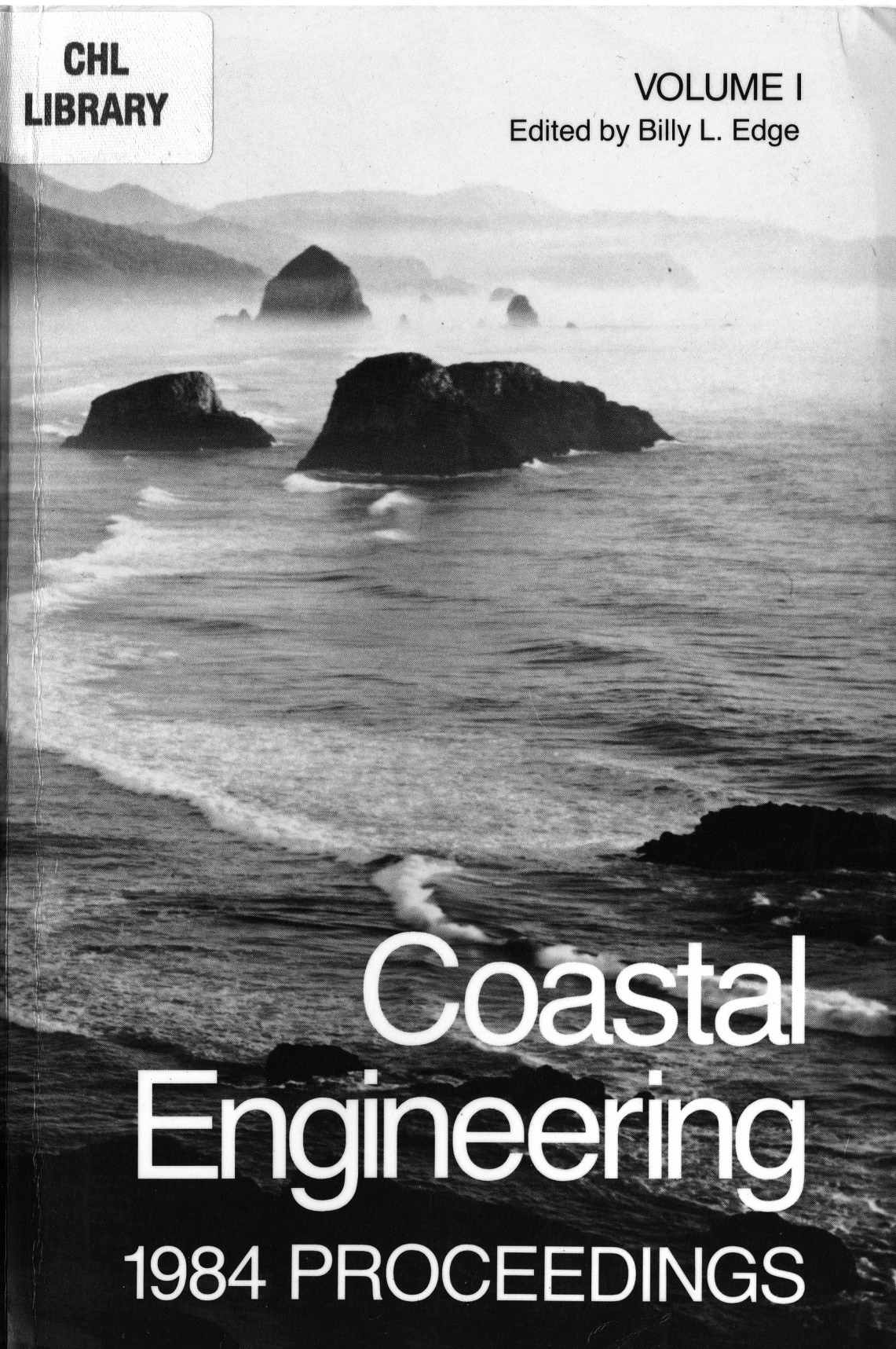


**CHL  
LIBRARY**

**VOLUME I**  
Edited by Billy L. Edge



**Coastal  
Engineering**  
**1984 PROCEEDINGS**

2828068 100

US-CE-C Property of the  
United States Government

TC203  
C6  
no. 19  
v. 1  
c. 4

# Nineteenth Coastal Engineering Conference

Proceedings of the International Conference  
**VOLUME I**

September 3-7, 1984  
Houston, Texas

Conference held under the auspices of the  
Coastal Engineering Research Council  
of the  
American Society of Civil Engineers

**BOOKS ARE ACCOUNTABLE PROPERTY CHARGED  
TO AN INDIVIDUAL BY NAME. PLEASE DO  
NOT LEND TO OTHERS WITHOUT CLEARING  
YOURSELF.**

and cosponsored by the  
International Association for Hydraulic Research  
Institute for Storm Research  
Marine Technology Society  
University of Houston  
Texas A&M University

Edited by Billy L. Edge



Published by the  
American Society of Civil Engineers  
345 East 47th Street  
New York, New York 10017-2398

~~LIBRARY BRANCH~~  
**TECHNICAL INFORMATION CENTER  
US ARMY ENGINEER WATERWAYS EXPERIMENT STATION  
VICKSBURG, MISSISSIPPI**

SS  
E



**The Society is not responsible for any statements  
made or opinions expressed in its publications.**

Copyright © 1985 by the American Society of Civil Engineers.  
All Rights Reserved.  
Library of Congress Catalog Card No.: 84-73359  
ISBN 0-87262-438-2  
Manufactured in the United States of America.

## FOREWORD

The 19th International Conference on Coastal Engineering was the first to be held in the Continental United States since 1970. This exemplifies the truly international scope and character of this conference series. The 19th ICCE, like the ones before it, was well organized with the primary objective being to share information and provide a forum for interaction with other engineers and scientists working on similar problems. The time and efforts contributed to that objective was extensive and the results have proven that the planning is a very vital part of each conference. All who attended the 19th ICCE will agree that it was a success in many ways.

At the beginning of the Conference a message was received from the President of the United States welcoming the attendees. His message is reproduced below:

TWX WHITEHOUSE WSH DLY PD  
260 GOVT DLY WHITE HOUSE DC AUG 31  
PMS MR. JOHN C. FREEMAN, //DLR DONT DWE//  
President, Institute For Storm Research  
University Of St. Thomas  
3600 Mt. Vernon  
Houston TX 77006

I am pleased to greet all participants in the Nineteenth International Conference on Coastal Engineering and to extend a special welcome to those from other countries.

Solving engineering problems associated with coastal and offshore areas is one of the most important environmental challenges we face. The many natural resources in these regions require careful management based on sound scientific and technical information. For example, our Commerce Departments National Ocean and Atmospheric Administration has storm surge problems underway that can serve as models for developing comprehensive hurricane preparedness plans.

I am confident that your conference will make an important contribution to the wise management of coastal resources and to the protection of the people who live, work and play in these areas.

You have my best wishes for every success in these deliberations.

RONALD REAGAN

92331

The papers in this Proceedings have been prepared by the authors who made presentations at the 19th International Conference on Coastal Engineering. The authors were asked to make their presentations and submit final papers based on review of the abstracts which were submitted well in advance of the conference. These abstracts were reviewed by a committee of four professionals including representation from the local organizing committee. All papers are eligible for discussion in the *Journal of Waterway, Port, Coastal and Ocean Engineering* and all papers are eligible for ASCE awards.

Venues for the 20th and 21st conferences are Taipei, Taiwan and Spain, respectively. Countries desiring to host a future conference should contact the Secretary of the Coastal Engineering Research Council to receive information on submitting a proposal.

Billy L. Edge, Secretary  
Coastal Engineering Research Council  
American Society of Civil Engineers

## **ACKNOWLEDGEMENTS**

### **ORGANIZING COMMITTEE**

Dr. John C. Freeman, Co-chairman  
Institute for Storm Research

Dr. Wayne Ingram, Co-chairman  
Sea Floor Engineering

Professor Robert Reid  
Texas A & M University

Mrs. Jill F. Hasling  
Institute for Storm Research

The Honorable Marla Forristall  
City of West University

Mr. David P. Hasling  
Institute for Storm Research

Mrs. Marjorie Freeman  
Houston, Texas

Dr. John B. Herbich  
Texas A & M University

Dr. William J. Graff  
University of Houston

Mr. Robert E. Haring  
Exxon Production Research Company

Dr. Herbert Beckman  
Rice University

### **SPONSORSHIP**

American Society of Civil Engineers  
Institute For Storm Research  
Marine Technology Society  
University Of Houston  
Texas A & M  
International Association For Hydraulic Research





# CONTENTS

Keynote Address . . . . .	1
<i>Morrough P. O'Brien</i>	

## PART I

### THEORETICAL AND OBSERVED WAVE CHARACTERISTICS

Chapter 1 THE EXPERIMENTAL VERIFICATION OF NUMERICAL MODELS OF PLUNGING BREAKERS . . . . .	15
<i>S.P. Kjeldsen</i>	
Chapter 2 BREAKING WAVE DESIGN CRITERIA . . . . .	31
<i>E.B. Thornton, C.S. Wu, and R.T. Guza</i>	
Chapter 3 REYNOLDS STRESS IN SURF ZONE . . . . .	42
<i>T. Sakai, I. Sandanbata, and M. Uchida</i>	
Chapter 4 WAVE ATTENUATION AND SET-UP ON A BEACH . . . . .	54
<i>I.A. Svendsen</i>	
Chapter 5 WAVE KINEMATICS AND DIRECTIONALITY IN THE SURF ZONE . . . . .	70
<i>J. van Heteren and M.J.F. Stive</i>	
Chapter 6 A MODEL FOR BREAKER DECAY ON BEACHES . . . . .	82
<i>W.R. Dally, R.G. Dean, and R.A. Dalrymple</i>	
Chapter 7 MODELING TURBULENT BORE PROPAGATION IN THE SURF ZONE . . . . .	99
<i>D.R. Basco and I.A. Svendsen</i>	
Chapter 8 EXTREMAL STATISTICS OF STORM SURGES BY TYPHOON .	115
<i>Y. Tsuchiya and Y. Kawata</i>	
Chapter 9 BAYWATER RESPONSE TO TSUNAMIS . . . . .	132
<i>T. Abe</i>	
Chapter 10 A RANKIN VORTEX NUMBER AS A GUIDE TO THE SELECTION OF A MODEL HURRICANE . . . . .	147
<i>C.L. Bretschneider and J.M. Lo</i>	

Chapter 11	
ESTIMATING ERROR OF COASTAL STAGE FREQUENCY CURVES.....	162
<i>M.D. Prater, T.A. Hardy, H.L. Butler, and L.E. Borgman</i>	
Chapter 12	
NUMERICAL SIMULATION OF STORM SURGES BY THE MULTI-LEVEL MODELS .....	174
<i>T. Yamashita and Y. Tsuchiya</i>	
Chapter 13	
NUMERICAL SIMULATION OF STORM SURGES INDUCED BY TROPICAL STORMS IMPINGING ON THE BANGLADESH COAST .....	190
<i>S.K. Dube, P.C. Sinha, and G.D. Roy</i>	
Chapter 14	
FREQUENCY OF OCCURRENCE OF STORM SURGES IN AN ESTUARY: A STOCHASTIC APPROACH.....	199
<i>M. Sas</i>	
Chapter 15	
UPDATE: THE NATIONAL FLOOD INSURANCE PROGRAM AND THE COAST.....	217
<i>W.G. Fry and P.A. Rhodes</i>	
Chapter 16	
SIMULATION OF TIDES AND STORM SURGES IN THE GREAT BARRIER REEF REGION.....	226
<i>K.P. Stark, L. Bode, and L.B. Mason</i>	
Chapter 17	
HURRICANE SURGE PROTOTYPE DATA COLLECTION .....	243
<i>T.H. Flor and S.C. Scott</i>	
Chapter 18	
HURRICANE ALICIA—STORM SURGES AND SHORE PROCESSES .....	257
<i>R.P. Savage</i>	
Chapter 19	
MEASUREMENT OF SURFACE WAVES FROM SUBSURFACE GAGE.....	271
<i>D.Y. Lee and H. Wang</i>	
Chapter 20	
A SHALLOW WATER DIRECTIONAL WATER RECORDER ...	287
<i>S.J. Buchan, R.K. Steedman, S.A. Stroud, and D.G. Provis</i>	
Chapter 21	
US ARMY CORPS OF ENGINEERS FIELD WAVE GAGING PROGRAM .....	304
<i>J.M. Hemsley</i>	

Chapter 22		
IRREGULAR WAVE OVERTOPPING RATES.....	316	
		<i>S.L. Douglass</i>
Chapter 23		
RUN-UP OF PERIODIC WAVES ON BEACHES OF NON-UNIFORM SLOPE .....	328	
		<i>Y. Ogawa and N. Shuto</i>
Chapter 24		
EFFECTS OF MEASUREMENT ERROR ON LONG-TERM WAVE STATISTICS .....	345	
		<i>B. Le Mehaute and S. Wang</i>
Chapter 25		
ON A DESIGN WAVE SPECTRUM .....	362	
		<i>P.C. Liu</i>
Chapter 26		
SHALLOW WATER WAVES: A SPECTRAL APPROACH.....	370	
		<i>C.L. Vincent</i>
Chapter 27		
WAVE COHERENCE IN COASTAL WATERS .....	383	
		<i>S.A. Hughes</i>
Chapter 28		
FIELD STUDIES OF RUN-UP ON DISSIPATIVE BEACHES ....	399	
		<i>C.T. Carlson</i>
Chapter 29		
A NONLINEAR MODEL OF IRREGULAR WAVE RUN-UP HEIGHT AND PERIOD DISTRIBUTIONS ON GENTLE SLOPES .....	415	
		<i>T. Sawaragi and K. Iwata</i>
Chapter 30		
A DYNAMICAL EXPRESSION OF WAVES IN SHALLOW WATER .....	435	
		<i>Y. Tsuchiya and T. Yasuda</i>
Chapter 31		
PREDICTION METHOD FOR THE WAVE HEIGHT DISTRIBUTION OFF THE WESTERN COAST OF TAIWAN ....	452	
		<i>F.L.W. Tang and J.T. Juang</i>
Chapter 32		
METHOD FOR ESTIMATING DIRECTIONAL WAVE SPECTRUM IN INCIDENT AND REFLECTED WAVE FIELD ..	467	
		<i>M. Isobe and K. Kondo</i>
Chapter 33		
CALCULATION OF DIRECTIONAL WAVE SPECTRA BY THE MAXIMUM ENTROPY METHOD OF SPECTRAL ANALYSIS ..	484	
		<i>M.J. Briggs</i>

Chapter 34		
NATURAL SEA STATES: THE COASTAL ENGINEER'S REQUIREMENTS TO THE REPRODUCTION IN MODELS.....	501	
		<i>H. Lundgren and Elias Davidsen</i>
Chapter 35		
NON-GAUSSIAN CHARACTERISTICS OF COASTAL WAVES..	516	
		<i>M.K. Ochi and W.C. Wang</i>
Chapter 36		
STATISTICAL PROPERTIES OF SHORT-TERM OVERTOPPING.....	532	
		<i>A. Kimura and A. Seyama</i>
Chapter 37		
SHALLOW-WATER SPECTRAL WAVE MODELING .....	547	
		<i>R.E. Jensen</i>
Chapter 38		
A TYPHOON WAVE HINDCASTING TECHNIQUE.....	561	
		<i>N.K. Liang and C.C. Chien</i>
Chapter 39		
INFLUENCE OF EL NINOS ON CALIFORNIA'S WAVE CLIMATE .....	577	
		<i>R.J. Seymour, R.R. Strange III, D.R. Cayan, and R.A. Nathan</i>
Chapter 40		
RUN-UP OF RANDOM WAVES ON GENTLE SLOPES.....	593	
		<i>H. Mase and Y. Iwagaki</i>
Chapter 41		
ON THE SEQUENTIAL BEHAVIOUR OF SEA-STATES .....	610	
		<i>A.S. Arcilla</i>
Chapter 42		
LOW FREQUENCY OSCILLATIONS ON THE DUTCH COAST .	625	
		<i>F. Gerritsen and J. van Heteren</i>
Chapter 43		
VERIFICATION OF KIMURA'S THEORY FOR WAVE GROUP STATISTICS .....	642	
		<i>J.A. Battjes and G.Ph. van Vledder</i>
Chapter 44		
CALIBRATION AND VERIFICATION OF A DISSIPATION MODEL FOR RANDOM BREAKING WAVES.....	649	
		<i>J.A. Battjes and M.J.F. Stive</i>
Chapter 45		
WAVE GROUP ANATOMY OF OCEAN WAVE SPECTRA.....	661	
		<i>W.C. Thompson, A.R. Nelson and D.G. Sedivy</i>

Chapter 46		
SWASH ON A NATURAL BEACH.....	678	
		<i>M. Mizuguchi</i>
Chapter 47		
WAVE GROUPS IN THE FREQUENCY AND TIME DOMAINS .	695	
		<i>R.J. Sobey and W.W. Read</i>
Chapter 48		
SWASH ON STEEP AND SHALLOW BEACHES.....	708	
		<i>R.T. Guza, E.B. Thornton, and R.A. Holman</i>
Chapter 49		
MEASUREMENTS OF SURF BEAT AND SET-DOWN		
BENEATH WAVE GROUPS.....	724	
		<i>J.K. Kostense</i>
Chapter 50		
THE PROBABILITY CHARACTERISTICS OF WAVE AND		
WAVE PRESSURES AT A VERTICAL BREAKWATER .....	741	
		<i>H. Peiji and Z. Binglai</i>
Chapter 51		
WAVE MEASUREMENT WITH DIFFERENTIAL PRESSURE		
GAUGES .....	755	
		<i>K.R. Bodge and R.G. Dean</i>
Chapter 52		
PREDICTION OF WAVE GROUP STATISTICS .....	770	
		<i>S. Elgar, R.T. Guza, and R.J. Seymour</i>
Chapter 53		
ESTIMATES OF LONG WAVES IN THE WESER ESTUARY....	782	
		<i>V. Barthel and E.R. Funke</i>
Chapter 54		
SHOALING PROPERTIES OF BOUNDED LONG WAVES .....	798	
		<i>E.P.D. Mansard and V. Barthel</i>
Chapter 55		
NUMERICAL SIMULATIONS OF THE 1964 ALASKAN		
TSUNAMI .....	815	
		<i>J.R. Houston and H.L. Butler</i>
Chapter 56		
A THREE-DIMENSIONAL MODEL OF THE BEAUFORT SEA .	831	
		<i>S.K. Liu and J.J. Leendertse</i>
Chapter 57		
MODEL HARBOUR SEICHING COMPARED TO PROTOTYPE		
DATA .....	846	
		<i>W.A.M. Botes, K.S. Russell, and P. Huizinga</i>



Chapter 58	
BOUNDARY CONDITION FOR LIMITED AREA MODELING ..	858
<i>H.L. Butler and Y.P. Sheng</i>	
Chapter 59	
IS SURF BEAT FORCED OR FREE? .....	871
<i>D.A. Huntley and C.S. Kim</i>	
Chapter 60	
EXTREME SEA LEVELS ON THE COAST OF CALIFORNIA...	886
<i>R.E. Flick and D.R. Cayan</i>	
Chapter 61	
NEW ASPECTS CONCERNING THE INCREASE OF SEA LEVEL ON THE GERMAN NORTH SEA COAST .....	899
<i>H. Rohde</i>	
Chapter 62	
SHORT-CRESTED BREAKING WAVES .....	912
<i>P.C. Machen</i>	
Chapter 63	
WAVE-INDUCED OSCILLATIONS IN HARBORS WITH WAVE-ABSORBING QUAY .....	929
<i>A. Yoshida, T. Ijima, and H. Okuzono</i>	
Chapter 64	
THE PHYSICAL BASIS OF THE MILD-SLOPE WAVE EQUATION .....	941
<i>L. Behrendt and I.G. Jonsson</i>	
Chapter 65	
STEEP UNSTEADY WATER WAVES: AN EFFICIENT COMPUTATIONAL SCHEME .....	955
<i>J.W. Dold and D.H. Peregrine</i>	
Chapter 66	
EXPLICIT SOLUTIONS TO PRACTICAL WAVE PROBLEMS ..	968
<i>P. Nielsen</i>	
Chapter 67	
THE INTERACTION OF SMALL AND FINITE AMPLITUDE LONG WAVES AND CURRENTS .....	983
<i>F. Raichlen and J.J. Lee</i>	
Chapter 68	
COMBINED REFRACTION-DIFFRACTION OF NONLINEAR WAVES IN SHALLOW WATER .....	999
<i>J.T. Kirby, P.L.F. Liu, S.B. Yoon, and R.A. Dalrymple</i>	
Chapter 69	
PROFILE ASYMMETRY OF SHOALING WAVES ON A MILD SLOPE .....	1016
<i>P.A. Hwang</i>	

Chapter 70	
THE EXACT SOLUTION OF THE HIGHEST WAVE DERIVED FROM A UNIVERSAL WAVE MODEL.....	1028
<i>Y. Y. Chen and F.L.W. Tang</i>	
Chapter 71	
COMBINED REFRACTION-DIFFRACTION CALCULATIONS WITH DIRECTIONAL WAVE SPECTRA.....	1040
<i>P. Gaillard</i>	
Chapter 72	
A NUMERICAL SOLUTION OF BOUSSINESQ TYPE WAVE EQUATIONS.....	1057
<i>H. Schaper and W. Zielke</i>	
Chapter 73	
INTERACTION OF NON-UNIFORM CURRENTS AND SURFACE WAVES .....	1073
<i>N.M. Ismail</i>	
Chapter 74	
A FINITE ELEMENT MODEL FOR WIND WAVE DIFFRACTION .....	1090
<i>O. Skovgaard, L. Behrendt, and I.G. Jonsson</i>	
Chapter 75	
CURRENT DEPTH REFRACTION OF REGULAR WAVES .....	1103
<i>I.G. Jonsson and J.B. Christoffersen</i>	
Chapter 76	
A NUMERICAL MODEL FOR REFRACTION OF LINEAR AND CNOIDAL WAVES.....	1118
<i>J.R. Headland and H.L. Chu</i>	
Chapter 77	
EFFECTS OF OPPOSING CURRENT ON WAVE TRANSFORMATION ON SLOPING SEA BED.....	1132
<i>S. Sakai and H. Saeki</i>	
Chapter 78	
MEASUREMENTS OF MASS TRANSPORT OVER A ROUGH BED.....	1149
<i>J.F.A. Sleath</i>	
Chapter 79	
NEAR-BOTTOM VELOCITIES IN WAVES WITH A CURRENT; ANALYTICAL AND NUMERICAL COMPUTATIONS.....	1161
<i>W.G.M. van Kesteren and W.T. Bakker</i>	
Chapter 80	
FIELD AND LABORATORY VERIFICATION OF THE WAVE PROPAGATION MODEL CREDIZ.....	1178
<i>M.W. Dingemans, M.J.F. Stive, A.J. Kuik, A.C. Radder, and N. Booij</i>	

Chapter 81	
CONFORMAL MAPPING SOLUTION OF A WAVE FIELD ON THE ARBITRARILY SHAPED SEA BOTTOM .....	1192
<i>K. Nadoaka and M. Hino</i>	

Chapter 82	
A FINITE ELEMENT METHOD FOR STORM SURGE AND TIDAL COMPUTATION .....	1209
<i>Y. Coeffe, S. Dal Secco, P. Esposito, and B. Latteux</i>	

**PART II**  
**COASTAL PROCESSES AND SEDIMENT TRANSPORT**

Chapter 83	
ADDED EVIDENCE ON NEW SCALE LAW FOR COASTAL MODELS .....	1227
<i>R.J. Hallermeier</i>	

Chapter 84	
ONSHORE-OFFSHORE SEDIMENT TRANSPORT NUMERICAL MODEL .....	1244
<i>A. Swain and J.R. Houston</i>	

Chapter 85	
MEASUREMENTS OF BEDLOAD TRANSPORT IN THE NEARSHORE ZONE USING RADIOISOTOPIC SAND TRACERS .....	1252
<i>G. Drapeau and B. Long</i>	

Chapter 86	
SAND TRANSPORT BY WIND ON A WET SAND SURFACE...	1265
<i>S. Hotta, S. Kubota, S. Katori, and K. Horikawa</i>	

Chapter 87	
TRANSPORT OF NILE SAND ALONG THE SOUTHEASTERN MEDITERRANEAN COAST .....	1282
<i>Z. Carmel, D.L. Inman, and A. Golik</i>	

Chapter 88	
FLUCTUATIONS IN LITTORAL DRIFT .....	1291
<i>R. Silvester</i>	

Chapter 89	
FLOW RESISTANCE DUE TO INTENSE BEDLOAD TRANSPORT .....	1306
<i>D.M. Hanes</i>	

Chapter 90	
A LABORATORY EXPERIMENT OF BEACH CUSPS .....	1311
<i>A. Kaneko</i>	

Chapter 91	
CALCULATION OF THE RATE OF NET ON-OFFSHORE SEDIMENT TRANSPORT ON THE BASIS OF FLUX CONCEPT	1325
<i>I. Deguchi and T. Sawaragi</i>	
Chapter 92	
EXPERIMENTAL VERIFICATION OF SIMILARITY CRITERIA FOR EQUILIBRIUM BEACH PROFILES	1342
<i>O.S.F.J. Sayao and J.C. Guimaraes</i>	
Chapter 93	
STABILITY OF MULTIPLE INLETS	1360
<i>J. van de Kreeke</i>	
Chapter 94	
SEDIMENT DYNAMICS FIELD EXPERIMENT: SUNDAY'S RIVER	1371
<i>D.H. Swart</i>	
Chapter 95	
SCALE-MODEL RELATIONSHIP OF BEACH PROFILE	1386
<i>M. Ito and Y. Tsuchiya</i>	
Chapter 96	
FORMATION OF TOMBOLO AT THE WEST COAST OF IWO-JIMA	1403
<i>T. Shigemura, J. Takasugi, and Y. Komiya</i>	
Chapter 97	
A MODEL FOR OFFSHORE SEDIMENT TRANSPORT	1420
<i>M.J.F. Stive and J.A. Battjes</i>	
Chapter 98	
A SYSTEM OF MATHEMATICAL MODELS FOR THE SIMULATION OF MORPHOLOGICAL PROCESSES IN THE COASTAL AREA	1437
<i>S. Boer, H.J. de Vriend, and H.G. Wind</i>	
Chapter 99	
A SIMPLIFIED MODEL FOR LONGSHORE SEDIMENT TRANSPORT	1454
<i>J.A. Bailard</i>	
Chapter 100	
AN ASSESSMENT OF BEACH NOURISHMENT SEDIMENT CHARACTERISTICS	1471
<i>D.K. Stauble, M. Hansen, and W. Blake</i>	
Chapter 101	
LONGSHORE SEDIMENT TRANSPORT ON DEAN BEACH PROFILES	1488
<i>W.G. McDougal and R.T. Hudspeth</i>	

Chapter 102	
TIME SCALES OF NEARSHORE PROFILE CHANGES .....	1507
<i>W.A. Birkemeier</i>	
Chapter 103	
BEACH RESPONSE TO COASTAL WORKS, GOLD COAST, AUSTRALIA.....	1522
<i>H.V. Macdonald and D.C. Patterson</i>	
Chapter 104	
METHOD FOR ASSESSING STORM DAMAGE TO BEACH HOUSES.....	1539
<i>L.C. Doyle and W.L. Fox</i>	
Chapter 105	
NUMERICAL MODEL FOR DUNE EROSION DUE TO WAVE UPRUSH .....	1553
<i>J.S. Fisher and M.F. Overton</i>	
Chapter 106	
A NEW OSCILLATORY FLOW TUNNEL FOR USE IN SEDIMENT TRANSPORT EXPERIMENTS.....	1559
<i>D.B. King, Jr., J.D. Powell, and R.J. Seymour</i>	
Chapter 107	
BEACH RESPONSE TO LONG PERIOD LAKE-LEVEL VARIATION .....	1571
<i>W.L. Wood and L.L. Weishar</i>	
Chapter 108	
BEACH AND DUNE RESPONSE TO SEVERE STORMS .....	1584
<i>D.L. Kriebel and R.G. Dean</i>	
Chapter 109	
THE NILE LITTORAL CELL AND MAN'S IMPACT ON THE COASTAL ZONE OF THE SOUTHEASTERN MEDITERRANEAN .....	1600
<i>D.L. Inman and S.A. Jenkins</i>	
Chapter 110	
GRADING EFFECTS IN CONCENTRATION MEASUREMENTS	1618
<i>J. van de Graaf and J.A. Roelvink</i>	
Chapter 111	
REDESIGN OF ENTRANCE STRUCTURES FOR SMALL CRAFT HARBORS IN OHIO.....	1635
<i>B.L. Edge, B.L. Sill, J.A. Swartzmiller, and J.S. Fisher</i>	
Chapter 112	
COASTAL CHANGES AT BETHANY BEACH, DELAWARE....	1650
<i>J.E. Dick and R.A. Dalrymple</i>	



Chapter 113	
PROCEDURE FOR DETERMINING DREDGING REQUIREMENTS IN COASTAL INLET CHANNELS.....	1668
<i>J.W. Forman, Jr. and L. Vallianos</i>	
Chapter 114	
THE COMPUTATION OF BED SHEAR IN A NUMERICAL MODEL .....	1685
<i>W. Leeuwenstein and H.G. Wind</i>	
Chapter 115	
NEARSHORE SEDIMENT TRANSPORT: ESTIMATES FROM DETAILED MEASUREMENTS OF THE NEARSHORE VELOCITY FIELD .....	1703
<i>A.J. Bowel and J.C. Doering</i>	
Chapter 116	
LABORATORY REPRODUCTION OF SEABED SCOUR IN FRONT OF BREAKWATERS .....	1715
<i>I. Irie and K. Nadaoka</i>	
Chapter 117	
NUMERICAL SIMULATION ON THE CHANGE OF BOTTOM TOPOGRAPHY BY THE PRESENCE OF COASTAL STRUCTURES .....	1732
<i>M. Yamaguchi and Y. Nishioka</i>	
Chapter 118	
NORTH SEA TIDE AND STORM SURGE INVESTIGATION....	1749
<i>W. Siefert</i>	
Chapter 119	
SUSPENDED SAND TRANSPORT ON A DISSIPATIVE BEACH	1765
<i>J.P. Downing</i>	
Chapter 120	
FIELD INVESTIGATIONS OF SUSPENDED SEDIMENT TRANSPORT IN THE NEARSHORE ZONE .....	1782
<i>R.W. Sternberg, N.C. Shi, and J.P. Downing</i>	
Chapter 121	
SEDIMENT RESPONSES TO NATURAL WAVES .....	1799
<i>A.F. Nielsen and A.D. Gordon</i>	
Chapter 122	
SHORE APPROACH AT THE DANISH NORTH SEA COAST, MONITORING OF SEDIMENTATION IN A DREDGED TRENCH .....	1816
<i>K. Mangor, T. Sorensen, and E. Navntoft</i>	

Chapter 123	
FIELD INVESTIGATIONS IN THE TOW STUDY PROGRAMME FOR COASTAL SEDIMENT TRANSPORT IN THE NETHERLANDS .....	1830
<i>H. Derks and M.J.F. Stive</i>	
Chapter 124	
FIELD OBSERVATION ON SUSPENDED-LOAD IN THE SURF ZONE .....	1846
<i>K. Katoh, N. Tanaka, and I. Irie</i>	
Chapter 125	
SEDIMENTATION IN DREDGED CHANNELS AND BASINS: PREDICTION OF SHOALING RATES .....	1863
<i>C.M. Vicente and L.P. Uva</i>	
Chapter 126	
SURVEY TECHNIQUES USED TO MEASURE NEARSHORE PROFILES.....	1879
<i>C.G. Gable and J.R. Wanetick</i>	
Chapter 127	
LONGSHORE VARIABILITY OF WAVE RUN-UP ON NATURAL BEACHES .....	1896
<i>R. Holman and A.H. Sallenger, Jr.</i>	
Chapter 128	
DUCK82—A COASTAL STORM PROCESSES EXPERIMENT ...	1913
<i>C. Mason, A.H. Sallenger, Jr., R.A. Holman, and W.A. Birkemeier</i>	
Chapter 129	
OFFSHORE BREAKWATER, WHEATLEY, ONTARIO .....	1929
<i>G.T. Beaulieu, M.G. Skafel, and W.F. Baird</i>	
Chapter 130	
ON PREDICTING INFRAGRAVITY ENERGY IN THE SURF ZONE .....	1940
<i>A.H. Sallenger, Jr. and R.A. Holman</i>	
Chapter 131	
SEDIMENT TRANSPORT ON THE SOUTH-EAST AUSTRALIAN CONTINENTAL SHELF.....	1952
<i>A.D. Gordon and J.G. Hoffman</i>	
Chapter 132	
BEACH FORESHORE RESPONSE TO LONG-PERIOD WAVES .	1968
<i>P.A. Howd and R.A. Holman</i>	
Chapter 133	
THE ROLE OF SUSPENDED SEDIMENT IN SHORE-NORMAL BEACH PROFILE CHANGES .....	1983
<i>B.E. Jaffe, R.W. Sternberg, and A.H. Sallenger, Jr.</i>	

Chapter 134	
CROSS-SHORE TRANSPORT OF BIMODAL SANDS .....	1997
<i>B.M. Richmond and A.H. Sallenger, Jr.</i>	
Chapter 135	
DEPOSITIONAL EFFECTS OF OFFSHORE BREAKWATER DUE TO ONSHORE-OFFSHORE SEDIMENT MOVEMENT .....	2008
<i>H. Noda</i>	
Chapter 136	
PERMEABLE GROYNES: EXPERIMENTS AND PRACTICE IN THE NETHERLANDS .....	2026
<i>W.T. Bakker, C.H. Hulsbergen, P. Roelse, C. de Smit and J.N. Svasek</i>	
Chapter 137	
STUDY OF THE EVOLUTION OF DREDGED MATERIAL DISCHARGES BY MEANS OF RADIOACTIVE TRACERS. ....	2042
<i>F. Tola, A. Caillot, G. Courtois, P. Gourlez, R. Hoslin, J. Massias, M. Quesney, G. Sauzay</i>	
Chapter 138	
A PRE-DREDGING SAND MOBILITY STUDY USING A RADIOISOTOPE TRACER .....	2063
<i>A. Davison</i>	
Chapter 139	
DEVELOPMENT OF A SEDIMENT TRANSPORT MEASURING SYSTEM .....	2077
<i>E. Renger</i>	
Chapter 140	
EFFECT OF RIP CURRENT BARRIER ON HARBOR SHOALING .....	2091
<i>T.O. Sasaki and H. Sakuramoto</i>	
Chapter 141	
SHORELINE CHANGE AT OARAI BEACH: PAST, PRESENT AND FUTURE .....	2107
<i>N.C. Kraus, H. Hanson, and S. Harikai</i>	
Chapter 142	
MECHANISM OF BEACH PROFILE DEFORMATION DUE TO ON-OFFSHORE SAND DRIFT .....	2124
<i>W.G. Pae and Y. Iwagaki</i>	
Chapter 143	
BEACH FILL BY TURNING THE COURSE OF SANDBARS ....	2140
<i>H.F. Erchinger</i>	
Chapter 144	
BEACH AND SURF ZONE EQUILIBRIA AND RESPONSE TIMES .....	2150
<i>L.D. Wright, S.K. May, A.D. Short, and M.O. Green</i>	

Chapter 145	
QUANTIFICATION OF SHORELINE RHYTHMICITY .....	2165
<i>H.C. Garrow</i>	
Chapter 146	
MODELLING OF THE DEPOSITIONAL PATTERNS IN HANGZHOU BAY.....	2181
<i>S. Jilan and X. Weiyi</i>	
Chapter 147	
UNIFORM LONGSHORE CURRENT MEASUREMENTS AND CALCULATIONS .....	2192
<i>P.J. Visser</i>	
Chapter 148	
MODELING OF NEARSHORE WAVE DRIVEN CURRENTS....	2208
<i>J.M. Hubertz</i>	
Chapter 149	
IMPROVED FORMULAS FOR ESTIMATING OFFSHORE WINDS.....	2220
<i>S.A. Hsu</i>	
Chapter 150	
ASPECTS OF WAVE CURRENT BOUNDARY LAYER FLOWS..	2232
<i>F.C. Coffey and P. Nielsen</i>	
Chapter 151	
A THEORETICAL AND EXPERIMENTAL STUDY OF UNDERTOW.....	2246
<i>J.B. Hansen and I.A. Svendsen</i>	
Chapter 152	
SOME TECHNIQUES TO CALCULATE DESIGN CURRENTS IN SHELF AND STRATIFIED COASTAL WATERS .....	2263
<i>S.P. Murray and M.H. Young</i>	
Chapter 153	
STEADY FLOWS IN THE NEARSHORE ZONE.....	2280
<i>J.W. Haines</i>	
Chapter 154	
OSCILLATORY BOUNDARY LAYER FLOW OVER RIPPLED BEDS.....	2293
<i>S. Sato, N. Mimura, and A. Watanabe</i>	
Chapter 155	
VARIATION OF SEDIMENT SUSPENSION IN OSCILLATORY FLOW.....	2310
<i>C. Staub, I.G. Jonsson, and I.A. Svendsen</i>	

Chapter 156	
SCALE EFFECTS IN LARGE COASTAL MOBILE BED MODELS .....	2322
<i>J.W. Kamphuis and R.B. Nairn</i>	
Chapter 157	
LOW PROFILE BARRIER ISLAND OVERWASH AND BREACHING ON THE GULF OF MEXICO .....	2339
<i>S. Penland and J.F. Suter</i>	
Chapter 158	
A NUMERICAL HINDCAST OF STORM-INDUCED CURRENTS ON THE NORWEGIAN SHELF.....	2346
<i>C.K. Cooper</i>	
Chapter 159	
REPRODUCTION OF NEARSHORE CURRENTS BY A MATHEMATICAL MODEL .....	2363
<i>H. Tanaka and A. Wada</i>	
Chapter 160	
A TURBULENT TRANSPORT MODEL OF COASTAL PROCESSES .....	2380
<i>Y.P. Sheng</i>	
Chapter 161	
BOTTOM TURBULENT BOUNDARY LAYER IN WAVE-CURRENT CO-EXISTING SYSTEMS.....	2397
<i>T. Asano and Y. Iwagaki</i>	
Chapter 162	
NUMERICAL SIMULATION OF SECONDARY CIRCULATION IN THE LEE OF HEADLANDS.....	2414
<i>R.A. Falconer, E. Wolanski, and L. Mardapitta-Hadjipandeli</i>	
Chapter 163	
ACCURATE MODELLING OF TWO-DIMENSIONAL MASS TRANSPORT .....	2434
<i>L. Bode and R.J. Sobey</i>	

**PART III**  
**COASTAL STRUCTURES AND RELATED PROBLEMS**

Chapter 164	
SAFETY AND RELIABILITY OF BREAKWATERS.....	2451
<i>A. Mol, R.L. Groeneveld, and A.J. Waanders</i>	
Chapter 165	
REHABILITATION METHODS FOR DAMAGED BREAKWATERS .....	2467
<i>R.L. Groeneveld, A. Mol, and E.H. Nieuwenhuys</i>	



Chapter 166	
STABILITY OF BREAKWATERS WITH VARIATIONS IN CORE PERMEABILITY.....	2487
<i>G.W. Timco, E.P.D. Mansard, and J. Ploeg</i>	
Chapter 167	
PHOTOGRAMMETRIC MONITORING OF DOLOS STABILITY, MANASQUAN INLET, NEW JERSEY.....	2500
<i>J.A. Gebert and J. Clausner</i>	
Chapter 168	
SHIP-WAVE ATTENUATION TESTS OF A PROTOTYPE FLOATING BREAKWATER.....	2514
<i>R.E. Nece and N.K. Skjelbreia</i>	
Chapter 169	
CASE HISTORY OF A SPACED PILE BREAKWATER AT HALF MOON BAY MARINA AUCKLAND, NEW ZEALAND... ..	2530
<i>P.S. Hutchinson and A.J. Raudkivi</i>	
Chapter 170	
NEW TYPE BLOCKS FOR SEAWALL SLOPE PROTECTION ...	2536
<i>O. Toyoshima</i>	
Chapter 171	
DETAILED DESIGN OF A WAVE ENERGY CONVERSION PLANT.....	2546
<i>G. Retief, F.P.J. Muller, G.K. Prestedge, L.C. Geustyn, and D.H. Swart</i>	
Chapter 172	
STRUCTURAL DESIGN PROCEDURES FOR CONCRETE ARMOUR UNITS .....	2563
<i>K.R. Hall, W.F. Baird, and D.J. Turcke</i>	
Chapter 173	
THE DESIGN OF BREAKWATERS USING QUARRIED STONES.....	2580
<i>W.F. Baird and K.R. Hall</i>	
Chapter 174	
FATIGUE IN BREAKWATER CONCRETE ARMOUR UNITS ...	2592
<i>H.F. Burcharth</i>	
Chapter 175	
STABILITY OF ARMOUR UNITS IN FLOW THROUGH A LAYER.....	2608
<i>A.C. Thompson and H.F. Burcharth</i>	
Chapter 176	
STABILITY OF RUBBLE MOUND SLOPES UNDER RANDOM WAVE ATTACK.....	2620
<i>J.W. van der Meer and K.W. Pilarczyk</i>	

Chapter 177	
SURVEYS OF COASTAL STRUCTURES USING GEOPHYSICAL TECHNIQUES .....	2635
<i>J.R. Dingler and R.J. Anima</i>	
Chapter 178	
REEF TYPE BREAKWATERS .....	2648
<i>J.P. Ahrens</i>	
Chapter 179	
RIGID BODY MOTION OF A FLOATING BREAKWATER.....	2663
<i>R.W. Miller and D.R. Christensen</i>	
Chapter 180	
ASPHALT STABILIZATION OF RUBBLE SLOPES .....	2680
<i>E.J. Schmeltz, M.J. McCarthy, and N. Lopez</i>	
Chapter 181	
REEF RUNWAY WAVE PROTECTIVE STRUCTURE, HONOLULU INTERNATIONAL AIRPORT, OAHU, HAWAII, STABILITY PERFORMANCE EVALUATION.....	2693
<i>R.S. Chun, E.K. Noda, and E.E. Tamaye</i>	
Chapter 182	
MARINE ROUGHENED CYLINDER WAVE FORCE COEFFICIENTS.....	2710
<i>J.H. Nath</i>	
Chapter 183	
TIME AND FREQUENCY LOADING ANALYSIS OF SUBMARINE PIPELINES.....	2726
<i>H.C. Alexander, P.L. Allen, and J.L. Warner</i>	
Chapter 184	
THE USE OF SAND IN BREAKWATER DESIGN .....	2737
<i>L.V. Van Damme, P.A. Kerckaert, R.L. Carpentier, J.N. De Rouck, and A. Bernard</i>	
Chapter 185	
A REVIEW OF BREAKWATER DEVELOPMENT IN AUSTRALIA.....	2751
<i>D.N. Foster</i>	
Chapter 186	
BREAKWATER ARMOR DISPLACEMENT THRESHOLDS: A POSSIBLE CORRELATION WITH CUMULATIVE WAVE ENERGY .....	2760
<i>D.L. Behnke and F. Raichlen</i>	
Chapter 187	
A DETAILED MODEL STUDY OF DAMAGE TO A LARGE BREAKWATER AND MODEL VERIFICATION OF CONCEPTS FOR REPAIR AND UPGRADED STRENGTH .....	2773
<i>O.J. Lillevang, F. Raichlen, J.C. Cox, and D.L. Behnke</i>	

Chapter 188	
ANALYSIS OF UPRIGHT STRUCTURE FOR WAVE DISSIPATION USING INTEGRAL EQUATION .....	2810
<i>K. Hagiwara</i>	
Chapter 189	
COASTAL DESIGN CRITERIA IN SOUTHERN CALIFORNIA..	2827
<i>J.R. Walker, R.A. Nathan, R.J. Seymour, and R.R. Strange III</i>	
Chapter 190	
A SIMULATION METHOD FOR SMALL CRAFT HARBOUR MODELS .....	2842
<i>D.S. Rosen and E. Kit</i>	
Chapter 191	
HYDRODYNAMIC FORCES ON A CIRCULAR CYLINDER DUE TO COMBINED WAVE AND CURRENT LOADING .....	2875
<i>Y. Iwagaki and T. Asano</i>	
Chapter 192	
WAVE POWER EXTRACTION AT COASTAL STRUCTURE BY MEANS OF MOVING BODY IN THE CHAMBER.....	2875
<i>H. Kondo, T. Watabe, and K. Yano</i>	
Chapter 193	
FULL-SCALE WAVE FORCES ON PILES IN SHALLOW WATER .....	2892
<i>U. Sparboom, N. Efthimiou, and A. Voigt</i>	
Chapter 194	
THE WAVE PRESSING PLATE FOR PROTECTING COOLING WATERWAYS OF COASTAL POWER PLANTS.....	2909
<i>S.C. Chow, F.L.W. Tang, and H.H. Hwung</i>	
Chapter 195	
WAVE FORCES AND IMPACTS ON A CIRCULAR AND SQUARE CAISSON.....	2920
<i>J.W. van der Meer and E. Benassai</i>	
Chapter 196	
ATTENUATION OF WAVE INDUCED OSCILLATION IN PORTS BY IMPROVING THE CONDITIONS AT THE HARBOR ENTRANCE.....	2933
<i>M. Kubo, S. Aoki, and J.J.A. Segura</i>	
Chapter 197	
DYNAMIC ANALYSIS OF PILE STRUCTURES TO PERIODIC WAVES.....	2952
<i>Hajime Ishida and Yoshimori Konda</i>	

\*

**PART IV**  
**COASTAL, ESTUARINE AND ENVIRONMENTAL PROBLEMS**

- Chapter 198  
EVOLUTION OF INTERFACIAL WAVES ALONG AN  
UNSTEADY SALT WEDGE ..... 2971  
*W. Nakano and I. Yakuwa*
- Chapter 199  
MODELING ESTUARIAL COHESIVE SEDIMENT  
TRANSPORT ..... 2985  
*E.J. Hayter and A.J. Mehta*
- Chapter 200  
WATER QUANTITY AND -QUALITY RESEARCH FOR THE  
RHINE MEUSE ESTUARY ..... 3001  
*A. Roelfzema, M. Karelse, A.J. Struijk and M. Adriaanse*
- Chapter 201  
SEDIMENTATION PATTERNS IN A TIDAL INLET  
SYSTEM/MORICHES INLET, NEW YORK ..... 3017  
*M.J. Vogel and T.W. Kana*
- Chapter 202  
NUMERICAL MODELING OF SHORELINE EVOLUTION  
AROUND THE RIVER MOUTH ..... 3034  
*M.C. Lin and J.C. Wang*
- Chapter 203  
SEDIMENTATION PROCESSES ALONG THE EAST FRIESIAN  
ISLANDS, WEST GERMANY ..... 3051  
*D.M. FitzGerald, S. Penland, and D. Nummedal*
- Chapter 204  
LATERAL DISTRIBUTIONS OF WATER, SALT, AND  
SEDIMENT TRANSPORT IN A PARTLY MIXED ESTUARY ... 3067  
*R.J. Uncles, R.C.A. Elliott, and S.A. Weston*
- Chapter 205  
STABILITY PARAMETERS OF WESTERN SCHELDT  
ESTUARY ..... 3078  
*H. de Jong and F. Gerritsen*
- Chapter 206  
EFFLUENT DISPERSAL IN EUROPEAN COASTAL WATERS.. 3094  
*D. Prandle*
- Chapter 207  
MATHEMATICAL MODELLING OF WATER-QUALITY FOR  
LONG TIME PERIODS ..... 3109  
*P. Huizinga*

Chapter 208	
THE EXCHANGE OF WATER IN FJORDS: A SIMPLE MODEL OF TWO-LAYER ADVECTIVE REACHES SEPARATED BY MIXING ZONES .....	3124
<i>E.D. Cokelet, R.J. Stewart, and C.C. Ebbesmeyer</i>	
Chapter 209	
SEWAGE DISPOSAL IN SHALLOW COASTAL WATERS .....	3134
<i>H.H. Dette</i>	
Chapter 210	
LARGE DIAMETER POLYETHYLENE SUBMARINE OUTFALLS .....	3148
<i>L.A. Jackson</i>	
Chapter 211	
OPTIMIZING DUMPING SITES NEAR DREDGED CHANNELS	3157
<i>U. Kogel and F. Ohlmeyer</i>	
Chapter 212	
A NEW NUCLEAR DENSITY GAUGE TO MEASURE DIRECTLY HIGH TURBIDITIES IN MUDDY AREAS.....	3172
<i>A. Caillot, G. Meyer, D. Chambellan, and J.C. Tanguy</i>	
Chapter 213	
CALIBRATION AND ADJUSTMENT PROCEDURES FOR THE RHINE-MEUSE ESTUARY SCALE MODEL.....	3180
<i>H.N.C.M. van der Heijden, P. de Jong, K. Kuijper, and A. Roelfzema</i>	
Chapter 214	
COMPARISON OF TURBULENT LATERAL MIXING MODELS	3197
<i>W.G. McDougal and R.T. Hudspeth</i>	

## PART V SHIP MOTIONS

Chapter 215	
SURGES AND WAVES GENERATED BY SHIPS IN A CONSTRICTED CHANNEL.....	3213
<i>J.B. Herbich and R.E. Schiller, Jr.</i>	
Chapter 216	
DEVELOPMENT OF SHIP WAVE DESIGN INFORMATION....	3227
<i>R.M. Sorensen and J.R. Weggel</i>	
Chapter 217	
THE EFFECT OF WAVE DIRECTION ON SHIP MOTIONS IN A HARBOUR ENTRANCE CHANNEL—MODEL STUDY APPROACH .....	3244
<i>A.C. van Wyk and J.A. Zwamborn</i>	

Chapter 218

SHIP WAVES IN SHALLOW WATER AND THEIR EFFECTS

ON MOORED SMALL VESSEL..... 3258

*K. Kurata and K. Oda*

Subject Index..... 3275

Author Index..... 3279



## COASTAL ENGINEERING

Morrrough P. O'Brien\*

These international conferences were at first organized by the Council on Wave Research of the Engineering Foundation, an organization sponsored by the engineering societies of the United States for the purpose of supporting research. Following the first conference, held in 1950 at Long Beach, California, it became clear that, in coastal engineering, the need was more for a forum at which to report and discuss results than for direct sponsorship of research. However, the charter of the Engineering Foundation did not quite encompass a council devoted solely to conferences, and the sponsorship was shifted to the American Society of Civil Engineers and the name became the Coastal Engineering Research Council.

I mention this bit of history to high-light the appropriateness of the original title -- the Council on Wave Research. The dominant agent active in the coastal zone is wave action -- wind-generated, ocean surface waves -- and it is this phenomenon which makes coastal engineering a distinct branch of the profession. In this respect, the outer coast and offshore areas, exposed to ocean waves, differ fundamentally from other shorelines -- estuaries, rivers, lagoons and small lakes. Familiarity with the theory and practice of wave phenomena is the hallmark of coastal engineering and of the coastal engineer.

Wave action has been studied intensely, theoretically and experimentally, in laboratory and field, but there remains much to be explored as the program of this conference amply illustrates.

My comments here deal with sandy beaches on the outer coast and with some problems of the interaction of ocean waves with the unconsolidated materials of the shore and bottom.

### PHYSICAL MODELS

Hydraulic models would be powerful tools for the investigation of phenomena of the outer coast -- provided that there were accurate methods for transferring model quantities to full scale. Unfortunately, there remains uncertainty regarding these "model laws," especially as applied to models with movable beds. The advantages of firmly establishing the model laws would be not only that specific locations could be studied with confidence but also that basic coastal processes could be reproduced under controlled conditions.

---

\* Dean and Professor of Engineering, College of Engineering, University of California, Berkeley.



Coastal models require relatively large surface areas, and large horizontal scale ratios, if the boundary conditions imposed by the wave climate are to be reproduced to scale: to obtain dynamically similar model waves, the depth should be as large as possible and the vertical scale ratio correspondingly small. In other words, practical considerations suggest distortion of hydraulic model of the outer coast. Unfortunately, the nature of surface waves is such that such distortion is questionable. In addition to the scale ratios, there are other limitations of applicability which need to be established such as the absolute size of the smallest dynamically similar waves and the smallest material size which avoids the effects of molecular forces. Establishing these restraints on design as well as the scaling laws is necessary for proportioning experimental basins suitable for basic studies.

#### **NUMERICAL MODELS**

The numerical model is a powerful tool -- if the validity of the underlying assumptions can be demonstrated. I am reminded of an old gag which seems pertinent here: "If you grant a mathematician his assumptions he's got you." For models of the outer coast, few field data are available for checking the validity of models: Do numerical model results stand as valid for the lack of comparative field data?

A problem of considerable importance in analyzing the material balance of a shore is the interaction of waves and currents with sediment at a tidal entrance. How, and in what quantity, does the littoral transport along the adjacent beaches cross the area seaward of the throat? Is the entrance a source or sink for sediment? What is the pattern of movement at jettied entrance? These and many other questions need to be answered. Wave action, including extreme conditions, as well as the tidal currents, must be represented in such a model, whether numerical or hydraulic.

A generally applicable numerical model representing the area seaward of tidal entrances would be a valuable tool -- but validation with field data alone seems almost an impossibility -- both because of the difficulty of field measurement and the elapsed time necessary to cover a representative range of wave conditions. I think of hydraulic models as an intermediate step between numerical models and full scale -- provided, of course, that the scaling laws are firmly established.

#### **MONITORING COMPLETED PROJECTS**

There are few complete records of the design, construction, maintenance, and demise of protective coastal structures. Failure of such works may occur (a) by physical impairment or destruction, (b) by not producing the predicted effect or (c) by either the initial or maintenance costs exceeding estimates, or by the effective life being very short. Such information on completed work is needed for the planning and design of future works. Little is available and for understandable reasons. On completion of construction, the engineers usually go on to other assignment. Seldom does the construction contract include provision for monitoring.

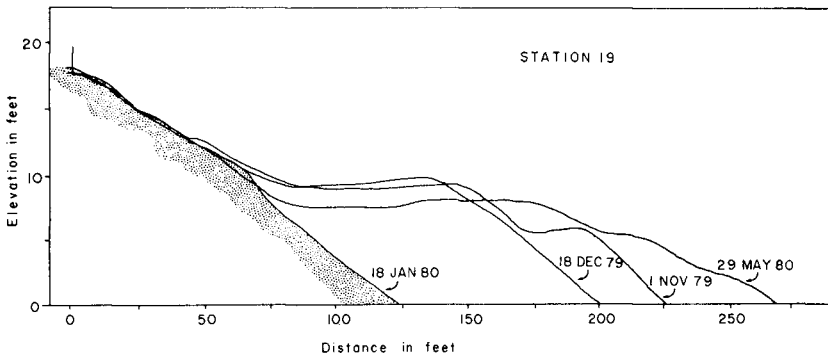
Monitoring structures of different types exposed to different wave climates, ranges of tide, and sand characteristics would, I believe, yield valuable data - not only for the continuing treatment of particular locations but also for basic studies. Shoreline changes develop slowly; apparently successful soon after construction, structures may show adverse effects years later.

It will be, I believe, possible to improve greatly the quantitative predictability of the effects of protective structures if a program of selective monitoring could be carried out on a national scale.

There are other studies which I would like to discuss here but my time is limited and I will devote the remainder of my talk to comments on a few completed projects. My prejudice in these matters is that beaches are primarily for use by people. Regulations, policies and laws, in many jurisdictions, represent a very different priority. An extreme view is that beaches should be allowed to go "back to nature" and that a "no structures" policy should be followed. I am convinced that the responsible public officials have been misinformed, sometimes deliberately, by enthusiasts who ignore the fact that the shorelines are the most popular areas for recreation and living.

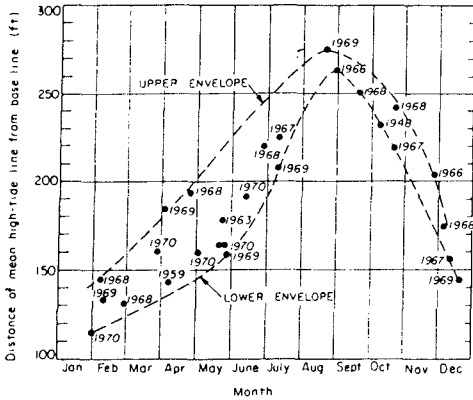
#### ANNUAL CYCLE OF BEACH CHANGES

The annual cycle of changes which a sandy beach exhibits is a phenomenon of great importance to the planning of beach development. Figure 1 shows the surveyed profiles of East Hampton Beach at different times of the year (1). The beach is wide in summer and fall and narrow in winter, due to seasonal variations in the wave climate. The average



**Figure 1.** Selected profiles at one station showing the magnitude of the seasonal changes (Reference 1)

change in width during the year at this beach is about 150 feet. Figure 2 (Bolinas Bay, California) shows the surveyed width of a beach at high-water at different seasons (2). The year of survey is shown. The average change in width is 200 feet.



**Figure 2.** Seasonal variation of the position of the mean high-tide line, Stinson Beach spit, 1948-1970, compiled from data supplied by the California State Lands Commission (Reference 2).

Beaches everywhere show similar wave effects but the amplitude of the annual change and the times of year for maximum and minimum width differs from beach to beach because of differences in sand size and wave climate.

A number of inferences may be drawn from Figures 1 and 2 and similar data, namely

- Two profiles taken at random times of the year may show either erosion or accretion, e.g., first survey in August, second in February, erosion.
- Underlying the annual cycle there may be long-term erosion or accretion. It is difficult to identify this trend if it is only a few feet per year.
- Erosion during storms is rapid and subsequently recovery is slow. Recovery after extremely severe storms may require several years.

Ignorance or disregard of this phenomenon has generated much misinformation regarding the erosional status of beaches and, frequently, to unwise decisions on public policy.

**SOME BEACH PROJECTS**

Ocean Beach, San Francisco, is the site of two interesting structures, a seawall near the south end and the O'Shaughnessy seawall at the North end.

The steel sheet-pile seawall (Fig. 3) protects a pedestrian underpass which was threatened by erosion during a storm more than 40 years ago. Accretion followed construction and the bulkhead remained buried in sand for so many years that its existence was forgotten until uncovered recently. It appears to be in perfect condition.



**Figure 3.** Taraval seawall at the South end of Ocean Beach, San Francisco.

The 2200-foot long seawall shown in Figure 4 was built in 1915 to the design of M.M. O'Shaughnessy, City Engineer, S.F. Today it shows no sign of settlement or deterioration.

I have visited this beach many times since 1930 and I believe that the configuration of the beach around the structures cited indicates that there has not been progressive erosion over the past 50 years.

In Figure 4, note the shallow landward indentation about midway between the seawall and the underpass. Photographs taken over the past 50 years all show this configuration. When the highway was built years ago, the desired alignment cut across this indentation and the bank was reveted to hold the shore seaward of its stable position.



**Figure 4.** O'Shaughnessy seawall at Ocean Beach Esplanade, San Francisco, California.

The recent history of this area is interesting. The shore seaward of the highway has been made a Seashore under the jurisdiction of the National Parks Service. Application of their "no structures" policy has brought some controversial proposals.

The groins at Westhampton Beach, Long Island, were the subject of a study by J.M. Heikoff (3) in which he traced the political maneuvers by which an apparently sound project became completely fouled up. Reading this small volume is recommended.

The shore of Westhampton Beach is within a project authorized by Congress for beach restoration and hurricane protection from Fire Island Inlet to Montauk Point. When the Westhampton Beach section was funded, the design recommended was to replenish the beach and dunes without groins and to monitor this work. Groins were to be added if the rate of loss of sand justified their cost. Execution of the project followed a diametrically opposed plan; groins were built in 1961 with no sand fill and in an unfavorable sequence. The net annual littoral transport here is from East to West, with seasonal reversal. The unfilled groins began trapping sand at the East end and, at first, erosion was general in the groin field and westward. Later, some sand was pumped to eroded areas and this volume plus the accumulated littoral transport has stabilized the shore within the groin field and eastward.

The original design of the groin field included groins, equally spaced, from the Moriches Inlet jetties updrift (eastward). However, local opposition caused groins to be omitted from 13,000 feet of beach just eastward of Moriches Inlet (Fig. 5). The breakthrough shown occurred during a storm on January 15, 1980. Erosion by currents had occurred on the bay side but the ocean beach has not been stabilized.

Omission of groins in the 13,000 foot reach was due, I understand, to a policy of "no structures" on the part of a park district, located in this reach. Closure of the gap cost approximately \$11,000,000.

In a groin field, the spacing between groins is short and, following a change in wave direction, re-orientation of the shoreline occurs between groins, with accretion at the down drift groin and erosion at the updrift groin. The extent of the shoreline movement at the groins is roughly proportional to the spacing. The 13,000 foot gap at Westhampton Beach permitted wide swings in waterline position. All of the reported destruction of housing at Westhampton Beach occurred in this section.

In 1957-58, Madeira Beach, Florida built a groin field along 2 miles of shore just north of Johns Pass. It has firmly stabilized the high-water line well seaward of the position reached during the storm which caused the groins to be built. Hurricane Agnes in 1972 reduced the general level of the beach about 1.5 feet; the beach built back rapidly after the storm. This groin field is an excellent example of what may be accomplished with designs suited to the local wave environment.

The remarkable fact about these groins is that, despite their obvious effectiveness, the State of Florida apparently would not permit their construction today.

Lorain, Ohio on the south shore of Lake Erie is situated many miles from a good bathing beach. With help from the Corps of Engineers, an artificial beach was built in the protection of a segmented offshore breakwater (Figure 6). A similar but larger structure, built at Winthrop, Mass, by the Works Progress Administration in the 30's has stabilized the protected beach. It has required substantially no maintenance over the intervening years.



Figure 5. Moriches Inlet jetties



**Figure 6.** Photograph of Lakeview Park, Lorain, Ohio, shows what can be done with offshore breakwaters and sand fill to form the only good bathing beach for many miles on the Lake Erie shoreline. The cliffs and streams in this vicinity supply very little beach material, and the natural beaches are narrow and not adequate for recreation (Corps of Engineers photograph).

There is a place for such structures in the plans for shoreline development, with due attention, of course, to their effect on adjacent shores.

Beaches for day-time visits, such as Jones Beach (Figure 7), represent the most generally desired and the least expensive type of facility for public recreation. Studies of the utilization of publicly supported recreational facilities have shown that the annual number of daily visits to public beaches almost equals the total number of visits to all other types of public recreational facilities combined -- and at a very low public cost per visit. Permanent facilities are required to handle such crowds; once these facilities are in place, the beach area seaward must be held to maintain capacity.

Miami Beach (Figure 8) serves a different clientele than Jones Beach. Overnight accommodations of all kinds -- hotels, motels, condominiums, single family dwellings and the related support and services are necessary. There are now hundreds of miles of the mainland shores



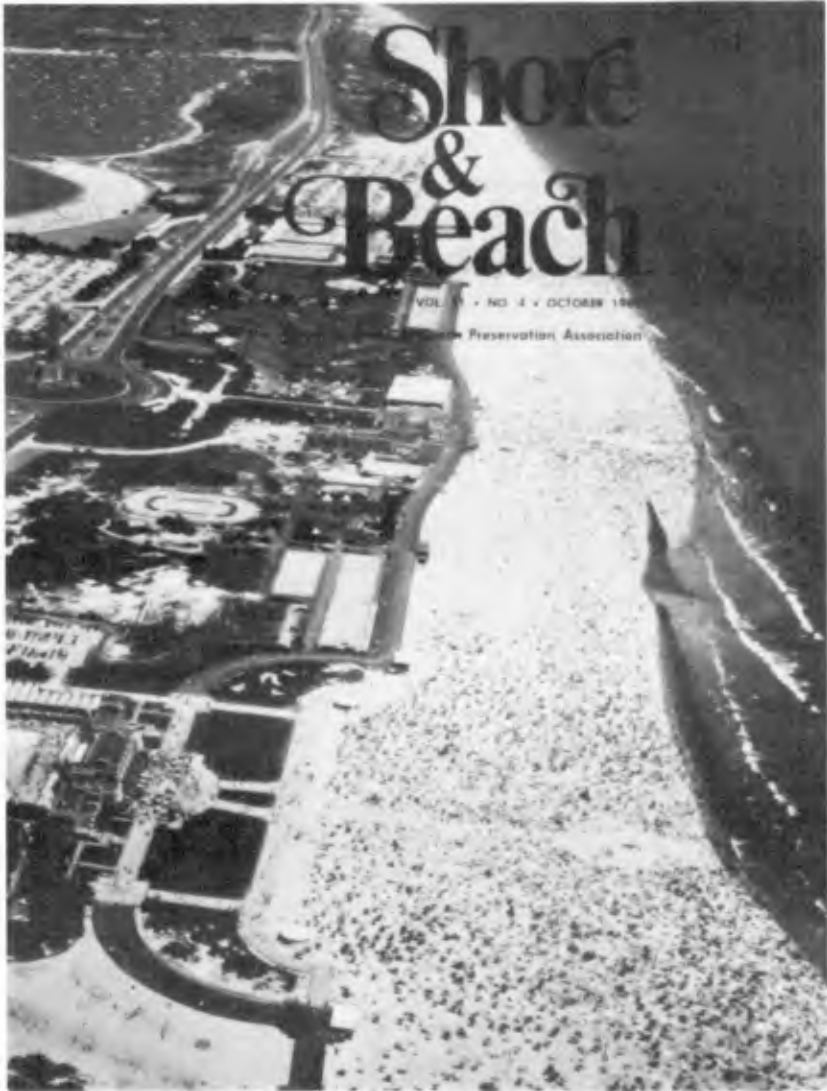


Figure 7. Jones Beach, New York

of the U.S. which are intensively developed -- much of it close to the present high-water line. This huge investment must be protected, if possible, against damage by the sea.



**Figure 8.** Beach fill at Bakers Haulover Inlet.

At Miami Beach, the 10.5 mile reach between Bakers Haulover Inlet and Government Cut, has been restored and expanded by placement of sand dredged from offshore. The minimum width of beach anywhere is 250 feet in May. The littoral transport along this shore is small; the net annual movement is southward. If erosion occurs, it should become apparent first at the North end. Figure 8 shows no evidence of erosion there.

This inadequate and random discussion of coastal projects could be greatly extended to demonstrate the effectiveness of modern coastal engineering practice. However, the policy of "no structures" and "let the beaches go back to nature" has gained acceptance. That such a negative attitude could be diffused widely among public officials and the public generally is difficult to understand when so many other examples of success are reported in the proceedings of the nineteen conferences in this series and in many similar publications. True it is that there have been ineffective, unduly expensive and even damaging projects in the past -- and some will occur in the future -- but I believe an objec-

tive review of coastal projects built in accordance with modern concepts of shore processes would arrive at strongly positive conclusions regarding the effectiveness of coastal structures, including beach replenishment. Monitoring would supply the facts. A means of getting these facts through to the public and their elected officials must be found.

#### REFERENCES

1. Bokuniewicz, H. J. The Seasonal Beach at East Hampton, New York. Shore & Beach, vol. 49, No. 3, July 1981.
2. Johnson, J. W. The Significance of Beach Changes in Tidal Boundaries. Shore & Beach, April 1971.
3. Heikoff, J. M. Politics of Shore Erosion: Westhampton Beach. Ann Arbor Science Publishers, Inc. 1970.



*Fishing Pier with accretion problems, Wildwood, N.J.*

**PART I**

**THEORETICAL AND OBSERVED CHARACTERISTICS**

*Estuaries of South Carolina*





## CHAPTER ONE

### THE EXPERIMENTAL VERIFICATION OF NUMERICAL MODELS OF PLUNGING BREAKERS

by

SØREN PETER KJELDSEN  
Senior Research Engineer

#### 1. ABSTRACT

Results of a WAVE-FOLLOWER EXPERIMENT are presented, in which a moving current meter entrained in the crest of a steep Stokes wave and a moving high-speed film camera follows the wave with its non-linear phase velocity. Measurements of wave particle velocities are then obtained both in non-breaking steep wave crests, and in breaking waves. The breaking waves in deep water conditions are obtained by the application of a non-linear sweep frequency modulation technique, and the Stokes wave becomes unstable due to interaction of 43 wave components focused into one single point in space and time, KJELDSEN 1982.

The result of this interaction is a large freak wave, breaking as a plunging breaker in deep water. Measured crest particle velocities obtained with the current meter exceeded the phase velocity of this wave with 36 %. Digitalisation of the high-speed film showed that particle velocities at the very tip of the plunging jet obtained the value 2.65 times the linear phase velocity. These results are then compared with predictions obtained from numerical simulations by LONGUET-HIGGINS & COKELET 1976 and VINJE & BREVIG 1980.

#### 2. INTRODUCTION

We still have a quite high frequency of damages to structures designed by engineers, and this implies both coastal structures and floating marine structures in deep waters such as semisubmersible platforms and smaller vessels. The Court of Inquiry has now released the report on the "Ocean Ranger" accident, where a semisubmersible platform capsized in severe sea conditions east of St. John's, Newfoundland, and more than 80 crew members lost their lives. The court of Inquiry's report says that a port hole was broken, and the rig gradually lost water tight integrity, partly due to wrong actions from the crew. (Some general information about this particular accident is found in NATIONAL TRANSPORTATION SAFETY BOARD, report 1983). - In Norway on the average 3 vessels are lost each winter in severe seas and over

- 1) NORWEGIAN HYDRODYNAMIC LABORATORIES  
Division: Ship and Ocean Laboratory  
P.O. Box 4118 - Valentinlyst  
N-7001 Trondheim, NORWAY

the 9 last years not less than 26 vessels and 72 people has been lost. In 13 cases surviving members of the crews has confirmed to Courts of Inquiry that the vessels actually capsized in severe seas, and in some cases it was confirmed that these severe seas actually were breaking waves. This is a most unsatisfying situation, and even more because most of the lost vessels fulfill the requirements given by the Norwegian Maritime Directorate to their stability. And the lost vessels are not really smaller vessels, it is trawlers and freighters with total lengths 50, 60 and even 70 meters. (See KJELDSSEN, LYSTAD, MYRHAUG 1981 and KJELDSSEN 1983). Also with regard to coastal structures and in particular with regard to new breakwaters, there is an extensive literature available with cases that documents large unwanted damages to new structures and severe economic losses. Sines harbour on the west coast of Portugal is the best known example, but far from the only one. (See BAIRD et al 1980, YAMAMOTO et al 1981 and BRUUN 1979).

This most unsatisfying situation, has been the severe background for the author, to initiate the present research involving severe efforts into the performance of detailed measurements of the kinematics in the very crests of breaking waves occurring in deep waters. - AND THE RESULTS SHOWED, THAT WAVES IN DEEP WATERS WITH PERIODS AS LONG AS 19 SECONDS COULD BREAK AS PLUNGING BREAKERS WITH CREST PARTICLE VELOCITIES EXCEEDING THE PHASE VELOCITY OF SUCH WAVES WITH 36%.

### 3. EXPERIMENTAL ARRANGEMENTS

The english LORD RAYLEIGH followed the waves in a canal and studied them, riding on a horseback with "phase velocity".

For the present experimental programme a unique WAVE - FOLLOWER EXPERIMENT was designed. The experimental programme was performed in a 260 m long, 10 m deep and 10 m wide wave flume equipped with a large double-flap hydraulic wave generator hinged 1.05 m and 2.62 m below mean water level respectively. Steep regular wave trains generated with this wave generator are Stokes waves with phase locked superharmonics, as shown by KJELDSSEN 1984a. Measurements of wave kinematics were performed in such wave trains. However in order to obtain control of violent plunging breakers at a fixed time and position in deep waters, a deterministic non-linear sweep-frequency modulation technique was applied, see KJELDSSEN 1982. This particular technique takes into account the non-linear dispersion properties of Stokes wave packets. A wave train consisting of 43 transient wave phases with frequencies in the range  $0.203 \text{ Hz} < \Delta f < 1.43 \text{ Hz}$  and all with the same steepness 0.10 were generated followed by a train of Stokes waves with constant frequency. A special WAVE-FOLLOWER-SYSTEM was designed, consisting of a carriage that was perfectly synchronized with the dispersion of one particular wave phase and kept a selected current meter submerged in the wave crest while the wave dispersed over a distance of 15 - 20 meters and developed asymmetry and finally broke as a violent plunging breaker in deep waters. The maintenance of the exact position of the current meter in the wave crest during the dispersion was monitored and controlled by a moving high-speed film camera also installed on the carriage. In advance of these experiments an in-depth dynamic calibration of 4 different types of current meters operating on 4 physically different principles were performed. 2 commercial available current meters were tested and 2 current meters under development at Norwegian Hydrodynamic Laboratories were also tested. Only one of these four types of current meters fulfilled the strict requirements to a satisfying dynamic response, and only these one was used in the WAVE-FOLLOWER EXPERI-

MENTS. Fig. 1. shows the princip for the WAVE-FOLLOWER-SYSTEM. The plunging breaker in deep water was obtained experimentally taking advantage of the fact that group velocity of wave components is a function of wave steepness. 43 non-linear wave components were then phase locked i a deterministic way at one preselected point in space and time, leading to a steep elevated deep water freak wave, that broke as a plunging breaker. In Fig. 1. the full lines are energy lines. In addition phase lines and the path line for the WAVE-FOLLOWER carriage are shown.

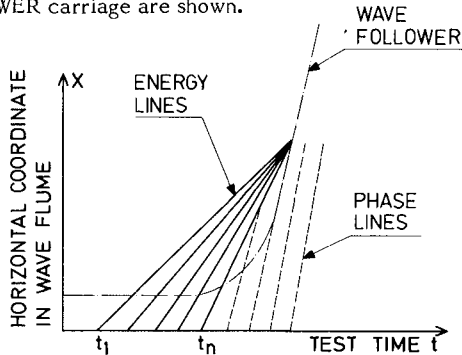


Fig. 1 Non-linear wave dispersion leading to freak waves breaking as plunging breakers in deep waters. Solid lines are energy lines. Further phase lines and the track of the WAVE-FOLLOWER carriage are shown.

Four different types of current meters based on 4 different physical principles, were selected for this particular investigation. The 4 types of instruments were the following:

- 1) Acoustic transit time current meter.
- 2) Acoustic doppler type current meter operated in backscatter mode. (Developed at NHL.)
- 3) Electromagnetic current meter based on Farady's principle.
- 4) Modified pitot tube developed at NHL.

All four types of current meters were then examined in depth during an extensive calibration programme. The evaluation of each current meter were then based on the following properties:

- a) Dynamic calibration.  
Attenuation of amplitude and phase delay in oscillatory flow mapped as a function of frequency.
- b) Surface penetration properties.
- c) Performance in a fluid containing air bubbles.

Only one of the four different types of current meters under evaluation, fullfilled the strict requirements to a satisfying dynamic response, a satisfying response in a fluid containing air bubbles, and a satisfying response when a liquid surface was penetracted by a current meter moving relatively to that surface. Thus the only current meter that passed the calibration tests and was selected for these WAVE-FOLLOWER-EXPERIMENT was an ultrasonic



transit time current meter with a working frequency of 4 Megahertz. This particular instrument measures the velocity of sound in the fluid and compensates automatically for any possible change of this velocity. It is well known, that it is impossible to use a low-frequency instrument because the velocity of sound drops significantly when air is entrained into the fluid. However, what is much less well known, is that at very high frequencies this effect disappears. Fig. 2 shows experimental results by FOX, CURLEY & LARSON 1968 and shows that in water containing air bubbles the velocity of sound stabilizes at very high frequencies close to the value for an air-free-fluid. In the present investigation a carrier frequency of 4 Megahertz was used, and this is well beyond and outside the critical limit shown in Fig. 2.

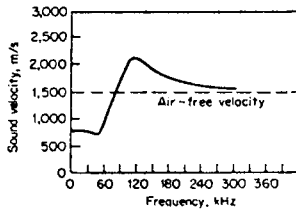


Fig.2 Velocity of sound as function of carrier frequency in a fluid containing air bubbles. (From FOX, CURLEY & LARSON 1968).

A special designed rig was used for dynamic calibration of the current meters, see Fig. 3. In this rig the current meters were oscillated at different frequencies, and amplitude attenuation as well as phase distortion were mapped. This calibration was first made with the current meter submerged at all times, and later it was performed with the current meter penetrating the free surface as shown in Fig. 3. A position galvanometer attached to the roof measured the exact position of the current meter at all times.

Fig. 4 shows an example of the obtained results from such a dynamic calibration. Above is the position of the moving current meter and below is the measured particle velocity.

Fig. 5 shows a comparison between the surface penetration properties of two different kinds of current meters. Above is shown the ideal curve for a surface penetrating instrument. The output shall be zero, and a moment later, it shall be 100 % of the true fluid velocity at that particular position. Further the intergrated velocity should be equal to the cross-hatched area. Below are shown the curves for the ultrasonic transit time current meter, and for the electromagnetic current meter. We observe that a time  $t$  elapses, that is 5 times the instrument time constant  $\tau$ , before the amplitude of the received signal has reached 95 % of the true value. As the time constant is as small as  $\tau = 0.01$  sec for the ultrasonic current meter it is nearly perfect for this kind of surface penetration experiments, while the electromagnetic current meter (Design Marsh McBirney) is much too slow and cannot be used for this kind of measurements in wave crests.

In order to further map the performance of the selected instrument in an air/fluid mixture, the current meters were installed in an oscillating water tunnel as shown in Fig. 6. From the bottom air bubbles were then released in a

controlled manner, the bubbles passed the current meter, and the response of the current meter to the passing of these free bubbles was then monitored.

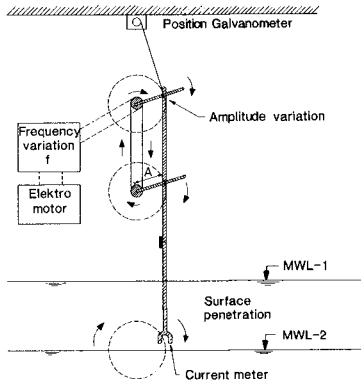


Fig. 3 Rig applied for dynamic calibration of current meters.

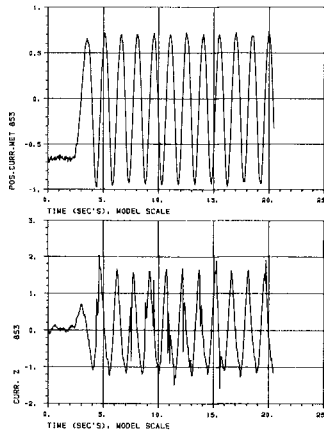


Fig. 4 Example of results from a dynamic calibration test. Above the position of the moving current meter, below the measured particle velocity.

A more comprehensive and complete description of the experimental arrangement and the development of the instruments are given by KJELDSEN 1984.

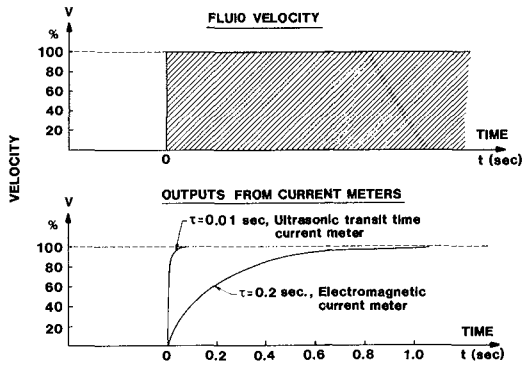


Fig. 5 Surface penetration properties of ultrasonic transit time current meter and electromagnetic current meter.

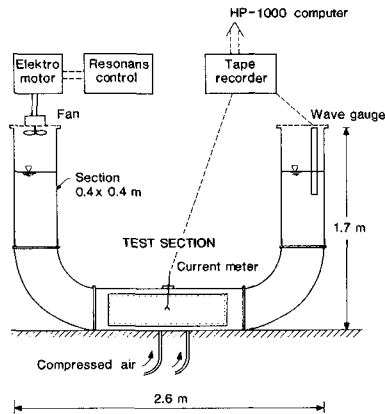


Fig. 6 Experimental arrangement used to map performance of current meters in an air-fluid mixture.

4. RESULTS - NON-BREAKING WAVES

Phase locked superharmonics contained in the generated Stokes waves are analysed by KJELDSEN 1984a. In order to further control the quality of the generated waves a non-dimensional plot of synoptic wave shape is prepared in which experimentally obtained values of wave shape are compared with calculations for high order Stokes waves made by COKELET 1977 using Padé approximations to an order of 110 with  $\epsilon$  as the expansion parameter. This plot is shown in Fig. 7. A strong coherence is observed between experimental values and calculations made with  $\epsilon^2 = 0.70$ . Steep wave crests and flat troughs are pronounced. Use of Stokes wave theory to represent the single experimentally obtained waves, then seems to be a very good approximation, until the Stokes wave finally becomes unstable and breaks due to the deterministic non-linear focusing and wave-wave interaction.

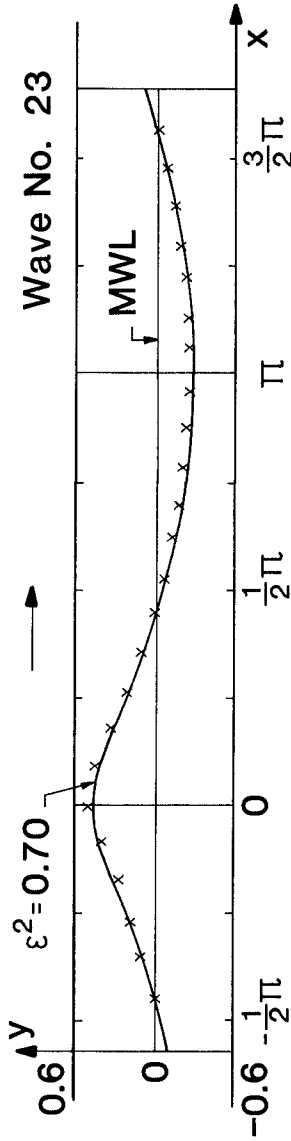


Fig. 7. Non-dimensional synoptic comparison between experimentally obtained Stokes wave and calculations made by COKELET 1977 using  $\epsilon^2 = 0.70$  as the expansion parameter. (Conversion from time domain to synoptic domain is made by application of equations given by COKELET 1977, page 210).

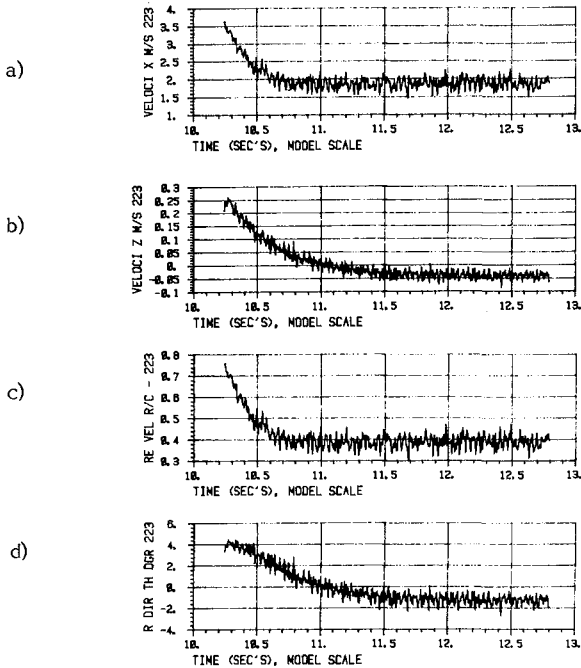


Fig. 8. Measurements of particle velocities with a moving current meter in steep Stokes waves 120 mm above mean water level.

Fig. 8 shows an example of the obtained results for steep Stokes waves. Fig. 8a is the horizontal particle velocity positive in the direction of wave dispersion. After entrainment of the current meter into the wave crest the horizontal particle velocity stabilizes at a value near 1.8 m/sec which shows, that a steady state condition is present in the interior of the wave crest, as it was expected. Fig. 8b shows the vertical particle velocity positive upwards. (In this case a slight negative vertical velocity  $-0.03$  m/sec is measured, which indicates that the position of the current meter has been slightly in the rear part of the wave. The expected value for the vertical particle velocity is 0, when the current meter is maintained directly below the wave crest. However this inaccuracy in alignment is very small as the ratio  $Z/X$  is less than 2 %). More important is it to observe that also the vertical particle velocity stabilizes at a fixed value, which proves that the current meter moves exactly with the phase velocity of the gravity wave. During these measurements the gravity wave dispersed over a distance of 16 m in the laboratory. A strong coherence is seen between the horizontal and the vertical particle velocities when the current meter is entrained. Fig. 8c then shows the resulting velocity vector normalized with respect to the phase velocity of the wave, and Fig. 8d finally shows the tilt of the velocity vector which in this case becomes  $-1.5$  degrees directed downwards from the horizontal.

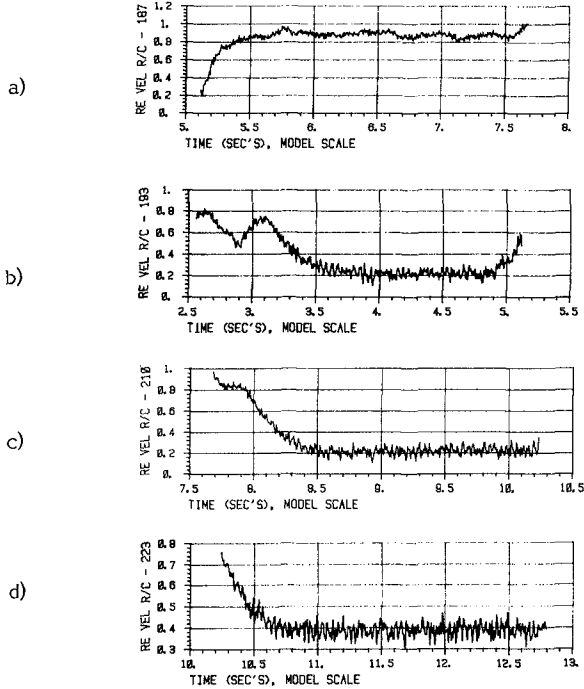


Fig. 9 Resulting velocity vector normalized with respect to phase velocity measured at 4 different vertical levels. a) 420 mm, b) 320 mm, c) 220 mm and d) 120 mm above mean water level. The crest height of the wave is 440 mm.

Fig. 9 then shows the resulting velocity vector obtained in 4 different vertical levels, namely 420 mm, 320 mm and 120 mm above mean water level. In the case where the current meter is moving in the level at 420 mm, it is entrained only 10 - 20 mm below the crest. It is then most remarkable to observe that the resulting velocity vector drops significantly when the current meter is lowered only 100 mm from the top position.

These experiments indicate that a velocity distribution above mean water level, as shown in Fig. 10 could be applied for design purposes. The very large particle velocities are confined to a very local region close to the upper part of the wave crest. In this local region the obtained recording of horizontal particle velocity in a coordinate grid moving with phase velocity is very close to zero in the entire recording period. It is therefore concluded that the Stokes 120 degrees corner flow is a good approximation to the interior flow field for such a local upper region in very steep Stokes waves.

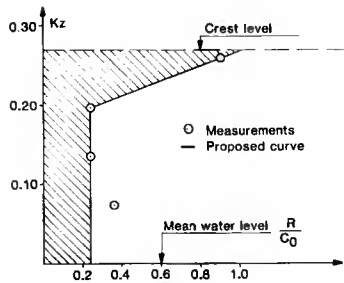


Fig. 10 Non-dimensional distribution of particle velocities above mean water level for non-breaking waves.

### 5. RESULTS - PLUNGING BREAKERS

Let us next consider the results obtained in breaking waves. The current meter then moved with phase velocity inside a steep Stokes wave over a distance as long as 16 meters until this particular wave phase due to the non-linear focusing suddenly becomes unstable and breaks as a plunging breaker, see Fig. 11.



Fig. 11 Moving current meter entrained in the very crest of a deep water plunging breaker at a level of 420 mm above mean water level.

This travel inside the wave takes less than 4 seconds, which means that the synchronisation has to be perfect. The position inside the wave crest was monitored with a moving high-speed film camera. This camera was operated with a speed of 200 frames/sec, and the camera was synchronized with a clock signal, that was recorded together with the measured particle velocities. Not less than 225 single experiments of this kind, with the current meter moving at different elevations above mean water level were performed. Fig. 12 shows the obtained horizontal and vertical particle velocities in one of these experiments. The current meter operated at a level of 420 mm above mean water level is entrained in the very crest of the wave at a time 5.1 seconds. The horizontal particle velocity then obtains the phase velocity of this particular wave which is 4 m/sec in the laboratory scale. It keeps this velocity for quite a

long time because the wave now appears as a steady wave. However suddenly the wave becomes unstable and the measured velocity increases in a burst with a value that reaches 5.42 m/sec in the laboratory scale! (Scaling of results to representative prototype values is treated in section 7). The corresponding vertical particle velocity is also displayed in Fig. 12. It has a more modest pattern and increases from 0 to 0.42 m/sec. It is directed vertically upwards.

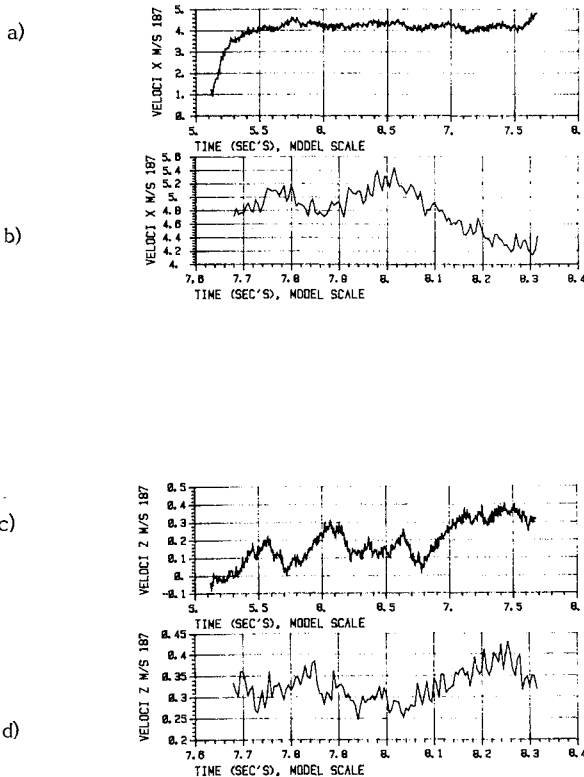


Fig. 12

Horizontal and vertical particle velocities measured 420 mm above mean water level in the plunging breaker shown in Fig. 11. The horizontal particle velocity is steady with a value near 4.00 m/sec until the wave breaks in a violent burst at a time  $t = 8$  seconds.

a) and b) horizontal particle velocity,  
 c) and d) vertical particle velocity.



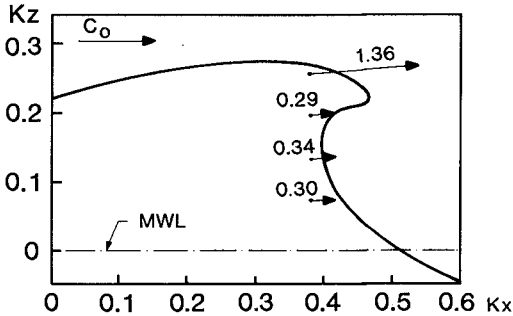


Fig. 13 Magnitude and tilt of resulting particle velocity vectors in the crest of a plunging breaker normalized with respect to the phase velocity.

The tilt and the total magnitude of the resulting particle velocity vector inside the breaking wave are shown in Fig.13 for 4 measured levels. The results are here normalized with respect to a linear phase velocity which is here taken as the velocity of the moving carriage. The measured tilt of the velocity vector at the very top of the wave crest is near 0. When the burst comes it obtains a small deflection 5.5 degrees upwards.

## 6. COMPARISON WITH MEASUREMENTS ON FILM

The experiments with non-linear focusing of wave components leading to violent plunging break waves in deep waters were repeated in a smaller wave flume with glass windows that permitted high-speed filming from the side. In order to obtain quantitative measurements from this film related to the tip of the plunging jet in the front of the wave, the velocity with which the film camera was operated was increased to 300 frames/sec. Fig. 14 shows above a typical stage in the development of the plunging jet and below the position of the tip of the jet measured on the frames of the film and plotted in a  $KX - KZ$  coordinate grid. It is then possible to obtain one of the two components of the particle velocity on the boundary, namely the one that is normal to the boundary. The time lapse between each frame is 3.33 milliseconds. At position 2, 3 locations of the tip of the jet is identified. The normal velocity is then measured and becomes 2.67 m/sec. 20 frames later at position 3, 3 new locations of the tip of the jet is identified. The normal velocity derived from these is 4.07 m/sec. Again 20 frames later at position 4, 3 locations are identified and the normal velocity becomes 4.07 m/sec. These values have then to be compared with a representative phase velocity for this particular plunging wave. This phase velocity is here defined as the linear phase velocity ( $C_0 = 1.54$  m/sec), that can be derived from the zero-downcross wave period  $T_{zd} = 0.984$  sec measured with a stationary instrument at the position of breaking. The rod visible in Fig. 14 is a stationary current meter, but also a wave gauge giving surface elevation might have been used for that purpose. The width of the wave flume is 1.00 m and the current meter is installed 0.5 m behind the tip of the jet viewed at the window. We then obtain the following non-dimensional results:

POSITION	$V_n$ (m/sec)	$\frac{V_n}{C_0}$
2	2.67	1.73
3	4.07	2.65
4	4.07	2.65

These results have then to be compared with available numerical simulations of plunging breakers in deep waters. LONGUET-HIGGINS & COKELET 1976 developed a model that in some cases achieved values as high as 2.8 times the linear phase velocity. This very high value occurred also in the numerical simulation at the very tip of the jet. The present experimental results thus confirms the physical existence of such very high values. VINJE & BREVIG 1980 developed a model that achieved values 1.8 times the linear phase velocity. This figure seems to be too low, and there is a discrepancy between the two numerical simulations, when the objective is evaluation of kinematics.

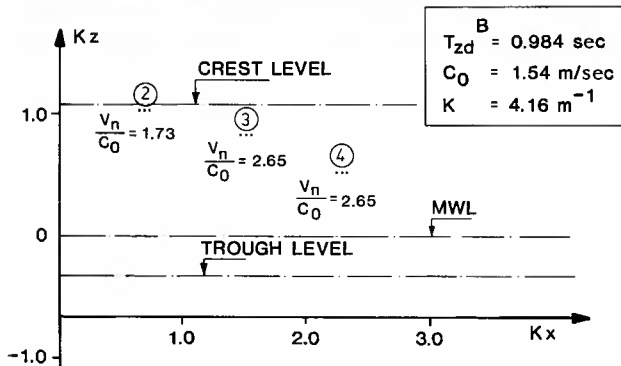


Fig. 14

Above tip of plunging jet obtained from the frames of a high-speed film. Below positions of the tip of the plunging jet viewed in a KX - KZ coordinate grid.

## 7. A NEW CRITERIA FOR INCEPTION OF BREAKING

The very high velocities in the crests of the waves of the kind reported here, have to be squared when drag forces on structures exposed to such waves are calculated. A study containing an attempt to evaluate the probabilities for encounter of such waves is available. This study is based on statistics of steepnesses of 25,000 waves observed during 22 gales on the Norwegian Continental shelf, see KJELDSEN 1981. Another most important aspect for design of structures is the crest length of breaking waves in a 3-dimensional sea, and such results are also available KJELDSEN 1984b.

The last and most important topic to consider is then the position of the violent plunging breaker relative to the envelope of the non-linear wave group in which it occurs. Fig. 15 shows the measured surface fluctuation of a focused freak wave converted to prototype values. It appears as a plunging breaker as shown on Fig. 11. However, it appears with a wave period  $T_{zd} = 19$  sec and a zero-upcross wave height  $H_{zu} = 30$  m. It thus breaks violently with a much lower steepness than the limiting steepness for monochromatic waves, and it contains very high particle velocities as measured with the current meter and plotted at the appropriate elevation. The present experiments confirm that violent breaking waves always appear in the front of the wave groups. Both the inception of wave breaking and the strength of the breaking of a particular wave phase is thus governed by a transition and a sudden jump in wave number, combined with a high wave energy flux. The breaking criteria valid for a sea containing wave groups can therefore be expressed as the joint probability of a certain wave number jump and the associated wave energy flux both exceeds certain critical thresholds (see KJELDSEN 1984 c.)

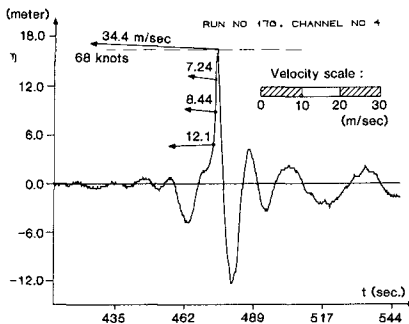


Fig. 15 The plunging breaker scaled to prototype values. The resulting particle velocity vectors obtained with the current meter are plotted at appropriate vertical elevations.

## 8. CONCLUSIONS

1) A moving current meter entrained in the very crests of focused plunging breakers showed that the ratio between the measured particle velocity vector and the phase velocity increased to a value 1.36 in a position a few millimeters below the crests in the centre of the waves.

2) Frame-to-frame analysis of a high-speed film showed that the particle velocity component normal to the boundary of the wave increased to a value that was 2.65 times the phase velocity valid for a position at the very tip of the plunging jet. This confirms the high values obtained at this particular position by LONGUET-HIGGINS & COKELET 1976 in their numerical simulation.

3) The violent breaking waves in deep waters always appeared in the front of the non-linear wave groups. Both the inception of wave breaking and the strength of the breaking of a particular wave phase within a wave group is thus governed by a transition and a sudden jump in wave number, combined with a high wave energy flux.

#### 9. ACKNOWLEDGEMENTS

Acknowledgements are given to a skilled highly professional staff at Norwegian Hydrodynamic Laboratories, that assisted during the performance of these demanding experiments. Further Norwegian Hydrodynamic Laboratories gratefully acknowledge a grant from the Continental Shelf Committee of the Royal Norwegian Council for Scientific and Industrial Research (NTNF), on the project "EXTREME RESPONSES FROM BREAKING WAVES IN DEEP WATERS".

#### 10. REFERENCES

BAIRD et al. 1980: "Report on the Damages to the Sines Breakwater, Portugal" Proc. 17th Coast. Eng. Conf. Sydney, Australia.

BRUUN P 1979: "Practical View on the Design of Mound Breakwaters" Report No. 7. Institute of Marine Civil Engineering. The Norwegian Institute of Technology. Trondheim, Norway.

COKELET 1977: "Steep Gravity Waves in Water of Arbitrary Uniform Depth" Philosophical Transactions of the Royal Society of London. No. 1335. Vol. 286, pp. 183-230.

FOX, CURLEY & LARSON, see MCGRAW HILL 1968: "Principles of Under-water Sound" pp. 223-228.

KJELDSSEN 1978: "Breaking Waves in Deep Water". Paper and 16 mm Film presented at Euromech Colloquium No. 102. Bristol University, England.

KJELDSSEN, LYSTAD, MYRHAUG 1981: "Forecast of Breaking Waves on the Norwegian Continental Shelf". Joint Report. The Norwegian Meteorological Institute and the Norwegian Hydrodynamic Laboratories, Trondheim, Norway.

KJELDSSEN 1981: "Design Waves" Report No. 1-81008. Norwegian Hydrodynamic Laboratories, Trondheim, Norway.

KJELDSSEN 1982: "2- and 3-Dimensional Deterministic Freak Waves". Proc. 18th International Conference on coastal Engineering. Cape Town, South Africa. 14-19 November, 1982.

KJELDSEN 1983: "Determination of Severe Wave Conditions for Ocean Systems in a 3-dimensional irregular Seaway". Proc. VIII Congress of the Pan-American Institute of Naval Engineering. Washington D.C. USA. September 12-17th 1983.

KJELDSEN 1984: "Freak Wave Hydrodynamics - and some of the Engineering Applications". Thesis submitted to the Institute of Technology at the University of Trondheim, Norway.

KJELDSEN 1984a: "New Wavemaker Design and Experience - Experience with Double-Flap Wavemakers". 17th International Towing Tank Conference. Gothenburg, Sweden. September 1984. Proc. Vol. II.

KJELDSEN 1984b: "Whitcapping and Wave Crest Lengths in Directional Seas". Proc. Symposium on Description and Modelling of Directional Seas. Technical University of Denmark, Copenhagen. June 1984.

KJELDSEN 1984c: "Dangerous Wave Groups". Norwegian Maritime Research Vol. 12, No. 2, 1984, pp. 4-16. Selvig Publishing. P.O. Box 9070. Oslo. Norway.

LONGUET-HIGGINS & COKELET 1976: "The Deformation of Steep Surface Waves on Water. I. A Numerical Method of Computation". Proc. Royal Society, London. Vol. A 350 pp. 1 - 26.

NATIONAL TRANSPORTATION SAFETY BOARD 1983: "Marine Accident Report". Report No. NTSB-MAR-2. Washington D.C. 20594 USA.

VINJE & BREVIG 1980: "Numerical Simulation of Breaking Waves". 3rd International Conference on Finite Elements in Water Resources. Proceedings. University of Mississippi, USA.

YAMAMOTO et. al 1981: "Random Wave Tests on a Damaged Breakwater in Himekawa Harbour, Japan". Coastal Engineering, Vol. 5, pp. 294-375.

## CHAPTER TWO

### BREAKING WAVE DESIGN CRITERIA

E.B. Thornton (M. ASCE)<sup>1</sup>, C.S. Wu (M. ASCE)<sup>1</sup>, R.T. Guza<sup>2</sup>

#### ABSTRACT

Breaking wave heights measured in both field and random wave laboratory experiments are examined. The dependence of breaker height and breaker depth on beach slope and deep water steepness is presented. The results are compared with the design curves of the Shore Protection Manual (SPM) and the predictions of the random wave model by Goda (1975). The comparisons indicate that the significant breaker height, based on Goda's model, is slightly conservative for the experimental cases; but the maximum breaker heights are reasonably predicted by the model. The design procedures in the SPM are based on a monochromatic wave breaking, and appear overly conservative, particularly for low wave steepness (less than 0.01) which occur frequently on the West Coast of the United States. The use of the Rayleigh distribution to predict wave height statistics is tested with random wave data for both deep and shallow water regions.

#### INTRODUCTION

The selection of breaking design waves is essential for the design of a coastal structure or for the coastal sediment problem. The present design practice is to specify maximum breaking waves based on empirical curves derived primarily from laboratory experiments of monochromatic waves (constant period and wave height). Several concerns arise from using monochromatic laboratory wave data as a basis for prototype design. Uncertainties exist in the scaling of laboratory waves to the prototype. More importantly, waves in nature are not monochromatic but random, having variable period, height and direction. The observed mean breaker height for random waves is generally 30-40% below the breaker inception height for periodic waves. Hence, uncertainty exists when applying criterion based on monochromatic waves to actual conditions in nature.

The objectives of this paper are to synthesize available random wave experiments, both in the field and laboratory, and to compare the

<sup>1</sup>Department of Oceanography, Naval Postgraduate School, Monterey, CA 93943

<sup>2</sup>Shore Processes Laboratory, Scripps Institution of Oceanography-A009, University of California, La Jolla, California 92093

results with the random wave model of Goda (1975) and the breaking wave design curves in the Shore Protection Manual (US Army Corps of Engineers, 1977).

#### RANDOM WAVE DATA

During the past decade, there has been a growing recognition that significant differences exist between the results of monochromatic and random wave experiments. At the same time, primarily due to better instrumentation, a large number of comprehensive nearshore field experiments have been conducted. A difficulty in synthesizing various experiments, particularly the field data, is that the data were collected in different manners. The requirements for inclusion in the data base here are: 1) the waves are random, either measured in the field or simulated in the laboratory; 2) the data are for dissipative, progressive waves on relatively plane sloping, unbarred beaches; 3) the wave measurement locations be close enough to accurately define the position of the mean breaking wave height; 4) the data be given in terms of either significant height,  $H_{1/3}$ , or maximum height,  $H_{max}$ . Based on the above requirements, two sets of field data collected under the Nearshore Sediment Transport Studies (NSTS) and two sets of laboratory experiments on wave shoaling are included in the present paper.

Torrey Pines Beach, San Diego, California. The beach and nearshore at Torrey Pines Beach is gently sloping with nearly parallel and plane contours. During the experiments, significant offshore wave heights varied between 60 and 160 cm. The average peak frequency of the incident wave spectra varied little during the experiments and was about 0.07 Hz. Shadowing by offshore islands and offshore refraction limit the angles of wave incidence in 10-m depth to less than 15°. It was shown by Guza and Thornton (1980) that because of the small incident angles, refractive effects can be neglected in calculating shoaling processes. The condition of nearly normally incident spilling (or mixed plunging-spilling) waves, breaking in a continuous way across the surf zone, prevailed during most of the experiments. Winds during the experiments were generally light and variable in direction. Surface elevation and horizontal, orthogonal velocity components were measured by using a closely spaced array of up to 17 instruments in a shore-normal transect from offshore at the 10-m depth contour to across the surf zone (see Figure 2 in Thornton and Guza [1983]).

Leadbetter Beach, Santa Barbara, California. The mean nearshore slope at Leadbetter Beach varied between 0.017 and 0.05 during the experiment, depending on the wave climate. No offshore bar was apparent. The shoreline has the unusual east-west orientation along a predominantly north-south coast. The open ocean waves are limited to a narrow window of approach (+9° centered on 270°) because of the protection from Point Conception to the north and the Channel Islands to the south. The generally highly filtered ocean swell type waves from almost due west must make a right angle turn to approach the beach normally. As a result, waves approach at large oblique angles to the bottom contours in the surf zone and drive a strong longshore current.

Because of the relatively large incident wave angles, refractive effects must be accounted for in the shoaling calculations. A similar array to that at Torrey Pines was used to measure the wave height transformation from 9-m depth to the shoreline (See Thornton and Guza, 1984).

Laboratory Experiments by Goda (1975) and CERC. Goda (1975) conducted a series of experiments in a 30 m long laboratory wave flume using random waves. Two beach slopes of 0.02 and 0.1 were used. Different wave spectra were employed simulating single peaked wind waves, double peaked sea and swell superposed, narrow swell waves, and relatively broad banded waves. Wave heights were calculated at six locations spanning the surf zone. Random wave laboratory experiments were also performed at CERC and have been variously described by Seelig et al (1983), Thompson and Vincent (1984), and Vincent (1984). The plane bottom slope was 1:30 in a 45.7 m long tank. Measurements were made at nine locations. Various theoretical wave spectra were simulated, including the Pierson-Moskowitz, JONSWAP and Ochi-Hubble Spectra.

The wave height statistics of  $H_{rms}$ ,  $H_{1/3}$  or  $H_{max}$  were calculated using the zero-up-cross technique. The surface elevations for the field data were first band-pass filtered ( $0.05-0.5 H_z$ ). Goda (1975) uses  $H_{1/260}$  for  $H_{max}$ , which is essentially the same statistic. All statistics are compared (nondimensionalized) using the deep water significant wave height  $H_0$  and deep water wave length defined as  $L_0 = (g/2\pi)T_p^2$ , where  $T_p$  corresponds to the wave period at the peak of the spectrum. Deep water wave heights were calculated by translating the measured nearshore wave heights to offshore accounting for shoaling and refraction using linear wave theory. For the data considered, refractive effects are needed to be accounted for only in the Santa Barbara data.

Monochromatic waves break on a plane beach at essentially a single location with a constant breaker height. Hence, a breaker height and depth are unambiguously defined. In contrast to monochromatic waves, there is no well-defined breakpoint for random waves; the largest waves tend to break farthest offshore and the smaller waves closer to shore. The result is a spatial distribution of breaking and unbroken waves. However, it is found that the use of a simple terminology for describing breaking wave parameters is informative and simplifies the analysis. For this reason, we introduce a mean breaker line for random waves. A "mean breaker line" is defined as the mean location where the averaged wave height reaches its maximum as the waves shoal from deep water and then dissipate due to breaking. As an example, the rms wave heights measured at Torrey Pines are shown in Figure 1. The mean rms breaker height  $H_B$  and surf zone width  $X_B$  are defined where  $H_{rms}$  reaches a maximum. Similar statistics are defined for  $H_{1/3}$  and  $H_{max}$ , and an example is shown in Figure 2. This definition of mean breaker height means that the  $H_{rms}$  and  $H_{1/3}$  statistic are made up of broken and unbroken waves. The  $H_{max}$  statistic



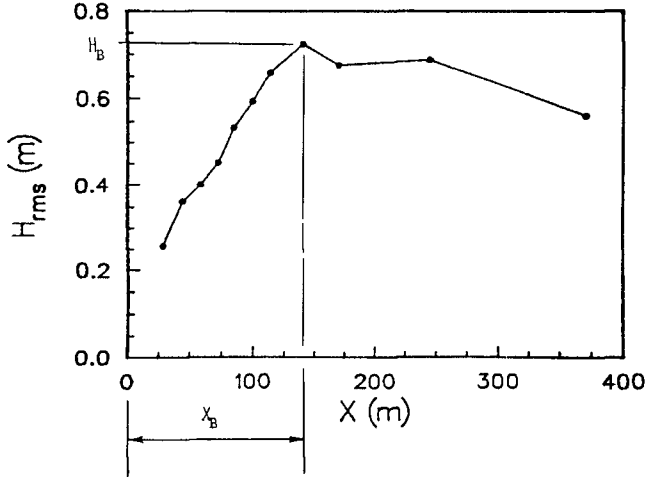


Figure 1. Definition of mean breaking wave height  $H_B$ , and corresponding surf zone width  $X_B$ .

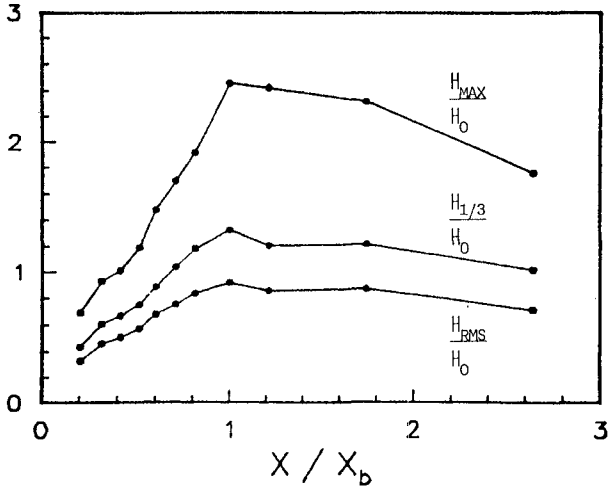


Figure 2. Wave height statistics  $H_{max}$ ,  $H_{1/3}$ , and  $H_{rms}$  normalized by deep water significant wave height  $H_0$ , as functions of distance offshore.

corresponds to the single largest wave measured during the experimental interval and presumably corresponds to a breaking, or incipient breaking wave.

The difficulty of using this definition for mean breaker height is that measurement locations need to be closely spaced to accurately locate the point of the maximum wave height. Also, in some of the data there appeared to be no maximum; this result occurred for both the field and laboratory data (where the obvious blame on refractive effects are not present).

## RESULTS

The breaking wave height data are compared with breaking wave design curves calculated by Seelig (1979), who employs the random wave height transformation theory by Goda (1975). Goda's theory describes the wave heights using a modified Rayleigh distribution in which the tail of the distribution is shortened, supposedly to represent the decrease in wave height due to breaking. Wave transformation is described using the nonlinear theory by Shuto (1974). Breaker height is expressed by

$$\frac{H_b}{H_0} = A \frac{L}{H_0} \left[ 1 - \exp\left(-1.5 \frac{h}{L_0} [1 + K \tan^s \beta]\right) \right] \quad (1)$$

where  $H_b$  is the breaking wave height,  $h$  is the local depth and  $\tan \beta$  is the beach slope. The breaking wave heights are described as varying linearly over a range of values from most frequent breaker height to maximum breaker height dependent on the coefficient  $A = (0.12, 0.18)$ , and other coefficients  $K = 15$  and  $s = 4/3$ . The coefficient values were suggested by Goda (1975). Goda's theory predicts the shoreward transformation of the distribution (non-Rayleigh) of wave heights, including both broken and unbroken waves, accounting for wave growth due to shoaling and attenuation due to breaking.

Seelig (1979) used Goda's theory to calculate the "mean breaker height" and breaker depth at that location. Seelig defined the mean random breaking wave height in the same manner as used to define the breaker line for the data, i.e. the location of the maximum wave height in the shoaling transformation of the waves from offshore to the beach. Seelig calculated a series of random wave breaking design curves for various beach slopes and initial deep water wave steepnesses.

The significant breaking wave heights,  $H_{1/3}$ , are compared for various beach slopes in Figure 3. Laboratory data are indicated by open symbols and field data by closed symbols. The field data have lower wave steepness due to the predominantly low frequency Pacific swell (0.07 Hz) that prevailed during the field experiments.

The curves by Seelig, corresponding to beach slopes 0.1, 0.05 and 0.01, are shown as solid lines. The SPM breaking wave design curve based on monochromatic wave data for beach slope 0.02 is presented for

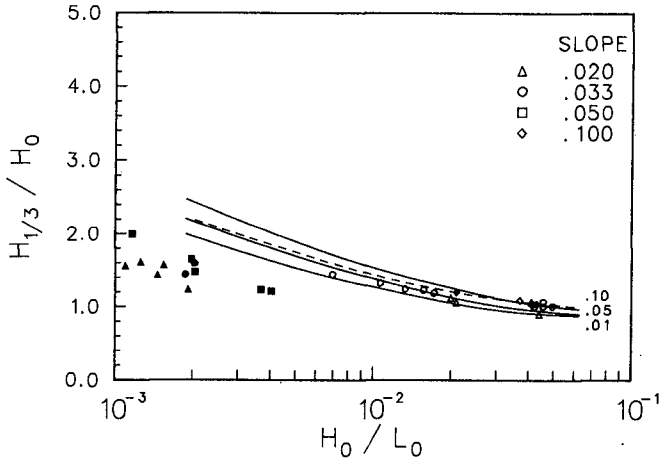


Figure 3. Significant breaking wave height,  $H_{1/3}$ , as a function of deep water wave steepness and beach slope. Shown are Seelig (1980) design curves for beach slopes 0.1, 0.05, and 0.01 based on Goda (1975) theory (solid lines) and SPM curve for beach slope 0.02 (dashed line).

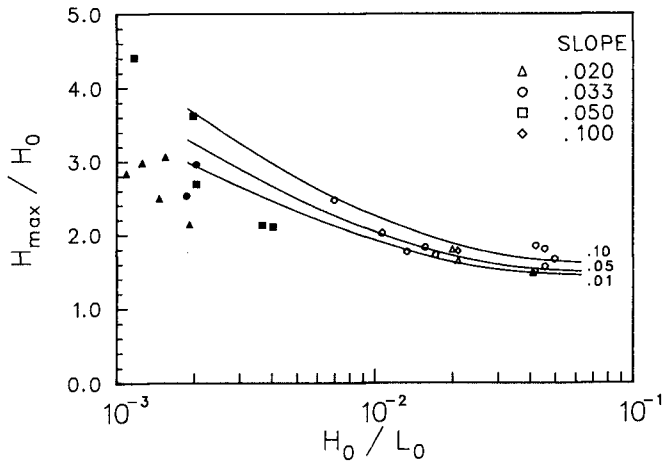


Figure 4. Maximum breaking wave height,  $H_{max}$ , as a function of deep water steepness and beach slope.

comparison (dashed line). The SPM curve is flatter, but generally falls within the range of the Seelig curves for random waves.

The Seelig curves reasonably predict the steeper wave slope laboratory data. This is expected since the coefficients used in (1) specifying Goda's theory are based on the same laboratory data collected by Goda. But the curves overpredict the significant breaker heights for initially low slope waves. Therefore, the Seelig curves appear to reasonably predict significant breaker heights for initially steeper waves ( $H_0/L_0 > 0.7 \times 10^{-3}$ ), but appear overly conservative for predicting significant breaker heights for initially low steepness waves.

The maximum breaking wave heights are compared with the Seelig design curves in Figure 4. The curves give reasonable predictions of maximum breaking waves, although the data do not align well with the beach slope dependence of the curves. It is pointed out that for the low wave steepness data, the maximum wave heights compare well with that by Goda's model, whereas the significant wave heights are over-predicted. This is fortuitous. The reason is that the actual wave heights conform more closely to a Rayleigh distribution than a Rayleigh distribution with a shortened tail. The Goda model, employing a modified Rayleigh distribution with a shortened tail, predicts a smaller increase in wave height from  $H_{1/3}$  to  $H_{max}$  than the data, so that the  $H_{max}$  curves do not overpredict the measured values as much.

Thornton and Guza (1983) showed that for the Torrey Pines data the Rayleigh distribution could be used to calculate the  $H_{max}$  with an average error of -7% (under-prediction). Comparisons of the Santa Barbara data with the Rayleigh distribution are shown for  $H_{1/3}$  in Figure 5 and for  $H_{max}$  in Figure 6. The Rayleigh distribution predicts

$$H_{1/3} = 1.41 H_{rms} \quad (2)$$

Figure 5 shows that most of the  $H_{1/3}$  wave heights plotted as a function of depth fall within +5% (dashed line) of (2). The wave heights in deeper water (depth  $> 4$  m) appear to agree better with the Rayleigh distribution than wave height in shallower water within the surf zone. The  $H_{max}$  data and values predicted from the Rayleigh distribution are compared in Figure 6. The average error of the regression curve (dashed line) from the 45° line is -9%, i.e., the Rayleigh distribution under-predicts the data by 9% on the average, although the scatter is considerably greater. This implies that the use of a modified Rayleigh distribution with a shortened tail as described by Goda (1975) to predict breaking wave height design conditions is nonconservative; it is found from field measurements that the use of Rayleigh distribution is also nonconservative.

The depth at the significant breaking wave height,  $d_b$ , is plotted as a function of wave steepness and beach slope in Figure 7. A beach slope dependence is evident. The data are reasonably represented by the Seelig curves and are only underestimated at the very lowest wave steepnesses.

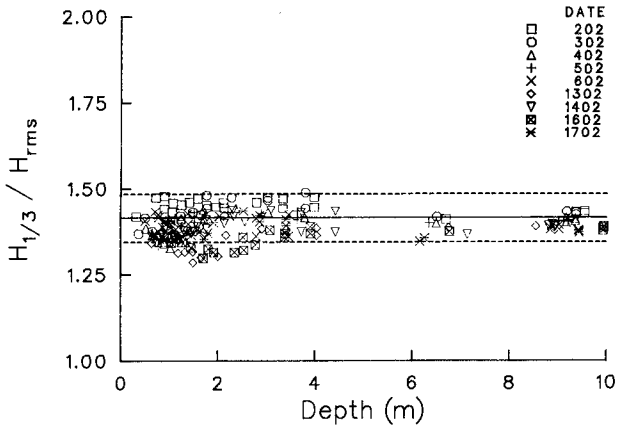


Figure 5. Significant wave heights,  $H_{1/3}$ , measured at Santa Barbara, California compared with wave height predicted by Rayleigh distribution (solid line) as a function of depth. Dashed lines indicate  $\pm 5\%$  error.

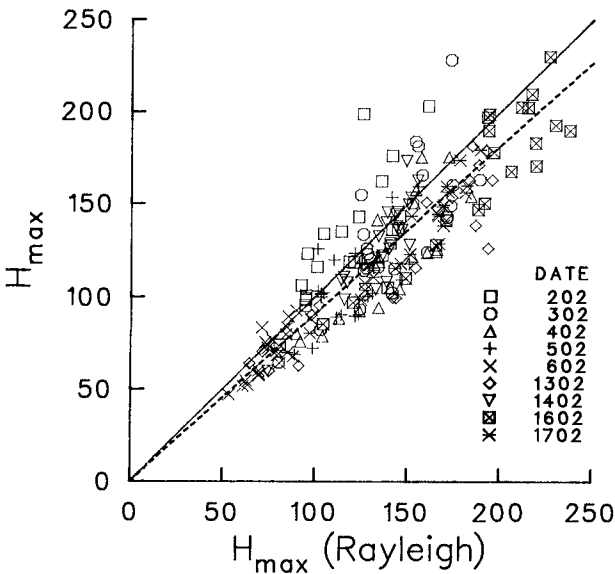


Figure 6. Maximum wave heights,  $H_{max}$ , measured at Santa Barbara, California compared with wave height predicted by Rayleigh distribution. Mean regression line is indicated by dashed line.

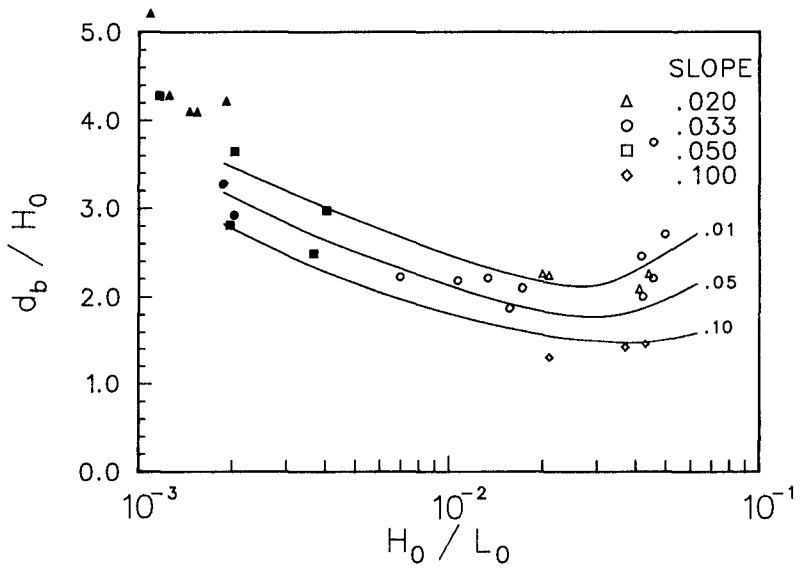


Figure 7. Depth at significant breaking wave height,  $d_b$ , as a function of wave steepness and beach slope.

## SUMMARY AND CONCLUSIONS

Breaking wave heights measured in the field and in random wave experiments in the laboratory are compared with the random wave model of Goda (1975) as calculated by Seelig (1980) and with the Shore Protection Manual (1977). The random wave model suggests that wave breaking is dependent on beach slope and wave steepness. The data spans a range of beach slopes (0.02, 0.033, 0.05 and 0.10) and deep water wave steepness. The dependence on beach slope is, however, not obvious from the data. The laboratory data are of higher wave steepness ( $H_0/L_0 > 0.7 \times 10^{-3}$ ). The field data corresponds to low wave steepness as the result of low frequency (0.07 Hz) Pacific Ocean swell waves.

The Goda's model reasonably predicts  $H_{1/3}$  and  $H_{max}$  for the higher wave steepness laboratory data; a reason being that much of the laboratory data is taken from Goda (1975), which is the same data used to calibrate the random wave model in the first place. For initially low steepness waves, the Goda model overpredicts  $H_{1/3}$ , but more reasonably predicts  $H_{max}$ . The  $H_{max}$  predictions are based on using a modified, shortened tail, Rayleigh distribution for which the  $H_{max}$  statistics are compensated for by the overprediction of  $H_{1/3}$ . Actual shallow water wave height data compare better, or are even underestimated in the tail, with a Rayleigh distribution as is demonstrated with the field data. Breaking wave heights do not exhibit a shortened or truncated, tail in their distributions.

The depth at breaking corresponding to the breaking wave height compared favorably with the Goda model for all wave steepness values. Depth at breaking exhibited a definite dependence on beach slope as suggested by the Goda model and the data.

## ACKNOWLEDGEMENTS

This research was supported by the Office of Naval Research, Coastal Sciences Branch, under contract numbers NR 388-114 (E.R. Thornton), Naval Postgraduate School Foundation (C.S. Wu) and N00014-75-C-0300 (R.T. Guza). Much of the analysis was performed by D.O. Burch.

Goda, Y., "Irregular wave deformation in the surf zone", Coastal Engineering in Japan 18, 13-26, 1975.

Guza, R.T. and E.B. Thornton, "Local and Shoaled Comparisons of Sea Surface Elevations, Pressures and Velocities", J. of Geophysical Research, 85, 1524-1530, 1980.

Seelig, W.N., "Maximum Wave Heights and Critical Water Depths for Irregular waves in the Surf Zone", Report No. 80-1, U.S. Army Corps of Engineers Coastal Engineering Research Center, 11 p., 1980.

Seelig, W.N., J.P. Ahrens and W.G. Grosskopf, "The Elevation and Duration of Wave Crests", Report No. 83-1, U.S. Army Corps of Engineers Coastal Engineering Research Center, 73 p., 1983.

- Shuto, N., "Nonlinear long waves in a channel of variable section", Coastal Engineering. in Japan, 17, 1-12, 1984.
- Thompson, E.F. and C.L. Vincent, Shallow Water Wave Height Parameters", J. Waterway, Port, Coastal and Ocean Engineering Division, ASCE, 110, 293-298, May, 1984.
- Thornton, E.B. and R.T. Guza, "Transformation of Wave Height Distribution", J. of Geophysical Research, 8, 5925-5938, 1983.
- Thornton, E.B. and R.T. Guza, "Longshore Current due to Random Waves", (Submitted to the J. of Geophysical Research) 1984.
- U.S. Army Corps of Engineers, Shore Protection Manual, Coastal Engineering Research Center, 1977.
- Vincent, C.L., "Energy Saturation of Irregular Waves During Shoaling", (Submitted to J. Waterway, Port, Coastal and Ocean Engineering, Division, ASCE) 1984.



## CHAPTER THREE

### REYNOLDS STRESS IN SURF ZONE

by  
T. Sakai<sup>1)</sup>, I. Sandanbata<sup>2)</sup> and M. Uchida<sup>3)</sup>

#### ABSTRACT

The on-offshore and the vertical components  $u, w$  of the velocity in a surf zone on a uniformly sloping beach in a wave tank were measured simultaneously with a laser-doppler velocimeter under two conditions. The time variation of the Reynolds stress  $-u'w'$  during one wave period is discussed. The Reynolds stress behaves as that in the oscillatory pipe flow does. The magnitude of the terms including the Reynolds stress terms in the on-offshore momentum equation is estimated. The Reynolds stress terms does not play any important role in the on-offshore momentum transfer during one wave period in the surf zone.

#### 1. INTRODUCTION

In the 18th Conference on Coastal Engineering, Cape Town, 1982, an experimental result on the turbulence generated by wave breaking on beaches in wave tanks was presented (Sakai et al. (1982), (6)). The vertical distribution of the turbulent intensity inside the surf zone was shown. The effects of the breaker type on this distribution was discussed. The variation of the vertical distribution of the turbulent intensity during one wave period was also shown. It was explained by extending the turbulent wake theory.

Similar works can be found in Stive (1980) (7), Flick et al. (1981) (2) and Nadaoka et al. (1982) (5). The turbulent intensity is discussed there. In oscillatory pipe flow, the turbulence generated by the shear on the boundary plays an important role in the momentum transfer (3, 4).

The Reynolds stress term is balanced with the local acceleration term and the pressure gradient term.

In the surf zone, it is believed that the turbulence generated by the wave breaking plays a role in the transfer of heat and material such as the sediment and the waste. Whether the turbulence generated by the wave breaking plays a role in the on-offshore momentum transfer during one wave period or not? Aono et al. (1981) (1) estimated the Reynolds stress in a surf zone on a horizontal bed in a wave tank. The data, however, are not sufficient to discuss this problem.

---

1) Assoc. Prof., Dept. of Civil Eng., Kyoto Univ., 606 Kyoto, Japan

2) Engineer, Technical Inst., Hazama-Gumi Ltd., 338 Yono, Japan

3) Engineer, Tokyo Civil Branch, Hazama-Gumi Ltd., 107 Tokyo, Japan

To answer this question, an experiment under two conditions was done in a wave tank. The on-offshore and the vertical components  $u$ ,  $w$  of the velocity inside a surf zone on a beach were measured simultaneously with a laser-doppler velocimeter. The turbulence  $u'$ ,  $w'$  generated by wave breaking was defined. The Reynolds stress  $-u'w'$  was estimated. Its time variation during one wave period and its role in the on-offshore momentum transfer during one wave period are discussed.

## 2. EXPERIMENTS

### 2.1 Experimental Arrangements

The experiment was done in a wave tank in Department of Civil Engineering, Kyoto University. The length of the tank is 30m, the width is 50cm, and the height is 70cm. This wave tank has glass walls on both sides in the central part. At the opposite end of the tank to a wave generator, a beach was installed.

A two-component laser-doppler velocimeter(abbreviated as LDV hereafter) was used to measure the water particle velocity field in the surf zone on the beach. The LDV used was a Spectra Physics Stabilite 15mW He-Ne laser, with a KANOMAX optical system 8143S and two data processors 8015( of the tracker type). This system utilizes the polarization of a laser beam in order to measure simultaneously two components of the velocity.

Since both sides of the wave tank has glass walls, the photo-detector and the other optical system used were set separately on both sides of the tank. The system was operated in fringe mode with forward scatter. Due to limited space beneath the tank, the total optical system was installed on a frame hanging over the tank. This frame could move in both a vertical and a longitudinal direction.

The length of the laser tube was 1.0m, and the the length of the optical system was 60cm. It made the frame unstable if both the laser tube and the optical system were set horizontally in one line normal to the tank. The laser tube was, therefore, set vertically, and the laser beam was reflected horizontally using a mirror.

Two wave gauges were used to measure the water level variation in the surf zone.

### 2.2 Experimental Conditions

The experiment was done under 2 conditions. The experimental conditions of 2 cases are listed in Table 1.  $i$  is the beach slope,  $h_1$  is the still water depth in the uniform depth region in front of the beach,  $T$  is the wave period,  $h_b$  is the still water depth at the wave breaking point,  $H_b$  is the breaking wave height,  $w$  is the surf zone width. In both cases, the waves broke on the beach.  $H_0/L_0$  is the deepwater wave steepness. The breaker types were a spilling breaker in case 1 and a plunging breaker in case 2. Fig.1 shows a comparison

of the size of the surf zone of two cases.

### 2.3 Experimental Procedures

The measurement of the velocity in case 1 was done in 6 positions. The deepest position was located 0.5m shoreward from the breaking point. The distance between the neighbouring positions was 0.5m. The thin vertical lines in Fig.1 show these positions. In case 2, the measurement of the velocity was done in 5 positions. The deepest position was located 45cm shoreward from the breaking point. The distance between the neighbouring positions was 5cm. The measurement in case 2 was done in a rather limited region. In each positions, the velocity was measured at about 7 levels from 1cm above the bottom to near the wave trough level.

Table 1 Experimental Conditions

case	i	$h_1$ (cm)	T (sec)	$h_b$ (cm)	$H_b$ (cm)
1	1/31	35.0	1.17	18.0	12.8
2	1/20	35.0	1.82	14.0	13.0

case	W (cm)	$H_0/L_0$	breaker type	instrument
1	530	0.063	spilling	LDV
2	275	0.019	plunging	LDV

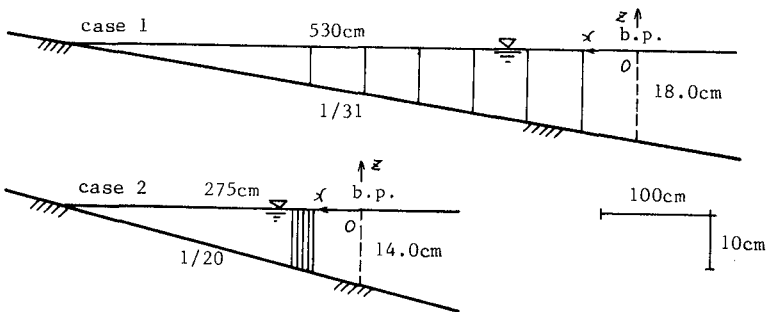


Fig.1 Surf Zone of 2 Cases

### 3. DATA ANALYSIS

The outputs from the wave gauges and the LDV were digitized every 0.01sec. The digitized data of the water level at the velocity measuring point, the on-offshore velocity, the vertical velocity and two dropout signals for two velocity components were plotted graphically. The time length of the plotted data was 48sec in case 1 and 70sec in case 2.

The time intervals in which the signal from the processor of the LDV did not drop out were determined. In these non-dropout intervals, the data of the two components of the velocity were moving averaged. The time width of this moving averaging was 0.1sec in case 1 and 0.2sec in case 2 (Fig.2). The turbulence ( $u'$  and  $w'$ ) was defined as the deviation of the original velocity from this moving averaged velocity (Fig.2).

At every 0.01sec, a cross product of  $u'$  and  $w'$  can be calculated. This quantity with a minus sign may be called "an instantaneous Reynolds stress". In oscillatory pipe flow, the Reynolds stress is usually defined as an ensemble average of this instantaneous Reynolds stress at a fixed phase for many waves (3, 4). The Reynolds stress is, however, originally defined as a time average of the instantaneous Reynolds stress. The Reynolds stress was therefore defined here as a moving average of the instantaneous Reynolds stress. The time width of this moving averaging was 0.1sec in case 1 and 0.2sec in case 2. As mentioned in the Introduction, here we are interested in the role of the turbulence during one wave period. The choice of this time width depends on this interest.

The Reynolds stress defined in this way was obtained every 0.01 sec in the non-dropout intervals for all waves. Now one wave period was divided into 12 sections of 0.1sec interval in case 1 and 18 sections in case 2 (In Fig.2, which is only a sketch, one wave period is divided into 10 sections.). To see an average trend of the time variation of the Reynolds stress, an average value of the Reynolds stress values for all waves in each section was calculated.

### 4. TIME VARIATION OF REYNOLDS STRESS DURING ONE WAVE PERIOD

Fig.3 shows an example of the time variation of the Reynolds stress during one wave period at several levels in the position 2.0m shoreward from the breaking point in case 1. The top figure is an averaged wave profile during one wave period. One clear trend is seen at the upper two levels. At  $z = -1.7\text{cm}$ , the Reynolds stress changes from negative to positive after the crest phase. At  $z = -3.2\text{cm}$ , a similar change occurs before the crest phase.

Fig.4 is a different expression of Fig.3, the time variation of the vertical distribution of the Reynolds stress. Above mentioned trend is seen in the upper region near the crest phase. Aono et al. (1981)(1) reported a similar time variation of the Reynolds stress defined in a different way in a surf zone on a horizontal bed in a wave tank.

In oscillatory pipe flow, it was found that the Reynolds stress takes a maximum when the mean flow velocity decreases (Hayashi et al. (1980) (3) and Hino et al. (1980) (4)). It seems that the Reynolds stress generated by the wave breaking in surf zone behaves as that in the oscillatory pipe flow does. Fig. 5 shows an example of the time variation of the Reynolds stress in the position 55cm shoreward from the breaking point in case 2. The trend seen in Fig. 3 is more evident.

The turbulence in the oscillatory pipe flow is a wall turbulence generated by the shear on the boundary. The turbulence in the surf zone is rather a free turbulence generated by the instability of the water surface. Considering this fact, there is no positive reason why the Reynolds stress in the surf zone behaves as that in the oscillatory pipe flow does.

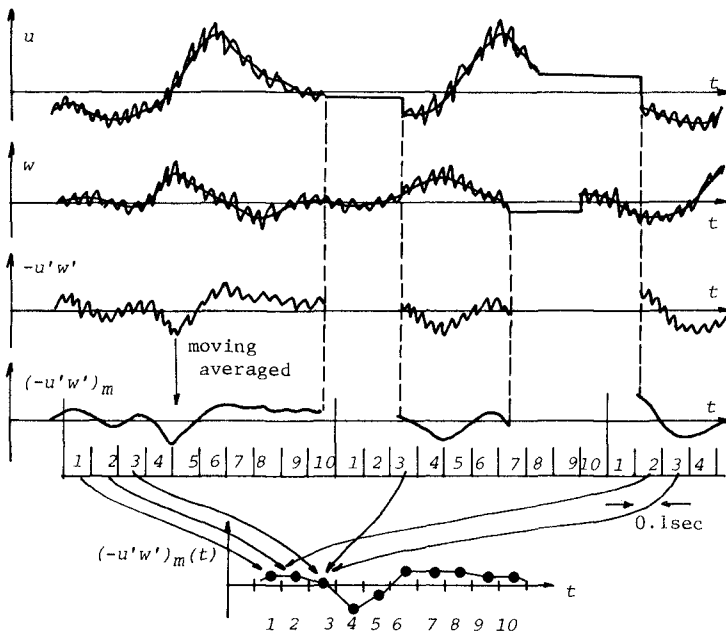


Fig. 2 Definition of Reynolds Stress

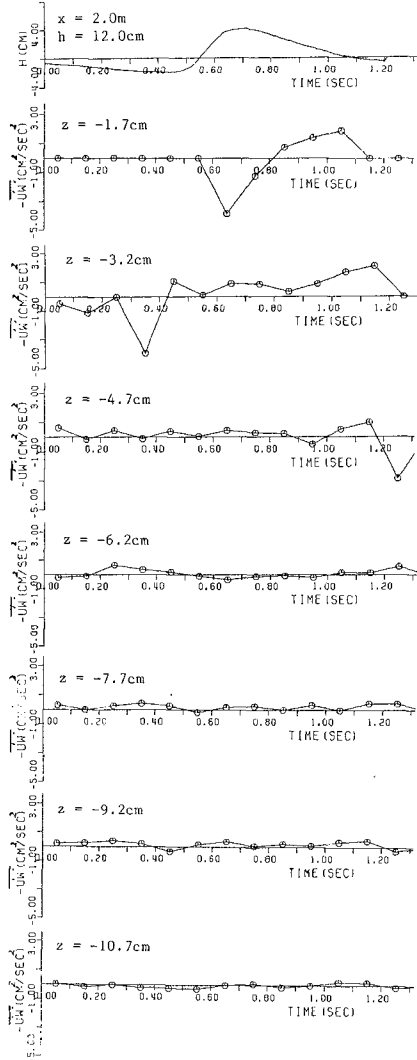


Fig.3 Time Variation of Reynolds Stress during One Wave Period(Case 1)

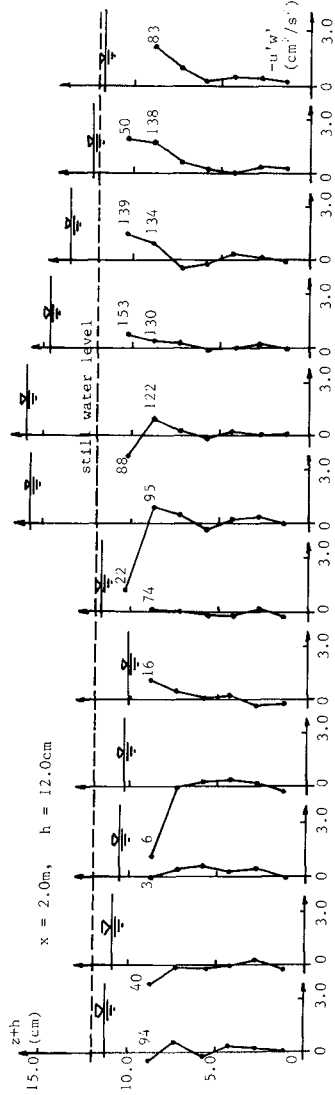


Fig.4 Time Variation of Vertical Distribution of Reynolds Stress during One Wave Period (Case 1)

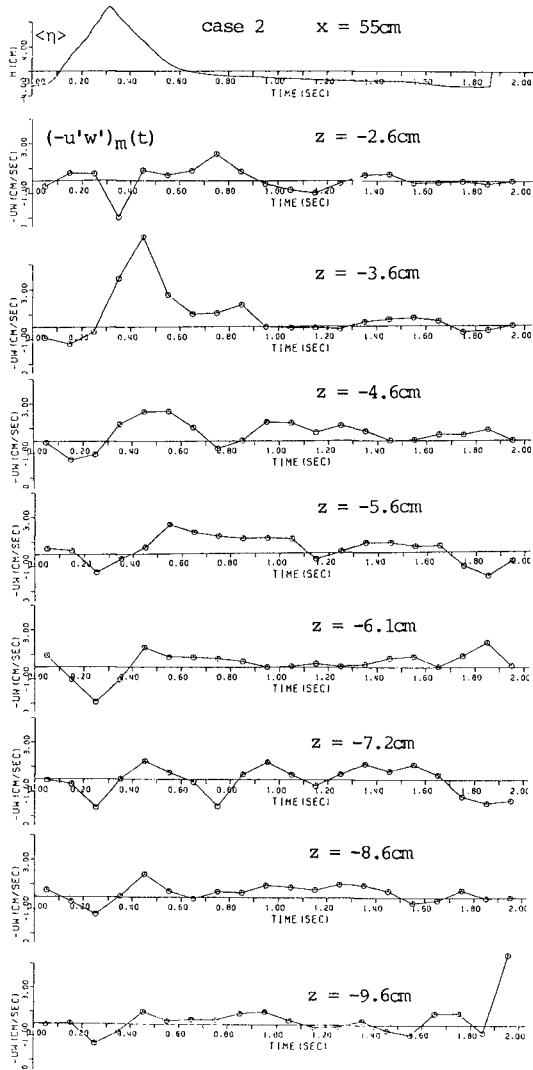


Fig.5 Time Variation of Reynolds Stress during One Wave Period(Case 2)



## 5. REYNOLDS STRESS TERM IN ON-OFFSHORE MOMENTUM EQUATION

### 5.1 Estimation of Magnitude of Terms

The on-offshore momentum equation is given as follows :

$$\frac{\partial u}{\partial t} + u \frac{\partial u}{\partial x} + w \frac{\partial u}{\partial z} = \frac{1}{\rho} \frac{\partial}{\partial x} (-p - \rho \overline{u'^2}) + \frac{1}{\rho} \frac{\partial}{\partial z} (-\rho \overline{u'w'}) \quad (1)$$

, where  $t$  is the time,  $x$  and  $z$  are two horizontal coordinates,  $u$  and  $w$  are two velocity components in  $x$  and  $z$  directions,  $\rho$  is the density of the fluid,  $p$  is the pressure, and  $-\rho \overline{u'^2}$  and  $-\rho \overline{u'w'}$  are two Reynolds stresses.

The magnitude of each term in Eq.(1) at one measuring point in case 2 is estimated by using the data obtained in the experiment. This point is located 5.5cm below the still water level and 60cm shoreward from the breaking point. As explained in 3., the Reynolds stress  $-\overline{u'w'}$  is obtained every 0.1sec during one wave period. To compare the magnitude of each term in Eq.(1) every 0.1sec during one wave period, the values of  $u$ ,  $w$  and  $\overline{u'^2}$  are estimated every 0.1sec as follows : The values of  $u$  and  $w$  in each section of 0.1sec for all waves were averaged, and these averaged values in each section were used as  $u$  and  $w$  in Eq.(1). A root-mean-square value of  $u'$  value in each section for all waves was calculated. This r.m.s. value was used as  $\overline{u'^2}$  in Eq.(1).

The value of the local acceleration term was estimated from a difference between the values of  $u$  in the neighbouring two sections. The value of the gradient in  $x$  direction was estimated from a difference between the values at this point and at the nearest point in the neighbouring offshore position. The phase difference between the values at two points was taken into account. The value of the gradient in  $z$  direction was estimated from a difference between the values at this point and at the point 1.0cm below in the same position. The value of the pressure gradient term was not able to estimate due to a trouble of the wave gauges.

### 5.2 Comparison of Magnitude of Terms

Table 2 shows the result of the calculation. The time origin is at the crest phase. It is clear that the local acceleration term is large. It is supposed that the local acceleration term is balanced with the pressure gradient term which was not able to estimate. In the time interval  $t > 0.65$ sec (the wave trough phase), however, the local acceleration term becomes as small as the other terms. Fig.6 shows the time variation of two convection terms and two Reynolds stress terms. It is found that two Reynolds terms are smaller than two convection terms. Only in  $0.5$ sec  $< t < 1.0$ sec, two Reynolds stress terms are as large as two convection terms.

For case 1, a simpler comparison of the magnitude of the convection term  $u \partial u / \partial x$  and the Reynolds stress term  $\partial \overline{u'w'} / \partial z$  was done. The selected measuring point is located 4.2cm below the still water level and 1.5m shoreward from the breaking point. The comparison was

made at an intermediate phase between the zero-up crossing phase and the creast phase. At this phase,  $u \approx 20\text{cm/sec}$ .

The distance between this point and the neighbouring point is too long to estimate the  $x$  gradient. So the value of  $\partial u/\partial x$  was estimated by using the small amplitude wave theory with the values of the wave period of 1.2sec, the still water depth of 15cm and the velocity amplitude of 30cm/sec. The estimated value of the convection term  $u\partial u/\partial x$  is 14cm/sec. The Reynolds stress term  $\partial u'w'/\partial z$  is estimated 4cm/sec, from the difference between the values at this point and at the neighbouring point in the same position. The Reynolds stress term is small again compared with the convection term.

Table 2 Comparison of Magnitude of Terms in On-Offshore Momentum Equation during One Wave Period in Surf Zone (Case 2, 5.5cm below still water level and 60cm shoreward from breaking point)

$t$ (sec)	$\frac{\partial u}{\partial t}$	$u \frac{\partial u}{\partial x}$	$w \frac{\partial u}{\partial z}$	$\frac{\partial u'^2}{\partial x}$	$\frac{\partial u'w'}{\partial z}$
		(cm/sec <sup>2</sup> )			
-0.25	-----	5.3	1.4	-0.3	0.4
-0.15	91.8	0.3	9.9	-1.1	0.4
-0.05	135.8	-5.7	10.5	0.1	0.7
0.05	49.9	1.3	1.9	0.5	1.1
0.15	-20.0	8.8	-1.2	1.4	-0.0
0.25	-56.3	4.4	-6.0	0.9	0.4
0.35	-52.3	-0.5	0.5	0.7	0.9
0.45	-58.8	0.5	3.3	0.6	1.3
0.55	-25.3	3.1	1.2	0.0	-0.2
0.65	-6.7	3.8	0.4	0.6	-1.1
0.75	13.4	1.7	-0.1	1.2	0.2
0.85	-0.3	1.7	0.4	0.1	1.1
0.95	-4.7	1.8	0.8	0.3	1.4
1.05	-24.3	2.9	-0.0	0.6	1.3
1.15	-5.6	0.6	-3.5	0.2	0.7
1.25	-8.2	-2.1	-9.3	-0.2	0.0
1.35	-25.6	-1.3	-5.1	0.3	-0.1
1.45	-12.2	----	-5.3	----	0.4

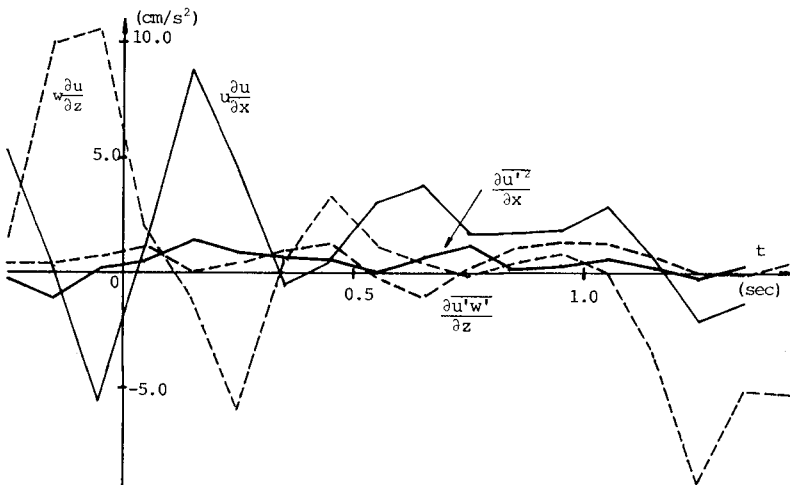


Fig. 6 Time Variation of Convection Terms and Reynolds Stress Terms in On-Offshore Momentum Equation during One Wave Period (Case 2, 5.5cm below still water level and 60cm shoreward from breaking point)

## 6. CONCLUSIONS

The on-offshore and the vertical components  $u$ ,  $w$  of the velocity in a surf zone on a beach were measured simultaneously with a laser-doppler velocimeter in a wave tank under two conditions. The time variation of the Reynolds stress  $-\overline{u'w'}$  during one wave period and its relative importance in the on-offshore momentum equation are discussed. The following conclusions are obtained :

- (1) The Reynolds stress  $-\overline{u'w'}$  changes from negative to positive near the crest phase. This is similar to the change of the Reynolds stress in the oscillatory pipe flow.
- (2) Since the turbulence in the surf zone is a free turbulence generated by the instability of the water surface, there is no positive reason why the Reynolds stress in the surf zone behaves as that in the oscillatory pipe flow.
- (3) The magnitude of the Reynolds stress terms in the on-offshore momentum equation during one wave period are small compared with the local acceleration term and the convection terms.
- (4) The turbulence generated by wave breaking has no significant role in the on-offshore momentum transfer during one wave period in the surf zone.

## 7. REFERENCES

- 1) Aono, T., Oohashi, M. and Hattori, M. : Experimental study on turbulence near wave breaking point, Proc. of the 13th Symp. on Turbulence, 1981, pp. 180-183, 1981(in Japanese).
- 2) Flick, R.E., Guza, R.T. and Inman, D.L. : Elevation and velocity measurements of laboratory shoaling waves, Jour. of Geophysical Res., Vol.86, No.C5, pp.4149-4160, 1981.
- 3) Hayashi, T., Oohashi, M. and Takeyasu, S. : Experimental study on boundary layer of oscillatory flow, Proc. of the 12th Symp. on Turbulence, 1980, pp.83-90, 1980(in Japanese).
- 4) Hino, M., Kashiwayanagi, M., Nakayama, T. and Hara, T. : Turbulence generation and energy transfer mechanism in oscillatory flow, Res. Rep. No.27, Dept. of Civil Eng., Tech. Univ. of Tokyo, pp.1-66, 1980 (in Japanese).
- 5) Nadaoka, K. and Kondoh, T. : Laboratory measurements of velocity field structure in the surf zone by LDV, Coastal Eng. in Japan, Japan Soc. of Civil Eng., Vol.25, pp.125-146, 1982.
- 6) Sakai, T., Inada, Y. and Sandanbata, I. : Turbulence generated by wave breaking on beach, Proc. 18th Conf. on Coastal Eng., ASCE, Vol.1, pp.3-21, 1982.
- 7) Stive, M.J.F. : Velocity and pressure field of spilling breakers, Proc. 17th Conf. on Coastal Eng., ASCE, Vol.1, pp.547-566, 1980.

## CHAPTER FOUR

### WAVE ATTENUATION AND SET-UP ON A BEACH

by

I. A. Svendsen <sup>\*</sup>)

#### ABSTRACT

A theoretical two-dimensional model for wave heights and set-up in a surf zone is described and compared to measurements. The integral wave properties energy flux  $E_f$ , and radiation stress  $S_{xx}$  are determined from crude approximations of the actual flow in surf zone waves. Some physical aspects of the outer region are discussed and found to agree with our knowledge of the waves seawards and shorewards of this region.

#### 1. INTRODUCTION

This paper examines waves in the surf zone on a beach with no long-shore bars. We also restrict the considerations to regular waves with constant period  $T$ . The theoretical results are compared with measurements on a plane beach but in general the results should be applicable to any bottom topography provided the waves continue to break shoreward of the breaking point.

We only consider integral properties of the waves and conservation equations time averaged over a wave period. Hence the only information that can be obtained from the model is the variation of wave height, the associated energy dissipation and the set-up. In this respect the model to be described follows a long tradition of earlier investigations, although some of those only consider the wave height variation, not the set-up. The model deviates, however, from earlier contributions in the way the basic properties of the broken waves are determined.

The time averaged properties we need for the broken waves are energy flux,  $E_f$ , radiation stress,  $S_{xx}$ , and energy dissipation  $D$ . In previous models various non breaking wave theories have been used to determine  $E_f$  and  $S_{xx}$  in combination with either elaborate turbulent mixing models (Horikawa & Kuo, 1966) or energy dissipation equal to or related to the dissipation in a bore of the same height. References are Le Mehauté (1962), Divoky et al. (1968), James (1974). A somewhat different approach has been used by Dally (1980) who assumes the energy dissipation is proportional to  $E_f - E_{f,0}$  where  $E_{f,0}$  represents the energy flux in the smallest possible breaking wave which is empirically determined to be about  $H = 0.4 h$ . Sine wave theory is used for the wave integral properties.

The model presented here follows the numerical part of the solution described by Svendsen (1984) who also showed, however, that an analytical solution is possible under certain conditions. The following presentation also includes a discussion of the conditions at the shoreline.

\* Inst. of hydrodynamics and Hydraulic Engrg. Techn. Univ., DK-2800 Lyngby, Denmark.

2. THE BASIC EQUATIONS

We consider the two-dimensional problem sketched in Fig. 1 which also shows the definition of variables.

The three basic equations to be satisfied represent the conservation of mass, momentum and energy, integrated over depth and averaged over a wave period  $T$ .

The conservation of mass will not be invoked explicitly but used in the way the particle velocities in the wave are determined.

We consider regular progressive waves only and hence the momentum equation simply reads:

$$\frac{\partial S_{xx}}{\partial x} = -\rho g (h_0 + b) \frac{\partial b}{\partial x} \tag{2.1}$$

where  $S_{xx}$  is the radiation stress defined (exactly) by:

$$S_{xx} = F_m + F_p$$

$$F_m = \int_{-h_0}^{\eta+b} \rho u^2 dz ; F_p = \int_{-h_0}^{\eta+b} \rho p dz - \frac{1}{2} \rho g \overline{\eta^2} \tag{2.2}$$

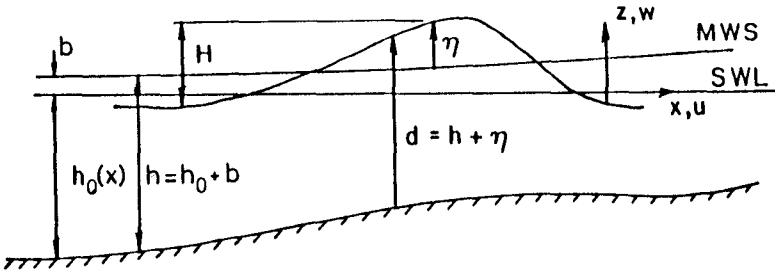


Fig. 1. Definition sketch.

with  $\overline{\quad}$  denoting average over a wave period, and the dynamic pressure  $p_D$  given by:

$$p_D = \rho g (z-b) + p \tag{2.3}$$

i.e.  $p_D$  is defined on the basis of the local mean water depth. Notice that  $\eta$  is measured from the level  $z = b$  so that  $\overline{\eta} = 0$ . In (2.1) we have also neglected the mean bed shear stress.

Using  $E_f$  for mean energy flux and  $D$  for the gain in energy (i.e.  $D < 0$  for dissipation), the energy equation (also averaged over a wave period) becomes:

$$\frac{\partial E_f}{\partial x} = D \tag{2.4}$$

The definition of  $E_f$  is

$$E_f = \int_{-h_0}^{\eta+b} \left[ p_D + \frac{1}{2} \rho (u^2 + v^2 + w^2) \right] u \, dz \quad (2.5)$$

(which with  $p_D$  from (2.3) presumes no net current)

In both eqs. (2.2) and (2.5) velocities and pressures are the instantaneous values, so that these definitions also cover the turbulent flow situations in a surf zone.

In equation (2.4) we may choose at will the division between which type of energy belongs to  $E_f$ , and which is already considered lost (and hence belongs to  $D$ ). Since energy once turned into turbulence will be dissipated to heat mostly with one wave period we choose to consider turbulent energy as energy already dissipated.

This highly simplifies the computations since it implies that we do not have to keep trace of the amount of turbulent energy present at the different phases of the breaking process.

The drawback of this is of course that we cannot evaluate the contribution to the momentum balance from the turbulent velocity fluctuations ( $u', v', w'$ ). These contributions, however, are proportional to  $\tilde{u}'^2 - \tilde{w}'^2$  where  $\tilde{\phantom{x}}$  represents ensemble averaging. And the measurements of Stive & Wind (1982) shows that these contributions only increase the radiation stress by a few per cent, mainly because  $u'$  and  $w'$  are not very different.

The conclusion of this is that  $E_f$  in (2.4) is taken as the ordered wave energy defined as

$$E_f = E_{f,w} = \int_{-h_0}^{\eta+b} \left( \tilde{p}_D + \frac{1}{2} \rho (\tilde{u}^2 + \tilde{w}^2) \right) \tilde{u} \, dz \quad (2.6)$$

and  $D$  represents minus the production of turbulent energy.

To facilitate the analysis we introduce non-dimensional measures of both  $E_{f,w}$ ,  $S_{xx}$  and  $D$  using the definitions

$$B = E_{f,w} / (\rho g c H^2) \quad (2.7)$$

$$P = S_{xx} / \rho g H^2 \quad (2.8)$$

$$D = D / (4hT / \rho g H^3) \quad (2.9)$$

where  $T$  is the wave period and  $c$  the speed of propagation for the wave.

These definitions are inspired by our knowledge from, say, linear wave theory which for  $B$  would yield the result  $c(1+G)/8$  where  $(G = 2kh/\sinh 2kh)$  and for  $P$  similarly  $P = (1+2G)/16$ . The form chosen for the definition of  $D$  is related to the energy dissipation in a bore or hydraulic jump.

Thus the idea behind the dimensionless quantities  $B$ ,  $P$ , and  $D$  is that the major part of the variation of  $E_{f,w}$ ,  $S_{xx}$  and  $D$  has been factored out so that  $B$ ,  $P$ , and  $D$  may be expected to vary only slightly.

Substituting into (2.1) and (2.4) we therefore find the equations

$$\frac{d}{dx} (H^2 P) = - (h_0 + b) \frac{db}{dx} \quad \text{and} \quad (2.10)$$

$$\frac{d}{dx} (c H^2 B) = \frac{H^3}{4hT} D \quad (2.11)$$

Thus, provided we can describe B, P, D and c in terms of  $h_0$ , b, T and H then (2.10) and (2.11) represent two simultaneous equations from which  $E(x)$  and  $b(x)$  may be determined.

3. THE INTEGRAL PROPERTIES OF SURF ZONE WAVES

The ideas used in the determination of the three quantities B, P, and D are associated with the observation (see e.g. Svendsen et al., 1978) that from a point somewhat after breaking the waves become bore-like irrespective of the initial type of breaking.

B & D are determined from the definitions of  $E_{F,W}$  and  $S_{XX}$ , i.e. (2.6) and (2.2), respectively. In essence this means that we need relevant approximations for  $\tilde{u}$ ,  $\tilde{w}$  and  $\mathcal{D}_D$  in these expressions.

The important feature dominating the bore-like wave motion is the surface roller, which in essence is a volume of water carried shorewards with the breaker: Figure 2a shows a typical situation, and also indicates a typical velocity distribution along a vertical at the front of the wave.

The roller is defined as the recirculating part of the flow above the dividing streamline (in a coordinate system following the wave). Since it is resting on the front of the wave, the absolute mean velocity in the roller equals the propagation speed c for the wave, and in the following we use this value for the velocity in the roller, neglecting the z-variation.

In the present two-dimensional study we assume a zero net mass flux which of course implies that there is a return flow compensating for the surface drift.

From observations we know that in the inner region the change in wave shape is slow so the instantaneous volume flux:

$$Q = \int_{-h_0}^{\eta+b} u(x,z,t) dz \tag{3.1}$$

may for  $\bar{Q} = 0$  be determined as:

$$Q = c\eta = Ud \tag{3.2a,b}$$

where the surface profile is specified so that  $\bar{\eta} = 0$ . U is the wave particle velocity averaged over depth.

Thus assuming the particle velocity distribution shown in Fig. 2b we are able from (3.2) at any phase of the wave to express the velocity  $u_0$  below the roller in terms of  $\eta$  and  $e$  ( $e = e(x,t)$  being the vertical thickness of the roller). The resulting full expression is

$$u_0 = c \frac{\eta - e}{d - e} \tag{3.3}$$

where  $e = 0$  away from the wave front. We also assume that  $w^2 \ll u^2$  can be neglected.

The pressure is assumed to be hydrostatic. This is of course not quite correct, but in combination with the rather crude assumptions for u and in view of the very small deviations from hydrostatic pressure actually measured by Stive (1980) this is the most relevant approximation. Thus we have

$$P_D = \rho g \eta \tag{3.4}$$



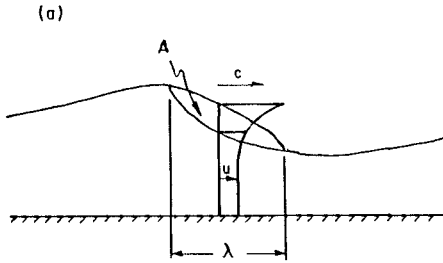


Fig. 2a. Velocity distribution under the front of a breaking wave.

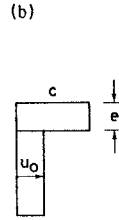


Fig. 2b. Approximations for the horizontal velocities in the surf zone waves.

When these approximations are substituted into (2.6) we find after some manipulations and further omission of small terms, that the leading approximation for B may be written

$$B = B_0 + \frac{1}{2} \frac{A}{H^2} \frac{h}{L} \quad (3.5)$$

where

$$B_0 \equiv \overline{(\eta/H)^2} \quad (3.6)$$

and A is the vertical cross sectional area of the roller (see Fig. 2a). The mentioned omission of small terms are based on the following approximations

$$\overline{(\eta/H)^3}, \overline{(\eta/H)^4} \ll \overline{(\eta/H)^2}$$

$$\text{and } \overline{\eta^3 e/h^4} \ll \overline{(\eta/H)^2}$$

The "wave length" L in (3.5) is defined as  $L(x) = c(x) T$ . Hence L is not the distance between two consecutive wave crests.

We have also assumed that  $c \sim \sqrt{gh}$  based on the measurements by Svendsen et al (1978) who found  $c \sim 1.05 - 1.10 \sqrt{gh}$ .

A similar procedure yields P by substitution of the assumptions for u and  $p_D$  into (2.2). The result may be written

$$P = \frac{3}{2} B_0 + \frac{A}{H^2} \quad (3.7)$$

Here the small terms omitted are of the type  $\overline{(e/H)^2}$ ,  $\overline{ne/\eta^2}$ .

Experimental information on the roller area A is only available for waves breaking behind a hydrofoil (Duncan, 1981). Fig 3 shows a plot of Duncan's data for A which suggests that we can use the approximation

$$A = 0.9 H^2 \quad (3.8)$$

by which B and P reduce to

$$B = B_0 + 0.45 h/L \quad (3.9)$$

$$P = \frac{3}{2} B_0 + 0.9 h/L \quad (3.10)$$

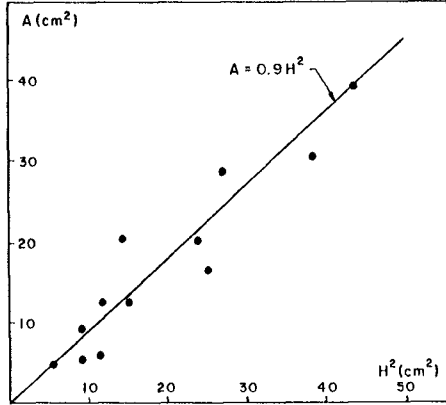


Fig. 3. The cross sectional area for A for the roller. Measurements by Duncan 1981.

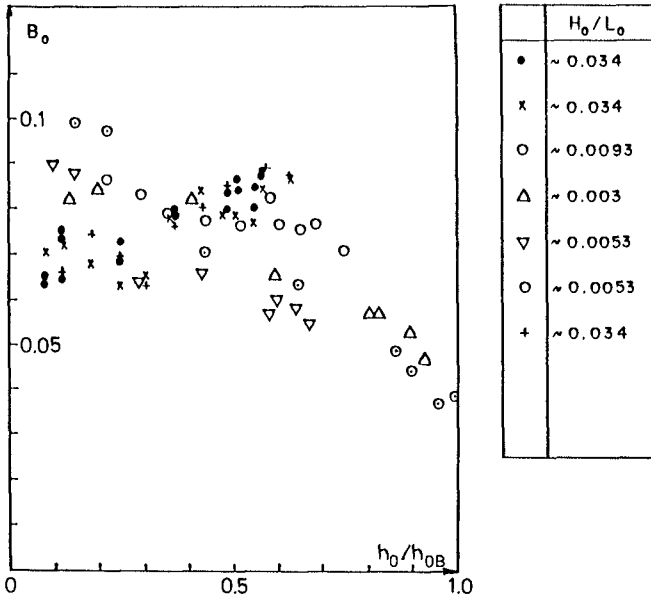


Fig. 4. Measured values of  $B_0$  defined by (3.6.). Hansen (1982).

The energy dissipation  $D$  was analysed theoretically by Svendsen et al (1978) and more explicitly by Svendsen & Madsen (1981). The conclusion which can be derived from the expression they find for  $D$  is that the energy dissipation will normally be almost equal to that in a hydraulic jump of the same height. Deviations (in particular in the upward direction) depend on the detailed velocity and pressure distributions in the wave - particularly in the wave trough, but normally they do not seem to exceed 20%.

For the present rather crude model it is natural simply to use  $D$  equal to the value in a hydraulic jump of the same height, and this yields

$$D = \frac{-h^2}{d_c d_t} \quad (3.11)$$

where  $d_c$  and  $d_t$  are the water depths under wave crest and wave trough, respectively.

It is convenient to express  $d_c$  and  $d_t$  in terms of the crest elevation  $\eta_c$  and the wave height  $H$ . With

$$d_c = h + \eta_c, \quad d_t = h + \eta_c - H$$

(3.11) may be written:

$$D = - \left[ \left( 1 + \frac{\eta_c}{H} \frac{H}{h} \right) \left( 1 + \frac{H}{h} \left( \frac{\eta_c}{H} - 1 \right) \right) \right]^{-1} \quad (3.12)$$

which shows that for fixed  $(\eta_c/H)$ ,  $D$  depends slightly on  $H/h$ . Figure 5 shows the variation and Fig 6 gives values of  $\eta_c$  from the experiments by Hansen quoted above. As was the case for  $B_0$  the results for  $\eta_c/H$  show significant scattering but in the inner region of the surf zone the value is mostly 0.6-0.7 which from Fig. 5 is seen to represent a  $D$  nearly independent of  $H/h$ .

Figure 5 also shows that  $D$  only varies slightly with  $\eta_c/H$ . In other words the primary variation of the energy dissipation is represented by the  $H^3/h$  dependence already accounted for in the definition (2.9).

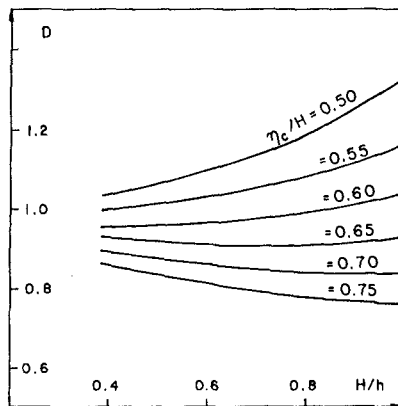


Fig. 5. The variation of  $D$  with  $H/h$  and  $\eta_c/H$  according to (3.12).

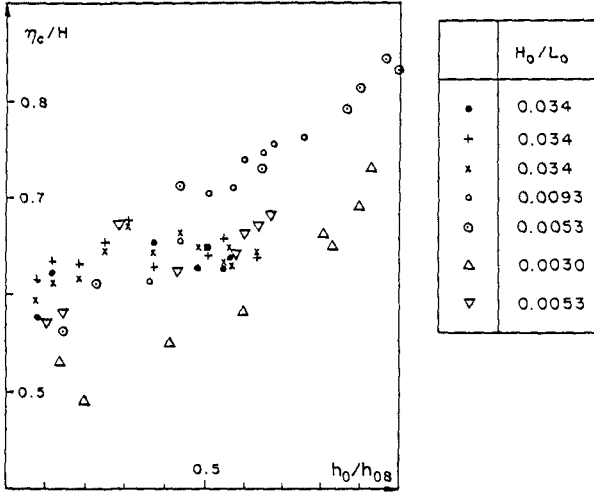


Fig. 6. Measurements of  $\eta_c/H$  in the surf zone. Hansen (1982).

4. COMPARISON WITH MEASUREMENTS

The outer and the inner region

The original concept of an outer (transition) region and an inner (bore) region was primarily based on the visual observations of wave behaviour after breaking (see Svendsen et al., 1978). The impression is one of a gradual change towards the bore shape found in the inner region. Consequently, no attempt was made to define a proper limit between the two regions, and wave height measurements truly do not suggest a natural definition.

The situation is quite different, when the variations in mean water level are considered. Figure 7 shows some examples from Hansen and Svendsen (1979) covering a wide range of deep water steepnesses. Most of them exhibit a marked change in the slope of the mean water level at some distance shoreward from the breaking point. A similar variation can also be seen in other investigations such as Bowen et al. (1968) and Stive and Wind (1982). The mean water level is horizontal or weakly sloping after the start of breaking over a distance of 5-8 times the breaker depth and then a rather sharp increase in slope occurs. The distance of nearly horizontal mean water level is comparable to the distance of the most obvious transformations of the wave shape following after the initiation of breaking, and so it will be coherent with the original concept to *define* the limit between the outer and the inner region as the point where the slope of the mean water level changes. In the following this is termed the *transition point*.

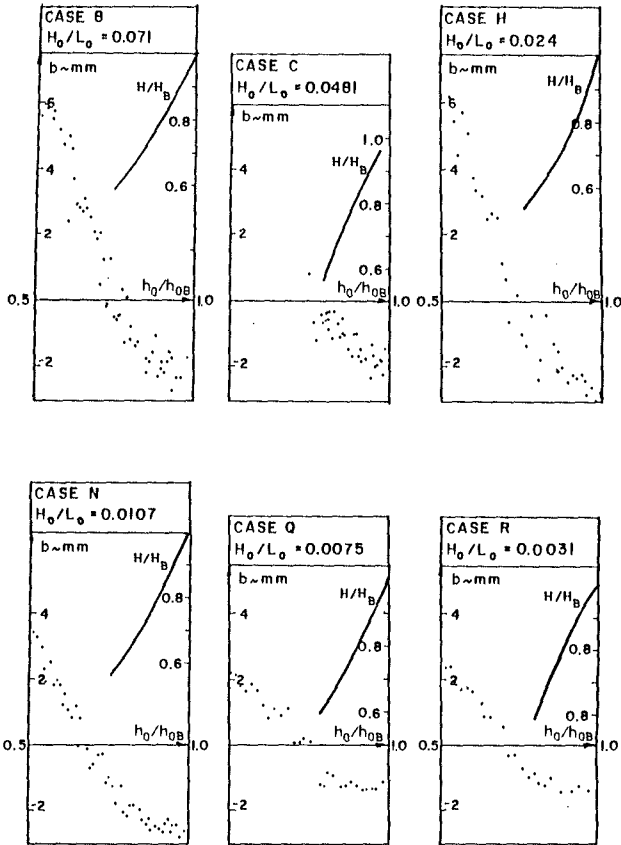


Fig. 7. Measurements of the mean water level shoreward of the breaking point. The figure also shows the simultaneous change in wave height relative to the value  $H_B$  at the breaking point (Measurements from Hansen & Svendsen, 1979).

Wave conditions in the inner region

Physical explanations for these changes are sought in section 5. First, however, we notice that since the results derived above for the parameters B, P and D are based on the wave properties in the inner zone, comparisons with experimental data should start at the transition point.

Numerical solution of equations (2.10) and (2.11) using (3.9), (3.10) and (3.12) then yields results for  $H$  and  $b$  in the inner surf zone. In the computations we have neglected the variation of  $B_0$  and  $\eta_c/H$  using the constant values  $B_0 = 0.075$  and  $\eta_c/H = 0.6$ . This, however, may not always be sufficient for obtaining reliable results but a more systematic investigation of the variation of  $B_0$  and  $\eta_c/H$  with wave parameters and bottom topography is required. For  $h/L$  is used  $T\sqrt{g/h}$  corresponding to  $c = \sqrt{gh}$ , with  $h = h_0 + b$ .

*Discussion of results*

Figures 8, 9, and 10 show a comparison with results for three rather different wave steepnesses, all on a plane slope 1/34.3. In general the agreement is quite good, particularly for the set-up. The latter is of particular interest because the calculations show that  $b$  is much more sensitive to the assumptions made than is the wave height variation. As can be expected from what was said above about  $D$ , the  $H$  variation turns out to be virtually independent of the choice of  $\eta_c/H$ .

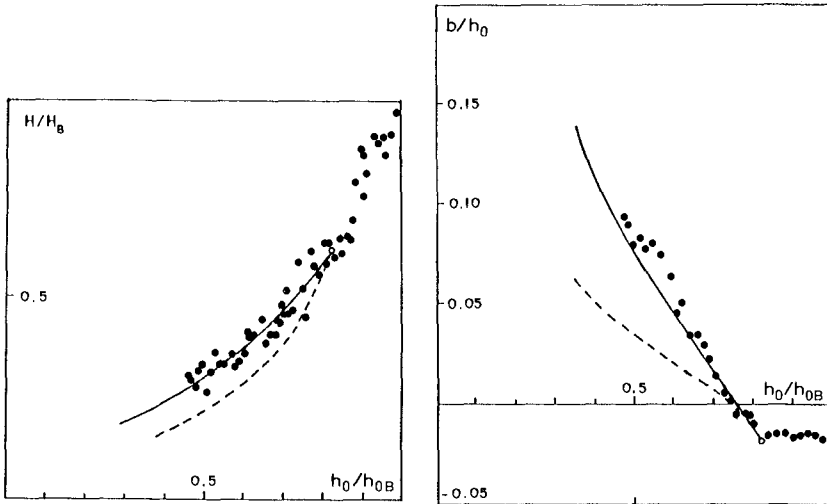


Fig. 8. Wave heights and set-up for a wave with deep water steepness  $H_0/L_0 = 0.071$  - theory using eqs. (3.9) and (3.10) - - theory without a surface roller;  $\cdot$  measurements by Hansen and Svendsen (1979), Case B.

It is noticed that in some of the cases the  $H$ -variation is slightly less curved than corresponding to the best fit of measurements, and the values of  $H$  become a little too large. This can be adjusted by using a value of  $D$  perhaps 20-30% larger than given by eq. (3.12), which is quite consistent with the results reported earlier (see Svendsen et al., 1978; Svendsen and Madsen, 1981) that the actual energy dissipation in a surf zone wave is generally larger than in a hydraulic jump of the same height.

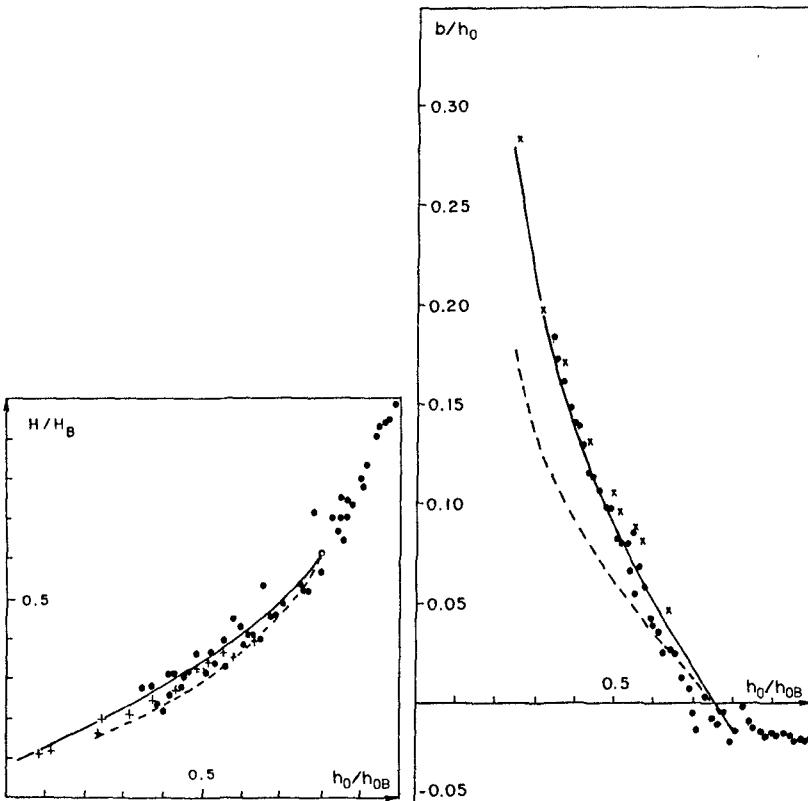


Fig. 9. Wave heights and set-up for a wave with deep water steepness  $H_0/L_0 = 0.024$ . - theory using eqs. (2.10) and (2.11) --- theory without a surface roller; • Measurements by Hansen & Svendsen (1979) Case H.+ Measurements by Hansen (1982).

In Fig. 8-10 are also included results obtained by omitting the surface roller (dotted curve corresponding to  $B = B_0$  and  $P = 3/2 B_0$ ). The effect is quite appreciable. On the other hand, considering that the presence of the surface roller significantly increases the energy flux and radiation stress, the difference between the full and the dotted lines in these figures indicates that the effect of also including turbulence, deviation from static pressure, etc. would hardly be discernible.

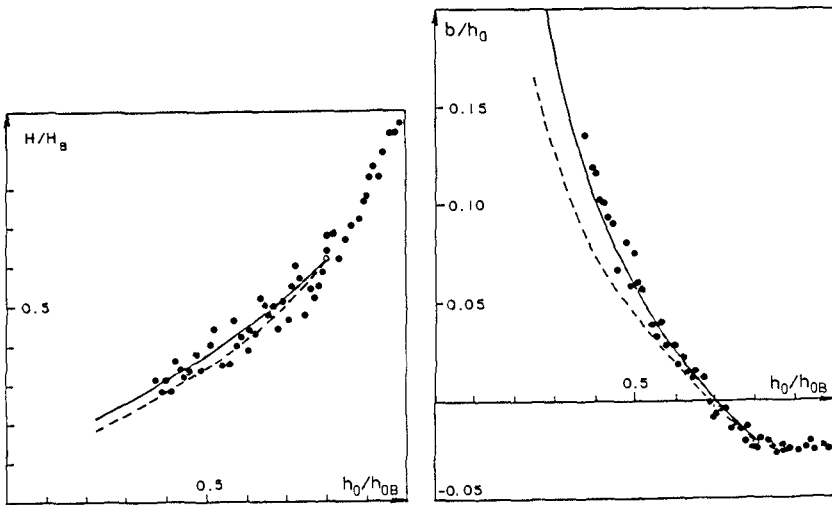


Fig. 10. Wave heights and set-up for a wave with deep water steepness  $H_0/L_0 = 0.010$ . — theory using eqs. (2.10) and (2.11); - - theory without a surface roller; • measurements by Hansen and Svendsen (1979), Case N.

*The situation at the shoreline*

Svendsen (1984) found that for  $D$  and  $B$  constant an analytical solution can be obtained to the energy equation. This solution is given by

$$\frac{H}{h} = \frac{H_r}{h_r} \frac{1}{h' \frac{5}{4} [1 + KD(h'^{-3/4} - 1)]} \quad \text{with } h' = \frac{h_0 + b}{h_r} \quad (4.1)$$

where  $H_r/h_r$  corresponds to values at a reference point (boundary condition) and  $K$  is a constant also depending on the wave properties at that boundary point.

This solution predicts a (very flat) minimum for  $H/h$  at some point and shoreward from that point  $H/h$  increases with  $H/h \rightarrow \infty$  as  $h \rightarrow 0$ .

Clearly this is not in accordance with reality and turns out to be associated with the assumption that  $D$  is constant. As  $h \rightarrow 0$ ,  $D$  will



increase similarly and prevent the singularity. This can be seen by considering the energy equation in the form

$$\left(\frac{H}{h}\right)_x = - \left( \frac{h_x}{h} + \frac{c_x}{2c} + \frac{B_x}{2B} \right) \frac{H}{h} + \frac{D}{8cTB} \left(\frac{H}{h}\right)^2 \quad (4.2)$$

(For derivation see Svendsen et al., 1978). As  $h \rightarrow 0$  we assume the wave has deformed to a perfect sawtooth so that  $\eta_c = -\eta_t = \frac{1}{2}H$ . Thus we get from (3.12)

$$D = \frac{-1}{1 - \frac{1}{4}(H/h)^2} \quad ; \quad B_x = 0 \quad (4.3)$$

With  $c \sim \sqrt{gh}$  we also have  $c_x/c \sim h_x/4h$ . Substitution of (4.3) into (4.2) yields the relation

$$\left(\frac{H}{h}\right)_x = - \frac{5h_x}{4h} \frac{H}{h} - \frac{1}{1 - \frac{1}{4}(H/h)^2} \frac{1}{8T\sqrt{gh}B} \left(\frac{H}{h}\right)^2 \quad (4.4)$$

$h \rightarrow 0$  yields  $H/h$  increasing. But as  $H/h \rightarrow 2^-$  the dissipation grows. Hence

$$\frac{H}{h} \rightarrow 2 \quad \text{as } h \rightarrow 0 \quad \text{i.e. } d_t \rightarrow 0 \quad (4.5)$$

Thus the model described above has the limiting value of  $H/h = 2$  at the shoreline, not  $\infty$ .

Even this limit is considerably higher than the observed values. As  $h \rightarrow 0$ , however, we also get  $L/h \rightarrow \infty$  which implies that the parameter  $h_x L/h$  is no longer small. That is the bottom slope is not negligible and the assumption of locally horizontal bottom does not hold.

## 5. THE WAVE MOTION IMMEDIATELY AFTER BREAKING

It is tempting and illustrative to try if the solution presented in the previous chapters also applies to the region of rapid transition right after the initiation of breaking.

Figure 11a shows a computation of the wave height variation, starting at the breaking point. The agreement is surprisingly good. This, however, does not apply to Fig. 11b which gives a similar comparison for the set-up  $b/h_0$ . The two figures together show the paradoxical fact already hinted at earlier that the radiation stress in the transition region stays nearly constant even with a 30-40% decrease in wave height. Recalling eq. (2.8) this can only be true if  $P$  is increasing, roughly as  $H^{-2}$ .

By considering what happens when the breaking starts, it becomes clear that the overturning of the wave cannot immediately be matched by dissipation of a similar amount of energy. In the first transformation a large amount of the lost potential energy is converted into forward momentum flux which eventually is concentrated mainly in the roller, and this must be the reason for the simultaneous increase in  $P$ .

This is also consistent with the fact that  $P$  for very high waves is rather small. There are no results available for the skew waves at the breaking point, but the high order results for Stokes waves presented

by Cokelet (1977) can be used to determine  $P$  for very high, symmetrical waves. Values found are typically around  $P = 0.07$ , i.e. less than half the value of  $3/16$  for linear long waves and considerably less than for cnoidal waves of the same height.

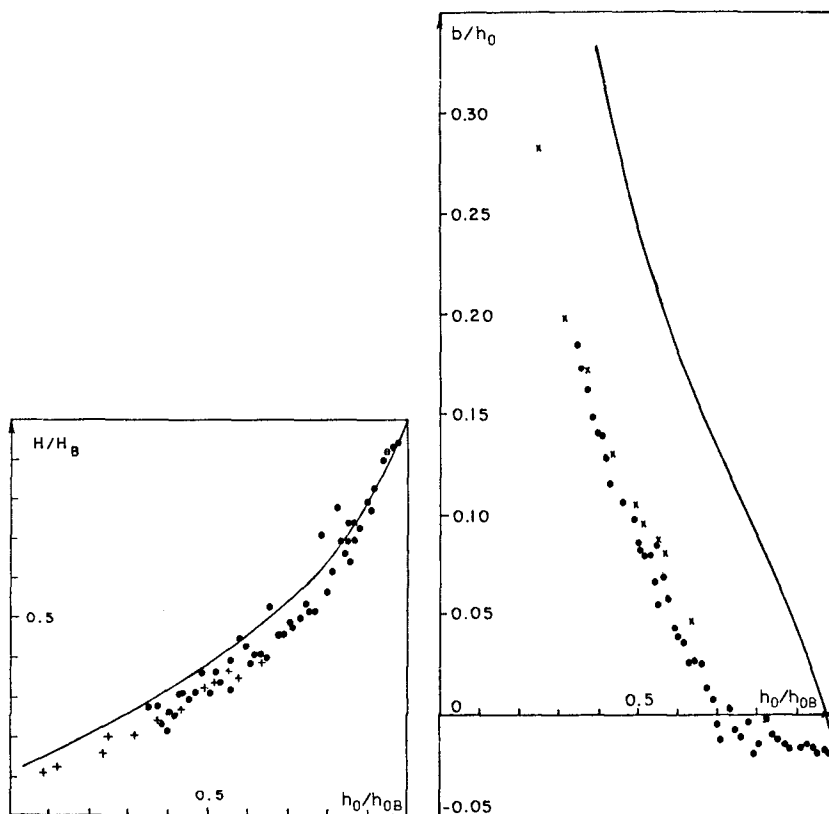


Fig. 11a and b. Wave height and set-up using the theoretical results for  $B$ ,  $P$  and  $D$  from the breaking point.  
 • Measurements by Hansen & Svendsen (1979), Case H,  
 + measurements by Hansen (1982).

The increase in P, however, is inevitably associated with a similar increase in B, the energy flux for a wave of unit height and propagation speed. The mechanism is the same as for P: very steep waves with peaky crests represent a very small energy flux relative to their height and the collapse of the crest in the initial stage of breaking leads to a significant increase in B.

It may be shown that these shifts in P and B are also consistent with the result found in section 3, that waves in the inner region represent rather high values of radiation stress and energy flux relative to their height and speed.

But even with no energy dissipation an increase in B will in itself require a decreasing wave height. Hence the question arises: how much of the wave height decrease in the outer transition region is actually due to redistribution of momentum and energy (represented by the changes in P and B) and how much is real energy dissipation?

This problem and the change in B and P can be analysed by considering the conservation of momentum and energy over the transition region as a whole in analogy to the jump conditions which apply to bores and hydraulic jumps in open channel flow and to shocks in compressible flows.

Svendsen (1984) found for a specific example that the wave height in the outer region with  $S_{xx} = \text{constant}$  decreased to  $0.65 H_B$  at the transition point that,  $H^2 = 0.423 H_B^2$  corresponding to an apparent energy reduction (had B been constant) of 57.7% of the energy at the breaking. Due to the simultaneous increase in B, however, the actual energy dissipation is only about 20%, or 1/3 of the 57.7%.

## 6. ACKNOWLEDGEMENT

The author wishes to thank J. Buhr Hansen for the access to unpublished data referred to as Hansen (1982).

## REFERENCES

- Bowen, A.J., D.L. Inman & V.P. Simmons (1968). Wave 'set-down' and set-up. *J. Geophys. Res.*, 73, 8, 2569-2577.
- Dally, W.R. (1980). A numerical model for beach profile evaluation MSc' dissertation, Univ. of Delaware.
- Divoky, D., B. LeMehaute & A. Lin (1968). Breaking waves on gentle slopes *J. Geophys. Res.*, 75, 9, 1681-1691.
- Duncan, J. H. (1981). An experimental investigation of breaking waves produced by a towed hydrofoil. *Proc. Roy. Soc. Lond.*, A 377, 331-348.
- Hansen, J. B. (1982). Wave measurements in the surf zone. Unpublished data.
- Horikawa, K & C. T. Kuo (1966). A study on wave transformation inside surf zone. *Proc. 10th Coast. Eng. Conf.*, Tokyo, Chap. 15, 217-233.
- James, I. D. (1974). Non-linear waves in the nearshore region: shoaling and set-up. *Estuarine & Coast. Mar. Sci.*, 2, 3, 207-34.
- Le Mehauté, B. (1962). On the non-saturated breaker theory and the wave run-up. *Proc. 8th Coast. Eng. Conf.*, 77-92.

- Stive, M. J. F. (1980). Velocity and pressure field in spilling breakers. Proc. 17th Int. Coast. Engrg. Conf., Chap. 34, 547-566.
- Stive, M. J. F., & H. G. Wind (1982). A study of radiation stress and set-up in the nearshore region, Coastal Engrg. 6, 1-25.
- Svendsen, I. A., P. A. Madsen & J. Buhr Hansen (1978). Wave characteristics in the surf zone. 16th Int. Coastal Engrg. Conf., Hamburg, Chap. 29, 520-539.
- Svendsen, I. A. & P. A. Madsen (1981). Energy dissipation in hydraulic jumps and breaking waves. Prog. Rep. 55, Inst. Hydrodyn. & Hydraulic Engrg., 39-47.
- Svendsen, I. A. (1984). Wave heights and set-up in a surf zone. Coastal Engineering, 8, 4, 303-329.

## CHAPTER FIVE

### WAVE KINEMATICS AND DIRECTIONALITY IN THE SURF ZONE

J. van Heteren\*, Staff member Hydraulic Division, Rijkswaterstaat.  
M.J.F. Stive \*\*, Research Engineer, Delft Hydraulics Laboratory.

#### ABSTRACT

Measurements of surface elevations and internal velocities have been conducted in a natural surf zone. The results were used to investigate the quantitative performance of linear theory in predicting the wave kinematics from the surface elevations. It appears that linear theory systematically overpredicts the horizontal velocities by 20 % in the frequency range around the peak, where the coherence with the surface motion is high, by 15 % at 2 times the peak frequency, changing in an underprediction of 15 % at higher frequencies. In these higher frequency ranges the rate of turbulent energy induced by breaking, contributes to the variance, so that the ratio of measured to theoretical r.m.s. fluctuation shows a trend of 25 % theoretical overprediction at negligible turbulent energy rates to 5 % underprediction at high turbulent energy rates. Furthermore the results were used to investigate the linear prediction of radiation stress and the effect of directionality on the radiation stress. Prediction of the radiation stress by unidirectional, linear theory gives an overestimation of 50 % at negligible turbulent energy rates to 35 % at high energy rates, which percentages reduce to 45 % and 25 % when the effect of shortcrestedness is taken into account.

#### 1. Introduction

The T.O.W. programme for Coastal Sediment Transport in the Netherlands consists of theoretical studies, laboratory investigations and investigations in the field and is carried out by 8 task groups. Within the framework of this study programme field campaigns were held in 1981 and 1982/83 covering simultaneous measurements of currents, surface elevations, wave kinematics and sediment concentrations in the surf zone on the Dutch coast near Egmond (Derks and Stive, 1984). The data are used to investigate several aspects of coastal processes. In the task group "Velocity Field in Waves" specific attention is given to the investigation of the relation between surface elevation and wave kinematics. This paper presents an analysis of the 1981 field measurements as carried out by this task group.

The quantitative performance of linear theory in predicting the wave kinematics from the surface elevation is investigated on basis of the squared coherence-, gain- and phase spectra between surface elevation and both horizontal and vertical velocity. In addition the measured

\* Directorate for Water Management and Hydraulic Research, Coastal and Maritime District, Hellevoetsluis Division, p.o. box 3, 3220 AA HELLEVOETSLUIS, The Netherlands.

\*\* Delft Hydraulics Laboratory, p.o. box 177, 2600 MH DELFT, The Netherlands.

and theoretical r.m.s. values are compared. Relevant earlier studies on this topic are e.g. those of Mitsuguchi et al. (1980) and of Guza and Thornton (1980). Their findings are that linear theory generally overestimates wave induced horizontal velocities by 10 % to 30 %. Mitsuguchi et al. merely state their conclusion without analysing apparent trends in their data with e.g. increasing frequency. They only consider a limited set of horizontal velocity data. Guza and Thornton obtain their overall conclusion merely on basis of the r.m.s. fluctuation of the horizontal velocity as measured and as predicted with linear theory. The present study confirms the conclusions of the above investigation by and large, but extends the analysis in depth by investigating the relation with the rate of turbulent kinetic energy generated by breaking.

A second topic of attention is the directional spreading of the wave motion in the surf zone, which aspect has received very little attention sofar. The directional spreading is used to investigate the effects of non-linearity and directionality on the prediction of the principal radiation stress component. Knowledge of the radiation stress is important for the study of phenomena as set-up and long-shore currents.

In this paper only a limited number of results is presented. A more extended publication will appear elsewhere.

## 2. Measurements

### 2.1 Introduction

The field experiments were conducted on the Dutch coast near Egmond in May/June 1981. The Dutch coast is part of a concave sandy beach with coastal dunes extending from Cape of Gris Nez to the island of Texel, see fig. 1. The exposed sandy beach is typically gently sloped and barred with fairly parallel bottom contours.

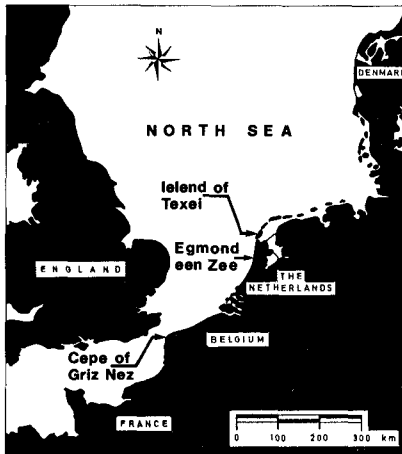


fig. 1 : Situation.

The measurements were made at three locations 20 m apart in the surf zone along a line normal to the shore. In addition measurements were made at two stations outside the surfzone as reference. The stations were numbered 1 to 5 from shore to sea. The local mean tidal range is approximately 2 m. This implies that at low tide station 1 was situated on the dry beach and nearly all wave energy was dissipated on the first breaker bar, see fig. 2. Therefore, all measurements were made around high tide.

During the 5 week campaign actual measurements were made at five different days, each with a duration of about 4 hours. Offshore significant wave heights were varying from 0.50 m - 1.80 m.

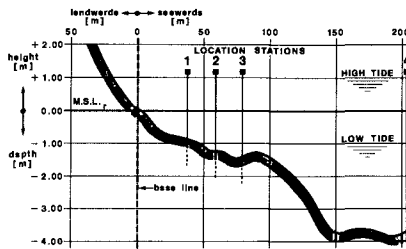


fig. 2: Location stations

## 2.2 Measuring stations

The stations in the surfzone consisted of a platform resting on transparent space trusses, a sensor pile and, with exception of station 1, a wave gauge. The sensor pile and wave gauge were spaced 2 m apart along a line nearly parallel to the shore. The sensor pile was placed 1 m seaward from the platform and was equipped with a measuring car in order to change the elevation of the sensors. On both sides of the socket longitudinal pipes were welded in a direct line parallel to the coast in order to intercompare different types of velocity meters at the same depth. Nearly all measurements were made at an elevation of about 1 m above the bottom. Some measurements were made at 0.20 m above the bottom.

## 2.3 Instruments

Velocities were measured at each of the three locations, both with conventional current meters and a newly developed current meter, viz. a so called vector-akwa, a three-dimensional meter based on the principle of travel time of acoustic pulses. Temperature and salinity variations are automatically corrected for. A meter of this type designed for use in physical models has been described by Botma (1978), who also designed the vector-akwa. The sensor is highly transparent and has four 0.23 m long survey lines (see fig. 3). The advantage of the fourth survey line is, that for the calculation of the three mutually orthogonal velocity components the survey line most influenced by the sensor itself can be eliminated. From calibration tests it was found that the inaccuracy of this instrument is  $\pm 5\%$ .

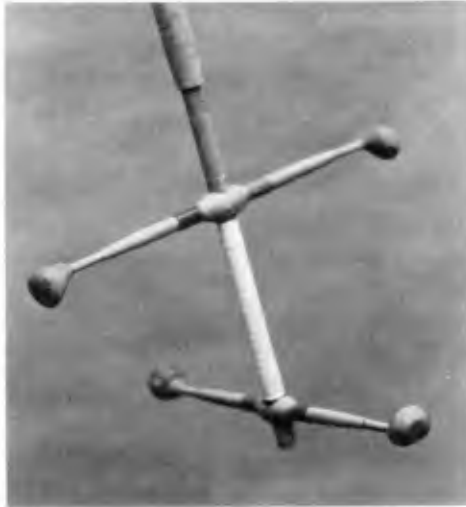


fig. 3: Vector-akwa velocity meter.

Surface elevations were measured using resistance wave gauges. These gauges consisted of resistance wires mounted inside a protection tube provided with slits. The tube caused a wave height reduction as well as a phase shift. To investigate the influence of this tube experiments were carried out in a large scale laboratory flume. This experiment showed a maximal reduction of 6% depending on the steepness of the waves. Since in the laboratory flume the conditions of Egmond were not reproduced exactly, the maximal reduction is estimated to be 10%.

The phase shift due to the tube appeared to be not considerable, but difficult to determine, since it is neither linear nor constant. This phase shift was modelled mathematically. It appeared to depend on a large number of parameters. Since several of these parameters, such as the shape of the wave, are difficult to determine, the phase shift can only be estimated with a limited accuracy. The maximal phase shift due to the tube appeared to be  $13^\circ/\text{Hz}$ .

For data storage during the experiment a pulse code modulator system (P.C.M.) was used. With this system 112 channels can be sampled and recorded simultaneously. The data were recorded with a 14 track tape recorder. The sample frequency of the system at the lowest record speed ( $1\frac{7}{8}$  i.p.s.) is 133 samples per second per channel.

### 3. Data analysis procedure

Standard procedures as described by Bendat and Piersol (1971) and Jenkins and Watts (1968) have been used to calculate mean values, variances, auto- and cross spectra, which yield coherence, gain- and phase spectra. The main procedure of the computer program is Singleton's F.F.T. procedure (Singleton, 1969) using subrecords. The length of the analysed records has been taken 1800 s. For the calculation of the spectra the records are divided in 30 subrecords. Because no data window has been



used the number of degrees of freedom is 60 and the resolution is 1/60 Hz.

Mean values, variances and auto spectra were calculated of the surface elevation ( $\zeta$ ) and the three orthogonal velocity components ( $u, v, w$ ).

To intercompare the velocity meters cross spectral calculations were carried out between the onshore wave velocity components ( $v$ ) of the two velocity meters fixed at the same sensor pile. For the same reason cross spectral calculations were used between these components and the surface elevation. These calculations have also been used to calculate the coherence-, gain- and phase spectra. However, this method cannot be used for the calculation of the coherence-, gain- and phase spectra of the surface elevation and the resultant velocity component in the horizontal plane ( $\hat{u}$ ) because of the shortcrestedness of the waves. Therefore, the gain spectrum of  $\zeta$  and  $\hat{u}$  has been calculated from:

$$H_{\zeta\hat{u}}^{\sim} = \{ (S_{uu} + S_{vv}) / S_{\zeta\zeta} \}^{1/2}$$

in which  $S_{uu}$ ,  $S_{vv}$  and  $S_{\zeta\zeta}$  are the auto spectra of the two horizontal velocity components,  $u$ ,  $v$ , and the surface elevation  $\zeta$ . This procedure does not permit the estimation of confidence intervals. For the coherence- and phase spectra the spectra of  $\zeta$  and  $v$  are used, since  $v$  contains the major part of the wave energy in the horizontal plane.

Assuming the water motion and the measurements to be linear and noise-free, the calculated auto- and cross spectra of ( $u, v, w$ ) can be used to estimate the directional properties of the waves by standard procedures (see Borgman, 1979). Using the auto- and cross spectra the truncated Fourier series and the parameters of the  $\cos^2$  ( $\theta/2$ )-model of the directional spectrum have been calculated for different frequencies (Longuet-Higgins et al., 1963 and Mitsuyasu et al., 1975). The spreading parameter of this model can easily be expressed in degrees.

#### 4. Intercomparison of velocity meters

One of the objectives of the field campaign was to investigate the performance of several types of current meters in a natural surf zone by intercomparison. To this end the velocity meters were closely placed at the same height above the bottom. The meters have been compared on basis of the r.m.s. values of  $\hat{u}$  and of the squared coherence and gain of the two onshore wave components at the peak frequency,  $f_p$ . Due to the lack of an absolute measurement result and of insight into the spatial variability of the velocity field these comparisons give no definite answer to the question which meter is the better one. The only quality assessment of the meters may be based on the squared coherence between  $\zeta$  and  $v$ . The results of the 1981 campaign indicate that the hydrodynamically well-designed vector-akwa shows in general a higher coherence (0.80 - 0.95) with the surface elevation than the signals of the other types of current meters. This intercomparison is based on a limited set of data obtained in the lower half of the water column. An extension of the intercomparison was realized in the 1982/83 field campaign of which the results are summarized in Derks and Stive (1984).

#### 5. Wave kinematics results

##### 5.1 Introduction

A comparison of measurement results with linear theory has been made in two ways. Firstly, the gain- and phase spectra are considered and compared with those according to linear theory. Secondly, the r.m.s.

values of the horizontal and vertical velocity components are compared with the estimated variances derived from the surface elevation spectra with linear theory.

This paper presents one typical example of squared coherence-, gain- and phase spectra of surface elevation and horizontal velocity component of one of the stations in the surf zone and the r.m.s. values of all horizontal velocity results.

## 5.2 The spectra

The surface elevation spectrum,  $\hat{S}_{\zeta\zeta}$ , and the corresponding 90% confidence interval is shown in fig. 4. The peak frequency appears at 1/6 Hz and, since we are dealing with breaking waves, second harmonics appear around twice the peak frequency. The local significant wave height in this example was about 1 m, the elevation of the velocity meter above the bottom was 0.80 m and the mean water depth was 2.30 m.

The squared coherence spectrum between surface elevation and on-shore velocity component,  $\hat{\gamma}_{\zeta v}^2$ , is shown in fig. 5. The dashed lines indicate the 90% confidence interval. In the frequency range where the bulk of the energy is concentrated the coherence is quite high. This implies a nearly linear relationship between  $\zeta$  and  $v$  and a relatively small contribution to the variance of the turbulent motion.

Fig. 6 exemplifies the gain spectra of surface elevation and horizontal velocity component in the propagation direction  $\hat{H}_{\zeta v}^{\gamma}$ . This example shows a typical overestimation of the horizontal velocity component by linear theory for the frequency range of 0.1 to 0.4 Hz of about 10 %, which changes in an underprediction of 20 % at higher frequencies. This can be seen more clearly in figure 7, where the ratio between the measured and the theoretical gain according to linear theory has been plotted versus frequency. It must be noted that this result is not corrected for the reduction caused by the tube of the wave gauge, which was estimated to be maximally 10 %. The phase spectrum of  $\zeta$  and  $v$ ,  $\hat{\phi}_{\zeta v}$ , is shown in fig. 8. This phase spectrum has been corrected for time delays due to: the tube of the wave gauge, the electronics of the wave gauge and the distance between wave gauge and velocity meter. The magnitude of these delays could only be estimated. The inaccuracy of the estimated phase corrections for this example is  $-28^\circ/\text{Hz}$  to  $+33^\circ/\text{Hz}$ . This phase spectrum shows a slight trend with frequency which, however, may be explained by the inaccuracies of the applied corrections, indicated by the thick broken line. Another reason may be that for the correction due to the spacing the main wave direction was used. Neglect of the wave spreading results in an overestimation of the time delay. Summarizing, it can be concluded that the phase spectrum of  $\zeta$  and  $v$  is consistent with linear theory within the accuracy margin.

In view of the above results concerning the phase spectrum of the horizontal onshore velocity component and the vertical velocity component,  $\hat{\phi}_{wv}$ , are of particular interest since this spectrum is neither influenced by a lag between two instruments nor by a spacing. This spectrum is shown in fig. 9. The theoretically expected value between these components is within the 90 % confidence interval of the estimate, confirming the theoretically predicted quadrature relation between these velocity components.

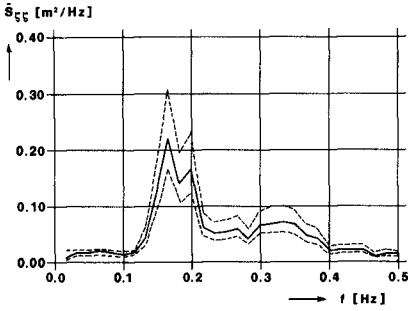


fig. 4 : surface elevation spectrum.

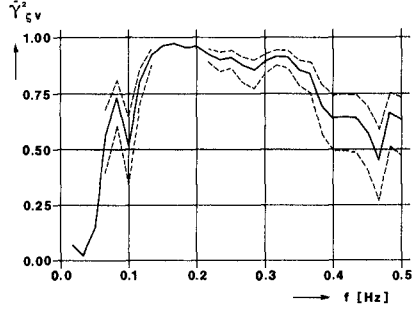


fig. 5 : squared coherence spectrum of surface elevation and onshore velocity component.

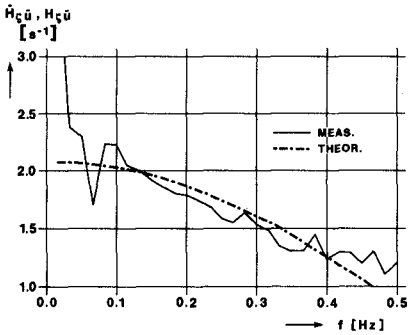


fig. 6 : gain spectrum of surface elevation and horizontal velocity component in the propagation direction.

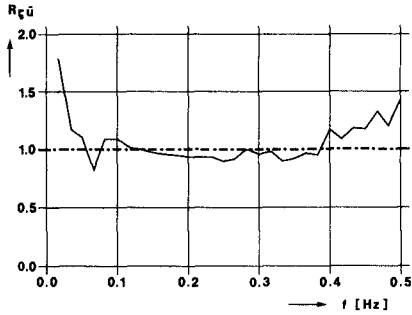


fig. 7 : ratio measured to the theoretical gain spectrum of surface elevation and horizontal velocity component in the propagation direction.

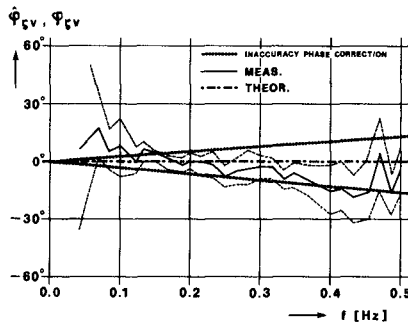


fig. 8 : phase spectrum of surface elevation and horizontal onshore velocity component.

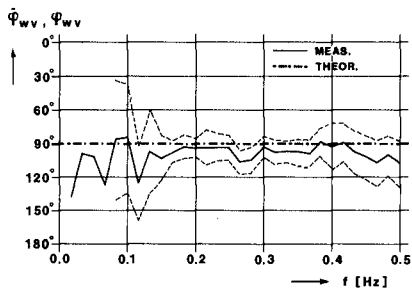


fig. 9 : phase spectrum of vertical and horizontal onshore velocity component.

5.3 The r.m.s. values

A correlation between the measured and theoretical r.m.s. values of the horizontal velocity component in the propagation direction is shown in fig. 10. No discrimination has been made between the r.m.s. values calculated from the measurements made at different elevations, because of the depth-uniformity of the horizontal velocity field in the lower water column. For the low r.m.s. values the deviations are generally outside the  $\pm 10\%$  interval, for the higher values they are generally within this interval. Again : these values are not corrected for the reduction due to the tube of the gauge (which would increase the theoretical estimate by 10 % maximally).

To investigate whether a systematic relationship between the discrepancy with linear theory and the relative turbulent energy level exists, a dimensionless parameter for this energy level has been used, defined as  $\hat{q}^2$ :

$$\hat{q}^2 = \rho h q^2 / E_{kin, inc}$$

in which  $\rho$  = water density [ kg/m<sup>3</sup> ],  $h$  = local water depth [ m ],  $q^2$  = turbulent kinetic energy [ m/s ],  $E_{kin, inc}$  = incident kinetic energy =  $\frac{1}{16} \rho g H_{rms}^2$  [ J/m<sup>2</sup> ],  $g$  = gravity acceleration [ m/s<sup>2</sup> ].

The turbulent kinetic energy is derived from :  $q^2 \approx (D/\rho)^{2/3}$  Battjes (1975). Here  $D$  is the energy dissipation due to breaking which is approximated by :  $D = \frac{1}{4} \rho g f_p Q_b H_m^2$ , according to Battjes and Janssen (1978),  $H_m$  being the maximum wave-height and  $Q_b$  the fraction of breaking waves.

The relation between this parameter and the ratio of the measured r.m.s. value of the horizontal velocity component to the theoretical one is shown in fig. 11. The results indicate that the discrepancy with linear theory is correlated with the rate of turbulent energy.

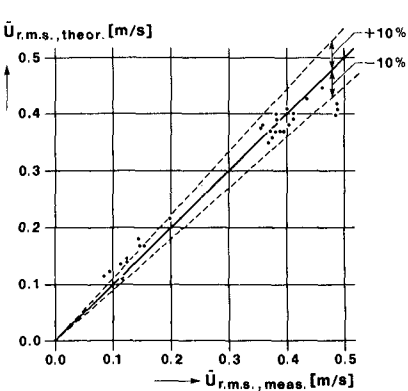


fig. 10 : Correlation measured and theoretical r.m.s. values of the horizontal velocity component in the propagation direction.

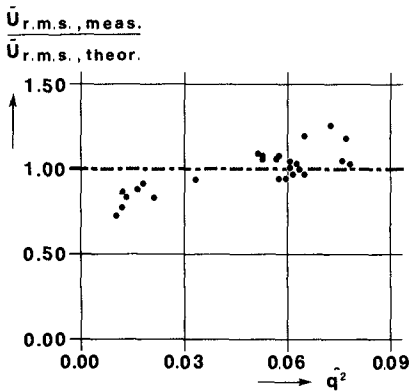


fig. 11 : ratio measured r.m.s. values of the horizontal velocity component in the propagation direction to the theoretical ones as a function of the relative turbulent energy level.

6. Wave directionality and radiation stress

An example of the wave direction results is shown in fig. 12. The upper diagram gives the main wave direction,  $\theta_0$ , as a function of frequency for the three stations in the surfzone. The lower diagram in this figure gives the spreading of the waves as a function of frequency. This spreading has been defined more or less analogously to the standard deviation of the Gaussian distribution and is expressed in degrees, see Van der Vlugt et al. (1981). Between this parameter and the spreading parameter of the  $\cos^2 s(\theta/2)$  model the following relation exists (Kuik et al., 1984):

$$\sigma = \sqrt{\frac{2}{s+1}} \cdot \frac{360^\circ}{2\pi}$$

The upper diagram shows that two different wave fields were present, one coming from the sea with a frequency of 0.10 Hz - 0.30 Hz and another caused by local winds at higher frequencies with the same direction as the wind direction,  $\theta_w$ . The wave directions of both wave fields clearly show refraction effects (station 3 is the most seaward station).

The spreading of the waves has a minimum at the peak frequency, which was also noticed from measurements made in deeper water, see Mitsuyasu et al. (1975). Another phenomenon which is clearly shown in this example is the decrease in spreading as the waves travel towards the shore. This can also be ascribed to refraction.

One of the effects of shortcrestedness is a decrease of the radiation stress. In a statistically homogeneous and stationary wave field the principal radiation stress component in the main wave direction is

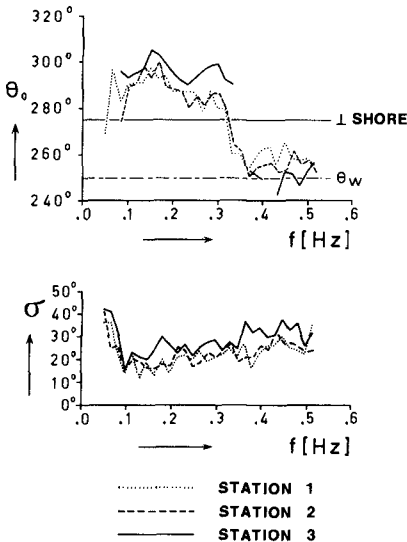


fig. 12 : Main wave direction (upper diagram) and wave spreading (lower diagram) as a function of frequency for the three stations located in the surf zone.

given, correct to second order in wave elevation (Battjes 1972), by :

$$S_{11, meas} = \frac{1}{2} \rho g \zeta^2 + \rho \int_0^{\infty} (\overline{v_*^2} - \overline{w^2}) dz$$

where  $\overline{v_*^2}$  is the variance of the horizontal orbital velocity in the main wave direction, which term can be derived from the measured variances  $\overline{u^2}$ ,  $\overline{v^2}$  and the cross variance  $\overline{u.v}$  (Battjes and Van Heteren, 1980). Assuming a linear longcrested wave field, the above expression reduces to an expression in which the main principal radiation stress component is :

$$S_{11, theor} = \int_0^{\infty} S_{\zeta\zeta}(f) \cdot \{2kh/\sinh(2kh) + \frac{1}{2}\} df$$

where k is the linear wave number. Battjes (1972) shows how the reducing effect of shortcrestedness on  $S_{11,theor}$  may be incorporated. For the simplified case of shallow water the reduction factor is given by  $(1-2/3.\epsilon)$  where  $\epsilon = (2s_0 + 1) \cdot (s_0 + 1)^{-1} \cdot (s_0 + 2)^{-1}$  in which  $s_0$  is the spreading parameter of the  $\cos^2 s(\theta/2)$  model. The radiation stress has been calculated for  $S_{11,meas}$  and for  $S_{11,theor}$  and for  $S_{11,theor}$  corrected for shortcrestedness. The results are shown in fig. 13. The results show that the reducing effect of shortcrestedness is 10% typically.

The correlation between the ratio of measured to theoretical estimates of the principal radiation stress component and the relative turbulent energy level is presented in fig. 14. This result clearly shows a trend with the rate of turbulent energy. The unidirectional linear theory overestimates the radiation stress by 40 % at negligible turbulent energy rates and by 25 % at higher rates. Corrected for shortcrestedness these percentages decrease to 35 % and 15 % respectively (these percentages are not corrected for the reduction caused by the tube of the gauge).

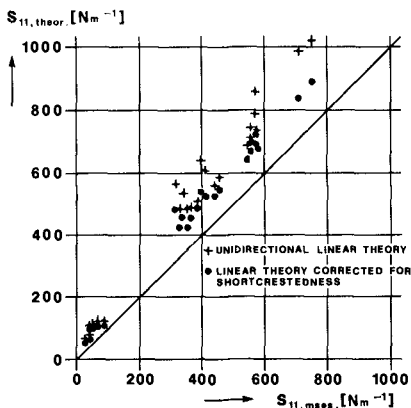


fig. 13: correlation measured and theoretical values of principal radiation stress component.

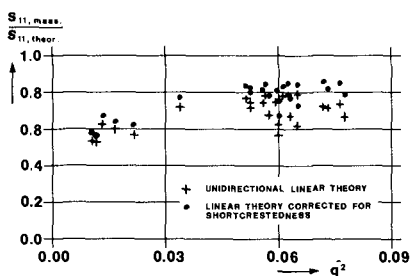


fig. 14: ratio measured values of principal radiation stress component to theoretical ones as a function of the relative turbulent energy level.

### 9. Conclusions

The following conclusions have not only been based on the examples presented in this paper, but more generally on the results of all measurements made in the surf zone of the beach near Egmond during the 1981 T.O.W. measuring campaign. All given values in this paragraph have been corrected for the reduction of surface elevation caused by the tube of the wave gauge which was estimated to be maximally 10 %. For this correction the mean value was used (5 %) accepting a random error of  $\pm 5\%$ . Furthermore, the inaccuracy of the velocity meter must be taken into account, which was found to be also  $\pm 5\%$ .

(1) In the surf zone linear theory systematically overpredicts the horizontal velocity component in the frequency range of high coherence with surface elevation. Average values of 21 % at the peak frequency and 17 % at two times the frequency have been found. This overprediction changes in an underprediction (in some cases as high as 15 %) at higher frequencies which is due to the presence of turbulent energy. Resultingly, the ratio of measured to theoretical r.m.s. fluctuations of the horizontal velocity shows a trend correlated with the turbulent energy rate from 25 % theoretical overprediction at negligible turbulent energy rates to 5 % underprediction at high turbulent energy rates.

(2) The estimated phases of the horizontal velocity component and surface elevation are generally consistent with linear theory within the margin of the sampling variability and the accuracy of the corrections applied. Corrections were needed due to the time delays caused by the sensor systems as well as by the distance between wave gauges and velocity meters.

(3) The wave direction results clearly show refraction effects. The spreading of the waves has a minimum at the peak frequency and decreases in onshore direction. Shortcrestedness decreases the magnitude of the radiation stress. Prediction of the radiation stress by unidirectional linear theory leads to an overestimation of 45 % at negligible turbulent energy rates and of 30 % at higher rates. These percentages reduce to 40 % and 20 % after correction for the effects of shortcrestedness.

REFERENCES

1. Battjes, J.A., 1972 : Radiation stress in shortcrested waves. *Journal of Marine Research*, 30, p.p. 56-64.
2. Battjes, J.A., 1975 : A turbulence model for the surf zone, *Proc. Symp. on modelling Techniques*, p.p. 1050-1061, American Society of Civil Engineers, New York.
3. Battjes, J.A., and J.P.F.M. Janssen, 1978 : Energy loss and set-up due to breaking of random waves. *Proc. 16 ICCE, Hamburg, Vol. I*, p.p. 569-587.
4. Battjes, J.A., and J. van Heteren, 1980 : Field measurements of wind wave kinematics. *Proc. 17th ICCE Sydney, Vol I*, p.p. 347-362.
5. Bendat, J.S., and A.G. Piersol, 1971 : *Random data : analysis and measurement procedures*, Wiley-Interscience, New York.
6. Borgman, L.E., 1979 : *Directional wave spectra from wave sensors*. *Marine Science* 8, Plenum Press, New York.
7. Botma, H.C., 1978 : *Acoustic flow meter for use with hydraulic models*, *Flow Measurements of Fluids*, North-Holland Publishing Company, p.p. 285-390.
8. Derks, H., and M.J.F. Stive, 1984 : Field investigation in the T.O.W. study programme. *Proc. 19th ICCE Houston*.
9. Guza, R.T., and E.B. Thornton, 1980 : Local and shoaled comparison of sea surface elevations, pressures and velocities, *Journal of Geophysical Research*, Vol. 85, No (3), p.p. 1524-1530.
10. Jenkins, G.M., and D.G. Watts, 1968 : *Spectral analysis and its applications*, Holden - day, San Francisco.
11. Kuik, A.J. et al., 1984 : Proposed method for the routine analysis of pitch-roll buoy data. *Proc. Symp. on Description and Modelling of Directional Seas*, Copenhagen.
12. Longuet - Higgins, M.S., et al., 1963 : Observations of the directional spectrum of sea waves using the motions of a floating buoy. *Proc. Conf. Ocean Wave Spectra*, Prentice - Hall, p.p. 111-132.
13. Mitsuguchi, M., et al. 1980 : Field observations of the wave-induced particle velocity in the surf zone. *Coastal Eng. in Japan*, Vol. 23, p.p. 81-89.
14. Mitsuyasu, H., et al. 1975 : Observations of the directional spectrum of sea waves using a cloverleaf buoy. *J. Phys. Oceanography*, Vol. 5, no. 2, p.p. 750-760.
15. Singleton, R.C., 1969 : An algorithm for computing the mixed radix fast Fourier transform. *IEEE Trans. Audio Electro - Acoustic*, AU - 17,2,p.p.93-103.
16. Van der Vlugt, A.J.M., et al., 1981 : The wavec directional buoy under development. *Proc. Conf. on Directional Wave Spectra Application*, Berkeley, p.p. 50-61.



## CHAPTER SIX

### A Model for Breaker Decay on Beaches

William R. Dally<sup>1</sup>, Robert G. Dean<sup>1</sup>, and Robert A. Dalrymple<sup>2</sup>

#### ABSTRACT

Based on the observation that a shallow water breaking wave propagating over a region of uniform depth will reform and stabilize after some distance, an intuitive expression for the rate of energy dissipation is developed. Using linear wave theory and the energy balance equation, analytical solutions for monochromatic waves breaking on a flat shelf, plane slope, and "equilibrium" beach profile are presented and compared to laboratory data from Horikawa and Kuo (1966) with favorable results. Set-down/up in the mean water level, bottom friction losses, and bottom profiles of arbitrary shape are then introduced and the equations solved numerically. The model is calibrated and verified to laboratory data with very good results for wave decay for a wide range of beach slopes and incident conditions, but not so favorable for set-up. A test run on a prototype scale profile containing two bar and trough systems demonstrates the model's ability to describe the shoaling, breaking, and wave reformation process commonly observed in nature. Bottom friction is found to play a negligible role in wave decay in the surf zone when compared to shoaling and breaking.

#### INTRODUCTION

A major problem encountered in modeling nearshore wave-induced phenomena is the description of wave parameters subsequent to the initiation of wave breaking. Specifically, wave height and its spatial gradients generate or have direct impact on sediment mobilization and suspension, littoral currents in both the alongshore and on/offshore directions, wave induced set-down/up in the mean water level, and forces on coastal structures. While the "0.78" criterion (ratio of breaker height to water depth = 0.78) appears to provide a reasonable prediction of incipient breaking on mildly sloping beaches, data show that this criterion does not hold farther into the surf zone (Horikawa and Kuo (1966), Nakamura, Shiraishi, and Sasaki (1966), Divoky, LeMéhauté and Lin (1970)). In fact, this data shows that such a similarity model is especially inappropriate on mild slopes - just where many coastal scientists assume it is most valid. Another shortcoming of this and most other representations developed to date is that they are not applicable on non-monotonic beach profiles such as those containing bar/trough formations. Such a model, capable of describing wave

- 1) Department of Coastal and Oceanographic Engineering, 336 Weil Hall, University of Florida, Gainesville, Florida 32611 (U.S.A.)
- 2) Department of Civil Engineering, 355 DuPont Hall, University of Delaware, Newark, Delaware 19711 (U.S.A.)

transformation across beaches of irregular profile shape, is essential to an adequate understanding of nearshore hydrodynamics and sediment transport.

#### BACKGROUND AND LITERATURE REVIEW

Aside from the similarity model which assumes that breaker height is strictly controlled by and directly proportional to water depth, investigations carried out over the past two decades have been based on the steady state equation governing energy balance for waves advancing directly toward shore:

$$\frac{\partial EC_g}{\partial x} = - \delta(x) \quad (1)$$

in which E is the wave energy per unit surface area,  $C_g$  is the group velocity, and  $\delta$  is the energy dissipation rate per unit surface area due to boundary shear, turbulence due to breaking, etc. The main thrust in previous studies has been the development of a rational and universally valid formulation for  $\delta$ . The most physically appealing approach, first advanced by LeMéhauté (1962), has been the approximation of a breaking wave as a propagating bore (hydraulic jump). The energy dissipation appears to be proportional to wave height cubed in this model. However, the adaptation of  $\delta$  from a jump to a breaking wave is not as straightforward as one might expect, and order of magnitude arguments by Battjes and Janssen (1978) produced a bore model in which  $\delta$  was proportional to wave height squared, with good results.

Horikawa and Kuo (1966) represent the internal energy dissipation in terms of turbulent velocity fluctuations which are assumed to decay exponentially with distance from the wave break point, while Mizuguchi (1981) applies the analytical solution for internal energy dissipation due to viscosity (Lamb, 1932) with the molecular kinematic viscosity replaced by the eddy viscosity. In these last two models the energy dissipation goes like wave height squared as well. All the dissipation models have coefficients which must be fitted empirically. It appears that until a precise model for breaking waves is developed, the existing ones must be judged by their abilities to predict accurately over the ranges of beach slope/shape, wave height, and wave period found in nature without changing these coefficients, or at least changing them in a systematic and easily applied manner. A summary of the studies which dealt with regular waves is presented in Table 1, including the dissipation model used in each.

Table 1 - Previous Investigations of Regular Breaking Waves

<u>Author(s)</u>	<u>Dissipation Model Used</u>
LeMéhauté (1962)	propagating bore
Horikawa & Kuo (1966)	turb. vel. fluc.
Divoky, LeMéhauté, & Lin (1970)	propagating bore
Hwang and Divoky (1970)	propagating bore
Svendsen, Madsen, & Hansen (1978)	propagating bore
Peregrine & Svendsen (1978)	propagating bore
Mizuguchi (1981)	internal energy

One of the features of breaking waves that is not represented in most of these models is that of the wave height stabilizing at some value in a uniform depth following the initiation of wave breaking. The laboratory data of Horikawa and Kuo (1966), general observations, and intuition support such a phenomenon, yet none of the dissipation models based on the moving hydraulic jump predict this effect. Although the model by Mizuguchi (1981) includes this stabilization, it is only included when waves are breaking in a surf zone of constant depth and does not play a role in governing the wave decay on a uniformly sloping beach - no matter how mild the slope. In fact, on a plane beach this model reverts to the similarity model, which as previously stated (and subsequently shown) does not compare well to the data collected on laboratory beaches of realistic slope.

In the present paper we concentrate on the development and evaluation of a somewhat intuitive model for monochromatic waves originally proposed in Dally (1980) which includes the wave height "stabilization". The model is calibrated using laboratory data, verified both qualitatively and quantitatively, and tested at prototype scale. Although one could question the significance of comparison against laboratory data when some field data are available, the field data are much more limited. Also, while the dependence of breaker decay on beach slope and wave steepness appear only as vague trends in the random wave data, it is clearly discernible and tractable in the monochromatic data. So it appears that the evaluation of a model by laboratory data would provide a useful step toward an understanding of the problem of greater interest in nature.

#### MODEL DEVELOPMENT

Consider a beach profile that rises from deep water in a gently sloping manner and at some point in shallow water becomes horizontal (see Figure 1). Consider further, a wave propagating onto this profile with characteristics such that breaking starts at the point where the bottom becomes horizontal. The wave will not instantaneously stop breaking because the bottom becomes horizontal (as dictated by the similarity model), but breaking would continue until some stable wave height is attained. Breaking would be most intense just shoreward of line AA and would decrease until the approximate stable wave height is reached at line BB. The rate of energy dissipation per unit plan area,

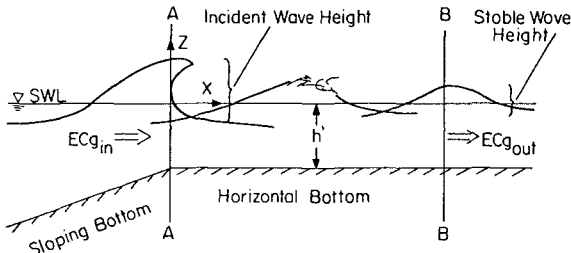


Figure 1 - Shelf beach presentation of the surf zone.

$\delta(x)$ , used in (1) is assumed to be proportional to the difference between the local energy flux and the stable energy flux, i.e.

$$\frac{\partial ECg}{\partial x} = \frac{-K}{h'} [ECg - ECg_s] \tag{2}$$

$ECg$  is now taken to be the depth-integrated time-averaged energy flux as given by shallow water linear wave theory,  $K$  is a dimensionless decay coefficient,  $h'$  is the still water depth, and  $ECg_s$  is the energy flux associated with the stable wave that the breaking wave is striving to attain. Horikawa and Kuo (1966) conducted laboratory tests with a bottom configuration identical to the one described. As shown in Figure 2, their data indicate a stable wave criterion given by

$$H_s = \Gamma h' \tag{3}$$

where  $H_s$  is the stable wave height, and  $\Gamma$  is a dimensionless coefficient whose value appears to lie somewhere between 0.35 and 0.40. Examination of another figure in their paper, where wave height was plotted versus still water depth for a uniform beach slope of 1/65, revealed that the breaking waves tended to approach asymptotically the line  $H = 0.5h'$ . In any event (3) appears to be a reasonable supposition and (2) can then be written:

$$\frac{\partial (H^2 \sqrt{h'})}{\partial x} = \frac{-K}{h'} [H^2 \sqrt{h'} - \Gamma^2 (h')^{5/2}] \tag{4}$$

where  $Cg$  is taken as  $\sqrt{gh'}$ . It should be noted that (2), (3), and (4) can be applied to a bottom of varying depth and slope until the stable wave criterion is reached because shoaling is included implicitly (if  $K = 0$ , the model satisfies conservation of energy, i.e. Green's Law).

ANALYTICAL SOLUTIONS

The problem to ultimately be addressed includes set-up, bottom friction, and beach profiles of irregular shape and consequently must be solved numerically. However, closed form solutions which exist for the

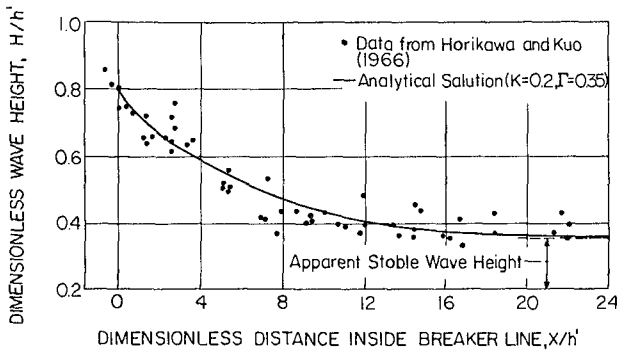


Figure 2 - The stable wave criterion, and comparison of analytical solution (7) with experimental results of Horikawa and Kuo (1966) for waves breaking on a shelf as shown in Figure 1.

simpler case of breaking on beaches of more idealized shapes, without including set-up, are both enlightening and potentially valuable for future analytical work with wave-induced currents and sediment transport. For brevity, the final results of the analytical solutions will just be stated here, but their full derivation can be found in Dally, Dean, and Dalrymple (1984).

Shelf Beach - For the idealized beach with a horizontal bottom described in the previous section given by,

$$h'(x) = \text{constant} = h' \quad (5)$$

and applying the boundary condition

$$G = G_b = H_b^2 \sqrt{h'} \quad , \quad x = 0 \quad (6)$$

the decay in wave height on a shelf beach in dimensionless form is

$$\frac{H}{h'} = \left( \left[ \left( \frac{H}{h'} \right)_b^2 - \Gamma^2 \right] \exp\left(-K \frac{x}{h'}\right) + \Gamma^2 \right)^{1/2} \quad (7)$$

where the subscript b denotes conditions at incipient breaking and x has its origin at the breaker line and is directed onshore. This expression dictates that the energy flux decays exponentially across the surf zone, never quite reaching the stable wave state known to exist. However, (7) may still be valid because internal and bottom friction losses could be accountable for the last bit of energy dissipation required to reach the stable condition. Note that if  $K = 0$  (no breaking), the wave height remains constant as would be expected. Equation (7) is plotted in Figure 2 with  $K = 0.2$ ,  $\Gamma = 0.35$ , and  $(H/h')_b = 0.8$ .

Plane Beach - The same general solution and boundary condition is applied to determine the analytical solution for the breaker model on a plane beach given by

$$h'(x) = h'_b - mx \quad (8)$$

where m is the beach slope. The result in dimensionless form is

$$\frac{H}{H_b} = \left[ \left( \frac{h'}{h'_b} \right)^{K/m - 1/2} \left( 1 + \alpha \right) - \alpha \left( \frac{h'}{h'_b} \right)^2 \right]^{1/2} \quad (9)$$

$$\text{where} \quad \alpha = \frac{K \Gamma^2}{m(5/2 - K/m)} \left( \frac{h'_b}{H_b} \right)^2 \quad (10)$$

Note that the solution is invalid if  $K/m = 5/2$ . For this special case the solution is

$$\frac{H}{H_b} = \left( \frac{h'}{h'_b} \right) \left[ 1 - \beta \ln \left( \frac{h'}{h'_b} \right) \right]^{1/2} \quad (11)$$

$$\text{where} \quad \beta = \frac{5}{2} \Gamma^2 \left( \frac{h'_b}{H_b} \right)^2 \quad (12)$$

Also note that if  $K$  is set equal to zero, (9) becomes Green's Law. If  $\alpha = -1.0$ , (9) reverts to the common similarity model  $H \sim h'$ . Equations (9) and (11) are plotted in Figure 3a for several values of  $K/m$  and  $(h'_b/H_b)$ . Figure 4 compares (9) to the data presented in Horikawa and Kuo (1966). Here  $K = 0.17$  and  $\Gamma = 0.5$  which are the recommended values for use with the "still water" model on a plane beach of slope less than approximately  $1/20$ .

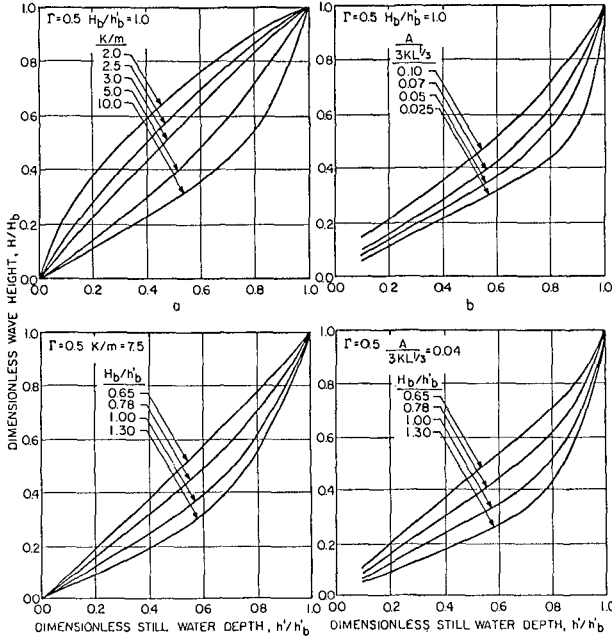


Figure 3a,b - Dependence of analytical solutions for plane beach (9) and equilibrium beach (14) on incipient conditions, and  $K/m$  and  $\phi$  respectively.

"Equilibrium" Beach Profile - The final closed form solution to be presented is for the profile shape which seems to best represent "equilibrium" beach profiles as determined by Dean (1977), and is expressed by

$$h'(x) = A(L - x)^{2/3} \tag{13}$$

where  $A$  is a parameter dependent on fluid and sediment characteristics,  $L$  is the distance from the still water line to the breaker line, and the origin of  $x$  remains at the breaker line directed onshore. Again with the same boundary condition as the two previous cases, the breaker decay on an equilibrium beach profile in dimensionless form is

$$\frac{H}{H_b} = \left( \left\{ -\Gamma^2 \left( \frac{H_b}{h'_b} \right)^{-2} \sum_{n=0}^5 \left[ x - \left( \frac{h'}{h'_b} \right)^{\frac{4-n}{2}} \right] \frac{\phi^n}{(5-n)!} \right\} + x \right)^{1/2} \tag{14}$$

where

$$x = \left( \frac{h'}{h'_b} \right)^{-1/2} \exp \left\{ \frac{1}{\phi} \left[ \left( \frac{h'}{h'_b} \right)^{1/2} - 1 \right] \right\} \tag{15}$$

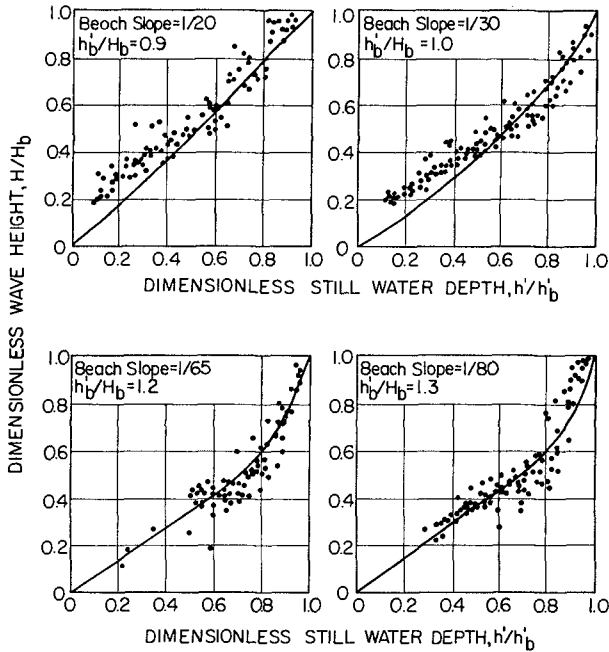


Figure 4 - Comparison of analytical solution (9) to wave decay data on a plane beach as presented in Horikawa and Kuo (1966) for various beach slopes ( $K = 0.17$ ,  $\Gamma = 0.5$ ).

and  $\phi$  is a similarity parameter given by

$$\phi = \frac{A}{3K L^{1/3}} \quad (16)$$

The effects of the incipient conditions and the parameter  $\phi$  on breaker decay on an equilibrium beach profile given by (14) are shown in Figure 3b. Note that the curves do not extend to the shoreline. This is because as the beach slope approaches infinity, shoaling causes the solution to become unbounded.

#### SET-UP AND BOTTOM FRICTION

During initial examination of the complete raw data set collected by Horikawa and Kuo, it was noticed that in all cases where measurements were taken in the inner portion of the surf zone, as the still water depth approached zero the wave height did not. This may also be apparent to the reader in Figure 4. To better model this phenomenon, including wave-induced set-up/down of the mean water level is necessary - the same conclusion reached originally by Hwang and Divoky (1970). From Longuet-Higgins and Stewart (1963), the slope of the mean water level,  $\bar{\eta}$ , is given by

$$\frac{\partial \bar{\eta}}{\partial x} = \frac{-3}{16} \frac{1}{(h' + \bar{\eta})} \frac{\partial H^2}{\partial x} \quad (17)$$

and can be used in conjunction with a slightly different form of (4) in which  $h'$ , the still water depth, is replaced by the mean water depth,  $h$ , given by  $h = h' + \bar{\eta}$ .

Although energy dissipation due to bottom friction will be negligible when compared to breaking in the cases to be examined, it will be incorporated in an elementary form for completeness. The average rate of energy dissipation per plan area due to bottom friction for shallow water (see Putnam and Johnson (1949)) is expressed by

$$\delta_{BF} = \rho \frac{f H^3}{12\pi h} \quad (18)$$

where  $f$  is a drag coefficient dependent on flow and bottom/sediment characteristics, and shallow water linear wave theory has been applied. (The bottom shear stress is defined as  $\tau = \rho \frac{f}{2} u|u|$ ).

#### NUMERICAL SOLUTION

Closed form solutions for the breaker model with the inclusion of set-up, beach profiles of more realistic shape, or bottom friction have not yet been discovered. A numerical scheme was therefore developed, which is capable of describing the one-dimensional transformation of wave height over bottoms of arbitrary shape due to shoaling, breaking, reformation, and bottom friction, including the effects of set-up in mean water level. Briefly outlining this scheme, (4) (with  $h$  replacing  $h'$ ) and (17) are explicitly finite differenced using a central average for each of the quantities on their right-hand sides. Before the wave height at the next spatial step can be calculated, the mean water level is required, but not known a priori. Using the mean water level at the present location as an initial guess, the program iterates between the wave height and set-up equations until the updated value for the mean water depth is close to the previous value. In the calibration runs, it usually required only one or two iterations for the difference in estimates to become less than a millimeter.

Early on in this investigation the decay in wave energy due to bottom friction was included in the model in an uncoupled fashion. That is, after utilizing the scheme described above at an individual cell, additional energy was then extracted using a finite-differenced form of (18) and energy flux considerations. As will be shown subsequently, for realistic values of the drag coefficient the energy dissipation due to bottom friction was found to be negligible for all cases examined, and this mechanism was therefore dropped from the model.

To apply the model in a given situation, the following information is required: 1) the wave height and still water depth at a known near-shore location, 2) the wave height to water depth ratio at incipient breaking, 3) the bottom friction coefficient, and 4) the bottom profile. The breaking height to depth ratio is not easily predicted and was not treated in an extensive manner in this study. Assuming the starting point is in shallow water and outside the surf zone, the set-down in mean water level as given by Longuet-Higgins and Stewart (1963) is



$$\bar{\eta}_1 = -H_1^2 / 16 h_1 \quad (25)$$

From these initial conditions and using the method described, the wave height will increase (with some losses due to bottom friction) as the wave moves shoreward until the incipient breaking criterion is reached. The wave then breaks to a location where local stability, as defined by (3), is achieved (if at all). On barred profiles, the combination of the wave decay and the increasing water depth as the wave passes over the trough enable the wave to reach stability, where the breaking aspect of the model is shut off. The "reformed" wave then shoals again until the breaking criterion is reached, and the process repeats until the mean water depth reaches an arbitrarily chosen small value (0.25 meters is a reasonable choice at prototype scale).

#### CALIBRATION

The model is calibrated by determining the best values for the stable wave factor ( $\Gamma$ ) and the wave decay factor ( $K$ ) using a least squares procedure. The original raw laboratory data of waves breaking on plane slopes obtained by Horikawa and Kuo and used in their paper (1966) were examined. Starting at incipient breaking, they measured wave heights at known distances across the surf zone under monochromatic wave conditions for plane smooth rubber and concrete slopes of 1/20, 1/30, 1/65, and 1/80. The wave period varied from 1.2 to 2.3 seconds and the incipient breaker height from 7 to 27 cm. Although not specifically stated, the breakers must have spanned both the plunging and spilling types because the ratio of wave height to water depth at incipient breaking ranged from 0.63 to 1.67. Over 85 waves from the 1/30, 1/65, and 1/80 slopes containing more than 750 data points were analyzed. Data from the 1/20 slope were not included in the calibration because the measurements were taken too far apart for the model to remain numerically stable. The error function to be minimized is defined by

$$\epsilon(\Gamma, K) = \left( \sum_{j=1}^N [H_{p_j}(\Gamma, K) - H_{m_j}]^2 / \sum_{j=1}^N H_{m_j}^2 \right)^{1/2} \quad (26)$$

where  $H_{m_j}$  is the measured wave height,  $H_{p_j}$  is the wave height at that location as predicted by the numerical scheme for given incipient conditions and values of  $\Gamma$  and  $K$ , and  $N$  is the number of data points analyzed. Attempts to best fit  $\Gamma$  and  $K$  using a non-linear least squares iterative procedure were unsuccessful, apparently because the error surface is too highly non-linear. However, by calculating the error at regular intervals of  $K$  and  $\Gamma$ , a discretized error surface can be generated whose low point occurs near the best-fit values for the factors. The surfaces for all three slopes were found to have recurved shapes, with the 1/65 and 1/80 surfaces also containing saddle points. The best fit values for  $\Gamma$  and  $K$  for the three slopes analyzed are presented in Table 2.

The best fit values for the two factors do vary with beach slope, especially as the beach gets very steep. However, it would be preferable to choose single values for  $\Gamma$  and  $K$  which give satisfactory results for all beach slopes, allowing the model to be used on beach

Table 2 - Best Fit Values for  $\Gamma$  and K

Slope	$\Gamma$	K	Minimum Error
1/80	0.350	0.100	0.1298
1/65	0.355	0.115	0.1054
1/30	0.475	0.275	0.1165

profiles of more realistic shape. Fortunately, the error surfaces for the three slopes tested are relatively broad and flat in the vicinity of their minimums (probably due to the reasonable scatter in the data), so the factors can be changed somewhat without excessively increasing the combined error. The procedure followed was to superimpose the contour plots for each of the three slopes and find the location where the sum of the three error values is minimized. This point occurs where:  $\Gamma = 0.40$ ,  $K = 0.15$ , and the mean error was 0.1423. It is recommended that these values be used in situations where the bottom slope varies over a wide range. If the beach is nearly planar, the values from Table 2 may be used accordingly.

#### RESULTS AND DISCUSSION - LABORATORY CONDITIONS

Wave Height - Figures 5, and 6 display a representative sample of model-predicted breaker decay as compared to the aforementioned laboratory data for plane beaches of 1/20, 1/30, 1/65 and 1/80 slopes. They are dimensional plots of wave height versus still water depth. In all cases, the wave decay factor K was set equal to 0.15 and the stable wave factor  $\Gamma$  was taken to be 0.40. Bottom friction was considered negligible. Each curve was generated by inputting the wave height and still water depth at incipient breaking as given in the data, and calculating stepwise ( $\Delta x = 1/\text{beach slope (cm)}$ ) the set-up and decay profiles.

Examination of these results shows that the model developed in this study appears to provide a good representation of breaking wave decay on plane beaches of laboratory scale. It is important to note that the model is in good quantitative agreement over the wide range of slopes tested (including the 1/20 slope not involved in the calibration), even with the two factors held constant at values that are not necessarily the best fit values for each particular slope. Coupled with the fact that the error surfaces are broad and flat in the vicinity of their minimums, this indicates the proposed governing equation (2) has the correct form, and that varying the empirical factors does not significantly affect the accuracy when considering the reasonable scatter already present in the data.

The line  $H = 0.78 h'$  is plotted in each of the figures, and appears to be an acceptable description of breaker decay only for the 1/30 slope (Figure 5). In fact, the similarity model ( $H \sim h'$ ) so prevalent in the coastal literature seems to be approximately valid only for beaches of much greater slope than those commonly found in nature. The dependence of breaker decay on beach slope is clearly observed in this monochromatic data, with the decay approaching an increasingly steeper asymptote as the beach slope increases. The model displays the exact same behavior, which is also explicitly derived in the closed form solution (9) as was shown in Figure 3a. Those collecting random wave

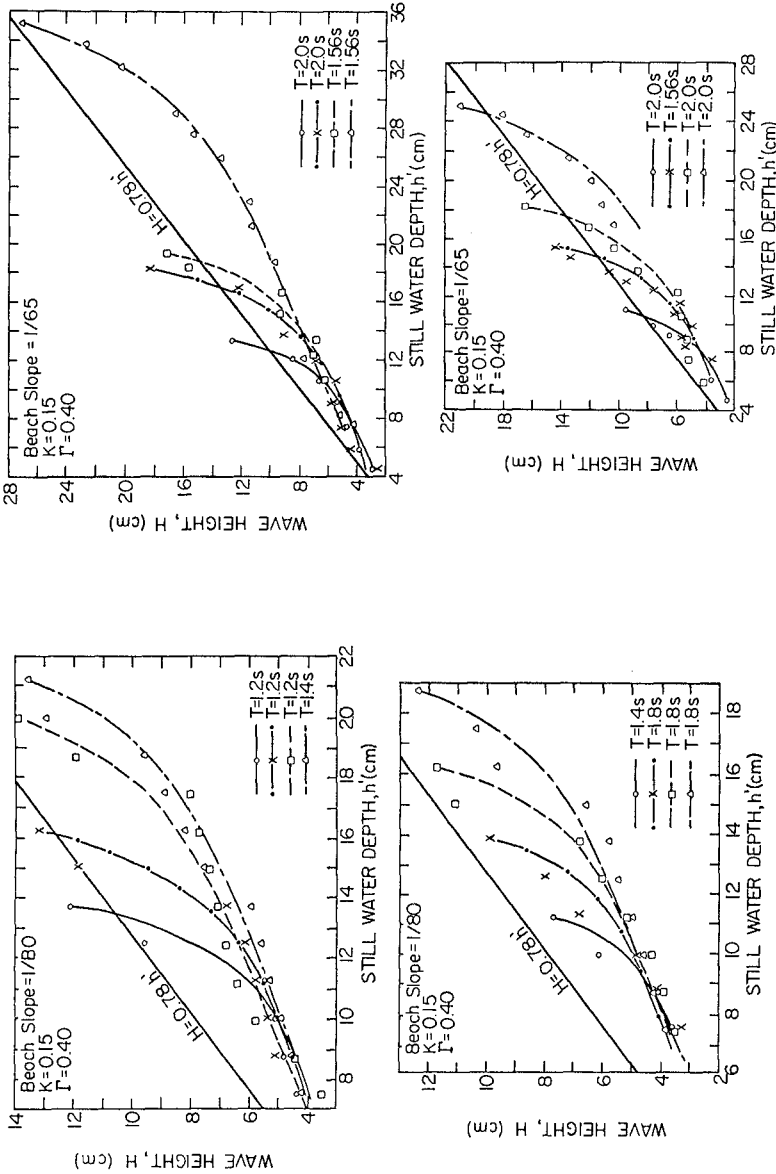


Figure 5 - Model comparison to laboratory data of Horikawa and Kuo (1966) for 1/80 and 1/65 beach slopes.

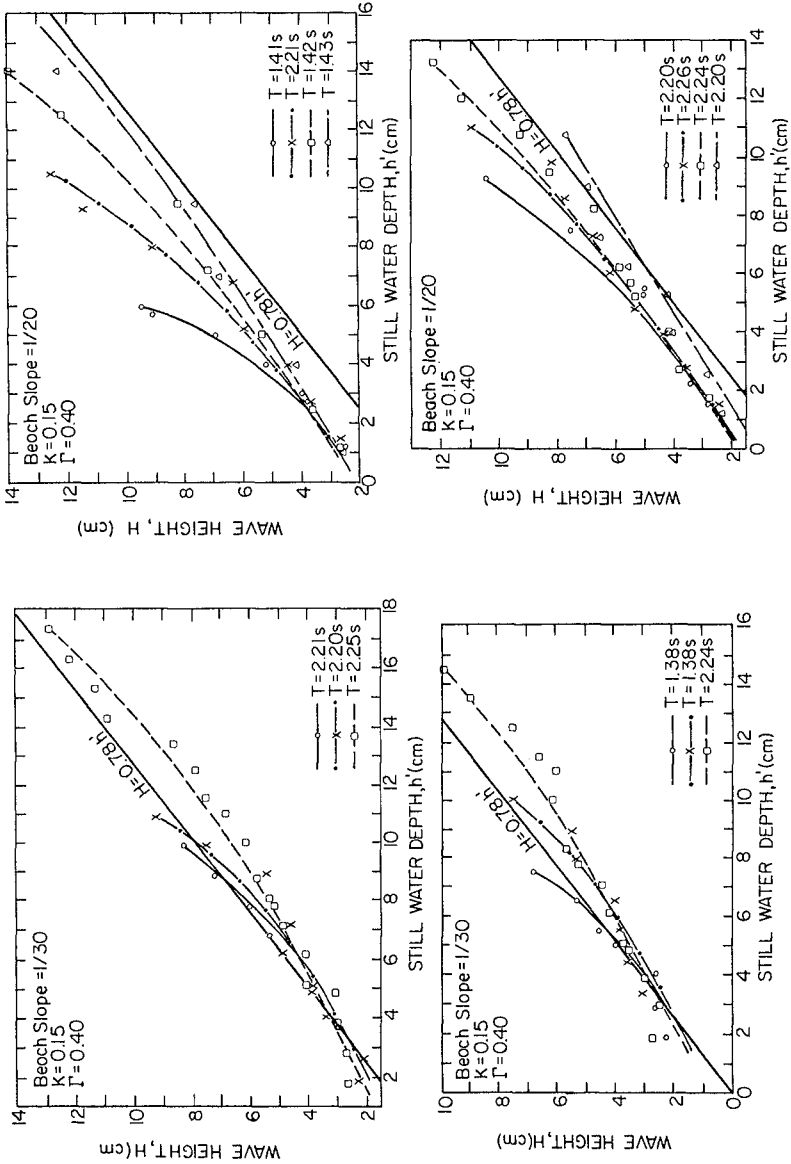


Figure 6 - Model comparison to laboratory data of Horikawa and Kuo (1966) for 1/30 and 1/20 beach slopes.

data in the laboratory and the field are also beginning to acknowledge this behavior, which is understandably less tractable when both breaking and non-breaking waves are present.

Although the range in wave period in the data is limited (1.2 - 2.26 s), it appears that wave period is not a primary factor in the decay of wave height after breaking is initiated. Wave period does affect the wave height to water depth ratio at incipient breaking (along with beach shape/slope and deepwater wave height) and therefore affects the shape of the decay profile through the initial condition.

Figure 7 demonstrates the negligible effect bottom friction losses have on the wave decay profile when compared to breaking. The upper curve is a test case of the model without bottom friction. The lower curve was generated with the same conditions, except greatly exaggerated bottom friction losses were included using the uncoupled scheme. The bottom drag coefficient,  $f$ , was set equal to a value (0.1) about two orders of magnitude greater than is realistic for the smooth rubber and concrete slopes used by Horikawa and Kuo in order for the two curves to be distinguishable from each other.

Set-down/up. - The Horikawa and Kuo data set does not include measurements of setdown/up in mean water level, and so data presented in Bowen, Inman, and Simmons (1968) was examined. Wave height and mean water level measurements were made on a relatively steep plane beach of 1/12 slope and the results of one test are presented in Figure 8, along with decay and set-down/up as predicted by the model. It was required to set  $K = 0.25$  and  $\Gamma = 0.35$  due to the unrealistically steep beach slope. With these values, the breaker decay now compares well, and the maximum set-up values are reasonable if the

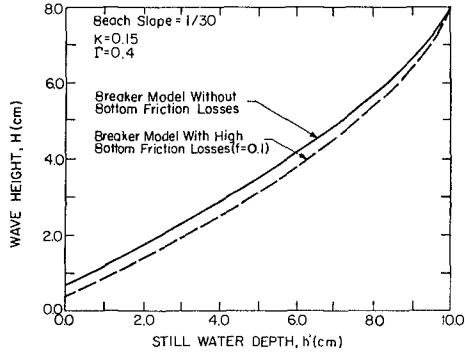


Figure 7 - Comparison of model-predicted wave decay with and without bottom friction losses.

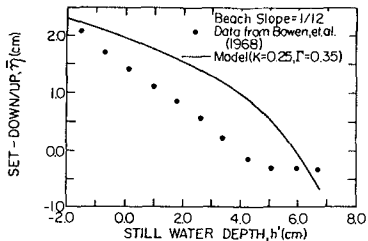
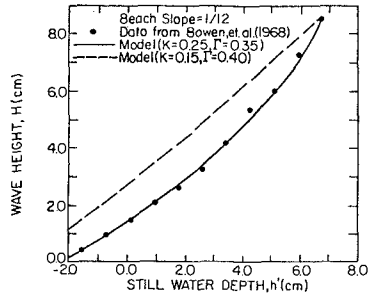


Figure 8 - Model-predicted wave decay and set-down/up as compared to laboratory data from Bowen, et. al. (1968).

swash zone is neglected; however, the predicted set-down/up curves do not follow the data. Apparently, linear wave theory does not provide a good representation of the onshore excess momentum flux for near breaking and breaking conditions, as might be expected. Higher order wave theories yield significantly less momentum flux for a given wave height than linear theory (see Stive and Wind (1982)), and this difference is the most likely explanation for the discrepancy between the measured and predicted set-down/up profiles.

#### RESULTS AND DISCUSSION - LARGE SCALE CONDITIONS

In order to demonstrate use of the model for waves breaking on beach profiles containing bars, and to lend some validity to the model for prototype situations, computations for large scale conditions were carried out. Prototype scale beach profiles measured by Saville (1957) in the Beach Erosion Board large wave tank were utilized and one is displayed in Figure 9. The profile is characterized by two offshore bar/trough systems, along with a monotonic section in the nearshore region. Test conditions, although not completely documented, were taken from the lab notes to be:

Wave period,  $T = 3.75$  s

Wave height at incipient breaking,  $H_b = 1.83$  to  $1.98$  m

Location of primary breaker line =  $75.6$  to  $78.0$  m from datum

Location of secondary breaker line =  $39.6$  m from datum

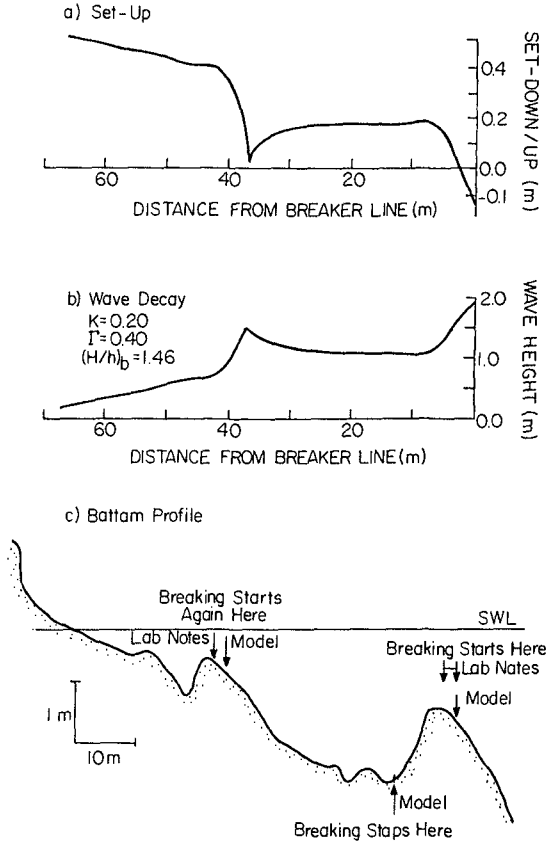
Mean sediment diameter,  $D = 0.2$  mm

In applying the model,  $\Gamma$  was set equal to  $0.4$ , but with  $K = 0.15$  conditions would not permit the broken wave to reform and break again as stated in the lab notes. It was necessary to increase  $K$  to a value of  $0.2$ , due to the extremely steep seaward faces of the bars - much steeper than those found in nature. Following the procedure described by Kamphuis (1975) and assuming the bottom was not rippled, the bottom friction factor,  $f$ , was found to be approximately  $0.005$ . Initial runs showed that bottom friction caused decay only on the order of millimeters, and friction was again left out of the model for this test. The distribution of model predicted set-down/up and wave height are shown in Figures 9a and b respectively. Note that the wave reaches the stable criterion in the deepest portion of the outermost trough as might be expected, shoals on the inner bar until the incipient condition is again attained (at a location close to that quoted in the lab notes), and then breaks continuously until the shoreline is reached.

The results of the application of the model under large scale conditions seem reasonably valid, at least in a qualitative sense. The example has demonstrated the ability of the model to describe wave breaking and reformation - a commonly observed process on natural beaches. The predicted wave decay and set-down/up profiles are continuous and well-behaved until the mean water depth becomes quite small ( $h < 0.25$  meters), where a swash zone model would be more appropriate.

#### SUMMARY AND CONCLUSIONS

Based on laboratory data collected by Horikawa and Kuo (1966) for regular wave conditions, the parameters found to most affect the decay in wave height due to breaking in the surf zone are the ratio of wave height to water depth at incipient breaking, and the beach slope.



**Figure 9** - Test of wave transformation model at prototype scale on large wave tank profile from Saville (1957).

Wave-induced set-down/up in mean water level plays a smaller but by no means trivial role in governing the shape of the wave decay profile, especially in the inner region of the surf zone. The similarity model,  $H \sim h'$ , commonly used by the coastal profession appears to be reasonable only on steep beaches ( $1/20$  to  $1/30$  at laboratory scale), and the "0.78" criterion predicts with marginal accuracy only for a  $1/30$  slope.

The model developed herein appears to qualitatively and quantitatively describe wave transformation in the surf zone due to shoaling, breaking, and reformation over a wide range of beach slopes ( $1/80$  to  $1/12$ ) and incipient conditions ( $0.63 \leq (H/h)_b \leq 1.67$ ). Closed form solutions neglecting set-up and bottom friction for the idealized profile shapes of a flat shelf, plane slope, and "equilibrium" beach

profile provide valuable insight because the apparently correct dependence on beach slope and incipient conditions appears explicitly. The best-fit values of the two assignable parameters in the model,  $\Gamma$  and  $K$ , were found to be relatively constant for beaches encompassing natural slope ranges (1/80 to 1/20). The greatest assets of the model are its simplicity and ease of application. Although it is most successful on profiles of monotonic shape, it is also employable when multiple bar/trough systems are present.

The model predicts maximum set-up values with reasonable accuracy for test cases presented by Bowen, et al. (1968); however, it does not describe the distribution of set-down/up across the surf zone satisfactorily.

From calculations based on the work by Kamphuis (1975), it can be concluded that bottom friction plays a negligible role in wave decay in the surf zone for most naturally occurring conditions when compared to the effects of breaking and shoaling. Bottom friction could be significant in nearshore regions that have very mild slopes or rough bottoms. This same conclusion was reached by Thornton and Guza (1983).

With the knowledge gained from this regular wave model, the irregular wave problem found in nature can now be investigated with greater insight and confidence.

#### ACKNOWLEDGEMENTS

The authors would like to thank Professor Kiyoshi Horikawa of the University of Tokyo for graciously providing the laboratory data used in this work. They would also like to express their appreciation to Mr. Philip Vitale for his assistance in generating the contour plots of error.

#### REFERENCES

- Battjes, J. A. and Janssen, J.P.F.M., "Energy Loss and Set-up Due to Breaking of Random Waves," Proceedings of the Sixteenth Conference on Coastal Engineering, American Society of Civil Engineers, Vol. 1, 1978, pp. 569-587.
- Bowen, A. J., Inman, D. L., and Simmons, V. P., "Wave Set-Down and Set-Up," Journal of Geophysical Research, Vol. 73, No. 8, 1968, pp. 2569-2577.
- Dally, W. R., "A Numerical Model for Beach Profile Evolution," Master's Thesis, University of Delaware, Department of Civil Engineering, 1980.
- Dally, W. R., Dean, R. G., and Dalrymple, R. A., "Wave Height Transformation Across Beaches of Arbitrary Profile," paper submitted to Journal of Geophysical Research, 1984.
- Dean, R. G., "Equilibrium Beach Profiles: U.S. Atlantic and Gulf Coasts," University of Delaware, Department of Civil Engineering, Ocean Engineering Report No. 12, January, 1977.
- Divoky, D., LeMehaute, B. and Lin, A., "Breaking Waves on Gentle Slopes," Journal of Geophysical Research, Vol. 75, No. 9, March 1970, pp. 1681-1692.
- Horikawa, K. and Kuo, C. T., "A Study of Wave Transformation Inside Surf Zone," Proceedings of Tenth Conference on Coastal Engineering, American Society of Civil Engineers, Vol. 1, 1966, pp. 217-233.



- Hwang, L. S., and Divoky, D., "Breaking Wave Set-Up and Decay on Gentle Slopes," Proceedings of Twelfth Conference on Coastal Engineering, American Society of Civil Engineers, Vol. 1, 1970, pp. 377-389.
- Kamphuis, J. W., "Friction Factor Under Oscillatory Waves," Journal of the Waterways and Harbors Division, American Society of Civil Engineers, Vol. 101, No. WW2, May 1975, pp. 135-144.
- Lamb, H., Hydrodynamics, 6th ed., Cambridge University Press, 1932.
- LeMehaute, B., "On Non-Saturated Breakers and the Wave Run-up," Proceedings of Eighth Conference on Coastal Engineering, American Society of Civil Engineers, 1962, pp 77-92.
- Longuet-Higgins, M. S. and Stewart, R. W., "A Note on Wave Set-Up," Journal of Marine Research, Vol. 21, 1963, pp. 4-10.
- Mizuguchi, M., "An Heuristic Model of Wave Height Distribution in Surf Zone," Proceedings of the Seventeenth Coastal Engineering Conference, American Society of Civil Engineers, Vol. 1, 1981, pp. 278-289.
- Nakamura, M., Shiraishi, H., and Sasaki, Y., "Wave Decaying Due to Breaking," Proceedings of Tenth Conference on Coastal Engineering, American Society of Civil Engineers, Vol. 1, 1966, pp. 234-253.
- Peregrine, D. H. and Svendsen, I. A., "Spilling Breakers, Bores, and Hydraulic Jumps," Proceedings of Sixteenth Conference on Coastal Engineering, American Society of Civil Engineers, Vol. 1, 1978, pp. 540-550.
- Putnam, J. A. and Johnson, J. W., "The Dissipation of Wave Energy by Bottom Friction," Transactions of the American Geophysical Union, Vol. 30, No. 1, 1949, pp. 67-74.
- Saville, T., "Scale Effects in Two-Dimensional Beach Studies," Transactions of the Seventh Meeting of the International Association of Hydraulic Research, 1957, pp. A3.1-A3.10.
- Stive, M.J.F., and Wind, H. G., "A Study of Radiation Stress and Set-Up in the Nearshore Region," Coastal Engineering, Vol. 6, 1982, pp. 1-25.
- Svendsen, I. A., Madsen, P. A., and Hansen, J. B., "Wave Characteristics in the Surf Zone," Proceedings of Sixteenth Conference on Coastal Engineering, American Society of Civil Engineers, Vol. 1, 1978, pp. 520-539.
- Thornton, E. B. and Guza, R. T., "Transformation of Wave Height Distribution," Journal of Geophysical Research, Vol. 88, No. C10, July 1983, pp. 5925-5938.

## CHAPTER SEVEN

### Modeling Turbulent Bore Propagation in the Surf Zone

David R. Basco<sup>1</sup> and Ib A. Svendsen<sup>2</sup>

#### Abstract

Initial efforts to numerically simulate surf zone waves by using a modified form of the nonlinear shallow water equations are described. Turbulence generated at the front of the moving bore-like wave spreads vertically downward to significantly alter the velocity profile and hence the horizontal momentum flux. This influence of turbulence is incorporated into the momentum balance equation through a momentum correction coefficient,  $\alpha$  which is prescribed based in part upon the theoretical  $\alpha(x)$  distribution beneath stationary hydraulic jumps. The numerical results show that with a suitably chosen  $\alpha(x)$  distribution, the equations not only dissipate energy as the waves propagate, but also that the wave shape stabilizes as a realistic profile rather than progressively steepening as when the nonlinear shallow water equations are employed. Further research is needed to theoretically determine the appropriate  $\alpha(x,t)$  distribution.

#### 1. Introduction

The transformation of breaking and broken waves in the surf zone is the dominant factor in the hydrodynamics of nearshore circulation, runup and sediment transport. Development of rational theories to describe breaking waves is just beginning.

After the moment the plunging jet strikes the onrushing trough, the wave undergoes a rapid transition in the region termed the outer surf zone (Fig. 1). Soon a bore-like shape appears which is maintained onto the beach or onto a bar profile as long as the depth decreases. This inner surf zone region involves the propagation of unsteady bores of non-constant form as they shoal, dissipate energy and create a mean water level setup on the beach.

This paper describes initial efforts to numerically model surf zone waves by using a modified form of the nonlinear shallow water equations (SWE) with additional momentum flux induced by the mean velocity profile through the bore. Numerical integration is by the finite-difference method and emphasis is on the many factors influencing the numerical results when compared with laboratory data.

---

<sup>1</sup>Professor, Civil and Ocean Engineering, Texas A&M University, College Station, TX 77843.

<sup>2</sup>Professor, Institute of Hydrodynamics and Hydraulic Engineering (ISVA), Technical University of Denmark, Building 115, DK-2800, Lyngby, Denmark.

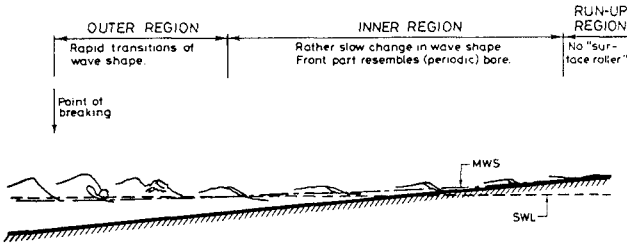


Fig. 1 Wave characteristics in the surf zone. (from Svendsen, et al., 1978)

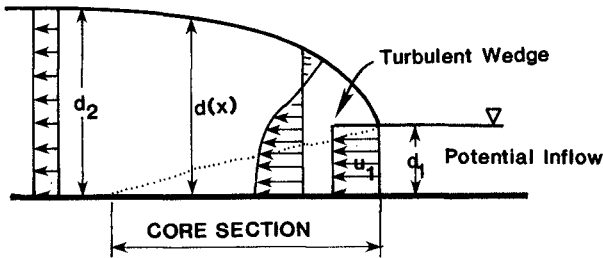


Fig. 2 Moving bores and jumps - relative coordinate system.

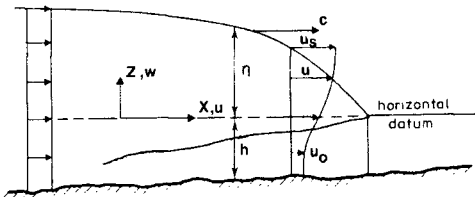


Fig. 3 Nonconstant form bores - fixed coordinate system.

An early approach to this problem idealized the moving bore front as a sharp discontinuity in the flow and used a "shock-fitting" procedure from classic hydraulic jump theory across the front (Meyer and Taylor, 1972, give a review). Others (Lax and Wendroff, 1960; Hibberd and Peregrine, 1979) rely on numerical viscosity induced by the coarse grid resolution at the front to produce a dissipative effect. Both methods do not permit details of the front wave shape nor internal dynamics to be resolved and consequently the wave propagation celerity is questionable.

As physically demonstrated by Peregrine and Svendsen (1978), turbulence is generated at the "toe" or front of the moving bore and spreads vertically to significantly influence the velocity profile in this high shear flow region. Madsen and Svendsen (1983) quantify this concept to develop an analytical model for steady flow, classic hydraulic jumps or moving bores on constant water depth. Turbulence closure is by a one-equation ( $k-\epsilon$ ) theory for transport of turbulent kinetic energy. The mixing-length is related to the turbulent wedge (Fig. 2) spreading from the surface at the toe and adjusting the similarity velocity profile in the downstream direction. Four dependent variables result that require solution of the depth-integrated continuity, total momentum, energy, and potential core-region momentum (Bernoulli) equations.

These ideas and methods were generalized and extended to unsteady, non-permanent form, propagating bores by Svendsen and Madsen (1984, in review). In a fixed frame of reference, a hyperbolic system of four simultaneous partial differential equations result. Additional turbulence closure relations are also required. Specification of the boundary conditions becomes difficult for the numerical solution of the four equation system. Without turbulence, the four equations reduce to the SWE.

In the present paper we only consider the depth-integrated equations of continuity and total momentum and include the influence of turbulence on the momentum flux through a momentum correction coefficient,  $\alpha$  which is prescribed. The purpose is to show that with a suitably chosen  $\alpha(x)$  - distribution, the equations will not only dissipate energy as the waves propagate, but the wave shape will stabilize as a realistic profile instead of progressively steepening as when the ordinary SWE are employed.

The basic equations of the four equation system are summarized in Section 2, where the theory for the two equation method is also presented. Section 3 summarizes the theoretical  $\alpha(x)$  - distribution in steady jumps and what has been postulated for a non-constant form, periodic bore wave including the model used in this paper. The numerical model is discussed in Section 4. Section 5 gives the results of some laboratory measurements of inner surface zone waves used as input boundary conditions and to check the numerical experiments as discussed in Section 6.

## 2. Theory - Basic Equations

For non-permanent form propagating bores in a fixed reference frame, the four equation system employed by Svendsen and Madsen (1984) is (see Fig. 3) in conservation form:

conservation of mass,

$$\eta_t + Q_x = 0 \quad (2.1)$$

conservation of total momentum,

$$Q_t + \left( \int_{-h}^{\eta} u^2 dz + \frac{1}{2} g d^2 \right)_x = g d h_x \quad (2.2)$$

conservation of mean energy,

$$E_t + (E_f)_x = D \quad (2.3)$$

and the

momentum conservation in core region,

$$(u_o)_t + u_o (u_o)_x + g \eta_x = 0 \quad (2.4)$$

where:

volumetric flowrate per unit width,

$$Q(x,t) = \int_{-h}^{\eta} u dz \quad (2.5)$$

total water depth,

$$d(x,t) = h(x) + \eta(x,t) \quad (2.6)$$

energy density per unit surface area,

$$E(x,t) = \int_{-h}^{\eta} \frac{1}{2} u^2 dz + \frac{1}{2} g \eta^2 \quad (2.7)$$

flux of energy through a vertical slice,

$$E_f(x,t) = \int_{-h}^{\eta} \frac{1}{2} u^3 dz + g \eta Q \quad (2.8)$$

loss of mean energy to turbulence,

$$D(x,t) = \int_{-h}^{\eta} \overline{u'w'} \frac{\partial u}{\partial z} dz \quad (2.9)$$

with  $u_o(x,t)$  the velocity in the lower constant-velocity, core region beneath the turbulent wedge with  $\overline{u'w'}$  the Reynolds shear stresses resulting from the turbulence and correlated by ensemble averaging. The subscripts  $x$  or  $t$  means partial differentiation with respect to  $x$  or  $t$ .

The primary assumption is that the horizontal length scale of the motion is much larger than the vertical scale so that the vertical

momentum balance is omitted and consequently a hydrostatic pressure distribution is taken. Normal turbulent stresses in (2.2) and bottom generated turbulence and shear stress are also neglected.

To solve the four equation system (2.1-2.4) requires relating the turbulent shear stress,  $\overline{u'w'}$  to the mean flow properties. The turbulence closure methods employed permit local nonequilibrium between turbulence advection and dissipation, but further details are beyond the scope of this paper.

This system (2.1-2.4) with closure represents one possible extension of the nonlinear shallow water equations (SWE) that includes the effects of turbulence.

Another approach as followed in this paper is to only invoke the following two, depth-integrated conservation laws:

conservation of mass,

$$\eta_t + Q_x = 0 \quad (2.10)$$

and

conservation of total momentum,

$$Q_t + \left( I + \frac{1}{2} g d^2 \right)_x = g d h_x \quad (2.11)$$

where:

momentum flux density,

$$I(x,t) \equiv \int_{-h}^{\eta} u^2 dz \quad (2.12)$$

and the effects of turbulence are now singularly brought in through  $I(x,t)$  which itself only depends on the mean velocity profile  $u(x,z,t)$ . All the assumptions in the four equation system are retained. The problem reduces to finding  $I(x,t)$ .

One possibility is to introduce a momentum flux correction coefficient,  $\alpha(x,t)$  so that

$$I(x,t) \equiv \frac{\alpha Q^2}{d} \quad (2.13)$$

where

$$\alpha(x,t) \equiv \frac{d}{Q^2} \int_{-h}^{\eta} u^2 dz \quad (2.14)$$

Now the problem is to find  $\alpha(x,t)$  for non-permanent form, surf zone waves. When  $\alpha(x,t) = 1.0$ , the SWE are recovered and the front face continuously steepens with no turbulence effects since the velocity profile remains uniform. In real propagating bores, water spills down the front face generating turbulence at the toe and creating a strongly non-uniform velocity profile, so that behind the toe  $\alpha(x,t) > 1.0$ .

### 3. Velocity and $\alpha$ -Distribution Models

It is instructive to review some typical  $u(z)$  profiles and resulting  $\alpha$  values as shown in Fig. 4. A log profile in uniform, open channel flow (Fig. 4b) gives  $\alpha = 1.05$  (Chow, 1955). The roller of a hydraulic jump causes a flow reversal (Fig. 2 and Fig. 4c) and significantly enhances the total momentum flux. The extreme case is a complete flow reversal (Fig. 4d) which essentially doubles the momentum flux created by each half.

The velocity distribution  $u(z)$  employed for this paper is the similarity profile used by Madsen and Svendsen (1983) for steady jumps:

$$f(\sigma) = \frac{u - u_0}{u_s - u_0} \quad 0 \leq \sigma \leq 1 \quad (3.1)$$

where

$$\sigma = \frac{z-d}{b} \quad b = d-a \quad (3.2)$$

with  $u_s(x,t)$  at the free surface, and  $b(x,t)$  the width of the turbulent wedge. The choice of  $f(\sigma)$  depended somewhat on the turbulent closure and a third order polynomial of the form

$$f(\sigma) = -A\sigma^3 + (1+A)\sigma^2 \quad (3.3)$$

with  $A = 1.4$  was found to give a good fit to measured mean velocity profiles for a wide range of inlet Froude numbers,  $F_1^2 = u_1^2/gd_1$ , with  $u_1, d_1$  the entrance jump conditions.

The  $\alpha$ -distribution that results from the Madsen and Svendsen (1983) theory is found by putting (3.1-3.3) into (2.14) to give

$$\alpha_r(x) = \xi \left[ 1 + \frac{1}{F_1^2} (1 - \xi^2) \right] \quad \xi = \frac{d(x)}{d_1} \quad (3.4)$$

with  $d(x)$  part of the solution for the jump profile. Here  $\alpha_r(x)$  is the distribution for a steady hydraulic jump or a moving bore on a horizontal bottom in a relative coordinate system moving with the bore celerity (Fig. 2). Some typical distributions of  $\alpha_r(x)$  for  $F_1^2 = 3.0, 3.95$  and  $8.0$  are shown by the solid line in Fig. 6.

For a fixed coordinate system (Fig. 3) and the  $\alpha(x)$  required by (2.11) and (2.13) it can be shown that

$$\alpha(x) = \left(\frac{h}{\eta}\right)^2 (\alpha_r - 1) + 1 \quad (3.5)$$

For example, when  $F_1^2 = 3$  (a weak jump) and at  $\eta/h = 0.3$ , then  $\alpha_r = 1.2$  and  $\alpha = 3.2$ . The turbulence significantly alters the velocity profile and enhances the momentum flux.

For constant form steady jumps and propagating bores, the water depth gradually increases so that  $\alpha_r$  gradually rises above 1.0 to a peak value  $\alpha_p$  within the jump at some distance  $x_p$  from the toe then gradually decreases back to 1.0 downstream. This is shown

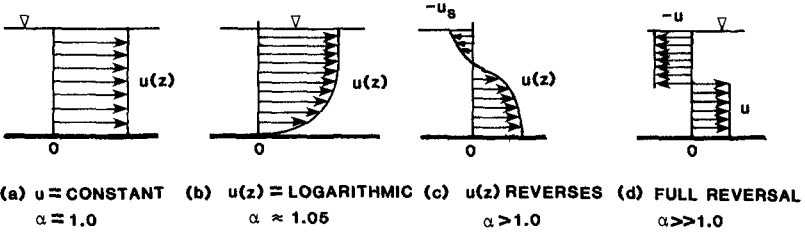


Fig. 4 Some velocity profiles and resulting momentum coefficients.

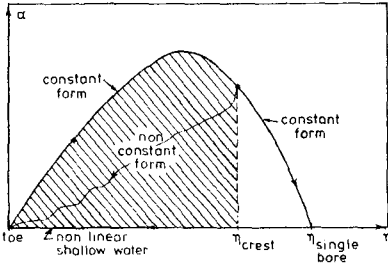


Fig. 5 Schematic variation of momentum coefficient  $\alpha$  with downstream water surface elevation  $\eta$ . (after Madsen, 1981)

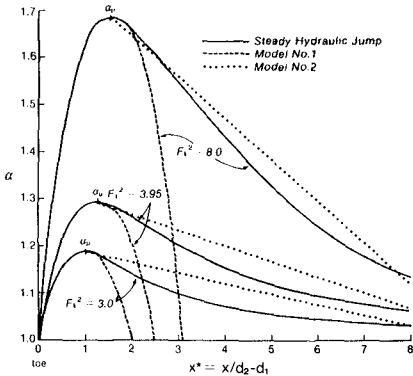


Fig. 6 Typical momentum coefficient distributions. The solid line is for the hydraulic jump. The dashed line (Model No. 1) is for a propagating wave-like bore of nonuniform shape. Model No. 2 is a variation not tested.



schematically in Fig. 5 (from Madsen, 1981) and for typical values in Fig. 6. The theory was exercised for a large range of  $F_1^2$  values and least squares curve fitting employed to find that for constant form jumps

$$\alpha_p(F_1^2) = 0.098F_1^2 + 0.902$$

and

$$X_p(F_1^2) = \begin{cases} 0.3F_1^2 + 0.05 & F_1^2 \leq 4 \\ 0.0833F_1^2 + 0.92 & F_1^2 > 4 \end{cases} \quad (3.6)$$

$$(3.7)$$

But what is the  $\alpha_r(x)$  distribution beneath non-permanent form, surf zone waves? Experimental evidence (Svendsen, et al., 1978) suggests that surf zone waves have similar-shaped fronts but changing backs as the broken wave shoals and dissipates energy up a slope. Fig. 5 schematically illustrates that non-constant form waves have an  $\alpha_r(x)$  distribution that must return to 1.0 as  $\eta(x)$  also decreases. This suggests an  $\alpha_r$ -distribution similar to the steady, constant form jumps up to  $\alpha_p$  on the front side (from trough to near the crest) but then rapidly decreasing again on the back side.

The initial, empirical  $\alpha_r$ -distribution chosen for this study was a parabolic shape as shown by the dashed line in Fig. 6 and labeled Model No. 1. The vertex ( $\alpha_p, x_p$ ) was found from (3.6) and (3.7) as key variables in the parabolic distribution with one limb passing through the toe ( $x=0, \alpha=1.0$ ). A procedure to theoretically calculate the  $I(x,t)$  distribution can be developed from the four equation system of Svendsen and Madsen (1984). Model No. 2 (Fig. 6, dotted) was never tested.

#### 4. Numerical Model

An explicit, finite-difference code based on the Lax-Wendroff, 2-Step algorithm (LW2S) has been developed for numerical solution of (2.10) and (2.11) using (2.13) and the parabolic model for the  $\alpha(x)$  distribution. The code uses the method of characteristics and interpolation subroutines to provide the needed additional boundary data. For example, when  $\eta(t)$  is specified on the incoming boundary, the code calculates  $Q(t)$  values at upper level time steps on the boundary as required by the LW2S algorithm. At the opposite, outgoing boundary a radiation boundary condition together with excessive numerical dissipation is introduced over a short reach to prevent wave energy reflections.

A large number of initial and boundary conditions with  $\alpha(x,t) = 1.0$  giving known analytical solutions for simple cases were employed during development and testing to insure the validity of the code and given confidence in the results.

The toe location was a key variable in the model since the parabolic  $\alpha$ -distribution began from this point. For a steady jump or constant form bore the toe is well defined since fixed in space. For the non-permanent form bore on a sloping bed, Svendsen and Madsen (1984) used as initial conditions a permanent bore starting seaward of the

slope with well defined toe. They then propagated the toe point itself at a celerity calculated by

$$C = \frac{Q_x}{\eta_x} \approx \frac{Q_j - Q_{j-1}}{\eta_j - \eta_{j-1}} \quad (4.1)$$

as a first order, upwind difference with  $j$  as the first grid point behind the toe.

For surf zone waves the toe position is ill defined since the approaching trough is a continuously varying curve. The toe position for these initial tests was heuristically taken midway between the trough (maximum negative  $\eta$ ) and the maximum front face slope. This was from observations in the laboratory that showed the toe point slightly up the curved trough. The toe position was then reestablished by this procedure each time step rather than propagating the initial toe position. This method proved to be expensive on the computer and caused problems as discussed in Section 7.

To numerically calculate  $F_1^2$  and hence  $\alpha_p$  and  $x_p$  to derive the  $\alpha$ -distribution, (4.1) was employed to calculate  $C$ , but with  $j$  at the point of maximum slope. The relative volumetric flowrate,  $Q_m$  was found from

$$Q_m = cd - Q \quad (4.2)$$

and finally

$$F_1^2 = \frac{Q_m^2}{gd^3} \quad (4.3)$$

with  $d$  and  $Q$  taken at the trough position to give an overall, representative value of  $F_1^2$ .

## 5. ISVA Experiments

Results of laboratory experiments at the Institute of Hydrodynamics and Hydraulic Engineering (ISVA), Denmark as performed by Hansen (1980,1982) were adapted for numerical testing. The experiments were made in a 60 cm wide, 32 m long and 36 cm deep (SWL) wave basin with a 1:34 plane sloping beach. Twelve wave gages spaced throughout the inner surf zone monitored the change in wave height and shape. Of the twenty test runs available, one test with wave period,  $T = 2.22$  sec and initial, "deepwater" wave height,  $H_0 = 10$  cm was selected for numerical simulation. Within the surf zone, surface wave measurements averaged over 20 waves at the first gage (CHANNEL 00,  $H_i = 5.48$  cm) became the boundary data as input into the numerical model.

The experimentally measured results of this particular test (Run No. 201) are summarized in Fig. 7 for relative variation of wave height,  $H/H_i$  versus distance up the slope and in Fig. 8 for the wave shape at four selected locations. The last gage (CHANNEL 11) was located 2.8 m from the first gage (CHANNEL 00). Fig. 8 shows rapidly changing back side slopes of these waves whereas the front slopes are relatively unchanged. The wave is clearly of non-constant form.

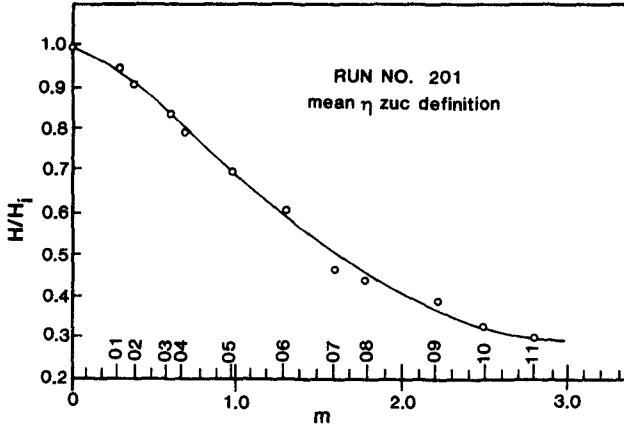


Fig. 7 Relative wave height versus position up the beach for run no. 201. (courtesy J.B. Hansen, 1982)

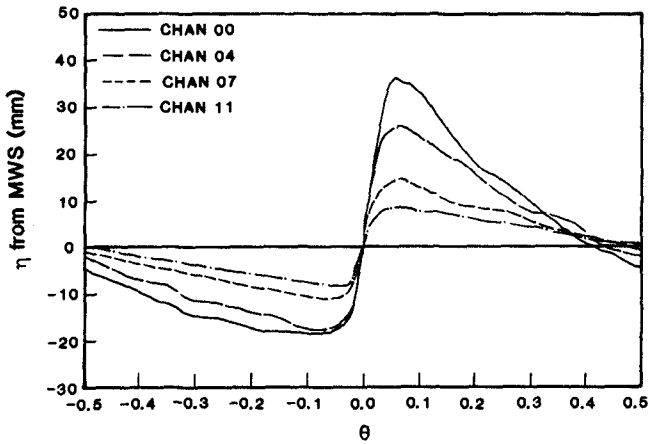


Fig. 8 Variation of wave shape at four locations for run no. 201. (courtesy J.B. Hansen, 1982)

Further details regarding the facilities, instrumentation and data analysis procedures employed can be found in Hansen and Svendsen (1979).

## 6. Numerical Experiments

The numerical experiments investigated the initial shape and wave height changes and celerity of the broken wave (labelled CHAN 00 in Fig. 8) as it shoaled and dissipated energy further up the beach. The detailed wave profile used as input boundary conditions is shown in Fig. 9. An arbitrary, smaller wave was placed in the "numerical" wave basin as initial conditions to avoid a completely "cold start" condition. Mean water depth (MWS) from the laboratory experiments which included wave induced setup was used as datum.

For an incoming wave length of about 2.5 m, the use of  $\Delta x = 0.025$  m gave roughly 50 grid intervals per wave for the staggered computational mesh of the LW2S scheme. This resulted in very low numerical dissipation. The  $\Delta t = 0.014$  sec was determined by using the maximum expected wave celerity together with the Courant number,  $Cr < 1.0$  restriction inherent in all explicit numerical schemes. As a result, for a wave period,  $T = 2.22$  sec,  $N = 80$  time steps correspond to about one-half a wave cycle. The shoreline ( $d = 0$ ) is about 3.3 m from the input boundary or at a grid index  $j = 133$ .

Fig. 10 is a baseline test result. It shows a wave propagating from left to right up the beach for the case when  $\alpha(x,t) = 1.0$  for all time and space and represents a solution to the SWE. The wave shoals and a secondary wave forms behind as the front face steepens. No mechanism exists in the numerical model to dissipate energy. The reason for the formation of the secondary wave is unclear but may be due to the original input wave shape (Fig. 9); the nonlinear advection term in the SWE creating harmonic components or, there being no real mechanism in the model to dissipate higher wave number energy. Running longer caused the scheme to go unstable. Fig. 11 demonstrates the use of a numerical smoothing filter on these results where

$$\eta_j^n = \gamma \eta_{j+1}^n + (1-2\gamma)\eta_j^n + \gamma \eta_{j-1}^n \quad (6.1)$$

with  $\gamma = 0.125$ , and using the filter every other time step ( $NR=2$ ) or every ten time steps ( $NR=10$ ). The use of this filter smoothed out the smaller oscillations and permitted the scheme to run beyond a full wave cycle. The crest elevation at  $N=80$  is 0.063 m and 0.046 after filtering. This filter behaves as an energy dissipative mechanism to remove higher wave energy (like turbulence) and changes the front face slope but not the phase speed of the wave.

Figures 12 and 13 show analogous plots but now with Model No. 1 used for the parabolic  $\alpha$ -distribution beneath the wave crest so that  $\alpha(x,t)$  varies in space and time. The effect of broken wave generated turbulence alters the velocity profile to enhance the momentum flux beneath the wave crest and behind the toe of the bore. Fig. 12 includes the numerical filter ( $NR=10$ ) to give a smoothed, clearer picture of the wave shape changes. The wave is seen to initially shoal

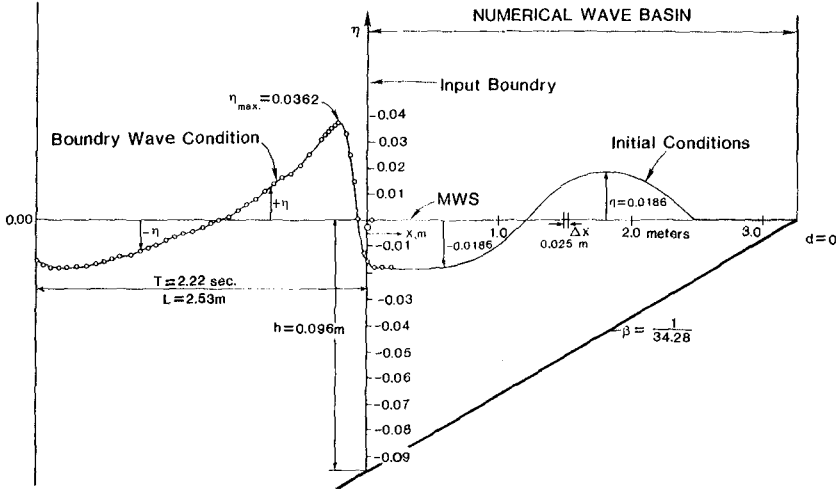


Fig. 9 Initial conditions and input wave boundary conditions for numerical simulation.

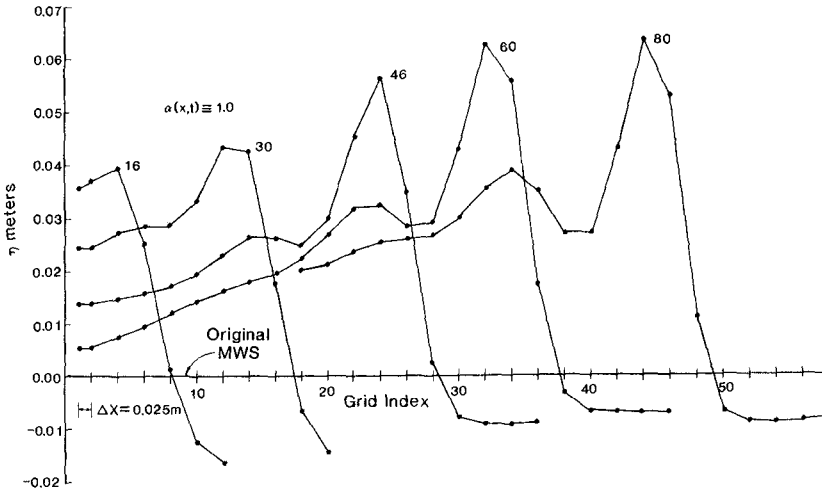


Fig. 10 Baseline numerical test results with no turbulence ( $\alpha=1.0$ ) for the five time steps.  $N=80$  equivalent to one-half wave period. A 2.22 sec wave with initial height of 0.055 m moves up a 1:34 slope.

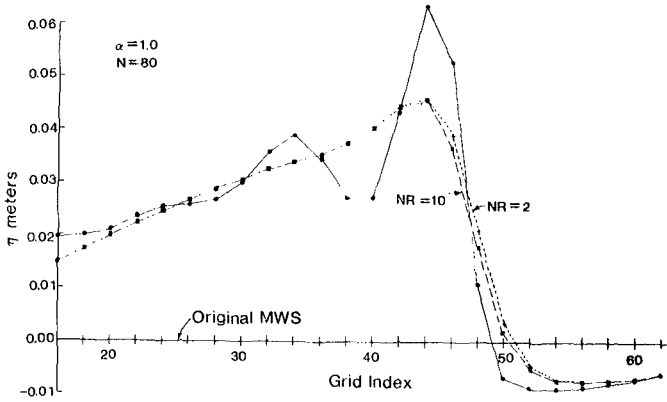


Fig. 11 Same as Fig. 10 at  $N=80$  except includes use of numerical filter every other ( $NR=2$ ) and every ten ( $NR=10$ ) time steps.

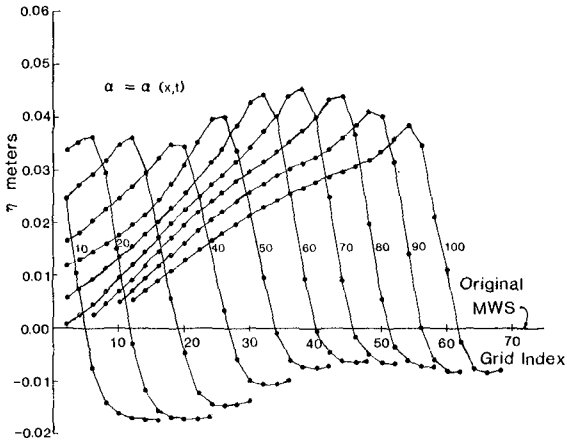


Fig. 12 Numerical test results with parabolic  $\alpha$ -distribution (Model No. 1) for 10 different time steps.

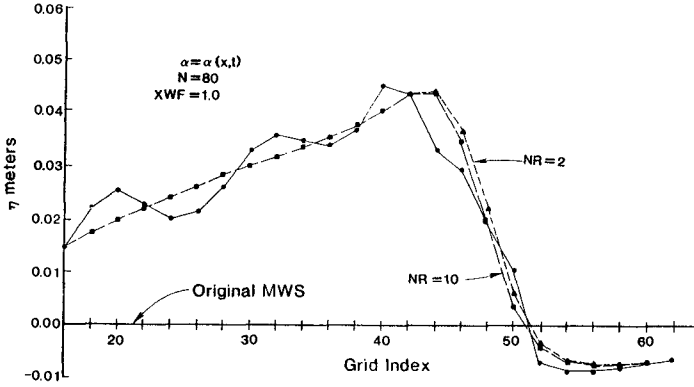


Fig. 13 Same as Fig. 12 at  $N=80$  including raw results and the effect of numerical filters.

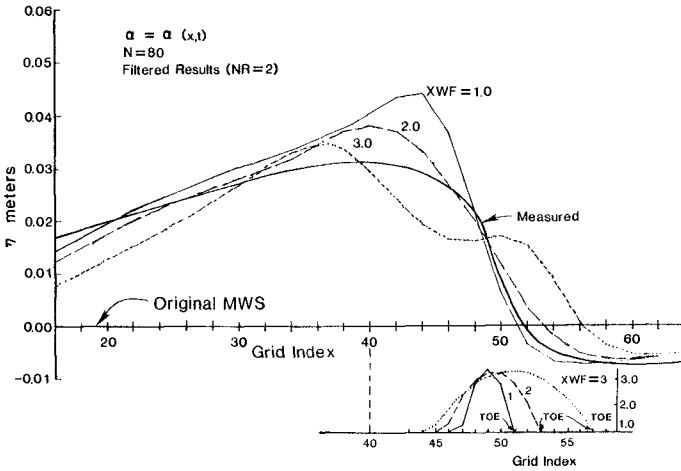


Fig. 14 The effect of different widths of the parabolic,  $\alpha$ -distribution model on the wave shape at  $N=80$ . Double width ( $XWF=2$ ) and trebled width ( $XWF=3$ ) shapes are shown below. Also shown is the laboratory measured wave shape as thick solid line.

in crest elevation (while dissipation takes place) and the trough elevation also rises. This is felt to be due to the initial conditions in the numerical basin. Beyond  $N=70$ , the numerical wave has established some type of equilibrium within the basin and dissipation dominates. Fig. 13 shows the wave shape after  $N=80$  time steps (one-half period) and demonstrates that high wave number oscillations (solid line) are still present when no numerical filtering is employed. Clearly, Fig. 13 reveals that the  $\alpha$ -distribution model must be responsible for the wave crest elevation reduction for now  $\eta_{\max} = 0.045$  m as compared to  $\eta_{\max} = 0.063$  m for the SWE ( $\alpha=1.0$ ) and the unfiltered results. It is also evident in Fig. 13 that additional numerical smoothing actually increases the front face steepness while smoothing out the higher wave number oscillations. Thus although both the  $\alpha$ -distribution mechanism and the numerical smoothing effectively result in energy dissipation, the general wave shape changes are primarily controlled by the  $\alpha(x,t)$  model.

This is demonstrated further in Fig. 14 for three different widths of the  $\alpha$ -distribution model. The results again show the wave shape at  $N=80$  with numerical filtering included. The width of the parabolic  $\alpha$ -distribution is arbitrarily doubled ( $XWF=2$ ) and trebled ( $XWF=3$ ) and this results in a significant change in both the crest elevation and slope of the front face. The  $\alpha$ -distributions are also shown below the wave with the toe located as discussed in Section 4. Widening the  $\alpha$ -distribution is seen to flatten the front shape. Entirely different results would be expected if the initial toe position were itself propagated as part of the solution procedure.

The thick solid line in Fig. 14 is from the measured laboratory results at a comparable position in space. The wave profile in time was converted to a space profile using the celerity of a local measured bore wave as reference. This wave was taken from the CHANNEL 05 position (see Fig. 7) so that the comparison is not exact. The measured shape in Fig. 14 is only included to give some rough idea of how the numerically calculated wave compares with that reported from the laboratory measurements.

## 7. Summary

This paper summarizes initial efforts to model surf zone wave shoaling and energy dissipation through the use of a semi-empirical, momentum correction coefficient distribution,  $\alpha(x,t)$  in the nonlinear SWE. The qualitative trends are correct in that energy is lost and the wave shape stabilizes rather than steepening. The numerical model can be improved by independently propagating the initial toe position as part of the solution procedure and by the development of a more rational theory for the  $\alpha(x)$ -distribution beneath the wave. In addition, many more waves need to be propagated through the numerical basin to reach an equilibrium state as found in the laboratory basin in order to make a proper comparison. Some additional energy loss occurs in boundary layer shear that should also be accounted for in the numerical model.



Further research is needed to theoretically determine the appropriate  $\alpha(x,t)$ -distribution.

#### References

- Chow, V.T. (1955) Open Channel Hydraulics, McGraw-Hill, NY.
- Hansen, J.B. (1980) "Experimental Investigations of Periodic Waves Near Breaking", Proceedings, 17th Int'l Conf. Coastal Engng., Sydney.
- Hansen, J.B. (1982) Personal communication.
- Hansen, J.B. and I.A. Svendsen (1979) "Regular Waves in Shoaling Water - Experimental Data", Series Paper 21, ISVA, Technical Univ. Denmark, Lyngby.
- Hibberd, S. and D.H. Peregrine (1979) "Surf and Run-Up on a Beach: A Uniform Bore", J. Fluid Mech., Vol. 95, No. 2, pp. 323-345.
- Lax, P.D. and Wendroff (1960) "Systems of Conservation Laws", Comm. Pure and Applied Math., Vol. 13, pp. 217-237.
- Madsen, P.A. (1981) "A Model for a Turbulent Bore", Series Paper 28, ISVA, Technical Univ. Denmark, Lyngby.
- Madsen, P.A. and I.A. Svendsen (1983) "Turbulent Bores and Hydraulic Jumps", J. Fluid Mech., Vol. 129, pp. 1-25.
- Meyer, R.E. and A.D. Taylor (1972) "Run-Up On Beaches" in Waves on Beaches and Resulting Sediment Transport, Academic Press, NY, pp. 357-411.
- Peregrine, D.H. and I.A. Svendsen (1978) "Spilling Breakers, Bores and Hydraulic Jumps", Proceedings, 16th Int'l. Conf. Coastal Engng., Vol. I, pp. 540-550.
- Svendsen, I.A., P.A. Madsen and J.B. Hansen (1978) "Wave Characteristics in the Surf Zone", Proceedings, 16th Int'l. Conf. Coastal Engng., Vol. I, pp. 520-539.
- Svendsen, I.A. and P.A. Madsen (1984) "A Turbulent Bore on a Beach", J. Fluid Mech., in review.

## CHAPTER EIGHT

### EXTREMAL STATISTICS OF STORM SURGES BY TYPHOON

Yoshito TSUCHIYA, M. ASCE<sup>\*</sup> and Yoshiaki KAWATA, M. ASCE<sup>\*\*</sup>

#### ABSTRACT

The objective of this paper is to propose a new approach based on the direction of the typhoon track for determining the probability of occurrence of extremal tides due to storm surges, as well as their return period. The study includes the effects of periods in tidal data and of tidal variation stemming from extensive reclamation along coasts on the fitness of the extremal data to probability density functions. The method is justified by application to an analysis of the probability of occurrence of storm surges in Osaka bay.

#### INTRODUCTION

Storm surges generated by typhoons have caused extensive damage at estuaries facing the Pacific Ocean in Japan. Historically, we know that there have been many storm surge disasters. There are records of 188 such disasters in certain zones between 701 and 1865, and 100 more have been recorded since 1865. It is, thus, clear that there is a high probability of occurrence of large storm surges in Japan during the typhoon season.

Unfortunately, methods available for the estimation of the return period of an abnormal tide have not as yet been completely established. This is due to not only the limited availability of long-term tidal data (usually more than 100 years are needed for reliable design predictions), but also the inaccuracy of absolute ground elevation measurements coupled with land subsidence in coastal industrial regions. Moreover, the hydrodynamic behavior of storm surges in the estuaries may have changed due to large-scale reclamation along the coast during the last two decades. To overcome these limitations and inaccuracies in the data, much effort has been expended. Generally, the extreme tidal data do not conform to any probability density function. Therefore, the main objective of these investigations is to discover why systematic divergence from the theoretical probability distribution curves appears at extreme tidal values. Führböter(1978) tried to

---

\* Professor, Disaster Prevention Research Institute, Kyoto University, Kyoto, Japan

\*\* Associate Professor, Disaster Prevention Research Institute, Kyoto University, Kyoto, Japan

explain this discrepancy as the nature of time-dependent tidal data and proposed a hypothetical model for practical use. Graff et al.(1978), Pugh et al.(1978), DeYong et al.(1975) and Tayfun (1979) discussed the joint probability of astronomical tides and storm surges after excluding their trend effects, even those for annual maximum anomaly which is a highly random occurrence relative to the astronomical tide. However, no one has successfully shown significant agreement between the data and any probability density function.

#### REARRANGEMENT OF DATA AND TRADITIONAL ANALYSIS

##### [a] Outline of the data

In Osaka and Kobe, tidal observations have been made since 1900 and 1927 respectively. During the Showa Era (since 1925), there have been three large storm surge disasters, in 1934, 1950 and 1961. A map of the region is shown in Fig. 1. Firstly, the characteristics of extreme tidal data in Osaka and Kobe such as the highest tidal level, the maximum anomaly and the lowest tidal level (not very widely used) need to be discussed in detail.

1] Highest tidal level: Fig. 2 shows the annual variation in the highest tidal levels in kobe and Osaka, including those in Tannowa and Kushimoto. The data for Osaka covers the longest period, but the data before 1946 is questionable for two reasons. One is the correction of ground level due to land subsidence. Local benchmarks, which in most cases corresponded to the original Osaka Pile, cannot be completely corrected from records of land subsidence. For Kobe, however, the correction of ground levels was made by the Kobe Marine Observatory. The other reason is the malfunction of an old tidal gage. A few slip between the pulley and the measuring rope connected to the float are needed to be justified, but attempts have as yet been unsuccessful.

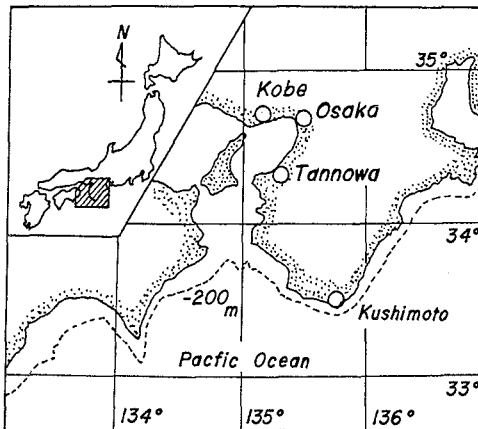


Fig. 1 Location map of study area

Fig. 2 reveals that the highest tidal level has exceeded 2 m T.P. [Tokyo Pile] four times since 1925. The highest tidal levels in Osaka and Kobe were recorded in 1934 (Muroto typhoon) and the second highest, in 1961 (Daini-Muroto typhoon). Third and fourth highest were recorded in 1950 (Jane typhoon) and for Typhoon 6420. There seems to be a periodic variation of three to five years and to be characterized by the group occurrence of storm surges between the end of World War II and 1970. This period will be studied by time series analysis in a later section. The data from Tannowa show the locality of storm surge generation and the influence of the typhoon path as in 1964 the rise of the sea level due to the typhoon was not marked in comparison with those in Osaka and Kobe. In Kushimoto, meteorological tides due to storm surges on the open coast affected the records. Therefore, it is valuable to have a boundary condition when the numerical simulation of a storm surge is attempted.

2] Maximum anomaly: Data for the annual maximum anomaly generated by typhoons and cyclones (low pressure) have been recorded since 1928 in Osaka and since 1931 in Kobe. Both have a few gaps, but from the historical reports of storm surges during these gaps, it has been determined that no large storm surges could have hit the area then. An annual maximum anomaly of over 2m was recorded four times in Osaka due to the large typhoons mentioned, but in Kobe there was only one recorded incidence, in 1934. This is proof that the probability of a storm surge disaster occurring in Osaka is much higher than in Kobe.

3] Lowest tidal level: The period covered by the time series data for the lowest tidal level is the same as for the highest tidal level. There are no extreme peak values, as for the highest tidal level and

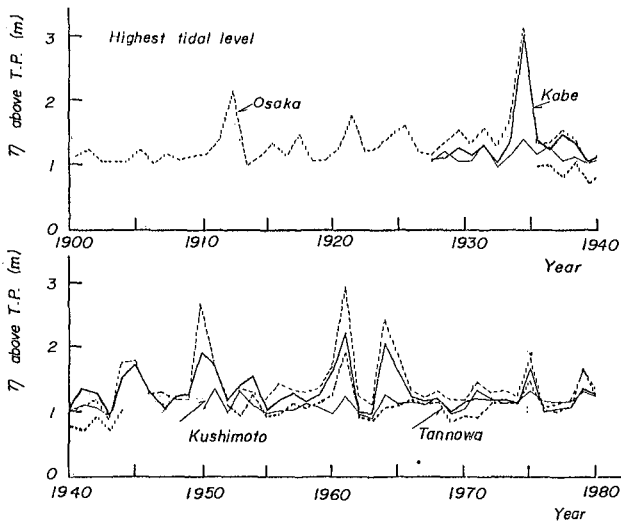


Fig. 2 Annual variation in the highest tidal levels in Kobe and Osaka

maximum anomaly. The occurrence of extremely low tides depends on the northwesterly monsoons in December or January. The low tidal levels due to the resurgence of a storm surge are not significant in comparison with those in monsoon season.

[b] Extremal statistics by traditional methods

To obtain the return period of occurrence of a storm surge, traditional methods of extremal statistics are usually applied to data such as the highest tidal level and the maximum anomaly. Originally, these methods were applied for the analysis of the statistical characteristics of other hydrological events, such as precipitation and river discharge. It has always been held that the fitness of data to any probability density function depends chiefly on the sampling size. For the application of extremal statistics, the period of the tidal records must usually be much shorter than the return periods. For practical use, however, the design tidal level or the maximum anomaly has to be determined in order to take countermeasures against storm surges. In any analysis, some risks are inevitable, so that slight overestimates are preferable for engineering application.

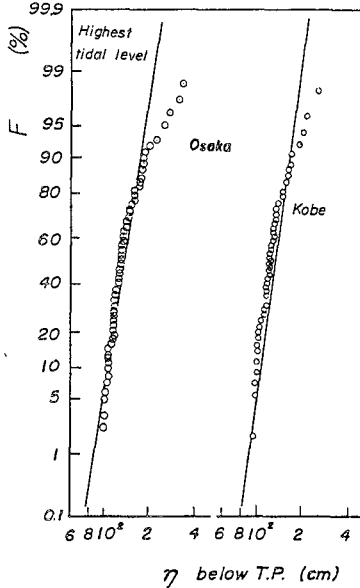
A statistical analysis of storm surges in Osaka has already been carried out by Nachi (1972). Now, about ten years of new data can be added to the old ones and improvement in the fitness due to this increment in the amount of data is studied in this section. A Gumbel distribution and a log-normal distribution have already been found to give a relatively reasonable description of the tendencies of the data. They are used here for the analysis of the new data set with a  $\chi$ -square test of fitness.

1] Highest tidal level: Figs.3(a) and(b) show the occurrence of highest tidal level in Osaka and Kobe on the probability papers of a Gumbel distribution and a log-normal distribution with Thomas plot. No distribution could follow the tendency of the data exactly because, especially for very large tidal levels, the discrepancy is remarkable. The statistical characteristics of the data from Osaka are very similar to those from Kobe. Comparison of these results with Nachi's fails to show any improvement in the degree of fitness. It is, therefore, concluded that the degree of fitness of the data to a probability density function does not necessarily depend only on the period of the data recorded.

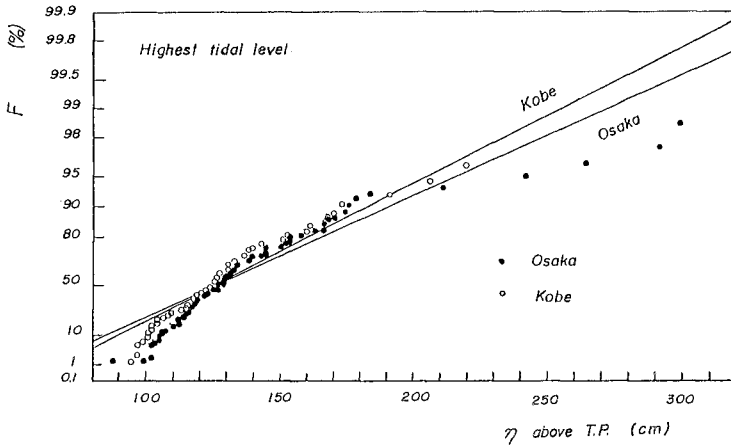
For further improvement, Führböter proposed a new method of treatment for tidal data which had been recorded for over 120 years in West Germany. In the method, he has not described any physical background for selecting the annual highest tidal levels every two or three years. It was, however, shown that the estimated tidal levels corresponding to the 100 year return period approach a constant value with the increment in sampling years. Fig. 4 shows the results in Kobe by applying this method. The same characteristics are recognizable in Osaka. The method includes the smoothing of annual variations in the highest tidal level, so that the clearly small sample size leads to a rough prediction of the return period of storm surges.

2] Lowest tidal level: Fig. 5 shows the probability distribution for

the occurrence of lowest tidal levels in Osaka and Kobe. The data fit well into a Gumbel distribution. This agreement has never been found in any other extremal statistics for tidal data except for the lowest tidal level. Annually, the lowest tidal levels occur in January or in December. During these months, the northwesterly monsoon blows continuously for one or two days after reaching a stable distribution of atmospheric pressure (in this situation, an anticyclone stagnates in western Siberia and a developing cyclone slowly moves eastward in the central part of the Japan Sea ) causing extraordinarily low tide. Under these circumstances, the lowest tidal level can be treated as statistically independent variables. This will be discussed later with the time series for the lowest tidal level. The effect of sampling interval on the return period is not evident as has already been shown in Fig. 4.



(a) Log-normal distribution



(b) Gumbel distribution

Fig. 3 Probability of occurrence of the highest tidal level by traditional methods

3) Maximum anomaly: Fig. 6 shows the probability distribution for the occurrence of the maximum anomaly. The discrepancies between the data and theoretical curves are marked, as for as the highest tidal level. The scattering of the data in Osaka resembles that in Kobe, so that on the basis of the physical background of storm surges, the occurrence of the maximum anomaly may be analyzed.

[c] Effect of tidal observation period on degree of fitness

The tides have been recorded for more than ten years since the last study done by Nachi(1972). However, in spite of this increase in the available sample size, the degree of fitness of the data to the probability distribution did not improve as was hoped. Thus, the sample size is not the dominant factor determining the degree of fitness. Even if the maximum anomaly can be regarded as a statistically independent variable, the "accidental" data do not agree with the theoretical curves. From Figs. 3 and 6, it is evident that the fitness of the maximum anomaly to a Gumbel distribution is worse than in the case of the highest tidal level. The influence of the period of the data is, of

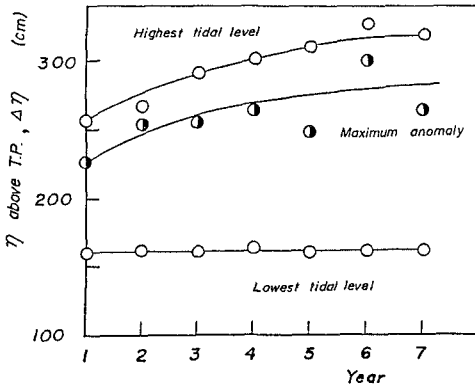


Fig. 4 Changes in estimated tidal values in Kobe with sampling years corresponding to 100 year return period analyzed by Führbötter's method

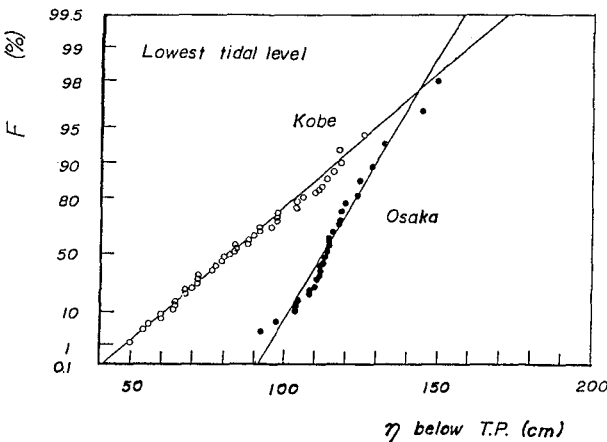


Fig. 5 Gumbel distribution for the lowest tidal level

course, part of this difference in fitness.

One of the probable explanations for this discrepancy is the effect of marked reclamation along the coast in Osaka Bay. Reclamation was rapid in the 1960's and since Osaka is located at the northeast end of the bay, as shown in Fig. 1, the effect is easily amplified. If the characteristics of the data have statistically changed due to this reclamation, it is necessary to divide them into two groups, for example, into the annual extremal values before and after reclamation. At the same time, the statistical independency of the data has to be justified. For example, if periodicity is to be found in the number of typhoons and cyclones which hit or move alongshore, the tide will consequently include their influences to some degree and careful editing should show the periodicity.

Attention must also be paid to changes in tidal characteristics due to differences in the wind fields along the tracks of typhoons. When a typhoon passes the west side of the bay, it results in a large storm surge by strong winds blowing over the sea counterclockwise. Therefore, the effect of wind drift on sea water accumulating in the semicircle is more remarkable than that in a western one. In this process, the influences of solid boundaries, such as the geographic shape of reclaimed areas and the general direction of coastlines, are also significant.

INFLUENCE OF RECLAMATION ON TIDE AND ITS TREND

[a] Influence of reclamation

Fig. 7 shows the cumulative curve for reclamation on Osaka Bay.

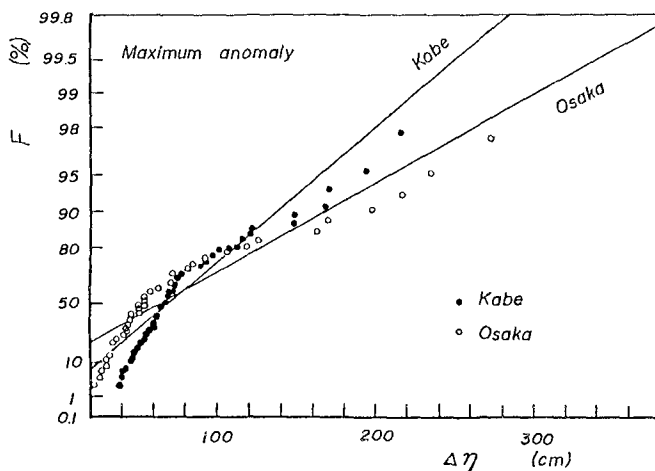


Fig. 6 Gumbel distribution for maximum anomaly



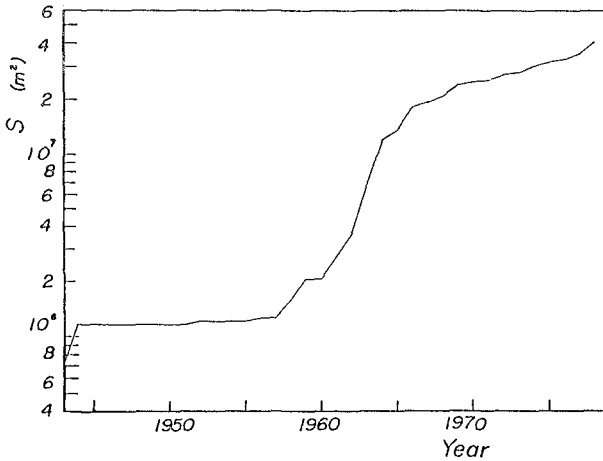


Fig. 7 Cumulative curve of reclamation area around Osaka Bay

The survey covers the coast between Akashi and Tannowa, a distance of about 90km. The acceleration in reclamation in the 1960's was a result of the rapid economic growth in Japan. According to an environmental white paper, natural beach, such as Nishikinohama and Suma beaches, occupies less than two percent of the length of the coastline. In general, the coast can be divided into rectangular areas of reclamation having sides less than several hundred meters in length continuously located along the coast. In small strips, behavior of storm surges may be amplified. In Kobe, man-made Port Island and Rokko Island are relatively large in comparison with the reclaimed areas in Osaka, so that the former unevenness in shape is not remarkable enough to make small rectangular strips of reclaimed areas.

It is very difficult to estimate quantitatively the effects of the reclamation on the tide because changes in astronomical tides are a slowly varying phenomenon. However, every tidal observations are carried out close to coast, and so the geographical boundary conditions must surely affect the tidal measurements. For this reason, changes in tidal constituents are first discussed on the basis of a comparison of predicted and observed tides, and secondly, the annual variation in high water level in the spring tide during typhoon season (July to September) is studied.

Fig. 8 shows the annual changes in the amplitude and phase angle of the tidal constituent M2 in tidal predictions. In Kobe, the changes are trivial, but in Osaka, an annual increase in the amplitude and a decrease in the phase angle can be seen. Other tidal constituents such as S2, K1 and O1 have also been found to have similar clear trends in Osaka. In order to confirm this phenomenon, further investigation is required, but at present, it can be surmised that the cumulative influences due to wide reclamation near Osaka have changed the behavior of the tide.

Fig. 9 shows the annual variation in the high water level of the spring tide during the typhoon season since 1950. A period of three to four years is evident in Osaka and Kobe with no phase lag between the two places. This phenomenon has also been detected at other tidal observation points around Osaka Bay, but the variations in amplitude are smaller than those in Osaka and Kobe. Probable factors which generate these variations, that is, the influence of typhoons and the meandering of the Kuroshio along the southwest coast of Japan have been investigated with field data; however, it appears that they do not contribute to this periodic variation in the high water level.

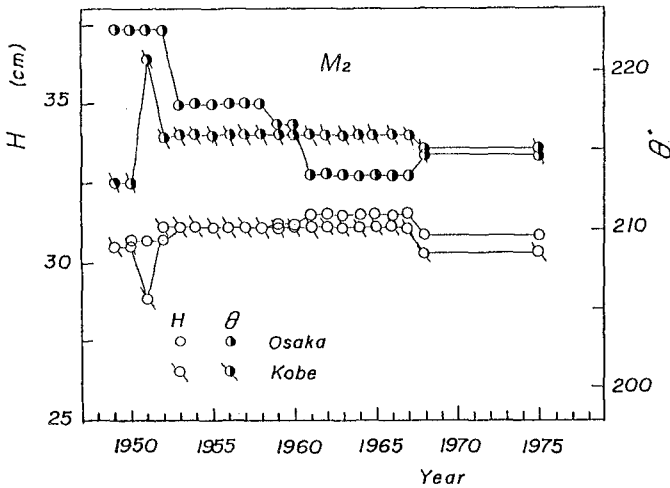


Fig. 8 Annual changes in amplitude and phase angle of tidal constituent  $M_2$

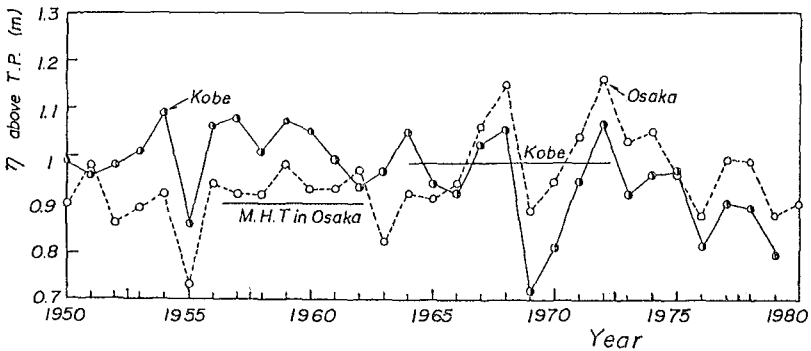


Fig. 9 Annual changes in high water level of spring tide in typhoon season

Next, hourly changes of the tide are studied to see if the reclamation could be causing the unusually high water levels. Fig. 10 shows the hourly changes in the tide in Osaka for four days around the spring tide of August 14 and 27, 1965. The discrepancies between the predicted and observed tides are clearly greater just before and after the spring tide. Such systematic discrepancies are usually observed during the rising stage of a tide. Moreover, flattening of the high tidal level peaks in the spring tide has been pointed out by the Kobe Marine Observatory since 1970, which almost coincides with the construction of Port Island in Kobe. Therefore, the tide may be under the influence of the reclamation

The above investigation gives the quantitative effects of the reclamation on the tide and shows that the tidal level tends to be amplified by a rapid increment in reclaimed areas.

[b] Time series of tide and its trend

Trends may be included in the time series for extremal values, such as the highest tidal level and the maximum anomaly. Such trends are due to long-term natural changes or to artificial impacts, such as rise of sea level or reclamation along the coast, land subsidence, etc.

The trend index is given with the rank correlation by

$$IT = \sqrt{18} \left( \sum_{i=1}^{N-1} n_i - N(N-1)/2 \right) / \sqrt{N(N-1)(2N+5)} \quad (1)$$

in which  $N$  is the number of samples,  $n_i$  the number of events larger than  $x_i$  after the occurrence of  $x_i$ . If  $IT > 1$ , the time series includes an increasing trend. On the contrary, if  $IT < -1$ , there is a decreasing trend. In the case of the highest tidal level,  $IT$  is 2.08 in Osaka and -0.78 in Kobe. The same tendency can be detected in the lowest tidal level, but there is no trend in the maximum anomaly for either place.

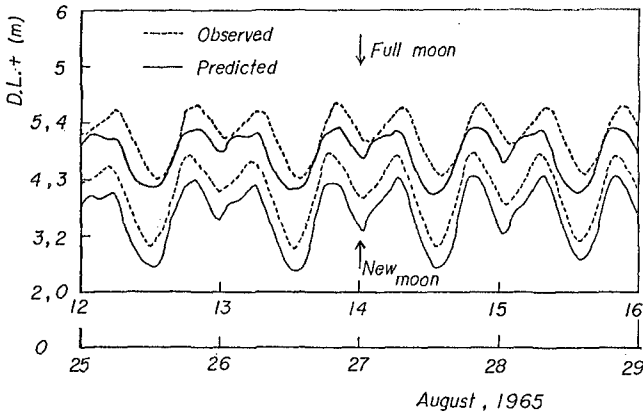


Fig. 10 Hourly changes in tide in Osaka

When the trend is detected, it is usual to eliminate it from the data by applying a polynomial expression. However, it is also evident that in the future, the situations affecting the tidal level will inevitably change. Reclamation, as mentioned affects the characteristics of the tide, but the trend that results will change again with more reclamation. Moreover, the rising trend of the highest tidal level in Osaka is due to a group occurrence of storm surges after World War II. In this paper, therefore, the trend due to natural factors are also included in the analysis.

Fig. 11 shows the auto- and serial-correlation coefficients of time series of the extreme tidal data in Kobe. From this figure, it is recognized that the maximum anomaly changes in periods of four, twelve and fourteen years. This situation is almost the same in Osaka. The reason this clear periodicity exists is mainly due to the characteristics of typhoons as the external force causing storm surges. Fig. 12 shows the auto-correlation coefficients of the number of typhoons generated and the number of typhoons which struck. The observation period of the data is the same as in Fig. 11. A periodicity of four, twelve and sixteen years can be found in the number of typhoons which struck. This result has also been confirmed by analysis with a periodogram. It is clear that the occurrence of the maximum anomaly strongly depends on characteristics of typhoons approaching Japan.

Another problem is revealed by this analysis. When the maximum anomaly is not made up of statistically independent variables, as shown in Fig. 12, it is, in a strict sense, impossible to apply the theory of extremal statistics, but as Gumbel (1957) said, it is reasonable that the probabilistic distribution of statistically dependent variables has some of asymptotic characteristics found in independent variables. Therefore, practically speaking, extremal statistics is also applicable to the maximum anomaly.

#### EXTREMAL STATISTICS OF STORM SURGES

##### {a} Changes of tide with typhoon track

As already pointed out, acceptable fitness of the highest tidal level and the maximum anomaly to a Gumbel distribution is not obtainable by traditional methods. The investigation shows that the shortness of the observation period is not always the main reason for the discrepancy between the observed data and theoretical distribution curves. On the contrary, for the lowest tidal level, the fitness of the data to a Gumbel distribution or a log-normal distribution is good.

For improvement in the degree of fitness, the process of the occurrence of an extremal tide should be studied. Most extremal data, except those in recent years, are due to typhoons. In the east area of the typhoon track, in which the moving speed of a typhoon is superposed on the gradient wind, strong wind are blown. Therefore, storm surges in the east semicircle are generally larger than those in the west one. Thus, the extremal data can be divided into two groups according to the directional characteristics of the typhoon tracks. Weather charts can

be used to clarify the position of typhoons.

Fig. 13 shows the auto correlation coefficients of the highest tidal level in Kobe when the typhoon tracks are considered. The characteristics of variation of the auto-correlation coefficients differ from those shown in Fig. 12 where the directional characteristics of the typhoons are not considered. This situation is the same in Osaka. Furthermore, comparison of the auto-correlation coefficients for west-

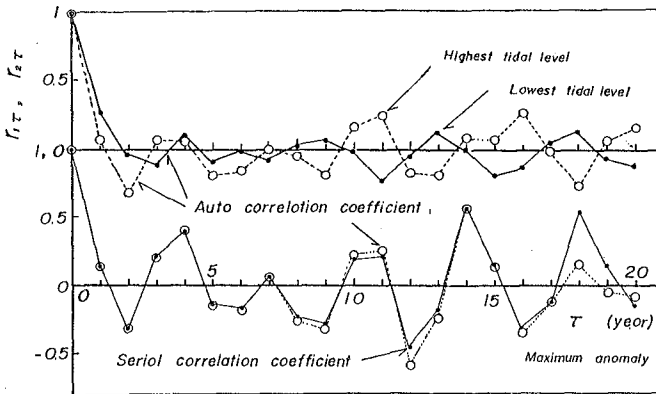


Fig. 11 Auto- and serial-correlation coefficients of time series for extreme tidal values in Kobe

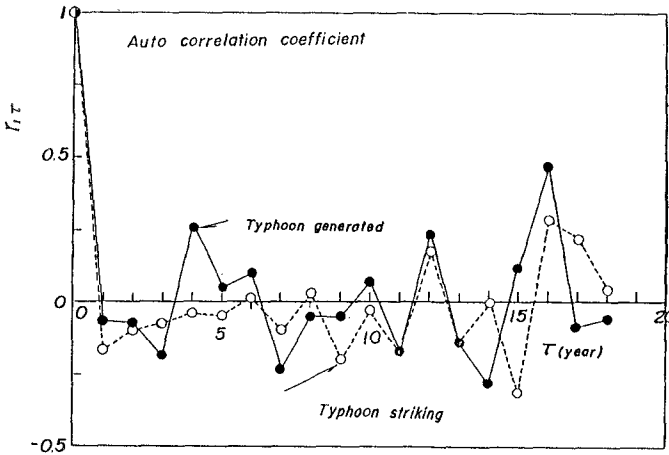


Fig. 12 Auto-correlation coefficients of numbers of typhoons generated and of typhoons striking Japan

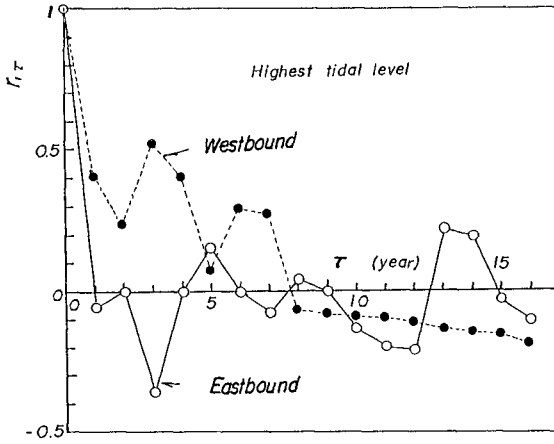


Fig. 13 Auto-correlation coefficients of the highest tidal level in Kobe, considering direction of typhoon track

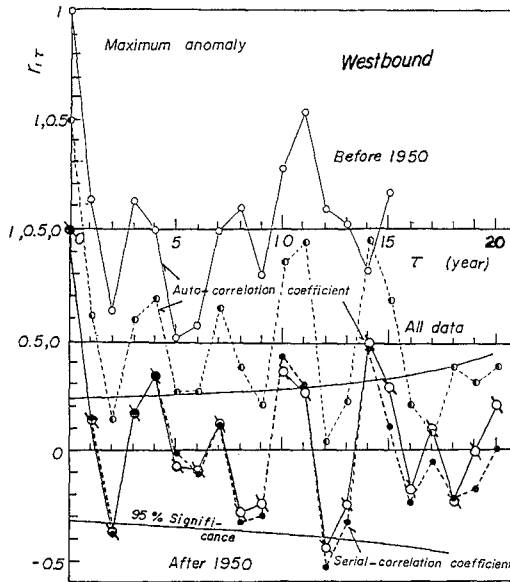
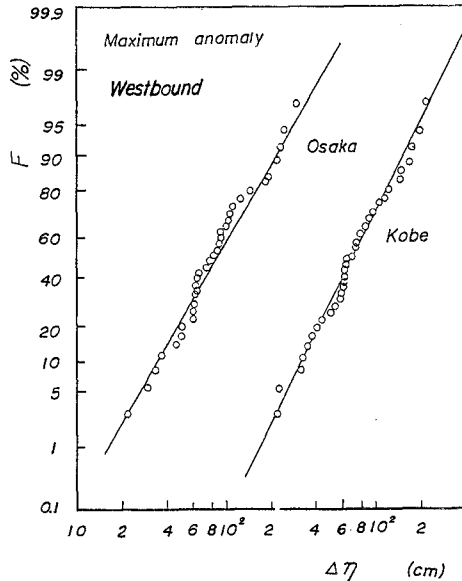


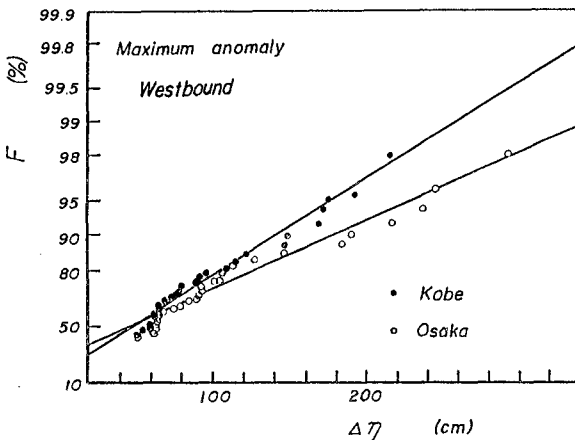
FIG. 14 Auto- and serial-correlation coefficients of maximum anomaly in the case of westbound typhoons

bound and eastbound typhoons shows that their phases are different. At the same time, the auto-correlation coefficients of the highest tide due to a cyclone are quite different from those due to typhoons. Therefore, the typhoon tracks and the source of generation of the highest tidal level govern the characteristics of the time series. In other words, the highest tidal level data are usually composed of three different ensembles, so that it is difficult to make a single law of extremal statistics.

From a practical point of view, the data associated with a westbound typhoon is the most important among them because it corresponds to the generation of big storm surges. In the case of eastbound typhoons, however, there seems to have upper



(a) Log-normal distribution



(b) Gumbel distribution

Fig. 15 Probability of occurrence of maximum anomaly generated by typhoons passing through area west of Osaka and Kobe

limit of wind speed in their west side, a scale of storm surges may be under certain level.

Fig. 14 shows the auto and serial correlation coefficients of the maximum anomaly for westbound typhoons. In comparison with Fig. 13, the overall characteristics of the maximum anomaly in Osaka are governed by the typhoons which pass through its western side. In the figure, the data are divided into two groups, just before and after 1950. In both groups, an eleven-year period can be seen. This periodicity coincides with that of the typhoons striking Japan.

[b] Extremal statistics of storm surges

Fig. 15 shows the probability of occurrence for the maximum anomaly generated by typhoons passing through the western side of the bay. From this figure, it is clear that the fitness of the data to a Gumbel distribution or a log-normal distribution improves in comparison with Fig. 3. In Fig. 16, data smaller than 50cm are included in order to obtain a larger sampling period. Every newspapers, weather charts and meteorological reports show that there was no storm surges at those years. The fitness of the data in Fig. 16 also improves over that in Fig. 15. From these figures, it is clear that Osaka is more susceptible to storm surges than Kobe. In this analysis the distance between the eye of a typhoon and the tidal measuring points has not been included. Its consideration would further improve this method.

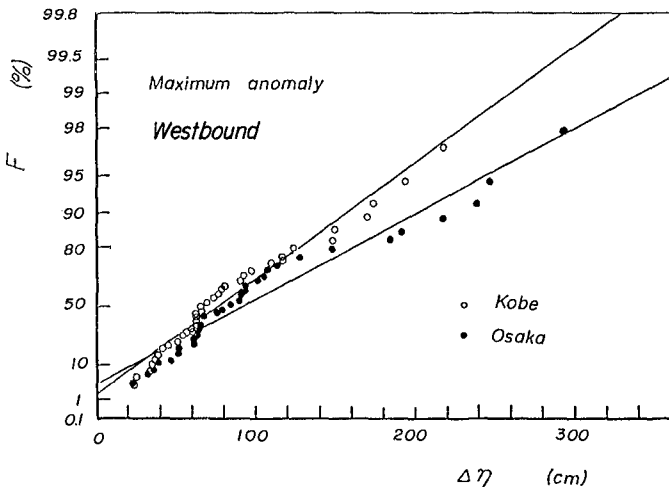


Fig. 16 Gumbel distribution of maximum anomaly in which data less than 50cm are newly added to those in Fig. 15



The frequency distributions for the highest tidal level in Osaka analyzed by the method proposed here are shown in Fig. 17. It is found that the fitness of the data to a Gumbel distribution is fairly good in comparison with Fig. 3. In particular, the scattering of the data is much improved for portion of relatively large tidal levels generated by typhoons passing through the western side of the bay. For eastbound typhoons, a certain upper limitation for the highest tidal level can be observed. Therefore, this classification of typhoon by track contributes much to the improvement of fitness.

#### CONCLUSIONS

We have developed a method for estimating the occurrence probability of abnormal tides by considering the characteristics of typhoon tracks. It is clear that the fitness of the data to any probability density function cannot be improved by lengthening the period of tidal data or by taking into consideration the effects of extensive reclamation on characteristics of tides. It is concluded that this method has high applicability for determination of the return periods of abnormal tides due to storm surges.

The study reported here was supported by Grant-in-Aids for Scientific Research from the Ministry of Education, Science and Culture of Japan, under Grant No. 302027.

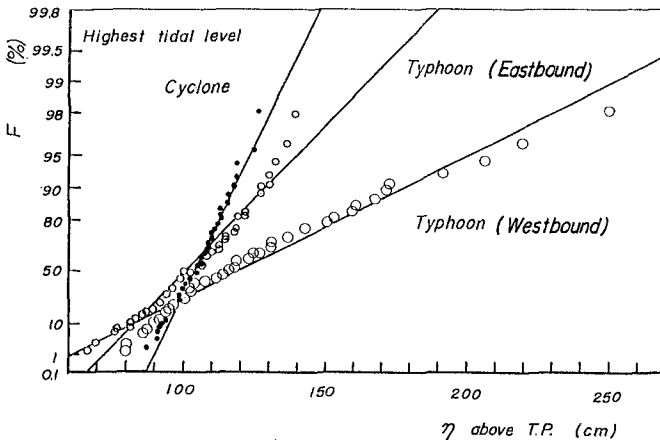


Fig. 17 Gumbel distribution for the highest tidal level in Osaka for east- and westbound typhoons and cyclones

## REFERENCES

- DeYong, R. K. and J. R. Pfattlin; Extreme sea levels from tide and surge probability, Proc. Civil Eng. in the Oceans, ASCE, 1975, pp. 79-82.
- Führböter, A.; Frequencies and probabilities of extreme storm surges, Proc. 16th Coastal Eng. Conf., ASCE, 1978, pp. 949-964.
- Graff, J. and D. L. Blackman; Analysis of maximum sea levels in Southern England, Proc. 16th Coastal Eng. Conf., ASCE, 1978, pp. 931-948.
- Gumbel, E. J.; Statistics of extremes, Columbia Univ. Press, 1957.
- Nachi, T; Some river engineering problems in relation to counter-measures against storm surges, Dr. of Eng. Dissertation, Kyoto Univ., pp. 1-240 (in Japanese).
- Pugh, D. T. and J. M. Vassie; Extreme sea levels from tide and surge probability, Proc. 16th Coastal Eng. Conf., ASCE, 1978, pp. 911-930.
- Tayfun, T.; Joint occurrence in coastal flood, Proc. ASCE, WW2, 1979, pp. 107-123.

## CHAPTER NINE

### BAYWATER RESPONSE TO TSUNAMIS

Tetsuo Abe\*

#### ABSTRACT

To investigate the transient characteristics of the tsunami-induced oscillations, records of tsunami caused by the Off-Miyagi earthquake in June, 1978 were analysed on the basis of theories on stationary and non-stationary stochastic processes. The stationary spectra show the average feature of the phenomenon. Discrepancies, however, are recognized between the first half oscillations and the second half oscillations during the tsunamis. Besides, the energy densities of non-stationary spectra do not always indicate stationary value at the periods which correspond to the predominant ones of the stationary spectra. These suggest that tsunami-induced oscillations are translative.

#### 1.0 INTRODUCTION

Tsunami waves are basically generated by dislocation of sea-bottom in earthquakes of magnitudes of over 6.5. Waves which attack the coast give greater height as the magnitude of an earthquake increases. Such waves are still in the dispersive process even at the coastline, because the source regions of tsunamis which attack the Japan Island are usually at the western slope of the Japan Submarine Trench and the distance to the coast is nearly the same order of the breadth of the source. Moreover, these waves are transformed by reflection and refraction superimposed by shelf resonance and the edge waves to give complicated dynamic phenomena near-coast offshore region( Iwasaki(4) ).

Dynamic phenomena such as baywater oscillations have been of considerable interest to coastal engineers in relation to engineering evaluation of structures against tsunami disaster. Many researchers have treated them so far, both theoretically and experimentally. Consequently, the understanding of the response of water bodies to external disturbance has progressed greatly. However, less attention has been paid on the investigations based on the actual tide gauge records, because of the limited amount of the tide gauge stations and tide gauge records available in ordinary bays. So that the detailed behaviours of actual bay oscillations were not so well investigated and the verification of experimental or numerical results by observed data is often hindered.

Then, the transient process of baywater response to tsunamis should be investigated based on the observation data, which is the object of this study.

#### 2.0 OUTLINE OF THE OFF-MIYAGI TSUNAMI IN JUNE, 1978

The Sanriku Coast is the name of the coast which is situated in the northeastern part of the mainland of Japan facing the Pacific Ocean and stretching from 38°N to 41.5°N in latitude. Although this coast is famous

\* Professor of Tohoku Institute of Technology, 35/1 Yagiyama-Kasumicho Sendai 982, JAPAN.

by the inundation of tsunamis and a lot of tsunamis attacked there in the past, there were only three cases for which scientific records were obtained among those which originated off this coast and severe damage. They were the Sanriku Tsunami in 1896, the Sanriku Tsunami in 1933 and the Tokachi-oki Tsunami in 1968. Thus, data acquisition of tsunami waves is not easy, because earthquakes of magnitude of over 7.0 are very much seldom.

In 1978, small tsunamis were caused by an earthquake of the magnitude of 7.4 which originated off the coast of the Miyagi Prefecture, the southernmost part of the Sanriku Coast, at 17:14 on June 12. Its source was reported to be at  $142^{\circ}14'E$  longitude,  $38^{\circ}10'N$  latitude and about 25 km deep. According to records of the present tsunamis, the initial motion of tsunamis was in the upward direction at the whole stations in the Sanriku Coast, suggesting the uplift of the sea-bottom in the tsunami source area. The tsunami source area which was estimated by using the adverse refraction diagram was reported by Iwasaki and Mano(5) as shown in Fig. 1, of which the longer axis of 65 km lies in the E-W direction and the shorter one of 50 km lies in the N-S direction, roughly along a bathymetric line of 600 m deep.

As to the Miyagi district, Hatori(3) reported two historical tsunamis as shown in Fig.1. These tsunamis caused by the earthquakes of magnitude of 7.5 and 7.4, respectively, whose seismic intensities were inferred from old documents. The present area of aftershocks coincided with the wave source area of the historical tsunami caused by the earthquake on October 21, 1861. This historical tsunami caused waves of 3 to 4 m high at Ryori near Ofunato Bay. However, wave heights of the present tsunamis were small in compare with those in 1861. The maximum height was only about 1.22 m at Onagawa Bay and about 1.18 m at Kesennuma Bay in the north of the Miyagi Prefecture. Generally speaking, historical tsunamis were generated at the similar locations to the source regions of recent tsunamis. Then, the area in the sea near the Miyagi district may still be considered a region of relatively high tsunami risk, because no conspicuous tsunami has been generated in this region since 1861, as pointed out by Hatori(3).

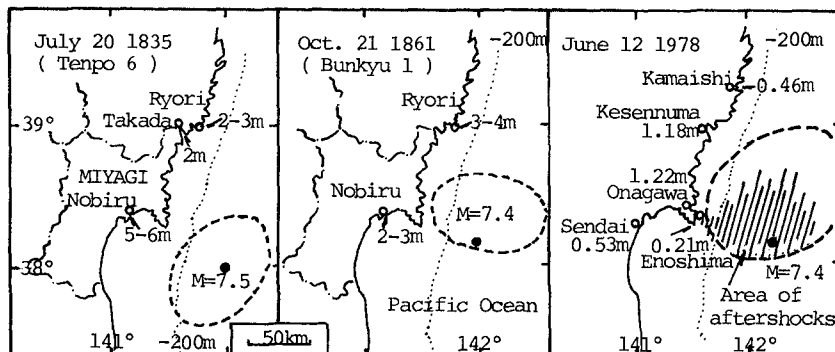


Fig. 1 Tsunami heights and tsunami source areas of the 1835 Tenpo and the 1861 Bunkyo earthquakes inferred from old documents by Hatori ( 3 ), and the tsunami source area caused by the Off-Miyagi Earthquake in 1978 as defined by Iwasaki and Mano( 4 ).

3.0 STATIONARY CHARACTERISTICS OF THE BAYWATER RESPONSE TO TSUNAMIS

3.1 Stationary Spectrum of Oscillation by Tsunamis

Onagawa Bay and Kesennuma Bay were selected for the analysis of gauge records, because the tsunami heights at two bays were relatively high in compare with those of other stations in the Sanriku Coast. Besides, Onagawa Bay was just located near the present tsunami source area and Kesennuma Bay was just opened to that. In Onagawa Bay, there are a tidal gauge station at the head and a tsunami observatory of the Earthquake Research Institute, University of Tokyo, at Enoshima Island offshore of the bay. In particular, Enoshima data may be used to estimate the spectral characteristics of wave offshore. In Kesennuma Bay, there is a big island inside the bay, so that the bay is almost like a long and narrow bay.

Table 1 shows the general discription of wave data and Fig. 2 shows the time sequence records of water level, namly tsunami waves, which were deduced from gauge records by subtracting meteorological tides estimated by the moving average method. Wave data at Onagawa and at Kesennuma were divided into two parts, "before the tsunamis" and "after the tsunamis". Furthermore, data after the tsunamis were divided into "first half" and "second half" for the spectral analysis on the basis of stationary stochastic process.

Spectrum is a widely used idea for presenting the constitution of a given time series. Wave oscillations originated in the open sea or induced within the bay are, in fact, typical time series in nature. There are several methods which can be used to estimate the spectrum of the stationary band-limited time series. The " Maximum Entropy Method " as introduced by Burg(2) is used here. This method is very convenient for the analysis of tsunani waves, because it can produce a highly resoluted spectrum with accurate frequencies and power estimates, even for the observed time series with very few samples.

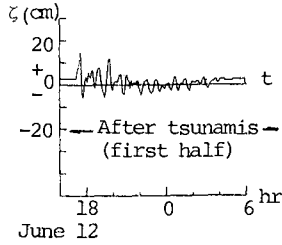
For a given stationary time series, the maximum entropy power spectrum is defined by the following power spectrum, S(f), which maximizes the entropy of the given time series:

$$S(f) = \frac{\Delta t \sigma_{M+1}^2}{\left| \sum_{m=0}^M \gamma_{m+1, K+1} \exp(i2\pi f m t) \right|^2} \quad (1)$$

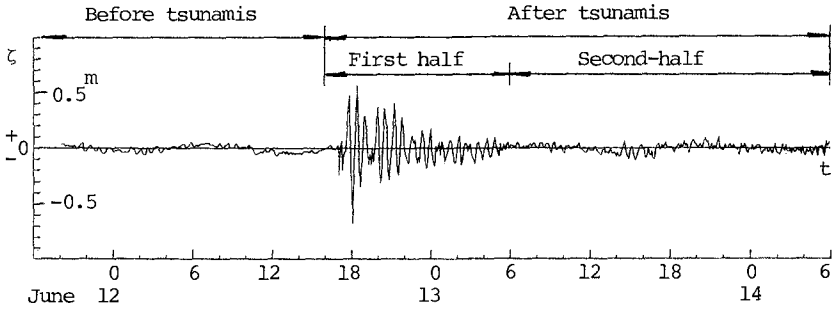
Hereafter, S(f) is called MEM-spectrum, where  $\sigma_{M+1}^2$  and  $\gamma_{m+1, K+1}$  are the variance of prediction errors and the prediction error filter for the filter number K+1, respectively. M is the number of the maximum correlation lag, and f is the frequency. The actual time step,  $\Delta t$ , was determined by the chart speed of tide gauge. Since  $\Delta t$  was selected as 5 min, the maximum frequency available is 1/15(HZ), that is, the minimum period available is 15 minutes here. The frequency range was, then,

Table 1 Tide gauge stations and analysis data

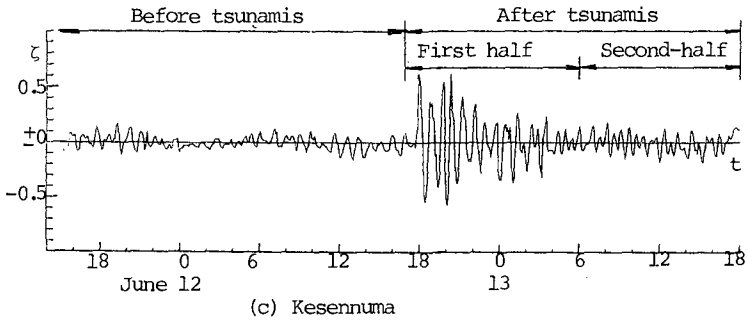
Bay	Onagawa				Kesennuma		
	Enoshima	Onagawa		Kesennuma	Kesennuma		
Tide gauge station	Enoshima	Onagawa		Kesennuma	Kesennuma		
Time origin (t=0)	After the tsunami	Before the tsunami	After the tsunami	Before the tsunami	After the tsunami	After the tsunami	
		First half data	Second-half data	First half data	Second-half data	Second-half data	
June, 1978, JST	12th 16:00	11th 18:00	12th 16:00	13th 6:00	11th 14:00	12th 17:00	13th 6:00
Sampling time ( $\Delta t$ )	5 minutes	5	5	5	5	5	5
Number of data (N)	169	265	169	289	324	156	145
Number of filters (K)	15	20	15	20	20	14	14



(a) Enoshima



(b) Onagawa



(c) Kesenuma

Fig. 2 Time sequence records of water level deduced from tide and tsunami gauge records.

divided into 100 unites, which enabled the calculation of MEM-spectrum. The number of filter terms was tentatively selected by the "Final Prediction Errors Standard", and the optimal one was decided so that the spectrum would include the first mode which had been estimated by a preliminary test with fewer filter terms.

Fig. 3 shows the MEM-spectra of Onagawa Bay, where the broken line was derived from the first half data after the tsunamis at Enoshima near the bay mouth and chain line is the one at Onagawa in the bay head. In this spectra, ordinate of  $S(f)$  is normalized such that 100 and 1 are the reference maximum and minimum values of spectra. According to the results of Onagawa, there are four predominant oscillation modes during the tsunamis. Their periods are 41, 32, 18 and 13 minutes. The oscillation of 41 min is the basic mode along the bay axis, whose node exists near bay mouth. The oscillation with the period of 18 min is corresponding to the first longitudinal mode, whose node exists near the branched bay at the bay head as reported by Aida(1). The oscillation with the period of 13 min may be corresponding to the second lateral mode between two branched bays. Spectra of Enoshima show four peaks at the period of 43, 26, 18 and 12 minutes. The predominant oscillation period 43 min shows that the water oscillation at Enoshima, although the tide gauge station is considered to be located at the open sea, is affected by the existence of Onagawa Bay. The oscillation of rather longer period is evidently reflecting the effect of the continental shelf off Onagawa Bay. Enoshima is located at the mouth of Onagawa Bay and was just on the edge of the present tsunami source area. So, the spectra at Enoshima may provide information on the waves in the tsunami source area. The oscillation of the period of 26 min seems to be related to the waves in the present tsunami source area. However, further data and considerations are needed to specify it. The oscillation energy is developed mainly with respect to the basic mode. Their magnitudes at the bay head are much higher than those at the bay mouth.

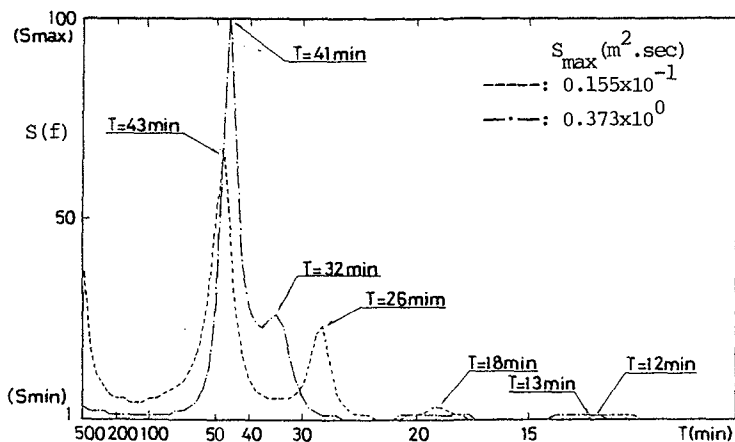


Fig. 3 MEM spectrum of Onagawa Bay, where the broken line is derived from the first half data after the tsunami at Enoshima, and the chain line at Onagawa.

Fig.4 shows the MEM-spectra at Onagawa and Kesennuma. The spectra at Onagawa show the several predominant oscillation periods of 38, 27, 18 and 15 minutes for the wave data before the tsunamis invade; for the first half data after the tsunamis, those of 41, 32, 18 and 13 minutes; and for the second half data after the tsunamis, those of 37, 30, 16 and 12 minutes, respectively. The oscillation of 38 min is the basic mode along the bay axis and the oscillation period of 18 min is corresponding to the first longitudinal mode. The oscillation with the period of 15 min is corresponding to the first lateral mode. It represents the interaction of oscillations in two branched bays, named Onagawa Harbour and Gobaura Bay, and may be considered a lateral oscillation between these two bays. By the intrusion of tsunamis, the basic mode with the period of 38 min in ordinary times before the tsunamis is slightly shifted to the longer period range, 41 min, in the first half of the tsunamis; and to shorter period range, 37 min, in the second half of the tsunamis, suggesting that the position of node moves toward the open sea; and moves back into the bay during the tsunamis. The oscillation energy is especially amplified in the basic mode in the first half of tsunamis. One of another typical facts is that rather remarkable rise in the spectrum is recognized at around 71 minutes in the final stage, evidently reflecting the effect of the continental shelf off Onagawa Bay.

As to Kesennuma Bay, three remarkable peaks were noticed at 52, 33 and 19 minutes in the spectra derived from data before the tsunamis; Two remarkable peaks were noticed at 50 and 32 min in the first half data after the tsunamis; and at 59 and 30 minutes in the second half data after the tsunamis. The largest period is corresponding to the basic oscillation mode of the bay whose node exists near the bay mouth, and the others are related to the oscillations near the bay head. However, the response features are different from the ones of Onagawa Bay. In the first stage of tsunami times, the mode at the period of 19 min disappears and the others are slightly shifted to shorter periods of 50 and 32 min. The energy of the basic oscillation is especially developed in this stage. It can be said that the location of the node of the basic mode moves into the bay and moves toward the open sea by the intrusion of the tsunamis.

### 3.2 Numerical Analysis

In contrast to the spectral analysis of the observed wave data, a theoretical investigation on the resonant oscillation in Onagawa Bay would be done in this study. Through this investigation, a discrete set of natural oscillation modes of Onagawa Bay and the corresponding relative wave heights at every point inside the bay are estimated, from which the system function of the baywater oscillation system can then easily be found. Furthermore, on the basis of the power spectrum of the waves observed at Enoshima near the bay mouth, the response power spectrum at various sites inside the bay can also be estimated.

Records of wave gauge set in bays show very much different behaviour in each locality where the gauges are set. It is the influence of the local features, the transient nature of the incident waves and the bay dynamics. From the foregoing statement, a simple concept is realized that the occurrence of the baywater oscillations, at least, is concerned with two parameters; one is the natural periods of the bay, the other is the period range of the incident waves. For the case of a long and narrow bay, only longitudinal oscillations are importance. Then, the natural period of the first mode of free oscillation on continental shelves or bays is



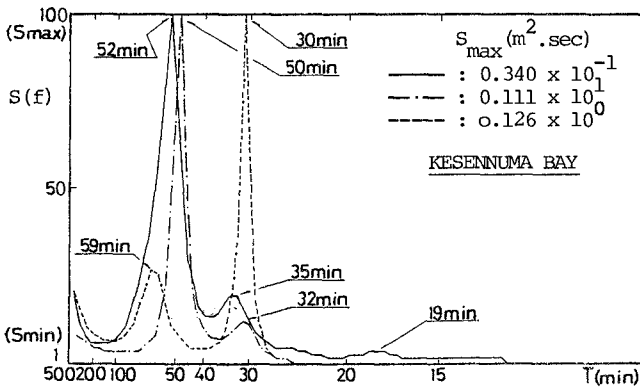
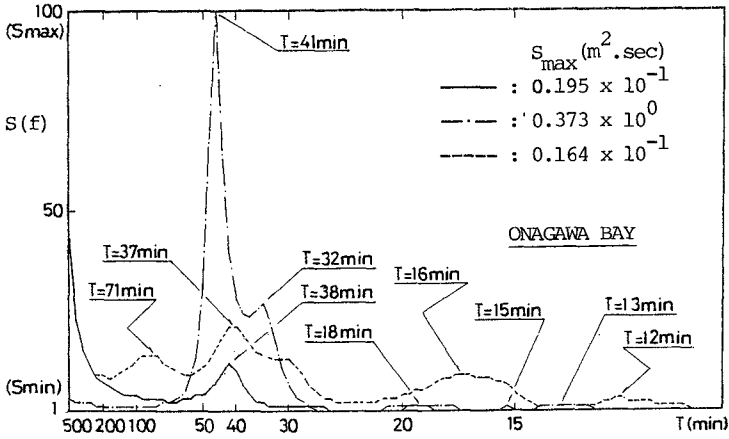


Fig. 4 MEM spectra at Onagawa and at Kesennuma, where the solid line is derived from data before the tsunami; the chain line is derived from first half data; and the broken line from second-half data after the tsunami.

calculated by  $T=4\ell / 60\sqrt{gh}$  (min.), where  $h$  and  $\ell$  are the average depth and length. However, tsunami-induced oscillations in bays are different from the free oscillations. They should be considered as forced oscillations. In this study, the basic equation used to analyse numerically this problem is the Helmholtz equation, which describes the spatial variation of the linear oscillation in a bay; that is,

the long wave equation for periodic waves is

$$\frac{\partial}{\partial x} \left( h \frac{\partial \zeta}{\partial x} \right) + \frac{\partial}{\partial y} \left( h \frac{\partial \zeta}{\partial y} \right) - \frac{1}{g} \frac{\partial^2 \zeta}{\partial t^2} = 0 \quad ( 2 )$$

where  $\zeta$  is the surface elevation,  $g$  is the acceleration of gravity. To obtain a solution of the steady oscillations for the bay, we assume that the induced wave oscillation is a simple harmonic; that is,

$$\zeta(x,y,t)=A(x,y)\exp(i\sigma t) \quad ( 3 )$$

where  $\sigma$  is the angular frequency. Then, the long wave equation is converted to the well-known Helmholtz equation;

$$\frac{\partial}{\partial x} \left( h \frac{\partial A}{\partial x} \right) + \frac{\partial}{\partial y} \left( h \frac{\partial A}{\partial y} \right) + \frac{\sigma^2}{g} A = 0 \quad ( 4 )$$

To solve this equation is then equivalent to finding out the unknown function  $A(x,y)$ . In this study, one of the numerical methods, that is, " Finite Element Method " is used to solve that equation. Then, the solution of the Helmholtz equation is finally converted to the problem of solving an eigen-value system given by

$$[ K ] \{ A \} - \lambda [ M ] \{ A \} = 0 \quad ( 5 )$$

with the boundary conditions of  $A=A_0$  at the entrance of the bay and  $\frac{\partial A}{\partial n} = 0$  at the rigid boundary, where  $\lambda=\sigma^2$ ,  $\{ A \}$ : unknown node value vector,  $[ K ] = \sum_{k=1}^m [ K ]_k$  : the stiffness matrix,  $[ M ] = \sum_{k=1}^m [ M ]_k$  : the mass matrix.

The solution domain defined in this study covers not only the confined water area, but also some area of open sea. In fact, the seaward boundary of the domain is just located at the edge of the bay mouth and the width of the extended part is almost the same as that of the confined part. The domain was divided into 98 triangular elements with 71 nodes. According to the above definition of the solution domain, the seaward boundary is assumed to be the entrance and all the others are taken as rigid boundary.

Next, from the Fourier analysis, we know that

$$S_y(f) = |H(f)|^2 S_x(f) \quad ( 6 )$$

where  $H(f)$  is the Fourier transform of the impulse response function of a given system;  $S_x(f)$  and  $S_y(f)$  are the power spectrum functions of the input  $x(t)$  and the output  $y(t)$ , respectively. Then, the output power spectrum can easily be computed if the input power spectrum and the system function are given. An example of the system functions of Onagawa Bay referred to Enoshima has been computed and the power spectrum of the waves observed at Enoshima has also been estimated as shown before.

Fig. 5 shows examples of the system function and the power spectrum estimated in this way. From this figure, it can be seen that the oscillations of natural mode theoretically obtained for Onagawa Bay are those with the periods of 38.5, 14.8, 9.0 and 7.9 minutes. Among them, the oscillations with the periods of 38.5 and 14.8 min are almost the same as the predominant oscillations of the first half after the tsunami records of Onagawa. The system functions say that oscillations on the bay and harbour cause greatly the amplification of oscillation energy at the bay head. Table 2 is the summary of the results of spectral analyses and numerical analyses on the stationary characteristics of the tsunami-induced oscillations, including the results reported by Aida(1).

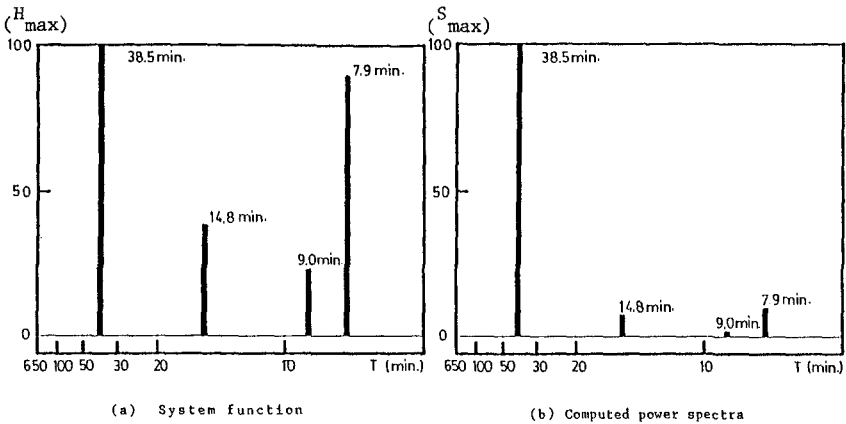


Fig. 5 System functions and computed power spectra at Onagawa in Onagawa Bay.

Table 2 Periods of oscillations in Onagawa and Kesennuma bays

Bay	Tide gauge station		Period (minutes)								
			Oscillation on continental shelves				Oscillation in bay				
			NR	ENR	E	ESE	SE	F	L <sub>1</sub>	T <sub>1</sub>	L <sub>2</sub>
Onagawa		Observation (Long-period waves)*	98-120								
		Numerical model†	36.0	18.1	14.4	12.8	10.0	9.0	8.0		
	Enoshima	Observation After tsunamis (Tsunamis) First half	43	26	18		12				
		Observation (Tsunamis) Before tsunamis	38	27	18	15					
	Onagawa	Observation (Tsunamis) After tsunamis	First half	41	32	18	13				
			Second half	71	37	30	16	12			
	Numerical model	38.5			14.8				9.0	7.9	
Kesennuma		Seiche: T=4ℓ/60√gh (min.)	97	76	77	83	89				8
		Observation (Tsunamis) Before tsunamis	52, 35, 19								
	Observation (Tsunamis) After tsunamis	First half	50, 32								
		Second half	59, 30								
	Seiche: T=4ℓ/60√gh (min.)	152	-	72	-	80					
Remarks	*; and F: fundamental mode; L <sub>1</sub> , L <sub>2</sub> : longitudinal 1st and 2nd modes; T <sub>1</sub> , T <sub>2</sub> : lateral 1st and 2nd modes [after Aida (1)].										

3.3 Amplification Factor

Fig. 6 shows the amplification factors at various sites within Onagawa Bay relative to Enoshima, which are directly estimated through the computation by using the numerical model based on finite element method as a set of natural oscillation modes and corresponding relative wave height vectors. The amplification factor at the period of 38.5 min is corresponding to the basic mode of the bay and the part at the period of 7.9 min is respect to the harbour resonance. However, values of the amplification factors seem to be large.

Then, the amplification factor at Onagawa relative to Enoshima (i.e. bay head vs. bay mouth) was computed from the MEM-spectrum at Enoshima,  $S_E(f)$ , and at Onagawa,  $S_O(f)$ , with the assumption of no reflection at the bay mouth; that is,

$$R(f) = \sqrt{\frac{(1 + \mu) S_O(f)}{S_E(f)}} \quad (7)$$

where  $\mu=0$  (without reflection). The results are shown in Fig.7 and Table3, from which the amplification factors estimated from the MEM-spectrum in this way seem to be explained, to a reasonable degree, by the relative tsunami heights obtained from the tsunami records which are shown in Table 4. They are very much dependent on the oscillatory periods.

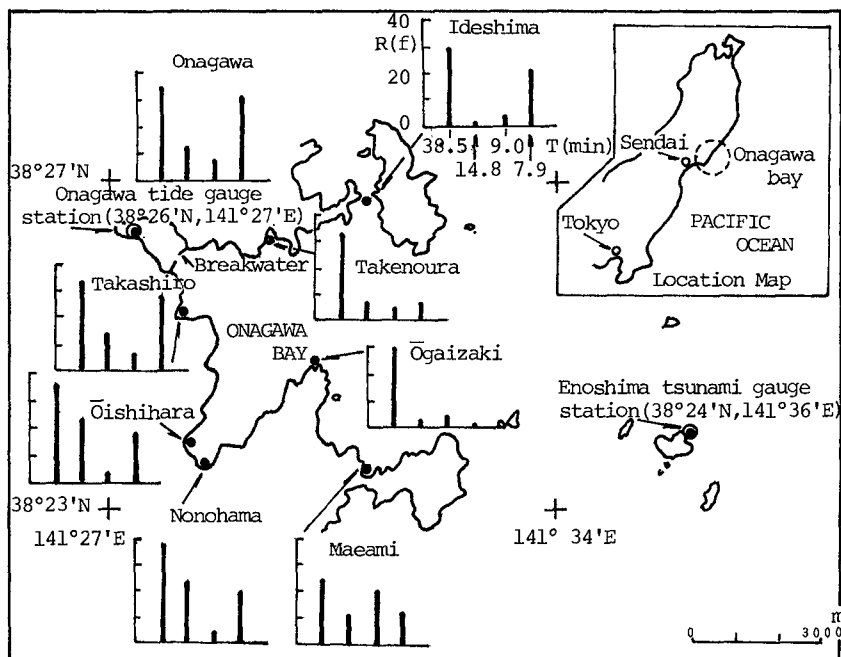


Fig. 6 Amplification factor at various sites within Onagawa Bay relative to Enoshima.

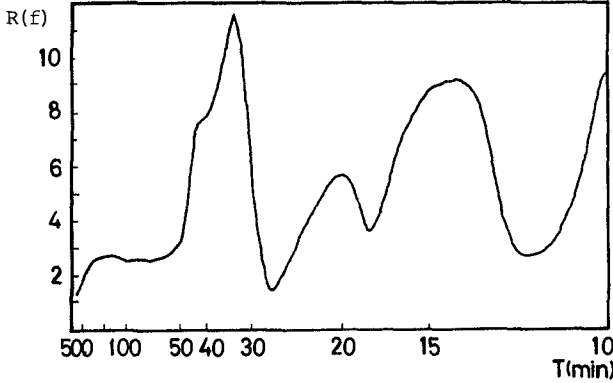


Fig. 7 Amplification factor at Onagawa (bay head) vs. Enoshima (bay mouth), which is derived from the MEM-spectra for the first half data after the tsunamis.

Table 3 Amplification factor at Onagawa relative to Enoshima, for predominant periods of oscillations derived from MEM-spectra.

Period (min.)	F						L <sub>1</sub>		T <sub>1</sub>	L <sub>2</sub>		
	45	43	42	36	32	29	26	19	18	15	13	12
Amplification factor	2.3	5.1	7.3	8.8	11.5	6.2	1.4	5.2	3.9	8.7	8.0	3.0

Table 4 Relative tsunami heights at Onagawa vs. Enoshima [from tide gauge records].

	Zero upcrossing waves					Remarks
	(a <sub>c</sub> ) <sub>O</sub>	(a <sub>T</sub> ) <sub>O</sub>	(H) <sub>O</sub>	Period (min.)		
	(a <sub>c</sub> ) <sub>E</sub>	(a <sub>T</sub> ) <sub>E</sub>	(H) <sub>E</sub>	(T) <sub>E</sub>	(T) <sub>O</sub>	
1st wave	3.1	12.5	5.8	35	40	( ) <sub>O</sub> :Onagawa ( ) <sub>E</sub> :Enoshima 
2nd wave	8.0	17.5	10.1	50	35	
3rd wave	3.6	2.7	3.2	50	55	
4th wave	3.3	10.3	4.7	30	35	
5th wave	7.2	7.0	7.1	55	40	
6th wave	8.2	12.0	9.3	25	40	
7th wave	14.5	2.8	6.1	55	40	
8th wave	4.0	3.5	3.7	45	50	
9th wave	5.7	6.0	5.8	30	40	
10th wave	-	8.5	13.0	20	30	

Water bodies on the continental shelf and in a bay usually oscillate by themselves. Such water oscillations are excited more by tsunami. The mechanisms of the wave amplification have been mainly considered to be energy concentration and resonance. The former has been discussed by Green's law and as to the latter, there are many solutions of the steady state oscillations for bays with various topography. However, as I was saying just now, the results are still unreliable enough to apply to the tsunami-induced oscillations, because of their transient characteristics as pointed out by Mano(7).

#### 4.0 NON-STATIONARY CHARACTERISTICS OF THE BAYWATER RESPONSE TO TSUNAMI

Through the results of stationary spectrum, discrepancies were recognized between the first half oscillations and the second half oscillations. It will suggest that the further advanced considerations on the characteristics of the baywater oscillations due to tsunamis will be needed. Then, in order to investigate a non-stationary stochastic time series, a so called "instantaneous Fourier spectrum" was used, which represents the constitutions of the given time series at each time steps. The definition and the estimation scheme of the instantaneous Fourier spectrum which adopted in this study are as follows:

Let  $x(t)$  be a given non-stationary time series, and let  $y_n(t)$  be outputs through a series of system functions  $H_n(f)$ . In linear systems, the following relationship is well known( Papoulis(8) ).

$$Y_n(f) = H_n(f) X(f) \quad ( 8 )$$

where  $X(f)$  and  $Y_n(f)$  are the Fourier transform of the input  $x(t)$  and the outputs  $y_n(t)$  of the system, respectively. Taking inverse transforms of these separated transform functions,  $Y_n(f)$ , respectively, the outputs are then derived as

$$y_n(t) = \int_{-\infty}^{\infty} X(f) H_n(f) \exp(i2\pi ft) df \quad ( 9 )$$

This set of time functions referred to different frequency indicates the components of the given time series at every time step. The envelope of these time functions is, then, defined as the instantaneous Fourier spectrum,  $F(f,t)$ , in this study( Kamiyama(6) ).

To estimate this instantaneous Fourier spectrum, the system function with the Gaussian type is assumed here, i.e.,

$$H_n(f) = \exp\left(-\alpha \frac{f-f_n}{f_n}\right)^2 \quad ( 10 )$$

Because the parameter  $\alpha$  and the band width of the frequency  $\Delta f_n$  can not be determined uniquely, values of  $\alpha$  and  $\Delta f_n$  were chosen as  $50 f_n$  and  $0.15$ , respectively, after the several trial tests. Furthermore, the numerical Fourier integration were carried out based on the well known "fast Fourier transform method".

Fig. 8 shows the instantaneous Fourier spectra at Enoshima in Onagawa Bay. According to the results, oscillation in the period range between 43 and 49 min, in which the basic oscillation mode of the bay is included, are at first excited remarkably. As time was elapsed, the energy was slightly transferred to shorter spectrum bands. Spectra in the period bands between 25 and 35 min are also developed, which corresponds to the waves in the present tsunami source area. The energy densities depend on the oscillatory periods. However, they do not always keep the constant.

Fig. 9 shows the instantaneous spectra at Onagawa. It is quite natural that the energy density before the tsunamis invade is very small. However, the oscillation energies are excited remarkably by the intrusion of the tsunamis. In the first half after the tsunamis, two remarkable oscillations around 39 to 43 minutes and 33 minutes are noticed in which the natural period of the bay is included. After that, at the 3rd wave, the above two remarkable oscillation modes become much more clear with the center periods at 31 and 41 minutes, respectively. And at the 4th wave, the oscillation becomes simple with the center period of 41 min. The oscillation energies in the range between 31 and 41 minutes occupy the major portion of baywater oscillations, and the period of these oscillation modes changes slightly with the lapse of time, which suggests the energy transfers among these modes. And the results agree with the ones of the stationary spectra.

Fig.10 shows the instantaneous Fourier spectra at Kesennuma. Although the spectral energies in the period range 45 and 51 min are excited by the intrusion of tsunamis, the oscillatory mode is relatively simple. The predominant oscillation with the center period at 53 minutes is noticed, which is corresponding to the basic mode of the bay. However, as time elapsed, the energy is gradually transferred to shorter spectrum band and the oscillations are superimposed to give complicated spectra.

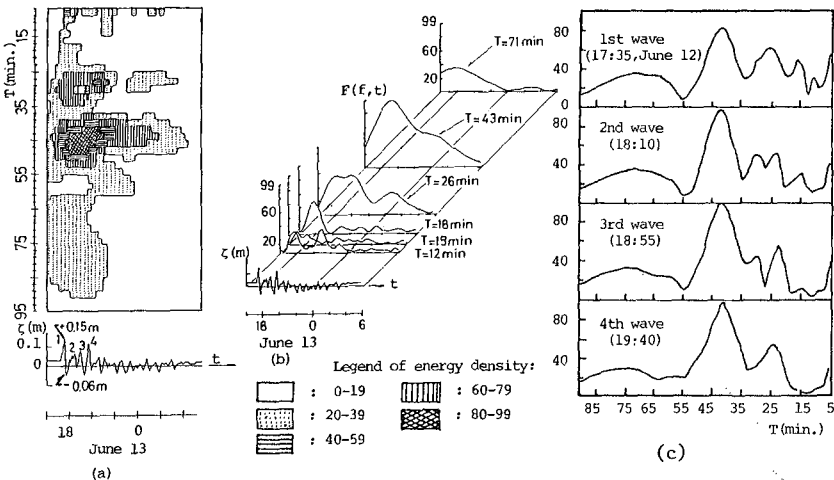


Fig. 8 (a) is energy densities in contour plotted by elapsed time  $t$  and periods  $T$ (min.). Values of energy density function  $F(f, t)$  were normalized 0 (minimum) to 99 (maximum). (b) is the time history of instantaneous Fourier spectra plotted for the predominant periods of oscillation in the stationary spectra. And (c) is the instantaneous spectra at 4 instants selected from the time sequence records of water level, which correspond to from the 1st wave to the 4th wave.

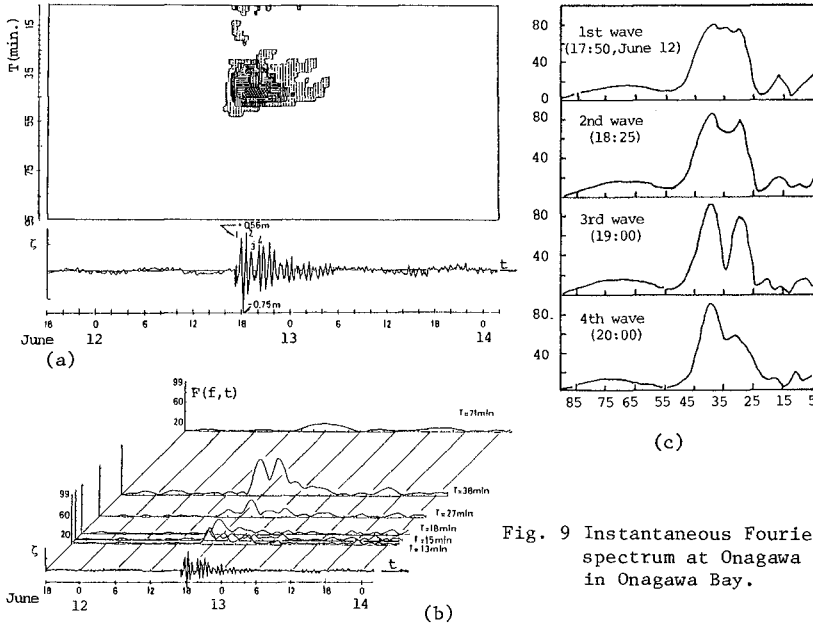


Fig. 9 Instantaneous Fourier spectrum at Onagawa in Onagawa Bay.

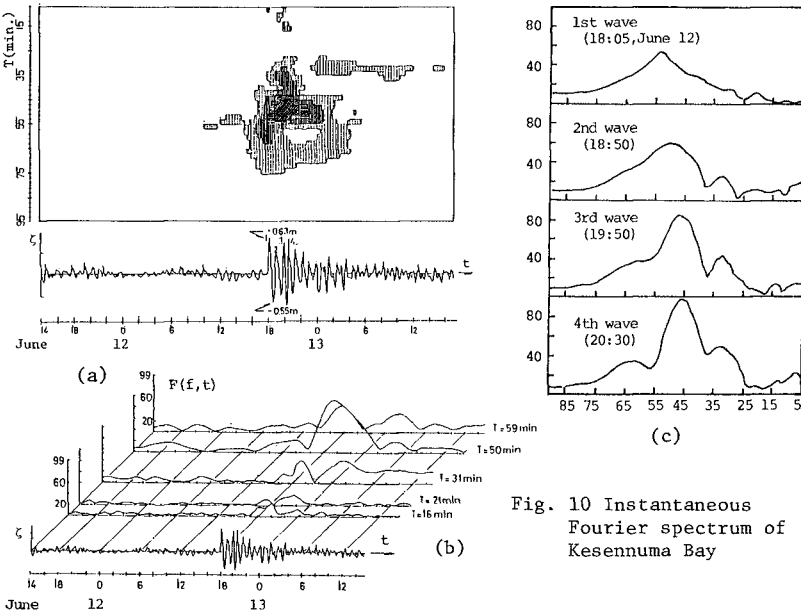


Fig. 10 Instantaneous Fourier spectrum of Kesennuma Bay



## 5.0 CONCLUSIONS

Stationary and non-stationary characteristics of tsunami-induced oscillations in bays were mainly investigated on the basis of records of tsunami caused by the Off-Miyagi earthquake in June, 1978. The estimated stationary spectra show that the main part of the oscillation energy is included in the basic mode and the secondary mode of oscillations based on the locality of bays, including the effect of continental shelf. The predominant period of these modes shifts to longer and/or shorter period ranges with the lapse of time, suggesting that the position of node moves toward the open sea and moves back into the bay during the tsunamis. The energies of non-stationary spectra do not always indicate stationary value at the periods which correspond to the predominant ones of stationary spectra, because of the transient characteristics of tsunami waves. Then, the results of the steady state oscillations are still not reliable enough to apply directly to the tsunami-induced oscillations.

## ACKNOWLEDGEMENTS

The author is most indebted to Professor Toshio Iwasaki, Ashikaga Institute of Technology, for his helpful criticisms and suggestions.

## REFERENCES

- 1) Aida, I.,1974: Long-period waves in the vicinity of Onagawa Bay (II). J. Oceanog. Soc. Japan, 30, 34-41.
- 2) Burg, J.P.,1972: The relationship between maximum entropy spectra and maximum likelihood spectra. Geophysics, 37, 375-376.
- 3) Hatori, T.,1975: Tsunami magnitude and wave source regions of historical Sanriku tsunamis in northeast Japan. Bull. Earthq. Res. Inst., 50, 397-414( in Japanese ).
- 4) Iwasaki, T.,1974: Computer aid for optimum design of tsunami waves. Proc. 14th Coastal Engineering Conference, 642-659.
- 5) Iwasaki, T. and A. Mano,1978: On the tsunamis due to the Miyagi-oki earthquake of 1978. Proc. 15th Symp. Natural Disaster Science, 582-584 ( in Japanese ).
- 6) Kamiyama, M.,1979: Non-stationary characteristics and wave interpretation of strong earthquake ground motions. Proc. JSCE,284, 35-48 ( in Japanese ).
- 7) Mano, A.,1982: Amplification of linear long waves in bays. Tsunami-Their Science and Engineering, Terra Scientific Pub. Co., 329-337.
- 8) Papoulis, A.,1962: The Fourier Integral and Its Application, McGraw-Hill.

## CHAPTER TEN

### A RANKIN VORTEX NUMBER AS A GUIDE TO THE SELECTION OF A MODEL HURRICANE

Charles L. Bretschneider

Professor Emeritus  
University of Hawaii Manoa

Jen-Men Lo

Environmental and Earth Sciences Division  
Kuwait Institute for Scientific Research  
P.O. Box 24885, Safat  
Kuwait

#### 1. INTRODUCTION

A model hurricane is defined by a model pressure profile, which is the same in all radial directions from the center of the hurricane. The model describes concentric circles of constant pressure known as isobars. The slope of the pressure profile gives the pressure gradient used in the gradient wind equation, together with other considerations determines the time history moving hurricane wind and pressure fields. The appropriate model hurricane can then be coupled with various other models for the determination of design criteria such as wind, waves, currents, wave forces, storm surge, wave run-up, coastal flooding and inundation limits. Because of the many requirements for accurate output data, there have always been concerns of the proper use of and selection of the appropriate hurricane model for a particular task and location.

The primary purpose of the paper is to begin to build a guide for determining the appropriate model to be used for a particular situation and criteria. When the data pressure profile is available, there is no need for a model since the slope of the data pressure profile gives the pressure gradient, which can be used directly in the gradient wind equation. The data pressure profile can also be fitted to the most appropriate model by various techniques of correlation.

After a sufficient number of data pressure profiles have been determined and correlated with various models, to determine the most appropriate model, then one should be able to extend the guide for better selection of model. One can then make better use of the standard project, maximum probable and actual tabulated hurricane data ( $R_G$ ,  $P_0$ ,  $P_W$ ,  $\phi$ ,  $V_F$ , etc.) given in the NOAA Report by Schwerdt, Ho and Watkins (1979).

The present guide for selection of a particular model has to do with the hurricane parameters  $R_G$ ,  $P_0$ ,  $P_N$ , and  $\phi$  as related to the cyclostrophic and gradient wind equations. For the convenience, in this paper  $R$  is the radius of maximum cyclostrophic wind as distinguished from  $R_G$ , the radius of maximum wind in the report by Schwerdt, et al. (1979). The

parameters determined by data pressure profile analysis are:

1.  $R$  = radius of maximum cyclostrophic wind,
2.  $P_R$  = pressure from the data pressure profile at  $R$ , and
3.  $\text{MAX} [rdP/dr]$  = related to the maximum cyclostrophic wind and determine the location of  $R$ .

## 2. DATA PRESSURE PROFILE

The data pressure profile is determined from the cyclone weather chart, and is an average of eight traverses from the center of the cyclone crossing identical isobars to the last closed or nearly closed isobar. The average distance  $r$  is plotted versus the corresponding isobar pressure. This method of analysis eliminates or at least minimizes the distortions in the isobar pattern due to personal judgement in construction of the isobars, possible effects due to forward motion to the cyclone and blocking effects due to adjacent pressure systems or land effects. The net result is a cyclone having concentric circular isobars, the definition of a model cyclone.

The step-by-step procedure is simple and straightforward in this method of analysis. A smooth S-curve is constructed through the data points, defining the data pressure profile. It is not necessary to have a complete data pressure profile, including  $P_0$  and  $P_N$ , which can be calculated by theory depending on choice of the model. The pressure gradient is a smooth profile through points calculated from the slope of the data pressure profile. The cyclostrophic profile is calculated from the smooth pressure gradient profile by multiplying corresponding points of the slope of the pressure profile by the radial distance  $r$ . Some fine tuning may be required to increase the accuracy in the range of radius of maximum wind, which can easily be estimated at a distance equal to about twice that of the maximum or peak of the pressure gradient profile, which occurs at the inflection point of the data pressure profile. Three important parameters are then determined as follows:

1.  $R$  = radius of maximum cyclostrophic wind at  $\text{max} [r dp/dr]$ ,
2.  $\text{max} [r dp/dr]$  at  $R$ , and
3.  $P_R$  the pressure from that data pressure profile at  $R$ .

It then follows by theory that  $P_0$  and  $P_N$  can be calculated from the following relations:

$$\Delta P_0 = P_N - P_0 = 1/C_1 \text{max} [r dp/dr] \quad (1)$$

$$P_0 = P_R - C_2 \Delta P_0, \text{ and} \quad (2)$$

$$P_N = P_0 + \Delta P_0 \quad (3)$$

where  $C_1$  and  $C_2$  are theoretical constants depending on the choice of the model.

The theoretical maximum cyclostrophic wind speed can be determined from:

$$V_C = \sqrt{1/\rho_a \text{MAX} [rdP/dr]} = K \sqrt{\text{MAX} rdp/dr} \quad (4)$$

where  $\rho_a$  = air density of  $P_R$  at  $r = R$ , radius of maximum wind.

Eq. 4 is independent of choice of model, and  $K = 18.7$  to  $19.3$  for all pressure profiles.

All theoretical pressure profiles will be in agreement with the data pressure profile at  $P_R$ ,  $R$ , and  $\max [r dp/dr]$  by the very nature of the analysis of the cyclone weather charts. Furthermore all model pressure profiles will be in very close agreement with the data pressure profile over the range of  $0.5 R < R < 1.5 R$  approximately, but there will be deviations outside this range. A high correlation will always be achieved between data pressure profile and model pressure profile because of the above range in agreement, but the choice of the model will be that model which has the overall best correlation with the data pressure profile, excluding  $P_0$  and  $P_N$ , except when available by measurements. Spot check data points such as  $P_0$ ,  $P_N$ ,  $V_{max}$ , etc. if available by measurements should also be considered.

Six Indian Seas cyclones have been analyzed by the above method. Regression analysis between the original data of the data pressure profile and the corresponding theoretical pressure points for BRET MODEL-X was made, and the following regression coefficients were obtained:  $\rho = 0.9890$ ,  $0.9995$ ,  $0.9993$ ,  $0.9824$  and  $0.9996$ . Figure 1 presents the example theoretical hurricane relations for BRET MODEL-X, and Figures 2 to 7 are the Indian Seas cyclones data pressure profile analysis. Because of the very nature of the method of determination of  $R$ ,  $P_R$  and  $\max [r dp/dr]$ , high regression correlations are expected, and therefore one might reject those cyclones for which  $\rho < 0.98$  or  $0.99$ .

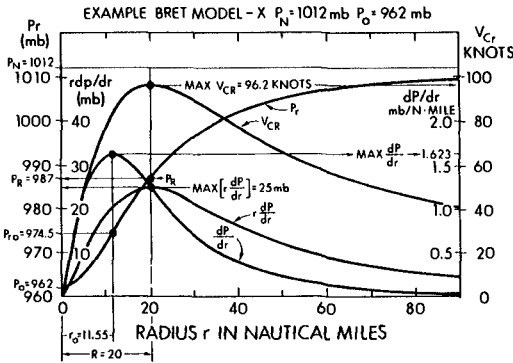


FIG. 1 EXAMPLE THEORETICAL HURRICANE RELATIONS FOR BRET MODEL - X

The choice of the model can also be based in part on previous investigations reported in the literature. By theory the maximum cyclostrophic wind speed for model hurricanes is given by:

$$V_c = K_1 \sqrt{P_N - P_0} \quad (5)$$

where

$$K_1 = (C_1 / \rho_a)^{1/2} \quad (6)$$

where  $\rho_a$  is the air density and generally increases slightly with latitude.  $C_1$  is a theoretical constant, depending on choice of model.

Obviously the choice of model depends on  $V_c$  of Eq. 5 is equal to  $V_c$  of Eq. 4.

It would seem prudent to analyze cyclones, hurricanes and typhoons by the simple straightforward method introduced in this paper, and determine a large number of values for  $R$ ,  $P_R$  and  $\max [r dp/dr]$ .  $P_0$  and  $P_N$

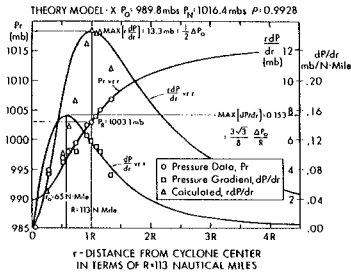


FIG. 2 BAY OF BENGAL CYCLONE 5 MAY 1975 2130 IST COMPARED WITH HURRICANE MODEL - X

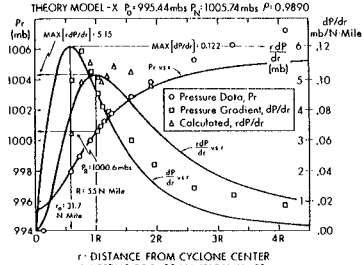


FIG. 3 BAY OF BENGAL CYCLONE 8 DEC. 1965 0830 IST COMPARED WITH HURRICANE MODEL - X

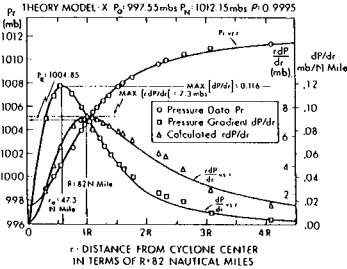


FIG. 4 ARABIAN SEA POST-TROPICAL CYCLONE 28 OCT. 1972 1800 GMT COMPARED WITH HURRICANE MODEL - X

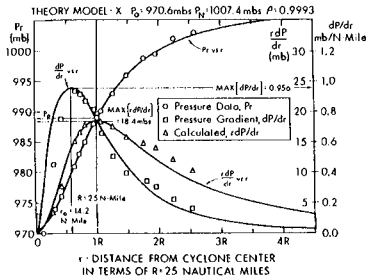


FIG. 5 ARABIAN SEA POST-TROPICAL CYCLONE 21 OCT. 1975 0200 - 1500 GMT COMPARED WITH HURRICANE MODEL - X

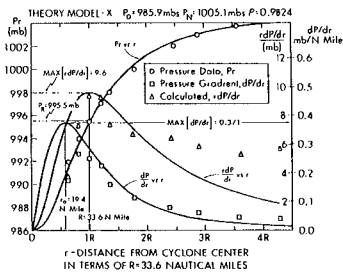


FIG. 6 BAY OF BENGAL CYCLONE 6 MAY 1975 0530 IST COMPARED WITH HURRICANE MODEL - X

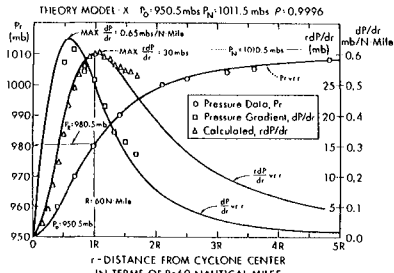


FIG. 7 BAY OF BENGAL ANDHRA CYCLONE 17 NOV. 1977 0930 IST COMPARED WITH HURRICANE MODEL - X

can then be determined for choice of model for correlation purposes.

In summary the uniqueness of this paper is the method of analyzing cyclone weather charts to determine the three parameters  $R$ ,  $P_R$  and  $\max [r dp/dr]$ , the determination of  $P_0$  and  $P_\infty$  by theory depending on choice of model, and the correlation between the data pressure profile and the theoretical pressure profile over the range of isobaric pressure data.

3. MODEL PRESSURE PROFILES

Besides, the Hydromet model pressure profile, there are a number of other available model pressure profiles found in the literature. A modification of the Hydromet model was made by Holland (1980) giving a family of pressure profiles, of which one of the pressure profiles reduces to the Rankin Vortex model. This family of pressure profiles has been in use with some success by Rosendal (1982).

A number of other pressure profile models from various sources are given in the NOAA Report by Schwerdt, Ho and Watkins (1979). Fujita (1962) proposed a different model, which Uji (1975) fitted quite well to Typhoon Vera, 22-27 September 1959, a very large western north pacific typhoon. Bretschneider (1982) proposed a new general form of hurricane models, of which Fujita (1962) model is a special case. Jelenianski (1966) used a non-dimensional surface profile corresponding to the BRET MODEL-X non-dimensional cyclostrophic wind profile.

In summary there are two general types of hurricane models: (1) the modified Rankin Vortex model by Holland (1980), of which the Hydromet model is a special case; and, (2) the BRET-General model of which the BRET MODEL-X, the Fujita model and Jelenianski model are all special cases. The mathematical form of the pressure profiles for the two families of models are:

$$\frac{P_r - P_0}{P_\infty - P_0} = A e^{-B [R/r]} \tag{7}$$

and

$$\frac{P_r - P_0}{P_\infty - P_0} = 1 - \left[ 1 + a \left( \frac{r}{R} \right)^2 \right]^{-b} \tag{8}$$

where

- $P_0$  = central pressure of hurricanes
- $P_r$  = pressure at radial distance  $r$
- $P_\infty$  = pressure at infinite distance  $r$
- $R$  = radius of maximum cyclostrophic wind

The constants  $A = B^{-1}$  and  $a = b^{-1}$  must always hold true to satisfy the mathematics of the cyclostrophic wind equation.

Eq. 7, proposed by Holland (1980), and when  $A = B = 1$ , becomes the original Rankin Vortex model after Schloemer (1954) or before. Eq. 8 was proposed by Bretschneider (1981) after pressure profile data analysis.

When  $a = b - 1$ , Eq. 8 is called BRET MODEL-X. When  $a = b^{-1} = 2$ , Eq. 8 becomes the same as Fujita model (1962).

Eqs. 7 and 8 above represent families of models that overlap. The deviations between models have to do with (1) the size of the hurricane as governed by the radius of maximum cyclostrophic wind, (2) the wind intensity of the hurricane as governed by the central pressure reduction, and (3) an assumption that there is a latitude affect as governed by the Coriolis parameter. The above assumptions lead to the introduction of a non-dimensional Coriolis or Rankin Vortex number for hurricane classification. Table 1 presents the theoretical constants  $K_1$  for four hurricane models -- Hydromet Model, NOAA Model-I, Fujita Model-J, and BRET MODEL-X. Table 2 presents the parameters for the six Indian Seas cyclones data pressure profile analysis.

Table 1: THEORETICAL CONSTANTS FOR FOUR HURRICANE MODELS				
	HYDROMET MODEL-HM	NOAA MODEL-I	FUJITA MODEL-J	BRET MODEL-X
$K_1 = \left(\frac{C_1}{\rho a}\right)^{1/2}$	$\left(\frac{1}{e\rho a}\right)^{1/2}$	$\left(\frac{1}{\pi\rho a}\right)^{1/2}$	$\left(\frac{2}{3\sqrt{3}\rho a}\right)^{1/2}$	$\left(\frac{1}{2\rho a}\right)^{1/2}$
FOR V = KNOTS and P = INCHES Hg				
$K_1$	66.0 68.0	61.39 63.25	67.51 69.56	76.74 79.28
FOR V = KNOTS and P = millibars				
$K_1$	11.34 11.68	10.55 10.87	11.60 11.95	13.22 13.62

#### 4. THE GRADIENT WIND EQUATION

The radius of maximum gradient wind and the maximum gradient wind, respectively are not identical to the corresponding radius of maximum cyclostrophic wind and the gradient wind at the radius of maximum cyclostrophic wind. The above was shown to be the case by Bretschneider (1959), using the Hydromet-Rankin Vortex model after Schloemer (1954) and Myers (1954). This will be true for any wind field developed from the pressure gradient by the very nature of the gradient wind equation.

The gradient wind equation for a stationary cyclone can be given as follows:

$$V_g^2 + frV_g = \frac{r}{\rho a} \frac{dp}{dr} \quad (9)$$

Table 2 Summary Parameters from Six Indian Seas Cyclones

Cyclone No. - Figure No. Area and Latitude $\phi$ Date and Time of Weather Chart	I 6 Bay of Bengal 14, 8 5 May 1975 2330 IST	II 7 Bay of Bengal 10 8 Dec 1965 0830 IST	III 8 Bay of Bengal 14 28 Oct 1977 1800 GMT	IV 9 Arabian Sea* -23 22 Oct 1975 0200-1500 GMT	V 10 Bay of Bengal 14, 3 6 May 1975 0530 IST	VI 11 Bay of Bengal 10 17 Nov 1977 0830 IST
From Data Pressure Profile and Derivative						
R, Radius of Maximum Cyclone Wind Nautical Miles	113	55	82	25	33.6	60
P <sub>P</sub> Pressure at R (mbs)	1003.1	1000.6	1000.85	989.0	995.5	980.5
M <sub>ax</sub> r dp/dr at R (mbs)	13.3	5.15	7.3	18.4	9.6	30
V <sub>GR</sub> (max) Knots	70.24	43.71	52.04	82.62	59.67	105.5
From Theory, Each Model						
Hyromet Model - RH						
K <sub>1</sub> = 11.66; c <sub>1</sub> = 1/e, c <sub>2</sub> = 1/e						
$\Delta P$ (mbs)	36.15	14.00	19.84	50.02	26.10	81.60
P <sub>0</sub> (mbs)	989.8	995.44	997.55	970.60	985.90	950.50
P <sub>N</sub> (mbs)	1026.0	1009.44	1017.40	1020.80	1012.00	1032.10
NOAA Model - I						
K <sub>1</sub> = 10.87; c <sub>1</sub> = 1/ $\pi$ , c <sub>2</sub> = 1/2						
$\Delta P$ (mbs)	41.78	16.17	22.92	57.77	30.13	94.20
P <sub>0</sub> (mbs)	982.2	982.52	993.40	960.10	980.40	933.40
P <sub>N</sub> (mbs)	1024.0	1008.69	1016.30	1017.90	1010.60	1027.60
Fujita Model - J						
K <sub>1</sub> = 11.95; c <sub>1</sub> = 2/3 $\sqrt{3}$ c <sub>2</sub> = 1 - $\sqrt{3}/3$						
$\Delta P$ (mbs)	34.55	13.38	18.90	47.80	24.94	77.94
P <sub>0</sub> (mbs)	988.50	994.94	996.90	968.80	985.00	947.56
P <sub>N</sub> (mbs)	1023.60	1008.32	1015.80	1016.60	1009.90	1025.50
Bret Model - X						
K <sub>1</sub> = 13.62; c <sub>1</sub> = 1/2, c <sub>2</sub> = 1/2						
$\Delta P$ (mbs)	26.60	10.30	14.60	36.80	19.20	60
P <sub>0</sub> (mbs)	989.80	995.44	997.55	970.60	985.90	950.50
P <sub>N</sub> (mbs)	1016.40	1005.74	1012.15	1007.4	1003.1	1010.50
$\rho$ = correlation coefficient	.9928	.9890	.9995	.9993	.9824	.9990
FR <sub>C</sub> (knots)	15.1	4.99	10.4	5.10	4.33	5.44
FR <sub>C</sub> /V <sub>C</sub>	0.215	0.114	0.199	0.062	0.072	0.052

where

- V<sub>g</sub> = gradient wind speed at radial distance r from the center of the cyclone
- f = Coriolis parameter
- $\rho$  = air density
- dp/dr = pressure gradient

In the absence of the Coriolis term fr Eq. 9 becomes the cyclostrophic wind equation as follows:



$$V_r^2 = \frac{r}{\rho_a} \frac{dp}{dr} \quad (10)$$

where  $V_r$  is the cyclostrophic wind speed, resulting from the balance between the centripetal force directed toward the center of the cyclone and the force due to the pressure gradient.

Thus Eq. 9 can be written as follows:

$$V_g^2 + frV_g = V_r^2 \quad (11)$$

The maximum cyclostrophic wind velocity can be obtained from

$$V_c^2 = \frac{1}{\rho_a} \text{MAX} \left[ \frac{r dp}{dr} \right] \quad (12)$$

where  $V_c$  occurs at  $R$  radius of maximum cyclostrophic wind.  $R_g$  is the radius of maximum gradient wind, and is somewhat smaller than  $R$ , depending on the value of  $fr/V_c$  or  $frR/V_c$ .

The most accurate evaluation of Eq. 12 would be by use of an accurately determined pressure profile from data, but this is seldom possible because of lack of sufficient data. The procedure is to best fit a pressure profile to the data pressure. Then, an analytical pressure profile or model pressure profile can be selected which best fits all the data including the central pressure, if available. Ideally, it would be excellent to have available the pressure at the radius of maximum cyclostrophic wind.

Once the maximum cyclostrophic wind  $V_c$  is obtained, then one can obtain the gradient wind at  $R$  as follows:

$$V_{gR}^2 + fr V_{gR} = V_c^2 \quad (13)$$

or

$$V_{gR} = \frac{1}{2} - fr + \sqrt{(1/2 - fr)^2 + V_c^2} \quad (14)$$

As can be seen from the works of Bretschneider (1959) Eq. 13 or Eq. 14 does not give the maximum gradient wind  $V_g$  and consequently the maximum 10-meter level wind speed  $V_s$  at the radius of maximum wind. The radius of maximum gradient wind,  $R_g$  for  $V_g$  is not the same as the radius of maximum cyclostrophic wind  $R = R_c$  for  $V_c$ .

Actually  $R_g = R_c$  and  $V_g = V_c$  for the Rankin Vortex model only, which implies that  $R_c = R_g$  as  $R \rightarrow 0$ ,  $V_g = V_c$  as  $V \rightarrow \infty$ . Otherwise everything can only be approximate, the approximation depends upon the Rankin or the Coriolis non-dimensional number, which can be defined as follows:

$$N_c = fr/V_c \quad (15)$$

where

$f$  = the well known Coriolis parameter  
 $R$  = radius of maximum cyclostrophic wind  
 $V_C$  = maximum cyclostrophic wind

When  $N_C$  is very small (0.01 to 0.05) the Rankin Vortex model applies. When  $N_C > 0.1$  the Rankin vortex cannot apply. The problem is when does some other model or modification of the Rankin Vortex model become important?

What is required is to establish certain relationships between cyclostrophic wind, gradient wind, and surface wind, usually defined as the 1-minute or the 10-minute average at the 10-meter standard anemometer level.

In sequence of maximum cyclostrophic wind  $V_C$ , maximum gradient wind  $V_G$  and maximum surface wind  $V_S$  we have

$$V_G > V_C \quad \text{and} \quad V_S R_G = C_f V_G \quad (16)$$

where  $C_f$  is the friction reduction factor.

What has not been recognized for hurricane is that the radii of maximum of the above types of winds are not the same. It is very easy to state that:

$$R_S = R_G < R_C \quad (17)$$

In fact one can prove always for a stationary model hurricane that:

$$R_G < R_C \quad (18)$$

However it is not apparent that  $R_G$  is not the same as  $R_S$  because of different relationships for reduction friction factors. Unlike  $R_C$  and  $R_G$  which are quite apparent, it is quite probable that  $R_G = R_S$ .

## 5. AN INVESTIGATION OF MODEL HURRICANE

To begin with, all model hurricane pressure and wind fields are assumed to be stationary models, after which forward speed of translations are applied to change only the winds but not the pressures.

What is required here is to establish relationships for the stationary hurricane between  $R_G$ , radius of maximum gradient wind,  $V_{GR}$  and  $R$ , the radius of maximum cyclostrophic wind,  $V_C$ .

It is important to note here that  $R_G$  and not  $R$ , the appropriate parameters to establish the radial distance at which  $V_G$  applies.

Three cases will be worked out here: (1) the Hydromet-Rankin Vortex model, (2) the BRET MODEL-X and (3) the Fujita model. Similar approaches can be worked out for the other models.

HYDROMET-RANKIN VORTEX MODEL, A=B=1

The pressure profile is given by:

$$\frac{P_r - P_0}{P_N - P_0} = e^{-R/r} \quad (19)$$

The pressure gradient is obtained as follows:

$$\frac{dp}{dr} = \frac{P_N - P_0}{R} \left(\frac{R}{r}\right)^2 e^{-(R/r)} \quad (20)$$

and the cyclostrophic wind equation by:

$$V_r^2 = \frac{1}{\rho_a} \frac{rdp}{dr} = \frac{1}{\rho_a} (P_N - P_0) \left(\frac{R}{r}\right) e^{-R/r} \quad (21)$$

The maximum cyclostrophic wind velocity occurs at  $r = R$ . Whence

$$V_c^2 = \frac{1}{\rho_a} \text{MAX} \left(\frac{rdp}{dr}\right) = \frac{1}{\rho_a} (P_N - P_0) e^{-1} \quad (22)$$

Dividing Eq. 21 by 22 we obtain

$$V_r^2 = V_c^2 \left(\frac{R}{r}\right) e^{(1 - R/r)} \quad (23)$$

Substituting Eq. 23 into Eq. 11 we obtain

$$V_g^2 + fr V_g = V_c^2 \frac{R}{r} e^{(1 - R/r)} \quad (24)$$

To find the maximum gradient wind  $V_G$  at radius of maximum wind  $R_G$ , we differentiate Eq. 24 and set the results equal to zero and let  $r = R_G$ .

$$\frac{V_G}{fR_G} = \left(\frac{V_c}{fR}\right)^2 \left(\frac{R}{R_G}\right)^3 \left(\frac{R}{R_G} - 1\right) e^{(1 - R/R_G)} \quad (25)$$

For any particular set of conditions

$$\frac{fR}{V_c} = \text{const} = \text{cyclostrophic Coriolis number}$$

$$\text{when } \frac{R}{R_G} = 1$$

$$fR_G = fR = 0$$

$$\frac{V_G}{V_c} = 1$$

The simultaneous solution of Eq. 25 and Eq. 14 will give the proper relationships between  $R/R$  and  $V_G/V_c$  as functions of the Coriolis number  $N_c = fR/V_c$ .

FUJITA MODEL,  $a=b^{-1}=2$

The cyclostrophic wind relationship for the Fujita model is given by

$$V_r^2 = V_c^2 \frac{3\sqrt{3} \left(\frac{r}{R}\right)^2}{\left[1 + 2 \left(\frac{r}{R}\right)^2\right]^{3/2}} \quad (26)$$

Substituting Eq. 26 into Eq. 11, the gradient wind equation becomes

$$V_g^2 + frV_g = V_c^2 \frac{3\sqrt{3} \left(\frac{r}{R}\right)^2}{\left[1 + 2 \left(\frac{r}{R}\right)^2\right]^{3/2}} \quad (27)$$

In a similar manner as was done for the Hydromet Rankin Vortex model, differentiate Eq. 27 and set  $dV_g/dr = 0$  to find the radius,  $R_G$  of maximum gradient wind  $V_G$

$$\frac{V_G}{fR_G} = 6\sqrt{3} \left(\frac{V_c}{fr}\right)^2 \frac{1 - \left(\frac{R_G}{R}\right)^2}{\left[1 + 2 \left(\frac{R_G}{R}\right)^2\right]^{5/2}} \quad (28)$$

and from Eq. 27, let  $r = R_G$  it becomes

$$V_G^2 + fR_G V_G = \frac{3\sqrt{3} V_c^2 \left(\frac{R_G}{R}\right)^2}{\left[1 + 2 \left(\frac{R_G}{R}\right)^2\right]^{3/2}} \quad (29)$$

The simultaneous solution of Eqs. 28 and 29 gives relationships between  $fR/V_c$  and  $R_G/R$ .

BRET MODEL-X,  $a=b=1$

The cyclostrophic wind relationship for the BRET MODEL-X is given by:

$$V_r^2 = V_c^2 \frac{4(r/R)^2}{(R^2 + r^2)^2} \quad (30)$$

and the gradient wind equation becomes

$$V_g^2 + frV_g = \frac{4(r/R)^2}{(R^2 + r^2)^2} V_c^2 \quad (31)$$

In a similar manner as was done for the Hydromet Rankin Vortex model differentiate Eq. 31 and set  $dV_g/dr = 0$  to find the radius,  $R_G$  of maximum gradient wind  $V_G$ .

$$\frac{V_G}{fR_G} = 8 \left( \frac{V_C}{fR} \right)^2 \left( \frac{R}{R_G} \right)^4 \frac{\left( \frac{R}{R_G} \right)^2 - 1}{\left[ \left( \frac{R}{R_G} \right)^2 + 1 \right]^3} \quad (32)$$

and from Eq. 31 let  $r = R_G$ , we have

$$V_G + fR_G V_G = \frac{4V_C^2 \left( \frac{R}{R_G} \right)^2}{\left[ 1 + \left( \frac{R}{R_G} \right)^2 \right]^2} \quad (33)$$

The simultaneous solution of Eqs. 32 and 33 gives relationships between  $fR/V_C$  and  $R_G/R_C$ .

Table 3 presents the relationships between the ratio of radius of maximum gradient wind versus radius of maximum cyclostrophic wind and the Rankin Vortex number for Hydromet Rankin Vortex model, Fujita model, and BRET-X model. Table 3 can be used in two ways.

1. Where  $R_G$  is given such as for the conditions of previous studies for the Gulf of Mexico, one can calculate the approximate  $R$  for the maximum cyclostrophic wind,  $V_C$ .
2. Where  $R$  is obtained by analysis by pressure profiles, then  $R_G$  can be used for the maximum gradient wind  $V_G$ .

## 6. NON-DIMENSIONAL RANKIN VORTEX NUMBER

The non-dimensional Rankin Vortex number,  $N_C$  has been defined in Eq. 15. It presents the ratio between the Coriolis velocity (a fictitious velocity) and the cyclostrophic wind velocity (a theoretical velocity) at the radius of the maximum cyclostrophic wind velocity. When  $\Delta P_0 = P_N - P_0$  (Eq. 1) is given in millibar,  $R$  in nautical miles, and  $V_C$  in knots, Eq. 15 becomes

$$N_C = \frac{0.522 R \sin \phi}{K \sqrt{\Delta P_0}} \quad (34)$$

where  $\phi$  is the latitude,  $K = 11.3$  to  $11.7$  depending on the air density at  $P_R$ .

Tabulated data from Schwerdt, et al. (1979) for 51 U.S. East Coast and 71 Gulf of Mexico hurricanes were used to calculate values of  $N_{CR}$  from Eq. 34 using  $K = 11.7$ . There was found a wide scatter of the data with respect to latitude. The average values of  $N_{CR}$  increased from 0.05 at  $\text{lat } \phi = 24^\circ$ , to 0.07 at  $30^\circ$  to 0.165 at  $41^\circ$ , where existing models probably do not apply any way. Two lowest values for  $N_{CR}$  were 0.01 for Key West (1909) and 0.018 for Camille (1969), both of which can be

Table 3: RADIUS OF MAXIMUM GRADIENT WIND VERSUS RADIUS OF MAXIMUM CYCLOSTROPHIC WIND RELATIONSHIPS FOR HYDROMET RANKIN VORTEX MODEL, FUJITA MODEL AND BRET-X MODEL

$\frac{fR}{V_c}$	HYDROMET $\frac{R_g}{R}$	FUJITA $\frac{R_g}{R}$	BRET-X $\frac{R_g}{R}$
0.0	1.0	1.0	1.0
0.01	0.9903	0.9926	0.9951
0.02	0.9809	0.9856	0.9902
0.03	0.9721	0.9787	0.9855
0.04	0.9636	0.9720	0.9809
0.05	0.9554	0.9656	0.9765
0.06	0.9476	0.9594	0.9721
0.07	0.9401	0.9534	0.9678
0.08	0.9329	0.9476	0.9635
0.09	0.9259	0.9419	0.9594
0.1	0.9192	0.9363	0.9554
0.11	0.9127	0.9310	0.9514
0.12	0.9064	0.9258	0.9476
0.13	0.9003	0.9207	0.9438
0.14	0.8945	0.9158	0.9401
0.15	0.8888	0.9109	0.9364
0.16	0.8832	0.9062	0.9328
0.17	0.8779	0.9016	0.9293
0.18	0.8727	0.8971	0.9259
0.19	0.8676	0.8928	0.9225
0.2	0.8625	0.8884	0.9191

considered as classical examples of the Rankin Vortex model. Maximum values for the Gulf were between 0.12 and 0.15, and for the East Coast 0.15 to 0.30.  $N_{CR} = 0.15$  for Western Pacific Typhoon Vera (1959), and for Hawaii Hurricane Iwa,  $N_{CR} = 0.15$  to 0.22.  $N_{CR} = 0.052$  to 0.22 for the Indian Seas cyclones. Data pressure profiles for Vera (1959), Iwa (1982) and Indian Seas cyclones, and also mean, minimum and maximum values of  $N_{CR}$  for the U.S. East and Gulf Coast hurricanes were used to suggest a guide for selection of model pressure profiles, given in Table 4.

Table 4: A SUGGESTED GUIDE FOR SELECTION OF MODEL

HYDROMET RANKIN VORTEX MODEL (Eq. 7)

A=B=1  $0.0 < N_{CR} < 0.05$   
 A=B=5/4 (approx. est.)  $0.03 < N_{CR} < 0.08$

BRET MODELS (Eq. 8)

Fujita (b = 1/2)  $0.03 < N_{CR} < 0.08$   
 BRET-X (b = 1)  $0.06 < N_{CR} < 0.15$

NOTE: The above table is only suggested. Revisions will be in order after sufficient hurricane analyses.

## 7. SUMMARY

The radius of maximum gradient wind and the maximum gradient wind to the corresponding radius of maximum cyclostrophic wind and the maximum cyclostrophic wind have been carefully studied with various theoretical hurricane models. The accuracy of the predicted hurricane wind field heavily depends on the choice of the hurricane model. In the current study, it found that the selection of the hurricane model are determined by the range of the non-dimensional Rankin Vortex number. This number presents the ratio between the Coriolis velocity and the cyclostrophic wind velocity at the radius of the maximum cyclostrophic wind velocity. Table 4 gives a suggested guidance for the selection of the hurricane model. But it is only a general guide. Additional data pressure profiles need to be analyzed for various  $P_R$ , hurricane intensive  $V_{CR}$ , and for different latitude  $\phi$ , as well as regional locations.

## 8. REFERENCES

- Atkinson, G.D. and C.R. Holliday, 1977: Tropical Cyclone Minimum Sea Level Pressure Maximum Sustained Wind Relationship for Western North Pacific. *Monthly Weather Review*, 105, 421-427.
- Bretschneider, C.L., 1982: Hurricane Models for Investigating Cyclones of the Indian Seas. Technical Report ANNEX I prepared for Government of India/United Nations Industrial Development Organization (in publication).
- Chin, P.C., 1972: Tropical Cyclone Climatology for the China Seas and Western Pacific from 1884 to 1970. Vol. I Basic Data, Royal Observatory, Hong Kong, R.O. T.M. No. 11.
- Fletcher, R.D., 1955: Computation of Maximum Surface Winds in Hurricanes. *Bull. Amer. Meteor. Soc.*, 36, 246-250.
- Fujita, 1962 (see T. Uji, 1975): Numerical Estimation of Sea Waves in a Typhoon Area. *Meteorol. Res. Inst. (JMRI) Tokyo, Papers in Meteorol. and Geophys.* Vol. 26, No. 4, 199-217.
- Gupta, G.R., D.K. Mishra and B.R. Yadav, 1977: The Porbandar Cyclone of October (1975). *Indian J. Met. Hydrol. Geophys.* (1977) Vol. 28, No. 2, 177-188.
- Holland, G.J., 1980: An Analytical Model of the Wind and Pressure Profiles in Hurricanes. *Monthly Weather Review*, 108, 1212-1218.
- Holliday, C.R., 1969: On the Maximum Sustained Winds Occurring in Atlantic Hurricanes. *Tech. Memo. WBTM-SR-45*, 6 pp.
- Jelesnianski, C.P., 1966: Numerical Computations of Storm Surges without Bottom Stress. *Monthly Weather Review*, Vol. 4, No. 6, 379-394.
- Jelesnianski, C.P., 1973: A Preliminary View of Storm Surges before and after Storm Modifications. NOAA Tech. Memo ERLWMP0-3.
- Kraft, R.H., 1961: The Hurricane's Central Pressure and Highest Wind. *Mariners Weather Log*, 5, 157.
- Myers, V.A., 1954: Characteristics of United States Hurricanes Pertinent to Levee Design for Lake Okechobee, Florida. *Hydromet Report* 32, 126 pp (GPO No. C30-70:32).
- Mishra, D.K. and G.R. Gupta, 1976: Estimating Maximum Wind Speeds in Tropical Cyclones Occurring in Indian Seas. *Indian Jour. Met. Hydrol. Geophys.* (1976) 273, 285-290.
- Natarajan, R. and K.M. Ramamurthy, 1975: Estimation of Central Pressures of Cyclonic Storms in the Indian Seas. *Indian J. Met. Hydrol. Geophys.* 26, 60-65.

- Rosendal, Hanse & Samuel L. Shaw, 1982: Relationships of Maximum Sustained Winds to Minimum Sea Level Pressure in Central North Pacific Tropical Cyclones. NOAA Technical Memo NWSTM PR-24.
- Schlomer, R.W., 1954: Analysis and Synthesis of Hurricane Wind Patterns over Lake Okechobee, Florida. Hydromet Report 31, 49 pp (GPO No. C30. 70:31).
- Schwerdt, R.W., F.P. Ho, and R.R. Watkins, 1979: Meteorological Criteria for Standard Project and Probable Maximum Hurricane Wind Fields, Gulf and East Coasts of United States, NOAA Technical Report. NWS 25 Dept. of Comm. NOAA NWS.
- Takahashi, K., 1939: Oistribution of Pressure and Wind in a Typhoon Circulation. J. Meteor. Soc. Japan, Ser. II, 17, 417-421.
- U.S. Dept. of Commerce, NOAA, Marine Environmental Data and Information Services, *Marine Weather Log*, Vol. 1979, 1979, 1980 and 1981.

#### LIST OF SYMBOLS

- $R = R_C$  = Radius of maximum cyclostrophic wind  
 $R_G$  = Radius of maximum gradient wind (corresponding to radius of maximum wind of published data on  $R = R_G$ )  
 $r$  = Distance from center of hurricane  
 $V_C$  = Maximum cyclostrophic wind at  $R$   
 $V_r$  = Cyclostrophic wind at radial distance  $r$   
 $V_G$  = Maximum gradient wind at  $R_G$   
 $V_g$  = Gradient wind at radial distance  $r$   
 $P_R$  = Atmospheric pressure at radius of maximum cyclostrophic wind  
 $P_r$  = Atmospheric pressure at radial distance  $r$

#### 9. ACKNOWLEDGEMENTS

The original work on the data pressure profiles Figures 2 through 6 was done by various members of Engineers India Limited under the support of UNIDO (United Nations Industrial Organization) and Figure 7 at the Coastal Engineering Research Center-Poona under the support of UNDP (United Nations Development Program). The drafting of the figures was done by HIG (Hawaii Institute of Geophysics) and typing of the final manuscript by the Department of Ocean Engineering.



## CHAPTER ELEVEN

### Estimating Error of Coastal Stage Frequency Curves

Mark D. Prater<sup>1</sup>, A.M. ASCE, Thomas A. Hardy<sup>1</sup>,  
H. Lee Butler<sup>2</sup> M. ASCE, and Leon E. Borgman<sup>3</sup> M. ASCE

#### Abstract

A computer intensive statistical procedure known as the bootstrap has been used to estimate the error in coastal stage-frequency relationships due to uncertainties in hurricane meteorological distributions. These stage-frequency relationships are developed through the use of a joint probability method, so that the probability of a storm event is the product of the probabilities of the individual independent components which comprise that storm event. The bootstrap technique provides an estimate of the error of the stage-frequency by determining the variation possible in each component's probability distribution. This variability is due to the construction of the distribution from a finite set of historical events. An example of the bootstrap is given and stage-frequency results and error estimates typical of a coastal region are shown.

#### Introduction

Efficiency in design of coastal protection is becoming more and more important. Development of coastal regions, costs of damages from storm induced water levels, and costs of protection from these waters are all increasing. Adequate protection for coastal regions is desired; however, due to monetary constraints what amount of water level protection that can be considered adequate becomes a question for which there is no easy answer. Therefore, inherent in any coastal protection project, there is a need to develop the best possible estimate of the stage-frequency relationship for the project area, as well as an estimate of the error in this relationship.

The tool in most widespread use for the development of coastal flood frequency, especially from hurricane induced water levels, is the joint probability method (4). However, a generally accepted method to judge the correctness of the produced flood frequency, or to estimate

<sup>1</sup>Research Hydraulic Engineer, Research Division, Coastal Engineering Research Center, U. S. Army Engineer Waterways Experiment Station, P. O. Box 631, Vicksburg, MS 39180-0631

<sup>2</sup>Chief, Coastal Processes Branch, Research Division, Coastal Engineering Research Center, U. S. Army Engineer Waterways Experiment Station, P. O. Box 631, Vicksburg, MS 39180-0631

<sup>3</sup>Department of Statistics, University of Wyoming, Laramie, Wyoming 82070

the error of these frequencies, is not available. This paper introduces a method which can be used to develop error estimates from meteorological uncertainty for stage-frequency relationships derived through the joint probability method.

This paper will first outline the joint probability method as it is used to develop stage frequency relationships for regions whose extreme water levels are dominated by hurricane surges. Secondly, a computer intensive statistical tool known as the "bootstrap" (1,2) will be introduced and a procedure will be described which uses the bootstrap to obtain error estimates from meteorological uncertainties. Finally, an example will be given showing the use of the bootstrap technique for developing confidence intervals for a coastal stage-frequency curve.

#### Joint Probability Method

When developing a hurricane stage-frequency relationships, it is not necessary, or even possible, to model all hurricane windfield configurations that are possible in the region of interest. It is assumed that a storm's configuration can be completely and uniquely described by a set of parameters. Therefore, all possible hurricanes are represented by a large number of synthetic storms, each with its own specified configuration, defined by the values of its parameters.

Commonly, five parameters are used to describe the configuration of a hurricane windfield (Figure 1). The central pressure deficit is the difference between the ambient atmospheric pressure and the extreme low pressure in the center of the hurricane, and is directly related to the intensity and magnitude of the storm. The radius of maximum winds is the distance from the center of the storm to the region of the strongest winds, and is a measure of the size of the hurricane. The forward speed is the storm's rate of translation. The direction of storm motion and location of landfall determine the track of the storm.

General relationships can be expressed which relate the movement and distribution of wind magnitudes and directions with specific values of the above parameters (6). If these parameters can be shown to act independently of one another, the probability of a hypothetical storm occurring is the product of the probabilities of the component parameter values. If independence of parameters cannot be justified, the joint probability method and the bootstrap can still be used, but procedures become more complex. For simplicity, independence will be assumed in the following discussion.

Probability distributions for hurricane parameters are derived by ranking historical values observed for each parameter. A plotting position method such as the Weibull formula (3) is then used to relate rank of parameter value to a probability of exceedance for that value (Figure 2).

Specific values of each parameter are then chosen to represent the entire range of parameter values obtainable in the area of interest. These representative values are chosen through a series of sensitivity tests by simulating the storm surge at a specified location with the

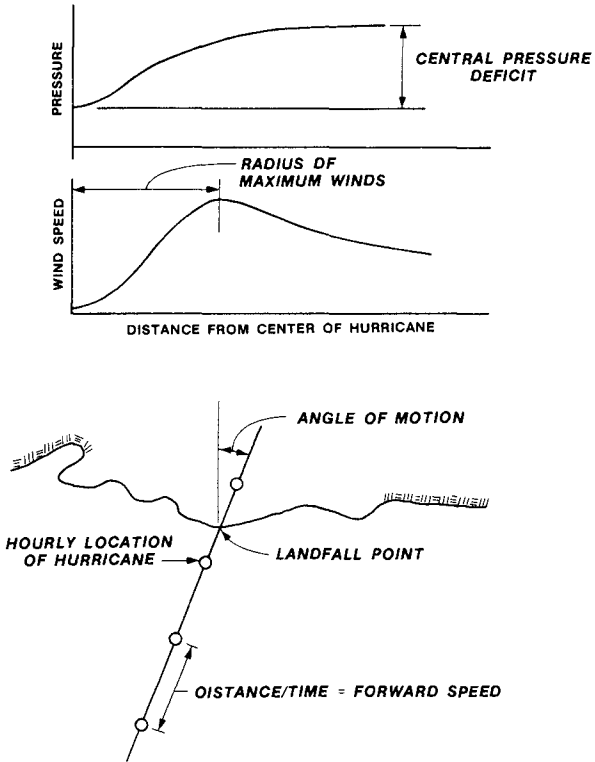


Figure 1. Schematic of Hurricane Parameters

WEIBULL FORMULA

$$\text{PROBABILITY OF EXCEEDANCE} = \frac{m}{N+1}$$

WHERE  $m$  IS THE RANK OF THE VALUE  
 $N$  IS THE NUMBER OF VALUES  
 (IN THIS EXAMPLE,  $N = 8$ )

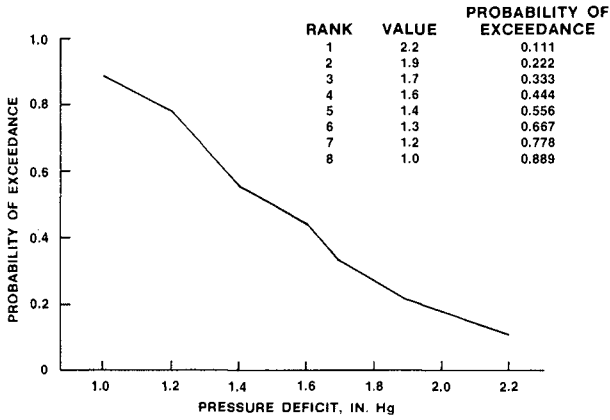


Figure 2. Exceedance Distribution From Plotting Positions

$V_i$  = REPRESENTATIVE PARAMETER VALUE  
 $P_i$  = ASSIGNED PROBABILITY

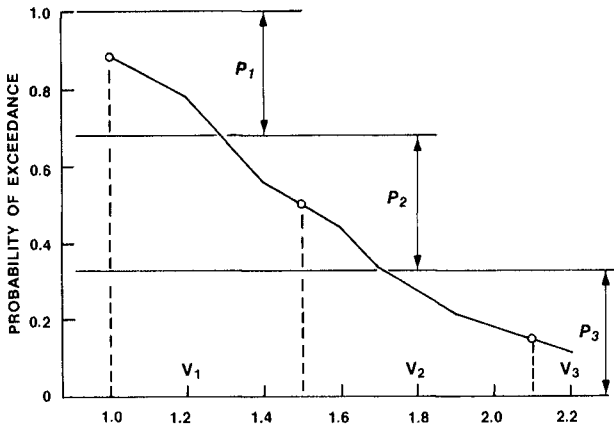


Figure 3. Parameter Value Probability Assignment

use of a parameterized model which produces a windfield from the hurricane parameter values, and a numerical hydrodynamic model. The purpose of these tests is to determine the variability of the surge level purely due to the variation in the value of a specific parameter. Often, all of the other parameters are assigned mean values while the remaining parameter is varied through the range of possible values. If the resulting surge levels vary greatly, more parameter values may be needed to represent the parameter probability distribution. Fewer values are needed for representation if little variation in surge is observed or if the variation in surge can be defined mathematically, i.e., by a linear function. The amount of probability which a parameter value receives is proportional to the amount of the probability distribution that the value is to represent (Figure 3).

The total number of storms simulated is the product of the number of representative values chosen for each parameter. If three values are chosen for each parameter, then  $(3)(3)(3)(3)(3)=243$  different synthetic hurricanes will be modeled, with each simulation resulting in a surge time history. The total number of storms will vary greatly with the number of values chosen to represent each parameter. Often, the outcome of a hurricane simulation is not reported as a surge time history, but as the maximum surge height obtained. The effect of the hurricane, in this case the maximum surge height, is assumed to have the same probability as the hurricane itself. However, this refers to the probability of the maximum surge height from an individual event occurring, not the probability of the same maximum surge height occurring from any other event. For example, a hurricane is given a probability  $P_1$ ; therefore, its maximum surge height of  $H$  is given probability  $P_1$ . Another storm can occur with probability  $P_2$  which also produces a surge height of  $H$ . The probability of the  $H$ -level surge height, however, is neither  $P_1$  or  $P_2$ , but the accumulative probability of all events causing a surge height of  $H$ .

To include the effect of tidal action on the total water level experienced at the coast, all of the computed surge records are convolved with a tidal record which is representative of the tides that the hurricane might encounter at the study site. This is possible if the water depth and other physical features allow the linear addition of surge and tide level to obtain a total water level. The hurricane surge and the tide both behave as shallow water waves, and thus their behavior depends on the water depth. In shallow areas the height of the surge or tide is a significant portion of the total water depth. In deep water, the surge and tide heights are a small fraction of the water depth, so that the behavior of the surge would be the same whether the tide is present or not. In most cases this linearity condition is met. The length of record used for the convolution process can vary from a minimum of a lunar month as long as 18.6 years, which is the cycle length for tidal activity. The length of tidal record is a decision which must be made on a case-by-case basis. For the following example, one lunar month was used.

The process of convolution involves creating all possible combinations of the surge and the tide records. This is achieved by adding the surge height time history produced through simulation to a

continuous tidal record of equal length to form a total water level record. In most cases, convolution is done by sampling the tidal and surge records at small time intervals, in this case one hour. The tidal record is then shifted one hour and the process is repeated (Figure 4). A lunar month is roughly 672 hours, so a convolution of a single synthetic storm surge record produces 672 different surge-tide combinations. Since the occurrence of a storm and a tide in nature is a random event, a storm can occur at any time of the month. Thus the probability of any hourly tidal height occurring is uniform and equal to  $1/672$ . When all of the storm surge records have been treated in the above manner, using the previous example,  $(243)(672)=163,296$  different surge-tide combinations will have been produced. The maximum water level is then found for each combination, and the water level's probability is the product of the probabilities of the producing storm and tide.

The final stage of this process is the construction of a water level vs. return period relationship, usually expressed as a curve. An array of intervals is created, each labeled with a unique water level value and spaced by a specified increment, for example 0.1 ft (0.03 m). The large number of maximum water levels are sorted and their probabilities are added to the appropriate interval. This process generates a water level probability distribution (Figure 5). The cumulative summation of the probabilities at each height produces an exceedance distribution, thereby providing the probability of a specified water level being equaled or exceeded.

A major factor not yet mentioned is the average recurrence interval for hurricanes. This value is found by dividing the number of recorded hurricanes into the record length. If the occurrence of hurricanes can be taken to be a Poisson process, then the average return interval, or return period between occurrences of a specified water level or greater, is the average recurrence interval divided by the exceedance probability. This produces a water level vs. return period relationship which is often the end result of the stage-frequency study (Figure 6).

The magnitude of error needs to be addressed before the above relationships should be used. The stage-frequency curve would give an exact reproduction of the behavior of the water level if absolutely no errors or uncertainties were introduced. This unfortunately is not possible. The parameterization of the hurricanes by only five parameters may not completely describe the windfield. The windfield and storm surge model may be either biased or inaccurate. These are factors which should be considered but are not the focus of this paper. A remaining problem is in the selection and assignment of parameter value probabilities. In the northern latitudes of the Atlantic Ocean for example, adequately monitored hurricane occurrences are scarce, and developing accurate parameter distributions with limited data becomes difficult. It is through the uncertainty of these parameter distributions that the error estimates on the stage-frequency curve are derived.

#### Bootstrap Method

The bootstrap (1,2) is a recently developed statistical tool which utilizes the computational speed of modern computers. This technique

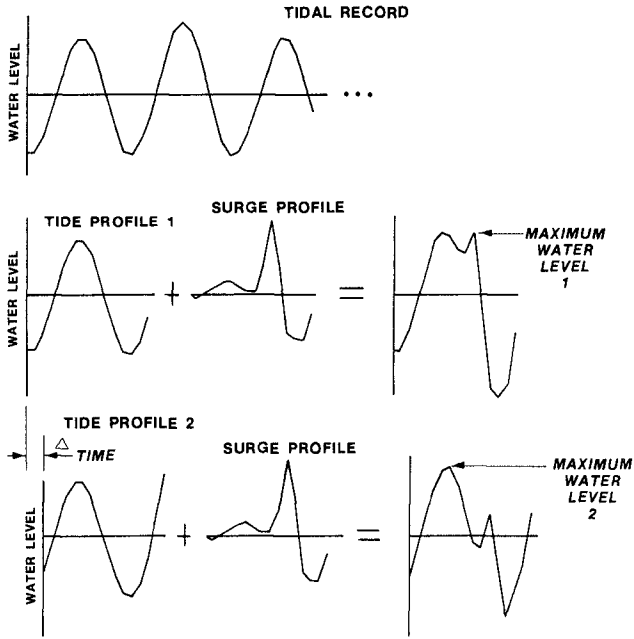


Figure 4. Tide Plus Surge Convolution Process

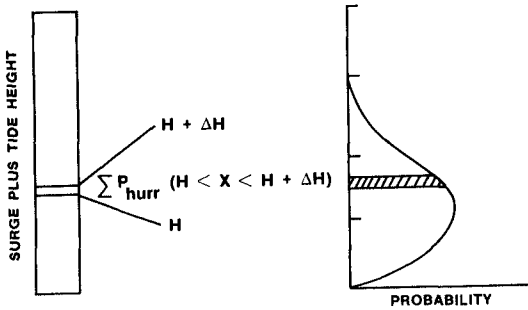


Figure 5. Probability Distribution for Total Water Level

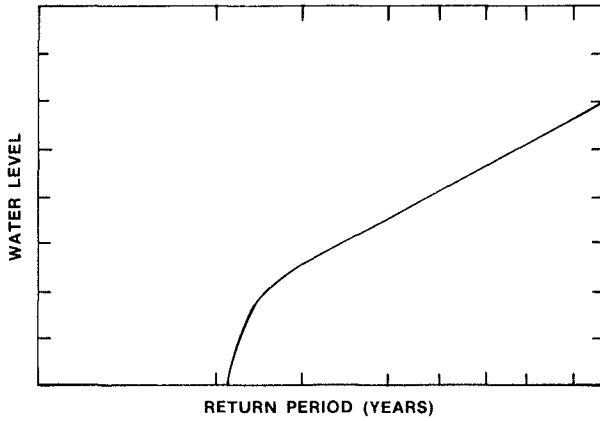


Figure 6. Stage-Frequency Curve From Joint Probability Method

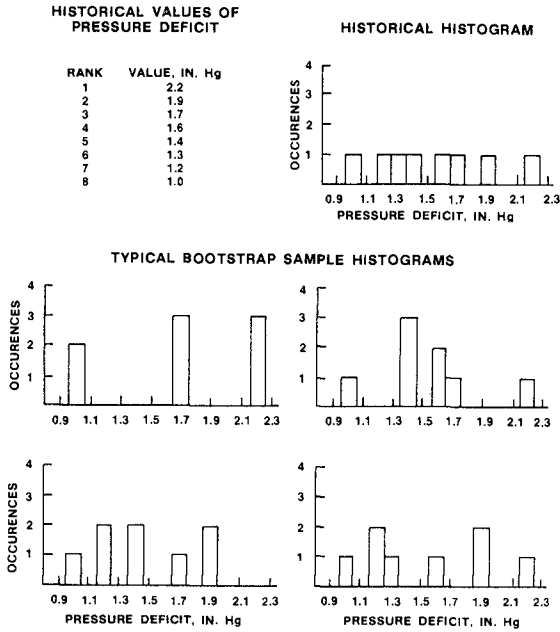


Figure 7. Variability of Synthetic Samples



is used here to develop stage-frequency relationships while accounting for the uncertainties of the parameter distributions due to a finite record length of hurricane occurrences. This section of the paper will give some insight on how the method works.

In the northeast coast of the United States, for example, only eight values of hurricane central pressure deficit have been recorded. The central pressure deficit is the most influential of the five hurricane parameters, and is directly responsible for the intensity, and therefore the surge height produced by the hurricane simulation. A stage-frequency curve developed on only eight values may be unreliable; therefore, the uncertainty inherent in such a small sample must be accounted for. These eight central pressure values can be thought of as being a random sample from a population whose distribution is unknown. It is desirable to estimate the unknown distribution as best possible, as well as calculate the possible difference, or error, between the true and estimated distributions. It is also advantageous if this can be done without the constraint of using a theoretical distribution.

The bootstrap method approximates the unknown population distribution with the historical sample distribution. This is what is done in most joint probability studies. However, instead of having only one historical sample from which to develop distributions, the bootstrap technique proposes to sample from the assumed population many thousands of synthetic "historical" sets. Each synthetic set generated by the bootstrap mimics how the parameter values might have occurred historically, since the synthetic bootstrapped set and the historical set are assumed to have been sampled from the same population. In this manner, the variation of the synthetic distributions about the assumed population can be quantified. The underlying assumption of the bootstrap is that all relationships between the assumed population and the synthetic samples also apply to the actual unknown population and the historical sample.

The bootstrap is performed in the following manner. For our example, the eight historical values are, in effect, placed in a box. A value is then randomly selected from the box, recorded, and replaced. This process continues until eight values, the size of the original set, have been chosen (Figure 7). This set of values constitutes a synthesized sample, from which a probability distribution of the sample can be formed. This new distribution is as likely to exist as the original historical distribution, since they both were assumed to have been sampled from the same population. The above process is repeated over and over, on the order of several thousand times, thus creating a large number of equally likely distributions. The variation among the synthesized distributions is caused by creating distributions from small samples, even though the population distribution is assumed to be known. This variability is not observed with historical sets since only one set of each parameter exists. This variability, estimated through the bootstrap process, indicates that the single historical parameter set should not be taken as an exact representation of the population distribution, but does not show the variability of the sample distributions.

The bootstrap is then applied to the remaining four parameters, creating several thousand synthesized probability distributions for each parameter. The stage-frequency curve discussed earlier was developed from the distributions of the five historical parameter sets. Other stage-frequency curves could just as well be generated from the synthetic parameter distributions. No additional hydrodynamic simulations need to be made in order to create these new curves. The change of a probability distribution for a parameter only changes the probability assigned to the parameter values, not the values themselves.

A new bootstrapped stage-frequency curve is generated by choosing one synthesized probability distribution at random for each parameter. A new probability assignment is made for each parameter value, and a new probability is calculated for each hurricane previously simulated. The tidal convolution process can be by-passed since only the probabilities of the water levels change, not the heights. Finally, a stage-frequency curve is created which can be considered as likely a representation of the true, unknown stage-frequency curve as was the stage-frequency curve generated from historical sample sets. If this process is repeated 1000 times, a family of 1000 such stage-frequency curves will be generated.

It is common for water levels to be determined at return periods of 10, 25, 50, 100, 200, 500 and 1000 years. After the bootstrapping process, 1000 possible values of water level, one from each of the bootstrapped stage-frequency curves, is obtained at each return period. If the 1000 values found at each return period are ranked in decreasing order, the 500th value will be by definition the 50th percentile, or median, value. This value will be the best estimate of the water level for the given recurrence interval. Estimates of confidence intervals can be obtained from other percentile levels. The 90th percent confidence interval can be estimated as the interval between the 95th percentile value (rank 950) and the fifth percentile value (rank 50). When the above process is done at each return period, an estimate of the uncertainty of a stage-frequency curve is obtained (Figure 8). This uncertainty is purely due to the small sample size of the hurricane parameters.

The bootstrap was used to estimate the error in stage-frequency curves during a project performed at the U. S. Army Engineer Waterways Experiment Station by the Coastal Engineering Research Center (CERC) for the U. S. Army Engineer District, New York. The details of the study are found elsewhere (5) and will not be discussed here.

For the study performed at CERC, it was found that 4000 synthetic parameter distributions and 1000 synthetic stage-frequency curves gave very stable results, stability defined as little change in final result with increased number of bootstrapped samples. The stability also increased as the historical sample size increased. The bootstrap procedure is fairly simple to program and implement, and when performed on a CRAY-1 computer, cost less than a single hurricane simulation.

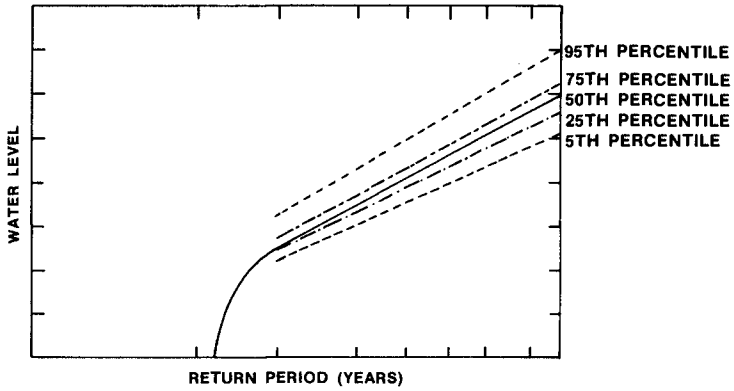


Figure 8. Bootstrapped Stage-Frequency Confidence Intervals

### Summary and Conclusion

A bootstrap procedure has been introduced which estimates the error due to meteorological uncertainty in coastal stage-frequency curves produced by the joint probability method. The procedure consists of assuming that the unknown population distribution for each hurricane parameter is the same as the parameter distribution obtained from historical data. Synthetic parameter distributions are created by repeated sampling from this assumed population. The variation of the synthetic parameter distributions is due to the small sample sizes. Synthetic stage-frequency curves are then generated by randomly selecting a synthetic distribution for each parameter. A large number of these stage-frequency curves are then used to estimate confidence intervals. The bootstrap method is flexible, simple to program, and inexpensive to implement.

### Acknowledgments

The methods developed in this paper were part of a numerical investigation of extreme water levels along the southern coast of Long Island funded by the U. S. Army Engineer District, New York. Permission was granted by the Chief of Engineers to publish this information.

### Appendix.-References

1. Efron, Bradley, "Computers and the Theory of Statistics: Thinking the Unthinkable," SIAM Review, Vol. 21, No. 4, October, 1979, pp. 460-480.
2. Diaconis, Persi, and Efron, Bradley, "Computer Intensive Methods in Statistics," Scientific American, May 1982, pp. 116-130.
3. Linsley, R.K., Kohler, M.A., and Paulhus, J.H.L., Hydrology for Engineers, 2d Ed., McGraw-Hill Book Co., New York, 1975.
4. Myers, Vance A., "Joint Probability Method of Tide Frequency Analysis Applied to Atlantic City and Long Beach Island, N.J.," ESSA Tech Memo WBTM HYDRO 11, April, 1970.
5. Prater, M.D., Hardy, T.A., and Butler, H.L., "Fire Island to Montauk Point Phase II Storm Surge Model," U.S. Army Engineer Waterways Experiment Station Technical Report in progress.
6. Schwerdt, R.W., Ho, F.P., and Watkins, R.R., "Meteorological Criteria for Standard Project Hurricane and Probable Maximum Windfields, Gulf and East Coasts of the United States," NOAA Tech Report NWS 23, National Weather Service, September, 1979.

## CHAPTER TWELVE

### Numerical Simulation of Storm Surges by Multi-Level Models

by

Takao Yamashita<sup>1</sup> and Yoshito Tsuchiya<sup>2</sup>, M. ASCE

**Abstract** The numerical simulation of storm surges in shallow bays is investigated by multi-level models such as the 2-level and FE-FD models which are used to consider the velocity profiles in wind-induced currents. These models were applied to hindcast the storm surge caused by Typhoon 7916 in Osaka Bay with the result that the water surface elevations and currents induced by the storm surge were successfully simulated.

#### 1. Introduction

In the recent years, rapid advancement in both the physical sciences for marine modeling and in the numerical calculation techniques for the governing differential equations have made new developments in fields such as storm surges, tides, mixing in the upper ocean and the air-sea interactions possible. We investigate here numerical simulation models of the storm surge which is one of the most complex, large scale and disastrous natural air-sea interaction phenomena in the ocean and coastal zones.

Such numerical calculation techniques have advanced greatly, particularly in the fields of computer-aided engineering and mathematics. Until now, the FEM(Finite Element Method), BEM (Boundary Element Method) as well as the classical FDM(Finite Difference Method) have prevailed as the techniques most used to solve differential equations in fluid dynamics. However, a number of types of numerical schemes have been proposed to carry out such calculations more accurately and stably, particularly in the case of the application of the FDM to a time-evolutional equation.

The physical modeling for storm surges is generally constructed by combining the wind and pressure fields of an atmospheric low pressure area with its accompanying tides and progressive waves of long periods. Assuming incompressive, viscous fluid, the basic equations for storm surges can be described by the Navier-Stokes equations. The most typical modeling is the so-called 1-level model based on depth-integrated equations in which velocity profiles are uniform.

---

1 Instructor, Disaster Prevention Research Institute, Kyoto University, Kyoto 611, JAPAN.

2 Professor, Disaster Prevention Research Institute, Kyoto University, Kyoto 611, JAPAN.

Considering, however, the dynamics of storm surges in partially enclosed shallow water, the flow structure and patterns of induced currents should be three dimensional because of the co-existence of wind driven currents and their return flows. In such regions, not only the nonlinearity of governing equations and complex geometrical features of coastlines but the three dimensionality of flow structures must be taken into consideration, so many types of models have been proposed.

Previous studies of the numerical simulation of storm surges have been made in three directions. The first direction has been to search for optimal schemes for time discretization in the FDM, which has resulted in schemes such as the leap-frog scheme (explicit) and the ADI (Alternating Direction Implicit) scheme. These are usually adopted for their time-efficiency scheme. In the second direction, researchers have made efforts to reproduce coastlines in calculations by using triangular grid systems. Thacker(1979) proposed the irregular-grid, finite-difference techniques for curving coastlines by approximating partial derivatives using the slopes of planar surfaces associated with the triangular components of the grid. This offers the advantages of greater flexibility than the coordinate transformation method (Wanstrath et al(1976)); and greater economy than the finite-element method (Pinder and Gray(1977), Tanaka(1978)), which have been used to include curving coastlines in calculations. The third direction has been to study mathematical modeling in order to introduce the three-dimensionalities of flow features into calculations of storm surges in shallow bays and estuaries. Koutitas and O'Connor(1980), examined the computer modeling of three-dimensional coastal currents induced by winds by the application of a composite finite-element/finite-difference procedure (referred to here as it the FE-FD model). The authors(1982) have modified the FE-FD model into a 3-level model which is more economical and more applicable generally than the previous multi-level models.

In this paper, we discuss the applicabilities and present limitations of the multi-level models by comparison of the theoretical results generated and the actual currents and tides observed at the storm surge caused by Typhoon 7916 in Osaka Bay, Japan.

## 2. Multi-Level Models

### 2.1 The 2-level model

The vertical distribution of the horizontal velocity component of wind-induced current in partially enclosed shallow water have been investigated theoretically and experimentally. It has been shown that there is a conversion point of mean velocity in the range from 0.2 to 0.4 in nondimensional depth (Baines and Knapp(1965)). This suggests that bottom stresses evaluated in the 1-level model are questionable in their magnitude and direction. To overcome these inconsistencies, the authors (8) have proposed the 2-level model, in which the upper level represents the wind-driven current and the lower, the return flow.

Using the definition sketch and notations for the 2-level model shown in Figure 1, the model equations for both the upper and lower levels, and for the continuity equation are written as

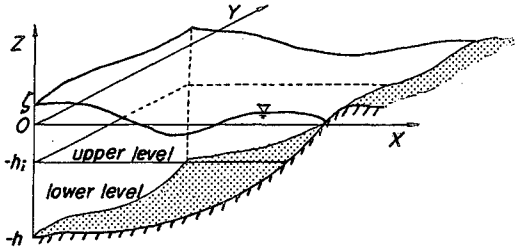


Figure 1. Definition sketch and notations for the 2-level model.

a) for the upper level

$$\frac{\partial M_u}{\partial t} + (NL)_{ux} + (uw)_i = fN_u - gH_u \frac{\partial \zeta}{\partial x} - \frac{1}{\rho_w} \frac{\partial p}{\partial x} + \frac{\tau_{sx}}{\rho_w} - \frac{\tau_{ix}}{\rho_w} + (HM)_u \quad (1)$$

$$\frac{\partial N_u}{\partial t} + (NL)_{uy} + (vw)_i = -fM_u - gH_u \frac{\partial \zeta}{\partial y} - \frac{1}{\rho_w} \frac{\partial p}{\partial y} + \frac{\tau_{sy}}{\rho_w} - \frac{\tau_{iy}}{\rho_w} + (HM)_u \quad (2)$$

b) for the lower level

$$\frac{\partial M_l}{\partial t} + (NL)_{lx} - (uw)_i = fN_l - gH_l \frac{\partial \zeta}{\partial x} - \frac{1}{\rho_w} \frac{\partial p}{\partial x} + \frac{\tau_{ix}}{\rho_w} - \frac{\tau_{bx}}{\rho_w} + (HM)_{lx} \quad (3)$$

$$\frac{\partial N_l}{\partial t} + (NL)_{ly} - (vw)_i = -fM_l - gH_l \frac{\partial \zeta}{\partial y} - \frac{1}{\rho_w} \frac{\partial p}{\partial y} + \frac{\tau_{iy}}{\rho_w} - \frac{\tau_{by}}{\rho_w} + (HM)_{ly} \quad (4)$$

where the discharges per unit width are defined by

$$M_u = \int_{-h_i}^{\zeta} u dz, \quad N_u = \int_{-h_i}^{\zeta} v dz, \quad M_l = \int_{h_i}^h u dz, \quad N_l = \int_{h_i}^h v dz$$

and  $H_u = \zeta + h_i$ ,  $H_l = h - h_i$ ,  $(NL)$  and  $(HM)$  indicate the nonlinear and horizontal mixing terms respectively,  $(uw)_i$  and  $(vw)_i$  are the mass fluxes at the interface, and  $f$  is the Coriolis parameter. The shearing stresses at the sea surface and the sea bottom are expressed in quadratic form, using the drag coefficients  $C_D$  and  $C_f$ , as

$$\left. \begin{aligned} \tau_{sx} &= \rho_w C_D W_x \sqrt{W_x^2 + W_y^2}, & \tau_{sy} &= \rho_w C_D W_y \sqrt{W_x^2 + W_y^2}, \\ \tau_{bx} &= \rho_w C_f U_l \sqrt{U_l^2 + V_l^2}, & \tau_{by} &= \rho_w C_f V_l \sqrt{U_l^2 + V_l^2} \end{aligned} \right\} \quad (5)$$

The shearing stress at the interface is given in the linear form.

$$\tau_{ix} = -2C_i \rho_w \nu_i (U_u - U_l)/h, \quad \tau_{iy} = -2C_i \rho_w \nu_i (V_u - V_l)/h \quad (6)$$

where,  $\nu_i$  is the eddy viscosity. The coefficient  $C_i$  of Eq.(6) has been determined as 3/2, assuming a steady, uniform current in the enclosed domain with uniform water depth.

The continuity equation is given by

$$\frac{\partial \zeta}{\partial t} + \frac{\partial}{\partial x}(M_u + M_l) + \frac{\partial}{\partial y}(N_u + N_l) = 0 \tag{7}$$

The model equations mentioned can be integrated numerically by the finite-difference technique.

2.2 The FE-FD model

Using the Navier-Stokes equation for fluid elements and the continuity equations for a water column, neglecting the horizontal diffusion of momentum and using the notations shown in Figure 2, where  $H$  is the total water depth,  $h$  the water depth in the M.W.L. and  $\zeta$  the water elevation induced by the storm surge, the fundamental equations can be described as

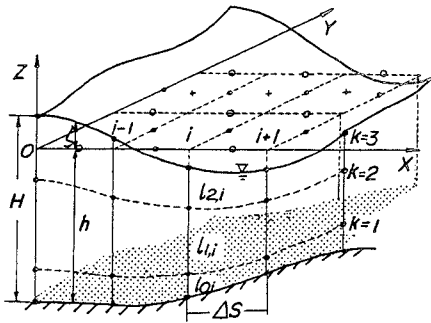


Figure 2. Definition sketch and notations for the FE-FD model.

$$L_u(x, y) = \frac{\partial u}{\partial t} + u \frac{\partial u}{\partial x} + v \frac{\partial u}{\partial y} - fv + g \frac{\partial \zeta}{\partial x} - \nu_i \frac{\partial^2 u}{\partial z^2} = 0 \tag{8}$$

$$L_v(x, y) = \frac{\partial v}{\partial t} + u \frac{\partial v}{\partial x} + v \frac{\partial v}{\partial y} + fv + g \frac{\partial \zeta}{\partial y} - \nu_i \frac{\partial^2 v}{\partial z^2} = 0 \tag{9}$$

The continuity equation is written as

$$\frac{\partial \zeta}{\partial t} + \frac{\partial}{\partial x} \left( \int_{-h}^{\zeta} u dz \right) + \frac{\partial}{\partial y} \left( \int_{-h}^{\zeta} v dz \right) = 0 \tag{10}$$

As to the three-dimensional problem, the coastal area is first covered by a regular-grid network in the x-y plane, and the water depth is divided into the same number of elements in the vertical water column. Next, the finite-element method is applied to Eqs.(8) and (9) and the finite difference method of fractional step is applied to Eq.(10) to obtain the components of currents  $(u_k(x, y), v_k(x, y))$  at the



nodal point  $k$  and water surface  $\zeta(x,y)$ . In the case of the three-level model, the equations of motion are, consequently, written in matrix form, by

$$\{A_x\} \cdot \{u\} = \{B_x\} \text{ FINAL-BRACKET, } \quad \{A_y\} \cdot \{v\} = \{B_y\} \quad (11)$$

in which, for example, the matrices and vectors of the x-components are respectively expressed as

$$\{A_x\} = \begin{bmatrix} l_{x,1ij}/3\Delta t & l_{x,1ij}/6\Delta t & 0 \\ l_{x,1ij}/6\Delta t & (l_{x,1ij}+l_{x,2ij})/3\Delta t & l_{x,2ij}/6\Delta t \\ 0 & l_{x,2ij}/6\Delta t & l_{x,2ij}/3\Delta t \end{bmatrix} \quad (12)$$

$$\{u\} = \begin{bmatrix} u_{1j}^{n+1} \\ u_{2j}^{n+1} \\ u_{3j}^{n+1} \end{bmatrix} \quad \{B_x\} = \begin{bmatrix} B_{1x} \\ B_{2x} \\ B_{3x} \end{bmatrix} \quad (13)$$

where  $B_i$  is the vector of known variables calculated at the time step of  $n-1/2$  in the fractional method, whose components include the atmospheric pressure gradients, and the shearing stresses at the water surface, interfaces and bottom.

### 3. Hindcast of Storm Surge Caused by Typhoon

#### 3.1 The calculation conditions

Using the 2-level and FE-FD models, the storm surges caused by Typhoon 7916 are hindcasted in the region shown in Figure 3. This typhoon which passed through Osaka Bay on November 30, 1979 caused peculiar tidal changes in the inner part of the bay. The tidal records measured at 9 points along the bay are shown in Figure 4. Resurgences are remarkable immediately after the peak of storm surge.

The computation was made by the leap-frog staggered system, in which the horizontal grid spaces were chosen as  $\Delta s=1.5$  km in order to approximately cover the two channels in computation, and time space  $\Delta t=20$  sec. And the depths at two channels were adjusted to cover the same area of the cross section. Considering that the mean water depth of the bay is 28m, the upper level depth in the 2-level model is determined as  $h_i = 8$  m. The open boundary conditions are given by the surface elevations which were estimated by interpolation of the observed anomaly of meteorological tides at the points Nushima, Kainan, Akashi and Higashi-Futami, and the so-called fixed boundary conditions are used along the coastlines.

It is important in numerical modeling for storm surges to determine the unknown physical parameters such as the drag-coefficients at the water surface  $C_b$ , the at the bottom  $C_f$ , the friction coefficient  $C_f$ , and the eddy viscosity  $\nu_i$ , which are expressed practically as,

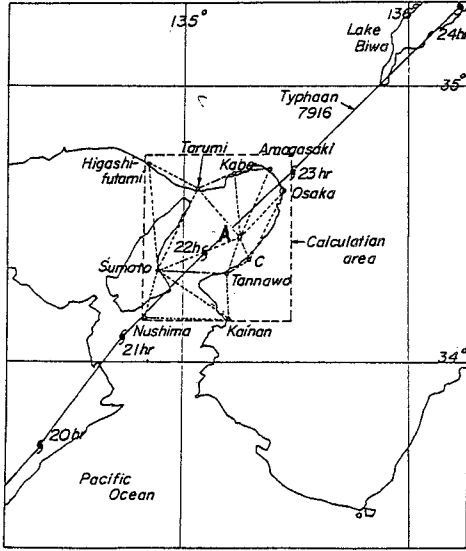


Figure 3. The computation region.

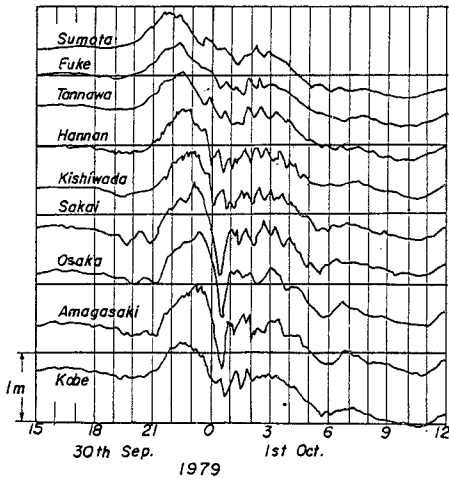


Figure 4. Observed tidal records showing anomalies in meteorological tides caused by Typhoon 7916 in Osaka Bay.

$$(C_{x0}, C_{y0}) = 1.50 \times 10^{-3} (w_x^{0.19}, w_y^{0.19}) \quad \text{for } w_x, w_y \leq 8 \text{ (m/sec)} \quad (14)$$

$$(C_{x0}, C_{y0}) = 2.04 \times 10^{-4} (w_x^{0.74}, w_y^{0.74}) \quad \text{for } w_x, w_y > 8 \text{ (m/sec)} \quad (15)$$

respectively and

$$C_f = 0.0026 \quad , \quad \nu_i = 0.01 \text{ (m}^2\text{/sec)} \quad (16)$$

where Eqs. (14) and (15) for the drag coefficient at the surface are those proposed by Mitsuyasu (1981).

### 3.2 Computation of tides

The dominant tides in the Seto Inland Sea including Osaka Bay are the  $M_2$  semi-diurnal lunar tide which is a semi-diurnal lunar tide coming in through the Kitan Channel in the south of the bay which flows out through the Akashi Channel in the west. The duration of the tide is about 2 hours and its amplitude reduces to 1/3 in the bay. The  $S_2$  tide is also similar to the  $M_2$  in these tendencies. We here consider only the semi-diurnal tides ( $M_2$ ,  $S_2$ ) whose amplitudes and phases are listed in Table 1.

Table 1 Amplitudes and phases of tides

Points	Amplitudes ( $M_2 + S_2$ )	Phases (deg.)
Nushima	0.629 m	179.8°
Kainan	0.661 m	188.2°
Higashi-Futami	0.285 m	294.6°
Ei	0.334 m	327.7°

The computation of tides was carried out by the 1-level model for four periods to obtain the initial flow conditions prior to the computation for storm surges.

### 3.3 Typhoon model

The wind and pressure gradients of a typhoon are expressed practically by Fujita model as

$$\left. \begin{aligned} \frac{\partial P}{\partial x} &= -\frac{P_0 r_0 x}{(r^2 + r_0^2)^{3/2}}, & \frac{\partial P}{\partial y} &= -\frac{P_0 r_0 y}{(r^2 + r_0^2)^{3/2}} \\ W_x &= C_1 F_x - C_2 G_x, & W_y &= C_1 F_y + C_2 G_y \end{aligned} \right\} \quad (17)$$

In this case, the wind field associated with the moving speed of a typhoon  $(V_x, V_y)$  (m/sec) and the baroclinic wind field are expressed, respectively as

$$\left. \begin{aligned} F_x &= V_x \exp\left(\frac{-r\pi}{5 \times 10^5}\right), & F_y &= V_y \exp\left(\frac{-r\pi}{5 \times 10^5}\right) \\ G_x &= \left(\sqrt{3y/2+x/2}\right) \left\{ \sqrt{f^2/4 + (\rho_w/\rho_a)gP_0 r_0 / (r_0^2 + r^2)^{3/2}} - f/2 \right\}, \\ G_y &= \left(\sqrt{3x/2-y/2}\right) \left\{ \sqrt{f^2/4 + (\rho_w/\rho_a)gP_0 r_0 / (r_0^2 + r^2)^{3/2}} - f/2 \right\} \end{aligned} \right\} \quad (18)$$

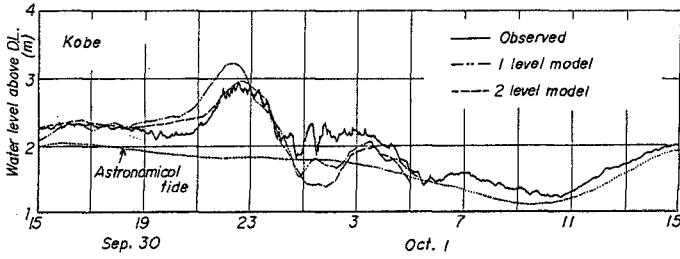
where  $r = \sqrt{x^2 + y^2}$  is the distance from the center of typhoon,  $P_0$  (m) the pressure head corresponding to the atmospheric pressure drop, and  $r_0$ ,  $C_1$ ,  $C_2$  are the typhoon parameters for which values for Typhoon 7916 were 60(km), 0.6 and 0.6, respectively.

### 3.4 Computations for the storm surge

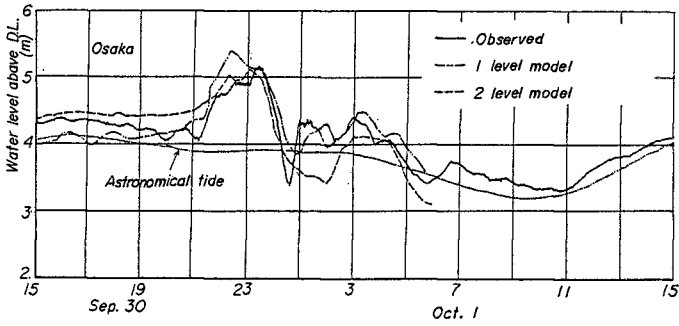
#### a) The 2-level model

Using the finite-difference method, the computation of storm surge was performed by the 1- and 2-level models. The calculated anomalies in meteorological tides at points, Kobe, Osaka and Sumoto are shown in Figure 5 with the astronomical tides. Figure 6 shows the flow patterns calculated by the 2-level model. We conclude that the results obtained by the 2-level model agree well with the observed tides around the peak of storm surge, including its forerunners. Disagreement at the resurgences appearing immediately after the peak can be seen in the results of both models, which may be caused by the rapid changes in its pressure fields. This fact has already been suspected by the authors(1981).

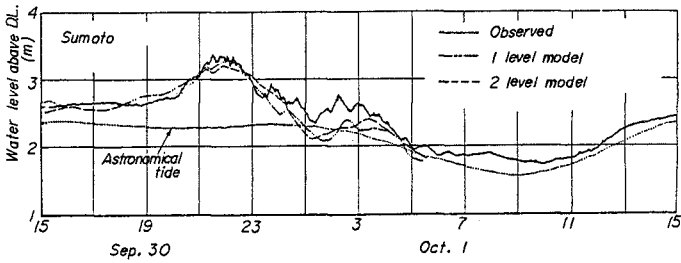
The current measurements have been carried out at point A shown in Figure 3, using magnetic current meters at three points of which the depths are 3, 9 and 16m. Comparison between the calculated and observed west-east components of currents at the point 3m deep is shown in Figure 7. In contrast to the agreement for surface elevation, both currents calculated by the 1- and 2-level models do not agree well with the observations at point A. The effects of the 2-level modeling are, however, remarkable in this figure in that changes in current velocities with time calculated by the 2-level model approach those observed.



(a) At Kobe

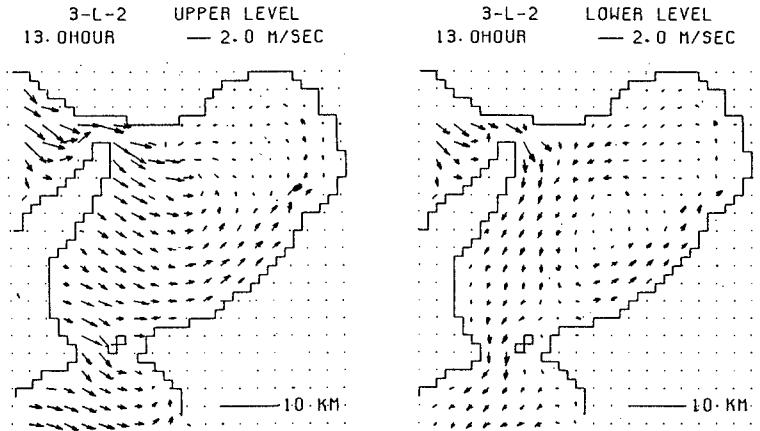


(b) At Osaka

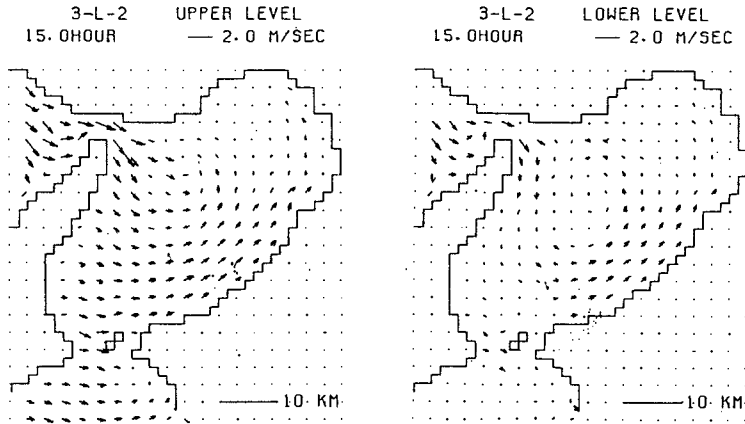


(c) At Sumoto

Figure 5. Comparisons between computations and observations of storm surges.



(a) At 22:00 Sept. 30



(b) At 0:00 Oct. 1

Figure 6. Flow patterns computed by the 2-level model.

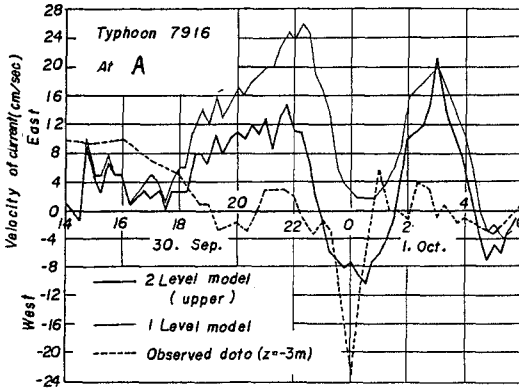


Figure 7. Comparison of calculated and observed east-west velocity components at point A.

b) The FE-FD model

Koutitas and O'Connor have made reference to the importance of an accurate estimate of the value for the vertical eddy viscosity  $\nu_i$  when applying the FE-FD model to a wind-induced flow. It is important, of course, to make clear its value physically and empirically. In this paper, the FE-FD modeling procedure is employed as a tool of new approach to establish a 3-level model which has simplicity and generality, so that the same values for  $\nu_i$  used in the 2-level model can be used, without further discussion. The ratios of thickness of the upper, middle and lower layers to the water depth at each level (element) are set respectively as 3:6:1, and the shearing stresses at the surface are determined as

$$\left. \begin{aligned} S_x &= \rho_a C_D W_x \sqrt{W_x^2 + W_y^2} = \rho_a \nu_i \left. \frac{\partial u}{\partial z} \right|_{\text{surface}}, \\ S_y &= \rho_a C_D W_y \sqrt{W_x^2 + W_y^2} = \rho_a \nu_i \left. \frac{\partial v}{\partial z} \right|_{\text{surface}} \end{aligned} \right\} \quad (19)$$

In addition the non-slip condition can be used at the bottom because the bottom shearing stresses can be automatically determined from the velocity gradient. This simplicity is one of remarkable features of the model.

The computational results for water surface elevations and currents in the vertical direction (east-west and north-south components) at point A are shown in Figures 8 and 9, respectively. Comparison with the results of the 1- and 2-level models shows that the water surface elevations are over-estimated at the inner part of the bay. In Figure 9, the solid lines show the velocity profiles of the currents due to the anomalies in the meteorological tides and the dotted lines, those caused by the storm surge. The flow patterns in the upper and lower levels at 13hr (actually 22:00 Sept. 30) and 15hr (actually 0:00 Oct. 1) are shown

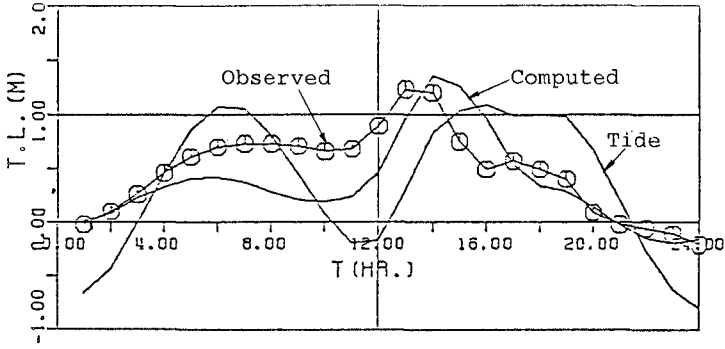


Figure 8. Surface disturbances computed by the FE-FD model at point A.

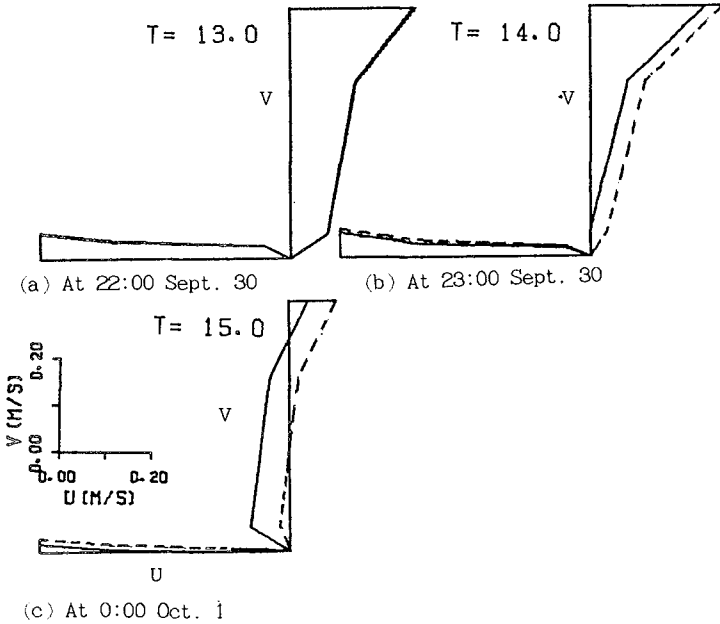


Figure 9. Velocity distributions calculated by the FE-FD model at point A.



in Figure 10, in which opposite currents in the upper and lower levels are recognized clearly, but no opposite ones exist in the results from the 2-level model as shown in Figure 6. Comparison of the calculated and observed current vectors is shown in Figure 11, in which the solid lines are the observed current vectors, the dotted lines calculated ones by the FE-FD model. 1-L and 2-L express the vector obtained by the 1- and 2-level models, respectively. The current vectors calculated by the FE-FD model are in better agreement with the observed ones than those calculated by the 1- or 2-level models, however the strong current to the southeast observed at 15hr (actually at 0:00 Oct. 1) is still not completely simulated.

#### 4. Discussions and Conclusions

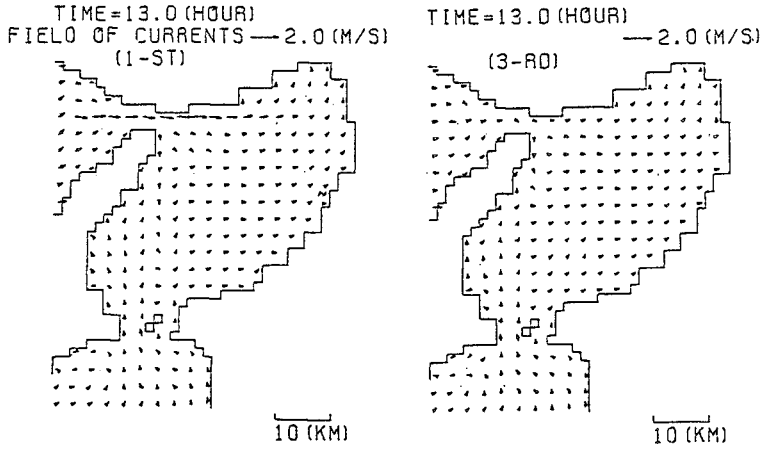
Thus far, we have presented the multi-level model numerical calculation methods and the results of storm surge hindcasting, with considerations. The multi-level models used in this paper are fundamentally based on the concept of introducing the effects of three-dimensionality of currents into the calculations for the storm surge.

Using the 2-level model, which is a modification of the 1-level model, water surface elevations and currents caused by storm surges in shallow bays can be simulated by estimating the shearing stresses at the interface between the upper and lower levels more reasonably. As the above formulation, of course, depends on the accuracy of the eddy viscosity estimate, the optimal coefficients in the model should be found practically by applying the model proposed to many cases of storm surges.

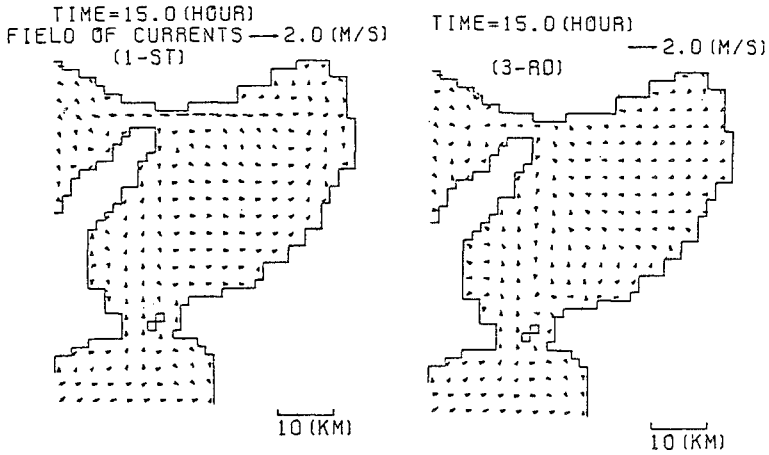
The FD-FE model proposed here deals with the modified 3-level model which has more simplicity and flexibility than previous multi-level models. This model is so economical in calculation time that the actual prediction of storm surges including their induced-currents as well as their associated tides even without using a so-called "super computer" may be feasible in the near future. But this model as yet requires practical improvement to determine reasonable formulas for shearing stresses at the bottom and the water surface.

It is concluded that the multi-level models are applicable to the numerical prediction of storm surges in shallow bays. As to further developments in the multi-level models, we think that it is possible and useful to introduce the BEM (Boundary Element Method) into this model instead of the finite-element technique to calculate the equations of motion and the irregular-grid finite-difference method for solving the continuity equation.

We are grateful to Messrs. T. Oka and T. Hiraishi, former graduate students for their kindest assistance in the numerical computations. This study was supported by Grant-in-Aid for Scientific Research from the Ministry of Education, Science and Culture of Japan, under Grant No.302027.

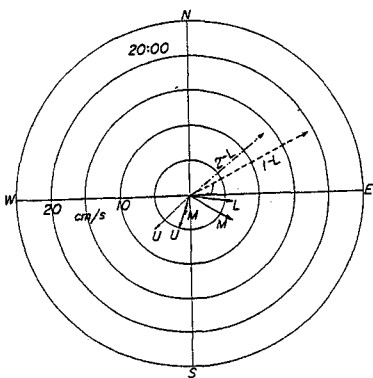


(a) At 22:00 Sept. 30

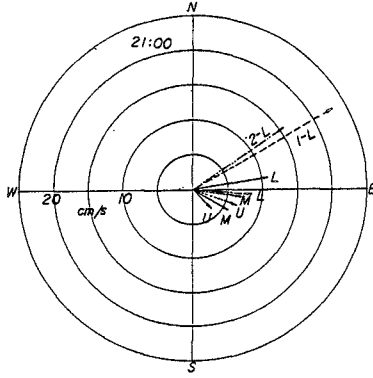


(b) At 0:00 Oct. 1

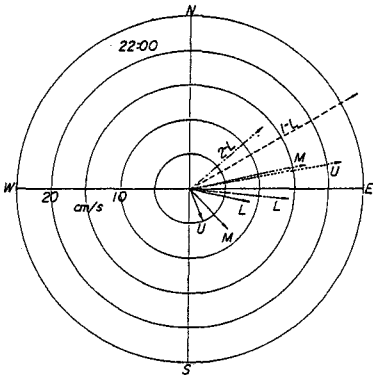
Figure 10. Flow patterns in the upper and lower levels.



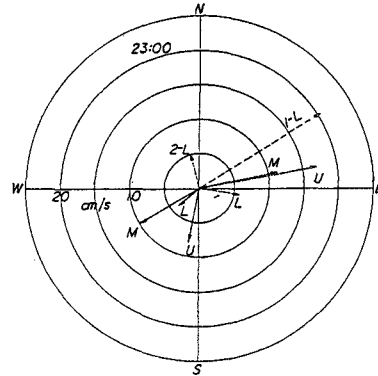
(a) At 20:00 Sept. 30



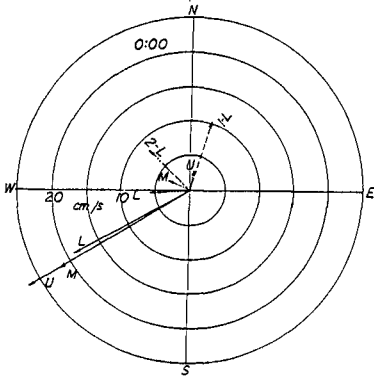
(b) At 21:00 Sept. 30



(c) At 22:00 Sept. 30



(d) At 23:00 Sept. 30



(e) At 0:00 Oct. 1

Figure 11. Comparisons between calculated and observed velocity vectors at point A.

## Appendix-References

- 1) Baines W. D. and D. J. Knapp, Wind driven water currents, Jour. ASCE, HY2, pp.205-221, 1965.
- 2) Koutitas C. and B. O'Conner, Modeling three-dimensional wind-induced flows, Jour. Div., ASCE, HY11, pp.1843-1865, 1980.
- 3) Mitsuyasu H., Formulation of water surface shearing stress extended by strong winds, in "Prediction of storm surges and related phenomena, and their extremes" (Head Investigator Y. Tsuchiya), Report of Grant-in-Aid for Research Project in Natural Disasters, The Ministry of Education, Science and Culture of Japan, No. A-56-4, pp.10-20, 1981 (in Japanese).
- 4) Pinder, G. F. and W. G. Gray,, Finite element simulation in surface and sub surface hydrology, Academic Press, London, 295p., 1979.
- 5) Tanaka T. and Y. Ono, Finite element analysis of typhoon surge in Ise Bay, U.S.-Japan Seminar on Interdisciplinary Finite Element Methods, Cornell Univ., pp.307-332, 1978.
- 6) Thacker, W. C., Irregular-grid finite-difference technique for surge calculations for curving coast-lines., in "Marine Forecasting", Elsevier Oceanography Series, pp.261-283, 1979.
- 7) Tsuchiya Y., T. Yamashita and T. Hiraishi, Numerical simulation of storm surges by the FE-FD model, Proc. 28th Japanese Conf. on Coastal Eng., JSCE, pp.31-35, 1982(in Japanese).
- 8) Tsuchiya Y., S. Nakamura, T. Yamashita and T. Oka, Characteristics of the storm surge due to Typhoon 7916 in Osaka Bay through the Kii Strait, Annuals of Disas. Prev. Res. Inst., Kyoto Univ., No.24-B2, pp.475-484, 1981(in Japanese).
- 9) Wanstrath, J. J., R. E. Whitaker, R. O. Reid and A. C. Vastano,, Storm surge simulation in transformed coordinates, Vol.I, Theory and Application, U.S. Army, Corps of Engineers, Tech. Rept., No.76-3, 166p., 1976.

## CHAPTER THIRTEEN

### NUMERICAL SIMULATION OF STORM SURGES INDUCED BY TROPICAL STORMS IMPINGING ON THE BANGLADESH COAST

S.K. Dube<sup>1</sup>, P.C. Sinha<sup>2</sup>, and G.D. Roy<sup>3</sup>

**ABSTRACT:** In the present paper a vertically integrated coastal zone numerical model has been described for the simulation of the surges generated by the tropical storms striking the Bangladesh coast. The model is fully nonlinear and uses a conditionally stable explicit finite-difference scheme for solving the relevant equations of motion. In this model the analysis area extends from 87°E to 93°E along the south coast of Bangladesh and there are three open-sea boundaries situated along 87°E, 93°E and 19°N. The model utilises a curvilinear boundary treatment to represent the coastline and uses a non-uniform off-shore grid spacing adjacent to the coastal boundary. This allows an increased resolution near the Bangladesh coast.

Using a forcing wind-stress distribution representative of the 1970 Chittagong cyclone, we compare the model predicted surges with the observed sea-surface elevations along the Bangladesh coast. The predicted peak surge elevation above mean sea level compares well with the observed values at Chittagong port. A comparison of the results has also been made with those obtained from the corresponding model having uniform off-shore grid spacing.

#### INTRODUCTION

The tropical storms and the associated surges are very common occurrences along the coastal regions of Bangladesh. These systems directly affect the life and property of the habitants which is a heavy burden on the country's exchequer. About 500,000 lives were lost in one of the most severe cyclones that hit Bangladesh (then East Pakistan) in November, 1970. There can be little doubt that the number of casualties would have been considerably lower if the storm surges could have been predicted well in advance to allow effective warnings in the threatened areas.

In an earlier paper, Dube et al.(4) have developed a vertically integrated coastal zone numerical model for the simulation of storm

<sup>1</sup>Senior Scientific Officer, Centre for Atmospheric Sciences,  
Indian Institute of Technology, New Delhi, India.

<sup>2</sup>Principal Scientific Officer, Centre for Atmospheric Sciences,  
Indian Institute of Technology, New Delhi, India.

<sup>3</sup>Research Scholar, Centre for Atmospheric Sciences,  
Indian Institute of Technology, New Delhi, India (on leave from  
Dhaka College, Dhaka, Bangladesh).

surges along the Bangladesh coast. This model uses a staggered finite-difference grid on which the sea-surface elevation and components of velocity are computed at different computational points. The sea-surface elevations are not directly carried out at points along the coastline. Thus, the coastal surge elevations are derived by extrapolating from the computed elevations of those adjacent off-shore grid points at which they are carried. In this model the grid spacing across the coastal zone is uniform and relatively coarse. Consequently, the extrapolated coastal surge elevations may not be very realistic as these are dependent on the elevations computed directly at those off-shore points which are far away from the coast. This deficiency may be overcome by overall increasing the off-shore resolution in the model which would lead to a substantial increase in the computational overheads and is, in any case, unnecessary far away from the coastline.

Accordingly, in the present paper, the model described by Dube et al.(4) has been extended to allow for an increased resolution near the Bangladesh coast. The noteworthy difference in our method from those earlier used by Jelesnianski (5), Das et al. (1) and Johns and Ali (6) is that it does not depend on the patching together of computational regions having different uniform grid spacings. Our approach is analogous to that used by Johns et al.(8) for the simulation of surges along the east coast of India. The model uses a continuously contracting non-uniform off-shore grid spacing adjacent to the coastal boundary which permits an increased resolution near the Bangladesh coast.

The model covers an analysis area lying between 87°E and 93°E, and between 19°N and the south coast of Bangladesh. There are three open-sea boundaries situated along 87°E, 93°E and 19°N. Numerical experiments performed with this model for simulating the surge generated by the November 1970 Chittagong cyclone lead to a surge response along the Bangladesh coast which is in good agreement with the observed values.

FORMULATION OF THE MODEL

The sphericity of the earth's surface is neglected and we use a system of rectangular Cartesian coordinates in which the origin, *o*, is in the equilibrium level of the sea-surface. *ox* points towards the south, *oy* points towards the east and *oz* is directed vertically upwards. The displaced position of the sea-surface is given by  $z = \zeta(x, y, t)$  and the position of the sea-floor by  $z = -h(x, y)$ . A northern coastal boundary (the south coast of Bangladesh) is situated at  $x = b_1(y)$  and the southern open-sea boundary is at  $x = b_2(y)$ . The western and the eastern open-sea boundaries are at  $y = 0$  and  $y = L$  respectively. This configuration is shown in Fig.1.

The basic equations of continuity and momentum in the vertically integrated form may then be given by

$$H_t + (Hu)_x + (Hv)_y = 0 \tag{1}$$

$$u_t + uu_x + vv_y - fv = -g \zeta_x + \frac{1}{H\rho} \{ \tau_x^\zeta - c_f \rho u(u^2 + v^2)^{\frac{1}{2}} \} \tag{2}$$

$$v_t + uv_x + vv_y + fu = -g \zeta_y + \frac{1}{H\rho} \{ \tau_y^\zeta - c_f \rho v(u^2 + v^2)^{\frac{1}{2}} \} \tag{3}$$

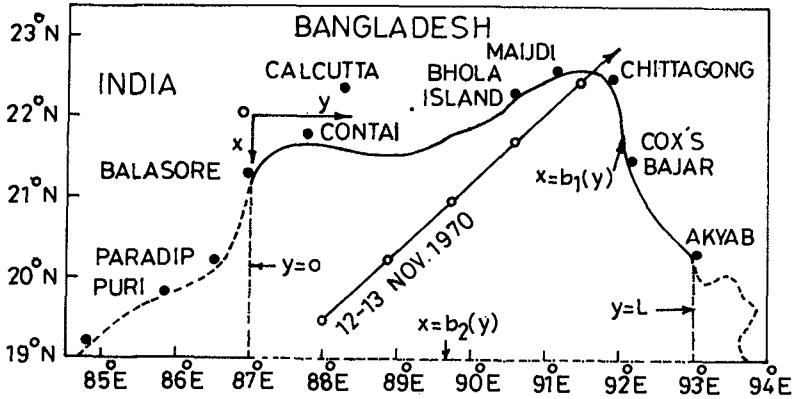


Fig.1 The analysis area and idealised track,  
 -.-.- open-sea boundaries  
 o 5 hourly positions of the centre of the cyclone (on the track)

where  $f$  denotes the Coriolis parameter, the pressure is taken as hydrostatic and  $H$  is the total depth  $\zeta + h$ . ( $\tau_x^\zeta, \tau_y^\zeta$ ) denotes the applied surface wind-stress and the bottom stress is parameterised in terms of a quadratic law.  $\rho$  denotes the water density and the friction coefficient,  $c_f$ , is taken as  $2.6 \times 10^{-3}$ .

Following Dube et al.(4), the appropriate boundary conditions are given by

$$u - v (b_1)_y = 0 \quad \text{at } x = b_1(y) \quad (4)$$

$$u - v (b_2)_y - (g/h)^{1/2} \zeta = 0 \quad \text{at } x = b_2(y) \quad (5)$$

$$v + (g/h)^{1/2} \zeta = 0 \quad \text{at } y = 0 \quad (6)$$

$$v - (g/h)^{1/2} \zeta = 0 \quad \text{at } y = L \quad (7)$$

COORDINATE TRANSFORMATION

In order to facilitate the numerical treatment of an irregular boundary configuration and to incorporate increased resolution adjacent to the coastline, we introduce the following coordinate transformations (Das et al.(3)).

$$\xi = \{ x - b_1(y) \} / b(y) \tag{8}$$

$$\eta = \xi + \epsilon \ln(1 + \xi / \xi_0) \tag{9}$$

where  $b(y) = b_2(y) - b_1(y)$  is the breadth of the basin and,  $\epsilon$  and  $\xi_0$  are disposable parameters.

Taking  $\eta$ ,  $y$  and  $t$  as new independent coordinates, Eqs.(1)-(3) may be transformed to

$$(b \xi)_t + F(\eta) (bU)_\eta + \tilde{v}_y = 0 \tag{10}$$

$$\begin{aligned} \tilde{u}_t + F(\eta) (U\tilde{u})_\eta + (v\tilde{u})_y - f\tilde{v} = & -gHF(\eta) \zeta_\eta + b \tau_x^\zeta / \rho \\ & - c_f \tilde{u} (u^2 + v^2)^{1/2} / H \end{aligned} \tag{11}$$

$$\begin{aligned} \tilde{v}_t + F(\eta) (U\tilde{v})_\eta + (v\tilde{v})_y + f\tilde{u} = & -gH \{ b \zeta_y - (b_{1y} + \xi b_y) \\ & F(\eta) \zeta_\eta \} + b \tau_y^\zeta / \rho - c_f \tilde{v} (u^2 + v^2)^{1/2} / H \end{aligned} \tag{12}$$

where,

$$bU = u - (b_{1y} + \xi b_y)v \tag{13}$$

$$(\tilde{u}, \tilde{v}) = bH (u, v) \tag{14}$$

$$F(\eta) = 1/\xi_\eta = 1 + \epsilon / (\xi + \xi_0) \tag{15}$$

The boundary conditions (4) and (5) become

$$U = 0 \quad \text{at } \eta = 0 \tag{16}$$

$$bU - (g/h)^{1/2} \zeta = 0 \quad \text{at } \eta = \eta_m \tag{17}$$

where  $\eta_m = 1 + \epsilon \ln(1 + 1/\xi_0)$ .

Eqs. (10)-(12) form the basic set for the numerical solution process.

NUMERICAL PROCEDURE

For the solution of the Eqs. (10)-(12) subject to the relevant boundary conditions, a conditionally stable explicit finite-difference scheme with a staggered grid is used. The details of the discretization procedure and the finite-difference grid selection are completely analogous to those reported in Das et al.(3).

The stability characteristics of this computational scheme have



been discussed in detail by Johns et al.(7). In fact, stability is only conditional upon the time step being limited by the space increment and the gravity wave speed.

#### NUMERICAL EXPERIMENTS

Numerical experiments are performed by using the analysis area which extends from 87°E to 93°E along the south coast of Bangladesh and there are three open sea boundaries situated along 87°E, 93°E and 19°N (Fig.1). Thus, on an average, the width of the coastal zone is about 168 miles (270 km) while the east-west extent,  $L$ , of the analysis area is about 375 miles (600 km). An idealised cyclone moves along the indicated straight-line track with uniform speed of translation for about 21 hours before landfall near Chittagong port (Fig.1). The five hourly positions of the centre of the cyclone is also indicated in the figure.

The wind field associated with this cyclone is simulated by applying the following empirically based formula suggested by Jelesnianski (5)

$$V = \begin{cases} V_0 (r/R)^{3/2} & \text{for } r \leq R \\ V_0 (R/r)^{1/2} & \text{for } r > R \end{cases}$$

where  $V_0$  is the maximum sustained wind,  $R$  the radius of maximum wind and  $r$  is the distance from the centre of the cyclone. Following Das et al.(1), we take

$$V_0 = 164 \text{ ft s}^{-1} (50 \text{ ms}^{-1}) \text{ and } R = 25 \text{ miles (40 km)}.$$

The optimum grid resolution in the computational plane is chosen with  $m = 10$ ,  $n = 21$ ,  $\epsilon = 0.04$  and  $\xi_0 = 0.001$ . Thus,  $\eta_m \approx 1.27$  and  $\Delta\eta \approx 0.14$ . This is obtained as a result of several experiments performed with the 1970 Chittagone cyclone for testing the adequacy of the resolution. It may be seen that with the above selection of parameters, the first off-shore grid point at which the elevation is computed is, on an average, about 3 miles (5 km) from the coastline and  $\Delta y \approx 18.5$  miles (30 km).

In our numerical experiments we prescribed an initial state of rest and integrated the governing equations ahead in time for a period of 50 hours. A time-step of 3 min. was found to be consistent with the computational stability. We also considered the sea-surface response during several hours after landfall when the system starts to enter the resurgence phase.

#### RESULTS AND DISCUSSIONS

The surges associated with the 1970 Chittagong cyclone have been computed by using a number of off-shore grid resolutions. However, the results are presented only for two resolutions corresponding to  $m = 10$ ,  $n = 21$  and  $m = 20$ ,  $n = 21$  for comparison and for an optimal selection of the grid size.

In Fig.2 we give the distribution of the predicted maximum sea-surface elevation (peak surge envelope), its time of occurrence and the

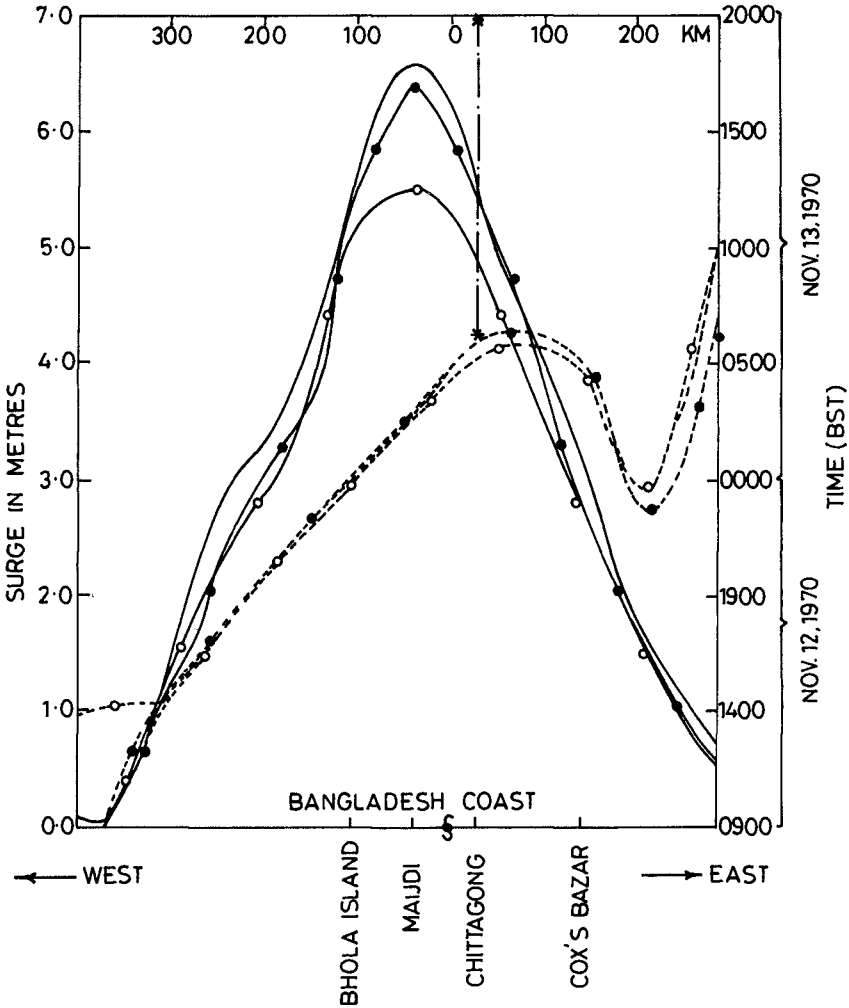


Fig.2 Maximum predicted surge and its time of occurrence  
 Place of landfall ● Time of landfall (on time axis)  
 — Peak surge envelop ( $m=10$ ) --- Time of occurrence ( $m=10$ )  
 —●— Peak surge envelop ( $m=20$ ) —●— Time of occurrence ( $m=20$ )  
 —○— Peak surge envelop ( $m=20$ , obtained in (4))  
 —○— Time of occurrence ( $m=20$ , obtained in (4))

observed surge along the Bangladesh coast. It may be seen from the figure that by increasing the number of off-shore grid points from 10 to 20 the maximum change in the peak surge values at various coastal stations is within two percent. Further, the time of occurrence of the peak surge in the two cases is almost same. A further increase in the number of off-shore grid points also show similar results.

The adequacy of the alongshore resolution has also been tested by increasing the value of  $n$ , which has not resulted in any significant change in the elevations and their time of occurrence along the coastal stations.

These tests on the selection of optimum resolution indicate that there is insignificant quantitative change in the results for the two resolutions (10X21 and 20X21). However, the computer overheads in the later case are much higher. Keeping these facts in view, it is appropriate to use a 10X21 grid for the present numerical experimentation.

The Fig.2 provides an idea of the coastal stretch upto which the significant surge may be expected. It may be seen from the figure that the maximum surge height of 21.6 ft (6.6m) is predicted at Maijdi which is about 25 miles (40 km) to the left of the landfall. A maximum surge of about 18.0 ft (5.5m) is predicted at Chittagong port (about 17.5 miles (28 km) to the right of the landfall point) at 0540 hrs BST on 13 November, 1970. A peak elevation of 19.7 - 29.5 ft (6-9 m) was reported at this tidal station on the morning of 13 November while according to the Tide-Table the predicted astronomical tide was 5.9 ft (1.8m) at about the same time. Thus, if we assume that the total sea-surface elevation is the result of purely linear superposition of surge and tide, it may be noted that the observed sea-surface elevation at Chittagong was in excess of 13.8 - 23.6 ft (4.2 - 7.2m) over the usual high-tide (Das et al.(2)). Hence, it may be seen that our predicted surge of 18.0 ft (5.5m) is in good agreement with the observed range of maximum surge of 13.8 - 23.6 ft (4.2 - 7.2 m) at Chittagong.

Further, it is worthwhile to compare the results of the present study with those obtained by Dube et al.(4) who have used a uniform off-shore grid spacing for the simulation of surges along the Bangladesh coast. It may be seen from Fig.2 that there is significant improvement in the computed surge heights by using a non-uniform off-shore grid spacing which allows an increased resolution adjacent to the coast.

Fig.3 depicts the time variation of the storm surge at four stations along the Bangladesh coast. All the three stages of the surge-forerunner, the main surge, and the resurgence phase may clearly be seen from the temporal variation of the coastal sea-surface elevations. The maximum surge height of 21.6 ft (6.6m) is predicted at Maijdi. The peak occurred at 0240 hrs BST on the morning of 13 November. This main surge remains for a very short period (about 30 min.) and is followed by the resurgence phase. During resurgence phase the sea-surface elevation falls rapidly from its maximum value and becomes negative after about the next 6 hours period and a sea-surface depression of 10.2 ft (3.1m) is predicted at 1700 hrs BST on 13 November.

The predicted surge height at Chittagong is about 18.0 ft (5.5m) which occurs in the morning of 13 November at about 0540 hrs BST. It may be seen that the time of occurrence of the peak surge is in exce-

llent agreement with the time of landfall. This main surge persists for about half an hour before falling rapidly and becoming negative at 1430 hrs BST. At Chittagong, a maximum sea-surface depression at 7.2ft (550mm) is predicted at about 1800 hrs BST on 13 November with a subsequent increase in the water height leading to a depression of about 15 cm in the early morning of 14 November.

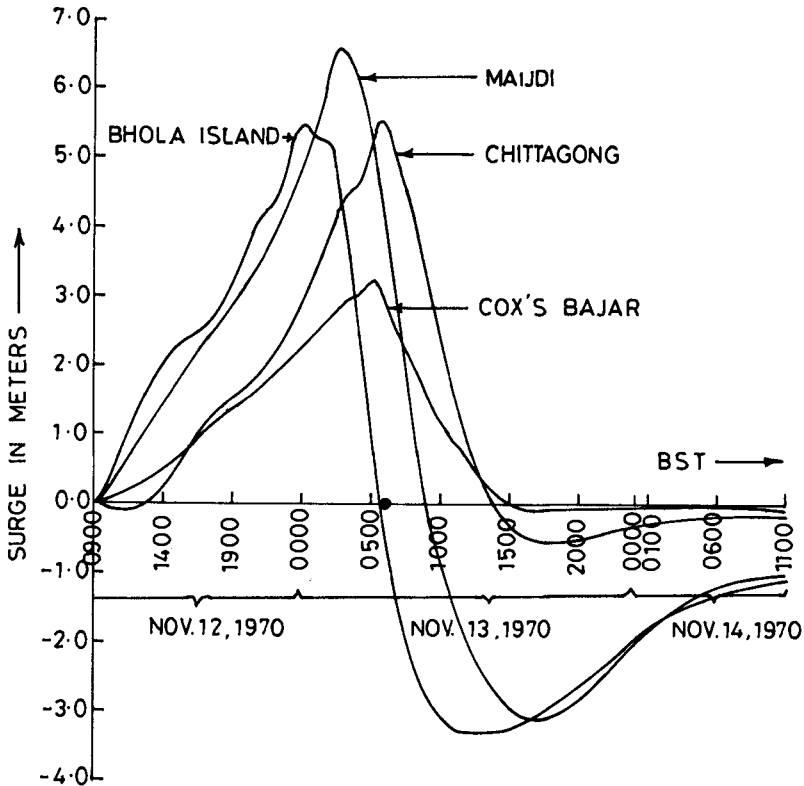


Fig. 3. Time variation of the predicted sea-surface elevation at four coastal stations.

● Time of landfall

At Bhola Island which is about 68 miles (110 km) to the west of landfall, the sea-surface elevation rises gradually to attain its peak value of about 18.0 ft (5.5m) at 0000 hrs BST on 13 November. Here again the main surge is short-lived (about 40 min.) and the surge becomes negative within 6 hours of the occurrence of its peak value. A sea-surface depression of about 10.8 ft (3.3m) is predicted at 1230 hrs BST on 13 November.

The predicted time history of the surge at Cox's Bazar which is about 87 miles (140 km) to the SE of landfall, indicate a maximum sea-surface elevation of 10.5 ft (3.2m) in the morning of 13 November at about 0500 hrs BST. This main surge is again very short-lived and it falls gradually to become negative in the afternoon of 13 November.

#### APPENDIX - REFERENCES

1. Das, P.K., Sinha, M.C., and Balasubramanyam, V., "Storm surges in the Bay of Bengal", *Quart. J. Roy. Met. Soc.*, Vol.100, 1974, pp. 437-449.
2. Das, P.K., Miyazaki, M., and Jelesnianski, C.P., "WMO Report No. 13 on Mar.Sci. Aff.", Vol. 28, 1978, p.3.
3. Das, P.K., Dube, S.K., Mohanty, U.C., Sinha, P.C., and Rao, A.D., "Numerical simulation of the surge generated by the June 1982 Orissa cyclone", *Mausam*, Vol.34, 1983, pp. 359-366.
4. Dube, S.K., Sinha, P.C., and Roy, G.D., "The numerical simulation of storm surges along the Bangladesh coast", *CAS Tech.Rep.No.6A/1983*, IIT Delhi.
5. Jelesnianski, C.P., "A numerical calculation of storm tides induced by a tropical storm impinging on a continental shelf", *Mon. Wea.Rev.*, Vol.93, 1965, pp. 343-358.
6. Johns, B., and Ali, A., "The numerical modelling of storm surges in the Bay of Bengal", *Quart. J. Roy.Met.Soc.*, Vol.106, 1980, pp. 1-18.
7. Johns, B., Dube, S.K., Mohanty, U.C., and Sinha, P.C., "Numerical simulation of the surges generated by the 1977 Andhra Cyclone", *Quart. J. Roy. Met. Soc.*, Vol. 107, 1981, pp. 919-934.
8. Johns, B., Sinha, P.C., Dube, S.K., Mohanty, U.C., and Rao, A.D., "On the effect of bathymetry in numerical storm surge simulation experiments", *Computers and Fluids*, Vol.11, 1983, pp.161 - 174.

## CHAPTER FOURTEEN

### Frequency of occurrence of storm surges in an estuary : a stochastic approach

Marc Sas\*

#### Abstract

This paper presents the results of a study on the frequency of occurrence of storm surge levels in the river Scheldt at Antwerp, related to the design of a storm surge barrier and the evaluation of the dike safety in the Scheldt basin.

The basic principles of the extreme value distribution methods, the joint probability methods and simulation models are examined.

A new technique, based upon the simulation of storms by variables characterizing the resulting surge is proposed.

Results are compared with those of other methods.

#### 1. Introduction

This study concerns a statistical evaluation of extreme waterlevels on the river Scheldt near Antwerp, for which the highest registered level is NKD+8m with an "estimated frequency of 1/100 years, based upon extrapolation of data along the Dutch North Sea coast.

Due to hydrodynamic and hydraulic actions in the estuary, the accuracy of such frequencies is poor, and since enough observations are available for Antwerp (1902 - present), the frequency of occurrence of storm levels was investigated for this city itself.

At this moment all levels exceeding NKD+6.5m are called "storm surges" (till 1954 that datum was NKD+6.0m).

This study doesn't analyse tidal characteristics either in a statistical way, nor in a fundamental, physical and hydrodynamic way.

#### 2. Analysis of storm surge levels

The different components of a surge level on the river Scheldt are represented in Fig. 1.

\*Marc Sas, Research Engineer, Hydraulics Laboratory,  
Katholieke Universiteit Leuven, de Croylaan 2/4,  
B-3030 Heverlee, Belgium

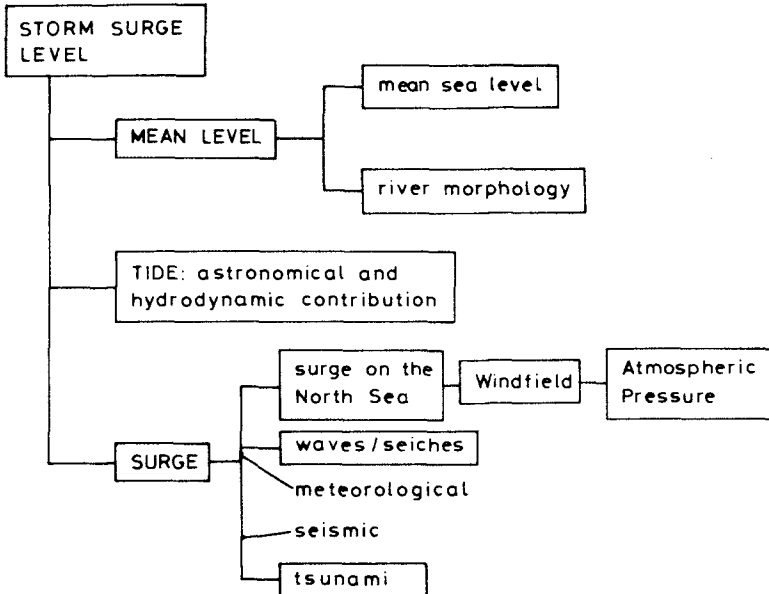


Fig.1: Components of storm surge level

### 2.1. Mean level

The variation of mean level, dealt with in this paragraph consists of periodic and secular changes, in which periodic means 'with a period of at least one year', thus excluding diurnal and shorter-period oscillations, classified as tidal effects. The variation in mean level, often substituted for by 'mean tidal level', is caused by mean sea level variations and by morphological changes of the river, due to the dynamic physical processes in the river and due to human interventions (35, 40). The most important causes of mean sea level variation are: changes in the total water balance, movements in the land reference level (bench mark), time variations in the atmospheric forces (wind stress and air pressure), time variations in the oceanographic forces (temperature, salinity, currents) and finally long period astronomical tides. For a description of these phenomena reference is made to specific geophysical literature (24, 35, 37, 39). With a view to obtain an homogeneous set of water level data along an estuary, one has to investigate not only mean sea level variations, but (depending upon the calculation procedure to determine frequencies of occurrence) also trends in annual maxima and in tidal amplitude must be considered (see § 3.1.).

## 2.2. Tidal movements

In the river Scheldt tidal activity is a cooscillating tide in an estuary, propagated in the basin and caused by tidal movements on the North Sea. The principal constituents are the M2 lunar semidiurnal tide, with a period of 12.42 hours and the S2 solar semidiurnal tide (period = 12h). Furthermore it must be mentioned that both observed and predicted tidal levels consist of pure "astronomical tides" and hydrodynamic influences.

## 2.3. Surge elevation

Surges on the river Scheldt are mainly caused by meteorological activities, acting on the water mass in the North Sea. For a description of the sources, physical phenomena and mathematical calculation schemes we refer to literature (32, 42). Waves and oscillations have neglectable influence on resulting water levels, while seismic surges didn't occur till now.

## 2.4. Interaction of surge and tide

The interaction effects between surge and tide are caused by frictional resistance and variations in the celerity of waves (due to differences in waterdepth), modifying surges in tidal regions (2, 15, 21, 28, 36, 38, 48).

The main conclusions of several investigators are :

Keers deduced that the interaction increases linearly with the surge height and that the degree of interaction is quite correlated with the tidal amplitude and with the ratio of the amplitude and mean waterdepth (21). Banks stated that the most important interaction is between the M2 semidiurnal tide and the surge (2). Although Pugh and Vassie (30) concluded that any interactions were of second order, so that surge and tide can be treated statistically independent, it seems important to mention the qualitative investigations of the dutch 'Deltacommissie' (33) : the increasing levels due to surge cause an advancement with regard to the predicted tide (in absence of surge), they cause a enfeeblement of the tide since low levels remain higher and finally they cause a deformation because geometrical elements, such as the topography of banks and gullies) which are boundaries for the tidal movement are oriented in a different way. Walden, Prescott and Webber (48) compared two methods to determine the degree of interaction, based upon hourly surge residuals : a first approach is to examine the distribution of these residuals at various phases of the tidal cycle (see also (28)), whilst the second method determines the distribution of residuals at different tidal levels (see also (29)). They concluded that the more a port is remote from the open sea, the more the interaction is prominent. This implies that the use of the joint probability method (see § 3.2.) is justified if the degree of interaction is negligible.

## 3. Methods to determine the frequency of occurrence of high surge levels

Depending upon the set of available tidal records, two principal methods can be used to determine the frequency of occurrence of high



water levels : extreme value distributions and methods based upon the joint surge-tide probability.

### 3.1. Extreme value distributions

For a series of M annual maximum water levels an extreme value distribution is assumed, characterized by a set of parameters, which are estimated in procedures such as the method of moments, maximum likelihood, etc. (4). Some of these distributions, such as Fisher-Tippet-distribution (10), Barricelli (3), Gumbel (14) and Jenkinson (19, 20), have been applied to estimate the frequency of occurrence of extreme sea-levels. Suthons (44) and Lennon (22) published studies with respect to the south-east and the west coast of England. Akers e.a. (1), Webber e.a. (9, 50), Blackman e.a. (6, 12) reviewed these reports to add more recent information. For the Scheldt estuary frequencies were calculated by SVKS (43), Janssens e.a. (19), Sas e.a. (40) and Berlamont e.a. (5). The results are listed in Table 1.

As conclusion, we believe that

1. Although no exact information is available, frequencies depending upon the extreme value distributions are reliable for design periods up to 4 times the length of the series of observed data (12).
2. Using the method of extreme value distributions includes the disadvantage of neglecting important information about exceptional but not maximal events : such as the increase of the frequency of occurrence of high water levels from 1960 on (see Table 2, and (40)).
3. If a persistent trend is apparent, its effect must be estimated and data must be adjusted accordingly in order to get a homogeneous set of data (6, 44, 47), using for example Suthon's adjustment method, based upon 10-year forward or backward accumulation (13, 44) or 19-yearly mean values to eliminate nodal periodic variations of mean sea level (34, 40).
4. To achieve any reliability, the observed data must cover a period of a least 30 years (11).

### 3.2. Joint surge tide probability methods

If the set of observed tidal data is not long enough, extreme value distributions can't provide reliable information concerning the frequency of occurrence. In this case several methods based upon the principal of joint probability can be applied. A recorded level (H) can be split up into three constituents, after filtering for wave influences :

$$H(t) = Z_0(t) + G(t) + M(t) \quad [1]$$

in which  $Z_0(t)$  : mean level (i.e. mean sea level),  $G(t)$  : tidal component,  $M(t)$  : meteorological component (i.e. surge).

#### 3.2.1. The convolution method

From a series of observations H the hourly surge component M can be derived by calculating the mean level  $Z_0(t)$ , and the tidal component  $G(t)$  from its harmonic constituents. If surge and tide can be treated as statistically independent (see § 2.4.); the probability density function  $p(h)$  can be written as the convolution of the individually

estimated density functions of tide  $p_G$  and surge  $p_S$ .

$$p(h) = \int_{-\infty}^{\infty} p_G(h-y) p_S(y) dy \quad [2]$$

with  $h = H(t) - Z_0$ ,  $y = M(t)$  and  $x = h - y = G(t)$ .

Eq. [2] is valid only if  $h$ ,  $y$  and  $x$  are deduced from a stationary stochastic process, which condition is nearly never completely satisfied. The probability of exceedance of a level  $h_0$  can be evaluated from the cumulative distribution function  $P_h(h_0)$  :

$$P_h(h_0) = 1 - \int_{h_0}^{\infty} p(h) dh = \int_{-\infty}^{\infty} P_G(h_0-y) p_S(y) dy \quad [3]$$

and the return period of height  $h_0$  :

$$T(h_0) = 1 / [ (1 - P_h(h_0)) \cdot (\text{average number of hourly values in a year}) ] \quad [4]$$

Pugh e.a. (30, 31) applied this method to the English south coast port of Portsmouth over a period of 12 years. For return periods of 50, 100 and 250 yr, they estimated sea levels of 2.86, 2.91 and 2.98 whereas application of the extreme value theory using the 12 annual maxima resulted in 2.69, 2.71 and 2.74 : which is an underestimate of 6, 7 and 8 % respectively.

### 3.2.2. Duration methods

In the aforementioned methods the duration of the storm is not considered; the surge is characterized by its magnitude only. Other methods however account for the transient nature of the surge event by considering the effective duration of the process.

Tayfun (45) developed an analytical procedure to determine the probability distribution function of extreme levels, caused by coincidence of a rare event with the astronomic tide. If we consider tide and surge to be statistically independent and if we characterize a storm surge by an equivalent magnetidue  $X$  and an effective duration  $\tau$  (Fig. 2) and if

$$Z = \max_{t_0 \leq t \leq t_0 + \tau} [G(t) + M(t)]$$

in which  $M(t)$  is a positive surge, starting at any time  $t_0$  of the tidal cycle, and if we assume that the water level increase caused by  $M(t)$  is gradual enough that an approximation by a constant height surge  $X$  is allowed over the period  $(t_0, t_0 + \tau)$  then

$$Z \approx \max_{t_0 \leq t \leq t_0 + \tau} [G(t) + X]$$

in which  $\tau$  and  $X$  are random variables. Considering the conditional probability function of  $Z$  for given value of  $\tau$  :

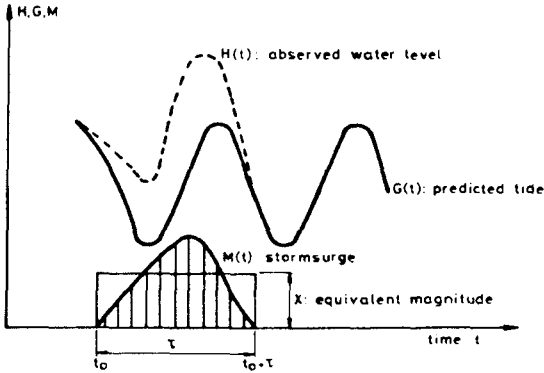


Fig 2: Tayfun method

$$\begin{aligned}
 P_{Z/\tau}(z/\tau) &= \text{Prob} [G(t) + X < z \text{ for } t \leq t \leq t_0 + \tau/\tau] \\
 &= \int_{-\infty}^z P [X < z - g / (G = g \text{ for } t_0 \leq t \leq t_0 + \tau/\tau)] \\
 &\quad \cdot P_{G/\tau}(g/\tau) dg \qquad [5]
 \end{aligned}$$

and assuming that the non-negative X is statistically independent of  $\tau$  and G :

$$P [X < z - g / (G = g \text{ for } t_0 \leq t \leq t_0 + \tau/\tau)] = P_X(z - g) \qquad [6]$$

and

$$P_{G/\tau}(g/\tau) dg = \text{Prob} (g \leq G \leq g + dg \text{ for } t_0 \leq t \leq t_0 + \tau/\tau) \qquad [7]$$

in which tide is assumed to be a Gaussian process.

For  $\tau$  varying over all possible values :

$$P_Z(z) = \int_0^\infty \int_{-\infty}^z P_X(z - g) P_{G/\tau}(g/\tau) p_\tau(\tau) dg d\tau \qquad [8]$$

so that the return period for a water level  $z = h_0$  caused by positive surges, occurring at a mean rate of  $\sigma$  per year :

$$T(h_0) = 1 / [\sigma (1 - P_Z(h_0))] \qquad [9]$$

Walden, Prescott and Webber (49) developed an adapted Tayfun method for use in European waters since tide can not be represented by a Gaussian process because frequency distributions tend to be bimodal (30). Furthermore, surge duration is longer than one tidal cycle ( $\approx 13$  hours) and the magnitude is rather moderate compared with the tidal

amplitude. For surges with duration  $\tau$  greater than 13 hours ( $= T_0$ ), only the largest equivalent magnitude  $X$  over a 13-hour interval must be considered. This  $X$  value results from moving the  $T_0$ -interval through the  $\tau$ -interval (= surge) in steps of one hour, and at each step  $T_1$  equating the area above  $(T_1, T_1 + T_0)$  to  $T_0X$  (in general  $\tau \leq 50$  hours (18, 49)). The conditional density function  $P_{G/\tau}(g/\tau)$  can be obtained from the conditional probability distribution function

$$P_{G/\tau}(g/\tau) = \text{Prob} \{G(t) \leq g \text{ for } t_0 \leq t \leq t_0 + \tau/\tau\} \quad [10]$$

by numerical differentiation.

Such probability can be estimated for different values of  $\tau$  for a series of  $g$  values by moving the interval of duration  $\tau$  through the hourly predicted  $G(t)$  series and dividing the number of hours for which the condition of eq. 10 is satisfied by the total number of  $G(t)$  values. The conditional distribution function of the maximum sea level  $Z$  for given  $\tau$  is derived in the following way. If  $g_{\min}$  and  $g_{\max}$  are the lowest and highest hourly predicted tides and if  $Z$  is chosen as a sea level which can occur only by adding a positive surge to  $g_{\max}$ , i.e.  $z \geq g_{\max}$ , then  $\text{Prob} (X \leq z - g/\tau) = 1$  for a range of  $g$  values between  $g_{\min}$  and  $g_{\max}$ . Let us denote this boundary by  $g_b$ , hence

$$P_{Z/\tau}(z/\tau) = \int_{g_{\min}}^{g_{\max}} P(X \leq z - g/\tau) P_{A/\tau}(g/\tau) dg$$

Further derivation leads to

$$P_{Z/\tau}(z/\tau) = 1 - \int_{g_b}^{g_{\max}} [1 - P(X \leq z - g/\tau)] P_{G/\tau}(g/\tau) dg \quad [11]$$

The adapted Tayfun method is completed by using eq. [8] and [9]. For return periods of 50, 100 and 250 yr, Walden, Prescott and Webber (49) estimated water levels of 2.74, 2.78 and 2.83 differing from the "convolution estimates" by 4.3, 4.7 and 5.3 % respectively (see § 3.2.1.).

Beside these analytical methods to calculate the frequency of occurrence of high water levels, several simulation procedures were developed in which the transient event is reconstructed.

1. Myers (25) pointed out three important aspects in developing a simulation procedure
  - assess the behaviour of surges from past records, analyze all factors causing and determining the event, such as atmospheric pressure, forward speed and direction of the storm
  - develop a hydrodynamic mathematical model to simulate storms (hurricanes) from a random input of the stochastic parameters, determined in the first step, and calculate the resultant surge
  - calculate density distributions and probability functions for all parameters and deduce the frequency of occurrence of the rare event, simulated in step 2.

This method has been applied several times in the U.S.A. (ref. 16, 17, 25, 26, 27). The major disadvantage is the development of the hydrodynamic model and the required calculation time for each simulation.

2. For this reason, the author proposes a simulation technique, based upon the parameters, characterizing the resulting surge (and not

based upon the event-causing parameters), such as duration and magnitude of surge and tidal amplitude and phase angle. Application of the Tayfun method is rejected since hourly water level data had to be digitized over a period of several years. As a list of storm events, exceeding the storm level of  $NKD+6.5m$  was available from 1900 on, this information was used to determine surge characteristics.

#### 4. Determination of surge

##### 4.1. Predicted tide during storm

For all storm periods predicted levels of high and low tide were available, as well as the time of occurrence. In order to avoid harmonic calculation of tidal levels, tide is reconstructed using the typical (mean) tidal cycle of the period 1961-1970 (8). This curve is transformed both in time and height (so that in the extremes coincide with the predicted values) by linear interpolation. In this way the tidal component during the storm is reconstructed similar with the typical tidal curve.

##### 4.2. Surge

To determine the surge from the observed levels and from the tidal elevations, several methods were examined. The Dutch Deltacommission (32) suggests to subtract predicted tide from observations which leads to inadequate surge levels, since the interaction between storm and tide causes transformations in the tidal phenomenon. Theuns (46) draws a smooth curve  $S$  through the registered storm water levels  $R$ , so that the area above and below  $S$  and limited by  $R$  are equal one to the other. Subtraction of mean water level from curve  $S$  gives the surge event. This is a practical method, producing reliable information in regions where mean water level doesn't vary with time. Due to the secular and periodic variations (Fig. 3) on the river Scheldt this method was rejected. Schalkwijk (42) proposes a method based upon harmonic analysis and recalculation of tidal levels. Subtraction of these levels from the observations and application of forward and backward means over 3 hours each to eliminate the  $M_4$  lunar component, produces a reliable approximation of the surge in the "linear" parts of the tidal cycle. To improve the surge residue in the neighbourhood of the extremes a flattening procedure is developed, based upon a trial and error method to draw a smooth curve through the surge residue. This method was also rejected for it requires a harmonic tidal calculation and because of the 'trial and error'-nature of the graphical flattening procedure. Janssens & Sas (18) propose a numerical technique. Subtraction of predicted tide, calculated in the aforementioned way (§ 4.1.), from the observed levels doesn't account for tide-surge interaction. Since no quantitative data are available on this interaction mechanism, the predicted tide is moved through the observations until no periodically oscillating surge residue is obtained. In this way the tidal 'advancement' due to storm is accounted for. The flattening procedure is realized by an approximation of the surge residue by a third order polynomial (higher order approximations cause inflexions and successive maxima), determined by the least square method and applying a Lagrangian multiplier so that the area below the resultant surge equals the one below the first non-oscillating surge approximation

## ANTWERPEN - SCHELDE

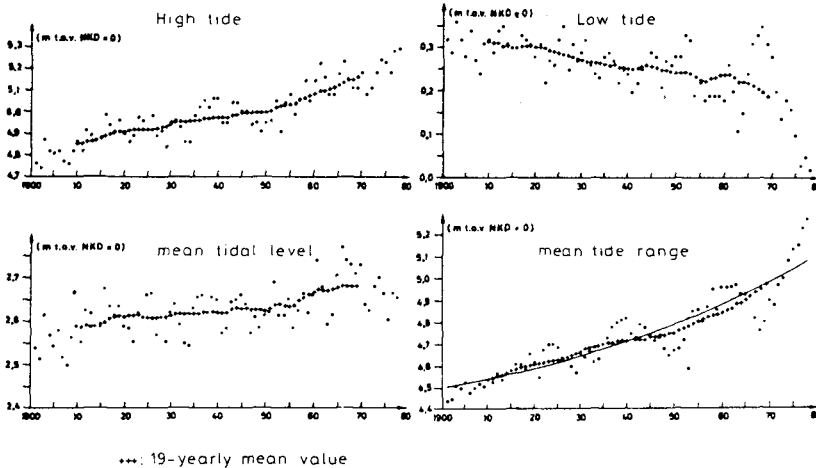


Fig. 3: Variation of tidal variables

(Fig. 4). For 33 storm periods the surge elevation was calculated in this way. It was discovered that there was no tendency at all for the maximum surge to occur at high tide, nor at any other stage of the tidal cycle, which is in strong agreement with the statements of Heaps (15) and Wemelsfelder (32). The resultant duration and magnitude for each surge was derived: 'Duration' is determined (with an accuracy of 0.5 hour) by comparing the time between the zero-points of the surge, the time between the minima of the surge and the time between the points of coincidence of predicted and observed water level. The 'magnitude' is assumed to be the maximum of the polynomial. After checking the dependency of both characteristics, it seems that there is no linear correlation (coefficient = 0.013). Hence magnitude and duration are treated as statistically independent stochastic variables. The probability distribution functions are a normal distribution ( $\mu = 42.5$  h,  $\sigma = 11.6$  h) for the duration and a Gumbel distribution

$$p(x) = \alpha \exp \{-\alpha(x - u) - \exp[-\alpha(x - u)]\}, u = 1.32, \alpha = 3.04$$

for the magnitude.

#### 4.3. Frequency of occurrence of storms

On the basis of the information concerning the penetration of storms in the Scheldt estuary (50 arrivals in 77 years) a uniform distribution of these storms was assumed. The time interval  $\Delta t$  of this Poisson process has a distribution function

$$p(\Delta t) = a \exp(-a\Delta t)$$

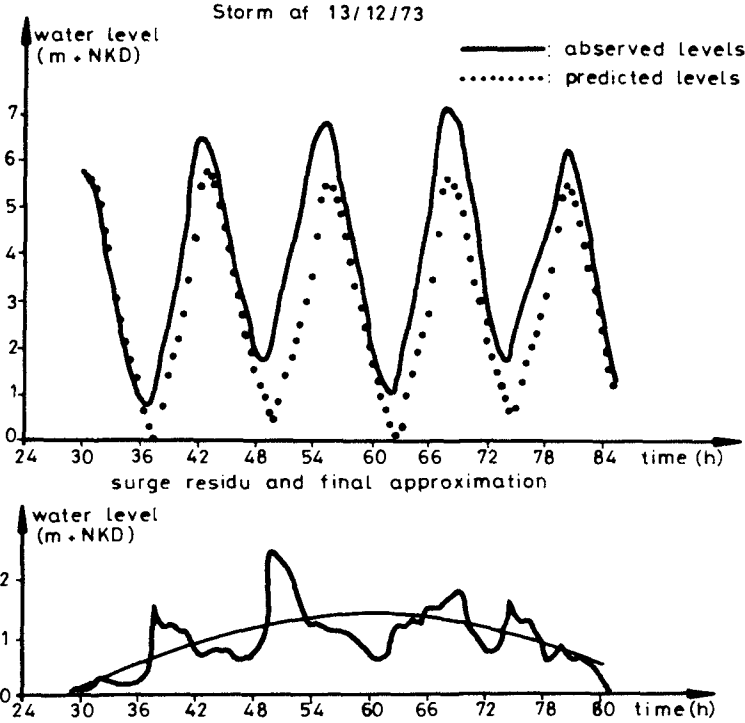


Fig. 4: Determination of a storm surge

with  $a = 1/E(\Delta t)$ . Since more storms occur during winter (October till March) :  $E_{winter}(\Delta t) = 10.74$  winter months and  $E_{summer}(\Delta t) = 66$  summer months (or 1 storm occurs in summer during 11 years).

4.4. Simulation of surge

From the set of surges, determined as explained in § 4.2., the most suitable shape was found to be a polynomial of order 3. For a surge of duration  $D$  and magnitude  $M_{max}$ , the component reads (Fig. 5)

$$M(t) = 6.75 M_{max} \left[ \left(\frac{ts}{D}\right)^3 - \left(\frac{ts}{D}\right)^2 \right] + M_{max}$$

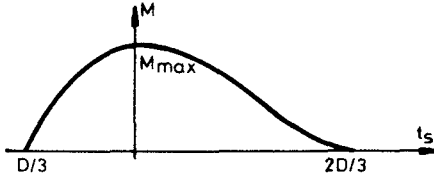


Fig. 5: Surge

5. Determination of tidal variables

As described in § 3.1. and illustrated in Fig. 3 tidal variables vary with time. Since the simulated tide is characterized by mean water level and tidal amplitude, the appropriate values of those variables must be determined. To eliminate secular, i.e. nodal, variations 19-yearly (forward and backward) mean values are calculated and are used to estimate actual values of both mean tidal level (= NKD+2.70m) and tidal amplitude (= 2.54 m). To account for variations of amplitude between neap and spring tide (= luni-solar fortnightly  $M_{sf}$  constituent) with a period of 14.76 days, the tidal amplitude is assumed to vary in a sinusoidal way with amplitude = 0.42 m. Variations in tidal amplitude of periodic nature are determined from annual mean amplitudes so that relative magnitude of all effects can be analysed :

$$\text{amplitude (t)} = A \cos \left( \frac{2\pi}{T} t \right) + B \sin \left( \frac{2\pi}{T} t \right) + C + DT \quad [12]$$

(where T = period of variation, t = time in years, C + DT is the trend due to secular variation). Using the method of least squares, the most important long term period can be determined. For the river Scheldt the nodal tide (T = 18.67 years, amplitude = 0.06 m) was found to be the most important). If tide is simulated by a simple sinusoidal variation; the tidal constituent during the surge event can be represented by

$$G(t) = A(t) \sin \left( \frac{2\pi}{12.42} t_s + \varphi_0 \right) \\ = (\bar{A} + A_{nodal}^* + A_{M_{sf}}^*) \sin \left( \frac{2\pi}{12.42} t_s + \varphi_0 \right)$$

$$G(t) = [\bar{A} + A_{nodal} \sin \left( \frac{2\pi}{18.67} t \right) + A_{M_{sf}} \sin \left( \frac{2\pi}{14.76 \times 24} t_h + \varphi_{M_{sf}} \right)] \\ \cdot \left[ \sin \left( \frac{2\pi}{12.42} t_s + \varphi_0 \right) \right] \quad [13]$$

(with t = time in years since the beginning of the simulation,  $t_h$  = hours since the surge in started,  $\varphi_{M_{sf}}$  = phase angle of the  $M_{sf}$  constituent,

$\bar{A}$  = annual mean amplitude,  $A_{nodal}$  = nodal amplitude,  $A_{M_{sf}}$  = luni-solar fortnightly amplitude).

For Antwerp  $\bar{A}$  = 2.54 m,  $A_{nodal}$  = 0.06 m,  $A_{M_{sf}}$  = 0.42 m.



## 6. The simulation model

In this model tide during the surge is described as observed during recent years, including periodic variations over a nodal period. Surge and interaction are treated together and their magnitude is based upon observations of the last century. From the probability distribution functions and the frequency distribution, the model parameters to reconstruct all components are generated by random numbers. These parameters, treated as stochastic variables are :  $\Delta t$ ,  $D$ ,  $M_{\text{Max}}$  and  $\varphi_0$ . Superposition of  $Z_0$ ,  $G(t)$  and  $M(t)$  each 10 minutes (according to eq[1]) during a storm (Fig. 6) leads to a series of  $n$  maximal storm levels  $H_{\text{max}}$  over a range of  $j$  simulated years. The return period  $T$  of a level  $h_0^{\text{max}}$  is calculated as  $j/m$ , with  $m$  the number of surges exceeding level  $h_0^{\text{max}}$ :

$$T(h_0) = \frac{\text{simulated years}}{\text{number of storms with } H_{\text{max}} > h_0} \quad [14]$$

To obtain suitable results :

- the simulation model must use enough random numbers so that the results are not influenced by the initial random number
- the simulation must cover a span of years of at least 10 times the largest requested return period
- the simulation results must be compared with historical data and if possible with other calculation methods.

Furthermore it seems obvious that the model can not give more information or more accurate data than those included in the set of observations. Hence one should try to collect as much data as possible to increase the reliability of the model parameters and their probability distributions. For the river Scheldt near Antwerp 10000 years were simulated, in which 5952 storms exceeded the lower limit level of NKD+6m. The results are given in Table 1 and Fig. 7.

## 7. Comparison of results - conclusions

The results in Table 1 indicate that the simulation model gives a higher water level than the extreme value distributions, for the same return period. Since the frequency of occurrence of high levels increases with time (Table 2), one should account for trends in determining the frequency of occurrence of extreme water levels. Classical extreme value distributions assume the series of annual maximal water levels as homogeneous, and thus underestimate the frequencies. To avoid inhomogeneity, trends must be corrected for, but one must be aware of the different possible estimates of these trends (Table 3) and the influence on the water levels corresponding to several return periods. The proposed simulation technique avoids these difficulties by using tidal variables based upon recent years observations and by simulating surge events as they happened over the last century. Examination of Table 1 shows that the extreme value distributions give estimates of water levels which become higher the more recent years are considered or the more a homogeneous set of annual maxima is used, whilst the estimates derived from the simulation model are greater than the pure annual maxima results but smaller than the estimates obtained after correction for trends.

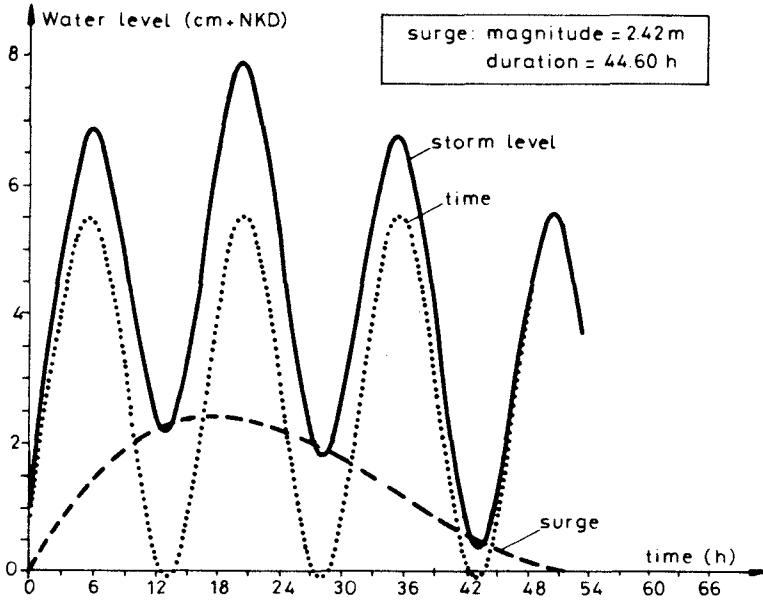


Fig. 6: Simulated storm

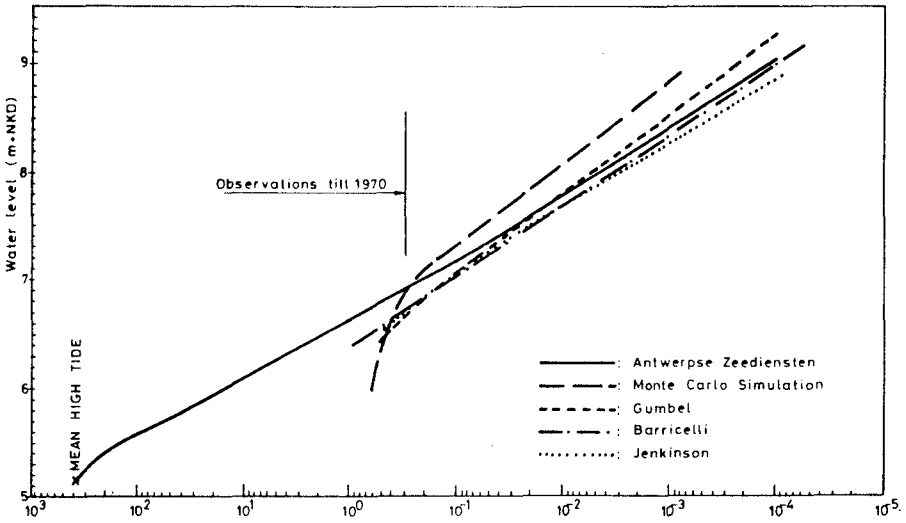


Fig. 7: Frequency of occurrence =  $1/T$  ( $T$ : return period in year)

The simulation technique overcomes the difficulties of applying extreme value distributions. Compared with the joint probability methods it avoids the problem of correlated residuals of the convolution method by considering surge duration and magnitude. It has been illustrated that in comparison with the Tayfun method, detailed observations are required in storm periods and not hourly values over 10 or 15 years. In this way laborious work of data collection is avoided. Compared with the simulation model the proposed technique has the big advantage of not using a hydrodynamic model, since surges are simulated depending on surge-characterizing parameters and not on surge-causing parameters. Although it remains difficult to draw any firm conclusions this simulation technique seems quite promising, especially in estuaries where shallow water components influence surge propagation so that hydrodynamic models become complex, and where trends in annual maxima are apparent. The technique serves to calculate a best estimate for extreme water level frequencies, which is a problem for which no definitely correct answer exists.

Table 1 : Water Levels  $h_0$  (m + NKD) and corresponding return periods

<sup>x</sup>extrapolation of results calculated till T = 1000 yr.

1901 - 1978		Return period (years)					
		10	50	100	1000	10000	
Simulation		7.29	7.82	8.06	8.85	9.58 <sup>x</sup>	
Barricelli		7.03	7.48	7.68	8.33	8.99	
Jenkinson		7.01	7.47	7.56	7.87	7.94	
GUMBEL + homogeneous annual maxima, with reference 1978	Trend (m/year)	Case					
	0.000	(0) no adaptation					
	0.0029	(1)					
	0.0032	(2)					
	0.00304	(3)					
	0.0025	(4)					
	0.0040	(5)					
	0.0020	(6)					
	0.0050	(7)					
	0.0014	(8)					
	0.0046	(9)					
	0.009/0.0067/0.0020	(10)					
	0.0037/0.009	(11)					
	0.0070	(12)					
	0.0096	(13)					
	0.0084	(14)					
	0.0071	(15)					
	0.0118	(16)					
	1941 - 1978						
	0.0000		(17) no adaptation				
	0.0046		(18)				
1951-1978							
0.0000		(18) no adaptation					
0.0046		(20)					
0.0092		(21)					

Table 2 : Frequency of occurrence (number of tides exceeding level  $h_o$ )

Waterlevel	1901	1911	1921	1931	1941	1951	1961
$h_o$	-	-	-	-	-	-	-
m + N.K.D.	1910	1920	1930	1940	1950	1960	1970
5	211	297	319	359	383	399	471
5,5	29	40,7	40	41	75	86	131
6	3,2	3	4,2	4,2	5,1	8,4	14,7
6,5	0,5	0,5	0,3	0,6	0,8	0,7	1,4

Table 3 : Trends in tidal observations

	Period	Trend (cm/century)				Reference
		Mean tidal level	Mean see level	High tide	Annual maximum	
Vlissingen	1900-1962 (x)	+29 (1)		+32 (2)		20
	1890-1962		+30.4 (3)			26
	1880-1970	+25 (4)		+40 (5)		61
Antwerpen	1888-1970	+20 (6)		+50 (7)		61
	1910-1969 (x)	+14 (8)		+46 (9)		20
	1910-1954 (x)	+9		+37		20
	1955-1961 (x)	+67 (10)		(11)		20
	1961-1969 (x)	+20				20
	1955-1969 (x)			+97		20
	1925-1978				70 (12)	18
		Annual maxima				
		Mean values during 40 years starting in 1920 till 1925 taken over				
		5 year	10 year	15 year	20 year	
mean	+96 (13)	+84 (14)	+71 (15)	+71	18	
minimum	+70	+45	+48	+68	18	
maximum	+118 (16)	+105	+108	+73	18	

(x) 19-yearly mean values; data cover a period of 9 years forward and backward to the indicated period.

( ) case number of adaptation to obtain homogeneous data (see also Table 1).

## References

1. Akers, P., and Ruxton, T.D., "Extreme levels arising from meteorological surges", *Proc. 14th Coastal Eng. Conf.*, Copenhagen, 1974, pp 70-86.
2. Banks, J.E., "A mathematical model of a river-shallow sea system used to investigate tide, surge and their interaction in the Thames southern North Sea region", *Philos. Trans. R. Soc. London, Ser. A*, 275, 1974, pp 567-609.
3. Barricelli, N.A., "Les plus grands et les plus petits maxima ou minima annuels d'une variable climatique", *Arch. Math. Naturv.*, Oslo, Vol. 46, No. 6, 1943.
4. Benjamin, J.R. and Cornell, C.A., "Probability, Statistics and Decision for Civil Engineers", McGraw-Hill Book Company, New York, 1970.
5. Berlamont, J., Sas, M., Van Langenhove, G., and Thienpont, M., "Multi- en Interdisciplinaire Evaluatiestudie betreffende de stormvloedkering te Antwerpen (Oosterweel). Deelstudie Waterbouwkundige Aspecten", Niet uitgegeven rapport in opdracht van het Ministerie van Openbare Werken, 1982.
6. Blackman, D.L., Graff, J., "The analysis of annual extreme sea-levels at certain ports in southern England", *Proc. Inst. Civ. Eng.*, Part 2, 65, 1978, pp 339-357.
7. Coen, I., "Nota over de evolutie van het getij in de Westerschelde", Ministerie van Openbare Werken, Antwerpse Zeediensten, 1973, (niet gepubliceerd).
8. Coen, I., and Theuns, J., "Overzicht van de tijwaarnemingen in het Zeescheldebekken gedurende het tijdperk 1961-1970", *Tijdschrift der Openbare Werken van België*, No. 3, 1972-1973.
9. Davies, J.R., Webber, N.B., "An investigation of the frequency of occurrence of extreme high water levels at Portsmouth", *Internal report*, Dept. of Civil Eng., University of Southampton, 1976.
10. Fischer, R.A., and Tippett, L.H.C., *Proc. Camb. Phil. Soc.*, 1928, pp 180.
11. George, K.J., Bates, D.J., "The 60 year sea level at Barnstaple as estimated using the convolution method", *Proc. Inst. Civ. Eng.*, Part 2, 69, 1980, pp 827-834.
12. Graff, J., and Blackman, D.L., "Analysis of maximum sea levels in southern England", *Proc. 16th Coastal Eng. Conf.*, Hamburg, 1978, pp 931-948.
13. Graff, J., "Concerning the recurrence of abnormal sea-levels, *Coastal Engineering*, Vol. 4, 1979, pp 177-181.
14. Gumbel, E.J., "Statistics of extremes, *Columbia University Press*, New York and London, 1958.
15. Heaps, N.S., "Storm Surges", *Oceanogr. Mar. Biol. Ann. Rev.*, 5, 1967, pp 11-47.
16. Ho, F.B., and Tracey, R.J., "Storm Tide Frequency Analysis for the Coast of North Carolina, North of Cape Lookout", *NOAA Technical Memorandum NWS-HYDRO-27*, National Oceanic and Atmospheric Administration, National Weather Service, 1975.
17. Ho, F.B., Tracey, R.J., Myers, V.A., and Foat, N.S., "Storm Tide Frequency Analysis for the Open Coast of Virginia, Maryland and Delaware", *NOAA Technical Memorandum NWS-HYDRO-32*, National Oceanic and Atmospheric Administration, National Weather Service, 1976.

18. Janssens, C., and Sas, M., "Studie van de extreme getijwaterstanden op de Schelde", Eindejaarsverhandeling, K.U. Leuven, 1979.
19. Jenkinson, A.F., "Frequency distribution of the annual maximum (or minimum) values of meteorological elements", *Quart. J. Roy. Met. Soc.*, Vol. 81, 1955, pp 158-171.
20. Jenkinson, A.F., "Statistics of extremes", *Technical Note 98*, World Meteorological Office, 1969.
21. Keers, J.F., "An empirical investigation of interaction between storm surge and astronomical tide on the east coast of Great-Britain" *Dtsch. Hydrogr. Z.*, 21, 1968, pp 118-125.
22. Lennon, G.W., "A frequency investigation of abnormally high tidal levels at certain west coast ports", *Proc. Inst. Civ. Eng.*, 25, 1963, pp 451-487.
23. Lennon, G.W., "An investigation of secular variations of sea level in European waters", *Ann. Acad. Sci. Fennicae*, A.3, 90, 1966, pp 225-236.
24. Lennon, G.W., "Coastal Geodesy and the relative movement of land and sea levels", *Geodynamics Today*, A review of the Earth's Dynamic Process, London, 1975, pp 97-102.
25. Myers, V.A., "Joint Probability Method of Tide Frequency Analysis Applied to Atlantic City and Long Beach Island", N.J., *ESSA Technical Memorandum WBTM Hydro11*, U.S. Department of Commerce, 1970.
26. Myers, V.A., "Storm Tide Frequencies on the South Carolina Coast", *NOAA Technical Report NWS-16*, National and Atmospheric Administration, National Weather Service, 1975. Oceanic
27. Myers, V.A., and Overland, J.E., "Storm Tide Frequencies for Cape Fear River", *J. of Waterway, Port, Coastal and Ocean Division*, Proc. ASCE, 103, 1977, pp 519-535.
28. Prandle, D., and Wolf, J., "The interaction of surge and tide in the North Sea and River Thames", *I.O.S. Rep. No. 64*, (unpublished), 1978.
29. Pugh, D.T., and Vassie, J.M., "Tide and surge propagation offshore in the Dowsing Region of the North Sea", *Dtsch. Hydrog. Z.*, 29, 1976, pp 163-213.
30. Pugh, D.T., and Vassie, J.M., "Extreme sea levels from tide and surge probability", *Proc. 16th Coastal Eng. Conf.*, Hamburg, 1978, pp 911-930.
31. Pugh, D.T., and Vassie, J.M., "Applications of the joint probability method for extreme sea level computations", *Proc. Inst. Civ. Eng.*, Part 2, 69, 1980, pp 959-978.
32. *Rapport Deltacommissie*, Staatsdrukkerij- en uitgeverijbedrijf, 's Gravenhage, 1962.
33. *Rapport Deltacommissie*, Eindverslag, Staatsdrukkerij- en uitgeverijbedrijf, 's Gravenhage, 1962.
34. Rohde, H., "Sturmfluthöhen und säkularer Wasserstansanstieg an der deutschen Nordseeküste", *Die Küste*, 30, 1977, pp 52-143.
35. Rohde, H., "Changes in sea level in the German Bight", *Geophys. J.R. Astr. Soc.*, 62, 1980, pp 291-302.
36. Rossiter, J.R., "Interaction between tide and surge in the Thames", *Geophys. J.R. Astron. Soc.*, 6, 1961, pp 29-53.
37. Rossiter, J.R., "Long-term variations in sea-level", *The Sea*, Vol. 1, M.G. Hill, Interscience Publishers, New York - London, 1962, pp 590-610.

38. Rossiter, J.R., and Lennon, G.W., "Computation of tidal conditions in the Thames estuary by the initial value method", *Proc. Inst. Civ. Eng.*, 31, 1965, pp 25-26.
39. Rossiter, J.R., "An Analysis of Annual Sea Level Variations in European Waters", *Geophys. J.R. Astr. Soc.*, 12, 1967, pp 259-299.
40. Sas, M., Smets, E., Van Langenhove, G., and Berlamont, J., "Gebruik van de simulatietechniek ter bepaling van overschrijdingsfrequenties van de extreme hoogwaterstanden op de Schelde, *Intern rapport van het Laboratorium voor Hydraulica (06-HV-03)*, K.U.Leuven, 1979.
41. Sas, M., and Berlamont, J., "The influence of mean sea level variation on the frequency of occurrence of high water levels in Antwerp", *Hydraulics Laboratory Report 10-HV-06*, K.U.Leuven, 1982.
42. Schalkwijk, W.F., "A contribution to the study of storms surges on the Dutch coast", Algemene Landsdrukkerij, 's Gravenhage, 1947.
43. S.V.K.S., "Analyse der hoogste hoogwaterstanden te Antwerpen", *Deelrapport 5B-Hydraulica*, Variantenstudies, 1979.
44. Suthons, C.T., "Frequency of occurrence of abnormally high sea-levels on the east and south coast of England", *Proc. Inst. Civ. Eng.*, 25, 1963, pp 443-449.
45. Tayfun, M.A., "Joint Occurrences in Coastal Flooding", *J. of Waterway, Port, Coastal and Ocean Division*, Proc. ASCE, 105, 1979, pp 107-123.
46. Theuns, J., "De Buitengewone Stormvloed van 3 januari 1976", *Ministerie van Openbare Werken - België, Antwerpse Zeediensten*, AZ 76/4, 1976.
47. Walden, A.T., Prescott, P., and Webber, N.B., "Some important considerations in the analysis of annual sea-levels", *Coastal Engineering*, Vol. 4, No. 4, 1981, pp 335-342.
48. Walden, A.T., Prescott, P., and Webber, N.B., "The examination of surge-tide interaction at two ports on the central south coast of England", *Coastal Engineering*, Vol. 6, 1982, pp 59-70.
49. Walden, A.T., Prescott, P., and Webber, N.B., "An alternative approach to the joint probability method for extreme high sea level computations", *Coastal Engineering*, 6, 1982, pp 71-82.
50. Webber, N.B., and Davies, J.R., "Research on exceptional levels in the Solent", *Dock. Harb. Auth.*, 1976, pp 158-171.

## CHAPTER FIFTEEN

UPDATE: THE NATIONAL FLOOD INSURANCE PROGRAM AND THE COAST

By: William G. Fry, P.E., and Perry A. Rhodes, P.E.,  
Respectively, Principal and Civil Engineer for  
Dewberry & Davis, Fairfax, Virginia

### ABSTRACT

This report will update the coastal zone practitioner on the National Flood Insurance Program (NFIP) as it affects the implementation of manmade changes along the coastline.

It is our intent to place in proper perspective this fast-changing and often difficult to interpret national program. Readers will achieve an overall understanding of the NFIP on the coast, and will be in a position to apply the program's requirements in their efforts.

We will begin with a history of the application of the NFIP to the coastal zone. The history of the problems encountered will lead into current regulations, methodologies, and the changes the Federal Emergency Management Agency plans for the future.

### INTRODUCTION

The NFIP, operated by the Federal Emergency Management Agency (FEMA), has been in existence since 1968. This program has been a major force in directing the course of development in the U.S., not only on the coast, but throughout all the flood-prone areas of the country. However, with regard to the coastal areas, the program was slow to get and to give direction to development, and the application of the program in coastal areas was an area of major criticism during its early years.

It is only now, 1984, that we feel the NFIP has achieved a steady state in the coastal areas. It has established a sound technical backing for its requirements, gained a national understanding, and achieved a fairly strong assurance of being accepted by local governments.

The achievement of this steady state has been made only after a period of loosely defined rules and regulations for the coastal areas. This has left considerable confusion to builders and developers, engineers and architects, the insurance industry, and local governments. The purpose of this paper is to summarize the current rules, regulations, and technical bases of the NFIP in the coastal area. This paper will also present what can be expected in the foreseeable future.



Our presentation will cover the following topics:

- o History of the coastal zone and the NFIP
- o Flood insurance zones in the coastal areas
- o The flood plain management and construction regulations of the NFIP
- o Representative examples of flood insurance rates
- o A summary of the storm surge models
- o A summary of the wave height and wave runup models
- o A brief discussion of the application of the barrier island regulations
- o Current updates to the surge and wave height models now being completed and contemplated by FEMA

#### HISTORY OF THE COASTAL ZONE DESIGNATIONS

Itemized below are the key dates for the NFIP in the coastal areas.

1969 - Inundation of the 100-year flood (A zones) was identified in the coastal zone.

1972 - First V zones (coastal high hazard area<sup>1</sup>) in areas of obvious wave action were applied to the coastal area. Zones V1 through V30, when determined, utilized the popular surge models of the early 1970s.

1975 - The Galveston District Corps of Engineers established the three-foot wave as that wave which will induce significant damage above and beyond inundation to structures (Reference 1). From this, using a convention of maximum wave height equaling 78% of the depth, a four-foot stillwater storm depth was established to identify V zones. In other words, areas of stillwater inundation with depths greater than four feet which had significant exposure to waves were considered V zones.

1977 - The National Academy of Sciences (NAS) completed its wave height methodology for V zone identification (Reference 2). It was to be applied using established stillwater elevations.

1979 - A cost benefit study, undertaken by FEMA, showed a positive ratio, as high as 8:1 in some instances, for implementation of the wave height methodology.

September 1979 - Hurricane Frederick occurred, establishing itself as the most costly natural disaster in U.S. history.

April 1980 - The first wave height study became effective on the coast of Alabama. The Federal Insurance Administration (FIA) initiated a major program to study communities on the Gulf and Atlantic coasts.

---

<sup>1</sup>"Coastal high hazard area" means the area subject to high velocity waters including but not limited to hurricane wave wash or tsunamis.

1981 - A storm surge model by Tetra Tech was published by FEMA (Reference 3). The purpose was to standardize coastal storm elevation determination for flood insurance applications.

1984 - Virtually all communities requiring coastal studies have studies in progress or completed.

1984 - Refinements to the NAS wave height model and the Tetra Tech surge model have been undertaken and evaluated by FEMA.

It should be noted that the coastal studies have been a major area of criticism for the Program. With the early utilization of only storm surges to identify the coastal hazards, it was well recognized that the overall coastal hazards were vastly underrated. As a result, allegations were made that the NFIP was encouraging development along the coast by providing unrealistically low insurance rates to protect those who built. Changes in technology and insurance premiums made in the past few years have done much to nullify this argument.

#### FLOOD INSURANCE ZONES

The medium by which the flood insurance zones are identified for a community is the Flood Insurance Rate Map (FIRM). A FIRM is created for every community participating in the NFIP. The definitions below are for effective FIRMs with detailed studies.

- o Zones V1-V30 - Coastal high hazard areas inundated by the 100-year flood where a three-foot or greater wave could occur. Wave crest elevations are shown as the base flood elevation.
- o Zone V - Areas of estimated inundation by the 100-year flood with depths greater than four feet and exposed to provide wave generation. No base flood elevations shown.
- o Zones A1-A30 - Special Flood Hazard Areas (SFHAs) inundated by the 100-year flood with waves less than three feet. The wave crest elevations are shown as the base flood elevations.
- o Zone A - Areas of approximate determination of 100-year inundation. No base flood elevations shown.
- o Zone A0 - SFHAs of shallow flooding caused by sheetflow from the 100-year flood. Depths are between one and three feet and are shown.
- o Zone AH - SFHAs of shallow flooding caused by ponding. Depths are between one and three feet, with the ponding elevations shown.
- o Zone B - Areas of moderate flood hazard, usually expected to be inundated by the 500-year flood. In coastal areas, only the stillwater elevations are utilized. No base flood elevations are shown.
- o Zone C - Areas of minimal flood hazard.

## FLOOD PLAIN MANAGEMENT REGULATIONS FOR ALL FLOOD-PRONE AREAS

The next two sections summarize briefly the requirements of Part 60.3, Title 44, Code of Federal Regulations (Reference 4). These are four very readable pages of the Federal Regulations, which should be reviewed by anyone practicing engineering in the coastal zone. Communities are required to adopt and enforce these minimum standards in order to be eligible for participation in the NFIP. The regulations for all flood-prone areas are discussed below and the additional regulations applicable to the coastal high hazard areas are discussed in the following section.

## REGULATIONS FOR SPECIAL FLOOD HAZARD AREAS

1. Participating communities must require permits for all proposed construction in SFHAs.
2. Participating communities must review proposed development to assure approval of all state and Federal regulations including Section 404 of the Federal Water Pollution Control Act.
3. Participating communities must review all development to assure safety from flooding with appropriate building standards.
4. Participating communities must assure that all subdivisions are designed with flood damage mitigation standards, applying to both structures and utilities.
5. For subdivisions of 50 lots or five acres or greater, if base flood elevations have not been established by the NFIP, they must be developed. This implies that where only Zones V or A are shown on a map, it is a requirement that studies be undertaken to establish base flood elevations.
6. Communities must utilize any available base flood elevation data available to them.
7. Communities must notify all neighboring communities of watercourse alterations and they must ensure the conveyance of all existing watercourses.
8. Mobile homes in SFHAs must be elevated and anchored using specific design standards.
9. Communities must maintain evacuation plans for mobile home parks and subdivisions.
10. New construction of, or substantial improvements to, residential structures in Zones A1-A30 and AH zones (ponding) must have the lowest floor, including the basement, elevated to or above the base flood elevation. For non-residential structures, certified waterproofing may be utilized.
11. In A0 zones (sheetflow) residential structures must have their lowest floor elevated above the adjacent grade by the depth of flooding identified (1-3 feet). Again, floodproofing is permitted for non-residential structures if certified by a registered architect or engineer.
12. There must be adequate drainage paths around all structures in Zones AH (ponding) and A0 (sheetflow).

13. Floodways (that portion of a reduced flood plain which would carry the 100-year flood without greater than a one-foot surcharge to the flood elevation) must not have any construction in them which will result in any increase in flood elevations. Mobile homes are prohibited except in existing parks.

#### SUMMARY OF ADDITIONAL REGULATIONS FOR THE COASTAL HIGH HAZARD AREAS

1. All new construction and substantial improvements must be landward of mean high tide.
2. All new construction and substantial improvements must be on piles, secured with the lowest structural member above the base flood elevation.
3. All new construction and substantial improvements must be certified by a registered architect or engineer to be designed to withstand the wave and water forces of the 100-year storm.
4. For all new construction and substantial improvements, the space below the lowest floor is prohibited for use for habitation. It must be free of obstructions and may utilize only breakaway walls for enclosure.
5. No fill is allowed for structural support.
6. No new mobile homes may be placed, except in existing parks.
7. There must be no degradation of sand dunes and mangroves.

In summary, for the coastal high hazard area, there are additional locational requirements, structural certification requirements, structural design requirements, and environmental requirements. Of particular note is the unique requirement that the lowest structural member must be above the base flood elevation as opposed to simply the lowest habitable floor.

The NFIP is voluntary. If a community chooses not to participate, flood insurance is not available, and grants, loans, or guarantees made by Federal agencies such as the Small Business Administration, Federal Housing Administration, and Veterans' Administration are prohibited for acquisition or construction in identified areas. Lending institutions insured or regulated by a Federal agency may make conventional loans at their own discretion in these areas. By law, if a flood disaster situation occurs in a nonparticipating flood-prone community, no Federal assistance for acquisition or construction may be provided in flood hazard areas. Individual and Family Grant assistance for housing and personal property is also not available after a flood disaster.

#### REPRESENTATIVE INSURANCE RATES

For comparison, indicated below are the annual premiums for three different structures. The premiums are based on the maximum structure insurance of \$185,000, and the maximum contents insurance of \$60,000 (References 5 and 6).

- o For a structure in Zones A1-A30 with the lowest habitable floor at the base flood elevation, the annual premium is \$287.50.

- o For a structure in Zones V1-V30 with the lowest structural member at the base flood elevation, the annual premium is \$2,442.00.
- o For a structure in Zones V1-V30 with the lowest structural member at four feet or more above the base flood elevation, the annual premium is \$946.00.

#### STORM SURGE MODELS

In performing coastal Flood Insurance Studies (FISs), determination of the stillwater elevations is the initial step. FEMA has used many different sources for stillwater elevations. These sources include frequency analyses of tidal gage data and storm surge models. In 1981, FEMA adopted Tetra Tech's storm surge model for use on the East and Gulf coasts (Reference 3). This model incorporates two separate models: a hurricane model to generate hurricane wind and pressure fields and a finite difference hydrodynamic model to generate storm surges using the hurricane data. The hurricane model uses an array of five hurricane parameters to simulate the wind and pressure fields of selected storms. The storm model uses a variable grid mesh which incorporates water depth, bottom friction, shoreline configuration, barrier islands, and inlets. The model results in a time history of storm surges. These are combined with the predicted astronomical tide for the same time period to produce the stillwater elevation. A joint probability analysis is used to assign frequencies to the stillwater elevations. This model has been applied extensively in the Gulf and South Atlantic states.

For Virginia, Maryland, and Delaware, FEMA has used a joint probability analysis by the National Oceanic and Atmospheric Administration (NOAA), which utilizes the SPLASH model with modifications similar to those in SLOSH (Reference 7). It should be noted that FEMA is using SLOSH for hurricane evacuation studies. Because these studies do not assign a frequency to the storm being modeled, the results from the SLOSH model cannot be used in FISs.

In the New England states, an additional model is applied for consideration of the effects of northeasters. FEMA has adopted a model developed by Stone & Webster (S&W) which simulates wind and pressure fields for northeasters (Reference 8). This data is then used in the same manner as the hurricane fields to generate storm surges and stillwater elevations.

#### WAVE HEIGHT AND RUNUP MODELS

To evaluate the wave action effects, FEMA had the NAS prepare a methodology applicable to most areas along the Gulf and Atlantic coasts (Reference 2). This methodology considers the effects of wind fetches, stillwater depths and all types of stationary obstructions in determining wave heights and corresponding wave crest elevations. An incident wave height is calculated at the shoreline based on available fetch and stillwater depth. This wave height is modeled as it propagates inland. Energy losses due to vegetation, buildings, and other structures are considered, as well as wave generation over unobstructed

areas. The calculated wave heights are used to determine the wave crest elevations which become the regulatory base flood elevations. This methodology has been applied to nearly all of the Gulf and Atlantic coastal communities.

The NAS methodology does not account for wave runup on steep shorelines subject to intense long period waves. In the New England states, many structures above the stillwater elevation were damaged by runup during the 1978 northeaster. To account for this hazard, FEMA contracted S&W to develop a model to determine the height of wave runup. S&W's computer model incorporates laboratory runup data from Phillip Stoa and uses the composite beach slope method developed by Thorndike Saville (Reference 9). The height of calculated runup is a function of beach slope and roughness, deepwater wave height and wave period. The maximum runup elevation is combined with the results of the NAS methodology to produce a simple yet realistic wave profile consistent with existing state-of-the-art technology to describe wave height variation in the surf and runup zones.

#### WEST COAST FLOODING

Most of the above-mentioned models and methodologies are not applicable to the West Coast. The West Coast is subject to severe flooding from tsunamis, winter storms, tropical storms, extratropical storms and the swells from these types of storms. For a large part of the West Coast, including Hawaii, the phenomenon that was determined to result in the worst flooding was modeled and mapped. For southern California, a joint probability analysis of astronomical tides, tsunami, offshore storms and landfalling storms is being performed for the coastline between the Mexican border and Morro Bay. FEMA has also just contracted for a tsunami model of the entire coast of Alaska. These last two models will complete the study of the areas of the West Coast subject to coastal flooding.

#### COASTAL BARRIER RESOURCES ACT

Another service provided by FEMA is the placing on the FIRMS of the "undeveloped barriers" identified under the Coastal Barrier Resources Act of 1982, by the Department of the Interior. Any development after October 1, 1983, in these areas is not eligible for any Federal funds, including flood insurance and disaster assistance. The classification of areas as "undeveloped barriers" has been challenged in court many times regarding the definition of "undeveloped" and "barrier." Most cases have been unsuccessful. Although not involved in the identification of the undeveloped barriers, FEMA has mapped these areas on the FIRMS for all of the affected communities. This was completed by October 1, 1983.

#### FUTURE ACTIONS

So far, we have briefly covered the flood hazard zones and regulations for coastal communities, and the methods of determining the flood hazards. We would now like to discuss FEMA's future involvement with coastal analyses.

Due to recent technological advances in the state of the art, unique situations encountered, and experience gained from application of their models, FEMA is currently reviewing and/or updating several of their methodologies. The National Weather Service of NOAA has been contracted to develop a comprehensive and authoritative set of hurricane climatological statistics to be utilized in future FISs. This will update a 1975 hurricane climatology study, NWS-15. All previous storms influencing the Gulf and Atlantic coasts will be analyzed to provide tabulated data of hurricane frequency parameters for determination of the wind and pressure fields for storm surge calculations. This will make variations of storm parameters smooth enough so that contractors can use the information directly. Decisions on the statistical representativeness of the sample size and final analysis will be made by NOAA and not left to individual contractors. It is estimated that this will be completed within 2 years.

In addition, FEMA has contracted a review of the complete Tetra Tech model for areas that could be potentially updated due to advances in the state of the art. Upon completion of this review, necessary updates will be made.

FEMA has just completed two updates to the NAS wave height methodology. These updates are really additions to account for unique situations. The first concerns the Mississippi Delta. The Mississippi River has deposited millions of tons of fine sediments into the Gulf of Mexico to form a soft mud bottom in contrast to the typical sand bottom of most coastal areas. This plastic, viscous bottom deforms under the action of a surface wave. This wave-like reaction requires energy from the surface waves, thus reducing the surface waves. Joseph Suhayda has just completed a methodology for FEMA to account for the wave energy losses in the Mississippi Delta. Waves in the offshore area are tracked over the muddy bottom resulting in lower wave heights at the shoreline. This methodology will be applied only to the Louisiana communities affected by this phenomenon.

The other situation FEMA has investigated is the effect of marsh grass on wave dissipation. The NAS methodology models vegetation as a rigid cylinder. This does not account for the flexibility of marsh plants. A FEMA task force is in the process of completing a methodology that accounts for different types of marsh plants, flexure of the plants, and wind energy input.

e Another service provided by FEMA is their "Design and Construction Manual for Residential Buildings in Coastal High Hazard Areas." FEMA is currently negotiating a contract for an updated and more detailed version.

#### CONCLUSION

By the end of FY 85, all of the coastal communities in the United States will have detailed studies completed or in progress. This will not be the end of FEMA's involvement in the coastal areas. Refinements will continue to be made with advances in the state of the art. Although FEMA does not plan any massive restudies as a result of upgrades

to their methodologies, these advances will be incorporated in future revisions and restudies as they become necessary.

To summarize, we have seen the Coastal Flood Insurance Program go from being controversial and very subjective to a program utilizing recent technical developments with well defined criteria and regulations. FEMA has provided a reasonable representation of potential flood hazards for nearly all of the coastal communities in the U.S. Along with its regulations, the FIRM becomes a flood plain management tool available to the coastal areas. While not promoting development, FEMA has provided this tool so that future development in the coastal areas will be constructed to minimize potential flood damage. Without FEMA's involvement in the coastal areas, development could be rampant and unsafe, with yearly flood losses drastically escalating.

## REFERENCES

1. U.S. Army Corps of Engineers, Galveston District, Guidelines for Identifying Coastal High Hazard Zones, Galveston, Texas, June 1975.
2. National Academy of Sciences, Methodology for Calculating Wave Action Effects Associated with Storm Surges, Washington, D.C., 1977.
3. Tetra Tech, Inc., Coastal Flooding Storm Surge Model, Parts I and II, Pasadena, California, May 1978.
4. Code of Federal Regulations, Title 44, Parts 59 and 60, Washington, D.C., 1984.
5. Federal Emergency Management Agency, National Flood Insurance Program, Flood Insurance Manual, Washington, D.C., June 1, 1982, revised October 1, 1983.
6. Federal Emergency Management Agency, National Flood Insurance Program, Adjusters Workshop and Handbook, 1984 edition, Washington, D.C., December 1983.
7. National Oceanic and Atmospheric Administration, National Weather Service, Storm Tide Frequency Analysis for the Open Coast of Virginia, Maryland, and Delaware, NOAA Technical Memorandum NWS HYDRO-32, Silver Spring, Maryland, August 1976.
8. Stone and Webster Engineering Corporation, Development and Verification of a Synthetic Northeaster Model for Coastal Flood Analysis, Boston, Massachusetts, 1978.
9. Stone and Webster Engineering Corporation, Manual for Wave Runup Analysis, Coastal Flood Insurance Studies, Boston, Massachusetts, November 1981.



## CHAPTER SIXTEEN

### SIMULATION OF TIDES AND STORM SURGES IN THE GREAT BARRIER REEF REGION

K.P. Stark,<sup>1</sup> L. Bode<sup>2</sup> and L.B. Mason<sup>3</sup>

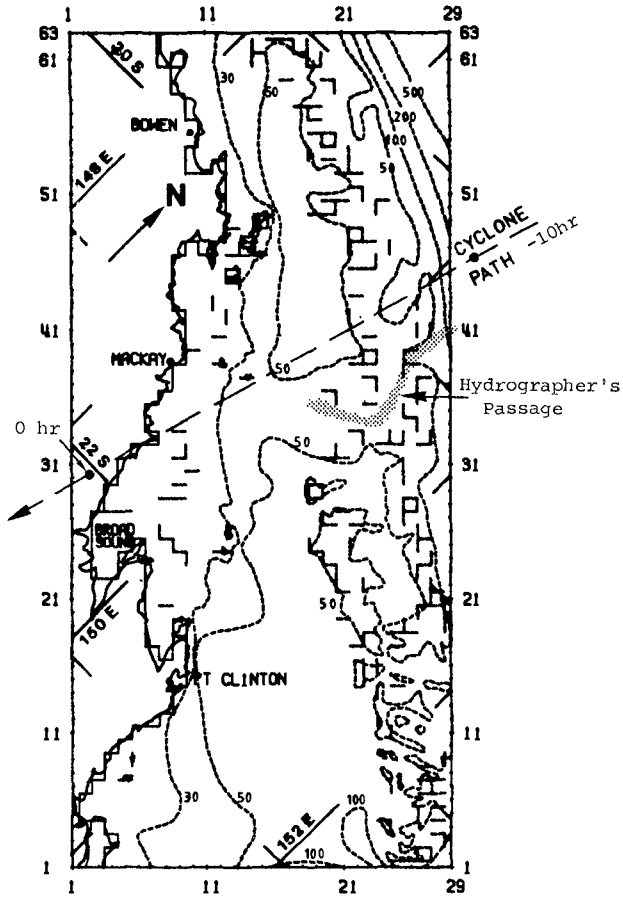
The Great Barrier Reef Region which constitutes the north-eastern continental shelf waters of Australia, is an area that is subject to both large astronomical tides and the passage of tropical cyclones (hurricanes). One section of this area, centred on Mackay, is characterised by particularly high tides, with a springs range of order 10 metres. Numerical hydrodynamic modelling is used in the present study to: (a) simulate the M<sub>2</sub> tide to investigate possible effects of the reef barrier on tidal amplification; (b) simulate the passage of a tropical cyclone across the continental shelf; (c) investigate the effect and consequences of non-linear surge/tide interactions. The recent discovery of a major shipping route through the reef in this area and the continuing development of natural resources makes a much more detailed understanding of the region's hydrodynamics essential for coastal engineering.

#### INTRODUCTION

The Great Barrier Reef (GBR) extends in an almost unbroken chain along some 1200 miles of the Queensland coast of Australia. The area between the coastline and reef (the 'lagoon') is of key importance to engineers, oceanographers, development consultants and shipping; it is of unique biological importance and supports significant fishing and tourism industries. The area of particular interest to the present study is centred on the city of Mackay, with the model's location and extent being delineated in Fig. 1. This area's hinterland is rich in natural resources and this has resulted recently in an upsurge of development, particularly in the exploitation of massive nearby coal reserves. The possibility also exists of large scale development of extensive shale-oil deposits in the longer term.

Shipping within the GBR Region is therefore very important and coastal engineering projects range from the development of port and harbour facilities, and the construction of deep-water ports to consideration of environmental problems associated with potential shipping disasters. The newly-discovered shipping channel through the main reef, Hydrographer's Passage, is also shown in Fig. 1. This provides much easier and more economical access for international shipping to Mackay.

1. Professor and Head of Dept., 2. Research Fellow, 3. Research Officer, Department of Civil and Systems Engineering, James Cook University of North Queensland, Townsville. Q. 4811. AUSTRALIA.



**Fig. 1** Model region with solid rectilinear boundaries of computational region superimposed on the actual coastline. Dashed curves depict bathymetry (m); dashed rectilinear elements represent reef and low barriers. The hatched region is Hydrographer's Passage. Also shown is the cyclone track through the region. Latitude and longitude of the region are indicated.

However, it is also clear that although the initial shipping traffic through the new passage will be relatively small, it will be necessary to evaluate the additional risks, environmental and ecological, that will be superimposed on the region. Such evaluations require a detailed understanding of the hydrodynamic interactions of the complex tidal and meteorological forcing mechanisms that apply in this area.

In this southern (Mackay) section of the GBR Region, the pattern of the astronomical tides is of considerable scientific and applied interest. Tides are much higher than, and exhibit large phase lags relative to areas to the north and south. Spring tides can have a range of up to 10 metres. Recent numerical studies by the authors have lent weight to the hypothesis [first proposed, incidentally, by the maritime explorer Matthew Flinders in 1814], that the reef chain itself plays a key role in the attainment of such large water levels (1). The area is also subjected to the influence of strong and persistent longshore winds for a large part of the year. In addition, the occasional incidence of the passage of tropical cyclones means that such extreme meteorological forcing and the associated water levels and currents, must be included in any coastal engineering assessment of the area.

#### Aims and Objectives

The work to be discussed in this paper comprises three parts. The first is an investigation of the factors which lead to the large amplification of the semi-diurnal astronomical tides. In particular the role played by the dense reef barrier in the tidal dynamics is considered by means of numerical modelling. The second part of the work considers the effect of the passage of a tropical cyclone through this area. In view of the extremely large water levels that are attainable from each of these forcing mechanisms, the ultimate effect of surge/tide interactions on the total water level and currents could well be considerable and should be incorporated in the design of important coastal engineering works in this area, since variations of fractions of a metre in levels could have significant economic implications. This aspect of the coastal hydrodynamics is often neglected and forms the third part of the study.

#### METHOD OF SOLUTION

The above cases are treated numerically by the solution of the two-dimensional (depth-integrated) long wave equations. Solution techniques for such models are by now more or less conventional and will not be referred to in any detail. Further details of the model can be found in Refs. (1,7,11,12). The equations of motion to be solved are:

$$\frac{\partial U}{\partial t} + \frac{\partial}{\partial x} \left( \frac{U^2}{H} \right) + \frac{\partial}{\partial y} \left( \frac{UV}{H} \right) - fV = -H \frac{\partial}{\partial x} \left[ g \eta + \frac{p_a}{\rho} \right] + \frac{1}{\rho} (\tau_{sx} - \tau_{bx}), \quad (1)$$

$$\frac{\partial V}{\partial t} + \frac{\partial}{\partial x} \left( \frac{UV}{H} \right) + \frac{\partial}{\partial y} \left( \frac{V^2}{H} \right) + fU = -H \frac{\partial}{\partial y} \left[ g \eta + \frac{p_a}{\rho} \right] + \frac{1}{\rho} (\tau_{sy} - \tau_{by}), \quad (2)$$

$$\frac{\partial \eta}{\partial t} + \frac{\partial U}{\partial x} + \frac{\partial V}{\partial y} = 0, \quad (3)$$

The notation used is:

t	time,
x, y	local horizontal Cartesian co-ordinates,
$\eta = \eta(x, y, t)$	sea-surface elevation, referred to M.S.L. datum,
$h = h(x, y)$	undisturbed water depth,
$H = h + \eta$	total water depth,
f	Coriolis parameter, assumed constant
g	gravitational acceleration,
P	atmospheric pressure
$\rho^a$	water density, assumed constant,
$\tau_{sx}, \tau_{sy}$	components of surface stress $\tau_s$ due to wind forcing,
$\tau_{bx}, \tau_{by}$	components of bottom stress $\tau_b$ ,
U, V	components of horizontal transport per unit width of cross section, defined by
$U = \int_{-h}^{\eta} u \, dz$	where u is the average velocity and $\bar{u}$ the depth averaged mean velocity, in the x-direction.
$= \bar{H}u$	

A similar definition holds for V (and  $\bar{v}$ ). The equations are solved by an explicit finite-difference technique on a uniform grid that is staggered both spatially and temporally (a Richardson lattice).

An additional and complicating factor in this region, however, is the necessity of formulating a suitable physical model of the GBR chain that can be incorporated within the numerical model. The reef would appear to play a number of roles, acting as a possible means for both large-scale tidal amplification plus considerable smaller-scale dissipation, a generator of extreme currents locally, and as possible offshore protection from even more extreme storm surge levels. In this and the works cited above, reefs and other low barriers (such as the extensive band of sandbanks at the mouth of Broad Sound) are modelled as weirs - after the approach of Reid and Bodine (11) and Sobey *et. al.* (12,13).

The model region has been shown already in Fig. 1. Both the actual coastline and its model approximation on the square grid of spatial resolution,  $\Delta s = 5$  n miles are shown. This value allows considerable, although not complete resolution of individual reef elements. The figure also shows the region's bathymetry as well as the model's approximation of the reef structure and submerged barriers, which are represented by the dashed rectilinear elements. For the purposes of comparison of the various results that follow, particular attention will be paid to grid point (5,29) in the mouth of Broad Sound. This is the location of Flat Isles where, in fact, Flinders was moored for two weeks in 1814. This point is in the area of maximum tides as well as surge for the chosen model cyclone.

## TIDAL MODEL

In the Mackay region, tides are predominantly semi-diurnal. In particular the  $M_2$  constituent accounts for roughly 50% of the total tidal range, as seen from Table I. As a result,  $M_2$  can be taken as representative of a mean tide over the spring-neap cycle. It should be remembered, however, that total tidal water levels can be up to double these values. The tidal model is driven by imposing the  $M_2$  tide (amplitude and phase) along the three open boundaries. The tidal amplitude is increased from zero to its full value over a build-up period of 6 hours in order to reduce the unwanted effects of initial transients (1,2).

TABLE I

RANGE OF PRINCIPAL TIDAL CONSTITUENTS (METRES) AT SELECTED LOCATIONS IN THE STUDY AREA, TOGETHER WITH THEIR SUM

Location	$M_2$	$S_2$	$N_2$	$K_1$	$O_1$	$P_1$	Sum
Bowen	1.50	0.61	0.40	0.64	0.34	0.21	3.70
Hook Island	1.72	0.63	0.45	0.71	0.35	0.24	4.10
Mackay	3.36	1.20	0.80	0.76	0.40	0.23	6.75
Broad Sound (McEwin Islet)	4.84	1.42	0.43	0.92	0.42	0.25	9.28
Pt. Clinton	2.74	1.10	0.63	0.64	0.32	0.21	5.64
Bell Cay	2.26	1.20	0.42	0.46	0.32	0.21	4.87
Gladstone	2.32	0.84	0.53	0.50	0.28	0.16	4.63

[(1,1) on Fig.1]

At present, there remains some uncertainty about this specification of the open boundary conditions, particularly along the edge of the continental shelf. Obtaining data along this stretch is made difficult by the fact that, apart from Hydrographer's Passage, no approach to the shelf edge can be made from the lagoon. Outside the reef, seas are generally too large for safe and recoverable deployment of instruments. Fortunately, this situation is improving and proposed field experiments should help to remedy some of the inevitable uncertainties.

Tidal Results

Fig. 2 shows the results of a simulation of the  $M_2$  tide in this region. The notable feature is the effect of the 'reef': the relatively large gradients of surface elevation and the large phase change across the central (and densest) portion of the reef chain, indicate considerable flow retardation. The mechanism of tidal amplification can also be seen from this figure. The phases of the resultant tidal streams from the north and south are such that they tend to reinforce each other in the central part of the region. The resulting pattern is essentially a standing wave, with almost uniform phase over this large central portion. The tide subsequently progresses up Broad Sound with considerable further amplification.

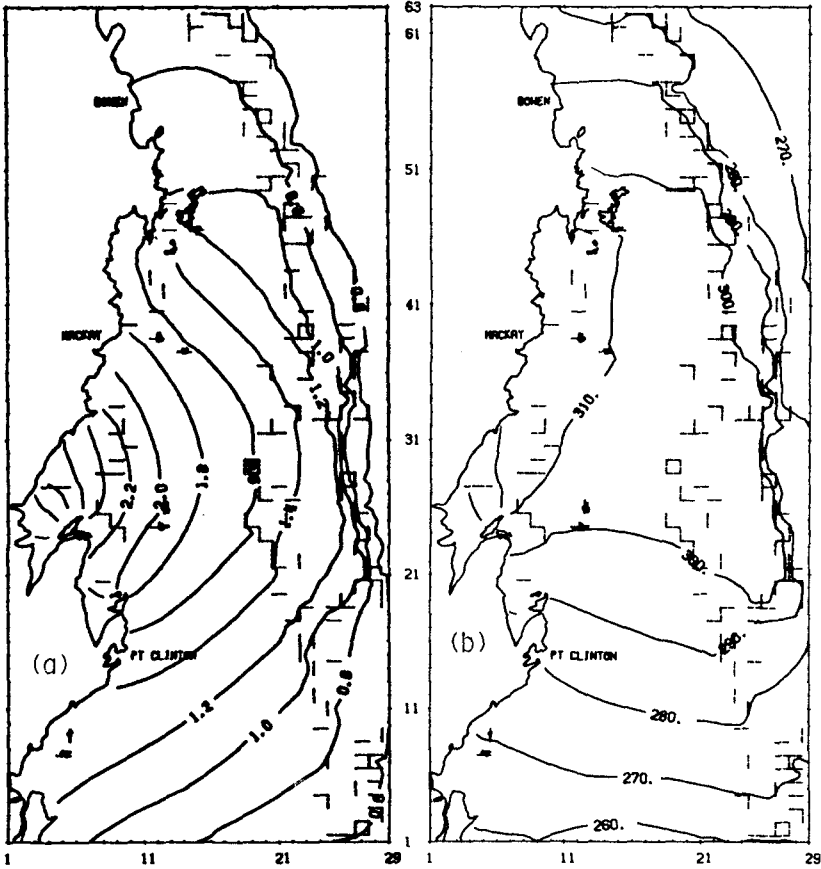
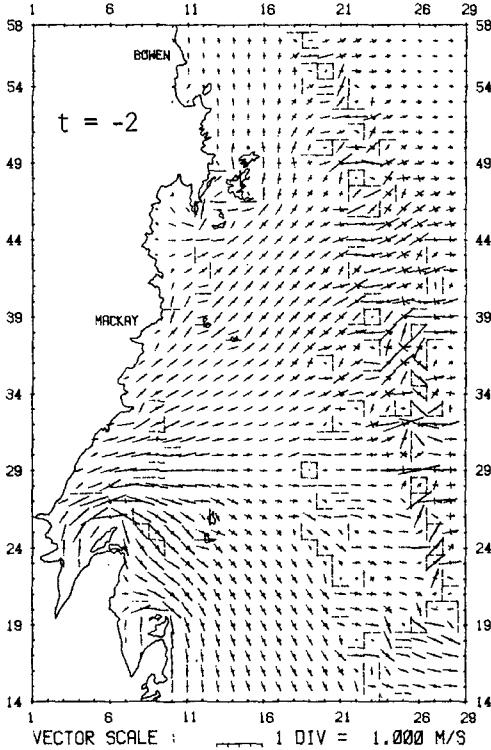


Fig. 2. Co-amplitude (m) and co-phase ( $^{\circ}$ ) contours for  $M_2$  tide. Grid size is 5 n miles; rectilinear elements depict reefs, etc.

$M_2$  tidal ellipses, shown at every grid point in each coordinate direction, are presented in Fig. 3. They show the essential pattern of the tidal streams, while the indicated phase depicts the variation from an essentially progressive wave towards a standing wave pattern. The maximum amplitude of the tidal current is  $1.8 \text{ ms}^{-1}$  (or roughly 3.5 knots) near grid point (25,32). However, personal observations indicate that for the area of the outer reef, tidal currents of order 6 knots are not uncommon between individual reefs.



**Fig. 3**  $M_2$  tidal ellipses for central 'window' of model region.

The effects of the reef on the propagation of the tides can be further demonstrated with a numerical model by the complete removal of the reef elements from the model. The results of this numerical experiment are shown in Fig. 4. The amplification of the tides is now much reduced. For example, at grid point (5,29), the  $M_2$  amplitude is reduced from 2.66 m in Fig. 2 to 2.01 m in Fig. 4. In addition, the tides are no longer so retarded at the edge of the shelf and phases and, as a result, are significantly earlier - by roughly 0.7 h - in the central coastal portion of the model region. The results of this simulation lend strong support to the original Flinders hypothesis of reef retardation leading to longshore lagoonal resonance - see also Ref. (9).

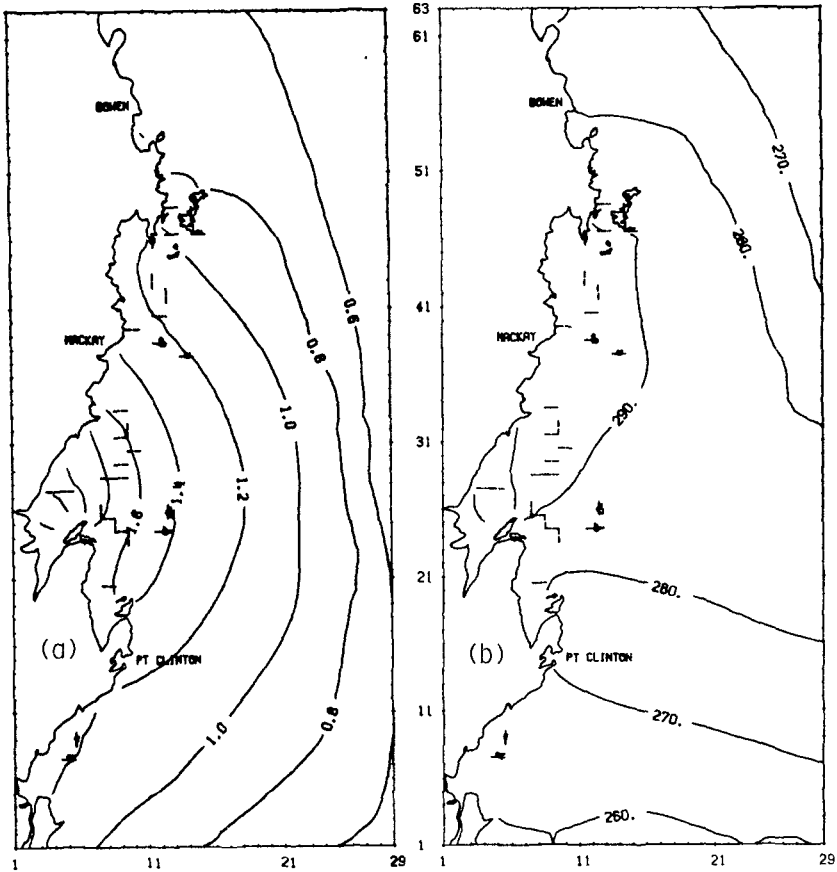


Fig. 4 As for Fig. 2 but without 'reef'.

#### STORM SURGE SIMULATION

In 1918 Mackay was hit by a tropical cyclone with an estimated central pressure of 940 mb. A significant component of the damage was due to the effects of storm surge (estimated at over 3.6 m at Mackay) and wave action, with the storm crossing the coast near the time of high tide. The combination of extreme winds and very high surge water levels devastated the town.



An engineering study of the effects of storm surges without tides at Mackay has been carried out previously - Ref. (5). In the present study, a simulated tropical cyclone of similar estimated magnitude to the 1918 storm is allowed to pass through the model region along the track indicated in Fig. 1. Altogether, a number of different simulations were effected, mainly to investigate the effect of the speed of forward movement and the phase of the storm relative to the tides, on the strength of the surge/tide interaction. The prototype storm, however, is identical to that used by Bode and Stark (3), although some recent modifications to the parameterisation of the wind stress field, suggested by Bode and Sobey (4) have been incorporated subsequently. The actual parameters governing the storm are detailed in Table II.

TABLE II  
PHYSICAL PARAMETERS GOVERNING THE SIMULATED  
TROPICAL CYCLONE OF THIS STUDY

Return Period	500 years
Central Pressure	940 mb
Ambient Pressure	1013 mb
Radius of Max. Winds	30 km
Track (Bearing)	255°
Speed of forward movement	30 kph
Simulation Time	- 10 h to + 1 h
Initial Grid Position	(30.9, 46.1)
Final Grid Position	(0.2, 28.4)
Build-Up Time	4 hours

As with the tidal modelling, the storm is built up in magnitude over a number of hours, in order to minimise the unwanted effects of initial transients. The landfall position and path (Fig. 1) have been designed deliberately to cause maximum enhancement of the storm surge in the region of maximum tides (Fig. 2). According to Sobey *et al.* (11), the maximum surge for Southern Hemisphere cyclones should be situated a distance of order  $R$ , the radius of maximum winds, to the left of the eye at landfall, looking along the track of the storm. Thus both maximum tides and surge should occur around the mouth of Broad Sound, and it is hypothesised that this should result in a very considerable surge/tide interaction, to be discussed in the following section.

Figs. 5(a) and (b) show storm surge water levels for the standard run, at times of one hour before and after landfall ( $t = -1$  and  $+1$ ) respectively. At the chosen point (5,29), the maximum surge is of order 4.3 m, although larger values are obtained farther up Broad Sound. Longshore currents are particularly intense and reach a maximum value roughly two hours prior to landfall ( $t = -2$ ), as shown in Fig. 6. Maximum currents at this time are of order  $1.7 \text{ ms}^{-1}$ , or roughly 3.3 knots.

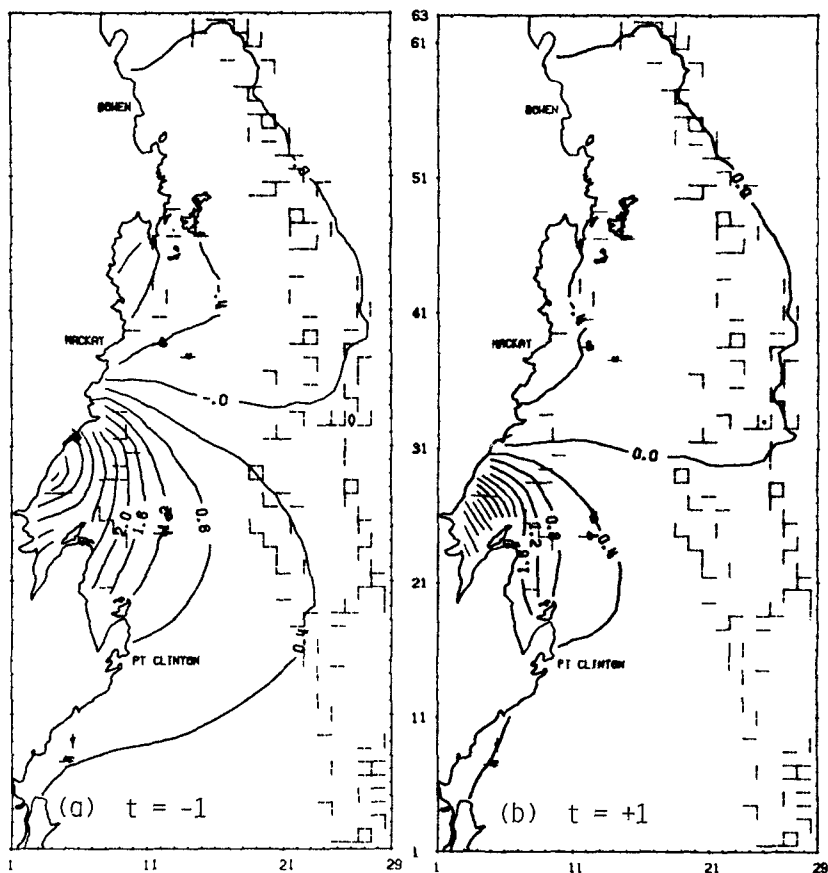
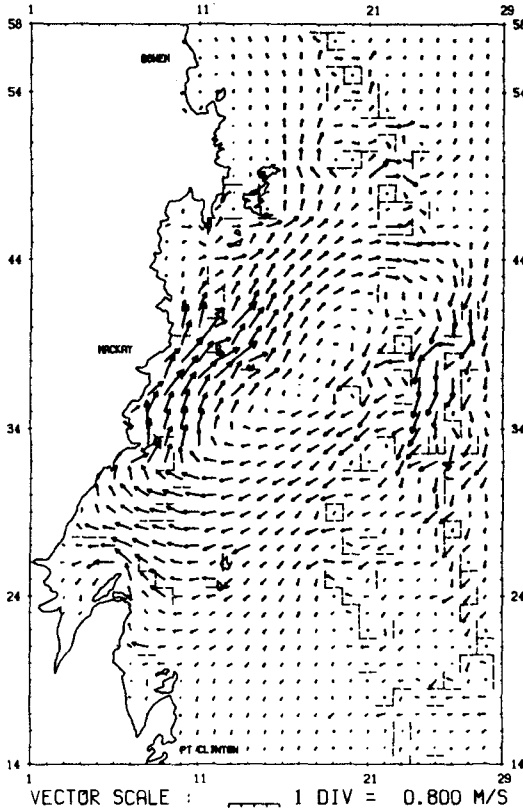


Fig. 5 Sea surface elevation (m) above MSL for surge alone at times (a)  $t = -1$  h and (b)  $+1$  h with respect to landfall.

Fig. 7 shows the results of the standard surge simulation, but without reef elements at  $t = -1$  - c.f. Fig. 4 for the corresponding tidal result. When compared with Fig. 5, it can be seen that, unlike the tides, storm surge water levels (and currents) are insensitive to the presence of even such dense reef structure as in the model region - see also Ref. (12). Apart from some minor differences, surge levels are almost unchanged by the absence of reef and peak levels are identical. Presumably, the transient nature of the rapidly moving cyclone, together with the intensely local nature of the forcing dictates such a response.



**Fig. 6** Depth-averaged currents for 'window' region at  $t = -2$ .

#### **SURGE/TIDE INTERACTION**

The calculations of the previous two sections have shown that both the storm surge and tidal phenomena have substantial magnitude, that are roughly of the same order. When this is considered along with the non-linearities of Eqs. (1)-(3), it would appear essential to consider the possible effects of surge/tide interactions. In other circumstances, this may not be necessary. For example, if the tide is the dominant effect, then it is possible to linearise the surge equation by appropriate techniques. Here, however, surge and tide are of the same order, but this presents no real difficulty with numerical modelling - boundary conditions and forcing terms from the individual simulations are added. The basic question is whether or not surge plus tide provided a sufficiently accurate estimate of the combined surge/tide simulation, and, if not, by how much does it under-estimate or possibly even over-estimate this?

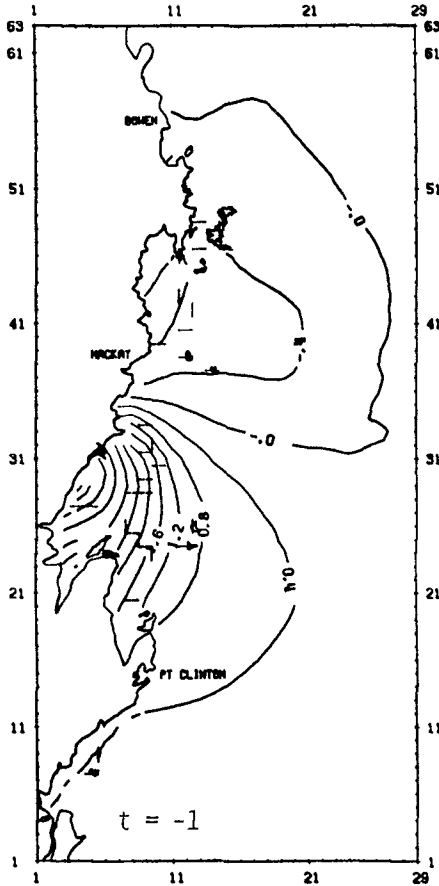


Fig. 7 As for Fig. 5(a) but without reef.

In spite of the above, there has been scant attention given to hurricane surge/astronomical tide interactions, although there are some good reasons for this omission. Hurricanes in the US impact predominantly in the Gulf of Mexico where the astronomical tide is negligible, and hence total water loads are basically provided by the storm surge alone. In the UK and Europe tides are quite significant, particularly in the North Sea region, which has been subject to a number of devastating storm surges (10). However storms are of the mid-latitude variety: they are almost always less intense and slower moving than hurricanes and

consequently differ considerably in their hydrodynamic response. The mid-latitude storm surge would appear also to be more amenable to analytical techniques. In this case, however, numerical modelling has demonstrated the importance of surge/tide interactions. Flather (5,8) has shown that surge hindcasts in the North Sea have been improved quite appreciably by joint consideration of the two effects.

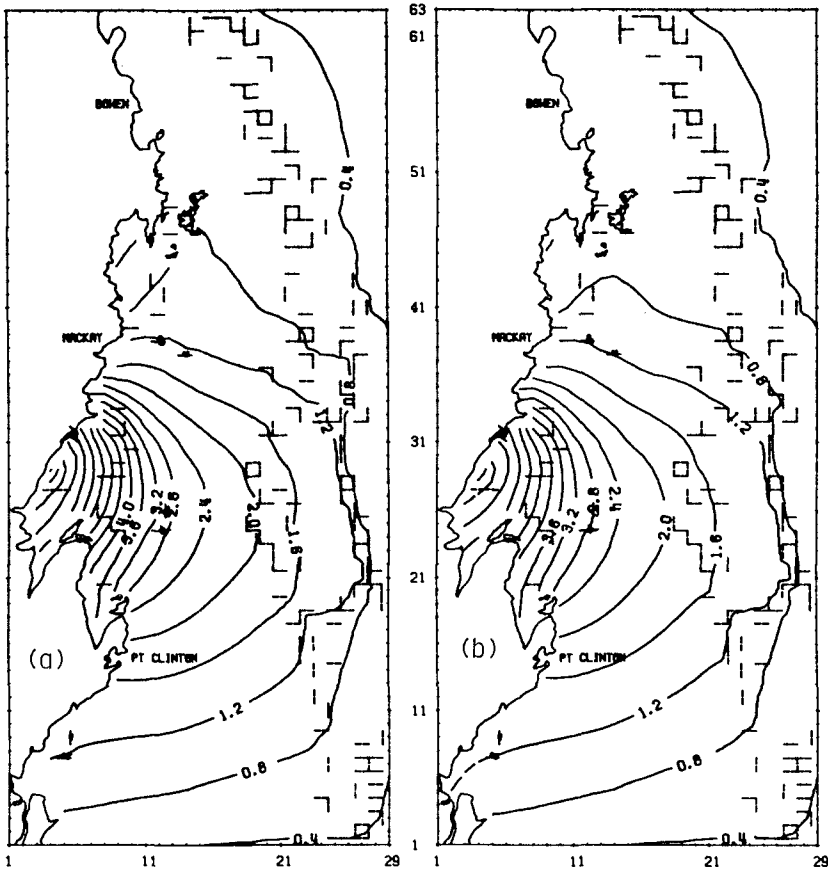
#### Theoretical Considerations

The essential non-linearity of the problem has also made it difficult to assess analytically. One approach that has managed some progress is that of Prandle and Wolf (10), through a combination of statistical, analytical and numerical techniques, that concentrated mainly on the (one-dimensional) response of the Thames Estuary to a North Sea surge. Here it has been observed that the net surge tends to peak on the rising tide but not at high tide. In addition, it appears possible in some circumstances for there to be surge *amplification* as well as a change in the phase of the surge (10).

There are two main non-linear terms in the equations of motion. In Eq. (1), these are the pressure terms  $(h+\eta)\partial\eta/\partial x$  and the quadratic bottom friction term. The first is affected by changes in the background water level and can be expected to change the propagation characteristics of a surface wave (its phase, principally), the second term is dissipative and is also affected by changes in water level - Eq. (1) - but the predominant effect is clearly due to the quadratic velocity term. Overall, the effect of a combined surge/tide might be expected to provide enhanced dissipation (by up to a factor of two!) if the surge and tide are of comparable magnitudes. An exception to this in one dimension is the case of opposing streams where the reduced dissipation may lead to possible surge amplification. An examination of the present two-dimensional case indicates that surge magnification would be most unlikely. In the case of a tropical cyclone storm surge, intense longshore currents (Fig. 6) are associated with the storm's passage across shallow continental shelf waters are . These provide a background against upon the quadratic friction term is applied, and the overwhelmingly likely result is a much higher dissipation rate with consequent damping in resultant elevation and current values. Prandle and Wolf (10) were able to show that the primary mechanism for surge dissipation was bottom friction; the pressure term had a negligible effect on surge levels, although, as noted above, the increase in background water level in the combined surge/tide case can result in higher wave celerities and consequent phase leads of peak surge levels. Both of these points are addressed below.

#### Results

Fig. 8 is a comparison of the sea surface elevations at 1 hour before landfall for the two cases: the sum of surge alone plus tide alone in (a) and the combined surge/tide simulation in (b). At the test position, grid point (5,29) the elevation at  $t = -1$ , which corresponds closely to the time of maximum surge, the elevations are 6.9 m and 6.1 m respectively. The marked reduction in total water levels for the combined simulation is apparent and is a most significant result.



**Fig. 8** Comparison of surface elevations (m) at  $t = -1$  for (a) Surge + Tide, (b) combined Surge/Tide simulations.

The net surge at  $t = -1$  is depicted in Fig. 9(a). This is obtained by subtracting the tidal elevation at  $t = -1$  from the combined surge/tide elevation at the same time. The elevation at (5,29) is 3.5 m. This result can be compared with the case of surge alone in Fig. 5(a) for which the corresponding elevation is over 4.3 m. An alternative representation is shown in Fig. 9(b) which is a 'window' view of the central portion of the model region - reefs are omitted for clarity, although they were retained in the simulation. This figure gives the

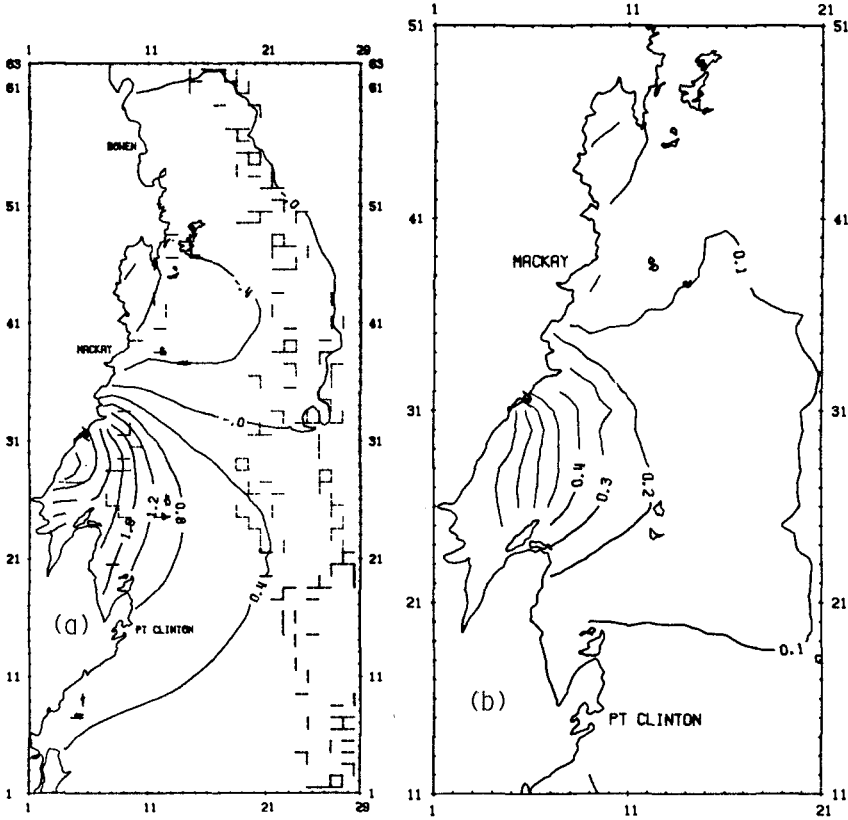
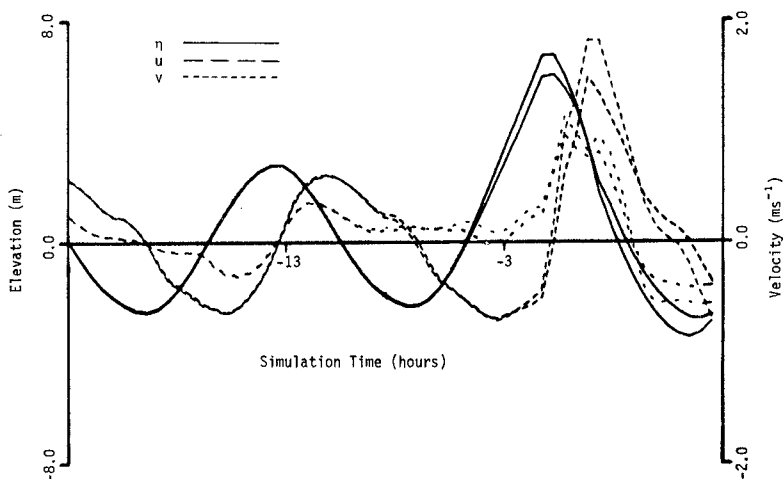


Fig. 9 (a) Net surge at  $t = -1$  for combined surge/tide; (b) Excess elevation (m) of surge plus tide over surge/tide at  $t = -1$ .

excess elevation obtained from the addition of surge plus tide at  $t = -1$  over the combined surge/tide elevations at the same time. This is obtained by subtracting the elevations of Fig. 9(a) from those of Fig. 5(a) and provides a measure of the extent to which the surge + tide result is conservative. Fig. 10 shows traces or time histories of the elevation and depth-averaged velocity components at (5,29). The chipping of the peaks is artificial and is due to the results of the numerical simulations being sampled much less frequently than the time step. Again, the reduction due to interaction, of both  $\eta$  and the velocity, particularly around the time of landfall, is clearly seen.



**Fig. 10** Traces of elevation and velocity components for surge plus tide and surge/tide simulations.

#### CONCLUSIONS

A number of important conclusions can be drawn from the present study. Firstly, the active role of the GBR chain in tidal amplification has been demonstrated. This is an unusual result, since elsewhere in the GBR Region, the reef appears to have a slightly dissipative effect on the tides, although in no way does it appear to act as a significant barrier. Here, by acting as a partial barrier to cross-shelf motion, longshore tidal streams are enhanced leading to an amplification, by the mechanism outlined. Storm surge levels, particularly for a track similar to that of the model storm of Fig. 1, would be very high in Broad Sound while longshore currents between there and Mackay would be of such magnitude as to cause significant changes to coastal morphology. The major result, however, is to show the significance of the surge/tide interaction. A reduction of total water levels of 1 metre is shown to be quite feasible and the corresponding economic and engineering implications warrant further attention in major coastal engineering studies.

#### ACKNOWLEDGEMENT

This work has been supported by a Marine Sciences and Technologies grant from the Australian Government.



## APPENDIX - REFERENCES

1. Bode, L., L.B. Mason, R.J. Sobey and K.P. Stark, "Hydrodynamic Studies of Water Movement within the Great Barrier Reef Region. I", *Research Bulletin No. CS27*, Dept. of Civil & Systems Engineering., James Cook Univ., 1981.
2. Bode, L. and R.J. Sobey, "Initial Transients in Long Wave Computations", *Journal of Hydraulic Engineering, ASCE*, Vol. 106, 1984.
3. Bode, L., and K.P. Stark, "Simulation of Tide and Currents in the Mackay Region", *Proceedings of the 6th Australian Conference on Coastal Engineering*, I.E. Aust., Gold Coast, 1983, pp.85-89.
4. Bode, L., and Sobey, R.J., "Hurricane Storm Surge", in *Tides and Surges*, B.J. Noye, editor, American Geophysical Union, 1985 (in press).
5. Flather, R.A., "Results from a Storm Surge Prediction Model of the North-West European Continental Shelf for April, November and December 1973", Institute of Oceanographic Sciences UK, Report No. 24, 1976.
6. Harper, B.A., Sobey, R.J., and Stark, K.P., "Numerical Simulation of Tropical Cyclone Storm Surge along the Queensland Coast - Part VIII Mackay", Department of Civil and Systems Engineering, James Cook University, 1977.
7. Harper, B.A., and R.J. Sobey, "Open-Boundary Conditions for Open Coast Hurricane Storm Surge", *Coastal Engineering*, Vol. 7, 1983, pp.41-60.
8. Heaps, N.S., "Storm Surges, 1967-1982", *Geophysical Journal of the Royal Astronomical Society*, Vol. 74, 1983, pp.331-376.
9. Middleton, J.H., Buchwald, V.T., and Huthnance, J.M., "The Anomalous Tides near Broad Sound", *Continental Shelf Research*, Vol. 3, 1984 (in press).
10. Prandle, D., and Wolf, J., "The Interaction of Surge and Tide in the North Sea and River Thames", *Geophysical Journal of the Royal Astronomical Society*, Vol. 55, 1978, pp.203-216.
11. Reid, R.O., and Bodine, B.R., "Numerical Model for Storm Surges in Galveston Bay", *J. Waterways Harbors Div.*, ASCE, Vol. 94, 1968, pp.33-57.
12. Sobey, R.J., Harper, B.A., and Stark, K.P., "Numerical Simulation of Tropical Cyclone Storm Surge", *Research Bulletin No. CS14*, Dept. of Civil and Systems Engineering, James Cook Univ., 1977.
13. Sobey, R.J., Harper, B.A., and Mitchell, G.M., "Numerical Modelling of Tropical Cyclone Storm Surge", *Civil Engineering Transactions*, I.E. Aust., Vol. 24, 1982, pp.151-161.

## CHAPTER SEVENTEEN

### HURRICANE SURGE PROTOTYPE DATA COLLECTION

Thomas H. Flor<sup>1</sup>, and Susan C. Scott<sup>2</sup>

#### INTRODUCTION

Storm surges from hurricanes have even more devastating effects on human lives and property than the high wind velocities associated with such storms. Storm surge forecasts are necessary as a guide for emergency action to prevent disasters due to coastal flooding caused by tropical storms. The design and evaluation of coastal structures are also dependent on estimates of storm surge levels. Several numerical models have been developed that appear to reasonably predict the surge from storms of given size and intensity, but they sometimes differ significantly among themselves. A comprehensive data set is needed to quantitatively evaluate these models. These data will also provide a better understanding of coastal processes during periods of severe wave activity and high water levels, and will better define coastal and inland water elevation time histories, high water marks, and water velocity fields caused by tropical storms and hurricanes.

The U. S. Army Engineer Waterways Experiment Station (WES), Coastal Engineering Research Center (CERC), under the sponsorship of the Office Chief of Engineers (OCE), has been involved for several years in a project entitled Hurricane Surge Prototype Data Collection Work Unit, the primary objective of which is to collect such a data set. In addition to the work being performed by CERC personnel, a cooperative program has been established with the Nuclear Regulatory Commission (NRC) and the University of Florida to collect surge data along the coast of Florida. A cooperative program has also been established with the National Ocean Service (NOS) to "harden" tide stations in the Gulf of Mexico and along the Atlantic Coast of Florida to survive hurricane forces and record the full range of anticipated surge levels.

This paper describes CERC's long term, ongoing Hurricane Surge Prototype Data Collection project, as well as the data collected.

<sup>1</sup>Physical Scientist, Coastal Engineering Research Center, U. S. Army Engineer Waterways Experiment Station, P. O. Box 631, Vicksburg, Miss. 39180-0631.

<sup>2</sup>Civil Engineer, Coastal Engineering Research Center, U. S. Army Engineer Waterways Experiment Station, P. O. Box 631, Vicksburg, Miss. 39180-0631.

## SURGE CHARACTERISTICS

The most destructive element of a hurricane is the storm surge. Simpson and Riehl (3) define it as "a shoal water process generated by hurricanes resulting in a superelevation due to a combination of direct wind driven water and an uplift induced by the pressure drop; together they reach maximum heights as the hurricane center arrives at an ocean or bay shore". In addition to the wind and pressure induced rise in water level, astronomical, secular and seasonal tides, freshwater runoff from heavy rains, and the outfalls from rivers and streams all have a hand in the creation of a massive still water platform. This platform can reach far inland to places that ordinarily would remain quite safe and dry.

The hurricane storm surge height,  $H_s$ , is a function of three principal sources of setup (Simpson and Riehl, 3):

$$H_s = f(S_b, S_w, S_v)$$

where,

$S_b$  = setup due to the dynamic inverse-barometer effect, and is concentric to the low pressure center

$S_w$  = setup due to the stresses from the irrotational component of the wind

$S_v$  = setup due to the stresses from the rotational component of the wind

$S_w$  is the major component of the surge in more protected areas, such as basins, bays, or estuaries; whereas,  $S_v$  is the major component of storm surge along the open coast.

When a hurricane reaches landfall at an open coast, its peak surge height will be larger with lower central pressures; with an increase in the radius of maximum winds up to 30 miles (48 km); with increased speed of coastal approach; and with a decreasing slope of the bottom surface from the beach seaward for a distance equal to the diameter of the maximum winds (1,3). Storm surges in bays and estuaries may be larger than those at an open coast by 50% or more for slow moving storms.

## HURRICANE SURGE DATA COLLECTION

The approach selected to provide a high quality, comprehensive data set was to develop rapidly deployable instrument packages that could be installed at preselected sites 24 to 48 hours before predicted landfall of a hurricane or tropical storm. To provide a sufficient quantity and quality of data, site surveys were undertaken approximately every 10 miles (16 km) along the entire Gulf Coast and the Atlantic Coast of Florida to select onshore locations for instrument deployment. More closely spaced sites were selected to provide

a better picture of the time histories of hurricane induced water levels in major bays and estuaries in the project area.

Selection criteria for the onshore sites were as follows:

- a. Smooth, flat terrain where possible, to minimize small scale effects on the storm surge measurements.
- b. Absence, or a minimal number, of man made or natural structures near the site that could influence propagation of surge, but would not be represented in numerical surge models.
- c. The existence of a structure on which to mount instrument packages that had a high probability of surviving a major hurricane.

Obviously, not many sites could meet the criteria exactly. The site selection process required numerous compromises in selecting locations that would both provide quality data and withstand the rigors of a severe storm. At this time, 265 sites have been selected and catalogued in Texas, Louisiana, Mississippi, Alabama, and Florida. These locations are depicted in Figure 1.

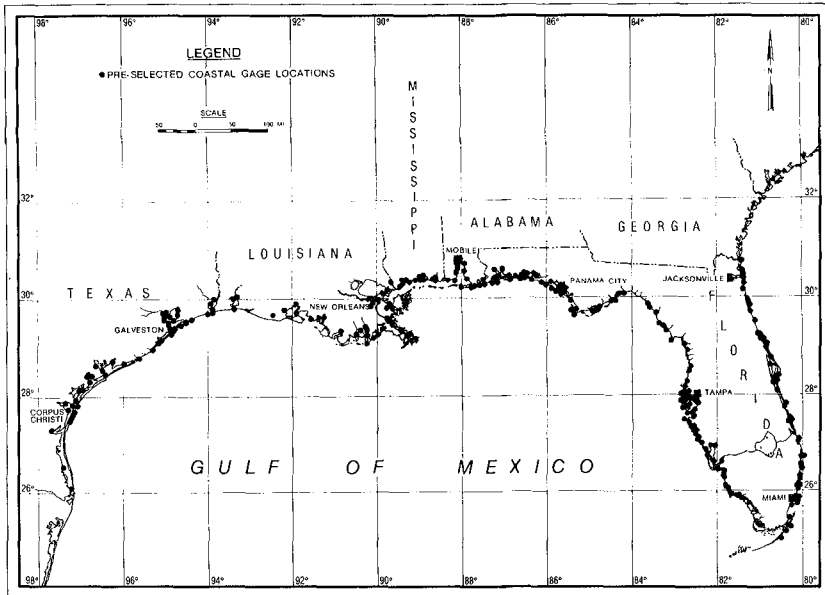


Figure 1. Preselected sites for onshore surge gages.

When a hurricane or tropical storm threatens the coast and the area most likely to be inundated is identified, water level instruments and mounting hardware necessary to occupy the preselected sites are loaded aboard a specially equipped deployment vehicle and the

field team proceeds to that area. The final decision on which preselected sites to occupy is made as more specific information on the expected point of landfall becomes available from the National Weather Service (NWS).

As soon as possible after landfall, the CERC field team recovers all instruments and surveys the area to delineate points of maximum inundation and the areal extent of hurricane induced flooding. The elevation of each instrument is marked and later tied into the National Geodetic Vertical Datum (NGVD) during post storm high water mark surveys.

In coastal areas without substantial structures on which to mount the instruments (e.g. south Louisiana), instrument packages are operated continuously throughout each hurricane season on available offshore structures. Three instruments are currently maintained on Shell Oil Company Platforms. These offshore sites are particularly useful since they provide surge data with virtually no small scale local effects from the coastal terrain, so that the data can be used in establishing boundary conditions in offshore areas. All three offshore sites are shown in Figure 2 as WES instruments.

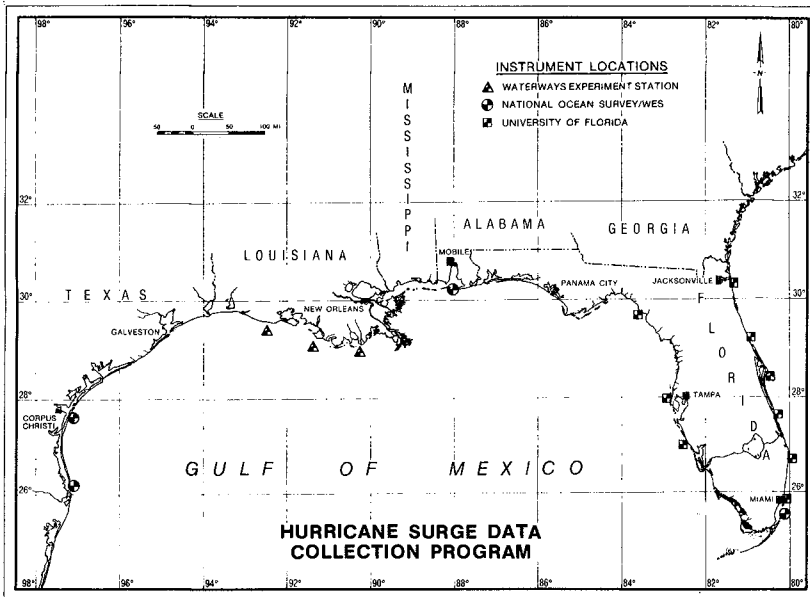


Figure 2. Permanent offshore surge gage sites.

Those instruments shown in Figure 2 as National Ocean Survey/WES sites are maintained as part of a cooperative effort with NOS. The sites in Miami, Dauphin Island, Alabama and Corpus Christi, Texas are NOS primary tide stations that have been "hardened" to survive hurricane conditions and contain a dedicated surge gage in addition to a

standard float-well type tide gage. The fourth NOS/WES instrument in Cameron County near the southern end of Padre Island was installed specifically for hurricane surge measurements. The nine University of Florida sites on the Atlantic and Gulf coasts of Florida are wave and surge gages maintained as part of a cooperative effort with the Nuclear Regulatory Commission and the University of Florida.

#### INSTRUMENTATION

In order to quickly deploy large numbers of instruments prior to landfall of a threatening hurricane, the instrument packages needed to be compact, rugged, and easily deployable by a 2-man team in a conventional size truck. Other desirable factors were: an independent power supply for continuous data collection throughout the storm, and digital recording capability to interface with existing data processing systems.

Twenty internally recording pressure sensors were acquired for this purpose. These instruments are microprocessor controlled data loggers which use a strain gage sensor to measure pressure at selectable time intervals and record data on small, continuous loop tape wafers. The submersible instruments can be quickly clamped to a bridge or pier pile.

For the sites at which a water level gage is maintained throughout each hurricane season, it was necessary to acquire instruments that could operate unattended for long periods and still collect data at short time intervals. Digitally recording wave and tide gages were selected to meet this requirement and to fulfill an additional objective, collection of wind generated wave data during a hurricane or tropical storm. These instruments sense pressure with a quartz crystal transducer and record both instantaneous wave heights and time integrated tide heights on four track data cassettes.

The hardened surge gages maintained by WES and NOS employ a gas purged pressure gage to measure surge due to tropical storms or hurricanes. Gas purged pressure gages, commonly known as bubbler gages, use a compressed dry gas, usually nitrogen, to activate a pressure sensitive diaphragm. Changes in water level are detected through an open-ended gas filled tube and recorded on a clock driven strip chart.

#### CORRECTION OF ABSOLUTE PRESSURE TIDE RECORDERS

Use of uncompensated pressure measuring sensors such as those employed at the preselected sites requires the data to be compensated for changes in atmospheric pressure during passage of the storm. A change of 1 mb in atmospheric pressure is approximately equivalent to a change of 1 cm in water level. Changes in atmospheric pressure of 50 mb are common during passage of a storm, consequently, it is essential such changes be taken into account when computing a hydrograph from uncompensated pressure data.

The simplest and most accurate means of compensating the pressure record would be to place a barograph near the tide gage; however,

this is seldom feasible both from logistic and economic standpoints. An alternative method is via an analytic model to interpolate in time and space using data observed elsewhere in the affected area. There are a number of models to choose from, some developed from theoretical considerations, others by empirical best fit to the smoothed pressure profiles of several hurricanes.

The model found to give the best fit to the observed data for previous hurricanes is:

$$\frac{P - P_0}{P_\infty - P_0} = C (\text{Arctangent } r/R)$$

where

- P - pressure to be computed
- $P_0$  - central pressure of storm
- $P_\infty$  - far field pressure
- R - radius to maximum winds
- r - distance from storm center at which pressure is to be computed
- C - constant

## RESULTS

Since the Hurricane Surge Data Collection program was initiated in 1980, Hurricane Alicia (August 1983) gave the CERC field team its first opportunity to use the technique described under actual hurricane conditions. Alicia was the first storm of the 1983 hurricane season and the first to make landfall in the continental U. S. since Allen in August 1980. Hurricane Alicia was unusual in that it developed in the central Gulf of Mexico and made landfall less than 2 days after showing signs of becoming a significant storm. Alicia was classed as a minimal category 3 at landfall on the SAFFIR/SIMPSON scale, which ranges from one to five.

Alicia was declared a hurricane at 0000 GMT 17 August 1983 with a central pressure of 991 mb and maximum sustained winds of 75 mph (120 kmph). The hurricane continued to intensify until it made landfall at the western tip of Galveston Island, Texas at approximately 0700 GMT 18 August. Its central pressure at that time was 963 mb with maximum sustained winds close to 115 mph (185 kmph).

The staff of CERC had been closely monitoring Alicia's development, when it became evident at 1700 GMT on 16 August that the storm was rapidly deepening, the field team was sent to the Houston-Galveston area, arriving at daybreak on 17 August. Galveston Island by this time was being evacuated. Since coastal water levels had already risen and the sea state was high, it was not possible to deploy onshore gages along the gulf side of Galveston Island and lower Galveston Bay. Information from the National Hurricane Center

at the time indicated the storm would make landfall between Corpus Christi and Freeport, Texas. The field team thus departed from the Houston-Galveston vicinity for the Matagorda Bay area. Enroute, the team deployed one gage package at Baytown, Texas near the head of Galveston Bay, in the event that Alicia turned northward as it later did.

In the time remaining before landfall, the field team deployed gage packages at Port Lavaca and Palacios, Texas in the Matagorda Bay area. At 0300 GMT, 18 August, approximately four hours before landfall, the field team retreated to Houston to wait out the storm.

Hurricane Alicia made landfall at the western tip of Galveston Island, traveled northward and was classified as a tropical depression after moving past Houston at 0600 GMT 19 August.

After the passage of the storm, the field team returned to the Galveston area to recover the instrument packages and begin a survey of high water marks.

The final compiled data set was obtained from a variety of sources including gage records from the Corps of Engineers, National Ocean Service, and private corporations.

The data set contains:

- a. Maximum water elevations from post-storm high water mark surveys.
- b. Histories of the time averaged water level at both coastal and inland locations.
- c. Areal extent of inundation.

Table 1 lists the gage location, responsible agency or institution for data, maximum water elevation, time and date, and reference datum. Figure 3 shows the locations of instruments that recorded water level data in the Galveston Bay area during hurricane Alicia.

Hydrographs at the Pleasure Pier and Pier 21 in Galveston (Figures 4 and 5) show the peak of the surge coincided with the predicted high tide. Assuming the tide and surge effects were linearly superimposed, the surge relative to the predicted tide was about 7.4 ft (2.25 m) at the Pleasure Pier on the ocean side and 4.9 ft (1.5 m) at Pier 21 on the bay side of Galveston Island. At Freeport, Texas, there were three peaks, two on 17 August, one day prior to landfall and one approximately coinciding with landfall. The three peaks were about 2.9 ft (0.88 m), 3.1 ft (0.94 m), and 2.5 ft (0.76 m) relative to the predicted tide. The highest surge value did not occur at landfall because Freeport was on the "backside" of the storm, i.e., the winds at Freeport were primarily offshore at the time.

As shown in Figure 3, the Pier 21 and Pleasure Pier gages are located quite close to one another and the hydrographs reflect this. The Hanna Reef gage, located on the opposite side of the bay, shows a



Table 1

<u>Location</u>	<u>Agency</u>	<u>Maximum Elevation ft (m)</u>	<u>Time CDT</u>	<u>Datum</u>
Freeport, TX	NOS	4.0 (1.22)	0630/17/08/83	NGVD
Pleasure Pier, Galveston, TX	NOS	9.0 (2.74)	0130/18/08/83	NGVD
Pier 21, Galveston, TX	NOS	5.8 (1.77)	0200/18/08/83	NGVD
Fort Point, Galveston, TX	CE	6.2 (1.86)	0200/18/08/83	NGVD
Seabrook, TX <sup>1</sup>	CE	8.5 (2.59)	0430/18/08/83	NGVD
T-14, Baytown, TX	CE	6.1 <sup>2</sup> (1.86)	0245/18/08/83	NGVD
Baytown Refinery, TX	EXXON Corporation	10.2 (3.11)	0730/18/08/83	MSL
Anahuac, TX <sup>2</sup>	Texas State Water Resources Board	8.0 <sup>2</sup> (2.44)	0800/18/08/83	NGVD
Hanna Reef, TX <sup>1</sup>	CE	6.0 (1.83)	0400/18/08/83	NGVD
Sabine Lake, TX <sup>1</sup>	CE	4.1 (1.25)	1400/17/08/83	NGVD
Calcasieu Pass, LA	CE	4.0 (1.22)	1600/17/08/83	NGVD

NOS - National Ocean Service

CE - Corps of Engineers

1. Time of peak surge estimated.
2. Incomplete hydrograph, see text.

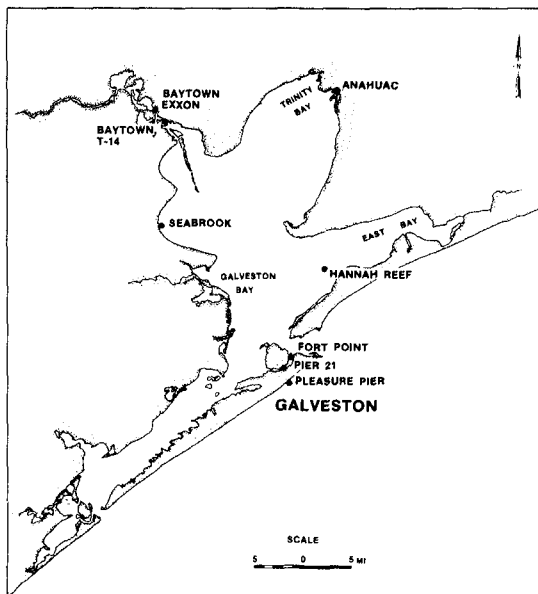


Figure 3. Tide gages operating in the Galveston Bay area during hurricane Alicia.

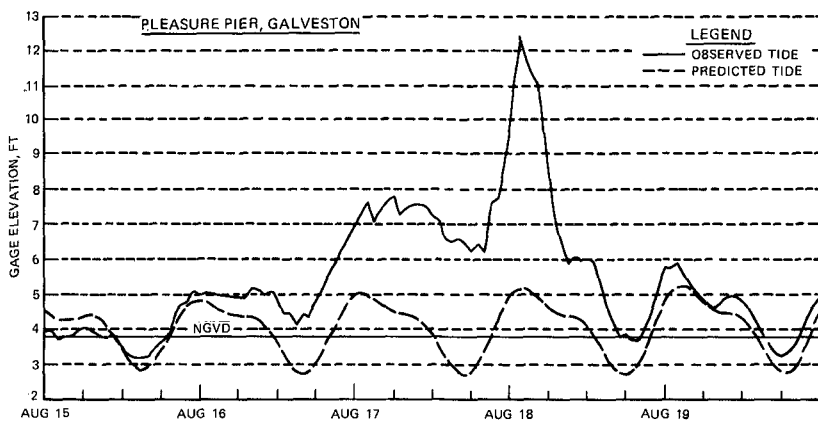


Figure 4. Hydrograph from NOS tide gage at the Pleasure Pier in Galveston.

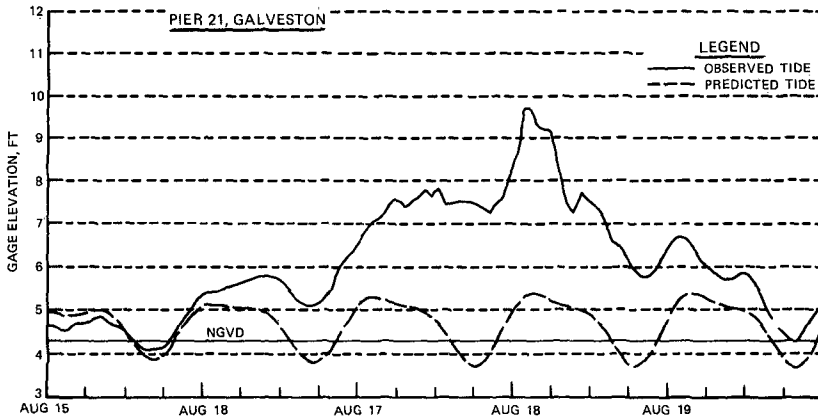


Figure 5. Hydrograph from NOS tide gage at Pier 21 inside the entrance to Galveston Bay.

broader peak followed by a relatively long tail. The broader peak and slower fall in water level were probably caused by waters that had been blown into the northwest reaches of the bay by the predominantly southeast winds during the storm flowing back into the Hanna Reef area after the storm had passed.

The gage at Anahuac recorded until submerged; attempts were made to determine a high water elevation nearby but the adjacent land is flat and featureless and overgrown with scrub vegetation.

The data obtained at the EXXON Corporation Baytown Refinery are a combination of readings from a strip chart recorder and digital readout. The strip chart recorder had a maximum excursion corresponding to about eight ft elevation. The water level sensor continued to function normally driving a remote readout from which surge heights were logged manually. The maximum surge recorded at the Baytown Refinery agrees very closely with nearby high water marks.

The CERC field team deployed two surge packages in Matagorda Bay, one at Port Lavaca and one at Palacios, Texas. Data from these gages showed no significant departure from the expected tide during passage of the storm. This is not unexpected as these gages were on the "backside" of the storm about 70 miles (112 km) from the point of closest approach.

The CERC gage T-14 functioned until about 0300 CDT 18 August when it failed. The cause of the failure was determined to be a defective pressure case which allowed water into the electronic circuits.

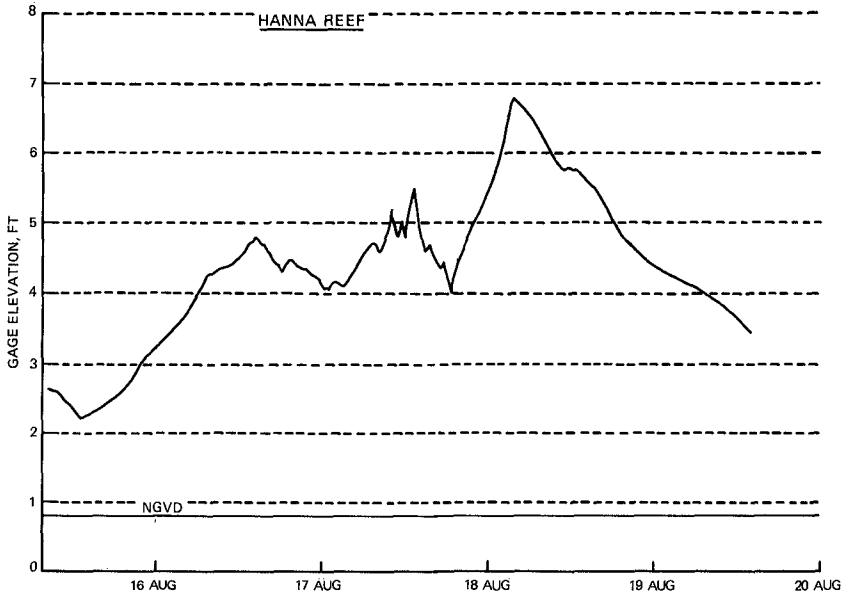


Figure 6. Hydrograph from tide gage at Hanna Reef in Galveston Bay.

#### POSTSTORM SURVEY OF HIGH WATER LEVELS

A poststorm visual survey of high water marks was made from Matagorda Bay east to High Island, Texas, including the shoreline of Galveston Bay, during the period 21-23 August 1983. The westernmost extent of surge induced flooding appeared to have been in the vicinity of Sargent, Texas at the eastern end of Matagorda Bay. Coastal flooding in this area, due to storm surge and wave setup, overtopped the low berm on the beach and built numerous washover fans on vegetated wetlands between the beach and a high man-made dune along the Intracoastal Waterway. The surge generated component of this rise in water level appeared not to exceed +3 ft (0.9 m) NGVD. Debris lines along the banks of the Intracoastal Waterway indicated a rise in water level of approximately +2 ft (0.6 m) NGVD.

At the U. S. Coast Guard Station in Freeport near the mouth of the Old Brazos River, high water overtopped a low bulkhead approximately 3 ft (0.9 m) above the normal water line but caused minimal flooding of the station itself. On Follets Island, located between Freeport and San Luis Pass, highwater overtopped highway 257 which is at an elevation of +8 ft (2.4 m) NGVD and caused numerous cuts through the dunes and sections of the roadbed. As described by Savage et. al., (2), these cuts were formed by highwater flowing from

Christmas Bay across the barrier island and out into the Gulf. The entire eastern tip of Follets Island at San Luis Pass appeared to have been inundated by the surge.

Between San Luis Pass and Jamaica Beach, 10 miles (16 km) to the east, the surge exceeded +9 ft (2.7 m) NGVD, overtopping Highway 257, the highest point on the western end of Galveston Island. Residences in this area exhibited extensive damage primarily from wind action. The total rise in water level reached approximately +11 ft (3.4 m) NGVD in Jamaica Beach and tapered to about +7 ft (2.1 m) NGVD near the western end of the Galveston seawall. Water levels rose from both the Gulf of Mexico and East Bay sides on this portion of the island but did not exceed the elevation of the coastal highway.

In the city of Galveston the storm surge did not exceed the +15 ft (4.6 m) NGVD elevation of the seawall. Storm damage was limited to wind damage, some wave overtopping of the seawall and flooding of low lying areas near the causeway on the bay side. At East Beach, seaward of the Galveston seawall, the surge reached approximately +7 ft (2.1 m) NGVD, causing extensive damage to residences and commercial buildings and leaving large debris piles at the base of the seawall. Surge levels on the Bolivar Peninsula reached +7 to +8 ft (2.1 to 2.4 m) NGVD between the western end of the peninsula and Crystal Beach, rising from both the Gulf and Bay sides of the peninsula but failing to inundate Highway 87 and many homes built on high ground along the highway. At High Island, 50 miles (80 km) east of the point of landfall, the surge reached +4 to +5 ft (1.2 to 1.5 m) NGVD flooding extensive low lying marsh areas and depositing large amounts of sand on Highway 87.

At Virginia Point, just north of Galveston Island, the surge covered the Gulf Freeway up to approximately +7 ft (2.1 m) NGVD, cutting off access to the island during the height of the storm. The Texas City Dike was overtopped along most of its length but the Texas City Levee system protected the city from surge induced flooding. The surge along this section of the bay is estimated to have been between +7 and +10 ft (2.1 and 3.0 m) NGVD. At Seabrook, 15 miles (24 km) north of Texas City, the storm surge reached approximately +9 ft (2.7 m) NGVD, the water level remained considerably higher than normal in this area for at least 3 days after landfall.

High water marks at Baytown indicated a surge at the north end of Galveston Bay of approximately +10 ft (3.0 m) NGVD. The water level in this area rose 3 to 4 ft (0.9 to 1.2 m) above normal by the morning of 17 August 1983 and remained several feet higher than normal for at least 3 days after landfall. East of Baytown, in the Houston Point area, the shoreline is backed by bluffs 15 ft to 20 ft (4.5 to 6.0 m) high which prevented significant surge damage. No distinct highwater marks were located in this area.

The maximum water level at Anahuac, in the northeast corner of the bay exceeded +8 ft (2.4 m) NGVD, flooding a Texas Water Resources Board recording tide gage. The topography in this area is flat and low lying, allowing the surge to propagate north past the Interstate 10 crossing of the Trinity River 7 miles (11 km) north of Anahuac.

Debris along the I-10 causeway indicated a surge level near +10 ft (3.0 m) NGVD. At Smith Point, 15 miles (24 km) south of Anahuac, high water marks in a county park indicated a rise in water level of approximately +5 ft (1.5 m) NGVD. Smith Point and the bay shoreline to the east are low lying wetland areas that were inundated by the surge except for high ground along Highway 562 and isolated highspots 5 to 10 ft (1.5 to 3.0 m) above NGVD.

#### FUTURE PLANS

While much of the coastline presently encompassed by the study is either accessible from inland or has some offshore structure suitable for semi-permanent instrumentation, there are some lengthy reaches where the only feasible means of data acquisition is by use of a temporarily deployed offshore device. To address this need, WES, with the assistance of the U. S. Army Research and Development Center, Natick, MA, has under development an air deployable wave/surge gage. The primary goal of this effort is the development of a launch vehicle and the methodology to successfully deploy the device from a C-130 type aircraft. Presently, the system is designed to accommodate acoustic or electromagnetic type water level and current meters.

In October, 1983, an agreement was reached with the National Hurricane Center (NHC) to provide manpower and equipment (trucks, helicopters, etc.) to deploy surge gages when a storm threatened the South Florida coastline. Since storms tend to travel parallel to the south Florida coast, a small error in predicted track can translate to a large error in point of landfall. The assistance of supplemental field teams allows coverage of a greater reach of coastline thereby increasing the probability that the storm will be intercepted.

Hopefully, more joint programs with District CE offices can be established to provide additional benefits to the surge data collection effort. Two field teams and twenty instrument packages will be maintained in a state of readiness for the next 3 to 4 hurricane seasons to collect data from any hurricane making landfall on the U. S. Gulf Coast. Individual data reports for each storm will be published by CERC.

#### ACKNOWLEDGEMENTS

This paper was prepared as part of the Hurricane Surge Prototype Data Collection Work Unit, Coastal Flooding and Storm Protection Program, Coastal Engineering Area of Civil Work R&D. The work unit is a multiyear project of the U. S. Army Engineer Waterways Experiment Station, Coastal Engineering Research Center. The authors wish to acknowledge the Office, Chief of Engineers, U. S. Army Corps of Engineers, for authorizing publication of this paper.

Additional thanks go to Mr. Andrew Garcia, principal investigator of the Hurricane Surge Prototype Data Collection Work Unit, and Ms. Joe Ann Green, Ms. Mary M. Logan and Mr. Toby Wilson for their assistance.

## REFERENCES

1. JELESNIANSKI, C. P. 1972. SPLASH (Special Program to List Amplitudes of Surges from Hurricanes): 1. Landfall Storms, Technical Memo II NWS TDL-46, National Weather Service, NOAA, Rockville, MD.
2. SAVAGE, R. P., BAKER, J., GOLDEN, J. H., KAREEM, A., and MANNING, W.R. 1984. Hurricane Alicia, Galveston and Houston, Texas, August 17-18, 1983, Committee on Natural Disasters, National Academy of Sciences, National Academy Press.
3. SIMPSON, R., and RIEHL, H. 1981. The Hurricane and Its Impact, Louisiana State University Press, Baton Rouge.

## CHAPTER EIGHTEEN

### Hurricane Alicia Storm Surges And Shore Processes

R. P. Savage\*

#### Abstract

Hurricane Alicia moved inland over the Texas coast during the night of August 17, 1983 creating waves and surges in the Gulf of Mexico and adjacent bays. Waves eroded beaches and dunes and surges overtopped low-lying areas of barrier islands and inland areas adjacent to the bays behind the barriers. A three-day survey of field evidence of water levels and flow directions was carried out one week after the storm. Physical evidence, such as the elevation of debris lines, water marks in buildings and debris caught on fences was used along with additional data from tide gages operating in the area to estimate the maximum flood levels and flow directions associated with the storm. Before and after aerial photography was used to obtain data on beach recession, retreat of the vegetation line behind the beach and extent of overwash deposits. The evidence gathered shows that the barrier islands were overtopped from front-to-back in some areas and from back-to-front in other areas with quite different results. There was little or no beach erosion to the left of the storm as it came ashore; however, serious beach erosion occurred for 18 miles (29.0 km) to the right of the storm and there was significant erosion for 55 miles (88.5 km) to the right of the storm. Maximum water levels in the Gulf, including the effects of normal tides and storm effects, were 9 to 11 feet (2.74 to 3.35 m) and maximum water levels along the northern portion of Galveston Bay were 11 to 14 feet (3.35 to 4.27 m).

#### Introduction

Hurricane Alicia made landfall near the western end of Galveston Island (Figure 1) during the predawn hours of Thursday, August 18, 1983. At landfall, the storm was a little above average in size and intensity with highest winds near 100 miles per hour (44.73 m/sec-ond). The area of high winds covered most of Galveston Island and extended eastward along Bolivar Peninsula. High storm water levels and waves overtopped western Galveston Island, Galveston's East Beach and the front of western Bolivar Peninsula. Surges also created high water levels in the bays behind the islands. Waves and surges modified beaches and dunes creating overwash deposits and cutting channels through dunes. This paper presents and discusses field and other evidence of the magnitude and effects of Alicia's waves and water levels.

\* Member, 8300 Kingsgate Rd., Potomac, MD 20854



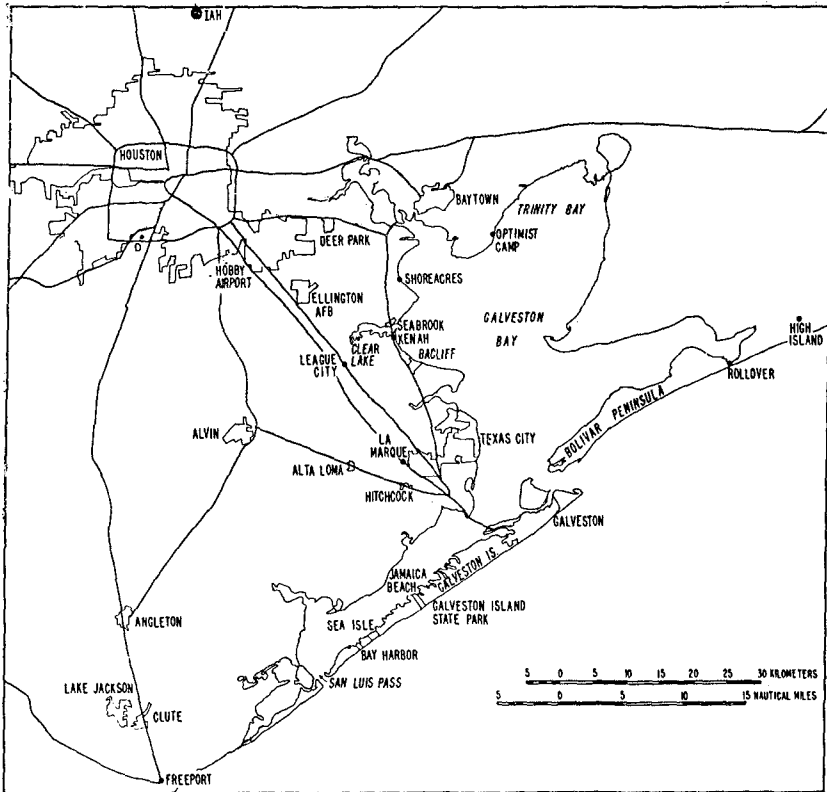


Figure 1. The Houston - Galveston area of Texas

### Data Collection

#### Storm Water Levels

Water level estimates were obtained from field evidence gathered during a field survey on 23, 24 and 25 August (Savage et al. 1984). Field observations included water marks in buildings, debris lines, beach and dune changes, overwash deposits and scour marks. Unless otherwise noted, all elevations refer to the National Geodetic Vertical Datum (NGVD).

Watermarks in closed buildings are good indicators of maximum water levels that do not include the effects of wave action. However, during the field survey, watermarks were difficult to distinguish, probably because the flood waters contained little or no sediment. No water marks were observed on the outside of buildings, and water

marks inside buildings were composed of bits of vegetation, including seeds. Debris lines, usually composed of loose vegetation, were common and were usually a clear, though not precise, indicator of maximum water level. Where their height spanned the flood level range, fences were also a good indicator of maximum water level because bits of floating vegetation were caught by the individual fence strands. Thus the line between bare and "clothsline" strands clearly indicated the maximum water level. Estimates of water levels from water marks, debris lines and fences were made by visually estimating the distance of the evidence above the ground level. The elevation of the ground level was obtained from the 7.5 minute series of topographic quadrangle sheets (quad sheets) published by the U. S. Geological Survey (USGS). Maximum water level estimates are probably accurate to plus or minus 1.5 feet (0.46 m). Water level estimates were also obtained from operating tide gages. NOAA maintains two gages in the immediate Galveston area and other gages at Freeport and Sabine Pass, however the Sabine Pass gage did not operate during Alicia's landfall. Other gages, operated by companies, The Corps of Engineers, and Civil Defense Offices were operating in the area affected by the storm (U. S. Army Corps of Engineers, Galveston District, 1984).

#### Shore Processes

Estimates of horizontal beach, dune and vegetation line changes were obtained from aerial photographs taken before and after the storm by NOAA. The "before" set (nominal scale 1 to 40,000) was taken on October 15, 1982 and November 5, 1982. The "after" set (nominal scale 1 to 30,000) was taken on August 24, 1983, seven days after storm passage. Ground measurements between points visible on the aerial photographs were made from Geological Survey (GS) quadrangle sheets and used to establish scales for individual photographs. Data was scaled from the photographs along selected lines, usually along streets perpendicular to the beach, using a scale divided into 600 parts/foot (1962 parts/m). Though individual measurements were estimated to a tenth of the smallest division, ground distance errors as large as plus or minus 30 feet (9.14 m) are possible. Measurements were made from the cross street nearest the beach to the feature of interest. Horizontal features measured were the high water line, the vegetation line just behind the beach and the scarp line where a scarp existed.

#### Storm Water Levels and Flow Patterns

Maximum water levels along the Gulf side of Galveston Island varied from 9 to possibly 11 feet (2.74 to 3.35) above NGVD. The NOAA tide gage on Pleasure Pier recorded a maximum water level of 9.0 feet (2.74 m) at 1:24 a. m. Central Standard Time (CST), August 18th (Figure 2). Since the peak of the storm surge occurred at high tide, which should have been at el. 1.7 feet (0.52 m), the storm surge portion of the high water level was about 7.3 feet (2.23 m). Observations along the front of Galveston Island during the field survey showed considerable overtopping of East Beach (a 3.5-mile (5.6 km) beach fronting the Galveston seawall just west of Galveston Inlet)

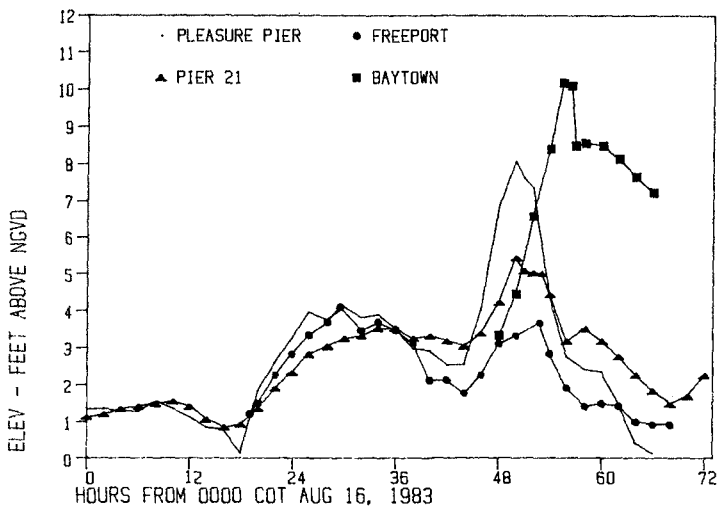


Figure 2. Tide hydrographs from gages at Baytown, Pleasure Pier, Pier 21, and Freeport during Hurricane Alicia. The reference level for the Baytown gage is mean sea level.

and the western portion of Galveston Island all the way to San Luis Pass. Maximum water levels along the back of Galveston Island varied from 6 feet (1.82 m) to as much as 9 feet (2.74 m). The NOAA tide gage on Pier 21 in Galveston Channel (behind Galveston) recorded a maximum water level of 5.8 feet (1.77m) at 2:12 a. m. CST on August 18th (Figure 2). Observations along the back of Galveston Island indicated that the maximum water level was generally not more than 1 to 2 feet (0.31 to 0.62 m) above the land level - estimated at 5 to 7 feet (1.52 to 2.13 m) from quadrangle sheets. Maximum water levels along the back of the island increased from about 6 feet (1.82 m) at the eastern end of the island to about 9 feet (2.74 m) 3 miles (4.8 km) east of San Luis Pass. To the west, water level elevations exceeded 10 feet (3.05 m) in the bays behind Follets Island.

Along the front of East Beach, the beach was overtopped by 2 to 4 feet (0.62 to 1.24 m) of water which then flowed landward toward the seawall. When the overtopping water reached the seawall, it turned eastward and ran over the shoreward part of the north jetty into Galveston Inlet. The higher dunes on the front of East Beach were not overtopped, but were partially eroded while acting as headlands that created accelerated flow and scour channels in low areas between dunes (Figure 3). Observations along the front of Galveston Island west of the seawall showed that the front of the island had been overtopped by a foot (0.31 m) or more of water along most of the island length. Two areas not overtopped, a half-mile (0.8 km)



Figure 3. View toward Gulf showing channel cut by overtopping Gulf water on East Beach. Note vegetation along back of beach, showing cut did not extend through beach, and beginning of outwash fan that forms the landward end of the cut.

section about one-half mile (0.8 km) east of Galveston Island State Park and a two and one-half mile (4.0 km) section eastward from Sea Isle (Figure 1), had dunes higher than 10 feet (3.05 m) in elevation. In other areas, debris lines on fences and against embankments and dunes along the highway indicated maximum Gulf water elevations of 8 to 11 feet (2.44 to 3.35 m), including the effects of wave action. Evidence of water flow across the body of the island from the bay toward the Gulf began about 3 miles (4.8 km) east of San Luis Pass. Otherwise, all evidence pointed to water flow from the Gulf toward the bay.

Follets Island is immediately west of Galveston Island across San Luis Pass. Only the eastern eight and one-half miles (13.7 km) of this island were covered by the ground survey. In this area, flow evidence was remarkably consistent - water flowed only from the bays toward the Gulf. Maximum water elevations in the bays were about 10 feet (3.05 m) or more. Maximum water level evidence consisted of debris lines on the bay side of the dunes at distances of 1.5, 2.0, 4.5, 7.5 and 8.5 miles (2.4, 3.2, 7.3, 12.1 and 13.7 km) from the eastern end of the island and a stranded houseboat between the highway and the dunes fronting the Gulf at the 4.5 mile (7.3 km) point. Evidence for flow direction was the location of debris lines on the bay side of the dunes, the location of the grounded houseboat and the characteristics of several cuts through the dunes and body of the island between the highway and the Gulf (Figures 4-6).



Figure 4. Aerial view of cut formed by Gulfward flowing water on Follets Island.

These cuts started at the beach and ended seaward of or at the highway; however, one cut extended completely through the highway and other cuts ended in the highway pavement (Figures 4 & 6).

Bolivar Peninsula lies eastward across Galveston Inlet from Galveston Island. Only the first 11 miles (17.7 km) of the Peninsula were surveyed during the ground survey. The 3 miles (4.8 km) of the island immediately east of Galveston Inlet is low with maximum elevations of 6 feet (1.83 m) or less. East of this point, a relic dune ridge rises near the middle (front-to-back) of the island and extends eastward to Caplen (1.5 miles (2.4 km) west of Rollover Pass - Figure 1) where the dune ridge joins the dunes behind the beach. Maximum elevations of the dune ridge vary from 9 to 11 feet (2.74 to 3.35 m). Debris lines on fences, scour adjacent to the highway and the way the grasses were bent showed that the first 5 miles (8.1 km) of the road along the Peninsula had been overtopped by water flowing from the Gulf toward the sound. Evidence of overtopping ended abruptly where the road rose from the lower elevation to cross and run behind the relic dune ridge. Thus, water levels in the Gulf along the western part of Bolivar Peninsula were higher than 6 feet (1.83 m), but lower than 10 feet (3.05 m).



Figure 5. Gulfward view of Follets Island cut showing erosion of dunes behind beach. Highway pavement is in foreground.



Figure 6. Landward end of a Follets Island cut showing undercutting of road pavement.

Study of the aerial photographs of Bolivar Peninsula taken after the storm showed that the front of the western 17 miles (27.4 km) of the Peninsula had been overtopped by the Gulf storm surge. Though water flowed across the western 3 miles (4.8 km) of the Peninsula, the relic dune ridge running from the center (front-to-back) of the Peninsula at the 3-mile (4.8 km) point to the beach at Caplen caused the overtopping water to pond between the Gulf frontal dunes and the relic dune ridge. When the water level in the Gulf dropped, the ponded water flowed back into the Gulf through a series of low points (at least 4) in the frontal dunes creating cuts across the beach and through the frontal dunes similar to those on Follets Island (Figure 4). However, the cuts were different in that they were triangular - wide at the beach and narrow inland - presumably because the cutting flow rates diminished as the level of the ponded water level dropped.

Only two mainland areas adjacent to Galveston Bay were covered by the ground survey - Seabrook and the Texas City hurricane flood protection dike, both on the western side of the Bay. The debris line on the Texas City dike was low on the front of the dike indicating maximum water levels there of about 5 feet (1.52 m). At Seabrook, along Todville Road, scour in the yards of houses and damage to structures showed water levels had been at least 3 feet (0.93 m) above the ground level. In the Baytown area, tide gage records (Figure 2) and debris line measurements showed maximum water levels of 10 to 11 feet (3.05 to 3.35 m).

#### Shore Processes

A total of about 70 miles (112.7 km) of coastline are covered by the aerial photograph measurements; about 55 miles (88.6 km) to the east (right) of the storm and about 15 miles (24.2 km) to the west (left) of the storm. No measurements were made in front of the Galveston seawall or just east of Galveston Inlet. Results of the measurements are presented in Table 1 and Figures 7-9 where the inland direction is positive. Change in the high water line and vegetation line is shown in columns 2 and 3 of Table 1 for the distances in column 1. Columns 4 and 5 contain data only where a beach or dune scarp existed after the storm. The change in high water line (column 2) is a rough measure of beach retreat during the storm. The measure is rough because the data (aerial photographs) were taken about a year apart and some of the change may have occurred before the storm. In addition, the measurement technique could result in errors of 50 feet or more in the change figures. The meaning of the change in the vegetation line (column 3) varies with conditions after the storm at the measurement point. In overwash areas the change in the vegetation line measures the magnitude of both erosion and overwash. Where there was beach and dune erosion that ended in a scarp, the change in the vegetation line is a measure of the beach and dune recession (column 4). In some areas overwash deposits extended inland from scarps. In these cases, the horizontal magnitude of both the beach and dune erosion and the overwash deposits (column 5) were defined.

# HURRICANE ALICIA

265

TABLE 1. Changes in Beach and Nearshore Features From High Island  
Westward to Freeport Inlet.

Location	Distance From Storm Center-Miles	Change in Water Line (feet)	Change in Vegetation Line (feet)	Erosion of Vegetation Line (feet)	Overwash (feet)
High Island	55.5	-38	18	---	---
	53.5	-92	24	---	---
	52.6	23	26	26	0
		32	193	---	---
	49.4	49	250	---	---
	48.4	-9	146	---	---
	48.2				
Rollover Pass	47.7	-21	208	---	---
Caplen	46.7				
	46.4	118	208	---	---
	45.0	-22	136	55	81
	43.6	-62	86	---	---
Crystal Beach	42.0	101	116	---	---
	39.1	62	67	16	51
	37.1	21	31	15	16
Flake	35.3				
	34.8	-18	92	62	30
Galveston Seawall extends from 18.9 miles to 28.5 miles					
	17.9	13	238	134	104
	16.9	102	171	161	10
	15.9	91	210	75	135
	14.7	128	156	80	76
	13.1	151	177	152	25
State Park	12.3				
Jamaica Beach	11.4	166	233	65	16
	11.1	127	194	107	87
	10.0	144	164	---	---
	8.7	108	61	61	0
	8.3	108	70	70	0
	7.5	48	114	73	41
	6.5	145	145	---	---
Sea Isle	6.1				
	5.7	77	138	---	---
	5.1	172	1,058	---	---
Bay Harbor	4.6	182	245	91	154
	4.4				
	4.3	168	310	79	231
	2.9	166	141	89	52
	2.2	195	170	88	82
San Luis Pass	1.6	110	146	28	118
	0.0				
	2.1	-30	45	---	---
	3.5	-58	8	---	---
	5.5	-58	-21	---	---
	7.5	-51	---	---	---
	9.1	9	---	---	---
	11.2	-6	-11	---	---
	12.5	78	16	---	---
	13.4	-35	-4	---	---
Surfside Beach	13.9	-33	55	---	---
	14.5	-3	28	---	---
Freeport Inlet	14.7				



A striking aspect of the high water line changes is the abrupt change where the center of the storm crossed the coast. Recession prevailed to the right of the storm and accretion to the left of the storm. The demarcation at the center of the storm is a strong indication that the large, erosive waves generated by the onshore winds to the right of the storm during the nearshore storm surge were closely confined to the area of the strong onshore winds. A second, somewhat unexpected result, is the advance of the high water line immediately to the left of the storm. Two phenomena could account for this. First, flattening of the beach profile by the storm could shift the high water shoreline seaward even though there had been volumetric erosion of the beach and dunes. Second, from Figure 4 it is apparent that considerable beach accretion (50 feet (15.24 m) or more) occurred after the storm, but before the photograph was taken. Since the Figure 4 photograph was taken on August 26 and the aerial photographs were taken on August 24, it is likely that the accretion is included in the beach change measurements. If so, similar accretion is probably included in the high water line change measurements to the right of the storm. Thus, the column 2 figures probably underestimate the beach recession by as much as 50 feet (15.24 m).

The largest recession rates occurred just to the right of the storm center and measured recession of 100 feet (30.5 m) or more extended up to 17 miles (27.4 km) to the right of the storm center where the Galveston seawall starts. There was little or no beach in front of the seawall either before or after the storm and no measurements were made there. While recession of more than 100 feet (30.48 m) was measured on Bolivar Peninsula, not many points changed that much. Recession appeared to be tapering off at High Island, 55 miles (88.6 km) to the right of the center of the storm.

Changes in the vegetation line generally followed the pattern of high water line changes. Changes in the vegetation line were larger because the vegetation line can be changed by both erosion (the vegetation is carried away) and overwash (the vegetation is buried). The largest change in the vegetation line (over 1000 feet (304.8 m)) was measured at Terramar Beach. From both the ground survey and the photographs, it was obvious that most of this change was caused by overwash which buried the vegetation under up to three feet of sand. On western Galveston Island, the vegetation line receded over 100 feet (30.48 m) at all points where measurements were made except for two adjacent points between Jamaica Beach and Sea Isle. The ground survey showed that this area was one of the limited areas not overtopped by the storm surge on western Galveston Island. Vegetation line retreat was over 200 feet (60.96 m) at three of the measurement points on Bolivar Peninsula and over 100 feet (30.48) at three others, but tapered off in the vicinity of High Island, 55 miles (88.6 km) to the right of the center of the storm.

Figures 7-9 present the Table 1 data as averages over 5-mile (8.1 km) intervals along the coast. The number of measurements used in 5-mile (8.1 km) intervals varies from none along the seawall, across Galveston Inlet and the western portion of Bolivar Peninsula to as many as 7 along part of western Galveston Island.

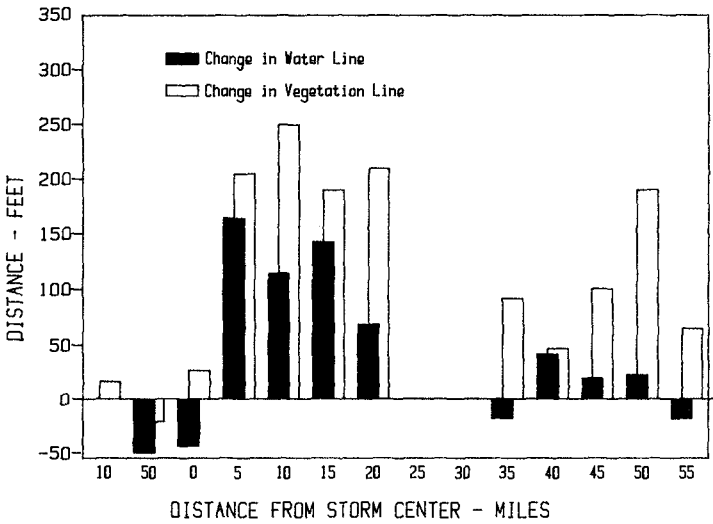


Figure 7. Change in high water line compared to the change in the vegetation line.

Beach and dune erosion and the width of overwash deposits could be measured separately where a scarp existed. A scarp was common along western Galveston Island, uncommon along Bolivar Peninsula and non-existent in the measurements made to the right of the storm center. Where measured separately (Figure 8), beach and dune recession on western Galveston Island averaged 90 feet (27.43 m) with a maximum of 160 feet (48.76 m). Overwash deposit widths on western Galveston Island that could be measured separately (Figure 9) averaged 87 feet (26.52 m) with a maximum of 154 feet (46.92 m).

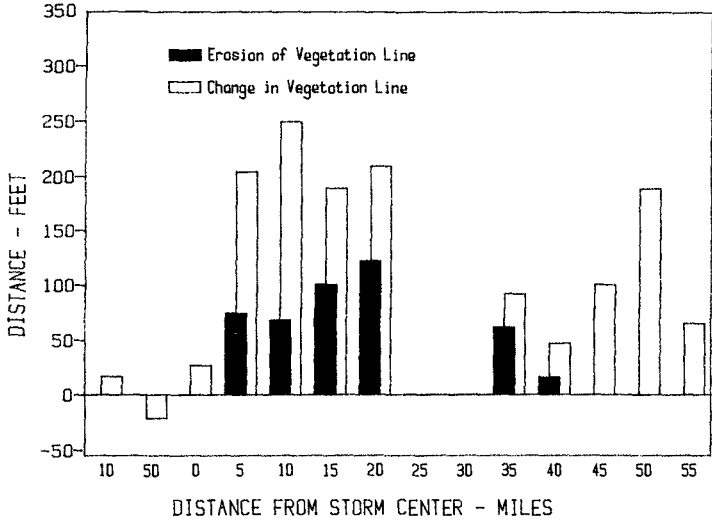


Figure 8. Erosion of vegetation line as shown by erosion scarps compared to the total change in the vegetation line.

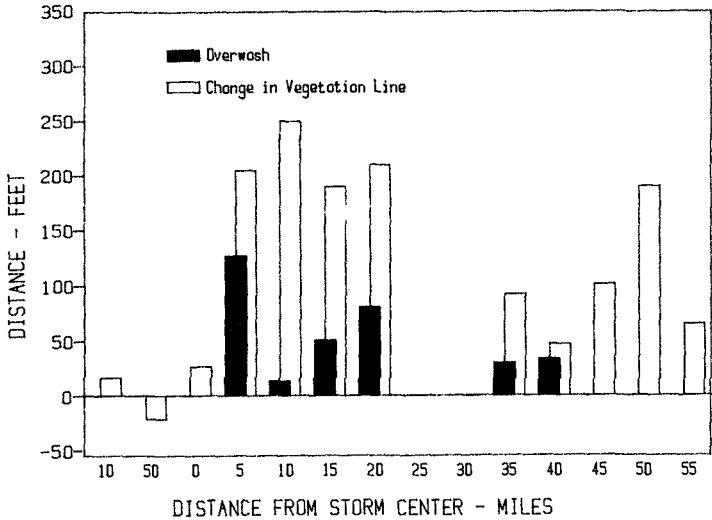


Figure 9. Width of overwash fans landward of erosion scarps compared to the magnitude of the change in the vegetation line.

## Conclusions

### Coastal Surges

1. Storm water levels in the Gulf of Mexico reached a maximum level of 9 to 10 feet (2.74 to 3.35 m) in the area from the west jetty of the Galveston entrance westward to and just past Bay Harbor on western Galveston Island, a distance of about 25 miles (40.3 km). Maximum water levels decreased slowly with distance both eastward and westward of this central area.

2. Maximum water levels in East and West Bays just behind Bolivar Peninsula and Galveston Island were generally 6 to 7 feet (1.83 to 2.13 m). However, in the Bays behind Follets Island, water levels increased reaching elevations of from 8 to 10 feet (2.44 to 3.05 m).

3. Maximum water levels around the west side of Galveston and Trinity Bays reached elevations ranging from around 8 feet (2.44 m) near Texas City and Baycliff to between 10 and 11 feet (3.05 to 3.35 m) in the Baytown area.

4. With the exception of the 9.5-mile (15.3 km) section protected by the Galveston seawall, almost all of Galveston Island was overtopped by a foot or more of water from the Gulf of Mexico. East Beach, in front of the Galveston Seawall, was overtopped by 3 to 6 feet (0.91 to 1.83 m) of water.

5. Follets Island was overtopped by the high water level in the bays behind the island from San Luis Pass to within 4 miles (6.4 km) of the Freeport entrance channel. This overtopping from bays-to-Gulf cut more than 30 distinctive channels starting at the beach, through the frontal dunes, toward, to, and in some cases into, the highway running behind the beach.

6. The western 3 miles (4.8 km) of Bolivar Peninsula was overtopped by water from the Gulf of Mexico. East of that point the front of the Peninsula was overtopped, with water ponding between the foredunes behind the beach and a relic dune ridge inland on the island. When the Gulf surge retreated, the ponded water ran back into the Gulf, cutting at least four large, triangular channels through the frontal dunes and beach.

### Shore Processes

1. A striking aspect of the shore processes during the storm was the strong demarcation between high-water line recession to the right of where the center of the storm crossed the coastline, and high water line advance just to the left of the storm center.

2. Retreat of the high-water line on western Galveston Island, measured from before and after aerial photographs, ranged from about

15 feet (4.57 m) near the seawall to almost 200 feet (60.96 m) near San Luis Pass. Along most of the beach from Jamaica Beach westward, retreat was more than 100 feet (30.48 m). At Terramar Beach and westward, high-water line recession was 170 feet (51.82 m) or more.

3. The vegetation line retreated more than 1,000 feet (304.8 m) at Terramar Beach, with an average retreat of 200 ft or more on western Galveston Island.

4. On Follets Island, the mean high-water line advanced an average of about 30 feet (9.14 m). Vegetation line retreat was small, usually less than 25 feet (7.62 m).

5. There was serious retreat of the high-water line (100 feet (30.48 m) or more) for the first 17 miles (27.4 km) to the right of the storm and significant retreat (20 feet (6.10 m) or more) for at least 55 miles (88.6 km).

6. Changes in the vegetation line generally followed the pattern of changes in the high-water line, but vegetation line changes were larger because they were a result of both erosion and overwash.

7. There was a marked difference in the frequency and appearance of scour cuts made in areas where water flowed from Gulf to bay as opposed to areas where water flowed from bay to Gulf. Where water flowed from Gulf to bay, there were few scour cuts and the cuts that were found were short and shallow, starting behind the beach and ending in an outwash deposition fan. Where water flowed from bay to Gulf, cuts were frequent and deep and it appears that if flow had continued long enough, scour would have cut completely through the island.

#### Acknowledgements

The Hurricane Alicia post-storm ground survey was carried out by a survey team of the Committee on National Disasters, National Research Council. Data analysis and report preparation was supported by The U. S. Army Coastal Engineering Research Center and Offshore & Coastal Technologies, Inc.

#### References

Savage, R. P., Jay Baker, J. H. Golden, Ashan Kareem and B. R. Manning, "Hurricane Alicia, Galveston and Houston, Texas, August 17-18, 1983," Committee on Natural Disasters, National Research Council, Washington, D. C., 1984.

U. S. Army Corps of Engineers - Galveston District, "Report on Hurricane Alicia," Galveston, Texas, 1983.

## CHAPTER NINETEEN

### MEASUREMENT OF SURFACE WAVES FROM SUBSURFACE GAGE

Dong-Young Lee and Hsiang Wang\*

#### ABSTRACT

Wave measurement using subsurface pressure gage has many advantages, especially in coastal waters. However, there are some disadvantages associated with indirect measurement of surface waves. This paper deals with the problems in the recovery of surface waves from the subsurface pressure measurement. Two problems are examined: more exact recovery of the surface waves from subsurface pressure signal and a simple real time recovery of surface waves from the pressure record.

The commonly used linear transformation from the subsurface pressure to surface elevation is evaluated and possible sources of error are examined. The effect of nonlinearity and effect of current are shown to be small in the intermediate water depth. For the case of shallow water where effects of nonlinearity and current are not negligible, a method of proper recovery of surface waves from the combination of pressure and current measurements is given.

A simple method to recover the time series surface waves from subsurface record is proposed which enables speedy near real-time recovery of surface waves from pressure measurement using a micro-processor.

#### 1. INTRODUCTION

Subsurface pressure transducer has been extensively used in measuring surface waves. It is particularly suitable for application in shallow and intermediate depth water. It does not require a supporting structure which penetrates the surface, hence is less susceptible to being damaged by ships and fishing activities and has better survivability in severe sea conditions due to storms. It is also not affected by high tidal range or storm surge which make the surface piercing gage impractical. In addition, it provides information for the mean water level variation due to tide and storm surge, that can not be obtained from moored surface gage such as pitch and roll buoy.

\* Department of Coastal and Oceanographic Engineering, University of Florida, Gainesville, Florida 32611

However, since the device measures the subsurface pressure, a proper transformation has to be carried out to obtain surface wave information. The commonly used practice is to recover the surface wave information by means of a transfer function based on the linear first order wave theory. There are several sources of error such as instrumental noise, nonlinearity, effect of current, etc. A number of these sources of error are examined here to establish the reliability and limitations of the subsurface wave measurement and a refined method of recovery is proposed.

As a second objective, a simple numerical filter is introduced here which can perform fast recovery of time series of surface wave from pressure record with minimum computation.

## 2. ANALYSIS OF SUBSURFACE PRESSURE RECORD

The record from the subsurface pressure gage contains signals of two widely separated time scales; small time scale signal due to wave induced motion and larger time scale signal due to tide, storm surge etc. The data measured from the subsurface gage is considered as a linear summation of various contributing components :

$$P(t) = P_a + \rho g[(h - H_g) + K_p \eta] \quad (1)$$

where  $P(t)$  is the measured pressure at gage and  $P_a$  is the atmospheric pressure at the surface,  $h$  and  $H_g$  denote mean water depth and gage height above bottom, respectively, and  $\eta$  is surface wave and  $K_p$  is the pressure response function, and  $\rho$  is water density and  $g$  is gravitational acceleration.

By averaging the time series with a time interval much larger than the time scale of gravity waves but smaller than the large time scale phenomena, the mean water depth ( $h$ ) is obtained as

$$h(t) = (\bar{P} - p_a) / (\rho g) + H_g \quad (2)$$

where  $\bar{P}$  denotes the time averaged mean pressure at the gage. The tide and storm surge information can be deduced from  $h(t)$  (Howell et al., 1983).

The pressure ( $p$ ) induced by surface gravity waves can be obtained from

$$p = \rho g K_p \eta = [P(t) - \bar{P}] \quad (3)$$

The pressure response function,  $K_p$ , is usually defined through linear wave theory as follows

$$K_p(\omega_n) = \{ \text{Cosh } k_n(h+z) / \text{Cosh } k_n(h) \} \quad (4)$$

such that

$$p(t) = \rho g \sum_n A_n \text{Cos}(\omega_n t - \epsilon_n) \quad (5)$$

$$\eta(t) = \sum_n \frac{A_n}{K_p(\omega)} \cos(\omega_n t - \epsilon_n) \quad (6)$$

where  $h$  is water depth and  $z$  is location of pressure gage, and  $A_n$ ,  $\omega_n$ ,  $\epsilon_n$  and  $k_n$  are wave amplitude, frequency, phase and wave number of  $n$ -th component wave, respectively. The wave number and the frequency are related by

$$\omega_n = \sqrt{gk_n \text{Tanh}(k_n h)} \quad (7)$$

The surface variance spectrum,  $E_{\eta\eta}(\omega)$ , commonly known by wave energy spectrum can be obtained from the subsurface pressure spectrum,  $E_{pp}(\omega)$ , by the following relation:

$$E_{\eta\eta}(\omega) = E_{pp}(\omega)/K_p^2 \quad (8)$$

The time series of the surface waves can be obtained by Eq. (6) where  $A_n$ ,  $\omega_n$  and  $\epsilon_n$  are obtained from the Fast Fourier Transform (FFT) of the pressure data. Another method of recovery of  $\eta(t)$  is obtained by means convolution integral,

$$\eta(t) = \int_{-\infty}^{\infty} h(\tau) p(t-\tau) d\tau \quad (9)$$

where

$$h(\tau) = \int_{-\infty}^{\infty} H(\omega) \text{Exp}(i\omega\tau) d\omega \quad (10)$$

$$H(\omega) = \frac{1}{K_p(\omega)}$$

The convolution integral method is usually more time consuming than the FFT method.

### 3. SOURCES OF ERROR AND IMPROVEMENT

#### 3.1. Noise

The signal due to high frequency wave components is small due to depth attenuation and sometimes is completely lost due to the instrument limitation. The electronic noise in the power system, pressure transducer, and the analog filter, and the numerical noise associated with analog-to-digital conversion, on the other hand, are introduced. These noise components are amplified when converting into surface waves.

The noise from many possible sources cannot be totally avoided, hence, the true surface elevation information in the high frequency range is very difficult to recover from pressure record.

In theory, the pressure signal can be corrected if the noise is a known function of frequency. Unfortunately, such is not the case. It is, thus, suggested to remove the averaged overall noise level for the higher frequency range as



$$E_{\eta\eta} = (E_{pp} - C)/K_p^2 \quad (11)$$

where C is the overall noise level in high frequency range. This seemingly trivial process is important as a slight error in the high frequency region may produce a significant error in the surface elevation through amplification. A simple way that is commonly used to resolve this problem is the application of windowed transfer function simply by cutting off the high frequency range above a certain cut-off frequency ( $\omega_a$ ) such that

$$\begin{aligned} H(\omega) &= H(\omega) & \text{for } \omega < \omega_a \\ &= 0 & \text{for } \omega > \omega_a \end{aligned} \quad (12)$$

The pressure record is usually represented as discrete and finite record. The use of finite record length, i.e. rectangular window results in an undesirable energy leakage to the neighboring frequency components. The spill over error in pressure spectrum is amplified in wave energy spectrum. A data window is to be applied to the data to reduce spectral leakage.

### 3.2 Nonlinearity of Coastal Waves

Many of the nonlinear wave theories are confined to cases of monochromatic waves, which are not practical to apply to the random waves. The higher order correction to the first order random (free) waves using perturbation method is used here to deal with the weakly nonlinear irregular waves. The surface elevation  $\eta$  is expressed up to second order as (Sharma et al., 1981),

$$\eta = \eta_1 + \eta_2 \quad (13)$$

where

$$\eta_1 = \sum_i A_i \cos(\omega_i t - \epsilon_i) \quad (14)$$

and

$$\begin{aligned} \eta_2 = \frac{1}{4} \sum_i \sum_j C_{ij}^- A_i A_j \cos[(\omega_i - \omega_j)t - (\epsilon_i - \epsilon_j)] \\ + \frac{1}{4} \sum_i \sum_j C_{ij}^+ A_i A_j \cos[(\omega_i + \omega_j)t - (\epsilon_i + \epsilon_j)] \end{aligned} \quad (15)$$

where

$$C_{ij}^- = \frac{D_{ij}^- + (\vec{k}_i \cdot \vec{k}_j + R_i R_j)}{\sqrt{R_i R_j}} + (R_i + R_j) \quad (16)$$

$$C_{ij}^+ = \frac{D_{ij}^+ - (\vec{k}_i \cdot \vec{k}_j + R_i R_j)}{\sqrt{R_i R_j}} + (R_i + R_j) \quad (17)$$

where

$$\begin{aligned}
 D_{1j}^- &= \{(\sqrt{R_1} - \sqrt{R_j}) [\sqrt{R_j} (k_1^2 - R_1^2) - \sqrt{R_1} (k_j^2 - R_j^2)] \\
 &\quad + 2(\sqrt{R_1} - \sqrt{R_j})^2 (\vec{k}_1 \cdot \vec{k}_j + R_1 R_j)\} \\
 &\div [(\sqrt{R_1} - \sqrt{R_j})^2 - k_{1j}^- \tanh k_{1j}^- h]
 \end{aligned} \tag{18}$$

$$\begin{aligned}
 D_{1j}^+ &= \{(\sqrt{R_1} + \sqrt{R_j}) [\sqrt{R_1} (k_j^2 - R_j^2) + \sqrt{R_j} (k_1^2 - R_1^2)] \\
 &\quad + 2(\sqrt{R_1} + \sqrt{R_j})^2 (\vec{k}_1 \cdot \vec{k}_j - R_1 R_j)\} \\
 &\div [(\sqrt{R_1} + \sqrt{R_j})^2 - k_{1j}^+ \tanh k_{1j}^+ h]
 \end{aligned} \tag{19}$$

and  $R_1 = k_1 \tanh k_1 h$ ,  $k_{1j}^- = |\vec{k}_1 - \vec{k}_j|$ ,  $k_{1j}^+ = |\vec{k}_1 + \vec{k}_j|$

The subsurface pressure at location  $z$  can be written as

$$p = p_1 + p_2 \tag{20}$$

where  $p_1 = \rho g \sum_1 \cosh[k(h+z)]/\cosh(kh) A_1 \cos(\omega_1 t - \epsilon_1)$  (21)

$$\begin{aligned}
 p_2 &= \frac{1}{4} \rho g \sum_1 \sum_j G_{1j}^- A_1 A_j \cos[(\omega_1 - \omega_j)t - (\epsilon_1 - \epsilon_j)] \\
 &\quad + \frac{1}{4} \rho g \sum_1 \sum_j G_{1j}^+ A_1 A_j \cos[(\omega_1 + \omega_j)t - (\epsilon_1 + \epsilon_j)]
 \end{aligned} \tag{22}$$

where  $\sqrt{R_1 R_j} G_{1j}^- = \frac{\cosh k_{1j}^- (h+z)}{\cosh k_{1j}^- h} D_{1j}^-$

$$\begin{aligned}
 &- \frac{k_1 k_j}{\cosh k_{1j}^+ h + \cosh k_{1j}^- h} \{ \cosh k_{1j}^+ (h+z) \\
 &\quad \cdot [1 + \cos(\theta_1 - \theta_j)] - \cosh k_{1j}^- (h+z) \\
 &\quad \cdot [1 - \cos(\theta_1 - \theta_j)] \}
 \end{aligned} \tag{23}$$

and  $\sqrt{R_1 R_j} G_{1j}^+ = \frac{\cosh k_{1j}^+ (h+z)}{\cosh k_{1j}^+ h} D_{1j}^+$

$$\begin{aligned}
 & - \frac{k_i k_j}{\cosh k_{ij}^P h + \cosh k_{ij}^M h} \{ \cosh k_{ij}^P (h+z) \\
 & \cdot [-1 + \cos (\theta_i - \theta_j)] + \cosh k_{ij}^M (h+z) \\
 & \cdot [1 + \cos (\theta_i - \theta_j)] \} \tag{24}
 \end{aligned}$$

where  $k_{ij}^P = |\vec{k}_i| + |\vec{k}_j|$ ,  $k_{ij}^M = |\vec{k}_i| - |\vec{k}_j|$   
 and  $\theta_i$  is wave angle.

By comparing the surface elevation and subsurface pressure, we may define two or more transfer functions as

$$K_{1i} = \cosh[k(h+z)] / \cosh(kh) \tag{25}$$

$$K_{2ij}^- = C_{ij}^- / G_{ij}^- \tag{26}$$

$$K_{2ij}^+ = C_{ij}^+ / G_{ij}^+ \tag{27}$$

The transfer function for the first order free component is shown in Figure 1.

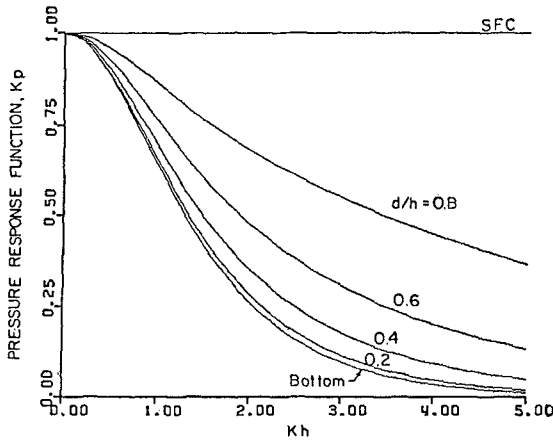


Figure 1. Variation of Linear Pressure Transfer Function with Dimensionless Water Depth (kh) for Various Dimensionless Gage Depth (d/h).

The transfer function for second order nonlinear component depends on the combination of the first order frequency components and their directions. Figure 2 shows the ratio of transfer function for the second order component to the linear transfer function for the simple case where all wave components propagate in the same direction. We can see that the transfer functions for the second order terms are slightly smaller than the linear transfer function for the subharmonics (frequency difference components) and slightly higher for the superharmonic (frequency sum components).

For example, considering just one free waves with its harmonics, the surface elevation  $\eta$  expressed by Stoke's wave is

$$\eta(t) = \eta_1 + \eta_2 \quad (28)$$

where

$$\eta_1 = a \cos(kx - \omega t) \quad (29)$$

$$\eta_2 = 1/2 k a^2 \cosh(kh) [2 + \cosh(2kh)] / \sinh^3(kh) \cos(2kx - 2\omega t) \quad (30)$$

The pressure at elevation of  $z$  can be expressed as

$$p(t) = K_1 \eta_1 + K_2 \eta_2 \quad (31)$$

where  $K_1 = \cosh[k(h+z)] / \cosh(kh)$

$$K_2 = \frac{3/4 k a^2 \tanh(kh) / \sinh^2(kh) [\cosh[2k(h+z)] / \sinh^2 kh - 1/3]}{\cosh(kh) [2 + \cosh(2kh)] / \sinh^3(kh)} \quad (32)$$

The second harmonic which is phase locked to the fundamental wave shows different characteristics from the free waves with the same frequency or wave length. The response function of the phase locked second order components is different from that of the free linear wave with the same frequency as shown in Figure 3. The pressure correspondent to second order superharmonic decays with depth at a slower rate than those of free waves with same frequency.

The nonlinearity effect is not significant in the intermediate depth water waves since the contribution of the nonlinear components are comparatively small and the difference of the transfer functions between the linear term and nonlinear term is not significant. However, in shallow water or in surf zone, the nonlinearity correction is essential.

### 3.3 Effects of Current

Current affects waves in two respects: the kinematic effect leading to the change of wave number and the dynamic effect leading to the change of dynamic pressure. Both will affect the pressure transfer function.

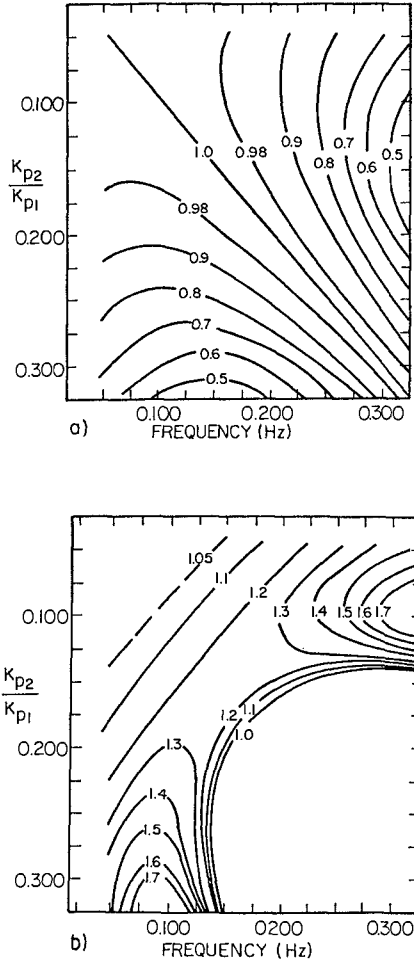


Figure 2.

Example of the Pressure Transfer Function for the Second Order Component Compared to that of Linear Component for Simple Case of Unidirectional Wave When  $h=7.5$  m,  $d=1.0$  m. (2-a). Subharmonic ( $\omega_1-\omega_j$ ) component. (2-b). Superharmonic ( $\omega_1+\omega_j$ ) component.

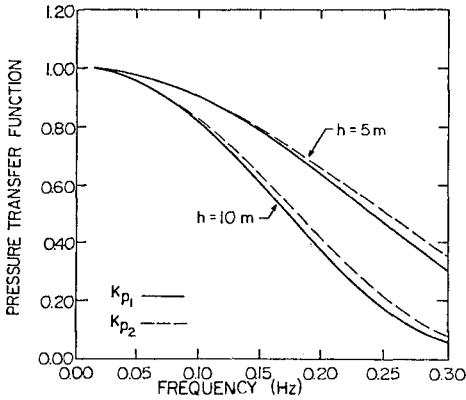


Figure 3. Pressure Transfer Function of the Second Order Harmonic of Stoke's Wave Compared to that of First Order Linear Wave Component.

As shown in Eq. 6, the transfer function,  $K_p$ , is related to the wave number. In the presence of current, the change of wave number can be obtained by following equation

$$n = \vec{k} \cdot \vec{u} + \sqrt{gk \tanh(kh)} \tag{33}$$

where  $n$  is the intrinsic wave frequency and  $\vec{u}$  is current vectors. This effect becomes increasingly significant in higher frequency range especially for the current against the waves.

The wave induced dynamic pressure by the combined current and wave motions is

$$\begin{aligned} p &= \frac{1}{2} \rho \left\{ \left( \sum_i U_i \cos(\omega_i t - \epsilon_i) + U_c \cos \alpha \right)^2 + (U_c \sin \alpha)^2 \right\} \\ &= \frac{1}{2} \rho \sum_i \sum_j U_i U_j \cos(\omega_i t - \epsilon_i) \cos(\omega_j t - \epsilon_j) \\ &\quad + \rho U_c \cos \alpha \sum_i U_i \cos(\omega_i t - \epsilon_i) + \frac{1}{2} \rho U_c^2 \end{aligned} \tag{34}$$

where  $U_i$  is the amplitude of wave induced velocity and  $U_c$  is the current speed and  $\alpha$  denotes the angle between the wave propagation and current direction. The first term in the right hand side of Eq. 34 is the second order components with frequency components of  $(\omega_i - \omega_j)$  and

$(\omega_1 + \omega_2)$  that contribute a part of  $p_2$  in Eq. 22. Its effect has been considered from the nonlinearity point of view. The third term gives only a constant drift. The effect of the superimposed current on the recovery of pressure data comes from the second term, which is proportional to the wave induced flow and the proportionality factor  $U_c \cos \alpha$  depends on the current speed and the angle between current and wave  $\alpha$ .

The relation between the pressure fluctuation and surface wave is now

$$p(t) + p_2(t) = \rho g K_p' \eta \quad (35)$$

where  $K_p$  is corrected transfer function. It can be shown that

$$\begin{aligned} K_p' &= [1 + U_c \cos(\alpha) k_n / \omega_n] K_p \\ &= (1 + \cos(\alpha) U_c / C) K_p \end{aligned} \quad (36)$$

where  $C$  is the wave phase speed.

Figure 4 shows the effect of the current on the transfer function,  $H(\omega)$  due to current effect in the change of wave number, and in the change of dynamic pressure. These two effects are in opposition hence somewhat neutralize each other. The resultant effect is dominated by the dynamic effect in the lower frequency range whereas it is dominated by the kinematic effect in the higher frequency range.

#### 4. APPLICATION TO THE FIELD DATA

##### 4.1. Comparison of the Surface and Subsurface Measurements

To determine the validity of the linear pressure transfer function, surface data and subsurface data obtained simultaneously during ARSLOE experiment are analysed and compared. The pressure gage is located at 0.9 meter above the bottom at the water depth of about 7.5 meter. The surface gage is the Baylor type gage at water depth of about 9.0 meter. The distance between the two gage is about 40 meters. Figure 5 shows an example comparing wave spectrum obtained from surface gage to that from subsurface gage using linear transfer. The pressure response function obtained from the measured data and from the theoretical linear transfer function are also compared in Figure 5.

The linear transfer function is found to perform well in the energy containing region but underestimates energy in the lower frequency range while slightly over estimates energy in the higher frequency range. This trend is consistent with other investigators (Cavaleri et al., 1978; Forristal, 1982). This may be partially explained by the nonlinear effect discussed earlier. The transfer function of the second order term for the frequency difference components (lower frequency) is smaller than that of the linear component at the same frequency, while the opposite is true for the

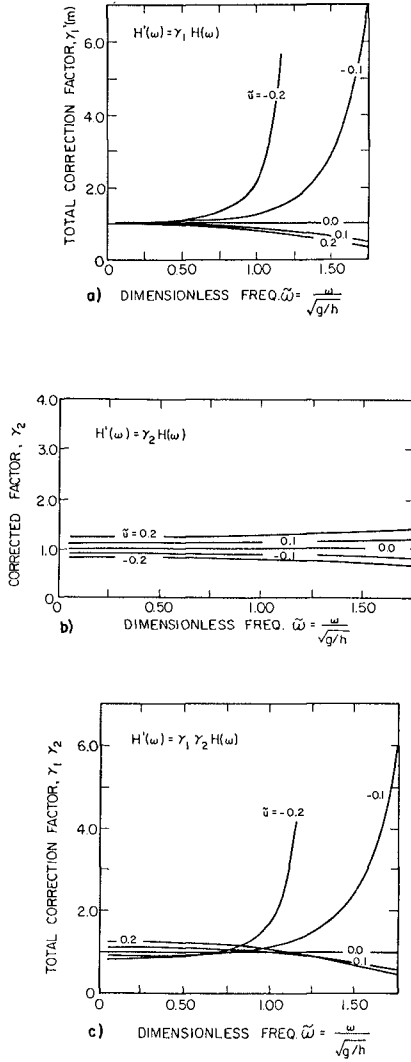


Figure 4. Variation of the Correction Factor to the Transfer Function  $H(\omega)$  due to the change of wave number (4-a) and due to the Dynamic Pressure (4-b) and the Total Effect (4-c).



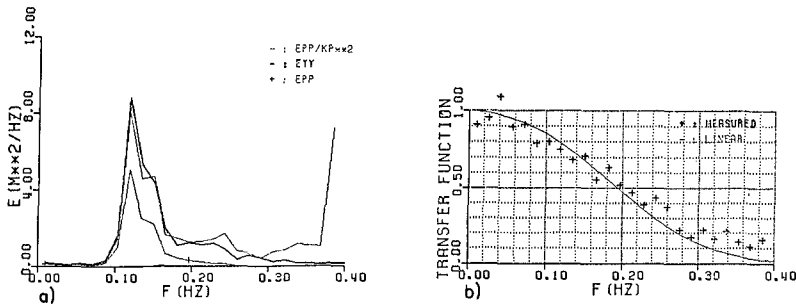


Figure 5. Example of the Comparison of Wave Energy Obtained from Surface Gage and that from Subsurface Pressure Gage (5-a) and Comparison of Linear Pressure Transfer Function with the Measured One (5-b).

frequency summation components (high frequency) as shown in Figures 2 and 3. However, the nonlinearity effect cannot fully account for the differences revealed by the data. Another possible contribution to this discrepancy may be due to the effect of current as shown in Figure 4. For the storm waves generated by the local wind force, the wave propagation is considered to be approximately in the same direction with the wind drift surface current. In this case the resultant effect of current on the transfer function overestimates energy in comparison to the linear transfer function in the higher frequency range, while it underestimates energy in the lower frequency range, which is consistent with the measured data.

#### 4.2 Surface Wave Recovery from the Simultaneous Subsurface Pressure and Current Measurement

When the nonlinearity and/or the current effects become significant, adequate surface wave recovery requires the information of current as well as wave direction for each frequency component. In this case, both pressure and horizontal current vector should be measured by using p-u-v gage or other means. The procedures of correctly recovering the surface waves information are outlined here.

- 1). obtain directional wave spectrum using p-u-v data and linear pressure and current transfer functions.
- 2). decompose spectral components of pressure and velocity components into linear and second order components by means of Eqs. 13 - 24 for p and similar equations for u and v using iteration method.
- 3). recompute wave directions using linear components, i.e.,  $p_1$ ,  $u_1$  and  $v_1$  only using linear transfer functions.

- 4). recompute wave number and thus transfer function including the effect of current using the mean current data.
- 5). recompute the wave energy spectrum with the inclusion of the second order correction and current interaction term.

This method has been implemented for the Coastal Data Network System at the University of Florida. The general experience is that the effect of nonlinearity and current are small in intermediate water depth such as the case of the Data Network. The details will be reported separately in the future.

Since the directional spectrum is expressed by only five Fourier coefficients, it is not possible to separate wave direction for two or more trains. One of the interesting case is where wind driven sea and swell are present at the site. The proper estimation of the swell component from the measurement is practically important. The signal in the low frequency component is contaminated by the nonlinear components of local wind waters. The wave energy of the free waves of the local wind waves may not be significant in high frequency. But in case that the second order nonlinear component is substantial, it is difficult to subtract the swell components from the measured data. By mean of the above mentioned detailed analysis, the swell components may be more reliably obtained.

#### 5. A SIMPLE FILTER TO RECOVER THE SURFACE WAVES FROM SUBSURFACE PRESSURE MEASUREMENT

The second topic of this paper is the introduction of a simple filter for the recovery of surface wave information from subsurface pressure measurement. The spectral analysis method used to compensate the depth attenuation to recover the surface elevation from subsurface pressure record requires a fast computing machine to handle FFT algorithm, which makes the pressure gage inconvenient and sometimes impractical if real-time wave information is needed.

As discussed earlier, the time series of surface elevation,  $\eta(n\Delta t)$ , can be obtained by means of inverse FFT or convolution integration. In the convolution integral method,  $N$  discrete points of pressure data sampled at  $\Delta t$ , are used to recover the surface wave time series through the following equation:

$$\eta(n \Delta t) = C_0 p(n \Delta t) + (1/2) \sum_m^{N/2} C_m [p((n+m) \Delta t) + p((n-m)\Delta t)] \quad (37)$$

where  $C_m$  is defined as

$$H(k \pi/N) = C_0 + \sum_{m=1}^{N/2} C_m \cos (mk\pi/N) \quad (38)$$

Thus, the surface elevation  $\eta(n \Delta t)$  is recovered from the  $N$  points of pressure record. A certain window function is to be applied to the transfer function to avoid problems of noise in the high frequency. Usually a simple window to cutoff the high frequency above a certain

value as in Eq. 16. In general the computation is cumbersome and takes longer than FFT method.

A very convenient windowed transfer function is proposed here which drastically reduces the computation, thus, renders the convolution integral method more effective. The proposed windowed transfer function takes a simple form:

$$H'(\omega) = A + B \cos(\omega) \tag{39}$$

here A and B are constant to fit the original transfer function,  $H(\omega)$ , for the desired frequency range for a specific water depth. Since  $H(\omega)$  is function of water depth (h) and gage-bottom distance (d), the constant A and B are also functions of h, d. Figure 6 compares the simple windowed transfer function in Eq. 39 and original transfer function for water depth of 6.0 meter where  $d=0.5$  meter.  $H'(\omega)$  fits the original transfer function for the low frequency region and smoothly reduces the value at high frequency. The simplified transfer function fit the original one well for the energy containing range and the blowing in the high frequency is reduced to avoid the serious problems of the errors in high frequency range. The transfer function is simple and defined by just two constants A and B for a given water depth.

Using the windowed transfer function,  $H'(\omega)$ , the recovery of the surface elevation can be done by means of simple three point convolution.

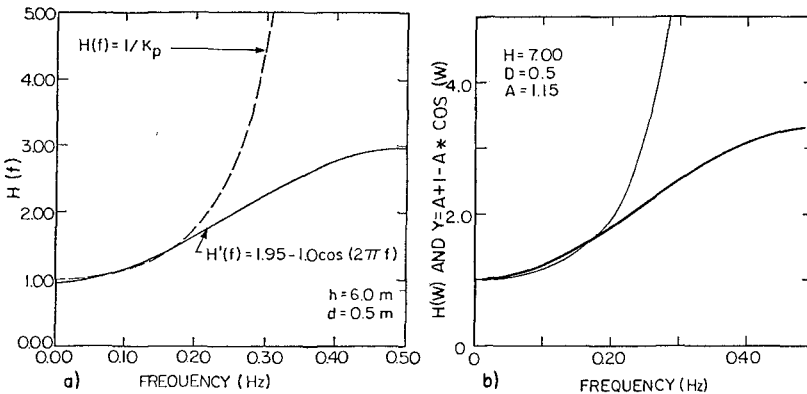


Figure 6. Simple Windowed Transfer Function Compared Original Linear Transfer Function. Two Parameter Filter (6-a) and One Parameter Filter (6-b).

$$\eta(n \Delta t) = A p(n \Delta t) + 1/2 B [P(n+1)\Delta t) + P(n-1)\Delta t)] \quad (40)$$

Three point convolution recovery is equivalent to that of surface waves from pressure and its local curvature. The filter is so simple that a small micro processor attached to the underwater package can easily handle the computation.

An even simpler one parameter filter of the following form also performs well:

$$H'(\omega) = (1 + A') - A' \cos(\omega) \quad (41)$$

where  $A'$  is a parameter depend on water depth (for fixed gage) obtained by curve fitting to the original  $H(\omega)$ . As shown in Figure 6, this filter has a slightly larger value than  $H(\omega)$  in the low frequency but is smaller in the high frequency range, which has the same trend as the nonlinear transfer function or measured transfer function discussed above. Therefore, it can be considered as an empirical fitting to a nonlinear transfer function.

When more accurate recovery is desired, we may increase number of convolution with more coefficients. The improvement will be largely in the high frequency range.

One of the application of the above simple filter is the real-time detection of the sea condition without using fast computing machine. A simple but reliable way of detection of sea state can be obtained by use of the significant wave height is estimated as

$$H_s = 4 H_{rms} \quad (42)$$

where  $H_{rms}$  is the root mean square height calculated from a record of recovered time series of surface elevation.

Since the values of  $A$  and  $B$  depend on water depth, for fixed gage height, the functional dependency of  $A$  and  $B$  on  $h$  can be precalculated by means of computer and stored in the microprocessor.

## 6. CONCLUSIONS

In spite of its many advantages, there is still hesitation by many to use subsurface pressure gage as a means to recover the surface wave information owing to the problems associated with signal recovery technique. The center of the problem is the dispute on the appropriateness of the linear transfer function and its limitation. A rather detailed analysis was performed to examine various sources of error involved in the conventional recovery technique.

In terms of wave energy spectrum, the linear transfer function is found to be good for intermediate-water-depth application. The bulk of the spectral components can be faithfully recovered except in the high frequency range. As water becomes shallower, nonlinearity effect and current influence may also become more prominent. In this case,

the linear transfer function should be modified to account for these effects. Methods of modification are proposed. When water becomes real shallow, the wave spectral approach may eventually become unsuitable. A transfer function should be developed to facilitate wave-by-wave recovery.

For more complete recovery of surface information, p-u-v gage should be used in shallow water. It not only provides directional information but also gives more correct estimation of wave energy.

The simple filter method proposed here has the potential of providing real-time wave information by using micro-electronic component instead high-speed computer. It will be a major asset from the operational point of view.

The subsurface pressure instrument is definitely a viable solution for surface wave measurement. The operational convenience reliability and cost of maintenance make it an attractive choice.

#### ACKNOWLEDGEMENT

This paper is prepared as part of the work for Coastal Data Network (CDN), University of Florida. The system is partially supported by Coastal Engineering Research Center, U.S. Army Corp of Engineer DACW39-80-C-0118. The authors wish to thank Jean Branson and Lillean Pieter for preparing the manuscript.

#### REFERENCES

- Cavaleri, L. et al. (1978), "Measurement of the Pressure and Velocity Field Below Surface Waves, in Turbulent Fluxes Through the Sea Surface, Wave Dynamics, and Prediction, Ed. A. Favre and K. Hasselmann, Plenum, New York.
- Dean, R.G. et al. (1984), "Analysis and Evaluation of Hurricane David Wave Data in Shallow Water," Department of Coastal and Oceanographic Engineering, University of Florida, Gainesville, Unpublished, May 1984.
- Forristall, G.Z. (1982), "Subsurface Wave Measuring Systems," in Measuring Ocean Waves: Proceedings of a Symposium and Workshop on Wave-Measurement Technology, Marine Board of the National Research Council, Washington.
- Howell, G.L, D.Y. Lee and H. Wang, (1983), "Storm Surge Measurement and Computations for Hurricane David," NUREG/CR-2860, U.S. Nuclear Regulatory Commission, Washington, D.C.
- Peregrine, D.H. (1976), "Interaction of Water Waves and Currents," Adv. Appl. Mech., 16, 99-117.
- Sharma, J.N. et al. (1981), "Second Order Directional Seas and Associated Wave Forces," Soc. of Petroleum Eng. Jour., Vol. 21, pp 129-140.

## CHAPTER TWENTY

### A SHALLOW WATER DIRECTIONAL WAVE RECORDER

S.J. Buchan, R.K. Steedman, S.A. Stroud, D.G. Provis

#### ABSTRACT

Shallow water wave theory shows that estimates of directional wave climate may be obtained from the measurement of near-bottom pressure and horizontal velocity components. Recent developments in low powered sensors and high density data loggers, incorporated into a bottom-mounted directional wave recorder, make the collection of directional shallow water wave data possible on a routine basis. The instrument is compact, robust, reliable and easily manageable from small craft, providing deployment capacities of up to four months. Analysis methods have been developed which provide for conversion of the recorded data to useful, convenient information.

#### 1. INTRODUCTION

During recent years, recognition of the importance of directional wave information in many facets of coastal and ocean engineering design has been increasing. Goda et al. (1978) have illustrated the importance of wave directionality for studies of wave diffraction and refraction in harbours; Forristall et al. (1978) have demonstrated the inadequacies of uni-directional wave theories in describing wave kinematics; and Sand et al. (1981) have discussed the applications of directional wave information to the hydrodynamics and design of offshore structures and pipelines.

Advances in remote low powered logger and sensor technology have allowed the development of reliable, compact, robust and manageable water current and pressure measuring devices. In May 1980, Sea Data Corporation were commissioned to modify their 635-11 Wave and Tide Recorder (based on bottom-mounted pressure measurements) to include synchronous horizontal velocity measurements within each "burst" of pressure data. The result was the Sea Data 635-12S Directional Wave and Tide Recorder, the use of which is the subject of this paper. Reference is made to the instrument operation and to the underlying theory on which the data analyses are based. Various analysis techniques are illustrated, and verification of instrument and analysis performance is provided.

---

\* R.K. Steedman & Associates  
384 Rokeby Road, Subiaco 6008, Western Australia

## 2. INSTRUMENTATION

The instrument measures fluctuations in absolute pressure and horizontal current velocity, at both tide and wind wave frequencies. Instrument temperature is also logged. A complete description of the instrument is given by Aubrey and Hill (1984), and a detailed analysis of sensor specifications is given by Grosskopf et al. (1983).

In operation the 635-12S runs two separate sampling schemes in parallel. These are the mean (tide) and burst (wave) recording modes. Data from each mode are recorded in an interleaved format on a magnetic cassette tape.

In the mean mode, water pressure is integrated continuously over a specified sample interval. To conserve battery power, the mean current is computed only over every eighth mean pressure sample interval. The mean sample interval may be selected in the range 3.75 to 60 minutes. An instantaneous temperature measurement from a thermistor within the instrument housing is sampled after every 8 mean pressure samples. Data recording takes place every 8 sample intervals when an elapsed time, 8 tide measurements, a water temperature measurement and the mean current components are recorded.

In burst mode, the instrument rapidly samples the water pressure and the two current velocity components at a preset interval in the range 0.5 to 4 seconds. The number of samples in each burst may be adjusted in steps between 64 and 2048, or alternatively the instrument may be set to run continuously. The interval between bursts may be varied from 0.5 to 24 hours. The burst samples are recorded as triples of the water pressure, easterly and northerly current components.

## 3. DEPLOYMENT AND RETRIEVAL

The directional wave recorder is usually deployed in an aluminium tripod which is lowered to the sea bed by winch from a work vessel. The tripod is attached to small surface floats by a buoyant line, to facilitate recovery. Thus, deployment and retrieval operations can be carried out without diver assistance.

Within the tripod, the velocity and pressure sensors are located at 1.5 m above the base. Provided the sea bed is relatively smooth and flat (easily checked using an echo sounder), then the sensors should be located above the bottom boundary layer.

An alternative deployment arrangement is provided by fixing the directional wave recorder to an offshore pile. This arrangement allows the sensors to be located near the water surface, but can only be used when the pile wake effects are not of significance. Deployment and retrieval of the instrument using this arrangement does require diver assistance.

#### 4. UNDERLYING THEORY

To obtain a representation of the surface sea state from subsurface measurements of pressure and velocity, an appropriate theory describing the kinematics of flow beneath surface waves must be applied. An assessment of available wave theories is presented in Forristall et al. (1978).

The simplest approach is to use linear wave theory which may be extended through spectral concepts to model irregular (i.e. aperiodic) sea. The most serious deficiency of linear theory occurs due to the non-linearity of the free surface boundary condition.

Higher order regular (periodic) and irregular (aperiodic) theories provide a better match to the free surface boundary condition, but their complexity precludes their incorporation in any practical analysis of directionally spread sea states.

From analysis of measurements conducted during Tropical Storm Delia in the Gulf of Mexico, Forristall et al. (1978) demonstrated that using a linear theory which accounted for the directional nature of the measured sea state provided a better representation of wave kinematics than higher-order, uni-directional wave theories.

Linear Wave Theory : A linear representation of the surface elevation  $\eta$ , above or below the equilibrium water level, of an arbitrary cosine wave component of a random sea is given by,

$$\eta = \alpha \cos(kx \cos\theta + ky \sin\theta - 2\pi ft + \phi) \quad (1)$$

This formulation has been set in a right-hand, rectangular coordinate system (x,y,z) with z chosen as positive upward from the sea bed where

$\alpha$  is the wave amplitude;

$\theta$  is the direction of phase propagation, measured counter-clockwise from the x axis;

$\phi$  is the wave phase;

t is time;

k is the horizontal wave number;

f is the wave frequency in cycles per second.

The horizontal wave number  $k = 2\pi/\lambda$ , where  $\lambda$  is the wave length.

A freely propagating surface gravity wave described by the above formula should satisfy a dispersion relation given by,

$$(2\pi f)^2 = gk \tanh kd \quad (2)$$

where g is the acceleration due to gravity, and d is the water depth.



At any level  $z$  in the water column below such a wave, the horizontal velocity components are described by,

$$u = \alpha 2\pi f \frac{\cosh kz}{\sinh kd} \cos\theta \cos(kx \cos\theta + ky \sin\theta - 2\pi ft + \phi) \quad , \quad (3)$$

and

$$v = \alpha 2\pi f \frac{\cosh kz}{\sinh kd} \sin\theta \cos(kx \cos\theta + ky \sin\theta - 2\pi ft + \phi) \quad . \quad (4)$$

the wave-induced pressure at  $z$  is given by,

$$p = \alpha \rho g \frac{\cosh kz}{\cosh kd} \cos(kx \cos\theta + ky \sin\theta - 2\pi ft + \phi) \quad , \quad (5)$$

where  $\rho$  is the water density.

A confused sea state may be represented by a summation of linear waves, given by (1), at various frequencies, propagation directions and phases, and may be described by a "random" sum

$$\eta(x, y, t) = \sum_m \sum_n \alpha_{mn} \cos\psi_{mn} \quad , \quad (6)$$

where the indices  $m, n$  run over selected frequencies and directions respectively, and the composite phase function is given by

$$\begin{aligned} \psi_{mn} &= \psi_{mn}(x, y, t) \\ &= k_m x \cos\theta_n + k_m y \sin\theta_n - 2\pi f_m t + \phi_{mn} \end{aligned} \quad . \quad (7)$$

In the above,  $\phi_{mn}$  is the random phase for the  $(m, n)$  wavelet, assumed to be uniformly distributed over the direction interval  $(0, 2\pi)$  and independent from wavelet to wavelet.

According to linear theory, the kinematics of a confused sea state described by (6) may be obtained by superposition from equations (3) to (5) as:

$$u(x, y, z, t) = \sum_m \sum_n \alpha_{mn} 2\pi f_m \frac{\cosh k_m z}{\sinh k_m d} \cos\theta_n \cos\psi_{mn} \quad , \quad (8)$$

$$v(x, y, z, t) = \sum_m \sum_n \alpha_{mn} 2\pi f_m \frac{\cosh k_m z}{\sinh k_m d} \sin\theta_n \cos\psi_{mn} \quad , \quad (9)$$

and

$$p(x, y, z, t) = \sum_m \sum_n \alpha_{mn} \rho g \frac{\cosh k_m z}{\cosh k_m d} \cos\psi_{mn} \quad , \quad (10)$$

where  $u(x, y, z, t)$  is the  $x$  component of the water particle velocity at space location  $(x, y, z)$  at some time  $t$ . Similarly,  $v(x, y, z, t)$  is the  $y$  component velocity and  $p(x, y, z, t)$  is the pressure.

Spectral Representation of Wave Properties : In practice, p,u,v measurements are taken over time at the same horizontal location, i.e. setting (x,y) = (0,0). Further, (u,v) measurements are made at the same height z = z<sub>v</sub> above the sea bed. Pressure measurements may be made at a different height z = z<sub>p</sub>. It is important that z<sub>p</sub> and z<sub>v</sub> are chosen to be above the bottom boundary layer.

We may introduce a frequency domain description of the wave field. The spectral density, S(f<sub>m</sub>, θ<sub>n</sub>), of the surface elevation is related to the mean (or expectation) of the square of the random amplitude, E(α<sub>mn</sub><sup>2</sup>), by

$$S(f_m, \theta_n) = \frac{1}{2\Delta f_m \Delta \theta_n} E(\alpha_{mn}^2) \quad , \quad (11)$$

where Δf<sub>m</sub> and Δθ<sub>n</sub> are the increments of frequency and direction "occupied" by the (m,n) wave component.

By taking lagged products of measured quantities (p,u,v) and passing from summation to integration, cross-covariances of p,u and v may be formed (Borgman, 1979). Fourier transformation of the cross-covariances provides the following cospectral expressions which may be used to estimate the direction surface sea state:

$$c_{uu}(f) = A^2(f) \int_0^{2\pi} S(f, \theta) \cos^2 \theta \, d\theta \quad , \quad (12)$$

$$c_{uv}(f) = A^2(f) \int_0^{2\pi} S(f, \theta) \sin \theta \cos \theta \, d\theta \quad , \quad (13)$$

$$c_{vv}(f) = A^2(f) \int_0^{2\pi} S(f, \theta) \sin^2 \theta \, d\theta \quad , \quad (14)$$

$$c_{pp}(f) = B^2(f) \int_0^{2\pi} S(f, \theta) \, d\theta \quad , \quad (15)$$

$$c_{up}(f) = A(f)B(f) \int_0^{2\pi} S(f, \theta) \cos \theta \, d\theta \quad , \quad (16)$$

$$c_{vp}(f) = A(f)B(f) \int_0^{2\pi} S(f, \theta) \sin \theta \, d\theta \quad , \quad (17)$$

where

$$A(f) = 2\pi f \frac{\cosh kz_v}{\sinh kd} \quad , \quad (18)$$

and

$$B(f) = \rho g \frac{\cosh kz}{\cosh kd} \quad , \quad (19)$$

represent velocity and pressure attenuation functions, respectively.

The Directional Spreading Function : Progress in the determination of the spectral density function  $S(f, \theta)$  is made by recasting the function as

$$S(f, \theta) = E(f) H(f, \theta) \quad , \quad (20)$$

with the constraint

$$\int_0^{2\pi} H(f, \theta) d\theta = 1 \quad . \quad (21)$$

In the above, the directional energy spectrum  $S(f, \theta)$  has been separated into a non-directional energy spectrum  $E(f)$ , and a directional spreading function  $H(f, \theta)$ .  $E(f)$  represents the surface wave energy summed over all propagation directions, i.e.

$$E(f) = \int_0^{2\pi} S(f, \theta) d\theta \quad . \quad (22)$$

$H(f, \theta)$  describes the distribution of the total energy  $E(f)$  over all possible propagation directions  $\theta$ . Its estimation is the key to obtaining a directional description of a sea state.

Following Longuet-Higgins et al. (1963), a convenient approximation to the directional spreading function may be obtained by expansion of  $H(f, \theta)$  in a truncated Fourier series, such that

$$H(f, \theta) = \frac{1}{2\pi} + \sum_{m=1}^M (a_m \cos m\theta + b_m \sin m\theta) \quad . \quad (23)$$

The  $p, u, v$  measurements which form the basis of this directional wave analysis contain sufficient information for the estimation of the above Fourier series truncated at  $M = 2$ .

Parametric Description of the Directional Spreading Function :

Further improvement to the description of the directional sea state may be obtained by introducing a subjectively selected, parametric approximation to the directional spreading function,  $H(f, \theta)$ . A model which has been widely used is that of Longuet-Higgins et al. (1963),

$$\begin{aligned} H(f, \theta) &= \frac{\Gamma(s+1)}{2\sqrt{\pi} \Gamma(s+1/2)} \cos^{2s}[(\theta - \theta_0)/2] \\ &= (1/\pi) \left[ 1/2 + \sum_{n=1}^{\infty} (r_n \cos n\theta_0) \cos n\theta \right. \\ &\quad \left. + \sum_{n=1}^{\infty} (r_n \sin n\theta_0) \sin n\theta \right] \quad , \quad (24) \end{aligned}$$

where

$$r_n = \frac{\Gamma^2(s+1)}{\Gamma(s+n-1) \Gamma(s-n+1)}$$

In the above,  $s$  is referred to as the "sharpness index", and  $\theta_0$  is the predominant direction of wave propagation. The multiplying term involving the Gamma function  $\Gamma$  arises from the constraint equation (13). This model should provide a satisfactory description of a uni-modal wave field with wave directions dispersed over a narrow sector centred about  $\theta_0$ . A high value of "sharpness index" indicates that all wave directions are concentrated about  $\theta_0$ .

5. ANALYSIS TECHNIQUES

Primary Data Plots : The wave-induced velocity data returned from each "burst" of the Sea Data 635-12S are illustrated by the cross plots of the horizontal current velocity components (figure 1).

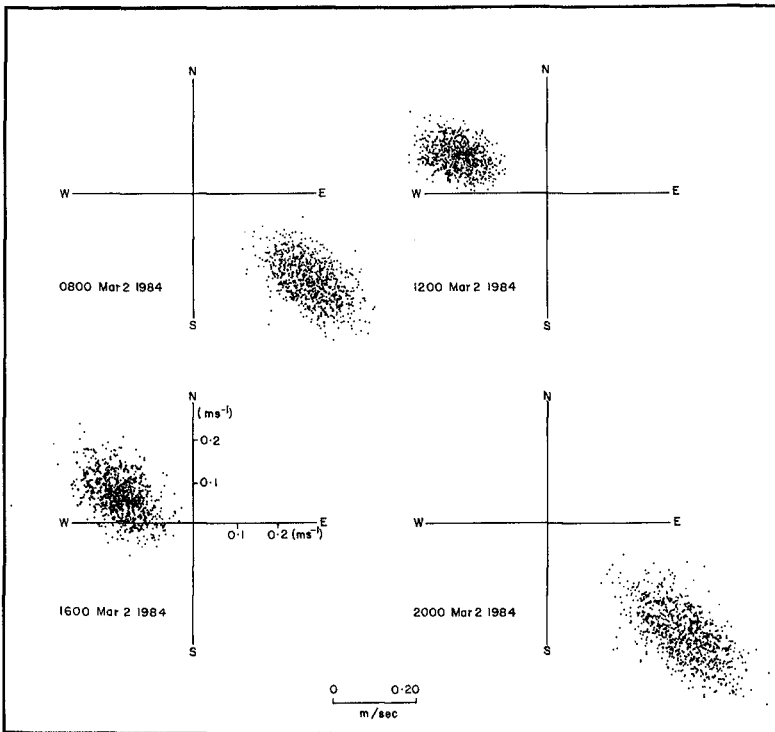


Figure 1 Example cross plots of the u-v horizontal current velocities measured near the sea bed. The elliptical scatter is caused by wave-induced currents, and displaced by tidal currents.

The velocity cross plot shows the elliptical spread of horizontal wave-induced motions. The principle direction of wave propagation is along the major axis of the ellipse. The 180° ambiguity about the direction of phase propagation is resolved by examination of the pressure time history. Horizontal wave-induced velocities under wave crests are in the same direction as the phase propagation.

Frequency Domain Estimation of Directional Parameters : The directional spectrum of a random sea state may be estimated from Fourier transformations of a set of N triplets of simultaneous u,v,p measurements, consecutively sampled at a time spacing of  $\Delta t$ .

Fourier transformations of the measured p,u,v time series provide estimates of the left-hand sides of equations (12) to (17), the p,u,v cospectra. Using the velocity and pressure attenuation functions (18) and (19) determined from linear wave theory, and the description of the spectral density function given by (20) to (22), the coefficients  $a_1, b_1, a_2$  and  $b_2$  of the truncated Fourier expansion of the spreading function (23), may be estimated from the p,u,v cospectra.

First order estimates of the directional spectral parameters of the  $\cos^{2S} [(\theta - \theta_0)/2]$  model may be obtained by comparing equation (24) with equation (23), from which

$$s = \frac{r_1}{1-r_1} \quad (25)$$

where

$$r_1^2 = a_1^2 + b_1^2 \quad , \quad (26)$$

and

$$\theta_0 = \arctan \left( \frac{b_1}{a_1} \right) \quad , \quad (27)$$

which are obtained from the pressure-velocity cospectra.

An alternative estimate of s and  $\theta_0$ , known as the second order fit, is also available, as

$$s = \frac{(1+3r_2) + (1-14r_2 + r_2^2)^{1/2}}{2(1-r_2)} \quad (28)$$

where

$$r_2^2 = a_2^2 + b_2^2 \quad , \quad (29)$$

and

$$\theta_0 = \frac{1}{2} \arctan \left( \frac{b_2}{a_2} \right) \quad . \quad (30)$$

which is obtained from velocity-velocity cospectra.

An example of the directional spectral information attainable from each "burst" of p,u,v measurements of the Sea Data 635-12S Directional Wave and Tide Recorder is presented in figure 2. First and second order estimates of wave direction agree very well. First and second order estimates of sharpness index are not theoretically equivalent, but are expected to display similar trends.

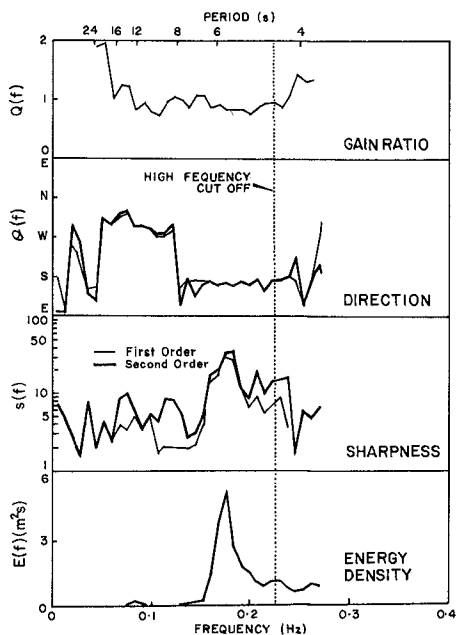


Figure 2 Example of the spectral information attainable from each "burst" of a directional wave recorder. First and second order estimates are derived from equations (25) to (27) and (28) to (30), respectively.

Following the example of Forristall et al. (1978) the gain ratio  $Q(f)$  has also been calculated. It represents the ratio of the measured pressure to velocity transfer function and that predicted by linear theory. From equations (18) and (19),  $Q(f) = A(f)/B(f)$ . If  $Q(f)$  remains near unity, linear theory is providing a satisfactory description of wave kinematics. Figure 2 shows that  $Q(f)$  departs from unity for very high frequencies where ambient turbulence contaminates the data, and for low frequencies where surface wave energy is very low.

Also presented on this plot is a dotted vertical line which marks where the spectral moment computations have been truncated (high frequency cut off), to avoid the increasing noise contamination of the wave signal.

Time Domain Estimation of Directional Parameters : The mean wave direction and sharpness index estimates may be obtained without recourse to spectral analysis, from the covariance (time domain) equivalents of equations (25), (27), (28) and (30). For each set of  $N$  triplets of  $p, u, v$  the variances and covariances  $C_{\gamma\zeta}$  of the measured quantities are computed by taking the dot products as follows:

$$C_{\gamma\zeta} = \frac{1}{N} \sum_{i=1}^N (\gamma_i - \bar{\gamma})(\zeta_i - \bar{\zeta}) \quad ,$$

where the overbars denote sample means, and the subscripts  $\gamma$  and  $\zeta$  denote  $p, u$  or  $v$ .

First order estimates of mean direction  $\bar{\theta}$  and sharpness index  $\bar{s}$  are obtained explicitly from

$$\bar{\theta} = \arctan \left\{ \frac{C_{pv}}{C_{pu}} \right\} \quad , \quad (31)$$

and

$$\bar{s} = \frac{r_1}{1-r_1} \quad , \quad (32)$$

where

$$r_1^2 = \frac{C_{pu}^2 + C_{pv}^2}{\{C_{uu} + C_{vv}\} C_{pp}} \quad . \quad (33)$$

The second order estimates are obtained from

$$\bar{\theta} = \frac{1}{2} \arctan \left\{ \frac{2C_{uv}}{C_{uu} - C_{vv}} \right\} \quad , \quad (34)$$

and

$$\bar{s} = \frac{(1+3r_2) + (1-14r_2 + r_2^2)^{1/2}}{2(1-r_2)} \quad , \quad (35)$$

where

$$r_2^2 = \frac{\{C_{uu} - C_{vv}\}^2 + 4C_{uv}^2}{C_{uu} + C_{vv}} \quad . \quad (36)$$

It should be noted that these estimates are derived from measurements of wave kinematics which have suffered frequency dependent depth attenuation. As the depth of measurements increases, these estimates become more biased towards longer period waves.

## 6. INSTRUMENT PERFORMANCE

Local deployments of the Sea Data 635-12S Directional Wave and Tide Recorder have now returned in excess of two years of data. Improvements in the design and operation of the instrument, and in the data transcription and processing techniques, now allow better than 98% data recovery.

Experience with deployments at various locations around Australia shows that minimum wave periods of 2, 5 and 8 seconds may be satisfactorily resolved in water depths of 2, 20 and 50 metres, respectively. The directionality of recorded wave fields has been evident in all deployments.

The performance of the 635-12S is illustrated by measurements conducted in 20 metres of water at a location 30 km south of Barrow Island off the north west coast of Australia, during the passage of tropical cyclone "Chloe". The measurement location and tropical cyclone track are shown in figure 3. The storm track passed about 150 km to the south east of the measurement location.

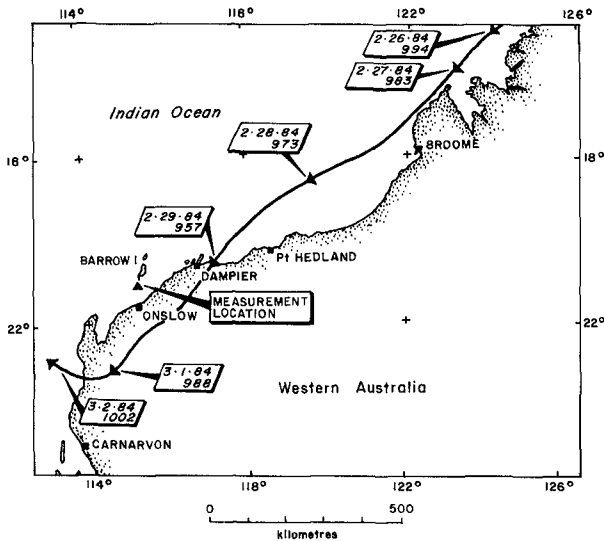


Figure 3 Location diagram showing directional wave measurement site and the track of tropical cyclone "Chloe". Arrow heads on the track correspond to 1200 hours GMT. Date and storm central pressure (mb) are shown adjacent each mark.



Figure 2 shows the directional spectral information obtained from one "burst" of the 635-12 near the time of closest approach of the storm. This includes the presentation of  $\theta(f)$  and  $s(f)$  as a function of frequency, derived from equations (25) to (30). In this figure, the distinct bimodality of the sea state is evident, with swell waves (periods longer than 8 seconds) propagating from the north west, and short period, locally generated wind waves propagating from the south.

Averages weighted by the non-directional energy spectrum were taken to produce burst mean estimates, denoted by  $\bar{\theta}$  and  $\bar{s}$ . Figure 4 shows the variation of the directional wave climate during the passage of tropical cyclone "Chloe", using burst mean parameters.

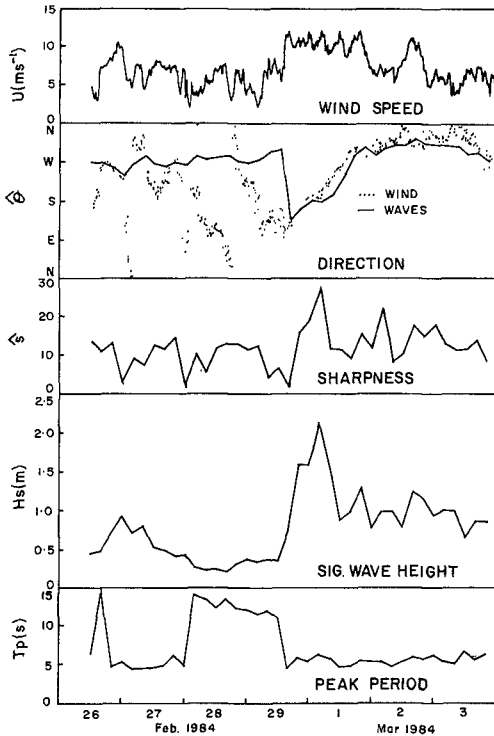


Figure 4 Description of the temporal variation of the directional climate using mean spectral parameters, for the period of the passage of tropical cyclone "Chloe".

Wind speeds and directions shown are 20 minute mean values recorded on Barrow Island, about 30 km north of the measurement location. The first order estimate of the wave direction  $\theta$ , initially shows the incidence of westerly to north westerly swell, then tracks the wind direction after the onset of the storm. The sharpness index  $s$  peak is observed to coincide with the storm peak, as also noted by Mitsuyasu et al. (1975).

Non-directional spectral parameters  $H_s$  (significant wave height) and  $T_p$  (period of the spectral peak) illustrate the incidence of low amplitude, long period swell prior to the arrival of the storm, followed by the generation of a high energy, short period sea state.

The 635-12S may also be used to establish frequency dependent variations in the wave climate. This is achieved by taking averages of  $E(f)$ ,  $s(f)$ ,  $\theta(f)$  and  $Q(f)$  for each spectral ordinate over entire deployments. Figure 5 illustrates the result of averaging the spectral parameters over a six week deployment period.

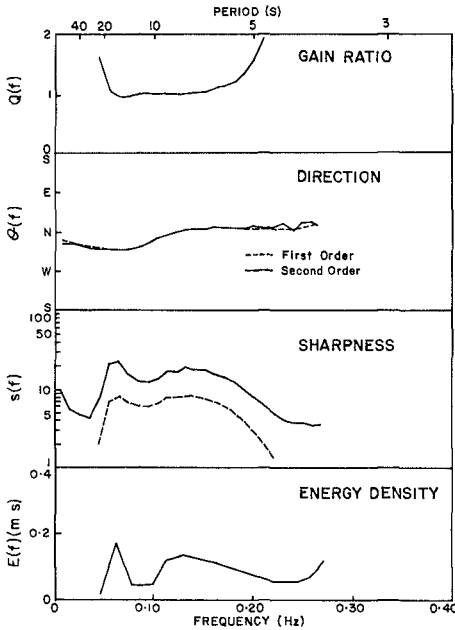


Figure 5 Spectral parameter means providing a description of the frequency dependent variation of the directional wave climate, over the period of an entire deployment.

$Q(f)$  determines the limits of applicability of the frequency dependent wave climate description, which holds only while  $Q(f)$  is near unity. Within this frequency range, the wave climate is seen to be distinctly bimodal, with swell periods in excess of 10 seconds typically incident from the north west, and shorter period wind waves (6 to 10 seconds) typically incident from the north-north-east. For this deployment, bathymetric constraints limit wave propagation from the east. The sharpness and energy density estimates also reflect the bimodality of the wave climate.

Comparison of Analysis Techniques : Figure 2 shows that first and second order estimates of  $\theta$  are very similar. Estimates of  $s$  vary, but they do display similar trends.

Estimates of  $\bar{\theta}$  and  $\bar{s}$  may be obtained without recourse to spectral analysis, using the covariance equations (31) to (36). A comparison of these estimates with their spectral equivalents,  $\hat{\theta}$  and  $\hat{s}$ , (weighted by the energy density) is presented in figure 6, again using data recorded during the passage of tropical cyclone "Chloe".

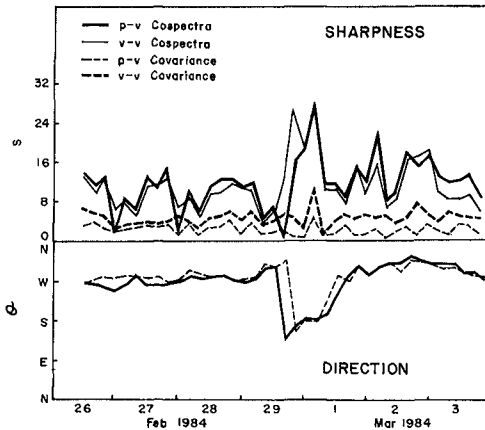


Figure 6 Comparison of mean wave directions and sharpness indices derived by time domain (covariance estimates  $\bar{\theta}$  and  $\bar{s}$ ) and frequency domain (cospectral estimates  $\hat{\theta}$  and  $\hat{s}$ ) techniques.

First and second order estimates of  $\theta$  in either the time domain (covariances) or frequency domain (cospectra), are almost indistinguishable. However, small differences are evident between time domain and frequency domain estimates, particularly during periods of rapid change in the sea state.

First and second order estimates of  $s$  show the expected similar trends, but time domain estimates are generally less than the frequency domain estimates.

Comparison with Surface Wave Measurements : A Datawell Waverider buoy was deployed concurrently with the Sea Data 635-12S, at the same location during the passage of tropical cyclone "Chloe". This allowed comparison of non-directional wave parameter estimates, which are presented in figure 7.

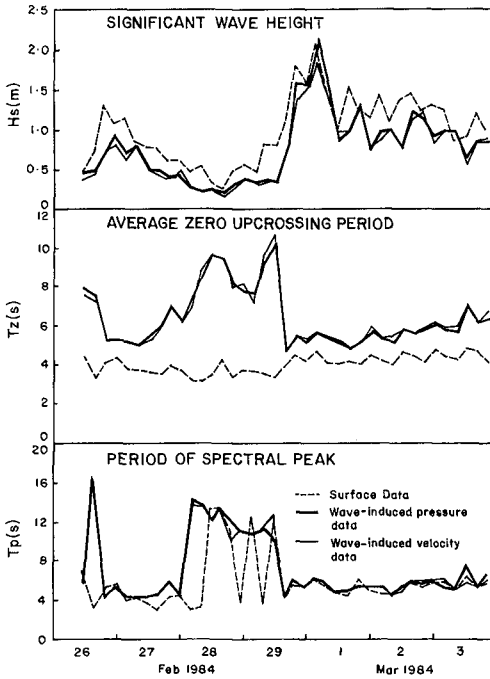


Figure 7 Comparison of non-directional spectral surface wave parameters derived from surface displacement measurements, and near-bottom pressure and velocity measurements.

Estimates of significant wave height derived from both near-bottom pressure and velocity measurements agree very well, except at the storm peak where dynamic pressure effects may have become important. Generally, Waverider estimates of significant wave height exceed those derived from the near-bottom measurements due to the depth attenuation of short period waves (5 seconds or less). At the storm peak, estimates from the Waverider and the near-bottom pressure measurements coincide.

Estimates of average zero upcrossing period and spectral peak period derived from both near-bottom pressure and velocity measurements also agree very well. While Waverider measurements provide good agreement for spectral peak period, average zero upcrossing periods are seen to be much lower than those derived from near-bottom measurements, because of the predominance of short period surface waves.

In accordance with Forristall et al. (1978), comparisons of measured near-bottom wave-induced velocity spectra with those derived from surface wave measurements using non-directional linear wave theory, show the theory to overpredict near-bottom velocities by about 20%.

#### 7. COMMENTS AND CONCLUSIONS

The Sea Data 635-12S Directional Wave and Tide Recorder provides a reliable means of measurement of near-bottom wave-induced kinematics and of shallow water directional wave climate.

Uni-directional linear wave theory is seen to overpredict near-bottom wave-induced velocities derived from surface wave measurements.

A variety of analysis techniques are available, several of which have been applied to the measured data. Analyses undertaken to date have not indicated a preference for first or second order estimates of directional wave parameters. Maximum likelihood techniques which combine both estimates have been successfully applied to simulated data, but small (sensor induced) phase differences between measured pressures and velocities inhibit application to field data. It is hoped to apply these types of data adaptive techniques in the future.

The Sea Data 635-12S Directional Wave and Tide Recorder can routinely provide important information for determination of wave-induced forces on coastal structures and submarine pipelines, for shallow water wave refraction and diffraction studies and for sediment transport studies.

#### 8. REFERENCES

- Aubrey, D.G. and W. Hill, 1984. Performance of bottom-mounted directional wave gauges. Conference Record, Oceans '84, Marine Technology Society, IEEE Ocean Engineering Society, Washington D.C.
- Borgman, L.E., 1979. Directional wave spectra from wave sensors. In Ocean Wave Climate edited by M.D. Earle and A. Malahoff. Marine Science, 8, 269-300. Plenum Press (N.Y.).

- Forristall, G.Z., Ward, E.G., Cardone, V.J. and Borgman, L.E., 1978. The directional spectra and kinematics of surface gravity waves in tropical storm Delia. *J. Phys. Oceanogr.*, 8, 888-909.
- Goda, Y., Takayama, T. and Y. Suzuki, 1978. Diffraction diagrams for directional random waves. *Proc. 16th Coastal Eng. Conf. Hamburg*. Published by ASCE, New York.
- Grosskopf, W.G., Aubrey, D.G., Mattie, M.G. and M. Mathiessen, 1983. Field intercomparison of nearshore directional wave sensors. *IEEE J. Oceanic Eng.*, OE-8, 254-271.
- Longuet-Higgins, M.S., Cartwright, D.E. and N.D. Smith, 1963. Observations of the directional spectrum of sea waves using the motions of a floating buoy. *Ocean Wave Spectra*, Prentice-Hall Inc. (NY), pp. 111-136.
- Mitsuyasu, J., Tasai, F., Suhara, T., Mizuno, S., Ohkusu, M., Honda, T. and K. Rikiishi, 1975. Observations of the directional spectrum of ocean waves using a cloverleaf buoy. *J. Phys. Oceanogr.*, 5, 750-760.
- Sand, S.E., Brink-Kjaer, O. and J.B. Nielson, 1981. Directional numerical models as a design basis. *ARAE International Symposium, Wave and Wind Directionality with Applications to the Design of Structures*. Paris.

## CHAPTER TWENTY ONE

US Army Corps of Engineers  
Field Wave Gaging Program

J. Michael Hemsley, M. ASCE\*

### Introduction

While the timely collection and reporting of climatological and environmental data have become routine in many countries, a similar capability for waves, currents, and coastal winds has not. The need for long-term, high quality wave data, in particular, has long frustrated the coastal engineer. In 1974, both Prof. Robert Wiegel and Dean Morrrough P. O'Brien commented publically on the need for information on the nearshore wave climate comparable to data routinely available on many other natural phenomena. O'Brien further expressed his concern for improving the accuracy of wave forecasting and hind-casting techniques through comparison with reliable measurements (2).

The need for characterizing the nearshore wave climate is much like the experience of conventional meteorological measurement programs. Along coastlines with high population densities, usage of the resource is intense. Ignorance of the processes at work carries a significant penalty. Past programs either have emphasized the collection of deepwater wave climatology or have been too regional or even site specific. With the Field Wave Gaging Program (FWGP), the US Army Corps of Engineers intends to collect the long-term, nearshore wave data that are necessary for planning, design, construction, operation, and maintenance of coastal projects.

### History and Objectives

In 1974, the American Society of Civil Engineers (ASCE) sponsored a Conference on Ocean Wave Measurement and Analysis. As a direct result of that conference, Scripps Institution of Oceanography installed a regional wave monitoring network for the State of California in 1975. The network began modestly, with only four stations operating by mid-1976, supported by the California Department of Boating and Waterways (Cal Boating) and the National Oceanographic and Atmospheric Administration (NOAA) Sea Grant Program. In 1978, the Corps of Engineers' South Pacific Division (SPD) became involved and provided funding to begin the expansion of this network throughout California. The Coastal Data Information Program (CDIP) became a cooperative effort between the Corps and Cal Boating, with Scripps acting as a contractor for data collection, analysis, and reporting (6).

---

\* Research Hydraulic Engineer, Coastal Engineering Research Center, USAE  
Waterways Experiment Station, PO Box 631, Vicksburg, MS 39180-0631

Almost concurrently with the formation of the CDIP, the Corps established a nationwide Coastal Field Data Collection Program (CFDCP), one element of which was the FWGP. The goals of the FWGP are to collect nearshore and relatively deepwater wave data to satisfy the immediate needs of the coastal planner, designer, and project operator; to support the Corps' effort to develop a wave hindcast/forecast model; and to provide a long-term data record for all of the nation's coastlines.

In addition to the FWGP, the CFDCP funds efforts to (1) hindcast 20 years of wave information from available wind data in the Atlantic, Gulf of Mexico, and Pacific; (2) identify, catalog, and make available beach profile data already obtained on the US coasts and obtain additional profile data in areas of particular interest; (3) identify, catalog, make available, and continue to update shoreline change maps; (4) continue Littoral Environmental Observations (LEO) in areas of interest; and (5) develop a database management system for the archiving of coastal data that have been and continue to be collected. The CFDCP also provides the mechanism through which valuable coastal data are collected, analyzed, distributed, and archived.

The existence of the CDIP has been very beneficial to the FWGP in two ways: (1) by having begun development on the automated data collection, analysis, and reporting system, and (2) by establishing a network of CDIP gages to provide a starting point from which the national wave gaging system could expand.

#### Gage Network

Eventually, the FWGP will acquire wave data along each of the nation's coasts. Primary data for the program will be collected at a number of deepwater, or index sites (Figure 1). These stations will be operated continuously in order to provide reliable long-term statistical wave data for use in planning, design, operation, and maintenance of coastal engineering projects. They are located in water sufficiently deep to minimize bathymetric effects on the measured waves, often as deep as 200 m (650 ft). An additional and unfortunately critical consideration in siting the index gages is to find a location that is not in a commercially fished area. Commercial fishermen using bottom-dragging equipment can break a deepwater mooring with their nets. This is an all too frequent occurrence in commercial fishing grounds even though instruments are reported in the US Coast Guard "Notice to Mariners."

Augmenting the index stations are nearshore gages located in areas generally representative of long stretches of coastline. These nearshore gages are, on occasion, single pressure gages, or, more often, slope arrays. Data are to be collected from these stations for five years to provide the nearshore wave information so necessary to coastal projects and to assist in verification of the numerous wave propagation models. Site selection for slope arrays requires reasonably straight, parallel offshore contours and, like the index stations, consideration of commercial fishing activity. A bottom-mounted sensor can be destroyed by the heavy nets used on large trawlers.



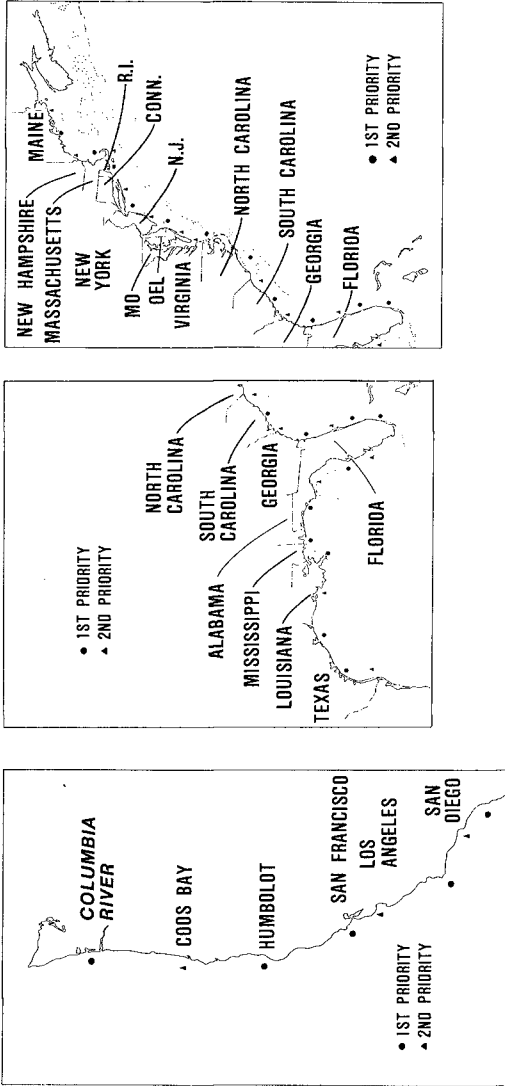


Figure 1. Proposed Index Sites

To date, Datawell Waverider buoys have been used in all of the index station installations; the depth of these installations precludes the use of bottom-mounted sensors. The Waverider buoy is a proven instrument which uses a vertically stabilized accelerometer to sense the vertical component of the buoy's motion. Heave data from the buoy are transmitted up to 50 km (31 miles) to shore.

Nearshore wave measurements, in depths of up to 15 m (50 ft), are made using a bottom-mounted Kulite semiconductor strain gage pressure transducer. The transducer and its circuitry are housed in a plastic pressure case mated to an underwater cable by a plastic underwater connector. The cable is used both to carry the signal ashore and to supply power to the sensor. Sufficient cable is stored in a service loop to allow the sensor housing to be brought to the surface for servicing, thereby increasing the system's reliability (9).

An array of four pressure sensors has been developed by Scripps to obtain directional wave data. This array is 6m (20 ft) square on a side and uses a specially designed armored underwater cable for data and power transmission. This cable has effective abrasion resistance, waterblocking integrity, tensile strength, and resistance to cutting which greatly enhance the system's reliability. Details of the array are described by Seymour and Higgins (8), and results of laboratory and field tests are discussed by Higgins, Seymour, and Pawka (3). Seymour, Domurat, and Pirie (7) describe a test at Santa Cruz, CA, where the estimates of gross and net longshore transport calculated from the array compared favorably with the actual sediment volume dredged from the harbor entrance.

Installation of the Waverider buoy and single pressure sensor is fairly straightforward, requiring only a small craft. The standard Datawell mooring has been employed successfully with few modifications. A tripod or jetted pipe is most often used for the single pressure sensor installation. Some innovation is needed when installing the array because of its size. When available, an amphibious vehicle can be effectively used to deploy the array and lay the cable from offshore across the surf zone and beach to the shore station. On two occasions when an amphibious vehicle was unavailable, an array was carried as a sling load beneath a US Army Reserve Chinook helicopter. The cable spool was carried inside its cargo area.

Figures 2 and 3 show the data collection sites currently being operated under the FWGP and provide information on gage type, percent data return, operational status, and gage ownership in programs other than this one. Operation of the system has been successful. Many of the stations that are not operational were lost or damaged during the severe storms in the early months of 1983 or as a possible result of that year's persistent "El Nino" current. Several arrays sustained cable damage as a result of beach protection or restoration efforts. An increase in buoy losses was experienced that appears attributable to the migration of commercially fished species as a result of "El Nino" and the expansion of the commercial fishing market to include species not previously considered marketable. All but one of the gages should be operational in 1984.

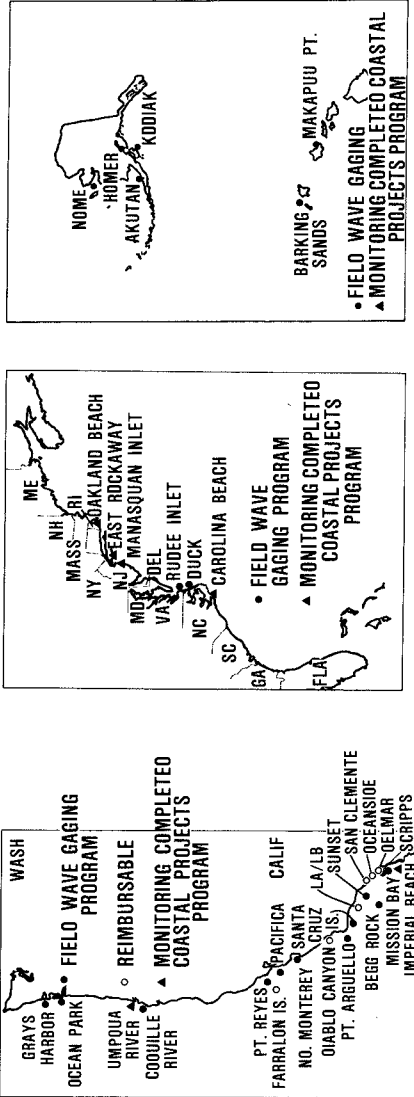


Figure 2. Data Collection Sites

## FIELD WAVE GAGING PROGRAM

309

## DATA COLLECTION REPORT

MONTH OF: June 1984

Program	Gage Location	Gage Type	Current Month	Year To Date	Comments
FWCP	Mission Bay, CA	Buoy	Hit by barge - to be replaced		
	Mission Bay, CA	Array - Energy - Direction	Cable damage - to be replaced		
	Scripps, CA	Single pressure	98.3%	90.9%	
	Begg Rock, CA	Buoy	95.8%	83.4%	USN owned
	Santa Cruz Is., CA	Buoy	85.4%	85.9%	USN owned
	Sunset, CA	Array - Energy - Direction	Cable damage - to be replaced		
	Pt Arguello, CA	Buoy	To be replaced		
	N. Monterey Bay, CA	Buoy	Lost to trawler - to be replaced		
	Pacifica, CA	Array - Energy - Direction	To be replaced		
	Humboldt, CA	Buoy	To be replaced		
	Coquille R., OR	Buoy	To be replaced		
	Coquille R., OR	Array - Energy - Direction	98.3% 0.0%	91.4% 0.0%	Cable damaged by vandals
	Ocean Park, WA	Array - Energy - Direction	94.2% 91.7%	93.3% 89.7%	
	Grays Harbor, WA	Buoy	To be replaced		
	Makapu'u Pt, HI	Buoy	100.0%	95.4%	
	Barking Sands, HI	Buoy	To be replaced		USN owned
Duck, NC	Array - Energy - Direction	96.7% 93.3%	95.4% 91.8%		
Rudee Inlet, VA	Array - Energy - Direction	Abandoned			
MCCP	Imperial Beach, CA	Array - Energy - Direction	99.2% 20.8%	93.5% 63.2%	MCCP owned
	Umpqua R., OR	Buoy	99.2%	77.1%	Installed May 20, 1984
CCSTWS	Del Mar, CA	Array - Energy - Direction	97.5% 95.8%	93.4% 92.1%	CCSTWS owned
	San Clemente, CA	Array - Energy - Direction	90.0% 90.0%	91.6% 89.9%	
SPL	Oceanside, CA	Array - Energy - Direction	97.5% 97.1%	92.0% 91.2%	SPL owned
City of SF	Farallon Is., CA	Buoy	98.3%	91.2%	City of SF owned
PG&E	Diablo Canyon, CA	Buoy	90.8%	85.4%	Adamo-Rupp Installation for PG&E

Figure 3. System Status

Nearshore gages installed in support of specific projects supplement the data collected under the FWGP. On the Pacific coast, nine project-supported gages are operated through the FWGP network and the data reported by Scripps in the program's reports. The program, therefore, provides an existing system through which project-specific data can be collected, analyzed, and reported, taking advantage of the FWGP computers at Scripps. The system provides the considerable capacity and flexibility needed for coastal data collection and can accommodate any continuously reporting instrument. Tide, surge, current, wind, and wave data are being or have been collected on the system.

#### Related Data Collection Programs

Alaska's coastal data needs are unique. The State has approximately 54,500 km (33,900 miles) of coastline with a climate varying from temperate to arctic. With communities heavily dependent on the sea scattered along the entire coast, the State needed a planned approach to its coastal data collection efforts. In 1982, a cooperative agreement was signed between the State of Alaska and the Corps of Engineers to collect coastal wind and wave data. The goals stated in that agreement were, briefly, to collect, analyze, report, and archive coastal data collected by either party; to develop a plan for the collection of coastal data; and to develop instruments, telemetry systems, and analysis procedures suited to the needs and environment of Alaska (1).

Figure 2 includes the sites currently instrumented in Alaska. The Alaska Coastal Data Collection Program (ACDCP) is supported by funds from the State Department of Transportation and Public Facilities (DOT/PF), the Corps of Engineers, Alaska District, and the FWGP. Short-term (two to three years) data collection is planned to begin at 17 sites over the next 5 years.

Two types of stations have been developed: one for deep water and the other for nearshore measurements; both include a remote anemometer. For the deepwater sites, Waverider buoys are used. Nome is the only station currently in shallow-water operation. There the instrumentation consists of a pressure gage and current meter to provide directional wave data. Data from both station types are telemetered to a shore station and recorded on magnetic tape. Because data transmission over telephone lines is not reliable in Alaska, a meteor burst transmitter is used to send real-time data to the Corps office in Anchorage. The system uses meteor trails in the upper atmosphere as the medium from which the data are reflected. Meteor burst allows the data to be transmitted over great distances without the use of satellites or telephone lines and provides an inexpensive system check.

US Army Engineer District, Alaska, publishes data reports periodically as data are processed. To date, two reports have been produced for the station at Kodiak. The data reports provide the average wind speed and direction, maximum wind speed, and standard deviation of the wind speed and direction for each data collection. Both wind and wave data are reported every three hours. Wave data reported include the significant wave height, total energy in the spectrum, and the percent of the energy in frequency bands of 0.02148 Hz

width. As more stations become operational, the data reports will be published more frequently.

Another cooperative effort that receives some support from the FWGP involves a contract with the University of Florida to collect, analyze, and report wave data from the Florida coast. The gaging effort is funded by the Corps of Engineers through the Hurricane Surge Prototype Data Collection Work Unit and the FWGP, by the State of Florida, and by the US Nuclear Regulatory Commission. Eight sites in Florida are operated by the University as the Florida Coastal Data Network (FCDN) using bottom-mounted single pressure transducers. Recently, three P-U-V in situ recording meters were added to provide directional wave data.

The FCDN provides real-time data in support of the hurricane surge work unit. Data reports are produced monthly by the University of Florida for each of the sites operated under the contract. Both tables and plots are used to report the wave data, which are collected every 6 hours. Plots of maximum period and significant wave height versus time are included in the reports. The tables provide significant wave height, total energy in the spectra, and the percent energy in various period bands from 4 to 22+ seconds for each data collection (4).

#### Data Collection, Analysis, and Reporting

The data collection system developed by Scripps and used by the FWGP is based on burst rather than continuous sampling. While sampling frequency is field selectable, depending on the data to be collected, it is typically set at 1 hertz for ocean waves measured for the FWGP. The standard sample size is 1024 points, yielding 17 minutes of data. Normally each instrument is interrogated once every 6 hours, although certain critical stations are called every 3 hours and the data transmitted to the National Weather Service.

A block diagram of the collection and analysis system is shown in Figure 4. Signals from as many as eight input channels are received by a weatherproof shore station near the sensors. This station, which contains the data conversion and storage capability, control and power systems, and telephone interfaces, is modular. All electronics are on plug-in cards to facilitate the replacement of faulty components and minimize a station's down-time. Current incoming data are maintained in a digital buffer memory which expels the oldest words on a first-in first-out basis, ensuring that the most recent data set is in the buffer.

A control computer (a NOVA 1200 located at Scripps) initiates a telephone call to the shore station using an autodialer and normal telephone lines. The shore station, when called, locks the most current words in memory and transmits the data in a special 1200 Baud synchronous format to a digital data receiver at Scripps. Once all the data are transmitted, typically in slightly over one minute for four data channels, the shore station disconnects itself from the telephone line. Header information is then added, and the record is written on magnetic tape. During data transmission from the shore station, signal quality checks are performed. Failure of a quality check results in a second

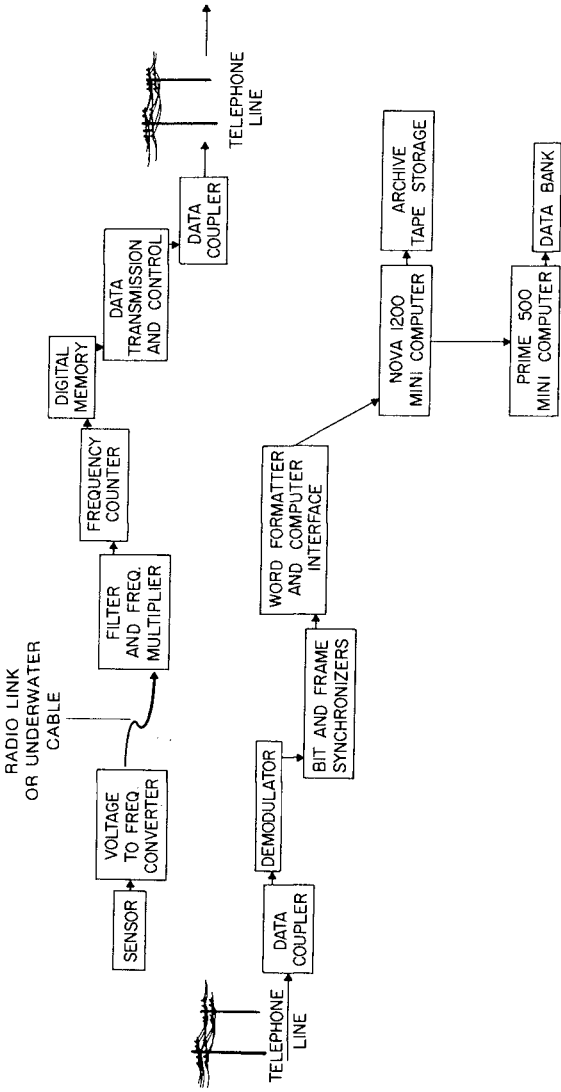


Figure 4. Data Collection and Analysis System

From Seymour, et.al., in press

call causing the immediate retransmission of the original data from the shore station. This protocol is important in the correction of transmission errors (9).

After the quality check, the raw data are put onto disks in a large mini-computer (a Prime 500 which serves as the central processing computer) for quasi-real-time analysis. The Prime and the NOVA are connected with a bidirectional serial link, allowing data and command flow in both directions. The NOVA can be remotely accessed through the Prime to make functions such as test calls, status checks, and raw statistics available from remote terminals.

Data analysis is composed of three phases. The first phase involves the receipt of the raw data from the NOVA and extensive data verification and editing in preparation for the second phase. An analysis phase performs the Fast Fourier Transform operations on the edited time series. The final phase operates on the analyzed data to produce the end products, monthly and annual reports.

In the first phase, an editing routine provides an automated data assurance scheme operating on the massive daily influx of data after their acceptance by the central computer. The editor is programmed to objectively recognize certain anomalies, to correct the more obvious ones, and to reject the others as bad data. It also compiles daily summaries and monthly statistics on the frequency and type of errors. The types of errors are spikes (the most frequent cause of data rejection), flat spots, mean shift exceedence, absence of zero crossings, and maximum and minimum wave height exceedence. Additionally, the editor filters the time series to remove tidal components and intercompares the individual sensor variances to evaluate acceptability of data for determining wave direction from the arrays.

Edited data for both gravity and infragravity waves are then Fourier transformed and the energy spectra calculated. Spectral values are grouped into period bins and summed to yield the variance. From the variance, the significant wave height is determined and the period band containing the maximum energy in the spectrum is identified. The data analysis routine also determines the percent of energy in each of nine period bands ranging from 4 to 22+ seconds.

Higgins, Seymour, and Pawka (3) describe the analytical method for extracting wave directionality from the sea surface slope components measured by the array. The method developed by Longuet-Higgins, Cartwright, and Smith (5) for use with a pitch-and-roll buoy is adapted for use with the array. An estimate of the longshore component of radiation stress,  $S_{xy}$ , can be extracted when surface elevation and components of sea surface slope are known at a point. The components of the slope are determined from differences between a pair of sensors. While only three sensors are required for this analysis, four are used for redundancy.

Routine analyses of wave direction involves calculation of a spectrum of the longshore component of shoreward-directed radiation stress, which, with the energy spectrum, allows the estimation of an apparent arrival direction for each band of



periods. Summing the radiation stress components over all frequencies yields total  $S_{xy}$ . From this, and the total energy, a significant angle of arrival for all the wave energy can be estimated (9).

In addition to the products previously discussed, the distribution of  $S_{xy}$  in the period bands is reported.

The significant data collected under the FWGP are available to users in three forms: direct access via remote terminals, data archives at Scripps and the US Army Engineer Waterways Experiment Station (WES), and monthly and annual reports. Data processed since the program's inception are directly available to any user with a computer terminal capable of remote telephone access of the Prime at Scripps. A user-friendly program has been developed to call up tabular and plotted data, including data for single or multiple stations on a single day, a single station on multiple days, or overplotted spectra to allow visualization of a storm's passage. Edited raw data are archived on tape at both Scripps and WES and can be made available to users under certain conditions.

Monthly and annual reports produced by Scripps provide the widest dissemination of wave data collected within the FWGP. After the first month of operation of the original program in 1975, a report was issued showing spectra and other wave parameters for Imperial Beach, CA. Every month since, analyzed data have been provided through these reports to a large group of public and private users. These data are summarized in an annual report which includes descriptive statistics on wave height and period as well as longshore sediment transport.

#### Future Effort

A nationwide network of index sites, including the Great Lakes, is the goal of the FWGP, and that goal will be pursued during the next few years. Growth of the program will be gradual, but the importance of obtaining long-term wave data should ensure that expansion.

#### Acknowledgement

The program described in this paper is an ongoing effort undertaken by WES for the Civil Works Program of the Corps of Engineers with the support of California, Florida, and Alaska. The author wishes to acknowledge the Office, Chief of Engineers, US Army Corps of Engineers for permission to publish this paper.

#### References

1. Bales, J. T. 1984 (Jun). "Alaska Coastal Data Collection Program," Proceedings of the Forty-First Meeting of the Coastal Engineering Research Board, Seattle, Washington, pp. 283-289.
2. Edmisten, J. R. 1978 (Jul). "Toward Fulfillment of an Urgent Need, Coastal Wave Data Acquisition and Analysis," Shore and Beach, Vol 46, No. 3, pp. 3-14.

3. Higgins, A. L., Seymour, R. J., and Pawka, S. S. 1981. "A Compact Representation of Ocean Wave Directionality," Applied Ocean Research, Vol 75, No. 33, pp. 6778-6801.
4. Howell, G., 1980. "Florida Coastal Data Network," Proceedings 17th International Conference on Coastal Engineering, ASCE, Sydney, Australia, Vol 1, pp. 421-431.
5. Longuet-Higgins, M. S., Cartwright, D. E., and Smith, N. D. 1963. "Observations of the Directional Spectrum of Sea Waves Using the Motions of a Floating Buoy," Ocean Waves Spectra, Proceedings of a Conference, pp. 111-136.
6. Seymour, R. J. 1979. "Measuring the Nearshore Wave Climate: California Experience," Marine Science, Vol 8, in Ocean Wave Climate, Marshall D. Earle and Alexander Malahoff, eds, Plenum Press, N. Y., pp. 317-327.
7. Seymour, R. J., Domurat, G. W., and Pirie, D. M. 1980. "A Sediment Trapping Experiment at Santa Cruz, CA." Proceedings of the 17th International Conference on Coastal Engineering, ASCE, Sydney, Australia, Vol II, 1416-1435.
8. Seymour, R. J. and Higgins, A. L. 1978. "Continuous Estimation of Longshore Sand Transport," Coastal Zone '78, ASCE, pp. 2308-2318.
9. Seymour, R. J., Sessions, M. H., and Castel, D. In press. "Automated Remote Recording and Analysis of Coastal Data," submitted to Journal of Waterways, Ports, Coastal, and Ocean Division of the American Society of Civil Engineers.

## CHAPTER TWENTY TWO

### IRREGULAR WAVE OVERTOPPING RATES

Scott L. Douglass\*  
A.M., ASCE

**ABSTRACT:** Methods for estimating wave overtopping of coastal structures are reviewed and compared with the very limited available data and with each other. The different methods yield results which can vary more than an order-of-magnitude. For vertical seawalls, the U. S. Army Engineer Shore Protection Manual method estimates more overtopping than Goda's method except in very shallow water. For sloped structures, the Shore Protection Manual method usually estimates less overtopping than Battjes' method and Owen's method. However, data for adequately evaluating how well these methods predict overtopping has not been published.

#### INTRODUCTION

Accurately estimating the amount of water which will wash over a coastal structure can be vital to design engineers. Building seawalls high enough to completely prevent overtopping is often unacceptable because of aesthetics and costs. For example, at Roughan's Point, Massachusetts, a coastal suburb of Boston, overtopping of the existing seawall causes flooding. A moderately higher seawall with improved backside drainage will reduce the flooding. In such situations, a reliable method for estimating overtopping rates for proposed seawall designs is imperative. Kobayashi and Reece (9) have pointed out that overtopping is also important in the design of arctic, gravel islands.

Overtopping is an extremely complex coastal phenomenon. Variables include structure characteristics (shape, height, slope, roughness, porosity, berm width, offshore slope, etc.) wave characteristics (height, period, direction, and the statistical descriptions of the wave field such as spectral widths and the correlation between height and period), water depth, wind speed and direction, air and water densities and viscosities, etc. Most overtopping

\*Hydraulic Engineer, Coastal Engineering Research Center, US Army Engineer Waterways Experiment Station, Vicksburg, Mississippi 39180-0631.

investigations have ignored the effects of local winds and wave direction in order to concentrate on the relationship between overtopping and the other variables.

#### METHODS FOR ESTIMATING OVERTOPPING

The US Army Corps of Engineers Coastal Engineering Research Center's (CERC) Shore Protection Manual (SPM) (17) presents a method for estimating overtopping due to irregular waves. The method uses results from three separate CERC investigations. Weggel (18) used Saville's (13) monochromatic wave overtopping data to derive an equation for overtopping due to monochromatic waves. Ahrens (2) extrapolates Weggel's equation to irregular waves by assuming that runup is Rayleigh distributed and by holding Weggel's empirical coefficients constant. These assumptions allow Ahrens to sum the overtopping contributions from each runup in an irregular sea.

Tsuruta and Goda (16) and Goda (7) use Saville's data and some Japanese data to generate dimensionless curves for monochromatic wave overtopping. The monochromatic wave curves are extrapolated to irregular seas by assuming that wave height is Rayleigh distributed and summing the overtopping contributions of each wave in the irregular sea. This method is called Goda's method in this paper.

Battjes (3) uses Saville's data to derive a different equation for monochromatic wave overtopping. Battjes then accounts for the irregularity of the seas by assuming deepwater wave height and length are jointly Rayleigh distributed. The overtopping contribution from each wave in the irregular sea is summed to estimate the overtopping rate.

All three of the methods use a form of what Tsuruta and Goda (16) call a "linear summation" procedure. They use an overtopping relationship derived for monochromatic waves and assume that the relationship holds for each component (wave or runup) in the irregular sea.

Recently, versions of the "summation" procedure have been presented which are computationally less direct. Kobayashi and Reece (9) and Gadd, et. al. (6) begin with assumed joint probability distributions of wave height and period. Then, a monochromatic runup formula is used to calculate the runup associated with each probability cell (H-T group). Thirdly, some form of Weggel's equation is used to calculate the overtopping contribution associated with each probability cell. And finally, all of these overtopping contributions are summed.

A different approach to estimating overtopping due to irregular waves has been taken by Owen (10, 11). He has related overtopping to irregular wave field parameters by conducting small-scale laboratory tests with irregular waves. However, Owen does not discuss scale effects in his 1:25 scale laboratory data. Aaen (1) found scale

effects at a 1:8 scale to be 60-150% and at a 1:10 to be 50-200%. Jensen and Sorensen (8) also suggest small-scale laboratory tests with irregular waves for estimating overtopping.

The rest of this paper focuses on four of the above mentioned methods:

SPM  
Goda  
Battjes  
Owen

The three basic questions which are addressed are:

- For what situations are the methods most applicable?
- How do estimates from the different methods compare?
- How good are the methods at estimating overtopping?

#### APPLICABILITY OF METHODS

Each of the four methods for estimating overtopping is applicable to specific design situations. The SPM method is limited by the range of situations which Saville tested: vertical and curved structures, smooth-slope structures, stepped structures, and a 1:1.5 slope impermeable quarrystone structure. While it may be necessary to extrapolate from these situations, particularly for composite walls and quarrystone structures at other slopes, Weggel derived his empirical coefficients only for those situations tested by Saville.

Goda's method is for vertical seawalls. He duplicated his work with seawalls covered with concrete blocks, but does not clearly define the situation.

Battjes' method is applicable to gently-sloped smooth structures. He did not attempt to apply the method to rough slopes.

Owen's method is for structures with slope between 1:1 and 1:4. Owen does not recommend using the method for situations outside of the range of wave and structure variables he tested. However, he does suggest an unverified way to apply his smooth-slope results to rough slopes.

These general regions of applicability are schematically represented in Figure 1.  $H_s$  is the offshore significant wave height and  $d$  is the water depth at the toe of the structure. The dashed portion of Battjes region represents the breaking wave limit, which will vary with wave steepness. Battjes' method is based on the assumption that the waves break on the structure.

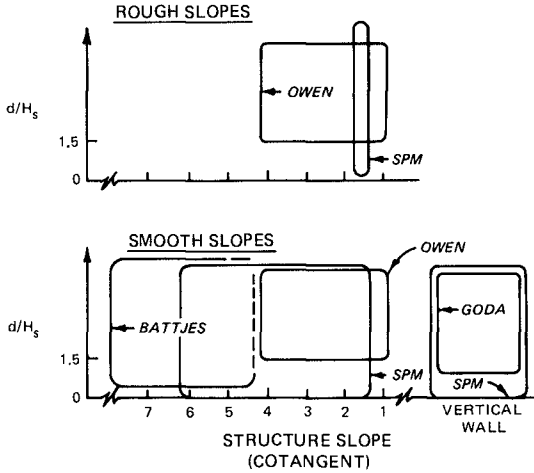


Figure 1. General regions of applicability of methods for estimating overtopping.

COMPARISON BETWEEN METHODS

The method's estimates can be compared in design situations for which more than one method is applicable. Figure 1 shows that both Goda's method and the SPM method can be used for estimating overtopping over a vertical wall. The methods can be compared in dimensionless form as in Figure 2.  $F$  is the freeboard (the height of the structure above the still water level),  $g$  is the acceleration due to gravity, and,  $Q$  is the volume rate of overtopping per unit length of structure. The four  $d/H_s$  ratios correspond to situations tested by Saville. The vertical spread of the SPM method is the effect of the variability of peak wave period, which Goda ignores.

The relationship between SPM and Goda estimates is dependent on the relative depth,  $d/H_s$ . For relative depths of 3 and 1.5, the SPM method estimates more overtopping than Goda's method. For a relative depth of 0.75, the two methods yield similar results. For a relative depth of 0.4, i.e. very shallow water, the SPM method estimates less overtopping than Goda's method. This dependence on relative depth implies a dependence on wave breaking and appears to be a result of

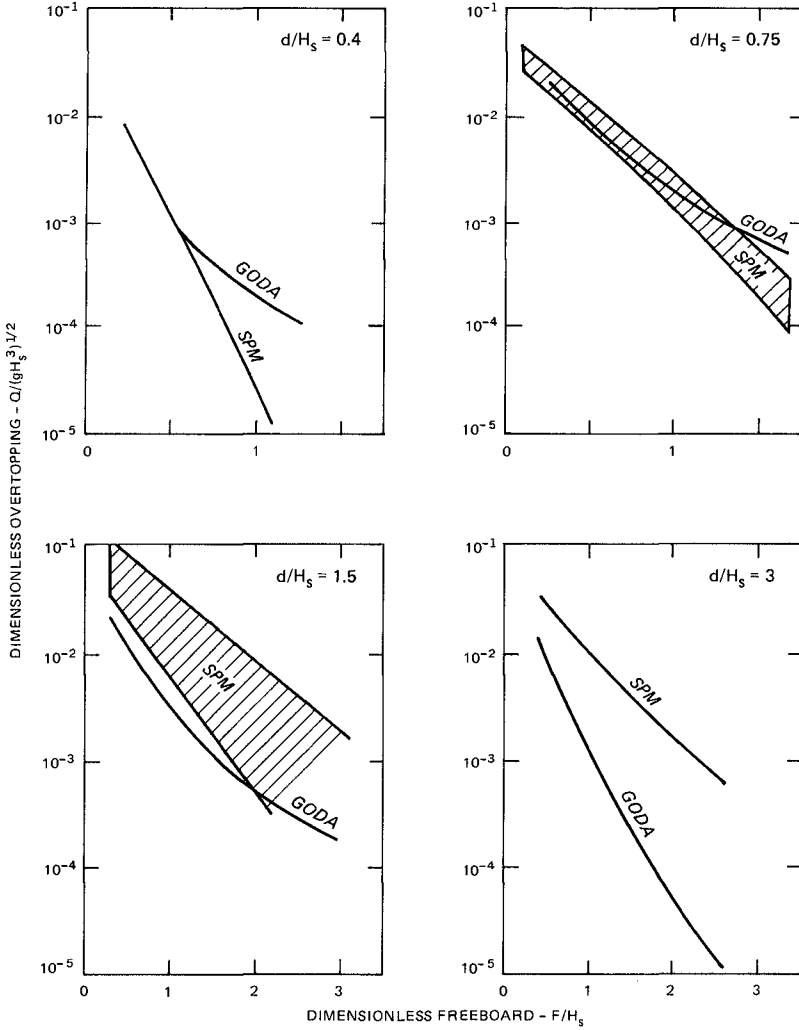


Figure 2. Goda's method and SPM method. Overtopping of a vertical wall.

the different approaches used to extrapolate monochromatic wave overtopping results to irregular seas.

Figure 2 clearly shows the sensitivity of overtopping to the freeboard. Since the freeboard is merely the difference between the structure height and the water level, overtopping is extremely sensitive to changes in either parameter. A varying water level, such as a tide or storm surge, will cause the overtopping rate to vary significantly with time.

Similar dimensionless plots can be generated to compare the SPM method with Battjes method for mildly-sloped, smooth structures. Figure 3 shows that Battjes method estimates more overtopping than the SPM method.  $\bar{T}$  is the average wave period. The spread of Battjes method is due to  $\kappa$ , a parameter which varies from 0 to 1 and is a function of the correlation between wave height and lengths.

Figure 1 shows that Owen's method can be compared with the SPM method. Figure 4 shows the comparison for 1:3 smooth slopes. Owen's method estimates more overtopping than the SPM method. The same result is found for both rough and smooth 1:1.5 slopes.

#### COMPARISON WITH DATA

The four overtopping methods should be evaluated by seeing how they agree with laboratory and field overtopping data. Unfortunately, no conclusive, comprehensive set of overtopping rates due to irregular waves has been published. Paape (12), Sibul and Tickner (14), and Tsuruta and Goda (16) conducted laboratory experiments before the present generation of irregular wave generators was developed. They could not generate a controlled, realistic irregular sea. Neither Owen (10, 11) nor Jensen and Sorensen (8) published their data. However, two studies provide rough "spot checks" of three of the overtopping methods.

Aaen (1) measured actual overtopping rates at a breakwater in Denmark. He then reproduced the structure and storm conditions in the laboratory at two scales, 1:8 and 1:10. The breakwater had a 1:2 slope of rounded sea stones. Figure 1 shows that Owen's method for rough slopes is applicable. The SPM method will be used for the sake of comparison by ignoring the difference in slope (1:2, not 1:1.5) and the difference in armor (rounded sea stone, not angular quarrystone). Aaen's data for these storms are plotted with the method's estimates in Figure 5.

The SPM method underpredicts Aaen's data and Owen's method overpredicts Aaen's data. Note that the relationship between the two estimates agrees with the trend in Figure 4; that is, for low overtopping rates, Owen's method estimates much more overtopping than the SPM method.



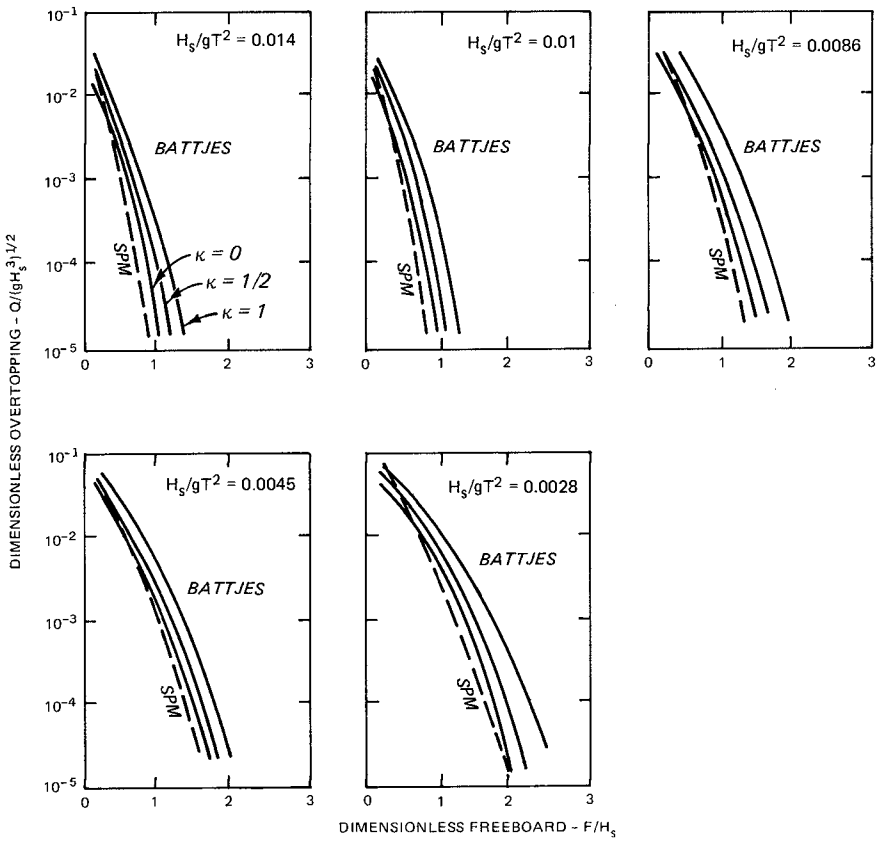


Figure 3. Battjes method and SPM method. Overtopping of a 1:6 smooth-slope structure.

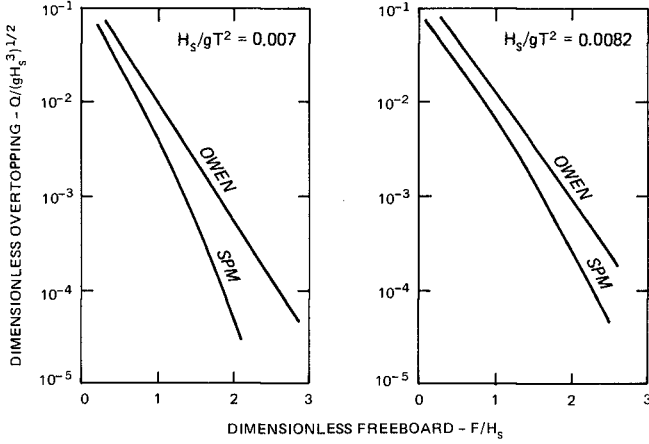


Figure 4. Owen method and SPM method. Overtopping of a 1:3 smooth-slope structure.

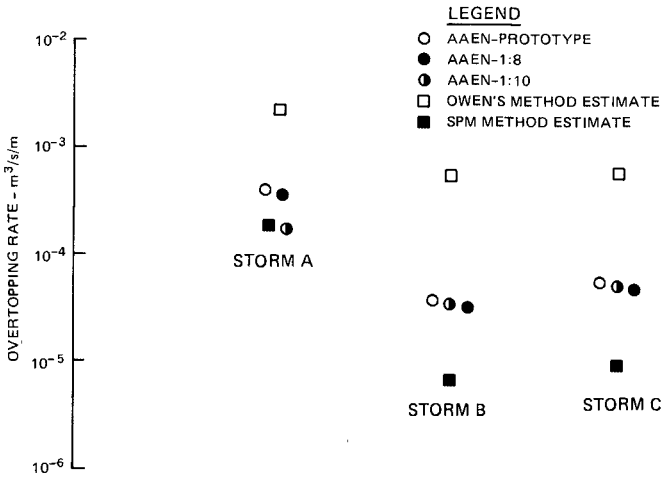


Figure 5. Aaen's overtopping data with estimates by Owen's method and the SPM method.

There are several possible explanations for the discrepancies shown in figure 5. Considering the inherent assumptions in the method, the unverified wind correction factor, and the ignored differences in slope and stone, the difference between the SPM estimate and the data is not discouraging. The difference between Owen's estimate and the data could be due to the unverified wind and roughness corrections and to scale effects. It must be strongly pointed out that Aaen measured only small rates of overtopping. Conclusions from Aaen's data apply to overtopping rates which may be less than the design engineer is considering.

Fukuda, Uno, and Irie (5) measured actual overtopping rates at a seawall fronted by artificial concrete blocks. They found that Goda's curves for seawalls covered with artificial blocks overpredicted their data by between one and two orders of magnitude. Fukuda, et. al. believe this drastic difference is due to energy dissipation across their offshore slope (1:80), which was much flatter than Goda's offshore slope (1:10 to 1:30).

#### OTHER PARAMETERS WHICH EFFECT OVERTOPPING

Several parameters which effect overtopping are ignored in the four methods. Onshore winds should increase the overtopping rate at a seawall. The SPM recommends an unverified wind correction factor which varies from 1 to 3.2. Owen uses the SPM wind correction factor and the other two methods do not address the problem. It must be realized, however, that the SPM correction is merely an engineering judgement approximation of a very complex phenomenon. Gadd et. al. (6) discuss some qualitative trends in the wind effect and conclude that more data is needed to improve upon the SPM correction.

Very little information exists concerning the effect that angle of wave attack has on overtopping. In the absence of data, engineers have usually assumed that overtopping is maximum when waves hit the structure head on, i.e. perpendicularly, and tapers off to zero as the angle of attack lessens. However, Owen found that overtopping is maximum not when waves approach the structure perpendicularly, but at an angle of 15°. Owen (10, 11) has no explanation for his results. Similar results have been seen for monochromatic wave runup by Tautenhain, Kohlhasse, and Partenscky (15). Until data is available to better define this phenomenon, care should be taken to not assume too much overtopping reduction for oblique angles of wave attack.

#### CONCLUSIONS

There are a number of methods for estimating wave overtopping rates. Some of the methods are based on "summation" extrapolations of monochromatic wave overtopping theory. Some of the methods are based on small-scale overtopping tests with irregular waves. For vertical walls, the SPM method estimates more overtopping than Goda's

method except in very shallow water. For sloped structures, the SPM method generally estimates less overtopping than Battjes' method and Owen's method.

Better data is sorely needed. The US Army Engineer Coastal Engineering Research Center (CERC) plans to conduct site-specific and general research overtopping tests. The tests will begin this fall in CERC's two-dimensional flumes with irregular waves. Also, prototype data is needed to determine scale effects in overtopping modelling, and data is needed to better understand the effects of wind and angle of attack.

The question, "how well do the available methods estimate overtopping?," cannot be conclusively answered at this time. The methods discussed in this paper provide the best available estimate. Until better data is available, these estimates should be considered to be within, at best, a factor-of-three, and conservatively, an order-of-magnitude of the actual overtopping rate. This final conclusion is made considering:

- a. The lack of comprehensive, conclusive data and the discrepancies between the methods' estimates and the very limited published data
- b. The assumptions made in the derivations of the methods
- c. The factor-of-three confidence band that Owen claims for his method, which is the only method of the four based on irregular wave overtopping data
- d. The scale effects found by Aaen, and
- e. The order-of-magnitude difference between estimates from different methods

#### ACKNOWLEDGEMENTS

Much more detail about the existing overtopping estimation methods and the methodology of this investigation is being published in a US Army Engineer Waterways Experiment Station Technical Report (4). The results presented herein, unless otherwise noted, were obtained from the research conducted under the Wave Runup and Overtopping Work Unit, Coastal Structure Evaluation and Design Program of the United States Army Corps of Engineers by the Waterways Experiment Station, Coastal Engineering Research Center. Permission was granted by the Chief of Engineers to publish this information.

## APPENDIX - REFERENCES

1. Aaen, S., Oversprojt (Overtopping), Bachelor Thesis, Danish Academy, Department of Civil Engineering, Copenhagen (in Danish), June 1977.
2. Ahrens, J., "Prediction of Irregular Wave Overtopping," CETA 77-7, US Army Corps of Engineers, Coastal Engineering Research Center, Fort Belvoir, Virginia, December 1977.
3. Battjes, J.A., "Computation of Set-up, Longshore Currents, Runup and Overtopping Due to Wind-Generated Waves," Report No. 74-2, Delft University of Technology, Department of Civil Engineering, 1974.
4. Douglass, S.L., "Methods for Estimating Overtopping Rates," Technical Report (in publication), US Army Engineering Waterways Experiment Station, Vicksburg, Mississippi, 1984.
5. Fukuda, N., Uno, F., and Irie, S., "Field Observations of Wave Absorbing Revetment," Coastal Engineering in Japan, Vol. 17, 1974.
6. Gadd, P.E., Potter, R.E., Safaie, B., and Resio, D., "Wave Runup and Overtopping: A Review and Recommendations," Proceedings of the 1984 Offshore Technology Conference, Houston, Texas, May 1984.
7. Goda, Y., "Expected Rate of Irregular Wave Overtopping of Seawalls," Coastal Engineering in Japan, Vol. 14, 1971.
8. Jensen, O.J., and Sorensen, F., "Overspilling/Overtopping of Rubble-Mound Breakwaters," Coastal Engineering, Vol. 3, No. 1, 1979.
9. Kobayashi, N., and Reece, A.M., "Irregular Wave Overtopping on Gravel Islands," ASCE Journal of Waterway, Port, Coastal and Ocean Engineering, WW4, Vol. 109, pp. 429-444, November 1983.
10. Owen, M.W., "Design of Seawalls Allowing for Wave Overtopping," Report No. EX924, Hydraulics Research Station, Wallingford, Oxfordshire, England, June 1980.
11. Owen, M.W., "Overtopping of Sea Defences," International Conference on the Hydraulic Modelling of Civil Engineering Structures, Coventry, England, pp. 469-480, September 1982.
12. Paape, A., "Experimental Data on the Overtopping of Seawalls by Waves," 7th Conference on Coastal Engineering, The Hague, Netherlands, pp. 674-681, 1960.

13. Saville, T., Jr., "Laboratory Data on Wave Runup and Overtopping on Shore Structures," TM-64, Beach Erosion Board, US Army, Corps of Engineers, 1955.
14. Sibul, O.W., and Tickner, E.G., "Model Study of Overtopping of Wind-Generated Waves on Levees with Slopes of 1:3 and 1:6," TM-80, Beach Erosion Board, US Army Corps of Engineers, 1956.
15. Tautenhain, E., Kohlhase, S., and Partenscky, H.W., "Wave Runup at Sea Dikes Under Oblique Wave Approach," 18th International Conference on Coastal Engineering, Capetown, South Africa, pp. 804-810, 1982.
16. Tsuruta, S., and Goda, T., "Expected Discharge of Irregular Wave Overtopping," 11th Conference on Coastal Engineering, London, England, pp. 833-852, 1968.
17. US Army Corps of Engineers, Coastal Engineering Research Center, Shore Protection Manual, 3rd ed., US Government Printing Office, Washington, D.C., 1977.
18. Weggel, J.R., "Wave Overtopping Equation," Proceedings of the 15th Coastal Engineering Conference, Honolulu, Hawaii, pp. 2737-2755, 1976.

## CHAPTER TWENTY THREE

### RUN-UP OF PERIODIC WAVES ON BEACHES OF NON-UNIFORM SLOPE

Yoshinobu Ogawa\* and Nobuo Shuto\*\*

#### ABSTRACT

Run-up of periodic waves on gentle or non-uniform slopes is discussed. Breaking condition and run-up height of non-breaking waves are derived by the use of the linear long wave theory in the Lagrangian description. As to the breaking waves, the width of swash zone and the run-up height are obtained for relatively gentle slopes (less than  $1/30$ ), on dividing the transformation of waves into dissipation and swash processes. The formula obtained here agrees with experimental data better than Hunt's formula does. The same procedure is applied to non-uniform slopes and is found to give better results than Saville's composite slope method.

#### 1. INTRODUCTION

Attempts are recently made to establish, in the prediction of beach process, a two-dimensional model which is more realistic than the conventional one-line or two-line models [Watanabe(1981)]. In the modelling to be developed, no sufficient knowledges have yet been accumulated on the swash zone which is the most remarkable output of the beach process. As the first step to fill this lack, run-up of periodic waves is discussed both on uniform gentle slopes and on beaches of non-uniform slopes which are often seen at natural sandy beaches.

Many studies have been made on run-up of periodic waves on uniform slopes, as are summarized below. Run-up of periodic waves is roughly divided into two types; run-up of surging (standing) waves and that of breaking (progressive) waves.

For non-breaking waves, the run-up height and the breaking condition as a standing wave can be estimated well by the modified Miche's(1944) solution [Le Méhauté et al.(1968), Van Dorn(1966), Takada(1970)] and Miche's condition(1951).

On the other hand, for breaking waves, the run-up height is empirically correlated directly to the offshore wave characteristics and the beach slope [Hunt(1959), Savage(1958)]. This is partly due to a lack of

---

\* Research Associate, Dept. of Civil Eng., Tohoku University,  
Aoba, Sendai 980, Japan

\*\* Professor, Dept. of Civil Eng., Tohoku University,  
Aoba, Sendai 980, Japan

knowledge about breaking waves. In addition, most of them deal with the run-up height on dikes which have relatively steep slopes.

Recently, some studies are performed on the size of the swash zone. Roos & Battjes(1976) showed from run-up experiments on relatively steep slopes (greater than 1/7) that the run-up height  $R$  was estimated well by Hunt's formula(1959) and that the run-down height  $R_r$  was expressed as  $R_r = R(1-0.4\xi)$ , in which  $\xi$  was the surf similarity parameter. Guza & Bowen(1976) and Van Dorn(1978) showed that the swash parameter  $\epsilon = a \sigma^2 / g s^2$  is almost constant for breaking waves. Although some people tried to discuss the run-up height in relation to the wave set-up [Van Dorn(1976), Michi & Watanabe(1982)], they did not formulate the results.

In the case of non-uniform slopes, one can use Saville's composite slope method (1958) to calculate the run-up height for breaking waves. Taylor(1980) applied this method to natural beaches by expressing beach profile as a parabolic curve. However, the physical meanings of this method is not always clear.

In the present study, the authors first obtain the run-up height of surging waves and the breaking condition as a standing wave on non-uniform slope by the use of the linear long wave theory in the Lagrangian description. The non-uniformity of profiles means steps, bars and foreshores with different inclination from those of inshore. Secondly, for breaking waves, we divide the wave deformation after breaking into two processes. One is the "Dissipation Process" and another is the "Swash Process". Combining these two processes in terms of wave height, we derive the run-up height on uniform gentle slopes. This technique is also applied to non-uniform slopes and is compared with Saville's method.

## 2. RUN-UP OF NON-BREAKING WAVES

Run-up height,  $R$ , of a linear standing wave on a uniform slope connected to the water of a constant depth,  $h$ , is given by the following equation, as was analysed by Shuto(1972) by using the Lagrangian description.

$$\frac{R}{H_i} = [J_0^2(4\pi\frac{L}{L}) + J_1^2(4\pi\frac{L}{L})]^{-1/2} \quad (1)$$

where  $H_i$  and  $L$  are the height and length of the incident wave in the channel of constant depth,  $l$  the horizontal distance between the shoreline and the toe of slope, and  $J_0$  and  $J_1$  the Bessel functions of the zeroth and the first order. As  $l$  tends to  $\infty$ , the relationship becomes

$$\frac{R}{H_i} = \sqrt{\frac{\pi\sigma}{s}} \left(\frac{h_1}{g}\right)^{1/4} \quad (2)$$

where  $\sigma$  is the angular frequency and  $s$  the angle of slope. In order to replace  $H_i$  by the height of incident wave in deep water  $H_0$ , the law of energy conservation is applied. Then Eq.(2) is reduced to Eq.(3) which is similar to Miche's solution(1944).

$$\frac{R}{H_0} = \sqrt{\frac{\pi}{2s}} \quad (3)$$

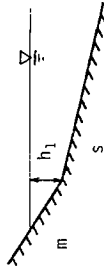
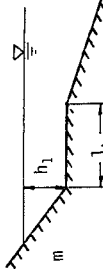
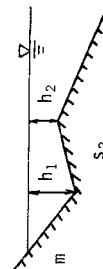


Table 1. Solutions of run-up height and breaking condition of standing waves.

$$\frac{R}{H_0} = \frac{1}{Z} \sqrt{\frac{\pi}{2S}}$$

$$\left(\frac{H_0}{L_0}\right)_{cr} = Z \sqrt{\frac{2S}{\pi}} \frac{m^2}{\pi}$$

$J_0, J_1, N_0, N_1$  : Bessel and Neumann function of the zeroth and the first order.

Profile	Value of coefficients
	$z = \sqrt{\left(\frac{J_0(d)N_1(e) - J_1(d)N_0(e)}{J_0(e)N_1(e) - J_1(e)N_0(e)}\right)^2 + \left(\frac{J_0(d)J_1(e) - J_1(d)J_0(e)}{N_0(e)J_1(e) - N_1(e)J_0(e)}\right)^2}$ $d = \frac{2\sqrt{2\pi}}{m} \left(\frac{h_1}{L_0}\right)^{0.5} \quad e = \frac{2\sqrt{2\pi}}{S} \left(\frac{h_1}{L_0}\right)^{0.5} \quad L_0 = \frac{g}{2\pi} T^2$
	$z = \sqrt{\left(\frac{u N_1(e) - v N_0(e)}{J_0(e)N_1(e) - J_1(e)N_0(e)}\right)^2 + \left(\frac{u J_1(e) - v J_0(e)}{N_0(e)J_1(e) - N_1(e)J_0(e)}\right)^2}$ $u = J_0(d) \cos k l_b - J_1(d) \sin k l_b \quad d = \frac{2\sqrt{2\pi}}{m} \left(\frac{h_1}{L_0}\right)^{0.5} \quad e = \frac{2\sqrt{2\pi}}{S} \left(\frac{h_1}{L_0}\right)^{0.5}$ $v = J_1(d) \cos k l_b + J_0(d) \sin k l_b$
	$Z = \sqrt{\left(\frac{u N_1(q) - v N_0(q)}{J_0(q)N_1(q) - J_1(q)N_0(q)}\right)^2 + \left(\frac{u J_1(q) - v J_0(q)}{N_0(q)J_1(q) - N_1(q)J_0(q)}\right)^2}$ $u = J_0(p) \frac{J_0(d)N_1(e) - J_1(d)N_0(e)}{J_0(e)N_1(e) - J_1(e)N_0(e)} + N_0(p) \frac{J_0(d)J_1(e) - J_1(d)J_0(e)}{N_0(e)J_1(e) - N_1(e)J_0(e)}$ $v = J_1(p) \frac{J_0(d)N_1(e) - J_1(d)N_0(e)}{J_0(e)N_1(e) - J_1(e)N_0(e)} + N_1(p) \frac{J_0(d)J_1(e) - J_1(d)J_0(e)}{N_0(e)J_1(e) - N_1(e)J_0(e)}$ $d = \frac{2\sqrt{2\pi}}{m} \left(\frac{h_1}{L_0}\right)^{0.5} \quad e = \frac{2\sqrt{2\pi}}{S_2} \left(\frac{h_1}{L_0}\right)^{0.5} \quad p = \frac{2\sqrt{2\pi}}{S_2} \left(\frac{h_2}{L_0}\right)^{0.5} \quad q = \frac{2\sqrt{2\pi}}{S} \left(\frac{h_2}{L_0}\right)^{0.5}$

A similar manipulation yields the following breaking condition of standing waves which is analogous to Miche's result(1951), from the breaking condition obtained by Shuto(1972).

$$\left(\frac{H_0}{L_0}\right)_{cr.} = \sqrt{\frac{2s}{\pi}} \frac{s^2}{\pi} \tag{4}$$

Run-up on a slope of more complicated shape can be obtained as follows. Divide the whole beach into segments of uniform slope with the inflection points of bottom slope as their end points. For each segment, solutions of the linear standing long waves in the Lagrangian description are determined, corresponding to its own slope. These local solutions are connected to build the solution over the whole slope. The continuation is carried out for the horizontal and vertical displacements of the water particles which are on the boundary between the two different slopes at the initial instant. As for the procedure, one may read the reference (22). Once the solution is established, the run-up height is correlated with the height of incident waves in deep water, as is shown above.

Solutions are obtained for bi-linear sloped beach, step-type beach and bar-type beach. Equations are summarized in Table 1. Numerical examples for the offshore slope  $s = 0.03$  and the foreshore slope  $m = 0.1$  are shown by circles and triangles in Fig.1. The dotted lines in Fig.1 are the result given by Eqs.(3) & (4), by setting  $s = m = 0.1$ . Even though the equations are functions of not only  $m$  but also  $s$ ,  $R/H_0$  and  $(H_0/L_0)_{cr.}$  are mainly governed by  $m$ . One may consider that the solutions of  $R/H_0$  (or  $(H_0/L_0)_{cr.}$ ) for  $m = 0.1$  and  $s = 0.03$  are between the values of Eq.(3) (or Eq.(4)) for  $s = 0.1$  and for  $s = 0.03$ . However, this is not

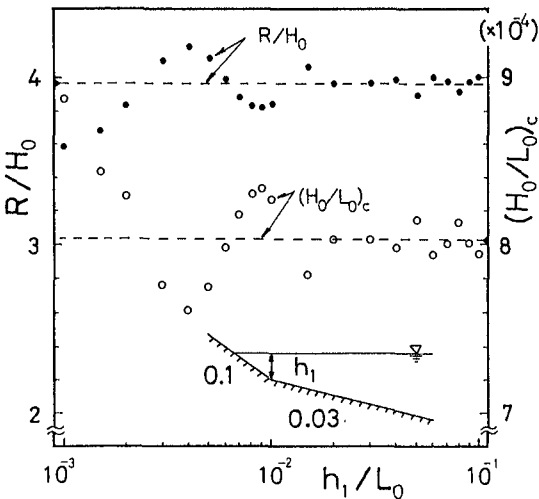


Fig.1(a) Numerical Examples of run-up height and breaking condition of standing waves (bi-linear sloped beach)

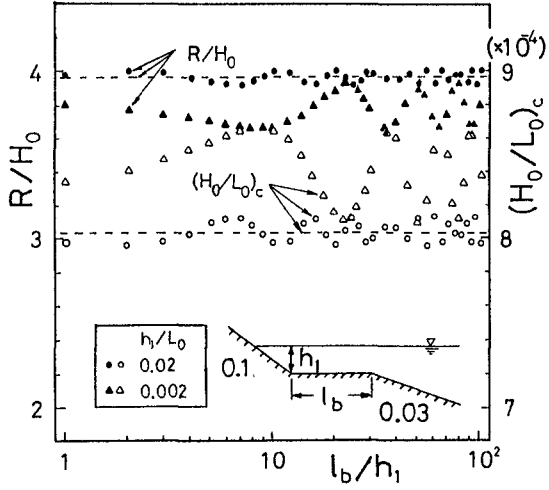


Fig.1(b) Numerical examples of run-up height and breaking condition of standing waves (step-type beach)

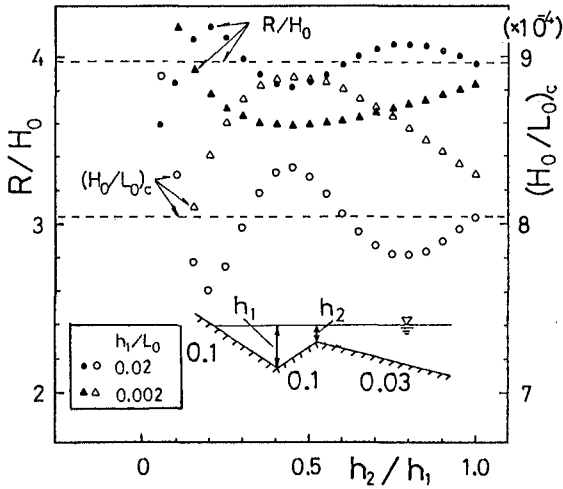


Fig.1(c) Numerical examples of run-up height and breaking condition of standing waves (bar-type beach)

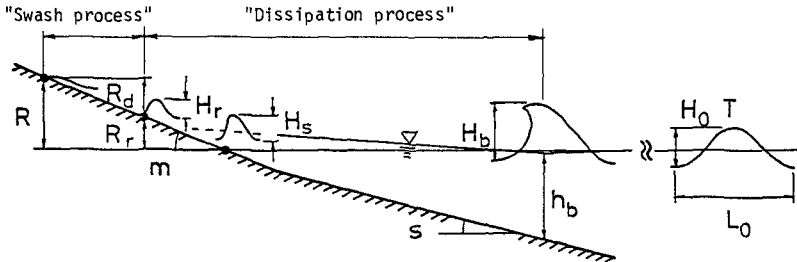
true in case of the standing waves in contrast to the case of the breaking waves. This result suggests that the foreshore slope is the most important in problems of the run-up, the breaking condition and the reflection of standing waves.

3. RUN-UP OF BREAKING WAVES

Deformation of progressive waves after breaking is divided into the following two processes; i) the dissipation process in which the kinematic and potential energies are consumed due to breaking, and ii) the swash process in which the kinematic and potential energies alternates to each other on a dry bed. The run-up height and the width of swash zone are calculated by continuing the wave height between the two processes. Figure 2 gives the definition sketch.

3.1 Dissipation process: decay of wave height due to breaking

According to the experimental curves of Sasaki & Saeki(1974) for waves after breaking on a uniform slope, the decay in wave height is almost independent of the wave steepness. It is also shown in their results that if  $h/h_b$  is smaller than 0.5,  $H/H_b$  is linearly proportional to  $h/h_b$  with the coefficient of proportionality  $\beta = 0.6$ , independent of the beach slope. Assume that their experimental curves can be extended to the points where the curves intersect the beach profile. The height,  $R_r$ , of the points of this intersection which are hereafter called as the beginning points of run-up are given by



- $H_0$  : Offshore wave height
- $T$  : Wave period
- $L_0$  : Offshore wave length
- $H_b$  : Breaking wave height
- $h_b$  : Breaking water depth
- $s$  : Tangent of slope in the surf zone
- $H_s$  : Wave height at the shoreline of still water level
- $H_r$  : Wave height at the beginning point of run-up
- $m$  : Tangent of foreshore slope
- $R$  : Total run-up height above still water level
- $R_d$  : The width of swash zone
- $R_r$  : The height of the beginning point of run-up

Fig.2 Definition sketch.

$$\frac{R_r}{h_b} = \frac{1}{\beta} \left( \frac{H_s}{H_b} - \frac{H_r}{H_b} \right) \tag{5}$$

The wave height,  $H_r$ , at the shoreline of still water level is given by black circles in Fig.3, from experimental results of Sasaki & Saeki (1974) and Roos & Battjes (1976). It is expressed by

$$\frac{H_s}{H_b} = \begin{cases} 3.04 s^{1.07} & \text{for } 0.01 < s < 0.2 \\ 0.55 & \text{for } 0.2 < s \end{cases} \tag{6}$$

With these informations,  $R_r$  can be obtained as a function of  $H_r$ , the wave height at the beginning point of run-up if the breaking wave height  $H_b$  and the breaking water depth  $h_b$  are given.

For a non-uniform slope for which no simple relations similar to Eqs.(5) and (6) are available at present, numerical computation such as proposed by Mizuguchi (1980) may be used.

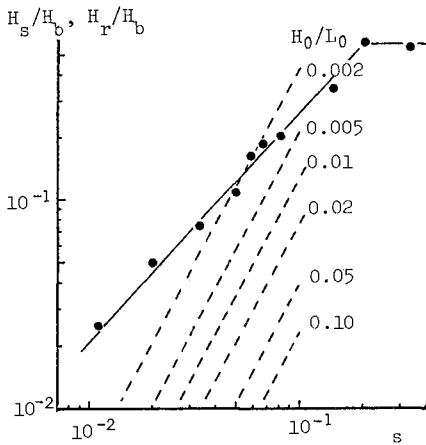


Fig.3 Relative wave heights  $H_s/H_b$ ,  $H_r/H_b$  and beach slope.

3.2 Swash Process: run-up of waves

Trajectory of the wave front when waves are climbing a uniform slope is given by Freemann & Le Méhauté (1964) as follows.

$$x_f(t) = -\frac{1}{2} gAm \left( t - \frac{u_s}{gAm} \right)^2 + \frac{1}{2} \frac{u_s^2}{gAm} \tag{7}$$

$$A = \frac{1+f/(a^2m)}{(1+2a)(1+a)} \tag{8}$$

where  $x_f(t)$  is the horizontal coordinate of the wave front measured from

the beginning point of run-up,  $t$  the elapsed time after the wave front passes the beginning point of run-up,  $u_s$  the water particle velocity of rarefaction waves at the beginning point of run-up,  $a$  the ratio of the wave propagation velocity  $c = \sqrt{g(h+\eta)}$  to the water particle velocity, and  $f$  the friction coefficient defined by  $\tau = \rho f u^2$ . According to the experiments of Iwagaki et al.(1966),  $a = 0.26$  and  $f = 0.005 - 0.01$  for a smooth bottom in case of  $m > 0.1$ .

Trajectory of the wave front when waves are descending is given as follows, on continuing the solution of Brandtzaeg(1964) with Eq.(7).

$$x_f(t) = \frac{u_s^2}{2gAm} - \frac{2z}{f'} \ln[\cosh \sqrt{\frac{f'g(m-\tan \gamma)}{2z}} (t-\zeta T)] \quad (9)$$

$(f' \neq 0)$

$$x_f(t) = \frac{u_s^2}{2gAm} - \frac{1}{2} g(m-\tan \gamma)(t-\zeta T)^2 \quad (f' = 0) \quad (10)$$

where  $\zeta T$  is the time when the maximum run-up height appears,  $T$  the wave period,  $z$  the thickness of water of descending waves,  $f'$  the friction coefficient and  $\gamma$  the angle between water and beach surface. With the assumptions that  $f = f'=0$  (or  $A = 1$ ) and that the water surface displacement at the shoreline varies linearly with respect to time, we have  $\zeta = 0.46$ .

The value of  $u_s$  is assumed to be given as follows in terms of  $H_r$ .

$$u_s = F\sqrt{gH_r} \quad (11)$$

Figure 4 shows empirical relationships between  $u_s$  and  $H_r$ . The experimental results are taken from one of the present authors(1982) for single bores on  $m = 1/20$ , Iwagaki et al.(1966) for solitary waves on  $m > 1/10$  and Roos & Battjes(1976) for regular wave trains on  $m = 1/3$  and  $1/7$ .

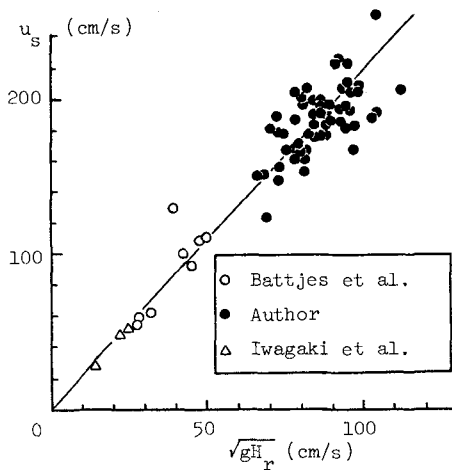


Fig.4 Relationship between  $u_s$  and  $\sqrt{gH_r}$  (for smooth fixed bottom)

It was assumed  $\zeta = 0.46$  in case of regular waves. From the figure, the coefficient of proportionality which is a kind of Froud number is 2.2 on an average for both single waves and regular wave trains. This is nearly equal to the wave front condition of Iwasaki & Togashi(1969).

From Eqs.(7) and (11),  $H_r$  and  $R_d$  are derived as follows.

$$H_r = \frac{gm^2T^2}{F^2} A^2\zeta^2 \tag{12}$$

$$R_d = \frac{gm^2T^2}{2} A\zeta^2 \tag{13}$$

Figures 5 and 6 compare the calculated results of  $H_r$  and  $R_d$  for  $F = 2.2$ ,  $f = 0.005$  and  $\zeta = 0.46$  with experimental results of  $R_oos$  &  $Battjes(1976)$ , Van Dorn(1976) and Michi(1982). Since the value of  $a = 0.26$  according to Iwagaki et al.(1966) makes the calculated value too big in case of a gentle slope, the followings are used for convenience.

$$a = \begin{cases} 0.26 & \text{for } 0.1 < m \\ 0.13 m^{-0.3} & \text{for } 0.01 < m < 0.1 \end{cases} \tag{14}$$

In the result of Van Dorn(1976) who discussed  $R_d$ , the calculated values were about twice the experimental results in case of a steep slope. From Eq.(13), swash parameter  $\epsilon = a_s \sigma^2/gm^2$  is calculated as  $\pi^2\zeta^2A$  ( $= 2.09 A$ ) and is found to be a function of  $s$  foreshore slope and friction factor.

Equation (12) (or Eq.(13)) shows that  $H_r$  (or  $R_d$ ) is mainly governed by the foreshore slope  $m$  and the wave period  $T$ , whereas  $H_s$  is a function of the slope  $s$  alone. For a comparison, values of  $H_r/H_b$  for different wave periods are drawn by dotted lines in Fig.3 which is originally given to show the relationship  $H_s$  and the slope angle.

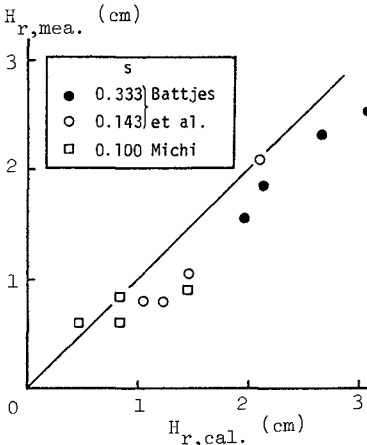


Fig.5 Comparison of  $H_r$  between measured and calculated. (for smooth fixed bottom)

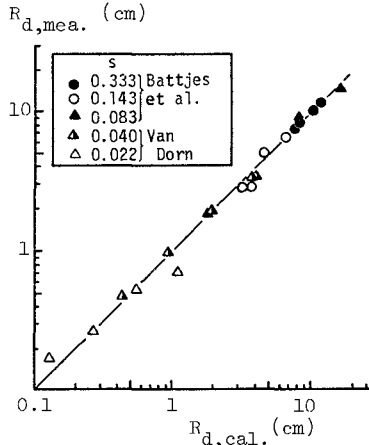


Fig.6 Comparison of  $R_d$  between measured and calculated. (for smooth fixed bottom)

3.3 Run-up on a gentle, uniform slope

Run-up height  $R$  is given by a sum of  $R_r$  and  $R_d$ .

$$\frac{R}{H_0} = \frac{0.46}{\beta} s^{-0.12} \left(\frac{H_0}{L_0}\right)^{-0.2} [3.04 s^{1.07} - \frac{2.94\pi\zeta^2 A^2}{F^2} s^{-0.09m^2} \left(\frac{H_0}{L_0}\right)^{-0.75}] + \pi A \zeta^2 m^2 \left(\frac{H_0}{L_0}\right)^{-1} \tag{15}$$

for  $0.02 < m < 0.33$ ,  $0.01 < s < 0.1$  and  $0.003 < H_0/L_0 < 0.07$

The first term on the right-hand side is  $R_r/H_0$  which is equal to the wave set-up and the second term is  $R_d/H_0$ , the width of swash zone. Breaking conditions are determined by the following formulas obtained from the same data as Goda(1970) used.

$$\frac{H_b}{H_0} = 0.68 s^{0.09} \left(\frac{H_0}{L_0}\right)^{-0.25} \quad \text{for } 0.01 < s < 0.1 \tag{16}$$

$$\frac{h_b}{H_0} = 0.46 s^{-0.12} \left(\frac{H_0}{L_0}\right)^{-0.20} \quad \text{for } 0.003 < H_0/L_0 < 0.07 \tag{17}$$

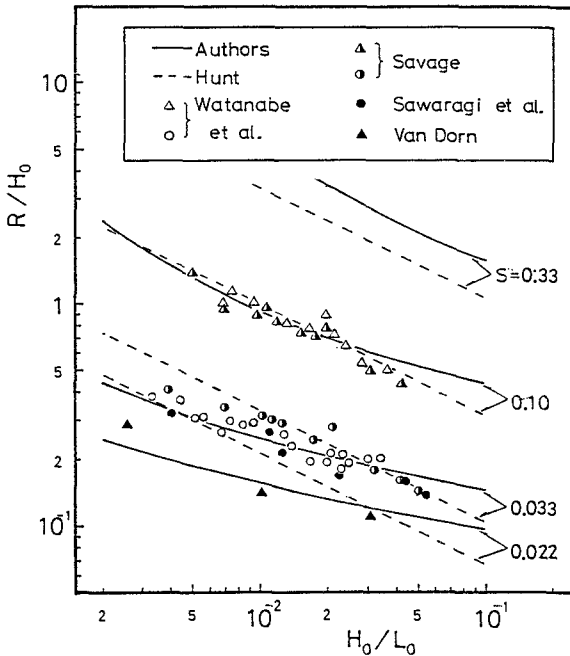


Fig.7 Comparison of calculated  $R/H_0$  with experimental data.



Figure 7 compares experimental results of Michi & Watanabe(1982), Van Dorn(1976), Sawaragi et al.(1976) and Savage(1958) with the calculated ones for  $\beta = 0.6$ ,  $F = 2.2$ ,  $f = 0.005$  and a obtained from Eq.(14). Calculated run-up heights agree better with experimental results than Hunt's formula(1959) does. Figure 8 shows the relative magnitude of  $R_r/H_0$  and  $R_d/H_0$  for  $s = 1/10, 1/30$  and  $1/90$ . The gentler the slope is and the greater the wave steepness is, the contribution of the wave set-up  $R_r$  is the greater, although the greater wave steepness does not always yield the greater  $R_r/H_0$ .

The discussion above is for a fixed bottom of smooth surface and is not directly applicable to a natural beach which is of movable and rough surface. According to Sawaragi's experiments(1962), effects of bottom roughness is not dominant on the breaking condition and is negligible for a natural, sandy beach.

Effects of bottom roughness in the swash process is shown in Fig.9. Equation (13) is used to calculate the run-up height for different values

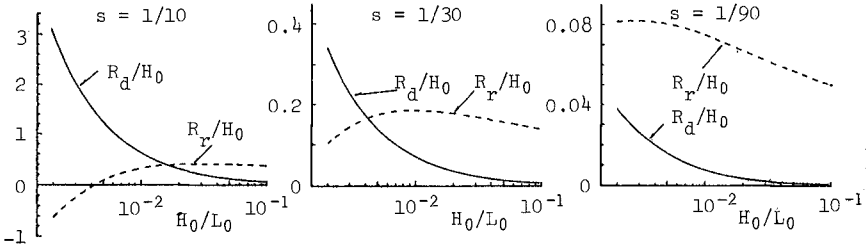


Fig.8  $R_d/H_0$  vs.  $R_r/H_0$  for various slopes.

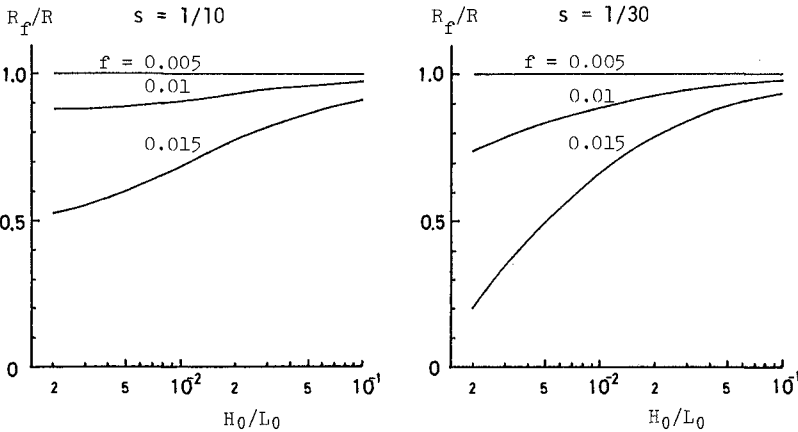


Fig.9 Effect of the value  $f$  on run-up height.

of  $f$  and the results are made dimensionless, divided by the run-up height on a smooth bottom for which  $f$  is 0.005. Tsuchiya et al.(1978) reexamined Savage's data(1958) and obtained the effect of roughness on run-up height, which is similar to Fig.9. However, we must take notice of the fact that  $f$  used here is somewhat different from the original definition of the bottom shear stress but is a virtual friction coefficient which includes several other effects such as turbulence effect caused by breaking in the name of the friction coefficient. No method is available to determine the value of  $f$  from hydraulic conditions near the bottom.

From prototype experiments by the Central Research Institute of Electric Power Industry, relationships similar to Fig.4, 5 and 6 are shown in Fig.10,11 and 12. As for the experimental channel, one may read the reference(8). All experiments were conducted with a constant still water depth of 4.5 m and on initial slope inclination of 1/20. The slope consists of movable sands with the median diameter of 0.27 mm. Foreshore slopes formed by waves ranged from 0.033 to 0.186. In these experiments, the value of  $F$  is also about 2 on an average. The friction coefficient is found to be 0.8 so as that calculated values of  $R_d$  and  $H_r$  give the best fit to the measured data. Values of  $f$  as well as  $\bar{a}$  should be experimentally determined, after all.

3.4 Run-up on a non-uniform slope

The same procedure is applied to the run-up on a non-uniform slope, based on the following assumptions.

- i) Dissipation process does not vary by changing foreshore profiles.
- ii) Water particle velocity is continuous at the point where profile changes and the value of  $a$  depends on local slopes.

Examples are given in case of bi-linear sloped beaches, the inflection point of which coincides with the shoreline. If  $R_r > 0$ , Eq.(15) can be used. For  $R_r < 0$ , the following equation is used.

$$\frac{R}{H_0} = \frac{F^2}{2A_2} \left( \frac{H_r}{H_0} \right) - \frac{A_1}{A_2} s \left( \frac{x_1}{H_0} \right) \tag{18}$$

$$\frac{x_1}{H_0} = \frac{-0.676}{8} s^{-1.21} \left( \frac{H_0}{L_0} \right) 0.05 [2.07s^{1.16} \left( \frac{H_0}{L_0} \right) - 0.25 \frac{H_r}{H_0}]$$

$$2\zeta \left( \frac{H_0}{L_0} \right)^{-1/2} = \frac{F}{A_1 s} \sqrt{\frac{H_r}{H_0}}^{1/2} + \sqrt{\frac{2}{\pi} \frac{A_1 s - A_2 m}{A_1 A_2 s m} F^2 \left( \frac{H_r}{H_0} \right) - 2A_1 s \left( \frac{x_1}{H_0} \right)}$$

where  $A_1$  and  $A_2$  are the values of  $A$  obtained from Eqs.(8) and (14) for  $s$  and  $m$ ,  $x_1$  the horizontal distance between the beginning point of dry bed and the inflection point of the slope.

Figure 13 shows comparisons of the calculated results with experimental results of Toyoshima et al.(1964) and Saville(1958). Full lines in Fig.13 are Eqs.(15) & (18) and broken lines are calculated by Saville's composite slope method(1958). The composite slope method always gives smaller values. The present method agrees fairly well with the experimental results, although the effect of the foreshore slope on the deformation of waves after breaking is not taken into consideration.

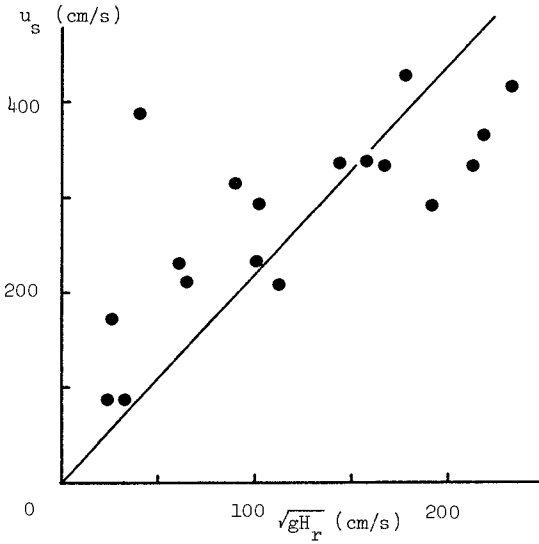


Fig.10 Relationship between  $u_s$  and  $\sqrt{gH_r}$  (for movable sand bottom)

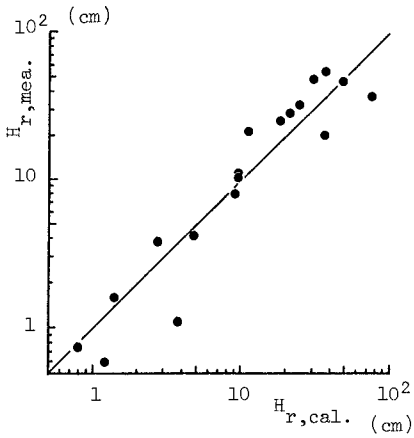


Fig.11 Comparison of  $H_r$  between measured and calculated. (for movable sand bottom)

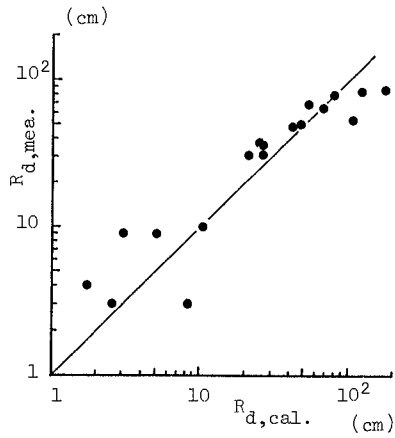


Fig.12 Comparison of  $R_d$  between measured and calculated. (for movable sand bottom)

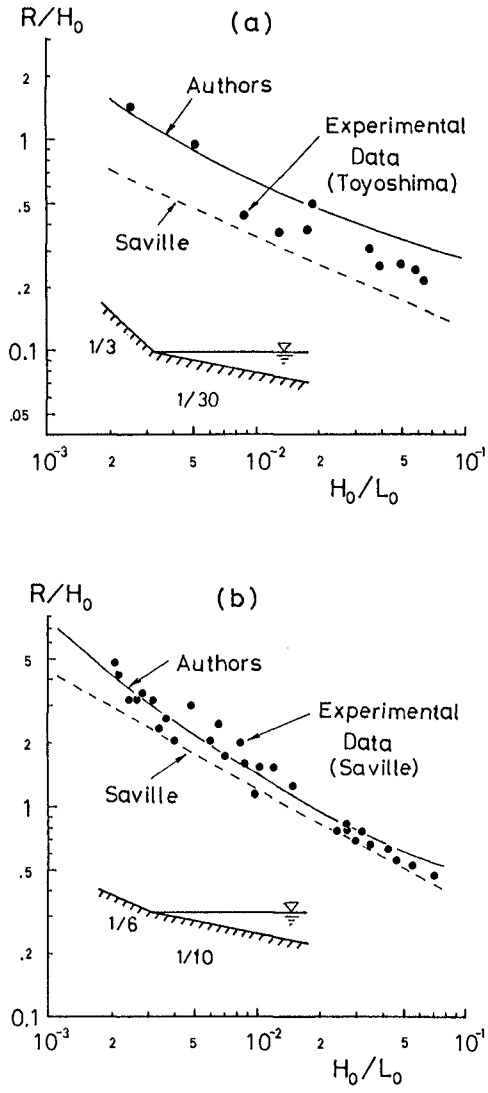


Fig.13 Comparison between Saville's method and the present method.

#### 4. CONCLUSIONS

Run-up of periodic waves is discussed, *considering the wave deformation*, especially for *gentle and non-uniform slopes* (with steeper foreshore slopes, steps and bars) which are often seen at *natural beaches*. Results are summarized as follows.

- (1) The run-up height and the breaking condition for non-breaking waves on non-uniform sloping beaches are derived as shown in Table 1. Foreshore slopes are found to be dominant in these values. The procedure to obtain the solution can be applied to understand the behavior of long period waves in the surf zone.
- (2) For breaking waves, run-up phenomena can be explained well by connecting dissipation and swash processes.
  - i) The width of swash zone is mainly determined by the foreshore slope and wave period. It can be calculated by Eq.(13) if the foreshore slope is within the range of  $1/3 - 1/50$ .
  - ii) For gentle uniform slopes ( $1/10 - 1/100$ ), the run-up height formula, Eq.(15), obtained by setting  $m = s$  can be used instead of Hunt's formula(1959) which is originally applicable to steeper slopes than  $1/10$ .
  - iii) The procedure to connect dissipation and swash processes is applied to calculate the run-up height in the case of steeper foreshore profiles which are generally found at natural beaches. The procedure gives not only better results than Saville's method(1958), but also a physically sound explanation of run-up. We can also obtain the size of the swash zone which is closely connected with the stability of dikes built near and above the shoreline and which is also important in estimating sand movement near swash zone.
  - iv) Further studies are necessary for wave run-up on more complicated slopes and for estimation of values of friction coefficient.

#### ACKNOWLEDGEMENTS

The authors express their thanks to Mr. R. Kajima, Mr. T. Shimizu and Mr. S. Saito, Civil Engineering Laboratory of the Central Research Institute of Electric Power Industry (CRIEPI) for their permission to use their data which were obtained in one of their special project. Only a part of the data was published, for example, at the 18th I.C.C.E. [see reference (8)]. A part of this research was supported by a grant from the Ministry of Education, Science and Culture, the Japanese Government.

#### REFERENCES

1. Brandtzaeg, A. : A simple mathematical model of wave motion on a rubble mound breakwater slope, Proc. 8th Coastal Eng. Conf., pp. 444-467, 1964.
2. Freemann, J.C. and B. Le Méhauté : Wave breakers on a beach and surges on a dry bed, Proc. A.S.C.E. Vol.90, HY2, pp.187-216, 1964.

3. Goda, Y. : A synthesis of breaker indices, Proc. J.S.C.E. No.180, pp.39-49, 1970 (in Japanese).
4. Guza, R.T. and A.J. Bowen : Resonant interaction for waves breaking on a beach, Proc. 15th Coastal Eng. Conf., pp.560-579, 1976.
5. Hunt, I.A. : Design of seawalls and breakwaters, Proc. A.S.C.E. Vol. 85, WW3, pp.123-152, 1959.
6. Iwagaki, Y., M. Inoue and K. Ohbori : Experimental study on the mechanism of run-up on sloping beach, 13th Japanese Conf. on Coastal Engg., pp.198-205, 1966 (in Japanese).
7. Iwasaki, T. and H. Togashi : Wave front condition and computation method of tsunami during run-up, 16th Japanese Conf. on Coastal Engg., pp.359-364, 1969 (in Japanese).
8. Kajima, R., T. Shimizu, K. Maruyama and S. Saito : Experiments on beach profile change with a large wave flume, Proc. 18th Coastal Eng. Conf., pp.1385-1404, 1982.
9. Le Méhauté, B., R.C.Y. Koh and L.S. Hwang : A synthesis on wave run-up, Proc. A.S.C.E. Vol.94, WW1, pp.77-92, 1968.
10. Miche, R. : Mouvements ondulatoires de la mer en profondeur constante ou décroissante, Annales des Ponts et Chaussées, 114e Année, 1944.
11. Miche, R. : Le pouvoir réfléchissant des ouvrages maritimes exposés à l'action de la houle, Annales des Ponts et Chaussées, 121e Année, pp.285-319, 1951.
12. Michi, M. and A. Watanabe : On the relationship between run-up and wave set-up, Proc. of the 37th Annual Technical Meeting of J.S.C.E., pp.869-870, 1982 (in Japanese).
13. Michi, M. : Study on hydraulic characteristics in the swash zone, Master Thesis of Tokyo University, 1982 (in Japanese).
14. Mizuguchi, M. : An heuristic model of wave height distribution in surf zone, Proc. 17th Coastal Eng. Conf., pp.278-289, 1980.
15. Muroi, S. and N. Shuto : Trajectory of wave front on sloping beach, Proc. of Annual Technical Meeting of J.S.C.E. in the Tohoku district, pp.103-104, 1982 (in Japanese).
16. Roos, A. and J.A. Battjes : Characteristic of flow in run-up of periodic waves, Proc. 15th Coastal Eng. Conf., pp.781-795, 1976.
17. Sasaki, M. and H. Saeki : Study on the deformation of waves after breaking, Proc. 21th Japanese Conf. on Coastal Engg., pp.39-44, 1974 (in Japanese).
18. Savage, R.P. : Wave run-up on roughened and permeable slopes, Proc. A.S.C.E. Vol.84, WW3, pp.1640-1 - 1640-38, 1958.

19. Saville, T.Jr. : Wave run-up on composite slopes, Proc. 6th Coastal Eng. Conf., pp.691-699, 1958.
20. Sawaragi, T. : Effects of bottom roughness on the decay of wave height after breaking, Proc. 9th Japanese Conf. on Coastal Engg., pp.85-89, 1962 (in Japanese).
21. Sawaragi, T., K. Iwata and M. Morino : On the characteristics of run-up on gentle beaches, 23th Japanese Conf. on Coastal Engg., pp. 164-169, 1976 (in Japanese).
22. Shuto, N. : Standing waves in front of a sloping dike, Coastal Engg. in Japan, Vol.15, pp.13-23, 1972.
23. Takada, A. : On relations among wave run-up, overtopping and reflection, Proc.J.S.C.E. No.182, pp.19-30, 1970 (in Japanese).
24. Taylor, R.B., E. Ozsoy and J.T. Thomas : Wave run-up on variable beach profiles, Proc. A.S.C.E., WW2, pp.169-192, 1980.
25. Toyoshima, O., N. Shuto and H. Hashimoto : Run-up height of waves on sea dikes — for slope of 1/30 —, 11th Japanese Conf. on Coastal Engg., pp.260-265, 1964 (in Japanese).
26. Tsuchiya, Y., Y. Kawata and T. Yashita : Effects of roughness and permeability on wave run-up, 25th Japanese Conf. on Coastal Engg., pp.160-164, 1978 (in Japanese).
27. Van Dorn, W.G. : Run-up recipe for periodic waves on uniformity sloping beach, Proc. 10th Coastal Eng. Conf., pp.349-363, 1966.
28. Van Dorn, W.G. : Set-up and run-up in shoaling breakers, Proc. 15th Coastal Eng. Conf., pp.738-751, 1976.
29. Van Dorn, W.G. : Breaking invariants in shoaling waves, Jour. of Geophy. Res., Vol.83, No.C6, pp.2981-2988, 1978.
30. Watanabe, A. : Numerical simulation of nearshore current and beach transformation, 28th Japanese Conf. on Coastal Engg., pp.285-289, 1981 (in Japanese).

## CHAPTER TWENTY FOUR

### EFFECTS OF MEASUREMENT ERROR ON LONG-TERM WAVE STATISTICS

by Bernard Le Mehaute<sup>1</sup> and Shen Wang<sup>2</sup>

KEY WORDS: Water waves, wave statistics

SUMMARY: An analysis of errors in the determination of extreme waves of low frequency of occurrence is presented. The result of the analysis provides a better understanding toward determining safety coefficients in the design of offshore structures.

ABSTRACT: The effect of sample size on confidence band in predicting the extreme wave height is related to the return period and the duration of the sample record length. An estimate of errors resulting from various methods of data acquisition is given. The uncertainties corresponding to various number of years of observation and various measurement errors are analyzed for various return intervals. It is shown that data accuracy and record length are equally important in long term wave predictions. At the present time, the determination of extreme event benefits more from relatively less accurate long-term hindcast calculation rather than short-term high quality measurements. In the long run, a long-term accurate measurement program is imperative if more definite descriptions of extreme events are sought.

---

<sup>1</sup> and <sup>2</sup> Prof., Rosenstiel School of Marine and Atmospheric Science, University of Miami, Miami, Fl 33149.



## INTRODUCTION

The uncertainties in the determination of extreme wave heights from observations may result from three causes of errors:

1. Errors due to climatological variations and extrapolation of the statistical compilation of small sample to extreme wave events of low probability of occurrence.
2. Errors in measurements, visual estimates, or (hindcast) calculations of wave input data on which the wave statistics are established.
3. Errors resulting from the lack of knowledge on the functional relationship characterizing the "true" long-term, underlying distribution, particularly at low probability level.

In a paper by Earle and Baer (6), the effects of uncertainties resulting from causes 1 and 2 have been addressed and analyzed through a Monte Carlo simulation, assuming that the long-term distribution of wave heights was log-normal. Patruskas and Aagaard (19) addressed the problems in extrapolating historical storm data. In particular, they examined the errors resulting from causes 1 and 3. While it was impossible to assess accurately the effect due to the uncertainty in underlying distribution laws, they concluded that it should be less significant than the uncertainty resulting from small sample size. The error resulting from small size samples was investigated analytically by Wang and Le Mehaute (25). The fact that small size samples cannot accurately establish the underlying distribution was particularly discussed. Confidence bands of uncertainties were possibly determined at low probability level as a function of sample size, assuming the error due to other sources to be absolutely negligible and the population distribution to be Weibull.

The purpose of this paper is to establish a rationale by comparing various methods of data gathering and to establish the confidence bands of prediction for extreme wave events. This also allows us to answer a number of practical questions such as: to determine the "100-year wave", is five years of good reliable wave measurements better than say 20 years of more questionable hindcasted data or ship observations?

As such, this paper is considered as a sequel to the previous paper already mentioned (25). Considerations and assumptions which have been raised in that paper concerning duration between uncorrelated events, measurement intervals, return periods, etc., are therefore not repeated here. Recalled only is that the translation of long-term wave statistics from a variety of causes of oceanic events (hurricane, storm, local sea state, swell, etc.) into a single distribution - Weibull, log-normal or else - is a gross simplification. It may be justified by curve fitting and found good or bad, but it cannot be proven right or wrong on a rational basis. The actual distribution in fact represents a sum of different populations corresponding to different classes of oceanic events and each having its own characteristics. It also varies with water depth and becomes very site

specific in shallow water.

Different forms of distribution have been examined and reviewed by Isaacson (13). Ochi and Whelan (17) and Ochi (18) have attempted to rationalize some of these. Even though the fact of no well-proven law of distribution could be a significant cause of error at low probability level, this subject will not be considered in the present paper. Instead, the Weibull distribution considered in (25) will remain as the foundation in the present discussion. There is enough evidence to support the Weibull distribution at low probability level down to  $10^{-3}$ , below which the probability of exceedance curves tend to depart on the high wave height side from the Weibull distribution due to the superposition of rare classes of oceanic events such as winter storms or tropical depressions. Indeed the Weibull distribution may not be truly representative of the population distribution, any conclusion which is obtained with the Weibull distribution however is anticipated to be equally valid for other forms of distributions.

#### EFFECT OF SAMPLE SIZE

Under the assumptions made in (25) the probability of exceedance of wave height at a given location is given by

$$Q(h) = \exp [-h^\gamma] \quad (1)$$

where the variate  $h$  is defined by

$$h = \frac{H - H_0}{\bar{H}} \quad (2)$$

Here  $H$  is the significant wave height characterizing a sea state, typically obtained by analyzing a 20-minute continuous wave record;  $H_0$  is the so called location parameter signifying a lower bound of the wave height,  $H$  the scale parameter and  $\gamma$  the shape parameter which varies between 0.9 and 1.5. The parameter  $\gamma$  tends to be toward the lower limit in shallow water.

Confidence bands at any given level of  $Q(h)$  can be determined with respect to errors arising from small sample size. The widths of these bands are given in terms of the standard deviation of the sample quantile at various probability levels. Recalled from (25), the standard deviation is given by

$$\sigma_s = \frac{1}{f(h)} \left[ \frac{Q(h)[1-Q(h)]}{N} \right]^{1/2} \quad (3)$$

in which  $f(h)$  is the probability density function, which can be obtained by

$$f(h) = -\frac{d}{dh} Q(h) \quad (4)$$

Note that  $\sigma_s$  is dimensionless because  $h$  is dimensionless. Referring to Eq. 2, the absolute value of the standard deviation  $\sigma_s$  maybe obtained by multiplying  $\sigma_s$  with  $H$ .

$$\bar{\sigma}_s = \sigma_s \cdot \bar{H} \quad (5)$$

Let  $N$  be the size of the sample which may be defined in terms of the number of years of measurements  $Y$  and the time interval between uncorrelated events  $\Delta t$  (expressed in hours) so that

$$N = \frac{365 \times 24 \times Y}{\Delta t} \quad (6)$$

The sensitivity of the exact definition of  $\Delta t$  on the confidence band for  $h$  has been examined in (25). The confidence bands which define the error in  $h$  due to small sample size generally envelop the error resulting from an imprecise definition for  $\Delta t$ . This allows some flexibility in the choice of  $\Delta t$  to assimilate the number of observations  $N$  to the number of uncorrelated events. Even though a  $\Delta t$  of 6 hours is probably small for the latter, it is common practice to sample the sea state every six hours. This number will be retained in most cases of the following discussion.

The standard deviation relative to the variate  $h$  is now defined by

$$\sigma'_s(h) = \frac{\sigma_s}{h} = \frac{\bar{\sigma}_s}{H - H_0} \quad (7)$$

Equation 7 shows that  $\sigma'_s(h)$  is equivalent to the dimensional quantity of the standard deviation normalized by the variable  $(H - H_0)$  or  $H$  if  $H_0$  is zero. This normalized standard deviation therefore can be expressed in percentages of wave height  $(H - H_0)$  or  $H$ . Inserting  $Q(h)$  and  $f(h)$  from Eqs. 1 and 4 into 3, the normalized standard deviation is given by

$$\sigma'_s(h) = \gamma^{-1} h^{-\gamma} \left[ \frac{[1 - \exp(-h^\gamma)] \exp(h^\gamma)}{N} \right]^{1/2} \quad (8)$$

Let  $R$  be the return interval (in years); by definition it is given by

$$R = \frac{\Delta t}{Q(h) \times 365 \times 24} = \frac{1}{Q(h) v} \quad (9)$$

where  $v$  is the number of observations per year. At low probability levels  $1 - Q(h) \approx 1$ , Eq. 8 then can be written as

$$\sigma'_s = \frac{1}{\gamma \ln(Rv)} \left( \frac{R}{Y} \right)^{1/2} \quad (10)$$

This relation indicates that the error due to extrapolation from short

sample is proportional to the square root of the return period but inversely proportional to the square root of the sample record length. The fact that the accuracy of prediction requires a long record length is obvious. The uncertainty in predicting events of long return period being not very sensitive to the value of  $\nu$  or the definition of  $\Delta t$  has been discussed in (25).

#### ERRORS FROM MEASUREMENT OR HINDCAST - ERROR IN DATA SAMPLE

The analysis presented in the previous section has assumed that the sample data are accurate with no error. The uncertainty involved, therefore, comes only from the fact of finite short length of sample. In this section, the error and uncertainty in the data are particularly addressed.

The methods used to constitute the population sample on which wave statistics are established, are numerous and various. The errors made in gathering the data depends on the specific instruments and processes used to analyze the records. Specific information on each method can be found in the literature (3,4,5,7,12,15,16,19,20,21,23,24).

The primary methods which have been used include wave staff (continuous or step), pressure gage in shallow water, wave rider and accelerometer in deep water, visual observations and estimates from ships, hindcasts from weather maps, either storm by storm or systematically. Remote observations by radar from airplane or satellite have also been used recently, but the corresponding data do not provide any kind of long-term statistical information at this time.

For a given wave height the random errors corresponding to all methods are normally distributed and can be characterized by a standard deviation  $\sigma_M$ . The systematic error or bias is obtained by "calibration in comparing the results of a less accurate method with the most accurate for the same period of time. In general,  $\sigma_M$  is a function of the wave height, and increases with the wave height. As  $\sigma_s$ , a standard deviation expressed in percentages of the wave height  $H$ , is defined by

$$\sigma_M' = \frac{\sigma_M}{H - H_0} \quad (11)$$

and in general  $\sigma_M'$  can be assumed as a constant. It is not, however, for the case of wave measurements made by step wave staff where  $\sigma_M$  rather than  $\sigma_M'$  is a constant. Indeed, the error is a function of the distance between sensors on the wave staff, and for small amplitude waves, the recorded signal appears as a square function making Fourier analysis of the signal meaningless. Also in the case of wave rider, the response is influenced by the wave period and sometimes the phenomena of jerking due to poorly designed mooring attachments.

Before attempting to give an order of magnitude estimate for  $\sigma_M'$  a general remark applies: given a true signal - such as given nearly by a high quality continuous wave staff - any comparison between this signal

and the data given by the other methods in the time domain, generally exhibit very large errors. For example, comparisons of recorded time series characterized by an energy spectrum or more simply a significant wave height with hindcasted wave results, display large discrepancies corresponding to a  $\sigma_M$  near 50%, (4, 14).

If, instead of comparing the sea state in the time domain, both data are ranked statistically, the random error becomes very small by comparison and the only discrepancy left would be the sum of the systematic error or bias, and the "ranked random errors." This applies also to short-term wave analysis. For example, free surface waves determined from pressure gage differ significantly from free surface measured concurrently by a wave staff. But, when the results are ranked statistically, the two (Rayleigh) distributions are alike (Brebner & LeMehaute, 2). Much of the random errors in these comparisons must be attributed to phase shifts. Figure 1 illustrates an example of a comparison of data obtained by hindcast calculations with data obtained by measurements given by Carson and Resio (4). On the left the data is compared point by point in the time domain. On the right the data is first ranked statistically and the comparison is made by rank, leading to a much smaller deviation.

It has been mentioned that the most accurate method for acquiring wave data is a continuous wave staff. The only error is from the calibration of the wave recorder and the data analysis which translates a limited size sample, say 20 minutes, into a wave energy spectrum. For practical purposes, this method provides a negligible error and can be used to calibrate the bias in other methods of data acquisition.

Step wave staff yields too much of a large error for small wave heights as already mentioned. Buoys, wave riders and accelerometers have been used in deep water. They also give reliable data when properly calibrated as function of frequency.

The most common mode of wave measurement has been by pressure gage. The free surface is then obtained by convolution of the pressure signal based on the linear wave theory. The original method which was developed on a wave by wave basis leads to an underestimation of the surface wave height by 25 to 30% because of nonlinear convective effects and inadequate consideration to shorter waves. A more accurate procedure is to compute the spectrum of the pressure record and to compensate each frequency band of the spectrum for the effect of gage submersion as function of the relative depth (Harris, 9). With the proper method of analysis and compensation factor, the error is then very small, even in the time series presentation. For a pressure gage on the seafloor, the normalized standard deviation  $\sigma_M$  does not exceed 5% when the results are statistically ranked (see Harris (9), Homma et al (11), Grace (8)).

Statistical wave summaries from ship observations have often been the only source of long-term wave data. For this, they have been the most widely used. Unfortunately they are the most inaccurate, particularly for large amplitude wave which ships tend to avoid. However, when the results are ranked statistically, the discrepancies between measured

R in years	1	10	100
$\gamma = 1.0$	13.7	10.4	8.4
$\gamma = 1.2$	11.5	8.6	7.0
$\gamma = 1.4$	8.1	7.4	6.0

TABLE 1  
 Climatological variations  $\sigma^*(R)$  as function of  $\gamma$   
 (assume  $\Delta t = 6$  hr)

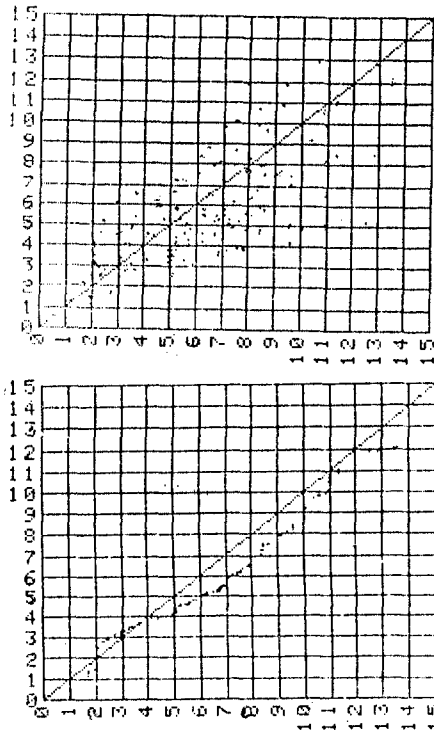


Fig. 1. Case example of a comparison of the calculated (hindcast) data vs. measured data. On the top the comparison is made point by point in the time domain, on the bottom the data is initially ranked statistically.

and observed data appear much smaller (Hogden and Lumb (12), Bell (1)).

Many comparisons between ship observations and measurements are reported in the literature and a number of quite different formulae have been proposed to "calibrate" ship observations. The problem is not settled. Harris (10) has presented an analysis on the reasons for these discrepancies, which include, singularities of the codes, ship operational procedures, etc.

The uncertainty in statistical information from wave hindcasting is of a different nature. Here again, an abundance of literature can be found offering comparisons between hindcast data and measurements. Errors in wave hindcasting result from: 1) the state of the art in relating wind and sea state, and 2) inaccuracy of weather maps, and the interpretation of weather maps.

The most recent assessment of the state of the art formulation can be found in a report on the SWAMP (Sea Wave Modeling Project) experiment (22). In this report, a comparison of 10 different mathematical models of wave generation was done based on seven hypothetical test wind fields. The wide spread between the results of these models gives an indication of the uncertainties which remain, even though all these models are initially based on specific experimental data.

Many differences found in the model wave growth are attributed to the uncertainties as to whether the friction velocity  $u$  or the wind velocity  $U_{10}$  control the growth rate of waves. Also, uncertainty is due to the lack of accurate information on the value of the drag coefficient as well as on the relationship between  $u_*$  and  $U_{10}$ .

Furthermore, since the comparison of the model is based on hypothetical, simple wind field, results corresponding to real situations may be expected to exhibit more divergence than for the cases studied by SWAMP. Uncertainties due to the lack of accuracy of weather maps and their interpretation are also a significant cause of error. In theory, more than 50 years of weather maps have been archived and can be used for wave hindcasting. But in reality, only the last 30 years are considered reliable. The lack of enough pressure measurements in the southern hemisphere still hindered wave hindcast. In general, the accuracy is better for a small body of water where the fetch is limited, such as the Great Lakes. It is also better for the Atlantic Ocean than it is for the Pacific because of the interference of swell on local sea states. The worst hindcasting uncertainty is for the case of hurricanes and tropical storms.

Still when the results are ranked statistically the large discrepancy due to random error disappears, and wave hindcasting methods appear in a more favorable shape. One of the latest comparisons between hindcast vs measurements, excluding hurricanes, is due to Carson and Resio (4). It indicates that a 20% deviation is still possible.

As a conclusion of this broad and rapid survey, one will retain for the sake of simplicity, the following normalized standard deviations applicable when the sample populations are ranked statistically:

Direct wave measurement	$\sigma_M' = 0.05$	bias	0.00
Ship observations	$\sigma_M' = 0.20$	bias	0.05
Wave hindcast	$\sigma_M' = 0.15$	bias	0.05

COMBINED ERRORS DUE TO SHORT SAMPLE AND INACCURATE DATA

It has been assumed that the errors due to small sample size and the random errors from measurements were normally distributed and characterized by the normalized standard deviation  $\sigma_s'$  and  $\sigma_M'$ , respectively. Because of their independence and the convolution of the Gaussian functions, the total errors are also normally distributed and the total variance is given by:

$$\sigma'^2 = \sigma_M'^2 + \sigma_s'^2 \tag{12}$$

In the case of a Weibull distribution,  $\sigma_s'$  is given by Eq. (8), or approximately by Eq. (10).

If one retains this last formulation, it is found that the number of years Y required for predicting an event of return period R with a maximum uncertainty not greater than  $\epsilon$  (in terms of standard deviation) is given by

$$Y > \frac{R}{[\gamma \text{Ln}(Rv)]^2} \frac{1}{\epsilon^2 - \sigma_M'^2} \tag{13}$$

It is seen that there is a lower limit to the level of uncertainty,  $\epsilon = \sigma_M'$ , for which the required number of years Y approaches infinity. This indicates beyond a certain number of years Y, the error introduced by small sample size becomes less important than the accuracy limited by the error of the data. This is further evidenced if one writes:

$$\sigma' = \left[ \sigma_M'^2 + \frac{1}{[\gamma \text{Ln}(Rv)]^2} \left( \frac{R}{Y} \right)^{1/2} \right]^{1/2} \tag{14}$$

which allows us to determine the normalized total standard deviation  $\sigma'$  for various return interval R as a function of the number of years of observation Y for various values of the data errors  $\sigma_M'$ . The corresponding results calculated for  $\Delta t = 6$  hours,  $\gamma = 1, 1.4$ ,  $R = 20, 50, 100$  years, and various values of  $\sigma_M'$  are shown in Figs. 2, 3 and 4. These results compared well with the results of Earl and Baer (6) obtained by a Monte Carlo simulation. (The case  $\sigma_M' = 0$  yields the same results as the one presented in (25) except for the multiplier of 1.28 for insuring a confidence level of 90%). From these results the asymptotic value of  $\sigma'$  at  $\sigma' = \sigma_M'$  clearly appears.

The derivative  $\partial\sigma'/\partial Y$  yields the fact that as Y increases the gain in accuracy decreases much less rapidly when  $\sigma_M'$  is large than when,  $\sigma_M'$  is small. This reveals that long-term accurate measurements ( $\sigma_M' = 0.05$ ) corresponding to, for example,  $Y/R \approx 0.4$  (40 years for the 100-



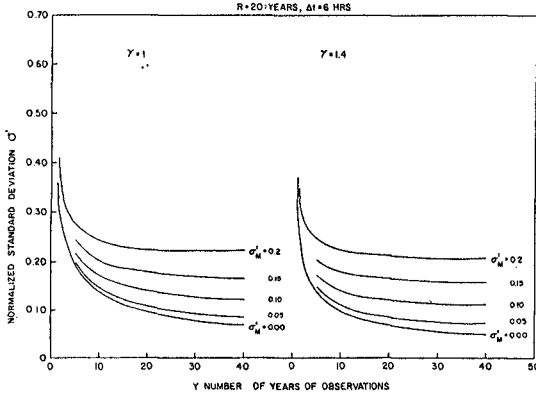


Fig. 2

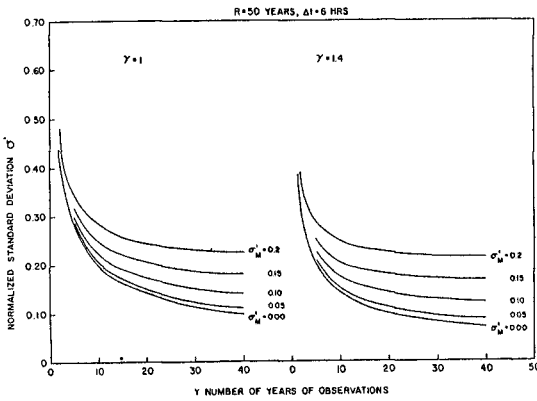


Fig. 3

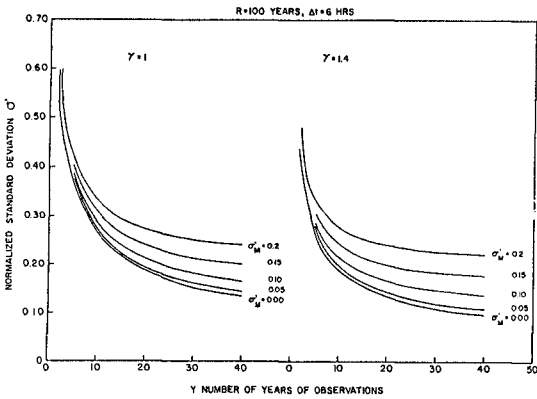


Fig. 4

Fig. 2 Normalized standard deviation as function of the number of years of observations and relative measurement error  $\sigma_M$ .

year wave) seems to be a worthwhile investment since the normalized standard deviation decreases to 16%. It decreases rather slowly for longer periods of measurements.

On the other hand, for data with  $\alpha_M = 0.2$ , such as given by wave hindcasts or ship observations, processing more data than given by  $Y/R = 0.15$  (15 years for the 100 year wave) gains little accuracy. This result of course contradicts what is done in practice where there is a tendency to carry out small-term wave measurements and long-term hindcast. Therefore, it would appear that long-term hindcast (or ship observations) should only be considered as a temporary measure, not a substitute for long-term wave measurements. The measurement accuracy characterized by  $\alpha_M = 0.05$  is adequate since with this accuracy the error due to sample size is more significant. Figures 2, 3 and 4 also yield directly the number of years which give the same level of accuracy by the various methods. For example, it is seen from Fig. 3 ( $R = 100$  y,  $\gamma = 1$ ) that 40 years of hindcast ( $\alpha_M = 0.15$ ) is equivalent to 18 years of accurate measurements ( $\alpha_M = 0.05$ ) since both yield a value of  $\sigma$  of 0.20.

As a part of the presumption of this paper, it has been implicitly assumed that all the cases had the same underlying distribution of Weibull type in the above discussion. This assumption is justified because of the lesser significance of the exact distribution than the causes of small sample size and relatively larger errors from measurements. It must be noted, however, that in most cases extreme wave heights are determined from a multiplicity of information which may include both short-term measurement and long-term hindcast or ship observations, and the probability functions fitted by different methods are not necessarily the same even though they correspond to the same time period because of the inherent errors of the methods. If part of the hindcast period overlaps the measurement period, the measurements may certainly be used to "calibrate" the hindcast results. The correction factor, which is valid for the lower level of probability, may then correct, in part, the systematic error of the hindcast and modify the underlying distribution. This kind of calibration is particularly useful in shallow water where the wave climatology is site-specific and directional.

For the convenience of discussion without jeopardizing the accuracy of the outcome, we shall continue to assume a single underlying distribution applying to all methods of data acquisition. In particular, we consider a Weibull distribution with  $\gamma = 1$ , and the distribution of a combined error (in terms of standard deviation) due to joint causes of limited observation ( $Y$ ) and measurement inaccuracy ( $\alpha_M$ ) are presented in Fig. 5. This figure reveals the trade-off between the data accuracy and the record length. Specifically, it shows that a 5-year accurate record ( $\alpha_M = 0$ ) is equivalent to 20 years less accurate hindcasts ( $\alpha_M = 0.10$ ) for prediction of 5.7-year return waves. Particularly of interest is that, in long return period predictions, the long record of less accurate data is far more superior than short, accurate data. This result shows the extreme importance of record length on the extrapolation of long-term wave statistics. On the other hand, in Fig. 6, one may find that good measurements ( $\alpha_M = 0.05$ ) of 5 years are just

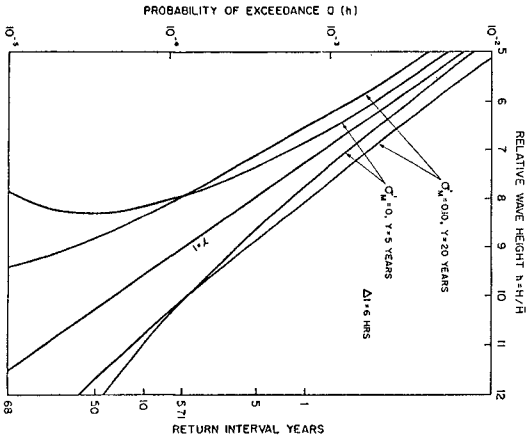


Fig. 5 Comparison of confidence bands about probability of exceedance curve based on 20 years of observations and measurement error  $\alpha_M = 0.10$ ; and 5 years of observations and measurement error  $\alpha_M = 0$ .

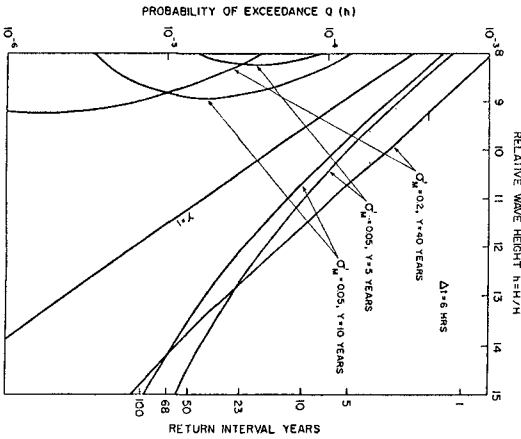


Fig. 6 Comparison of confidence bands about probability of exceedance curve. Corresponding to number of years of observations Y and relative measurement error  $\alpha_M$ :

$\alpha_M = 0.05$	Y = 5 years
$\alpha_M = 0.05$	Y = 10 years
$\alpha_M = 0.20$	Y = 40 years

as good as 40 years of ship observations ( $\sigma_M^2 = 0.2$ ) for 23-year return waves and good measurements of 10 years would predict 68-year return waves as the 40 years less accurate observations. In general, a high frequency event, say the 5-year or 10-year wave should be determined from 5 years of good measurements rather than 20 years of questionable hindcast. This figure, therefore, specifically emphasizes the importance of the measurement accuracy. It also indicates, however, that in order to improve the long-term predictions, long-term commitment of accurate measurements is imperative. At the present time, a deeper insight into extreme events can be provided only by lengthy hindcast, say 30 or 40 years, because of the nonexistence of long-term accurate measurements.

#### CLIMATOLOGICAL VARIATIONS

The foregoing discussion reveals indubitably two important errors which may be involved in long-term wave statistics, the error of extrapolation from short-term data and the error due to the inaccuracy in the data themselves. Consequently, it is not difficult to conclude that a long-term investment on the acquisition of accurate data is necessary, especially when there are only 5-7 years of good measurements available today. The improvement in the measurement accuracy always benefits wave analysis. The combination of error due to measurements and small sample size demonstrates that large measurement errors practically limit the accuracy of the prediction of extreme wave heights regardless of the number of years of observation. On the other hand, when the record length is longer than a certain period of time, the improvement in prediction accuracy becomes negligible. As shown in the foregoing analysis, a period of 30-40 years of good measurements appear to be sufficient for establishing 100-year wave statistics.

Statistical estimates can be improved by reducing the source of uncertainties. For the present problem, the reduction is limited by the facts of the data accuracy and sample extrapolation. The former is governed by the state of the art in wave measurements and data analysis; the latter is governed by the law of statistics. Still, there is an additional source of uncertainty attributed to the nature, the natural variations of the wave climate.

Now, assuming the natural climatology is ergodic and stationary and indeed governed by the statistical law of Weibull distribution, the result derived in Eq. (10) can also be used to determine the periodical climatological variations. Setting  $Y = R$  in Eq. (10), one obtains:

$$\sigma^*(R) = \frac{1}{\gamma \ln(Rv)} \quad (15)$$

This parameter, in theory, characterizes the climatological variation of  $R$  years for the Weibull nature. In particular, when  $R = 1$ , one obtains the annual climatological variation

$$\sigma^*(1) = \frac{1}{\gamma \text{Ln}(v)} \quad (16)$$

This parameter represents the characteristics of the nature indicating the spread of yearly climatological variations at a particular location. This parameter is unique under the assumption of Weibull distribution and the definition of  $\Delta t$ . The values of this parameter are tabulated in Table 1 for three values of  $R$  with  $\Delta t = 6$  hr. From this table, it is seen that  $\sigma^*(1)$  is on the order of 11%, for  $\gamma = 1.0 - 1.4$ . The result indicates that there is a variation of about 11% (in term of standard deviation) from year to year in the Weibull nature. This value reduces to about 9% for 10 years and 7% for 100 years. Indeed, when making an estimate on 100-year events in a Weibull world, there is always a 7% standard deviation from the expectation attributed to the climatological variations of the nature, regardless of the data quality or the sample length used for extrapolation. In other words, the average prediction accuracy is limited by the climatological variations of the nature. It becomes more evident to relate this parameter with the risk of exceedance. It is well known that the risk for a  $R$  year-wave to be exceeded in  $R$  years is

$$R_e = 1 - \left(1 - \frac{1}{R}\right)^R \quad (17)$$

which tends toward 0.63 or 63% when  $R$  is large. Knowing the climatological variation in  $R$  years makes it further possible to determine the standard deviations of the risk from expectations.

#### CONCLUSION

Large errors in the prediction of sea state, such as given by wave hindcast, limit the accuracy of the prediction of extreme event, and improvement in prediction accuracy with the number of years of observation becomes rapidly negligible. Long term measurements are only worthwhile if they are accurate. For an accurate prediction of extreme events, a long term program of accurate measurements is necessary, as it reduces both the error  $\sigma_s$  due to short sampling and  $\sigma_M$  due to measurement or hindcasting calculation.

The errors due to natural climatological variations are predictable, assuming a stochastic and Gaussian world. This error is of the order of 11% for the yearly wave and 7% for the hundred year wave. In a non-ergodic and unstationary nature, it could be larger. This parameter directly relates with the risk of exceedance and should be carefully taken into account in the design of offshore structures.

The uncertainty of prediction as well as the errors involved in short sampling and data accuracy is characterized in terms of standard deviation. Confidence bands of uncertainties for various levels of probability can be derived from the standard deviation under the law of normal distribution (25).

## Appendix

PROBABILITY OF EXCEEDENCE CURVE INCLUDING UNCERTAINTIES.

Both  $h$  and  $\sigma'_s$  can be expressed in term of  $Q$ . Indeed referring to equation (1).

$$h = [-\text{Ln } Q]^{1/\delta}$$

Also, referring to equation (8)

$$\sigma'_s = \frac{1}{\gamma \text{Ln } Q (\sqrt{Y})^{1/2}} \left( \frac{1-Q}{Q} \right)^{1/2}$$

Therefore, the total error  $\sigma'^2 = \sigma_M'^2 + \sigma'_s'^2$  can entirely be defined in terms of  $Q$ . Furthermore, multiplying  $\sigma'$  by a coefficient  $\alpha$  allows to calculate the uncertainty spread corresponding to various confidence levels. For example,  $\alpha = 0.84, 1.28, 1.65, 2.32$  corresponds to confidence level  $C_1 = 80, 90, 95, \text{ or } 99\%$  that the spread will not be exceeded. By adding  $\alpha\sigma'h$  to  $h$  gives the upper bound corresponding to these confidence levels. (By subtracting  $\alpha\sigma'h$ , the lower bound is obtained.) Accordingly, the upper bound characterizes a new probability of exceedence curve which is now defined by the function

$$h_E = h(1+\alpha\sigma) = [-\text{Ln}Q]^{1/2} \left\{ 1 + \alpha \left[ \sigma_M'^2 + \frac{1}{\gamma^2(\text{Ln}Q)^2 \sqrt{Y}} \left( \frac{1-Q}{Q} \right)^{1/2} \right] \right\}$$

It is an inverse Weibull distribution defining the upper bound due to statistical uncertainties. The inclusion of the correction due to these uncertainties establishes the basis for the determination of the safety coefficients for various confidence level  $C_1(\alpha)$ . As a result it appears that tradeoff or risk analysis for the design of offshore structures should rather be based on  $h_E(Q)$  instead of  $h(Q)$ . The importance of each cause of error, and the need for long term accurate measurements then become apparent.

## ACKNOWLEDGEMENTS

This study was sponsored by the National Science Foundation as part of a study under Grant No. CEE-7911930 and by the NOAA under contract No. NA83AA-D-00041. The authors acknowledge Dr. L. Baer for his encouragements and challenging discussions. M. Soldate reviewed the manuscript critically and is acknowledged for his pertinent remarks. Dr. Max Sheppard of Mobil Research and Development Corp., is also acknowledged for fruitful discussions during the course of this investigation.

## References

1. Bell, A. O. (1974) Service performance of a drilling unit. Trans. Roy. Inst. Nav. Architects.
2. Brebner, A., and Le Mehaute, B. (1961). Wind and waves at Cobourg Lake Ontario. CE Research Report No. 19, Queens Univ., Kingston, Ontario.
3. Cartwright, D. E. (1962). A comparison of instrumental and visually established wave lengths and periods recorded on ocean weather ships, NIO.
4. Corson, W. D. and D. T. Resio (1981). Comparisons of hindcast and measured deep water significant wave heights. U. S. Army, Corps of Engineers, WES, WIS Report No. 3, May.
5. Deleonibus, P. S. and L. S. Simpson (1972). Case study of duration limited wave spectra observed in an open ocean tower, Journal of Geological Research, Vol. 77, No. 24, pp 4555-4569.
6. Earl, H. D. and L. Baer (1982). Effects of uncertainties on extreme wave heights, Journal of Waterway, Port, Coastal and Ocean Division, ASCE, Vol. 108 (WW4), Nov. pp 456-478.
7. Estava, O, and D. L. Harris (1970). Analysis of pressure wave records, and surface wave records, Proc. 12th Conf. ASCE, Washington.
8. Grace, R. A. (1970). How to measure waves, Ocean Industry, 5, pp 65-69.
9. Harris, D. L. (1972). Wave estimates for coastal regions. Shelf sediment transport, ed. Swift, Duane, Pilkey, Chapter 5, Dowden, Hutchinson and Ross, Inc., Stroudsburg, Pa., pp 99-125.
10. Harris, D. Lee and p. Turner (1973). The consistency of ship-board reports of waves and winds, CERC, U. S. Army Corps of Engineers, Wash. D.C.
11. Houma, M., K. Horikawa and S. Komori (1966). Response characteristics of underwater wave gage, Proc. 10th Conf. Coastal Eng., (Tokyo) pp 99-119.
12. Hogden, N. and F. E. Lumb (1967). Ocean wave statistics, National Physics Lab. Her Majesty's Printing Office, U.K.
13. Isaacson, M. de St. Q. and N. G. MacKenzie (1981). Long-term distribution of ocean waves: A review, Journal of Waterway, Port Coastal and Ocean Division, ASCE, Vol. 107, (WW2), pp 93-109.

14. Leung, T. and M. Bransdma (1979). Validation of the U. S. Navy spectral ocean wave model for hindcasting wave conditions at Point Conception, Tetra Tech Report TC-3917-14.
15. Michelena, E. D., et al (1974). A reliable wave measurement system for NOAA buoys. Unpublished NOAA Report.
16. Moskowitz, L. W. J. Pierson and J. Mehr (1962). Wave spectra from wave recores obtained by the OWS Weather Explorer and the OWS Reporter, NYU, Dept of Meteorology and Oceangraphy, Tech. Report.
17. Ochi, M. K. and J. E. Whalen (1980). Prediction of the severest significant wave height, Proc. 17th Conf. Coastal Eng., Vol. 1, pp 587-599.
18. Ochi, M. K. (1982). Stochastic analysis and probability prediction of random seas. Advances in Hydrosiences, Academic Press, Vol. 13, pp. 217-375.
19. Petruskas, C. and P. M. Aagaard (1971). Extrapolation of historical storm data for estimating design wave heights, Journal of Society of Petroleum Engineers, 2, pp 25-35.
20. Pickett, R. L. (1964). Argus Island wave recorder, Report. No. O-20-64, U. S. Naval Oceanographic Office.
21. Pitt, E. G., J. S. Driver and J. A. Ewing (1978). Some inter-comparison between wave recorders, Report No. 43, Institute of Oceanographic Sciences.
22. Sea wave modeling project (SWAMP), (1983). An intercomparison study of wind wave prediction models, to be published,
23. Tucker, M. H. (1956). A ship bourne wave recorder, Royal Institution of Naval Architects, Vol. 98, pp 236-250.
24. Tucker, M. H. (1956). The NIO wave analyzer, Proc. 1st Conf. on Coastal Eng. Instruments, R. L. Wiegel, ed., pp 129-133.
25. Wang, S., and Le Mehaute, B. (1983). Duration of measurements and long term statistics, Journal of Waterway, Port, Coastal and Ocean Engineering, ASCE, Vol. 190, No. 2.



## CHAPTER TWENTY FIVE

### On A Design Wave Spectrum\*

Paul C. Liu<sup>†</sup>, M. ASCE

We propose the use of a generalized representation for acquiring a design wave spectrum. The generalized form, free from any predetermined coefficients and exponents, requires only significant wave height and average wave period as input for practical applications. The usefulness of this representation has been demonstrated with over 2000 measured deep-water wave spectra recorded from NOMAD buoys in the Great Lakes during 1981.

#### Introduction

Since Neumann (1953) first introduced his representation for wind-wave spectra to facilitate wave prediction, coastal engineers have endeavored for over three decades to develop a realistic representation of wave spectra. The two-parameter spectrum of Bretschneider (1959), the fully developed spectrum of Pierson and Moskowitz (1964), and the fetch-limited spectrum of JONSWAP (Hasselmann et al., 1973) are notable examples. Among these, the JONSWAP spectrum is perhaps the one most widely used in wave modeling and engineering designs during the last decade.

All of these proposed spectral forms consist of a number of empirical coefficients and exponents that differ among various authors, while the overall forms are basically similar. The applicability and universality of these coefficients and exponents has frequently been the subject of question or dispute. For instance, the rear face of the spectrum in the high frequency range was first intuitively set by Neumann to be proportional to the -6th power of frequency. Later Phillips (1958) deduced from dimensional considerations that the exponent should be -5. The -5th power dependence on the high frequency side of the spectrum seems to have been substantiated by many laboratory and field measurements. Most of the spectral forms use the -5 formulation. More recently, however, Kitaigorodskii (1983) found theoretical as well as experimental evidence that the exponent should be -4 instead. The situation remains unsettled. Moreover, the widely used average JONSWAP spectrum consists of four numerical parameters, three of which are averaged from largely scattered empirical data points. When applying the formula with these empirical numbers in

---

\*GLERL Contribution No. 435.

<sup>†</sup>Oceanographer, NOAA/Great Lakes Environmental Research Laboratory, 2300 Washtenaw Avenue, Ann Arbor, MI 48104.

practice, it is seldom certain how close the representation is as compared to the actual modeling or design conditions.

In this paper, we propose an alternative approach by using a generalized form (Liu, 1983) that avoids predetermining any coefficient and exponents in the spectrum representation. They can all be obtained from known spectral parameters. Hence, if design wave conditions are given, relevant spectral parameters can be estimated and a design wave spectrum can be readily determined.

### The Spectral Form

The generalized spectral form given by Liu (1983) in representing a one-dimensional, single peak frequency wave spectrum is

$$S(f) = C_1(E/f_m)(f/f_m)^{-C_2}\exp[-C_3(f/f_m)^{-C_2/C_3}] \quad (1)$$

where  $E = \int S(f)df$  is the variance of the surface displacement,  $f_m$  is the frequency of the spectral peak, and  $C_i$ 's are dimensionless coefficients and exponents that can be determined from given spectral parameters.

To show how the  $C_i$ 's are determined, we note first in eq. (1) that for  $f = f_m$

$$C_1 = \exp(C_3)S(f_m)f_m/E \quad (2)$$

Furthermore from the definition of  $E$  and using the gamma function  $\Gamma$  with eqs. (1) and (2), we find

$$E/(S(f_m)f_m) = \exp[C_3 + (1 - C_3 + C_3/C_2)\ln C_3]\Gamma(C_3 - C_3/C_2)/C_2 \quad (3)$$

which is an equation for  $C_2$  and  $C_3$ . Now if we use the average frequency  $f_a$  defined by Rice (1944)

$$f_a^2 = [\int f^2 S(f)df]/[\int S(f)df] \quad (4)$$

and substituting  $S(f)$  from eq.(1) and using the gamma function again, we have another equation for  $C_2$  and  $C_3$

$$(f_a/f_m)^2 = \exp(2C_3)\ln C_3/C_2\Gamma(C_3 - 3C_3/C_2)/\Gamma(C_3 - C_3/C_2) \quad (5)$$

Thus we have two equations [(3) and (5)] that can be solved for  $C_2$  and  $C_3$  if the parameters  $E$ ,  $f_a$ ,  $f_m$ , and  $S(f_m)$  are given. Then  $C_1$  can be found from eq. (2) and the spectrum is fully determined.

The representation eq. (1) has been applied to over 2000 sets of deep-water wave spectra measured from NOMAD buoys moored in the Great Lakes with water depth ranging from 15 m to 250 m. Sample comparisons are presented in Liu (1983). It was found that the spectral form fits the measured spectra very well under a variety of wave conditions. The close fit was especially evident for large storm waves. Perhaps the spectra that eq. (1) does not fit well were those multimodal ones that occur mainly during the early stage of wave growth.

The process for solving eqs. (3) and (5) can best be achieved iteratively. Liu (1983) presented a workable empirical trial and error procedure. A more effective approach is to apply the iteration procedure using the Newton method to solve eq. (3) (Liu, 1984a; Fullerton, 1984) for  $C_3$  with an initial  $C_2$ . These values are then substituted into the right-hand side of the following equation obtained from eqs. (3) and (5)

$$C_2 = \exp[C_3 + (1 - C_3 + 3C_3/C_2)\ln C_3]\Gamma(C_3 - 3C_3/C_2)/D \quad (6)$$

where  $D = (f_a/f_m)^2 E / (S(f_m)f_m)$ . If the  $C_2$  calculated from eq. (6) is not nearly equal to the previous one, then the new  $C_2$  will be used for input and the procedure is repeated again until  $C_2$  converges.

### The Applications

The practical applications of the generalized spectrum form eq. (1) require the parameters  $E$ ,  $f_a$ ,  $f_m$ , and  $S(f_m)$  to be known. With these four parameters, all the useful spectral properties can be readily deduced. For example, the  $n$ th moment of the wave spectrum is given by

$$\begin{aligned} M_n &= (2\pi) \int f^n S(f) df \\ &= E(2\pi f_m)^n (C_1/C_2)^n \exp[(1-n)\ln C_3] \Gamma(Z) \end{aligned} \quad (7)$$

where  $Z = C_3 - (n+1)C_3/C_2$ . From eq. (7), the spectrum-width parameter is then

$$\begin{aligned} \epsilon^2 &= 1 - M_2^2 / (M_0 M_4) \\ &= 1 - \Gamma^2(C_3 - 3C_3/C_2) / [\Gamma(C_3 - C_3/C_2)\Gamma(C_3 - 5C_3/C_2)] \end{aligned} \quad (8)$$

Therefore, relevant spectral characteristics can generally be estimated if we know the four essential parameters.

Among the four parameters,  $E$  and  $f_a$  are obtainable from design wave information (e.g.,  $E = (H_{1/3}/4)$ , where  $H_{1/3}$  is the significant wave height). The parameters  $S(f_m)$  and  $f_m$  are in general, however, not readily obtainable without actual measurements. For practical applications, Liu (1983) found that for  $f_a$  and  $f_m$  in Hz,  $S(f_m)$  in  $m^2/Hz$ , and  $E$  in  $m^2$  the following empirical correlations exist for deep-water wave spectra

$$f_a = 0.82(f_m)^{0.74} \quad (9)$$

and

$$S(f_m) = 17.0(E)^{1.13} \quad (10)$$

which effectively reduced the necessary parameters to only two. Applying eqs. (9) and (10) in practice, we can always acquire a reasonably accurate deep-water design wave spectrum with only customarily available design wave conditions, e.g., a significant wave height and an average wave period. The applicability of eqs. (9) and (10) has been further corroborated with over 2000 measured wave spectra as shown in Fig. 1. These measured data, recorded from the eastern Lake

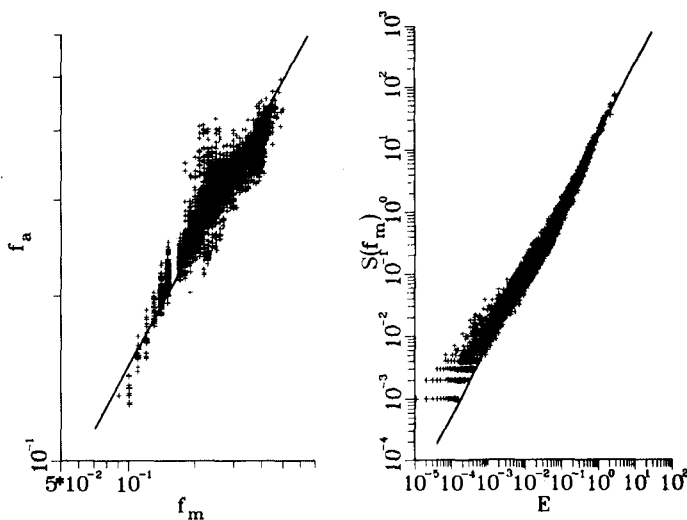


Figure 1. The correlations between  $f_a$  and  $f_m$  and between  $S(f_m)$  and  $E$ . The straight lines correspond to eqs. (9) and (10), respectively.

Superior buoy during 1981, consist of waves ranging from 0.2 to over 8 m in significant wave height. Although dimensionally inhomogeneous, the obvious existence of the empirical correlations eqs. (9) and (10) has provided a useful modification that simplifies and enhances the applicability of the generalized wave spectrum representation eq. (1).

#### Assessment of the Representations

To demonstrate the actual applicability of the generalized spectrum form, we use the following deviation index, D.I., defined in Liu (1983) as a measure of the accuracy of the representations:

$$D.I. = \sum_i \left[ \frac{S(f_i) - S_R(f_i)}{S(f_i)} \times 100 \right] \left[ \frac{S(f_i)\Delta f}{E} \right] \quad (11)$$

where  $S(f_i)$  and  $S_R(f_i)$  are, respectively, measured spectral density at frequency  $f_i$  and that calculated from eq. (1);  $\Delta f$  is the frequency interval used in calculating the spectrum. Simply stated, this deviation index is the sum of percentage deviations of calculated from measured and weighted by the relative magnitude of the measured spectral density. A perfect representation will yield a zero D.I. Hence, a smaller D.I. implies a better fit.

Based on over 2000 measured wave spectra recorded from the eastern Lake Superior NOMAD buoy during 1981, our representation with all four required parameters had an average D.I. of  $30.875 \pm 8.756$ . The modified application with only two parameters leads to an average D.I. of  $41.896 \pm 13.425$ .

For comparison, we also applied the JONSWAP representation to the same data set with the coefficients determined through fitting the measured spectrum. The resulted average D.I. is  $44.056 \pm 27.203$ . Furthermore, when the average JONSWAP representation with predetermined parameters is used, the average D.I. becomes  $101.31 \pm 82.022$ .

Since the data used in the analysis are from both large and small waves, it is of interest to eliminate the smaller waves for design purposes. For over 900 spectra with significant wave heights greater than 1 m, the average D.I.'s are  $28.510 \pm 6.720$  and  $38.136 \pm 11.011$ , respectively, for the original and modified applications of representation (1). Similarly, average D.I.'s of  $27.802 \pm 8.428$  and  $52.549 \pm 23.032$  are found for the JONSWAP and average JONSWAP representations, respectively.

From the above discussion, it appears that the JONSWAP representation gives a better fit for waves having a significant wave height greater than 1 m. However, JONSWAP only has the advantage when the spectra are given and the parameters can be obtained through fitting the known spectrum. For practical applications where a wave spectrum is not expected to be available, the proper JONSWAP parameters cannot be readily obtained; then the generalized representation is certainly

more advantageous. A comparison of the various average D.I.'s we have calculated makes it evident that the modified approach of eq. (1), which renders a reasonably accurate representation with only  $H_{1/3}$  and  $f_a$  as required inputs, is the most useful and feasible approach for acquiring a deep-water design wave spectrum.

#### The Equilibrium Range Exponent

The generalized wave spectrum representation eq. (1) is characterized by the nonpredetermined coefficients and exponents  $C_i$ 's. What is the significance of these  $C_i$ 's? Basically, they are simply scale factors for the spectrum. Liu (1983) found evidence that the  $C_i$ 's are correlated with the wave growth process; i.e., the  $C_i$ 's are large during early growth and approach some asymptotic value as waves become well developed. This is generally the case. We are particularly interested in  $C_2$ , which is the equilibrium range exponent corresponding to the high frequency side of the spectrum. Its exact value has been the subject of some controversy.

Fig. 2 presents a correlation between  $C_2$  and the significant wave height  $H_{1/3}$  based on the 2000 and more data sets used in this study. For smaller wave heights,  $C_2$  is generally larger and quite scattered. For larger wave heights, the scatter reduces significantly and  $C_2$  appears to cluster around the value 5, which is consistent with many of the previous studies. There is no indication, however, that the exponent  $C_2$  should approach a value of 4.

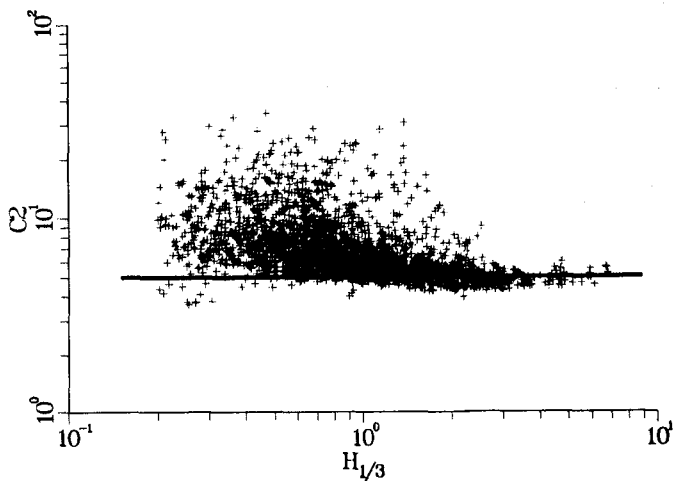


Figure 2. The correlation between  $C_2$  and  $H_{1/3}$ .  
The straight line represents  $C_2 = 5$ .

It should be noted that in most of the previous studies the equilibrium range exponent was generally obtained by fitting only the high frequency side of the spectrum, which basically ignores the total spectrum. The  $C_2$ 's deduced in this study relate to the entire spectrum and are therefore more representative of the true equilibrium range exponent.

#### Concluding Remarks

We have shown that the generalized form eq. (1) provides a reasonably accurate representation for the deep-water wave spectrum. The spectrum is fully determined from four internal parameters: the variance of the surface displacement  $E$ , the average frequency  $f_a$ , the frequency of the spectral peak  $f_m$ , and the energy density at the spectral peak  $S(f_m)$ . Because some of these parameters are not readily accessible, we have also found empirical correlations between  $S(f_m)$  and  $E$  and between  $f_a$  and  $f_m$  that can be used to reduce the essential parameters to two. This is useful in many coastal and oceanic engineering applications when spectral properties are needed and only design wave height and wave period are available.

The analysis presented here has concentrated on deep-water waves. One of the immediate interests related to coastal engineering problems is the finite depth effect. We have found from a separate analysis (Liu, 1984b) that, with four parameters given, the representation also applies satisfactorily to shallow-water waves. The depth clearly affects the spectral parameters but not the generalized form of representation. There is at present not enough shallow-water wave measurements to allow a more detailed analysis.

The contention that spectral characteristics can be obtained from given wave height and wave period can also lead to a simplified wave prediction process. That is, instead of using complicated spectral model predictions, a simpler model can be developed to predict wave height and wave period only. One such model has been developed for the Great Lakes (Liu et al., 1984; Schwab et al., 1984) with satisfactory results. Thus, by combining the output from this model with the generalized spectrum representation, we can obtain results similar to those produced from a general spectral model, but using a simpler approach and with greater computational economy.

## Appendix A.--References

- (1) Bretschneider, C.L., 1959: Wave variability and wave spectra for wind generated gravity waves. Tech. Memo. 118, U.S. Army Corps of Engineers, Beach Erosion Board, 192 pp.
- (2) Fullerton, L.W., 1984: Solution to an iteration problem. SIAM Review, 26, 279-281.
- (3) Hasselmann, K., Barnett, T.P., Bouws, E., Carlson, H., Cartwright, D.E., Enke, K., Ewing, J.A., Gienapp, H., Hasselmann, D.E., Kruseman, P., Meerburg, A., Muller, P., Olbers, D.J., Richter, K., Sell, W. and Walden, H., 1973: Measurements of wind-wave growth and swell decay during the Joint North Sea Wave Project (JONSWAP). Dtsch. Hydrogr. Z. Ergangzungsheft, A12, 95 pp.
- (4) Kitaigorodskii, S.A., 1983: On the theory of the equilibrium range in the spectrum of wind-generated gravity waves. J. Phys. Oceanogr., 13, 816-827.
- (5) Liu, P.C., 1983: A representation for the frequency spectrum of wind-generated waves. Ocean Eng., 10, 429-441.
- (6) Liu, P.C., 1984a: An iteration problem. SIAM Review, 26, 279.
- (7) Liu, P.C., 1984b: Representing frequency spectra for shallow water waves. Ocean Eng. (In press).
- (8) Liu, P.C., Schwab, D.J. and Bennett, J.R., 1984: Comparison of a two-dimensional wave prediction model with synoptic measurements in Lake Michigan. J. Phys. Oceanogr., 14, (In press).
- (9) Neumann, G., 1953: On ocean wave spectra and a new method of forecasting wind-generated sea. Tech. Memo. 43, U.S. Army Corps of Engineers, Beach Erosion Board, 42 pp.
- (10) Phillips, O.M., 1958: The equilibrium range in the spectrum of wind-generated waves. J. Fluid Mech., 4, 426-434.
- (11) Pierson, W.J., Jr., and Moskowitz, L., 1964: A proposed spectral form for fully developed wind seas based on the similarity theory of S.A. Kitaigorodskii. J. Geophys. Res., 69, 5181-5190.
- (12) Rice, S.O., 1944: Mathematical analysis of random noise. Reprinted in: Noise and Stochastic Processes, pp. 133-294. Ed. Wax, N., Dover Pub., N.Y.
- (13) Schwab, D.J., Bennett, J.R., Liu, P.C. and Donelan, M.A., 1984: Application of a simple numerical wave prediction model to Lake Erie. J. Geophys. Res., 89(C3), 3586-3592.



## CHAPTER TWENTY SIX

### Shallow Water Waves: A Spectral Approach

Charles L. Vincent,\* M. ASCE

#### Introduction

Bouws et al. (1983, 1984) have shown that wind sea spectra in finite depth water can be described by a self-similar spectral equation that in the deep water limit is the JONSWAP spectrum (Hasselmann et al. 1973). This paper shows that the spectral parameter  $\alpha$  is linked to wave steepness, for wind sea and swell; presents a simple model for wave transformation across the surf zone; and shows that the spectral theory provides data similar to the results of Bretschneider (1958) for shallow water wave growth.

#### TMA Spectral Spectrum

Examination of the free wave spectrum of wind generated gravity waves in water of finite depth indicates that the shape of the spectrum may be specified by an equation (Bouws et al., 1983) which Bouws et al. termed the TMA-spectrum

$$S(\omega, H) = \alpha g^2 \omega^{-5} \exp[-5/4(\omega/\omega_m)^{-4}] \times \exp[-(\omega - \omega_m)^2 / 2\omega_m^2 \sigma^2] \times \phi(\omega_H) \quad 1$$

with

$$\phi(\omega_H) = \frac{(k^{-3}(\omega, H) \partial k(\omega, H) / \partial \omega)}{(k^{-3}(\omega, \infty) \partial k(\omega, \infty) / \partial \omega)} \quad 2$$

$$\omega_h = 2\pi f(H/g)^{1/2}$$

where the parameters  $\alpha, \gamma$  and  $\sigma$  can be derived by curve fit analysis to a particular spectrum or estimated by prognostic equations. Although the most useful form of the equation is in frequency space, Bouws et al. (1983, 1984) indicate that the spectrum is better expressed in wave number space because depth is included explicitly through wave number. The resulting equation has a simple form in which the spectral density is related to a constant power of wave number, i.e.

$$F(k) = \frac{\alpha}{2} k^{-3} \Psi(\gamma, \omega_m, \omega, \sigma) \quad 3$$

\*Chief Scientist, Offshore & Coastal Technologies, Inc., 10378 Democracy Lane, Fairfax, VA 22030

where  $\Psi$  is dimensionless. Equation 1 goes to the JONSWAP equation in deep water.

The prognostic equations for  $\alpha$  and  $\gamma$  are derived in terms of the wave number for the peak frequency of the spectrum, gravitational acceleration and wind speed (Table 1). The spectral equation was derived as an extension of the deep water similarity principles used to develop the JONSWAP equation to shallow water using the results of Kitaigorodskii et al. (1975). The results were checked against nearly 3000 wind sea spectra observed off the North Carolina coast and in the North Sea. The bottom slopes ranged from nearly flat to about 1:100, bottom materials ranged from fine to coarse sands, and wind speeds ranged up to 30 meters per second.

TABLE 1

## TMA PARAMETRIC RELATIONS

$$\alpha = 0.0078 \kappa^{0.49}$$

$$\gamma = 2.47 \kappa^{0.39}$$

$$\sigma = 0.7 \quad f \leq f_m; \quad \sigma = 0.9 \quad f > f_m$$

where

$$\kappa = \frac{U^2 k_m}{g}$$

U wind speed at 10m elevation, g gravitational acceleration  
wave number corresponding to peak frequency

## Steepness and Alpha

The general fit of the TMA spectrum to data implies that the Kitaigorodskii et al. (1975) wave number expression

$$F(k) = \alpha k^{-3/2} \quad 4$$

is a reasonable scaling of the spectrum up to the peak wave number (recognizing some modification due to the shape factors near the peak) if  $\alpha$  is allowed to vary. An approximation of the total energy in the spectrum may be obtained by integrating equation 4 from  $k_m$  to

$$E_t = \int_{k_m}^{\infty} F(k) = 1/4 \alpha k_m^{-2} \quad 5$$

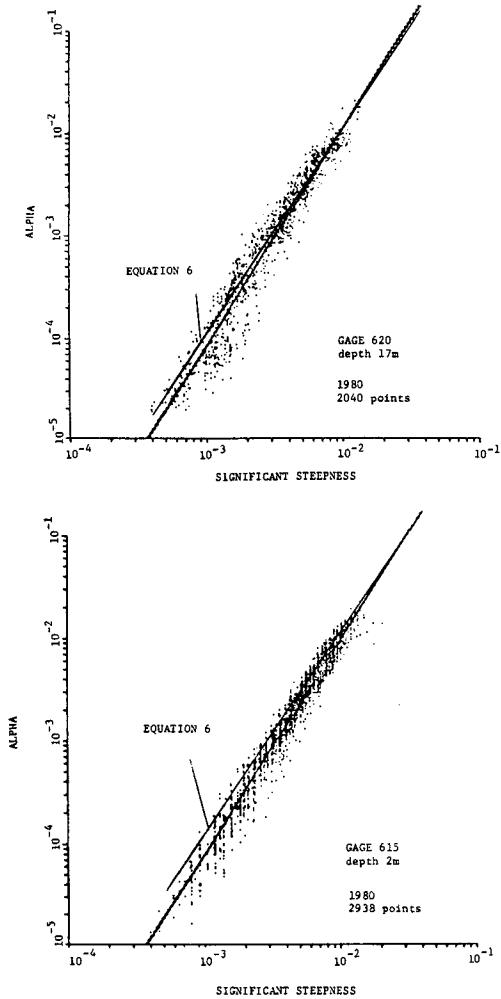


Figure 1. Alpha versus Significant Steepness. Theoretical equation (6) is compared to data taken at two average depths. Unlabelled line is the regression line for the data in each graph.

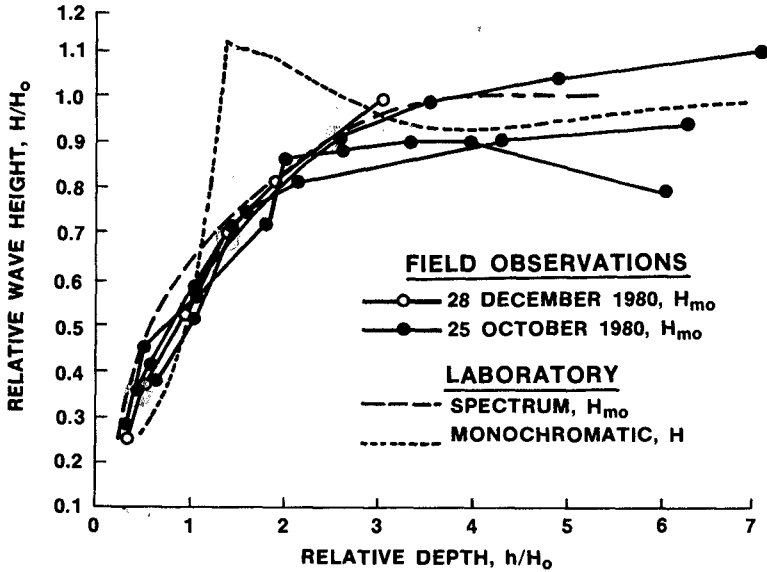


Figure 2. Depth Variation of Zero Moment Wave Height. The zero moment estimate of significant wave height  $H_{mo}$  is normalized by the offshore value (ratio denoted as  $H/H_0$ ) and plotted as a function of depth normalized by the offshore wave height (denoted as  $h/H_0$ ). Two field data sets and one laboratory data set are plotted. The equivalent variables are plotted for a monochromatic wave from laboratory tests with similar initial steepness.

By inverting equation 5 a relationship between  $\alpha$  and a steepness parameter  $\epsilon$  may be obtained

$$\alpha = 4E_t k_m^2 = 16\pi^2 \epsilon^2 \quad 6$$

where

$$\epsilon = E_t^{1/2} / L_m \quad 7$$

with

$$L_m = 2\pi / k_m \quad 8$$

Huang et al. (1980) had arrived at the same relationship for deep water. Equation 6 is valid for any depth where equation 4 holds. Figure 1 shows a plot of  $\alpha$  versus  $\epsilon$  from field data taken at the Coastal Engineering Research Center's Field Research Facility at Duck, North Carolina, for two average depths: 17m and 2m. Alpha was estimated by fitting equation 6 to both sea and swell spectra. The results indicate an excellent fit at high steepnesses. For low steepnesses there is some divergence. This results from a poor knowledge of depth over time in the surf zone and the irregularity of spectral shape for very low wave height conditions.

#### Energy Levels in the Surf Zone

Equation 5 was used by Vincent (1983) to derive an upper bound on energy in the surf zone by noting that the zero movement estimate of significant wave height is given by

$$H_{m0} = 4E_t^{1/2} = 2\alpha^{1/2} k_m^{-1} \quad 9$$

For depth limited conditions it is assumed that a linear shallow water dispersion relation

$$k_m = \omega_m (gh)^{-1/2} \quad 10$$

held and equation 9 becomes

$$H_{m0} = \frac{1}{\pi} (\alpha gh)^{1/2} f_m^{-1} \quad 11$$

If  $\alpha$  and  $f_m$  were constant across the surf zone (which is not generally the case) equation 11 would imply a square root of depth dependence for  $H_{m0}$ . Because of some variation of  $\alpha$  and  $f_m$ , some difference from square root dependence occurs. Figure 2 provides a comparison of field and laboratory data for high energy conditions compared to a monochromatic wave. The

SURF ZONE ALPHA

$$\alpha = 3.55 h / gT_m^2$$

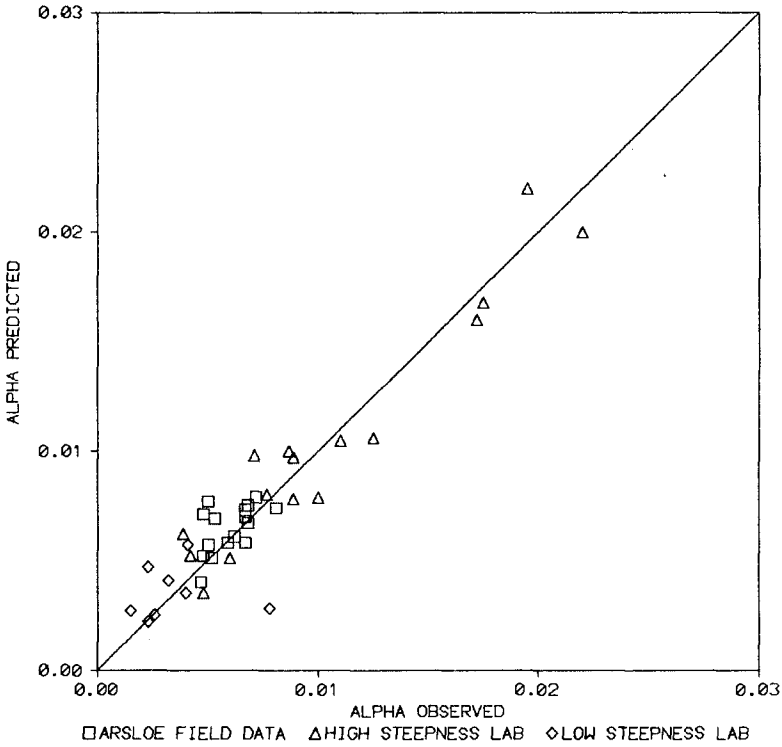


Figure 3. Surf Zone Alpha. Alpha was calculated from a curve fit to the spectra of waves measured in the surf zone in the field and the laboratory and compared to the maximum value of alpha expected from theory.

results show that  $H_{mo}$  has a curvilinear form similar to the square root of depth and that its variation with depth is distinctly different than the monochromatic case. In the shallowest water the dependence is not much different from the monochromatic case. Since equation 9 is directly related to equation 6, the data in Figure 1 suggest that the upper bound derived is a good approximation.

#### Surf Zone ALPHA

The relationship between  $\alpha$  and  $\kappa$  given in Table 1 is valid where there is a relative balance between energy gain and loss in the spectrum during wave growth. As the wave field propagates into the surf zone, breaking dominates and the  $\alpha, \kappa$  relation is no longer valid. Mathematically for fixed  $f_m$  as  $H \rightarrow 0$   $\kappa$  becomes infinite as does  $\alpha$ . Equation 6 provides a link between spectral shape and steepness. In the surf zone, the wave train is largely nondispersive and the largest waves are limited by depth, so it is possible to estimate  $\alpha$  by relating the variance in the wave relative to its height and obtain a rough estimate on the maximum alpha for a given depth and peak frequency:

$$\alpha_{max} = 3.55hf_m^2/g \quad 12$$

Figure 3 provides a comparison of measured and estimated  $\alpha_{max}$  from field and laboratory data.

#### Simple Model for Surf Zone Wave Heights

Equation 11 provides an estimate for the upper bound for a wind sea. In order to model the spectrum across a shoaling and breaking region for an arbitrary wind and depth field requires a complex numerical model. For many purposes an assumption of a uniformly varying slope in the along shore direction is not an unreasonable first approximation. A simple one-dimensional numerical code embodying the TMA relationship and extension has been developed to provide an intermediate step between the simplest equation and a full scale model.

The following are the elements of the model:

- (1) Refraction and shoaling is given by the method of Longuet-Higgins (1957).
- (2) The spectrum at any depth is given by equation 1.
- (3) For wind seas  $\alpha, \gamma, \sigma$  are given in Table 1.

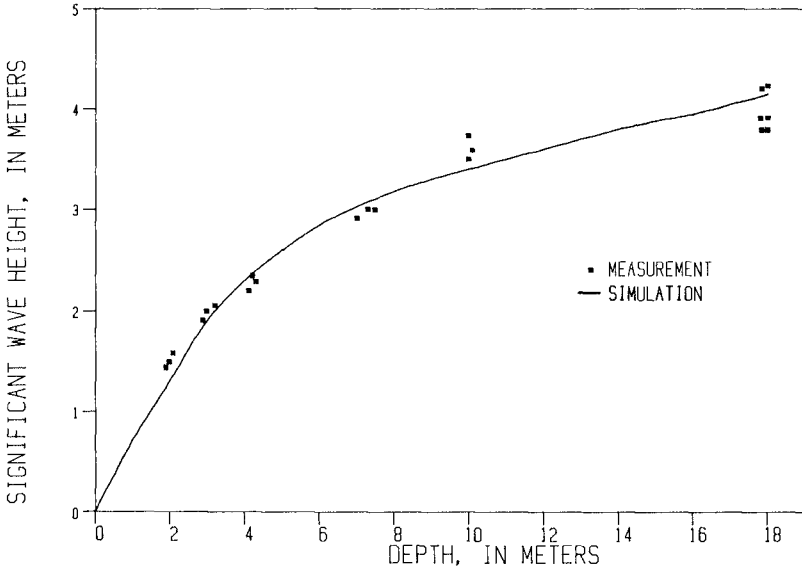


Figure 4. Comparison of Model Predictions to Field Data.

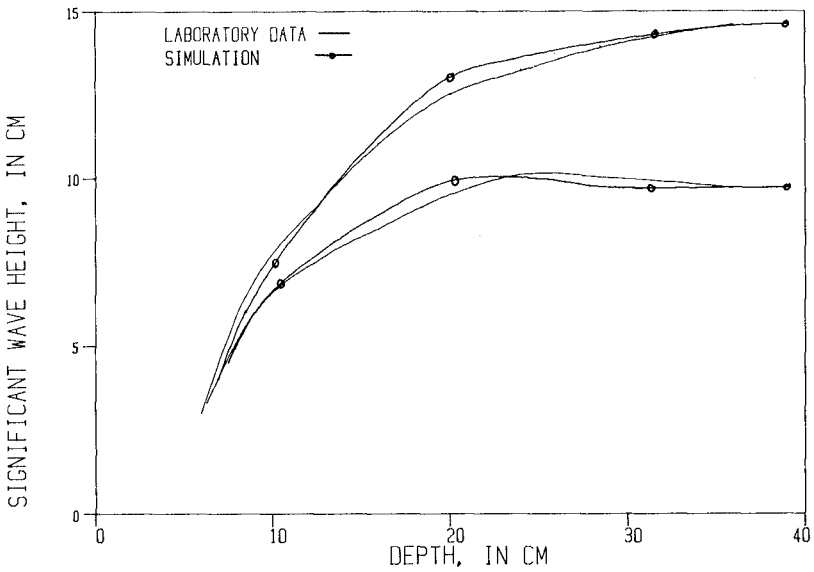


Figure 5. Comparison of Model Predictions to Laboratory Data.



- (4) For swell  $\alpha$  is provided by equation 6, with the wave steepness at a new computation estimated by projection of the next upstream wave steepness.
- (5) The maximum value of  $\alpha$  in the surf zone is given by equation 12.
- (6) If waves pass over a bar, and the depth then increases  $\alpha$  and  $\gamma$  remain fixed at the equilibrium values of the previous shallowest depth until a shallower depth is reached.
- (7)  $f_m$  remains fixed.

This model neglects bottom friction and overly simplifies the processes occurring. Its essential assumption is that once the depth becomes a dominant influence on the waves the spectrum rapidly approaches the equilibrium form.

The model allows input of initial TMA parameters and a peak wave direction. The directional spectrum is set to  $\cos 4\theta$  spread. Variation of this input may be made by reprogramming.

The model was run for a wind sea case using data from the CERC Field Research Facility Figure 4 and laboratory data from a CERC wave tank Figure 5. In both cases the simple model provided an approximation to energy decay across the shoaling region. Similar results using different field data and a more sophisticated numerical scheme are reported by Hubertz (1984).

#### Shallow Water Wave Growth Relationships

A discussion of deep water wave growth is required before the TMA spectrum can be related to the Bretschneider wave growth curves. In deep water, wind wave growth appears to stop for wave components whose speed is faster than the wind. In the open ocean for long duration winds the spectrum appears to reach an equilibrium fully developed form (Pierson and Moskowitz, 1964) with a peak frequency  $f$  with celerity  $C$  satisfying

$$U/C_m = 0.82$$

13

The observation that the peak frequency of spectrum occurs at a slightly lower frequency than would be expected from the constraint of zero wind input for  $C(f) > U$  has been explained by the nonlinear wave-wave interactions (Masselmann et al., 1976). Although atmospheric input ceases for waves with  $U/C < 1$ , the wave interactions can still shift wave energy to lower frequencies. If for a given  $U$ ,  $f_p$  is the frequency of waves such that  $U=C$ ,

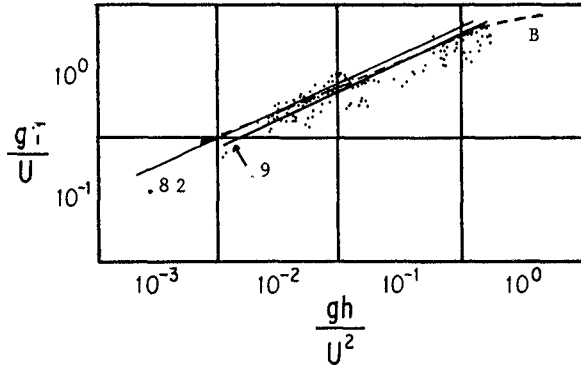


Figure 6. Depth Limited Wave Period. Bretschneider's empirical curve is labelled B; theoretical curves are given for values of A of 0.82 and .9.

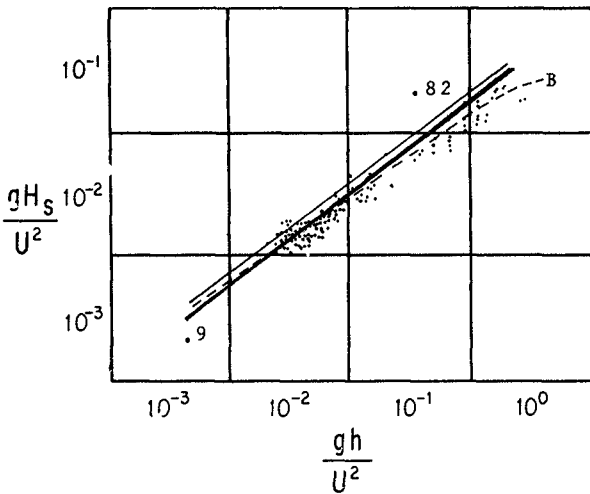


Figure 7. Depth Limited Wave Height. Bretschneider's curve for a friction factor of .01 is labelled B; theoretical curves corresponding to values of a of .082 and .09 for the depth limited period are provided.

once the peak frequency of the wind sea evolves to  $f_0$ , the frequency with maximum input from the wave-wave interactions are 0.8 to 0.9  $f_p$ , or approximately the peak frequency associated with the fully developed spectrum.

In shallow water of depth  $H$  the maximum celerity of waves is approximately  $(gH)^{1/2}$ . If  $H$  is sufficiently small, almost any wind speed  $U$  will exceed  $(gH)^{1/2}$ . Hence the mechanism for producing a cut-off to wave growth in deep water does not appear workable in shallow water. Yet the data of Bretschneider (1958) clearly suggest a cut-off value for the wave period. In essence this is a depth limited wave period which would be the shallow water analogy to the fully developed spectrum's peak frequency in deep water.

In the TMA spectrum when  $\omega_H$  is less than one, the spectrum approaches the  $f^{-3}$  saturation dependence suggested by Kitaigorodskii et al. (1975). Thus, a hypothesis for a limit on the peak frequency can be suggested. Assuming a flat bottom, as waves grow and the peak frequency decreases, the waves at the spectral peak ultimately reach a value of  $\omega_H < 2$  in which depth begins to influence wave growth. With continued development to lower frequencies  $\omega_H$  approaches 1 and waves near the peak of the spectrum approach the saturation limit, i.e. cannot grow more without breaking. Thus, allowing for some influence of the wave-wave interactions, the peak frequency should not become less than

$$\omega_{H,m} = 2\pi f_m (H/g)^{1/2} = A \quad 14$$

where  $A$  lies between 0.8 and 1.0. Nondimensionalization to include wind speed and algebraic rearrangement provides an equation for a depth limited period

$$T = gT/U = 2\pi(gH/U^2)^{1/2}/A \quad 15$$

with  $A$  between 0.8 and 1.0. A plot of equation 15 versus Bretschneider's data (Figure 6) indicates reasonable agreement when the uncertainty in  $A$  and the differences in  $T_m$  and  $T_s$  are considered.

Vincent and Hughes (1985) have taken equations 11 and 15 with the  $\alpha, \kappa$  relationship and calculated an estimate of the  $H_{mo}$  for depth limited conditions assuming a shallow water dispersion relation. The results are displayed in Figure 7 for two values of  $A$  and are within the general scatter of the data. Pinpointing the correct value of  $A$  requires a yet to be performed analysis of the shallow water wave-wave interactions.

## Summary

Natural wave trains may be described in several ways: approximation as a monochromatic wave, representation by probability distributions and representation by a spectrum. The TMA spectrum and its extensions discussed here provide a unified wave theory that spans a range of conditions including deep, intermediate and shallow water through a continuous variation of the parameter  $\kappa$  for wind seas. For swell, the parameter  $\epsilon$  appears equally useful. The theory provides a description of the free wave components of the spectrum even into the surf zone and provides a prediction of energy levels of the same quality as the other methods without a requirement of a site specific dissipation mechanism tuning. Further, the theory provides an explanation of the apparent depth limited wave period which when combined with the spectral shape parameters yields a reasonable approximation to the shallow water wave growth data of Bretschneider (1958).

One useful element of the approach is its direct connection to spectral models for wave forecasts and hindcasts.

## References

- Bouws, E., Gunther, H., Rosenthal, W., and Vincent, C. L., "A Similarity Based Spectral Form for Finite Depth Water: Wave Growth Relationships for the Entire Depth TMA Spectral Form," International Association for Hydraulic Research, Conference, Moscow, 1983.
- Bouws, E., Gunther, H., Rosenthal, W., and Vincent, C. L., "Similarity of the Wind Wave Spectrum in Finite Depth Water, Part I - Spectral Form," Journal of Geophysical Research, in preparation, 1984.
- Bretschneider, C. L., "Revisions in Wave Forecasting: Deep and Shallow Water," Proceedings of the 6th Conference on Coastal Engineering, ASCE, pp. 30-67, 1958.
- Hasselmann, K., et al., Measurements of Wind-Wave Growth and Swell Decay During the Joint North Sea Wave Project (JONSWAP), Deutsches Hydrographisches Institute, Hamburg, 1973.
- Hasselmann, K., Ross, D. B., Muller, P., and Sell, W., "A Parametric Wave Prediction Model," Journal of Physical Oceanography, 1976, pp. 200-228.
- Huang, N. E., Long, S. R., Tung, C., Yyuen, Y., and Blinin, L., A Unified two-parameter wave spectral model for a general sea state, Journal of Fluid Mechanics, Vol. 112, p. 203, 1981.

Hubertz, J. M., Model of Nearshore Wave Driven Currents, to appear, Proceedings, 19th International Conference on Coastal Engineering, Houston, Tx., 1984

Kitaigorodskii, S. A., Krasitskii, V. P., and Zaslavskii, H. H., "On Phillip's Theory of Equilibrium Range in the Spectra of Wind-Generated Gravity Waves," Journal of Physical Oceanography, Vol. 5, pp. 410-420, 1975.

Longuet-Higgins, M.S., On the Transformation of a Continuous Spectrum by Refraction, Proc. Cambridge Phil., Soc. 53, 1957, pp. 226-229.

Pierson, W. J., and Moskowitz, L., "A Proposed Spectral Form for Fully Developed Windseas Based on the Similarity Theory of S. A. Kitaigorodskii," Journal of Geophysical Research, Vol. 69, 1964, pp. 5181-5190.

Vincent, C. L., "Depth-Limited Significant Wave Height: A Spectral Approach," TR 82-3, U. S. Army Corps of Engineers, Coastal Engineering Research Center, Fort Belvoir, Va., Aug. 1982.

Vincent, C. L. and Hughes, S. A., "A Note On Wind Wave Growth in Shallow Water," Journal of Waterway, Port, Coastal and Ocean Engineering, to be published, 1985.

## CHAPTER TWENTY SEVEN

### WAVE COHERENCE IN COASTAL WATERS

Steven A. Hughes\* , M.ASCE

**ABSTRACT:** The spatial variability of the near-shore wave field is examined in terms of the coherence functions found between five closely spaced wave gages moored off the North Carolina coast in 17 meters depth. Coherence was found to rapidly decrease as the separation distance increased, particularly in the along-crest direction. This effect is expressed as nondimensional coherence contours which can be used to provide an estimate of the wave coherence expected between two spatial positions.

#### INTRODUCTION

The coherence function between two spatially separated time series of ocean waves measures the extent to which the waves occurring at one position can be predicted from the wave field at the other position, assuming a linear dependence exists between the wave time histories at the two locations. The coherence function rapidly decreases as the distance between the two spatial positions increases. This decrease arises because most naturally occurring waves are not long-crested and the waves change form as they propagate. Ocean waves are conveniently described in terms of energy spectra, with empirically determined parameters relating the spectra between locations. In many applications a spectral representation of the wave field is sufficient, however, there are instances when it would be useful to estimate the wave coherence function between two positions. A case in point is an investigation by the Naval Civil Engineering Laboratory (NCEL) into ship motions and mooring forces for vessels anchored in coastal waters.

A mooring forces numerical model has been developed by the NCEL which simulates ship motions and resultant mooring loads under various mooring configurations and wave conditions, but field data are needed to verify the model's accuracy and to determine its limits of applicability. In the NCEL numerical model the wave field is to be applied at the ship's center of gravity. Since waves cannot be measured at this position, it is necessary in the course of a

---

\* Hydr. Engr., Coastal Engineering Research Center, U.S. Army Engineer Waterways Experiment Station, P.O. Box 631, Vicksburg, Mississippi 39180 USA.

field experiment to collect wave data a short distance away from the ship where the waves are free of excessive ship-induced interference. These waves, which are slightly different from those waves causing the ship motion, are used to drive the numerical model, producing a time history of the mooring loads.

Evaluation of the mathematical algorithms in the model can be performed by finding the coherence function between the measured ship response and the response predicted by the model. This response coherence is composed of the coherence due to the approximations made in the mathematical algorithms and the wave coherence between the position where the waves were measured and the ship's center of gravity. Therefore, it is necessary to either: 1) estimate or directly measure wave coherence as a function of spatial separation so that it may be factored out of the response coherence, or 2) position the wave gage in a location which helps maximize the wave coherence.

It was this application that prompted the NCEL to sponsor a month-long wave coherence experiment at the Coastal Engineering Research Center's Field Research Facility at Duck, North Carolina during the Spring of 1983. The primary objective of the experiment was to collect simultaneous wave data from an array of five closely spaced wave gages for events of wind seas, swell, and multi-directional wavetrains, and to then examine the spatial variability in the wave field. This paper presents the findings of the experiment.

#### DATA COLLECTION

Between April 23 and June 10, 1983, wave data were collected from an array of 5 Datawell Waverider wave gages moored in a depth of 17 meters. The array was positioned about 2 kilometers offshore of the Field Research Facility (FRF) at Duck, North Carolina (Fig. 1). The dimensions and orientation of the Waverider array, as shown in Fig. 2, were determined using a land-based laser surveying instrument during calm conditions after the array was installed. The local bottom slope in the area is on the order of 1:200, resulting in less than a meter difference in water depth over the site. All the buoys in the array were tethered to mooring lines of equal scope with the intent that any displacement due to a unidirectional current would result in a translation of the array with minimum distortion. There was some variation in the array dimensions and orientation due to wave induced excursions of the buoys, but these spatial differences are small compared to the dimensions of the array and should average out over the period of data collection.

Prior to deployment all the Waveriders were calibrated according to the manufacturer's recommendations using a ferris wheel arrangement, and all the gages met or exceeded the calibration specification required by Datawell. A check on two of the gages after the experiment indicated

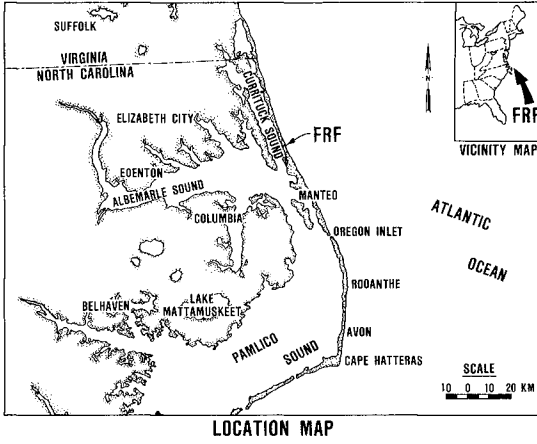


Figure 1. Field Research Facility Location Map

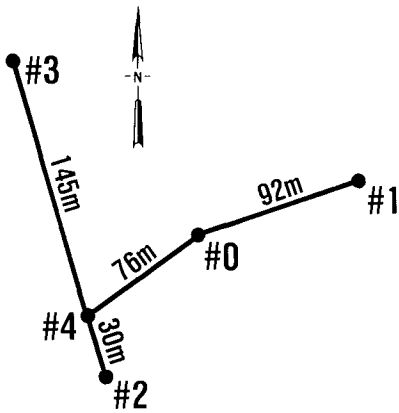


Figure 2. Waverider Wave Gage Array



that the calibration error for these two instruments was less than 4 percent.

The original data set is comprised of 38 data collection sessions lasting 80 minutes each. Each session involved the simultaneous recording of the wave height time series (as determined from buoy accelerations) from all gages at a sampling rate of 4 data points per second, resulting in a total record length of 19,200 data points per wave gage. The collection sessions were substantially longer than normal because it was realized that a fairly unique data set was being assembled and longer records might be of interest in future studies. The raw data were recorded by a digital computer and stored on magnetic tape.

The wave direction for each recording session was routinely obtained using an X-band imaging radar at the Field Research Facility, supplemented by visual observations. Mattie and Harris (5) report the direction measuring capability of the imaging radar to be accurate to within +4 degrees. During periods when two distinct wave trains were approaching from different directions, the direction of both the primary and secondary wave train was recorded. Pertinent weather data were noted during each recording session, and aerial photographs of the wave field were obtained several times over the duration of the experiment.

Realtime monitoring of the instruments during collection sessions helped insure that reasonable data were being obtained. Buoy number 2 (the buoy at the most southerly location on Fig. 2) produced erratic results from the onset of the experiment, and was replaced with a backup buoy as soon as possible. Consequently, the data from the first 22 collection sessions do not include results from this location. The 16 sessions after run number 22 include results from all locations in the array.

#### DATA ANALYSIS

Nine of the data collection sessions, representing a fairly broad range of conditions, were selected for detailed analysis (Table 1). For each selected data session the energy density spectrum for each gage was calculated and cross-spectral analysis was performed to determine the coherence and phase functions between all possible gage pairings. By definition the coherence function is given as

$$\gamma_{xy}(f) = \frac{|G_{xy}(f)|}{[G_{xx}(f) G_{yy}(f)]^{1/2}} \quad (1)$$

where

$G_{xx}(f)$  = autospectral density function of gage X,

$G_{yy}(f)$  = autospectral density function of gage Y, and

$G_{xy}(f)$  = cross-spectral density function between X and Y.

TABLE 1. Analyzed Data Set

Data Ref. No.	Date	$H_{mo}^1$ (m)	$T_p^2$ (sec)	Wave Direction <sup>3</sup> (degrees)	Ave. Wind Speed (m/s)	Ave. Wind Direction (degrees)
1	23 Apr	0.5	8.5	130/55 <sup>4</sup>	4.0	133
2	23 Apr	0.8	3.6	127	10.0	142
3	24 Apr	2.5	9.3	125	6.7	203
4	24 Apr	1.6	9.5	125	7.0	225
5	25 Apr	1.1	10.5	45/125	7.5	290
6	17 May	2.0	7.0	55	12.0	32
7	17 May	1.3	6.5	55	7.0	32
8	19 May	1.1	5.5	110/80	5.0	146
9	10 Jun	1.9	6.5	80	9.4	34

- <sup>1</sup> Significant wave height (four times the standard deviation of the sea surface elevations).
- <sup>2</sup> Peak spectral wave period.
- <sup>3</sup> Direction from which waves are approaching.  
0 -North; 90 -East; 180 -South; 270 -West.
- <sup>4</sup> Primary wave direction/Secondary wave direction (when two distinct wavetrains were present).

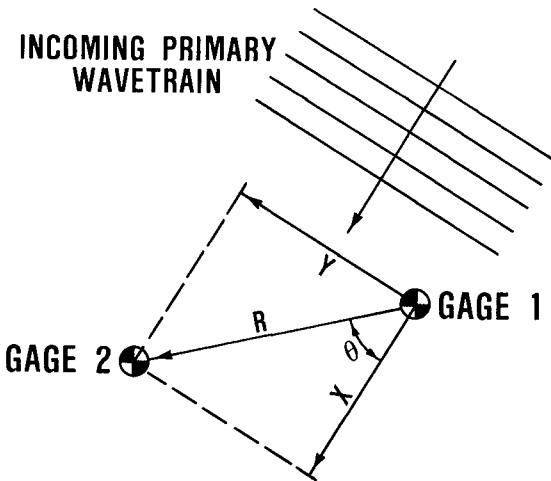


Figure 3. Reference Coordinate System

The coherence values are bounded between zero (no dependence) and one (complete linear dependence).

The data were processed with a fast Fourier transform routine using every other data point in the first 2048 seconds of the recorded time series. Thus the analysis subset contained 4096 points sampled at a 2 hertz rate (1/2 second interval). There is evidence that coherence estimates are not appreciably improved by increasing the length of the time series beyond 2048 data points (1). The resolution in the frequency domain is 0.0004883 hertz. Attention was concentrated on the frequency range 0- to 0.25-hertz since coherences at higher frequencies are expected to be quite small. Within this range spectral values are given at 512 discrete frequencies. A Tukey filter was applied to the cross-spectrum Fourier coefficients to increase the statistical stability of the results with only a minor loss in resolution. Coherence and phase were computed from the smoothed cross-spectral values.

Using the rather arbitrary criterion that coherence values greater than 0.7 indicate a meaningful coherence between gages, the results were examined, and it was found that about half (36) of the gage pairings had meaningful coherence in at least part of the frequency range. The autospectra and coherence functions for those gage pairings selected by this criterion are given in Hughes (3). The cases without meaningful coherences represented gage pairings with large spatial separation.

#### QUALITATIVE OBSERVATIONS

For each incident wave direction the distance vector separating any wave gage pairing can be resolved into a crest-parallel (along-crest) component, Y, and a crest-perpendicular (down-crest) component, X, as illustrated in Fig. 3. By comparing gage pairings with similar values for X and Y, several qualitative trends were observed. For example, Runs 3 and 7 (Fig. 4) and Run 6 (Fig. 5) have similar spatial separation for the selected gage pairings, and the coherence plots for these three runs are quite similar even though the autospectra differ considerably between runs. This comparison and other similar comparisons suggest that the coherence function is weakly, if at all, dependent upon the shape of the spectrum (compare Runs 3 and 7), the total energy contained in the spectrum, or the location of the spectral peak (compare Runs 3 and 6) for the range of conditions examined. Reasonably high coherence is observed at frequencies lower than the peak frequency so long as there is at least a small amount of energy present. The relatively high coherences at low frequencies could be attributed to the fact that waves at these frequencies are rendered less dispersive by the depth than waves at higher frequencies, and hence, can propagate with less alteration in form and celerity than higher frequency waves. These trends appear to be fairly consistent throughout the examined data. Run 5 (Fig. 5) was

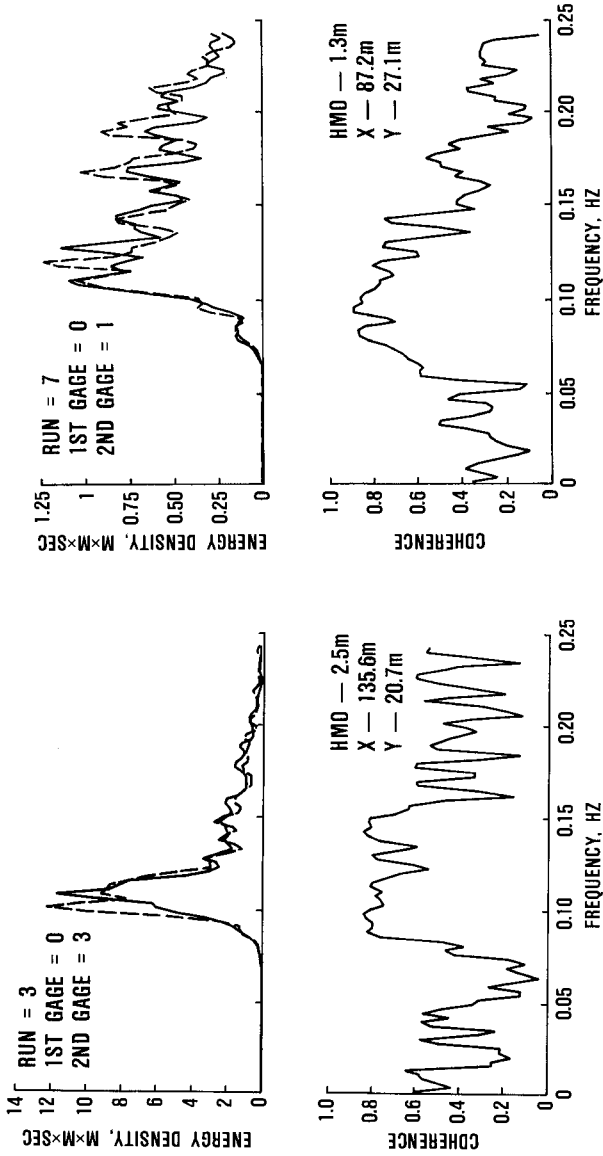


Figure 4. Comparison of Coherence Functions, Runs 3 and 7

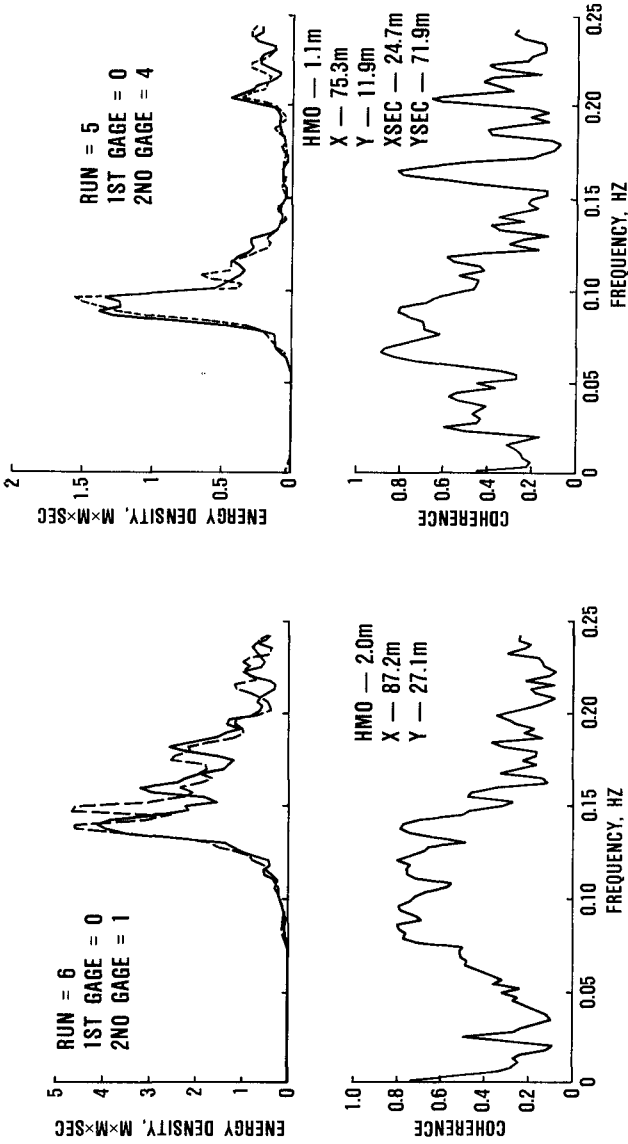


Figure 5. Comparison of Coherence Functions, Runs 6 and 5

included to illustrate the decrease in wave coherence caused by the visually observable presence of two wave trains propagating from different directions.

The most apparent influence on the wave coherence function is the spatial separation of the wave buoys. The observed trend is for a decrease in wave coherence, particularly at higher frequencies, as the spatial separation increases, and the trend is more evident with increases in along-crest separation than with down-crest separation. In other words the coherence found between gages separated by 30 meters in the down-crest direction will be somewhat better than the coherence between gages 30 meters apart in the along-crest direction.

#### WAVE COHERENCE CONTOURS

One of the goals of this study was to arrive at a method for estimating the wave coherence function in terms of the important parameters, which appear to be mainly frequency and spatial separation. A convenient way of incorporating frequency into the analysis was to nondimensionalize the along-crest ( $Y$ ) and the down-crest ( $X$ ) distances by the wavelength associated with each discrete frequency at the 17-meter water depth (linear theory). Then all discrete coherence values can be plotted against separation distances given in terms of relative wavelength. A survey of the discrete coherence values revealed that meaningful coherence values (greater than 0.7) were almost exclusively contained within the frequency range 0.08 - 0.16 hertz (wave periods 12.5 - 6.3 seconds). Since this frequency range covers the region where most coastal wave energy is concentrated, it was decided to limit the ensuing analysis to the discrete coherence values within this range.

Plotting of coherence values as a function of relative down-crest separation ( $X/L$ ) and relative along-crest separation ( $Y/L$ ) led to the subjective sketching of contours of equal coherence. These contours resembled those of an elliptic surface, suggesting that a satisfactory approximation might be obtained by the fitting of an elliptic surface to the data, i.e.,

$$\frac{(X/L)^2}{a^2} + \frac{(Y/L)^2}{b^2} = 1 \quad (2)$$

where  $a$  and  $b$  are some function of the wave coherence. Under the assumption that coherence decays exponentially as a function of the magnitude and direction of the vector separating the two positions, coherence can be expressed as

$$\gamma = e^{-f(R/L, \theta)} \quad (3)$$

where

$$\begin{aligned} \gamma &= \text{coherence,} \\ L &= \text{wavelength by linear theory,} \\ R &= (X^2 + Y^2)^{1/2}, \text{ and} \\ \theta &= \arctan (Y/X) \end{aligned} \quad (4)$$

The cylindrical coordinate system (Eqs. 4 and 5) is oriented so that the down-crest direction (X/L) corresponds to 0 degrees and the Y/L axis aligns with 90 degrees.

Transforming Eq. 2 into cylindrical coordinates and taking the square root of both sides yields

$$\frac{R}{L} \left[ \frac{\cos^2 \theta}{a^2} + \frac{\sin^2 \theta}{b^2} \right]^{1/2} = 1 \quad (6)$$

Taking the logarithm of Eq. 3 and rearranging gives

$$\frac{f(R/L, \theta)}{-\ln(\gamma)} = 1 \quad (7)$$

By equating Eqs. 6 and 7, it is seen that one expression for the unknown function,  $f$ , is

$$f(R/L, \theta) = \frac{R}{L} [(c \cos \theta)^2 + (d \sin \theta)^2]^{1/2} \quad (8)$$

where

$$c = \frac{-\ln(\gamma)}{a} \quad \text{and} \quad d = \frac{-\ln(\gamma)}{b} \quad (9)$$

and  $c$  and  $d$  are the constants to be determined from the coherence data.

After discarding coherence values less than 0.5, the remaining 4000 discrete values of coherence as a function of X/L and Y/L were used to determine the values of  $c$  and  $d$  which minimized the sum of the square of the errors between the observed and predicted coherence values. The data collected when multiple wave trains were approaching from different directions were not included in this formulation. The resulting "best-fit" equation is

$$\gamma = \exp\left\{-\frac{R}{L} [(0.18 \cos \theta)^2 + (0.39 \sin \theta)^2]^{1/2}\right\} \quad (10a)$$

or in rectangular coordinates,

$$\gamma = \exp\left\{-[(0.18 X/L)^2 + (0.39 Y/L)^2]^{1/2}\right\} \quad (10b)$$

There are certainly a multitude of other surfaces which could be fit to the data with equal or slightly better success, but the present solution offers reasonable simplicity. As an indication of the scatter present in the data, the root-mean-square error between the measured coherence and that predicted by Eq. 10 was calculated and found to be 0.126, which is quite large.

The coherence contours found from Eq. 10 are presented in Fig. 6 as a function of nondimensional along-crest separation distance (horizontal axis) and nondimensional down-crest separation distance (vertical axis). The contours are a crude estimate at best, however, they do provide a means of getting a first estimate of the wave coherence function between two locations. Fig. 7 is a plot of Eq. 10 for constant values of theta.

Fig. 8 shows four coherence plots from this experiment along with the estimate of coherence obtained from Eq. 10. The dashed portion of the estimate represents application of Eq. 10 outside the frequency range 0.08 - 0.16 hertz. The estimate for Run 8 is the product of the separate coherence functions determined for the primary and secondary wave directions. Eq. 10 is seen to reproduce a reasonable estimate for planning purposes.

The estimation technique was also applied to the data of Kuo, et al. (4) which were collected from a triangular array, 7 meters on a side, located in 15.5 meters depth. The estimate (see Fig. 9) is reasonable even well outside the frequency range used to establish the empirical constants. This is probably because of the close proximity of the gages.

## DISCUSSION

An empirical equation for estimating wave coherence in terms of spatial separation has been formulated using a select portion of the original data set, and thus, the limits of applicability have been defined. Within the frequency range 0.08 - 0.16 hertz, the empirical equation can be expected to provide a fair estimate of wave coherence. At higher frequencies the coherence decreases more rapidly than Eq. 10 would predict. This indicates that the parameterization of frequency in terms of wavelength is incorrect at higher frequencies.

There was no clear difference in wave coherence between conditions representing swell and storm seas in the data analyzed. Swell waves can be expected to be longer-crested and less dispersive and thus less sensitive to spatial separation, but this was not clearly evident in the data. This observation may be a consequence of the finite depth influence, and the difference between sea and swell might become more apparent in deeper water. Since the results were obtained in a water depth of 17 meters, it is reasonable to expect some signature of the depth in the coherence function. The high coherence values observed in the frequency range 0.08 - 0.10 hertz are quite possibly



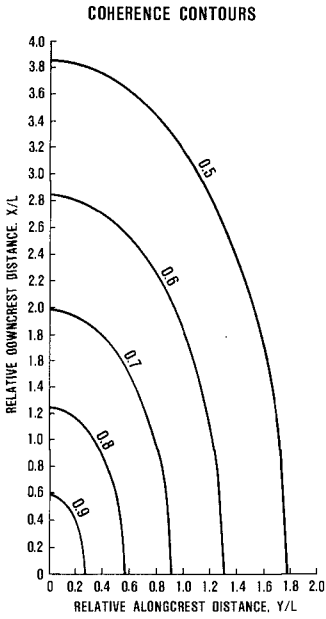


Figure 6. Wave Coherence Contours

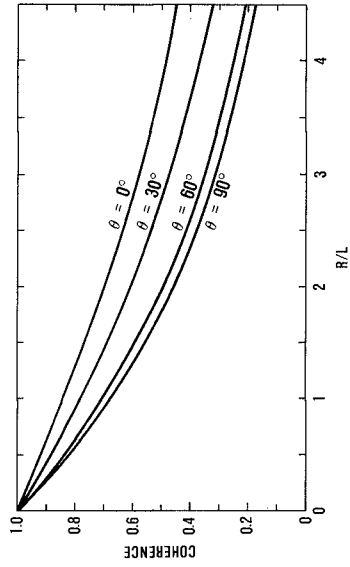


Figure 7. Coherence Curves of R/L Versus  $\theta$

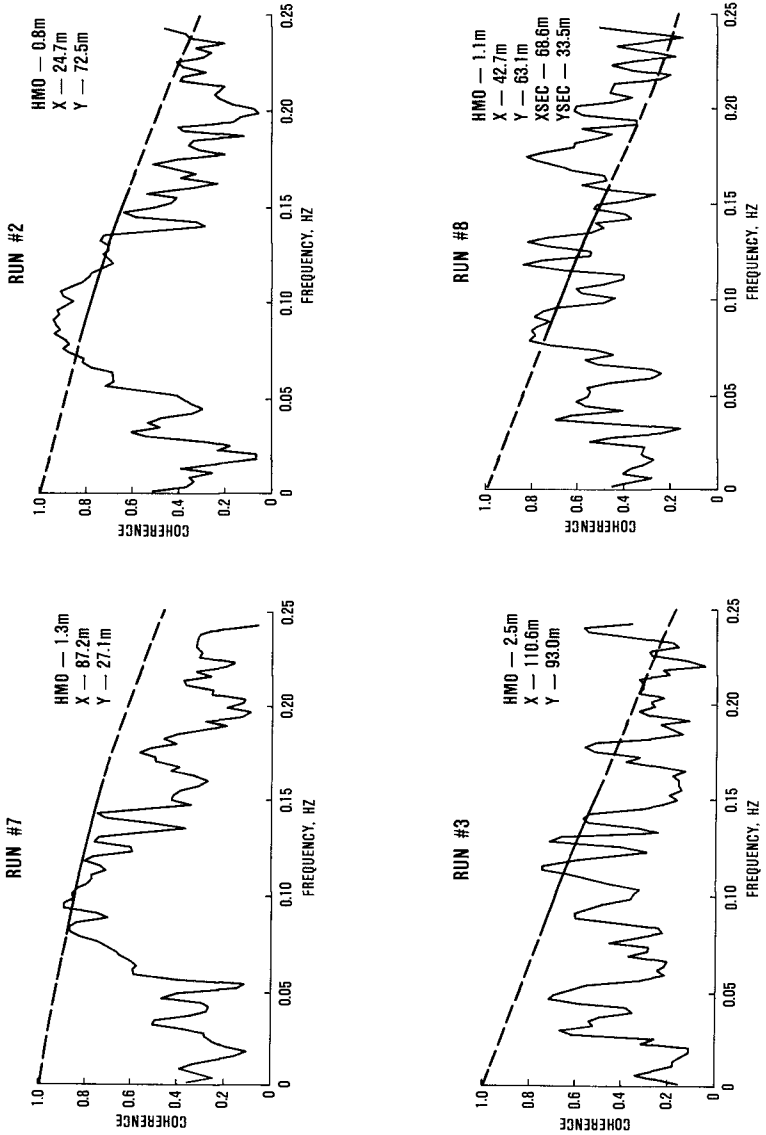


Figure 8. Coherence Estimates (This Experiment)

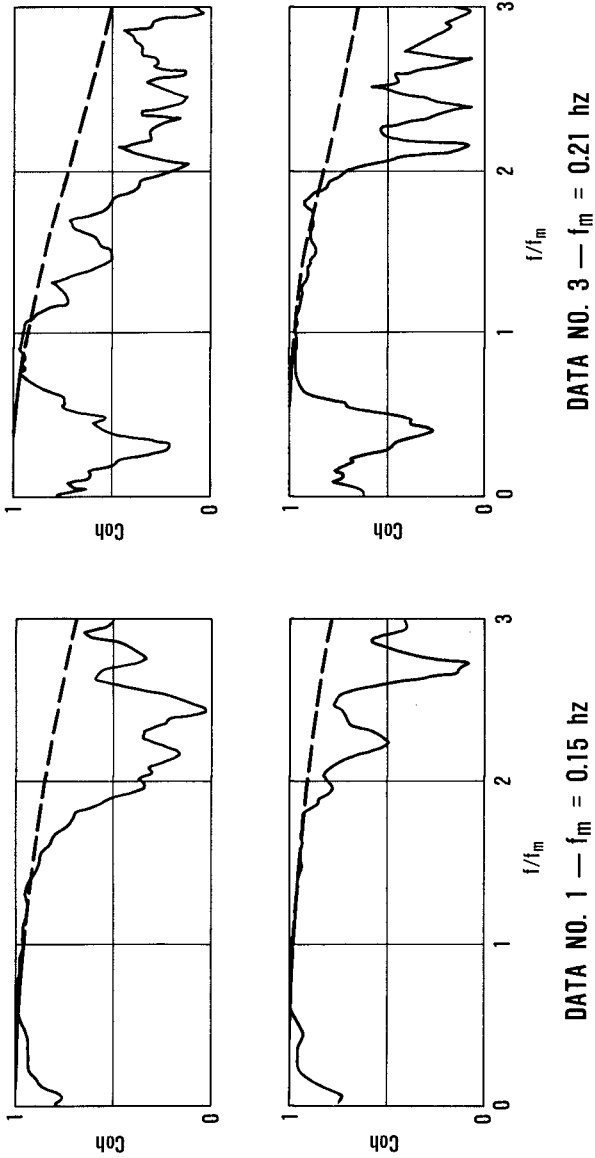


Figure 9. Coherence Estimates (Kuo, et al. Data)

related to the fact that waves at these frequencies have been rendered less dispersive by the finite depth. The observed decrease in coherence values at frequencies less than about 0.07 hertz may well be due to the minuscule amounts of energy at these low frequencies.

It must be emphasized that the equation for estimating wave coherence was obtained from data gathered in a water depth of 17 meters. It is expected that Eq. 10 could be applied at other water depths because of the nondimensionalizing by wavelength, however, more data are needed to support this generalization.

One interesting observation comes from comparing the theoretical wave coherence plots presented by Georgiadis and Hartz (2) with the empirical result given by Fig. 7. The theoretical coherence curves were obtained by assuming a JONSWAP spectrum in conjunction with selected directional spreading functions, and the results assume that the coherence function between two positions is strictly determined by the directional spreading. The theoretical curve which best follows the down-crest (0 degree) curve on Fig. 7 turns out to be the one found for a cosine to the sixth power. However, the corresponding theoretical curve for the along-crest direction (90 degrees) drops off to zero coherence before the value of  $R/L$  reaches 1.0. This is not the case for the empirical representation of the field data, as seen in Fig. 7. Thus, the along-crest coherence in shallow water is much better than predicted from the stated theoretical considerations. This could once again be a depth influence and possibly an indication that energy and directional spreading are not completely uncoupled in finite depth water.

Finally, the empirical equation presented for estimating the wave coherence function between two spatial locations should be used primarily as a planning tool due to the considerable variation present in the observed values. Attempts to use Eq. 10 to remove the effects of wave coherence from a system response might not be satisfactory in many cases. If the wave coherence between two positions is required during the course of an experiment, it is advisable to measure this coherence directly, using Eq. 10 as a planning guide.

#### SUMMARY

The Coastal Engineering Research Center has collected wave data from a closely spaced array of five wave gages at the Field Research Facility at Duck, North Carolina. The objective was to examine the spatial variability of the wave field in terms of the wave coherence function for a variety of incident wave conditions.

Qualitatively, the coherence function appears relatively independent of the shape of the spectrum, the spectral energy content, and the location of the spectral peak frequency for the range of conditions examined. The finite water depth at the site appears to render the lower fre-

quency waves less dispersive, and hence, more coherent so long as sufficient energy is present at those frequencies. The most apparent influence on the coherence is the spatial separation, and this effect was empirically quantified in terms of the relative wavelength. The resulting equation can be used to estimate the wave coherence function in finite depth water, but the uncertainty involved is substantial. A reasonable estimate is provided in the region between 0.08 - 0.16 hertz, but coherence is overestimated at higher frequencies. Consequently, these results are more suited for planning considerations.

#### ACKNOWLEDGMENTS

The research results contained in this paper were sponsored by the Naval Civil Engineering Laboratory. Field data collection was performed by the staff of the Field Research Facility. Permission to publish these findings was granted by the Naval Civil Engineering Laboratory and by the U.S. Army Chief of Engineers.

#### APPENDIX.—REFERENCES

1. BRIGGS, M.J., "Multichannel Maximum Entropy Method of Spectral Analysis Applied to Offshore Structures," WHOI-81-69, Woods Hole Oceanographic Institution, Woods Hole, Massachusetts, August 1981.
2. GEORGIADIS, C., and HARTZ, B.J., "Wave Coherence Along Continuous Structures For Directional Spectral Models," STF71 A82004, The Foundation of Scientific and Industrial Research at the Norwegian Institute of Technology, Trondheim, Norway, March 1982.
3. HUGHES, S.A., "Spatial Variability in the Nearshore Wavefield," Misc. Paper CERC-84-7, U.S. Army Engineer Waterways Experiment Station, Coastal Engineering Research Center, Vicksburg, Mississippi, 1984.
4. KUO, Y., MITSUYASU, H., and MASUDA, A., "Experimental Study on the Phase Velocity of Wind Waves, Part 2: Ocean Waves," Reports of Research Institute for Applied Mechanics, Vol. XXVII, No. 84, September 1979.
5. MATTIE, M.G., and HARRIS, D.L., "A System for Using Radar to Record Wave Direction," TR 79-1, U.S. Army, Corps of Engineers, Coastal Engineering Research Center, Ft. Belvoir, Virginia, September 1979.

## CHAPTER TWENTY EIGHT

### Field Studies of Run-up on Dissipative Beaches

Christopher T. Carlson\*, A.M. ASCE

#### Abstract

Field measurements of narrow-band incident wind waves and the resulting run-up were made photographically at two different natural sand beaches along San Francisco Bay. The run-up spectra derived from the field-measured time series show some energy at the incident-wave peak frequency, with the predominant run-up spectral energy concentrated in frequency bands below the incident-wave peak frequency. Observations of the swash time series recorded at both beaches indicate that the low-frequency run-up is generated on the beach face by the interaction between the run-up and backwash during the swash cycle.

Coherence analyses indicate that the offshore incident waves and run-up on the beach are not linearly correlated but that the run-up is correlated in the alongshore direction. The slopes of the log-log run-up spectra computed over the frequency band of the incident waves are all approximately -3. Statistical hypothesis tests were used to compare the empirical run-up cumulative distribution functions with both normal and Rayleigh distribution functions.

#### Introduction

The frequency band containing the dominant run-up spectral energy is generally not the same as the frequency band of the predominant incident-wave energy. For this reason, offshore wave statistics may not provide good estimates of the frequency distribution of wave energy expected at the shoreline or on the beach. A shift in the run-up spectral energy to frequencies lower than the predominant incident-wave frequencies has been observed for the run-up generated by a broadband incident-wave field. Field measurements of wave run-up reported in the open literature are very limited and most are by-products of edge wave or standing wave studies conducted on open ocean coasts where the incident-wave fields were usually swell dominated. The incident-wave/beach slope combinations generally produced highly reflective conditions, and the low-frequency (LF) run-up observed or measured during the experiments was attributed to modulation of the run-up by standing waves or edge waves present near the shoreline. No measurements have been reported for the run-up generated on a dissipative beach by narrow-band wind waves only.

\*Oceanographer, Sohio Petroleum Co., One Lincoln Centre,  
5400 LBJ Freeway, Suite 1200-LB 25, Dallas, TX 75240

LF swell-derived components in the run-up spectrum can often obscure other low-frequency contributions to the run-up that are developed on the beach by the higher-frequency wind waves in the incident-wave field.

### Objective

The objective of this study was to measure LF run-up generated on the beach face by the interaction between the run-up and backwash during the swash cycle. The experiments were designed to measure run-up on dissipative beaches exposed only to relatively high-frequency, narrow-band wind waves that broke near the shoreline by plunging. These conditions generally minimize or eliminate standing wave, edge wave, or very-low-frequency surf-beat components from the run-up that are derived from the swell component in an incident-wave field.

### Field Experiments

On 14 December 1977, incident wave and run-up measurements were made at the R.W. Crown Memorial State Beach on the eastern shore of San Francisco Bay (western shore of Alameda Island); similar measurements were subsequently made along the western shore of the bay on 14 May 1982 at Coyote Point Beach (Figure 1). Two separate field sites were selected to provide independent data sets for different beach slopes exposed to different incident wind-wave fields. It was necessary to avoid reflective beach conditions for which nonlinear perturbation of the incident-wave field by edge or standing waves might affect the frequency distribution of the run-up on the beach face. The field measurements were therefore conducted for dissipative beach conditions.

Beach reflectivity and inshore resonance may be characterized by the surf scaling parameter,  $\epsilon = a\omega^2/g \tan^2\beta$ , where  $a$  is the incident wave amplitude,  $\omega$  the radian wave frequency and  $\beta$  the beach slope. Reflective, dissipative and highly dissipative beach conditions are characterized by respective  $\epsilon$  values of less than about 2.5, greater than 2.5 and greater than 33. The moderately dissipative regime studied here, is identified by a relatively narrow surf zone, plunging breakers, and strong run-up. Beach reflectivity conditions for these field experiments yielded ideal  $\epsilon$  values of 6 (Alameda) and 19 (Coyote Point).

#### Alameda Beach

The Alameda Beach was composed of fine- to medium-grained silica sand and was openly exposed to westerly and southwesterly winds (Figure 1). The angle of wave approach was nearly normal to the shoreline as wind speeds increased from 3 m/s to over 5 m/s from 170

degrees true. A single breaker zone was located approximately 3 m (9.8 ft) from the shoreline, and all waves broke by plunging. The measurements were made during the peak of the afternoon high tide.

A 16-mm Bolex movie camera was used to simultaneously record time series of the offshore incident waves and the run-up on the beach face along a single line of 25 aluminum reference stakes. The reference stakes were positioned in a linear transect normal to the shoreline extending about 14 m (45.9 ft) in the offshore direction (Figure 2) and were used to calibrate the time series of the incident waves and run-up measurements. The camera was positioned on a 1-m (3.3 ft) high bluff just shoreward of the reference stake array.

Transit and level field survey methods and direct tape measurements were used to establish the position and elevation of the reference stakes relative to a fixed datum stake and the camera. The elevations were surveyed accurate to 0.3 cm (0.01 ft), as were the horizontal distances. Reference surveys that included offshore profiles were made both before and after the experiment and confirmed that no measurable change occurred in the offshore profile during the experiment. Agreement between the measured and computed heights and positions of the reference stakes was better than 1 cm (0.03 ft) in all cases. The Alameda beach had a nearly linear slope of approximately  $0.11 (6.2^\circ)$ , becoming nearly horizontal about 12 m (39.4 ft) offshore.

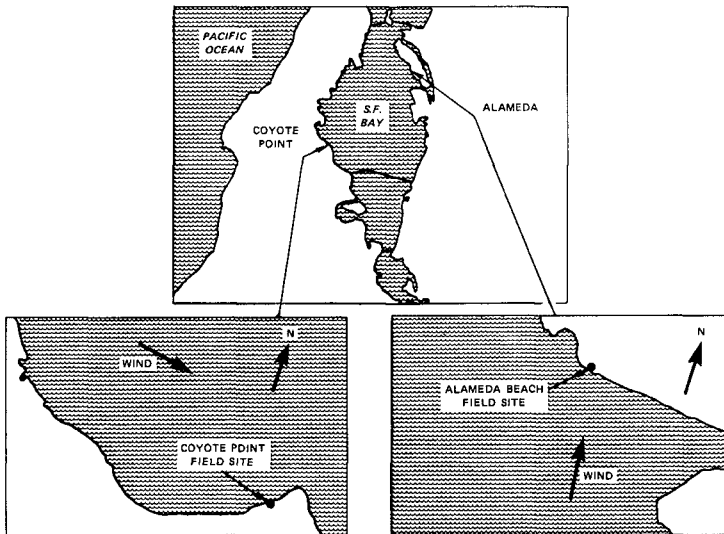


FIGURE 1 MAP SHOWING THE LOCATION OF THE ALAMEDA AND COYOTE POINT FIELD SITES AND THE PREDOMINANT WIND DIRECTIONS THAT PREVAILED DURING EXPERIMENTS



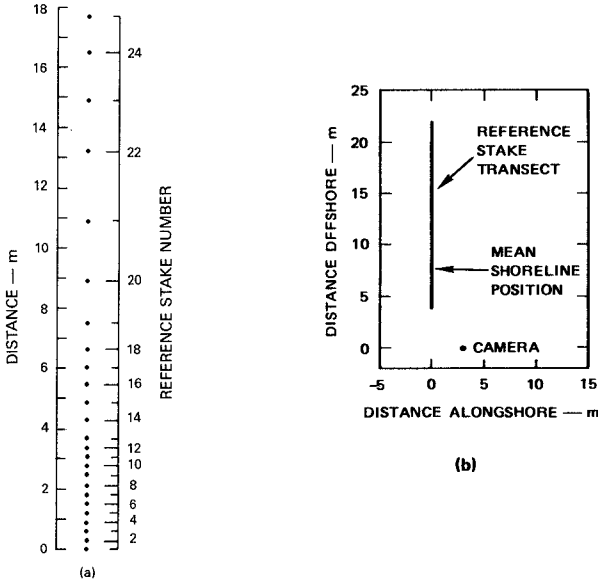


FIGURE 2 PLAN VIEWS OF ALAMEDA BEACH REFERENCE STAKE ARRAY SHOWING (a) REFERENCE STAKE NUMBERS AND SPACING BETWEEN STAKES AND (b) LOCATION OF CAMERA RELATIVE TO REFERENCE STAKE TRANSECT AND APPROXIMATE SHORELINE POSITION.

### Coyote Point Beach

The beach at Coyote Point was openly exposed to northerly and northwesterly wind waves (Figure 1) and the beach was composed of very small gravel and coarse sand. The beach slope was nearly constant in both the alongshore and offshore directions and formed a low-energy dissipative system with the incident-wave conditions present during the experiment.

The movie camera used for the Alameda field experiment was also used for the Coyote Point measurements. A two-dimensional grid of 80 wooden reference stakes arranged in 10 shore-normal transects provided the datum control for the Coyote Point experiment (Figure 3). Level and transit field survey techniques described for the Alameda measurements were used to establish datum control with the same accuracies. Three long transects and seven shorter ones crossed the beach face and extended offshore. The stakes located on the beach face were spaced closer together than those offshore to increase the available resolution for the run-up measurements. Figure 4 shows the orientation of the reference stake array relative to the camera, which is positioned at the origin of the plot. Also shown is a triangular array of three stakes located well seaward of the breaker zone and used for definition of the offshore incident-wave field.

To maintain continuity of the mean water level during the experiment, time series were recorded during the peak of the high tide. The winds were quite strong (about 8 m/s) and were nearly constant in their direction ( $250^{\circ}$  true) throughout the experimental period. The waves were nearly normal in incidence to the beach at the location of the reference stake array and plunging breakers were observed throughout the experiment. No visible signs of edge wave activity, such as beach cusps or regular alongshore spatial modulation of the run-up, were observed at any time during the experiment. Only one breaker zone was present near the shoreline.

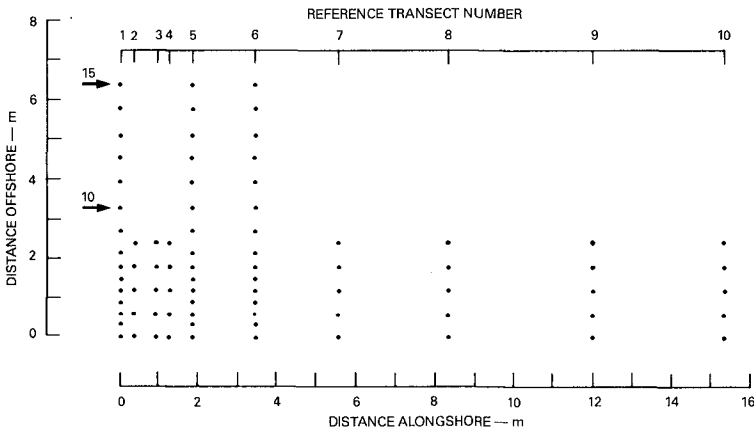


FIGURE 3 PLAN VIEW OF THE TWO-DIMENSIONAL ARRAY OF REFERENCE STAKES USED FOR THE COYOTE POINT RUN-UP FIELD EXPERIMENT

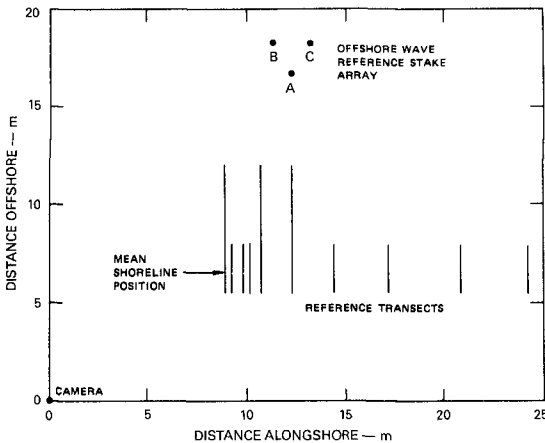


FIGURE 4 PLAN VIEW SHOWING LOCATION OF THE CAMERA RELATIVE TO REFERENCE STAKE TRANSECTS AND OFFSHORE INCIDENT-WAVE REFERENCE STAKE ARRAY

### Data Analysis

Time series of the incident waves were derived from the 16-mm photographic record by digitizing the amplitude fluctuations of the waves where they passed the offshore reference stakes. Similarly, the run-up time series were developed from the movie record by digitizing the position of the leading edge of the run-up on the beach face.

The movie frames were digitized manually using an electronic photodigitizer. The oblique photographic image was projected onto a Tektronix 4956 Graphics Tablet connected to a Tektronix 4052 terminal; an electronic pad with crosshairs was used to digitize the photograph. The digitized points were stored on cassette tape and subsequently transferred from the Tektronix terminal to a DEC VAX 11-782 computer for processing and analysis.

The leading edge of the run-up on the beach face was digitized in the photographs along the reference stake transect. It was relatively easy to identify the position of the leading edge of the run-up in the photographs due to the presence of seafoam on the beach. The seafoam provided an effective tracer of run-up in the photographs since it closely followed the moving shoreline. In addition, the flow pattern around other inundated reference stakes was readily evident and proved helpful in verifying the continuity of the swash layer on the beach face. The run-up time series were calibrated into physical units directly from the photographs by using the surveyed reference stake positions. The positions of the reference stakes computed from the photographs agreed to within 2.5 cm (0.08 ft) of the measured positions.

The incident-wave amplitude time series were developed by digitizing the fluctuating water surface at the stakes. As with the digitized run-up time series, the product of digitizing was a digital time series of oblique photo coordinates in arbitrary digitizer units. No calibrations were available for the middle of the unmarked offshore reference stakes, near the mean water level, where the waves passed the stakes, thus precluding direct calibration. Photogrammetric analysis techniques were used to calibrate the incident-wave time series. The equivalent vertical photograph method of analysis (2,8,13) was used to compute the real ground coordinates of the offshore reference stakes and to calibrate the wave amplitude time series.

All incident-wave and run-up time series data computed from the Alameda and Coyote Point photographs were processed identically using standard digital time series analysis techniques. The results of four primary categories of processing are presented; spectral analysis, coherence and phase analysis, computation of spectral slopes, and statistical hypothesis testing on the empirical cumulative distribution functions (CDFs). Both chi-square ( $\chi^2$ ) and Kolmogorov-Smirnov (KS) goodness-of-fit tests were used to compare the empirical CDFs to both normal and Rayleigh distributions.

Results

Alameda Beach

Due to preset camera exposure rates, the raw time series data were recorded at 10.66 Hz and were subsequently down-sampled to 5.33 Hz during the digitizing process. A total of 1024 time series points were processed for both the incident waves and run-up, representing approximately 192 s of data. A 128-point FFT window was used, which corresponded to a 24-s time series segment, giving a Nyquist frequency of 2.67 Hz and a spectral resolution of 0.042 Hz. The use of a 50% spectral overlap with the power-normalized Hanning window produced 26 equivalent degrees of freedom for the spectral estimates (12).

Figure 5 shows the power spectral density (PSD) computed for (a) the incident waves recorded at reference stake 19 (Figure 2) and (b) the run-up recorded on the beach face plotted against frequency in Hertz. The predominance of LF run-up spectral energy at frequencies not containing high energy densities in the incident-wave spectrum is striking. The absolute magnitude of the power in the run-up spectrum is greater than that of the incident-wave spectrum. This is because the component of swash motion measured parallel to the plane of the beach face was recorded in these experiments and is reported here. If the vertical component of run-up had been computed, the absolute magnitude of the run-up spectral values would have been smaller, but the frequency distribution of the energy would remain the same.

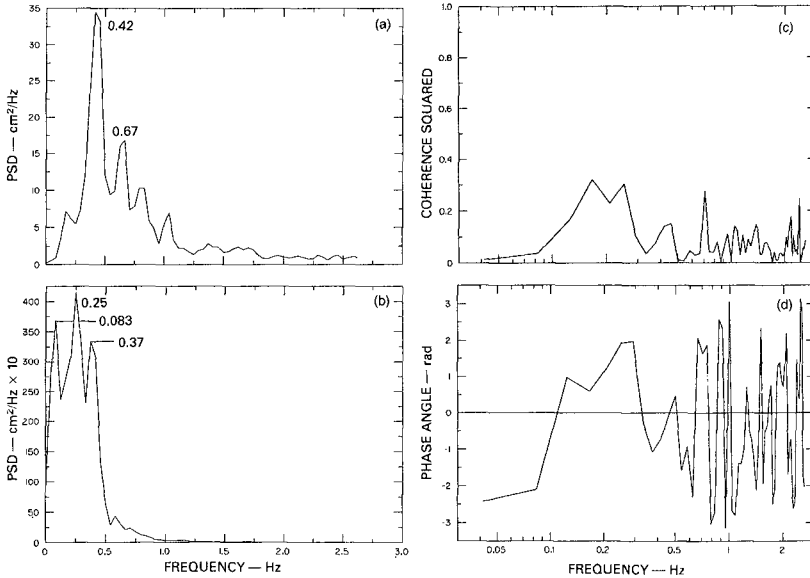


FIGURE 5 ALAMEDA BEACH (a) INCIDENT-WAVE AND (b) RUN-UP SPECTRA WITH THE ASSOCIATED (c) COHERENCE AND (d) PHASE.

The frequencies of the dominant peaks in the spectra are indicated on the plots. The frequency resolution is 0.042 Hz, and the absolute position of any given spectral peak with respect to frequency may vary by a single resolution cell in either direction. The 0.42-Hz peak in the wave spectrum can be assumed to match the 0.37-Hz peak in the run-up spectrum. Guza and Thornton (6) also report the presence of a peak in the run-up spectrum at the incident-wave frequency for run-up measured on steep beaches with narrow surf zones. The wave spectrum is virtually devoid of energy at the 0.083- and 0.25-Hz frequencies containing the majority of the energy in the run-up spectrum. Conversely, the run-up spectrum does not exhibit energy at frequencies higher than about 0.5 Hz, whereas significant wave energy is present at frequencies greater than 0.5 Hz.

The incident-wave and run-up spectra were recomputed using a log-log format. Spectral slopes were then computed for these spectra over the so-called saturation frequency band of the incident wind waves by using a linear least-squares regression analysis. The slope computed for the wave spectrum is -1.9 and for the run-up spectrum is -3.2. The saturation band was defined over the frequency band of the incident wind waves that broke near the shore (6,7). Since the data recorded for the Alameda and Coyote Point field experiments contained only wind-wave characteristics, the saturation region of the spectrum was defined as all frequencies equal to and greater than the incident-wave peak frequency.

Figure 5 also shows the (c) coherence squared and (d) phase computed between the incident-wave and run-up time series. Following Bendat and Piersol (4), the 95% confidence limits are given in the Appendix (Table A-1) as a function of coherence. At the 5% level of significance ( $\alpha = 0.05$ ), the hypothesis that  $\gamma_{xy} = 0$  results in an acceptance region for the variable equal to 0.19. The coherence is generally low across the entire frequency band, and the phase is random, indicating that the waves and run-up are not linearly correlated. This lack of linear coherence between the offshore incident waves and the run-up on the beach face is not surprising and has been observed by others. The coherence between the time series was computed both with and without compensation for the spatial separation between the measurement locations.

The CDFs were computed for the Alameda incident waves and run-up. Two different data formats were used in comparing the empirical CDFs with normal and Rayleigh CDFs. For hypothesis testing of the measured data with respect to the model normal distribution, the incident-wave and run-up amplitude time series were converted to time series of standard deviations using:  $x(t) = (x(t) - E[x(t)]) / \sigma_x$  where  $E[\ ]$  is the expected value and  $\sigma_x$  is the standard deviation. Prior to computing the Rayleigh CDFs, the run-up and incident-wave time series were redefined for the comparisons using:  $x(t) = x^2(t) / \langle x^2(t) \rangle$ .

With the exception of the Rayleigh distribution for the waves, the empirical distributions provide a very close fit to both the normal and Rayleigh distributions and it might be tempting to conclude that

both distributions provide a good fit to the data. A KS goodness-of-fit test was used to quantify the agreement between the empirical, normal, and Rayleigh distributions. Only the incident-wave and normal CDFs appeared to be statistically the same with respect to the KS test statistic. That is, the two CDFs were not statistically different based on the KS test statistic. It should be emphasized here that these statistical tests do not indicate the distribution to which the empirical data conform; rather, the tests identify model statistical distributions from which the empirical distribution is not different. It is also possible that some other statistical distribution, not tested here, may fit the empirical run-up and incident-wave distributions.

#### Coyote Point Beach

The Coyote Point reference stakes were numbered consecutively in the offshore direction from 1 to 15 in transect 1 (Figure 3). The incident waves were measured at four offshore locations, which included reference stakes 10 and 15 in transect 1 and points A and B in the offshore reference stake triangle shown in Figure 4. The waves were steepening or just beginning to break as they reached stake 15; the largest waves broke by plunging just seaward of stake 15, while the smaller waves broke by plunging just shoreward of stake 15. The waves measured at stake 10 were actually bores moving shoreward toward the beach. The run-up was measured along transects 1, 3, 5, and 6 spanning an alongshore distance of approximately 3.5 m (11.5 ft).

The Coyote Point series data were recorded at 14 Hz and were downsampled to 3.5 Hz during digitizing. All eight time series were time-registered. Spectral analysis of these data was accomplished using 36-s, 128-point FFTs, producing a spectral resolution of 0.027 Hz and a Nyquist frequency of 1.75 Hz. The 50% spectral overlap, Hanning window, and other processing techniques described for the Alameda data were used to produce the spectra with 23 equivalent degrees of freedom.

The incident-wave spectra computed for the data recorded at offshore stakes A and B and along transect 1 at stakes 10 and 15 are shown in Figure 6. The spectral peak frequencies between all four of the spectra agree to within 1 frequency resolution cell. The spectra measured at all four locations are uniformly narrow-band, with one primary frequency. Virtually no LF energy is observed in any of the incident-wave spectra measured either well offshore at stakes A and B or nearer the shoreline at stakes 10 and 15.

A net decrease in wave height was observed across the reference stakes moving shoreward in order B-A-15-10. Respective rms wave heights of 10.0, 9.7, 8.6 and 5.1 cm (0.33, 0.32, 0.28, 0.17 ft) were computed for these locations both directly from the time series variance and by integration of the spectra from zero to the Nyquist frequency. Agreement between the two methods was uniformly better than 1%. Some transfer of spectral energy from lower to higher frequencies is observed in the spectra computed for stakes 10 and 15.

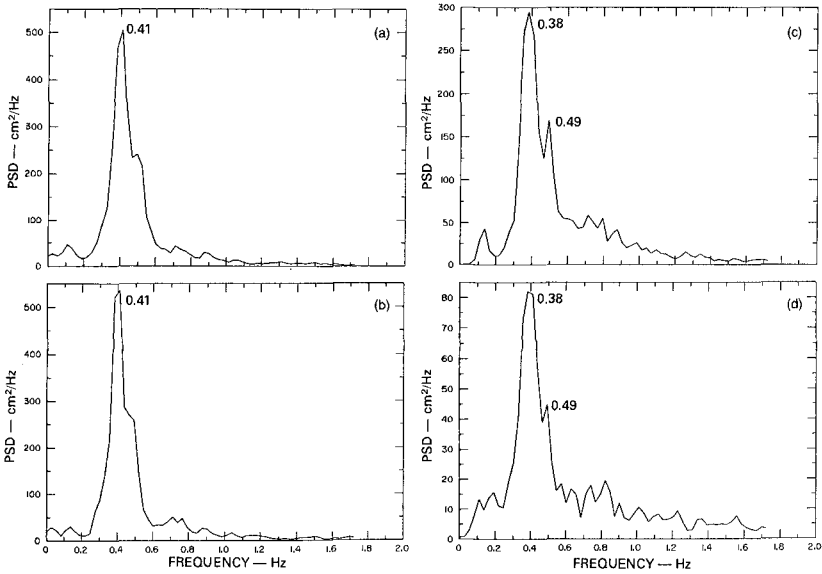


FIGURE 6 COYOTE POINT INCIDENT-WAVE SPECTRA MEASURED AT REFERENCE STAKES (a) B, (b) A, (c) 15 AND (d) 10

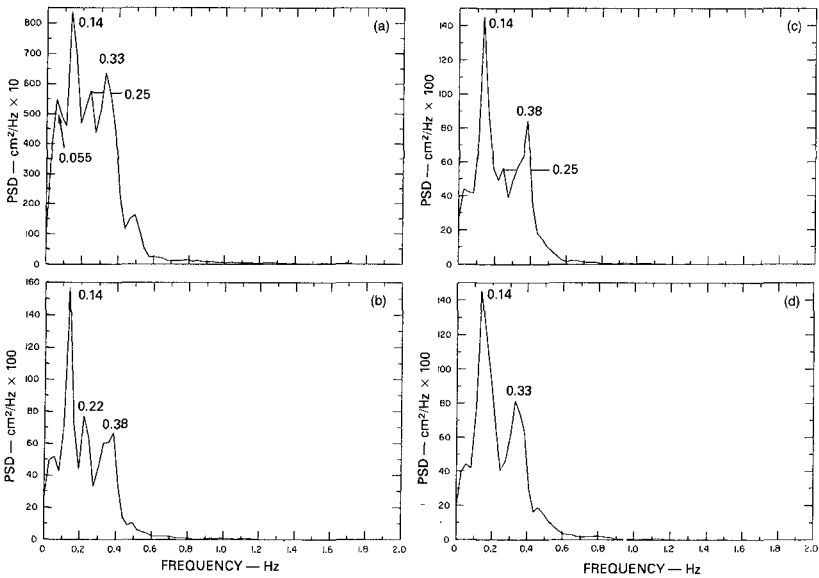


FIGURE 7 COYOTE POINT RUN-UP SPECTRA MEASURED ALONG REFERENCE TRANSECTS (a) 1, (b) 2, (c) 5 AND (d) 6

The run-up spectra measured at reference transects 1, 3, 5 and 6 are shown in Figure 7. The predominance of the LF energy in each run-up spectrum is the most noteworthy feature. The spectral peak frequency of the incident waves was approximately 0.38 Hz and although each of the measured run-up spectra show some energy at this frequency, the predominant run-up energy is located at much lower frequencies as observed for the Alameda Beach data. The 0.14 Hz spectral peak is observed in all of the run-up spectra measured at Coyote Point. A peak at 0.22 to 0.25 Hz (1 resolution cell apart) is observed in the run-up spectra measured at transects 1, 3 and 5.

The predominant run-up and backwash motions at frequencies 0.14 and 0.38 Hz were readily observed along all of the transects analyzed here. Although the frequency resolution of all four run-up spectra is identical, there appears to be a loss of fine structure detail in the spectra moving from transect 1 to transect 6. This is attributed to the increased distance between the measurement point and the camera location (Figure 4), coupled with the photographic resolution of the small 16-mm film. During analysis, it was increasingly difficult to observe the fine structure of the swash motions as transects located further from the camera were analyzed. For this reason, the continuum of energy located in frequency bands surrounding the dominant 0.14- and 0.38-Hz peaks in the run-up spectra recorded at transects 3, 5 and 6 is not as pronounced as in the spectrum recorded at transect 1. The basic shape of the energy continuum surrounding the 0.14-Hz spectral peak is conserved in the spectra measured at transects 1, 3 and 5 as is the total energy in the spectra. The rms run-up computed in the plane of the beach face at transects 1, 3, 5 and 6 was respectively 50.3, 55.2, 53.4 and 55.4 cm (1.65, 1.81, 1.75, 1.82 ft).

The spectral slopes were also computed over the saturated frequency band of the breaking incident wind waves for the run-up and incident-wave data recorded at Coyote Point. The slopes given in Table 1 compare favorably with the slopes computed for the Alameda data and show good agreement with slopes reported recently by others (6,7) for measurements made at beaches exposed to both swell and wind waves simultaneously. The slopes of the incident-wave spectra decrease in the shoreward direction. This appears to be explained by the transfer of energy in the spectrum from lower to higher frequencies as the waves shoal and break.

Table 1  
COYOTE POINT SPECTRAL SLOPES

Run-up Location	Slope	Wave Location	Slope
1	-2.8	B	-3.1
3	-3.0	A	-3.0
5	-2.9	15	-2.7
6	-3.1	10	-1.8



To estimate the onshore-to-offshore correlation between the run-up and the incident waves, the coherence and phase were computed between the run-up measured at reference transect 1 and the incident waves measured at reference stakes B, 15 and 10. Figure 8(a) shows the coherence squared and the phase computed between the run-up and the waves measured at offshore stake 15. The acceptance region for  $\gamma_{xy} = 0$  at the 95% confidence interval is 0.21. These results are typical of those computed between measurements made at the other locations. In each case, the correlation between the incident waves and the run-up is low.

The alongshore correlation in the run-up was also examined by computing the coherence and phase between all combinations of the run-up time series measured at transects 1, 3, 5 and 6. The coherence and phase between the run-up measured at transect 1 and 3 shown in Figure 8(b) is representative of all transects. Phase in the run-up correlations is generally random above 0.4 Hz, and coherence is low. Coherence squared was generally high between all four run-up transects across the lower frequency bands containing the predominant run-up spectral energy, reaching a maximum of approximately 0.8. The alongshore correlation in the run-up tends to decrease, however, with increasing separation between measurement points. Across all transects, the coherence remains consistently high near 0.14 and 0.38 Hz, the frequencies of the dominant peaks in the run-up spectra. The phase is nearly constant and is approximately zero in the band of frequencies less than 0.3 Hz, where the coherence is high, indicating that the time series are in phase.

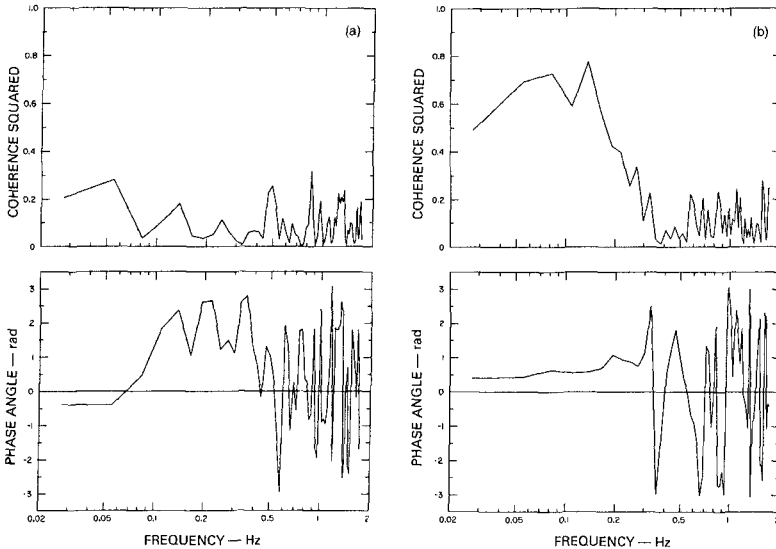


FIGURE 8 COYOTE POINT COHERENCE AND PHASE BETWEEN THE RUN-UP ALONG TRANSECT 1 AND THE (a) INCIDENT WAVES AT STAKE 15 AND (b) THE RUN-UP ALONG TRANSECT 3

The CDFs computed for the run-up measured at transects 1, 3, 5 and 6 and for the incident waves measured at stake A were compared to model normal and Rayleigh distributions using  $X^2$  and KS statistical hypothesis tests. In each instance, the fit between the normal and data-derived run-up CDFs is very close. The KS tests results show that the null hypothesis cannot be rejected at the 95% confidence interval in any of the tests, and thus a normal distribution is not statistically different from the distribution of the Coyote Point run-up data for all four transects reported here. The observed value of the  $X^2$  statistic was less than the expected value in each case, and thus, the  $X^2$  test also confirms that the Coyote Point run-up data are not different from a normal distribution at the 95% confidence interval.

When tested against a Rayleigh distribution, the tests show that the Coyote Point run-up is statistically different from a Rayleigh distribution at the 95% confidence interval. The distribution of wave heights measured at A is statistically different from both the Rayleigh and normal distributions at the 95% confidence interval but is not different from a normal distribution at 99%.

#### Discussion

Two different field sites were selected, each with similar yet statistically different incident-wave and beach slope conditions, and in both cases low-frequency wave run-up was observed with similar characteristics. A small percentage of run-up energy was observed at the incident-wave peak frequency, but the largest percentage of the run-up energy was located at frequencies that were significantly lower. The fact that some run-up spectral energy is located at the predominant incident-wave frequency indicates that although wave-breaking by plunging is highly nonlinear, there is some memory involved whereby incident-wave frequency information is transferred to the run-up. The mechanism for this transfer may be the collision between the seaward-moving backwash and the shoreward-moving incident bore.

Observations of the run-up made during the field experiments revealed a typical swash-cycle scenario. A wave broke by plunging in the shallow water near the shoreline forming a bore that traveled a very short distance before running up the beach. Before this first wave reached the run-up limit and began its backwash, a second or even third wave plunged and surged up the beach face over the top of the moving layer of water created by the first wave(s). The backwash generated by the combination of these earlier waves would often attenuate the run-up of the subsequent wave, producing a modulation of the swash. Because a spectrum of incident-wave frequencies was present, albeit a narrow one, the relative timing between the run-up and backwash was not constant, thus creating the spectrum of low run-up frequencies.

The red-shift observed in run-up spectra may be caused by different mechanisms. The beach can behave as a low-pass filter to

the incident waves when exposed to a broadband spectrum of incident-wave energy. When exposed to both long swell waves and shorter wind waves, the longer waves produce the dominant, large run-up excursions, and the run-up generated by the shorter waves becomes embedded in the long-wave run-up. As a result, the run-up spectrum shows a prominent peak at the long-wave frequency, as well as at other frequencies.

Unlike the run-up field data reported in the open literature, however, the Alameda and Coyote Point run-up measurements were made for wind-wave conditions exclusively. The Alameda and Coyote Point incident-wave fields were narrow-band in frequency and contained only one predominant wind-wave component. The peak in the run-up spectrum coincident with the incident-wave peak frequency was not produced by long waves masking the run-up generated by shorter waves. Instead, the incident wind waves produced components in the run-up at their characteristic frequency and at lower frequencies through the interaction of the run-up and backwash during the swash cycle. If the beach were simply acting as a low-pass filter to the incident waves, the run-up spectral energy would be observed primarily at the wind-wave frequency only. There was no broadband distribution of incident-wave energy to be low-passed by the beach, but instead only one predominant forcing frequency.

No regular alongshore modulation of the run-up was observed at any time during the field experiments. The mean shoreline remained straight, and no edge wave derived cusps or regularly spaced deposits of seafoam or debris were observed along the shore. The time series of the run-up measured at transects 1, 3, 5 and 6 all showed approximately the same mean value. Thus, no quantitative alongshore variability of the mean run-up was observed over the 3.5-m (11.5 ft) distance between transects 1 and 6.

Huntley et al. (7) proposed a universal form for swash spectra. They observed an  $f^{-4}$  frequency dependence over the saturated portion of the run-up spectrum corresponding to the wind-wave band. Thornton (10) and Guza and Thornton (6) reported swash measurements for which an  $f^{-3}$  frequency dependence was observed. While a -3 slope was measured for the Alameda and Coyote Point run-up spectra, these data do not identify whether the same mechanisms produce both the -3 and -4 spectral slopes. These data do, however, support the idea of a saturated run-up spectrum.

Both normal and Rayleigh distributions appear to provide reasonable models for the run-up amplitude distribution. Webber and Bullock (11) indicate laboratory measured run-up was best described by a normal distribution. Battjes (3) suggests that run-up is more appropriately modeled using a Rayleigh distribution based on an assumed Rayleigh distribution for the incident-wave heights and squared wave periods. Sawaragi et al. (9) used a Weibull distribution in their run-up distribution model and Ahrens (1) assumed a Rayleigh distribution for the run-up in his proposed method for predicting the run-up due to irregular waves. Formal statistical hypothesis test

results are often not reported in the open literature for comparisons between empirical data and a chosen model probability distribution. The agreement may not be acceptable quantitatively based on formal hypothesis tests. If the run-up distribution model proposed for use in a predictive capacity does not match the field conditions, the accuracy of the prediction may not be acceptable.

#### Conclusions

Field measurements of narrow-band, incident wind waves and the resulting run-up on the beach face were made at two different natural beaches. The run-up spectra measured at both beaches show LF energy concentrated at frequencies much lower than the frequency band of the predominant incident waves. No LF energy was observed in any of the incident-wave spectra measured either offshore or near the shoreline. No continuous offshore-to-onshore red-shifting of spectral energy was observed. Photographic observations of the swash cycle on the beach face indicate that the interaction between the run-up and the backwash appears to be the source of the low-frequency energy.

Coherence between the incident waves and the run-up is very low across the surf zone. Although some run-up spectral energy is present at the dominant incident-wave frequency, the coherence level in this frequency band is not statistically significant. Some incident-wave information appears to be transmitted to the run-up, but linear coherence estimates do not identify the mechanism.

An equilibrium region of the run-up spectrum appears to exist over the frequency band of the incident waves. Run-up spectra measured during both field experiments show consistent  $-3$  slopes over the frequency band defined by frequencies greater than or equal to the incident-wave peak frequency.

The CDF computed for the Coyote Point run-up amplitude data is not statistically different from a standard  $(0,1)$  normal distribution. The Alameda run-up was statistically different from both normal and Rayleigh distributions, although qualitatively the data were more nearly normally distributed.

#### Acknowledgements

This work represents a portion of the author's Ph.D. dissertation research (5) conducted at the University of California, Berkeley, CA (UCB). The writer thanks Professors R.L. Wiegell and J.R. Paulling of UCB and Professor J.L. Hammack of the University of Florida for their advice and suggestions during this study. A special thanks to Dr. J.W. Maresca, Jr. of Vista Research, Inc. and Dr. E. Seibel of San Francisco State University, for their help during the field experiments. This study was completed with the generous support of SRI International, Menlo Park, CA and the Department of Hydraulic and Coastal Engineering at UCB. The author thanks Lynnett Doeden for typing the text and the Sohio Petroleum Company for supporting the preparation of this manuscript.

## References

1. Ahrens, J., "Prediction of Irregular Wave Run-up," Coastal Engineering Technical Aid No. 77-2, U.S. Army, Coastal Engineering Res. Center, Fort Belvoir, VA, (1977).
2. American Society of Photogrammetry, Manual of Photogrammetry, 3rd Ed., Washington, DC, (1966).
3. Battjes, J.A., "Run-up Distributions of Waves Breaking on Slopes," J. Waterways, Harbors and Coastal Engineering Div., ASCE, No. WW1, pp 91-114, (1971).
4. Bendat, J.S. and A.G. Piersol, Random Data: Analysis and Measurement Procedures, (Wiley - Interscience, New York, NY 1971).
5. Carlson, C.T., "Field Studies of Run-up Generated by Wind Waves on Dissipative Beaches," Ph.D. Dissertation, Univ. of California, Berkeley, CA, (1983).
6. Guza, R.T. and E.B. Thornton, "Swash Oscillations on a Natural Beach," J. Geophys. Res., Vol. 87, No. C1, pp 483-491, (1982).
7. Huntley, D.A., R.T. Guza, and A.J. Bowen, "A Universal Form for Shoreline Run-up Spectra?," J. Geophys. Res., Vol. 82, No. 18, pp 2577-2581, (1977).
8. Maresca, J.W., Jr. and E. Seibel, "Terrestrial Photogrammetric Measurements of Breaking Waves and Longshore Currents in the Nearshore Zone," Proc. Fifteenth Coastal Engineering Conf., ASCE, Honolulu, HI, pp 681-900, (1976).
9. Sawaragi, T., K. Iwata and A. Morino, "Wave Run-up Height on Gentle Slopes," Coastal Engineering in Japan, 20, pp 83-94, (1977).
10. Thornton, E.B., "Energetics of Breaking Waves Within the Surf Zone," J. Geophys. Res., Vol. 84, No. C8, pp 4931-4938, (1979).
11. Webber, N.B. and G.N. Bullock, "A Model Study of the Distribution of Run-up of Wind-Generated Waves on Sloping Sea Walls," Proc. Eleventh Coastal Engineering Conf., ASCE, London, England, pp 870-887, (1968).
12. Welch, P.D., "The Use of Fast Fourier Transform for Estimation of Power Spectra: A Method Based on Time Averaging Over Short Modified Periodograms," IEEE Trans. Audio and Electroacoust., Vol. AU-15, pp 70-73, (1967).
13. Wolf, P.R., Elements of Photogrammetry, (McGraw-Hill, Inc., 1974).

## Appendix

Table A-1

THE 95% CONFIDENCE LIMITS FOR  $\gamma^2(f)$  WHEN DF = 26

$\gamma^2(f)$	0.4	0.5	0.6	0.7	0.8	0.9
Upper limit	0.64	0.72	0.78	0.84	0.90	0.95
Lower limit	0.087	0.17	0.28	0.42	0.58	0.78

DF = Number of degrees of freedom

## CHAPTER TWENTY NINE

### A Nonlinear Model of Irregular Wave Run-up Height and Period Distributions on Gentle Slopes

Toru SAWARAGI\* and Koichiro IWATA\*\*

Member, JSCE and ASCE

#### ABSTRACT

This paper discusses the probability distributions of irregular wave run-up height and period on gentle slopes.

Assuming that the long period component appeared on the run-up oscillation corresponds to the incident envelope wave period, a nonlinear model to estimate the probability distributions of run-up heights and periods is proposed.

Laboratory experiments on gentle slopes of 1/15, 1/30 and 1/40, and field measurements on a natural sandy beach with swash slopes of 1/6 to 1/14 were performed to examine the proposed model. The proposed model is shown to agree with the experiments.

#### 1. INTRODUCTION

The elucidation of irregular wave run-up mechanism on a gently sloping beach is one of the important Coastal Engineering problems. The run-up oscillation presents a shoreward boundary condition for the onshore-offshore sediment transport which results in the change of beach profile, and a precise prediction of the swash oscillation, especially run-up heights give a significant information for the construction site of dikes, beach nourishment works, etc.,

So far, investigations have been performed to verify the nature of the swash oscillation on gentle slopes from field measurements<sup>1)-4)</sup> and laboratory experiments<sup>5)-9)</sup>. Most of the foregoing researches have pointed out that the swash oscillation has long period components which are not included in an incident wave outside the surf-zone, and the power level in the low frequency range of the swash oscillation becomes larger than that of the incident individual wave.

Some theoretical models<sup>10)-13)</sup> to predict a probability distribution of run-up heights have been proposed. All the foregoing models, however,

---

\* Professor, Dr. of Eng., Dept. of Civil Eng., Osaka Univ., Osaka 565, Japan

\*\* Associate Professor, Dr. of Eng., Dept. of Civil Eng., Nagoya Univ., Aichi 464, Japan

assumed that run-up heights of individual waves in an irregular wave train indicate the values following a formula proposed for a regular wave, such as Hunt's equation<sup>14</sup>). Therefore, the long period component observed in field and laboratory measurements has not been taken into consideration. In this sense, the foregoing models should be called a "linear model". Then, a "nonlinear model" considering the long period components is expected to be settled down.

With this situation, the present paper is intended to propose a nonlinear model to evaluate the probability distribution of the run-up height and period of irregular waves on gently sloping beaches, from engineering purposes in mind.

First of all, the nature of wind wave-generated run-up oscillations on a sandy beach is discussed. Secondly, two-component composite waves showing a strong wave grouping are treated and the effect of wave groupiness on the run-up oscillation is revealed in laboratory flume. Lastly, the irregular wave-induced swash oscillation is investigated in an indoor wave tank. Based on the experimental fact that the long period on the swash oscillation is highly correlated with the incident envelope wave period, the probability distribution of swash oscillation periods is proposed to be given by a combined distribution of the incident individual wave and their envelope wave periods. By extending the idea, the probability distribution of run-up height is also proposed to be given by a combined distribution of the incident individual waves and their envelope waves-induced run-up height distributions. The proposed model is shown to agree with experiments.

## 2. FIELD MEASUREMENT

### 2-1. Measurements

Field measurements were conducted at Kanaiwa Beach, Ishikawa Pref., in Honshu Island, during Sept., 1981 and Nov., 1983. The Kanaiwa Beach which faces to the Japan Sea is moderately well sorted sandy beach and the sand has a diameter of 0.5 mm and the coefficient of permeability of the beach is 0.124 cm/s.

A typical beach face topography is shown in Fig.1. The local beach slope where the run-up oscillation was measured was between 1/14 and 1/6. The slope in the surf-zone and just offshore was more gentle ( $< 0.01$ ). Bar-trough topography was in general weak or absent, and the beach bottom counter was relatively uniform in the longshore direction (see Fig.2).

The change of tidal level at Kanaiwa Beach was so small enough to be constant during 45 min measurement. The swash oscillation was measured at three different locations (O, R and L in Fig.2), where the distances between R and O, and O and L were about 300 m. Most of the run-up oscillation data were collected at location O.

The run-up meter was a capacitance wire, and its length was 50 m and the diameter was 2 mm, and it was supported about 0.5 cm above the bed. Sand level changes required raising and lowering the support wood stakes. The run-up meter was calibrated before and after each data acquisition by shorting the wire at three different locations.

Nanao Harbor Construction Office at 1st Harbor Construction Bureau of Transportation Ministry has been measuring regularly 20 min wave data at 2 hours intervals at the depth of 20 m with the ultrasonic-type wave gauge

( see Fig.2 ). The tidal level has been also measured by the Office at the adjacent Kanazawa Port. In this research, the wave and tidal data measured by the Nanao Harbor Construction Office were used as an incident wave and an initial stillwater level, respectively.

The run-up oscillation was recorded on a magnetic tape with 45 min. The wave and run-up oscillation were cut discretely at 1 Hz intervals and a power spectrum was calculated by FFT method with 1024 points. The incident individual and envelope waves were defined by the zero-upcrossing method. On the other hand, the individual wave of run-up oscillation was defined here both by the zero-upcrossing and trough-to-trough methods. This is due to the following reason. The zero-upcrossing method is very objective, but it sometimes fails to define small waves which donot cross the mean water level. On the other hand, the trough-to-trough method is subjective, in general, and it can define noise-like small waves. Thus, both definitions have its own merits and demerits. Since there have been little discussions on which definition is better, this paper uses the two definitoins.

### 3-2. Results and Discussions

Fig.3 is one example indicating an incident wave profile at the depth of 20 m and the corresponding run-up oscillation measured at the location O. It can be pointed out that the run-up oscillation has flat crests and sharply edged troughs in general.

Fig.4 shows an effect of the swash zone slope  $S$  on the non-dimensional period of run-up oscillation  $\bar{T}_R/\bar{T}_I$ , where  $\bar{T}_R$  is the mean period of the run-up oscillation and  $\bar{T}_I$  is the mean period of incident individual waves. The mean period of run-up oscillation defined by the trough-to-trough method as well as by the zero-upcrossing method becomes longer with decreasing of the swash zone slope  $S$ .  $\bar{T}_R/\bar{T}_I$  defined by the zero-upcrossing

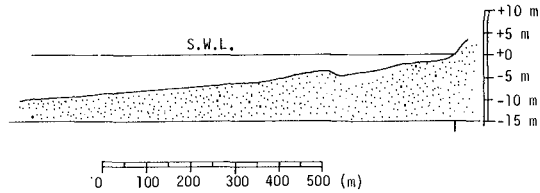


Fig.1 Typical beach topography

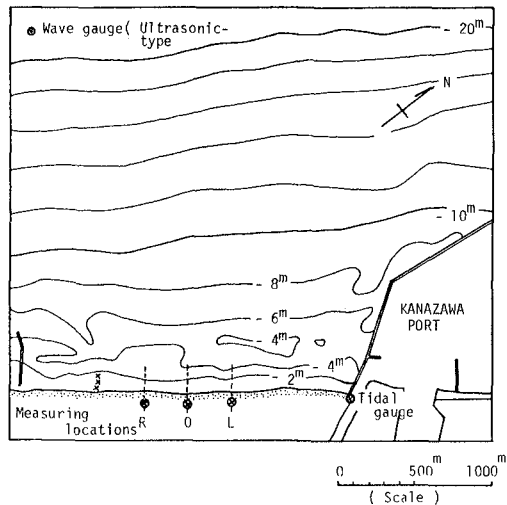


Fig.2 Measuring locations



method is about two times larger than those defined by the trough-to-trough method. The reason is that the former method neglects short period waves which do not cross the mean water level, on the other hand the latter method defines noise-like short period waves.

Thus, the swash oscillation cycle becomes longer than the incident individual wave periods on gentle slope such as 1/14 in our field measurement. The mechanics of generation of the long period component have been pointed out as follows<sup>1)-8)</sup>.

- (1). marked decay of wave energy around a spectral peak frequency by wave breaking ( see Fig.5 ),
- (2) amplification of long period components by nonlinear wave-wave interactions in the surf-zone,
- (3) nonlinear wave-wave interaction on the swash zone, i.e. large bores overtaking and capturing smaller ones in the up-rush and downrush process,
- (4) edge wave or standing long long wave, et..

Therefore, a new model considering the long period component for predicting the swash oscillation is needed to be established.

Fig.5 indicates that the power spectral shape(A) of the run-up oscillation in low frequency range resembles approximately to that of the incident envelope wave(A'). On the other hand, the spectral shape(B) of the run-up oscillation in high frequency range (> 0.1 Hz ) can be seen to correspond to that of the incident individual wave (B'). From Fig.4 and Fig.5, we assume here that the probability distribution of run-up oscillation  $P_{R}(T_R)$  is, for 1st approximation, given by a combined distribution of the incident individual wave period distribution  $P_{I}(T_I)$  and the incident

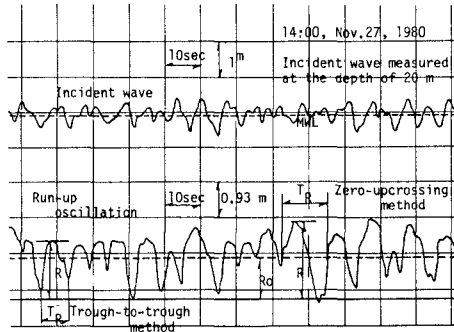


Fig.3 Incident wave and swash oscillation

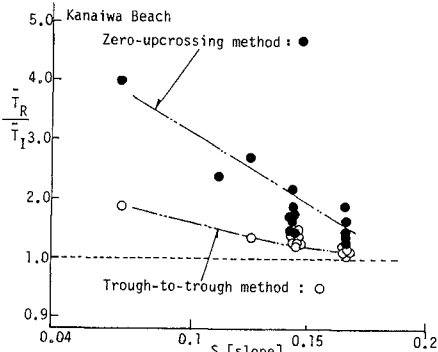


Fig.4 Effect of swash beach slope on period of run-up oscillation

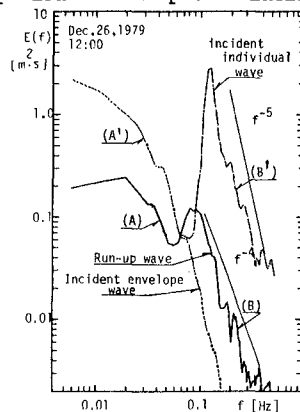


Fig.5 Power spectra of incident individual and envelope waves and run-up wave

envelope wave period distribution  $P_{rE}(T_E)$ , as expressed by Eq.(1).

$$P_{rR}(T_R) = \alpha P_{rI}(T_I) + \beta P_{rE}(T_E) \tag{1}$$

$$\alpha + \beta = 1$$

In Eq.(1),  $\alpha$  and  $\beta$  are weight coefficients. In case of  $\alpha = 1$ , the swash oscillation periods equal the incident individual wave periods and there is no long period component. On the other hand,  $\beta = 1$  presents a situation where only long period components appear on the run-up oscillation. Therefore,  $\beta$  is an index showing a degree of nonlinear interaction in the surf and swash zones.

Fig.6 shows that the probability distribution of run-up oscillation period can be estimated by Eq.(1) for moderate values of  $\alpha$  and  $\beta$ . The value of  $\beta$  for the zero-upcrossing wave is generally larger than that for the trough-to-trough wave.

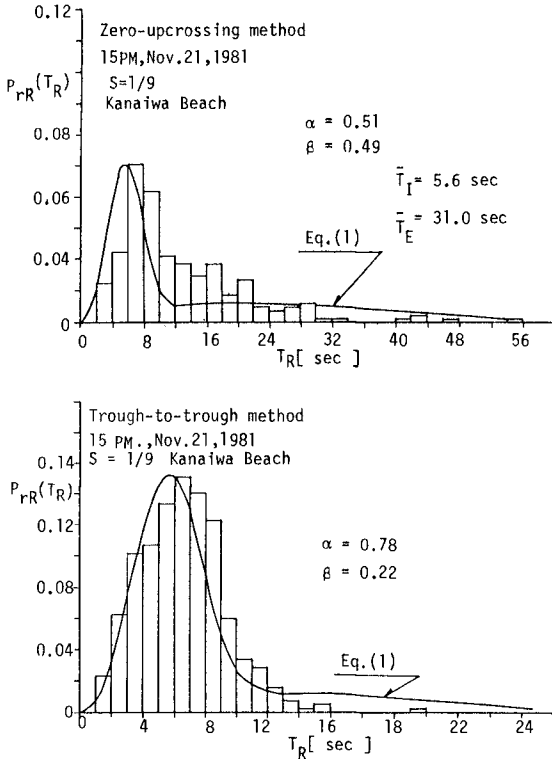


Fig.6 Probability distribution of run-up oscillation period ( Comparison between measurements and Eq.(1) )

### 3. TWO-COMPONENT COMPOSITE WAVE

#### 3-1. Equipment and Procedure

Experiments were conducted to examine the effect of wave groupiness on run-up heights and periods on gentle slopes. In the experiments, an indoor wave tank in 0.75 m width, 0.9 m height and 30 m length was used. At one end of the wave tank, a uniform slope was installed. The slopes of 1/40, 1/30 and 1/15 were used in this experiment. At the other end of the tank, a flap-type wave generator was set, which is controlled by an electric dynamic shaker. The electric dynamic shaker is activated by an electric voltage input. Throughout the experiments, the stillwater depth was kept constant ( 73 cm ) in front of the wave board.

Two-component composite waves were generated by composing two monochromatic waves ( [  $H_1, T_1$  ] and [  $H_2, T_2$  ] ) with use of a multi-wave composer, where  $H$  and  $T$  are the wave height and period, respectively. Wave periods of  $T_1$  and  $T_2$  were changed from 0.67 sec to 1.47 sec and were chosen to be almost equal each other in order to produce grouping or beat waves.  $H_1$  and  $H_2$  were also determined to have almost an equal value. The envelope wave period  $T^*$  and height  $H^*$  were 3.1 sec to 47.0 sec and 2.0 cm to 15.8 cm, respectively.  $T^*$  and  $H^*$  are indicated in Fig.7(c). The number of experimental waves were about 70.

The incident water surface profile was measured by a capacitance-type wave gauge, and a time history of the run-up oscillation was measured by the run-up measuring instrument<sup>13)</sup> which was set along the surface of slope bed. All the measured wave profiles were recorded onto magnetic tapes in about 120 sec.

Incident individual and envelope waves were defined by the zero-up-crossing method which is more objective than the trough-to-trough method. The run-up wave which is discussed in this paper is a *time history of run-up wave front* ( swash oscillation ) measured by the run-up measuring instrument. The run-up oscillation waves were defined by the zero-up-crossing and trough-to-trough methods.

#### 3-2. Results and Discussions

##### (1) Time history of run-up oscillation

Fig.7 shows some typical examples of time histories of incident two-component composite waves and their corresponding run-up oscillations. As indicated in Fig.7(a), (b) and (c), incident individual wave periods do not, in general, appear on a time history of the run-up oscillation with decreasing of the bottom slope. And, the period of run-up oscillation becomes to close to the incident envelope wave period  $T^*$  with decreasing the beach slope( Fig.7(c)). This is very different from the case of the regular wave as in Fig.7(d). The physical explanation of this seems to be following. Since the individual wave heights change gradually and regularly with the beat period, the nonlinear wave-wave interaction, e.g. big waves overtaking and capturing smaller waves in the run-up and run-down process occur regularly and smoothly in the swash zone, which smooths out variation generated by incoming incident individual wave components. Therefore, it can be understood that the time history of the swash oscillation shows a change of the mean water level. Its oscillation period comes to close to the incident envelope wave period with decrease of the bottom slope.

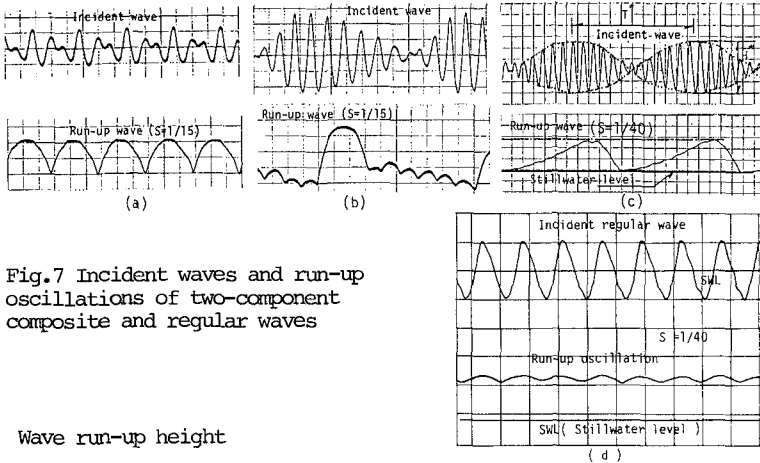


Fig.7 Incident waves and run-up oscillations of two-component composite and regular waves

(2) Wave run-up height

The run-up height is defined by a vertical distance of the run-up oscillation crest from the stillwater level. Based on a dimensional consideration, the run-up height  $R$  is dominated by 6 physical quantities,

$$R = F ( T^*, H^*, T_1, h, g, S ) \tag{2}$$

here,  $h$  is the stillwater depth,  $g$  is the gravitational acceleration, and  $S$  is the beach slope. From Eq.(2), a non-dimensional run-up height  $R/H^*$  is governed by 4 factors;

$$R/H^* = F ( H^*/L_o^*, T^*/T_1, h/L_o, S ) \tag{3}$$

where,  $L_o^* = gT^{*2}/2\pi$  and  $L_o = gT_1^2/2\pi$ .

The run-up height  $R$  of the two-component composite wave increases with increasing of  $H^*$  and  $T^*$ , in general, as indicated in Fig.8. This is very similar to the case of the regular wave<sup>13</sup>). The run-up height of two-component waves are generally higher than those of the regular waves. Putting it in another way, a grouping wave is apt to produce higher run-up height than the regular wave which does not show a grouping wave. The same thing can be said from Fig.9, where the wave height and period of the regular wave are equal to the maximum wave period and height among the incident individual waves. This experimental fact would imply that the run-up height of irregular waves becomes possibly higher than that of the regular wave.

By the way, the non-dimensional run-up height of the two-component composite wave  $R/H^*$  decreases as the incident envelope wave steepness  $H^*/L_o^*$  becomes larger, as indicated in Fig.10. In our experiments, the effect of  $h/L_o$  on  $R/H^*$  was little (the figures are not presented in this paper). From Fig.10, the non-dimensional run-up height  $R/H^*$  can be approximated by the following equations.

$$R/H^* = 0.05 ( H^*/L_o^* )^{-0.1} \quad \text{for } S = 1/40$$

$$\left. \begin{aligned}
 R / H^* &= S \sqrt{H^0/L^0} && \text{for } H^0/L^0 \geq 0.05 \\
 &= 0.15 && \text{for } H^0/L^0 < 0.05 && \text{for } S=1/30 \\
 \\
 \text{where, } H^0/L^0 &= 0.766 (T^*/T_1)^{2.18} (H^*/L_0^*) \\
 \\
 R / H^* &= S \sqrt{H^0/L^0} && \text{for } H^0/L^0 \geq 0.022 && \text{for } S=1/15 \\
 &= 0.45 && \text{for } H^0/L^0 < 0.022 \\
 \\
 \text{where, } H^0/L^0 &= 0.309 (T^*/T_1)^{2.18} (H^*/L_0^*)
 \end{aligned} \right\} (4)$$

Eq. (4) will be used for calculating run-up heights caused by the incident envelope waves in an irregular wave train in the next section.

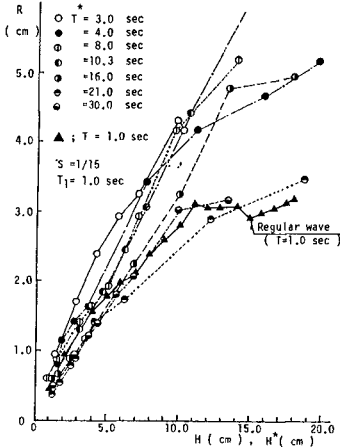


Fig.8 Run-up height of two-component composite waves ( $T_1=1.0$  sec)

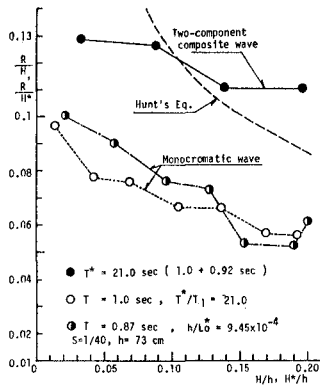


Fig.9 Comparison between run-up heights of regular and two-component composite waves

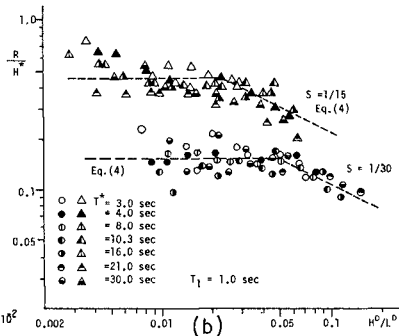
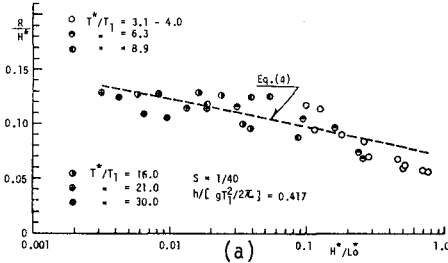


Fig.10 Non-dimensional run-up height of two-component composite wave

4. IRREGULAR WAVE

4-1. Equipment and Procedure

Experiments were carried out by using the same wave tank and instruments used for two-component composite wave experiments.

Irregular waves were generated to have a Bretschneider spectrum. In this work, 11 random waves (W.-1 - W.-11) were produced, and their power spectral and statistical quantities are given in Table 1. Time histories of incident individual and envelope waves and run-up waves were cut discretely, respectively, at each 0.05 sec, 0.5 sec, and 0.2 sec intervals, and the corresponding power spectra were calculated by BT-method with data of 4000 and freedom of 40, data of 6000 and freedom of 60 and data of 2400 and freedom of 30, respectively.

Incident individual and envelope waves were defined by the zero-upcrossing method. The run-up waves were defined both by the zero-upcrossing and trough-to-trough methods.

Table 1. Experimental waves

Wave	$H_{1/3}$	$\bar{H}$	$T_{1/3}$	$\bar{T}$	$Q_p$	$H_0/L_0$	S
W.- 1	3.5	2.2	2.2	1.9	2.17	0.005	1/40
W.- 2	5.0	3.3	2.1	1.9	2.22	0.008	
W.- 3	5.0	3.2	1.8	1.5	2.32	0.011	
W.- 4	7.4	4.9	1.3	1.2	2.18	0.027	
W.- 5	8.9	5.7	1.2	1.0	1.89	0.043	
W.- 6	6.0	3.9	0.8	0.7	1.48	0.060	
W.- 7	2.8	1.8	1.2	1.0	1.47	0.013	1/30
W.- 8	3.9	2.6	1.1	0.9	1.55	0.021	and
W.- 9	8.0	5.1	1.2	1.1	1.94	0.037	1/15
W.-10	7.9	5.1	1.0	0.9	1.98	0.051	
W.-11	10.3	6.8	1.1	1.0	2.08	0.062	

$H_{1/3}$ : significant wave height,  $\bar{H}$ : mean wave height,  $T_{1/3}$ : significant wave period,  $\bar{T}$ : mean wave period,  $Q_p$ : spectral peakedness,  $H_0/L_0$ : equivalent deep water wave steepness, S; beach slope  
Unit: cm for  $H_{1/3}$  and  $\bar{H}$ , and sec for  $T_{1/3}$  and  $\bar{T}$

4-2. Results and Discussions

(1) Time history and power spectrum of run-up oscillation

Fig.11 shows time histories of run-up oscillation. Different from the regular wave, the irregular wave-caused run-up oscillation contains long period components which are not included in the incident wave at the wave board. Therefore, this fact shows that the assumption "run-up heights of individual waves in an irregular wave train indicate the values following the formula, such as Hunt's formula, deduced for the regular wave" is not established on the gentle slopes of 1/15, 1/30 and 1/40.

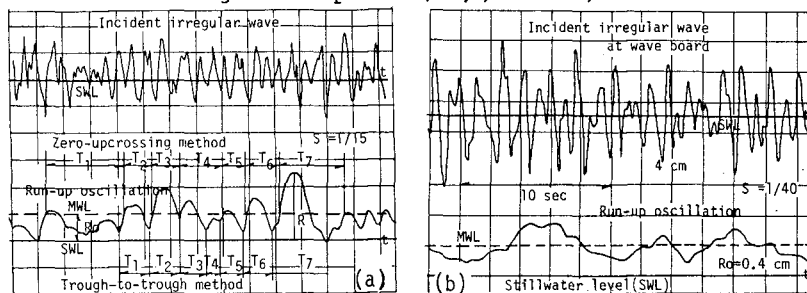


Fig.11 Time histories of incident wave and run-up oscillation

Fig.12(a) shows one example of power spectra of run-up oscillations. The remarkable feature of run-up oscillation is a marked increase of power density in a low frequency range than the spectral peak frequency of the incident individual wave. A predominant power peak is always recognized to appear at a little lower frequency side than the power spectral peak frequency of the incident individual wave. This is due to the reason of rapid decay of the wave energy around the spectral peak frequency by wave breaking and nonlinear wave-wave interactions in the swash and surf zones, etc..

The power spectral shape of run-up oscillation in a low frequency band is very similar to that of the incident envelope wave, different from the spectral shape of the incident individual wave. This would imply that the long period components which are supposed to be caused by nonlinear interactions including wave-wave interaction can be estimated from incident envelope wave periods. Typical examples are the cases of two-component composite waves discussed in the previous section.

Therefore, it may be possible to assume that the power spectrum of run-up oscillation is constructed by the two components, i.e. the individual wave and its envelope wave power spectra.

By the way, as indicated in Fig.12(a) and (b), the spectral slope of the run-up wave on high frequency range is proportional to  $f^{-4}$  (  $f$ ; frequency ). This fact coincides with experiments of Sutherland et al.<sup>6)</sup>

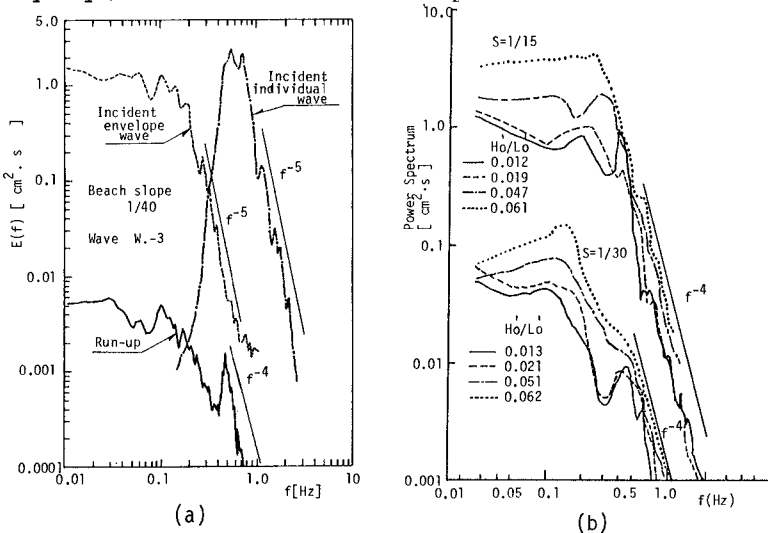


Fig.12 Power spectra of run-up oscillation on gentle slopes

(2) Distribution of run-up wave period

The distribution of run-up wave periods ( run-up oscillation periods ) is different from  $T^2$ -Rayleigh distribution which is usually observed for the incident individual wave, as indicated in figure 13. The run-up

wave periods distribute comparatively widely from short periods to long periods, and the distribution becomes to have two peaks with increasing of individual wave steepness  $H_0/L_0$ , as in Fig.14. The second peak period appears in the period domain corresponding to the incident envelope wave period.

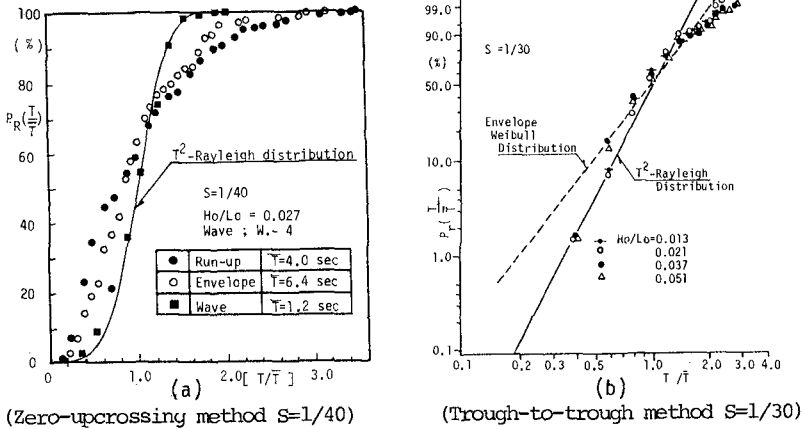


Fig.13 Cumulative distribution of period of run-up oscillation ( $T$  ; mean wave period )

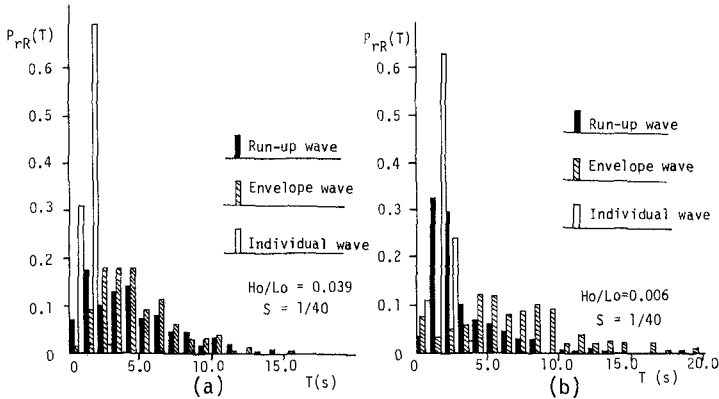


Fig.14 Probability distribution of period of run-up oscillation ( Waves defined by zero-upcrossing method )

As already cited in this paper, the foregoing theoretical distributions for run-up heights are strongly based on the assumption of "Equivalency". The assumption is, however, inconsistent with experimental facts described above.

Since the period of long period components of run-up waves almost equals incident envelope wave periods and the spectral shape of swash oscillation



in low frequency resembles that of the incident envelope wave, this paper uses the following assumption. That is, the long periods are appearances of incident envelope wave periods, and the occurrence frequency of short periods (individual wave periods) and long periods (envelope wave periods) on the run-up oscillation is probabilistic, because of extreme complexity of nonlinear wave-wave interaction in the surf and swash zones.

Following the above-mentioned assumption, the probability density function of run-up wave period,  $P_{rR}(T)$  is defined here, like the field measurement, by a following combined probability density function,

$$\left. \begin{aligned} P_{rR}(T) &= \alpha P_{rI}(T) + \beta P_{rE}(T), \\ &= \alpha \left[ \frac{m_{I1}}{n_{I1}} T^{m_{I1}-1} \exp\left(-\frac{1}{n_{I1}} T^{m_{I1}}\right) \right] + \beta \left[ \frac{m_{E1}}{n_{E1}} T^{m_{E1}-1} \exp\left(-\frac{1}{n_{E1}} T^{m_{E1}}\right) \right] \\ \alpha + \beta &= 1, \end{aligned} \right\} (5)$$

here,  $P_{rI}(T)$  and  $P_{rE}(T)$  are the probability density functions of the incident individual and envelope wave periods, respectively. Since there are no established expressions for  $P_{rI}(T)$  and  $P_{rE}(T)$ , they are given by Weibull probability density functions. In Eq. (5),  $n$  and  $m$  are, respectively, a scale and shape parameters,  $\alpha$  and  $\beta$  are weight coefficients whose meaning is the same as in Eq. (1), and subsuffixes  $R, I$  and  $E$  indicate quantities regarding the run-up, incident individual and envelope waves. The subsuffix  $l$  shows quantities concerning incident wave periods.

The mean of the largest  $l/k$  wave period,  $\bar{T}_{l/k}$  is defined by Eq. (6).

$$\bar{T}_{l/k} \int_{\bar{T}_{l/k}}^{\infty} P_{rR}(T) dT = \int_{\bar{T}_{l/k}}^{\infty} T P_{rR}(T) dT \quad (6)$$

From Eqs. (5) and (6),  $\bar{T}_{l/k}$  is expressed by

$$\bar{T}_{l/k} = \frac{\left[ \alpha n_{I1}^{1/m_{I1}} \Gamma\left(\frac{1}{m_{I1}} + 1, \frac{1}{n_{I1}} \bar{T}_{l/k}^{m_{I1}}\right) + \beta n_{E1}^{1/m_{E1}} \Gamma\left(\frac{1}{m_{E1}} + 1, \frac{1}{n_{E1}} \bar{T}_{l/k}^{m_{E1}}\right) \right]}{\left[ \alpha \exp\left(-\frac{1}{n_{I1}} \bar{T}_{l/k}^{m_{I1}}\right) + \beta \exp\left(-\frac{1}{n_{E1}} \bar{T}_{l/k}^{m_{E1}}\right) \right]} \quad (7)$$

where,  $\Gamma\left(\frac{1}{m_{j1}} + 1, \frac{1}{n_{j1}} \bar{T}_{l/k}^{m_{j1}}\right)$ ,  $j=I$  and  $E$ , are incomplete Gamma functions.

Figure 15 shows some comparisons between calculations and experiments. As indicated in Fig. 15, agreement of the estimated values using Eq. (5) with experimental values is good for moderate values of  $\alpha$  and  $\beta$  in both waves defined by the zero-upcrossing and trough-to-trough methods. The run-up oscillation period defined by the zero-upcrossing method is, in general, longer than that defined by the trough-to-trough method. The reason is, as mentioned already, that the zero-upcrossing method cannot define small period waves which do not cross the mean water level, on the other hand, the trough-to-trough method is apt to define or pick up noise-like short period waves.

Following comparisons between calculations and experiments, it seems that correspondence between estimated values and experiments for the zero-upcrossing method-defined wave is better than that for the trough-to-trough

method-defined wave .

In calculating Eq. (5), the scale and shape factors of  $n$  and  $m$  were determined, by a least square method, to fit best the incident experimental wave.  $\alpha$  and  $\beta$  were also decided by the least square method in order for the estimated value of Eq. (5) to agree with experimental distributions.

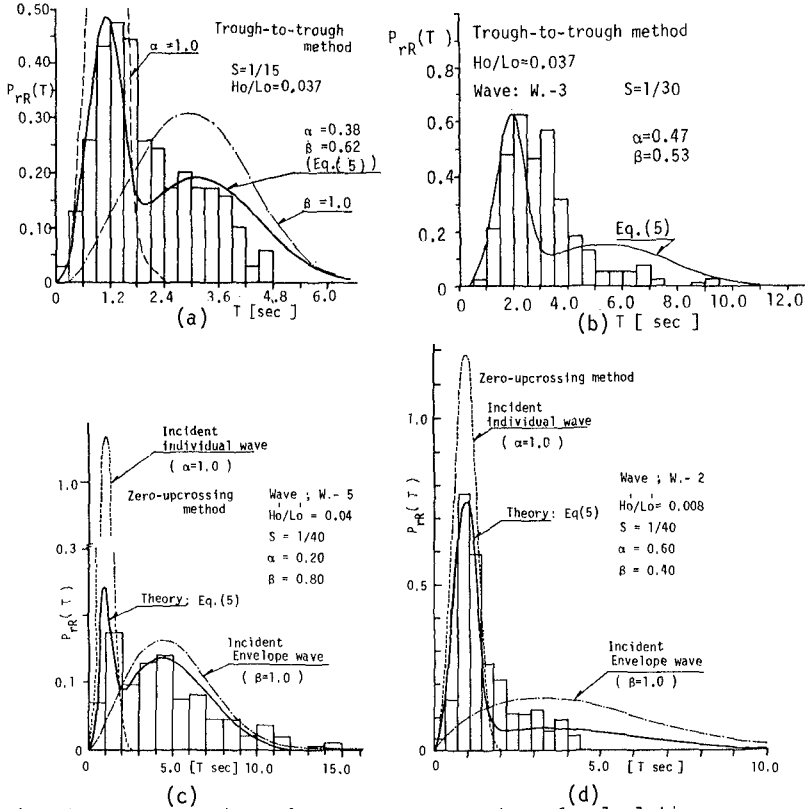


Fig.15 Some comparisons between measurements and calculations ( probability distribution of run-up wave period )

The values of  $\beta$  thus determined are shown in Fig.16, where  $H_o/L_o$  is the incident significant wave steepness (for an individual wave) in deep water depth and  $S$  is the beach slope. The value of  $\beta$  which implies a degree of nonlinear interaction increases with increasing of  $H_o/L_o$  and decreasing of  $S$ . That is, the gentler the beach slope and the steeper the wave steepness become, the more long period components are generated. Due to the shortage of experimental values, we cannot propose an empirical expression for  $\beta$  in relation to  $H_o/L_o$  and  $S$ . Further elaborate experiments are needed to set up an experimental formular for  $\beta$ , which will be done in the near future by the present authors.

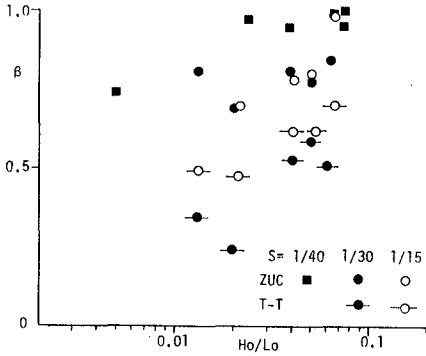


Fig.16 Variation of  $\beta$  with  $H_o/L_o$  and  $S$  ( T-T;Trough-to-trough method, ZUC;Zero-upcrossing method )

(3) Distribution of run-up heights

The distribution of run-up heights is, like that of run-up wave period, assumed to be given by a combined distribution of the incident individual wave-induced run-up height distribution and the incident envelope wave-induced run-up height distribution.

The probability density function  $P_{rR}( R )$  of run-up height distribution is then given by Eq. (8a) and Eq. (8b).

$$P_{rR}( R ) = \alpha P_{rI}( R ) + \beta P_{rE}( R ) \tag{ 8a }$$

( for trough-to-trough method )

$$P_{rR}( R ) = \alpha \frac{P_{rI}( R )}{\int_{R_0}^{\infty} P_{rI}(R) dR} + \beta \frac{P_{rE}( R )}{\int_{R_0}^{\infty} P_{rE}(R) dR} \tag{ 8b }$$

( for zero-upcrossing method )

where,  $\alpha$  and  $\beta$  are weight coefficients determined by Eq. (5), and  $R_0$  is the vertical distance of the mean water level from the stillwater level.

$P_{rI}( R )$  is the probability density function of run-up heights induced by the incident individual waves, and Eq. (9) proposed by the authors<sup>13)</sup> is used for  $P_{rI}( R )$ .

$$P_{rI}( R ) = K_1( R ) \int_0^{\infty} K_2( R ) dt \tag{ 9 }$$

$$K_1( R ) = [2P(S) h^{Q(S)} (g/2\pi)^{1/2-Q(S)} ] [ \frac{m_{I2}}{n_{I2}} \frac{m_{I1}}{n_{I1}} R^{2m_{I2}-1} ]$$

$$\left. \begin{aligned} P(S) &= 4.56 \times 10^{-2} \times S^{-0.133} \\ Q(S) &= 5.85 \times 10^{-3} \times S^{-1.246} \quad (\text{for } 1/10 \leq S \leq 1/40) \\ a(S) &= 2(1/2 - Q(S)) \end{aligned} \right\}$$

In Eq. (9), subsuffixes 1 and 2 indicate quantities regarding the incident wave period and height, respectively.

$P_{rE}(R)$  is the probability density function of run-up heights produced by the incident envelope wave. Eq. (4) is adopted here as  $P_{rE}(R)$ , for the 1st approximation. In case of  $S=1/40$ ,  $P_{rE}(R)$  is expressed by Eq. (10).

$$\left. \begin{aligned} P_{rE}(R) &= K_3(R) \int_0^\infty K_4(t) dt \\ K_3(R) &= \frac{b(S)}{1-C(S)} \frac{m_{E1}}{n_{E1}} \frac{m_{E2}}{n_{E2}} R^d(S) \\ d(S) &= (m_{E2} + 2C(S) - 1) / (1 - C(S)) \\ K_4(t) &= t e^{e(S)} \exp\left[-\frac{1}{n_{E1}} t^{m_{E1}} - \frac{1}{n_{E2}} R^j(S) t^{-2j(S)C(S)}\right] \\ b(S) &= 0.137, C(S) = 0.100, e(S) = m_{E1}^{-1} - [2C(S)m_{E2}/(1-C(S))] \\ j(S) &= m_{E2}/(1-C(S)) \end{aligned} \right\} (10)$$

In cases of  $S=1/15$  and  $S=1/30$ , we can deduce similar but a little different expressions, which are not presented in this paper because of limited pages.

By the way, using the same definition as in deriving Eq. (7), the mean of the largest  $1/k$  run-up height  $R_{1/k}$  is expressed by

$$\bar{R}_{1/k} = \frac{\alpha \int_{R_{1/k}}^\infty R P_{rI}(R) dR + \beta \int_{R_{1/k}}^\infty R P_{rE}(R) dR}{\alpha \int_{R_{1/k}}^\infty P_{rI}(R) dR + \beta \int_{R_{1/k}}^\infty P_{rE}(R) dR} \quad (11a)$$

( for trough-to-trough method )

$$\bar{R}'_{1/k} = \frac{\alpha \int_{R_{1/k}}^\infty R P_{rI}(R) dR + \beta' \int_{R_{1/k}}^\infty R P_{rE}(R) dR}{\alpha \int_{R_{1/k}}^\infty P_{rI}(R) dR + \beta' \int_{R_{1/k}}^\infty P_{rE}(R) dR} \quad (11b)$$

$$\alpha' = \alpha \int_{R_0}^\infty P_{rI}(R) dR, \quad \beta' = \beta \int_{R_0}^\infty P_{rE}(R) dR$$

( for zero-upcrossing method )

Thus, as described above, the probability density function of run-up wave heights  $P_{rR}(R)$  can be calculated by putting Eq. (9) and Eq. (4) or Eq. (10) (in case of  $S=1/40$ ) into Eq. (8a) or Eq. (8b).

Fig.17 shows some comparisons between calculated values and experiments. Run-up waves in Fig.17 are all defined by the trough-to-trough method. The correspondence of the calculated values to the experimental values is, in general, good on the slopes of 1/15 and 1/30. In particular, quantitative agreement of calculations with experiments is recognized on the slope of 1/15 ( see Fig.17(a) and (b)). On the beach slope of 1/30, however, the discrepancy between calculated values and measurements is sometimes observed for steep waves such as W.-10 ( see Fig.17(d)) and W.-11 listed in Tabel 1. This may be partly caused by the reason that Eq. (4) is not the best formula for estimating the envelope wave-induced run-up heights.

In calculating Eq. (8a),  $m_{I1}$ ,  $m_{I2}$ ,  $m_{E1}$ ,  $m_{E2}$ ,  $n_{I1}$ ,  $n_{I2}$ ,  $n_{E1}$  and  $n_{E2}$  were all determined by the least square method with use of incident wave statistics measured in our experiments.

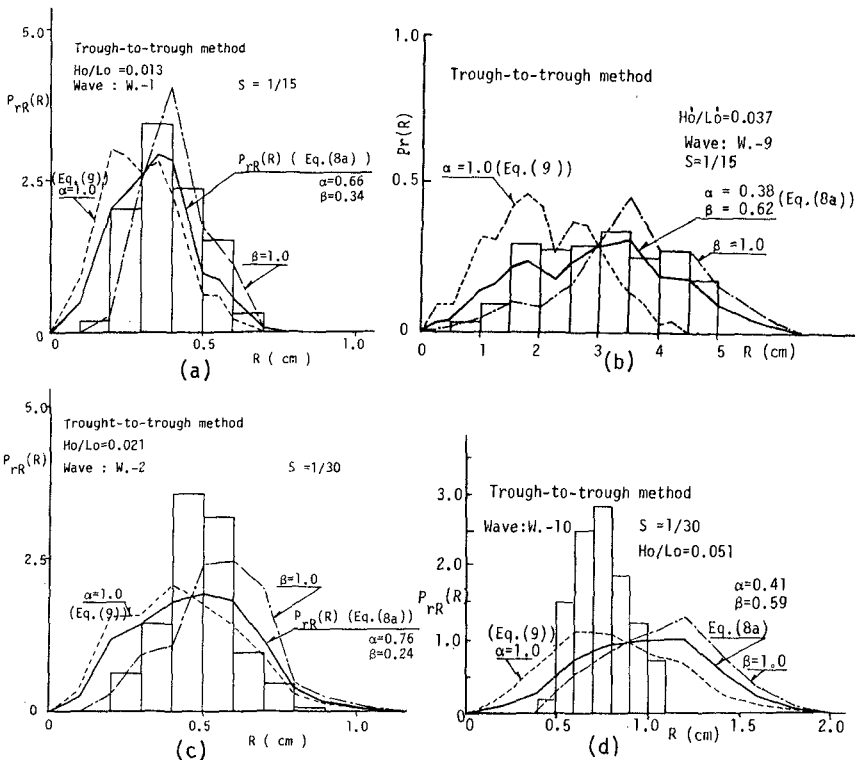


Fig.17 Comparisons between calculations and experimental values ( Trough-to-trough method )

Fig.18 shows some comparisons between measurements and calculations. In Fig.18, waves are defined by the zero-upcrossing method. The agreement of calculated values with experimental values is also good, like the case for waves defined by the trough-to-trough method. However, in some cases on the slope of 1/15; the calculated values of W.-10 and W.-11 do not correspond well to the experiments. The reason may be the same as that described for waves defined by the trough-to-trough method.

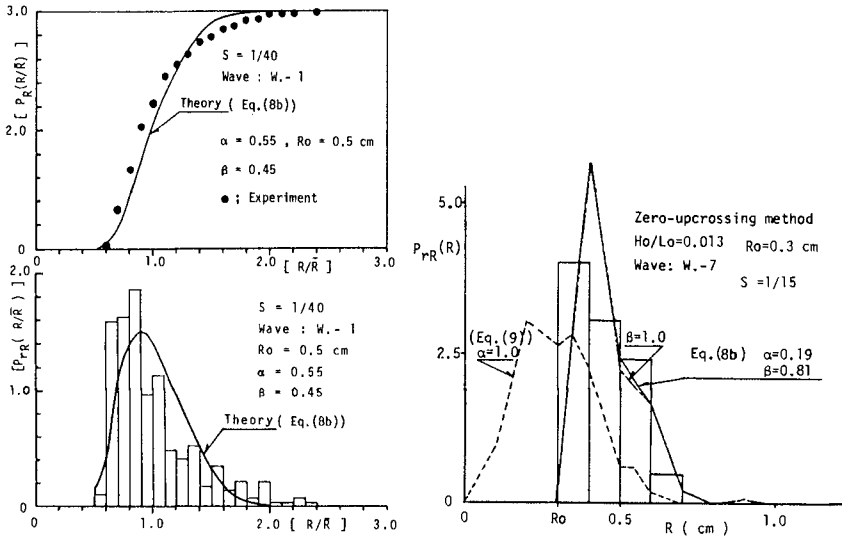


Fig.18 Comparison between measurements and calculations  
( Zero-upcrossing method )

In the calculations,  $m_{T1}$ ,  $m_{T2}$ ,  $m_{E1}$ ,  $m_{E2}$ ,  $n_{T1}$ ,  $n_{T2}$ ,  $n_{E1}$ , and  $n_{E2}$  were all the same values as those for waves defined by the trough-to-trough method.  $R_0$  was decided as the mean value over 8 minutes.

(4) Extreme distribution of run-up height and period

The estimation of the maximum values of run-up height  $R_{max}$  and period  $T_{max}$  is usefull for engineering purposes.

The maximum run-up wave period  $T_{max}$  is defined by

$$N ( 1 - P_r ( T < T_{max} ) ) = 1 \tag{12}$$

In Eq.(12),  $N$  is the number of wave ,  $P_r ( T < T_{max} )$  is the cumulative probability that  $T$  does not exceed  $T_{max}$ .

From Eq. (5) and Eq. (12),  $T_{max}$  can be determined by solving the following equation,

$$\alpha \exp\left(-\frac{1}{n_{I1}} \frac{m_{I1}}{T_{max}}\right) + \beta \exp\left(-\frac{1}{n_{E1}} \frac{m_{E1}}{T_{max}}\right) = \frac{1}{N} \quad (13)$$

The same argument is applied to the maximum run-up height  $R_{max}$ . The maximum run-up height  $R_{max}$  is obtained by solving the following equations.

$$\alpha \int_{R_{max}}^{\infty} P_{rI}(R) dR + \beta \int_{R_{max}}^{\infty} P_{rE}(R) dR = 1/N \quad (14a)$$

( for trough-to-trough method )

$$\alpha \int_{R_{max}}^{\infty} P_{rI}(R) dR + \beta \int_{R_{max}}^{\infty} P_{rE}(R) dR = 1/N \quad (14b)$$

( for zero-upcrossing method )

One example of calculations is given in Fig.19. As indicated in Fig.19, the correspondence of the calculation using Eqs.(5)-(14) to the experiment is not bad.

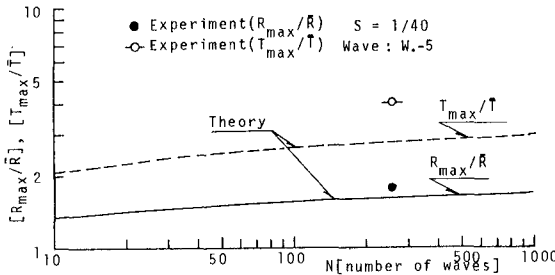


Fig.19 Nondimensional maximum run-up height and period ( Zero-upcrossing method )

5. CONCLUDING REMARKS

In this paper, the distributions of the run-up height and period of irregular waves on gentle slopes of 1/15, 1/30 and 1/40 are mainly discussed from engineering viewpoint. The theoretical distributions of run-

up heights and periods which consider long period components generated by nonlinear wave-wave interactions in the surf and swash zones are proposed.

The theoretically estimated values are seen to agree with experiments. The proposed model is, however, largely based on the assumption that the long period components can be represented by the incoming envelope wave periods. It should be stressed that the energetic investigations on mechanics of long period wave generation by wave-wave interactions in relation to the incident wave characteristics are needed to develop more elaborate theoretical distributions for the run-up oscillation.

## REFERENCES

- 1) Waddell, E., : Field measurements of characteristics of run-up waves on natural beach, Proc. 20th Japanese Conf. on Coastal Eng., JSCE, 1973, pp. 545-551 ( in Japanese ).
- 2) Sonu, C.J., Pettigrew, N. and R.G. Fredricks : Measurement of swash profile and orbital motion of the beach, Proc. Inter. Sympo., Louisiana, USA, 1974, pp. 621- 638.
- 3) Huntley, D.A., Guza, R.T. and A.J. Bowen : A universal form for shoreline run-up spectra ? , Jour. Geophysical Res., Vol. 82, No. 18, 1977, pp. 2577 - 2581.
- 4) Guza, R.T. : Swash oscillations on natural beach, Jour. Geophysical Res., Vol. 87, 1982, pp. 483 - 490.
- 5) Webber, N.B. and G.N. Bullock : A model study of the distribution of run-up of wind-generated waves on sloping sea wall, Proc. 11th ICCE, 1968, pp. 870 - 887.
- 6) Sutherland, A.J., Sharma, J.N., and O.M. Shemdin : Wave run-up on a simulated beach, Proc. 15th ICCE, ASCE, 1976, pp. 752 - 765.
- 7) Sharma, J.N. : Nonlinear modeling of wave runup on sloping beach, Proc. ASCE, WW2, 1979, pp. 125 - 129.
- 8) Iwata, K., Sawaragi, T. and W. Nobuta : Irregular wave run-up heights and periods on gentle slopes, Proc. 28th Japanese Conf. on Coastal Eng., JSCE, 1981, pp. 330 - 334 ( in Japanese ).
- 9) Sawaragi, T., Iwata, K. and W. Nobuta : Run-up height and period of irregular waves on gentle slopes, Coastal Engineering in Japan, Vol. 26, 1983, pp. 163 - 174.
- 10) Saville, T.J. : An approximation of the run-up frequency distribution, Proc. 8th ICCE , 1963, pp. 48 - 59.
- 11) Shuto, N. : Relation between significant wave and run-up height, Rept.,



Public Works Res.,Inst., No.126, 1965.

12) Battjes,J.A. : Run-up distributions of waves breaking on slopes, Proc. ASCE, Vol.97, WW1, 1971,pp. 91 - 113 .

13) Sawaragi,T.,Iwata,K. and A.Morino : Wave run-up height on gentle slopes, Coastal Engineering in Japan, Vol.20,1977,pp. 83 - 94 .

14) Hunt,I.A.J. : Design of seawalls and breakwaters,Proc. ASCE, Vol.85, WW3, 1959, pp.123 - 152 .

## CHAPTER THIRTY

### A Dynamical Expression of Waves in Shallow Water

Y. Tsuchiya<sup>1</sup>, M. ASCE and T. Yasuda<sup>2</sup>

Making the assumptions that solitons are one of the most elementary excitation in random nonlinear waves in shallow water and that the waves have a coherent dynamic structure of solitons, we attempt to describe the swell-like waves theoretically by deriving the asymptotic multi-soliton solution for the KdV equation. Formulations of the random wave profiles and internal properties are also made. We conclude from the comparisons between observed and theoretical results of the propagation characteristics of the swell-like random waves and their water particle velocities, that the waves in shallow water have a coherent dynamic structure of solitons and that the theoretical expression for the waves has practically sufficient accuracy in estimating their propagation.

#### 1. INTRODUCTION

One of the outstanding features of swell-like waves propagating on shallow water is the coupling between their nonlinearity and randomness. How to express them theoretically is clearly of basic importance for coastal engineering because of the need to accurately calculate forces on coastal structures and to rationally estimate design waves and so on. Various attempts have been made to formulate them theoretically, for example, by using the nonlinear spectral analysis based on a perturbative approach from a linear mode, which was developed by Tick(1959), Phillips (1961) and Hasselmann(1962). However, the application of the nonlinear spectral analysis requires much labor because the nonlinear effects of the waves are remarkably stronger than those of ocean waves. As the result, the design of coastal structures is generally carried out by using the individual wave method which is a mere statistic approach and has no basis of the dynamics.

The coupling between nonlinearity and randomness of the waves makes their dynamics seriously difficult, because it provides active exchanges of energy among different modes and brings the above perturbative approach to the chaotic situation. From the new viewpoint of the dynamics of nonlinear waves, therefore, another approach may be needed in establishing the dynamics of the waves, instead of the usual perturbative approach mentioned above.

In this study, we attempt to propose a dynamical expression of the swell-like waves based on soliton modes, including simultaneously both effects of their nonlinearity and randomness. Further, applicability of the expression to field waves is examined by comparing it with observed data of wave propagation in the field.

---

1 Professor, Disaster Prevention Research Institute, Kyoto University, Uji 611, Kyoto, JAPAN

2 Associate Professor, Department of Civil Engineering, Gifu University, Gifu 501-11, Gifu, JAPAN

2. WAVE EQUATION OF SWELL-LIKE WAVES IN SHALLOW WATER

Consider swell-like waves in shallow water of uniform depth and define the two-dimensional coordinate system as shown in Fig. 1. By assuming that viscosity is ignorable in the swell-like waves, we derive the equations governing them as

$$\left. \begin{aligned} \nabla^2 \Phi &= 0 \\ \Phi_t + (\Phi_x^2 + \Phi_z^2) / 2 + gz' |_{z=h+z'} &= 0 \\ \eta_t + \Phi_x \eta_x - \Phi_z |_{z=h+z'} &= 0 \\ \Phi_z |_{z=0} &= 0 \end{aligned} \right\} (1)$$

where  $\phi$  is the velocity potential,  $z'$  the water surface displacement from the mean water level,  $x$  and  $z$  the coordinate system,  $t$  the time,  $h$  the water depth, and  $g$  the acceleration of gravity.

Furthermore, assuming that the effects of nonlinearity and frequency dispersion of waves are of the same order and considering progressive waves of temporal evolution, we introduce the so-called Gardner-Morikawa transform

$$\xi = \epsilon^{1/2} (x^* - t^*), \quad \tau = \epsilon^{3/2} t^*, \quad x^* = x/h, \quad t^* = t\sqrt{g/h}, \quad z^* = z/h, \quad \epsilon = (h/L)^2 \quad (2)$$

and the perturbed solution

$$\left. \begin{aligned} z' / h (= \epsilon \eta) &= \epsilon \eta_1 + \epsilon^2 \eta_2 + \dots \\ \Phi / h \sqrt{gh} &= \epsilon^{1/2} \Phi_1 + \epsilon^{3/2} \Phi_2 + \dots \end{aligned} \right\} (3)$$

where  $L$  is the representative wave-length.

By substitution of Eqs. (2) and (3) into Eq.(1), we can rewrite Eq. (1) as

$$\eta_\tau + 3 \eta \eta_\xi / 2 + \eta \xi \xi \xi / 6 = \epsilon F(\eta, \eta_\xi, \Omega_\tau, \dots) + O(\epsilon^2) \quad (4)$$

$$\Omega_\xi - \eta = \epsilon (\eta \xi \xi / 2 + \eta^2 / 2) + O(\epsilon^2) \quad (5)$$

The relation between the new velocity potential  $\Omega$  and the original one  $\phi$  is given as

$$\Phi / h \sqrt{gh} = \epsilon^{1/2} (\Omega - \epsilon z^{*2} \Omega_\xi \xi / 2 + \dots) \quad (6)$$

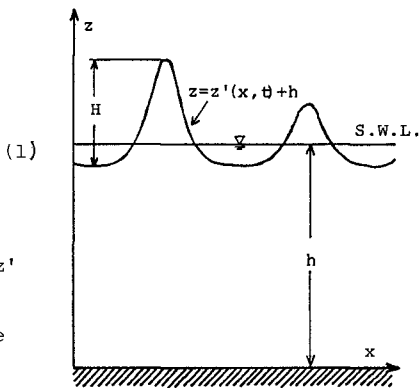


Fig. 1 Coordinate system and symbols used

Taking  $\epsilon = 0$  in Eq.(4), we obtain the well-known Korteweg de Vries(KdV) equation as the lowest order equation of the swell-like waves as

$$\eta_\tau + 3\eta\eta_\xi/2 + \eta\xi\xi\xi/6 = 0 \quad (7)$$

Fig. 2 which was calculated by the authors(1982) indicates the comparison of wave transformation in evolution process between the numerical solutions of Eqs.(4) and (7) and the experimental results obtained by giving sinusoidal waves a initial condition of waves. From this figure, it can be considered that the second order correction when compared with that of the first order is relatively small for the wave transformation and that the soliton development can sufficiently be explained by the KdV equation. Hence, from the viewpoint that the swell-like waves should be described as simple as possible, we may use the KdV equation as the governing equation.

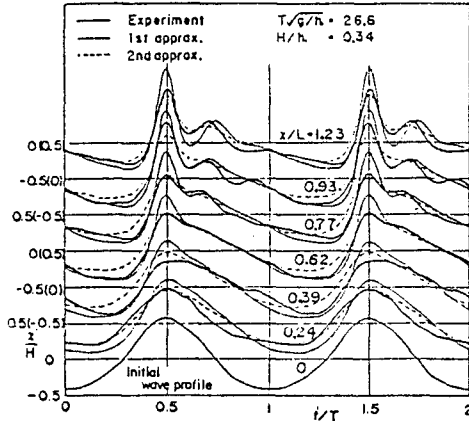


Fig. 2 Comparison between numerical and experimental wave profiles

### 3. WAVE SOLUTION OF THE KDV EQUATION BASED ON SOLITON MODES

#### 3.1 Elementary Excitation in the Wave Field Governed by the KdV Equation

We can derive the solution of the KdV equation perturbed from a sinusoidal wave solution by using Stokes expansion as

$$\left. \begin{aligned} \eta &= A \cos \theta + (3A^2/4\gamma) \cos 2\theta + (27A^3/64\gamma^2) \cos 3\theta + \dots, \\ \gamma &= (2\pi h/L)^2, \quad \theta = 2\pi x/L - \omega t \end{aligned} \right\} \quad (8)$$

where A is the Ursell number and  $\omega$  the angular frequency. The above expression describes that a sinusoidal wave becomes an elementary excitation of the wave field to be governed by the KdV equation. It is, however, noticed that the reduction of higher order terms requires much labor and that the number of sinusoidal modes is undetermined. We may conclude that sinusoidal waves are inadequate as elementary excitation in the wave field to be governed by the KdV equation.

The exact stationary solution of the KdV equation is known as cnoidal waves which is given as

$$\eta = A \left[ \text{cn}^2 \left\{ (\sqrt{3A}/2k) \vartheta \right\} - (E/K + k^2 - 1)/k^2 \right] \quad (9)$$

where  $\vartheta = (x/h - ct/h)$ , c is the wave-celerity, K and E the complete elliptic integrals of the first and the second kind, respectively, of

which the modulus is denoted by  $k$  and  $cn$  the Jacobian  $cn$ -function. Eq. (9) describes the stationary waves which is simpler than Eq.(8), although it contains an elliptic function.

It is well-known that Eq.(9) expresses a solitary wave(soliton), when the wave-period of cnoidal waves is taken infinite, as

$$\eta = A \operatorname{sech}^2 \left\{ (\sqrt{3A}/2) \vartheta \right\} \quad (10)$$

This means that the cnoidal waves contain solitons as their limiting and are rather elementary than solitons. However, using the relation between Jacobian  $dn$ -elliptic and hyperbolic functions obtained by Toda(1970)

$$\operatorname{dn}^2 \chi = (\pi/2K')^2 \sum_{l=-\infty}^{\infty} \operatorname{sech}^2 \left\{ (\pi K/K') (\chi/2K - l) \right\} - k/2KK' + E/K \quad (11)$$

we can transform Eq.(9) into

$$\eta = \sum_{l=-\infty}^{\infty} a \operatorname{sech}^2 \left\{ (\sqrt{3a}/2) \vartheta - l \pi K/K' \right\} - (4aK'^2/3\pi^2) \left\{ 3(E/K) + 2k^2 - 2 \right\} \quad (12)$$

where

$$\left. \begin{aligned} \vartheta &= \varepsilon^{-1/2} (\xi - c^* \tau) = (x/h - ct/h), \quad c = 1 - (2aK'^2/\pi^2) \left\{ 3(E/K) + k^2 - 2 \right\}, \\ a &= A(\pi/2kK')^2, \quad \varepsilon = (h/L)^2 \end{aligned} \right\} \quad (13)$$

Eq.(12) shows that a cnoidal wave train with the amplitude  $A$  consists of a periodic sequence of pulse-like waves, that is, solitons with the amplitude  $a$ , and that the cnoidal wave train can be expressed by making solitons its elementary excitation. As the modulus  $k$  becomes large, the number of solitons expressing a single wave crest of the cnoidal wave decreases. When the value exceeds about 0.98,  $a$  is approximated by  $A$  so that the influence of the adjacent waves become negligible and the cnoidal waves can be expressed as the regular train of solitons with the same amplitude. This means that periodic wave motion can be expressed by using a particle-like waves such as solitons, and that solitons are superior to cnoidal waves as elementary excitation in the wave field governed by the KdV equation. We, therefore, may describe theoretically nonlinear random waves in shallow water by making solitons elementary excitation.

### 3.2 Expression of the Swell-Like Waves Based on Soliton Modes

It is possible to express approximately the swell-like waves by the perturbed approach from sinusoidal modes as made by Freilich and Guza (1984). However, the calculation becomes very complicated, so that the approach is not applicable to explain nonlinear random waves completely. Some attempts[Nakamura and Matsuno(1980) and Hirota and Ito(1981)] were carried out of the theoretical expression of nonlinear random waves by making cnoidal waves elementary excitation, but they merely succeed in the case of two-periodic waves in shallow water. Consequently, the approach making solitons elementary excitation may give the sole and possible expression of nonlinear random waves in shallow water. Hence, considering that the swell-like waves in shallow water are the typical nonlinear random waves, we assume that the swell-like waves have a coherent

dynamic structure making solitons elementary excitations, that is, the soliton structure, as far as concerned with the dominant portions of them. In order to describe theoretically the swell-like waves under the above assumption and the condition of nondegeneration, we derive the exact multi-soliton solution of the KdV equation satisfying the continuity condition for wave profiles around the mean water level(1984) as

$$\eta = (4/3) (\log F)_{\xi\xi} - \eta_0 \tag{14}$$

where

$$F = \lim_{N \rightarrow \infty} \det \left| \delta_{ij} + \frac{2B_i}{B_i + B_j} f_i \right|, \quad 1 \leq i, j \leq N \tag{15}$$

$$\left. \begin{aligned} f_i &= \exp \{ B_i (\xi - c_i \tau - \tilde{\delta}_i) \}, \quad B_i = \sqrt{3A_i} \\ c_i &= A_i/2 - 3\eta_0/2 \end{aligned} \right\} \tag{16}$$

in which both of  $A_i$  and  $\tilde{\delta}_i$  are integral constants,  $A_i$  denotes the amplitude of a soliton expressing its energy level,  $\tilde{\delta}_i$  the phase constant determining the position of the soliton with the amplitude  $A_i$ ,  $c_i$  the wave-celerity of the soliton, and  $\delta_{ij}$  Kronecker's  $\delta$ . And,  $\eta_0$  is a statistical quantity defined as an ensemble mean of solitons satisfying the continuity condition and given as

$$\eta_0 = \lim_{\zeta \rightarrow \infty} (2/3\zeta) (\log F)_{\xi} \Big|_{-\zeta}^{\zeta} \tag{17}$$

under the assumption that disturbances exist at infinity and the period of observation( $\xi: -\zeta - \zeta$ ) is sufficiently long to describe the wave phenomena.

In analyzing the swell-like waves with the soliton structure, we may assume the following relation for spacings between the crests of solitons, which states that interactions of solitons are negligibly small.

$$|\xi_i - \xi_j| > \beta, \quad e^{-\beta} \ll 1, \quad -\infty < \dots < \xi_i < \xi_j < \dots < +\infty \tag{18}$$

where  $\xi_i$  is the coordinate of the crest position of the soliton with the amplitude  $A_i$  at  $\tau = \tau_0$ . Under the above assumption, Eq.(15) can asymptotically be rewritten as

$$F = \prod_{i=1}^{\infty} \{ 1 + f_i \exp(-B_i \Delta_i) \} \tag{19}$$

where

$$\Delta_i = -(1/B_i) \log \left\{ \prod_{j=1}^{i-1} (B_i - B_j)^2 / (B_i + B_j)^2 \right\} \tag{20}$$

Substituting Eq.(19) into Eq.(14), we can obtain the asymptotic expression of the swell-like waves based on soliton modes as

$$\eta = \sum_{i=1}^{\infty} A_i \operatorname{sech}^2 \vartheta_i - \eta_0, \quad \vartheta_i = (\sqrt{3A_i}/2) (\xi - c_i \tau - \delta_i), \quad \delta_i = \tilde{\delta}_i + \Delta_i \tag{21}$$

This expression asymptotically agrees with the exact solution of the KdV equation even when the value of  $\tau$  is finite not but  $\tau \rightarrow \infty$ , only if the

relation of Eq.(18) is satisfied. It is emphasized that this expression admits arbitrary degeneration of the amplitudes of solitons and is independent of evolution type. Moreover, we can easily determine the integral constants  $A_i$  and  $\delta_i$  from the observed data of swell-like waves by using the asymptotic solution, although it is very difficult to determine them and transform the exact solution with unknown constants into the particular solution expressing actually the swell-like waves as far as the exact solution is used.

Taking into account these facts in addition to that the usual swell-like waves can be expressed by the asymptotic multi-soliton solution as the authors recently pointed out(1984), any wave motion to be governed by the KdV equation may asymptotically be expressed as a train of solitons with various amplitudes under the assumption of Eq.(18). Macro-scopic properties of the waves then may uniquely be described by using the ensembles of  $A_i$  and  $\delta_i$ .

3.3 A Complete Orthonormal System

If the right-hand side of Eq.(21) is transformed into a linear combination of orthonormal system,  $\{\phi_i\}$ , by using Schmidt's method, it becomes a complete orthonormal system because Eq.(21) is a solution of the swell-like waves having a soliton structure. Eq.(21) is then rewritten by the linear combination of complete orthonormal systems

$$\eta = \lim_{N \rightarrow \infty} \sum_{i=1}^N A_i \psi_i(\vartheta_i) - \eta_0 = \lim_{N \rightarrow \infty} \sum_{i=1}^N A_i \sum_{l=1}^i c_{il} \phi_l(\vartheta_i) - \eta_0 \tag{22}$$

where

$$\psi_i = \text{sech}^2 \vartheta_i$$

$$\phi_i = \psi_i / \|\psi_i\|,$$

$$\phi_l = |F| \cdot G(\psi_1, \dots, \psi_{l-1})^{-1/2} \cdot G(\psi_1, \dots, \psi_l)^{-1/2}, \quad (l \geq 2)$$

$$|F| = \begin{bmatrix} (\psi_1, \psi_1) & & (\psi_1, \psi_l) \\ \vdots & & \vdots \\ (\psi_{l-1}, \psi_1) & \dots & (\psi_{l-1}, \psi_l) \\ \psi_1 & \dots & \dots & \psi_l \end{bmatrix}$$

$$G(\psi_1, \dots, \psi_l) = \begin{vmatrix} (\psi_1, \psi_1) & \dots & (\psi_1, \psi_l) \\ \vdots & & \vdots \\ (\psi_l, \psi_1) & \dots & (\psi_l, \psi_l) \end{vmatrix}$$

$$c_{il} = D_{li} (d_{11} \cdot d_{22} \dots d_{ll})$$

(23)

in which  $(\psi_i, \psi_j)$  is the dot product defined by

$$(\psi_i, \psi_j) = \int_0^\infty \psi_i \psi_j d\xi \tag{24}$$

and  $D_{1j}$  a cofactor of  $d_{1i}$  element of the matrix [D] defined by

$$[D] = \begin{bmatrix} d_{11} & 0 \\ \vdots & \ddots \\ d_{N1} & \dots & d_{NN} \end{bmatrix} \quad (25)$$

where

$$\left. \begin{aligned} d_{li} &= \left| \sum_{j=1}^{l-1} d_{ji}(\psi_l, \phi_j) / \left| \psi_l - \sum_{j=1}^{l-1} \phi_j(\psi_l, \phi_j) \right| \right|, \quad (l > i \geq 1) \\ d_{li} &= 1 / \left| \psi_l - \sum_{j=1}^{l-1} \phi_j(\psi_l, \phi_l) \right| \end{aligned} \right\} \quad (26)$$

4. EXPRESSION OF THE INTERNAL PROPERTIES OF SWELL-LIKE WAVES BASED ON SOLITON MODES

4.1 Reduction of the Velocity Potential

Not only the number of solitons but both of the amplitude  $A_i$  and the integral constant  $\eta_0$  are invariant, so that the wave-celerity  $c_i$  also become invariant and each soliton propagates with a constant speed. We then introduce the following transform of variables into each soliton.

$$\sigma_i = \xi - c_i \tau \quad (27)$$

Assuming that both  $\eta_i$  expressing the wave profile of the soliton with the amplitude  $A_i$  and  $\Omega_i$  being the velocity potential are functions of  $\sigma_i$ , we obtain the relations

$$\left. \begin{aligned} \partial \eta_i / \partial \tau &= -c_i \partial \eta_i / \partial \sigma_i, \quad \partial \eta_i / \partial \xi = \partial \eta_i / \partial \sigma_i \\ \partial \Omega_i / \partial \tau &= -c_i \partial \Omega_i / \partial \sigma_i, \quad \partial \Omega_i / \partial \xi = \partial \Omega_i / \partial \sigma_i \end{aligned} \right\} \quad (28)$$

Substituting Eqs.(27) and (28) into the relation between  $\Omega$  and  $\eta$  derived from Eqs.(5) and (6),

$$(\partial \Phi / \partial x) / \sqrt{gh} = \varepsilon \eta + \varepsilon^2 \{ \eta^2 / 2 + (1/2)(1 - \alpha^{*2}) \partial^2 \eta / \partial \xi^2 + \partial \Omega / \partial \tau \} + \dots \quad (29)$$

which may be transformed to

$$\begin{aligned} (\partial \Phi / \partial x) / \sqrt{gh} &= \sum_i \eta_i - \eta_0 + \left( \sum_i \eta_i - \eta_0 \right)^2 / 2 + (1 - \alpha^{*2}) / 2 \sum_i \partial^2 \eta_i / \partial \sigma_i^2 \\ &\quad - \sum_i c_i (\eta_i - \eta_0) + \dots \end{aligned} \quad (30)$$

It is found that the water particle velocities of the waves having the soliton structure have the particle-like property to be governed directly by the amplitude of each soliton and the periodic property dependent on the ensemble of solitons through the continuity condition for wave profiles.



#### 4.2 Expression of the Water Particle Velocities

Substituting Eq.(21) into Eq.(30) and evaluating the velocity potential of the waves to the second-order approximation, the horizontal and vertical velocities in the Eulerian coordinates  $u$  and  $w$  are obtained respectively as

$$\begin{aligned} \frac{u}{\sqrt{gh}} = & \sum_i A_i \operatorname{sech}^2 \vartheta_i - \eta_0 + \sum_i A_i \operatorname{sech}^2 \vartheta_i \left[ \frac{\eta_0}{2} + \frac{A_i}{2} \left\{ 2 - 3 \left( \frac{z}{h} \right)^2 \right\} - \frac{9}{4} A_i \left\{ 1 - \left( \frac{z}{h} \right)^2 \right\} \operatorname{sech}^2 \vartheta_i \right] \\ & + \frac{1}{2} \left( \sum_i A_i \operatorname{sech}^2 \vartheta_i \right)^2 - \eta_0^2 + \frac{1}{2N} \eta_0 \sum_i A_i \end{aligned} \quad (31)$$

$$\begin{aligned} \frac{w}{\sqrt{gh}} = & \frac{1}{2} \left( \frac{z}{h} \right) \sum_i \sqrt{A_i^3} \operatorname{sech}^2 \vartheta_i \tanh \vartheta_i \left[ 2 + \left\{ \left( \frac{z}{h} \right)^2 - 1 \right\} A_i (3 \operatorname{sech}^2 \vartheta_i - 1) \right. \\ & \left. + 2 \sum_j A_j \operatorname{sech}^2 \vartheta_j + 2 \eta_0 - A_i \right] \end{aligned} \quad (32)$$

Further, those in the Lagrangian coordinates  $U$  and  $W$  are expressed as

$$\frac{U}{\sqrt{gh}} = \frac{u}{\sqrt{gh}} + 2 \sum_i \sum_j \frac{\sqrt{A_i A_j}}{c_i} \tanh \vartheta_i \Big|_0^\infty \tanh \vartheta_j \operatorname{sech}^2 \vartheta_j + \eta_0 t^* \sum_i \sqrt{3 A_i^3} \tanh \vartheta_i \operatorname{sech}^2 \vartheta_i \quad (33)$$

$$\begin{aligned} \frac{W}{\sqrt{gh}} = & \frac{w}{\sqrt{gh}} - \left( \frac{z}{h} \right) \left( \sum_i \sum_j \frac{A_j \sqrt{3 A_i}}{c_i} \tanh \vartheta_i \Big|_0^\infty \operatorname{sech}^2 \vartheta_i (3 \operatorname{sech}^2 \vartheta_j - 2) \right. \\ & \left. - \frac{3}{2} \eta_0 + \sum_j A_j^2 \operatorname{sech}^2 \vartheta_j (3 \operatorname{sech}^2 \vartheta_j - 2) - \sum_i \sum_j \frac{A_i \sqrt{3 A_j^3}}{c_i} \operatorname{sech}^2 \vartheta_i \operatorname{sech}^2 \vartheta_j \tanh \vartheta_j \right] \end{aligned} \quad (34)$$

#### 4.3 Expression of the Mass Transport Velocities

In this study, the expression of the velocity potential has been derived under the assumption of Eq.(28) as shown already, so that the water particle velocity is independent of the restriction caused by the so-called Stokes' definition of wave-celerity. The mass transport velocities can then be defined both in the Eulerian and Lagrangian coordinates. Denoting the observed period as  $T^*$ , the mass transport velocity in the Eulerian coordinate:  $\bar{u}$  is defined as

$$\frac{\bar{u}}{\sqrt{gh}} = \frac{1}{T^*} \int_0^{T^*} \frac{u}{\sqrt{gh}} dt^* \quad (35)$$

Rewriting Eq.(31) into the expression of  $N$  solitons which are included in observed data within the period of  $T^*$  and introducing this into Eq.(35), we obtain

$$\frac{\bar{u}}{\sqrt{gh}} = \frac{1}{2T^*} \int_0^{T^*} \left( \sum_i^N A_i \operatorname{sech}^2 \vartheta_i \right)^2 dt^* - \frac{1}{2} \eta_0^2 - \frac{1}{2T^*} \left\{ 1 - \left( \frac{z}{h} \right)^2 \right\} \sum_i^N \frac{\sqrt{3 A_i^3}}{c_i}$$

$$\begin{aligned} & \times \left\{ 2 \tanh \vartheta_i \Big|_0^{T^*} - \tanh \vartheta_i (\operatorname{sech}^2 \vartheta_i + 2) \Big|_0^{T^*} \right\} \\ & - \sum_i^N c_i \left\{ \frac{\eta_0}{N} + \sqrt{\frac{A_i}{3}} \frac{2 \tanh \vartheta_i}{c_i T^*} \Big|_0^{T^*} \right\} \end{aligned} \quad (36)$$

By the same means, the mass transport velocity  $\bar{U}$  in the Lagrangian coordinates is derived by the horizontal velocity for the observed period as

$$\begin{aligned} \frac{\bar{U}}{\sqrt{gh}} &= \frac{\bar{u}}{\sqrt{gh}} + \frac{2\eta_0}{T^*} \sum_i^N \frac{1}{c_i^2} \sqrt{\frac{A_i}{3}} \left\{ \frac{\sqrt{3}A_i}{2} c_i t^* \operatorname{sech}^2 \vartheta_i + \tanh \vartheta_i \right\} \Big|_0^{T^*} \\ & - \frac{2}{T^*} \sum_i^N \sum_j^N \frac{A_j}{c_i c_j} \sqrt{\frac{A_i}{3}} \tanh \vartheta_i \Big|_0 \operatorname{sech}^2 \vartheta_j \Big|_0^{T^*} + \frac{2}{T^*} \sum_i^N \sum_j^N \frac{\sqrt{A_i A_j}}{c_i} \\ & \times \int_0^{T^*} \tanh \vartheta_i \tanh \vartheta_j \operatorname{sech}^2 \vartheta_j dt^* \end{aligned} \quad (37)$$

5. APPLICATION TO FIELD WAVES

5.1 Soliton Analysis and Synthesis of Observed Data

For expressing theoretically observed waves on soliton modes, we must decompose them into a number of solitons to determine their amplitude  $A_i$  and phase constant  $\delta_i$ . Then, employing these values of  $A_i$  and  $\delta_i$  into Eq.(21) may yield a theoretical expression of the waves with a soliton structure.

Under the assumption that the right-hand side of Eq.(23) is a complete orthonormal system, moreover, the ensemble of the amplitude  $\{A\}$  by making the inner product between the theoretical wave profile  $\eta$  given by Eq.(23) and the observed wave profile  $Y$  can be calculated by

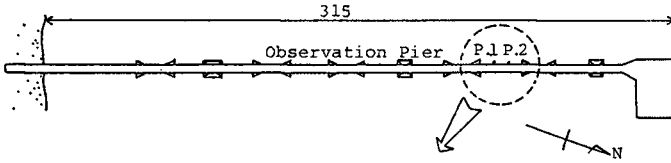
$$\begin{Bmatrix} A_1 \\ \vdots \\ A_N \end{Bmatrix} = \begin{bmatrix} d_{11} & \cdots & d_{N1} \\ \vdots & \ddots & \vdots \\ 0 & & d_{NN} \end{bmatrix} \begin{Bmatrix} (Y + \eta_0, \phi_1) \\ \vdots \\ (Y + \eta_0, \phi_N) \end{Bmatrix} \quad (38)$$

5.2 Accuracy of the Expression of the Swell-Like Waves

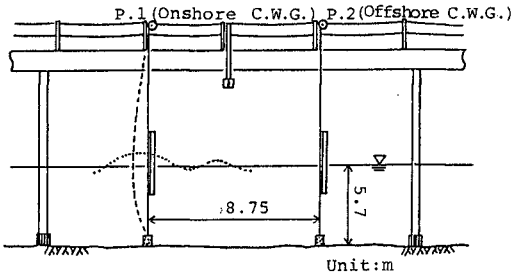
An observation of the swell-like waves was carried out on the 7th of March, 1981, by using the wave observation system, at the Ogata Wave Observatory, Disaster Prevention Research Institute, Kyoto University.

Fig. 3 describes the position of the wave gauges of capacitance type installed along the observation pier 315m long in the offshore direction. The water depths at which the wave gauges are installed are shown in the figure. Wind speed and direction during the observation were about 3m/s and S, respectively. Incident waves were long crested and approaching parallel with the pier as swell-like waves suffering from no influence of wave breaking.

A comparison of power spectra computed by the FFT method between the waves observed at P. 1 and P. 2 is shown in Fig. 4 with their values of skewness and kurtosis of the water surface displacement. And, the Ursell



(a) Plane view of observation pier



(b) Side view of observation pier and wave gauges installed

Fig. 3 Positions and number of installed wave gauges

number( $U_r$ ) at P. 1 calculated by the zero-up crossing method is 45.9. The power spectra exhibit pronounced secondary peaks at frequencies about twice the main peak frequencies due to nonlinear interaction among sinusoidal modes. It is considered from this figure that the waves are swell-like with fully developed nonlinearity. Low frequency components of the waves have considerable energy which is probably due to water surface displacements with long periods, such as surf-beat, independent of the soliton modes. Mechanism of their excitation is different from that of the waves. The approach based on soliton modes can therefore be applied to the observed data, if the low frequency components under 0.04Hz are excluded with a numerical low-cut filter of critical frequency of  $f_c = 0.04$ Hz.

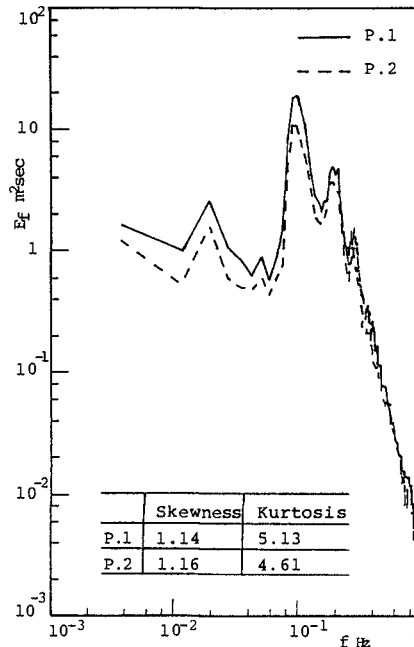


Fig. 4 Spatial variation of power spectra

Fig. 5 shows comparisons of wave profiles between the data observed at P. 1 and P. 2 mentioned above and the theoretical results obtained by the expression of Eq.(21). Clearly, Eq.(21) has sufficient accuracy in expressing the wave profiles under the swell-like sea condition.

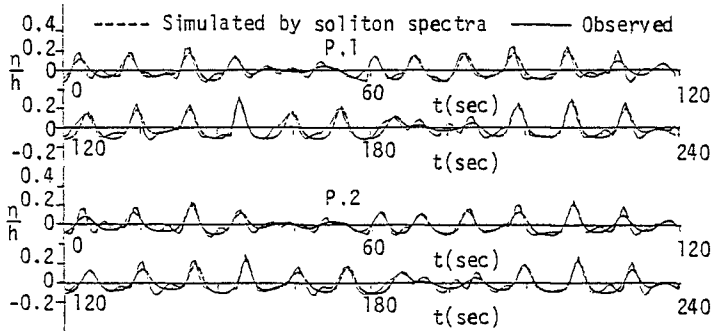


Fig. 5 Comparisons of wave profiles between the observed data and the theoretical results

One of the comparisons between the observed data and the theoretical profiles of the waves propagated from P. 1 to P. 2 is shown in Fig. 6. This figure states that this approach can express the propagation of the waves, as well as the wave profiles with satisfactory accuracy.

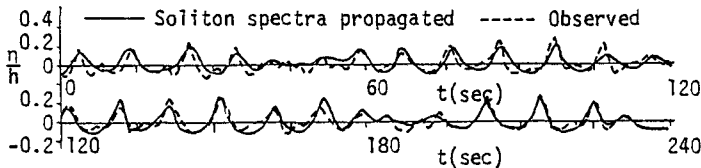


Fig. 6 Comparison of wave propagation between the observed and theoretical data

Figs. 7 and 8 show another comparison on swell-like waves with the Ursell number 22.4 at P. 1. The observed data in these figures were obtained by the same observation system under the similar sea condition and analyzed as well. The expression has sufficient accuracy, so that the dominant part of these waves have the soliton structure for which the formulation can be made by the soliton modes.

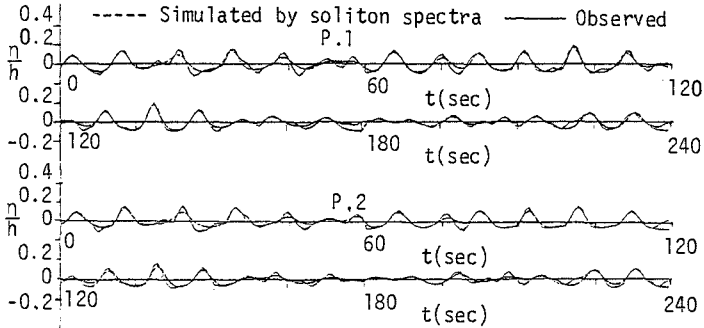


Fig. 7 Comparisons of wave profiles between the observed data and the theoretical results

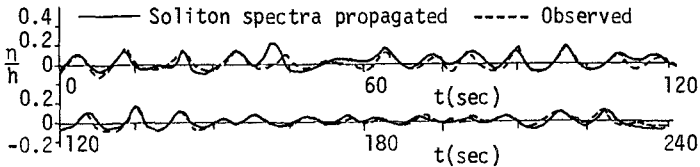


Fig. 8 Comparison of wave propagation between the observed and theoretical data

### 5.3 Extensive Application to Waves Under the Various Sea Conditions

Observations of waves were carried out by use of both the array consisting of nine capacitance-type wave gauges installed along the observation pier mentioned above and the line array of four ultra-sonic-type wave gauges installed at the offshore end of the pier to obtain directional spectra. Fig. 9 shows the positions of the wave gauges at which the water depths are also shown. Fig. 10 indicates the changes in wind speed and direction within a period of the observation and the relation between them together with the data numbers of which abbreviation is expressed by DNO.

Fig. 11 shows some comparisons of wave profiles at the points of U<sup>4</sup>, CW5, CW7 and CW9 between the observed data of DNOs 27, 31 and 34 and the theoretical results by soliton modes. The Ursell numbers at U<sup>4</sup> of DNOs 27, 31 and 34 are 4.7, 18.0 and 11.1, respectively. We may conclude that the expression by soliton modes has sufficient accuracy in expressing the wave profiles under various sea conditions, as far as their

dominant portions are concerned, although the influence of wave breaking is not negligible in these comparisons where about a few ten's percent or more of the waves are broken.

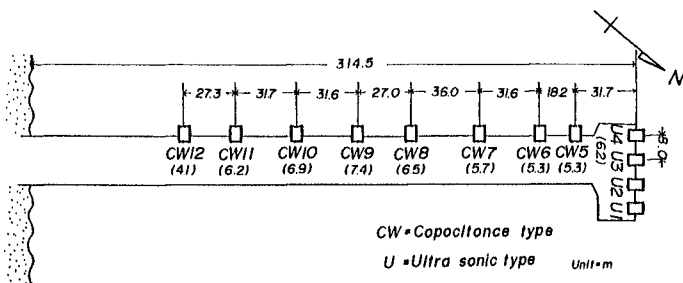


Fig. 9 Positions and their numbers of the installed wave gauges (figures in parentheses indicate the water depths)

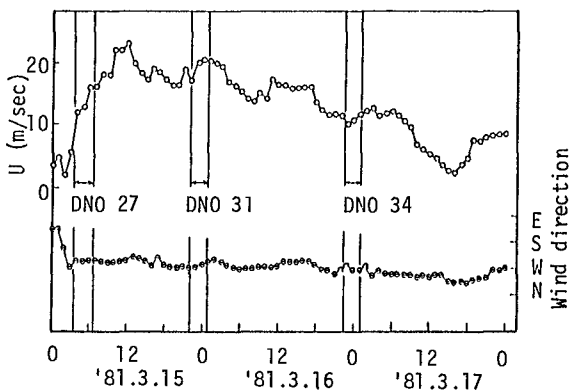
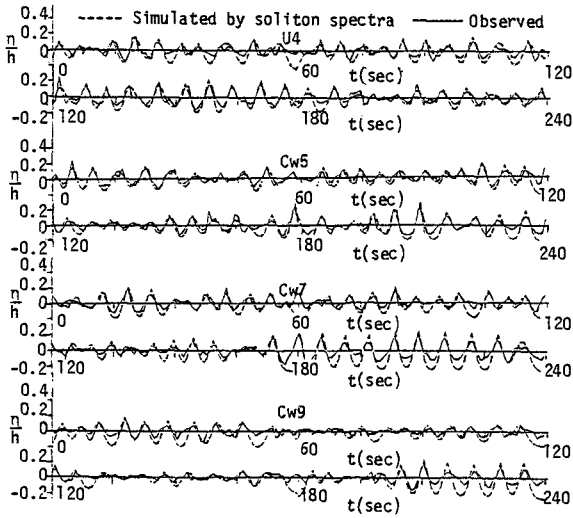
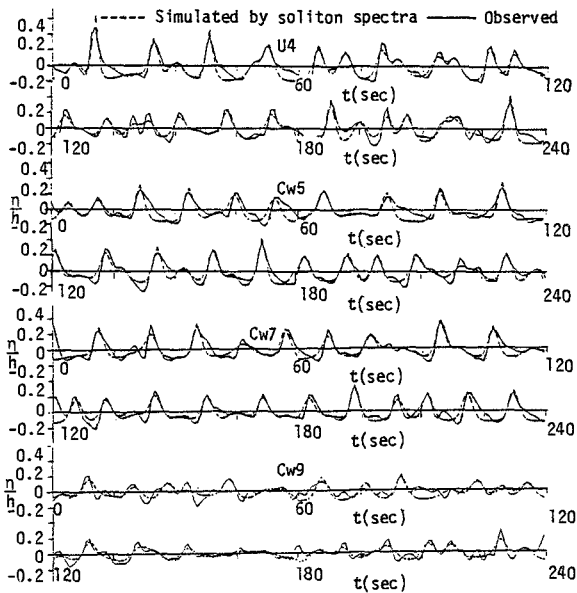


Fig. 10 Wind speed and direction during the wave observations



(a) DNO 27



(b) DNO 31

Fig. 11 Comparisons of wave profiles in a period of growing state to damping, one between the observed data and the theoretical results

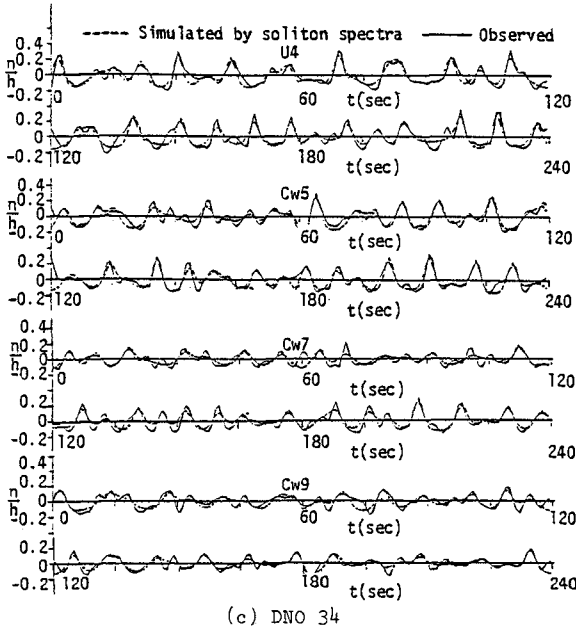


Fig. 11 Comparisons of wave profiles in a period of growing state to damping one between the observed data and the theoretical results

5.4 Accuracy of the Expression of Internal Properties

An observation of horizontal water particle velocities of the swell-like waves with the Ursell number 19.6 was carried at Ajigaura coast facing the Pacific ocean by Horikawa et al. The velocities were measured at the water depth of 2.28m by using an electro-magnetic current meter which is installed at the height of 0.62m above the sea bottom.

Fig. 12 shows part of the comparison of the velocities between their observed data and the theoretical result calculated by Eq.(31). Fig. 13 also shows similar comparison of wave profiles. It is found from these

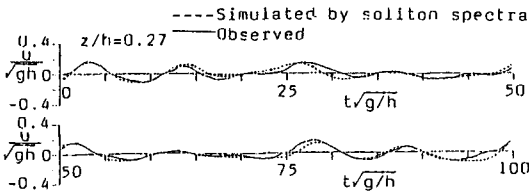


Fig. 12 Comparison of horizontal water particle velocity between the observed data and the theoretical results



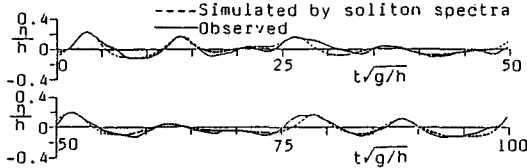


Fig. 13 Comparison of wave profiles between the observed data and the theoretical results

results that the expression of the water particle velocity based on soliton modes has accuracy similar to that for wave profiles as far as the expression of wave profiles has sufficient accuracy.

## 6. CONCLUSIONS

From the viewpoint that the soliton is one of the most elementary excitation in the nonlinear random waves, we have attempted to describe swell-like waves in shallow water theoretically by deriving the asymptotic multi-soliton solution under the assumption that the waves have a coherent dynamic structure composed of solitons alone. The expressions of wave profiles and internal properties such as water particle and mass transport velocities were derived by using the asymptotic solution, independently of both the evolution type and the degeneration of the amplitudes.

Further, applicability of the expressions by soliton modes was examined by comparisons between observed and theoretical wave profiles and internal properties. We conclude from these comparisons that the expressions by soliton modes practically have sufficient accuracy in expressing various properties of the swell-like waves.

## 7. ACKNOWLEDGEMENT

Figs. 12 and 13 were drawn from the wave data observed by Professor Horikawa et al. of Tokyo University and their permission for publication is gratefully acknowledged.

## 8. REFERENCES

- Freilich, M.H. and Guza, R.T. 1984 Nonlinear effects on shoaling surface gravity waves, *Phil. Trans. R. Soc. Lond.* A311, 1-41.
- Hasselmann, K. 1962 On the non-linear energy transfer in a gravity-wave spectrum Part 1 General theory, *J. Fluid Mech.* 12, 481-500.
- Hirota, R. and Ito, M. 1981 A direct approach to multi-periodic wave solutions to evolution equations, *J. Phys. Soc. Japan* 50, 338-342
- Nakamura, A. and Matsuno, Y. 1980 Exact one- and two-periodic wave solutions of fluids of finite depth, *J. Phys. Soc. Japan* 48, 653-657.
- Phillips, O.M. 1961 The dynamics of random finite amplitude gravity waves, in *Ocean Wave Spectra*, Prentice-Hall inc., 171-178.
- Tick, L.J. 1959 A non-linear random model of gravity waves I, *J. Math. & Mech.* 8, 643-652.

Toda, M. 1970 Waves in nonlinear lattice, Progr. Theor. Phys. Suppl. 45, 174-200

Tsuchiya, Y. and Yasuda, T. 1984 Waves in shallow water and soliton modes, J. Fluid Mech. (submitted)

Yasuda, T., Yamashita, T., Goto, S. and Tsuchiya, Y. 1982 Numerical calculations for wave shoaling on a sloping bottom by KdV equation, Coastal Eng. in Japan JSCE 25, 1-23

Yasuda, T., Nagata, M. and Tsuchiya, Y. 1984 Expression of nonlinear random waves based on the multi-soliton solution, Proc. 31st Conf. on Coastal Eng. JSCE, 61-65

## CHAPTER THIRTY ONE

### PREDICTION METHOD FOR THE WAVE HEIGHT DISTRIBUTION OFF THE WESTERN COAST OF TAIWAN

Frederick L. W. Tang\*  
Jea - Tzyy Juang\*\*

#### Introduction

Taiwan Strait locates on the continental shelf of the western Pacific Ocean. The water depth is less than 100 meters. Furthermore, the bathymetry of the eastern side namely the offing of western coast of Taiwan shoals gradually. In consequence, in case of the wind blows from the north to south, waves in the deeper part of the strait refract to be north west direction while they are approaching the shore and local waves directly generated by the wind still keep the same direction of the wind. The situation is shown in Figure 1.

From September to April of the next year, anticyclones come from Mongolia causes monsoon in this area. The wind velocity in the monsoon sometimes exceeds 20 meters per second, but it is around 10 meters per second in general. However, the duration of winds over 5 meters per second has been recorded more than 50 days. Engineering works such as towing caissons for building breakwater as well as dredging offshore have to be done in these days. Furthermore, navigation operations should not be stopped unless the wind is too strong. Of course, waves are forecast every day, however, more precise information about the probability of the occurrence of certain wave height is of great significance.

In last conference, the authors submitted a probability density function of wave heights in this area. This distribution model is to be remended by considering energy loss in this paper, and concrete forecasting procedure is submitted for engineering and navigation practice.

#### The Distribution Model

In last conference which was held in Capetown the authors ( Tang et. al. 1982 ) submitted a probability density function of wave heights off the western coast of Taiwan namely the eastern side of Taiwan Strait. The bathymetry of this area is rather flat and the prevailing wind direction is almost in the longshore direction. Waves in this area are considered to be the combination of the refracted waves from the deeper sea in the central part of Taiwan Strait and the local waves generated directly by the wind. The wave height is proportional to the square root of the sum of energies from refracted and local wave.

---

\* Dr. Eng., Professor, Graduate School of Hydraulic and Ocean Eng., National Cheng-Kung University, Tainan City 700, Taiwan, R.O.C.

\*\* Asso. Prof., Dept. of Civil Engineering, National Central University, Chungli City 320, Taiwan, R.O.C.

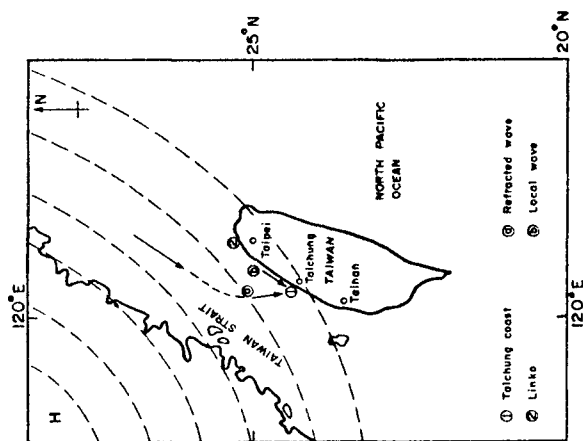


Fig.1 Wind and wave situation in the winter

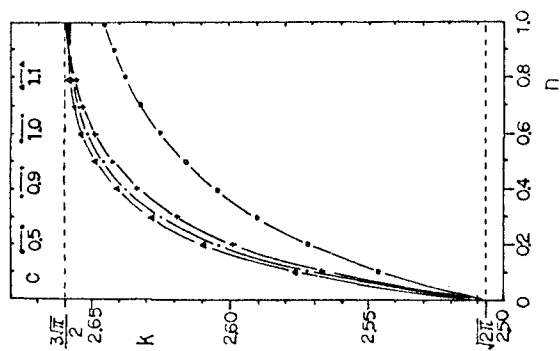


Fig.2 Relationship between  $k$  and  $n$

From such an assumption the wave height probability distribution was to be worked out as follows :

$$\psi(H) = \frac{H}{a-b} \left[ \exp\left(-\frac{H^2}{2a}\right) - \exp\left(-\frac{H^2}{2b}\right) \right] \quad (1)$$

where  $a$  : energy of the refracted waves,  $a = 4 \sigma_1^2$   
 $b$  : energy of the local waves,  $b = 4 \sigma_2^2$   
 $\psi(\cdot)$  : probability density function  
 $H$  : wave height  
 $\sigma_{1,2}^2$  : area under the wave spectral density function curve, subscript 1, 2 denote the refracted and local wave respectively.

The ratio between the mean wave height  $\bar{H}$  and the combined energy  $\sigma$  is

$$k = \frac{\bar{H}}{\sigma} = \sqrt{2\pi} \cdot \frac{1 - n^{3/2}}{(1-n)\sqrt{1+n}} \quad (2)$$

where  $\sigma = \sqrt{\sigma_1^2 + \sigma_2^2}$ ,  $n = \frac{b}{a} = \left(\frac{\sigma_2}{\sigma_1}\right)^2$

when  $n \rightarrow 0$ , it means that no local wave existing,  $k = \sqrt{2\pi}$ , as shown in Fig.2.

Above equation fits the reality better than Rayleigh's distribution in comparison with the measured data as shown in Fig.3.

#### Modification of The Model

In navigation and engineering practice, the wave height distribution must be predicted in advance of operation and being much more accurate is required.

In equation(1), the ratio of  $\sigma_1$  and  $\sigma_2$  is to alter the steepness and location of the peak of the curve sensitively. In addition, the wave energy dissipation should also be taken into consideration.

Denoting  $E_1$ ,  $E_2$  to be the wave energy of refracted and local wave respectively, considering the energy dissipation, the total wave energy  $E$  at the location of interest is assumed to be the following linear combination.

$$E = r E_1 + c r E_2 ; 0 < r \leq 1, c > 0, c r \leq 1 \quad (3)$$

From probability transform and convolution integration operations the revision of equation(1) is worked out as follows :

$$\psi(H) = \frac{H}{r(a-cb)} \left[ \exp\left(-\frac{H^2}{2ra}\right) - \exp\left(-\frac{H^2}{2crb}\right) \right] \quad (4)$$

The expected value namely the average wave height and the variance, can be calculated respectively as

$$\bar{H} = \sqrt{\frac{\pi}{2}} \cdot \frac{r^{1/2}}{a-cb} \left[ a^{3/2} - (cb)^{3/2} \right] \quad (5)$$

$$\sigma_H^2 = 2r(a+cb) - \frac{\pi r}{(a-cb)^2} \left[ \frac{a^3 + c^3 b^3}{2} - (cab)^{3/2} \right] \quad (6)$$

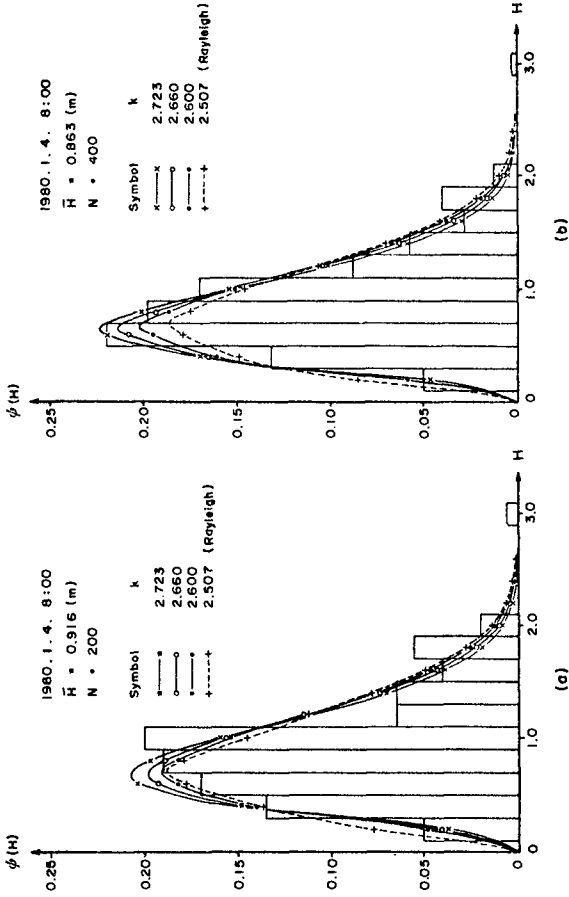


Fig.3 New probability density curve and measured data

The skewness and kurtosis of the curve are also to be evaluated as follows.  
Skewness :

$$\sqrt{\beta_1} = \frac{1}{\left\{ 2(a+cb) - \frac{\pi}{(a-cb)^2} \left[ \frac{a^3+c^3b^3}{2} - (c \cdot a \cdot b)^{3/2} \right] \right\}^{3/2}} \cdot \frac{\sqrt{\pi/2}}{a-cb} \cdot \left\{ 3 \left[ a^{5/2} - (cb)^{5/2} \right] - 6(a+cb) \left[ a^{3/2} - (cb)^{3/2} \right] + \frac{\pi}{(a-cb)^2} \left[ a^{3/2} - (cb)^{3/2} \right]^3 \right\} \quad (7)$$

Kurtosis :

$$\beta_2 = \gamma^{-3} = \frac{1}{\left\{ 2(a+cb) - \frac{\pi}{(a-cb)^2} \left[ \frac{a^3+c^3b^3}{2} - (cab)^{3/2} \right] \right\}^2} \cdot \left\{ 8(a^2+cab+c^2b^2) - \frac{6\pi}{(a-cb)^2} \left[ a^{3/2} - (cb)^{3/2} \right] \cdot \left[ a^{5/2} - (cb)^{5/2} \right] + \frac{6\pi(a+cb)}{(a-cb)^2} \left[ a^{3/2} - (cb)^{3/2} \right]^2 - \frac{3\pi^2}{4(a-cb)^4} \left[ a^{3/2} - (cb)^{3/2} \right]^4 \right\} - 3 \quad (8)$$

And the ratio k becomes

$$k = \frac{\sqrt{2\pi} \left[ 1 - (cn)^{3/2} \right]}{(1-cn)\sqrt{1+cn}} \quad (9)$$

For evaluating the influence of coefficients k, r, c, on the shape of the curves, several calculations are made and illustrated in Figures 4, 5, 6.

These coefficients, however, should be determined by calculations of refraction effect, friction of sea bottom as well as wave-wave interaction. Such computations are too complicate to be done. Besides, the theories have not yet fully developed. Approximate evaluations are to be carried out by comparing calculated curve and measured data as shown in Fig.7.

Through these comparison, coefficient r, which represent the ratio of remainder of energy after dissipation, should be taken to be 0.95, and the coefficient c, which denotes the ratio of energy loss of refracted and local waves is of minor significant, so it can be consider as unity. The coefficient k, its definition is shown in equation(2)and(9), is merely the function of the ratio of local wind wave energy and the refracted wave, which will depend on the weather situation and can not be decided in advance and will not be a constant. The probability density function is as follows in consequence.

$$f(H) = \frac{H}{0.95(a-b)} \left[ \exp\left(-\frac{H^2}{1.9a}\right) - \exp\left(-\frac{H^2}{1.9b}\right) \right] \quad (10)$$

Prediction Procedure

If the weather forecasting data are available, the waves and wave height distribution off the western coast of Taiwan are to be forecasted as follows.

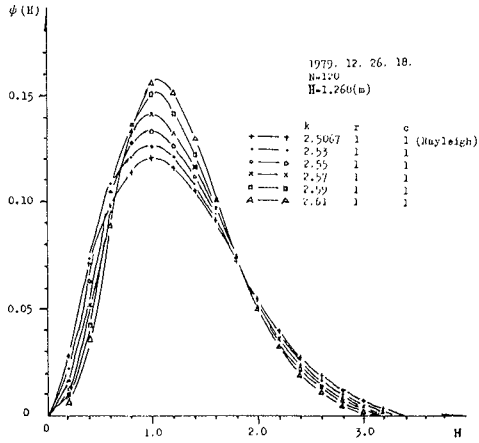


Fig.4 Coefficient k influences the shape of distribution (1)

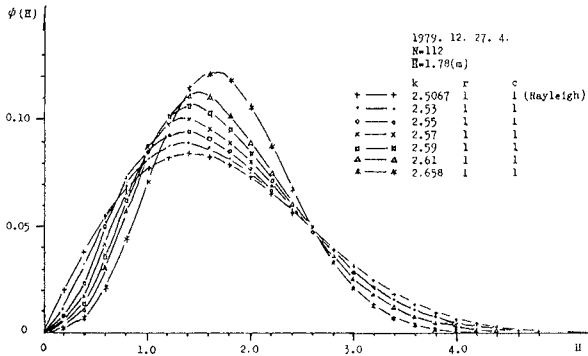


Fig.4 Coefficient k influences the shape of distribution (2)



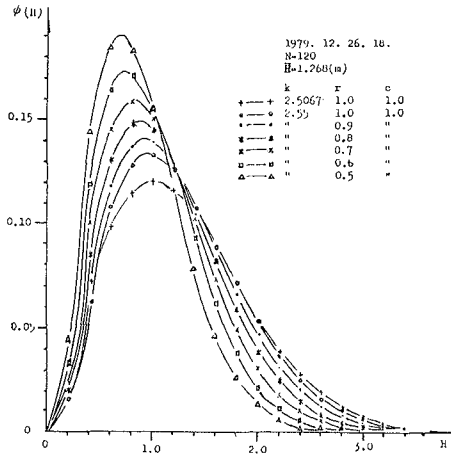


Fig.5 Coefficient r influences the shape of distribution(1)

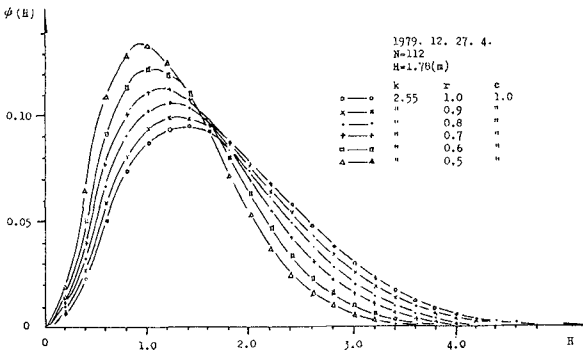


Fig.5 Coefficient r influences the shape of distribution(2)

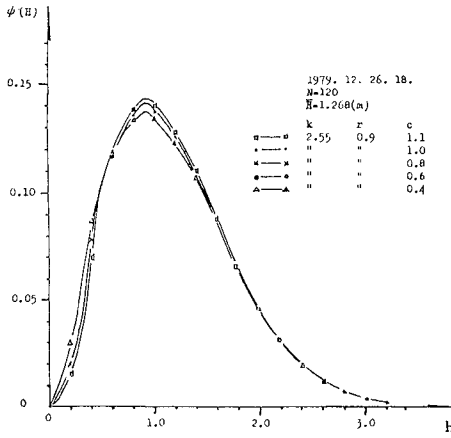


Fig.6 Coefficient c influences the shape of distribution(1)

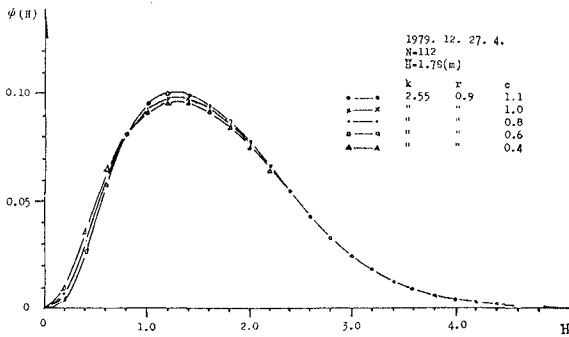


Fig.6 Coefficient c influences the shape of distribution(2)

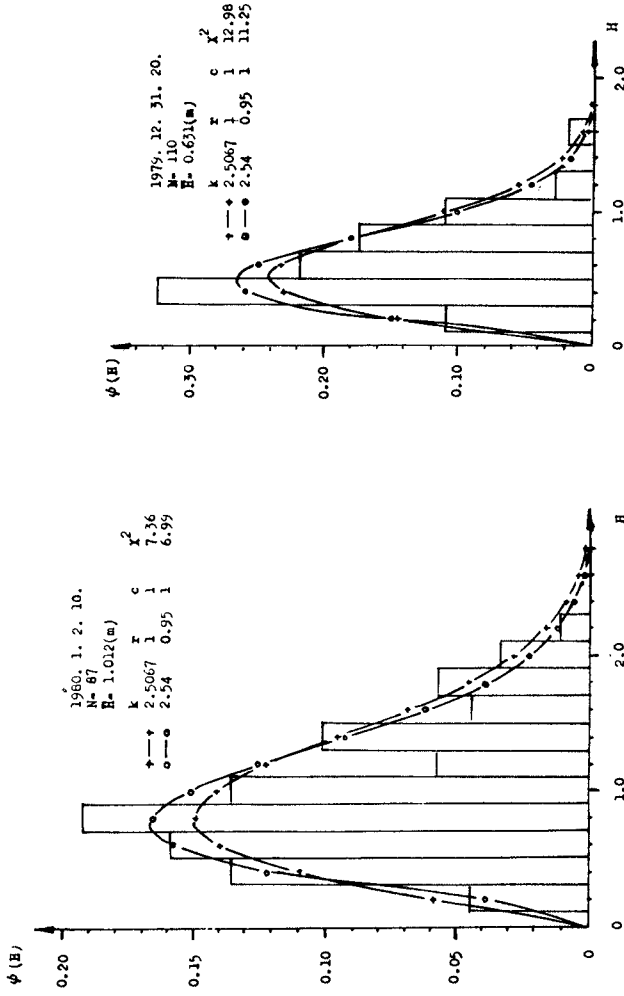


Fig.7 The measured data and the new distribution curve in comparison to Rayleigh's

Waves come from the East China Sea and Taiwan Strait are evaluated by Liang's (1976) element wave prediction model

$$E_I = \frac{2}{\pi G} \int_r \int_\theta \bar{\xi}(r, \theta) \bar{U}^2(r, \theta) \cos^2[\beta(r, \theta)] \cdot \exp\left(-\frac{0.08 r}{\bar{U}^2}\right) dr d\theta \quad (11)$$

- $E_I$  : wave energy in the point of interest.
- $G$  : group velocity
- $\bar{U}(r, \theta)$  : wind velocity at 10 meters above sea level.
- $\beta(r, \theta)$  : the angle between the wind direction and the line.

Such definitions are illustrated in Fig.8.

In practical calculations,  $\bar{\xi}$  can set to be constant.  $H_{1/3,1}^2$  is to replace  $E_I$  and  $T_{1/3,1}$  can calculated from fetch and wind velocity.

$$H_{1/3,1}^2 = \frac{2\bar{\xi}}{\pi G_{1/3}} \sum_r \sum_\theta \bar{U}^2(r, \theta) \cos^2[\beta(r, \theta) \exp\left(-\frac{0.08 r}{\bar{U}^2}\right) \Delta r \Delta \theta \quad (12)$$

$$T_{1/3,1} = \frac{0.0552 \cdot \pi \cdot \bar{U}}{g} \left(\frac{g F}{\bar{U}^2}\right)^{0.3269} \quad (13)$$

The local wave height  $H_{1/3,2}$  and period  $T_{1/3,2}$  are to be computed by following formula ( Tang, 1970 )

$$H_{1/3,2} = \frac{0.26 U^2}{g} \tanh\left\{0.578 \left(\frac{g D}{U^2}\right)^{3/4}\right\} \tanh\left\{\frac{0.01 \left(\frac{g F}{U}\right)^{1/2}}{\tanh\left[0.578 \left(\frac{g D}{U^2}\right)^{3/4}\right]}\right\} \quad (14)$$

$$T_{1/3,2} = \frac{2.8 \pi U}{g} \tanh\left\{0.52 \left(\frac{g D}{U^2}\right)^{3/8}\right\} \tanh\left\{\frac{0.0436 \left(\frac{g F}{U^2}\right)^{1/3}}{\tanh\left[0.52 \left(\frac{g D}{U^2}\right)^{3/8}\right]}\right\} \quad (15)$$

- where  $U$  : local wind velocity
- $g$  : gravitational acceleration
- $D$  : water depth
- $F$  : fetch length

The wave height  $H_{1/3}$  can be calculated by

$$H_{1/3} = \sqrt{r H_{1/3,1}^2 + c \cdot r \cdot H_{1/3,2}^2} \quad (16)$$

According to Liang (1982) the period in this case can be calculated as follows

$$T_{1/3} = \frac{H_{1/3,1}^2 \times T_{1/3,1} + H_{1/3,2}^2 \times T_{1/3,2}}{H_{1/3,1}^2 + H_{1/3,2}^2} \quad (17)$$

Examples of such prediction are shown in Fig.9

Finally, since

$$a = 4 \sigma_1^2 = 4 \left(\frac{H_{1/3,1}}{3.8}\right)^2 \quad (18)$$

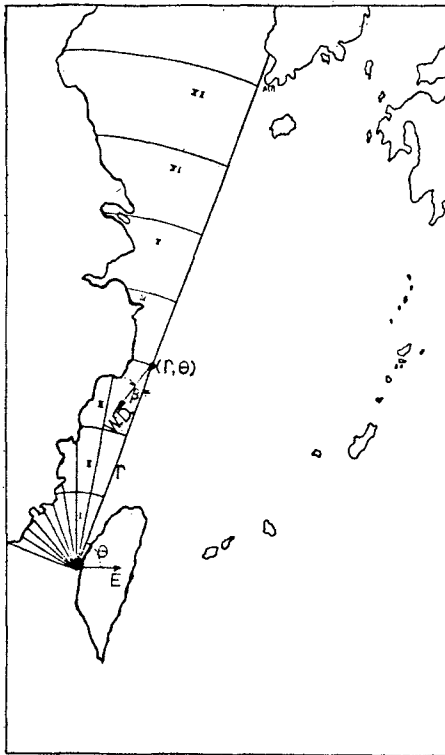


Fig. 8 Illustration of element wave method

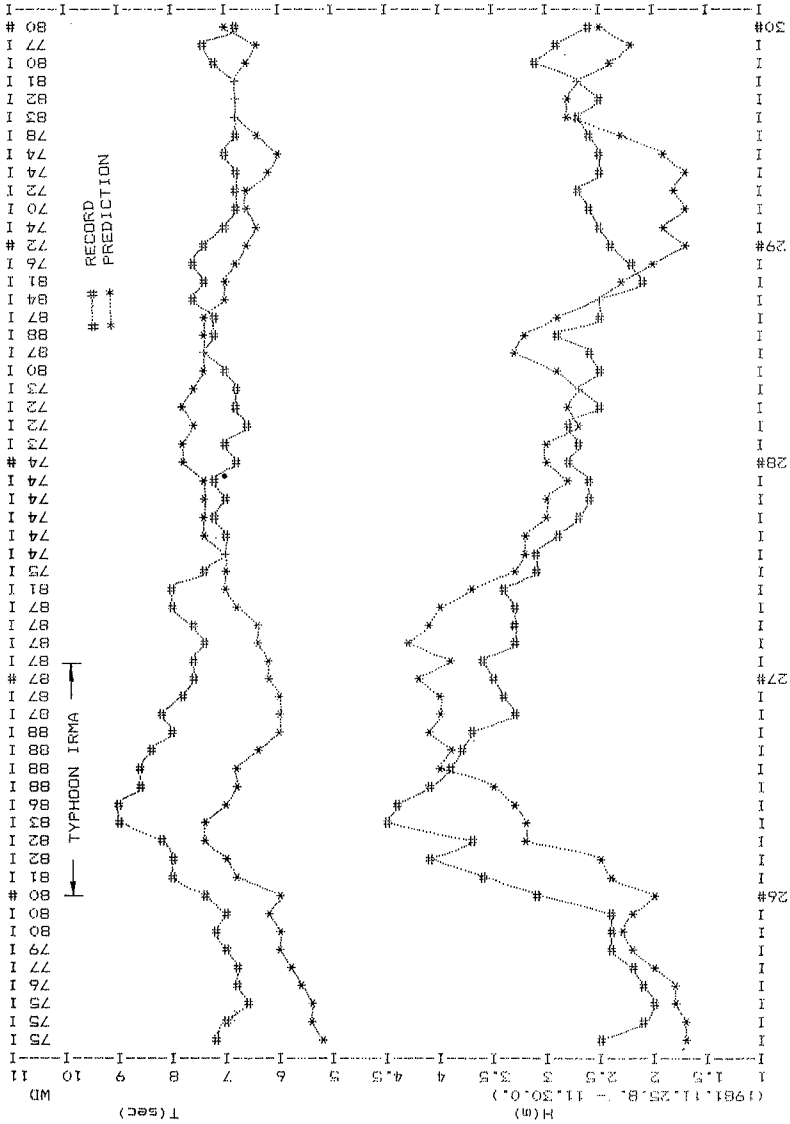


Fig.9 Results of wave prediction (1)

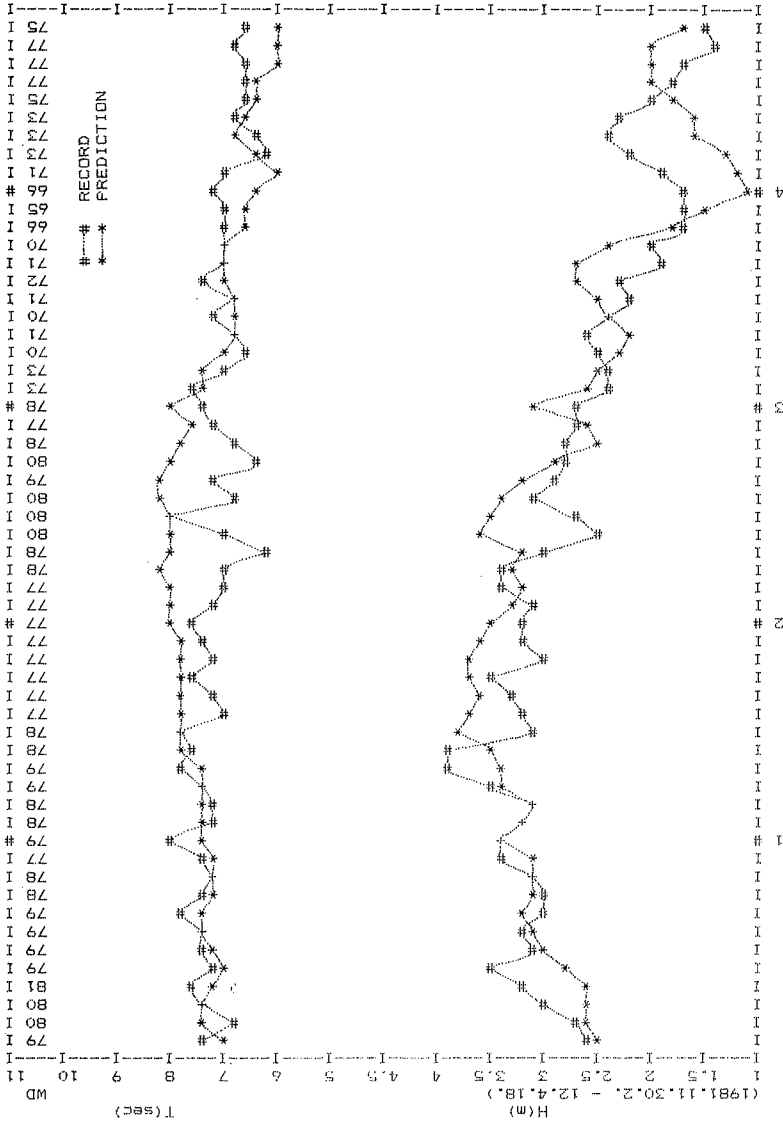


Fig.9 Results of wave prediction (2)

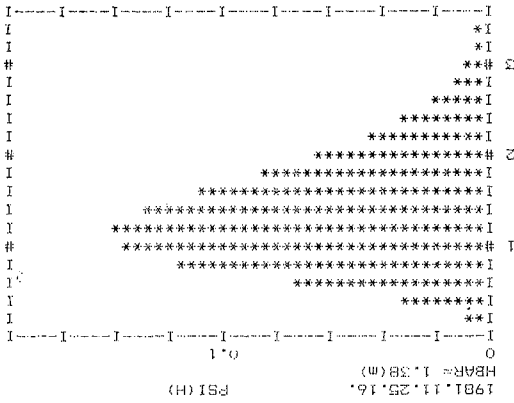
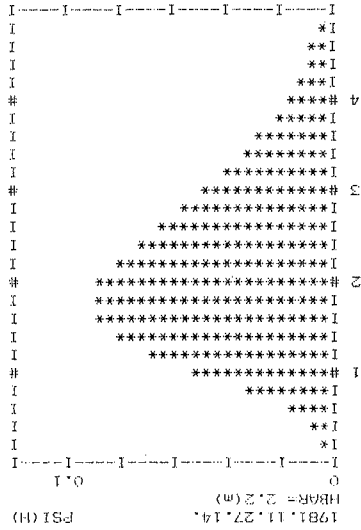


Fig. 10 Predicted wave height distribution



$$b = 4 \sigma_2^2 = 4 \left( \frac{H_{1/3, 2}}{3.8} \right)^2 \quad (19)$$

after substitute into equation(10), the wave height distribution can be predicted as Fig.10.

#### Conclusion

The wave height distribution of the waves generated by monsoon is to be predicted by following procedure.

1. Calculate the waves by element wave prediction method from weather data.
2. Calculate local waves by empirical formulas.
3. Add wave energies linearly but the coefficient of energy remainder is considered.
4. Calculate a and b by equations (18) and (19)
5. Substitute a, b to equation (10), the probability density equation is obtained.

These distribution model only can be applied in monsoon season, because the wind direction remains to be constant and the waves are moderate. Navigation and offshore engineering activities have to be done if the probability of waves exceeding certain height is negligible. However, during typhoon assailing, wave directions change frequently, navigation should be stop and no engineering work would take place. Neither the necessary to predict the probability of wave height nor the above model can be applied in such a case.

If the bathymetry and climate situation are similar to the offing of western coast of Taiwan, namely the sea bottom shoals gradually and the wind direction along the shore such as the southern part of German bight, this model might be adoptable.

#### References

- Liang N.K., S.T. Tang and B.J. Lee  
Application of Fetch Area Method in Monsoon Wave Hindcasting, Coastal Engineering - 1976, pp.258 - 272
- Liang N.K. and C.G. Jan  
Typhoon Wave Prediction, Symposium on Civil and Hydraulic Engineering, pp.277 - 293, 1982
- Tang F.L.W.  
Researches on the Calculation of Waves on Long Shoaling Beaches, J. of Civil and Hydraulic Engineering, NCKU, Vol.1, 1970

## CHAPTER THIRTY TWO

### METHOD FOR ESTIMATING DIRECTIONAL WAVE SPECTRUM IN INCIDENT AND REFLECTED WAVE FIELD

by

Masahiko Isobe\* and Kosuke Kondo\*\*

#### ABSTRACT

The relationship between the directional spectrum and the cross-power spectra in an incident and reflected wave field differs from the situation with no reflected waves because the phase lag between the incident and reflected waves is not random. Extra terms, which may be called phase interaction terms, exist. Hence standard methods for estimating the directional spectrum are not applicable. In the present study, the MLM is modified for this situation and the method is termed the MMLM (Modified Maximum Likelihood Method).

The validity of the MMLM is examined by numerical simulation. The results indicate that the MMLM has a high resolution power. Formulas to determine the reflection coefficient are derived and their accuracy and suitability are examined.

#### 1. INTRODUCTION

This paper describes a method to measure the directional spectrum in an incident and reflected wave field and to determine the reflection coefficient of a structure in a directional sea. The directional spectrum represents the energy distribution in wave direction, so that in principle the incident and reflected wave energies can be separated by measuring the directional spectrum near a structure and then the reflection coefficient can be determined. However, standard methods of estimating the directional spectrum are not valid because the phase lag between the incident and reflected waves is not random. Therefore, these methods should be modified for application in such a situation.

Many methods have been proposed for directional spectrum estimation. These are the DFT method (Direct Fourier Transform Method; Barber, 1963), parametric methods (Longuet-Higgins et al., 1963; Panicker and Borgman, 1974), the MLM (Maximum Likelihood Method; Capon,

---

\* Associate Professor, Department of Civil Engineering, Yokohama National University, 156 Tokiwadai, Hodogaya-ku, Yokohama, 240 Japan

\*\* Principal Engineer, Design and Engineering Department, Penta-Ocean Construction Co., Ltd., 2-2-8 Koraku, Bunkyo-ku, Tokyo, 112 Japan

1969), and others. Of all the proposed methods of calculation, the MLM has the highest resolution power, so that it is favorable to use to separate the incident and reflected wave energies. Therefore, in the present study, the MLM is modified to estimate the directional spectrum in an incident and reflected wave field.

Numerical simulations were carried out to examine the validity of the MMLM. By this means, accuracies of various formulas to determine the reflection coefficient could be examined.

The MLM was originally applicable only to wave gage arrays, but recently it has been extended for use with mixed gage arrays such as a pitch-roll buoy system, a clover-leaf buoy system, a wave gage plus current meter system, and so on (Isobe et al., 1984; Oltman-Shay and Guza, 1984). Hence it is also possible to extend the present method to mixed measuring systems.

## 2. DERIVATION OF MMLM

### 2.1 Relationship between Directional Spectrum and Cross-Power Spectra

Suppose that the wave amplitude is small, and that the water surface elevation can be expressed as the superposition of component waves with wavenumber (vector),  $\mathbf{k}$ , and angular frequency,  $\sigma$ . The water surface elevation due to the incident waves,  $\eta_i$ , at the point,  $\mathbf{x}$ , and the time,  $t$ , can be expressed as:

$$\eta_i(\mathbf{x}, t) = \int_{\sigma} \int_{\mathbf{k}} e^{i(\mathbf{k}\mathbf{x} - \sigma t)} Z(d\mathbf{k}, d\sigma) \quad (1)$$

This was called the spectral representation by Koopmans (1974). From the physical point of view,  $Z(d\mathbf{k}, d\sigma)$  means the amplitude which represents the energy within  $[\mathbf{k}, \mathbf{k} + d\mathbf{k}]$  and  $[\sigma, \sigma + d\sigma]$ . The quantity  $Z$  is a complex number. The absolute value of  $Z$  gives the amplitude of the component waves and the argument gives the phase at  $\mathbf{x} = \mathbf{0}$  and  $t = 0$ . Since the phase lag between different wave components can be assumed to be random,  $Z(d\mathbf{k}, d\sigma)$  and  $Z(d\mathbf{k}', d\sigma')$  are independent for  $\mathbf{k} \neq \mathbf{k}'$ , i.e.,

$$\langle Z(d\mathbf{k}, d\sigma) Z^*(d\mathbf{k}', d\sigma') \rangle = 0 \quad (\mathbf{k} \neq \mathbf{k}') \quad (2)$$

where the symbol  $\langle \rangle$  denotes the ensemble mean. The wavenumber-frequency spectrum,  $S(\mathbf{k}, \sigma)$ , represents the power density (square of the amplitude), and is therefore defined as:

$$\langle Z(d\mathbf{k}, d\sigma) Z^*(d\mathbf{k}, d\sigma) \rangle = S(\mathbf{k}, \sigma) d\mathbf{k} d\sigma \quad (3)$$

where the symbol  $*$  denotes the complex conjugate. The wavenumber vector,  $\mathbf{k}$ , is expressed by the wavenumber,  $k$ , and the wave propagation direction,  $\theta$ . Hence, the wavenumber-frequency spectrum is a function of  $k$ ,  $\theta$ , and  $\sigma$ . For water surface waves, since  $k$  is uniquely determined from  $\sigma$  by the dispersion relation, the spectrum becomes a function of  $\theta$  and  $\sigma$  and is called directional spectrum.

As shown in Fig. 1, if waves are reflected at the y-axis, the water surface elevation due to the reflected waves,  $\eta_r$ , can be expressed as:

$$\eta_r(\mathbf{x}, t) = \int_{\sigma} \int_{\mathbf{k}} r e^{i(\mathbf{k}_r \mathbf{x} - \sigma t)} Z(d\mathbf{k}, d\sigma) \quad (4)$$

where  $\mathbf{k}_r$  denotes the vector symmetrical to  $\mathbf{k}$  with respect to the reflection line, and  $r$  is the reflection coefficient which can be a function of  $\mathbf{k}$  and/or  $\sigma$ . Even though the amplitude of the reflected waves may change by the factor  $r$ , the phase on the reflection line is the same as that of the corresponding incident waves. Therefore the phase lag between the incident and reflected waves is not random. Let  $\mathbf{x}_r$  be the vector symmetrical to  $\mathbf{x}$ , then Eq. (4) can be written as:

$$\eta_r(\mathbf{x}, t) = \int_{\sigma} \int_{\mathbf{k}} r e^{i(\mathbf{k} \mathbf{x}_r - \sigma t)} Z(d\mathbf{k}, d\sigma) \quad (5)$$

From Eqs. (1) and (5), the total water surface elevation,  $\eta = \eta_i + \eta_r$ , can be expressed as:

$$\eta(\mathbf{x}, t) = \int_{\sigma} \int_{\mathbf{k}} [ e^{i(\mathbf{k} \mathbf{x} - \sigma t)} + r e^{i(\mathbf{k} \mathbf{x}_r - \sigma t)} ] Z(d\mathbf{k}, d\sigma) \quad (6)$$

Thus the complex amplitude,  $X(\mathbf{x}, d\sigma)$ , which represents the energy in  $[\sigma, \sigma + d\sigma]$  at the point  $\mathbf{x}$ , becomes

$$X(\mathbf{x}, d\sigma) = \int_{\mathbf{k}} [ e^{-i\mathbf{k} \mathbf{x}} + r e^{-i\mathbf{k} \mathbf{x}_r} ] Z^*(d\mathbf{k}, d\sigma) \quad (7)$$

The cross-power spectrum,  $\Phi_{mn}(\sigma)$ , between the water surface elevations at  $\mathbf{x} = \mathbf{x}_m$  and  $\mathbf{x} = \mathbf{x}_n$  is defined as the ensemble mean of the product of the complex amplitude,  $X(\mathbf{x}_m, d\sigma)$ , the the complex conjugate amplitude,  $X^*(\mathbf{x}_n, d\sigma)$ . That is,

$$\Phi_{mn}(\sigma) d\sigma = \langle X^*(\mathbf{x}_n, d\sigma) X(\mathbf{x}_m, d\sigma) \rangle \quad (8)$$

If  $m = n$ , then  $\Phi_{mn}(\sigma)$  represents the power spectrum, and if  $m \neq n$ ,  $\Phi_{mn}(\sigma)$  represents the cross spectrum. Substitution of Eq. (7) into Eq. (8) yields

$$\begin{aligned} \Phi_{mn}(\sigma) d\sigma = \int_{\mathbf{k}} \int_{\mathbf{k}'} [ e^{i\mathbf{k} \mathbf{x}_m + r e^{i\mathbf{k} \mathbf{x}_m}} ] [ e^{-i\mathbf{k}' \mathbf{x}_n + r e^{-i\mathbf{k}' \mathbf{x}_n}} ] \\ \times \langle Z(d\mathbf{k}, d\sigma) Z^*(d\mathbf{k}', d\sigma) \rangle \end{aligned} \quad (9)$$

From Eqs. (2) and (3), Eq. (9) becomes

$$\Phi_{mn}(\sigma) = \int_{\mathbf{k}} [ e^{i\mathbf{k} \mathbf{x}_m + r e^{i\mathbf{k} \mathbf{x}_m}} ] [ e^{-i\mathbf{k} \mathbf{x}_n + r e^{-i\mathbf{k} \mathbf{x}_n}} ] S(\mathbf{k}, \sigma) d\mathbf{k} \quad (10)$$

This is the relationship between the wavenumber-frequency (or directional) spectrum and the cross-power spectrum in an incident and reflected wave field and will be used to derive the basic formula for

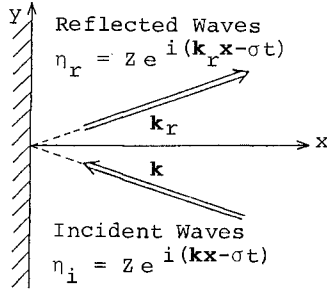


Fig. 1 Definition sketch of incident and reflected wave field.

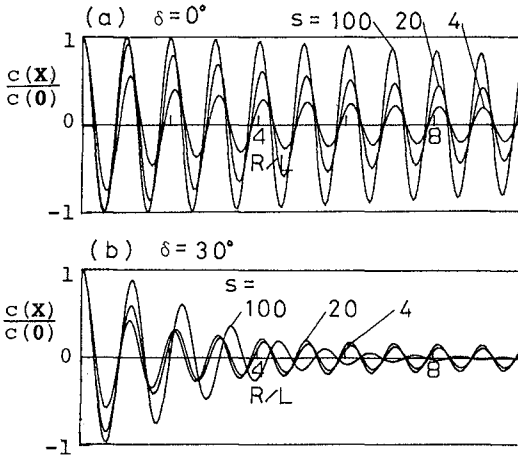


Fig. 2 Co-spectrum for Mitsuyasu-type directional distribution functions.

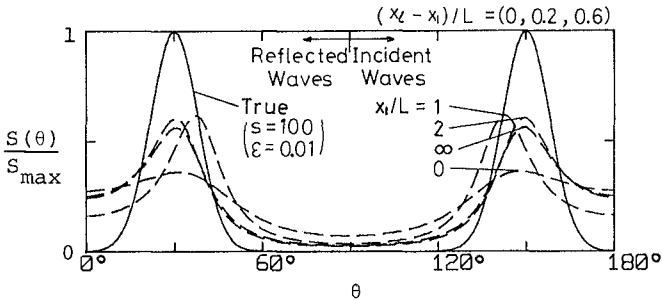


Fig. 3 Result of directional spectrum estimation by the standard MLM in incident and reflected wave field.

estimating the directional spectrum. The product of the first terms in the two brackets in Eq. (10) represents the incident wave component and the product of the second terms represents the reflected wave component. The other two products are extra terms describing the interaction of the incident and reflected wave fields. Since these terms appear because the phase lag between the incident and reflected waves is not random, they may be called phase interaction terms.

2.2 Magnitude of Phase Interaction Contribution

Before proceeding to the discussion of the directional spectrum estimation, it is worth examining the relative magnitude of the phase interaction terms. Any combination of terms in the brackets in Eq. (10) has the following form:

$$\phi(\mathbf{X}) = \int_{\mathbf{k}} e^{-i\mathbf{k}\mathbf{X}} S(\mathbf{k},\sigma) d\mathbf{k} \tag{11}$$

Mitsuyasu et al. (1974) proposed a standard directional distribution function with two parameters,  $\theta_0$  and  $s$ , as:

$$S(\mathbf{k},\sigma) = \left[ \cos \frac{\theta - \theta_0}{2} \right]^{2s} \tag{12}$$

If Eq. (12) is substituted into Eq. (11), the following result can be obtained after some manipulation:

$$\frac{c(\mathbf{X})}{c(\mathbf{0})} = J_0(kR) + 2 \sum_{l=1}^{[[s/2]]} (-1)^l \left[ \frac{s!}{(s-2l)!} \right] \left[ \frac{s!}{(s+2l)!} \right] \times J_{2l}(kR) \cos\{2l(\theta_0 - \theta)\} \tag{13}$$

$$\frac{q(\mathbf{X})}{c(\mathbf{0})} = 2 \sum_{l=0}^{[(s-1)/2]} (-1)^l \left[ \frac{s!}{(s-2l-1)!} \right] \left[ \frac{s!}{(s+2l+1)!} \right] \times J_{2l+1}(kR) \cos\{(2l+1)(\theta_0 - \theta)\} \tag{14}$$

where  $[[x]]$  denotes the maximum integer not larger than  $x$ ,  $J_n$  is a Bessel function of the  $n$ 'th order, and  $c$  and  $q$  are the co- and quadrature-spectra:

$$\phi(\mathbf{X}) = c(\mathbf{X}) - iq(\mathbf{X}) \tag{15}$$

and

$$\mathbf{X} = (R \cos\theta, R \sin\theta) \tag{16}$$

Figure 2 shows the relative co-spectrum as a function of relative distance  $R/L$  ( $L$ : wave length) for  $\delta = \theta_0 - \theta = 0^\circ$  and  $30^\circ$ . For the quadrature-spectrum, the shapes of the curves are similar to the co-spectrum, but the maximum and minimum occur at the zero-crossing points of the co-spectrum. Thus the amplitude of  $\phi$  becomes the envelope of the curve. Therefore, the relative magnitude of  $\phi$  is small for large

relative distance, unless the directional distribution is very narrow ( $s$  is large) and the principal direction almost coincides with the direction of the distance vector ( $\theta = \theta_0$ ).

For the phase interaction terms, we have  $\mathbf{X} = \mathbf{x}_{nr} - \mathbf{x}_m$ ,  $\mathbf{x}_n - \mathbf{x}_{mr}$ , so that  $R$  becomes about twice the distance between the measuring point and the reflection line. Hence the phase interaction terms generally become small if the wave gage array is located far from the reflection line. Therefore, if the structure is long enough, the incident and reflected directional spectrum can be observed in the far field by applying the standard methods of estimation.

Figure 3 is an example of a numerical simulation which shows the effect of the phase interaction terms. The peak incident wave direction is  $150^\circ$  and the reflection coefficient is 1, so that a spectral peak due to reflected waves appears at  $\theta = 30^\circ$ . The separation distance in the 3-sensor linear wave gage array are  $0.2L$  and  $0.4L$ . The estimated directional spectra by the standard MLM are shown by the dashed lines for the cases that the distances between the nearest wave gage and the reflection line are  $0$ ,  $L$ ,  $2L$ , and  $\infty$ . The accuracy becomes higher as the distance increases. This is because the phase interaction terms become small. However, a 3-sensor array may not be sufficient to measure a bimodal directional spectrum.

### 2.3 Formula for Estimating the Directional Spectrum

In this subsection a formula for estimating the directional spectrum is derived from the relationship between the directional spectrum and the cross-power spectra, as given by Eq. (10). The maximum likelihood technique is used and the process is similar to that given by Davis and Regier (1977), and Isobe et al. (1984).

Let

$$\gamma_{on}(\mathbf{k}) = e^{-i\mathbf{k}\cdot\mathbf{x}_{om}} + r e^{-i\mathbf{k}\cdot\mathbf{x}_{mr}} \quad (17)$$

and

$$T_{mn}(\mathbf{k}) = \gamma_{on}^*(\mathbf{k}) \gamma_{on}(\mathbf{k}) \quad (18)$$

Then Eq. (10) can be rewritten as follows:

$$\phi_{mn}(\sigma) = \int_{\mathbf{k}'} T_{mn}(\mathbf{k}') S(\mathbf{k}', \sigma) d\mathbf{k}' \quad (19)$$

In general, the estimated wavenumber-frequency spectrum, denoted with a caret as  $\hat{S}(\mathbf{k}, \sigma)$ , can be formally expressed as a linear combination of the known cross-power spectra:

$$\hat{S}(\mathbf{k}, \sigma) = \sum_m \sum_n \alpha_{mn}(\mathbf{k}) \phi_{mn}(\sigma) \quad (20)$$

where  $\Sigma$  means a summation over all measuring points and the  $\alpha_{mn}(\mathbf{k})$  are coefficients. Then, substitution of Eq. (19) into Eq. (20) yields

$$\hat{S}(\mathbf{k}, \sigma) = \int_{\mathbf{k}'} S(\mathbf{k}', \sigma) w(\mathbf{k}, \mathbf{k}') d\mathbf{k}' \tag{21}$$

where

$$w(\mathbf{k}, \mathbf{k}') = \sum_m \sum_n \alpha_{mn}(\mathbf{k}) T_{mn}(\mathbf{k}') \tag{22}$$

Equation (21) indicates that the estimated wavenumber-frequency spectrum is a convolution of the true wavenumber-frequency spectrum and the window function,  $w(\mathbf{k}, \mathbf{k}')$ , which is expressed by Eq. (22).

Now  $\alpha_{mn}$  is assumed to be of factorable form as

$$\alpha_{mn}(\mathbf{k}) = \gamma_m(\mathbf{k}) \gamma_n^*(\mathbf{k}) \tag{23}$$

Then Eqs. (20) and (22) become

$$\hat{S}(\mathbf{k}, \sigma) = \sum_m \sum_n \gamma_m(\mathbf{k}) \phi_{mn}(\sigma) \gamma_n^*(\mathbf{k}) \tag{24}$$

and

$$w(\mathbf{k}, \mathbf{k}') = \sum_m \sum_n \gamma_m(\mathbf{k}) T_{mn}(\mathbf{k}') \gamma_n^*(\mathbf{k}) \tag{25}$$

Substitution of Eq. (18) into (25) yields

$$w(\mathbf{k}, \mathbf{k}') = \left| \sum_m \gamma_m(\mathbf{k}) \gamma_{\text{cm}}^*(\mathbf{k}') \right|^2 \tag{26}$$

which shows the value of the window function is non-negative. Then the estimated directional spectrum is always non-negative because the integrand in Eq. (21) is non-negative.

The window function is normalized by putting

$$w(\mathbf{k}, \mathbf{k}) = 1 \tag{27}$$

In order for  $\hat{S}(\mathbf{k}, \sigma)$  to closely approximate  $S(\mathbf{k}, \sigma)$ , it is seen from Eq. (21) that  $w(\mathbf{k}, \mathbf{k}')$  should approach the Dirac delta function as closely as possible. Since  $S(\mathbf{k}, \sigma)$  and  $w(\mathbf{k}, \mathbf{k}')$  in Eq. (21) are non-negative, this can be attained by minimizing the value of  $\hat{S}(\mathbf{k}, \sigma)$ :

$$\hat{S}(\mathbf{k}, \sigma) \rightarrow \min. \tag{28}$$

From Eqs. (24), (25), (27), and (28), this problem becomes as follows:

$$\frac{\sum_m \sum_n \gamma_m(\mathbf{k}) T_{mn}(\mathbf{k}) \gamma_n^*(\mathbf{k})}{\sum_m \sum_n \gamma_m(\mathbf{k}) \phi_{mn}(\sigma) \gamma_n^*(\mathbf{k})} \rightarrow \max. \tag{29}$$



This is equivalent to the problem of finding the maximum eigenvalue for given matrices,  $\phi_{mn}$  and  $T_{mn}$  such that

$$\sum_n T_{mn} \gamma_n^* = \lambda \sum_n \phi_{mn} \gamma_n^* \tag{30}$$

and hence

$$\sum_m \sum_n \phi_{lm}^{-1} T_{mn} \gamma_n^* = \lambda \gamma_l^* \tag{31}$$

where  $\phi_{lm}^{-1}$  is the inverse matrix of  $\phi_{lm}$ . From Eq. (29), the maximum eigenvalue,  $\lambda_{max}$ , is inversely proportional to the estimated directional spectrum:

$$\hat{S}(k, \sigma) \propto 1/\lambda_{max} \tag{32}$$

It can be seen from Eq. (18) that any vector orthogonal to  $\gamma_{0n}$  is an eigenvector with eigenvalue  $\lambda = 0$  in Eq. (31). Hence the only possible choice of  $\gamma_n$  for a positive eigenvalue is of the form

$$\gamma_n = \gamma_{0n} + \gamma_{0n}^\perp \tag{33}$$

where  $\gamma_{0n}^\perp$  is a vector orthogonal to  $\gamma_{0n}$ . If Eqs. (18) and (33) are substituted into Eq. (31) and then multiplied with  $\gamma_{0l}$  from the left, the maximum eigenvalue,  $\lambda_{max}$ , can be obtained as

$$\lambda_{max} = \sum_m \sum_n \gamma_{0m} \phi_{mn}^{-1} \gamma_{0n}^* \tag{34}$$

As seen from Eq. (17),  $\lambda_{max}$  is a function of  $r$ . In order to determine the value of  $r$ , a relationship which is strictly satisfied in the uni-directional case was derived. That is

$$d\lambda_{max} / dr = 0 \tag{35}$$

This relationship is assumed to be valid in a general case and then substitution of Eq. (17) and (34) into Eq. (35) yields

$$r_0 = - \frac{\sum_m \sum_n \phi_{mn}^{-1}(\sigma) [ e^{ik(x_n - x_{nr})} + e^{ik(x_{nr} - x_n)} ]}{2 \sum_m \sum_n \phi_{mn}^{-1}(\sigma) e^{ik(x_{nr} - x_{nr})}} \tag{36}$$

Since the value of the reflection coefficient is non-negative the estimated reflection coefficient becomes

$$\hat{r} = \begin{cases} 0 & (r_0 \leq 0) \\ r_0 & (r_0 > 0) \end{cases} \tag{37}$$

Finally, from Eqs. (17), (32), (34), and (37), the estimated directional spectrum becomes as follows:

$$\hat{S}(\mathbf{k}, \sigma) = \begin{cases} \kappa / \left[ \sum_m \sum_n \Phi_{mn}^{-1}(\sigma) e^{i\mathbf{k}(\mathbf{x}_n - \mathbf{x}_m)} \right] & (r_0 \leq 0) \\ \kappa / \left[ \sum_m \sum_n \Phi_{mn}^{-1}(\sigma) e^{i\mathbf{k}(\mathbf{x}_n - \mathbf{x}_m)} \right. \\ \left. - \frac{\left\{ \sum_m \sum_n \Phi_{mn}^{-1}(\sigma) \left[ e^{i\mathbf{k}(\mathbf{x}_n - \mathbf{x}_{nr})} + e^{i\mathbf{k}(\mathbf{x}_{nr} - \mathbf{x}_m)} \right] \right\}^2}{4 \sum_m \sum_n \Phi_{mn}^{-1}(\sigma) e^{i\mathbf{k}(\mathbf{x}_{nr} - \mathbf{x}_{mr})}} \right] & (r_0 > 0) \end{cases} \quad (38)$$

where  $\kappa$  is a proportionality constant which can be determined from the relationship between the directional spectrum and the power spectrum. This relationship can be obtained by putting  $m = n$  in Eq. (10). The result is

$$\Phi_{mn}(\sigma) = \int_{\mathbf{k}_i} \left[ \hat{S}(\mathbf{k}_i, \sigma) + 2 \sqrt{\hat{S}(\mathbf{k}_i, \sigma) \hat{S}(\mathbf{k}_r, \sigma)} \cos \mathbf{k}_i(\mathbf{x}_m - \mathbf{x}_{nr}) + \hat{S}(\mathbf{k}_r, \sigma) \right] d\mathbf{k}_i \quad (39)$$

where  $\mathbf{k}_i$  represents the wavenumber vector within the incident wave direction and  $\mathbf{k}_r$  is the reflected wavenumber vector corresponding to  $\mathbf{k}_i$ . The symbol  $\hat{S}(\mathbf{k}_r, \sigma) = r^2 \hat{S}(\mathbf{k}_i, \sigma)$  represents the reflected wave spectrum. If Eq. (38) is substituted into Eq. (39), the equation for determining the value of  $\kappa$  can be obtained for each measuring point. Hence  $\kappa$  can be obtained by the least square method.

Equation (38) was derived by modifying the standard MLM for use in an incident and reflected wave field. Therefore, the present method is named the MMLM (Modifiend Maximum Likelihood Method).

The procedure for calculating the directional spectrum by the MMLM is summarized as follows:

- 1) For a given data set, compute the cross-power spectra,  $\Phi_{mn}(\sigma)$ , for all possible combinations.
- 2) For a fixed value of  $\sigma$ , determine  $k$  from the dispersion relation and the compute the directional spectrum by using Eq. (38), except for  $\kappa$ . The computation range of the wave direction includes both the incident and reflected wave directions.
- 3) Determine the value of  $\kappa$  from Eq. (39); then the directional spectrum is completely determined by Eq. (38).

### 3. NUMERICAL SIMULATION

#### 3.1 Procedure of Numerical Simulations

Numerical simulations were performed to examine the validity of the MMLM. The procedure is similar to the one used for examining the EMLM (Isobe et al., 1984). Since from the theoretical viewpoint the energies distributed among the wave frequency can be separated by cross-power spectral analysis, the directional spectrum is described as a function of only the wave direction,  $\theta$ .

The procedure for the numerical simulation is as follows:

- 1) Specify a functional form for the directional spectrum,  $S_{\theta}(\theta)$ , and reflection coefficient,  $r(\theta)$ . Here, the Mitsuyasu-type directional distribution expressed by Eq. (12) is used. To fabricate a bimodal distribution, two Mitsuyasu-type distribution functions with different  $\theta_0$  and  $s$  are superimposed.
- 2) Calculate  $\phi_{mn}$  for a given wave gage array from Eq. (10). For the power spectra,  $\phi_{mm}$ , a fraction of the total incident wave energy is added as a noise component.
- 3) Calculate  $\hat{S}_{\theta}(\theta)$  from Eq. (38) and compare to  $S_{\theta}(\theta)$ .

#### 3.2 Results

Figure 4 shows an example of the numerical simulation. A 3-sensor linear wave gage array in which the gages are set at  $(x, y) = (0.2L, 0)$ ,  $(0.4L, 0)$ ,  $(0.8L, 0)$  is used. This arrangement is the same as in Fig. 3. For all the figures in this paper, the reflection line coincides with the  $y$ -axis. The solid line represents the true (given) directional spectrum. The peak direction of the incident waves is  $150^\circ$  and the reflection coefficient is 1, so that the spectral peak due to the reflected waves appears at  $\theta = 30^\circ$ . The estimated results are shown for various values of  $\epsilon$ , the ratio of the noise power to the total incident wave energy. The resolution power decreases with increasing noise component; however, the MMLM has higher resolution power than the (standard) MLM for the same amount of noise (cf. Fig. 3).

Numerical simulations were carried out for a wide range of wave gage arrangements in order to study adequate arrangements. Results were similar to the case of the standard MLM. The minimum and maximum distance between wave gages should be about  $0.2L$  and  $1.5L$ . As can be seen from Fig. 5, the resolution power increases as the number of wave gages increases. The detailed shape of the array does not influence the result very much. This is quite different from the DFT method.

Figure 6 shows one problem in the MMLM. If the wave gages are located far from the reflection line, spurious peaks can appear in the estimated spectrum, as shown in the figure. This occurs when the modes of the standing waves at the measuring points are the same for the true and spurious peak direction. It should be possible to remove these false peaks after calculation, since they are always very sharp and recognizable. If one wave gage is located within  $0.2L$  from the

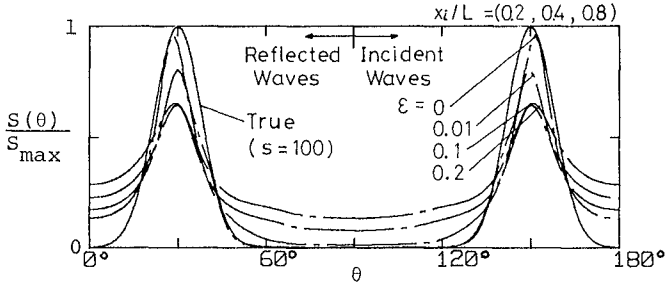


Fig. 4 Influence of noise on the resolution power of the MMLM.

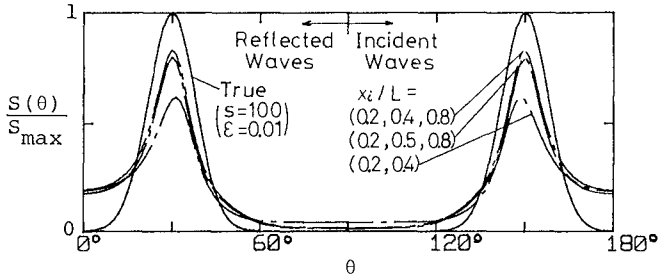


Fig. 5 Comparison among true and estimated directional spectra for various wave gage arrays.

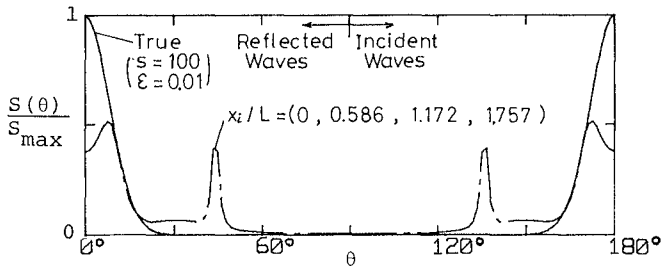


Fig. 6 Example of spurious peaks resulting from the MMLM.

reflection line and another one is about  $0.2L$  from the first one, this trouble can be avoided.

From these results, linear arrays in which the distances between the reflection line and the wave gages are  $0.2 l$ ,  $0.4 l$ ,  $0.8 l$ ,  $1.6 l$ , ..... ( $l$  is the minimum wave length to be observed.) can be recommended. However, as will be seen later in Fig. 7(a), a 2-dimensional array is necessary to improve resolution power near the normal direction.

Figure 7 shows the results for various true directional spectra. The numbers of wave gages used are 2, 3, and 4. The array types are linear and the locations of gages are indicated in Fig. 7(a). Figure 7(a) corresponds to normal incidence. Accuracies are not high because the resolution power of the linear array in the array direction is low. A 2-dimensional array is necessary to improve resolution power in this direction. The peak incident wave direction is  $120^\circ$  for Fig. 7(b). Three or four-sensor arrays may have sufficient accuracy. Figure 7(c) shows the results for a uni-directional case. If the noise component is excluded, the estimated spectra should approach the true spectrum. However, since the relative noise amount of 1% was added in the numerical simulation, the resolution power for the smaller number of gages decreases significantly. Figure 7(d) corresponds to a broad spectrum. The estimated spectrum by the 4-sensor array becomes bimodal. In order to avoid this, the distance between the wave gages should be reduced. Figure 7(e) is for the bimodal incident wave spectrum. The 4-sensor array gives an accurate estimation even in this case. The reflection coefficient for Fig. 7(f) is 0.5 and the MLM is valid.

Figure 8 shows the result for a complex situation. The incident directional spectrum is bimodal and the reflection coefficient changes with direction as indicated by the solid line in the lower figure. It can be seen that many wave gages are necessary for this case.

### 3.3 Estimation of Reflection Coefficient

There are several possible ways to estimate the reflection coefficient. Equation (37) gives an estimation of the reflection coefficient at the peak direction,  $\theta_m$ . This can be defined as a representative reflection coefficient, denoted by  $r_m$ :

$$r_m = r(\theta_m) \quad (40)$$

A second definition is as the square root of the ratio between the reflected and incident spectra estimated at the peak direction:

$$r_{sm} = \sqrt{\hat{S}(\theta_{mr}) / \hat{S}(\theta_m)} \quad (41)$$

where  $\theta_{mr}$  is the reflected wave direction corresponding to the incident peak direction. A third definition is as the square root of the ratio between the integrated reflected and incident wave energy:

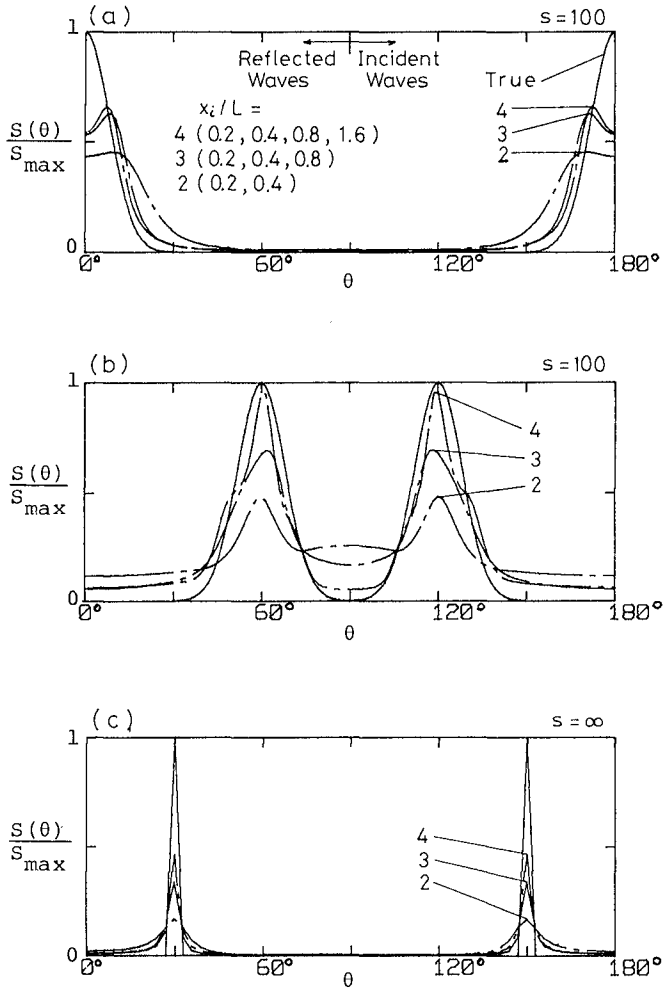


Fig. 7 Comparison among true and estimated directional spectra for various true spectra. (continued)

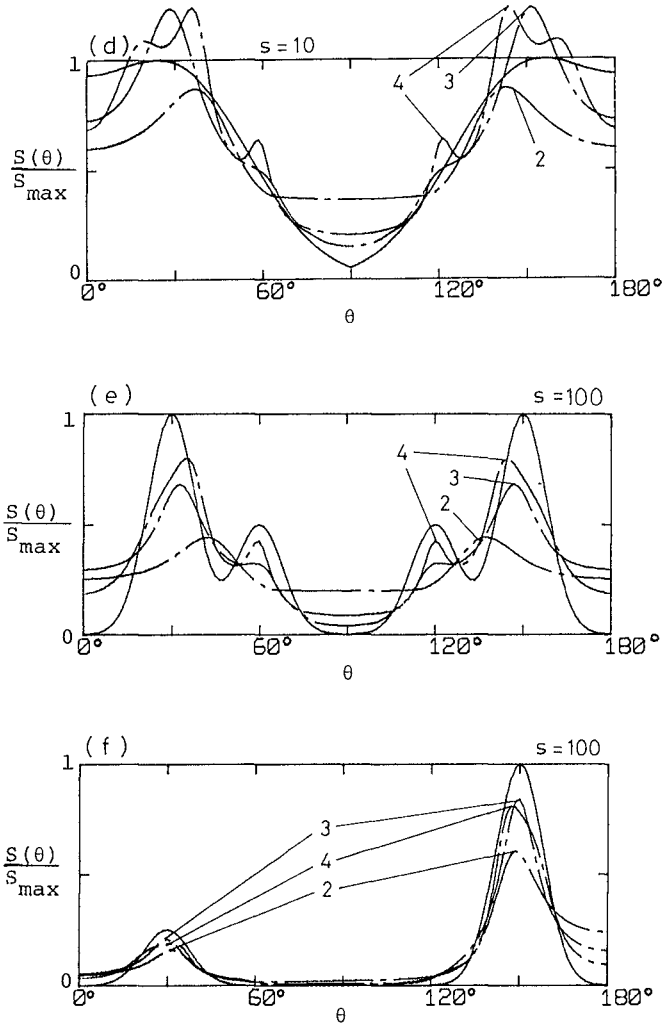


Fig. 7 Comparison among true and estimated directional spectra for various true spectra.

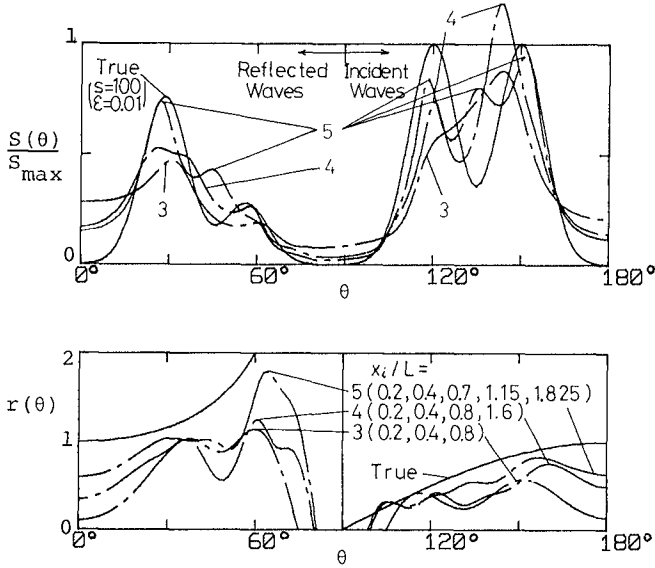


Fig. 8 Comparison among true and estimated directional spectra and reflection coefficients for a complex wave field.

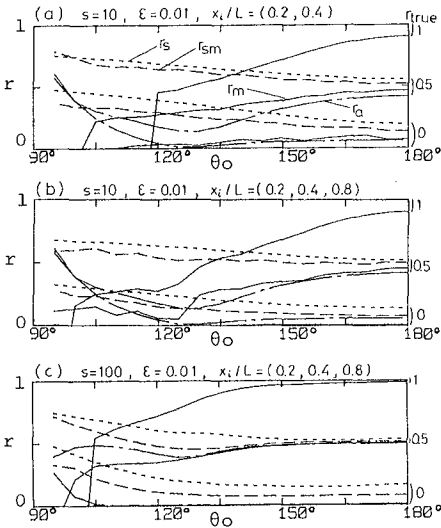


Fig. 9 Comparison among true and estimated reflection coefficients.



$$r_s = \sqrt{\frac{\int_{\text{ref.}} \hat{S}(\theta) d\theta}{\int_{\text{in.}} \hat{S}(\theta) d\theta}} \quad (42)$$

For the uni-directional case, the reflection coefficient can be calculated from data records at two points (Goda and Suzuki, 1976, for example). When the two points are on the x-axis, this can be written by using the results of a spectral analysis as

$$r_a = \sqrt{\frac{1 + c^2 - 2c \cos(kd \cos\theta_0 - \Delta)}{1 + c^2 + 2c \cos(kd \cos\theta_0 - \Delta)}} \quad (43)$$

where  $c$  is the ratio of the power spectra,  $\Delta$  is the phase lag, and  $d$  is the distance between the measuring points.

Figure 9 compares the true and estimated reflection coefficients. The Mitsuyasu-type directional distributions were used with  $s = 10$  for Fig. 9(a) and (b) and  $s = 100$  for Fig. 9(c). For true reflection coefficients of 0, 0.5 and 1, the estimated values are plotted against the peak incident wave direction. The solid, dashed, dotted, and chain lines indicate the values of  $r_m$ ,  $r_{sm}$ ,  $r_s$  and  $r_a$ , respectively. As seen from Fig. 9(a), a 2-sensor array may not be sufficient. If a 3-sensor array is used,  $r_m$  gives a fairly accurate value when the true reflection coefficient is small, whereas  $r_{sm}$  is relatively accurate for large values. However, the error is large when the peak incident direction is nearly parallel to the reflection line.

#### 4. CONCLUSION

In an incident and reflected wave field, extra terms which may be called phase interaction terms, appear in the relationship between the directional spectrum and the cross-power spectrum. If the wave gage array is located near the reflection line, this contribution becomes significant and therefore the standard MLM is not applicable. The MLM was modified for estimating the directional spectrum in such a situation and the method was named the MMLM (Modified Maximum Likelihood Method). The final result is expressed by Eq. (38).

Numerical simulations were carried out to examine the validity of the MMLM. The results demonstrated that the MMLM has high resolution power and can separate incident and reflected wave energies. The resolution power increases with increasing number of wave gages, but the effect of the detailed wave gage arrangement is small. In general, the minimum and maximum distance between the wave gages should be about  $0.2L$  and  $1.5L$ . However, these criteria depend upon the number of gages and the width of the directional distribution. Spurious spectral peaks appear if the wave gages are located far from the reflection line. If the wave gages are located at  $0.2l$ ,  $0.4l$ ,  $0.8l$ ,  $1.6l$ , ... ( $l$  is the minimum wave length to be observed) from the reflection line, the array is effective for wide range of wave length. A 2-dimensional array is necessary to improve the resolution power near the direction normal to the reflection line.

Various formulas to estimate the reflection coefficient were examined. As long as the peak incident wave direction is not coincident with the reflection line, the reflection coefficient,  $r_m$ , determined directly by the MMLM is accurate for small values of the true reflection coefficient, whereas the reflection coefficient determined from the resulting power ratio of the incident and reflected waves,  $r_{sm}$ , is accurate for large values.

## REFERENCES

- 1) Barber, N.F. (1963): The directional resolving power of an array of wave detectors, *Ocean Wave Spectra*, Prentice-Hall, Inc., New Jersey, pp. 137-150.
- 2) Capon, J. (1969): High-resolution frequency-wavenumber spectrum analysis, *Proc. IEEE*, Vol. 57, No. 8, pp. 1408-1418.
- 3) Davis, R.E. and L.A. Regier (1977): Methods for estimating directional wave spectra from multi-element arrays, *J. Mar. Res.*, Vol. 35, No. 3, pp. 453-477.
- 4) Goda, Y. and Suzuki, Y. (1976): Estimation of incident and reflected waves in random wave experiments, *Proc. 15th Coastal Eng. Conf.*, ASCE, pp. 828-845.
- 5) Isobe, M., K. Kondo and K. Horikawa (1984): Extension of MLM for estimating directional wave spectrum, *Proc. Symp. on Description and Modelling of Directional Seas*, Copenhagen, pp. A-6-1 - A-6-15.
- 6) Koopmans, L.H. (1974): *The Spectral Analysis of Time Series*, Academic Press, New York, 366p.
- 7) Longuet-Higgins, M.S., D.E. Cartwright and N.D. Smith (1963): Observations of the directional spectrum of sea waves using the motions of a floating buoy, *Ocean Wave Spectra*, Prentice Hall, Inc., New Jersey, pp. 111-136.
- 8) Mitsuyasu, H., F. Tasai, T. Subara, S. Mizuno, M. Okusu, T. Honda and K. Rikiishi (1975): Observation of the directional spectrum of ocean waves using a clover-leaf buoy, *J. Phys. Oceanogr.*, Vol. 5, pp. 750-760.
- 9) Oltman-shay, J. and R.T. Guza (1984): A data adaptive ocean wave directional spectrum estimator for pitch and roll type measurements, *J. Phys. Oceanogr.* (in press)
- 10) Panicker, N.N. and L. E. Borgman (1974): Enhancement of directional wave spectrum estimates, *Proc. 14th Coastal Eng. Conf.*, ASCE, pp. 258-279.

## CHAPTER THIRTY THREE

### CALCULATION OF DIRECTIONAL WAVE SPECTRA BY THE MAXIMUM ENTROPY METHOD OF SPECTRAL ANALYSIS

Michael J. Briggs,\* M. ASCE

#### Abstract

Two analysis techniques for calculating directional wave spectra from measured pressure and biaxial current components were inter-compared using data from the 25 October 1980 Atlantic Remote Sensing Land Ocean Experiment (ARSLOE) storm. The two methods are the conventional Fast Fourier Transform (FFT) method and a Maximum Entropy Method (MEM). The MEM is a nonlinear data adaptive method of spectral analysis which is capable of generating higher resolution spectral estimates from shorter data records than conventional FFT methods. The MEM has shown good agreement with the frequency and directional wave spectra calculated using conventional methods.

#### Introduction

The accurate calculation of directional wave spectra is important in the coastal zone for determination of coastal erosion, littoral sediment transport, diffraction and refraction of waves, and interaction with marine structures. One of the top research priorities of the National Research Council's Workshop on Wave Measurement Technology conducted in Washington in 1981 was the development of more efficient analysis techniques for the calculation of directional wave spectra (6). Considerable interest was generated at the ASCE Conference on Directional Wave Spectra Applications held in Berkeley on the Maximum Likelihood Method (MLM) for calculating directional spectra (8). Borgman (1) presented a proposal during the Second Workshop on Maximum Entropy and Bayesian Methods in Applied Statistics for comparisons of directional wave spectra instrument systems and analysis methods. Among the methods discussed were the conventional FFT, MEM, MLM, variational fitting, and linear programming. The four latter methods are all data-adaptive procedures which are capable of generating a higher resolution spectral estimate from shorter data records than conventional FFT methods. The primary objective of this paper is to demonstrate the promise of the MEM as a technique to increase directional resolution in directional wave spectra estimates.

Grosskopf (7) reported the results of an intercomparison of five different measurement systems and analysis techniques for calculating directional wave spectra from data obtained during the ARSLOE

---

\* Coastal Engineer, Coastal Engineering Research Center, US Army Engineer Waterways Experiment Station, Vicksburg, Mississippi.

experiment. The five measurement systems included two pressure/biaxial current meter arrays belonging to the Coastal Engineering Research Center (CERC) and Woods Hole Oceanographic Institution (WHOI), respectively, a Scripps  $S_{xy}$  array, an NHL triaxial current meter array, and a CERC X-Band Surface imaging radar (XERB). In this paper, an intercomparison with the CERC pressure/biaxial current meter (PUV) array is presented. Data representative of storm conditions during 25 October 1980 of the ARSLOE experiment are used.

#### Techniques Used

In 1965 Cooley and Tukey sparked a revival of the Fast Fourier Transform (FFT) which had been known for years but was not practical until the advent of the high speed digital computer. The direct method of calculating spectral estimates involving magnitude squaring of the transform of windowed data records became popular. Unfortunately, this method unreasonably assumes the data to be zero outside the selected number of points and repeats itself periodically.

In 1967, Burg (3) introduced the concept of MEM of autospectral analysis. Entropy is a measure of the information content contained in a signal. Maximizing entropy, therefore, maximizes the information transmitted in a signal. The concept involves finding a spectral estimate corresponding to the most random or unpredictable time series whose extended correlation function satisfies the constraint that it agrees with known values. Since then researchers have successfully applied MEM to such diverse fields as geophysics, neurophysics, and ocean engineering. Campbell (4) accurately estimated natural frequency and damping ratio parameters and their 95 percent confidence limits for offshore platforms. The multichannel MEM was shown to be a useful tool in mode shape identification of offshore structures (2). Houmb (9) showed that MEM is a powerful tool for estimation of wave spectra and proposed a data acquisition system based on the technique.

In conventional FFT analysis of PUV arrays, the data are windowed and Fourier transformed; and the variance lost due to windowing is restored to the line spectra. The auto and cross-spectra terms are calculated from the line spectrum and used to obtain the first five directional Fourier series coefficients (truncated series representation for three independent measurements). These coefficients are usually band or ensemble averaged to decrease the variance of the estimate. Finally, the directional wave spectrum is calculated from the averaged coefficients using a smoothing or weighting function such as Longuet-Higgins, et al. (11) to eliminate negative side lobes.

Because the MEM is data adaptive, it does not suffer from the "bias vs. variance" tradeoff due to finite record length requirements of conventional methods. When calculating spectral estimates at one frequency, it is able to adjust itself to be least disturbed by power at neighboring frequencies. In this paper, the MEM method is used instead of conventional FFT techniques to calculate the auto- and cross-spectra for input to the directional Fourier series coefficient algorithm. Other portions of the algorithm are unchanged.

## Multichannel Maximum Entropy Method of Spectral Analysis

In order to assist understanding of the multichannel MEM algorithm, a brief review of the single-channel MEM model as a prediction error (PE) filter will be presented. An error series,  $e(n)$ , is defined as the difference between the desired signal,  $d(n)$ , and the actual signal,  $y(n)$ . The desired value is chosen as the input signal advanced one time unit ahead. The actual signal represents past values of the input signal. These past or previous values of the time series are used to predict the next value. According to least squares theory, a mean square error or error power,  $P(L)$ , is defined as the expected value of the square of the error signal. The energy contained in this error power must be minimized in such a way that the input signal is whitened as the filter order is increased. The Normal or Wiener-Levinson equations are obtained as a result of this minimization and are given by

$$[R]\{A\} = \{P\} \quad (1)$$

where

$[R]$  = matrix of autocorrelation coefficients, 0 to 1 lags

$\{A\}$  = column vector of prediction error filter coefficients

$\{P\}$  = column vector of prediction errors

The Normal equations are then solved by the Levinson-Durbin recursion to obtain the PE filter coefficients,  $A$ . The MEM spectral estimate,  $S_x$ , defined between the Nyquist frequency,  $f_{ny}$ , is then given by

$$S_x(f) = |A(f)|^2 S_w(f) \quad -f_{ny} \leq f \leq f_{ny} \quad (2)$$

$$= \frac{2\sigma^2(L)\Delta}{\left| 1 - \sum_{m=1}^L A(m) \exp(-j2\pi f m \Delta) \right|^2}$$

where  $\sigma^2(L)$  or  $S_w(f)/2\Delta$  is the prediction error or white noise variance and the denominator is the magnitude squared of the Fourier transform of the PE filter coefficients. The  $\Delta$  is the time increment in seconds between sampled data points.

Thus, the single-channel MEM filter can be written in a form familiar to engineers. The MEM spectral estimate,  $S_x(f)$ , (i.e. output spectrum) is the product of the prediction error spectrum,  $S_w(f)$  (i.e. input spectrum), and the magnitude squared of the transfer function of the PE filter,  $A(f)$ . The MEM spectral estimate is obtained by (1) calculating the PE filter coefficients out to the desired filter order of length  $L$  (as determined by Akaike's Final Prediction Error (FPE) or other suitable model order criterion), (2) calculating the PE due to a white noise signal at filter order  $L$ , (3) taking the magnitude squared of the Fourier transform of the PE coefficients, and (4) performing the operations indicated in Equation 2.

For the multichannel MEM algorithm, the development is analogous to the single-channel case. The expected mean square values of forward and backward errors of length  $M$  ( $M \leq L$ ) are minimized for the optimum filter. As a result, the Normal equations for the two-channel case forward filter coefficients,  $CF$ , are given by

$$[RF] \{CF(M,m)\} = \{V\} \quad (3)$$

where

$[RF]$  = forward R-matrix, Toeplitz, square block submatrices

$\{V\}^T$  = forward power matrix,  $[P(M) \ 0 \ 0 \dots 0]$

$m$  = coefficient number

The  $R_4$  element or  $2 \times 2$  submatrix of the RF matrix for a lag of 4 for the two-channel case is

$$\{R_4\} = \begin{bmatrix} R_{11}(4) & R_{12}(4) \\ R_{21}(4) & R_{22}(4) \end{bmatrix} \quad (4)$$

where the diagonals are the autocorrelations and the off-diagonals are the cross-correlations between channels 1 and 2.

The single-sided multichannel MEM spectral estimate matrix is a function of the Fourier transform of the forward filter coefficient matrix and is given by

$$G(f) = 2\Delta [CF^{-1}(1/z)]^* P(M) [CF^{-1}(1/z)] \quad (5)$$

where  $z = \exp(-j2\pi f\Delta)$ . Equation 5 reduces to Equation 2 for the single channel case if matrices are replaced by vectors and vectors by scalars. The inverse matrix operations become divisions, and the product of the filter coefficients with their complex conjugates gives the magnitude squared as before.

#### Directional Wave Spectral Theory

The directional wave spectrum is given by

$$S(\sigma, \theta) = S(\sigma) D(\sigma, \theta) \quad (6)$$

where  $S(\sigma)$  is the one-dimensional frequency spectrum

$$S(\sigma) = \int_0^{2\pi} S(\sigma, \theta) d\theta \quad (7)$$

and  $D(\sigma, \theta)$  is a directional spreading function which satisfies

$$\int_0^{2\pi} D(\sigma, \theta) d\theta = 1 \quad (8)$$

For a pressure/biaxial current meter combination (PUV), the derivation of the wave directional spectra is analogous to that of Longuet-Higgins et al. (11) and Cartwright (5) for heave-pitch-roll buoys. The water surface elevation is given by

$$\eta(x, y, t) = \int_{-\infty}^{\infty} \int_0^{2\pi} A(\sigma, \theta) \exp [i\psi(x, y, t, \sigma, \theta)] d\theta d\sigma \quad (9)$$

The dynamic wave pressure and horizontal u- and v-water particle velocities in the x and y directions are, respectively,

$$p(x, y, t) = \int_{-\infty}^{\infty} \int_0^{2\pi} A(\sigma, \theta) K_p(\sigma) \exp [i\psi(x, y, t, \sigma, \theta)] d\theta d\sigma \quad (10)$$

$$u(x, y, t) = \int_{-\infty}^{\infty} \int_0^{2\pi} A(\sigma, \theta) K_u(\sigma) \cos \theta \exp [i\psi(x, y, t, \sigma, \theta)] d\theta d\sigma \quad (11)$$

$$v(x, y, t) = \int_{-\infty}^{\infty} \int_0^{2\pi} A(\sigma, \theta) K_u(\sigma) \sin \theta \exp [i\psi(x, y, t, \sigma, \theta)] d\theta d\sigma \quad (12)$$

where

$$A(\sigma, \theta) = \text{amplitude spectrum} = \sqrt{2S(\sigma)d\sigma} \sqrt{D(\sigma, \theta)d\theta} \quad (13)$$

$$\psi(x, y, t, \sigma, \theta) = \text{random phase angle} = \sigma t - k_x x - k_y y \quad (14)$$

$$K_p(\sigma) = \gamma \frac{\cosh k(h+z)}{\cosh(kh)} \quad (15)$$

$$K_u(\sigma) = \sigma \frac{\cosh k(h+z)}{\sinh(kh)} \quad (16)$$

The single-sided autospectra for pressure and u- and v-velocities are, respectively,

$$G_{pp}(\sigma) = \int_0^{2\pi} S(\sigma, \theta) K_p^2(\sigma) d\theta \quad (17)$$

$$G_{uu}(\sigma) = \int_0^{2\pi} S(\sigma, \theta) K_u^2(\sigma) \cos^2 \theta d\theta \quad (18)$$

$$G_{vv}(\sigma) = \int_0^{2\pi} S(\sigma, \theta) K_u^2(\sigma) \sin^2 \theta d\theta \quad (19)$$

The single-sided cross-spectra are given by

$$S_{pu}(\sigma) = \int_0^{2\pi} S(\sigma, \theta) K_p(\sigma) K_u(\sigma) \cos \theta d\theta \quad (20)$$

$$S_{pv}(\sigma) = \int_0^{2\pi} S(\sigma, \theta) K_p(\sigma) K_u(\sigma) \sin \theta d\theta \quad (21)$$

$$S_{uv}(\sigma) = \int_0^{2\pi} S(\sigma, \theta) K_u^2(\sigma) \sin \theta \cos \theta d\theta \quad (22)$$

Since a PUV gage has only three independent measurements, only the first five directional Fourier coefficients can be derived. They are expressed as

$$A_0(\sigma) = \frac{S_{pp}(\sigma)}{2\pi K_p^2(\sigma)} = \frac{S_{uu}(\sigma) + S_{vv}(\sigma)}{2\pi K_u^2(\sigma)} \quad (23)$$

$$A_1(\sigma) = \frac{S_{pu}(\sigma)}{\pi K_p(\sigma) K_u(\sigma)} \quad (24)$$

$$B_1(\sigma) = \frac{S_{pv}(\sigma)}{\pi K_p(\sigma) K_u(\sigma)} \quad (25)$$



$$A_2(\sigma) = \frac{G_{uu}(\sigma) - G_{vv}(\sigma)}{\pi K_u^2(\sigma)} \quad (26)$$

$$B_2(\sigma) = \frac{2S_{uv}(\sigma)}{\pi K_u^2(\sigma)} \quad (27)$$

Ideally, the number of directional Fourier coefficients would be infinite, and perfect frequency and directional resolution would be obtained. However, due to the limited number of coefficients, a loss of resolution and negative side lobes results in a broadened spectra with lost total energy (variance). A binominal weighting function given by Longuet-Higgins et al. (11), although ensuring a non-negative directional spectra, still results in some loss of directional resolution. It is given by

$$S(\sigma, \theta) = A_0 + 2/3(A_1 \cos \theta + B_1 \sin \theta) \\ + 1/6(A_2 \cos 2\theta + B_2 \sin 2\theta) \quad (28)$$

Some of the statistical parameters which are compared in this paper are significant wave height, peak frequency, peak wave direction, and peak directional spread. The significant wave height is related to the zeroth moment of the directional wave spectrum by

$$H_{mo} = 4.0 \sqrt{M_0} \quad (29)$$

where  $M_0$  is the sum of the energy or variance over all frequencies and directions. The peak frequency is the center frequency of the band containing the maximum energy. The peak wave direction is the mean direction the waves travel toward in the band of maximum energy. It is defined as

$$\bar{\theta}(\sigma) = \arctan \left[ \frac{B_1(\sigma)}{A_1(\sigma)} \right] \quad (30)$$

The peak directional spread is an estimate of the spread of energy about the peak wave direction. It is given by

$$\theta_s(\sigma) = \left\{ 2 - \frac{2 \left[ A_1^2(\sigma) + B_1^2(\sigma) \right]^{1/2}}{A_0(\sigma)} \right\}^{1/2} \quad (31)$$

#### Description of Arsløe Experiment

The ARSLØE was conducted during October and November 1980 by CERC's Field Research Facility (FRF) at Duck, NC (see Figure 1). The purpose was to evaluate various types of in situ and remote sensing

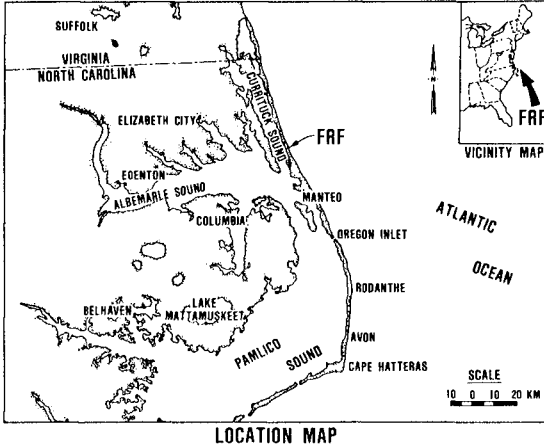


Figure 1. CERC Field Research Facility (FRF)

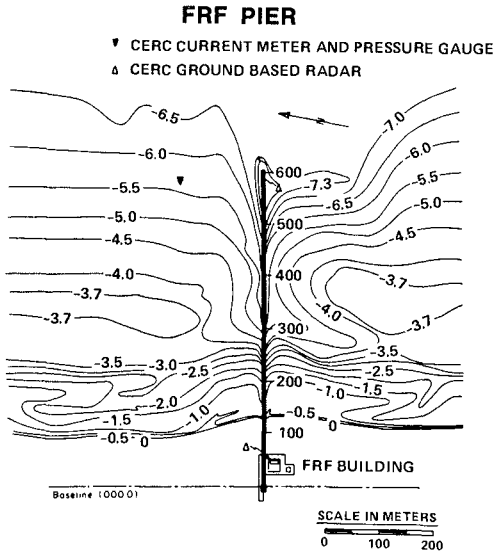


Figure 2. CERC FRF pier bathymetry

devices for measuring directional wave spectra in shallow water. All in situ instruments were installed on or near the end of the FRF pier (see Figure 2).

A major storm moved through the area during the period 23-25 October 1980. A total of 15 data records during the hours of 0915 to 1415 on 25 October was selected for intercomparisons with the CERC FFT and MEM directional wave spectra programs. The weather conditions during this time period were characterized by winds of 10-15 m/s (22-34 mph). Wind directions were initially from the northeast, then from the east followed by a rapid shift southward then around to the west and north-west (12). Figure 3 shows the mean current speed and direction during this time as determined from the PUV data records.

The gage used for software comparisons in this paper is the CERC PUV gage: a Model 551 Marsh McBirney biaxial current meter with a Bell and Howell pressure gage. The table below summarizes the sampling parameters used. The water depth at this location was 5.5-6 meters (18.0-19.7 ft) (see Figure 2).

#### Sampling and Analysis Parameters

Sampling Frequency, Hz	4
Burst Interval, min	20
Total Number of Points per Record	4096
Record Length, sec	1024
Bandwidth, Hz	0.00781

#### Results and Discussion

Intercomparisons are made between the directional wave spectra and moment generated parameters calculated by the CERC and MEM analysis methods for the 15 data records collected during the period 25 October 1980. For the MEM auto- and cross-spectra estimates, a constant model order (filter length L) was selected for each record based on the results for each from Akaike's FPE criterion. Figures 4, 5, and 6 are sample plots of frequency and peak directional wave spectral estimates for records 12, 13, and 14 (i.e., 1315, 1335, and 1355), respectively. The solid curve in all figures corresponds to the FFT-generated spectral estimates; the dashed line represents the MEM spectral estimates. The table on the following page compares the results for the significant wave height, peak frequency, peak wave direction, and peak directional spread for these three data records. Figures 7 and 8 are time series plots of significant wave height, peak frequency, peak direction, and peak directional spread for all of the 15 data records intercompared.

In general, the MEM frequency spectral estimates are smoother than those of the FFT, with the peaks shifted slightly in frequency. Records 13 and 14 peak frequencies differ by one bandwidth interval (which is the minimum resolveable with the band averaging procedure used). As a

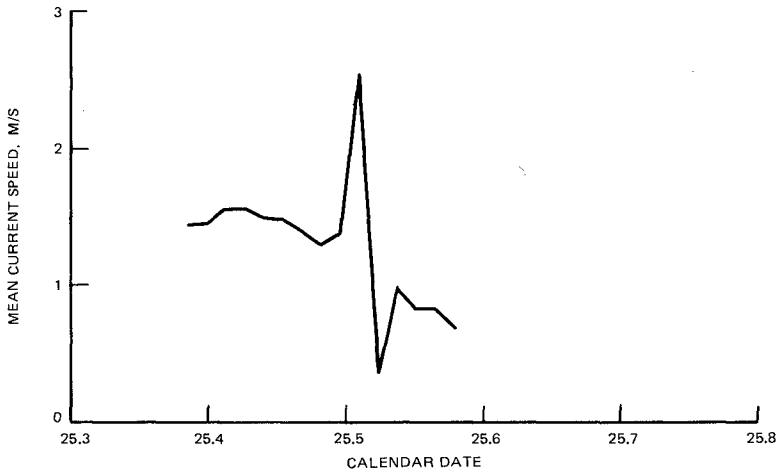
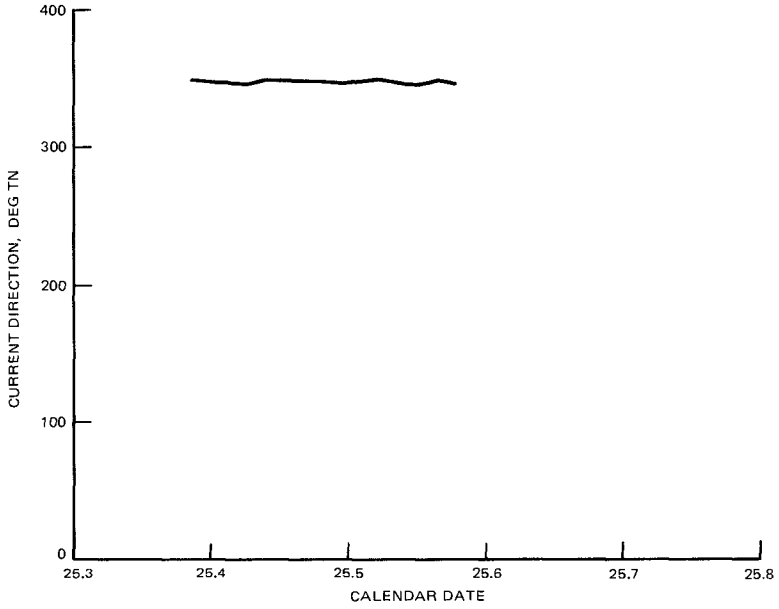
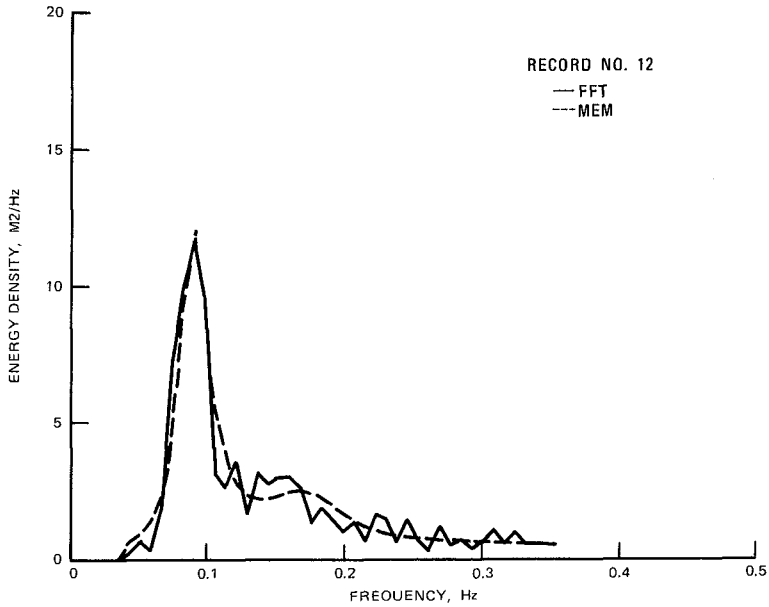
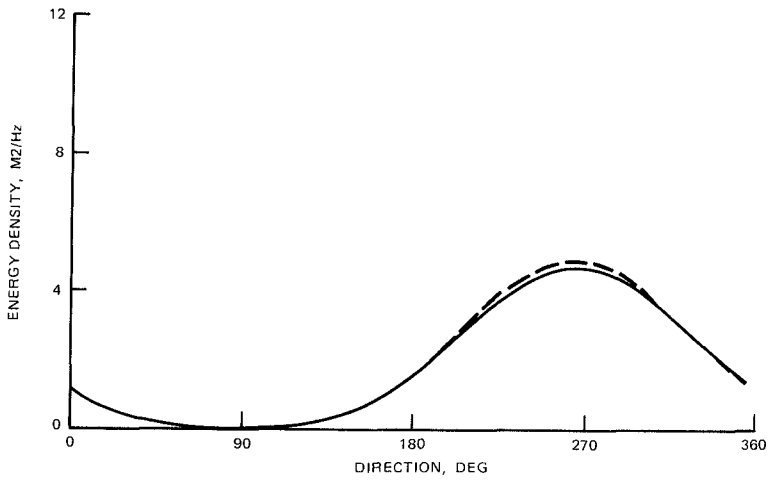


Figure 3. Mean current speed and direction estimates

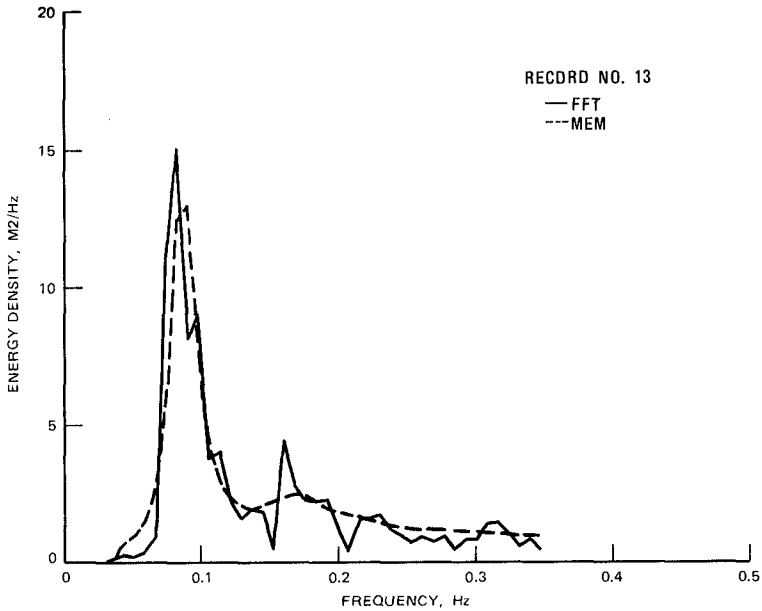


a. Frequency spectra

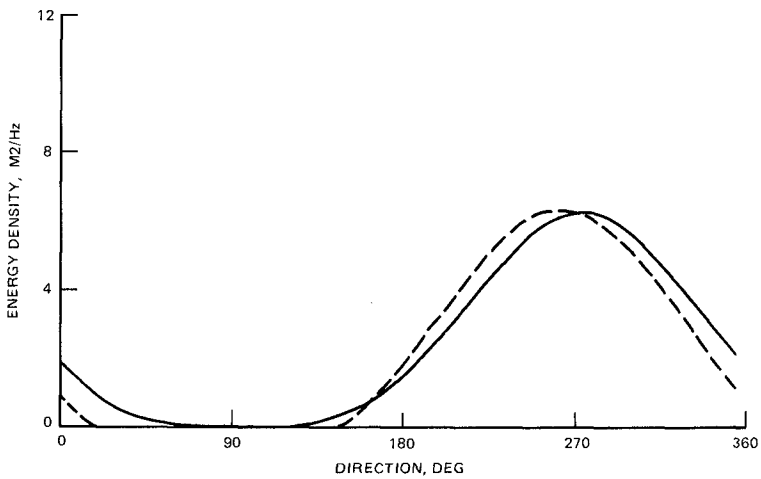


b. Directional wave spectra

Figure 4. Record 12 spectra intercomparison

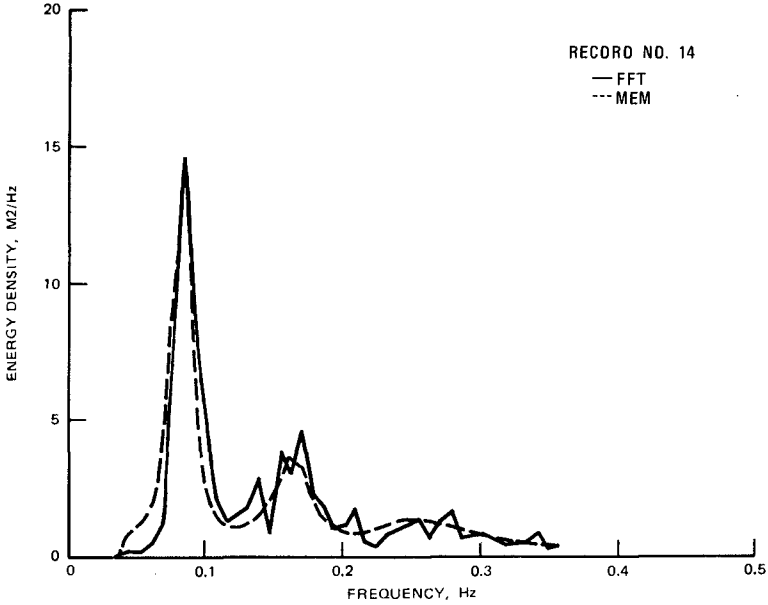


a. Frequency spectra

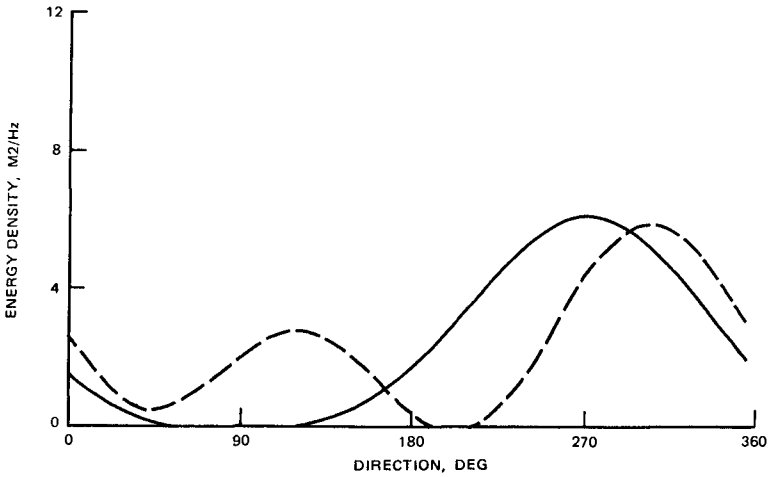


b. Directional wave spectra

Figure 5. Record 13 spectra intercomparison



a. Frequency spectra



b. Directional wave spectra

Figure 6. Record 14 spectra intercomparison

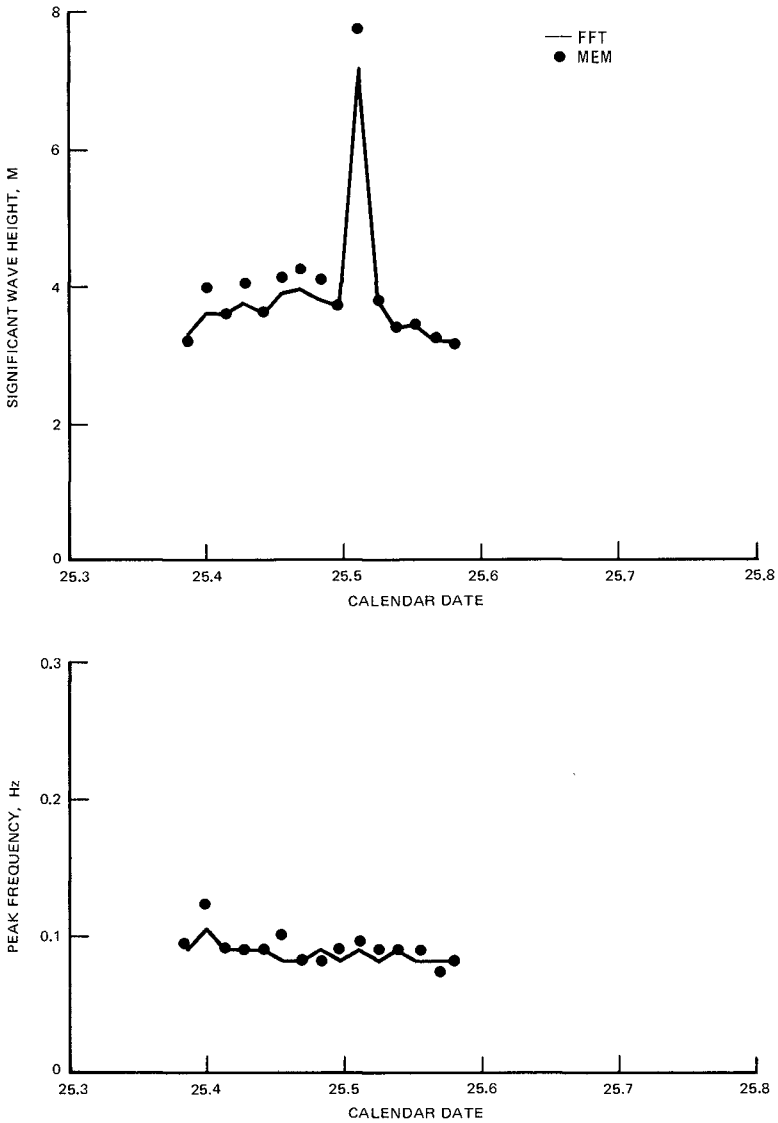


Figure 7. Significant wave height and peak frequency estimates



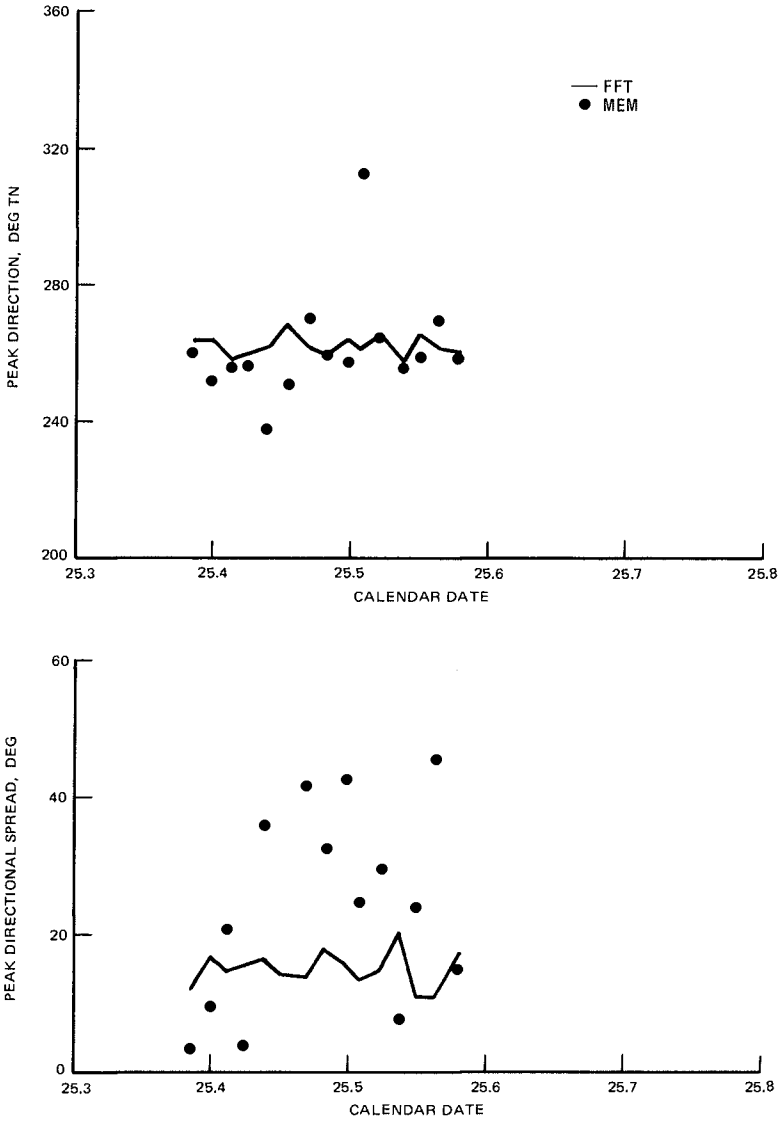


Figure 8. Peak direction and peak directional spread estimates

result, the significant wave height and peak frequency time series curves (Figure 7) agree quite well.

Comparison of MEM and FFT Method

Record No.	Hs, M		fp, Hz		$\bar{\theta}$ , deg TN		$\theta_s$ , deg	
	FFT	MEM	FFT	MEM	FFT	MEM	FFT	MEM
12	3.39	3.39	0.0898	0.0898	256.9	255.1	20.2	8.3
13	3.45	3.53	0.0820	0.0898	265.0	257.3	10.7	24.1
14	3.21	3.20	0.0820	0.0742	261.7	269.0	10.7	45.7

The MEM peak directional spectral estimates intercompare less favorably, however. The ARSLOE data used here were characterized by a combination of factors which would tend to increase the variability of the peak directional spread estimates (see Figure 8). Among these factors were unsteady wind conditions, reflections from the beach, and pier effects. Irregular bathymetry, short-term disruptions in wave patterns, and shallow-water induced spatial variability as reported by Grosskopf et al. (7) have a pronounced effect on the data analysis.

Figures 4 and 5 agree reasonably well with some slight shifts in direction being apparent. Figure 6, however, indicates two peaks of differing amplitude occurring at the same peak frequency. This bidirectional wave spectrum of two wave trains agrees with results obtained by XERB radar during the ARSLOE experiment. More than one wave train occurring at the same wave frequency was resolved by the XERB but not by the other systems using conventional FFT analysis methods (12).

Jefferys (10) demonstrated the substantial effect reflections and phase locking have on the spread predictions even for MLM methods. Phase locking occurs when two waves of the same frequency but differing amplitudes and directions are produced. Even when the amplitudes were equivalent, only a unimodal spectrum was produced. As the amplitude of one of the waves is decreased, the peak remains unimodal but shifts slightly. When the waves were no longer identical in frequency but still equal in amplitude, the bidirectional nature of the waves could be resolved. This would explain the differences in the MEM-generated peak directional spectra of Figures 4, 5, and 6.

#### Conclusions

In general, the MEM and CERC FFT method intercompared reasonably well. Comparisons were made with frequency and directional wave spectral estimates, significant wave height, peak frequency, peak wave direction, and peak directional spread. The MEM spectral estimates were generally slightly shifted in frequency and direction. The MEM tended to resolve multiple wave trains of similar frequency coming from different directions better than did the FFT method. The lack of band averaging in the MEM also tended to make the spread calculations more erratic. Further research with MEM and other data adaptive methods should be encouraged.

### Acknowledgements

The research contained in this paper was conducted under the auspices of the Prototype Measurement and Analysis Branch, Coastal Engineering Research Center, Waterways Experiment Station, of the U. S. Army Corps of Engineers. Permission to publish this paper was granted by the Chief of Engineers.

### References

1. Borgman, L. E. 1982. "Maximum Entropy and Data-Adaptive Procedures in the Investigation of Ocean Waves," Second Workshop on Maximum Entropy and Bayesian Methods in Applied Statistics, Laramie, WY.
2. Briggs, M. J. and J. K. Vandiver. 1982. "Multichannel Maximum Entropy Method of Spectral Analysis Applied to Offshore Platforms," Offshore Technology Conference 4286, Houston, TX, pp 647-660.
3. Burg, J. P. 1967. "Maximum Entropy Spectral Analysis," 37th Society of Exploration Geologists Winter Meeting, Oklahoma City, OK.
4. Campbell, R. B. and J. K. Vandiver. 1980. "The Estimation of Natural Frequencies and Damping Ratios of Offshore Structures," Offshore Technology Conference 3861, Houston, TX.
5. Cartwright, D. E. 1963. "The Use of Directional Spectra in Studying the Output of a Wave Recorder on a Moving Ship," Ocean Wave Spectra, Prentice-Hall, Englewood Cliffs, NJ, pp 203-218.
6. Dean, R. G. 1981. "The NRC Workshop on Wave Measurement Technology," Proceedings of the Conference on Directional Wave Spectra Applications, ASCE, Berkeley, CA, pp 220-232.
7. Grosskopf, W. G., D. G. Aubrey, M. G. Mattie, and M. Mathiesen. 1983. "Field Intercomparison of Nearshore Directional Wave Sensors," IEEE Journal of Oceanic Engineering, Vol OE-8, No. 14, pp 254-271.
8. Hogben, N. 1981. "Directional Wave Spectra Applications '81," Journal of the Society for Underwater Technology. Summer 1982, pp 4-8.
9. Houmb, O. G. and T. Overvik. 1981. "Some Applications of Maximum Entropy Spectral Estimation to Ocean Waves and Linear Systems Response in Waves," Applied Ocean Research, Vol 3, No. 4, pp 154-162.
10. Jefferys, E. R., G. T. Wareham, N. A. Ramsden and M. J. Platts. 1981. "Measuring Directional Spectra with the MLM," Proceedings of the Conference on Directional Wave Spectra Applications, ASCE, Berkeley, CA, pp 203-219.
11. Longuet-Higgins, M. S., D. E. Cartwright, and N. D. Smith. 1963. "Observations of the Directional Spectrum of Sea Waves Using the Motions of a Floating Buoy," Ocean Wave Spectra, Prentice-Hall Englewood Cliffs, NJ, pp 111-132.
12. Vincent, C. L. and D. E. Lichy. 1981. "Wave Measurements in ARSLOE," Proceedings of the Conference on Directional Wave Spectra Applications, ASCE, Berkeley, CA, pp 71-86.

## CHAPTER THIRTY FOUR

### DESCRIPTION OF NATURAL SEA STATES

#### REQUIREMENTS TO THE REPRODUCTION IN MODELS

H. LUNDGREN<sup>1</sup>

ELIAS DAVIDSEN<sup>2</sup>

#### ABSTRACT

In order to attain a satisfactory reproduction in physical and numerical models of Nature's sea states, much development of the description of these sea states has to take place. This paper gives a *discussion* (i) of the problems that can be considered as solved today, and (ii) of the problem areas where much research is still needed.

Firstly, the paper presents the basic definition of the *directional spread* of energy (for a given frequency) as derived from a field record. This definition is necessarily a statistical one and leads directly to the determination in practice of the directional spectrum.

Secondly, the parameterization of spectra is discussed and it is proposed to express one-dimensional storm spectra by means of the *four parameter F.I.-spectrum*, which is more manageable than the JONSWAP-spectrum.

Thirdly, it is concluded that the first order components of any spectrum have *random phases*.

#### 1. INTRODUCTION

In the modelling of a coastal engineering problem it is, of course, desirable to work with the best reproduction of the natural sea states. The degree of sophistication, however, depends on the size of the project and the type of model used.

For economic reasons, the study in *physical models of smaller projects* must be confined to the *1-D f-spectrum*, i.e. the one-dimensional frequency spectrum giving wide-crested waves, i.e. waves with (infinitely) wide crests.

The input wave data will often be given as, say, the

---

<sup>1</sup>Professor, Dr.Techn., Institute of Hydrodynamics and Hydraulic Engineering, Technical University of Denmark, Building 115, DK-2800 Lyngby - Denmark. Consultant to Danish Hydraulic Institute.

<sup>2</sup>M.Sc., Harbour Engineer, Government Engineering Office, Faroe Islands.

100 year storm, where  $H_s$  and  $f_p$  (peak frequency) have been found by *extrapolation* of wave statistics, based on (i) actual wave records, or (ii) meteorologically based wave hind-cast models, or (iii) a combination of both, for example, involving the forecast of extrapolated 'historical' storms.

It is quite usual to prescribe a *spectrum* corresponding to the average parameters determined during the JONSWAP-project. Because of the special characteristics of this project (offshore wind), this method is not in general completely satisfactory. It would seem better to parameterize the locally recorded spectra and to extrapolate the parameters to 100 years.

In order to obtain reliable results from models of *larger projects*, it is necessary to reproduce the 2-D ( $f, \theta$ )-*spectrum*, i.e. the directional spectrum giving narrow-crested waves. For physical models it is more expensive to work with the directional spectrum because of the large number of wave generators required and the equipment to control them. On the other hand, in a numerical model, when first established, the extra work involved in the use of the 2-D spectrum is often not essential.

In models of *disturbance inside harbours* the directional spread of wave energy can influence the diffraction considerably, cf. Sand et al., 1983 (Ref. 15). For *rubble mound breakwaters* preliminary tests have shown that unidirectional waves may give results on the conservative side in shallow water (see the reference in Lundgren, 1983 (Ref. 8)). On the other hand, recent failures of major breakwaters indicate that the directional spread may give catastrophic 3-D effects, perhaps as a result of the occurrence of freak waves. For *vertical and composite breakwaters*, which may be exposed also to shock forces, one could imagine that the directional spread of energy would give a higher local force but a smaller total force on a long caisson.

The *determination of directional spectra* is discussed in Sec. 2 in terms of what can be characterized as a complete analysis of the 3-D structure of waves. Unfortunately, rather many papers have dealt with computer simulations of directional spectra, and very few have given actual directional distributions from recorded data. Therefore, it would be premature to propose an empirical formula covering the essential part of the energy in directional spectra for storm waves. On the other hand, such a *parameterized formula* is definitely a prerequisite for the extrapolation to rare events. In addition, there is a great need for studies of the *spectrum development because of shoaling and currents*.

For *1-D spectra* the situation is considerably simpler. In this area several parametric formulae have been proposed. The JONSWAP-formula is the most frequently used. It has five parameters and exhibits a discontinuity in curvature

at the peak. In Sec. 3 a four-parameter spectrum (without discontinuities) is proposed for use in typical storm situations. It is called the *F.I.-spectrum* because it was conceived in connection with the analysis of thousands of spectra recorded around the *Faroe Islands* in the North Atlantic. A complete *procedure* for the determination of the *F.I.-parameters* is described in the Appendix.

In recent years many papers have been published about the *grouping of waves*. This is discussed in Sec. 4, and it is contended that all information about the grouping of first order components is inherent in the (directional) spectrum. It is therefore proposed that the international discussion of grouping be discontinued. Related to the grouping is the occurrence of *long waves*, a second order effect that is decisive for harbour resonance and for drift forces. In Sec. 4 the imminent necessity of recording long wave directional spectra is pointed out.

In some models it is sufficient to reproduce the first order components of the (directional) spectrum applying random phases. In other models, however, the higher order effects involved in the *wave shapes* must be included, as briefly discussed in Sec. 5.

## 2. DETERMINATION OF DIRECTIONAL SPECTRA

A survey of the methods hitherto used for the determination of directional spectra is given by Lundgren, 1984 (Ref. 9), as Opening Address at the Symposium on Description and Modelling of Directional Seas, organized June, 1984 by Danish Hydraulic Institute & Danish Maritime Institute.

If a fixed support of instruments cannot be provided, a pitch-roll buoy can be used. It records the water surface elevation  $\eta$  together with two slopes,  $\eta_x$  and  $\eta_y$ , of the water surface. If a fixed support, for example, an offshore platform is available,  $\eta$  can be recorded by a wave radar from above or an echo sounder from below, at the same time as two horizontal velocities,  $u$  and  $v$ , are recorded by a current meter placed below the deepest trough.

In principle, there is little difference between analysing the set  $(\eta, \eta_x, \eta_y)$  and the set  $(\eta, u, v)$ . The latter will be used as basis for the discussion below.

There are two different methods of analysis:

- A. The correlation method, which requires knowledge of all 3 time series,  $\eta(t)$ ,  $u(t)$  and  $v(t)$ , in one vertical. This method can deliver approximate information about only 4 parameters of the directional distribution of energy at each frequency.
- B. The complete FFT-method, which - for practical purposes - requires knowledge of only 2 time series,  $u(t)$  and

$v(t)$ . This method will deliver the most complete information about the directional distribution that can be obtained from the data recorded.

The *correlation method* was first developed by Longuet-Higgins et al., 1963 (Ref. 7). It is based on the 6 auto- and cross-spectra,  $S_{\eta\eta}, S_{uu}, S_{vv}, S_{\eta u}, S_{\eta v}, S_{uv}$ . From these can be derived the first 5 coefficients,  $a_0, a_1, b_1, a_2, b_2$ , in the fourier series development with respect to the direction  $\theta$ . A special correction had to be introduced in order to eliminate the negative side lobes, which would correspond to propagation of negative energy in directions away from the mean direction.

In recent years the correlation method has been further elaborated in a number of papers, cf. for example, Kuik and van Vledder, 1984 (Ref. 5), who give approximate formulae for 4 directional parameters, viz. the circular mean direction, standard deviation, skewness and curtosis. The basis is still the 6 spectra. The same applies to a recent paper by Isobe et al., 1984 (Ref. 4), who describe an extension of the maximum likelihood method to an arbitrary combination of instruments as wave gauges, current meters etc.

The principle of the *complete FFT-method* was first proposed by the senior author in February 1978 and worked out in details by Dr. S. E. Sand, cf. Sand and Lundgren, 1979 (Ref. 14) and, particularly, Sand, 1979 (Ref. 13). It can be described as follows: The FFT-analysis of the three time series delivers - at a particular frequency  $\omega = 2\pi f$  - the fourier coefficients  $A_\eta, B_\eta, A_u, B_u, A_v, B_v$ , where the three A pertain to  $\cos \omega t$  and the three B to  $\sin \omega t$ . ( $A_u, A_v$ ) constitute the velocity vector of a wavelet, for which the energy corresponds to  $|A_u, A_v|^2 = A_u^2 + A_v^2$ . If  $A_\eta$  is positive, the wavelet has a crest for  $t = 0$ , and the vector indicates the direction of energy propagation. If  $A_\eta$  is negative, the wavelet has a trough for  $t = 0$ , and the vector has to be rotated  $180^\circ$  in order to give the direction of energy. In this simplified description the numerical value of  $A_\eta$  is an (unused) redundant. It is possible to utilize it in a least square method (Ref. 13).

In 1984 the FFT-method has been further elaborated in connection with the analysis of data from the North Sea where the wave radar (recording  $\eta$ ) for practical reasons could not be placed vertically above the current meter. For simplicity, only the latter was used in the analysis. For a strong storm without essential swell the major part of the energy propagates within  $\pm 90^\circ$  from the mean direction. Therefore it is easy to distinguish between crests and troughs.

The explanation below will be illustrated with a one hour record from 1983-10-16 with practically constant wave weather with  $H_{m0} = 5.8$  m. With a scanning per 0.5 s there is 7200 data available. Traditionally, this can be divided into 14 subseries, each of 512 data. Each subseries gives

a frequency resolution of  $\Delta f = 1/256$  Hz. For each frequency there are four fourier coefficients,  $A_u, B_u, A_v, B_v$ . The total set of fourier coefficients for all frequencies gives a *complete, deterministic description* of the variation of the velocities (u,v).

Hence, for each subseries there is at each frequency *only* two energy vectors

$$|A_u, A_v| \cdot \{A_u, A_v\} \quad \text{and} \quad |B_u, B_v| \cdot \{B_u, B_v\} \quad (2-1)$$

Seen from a deterministic point of view, these vectors represent the energy spread for the subseries considered. Thus, for 14 subseries there are 28 vectors. This ensemble will already give some idea of the statistical spread of energy.

Much more directional information can be obtained, however, by the method of *overlapping subseries*. Overlapping was introduced by Welch, 1967 (Ref. 17) for reduction of the variance by the determination of spectra. Assuming a  $\cos^2$ -data taper for the subseries and a large number of subseries, giving a variance of one of the spectral value at a certain frequency, the use of overlapping will, according to Welch's formulae, reduce the variance as indicated in Table 1.

Table 1: Reduced variance by overlapping

Overlap of each subseries with the previous one	50%	66.7%	75%	80%	83.3%
5% taper each end	0.730	0.683	0.667	0.660	0.656
10% - - -	0.709	0.660	0.645	0.639	0.636

By 50% overlap the computer work is doubled and the variance reduced to about 70%. For the determination of 1-D spectra it does not pay to go any further.

For 2-D spectra, however, the situation is completely different. Here, *overlapping time series will increase the directional information decisively*. Whereas the one hour record mentioned above gave 28 vectors at each frequency for 14 non-overlapping subseries, an 85% overlap (i.e. a shift of  $0.15 \cdot 512 = 77$  data for each subseries) will give 87 subseries, or 174 energy vectors.

This is illustrated by Fig. 1, showing the directional distribution at the peak frequency 102 mHz. The trough vectors have been rotated  $180^\circ$ , and each vector is referred to one of 180 boxes, each  $1^\circ$  wide. For smoothing, a triangular window with a base width of only  $5^\circ$  has been applied.



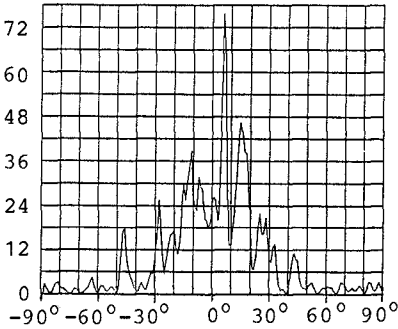


Fig. 1 Directional distribution for 85% overlapping

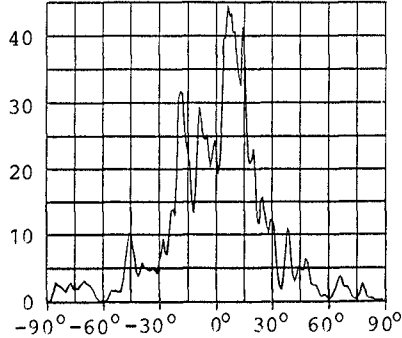


Fig. 2 Directional distribution for 95% overlapping

For comparison, the directional distribution for 95% overlapping is shown in Fig. 2. It is seen to be much smoother. In both cases a 10%  $\cos^2$ -taper has been applied at the ends of a subseries.

It is a fundamental fact that the 1-D spectrum of a field record can be defined only statistically, by a sufficiently long record or by a spectral window. Analogously, the overlapping method leads to the very statistical definition of the directional distribution of energy in a field record.

If the length of the velocity vector  $(A_u, A_v)$  is squared, the vector  $(A_u, A_v) \cdot (A_u^2 + A_v^2)^{1/2}$  is obtained. It is proportional to the energy. Thus, each of these vectors defines an "energy point" in the plane where  $\theta = 0$  is the u-axis and  $\theta = 90^\circ$  the v-axis. Half the points correspond to crests of wavelets, the other half to troughs, which - on the whole - are in the opposite directions.

The first principal axis, with direction  $\theta_0$ , is the mean energy direction. It is found from the equation

$$\tan 2\theta_0 = \frac{\sum A_u A_v (A_u^2 + A_v^2) + \sum B_u B_v (B_u^2 + B_v^2)}{\sum (A_u^2 - A_v^2) (A_u^2 + A_v^2) + \sum (B_u^2 - B_v^2) (B_u^2 + B_v^2)} \quad (2-2)$$

Before Figs. 1-2 were plotted, the coordinate system was rotated the angle  $\theta_0$ , so that the mean energy is in direction  $0^\circ$ . In addition, all energy vectors with directions between  $90^\circ$  and  $270^\circ$  were assumed to correspond to troughs and were rotated  $180^\circ$ . This method implies that the small amount of energy that propagates in directions beyond  $+90^\circ$  or  $-90^\circ$  is mirrored in these directions. At frequencies far from the peak frequency, or if essential swell is involved, it is necessary to include information from the fourier series of  $\eta(t)$  in order to determine the full distribution over  $360^\circ$ .

It should be noted that with the method developed in 1978 a good resolution of the spectrum with respect to frequencies was accompanied by a poor resolution with respect to directions and vice versa. With the overlapping method a *good resolution* can be obtained simultaneously in frequencies and directions.

With this method it should also be possible to study the spectral properties that give rise to *freak waves*.

Excellent *deterministic reproduction* of the 3-D structure of waves may be obtained by means of 60 wave generators, as shown by Agee and Sand, 1984 (Ref. 1).

### 3. F.I.-SPECTRUM

Four waveriders placed around the Faroe Islands have delivered a comprehensive material, for the analysis of which the so-called F.I.-spectrum has been chosen

$$S(f) = A_p (f/f_p)^{-\varphi_1} \exp\left[-B_p (f/f_p)^{-\varphi_2}\right] \quad (3-1)$$

This formula is a generalization of the P-M-spectrum, for which  $\varphi_1 = 5$  and  $\varphi_2 = 4$ . The Ochi-spectrum is the sum of two similar terms, both with  $\varphi_2 = 4$ . At the 19th ICCE in Houston, 1984, Liu (Ref. 6) has, independent of the present authors, reported the use of a formula that differs from (3-1) only in the symbols.

The F.I.-formula can be fitted with good accuracy to more than 95% of all spectra of larger waves. It has only four parameters, because the powers of  $f_p$  may be included in  $A_p$  and  $B_p$ .

A procedure for the determination of  $A_p$ ,  $B_p$ ,  $\varphi_1$ ,  $\varphi_2$  is described in the Appendix. It is based on the moments of (3-1), which can be expressed by means of the  $\Gamma$ -function, see Eq. (A-4). This circumstance has previously been utilized by Ochi and Hubble, 1977 (Ref. 11) and by Houmb, 1984 (Ref. 3). The advantage of using the moments is that they have a much smaller variance than the individual spectral values  $S(f)$ .

An example of an F.I.-fit is shown in Fig. 3 for a 20 minute record with 9 non-overlapping subseries, each of 256 data. (With a 10% data taper it is recommended to use 55% overlapping, cf. Table 1, Sec. 2.) The abscissa is the frequency number  $i = f/\Delta f$ , where  $\Delta f = 1/128$  Hz. The moment  $M(n)$  in (A-2) and its derivatives in (A-12/14) have been taken at  $n = -2$ , with summations extending from  $i_{\min} = 5$  to  $i_{\max} = 30$ .

The spectrum of the wave record is shown with dots. For this spectrum, with  $H_{m0} = 11$  m, the values  $\varphi_1 = 3.5$  and  $\varphi_2 = 10.6$  have been found.

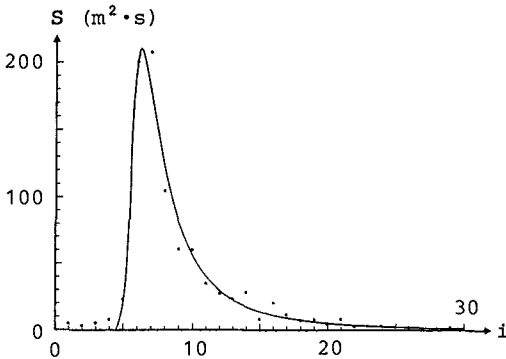


Fig. 3 F.I.-spectrum

#### 4. WAVE GROUPING AND LONG WAVES

It is well known that there is a steadily ongoing *multi-exchange of energy* (or rather wave action) between infinitely many combinations of four wave number vectors. Because of this exchange, *the phases of the infinite number of first order wave components are random*. It is excluded to define a "phase spectrum".

Hence, the *grouping of waves* in a stochastic ensemble of shorter and longer groups is determined uniquely by the spectrum. On the average, a narrow spectrum gives long groups and a wide spectrum short ones. A very long wave record is required in order to obtain a complete statistical picture of the grouping.

For a *steady wave state* the grouping is associated with a pattern of *second order long waves* (SOLW) in such a manner that the long waves have troughs where the short waves are high, and crests where the short waves are small. Formulae for the SOLW for an arbitrary directional sea in arbitrary depth were given by Sharma and Dean, 1979 (Ref. 16). Independently, Ottesen Hansen et al., 1981 (Ref. 12) established the corresponding formulae for a unidirectional sea. The SOLW have frequencies and wave number vectors equal to the differences between frequencies and wave number vectors of pairs of first order wave components.

In practice, however, *all wave states are unsteady*. Because of the movement and the change of the wind field, the change in water depth and current as the waves propagate, wave-wave interaction and energy decay, there is a continuous change of the (directional) spectrum. Since the characteristic frequencies of the long waves are the differences between frequencies of the short ones, the long waves can only gradually adjust themselves to the changing short wave spectrum. If, for instance, the wind field changes direction, the short waves may turn relatively fast, whereas

the long waves will turn much more slowly. Hence, it is possible to speak of a *partial separation* of the long waves from the short ones.

The long waves are responsible for harbour resonance and will often be the dominant cause of drift forces, cf. Lundgren et al., 1982 (Ref. 10). Hence, there is an *urgent need for good records of directional spectra of long waves*. Since long waves have a much larger directional spread than the short ones, it is necessary to determine their distribution over the full circumference of  $360^\circ$ . This cannot be done with a pitch-roll buoy because of its poor response for low frequency heave motions. Therefore, it is necessary to record three time series ( $\eta, u, v$ ) with a fixed installation and analyse the data with the overlapping method.

#### 5. WAVE SHAPE EFFECTS

The spectrum represents the superposition of a large number of small sinusoidal components. In contrast to sine curves, high waves have *elevation skewness*, i.e. the crest height is larger than the trough depth, and they may have *slope skewness*, i.e. the wave front is steeper than its back.

In some model tests, for example with vertical and composite breakwaters, it is necessary to also reproduce the natural wave shapes. The deviations from the "sinusoidal" shapes are *second order short waves* (SOSW), generated by the first order components through the nonlinear surface conditions or the bed slope. The SOSW have frequencies and wave number vectors equal to the sums of frequencies and wave number vectors of pairs of first order wave components, cf. Sharma and Dean, 1979 (Ref. 16).

Because of the high frequencies of the SOSW, they have a good possibility of adjusting themselves to the local first order wave conditions, provided that the bed slope is not too large. By abrupt changes, however, a *partial separation* may take place. This was shown by Biésel, 1963 (Ref. 2) in connection with the diffraction of regular high waves into a harbour model and the refraction across a shoal. In both cases the height of the first order waves changes over a rather short distance and, if the first order wave is reduced to 90%, the corresponding SOSW is reduced to 81%. Therefore, some SOSW energy is released and diffracted/refracted in a different manner.

A particularly strong nonlinear effect is present in *freak waves*, where a very high 3-D crest is surrounded by troughs of normal depth, cf. Fig. 4.

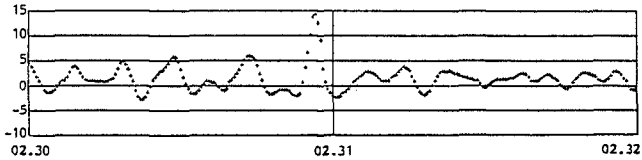


Fig. 4  
Record with  
freak wave  
from the  
North Sea,  
1981-11-25

#### ACKNOWLEDGEMENTS

The large Faroe Islands Wave Project has been executed under the auspices of and vigorous support from Mr. M. A. Helmsdal, Government Engineer, Head of Public Works. The wave recorders were installed with the valuable assistance of the Faroe Islands' Coast Guard. The instrumentation, programming and data analysis have profited greatly from the cooperation with Mr. Flemming Lindenstrøm and Mr. Signar Heinesen and their keen interest in the project.

The results presented in this paper could not have been produced without valuable support from management and staff members of Danish Hydraulic Institute, including the use of North Sea data available in the institute. Special thanks go to Mr. Ebbe W. Frederiksen and Mr. Bjarne Donslund for their work with 1-D and 2-D spectra.

#### REFERENCES

1. Aage, C., and Sand, S. E., "Design and Construction of the DHI 3-D Wave Basin", June, 1984, *Symposium on Description and Modelling of Directional Seas*, Technical University, Denmark, Paper B2, 20 p.
2. Biéssel, F., "Radiating Second-Order Phenomena in Gravity Waves", 1963, London, *International Association for Hydraulic Research, Tenth Congress*, Vol. 1, Paper 1.27, pp. 197-203.
3. Houmb, O. G., "Private Communication", 1984.
4. Isobe, M., Kondo, K., and Horikawa, K., "Extension of MLM for Estimating Directional Wave Spectrum", June, 1984, *Symposium on Description and Modelling of Directional Seas*, Technical University, Denmark, Paper A6, 15 p.
5. Kuik, A. J., and van Vledder, G. P., "Proposed Method for the Routine Analysis of Pitch-Roll Buoy Data", June, 1984, *Symposium on Description and Modelling of Directional Seas*, Technical University, Denmark, Paper A5, 13 p.
6. Liu, P. C., "Great Lakes Environmental Research Laboratory/NOAA", September, 1984, *Nineteenth Coastal Engineering Conference*, Houston, Texas, Abstract, p. 104.
7. Longuet-Higgins, M. S., Cartwright, D. E., and Smith, N. D., "Observations of the Directional Spectrum of Sea Waves using the Motions of a Floating Buoy", Easton, Maryland, 1961, *Ocean Wave Spectra, Proceedings of a Conference*, National Academy of Sciences, 1963, pp. 111-132.

8. Lundgren, H., "Trends in Coastal and Port Engineering Research", March, 1983, Colombo, Sri Lanka, *International Conference on Coastal and Port Engineering in Developing Countries*, Opening address, pp. 1-17.
9. Lundgren, H., "Description and Modelling of Natural Seas", June, 1984, *Symposium on Description and Modelling of Directional Seas*, Technical University, Denmark, Opening address, Paper A0, 13 p.
10. Lundgren, H., Sand, S. E., and Kirkegaard, J., "Drift Forces and Damping in Natural Sea States - A Critical Review of the Hydrodynamics of Floating Structures", Cambridge, Massachusetts, August, 1982, *Proceedings of the Third International Conference of Off-Shore Structures (BOSS '82)*, Massachusetts Institute of Technology, Vol. 2, pp. 592-607.
11. Ochi, M. K., and Hubble, E. N., "Six-Parameter Wave Spectra", Honolulu, Hawaii, July, 1976, *Proceedings Fifteenth Coastal Engineering Conference*, ASCE, New York, 1977, Vol. 1, pp. 301-328.
12. Ottesen Hansen, N.-E., Sand, S. E., Lundgren, H., Sørensen, T., and Gravesen, H., "Correct Reproduction of Group-Induced Long Waves", Sydney, Australia, March, 1980, *Proceedings Seventeenth Coastal Engineering Conference*, ASCE, New York, 1981, Vol. 1, pp. 784-800.
13. Sand, S. E., *Three-Dimensional Deterministic Structure of Ocean Waves*, Institute of Hydrodynamics and Hydraulic Engineering, Technical University of Denmark, Ph.D.-thesis, 1979, Series Paper 24, pp. 177 + XI.
14. Sand, S. E., and Lundgren, H., "Three-Dimensional Structure of Waves", London, England, August, 1979, *Proceedings of the Second International Conference on Behaviour of Off-Shore Structures (BOSS '79)*, Vol. 1, pp. 117-120.
15. Sand, S. E., Kirkegaard, J., Larsen, J., and Rodenhuis, G. S., "Numerical and Physical Modelling of Directional Diffraction of Waves", Colombo, Sri Lanka, March, 1983, *International Conference on Coastal and Port Engineering in Developing Countries*, pp. 1290-1303.
16. Sharma, J. N., and Dean, R. G., "Development and Evaluation of a Procedure for Simulating a Random Directional Second Order Sea Surface and Associated Wave Forces", 1979, *Ocean Engineering*, University of Delaware, Rep. 20.
17. Welch, P. D., "The Use of FFT for the Estimation of Power Spectra: A Method based on Time Averaging over Short, Modified Periodograms", 1967 and 1978, *IEEE Transactions Audio and Electroacoustics*, AU-15, pp. 70-73. Reprinted in: Childers, D. G. (edit.) *Modern Spectrum Analysis*, IEEE, Inc., New York, 1978, pp. 17-20.

## APPENDIX: DETERMINATION OF F.I.-PARAMETERS

From the FFT-analysis the empirical spectrum  $S(f)$  is determined at the equidistant values  $f = i \cdot \Delta f$ , with  $i = 1, 2, 3, \dots$ . For simplicity, the spectrum is considered a function of the *frequency number*  $i$ , i.e.

$$S(i) = A i^{-\varphi_1} \exp[-B i^{-\varphi_2}] \quad (\text{A-1})$$

Expressed in frequency numbers, the moment of order  $n$  is

$$\begin{aligned} M(n) &= \sum_{i=1}^{\infty} i^n S(i) \approx \int_0^{\infty} i^n S(i) di \\ &= A \int_0^{\infty} i^{n-\varphi_1} \exp[-B i^{-\varphi_2}] di \end{aligned} \quad (\text{A-2})$$

After introduction of the parameter

$$z = z(n) = (\varphi_1 - n - 1) / \varphi_2 \quad (\text{A-3})$$

and the substitution  $t = B i^{-\varphi_2}$ , (A-2) may be written

$$M(n) = A \varphi_2^{-1} B^{-z} \int_0^{\infty} t^{z-1} e^{-t} dt = A \varphi_2^{-1} B^{-z} \Gamma(z) \quad (\text{A-4})$$

the infinite integral being the definition of the gamma function.

Hence, the problem is, from a knowledge of the moments  $M(n)$ , to determine the four parameters  $A, B, \varphi_1, \varphi_2$ . Since  $\varphi_1$  and  $\varphi_2$  through the parameter  $z$  are 'well hidden' under the  $\Gamma$ -function, this is a seemingly difficult problem. It may be tackled in the following manner: The *logmoment*  $P(n)$  is introduced by taking the logarithm of (A-4)

$$P(n) = \ln M(n) = \ln A - \ln \varphi_2 - z \ln B + \ln \Gamma(z) \quad (\text{A-5})$$

In the following,  $M(n)$  and  $P(n)$  are considered functions of the *continuous variable*  $n$  and may be differentiated with respect to  $n$ .

Since  $z'(n) = -\varphi_2^{-1}$ , the first derivative of (A-5) is

$$P' = P'(n) = M'/M = \varphi_2^{-1} \ln B - \varphi_2^{-1} \psi(z) \quad (\text{A-6})$$

where

$$\psi(z) = \Gamma'(z) / \Gamma(z) \quad (\text{A-7})$$

is the digamma function, also called the psi function.

The derivative of (A-6) is

$$P'' = M''/M - (M'/M)^2 = \varphi_2^2 \psi'(z) \quad (\text{A-8})$$

where  $\psi'(z)$  is the trigamma function. Finally, the derivative of (A-8) is

$$\begin{aligned} P''' &= M'''/M - 3 (M''/M) (M'/M) + 2 (M'/M)^3 \\ &= -\varphi_2^3 \psi''(z) \end{aligned} \quad (\text{A-9})$$

where  $\psi''(z)$  is the tetragamma function.

In (A-8) and (A-9) both  $\varphi_2$  and  $z$  are unknown. Therefore,  $\varphi_2$  is eliminated by introducing the *ratio function*

$$R(z) = (P''')^2 / (P'')^3 = (\psi'')^2 / (\psi')^3 \quad (\text{A-10})$$

where  $P$  is differentiated with respect to  $n$  and  $\psi$  with respect to  $z$ . In principle,  $R(z)$  may be tabulated from published tables of the  $\psi''$  and  $\psi'$  functions.

Assuming that  $P'''$  and  $P''$  have been calculated from the given spectrum for a chosen value of  $n$ , the *procedure* is now: Calculate the value of  $R$  from the first expression in (A-10), and find the corresponding value of  $z$  as the *inverse function*

$$z = z(R) \quad (\text{A-11})$$

from the table mentioned. In practice, no table is needed because an approximate formula for  $z(R)$  is given below.

According to (A-6,8,9), the derivatives  $P'$ ,  $P''$ ,  $P'''$  of the logmoment  $P$  can be found from the moment  $M$  and its derivatives  $M'$ ,  $M''$ ,  $M'''$ . For these derivatives the following formulae are easily derived from (A-2)

$$M'(n) = \sum_{i=1}^{\infty} \ln i \cdot i^n S(i) \quad (\text{A-12})$$

$$M''(n) = \sum_{i=1}^{\infty} \ln^2 i \cdot i^n S(i) \quad (\text{A-13})$$

$$M'''(n) = \sum_{i=1}^{\infty} \ln^3 i \cdot i^n S(i) \quad (\text{A-14})$$

Based on analyses of a number of Faroe Island spectra, the present authors recommend the following *procedure*:

(a) In the sums (A-2,12,13,14) choose  $n = -2$ . ( $n = -1$  has been found not to reproduce a sharp peak in the spectrum sufficiently well.  $n = -3$  has been found to give practically the same spectral shape as  $n = -2$ .) In order to compare the F.I.-parameters for different storms, it is advantageous to use the same  $n$  for all spectra.

(b) The summations in (A-2,12,13,14) must *not* start from  $i = 1$ . The reason is that the left hand side of the F.I. spectral shape is very steep down to extremely small values. Therefore, if the empirical spectrum has points above this steep slope - for example, because of the presence of some swell - such points would influence the F.I.-parameters in a *most disturbing* manner if they were included in the summations. In most cases the following rules may be applied:

- (i) To the left of the maximum,  $S_{\max}$ , of the given spectral values all points are included for which  $S(i) > 0.25 S_{\max}$ .
- (ii) Below  $0.25 S_{\max}$  at least one more point is included but



otherwise the summations stop at the value  $i_{min}$  for which

$$S(i_{min}) - S(i_{min}-1) < 0.8 [S(i_{min}+1) - S(i_{min})] \quad (A-15)$$

this inequality indicating that the steep slope does not continue further to the left.

(c) The summations (A-2,12,13,14) need only extend to a value,  $i_{max}$ , for which the spectral values are so small that they do not influence the sums essentially. In this respect the value  $n = -2$  helps in reducing the influence of large  $i$ -values.

(d)  $M, M', M''$  and  $M'''$  are calculated.

(e)  $P', P''$  and  $P'''$  are calculated.

(f)  $R$  is calculated from (A-10).

(g)  $q$  is calculated from

$$q = \left(1 - \frac{R}{4}\right)^{\frac{1}{2}} \quad (A-16)$$

(h)  $z$  is calculated from the approximation

$$Rz = 1.8024 q + 0.7906 q^2 - 1.5920 q^{4.640} - 2.252 q^{3.379} (1-q)^{1.589} \quad (A-17)$$

The error on  $z$  according to this formula is numerically less than 0.17% for  $z < 1.5$  and less than 0.29% for all  $z$ .

(i) Calculate  $\Gamma(z)$  from the formula

$$1/\Gamma(z) = \sum_{k=1}^{\infty} c_k z^k \quad (A-18)$$

where

k	$c_k$	k	$c_k$
1	1.00000 00000 000000	11	0.00012 80502 823882
2	0.57721 56649 015329	12	-0.00002 01348 547807
3	-0.65587 80715 202538	13	-0.00000 12504 934821
4	-0.04200 26350 340952	14	0.00000 11330 272320
5	0.16653 86113 822915	15	-0.00000 02056 338417
6	-0.04219 77345 555443	16	0.00000 00061 160950
7	-0.00962 19715 278770	17	0.00000 00050 020075
8	0.00721 89432 466630	18	-0.00000 00011 812746
9	-0.00116 51675 918591	19	0.00000 00001 043427
10	-0.00021 52416 741149	20	0.00000 00000 077823

(j) Calculate  $\psi(z)$  from the formula

$$\psi(z) = -\gamma - \frac{1}{z} + \sum_{m=1}^{10} \frac{z}{m(z+m)} + z \Sigma_2 - z^2 \Sigma_3 + z^3 \Sigma_4 - \dots \quad (A-19)$$

where

$$\gamma = 0.57721 56649 \quad \text{and} \quad \Sigma_k = \sum_{m=11}^{\infty} m^{-k} \quad (A-20)$$

[The formula for  $\psi(z)$  has been derived by differentiation of the logarithm of Euler's infinite product for  $1/\Gamma(z)$ . Since  $\psi(z)$  has simple poles at the points  $0, -1, -2, \dots$ , the convergence of the series (A-19) has been improved by separating the first 11 poles with their respective residues.] The numerical values of  $\Sigma_k$  are \*)

$$\begin{aligned} \Sigma_2 &= 9.516\ 633\ 568 \cdot 10^{-2}; & \Sigma_3 &= 4.524\ 917\ 486 \cdot 10^{-3}; \\ \Sigma_4 &= 2.866\ 502\ 175 \cdot 10^{-4}; & \Sigma_5 &= 2.041\ 379\ 870 \cdot 10^{-5}; \\ \Sigma_6 &= 1.549\ 542\ 998 \cdot 10^{-6}; & \Sigma_7 &= 1.224\ 317\ 311 \cdot 10^{-7}; \\ \Sigma_8 &= 9.942\ 690\ 896 \cdot 10^{-9}; & \Sigma_9 &= 8.236\ 974\ 0 \cdot 10^{-10}; \\ \Sigma_{10} &= 6.927\ 213 \cdot 10^{-11}; & \Sigma_{11} &= 5.89777 \cdot 10^{-12}; \\ \Sigma_{12} &= 5.0683 \cdot 10^{-13}; & \Sigma_{13} &= 4.388 \cdot 10^{-14}; \\ \Sigma_{14} &= 3.80 \cdot 10^{-15}; & \Sigma_{15} &= 3.3 \cdot 10^{-16}. \end{aligned}$$

(k) Calculate  $\psi'(z)$  from the formula

$$\psi'(z) = \sum_{m=0}^{10} \frac{1}{(z+m)^2} + \Sigma_2 - 2z \Sigma_3 + 3z^2 \Sigma_4 - 4z^3 \Sigma_5 + \dots \quad (\text{A-21})$$

(l) Find  $\varphi_2$  from (A-8) as

$$\varphi_2 = \left[ \psi'(z) / P''(n) \right]^{\frac{1}{2}} \quad (\text{A-22})$$

(m) Find  $\varphi_1$  from (A-3) as

$$\varphi_1 = z \varphi_2 + n + 1 \quad (\text{A-23})$$

(n) Find B from (A-6) as

$$\ln B = P'(n) \varphi_2 + \psi(z) \quad (\text{A-24})$$

(o) Find A from (A-4) as

$$A = M(n) \varphi_2 B^z / \Gamma(z) \quad (\text{A-25})$$

(p) Plot the graph of  $S(i)$  according to the F.I.-formula (A-1) and compare with the given spectral values. In special cases it may be necessary to choose another value of  $i_{\min}$  than given by the rules (i) and (ii) under item (b) above. In some cases another value than  $n = -2$  may have to be chosen; see (a) above.

(q) Calculate the peak frequency from

$$i_p = \left[ B \varphi_2 / \varphi_1 \right]^{1/\varphi_2} \quad (\text{A-26})$$

and the peak spectral value from

$$S_p = A i_p^{-\varphi_1} \exp\{-\varphi_1 / \varphi_2\} \quad (\text{A-27})$$

\*) The last few decimals in these values are not reliable.

## CHAPTER THIRTY FIVE

### NON-GAUSSIAN CHARACTERISTICS OF COASTAL WAVES

Michel K. Ochi\* and Wei-Chi Wang\*

#### ABSTRACT

This paper presents the results of a study on non-Gaussian characteristic of coastal waves. From the results of the statistical analysis of more than 500 records obtained in the growing stage of the storm, the parameters involved in the non-Gaussian probability distribution which are significant for predicting wave characteristics are clarified, and these parameters are expressed as a function of water depth and sea severity. The limiting sea severity below which the wind-generated coastal waves are considered to be Gaussian is obtained for a given water depth.

#### INTRODUCTION

The profile of wind-generated waves observed in coastal waters is significantly different from that observed in deep water because of finite water depth effects, and the difference is particularly pronounced in severe seas. In general, time histories of coastal waves show a definite excess of high crests and shallow troughs in contrast to those of waves in deep water as demonstrated in Figure 1. This implies that waves in coastal waters where the effect of water depth on wave characteristics is present cannot be considered as a Gaussian random process. Hence, clarification of the non-Gaussian characteristics of coastal waves is highly desirable to provide a basis for statistical prediction of wave characteristics such as wave height, breaking, groupiness, etc.

The purpose of this study is to clarify the non-Gaussian properties of coastal waves which depend on water depth as well as sea severity. In particular, effort is made to clarify the extent to which coastal waves deviate from a Gaussian random process for a given water depth in order to develop more accurate and rational prediction techniques of random wave characteristics. To achieve this goal, a statistical analysis is carried out on wave time histories obtained during a storm by the Coastal Engineering Research Center (CERC) in the Atlantic Ocean Remote Sensing Land-Ocean Experiment (ARSLOE) Project.

---

\* Coastal and Oceanographic Engineering Department, University of Florida, Gainesville, Florida, 32611

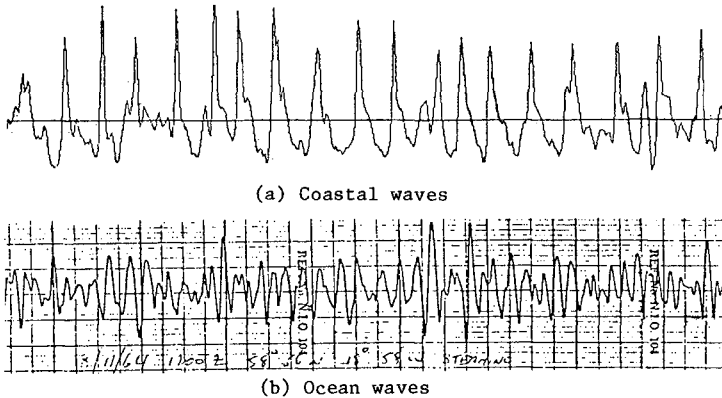


Figure 1: Comparison of coastal and ocean wave profile

The paper consists of three sections. The first section summarizes the results of the statistical analysis based on the non-Gaussian probability density function. From analysis of more than 500 wave records measured at various water depths during the growing stage of the storm, it is found that two parameters associated with skewness and kurtosis, respectively, involved in the Longuet-Higgins' non-Gaussian probability density function are significant for predicting wave characteristics in finite water depth. The second section presents the results of the analysis in which these two parameters are expressed as a function of water depth and sea severity (significant wave height). The third section discusses the limiting sea severity below which wind-generated coastal waves can be considered Gaussian. It is shown that coastal waves in seas for which the parameter representing the skewness is less than 0.2 can be considered as a Gaussian random process irrespective of water depth.

#### PROBABILITY DISTRIBUTION OF WAVE PROFILES

As stated in the introduction, waves in coastal waters cannot be considered as a Gaussian random process, and hence a non-Gaussian probability density function has to be applied for representing the wave profile. Several probability density functions have been introduced to describe non-Gaussian random processes. These can be categorized as being derived from two different approaches: one based on probability theory in which no specific consideration is given to the wave profile, the other based on an approximation to the wave profile. The Gram-Charlier probability density function (Cramér 1946) derived from the concept of orthogonal polynomials is a well-known example of the former approach. Since Hermite polynomials are orthogonal with respect to the normal distribution,

the probability density function is expanded in a series of Hermite polynomials. The Edgeworth series probability density function (Edgeworth 1905) is derived following the same basic concept as the Gram-Charlier series but the series expansion method is different and the expanded terms are expressed in terms of cumulants. On the other hand, the Longuet-Higgins series probability density function (Longuet-Higgins 1963) is derived by applying the cumulants generating function. In his approach, the integrations involved in the derivation are expressed in terms of Hermite polynomials. Although these three probability density functions are derived by applying different theorems in probability theory, the results are similar.

In contrast to the approach considered for the above three probability density functions, Tayfun (1980) and Huang et al. (1980) (1983) derived probability density functions based on the approximation that waves can be expressed as a Stokes expansion to the 2nd and 3rd order components. This is certainly one way to present non-Gaussian characteristics of coastal waves. However, an important object of the present study is to clarify the extent to which coastal waves deviate from a Gaussian random process; hence, it may be well not to impose any preliminary form on wave profile representation in analyzing data obtained in coastal waters. Hence, the following non-Gaussian probability density function derived by Longuet-Higgins is considered in the present study:

$$f(x) = \frac{1}{\sigma\sqrt{2\pi}} e^{-\frac{x^2}{2\sigma^2}} \left[ 1 + \frac{\lambda_3}{3!} H_3\left(\frac{x}{\sigma}\right) + \frac{\lambda_4}{4!} H_4\left(\frac{x}{\sigma}\right) + \frac{\lambda_5}{5!} H_5\left(\frac{x}{\sigma}\right) + \dots \right] \quad (1)$$

where,  $\sigma^2$  = variance of wave deviation from the mean

$$\lambda_3 = \kappa_3 / (\sqrt{\kappa_2})^3 = \text{skewness}$$

$$\lambda_4 = \kappa_4 / (\kappa_2)^2 = \text{kurtosis} - 3$$

$$\lambda_5 = \kappa_5 / (\sqrt{\kappa_2})^5$$

$\kappa_j$  = cumulants

$H_n\left(\frac{x}{\sigma}\right)$  = Hermite polynomial of degree n

In applying the above probability density function to the analysis of coastal waves, the following remarks are made:

(1) The probability density function given in Equation (1) at times becomes negative for large negative x depending on the value of  $\sigma$ . However, this should not cause any trouble in practice, since the

x-values where the function becomes negative are usually outside the range where the histogram exists as will be shown later.

(2) The accuracy of a function which is expressed in the form of a series increases with increase in higher order terms, in general. However, this is not the case for the probability density function given in Equation (1). The results of comparisons between histograms and the probability density function have shown that higher order terms do not necessarily yield better agreement. Therefore, it is highly desirable to examine terms of the series which significantly contribute to the distribution.

In order to clarify questions that might surface from the above remarks, more than 500 wave records measured at various water depths during the growth stage of the storm in the ARSLOE Project are analyzed. Details of wave data used in the present study are summarized in the Appendix.

Figure 2 shows an example of a comparison between the probability density function given in Equation (1) with a histogram of the wave profile obtained at a water depth of 1.4 m. The significant wave height is 2.05 m which is considered to be severe for this water depth. Four variations of the probability density function are compared with the histogram. These four variations represent, respectively, the first term of the series (which is the normal distribution), the first two terms (including the parameter  $\lambda_3$ ), the first three terms (including the parameters  $\lambda_3$  and  $\lambda_3^2$ ), and the first four terms (including the parameters  $\lambda_3$ ,  $\lambda_3^2$ , and  $\lambda_4$ ). As can be seen in the figure,

(1) The histogram deviates substantially from the normal distribution.

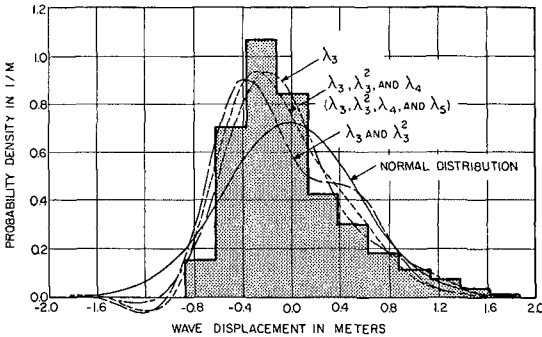


Figure 2: Comparison between observed histogram, Gaussian distribution (heavy line), and Non-Gaussian distribution: Water depth 1.4 m, Significant wave height 2.1 m

(2) The probability density function becomes negative for large negative  $x$ . However, the magnitude of the negative probability density function is relatively small; on the order of 2 percent or less. Furthermore, the negative density occurs outside the range of the histogram. Therefore, it will not cause any serious problem if we assume this negative probability density to be zero and, in turn, normalize the entire probability density function so that the area of the density function becomes unity.

(3) The probability density function which includes the parameter  $\lambda_3$  only agrees reasonably well with the histogram.

(4) The agreement with the histogram becomes poor if the term with the parameter  $\lambda_3$  is included in addition to the  $\lambda_3$ -term in the probability density function. Although not included in Figure 1, the same trend is obtained if the term with the parameter  $\lambda_4$  is included in addition to the  $\lambda_3$ -term.

(5) The probability density function consisting of terms with the parameters  $\lambda_3, \lambda_3^2, \lambda_4$  agrees well with the histogram.

(6) The addition of the parameter,  $\lambda_5$ , to the probability density function does not yield any appreciable change in the shape of the probability density function.

The same trend as stated above was also observed for many other wave records obtained at various water depths in various sea severities. Some examples are shown in Figures 3(a) through 3(c) for which the water depth ranges from 3.7 m to 8.8 m.

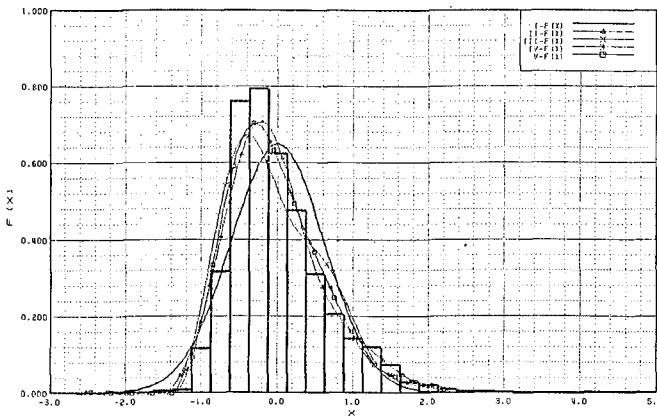
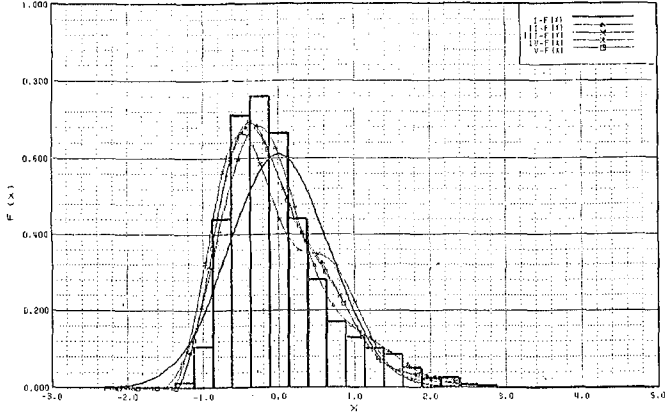
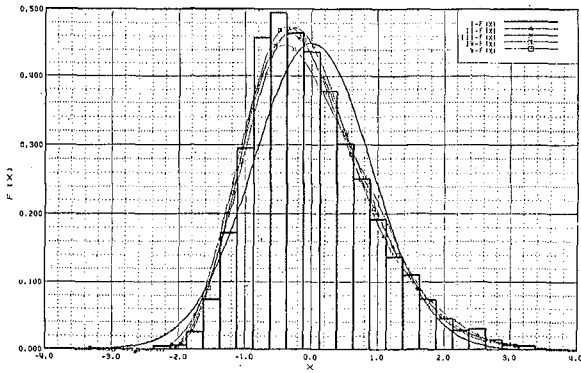


Figure 3: Comparison between observed histogram, Gaussian distribution (heavy line), and non-Gaussian distribution:

(a) Water depth 3.7 m, significant wave height 2.45 m



(b) Water depth 6.0 m, significant wave height 2.60 m



(c) Water depth 8.8 m, significant wave height 3.55 m

ANALYSIS OF PARAMETERS OF THE PROBABILITY DISTRIBUTION FUNCTION

It was shown in the previous section that  $\lambda_3$  and  $\lambda_4$  in Equation (1) are the significant parameters which govern the non-Gaussian probability density function for representing the distribution of wave profiles. Since the non-Gaussian characteristics of coastal waves depend on water depth and sea severity, it may be well to examine these parameters as a function of water depth and sea severity.



It was first thought that the parameter  $\lambda_3$  was a function of significant wave height and wave period. However, wave records show that  $\lambda_3$  appears to depend on significant wave height only. To substantiate this, an example of the variation of significant wave height, water depth, and the parameter  $\lambda_3$  with time during the growing stage of the storm are shown in Figure 4. The data were obtained at an average water depth of 1.4 m during the storm. As can be seen in the figure, the water depth varies with time by a substantial amount due to the tide. This results in an increase and decrease in significant wave height with the same period as the tide but the magnitude at high tide increases consistently during the growing stage of the storm. The time history of the magnitude of the parameter  $\lambda_3$  computed at hourly intervals (although a few points are missing) demonstrates nearly the same pattern as that of the significant wave height. Thus, it is clear that the parameter  $\lambda_3$  has a functional relationship with significant wave height.

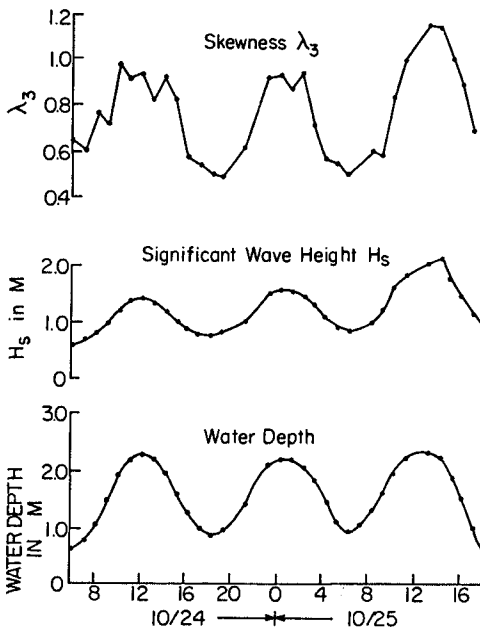
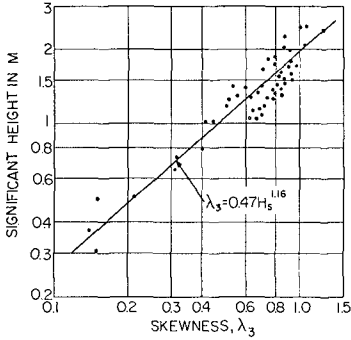


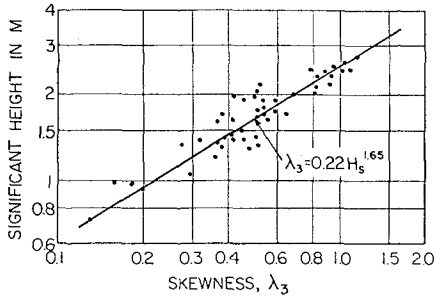
Figure 4:

Variation of water depth, significant wave height, and skewness with time: Water depth 1.4 m

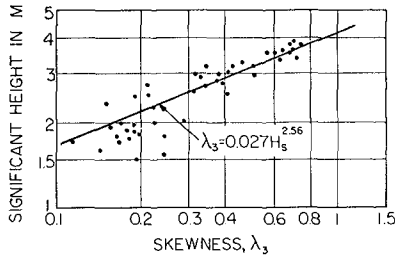
The parameter  $\lambda_3$  computed from records measured at various water depths is plotted against significant wave height, and some examples are shown in Figures 5(a) through 5(c). It is noted that the results presented in these figures are at locations where waves were measured, and that the water depth given in each figure is the average water depth during the storm at that location (see Figure 13



(a) Water depth 2.0 m



(b) Water depth 3.7 m



(c) Water depth 8.8 m

Figure 5:  
Parameter  $\lambda_3$  as a function of significant wave height

in the Appendix). Included in each figure is the functional relationship between  $\lambda_3$  and significant wave height expressed in the form of  $\lambda_3 = a(H_s)^b$ , where  $H_s$  is the significant wave height and the coefficients "a" and "b" are obtained by drawing the average line in the figure.

The coefficients "a" and "b" obtained from Figure 5 are plotted against the (average) water depth and the results are shown in Figure 6(a) and 6(b), respectively. As can be seen in these figures, the values of the coefficients "a" and "b" evaluated at a location where the water depth was in the range of 5.5 m to 6.0 m deviate from the average line drawn in the figure. That is, for a given significant wave height, the skewness evaluated from the record is greater than that evaluated by using the values obtained from the average line. This implies that the water depth of 5.5 m to 6.0 m appears to be the breaker depth during the storm, and hence the non-Gaussian characteristics of the waves in this particular water depth range are relatively more pronounced.

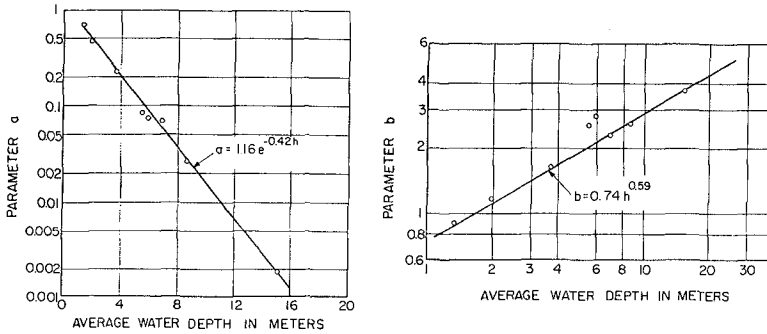


Figure 6: Parameters "a" and "b" as a function of water depth

The coefficients "a" and "b" are expressed as a function of the average water depth,  $h$ , as shown in Figure 6, and thereby the parameter  $\lambda_3$  can be evaluated in terms of water depth and sea severity as follows:

$$\lambda_3 = 1.16 e^{-0.42h} \cdot H_s^{0.74} h^{0.59} \quad (2)$$

where,  $h$  = average water depth in meters  
 $H_s$  = significant wave height in meters

Next, the parameter  $\lambda_4$  is evaluated from the records and its values are plotted against the parameter  $\lambda_3$  as shown in Figure 7. Several interesting features of the results shown in the figure are apparent. These are,

(1) There is considerable scatter in the values of  $\lambda_4$  for values of  $\lambda_3$  less than 0.2. These are values obtained from records taken at locations where the water depth is relatively deep; on the order of 15 to 25 meters. Although the values of  $\lambda_4$  vary considerably for  $\lambda_3$  less than 0.2, the shape of the distribution appears to be very close to that of the normal distribution. As an example, Figure 8 shows a comparison between the non-Gaussian probability density function with  $\lambda_3 = 0.2$  and  $\lambda_4 = -0.15$  and the normal probability density function in the standardized form. As can be seen, there is no difference between these two probability density functions. From the results of many similar comparisons, it may safely be concluded that the non-Gaussian presentation of coastal wave profiles (in standardized form) with a value of  $\lambda_3$  less than 0.2 can be approximated by the Gaussian probability density function (in standardized form).

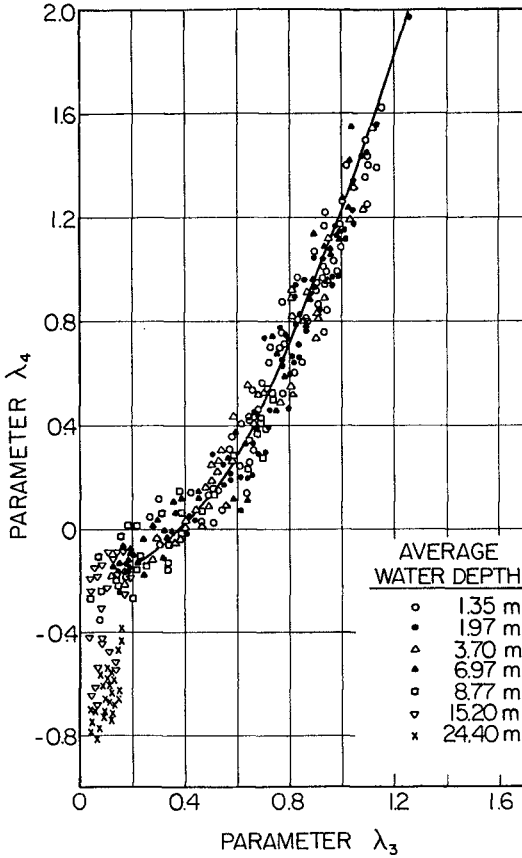
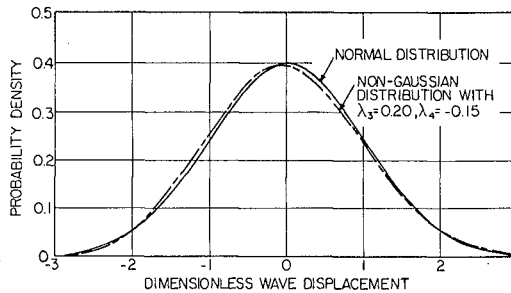


Figure 7:  
Parameter  $\lambda_4$  as a function of parameter  $\lambda_3$

Figure 8:  
Comparison between normal probability distribution and non-Gaussian distribution with  $\lambda_3 = 0.20$  and  $\lambda_4 = -0.15$



(2) The largest value of the parameter  $\lambda_3$  obtained in the present analysis is 1.26 with the parameter  $\lambda_4$  of 1.98. This is observed in a severe sea of significant wave height 2.31 m at a water depth of 1.97 m. Figure 9 shows the histogram of the wave profile together with a portion of the wave record.

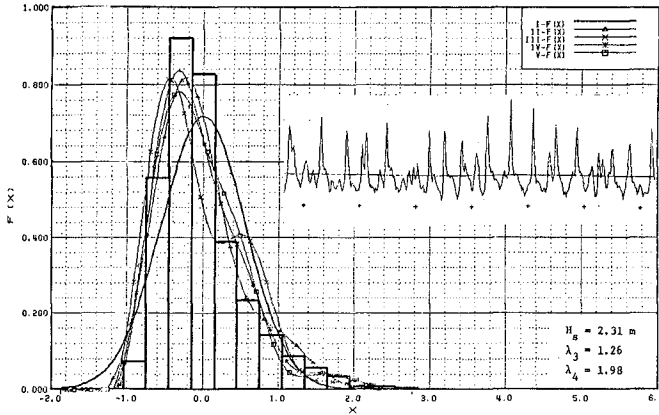


Figure 9: Histogram, probability distribution and portion of wave record for significant wave height 2.31 m at water depth 2.0 m

(3) There is some scatter in the  $\lambda_4$ -values for a specified  $\lambda_3$ . For example, the value of  $\lambda_4$  spreads from 0.45 to 0.90 with an average value of 0.70 for  $\lambda_3 = 0.8$ . However, the difference in the  $\lambda_4$ -values for a specified  $\lambda_3$  does not seriously affect the shape of the non-Gaussian probability density function. For instance, Figure 10 shows a comparison between three probability density functions having the same  $\lambda_3$ -value (0.8), but with values of  $\lambda_4$  of 0.45, 0.70 and 0.90. Included also in the figure is the Gaussian probability density function. As can be seen, the shape of the non-Gaussian probability density functions computed by Equation (1) differ significantly from that of the Gaussian density function, but there is no substantial difference between the shapes of the non-Gaussian distributions. In other words, the scatter in the  $\lambda_4$ -values for a given  $\lambda_3$  does not result in any serious difference in the shape of the probability density function.

From the discussion and subsequent conclusions stated in Items (1) and (3) above, the relationship between  $\lambda_3$  and  $\lambda_4$  can be formulated by taking the average value of  $\lambda_4$  for a specified  $\lambda_3$ -value. That is,

$$\lambda_4 = \begin{cases} -0.15 + 1.10 (\lambda_3 - 0.20)^{1.17} & \text{for } 0.2 < \lambda_3 < 0.5 \\ -0.15 + 1.10 (\lambda_3 - 0.20)^{1.17} + 1.48 (\lambda_3 - 0.50)^{1.47} & \text{for } \lambda_3 > 0.5 \end{cases} \quad (3)$$

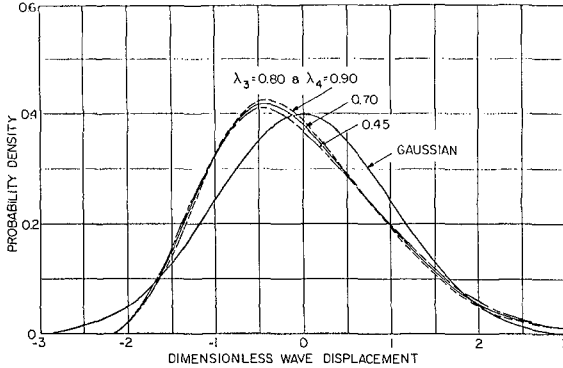


Figure 10: Comparison between normal probability distribution and non-Gaussian distribution with  $\lambda_3 = 0.80$  and  $\lambda_4 = 0.45, 0.70,$  and  $0.90$

#### NON-GAUSSIAN PROPERTIES AND WATER DEPTH

As discussed earlier, the non-Gaussian characteristics of wind-generated coastal waves depends on water depth as well as sea severity. That is, even though the water depth is shallow, waves may still be considered to be a Gaussian random process if the sea severity is mild. Therefore, it may be of considerable interest to examine the limiting sea severity below which wind-generated coastal waves are considered to be Gaussian.

In the discussion of Figure 8, it was stated that the non-Gaussian presentation of coastal wave profiles with a value of  $\lambda_3$  less than 0.2 can be approximated by the Gaussian probability distribution, where  $\lambda_3$  is expressed as a function of water depth and sea severity in Equation (2). Therefore, it may be well to confirm whether or not the significant wave height which yields  $\lambda_3 = 0.2$  computed from Equation (2) for a given water depth represents the limiting sea severity below which the seas can be considered to be a Gaussian random process.

For this, histograms of the wave profile obtained at various water depths are examined to find the severest sea state (significant wave height) below which the histograms approximate a normal distribution. As an example, Figure 11 shows the histogram as well as a portion of the wave record obtained in a sea of significant wave height 1.52 m at a location of water depth 7.0 m. This is the largest significant wave height below which Gaussian characteristics were observed during the storm at this location. The computed value of the parameter  $\lambda_3$  is 0.19. A similar analysis was made at various water depths and the results are shown in Figure 12. Included also

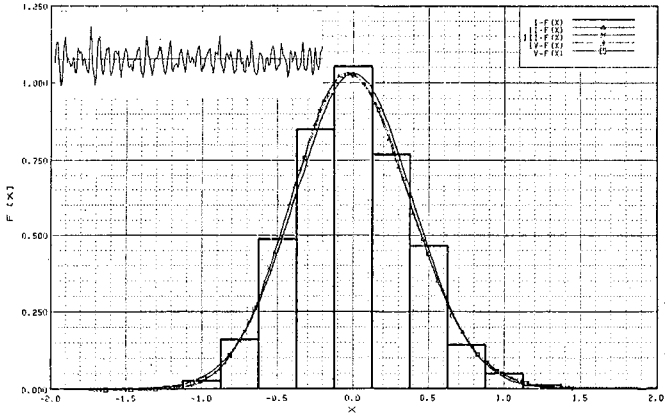


Figure 11: Histogram, probability distribution and portion of wave record for significant wave height 1.52 m at water depth 7.0 m

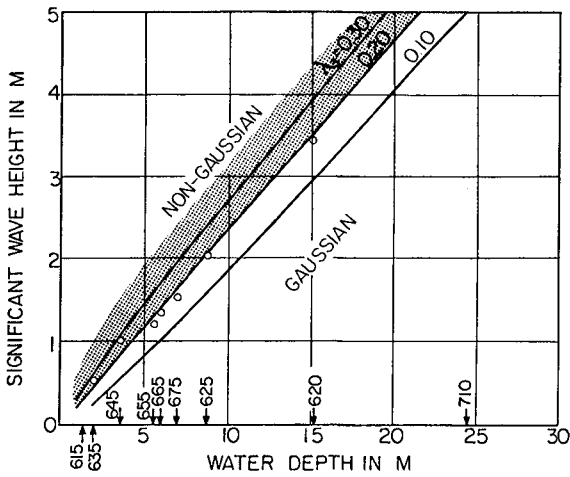


Figure 12: Largest significant wave height below which non-Gaussian characteristics are expected as a function of water depth

in the figure are the lines indicating various  $\lambda_3$ -values computed from Equation (2). As can be seen, the largest significant wave height below which Gaussian characteristics are observed for water depths up to 15 m agrees well with the line for  $\lambda_3 = 0.20$ .

It is noted that the largest significant wave height observed at a water depth of 24.4 m was 4.34 m during the storm, and that all histograms of the wave profile obtained at this location approximate a normal probability distribution. It thus appears that the sea severity at this location did not reach a level during the storm to produce non-Gaussian characteristics. Thus, although confirmation could not be made for a water depth of 24 m, it may safely be concluded from Figure 12 that coastal waves in seas for which the parameter  $\lambda_3$  (skewness) is less than 0.2 can be considered as a Gaussian random process irrespective of water depth.

#### CONCLUSIONS

This paper presents the results of a study on non-Gaussian properties of coastal waves. From the results of statistical analysis of more than 500 records obtained in the growing stage of the storm, the following conclusions are drawn:

1. Time histories of coastal waves show a definite excess of high crests and shallow troughs, in general, and waves are considered to be a non-Gaussian random process. The non-Gaussian characteristic depends on water depth and sea severity.
2. The parameter  $\lambda_3$  which represents the skewness of the wave profile is the dominant parameter affecting the non-Gaussian characteristics of coastal waves, and that the combination of the parameters  $\lambda_3$ ,  $\lambda_2$ , and  $\lambda_4$  (where  $\lambda_4 = \text{kurtosis} - 3$ ) best represent the non-Gaussian probability density function (see Equation 1) applicable to coastal waves.
3. The parameter  $\lambda_3$  can be evaluated from Equation (2) as a function of water depth and sea severity. However, the non-Gaussian presentation (in standardized form) of coastal wave profiles with a value of  $\lambda_3$  less than 0.2 can be approximated by the Gaussian probability density function (in standardized form).
4. The parameter  $\lambda_4$  can be evaluated from Equation (3) as a function of  $\lambda_3$ .
5. From the conclusion stated in Item 3, it is possible for a given water depth to evaluate the limiting sea severity below which wind-generated coastal waves are considered to be Gaussian. That is, coastal waves in seas for which the parameter  $\lambda_3$  (skewness) is less than 0.2 can be considered as a Gaussian random process irrespective of water depth.



ACKNOWLEDGEMENTS

Part of this study was carried out under the sponsorship of the Office of Naval Research, Ocean Technology Program through Contract N00014-83-K-0157 to the University of Florida in connection with a project on prediction of wind-generated waves in finite water depth. The authors would like to express their appreciation to Dr. Silva, Office of Naval Research, for his encouragement and valuable discussion received during the course of this project.

APPENDIX: WAVE DATA

The wave data used in the present study were obtained by the Coastal Engineering Research Center (CERC), U.S. Army, at its Field Research Facility, located at Duck, North Carolina. The Field Research Facility has a 550-meter-long research pier extending into the Atlantic Ocean, equipped with seven Baylor resistance-type wave gages (see Figure 13). Extensive wave measurements were made at this site for two months in 1980 under the Atlantic Ocean Remote Sensing

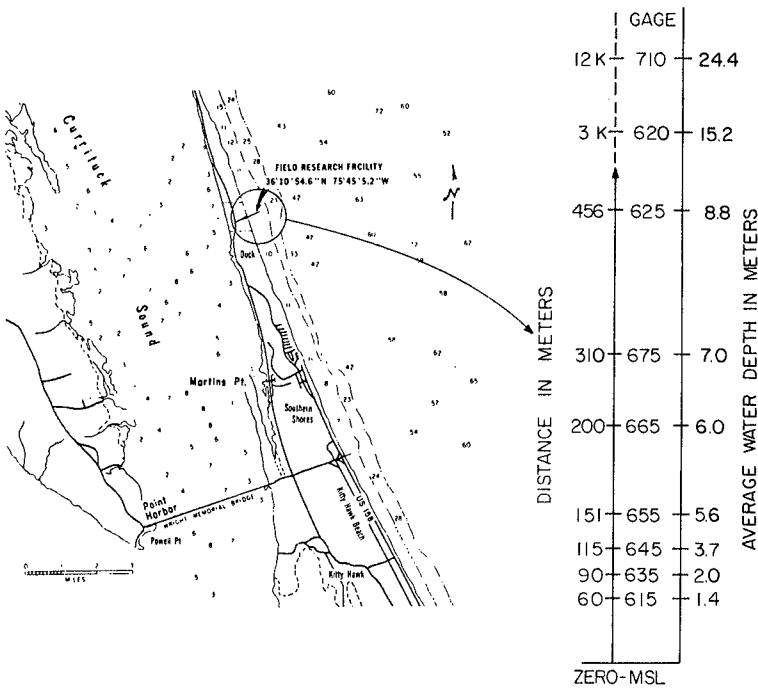


Figure 13: Coastal Engineering Research Center (CERC) Field Research Facility, Duck, North Carolina (By courtesy of CERC)

Land-Ocean Experiment (ARSLOE) Project. The details of this project may be found in several publications, Vincent and Lichy (1981), for example.

During October 23-25, an extratropical cyclon moved directly through the experimental area with wind speeds on the order of 10-15 m/sec. Continuous wave records were taken by the CERC Field Research Facility during the storm. The wave data analyzed in the present study are those recorded at the seven locations along the research pier and an additional two buoys (wave riders) located offshore along the extended line of the pier. The location of the wave gages and wave riders as well as the average water depth measured on October 21 and 27 by CERC are given in the figure.

#### REFERENCES

- Cramer, H., (1946): Mathematical Methods of Statistics", Princeton Univ. Press.
- Edgeworth, F.Y., (1905): "The Law of Error", Trans. Camb. Phil. Soc., Vol. 20, pp 36-65.
- Huang, N. and Long, S.R., (1980): "An Experimental Study of the Surface Elevation Probability Distribution and Statistics of Wind-Generated Waves", Journal Fluid Mech., Vol. 101, Part 1, pp 179-200.
- Huang, N.E., et al., (1983): "A Non-Gaussian Statistical Model for Surface Elevation of Non-Linear Random Wave Fields", Journal, Geophy. Res., Vol. 88, No. C12, pp 7597-7606.
- Longuet-Higgins, M.S., (1963): "The Effect of Non-Linearities on Statistical Distribution in the Theory of Sea Waves", Journal Fluid Mech., Vol. 17, Part 3, pp 459-480.
- Tayfun, M.A., (1980): "Narrow-Band Non-Linear Sea Waves", Journal, Geophy. Res., Vol. 85, No. C3, pp 1548-1552.
- Vincent, C.L. and Lichy, D.E., (1981): "Wave Measurements in ARSLOE", Proc. Conf. Directional Wave Spect. Applications, pp 71-86.

## CHAPTER THIRTY SIX

### STATISTICAL PROPERTIES OF SHORT-TERM OVERTOPPING

Akira Kimura\* and Akira Seyama\*\*

#### 1. INTRODUCTION

It has been recognized recently that large waves tend to form a group in random sea waves. Overtopping tends to occur particularly when a group of high waves attacks a sea wall. If the capacity of a storage reservoir inside the sea wall is not sufficiently large enough to store a total amount of overtopping brought about by a single group of consecutive high waves, and if a drainage facility is not large enough to pump out sufficient water from the storage reservoir before the next overtopping starts, there is a danger of flooding inside the sea wall. Hence, storage and drainage facilities should be planned to be able to cope with the total amount of overtopping produced by a single group of high waves which overtop the sea wall consecutively. The term "short-term overtopping" referred in this study is that caused by a single group of high waves (see Fig.1). This study aims to clarify the following points:

- (1) the statistical properties of the amount of short-term overtopping,
- (2) the method to evaluate a security factor inside a sea wall against flooding by overtopping and an extension of the theory to the short-term overtopping from a comparatively long sea wall.

#### 2. PROBABILITY DISTRIBUTION OF SHORT-TERM OVERTOPPING

Short-term overtopping from a vertical (steep) sea wall located off a breaking zone is investigated in this paper. Following three assumptions are made to introduce statistical properties of short-term overtopping amount from a sea wall:

- (1) characteristics of an overtopping of zero-up-crossing wave from a sea wall can be approximated by a existing theory for periodic wave,

\* Associate Professor, \*\* Professor of the Dept. of Ocean Civil Engg., Faculty of Engg., Tottori Univ., Tottori, Japan

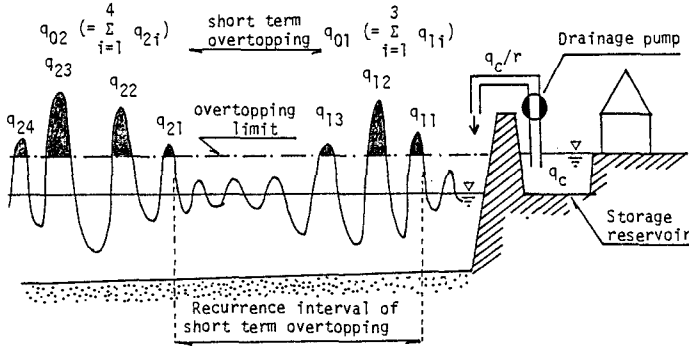


Fig.1 Explanation of the short-term overtopping and schematic illustration of the sea wall, storage reservoir and drainage pump

- (2) characteristic of an overtopping is not affected by neighboring waves but can be evaluated only by properties of an individual wave,
- (3) statistical distribution of wave height can be approximated as the Rayleigh distribution.

Beside above assumptions, wave period of overtopping waves are assumed to be constant, since high waves in random sea tend to have a constant wave period as recent studies on the joint probability distribution of wave height and period have pointed out<sup>4),7)</sup>.

The overtopping equation by Kikkawa et al.<sup>5)</sup> was applied in this study. They gave a simple overtopping equation in terms of a wave height, period and properties of a sea wall as follows.

$$q' / TH\sqrt{2gH} = 2/15 \cdot m_0 k^{3/2} (1 - Z/kH)^{5/2} \tag{1}$$

in which  $q'$ : overtopping amount of a wave from a unit length of a sea wall,  $H$ : incident wave height just outside a sea wall,  $T$ : wave period,  $Z$ : sea wall height,  $m_0, k$ : constants which characterize a shape and location of a sea wall (for a vertical sea wall located off a breaking zone, the value of

$m_0=0.5, k=0.6$  are recommended by Kikkawa et al.<sup>5)</sup>,  $g$ : gravitational acceleration. From eq.(1) an overtopping amount of the mean wave ( $\bar{H}, \bar{T}$ ) in case of  $Z=0$  is given by

$$\bar{q} = \sqrt{8}/15 \cdot m_0 k^{3/2} g^{1/2} \bar{T} \bar{H}^{3/2} \tag{2}$$

q' in eq.(1) is normalized with  $\bar{q}$  to yield

$$q = q'/\bar{q} = th^{3/2} (1 - \frac{z}{h})^{5/2} \tag{3}$$

in which  $t=T/\bar{T}$ ,  $h=H/\bar{H}$  and  $z=Z/k\bar{H}$ .

Analyzing the results presented by Goda<sup>4)</sup>, it appears that wave periods of high waves tend to distribute around 1.1 times of the mean wave period. t is put equal to 1.1 in this study. Thus a normalized overtopping amount is given only in terms of h when the properties of the sea wall are given. An amount of a short-term overtopping brought about by n high waves  $(h_1, h_2, \dots, h_n)$  which overtop the sea wall consecutively is determined as

$$q_0 = \sum_{i=1}^n q(h_i) \tag{4}$$

in which  $q(h_i)$  ( $i=1,2,\dots,n$ ) is given by eq.(3).

If the above-mentioned n wave heights are classified into following ranks

$$\begin{array}{lll}
 \text{rank} & 1 & : \quad 0 < h_i \leq z \\
 & " & 2 & : \quad z < h_i \leq z + \Delta h \\
 & \dots & \dots & \dots \dots \dots \dots \dots \\
 & " & j & : \quad z + (j-2)\Delta h < h_i \leq z + (j-1)\Delta h \\
 & \dots & \dots & \dots \dots \dots \dots \dots
 \end{array} \tag{5}$$

and if these n waves belong to the ranks  $j_1, j_2, \dots, j_n$  respectively and since the time series of zero-up-crossing wave height has close properties to those of the Markov chain<sup>6)</sup>, the probability that they appear in this order is given as

$$p(j_1, j_2, \dots, j_n) = p_{j_1} p_{j_1 j_2} \dots p_{j_{(n-1)} j_n} \tag{6}$$

in which  $p_{j_i}$ : probability that wave  $h_i$  belongs to the rank  $j_i$ ,  $p_{j_i j_{(i+1)}}$  ( $i=1,2,\dots$ ): probability that consecutive two waves belong to the rank  $j_i$  and  $j_{(i+1)}$  in this order respectively and so on. These probabilities are given as follows in this study<sup>6)</sup>.

$$P_{ji} = \int_{z+(ji-2)\Delta h}^{z+(ji-1)\Delta h} P(h) dh \quad (7)$$

and

$$P_{jij(i+1)} = \frac{\int_{z+(ji-2)\Delta h}^{z+(ji-1)\Delta h} \int_{z+[j(i+1)-2]\Delta h}^{z+[j(i+1)-1]\Delta h} P(h_1, h_2) dh_1 dh_2}{\int_{z+(ji-2)\Delta h}^{z+(ji-1)\Delta h} P(h) dh} \quad (8)$$

from the third assumption,  $P(h)$  and  $P(h_1, h_2)$  are given as<sup>6)</sup>

$$P(h) = \pi h/2 \cdot \exp(-\pi h^2/4) \quad (9)$$

$$P(h_1, h_2) = h_1 h_2 \cdot I_0[h_1 h_2 \rho/A] \cdot \exp[-(h_1^2 + h_2^2)/\pi A]/A \quad (10)$$

and

$$A = 4/\pi^2 - \rho^2$$

in which  $I_0$ : modified Bessel function of order 0,  $\rho$ : the correlation parameter which has the following relation with the correlation coefficient of the consecutive two wave heights<sup>1), 6)</sup>.

$$\gamma_h = \{E(\pi\rho/2) - (1/2)(1 - \pi^2\rho^2/4)K(\pi\rho/2) - \pi/4\} / (1 - \pi/4) \quad (11)$$

in which  $\gamma_h$ : correlation coefficient of consecutive wave heights,  $K$  and  $E$ : complete elliptic integrals of the 1st and 2nd kinds. When  $\Delta h$  in eq.(5) is sufficiently small, eqs.(7) and (8) can be replaced by eqs.(7)' and (8)'<sup>6)</sup>.

$$P_{ji} = \pi h_i/2 \cdot \exp(-\pi h_i^2/4) dh \quad (7)'$$

and

$$P_{jij(i+1)} = 2h_{i+1}/\pi A \cdot I_0(h_i h_{i+1} \rho/A) \cdot \exp[-(h_i^2 + h_{i+1}^2)/\pi A + \pi h_i^2/4] dh \quad (8)'$$

The probability that a short-term overtopping amount becomes  $q_0$ , when the above mentioned  $n$  waves overtop consecutively

in this order from a unit length of the sea wall, is given as

$$P_1(q_0) dq = \int \int \dots \int_D p_{j1} p_{j1j2} \dots p_{j(n-1)jn} dh_1 dh_2 \dots dh_n \tag{12}$$

where D is the region which is determined as

$$D : q_0 < \sum_{i=1}^n q(h_i) \leq q_0 + dq \tag{13}$$

D is schematically shown in Fig.2 when n=2 for example.

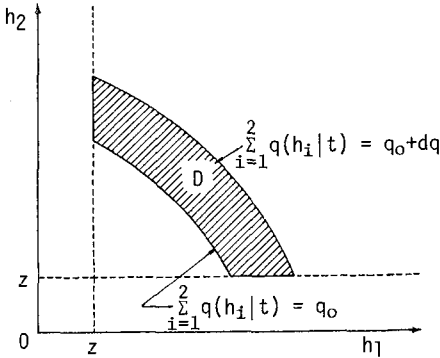


Fig.2 Region D (hatched area)

Region D (hatched area) the boundaries of which are given by the equations

$$\begin{aligned} \sum_{i=1}^2 q(h_i | t) &= q_0 \\ \sum_{i=1}^2 q(h_i | t) &= q_0 + dq \\ h_1 &> z \quad h_2 > z \end{aligned}$$

in which z: normalized sea wall height (eq.3). No over-topping takes place when an incident wave height is not larger than z. Since the region D and the probabilities  $p_{ji}$  and  $p_{jij(i+1)}$  in eq.(12) have complex forms, this equation is integrated numerically in this study. In such a case, the

more number of waves in a high wave group increases the longer becomes the computing time. But if a sea wall height is not so low, the expected run of waves in the longest high wave group which may appear during a single storm period is not so large. From the theory of a run of waves<sup>6)</sup>, the probability distribution of a run of high waves is given as

$$P_2(\ell) = p_{22}^{\ell-1} (1-p_{22}) \quad (14)$$

where  $p_{22}$ : probability that consecutive two waves exceed the threshold wave height  $h_*$ , which is given by

$$P_{22} = \frac{\int_{h_*}^{\infty} \int_{h_*}^{\infty} P(h_1, h_2) dh_1 dh_2}{\int_{h_*}^{\infty} P(h) dh} \quad (15)$$

$P(h)$  and  $P(h_1, h_2)$  are given by eqs.(9) and (10) respectively. Therefore, the probability that a run of high waves does not exceed  $\ell_* - 1$  is

$$P_3(\ell_* - 1) = \sum_{\ell=1}^{\ell_* - 1} p_{22}^{\ell-1} (1-p_{22}) = (1-p_{22}^{\ell_* - 1}) \quad (16)$$

Among  $N$  sets of independent high wave runs, the probability that no run exceeds  $\ell_* - 1$  is given by  $(1-p_{22}^{\ell_* - 1})^N$ . Therefore the probability that at least one run exceeds  $\ell_* - 1$  is given by  $1 - (1-p_{22}^{\ell_* - 1})^N$ . In the same manner, the probability that at least one run exceeds  $\ell_*$  is  $1 - (1-p_{22}^{\ell_*})^N$ . Probability distribution of the maximum run among  $N$  sets of high wave runs becomes  $\ell_*$  is given as<sup>8)</sup>

$$\begin{aligned} P_4(\ell_*) &= (1-p_{22}^{\ell_*})^N - (1-p_{22}^{\ell_* - 1})^N \\ &= \exp[N \cdot \ln(1-p_{22}^{\ell_*})] - \exp[N \cdot \ln(1-p_{22}^{\ell_* - 1})] \end{aligned} \quad (17)$$

in which  $\ln$ : natural logarithms.  
Its expectation is<sup>8)</sup>



$$\begin{aligned}
 E(\ell_*)_{\max} &= \sum_{\ell_*=1}^{\infty} \ell_* (1-p_{22}^{\ell_*})^N - \ell_* (1-p_{22}^{\ell_*-1}) \\
 &= \sum_{n=1}^N \frac{(-1)^{n+1} N C_n}{1-p_{22}^n} \\
 &\approx -[\ln(N) + 0.5772] / \ln(p_{22}) + (2p_{22}+1)/(3+3p_{22})
 \end{aligned} \tag{18}$$

Fig.3 shows probability distribution of the maximum run among 1000 sets of high wave runs, for example, for several threshold wave heights. (the value of  $\rho$  in eqs.(10) and (8)' is about 0.25 in case of the Pierson-Moskowitz type random waves). Solid lines in Fig.4 show the relation between  $E(\ell_*)_{\max}$  and  $N$  when the same value of  $\rho$  and  $z$  as Fig.3 are used. From this figure, the expected maximum run during a single storm is evaluated as follows. The mean interval of a run of high waves (mean total run) is given as<sup>6)</sup>

$$\bar{\ell}_0 = \frac{1}{1-p_{11}} + \frac{1}{1-p_{22}} \tag{19}$$

where

$$p_{11} = \frac{\int_0^{h_*} \int_0^{h_*} P(h_1, h_2) dh_1 dh_2}{\int_0^{h_*} P(h) dh} \tag{20}$$

$p_{22}$  is given by eq.(15).

The total number of waves which arrive during a single storm of duration  $I_e$  is  $N=I_e/(\ell_0 T)$  ( $\ell_0$ : mean total run). Substituting this value into eq.(18), the expected value of the longest run can be evaluated. For example, in case of  $h_* = h_{1/10}$  ( $=H_{1/10}/H=1.80$ ),  $T=10s$  and  $I_e=24$  hours in the Pierson-Moskowitz type random waves,  $N$  is about 860.  $E(\ell_*)_{\max}$  can be calculated by eq.(18) or read off from Fig.4 as about 4.3. In case of the non-dimensional sea wall height  $z=5$ ,  $E(\ell_*)_{\max}$  is about 2.5. For the practical use these values should be raised to the next whole number.  $n$  in eq.(12) for above examples are 5 and 3.

Fig.5 shows an example of a cumulative distribution of the short-term overtopping amount  $q_0$  which is given by

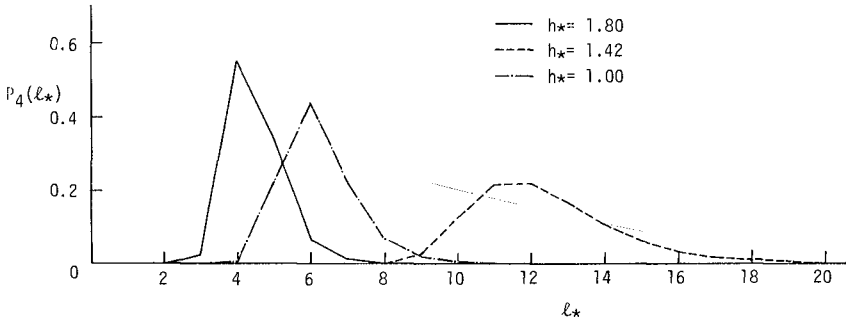


Fig.3 Probability distribution of the maximum run (N=1000)

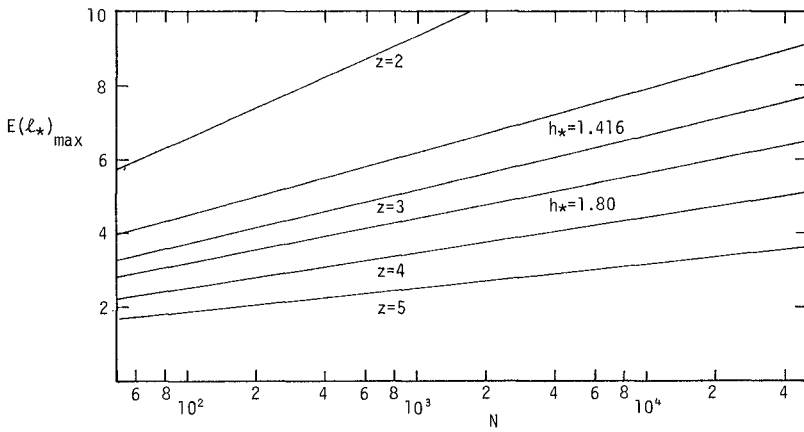


Fig.4 Relation of  $E(\ell_*)_{\max}$  and N

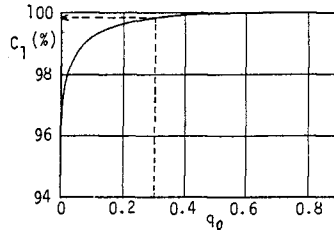


Fig.5 Cumulative distribution of the short-term overtopping amount  $q_0$  ( $z=3, n=6$ )

$$C_1 = \int_0^{q_0} P_1(q) dq \quad (21)$$

when  $z=3.0, n=6$  are used for the Pierson-Moskowitz type random waves.

The security factor  $C_1$  against a temporal flooding by a single short-term overtopping inside the sea wall can be read off from this Fig.5 in terms of a capacity of the storage reservoir  $q_c$ . For example, when a normalized capacity of the reservoir ( $q_c/\bar{q}$ ) is 0.3,  $C_1$  is about 0.998 in this case (dotted line in Fig.5).

### 3. SECURITY FACTOR AGAINST FLOODING

The total run of high waves is determined by a sum of a pair of one high wave group and the next one low wave group. Therefore if an amount of a short-term overtopping  $q_0$  brought about by a single high wave group is pumped out until the next overtopping starts (within a total run), no flooding inside the sea wall takes place. When a drainage pump the capacity of which per 1 wave period ( $1.1T$ ) equals  $q_c/r$ , is facilitated inside the sea wall (it takes  $r$  times of the wave period to pump out water of volume  $q_c$  (Fig.1) from the reservoir) and if the next total run is longer than  $r+1$ , no overtopping takes place.

Since the probability distribution of the total run is given as<sup>6)</sup>

$$P_5(\ell_0) = \frac{(1-p_{11})(1-p_{22})}{p_{11}-p_{22}} (p_{11}^{\ell_0-1} - p_{22}^{\ell_0-1}) \quad (22)$$

The probability that a total run exceeds  $r$  ( $\ell_0 \geq r+1$ ) is given as

$$C_2(r) = \sum_{\ell_0=r+1}^{\infty} P_5(\ell_0)$$

$$= \frac{(P_{11}-1)P_{22}^r - (P_{22}-1)P_{11}^r}{P_{11} - P_{22}} \tag{23}$$

Since the expected maximum run of high wave of which length equals  $n$  is being discussed now, the total run is always longer than  $n$ . Therefore

$$C_2(r) = 1 \quad (r < n) \tag{24}$$

Finally, the security factor during a single storm inside the sea wall is given by  $C_1(q_c)C_2(r)$  when the given capacities of the storage reservoir and drainage pump per 1 wave period are  $q_c$  and  $q_c/r$ , respectively. Fig.6 shows examples of the security factor  $C_1C_2$  when the given  $q_c$  can cope with 99% of short-term overtoppings ( $C_1=0.99$ ) among entire short-term overtoppings brought about by high wave groups of length 6 (Fig.5). The parameter in the figure is the normalized sea wall height  $z$ .

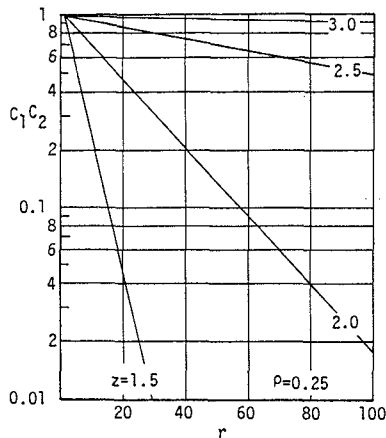


Fig.6 Security factor in the case drainage pump is facilitated ( $C_1=0.99$ )

## 4. SPATIAL DISTRIBUTION OF WAVE HEIGHTS

Short-crestedness of random waves has to be taken into account to cope with the short-term overtopping from a comparatively long sea wall. In this study, such a long sea wall is divided into sections in which the water surface profile along the sea wall can be assumed to be uniform within the individual sections but independent of those of other sections. Overall security inside the sea wall is derived from the synthesis of the securities of all sections. In this respect, a simultaneous spatial correlation coefficient of wave profile along the sea wall may be a good property to determine the above mentioned range along the sea wall.

Short crested random wave profile is usually expressed as<sup>3)</sup>.

$$\eta(x,y,t) = \sum_{i=1}^{m_f} \sum_{j=1}^{m_\theta} \sqrt{2S(f_i)G(f_i,\theta_j)} \Delta f \Delta \theta \cdot \cos(k_1 \cos \theta_j x + k_1 \sin \theta_j y - 2\pi f_i t + \epsilon_{ij}) \quad (25)$$

in which  $m_f$ ,  $m_\theta$  : numbers of partitions of the energy spectrum  $S(f)$  and directional function  $G(f,\theta)$ ,  $\Delta f$ ,  $\Delta \theta$  : interval of  $S(f)$  and  $G(f,\theta)$ ,  $k_1$  and  $\theta_j$  : wave number and direction of propagation,  $\epsilon_{ij}$  : initial phase. Directional

function used is of Mitsuyasu type<sup>9)</sup>.  $S_{\max} = 50$  at non-dimensional water depth  $d/L_{1/3} = 0.1$ . Fully developed wind wave directional spectra usually take around this value of

$S_{\max}$  in this water depth range<sup>3)</sup>. ( $L_{1/3}$ : significant wave length), significant wave period is 5s and main direction of wave propagation is normal to the sea wall.

Fig.7 shows an example of a simultaneous spatial correlation coefficient along the infinitely long straight sea wall when a bottom slope is uniform and x-axis is set on the sea wall, y-axis is normal to the sea wall.

$$R(x_0, y_0) = \int_{t=0}^{\infty} \eta(x,y,t) \eta(x+x_0, y+y_0, t) dt \quad (26)$$

This correlation coefficient  $R$  was approximated with the following function  $R'$  (dotted line in Fig.7) in this study.

$$R'(x) = \begin{cases} 1 & ; L_c \leq |x_0| \\ 0 & ; \text{otherwise} \end{cases} \quad (27)$$

where  $L_c$  was selected so that the integration of

$R(x_0) - R'(x_0)$  from  $x_0=0$  to the point where  $R(x_0)$  first takes on 0, becomes 0. The long sea wall is divided into sections, the interval of which is  $2L_c$ . If there are topographical configurations on the sea bottom, the local change of  $L_c$  due to the refraction, diffraction and shoaling<sup>3)</sup> should be changed locally. To cope with the spatial changes in wave height and  $L_c$  due to sea bottom configuration, probability distribution  $P_1$  (or cumulative distribution  $C_1$ : Fig.5) for individual sections should be transformed so that they are expressed in terms of the real (not normalized) amount of short-term overtopping by multiplying  $2L_c \bar{q}$  to the horizontal axis at individual sections.

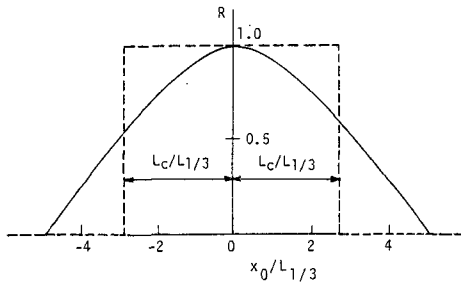


Fig.7 Spatial correlation coefficient of wave profile along the sea wall ( $S_{max}=50, d/L_{1/3}=0.1, T_{1/3}=5s$ )

5. SECURITY FACTOR INSIDE THE COMPARATIVELY LONG SEA WALL AGAINST FLOODING

In case the sea wall is divided into  $M$  independent sections and simultaneous amount of short-term overtoppings brought about by a single group of  $n$  consecutive waves from individual sections are  $q_1, q_2, \dots, q_M$ , respectively, the probability that the overall amount of a short-term overtopping becomes  $Q$  is

$$P_6(Q) = \iiint \dots \int_S P_{11}(q_{*1}) P_{12}(q_{*2}) \dots P_{1M}(q_{*M}) dq_{*1} dq_{*2} \dots dq_{*M} \tag{28}$$

in which  $P_{1i}(q_{*i})$  ( $i=1, 2, \dots, M$ ): probability that an amount of the short-term overtopping at the section  $i$  becomes  $q_{*i}$ ,  $S$ : the region where

$$S : Q < \sum_{i=1}^M q_{*i} \leq Q+dQ$$

Since  $P_{1i}$  are introduced numerically in this study, eq.(28) is rewritten as

$$P_6(Q) = \sum_{i_1=0}^{i_Q} \sum_{i_2=0}^{i_{Q_1}} \sum_{i_{M-1}=0}^{i_{Q_{M-2}}} P_{11}(i_1 \Delta q) \dots \cdot P_{1(M-1)}(i_{M-1} \Delta q) P_{1M}(i_{Q_{M-1}} \Delta q) \tag{29}$$

in which

$$i_m \Delta q = q_m, \quad i_Q \Delta q = Q, \quad i_{Q_m} \Delta q = i_Q \Delta q - \sum_{j=1}^m i_j \Delta q$$

( $m=1, 2, \dots, M-1$ )

When an amount of a single overall short-term overtopping  $Q$  is less than the capacity of the storage reservoir  $Q_0$ , no flooding inside the long sea wall takes place. This probability is given by

$$P_7(Q_0) = \text{Prob.}[Q \leq Q_0]$$

$$= \sum_{i_1=0}^{i_{Q_0}} \sum_{i_2=0}^{i_{Q_1}} \dots \sum_{i_M=0}^{i_{Q_{M-1}}} P_{11}(i_1 \Delta q) \dots P_{1M}(i_M \Delta q) \tag{30}$$

in which

$$i_{Q_0} \Delta q = Q_0$$

When the drainage pump the capacity of which per 1 wave period is  $Q_u$  (it takes  $r_u$  times of one wave period to pump out water of the volume of  $Q_0$  from the reservoir :  $r_u=Q_0/Q_u$ ) is facilitated, no overtopping takes place as far as the simultaneous total runs at all sections are longer than  $r_u+1$ . Since the probability that a total run exceeds  $r$  is given by eq.(23), the simultaneous probability that total runs at all sections exceed  $r_u$  is given as

$$P_8(r_u) = \prod_{i=1}^M C_{2i}(r_u) \quad (31)$$

Suffix  $i$  refers to the properties of the section  $i$ . Totally, the security factor against flooding inside the sea wall becomes

$$P_7(Q_0)P_8(r_u) \quad (32)$$

Supplemental security can be incorporated into eq.(32) even in the case a certain amount of water is left unpumped from the reservoir. Because if the total amount of unpumped water from the reservoir and that brought about by the next short-term overtopping do not exceed  $Q_0$ , no flooding takes place. When the total run of the first high wave group becomes longer than  $r_u - j$  at every section, an amount of  $jQ_u$  is left unpumped from the reservoir at most. And in case the next short-term overtopping is  $Q'$ , to pump out the total amount of  $Q' + jQ_u$  within the second total run, the second total run should exceed  $j + \ell' + 1$  ( $\ell' = Q'/Q_u$ ). Therefore the security against flooding in this case becomes

$$P_7(Q_0 - jQ_u)P_8(r_u + j) \quad (33)$$

The maximum possible amount carried over to the second total run is  $Q_0 - (n+1)Q_u$  because the minimum total run is  $n+1$  in the present discussion. The security against flooding when a single carry-over of water to the next total run is permitted, is given as

$$\sum_{j=0}^{n+1} P_7(Q_0 - jQ_u)P_8(r_u + j) \quad (34)$$



## 6. DISCUSSION

The overtopping equation by Kikkawa et al<sup>5)</sup> was used in this study. But to the extent which the three assumptions made in section 2 holds, other overtopping equations which are suitable for various situations considered may be utilized.

The method to divide the long sea wall into independent sections used in this study is found not always appropriate one. Therefore a more effective method needs to be introduced<sup>2)</sup>.

Some supplemental security factor was discussed in the last part of the section 5. Further supplements are possible, however, in the same way by allowing carry overs of unpumped amounts from the reservoir to occur more than twice. Needed supplements should be determined in accordance with the degree of accuracy of the assumptions made for various situations considered.

## REFERENCES

- 1) Battjes, J.A. (1971): Run-up distributions of waves breaking on slopes, Proc. ASCE, 97, WW-1, pp.91-114.
- 2) Battjes, J.A. (1982): Effects of short-crestedness on wave loads on long structures, Applied Ocean Res., Vol.4, No.3, pp.165-172.
- 3) Goda, Y. and Y. Suzuki (1975): Computation of refraction and diffraction of sea waves with Mitsuyasu's directional spectrum, Tech. Note of Port and Harbour Research Institute, No.230, pp.1-45. (in Japanese)
- 4) Goda, Y. (1978): The observed joint distribution of periods and heights of sea waves, Proc. 16th Conf. on Coastal Engg., pp.227-246.
- 5) Kikkawa, H., H. Shiigai and T. Kohno (1967): Fundamental study on wave overtopping from sea wall, Proc. 14th Japanese Conf. on Coastal Engg., pp.118-122. (in Japanese)
- 6) Kimura, A. (1980): Statistical properties of random wave groups, Proc. 17th Conf. on Coastal Engg., pp.2955-2973.
- 7) Kimura, A. (1981): Joint distribution of the wave heights and periods of random sea waves, Coastal Engg. in Japan, pp.77-92.
- 8) Kimura, A. (1984): Statistical properties of the maximum random sea wave groups.
- 9) Mitsuyasu, H. and S. Mizuno (1976): Directional spectra of ocean surface waves, Proc. 15th Conf. on Coastal Engg., pp.329-348.

## CHAPTER THIRTY SEVEN

### Shallow-Water Spectral Wave Modeling

Robert E. Jensen, PhD\*

#### ABSTRACT

A parametric shallow-water spectral wave modeling technique is developed and is tested against extensive field measurements of wave height, period and spectral shape. The wave model considers wave growth and finite water depth mechanisms such as spectral wave shoaling, wave-bottom interactions, wave-wave interactions and wave breaking. The key to this approach is that the resulting wave conditions are provided by transformation mechanisms rather than transforming spectral components during wave propagation. Thus long-term wave hindcasts can be performed economically without the loss in accuracy.

#### INTRODUCTION

The predictions of shallow-water wave characteristics have become a focal point of research activities across the world. Because construction, shipping, and dredging operation costs have drastically increased over the years, coastal engineers have been faced with more accurately defining the shallow-water wave climate. A better understanding of shallow-water wave growth and transformation mechanisms is slowly evolving through controlled wave-measuring programs such as ARSLOE [Vincent and Lichy (21)]. However, not all of the questions have been answered, and it will take some time before all shallow-water wave transformation mechanisms are quantified [Vincent (19)]. In light of this, the shallow-water wave modeling technique employed in this study adopts recently derived mechanisms currently available. The main intent in the development of the wave model is to describe the physical processes as accurately as possible while simplifying the computational procedures to a degree where shallow-water wave hindcasting is economically feasible. The wave model is designed to compute wave conditions (frequency spectra and various wave parameters derived from the spectra) at site-specific locations. Study areas are restricted to semi-enclosed bodies of water. Also, wind conditions are assumed to be uniform over the area and remain constant for a given duration. Wave propagation is assumed to be restricted to the direction described by the winds, and the bottom topography is represented by straight and parallel bottom contours. The model is applied to Saginaw Bay, Michigan.

#### THEORY

Hasselmann et al. (7) introduced a parametric model of wind-wave generation relating the rate of energy growth to nondimensional

\*Research Hydraulic Engineer, US Army Engineer Waterways Experiment Station, Coastal Engineer Research Center, Vicksburg, Miss. 39180-0631.

characteristics of the wind field. The energy growth (in space or time) is governed by a self-similar process and verified through extensive prototype data [Hasselmann (5), Hasselmann et al. (7)]. In these studies, the dominant energy input to the forward face of the spectrum is related to convergence of energy flux due to nonlinear, resonant wave-wave interactions (Fig. 1) of the form described by Hasselmann (6). Studies by Mitsuyasu (13, 14) and Kitaigordskii (11) also displayed similar results.

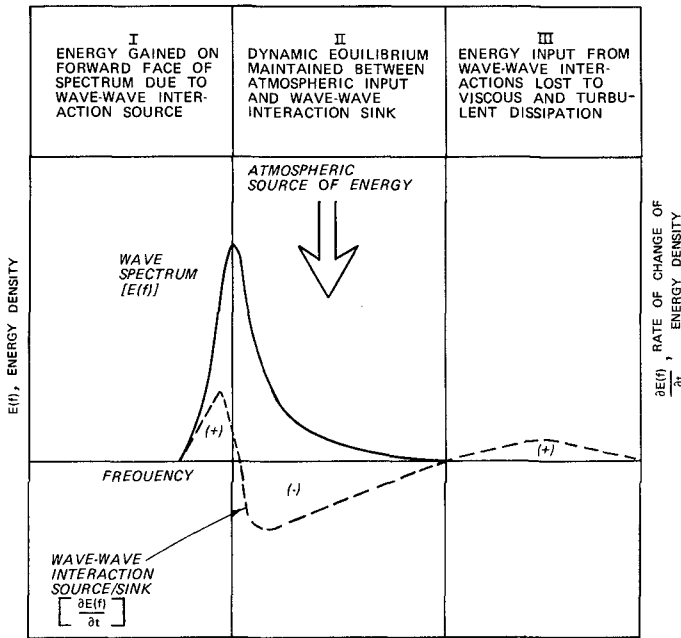


Fig. 1. Schematic representation of the nonlinear wave-wave interactions

The rate of wave growth under ideal conditions of fetch limitations or duration limitation and a stationary wind field can be computed [Hasselmann et al. (7)]. For growth along a fetch the solution is

$$E_o = 1.6 \times 10^{-7} U^2 \frac{F}{g} \tag{1}$$

and for growth through time, it becomes

$$E_o = 4.3 \times 10^{-10} U^{18/7} g^{-4/7} t^{10/7} \tag{2}$$

where  $E_o$  is the total energy resulting from a wind speed  $U$  [assumed to be overwater wind conditions adjusted to 33 ft (10m) elevation], blowing over a given fetch length  $F$ . The gravitational

acceleration is denoted by  $g$ ;  $t$  is the time since the wind began to blow.

Two additional pieces of information are required to quantify the distribution of  $E_0$  given in the form of an energy density spectrum. The nondimensional peak frequency,  $\tilde{f}_m$ , and the Phillips' equilibrium constant  $\alpha$  [Phillips (17)] and are written as

$$\alpha = 0.076\tilde{X}^{-0.22} \quad (3)$$

and

$$\tilde{f}_m = 3.5\tilde{X}^{-0.33} \quad (4)$$

where  $\tilde{X}$  is the nondimensional fetch length

$$\tilde{X} = \frac{gF}{U^2} \quad (5)$$

Although Hasselmann, et al. (7) found that wave growth followed the parametric forms defined in terms of distance and time, it will be shown that for all wave generating conditions in Saginaw Bay, wave growth is adequately described only by spatial variations. Therefore, it becomes a matter of comparing the prototype results (wave height, period and spectral shape) to the hindcast model that employs Eqs. 1 and 4.

The parameterization of the wave growth is restricted such that when the nondimensional peak frequency attains a value of 0.13 or less, a fully developed sea state is achieved and wave growth is halted. Over long fetch lengths and low wind speeds, this condition can occur with some degree of regularity. Thus Eqs. 1, 3-5 are then redefined by

$$Q = K \sum_{i=1}^{10} \zeta_i \quad (6)$$

where  $K$  is defined as the nonvarying parameters (and constants),  $Q$  is defined as the dependent parameters, and  $\zeta_i$  is recognized as the independent parameters ( $F$  and  $\tilde{X}$ ) found in Eqs. 2-5. The parameter  $i$  is the increment counter. After each discrete fetch length  $F_i$ , the nondimensional peak frequency is evaluated to determine if  $\tilde{f}_m < 0.13$ . If this occurs wave growth is terminated, and wave decay is initiated for the remainder of the fetch length. Wave decay is parameterized following the work conducted by Bretschneider (1) and Mitsuyasu and Kimura (15) for the peak frequency  $f_m$  (where  $f_m = \tilde{f}_m g/U$ ) while the total energy decay rate follows that described by Jensen (10).

Wave conditions generated in Saginaw Bay also must consider dispersion effects resulting from finite water depth conditions. When the water depths vary from  $F_i$  to  $F_{i+1}$ , the conservative transformation mechanisms of shoaling and refraction must be considered. Wave shoaling is determined from the evaluation of group speed determined by linear theory. Wave refraction is neglected under the assumption

that: the bottom topography is assumed to be straight and parallel for every fetch length. Considering the water depths in Saginaw Bay and peak wave periods ( $T_p = 1/f_m$ ) in the range of 2 to 8 sec, wave-refraction effects (and subsequent "errors") would be on the order of 2 to 25 percent in terms of the wave direction. This is assuming that the angle between the wave crest and bottom contour is at most,  $30^\circ$ . The initial direction of wave propagation is limited to 18 angle classes at  $10^\circ$  increments (because of the wind data employed in this study); thus the accuracy in the resultant refracted wave condition, by similarity, also would be constrained to the 18 angle classes.

Finite water depth conditions also lead to bottom dissipation effects on the growing seas. Energy losses associated with bottom friction are empirically modeled using the following sets of equations developed by Bretschneider (2).

The second theoretical aspect of wave model deals primarily with the distribution of the total energy ( $E_o$ ) in the form of a one-dimensional discrete frequency spectrum  $E(f)$ . Through the use of similarity principles, Kitaigorodskii, Krasitskii, and Zaslavaskii (12) extended Phillips' deepwater hypothesis [Phillips (17)] of the equilibrium range in the spectrum of wind-generated surface waves to finite depth conditions. The spectral form is defined by

$$E(f) = \alpha g^2 (2\pi)^{-4} f^{-5} \phi(\omega_h) \quad f \geq f_m \quad (7)$$

where  $E(f)$  is the energy density at each discrete frequency band  $f$  and  $\phi(\omega_h)$  is a nondimensional function dependent on  $\omega_h$  given by

$$\omega_h = 2\pi f(h/g)^{1/2} \quad (8)$$

The function  $\phi(\omega_h)$  varies from 1.0 in deep water to 0.0 when  $h = 0.0$  as shown by Fig. 2. When  $\omega_h$  is less than 1.0,  $\phi(\omega_h)$  can be approximated by:

$$\phi(\omega_h) \approx \frac{1}{2} \omega_h^2 \quad (9)$$

and therefore,

$$E(f) = \frac{1}{2} \alpha g h (2\pi)^{-2} f^{-3} \quad f_j \geq f_m \quad (10)$$

or, the spectral shape changes from  $f^{-5}$  to  $f^{-3}$  in the tail of the energy density spectrum, and more importantly, becomes a function of the water depth.

The forward face of the spectrum is assumed to be represented by:

$$E(f) = \alpha g^2 (2\pi)^{-4} f_m^{-5} \exp \left[ 1 - \left( \frac{f}{f_m} \right)^4 \right] \phi^*(\omega_h) \quad f < f_m \quad (11)$$

where  $\phi^*(\omega_h)$  is evaluated from the  $\omega_h$  defined at  $f_m$ . Field and laboratory data by Goda (4), Thornton (18), Ou (16), Iwata (8), and Vincent (20) support the form given by Eq. 7. The verification of Eq. 11 is supported by Garcia and Jensen (3), Jensen (9, 10).

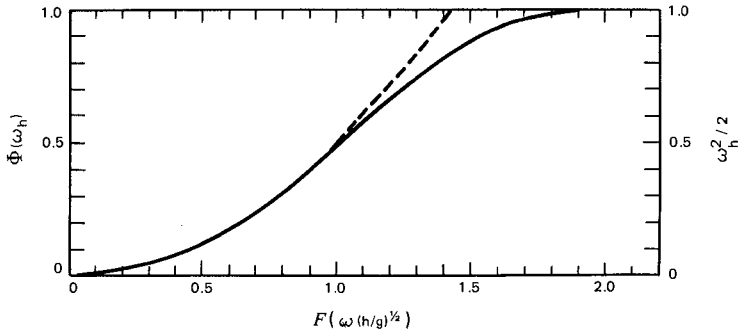


Figure 2. The universal dimensionless function  $\phi$  (solid curve) and the function  $\omega_h^2/2$  (dashed curve), from Kitaigorodskii, Krasitskii, and Zaslavskii (12).

The parametric representation of wave growth assumes a dynamic balance between atmospheric sources and transfers of energy resulting from wave-wave interactions (Fig. 1). This parameterization was based on deep-water wave conditions, Hasselmann et al. (7). During the Saginaw Bay study, it was determined that over moderately short fetch lengths [10 to 20 nautical miles (18.5 to 37 km)], this deep-water growth rate expression (Eq. 1) consistently underpredicted the total energy found in the measured data. The only theoretically consistent location to add the energy would be on the forward face of the spectrum (Fig. 3). The function,  $E(f,h)_{THEORY}$  is the saturated spectrum based on Eqs. 7 and 11, and  $E(f,h)_{WEIGHTED}$  is the spectrum based on  $E_0$  after wave growth. This process also shifts  $f_m$  to a lower frequency which has been noticed in field data. As the fetch length increases, the relative amount of added energy decreases, where eventually no additional energy is incorporated into the resulting spectrum.

It has been shown that the water depth greatly influences the spectral shape and in so doing will influence the maximum wave conditions. The parametric formulation follows the work conducted by Vincent (20). The depth limiting maximum wave condition is given by,

$$H_m = 4 \int_{f_c}^{\infty} E_m(f) df \quad (12)$$

where

$H_m$  is the maximum wave condition;  $f_c$  is the lower frequency bounding the total energy (equal to  $0.9 f_m$ ); and  $E_m(f)$  is defined from Eq. 10. Integrating Eq. 12 the absolute limit on the wave condition at a particular water depth is obtained, where

$$H_m = \frac{(\alpha gh)^{1/2}}{\pi f_c} \quad (13)$$

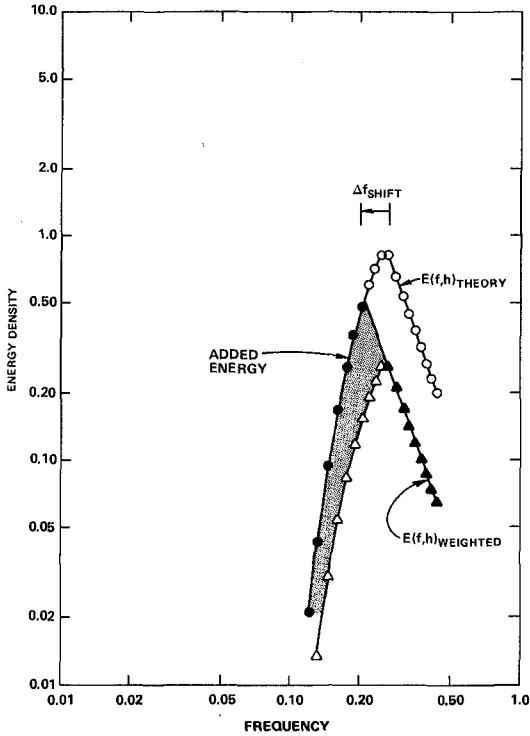


Fig. 3. Construction of the final energy density spectrum (solid symbols) caused by shallow-water wave generation

In summary, the physical process governing wave generation and transformations has been theoretically determined using available, state-of-the-art techniques. It must be emphasized that not all shallow-water transformation processes have (or can be) measured to determine their relative effect on the total energy, spectral shape, and peak frequency. Therefore the development of the wave model as employed in this study attempts to model the physics of the problem in a general sense while maximizing computational efficiency.

#### VERIFICATION

In all wave hindcasting studies, comparisons to gage measurements are a necessary element in the development of a wave model. The initial calibration test was conducted on a data set that contained the largest wave conditions measured during the wave gaging portion of this study.

The wave gages were deployed in April 1981 shortly after the bay became ice-free (Fig. 4). Early on 10 May 1981, winds began to increase and by noon were steady at 25 to 30 mph (11.1 to 13.4 m/s) from a direction of about  $40^\circ$  east of north. The winds held a remarkably constant speed and direction for about a day and a half before beginning to diminish. The predominant direction coincided with the axis of the bay and alignment of the gage array, the most favorable condition for generation of the largest waves and for studying changes in the wave climate.

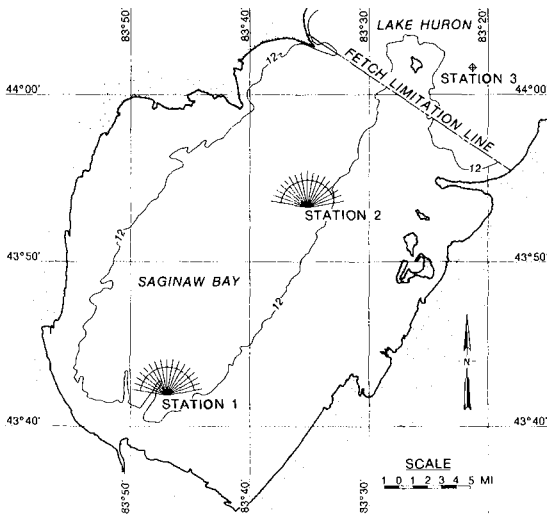


Fig. 4. Saginaw Bay wave gage and hindcast station locations, (Note: 1 mile = 1.61 km)

Because of the constancy in the wind speed and direction during the period 10-12 May 1981, any variation in the wave climate would be a function only of the wind speed. Fig. 5 shows the wind data obtained at the Saginaw Projects Office, of the U. S. Army Engineer District, Detroit, during this period of time. The anemometer elevation was about 60 ft (18.3 m) and located about 3 miles (4.8 km) south of Station 1.

Results of the comparisons for gage sites 1 and 2 are shown in Fig. 6 where  $H_{mo}$  is the characteristic wave height and  $T_p$  is the peak period defined as:

$$H_{mo} = 4 \int_0^{\infty} E(f) df \quad (14)$$

$$T_p = f_m^{-1} \quad (15)$$



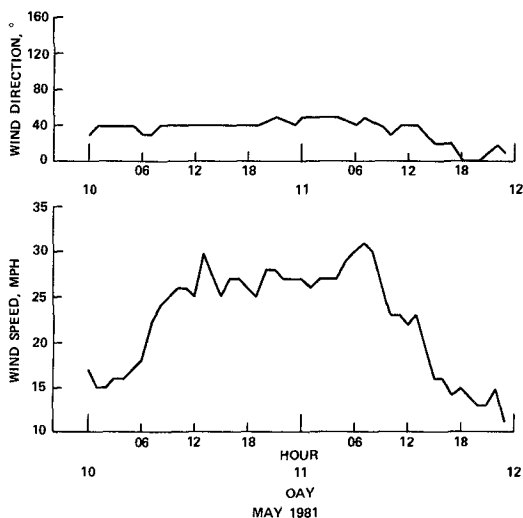


Fig. 5. Wind data used for verification test,  
(Note: 1 mph = 0.447 m/s)

There is a slight phase difference between the measured and hindcast data sets. This is due to the wave model assumption that wave conditions are generated instantaneously, i.e., there is no time-dependency associated with the effects of wave propagation on the wave climate. The small-scale temporal fluctuations in the measured data cannot be simulated in the wave model because of the assumption of uniform wind conditions.

Energy density comparisons are also made between the measured and hindcast data. It is helpful to recognize that a spectral representation of the wave phenomena is an estimate of the actual wave conditions existing at a specific point in space and time. To illustrate this, all measured wave spectra are plotted with an accompanying 90 percent CHI-squared distribution confidence band. Although numerous comparisons were performed, a limited number of Station 1 results are presented. The three energy density spectral plots shown in Figs. 7-8 represent three phases in the 10-12 May 1981 storm; Fig. 7 illustrates the initial growth phase, and the peak of the storm; Fig. 8 illustrates the final decay stage. The wave model spectral results are adjusted in time to compensate for the lag associated with the wave propagation. The adjustment varies from 2 to 4 hours depending on propagation time.

The energy plots [ $E(f)$  versus  $f$ ] are plotted in a nondimensional frequency domain defined by  $f/f_m$  where  $f_m$  is the frequency at the spectral peak. The greatest discrepancy in the comparison of measured and hindcast peak frequencies was one discrete frequency band or 0.0156 Hz. Figs. 7-8 show that from initial growth to final decay,

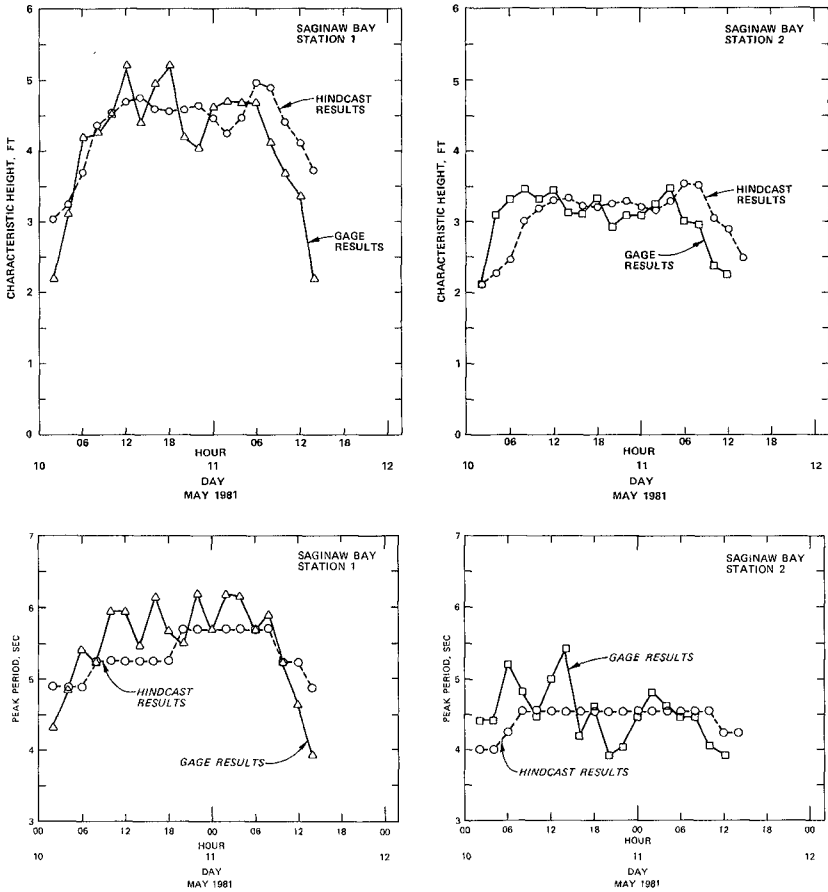


Fig. 6. Comparison of wave height and period for hindcast and measured conditions, (Note: 1 ft = 0.305 m)

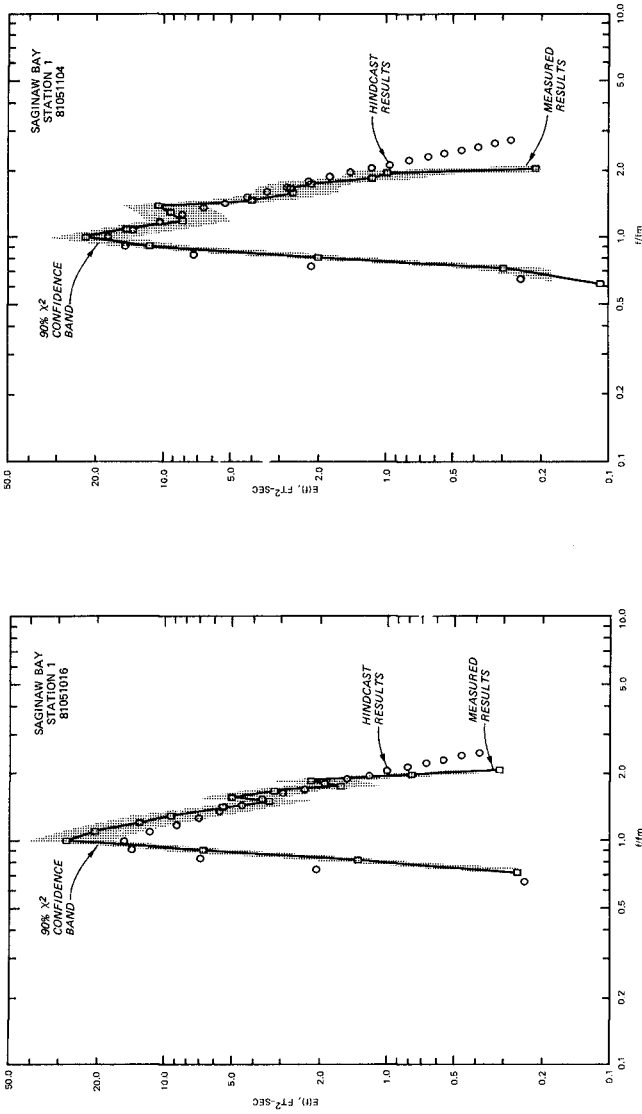


Fig. 7. Comparison between measured and hindcast wave spectra estimates for Station 1, 1600 hours, 10 May 1981 and 400 hours, 11 May 1981, (Note:  $1 ft^2 = 0.093 m^2$ )

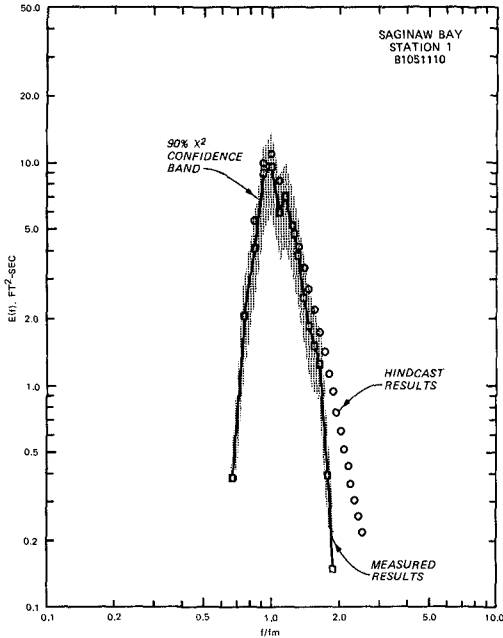


Fig. 8. Comparison between measured and hindcast wave spectra estimates for Station 1, 1000 hours, 11 May 1981,

(Note:  $1 \text{ ft}^2 = 0.093 \text{ m}^2$ )

the wave model energy density spectrum follows the measured spectrum to within the 90 percent confidence limits. The forward face of the measured spectra conforms with the assumption of the spectral shape defined in Eq. 11. The tail of the hindcast spectra conforms with the measured data except for small-scale temporal variations in the measured data and the extreme tail of the distribution, i.e., when  $f/f_m > 2$ . The discrepancy between the measured and hindcast spectra when  $f/f_m > 2$  is a characteristic of a pressure sensing gage system such as used in this study. Assuming a linear transformation exists between the recorded pressure response and the free surface, individual wave component frequencies greater than 0.35 Hz will be increasingly damped with water depth. Thus representation of the energy density at frequencies greater than  $\approx 0.35$  Hz are very approximate. The relative energy at frequencies greater than 0.35 Hz is plotted but represents only an unknown fraction of the energy in a particular wave record.

The secondary peaks displayed in the measured spectra may be caused by several different mechanisms such as secondary wave trains propagating into the area or backscattering due to variations in bottom topography, the decomposition of finite amplitude waves into secondary harmonics, or in artifact of the analysis procedure.

#### CONCLUSIONS

Many more comparisons were performed than are presented here without adjustment of coefficients or modification to the hindcast model to account for changes in location. The comparisons convincingly demonstrate the ability of the wave model to accurately hindcast wave conditions in Saginaw Bay to within  $\pm 0.5$  ft ( $\pm 0.15$ m) significant height and  $\pm 1.0$  sec peak period. Moreover, the theoretically derived spectral shapes generally conform within the 90 percent CHI-squared confidence limits of the measured spectra, [Garcia and Jensen (3)].

The wave model has been extensively used in other site specific hindcast studies [Jensen (9, 10)]. The mechanisms describing the physical processes found in the wave model have remained unchanged from study to study. The differences between the hindcast and prototype wave estimates were found to closely approximate the aforementioned ranges.

#### ACKNOWLEDGMENTS

I would like to thank the Office, Chief of Engineers for permission to publish this manuscript and the U. S. Army Engineer, Detroit District for sponsoring the project on which this work was accomplished. Ms. Janie Daughtry assisted in preparing this report.

## REFERENCES

1. Bretschneider, C. L., "The Generation and Decay of Wind Waves in Deep Water," Transactions, American Geophysical Union, Vol 33, No. 3, 1952, pp 381-389.
2. Bretschneider, C. L., "Modifications of Wave Height due to Bottom Friction, Percolation and Refraction," Technical Memorandum No. 45, U. S. Army Corps of Engineers, Beach Erosion Board, Washington, D. C., Oct. 1954.
3. Garcia, A. G. and Jensen, R. E., "Wave Data Acquisition and Hindcast for Saginaw Bay, Michigan," Technical Report HL-83-14, U. S. Army Engineer Waterways Experiment Station, CE, Vicksburg, Miss., June 1983.
4. Goda, Y., "Estimation of Wave Statistics from Spectral Information," Proceedings, International Symposium of Ocean Wave Measurement and Analysis, American Society of Civil Engineers, Vol 1, 1974, pp 320-337.
5. Hasselmann, K., "A Parametric Wave Prediction Model," Journal of Physical Oceanography, Vol 6, 1976, pp 200-228.
6. Hasselmann, K., "On the Non-Linear Energy Transfer in a Gravity Wave Spectrum-General Theory," Journal of Fluid Mechanics, Vol 12, Part 1, 1962, pp 481-500.
7. Hasselmann, K., et al., "Measurements of Wind-Wave Growth and Swell Decay During the Joint North Sea Wave Project JONSWAP," Dtsch, Hydrogr. Z., Vol 8, Supplement A8, No. 12, 1973.
8. Itwata, Koichiro, "Wave Spectrum Changes due to Shoaling and Breaking; I, Minus - Three - Power - Law on Frequency Spectrum," Osaka University, Technical Report, Vol 30, No. 1517-1550, 1980, pp 269-278.
9. Jensen, R. E., "The Atchafalaya River Delta, Report 10, Wave Hindcasts," Technical Report HL-82-15, U. S. Army Engineer Waterways Experiment Station, CE, Vicksburg, Miss., (in preparation).
10. Jensen, R. E., "Mississippi Sound Wave Hindcast Study," Technical Report HL-83-8, U. S. Army Engineer Waterways Experiment Station, CE, Vicksburg, Miss., April 1983.
11. Kitaigorodskii, S. A., "Application of the Theory of Similarity to the Analysis of Wind-Generated Wave Motion as a Stochastic Process," Bull. Acad. Sci. USSR Ser. Geophys., Vol 1, No. 1, 1962, pp 105-117.
12. Kitaigorodskii, S. A., Krasitskii, V. P., and Zaslavskii, M. M., "On Phillips' Theory of Equilibrium Range in the Spectra of Wind-Generated Gravity Waves," Journal of Physical Oceanography, Vol 5, 1975, pp 410-420.

13. Mitsuyasu, Hisashi, "On the Growth of the Spectrum of Wind-Generated Waves (I)," Reports of Research Institute for Applied Mechanics, Kysusha University, Vol 16, No. 55, 1968, pp 459-482.
14. Mitsuyasu, Hisashi, "On the Growth of the Spectrum of Wind-Generated Waves (II)," Reports of Research Institute for Applied Mechanics, Kysusha Univeristy, Vol 17, No. 59, 1969, pp 235-248.
15. Mitsuyasu, Hisashi, and Kirmura, Hisao, "Wind Wave in Decay Area," Coastal Engineering in Japan, Vol 8, 1965, pp 221-235.
16. Ou, Shan-Hwei, "The Equilibrium Range in the Frequency Spectra of the Wind Generated Gravity Waves," Proceedings, Fourth Conference on Ocean Engineering in the Republic of China, Sep 1980.
17. Phillips, O. M., "On the Generation of Waves by Turbulent Wind," Journal of Fluid Mechanics, Vol 2, 1957, pp 417-445.
18. Thornton, E. G., "Rederivation of the Saturation Range in a Frequency Spectrum of Wind-Generated Gravity Waves," Journal of Physical Oceanography, Vol 7, pp 137-140.
19. Vincent, C. L., "Shallow-Water Wave Modeling," 1st International Conference on Meteorology and Air-Sea Interaction in the Coastal Zone, The Hague, the Netherlands, American Meteorological Society, Boston, Mass., May 1982, pp 920-925.
20. Vincent, C. L., "A Method for Estimating Depth-Limited Wave Energy," CETA No. 81-16, U. S. Army Coastal Engineering Research Center, CE, Fort Belvoir, Va., 1981.
21. Vincent, C. L. and Lichy, D. E., "ARSLOE Wave Measurements," Proceedings Conference on Directional Wave Spectra Applications, American Society of Civil Engineers, Sep 1981, pp 71-86.

## CHAPTER THIRTY EIGHT

### A Typhoon Wave Hindcasting Technique

N.K. Liang\*      C.C. Chien\*\*

#### ABSTRACT

The typhoon wave forecasting technique proposed by C.L. Bretschneider (1) is a good simple method. However, the measured maximum wave height at Nan-Wan Bay (at southern tip of Taiwan) of Ida typhoon is about twice of the hindcasted maximum wave height. In general, the hindcasted maximum typhoon wave height arrives earlier than the measured data for Bretschneider's method as well as the other methods, such as Tang's and Ijima's methods. And as the typhoon is approaching the station, the hindcasted wave heights are smaller than the measured ones. On the contrary, as the typhoon is leaving the station, the hindcasted wave heights are greater than the measured heights. In order to improve these defects, the typhoon swell proposed by Liang (7) is superimposed upon the typhoon wind wave according to the energy conservation principle. The modified wave period is calculated by the energy-weighted method.

In this paper 8 typhoons are as examples to show that the new method has amended the above-mentioned defects.

\* Director, Institute of Harbor & Marine Technology, (435) Wuchi, Taiwan, Rep. of China

\*\* Assistant Researcher, Institute of Harbor & Marine Technology, (435) Wuchi, Taiwan, Rep. of China



## 1. INTRODUCTION

There are approximately 4 typhoon wave hindcasting techniques : (1) Wilson's graphical method (2) Tang's numerical technique. (3) Ijima's tracing method, and (4) Bretschneider's empirical method. Liang (3) has used Tang's method to hindcast typhoon wave at South Taiwan strait of Typhoon Elsie (Oct., 1975). The result is that the hindcasted peak wave arrived 7 hours ahead of the measured data. And the hindcasted peak wave height is 2 meters less than the measured one. However, Tang's method is proved to be quite good for typhoon wave on shoaling beaches.

Tsai (10) has used Ijima's tracing method to hindcast waves of typhoons Nina (Aug., 1975), Betty (Sept., 1975), Bess (Sept., 1971) and Judy (May, 1966). The results show that in the approaching period the measured wave heights are much higher than those of hindcasted wave heights, and vice versa for the leaving period. However, the hindcasted peak wave heights are close to the measured ones. Therefore, Ijima's method can be used to determine the design wave.

Bretschneider's empirical method is very simple. Liang & Lin (4) have used it to hindcast waves of Typhoon Vera (July, 1977). It was found that in the initial stage the hindcasted wave heights are higher than the measured data and the hindcasted peak wave height is close to the measured one. The former result may be due to the sheltering effect of the land. However, Liang has hindcasted wave of Typhoon Ida (July, 1980). The measured wave heights are much higher than the hindcasted data (Fig. 7). The reason is that Typhoon Ida's center did not pass through the wave station at Nan-Wan (at the southern tip of Taiwan) as Typhoon Vera did. Therefore, more typhoon swell energy overlapped on the typhoon wind wave for the latter case.

Hou, Kou & Tzeng (2) have modified Bretschneider's method by reducing the R value (radius of maximum wind speed) and found that the hindcasted peak wave heights are close to the measured ones. But, if the variation of the typhoon track changes greatly, the hindcasted data do not match the measured data, such as for Typhoon Judy (Fig. 1).

This paper is going to use Bretschneider's method to calculate typhoon wind wave and Liang's typhoon swell method to estimate typhoon swell. Then, by the energy superposition principle and wave energy weighting method, the typhoon wave height and wave period are estimated.

## 2. THEORY

A simple introduction of Bretschneider's method and Liang's method is as follows:

(A) Typhoon wind wave hindcasting method (for area within the radius  $10R$ )

(1) Typhoon wind field

$$\frac{U_r}{U_R} = -\frac{1}{2} \frac{fR}{U_R} \frac{r}{R} + \left[ \left( 1 + \frac{fR}{U_R} \right) \frac{R}{r} e^{\left( 1 - \frac{R}{r} \right)} + \left( \frac{1}{2} \frac{fR}{U_R} \frac{r}{R} \right)^2 \right]^{\frac{1}{2}} \quad (1)$$

in which,

- r radius of typhoon measured from typhoon center.
- R radius of maximum wind speed.
- f Coriolis force coefficients.
- U<sub>r</sub>, U<sub>R</sub> Geostrophic wind speed at radius r or R.

By Graham and Nunn, an empirical formula for maximum wind speed radius is as follows:

$$R' = \{ 28.52 \tanh [ 0.0873 ( \phi - 28 ) ] + 12.22 \exp [ ( p_o - 1013.2 ) / 33.86 ] + 0.2 V_F \times 1.852 + 37.22 \} / 1.852 \quad (N.M.) \quad (2)$$

in which,

- φ latitude
- p<sub>o</sub> typhoon center atmospheric pressure in mb
- V<sub>F</sub> typhoon moving speed in knots

Here, R is modified by the following equation

$$R = R' - [ ( U_{R'} - 100 ) / 6 + 6 ] \quad (3)$$

where

$$U_R = K \sqrt{\Delta p} - 0.5 fR \quad (4)$$

$$K = -\phi / 7.5 + 70 \quad (5)$$

after Liaw (8), typhoon center atmospheric anomaly in inches of mercury column is as follows:

$$\Delta p = \frac{1}{33.86} \left[ 1000 + \frac{(1000 - p_o)}{10} p_o \right] \quad (6)$$

The mean (10 minute) sea surface wind speed at 10 meter height at radius R is as follows:

$$U_{RS} = 0.865 U_R \quad (7)$$

for moving typhoon

$$U_{RSS} = U_{RS} + \frac{1}{2} V_F \cos \theta \quad (8)$$

in which,

- θ angle between the line connecting typhoon center and wave station and the direction of typhoon motion

Similarly, we have

$$U_{rs} = 0.865 U_r \quad (9)$$

$$U_{rss} = U_{rs} + \frac{1}{2} V_F \cos \theta \tag{10}$$

(2) Estimation of wave height and wave period

For stationary typhoon, the wave height at radius R is

$$H_R = K' \sqrt{R \cdot \Delta p} \quad (\text{ft}) \tag{11}$$

$K'$  is a function of  $\frac{fR}{U_R}$  and can be approximated by the equation:

$$K' = 7.59 - 41.21 \left( \frac{fR}{U_R} \right) + 160.51 \left( \frac{fR}{U_R} \right)^2 - 219.32 \left( \frac{fR}{U_R} \right)^3 \tag{12}$$

$$\frac{T_o}{U_{RS}} = 0.4 \tanh \left\{ \ln \left( \frac{1 + \frac{40 H_R}{U_{RS}^2}}{1 - \frac{40 H_R}{U_{RS}^2}} \right)^{0.5} \right\}^{0.6} \tag{13}$$

$$T_R = (4/5)^{\frac{1}{4}} T_o \tag{14}$$

$T_R$  is the wave period at radius R.

$H_r$  is the wave height at radius r,  $H_r/H_R$  is a function of  $r/R$  and  $fR/H_R$  (1).  $T_r$  is the wave period at radius r.

$$\frac{T_o}{U_{rs}} = 0.4 \tanh \left\{ \ln \left( \frac{1 + \frac{40 H_r}{U_{rs}^2}}{1 - \frac{40 H_r}{U_{rs}^2}} \right)^{0.5} \right\}^{0.6} \tag{15}$$

$$T_r = (4/5)^{\frac{1}{4}} T_o \tag{16}$$

For moving typhoon,

$$H_{RS} = H_R \left( 1 + \frac{\frac{1}{2} V_F \cos \theta}{U_{RS}} \right)^2 \tag{17}$$

$$H_{rs} = H_r \left( 1 + \frac{\frac{1}{2} V_F \cos \theta}{U_{rs}} \right)^2 \tag{18}$$

(B) Typhoon swell estimation (for radius r greater than 10R)

After Liang (7), the swell height is as follows:

$$H_s = C H_{RS} \frac{R}{\sqrt{DD}} \quad (\text{Meter}) \tag{19}$$

DD distance between typhoon center and station in N.M.  
 C a constant, about 0.11

The swell period is as follows:

$$T_s = C' T_{RS} \quad (20)$$

$C'$  is always greater than 1 and empirically equal to

$$C' = 0.0021 \left( \frac{DD \cdot T_{RS}}{R \cdot U_{RSS}} \right)^2 + 0.0021 \left( \frac{DD \cdot T_{RS}}{R \cdot U_{RSS}} \right) + 1.21 \quad (21)$$

The time lag for the swell to arrive the station is:

$$T_{lag} = \frac{DD}{1.516 \times T_s} \quad (\text{hours}) \quad (22)$$

As the typhoon moves to the station,  $T_{lag}$  decreases; and as the typhoon moves away from the station,  $T_{lag}$  increases. By using the principle of energy flux conservation, a swell wave height correction coefficient  $\lambda$  is obtained (7).

$$\lambda = \left( \frac{T_D}{T_{D'}} \right)^{\frac{1}{2}} \quad (23)$$

in which

$T_D$  Duration of swell if the typhoon were stationary

$T_{D'}$  The real duration

The swell wave height is then as follows,

$$H_s' = \lambda H_s \quad (24)$$

By the principle of energy conservation, the typhoon wave can be estimated as follows:

$$H_{1/3} = (H_s'^2 + H_w^2)^{\frac{1}{2}} \quad (\text{meter}) \quad (24)$$

$$T_{1/3} = \frac{H_s'^2 T_s + H_w^2 T_{rs}}{H_s'^2 + H_w^2} \quad (\text{sec}) \quad (25)$$

where

$$H_w = 0.3048 \text{ Hrs} \quad (\text{meter}) \quad (26)$$

### 3. COMPARISONS OF HINDCASTED AND MEASURED DATA.

In the paper 8 typhoons are used to check the different models by the measured wave data. The typhoons and the wave stations are shown in Table 1.

Table 1

Typhoon	Time	Wave Station	Water Depth
Judy	May, 1966	Kaoshiung Harbor	12 m
Agnes	Sept., 1971	Taichung Harbor	19 m
Bess	Sept., 1971	Taichung Harbor	19 m
Nina	Aug., 1975	Su-Ao Harbor	28 m
Betty	Sept., 1975	Su-Ao Harbor	28 m
Elsie	Oct., 1975	South Taiwan Strait	104 m
Vera	July, 1977	Keelung Harbor	38 m
Ida	July, 1980	Nan-Wan Bay	16 m

Because the wave stations are not at deep sea (except Elsie Typhoon), shoaling effect is considered. The measured data and hindcasted data of the above eight Typhoons are shown in Fig 1 - Fig 8.

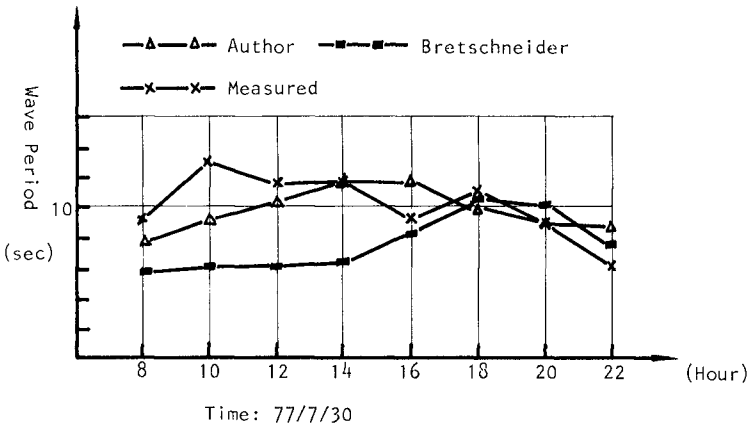
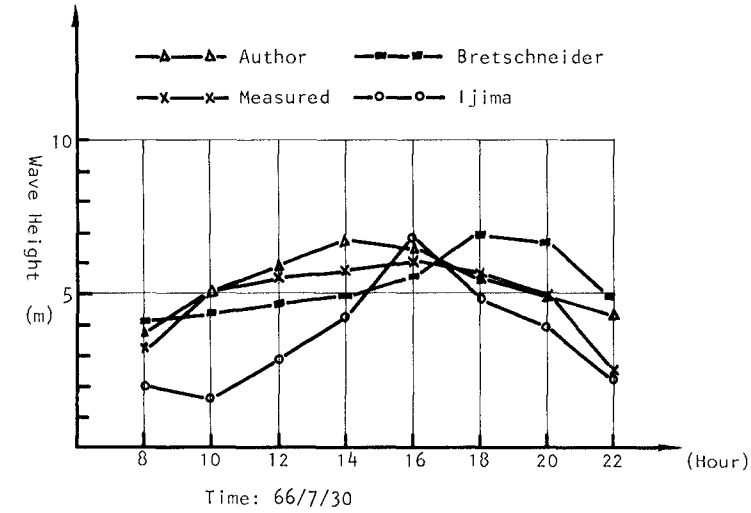


Fig 1 Judy Typhoon

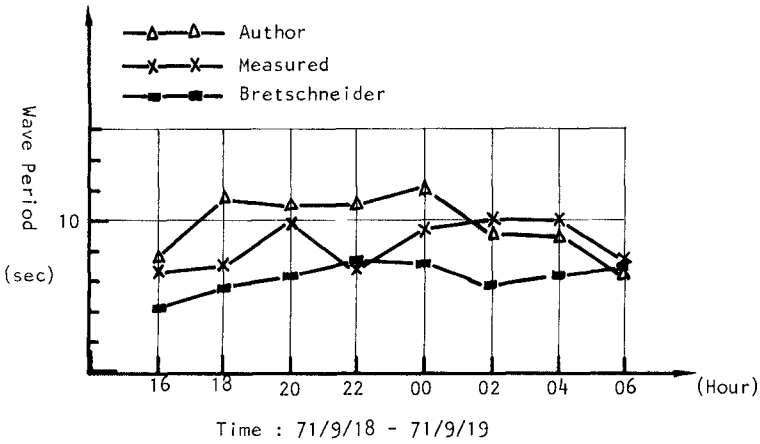
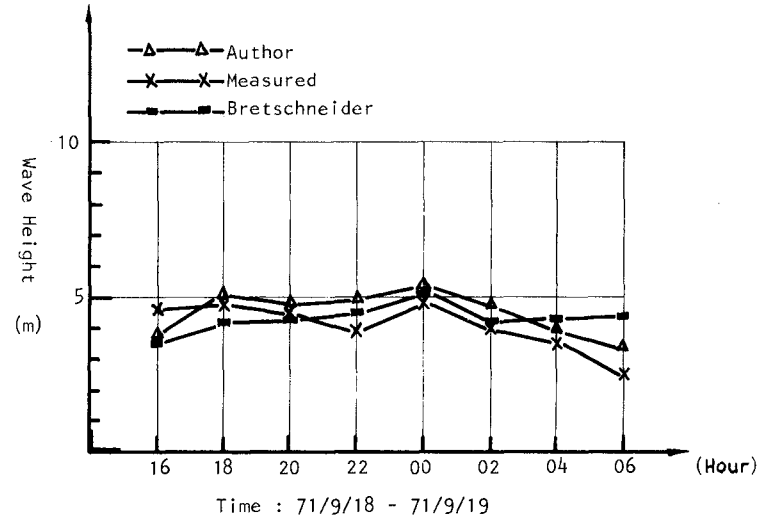


Fig 2 Agnes Typhoon

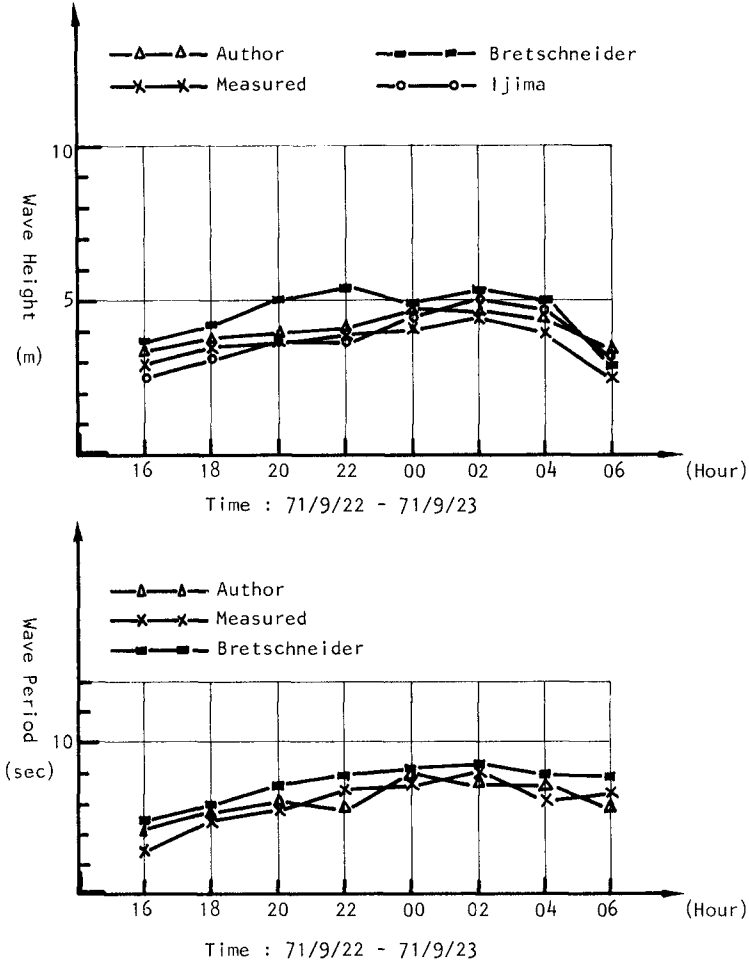
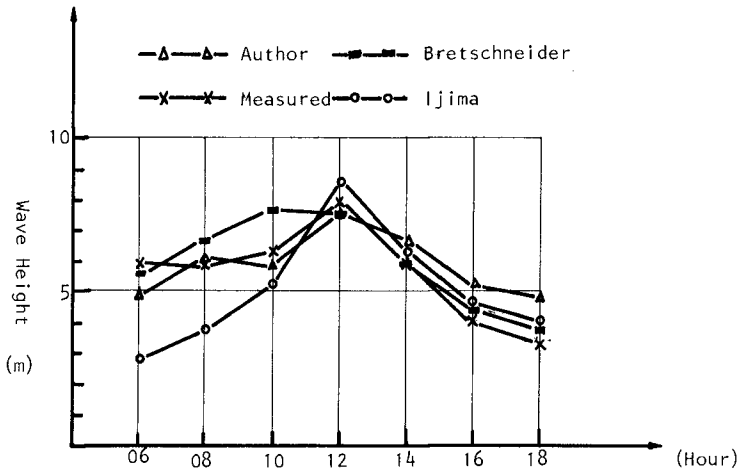
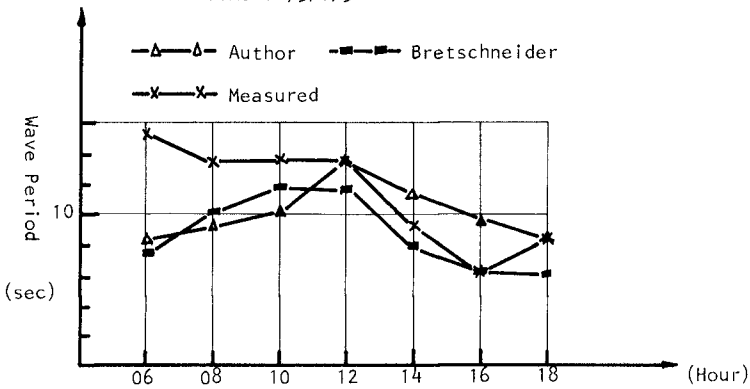


Fig 3 Bess Typhoon





Time : 75/8/3



Time : 75/8/3

Fig 4 Nina Typhoon

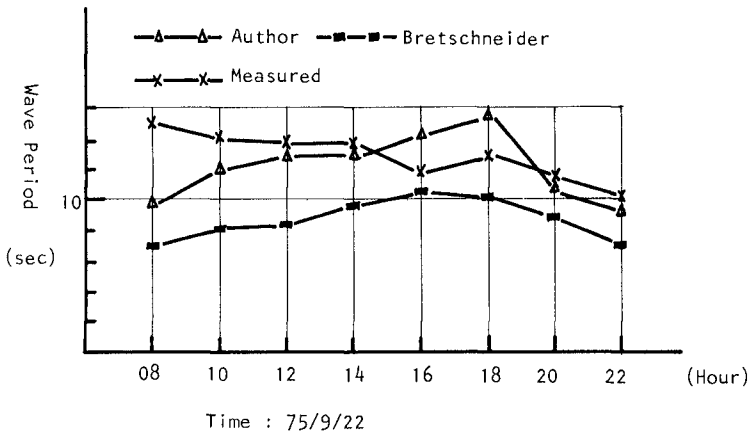
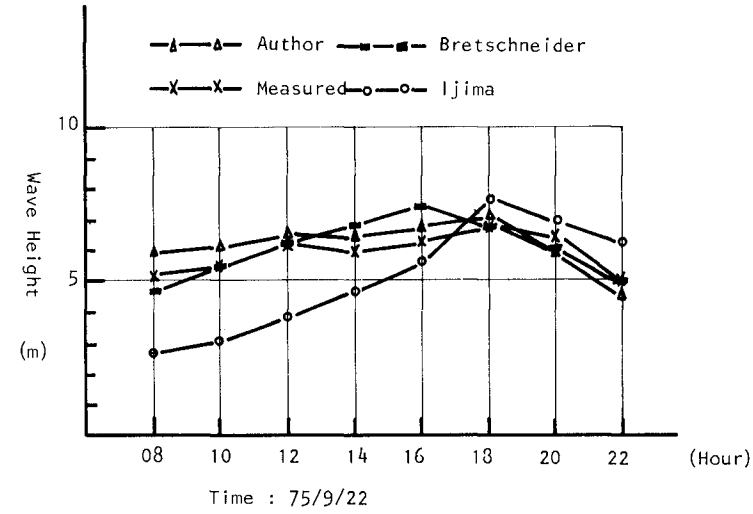


Fig 5 Betty Typhoon

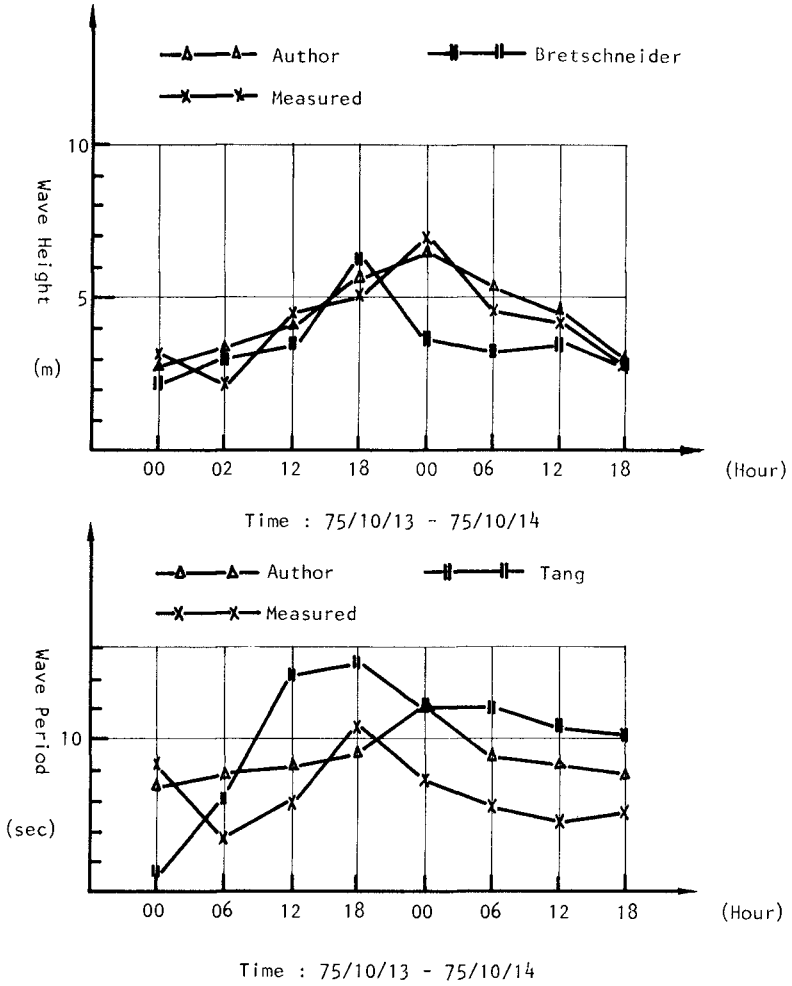


Fig 6 Elsie Typhoon

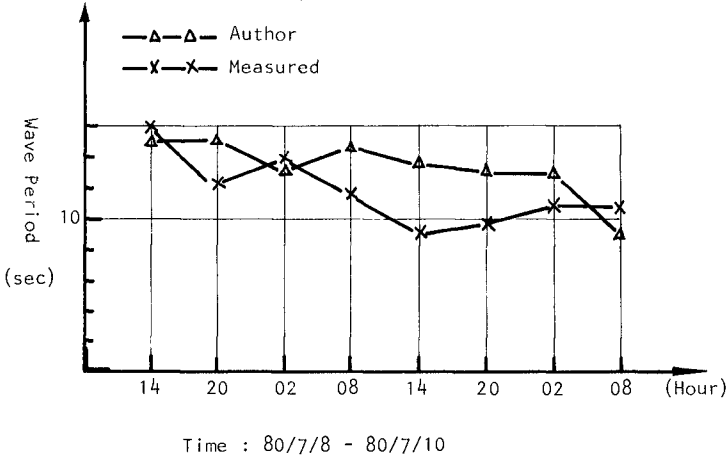
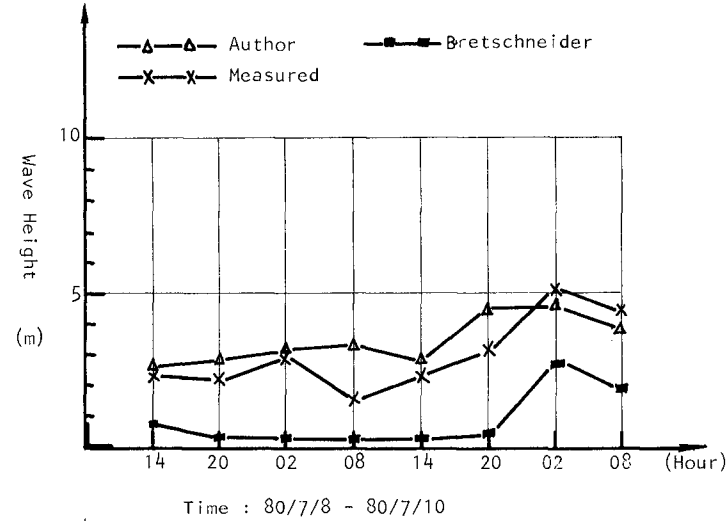
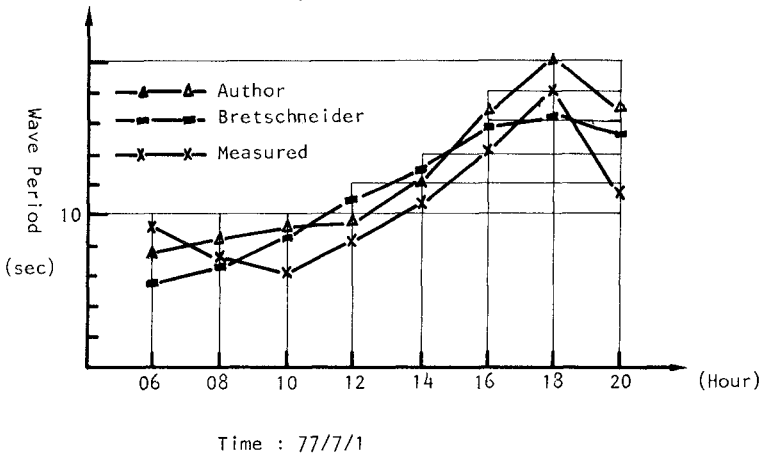
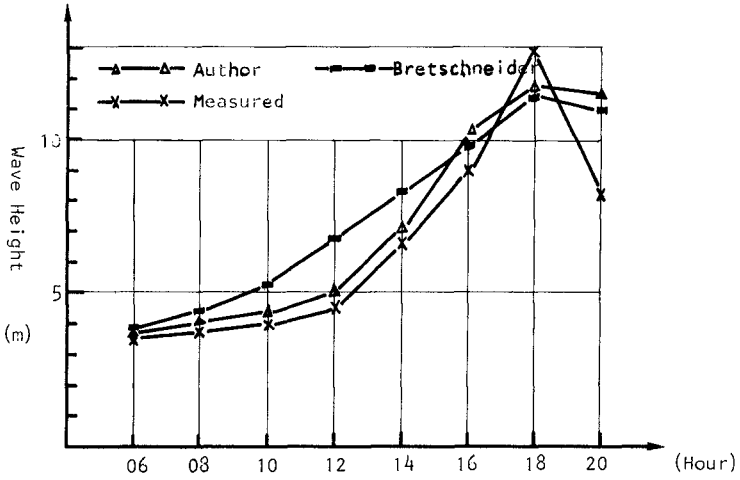


Fig 7 Ida Typhoon



#### 4. CONCLUSIONS

This paper proposes a new typhoon wave hindcasting method which has improved several defects of the other models. Basically, this method is based on Bretschneider's method and Liang's typhoon swell method. Which is also partially originates from Bretschneider's method. Hence, it is sure that, (1) Bretschneider's method is a good typhoon wave predication method. (2) The effect of swell has not been considered in Bretschneider's method. Finally, there are two other things which should be further studied. One is R value (radius of maximum wind speed). Another is the wave period. However, the method proposed in this paper can be used in the wave climate prediction.

#### 5. REFERENCE

- 1) Bretschneider C.L. and E.E. Tamaya (1976):  
Hurricane Wind and Wave Forecasting Techniques, Proc. 15th International Coastal Engineering Conference. ch. 13, pp.202-237  
Published by ASCE.
- 2) Hou, Kou, & Tzeng (1982) :  
Study of Hurricane Waves around Taiwan Coast, Proc. 6th Ocean Engineering Conference, R.O.C.
- 3) Liang, N.K. (1978):  
Wave Data Processing and Hindcasting Model, Institute of Oceanography, National Taiwan University, pp. 122 (in Chinese).
- 4) Liang & Lin (1978):  
Comparisons of Hindcasted and Measured Wave of Vera Typhoon, Proc. 2th Ocean Engineering Conference, R.O.C. (in Chinese)
- 5) Liang, N.K., J. Wang, C.Y. Liou and H. Pien (1981):  
Current and Wave Measurement in the Vicinity of Hsien-Da-Kang and Tung-Kang, Speical Publication No.28, Institute of Oceanography, National Taiwan University.
- 6) Liang, Tzeng & Wang (1981):  
Wave Measurement and Analysis in Nan-Wan Bay, special Publication No.38, Institute of Oceanography, National Taiwan University (in Chinese).
- 7) Liang, N.K. (1982):  
A Typhoon Swell Predication Method, Proc. 6th Harbor Engineering Conference, R.O.C. (in Chinese).
- 8) Liaw (1980):  
Introduction to Japan Typhoon Prediction, Proc. Conf. on Typhoon Prediction, 1980, R.O.C. (in Chinese).

- 9) F.L.W. Tang (1971):  
Coastal Engineering Plan and Design, Joint Commission on Rural Reconstruction. (in Chinese)
- 10) Tsai (1977):  
Study of Application of the Tracing Method at Taiwan, Proc. 1th Ocean Engineering Conference, R.O.C. (in Chinese)

## CHAPTER THIRTY NINE

### INFLUENCE OF EL NINOS ON CALIFORNIA'S WAVE CLIMATE

Richard J. Seymour, M.ASCE (1)

R. Rea Strange III (2)

Daniel R. Cayan (3)

Robert A. Nathan AM.ASCE (4)

#### ABSTRACT

Waves with exceptional height and periods caused severe damage along the coast of California in 1982-83. Because these large wave events coincided with a strong El Nino-Southern Oscillation (ENSO) climatic anomaly, which occurs 20-25 times per century, there was interest in determining if the extreme waves resulted from the ENSO or its related features. The meteorological setting featured a very large and intense low pressure zone over the north-central Pacific. Associated with this Pacific-wide pattern, a series of large mid-latitude storms developed at about weekly intervals and produced exceptionally long fetchs directed at the California Coast.

Two time series of extreme wave events, using buoy data after 1981 and hindcasts before, were used covering the period from 1900 to 1984. One series considered waves with significant heights greater than 3 m (10 ft) and the second for those greater than 6 m (20 ft.) These were compared with a time history of ENSOs for the same period. A strong association was established between northern hemisphere winters during ENSO years and large wave events in Southern California. Strong ENSO winters had the largest storm waves, moderate ENSOs less intense waves, and weak ENSOs tended not to have storm waves greater than the threshold value used in this study. The correlation between large waves and ENSO years is significant at the 1% level. The correlation between lack of large waves and non-ENSO years is significant at the 0.5% level.

Because of the great southerly extent of the most energetic storms, a large number of energetic wave trains approach the coast from the west, rather than the northwest, as previously assumed by many. ENSO winters are responsible for producing all of the wave events in this study with both heights greater than 6 m and periods of peak energy longer than 19 seconds.

Five out of nine eastern Pacific tropical storms making landfalls on California in the 85 year period occurred during the late northern summer of ENSO years.

(1) Hd., Ocean Engr. Research Group, Scripps Inst. of Oceanography, La Jolla, CA

(2) President, Pacific Weather Analysis, Santa Barbara, CA

(3) Research Assoc., Scripps Inst. of Oceanography, La Jolla, CA

(4) Coastal Engineer, Moffatt & Nichol, Engineers, Long Beach, CA



## INTRODUCTION

During the Winter of 1982-83, a series of extraordinary storms attacked the coast of California. Shoreline damage was severe, particularly in Southern California, and was accompanied by unusual coastal plain flooding in many areas. The extreme sea levels causing this flooding and an assessment of the nearshore waves and their impacts are discussed in two papers in these proceedings (see Flick and Cayan, 1984 and Walker, Nathan, Strange and Seymour, 1984.) The wave fields associated with these storms attracted particular attention because of the extremely long peak periods as well as the great wave heights. To many observers, the number and intensity of these storms exceeded that of any winter within memory.

The year 1982, which immediately preceded the most intense storms during January-March of 1983, was climatologically exceptional. We now know that a very strong El Nino - Southern Oscillation (ENSO) event began in the late spring of 1982. At the time, the time sequence of equatorial oceanic warming and trade wind reversal was several months later than most previous ENSOs, causing lively debate among oceanographers and climatologists as to whether there really was an ENSO occurring (see Kerr, 1983.) The impact of ENSOs on productivity in South American coastal waters has been well studied for many years. Only recently, motivated in part by the extreme nature of the 82-83 ENSO, have scientists understood the global impacts of the event, including droughts and excessive rainfall over large areas outside of the tropics. (For a review of ENSO see Philander, 1983.) There was a second major climatological perturbation almost coincident with the onset of the ENSO - the eruption of the Mexican volcano, El Chichon. Although its total ejected mass was much smaller than, say, Mount St. Helens, it was one of those rare eruptions that results in very large quantities of sulfuric acid in the stratosphere. This contaminant, with a long persistence, spread completely around the globe in a broad band straddling the equator. There is evidence from historical climate records that this kind of eruption can have pronounced effects on global climate (see Sigurdsson, 1982.) The superposition of the strong ENSO and El Chichon makes it very difficult to sort out the climatic effects of each event. The severity of the 1982 ENSO may even have been augmented by the influence of the El Chichon cloud, but our present level of understanding of climatology does not allow us to confirm or reject such interactions.

Volcanos rarely vent sulfides all the way to the stratosphere, but ENSOs occur perhaps 20 times in a century. It is therefore important, from a wave climatology standpoint, at the least to determine if ENSOs are likely to have been paramount in driving these severe storms. Therefore, the authors decided to test the relationship between ENSOs and large wave events by comparing time series from historical records.

### THE 1982-83 LARGE WAVE EVENTS OFF CALIFORNIA

The NOAA observation buoy moored at approximately 35 N latitude and 121 W longitude measured six large wave events, each related to a massive storm in the Pacific Basin, that occurred in the period from December, 1982 to March, 1983. The significant wave height exceeded 6 m (20 ft) in each of these events, as shown in Table I. These observations were made in deep water in unsheltered offshore locations.

The storm of 10 February, 1983, which produced the longest periods of this series, was studied in detail (see Earle et al., 1984.) Using all of the NOAA buoy data, this work showed that the significant wave height at the site closest to the storm was 12.9 m (43 ft) and that there was considerable energy up to periods as long as 25 seconds. This energy level would predict a maximum wave height of about 24 m (79 ft.)

In later sections of this paper, it will be shown that these storms rank as very extreme events in recent history.

### THE METEOROLOGICAL SETTING

From a meteorological standpoint, the 1982-83 ENSO winter was most extraordinary, especially over the Pacific and adjacent continental margins. Not only was the Gulf of Alaska-Aleutian low pressure center unusually deep (as is often the case with northern hemisphere ENSO winters), but the low was, on average, large enough in areal extent and displaced eastward sufficiently to affect the West Coast and particularly California. This has not always been the case with ENSO winters (see Namias and Cayan, 1984.) Figure 1 shows the departure from normal of the 700 millibar (mb) height surface for winter, which is nearly equivalent to the anomalous pressure pattern at about 3 km (10,000 ft) aloft. It is shown to be abnormally low (negative) in a broad region centered in the southern Gulf of Alaska, and very high (positive) in the central Pacific subtropics. Symptomatic of this pressure distribution were the frequent massive and vigorous storms that tracked across the central North Pacific to make landfall along virtually the entire West Coast of the United States. In a more usual winter, storms would be confined to landfalls at latitudes much further north.

The anomalous atmospheric angular momentum associated with these wind fields was studied by Rosen et al., (1984). This work shows that the transfer of angular momentum between the earth and the atmosphere was sufficient to change the length of the day by a few milliseconds during the winter of 1982-83.

Note that, although these storms were associated with an ENSO (a tropically based phenomenon), they were definitely extratropical disturbances. This is shown in Figure 2 by the cyclone tracks for March 1983. Figure 3 shows an infrared satellite image of two of the March 1983 storms. The storm fronts show greater development and a more southerly displacement than usual. Also note that there is no obvious connection of these storm systems with the tropics.

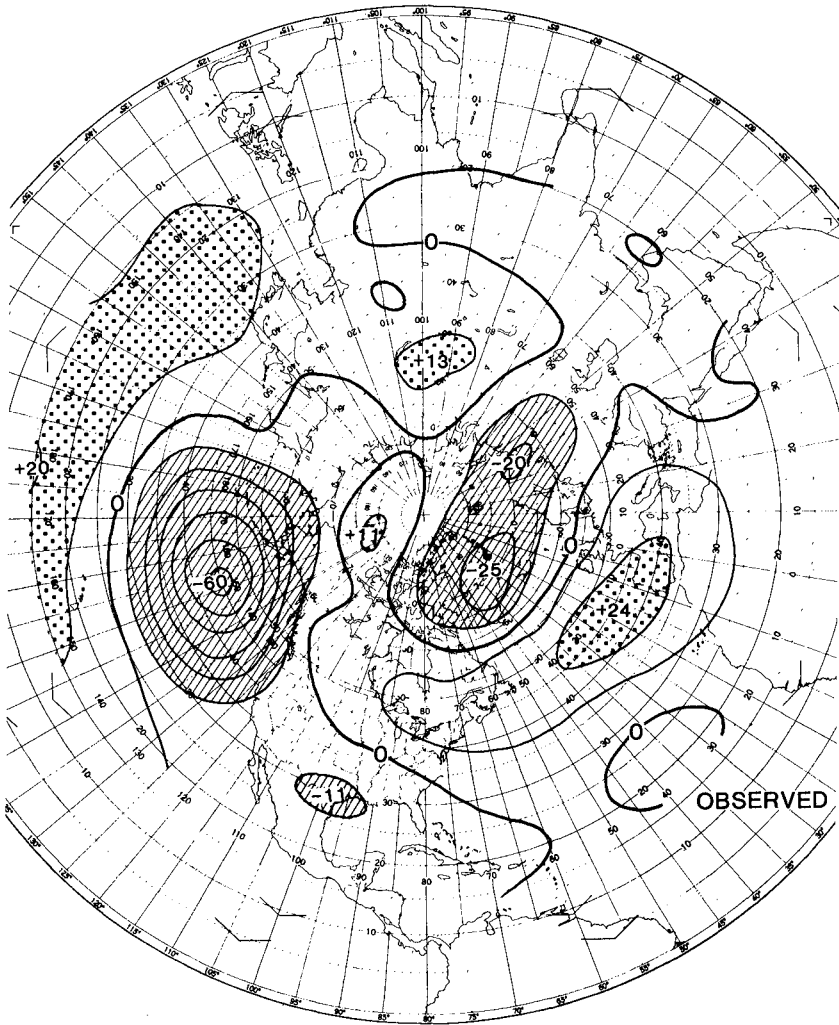


FIGURE 1

Winter 1982-1983 mean 700 mb. height anomaly in tens of feet. This is roughly analogous to the sealevel pressure anomaly. Winter is defined as December through February. Anomaly calculated against mean of 1947-1972 winters.

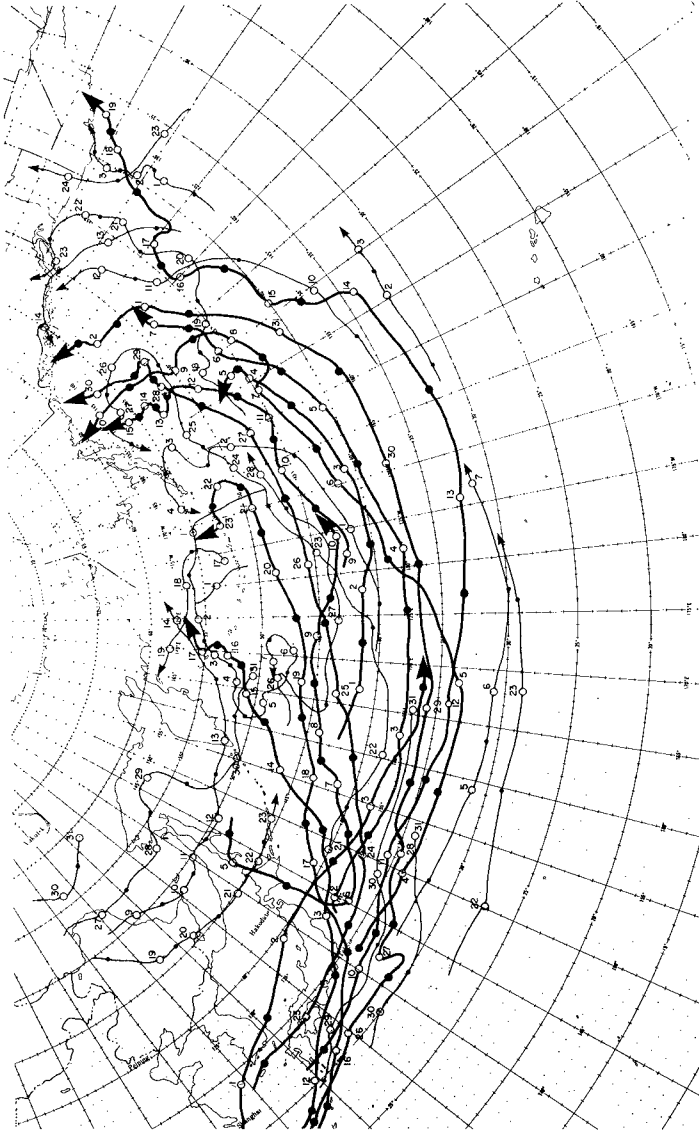


FIGURE 2

North Pacific cyclone (extratropical storm) tracks for March, 1983.  
[From NOAA Mariner's Weather Log, :27, pl82]

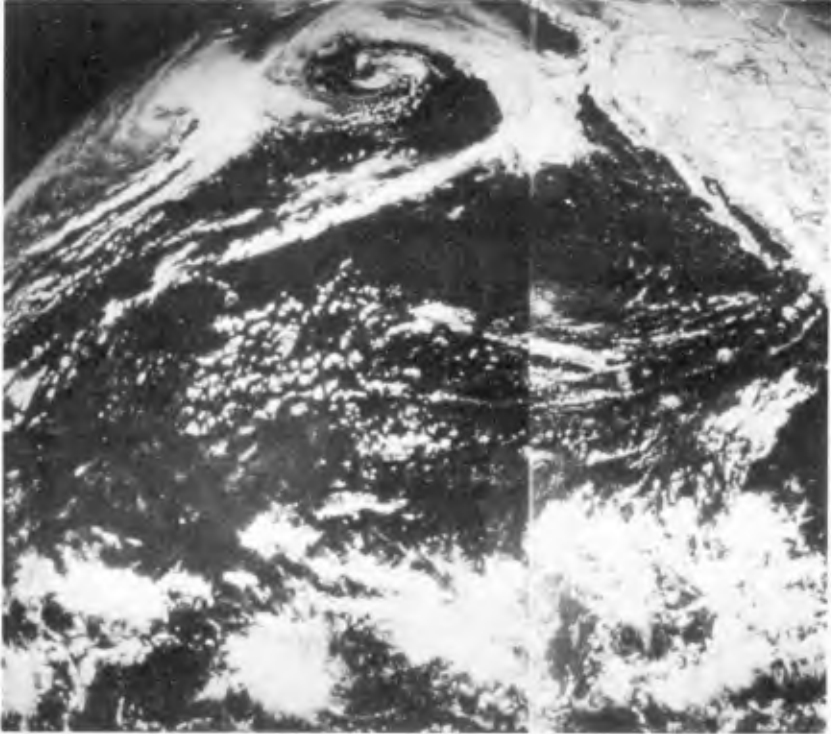


FIGURE 3

Satellite infrared image over North Pacific, March 4, 1983. High clouds (coldest) are shown in white. Low clouds (warm) are not distinguishable here. Note extensive frontal systems extending southward to 30 deg N, and lack of connection to intertropical convergence zone near equator.

TABLE I  
 NOAA BUOY OBSERVATIONS OF WAVES FROM MAJOR STORMS  
 WINTER 1982-83

DATE	SIG.HT. (m)	MAX. PERIOD	DIRECTION
01 DEC 82	6.4	14	295
18 DEC 82	6.4	20	288
25 JAN 83	6.1	17	278
27 JAN 83	7.3	22	279
10 FEB 83	6.7	25	281
01 MAR 83	8.2	20	258

These very large and intense low pressure centers resulted in fetches on the order of 1000 km (550 nm) and wind speeds up to 30 m/s (60 kts.) Previous empirical models, still widely used today, would predict peak periods of only about 17 seconds for such conditions. Contemporary spectral wave generation models containing nonlinear wave interaction terms, however, are capable of predicting the very long periods actually generated in these storms.

It can be seen from Figure 1 that the wind vectors can be expected to rotate to the north as the storms approach the continent. In typical winters, this northward shift occurs (on average) about 2200 km (1200 nm) offshore. At this point, the winds no longer continue to increase wave height. Dispersion causes the swell to decay over these long distances, reducing the height of the waves as they approach the shore. During the winter of 1982-83, because of the very large size of the low pressure zone and the increased strength of the westerlies, the average decay distance was reduced to about 1600 km (900 nm.) These factors account for the increase in the swell height during these storm wave events. It should also be noted that the locally generated waves may be travelling north almost orthogonally to the swell, producing a very confused sea state in deep water.

#### HISTORICAL WAVE DATA FOR THE CALIFORNIA COAST

Systematic wave measurements in deep water off the West Coast of the United States have been available only since 1980. Therefore, any meaningful historical assessment must depend largely upon wave hindcasts. Contemporary hindcasts, based upon reliable pressure field data and satellite imagery, can provide wave energy spectra and directional estimates with satisfactory accuracy for engineering analyses. However, for pre-satellite years, and particularly prior to the mid-1940's, the meteorological data become less satisfactory and the accuracy of the wave hindcasts is degraded. There are a number of storm hindcast studies that have been performed for the California

Coast (e.g., see Marine Advisers, 1960 and Meteorology International, 1977.) These works suffered from short observation periods and, in at least one case, from serious methodological problems. The earlier works used a singular wave approximation, compared with the spectral approach now employed by contemporary hindcasters. Rather than attempting to patch together the work of several hindcasting studies in an attempt to acquire a long enough time history, we decided to use the work of a single hindcaster which spanned the whole interval from the inception of meteorological data (approximately 1900) to the advent of continuous deep water measurements in late 1980. One of us (RRS) has prepared such a series. It was hindcast for a location in Southern California at a latitude of about 35 N. This series was an attempt to identify wave trains expected to have a significant impact on the shoreline. Therefore, it included only those events with deep water approach directions in the zone between SW and WNW. Waves approaching more obliquely would be diminished considerably by refraction as they approached the shore. Further, the waves were ranked by their power (energy multiplied by period.) This resulted in a list of 59 storms in which the resulting offshore significant wave height exceeded 3 m (10 ft), all having periods equal to or exceeding 12 seconds. The tropical cyclone of September, 1939, a major wave event in Southern California, was added for a total of 60 storms. These storms are listed in Table II.

A second series was obtained by considering only the very largest events. The threshold significant wave height was raised to 6 m (20 ft.) The second series contains only 18 storms because of its higher limit value, as shown in Table III.

It should be clearly recognized that the possible quality of hindcast decreases with the age of the data, particularly prior to the 1950's. It is likely that some major storms in the early years were excluded because there was insufficient pressure field resolution and accuracy to estimate the real wind speeds. This is particularly true for small, intense storms like tropical cyclones. It is almost impossible to hindcast these storms prior to the availability of satellite imagery. However, since no series of this length had previously been published, and since the work used a consistent methodology throughout, we felt that they would make a valuable contribution to our knowledge of the wave climate off California.

#### HISTORICAL RECORDS OF ENSO CONDITIONS

Using anomalies in the surface barometric pressure in the Indian and Pacific Oceans, combined with observations of fisheries in Peru and other similar data, Quinn et al. (1978) were able to develop a series of ENSO events covering more than 200 years. They also rated each event as strong, moderate or weak. The ENSOs since 1900 from this record are shown in Table IV. Quinn et al.'s ENSO series identifies events according to their onset years. For our purposes, it is the winter following the onset, when the mid-latitude connections are strongest, that would have possible consequences for Pacific waves.

TABLE II

EXTREME WAVE EPISODES EXCEEDING 3 M. (BASIC SERIES)  
1900 - 1984

DATE	SIG. HT. (m)	MAX. PERIOD	DIRECTION
13 MAR 05	8.8	15	247
17 NOV 05	3.3	17	286
31 DEC 07	5.3	16	282
12 MAR 12	3.2	12	220
26 JAN 14	5.8	13	223
03 FEB 15	7.5	14	235
01 JAN 18	3.7	16	280
12 FEB 19	5.3	12	299
20 DEC 20	4.7	13	301
15 OCT 23	3.7	16	296
01 FEB 26	6.9	15	257
03 JAN 27	5.8	20	287
06 NOV 28	4.0	17	294
01 JAN 31	3.9	16	276
28 DEC 31	7.4	18	288
19 DEC 35	4.7	16	267
13 DEC 37	4.5	16	272
06 JAN 39	7.9	19	285
25 SEP 39	4.5	15	205
24 JAN 40	4.3	16	267
25 DEC 40	5.7	16	270
20 OCT 41	3.3	17	294
30 DEC 45	3.9	19	285
13 FEB 47	3.9	16	265
04 NOV 48	4.7	18	300
15 NOV 53	5.7	17	269
15 JAN 58	3.1	22	280
26 JAN 58	6.8	14	259
05 AER 58	7.7	18	289
16 FEB 59	5.1	14	244
09 FEB 60	8.1	19	295
22 DEC 60	3.4	17	276
31 JAN 63	4.2	16	260
10 FEB 63	5.9	15	256
19 NOV 65	4.0	15	277
07 DEC 67	4.0	15	298
06 FEB 69	4.7	13	222
04 DEC 69	3.6	17	278
06 DEC 69	4.9	22	274
14 DEC 69	5.7	17	290
19 DEC 69	4.7	18	281
26 DEC 72	4.1	15	289
21 FEB 77	5.2	18	280
29 OCT 77	5.5	20	299
16 JAN 78	6.0	13	240



TABLE II (cont.)

01 JAN 80	4.7	20	272
17 FEB 80	6.1	18	249
22 JAN 81	4.3	20	258
28 JAN 81	7.0	17	262
13 NOV 81	4.9	18	284
01 DEC 82	6.4	14	295
18 DEC 82	6.4	20	288
25 JAN 83	6.1	17	278
27 JAN 83	7.3	22	279
10 FEB 83	6.7	25	281
13 FEB 83	4.9	17	268
01 MAR 83	8.2	20	258
14 NOV 83	5.0	17	290
03 DEC 83	7.0	17	285
25 FEB 84	6.4	17	300

TABLE III

EXTREME WAVE EPISODES EXCEEDING 6 M.  
1900 - 1984

DATE	SIG.HT. (m)	MAX. PERIOD	DIRECTION
13 MAR 05	8.8	15	247
03 FEB 15	7.5	14	235
01 FEB 26	6.9	15	257
28 DEC 31	7.4	18	288
06 JAN 39	7.9	19	285
26 JAN 58	6.8	14	259
05 APR 58	7.7	18	289
09 FEB 60	8.1	19	295
17 FEB 80	6.1	18	249
28 JAN 81	7.0	17	262
01 DEC 82	6.4	14	295
18 DEC 82	6.4	20	288
25 JAN 83	6.1	17	278
27 JAN 83	7.3	22	279
10 FEB 83	6.7	25	281
01 MAR 83	8.2	20	258
03 DEC 83	7.0	17	285
25 FEB 84	6.4	17	300

In four cases, one year adjustments were made in the onset years suggested by Quinn et al. The 1929 onset was changed to 1930 and the 1905, 1914 and 1939 onsets were changed to two year spans (1904-05, 1913-14, and 1939-40, respectively.) The basis for this was the timing of the peak of the Southern Oscillation (as determined from the Santiago-Darwin anomaly.) The onset year was adjusted to provide a uniform condition throughout the series in which the peak of the pressure anomaly occurred in the Spring or Summer. In addition, the

TABLE IV  
 ONSET YEARS OF ENSOS, 1900-1984  
 (From Quinn et al., 1978)

ONSET YEAR	SEVERITY
1902	Moderate
* 1904-05	Moderate
1911	Strong
* 1913-14	Moderate
1917	Weak
1918	Strong
1923	Weak
1925	Strong
* 1930	Moderate
1932	Weak
* 1939-40	Moderate
1941	Strong
1943	Weak
1951	Weak
1953	Moderate
1957	Strong
1965	Moderate
1969	Weak
1972	Strong
1976	Moderate
* 1982	Strong

\* Modified from Quinn et al.

1969 ENSO was reclassified from weak to moderate, in the context of this study, because the pressure anomaly persisted for more than a year. The 1982 ENSO, which occurred after the Quinn et al. paper, was classified by us as strong. The ENSO predictions for the first half of the century are expected to be of higher quality than the wave hindcasts, since they did not depend upon the density of pressure measurements.

#### CORRELATIONS BETWEEN ENSO YEARS AND LARGE WAVE EVENTS

As was observed in 1982-83, increased storminess as a result of an ENSO condition would likely occur during the winter following onset. Therefore, storms in January through April of the year following the onset could be assumed to have been influenced by the ENSO.

Applying this criterion to the time series of ENSOs and of large wave events produces the following results. For the basic wave series, 32 of the 60 wave events were associated with ENSOs. For the series of very large waves, 12 of the 18 wave events were associated with ENSOs.

Not all ENSOs resulted in large wave events. Table V shows a comparison between the occurrence of large storms and the ENSO strength categories of Quinn et al.

Table V shows that all seven strong ENSOs resulted in a wave event where the height exceeded 3 m (10 ft) with an average of 2.1 such events per ENSO. Three out of seven of these strong ENSOs produced wave heights over 6 m (20 ft) for an average of 1.3. All but one of the nine moderate ENSOs yielded waves above 3 m, with an average of 1.7 events per ENSO. Only two of these produced waves above 6 m and the average dropped to 0.3. Two of the five weak ENSOs met the lower height limit with an average of 0.4 occurrences per ENSO. Weak ENSOs produced no wave events exceeding the 6 m limit.

Table V shows a consistent series of relationships between ENSOs and large wave events. Strong ENSOs result in significant numbers of storms with waves exceeding both the 3 m and the 6 m thresholds. Moderate ENSOs produce storms with waves exceeding the 3 m limit, but not the 6 m value. Weak ENSOs have only a slight tendency to produce storm waves that exceed the 3 m threshold.

Eliminating the weak ENSOs, a total of 16 strong and moderate events were recorded in the 85 year period considered. Allowing for the three multi-year events, there were 19 ENSO years during the 85 year interval that would be classified as greater than weak events. Considering the 3 m (10 ft) threshold wave events, there was an average of 0.71 events per year over all years. During the moderate or strong ENSO years, there was an average of 1.58 events per year. Applying the Student's t test to determine the probability of the mean during these ENSO years exceeding the mean over all years by this amount, the probability was shown to be about 0.01 (one chance in a hundred.) The mean value of large wave events during non-ENSO years was found to be 0.45. The probability of the mean being this much lower than the mean over all years was found, by Student's t test, to be less than 0.005 (five chances out of a thousand.) Thus, the incidence of large wave events in association with ENSOs and the reduction in large storm waves during non-ENSO years are established statistically with little question.

#### WAVE APPROACH DIRECTIONS AND CHARACTERISTIC PERIODS

Because of the frequent winter storms that are spawned by the Aleutian Low during most years, it has generally been assumed that the track for major storms affecting California is usually out of the northwest. Table II shows, however, that a large number of severe storm waves come out of the west. This is shown in Figure 4, which plots the incidence of wave approach directions for the Table II series. A strong peak is found at about 285 deg. for both the total data set and also the ENSO year subset. The ENSO year occurrences also are observed to fall off rapidly at approach directions slightly north of this peak.

TABLE V  
ASSOCIATION OF ENSOS AND LARGE WAVES

ONSET YEAR	NUMBER OF LARGE WAVE EVENTS	
	Central California	Southern California
<b>STRONG ENSOS</b>		
1911	1	0
1918	1	0
1925	1	1
1941	1	0
1957	3	2
1972	1	0
1982	7	6
<b>MODERATE ENSOS</b>		
1902	0	0
1904-05	2	1
1913-14	2	1
1930	1	0
1939-40	3	0
1953	1	0
1965	1	0
1969	4	0
1976	1	0
<b>WEAK ENSOS</b>		
1917	1	0
1923	1	0
1932	0	0
1943	0	0
1951	0	0

Conventional wisdom has also suggested that severe storms along the California Coast produced periods of peak energy of no greater than about 19 seconds. The storms of 1982-83 showed very clearly that this limit was much too low. Figure 5 depicts the incidence of peak periods in the very large wave events contained in the Southern California series. It can be readily seen from Figure 5 that all storms that produced peak energy wave periods greater than 20 seconds were associated with ENSO years. This is, of course, consistent with the meteorological setting during most ENSO events in which there are very long fetches directed at the California Coast.

#### TROPICAL STORMS

The pronounced warming of the surface waters along the California Coast during a strong El Nino condition could be expected to allow the northward excursion of tropical cyclones (hurricanes) in late summer and early fall to latitudes excluded in non-ENSO years. As previously noted, it is not generally possible to develop a wave hindcast series

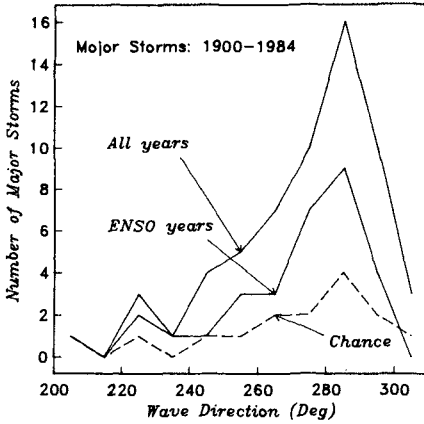


FIGURE 4

Number of occurrences of major wave events from various approach directions for events in Table II.

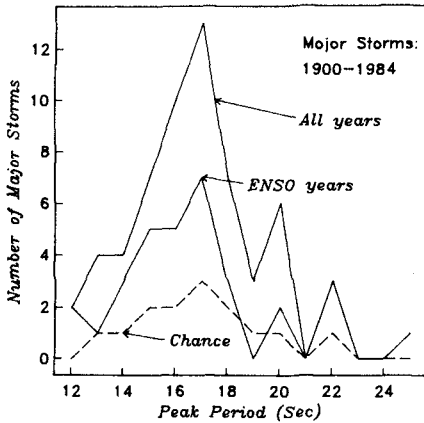


FIGURE 5

Number of occurrences of major wave events with the energy spectra peaked at various wave periods. Events are from Table II.

for these storms which are so small in diameter compared to a typical extra-tropical cyclone. However, Court (1980) has compiled a record of hurricane tracks since 1900. This was extended through 1983 using DeAngelis (1983). The tracks of these storms are shown in Figure 6. Of all of the hurricanes observed in this period, only nine made landfalls in California. Five of these nine were in ENSO initiation years, when warm water would be expected along the West Coasts of Mexico and California during the Fall hurricane season. One of these was the storm of 25 September, 1939, which is one of the events in the basic series. Therefore, the data suggest that late summer and fall hurricane-driven wave events in Southern California are much more likely in ENSO years than during the intervening periods.

#### DISCUSSION AND CONCLUSIONS

A very convincing statistical relationship has been demonstrated between ENSOs and the large wave events that dominate the wave climate of Southern California. Because ENSOs also tend to increase sea level along the California Coast in rough proportion to their intensity, the coastal damage resulted from large waves will be exacerbated during ENSO events.

The scheme adopted by Quinn et al. (1978) for designating the intensity of the ENSOs is in good qualitative agreement with the number and intensity of large hindcast wave events in California.

ENSOs appear to be among the more predictable of the major global climate events. Therefore it may be possible to forecast severe winter wave climates with some skill for the California Coast.

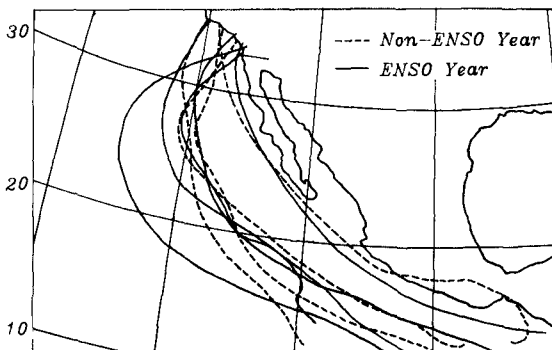


FIGURE 6

Tracks of tropical cyclones (hurricanes) that made landfalls in Southern California during the period 1900-1983.

Wave periods much longer than typically assumed for this coast were recorded. These very long periods have particular significance both for wave runup intensity and for drastic intensification of mooring loads on large floating structures with the potential for reaching a near-resonant condition at approximately 0.04 hz.

## REFERENCES:

- Court, A, 1980. "Tropical Cyclone Effects on California", NOAA Tech Memo NWS WR-158, 41 p.
- DeAngelis, D., 1983. "Hurricane Alley", Mariners Weather Log 27:1, pp 34-40.
- Earle, M.D., K.A. Bush and G.D. Hamilton, 1984. "High Height Long Period Ocean Waves Generated by a Severe Storm in the Northeast Pacific Ocean during February 1983", Journ. Phy. Ocean. In press.
- Flick, R.E., and D.R. Cayan, 1984. "Extreme Sea Levels on the Coast of California", Proc. 19th Intl. Conf.Coast. Engr., Houston, TX.
- Kerr, R.A., 1983."Fading El Nino Broadening Scientists' View", Science 221:4614, pp 940-941.
- Marine Advisers, 1960. "Design Waves for Proposed Small Craft Harbor at Oceanside, California", Report prepared for the U.S. Army Engineer District, Los Angeles, CA.
- Meteorology International, 1977. "Deep-Water Wave Statistics for the California Coast", Report prepared for the Dept. of Navigation and Ocean Development, Sacramento, CA.
- Namias, J., and D.R. Cayan, 1984. "El Nino: Implications for Forecasting", Oceanus 27:, pp 41-47.
- Philander, S.G.H., 1983. "El Nino Southern Oscillation Phenomena", Nature 302:5906, pp 295-301.
- Quinn, W.H., D.O. Zopf, K.S. Short and R.T.W. Kuo Yang, 1978. "Historical Trends and Statistics of the Southern Oscillation, El Nino, and Indonesian Droughts", Fishery Bull. 76:3, pp 663-678.
- Rosen R.D., D.A. Salstein, T.M. Eubanks, J.O. Dickey, and J.A. Steppe, 1984. "An El Nino Signal in Atmospheric Angular Momentum and Earth Rotation", Science 225:4660, pp 411-414.
- Sigurdsson, H., 1982. "Volcanic Pollution and Climate: The 1783 Laki Eruption", Trans. Amer. Geophysic. Union 63:32, pp 601-602.
- Walker, J.R., R.A. Nathan, R.J. Seymour, and R.R. Strange III, 1984. "Coastal Design Criteria in Southern California", Proc. 19th Intl. Conf.Coast. Engr., Houston, TX.

## CHAPTER FORTY

### RUN-UP OF RANDOM WAVES ON GENTLE SLOPES

Hajime Mase\* and Yuichi Iwagaki, M.ASCE\*\*

#### ABSTRACT

This paper investigates the following characteristics of run-up of random waves on gentle slopes experimentally: (1) the run-up wave energy spectrum, (2) the ratio of the number of run-up waves to that of incident waves, (3) the relationship between the representative run-up height, the deep-water wave steepness and the beach slope, (4) the run length of run-up heights, and (5) the effect of wave grouping on representative run-up heights.

Main results are summarized in the chapter of conclusions.

#### 1. INTRODUCTION

Wave up-rush and back-rush on beaches are significant external forces for the change of beach profile near the shoreline. Besides, the height of wave run-up is important in determining for the height of coastal structures such as seawalls, dykes and surge barriers, and is the limit of onshore side for on-offshore and littoral sand transports.

A number of studies for run-up of random waves on steep slopes, as well as for run-up of monochromatic waves, have been performed, because front faces of traditional coastal structures are generally steep and accurate design data of wave run-up on steep slopes have been needed. Recently, seawalls and dykes with gentle slopes have been recommended, if possible, from the reason that sand beaches in front of the structures with steep slopes are apt to be lost during storms and from the reason of a good view and utilization of the beaches. However, studies for run-up of random waves on relatively gentle slopes like natural beaches are very few.

---

\* Research Associate, Dept. of Civil Eng., Kyoto Univ., Kyoto, Japan  
\*\*Professor, Dept. of Civil Eng., Kyoto Univ., Kyoto, Japan



When a beach slope becomes gentle, a period of one cycle of up-rush and back-rush of a wave becomes long and the interaction between a back-rush and a subsequent up-rush (or, overtaking and capturing of bores on beaches) becomes remarkable. The characteristics of run-up of random waves will depend on the time series of waves coming to the shoreline, and also on wave grouping of incident waves in deep water.

The purpose of this paper is to examine the following characteristics of run-up of random waves on gentle slopes experimentally by using random waves with two different groupiness factors defined by Funke and Mansard<sup>1</sup>), but with the same spectrum of Pierson-Moskowitz type: (1) the run-up wave energy spectrum, (2) the ratio of the number of run-up waves to that of incident waves, (3) the relationship between the representative run-up height, the deep-water wave steepness and the beach slope, (4) the run length of run-up heights, and (5) the effect of wave grouping on representative run-up heights.

## 2. EXPERIMENTS

A series of tests was carried out in a 50cm wide, 27m long and 75cm deep wave flume. At one of the ends of the wave flume, a random wave generator is installed. Beach slopes were selected as 1/5, 1/10, 1/20 and 1/30. The depth of water,  $h$ , in a uniform section of the flume was kept 45cm, but 43cm only in the case of a 1/30 beach slope. The outline of experimental apparatus is shown in Fig.1.

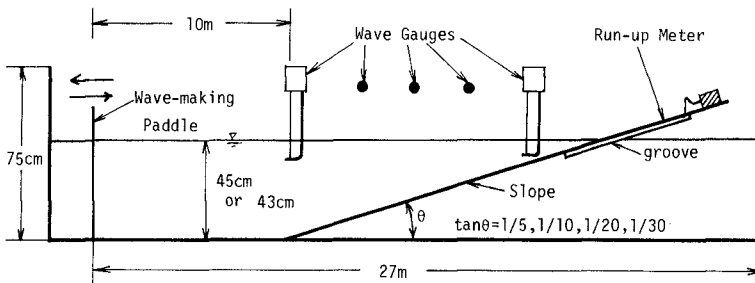


Fig.1 Experimental apparatus.

A wave gauge of capacitance type was used as a run-up meter, which was installed in a groove (3cm wide and 1cm deep) along a centerline of the slope to coincide the height of the capacitance wire (2.2mm diameter and 2m long) with the slope surface, see Photo.1. The run-up meter was calibrated by moving every 10cm along the slope surface. The calibration curve was closely approximated by a straight line. Additional calibrations of the run-up meter were done comparing



Photo.1 Run-up meter.

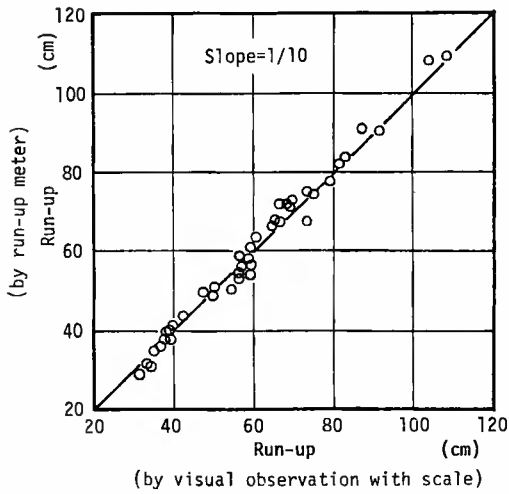


Fig.2 Comparison of run-up heights by run-up meter and by visual observation with scale.

run-up heights measured by the run-up meter and by a visual observation with a scale. Both run-up heights were nearly the same. An example of the comparison is shown in Fig.2, and the correlation coefficient of both run-up heights is about 0.99. We believe that the run-up meter used here is sufficient to measure run-up of random waves.

Random waves used here were simulated<sup>2)</sup> to have Pierson-Moskowitz type spectra with six kinds of peak frequencies of 0.4, 0.5, 0.6, 0.8, 1.0 and 1.2Hz, and with two kinds of groupiness factors of 0.74 (Case 1) and 0.53 (Case 2), based on the study of Funke and Mansard<sup>1)</sup>. Electric signals for generating the random waves have been recorded by an analog data recorder. Three kinds of input levels of the electric signals were used to generate random waves with the peak frequency from 0.4 to 0.8Hz (in Cases 1 and 2) and two kinds were used for random waves with the peak frequency of 1.0Hz (in Cases 1 and 2) and 1.2Hz (in Case 1). A series of totally 30 tests were carried out for each beach slope.

Water surface variations were measured by using five wave gauges of capacitance type at water depths of 45 (40cm for a 1/30 beach slope), 20, 15, 10 and 5cm (W-1 ~ W-5).

Both of water surface variations and run-up variations (shoreline oscillations) were recorded simultaneously by an analog data recorder. The records were digitized by an A-D converter at the sampling interval of 0.04 second. The numbers of data are 40 000, 31 000, 26 500, 19 500, 15 500 and 12 500 for cases of random waves with peak frequencies of 0.4, 0.5, 0.6, 0.8, 1.0 and 1.2Hz. The numbers of individual waves at the wave gauge W-1 in each record are from 650 to 900.

### 3. EXPERIMENTAL RESULTS AND CONSIDERATIONS

#### 3.1 Characteristics of incident waves

Table 1 shows representative quantities of waves measured at the wave gauge W-1 (40cm water depth), and the wave height and wave steepness in deep water,  $H_0$  and  $H_0/L_0$ , calculated from the significant wave, for the experiments of a 1/30 beach slope. Individual waves are defined by the zero-up-cross method.

Fig.3 shows two examples of energy spectra of incident waves, in which (a) is for S30-Case 1-7 and S30-Case 2-7, and (b) for S30-Case 1-13 and S30-Case 2-13. The energy spectra of waves with the same case number of Cases 1 and 2 are almost the same except in the region of low frequency smaller than 0.3Hz. The difference of energy spectra in the low frequency region depends mainly on long waves generated by short waves with the different wave groupiness factors.

Fig.4 shows the groupiness factor,  $GF$ , against the deep-water wave steepness  $H_0/L_0$ . The average values of  $GF$  in Cases 1 and 2 are 0.73 and 0.57 respectively, while the expected values of  $GF$  are 0.74 and 0.53<sup>2)</sup>. Random waves with a small  $GF$  cannot be well reproduced in a wave tank when the deep-water wave steepness is larger than 0.03 (this corresponds to  $kh > 1.36$ ,  $k$ : the wave number), which is discussed in another paper<sup>3)</sup>.

Statistical properties of random waves related to wave groups have been examined in the previous paper<sup>2)</sup>.

Table 1 Representative quantities of incident waves in case of 1/30 beach slope.

Slope	F <sub>p</sub>		H <sub>0</sub>	H <sub>0</sub> /L <sub>0</sub>	H <sub>max</sub>	H <sub>1/3</sub>	H	T <sub>max</sub>	T <sub>1/3</sub>	T	
1/30	0.4	S30-Case1-	1	4.685	0.0061	9.549	4.762	2.841	2.680	2.222	1.732
			2	3.560	0.0047	7.108	3.612	2.137	2.680	2.212	1.704
			3	2.641	0.0035	5.265	2.678	1.542	2.600	2.208	1.630
	0.5		4	6.085	0.0128	10.479	5.773	3.550	2.000	1.743	1.431
			5	4.761	0.0100	8.186	4.517	2.777	1.960	1.744	1.433
			6	3.447	0.0071	5.860	3.277	1.973	2.040	1.760	1.408
	0.6		7	7.664	0.0208	12.243	7.100	4.434	1.560	1.536	1.300
			8	5.305	0.0162	9.977	5.466	3.389	1.480	1.528	1.292
			9	4.748	0.0137	21.126	4.390	2.626	0.320	1.491	1.267
	0.8		10	9.993	0.0467	25.002	9.148	5.849	0.240	1.171	1.075
			11	7.830	0.0364	13.676	7.168	4.576	1.240	1.174	1.050
			12	5.720	0.0272	9.910	5.240	3.352	1.240	1.162	1.033
	1.0		13	6.576	0.0496	10.657	6.244	3.979	0.960	0.922	0.865
			14	5.357	0.0412	8.982	5.097	3.287	0.880	0.913	0.838
	1.2		15	6.839	0.0646	10.536	6.642	4.263	0.760	0.824	0.819
			16	5.881	0.0584	8.941	5.736	3.617	0.760	0.804	0.778
1/30	0.4	S30-Case2-	1	4.754	0.0059	7.000	4.872	3.176	1.880	2.278	1.846
			2	3.472	0.0042	5.158	3.565	2.312	1.880	2.290	1.828
			3	2.871	0.0035	4.251	2.945	1.872	1.880	2.282	1.785
	0.5		4	6.187	0.0117	9.302	5.949	3.906	1.440	1.843	1.527
			5	4.701	0.0090	7.287	4.514	2.918	1.400	1.833	1.497
			6	3.851	0.0073	5.939	3.692	2.390	1.400	1.840	1.502
	0.6		7	8.105	0.0223	12.088	7.502	4.955	1.280	1.526	1.356
			8	6.085	0.0165	9.017	5.639	3.717	1.280	1.538	1.351
			9	4.997	0.0134	7.313	4.634	3.054	1.240	1.546	1.349
	0.8		10	9.989	0.0464	14.869	9.143	5.953	1.120	1.174	1.063
			11	7.492	0.0360	10.991	6.867	4.483	1.200	1.155	1.030
			12	6.344	0.0308	8.534	5.817	3.835	1.120	1.149	1.035
	1.0		13	5.514	0.0434	9.069	5.259	3.369	0.920	0.902	0.828
			14	6.996	0.0528	10.701	6.617	4.260	0.960	0.919	0.865

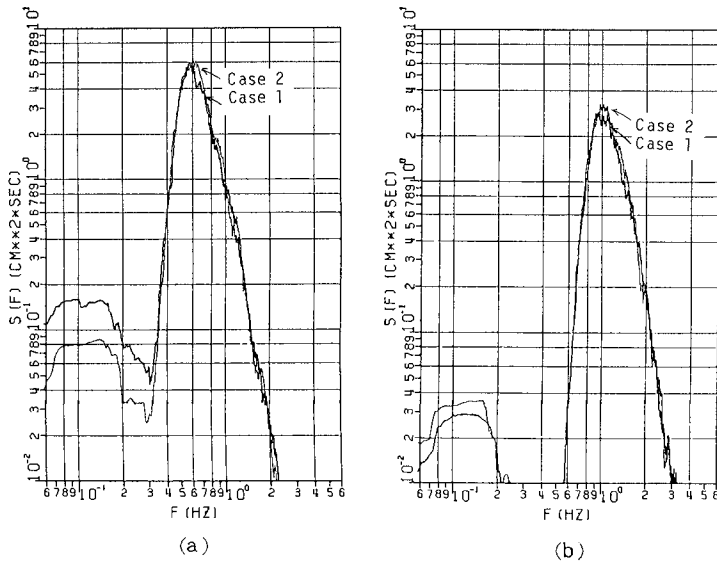


Fig.3 Energy spectra of incident waves at the wave gauge W-1 in case of 1/30 beach slope. (a)  $f_p=0.6$ Hz, (b)  $f_p=1.0$ Hz.

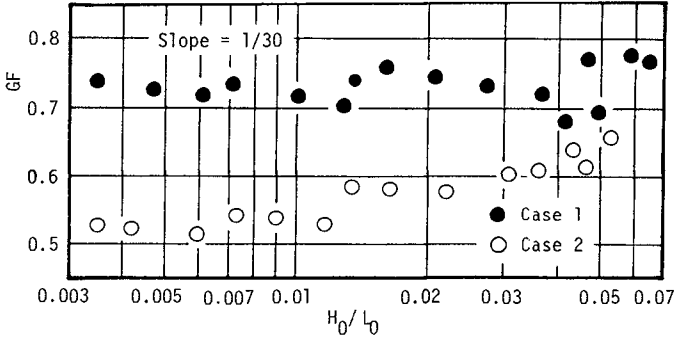


Fig.4 Groupiness factor of incident waves at the wave gauge W-1. Groupiness factor was defined by Funke and Mansard<sup>1)</sup> to represent wave groupiness.

### 3.2 Energy spectrum of run-up waves (run-up variations)

Huntly, Guza and Bowen<sup>4)</sup> remarked that run-up wave energy spectra have a universal 'saturation' form of  $f^{-4}$  dependence for the frequency region over which incident waves are large enough to break. Guza and Thornton<sup>5)</sup> mentioned that run-up wave energy spectra in the saturation region show a  $f^{-3}$  dependence and spectral energy densities are independent of incident wave energies. The difference of both results is the  $f^{-4}$  or the  $f^{-3}$  dependence, which is considered as the effect of beach slopes by Guza et.al.

Fig.5 shows run-up wave energy spectra when the energies of incident waves with the peak frequency 0.6Hz (Case 1) are changed, for 1/5, 1/10, 1/20 and 1/30 beach slopes. It is seen from these figures that run-up wave energy spectra are saturated and show the  $f^{-4}$  dependence in the region of high frequency independently of incident wave energies and of beach slopes.

Fig.6 shows the relationship between the beach slope and the spectral energy density of run-up waves in the saturation region, in which values of the spectral energy density are plotted by the mean value and the standard deviation. It is found from this figure that the spectral energy density at a given frequency in the saturation region depends on the beach slope and is nearly proportional to  $\tan^4\theta$ .

These results of run-up wave energy spectra such as the  $f^{-4}$  and  $\tan^4\theta$  dependence are the same as those estimated from the theoretical consideration by Huntly et.al<sup>4)</sup> and Guza et.al<sup>5)</sup>.

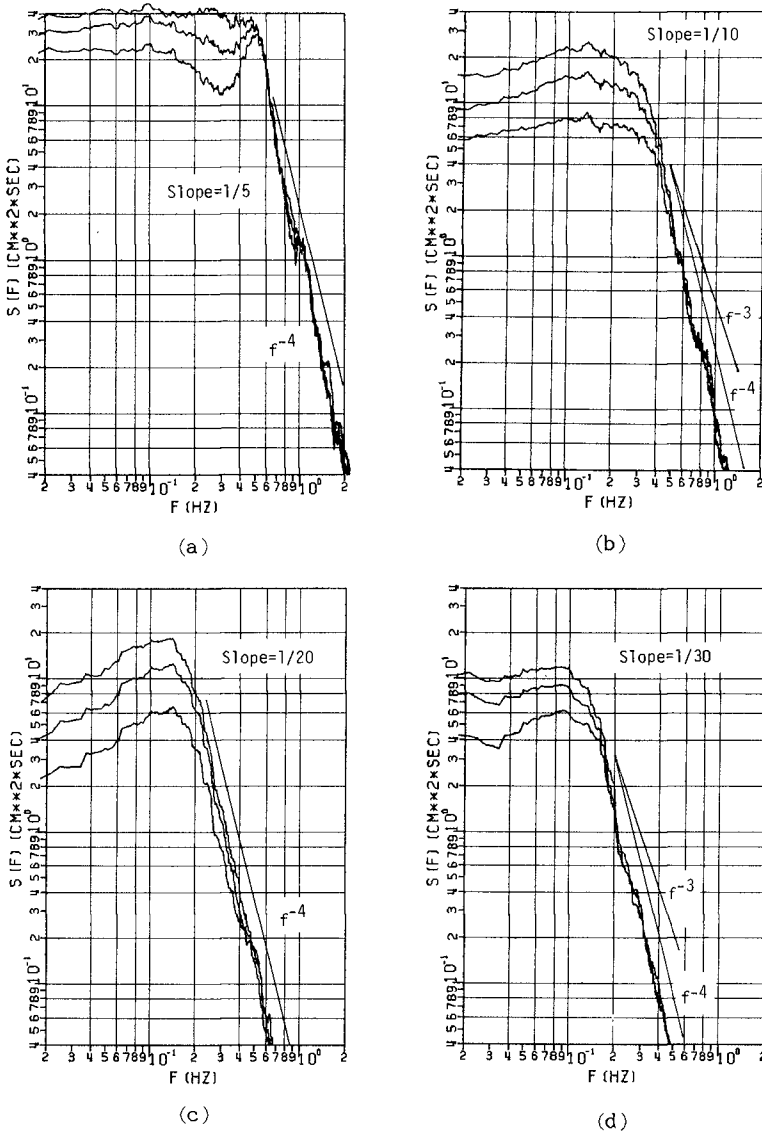


Fig.5 Run-up wave energy spectra. (a)  $\tan\theta=1/5$ , (b)  $\tan\theta=1/10$ , (c)  $\tan\theta=1/20$ , (d)  $\tan\theta=1/30$ .

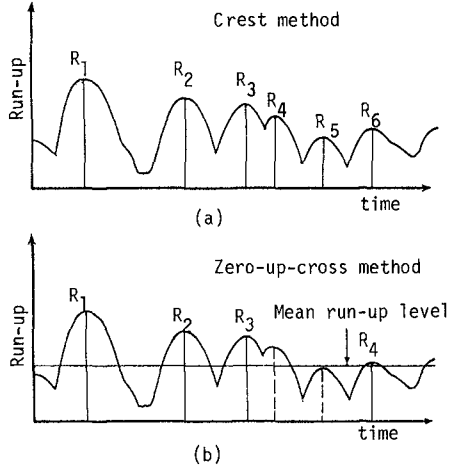
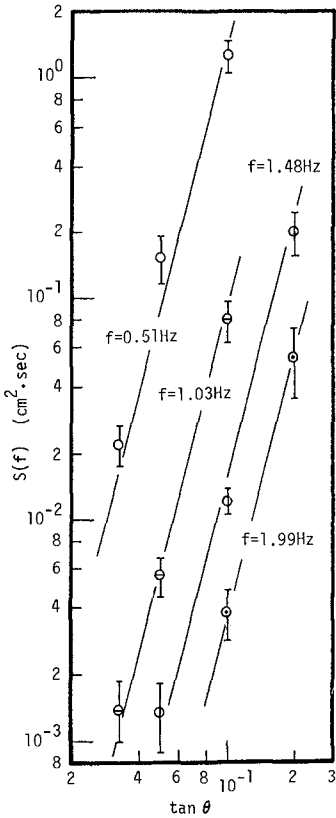


Fig.7 Definition method of run-up waves.

Fig.6 Relationship between beach slope and spectral energy density of run-up waves in saturation region.

**3.3 Individual wave analysis of run-up waves**

**(1) Definition of an individual run-up wave**

There are several definition methods of an individual wave of run-up wave such as a zero-up-cross, a zero-down-cross, a crest-to-trough and so on. The number of individual run-up waves and the representative run-up heights change with the definition method. Fig.7 shows an example of definition of an individual wave, in which (a) is the crest method, (b) the zero-up-cross method. The number of run-up waves by the crest method is two waves more than that by the zero-up-cross method. In our experimental results, the ratio of the number of individual run-up waves defined by the zero-up-cross method to that by the crest method is from about 0.4 to 0.9 depending on the

beach slope, and the ratio of significant run-up height is about 1.1 and the ratio of mean run-up height is about 1.2.

In the following sections, an individual run-up wave is defined by the crest method.

(2) Number of individual run-up wave

In the case of gentle slopes, it takes place that a wave (bore) coming to the shoreline cannot run up if the back-rush of a preceding wave (bore) is large and that a wave (bore) running up on the beach face is overtaken and captured by a subsequent wave (bore) before the wave (bore) reaches a maximum run-up height. Therefore, the number of run-up waves (the frequency of run-up waves) will be reduced compared to that of incident waves. Fig.8 shows the ratio  $\alpha$  of the number of run-up waves to that of incident waves at the wave gauge W-1. The experimental data can be well arranged by the surf similarity parameter,  $\xi (= \tan\theta / \sqrt{H_0/L_0})$ , as shown in Fig.8. The ratio  $\alpha$  becomes small as  $\xi$  becomes small (or the beach slope becomes gentle and the deep-water wave steepness becomes large). In this result, the effect of wave grouping is not clear.

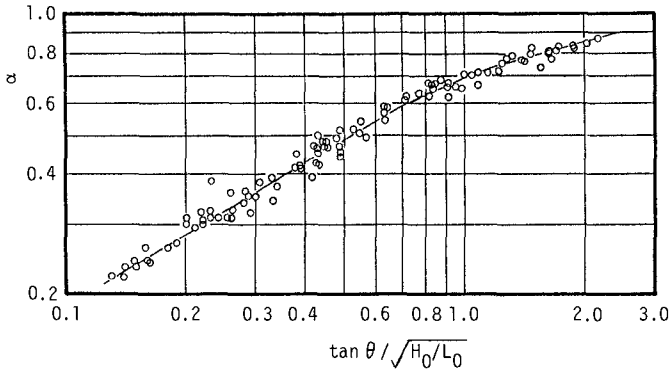


Fig.8 Ratio of the number of run-up waves to that of incident waves.

(3) Representative run-up heights

According to the dimensional analysis, the height of run-up,  $R$ , on an impermeable, smooth slope is expressed as follows:

$$\frac{R}{H_0} = f\left(\frac{H_0}{L_0}, \tan\theta, \frac{h_0}{H_0}\right), \quad (1)$$

in which,  $h_0$  is the water depth at the toe of a slope. When  $h_0/H_0$  is larger than 3.0, the effect of  $h_0/H_0$  is negligible<sup>6)</sup> and Eq.(1) becomes

$$\frac{R}{H_0} = f\left(\frac{H_0}{L_0}, \tan\theta\right). \quad (2)$$

Hunt<sup>7)</sup> proposed the following equation for run-up heights of monochromatic waves based on the experimental data:



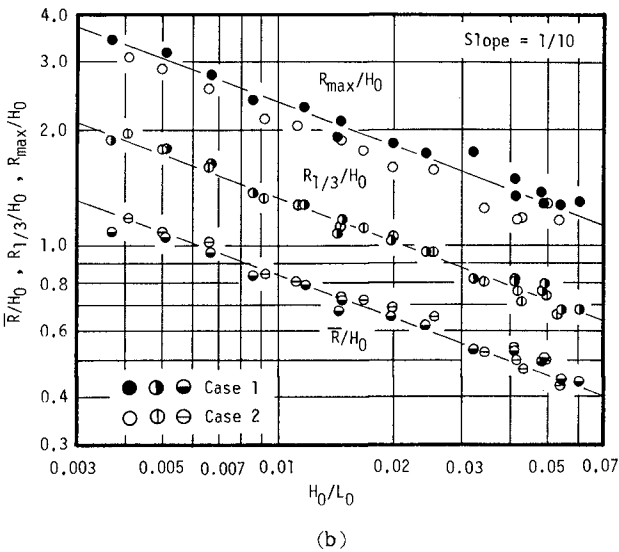
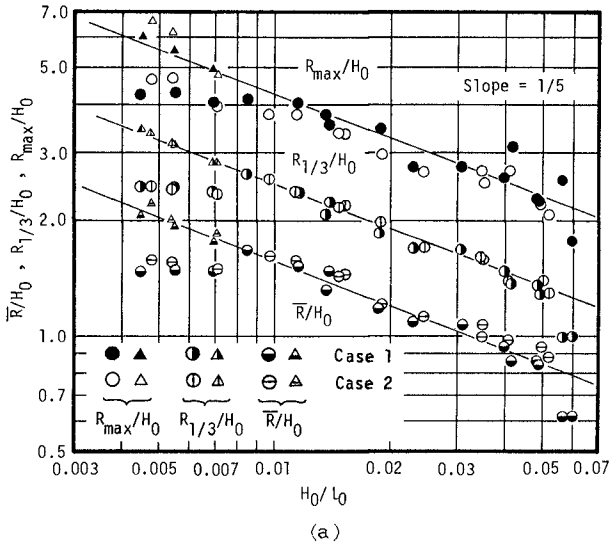
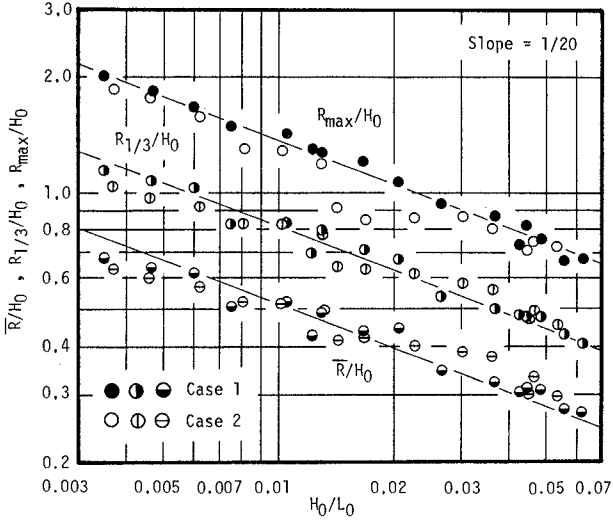
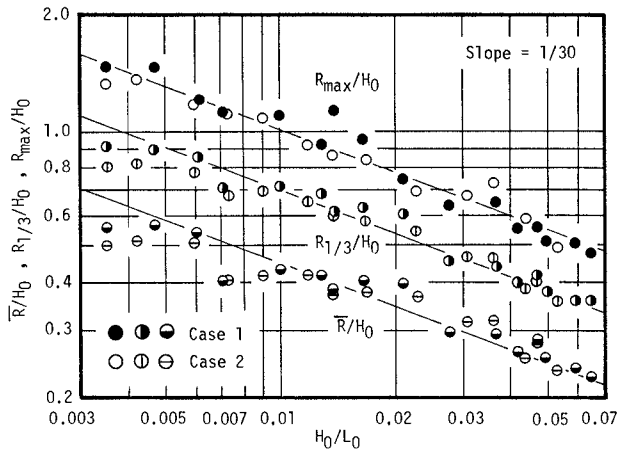


Fig.9 Relationship between representative run-up heights and deep-water wave steepness. (a)  $\tan\theta=1/5$ , (b)  $\tan\theta=1/10$ , (c)  $\tan\theta=1/20$ , (d)  $\tan\theta=1/30$ .



(c)



(d)

Fig.9 (c) (d) (Continued).

$$\frac{R}{H_0} = \tan\theta / \sqrt{H_0/L_0} \quad (3)$$

In this paper, representative run-up heights of random waves are examined based on Eq.(2), in which  $H_0$  and  $L_0$  are taken as the significant wave height and wave length in deep water (see Table 1).

Fig.9 shows the relationship between the representative run-up heights ( $R_{max}$ : maximum run-up height,  $R_{1/3}$ : significant run-up height,  $\bar{R}$ : mean run-up height) and the deep-water wave steepness. Straight lines were drawn parallel to each other in all figures, so as to represent the tendency of the experimental data of which the deep-water wave steepness is larger than 0.008. The gradient of the lines is  $-0.37$ , which is a little different from  $-0.5$  by Hunt. In the cases of smaller deep-water wave steepness than 0.005 for  $1/20$  and  $1/30$  beach slopes, the values of  $R_{1/3}/H_0$  and  $\bar{R}/H_0$  are a little smaller than the values by the straight lines. Especially for the  $1/5$  beach slope, all representative run-up heights are considerably smaller than the values by the straight lines in the region of smaller deep-water wave steepness than 0.008. Although we used the same electric signal to generate random waves, the significant wave height at the wave gauge W-1 in the case of the  $1/5$  beach slope was large compared with the results in other gentler slopes  $1/10$ ,  $1/20$  and  $1/30$  due to the wave reflection at the slope. The larger value of  $H_0$  causes the smaller values of  $R_{max}/H_0$ ,  $R_{1/3}/H_0$  and  $\bar{R}/H_0$ . When we use the mean value of  $H_0$  obtained in other gentler slopes, the run-up heights are plotted with triangular shape symbols (in Fig.9(a)) represented well by the straight lines.

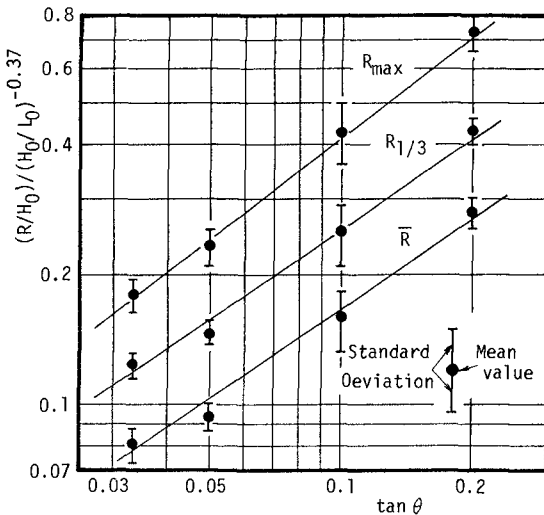


Fig.10 Relationship between run-up heights and beach slope.

The maximum run-up height in Case 1 of which the groupiness factor is about 0.73 is about 10% larger than that in Case 2 of which the groupiness factor is about 0.57. However, there is little effect of wave grouping on other representative run-up heights of  $R_{1/3}/H_0$  and  $\bar{R}/H_0$ .

Fig. 10 shows the relationship between the representative run-up heights and the beach slope  $\tan\theta$ , in which experimental data are plotted by the mean value and the standard deviation. It is seen from this figure that the representative run-up heights increase as the beach slope becomes steep. The gradients of the straight lines are 0.69 for the significant and mean run-up heights, and 0.77 for the maximum run-up height.

(4) Experimental formula for run-up height of random waves

Here, we formulate the run-up height by the following two equations:

$$\frac{R}{H_0} = a(\tan\theta)^b (H_0/L_0)^c, \quad (4)$$

$$\frac{R}{H_0} = d(\tan\theta/\sqrt{H_0/L_0})^e. \quad (5)$$

The coefficients in Eqs. (4) and (5) are determined by the least squares method, based on the experimental data of which the deep-water wave steepness is larger than 0.008 for the 1/5 beach slope and larger than 0.005 for the 1/20 and 1/30 beach slopes.

Table 2 shows the result, in which  $\sigma$  denotes the standard deviation of the difference between the experimental value and the formula. The standard deviation in Table 2(b) is almost the same as that of Table 2(a). We propose the simple experimental formula for run-up heights of random waves, represented by the surf similarity parameter of Eq. (5).

(5) Run length of run-up heights

The highest wave in a wave record does not appear alone but usually appears with several high waves. Such a phenomenon was firstly studied by Goda<sup>8)</sup>. On the other hand, the highest run-up appears singly very often. Table 3 shows the distribution of run length of run-up heights exceeding the significant run-up height and the mean run-up height, based on all 120 test runs containing 54 244 run-up waves. The mean length of runs of run-up heights is 1.18 for  $R > R_{1/3}$  and 1.95 for  $R > \bar{R}$ , which is smaller than the mean length of runs of wave heights (1.42 for  $H > H_{1/3}$  and 2.37 for  $H > \bar{H}$ ). The mean length of conditional runs of run-up heights containing the highest run-up is 1.15 for  $R > R_{1/3}$  and 1.78 for  $R > \bar{R}$  (2.37 for  $H > H_{1/3}$  and 4.82 for  $H > \bar{H}$ ). The highest run-up occurs when the preceding back-rush is small, and the subsequent run-up height is reduced by the back-rush of the highest run-up. Therefore, the highest run-up is apt to appear alone.

(6) Effect of wave grouping on run-up heights

It was demonstrated by Carstens, Torum and Traetteberg<sup>9)</sup> and Johnson, Mansard and Ploeg<sup>10)</sup> that random waves with large wave grouping cause larger wave run-up and therefore severer damage to rubble mound breakwaters than waves with poor wave grouping. Van Ooschot<sup>11)</sup> reported that random waves with a large spectral width parameter cause larger wave run-up than waves with a small spectral width parameter, which means random waves with poor wave grouping

Table 2 Experimental formulas for run-up heights of random waves.

(a)  $\frac{R}{H_0} = a(\tan \theta)^b (H_0/L_0)^c$

	Crest Method				Zero-up-cross Method			
	a	b	c	$\sigma$	a	b	c	$\sigma$
$R_{max}$	2.565	0.783	-0.367	0.151	2.565	0.783	-0.367	0.151
$R_{1/3}$	1.308	0.696	-0.361	0.095	1.375	0.686	-0.363	0.088
$\bar{R}$	0.946	0.697	-0.330	0.072	0.992	0.668	-0.356	0.079

(b)  $\frac{R}{H_0} = d \left( \frac{\tan \theta}{\sqrt{H_0/L_0}} \right)^e$

	Crest Method			Zero-up-cross Method		
	d	e	$\sigma$	d	e	$\sigma$
$R_{max}$	2.319	0.771	0.159	2.319	0.771	0.159
$R_{1/3}$	1.378	0.702	0.094	1.497	0.695	0.086
$\bar{R}$	0.878	0.688	0.074	1.085	0.678	0.077

Table 3 Distribution of run length of run-up heights.

Run Length <i>j</i>	Ordinary Runs		Runs containing $R_{max}$	
	$R > R_{1/3}$	$R > \bar{R}$	$R > R_{1/3}$	$R > \bar{R}$
1	5396	6449	102	58
2	800	3162	18	36
3	138	1630		16
4	1	777		6
5	13	373		1
6	1	174		1
7		86		
8		36		
9		14		
10		12		
11		3		
mean	1.18	1.95	1.15	1.78

(120 test runs, containing 54,244 run-up waves)

cause larger wave run-up. In our results, the maximum run-up height in Case 1 (large wave grouping) is about 10% larger than that in Case 2 (poor wave grouping). However, there is little effect of wave grouping on the significant and mean run-up heights.

Fig.11 shows the groupiness factor at the wave gauge W-5 in 5cm water depth, which shows the degree of wave grouping before waves run up. It is seen from this figure that the values of  $GF$  in cases 1 and 2 become small compared with the results shown in Fig.4 and the difference of wave grouping between in Cases 1 and 2 diminishes due to wave breaking in the surf zone.

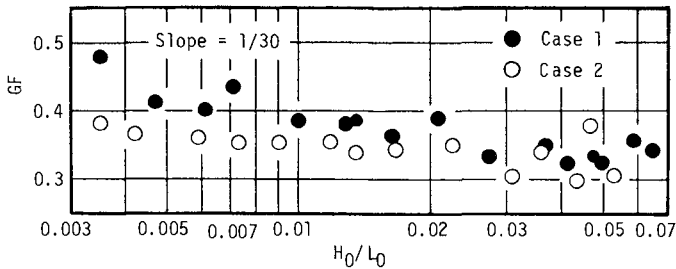


Fig.11 Groupiness factor at the wave gauge W-5 after wave breaking.

The change of wave grouping in shallow water has been investigated by the authors (2), (3), (4).

In the experiments by Carstens et.al and Johnson et.al, it seems that since the slope of a breakwater is very steep such as 1:1.25 and 1:1.5, the properties of wave grouping are not changed on the slope and the effect of wave grouping on wave run-up and stability of the breakwater was remarkable.

#### CONCLUSIONS

This paper examined the characteristics of wave run-up of random waves on gentle slopes experimentally by using random waves having the same spectrum and two different groupiness factors. Main results of this paper are summarized as follows:

1) Run-up wave energy spectra show a  $f^{-4}$  dependence in the region of high frequency (saturation region) independently of incident wave energies and beach slopes, and also show a  $\tan^4\theta$  dependence in the saturation region.

2) The ratio of the number of run-up waves to that of incident waves at the deepest water (45cm or 40cm in our experiments) becomes small as the beach slope becomes gentle and the deep-water wave steepness becomes large. The experimental data can well be arranged by the surf similarity parameter as shown in Fig.8. Reducing of the number of run-up waves is caused by overtaking and capturing of bores in the surf zone and on the beach face, and by large back-rushes suppressing

following running up waves.

3) A linear relation is obtained when two pairs of representative run-up heights vs. deep-water wave steepnesses and representative run-up heights vs. beach slopes are plotted on a log-log scale. We propose the simple experimental formula for run-up heights of random waves represented as a function of the surf similarity parameter by Eq. (5).

4) The highest run-up of each test run appears singly very often because the highest run-up occurs when the preceding back-rush is small, and the subsequent run-up height is reduced by the back-rush of the highest run-up.

5) The maximum run-up height of random waves in Case 1 of which the groupiness factor is about 0.73 is 10% larger than that in Case 2 of which the groupiness factor is 0.57 on the average. However, there is little effect of wave grouping on other representative run-up heights  $R_{1/3}/H_0$  and  $\bar{R}/H_0$ . This is due to the fact that the difference of wave grouping of random waves between in Cases 1 and 2 becomes small in very shallow water by wave breaking in the surf zone in the case of gentle beach slopes.

#### ACKNOWLEDGEMENT

This investigation is supported by a Grant-in-Aid for Encouragement of Young Scientist of The Ministry of Education, Science and Culture.

#### REFERENCES

- 1) Funke, E.R. and E.P.D. Mansard : On the synthesis of realistic sea states in a laboratory flume, Hydraulics Laboratory Rept. LTR-HY-66, National Res. Council of Canada, 54p., 1978.
- 2) Mase, H., N. Kita and Y. Iwagaki : Random wave simulation considering wave groups, Coastal Eng. in Japan, Vol.26, pp.61-75, 1983.
- 3) Mase, H., K. Furumuro and Y. Iwagaki : Transformation characteristics of wave grouping with wave propagation, Proc.31th Japanese Conf. on Coastal Eng., pp.36-40, 1984 (in Japanese).
- 4) Huntly, D.A., R.T. Guza and A.J. Bowen : A universal form for shoreline run-up spectra, Jour. Geophys. Res., Vol.82, No.18, pp.2577-2581, 1977.
- 5) Guza, R.T. and E.B. Thornton : Swash oscillations on a natural beach, Jour. Geophys. Res., Vol.87, No.C1, pp.483-491, 1982.
- 6) Saville, T. : Wave run-up on shore structures, Trans. ASCE, Vol.123, pp.139-150, 1958.
- 7) Hunt, I.A. : Design of seawalls and breakwaters, Proc. ASCE, Vol.85, No.WW3, pp.123-152, 1957.
- 8) Goda, Y. : On wave groups, Proc. Int. Conf. Behavior of Offshore Structures, pp.115-128, 1976.
- 9) Carstens, T., A. Torum and A. Traetteberg : The stability of rubble mound breakwaters against irregular waves, Proc.10th Coastal Eng. Conf., pp.958-971, 1966.
- 10) Johnson, R.R., E.P.D. Mansard and J. Ploeg : Effects of wave

grouping on breakwater stability, Proc.16th Coastal Eng. Conf., pp.2228-2243, 1978.

11) Van Ooschot, J.H. and K. d'Angremond : The effect of wave energy spectra on wave run-up, Proc.11th Coastal Eng. Conf., pp.888-900, 1968.

12) Mase, H. and Y. Iwagaki : Wave height distributions and wave grouping in the surf zone, Proc.18th Coastal Eng. Conf., pp.58-76, 1982.

13) Iwagaki, Y., H. Mase and K. Furumuro : Transformation characteristics of irregular wave including wave breaking, Disaster Prevention Res. Inst. Annuals, No.26 B-2, pp.559-575, 1982 (in Japanese).

14) Mase, H. and Y. Iwagaki : An analysis of wave data for wave grouping, Coastal Eng. in Japan, Vol.27, 1984 (in Printing).



## CHAPTER FORTY ONE

### On the Sequential Behaviour of Sea-States

A. Sánchez-Arcilla \*

#### Abstract

Probability distributions theoretically derived for gaussian, stationary processes are applied here to the sequential behaviour of sea-states. This behaviour defined by the curve of evolution of significant wave-height,  $H_s(t)$ , is characterized by variables such as: intensity of storm peaks, time between beginnings of storms, average duration of calms and storms, average number of consecutive storms, expected value of the extremal storm peak, etc.

The distributions obtained for these variables have been tested with 5 years of wave data, recorded in the north coast of Spain. The agreement obtained is satisfactory in most cases, showing the validity of the approach and its applicability to situations in which only a limited amount of data is available. However, in cases where a large volume of data exists, empirically selected distributions could provide a marginally better fit.

#### 1. Background

Short-term analysis of wave records apply random process theory, (20), (1), to the curve of sea surface elevations,  $\eta(t)$ . The curve must be continuous, random, stationary and gaussian (for most results) to allow application of this technique. The results so obtained are probability distribution functions (PDF's) for variables such as wave-height ( $H$ ), wave period ( $T$ ), etc. in terms of a few (compact) parameters. These theoretically derived PDF enable a straightforward prediction of a wide range of characteristic values provided some basic parameters are known (e.g. mean value, variance, etc.).

The sequential behaviour of sea-states shall be defined here by the curve of evolution of  $H_s$  (significant wave-height) with time:  $H_s(t)$ . Any threshold level defines in this curve a sequence of calms (periods in which  $H_s$  is below the

---

\*Professor, Coastal and Harbour Eng. Dept. Univ. Politécnica de Catalunya. Jordi Girona Salgado, 31.08034 Barcelona. Spain

threshold) and storms (opposite event) whose analysis is the aim of the paper. However, to use random process theory for this purpose,  $H_s(t)$  must be continuous, random, stationary and gaussian.

A continuous evolution of  $H_s(t)$  and its first derivate is physically much more realistic than with a step-wise shape. This, in spite of having obtained  $H_s(t)$  from a set of values calculated from stationary, i.e.  $H_s$  constant, time periods. The difficulty is more apparent than real because an  $H_s(t)$  curve, with a continuous slope may be obtained from stationary periods by lagging  $\Delta t$  at the intervals. If  $\Delta t$  goes to zero the successive  $H_s$  values may be as close as desired, obviating the step-wise shape problem.

It is quite reasonable to assume  $H_s(t)$  is random since the stationary wave fields are generated by random winds. On the other hand, it is easy to understand that  $H_s(t)$  is not stationary in an average (typical) year. Nevertheless it is possible to hypothesize shorter, stationary periods (e.g. months) and test with wave data the validity of this hypothesis. In the paper the stationary periods selected have been months (from January to December) and winter (1st. October to 31st. March) and summer (1st. April to 30th September) seasons. In these periods the sequence of calms and storms obtained could be assumed to be homogeneous since the energy density (variance) of the  $H_s(t)$  curve was found to be reasonably constant.

The PDF of the  $H_s(t)$  process should be Gaussian to allow application of what has been called random process theory. However the long-term PDF of  $H_s$  is usually taken to be Weibull (16) with 3 free parameters for the fit. A Gaussian PDF can also be assumed empirically, providing only 2 free parameters for the fit, and therefore, an (expected) slightly worse visual agreement with data. In figure 1 and 2 the fit of 4 randomly selected months (out of the 5 years of wave data used in the paper) to a Weibull and Gaussian PDF, respectively, is shown. The agreement is acceptable in both cases and the predictions of  $H_s$  for a fixed probability level are very similar except in the tails of the distributions.

An acceptable fit of registered  $H_s$  values to the Gaussian PDF would allow application of random process theory such as is done in short term analyses. An important difference will be the spectral width of the process which, for this sequential behaviour analysis, turns out to be broad-banded in all cases. Apart from this, however, there is a close similarity

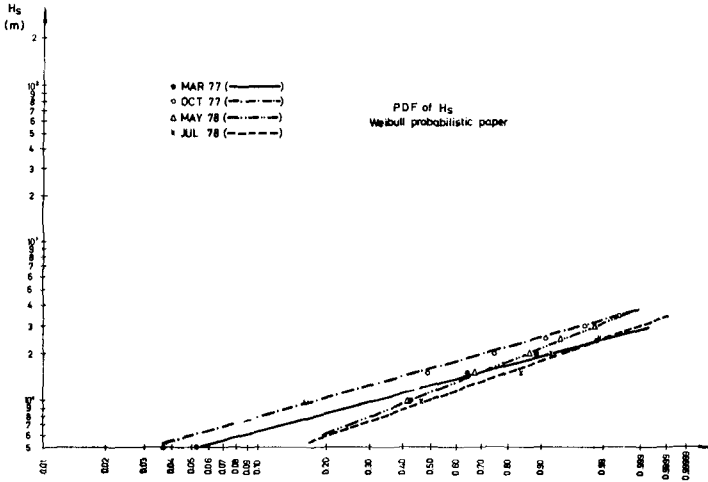


Figure 1 : Fit of the empirical distribution of  $H_s$  (as obtained from data) to a Weibull PDF for 4 randomly selected months.

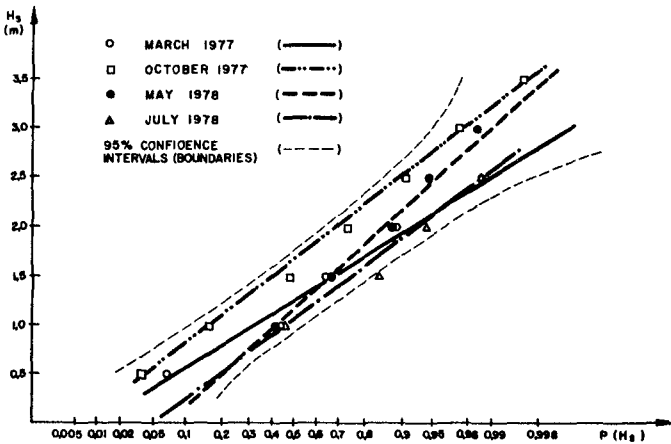


Figure 2 : Fit of the empirical distribution of  $H_s$  to a Gaussian PDF for the same 4 months of figure 1.

between both problems. As an illustration, local maxima in a wave record (short-term) would correspond to local storm peaks (sequential-behaviour), the zero-up-crossing wave period to the time between beginnings of storms, etc. A more detailed review of common points between both types of analysis, together with a summary of some of the empirical models used for storm analysis, may be found in (21).

## 2. Theoretical results compared with wave data

The data used for calibration are 6 years (1.975 to 1.980) of continuous wave recording near the entrance of the Bilbao Harbour in the north of Spain. The average depth at the recording location was 30 m., with records of 10 to 20 minutes every 3 or 4 hours, depending on the year.  $H_S$  was obtained by standard statistical analysis (Tucker's method). For part of the records  $H_S$  was also calculated with a standard spectral analysis, based on the FFT approach.

The first thing to check was the PDF of the  $H_S(t)$  process. A Gaussian distribution was proposed and a satisfactory visual fit was found for all stationary periods considered (months and winter and summer seasons). Quantitatively, the Gaussian PDF was found acceptable in 96.15% of cases, with a significance level of 0.05, applying a Kolmogorov-Smirnov goodness-of-fit test.

The spectral width of the process, measured by the  $\xi$  parameter, (13),(4) to facilitate comparisons between statistical and spectral analysis, was found to be between 0.90 and 0.99 except in 5 months in which it varied between 0,87 and 0,90. This means that the  $H_S(t)$  process is broad-banded for all stationary periods considered.

In these conditions the PDF of storm peaks,  $H_M$ , (local maxima) should be Gaussian, (21). An illustration of the fit obtained appears in figure 3. Negative values of  $H_M$  are, simply, values of  $H_M$  smaller than the mean value of  $H_S$  for the stationary period considered,  $H_{mean}$ . In other words, the height of storm peaks was measured from the  $H_{mean}$  level. The total range of  $H_S$  variation between two successive up-crossings of  $H_{mean}$  (i.e. range of  $H_S$  variation between storms defined with respect to  $H_{mean}$ ) should, for a gaussian process, follow a Rayleigh PDF irrespective of  $\xi$  (9). This total range shall be denoted  $H$  and is equivalent to the wave-height concept (zero-up-crossing definition) in short-term analysis. Figure 4 shows the fit obtained for 4 random months. The agreement was satisfactory for all stationary

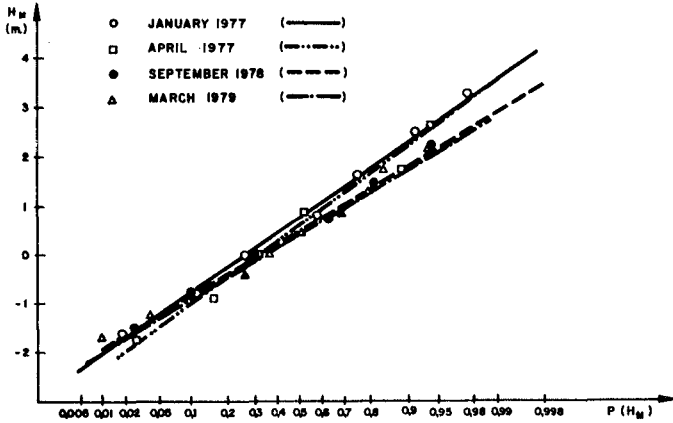


Figure 3 : Fit of the empirical distribution of  $H_M$  (intensity of storm peaks) to a Gaussian PDF for 4 randomly selected months.

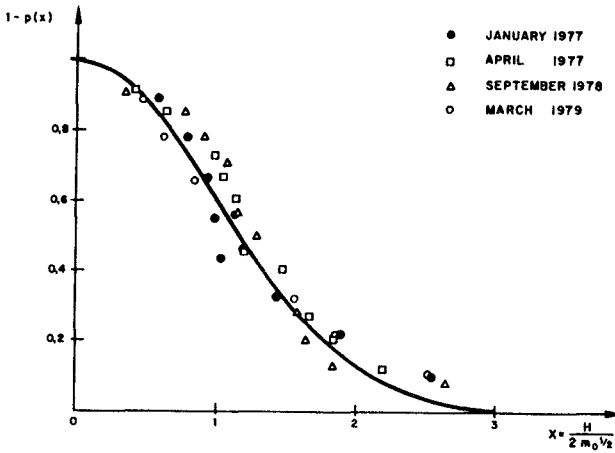


Figure 4 : Fit of the empirical distribution of  $H$  (range of  $H_S$  variation in a storm) to a Rayleigh PDF for the same 4 months of figure 3.

periods considered.

The zero-up-crossing wave period of short-term problems,  $T$ , corresponds here to the time between beginnings of storms (defined with respect to  $H_{S, \text{mean}}$ ). Three PDF were used for  $T$ : Bretschneider, (3), CNEXO, (5), and Longuet-Higgins (14). Only the last two provided a satisfactory fit for winter and summer seasons (figures 5 and 6), while giving a poor fit for monthly periods. This was attributed to the small size of  $T$  samples obtained for monthly periods. The poor agreement found for Bretschneider's PDF could be due to the lack of an  $\epsilon$  dependance for this distribution, the other two being  $\epsilon$ -dependent, (21).

The average number of storms (defined with respect to an arbitrary threshold  $H_S = h$ ) per unit time,  $n(h)$ , is identical to the average number of up-crossings of level  $h$ , per unit time, in short term analyses. It may, therefore, be written as, (2) :

$$n(h - H_{\text{mean}}) = \left(\frac{m_2}{m_0}\right)^{\frac{1}{2}} \exp\left(-\frac{(h - H_{\text{mean}})^2}{2m_0}\right)$$

in which  $m_0$  and  $m_2$  are, respectively, the zero and second order moments of the spectral density function of the  $H_S(t)$  process. If alternatively,  $\bar{T}$  (average value of  $T$ ) is known  $m_2$  may be evaluated from  $m_0$  and  $\bar{T}$  by considering that, for  $h = H_{\text{mean}}$

$$\bar{T} = \frac{1}{n(0)} = \left(\frac{m_0}{m_2}\right)^{\frac{1}{2}}$$

From these expressions it is easy to see that (21), the average duration of calms and storms, defined for an arbitrary threshold  $h$ , may be calculated as:

$$\bar{d}_S(h) = \frac{(1 - P(h))}{n(h - H_{\text{mean}})}$$

$$\bar{d}_C(h) = \frac{P(h)}{n(h - H_{\text{mean}})}$$

in which:

$\bar{d}_S(h)$  : average duration of storms at level  $h$ .

$\bar{d}_C(h)$  : average duration of calms at level  $h$ .

$P(h)$  : Prob ( $H_S \leq h$ )

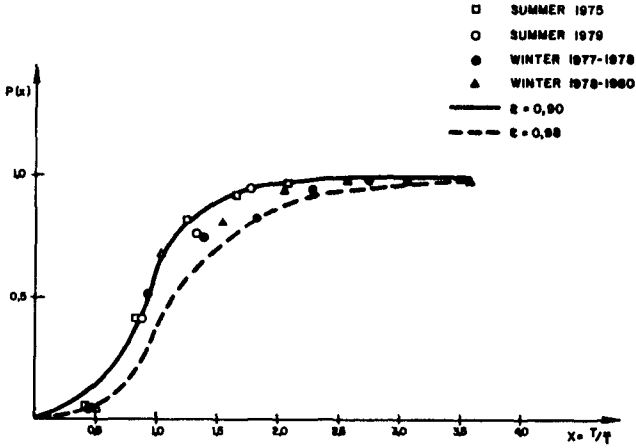


Figure 5 : Fit of the empirical distribution of  $T$  (time between beginnings of storms) to a CNEOX PDF for 4 randomly selected seasons.

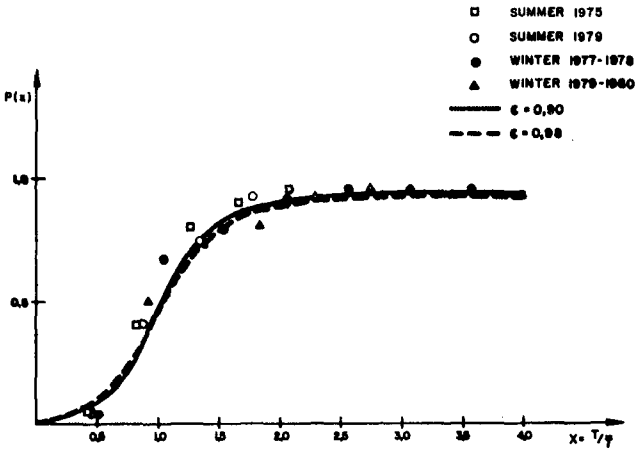


Figure 6 : Fit of the empirical distribution of  $T$  to a Longuet-Higgins PDF for the same 4 seasons of figure 5.

These formulae for  $\bar{d}_s$  and  $\bar{d}_c$  have been tested for all months and winter and summer seasons finding a qualitative fit in all cases. Figure 7 shows the agreement obtained together with predictions for  $\bar{d}_s$  and  $\bar{d}_c$  calculated from the empirical model of (10).

The PDF of the  $d_s(h)$  and  $d_c(h)$  variables was found (empirically) to agree well with a 3-parameters Weibull distribution (figure 8), as reported by other authors, (11), (12).

The number,  $j_1$ , of consecutive storms (defined with respect to  $H_{mean}$ ) exceeding level  $h$  is equivalent to the number of waves in a group exceeding a threshold  $h$  in short-term analyses. The number,  $j_2$ , of storms between groups exceeding level  $h$  is likewise equivalent to the number of waves between groups.

Three different expressions were tested for the mean values of  $j_1$  and  $j_2$ ,  $E(j_1)$  and  $E(j_2)$ . The formulae proposed by Nolte, (15), Ewing (7), and Goda (9) were found to give a very poor agreement with recorded data. This was attributed to existing differences between the  $H_s(t)$  process and the standard sea-surface elevation process. Furthermore the PDF of  $H$  used in the predictions of  $j_1$  and  $j_2$  could also introduce additional errors. It was, thus, decided to use Goda's formulae which provided a marginally better fit than the other two, reformulated in terms of the PDF of  $H_s$  instead of using the PDF of  $H$ . The original formulae can be written as (9):

$$E(j_1) = \frac{1}{P}$$

$$E(j_2) = \frac{1}{P} + \frac{1}{Q}$$

in which  $Q$  is the probability of occurrence of the event ( $H > h^*$ ) and  $P$  is :  $P = 1 - Q$ .

For a process symmetric with respect to  $H_{mean}$  the reference level  $h^*$  of the variable  $H$  can be written in terms of the reference level  $h$  of the variable  $H_s$  as:

$$h^* = 2(h - H_{mean})$$

Moreover  $H$ , for a symmetric process, may be expressed as:

$$H = 2(H_s - H_{mean})$$



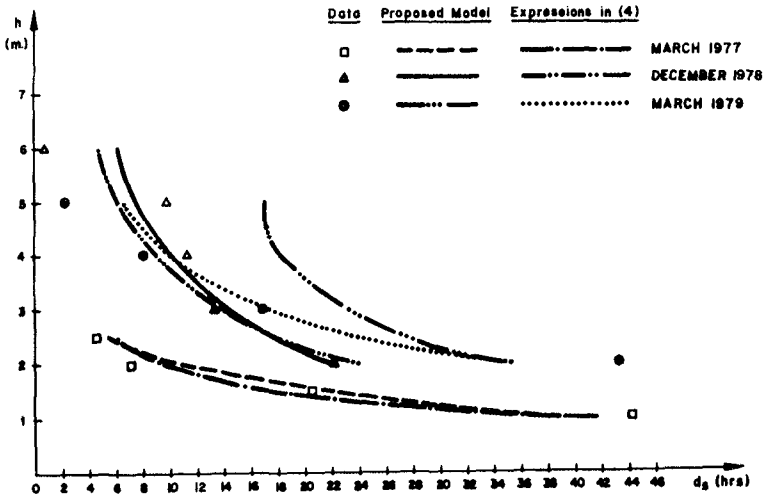


Figure 7 : Average duration of storms versus the threshold level, as obtained from registered data, the proposed model and the model of (10).

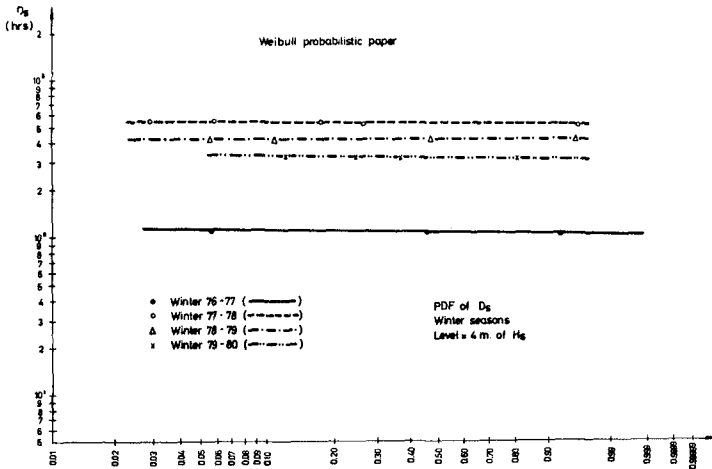


Figure 8 : Fit of the empirical distribution of  $d_s$  (duration of storms) to a Weibull PDF for 4 randomly selected winter seasons.

Hence :

$$Q = \text{Prob} (H > h^*) = \text{Prob}(H_s > h) = 1 - F(H_s)$$

$$P = F(H_s)$$

Substituting these equations in Goda's formulae the fit improves significantly though remaining still qualitative (figure 9).

The PDF of the extremum of  $H_s$  in a stationary interval of duration  $D$  may be obtained following the approach proposed in (6):

$$\phi_1(h) = \text{Prob} (H_s \text{ extr.} \leq h) = (F(h))^n$$

in which :

$$F(h) = \text{Prob} (H_s \leq h)$$

$$n(h) = \frac{D}{d_s(h)} = \frac{D}{1 - F(h)} \lambda (h - H_{\text{mean}})$$

The extremal distribution may be alternatively obtained treating storm occurrences as a Poisson process. The corresponding PDF, as used in short-term analyses, is shown in (1) and can be written as :

$$\phi_2(h) = \text{Prob} (H_s \text{ extr.} \leq h) = \exp \left[ -D \left( \frac{m_2}{m_0} \right)^{\frac{1}{2}} \exp \left( - \frac{(h - H_{\text{mean}})^2}{2m_0} \right) \right]$$

The distribution so obtained is only valid for  $h > H_{\text{mean}}$ , requiring extrapolation out of this region. A comparison of predictions obtained using  $\phi_1(h)$  and  $\phi_2(h)$  is shown in figure 10. To test these predictions with wave data the mean value of the extremum has been evaluated from  $\phi_1$  and  $\phi_2$ , being denoted, respectively,  $E_1$  and  $E_2$ .

An alternative estimate of this mean value,  $E_3$ , has been obtained applying the formula proposed in (4) for the expected value of the highest of  $N$  maxima. This expression, valid for large  $N$  and broad-banded gaussian processes, may be written as:

$$E_3 = H_{\text{mean}} + m_0^{\frac{1}{2}} \left[ m + \frac{0,5772m}{1 + m^2} \right]$$

$$m = \left( \ln \left( \frac{N}{2\pi} \right) - \ln \ln \left( \frac{N}{2\pi} \right) \right)^{\frac{1}{2}}$$

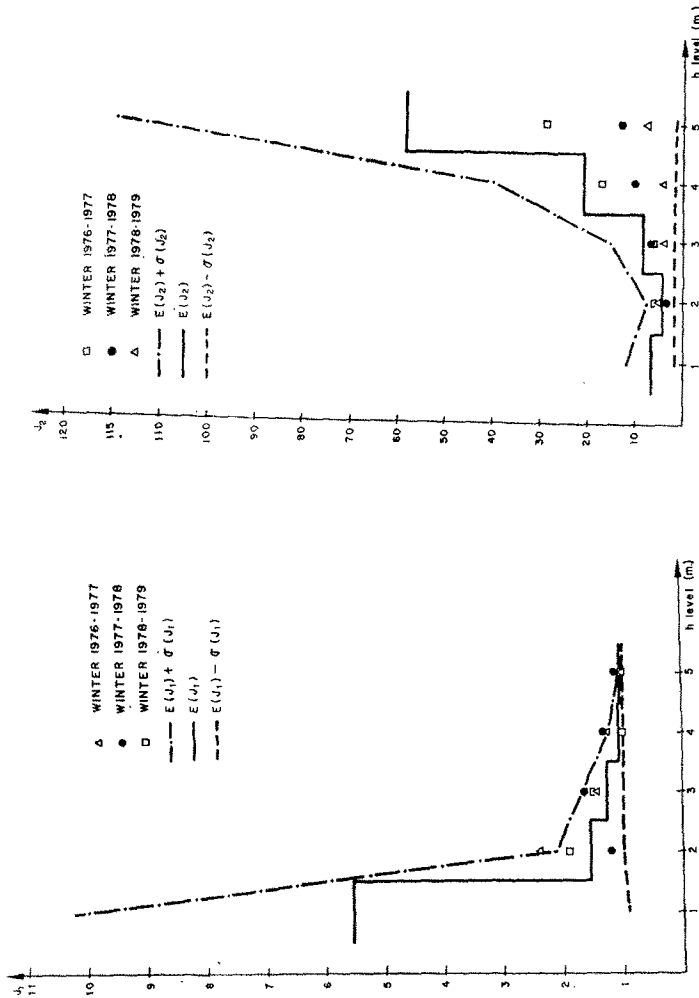


Figure 9 : Mean values of the number of consecutive high storms ( $j_1$ ) and storms between groups of high storms ( $j_2$ ) as a function of the threshold level for defining high storms.

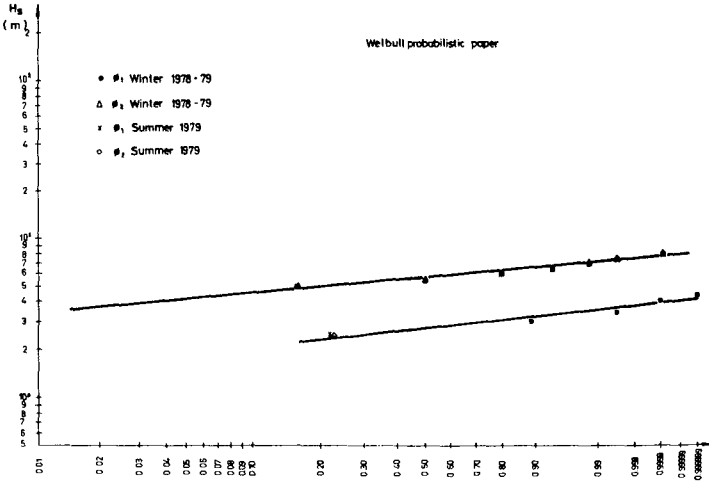


Figure 10 : Comparison of theoretical predictions of the extremal  $H_s$  value in a stationary period (randomly selected winter/summer seasons).

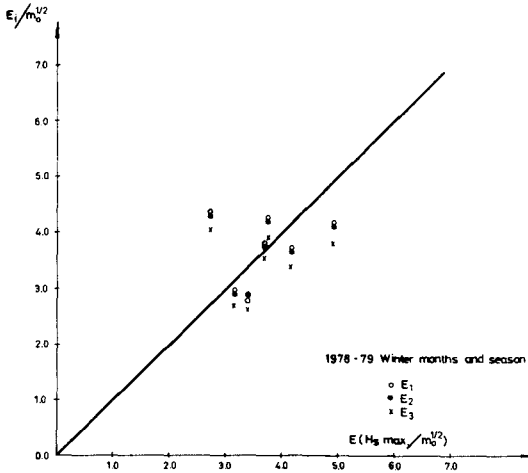


Figure 11 : Mean of the extremal  $H_s$  value in a stationary period as obtained from theory ( $E_1$ ), versus the corresponding value calculated from data (for a random winter season).

in which  $N = \frac{N_o}{r}$  ( $N_o = D \left( \frac{m_2}{m_o} \right)^{\frac{1}{2}}$ ) is the total number of local maxima for a process symmetric with respect to  $H_{\text{mean}}$ . This expression is easily obtained considering that the proportion of negative maxima is  $(1 - \alpha)$ , with  $\alpha$  given by  $\alpha = \frac{1}{2} (1 + r)$ , (1).

These three theoretical estimates for the mean value of the extremum have been tested with wave data showing a reasonable agreement in winter seasons (figure 11). The fit obtained for summer periods is significantly worse, probably due to the poor definition (in a probabilistic sense) of maxima in these seasons.

### 3. Concluding remarks

A satisfactory fit has been obtained for the theoretical distributions of  $H_M$  (storm peaks),  $H$  (range of  $H_S$  variation in a storm) and  $T$  (time between beginning of storms). Theoretical expressions for  $\bar{d}_c(h)$  (average duration of calms),  $\bar{d}_s(h)$  (average duration of storms),  $j_1(h)$  (number of consecutive storms) and  $j_2(h)$  (number of storms between groups exceeding level  $h$ ) show a qualitative agreement with wave data in all cases. Moreover, the fit obtained for these variables is also quantitatively correct in a high percentage of the stationary periods considered.

Theoretical expressions for the average value of the extremum of  $H_S$  in a stationary interval (month or winter/summer season) provide a good fit with data except for summer months and seasons.

The agreement between theory and data appears to be significantly improved when using results of the statistical analysis of the time-series  $H_S(t)$  (instead of results from spectral analysis) for the parameters of the theoretical expressions. All figures shown in the paper have been obtained with results from statistical analysis.

### 4. Acknowledgments

The author wants to express his acknowledgment to the Harbour Laboratory R. Iribarren for permission to use the wave data included in this paper. He is also indebted to Dr. J.J. Egozcue and J.R.-Marín, from the University of Barcelona for their help in handling and processing the data.

## Appendix-References

- 1.- Battjes, J.A. "Short-term Wave Statistics" IInd. WEGEMT Grad. School NTH, Trondheim, 1.979.
- 2.- Battjes, J.A. "Long-Term Wave Statistics" IInd. WEGEMT Grad. School, Norges Tekniske Hogskole, Trondheim, 1.979
- 3.- Bretschneider, C.L. "Wave variability and Wave Spectra for Windgenerated Gravity waves" U.S. Army Corps of Engineers Beach Erosion Board, Tech. Memo. No. 113. 1.959.
- 4.- Cartwright, D.E. and Longuet-Higgins, M.S. "The Statistical Distribution of the Maxima of a Random Function" Proc. Royal Soc. A, Vol. 237, 1.956.
- 5.- Cavanié, A., Arhan, M. and Ezraty, R. "A Statistical Relationship between Individual Heights and Periods of Storm Waves". Proceedings Boss 76. Trondheim 1.976.
- 6.- Copeiro, E. "Extremal prediction of significant wave-height" 16th. ICCE, Hamburg, 1.978.
- 7.- Ewing, J.A. "Mean Length of Runs of High Waves" Journal of Geophysical Research. Vol. 78 No. 12. April, 1.973
- 8.- Fang, Z.S. and Hogben, N. "Analysis and Prediction of Long-term Probability Distributions of Wave Height and Periods" National Maritime Institute Report R 146, 1.982
- 9.- Goda, Y. "Numerical Experiments on Wave Statistics with Spectral Simulation" Report of the Port and Harbour Research Institute. Vol. 9, No. 3. Sep. 1.970.
- 10.- Graham, C., "The Parameterisation and Prediction of Wave Height and Wind Speed Persistence Statistics for Oil Industry Operational Planning Purposes". Coastal Engineering. Vol. 6. Feb. 1.982.
- 11.- Houmb, O.G. and Vik, I. "Statistical Models for Estimating Storms duration" Division of Port and Ocean Engineering Norges Tekniske Hogskole. Trondheim, 1.975.
- 12.- Houmb, O.G. and Vik, I. "On the Duration of Sea State". Report of the Ship Research Institute of Norway. Trondheim. 1.977.
- 13.- Longuet-Higgins M.S. "On the Statistical Distribution of the Heights of Sea Waves". Journal of Marine Research. Vol. 11 No 3, 1.952.
- 14.- Longuet-Higgins, M.S. "On the joint Distribution of the Periods and Amplitudes of Sea Waves". Journal Geophysical Research. Vol. 80.

- 15.- Nolte, K.G. "Statistics of Larger Waves in a Sea State" Proc. ASCE WW4 November, 1.979.
- 16.- Nordenstrom, N. "Methods for predicting Long-term distribution of wave loads and probability of failure for ships" DnV Report 71-2-5, 1.972.
- 17.- Ochi, M.K. "Wave Statistics for the Design of Ships and Ocean Structures". Proc. SNAME. New York, 1.978
- 18.- Ochi, M.K. "Extreme Value of Wave and Ship Responses subject to the Markov Chain Condition". Journal of Ship Research. Vol. 23 N° 3. Sep. 1.979
- 19.- Overvik, T. and Houmb, O.G. "A Note on the Distribution of Wave Steepness" Division of Port and Ocean Engineering. Norges Tekniske Hogskole, Trondheim, 1.977.
- 20.- Rice, S.O. "Mathematical Analysis of Random Noise" Selected papers on Noise and Stochastic Processes. Dover Pub. Inc. 1.954
- 21.- Sánchez-Arcilla, A., "Long-term analysis of wave climate using short-term techniques" Trans. Journal of ASME New York, 1.984

## CHAPTER FORTY TWO

### LOW FREQUENCY OSCILLATIONS ON THE DUTCH COAST

by

F. Gerritsen<sup>1</sup> and J. van Heteren<sup>2</sup>

#### 1. INTRODUCTION

During several months in 1981 and 1982/1983 two extensive programs of field measurements were carried out at Egmond on the Dutch North Sea coast, one during the spring of 1981 and the other during the winter of 1982/83.

In these programs researchers of the Dutch "Rijkswaterstaat", of The Delft University of Technology and of the Delft Hydraulics Laboratory cooperated in the planning and execution of the measurements and are now involved in data analysis and evaluation of results.

During the year 1983 the senior author spent a sabbatical year with the Rijkswaterstaat in the Netherlands and joined the team effort in analyzing the data.

Reference is made to other papers presented at this conference, highlighting some aspect of this research program: Van Heteren and Stive (1984), Derks and Stive (1984).

The present paper deals with low frequency oscillations in the surfzone and their potential impact on certain aspects of coastal morphology.

The conclusions of this paper have to be considered as tentative and should be followed by further study.

Its main intention is to point to certain possible relationships regarding coastal morphology so that in future measurements the program can be designed in such a way that certain relationships can clearly and unmistakably be identified.

The programs of measurements carried out in 1981 and 1982/83 were primarily designed to evaluate the usefulness and accuracy of various types of instruments in the surfzone. The measurements were never designed for the use we have made of them and results may therefore not be fully conclusive and thus subject to discussion.

Nevertheless the authors found their tentative findings of sufficient interest to share them with their colleagues.

---

<sup>1</sup> Professor and Chairman, Dept. of Ocean Engineering, Univ. of Hawaii

<sup>2</sup> Staff member, Rijkswaterstaat, Hellevoetsluis, The Netherlands



In the group of low frequency oscillations a distinction has been made between edgewaves and surf beat in this paper.

Edgewaves are characterized as waves propagating parallel to the shoreline and surf beat as waves travelling perpendicular to the shoreline. It is known to the authors that often low frequency oscillations are considered to be in the surfbeat frequency range, without distinction for direction.

For the purpose of studying their effect on coastal morphology a distinction in the two types of waves as discussed above is meaningful.

## 2. VARIOUS TYPES OF LOW FREQUENCY OSCILLATIONS IN THE SURFZONE

Many phenomena play a role in the generation of low frequency oscillations in the nearshore zone.

In this paper we will limit ourselves to the discussion of some relevant aspects of this subject.

### Wave groups and mass transport

In recent years the presence of wave groups in a wave train has been recognized as an important feature, both in the development of coastal processes and in the design of coastal structures, such as breakwaters. In the past the study of the phenomena of wave groupiness has developed along two different lines; one is the correlation aspects of sequential waves in an observed or simulated wave record, the other is the analysis of the modulations in mean energy of a wave record. In this study a third approach is followed: the analysis of low frequency oscillations through spectral analysis.

Two important phenomena may be observed in wave groups:

- (1) a lowering of the mean waterlevel associated with high waves in the group and a rising of the mean waterlevel in the group of low waves. This phenomena arises from the concept of energy conservation.
- (2) a modulation in mass transport associated with the sequence of groups of high and low waves.

Outside the surfzone the first aspect demonstrates itself as a coupled long wave, which travels shoreward with the groupspeed of the waves, having a  $180^\circ$  phase difference with the center of the group of high waves. This wave is coupled to the wave height modulation of the group. At the breaking point the coherence of wave groups is destroyed; the low frequency wave is released from the group, travelling as a free wave toward the coastline, from which it is reflected in seaward direction. The reflected waves travels through the surfzone to deep water as a free wave.

With respect to the modulation in mass transport the breaking of high waves of a group induces larger onshore directed mass transport than the breaking of low waves. This phenomena again induces a free travelling long wave in the breaking zone, with a phase difference of

180° with respect to the first wave. The two waves cannot be distinguished from one another because they have the same frequency, associated with the group period.

### Surf beat

The low period oscillation that is induced by the above described phenomena is here called surf beat. Inside the surfzone the surfbeat demonstrates itself as a standing wave of low period. In this zone both the incoming and reflected wave travel with the speed of a free travelling long wave,  $c = \sqrt{gh}$ . Outside the surfzone the incoming wave has the speed of the group velocity and the reflected wave that of a free travelling long wave. The seaward propagating free wave is often larger than the incoming forced wave (7).

It has been established that the amplitude of the surfbeat waves is dependent on the wave amplitude of the incoming wave.

According to Munk (11) the ratio of the amplitudes of long period oscillations to wind wave amplitude is about 1:10. This is probably valid for areas outside the surfzone. Inside the surfzone the ratio can be higher depending on depth and location (10).

### Progressive edge waves

For a long time edge waves were regarded as a subject of pure hydrodynamical interest, with no or little practical significance. In more recent years, however, it has been established that the presence of edge waves can be of fundamental importance in the dynamics and sedimentology of the nearshore zone through their interaction with ocean swell and surfbeat to produce circulation cells and ripcurrent patterns.

Reports of the occurrence of edge waves in the literature indicate that they may come in vastly different dimensions (9).

Observations at Egmond in 1981 and in 1982/83 suggest that edge waves are also present along the Dutch coast.

Where surf beat waves were identified as waves which have their crest parallel to or almost parallel to the shoreline, edge waves have their crests perpendicular to the shoreline. A solution for the edge wave formulation for gently sloping beaches with constant inclination  $\beta$  can be obtained from the linearized shallow water equations (9).

The condition of trapping is reflected in the form of the dispersion relation, which for the shallow water wave approximation is given by

$$\sigma_n^2 = gk(2n + 1) \tan\beta \quad (n = 0, 1, 2, \dots) \quad (1)$$

where  $\tan\beta$  is the beach slope and  $n$  the edgewave mode.

The solution for a progressive edge wave is of the form

$$\zeta(x, y, t) = F(y) e^{i(kx - \sigma t)} \quad (2)$$

in which the x-direction is parallel to the coast and the y-direction perpendicular to the coast positive seaward.  $k$  is the longshore wave number and  $\sigma$  the angular frequency. The function  $F(y)$  depends on the mode of the edgewave.

Edge waves have velocities in the x and y-direction, respectively parallel and perpendicular to coastline.

Trapping of edgewaves can also occur with different coastal profiles. A profile which is more realistic than the straight beach (from 0 to  $\infty$ ) has the form

$$h = h_0 (1 - e^{-\alpha y}) \quad 0 < y < \infty \quad (3)$$

The behavior of edge waves for such a profile was studied by Ball (1). It can be shown (Huntley, (6)) that the entrapped modes must obey the condition:

$$\sigma_{CR} = [n(n+1)]^{1/2} \alpha \sqrt{gh_0} \quad (4)$$

Experiments by Huntley (6) have furthermore shown that the frequencies of spectral peaks in the spectrum can be identified with the frequencies  $\sigma_{CR}$  for the consecutive modes. For a given offshore profile this can be expressed by:

$$f_{CR} = \text{const.} [n(n+1)]^{1/2} \quad (5)$$

where  $f = \sigma/2\pi$ . This expression could be verified for the North Sea Coast near Egmond.

#### Cell circulation

A standing edge wave has surface variations according to:

$$\zeta(x, y, t) = F(y) \cos kx \sin \sigma t \quad (6)$$

Standing edge waves are of particular relevance to coastal morphology.

Both theoretically and experimentally it can be shown that standing edge waves induce a nearshore cell circulation. Kaneko (8) developed a numerical simulation for cell circulation under the influence of standing edge waves on a sloping beach. He considered three conditions:

- (a) Cell circulation due to edge waves only.
- (b) Cell circulation due to superposition of edge wave and leaky-mode wave (with crest parallel to shoreline) with leaky mode having half the period of the edge wave (subharmonic edge wave). Leaky mode waves are defined as waves, which are not trapped to the coast.
- (c) Cell circulation due to superposition of edge wave and leaky-mode wave of the same period (synchronous edge wave).

The leaky mode waves of interest here are the surfbeat waves. The numerical circulations showed that in the cases (a) and (b) the circulation cells which developed, had the same form whereby two circulatory

cells developed each in size equal to one half the wave length of the edge wave. In the second case the velocities were considerably stronger than in the first case. The third case (c) showed a different behavior. Two cells developed along the full length of the edge wave whereby circulatory velocities became fairly strong in case the amplitudes of the two waves had equal value.

3. ANALYSIS OF MEASUREMENTS

Measurements

For a complete description of the measurements reference is made to Derks (2). In 1982/1983 two parallel traverses A and B were erected. Traverse A contained four platforms, traverse B only piles.

In Figure 1 the offshore profile in Traverse A and the measuring stations (A1 - A9) are shown.

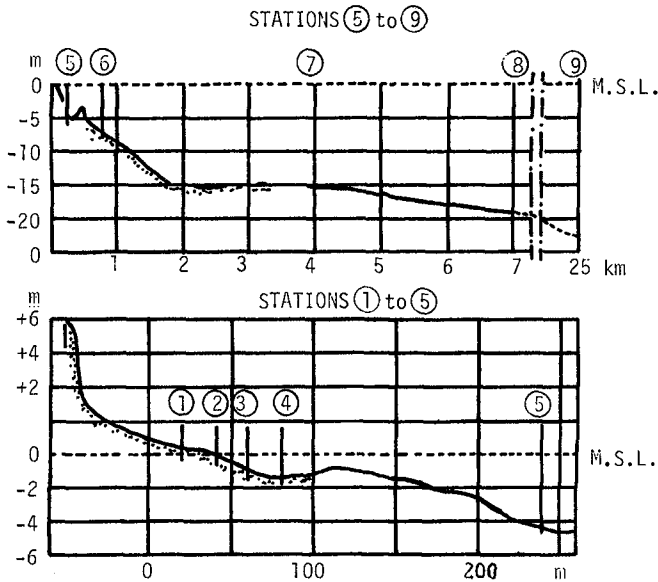


Figure 1: Depth-profile and measuring stations Traverse A, Stations A1 - A9.

Waves were measured with resistance gages where supporting piles were available and with wave buoys in deeper water. For currents various types of sensors were used.

### Digital filtering

A low pass filter has been developed, which suppresses the energy of wind wave frequencies of the spectrum. In order to remove the high frequency oscillations from a waterlevel or velocity record, a moving-average procedure is applied. The length of the record section to which the averaging is applied must be long enough to filter out the high frequency oscillation but short enough to retain the type of oscillations in which we are interested. As a general measure an averaging period of one to two times the peak period of the wave spectrum is an adequate procedure. The application of a moving average system in the time-domain corresponds with a frequency response in the frequency-domain.

If the window function in the time domain has a length  $2\tau$  and a height of  $1/2\tau$  then the frequency response function is

$$H(f) = \frac{\sin 2\pi f\tau}{2\pi f\tau} \quad (7)$$

This function has zero crossings for  $f\tau = 0.5, 1.0, 1.5, \dots$ . If a number of moving average procedures are applied in series, one finds the impulse response by convolution of the individual weighting functions and the frequency response as the product of the individual frequency response functions.

Based on the above described procedures various low pass filters were designed and applied to selected data. For the 1982/83 observations the original time series was sampled at a frequency of 10 Hz.

It was found that a reduction of the number of data points in ratio 1:24 could be applied without loss of relevant information. ( $\Delta t = 2.4$  sec).

Characteristics of the selected low pass filter were the following:

- (1) Use of the running average procedure 3 times in series with equal block length. This corresponds to a filtering characteristic

$$H(f) = \left( \frac{\sin 2\pi f\tau}{2\pi f\tau} \right)^3 \quad (8)$$

- (2) Selection of block length  $2\tau$  in such a manner that

$$H(f) = 0.5 \quad \text{at } f = \frac{1}{4T_p},$$

where  $T_p$  is the peak period of the wave or velocity spectrum. This condition gives  $2\tau = 1.465 T_p$ .

- (3) A further reduction of data points in sequential time series in ratio 1:8. The characteristic low pass filter obtained in this way is shown in Figure 2-a.

In addition a high pass filter of the form of Figure 2-b was applied to remove low frequency trends such as the tide. The combined effect is shown in Figure 2-c.

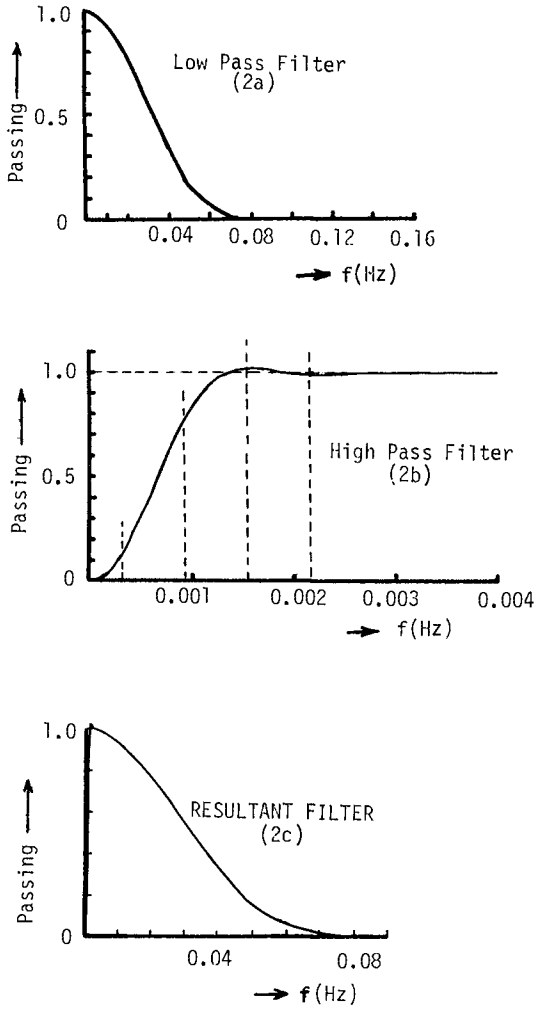


Figure 2. Numerical filter characteristics ( $T_p = 7.5$  sec).

### Required resolution of low pass filter

In the beginning of the study measuring series of about 1800 seconds in length were used for analysis. In order to obtain sufficient accuracy (10 subseries) the resolution step could not be smaller than  $\Delta f = 0.0029$  Hz. It appeared that this type of resolution would smooth most of the edge wave energies. To overcome this problem a longer length of time series was required. For this five hour records were selected which reduced the resolution step to  $\Delta f \approx 0.0006$  Hz. A five hour time series also has serious drawbacks. It is likely to violate the requirement of stationarity of the low frequency oscillations due to changes in tide and wave conditions over that period. In the future record lengths of 3 hours will be utilized. This period is selected before and after high water to have minimal effect of the tide on the low frequency phenomena.

## 4. RESULTS OF INVESTIGATIONS

The results of the investigations relate to three different aspects of the problem:

- (1) The characteristics of the low frequency spectra (both waterlevel and velocities)
- (2) The effect of low frequency oscillations on horizontal circulation (spacing of rip currents)
- (3) Relationship of low frequency oscillations to beach profile characteristics

### Low frequency spectra

The analyzed data included the measurements of Spring 1981 as well as of Winter 1982.

Space limitations do not allow us to present the results of both measurement series. In this paper only results of 1982 will be presented.

For this paper the measurements of 10 December 1982 were selected. This series is characterized by significant wave heights ( $H_s = 4\sqrt{m_0}$ ) and peak periods as follows:

Sta A9 :	$H_s = 2.56$ m	$T_p = 7.5$ sec
Sta A8 :	$H_s = 2.18$ m	$T_p = 6.95$ sec
Sta A6 :	$H_s = 2.14$ m	$T_p = 7.5$ sec
Sta A5 :	$H_s = 1.64$ m	$T_p = 6.75$ sec

The low pass filter, described in section 3 is based on a peak period for the offshore waves of 7.5 sec.

The wave spectrum in Sta A5 is presented in Figure 3.

The results of the low frequency spectra obtained by applying the low and high pass filters are presented in Figures 4 through 7.

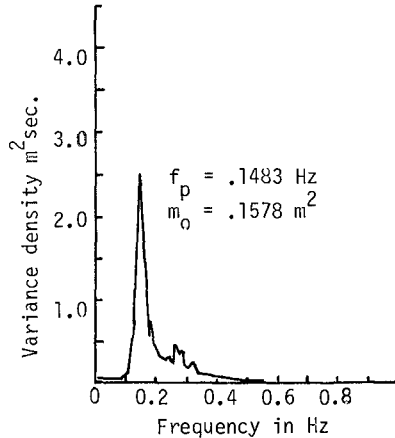


Figure 3. Wave spectrum in Station A5

In figure 4 the low frequency wave spectra are shown for stations A2, A3, A4, and A5 (stations 2-5 in traverse A).

The type of oscillations present in these spectra include the surfbeat types (waves travelling perpendicular to the shoreline) and the edgewave types (waves travelling parallel to the shoreline).

Without further information the distinction between these two types of oscillations is difficult to assess.

To assist in the distinction of these types the following additional information was utilized.

- (a) Directional information obtained from horizontal velocity components;
- (b) Phase spectra (phase of wave in one station compared to the next station).
- (c) Coherence spectra, giving correlation between one oscillation and another.
- (d) Horizontal circulation patterns.

By considering the above information in addition to the low frequency spectra the following picture emerges:

In almost all low frequency spectra a dominant peak occurs at a frequency between 0.0012 and 0.0033 Hz (This peak is clearly dominant in Figure 6<sup>a</sup> and 7<sup>a</sup>). This peak is attributed to the zero mode edge wave. The sharp peaks visible e.g. in Figure 4 are contributed to edge wave peaks of higher modes. The peaks in Stations A2, A3, and A4 are superimposed on three broad bands of low frequency energy. The middle one, between frequencies 0.012 Hz and 0.024 Hz contains the largest amount of energy and is believed to represent the major surfbeat mode.



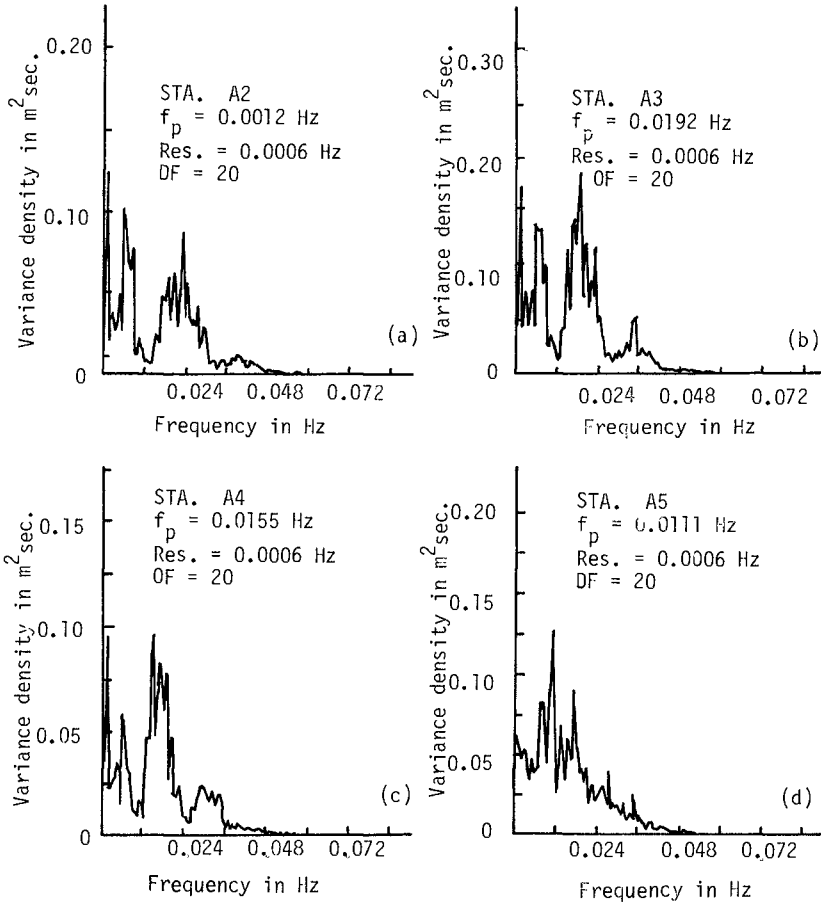


Figure 4: Low frequency wave spectra for stations A2 - A5

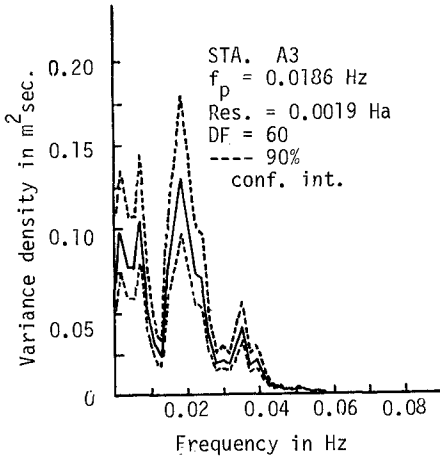


Figure 5. Low frequency wave spectrum for Sta. A3 for different resolution and degrees of freedom

The bands on either side also contain surfbeat energy. It is of interest to consider the frequency at which the major surfbeat energy has its maximum density and to relate this to the peak frequency of the offshore waves:

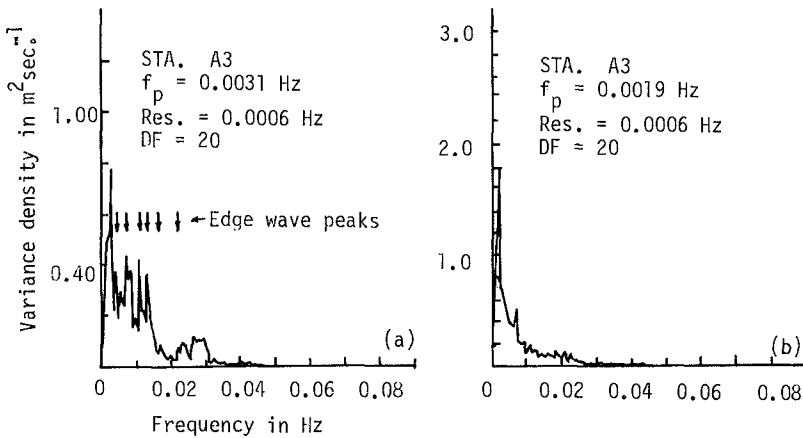


Figure 6. Low frequency spectra for velocity components (a) Perpendicular to coast; (b) parallel to coast

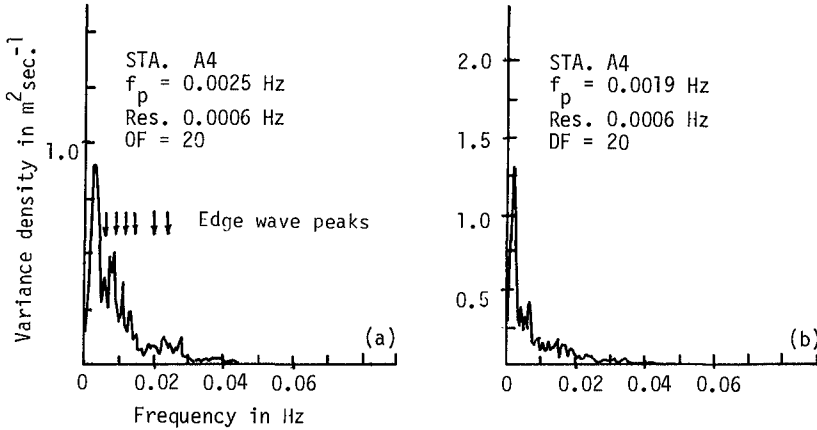


Figure 7. Low frequency spectra for velocity components  
 (a) perpendicular to coast;  
 (b) parallel to coast

In station A5,  $f_p = .1483$  Hz.

For stations 2-4 we have ( $f_{ps}$  denoting the peak of the surfbeat energy):

Sta A2:  $f_{ps} = 0.024$ ;  $f_p/f_{ps} = 6.2$

Sta A3:  $f_{ps} = 0.019$ ;  $f_p/f_{ps} = 7.8$

Sta A4:  $f_{ps} = 0.015$ ;  $f_p/f_{ps} = 9.9$

with an average value (for stations 2 to 4) of 8.0.

In order to compare total energy values for the three different surfbeat modes it must be realized that due to the application of the filter, energies in the higher frequencies are undervalued compared to the values corresponding to the lower frequencies. Since the filter characteristics are known this can be compensated for. However, this is not necessary where spectra are used to identify where peaks occur. In this study this compensation was not applied.

Keeping this in mind and going from Station A4 to Station A2 there is a shift of energies to lower frequencies in a relative perspective. The highest variance density ( $0.18 \text{ m}^2/\text{sec}$ ) is present in Station A3; this value however includes some edge wave energy as well. The sharp peaks in the spectra for stations A2 and A4 are also considered to represent edge wave energy. The grouping of surfbeat energy is less distinct at Station A5 (Figure 4d). The individual peaks are also considered edge wave peaks.

One method to filter edge wave energy is to use a larger resolution frequency step ( $0.0019$  Hz) and obtain a higher degree of accuracy (Degrees of freedom = 60). See Figure 5, showing an example of this approach for Station A3.

Figure 6 and 7 present the low frequency spectra for onshore and alongshore velocity components for Stations A3 and A4.

It is to be noted (Figure 6<sup>a</sup>) that where surfbeat energy is high ( $f \sim 0.02$  Hz) onshore velocities are low. This corresponds with the situation at standing waves, at a location close to the nodal point.

An example of the calculated phase spectrum between surface elevations of Stations A2 and A3, is presented in Figure 8. Both edge wave peaks of low frequency and surfbeat peaks have phase = 0, as expected (standing waves). The coherence function for the same quantities is shown in Figure 9, showing high coherence for the very low frequency oscillation as well as the surf beat modes.

The resolution of 0.0019 Hz used for the analysis in Fig. 8 and 9 smoothes the edge wave energy and therefore does not allow identification of edge wave peaks.

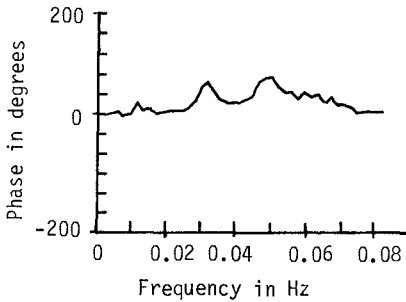


Figure 8. Phase spectrum (waterlevel) for Stations A2 and A3

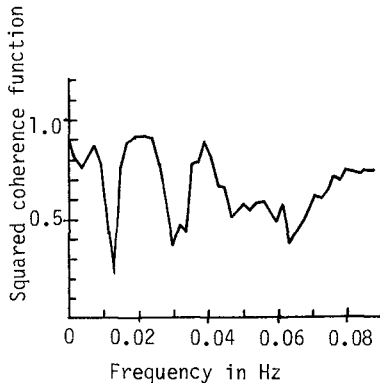


Figure 9. Squared coherence function (waterlevel) for Stations A2 and A3

Figure 6<sup>a</sup> and 7<sup>a</sup> have been used to plot the (assumed) edgewave frequency peaks as a function of the mode number. The results are plotted in Figure 10 and validate the relationship given in equation (5), with the value of the constant equal to 0.0031.

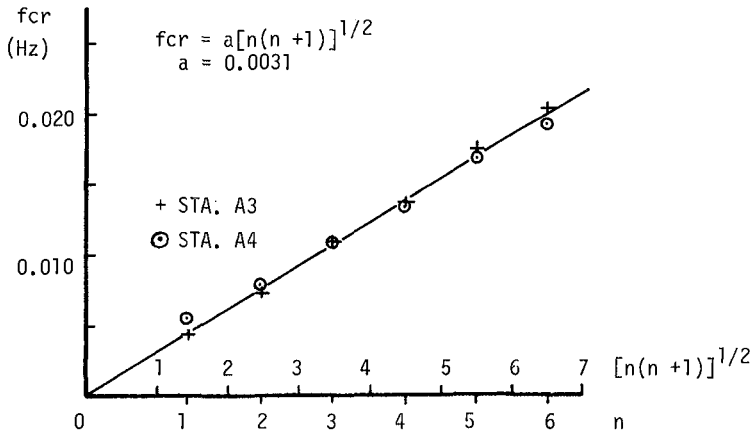


Figure 10. Edge wave frequency peaks as function of mode number for velocities perpendicular to coast. (reference Figure 6(a) and 7(a)).

Massel and Musielak (10) found for the Baltic Coast at Lubiatowe for the constant value 0.0041, which is somewhat higher but of the same order of magnitude.

An offshore profile of exponential shape is given by relation (3):

$$h/h_0 = 1 - e^{-\alpha y}$$

If  $h_0 = 16\text{m}$  and  $\alpha = 0.001315$  (obtained from equation(5)) a reasonable approximation for the offshore profile at Egmond is obtained.

#### The effect of low frequency oscillations on horizontal circulation

In section 2 a description is given of possible circulation patterns induced by edgewaves or by edge waves and surfbeat waves combined.

With respect to ripcurrent distances along the Dutch Coast reference is made to Ten Hoopen and Van Driel (5). They found that along the Dutch coast ripcurrent distances varied from 150 to 1850m with an average distance of 785m. Aerial photographs of the Egmond coastline in 1981 show an average distance of rips of about 1300-1400m whereas the 1983 photographs showed shorter distances, 600-700m. Unfortunately there is no extensive information available for the circulation patterns and rip current distances at the date of the measurements except some local observations near the measuring site showing ripcurrent distances of 500-700m.

In view of the characteristics of the low frequency spectra, discussed above, it is feasible that a zero mode edge wave occurs by itself or simultaneously with a surf beat wave of double frequency, a situation corresponding with respectively the conditions (a) or (b) of the combi-

nation listed in section 2. The length of the complete circulation cell is than half of the wave length of the edge wave. Taking 700m as the distance between ripcurrents the zero mode edge wave length is then 1400m and the corresponding frequency for the zero mode edge wave (equation (1) for  $n = 0$ ) is:  $\sigma = 1.92 \times 10^{-2}$  rad/sec and  $f = \sigma/2\pi = 0.0031$  Hz. The corresponding first mode is  $f(1) = f(0)\sqrt{3} = 0.0053$ Hz.

The value  $f(0) = 0.0031$  Hz corresponds with the major low frequency peak in Figure 6a (Station A3). In this figure the next peak is either at  $f = 0.004$ Hz or  $0.005$ Hz. The assumption of a zero mode edge-wave peak at  $f \sim 0.003$  corresponding to a wavelength of 1400m therefore appears to be in general agreement with observed rip current patterns.

Relationship between low frequency spectra and beach profile characteristics

It is beyond the scope of this paper to discuss the various mechanisms that contribute to the formation of longshore bars and troughs. In this study we will only investigate if the dimension of troughs between offshore bars has any relationships with the major surfbeat wave. It is suggested that the following mechanism may play a part in the bar and trough formation. During high wave conditions (storms), waves break on the second bar. During this process due to variable mass transport a surfbeat type standing wave is induced with its nodal points at the first and second bar (see Figure 11).

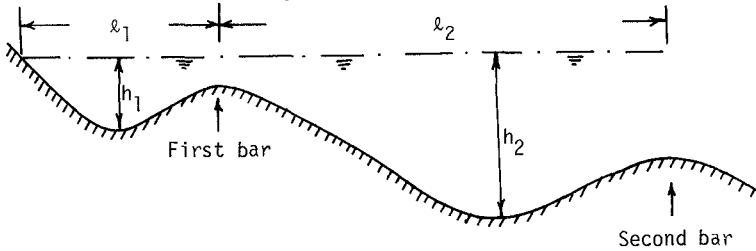


Figure 11. Schematic offshore profile

If such a concept would be correct the following relationship should be valid:

$$T = 2\lambda_2 \left[ \frac{1}{\sqrt{gh_2}} \right] \tag{9}$$

whereby  $T$  is the dominant surfbeat period and  $\lambda_2$  the distance between first and second bar.

The overbar signifies the average value over the trough of  $\left[ \frac{1}{\sqrt{gh_2}} \right]$ . In first approximation the above expression for  $T$  can be written as:

$$T = \frac{2\lambda_2}{\sqrt{gh_2}} \tag{10}$$

Expression (10) was tested for a significant number of profiles during different times of their development. See also Nanninga (12). It was found that for most of the observations the value of  $T$  ranged from 75 to 85 sec.

Observations during storms on December 21 and December 27, 1982 showed a peak period of waves offshore of 9.0 sec.

The conditions during storm are selected because it is assumed that under those conditions bedforming activities occur. The ratio of the values of  $T$  found above and the peak period during storms then ranges between 8.3 and 9.5, which is similar to the ratio found in section 4 for station A3 and A4 (respectively 7.8 and 9.9).

In station A5 which is located in the trough between first and second bar, an (assumed) surfbeat peak occurs around  $f=0.011$  Hz corresponding to a period of 90 seconds. The above suggests a fairly good correlation between the period  $T$ , defined above and the period at which surfbeat energy peaks. It is suggested that further investigations are in order to validate this relationship.

For the channel between first bar and coastline two possibilities are open:

- (1) The width of this channel could correspond to  $1/4$  wave length with an anti-node located at the coastline. In that case,  $T$  would range from 110 - 130 sec. and does not correspond to the same surfbeat peak period. However there is a possibility that a correlation with the surfbeat mode at lower frequencies may be found.
- (2) The width of this channel could correspond to  $1/2$  of the local wave length with an offshore bar starting to develop near the shoreline. In that case  $T$  would range from 55-65 sec. which is 6.1 to 7.2 times the peak period. This is close to the observed values listed in 4 for Station A2 and A3 (respectively 6.8 and 7.8).

## 5. CONCLUSIONS

- (1) It is concluded that low frequency oscillations in the surf-zone may contribute in different ways to bedforming conditions of the Dutch North Sea coast.
- (2) Evidence is found of the following specific influences of low frequency oscillations on the Dutch coastline:
  - (a) Edge waves in possible combination with surfbeat are likely to influence horizontal circulating patterns and the spacing of rip currents.
  - (b) Surfbeat oscillations seem to have a bedforming influence on the offshore profile.

## 6. ACKNOWLEDGEMENTS

The authors wish to thank A.P. Roskam for assistance in computer programming and data analysis.

The senior author wishes to express his appreciation to the Dutch Rijkswaterstaat for the opportunity to participate in their studies.

## 7. REFERENCES

1. Ball, F.K. (1967) "Edge waves in an ocean of finite depth", Deep Sea Research, 14, 179-88.
2. Derks, H. (1982, 1983) "Measurements in the surfzone near Egmond", Reports Delft Hydraulics Laboratory, R 1597, parts I - VI.
3. Derks, H. and M.J.F. Stive (1984) "Field investigation in the T.O.W. study program", Proceedings 19th ICCE, Houston.
4. Heteren, J. van and M.J.F. Stive (1984) "Wave kinematics and directionality in the surf zone", Proceedings 19th ICCE, Houston.
5. Hoopen, H.G.H. ten and G.B. van Driel, "Report aerial photographs, rip currents - investigations , nota WWKZ-79G.013., Rijkswaterstaat, The Netherlands.
6. Huntley, D.A. (1976) "Long period waves on a natural beach", J. Geophys. Res., 81, 6441-6449.
7. Huntley, D.A., T. Guza and E.B. Thornton (1981) "Field observations of surf beat, 1. Progressive edge waves", J. Geophys. Res., vol. 86, no. C7, pp. 6451-6466, July 20.
8. Kaneko, Arata (1983) "A numerical experiment on nearshore circulation in standing waves", Coastal Engineering, 7, 271-284.
9. Le Blond, Paul H. and Lawrence A. Mysak (1978) "Waves in the ocean", Elsevier Oceanographic Series 20, Elsevier Scientific Publishing Co., Amsterdam Oxford, New York.
10. Massel, Stanislaw, and Stanislaw Musielak (1980) "Long-period oscillations in surf zone", Polish Academy of Sciences, Institute of Hydroengineering - Gdansk, Hydrotechnical Transaction, vol. 41.
11. Munk, W. (1949) "Surf beats", Eos Trans., AUG 30, 849-854.
12. Nanninga, H. (1983) "Morphological behavior of the surfzone near Egmond, from local field measurements", Final Project Report, Delft University of Technology.



## CHAPTER FORTY THREE

### VERIFICATION OF KIMURA'S THEORY FOR WAVE GROUP STATISTICS

J.A. Battjes<sup>1</sup> and G.Ph. van Vledder<sup>1</sup>

#### ABSTRACT

North Sea wave records, obtained in conditions of active wave generation, have been analyzed with respect to the distribution of the length of wave groups. The results are compared to a theory by Kimura, in its original form as well as with the addition of a new spectral wave groupiness parameter, based on the theory of Gaussian processes. The results lend support to the validity of Kimura's theory; this in turn implies further evidence that the phenomenon of wave groups in sea waves can by and large be explained, both qualitatively and quantitatively, in terms of the linear, random phase model for the wave motion, even in conditions of active wave generation.

#### INTRODUCTION

The occurrence of groups of high waves in a seastate is a phenomenon of practical and theoretical interest. Two principal lines of approach have been used for the investigation of wave groupiness. One approach considers the wave envelope, the other uses the sequence of wave heights. In this paper, the latter approach is followed. A wave group is defined as a sequence of wave heights ( $H_n$ ;  $n=1,2,\dots$ ) in excess of a given threshold value ( $H_x$ ), preceded and followed by a height below that level. The length of a group ( $N$ ) is defined as the number of heights in that group.

Goda (ref. 5) derived an expression for the probability distribution of  $N$ , assuming all wave heights to be stochastically independent, each being Rayleigh distributed. This theory systematically underpredicts observed group lengths in wind waves. This is due to the neglect of dependence between wave heights. As shown by Rye (ref. 11) and others, successive wave heights are positively correlated. This was taken into account by Kimura (ref. 9). His theoretical results are in good agreement with results from numerical simulations (Kimura, ref. 9) as well as from field observations in old, narrow-banded swell (Goda, ref. 6).

A shortcoming of Kimura's formulation is that the parameter determining the groupiness is not defined in terms of the energy spectrum of the underlying process. However, a spectral shape parameter which is appropriate for this purpose can in fact be defined (Battjes, ref. 3), using Arhan and Ezraty's calculations of the joint pdf of consecutive wave heights (ref. 1), which in turn were based on Rice's theoretical results on envelope statistics (ref. 10).

Dept. of Civil Engineering, Delft University of Technology,  
Stevinweg 1, 2628 CN Delft, The Netherlands

The purpose of the present paper is to present results of an empirical check of Kimura's theory, including the spectral parameter referred to above. The check is based on analyses of North Sea wave records obtained during conditions of active generation. The presentation in this proceedings paper is kept brief. A full account will be published elsewhere.

RESUME OF KIMURA'S THEORY

Considering a sequence of random wave heights ( $H_1, H_2, \dots$ ) as a Markov process, Kimura (ref. 9) derives the following expression for the probability distribution of the group length ( $N$ ) :

$$P(N) \equiv \Pr \{N = N\} = (1 - q) q^{N-1} \tag{1}$$

in which  $q \equiv \Pr\{H_{-n+1} > H_* \mid H_n > H_*\}$  (2)

For a given threshold value  $H_*$ , the conditional probability  $q$  can be expressed in terms of the joint probability density function (pdf) of two consecutive wave heights ( $H_1, H_2$ ), for which Kimura uses the two-dimensional Rayleigh pdf. This pdf has one shape parameter,  $\kappa$ , say (Kimura's parameter  $\rho$  equals  $\frac{1}{2}\kappa$ ). The coefficient of linear correlation between  $H_n$  and  $H_{n+1}$  (denoted as  $\gamma$ ) can be expressed in terms of  $\kappa$ , with the result

$$\gamma = \frac{E(\kappa) - \frac{1}{2}(1 - \kappa^2)K(\kappa) - \pi/4}{1 - \pi/4} \tag{3}$$

in which  $K(\kappa)$  and  $E(\kappa)$  are the complete elliptic integrals of the first and second kind, respectively. Kimura uses this to estimate  $\kappa$  from a wave record via  $\gamma$ , which can be calculated directly from the given sequence of wave heights. (A direct time-domain estimate of  $\kappa$  is possible on the basis of the fact that  $\kappa^2$  equals the coefficient of linear correlation between  $H_n^2$  and  $H_{n+1}^2$ , as shown by Battjes (ref. 2).) Alternatively, one can use an approach developed by Arhan and Ezraty (ref. 1) and express  $\kappa$  in terms of the energy spectrum  $E(f)$  of the surface elevation (Battjes, ref. 3) :

$$\kappa = k(\tau) \quad \text{for } \tau = T_z = (m_0/m_2)^{1/2} \tag{4}$$

in which

$$k(\tau) \equiv \left| \int_0^\infty E(f) e^{i2\pi f\tau} df \right| / m_0 \tag{5}$$

In these expressions,  $m_0$  and  $m_2$  are the zeroth- and second moments of  $E(f)$  about  $f=0$ , and  $T_z$  is the mean zero-crossing wave period.

It is pointed out that this direct, spectral estimate of  $\kappa$  obviates the need to use the correlation coefficient of successive wave heights. Nevertheless, the results to be given below are presented in terms of  $\gamma$  for purposes of comparison with previous results. To this end, values of  $\kappa$  obtained from (4) and (5) have been transformed to values of  $\gamma$  using (3).

## WAVE DATA

An empirical check was made of Kimura's theory, based on an analysis of 33 wave records, collected in the southern North Sea using a Waverider buoy in swell and wave growth situations. These included some JONSWAP data as well as data of the severe storm of January 3, 1976 (described by Harding and Binding, ref. 8 and by Bouws, ref. 4). The wave records consist of time series (sampling rate 2 Hz) with a duration of approximately 20 minutes.

## ANALYSIS AND RESULTS

In the time domain, each wave record was analysed to obtain a sequence of zero upcrossing wave heights. Each of these sequences was used to estimate the coefficient of correlation between consecutive wave heights, denoted as  $\gamma_t$  (t for time domain). Furthermore, frequency distributions of group length were determined for two threshold values, viz. the mean wave height and the significant wave height, here defined as the mean of the one-third highest wave heights ( $H_{1/3}$ ). In this paper, results for  $H_{\kappa} = H_{1/3}$  only are presented.

Each record was Fourier-analysed via a direct FFT-method with a partial Hanning data window in the time domain, to obtain estimates of the variance spectral density.

In the spectral domain, values of  $\kappa$  were calculated using (4) and (5). The integration limits for this calculation were 0.045 Hz and 0.505 Hz. Values of  $\kappa$  were substituted in (3) to obtain spectral estimates of the correlation coefficient  $\gamma$ , denoted as  $\gamma_s$  (s for spectral domain).

The number of wave groups per record was too small to allow meaningful conclusions about the group length distribution per record. Therefore, all records with more or less the same value of  $\gamma$  were pooled, using a class width equal to 0.1 ( $\gamma$  between 0 and 0.1, between 0.1 and 0.2, etc.). The frequencies of observations of the group length  $N$  ( $N=1, N=2, \dots$ ) for all records with  $\gamma$  in a given interval were added so as to obtain an estimate of the group length distribution  $P(N)$  for the given range of  $\gamma$ . These were compared with the theoretical distributions.

For each observed pooled distribution the sample mean group length was calculated, and compared with Kimura's theoretical prediction for it, using either the time-domain estimate of the correlation coefficient of successive wave heights ( $\gamma_t$ ) or the spectral estimate ( $\gamma_s$ ), obtained via  $\kappa$ . The results are given in the figures 1 and 2, respectively.

The whole observed distribution of the group length is compared to the predicted one in figure 3 for two classes of  $\gamma_s$ . For other classes comparable agreement was obtained.

## DISCUSSION

Kimura's theoretical prediction of the mean group length ( $\mu_N$ ), using the time-domain estimate of  $\gamma$  as input, is in excellent agreement with the observations (figure 1). The agreement is slightly less in case the spectral estimate of  $\gamma$  is used (figure 2). In this case, there appears to be some tendency of underprediction, particularly for cases of high correlation. Removal of the bound higher harmonics from the spectrum,

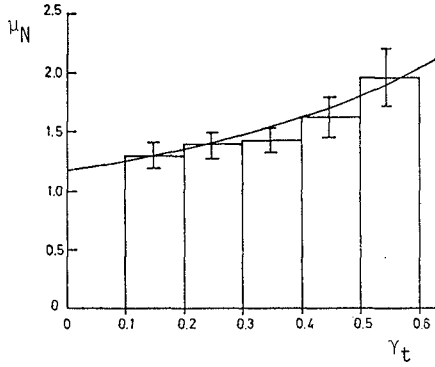


Figure 1 - Block diagram: sample mean group length ( $\mu_N$ ) and 90% confidence band vs. time domain estimate of  $\gamma$ . Curve:  $\mu_N$  vs.  $\gamma$  according to Kimura's theory.

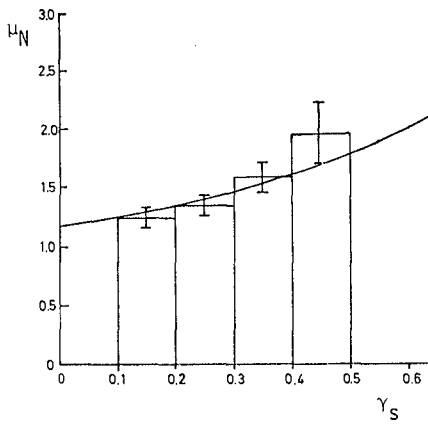


Figure 2 - Block diagram: sample mean group length ( $\mu_N$ ) and 90% confidence band vs. spectral domain estimate of  $\gamma$ . Curve:  $\mu_N$  vs.  $\gamma$  according to Kimura's theory.

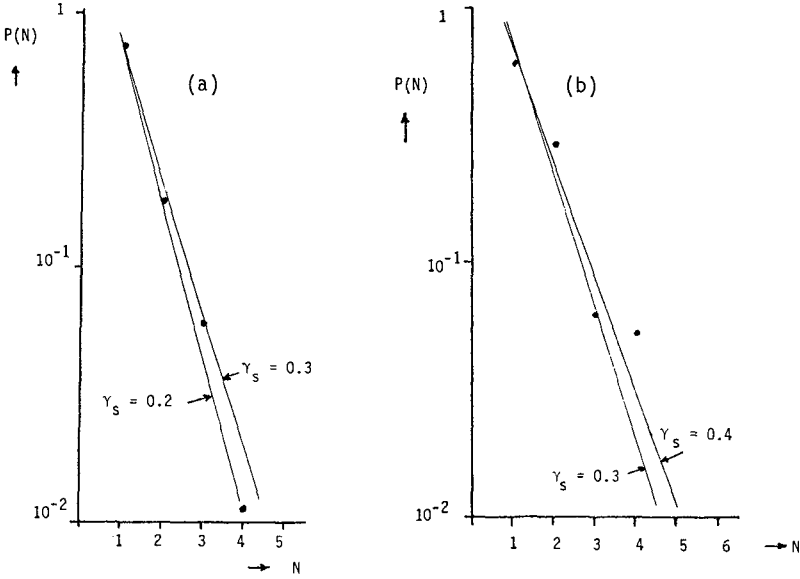


Figure 3 - Group length distribution for  $H_{*} = H_{1/3}$ ; records pooled according to values of spectral estimate of  $\gamma$ . Dots: observed values. Lines: theoretical values of  $\gamma_s$  at the limits of the class interval of the observations. (The lines have been drawn only for the purpose of visualisation; only the values for integer  $N$  have meaning.)  
 Fig. 3a: class interval  $0.2 < \gamma_s < 0.3$ ; fig. 3b: class interval  $0.3 < \gamma_s < 0.4$ .

as was done by Goda (ref. 6) using the theory for nonlinear wave-wave interactions by Tick (ref. 13) and Hamada (ref. 7), would result in less underprediction. This is because removal of the bound high-frequency energy from a given spectrum results in a narrower spectrum and a corresponding higher value of  $\kappa$ . The use of this higher value of  $\kappa$  in the estimation of the groupiness is legitimate because the principal effect of bound higher harmonics is wave profile distortion, and much less changes in wave height. An analysis along these lines of the data used in this study is carried out at the time of writing. Quantitative results are not yet available.

The theoretical prediction of the group length distribution is fair or good, as can be seen in the examples shown in figure 3. It is emphasized that the theory used in these predictions, and in those of the mean group length as well, does not contain any adjustable parameter.

The fair degree of agreement between theory and observations observed above lends further support to the validity of Kimura's theory, even in cases of active wave generation in storms. This in turn implies further evidence, in addition to that already presented by Rye and Lervik (ref. 12) and Goda (ref. 6), that the essential features of wave groups in sea waves can be explained on the basis of the linear, Gaussian model.

#### CONCLUSIONS

An analysis has been made of a series of North Sea wave records, including records obtained during storms. The analysis was aimed at an investigation of wave group statistics. The following conclusions were obtained:

- (1) The probability distribution and expected value of the length of groups of waves with height exceeding  $H_{1/3}$ , predicted by Kimura's theory, are in good agreement with observed frequency distributions and sample mean values.
- (2) The preceding conclusion holds for Kimura's theory in its original formulation, utilizing the correlation coefficient between consecutive wave heights estimated in the time domain, as well as in an alternative formulation, utilizing a spectral groupiness parameter based on Rice's theory for wave envelope statistics.
- (3) The preceding conclusions imply that the essential features of wave groups at sea, even in stormy conditions, can be explained on the basis of the linear, Gaussian model for the wave motion.

#### ACKNOWLEDGEMENTS

The authors thank E. Bouws of the K N M I (Royal Dutch Meteorological Institute) for providing the wave records used in this study.

#### REFERENCES

1. Arhan, M. and R. Ezraty, Statistical relations between successive wave heights, *Oceanologica Acta*, 1978, Vol. 1, No. 2, p.151-154
2. Battjes, J.A., Computation of set-up, longshore currents, run-up and overtopping due to wind-generated waves, thesis, Delft, 1974
3. Battjes, J.A., Lecture "Linear versus nonlinear models for wave groups" presented at IAHR Colloquium on "The propagation of non-linear free surface water waves", Delft, April 22-23, 1982 (manuscript in preparation, 1984)
4. Bouws, E., Spectra of extreme wave conditions in the southern North Sea considering the influence of water depth. AREA Conference on sea climatology, Paris, 1979
5. Goda, Y., Numerical experiments on wave statistics with spectral simulation, Rept. Port and Harbour Res. Inst., 1970, Vol. 9, No. 3, p. 3-57
6. Goda, Y., Analysis of wave grouping and spectra of long-travelled swell, Rept. Port and Harbour Res. Inst., 1983, Vol. 22, No. 1, p. 3-41
7. Hamada, T., The secondary interactions of surface waves, Rept. Port and Harbour Res. Inst., 1965, No. 10, 28 p.

8. Harding, J. and A.A. Binding, Windfields during gales in the North Sea and the gales of January 3, 1976. *Meteorological Magazine*, 1978, No. 107, p. 164-181
9. Kimura, A., Statistical properties of random wave groups, Proc. 17th Int. Conf. Coastal Engineering, Sydney, 1980, p. 2955-2973
10. Rice, S.O., Mathematical analysis of random noise (reprinted in Selected papers on noise and stochastic processes, Dover Pub. Inc.), 1944, par. 3.7
11. Rye, H., Wave group formation among storm waves, Proc. 14th Int. Conf. Coastal Engineering, Copenhagen, 1974, p. 164-183
12. Rye, H. and E. Lervik, Wave grouping studied by means of correlation techniques, Proc. Int. Conf. Hydrodynamics in Ocean Engineering, Trondheim, 1981, Vol. 1, p. 25-48
13. Tick, L.J., Nonlinear probability models of ocean waves, *Ocean Wave Spectra*, 1963, Prentice Hall Inc., p. 163-169
14. Uhlenbeck, G.E., Theory of random process, MIT Radiation Lab. Rept. 454, Oct. 1943 (citation quoted from D. Middleton, An introduction to statistical communication theory, McGraw-Hill, New York, 1960, p. 403)

## CHAPTER FORTY FOUR

### CALIBRATION AND VERIFICATION OF A DISSIPATION MODEL FOR RANDOM BREAKING WAVES

J.A. Battjes\* and M.J.F. Stive\*\*

#### ABSTRACT

A model describing the average rate of energy dissipation in random waves breaking in shallow water, published previously by the first author and Janssen (1978), has been applied to an extensive set of data for the purposes of calibration and verification. Both laboratory and field data were used, obtained on beaches with a more or less plane slope as well as on barred beaches, and for a wide range of wave conditions. Optimal values have been estimated for an adjustable breaking waveheight-coefficient in the model; these appear to vary slightly but systematically with the incident wave steepness, in a range which is physically realistic. A parameterization of this dependence allows the use of the model for prediction. Applied to the present data set, the correlation coefficient between measured and predicted rms wave heights is 0.98, with an rms normalized error of 6% and a bias which does not differ significantly from zero.

#### 1. INTRODUCTION

The principal physical process in the surfzone is the dissipation of the energy of incident windwaves and swell, due to wave breaking. Because of the randomness of wind-generated waves the occurrence of breaking at a fixed location is itself a random process. Realistic models for the prediction of the onshore variation of wave energy and radiation stress should take this randomness into account.

Battjes and Janssen (1978), hereafter referred to as BJ, presented an approach in which the mean local rate of energy dissipation is modelled, based on that occurring in a bore and on the local probability of wave breaking. The result is used as a sink in the energy balance, which is subsequently integrated to obtain the wave energy as a function of onshore distance. A few laboratory experiments performed by BJ, including cases with a bar-trough profile, indicated a very promising degree of agreement.

Thornton and Guza (1983) have presented a refinement of BJ's model, which however has negligible consequences for the predicted rms-variation. They also made a comparison between calculated and measured rms wave heights, using field data of low swell incident on a gently sloping, almost plane beach. Again, good agreement was found, with an rms relative error of about 9%.

---

\* Delft University of Technology, Delft, the Netherlands

\*\* Delft Hydraulics Laboratory, Delft, the Netherlands



The range of bottom profiles and incident wave parameters in the measurements referred to above is too restricted to allow a systematic investigation of the model performance and of the optimum values of the adjustable parameters. It was therefore decided to carry out an extensive calibration and verification of the model. The present paper briefly presents the results of this investigation. A full account will be published elsewhere.

The paper is made up as follows. A resume of BJ's model is given first. Then the observational conditions and procedures are described. The results are used for estimation of adjustable model coefficients as a function of the independent parameters (particularly the incident wave steepness). Finally, an overall assessment of the model performance with parameterized coefficients is presented, followed by a discussion.

## 2. RESUME OF BATTJES AND JANSSEN'S MODEL

In this section, we present a summary of BJ's model for reference in the remainder of this paper.

The essence of BJ's model is the estimation of the time-averaged rate of dissipation of wave energy per unit area due to breaking ( $\bar{D}$ ). Two aspects are distinguished: the rate of energy dissipation in periodic breaking waves, and the probability of occurrence of breaking waves of given height in a random wave field.

The energy dissipation in breaking waves is modelled after that in a bore of the same height. For periodic waves with frequency  $f$  and breaking waveheight  $H_b$  in water of mean depth  $h$ , BJ arrive at the following order-of-magnitude estimate for the mean dissipation rate per unit area:

$$D \sim \frac{1}{2} f \rho g H_b^2 \quad (1)$$

For application to random waves, the expected value of  $D$  (written as  $\bar{D}$ ) must be estimated, taking into account the randomness of the waves and the fact that not all the waves passing the point considered are breaking. In this estimate, BJ have used characteristic values for the frequency and the breaking waveheights, and they have derived a prognostic equation for the local fraction of breaking waves.

The characteristic frequency used in the following is  $f_p$ , the frequency at the peak of the energy spectrum of the incident waves.

The mean square of  $H_b$  is equated by BJ to the square of the nominal, depth-limited height of periodic waves ( $H_m$ ) in water of the local mean depth. BJ use a Miche-type expression for  $H_m$ , adapted through the inclusion of a parameter  $\gamma$  to account for influences of bottom slope and mean wave steepness:

$$H_m = 0.88 k_p^{-1} \tanh(\gamma k_p h / 0.88) \quad (2)$$

in which  $k_p = 2\pi/L_p$  is the wavenumber calculated on the basis of the linear theory dispersion equation for gravity waves with frequency  $f_p$ .

To determine the local fraction of breaking waves ( $Q$ ), BJ assume that the cumulative probability distribution of all waveheights (breaking or non-breaking) is of the Rayleigh-type, cut off discontinuously at  $H = H_m$ . This was shown to imply the following relation between  $Q$  and  $H_{rms}/H_m$ , in which  $H_{rms}$  is the rms of all waveheights:

$$\frac{1 - Q}{-\ln Q} = \left( \frac{H_{rms}}{H_m} \right)^2 \quad (3)$$

Substituting the approximations mentioned above in the averaged equation (1), and writing the order-of-magnitude relation in the form of an equation, gives

$$\bar{D} = \frac{1}{4} \alpha Q f_p \rho g H_m^2 \quad (4)$$

in which  $\alpha$  is a coefficient which is expected to be of order 1. It is pointed out that  $\bar{D}$  varies with  $H_{rms}$  through  $Q$ .

To close the model,  $\bar{D}$  is used as a sink in the wave energy balance, which in its most reduced form (statistically steady, uniform alongshore, no other sources or sinks than  $\bar{D}$ ) can be written as

$$\frac{\partial P_x}{\partial x} + \bar{D} = 0 \quad (5)$$

$P_x$  is the onshore energy flux per unit width, approximated as  $E c_g$ , in which  $E = \frac{1}{8} \rho g H_{rms}^2$  and  $c_g$  is the group velocity according to the linear theory for  $f = f_D$ .

The energy balance (5) is integrated simultaneously with the balance of onshore momentum (not reproduced here), resulting in the simultaneous determination of the onshore variation of  $H_{rms}$  and of the set-up of the mean water level ( $\bar{\eta}$ ).

### 3. OBSERVATIONS

Empirical data from various sources have been collected for calibration and verification of the theoretical model. These include laboratory data and field data, obtained for a variety of wave conditions and bottom profiles. The original data of BJ are included also.

All laboratory data used herein have been collected in wave flumes, using mechanically generated random waves. The field sites and conditions were selected so as to have more or less statistically uniform conditions alongshore and normal incidence (for the principal wave propagation direction). Direct wind influence was negligible in all cases considered here except one.

The laboratory bottom profiles include plane slopes and a schematized bar-profile in concrete, as well as concave and barred profiles in sand. Two field sites on the Dutch coast were used, one on a beach near Egmond, the other on a shoal in the mouth of the Haringvliet estuary. The beach has a typical double bar system. The measurements in the Haringvliet estuary were conducted in a line across an elongated shoal, with more or less parallel depth contours over a distance of about 5000 m. The minimum depth over the shoal is 0.1 m below Mean Sea Level, and about 1.5 m below Mean High Water Level.

For each combination of incident waves and bottom profile, measurements were made of the bottom profile, the mean water level, the rms wave height and the peak frequency at an offshore reference point, and the rms wave heights at various points in the profile. In some cases the variation of mean water level with distance onshore was measured also. The surface elevation signals were analyzed to estimate the variance,  $\sigma^2$ , and its spectral distribution. The measured variances were used to estimate  $H_{rms}$  according to

$$H_{rms} = 8^{\frac{1}{2}} \sigma. \quad (6)$$

A resume of the independent parameters is given in Table 1. The columns 4, 5 and 6 list the values of  $h$ ,  $H_{rms}$  and  $f_p$  in the offshore reference point (indicated with the subscript  $r$ ). Values of a mean deep-water wave steepness  $s_o = H_{rms}/L_{Op}$  are listed in column 7, based on  $L_{Op} \equiv g/(2\pi f_p^2)$  and a deep-water value of  $H_{rms}$  calculated from the values in the reference point using linear shoaling theory for periodic waves with frequency  $f_p$ , i.e.  $H_{rms}_o = H_{rms}_r (c_{gr}/c_{go})^{\frac{1}{2}}$ . The parameter  $\hat{\gamma}$  in column 8 will be explained below.

(1) Nr.	(2) Source	(3) Profile [m]	(4) $h_r$ [m]	(5) $H_{rms_r}$ [Hz]	(6) $f_{p_r}$ -	(7) $s_o$ -	(8) $\hat{\gamma}$
1	Battjes and Janssen (1978)	Plane (1:20)	.705	.144	.511	.026	0.73
2			.697	.122	.383	.012	0.60
3			.701	.143	.435	.018	0.70
4	Battjes and Janssen (1978)	Schematized bar-trough	.703	.137	.450	.019	0.72
5			.645	.121	.443	.016	0.69
6			.763	.104	.467	.016	0.70
7			.732	.118	.481	.019	0.70
8			.616	.143	.498	.024	0.72
9	Stive (1984)	Plane (1:40)	.700	.138	.341	.010	0.62
10			.700	.136	.633	.038	0.81
11			4.19	1.00	.185	.023	0.82
12	Van Overeem (1983)	Concave	.800	.211	.392	.022	0.73
13			.800	.096	.568	.022	0.80
14			.800	.132	.559	.029	0.80
15	Van Overeem (1983)	Bar-trough	.800	.132	.557	.029	0.83
16			.800	.212	.393	.022	0.75
17	Derks and Stive (1984)	Bar-trough	10.80	1.29	.157	.022	0.67
18			15.65	2.78	.115	.026	0.73
19	Dingemans (1983)	Bar	16.40	.94	.143	.013	0.70
20			11.10	2.43	.128	.028	0.82

Table 1 Experimental and environmental parameters; cases 1...16 laboratory experiments, cases 17...20 field experiments

## 4. MODEL CALIBRATION

The energy balance and the momentum balance have been numerically integrated with respect to the onshore distance ( $x$ ) for each case listed in Table 1, using chosen values of  $(\alpha, \gamma)$ . The peak frequency  $f_p$  and the coefficients  $(\alpha, \gamma)$  were kept constant with respect to  $x$ . Each integration gives two functions  $\eta(x)$  and  $H_{rms}(x)$  shoreward of the reference point, which can be compared to the measurements. Repeating the integration for several choices of  $(\alpha, \gamma)$ , optimal values of these coefficients have been estimated, such that a maximum agreement is obtained between computed and measured  $H_{rms}$  values.

The coefficients  $\alpha$  and  $\gamma$  can formally be varied independently of each other. However, in the calibration process just described there is a dependence between the two since in this process the model is forced to simulate a certain energy dissipation, which depends on  $\alpha$  and  $\gamma$  through its proportionality to the product  $\alpha Q H_m^2$  (see eq. 4). Therefore, there is effectively only one degree of freedom in tuning the model to a measured waveheight variation. The calibration was in fact carried out by estimating optimal values of  $\gamma$  (denoted as  $\hat{\gamma}$ ) under the constraint  $\alpha = 1$ . The resulting values of  $\hat{\gamma}$  are listed in column 8 of Table 1. They fall in the range from 0.60 to 0.83, which is physically realistic.

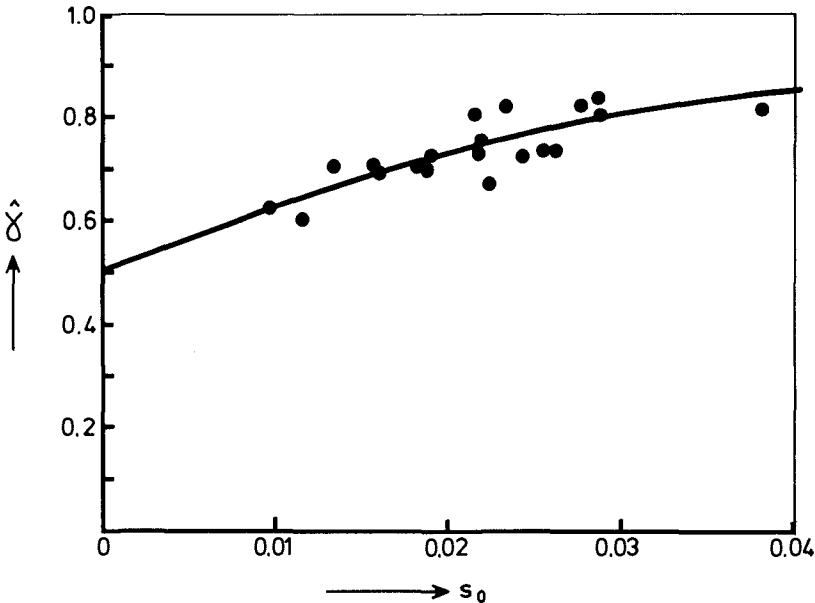


Fig. 1 Estimated values of breaker height coefficient  $\hat{\gamma}$  vs. deep-water steepness  $s_0$ ; data points: optimal value per case; full curve parameterization given by eq. 7.

It is known that the process of wave breaking in shallow water is influenced by the incident wave steepness and by the bottom slope. It was therefore investigated whether the estimated  $\hat{\gamma}$ -values varied systematically with these parameters. No significant variation of  $\hat{\gamma}$  with beach slope could be found. However, there did appear to be a systematic dependence of  $\hat{\gamma}$  on the deep-water steepness  $s_0$ , as can be seen in Fig. 1. A tanh-function has been fitted to these data, with the result

$$\hat{\gamma} = 0.5 + 0.4 \tanh(33 s_0) \quad (7)$$

This relation, indicated in Fig. 1 by the full line, can be used for purposes of prediction.

##### 5. EVALUATION OF MODEL PERFORMANCE

In order to gain an impression of the overall performance of the model, we have applied it again to each of the 20 cases considered, this time using the parameterization (7) described above. The model was found to be quite realistic in the simulation of the observed rms waveheights. Some examples of the results are shown in the Figs. 2 through 4. A comparison of normalized computed and measured  $H_{rms}$  values in the zone of wave shoaling and breaking covering all 20 cases is given in Fig. 5. The correlation coefficient is 0.98; the model bias based on the best-fitting proportional relationship is 0.01, and the rms relative error, normalized with the mean value of all measured values of  $H_{rms}/H_{rms_0}$  shown in Fig. 5, is 0.06. These numbers confirm in a quantitative sense the high degree of realism possessed by the model for the prediction of the waveheight variation in areas of wave breaking. The good model performance is remarkable in view of the complexity of the physical processes involved, and the relatively simple concept on which the model is based.

The maximum set up also is well predicted (Fig. 2), but in areas of large set-up gradient the predicted rise is systematically too far seaward. This phenomenon has been noted previously by Battjes (1972) and by BJ. It suggests that the decrease in momentum flux lags behind the decrease in wave energy as measured through the variance of the surface elevation. A possible explanation for this phenomenon would be a relative surplus of kinetic energy in the area of intensive wave energy dissipation. This might consist partly of a surplus of kinetic wave energy (coherent with the surface elevation) and partly of turbulence energy. The latter possibility can be investigated by adding turbulent Reynolds stresses to the radiation stresses, e.g. on the basis of the model for turbulence in the surf zone presented by Battjes (1975). However this matter has not been pursued in the present study.

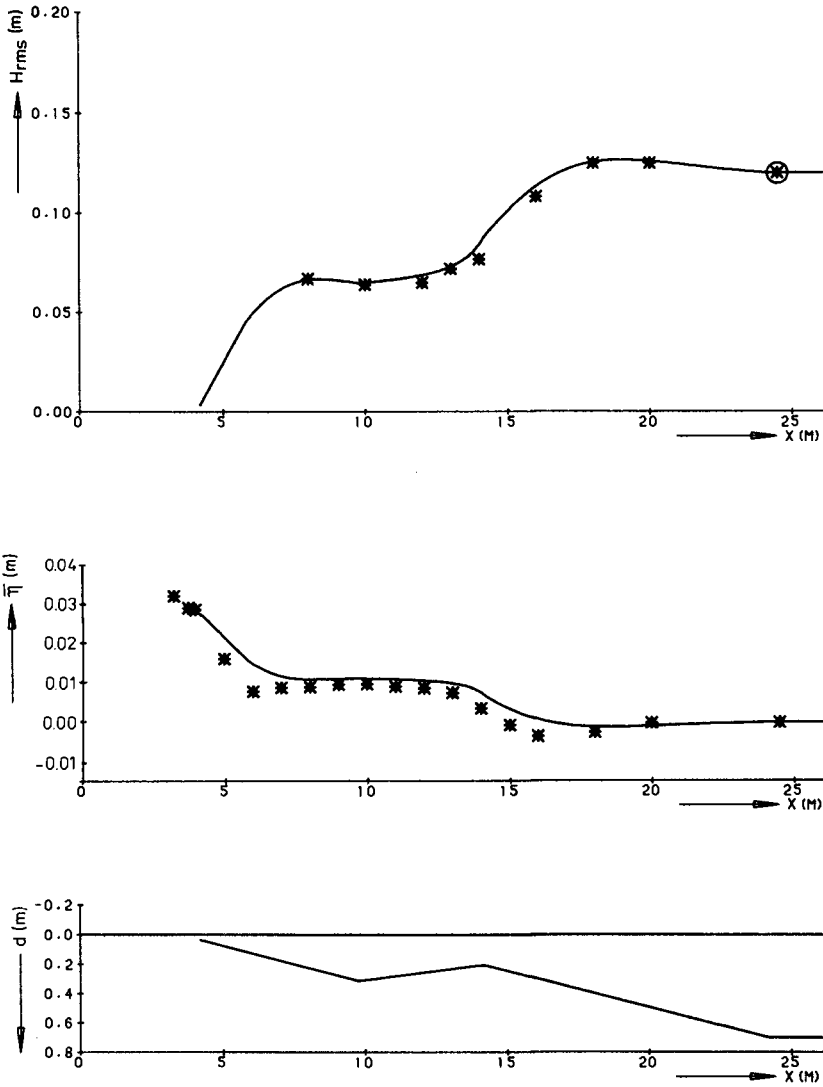


Fig. 2 Results for case 5 (laboratory); profiles of bottom elevation below MWL<sub>r</sub> ( $d$ ), mean water level above MWL<sub>r</sub> ( $\bar{\eta}$ ) and rms wave-height ( $H_{rms}$ ) vs. distance normal to shore ( $x$ ); data points: measured values with offshore reference value encircled; full curves: computed values of  $\bar{\eta}$  and  $H_{rms}$ , based on parameterization of  $\gamma$  given by eq. 7.

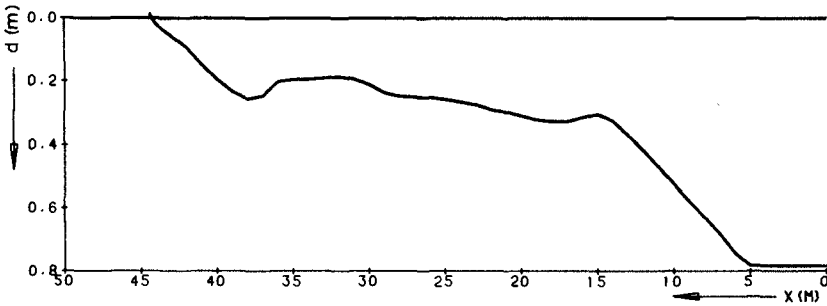
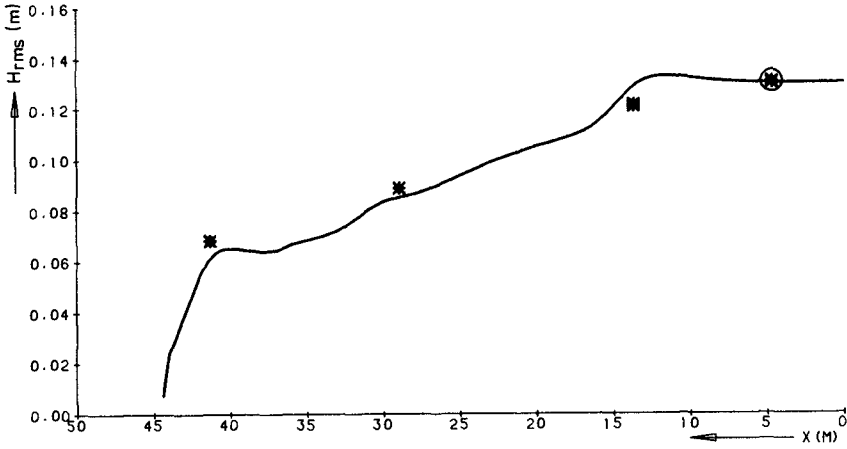


Fig. 3 Results for case 15 (laboratory); for legend see Fig. 3 (except  $\bar{\eta}$ ).

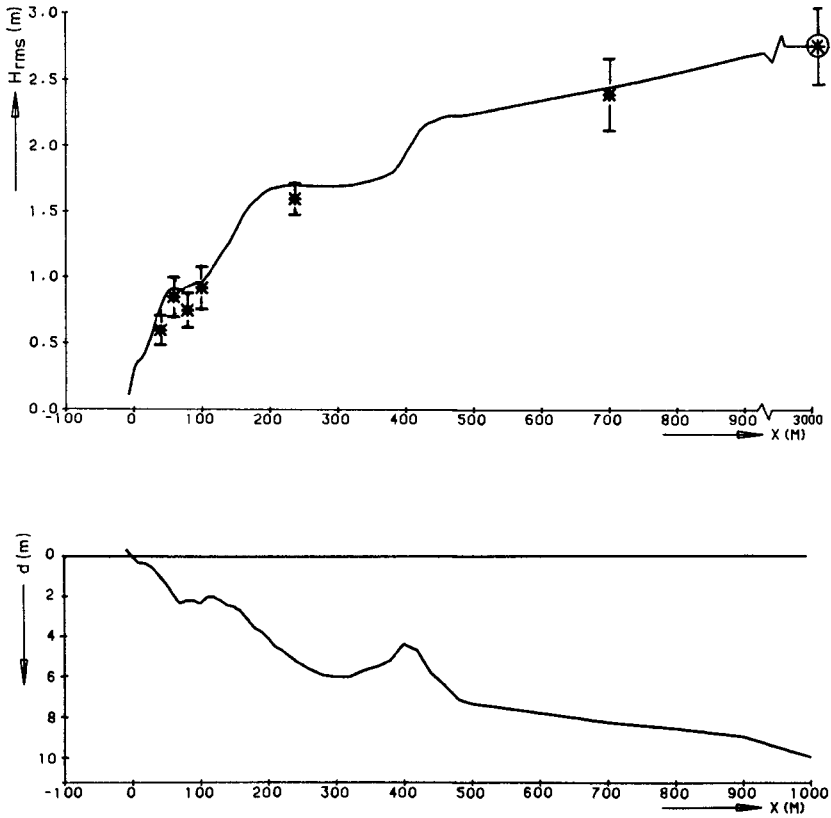


Fig. 4 Results for case 18 (field - Egmond beach); for legend see Fig. 3; the vertical line segments indicate one standard deviation on either side of the plotted data point.



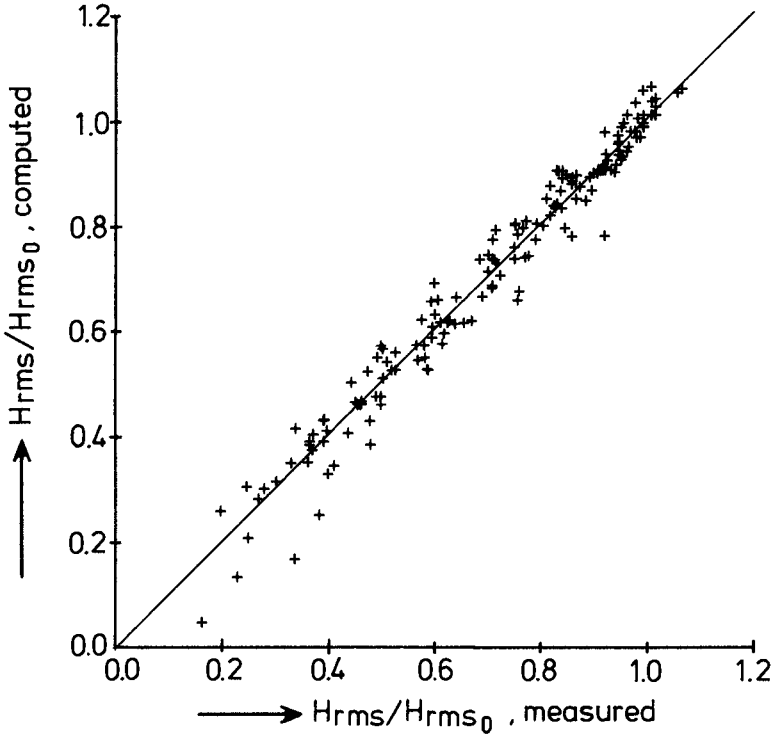


Fig. 5 Comparison of calculated and measured rms waveheights, normalized with the deep-water value. The calculated values are based on the parameterization given by eq. 7. The straight line is the least squares best-fit proportional relationship.

## 6. DISCUSSION

The model calibration described above is based on situations of one-dimensional wave propagation. However, the key element in the model is the estimate of the mean energy dissipation in random waves due to breaking, which is believed to apply equally well in cases of two-dimensional wave propagation.

In the situations used in the calibration described herein, there were no significant sources or sinks of energy between deep water and the surfzone. In these situations, a parameterization of the model coefficient(s) in terms of a characteristic deepwater wave steepness is meaningful, as in eq. 7. In applications, more complicated situations may arise, in which processes other than pure shoaling play a non-negligible role between deep water and the surfzone. Examples are

wave refraction, and energy dissipation in the near-bottom boundary layer. For such situations, we use the following procedure.

We distinguish areas of negligible breaking and areas of significant breaking. (In barred profiles, more than one area of significant breaking may occur). Somewhat arbitrarily, we define an area of significant breaking as the region of space (in the horizontal plane) where  $H_{rms}/h > 0.25$ . This corresponds roughly with  $H_{rms}/H_m > 0.35$ , approximately the limit above which the fraction of breaking waves is no longer negligible.

In a process of numerical integration along a wave ray in water of decreasing depth, in which refraction and various energy sources and sinks can be taken into account, the dissipation due to breaking is neglected as long as  $H_{rms} < 0.25 h$ . At the point where  $H_{rms} = 0.25 h$ , the local value of  $H_{rms}$  is converted to an equivalent deep-water value using linear shoaling only (i.e.  $H_{rms_o} = (c_g/c_{g_o})^2 H_{rms}$ ). This value is used to determine  $\hat{\gamma}$  according to eq. 7; the value of  $\hat{\gamma}$  so obtained is used in the integration of the energy balance (including the dissipation due to breaking according to eq. 4) across the area of non-negligible breaking downwave of the point of transition (i.e., as long as  $H_{rms}/h > 0.25$ ).

## 7. CONCLUSIONS

A calibration is performed of a theoretical model for the wave energy dissipation and resulting wave energy variation in random breaking waves. The theoretical model has effectively one adjustable parameter. Optimal values of this coefficient have been determined. These vary slightly in a physically realistic range with the incident wave steepness. A parameterization of this dependence is presented so that the model can be used for prediction. Using this parameterization, the overall performance of the model has been evaluated. The coefficient of correlation between predicted and observed  $H_{rms}$ -values is 0.98; the model bias is not significantly different from zero, and the rms relative error is 0.06. The maximum set-up of the mean water level also is well predicted.

## ACKNOWLEDGEMENT

The authors wish to express their gratitude to H. Derks, M.W. Dingemans and J. van Overeem, who supplied additional information on the measurement results obtained by them in their respective studies. Furthermore M.W. Dingemans is thanked for his support in developing the numerical model.

## REFERENCES

- BATTJES, J.A., Set-up due to irregular waves, in Proceedings of the 13th International Conference Coastal Engineering, pp. 1993-2004, American Society of Civil Engineers, New York, 1972.
- BATTJES, J.A., A turbulence model for the surf zone, in Proceedings Symposium on Modelling Techniques, pp. 1050-1061, American Society of Civil Engineers, New York, 1975.

BATTJES, J.A. and J.P.F.M. JANSSEN, Energy loss and set-up due to breaking of random waves, in Proceedings 16th International Conference Coastal Engineering, pp. 569-587, American Society of Civil Engineers, New York, 1978.

DERKS, H. and M.J.F. STIVE, Field investigations in the TOW Study programme for coastal sediment transport in the Netherlands, in Proceedings of the 19th International Conference Coastal Engineering, American Society of Civil Engineers, New York, 1984.

DINGEMANS, M.W., Verification of numerical wave propagation models with field measurements; Crediz verification Haringvliet, Report W 488, Delft Hydraulics Laboratory, 1983.

STIVE, M.J.F., A scale comparison of waves breaking on a beach, Accepted for publication J. Coast. Eng., 1984.

THORNTON, E.B. and R.T. GUZA, Transformation of wave height distribution, J. Geophys. Res., 88, 5925-5938, 1983.

VAN OVEREEM, J., Morphologic behaviour of beach fill with underwater dam, Report M 1891, Delft Hydraulics Laboratory, 1983.

## CHAPTER FORTY FIVE

### WAVE GROUP ANATOMY OF OCEAN WAVE SPECTRA

Warren C. Thompson<sup>1</sup>, Arthur R. Nelson<sup>2</sup>, and Dean G. Sedivy<sup>3</sup>

#### ABSTRACT

This paper inquires into the questions of how wave groups are related to the wave spectrum, and how they differ in sea versus swell. Some results are presented in the form of a wave group model for sea spectra and for swell spectra. The models were developed from statistical analysis of a large number of wave records and apply to deep water only.

#### INTRODUCTION

A universal characteristic of sea (wind waves) and swell is the occurrence of sets of consecutive quasiperiodic larger waves called wave groups; these occur at intervals of approximately one to two minutes, vary in their energy and length, and are preceded and followed by generally nondescript low waves.

Wave groups have been recognized by coastal engineers in recent years as the cause of damage and destruction to vessels, offshore platforms, and shore structures due to high wave runs and to their periodicity. They constitute the principal components of the wave spectrum which the coastal engineer uses, yet information on their relationship to the spectrum has been quite incomplete. A further reason for interest in wave groups is their relationship to sea versus swell, or more specifically to initial wave steepness ( $H'_0/L_0$  in linear wave theory), particularly because the initial wave steepness controls many shallow-water wave variables, including breaker type, breaker height and depth, wave runup and overtopping, and beach profile response.

With these areas of practical concern in mind, we explore in this paper the following questions:

- (a) How are wave groups related to the wave spectrum?  
(Or, given a spectrum what can be said about the

<sup>1</sup>Consultant; Emer. Prof., Naval Postgrad. Sch., Monterey, CA 93943

<sup>2</sup>Spec. Proj. Div., Fleet Numer. Ocean. Center, Monterey, CA 93940

<sup>3</sup>Div. of Math. & Sci., U. S. Naval Acad., Annapolis, MD 21402

characteristics of the wave groups occurring in the wave field?)

(b) How do wave groups differ in sea versus swell?

Some preliminary answers are given herein in the form of simple wave group models for sea and swell spectra. The models were constructed from statistical analyses of a large number of wave records for their wave group characteristics. The models apply to deep water only. Study of wave groups in shoal water is more complex due in part to differential shoaling of the various frequencies composing the spectrum and we have not probed this area in any depth. Such a study should logically follow and benefit from data developed for deep water.

In this paper a definition of wave group is given, wave group measures and associated wave record measures are specified, and some results from statistical analyses are presented leading to the models. The wave group definition was developed by Sedivy (1978), who also performed exploratory statistical analysis of wave records obtained from bottom pressure sensors in shallow water on the open California coast. Nelson (1980), applying this definition, probed wave group characteristics in deep water from a statistical analysis of records from a surface sensor on the California coast. It is Nelson's analyses that primarily provided the basis for constructing the deep water wave group models presented. The studies by Sedivy and Nelson were conducted at the Naval Postgraduate School in Monterey, California.

#### WAVE GROUP DEFINITION AND MEASURES

The analytical definition of the wave group presented by Sedivy (1978) is based on a comparison of the energy content in the group with that in the record, where energy is represented in terms of the statistical variance of the wave heights occurring in the group and in the record.

The procedure for identifying groups first involves computation of the variance of the whole record. The record, in digitized form, is then reanalyzed using a window of short duration over which a short-term variance is computed and plotted at the window midpoint. The window is moved along the wave record from beginning to end at one digital step at a time and produces a running short-term variance curve. The result of this procedure is illustrated in the upper diagram of Figure 1 for the record of mature swell shown. Those portions of the wave record where the running short-term variance values exceed the record variance indicate wave energy in excess of the record energy and identify possible wave groups.

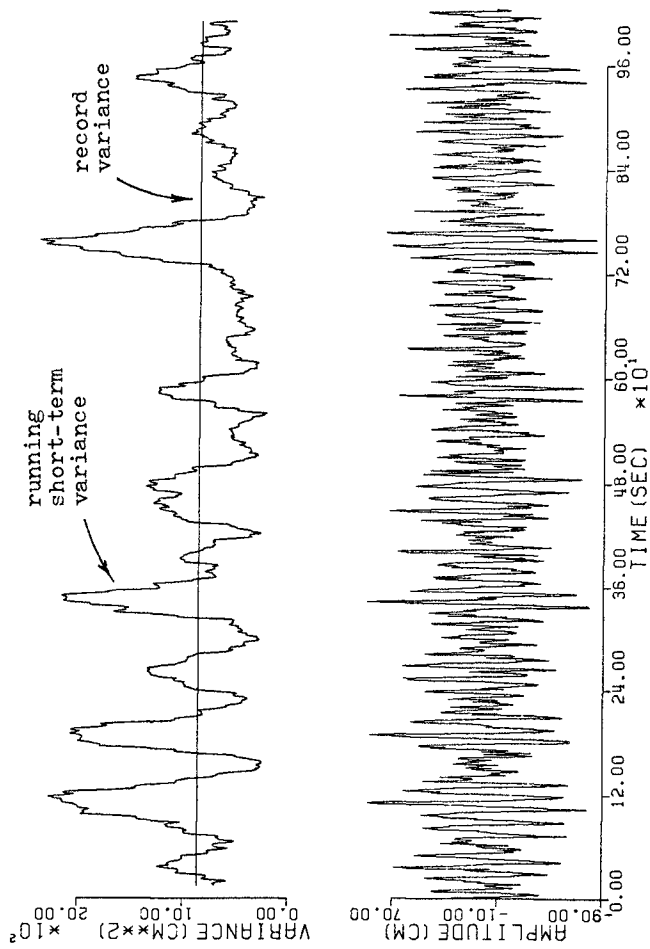


Figure 1: WAVE RECORD (lower) AND VARIANCE ANALYSIS (upper)  
 (from Nelson, 1980)

In choosing a suitable window width  $W$  for computing the short-term variance, the finding by Thompson (1972) and by Smith (1974) that the average period of the waves in prominent wave groups approximates the spectral peak period  $T_R$  of the wave record indicates that  $W$  should be an integer multiple of  $T_R$ . Sedivy experimented with real and artificial wave records  $T_R$  and settled on  $W = 2T_R$  as optimum. Nelson (1980) conducted additional experiments by varying  $W$  over the range from  $1/2$  to 4 times  $T_R$ . He found that wave groups having high energy relative  $T_R$  to the record energy were identified by all window widths and that the window width seldom affected the number of waves in the group. In low energy groups, however, as  $W$  was increased from  $1/2 T_R$  to  $4 T_R$  the number of groups identified decreased by approximately 50% and the number of waves per group increased somewhat. Nelson concurred with the choice of  $W = 2 T_R$  and concluded that it gives a short-term variance curve that is relatively smooth yet is reasonably sensitive to lower energy groups.

In addition to the requirement that the short-term variance must exceed the record variance, Sedivy specified three limitations on the definition of a wave group. First, the group must be composed of whole waves as defined by successive upcrossings of the mean water level by the wave-form. Since the short-term variance curve does not ordinarily cross the record variance "line" at an upcrossing, this specification was satisfied by placing the wave group boundaries at the first zero upcrossing met in moving away from the center of the wave group in either direction. Second, a wave group must contain a minimum of two waves; this limitation requires a minimum of order to the wave heights against a random wave field, and also rules out many occurrences where the short-term variance curve only just manages to rise above the record variance for a brief interval of time. Third, adjacent wave groups must be separated from one another by at least one-half the window width, otherwise they are treated as a single group; this condition was specified in order to prevent the possibility of including a given wave in two separate wave groups.

Following identification of the wave group using these procedures, various wave group characteristics may then be measured. Those wave group variables (designated with subscript  $G$ ) that are dealt with in this paper, along with wave record measures (subscript  $R$ ) and group-to-record parameters, are as follows:

#### Wave group measures

$T_G$  Mean wave group period--average of the periods of the individual waves composing the group, computed from the group duration divided by the number of waves in the group; the waves composing a group tend to be periodic so that  $T_G$  approximates this periodicity.

- $V_G$  Mean wave group variance--computed by averaging the digital short-term variance values over the group duration.
- $N_G$  Number of waves per group--given by the number of intervals between upcrossings within the group.

Wave record measures

- $T_R$  Spectral peak period--reciprocal of the frequency of maximum energy density obtained from spectral analysis of the record (using the Fast Fourier Transform with four windows).
- $V_R$  Wave record variance--computed by digital time-series analysis (and checked by spectral analysis): the significant wave height  $H_R$  is related to the record variance by the relationship  $H_R = 4 \sqrt{V_R}$ .
- $G_R$  Significant wave steepness--defined and described below; used in this study to categorize wave records by wave type, e.g., sea, young swell, mature swell, and old swell.

Group-to-record parameters--In order to compare wave group measures among records having different peak periods and energy levels, the group period and group variance were normalized by referencing them to the corresponding record measures as follows:

- $T_G/T_R$  Relative group period.
- $V_G/V_R$  Relative group variance.

The significant wave steepness of the record  $G_R$  was used as a measure of the wave type (Thompson and Reynolds, 1976). It is defined by analogy with the steepness  $H/L$  of monochromatic waves in deep water as given by the linear wave theory, where the linear theory wave height  $H$  and period  $T$  are replaced by the significant height of the record  $H_R$  and spectral peak period  $T_R$ , as follows:

$$\frac{H}{L} = \frac{H}{\frac{g}{2\pi} T^2} \quad \equiv \quad \frac{H_R}{\frac{g}{2\pi} T_R^2} = G_R$$

The wave type is then defined in terms of the significant wave steepness according to the table below:



Wave type	$G_R$	Significant height reduction ( $H_D/H_F$ )	Swell decay distance (naut. mi.)
Sea	1/12-1/40	1.00	0
Young Swell	1/40-1/100	1.00-0.50	0-250
Mature Swell	1/100-1/250	0.50-0.25	250-1600
Old Swell	< 1/250	< 0.25	> 1600

$H_F$  = significant height in generating area  
 $H_D$  = significant height at decay distance

The range of wave steepness for sea given in the table was evaluated from the Sverdrup-Munk-Bretschneider (SMB) wave generation graph (Bretschneider, 1958). The wave steepness boundaries between the types of swell were determined by specifying swell height reductions of 0.50 and 0.25 relative to the significant height of the waves in the fetch (column 3), and assuming wave generation in extratropical storms of average size. These height reduction factors, when entered into the SMB swell decay curves, yield both the swell steepness boundaries (column 2) and the approximate swell decay distances from the generating area (column 4). Since swell steepness diminishes with increasing travel time as well as travel distance from the generating area, the significant steepness may be considered a measure of the relative age of the swell (column 1), and provides the basis for designating swell as young, mature, or old.

#### WAVE RECORDS ANALYZED AND SOME RESULTS

The wave group models presented herein were constructed from the results obtained from statistical analysis of a large sample of ocean wave records. The wave records were recorded at an open ocean station off the central California coast that is exposed to an array of wave dimensions typical of the major oceans, ranging from locally generated wind waves to swell that has decayed over thousands of travel miles. The wave data were recorded by a Datawell Waverider accelerometer-type buoy and were digitized on magnetic tape at a sampling interval of one second. Each record analyzed was of 1,024 seconds duration, or approximately 17 minutes.

The sea surface sensor was positioned in a water depth of approximately 30 fathoms (55 meters). At that depth the linear theory shoaling coefficient  $K_G$  for 18-second waves, the longest spectral peak period dealt with, is 0.91. This

value of the coefficient places the relative water depth  $d/L_0$  for waves of 18-second period toward the deep water boundary of the intermediate relative depth zone as conventionally defined. Accordingly, we consider the findings of this study to effectively apply to deep water for all wave periods dealt with.

A large number of wave records were screened from which 338 unimodal records were selected for analysis which met criteria requiring a single spectral peak and a relatively narrow bandwidth. These criteria were chosen to avoid complication in the selection of a short-term variance window used to identify wave groups and also to ensure as fully as possible that the waves in each record originated in a single generating area in order for the wave type to be determined.

The selected records are well distributed in their characteristics and cover spectral peak periods from 4 to 18 seconds, significant wave heights from 0.6 to 3.4 meters, and significant wave steepnesses from 1/15 (young sea) to 1/530 (very old swell). The 5,598 wave groups identified in these records were then statistically examined for their properties and relationships.

To convey an idea, in the limited space available, of the nature of the findings from these analyses, we now look at some of the results obtained by Nelson (1980). By way of example we will focus on the measure  $N_G$ , the number of waves composing a group, and examine its frequency of occurrence with respect to other factors as displayed in a series of graphs.

In Figure 2 the graph shows the cumulative frequency of occurrence, in percent, of  $N_G$  in different parts of the wave spectrum. The position of a wave group in the spectrum is determined by its relative group period  $T_G/T_R$ ; values of the ratio near unity place the group close to the spectrum peak whereas groups having ratios  $\ll 1$  and  $\gg 1$  lie, respectively, well into the high frequency tail and the low frequency tail. The six curves in the figure are seen to form a tight-bundle, and we draw the conclusion from this and other data that the percentage distribution of  $N_G$  is fundamentally the same in the tails of the spectrum as at the peak, i.e., the spectrum can be sliced at any wave frequency and the percentage distribution of  $N_G$  among the wave groups occurring there can be expected, for a large group population, to be the same. The histograms for these six sets of data (not shown) are Rayleigh-like in form.

The distribution of  $N_G$  with respect to the relative energy content of wave groups  $V_G/V_R$  is shown in the cumulative distribution graph in Figure 3. As may be expected from the wave group definition, groups with the lowest energy content have an average group variance approximately equal to the record variance ( $V_G \doteq V_R$ ). It is evident from this

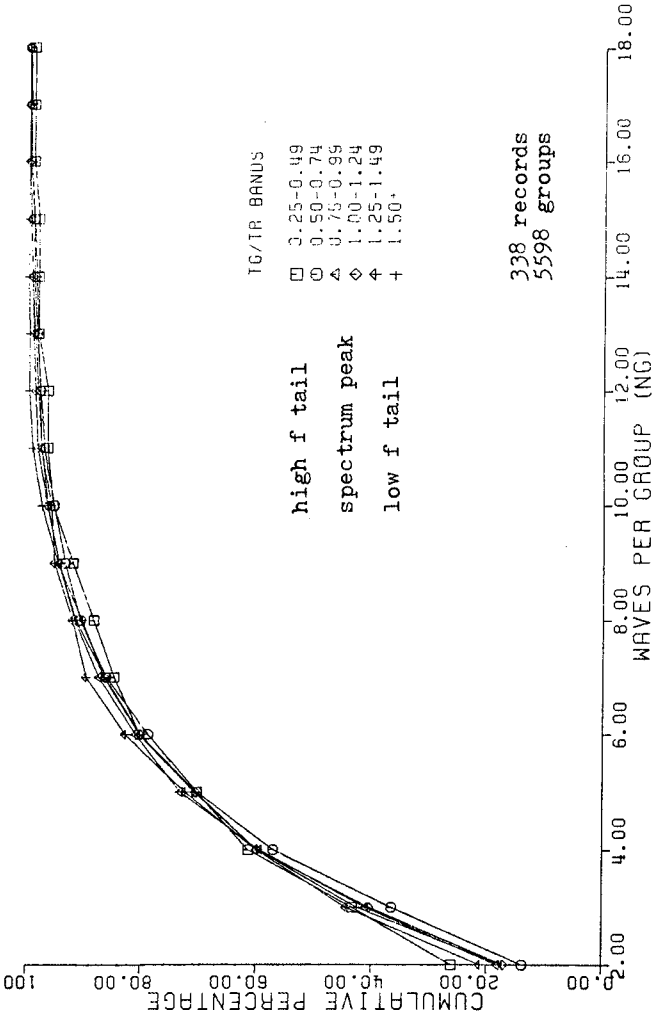


Figure 2: CUMULATIVE DISTRIBUTION OF  $N_G$  FOR  $T_G/T_R$  BANDS  
 (from Nelson, 1980)

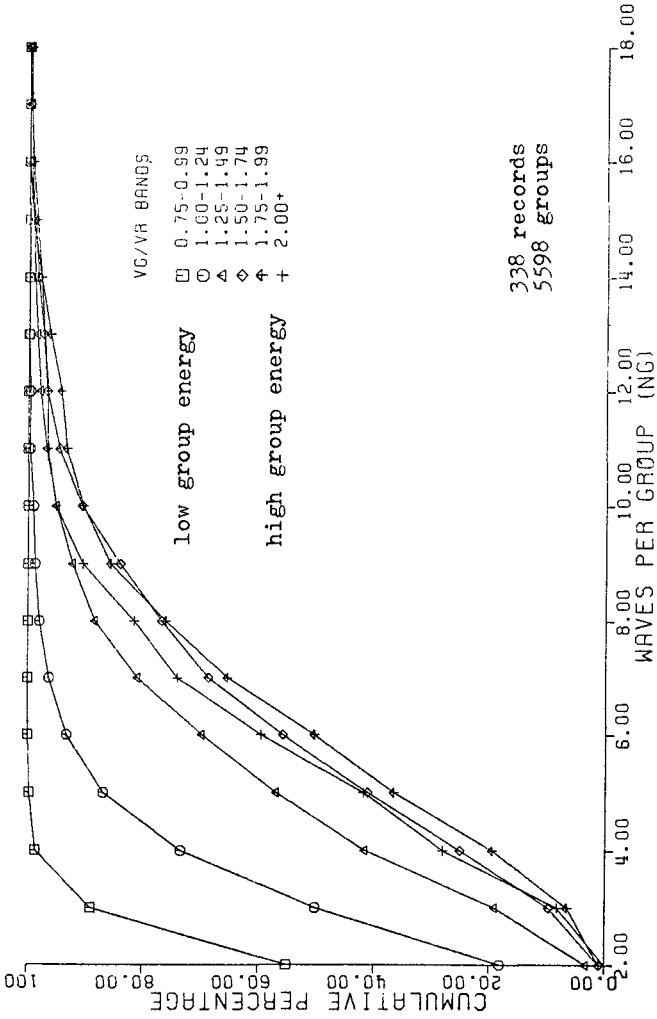


Figure 3: CUMULATIVE DISTRIBUTION OF  $N_G$  FOR  $V_G/V_R$  BANDS  
 (from Nelson, 1980)

figure that  $N_G$  is sensitive to the relative energy content of wave groups. The lowest energy groups most frequently contain 2 waves, the minimum taken to constitute a group, and seldom contain more than 4 waves. The highest energy groups, on the other hand, rarely contain 2 waves, most frequently have 6 waves, and exceed 10 waves in 10% of occurrences. Histograms for the six energy levels (not shown) appear as nested curves having a Rayleigh-like form in which the distribution becomes less peaked and extend over a wider range of  $N_G$  as the group energy level increases.

The frequency of occurrence of  $N_G$  with respect to wave type, represented by wave steepness intervals, is illustrated in the cumulative distributions shown in Figure 4. It may be concluded that the older the swell the larger tends to be the number of waves in a group at any given probability level. The associated histograms (not shown) also have a Rayleigh-like form.

#### WAVE GROUP MODELS

##### Sea Model

Figure 5 presents a model of the relationship between wave groups and the energy density spectrum for the case of waves under generation by the wind in deep water.

The reader's attention is directed to the table in the lower part of the figure which describes the three areas of the spectrum. The table indicates that most wave groups in a large population are concentrated about the frequency of maximum energy density of the spectrum, i.e., their relative group periods  $T_G/T_R$  lie at or close to 1.0. In moving away from the peak and toward the tails of the spectrum, group periods deviate increasingly from the spectral peak period and the number of groups falls rapidly. Groups are rare at values of  $T_G/T_R < 0.7$  and  $> 2.0$  (Figure 6).

Wave groups falling in the tails of the spectrum not only occur infrequently but they also have a low relative energy level in which the average group variance is close to the variance of the record. As the spectral peak is approached, low energy groups increase in occurrence and are joined by groups containing increasing amounts of energy. At and very close to the peak of the spectrum are found those groups with the highest energy levels but also the greatest occurrence of groups at all energy levels.

With regard to the number of waves per group, the percentage distribution of  $N_G$  is the same in all parts of the spectrum (noted in Figure 2). Thus, the percentage frequency of occurrence of groups having, for example, ten or more waves is the same in the spectrum tails as at the peak, but groups actually occur much less frequently in the tails.

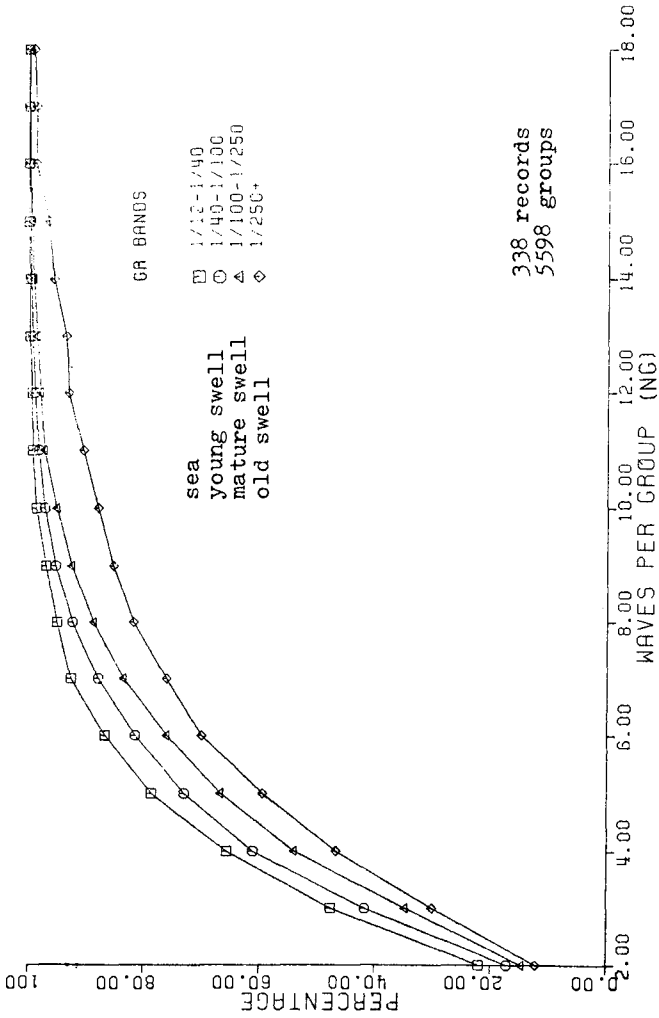
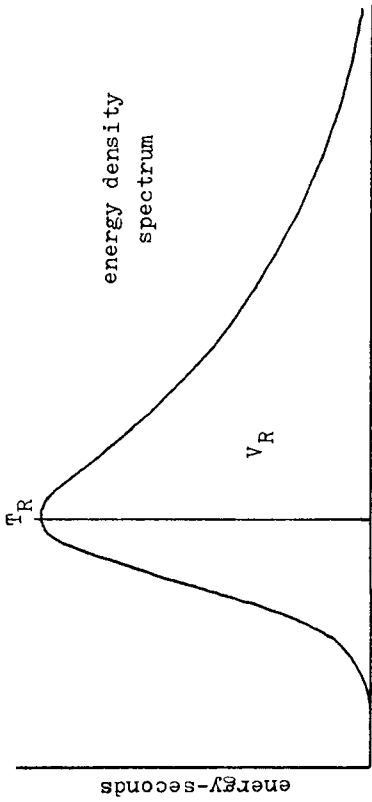


Figure 4: CUMULATIVE DISTRIBUTION OF  $N_G$  FOR  $G_R$  BANDS  
(from Nelson, 1980)



Low f tail	Spectrum peak	High f tail
few	max	few

$> T_R$   
 $\hat{=} V_R$   
 $\hat{=} V_R$  to  $>> V_R$   
 Same percentage distribution at all frequencies (Fig. 2).

Sea and Swell

As relative group energy ( $V_G/V_R$ ) increases:

$T_G \rightarrow T_R$   
 $N_G$  increases

Sea  
Distribution of groups:

Group period,  $T_G$ :

Group energy,  $V_G$ :

Waves per group,  $N_G$ :

Swell

Distribution of groups:

Group period,  $T_G$ :

Group energy,  $V_G$ :

Waves per group,  $N_G$ :

Figure 5: WAVE GROUP MODELS FOR SEA AND SWELL SPECTRA for unimodal spectra in deep water

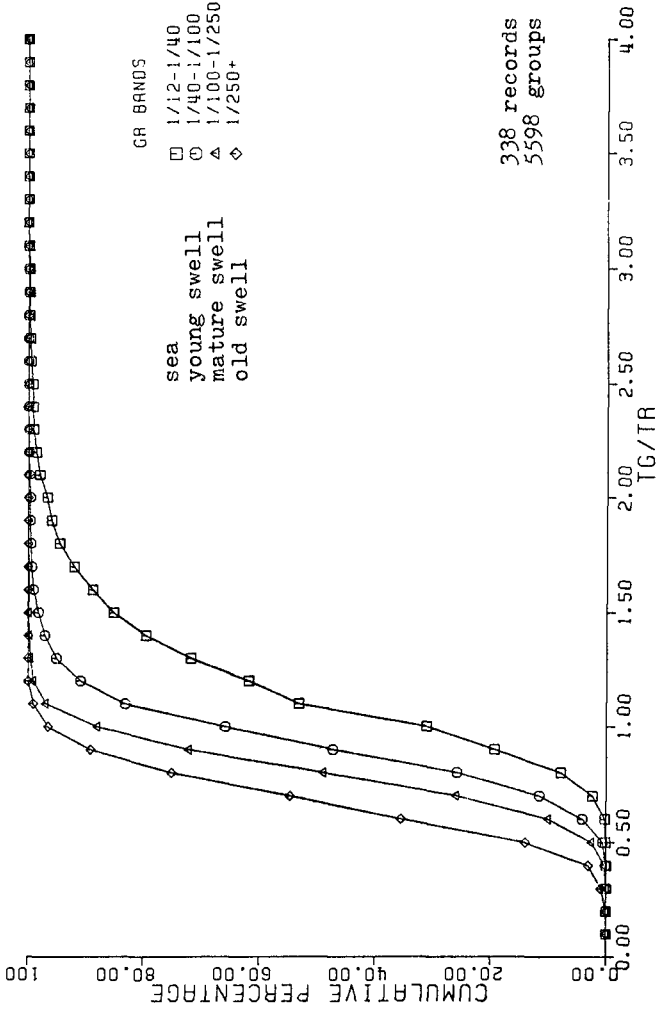


Figure 6: CUMULATIVE DISTRIBUTION OF  $T_G/T_R$  FOR  $G_R$  BANDS  
(from Nelson, 1980)



Directing attention to the statement to the left of the diagram in Figure 5, it may be noted further that in wave groups containing increasing amounts of energy relative to the wave record, the group period tends to approach the spectral peak period and the number of waves in the group tends to increase.

#### Swell Model

A general wave group model for swell in deep water is also presented in Figure 5. Swell is similar to sea in that the highest energy groups are most closely concentrated about the spectral peak and, indeed, control the position of the peak. However, swell contains many lower energy groups that differentially trail well into the high frequency tail of the spectrum. As a result, the most frequently occurring group period in a large population shifts away from the spectral peak toward shorter periods increasingly with increasing swell age.

The latter situation is illustrated in the cumulative distributions in Figure 6. The three swell curves represent normal distributions with similar standard deviations, but are displaced successively toward lower values of  $T_G/T_R$  with increasing swell age. For old swell, the median of the distribution is located at  $T_G/T_R \doteq 0.7$ . This means that in old swell having a spectral peak period of 14 seconds the most frequently expected group period should be about 10 seconds, although these are not the groups having the highest energy.

Swell groups are commonly observed to contain short waves due to apparent phase changes and other effects, and these bias the group period. Accordingly, when wave groups are filtered to remove anomalously short waves, most group periods increase substantially with the result that the median  $T_G/T_R$  value in any large population is shifted back toward unity for all swell types. A similar effect can be achieved by raising the record variance level that the running short-term variance must exceed in the definition of the wave group. This redefinition would have the additional effect of reducing the number of groups occurring in a given recording period and the number of waves per group.

Referring once again to Figure 5, the frequency of occurrence of the number of waves per group in swell is similar to that in sea in that the percentage distribution of  $N_G$  appears to be the same in all parts of the spectrum, and also in that  $N_G$  tends to increase as relative energy in groups increases. However, as the swell age increases the number of waves per group increases for any given percentage frequency of occurrence.

Further illustration, from a different perspective, of the relationship of swell groups to the wave spectrum is

given in Figure 7 for a mature swell record. For each wave in the record the square of the height is plotted against the reciprocal of its wave period. Since wave energy is proportional to  $H^2$ , the graph is effectively a plot of energy versus frequency for every wave. Waves belonging to wave groups are coded according to the relative energy of the group; all waves occurring in the intervals between wave groups are designated "interval" waves and are separately identified. The curve shown in the figure is the wave spectrum (the energy scales of the  $H^2$  values and the spectrum differ).

The manner in which the individual waves contribute to the wave spectrum is readily apparent in the figure. All waves having high and moderate energy lie close about the spectral peak frequency, and all are members of wave groups. There is also a number of low energy wave group members and these are clustered in the frequencies of highest energy density, although a few lie well into the high frequency tail. The interval waves, all of low energy, are most densely concentrated in frequencies above the spectral peak frequency, but extend well out along the high frequency tail in decreasing number and with diminishing range of energy. The occurrence of individual waves on the low frequency end is cut off sharply in this record.

The close association of individual waves with the wave spectrum shown can also be readily demonstrated by cumulating the  $H^2$  values with frequency and constructing a histogram from this cumulative distribution having the same frequency interval as the wave spectrum. This  $H^2$  histogram, if plotted in Figure 7, would resemble the wave spectrum closely (not shown due to clutter).

#### CONCLUSION

We hope that the wave group models for sea and swell presented herein will give practicing coastal engineers a better feel for wave spectra and the nature of the waves composing them, and that these models might also bring to the attention of theoreticians some areas that can benefit from application of their talents.

We recognize that the models are preliminary and believe that a great deal more is yet to be learned about wave groups from purely statistical analysis. Further work that profitably can be pursued includes: (1) Additional investigation of the relationships between swell groups and the wave spectrum in deep water, (2) examination of group-to-group relationships in deep water and how they are related to sea and swell, and (3) inquiry into all of the above relationships in shallow water.

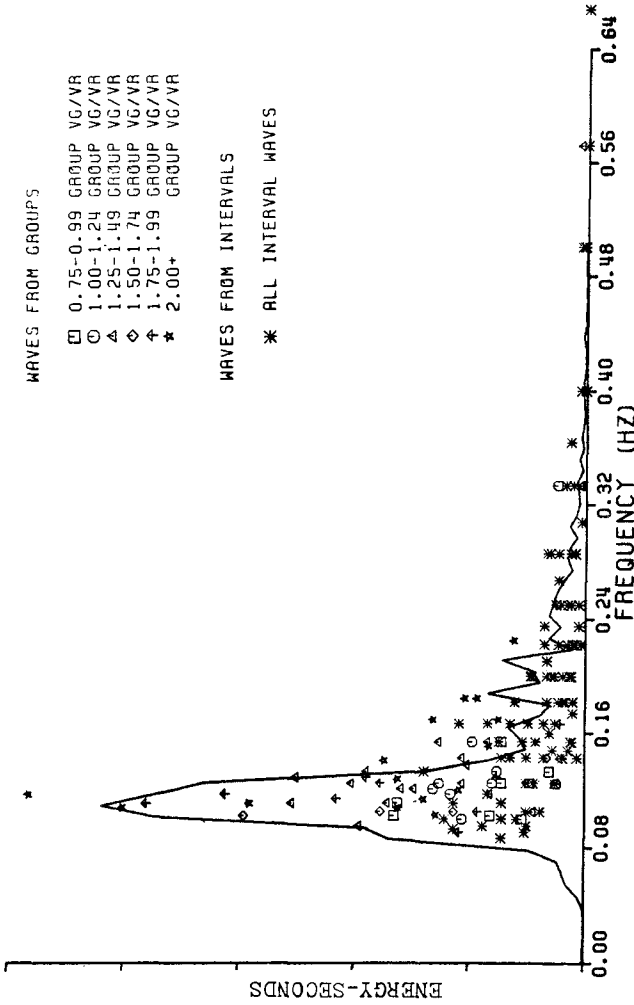


Figure 7: WAVE SPECTRUM WITH PLOT OF  $H^2$  VS.  $f$  FOR INDIVIDUAL WAVES  
(modified from Nelson, 1980)

We gratefully acknowledge receipt from M.S. Longuet-Higgins, following the presentation of our paper at this conference, of a copy of his theoretical paper titled "Statistical properties of wave groups in a random sea state" scheduled for publication in the Philosophical Transactions of the Royal Society of London.

## REFERENCES

- Bretschneider, C.L., 1958. Revisions in wave forecasting: Deep and shallow water, Proc. 6th Int. Conf. on Coastal Eng., pp. 30-67.
- Nelson, A.R., 1980. Statistical properties of ocean wave groups. Naval Postgraduate School, M.S. thesis, 133 pp.
- Sedivy, D.G., 1978. Ocean wave group analysis. Naval Postgraduate School, M.S. thesis, 90 pp.
- Smith, R.C., 1974. Ocean swell wave groups from wave record analysis. Naval Postgraduate School, 77 pp.
- Thompson, W.C., 1972. Period by the wave-group method. Proc. 13th Int. Conf. on Coastal Eng., pp. 197-214.
- Thompson, W.C., and F.M. Reynolds, 1976. Ocean wave statistics from FNWC spectral analysis. Proc. 15th Int. Conf. on Coastal Eng., pp. 238-257.

## CHAPTER FORTY SIX

### SWASH ON A NATURAL BEACH

Masaru Mizuguchi \*

#### Abstract

A field measurement was conducted in order to clarify the swash motion on a natural beach. It is found on this particular beach, which had a rather steep foreshore slope, that cross spectra calculated between the surface elevations, onshore velocities and the swash agree very well with those given by linear long two-dimensional standing wave theory in the lower frequency region than a certain value. This finding together with the observed  $f^{-4}$  ( $f$ ; frequency) high frequency saturation in swash spectra encourages a partial reflection model to describe the fluid motion in the inner surf zone, including the swash. The model developed shows a good agreement with the observed results, in which being employed an analogy to regular waves for the criticality of wave reflection. This model makes it possible to predict the swash spectrum for a given incident wave spectra and a given beach profile, as far as wave breaking takes place on a foreshore slope.

#### 1 INTRODUCTION

The boundary zone between the land and the sea provides interesting wave phenomena known as wave run-up. It is this zone where the incident waves show the swash motion which includes both the up-rush and the down-rush. Wave set-up due to wave breaking outside the swash zone contributes only to the mean water level change and the position of the mean swash motion, namely the shoreline.

The understanding of the wave dynamics in the swash zone on a natural beach is important in order to give a reasonable boundary condition at the shoreline when one tries to simulate the two- or three-dimensional beach transformation due to waves. Conventional assumption that the wave height is linearly proportional to the water depth gives zero wave height at the shoreline, resulting neither wave motion nor sand movement. This is clearly not what we observe in the field or in the laboratory, although one can imagine an extreme case where the wave energy would be completely dissipated before it arrives the swash zone on a very gentle beach.

On the other hand recent field observations reveal that the long period fluctuation may prevail among the fluid motion in the surf zone, especially near the shoreline (Guza & Thornton, 1982; Mizuguchi, 1982b). The long period motion is supposed to be a standing wave in the on-offshore direction, no matter if it is a two-dimensional one or a three-dimensional one like an edge wave. The long period standing wave form an antinode at the shoreline, exhibiting swash oscillations. There has been some discussions whether the observed long period fluctuations are

---

\* Associate Professor, Dept. of Civil Eng., Chuo Univ., Bunkyo-ku, Tokyo JAPAN 112

two- or three-dimensional. It is critically higher mode or cut-off mode edge waves that were employed to fit the data by Huntley (1976) and Sasaki & Horikawa (1978). It is shown, e.g. by Hotta et al. (1980), that the higher mode edge waves do not quantitatively differ from the two-dimensional standing waves as far as the fluid motion in the near-shore zone is dealt with. Therefore in this paper only two-dimensional motion is assumed as is done by Suhayda (1974).

This study comes from the first motivation mixed with the second findings. That is to test a hypothesis based on the linear long standing wave theory against a field experiment.

## 2. SWASH OF REGULAR WAVES

The wave run-up on a somewhat artificial beach has been studied for a long time and of their main concern has been the highest point of the up-rush. For example see Hunt (1959). The long history of the studies on its dynamics can be looked at from the following two viewpoints. There are a group of papers in which they looked at the swash motion as the highly nonlinear process and treated it as a bore on a dry bed. For example Shen & Meyer (1963). This approach indicates that the wave front shows a parabolic motion on a frictionless plane beach and that the total excursion width  $Y$  is given by the following relation for regular waves (Van Dorn, 1976).

$$Y = 1/18gT^2 \tan^2 \beta \quad (1)$$

where  $g$  is the gravitational acceleration,  $T$  is the wave period and  $\tan \beta$  is the bottom slope.

Another long history can be traced back to Lamb (1932). The swash motion is considered to be a standing wave on a sloping beach. The linear long wave theory gives the following well-known results for the water surface elevation  $\eta$  and the offshoreward velocity  $u$  for the perfectly reflected waves on a plane beach.

$$\eta = 2a_r J_0(z) \cos \sigma t \quad (2)$$

$$u = 2a_r \sqrt{a/h} J_1(z) \sin \sigma t \quad (3)$$

where  $z = \sqrt{\alpha x}$ ,  $\alpha = 4\sigma^2/g \tan \beta$  and  $2a_r$  is the amplitude of a standing wave at the shoreline. The  $x$  axis is taken offshoreward along the still water surface from the shoreline. The finite amplitude theory by Carrier & Greenspan (1956) shows that the amplitude of the swash motion does not differ from that given by the linear theory Eq.(2).

The standing wave solution, however, is no longer valid when the so-called swash parameter  $\epsilon_r$  which is defined as

$$\epsilon_r = 2a_r \sigma^2 / g \tan^2 \beta \quad (4)$$

exceeds a certain critical value  $\epsilon_{rc}$ . Miche (1951) argued that the surface slope at the shoreline should not be smaller than the beach slope and gave  $\epsilon_{rc} = 2$ . The finite amplitude wave theory gives  $\epsilon_{rc} = 1$  as

a necessary condition for the theory to yield a solution (Meyer & Taylor, 1972). The critical value  $r_c=1$  also corresponds to a condition that maximum downward acceleration of the swash is equal to the gravitational acceleration along the beach slope. Miche also proposed a hypothesis that the reflection coefficient for the incident waves on a plane beach may be given as follows.

$$r_0 = 2 / \epsilon_0 \quad \text{Eq. 11 of Guza} \quad (5)$$

$$\text{where } \epsilon_0 = \sqrt{2\pi} a_0 \sigma^2 / (g \tan^5 / 2 \beta) \quad \text{Guza Eq. of 1977} \quad (6)$$

and  $r_0$  is the reflection coefficient in deep water. The parameter  $\epsilon_0$  is equivalent to the swash parameter  $\epsilon_s$  and is calculated under the condition of perfect reflection, using the relation,

$$a_r = a_0 \sqrt{\pi / 2 \tan \beta} \quad \text{from setting } \epsilon_r = \epsilon_0 \quad (7)$$

Equation (5) simply states that the possible swash oscillation is always limited by his critical condition.

Guza & Bowen (1976) carried out detailed laboratory experiments in order to investigate the behaviour of the standing waves. They found (1) that the incident waves are perfectly reflected and the observed spatial distribution of the wave height agrees well with Eq.(3) when  $\epsilon_0 < 1$ , and (2) that Miche's hypothesis on the reflection coefficient given by Eq.(5) shows a reasonably good agreement with their experimental results when  $\epsilon_0 > 1.6$ , being taken into account the effect of bottom roughness. Their study confirmed that the swash oscillation can be considered at least on a rather steep beach as the antinode motion of two-dimensional standing waves, which survived wave breaking.

Comparing these two different approach to the regular wave swash, one may notice that Eq.(1) is quantitatively almost identical to Eq.(5). Substituting  $Y=2a_r$  into Eq.(1) gives  $\epsilon_r=2.5$ . Figure 1 compares the experimental data<sub>r</sub> by VanDorn (1976) with those two semi-theoretical results. It is clearly seen that the data agrees with Eq.(5) when the parameter  $L_0 \tan^2 \beta$  is large, in other words, high reflection coefficient.

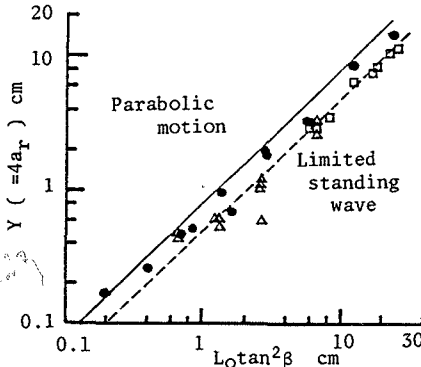


Fig. 1 Total excursion of swash (VanDorn, 1976).

Handwritten notes on the left side of the page:

- $2a_r = 2 \cdot 60 = 120$
- $2a_r = 200 \cdot 2 = 400$
- $\epsilon_0 = 2.26 \cdot 10^6 \cdot 10^6 \cdot 10^6 / (9.8 \cdot 10^6 \cdot 10^6 \cdot 10^6) = 2.26$
- $\epsilon_r = 2.5$
- $L_0 \tan^2 \beta = 200$
- $L_0 \tan^2 \beta = 200$

icients can be expected. As the parameter decreases, Eq.(1) tends to show a better agreement, although the difference between the two lines is small as already pointed out. However it should be noted that, in a strict sense, the wave amplitude should affect the transition.

It is tempting from the above discussion to make a statement that the swash oscillation is, in any case, the antinodal motion at the shoreline of a standing wave, which survives its breaking on the slope. Practically, as pointed by Guza & Bowen (1976), Miche's criterion Eq.(5) provides the "surviving" ratio, as far as wave breaking occurs only on the foreshore slope. The following viewpoint can be added to support this tempting conclusion. It is not an unreasonable conjecture that the swash oscillation, which might be given through a complicated non-linear process on a gently sloping beach, plays a role to generate an outgoing wave by its periodic or unsteady forcing. The outgoing wave forms a standing wave, coupling with the incident wave. Hence the swash motion may well be treated as that of a standing wave at least as a first approximation. Therefore the following expression would be applicable to describe the wave motion near the shoreline not only for a steep (reflective) beach as confirmed by Guza & Bowen (1976) but also for a gentle (dissipative) beach, again as a first approximation.

$$\eta = a_i \{J_0(z) \cos \sigma t - Y_0(z) \sin \sigma t\} + 2a_r J_0(z) \cos \sigma t \quad (8)$$

$$u = \sqrt{a/h} [a_i \{J_1(z) \cos \sigma t + Y_1(z) \sin \sigma t\} + 2a_r J_1(z) \sin \sigma t] \quad (9)$$

where  $a_i$  is the amplitude of the progressive wave, which should change to be zero at the shoreline. The local reflection coefficient  $r = a_r / (a_i + a_r)$  varies with the on-offshore location as  $a_i$  does. The bottom profile in the field scarcely shows a plane beach. Then Eqs.(8) and (9) can be easily extended to the case of a complex beach profile by applying a multi-linear profile approximation.

### 3. A MODEL FOR IRREGULAR WAVE SWASH

For irregular waves, one, who put the stress on the high non-linearity of the process, may introduce a model based on the joint probability distribution of the wave heights and periods. For examples Battjes (1971) and Sawaragi & Iwata (1984). It is generally accepted that the swash motion on a gently sloping beach is described in such a model. However the long period fluctuation in the swash is significant as reported in many field experiments. The individual wave analysis clearly fails to be meaningful when the long period fluctuation exists, unless it is removed before the analysis is applied (Mizuguchi, 1982a).

Here a tentative model is proposed based on the previous discussion and illustrated schematically in Fig. 2. The model implies that the Fourier component of the irregular wave behaves independently even through the very nonlinear process like wave breaking, as far as the long period motion is concerned. It is trivial that this model has the shortcomings, as not only the real swash motion but also the waves near the shoreline show some nonlinearity. However it is worth trying to see how well the simple model based on a linear theory can describe a result obtained in a field experiment.



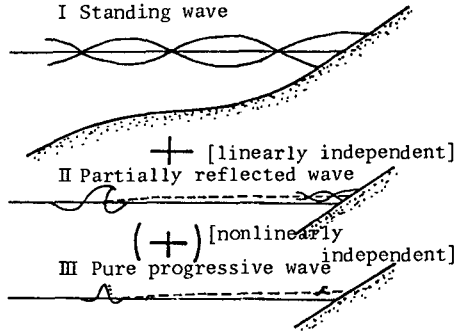


Fig. 2 A model for irregular wave swash

In relation to the critical condition for irregular wave reflection, there have been some field observations on the high frequency saturation of the swash spectra. Huntley et al. (1977) reported the form  $f^{-4}$  for the saturated high frequency range. Guza & Thornton (1982) found  $f^{-3}$  instead. When the concept of the critical condition could be applied for different frequency component independently, one can expect a kind of universal form for the saturated region, although it is not theoretically clear how the result for monochromatic waves is related to that on the irregular waves. The spectral shape of the high frequency region is also considerably affected by the profile of the main (peak frequency) component. The smoother the profile is, the smaller the power leaking to the high frequency region is. In addition, different techniques employed to measure the swash may produce different results (Guza & Thornton, 1984). Here we will not go further into this discussion.

#### 4. FIELD OBSERVATION

A field observation was carried out around noon on 9th Jan. 1982 at Yonezu-hama beach in Shizuoka Prefecture, Japan. The beach faces to the Pacific Ocean in south and has a straight extension of about 20 km. The beach cusp formation was observed on the previous day. However there remained only their ruins around the high water level on that day. The observation site was almost at the middle of the beach extension and the measuring section chosen on the line of the apex of a beach cusp ruin, so that the node of the edge waves had been expected if it had existed.

In Fig. 3 was shown the experimental setup with the bottom topography along the measuring section. Two artificial channels were placed, being extended into the water only to the position of the lowest run-down point, just covering the swash zone. The natural swash motion was measured between the two channels, by using the photographic technique. Small poles were placed standing on a line, every 50 cm, to give a scale. Several poles and two EMCM (Electro-Magnetic Current Meter) were also installed on the measuring section. The poles were photographed with 16mm camera, to obtain surface elevation records. Horizontal

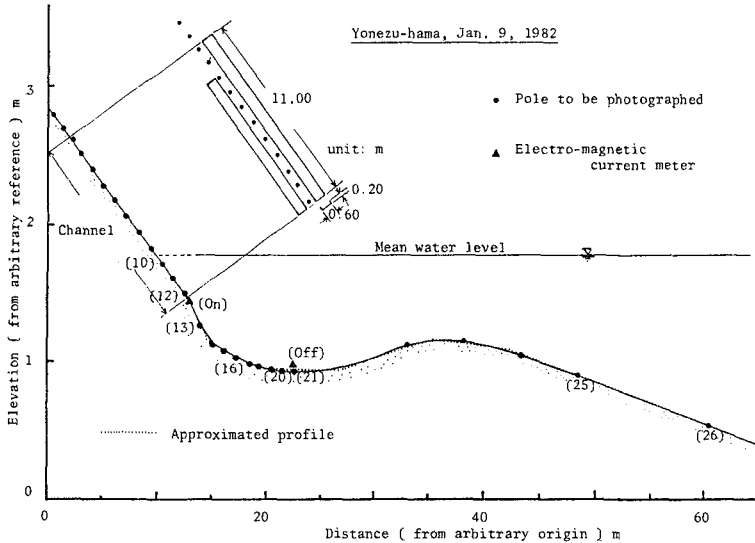


Fig.3 Beach profile and experimental setup. The poles with a number in brackets denote those analyzed. The approximated profile to be used for the later analysis is so close to the measured one that one cannot see the difference.

velocities were measured with EMCM. The EMCM(on) was situated just on the step. The bottom profile was a typical bar-trough one with a step at the foot of the swash zone. The slope of the swash zone was  $1/9$ . The beach material of that zone was well-sorted sand with  $\sqrt{d_{75}/d_{25}}=1.7$  and  $d_{50}=0.4$  mm. Visual observation showed (1) that the incident waves were long-crested swells with some white caps due to the strong westerly wind, (2) that the average breaking point was on the offshoreward slope of the bar between the poles (25) and (26), and (3) that the broken wave reformed almost completely in the trough region and made surging type breaker on the foreshore slope. The measurement was done for the duration of 10min 22s with the sampling interval of 0.2s, yielding 3110 total data points.

Examples of the obtained raw data are shown in Fig. 4. This figure shows the following features; (1) Short period waves disappear almost suddenly in the swash record, although they are still seen in the surface elevation at the pole (10), which was in the swash zone. (2) Both at the two locations where the horizontal velocity was measured as well as the surface fluctuation, they are not correlated, in contrast to the in-phase relation for the progressive wave theory. (3) The downward motion of the swash, for instance that of about 60s from the beginning of the data, shows a very good correlation with the strong offshoreward velocity, and the upward motion does with onshore one. The latter two features indicate a fact that the long period fluctuations were significant, forming the swash oscillations as the antinode of standing waves.

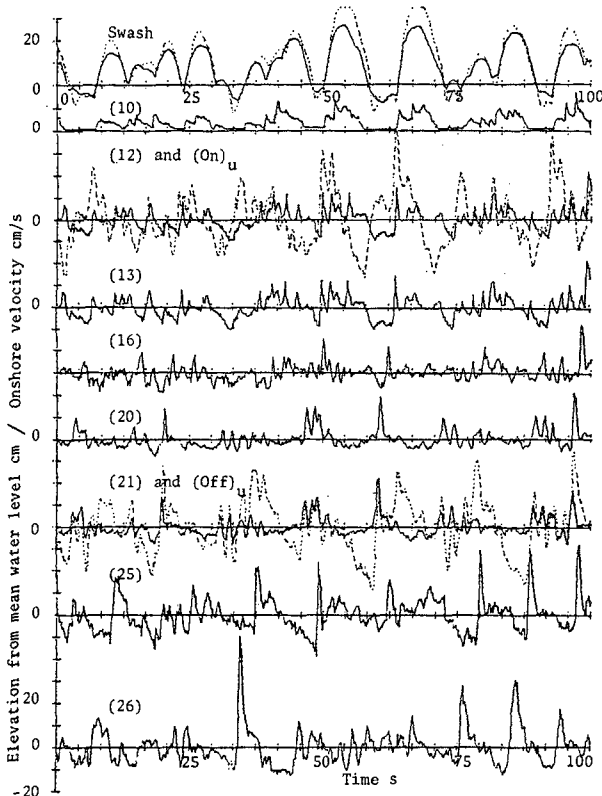


Fig. 4 Examples of raw data obtained. The dotted line on the top denotes the swash on a artificial channel. The broken lines denote onshore velocity.

## 5. ANALYSIS OF THE DATA

First, the individual wave analysis was applied to the surface elevation data, partly for the purpose to show how inappropriate to apply the method automatically. The results obtained in Table 1 show peculiar behaviors of the wave transformation in the surf zone. As reported by Mizuguchi (1982a) the individual waves propagate independently in its literal sense in a normal circumstance, showing almost no change of the wave period distribution. However this results shows a considerable change of the wave period in the surf zone, being affected by the standing waves of significant magnitude. The standing waves have a node and antinode structure, which results in the dominance of shorter period waves at the node and longer period waves at the antinode. Table 1 shows that the significant node lay at the pole (16) where minima of both wave period and height were observed. Figure 4 also shows only

Table 1 Wave statistics of the surface elevations

Location	Mean water level*	Water depth (cm)	$\eta_{rms}$ (cm)	$H_{1/3}^{**}$ (cm)	$T_{1/3}$ (s)	$H_{rms}$ (cm)	$\bar{T}$ (s)
Swash (Natural)	190.9	-	16.9	57.1	10.6	45.1	9.5
Swash (Channel)	194.7	-	22.7	77.0	10.9	60.9	9.5
No. 10	181.9	10.4	5.9	24.2	10.3	17.0	7.4
" 12	174.2	23.7	8.5	32.8	6.0	23.4	4.0
" 13	174.8	47.9	5.2	32.4	4.9	22.3	3.5
" 16	173.9	60.6	7.3	28.5	4.4	19.9	3.0
" 20	176.3	82.0	7.6	30.5	5.5	21.0	3.5
" 21	-	(83.5)	7.8	31.8	6.0	21.9	3.6
" 25	176.3	85.5	13.4	59.5	6.9	40.0	4.3
" 26	176.3	123.0	13.2	50.7	6.4	35.5	3.9

\* Reference is made to an arbitrary level as is in Fig. 3.

\*\* Zero-down crossing method is applied with a band width of 1 cm for the mean water level (Mizuguchi, 1982a).

short period fluctuation at this position. This result shows that it is essential to separate the long period fluctuations which are of standing waves, in order to discuss the transformation of the progressive waves in the surf zone. Table 1 also shows that the significant breaking wave height and period were about 60cm and 7s respectively.

Secondly the obtained surface elevations were studied in the frequency domains. Figure 5 shows the two-sided power spectra of  $S(f)$  at the representative locations as well as that of the swash on the natural beach. There are following two points to be noted.

1) There are seen three distinct regions of the high frequency saturation. One is the  $f^{-3}$  law for the high frequency region of the incident wave spectra around the breaker line. This is consistent with the result reported by Thornton (1977), however the physical argument is, Second and third ones, which are more interesting here, are the  $f^{-1}$  observed in the intermediate frequency range from 0.2Hz to 0.5Hz in the surf zone, and the  $f^{-4}$  for the entire high frequency region of the swash. The simplest argument to give the  $f^{-1}$  law is to assume that the power spectra is determined by the depth-controlled wave breaking where the wave height is almost proportional to the water depth  $d$  as done by Sawaragi & Iwata (1980). This assumption yields the relation  $S_{\eta}(f) \approx d^2 f^{-1}$ , based on a dimensional analysis. This relation may hold only for the lower frequency than the limit of the long wave assumption. However in this observation the  $f^{-1}$  law is seen to the higher frequency range than this limit. Third one, high frequency saturation of the swash, has been recently investigated as already mentioned. It is useless to repeat the argument, unless one can add the more convincing model to describe the swash motion on a natural beach. Here it is taken for granted that there is a saturation for the swash spectra and the form obeys the  $f^{-4}$  law as obtained.

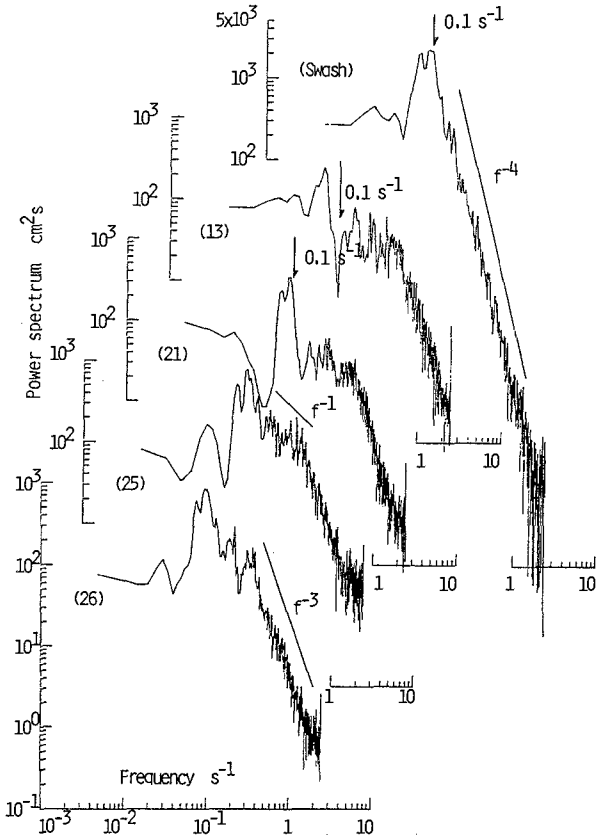


Fig. 5 Two-sided spectra of surface elevations at various points as well as of swash on natural beach.

2) The peak frequency of the swash is 0.1Hz as shown by the arrow. However the power corresponding to the peak almost disappears making a deep trough for the spectrum measured at the pole (13), which is just off the step at the foot of the swash zone. This fact suggests that the powers around the peak frequency are of standing waves.

Now it will be shown how well the linear long standing wave theory can describe the observed fluid motion including the swash. In the following three figures the results denoted by the solid lines for the perfect reflection model were calculated by using Eqs.(1) and (2) for the approximated multi-linear profile shown in Fig. 3. The dotted lines are those obtained by a partial reflection model which will be explained in the next section. Figure 6 shows the cross spectra between the surface elevations at the two different locations, (13) and (16), both of which were in the wave reforming zone. The agreement between

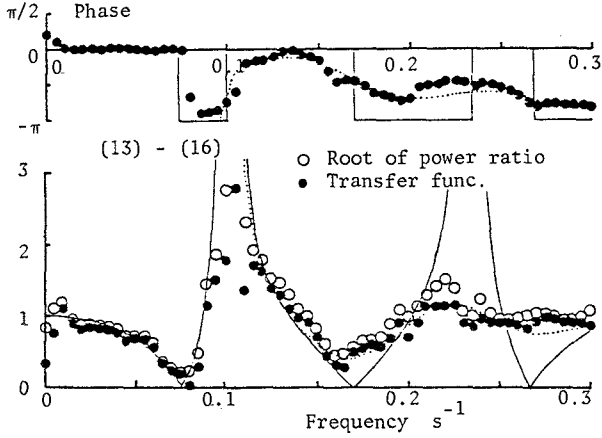


Fig. 6 Cross spectra between surface elevations at poles (13) and (16). The solid line denotes results for perfect reflection and the dotted lines those for a partial reflection model. Coherence is given by the ratio of transfer function to the root of power ratio.

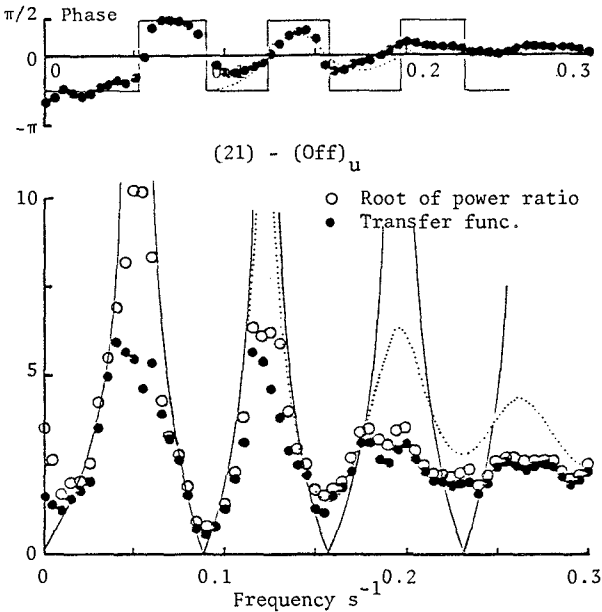


Fig. 7 Cross spectra between surface elevation and onshore velocity at pole (21).

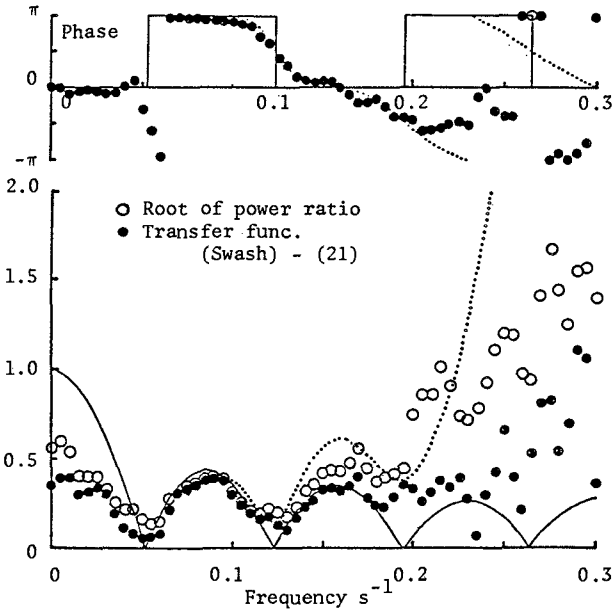
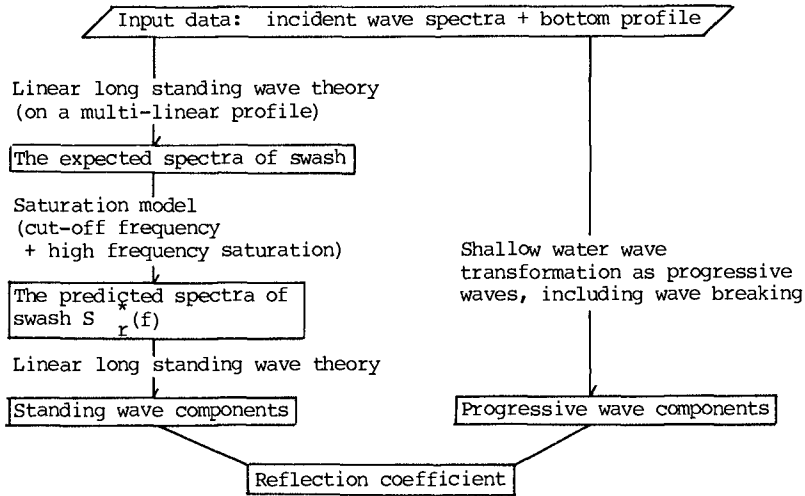


Fig. 8 Cross spectra between swash and surface elevation at pole (21).

the theory and the measurement is remarkably good for the lower frequency region than 0.1Hz, except very near the zero frequency. Figure 7 shows the cross spectra between the surface elevation and the onshore velocity at the point (21). In this figure one can obtain the same conclusion as in Fig. 6. The third figure, Fig. 8 shows the cross spectra between the swash and the surface elevation at the pole (21). The good agreement between the experiment and the perfect reflection model is only found around the peak frequency 0.1Hz, where the significant power of the spectra was observed. The following conclusions can be drawn from these three figures. (1) The long period fluid motion inside the surf zone is well described by the linear long standing wave theory. (2) The measured data in all of the figures shows large deviation from the theory in the higher frequency range beyond 0.1Hz. This corresponds to the inception of wave breaking. (3) In the low frequency range in Fig. 8, the swash motion tends to be about twice larger than that predicted by the theory, although the agreements are reasonably good in other two Figs. 6 and 7. This indicates that there might be taking place some nonlinear processes which work only in the swash zone to produce the longer period motion, transferring the energy from the shorter period one to the longer period one.

In concluding this section, it should be noted the magnitude of the power spectra of the alongshore velocity component was one-twentieth or less than that of the onshore component and can be maintained that there existed no significant edge waves.

Table 2 A model to predict the swash spectra as well as the reflection coefficient



6. PARTIAL REFLECTION MODEL AND THE SWASH SPECTRA

The observed swash motion as well as the fluid motion in the surf zone encourage the model discussed in the section 3. Table 2 illustrates the partial reflection model in terms of the flow of computation. The expected spectrum is defined as that which would be realized if all the incident wave powers were perfectly reflected. The concept of the saturation is introduced to calculate the predicted swash spectrum from the expected one. The assumption that the swash oscillations consist only of standing waves makes them equivalent evaluating the reflection coefficient at the specified location and determining the swash motion at the shoreline.

In order to obtain the predicted spectra, we exploit the following two results. First one is that there is a high frequency saturation. The  $f^{-4}$  law is employed here simply as it is the case observed. Second one is that the irregular wave trains may show a similar behavior as that of monochromatic waves in terms of the "surviving" process through the run-up. The method is not yet well established to relate properties of the irregular wave trains with those of the monochromatic waves. Here rms swash amplitude  $2a_r^*$  and mean frequency  $f^*$  are defined by the following relations after Longuet-Higgins (1969).

$$2a_r^* = \sqrt{2 \eta_r^2} = \int_0^\infty S_{\eta_r^*}(f) df \tag{10}$$

$$f^* = \left[ \int_0^\infty f^2 S_{\eta_r^*}(f) df / \int_0^\infty S_{\eta_r^*}(f) df \right]^{1/2} \tag{11}$$



These relations were applied to the measured swash spectra both on the natural beach and on the artificial channel. The representative swash parameter obtained by using these  $2a_T$  and  $f^*$  are respectively 1.18 and 1.50. These values are reasonably similar to those for the monochromatic waves so that the analogy between irregular waves and regular waves can be considered to work, as far as this experiment is concerned. However it could be wrong to take the zero frequency as the lower limit of the integral in Eqs.(10) and (11). The lower limit should be chosen such that the integral contains only the power of the spectral components affecting the phenomena considered. In this experiment the low frequency energy shown in Fig. 5 is not large and do not contribute to the integral. It is also true that the fact that the run duration of the experiment is the order of ten minutes automatically excludes the lower frequency energy contribution. The difference between the values on the natural beach and on the artificial channel is mainly due to the last moment up-rush which was only observed on the artificial channels as shown in Fig. 4. The reason should be attributed to the energy loss for the sand movement as well as peccolation on a natural beach.

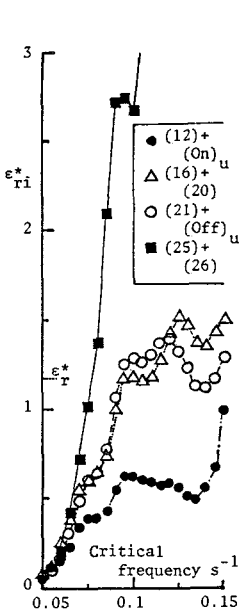


Fig. 9 Representative swash parameters versus critical frequencies

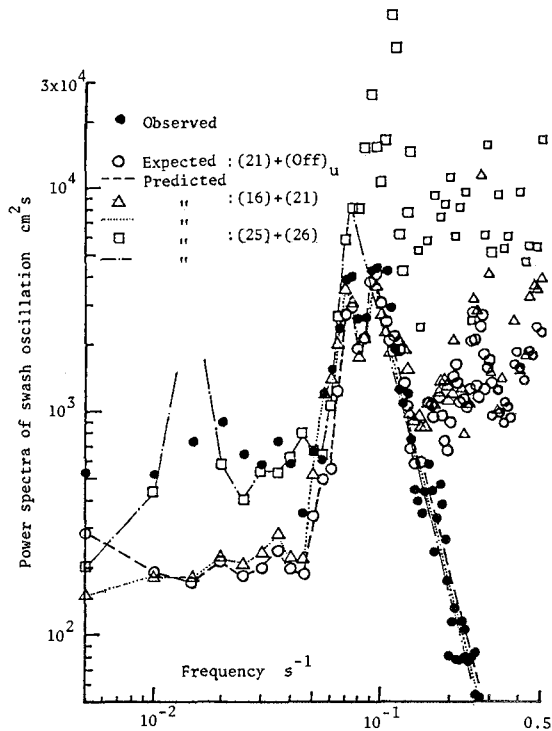


Fig. 10 Comparison of predicted swash spectra with observed one

Then the critical frequency  $f_c$  for the predicted spectra which is defined as the highest frequency for perfect reflection or as the lowest frequency of the saturation range is calculated so that the representative swash parameter is equal to the observed value 1.18. Figure 9 shows the changes of estimated swash parameters  $\epsilon_{ri}$  versus different critical frequencies. Here four pairs of the data were used. It is necessary to use a pair of data to estimate the expected swash spectrum, as standing waves give nodes for particular combinations of a offshore location and a frequency. A practical method to have an average of the two quantities is needed, in order to avoid infinite transfer function that the nodes give. In Fig. 9 it is seen that the two results calculated by the pairs of the data in the trough region are almost identical, showing that there is no significant wave transformation in that zone. The critical frequency  $f_c$  for these data is determined 0.095Hz. The result based on the data at the pole (12) show smaller values and do not reach the measured swash parameter, indicating that the pole was actually located within the swash zone and some part of the energy was already dissipated before reaching the pole (12). The results from the offshoreward data, on the contrary, show larger value for the given critical frequency compared with the other results. The application of this model yields that the critical frequency  $f_c$  should be 0.075Hz.

Figure 10 shows the comparison of the three predicted swash spectra thus-obtained with the observed swash spectrum. The predicted results (denoted by the dotted line or the broken line) based on the data obtained in the trough zone agrees very well with the observed one, except in the frequency domain lower than 0.05Hz. The reason of this difference is already mentioned in the discussion for Fig. 8. The poorer agreement of the chain line may mean that the model shown in Table 2 should be applied only for the data obtained in the location between which and the shoreline there is no wave breaking except that on the foreshore slope.

As shown in Table 2, reflection coefficient at any location can be estimated either if the transformation of progressive wave components could be estimated or when wave spectrum is measured. In Fig. 11 are shown the reflection coefficients calculated by using the observed swash spectra together with the observed local spectra. The results based on the data in the trough region (denoted by open circles or open triangles) are supposed to show the reflection coefficients at the slope of swash zone. The higher reflection coefficients than unity in the low frequency region again correspond to the larger swash oscillation compared with the theory as shown in Fig. 8. The most reliable frequency region around 0.1Hz shows perfect reflection for the lower frequency than the critical frequency 0.095Hz and the decrease of the reflection coefficient following  $f^{-2}$  law in the higher frequency region. The  $f^{-2}$  law can be understood as follows. As discussed in the previous section the high frequency saturation due to the depth-controlled wave breaking results in the  $f^{-1}$  law. Then the expected swash spectra would be constant in that frequency region, as the linear long standing waves show the following behavior as  $\alpha x$  is large,

$$\eta = 2a_r J_0(\sqrt{\alpha x}) \sim f^{-1/2} \quad (12)$$

Taking this into consideration, the  $f^{-4}$  saturation law of the swash

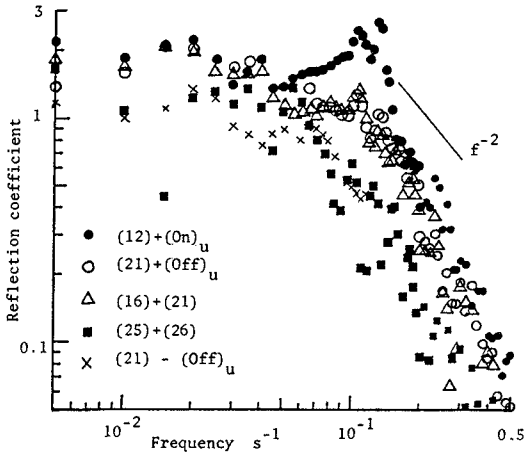


Fig.11 Reflection coefficients observed

spectra simply indicate the  $f^{-2}$  dependence of the reflection coefficient at the slope. The reflection coefficients for the combination of the poles (25) and (26) cannot be free from the effect of wave breaking on the shoreward slope of the bar and are considerably smaller than those for the swash slope only. In Fig. 11 is also plotted the reflection coefficient calculated from the phase lag between the water surface elevation and the onshore velocity at the pole (21). The result shows a quantitative agreement with others. The surveying of the position of EMC was not so accurate that one should expect some errors for the reflection coefficients especially for high frequency region.

Returning back to Figs. 6-8, one can see the agreement improved between the results of this partial reflection model and the observed results. Especially in Fig. 7, where it is assumed that the progressive components of the incident wave do not change during the travel over the distance, the agreement is excellent. The partial reflection model gives slightly higher values than the observed ones in the high frequency region in Fig. 9. This is not significant and not worth of further consideration at present. However in Fig. 8 the observed velocity is considerably smaller in the higher frequency region than that calculated by the linear long wave theory. This corresponds to the fact reported by Guza & Thornton (1980) and Mizuguchi et al. (1980), that the linear (long) wave theory gives larger values of transfer function for the progressive waves from the water surface elevation to the onshore velocity in the nearshore zone. Nonlinearity can partly explain the difference, as the air entrained may account for the rest.

Finally Fig. 12 shows the result of the comparison of the proposed model to the data around the breaker line. The agreement is still good particularly around the peak frequency region. In this sense, it should be pointed out that the measured swash oscillation makes it possible to rather easily evaluate the standing wave components by applying the two-

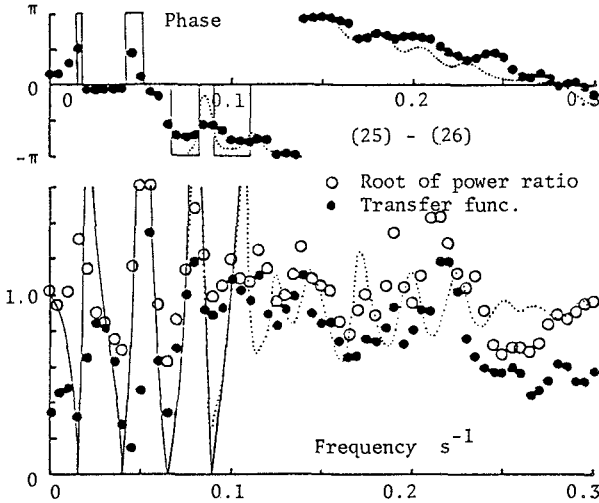


Fig. 12 Cross spectra between surface elevations around breaker line.

dimensional liner long standing wave theory for the multi-linearly approximated bottom topography.

## 7 CONCLUSION

A model to describe the swash motion on a natural beach is developed based on three hypotheses. First one is that the swash oscillations are considered to be antinode motion of the linear long standing waves. Second one is that the swash spectra exhibit the high frequency saturation for which the observed  $f^{-4}$  law is assumed. Third one is that a concept of the saturation developed for the regular waves swash is also applicable to the irregular wave trains, as an appropriate method to make them related being employed. A field observation was conducted on a natural beach with a rather steep foreshore slope. The results, in a general sense, confirm the applicability of the model. With regard to the three hypotheses, first one is strongly supported by the observation. The validity of the concept of the saturation for the irregular waves is not so clear and needs further study, although the model works very well for this experiment. The minor discrepancy found in the very low frequency region suggests that there might be the cases where one should take into account nonlinearity to achieve a better agreements. It is plausible that the gentle slope of the swash zone provides such cases. Another limitation of this model is that the effect of wave breaking can not be included, which takes place in other area than the swash zone.

## REFERENCES

- Battjes, J.A. (1971), Run-up distributions of waves breaking on slopes, Proc. ASCE, Vol. 97, WW1, pp. 91-113.
- Carrier, E.F. and H.P. Greenspan (1958), Water waves of finite amplitude on a sloping beach, Jour. Fluid Mech., Vol.4, pp. 97-109.
- Guza, R.T. and A.J. Bowen (1976), Resonant interaction for waves breaking on a beach, Proc. 15th Coastal Eng. Conf., pp. 560-579.
- Guza, R.T. and E.B. Thornton (1980), Local and shoaled comparison of sea surface elevations, pressures, and velocities, Jour. Geophys. Res., Vol. 85, pp. 1524-1530.
- Guza, R.T. and E.B. Thornton (1982), Swash oscillations on a natural beach, Jour. Geophys. Res., Vol. 87, C1, pp. 483-491.
- Guza, R.T. and E.B. Thornton (1984), Measuring run-up on a natural beach, Coastal Eng., Vol. 8, pp. 129-140.
- Hunt, I.A. (1959), Design of seawalls and breakwater, Proc. ASCE, Vol. 94, WW1, pp. 72-92.
- Huntley, D.A. (1976), Long-period waves on a natural beach, Jour. Geophys. Res., Vol.81, pp. 6441-6449.
- Huntley, D.A., R.T. Guza and A.J. Bowen (1977), A universal form for shoreline run-up spectra, Jour. Geophys. Res., Vol. 82, No. 18, pp. 2577-2581.
- Lamb, H. (1932), Hydrodynamics, 6th Ed., Cambridge Univ. Press, 186.
- Longuet-Higgins, M.S. (1969), On wave breaking and equilibrium spectrum of wind-generated waves, Proc. Roy. Soc. Lond. A-310, pp. 151-159.
- Meyer, R.E. and A.P. Taylor (1972), "Run-up on beaches" in WAVES ON BEACHES, Ed. by R.E. Meyer, Academic Press, New York, pp. 357-341.
- Miche, M. (1951), Le Pouvoir reflechissant des ouvrage maritimes exposes a l'action de la houle, Ann. Ponts. Chaussees, Vol. 121, pp. 285-319.
- Mitsuyasu, H. (1971), On the form of fetch-limited wave spectrum, Coastal Eng. in Japan, vol.14, pp. 1-7.
- Mizuguchi, M. (1982a), Individual wave analysis of irregular wave deformation in the nearshore zone, Proc. 18th Coastal Eng. Conf., pp. 485-504.
- Mizuguchi, M. (1982b), A field observation of wave kinematics in the surf zone, Coastal Eng. in Japan, Vol.25, pp. 91-107.
- Mizuguchi, M., M. Isobe, S. Hotta and K. Horikawa (1980), Field observation of the wave induced velocity in the surf zone, Coastal Eng. in Japan, Vol. 23, pp. 81-90.
- Sasaki, T.O. and K. Horikawa (1978), Observation of nearshore current and edge waves, Proc. 16th Coastal Eng. Conf. Vol. 1, pp. 791-809.
- Sawaragi, T. and K. Iwata (1980), Wave power spectrum slope on high frequency range in shallow water surf, Coastal Eng. in Japan, Vol. 23, pp. 91-99.
- Sawaragi, T. and K. Iwata (1984), A nonlinear model of irregular wave run-up height and period distributions on gentle slopes, 19th Coastal Eng. Abstract, pp. 210-211.
- Shen, M.C. and R.E. Meyer (1963), Climb of a bore on a beach, part 3 run-up, JFM, Vol.16, pp. 113-125.
- Suhayda, J.N. (1974), Standing waves on beaches, Jour. Geophys. Res. Vol. 79, pp.3065-3071.
- Thornton, E.B. (1977), Rederivation of the saturation range in the frequency spectrum of wind-generated gravity waves, J. Phys. Oceanogr., Vol.7, pp. 137-141.
- Van Dorn, W.G. (1976), Set up and run-up in shoaling breakers, Proc. 15th Coastal Eng. Conf., pp. 738-751.

## CHAPTER FORTY SEVEN

### WAVE GROUPS IN THE FREQUENCY AND TIME DOMAINS

Rodney J. Sobey<sup>1</sup>, M.ASCE and W. Wayne Read<sup>2</sup>

**ABSTRACT.** The identification of wave groups in wave records is sought in terms of the classical linear analysis techniques in the frequency and time domains. Unwrapping and detrending of the phase spectrum identifies apparent order where none is assumed in the Gaussian random wave model. Similarly unexpected order is observed in the tail of the correlogram of both the wave record and the Rice envelope function. These aspects are strongly suggestive of wave grouping.

#### INTRODUCTION

Sophisticated design and analysis in coastal and ocean engineering requires a detailed description of incident sea conditions. Wave groups, a finite run of higher than normal waves, are frequently observed at sea and in wave records. They have an important impact on a wide range of coastal and offshore activities and some measure of wave groupiness needs to be included among the standard analysis and synthesis techniques routinely adopted by data collection authorities and coastal and ocean design groups. Despite the growing literature, the true nature and extent of wave grouping remains unresolved. There is sufficient evidence that wave grouping exists but insufficient evidence to confirm the nature and extent of these groups. Neither theoretical investigations nor numerical simulations can resolve these issues. The information must be sought initially from field data. Considerable recent research effort has focussed on the development of new analysis techniques to accommodate wave grouping. In contrast, the present paper will concentrate on linear wave theory and classical time series analysis techniques in the frequency and time domains. There is evidence to suggest that wave grouping is reasonably well described by these classical linear techniques.

---

<sup>1</sup> Associate Professor, Department of Civil Engineering, University of California, Berkeley, CA 94720, U.S.A.

<sup>2</sup> Research Officer, Department of Civil and Systems Engineering, James Cook University, Townsville, Q. 4811, Australia.

### DATA SERIES FOR ANALYSIS

The basis of the present research is an extensive data base of deep water wave records assembled from sites off the eastern, western and southern coastlines of Australia. These are good quality records in computer compatible form. Data set A, obtained from the Maritime Services Board of New South Wales, comprises about fourteen hundred twenty-minute records off Newcastle and Botany Bay under generally winter storm conditions in the Tasman Sea. Data set B, obtained from Woodside Offshore Petroleum, comprises about three hundred twenty-minute records during six separate hurricanes on the North West Shelf. Data set C was obtained through Esso Australia for a site on the continental shelf of the Great Australian Bight. This region is exposed to Southern Ocean swell, recognized (Chelton, et al., 1981) as the most extreme wave climate in any of the world's oceans and the data set is an almost continuous record for several days of big, long-period swell. Together, these three data sets provide excellent samples of the common wave climate extremes.

Although the typical 20-minute wave record is the basic data series, considerable attention has recently been focussed on the data series of individual wave heights in the record, identified by the zero up-crossing method. Statistical parameters commonly extracted are  $R_H$ , the correlation coefficient between consecutive wave heights, and  $j_1$  and  $j_2$ , respectively the mean number of waves in a group and the mean number of waves between the start of one group and the start of the next group. Theoretical estimates consistent with the Gaussian random wave model have been developed by Goda (1970) for  $j_1$  and  $j_2$ , and Arhan and Ezraty (1978) for  $R_H$ . Field observations for  $j_1$  (Goda 1976, Su et al. 1982) and  $R_H$  (Arhan and Ezraty, Su et al.) are consistently above the theoretical values, although there is qualitative agreement in the trends. It is apparent that wave groups are rather longer and more coherent than predicted by the Gaussian random wave model. Battjes (1984) has, however, obtained adequate agreement between field records and a theory that is based on a finite lag one auto-correlation between consecutive wave heights.

As a sea state description, this data series of individual waves has considerable value, although the same cannot be said of its potential in the development of an appropriate sea state model. A predictive model is ultimately sought, in which the reversibility of analysis and synthesis is a required property. The data series of individual waves focusses attention on amplitude relationships and considers time relationships only in an averaged sense.

Much of the facility of the individual wave approach is implicit in the complex wave envelope  $A(t)$  introduced by Rice (1944, 1945). A carrier frequency,  $f_0$ , typically the

peak frequency  $f_p$ , is identified and removed from the record  $\eta(t)$ , such that

$$\eta(t) = \text{Real}[A(t) e^{i2\pi f_o t}] \quad (1)$$

In principle, the complex envelope function is the natural vehicle for wave group studies. No information is lost from the original record and attention is focussed on the envelope modulations. For typically narrow-banded sea states, the Rice envelope function  $|A(t)|$  is a good approximation to the wave envelope and the  $R_H$ ,  $j_1$  and  $j_2$  statistics are readily extracted.

#### FREQUENCY DOMAIN ANALYSIS OF DATA SERIES

The standard statistical summary in the frequency domain is the variance spectrum  $E(f)$  of the water surface time history  $\eta(t)$ . The common model of an irregular sea state, the Gaussian random wave model, was introduced by Rice (1944, 1945) as a model of random noise. The water surface time history is represented as the superposition of many linear waves of amplitude  $a_n = [2E(f_n)\Delta f]^{1/2}$  and random phase  $\phi(f_n)$ :

$$\eta(t) = \sum_n a_n \cos(2\pi f_n t + \phi_n) \quad (2)$$

The phase angle is randomly distributed over the range  $(-\pi, \pi)$ . This model has been the basis for analysis and design in coastal and ocean engineering for several decades.

There is a growing literature of detractors and defenders of the Gaussian random wave model. Rye (1983) and Goda (1983) argue that it is a sufficient description of wave grouping. Mollo-Christensen and Ramamonjiarisoa (1978), Hamilton et al. (1979) and Funke and Mansard (1980) propose supplementation to include wave grouping. Sobey and Colman (1982) have investigated a theoretical alternative, the nonlinear Schroedinger equation and the scattering transform. The field evidence is inconclusive, although the balance remains in favor of the Gaussian random wave model.

The intermediate step in the estimation of the variance spectrum is the complex Fourier transform  $F(\omega)$  of the wave record  $\eta(t)$ , defined as

$$F(\omega) = \int_{-\infty}^{\infty} \eta(t) e^{-i\omega t} dt \quad (3)$$

$F(\omega)$  is a complex function of the angular frequency  $\omega = 2\pi f$ , and may be represented as



$$F(\omega) = |F(\omega)| e^{i\Phi(\omega)} \quad (4)$$

where  $|F(\omega)|$  and  $\Phi(\omega)$  are respectively the amplitude and phase spectrums. The Gaussian random wave model assumes the phase spectrum to be completely random but Funke and Mansard (1981) have questioned whether it may indeed contain some useful information. Two problems are identified in interpretation of the phase spectrum, respectively phase unwrapping and phase trend removal, which may contribute to the apparently random character of computed phase spectra. These aspects will be considered separately.

### PHASE UNWRAPPING

Phase unwrapping refers to the modulo 2 operation on phase angles. The phase angle returned by the Fast Fourier Transform (FFT) algorithm is in the range  $-\pi$  to  $\pi$  and is termed the principal phase  $\Phi_p(\omega)$ . Any principal phase angle may in fact be  $\Phi_p(\omega) + 2n\pi$ , where  $n$  is any signed integer, without changing either the complex Fourier transform or the variance spectrum. The "true" phase is obtained by "unwrapping" the principal phase through addition or subtraction of multiples of  $2\pi$ ; this phase is called the unwrapped phase,  $\Phi_u(\omega)$ . The subscript  $u$  has been dropped but is implied in the subsequent discussion.

It remains to determine the signed integer  $n$ . The Schafer algorithm (Oppenheim and Schafer, 1975) assumes the unwrapped phase to be a continuous function of  $\omega$ , the only discontinuities being those introduced by the modulo  $2\pi$  operation in determining the principal phase. A discontinuity is defined to exist when the change in principal phase between adjacent values exceeds a given threshold. This process, however, is inconclusive and does not guarantee a unique result, as demonstrated by Tribolet (1977).

A unique result, however, does seem to be possible as the slope of phase spectrum is uniquely defined at all frequencies and uninfluenced by the modulo  $2\pi$  operation on the principal phase (Oppenheim and Schafer, 1975). Taking the natural logarithm of both sides of Eq. 4 and differentiating with respect to  $\omega$  gives

$$\frac{1}{F} \frac{dF}{d\omega} = \frac{d}{d\omega} (\ln|F|) + i \frac{d\Phi}{d\omega} \quad (5)$$

from which

$$\frac{d\Phi}{d\omega} = \text{Imag} \left( \frac{1}{F} \frac{dF}{d\omega} \right) \quad (6)$$

Similarly differentiating Eq. 3 with respect to  $\omega$  gives  $dF/d\omega$  as

$$\frac{dF}{d\omega} = -i \int_{-\infty}^{\infty} t \eta(t) e^{-i\omega t} dt \quad (7)$$

where the integral is recognized as the Fourier transform of  $t\eta(t)$ . The slope of the phase spectrum  $d\phi/d\omega$  is thus uniquely defined, at least in theory. Integration of Eq. 6 should yield the unwrapped phase spectrum but there are a number of problems in practice.

The first is a familiar one in discrete frequency domain analysis. The  $d\phi/d\omega$  estimates from the discrete Fourier transform of  $t\eta(t)$  are raw estimates and their erratic nature significantly complicates the numerical integration. Some theoretical assistance is available in that the principal phase prediction should be identical with that available from the Fourier transform of  $\eta(t)$ , but these discrete estimates are also raw estimates. Advantage can be taken of both estimates. The second problem is the specification of the phase and the phase gradient at zero or near zero magnitude points for the Fourier transform. This problem arises in the specification of the initial conditions for numerical integration of Eq. 6 and at any other frequency where  $|F(\omega)| \sim 0$  and  $1/|F(\omega)| \sim \infty$  in Eq. 6, a situation that is not uncommon given raw estimates of  $F(\omega)$ .

Tribolet (1977) considers the former problem in the context of the complex cepstrum, proposing an algorithm based on adaptive stepsize integration using the trapezoidal rule. If the difference between the unwrapped phase estimate and the principal phase estimate at each  $\omega$  is not sufficiently close to an integer multiple of  $2\pi$ , then the frequency interval  $\Delta\omega$  is continually halved until the specified accuracy is achieved. The discrete Fourier transform is used to estimate the Fourier transform by interpolation at intermediate points between those on the FFT raster. The initial phase was assumed to be zero, without discussion. The coding for this algorithm has been published and initial experiments utilized this code. Results were rather erratic for wave records and it was apparent that detailed consideration of the singular or near-singular points was essential.

These singular points can be accommodated by classical limit theory. L'Hospital's rule confirms that the principal phase and the phase derivative both exist and are given by

$$\phi_p(\omega) = \tan^{-1} \frac{F_I^{(k+1)}}{F_R^{(k+1)}} \quad (8)$$

$$\frac{d\phi}{d\omega} = \frac{1}{k+2} \frac{F_I^{(k+2)} F_R^{(k+1)} - F_I^{(k+1)} F_R^{(k+2)}}{F_R^{(k+1)} F_R^{(k+1)} + F_I^{(k+1)} F_I^{(k+1)}} \quad (9)$$

where  $|F^{(k)}(\omega)| = 0$ ,  $j = 0, 1, \dots, k$  and  $|F^{(k+1)}(\omega)| \neq 0$  and the bracketed superscripts represent differentiation with respect to  $\omega$ :

$$F_R^{(j)} + i F_I^{(j)} = \frac{d^j F(\omega)}{d\omega^j}$$

These higher derivatives can be calculated in a similar manner to Eq. 7, from the discrete Fourier transforms of  $t^j \eta(t)$  respectively. A further enhancement of the algorithm has been the adoption of Simpson's rule for numerical integration. Fourth order Runge-Kutta integration was initially utilized but Simpson's rule is numerically equivalent and has some coding advantages.

#### PHASE TREND REMOVAL

If the time origin of the record  $\eta(t)$  is shifted from  $t = 0$  to  $t = t_0$ , the Fourier transform of the origin-shifted record becomes  $F(\omega)e^{i\omega t_0}$ . The amplitude spectrum and hence the variance spectrum is not changed but the phase spectrum is changed by the addition of a linear trend  $\omega t_0$  to  $\phi(\omega) + \omega t_0$ . For an origin shift even as small as a few discrete record time steps  $\Delta t$ , this would impose a saw tooth variation on the principal phase, which potentially contributes to the random appearance of the principal phase spectrum. Although any linear trend is accommodated by phase unwrapping, the question of the "true" phase spectrum again arises. Interpretation of the phase spectrum will certainly be facilitated by the removal of any non-physical influences.

Funke and Mansard (1981) observe that a phase spectrum including a linear trend component will approach  $+\infty$  as  $\omega$  becomes very large and suggest that the correct choice of time origin (and this choice is arbitrary) will have zero slope,  $d\phi/d\omega \rightarrow 0$ , as  $\omega \rightarrow \infty$ . This is a compelling argument but there are difficulties in implementation. The phase spectrum is known only as far as the Nyquist frequency  $\omega_N = \pi/\Delta t$  and not to infinity. Also, energy levels beyond two to three times the peak frequency are very small for typical records and raw phase estimates are increasingly unreliable.

A reasonable compromise would be to take advantage of the phase estimates where they are expected to be most reliable, which is in the vicinity of the spectral peak. Accordingly the origin shift has been estimated from a least-squares curve fit of

$$\phi(\omega) = \phi(\omega = 0) + \omega t_0 \quad (10)$$

to the raw, unwrapped phase spectrum, weighted by the raw variance spectrum. This requires minimizing the sum

$$S(t_0) = \sum_i E(\omega_i) [\phi(\omega_i) - \phi(\omega = 0) - \omega_i t_0]^2 \quad (11)$$

where the  $\omega_i$  are the FFT raster points. The trend  $\omega t_0$  is then subtracted from the unwrapped phase spectrum. A number of variations on this approach and that suggested by Funke and Mansard (1981) were investigated but the Eq. 11 approach appeared to be the most consistent. This is recognized, however, as a subjective judgement.

Figures 1 and 2 are typical results from the phase unwrapping and detrending algorithms, showing the raw but unwrapped and detrended phase spectrum together with the raw variance spectrum. The results are presented non-dimensionally in terms of the peak frequency  $f_p$  and truncated at  $3f_p$  along the frequency axis. The oscillations in the tail of the phase spectrum are a computational effect in the phase unwrapping. A tolerance level must be set to define a near-singular point and to invoke the L'Hospital rule algorithm. These oscillations can be damped by appropriate choice of the tolerance level.

Similar results are consistently achieved, strongly indicating the existence of some coherent structure in the phase spectrum, against a background that has a distinctly random character.

#### TIME DOMAIN ANALYSIS OF WAVE RECORD

The standard statistical summary in the time domain is the correlogram  $R(\tau)$ , which forms a Fourier transform pair with the variance spectrum  $E(f)$ . In principle, both summaries describe the same information but from different perspectives. In practice, however, this equivalence becomes confused. The FFT algorithm yields the raw variance spectrum (Figures 1 and 2) which is then subjected to frequency domain smoothing, but the nature and extent of that smoothing is an especially subjective operation. Variations from a visually smooth result are commonly regarded as noise and given little attention; it remains possible that these variations from the smooth and expected result in fact describe wave grouping. This possibility is indeed sugges-

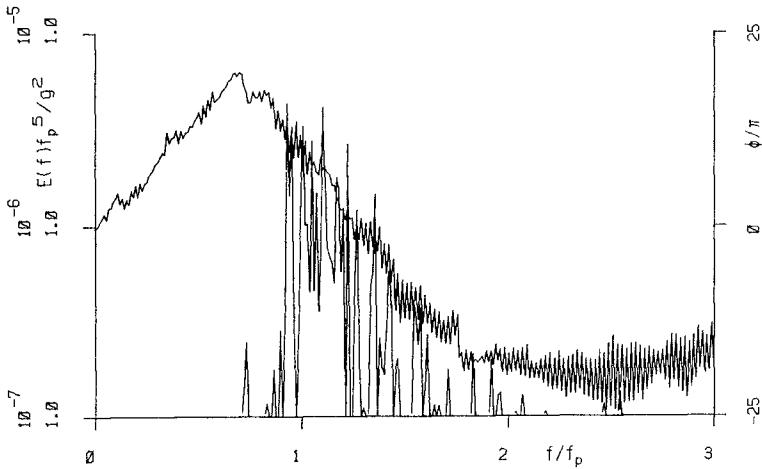


Fig. 1 Raw Variance and Unwrapped Phase Spectrum  
in Deep Water off Botany Bay, 5:20 hrs  
on 9 July 1981

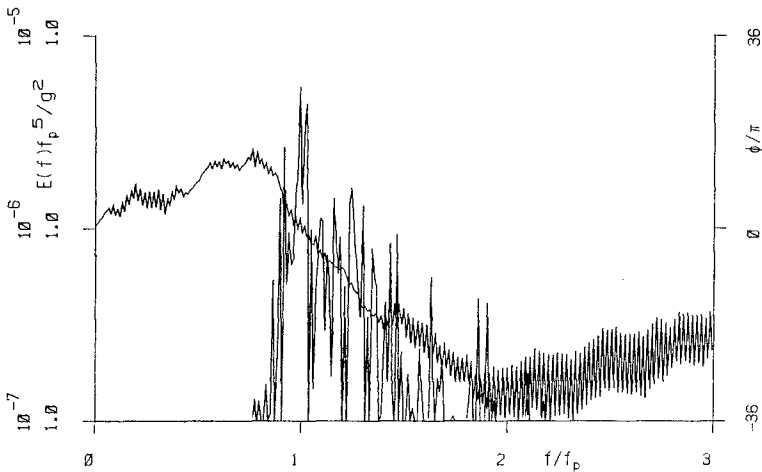


Fig. 2. Raw Variance and Unwrapped Phase Spectrum  
in Deep Water off Botany Bay, 7:20 hrs  
on 9 July 1981

ted by the correlograms in Figures 3 and 4, corresponding to the same records as Figures 1 and 2, where  $\tau$  is the time lag and  $\sigma^2$  the record variance. The time lag scale is non-dimensionalized by the peak frequency, as were the frequency domain results. If the phase spectrum is indeed random, the envelope of the correlogram should go asymptotically to zero in about five wave periods. This is not observed in Figures 3 and 4 (solid line), where the dominant feature is the ordered tail. The correlogram is inherently smoothed in a reasonably unbiased manner and the ordered tail is strongly suggestive of wave groups. These are typical results for moderate sea states and were not specially selected for presentation.

It remains possible that the oscillations in the correlogram tail are a computational effect. It is well known (Kendall and Stuart, 1966) that the correlogram for short series can be unreliable and may not damp out as rapidly as expected; as a rule of thumb, only the first twenty percent might be given any credence. Wave records are moderately long series, typically 2048 points over seventeen minutes. Figures 3 and 4 present the correlogram for non-dimensional lags  $f_p$  up to twenty. This corresponds to approximately twenty waves, about one-fifth of a typical wave record of one hundred waves. Further Kendall and Stuart give the 95% confidence limits of the correlogram for a random process as

$$CL = -1/N \pm 2/(N)^{1/2} \quad (12)$$

where  $N$  is the number of points in the record. For  $N = 2048$ , the 95% confidence limits are  $-0.00 \pm 0.04$ . The amplitude of the oscillations in the tail of Figures 3 and 4 is of order 0.15, well outside the 95% confidence limits for a random process. This conclusion is not influenced by the adoption of the "unbiased estimator" for the autocorrelation, which uses the factor  $1/(N-k)$  in place of  $1/N$  in the estimation of  $R(\tau = k\Delta t)$ . In this case both the correlogram tail and the confidence limits are scaled up by the factor  $N/(N-k)$ .

#### TIME DOMAIN ANALYSIS OF RICE ENVELOPE FUNCTION

In the initial discussion of data series for analysis it was observed that the complex envelope function  $A(t)$  defined by Eq. 1 appeared to be the natural vehicle for wave group analyses. A procedure for extracting the complex envelope function from the wave record is described by Sobey and Colman (1983). It involves the computation of the discrete Hilbert transform  $\hat{\eta}(t)$  from the wave record  $\eta(t)$  using the FFT and inverse FFT algorithms. Then follows the definition of the pre-envelope function

$$\eta(t) + i \hat{\eta}(t) = A(t)e^{i\omega_0 t} \quad (13)$$

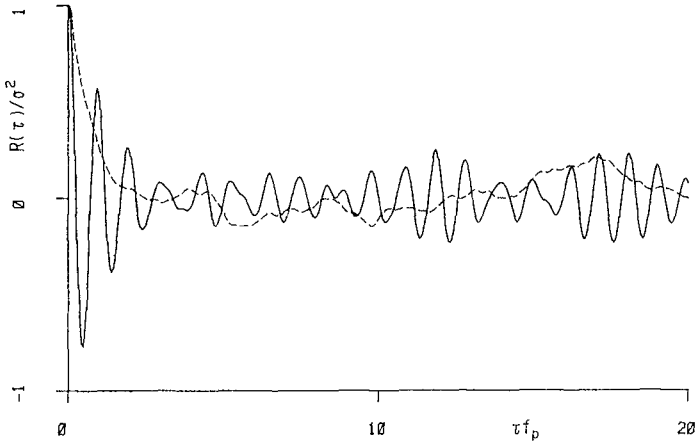


Fig. 3 Correlogram of Record and Rice Envelope Function in Deep Water off Botany Bay, 5:20 hrs on 9 July 1981

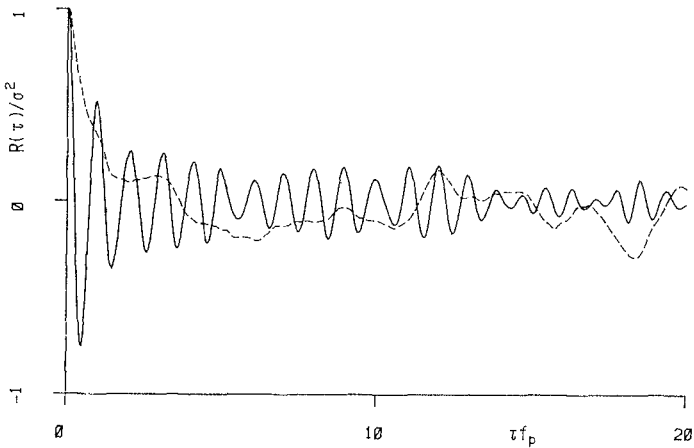


Fig. 4 Correlogram of Record and Rice Envelope Function in Deep Water off Botany Bay, 7:20 hrs on 9 July 1981

where  $\omega_0 = 2\pi f_0$  is the carrier frequency. The carrier frequency is identified as the peak frequency  $2\pi f_p$  and estimated as

$$f_p = \frac{\int f E^8(f) df}{\int E^8(f) df} \quad (14)$$

Multiplying both sides of Eq. 14 by  $\exp(-i\omega_0 t)$  recovers the complex envelope function  $A(t)$ . The Rice envelope is simply the modulus of  $A(t)$ .

Sample computations of the Rice envelope function and comparison with Rice envelope is simply the modulus of  $A(t)$ .

Sample computations of the Rice envelope function and comparison with the wave record confirm that it is indeed an excellent representation of the wave envelope. It is this property of the Rice envelope function that was used by Rice (1944, 1945) and later Longuet-Higgins (1952) to establish the Rayleigh distribution as an excellent approximation to the probability distribution for wave heights. In the context of wave grouping, the Rice envelope function very conveniently concentrates attention on the wave envelope and hence the wave groups. A similar identification of wave groups was the rationale for the definition of the SIWEH function by Funke and Mansard (1980).

The considerable attention recently given to the data series of individual wave heights might also be considered in the context of the Rice envelope function. Amplitude domain arguments led Rice and Longuet-Higgins to the Rayleigh distribution. Time domain or correlogram arguments appear to lead to  $R_H$  (the correlation coefficient between consecutive wave heights) and  $j_2$  (the average number of waves between the start of one wave group and the start of the next group). The correlogram of the Rice envelope function is shown as the dashed lines on Figures 3 and 4.

The initial exponential decay is closely related to typical statistics extracted from the data series of individual wave heights. In particular  $R_H$  might be defined as

$$R_H = R(\tau f_p = 1) / \sigma^2 \quad (15)$$

and  $j_2$  from the first zero crossing of the correlogram as

$$R(\tau f_p = 1/2 j_2) = 0 \quad (16)$$

Alternately the zero-crossing frequency rather than the peak frequency could be used in these definitions. The difference is typically small; the peak frequency has rather more dynamic significance while the zero-crossing frequency oc-



curs naturally in the theory of random noise. Note that  $R_H$  defined in terms of the zero crossing frequency is the parameter proposed by Battjes (1984) as the sole spectral shape parameter determining the group statistics.

The long period persistence in the tail of the Rice envelope correlograms is again suggestive of wave grouping.

### CONCLUSIONS

Evidence suggestive of wave grouping has been sought in the frequency and time domain. Ordered structures have been identified in the phase spectrum and in the tail of the correlogram, both for wave records and for the Rice envelope function. There is a reasonable expectation that wave grouping will be adequately described by these classical linear techniques of time series analysis.

### APPENDIX I - REFERENCES

- Arhan, M., and Ezraty, R. 1978. Statistical relations between successive wave heights. Oceanologica Acta, 1:151-158.
- Battjes, J.A. 1984. Manuscript in preparation.
- Chelton, D.B., Hussey, K.J. and Parke, M.E. 1981. Global satellite measurements of water vapour, wind speed and wave height. Nature, 294:529-532.
- Funke, E.R., and Mansard, E.P.D. 1980. On the synthesis of realistic sea states. Procs., 17th Int. Conf. Coastal Engineering, Sydney, pp. 2974-2991.
- Funke, E.R. and Mansard, E.P.D. 1981. On the meaning of phase spectra in the Fourier transform of random waves. Procs., Int. Conf. Hydrodynamics in Ocean Engineering, Trondheim.
- Goda, Y. 1970. Numerical experiments on wave statistics with spectral simulation. Report Port and Harbour Research Institute, 9:3-57.
- Goda, Y. 1976. On wave groups. Procs., Int. Conf. Behaviour of Offshore Structures, Trondheim, vol. 1, pp. 115-128.
- Goda, Y. 1983. Analysis of wave grouping and spectra of long-travelled swell. Report Port and Harbour Research Institute, 22:3-41.
- Hamilton, J., Hui, W.H., and Donelan, M.A. 1979. A statistical model for groupiness in wind waves. J. Geophysical Research, 84:4875-4884.

Kendall, M.G. and Stuart, A. 1966. The Advanced Theory of Statistics. Vol. 3, Hafner.

Longuet-Higgins, M.S. 1952. On the statistical distribution of the heights of sea waves. J. Marine Research, 9:245-266.

Mollo-Christensen, E. and Ramamonjiarisoa, A. 1978. Modeling the presence of wave groups in a random wave field. J. Geophysical Research, 83:4117-4122.

Oppenheim, A.V. and Schaffer, R.W. 1975. Digital Signal Processing. Prentice-Hall, Englewood Cliffs, N.J.

Rice, S.O. 1944. Mathematical analysis of random noise. Bell System Technical J., 23:282-332 (Also 1945, 24:46-156).

Rye, H. 1983. Ocean wave groups: their relation to spectral information and their reproduction by means of laboratory or numerical simulation. Procs., Int. Conf. Coastal and Port Engineering in Developing Countries, Colombo, pp. 1274-1289.

Rye, H., and Lervik, E. 1981. Wave grouping studied by means of correlation techniques. Procs., Int. Conf. Hydrodynamics in Ocean Engineering, Trondheim, pp. B1-B24.

Sobey, R.J., and Colman, E.J. 1982. Natural wave trains and scattering transform. J. Waterway, Port, Coastal and Ocean Division, ASCE, 108:272-290.

Sobey, R.J. and Colman, E.J. 1983. Scattering analysis and synthesis of wave trains. J. Aust. Mathematical Soc., Series B., Special Issue on Waves and Fluids, 25:44-63.

Su, M.-Y., Bergin, M.T., and Bales, S.L. 1982. Characteristics of wave groups in storm seas. Procs., Ocean Structural Dynamics Symp., Corvallis, pp. 118-132.

Tribolet, J.M. 1977. A new phase unwrapping algorithm. IEEE Trans. Acoustics, Speech, and Signal Processing. ASSP-25:170-177.

## CHAPTER FORTY EIGHT

### SWASH ON STEEP AND SHALLOW BEACHES

R. T. Gnza<sup>1</sup>, E. B. Thornton (M. ASCE)<sup>2</sup>, R. A. Holman<sup>3</sup>

#### Abstract

Extensive field observations of swash on natural beaches are used to relate the magnitudes of swash oscillations to incident wave conditions and the beach slope. Swash fluctuations at wind wave frequencies (defined here as  $f > .05$  Hz) appear to be "saturated." As in laboratory experiments with monochromatic waves, wave breaking prevents the magnitudes of swash oscillations at incident wave frequencies from increasing past a certain level which depends on the beach slope. All data sets considered support this conclusion. In contrast, the magnitude of swash oscillations at surf beat frequencies (defined as  $f < .05$  Hz) varies between data sets. Possible reasons for the discrepancy are discussed. Despite their differences, all data sets show that motions at surf beat frequencies dominate the swash spectrum on dissipative beaches. As in previous studies, the frequencies of spectral hills and valleys in the spectra of surf zone sensors suggests that a significant fraction of the surf beat energy is contained in motions which are standing in the cross-shore direction. Preliminary analysis indicates that shoreward propagating surf beat is coupled to incident wave groups.

<sup>1</sup> Associate Professor, Shore Processes Laboratory, Scripps Institution of Oceanography, A-009, University of California, La Jolla, CA 92093

<sup>2</sup> Professor, Naval Postgraduate School, Monterey, CA 93940

<sup>3</sup> Associate Professor, School of Oceanography, Oregon State University, Corvallis, OR 97331

## INTRODUCTION

The location of shoreline water level (run-up) is important in coastal dynamics. Run-up is composed of a super elevation of mean water level (set-up) and of fluctuations about the set-up level (swash). The present work concerns swash oscillations on natural beaches. The objective is to relate the amounts of swash energy in low (i.e. surf beat) and high (i.e. incident wave) frequency bands to incident wave conditions and the beach slope. Previously unreported field data is supplemented by the extensive field observations of swash reported in Guza and Thornton [1982; in press] and Holman and Sallenger [in press], hereafter referred to as GT and HS. Taken together, these observations span a wide range of incident wave conditions (significant wave heights 20-400 cm, most energetic spectral period 6-20 sec) and beach morphologies (foreshore slopes .025-.125).

The GT swash data were collected on the California coast with a resistance wire gauge. HS used time lapse photography of run-up during a month long experiment at Duck, North Carolina. In all experiments, incident wave heights were calculated from pressure sensor data collected directly offshore of the run-up measurements. Each HS run was 35 minutes long, while GT runs varied between 35 and 256 minutes. Roughly 150 hours of run-up data are considered here.

Huntley et al., [1977] suggested that naturally occurring swash consists of "saturated" high frequency and "unsaturated" lower frequency components, corresponding roughly to the incident wave and surf beat frequency bands. Swash motions at wind wave frequencies are discussed first. Laboratory experiments and theories for monochromatic incident waves are briefly reviewed because they suggest nondimensional parameters useful in discussing this frequency band. As suggested by Huntley et al., [1977], the magnitudes of wind wave swash oscillations in field data are saturated, qualitatively similar to monochromatic laboratory wave results. Surf beat frequencies are considered next. Apparent discrepancies, between data sets, in the magnitude of surf beat swash oscillations are discussed. Finally, some preliminary results concerning the relationship between surf beat and incident wave groups are presented.

## WIND WAVE FREQUENCY BAND

Monochromatic results

Miche [1951] hypothesized that the amplitude of swash oscillations due to monochromatic incident waves is proportional to the amount of shoreline reflection and thus to the standing wave amplitude. Furthermore, the standing wave amplitude at the shoreline with incident wave breaking was assumed equal to the maximum value which occurs without wave breaking. Thus, a maximum swash oscillation supposedly occurs with incident waves just large enough to break. Further increases in incident wave height were hypothesized to increase the amplitude of the progressive component (which is dissipated by breaking and has zero shoreline amplitude), while the standing component and swash amplitudes remain constant (i.e., saturated). Carrier and Greenapan [1958] used the fully nonlinear, inviscid, shallow water

equations to study the maximum possible size a standing wave can attain on an impermeable sloping beach. A review of their work, and of the general problem of waves on a sloping beach is given by Meyer and Taylor [1972]. Carrier and Greenspan found that a standing wave solution is possible if

$$\varepsilon_s = \frac{a_o^s \sigma^2}{g \tan^2 \beta} \leq 1 \quad (1)$$

where  $\beta$  is the slope of a plane beach,  $\sigma$  is the radian frequency,  $2a_o^s$  the vertical swash excursion, and  $\varepsilon_s$  a nondimensional swash parameter. According to inviscid, linear theory, the standing wave amplitude at the shoreline is amplified, relative to the standing wave amplitude in deep water ( $a_\infty^s$ ) by [Stoker, 1947; Meyer and Taylor, 1972].

$$a_o^s = a_\infty^s \left| \frac{\pi}{2 \tan \beta} \right|^{1/2} \quad (2)$$

The deep water condition for a standing wave which will not break at the shoreline is given by, using (1) and (2),

$$\frac{a_\infty^s \sigma^2}{g} \left| \frac{\pi}{2} \right|^{1/2} \tan^{5/2} \beta \leq 1 \quad (3)$$

In terms of the deep water progressive wave amplitude  $a_\infty^s (= \frac{a_\infty^s}{2})$ , the criterion for total reflection of incident waves is [Meyer and Taylor, 1972]

$$\varepsilon_i = \frac{a_\infty^s \sigma^2}{g} (2\pi)^{1/2} \tan^{-5/2} \beta \leq 1 \quad (4)$$

Combining the Miche saturation hypothesis with inviscid linear theory for the maximum amplitude standing wave yields

$$\begin{aligned} \varepsilon_i, \varepsilon_i &< 1. \\ \varepsilon_s &= \\ 1, a_i &> 1. \end{aligned} \quad (5)$$

According to this model, if  $\varepsilon_i$  is small, then increasing the incident wave height (i.e.  $\varepsilon_i$ ) results in an increased swash excursion ( $\varepsilon_s$ ) and the swash is "unsaturated." For large  $\varepsilon_i$ , increasing the incident wave height results in a larger breaker height and steady set-up, but the swash oscillations ( $\varepsilon_s$ ) do not increase. The swash is "saturated."

Several laboratory experiments with monochromatic incident waves have confirmed the basic saturated swash hypothesis. There are, however, some differences in the observed maximum values of  $\epsilon_s$  [ $\sim 1.25$ , Battjes, 1974;  $\sim 2.0$ ; Van Dorn, 1978;  $\sim 3.0$ , Guza and Bowen, 1976] and in the proper nondimensional form for the incident waves ( $\epsilon_i$  in eq. 5).

Typical laboratory data are shown in Figure 1 based on the data of Guza and Bowen [1976]. For  $\epsilon_i < 1.0$ , there was no visible wave breaking and  $\epsilon_s = \epsilon_i$  as predicted by eq. 5. For  $1.0 < \epsilon_i < 9.0$  the swash motion ( $\epsilon_s$ ) increases slowly with increasing  $\epsilon_i$  until reaching a saturated value of  $\sim 3.0$  at  $\epsilon_i \sim 9$ . Further increases in  $\epsilon_i$  do not increase  $\epsilon_s$ . A modification of the Miche hypothesis (eq. 5) which better fits this data (Figure 1) is

$$\epsilon_i \quad ; \quad \epsilon_i < 1. \tag{6a}$$

$$\epsilon_s = \epsilon_i^{1/2} \quad ; \quad 1. < \epsilon_i < 9. \tag{6b}$$

$$3 \quad ; \quad \epsilon_i > 9. \tag{6c}$$

The  $\epsilon_i^{1/2}$  dependence occurs in a transition region between complete reflection and spilling wave conditions. The  $\epsilon_i^{1/2}$  functional form does not correspond to any theory and is only a convenient and simple fit to the data. For comparisons with other results it is useful to recast eq. 6 in terms of the Irribarren, or surf similarity parameter [Battjes, 1974]

$$\xi_\infty = \tan\beta \left| \frac{L_\infty}{H_\infty} \right|^{1/2} = \left| \frac{\pi}{2 \tan\beta} \right|^{1/4} \epsilon_i^{-1/2} \tag{7}$$

with  $L_\infty$  and  $H_\infty$  the deep water wavelength and height. The ratio of the vertical swash excursion ( $R^v = 2a_s^0$ ) to  $H_\infty$  is then

$$3\xi_\infty^2/\pi \quad ; \quad \xi_\infty < \xi_c/3 \tag{8a}$$

$$\frac{R^v}{H_\infty} = (2\pi\beta)^{-1/4} \xi_\infty \quad ; \quad \xi_c/3 < \xi_\infty < \xi_c \tag{8b}$$

$$(\pi/2\beta)^{1/2} \quad ; \quad \xi_c < \xi_\infty \tag{8c}$$

where  $\xi_c = \left| \frac{\pi}{2\beta} \right|^{1/4}$  is the minimum  $\xi_\infty$  value for complete reflection (corresponding to  $\epsilon_i = 1.0$  in eq. 7) and the small slope assumption has been made ( $\beta \sim \tan \phi$ ). Note that large waves correspond to large  $\epsilon_i$  (eq. 6c) and small  $\xi_\infty$  (eq. 8a).

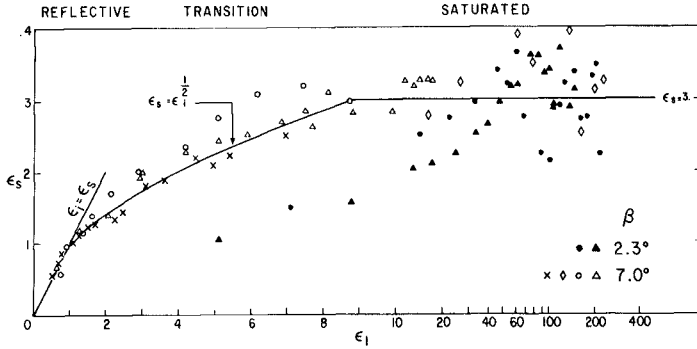


Figure 1. Nondimensional swash ( $\epsilon_s$ , eq. 1) versus nondimensional incident wave height ( $\epsilon_1$ , eq. 4) for monochromatic lab data [Guza and Bowen, 1976].<sup>1</sup> Solid lines correspond to a modified Miche hypothesis (eq. 6).

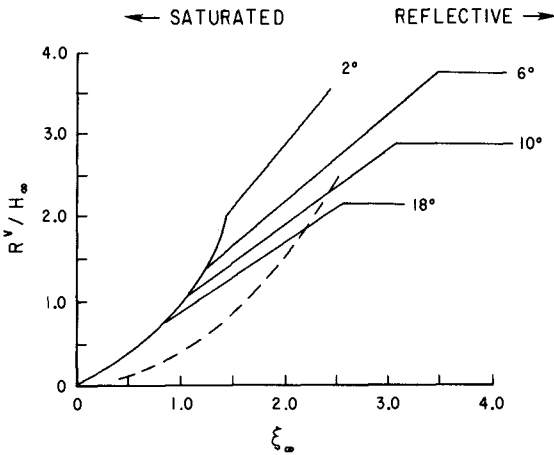


Figure 2. Swash/incident wave height ratio ( $R^V/H_0$ ) versus surf similarity parameter ( $\xi_\omega$ ). — Eq. 8 for indicated values of  $\beta$ ; ---- eq. 9.

As shown in Figure 2, eq. 8 is qualitatively similar to the result of Battjes [1974] based on laboratory experiments with breaking waves on relatively steep slopes

$$\frac{R_v}{H_\infty} = 1.25 \frac{\xi_\infty^2}{\pi} \quad .3 < \xi_\infty < 1.9 \quad (9)$$

In fact, in the saturated range eq. 9 has the same functional form as the modified Miche model (eq. 8a). The difference in the constants corresponds to the different observed saturated values of  $\xi_\infty$  (1.25 and 3.0 in eq 9 and 8a, respectively). The important point here is that eqs. 8 and 9 describe a large amount of monochromatic lab data. Although run-up studies with random waves exist, the data are generally not analyzed in a form suitable for the present application.

#### Field Data; magnitudes

Figure 3 shows the field data superimposed on eqs. 8 (with  $\beta = 6^\circ$ ) and 9. The "significant" swash and incident wave heights ( $R_v$  and  $H_{s,\infty}$ ) are defined as four times the observed variance above  $s_{inc}$ .05 Hz and  $L_\infty$  (which appears in  $\xi_\infty$ ) is based on the incident wave frequency with the maximum power. Because run-up heights can have non-Rayleigh distributions, the significant heights in the present context are simply characteristic heights defined in terms of the variance. Figure 3 also shows the best fit straight line given by HS for that data only. Note that a linear dependence of  $R_v/H_\infty$  on  $\xi_\infty$  does not correspond to the  $\xi_\infty$  dependence of the fully saturated Miche (eq. 8a) or Battjes (eq. 9) models, but is consistent with the transition range suggested by the Guza and Bowen [1976] laboratory data (Figure 1, eq. 8b). However, the field data is clearly too scattered to define a particular functional dependence on  $\xi_\infty$ .

Some of the scatter in Figure 3 is due to the subjectivity of digitizing the HS films and to nonconstant elevations above the bed of the GT resistance wires [Holman and Guza, 1984]. In addition to these instrumental errors, there are more fundamental problems associated with the definitions of  $\xi_\infty$  and  $R_v$ . The  $L_\infty$  term in  $\xi_\infty$  (eq. 7) should probably be defined using the entire incident wave spectrum rather than only the most energetic spectral component. The frequency range for  $R_v$  (here  $f > .05$  Hz) might be more reasonably selected as the range of saturated frequencies, or as having a particular relationship to a characteristic incident wave frequency. The present choice of .05 Hz as the low frequency cut-off corresponds very roughly to a lowest frequency wave band. There are considerable experimental and conceptual shortcomings in the present work. Nevertheless, the clear decrease in  $R_v/H_\infty$  with decreasing  $\xi_\infty$  (Figure 3) further confirms the idea that saturation is a relevant concept for swash on natural beaches.



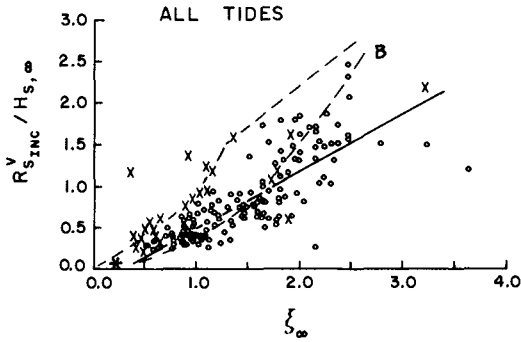


Figure 3. Ratio of observed significant swash height in the incident wave band ( $R_{s,inc}^V$ ) to significant incident wave height ( $H_{s,\infty}$ ) versus  $\xi_{\infty}$

- o, Holman and Sallenger [in press]
- x, Gnza and Thornton [1982] and new data
- \*, Holman and Bowen [1984]

Dashed lines are eq. 7 for  $\beta = 6^\circ$  and eq. 8 (labeled B).  
 Solid line is best fit line given by Holman and Sallenger.

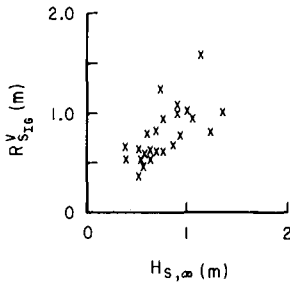


Figure 4. Significant swash height in the surf beat (infragravity) frequency band ( $R_{s,IG}^V$ ) versus  $H_{s,\infty}$ . Data is from Gnza and Thornton [in press].

## SURF BEAT FREQUENCIES

Field Data; magnitudes

In contrast to swash at wind wave frequencies, there are no comprehensive laboratory experiments which provide suggestions about the nondimensional parameters controlling the magnitude of swash oscillations at surf beat frequencies. Laboratory experiments have been hampered by both the generation of spurious free long waves (Bowers, 1977) and multiple reflections between the beach and wave generator [Flick et al., 1981]. Thus, although laboratory measurements with non-monochromatic incident waves do exist, the swash motions at surf beat frequencies are contaminated to an unknown degree. Work presented at the 19th ICCE (Kostense and Vis) describes the first variable depth experiments apparently free of both paddle generated free long waves and long waves re-reflected from the wavemaker. Such experiments, particularly when extended from two incident wave frequencies to a spectrum, will hopefully provide important insights into naturally occurring surf beat. There are no theories which claim to predict surf beat swash energy levels for a spectrum of incident waves. Bounded long wave theories [Longuet-Higgins and Stewart, 1962, 1964] are not valid in very shallow water. Symonds et al., [1982] model the generation of long waves in the surf zone, but the necessary extension of the model from a two frequency deterministic incident wave field to a random wave spectrum has not been done.

While theoretical work provides little guidance, field studies have indicated several general trends. The first is an apparent linear dependence between incident wave and surf beat energy levels [Tucker, 1950; Holman, 1981; Gnza and Thornton, 1982; in press]. Figure 4 shows the observed linear relationship between  $R_{s,IG}^V$  (the significant vertical swash excursion at infragravity frequencies) and  $H_{s,\infty}$  for the GT data. Figure 5 shows the same plot for the HS data. While there may be an indication of some dependence, the HS data are scattered. (Note that the GT data do fall within the general scatter of the HS data).

One reason for the great variability in the HS data lies in the longshore variability of the beach face slope. During the month the HS data were collected, the beach morphology was occasionally rhythmic with longshore length scales of several hundred meters. While these slope variations are small on an incident wave length scale (and the incident band data are correspondingly well behaved), they are large on the length scales associated with infragravity waves. The longshore variation of  $R_{s,IG}^V$  in the same data run, appears in Figure 5 as a wide range of  $R_{s,IG}^V$  values for the same  $H_{s,\infty}$ .

The second general trend that has been previously noted in the literature is that the presence of infragravity energy is in some way linked to the degree to which a beach is "dissipative" [Sasaki et al., 1976; and others]. Since  $s_i$  and  $\xi_\infty$  have been linked to the dissipative characteristics of a beach,  $H_{s,IG}$  plotted the non-dimensional infragravity band swash height,  $r_{IG} = R_{s,IG}^V/H_{s,\infty}$  against  $\xi_\infty$ . Figure 6 shows this plot, together with the best fit linear slope to the HS data. This parameterization does appear to reduce the scatter of the HS data. However, it also shows that the HS and GT data are systematically

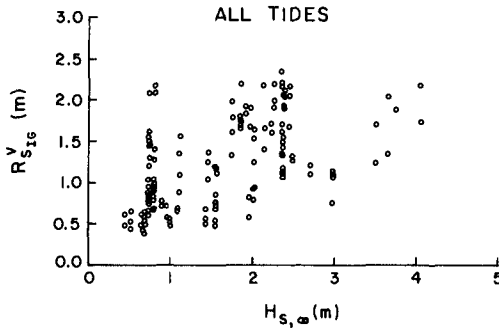


Figure 5. Same as Figure 4, but data is from Holman and Sallenger [in press, reprinted with permission of AGU].

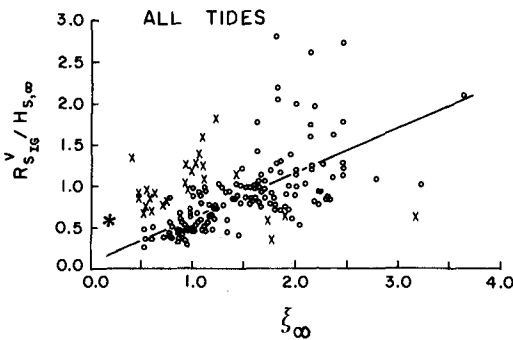


Figure 6.  $\frac{R_{s,IG}^V}{H_{s,\infty}}$  versus  $\zeta_{\infty}$   
 o, Holman and Sallenger [in press]  
 x, Guza and Thornton [1982; in press]  
 \*, Holman and Bowen [1984]

Solid line is best fit line to HS data.

different in this parameter space. While the HS data show a clear trend, the GT data show no significant slope when  $r_{IG}$  is regressed against  $\xi_\infty$ . Note that the linear dependence between  $r_{IG}$  and  $\xi_\infty$  in the HS data implies that  $R_{s,IG}^H/H_{s,\infty}$  (with the significant horizontal swash excursion  $R_{s,IG}^H = R_{s,IG}^V/\beta$ ) is independent of local  $\beta$ .

Perhaps the most important difference between the data sets are the inferred low Irriharren number (large waves) limiting values of  $r_{IG}$ . Based on linear regressions of  $r_{IG}$  against  $\xi_\infty$ , the limits are of the order of 0.1 and 1.0 for the HS and GT data sets respectively. Separate evidence from two highly dissipative beaches ( $\xi_\infty = 0.25$ ) tends to support the GT limit, with observed values of  $r_{IG}$  of at least 0.6 [Wright et al., 1982; Holman and Bowen, 1984].

A potentially simple explanation for the apparent discrepancy between the data sets lies in the rather arbitrary definition of the infragravity band. A cutoff frequency of 0.05 Hz may be generally appropriate for west coast swell, but may be too low for the higher frequency east coast waves. For Great Lakes data this cutoff would be ridiculous. It can be easily seen that variability in incident wave period could induce an artificial trend in a plot such as Figure 6, for a truly constant  $r_{IG}$ . For similar incident wave heights, shorter incident periods will be associated with smaller  $\xi_\infty$ , and will also have a smaller apparent infragravity energy since the fixed cutoff of .05 Hz will encompass a smaller portion of what may properly be considered true infragravity energy. Longer incident periods are associated with larger  $\xi_\infty$  and a proportionally larger  $r_{IG}$  since the .05 Hz cutoff encompasses more of the "true" infragravity energy. Thus the differences between the HS and GT data sets in Figure 6 may only represent the differences in incident wave frequencies encompassed by the data.

Summarizing, there are at least two potential factors contributing to the differences in the surf beat data sets. These are effects associated with three dimensional topography, and the arbitrariness of the present cut-off frequency separating the surf beat and wind wave bands. Note that altering the cut-off frequency will also alter the amount of wind wave energy, and improved agreement between the surf beat data sets may unfortunately be accompanied by increased differences in the wind wave band (Figure 3). Further research on this problem is clearly needed.

#### Field data: generation mechanisms

The idea that surf beat is a forced oscillation associated with incident wave groups originated with Munk [1949] and Tucker [1950]. They interpreted their low frequency observations, taken several hundred meters offshore, as being due to mass transport shorewards under high incident wave groups, with the release of low frequency free waves at the break point where the groups are destroyed by breaking. The long waves then reflect off the beach face and propagate offshore. Tucker [1950] found that high wave groups were correlated with troughs in the low frequency waves. The time lag of maximum correlation approximately equaled the sum of the travel times for incident wave groups to

propagate from the observation point to the break point, and seaward going long waves to return from the break point. Longuet-Higgins and Stewart [1964] subsequently showed that Tucker's observation that high wave groups were correlated with troughs in the low frequency waves agree with the predictions of second-order theory for forced waves if it is assumed that the long waves reflect at the beach. Munk's results were similar to Tucker's, except that with a similar time lag he found crests of long waves correlated with high wave groups, implying a  $180^\circ$  phase shift for the reflected long wave. Both Munk [1949] and Tucker [1950] imply that there is a small nonlinear forced long wave correction under shoreward propagating wave groups, and a larger seaward propagating low frequency wave released at the break point or beach face. In contradiction, Hasselman et al., [1962] presented evidence that the shoreward propagating nonlinearly forced motion is larger than any seaward propagating component. More recent observations suggest that incoming and outgoing waves are of roughly equal magnitude, forming a quasi-standing wave [Suhayda, 1974; and many others]. An example from the GT data set is shown in Figure 7 where measured surf beat run-up spectra are compared with numerical integrations of the long wave equations to predict the energy spectrum at offshore sensors, and the phase between offshore sensors and run-up meter. As in previous studies, valleys in the observed surf beat energy spectra at offshore sensors, and jumps in the relative phase between sensors, occur at the nodal frequencies of simple standing wave (either leaky or high mode edge wave) models.

The question of whether there are long waves associated with groups of incoming waves is addressed by calculating correlations between the two. The data considered here is from a 68 minute run at Torrey Pines on 21 November 1978. The envelope of the high frequency wind waves was obtained by squaring the wind wave time series, and then low pass filtering this signal. A similar approach has been independently taken by Kim and Huntley, and their results are also presented in this volume. Table 1 shows the maximum correlation, and the associated time lag, between the envelope of the deepest sensor (P4) and the envelope at other locations. The correlations are high for sensors outside the breaker region, seawards of W29 (Table 1). This indicates that well defined groups of waves propagate across the nearshore until shoaling and/or wave breaking radically alters the group structure. Theoretical travel times are approximated by using a group velocity equal to

$(gh)^{1/2}$ . These times are nearly equal to the observed times of maximum correlation except in very shallow water where bottom slope effects are not negligible, and the  $(gh)^{1/2}$  assumption breaks down.

Correlations between the low frequency motion and envelope at each sensor are also given in Table 1. At time lag 0, the correlation ( $C_2(\tau = 0)$ ) at the 5 deepest stations are all negative, as would be found with the bound long wave solutions of Longuet-Higgins and Stewart [1962, 1964]. Most of these correlations are barely significantly different than zero with 95% confidence. They are, however, comparable to the maximum correlations observed ( $C_2^{\max}$  in Table 1). At the shallowest three stations,  $C_2(\tau = 0)$  has substantially higher values

Table 1.  $C_1$  is the correlation between the wind wave envelopes at P4 and other sensors, and  $\tau_1^{\max}$  the time lag of maximum correlation, both observed and calculated.  $C_2$  values are correlations between the envelope and low frequency motion at the same sensor.  $C_2^{\max}$  is the maximum correlation (at lag  $\tau_2$ ), and  $C_2(\tau=0)$  the correlation at lag 0.

SENSOR	P4	P7	P7A	P10	P16	W29	P30	W38	W41
Offshore Location(m)	456.	360	303	233	159	103	73	47	17
Depth(cm)	1006.	736	669	553	381	173	130	85	47
$C_1^{\max}$	1.	.93	.92	.90	.87	.58	.50	.43	.43
$\tau_1^{\max}$ (sec) observed	0.	11	19	28	40	49	50	53	148
$\tau_1^{\max}$ (sec) theory	0.	10.	17.	26.	37.	48.	56.	64.	76.
$C_2^{\max}$	.16	-.20	-.14	-.18	-.30	-.17	.32	.51	.45
$\tau_2^{\max}$ (sec)	-225.	170	28	6.	4.	-91.	0.	4.	2.
$C_2(\tau=0)$	-.16	-.13	-.11	-.15	-.26	.00	.32	.46	.43

than at the deeper stations. The maximum correlations at the shallow stations occur at lags ( $\tau_2^{\max}$ ) very close to zero (a positive value of  $\tau_2^{\max}$  means the envelope leads the long wave). Curiously,  $C_2(\tau = 0)$  changes sign between deep and shallow water. The consistent pattern of correlations near zero lag suggests that there is a component of surf beat associated with local wave groups. However, the correlations are disturbingly low and there is no obvious indication of the outgoing long wave energy which contributes to the ubiquitous quasi-standing wave patterns observed by many investigators, and in this data set in particular (Figure 7).

Additional insights are obtained by using colocated pressure and current meters to decompose the long wave into seaward and shoreward propagating components. With  $\eta(t)$  and  $n(t)$  the long wave sea surface elevation and cross-shore velocity time series, plus and minus characteristic (PC(t), MC(t)) time series are defined as

$$PC(t) = (\eta + (\frac{h}{g})^{1/2} n)/2. \quad (10a)$$

$$MC(t) = (\eta - (\frac{h}{g})^{1/2} n)/2. \quad (10b)$$

If  $\eta$  and  $n$  are normally incident shallow water waves following the flat bottom dispersion equation, then PC(t) and MC(t) are the time series of shoreward and seaward propagating waves respectively. Figure 8 shows the time lags for maximum correlation between the envelope of sensor P10 (distance = 233 m) and PC and MC for the six available colocated pressure/current meters. The numbers on the figure are the values of the maximum positive and negative correlations. Correlation values between the P10 envelope and seawards propagating long wave characteristics are circled, while those between the envelope and the shoreward propagating wave are not circled.

In three cases ( $x = 233, 259, 47$  m) the time lag for one of the maximum correlations of the incoming characteristics was not between  $\pm 150$  sec., and these values are not shown. The solid lines on Figure 8 are the calculated travel times for groups of long waves to propagate from P10 to various locations, assuming reflection occurs at the shoreline and the phase speeds equal to  $(gh)^{1/2}$ . Incoming and outgoing long waves are both significantly correlated with the envelope at P10 ( $x = 233$  m). In fact, the maximum correlations of the outgoing long waves with the P10 envelope are comparable to those between the incoming long waves and the P10 envelope. Without the decomposition into incoming and outgoing long waves, the maximum correlations ( $C_2^{\max}$ , Table 1) are generally reduced because the envelope is correlated to both components, but with different time lags. Note the comparable magnitudes of the maximum positive and negative correlations between the seawards propagating long wave and the P10 envelope (circled values in Figure 8) at each position. Given their similar values, and the inaccuracies in the theoretical travel times in very shallow water, it is not possible to tell whether or not the outgoing long wave is phase shifted by  $180^\circ$

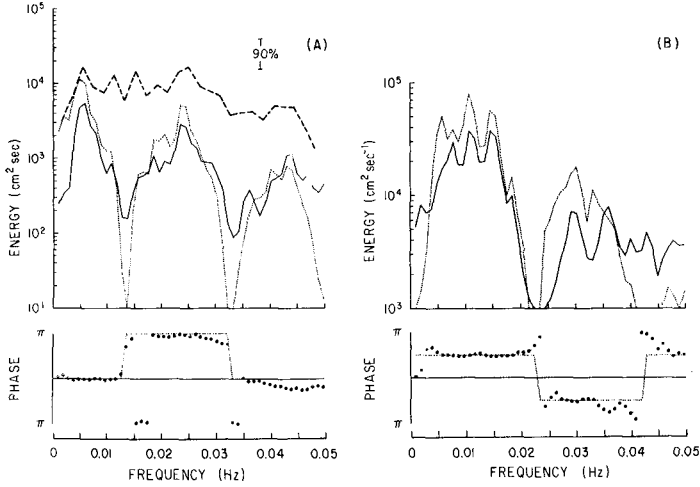


Figure 7. Upper panels compare measured surf beat elevation (A, —) and cross-shore velocity (B, —) energy spectra with predictions (.....) based on measured run-up spectra (A, ---) and hypothesis of standing long waves. Lower panels compare predicted (...) and measured (\*) phase difference between run-up and the offshore sensors (depth = 85 cm, x = 47 cm, 21Nov78, Torrey Pines Beach).

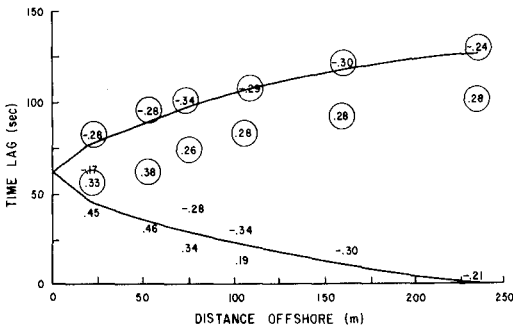


Figure 8. Time lags for maximum correlation between the wind wave envelope at a sensor 233 m offshore, and the seaward and shoreward propagating long waves at various offshore locations.



or not. It is clear, however, that both seaward and shoreward propagating components are correlated with the wind wave envelope. The variances of PC(t) and MC(t), at any particular location, differed by a maximum of 28%, with the shoreward propagating component larger at all positions. The average variance difference was 17%, or roughly an 8% difference in incoming and outgoing long wave amplitudes. This result is very preliminary, but the small differences in incoming and outgoing long wave amplitudes leads us to speculate that the outgoing long wave is simply the reflection of the incoming long wave. However, substantial improvements in several important aspects of the analysis, and consideration of a wider range of data sets are required before any firm conclusions can be reached. The present discussion demonstrates the potential value of decomposing the long wave into incoming and outgoing components and separately correlating these with the wind wave envelope.

#### Acknowledgements

This work was supported by the Office of Naval Research, Coastal Science Branch, under contracts N00014-83-C-0182 (RTG), NR388-114 (EBT), and NR388-168 (RAH). Joan Semler produced this manuscript in spite of a recalcitrant word processing system.

#### References

- Battjes, J. A., 1974, "Surf similarity," Proc. of the 14th Coastal Engineering Conf., p. 466-480, Amer. Soc. Civil Engin., New York.
- Bowers, E. C., 1977, "Harbor resonance due to set-down beneath wave groups," Jour. Fluid Mech., v. 79, p. 71-92.
- Carrier, G. F. and H. P. Greenspan, 1958, "Water waves of finite amplitude on a sloping beach," Jour. Fluid Mech., v. 4, p. 97-109.
- Flick, R. E., D. L. Inman, and R. T. Guza, 1981, "Two-dimensional surfbeat," Proc. of the 17th Coastal Engineering Conf., v. 1, p. 624-638, Amer. Soc. Civil Engin., New York.
- Guza, R. T. and A. J. Bowen, 1976, "Resonant interactions for waves breaking on a beach," Proc. of the 15th Coastal Engineering Conf., p. 560-577, Amer. Soc. Civil Engin., New York.
- Guza, R. T. and E. B. Thornton, 1982, "Swash oscillations on a natural beach," Jour. Geophys. Res., v. 87, n. C1, p. 483-491.
- Guza, R. T. and E. B. Thornton, "Observations of surf beat," Jour. Geophys. Res., in press.
- Hasselmann, K., W. H. Munk, and G. J. F. MacDonald, 1963, "Bispectra of ocean waves," p. 125 in M. Rosenblatt (ed) Time Series Analysis, John Wiley Sons, New York.
- Holman, R. A., 1981, "Infragravity energy in the surf zone," Jour. Geophys. Res., v. 86, n. C7, p. 6442-6450.
- Holman, R. A. and A. J. Bowen, 1984, "Longshore structure of infragravity wave motions," Jour. Geophys. Res., v. 89, n. C4, p. 6446-6452.

- Holman, R. A. and A. H. Sallenger, Jr., "Set-up and swash on a natural beach," Jour. Geophys. Res., in press.
- Holman, R. A. and R. T. Guza, 1984, "Measuring run-up on a natural beach," Coastal Engineering, v. 8, p. 129-140.
- Huntley, D. A., R. T. Guza and A. J. Bowen, 1977, "A universal form for shoreline run-up spectra?," Jour. Geophys. Res., p. 2577-2581.
- Longuet-Higgins, M. S. and R. W. Stewart, 1962, "Radiation stress and mass transport in gravity waves, with application to surfbeats," Jour. Fluid Mech., v. 13, p. 481-504.
- Longuet-Higgins, M. S. and R. W. Stewart, 1964, "Radiation stresses in water waves; a physical discussion, with applications," Deep-Sea Research, v. 11, n. 4, p. 529-562.
- Meyer, R. E. and A. D. Taylor, 1972, "Run-up on beaches," p. 357-411 in R. E. Meyer (ed) Waves on Beaches, Academic Press, New York.
- Miche, A., 1951, "Exposes a l'action de la houle," Ann. Ponts Chaussees, v. 121, p. 285-319.
- Munk, W. H., 1949, "Surf beats," EOS Trans., Amer. Geophys. Union, v. 30, p. 849-854.
- Sasaki, T., K. Horikawa and S. Hotta, 1976, "Nearshore currents on a gently sloping beach," Proc. of the 15th Coastal Engineering Conf., p. 626-644, Amer. Soc. Civil Engin., New York.
- Stoker, J. J., 1947, "Surface waves in water of variable depth," Quart. Appl. Math., v. 5, n. 1, p. 1-54.
- Suhayda, J. N., 1974, "Standing waves on beaches," Jour. Geophys. Res., v. 72, p. 3065-3071.
- Symonds, G., D. A. Huntley and A. J. Bowen, 1982, "Two-dimensional surf beat: long wave generation by a time-varying breakpoint," Jour. Geophys. Res., v. 87, n.C1, p. 492-498.
- Tncker, M. J., 1950, "Sea waves of 1 to 5 minute period," Proc. Roy. Soc. London, A202, p. 565-573.
- Van Dorn, W. G., 1978, "Breaking invariants in shoaling waves," Jour. Geophys. Res., v. 83, p. 2981-2987.
- Wright, L. D., R. T. Guza and A. D. Short, 1982, "Surf zone dynamics on a high energy dissipative beach," Marine Geology, v. 45, p. 41-62.

## CHAPTER FORTY NINE

### MEASUREMENTS OF SURF BEAT AND SET-DOWN BENEATH WAVE GROUPS

J.K. Kostense\*

#### ABSTRACT

A laboratory study was conducted to measure the amplitudes of long waves in shallow water as induced by wave grouping. In a 55 m long wave channel with a plane beach at the end, two primary waves of nearly equal frequency were generated. Due to a sophisticated control of the wave paddle - including second order wave generation as well as active wave absorption at the paddle face - the wave action at the difference frequency was limited to an incident forced wave, propagating at the group velocity, and a reflected free wave generated in the surf zone. For the incident forced - or bound - wave, also known as set-down, the experimental results show good agreement with the existing theory. Furthermore, the experiments confirm qualitatively a theoretical model by Symonds et al. (1982) explaining two-dimensional surf beat as a result of the time-varying breakpoint of the incident primary waves.

#### 1 INTRODUCTION

Long period sea-level fluctuations of several minutes in the nearshore zone were first observed by Munk (1949) and Tucker (1950). Their field records revealed a correlation between the amplitude of these fluctuations, since then termed surf beat, and the amplitude of the incoming swell. The mechanisms by which surf beat is generated have been discussed since then.

Several more recent field studies revealed that three-dimensional free edge waves can account significantly for nearshore long period energy. Gallagher (1971) was able to show theoretically that edge waves can be generated and resonantly excited by nonlinear interaction of obliquely incident wave groups. However, since the first observations there has been some evidence that, apart from the resonant excitation of edge waves, two-dimensional surf beat due to normally incident waves also exists and contributes significantly to the long period energy.

Using the concept of radiation stress, Longuet-Higgins and Stewart (1962 and 1964) presented a theoretical explanation for the existence of a nonlinear forced - or bound - wave associated with grouped waves. This wave, propagating at the group velocity, results in a set-down beneath wave groups. For a constant water depth Bowers (1977) and Ottesen Hansen (1978) derived expressions for the velocity

---

\* Delft Hydraulics Laboratory, the Netherlands

potential and the surface elevation of the bound long wave, using a Stokes expansion of the wave equations to the second order.

Referring to Tucker's observations, showing at some distance offshore a time lag of several minutes between the envelope of the incoming swell and the measured long wave, Longuet-Higgins and Stewart (1962) suggested that the incident bound wave is reflected from the surf zone and is radiated seaward as a free long wave, resulting in two-dimensional surf beat. However, no mechanism was proposed for this phenomenon. More recently, Symonds, Huntley and Bowen (1982) presented a theoretical model explaining the generation of free long waves, radiating seaward from a plane beach, as a result of the time-varying position of the breakpoint of normally incident grouped waves. Shoreward of the breakpoint standing wave solutions are found. This model has been extended by Symonds and Bowen (1984) to describe the long wave solutions generated over any offshore profile, including barred topographies.

Apart from coastal processes, surf beat is of special importance for the resonant excitation of harbour basins and moored structures. However, until recently a correct reproduction of these waves in physical models has been hampered for two reasons. Firstly, if a wave paddle is programmed to produce the primary waves only, the boundary conditions at the paddle are not fulfilled for the bound long waves. This results in the generation of spurious free long waves, as already pointed out by Bowers (1977). Secondly, disturbances occur when reflected long waves are re-reflected from the paddle. Flick et al. (1980) show that for critical frequencies this may even result in resonance, which makes model testing on surf beat phenomena virtually impossible. In the following sections methods to prevent both types of disturbances are discussed. Moreover, experimental results on both set-down beneath wave groups and free long waves generated in the surf zone and radiated seaward, are presented.

## 2 EXPERIMENTAL SET-UP

The experiments were carried out in a glass-wall wave channel of the Delft Hydraulics Laboratory. The channel is 55 m long, 1.0 m wide and 1.2 m high.

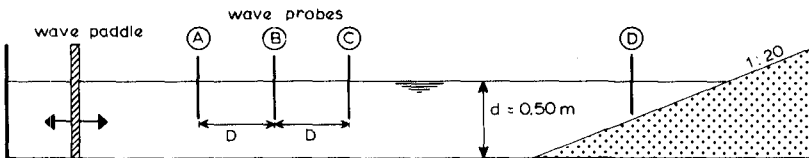


Fig. 1 Sketch of the wave channel

The facility is equipped with a hydraulically driven cradle-type wave generator which was operated in the piston mode only. For all tests a primary wave system made up of two frequencies was generated in a water depth of 0.50 m. These waves broke on a plane cemented beach of a 1:20 slope (see Fig. 1).

## 3 WAVE PADDLE CONTROL

Excluding reflection from the beach, the first-order water surface elevation in the wave channel is given by:

$$\eta = \hat{\eta}_1 \cos(\omega_1 t - k_1 x - \phi_1) + \hat{\eta}_2 \cos(\omega_2 t - k_2 x - \phi_2) \quad (1)$$

Application of the classical wave paddle control for the generation of these bichromatic waves will induce a secondary wave motion at the difference frequency, which may consist of the following four components:

- incident bound wave :  $\zeta_{ib} \cos(\Delta\omega t - \Delta kx - \phi_{ib})$
- incident free wave :  $\zeta_{if} \cos(\Delta\omega t - \kappa x - \phi_{if})$
- reflected bound wave :  $\zeta_{rb} \cos(\Delta\omega t + \Delta kx - \phi_{rb})$
- reflected free wave :  $\zeta_{rf} \cos(\Delta\omega t + \kappa x - \phi_{rf})$

where  $\Delta k$ , the wave number of the bound waves, equals  $k_1 - k_2$ , and the wave number of the free waves  $\kappa$  is coupled to the wave group frequency  $\Delta\omega$  by the dispersion relation:

$$(\Delta\omega)^2 = (\omega_1 - \omega_2)^2 = g\kappa \tanh \kappa d \quad (2)$$

Ottesen Hansen (1978) shows that the amplitude of a bound wave is proportional to the product of the amplitudes of the corresponding primary waves. For the present study the 1:20 slope results in reflection coefficients for the primary waves of a few per cent. Therefore, the amplitudes of the reflected bound waves are negligible.

One of the objectives of the study was to measure the amplitude of the outgoing free long wave generated in the surf zone. To be able to do this, it is essential that all reflected low frequency energy is related to the outgoing free long wave only. However, without taking any precautions, and in spite of the mild slope of the beach, any incident free long wave will almost fully reflect due to its low steepness. Consequently, incident free long waves have to be avoided. In a wave channel there are two main reasons for the occurrence of these waves. Firstly, if a wavemaker is programmed to produce the primary wave system without the associated secondary bound wave, the boundary conditions at the paddle face are not fulfilled to second order. This results in the generation of spurious free long waves propagating onto the beach. Ottesen Hansen et al. (1980) give the theoretical expressions for these waves. Barthel et al. (1983) describe in detail how to correct the control signal for the wave paddle to second order, and verify this method, both for bichromatic wave systems and random waves. Secondly, free long waves reflected from the surf zone will re-reflect from the paddle face, resulting in another incident free wave. To prevent this, a recently developed device for active wave absorption has been applied. The special features of this electronic compensation are the capability of absorbing both primary and secondary waves and the independency of the mass of the paddle on the absorbing capacity.

The effect of second-order wave generation as well as active wave absorption on the resulting wave motion in the wave channel is illustrated in Figures 2a to 2d. These figures show respectively, from above to below, the control signal for the wave paddle, the wave signal recorded by the middle probe, and filtered low frequency signals at three increasing distances from the paddle (see Figure 1). Comparing these figures the effect of active wave absorption is obvious. The low frequency recordings obtained without absorption show instabilities - partly due to resonances in the channel - which almost completely vanish in the recordings obtained with absorption. An extra advantage of active wave absorption is the drastic reduction in time for a test series. Without absorption the low frequency water motion continues quite some time after the wavemaker is stopped, whereas with absorption one test can be started almost immediately after another. The effect of second-order wave generation can be seen best in the left-hand side of the figures, when the reflected waves are not yet interfering with the incident ones. If the wave generation is restricted to first order, the earliest long waves have different amplitudes at different positions. This is due to the interaction between the bound waves and the spurious free waves, which have different phase velocities. As shown in Figures 2c and 2d second-order wave generation results in equal amplitudes of the earliest waves at all positions, indicating that the spurious free waves are suppressed effectively.

#### 4 MEASURING PROCEDURES

Water surface elevations were measured by means of resistance type wave gauges. Although incident bound waves and reflected free waves can be distinguished using two probes only, it was decided to use a set of three probes to check the effectiveness of the suppression of the incident free waves. These probes were positioned above the horizontal bed at equal distances  $D$  (see Figure 1).

The analysis to obtain surf beat amplitudes is restricted to waves having the wave group frequency  $\Delta\omega$ . Thus, at a specific position  $x = x_A$  in the channel, the low frequency surface elevation  $\zeta_A$  can be written as:

$$\zeta_A = \zeta_{ib} \cos(\Delta\omega t - \Delta kx_A - \phi_{ib}) + \zeta_{if} \cos(\Delta\omega t - \kappa x_A - \phi_{if}) + \zeta_{rf} \cos(\Delta\omega t + \kappa x_A - \phi_{rf}) \quad (3)$$

The recorded signals were low-pass filtered. To obtain the local amplitudes at the fundamental, the low frequency signals were decomposed by means of a Fourier analysis. The Fourier series of the signal recorded at  $x = x_A$  can be written as:

$$\zeta_A = \frac{a_{0,A}}{2} + a_A \cos \Delta\omega t + b_A \sin \Delta\omega t + \dots \text{higher harmonics} \quad (4)$$

For positions  $x = x_B$  and  $x = x_C$  similar equations can be formulated, resulting in a set of 6 equations. For the applied analysis it is essential that the Fourier series refer to the identical time interval of the simultaneous signals. Choosing the origin of the  $x$ -axis at the

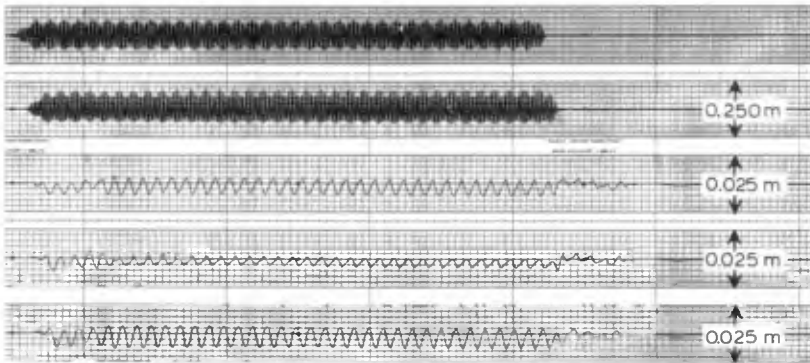
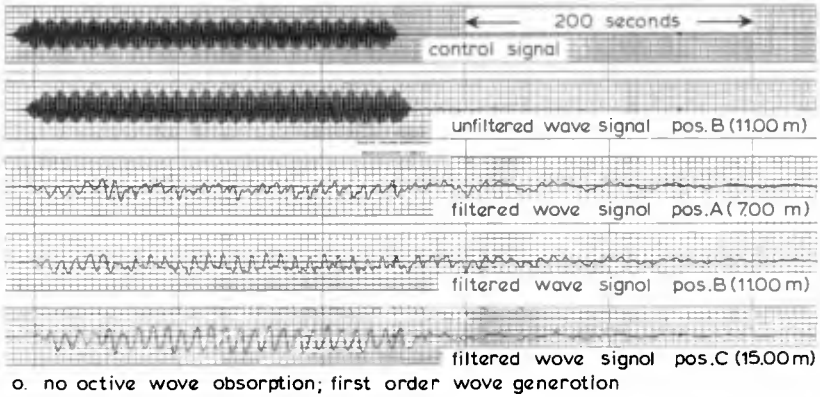
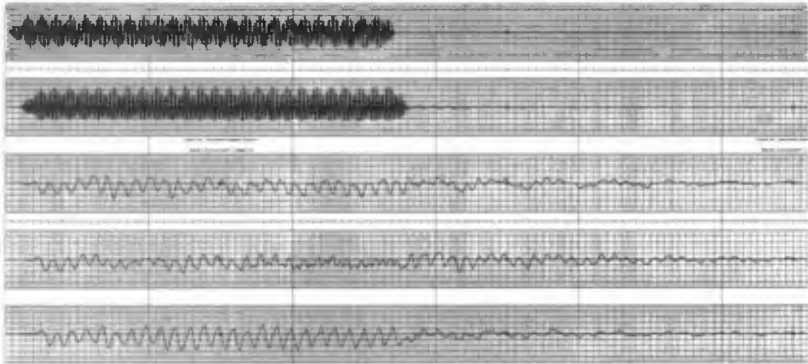
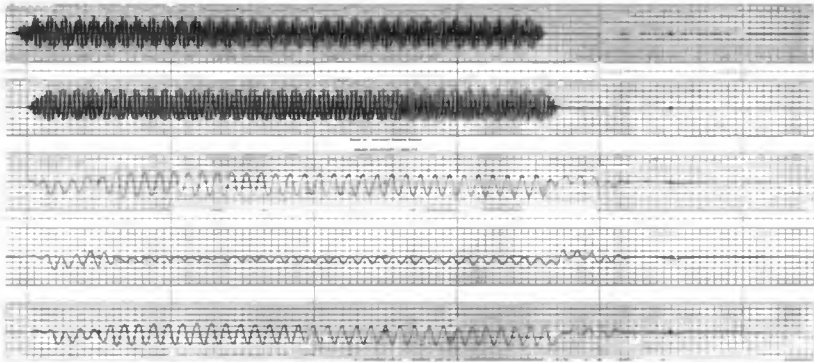


Fig. 2 Typical recordings for different wave-paddle control techniques



c. no active wave absorption; second order wave generation



d. with active wave absorption; second order wave generation

Fig. 2 (contd.) Typical recordings for different wave-paddle control techniques



middle probe, i.e.  $x_B = 0$ , after some trigonometry the following expressions can be obtained:

$$C_{ib} = \zeta_{ib} \cos \phi_{ib} = \frac{(a_A + a_C)/2 - a_B \cos \kappa D}{\cos \Delta \kappa D - \cos \kappa D} \quad (5)$$

$$S_{ib} = \zeta_{ib} \sin \phi_{ib} = \frac{(b_A + b_C)/2 - b_B \cos \kappa D}{\cos \Delta \kappa D - \cos \kappa D} \quad (6)$$

$$C_{if} = \zeta_{if} \cos \phi_{if} = \frac{(-b_A + b_C)/2 + a_B \sin \kappa D - C_{ib}(\sin \Delta \kappa D + \sin \kappa D)}{2 \sin \kappa D} \quad (7)$$

$$S_{if} = \zeta_{if} \sin \phi_{if} = \frac{(a_A - a_C)/2 + b_B \sin \kappa D - S_{ib}(\sin \Delta \kappa D + \sin \kappa D)}{2 \sin \kappa D} \quad (8)$$

$$C_{rf} = \zeta_{rf} \cos \phi_{rf} = a_B - C_{ib} - C_{if} \quad (9)$$

$$S_{rf} = \zeta_{rf} \sin \phi_{rf} = b_B - S_{ib} - S_{if} \quad (10)$$

The amplitudes of all long waves can be simply obtained from these expressions. The Fourier series were determined for 20 individual subsequent long waves. In this way, the average value as well as the standard deviation of  $\zeta_{ib}$ ,  $\zeta_{if}$ , and  $\zeta_{rf}$  could be obtained. Subsequently, the test was repeated with an adjusted control signal for the wave paddle. An extra long wave, having the same amplitude as the free incident wave obtained in the former test but with a phase shift of  $180^\circ$ , was generated. The test with an optimum control of the wave paddle, in other words the test resulting in the lower computed amplitude of the incident free wave - in most cases some tenths of a millimeter -, was selected for the final analysis. Sometimes, the original control was even better than the second one, suggesting that at the optimum control, the computed amplitude of the incident free wave should be considered as an indicator for the accuracy of the applied analysis instead of being considered as a real wave. Therefore, for the final analysis, it was assumed that there is no incident free wave at all, which means that the second term at the right-hand side of equation (3) is omitted. Now, the recordings of two probes suffice to compute  $\zeta_{ib}$  and  $\zeta_{rf}$ . Choosing the origin of the x-axis in between probes A and B yields the following set of equations:

$$C_{ib} = \zeta_{ib} \cos \phi_{ib} = \frac{(a_A + a_B) \sin(\kappa D/2) - (b_A - b_B) \cos(\kappa D/2)}{2 \sin\{(\kappa + \Delta \kappa)D/2\}} \quad (11)$$

$$S_{ib} = \zeta_{ib} \sin \phi_{ib} = \frac{(a_A - a_B) \cos(\kappa D/2) + (b_A + b_B) \sin(\kappa D/2)}{2 \sin\{(\kappa + \Delta \kappa)D/2\}} \quad (12)$$

$$C_{rf} = \zeta_{rf} \cos \phi_{rf} = \frac{(a_A + a_B)/2 - C_{ib} \cos(\Delta \kappa D/2)}{\cos(\kappa D/2)} \quad (13)$$

$$S_{rf} = \zeta_{rf} \sin \phi_{rf} = \frac{(b_A + b_B)/2 - S_{ib} \cos(\Delta kD/2)}{\cos(\kappa D/2)} \tag{14}$$

All presented results are obtained from the above set of equations.

A fourth probe was positioned above the slope just in front of the location where the highest waves break. In this way, it could be checked if the wave groups had the same modulation just before breaking as above the horizontal bed. No measuring devices were installed within the surf zone.

5 TEST PROGRAMME

The test conditions were selected to enable verification of the theoretical model presented by Symonds et al. (1982). They show that the zone between the minimum and the maximum positions of the breakpoint acts as a forcing region. Free long waves at the group period and harmonics are radiated away from this region both shoreward and seaward. As the waves which propagate shoreward are assumed to be fully reflected at the shoreline, standing waves are produced inshore of the forcing region. The reflected waves move through the forcing region and radiate seaward. Thus, the amplitudes of the resultant outgoing waves depend on the relative phase between the reflected waves and the waves radiated seaward directly from the forcing region. This is shown schematically in Figure 3 for the wave at the group frequency. The amplitude of this wave at the outer limit of the forcing

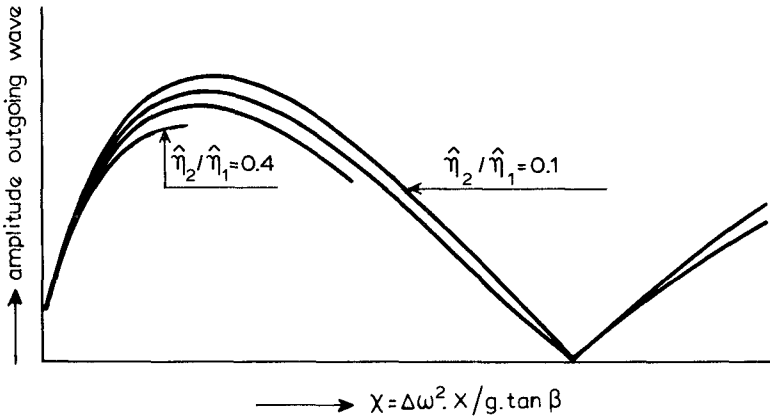


Fig. 3 Schematic representation of the results obtained by Symonds et al. (1982)

region, normalized by the variation about the mean of the steady state set-up, appears to be a function of the parameter  $\chi$  and the modulation ratio of the incident primary waves  $\hat{\eta}_1 / \hat{\eta}_2$ . The parameter  $\chi$  depends on the mean distance  $X$  between the breakpoint and the shoreline, the group frequency  $\Delta\omega$ , and the beach slope  $\beta$ .

Table 1 presents the test programme, which was divided up into five test series. For the tabulated values of  $\chi$  the mean position of the breakpoint had to be estimated. This quantity was obtained using the same equation as applied by Symonds et al.:

$$X = \frac{\hat{\eta}_1}{\gamma \tan \beta} \quad (15)$$

where the ratio of wave amplitude to water depth at breaking has been assumed to be  $\gamma = 0.4$  (see Bowen et al., 1968). The results of Symonds et al. imply among other things that the outgoing free wave does not depend on the individual primary wave frequencies  $\omega_1$  and  $\omega_2$ , but on their difference  $\Delta\omega$  only. To check this, series A and B, each repre-

test	$\chi$	$\hat{\eta}_1$ (m)	$\hat{\eta}_2$ (m)	$\omega_1$ (rad/s)	$\omega_2$ (rad/s)	$\Delta\omega$ (rad/s)
A-1	4.72	0.055	0.011	3.062	2.145	0.917
A-2	3.29	0.055	0.011	3.062	2.296	0.766
A-3	2.08	0.055	0.011	3.065	2.456	0.609
A-4	1.18	0.055	0.011	3.077	2.618	0.459
A-5	0.53	0.055	0.011	3.063	2.755	0.308
B-1	4.78	0.055	0.011	4.295	3.372	0.923
B-2	3.34	0.055	0.011	4.065	3.293	0.772
B-3	2.12	0.055	0.011	4.070	3.455	0.615
B-4	1.19	0.055	0.011	4.071	3.609	0.462
B-5	0.53	0.055	0.011	4.070	3.762	0.308
C-1	4.86	0.080	0.016	4.294	3.522	0.772
C-2=B-2	3.34	0.055	0.011	4.065	3.293	0.772
C-3	2.13	0.035	0.007	4.295	3.523	0.772
D-1=A-3	2.08	0.055	0.011	3.065	2.456	0.609
D-2	1.32	0.035	0.007	3.065	2.456	0.609
D-3	1.13	0.030	0.006	3.065	2.456	0.609
E-1	3.04	0.035	0.028	4.295	3.372	0.923
E-2	2.13	0.035	0.028	4.294	3.522	0.772
E-3	1.35	0.035	0.028	4.296	3.681	0.615
E-4	0.76	0.035	0.028	4.294	3.833	0.461
E-5	0.34	0.035	0.028	4.296	3.988	0.308

Table 1 Test programme

sents one specific wave frequency  $\omega_1$ , were designed to cover the same set of values for the parameter  $\chi$ . In these series the variation of  $\chi$  has been obtained by a change of  $\omega_2$ . In series C and D the wave frequencies are fixed and, instead, the amplitudes of the primary waves are changed. In the model of Symonds et al. the breakpoint is taken to vary sinusoidally, implying a weak modulation of the primary wave system. Therefore, series A, B, C and D all have the same low ratio of modulation ( $\hat{\eta}_2/\hat{\eta}_1 \approx 0.2$ ). Of course, in nature far higher ratios are encountered. To obtain an idea of the effect of such modulations, series E was added to the programme.

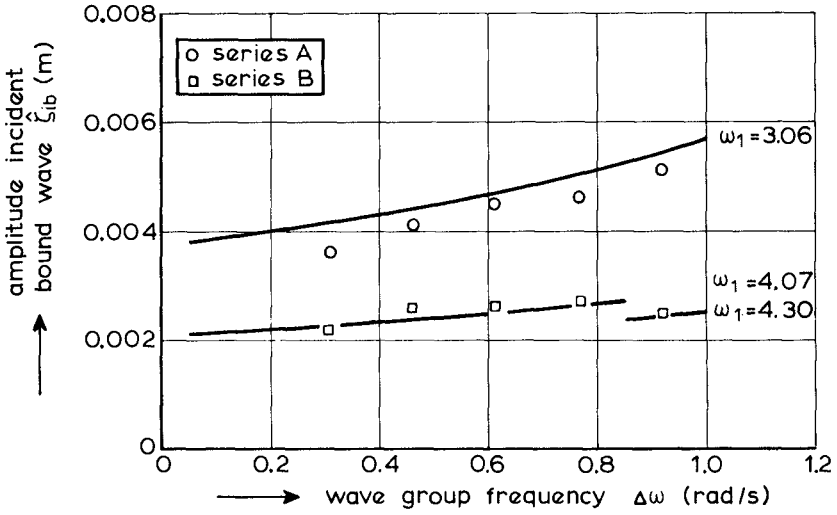


Fig. 4 Measured and theoretical bound long waves for weakly modulated primary waves,  $\hat{\eta}_2/\hat{\eta}_1 = 0.2$

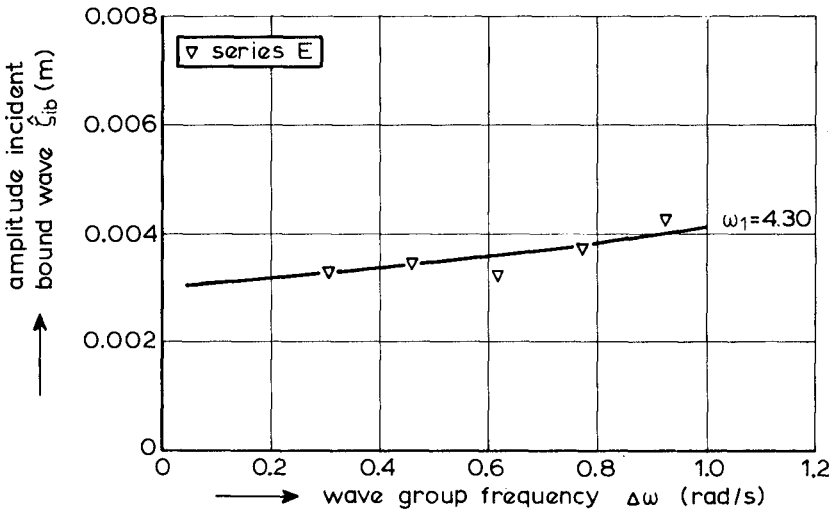


Fig. 5 Measured and theoretical bound long waves for almost fully modulated primary waves,  $\hat{\eta}_2/\hat{\eta}_1 = 0.8$

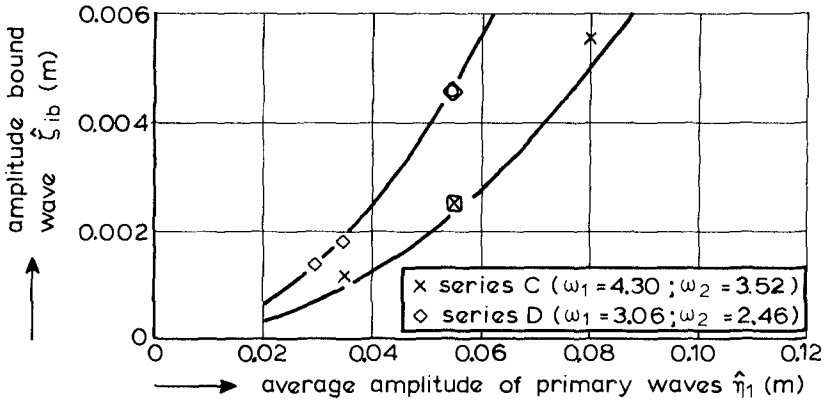


Fig. 6 The effect of the average amplitude of the primary waves on the bound long wave,  $\hat{\eta}_2/\hat{\eta}_1 = 0.2$

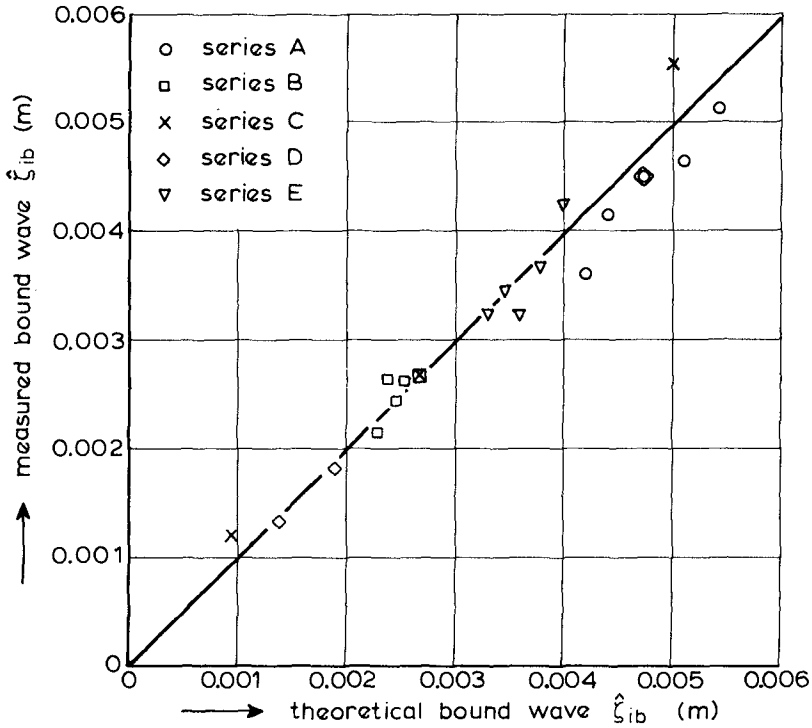


Fig. 7 Comparison of measured bound waves with theory, all tests

6 RESULTS

For all the test series, the measured amplitudes of the incident bound long waves are shown in Figures 4 to 6. The solid lines in these figures represent the theoretical values as given by Ottesen Hansen (1978). Both for weakly and almost fully modulated wave signals, the agreement between measured and theoretical values is quite satisfactory. According to the theory, the amplitude of the bound long wave should be proportional to the product of the primary wave amplitudes  $\hat{\eta}_1$  and  $\hat{\eta}_2$ . As shown in Figure 6, this is confirmed by the measurements. In Figure 7 the measured values are plotted against the theoretical ones for all test conditions. The high correlation shown in this figure gives an indication of the accuracy of the measuring procedure applied.

Longuet-Higgins and Stewart (1962) have suggested that the incident bound wave is reflected from the surf zone and radiated seaward as a free long wave. Using this concept, one would expect some correlation between both waves. However, as shown in Figure 8, the correlation is very poor. Moreover, for some conditions the reflected wave is even higher than the incident one. Both results support the relevance of the model of Symonds et al.

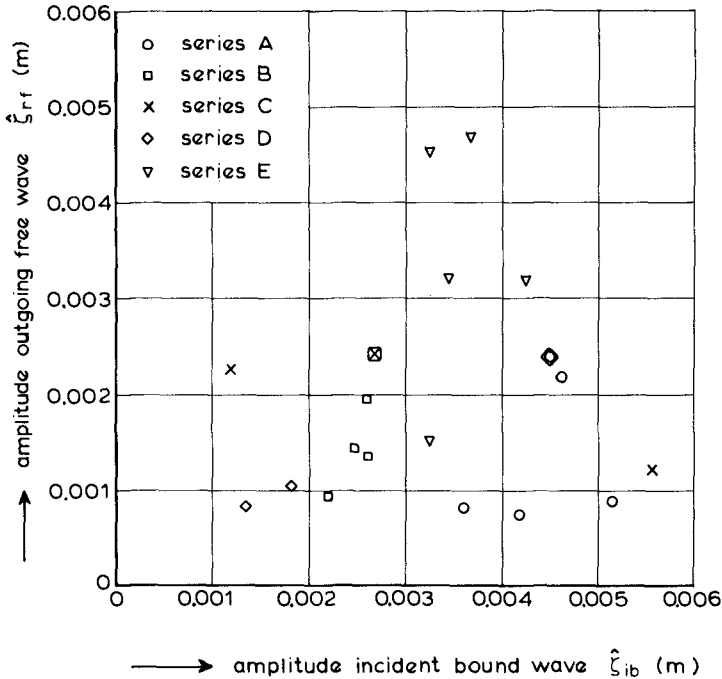


Fig. 8 Relation between incident bound long waves and outgoing free long waves

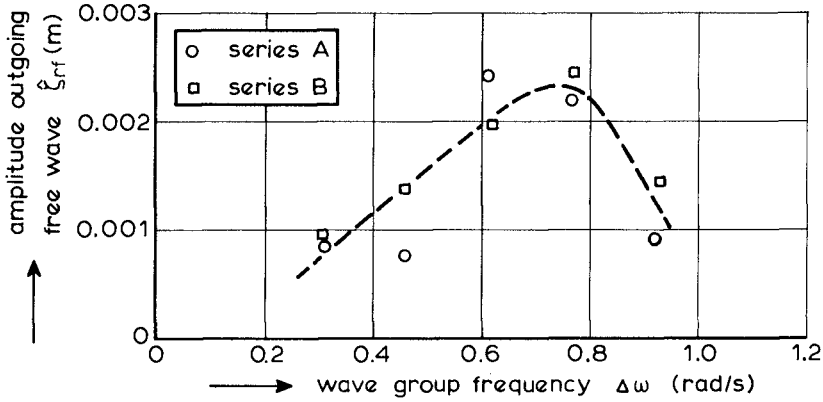


Fig. 9 Measured outgoing free long waves for weakly modulated primary waves,  $\hat{\eta}_2/\hat{\eta}_1 = 0.2$

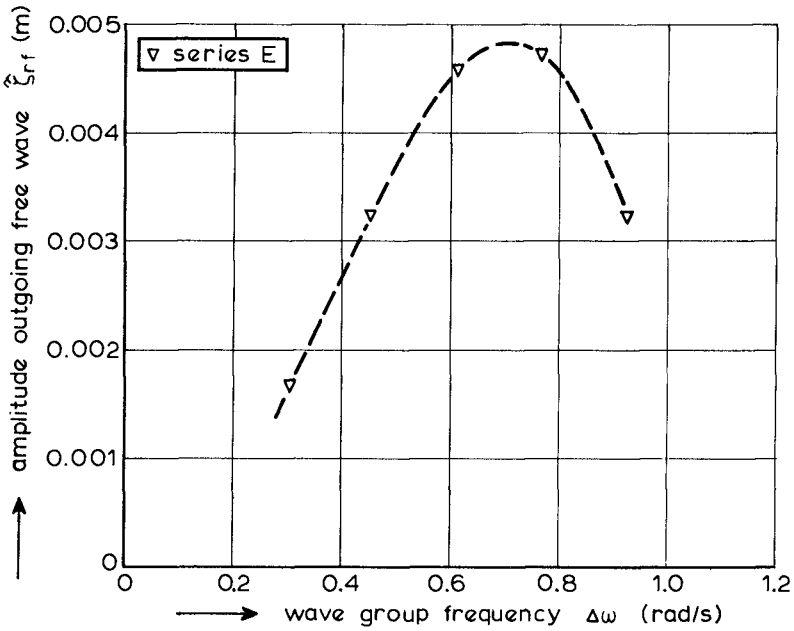


Fig. 10 Measured outgoing free long waves for almost fully modulated primary waves,  $\hat{\eta}_2/\hat{\eta}_1 = 0.8$

The measured amplitudes of the outgoing free waves are shown for each test series separately in Figures 9 to 11. The barred lines on these figures merely connect the measured values; they do not refer to any theory. Figure 9 shows that the results for series A and B compare quite well with one another, which is again in accordance with the model of Symonds et al. This model is also qualitatively confirmed by the results shown in Figure 11. This figure shows clearly that increasing the primary wave amplitudes, or, in other words, increasing the mean position X of the breakpoint, does not necessarily result in an increase of the amplitude of the outgoing wave. The results of the tests with almost fully modulated primary waves show the same trend as that found for the weakly modulated waves (see Figure 10).

To be able to compare the experimental results with the model of Symonds et al. in a quantitative way, some assumptions have to be made. Firstly, the mean position X of the breakpoint was not measured. This quantity was obtained using equation (15). Secondly, the experimental results are obtained at a water depth of 0.50 m, whereas the theoretical results refer to the amplitude of the outgoing wave at the outer limit of the wave breaking region. This amplitude was estimated as follows:

$$\hat{\zeta}_{rf,b} = \left(\frac{0.50}{d_b}\right)^{\frac{1}{2}} \cdot \hat{\zeta}_{rf} = \left(\frac{0.50 \gamma}{\hat{\eta}_1 + \hat{\eta}_2}\right)^{\frac{1}{2}} \cdot \hat{\zeta}_{rf} \tag{16}$$

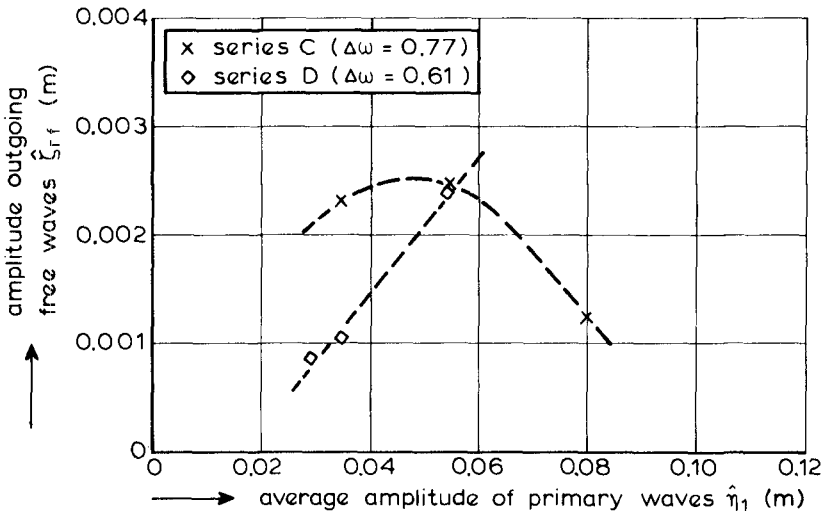


Fig. 11 The effect of the average amplitude of the primary waves on the outgoing free long wave,  $\hat{\eta}_2/\hat{\eta}_1 = 0.2$



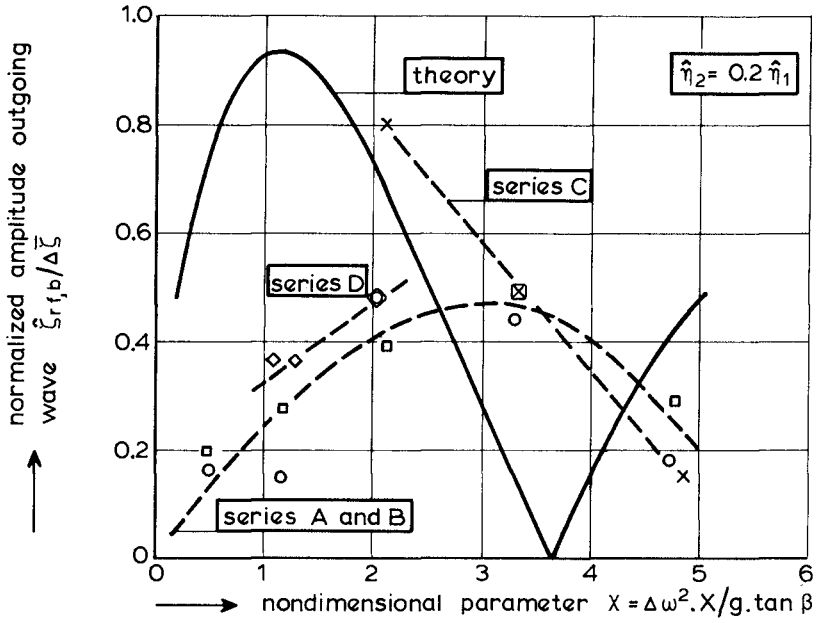


Fig. 12 Comparison of normalized outgoing long waves with the theory of Symonds et al., weakly modulated primary waves

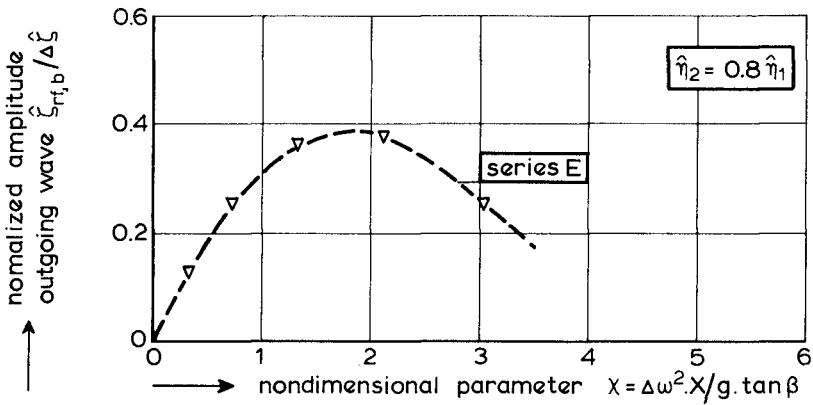


Fig. 13 Normalized outgoing long waves for almost fully modulated primary waves

Finally, the theoretical results are normalized by the variation about the mean of the set-up at the shoreline which would be obtained for monochromatic waves with the same amplitudes. Again in accordance with Symonds et al. this variation has been estimated to be:

$$\Delta \bar{\zeta} = \frac{3}{2} \gamma \hat{\eta}_2 \quad (17)$$

Using equations (15) to (17), the experimental results can be plotted against the theory. Figure 12 shows, in spite of a qualitative agreement, that the deviations are significant. It is presumed that this is due to the assumptions underlying the conceptual model. For instance, the bound wave associated with the incoming wave groups, has not been included in the model. Moreover, the formulation precludes any modulation of the primary waves inside the surf zone. Another major assumption of the theoretical model is that the long waves propagating shoreward are supposed to be fully reflected at the shoreline.

Symonds et al. also assume a sinusoidal variation of the break-point, which restricts a qualitative comparison between the theory and experiments to those tests carried out with weakly modulated primary waves. Nonetheless, for comparison, the normalized results of series E are presented in Figure 13. Studying Figures 12 and 13 reveals that the effect of the ratio of wave modulation qualitatively agrees with the theoretical trend presented in Figure 3.

## 7 CONCLUSIONS

Two-dimensional surf beat induced by bichromatic waves has been investigated experimentally. The following conclusions can be drawn:

- The wave action at the wave group frequency can be reproduced correctly, applying a sophisticated control of the wave paddle, including second-order wave generation and active wave absorption at the paddle face.
- Two-dimensional surf beat induced by incident wave groups should be considered as the result of two wave systems, viz. incident bound waves, propagating at the group velocity, and outgoing free waves, which are generated in the surf zone.
- The experiments confirm the theoretical values for the amplitude of the incident bound wave, which is often termed as set-down, as obtained with a Stokes expansion of the wave equations to second order.
- There is no correlation between the incident bound waves and the outgoing free waves.
- The theoretical model of Symonds et al. and the experimental results for the free waves, which are generated in the surf zone and radiated seaward, agree qualitatively.

## REFERENCES

- Barthel, V., E.P.D. Mansard, S.E. Sand, and F.G. Vis, 1983: Group-bounded long waves in physical models. *Ocean Engineering*, Vol. 10, No.4, pp 261-294
- Bowen, A.J., D.L. Inman, and V.P. Simmons, 1968: Wave set-down and set-up. *J. Geophys. Res.*, Vol. 73, No. 8, pp. 2569-2577
- Bowers, E.C., 1977: Harbour resonance due to set-down beneath wave groups. *J. Fluid Mech.*, Vol. 79, Part 1, pp. 71-92
- Flick, R.E., D.L. Inman, and R.T. Guza, 1980: Two-dimensional surf beat. *Proc. 17th Int. Conf. Coastal Engng.*, Sydney, Vol. 1, pp. 624-638
- Gallagher, B., 1971: Generation of surf beat by non-linear wave interactions. *J. Fluid Mech.*, Vol. 49, Part 1, pp. 1-20
- Longuet-Higgins, M.S., and R.W. Stewart, 1962: Radiation stress and mass transport in gravity waves, with application to "surf beats". *J. Fluid Mech.*, Vol. 13, pp 481-504
- Longuet-Higgins, M.S., and R.W. Stewart, 1964: Radiation stresses in water waves; a physical discussion, with applications. *Deep Sea Res.*, Vol. 11, pp. 529-562
- Munk, W.H., 1949: Surf beats. *Trans. Am. Geoph. Union*, Vol. 30, pp. 849-854
- Ottesen Hansen, N.E., 1978: Long period waves in natural wave trains. *Inst. Hydrodyn. and Hydraulic Engng.*, Techn. Univ. Denmark, Progress Rep. No. 46, pp. 13-24
- Ottesen Hansen, N.E., S.E. Sand, H. Lundgren, T. Sorensen, and H. Gravesen, 1980: Correct reproduction of group-induced long waves. *Proc. 17th Int. Conf. Coastal Engng.*, Sydney, Vol. 1, pp. 784-800
- Symonds, G., D.A. Huntley, and A.J. Bowen, 1982: Two-dimensional surf beat: long wave generation by a time-varying breakpoint. *J. Geoph. Res.*, Vol. 87, No. C1, pp. 492-498
- Symonds, G., and A.J. Bowen, 1984: Interactions of nearshore bars with incoming wave groups. *J. Geoph. Res.*, Vol. 89, No. C2, pp. 1953-1959
- Tucker, M.J., 1950: Surf beats: sea waves of 1 to 5 minutes period. *Proc. R. Soc., London, Ser. A*, Vol. 202, pp. 565-573

## CHAPTER FIFTY

### THE PROBABILITY CHARACTERISTICS OF WAVES AND WAVE PRESSURES AT A VERTICAL BREAKWATER

Huang Peiji\* and Zhao Binglai\*\*

#### ABSTRACT

In this paper, under the condition of waves in front of a breakwater being not broken, studies were made on the characteristics of probability distribution of waves and wave pressures, the regularity of the spectral component attenuation with depth and the constitution of the high frequency band of wave pressure spectrum.

The distributions of wave heights in front of a vertical breakwater, the range of wave pressure fluctuation at different subsurface levels, and the wave periods have shown that they are practically invariable with depth and can be determined theoretically. The spectral constitution of wave pressure field and the regularity of attenuation of spectral components were analyzed at the vertical breakwater, and a new expression describing the equilibrium range of wave pressure spectrum was obtained.

#### 1. INTRODUCTION

Along with the exploitation of the offshore oil fields and marine minerals as well as with the advance of marine navigation and transportation, it is necessary to build up much more marine structures or wharfs. As for those structures, the vertical-wall type marine structure is still adopted widely in the engineering construction at present. In order to select the optimum conditions for structure of this kind, we must research on the probability characteristics of the waves and wave pressures in front of it. This work directly concerns the calculations of the stability and the strength for such structure. It is very important to investigate, under natural conditions, the probability characteristics of the waves and the wave pressures in front of it.

Since the late 1960's, the effects of sea wave on the vertical breakwater have been studied and observed abroad(9, 10,12). In recent years, we have observed the wave and its action on the vertical breakwater at a certain harbour(1,3). The breakwater of this harbour is situated in the open sea ,

---

\* Associate Researcher . \*\* Assistant Researcher .  
First Institute of Oceanography, National Bureau of Oceanography, P.O. Box 98, Qingdao, China

and its body which is a caisson structure was placed on the basement. The sea bottom is comparatively even. The altitude of the basement is -6.0m and the tidal range 3--4m. The depth of water in front of the breakwater may reach about 10m at high tide. The observation station was built 40m from the head of this breakwater. The sensors which are used for measuring the wave pressure were mounted at different heights of the breakwater side facing the sea (its respectively altitudes are -5.2, -2.2, -0.2, +1.8, +2.8, and +3.8m, the altitude is regarded as zero at the tidal datum plane and is positive on the above and negative in the below). The resistance wire staffs are mounted on the breakwater side and on a location where it is 450m far from the breakwater in the open sea. The wave pressures at different heights on the breakwater side, the water surface elevations in front of it and the incident waves are synchro-recorded altogether continuously.

In this paper, as to the successive recordings of the waves and the wave pressure, we have carried on statistical and spectrum analyses on the basis of actually measured data in front of the vertical breakwater in this harbour. Meanwhile, we also investigated, without the wave breaking condition in front of the breakwater, the probability distribution characteristics of the wave and the wave pressure, the characteristics of the component of the wave pressure spectra attenuated with the depth, and the constitution of the wave pressure spectra in front of the breakwater.

## 2. THE PROBABILITY DISTRIBUTION OF WAVES AND WAVE PRESSURES IN FRONT OF THE BREAKWATER

The waves are random phenomena, the forces resulted from them also exhibit the stochastic behaviour. Therefore, when the interaction between the waves and the breakwater takes place, the wave height and the total pressure acted upon the breakwater, the intensity of pressure at any point on it and other dynamic parameters which characterize the action of wave on the breakwater, all these may be regarded as being of random quantities with the definite distribution law. In the case of deep water, this distribution law has ever been investigated by some researchers. They thought that the wave height in front of the breakwater, the range of wave pressure fluctuation at different heights on the breakwater, the crest value and the trough value of the total pressures all follow the Rayleigh Distribution(9,11). In the case of shallow water, this problem has not been studied yet.

### 2.1 The cumulative probability distribution function for both the wave height in front of the vertical breakwater and the range of wave pressure fluctuation at different heights on the breakwater

In the case of deep water, both the wave height in front of the breakwater and the range of wave pressure fluctuation

at any point on it follow the Rayleigh Distribution. In the case of shallow water, the wave height is no more in agreement with the Rayleigh Distribution. According to reference(2), we may obtain the following expressions:

$$F(h) = \exp \left[ - \Gamma^{K(H^*, B)} \left( \frac{1}{K(H^*, B)} + 1 \right) \left( \frac{h}{\bar{h}} \right)^{K(H^*, B)} \right], \quad (1)$$

$$K(H^*, B) = (5 - B)/(2 - 1.5H^*), \quad (2)$$

$$B = \begin{cases} \bar{C}/U = \bar{\tau}g/2\pi U, & \bar{C} \leq U \\ 1, & \bar{C} > U \end{cases}, \quad (3)$$

$$H^* = \bar{h}/d, \quad 0 \leq H^* \leq 0.5$$

here  $\bar{h}$  is the average wave height,  $\bar{\tau}$  the average wave period,  $d$  the water depth,  $U$  the wind velocity,  $g$  the gravitational acceleration,  $H^*$  the shallow water factor,  $B$  the stage factor of wind-wave growth. When  $B=1$ , the wind wave appears in a fully developed state. It is evident that the expression (1) is the Rayleigh Distribution, while  $H^*=0$ , and  $B=1$ .

In order to find out which kind of distributions will be reflected in the actually measured data, first of all, we have respectively computed the cumulative curve of the nondimensional wave height ( $h/\bar{h}$ ) and the nondimensional wave pressure range ( $p/\bar{p}$ ) at every recording, and then determined the values of the nondimensional wave height and the nondimensional wave pressure range which correspond to the cumulative probabilities as 1, 5, 10, 20, 30, 50, 70, and 90%. By making use of the values of every cumulative probability mentioned above, we have computed the points corresponding to the value  $K$  by the expression(2), and then plotted them on Fig. 1.

Fig. 1a illustrates the distribution of the actually measured wave heights on the vertical breakwater and Fig. 1b illustrates that of the range of wave pressure fluctuation measured at the basement layer of the breakwater. Other mediate layers have similar figures, too.

As seen from the above figures, the distances between the points of the actually measured data quite approximate the corresponding values of the theoretical cumulative probability in expression(1). Thus we may think that, in the case of shallow water, the wave height at the vertical breakwater and the wave pressure range at different heights on it are in agreement with the distribution law in expression(1). The distribution of wave pressure range, as a matter of fact, will not vary with the altitude of the measured points.

## 2.2 The cumulative distribution function of the surface wave period in front of the vertical breakwater and the wave pressure period at the different heights on it

Regarding the distribution of the wave period, analyses (6,8) of the researchers and results observed indicate that, under the first order approximation, the distribution curves

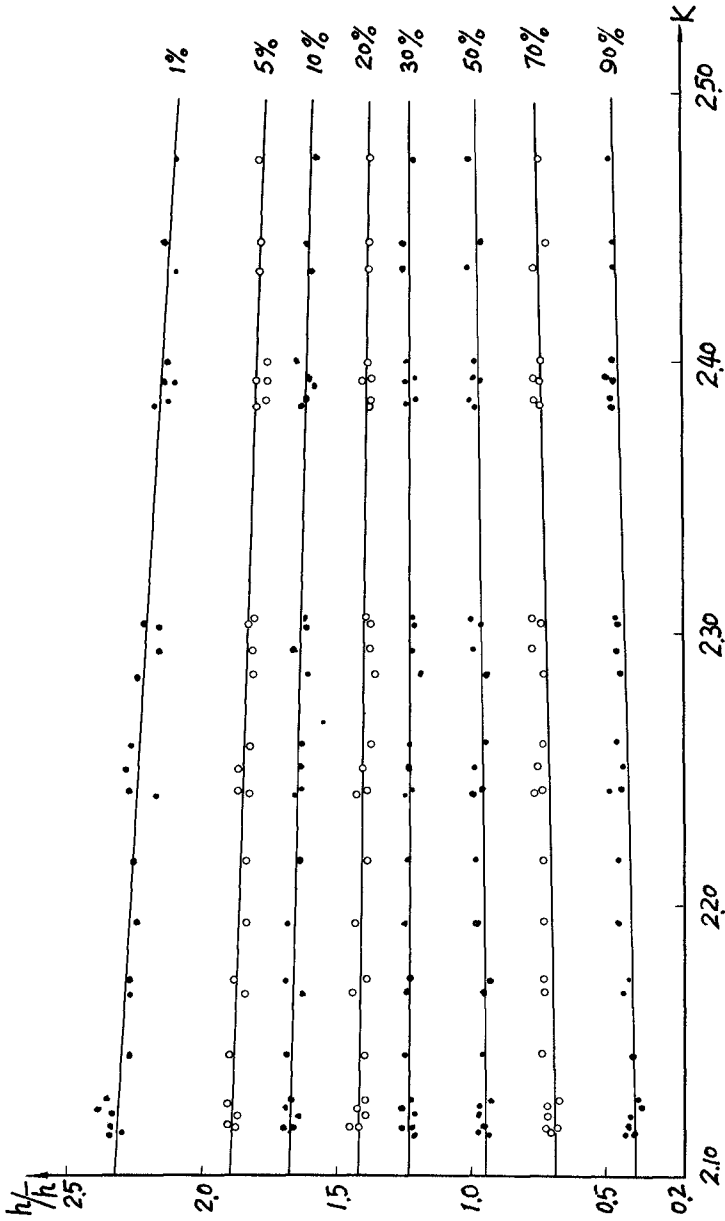


Fig. 1a Comparison of the empirical cumulative distribution (dots) of wave height with the value (line) calculated by eq.(1).

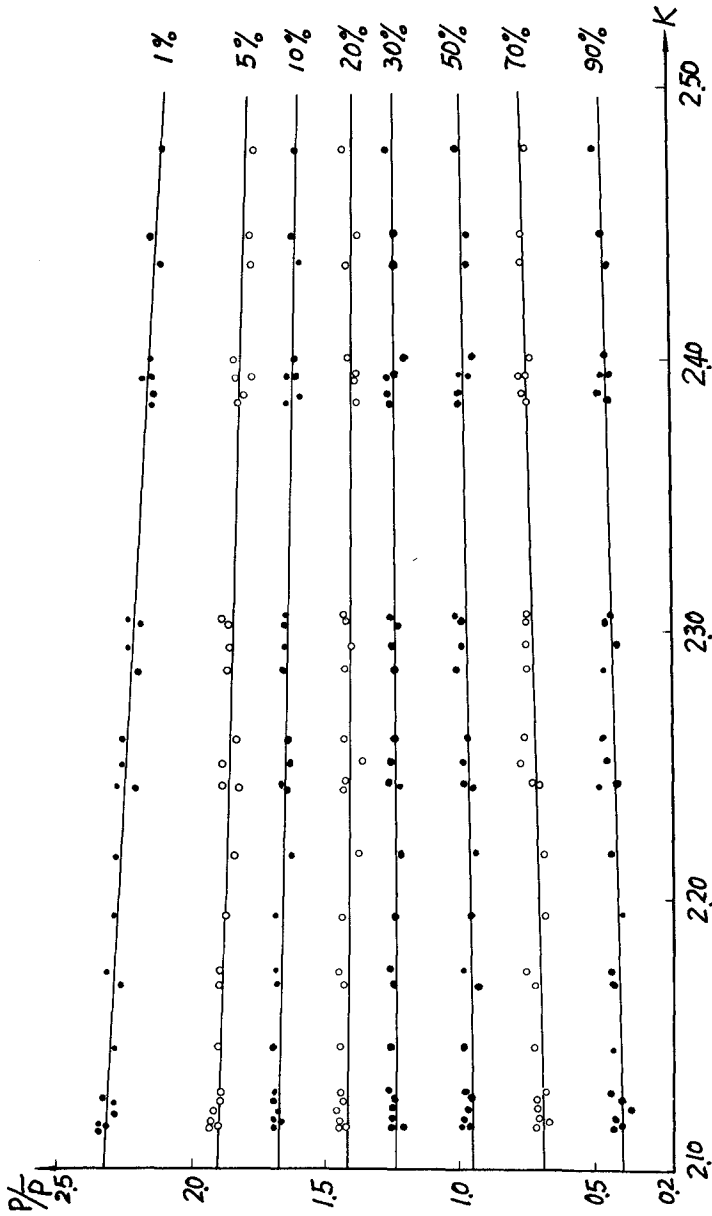


Fig. 1b Comparison of the empirical cumulative distribution (dots) of range of wave pressure fluctuation with the value (line) calculated by eq.(1).



of the nondimensional wave periods for the wind waves and the swell before the breaking area are, in fact, a constant no matter how deep the water is. Its distribution function is given as follows:

$$F(\tau) = \exp \left[ -\Gamma \left( \frac{5}{4} \right) \left( \frac{\tau}{\bar{\tau}} \right)^4 \right]. \quad (4)$$

To analyse the distributions of both the wave period in front of the breakwater and the wave pressure period at different heights on it, we have plotted the experimental cumulative distribution on the special coordinate paper such as Fig.2, whose curves denote the expression(4).

In Fig. 2,  $Z=0$  represents the distributions of the surface wave period in front of the vertical breakwater, and  $Z=-5.2\text{m}$ , the distributions of the wave pressure periods at the basement layer of the breakwater. There are also similar distribution for the mediate layers.

After analysing the experimental cumulative distributions of periods for the wave and wave pressure, it shows that, in the case of shallow water, the distribution of wave periods and wave pressure periods in front of the vertical breakwater may be calculated by expression(4), and that the distribution of period for the wave pressure does not vary with the altitudes of the measuring points practically.

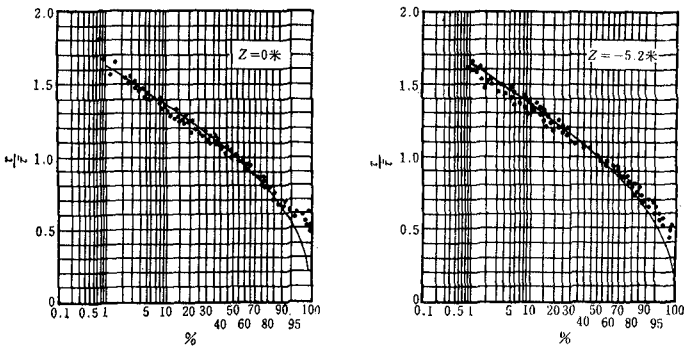


Fig. 2a,b The comparison of the experimental cumulative distribution of wave period and wave pressure period(points) with the theoretical cumulative distribution(curves).

### 2.3 The cumulative distribution function of the total pressure

The total pressure is one of the most important characteristic quantities for the wave acted on the vertical breakwater. At present, research on the total pressure is mainly

based on the analysis to the values of crest and trough of single wave hitted against the breakwater.

To analyse the distribution characteristics of the total pressure, we have calculated the crest value,  $R^+$ , and trough value,  $R^-$ , of the total pressure corresponding to the phases of every wave crest and wave trough based on 27 successive recordings. Then we obtained the cumulative distribution curves of the total pressures for the nondimensional crest ( $R^+_i/\bar{R}^+$ ) and trough ( $R^-_i/\bar{R}^-$ ). Furthermore, we determined the values of the total pressures of the nondimensional crest and trough corresponding to cumulative probability of 1, 5, 10, 20, 30, ..., 90%. According to the following expression(5)

$$F(R^\pm) = \exp \left[ -\Gamma \frac{5-B}{2-1.5H^*} \left( \frac{2-1.5H^*}{5-B} + 1 \right) \left( \frac{R^\pm_i}{\bar{R}^\pm} \right)^{(5-B)/2-1.5H^*} \right], \quad (5)$$

we computed the above mentioned total pressures of the nondimensional crest value and trough value for every cumulative probability as well as the relative differences between them and the actually measured value. Thus we have respectively made statistics of the occurrence probability for the relative differences within the given range (-5--+5%, -10--+10%). Then the mean absolute difference was calculated and the maximum relative differences corresponding to cumulative probability were obtained. Their results are shown in table 1.

Table 1

relative error		cumulative probability %							
		1	5	10	20	30	50	70	90
-5--+5%	$R^+$	100	100	100	100	100	100	100	81.48
	$R^-$	98.30	100	100	100	100	100	98.30	74.07
-10--+10%	$R^+$	100	100	100	100	100	100	100	96.30
	$R^-$	100	100	90	100	100	100	100	100
maximum relative error	$R^+$	-4.109	3.84	4.32	4.96	4.09	4.211	4.34	10.25
	$R^-$	7.272	3.261	3.012	3.543	4.065	-4.211	5.633	-8.888
average absolute error	$R^+$	0.030	0.022	0.0237	0.0200	0.0248	0.014	0.0155	0.014
	$R^-$	0.035	0.0229	0.0203	0.0174	0.0181	0.0155	0.0155	0.0163

Table 1 shows that the occurrence probability corresponding to every cumulative probability is quite high within the relative differences at -5--+5%, while the lowest is 74.07%. As for the mean absolute difference, its maximum is not more than 0.035. Therefore, it is deemed that the distribution function of the total pressures for the crest and trough of the wave acted upon the vertical breakwater in shallow water may be calculated by expression(5) and may be of identical distribution law of wave heights in front of the vertical breakwater.

As for the above cumulative distribution function of every parameter, the analysed results are of importance. In the case of shallow water, making use of these distribution law, we might obtain the required values of the arbitrarily given cumulative probability by the average wave height known in front of the vertical breakwater, the mean range of wave pressure fluctuation at different heights on it, the mean wave period and the mean total pressure. They are very useful to the engineering calculations.

### 3. ATTENUATION OF WAVE PRESSURE WITH DEPTH

The problem of the wave and the wave pressure attenuated with depth was first investigated on the open sea and ocean(6,13) or in the offshore area without any obstacles(6). Since the beginning of the 1970's, there were research results of both the waves and the wave pressures attenuated with the depth in front of the vertical breakwater under the deep water condition(9,11). On the basis of the actually measured data, we have analysed and investigated the regularity of the wave pressure spectral component attenuated with the depth and the constitution of the high frequency portion of the wave pressure spectrum in front of the vertical breakwater.

#### 3.1 The spectral component of wave pressure attenuated with depth

According to the ordinate data picked out by the same time interval( $t=0.75\text{sec.}$ ) for both the wave profile in front of the breakwater and the wave pressure fluctuations at different heights on it, we have obtained their spectrum densities respectively.

We regarded the frequency spectrum of the wave pressure at the levels  $-0.2$ ,  $-2.2$ , and  $-5.2\text{m}$  as original data used for analysing the spectral component of the wave pressure attenuated with the depth, then we compared the actually measured results with that of the wave theory for small amplitude at the limited depth. The attenuation coefficient of spectral component varied with the depth may be obtained, within the limited depth, by the wave theory

$$r(\omega, Z, d) = \text{ch}k(d + Z) / \text{ch}k(d + Z_0), \quad (6)$$

where  $d$  stands for water depth in front of the vertical breakwater,  $k$  stands for wave number; it has to be satisfied with the expression as follows:

$$\omega^2 = gk \text{th} k d. \quad (7)$$

Fig.3 shows the comparison of the measured attenuation coefficient of wave pressure spectral component at the level of water layers being  $-2.2$ , and  $-5.5\text{m}$  respectively with the values calculated(curve) by the expression(6).

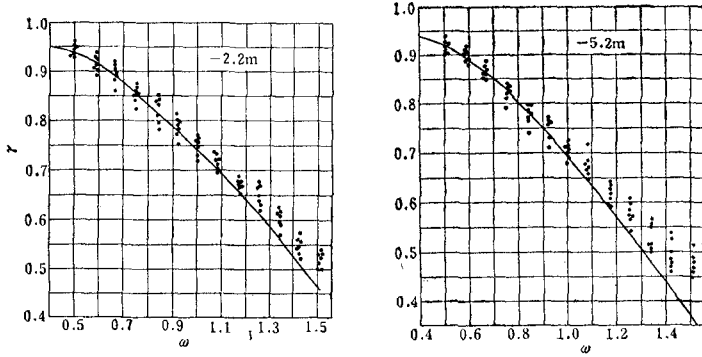


Fig.3 Comparison between the measured attenuation coefficient(dots) of wave pressure spectral components and the result(curve) of small amplitude wave theory

The above comparison shows that, within the whole range of  $0.5 < kd < 1.15$ , the low frequency components of the wave pressure spectra attenuated with the depth may be considered coincidence with the results of small amplitude wave theory for a limited depth. while  $kd > 1.15$ , the spectral component (corresponding to the high frequency portion of the wave pressure spectra) attenuated with the depth has a more even trend. This is due to the non-linear effect of the interaction between the wave and the vertical breakwater.

3.2 Equilibrium range of wave pressure spectrum varied with the depth

It is well known that there is a most important and specific hypothesis for the wind wave spectrum, namely, while the frequency is high enough, there is a range agreed with Phillips' equilibrium range(4,5,7). Within the equilibrium range, the wave energy is only related to the physical parameters characterized the mechanism of the wave crest breaking, but is independent of external factors of wind wave generation. If we only consider this range, in which the sea-water surface tension and sea-water molecular viscosity have no effect on the wave frequency, the constitution of the equilibrium range only depends on the frequency and the gravitational acceleration. Basing ourselves on the dimensional analysis, we may obtain:

$$S(\omega) = \beta g^3 \omega^{-5}, \tag{8}$$

where  $\beta$  is nondimensional constant, adopted as  $7.8 \times 10^{-3}$ (7).

At present, most measured wind wave spectra have primarily verified the expression(8) of the equilibrium range

worked out by Phillips(5,7). Until now we have studied very little of constitution of high frequency portion for the wave pressure spectra at different depth below the sea surface. In 1973, Цыплухин and Попов (14) analysed the wave pressure spectra at different depths on the vertical breakwater in the harbours of Сочи and Месхарис. They pointed out that, in the expression(8), the power of frequency varied with the depths from 5.0 of  $Z=-0.6m$  to 8.0 of  $Z=-11.2m$ . Such a result show that it is not proper to analyse by the dimension because the dimension of the spectrum density is varied with the power of the frequency in the expression(8).

We intend to investigate the constitution of the high frequency portion of the spectrum for both the wave in front of the breakwater and the wave pressure at different depth on it. We have plotted the points of the spectrum density values actually measured for the wave in front of the breakwater and the wave pressures at different depth on it onto the logarithmic paper, such as Fig. 4a shows the wind wave spectra in front of the breakwater, and Fig. 4b the wave pressure spectra at the level of  $-2.2m$ .

Fig. 4a, we see that the high frequency portion of the wind wave spectra in front of the vertical breakwater may be described by the expression(8)(rough inclined line in the Fig. ). From Fig. 4b, we see that the high frequency portion of wave pressure spectra almost parallelly deviates from the rough lines with the increase in depth. From this we may think that within the constitution of the equilibrium range of wave pressure spectrum, the power of the frequency is still equal to 5, and does not vary with the increase in depth, but its spectrum density values may get smaller with the increase in depth. From the expression(8), we may obtain:

$$\beta = S(\omega) \cdot \omega^5 / g^2, \quad (9)$$

Now we calculate the actually measured  $\beta$  values by expression(9), and then plot it (Fig. 5).

As an example, Fig. 5 gives the  $\beta$  values at the level of  $-0.2m$  through many observations; we can obtain similar diagram at other water levels, too. Since the tidal levels are not the same at each observation, the actual depths in every observation also are not the same at the level of  $-0.2m$ . Thus in Fig. 5, the  $\beta$  values measured in every observation always have some difference. While  $\omega > \omega_{max}$ , however, the  $\beta$  values actually measured in each time do not vary with the frequency primarily, and vary up and down at some  $\beta$  value. This is due to the errors in the observation and the spectrum analysis. As a result, after evaluating the average value of  $\beta$  actually measured at different depth, Fig. 6 is plotted with the average value of  $\beta$  as ordinate versus the nondimensional parameter  $Z\omega_{max}^2/g$  as abscissa. Here  $\omega_{max}$  is the spectral peak frequency.

Fig. 6 shows that, while the sea surface  $Z=0$ , the ave-

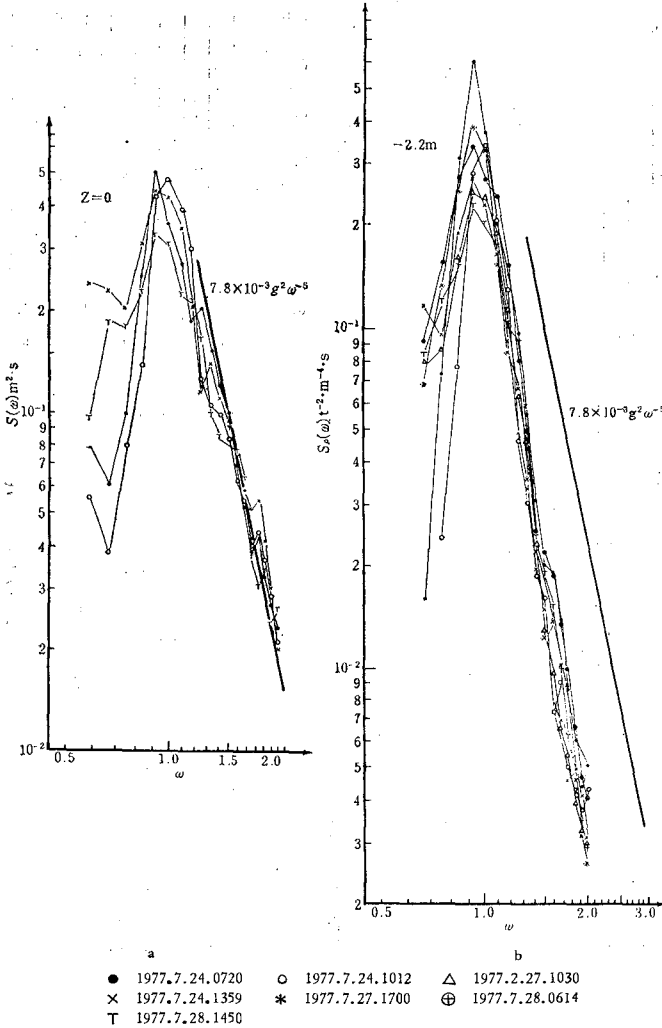


Fig. 4a,b The observed spectra of wave and wave pressure fluctuations at a vertical breakwater, declined line is expression(8).

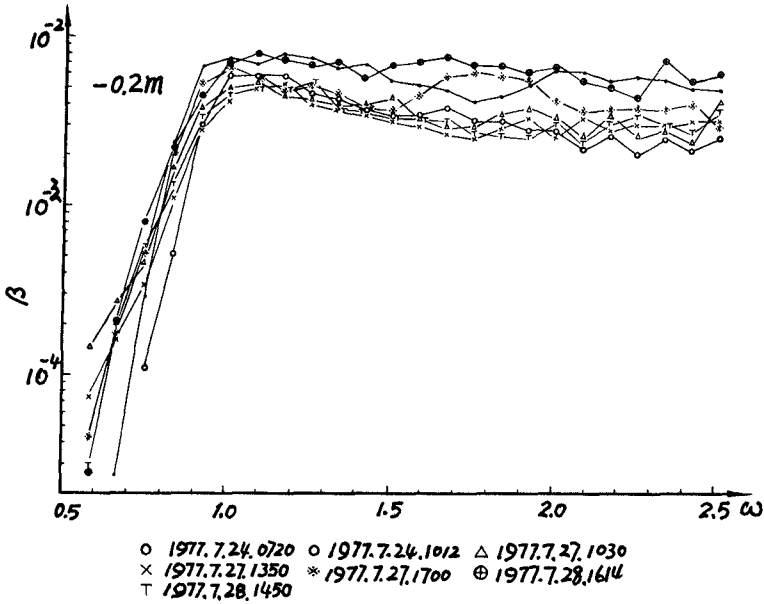


Fig. 5 The values of wave pressure spectra at level  $Z = -0.2m$ .

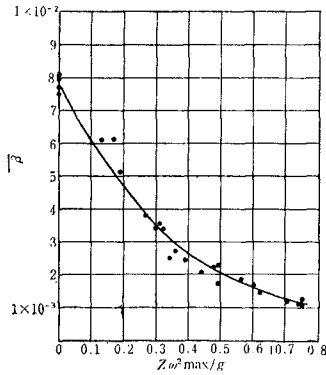


Fig. 6 The relationship between the measured value  $\beta$  and the nondimensional parameter  $Z\omega^2 \max/g$ , of which the curve from the eq.(10).

range value of  $\beta$  is  $7.8 \times 10^{-3}$ . Since the value of  $\beta$  get smaller with the increase of  $Z\omega_{max}^2/g$ , we can obtain:

$$\beta = \beta_0 \exp[-4\pi Z\omega_{max}^2/5g], \quad Z\omega_{max}^2/g \leq 0.75 \quad (10)$$

where  $\beta_0 = 7.8 \times 10^{-3}$ .

The above analyses, indicate that the equilibrium range of the wave pressure spectra at different depth on the vertical breakwater varied with depth may be described by the following expression:

$$S_p(\omega) = \beta_0 \omega^{-5} g^2 \exp[-4\pi Z\omega_{max}^2/5g], \quad (11)$$

#### 4. CONCLUSION

The results of this study are concluded as follows:

1. In the case of shallow water, the cumulative distribution of range of wave pressure fluctuation at different heights on the vertical breakwater actually does not vary with the heights of the measuring points on the breakwater, and it may be described by the expression(1). The cumulative distribution of both the crest value and the trough value of total pressure acted upon the breakwater agrees with that of wave height, and it may be calculated by expression(5).

2. The cumulative distribution of wave period also does not vary with the heights of measured points on the breakwater; it just follows the distribution law of expression(4).

3. The analysis of the wave pressure spectra at different altitudes in front of the vertical breakwater shows that within the whole range of  $0.5 < kd < 1.15$ , the low frequency portion of the wave pressure spectra attenuated with depth may be calculated according to the small amplitude wave theory within a limited depth. When  $kd > 1.15$ , the spectral component of the wave pressure (corresponding to the high frequency portion of the wave pressure spectrum) attenuated with depth has a more even trend. Thus we may think that it related to the nonlinear effect of the interaction between the wave and the vertical breakwater. In order to obtain a clear explanation, it is necessary to establish a nonlinear model of the interaction between the irregular wave and the vertical breakwater.

4. The high frequency portion of the spectra for both the wave in front of the vertical breakwater and the wave pressure at different altitudes on it agrees with the Phillips' equilibrium range. With the increase in depth, the power of the frequency in the constitution of the equilibrium range is basically unchanged, but the value of  $\beta$  may get smaller with the increase in the nondimensional parameter and can be described by the expression(10).



## REFERENCES

1. Huang Peiji, Yang Keji, Lu Changwu, Liu Laichen, 1979. A study on the force of ocean wave upon a vertical break-water. *Acta Oceanologica Sinica*, vol. 1, no. 2, 311--322. (in chinese).
2. Huang Peiji, Zhao Binglai, Liu Laichen, Pu Shuzhen, 1981. A distribution function for wind wave heights with parameter of wave growth stage. *Acta Oceanologica Sinica*, vol. 3, no. 4, 639--654. (in chinese).
3. Liu Laichen, Guo Dayong, Huang Peiji, 1980. The wave observation station of SHAZIKOU. *Transactions of Oceanology and Limnology*, 1, 71--75. (in chinese).
4. Phillips, O.M., 1958. The equilibrium range in the spectrum of wind-generated waves, *Jou. Fluid Mech.* 4, 426-434.
5. Гаджиев, Я.З., 1978. Изв. АН СССР, Физик атмосферы и океана, том. 14, вып. 3, 335--339.
6. Глуховский, В.Х., 1966. Исследование морского ветрового волнения. Л. Гидрометеиздат. 284.
7. Давидан, И.Н., Лопатухин, Л.И., Рожков, В.А., 1978. Ветровое волнение как вероятностный гидродинамический процесс. Л. Гидрометеиздат. 284.
8. Крылов, Ю.М., 1966. Спектральные методы исследования и расчета ветровых волн. Л. Гидрометеиздат, 254.
9. Крылов, Ю.М., Цыплухин, В.Ф., 1973. *Океанология*, том. 13, вып. 26, 203--209.
10. Крылов, Ю.М., Цыплухин, В.Ф., 1973. *Труды СОЮЗМОРНИИПРОЕКТА*, том. 34, вып. 40, 16--27.
11. Крылов, Ю.М., Цыплухин, В.Ф., 1974. *Труды СОКМОРНИИПРОЕКТА*, том. 36, вып. 42, 151--164.
12. Никеров, П.С. и др., 1971. Информационные материалы по Гидрометеорологическим приборам и методам наблюдений, сб. 46, М. Гидрометеиздат, 21--25.
13. Цыплухин, В.Ф., *Океанология*, 1963, том. 3, вып. 56, 833--839.
14. Цыплухин, В.Ф., Попов, Г.И., 1973. *Труды СОЮЗМОРНИИПРОЕКТА*, том. 34, вып. 40, 50--54.

## CHAPTER FIFTY ONE

### WAVE MEASUREMENT WITH DIFFERENTIAL PRESSURE GAUGES

by

Kevin R. Bodge<sup>1</sup> and Robert G. Dean<sup>2</sup>, M. ASCE

#### ABSTRACT

The potential error of estimating the small pressure gradient under a directional wave field through the subtraction or comparison of relatively large total-head signals from adjacent pressure transducers in an array is avoided through the use of differential pressure transducers which measure directly the pressure gradients. A device which utilizes four differential pressure transducers placed orthogonally about one absolute pressure transducer, (the "DPG"), was developed and field-tested at the U.S. Army Corps of Engineers Coastal Engineering Research Center Field Research Facility, Duck, North Carolina. The first five directional Fourier coefficients of the directional ocean spectra were developed from the DPG data, and although no other in situ directional wave monitors were available for comparison, the directional peak determined from the DPG agreed well with simultaneous High Frequency (HF) radar data. The DPG instrument is about one-half the size and less than one-sixth the weight of conventional pressure sensor arrays. The field establishment of the orientation of directional-measuring instruments is also discussed.

#### 1. INTRODUCTION

The "pressure-slope array" is a commonly used instrumentation technique to make in-situ point estimates of wave directionality. Such systems traditionally use a subsurface array of transducers which simultaneously measure the absolute pressure at a number of fixed locations under the wave field. Whereas the use of one pressure sensor to obtain wave height requires the measurement of the dynamic pressure sensed by a single gauge, the use of an array of pressure sensors to obtain wave direction requires intercomparison of the dynamic pressures sensed at adjacent gauges. The direction can be estimated by a number of methods. One is to cross-correlate each of the sensors' signals directly (2). Another is to calculate the

<sup>1</sup>Ph.D. Candidate, Coastal and Oceanographic Engineering Department, University of Florida, Gainesville, FL 32611; Formerly, Research Assistant, Department of Civil Engineering, University of Delaware, Newark, DE 19711.

<sup>2</sup>Graduate Research Professor, Coastal and Oceanographic Engineering Department, University of Florida, Gainesville, FL 32611; Formerly, Professor, Department of Civil Engineering and College of Marine Studies, University of Delaware, Newark, DE 19711.

pressure gradients between the sensors and cross-correlate this estimate of slope (4). In any case, the analysis methods are concerned with the difference in pressures sensed between points under the wave field. For a typical array, where pressure sensors might be spaced about 20 feet (6 m) apart, the instantaneous differences in the sensors' records due to wave action can be very small relative to the large total-head values that the sensors are required to record. Hence the pressure gradient across the array is calculated by comparing two large numbers in order to generate a very small number. This technique can lead to inherent inaccuracies, for example due to minor non-linear response or different noise levels in the sensors. The difference between adjacent sensor signals can be increased by enlarging the distance between transducers -- at the expense of a more physically unmanageable array, greater error in the assumption of linear surface slope, and possibly introduction of directional ambiguities for the higher frequencies present.

It is desirable, then, to measure directly the difference in pressure between two points. A differential pressure transducer (DPT) is ideally suited for this task. The DPT generates an electrical voltage proportional to the fluid pressure difference on opposite sides of a mechanical diaphragm, and can thus be considered an inherently more effective instrument for determining pressure gradient (and thereby wave direction) than conventional pressure sensors. Further, the variation with depth of the differential pressure is a maximum over a range of frequencies that is more representative of typical ocean gravity waves. For a pressure transducer located at height  $s$  above bottom, the dynamic pressure,  $P_{dyn}$ , can be expressed as a function of position  $(x,y)$  from linear theory, as:

$$P_{dyn}(x,y,s,t) = \gamma \frac{H}{2} K_p(s) \cos(k_x x + k_y y - \sigma t + \epsilon) \quad (1)$$

where  $K_p(s) = \frac{\cosh ks}{\cosh kh}$ , the pressure response factor

and  $H$  = wave height

$x,y$  = coordinate axes in the horizontal plane

$k_x = k \cos \theta$  = wavenumber in the x-direction

$k_y = k \sin \theta$  = wavenumber in the y-direction

$\theta$  = wave direction, measured counter-clockwise from the x-axis

$\sigma$  = wave frequency

$h$  = water depth

$\gamma$  = specific weight of seawater

$\epsilon$  = phase angle

The x- and y-components of pressure gradient are then:

$$dP(x,y,s,t) = -\gamma \frac{H}{2} k \begin{bmatrix} \cos \theta \\ \sin \theta \end{bmatrix} K_p \sin(k_x x + k_y y - \sigma t + \epsilon) \begin{bmatrix} dx \\ dy \end{bmatrix} \quad (2)$$

Figure 1 depicts the dynamic response of pressure for a DPT located in twenty feet (6.1 m) of water, three feet (0.91 m) off the bottom, with

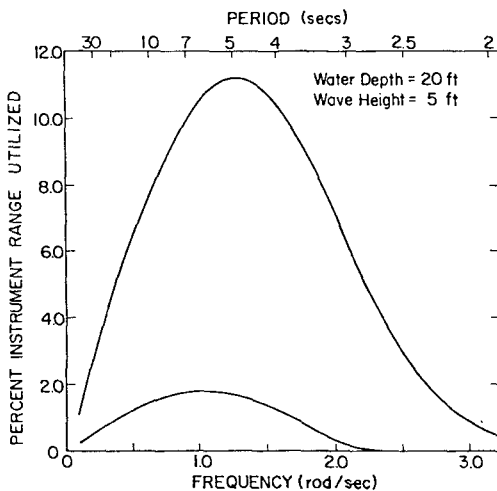


Figure 1. Upper curve: signal from differential pressure transducer sampling 3 feet (0.9 m) along wave ray. Lower curve: difference of signals from two absolute pressure transducers separated 20 feet (6.1 m) along wave ray. (Both curves normalized by typical rated capacity of the measuring instrument.)

a wave height of 5.0 feet (1.5 m). The DPT is assumed to sample two points separated by three feet (0.91 m) coincident with the wave ray. The lower curve represents the difference in pressure monitored by two absolute pressure transducers separated by twenty feet (6.1 m) along the wave ray. The response of each system is normalized by typical values of the rated capacity of the instruments: 35 psia (2460 cm H<sub>2</sub>O) for the absolute pressure transducer and  $\pm 0.5$  psid (70.3 cm H<sub>2</sub>O total differential) for the DPT. The differential pressure signal utilizes a greater portion of the instrument dynamic range than the difference between adjacent absolute pressure gauge signals and reaches its greatest response for waves between four and six second periods for the deployment described. The maximum response of the DPT shifts to longer period waves with increasing water depth or instrument deployment depth. The response of the DPT was developed over a pressure sampling space, or gage length, of only three feet (0.91 m) -- less than one-sixth the gage length of conventional pressure sensor array systems. The differential pressure gauge concept, then suggests that more efficiently measured directional information can be obtained with a considerably smaller instrument than is presently used.

## 2. THE DIFFERENTIAL PRESSURE GAUGE DIRECTIONAL WAVE MONITOR

To test the effectiveness of an array using differential pressure transducers, the differential pressure gauge directional wave monitor

(DPG) was developed and tested under field conditions. The DPG samples the pressure about its center using an absolute pressure transducer and simultaneously samples the pressure gradient along four arms oriented orthogonally about the instrument center using four DPT's, (Figure 2). There are two redundant slope measurements made along each axis in case one of the arm sensors should fail or so that directional spectra calculated from different combinations of gauges might be compared. It was also hoped that the pressure curvature could be developed through the subtraction of collinear slope terms.

### 3. SELECTION OF TRANSDUCERS AND DPT ARM LENGTH

The selection of the arm length which establishes the pressure difference to be measured by the DPT is dependent upon three criteria: (i) the characteristics of the transducer, (ii) the error in approximating the water surface slope as a linear function between the two sampled points, and (iii) reasonable size limitations of the instrument. The third criterion limits the gage length per transducer to a maximum of about 5 feet (1.5 m) if one imposes a design constraint of easy instrument manageability. At such small spacings, the maximum error in linearly approximating the water surface slope between sampled points is less than one and one-half percent for the shortest waves of interest, (say 3.2 seconds). The necessary rated capacity of the transducer R, is a function of the maximum pressure gradients expected and the ability of the transducer to detect and report a pressure difference of a minimum wave condition beyond the ambient and electrical noise level. From Eq. (2), the gage length between sensors can be found from

$$\Delta x = \frac{R}{\gamma H k K_p} \quad (3)$$

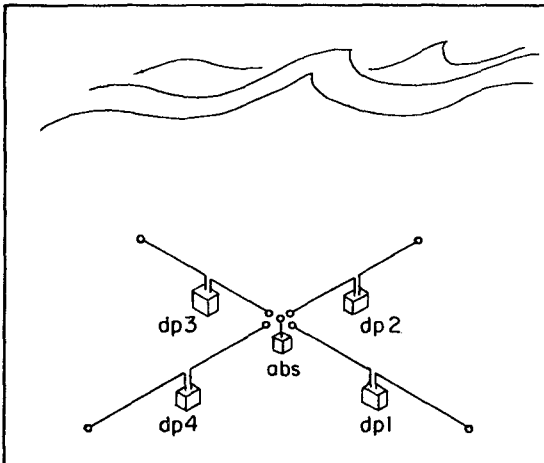


Figure 2. Schematic representation of the DPG directional wave monitor.

evaluated for the maximum wave height of interest (at the most sensitive wave frequency of the DPT at the selected deployment depth).

The site selected for field evaluation of the DPG was the United States Army Corps of Engineers Field Research Facility (FRF) at Duck, North Carolina, which is operated by the Coastal Engineering Research Center (CERC). The instrument was to be placed near and hard-wired to the Facility research pier. After examining the bathymetry near the pier, a nominal deployment depth of 20 feet (6.1 m) was selected. This indicated that the instrument would be most sensitive to waves of about 5 second period, (Figure 1). A design wave height of 16 feet (4.9 m) was chosen and considered with a gage length of 5 feet (1.5 m). This suggested the use of a  $\pm 0.6$  psid ( $\pm 42$  cm H<sub>2</sub>O) transducer which was unavailable. A  $\pm 0.5$  psid ( $\pm 35$  cm H<sub>2</sub>O) transducer was selected instead resulting in a gage length of 4.15 feet (1.27 m) from Eq. (3). The overall dimensions of the final instrument, then, became 9.75 feet (3 m) along each axis and 40 inches (1 m) in height to accommodate the electronics package. The sensors are approximately 3.9 feet (1.2 m) from the seafloor when the instrument is mounted in a supporting cradle.

#### 4. DPG HARDWARE

The in situ instrumentation is contained in a poly-vinyl chloride (PVC) structure that is secured to a steel cradle fixed to the seafloor. The PVC structure, or "instrument" as it is called hereafter, consists of a central tube, or "fuselage," and four arms that extend from near the top of the fuselage, (Figure 3). The fuselage section contains five pressure-sensing isolation diaphragms and a water-tight instrumentation cylinder that contains the pressure transducers. Each of the four arms contain a pressure-sensing isolation diaphragm near its end. The arms bolt into a PVC 4-pipe female junction within the fuselage so that the arms can be disconnected for greater ease in transportation, or potentially, a change in arm orientation. The ends of each arm and the top of the fuselage are punctured with 5/8 inch (1.6 cm) holes. Removable end-caps are fastened to the extreme ends of each arm and the fuselage in order to protect the isolation diaphragm sensors.

A typical DPT (Setra Systems Model 228) measures the pressure difference between the isolation sensor at the end of one arm and one of the five isolation sensors mounted within the fuselage near the center of the instrument. The fifth isolation sensor in the fuselage provides a signal measured by a Setra Systems Model 205-2 50 psia (3515 cm H<sub>2</sub>O) absolute pressure transducer. Each isolation sensor consists of a flexible 13 mil DuPont Fairprene® elastomer sealed to an acrylic housing by a 90-10 copper-nickel alloy ring and six Monel® bolts, (Figure 4). The exposed diameter of the elastomer is 1.625 inches (4.1 cm). The isolation sensors are connected to the transducers by flexible tubing -- 1/8 inch (3.2 mm) I.D. stainless steel armored teflon outside the water-tight cylinder and 1/16 inch (1.6 mm) I.D. nylon tubing inside. The tubing is back-filled with an ethanol-water mix (gin) such that the response time of a transducer to a static load placed on its isolation sensor was measured as 0.12 seconds for all sensors.

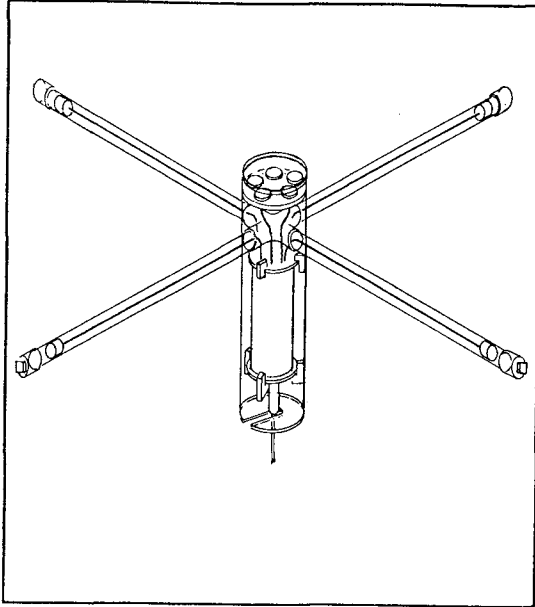


Figure 3. Rendering of the DPG instrument.

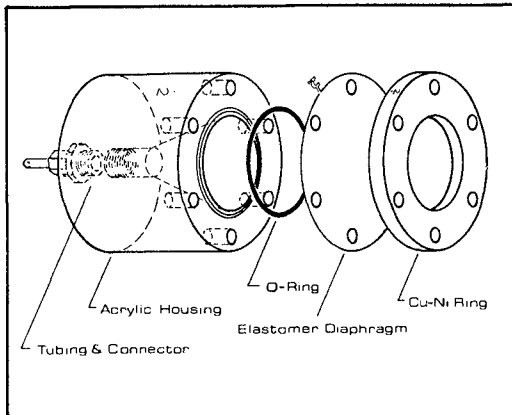


Figure 4. Assembly drawing of an isolation sensor chamber.

The instrument is anchored to the seafloor using a steel cradle which consists of two mutually perpendicular pieces of channel iron in plan view with a hole in the center, and legs to raise the channel off the seabed. The arms of the instrument fit into the channel and are made fast with heavy electrical cable ties. The cradle is anchored to the seafloor by chain that runs taut between each arm of the cradle and screw-anchors in the seabed. Alone, the cradle weighs about 200 pounds (91 kg) in air and about 280 pounds (127 kg) with the instrument attached (cable excluded).

The instrument is cabled to shore for power requirements and analogue data delivery. Eighty feet (24 m) of the seaward end of the cable is stripped of its armoring and stored in a plexiglass box immediately shoreward of the instrument. The top plate of the box is removable in order to access the extra cable if the instrument is to be moved or taken to the surface.

#### 5. CALIBRATION AND WAVE TANK EVALUATION

A relatively simple bench calibration system was designed consisting of two pressure chambers which secure around each isolation sensor of a DPT using a short length of motorcycle tire inner tube, (Figure 5). Each chamber is equipped with a pressure transducer and a bicycle tire valve. The two chambers are connected by tubing with a valve in the center to isolate, bleed, or allow the chambers to communicate with one another. The chambers are pressured with a bicycle tire pump and the pressures which are sensed simultaneously in each chamber and by the corresponding DPG transducer are recorded on a multi-channel strip chart. The response time for the DPG transducers was determined by measuring the passage of time between loading events as reported by the chamber transducers and by the DPG transducer. If an anomalous pressure difference or response lag was observed during a

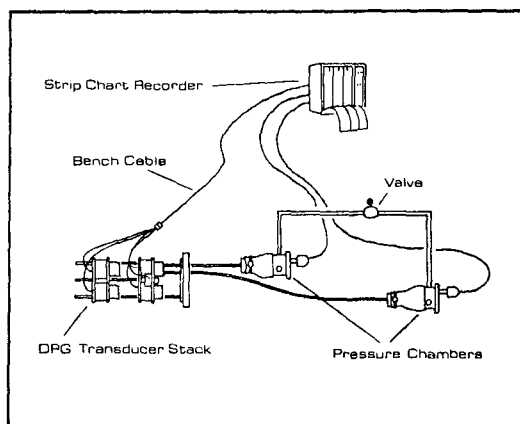


Figure 5. The DPG bench calibration system. One pair of sensors shown for clarity.



calibration test, it was assumed that air was present in the lines and the isolation sensors and connecting tubing were re-back-filled and re-calibrated. After the final back-filling and calibration, each of the transducers on board the DPG was found to respond linearly (1:1) to the pressure loads imposed on its isolation sensors.

The tubing length of the arm sensors is four times greater than that of the center sensors so that an ambient temperature change induces a slight differential pressure across each DPT. (Volumetric expansion of a fluid is linearly proportional to the change in temperature and initial volume of fluid, so that the expanded volume in the arm sensors due to a temperature increase will be four times that of the center sensors.) Temperature changes under twenty feet (6.1 m) of ocean water are typically of low frequency, so it is assumed that any temperature-induced drift during a sampling interval will be interpreted as a very long period wave or as a mean which changes from record to record. If the mean of a DPT record was known at some measured ambient temperature, then for any other sampling interval, the record mean could be used to approximate the water temperature during the time of that record, (neglecting the small lag of the transducer readings due to the thermal mass of the instruments).

An early version of the DPG was tested in the Coastal Engineering Research Center's large outdoor wave tank at Fort Belvoir, Virginia. This initial version of the instrument used semi-rigid 1/8 inch (3.2 mm) I.D. sensor tubing, and it is believed that three of the four arm tubings broke during the instrument assembly; (the tubing was subsequently changed to a flexible type for the field evaluation). The absolute pressure gauge and differential pressure channel dP3 appeared to be in satisfactory order, however, and their signals were recorded on a strip chart while the instrument operated under large amplitude, regular waves generated for another test in progress. The wave profile recorded by the tank's resistance wave staffs indicated non-linear waves of 5 second period and crest-to-trough height between 3.0 feet (0.925 m) and 3.36 feet (1.025 m). Because of the highly non-linear nature of the waves, stream function theory (3) was used to calculate the water surface displacement inferred by the signals of the DPG's absolute pressure gauge — approximately 3.2 feet (0.98 m) from crest to trough with a period of 5 seconds.

The DPG orientation relative to the unidirectional wave train was approximated from the signal of dP3 for each of the two DPG orientations tested. The average total magnitude of the dP3 signal was estimated from the strip chart and the maximum differential pressure expected along the direction of wave travel  $s$ , was calculated from stream function theory. The angle  $\theta$  between the wave ray and the dP3 arm is then:

$$\theta = \cos^{-1} \left[ \frac{\left| \frac{dP}{dx} \right|_{\text{measured by dP3}}}{\left| \frac{dP}{ds} \right|_{\text{max. calculated}}} \right] \quad (4)$$

where  $(dP/ds)_{\max}$  is the value applicable for  $\theta=0^\circ$  from stream function theory. The orientation of arm 3 of the DPG was measured approximately by divers as  $55^\circ$  to the tank centerline, or wave ray, for the first tests and  $35^\circ$  for the second tests. The calculated angle from (4) using the instrument data was  $51.3^\circ$  and  $35.4^\circ$  for each of the two sets of tests, respectively. The directional agreement -- as well as the ease with which the instrument was installed and removed -- was encouraging. Details of the wave tank evaluation are given in Bodge (1).

#### 6. FIELD INSTALLATION AND ORIENTATION MEASUREMENT

The DPG field prototype was deployed at the CERC Field Research Facility on May 14, 1982, using the Facility's Coastal Research Amphibious Buggy (CRAB). The CRAB is a large tripod that is capable of driving across the beach and into the surf zone under its own power. The DPG was hoisted beneath the operator's platform, and the CRAB driven toward the end of the pier where the cable was mated to the instrument and then driven to the installation site where the instrument and cradle were lowered and secured to the seafloor by divers. The relatively small and lightweight DPG hardware, combined with the flexibility of the CRAB, afforded a very smooth installation -- despite less than ideal wave conditions.

The DPG is installed on the relatively stable 20 foot (6.1 m) depth contour, approximately 735 feet (224 m) south of the pier and 1800 feet (549 m) offshore. The orientation of the instrument was determined using a submersible digital compass mounted at the end of a five-foot (1.5 m) length of aluminum angle which was placed atop the end of each PVC instrument arm. In this way, the digital compass was at least six feet (1.8 m) from the steel cradle. Compass headings were recorded for each arm twice -- once by each of two divers -- and then averaged. The orientation of each arm was also measured by securing a diver's compass around the end of each arm using the compass wrist strap. Measurements were taken three times for each arm using two different wrist compasses and then averaged. All of the values recorded for each technique along each arm agreed reasonably well within a technique.

As an experiment, the divers' compasses were placed on an arm above the end of the steel channel and then slid towards the end of the arm. The heading changed as the compass moved across the end of the steel and then remained relatively stable. It was therefore thought at the time that the readings taken at the ends of the PVC arms were sufficiently far from the steel cradle to avoid magnetic bias. However, this was found not to be the case. Since each arm is perpendicular to its neighboring arm, adjacent arm bearings are constrained to be  $90^\circ$  apart. Although the digital compass measurements approximate  $90^\circ$  separation, those of the wrist compasses clearly do not, (Table 1).

If the measured orientation  $\beta_n'$  is expressed in terms of the actual orientation,  $\beta_n$ , of the arm and the error,  $\epsilon_n$ , associated with that arm that is introduced by the metal mass of the cradle, one can write:

Table 1: ORIENTATION HEADINGS* OF THE DPG ARMS					
ARM	WRIST COMPASS		DIGITAL COMPASS		RESOLVED
	apparent	actual	apparent	actual	averaged
1	228.33	241.75	238.80	241.89	241.82
2	155.33	151.75	153.90	151.89	151.82
3	78.00	61.75	61.20	61.89	61.82
4	325.33	331.75	333.65	331.89	331.82

\*Headings are with respect to magnetic north, 6/15/82.

$$\beta_n' = \beta_n + \epsilon_n \quad (5)$$

Since the compasses were placed upon each arm at about the same distance from the center of the instrument, and if one assumes that the effect of the metal mass upon the compass readings is the same for each arm (i.e., radially inward), then the errors associated with each of two collinear arms should be equal and opposite in sense. Accordingly,

$$\sum_{n=1}^4 \epsilon_n = 0 \quad (6)$$

If one expresses the actual orientation of each arm in terms of the arm with the smallest value of apparent direction, (arm 3, in this case), Eq. (5) may be written:

$$\beta_3' = \beta_3 + \epsilon_3 \quad (7a)$$

$$\beta_4' = \beta_3 + 90^\circ + \epsilon_4 \quad (7b)$$

$$\beta_1' = \beta_3 + 180^\circ + \epsilon_1 \quad (7c)$$

$$\beta_2' = \beta_3 + 270^\circ + \epsilon_2 \quad (7d)$$

From the sum of Eqs. (7) and substituting (6);

$$\beta_3 = \frac{1}{4} \left[ \left( \sum_{n=1}^4 \beta_n' \right) - 540^\circ \right] \quad (8)$$

The corresponding orientation for each of the other three arms may be found by successively adding  $90^\circ$  to the orientation of the adjacent arm. The agreement between the corrected averages of the arm headings as found using the expensive digital compass and the two simple wrist

compasses is surprisingly good, within  $0.3^\circ$  (Table 1). This investigation indicates the importance of establishing the inherent inaccuracies in a compass and/or of careful redundant checks of instrument orientation when working near a steel structure.

## 7. DATA ANALYSIS AND RESULTS

If only the absolute pressure signal  $P$ , and one slope signal from each of the two axes,  $dP_x$  and  $dP_y$ , are processed, then the DPG yields the same information as a heave-pitch-roll buoy. The first five coefficients in a Fourier series representation of the directional wave spectrum ("directional Fourier coefficients," or DFC's, for short), can be found using the analysis technique described by Longuet-Higgins, Cartwright, and Smith (4).

If the absolute pressure and the four slope signals are measured and the curvature across each axis established, the first seven DFC's could be developed by the aforementioned technique (4). However, attempts to calculate curvature through the subtraction of collinear slope measurements were generally unsuccessful. This is not surprising since it requires the calculation of very small curvature terms by subtracting two already small (measured) slope terms. In principal, differential pressure transducers can be used to measure directly pressure curvature, however, and this technique will constitute the subject of a future investigation.

If one directly cross-correlates the instrument's signals using the technique outlined by Borgman (2), among others, higher order DFC's can generally be obtained. If one directly cross-correlates the instrument's signals using the technique outlined by Borgman (2), among others, higher order DFC's can be obtained if the gages are separated sufficiently to allow estimation of an accurate separation-related phase difference in the signals of the two gages. If the gages are so closely located that it is impossible to obtain meaningful phase differences due to their separation, it is possible to estimate only the first five DFC's. If it is known that waves approach only over a limited range of directions, it is possible to modify the analysis procedure to improve the directional description substantially. Altering the orientation of the arms as shown in Figure 6 would appear to improve the quality of the directional distribution information for waves approaching over a limited range of directions.

Inspection of the time series signals from the submerged DPG indicated that one of the differential transducers along the instrument's x-axis was suspect. Accordingly, only the absolute pressure signal and one measure of slope along each axis were processed. In particular, the pressure slope along each axis was calculated by dividing each differential pressure signal by the gauge length between DPT sensors, and the absolute pressure and pressure slope time series were then transformed to the frequency domain. The linear pressure response function and a low pass filter were applied to obtain the water surface displacement and slope spectra, and the analysis technique mentioned above, (4), was utilized in order to calculate the first five directional Fourier coefficients.

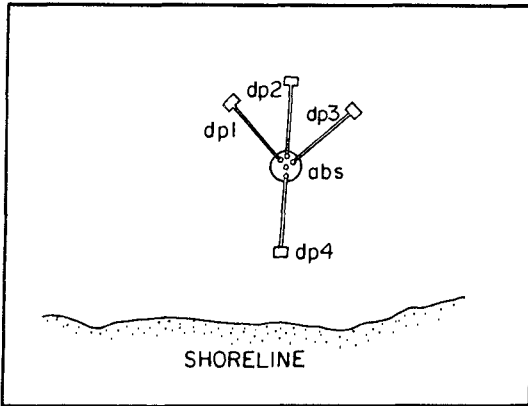


Figure 6. Plan view of DPG proposed to potentially improve resolution of directional wave distribution.

For several data sets, directional spectra were calculated using  $P$ ,  $dP_x$ , and one of the  $dP_y$  signals -- and then re-calculated using  $P$ ,  $dP_x$ , and the other  $dP_y$  signals from the redundant y-axis differential pressure transducer. Agreement between the calculated spectra using the two different y-axis DPT signals was satisfactory (1).

No other *in situ* directional wave monitors were operational during the first few months following the DPG installation. Therefore, the wave height and period information calculated from the DPG's absolute pressure sensor were compared to height and period estimates from nearby surface-piercing Baylor gauges, (Table 2). The direction of peak wave energy reported by the DPG was compared to visual estimates and HF radar images of the wave fields, (Table 2). The agreement between observed and DPG-generated height, peak period, and directional estimates, (all taken from the spectra for the DPG estimates), is encouraging.

It is theoretically possible to develop the water surface displacement energy spectrum from the slope spectra of the differential gauges:

$$S_{\eta\eta}(\sigma) = \frac{S_{\eta_x\eta_x}(\sigma) + S_{\eta_y\eta_y}(\sigma)}{k^2} \quad (9)$$

where  $S_{\eta\eta}$ ,  $S_{\eta_x\eta_x}$ , and  $S_{\eta_y\eta_y}$  represent the auto-spectra of water surface displacement, and x-axis and y-axis slopes respectively. Theoretically, it is also possible to estimate the principal wave direction without the absolute pressure signal if one assumes that there exists only one wave direction  $\theta$  per frequency  $\sigma$ . Specifically,

Table 2: COMPARISON OF DPG RESULTS WITH FRF MEASUREMENTS AND OBSERVATIONS

8 June - 11 June, 1982

<u>DATE</u>	<u>TIME</u>		<u>DPG</u>	<u>FRF</u> <u>OBSERVATIONS</u>
6/8	0700	dirxn	59°	58° <sup>a</sup> (50°) <sup>b</sup>
		H <sub>sig</sub>	1.39	1.41 <sup>c</sup>
		period	8.23	8.00 <sup>c</sup>
	1300	dirxn	59°	-
		H <sub>sig</sub>	1.28	1.33 <sup>c</sup>
		period	8.79	9.57 <sup>c</sup>
6/9	0700	dirxn	67°	68° <sup>a</sup> (50°) <sup>b</sup>
		H <sub>sig</sub>	1.34	1.33 <sup>c</sup>
		period	9.44	9.66 <sup>c</sup>
6/10	0700	dirxn	65°	66° <sup>a</sup> (55°) <sup>b</sup>
		H <sub>sig</sub>	1.23	1.56 <sup>c</sup>
		period	10.19	10.56 <sup>c</sup>
	1300	dirxn	85°	-
		H <sub>sig</sub>	1.71	1.82 <sup>c</sup>
		period	11.07	10.34 <sup>c</sup>
6/11	0700	dirxn	73°	69° <sup>a</sup> (60°) <sup>b</sup>
		H <sub>sig</sub>	1.32	1.53 <sup>c</sup>
		period	11.07	10.89 <sup>c</sup>

NOTES:  
 "dirxn" listed is the principal direction (peak energy), true north.  
 "H<sub>sig</sub>" is the significant wave height in meters.  
 "period" corresponds to the frequency band of greatest energy in seconds.  
<sup>a</sup>CERC Radar ( $\pm 2^\circ$ )  
<sup>b</sup>visual estimate from the end of the pier  
<sup>c</sup>CERC Baylor Gauge near the end of the pier

$$\tan 2\theta (\sigma) = \frac{2 S_{\eta_x \eta_y} (\sigma)}{S_{\eta_x \eta_x} (\sigma) - S_{\eta_y \eta_y} (\sigma)} \quad (10)$$

There exist four roots in the arc-tangent of  $2\theta$ , and it can be shown that two of these roots are associated with maxima (and separated by  $180^\circ$ ) and the other two (also separated by  $180^\circ$ ) are associated with minima and separated from the first two roots by  $90^\circ$ . Two of these roots (the minima) can be eliminated by considering the signs of the numerator and denominator. The remaining two might be resolved by considering the physical environment of the instrument deployment site; i.e., ruling out the possibility of dominant waves originating

from the beach. Equations (9) and (10) were tested on a frequency-by-frequency basis with DPG data and compared to the total energy from the absolute channel and the peak-energy direction found from the directional spectra, respectively. Agreement was poor (with errors often greater than 40% in energy and 70° in direction) -- presumably due to spectral leakage and because the noise of the differential pressure signals is potentially greater than that of the absolute pressure signals and because the wave energy is spread over many directions in reality.

Similarly, a directional estimate was considered (and found likewise unreliable) which uses only one differential pressure signal and the absolute pressure signal:

$$\theta(\sigma) = \cos^{-1} \frac{1}{k} \sqrt{\frac{S_{\eta_x \eta_x}(\sigma)}{S_{\eta\eta}(\sigma)}} \quad (11)$$

or

$$\theta(\sigma) = \sin^{-1} \frac{1}{k} \sqrt{\frac{S_{\eta_y \eta_y}(\sigma)}{S_{\eta\eta}(\sigma)}} \quad (12)$$

assuming one direction per frequency. Non-linearity in wavenumber,  $k$ , may contribute to the observed error of (11) and (12).

## 8. CONCLUSIONS

From the present work, it appears that differential pressure gauges provide an effective means of measuring the pressure gradient under a wave field -- enabling estimation of at least the first five coefficients in the Fourier series representation of the directional wave spectrum. The use of differential pressure sensors enables one to directly measure pressure gradients over small arrays instead of comparing large-valued point measurements of pressure over relatively large arrays. It appears that the development of higher order terms, such as curvature, are also best made directly.

## ACKNOWLEDGEMENTS

The DPG was reduced to practice under U.S. Army Corps of Engineers Coastal Engineering Research Center Contract No. DACW72-81-C-0025 and further supported by the Exxon Research Foundation while the authors were at the University of Delaware. The authors wish to thank James Coverdale, Ed Green, and Roland Essex of the University of Delaware Civil Engineering Shop Facility, Dr. Todd Walton of CERC, Curtis Mason and the staff of the FRF, and Brian Jacobs, "Chip" Fletcher, David Wiley, and Karen Francheschini for their dedicated assistance to the project.

## APPENDIX 1. - REFERENCES

1. Bodge, K. R., "The Design, Development, and Evaluation of a Differential Pressure Gauge Directional Wave Monitor," U.S. Army Corps of Engineers Coastal Engineering Research Center, MR82-11, October, 1982.
2. Borgman, L. E., "Directional Spectra Models for Design Use," Proceedings, Offshore Technology Conference, 1969.
3. Dean, R. G., "Evaluation and Development of Water Wave Theories for Engineering Application," Special Report No. 1, U.S. Army Corps of Engineers Coastal Engineering Research Center, Vols. I and II, Nov., 1974.
4. Longuet-Higgins, M. S., Cartwright, D. E., and Smith, N. D., "Observations of the Directional Spectrum of Sea Waves Using the Motions of a Floating Buoy," Ocean Wave Spectra, Proceedings of a Conference, Prentice-Hall, Inc., Englewood Cliffs, N.J., 1963.



## CHAPTER FIFTY TWO

### Prediction of Wave Group Statistics

Steve Elgar,<sup>1</sup> R.T. Guza,<sup>2</sup> and R.J. Seymour<sup>3</sup>

Two methods of numerically simulating random seas, given a target power spectrum, are discussed. Wave group statistics, such as the mean length of runs of high waves, produced by the different simulation schemes are compared. For a large number of spectral components, no significant differences are found in the wave group statistics produced by the two simulation techniques. Using the simulation techniques, it is shown that ocean gravity wave group statistics are not inconsistent with an underlying wave field composed of linearly superposed random waves. The majority of the field data examined were collected in 9-10 m depth, significant wave heights ranged from about 20 to 200 cm, and the spectral shapes ranged from fairly narrow to broad. For the 9-10 m depth data, observed mean run length, variance of run length, and the probabilities of runs of a given number of high waves were statistically consistent with the linear simulations. In contrast to the apparent linear behavior in 9-10 m depth, waves in 2-3 m depth showed substantial departures from the linear simulations.

#### Introduction

Groups of high waves are commonly observed in the ocean. A run or group of waves is defined as a sequence of waves, the heights of which exceed a particular level (Goda, 1970). It has been suggested that such runs of large waves effect coastal structures such as breakwaters (Burcarth, 1979) and pipelines (Dean, 1980), and influence the response of ships to the wave field (Pinkster and Huijsmans, 1982). Additionally, groups of waves can excite other fluid motions, which may in turn produce noticeable effects (Bowers, 1979).

There are several linear theories which predict wave group statistics, such as the mean group length, given only the energy spectrum. One such theory considers the wave field to be composed of a succession of discrete, independent waves, an assumption appropriate for broad band spectra. Results from the theory of runs are then employed to determine certain group statistics (Goda, 1970; Nagai, 1973). The mean length of such runs of waves greater than some critical height,  $H_c$  is (Goda, 1970)

$$E\{j\} = 1/(1-p) \quad (1)$$

where  $j$  is the number of discrete waves in a run,  $E\{\}$  is the expected value operator, and  $p$  is the probability that the height of a wave is greater than  $H_c$ . The standard deviation of run length is

$$\sigma\{j\} = p^{1/2}/(1-p) \quad (2)$$

For Rayleigh distributed wave heights, and for  $H_c = 4m_o^{1/2}$ , where  $m_o$  is the variance of the time series,  $p=0.1348$ . Thus, for these conditions

$$E\{j\} = 1.16$$

$$\sigma\{j\} = 0.42$$

On the other hand, for narrow band energy spectra, an expression for the mean length of runs can be derived from Rice's (1944, 1945) results for the envelope of a random process. For

<sup>1</sup> Research Assistant, Scripps Institution of Oceanography, A-022, La Jolla, CA 92093

<sup>2</sup> Associate Professor, Scripps Institution of Oceanography, Shore Processes Lab, A-009, La Jolla, CA 92093

<sup>3</sup> Head, Ocean Engineering Research Group, Institute of Marine Resources, SIO, A-022, La Jolla, CA 92093, M. ASCE

this case, the mean length of runs whose envelope lies above  $H_c/2$ , for the  $H_c$  given above, is given by (Vanmarke, 1972; Ewing, 1973)

$$E\{k\} = 1/2(m_2/2\pi\mu_2)^{1/2} \tag{3}$$

where  $m_2$  and  $\mu_2$  are the second moments of the spectrum about the origin and about the centroid, respectively, and  $k$  is the number of waves in the group, not necessarily discrete.

Extensive numerical simulations (Elgar, Guza, and Seymour, 1984) indicate agreement ( $\pm 10$  percent) with Goda's prediction of a constant mean run length, equation (1), for very broad spectra,  $Q_p < 2$ . Here  $Q_p$  is defined as (Goda, 1970)

$$Q_p = (2/m_0^2) \int_0^\infty f S^2(f) df \tag{4}$$

where  $f$  is frequency and  $S(f)$  is the power spectral density. Unfortunately, Elgar, et al. (1984) could find no simple shape parameter that quantitatively indicated the region of validity of equation (3). Indeed, for spectral shapes similar to those found in the ocean, neither of the theories described above adequately predicts mean run length. Consequently, in order to predict wave group statistics given an arbitrary spectral shape, a simulation procedure is utilized.

**Simulations**

The fundamental assumption of linear waves is that the sea surface can be represented as a linear combination of waves with random phases,

$$\eta(t) = \sum_{n=1}^N C_n \cos(\omega_n t - \phi_n) \tag{5a}$$

where  $N \gg 1$  and

$$C_n = (2S(f_n)\Delta f)^{1/2} \tag{5b}$$

are the Fourier amplitudes,  $\omega_n = 2\pi f_n$ ,  $f_n = n \Delta f$ , and  $\phi_n$  are random phase angles, uniformly distributed in  $[0, 2\pi]$ . An alternate expression for the sea surface is

$$\eta(t) = \sum_{n=1}^N a_n \cos(\omega_n t) + b_n \sin(\omega_n t) \tag{6}$$

where  $a_n$  and  $b_n$  are independent, Gaussian distributed random variables with zero mean and variance  $S(f_n)\Delta f$ . Simulations using equation (5), which will be referred to as a random phase scheme, have spectra that always exactly match the target spectrum,  $S(f)$ , while simulations with equation (6), a random Fourier coefficient scheme, have spectra with a statistical variation about  $S(f)$ . Both methods were implemented, and as discussed below, yield nearly identical results.

**Comparison of simulation schemes**

For the random phase scheme, Fourier coefficients were coupled with random phases produced by a numerical random number generator (equation (5)). An inverse fast Fourier transform of the unsmoothed spectrum results in a simulated time series with the identical spectral shape as the target spectrum, but with random phases. To obtain random Fourier coefficients (equation (6)), Gaussian distributed, zero-mean, unit-variance random variables were generated, and then multiplied by  $(S(f_n)\Delta f)^{1/2}$ , producing new Fourier amplitudes with the desired properties (Andrew and Borgman, 1982). Again, an inverse fast Fourier transform yields a simulated time series.

Rice (1944 and 1945), invoking the central limit theorem, points out that both representations (5) and (6) will yield the same statistics in the limit as  $N \rightarrow \infty$ . Nevertheless, both forms were used in the simulations because there is some question as to whether or not they produce the same results (Tuah and Hudspeth, 1982; Tucker, Challenor, and Carter, 1984).

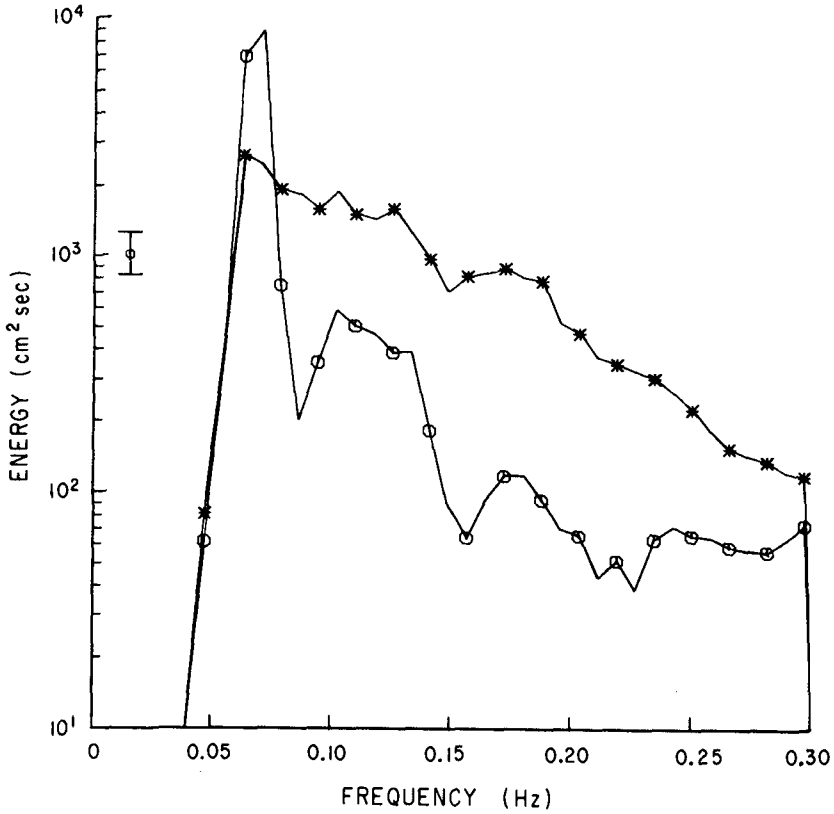


Figure 1. Power spectral density of sea surface elevation in water 10 m deep. Circle, narrow band; asterisk, broad band. The spectra have 128 degrees of freedom, and the 90 percent confidence limits are indicated by the bars. (Reprinted with permission of AGU.)

Each set of random phases or coefficients, via the simulations described above, produces a time series whose properties are statistics which fluctuate about mean values. To compare the two simulation methods for a particular target spectrum, 100 simulated time series were produced for each simulation scheme, each with its own set of random phases or Fourier coefficients. This procedure was repeated for 29 target spectra, thus a total of 5800 time series were produced.

The target spectra used to compare the two methods of simulating random waves were obtained from field measurements at Santa Barbara, California during the Nearshore Sediment Transport Study, conducted in January and February, 1980 (Gable, 1981). The time series used for this study were obtained from bottom mounted pressure sensors in water approximately 10 m deep. These spectra represent a wide range of ocean conditions, including very narrow (by ocean standards) and quite broad band spectral shapes. Figure 1, and significant wave heights between 20 and 200 cm. With typical peak periods from 8 to 20 seconds, the wave steepness (product of significant amplitude and wave number of the spectral peak) is in the range 0.006 to 0.1. Some of the field data were characterized by swell from distant storms, others by locally generated seas, and a few had multiple-peaked spectra, representing a combination of sea and swell.

Each time series used in this study was 8192 s (2.27 hr) long and was band-pass filtered between 0.04 and 0.3 Hz. The bottom pressures were converted to sea surface elevation using linear theory. Individual wave heights were determined using a zero-upcrossing definition, and were considered to belong to a group if the crest to trough distance exceeded  $4m_0^{1/2}$ , the significant wave height. The mean period of the waves was about 10 s, so there are approximately 800 waves per record, and about 80,000 waves per target spectrum for each of the two simulation schemes. The mean length of runs of waves greater than the significant wave height in the simulations varies from about 1 to 2.5, and the number of groups in each time series is between 30 and 100. It was shown in Elgar, et al. (1984) that simulations with 100 realizations as described above are extensive enough to estimate the mean length of runs and the frequency distribution of the number of waves per group to within a few percent of their true values.

For each realization, the mean run length and the frequency distribution of the number of waves per group were calculated. These quantities were then averaged over the 100 realizations per target spectrum. Higher order moments, such as the variance of run lengths, were calculated from the averaged frequency distributions. Average values were calculated for each simulation scheme, and compared to determine if there are any statistical differences between the two simulation schemes. Figure 2 shows that the mean run lengths from the random phase and random coefficient schemes are visually very similar. To test if the collection of mean run lengths from the random phase scheme was statistically consistent with the collection produced by the random coefficient scheme, Student's t test for paired data was calculated. Essentially, this test examines whether or not the two treatments (random phase and random coefficients) of the same data (target spectrum) produce the same result (mean run length). The t statistic obtained will be exceeded about 25 percent of the time due to random fluctuations. Thus, there is no support for the hypothesis that the mean group lengths produced by the random phase scheme are statistically different than those produced by the random coefficient simulations.

Similarly, the variances of run lengths obtained from the random phase and coefficient methods were compared. Figure 3 shows the two simulation procedures have negligibly different run length variances. The ratios of the square of run length coefficients of variation (standard deviation normalized by the mean, random phase and random coefficient schemes) for each of the 29 target spectra were compared to tabulated values of Fisher's F distribution. None of the values exceeded the tabulated values at the 99 percent significance level.

Finally, the frequency distributions of the number of waves per group produced by each simulation technique for each target spectrum were compared. A chi-square test was used to test if the entire collection of frequency distributions produced by the random phase scheme differed significantly from those produced by the random coefficient scheme. The chi-square value obtained (with 77 degrees of freedom) is such that the hypothesis that the two collections of frequency distributions come from the same population can be accepted with more than 99 percent confidence. Indeed, as displayed in Figure 4, when corresponding frequency distributions

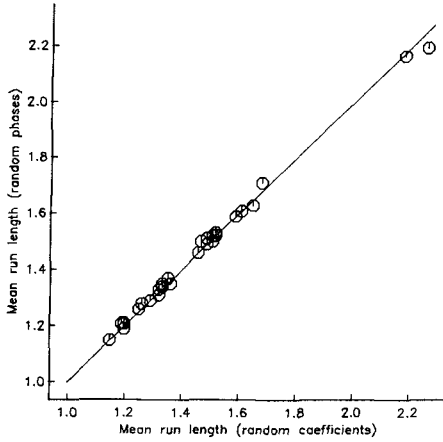


Figure 2. Mean length of runs greater than the significant wave height from the random phase scheme (equation (5)) versus mean length of runs greater than the significant wave height from the random coefficient scheme (equation (6)). The solid line indicates agreement between the two simulation methods.

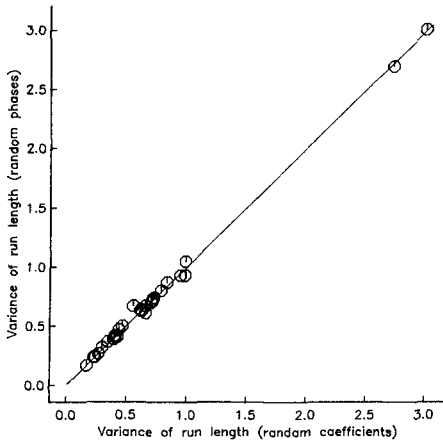


Figure 3. Variance of lengths of runs greater than the significant wave height from the random phase scheme (equation (5)) versus variance of the lengths of runs greater than the significant wave height from the random coefficient scheme (equation (6)). The solid line indicates agreement between the two simulation methods.

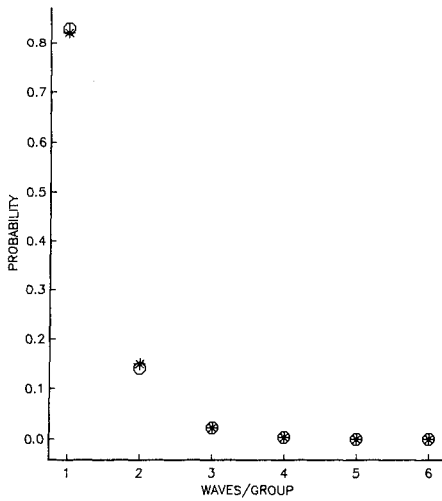
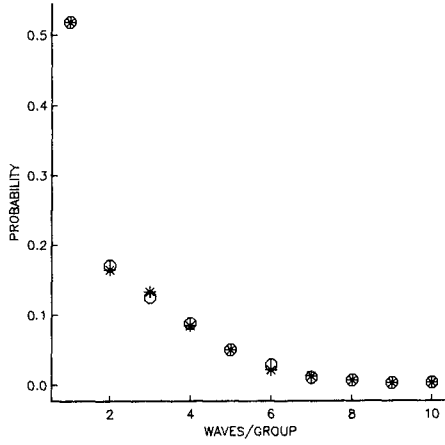


Figure 4. Frequently distribution of the number of waves per group corresponding to the spectra in Figure 1; circle, random coefficient scheme; asterisk, random phase scheme. (top) narrow band spectrum, (bottom) broad band spectrum.

from each simulation method are compared, they are seen to be almost identical. A more detailed discussion of the variability and statistics of the frequency distributions can be found in Elgar, et al. (1984).

The parameters investigated above indicate that the random phase scheme produces wave group statistics which do not differ from the random coefficient scheme statistics any more than two collections of random coefficient (or random phase) generated statistics would differ from each other. Further discussion of the similarities of and differences between the two simulation procedures can be found in Elgar, Guza, and Seymour (in Press).

### Simulation-data comparison

In order to determine whether or not linear simulations (i.e., random phase or random Fourier coefficient schemes) are adequate for predicting ocean wave group statistics, several different comparisons of measured and simulated data were made. The simulation procedures are the same as described above, but in this case statistics from ensemble averages of the 100 simulation realizations are compared to the actual field data values for each target spectrum. One such comparison is of the mean length of runs. Figure 5 shows that the mean run lengths from the ocean data are visually well correlated with the mean run lengths from the simulations. As shown in Elgar, et al. (1984), the  $E[j]$  for the 100 realizations for each target spectrum are Gaussian distributed, and the field values of  $E[j]$  deviated from the simulation mean no more than would be expected for a Gaussian distribution, with 77 percent of the ocean  $E[j]$  falling within one standard deviation of the simulation mean.

To test if the entire collection of ocean  $E[j]$  were statistically consistent with the simulated  $E[j]$ , Student's *t* test for paired data was calculated (Elgar, et al., 1984). The value obtained will be exceeded about 50 percent of the time due to random fluctuations. Hence, the hypothesis that the ocean mean group lengths are statistically consistent with linear wave theory cannot be rejected, and the simulation procedure successfully predicts ocean mean group lengths given a target spectrum.

Similarly, the variances of run length obtained from the ocean data were compared with the corresponding variances produced by the simulations, Figure 6. Fisher's *F* distribution was used to compare the ratios of the square of run length coefficients of variation. As shown in Elgar, et al. (1984), the hypothesis that the run length variances come from the same population cannot be rejected. Thus, the simulation procedure correctly predicts field values of run length variance given the energy spectrum.

Finally, a comparison of the frequency distributions of the number of waves per group was made, as shown in Figure 7. The details of this comparison can be found in Elgar, et al. (1984). Again, the conclusion is that the simulation schemes are capable of predicting field probability densities given only the power spectrum.

All the above statistical tests were applied to both the random phase simulations and the random Fourier coefficient simulations, with negligible differences as expected. The values presented above are from the random phase simulations.

### Simulations of shoaling waves

The results presented so far indicate that the assumption of a linear, Gaussian process, as expressed by equation (5) or equation (6), produces statistics consistent with observations of ocean wave group statistics in 10 m depth. However, as waves shoal they are expected to become more nonlinear. Consequently, a linear representation, such as (5) or (6) should not necessarily produce wave group statistics consistent with observations of shoaled waves. That this is the case is shown in Figure 8. Values of  $E[j]$ , both observed and simulated (from the measured spectrum at the appropriate depth) are shown as a function of depth, from 10 m, through the breaking region (about 2 m), and into 1 m of water. The simulated run length varies during shoaling because of substantial changes in the observed spectrum. Simulations and observations are similar in 9-10 m depth, but as the waves shoal the observed  $E[j]$  becomes much greater than

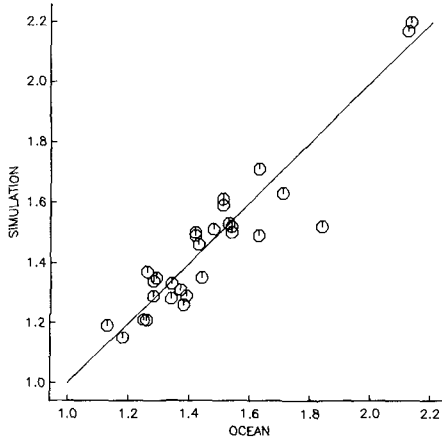


Figure 5. Mean length of runs greater than significant wave height from the numerical simulations versus mean length of runs greater than the significant wave height from the ocean field data. The 45° solid line indicates agreement between simulations and ocean field data. (Reprinted with permission of AGU.)

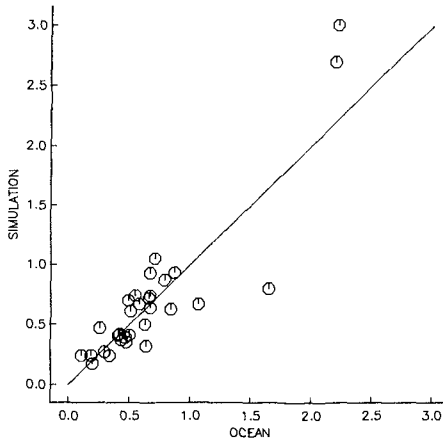


Figure 6. Variance of the lengths of runs greater than the significant wave height from the numerical simulations versus variance of the lengths of runs greater than the significant wave height from the ocean field data. The 45° solid line indicates agreement between simulations and field data.



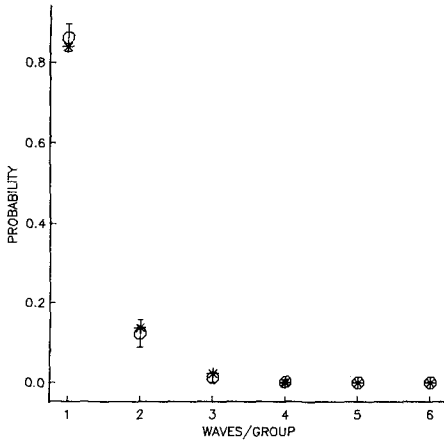
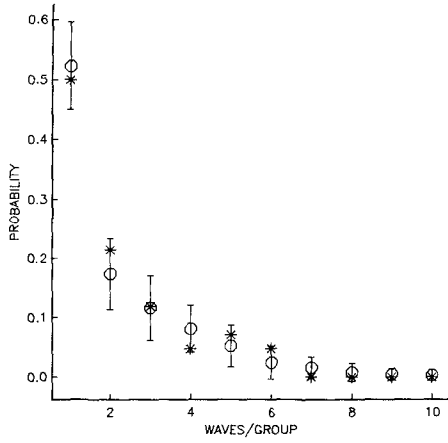


Figure 7. Frequency distribution of the number of waves per group corresponding to the spectra in Figure 1; circle, simulations; asterisk, ocean field data. (top) narrow band, February 2 (42 groups were observed in the field data); (bottom) broad band, February 15 (74 groups were observed in the field data). Bars indicate  $\pm 1$  standard deviation of simulated values. (Reprinted with permission of AGU.)

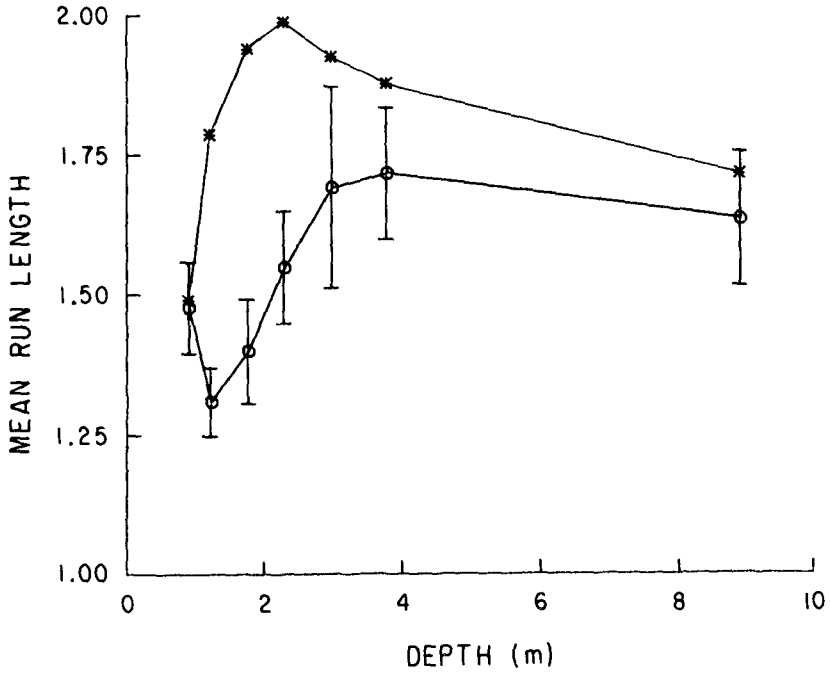


Figure 8. Mean length of runs greater than the significant wave height versus depth of water. Asterisk, ocean field data; circle, simulations, bars indicate  $\pm 1$  standard deviation of simulated values. (Reprinted with permission of AGU.)

linear simulations predict. The ocean  $E[\eta]$  remains higher than the corresponding value from the simulations until the waves break. This trend occurs in many of the data sets, and requires a nonlinear model to be predicted from a given deep water spectrum (Elgar, et al., in preparation). Other group statistics observed in the field data are also inconsistent with the linear simulations, as described in Elgar, et al. (1984). Consequently, it is inappropriate to use the linear simulation technique to predict wave group statistics for very shallow water waves.

### Conclusions

The theoretical models which predict wave groups statistics given only the power spectral density are not appropriate for the vast majority of ocean spectra. On the other hand, wave group statistics such as the mean length of runs of high waves, the run length variance, and the frequency distribution of the number of waves per group can be predicted by a linear numerical simulation from the energy spectrum. The two methods discussed here, a random phase scheme and a random Fourier coefficient scheme, produce nearly identical statistics for the spectra and conditions considered in this study.

Although the linear simulations accurately predict wave group statistics in water 8-10 m deep, very substantial disagreement with the simulations was found for shoaled waves in 2-3 m depth. Thus, the linear simulation procedure is inappropriate to use in shallow water where nonlinearities are important.

### Acknowledgements

This study was funded by the National Oceanic and Atmospheric Administration Office of Sea Grant contracts NOAA-04-8-MO1-193, R-CZ-N-4E (S.L.E. and R.J.S.) and Office of Naval Research contract N00014-75-C-0300 (R.T.G.) S.L.E. would like to thank Wayne Hager, chairman of the Engineering Science Department, University of Idaho, where the bulk of this manuscript was prepared, for providing a most hospitable environment during the summer of 1984.

### References

- Andrew, M.E., and L.E. Borgman, Procedures for studying wave grouping in wave records from California Coastal Data Collection Program, report, U.S. Army Corps of Eng., San Francisco, Calif., November, 1981.
- Bowers, E.C., Harbour resonance due to set-down beneath wave groups, *JFM* 79, 71-92, 1977.
- Burcharth, H.F., The effect of wave grouping on on-shore structures, *Coastal Engineering* 2, 189-199, 1979.
- Dean, R.G., Kinematics and forces due to wave groups and associated second-order currents, Proceedings Second International Conference on the Behavior of Offshore Structures (BOSS'80), London, paper # 6, 1980.
- Elgar, Steve, R.T. Guza, and R.J. Seymour, Groups of waves in shallow water, *Journal of Geophysical Research*, 89, 3623-3624, 1984.
- Elgar, Steve, R.T. Guza, and R.J. Seymour, Wave group statistics from numerical simulations of a random sea, *Applied Ocean Research*, in Press.
- Goda, Y., Numerical experiments on wave statistics with spectral simulation, report, volume 8, pp.3-57, Port and Harbor Research Institute, Nagase, Japan, 1970.
- Nagai, K., Runs of the maxima of the irregular sea, *Coastal Engineering Japan*, 16, 13-18, 1973.

Pinkster, J.A. and R.H.M. Huijmans, The low frequency motions of a semi-submersible in waves, Proceedings of the Third International Conference on Behavior of Off Shore Structures (BOSS'82), Boston, 1982.

Rice, S.O., The mathematical analysis of random noise, Bell System Technical Journal, *23*, 282-332, 1944.

Rice, S.O., The mathematical analysis of random noise, Bell System Technical Journal, *24*, 46-156, 1945.

Tuah, H. and R.T. Hudspeth, Comparisons of numerical random sea simulations, Journal of Waterway, Port, Coastal, and Ocean Division, American Society of Civil Engineers, *108*, 569-584, 1982.

Tucker, M.J., P.J. Challenor, and D.J.T. Carter, Numerical simulation of a random sea: a common error and its effect upon wave group statistics, Applied Ocean Research, *6*, 118-122, 1984.

## CHAPTER FIFTY THREE

### ESTIMATES OF LONG WAVES IN THE WESER ESTUARY

V. Barthel\* and E.R. Funke\*

#### ABSTRACT

Long waves of small amplitudes can excite harbour oscillations as well as the motion of floating structures or vessels. Field data from the Weser Estuary, German Bight of the North Sea were analysed with respect to waves with periods greater than 8 s. After preprocessing of the mostly noisy data records, special analysis incorporated the reconstruction of incorrectly recorded frequency components below .03 Hz and bivariate distributions of heights and periods. Results suggest that long wave activity increases towards the inner estuary. Grouping properties are dependent on wind direction and on directionality of the sea state. Further investigations and model studies for the response of travelling vessels to this wave climate are recommended.

#### 1.0 INTRODUCTION

It has been frequently suggested and generally accepted that long waves with a small amplitude can excite harbour oscillations. Pinkster (7) and Mansard and Pratte (6) demonstrated that significant motions of moored vessels can be induced as a result of these same waves. It is also being speculated that large vessels navigating with small underkeel clearance in restricted channels can hit bottom in response to these long waves. It is therefore important to know about and to understand long wave activity in coastal areas and estuaries.

Long waves in estuaries can appear as

- (a) free long waves, which are generated far from shore and travel at free wave velocity.
- (b) group-bound long waves, which represent a set-down under the wave group and travel at group velocity.
- (c) free long waves, which result from the shoaling process of bounded long waves.
- (d) reflected long waves, which derive from a reflection process of free or bounded long waves.

The existence of second order group-bound long waves as a result of the variation of radiation stress under a group of waves has already been shown by Longuet-Higgins and Stewart (5). Dependent on the amount

\*Hydraulics Laboratory, National Research Council, Ottawa, Ont. K1A 0R6  
Canada

of wave grouping the bounded long wave appears as a set-down under a group of larger waves and a set-up in between groups (Fig. 1). That this phenomenon is really present in nature can be shown by a low-pass filtering process presented in Figure 2 where the thick line superimposed on the measured wave train represents the second-order low frequency surface elevation. The encircled low frequency part of the variance spectral density is shown enlarged on the upper right part of the figure.

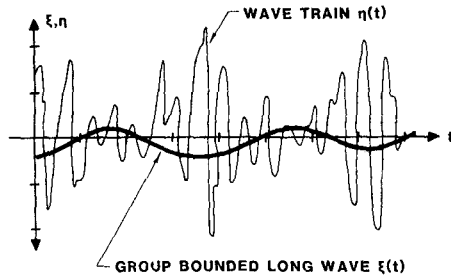


FIGURE 1: GROUP BOUNDED LONG WAVES - DIAGRAMMATIC SKETCH -

Long waves in deep water are typically considered to have periods longer than 30 seconds. However, as waves propagate into the shallower water of an estuary, there is a significant transformation of spectral energy towards the higher as well as the lower frequency part of the spectrum. As a result, long waves in estuaries may reasonably be considered as being those of periods longer than eight to ten seconds. This

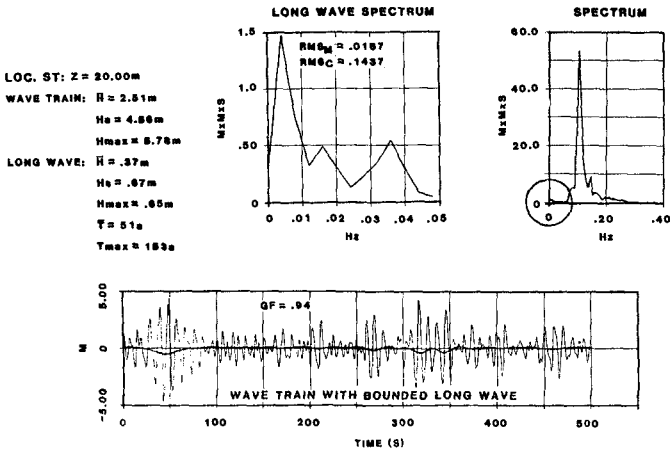


FIGURE 2: BOUNDED LONG WAVES IN NATURAL WAVE TRAINS

investigation was also undertaken in support of navigation services in the Weser Estuary, part of the German Bight of the North Sea, for which a specific interest in wave activity beyond a certain threshold had been expressed. Discussions taking estimated or well-established response frequencies of different types of vessels into consideration resulted in a cut-off frequency of 8 s. For the purpose of this analysis long waves - in deviation from a conventional definition - shall be considered as those which exceed this given threshold.

The behaviour of long waves propagating in a uniform channel at constant water depth is well known (Barthel et al., 1983) (2). However, when approaching the shore with progressively decreasing depth of water, these waves change due to shoaling, refraction, diffraction and reflection in a manner which is not yet understood. It is suspected that, e.g. bounded long waves depart from the wave groups and proceed as free long waves in the shoaling process. To complicate matters, some long wave components tend to follow deep channels into the inner estuary without much change in characteristics.

## 2.0 Field Data

Field investigations were carried out in the Weser Estuary, German Bight of the North Sea, between 1975 and 1981 and results were partly reported by Barthel (1). This study was to provide sufficient wave climate information for the prediction of waves and form the basis for design of coastal structures. Waverider buoys were deployed in seven

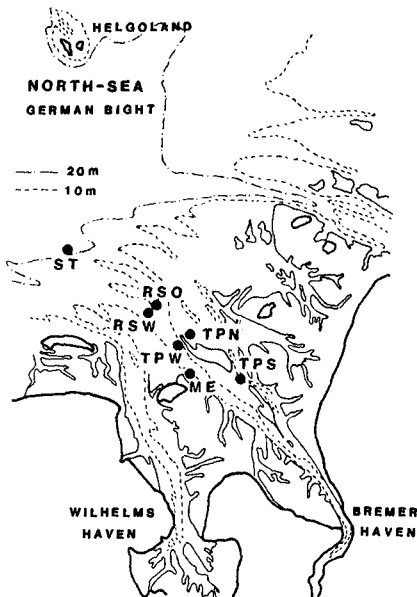


FIGURE 3: WESER ESTUARY WITH LOCATIONS OF MEASUREMENTS

different locations in the estuary, covering specific areas like the open sea, the edge of deep channels and the protected areas behind submerged bars (Fig. 3). This data set was also made available for the present investigation.

Data had been acquired for the conventional 20 minute periods and transmitted to shore for recording on digital magnetic tape. However, for reasons of cost, it had not been possible to record data from all buoys concurrently. Instead, data channels were selected consecutively for 20 minute periods. During different periods, different buoys participated in wave monitoring activity. Sometimes two, three or four buoys were selected consecutively so that the same buoy recorded every 40, 60 or 80 minutes. At other times a two-buoy sequence repeated every 60 or 80 minutes if one or two of the buoys in the sequence were inoperative.

### 3.0 INSTRUMENTATION

When the wave climate study was started in 1975 it could not be anticipated that the data might be used for long wave analysis. Consequently, the instrumentation selected which was most suitable for short wave measurements at that time, proved to be not ideal for this investigation.

The Waverider buoy has a dynamic response which starts dropping off at wave periods of 16 seconds. As Figure 4, which originates from the

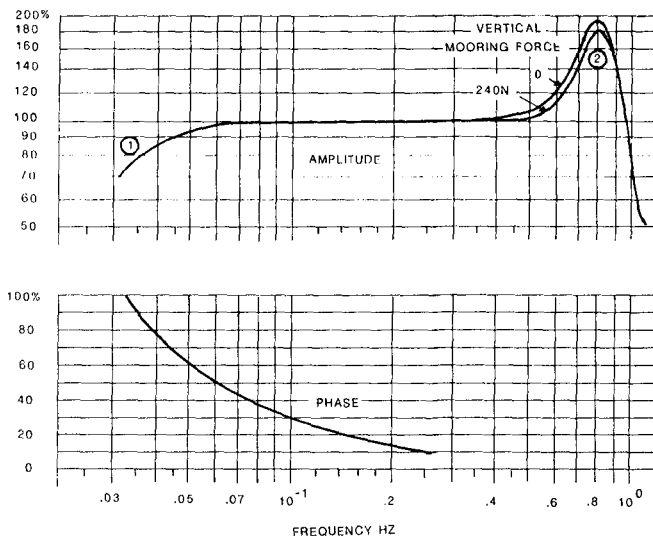


FIGURE 4: WAVERIDER TRANSFERFUNCTIONS (WAVERIDER MANUAL)



Waverider Manual, shows, the buoy is totally incapable of recording periods greater than 50 seconds. Typically, measurements of periods longer than 30 seconds should not be relied upon.

A further disadvantage stems from the fact that the radio transmission is susceptible to corruption by radio interference. The buoys and their receiver station had to be located in the vicinity of harbour services which were using short wave communication systems. CB-amateur activity in the region is very high. Hence, many of the records are influenced by interferences which lead to statistical "outliers" or "glitches". In order to make use of as many of the limited number of records as possible, programs had to be developed to detect and correct these erroneous portions of records.

#### 4.0 PREPROCESSING OF DATA

The procedure GLTFX which was created to recognize and repair noise records can be summarized as follows: The data vector is being differentiated by simple differencing. The resultant derivative is subjected to statistical analysis for the definition of a threshold which permits the separation of derivatives contributed by noise spikes on the one hand and those contributed by the uncorrupted signal on the other. The derivative record is then searched and on the basis of this threshold, a noise derivative is identified with the additional proviso that the derivative of the noise spike must be shorter than a given period and that the noise spike must be associated with a derivative exceedence of one polarity followed immediately by another derivative exceedence of the opposite polarity.

Figure 5 shows an example of a noisy record with its derivative and

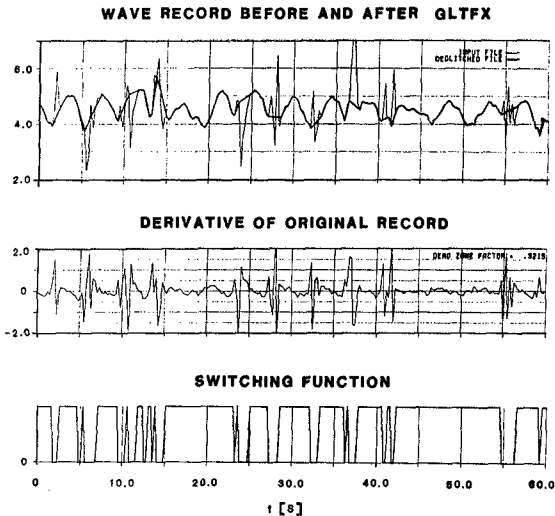


FIGURE 5: PREPROCESSING OF DATA

the switching function. The upper part shows the repaired wave record as a thick line superimposed on the original recorded time series of "surface elevations". As may be seen, the method can significantly improve the viability of wave data.

Another program was developed which can process erroneous prototype records and replace them by the best fitting quasi-synthetic time series. By using Fourier techniques, sinusoidal components are systematically removed from the original record until the variance of the extracted sum of sinusoids is greater than 90-95% of the RMS value of the original record. The superposition of all sinusoids at their computed amplitude and phase approximates the original function quite well.

By this method "glitches" and statistical "outliers" can be removed. However, since the process requires a comparatively long computation time, it can only be justified for very valuable records which cannot be recovered otherwise.

## 5.0 ANALYSIS OF WAVE DATA

### 5.1 Conventional Analysis

In order to assess the quality of data records after preprocessing, conventional analysis is applied on all records. This procedure incorporates:

- (a) Zero-downcrossing analysis, resulting in statistical parameters like  $H_s$ ,  $H_{max}$ ,  $T$ , etc.
- (b) Variance spectral density analysis giving peak frequency and RMS-values.
- (c) SIWEH-analysis as per Funke and Mansard (4) from which the groupiness factor  $GF$  is obtained.
- (d) Wave height probability distribution analysis including a comparison with model distributions.

After a visual control and selection process, data are subjected to a second analysis procedure.

### 5.2 Extended Long Wave Analysis

Since waves with a period longer than 33 s could not have been recorded correctly, all frequency components smaller than the given boundary were removed and replaced by a theoretical bounded long wave component. These second-order components were calculated using the method described by Ottensen-Hansen (7) and had been extensively tested for laboratory conditions (Barthel et al.) (2). The program uses Fourier techniques combining every possible combination of frequency pairs and their respective Fourier components. The second order surface elevations are given by

$$\eta_{nm}(t) = G_{nm}(f, \Delta f) \left[ (a_n a_m + b_n b_m) \cos(\Delta\omega_{nm}t) + (a_m b_n - a_n b_m) \sin(\Delta\omega_{nm}t) \right]$$

$G_{nm}(f, \Delta f)$  is the transfer function, the properties of which were extensively described by Sand (9). In order to save computational time the program lets the user remove all frequency pairs with an energy content below a defined threshold.

This procedure effectively reconstructs the long period portion of the energy spectrum which could not be correctly measured by the Wave-rider buoy. The low frequency part of the spectrum shown in Figure 2 is, in fact, a reconstructed, theoretical bounded long wave which adds remarkably to the energy content in this range. However, it accounts only for those long waves which belong to the category of "bounded long waves". It does not include any free long wave activity which may also be present in the natural sea state but has not been correctly recorded. Consequently the long wave activity computed and presented here represents an underestimation of the true situation.

Because of the specific interest in all "long wave" activity for wave periods longer than eight seconds, a special time series was constructed. The measured wave train was band-pass filtered between the low cut-off frequency of 0.03 Hz and the given boundary value of 0.125 Hz ( $T = 8$  s). The filtered time series was then superimposed with the "theoretical bounded long wave" and the resulting "long wave" subjected to the following analysis:

- (a) Zero-crossing analysis results in heights and periods of this artificial wave train. The effect of a wave field on a floating structure or travelling vessel can only be obtained by physical or mathematical modelling. However, certain boundary values (e.g. periods) are considered to initiate a - very often serious - response of a vessel. The RAO (response amplitude operator) of a vessel can be for example 0.6 for a frequency of .2 Hz and 1.0 for a frequency of 0.125 Hz. Therefore, a wave height  $H_R$  obtained from a measured wave train, which in Figure 6 as an example only consists of two superimposed frequencies, may not mean too much for a travelling vessel. The filtered, lower frequency component attached to a significantly smaller height  $H_F$ , however, can be of more consequence to its movement.
- (b) To evaluate the frequency of occurrence of pairs of height and period obtained from the zero-crossing analysis data are subjected to a bivariate distribution analysis resulting in a scatter diagram of heights and periods of the "long wave train". This procedure is performed on the data records of each station separately for a whole measurement period and results are accumulated in one data file to show the distribution of this specific period. Figure 7 shows the bivariate distributions of stations ST and RSW (42 records each) for the period of November 15-17, 1978. Leakage during the filtering process still lets waves appear in the region  $T < 8$  s. Due to the same filtering process, the asymmetry of a joint distribution as shown by Cavanie et al. (3) is not very distinct in this representation. As can be seen from the example, the maximum numbers of events occur within the periods of 8-10 s with heights from 0.4-1.0 m. These "long waves" may well

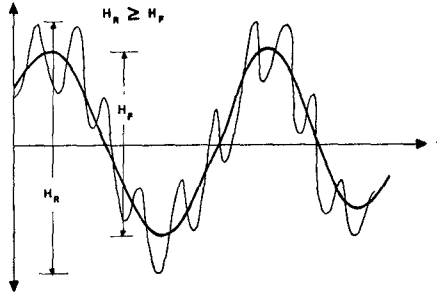


FIGURE 6: SUPERPOSITION OF LOW AND HIGH FREQUENCY COMPONENTS  
- SCHEMATIC PRESENTATION -

excite a travelling vessel to an extent which could cause dangerous situations. Multiple events in that period range go up to 3.6 m whereas very long waves ( $T > 22$  s) occur more than once with a height of .4-.6 m. However, it still remains to be accurately defined how these results have to be interpreted with respect to the behaviour of a certain type of vessel.

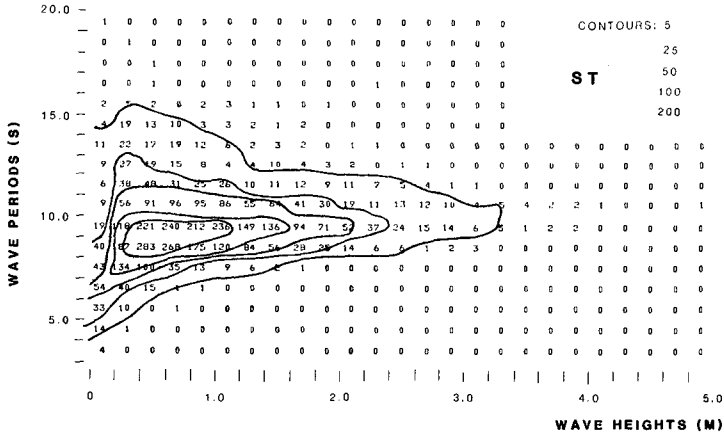
### 5.3 Distribution of Energy

Another method of showing the energy which is attached to certain frequency ranges is given with Figure 8. The cumulative distribution of spectral energy (RMS-value) for the frequency bands 0-0.05, 0.05-0.125, 0.125-0.25 and 0.25-0.5 Hz gives a very good indication of what is happening, e.g. in a storm. In the presented example the energy of "long waves" increases substantially with increasing wind velocity in both locations. However, real long wave activity for frequencies below .05 Hz ( $T > 20$  s) is much larger towards the inner estuary (RSW) than it is in deep water. This process of transfer of energy towards lower frequencies in storm situations could be observed quite often and appears to be enhanced with decreasing water depths. It implies that vessels moving into the estuary can expect more "long wave activity" and therefore possibly heavier motion towards the inner estuary where water depths normally provide less underkeel clearance.

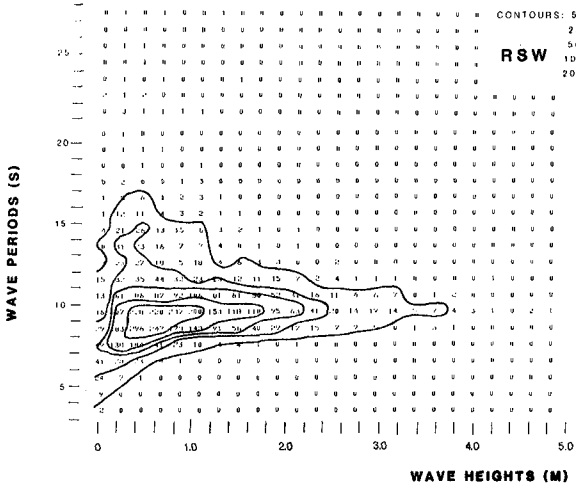
### 5.4 Grouping Properties

The concentration of energy in a group of higher waves in superposition with a second-order slow drift oscillation of a ship due to very long waves can affect its stability especially if it starts to respond in a resonant rise. Grouping properties of the sea state in terms of the groupiness factor

$$GF = \frac{\sqrt{m_0 \epsilon}}{m_0}$$



JOINT FREQUENCY OF OCCURENCE DIAGRAM



JOINT FREQUENCY OF OCCURENCE DIAGRAM

FIGURE 7: BIVARIATE DISTRIBUTION OF H AND T

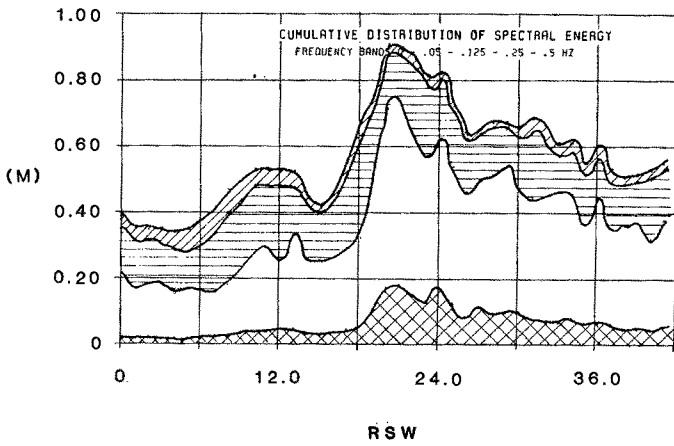
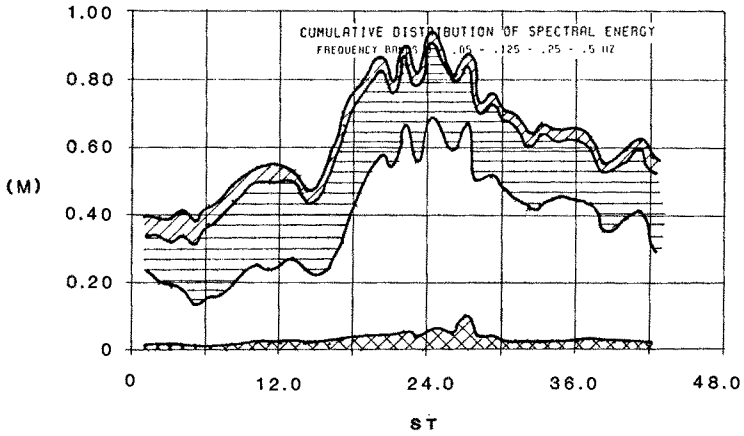


FIGURE 8: CUMULATIVE DISTRIBUTION OF SPECTRAL ENERGY

$m_{0E}$  = zeroth moment of the SIWEH spectral density

$m_0$  = zeroth moment of the SIWEH variance spectral density

SIWEH = Smoothed Intermediate Wave Energy History

as defined by Funke and Mansard (4), were determined for all records. The groupiness factor GF is the standard deviation of the SIWEH function about its mean normalized by its variance and gives a good indication of the concentration of higher and smaller waves in deviation from the Gaussian process. Table 1 presents the results of this specific analysis for different wind directions and the three main locations which were being looked at for navigation safety purposes. It appears that unusually high GF values only occur with certain prevailing wind directions (SE).

WIND DIRECTION	ST			RSW			TPW (TPN)		
	GF <sub>ave</sub>	GF <sub>max</sub>	H <sub>sig</sub> (m)	GF <sub>ave</sub>	GF <sub>max</sub>	H <sub>sig</sub> (m)	GF <sub>ave</sub>	GF <sub>max</sub>	H <sub>sig</sub> (m)
SW	0.64	0.66	1.6	0.56	0.70	1.6	---	---	---
WSW	0.61	0.73	2.4	0.63	0.74	2.1	---	---	---
SW-WNW	---	---	---	0.60	0.66	3.3	0.63	0.72	1.4
WSW-NE	---	---	---	0.59	0.75	1.4	0.62	0.63	0.7
SW-SE	---	---	---	0.56	0.66	2.0	0.60	0.75	0.6
SE	0.64	0.69	1.3	0.66	0.63	0.6	---	---	---
SE-SW	---	---	---	0.80	0.66	1.4	0.61	0.66	0.6
SE-SSW	0.65	0.63	1.6	0.63	0.62	0.9	---	---	---
NE-ESE	---	---	---	0.63	0.73	1.6	0.60	0.70	1.0
WNW	0.65	0.76	2.6	0.63	0.73	2.6	0.66	0.79	1.4
WNW	0.67	0.63	1.6	0.67	0.66	1.4	0.67	0.95	1.2

TABLE 1: GF AND H<sub>sig</sub> FOR DIFFERENT WIND DIRECTIONS FOR THE LOCATIONS ST, RSW AND TPW

Figure 9 shows the groupiness factors for only three wind directions. Interpretation of these results suggests that waves, generated by easterly winds, are not very much affected by topography and therefore only obey the boundary process of energy transfer from wind to water surface, which seems to govern or influence the grouping properties the most. On the other hand, waves penetrating the estuary are being affected by bottom-wave-interaction and superimposed by locally generated wind waves. Therefore, the grouping-process is disturbed and interrupted. Interaction of the group-bound long wave, which feels the bottom very early, and its constituent group could lead to a decay of the group. Finally, superposed wave fields coming from different directions can suppress grouping behaviour of the combined sea state.

Therefore, wave data used for groupiness analysis should be selected and treated very carefully. If superposed sea states like those shown in Figure 10 are being recorded, a separation of the two (or in some

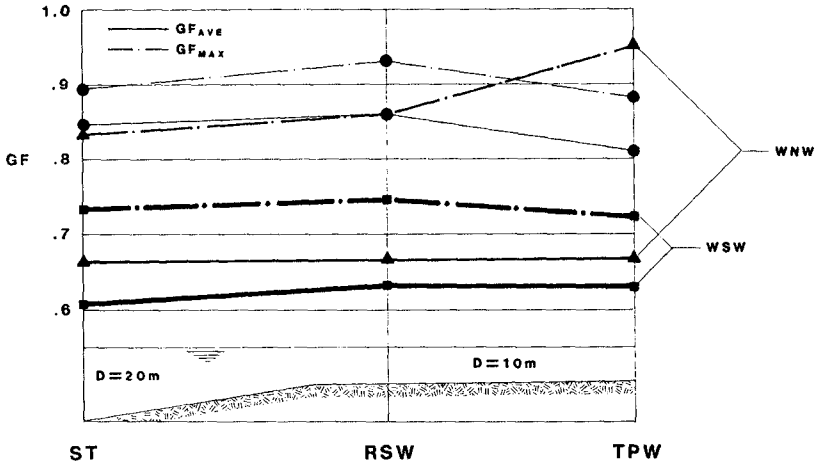


FIGURE 9: AVERAGE AND MAXIMUM GF - VALUES FOR 3 WIND DIRECTIONS

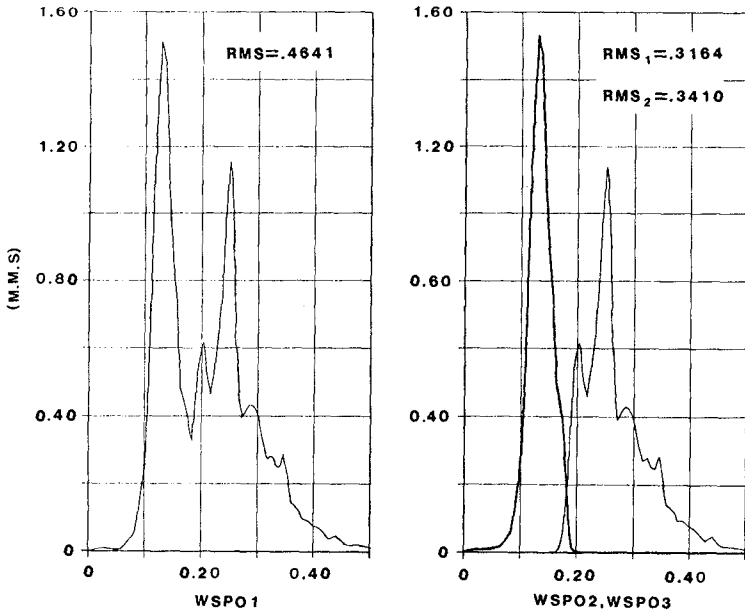
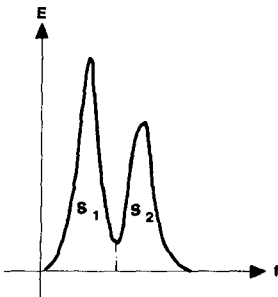


FIGURE 10: DOUBLE - PEAK - SPECTRUM - RW 609



cases even three) partial spectra is necessary to obtain valid grouping properly results. For a series of twelve records for four locations double-peak spectra were separated by filter techniques. Combined and separated time series were subjected to a grouping analysis, the results of which can be seen in Table 2. The GF value is generally much higher for the partial wave fields than for the combined record. Moreover, bounded long wave energy in terms of RMS-values of the bounded long wave is up to 25% higher if determined for the separated wave fields rather than for the superimposed and recorded sea state. This shows very much the need for directional information for further investigations if also groupiness properties are to be determined.



LOC.	GF	GF1	GF2	BLW (RMS1 + RMS2)/RMS
ST	0.82	0.82	0.73	1.23
TPW	0.58	0.88	0.80	1.18
RSO	0.57	0.83	0.80	1.18
RSW	0.88	0.83	0.82	1.25

TABLE 2: GROUPINESS OF DOUBLE - PEAK - SPECTRA  
AVERAGE OF 12 RECORDS

### 5.5 Parameter Sampling

To show the collected parameters of each measurement series consisting of more or less consecutive recordings of participating buoys over the course of a strong wind episode, analysis results were plotted for each location showing the time series of

- wind direction and velocity
- significant and maximum height of the measured wave train
- groupiness factor GF
- significant and maximum height of the "long waves" with  $T > 8$  s

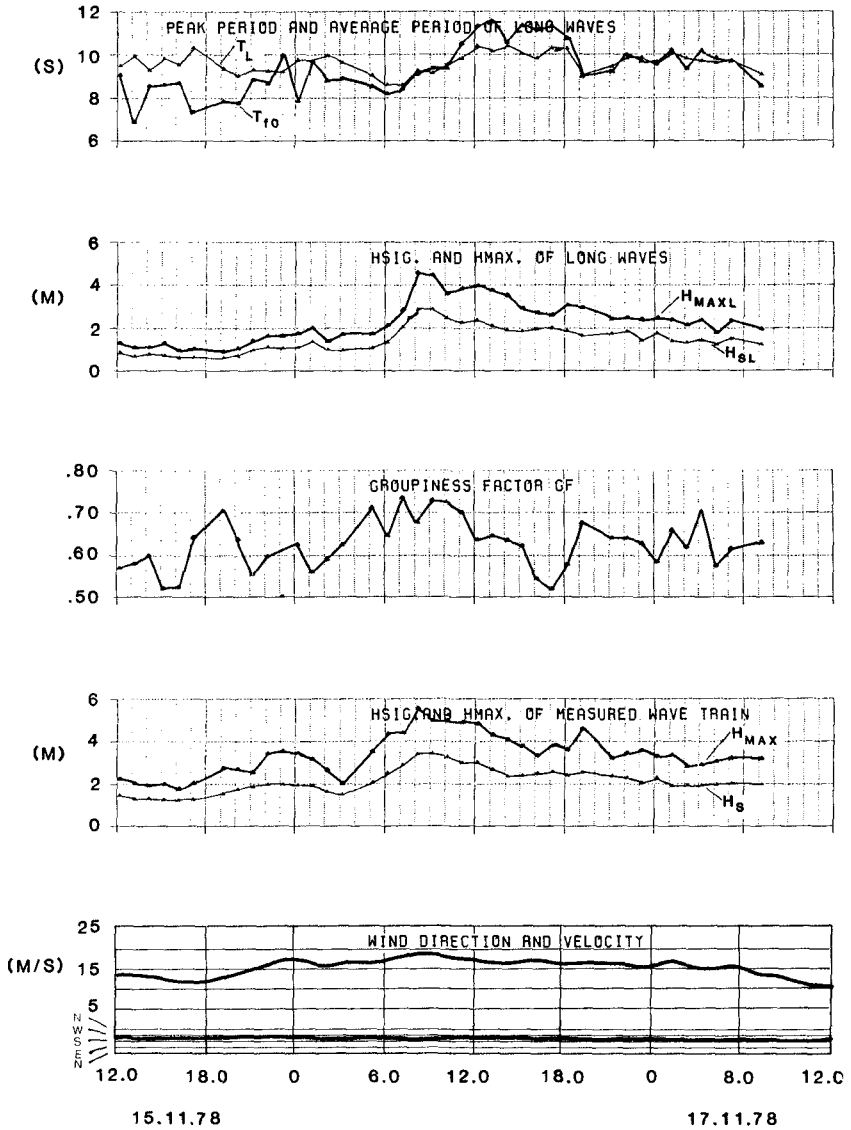


FIGURE 11: WESER WAVE PARAMETER - STATION RSW

- and the peak period (derived from spectral analysis) and average period (derived from zero-crossing analysis) of the "long waves".

Figure 11 presents the results for location RSW for the period of November 15-17, 1978.

#### 6.0 CONCLUSIONS

Analysis indicates that

- long waves with periods exceeding 8 s may well be in excess of 5 m in height.
- those waves of periods greater than 33 seconds, which provide only an underestimation of real long wave activity (theoretical bounded long wave) can reach .5 m in height.
- grouping of waves can be very much affected by decreasing water depth. With only wind-wave interaction groupiness is quite high, if waves travel offshore.
- grouping properties described by the groupiness factor  $GF$ , as defined by Funke and Mansard (4), are much more distinct for the directional components of a superimposed state than for the original record itself. This reflects on the theoretical energy content of the group bounded long wave as well.

It is recommended to perform further wave investigations in that area deploying measurement devices which are capable of recording the required range of frequencies. In addition to that, gustiness recordings and directional information are essential for a detailed analysis.

The response of different types of travelling ships to the existing wave climate has to be investigated in laboratory experiments.

#### 7.0 REFERENCES

1. Barthel, V., 1978, "Analysis of Storm Tide Waves", Proc. 16th ICCE, Hamburg, Germany.
2. Barthel, V., Mansard, E.P.D., Sand, S.E., Vis, F.C., 1983, "Bounded Long Waves in Physical Models", Ocean Engineering, Vol. 10, No. 4.
3. Cavainie, A., Arban, M. and Ezoaly, R., 1976, "A Statistical Relationship Between Individual Heights and Periods of Storm Waves", Proc. BOSS '76, Vol. II.
4. Funke, E.R., Mansard, E.P.D., 1979, "On the Synthesis of Realistic Sea States in a Laboratory Flume", National Research Council Technical Report LTR-HY-66, Ottawa, Canada.
5. Longuet-Higgins, M.S. and Stewart, R.W., 1964, "Radiation Stresses in Water Waves, a Physical Discussion with Application", Deep Sea Res., No. 11.

6. Mansard, E.P.D., Pratte, B.D., 1982, "Moored Ship Response in Irregular Waves", Proc. 18th Conf. on Coastal Engg., Cape Town, South Africa.
7. Ottensen-Hansen, N.E., 1978, "Long Period Waves in Natural Wave Trains", Progress Report 46, Inst. of Hydrodyn. and Hydraulic Engg., Techn. University of Denmark.
8. Pinkster, J.A., 1980, "Low Frequency Second Order Wave Exciting Forces on Floating Structures", Publication No. 650, Netherlands Ship Model Basin, Wageningen, Netherlands.
9. Sand, S.E., 1982, "Long Wave Problems in Laboratory Models", Journal of Waterways, Ports, Coastal and Oc. Div., ASCE, Vol. 108, No. WW4.

## CHAPTER FIFTY FOUR

### SHOALING PROPERTIES OF BOUNDED LONG WAVES

E.P.D. Mansard\* and V. Barthel\*

#### ABSTRACT

Group bounded long waves which appear as a set-down under a group of high waves and a set-up in between groups are well described for constant water depth. However, their propagation into shallow water and their interaction with the constituent wave groups are not well understood and theoretically described yet. Therefore, model investigations were carried out to study shoaling properties of these second order waves in terms of amplitudes and phases. The tests give a good insight into the phenomenon and suggest distinct shoaling properties. Moreover, experimental results provide a valuable basis for future theoretical considerations.

#### 1.0 INTRODUCTION

Recent investigations have shown that model tests of harbour basins and moored ships are highly dependent on the correct reproduction of grouped sea states. Using the concept of radiation stress, Longuet-Higgins and Stewart (4) have established that a set-down of the mean water level occurs under wave groups with a corresponding set-up in between the groups. This results in a variation of the mean water level known as a Bounded Long Wave (BLW) with its period equal to that of the wave groups. The Bounded Long Wave, which travels with the group velocity, is of second order and therefore cannot be reproduced in a model just by application of the first order classical wave generation, since the boundary conditions required at the paddle are not being satisfied. As a consequence the following spurious long wave components are generated in a model in addition to the inevitably produced Bounded Long Wave:

- a free parasitic long wave which is opposite in phase to the bounded long wave,
- a free displacement wave generated due to the moving boundary of the paddle, and
- a free long wave generated by the first order local disturbances (negligible amplitude with respect to the above two).

These spurious long waves, which propagate at free wave celerities, can travel back and forth along the flume since they are almost fully reflected even from beaches with mild slopes. The resulting standing wave system could therefore lead to incorrect and unrealistic responses of test structures depending on their location. However, these free long waves can be reduced by including correct suppression terms in the

\*Hydraulics Laboratory, National Research Council, Ottawa, Ont. K1A 0R6  
Canada

wave generation. This is basically achieved by generating, along with first order waves, long wave components which are equal in amplitude but opposite in phase to those spurious contributions. The theoretical expressions of these contributions are given by Ottensen-Hansen et al. (6) and their successful suppression in a physical model is demonstrated by Barthel et al. (1). These suppression techniques used in model investigations of moored ship response (Mansard and Pratte) (5) and wave run-up on beaches (Barthel et al.) (2) have clearly established their importance in obtaining a realistic response of the structure in the model.

## 2.0 OBJECTIVES

This paper describes the continuation of the research program and deals with the shoaling properties of the group-bound long waves. Although these waves are small in amplitude, their shoaling effects can significantly influence the model response. Harbour oscillations are one of the examples where these effects can be greatly felt; the long waves penetrating the harbour can induce long period seiches or resonance causing thereby enhanced slow drift motions of moored vessels or other floating structures.

At present there is no description (either theoretical or experimental) of the shoaling properties of these waves. Model investigations were therefore undertaken at the Hydraulics Laboratory of the National Research Council of Canada to study the propagation of Bounded Long Waves on a mild slope.

## 3.0 EXPERIMENTAL SET-UP

Investigations were carried out in a flume of dimensions 67 m x 1.2 m x 1.2 m (see Figure 1), equipped with a hydraulically driven wave generator operating in piston mode. The horizontal part of the flume in front of the wave paddle was 9 m long with a mean water depth of 0.7 m. A slope of 1:40 covering a distance of 17 m was used for shoaling purposes. This slope was then followed by a 16 m long horizontal part with a water depth of 0.28 m. A porous beach with a 1:30 slope was to dissipate wave energy at the end of the flume.

Considering wave length and velocity of these long waves, the experiments should ideally be carried out in very long flumes; however, such flumes are generally not available. Moreover, the distances used in this set-up represent some of the commonly encountered dimensions in model studies.

The shoaling slope and the following constant depth portion were constructed of sand covered with a thin layer of floated concrete. But subsequently the entire concrete surface had to be painted in order to make it smoother since preliminary investigations indicated a high degree of breaking and viscous loss due to the roughness of the bottom.

The permeable beach at the end of the flume was made up of 2 to 3 cm angular stones in order to allow the waves to penetrate through the stones and thereby dissipate as much energy as possible before being reflected at the vertical end of the flume. During a set of preliminary investigations a beach, with a slope of about 1:20 was originally used.

Under that set-up the results displayed a high degree of reflection, which could be detected particularly in the phases of long waves: in the first portion of the sampled record, the set-down and the corresponding set-up were properly reproduced but after about 50 s the phases were corrupted due to reflection.

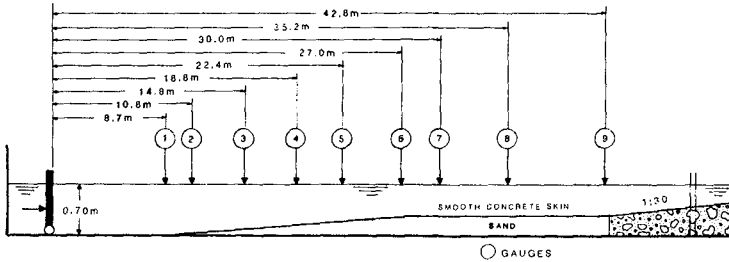


FIGURE 1  
EXPERIMENTAL SETUP IN THE 4' FLUME

The slope used in this study (1:30) provided an optimum "effective length" of the flume and at the same time guaranteed satisfactory absorption characteristics. Given the limited lengths of the constant depth zones, a satisfactory reflection analysis could not be carried out in the present configuration.

A set of nine twin wire capacitance gauges were used to monitor the waves of the salient locations of the set-up. Wave generation and data acquisition were controlled by an on-line computer.

#### 4.0 SELECTION OF TESTS

It has been shown by Barthel et al. (1) that the magnitude of bounded long waves and suppression terms used for the correct reproduction of bounded long waves change as a function of water depth and frequencies: higher amplitudes go with decreasing water depths and frequencies.

Since the amplitudes of the bounded long waves are generally very small in models ( a few mm), a careful selection of wave signals had to be done in order to obtain a distinct long wave with an amplitude well above the accuracy of the gauges and the signal noise level. As a result, a peak frequency of 0.43 Hz and a depth of water of 0.7 m were finally chosen since they provided reasonable amplitudes of the bounded long waves and at the same time an effective beach length for dissipation purposes. Jonswap spectra with three different characteristic wave heights (6 cm, 9 cm and 12 cm) were used on this study to establish the shoaling properties of the different amplitudes of the BLW. In addition, the amplitudes of BLW were varied by changing the grouping properties of the input wave which are described by the Groupiness Factor (GF), (Funke and Mansard) (3).

In a recent study Sand (7) has illustrated the direct relationship which exists between the bounded long wave and the Groupiness Factor. The Groupiness Factor, a measure of the wave group activity in a wave train, can be easily controlled in model tests using the synthesis techniques developed at the National Research Council of Canada (Funke and Mansard) (3). Using this technique, time series of 150 s with the same variance spectral density but with three different groupiness factors ( $GF = 0.60, 0.75$  and  $0.90$ ), were synthesised. This resulted in three combinations of bounded long wave amplitudes for each characteristic wave height. Besides varying the groupiness factor, the synthesis technique, indicated above, could also be used to control the ultimate shape of the bounded long wave spectrum in terms of peak frequency and width. For this study, a relatively narrow spectrum with a peak frequency of 0.05 Hz was used. Complete details of the various steps involved in this technique are well documented in the reference cited above.

Data sampling was always initiated a few seconds before the generation in order to monitor corruption of bounded long wave, if any, due to reflections. However, in order to be consistent with the length of the time series used in generation, the analysis was carried out only for a period of 150 s. The generation technique was such that the same driving signal was recycled every 150 s which meant that any part of the time series with a length of 150 s could be used in the analysis. For this study, it was decided to sample for a total period of 325 s and analyse two portions of the record: one from 25 s to 175 s and another 175 s to 325 s. The choice of 25 s as initial time was based on the propagation time of the waves up to the 9th wave gauge. The results presented in this paper correspond generally to the first section of the record while the second portion was useful to establish the effects of reflections, if any.

One of the main objectives of this study, besides establishing the shoaling properties of BLW, is to investigate the effects of spurious long waves on the amplitudes of long wave oscillations measured in the shallow water region. Hence each combination of input sea states described above was run with and without compensation for spurious long waves.

The compensation for the spurious long waves was performed, as indicated in Section 1.0, by generating long wave components equal in amplitude but opposite in phases to the spurious contributions. Generation of the suppression terms often requires large paddle excursions as illustrated in Figure 2. The graph presents two driving signals used for the generation of the same input sea state ( $f_p = 0.43$  Hz,  $HCHR = 12$  cm and  $GF = 0.9$ ). The driving signal corresponding to the classical wave generation (without suppression) is shown in Figure 2a while Figure 2b displays the signal with correct compensations for spurious long waves.

## 5.0 ANALYSIS TECHNIQUES

The various analysis techniques used in this study, can best be described with the help of the illustrations presented in Figure 3 displaying a sample of analysis results obtained for the first gauge with and without compensation for spurious long waves.



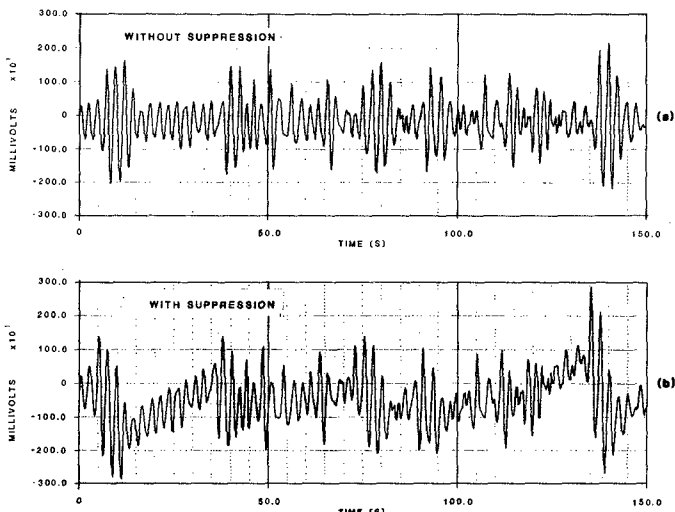


FIGURE 2

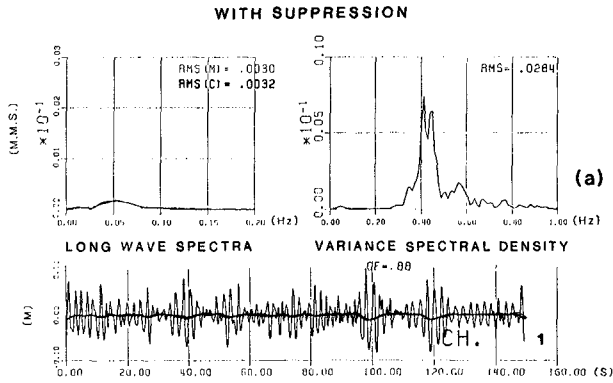
DRIVING SIGNALS FOR AN IRREGULAR WAVE TRAIN WITH AND WITHOUT SUPPRESSION OF SPURIOUS LONG WAVES

The wave train measured at the first gauge is shown together with the time series of measured and calculated long wave components. The spectra of these two long wave components are also presented in the same figure on the left hand side of the total spectrum.

The measured long waves (or the long waves prevailing in the model) were extracted from the total wave train by low pass filtering. Filtering was carried out using a time domain technique which convolved a data window with the input data. A 201 point Kaiser filter with a cut-off frequency 0.2 Hz was used for this purpose.

The expected (or calculated) long waves were obtained by theoretical relationships (Ottensen-Hansen et al.) (6) from the measured wave trains with a cut-off frequency excluding all the measured long waves (0.2 Hz).

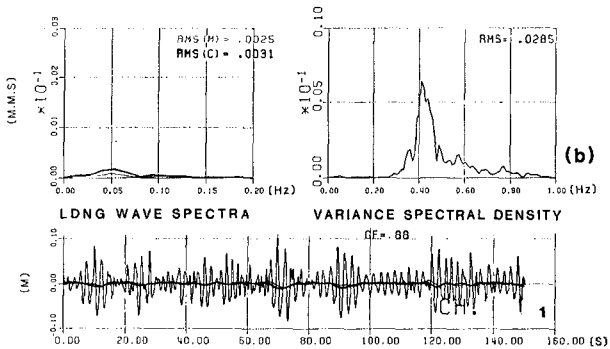
Frequency domain analysis of these two long wave components and the measured wave train directly provided their corresponding spectral densities and RMS values. The closer the RMS value of the measured long waves is to the theoretical RMS value, the more successful is the spurious long wave suppression (see Fig. 3a). However, perhaps more important than matching the amplitudes of the measured long waves to their respective expected values, it is necessary to obtain a good agreement in phase. This is usually demonstrated by a distinct proper set-down and set-up of the mean water level with respect to the wave groups. Without any suppression, this agreement would be difficult to achieve



WAVE TRAIN WITH MEASURED AND CALCULATED

LONG WAVE COMPONENTS

**WITHOUT SUPPRESSION**



WAVE TRAIN WITH MEASURED AND CALCULATED

LDNG WAVE COMPONENTS

FIGURE 3

ANALYSIS OF THE LONG WAVE CHARACTERISTICS

partly due to the differences in velocities between the free and bounded long waves. To verify the phase agreement between measured and calculated long waves, a cross correlation technique was used as follows:

$$C_{\eta_{LM}\eta_{LT}}(\tau) = \frac{1}{T-\tau} \int_{-T/2+\tau}^{T/2} \eta_{LM}(t) \cdot \eta_{LT}(t+\tau) dt / (RMS_{\eta_{LT}} \cdot RMS_{\eta_{LM}})$$

where,  $\eta_{LT}$  = time series of theoretical (or calculated) long waves

$\eta_{LM}$  = time series of measured long waves

If optimum suppression is achieved, the analysis should indicate zero shift for maximum correlation. In practice the time shift  $\tau$  (TAU) for maximum correlation is never quite zero. However, this variable proves to be a fair measure of success of suppression of spurious long waves. The maximum cross correlation coefficient is also never quite 1 due to small variations in the RMS values of the long waves which are very small themselves.

## 6.0 ANALYSIS OF RESULTS

### 6.1 Comparison Between Measured and Calculated Long Waves

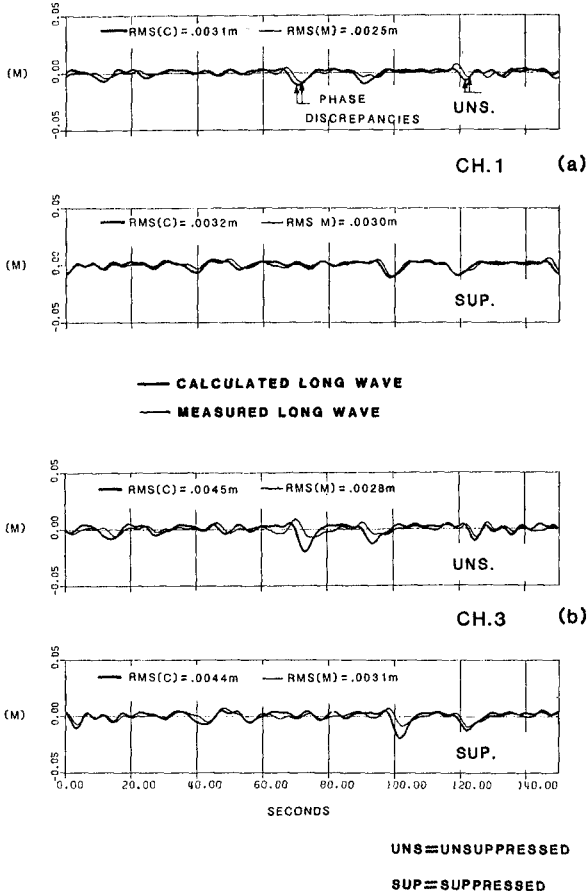
Figure 4 presents comparisons between measured and calculated long waves for four different locations in the flume. To illustrate the effectiveness of suppression, results from both types of generation (with and without suppression) are also included in this figure.

The characteristics of the bounded long wave, measured at the first gauge before any shoaling took place, are illustrated in Figure 4a. The measured amplitudes and phases of the long waves show good agreement with theory when compensation was applied. On the other hand, when no compensation was done, the amplitudes and especially the phases of the BLW are different from the theoretical predictions. To a certain extent, this figure demonstrates not only the effectiveness of suppression but also the minimal influence of reflection: If reflections were higher, it would be difficult to obtain such a good match in spite of compensation.

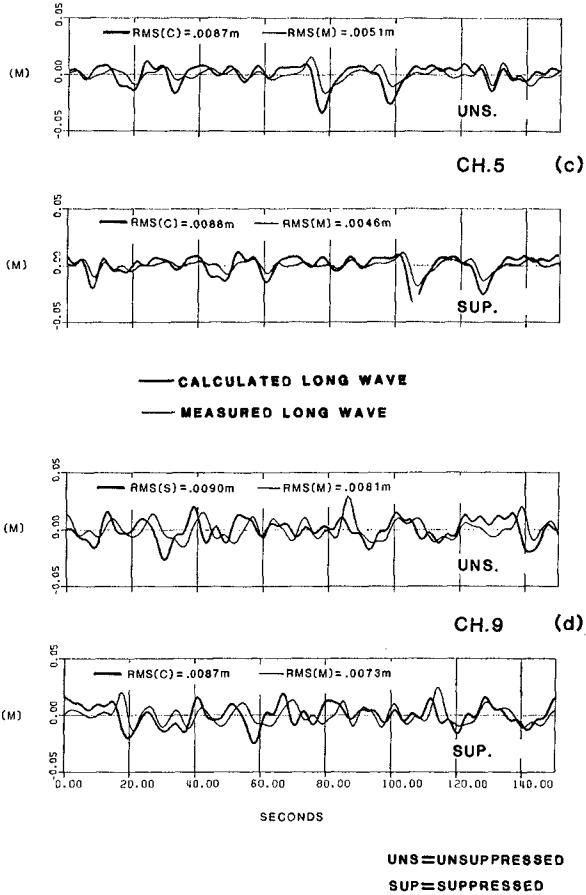
The long waves measured, at gauges 3 and 5, during shoaling, are presented in Figures 4b and 4c. In the case of generation with suppression, the phase agreement between theoretical predictions and measured values are more or less maintained, but differences in amplitudes can be detected. When no suppression was included, differences between theory and experiment are much larger in amplitudes as well as in phases.

Since a large amount of breaking was taking place between probes 6 and 7, the long waves measured at gauge 9 (Fig. 4d) show very little correlation between theory and experiment. This is possibly due to the fact that the long waves measured at the 9th gauge are a superposition of two different contributions:

- long waves released by breaking process, and



**FIGURE 4**  
**COMPARISON OF MEASURED AND CALCULATED**  
**LONG WAVES**



**FIGURE 4**  
**COMPARISON OF MEASURED AND CALCULATED**  
**LONG WAVES**

SHORT WAVE SPECTRUM RMS=0.03m, GF=0.90

- long waves which are bound to a grouped wave train reconstituted after breaking.

The calculated long waves presented in these figures for various locations of the flume, were computed using the local depth of water. But it should be pointed out that the theoretical relationships available now are strictly valid only for a constant depth of water. Hence the predictions which are presented here are only approximations of the true values. To calculate these true values it would be necessary to extend the existing theory by including terms for variable water depth and non-linear interactions between first order and bounded long waves. Since, at present, such a theory is not available, the equations of Ottensen-Hansen et al. (6) provide a useful comparison to the various trends in BLW behaviour.

#### 6.2 Amplitudes of the Measured Long Waves at Different Locations of the Flume

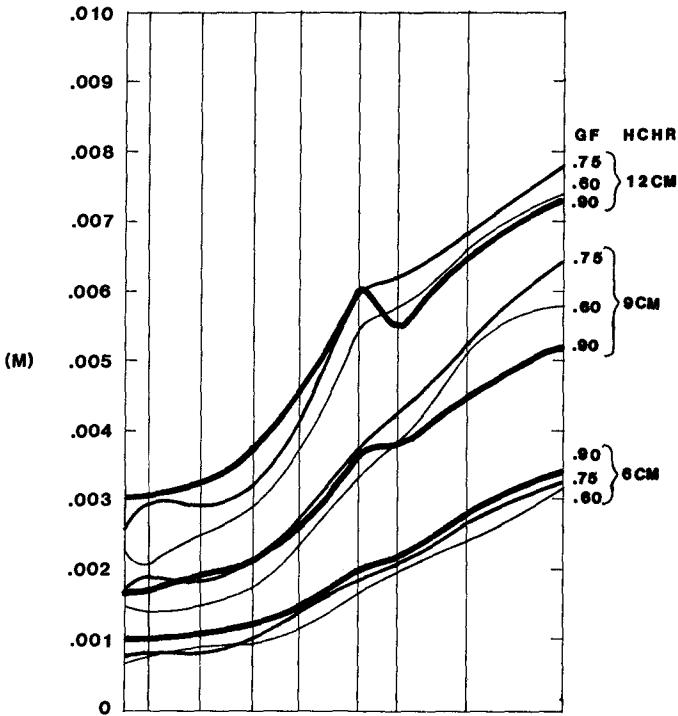
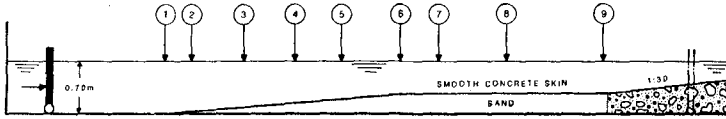
Figure 5 presents the variation of RMS values of the measured long waves along the flume. These results, only shown for the case of suppression of spurious long waves, illustrate very well some of the anticipated trends:

- The RMS value of the long waves increases with increasing wave height of the input sea state.
- For a given characteristic wave height of the spectrum (HCHR), an increase in GF results in large bounded long waves.

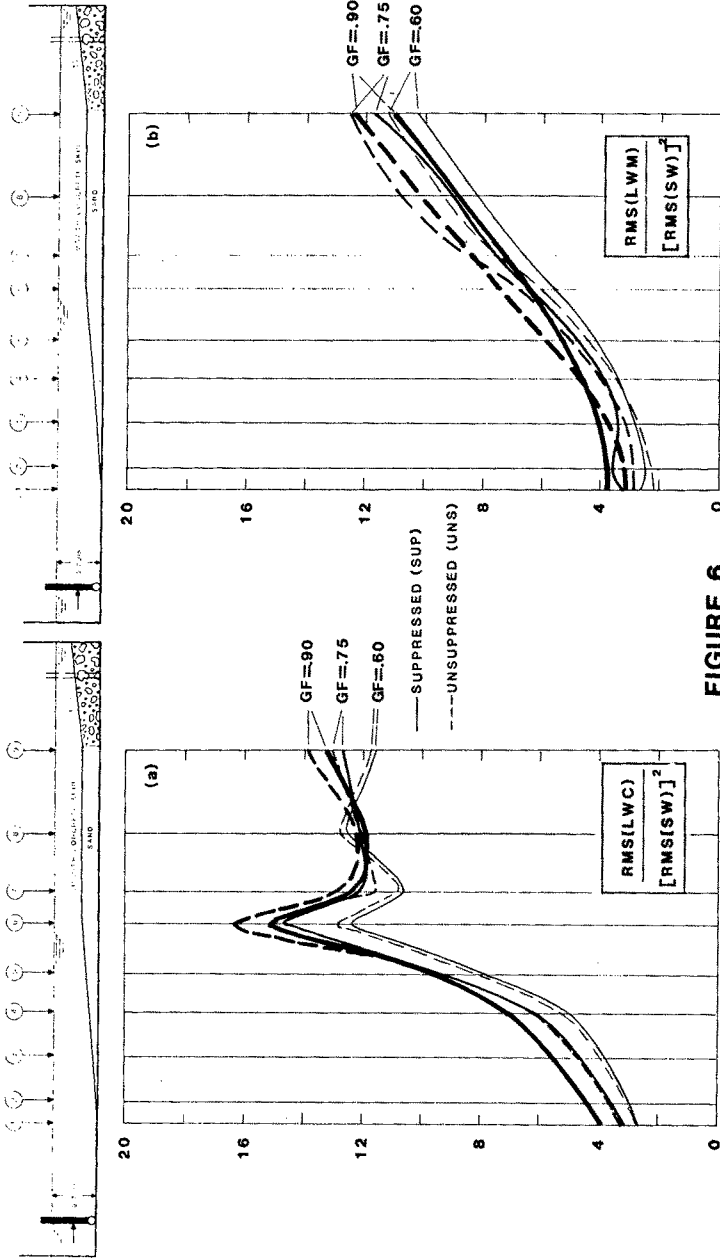
It is interesting to detect a reduction in the amplitudes of the long waves with increasing GF for the input sea states with HCHR = 9 and 12 cm at gauges 7, 8 and 9. This reduction could be attributed to the breaking of large waves due to the combination of high RMS value and large GF: a portion of the long wave energy could be expected to be dissipated with the breaking of short waves while the rest is released as free long waves.

Figure 6 presents a similar illustration of the amplitude of the long waves, but this time as a function of the amplitude of the measured short waves. With the amplitude of the long waves being proportional to the square of the amplitude of the primary wave train, the ratios of  $RMS_{LW}/[RMS_{SW}]^2$  are illustrated in Figures 6a and 6b. Figure 6a represents the ratio of the expected long wave, while the values actually measured are displayed in 6b. Results of  $RMS_{LW}/[RMS_{SW}]^2$  suggest that, for both cases of generation (SUP and UNS), this ratio increases towards the end of the flume. While this increase could be associated with the shoaling effect in the sloped area, it is not clear as to why the same tendency prevails in the post-breaking zone where the depth is constant (gauges 7, 8 and 9). A possible explanation could be the superposition of the long wave energy released during breaking process with the group-bound energy of the post-breaking time series. It could also be partly due to incomplete stabilisation process after breaking.

Because of additional free wave energy, the generation process without suppression generally results in a higher value of this ratio within the shoaling process.



**FIGURE 5**  
**RMS VALUES OF MEASURED LONG WAVES**  
**FOR 3 GF - VALUES AND 3 CHARACTERISTIC**  
**WAVE HEIGHTS OF THE SHORT WAVE SPECTRUM**  
**(SUPPRESSED)**



**FIGURE 6**  
**RATIO  $\frac{RMS_{LW}}{[RMS_{sw}]^2}$  (SUP.+UNS.)**  
 3 GROUPINESS FACTORS,  $RMS(SW) = 0.03m$



The ratio of expected long wave  $RMS_{LWC}/[RMS_{SW}]^2$  increases much more rapidly on the slope than the measured one. In the post breaking zone, it decreases as anticipated to a more or less constant value. As discussed above, these variations are based on the estimations of the theoretical long wave. However, it is not clear why this ratio is slightly higher for the unsuppressed cases (2% on the average and 8% at probe 6). This appears to be partly due to slight changes in the spectral shape caused by the difference in breaking pattern. It has been observed that the omission of suppression causes waves to break in different regions than observed in the presence of correct suppression.

### 6.3 Cross-Correlation Between Measured and Theoretical Long Waves

The results of the cross-correlation analysis between measured and calculated long waves are presented in Figure 7. These results correspond to the input sea states of  $RMS = 0.03$  m generated with different groupiness factors, each with and without suppression. The full lines indicate the suppressed case while the dotted lines represent the other. The effectiveness of suppression is well evident in this figure, since for all three groupiness factors the generation without suppression results in a poorer correlation and larger time shift as opposed to the generation with correct suppression. As anticipated, the correlation between theory and experiment decreases in the post breaking zone due to the superposition of energy from the bounded long waves and the long waves released by the breaking process. However, it is not clear why the time shift tends to decrease in that zone.

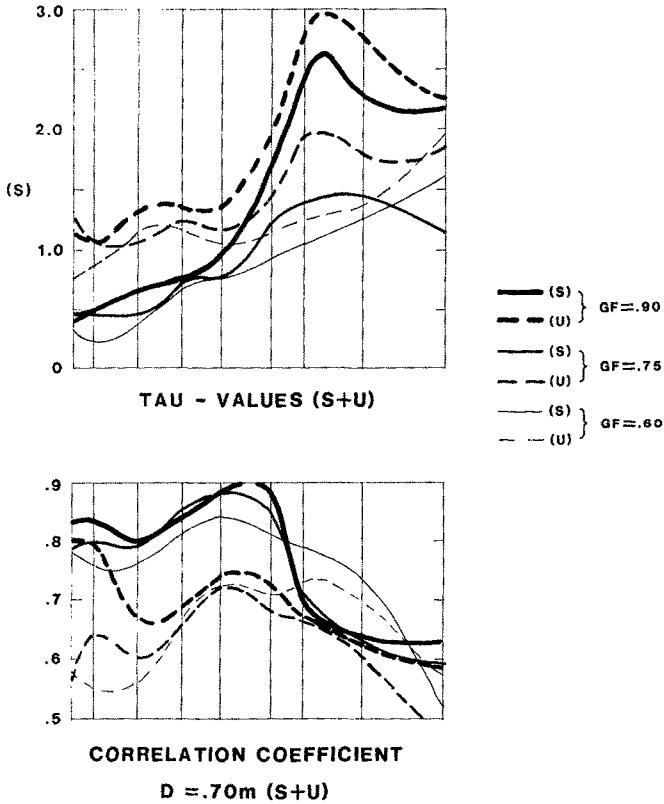
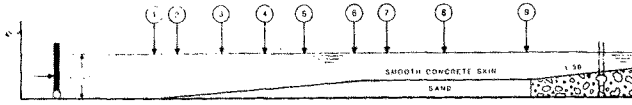
Similar cross correlation analyses were carried out to establish the effects of wave height of the primary spectrum and the influence of decreasing water depths.

As expected, a higher correlation and a smaller time shift value were achieved with lower wave heights resulting in less wave breaking.

With a shallower water depth ( $d = 0.6$  m), the number of breaking waves was comparatively higher than in 0.7 m depth resulting in an increasing mismatch between expected and measured values. Distinctly higher phase shifts and lower correlation coefficients ( $TAU > 3$  s and  $corr < 0.3$  at gauge 7) reflected this result.

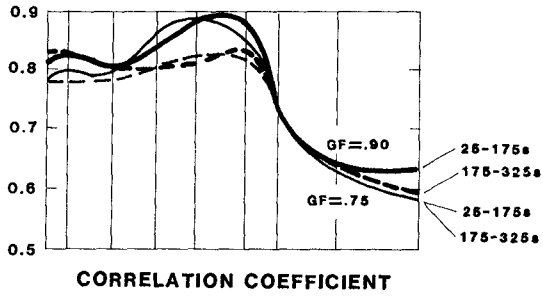
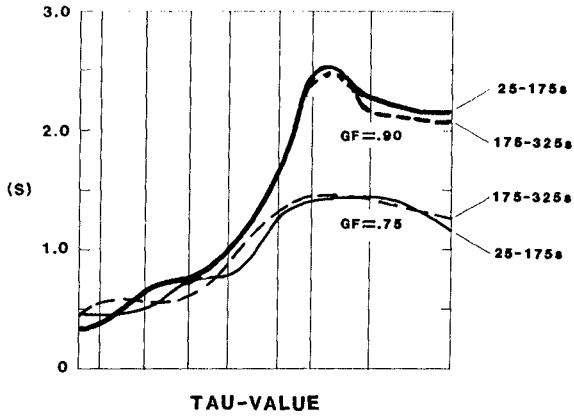
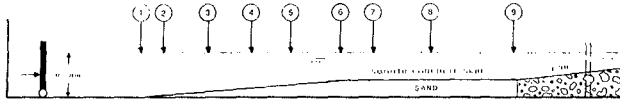
### 7.0 ENERGY BUILD-UP DUE TO REFLECTION

In order to establish the possible effect of reflection on the phases and amplitudes of BLW, the second portion of the record (175 s - 325 s) was subjected to similar analyses described above. The comparison of results of both portions of the records are presented in Figures 8 and 9 for two typical cases of GF. The cross-correlation between theoretical and obtained bounded long waves of both portions in Figure 8 show a good agreement in the TAU values while minor differences could be detected in the correlation coefficient. The match of the amplitudes of the long waves measured in different locations of the flume indicates a minimal effect of reflection (Fig. 9). In other words, the reflection coefficient was small enough not to substantially corrupt the progressive nature of the wave system in the set-up.

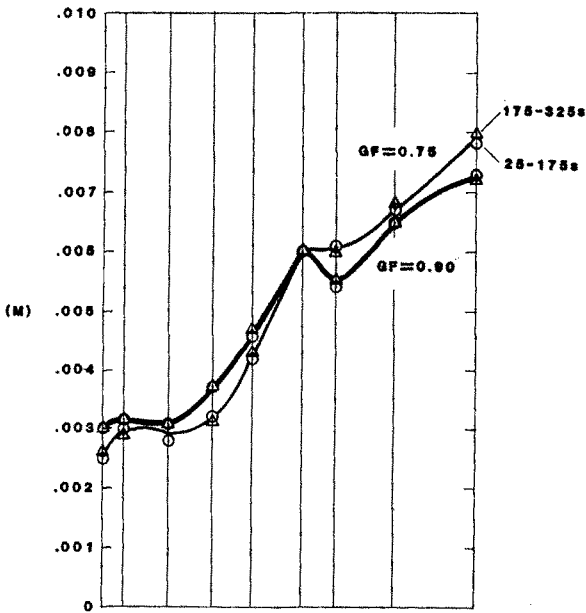
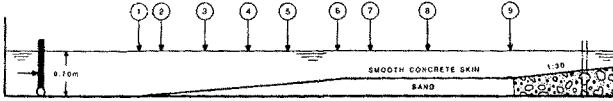


**FIGURE 7**  
**TAU-VALUES AND CORRELATION COEFFICIENTS**  
**FOR DIFFERENT GROUPINESS FACTORS (SUP+UNS)**

SHORT WAVE SPECTRUM RMS=0.03m



**FIGURE 8**  
**TAU-VALUES AND CORRELATION COEFFICIENTS**  
**BEFORE AND AFTER REFLECTION BUILD-UP (SUP)**  
 SHORT WAVE SPECTRUM RMS=0.03m



RMS VALUES OF MEASURED LONG WAVES

FIGURE 9

LONG WAVE CHARACTERISTICS  
 BEFORE AND AFTER BUILD-UP (SUP)

SHORT WAVE SPECTRUM RMS=0.03m

## 8.0 CONCLUSIONS

In the absence of a suitable theoretical description of bounded long wave propagation on a slope, this study provides useful experimental results on their shoaling properties. To date, the investigation suggests that

- there is a distinct trend in the increase of the BLW during shoaling.
- for nonbreaking waves, the relationship between BLW and GF is well documented.

In our experimental set-up, the classical wave generation, which does not include any suppression for spurious long waves, resulted in a higher magnitude of low frequency oscillations in the shallow region as opposed to those with suppression. However, this may not be true if the reflections had been high enough to set up a predominant standing wave pattern. Therefore it is recommended to suppress the spurious long waves in order to have a realistic model response. Further experiments are being carried out to study the effect of impervious beaches.

## 9.0 REFERENCES

1. Barthel, V., Mansard, E.P.D., Sand, S.E. and Vis, F.C., (1983), "Group Bounded Long Waves in Physical Models", Ocean Engineering, Vol. 10, No. 4.
2. Barthel, V., Mansard, E.P.D. and Funke, E.R., (1983), "Effect of Group-Induced Long waves on Wave Run-up", Proc. Coastal Structures 1983, ASCE, Arlington, U.S.A.
3. Funke, E.R. and Mansard, E.P.D., (1979), "On the Synthesis of Realistic Sea States", National Research Council of Canada, Hydraulics Laboratory Technical Report, LTR-HY-66.
4. Longuet-Higgins, M.S. and Stewart, R.W., (1964), "Radiation Stresses in Waver Waves, a Physical Discussion with Application", Deep Sea Research, Vol. 11.
5. Mansard, E.P.D. and Pratte, B.D., (1983), "Moored Ship Response in Irregular Waves", Proc. XVIII International Conference on Coastal Engineering, Cape Town, South Africa.
6. Ottensen-Hansen, N.E., Sand, S.E., Lundgren, H., Sorensen, T. and Gravesen, H., (1980), "Correct Reproduction of Group-Induced Long Waves", Proc. XVII International Conference on Coastal Engineering, Sydney, Australia.
7. Sand, S.E., (1982), "Wave Grouping Described by Bounded Long Waves", Ocean Engineering, Vol. 9, No. 6.

## CHAPTER FIFTY FIVE

### Numerical Simulations of the 1964 Alaskan Tsunami

James R. Houston<sup>1</sup> and H. Lee Butler<sup>2</sup>, A.M. ASCE

#### Introduction

Tsunamis are long-period water waves usually generated by earthquakes. They occur predominantly in the Pacific Ocean and can produce massive inundation and destruction. The last major tsunami that seriously impacted the United States was the 1964 Alaskan tsunami. This tsunami was generated in Alaska and caused damage in Alaska, the Hawaiian Islands, and on the west coast of the continental United States. It is the most documented of all tsunamis and the only tsunami for which there is information on the ground motion that generated the tsunami.

Numerical models have been used to simulate tsunami generation and propagation. A numerical simulation of the 1964 Alaskan tsunami that included deep ocean propagation was performed by Hwang et al. (1) and a comparison was made with a deep water gage at Wake Island. Houston (2) performed a numerical simulation of this tsunami including both deep ocean and nearshore propagation in the Hawaiian Islands and presented comparisons with tide gage recordings. Although Houston (2) demonstrated the ability of numerical models to propagate tsunamis from source regions to distant shorelines, the Hawaiian Islands considered in his simulation have a very short continental shelf and the conclusions of his study might not be applicable to typical continental areas that have significantly longer continental shelves.

There has been considerable controversy in recent years concerning the governing equations for tsunami generation, deep ocean propagation, propagation over the continental shelf, and land inundation. The importance of frequency dispersion and nonlinearity in tsunami propagation has been debated. However, research by a number of investigators in recent years has provided clear evidence of the relative significance of frequency dispersion and nonlinearities. The numerical simulation presented in this paper of the 1964 Alaskan tsunami and comparisons with tide gage recordings of this tsunami all along the west coast of the continental United States provide additional confirmation of the conclusions of these investigators. I show that for very large tsunamis such as the 1964 Alaskan tsunami, frequency dispersion is negligible during

<sup>1</sup>Chief, Research Division, Coastal Engineering Research Center, U. S. Army Engineer Waterways Experiment Station, P. O. Box 631, Vicksburg, MS 39180-0631.

<sup>2</sup>Chief, Coastal Processes Branch, Coastal Engineering Research Center, U. S. Army Engineer Waterways Experiment Station, P. O. Box 631, Vicksburg, MS 39180-0631

all phases of tsunami propagation except in rare circumstances when tsunamis exhibit a bore-like form in their final runup phase. Nonlinearities also are negligible except during tsunami land inundation, and they are not generally dominating even during inundation by non-bore waves.

It should be emphasized that the conclusions of this paper are valid only for spatially large tsunamis such as the 1964 Alaskan tsunami and for the first major waves recorded at distant locations. Frequency dispersion may be significant for the propagation of relatively short period tsunamis generated by ground displacements that are small and for the later waves of even large tsunamis. Waves near the tsunami source region may be influenced by details in the time-history of the ground motion or by small scale features of the permanent ground deformation.

#### Governing Equations

Tuck (3) made the following sweeping statement in a paper on models of tsunami propagation: "The linear long-wave equations are adequate to describe most of the tsunami generation, propagation and reception processes."

He primarily used intuitive arguments based upon the magnitudes of ratios of tsunami wave lengths and wave heights to water depths. Tuck (3) clearly stated that his conclusions applied only to large tsunamis such as the 1964 Alaskan tsunami, but the considerable disagreements with his conclusions that developed were a result of assumptions that his statement applied to smaller tsunamis.

Hammack (4) in a series of detailed laboratory experiments and calculations employing the Korteweg and deVries (KdV) equation (includes frequency dispersive and nonlinear terms) concluded that linear theory is applicable for determining tsunami generation for large tsunamis such as the 1964 Alaskan tsunami. In subsequent work using the KdV equation, Hammack (5) concluded ". . . the propagation of the lead wave of a two-dimensional tsunami is modeled by linear nondispersive theory for almost its entire trajectory. The KdV equation is valid, but unnecessary, while linear dispersive theory never applies." This trajectory was explained to extend from the source region to the vicinity of a beach. Nonlinearities were found to be negligible in the generation region and for deep ocean propagation. Frequency dispersion was shown to be negligible for the lead wave of the 1964 Alaskan tsunami until it propagated a length of time of approximately 100 hours (equivalent to a propagation distance of approximately 50,000 miles). Kajiura (6) in a separate analysis using linear but dispersive equations found "The remarkable similarity of results between dispersive and nondispersive theories is evident for  $P_a = 4$ ."  $P_a$  was defined as

$$P_a = 6(h/g)^2/t^3(b/h) \quad (1)$$

where

h = water depth

g = acceleration of gravity

t = time  
b = one-half the length of the major axis of an elliptical source region

Using parameters for the 1964 Alaskan tsunami,  $P_a$  decreases to a value of 4 after 105 hours. Thus Kajiura's analysis is in agreement with that of Hammack (4). Kajiura (6) also noted the calculations of Carrier (7) were in similar agreement.

The unimportance of nonlinearities and frequency dispersion for generation and deep ocean propagation of large tsunamis was confirmed by simulations of the 1964 Alaskan tsunami and comparisons of results with a deep water gage at Wake Island (1) and with tide gages in the Hawaiian Islands (2). These simulations did not confirm the negligibility of nonlinearities during propagation from the deep ocean to shore, since the Wake Island gage is in deep water and the continental shelf of the Hawaiian Islands is so short that the time scale for the growth of nonlinearities is small.

Hammack (5) considered tsunami propagation from the deep ocean to the nearshore area using the KdV equation and concluded that ". . . linear nondispersive theory can be used until the distance across the continental shelf (of uniform depth) that the lead wave propagates is given by . . . X = 200 miles." Goring (8) conducted laboratory experiments and calculations using Boussinesq equations (similar to the KdV equations, but allowing wave propagation in two directions) and also concluded ". . . the propagation of tsunamis from the deep ocean to the continental shelf-break and for some distance onto the shelf will be predicted as well by the linear nondispersive theory as by the nonlinear theories." The conclusions of Hammack (5) and Goring (8) may not be in agreement with calculations of Mader (9) who used a Simplified Marker and Cell (SMAC) code that included vertical accelerations and nonlinearities and a vertically integrated linear long wave code (SWAN). Significant differences were noted between the calculations of the SMAC and SWAN codes for long waves propagating over a simulated continental shelf (9). However, since experimental or field data are not presented, differences between the models noted by Mader (9) are likely attributable to inaccuracies of the solution techniques, methods of application, or boundary conditions rather than to differences in the equations solved.

Tsunamis are often portrayed as bore-like walls of water during their final stages as they inundate coastal areas. However, tsunamis only rarely appear as bore-like along coastlines distant from a source region. Instead they normally are described as having the appearance of "fast-rising" tides. In this form they are likely to be governed by nonlinear long wave equations that are successfully used for tidal inundation problems.

#### Simulation of the 1964 Alaska Tsunami

Tsunami generation and deep ocean propagation was simulated using a finite-difference numerical model (1). The model solves the linear long-wave equations on a spherical coordinate grid. One-third by one-third degree grid cells were used with the grid extending over much of the



north Pacific Ocean. The boundary condition employed on land boundaries of the grid was the component of the velocity normal to the boundary was equal to zero. On open (ocean) boundaries, a first-order approximation of total transmission was made.

The model solved an initial value problem starting with an uplift deformation of the water surface identical with the major features of the permanent deformation (permanent in the sense that the time scale associated with it is much longer than the period of the tsunami) of the seafloor following the 1964 earthquake. The transient movements within the time history of the ground motion of the 1964 earthquake were neglected because Hammack (4) has shown through laboratory experiments that these movements are unimportant in the far field for spatially large ground motions. Hammack (4) has further shown that the initial deformation of the water surface will closely approximate major features of the permanent deformation of the ocean floor, provided these features have characteristic lengths that are at least four times as great as the water depth (water depth was approximately 200 m in the tsunami source region of the 1964 earthquake). The neglect of smaller features is unimportant because Hammack (4) demonstrated in laboratory experiments such small-scale details produce waves negligible in the far field. These experiments (4) have great practical significance, since details of the time history of ground motion and small scale features of the ground deformation are unknown for the 1964 earthquake and other tsunamigenic earthquakes.

The permanent deformation of the ocean's bottom as a function of spatial location for the 1964 earthquake was adapted (1) from the field measurements of Plafker (10). It is identical to the uplift used earlier by others (1,2). Starting with this uplift as an initial condition, the numerical model propagated the 1964 tsunami across the deep ocean to the west coast of the continental United States.

The cell size of the deep ocean grid is too coarse to allow accurate simulations of tsunami propagation from the deep ocean to shore, since the tsunami wave length decreases in shallow water. Therefore, separate finite difference grids were used to propagate waves from a water depth of 500 m to shore. a variable rectilinear grid was used with grid cells that decreased in size as the water depth decreased. The smallest grid cells were less than 1 mi on a side. A finite-difference numerical model (11) was used to calculate nearshore propagation. The model uses a highly efficient implicit solution scheme that employs a centered, alternating-direction procedure. Nonlinear long wave equations including bottom function terms were solved. However, in agreement with the calculations of Hammack (5) and Goring (7) it was found that the results were insensitive to the nonlinear advective and bottom friction terms for reasonable values of bottom friction.

Figures 1-9 show comparisons between the numerical model calculations and tide gage recordings for nine tide gates on the west coast of the continental United States. These are all of the tide gages on the west coast that recorded the 1964 tsunami, except for gages in Puget Sound, the Columbia River, and San Francisco Bay (not covered by numerical grid). The tide has been extracted from all the comparisons except

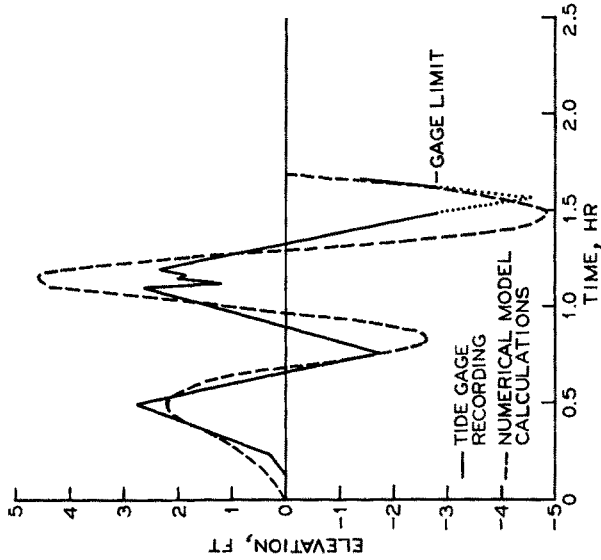


Figure 1. 1964 Tsunami at Rincon Island, California.

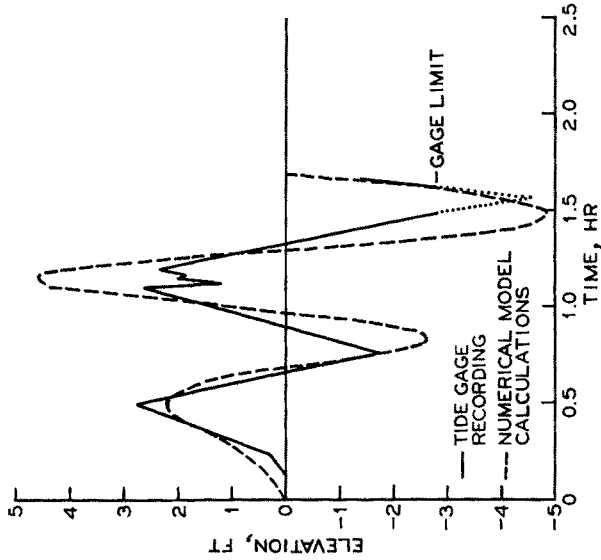


Figure 2. 1964 Tsunami at Santa Monica, California.

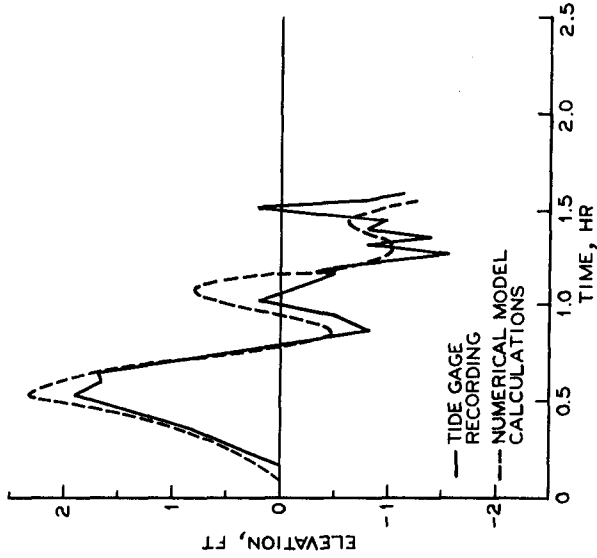


Figure 4. 1964 Tsunami at Alamites Bay, California.

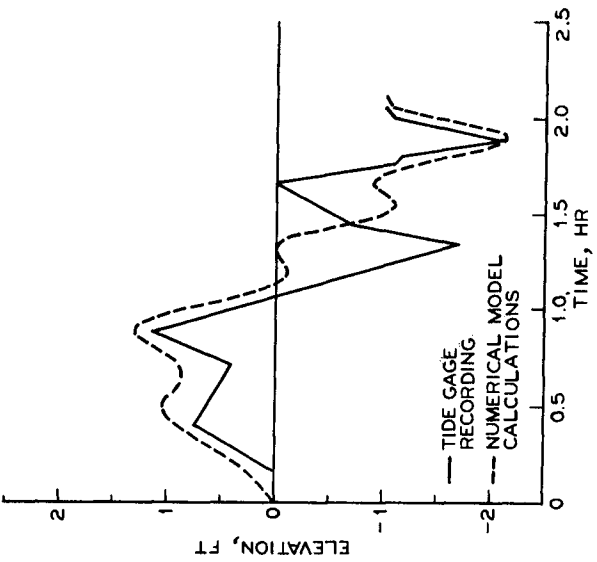


Figure 3. 1964 Tsunami at Los Angeles (Berth 60), California.

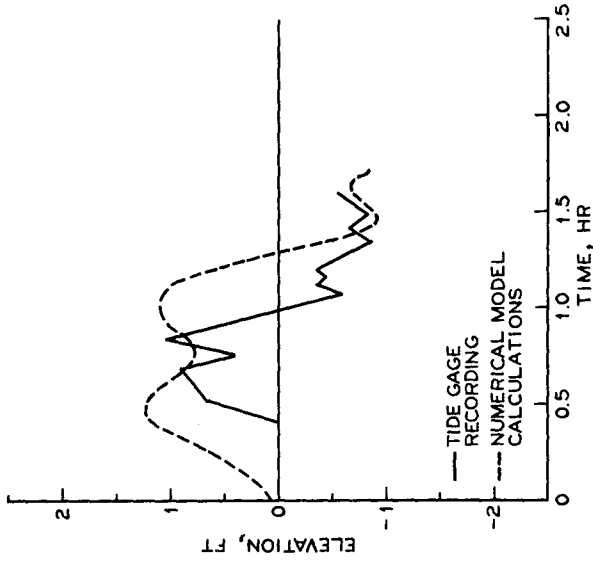


Figure 6. 1964 Tsunami at San Diego, California.

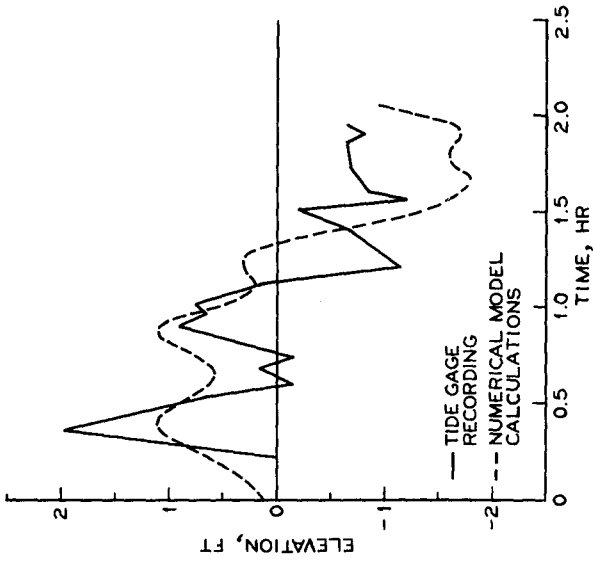


Figure 5. 1964 Tsunami at La Jolla, California.

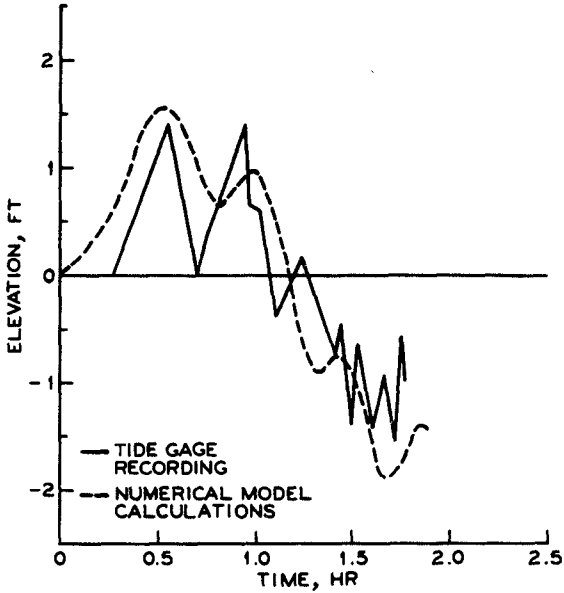


Figure 7. 1964 Tsunami at Newport Bay, California

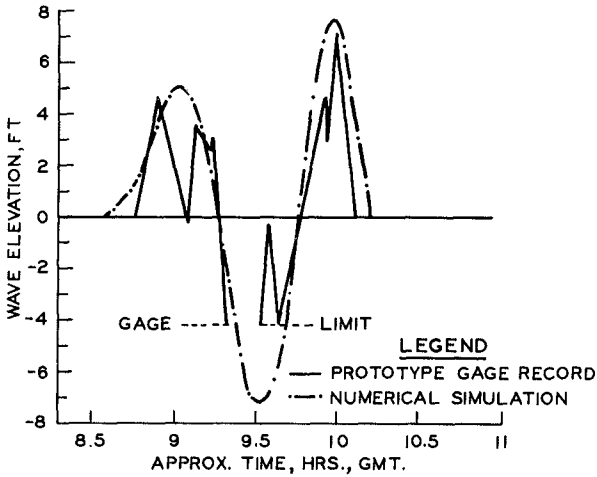


Figure 8. 1964 Tsunami at Avila Beach, California.

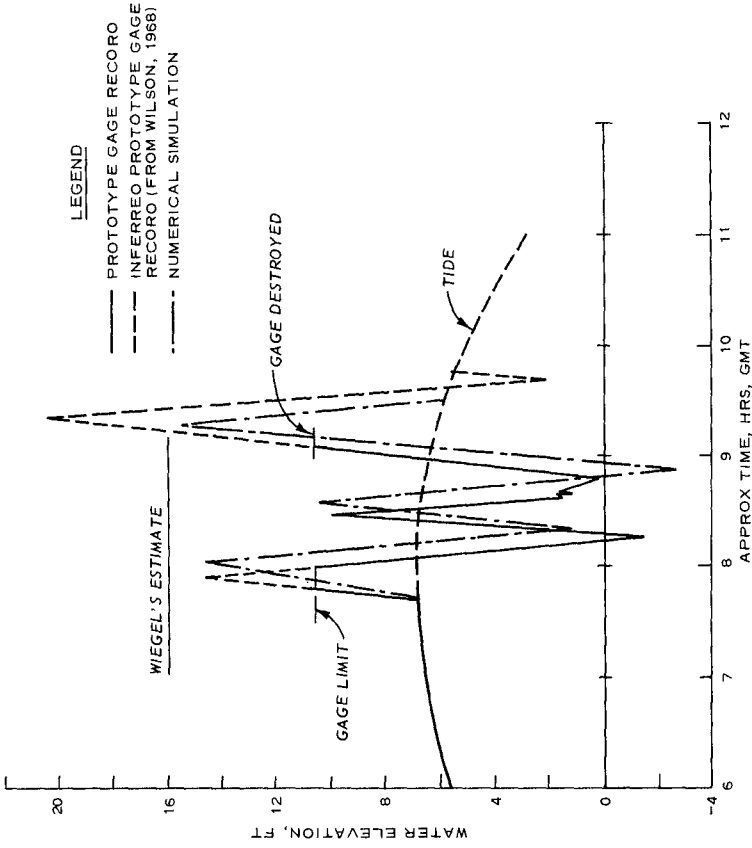


Figure 9. 1964 Tsunami at Crescent City, California.

the one at Crescent City, California. A tide gage record of the 1964 tsunami at Crescent City inferred by Wilson and Torum (12) is used for the comparison at Crescent City. In addition, an estimate by Wiegel (13) that differs somewhat from the estimate of Wilson and Torum (12) is presented. Each comparison is over a period of 1.5 to 2.0 hr.

Tide gages do not record tsunamis perfectly, but the heights and periods of the waves seen in Figures 1-9 are such that gage response is close to 100 percent (14). However, the standard sampling interval of tide gages is 6 minutes and this long sampling interval distorts the recorded wave form and can reduce apparent heights. Tide gages also experienced difficulties when gage limits were encountered. In addition to truncations of the waveforms as seen in Figures 2, 8, and 9, gage limit problems are seen in the inverted trough of Figure 8 and high frequency oscillations in the crests seen in Figures 2 and 8.

The wave form recorded at one location is remarkably different from those recorded at other locations. The waveforms for the 1964 tsunami calculated for the Hawaiian Islands (2) also show remarkable differences from gage to gage. The numerical calculations are in good general agreement with the waveforms. The shape of the waveforms, and wave heights and periods are in reasonable agreement in Figures 1-9 considering unknowns of the source region. Calculated maximum wave heights vary among the locations from as little as 1.5 ft to as much as 18.0 ft.

#### Land Inundation

The only gage location where the tsunami produced significant land inundation was at Crescent City, California. Figure 10 shows the numerical grid used to simulate land inundation at Crescent City. The grid was oriented such that the incident waves approached Crescent City from the direction predicted by Roberts and Kauper (15). The interaction of the tsunami with the Crescent City region was quite complex. For example, the Crescent City Harbor is protected by breakwaters, some of which were overtopped and others which were not. In the region there is a developed city area, mud flats, and an extensive riverine floodplain. Inland flooding was extensive in the floodplain area and extended as much as a mile inland. Sand dunes and elevated roads played a prominent role in limiting flooding in certain areas.

The input to the numerical model was a wave crest that, when propagated to shore, reproduced as accurately as possible the historical maximum elevation at the tide-gage location near the shoreline in Crescent City. There is some disagreement among investigators on the maximum elevation of the tsunami at the tide gage with estimates ranging from 18 to 20.7 ft above mean lower low water (mllw). A wave crest with an elevation of 19 ft above mllw at the tide-gage location was used in this simulation, based on a study by Keulegan et al. (16) that considered all available data and concluded the 19.0-ft level was the most likely.

There are several barriers in the Crescent City region. Wiegel (13) reports that there was little flow over the outer breakwater during the 1964 tsunami (Figure 10). Therefore, this breakwater was represented as a non-overtopping barrier. However, the breakwaters attached to Whaler

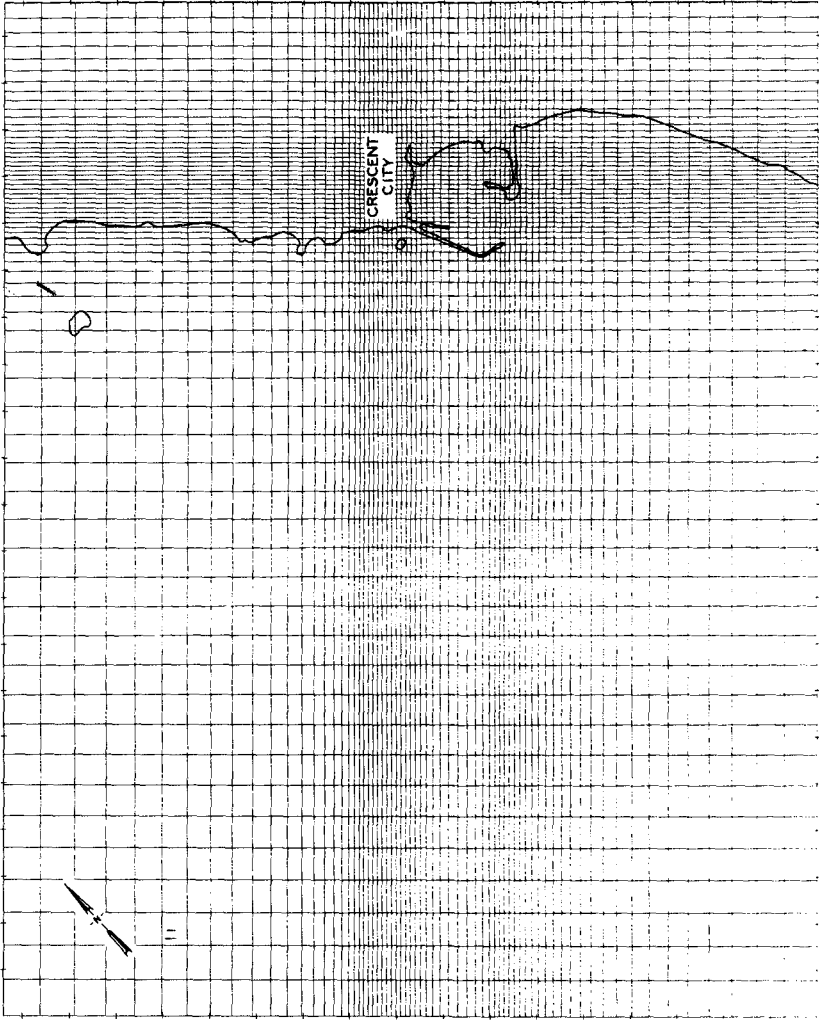


Figure 10. Numerical grid from Crescent City, California.



Island (Figure 11) were overtopped during a part of the tsunami and thus are represented as dynamic overtopping barriers. Similarly, Redwood Highway (Figure 11); and beach dunes along the crest were overtopped during the tsunami. Magoon (17) reported water flowed over these barriers with flow rates governed by weir equations.

Frictional effects in the numerical model are governed by Chezy frictional coefficients. Values of Manning's  $n$  suggested by Bretschneider and Wybro (18) for coastal terrain were used. Manning's  $n$  values were selected for very general categories of terrain, since detailed knowledge of vegetation and land roughness are not known. The ocean bottom, mud flats, and beaches were assigned a value of 0.024. Developed areas were assigned a value of 0.035 and the riverine flood-plain area and other heavily vegetated areas a value of 0.055. No attempt was made to force agreement of numerical calculations and historical recordings of elevations by varying local values of Manning's  $n$ .

The U. S. Army Corps of Engineers made surveys of the tsunami inundation at Crescent City in January, April, and May of 1965 (17). Figure 11 shows the location of 11 high-water marks recorded by the surveys. The tide gage was located near high-water mark No. 307 (Figure 11). Table 1 presents the measured elevations at the high-water marks and elevations calculated by the numerical model. The measured and calculated elevations are within 1 ft except at locations 307, 2, 3, and 5. However, Wiegel (13) reports that the measured elevation at

Table 1

High-Water Mark Number (Reference 17)	Measured Elevation mllw, ft	Calculated Elevation mllw, ft	Difference ft
302	18.35	17.95	+0.40
305	18.74	19.39	-0.65
307	20.70	19.45	+1.25
309	19.84	19.79	+0.05
312	19.41	20.23	-0.82
316	16.29	17.09	-0.80
1	15.90	15.43	+0.47
2	17.80	19.24	-1.44
3	19.30	18.89	+0.41
4	16.50	18.94	-2.44
5	20.50	19.13	1.37

location 307 was greater than the actual wave elevation by 1 to 2 ft due to local runup on a concrete wall. Thus the actual wave elevation and the calculated elevation are in good agreement at location 307. The measured elevation at location 4 is lower than the calculated elevation, since the measured high-water mark was inside a lumber building (17). Incomplete filling of the lumber building by water would result in lower elevations within the building than outside the building. Location 5 is almost 2 miles south of the tide gage. It is likely the wave approaching this shoreline had a greater elevation than the wave approaching the harbor area. The elevation calculated at this location could be increased by varying the incident wave form along the input boundary.

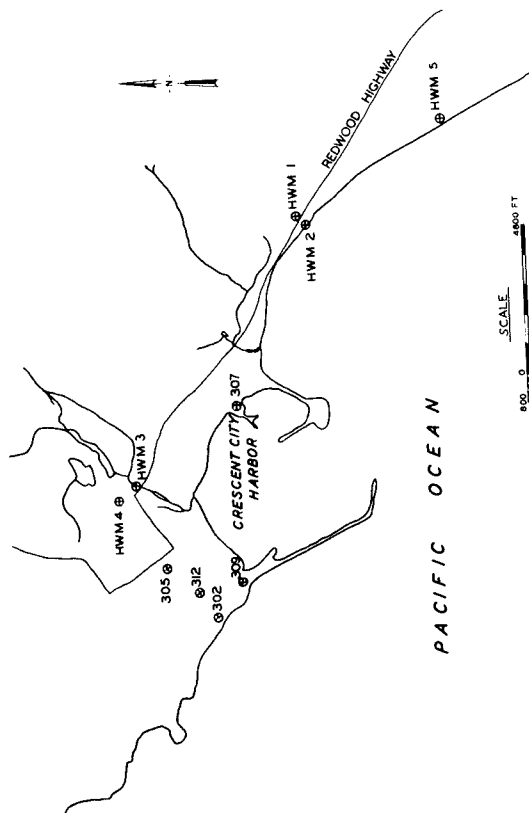


Figure 11. High-water mark locations for 1964 Tsunami (adapted from Magoon, 1965).

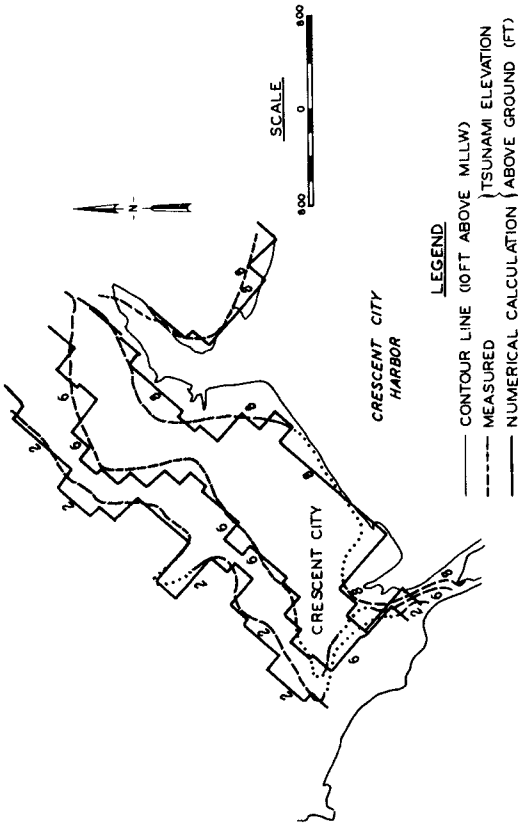


Figure 12. Inundation Lines, 1964 Tsunami (adapted from Magoon, 1965).

There is no apparent explanation for the disagreement at location 2, especially since there is good agreement at nearby location 1.

The agreement between the measured high-water marks and calculated elevations is quite good. The root-mean-square error is 0.7 ft (elevations at locations 307, 4, and 5 not included since differences attributable to factors other than the numerical model). Since the observed elevation at the tide gage used to choose an incident wave height is accurate to within no more than 0.5 to 1.0 ft, the agreement between measured and calculated elevations is good.

Figure 12 shows contour lines of the tsunami elevation above ground level within the developed area of Crescent City. The topography and tsunami elevations are known in much more detail in this developed area than any other area. The dotted parts of the measured elevation denote uncertain elevations. The contour lines for the calculated elevations were determined by linear interpolation. For example, if the elevation at the center of one cell was 9.0 ft above land and the elevation in an adjacent cell was 7.0 ft, the contour line was drawn halfway between the two cell centers. The agreement between the measured and calculated elevations shown in Figure 12 is good.

#### Conclusions

Linear long waves are adequate to simulate tsunami generation, propagation across the deep ocean, and propagation over the continental shelf of the west coast of the continental United States or the Hawaiian Islands when the uplift that generates the tsunami is large spatially (1964 Alaskan or 1960 Chilean tsunamis). Tsunamis usually appear as rapidly rising water levels along distant coastlines. Nonlinear long wave equations that include bottom function terms (typically used to model astronomical tides) can be used to model land inundation for tsunamis that appear as rapidly rising water levels. If information exists on the ground motion that generates a tsunami, the tsunami can be simulated over its complete path of propagation from a generation region up to terminal flooding at a distant coastline.

#### Acknowledgments

The authors wish to acknowledge the Federal Emergency Management Agency for funding the studies on which this paper is based and the Office, Chief of Engineers, U. S. Army Corps of Engineers for authorizing publication of this paper.

#### Appendix.-References

1. Hwang, L. S., Butler, H. L., and Divoky, H. L., "Tsunami Model: Generation and Open-Sea Characteristics." *Bulletin of the Seismological Society of America*, Vol. 62, No. 6, 1972, pp. 1579-1596.
2. Houston, J. R., "Interaction of Tsunamis with the Hawaiian Islands Calculated by a Finite-Element Numerical Model," *Journal of Physical Oceanography*, Vol. 8, No. 1, 1978, pp. 93-101.
3. Tuck, E. O., "Models For Predicting Tsunami Propagation." *Proceedings of the National Science Foundation Tsunami Workshop*, Coto de Caza, California, 1979, pp. 43-104.

4. Hammack, J. L., "Tsunamis - A Model of Their Generation and Propagation," Report No. KH-R-28, California Institute of Technology, Pasadena, California, 1972.
5. Hammack, J. L., and Segur, H., "Modeling Criteria for Long Waves," Journal of Fluid Mechanics, Vol. 84, Pt. 2, 1978.
6. Kajiura, K., "Tsunami Generation," Proceedings of the National Science Foundation Tsunami Workshop, Coto de Caza, California, 1979, pp. 15-42.
7. Carrier, G. F., "The Dynamics of Tsunamis," Mathematical Problems in the Geophysical Sciences, Geophysical Fluid Dynamics, American Mathematical Society, 1, 1970, pp. 157-187.
8. Goring, D. G., "Tsunamis - The Propagation of Long Waves Onto a Shelf," Report No. KH-R-38, California Institute of Technology, Pasadena, California, 1978.
9. Mader, C. L., "Numerical Simulation of Tsunamis," Hawaii Institute of Geophysics, HIG-73, 3, 1973.
10. Plafker, G., "Tectonics of the March 27, 1964, Alaska Earthquake," U. S. Geological Survey Professional Paper 543-I, pp. 11-174, 1969.
11. Butler, H. L., "Numerical Simulation of Coos Bay-South Slough Complex," Technical Report H-78-22, U. S. Army Engineer Waterways Experiment Station, CE, Vicksburg, Mississippi, 1978.
12. Wilson, B. W., and Torum, A., "The Tsunami of the Alaskan Earthquake, 1964: Engineering Evaluation," Technical Memorandum No. 25, U. S. Army Coastal Engineering Research Center, CE, Washington, D. C., 1968.
13. Wiegel, R. L., "Protection of Crescent City, California, from Tsunami Waves," prepared for the Redevelopment Agency of the City of Crescent City, Berkeley, California, 1965.
14. Loomis, H. G., "The Nonlinear Response of a Tide Gage to a Tsunami," Proceedings of the 1983 Tsunami Symposium, Hamburg, Germany, 1983.
15. Roberts, J. A., and Kauper, E. K., "The Effects of Wind and Precipitation on the Modification of South Beach, Crescent City, California," ARG64 FR-186, Office of the Chief of Research and Development, Washington, D. C., 1964.
16. Keulegan, G. H., Harrison, J., and Mathews, M. J., "Theoretics in Design of the Proposed Crescent City Harbor Tsunami Model," Technical Report H-69-9, U. S. Army Engineer Waterways Experiment Station, CE, Vicksburg, Mississippi, 1969.
17. Magoon, O. T., "Structural Damage by Tsunamis," Coastal Engineering Santa Barbara Specialty Conference of the Waterways and Harbors Division, American Society of Civil Engineers, pp. 35-68, 1965.
18. Bretschneider, C. L., and Wybro, P. G., "Tsunami Inundation Prediction," Proceedings of the 15th Coastal Engineering Conference, American Society of Civil Engineers, pp. 1000-1024, 1975.

## CHAPTER FIFTY SIX

### A THREE-DIMENSIONAL MODEL OF THE BEAUFORT SEA

Shiao-Kung Liu\* and Jan J. Leendertse\*

#### Introduction

The Beaufort Sea borders the northern coasts of the United States and Canada. During the last decade, oil discovered at the Prudhoe Bay field contributes a substantial amount of the petroleum needs of the U.S. At present, it represents approximately 20 percent of the total domestic production. However, according to estimates made by the Department of the Interior, gas and oil lie under the Alaskan coastal waters (mainly in the Beaufort Sea) accounts for about 40 percent of the total domestic reserve.

To assist government agencies in their assessment of offshore oil exploration, the authors have been engaged, during the past nine years, in three-dimensional modeling work of the the Alaskan coastal area (Fig. 1). Results from the modeling work involving the Bering Sea and the Chukchi Sea have been reported at an earlier conference (Ref. 1).

This paper describes the formulation, coupling, and other essential aspects of the Beaufort Sea model (Fig. 2).

The Beaufort Sea, occupying a larger portion of the Alaskan coastal water, is dynamically interactive with other modeled areas. Most importantly, the exchange of water mass with the Chukchi Sea interconnects the Bering Sea through the Bering Strait (Fig. 3). Under certain weather conditions, ice in the Beaufort Sea can be transported toward the Bering Sea by an "ice breakout" process through the Bering Strait.

The purpose of the modeling work is to address coastal hydrodynamic-related problems, in general, as well as the following specific objectives:

- o Tidal and density-induced baroclinic circulation patterns;
- o Water and ice movements induced by wind, including storm-surges;
- o The behavior of oil movements under various spill scenarios; and
- o Providing boundary conditions for the near-shore models of higher spatial resolutions (Fig. 3).

#### The Methodology and Modeling System

Formulated on an elliptical horizontal grid and variable vertical grid, the three-dimensional model solves the equations of motion for water and ice, continuity, state, the balance of heat, salt, pollutant, turbulent energy density, the dynamics and thermodynamics of ice. The model computes the generation, melting, and the movements of ice together with the nonlinear vertical shear coupling during cooling and heating processes. This is achieved by means of a turbulence-closure technique in which the potential and kinetic energetics are monitored and

---

\*The Rand Corporation, 1700 Main Street, Santa Monica, California

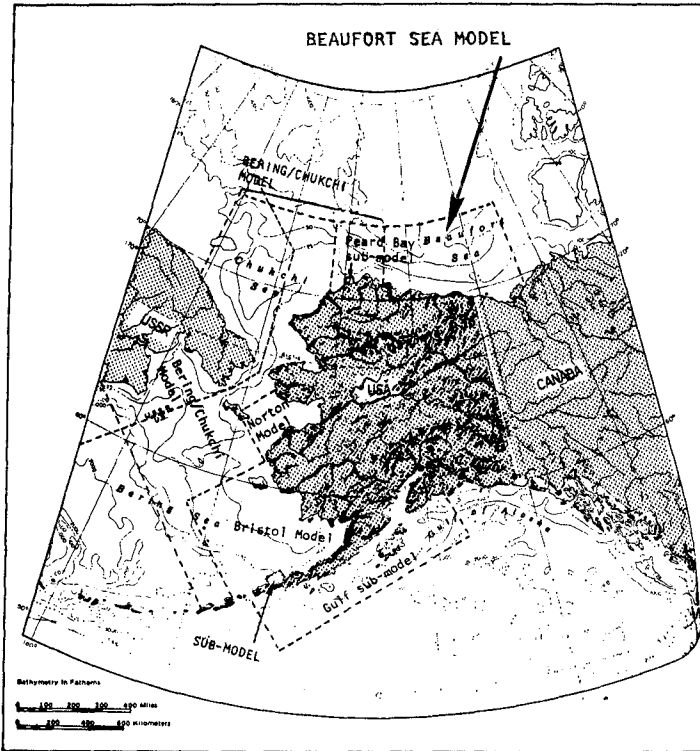


Fig. 1--Relative location between the Beaufort Sea model and other models covering the Alaskan coastal waters

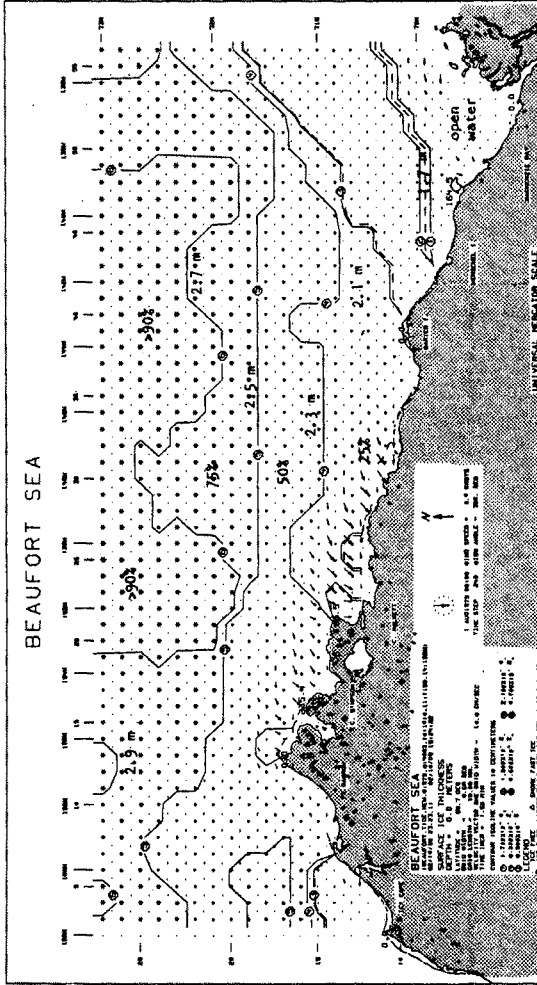


Fig. 2--Computational grid of the Beaufort Sea model plotted using the universal Mercator projection method. The map also shows the spatial distribution of ice concentration and ice thickness for the summer period.



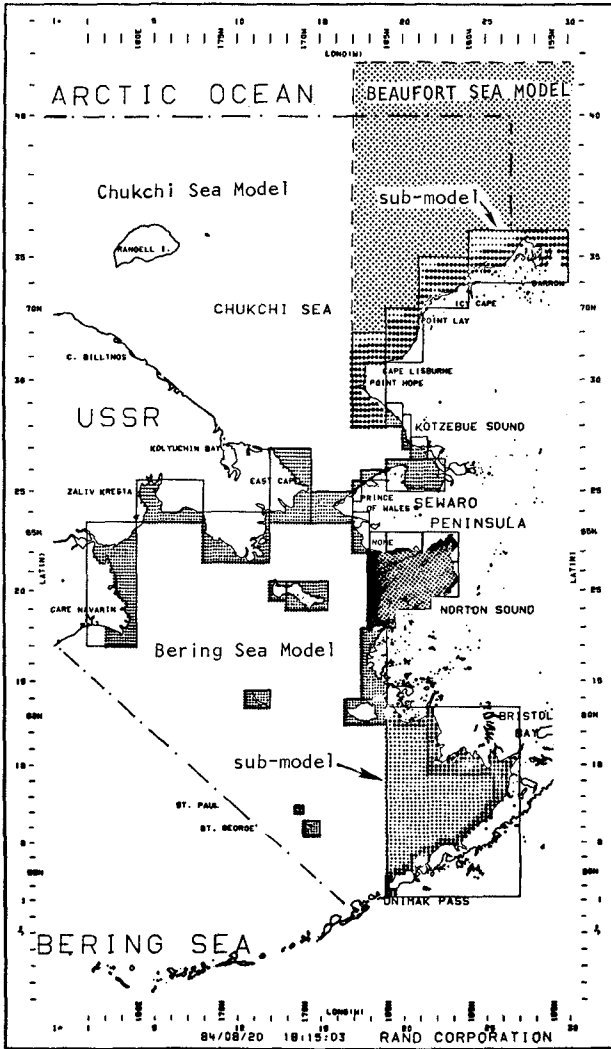


Fig. 3--Due to the interactive aspects, the western portion of the Beaufort Sea Model (shaded) is overlapped with the Chukchi Sea Model. This technique not only minimizes the boundary's effects on the computed residual currents but also would allow oil spill trajectory computations to be continued into the neighboring models. Submodels improve the near-shore resolution.

transferred in a closed form.

The hydrodynamic model is coupled to a two-dimensional stochastic weather model and an oil trajectory model. The important components and the flow of information are illustrated in Fig. 4.

The inclusion of the weather model is essential because the model covers the area where one of the world's major low pressure systems in the Northern Hemisphere (i.e. the Aleutian Low) is situated.

In developing the model we first treat the weather system over the modeled area as a stochastic process whose evolution is represented by a series of transitions between certain "state" of the process. When the number of the states is finite, the process is of the Markov type. It can be described or simulated if the probabilities of transition are known via the matrix of transitional probability. Also needed are the steady state behavior of the process chain and the amount of occupation time the chain spends in various states.

The required transitional probability matrices are generated using the daily synoptic weather data over the modeled area from 1945-1963. A  $11 \times 11$  matrix is determined for each oceanic season. Within the sampled period, 98 percent of the daily surface pressure pattern over Alaska can be classified into eleven types. The most frequent pattern (with 23 percent occurrence) during summer is a low pressure system with several centers over Alaska. Surface winds at various locations are analyzed for each weather type.

During the simulation with the stochastic weather model, wind fields generated by the Markov model are being interrupted by a storm track model which is of the Poisson type. The initial location of the extra-tropical-low is generated from a two-dimensional density function derived from the long-term observed data (Fig. 5). Figure 5 also gives the comparison between the wind rose generated from the model and those observed at three major weather stations showing zonal climatological variabilities. Detailed analyses of the probability distributions for the wind speed, direction, homogeneity and storm interruption are discussed in Ref. 2. Surface winds during the passage of a storm are computed by the gradient wind equation and modified for speed and veering angle according to local marine boundary layer stability conditions.

Another component of the modeling system is an oil-spill trajectory model which synthesizes the hydrodynamic responses of the coastal system obtained by the three-dimensional model under various forcing to compute the movement of oil resulting from simulations of the stochastic weather model. The 3-D model also provides energy densities and dispersion parameters for various layers for the oil trajectory computation. These trajectory computations have extended to eight months in elapse time at half-hourly intervals.

In addition to data synthesis, the oil trajectory model computes the surface and subsurface oil concentrations while the oil/weather processes take place.

#### Modeling Results

Our first step in the model development has been the determination of tidal and baroclinic residual circulation. The latter is caused by

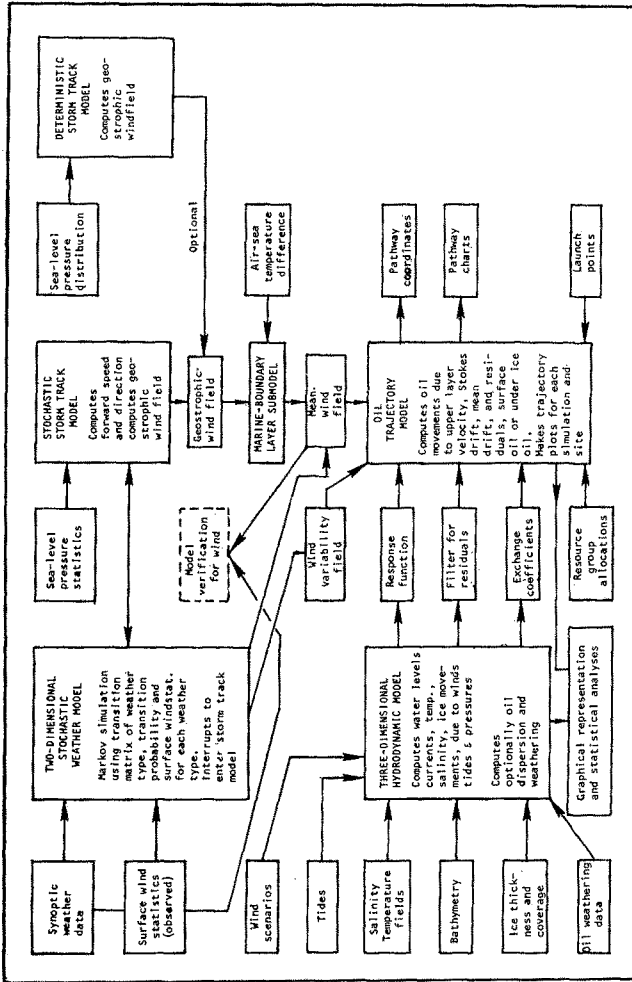


Fig. 4--Essential components of the two-dimensional stochastic weather simulation model; also showing their inter-relationship between the three-dimensional hydrodynamic model and the oil-spill trajectory model. Transitional probabilities of the weather states are derived from 19-year synoptic weather data.

		180°W	170°W	160°W	150°W	140°W	130°W	Σ
80°N	1	2	1	0	0	2	0	23
	2	1	1	1	2	1	1	23
	3	1	1	1	2	0	0	26
	4	1	1	1	2	0	0	26
	5	1	1	1	2	0	0	25
	6	1	1	1	2	0	0	25
	7	1	1	1	2	0	0	25
	8	1	1	1	2	0	0	25
	9	1	1	1	2	0	0	25
	10	1	1	1	2	0	0	25
70°N	1	2	3	4	5	3	2	40
	2	3	4	5	6	4	3	43
	3	4	5	6	7	5	4	45
	4	5	6	7	8	6	5	47
	5	6	7	8	9	7	6	49
	6	7	8	9	10	8	7	51
	7	8	9	10	11	9	8	53
	8	9	10	11	12	10	9	55
	9	10	11	12	13	11	10	57
	10	11	12	13	14	12	11	59
60°N	1	7	10	12	14	12	8	65
	2	8	11	13	15	13	9	68
	3	9	12	14	16	14	10	71
	4	10	13	15	17	15	11	74
	5	11	14	16	18	16	12	77
	6	12	15	17	19	17	13	80
	7	13	16	18	20	18	14	83
	8	14	17	19	21	19	15	86
	9	15	18	20	22	20	16	89
	10	16	19	21	23	21	17	92
50°N	1	18	22	26	31	26	18	142
	2	19	23	27	32	27	19	145
	3	20	24	28	33	28	20	148
	4	21	25	29	34	29	21	151
	5	22	26	30	35	30	22	154
	6	23	27	31	36	31	23	157
	7	24	28	32	37	32	24	160
	8	25	29	33	38	33	25	163
	9	26	30	34	39	34	26	166
	10	27	31	35	40	35	27	169
Σ		370	401	464	526	426	412	391 403 368 381 372 390 342 326 407 412 395 408 445 439 394 381 374 285 82

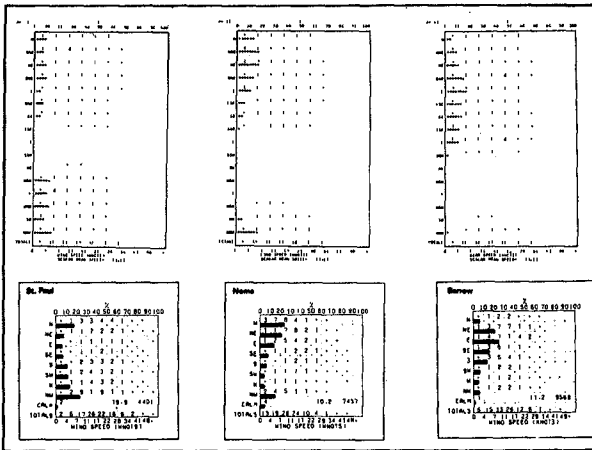


Fig. 5--Top graph shows the probability density function (pdfx10000) of the occurrence of extra-tropical cyclones within the modeled area. Lower graphs show the comparison between the wind roses generated by the long term simulation of the stochastic weather model and the observed wind roses at three ground stations for the month of July.

the density field and is interactive with the former. Originating from the Arctic Ocean, the tides in the Beaufort Sea generally move in a clockwise direction. The computed co-tidal chart for the semi-diurnal component is illustrated in Fig. 6. Also presented are the comparisons between the computed and the observed values at several locations. The agreement is generally quite good except near Herschel Island where the measured value is two centimeters higher. The difference may be attributable to the location of the gauge which, for practical reasons, was deployed behind the barrier island.

The computed tidal current ellipses, including baroclinic components for the surface layer is presented in Fig. 7. Figure 8, also for the surface layer, is the residual circulation pattern. The plotting scale for the current vector is two kilometers for each model grid-spacing.

The combined effects of residual circulation and the weather's effects can be illustrated by a map showing the trajectories of hypothetically spilled oil as they are released at various locations in the Beaufort Sea (Fig. 9), all under identical sequence of weather state. The daily movement of oil (depicted by a dot) reflects the local circulation as well as the evolution of weather states. The series of wind vectors plotted on top of the graph represent the 12-hour mean wind at Point Barrow. From Fig. 9, the shore's effect on the movement of oil is quite obvious.

In order to evaluate the risk (probability) associated with the oil development, a sequence of oil-spill scenarios have been selected at important locations representing platforms, pipelines, and transportation routes.

Figure 10 shows the comparison between trajectories of five satellite-tracked buoys deployed by the U.S. Coast Guard for a period of three months, and 30-day trajectories launched from five locations computed by the oil-spill trajectory model. They generally agree both in speed and in direction of movement.

Also needed for the evaluation of ecological impact, the concentrations of the spilled oil are computed. This computation includes the evaporation, dissolution, and spreading across the vertical layers.

Figure 11 shows the daily envelope of one-part-per-billion concentration contour of a hypothetical 30-day continuous spill of 500 barrels of crude oil per day under a summer condition. Loops in the plume's centerline indicating the occurrence of three low pressure centers move across the Bering Sea area. Under identical weather sequence, oil released from other areas, experiences an entirely different drift pattern.

The effects of shoreline and zonal climate difference on the movements of oil can be illustrated in Fig. 12. The peninsula in the figure exerts substantial influence on both near-shore residual currents as well as on the local wind pattern.

#### Conclusions and Discussions

Soon after the beginning of our modeling effort, it became clear that hydrodynamic computations per se cannot sufficiently address important policy issues. Other types of models such as for oil, ice, and weather related processes were needed. Weather models are of particular

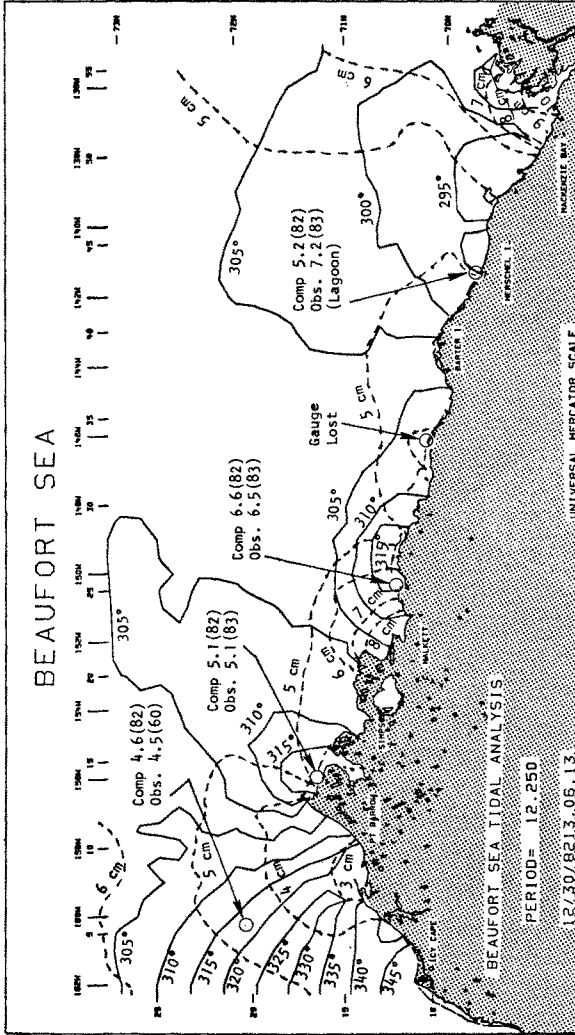


Fig. 6--Computed co-tidal chart for the semi-diurnal component in the Beaufort Sea showing amplitudes in cm and Greenwich phase in degrees. Computations were made in December 1982, and observations were made in September 1983 and published in 1984 (Pitman, 1984).

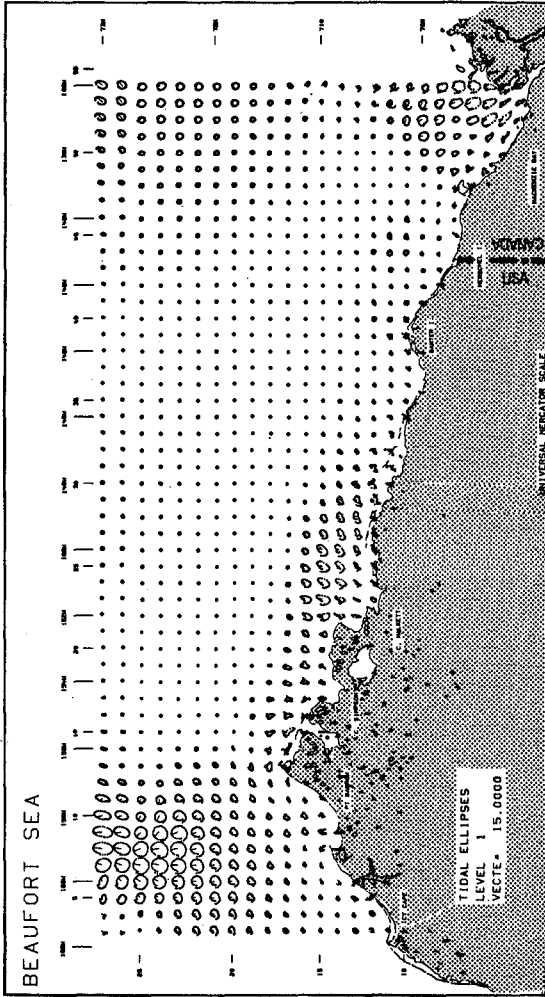


Fig. 7--Computed tidal and baroclinic current ellipses in the surface layer using a plotting scale of 15 cm/sec equal to a grid space

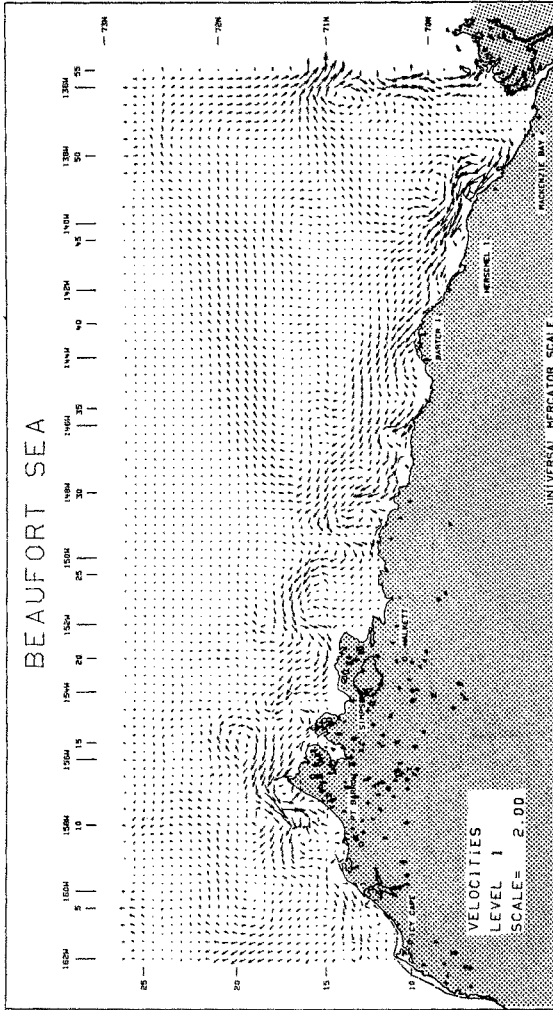


Fig. 8--Computed tidal and baroclinic residual current in the surface layer using a plotting scale of 2 km/day per grid space



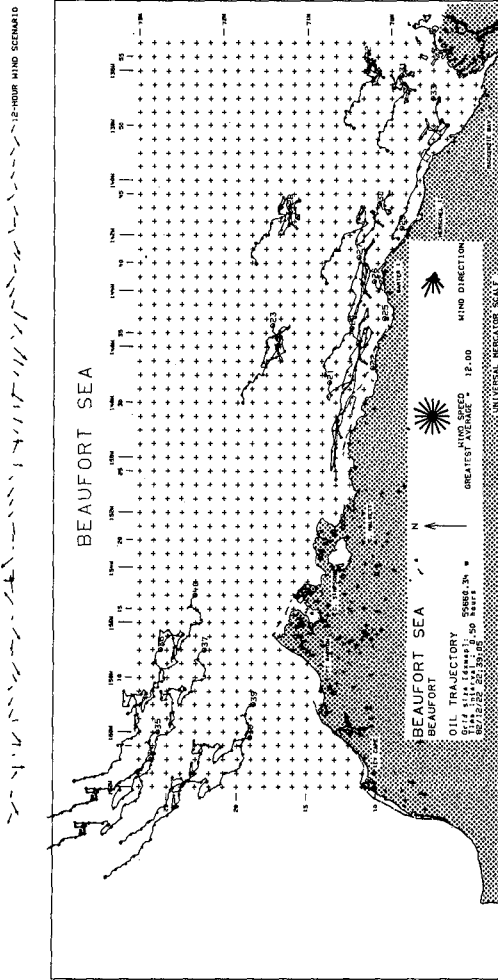


Fig. 9--Thirty day oil spill trajectories launched from hypothetical spill locations. Near shore trajectories within the ice-free area tend to move downwind whereas the oil in the offshore area tend to have various turning angles depending on the local ice concentration.

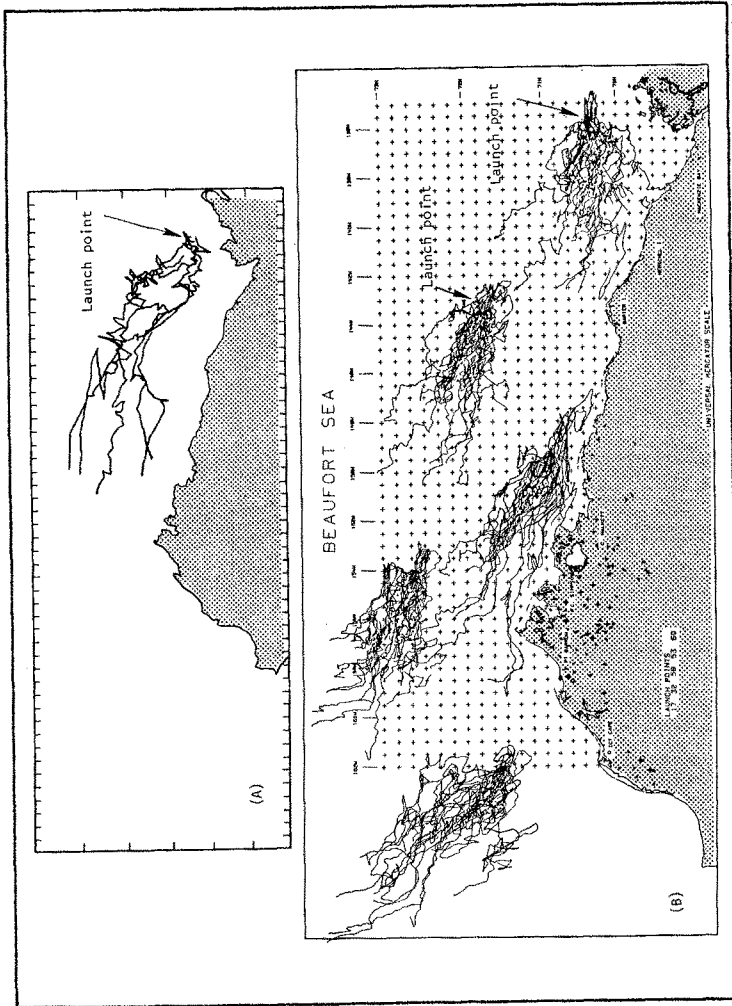


Fig. 10--Comparison between (A) trajectories of five satellite-tracked buoys deployed by the U.S. Coast Guard during the period between the months of August and October, 1979 from eastern Mackenzie Bay, Canada, and (B) 30-day trajectories launched from five locations computed by the oil spill trajectories model and the two-dimensional stochastic weather simulation model.

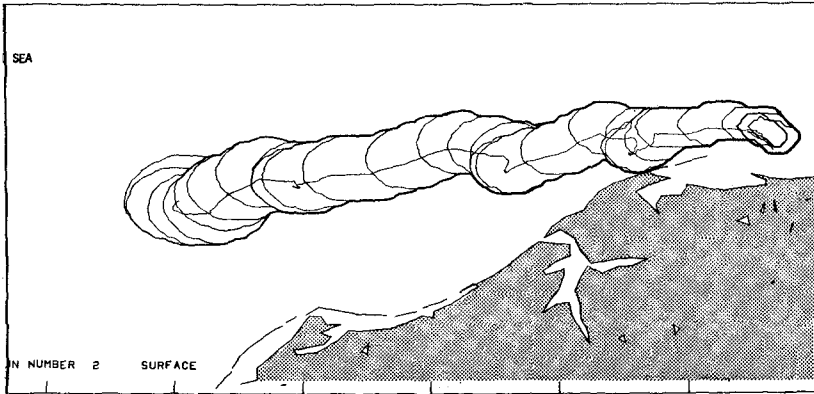


Fig. 11--Daily envelope of one-part-per-billion concentration contour of a hypothetical 30-day continuous spill of 500 barrels of crude oil per day under a summer condition.

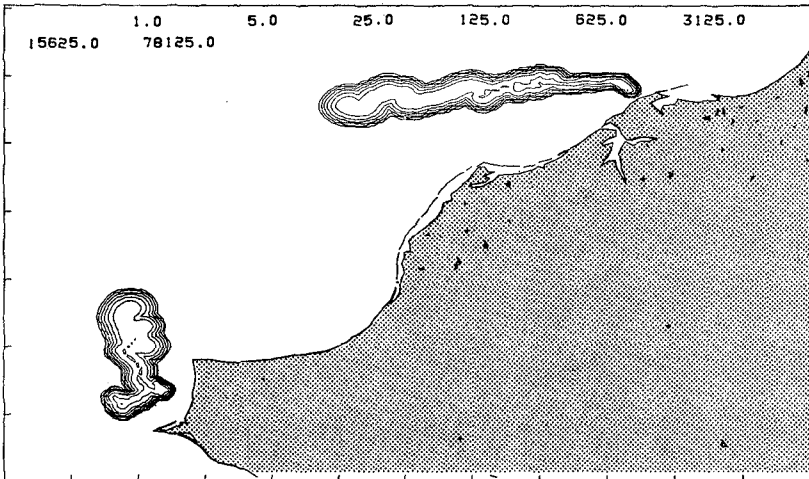


Fig. 12--The effects of shoreline and zonal climatic difference on the movements of oil

importance as the weather is often the major driving force for the generation of currents, movement of ice, and the dispersal of oil.

The stochastic-type of weather model is more suitable for the coastal area than the steady-state type of model in which winds are randomly generated based on a given wind rose. The latter method can be used under open ocean conditions where the drift duration is long and the nonlinear dynamic effects induced by the coasts are less significant. In coastal areas, the sequential occurrences of weather types tend to govern the final landfall location, particularly where coastal features and orographic influences have to be taken into consideration.

Finally, numerical models are particularly useful in remote areas where observed data are scarce and difficult to obtain, such as the one reported here. A preliminary model, formulated according to fundamental parameters and existing data, would serve as a starting point. Results from the initial analysis would then indicate the data needs. It can also assist in designing an effective field sampling program.

With new data, the investigators can thence improve the model formulation and proceed in an efficient manner.

#### ACKNOWLEDGEMENTS

This study was supported by the U.S. Bureau of Land Management through interagency agreement with the National Oceanic and Atmospheric Administration, under which a multi-year program responding to the needs of petroleum development of the Alaskan Continental Shelf is managed by the Outer Continental Shelf Environmental Assessment Program (OCSEAP) office. Thanks also go to our Rand colleagues, A. B. Nelson for his excellent programming effort and G. Coughlan for paper preparation.

#### REFERENCES

1. Liu, S. K., and J. J. Leendertse, *A Three-Dimensional Model of the Bering and Chukchi Sea*. The 18th International Conference on Coastal Engineering, Cape Town, South Africa, 1982.
2. Liu, S. K., *Stochastic Analyses and Control of Coastal Hydrodynamic and Water Quality Systems: Vol. II, a Two-Dimensional Stochastic Weather Model*, The Rand Corporation, in preparation.
3. Pitman, R. W., *Oceanographic Data from the Bering, Chukchi, and Beaufort Sea*, WASC-83-00114, Brown and Caldwell, 1984.
4. Murphy, D. L., P. A. Tebeau, and I. M. Lissner, *Long-Term Movement of Satellite-Tracked Buoys in the Beaufort Sea*, Office of Research and Development, U.S. Department of Transportation, CG-D-48-82, 1981.

## CHAPTER FIFTY SEVEN

### Model Harbour Seiching Compared to Prototype Data

W A M Botes\*, K S Russell\*, P Huizinga\*

#### 1. INTRODUCTION

Since 1978 a finite-difference numerical model based on that developed by Leendertse and adapted for resonance studies (Russell and Huizinga, 1978) has been applied to investigate harbour resonance in Table Bay Harbour and several other South African ports.

During April 1981 three long-wave recorders were installed in the cooling water intake basin of the Koeberg Nuclear Power Station to determine the occurrence and magnitude of the long waves and to measure the corresponding response of the basin. Koeberg is situated on the west coast of South Africa, 30 km north of Cape Town and is exposed to the approaching cyclonic weather systems which experience has shown to be associated with the occurrence of long waves. An example of an approaching low pressure system with the location of Koeberg is shown in figure 1.

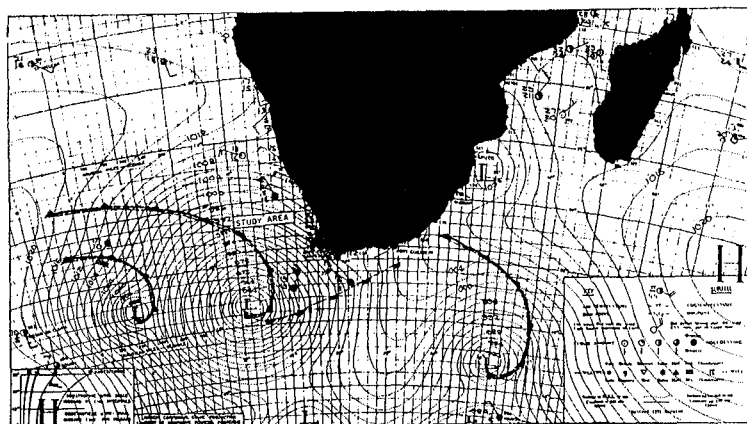


Figure 1. South Africa with approaching low-pressure systems, passing from west to east

Data were sampled over a period of two years and a paper on the characteristics of the long waves in the Koeberg basin was presented at the ICCE in 1982 by Botes, Russell and Huizinga (1982). In that paper the

\* National Research Institute for Oceanology, Stellenbosch, Republic of South Africa.

correlation between the occurrence of long-period waves and short-period waves was shown. During the sample period the recorders were switched to continuous mode during extreme weather conditions. These relatively long records could be analysed with a high degree of confidence and resolution for determining the response of the basin.

This paper presents further work using prototype results since they provide the basic data to calibrate and verify a numerical model of the Koeberg basin designed to study its resonance characteristics. This also allowed the investigation of aspects such as the sensitivity of the numerical model to grid sizes, computational time steps, friction, etc. The Koeberg intake basin provides an ideal configuration for the abovementioned investigations, as the basin is of medium size and situated on a straight coastline with a uniformly contoured seabed.

2. PROTOTYPE DATA SAMPLING

The water level recorders used consist of pressure transducers connected to magnetic tape recorders. Data were sampled at an interval of 1,0 s for a duration of 50 minutes every 12 hours. When resonance was visually observed the recorders were switched to continuous mode.

Three water-level recorders were installed in the basin and were in operation for the period April 1981 to March 1983. The characteristics of the long waves and the relation between the long- and short-period wave heights are described in Botes, Russell and Huizinga (1983). The long-period wave heights between 50 s and 110 s measured in the Koeberg basin are illustrated in Figure 2 where the wave height exceedance curves are drawn for the three recording positions.

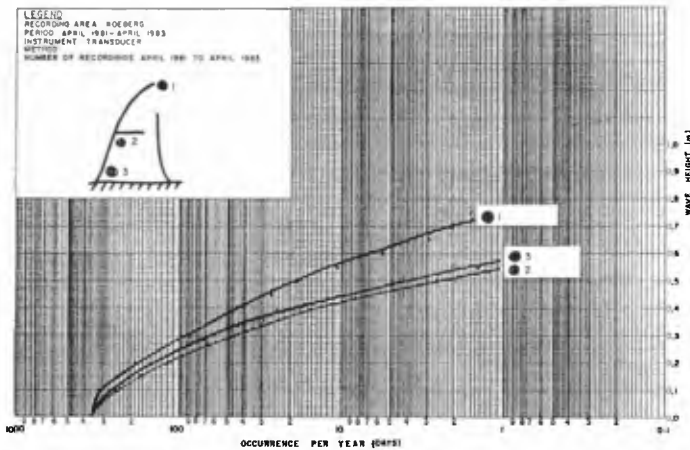


Figure 2. Long-period wave height exceedances

The analysis of the data was based on the auto-covariance method and is described in Botes (1980).

### 3. THE NUMERICAL MODEL

#### 3.1 General

The computations for this numerical model were based on the approximation of the hydrodynamic equations (conservation of mass and momentum equations in terms of the water elevation and depth average velocity) by using finite-difference techniques. The finite-difference modelling scheme, originally developed by Leendertse (1967), was adapted at the CSIR to accommodate any harbour layout (Russell and Huizinga, 1978). The modifications included radiative open boundaries, based on the method of characteristics which could be applied to any of the model boundaries to permit the passage of reflected waves. The same type of boundary was constructed on the side of the model which faced the main long-wave direction for the input wave conditions.

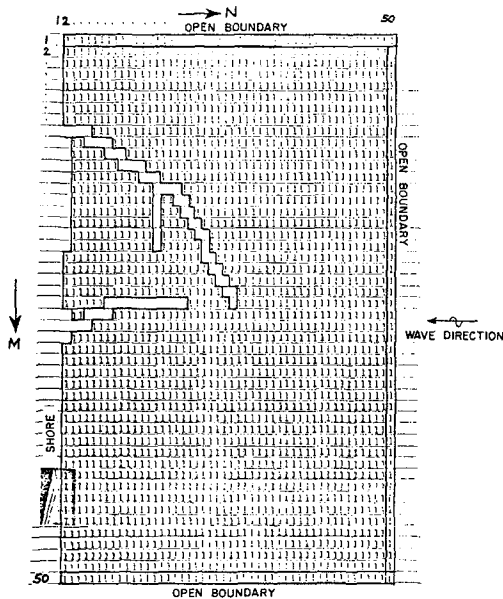


Figure 3. Computational field of the numerical model

The model area of Koeberg was represented by a two-dimensional grid system ( $50 \times 50$ ) with a grid size of 30 m which was the largest grid size which could describe this particular harbour configuration accurately.

At each grid point the depth and bottom friction were described and the velocities and water level fluctuations were calculated.

The computational field of the model was described by a notation of "1"'s and "0"'s with which the harbour configuration, shoreline, boundaries, etc. could be defined. The model created a computational notation by scanning this field vertically and horizontally. The computational field is described in Figure 3.

### 3.2 Input Conditions and Output of the Model

A method was developed to incorporate a range of frequencies in one model run by simulating an input wave spectrum which could be obtained by the bandpass filtering of a white noise spectrum. During the model run, time-series recordings were made at selected grid locations. These time-series were analysed in the frequency domain and the amplifications between two locations were obtained by the direct relation between the spectral density estimates of the two selected locations. The analysis was based on the auto-covariance method and is described by Botes (1983).

The advantages of this method were that the model and prototype data could be compared directly for calibration purposes and that it led to impressive savings over an approach where individual regular long waves were used in the model.

Frequencies which caused high amplifications were identified and the model was then operated with a sine wave input, with frequencies similar to the identified peaks. Maximum water level fluctuations over the entire harbour area were obtained as well as velocity vector fields at certain time steps.

### 3.3 Selection of Grid Size and Time Step

The computational time and cost of such a numerical model is directly related to the grid size and the computational time step.

The grid size must be small enough to provide not only a sufficient description of the coastline and harbour geometry but also to describe the bottom topography accurately. Bottom profiles can be very irregular with deep, narrow channels as at the entrance of the Koeberg basin. For adequate description of the Koeberg basin a maximum grid size of 30 m was needed for this study.

The computational system is unconditionally stable and is consistent so that the solution of the difference equations converge to the solution of the differential equations, the "true solution", as the grid size and time-step approach zero.



The stability, convergency and accuracy of the scheme is described by Leendertse (1967). The computational time-step can be determined theoretically with a few guidelines such as the Courant criterion and wave description, for the minimum phase and amplitude deformation. However, there was still a need to determine the sensitivity of the model compared to prototype measurements. If various layouts for a harbour are to be tested for a preliminary study, considerable cost can be saved if a bigger time-step than that theoretically decided on, can be used as long as the results are within acceptable limits.

The accuracy of the model (amplitude) compared to prototype responses for various time steps was determined with this series of tests.

#### 4. RESULTS

##### 4.1 Calibration

As mentioned, the grid size is controlled by the harbour geometry and topography. Initially a grid size of 30 m was chosen. For an average depth of 7 m the wave celerity is:

$$C = \sqrt{gd} = 8,29 \text{ m/s}$$

where  $d$  = depth (m)  
 $g$  = gravitational acceleration ( $\text{m/s}^2$ ).

For the best first approximation to a value for  $\Delta t$  we can put the Courant number,  $C_r$ , equal to 1:

$$C_r = C \cdot \Delta t / \Delta l = 1$$

where  $\Delta l$  = model grid size (m)  
 $\Delta t$  = model time step (s).

For  $C = 8,29$  and  $\Delta l = 30$

$$\Delta t = \frac{30}{8,29} \approx 3,62$$

$$\Delta \tau = 4,0 \text{ s.}$$

With a time step of 4,0 s and a grid size of 30 m the model was run with a random input between 0,0075 Hz (133,3 s) and 0,026 Hz (38,5 s). For the shortest wave, that is 38,5 s, the wave description (number of points per wave length) was  $T/\Delta t = 9,6$  and  $L/\Delta l = 10,6$ , which according to Leendertse (1967) is approximately the lower limit for wave description before considerable phase shift will occur.

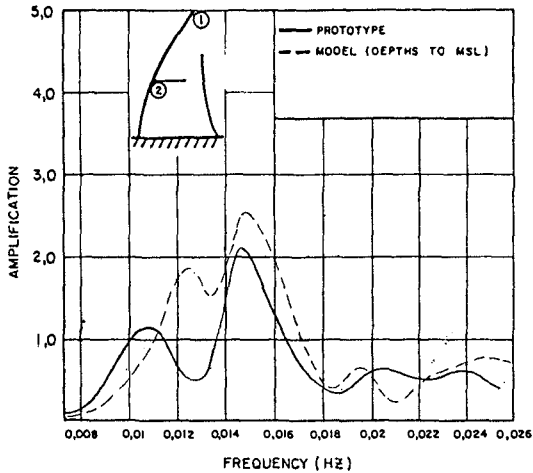


Figure 4. Prototype and model responses for  $\Delta t = 4,0$  s

The model responses between locations 1 and 2 are compared to the prototype data in Figure 4. The model topography was similar to the prototype topography that existed when the long waves were recorded.

The peak amplification at 0,015 Hz (66,67 s) compared well with the prototype data. This is the standing wave between the lateral arm and the shore side of the basin. Although the form of the total response wave tended to the shape of the prototype response curve, the correlation became worse from 0,013 Hz and lower. This is due to the lack of exact description of the topography in the outer basin which was still in the construction stage (dredging) during the time when the prototype data were recorded.

During 1978 an existing physical short-wave penetration model (scale 1:80) was used to investigate the response of the physical model to long waves.

This physical model had been constructed with a simplified harbour topography (a depth of 6,0 m throughout) and responded to a wave of 91 s. The numerical model responded to a wave of 85 s when an average depth of 6,0 m was also used in the model.

The resemblance between the velocity fields of the numerical and physical models is illustrated in Figure 5.

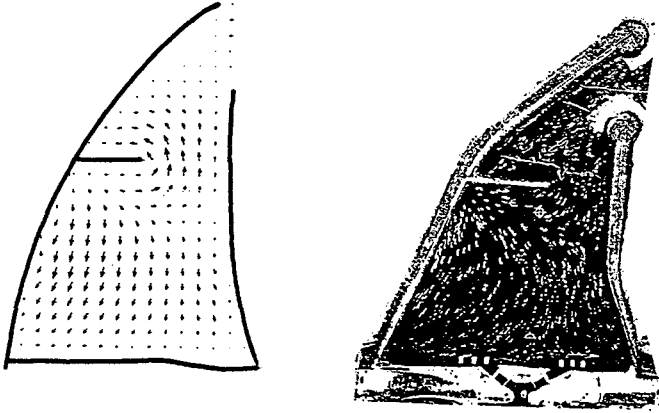


Figure 5. Velocity fields

Numerical model  
 $T = 85,7$  s

Physical model  
 $T = 91,0$  s

#### 4.2 Influence of Varying Time-steps on the Accuracy of the Model

As the grid size was fixed for the description of the layout it was attempted to increase the computational time-step in order to economize the model.

Although the shape of the response curve changed with a bigger time-step the peak response period and the magnitude of the amplification for the basin remained the same for a computational time-step of 6,0 s which resulted in a  $T/\Delta t$  of 6,4 and Courant number of 1,7. The result is illustrated in Figure 6.

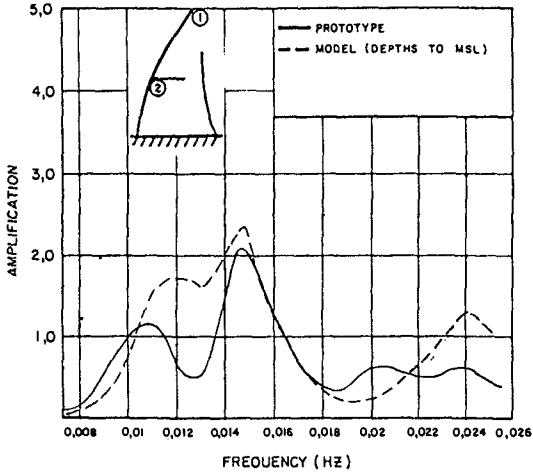


Figure 6. Prototype and model responses for  $\Delta t = 6,0$  s

The influence of the time-step on the accuracy of the model is best illustrated when the amplifications and velocity fields over the entire harbour area for the peak period of 66,67 s are compared as illustrated in Figures 7a-f.

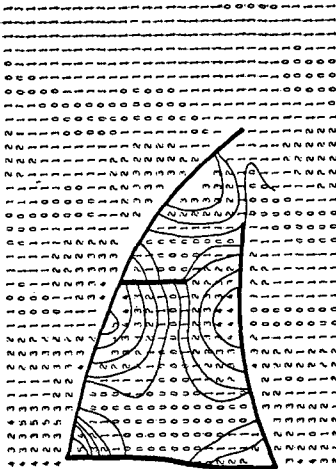


Figure 7a. Maximum amplifications  
 $\Delta t = 4,0$  s,  
 $T = 66,7$  s,  
 Input height = 0,1 m

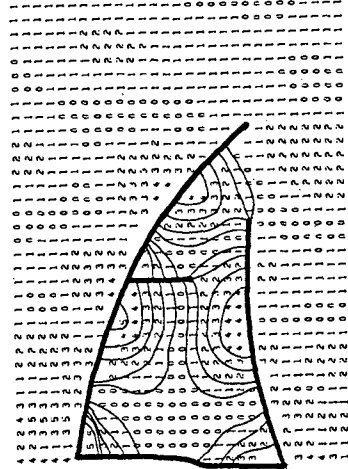


Figure 7b. Maximum amplifications  
 $\Delta t = 6,0$  s,  
 $T = 66,67$  s,  
 Input height = 0,1 m

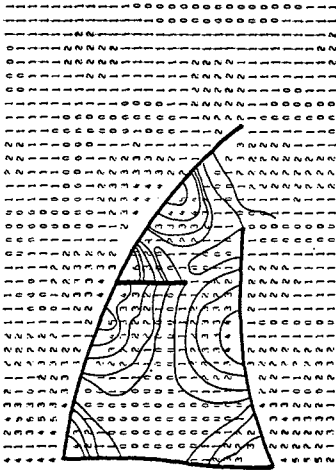


Figure 7c. Maximum amplifications  
 $\Delta t = 8,0$  s,  
 $T = 66,67$  s,  
 Input height = 0,1 m

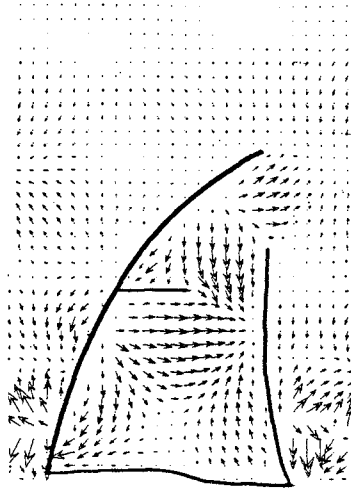


Figure 7d. Velocity field  
 $\Delta t = 4,0$  s,  
 $T = 66,67$  s,  
 Input height = 0,1 m

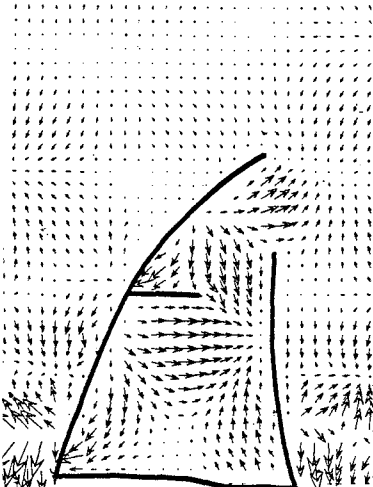


Figure 7e. Velocity field  
 $\Delta t = 6,0$  s,  
 $T = 66,7$  s,  
 Input height = 0,1 m

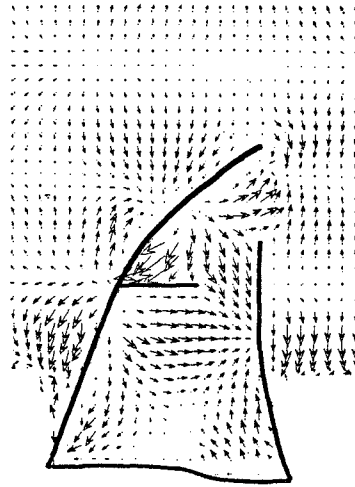


Figure 7f. Velocity field  
 $\Delta t = 8,0$  s,  
 $T = 66,7$  s,  
 Input height = 0,1 m

From these figures it can be seen that a computational time-step of 8,0 s ( $T/\Delta t = 4,81$ , Courant number = 2,2), which is twice the theoretically determined time-step, can still be used when numerous preliminary tests are necessary to determine an optimum layout. This results in considerable savings on computer cost and time.

However, for a time step of 10,0 s ( $T/\Delta t = 3,85$ , Courant number = 3,0). As shown in Figure 8, there is no sign of the characteristic response of the basin when compared to Figures 7a-c.

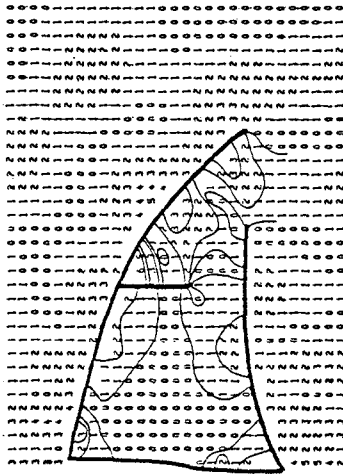


Figure 8. Maximum amplifications

#### 4.3 Influence of the Magnitude of the Input Wave

As the long-wave amplitudes range between 10 and 50 cm in the prototype, the influence of the magnitude of the input waves to the model was investigated.

As experienced with the prototype data the model response was consistent, irrespective of the magnitude of the input waves as illustrated in Figure 9 and compared to Figure 7b.

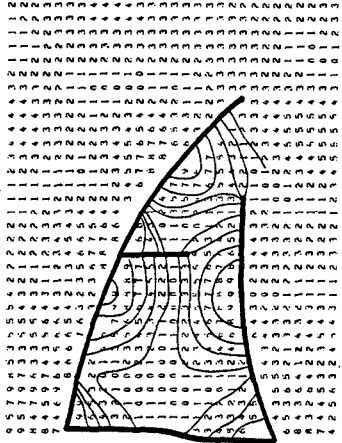


Figure 9. Maximum amplifications  
 $\Delta t = 6,0 \text{ s}$ ,  $T = 66,7 \text{ s}$ ,  
 Input height =  $0,2 \text{ m}$   
 Amplifications are the values divided by 2

4.4 Influence of Water Depth

In relatively shallow areas in a harbour layout the water levels are of great importance when comparing model results to prototype data as illustrated in Figure 10 where the responses of the model for water levels at spring, mean and neap tides are compared with prototype data.

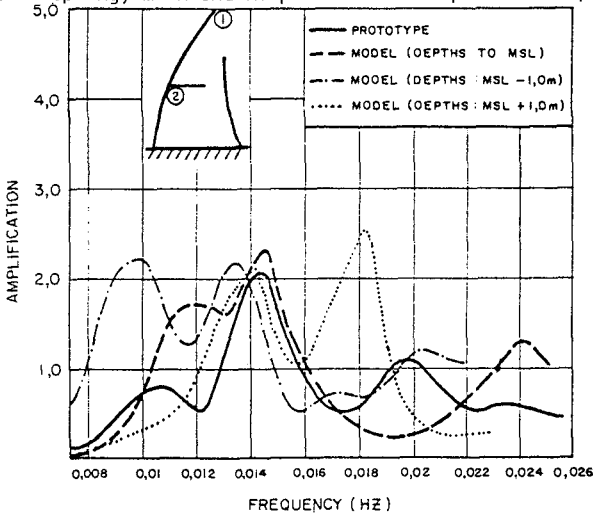


Figure 10 Model responses at different water levels compared to prototype data

## 5. CONCLUSIONS

- (1) The prototype data provided valuable information on wave-height exceedances, correlation between short and long-period wave heights, and response data to calibrate and verify the numerical model.
- (2) The numerical model could be calibrated with a computational time-step of 4,0 s.
- (3) Resemblance between the physical and numerical model results is very good.
- (4) For basic investigations with the response frequency, larger time-steps can be used in order to save cost and time.
- (5) For a wave description ( $T/\Delta t$ )  $< 4,8$  and a Courant number  $> 2,2$  the model results are completely inaccurate.
- (6) In relatively shallow harbours the response of the basin is strongly influenced by the water depths (tidal variation).
- (7) The response of a basin (i.e. pattern of oscillation and degree of amplification) is not influenced by the magnitude of the input wave height.

## REFERENCES

- BOTES, W A M (1980). Application of digital time series analysis to a resonance study at Table Bay Harbour. CSIR Report SEA 8006.
- BOTES, W A M, RUSSELL, K S and HUIZINGA, P (1982). Resonance in South African harbours. Proceedings ICCE 1982, Cape Town.
- LEENDERTSE, J J (1967). Aspects of a computational model for long period water wave propagation. The Rand Corporation, RM-5894-PR.
- RUSSELL, K S and HUIZINGA, P (1978). A two-dimensional finite-difference numerical model for the investigation of harbour resonance. CSIR Report IR 7804.



## CHAPTER FIFTY EIGHT

### Boundary Condition for Limited Area Modeling

H. Lee Butler<sup>1</sup>, and Y. P. Sheng<sup>2</sup>, M, ASCE

#### Abstract

A simple open boundary condition for limiting the computational domain in tidal simulations is presented. In modeling the impact of proposed coastal projects with a limited-area model, problems due to undesired reflection of gravity waves at open boundaries often occur. The boundary condition presented herein eliminates these problems in many instances and can be easily incorporated into a wide variety of models. The adapted procedure permits representation of appropriate forcing conditions while allowing propagation of internally-generated disturbances out of the open boundaries. Applications to real world engineering problems are presented.

#### Introduction

Numerical models are routinely used to assess the potential impact of proposed hydraulic or geometric modifications within coastal areas. A recurring problem in these applications is the establishment of appropriate boundary conditions for both baseline and improvement simulations. For tidal simulation by means of a vertically-integrated model, it is often sufficient to specify the surface elevation along the open boundaries based on existing tidal measurements at these boundaries. However, the presence of a proposed modification within the model domain may introduce enough disturbance to significantly alter the tidal conditions at the open boundaries.

In such a case, using existing tidal measurements at the boundaries of the limited-area model will lead to wave reflection and hence erroneous simulation results within the model domain. Traditionally, this problem has been resolved by moving the open boundaries to locations substantially further from the area of interest such that existing measurements there may be utilized without causing damaging wave reflections. This procedure leads to a much larger computational domain and hence extra computational cost. Moreover, there may exist little or no data at such far-away open boundaries and acquisition of such data can be expensive and difficult to obtain. In an effort to simulate the effect of tidal barriers in a limited-area model, Prandle (9) utilized the concept of Garrett (5) to objectively assess the validity of applying existing tidal measurements at various downstream boundary locations.

<sup>1</sup>Chief, Coastal Processes Branch, Coastal Engineering Research Center, U. S. Army Engineer Waterways Experiment Station, P. O. Box 631, Vicksburg, Mississippi 39180

<sup>2</sup>Senior Consultant, Aeronautical Research Associates of Princeton, Inc., P. O. Box 2229, Princeton, New Jersey 08540

## Wave Separation/Radiation Boundary Condition

The approach used is based on the concept that tidal data at a given coastal location (e.g., the open boundary) can be represented by the superposition of an incident and an outgoing component. The present formulation is a variation of the approach given by Orlanski (8) which did not include any external forcing, and is somewhat similar to the port boundary condition used by Reid and Whitaker (10) in the limiting case of negligible spatial variation of the wave phase speed. The application of Reid and Whitaker's condition, however, requires the explicit estimation of the tidal impedance according to the empirical formula of Garrett (5). The estimation of tidal impedance in the presence of proposed structures is not a straightforward matter.

Consider the scalar wave equation (or Sommerfeld radiation condition) as given by

$$\frac{\partial \phi}{\partial t} + c \frac{\partial \phi}{\partial x} = 0 \quad (1)$$

where  $\phi$  is the surface elevation or fluid velocity and  $c$  is the phase velocity of the wave. Let Figure 1 describe an area within the computational domain where we desire to establish an open-boundary condition that permits any internally-generated disturbances to pass through the boundary without undergoing significant distortion and without influencing the interior solution. Let  $p$  and  $q$  represent the outgoing and

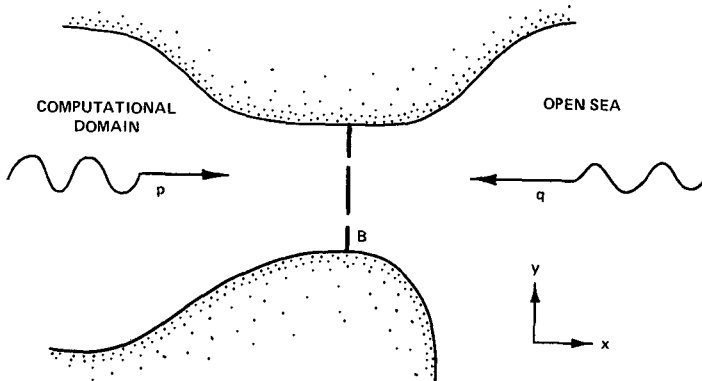


FIG. 1.-Typical Location for Applying the Wave Separation/radiation Boundary Condition

incoming tidal waves, respectively. The surface elevation ( $\eta$ ) at the boundary (B) is given by the superposition of  $p$  and  $q$ , or

$$\eta = p + q \quad (2)$$

Functional representations of  $p$  and  $q$  can be given in characteristic form as

$$p = f(x - ct) \quad \text{and} \quad q = g(x + ct) \quad (3)$$

Assuming flow through the open boundary is approximately normal to the boundary, the scalar wave equation can be used to approximate tidal behavior at B. Substituting the value of surface elevation given by expressions (2) and (3) into Equation 1 and evaluating the lefthand side at the boundary, we obtain

$$\begin{aligned} \frac{\partial(p+q)}{\partial t} + c \frac{\partial(p+q)}{\partial x} &= \frac{\partial p}{\partial t} + c \frac{\partial p}{\partial x} + \frac{\partial q}{\partial t} + c \frac{\partial q}{\partial x} \\ &= -cf' + cf' + cg' + cg' \\ &= 2cg' = 2q' \end{aligned} \quad (4)$$

The term  $q'$  is the time derivative of the incoming wave evaluated at B, i.e.,  $q'_B$  is given as

$$\left. \frac{\partial \eta}{\partial t} + c \frac{\partial \eta}{\partial x} \right|_B = 2q'_B \quad (5)$$

This formulation only requires knowledge of the incoming tidal wave. The proposed strategy is to (a) measure tidal elevation at the open boundary for some existing condition under various tidal events, (b) apply the interior hydrodynamic model under tidal forcing and evaluate the lefthand side of expression (5) to obtain  $q'_B$ , and (c) introduce proposed interior modifications for impact evaluation and apply Equation (5) as a forcing boundary condition at B.

In case of an open boundary on the left side of the computational domain, a corresponding condition can be derived as

$$\frac{\partial \eta}{\partial t} - c \frac{\partial \eta}{\partial x} = -2cf' = 2p' \quad (6)$$

If interior modifications to be investigated do not alter characteristics of the incoming tide, only a different combination of incoming and outgoing waves at the boundary will occur. The wave separation/radiation (S/R) open boundary condition prescribes the correct incident component,  $q$ , and allows the outgoing component,  $p$ , to be modified by any internally-generated disturbances. In the absence of tides, the S/R condition reduces to the simple Sommerfeld radiation boundary condition.

For simplicity, the above discussion has been given for the limiting case of subcritical flow and small amplitude wave. Extension of the basic concept to the more general case has been studied and will be

discussed elsewhere. The major difference is that the more general S/R condition involves both  $\eta$  and the velocity  $u$ .

Numerical Implementation

The S/R boundary condition application is not dependent on the type of numerical algorithm used for solving the equations of motion within the computational domain. In all application examples vertically-integrated two-dimensional implicit finite difference models were used (1,11). These schemes employ a three-time level alternating-direction implicit (ADI) algorithm to solve the equations of motion on a variable-stretched rectilinear grid. Any finite difference representation of Equation (5) or (6) must be consistent with the interior scheme. The ADI procedure in the models mentioned above uses the double-sweep method to efficiently solve for the dependent flow variables. For simplification we will consider the boundary to be parallel to the y-direction (Fig. 1) and hence only the x-sweep of the algorithm is affected. The index  $m$  ( $M$  in FORTRAN notation) will be used to mark the boundary location within a staggered grid system (Fig. 2). The grid stretching is of the exponential type and involves only a weighting factor ( $\mu$ ) with the second term in Equation (5). For the three time level ADI scheme (ADI3T)

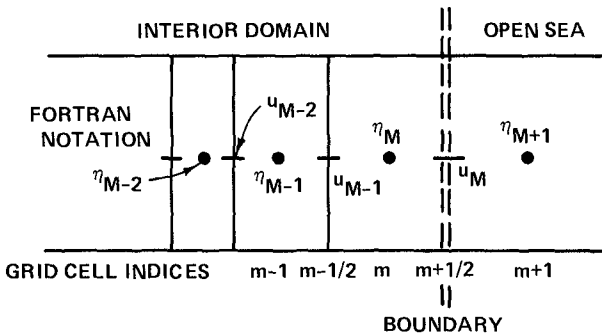


FIG. 2.-Staggered Grid Cell Definition at the Open Boundary

used in Butler (1), Equation (5) in finite difference form is

$$\left(\frac{\partial \eta}{\partial t}\right)_{m+1/2}^k + \left(\frac{c}{\mu}\right)_{m+1/2}^k \left(\frac{\partial \eta}{\partial x}\right)_{m+1/2}^k = 2(q')_{m+1/2}^k \quad (7)$$

where  $k$  is the time step counter and  $\mu_{m+1/2}^k$  is the weighting factor to account for the grid stretching (variability).

If

$$z_{m+\frac{1}{2}}^k = \frac{2 \Delta t c_{m+\frac{1}{2}}^k}{\mu_{m+\frac{1}{2}} \Delta x} \quad (8)$$

and

$$F^k = 8 \Delta t q'_{m+\frac{1}{2}}^k + \eta_{m+1}^{k-1} + \eta_m^{k-1} + z_{m+\frac{1}{2}}^k \left( \eta_{m+1}^k - \eta_m^{k-1} \right) \quad (9)$$

then the ADI3T approximation for Equation (5) can be written as

$$\left( 1 - z_{m+\frac{1}{2}}^k \right) \eta_m^{k+1} + \left( 1 + z_{m+\frac{1}{2}}^k \right) \eta_{m+1}^{k+1} = F^k \quad (10)$$

The last interior equation evaluated adjacent to the boundary is of the form

$$-a_M \eta_M^{k+1} + \bar{a}_{M+\frac{1}{2}} u_{M+\frac{1}{2}}^{k+1} + a_{M+1} \eta_{M+1}^{k+1} = D_{M+\frac{1}{2}}^k \quad (11)$$

where the coefficients  $a$  and  $\bar{a}$  are defined in terms of known quantities and where  $a_M = a_{M+1}$ . Substituting the expression for  $\eta_{M+1}^{k+1}$  from Equation (10) into (11), one obtains

$$-\frac{2a_M}{1 + z_{M+\frac{1}{2}}^k} \eta_M^{k+1} + \bar{a}_{M+\frac{1}{2}} u_{M+\frac{1}{2}}^{k+1} = D_{M+\frac{1}{2}}^k - \frac{a_M F^k}{1 + z_{M+\frac{1}{2}}^k} \quad (12)$$

To implement Equation (12) as a boundary condition in the ADI model, only a few recursion coefficients in the solution algorithm need to be changed. Note that no restrictions have been made on grid cell dimensions or time step.

Actual implementation of the S/R boundary condition in areas of complex geometries may result in high frequency oscillations superimposed on the derivative of the incident wave,  $q'$ . This problem can be eliminated by applying a temporal smoothing formula. In some applications presented herein a central smoothing formula of degree 3 over a subrange of 13 time steps was effective (6).

#### Tests and Applications

As stated previously the S/R boundary condition was used in conjunction with a vertically-integrated model (WIFM or WES Implicit

Flooding Model) developed at the U. S. Army Engineer Waterways Experiment Station. The governing equations and computational scheme are explained in the paper by Butler (1). This model, as well as a two time level ADI model used by Sheng (11), were employed in performing extensive tests of the S/R boundary condition in idealized basins with simple geometry and bathymetry. These included one-dimensional model tests with parameter variations of (a) constant depth or sloping bottom, (b) fixed or variable grid spacing, (c) uniform flow or tidal forcing, and (d) the introduction of internal modifications. Also tested were two-dimensional basins with similar parameter variations. Once the boundary condition algorithm was coded to be consistent with the ADI models all tests were successful in radiating the outgoing wave components without reflection or without disturbing the incoming signal.

To demonstrate the application of the S/R condition, we present a simple example of wave propagation in a one-dimensional channel with a length of 10 spatial units. Consider an external forcing of  $\sin(2\pi t/100)$  on the right boundary with radiation at the left boundary. For simplicity, but without loss of generality, we assume that  $\Delta t = 1$ ,  $\Delta x = 1$ , and  $c = 1$ . Based on these boundary conditions and parameter values, the results of the one-dimensional wave equation along the channel at a particular instant of time are shown by the solid line in Figure 3.

The dashed line in Figure 3 was obtained by using the S/R condition on the right boundary. In the separation mode the model was run with the conditions just described in the last paragraph. The term,  $q'$  (Equation 5), was evaluated at each time step on the right boundary (using one-sided differences) and stored on a file. The model was then run in the radiation mode with Equation (5) as a boundary condition on the right boundary.

The slight discrepancy shown in Figure 3 is associated with the fact that the interior numerical scheme is based on central differencing while one-sided differences were used at the boundary in computing  $q'$ . When central differences were used in the separation mode to compute  $q'$ , the radiation mode results agreed exactly with the result obtained by external forcing.

The primary motivation for a S/R boundary condition was a project impact study involving a proposed navigation lock and flood-control structure at the Lake Pontchartrain, Louisiana, end of the Inner Harbor Navigation Canal (IHNC). This application was part of a comprehensive study to evaluate effects of the Lake Pontchartrain and Vicinity Hurricane Protection Plan (3).

Lake Pontchartrain is adjacent to and just north of the city of New Orleans, Louisiana. In addition to two natural pass connections to the Gulf of Mexico, there is a man-made canal, including the IHNC and Mississippi River-Gulf Outlet (MR-GO), which connects the southernmost part of the lake with the Gulf of Mexico. The Gulf Intracoastal Waterway

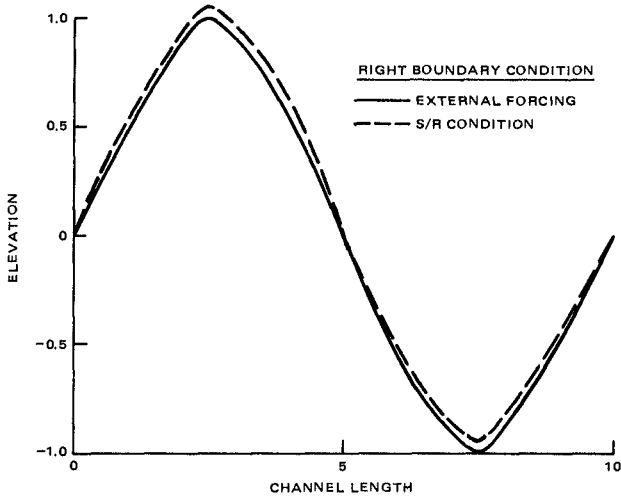


FIG. 3.—One-Dimensional Test of the S/R Boundary Condition

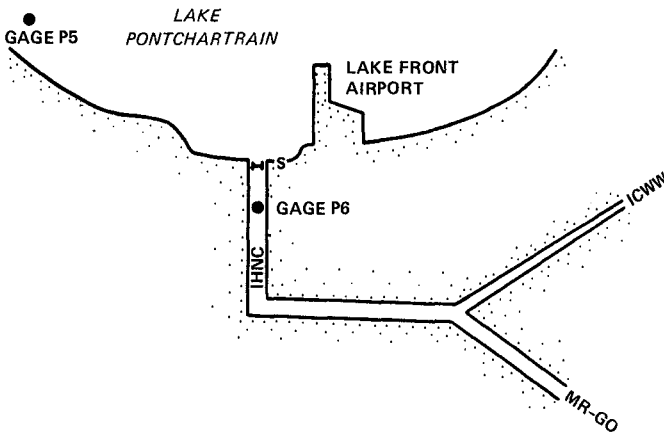


FIG. 4.—Vicinity and Gage Location Map for the Lake-IHNC Sectional Model

(ICWW) also joins with the MR-GO resulting in a highly complex lake-channel waterway.

A part of the study centered on investigating effects of the proposed lock and flow-control structure at the lake end of the IHNC. Figure 4 depicts the waterway subsystem geometry, location of the proposed structure (S), and locations of prototype measurement stations (P5 and P6). A numerical sectional model of the lake-IHNC complex was constructed and verified with tidal elevation and current data taken at locations P5 and P6. In addition, a physical hydraulic model of the same area was constructed, verified for existing conditions under steady state flow, and run for various flow rates and head differences between the lake and the IHNC. These results were used to define the structure hydraulic characteristics in order to permit proper numerical representation, and are reported by Butler, et al., (2). Results from the hydraulic model tests were used to verify the S/R boundary condition for peak flow conditions (near steady state).

The numerical sectional model of the lake-channel complex was calibrated and verified to simulate steady-state flow conditions generated in the undistorted hydraulic model of the same area. Frictional coefficients associated with barriers representing the existing bridge constriction at the lake entrance of the IHNC and those representing the lock/structure for various operating conditions were determined. In all cases the model was forced at the IHNC open boundary with discharge rates while lake levels were held at specified values.

Without changing any model parameters the numerical sectional model was forced with mixed tides (determined from analyzed constituent data at P5 and P6) at both the lake and IHNC open boundaries. Table 1 shows, for a series of average water levels in the lake and IHNC at peak flood conditions corresponding to a spring, mean, and neap tide, a comparison of discharge rates taken from the numerical and hydraulic model tests. Similar comparisons were noted for peak ebb discharge conditions.

TABLE 1. Comparison of IHNC Discharge Rates Predicted by the Hydraulic and Numerical Sectional Models for Existing Conditions

Tide Event	Water Levels (cm)		Discharge Rate ( $m^3/sec$ )	
	IHNC	Lake	Hydraulic	Numerical
Spring	12.8	2.4	490	496
Mean	7.9	1.2	408	382
Neap	1.5	-1.2	215	227

For each tide simulation the derivative of the incident wave at P6 was computed and stored for later use. Replacing the tidal forcing boundary condition at P6 with the S/R boundary condition resulted in identical model results throughout the computational domain. Figure 5 depicts a comparison of the elevation computed at the S/R boundary with analyzed prototype data for a mean tide.



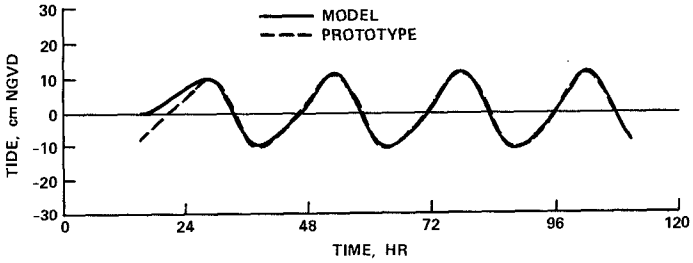


FIG. 5.-Comparison of Analyzed Prototype Surface Elevation Data at Gage P6 with Computed Results at P6

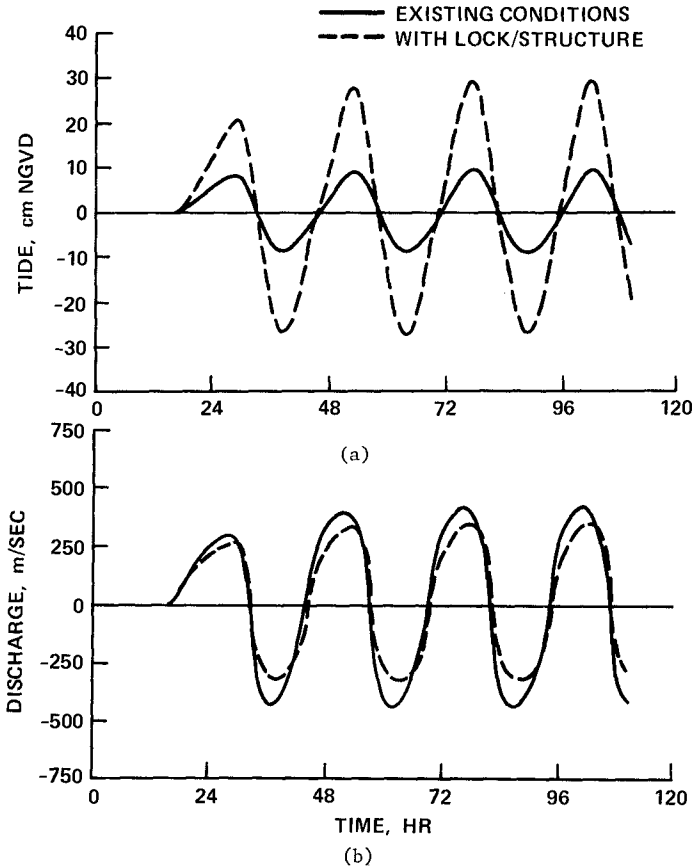


FIG. 6.-Impact of the Lock/Structure System on Tidal Elevations and Discharge Rates in the IHNC

The proposed lock/structure was placed in the model and runs were made for the three tidal conditions mentioned above, using the S/R boundary condition as a forcing condition. Results for the mean tide condition with and without the lock/structure modification are shown in Figure 6a (tidal behavior in the IHNC) and Figure 6b (changes in IHNC discharge rates). Table 2 shows a similar comparison as in Table 1 for differences between the numerical and hydraulic model tests. The results indicate a very good agreement was reached for the near steady-state portions of the tidal cycle. What is significant is that a small change in channel discharge may be associated with a large change in tidal amplitude in the IHNC. This is expected since the constriction of the lock/structure system in a fully-open operating condition reduces the existing cross-sectional area of the IHNC lake entrance by about 70 percent. Also as expected, the impact is significantly less during a neap tide event.

TABLE 2. Comparison of IHNC Discharge Rates Predicted by the Hydraulic and Numerical Sectional Models for Plan Conditions

Tide Event	Water Levels (cm)		Discharge Rate ( $m^3/sec$ )	
	IHNC	Lake	Hydraulic	Numerical
Spring	40.2	3.7	408	405
Mean	28.0	3.4	317	328
Neap	6.1	0.0	161	164

A second application of the S/R boundary condition involved its use as a simple radiation boundary condition. To implement such a condition one need only input a zero derivative for  $q'$  at the open boundary. The radiation condition was applied in a generalized numerical model for longshore currents (12). The vertically-integrated long wave equations were modified to include radiation stresses defined in terms of the local values of the wave height, wave number, and wave direction. For the bottom friction a linear formulation, similar to that of Longuet-Higgins (7), was used in all applications. The solution algorithm is similar to that used in WIFM and is computed on a variable-spaced rectangular grid. A wall condition was assumed at the still water line along the beach. A zero-gradient flux condition was used at the open-sea lateral boundaries extending seaward from the beach. Of primary concern was the selection of a proper boundary condition for the seaward boundary, parallel to the shore.

Use of a fixed elevation or wall boundary condition on the offshore boundary will develop transients in the numerical solution. Such transients are evident in the results (Fig. 7) present by Ebersole (4). If transients are present that reflect between the shore and the offshore boundary, a steady condition of no flow in the onshore and offshore direction is not achieved. If steady state is assumed, grid cells will have small but steady currents in onshore and offshore directions that will produce steady erosion and deposition when these currents are used as input to sediment transport models.

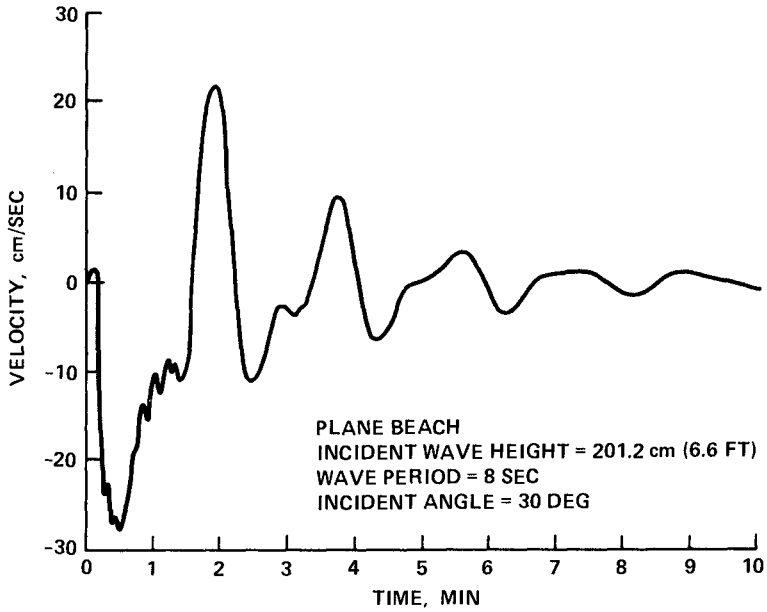


FIG. 7.-Velocity with Transients in the Offshore Direction (4)

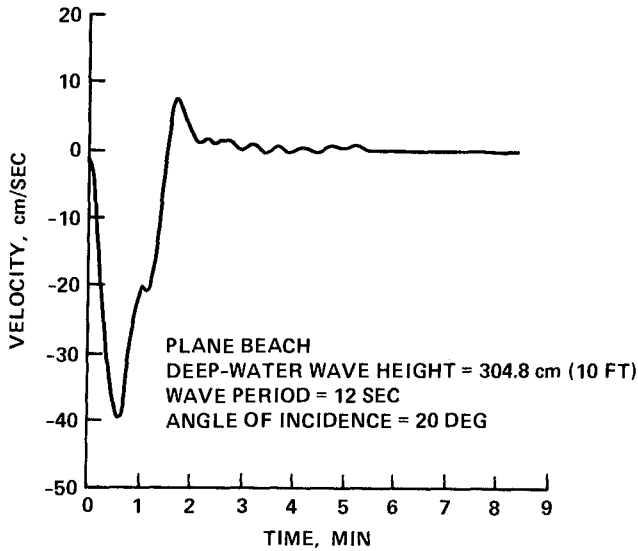


FIG. 8.-Velocity in the Offshore Direction Using the S/R Boundary Condition (12)

To eliminate the problem with transients, the S/R boundary condition was used as a simple radiation condition. Figure 8 shows a test (12) similar to the one run by Ebersole, except using the radiation boundary condition. Velocity in the offshore direction reached a steady zero velocity after approximately 6 minutes. Similar results were obtained for wave setup and the longshore velocity component. All tests demonstrated how well the S/R condition worked.

#### Conclusions and Remarks

The successful application of this type of boundary condition in various idealized and practical investigations has resulted in cost-effective analysis by permitting a reduction in model limits. The efficient numerical scheme and the ability to vary spatial coordinates at the boundary allows for realistic and easy application to a large number of coastal impact studies. Current research is aimed at expanding the S/R boundary condition approach to more complicated two- and three-dimensional model problems. In addition, the condition has been recently developed for application on a generalized curvilinear grid. These developments will be reported in forthcoming articles.

#### Acknowledgments

The work reported herein was supported by the U. S. Army Engineer District, New Orleans, and the Coastal Flooding and Storm Protection Research Program. The permissions given by the District as well as the Office, Chief of Engineers, U. S. Army Corps of Engineers, to publish this paper are hereby acknowledged. The findings of this paper are not to be construed as official Department of the Army position unless so designated by other authorized documents.

#### Appendix.-References

1. Butler, H.L., "Evolution of a Numerical Model for Simulating Long Period Wave Behavior in Ocean-Estuarine Systems," Estuarine and Wetlands Processes with Emphasis on Modeling, Marine Science Series, Vol. 11, Plenum Press, New York, 1980.
2. Butler, H.L., et al., "Lake Pontchartrain and Vicinity Hurricane Protection Plan; Physical and Numerical Model Investigation of Control Structures and the Seabrook Lock; Hydraulic and Mathematical Model Investigation," Technical Report HL-82-2, Report 2, U. S. Army Engineer Waterways Experiment Station, CE, Vicksburg, Mississippi, June 1982.
3. Butler, H.L., "Lake Pontchartrain and Vicinity Hurricane Protection Plan; Numerical Model Investigation of Plan Impact on the Tidal Prism of Lake Pontchartrain," Technical Report HL-82-2, Report 3, U. S. Army Engineer Waterways Experiment Station, CE, Vicksburg, Mississippi, October 1983.
4. Ebersole, B.A., and Dalrymple, R.A., "Numerical Modeling of Near-shore Circulation," Proceedings, 17th Conference on Coastal Engineering, 1980, Vol. III, Chapter 163, pp. 2710-2725.
5. Garrett, C. J. R., "Tides in Gulfs," Deep Sea Research, Vol. 22, 1975, pp. 23-35.

6. Hildebrand, F.B., Introduction to Numerical Analysis, McGraw-Hill, New York, 1956.
7. Longuet-Higgins, M.S., "Longshore Currents Generated by Obliquely Incident Sea Waves, 1 and 2," Journal of Geophysical Research, Vol. 75, No. 33, November 1970, pp. 6778-6789 and pp. 6790-6801.
8. Orlanski, I., "A Simple Boundary Condition for Unbounded Hyperbolic Flows," Journal of Computational Physics, Vol. 21, 1976, pp. 251-269.
9. Prandle, D., "Modeling of Tidal Barrier Schemes: An Analysis of the Open-Boundary Problem by Reference to AC Circuit Theory," Estuarine and Coastal Marine Science, No. II, 1980, pp. 53-71.
10. Reid, R.O., and Whitaker, R.E., "Numerical Model for Astronomical Tides in the Gulf of Mexico," Technical Report to be published, U. S. Army Engineer Waterways Experiment Station, CE, Vicksburg, Mississippi.
11. Sheng, Y. P., "Mathematical Modeling of Three-Dimensional Coastal Currents and Sediment Dispersion," TR CERC-83-2, U. S. Army Engineer Waterways Experiment Station, CE, Vicksburg, Mississippi, September 1983.
12. Vemulakonda, S.R., Houston, J.R., and Butler, H.L., "Modeling Longshore Currents for Field Situations," Proceedings, 18th Conference on Coastal Engineering, 1982, Vol. II, Chapter 100, pp. 1659-1676.

## CHAPTER FIFTY NINE

### Is Surf Beat Forced or Free?

David A. Huntley and Chang S. Kim\*

#### Abstract

Although many field experiments have shown that surf beat motion, with periods longer than incident wave periods, becomes the dominant feature of the nearshore velocity field as the shoreline is approached, the nature of this motion is still not fully understood. This paper describes a field experiment on a sheltered beach which was designed to distinguish between long wave motion directly forced by the incident wave envelope (as suggested by Longuet-Higgins and Stewart, 1962), and wave motion which is only weakly coupled to the local incident waves and therefore essentially free.

The results for on/offshore flows show that low frequency surf beat (frequency less than 0.03 Hz) is strongly correlated with the wave envelope, suggesting the dominance of forced wave motion at these frequencies. In a higher frequency band, between 0.06 and 0.095 Hz, the correlation is generally much lower, suggesting that free wave motion, possibly subharmonic edge waves, is significant in this band.

The longshore flows are much more weakly correlated to the envelope of either the longshore or on/offshore components of the orbital velocity. This is consistent with previous observations that edge wave motion dominates the longshore surf beat motion.

#### Introduction

It is now clear that water motion with periods substantially longer than incident wave periods generally dominates the velocity field near the shore, and may be the controlling mechanism for changes in coastal morphology in response to waves (Bowen and Huntley, 1984). However, despite extensive field and theoretical work, the precise nature of this long period motion is still unclear.

\* Department of Oceanography  
Dalhousie University  
Halifax, Nova Scotia  
B3H 4J1 Canada

Figure 1 shows schematically the possible forms of low frequency motion which have been suggested for the nearshore zone. Broadly they fall into two categories, occurring either as forced waves or free waves.

Forced motion is generated directly by the incident waves. Longuet-Higgins and Stewart (1962) showed theoretically, using the radiation stress concept, that there should be a depression of the mean water level under high waves and a corresponding rise in mean water level under low waves. Hence if incident waves are "groupy", i.e. have an alternating sequence of high waves and low waves, they will carry with them a forced wave component at the frequency of the wave groups.

Free wave motion, on the other hand, is presumed to have an existence which is decoupled from the local incident waves. It can, in principle, take a number of different forms. Free edge waves are trapped to the coast and propagate parallel to the shoreline. Although such edge waves at surf beat periods are probably generated by the groupy structure of the incident waves, their growth rate is relatively slow and depends upon a spatial average of the incident wave structure, in contrast to the immediate and local response of the forced waves (Gallagher 1971, Bowen and Guza 1978). Free waves might also be "leaky" in the sense of being able to propagate towards or away from the shoreline. There is no evidence that significant free long wave energy propagates to the shoreline from deep water, but free wave motion may be generated within the nearshore zone itself. For example Symonds et al (1982) show how the varying position of the breakpoint for groupy incident waves can generate freely propagating long waves at the group period. They predict a shoreward propagating long wave which reflects at the shoreline to set up standing wave motion in the surf zone, and a seaward propagating free wave seawards of the breakpoint. It has also been suggested that the forced wave brought to the breakpoint by incident wave groups might be released at the breakpoint and travel seawards and perhaps shorewards as a free wave, though the mechanism for this is not clear (Tucker, 1950, Longuet-Higgins and Stewart, 1962).

Surprisingly little published data addresses the problem of distinguishing between these possible forms of long period motion in the field. A number of studies confirm that edge waves contribute to the long period energy (e.g. Holman, 1981; Huntley et al., 1981). For example, Huntley et al (1981) show unambiguous evidence that edge wave motion dominates in the alongshore components of velocity, though the on/offshore velocities

showed additional energy which could not be clearly related to edge wave motion.

This paper describes field measurements of nearshore velocities designed to distinguish between forced and free long wave motion. In order to measure significant incident wave groups the measurements were made just seawards of the breakpoint. The test of whether the long period motion is forced or free then becomes simply a question of the degree of correlation between the local incident wave envelope and the long period motion at a point; if forced motion dominates the correlation should be very high while if free wave motion is significant the correlation should be correspondingly low.

### Theoretical considerations

#### Forced waves

Longuet-Higgins and Stewart (1962) showed theoretically that mean water level,  $\zeta$ , under wave groups and the onshore component of radiation stress,  $S_{xx}$ , are related by

$$\zeta = - S_{xx} / \rho(gh - c_g^2) + \text{const} \quad (1)$$

where  $\rho$  is the density of water,  $g$  the gravitational acceleration,  $h$  the local water depth and  $c_g$  the incident wave group velocity. Equation 1 should be valid where the wave group wavelength is long compared to the water depth. Since  $S_{xx}$  is proportional to the square of the incident wave amplitude equation (1) predicts a relative depression of mean water level where the wave amplitude is high.

As the incident waves travel into shallow water their group velocity tends to the wave phase velocity and the denominator in equation 1 tends to zero, suggesting very large changes of mean water level. At small Ursell numbers the shallow water form of (1) can be written

$$\zeta \sim -3/4 \frac{ga^2}{\sigma^2 h^2} \quad (2)$$

where  $a$  is the wave amplitude and  $\sigma$  is the wave radian frequency. However the large mean water level changes predicted by this formula are clearly inappropriate in the nearshore zone. As Longuet-Higgins and Stewart (1962) pointed out, not only is the small Ursell number condition violated, but also the shallow water resonance implied by equation (1) must be properly treated.

Unfortunately, although there has been some theoretical work addressing this problem (e.g. Foda and



Mei 1981) there is as yet no accepted theoretical prediction of water level changes under wave groups in shallow water. Nevertheless, for the purposes of this study we assume that, although the forms of equations 1 and 2 are not valid where our measurements were made, the mean water level response in shallow water will still be proportional to the square of the incident wave amplitude since the varying radiation stress remains the agent driving the forced waves.

The measurements discussed in this paper are of velocities rather than sea level changes. The only change this might make to the discussion above is in the sign of the long wave response relative to the wave envelope. For elevations the depression of mean water level under high waves results in the negative sign on the right hand side of equations 1 and 2. Under such a depression the forced velocity is in the opposite direction to the group propagation direction. In the discussion below we take the positive  $x$  direction to be the seaward-pointing normal from the shoreline, so that offshore flows under shoreward propagating wave groups are positive. Hence, while for elevation measurements we would expect to find a negative correlation between wave envelope and mean sea level (assuming positive sea level changes to be upwards), for our current measurements we would expect a corresponding positive correlation.

### Free waves

As we have shown in Figure 1 there are several different forms that free wave motion might take, but each is decoupled in some way from an immediate local response to incident wave groups.

Edge wave generation is generally considered to take one of two basic forms. Pairs of edge waves can be generated by the instability of a single incident wave component reflected at the shoreline, the most rapidly generated being zero mode edge waves at the subharmonic of the incident waves (Guza and Davis 1974; Guza and Bowen 1975). Edge waves can also be generated by the long period groupiness structure of the incident waves (Gallagher 1971, Bowen and Guza 1978). Theoretical and laboratory work on these generation mechanisms has been limited to monochromatic incident waves, but even in these studies edge wave growth rates have been found to be relatively slow (e.g. an e-folding time of 10 incident wave periods for the fastest growing subharmonic edge waves). On natural beaches with a stochastic spectrum of incident waves the growth rates should be substantially reduced below these monochromatic values and edge wave

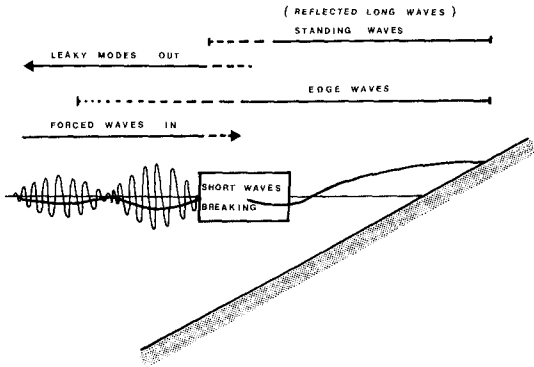


Figure 1. Possible forms of long waves on sloping beaches. The top three lines represent free wave modes and the bottom represents the forced wave.

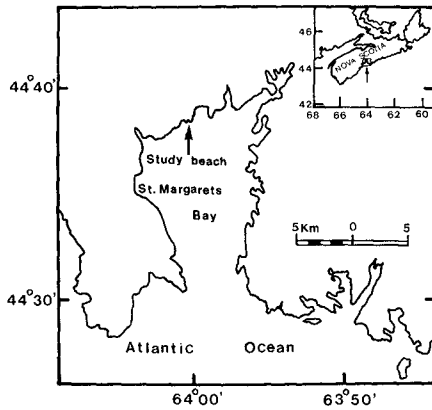


Figure 2. Location of Queensland beach.

amplitude is therefore expected to correspond to a time average of incident wave conditions rather than to the immediate local wave conditions. In addition, as Bowen and Guza (1978) point out, edge waves generated by incident wave groups will be linked only to that component of the groupiness whose spatial as well as temporal structure matches that of the edge wave. Again this suggests a low correlation between edge wave amplitude and local incident wave envelope.

Free waves generated by a time-varying breakpoint (Symonds et al. 1982) are clearly linked to the incident wave groupiness. However there are a number of reasons why correlation to incident wave amplitude may be small. The amplitude of the seaward propagating free waves is frequency dependent with free wave amplitude going to zero for some group frequency components. At each group frequency component, free waves at a range of harmonic frequencies are also predicted. In addition, for a sensor seawards of the breakpoint, there will be a time lag between the wave envelope and the long wave response corresponding to the travel time to the breakpoint and back. Without a more complete quantitative theory it is not possible to estimate the significance of the first two of these factors, and the third may be too small to detect in our data (see the discussion below). However a strong correlation over a broad frequency range would seem unlikely in this case.

### Field Observations

Measurements of the nearshore velocity field were made at Queensland Beach in St. Margaret's Bay, Nova Scotia, on the 25th and 26th June, 1979. Queensland is a pocket beach with direct exposure to the Atlantic in only a very narrow range of directions around normal incidence to the beach (Figure 2). The shoreline is essentially straight, about 170 m long, and is terminated at one end by a headland and at the other by a reef of bedrock which extends several tens of meters offshore. The local beach slopes in the region where the currents were measured varied between 0.08 and 0.10.

The flow field was measured using Marsh-McBirney electromagnetic flowmeters mounted on the single tripod at three heights above the bed (10, 45 and 100 cm). Each sensor, measuring two orthogonal axes of flow with a response time of about 0.2 s, was aligned to measure the onshore and longshore components of flow. Figure 3 shows the position of the tripod on which flowmeters were mounted, the mean run-up position visually observed midway

through each data run and tidal variation during the measurements.

Winds during the experiment were generally mild and variable in direction. Near-normally incident waves approached the shoreline with noticeable groupiness. Generally the significant wave heights were between 40-60 cm near the tripod, which was located 10-25 m from the shoreline. Most of the waves broke inshore of the sensors.

#### Data Acquisition and Analysis

Spectra of the measured currents show two consistent spectral troughs. A trough near 0.095 Hz, present in all spectra, is taken to separate the incident wave energy, centered at 0.12 Hz, from the low frequency motion. A second spectral trough is found near 0.06 Hz, and its frequency is independent of offshore distance for the range of distances shown in Figure 3. This trough separates the low frequency band into a higher frequency band which we term "subharmonic" and a lower frequency band which we term "surf beat". For all segments of the data there is significant long period energy. Long wave energy varies from 2% to 11% of the total incident wave height, the largest values occurring nearest the breakpoint.

A Kaiser-Reed (1977) filter is used to separate time series of velocity into low- and high-passed components, with the division at 0.095 Hz. To obtain the wave envelope, the high-passed time series is squared and then low-passed through the same filter. Means of both the wave envelope and the long period time series are then calculated and removed.

Cross-spectra between wave envelope and low frequency wave motion were computed using the IEEE cross-spectral algorithm described by Carter and Ferrie (1979). Each time series of 4096 data points was partitioned into 7 segments of 1024 data points with a 50-percent overlap, giving a frequency resolution of 0.0029 Hz. Nuttal (1971) shows that the number of degrees of freedom,  $n$ , for 50% overlapped data segments is given by:

$$n = 3.82 N_d - 3.24$$

where  $N_d$  is the number of disjoint (non-overlapping) segments. For our data runs this gives  $n = 12$ .

Cross-correlations between the two series were also calculated for time lags up to  $\pm 200$  seconds, to determine

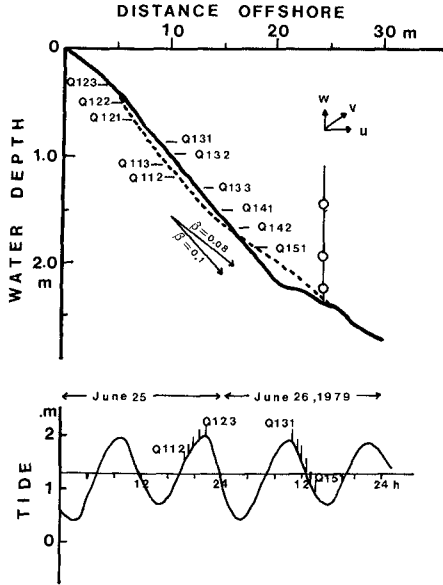


Figure 3. Tripod deployment and the variation of mean run-up positions with the tide.

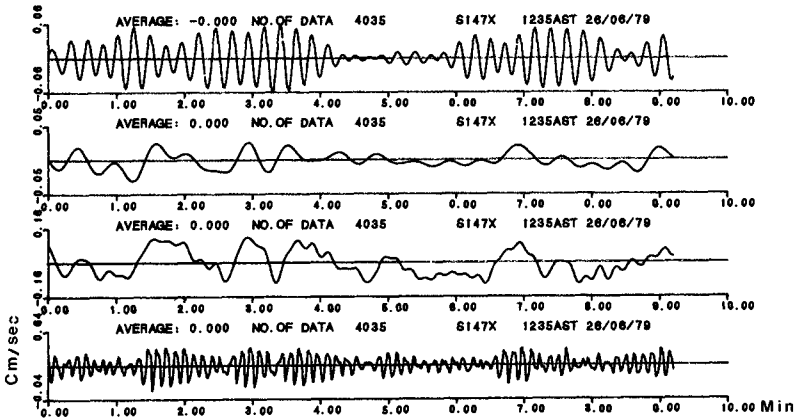


Figure 4. Sample segments of time series. From the bottom in ascending order the original data, the corresponding wave envelope, the very low frequency surf beat motion and, on top, the motion at sub-harmonic period.

any non-dispersive time lag between the series. The 95% significance level for cross-correlation is related to the effective number ( $N^*$ ) of independent points within each series. The number of independent points can be estimated from the auto-correlation of the product of the two series by (Garrett and Toulany, 1981),

$$(N^*)^{-1} = (N)^{-1} + \sum_{j=1}^{N'} (N-j) R_{11}(j) \quad (3)$$

where  $N$  is the actual number of observation,  $R_{11}(j)$  is the lagged auto-correlation of the product and  $N'$  is the number of lags up to the first zero crossing of  $R_{11}$ . Throughout our runs  $N^*$  lies in the range 150-600. The corresponding 95% confidence limits on zero correlation ranges between 0.18 to 0.10.

#### The On/Offshore Flow Response to Incident Wave Groups

The lowest plot of figure 4 is a segment of the time series of onshore velocity for run Q141, showing noticeable wave groupiness. Above this, in ascending order, are the corresponding wave envelope, the very low frequency surf beat motion and, on top, the wave motion at subharmonic periods. Clearly the surf beat energy is positively correlated with the wave envelope.

Figure 5 shows an example of the spectra, coherence and phase of wave envelope and long period motion. The cross spectra suggest that we can identify three spectral bands, a surf beat band (0.003 - 0.03 Hz), an intermediate band (0.03-0.06 Hz) and a subharmonic band (0.06-0.08 Hz).

In the surf beat band the coherence between the incident wave envelope and the long period motion is consistently above the 95% confidence level and the phase is close to zero degrees across the entire frequency band. These features occur in the surf beat band throughout the data set. They suggest that locally forced wave motion strongly dominates the on/offshore flow in this frequency band.

In the subharmonic band, on the other hand, the coherence is generally weak with a phase which, if not entirely random, varies significantly across the band. This suggests that free wave motion is significant in this band. This is not the case for all data runs, however. Where subharmonic energy occurs as a narrow high energy peak a corresponding narrow peak in coherence can occur, with again a phase close to zero degrees (Figure 6). Clearly this suggests that forced wave motions can occur

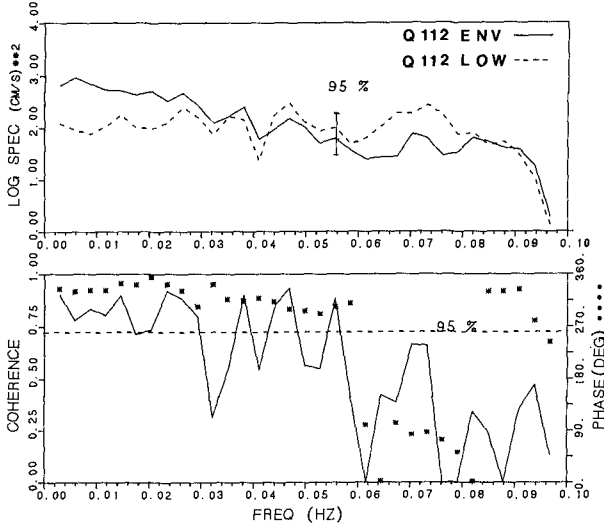


Figure 5. Cross-spectra between wave envelope and low frequency wave motion for Q112.

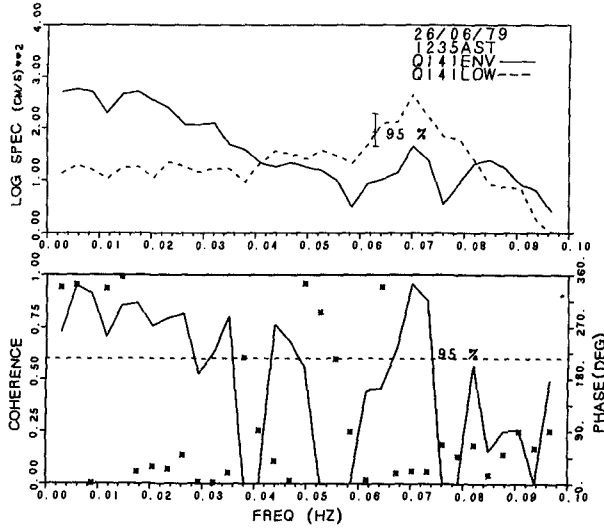


Figure 6. As Figure 5, but for Q141.

in a narrow frequency band within this "subharmonic" band, but the significance of this observation is not yet clear.

In the intermediate band between the lowest frequency band and the subharmonic band no consistent conclusion could be reached, the cross spectra suggesting the presence of both forced and free motion with neither dominating.

Figure 7 summarizes the band-averaged coherences and phases for the complete data set, for both the low frequency surf beat band and the subharmonic band. These confirm the conclusions discussed above. In the surf beat band the coherence averages about 0.8, suggesting that the long period energy is about 80% forced by the wave envelope. The phase, as expected from the Longuet-Higgins and Stewart (1962) theory, is very close to zero degrees. In contrast, the subharmonic band shows coherence values which, while sometimes above the 95% confidence level on zero coherence, are much lower, with an average value of around 0.55. The average phases are also scattered. Although definitive conclusions cannot be drawn from coherence values so close to the 95% level, it would appear that the forced wave motion can account for, at most, 55% of the long period energy present in this frequency band.

Cross-correlations between the incident wave envelope and the long period motion were also computed for the lowest frequency surf beat band to identify any time lags between the wave envelope and the long period response. Figure 8 shows the average cross-correlation function for the complete data set. The 95% confidence level is estimated as about 0.10. As expected, the largest correlation occurs at zero lag and the correlation drops rapidly for non-zero lags. In Figure 8 a positive lag implies that wave envelope leads the long period motion. In the case where the forced wave is released as a seaward propagating free wave at the breakpoint, the positive lag between wave envelope and long wave response was around 10 s for the present data set. This is too small to be clearly separated from the peak at zero lag, but the rapid decay of the peak at positive lag is suggestive of only a small seaward component, if any. The secondary, barely-significant peak at a positive lag of about 35 s is intriguing. It will be further mentioned in the following section.

#### The Longshore Flow Response

Huntley et al. (1981) used data from a California beach to show that the longshore component of flow was



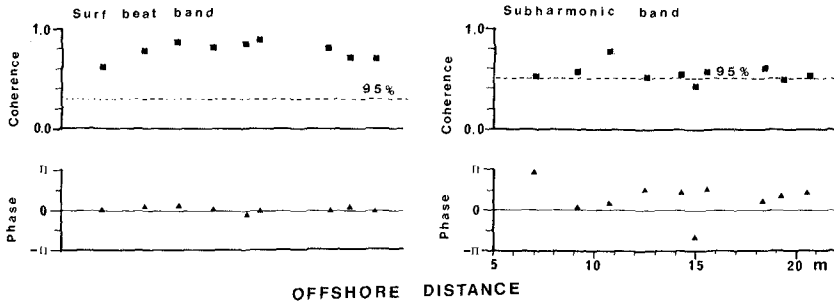


Figure 7. Band-averaged coherences and phases at surf beat and subharmonic frequencies.

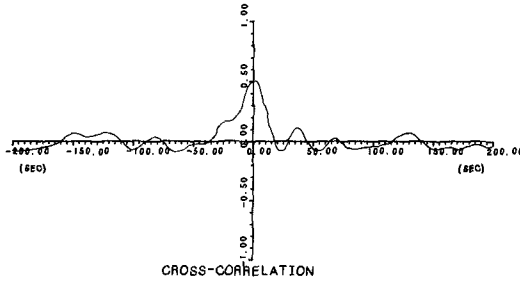


Figure 8. Cross-correlation between wave envelope and low frequency motion.

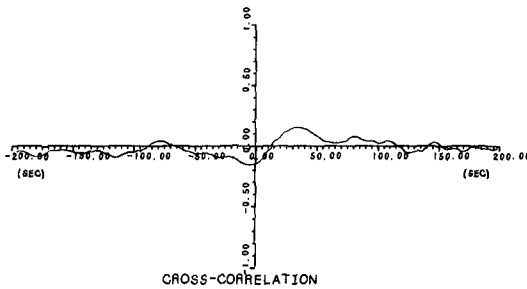


Figure 9. Cross-correlation between incident wave envelope and longshore surf beat energy.

dominated by free edge wave motion. It is therefore of some interest to ask whether the present data set is consistent with this observation or whether there is evidence for forced longshore motion correlated with incident wave groups.

Calculated cross-correlations between longshore current envelope and the longshore surf beat flow are low, below the 95% confidence level, for all time lags. Thus there is no evidence for longshore motion forced by longshore groupiness. However cross-correlation between the on/offshore envelope and the longshore surf beat flow does show a significant, though low, peak at a positive lag of around 35 s (Figure 9). This surprising result may be related to the peak at a similar lag observed in the on/offshore correlation (Figure 8). These observations and possible explanations for them will be the subject of a subsequent paper.

#### Discussion

This study clearly shows that, outside the surf zone, the long period surf beat motion at frequencies below 0.03 Hz is dominated by the locally forced response to the incident wave groupiness. This is contrary to the suggestion of Bowen and Guza (1978), based on laboratory and theoretical studies, that the free edge wave response should dominate.

Other studies of long period motion have emphasized its on/offshore structure, which is generally found to be consistent with shoreline-reflected standing waves or with edge waves (Suhayda, 1974; Huntley, 1976; Holman, 1981). The present data set cannot provide definitive evidence for or against the presence of a seaward propagating wave which could combine with the incoming forced wave to provide standing wave motion. The observed cross-correlation of figure 8 does not suggest the presence of an outgoing free wave at a lag expected for the wave envelope to travel to the breakpoint and a free wave to return to the sensor location, but the expected lag is within the peak centered at zero lag so no firm conclusions can be drawn. If there is a smaller seaward propagating component on Queensland Beach it may be related to the absence of long swell waves characteristic of many of the other sites studied.

The present data set is limited to measurements outside the surf zone, whilst many previous studies have concentrated on measurements within the surf zone. For data run Q151, when the sensor tripod was closest to the breakpoint, the cross-correlation between surf beat motion

and wave envelope was significantly lower than for runs further offshore. This is consistent with the observed saturation of wave amplitude on breaking, which reduces incident wave groupiness inside the surf zone. Thus previous measurements from within the surf zone which have emphasized the presence of edge waves will have been unable to identify forced wave motion by a direct correlation with the local wave envelope. It would be particularly interesting to correlate long period motion inside the surf zone with incident wave envelope just outside the breakpoint, to try to identify any free wave motion inside the surf zone released by wave breaking.

The lack of evidence for dominant free edge waves motion in the on/offshore flows on this relatively steep beach may require some modification of the hypothesis that edge waves are the most significant controlling factor for nearshore coastal geomorphology (Bowen and Huntley, 1984). However even small on/offshore standing wave components will be very significant in providing the mean flow divergences and convergences needed to create erosion and deposition. The observations of edge wave motion in the longshore flows (Huntley et al., 1981) is also consistent with the present data set and provides a further important component contributing to flow divergence and convergence.

#### References

1. Bowen, A.J. and R.T. Guza, Edge waves and surf beat, *J. Geophys. Res.*, 83, 1913-1920, 1978.
2. Bowen, A.J. and D.A. Huntley, Waves, long waves and nearshore morphology, *Mar. Geology*, 60, 1-13, 1984.
3. Carter, G.C. and J.F. Ferrie, A coherence and cross-spectral estimation program; in *Programs for digital signal processing*, edited by IEEE Acoustics, speech and signal processing society, 1979.
4. Foda, M.A. and C.C. Mei, Nonlinear excitation of long-trapped waves by a group of short swells, *J. Fluid Mech.*, 111, 319-345, 1981.
5. Gallagher, B., Generation of surf beat by non-linear wave interaction, *J. Fluid Mech.*, 49, 1-20, 1971.
6. Garrett, C.J.R. and B. Toulany, Variability of the flow through the Strait of Belle Isle, *J. Mar. Res.*, 39, 163-189, 1981.
7. Guza, R.T. and A.J. Bowen, The resonant instabilities

- of long waves obliquely incident on a beach, *J. Geophys. Res.*, 80, 4529-4534, 1975.
8. Guza, R.T. and R.E. Davis, Excitation of edge waves by waves incident on a beach, *J. Geophys. Res.*, 79, 1285-1291, 1974.
  9. Holman, R.A., Infragravity energy in the surf zone, *J. Geophys. Res.*, 86, 6442-6450, 1981.
  10. Huntley, D.A., Long-period waves on a natural beach, *J. Geophys. Res.*, 81, 6441-6449, 1976.
  11. Huntley, D.A., R.T. Guza and E.B. Thornton, Field observations of surf beat. Part I. Progressive edge waves. *J. Geophys. Res.*, 86, 6451-6466, 1981.
  12. Kaiser, J.F. and W.A. Reed, Data smoothing using low-pass filters, *Rev. Sci. Instrum.* 48., 1447-1457, 1977.
  13. Longuet-Higgins, M.S. and R.W. Stewart, Radiation stress and mass transport in gravity waves, with application to 'surf beat', *J. Fluid Mech.*, 13, 481-504, 1962.
  14. Nuttall, A.H., Spectral estimation by means of overlapped Fast Fourier Transforms of windowed data, NUSC rep. #4169, Dept. of Navy, USA, 1971.
  15. Suhayda, J.N., Standing waves on beaches, *J. Geophys. Res.*, 72, 3065-3071, 1974.
  16. Symonds, G., D.A. Huntley and A.J. Bowen, Two-dimensional surf beat: long wave generation by a time-varying breakpoint, *J. Geophys. Res.*, 87, 492-498, 1982.
  17. Tucker, M.J., Surf beat: Sea waves of 1 to 5 minutes period, *Proc. R. Soc. A*, 202, 565-573, 1950.

## CHAPTER SIXTY

### EXTREME SEA LEVELS ON THE COAST OF CALIFORNIA

Reinhard E. Flick<sup>1</sup> and Daniel R. Cayan<sup>2</sup>

#### 1. INTRODUCTION

During the winter of 1982-1983, a combination of high tides, higher than normal sea level and storm-induced waves were devastating to the coast of California. Damage estimates for public and private property destruction in the coastal counties of California total over \$100,000,000.

Much higher than average sea levels played a very important contributory role in the flooding damage. This report describes and examines the oceanographic and meteorological conditions prevailing during winter 1982-1983, and attempts to put them into perspective using historical information at San Diego. Emphasis is placed on the processes and forces that contribute to extreme sea levels in the hope that better understanding of these and more complete information on historical extremes will help the engineer in design and in assessment of risk.

The unusually high sea levels were due to a combination of higher than normal mixed layer temperature associated with a strong, 2-year El Nino, storm surge due to low atmospheric pressure and persistent onshore winds, and the cumulative effect of steady, "global" rise in relative sea level. Higher than average high tides coincided to an unusual extent with the peak sea levels reached during the numerous storms between November 1982 and March 1983. Important cyclical variations occur in California's tide regime and the consequences of these on extreme tides have not been considered previously.

#### 2. ASTRONOMICAL TIDES

During the time of the winter 1982-1983 storms, newspaper accounts of the damage referred to predictions of much higher astronomical tides in the early part of the next decade and led to increased public concern as to the future safety of many coastal structures. These concerns are unfounded since studies have shown that there are crucial differences in the California tide regime compared with those that were used as the basis for the alarming forecasts (Zetler and Flick, 1985).

Tides along the coast of California are of the "mixed" type meaning that the diurnal constituents are of the same order of magnitude as the semidiurnal components. This is crucial for explaining the

---

<sup>1</sup> California Department of Boating and Waterways, and  
Scripps Institution of Oceanography, La Jolla, CA

<sup>2</sup> Scripps Institution of Oceanography, La Jolla, CA

nature of the extreme ranges of tides. Different criteria determine the time of occurrence of maximum mixed tides as opposed to semidiurnal tides, which dominate, for example, the east coast of the U.S.

"Spring tides" are large semidiurnal tides that occur twice each month around the time of full and new moon. Spring tides tend to be larger than average twice each year during the equinoxes, that is, during the spring and autumn seasons. In contrast, "tropic tides" are large diurnal tides that also occur twice each month, but around the times of maximum lunar declination. Solar declination has a similar influence, and as a consequence, the tropic tides occurring in winter and summer (during maximum solar declination) are larger than average. In addition, the earth's yearly closest approach to the sun (perihelion) occurs during the northern hemisphere winter, thus increasing yet further the magnitude of the tropic tides that occur around December and January.

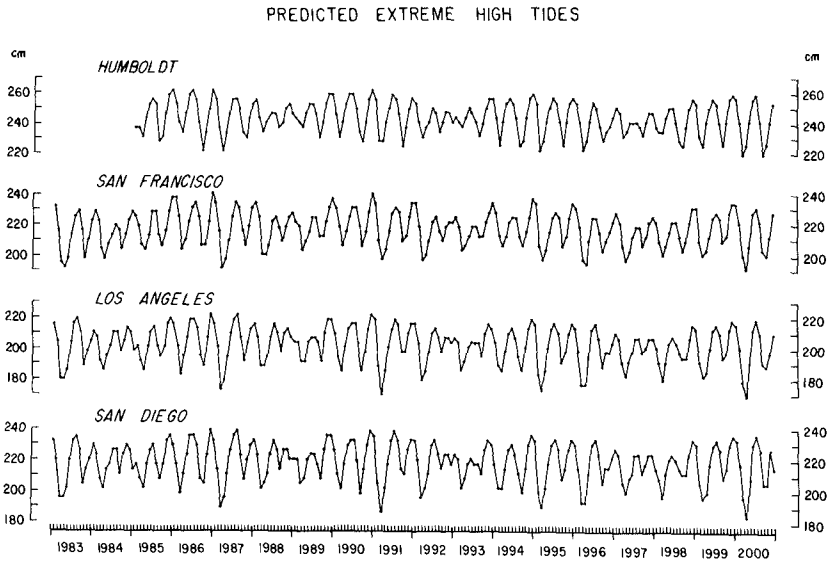


Figure 1. Predicted extreme high astronomical tide for four California ports through 2000. The extremes are dominated by the mixed tidal regime (Zetler and Flick, 1985).

Because of the complexities in the mixed tide regimes, the best way of forecasting times and heights of extreme tides is to prepare standard harmonic predictions and extract the desired extremes for tabulation. This has been done for the monthly extreme high tides at four California ports through the year 2000, and is shown in Figure 1 (from Zetler and Flick, 1985). The details of the interactions governing the variability of extreme predicted tides as well as tables of data corresponding to Figure 1 are given in Zetler and Flick (1985) and Zetler and Flick (in prep).

The effect of tropic tides dominates the extremes so that maximum tides occur in summer and winter. This maximizes the likelihood of coincidence of high tide levels with storm-induced sea level extremes. A second feature evident in Figure 1 is the regular 4.4 year beat which raises high tides about 0.5 foot every 4.4 years compared with times in between. This cycle peaked in 1982-1983 and contributed to the high levels observed.

### 3. MEAN SEA LEVEL

Recent studies of global mean sea level rise indicate a most probable value of about 0.5 foot/century (Hicks et al, 1983; Aubrey and Emery, 1983; Barnett, 1983; and many others). These estimates have a great deal of uncertainty and variability depending on how the analysis is done and due to a large number of other factors: errors in measurement, poor spacial distribution of stations around the world, wide variations in record length, wide variability of ground motions relative to sea level, etc.

Yearly mean values are likely contaminated very little by tidal errors and are very useful for displaying secular trends and longer term departures from the trends. Figure 2 shows annual average sea level at San Diego relative to MLLW computed over the 1960-1978 epoch, also shown in the figure. The light line is a least squares fit to all the data points and indicates an upward trend of 0.7 foot/century between 1906-1983. This is comparable to the global rate of rise and is typical of all long-term California stations, except for a few where

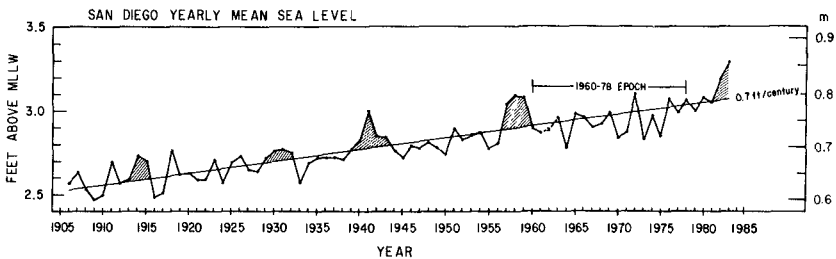


Figure 2. Secular increase in relative sea level at San Diego is close to global "average" of around 0.5 foot/century. Large positive departures are associated with major El Niño events.

local uplift or subsidence effects dominate the relative sea level signal.

Extreme estimates of rapidly accelerating rise in future mean sea levels have been published, and expressed as a mean rate, range as high as 10 feet/century to the year 2100 (Hoffman, 1983). These estimates depend upon a widely varying range of assumptions, or "scenarios," involving global warming and subsequent ice cap retreat and thermal expansion of the oceans. In our opinion, it is very difficult to know how much weight to assign to such extreme predictions and therefore how much to allow for them in design. On the other hand, it seems prudent to allow for at least the current rise of between 0.6-0.7 foot/century over the life of any particular planned coastal improvement.

Another feature of annual mean sea levels displayed in Figure 2 are the episodic (2-4 year) positive departures from the linear trend. These are shown shaded and are very pronounced in 1914, 1930-1931, 1941, 1957-1959 and 1982-1983, comprising 5 episodes in about 70 years of record. All these periods coincide with or are near in time to strong El Nino events. While there is no ability to forecast the year of onset, duration, and intensity of future El Nino occurrences, the historical record suggests that for engineering purposes, it would be sensible to design for the prolonged high sea level stands that occur during major episodes. The data in Figure 2. suggests these major events have an average return period of 14 years with departures from the trend on the order of 0.2 foot for durations of 2-3 years.

Seasonal variations in mean sea level are often displayed using monthly mean sea levels. The extremely unusual and persistent sea level heights reached during the 1982-1983 El Nino off San Diego are illustrated in Figure 3. The solid line shows the "average" seasonal cycle of sea level computed over the 19-year tidal epoch from 1960-1978. The light vertical bars around each average monthly data point show +/-1 standard deviation, indicating the typical variability of the fluctuations. The amplitude of the seasonal cycle is about 0.5 foot, with a variability of about 0.1-0.2 foot. This seasonal sea level cycle in San Diego is clearly related to seasonal heating and cooling of the ocean (Reid and Mantyla, 1976). On average, the water temperature is coolest in spring, leading to lower levels, and warmest in autumn, leading to higher levels. The light dashed line in Figure 3 shows the monthly averages for 1982. Until about July, observed sea level was close to normal, but by fall and early winter it exceeded the 1960-1978 average by up to 0.5 foot, or about 3 standard deviations. This condition persisted through 1983, illustrated in Figure 3 with the light solid line. Sea level finally returned to near normal in December 1983. The small vertical arrow labelled "trend" shows the increase in yearly mean sea level between 1969 (middle of the 1960-1978 epoch) and 1983. The magnitude of this increase is 0.1-0.2 foot or about 0.5 of a typical standard deviation. This shows that the unusually large deviations in 1982-1983 from the 1960-1978 mean were only due in small part to the cumulative secular increase.



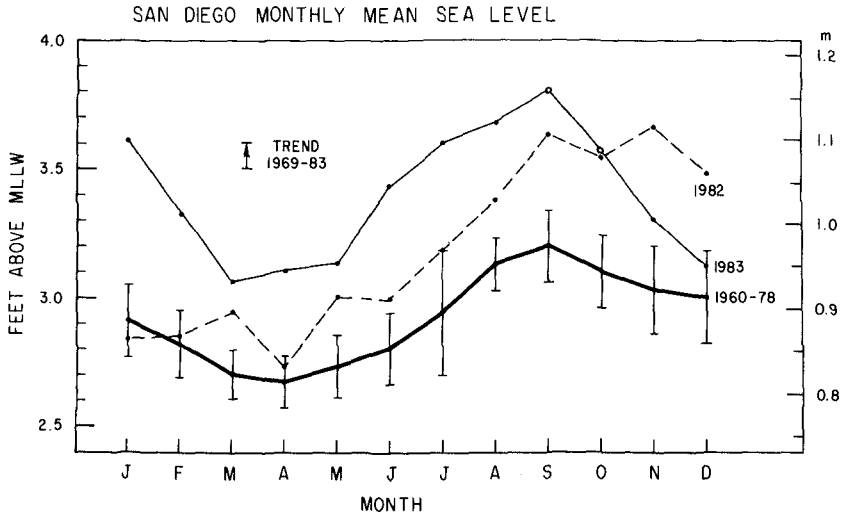


Figure 3. Seasonal cycle of sea level at San Diego associated with cooling in spring and warming in autumn. Curves for 1982 and 1983 show large departure from 1960-1978 average.

#### 4. METEOROLOGICAL INFLUENCES

The winter of 1982-1983, now commonly known as "El Nino Winter," was in many respects the most severe storm season in several decades along the North American Pacific Coast (Quiroz, 1983). The unusually active North Pacific storm conditions were associated with anomalously warm water in the eastern tropical Pacific that had its beginnings in the Summer of 1982 and by northern Winter, 1982-1983, had developed into the most intense such warmings of any within about a century of quantitatively recorded data.

Winter atmospheric conditions during El Nino events show a tendency for anomalously low barometric pressure in the region south of the Aleutian Islands, extending into the Gulf of Alaska, and higher than normal pressure in the North Pacific subtropics (Namias, 1976; Dickson and Livezey, 1984). This pressure distribution is associated with heightened storm activity across the central North Pacific. However, the pattern is not clear-cut along the West Coast: in some winters the storms take a northward course into British Columbia and Alaska, while in others they take a southward trajectory into Oregon and California (Namias and Cayan, 1984). As a measure of this activity during the winter of 1982-1983, the average westerly winds across the North Pacific subtropics were almost twice their normal speed. The

high winds and long fetch produced by these conditions during 1982-1983, caused the unusually long and high waves that pounded the California coastline (Seymour et al, 1984). The influence of atmospheric pressure and high winds during the winter 1982-1983 season on sea level is illustrated in Figure 4. The upper curve shows daily maximum observed sea level with each monthly maximum, shown circled. The second curve shows the anomaly, or the difference between the observed daily maximum and the predicted highest tide each day. This curve is very close to the daily mean sea level (curve 3) implying that the exceedence over the predicted tide is more or less constant over time scales of 1 day. The dashed line under the daily mean sea level shows the long-term (1960-1978) monthly mean sea levels and illustrates the approximate 0.5 foot excess due to the large-scale El Nino condition.

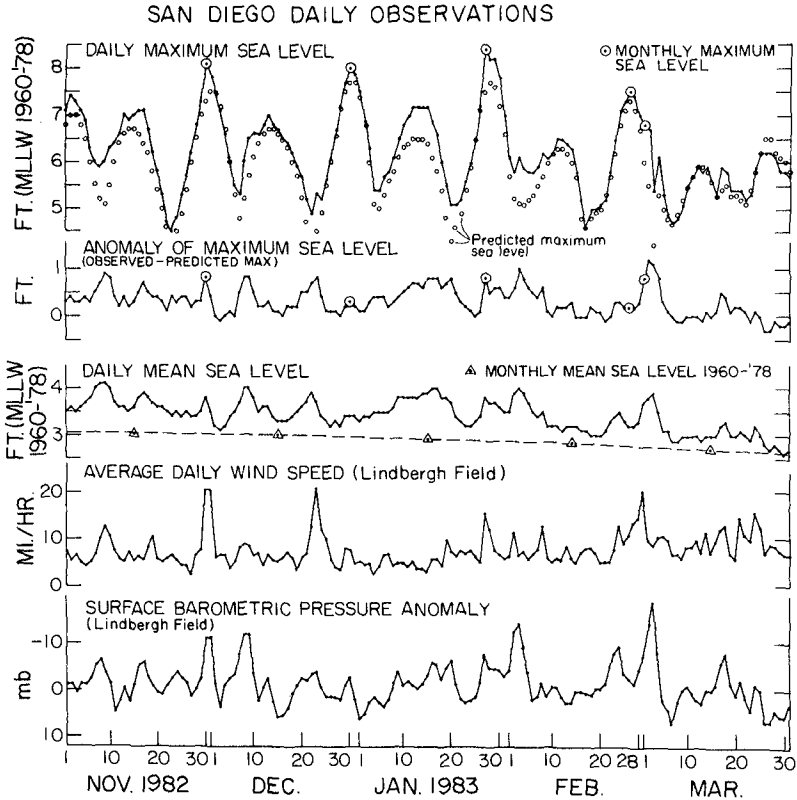


Figure 4. Daily observations at San Diego during winter 1982-1983. Storm episodes are marked with increased wind speed and anomalously low barometric pressure (bottom two curves).

The lowest 2 curves in Figure 4 show average daily wind speed and surface barometric pressure anomaly at San Diego. The storm episodes stand out clearly (9-10, 16-19, 29-30 Nov; 7-9, 22-23, 29 Dec; 17-19, 27-29 Jan; 2-4, 7-8, 24-27 Feb; 1-5, 17-18, 21-24 Mar) and these are highly correlated with the sea level anomalies. In general, the direct influence of lowered atmospheric pressure in the winter's storm events through the inverse barometer effect contributed about 1/3 of the observed anomalies of sea level. The average of surface pressure anomalies during the storms is in the range of 7-10 mb, with a maximum of 18 mb below normal on 3 March 1983.

Maximum winds recorded at San Diego during this time period were 39 mph on 1 December 1982. The wind direction (not shown) associated with high sea level anomalies varies from one event to the next. High sea level events were found under conditions of east, south, southwest and northwest wind. The largest anomalies (2-3 Mar 1983) occurred under southerly winds at San Diego. It is not known how open ocean wind conditions may differ from those measured at San Diego's Lindbergh Field.

In the five month winter 1982-1983 period shown, three of the five monthly high predicted tides (30 November 1982, 27 January 1983, and 1 March 1983) were coincident with unusually large anomalous daily average sea level (0.8, 0.7, 0.9, respectively). For any given month, with about 6 days of large sea level anomalies and only about 3 days of near monthly maximum predicted tide, the probability of these coinciding (assuming the two phenomena are independent) is about  $6/30 \times 3/30 = 1/50$ . The fact that this coincidence was realized in 3 out of 5 chances between November and March is even more unusual, and illustrates the extraordinary nature of this winter. This suggests a very small likelihood that such a concentrated run of severe winter months having high tides amplified by large non-tidal anomalies will recur with great frequency, even given sympathetic large-scale conditions.

## 5. MONTHLY EXTREME SEA LEVELS

Many published studies describe changes in mean sea level and their possible causes, but very few have concentrated on the extremes of sea level (Disney, 1955; Smith and Leffler, 1980). From an engineering viewpoint, the rationale behind such investigation is simple: the extreme sea level dictates design since it is what floods property and causes damage. Monthly sea level extreme values are routinely tabulated as one of the products of the National Ocean Service, NOAA. Plots have been prepared (Figures 5, 6, 7) each showing (at San Diego) observed monthly extreme sea level, maximum predicted tide on the date of the observed extreme, and two versions of the anomaly defined as the difference between the observed level and predicted tide. Movement of the tide station, installed in 1906, and other complications causes the analysis of the anomalies to be limited to the period 1940-1983.

The highest value of sea level recorded at San Diego is 8.35 feet above MLLW on 27 January 1983. The largest contribution to this level was from the extreme tide (7.6 feet) with the remainder due to the processes discussed above. Analysis in this study was limited to the statistics of the monthly anomalies at the time of maximum monthly sea level. In this sense, the statistics should not be expected to follow extreme value form since they are not the extremes drawn from the population of all (hourly or daily, say) exceedence values. Instead, they form a conditional sample from this population, the condition being that the total sea level be the monthly maximum.

The two versions of the anomaly plotted in Figures 5, 6, 7 are the "raw" anomaly, which is simply the difference between the observed sea level and the tide, and the "adjusted" anomaly which was corrected for a linear fit to the trend in sea level (shown in Figure 2). The raw anomaly figures show a secular increase which reflects the trend in the observed monthly extremes and the fact that the tide predictions do not include any trend. In effect, the "adjusted" anomalies represent the exceedence of the maximum sea level over the tide and the secular trend. To derive statistical estimates of future absolute

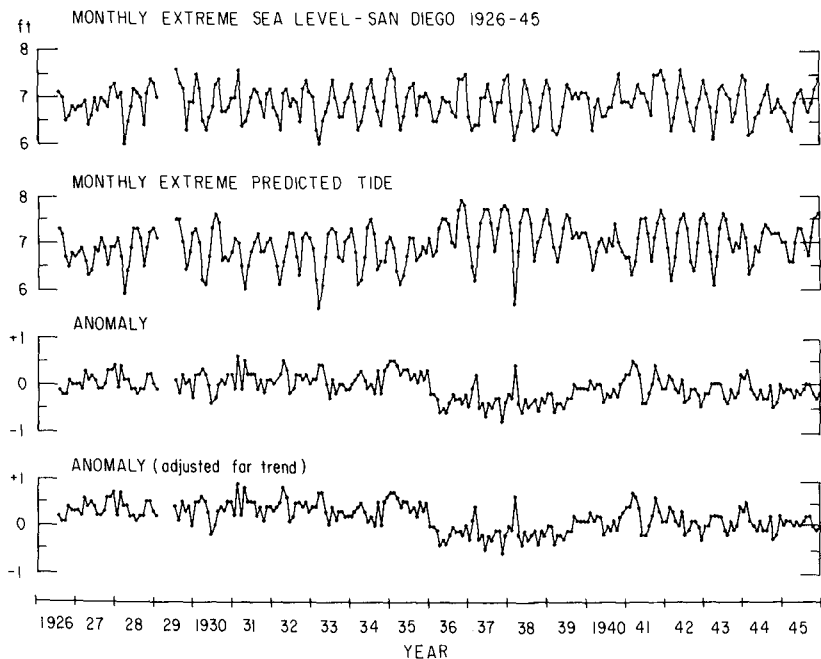


Figure 5. Monthly extreme sea level at San Diego 1926-1945 showing predicted tide on day of observed monthly maximum. Anomaly is difference between observed and predicted. Lower trace is anomaly adjusted for secular trend shown in Figure 2.

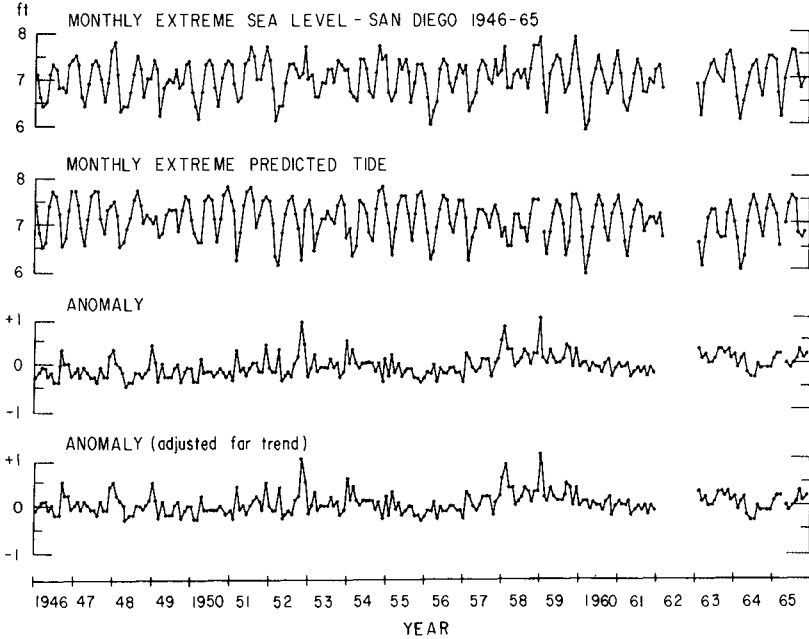


Figure 6. Monthly extreme sea level at San Diego 1946-1965. See Figure 5.

sea level heights, the estimate of exceedence must be added to the tide prediction plus an estimate of the increase due to the trend in mean sea level.

Several statistical analyses of the adjusted anomaly data have been carried out. First, Figure 8 shows the median anomaly as a function of month of year for the period 1940-1983. There is a clear seasonal variation with larger than normal anomalies in December through April, with median values around 0.1 to 0.15 foot. During the summer and in October and November, the median of the highest monthly sea levels are very close to the predicted tides with median anomalies not significantly different from zero. In September, there is a significant peak, with median anomalies over 0.1 foot higher than predicted tides at maximum sea level. This is apparently attributable to extratropical low pressure systems that are frequently observed west of San Diego in September. These systems cause depressions in atmospheric pressure of about 5-10 millibars compared with seasonal normals, roughly accounting for the magnitude of the anomalies.

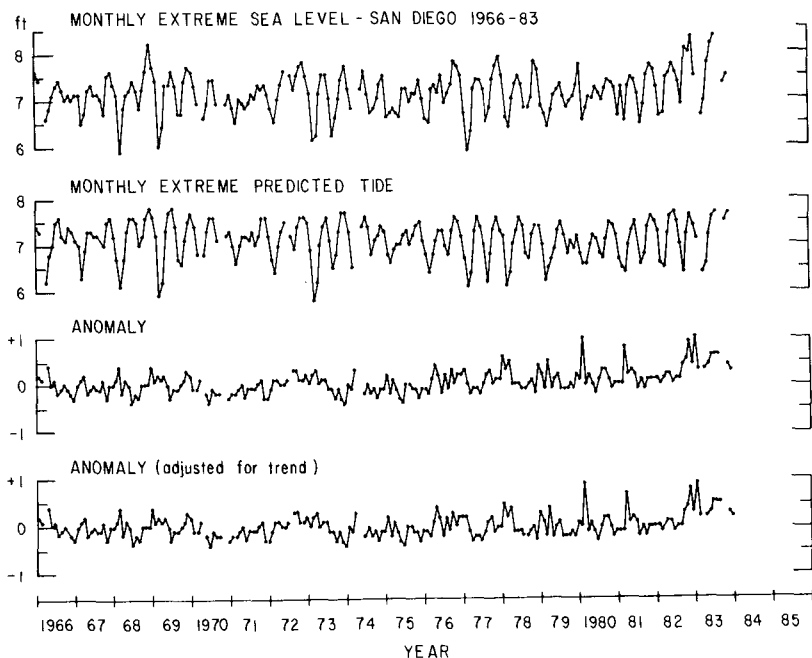


Figure 7. Monthly extreme sea level at San Diego 1966-1983. See Figure 5.

A return period statistic has been computed, and the results are shown in Table 1. The return period of any particular anomaly size can be defined as  $T$  where  $T = R/N$ , and  $R$  is the record length in months and  $N$  is the number of occurrences of that size in the record. Table 1 shows that the return period for 0.3 foot anomalies is about 20 months, or just under 2 years. Anomalies of 0.5 foot occur on average about every 50 months (4 years). The longer interval, larger anomalies have not recurred often enough to derive stable statistics, and not too much faith should be put in their return period. On the other hand, anomalies on the order of 1 foot are certainly possible, since they have been observed at San Diego, and at other stations on the California coast.

An added complication in the recurrence of the largest anomalies exists because their occurrence is not independent. Examination of the dates of occurrence of the 12 largest adjusted anomalies (greater than or equal to 0.6 foot) shows that 3 groups, containing 9 events cluster together (March, April and October 1941; January, February 1958, January 1959; and November 1982, January 1983). This is consistent with the observations that a large portion of the exceedence is related to the sympathetic, large-scale and persistent El Nino conditions.

Table 1

San Diego Sea Level Anomalies, 1940-1983

Adjusted Anomaly (ft)	Number of Occurrences	Return Period (mo.)
-0.4	4	132.0
-0.3	32	16.5
-0.2	58	9.1
-0.1	100	5.3
0.0	103	5.1
0.1	99	5.3
0.2	59	8.9
0.3	28	18.9
0.4	22	24.0
0.5	11	48.0
0.6	4	132.0
0.7	2	264.0
0.8	1	528.0
0.9	3	176.0
1.0	1	528.0
1.1	1	528.0

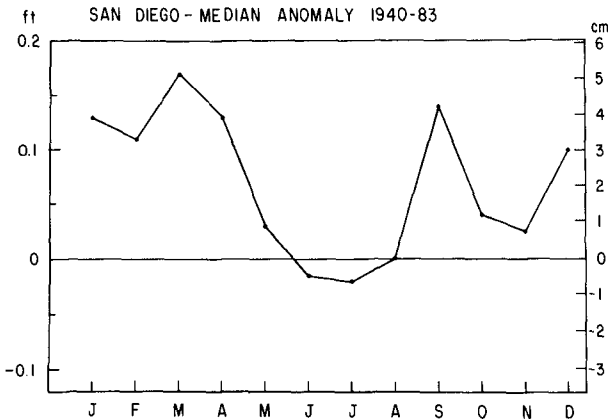


Figure 8. Median adjusted anomaly statistics, San Diego 1940-1983. Peak in September is associated with extra-tropical low pressure systems.

## 6. CONCLUSIONS

This investigation confirms the unusual nature of the 1982-1983 winter. Although individual months with relatively high sea level anomalies can be isolated, and some years exist with clusters of such anomalies, the concentrated run of extreme events that occurred in 1982-1983 is virtually unprecedented in the California sea level record. That is not to say that winters such as 1982-1983 won't happen again, but such recurrence should be quite rare.

Unusually high tides coincided with storm events to cause coastal flooding. The mixed tide regime in California predictably causes peak tides in summer and in winter. This maximizes the chances for such coincidences.

Sea levels in excess of predicted high tides during Winter 1982-1983 were the result of 1) large-scale meteorological and oceanic influences broadly known as "El Nino" that produced (among other effects) a tendency for anomalously high sea levels along the West Coast, probably contributing in the neighborhood of 0.1 to 0.4 foot in excess of normal. 2) Frequent vigorous North Pacific storms affected hundreds of miles of the West Coast over durations of 1-4 days. These heightened sea level by lowering surface barometric pressure via the "inverse barometer effect" (as much as 0.6 foot, but usually about 0.2 to 0.3 foot), and strong winds that piled up coastal waters.

## ACKNOWLEDGEMENTS

Financial support from the California Sea Grant College Program under Project R/CZ-69, NOAA, Grant No. NA80AA-D-00120 and from The Quest for Truth Foundation of Seattle, Washington is very gratefully acknowledged.



## REFERENCES

- Aubrey, D. G. and K. O. Emery, 1983, "Eigenanalysis of recent United States sea levels," Cont. Shelf Res., 2(1), p. 21-33.
- Barnett, T. P., 1983, "Recent changes in sea level and their probable causes," Climatic Change, 5, p. 15-38.
- Dickson, R. R. and R. Livezey, 1984, "On the contribution of major warming episodes in the tropical East Pacific to a useful prognostic relationship based on the Southern Oscillation," Jour. Climate and Appl. Meteorol., v. 23, p. 194-200.
- Disney, L. P., 1955, "Tide heights along the coasts of the United States," Proc. Hydraulics Div., Amer. Soc. Civil Eng., v. 81, n. 666, p. 1-9.
- Hicks, S. D., H. A. Debaugh, Jr., and L. E. Hickman, Jr., 1983, "Sea level variations for the United States 1855-1980," U. S. Dept. of Commerce.
- Hoffman, J. S., 1983, "Projecting sea level rise to the year 2100," Coastal Zone 83, p. 2784-2795.
- Namias, J., 1976, "Some statistical and synoptic characteristics associated with El Nino," Jour. Phys. Oceanog., v. 6, p. 130-138.
- Namias, J. and D. R. Cayan, 1984, "El Nino: implications for forecasting," Oceanus, v. 27, p. 41-47.
- Quiroz, R. S., 1983, "The climate of the El Nino winter of 1982-1983, a season of extraordinary climatic anomalies," Monthly Weather Rev., v. III, p. 1685-1706.
- Reid, J. L. and A. W. Mantyla, 1976, "The effect of the geostrophic flow upon coastal sea elevations in the northern North Pacific Ocean," Jour. Geophys. Res., v. 81, n. 18, p. 3100-3110.
- Seymour, R. J., R. R. Strange, III, D. R. Cayan and R. A. Nathan, 1984, "Influence of El Ninos on California's wave climate," Proc. 19th Coastal Eng. Conf., Amer. Soc. Civil Eng., in press.
- Smith, R. A. and R. J. Leffler, 1980, "Water level variations along California coast," Jour. Waterway, Port, Coastal and Ocean Div., Amer. Soc. Civil Eng., v. 106, n. ww3, p. 335-348.
- Zetler, B. D. and R. E. Flick, 1985, "Predicted extreme high tides for California, 1983-2000," Jour. Waterway, Port, Coastal and Ocean Div., Amer. Soc. Civil Eng., in press.
- Zetler, B. D. and R. E. Flick, in prep, "Predicted extreme high tides for mixed tidal regimes," submitted.

## CHAPTER SIXTY ONE

### New aspects concerning the increase of sea level on the German North Sea coast

Hans Rohde\*

#### ABSTRACT

The development of MThw on the German North Sea coast is probably related to the development of the climate. Other important contributing factors are discussed. For the last 20 years a relatively steep rise of MThw level is recognizable. An even steeper rise as a result of climate changes appears possible within the next 100 years. With regard to the great importance for coastal engineering, the necessity of attentive observation and international cooperation among different scientific disciplines is stressed.

#### 1. INTRODUCTION

The development of the water level changes on a coast is of great importance for coastal engineering. In general the water level in the oceans and also on the coasts has risen more than 100 m since the maximum of the last ice age about 20,000 years ago, when huge masses of water were stored in large ice-covered areas. The steepest increase amounted to 2 m per century (2 cm/a) (5) (12) (18) (10). This rise was caused primarily by the melting of the ice and the subsequent increase of the water volume in the ocean. All other influences on the development of the water level changes on the coasts were negligible by comparison.

The steep rise of water level ceased about 6,000 years ago. With the flattening of the water level curve other influences on the development of water level on the coasts became evident. The development wasn't uniform. Oscillations can be found which can differ in locality as well as with time as described by many authors (12) (10) (13).

The development of the water level changes on a coast depends essentially on three superimposed effects:

- 1) The height of mean sea level in the ocean: Its development with time depends primarily on the general behavior of the temperature and hence on the ratio between the volume of mainland ice and the volume of sea water (development of the climate).
- 2) The wind conditions: They depend essentially on atmospheric pressure conditions (meteorological conditions in general) and can change with time.
- 3) The geographical and geological conditions of the specific coastal region. Changes of the morphology or the topography - natural as

\*Dr.-Ing., Director of the Coastal Engineering Department of the Federal Institute of Waterways Engineering (Bundesanstalt für Wasserbau), Moorweidenstraße 14, D-2000 Hamburg 13, FR Germany

well as man-made - can produce a change in the development of water level. Tectonical changes of the sea-bottom and of the coast may also contribute to the water level changes.

These three factors are interdependent. A worldwide change of temperature can cause changes in the atmospheric circulation which affect the abundance and the paths of low-pressure systems. Changes of the wind-field and of the wind set up on the coast can be the consequence. A changing angle of attack of the sea against the coast can cause changes of the coastal configuration.

## 2. DEVELOPMENT OF WATER LEVEL FOR THE LAST 2,000 YEARS ON THE GERMAN NORTH SEA COAST

Figure 1 depicts schematically the probable development of MThw (Mean tidal high water, MThw) on the German North Sea coast for the last 2,000 years. If the levels of MThw and MThw (Mean tidal low water, MLW) change in the same direction and the shape of the tidal curve re-

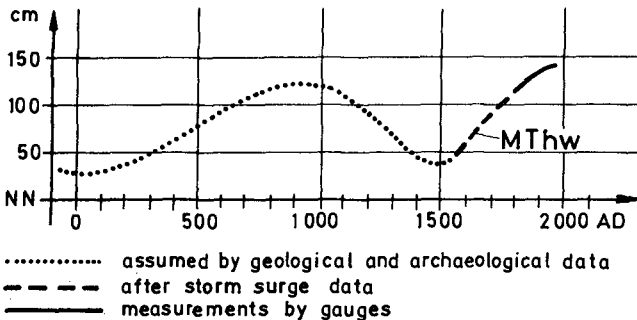


Figure 1. Probable behavior of MThw on the German North Sea coast for the last 2,000 years (schematic)

mains constant, the development of MThw will be in accordance with the development of the "Mean Sea Level". But in most cases the shape of the tidal curves were affected by changes of the meteorological, topographical and morphological conditions. The influences of these factors are different on the levels of MThw and MThw.

The curve of Figure 1 consists of three sections:

- 1) The period till the middle of the 16th century (dotted line): The data arise from geological and archaeological investigations. They are relatively uncertain in their magnitude and temporal classification. The topographical conditions of the coast are of great importance and are not exactly known for this period.
- 2) The period from the middle of the 16th century until the end of the 18th century (dashed line): There are already data of water levels on the German North Sea coast, namely of the height of severe and very severe storm surges. Figure 2 shows some sites on the German North Sea coast for which these data are known.

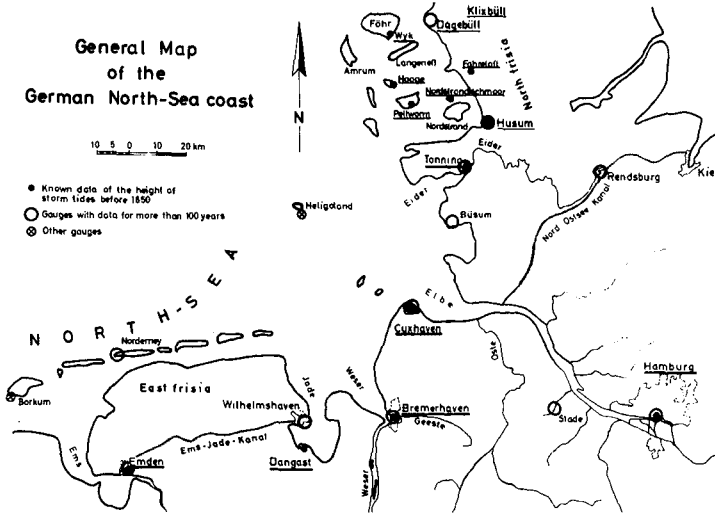


Figure 2: General map of the German North Sea coast with the sites of gauges and storm surge data

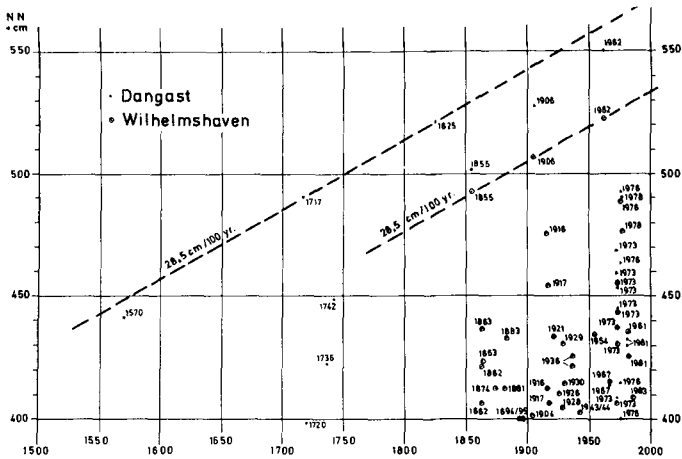


Figure 3: Maximum flood levels at Dangast and Wilhelmshaven since 1570 (15)

Figure 3 depicts the development of the maximum flood levels for one of these sites (Dangast/Wilhelmshaven) since 1570. One can recognize that the limiting line of the peaks of the highest storm surges 28.5 cm per century. A similar increase between 20 and 30 cm per century can be found at the other investigated sites (15) (16). Because the shape of the coast and the climatic conditions didn't change essentially in this

period, one may suppose that the level of the highest storm surges remains constant with respect to MThw and thus the increase of MThw also amounts to 20 - 30 cm per century i.e. an average of 25 cm per century.

- 3) The period from the end of the 18th century until present time (solid line): The shape of the coast and the climate have not changed fundamentally in this time. For this period records of some gauges are available (Figure 2). In the middle of the 19th century there were already as many gauges on the German North Sea coast as there are today (14). As long as gauges are not or only slightly affected by morphological changes of their environment, one can recognize an average increase of MThw of 25 cm per century. About 60 or 70 years ago the slope of the MThw curve began to decrease. The flat run of the curve is most pronounced on such gauges on which the man-made influences on the development of MThw are small (15) (16).

The graph in Figure 1 is in good agreement with the curve of temperature-development in Central England for the last 1000 years (7) (8) and a similar curve given by Benoist et al. (2) for the Antarctic. High water levels correspond to relatively high temperature, low water levels to a relatively low temperature. At the beginning of the second millennium A.D. the water level on the coast was relatively high. The height of the "Little Ice Age" was about 1600 A.D. and the water level was relatively low. This confirms assumptions that the development of water level change, shown in Figure 1, depends essentially on gradual changes of the climate (11). How much the water levels are influenced by other factors can only be determined from the careful analysis of gauge records. It was already said by (15) that the rise of MThw - see lower curve in Figure 4 - and correspondingly the rise of Mean Sea Level as well as the increase of the maximum flood levels - see upper curve in Figure 4 - depends essentially on changes of the climate. The frequency of the high

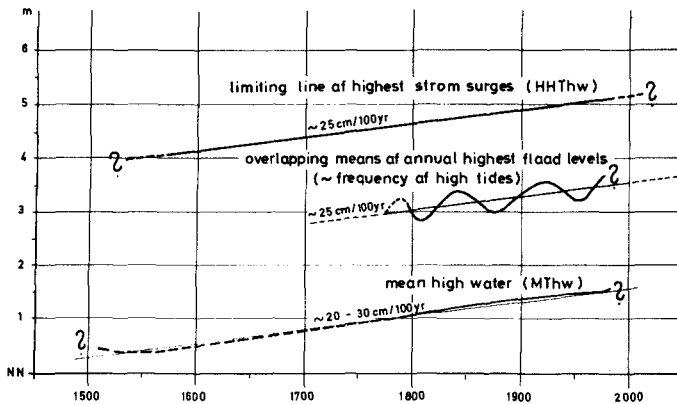


Figure 4: Development of water level on the German North Sea coast since the 16th century (15)

tides oscillates with long periods as the curve in the middle of Figure 4 shows. The oscillations depend on changes of the wind conditions and have meteorological causes (19).

3. ANALYSIS OF WATER LEVELS ON THE GERMAN NORTH SEA COAST FOR THE YEARS 1951 - 1980

For five gauges on the German North Sea coast - Borkum, Emden, Wilhelmshaven, Bremerhaven and Cuxhaven (Figure 2) - an exact analysis was made for the period from 1951 to 1980. Figure 5 shows as an example the frequency distribution of all Thw of the two years with the lowest MThw (1960) and the highest MThw (1967) at Cuxhaven. High water levels are produced by winds blowing towards the coast (from the directions north and west), low water levels by winds blowing away from the coast (from the directions south and east). In order to eliminate the influence of west winds on MThw, all Thw with a level of more than 50 cm above the arithmetical mean of all Thw for each year (MThw) were omitted. The hatched parts of the curves in Figure 5 show the omitted Thw. The number

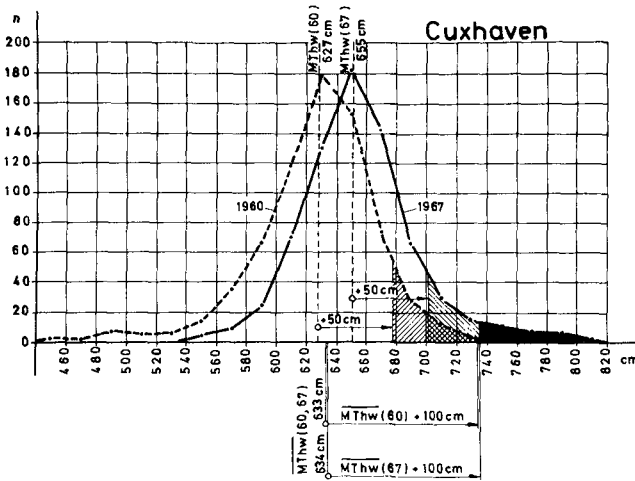


Figure 5: Frequency distribution of Thw at Cuxhaven for the years 1960 and 1967

of these high levels, caused by west winds, was much higher in 1967 than in 1960, a year with a relatively large number of low east wind tides. A new arithmetical mean was computed with the rest of the Thw for each year (MThw). All Thw, influenced by onshore winds were disregarded in the computation of this new mean.

Figure 6 shows for Cuxhaven, as one example, that the differences between MThw and  $\bar{MThw}$  are small. The figure also shows the 5 year overlapping means and their regression lines (A and B), determined by the method of the least squares. A clear increase of the  $\bar{MThw}$  is recognizable which is only a little less steep than the increase of MThw. The

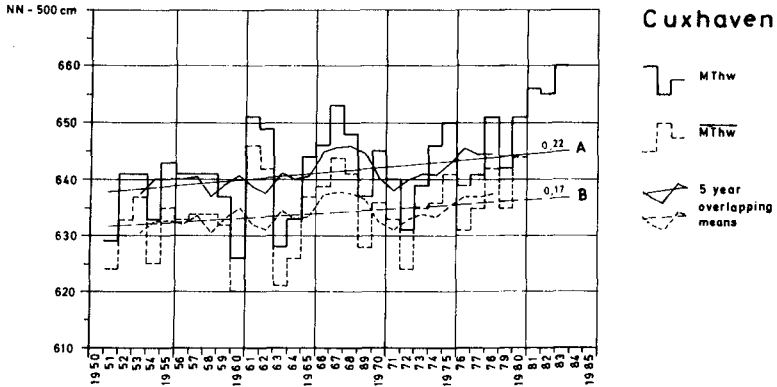


Figure 6: MThw and  $\overline{MThw}$  at Cuxhaven 1951 - 1983

slopes of the regression lines of the 5 year overlapping means of MThw and  $\overline{MThw}$  are collated for all 5 above mentioned gauges in the Columns 1 and 4 of Tabel 1.

	MThw	> MThw + 1 m number	+ 1 m level	$\overline{MThw}$	$\geq \overline{MThw}$ + 1 m number	+ 1 m level
	1	2	3	4	5	6
Borkum-Südstrand	0.23	0.12	0.37	0.20	0.18	0.27
Emden	0.23	0.18	0.42	0.20	0.17	0.59
Wilhelmshaven	0.22	0.09	0.50	0.19	0.17	0.32
Bremerhaven	0.22	0.14	0.51	0.18	0.22	0.30
Cuxhaven	0.22	0.17	0.55	0.17	0.26	0.29

Table 1: Slope "b" of the regression lines  $y = a + bx$  of the 5 year overlapping means 1951 - 1980

Now all Thw with a higher level of 1 m or more above the regression lines of MThw (line B in Fig. 6) were selected. These Thw are visible in Figure 5 for the years 1960 and 1967 on the right hand side and are shaded black in the frequency distribution curve. The upper graph in Figure 7 shows the annual number of these high Thw, the 5 year overlapping means and their regression line for Cuxhaven. In comparison with the number of the Thw  $\geq 1$  m above  $\overline{MThw}$  (line B in Fig. 6) the number of Thw  $> 1$  m above the yearly MThw (line A in Fig. 6) is also given (dashed line in Fig. 7). The number of the last mentioned Thw is 330 for the whole period 1951 - 1980, the number of the Thw  $\geq 1$  m above  $\overline{MThw}$  is 426. The

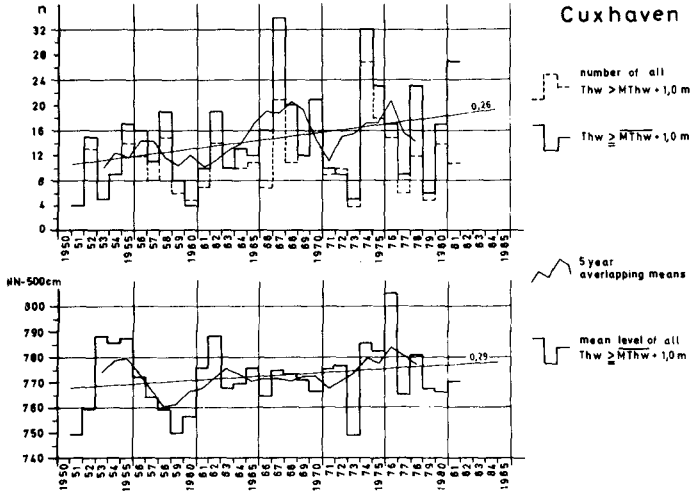


Figure 7:  $Thw > MThw + 1\text{ m}$  and  $\overline{Thw} \geq MThw + 1\text{ m}$  at Cuxhaven 1951 - 1981 (number and mean level)

mean levels, which are computed from the Thw with a level of 1 m or more above  $\overline{MThw}$ , the 5 year overlapping means and their regression line are shown in the lower graph of Figure 7 for Cuxhaven.

The mean level of the high Thw increases as well as their number for the period 1951 - 1980. This applies also for the  $Thw \geq 1\text{ m}$  above line B in Figure 6 and for the  $Thw > 1\text{ m}$  above line A in Figure 6 and has proved to be true for all 5 gauges as Table 1 shows (see Columns 2, 3, 5 and 6). The rise of the levels of the high Thw is remarkably steeper than the increase of  $\overline{MThw}$  or  $MThw$ , as the comparison of Column 3 with Column 1 and of Column 6 with Column 4 shows. This result doesn't change if the  $\overline{MThw}$  are not computed for the hydrological year (November to October) but for the year September to August.

The comparison between the Columns 1 and 4 in Table 1 shows that the greatest part of the rise of  $\overline{MThw}$ , observed on the German North Sea coast, is independent from the increase of the high Thw's which are influenced by west winds. The influence of the high tides on the rise of  $\overline{MThw}$  is relatively small. Therefore it is permissible, as a first approximation, to look at the rise of the common yearly  $\overline{MThw}$  for comparisons of the development of mean water level on the coast. This is important because the elimination of all tides influenced by stronger west winds has not been done for all gauges and for longer periods.

As Figure 7 shows, the number and the mean level of the high Thw is increasing. The last section of the middle curve in Figure 4 also shows this because a good correlation between the number of the high Thw in each year and the highest level of Thw in the same year exists. The factor of correlation lies between 0.61 and 0.73 for the five mentioned gauges. The middle curve in Figure 4 also gives an approximated scale



for the frequency of high tides. Periods with a high frequency of high tides always have been followed by periods with a lower frequency.

#### 4. POSSIBLE FUTURE DEVELOPMENTS

As already mentioned above and as described in previous papers, the records of most gauges on the German North Sea coast show an average rise of 25 cm per century since the beginning of the observations. Since about 1920, the curves of the 19 year overlapping means of MThw on several gauges became less steep (15) (16). In such cases where the decrease of the slope was less strong, effects of man-made influences are probable (e.g. dredging in the estuaries or the construction of dams). It seemed to be possible that the less steep increase of the MThw-curve could turn over in a gradual decreasing curve. Because a correlation between the development of temperature and water level obviously exists, a maximum of the water level curve could come after a maximum of the temperature. Some observations of temperature pointed out such a development (7) (15) (16) (19). The decrease of the temperature and of the water level could be the beginning of a new "Little Ice Age" or even a new major ice age.

Recently a turning-point seems to be recognizable. The graphs of MThw of all gauges on the German North Sea coast rise steeper again during the last years. Figure 8 shows the curves of the 19 years overlapping means of MThw at Emden, Cuxhaven and Büsum. The figure which was published already in (15) (16) has been expanded for the years up to 1983. Moreover the time-scale has been shifted in such a way that the mean values refer to the last year of the period respectively (e.g. mean value of 1932/50 = 1950). These three gauges show a very flat graph of

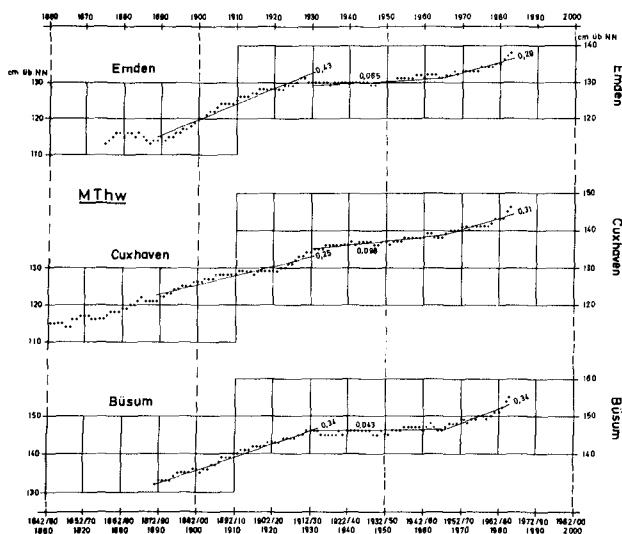


Figure 8: 19 year overlapping means of MThw at Emden, Cuxhaven and Büsum

MThw from 1920 to 1965. In the last years a steeper rise of the graphs is apparent. The slopes of the regression lines are quoted for the three periods 1871/89 - 1912/30, 1912/30 - 1947/65 and 1947/65 - 1965/83. Such a recent increase can also be observed on other gauges on the coast and in the estuaries (compare Columns 1 and 2 with Column 3 in Tabel 2).

		MThw			MTnw
		till 1955	1873-1955	1956-1983	1956-1983
		1	2	3	4
Emden	(1857)	0.25	0.23	0.54	-0.33
Wilhelmshaven	(1873)	0.23	0.23	0.37	-0.15
Cuxhaven	(1843)	0.25	0.24	0.51	-0.21
Büsum	(1871)	0.22	0.21	0.62	-0.25
Husum	(1870)	0.30	0.28	0.63	-0.09
Dagebüll	(1873)	0.28	0.28	0.65	-0.32

Table 2: Slope "b" of the regression lines  $y = a + bx$  of MThw in 3 different periods and of MTnw in the last period

Figure 9 gives a schematic curve of MThw generated by the graphs in Figure 8. The dashed line shows the development which seemed to be possible on the basis of the less steep graph of water level after 1920. On the basis of the new steeper rise one cannot exclude a development described by the dotted line. In the opinion of some climatologists an increase of the mean temperature of the atmosphere by 4° C during the next 50 or 100 years could be possible as a result of air pollution,

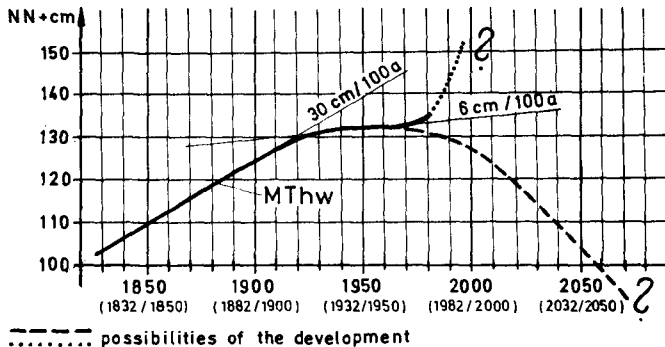


Figure 9: Schematic graph of MThw on the German North Sea coast since the middle of the 19th century and possible future developments

increase of carbon dioxide concentration etc. Such an increase of temperature would cause a change of the ice conditions in the polar regions. A rise of the sea level by some meters could be the consequence (1) (3) (4) (9).

There is no exact proof to date that the steeper rise of MThw, observed on the gauges on the German North Sea coast, is already the result of the beginning of a general increase of temperature. But such a development cannot be excluded. On the other hand a more or less decrease of MThw has been observed on most gauges on the German North Sea coast (see Column 4 in Table 2), that means an increase of the mean tidal range (MThb). If the rise of MThw had climatic causes, a simultaneous rise of MThw would be probable. Therefore it is possible that the increase of MThb - rise of MThw and a simultaneous decrease of MThw - has oceanographic causes. Investigations of Siefert (20) provide some hints of generally changing tidal conditions in the North Sea. But such a change can also be the consequence of the rising sea level. Investigations about this problem by means of a numerical model have been started already.

## 5. CONCLUSIONS

The knowledge of the probable development of the water level on the German North Sea coast - in general on all flat coasts - is of greatest importance for coastal engineering. In Germany an increase of MThw of 25 cm per century has been taken as a basis for dimensioning of coastal protection constructions (e.g. dykes or storm surge barrages) (6). If instead one had to reckon with a rise of MThw of 2 m or more in the next 100 years and with at least the same increase of the storm surge levels, all coastal protection works would be ineffective. It is doubtful that an elevation of the dykes for such a water level rise would be possible everywhere. As one can conclude from the development of MThw at all locations on the German North Sea coast for the last 400 years in connection with the development of temperature in Central England (7) (8), an increase of 2 m or more would be thinkable in the case of an increase of the temperature of about 4° C. The increase of temperature is assumed to be 1° C since the culminating-point of the "Little Ice Age". In the same period MThw rose about 1 m (Fig. 1). Some scientists even speak of a possible rise of mean sea level of 5 or 6 m during the next 100 years (3) (4).

Therefore it is necessary to intensify investigations in order to predict the probable development of the global sea level as well as that of certain coastal sections for the next 100 years as exactly as possible. Three routes of research are deemed necessary:

- 1) One has to analyse all the factors responsible for the development of water level in the ocean and on the coasts as exactly as possible. This demands an extensive and close co-operation of the different scientific disciplines of climatology, meteorology, oceanology, glaciology, geodesy and coastal engineering. This co-operation has to be international. Coastal engineers should contact such projects as the International Climate Research Program and the Project No. 200 of the International Geological Correlation Program "Sea-Level Correlation and Applications". The results of these projects are of greatest practical importance for coastal engineering.

- 2) One has to analyse all records of gauges on the coasts or near the coasts as far back in time as possible. The aim must be to discover relationships between the development of water level and other factors, e.g. climate and wind set up. Such relationships can be of importance for the estimation of the water level behavior in the future. In the Federal Republic of Germany the records of many gauges are available. They go back up to 180 years. But only the youngest data are available for an analysis with automatic data processing (ADP). We started to convert, at least for the most important gauges, the older data - all daily Thw and Thw level and time - to automatic data carriers. This requires careful examinations of the data. The older the data are, the more difficult become these examinations. Such investigations should also be done by all countries which possess gauge-records for long time periods.
- 3) One should try to erect new gauges at a greater distance away from the coast in order to receive water level records which are free from coastal influences. Also Ausubel (1) suggests an expansion of the present global tide gauge network. The new gauges have to have firm foundations: any vertical movement of the stations should be impossible. The water levels have to be recorded exactly for some decades. The German Coastal Engineering Board (KFKI), in which the federal authorities and the authorities of the German States work together, plans the construction of three such gauges in the North Sea (17). Figure 10 shows the sites of these gauges. They are situated at a distance of 25 to 35 km from the German North Sea coast in a water depth between 15 and 25 m below chart datum. The geo-

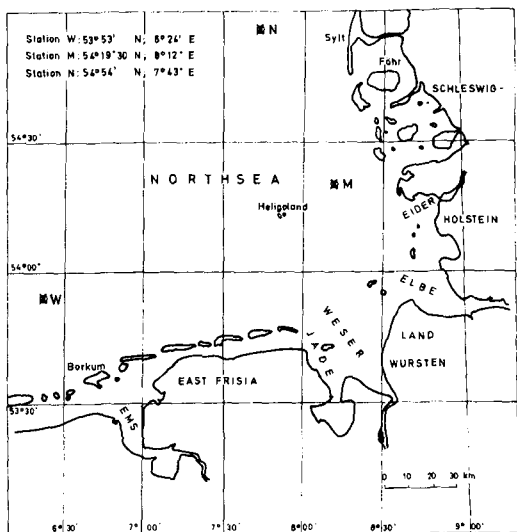


Figure 10: Sites of the three planned gauge-stations in front of the German North Sea coast

logical and morphological parameters are such that firm foundations are possible and movements are very unlikely. Gauge devices are planned which will stand on the sea-bottom and be fixed onto piles which are driven 10 or 20 m into the sea-bed. The devices work on the pressure transducer principle. The costs for the construction of the stations are not very high compared to the management and maintenance costs for several decades. The problem of an exact reference of the gauge-records to the altitude datum of the mainland is still unsolved. At first one can dispense with this reference. The gauge-stations are also of importance for other branches of research and practical tasks, e.g. for an exact surveying of the depths of the off-shore region and for storm surge research. The final design of the stations has not been completed. We hope to obtain the necessary financial support shortly so that the gauges may be operational by 1986 or 1987.

## REFERENCES

- (1) Ausubel, J.H.: The challenge of CO<sub>2</sub>. Aerospace America, April 1984.
- (2) Benoist, J.P., Lorius, C. et al.: Isotope climatic record over the last 2500 years from Dome C (Antarctica) ice cores. 3rd. Int. Symp. on Antarctic Glaciology, Columbia, Ohio, Sept. 1981.
- (3) Duphorn, K.: Kommt eine neue Eiszeit? Geolog. Rundschau 65, Bd. 55, 1976.
- (4) Flohn, H.: Modelle der Klimaentwicklung im 21. Jahrhundert. In: Das Klima, Springer Verlag, Berlin, Heidelberg, New York, 1980.
- (5) Jelgersma, S.: Holocene sea level changes in the Netherlands. Medel. Geol. Sticht., Ser. C, Vl, No. 7, 1961.
- (6) Kramer, J. et al.: Empfehlungen für die Ausführung von Küstenschutzwerken - EAK 1981. Empfehlungen A. Die Küste, H 36, 1981.
- (7) Lamb, H.H.: An approach for the study of the development of climate and its impact in human affairs, Review Papers Int. Conf. on Climate and History, Norwich, 1979.
- (8) Lamb, H.H.: Weather and climate patterns of the Little Ice Age. In: Das Klima, Springer Verlag, Berlin, Heidelberg, New York, 1980.
- (9) Lamb, H.H.: Climate, history and the modern world. S. Methuen + Co. Ltd., London and New York, 1982.
- (10) Linke, G.: Ergebnisse und Aspekte zur Klimaentwicklung im Holozän. Geol. Rundschau, Bd. 70, 1981.
- (11) Menke, B.: Vegetationsgeschichtliche Untersuchungen und Radiocarbon-Datierungen zur holozänen Entwicklung der schleswig-holsteinischen Westküste. Eiszeitalter und Gegenwart, Bd. 20, 1969.
- (12) Menke, B.: Befunde und Überlegungen zum nacheiszeitlichen Meeresspiegelanstieg. Probleme der Küstenforschung, Bd. 11, 1976.

- (13) Preuss, H., Streif, H. et al.: Abschlußbericht zum DFG-Forschungsvorhaben "Meeresspiegelschwankungen der Nordsee im Jungpleistozän und Holozän". Niedersächsisches Landesamt, für Bodenforschung, Hannover, 1981 (unveröffentlicht).
- (14) Rohde, H.: Wasserstandsbeobachtungen im Bereich der deutschen Nordseeküste vor der Mitte des 19. Jahrhunderts. Die Küste, H. 28, 1976.
- (15) Rohde, H.: Sturmfluthöhen und säkularer Wasserstandsanstieg an der deutschen Nordseeküste. Die Küste, H. 30, 1977.
- (16) Rohde, H.: Changes in sea level in the German Bight. Geoph. Journ. Royal astr. Sc., 62, 1980.
- (17) Rohde, H.: Die Forschungsarbeiten des KFKI 1981 bis 1983. Die Küste, H. 40, 1984.
- (18) Segota, T.: Radiocarbon measurements and the holocene and the late Würm sea level rise. Eiszeitalter und Gegenwart. Bd. 23/24, 1973.
- (19) Seliger, J.: Das Sturmflutgeschehen an der deutschen Nordseeküste. Diss. Univ. Kiel, 1983.
- (20) Siefert, W.: Detailed tide and storm surge investigations in coastal waters. Paper of 19th ICCE, Houston/Texas, 1984.

## CHAPTER SIXTY TWO

### SHORT-CRESTED BREAKING WAVES

P.C. Machen<sup>1</sup>

#### Abstract

The likely effects of short-crested (sc) breaking waves on ships and structures are summarised in the case of the simplest non-trivial sc sea at medium/high crossing angle. Typical experimental data of sc breaking wave-height and sc water particle speeds are given at model-scale.

#### 1. INTRODUCTION

In recent years, more attention has been devoted to extreme waves (e.g. 15). It is suggested that there are at least two classes of extreme waves, which frequently may break:

- a) "Tail of the distribution" - type waves where two or more waves are temporarily superposed (16).
- b) Current-wave interaction, producing high steepness waves (14, 17, 26). To these should probably be added a third category:
- c) Short crested waves, in particular where high waves come together from two or more directions at middle or high crossing angle. An inshore example is given in Figure 1.1

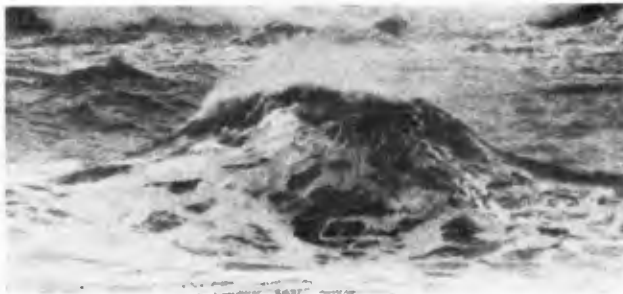


Figure 1.1: Near-shore short-crested breaking wave formed from two obliquely-crossing waves.

Little attention has been paid to the last of these. Salter (23) formed a three-dimensional deep-water plunging wave by arranging that the phases of waves from an array of generators came into coincidence at a point. Halliwell and Machen (10) pointed out that short-crested (sc)

<sup>1</sup> Senior Research Associate, University of Newcastle upon Tyne, U.K.

breaking waves could be higher than long-crested and gave some results for shallow water. Hsu and Silvester (12) and Hsu (13) compared these results with predictions based on a third-order perturbation analysis.

The term 'short-crested' sea is often used to describe any sea having components from more than one direction, but in this paper the simplest non-trivial case will only be considered, that is a sc sea composed of two equi-amplitude equi-period waves crossing obliquely. It is to be expected that before breaking the finite-amplitude standing wave research reported in the 1950s and 1960s may be relevant. A step towards three-dimensional behaviour was made by Verma and Keller (28), and a third-order perturbation analysis of two obliquely-crossing waves was made by Hsu et al (11). Roberts (21) generalised and extended the analysis of the resonance behaviour of steady sc waves, using the preferred term "harmonic resonance".

In this paper, we begin in Section 2 by examining the loss of HMS COBRA in 1901 to which sc waves may have contributed. After some general discussion of sc breaking waves, some results are given in Section 3 from an experimental facility of two intersecting channels and sc steepness is compared with limiting long-crested steepness. The measurement of sc water-particle speed is considered in Section 4 where some success with a hot-film anemometer is reported.

## 2. THE IMPORTANCE OF SHORT-CRESTED BREAKING WAVES FOR SHIPS AND STRUCTURES

In a wind-sea, the angles between directional components are small and whitecapping will accord to normal criteria. The short-crestedness of the sea might be described as of low entropy. On the other hand, if we imagine two separate long-crested waves (associated perhaps with a swell or highly peaked spectrum) crossing obliquely at medium or high angle, then a high energy event with modified breaking criteria is possible.

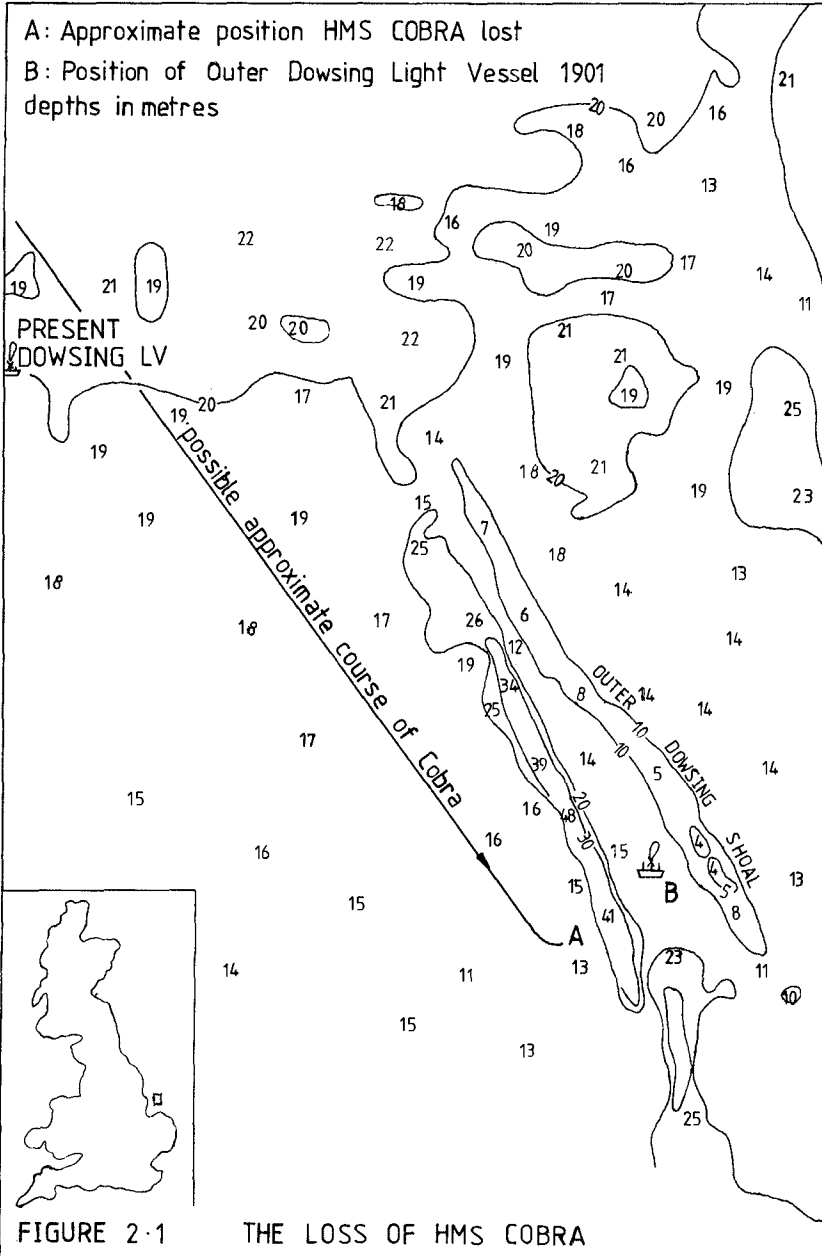
In the case of such a crossing event the secondary wave flux can be produced by refraction around a shoal, by reflection from a deep-channel or structure, or by similar action through the action of a current regime. Clearly in these cases the secondary source is an image source. High crossing waves due to an image source are in practice likely to be rather localised.

Equally a secondary source could be real in the sense of wave flux from a second storm or from a wind-shift, but there is some experience that the short steep seas caused by very strong winds attenuate quite quickly when the wind drops or changes direction (see for instance Fig. 2 of (22), (6) and (8)); a secondary real wave flux is therefore only likely to be of the same order as a high primary source in a localised region of time and space.

### 2.1 Loss of HMS COBRA

Pierson (19) discussed the loss of two trawlers in the North Sea, suggesting that crossing waves could be to blame. Recently Faulkner et al (7) re-examined the loss of the torpedo-destroyer HMS COBRA in the North Sea in 1901 (their principal interest being in the structural aspects of the vessel). In the case of COBRA, more information is available





regarding the position of the ship than in Pierson's and there is eye-witness evidence that it was lost in a crossing sea. The mate of the light vessel 2nm ( $3\frac{1}{2}$ Km) to the north-east reported winds NNW Force 6, the helmsman wind NW, and heavy rolling was experienced when heading slightly north of east. In spite of the sea being described by the light vessel mate as only "middling rough" the ship was seen to execute three terrific plunges with waves breaking over her fore-castle and the ship broke in two. Survivors described the sea as "a heavy sea, a cross sea, not a regular sea, the wind one way and the tide another, as though there had been a change in the wind" (7).

There was some ambiguity about the exact position but the COBRA was near the Outer Dowsing Channel, the general alignment of which is NNW/SSE (Fig. 2.1). At this point the west bank of the channel is steep with chart depths of 15m and 40m top and bottom respectively, and its lie is  $N16^{\circ} W$  over a 3Km length. Waves from the NW/NNW would have been obliquely incident on the discontinuity, and those of middle and higher period would have been reflected. A simple analysis by Snell's law indicates that, at the state of the tide at the time, waves from the NW would have been reflected for periods of 8 sec and more; from the NNW, of 5 sec and more. Faulkner et al (7) estimated the characteristic wave period as 7 sec.

A crossing-wave regime would have been set up near the discontinuity. 7-sec waves would have implied a depth-to-wavelength ratio of about 0.24, and the primary wave flux, the reflected secondary component(s) and any swell would have been approximately superimposed until a breaking limit were reached. There remains some doubts, however, whether the short-crested seas were breaking, what contribution additional swell made, what effect tidal currents had, and to what extent the present-day chart indicates the bathymetry of 1901.

## 2.2 Summary of Short-crested Breaking Effects

There are other examples of the importance of short-crested wave effects both offshore and inshore, but restrictions of space preclude inclusion here. The effects of sc (breaking) waves on ships and structures are as follows:

- a) The sc pyramidal or breaking waves may present a vessel or structure with a steeper than expected wave environment, which may exceed normal steepness criteria before reaching instability.
- b) Along the centre-line of the sc wave the wavelength is  $L \sec \alpha$  ( $\alpha$  being defined in Figure 3.1) and a ship steaming in that direction is more likely to be entirely in a trough immediately before the bow is struck by the three-dimensional crest. (In two dimensions, an abnormal length of trough has been advanced as an important factor in the casualties off the South African coast (17)).
- c) The sc wave profile speed may be high (higher by a factor of the order of  $\sec \alpha$ ).
- d) At breaking a sc jet or inverted saucer of water may issue from the crest. Little information is available about maximum water-particle speeds, but behaviour is likely to depend partly upon  $d/L$ . Some results

are given in Section 4.

- e) Silvester (25) discussed the effects of crossing waves on sediment movement. Increased sediment transport can accompany crossing waves.
- f) There are likely to be consequences for fatigue calculations.

3. SC BREAKING WAVES - THEIR MODELLING AND HEIGHT

3.1 Modelling

Although it might be expected by symmetry and neglecting energy losses at the wall, that two obliquely-crossing waves would be analytically the same as one wave obliquely reflected from a straight vertical wall, if the wall is of finite length the diffracted wave must be included. High energy crossing events are likely to be localised and the diffracted wave may have to be included in some general sc breaking waves. There are, therefore, two alternative crossing-wave circumstances which can be modelled, one including the diffracted wave (Set-up A) and the other not (Set-up B).

The decision which to model will be significant as the diffracted wave may be important for a considerable distance (2). Clearly A can be modelled by reflecting waves from a straight vertical wall, or alternatively by bringing together waves from two intersecting channels. B could be modelled in a large basin with an array of wave generator elements with their phases set such that two obliquely-crossing waves were generated, but depending upon the scale a diffracted wave may still make a significant contribution. There are further possible modelling problems.

The basin at the University of Western Australia has some attractive features (25) and perhaps lies somewhere between A & B. For reasons of finance and the need for a local facility, an A-type basin was built at Newcastle (Figure 3.1), in which the angle  $\alpha$  is variable. It is however not an ideal facility and suffers from the following deficiencies: diffraction of wave energy takes place into the adjacent channel which is then subject to reflection at the paddle; the test aperture is rather limited; and the channels, being of finite width, can support standing waves, in spite of cross-wave filters.

3.2 Short-crested Instability Criteria

As  $\alpha$  is varied (theoretically) between  $0^\circ$  and  $90^\circ$ , the sc behaviour changes from being purely progressive to purely standing. In the general case, the two principal instability criteria, as summarised in (10) & (13) are:

a) Kinematic:  $u_{max} > f(C_s)$  ..... (3.1A)

b) Dynamic:  $v_{max} > h(g)$  ..... (3.1B)

Where  $u_{max}$  and  $v_{max}$  are maximum water particle speeds parallel to the basin centre-line and vertically upwards respectively,  $f(C_s)$  is some function of short-crested celerity and  $h(g)$  is a function of gravitational acceleration. Here the terms kinematic and dynamic are preferred as used by Hsu (13) after Dean (5).

Clearly when  $\alpha$  is high, the dynamic condition is likely to dominate.

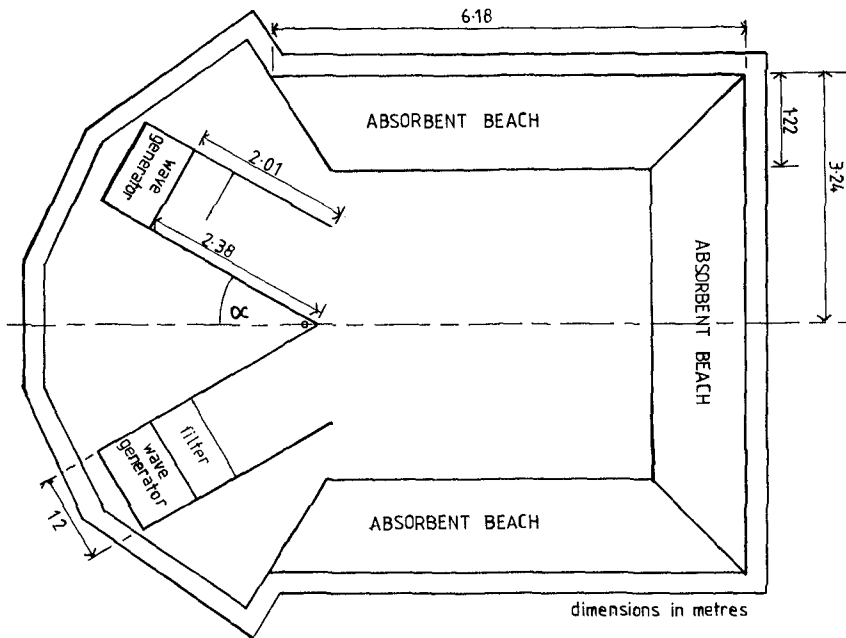


FIGURE 3.1 TWO-CHANNEL BASIN

Hsu (13) found a third-order solution to the dynamic stability criterion at all  $d/L$  from 0.05 to 0.5 for  $70^\circ \leq \alpha \leq 90^\circ$ . In the range  $55^\circ < \alpha < 70^\circ$  he found the stability equation unsatisfied in a number of  $d/L$  values. On the other hand at lower values of  $\alpha$  it may be expected that the kinematic condition will be dominant. In Equation (3.1A)  $f(C_s)$  may be approximately equal to  $C_s$ , or alternatively a long-crested kinematic condition may be more appropriate. In this respect Hsu (13) found that for part-range of  $d/L$  a maximum value of  $u$  occurred which was less than  $C_s$ , finding it questionable that  $u_{\max}$  was a valid criterion for the highest wave where it was less than  $C_s$ .

The author has watched a large number of in-shore sc breaking waves and there appears to be a maximum value of  $\alpha$  for a forward-breaking sc wave which is of the order of  $45^\circ$ . For wave-loading and slam considerations the kinematic condition is probably the more important criterion, but for ships experiencing pyramidal seas both conditions are likely to be of interest.

### 3.3 Short-crested wave height

In the model basin the sc breaking wave-height ( $H_{bs}$ ) varied with the parent wave steepness ( $K\bar{H}$ ), and there appeared to be a particular value of  $K\bar{H}$  which gave the highest acceptable value of  $H_{bs}$ . At values of  $K\bar{H}$

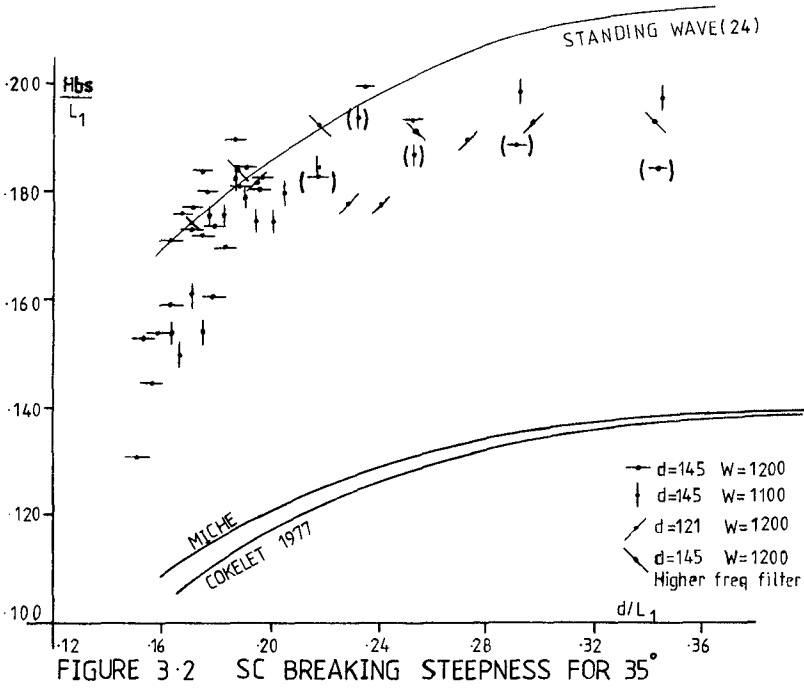


FIGURE 3-2 SC BREAKING STEEPNESS FOR 35°

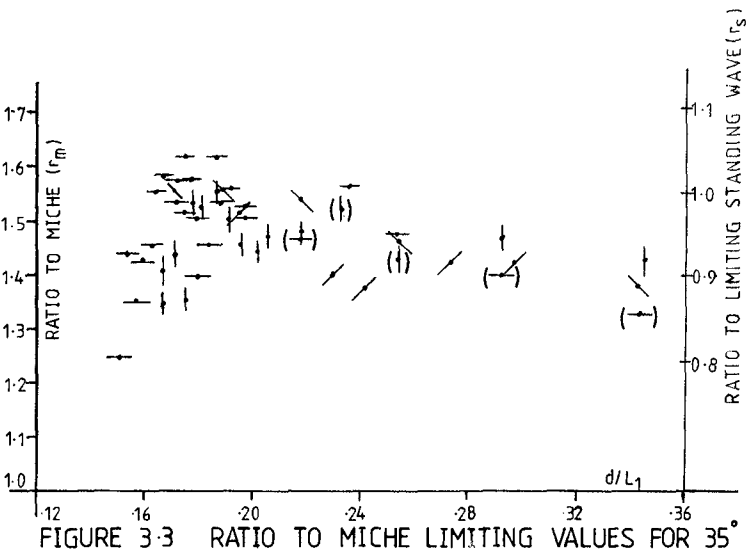


FIGURE 3-3 RATIO TO MICHE LIMITING VALUES FOR 35°

higher than the optimum, one of two circumstances applied, either  $H_{bs}$  decreased with the sc breaking wave being "pushed through" because of high energy concentration, or unacceptable spilling occurred in the channels. An envelope curve of  $H_{bs}/L_1$  versus  $d/L_1$  was plotted for  $\alpha = 35^\circ$  (Figure 3.2); two values of channel width ( $W = 1200$  &  $1100\text{mm}$ ) and two values of  $d$  ( $145$  and  $121\text{mm}$ ) were used. The bracketted points are those where, at one  $d/L_1$ ,  $W$  was changed but the  $KH$  setting was not re-optimised. A series was also carried with a higher frequency cross-wave filter. The data is compared with limiting progressive steepness (according to Miche, and Cokelet (3)) and limiting standing wave steepness (24)). Fig. 3.3 shows the ratios of the experimental data points to the Miche value ( $r_m$ ) and limiting standing wave ( $r_s$ ):-

$$\left( \begin{array}{c} r_m \\ r_s \end{array} \right) = \left( \begin{array}{c} 1/0.142 \\ 1/0.22 \end{array} \right) \frac{H_{bs}}{L_1 \tanh Kd} \dots\dots\dots (3.2)$$

Compare Figure 3.3 with Roberts' conclusion that deep water sc waves could be up to 60% steeper than progressive waves (21).

Daemrich et al (4) found that for  $\alpha = 20^\circ$  the height of a Mach Stem breaking wave did not exceed the predicted Miche limiting value for progressive waves. Further work needs to be done, but this may indicate the sensitivity of behaviour to variation of  $\alpha$  in the range  $20^\circ$ - $30^\circ$  (21 Fig. 4).

#### 4. WATER PARTICLE SPEED MEASUREMENTS

##### 4.1 Experimental Method

Available was a Thermo-Systems Inc. 1054 Constant Temperature Anemometer, with which conical hot-film probes (1231W) were used.

Breaking waves represent a hostile environment for hot-film anemometry. The problem of air entrainment was however likely to be less severe if measurements were made only up to the location where the front face of the sc waves became vertical.

Regarding the air-water interface, there have been conflicting views. Baldy et al (1) felt that the exploration, by fixed probes, of the air and water flows near the interface was "not generally feasible" and went on to use a wave-follower mounting. Wills (29) used a fixed hot-wire probe at the interface, but he was interested in the air flow above the surface. His discussion of the problems facing the experimenter at the air/water interface is illuminating. Van Dorn and Pazan (27) recognised that the frequency response of the equipment was sufficiently high for an equilibrium value to be measured within a small distance of the probe traversing from air to water (in their case  $0.1\text{mm}$ ).

To measure velocity on the water-side of the interface is easier than on the air-side. The reason for this is that if measurements are made on the airside a high overheat may be necessary to rapidly evaporate the water film and this degree of overheat may increase the rate of accretion of any contamination from the water-surface onto the sensing element.

In the two-channel basin a water-surface suction and filtering system was used to reduce contamination, but it was still likely to be a major

problem. It was decided to use a low value of overheat to reduce accretion, and the lowest value which would give adequate sensitivity to flow was used. 4% overheat was chosen. The usual heat balance equation is:

$$\frac{e_b^2 R}{(R + R_3)^2} = \left[ A + B (\rho V)^{\frac{1}{n}} \right] (T_s - T_e) \dots\dots\dots (4.1)$$

where  $e_b$  is the bridge voltage, R the probe resistance,  $R_3$  the resistance in the other bridge arm,  $\rho$  density, V speed,  $T_s$  the sensor operating temperature,  $T_e$  the water temperature and A, B constants. For good sensitivity to flow variation, a high  $T_s$  is required, that is high overheat. The choice of a low overheat of 4% necessitated close control of  $T_e$  to be maintained.

A simple test of the probe traversing the interface was conducted (at an overheat of 4%) at a constant speed in a towing tank. By means of a suitable mounting and a string and pulley, the probe was caused to traverse a number of times the water surface which had previously been

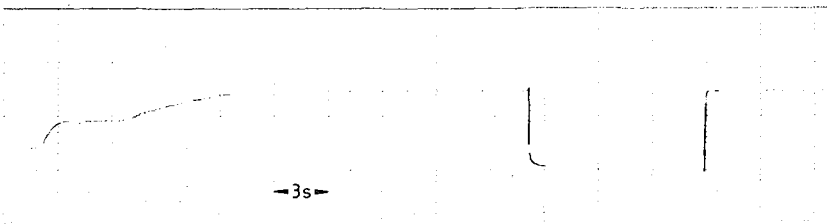


Fig. 4.1 Towing Tank Trial

swept clean, Figure 4.1 showing the bridge output voltage. The acceleration of the carriage to 1 m/s is clear, followed by traverses of the interface. The evaporation of the water film can just be seen. Upon successive immersion a consistent value of  $e_b$  was evident. The record was made on a heat recorder of bandwidth to about 50Hz which will therefore filter high frequency transients.

A calibration rig was constructed alongside the basin and water was drawn from the central area of the basin and discharged onto one of the absorbent beaches (Figure 4.2). The calibration rig had similarities to that used by Goodman and Sogin (9) who demonstrated that heat transfer was not affected by whether the flow was turbulent or laminar. In the calibration rig for the present work, Reynold's Numbers were in the range  $1.5 \times 10^4$  to  $4 \times 10^4$ . Temperature increase through the calibration rig was about  $0.05^\circ\text{C}$  which was equivalent to a change in speed of the order of 1%.

One would expect two principal reasons for changing calibration, dirt accumulation on the probe and temperature variation.

a) Dirt accumulation: Richardson and McQuivey (20) proposed that a dirty probe behaved as a clean probe at lower overheat, but Morrow and

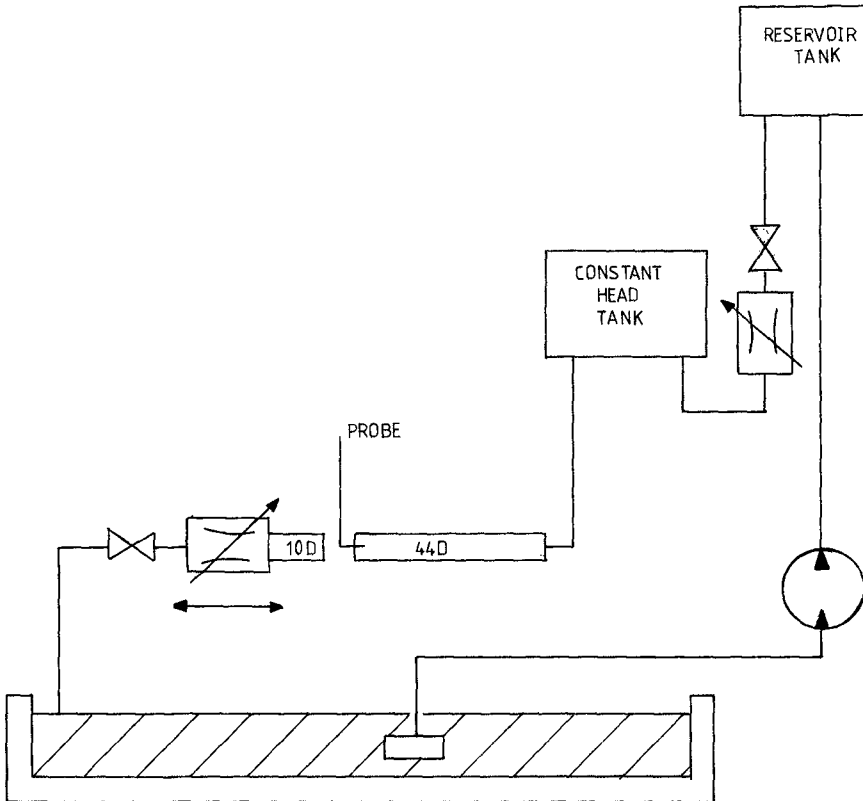


FIGURE 4-2 CALIBRATION RIG

Cline (18) concluded this was untrue. Because of the anticipated high drift from water surface contamination a second simple test was conducted with a highly contaminated water surface, at an overheat of 4%. The probe was mounted such that it was wetted by the crests of a series of waves. The output was monitored and it was noted that for the condition of the water at the time, rapid degradation occurred when the drying time between wave crests exceeded 0.7sec., but no degradation occurred for less than 0.6sec. This drift was probably due to the progressive accretion of water surface contamination onto the probe. Therefore for subsequent measurements small wave periods were chosen and the probe calibration was re-checked and the probe cleaned after every measurement.

b) Temperature variation: One standard method of allowing for a change of  $T_e$  by varying overheat slightly for the same  $e_{b0}$  was unsatisfactory in this case for the degree of control required. It can be easily shown from Equation (4.1) that for the same probe setting and the same flow one would



expect an approximately linear relationship between  $e_b^2$  and  $e_{bo}^2$ . Experimental confirmation is given in Figure 4.3 where the middle group of points relates to small changes in  $T_e$  and the low and high values are a result of dropping and raising overheat slightly, that is varying  $T_s$ . This linear relationship was used to correct measured values of  $e_b^2$  to a base

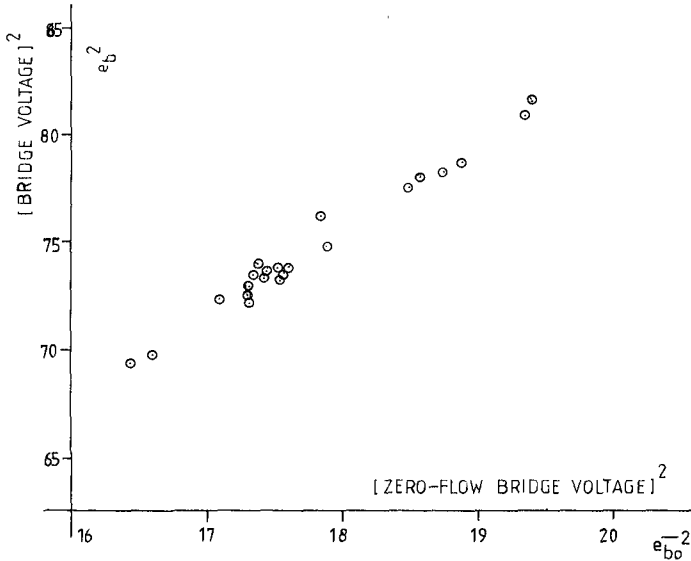


FIGURE 4-3 VARIATION OF  $e_b^2$  WITH  $e_{bo}^2$  FOR CONSTANT FLOW

value of  $e_{bo}^2$  the square mean zero-flow measurement before and after calibration. The procedure also corrected for variations in other resistances. In Table 4.1 Runs 1 and 2 were calibration runs for a cleaned probe at differing water temperatures with similar values of  $e_b^2$  after correction. For comparison Run 3 shows the calibration run for a lightly contaminated probe. The base value of  $e_{bo}^2$  was 17.56.

Calib- ration run	$T_e$	$e_{bo}$ BEFORE	CAL $e_b$	$e_{bo}$ AFTER	$e_{bo}^2$	Correct- ion Factor	Uncorr- ected $e_b^2$	Correc- ted $e_b^2$	Remarks
1	18.3	4.16	8.455	4.16	17.26	1.017	71.45	72.56	Uncontam.
2	17.45	4.24	8.64	4.25	18.02	0.974	74.65	72.71	Uncontam.
3	17.5	4.25	8.49	4.25	18.06	0.972	72.08	70.06	Light Con- tamination

TABLE 4.1: Effect of Temperature Variation and Contamination

#### 4.2 Results

Profiles of maximum total water particle speed  $U/C_1$  were measured along the basin centre-line (average of 5 consecutive waves), with the right-angled probe pointing towards the channel apex. Figures 4.4a and b show the development of the  $U/C_1$  profile (shown by the circled points) for  $d/L_1 = 0.34$  at four distances from the apex ( $X/L_1$ ). The corresponding sc  $L_1$  wave profiles are also shown. For comparison the horizontal speed profiles ( $u/C_1$ ) in a hypothetical long-crested wave of this height according to Van Dorn's hyperbolic equation is shown (27):

$$\frac{u}{C} = \frac{a}{b} \frac{z^1}{1-z^1} + \frac{u_0}{C}$$

Where  $z^1$  is the fractional ordinate from trough to crest at which  $u$  is given,  $a$  &  $b$  are arbitrary constants 0.10 and 1.125 respectively.  $u_0/C = 0.20$  and  $C$  is the wave celerity.

In Figures 4.5 to 4.7,  $U/C_1$  profiles are shown at breaking for  $d/L_1 = 0.29$ , 0.24 and 0.19. Differing values of  $d$  and  $W$  were used. It is seen that there is good consistency of the  $U/C_1$  profiles at breaking of the four values of  $d/L_1$ . Measurement accuracy is estimated as  $\pm 15\%$ .

Table 4.2 summarises the maximum values of  $U(U_{max})$  found for each  $d/L_1$ , and compares it with linear pattern speed ( $\sec\alpha$ ) and with a measured estimate of sc celerity  $C_s$ . It will be seen that maximum water particle speeds were less than pattern speeds except for  $d/L_1 = 0.24$  for which there was variation in the sc jet speed; at these values of  $d/L_1$  this is qualitatively not in disagreement with Figure 4 of (13). However higher speeds later in the breaking process cannot be ruled out.

Further work is desirable on the crest values of  $U$  as breaking develops: measurements are required at lower  $d/L_1$  values; and an increase of scale is desirable.

$d/L_1$	$\sec\alpha$	Measured $C_s/C_1$	Measured $U_{max}/C_1$
0.34	1.22	1.33	0.83
0.29	1.22	1.31	0.89
0.24	1.22	1.31	0.82-1.28
0.19	1.22	1.39	0.78

Table 4.2 Summary of  $U_{max}$

#### Acknowledgement

The work is funded by the UK Science and Engineering Research Council through its Marine Technology programme.

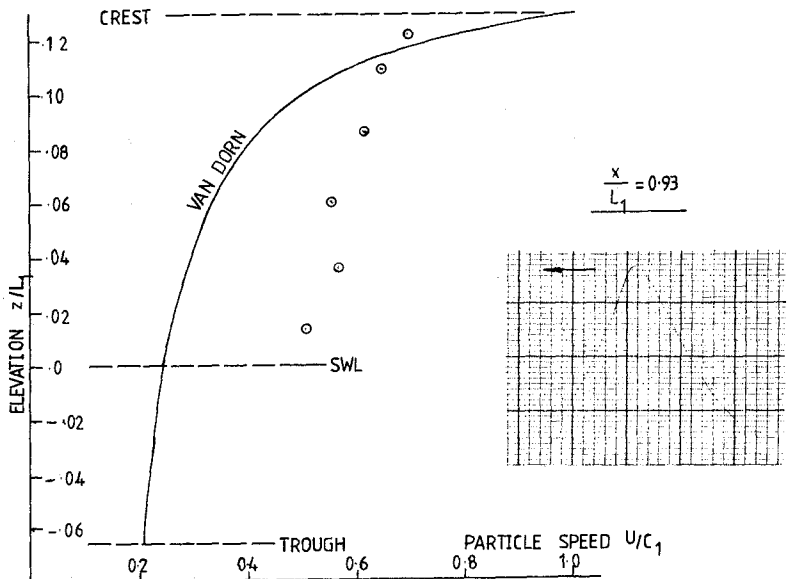
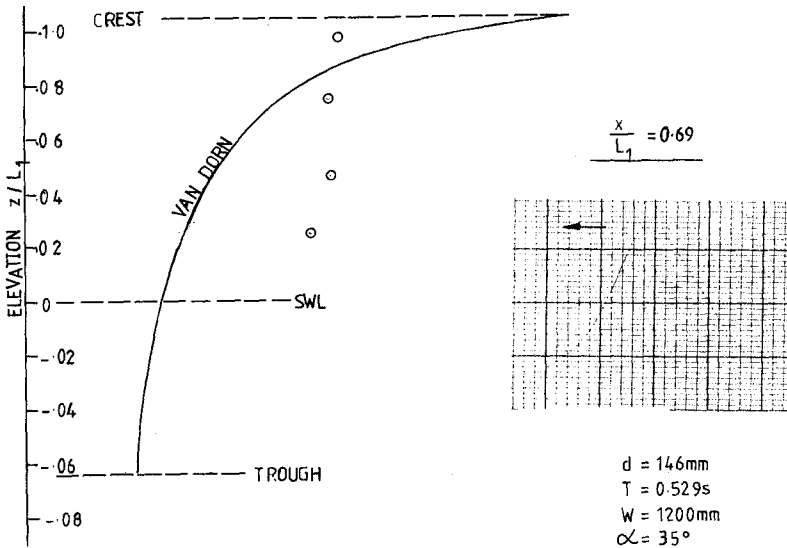


FIGURE 4-4a DEVELOPMENT OF SC WATER PARTICLE SPEED PROFILE ALONG CENTRE-LINE  $d/L_1 = 0.34$

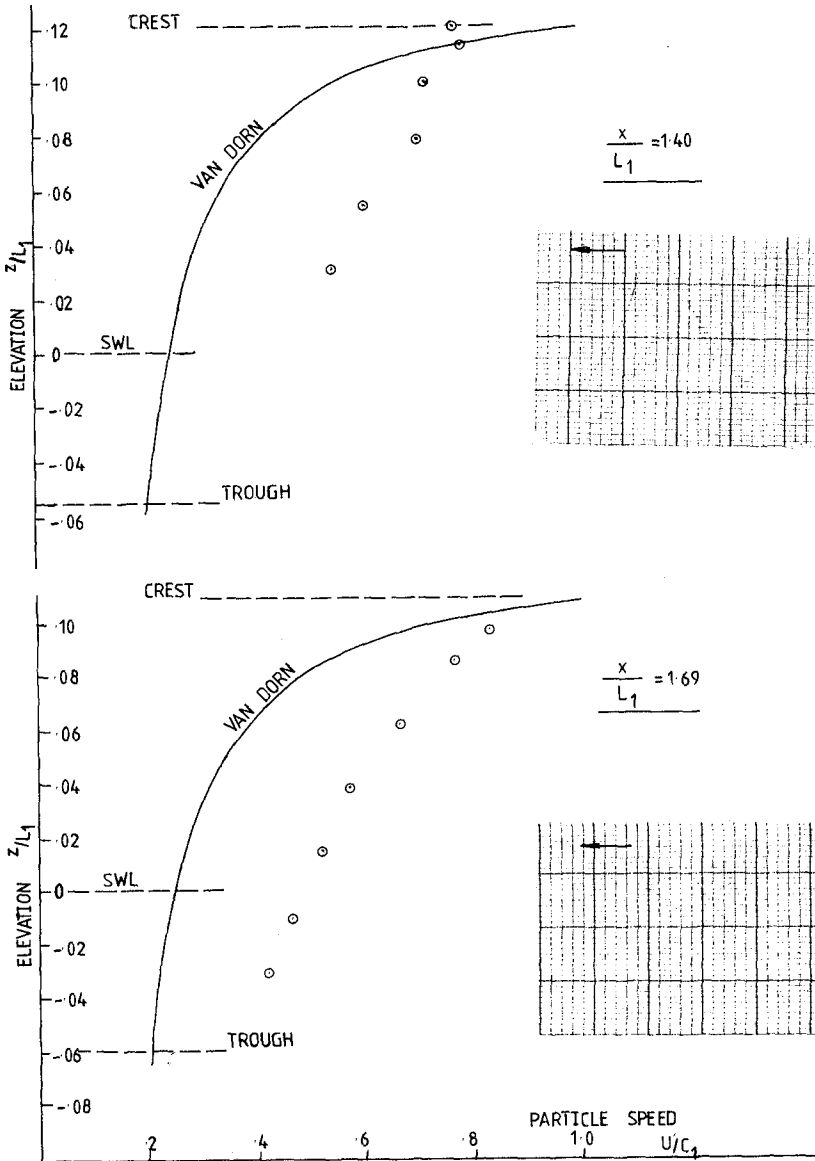


FIGURE 4.4b DEVELOPMENT OF SC WATER PARTICLE SPEED PROFILE ALONG CENTRE-LINE

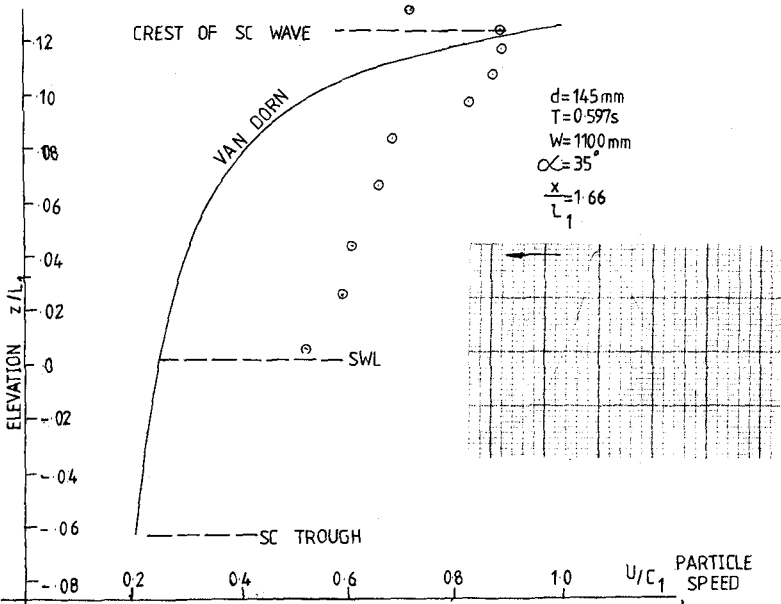


FIGURE 4.5 SC WATER PARTICLE SPEED PROFILE  $d/L_1=0.29$

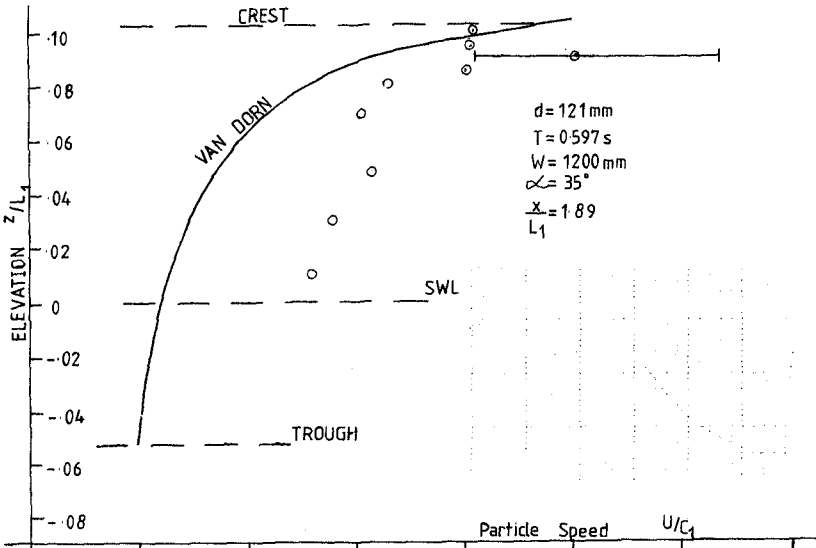
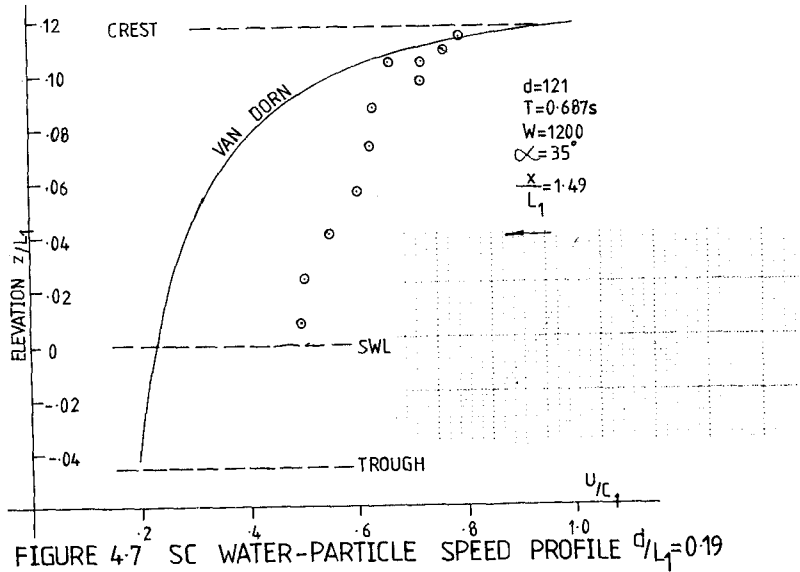


FIGURE 4.6 SC WATER PARTICLE SPEED PROFILE  $d/L_1=0.24$



## REFERENCES

1. BALOY, S. et al (1978). Description of characteristics of a wave follower system for energy exchange studies in the vicinity of an air water interface. *Rev. Sci Instrum.* 49(8).
2. BERGER, U & KOHLHASE, S (1976). Mach-reflection as a diffraction problem. *Proc. 15th Coast Eng. Conf.* 1, 796-814.
3. COKELET, E.D. (1977). Steep gravity waves in water of arbitrary uniform depth, *Phil Trans Roy Soc. Lond.* A.286, 183-230.
4. DAEMRICH, K-F. et al (1983). Investigation of Mach-reflection including breaking and irregular waves. *Conf. Coast and Port Eng. in Dev. Count.*
5. DEAN, R.G. (1968). Breaking wave criteria: a study employing a numerical wave theory. *Proc. 11th Coast. Eng. Conf.*, 108-123.
6. EARLE, M.D. (1975). Extreme wave conditions during Hurricane Camille. *JGR* 80.
7. FAULKNER, J.A. et al (1984). The loss of HMS COBRA - a reassessment. *RINA Spring Meeting 1984*.
8. GERRITSMAN, J. & BEUKELMAN, W. (1980). Seakeeping trials with HNLMS TYDEMAN. Report 494 Delft Univ. of Tech.
9. GOODMAN, C.H. & SOGIN, H.H. (1974). Calibration of a hot-film anemometer in water over veloc. range 0.5 to 200 cm/s. In *Flow - its Measure & Control in Sci and Ind.*, 1 Pt.2.
10. HALLIWELL, A.R. & MACHEN, P.C. (1981). Short-crested breaking waves in water of limited depth. *Proc. Instn. Civ. Engr. Part 2.*, 71, 663-674.

11. HSU, J. (1979). 3rd order approximation to short-crested waves, *JFM* 90, 179-196.
12. HSU, J & SILVESTER, R. (1982). Discussion on Halliwell and Machen (1981). *Proc. Instn. Civ. Engrs. Part 2*, 73, 489-491.
13. HSU, J. (1983) On the limiting conditions for short-crested waves. *Conf. Coastal and Ocean Eng., Gold Coast*, 13-15 Jul.
14. KJELOSEN, S.P. & MYRHAUG, D. (1979). Breaking waves in deep water and resulting wave forces, *Proc. OTC*, Paper OTC 3646.
15. KJELSDEN, S.P. (1982). 2- & 3- dimensional deterministic freak waves, *Proc. 18th Coast. Eng. Conf*, 1, 677-694.
16. LONGUET-HIGGINS, M.S. (1974). Breaking waves - in deep or shallow water. *Proc. 10th Symp. Nav. Hydrodyn. Office Nav.Res*, 24-28 Jun 74.
17. MALLORY, J.K. (1975). Abnormal waves off the S. African coast - a danger to shipping. *The Nav. Arch.* 5, 82-84.
18. MORROW, T.B. & KLINE, S.J. (1974). The performance of hot-wire and hot film anemometers used in water, In *Flow - its Measurement and Control in Sci & Ind.* 1, 555-562.
19. PIERSON, W.J. (1972). The loss of two British trawlers, a study in wave refraction, *J. Nav.*, 25, 291-304.
20. RICHARDSON, E.V. & McQUIVEY, R.S. (1968). Measurement of turbulence in water. *Proc. ASCE*, HY94, 411-430.
21. ROBERTS, A.J. (1983), Highly nonlinear short-crested water waves. *J. Fluid Mech*, 135, 301-321.
22. SAETRE, H.J. (1975) On high wave conditions in the northern North Sea. *Proc. Oceanology International*, 280-289.
23. SALTER, S.H. (1978). The development of the duck concept. *Proc. Wave Energy Conf. London*, 22 Nov. 78.
24. SILVESTER, R. (1974). *Coastal Engineering*, 1, Elsevier.
25. SILVESTER, R. (1977). The role of wave reflection in coastal processes. *Proc. Coastal Sediments 77*, 639-654.
26. SMITH, R. (1976) Giant waves, *J. Fluid Mech.*, 77, 417-431.
27. VAN DORN, W.G., PAZAN, S. (1975): Laboratory investigation of wave breaking Part 2, deep water waves. *Scripps*, SIO 75-21.
28. VERMA, G.R. & KELLER, J.B. (1962). 3-dimensional standing surface waves of finite amplitude. *Phys. Fluids* 5, 52-56.
29. WILLS, J.A.B. (1976). A submerging hot wire for flow measurements over waves. *OISA Info* 20, 31-34.

## CHAPTER SIXTY THREE

### WAVE-INDUCED OSCILLATIONS IN HARBORS WITH WAVE-ABSORBING QUAY

by

Akinori Yoshida, Takeshi Ijima  
and Hideaki Okuzono

Dept. of Civil Engineering Hydraulics  
Kyushu University, Higashi-ku, Fukuoka,  
812 Japan

#### 1. Introduction

An artificial wave-absorber (wave-absorbing quay) has come to be widely used to counteract excessive wave action on ships and structures in harbors. Its two-dimensional characteristics on wave absorption have been investigated with several types of the wave-absorbing quay theoretically as well as experimentally, e.g., Jarlan (5), Terret, Osorio and Lean (9), Ijima, Tanaka and Okuzono (3), and Ijima and Okuzono (4), but the effects on the wave reduction in harbors seem to be not fully clear. This may be due to the lack of analytical methods for solving wave-induced oscillations in harbors with the wave-absorbing quay.

When the side wall in the harbor basin is assumed to be perfectly reflective, many theoretical methods for solving wave-induced oscillations in harbors have been presented: Ippen and Goda (2) solved the problem of a rectangular harbor by using the Fourier Transform technique. Hwang and Tuck (1) presented powerful method, which is applicable to arbitrary shaped harbors, by using integral equation (source distribution along the boundary) for the expression of the velocity potential. A similar method to that of Hwang and Tuck, but more suitable one for numerical computation, was presented by Lee (6), who used integral equation separately in the harbor basin and in the open sea. Raichlen and Naheer (8), Mattioli (7), and Yoshida and Ijima (10) presented the methods being applicable to the harbors of arbitrary shape and variable depth by further extending Lee's method.

On the other hand, when the side wall in the harbor basin is partly or wholly composed of the wave-absorbing quay, a new boundary condition, replacing the usual solid boundary



condition  $\partial\phi/\partial\nu=0$  ( $\phi$  is the velocity potential and  $\nu$ , the normal to the boundary), is needed, and it can be expressed as  $\partial\phi/\partial\nu=\Omega\phi$ . The characteristics of the coefficient  $\Omega$  depend on the nature of the wave-absorbing quay, and  $\Omega$  generally takes complex values, in which  $\Omega=0$  gives perfect reflection and  $\Omega=ik$  ( $k$  is the wave number) gives perfect absorption. It is obvious that  $\Omega$  can not be determined either by theoretical approach or by experimental approach only, and both the approaches are required. And, If the boundary condition on the wave-absorbing quay is obtained, the methods presented so far for solving wave-induced oscillations can be directly extended to the harbors with the wave-absorbing quay.

The aim of this investigation is to derive the boundary condition on the wave-absorbing quay, and to check that the methods for perfectly reflective harbors are applicable to the harbors with the wave-absorbing quay by using the obtained boundary condition.

2. Theoretical Formulation

Figure 1 shows schematic drawing of the harbor with the wave-absorbing quay: an arbitrary shaped harbor of a flat bottom is directly connected to the open sea. The boundary line on the harbor basin as well as the straight coastline are assumed to be perfectly reflective except that on the wave-absorbing quay. If there is no wave-absorbing quay in the harbor, the problem is reduced to a usual harbor resonance problem, which has been already solved by, e.g., Hwang and Tuck (1), Lee (6), etc. The following theoretical formulation is devoted to derive the boundary condition on the wave absorbing quay.

The type of the wave-absorbing quay considered in this investigation is illustrated in figure 2. This type of the wave-absorbing quay is now widely used in practice. It comprises a uniformly perforated vertical wall and a water chamber behind the wall.  $b$  and  $d$  indicate the thickness of the wall and the length of the water chamber, respectively. The water chamber is further divided into small chambers along the perforated wall with partition walls.

The fluid region in front of the perforated wall is indicated as region (0), and the fluid region in the water chamber, as region (1). In each region, physical quantities such as the wave amplitude, the fluid velocity, etc., will be expressed with either subscript 0 or subscript 1 from now on.

The fluid is assumed to be inviscid and incompressible and the fluid motion to be irrotational; then, the velocity potential of the fluid motion can be expressed as

$$\Phi=(ga/\sigma)\phi \exp(i\sigma t) \dots\dots\dots(1)$$

where  $g$  is the gravitational acceleration,  $a$  and  $\sigma$  are the amplitude and the angular frequency, respectively, of the incident wave, and  $\phi$  is a non-dimensional function which satisfies the Laplace equation,

$$\nabla^2 \phi = 0 \quad \dots\dots\dots(2)$$

Assuming that the waves are shallow water waves, and that the distance between the adjacent partition walls is much smaller than the incident wave length so that the fluid motion in the  $y$ -direction can be negligibly small in each water chamber, we can express the distribution of the wave amplitude  $\zeta_1$ , and the horizontal fluid velocity  $u_1$ , as follows:

$$\zeta_1(x) = \eta \cos \{k(x+b+d)\} \quad \dots\dots\dots(3)$$

$$u_1(x) = -i(\eta g k / \sigma) \sin \{k(x+b+d)\} \quad \dots\dots\dots(4)$$

where  $\eta$  is the unknown amplitude of the standing wave in each water chamber. In the region (0), the distribution of the wave amplitude  $\zeta_0$  and the horizontal (in the  $x$ -direction) fluid velocity  $u_0$  can be expressed with the potential function  $\phi$  as follows:

$$\zeta_0 = -ia\phi \quad \dots\dots\dots(5)$$

$$u_0 = (ga/\sigma) \cdot \partial\phi/\partial x \quad \dots\dots\dots(6)$$

We assume that the energy dissipation caused by the wave-absorbing quay is represented by linearized fluid resistances proportional to the fluid velocity and to the fluid acceleration in the holes. Then, the equation of the fluid motion in the holes can be expressed as

$$\frac{dU}{dt} = -\frac{1}{\rho} \frac{\partial p}{\partial x} - \mu_1 U - \mu_2 \frac{dU}{dt} \quad \dots\dots\dots(7)$$

in which  $\rho$  is the fluid density,  $U$  is the fluid velocity in the holes,  $\mu_1$  and  $\mu_2$  are the coefficients of the fluid resistances proportional to the fluid velocity and to the fluid acceleration, respectively, and  $\partial p / \partial x$  is the pressure gradient in the holes, which is assumed to be given by the water level difference across the perforated wall as

$$\frac{\partial p}{\partial x} = \rho g \exp(i\sigma t) [\zeta_0(0, y) - \zeta_1(-b)] / b \quad \dots\dots\dots(8)$$

Then substituting equation (8) into equation (7), and writing the fluid velocity  $U = U_0 \exp(i\sigma t)$ , we have

$$U_0 = \frac{ig[\zeta_0(0, y) - \zeta_1(-b)]}{\sigma b[(1 + \mu_2) - i(\mu_1/\sigma)]} \dots\dots\dots(9)$$

The mass continuity must be satisfied both at the front (x=0) and at the rear (x=-b) of the perforated wall, and because the width of each water chamber is assumed to be much smaller than the incident wave length, the mass continuity equation can be expressed on each water chamber as follows:

$$U_0 V = u_0 \quad (x=0) \quad \dots\dots\dots(10)$$

$$U_0 V = u_1 \quad (x=-b) \quad \dots\dots\dots(11)$$

where V is the porosity ratio (the ratio of the hole area to the whole area of the perforated wall). In equation (10), the midpoint of the chamber width may be used as the value of y-coordinate in  $u_0$ .

From these mass continuity conditions and equations (4) and (6), the unknown quantities  $U_0$  and  $\eta$  can be expressed by  $\partial\phi/\partial x$  as follows:

$$U_0 = (ga/\sigma V) \cdot \partial\phi/\partial x \quad \dots\dots\dots(12)$$

$$\eta = i\{khV/\sigma \sin(kd)\} \cdot (ga/\sigma V) \cdot \partial\phi/\partial x \quad \dots\dots\dots(13)$$

Thus, substituting equations (3) and (5) into equation (9), and eliminating the unknown quantities  $U_0$  and  $\eta$  by using equations (12) and (13), we obtain the equation,

$$\frac{\partial\phi}{\partial x} = \left[ \frac{\cot(kd)}{k} - \frac{b}{V} \{(1 + \mu_2) - i(\mu_1/\sigma)\} \right]^{-1} \cdot \phi \quad \dots\dots\dots(14)$$

This gives a relation between the potential function  $\phi$  and its normal derivative  $\partial\phi/\partial x$ , and therefore can be used as the boundary condition on the wave-absorbing quay. However, this equation contains two coefficients of the fluid resistances,  $\mu_1$  and  $\mu_2$ , which have to be rationally determined before we use equation (14) for numerical calculations. They can be determined by sub-empirical way from theoretical and experimental approaches.

In order to estimate the values of the coefficients, we consider the case that a plane monocromatic wave is incident on the wave-absorbing quay, which is now assumed to be infinitely long, at an angle  $\theta$  with x-axis as shown in figure 2. The distribution of the wave amplitude  $\zeta_0$  and the horizontal fluid velocity  $u_0$  can be expressed in this case as follows:

$$\zeta_0(x, y) = a \exp(iky \sin \theta) \times [\exp(ikx \cos \theta) + K \exp(-ikx \cos \theta)] \dots (15)$$

$$u_0(x, y) = -\frac{agk \cos \theta}{\sigma} \exp(iky \sin \theta) \times [\exp(ikx \cos \theta) - K \exp(-ikx \cos \theta)] \dots (16)$$

in which K is the complex reflection coefficient of the wave absorbing quay: the absolute value |K| means the reflection coefficient and its argument means the phase angle of the reflected wave. The rest of equations, that is, the equation of motion in the holes, the mass continuity equation at the perforated wall, and the equation of  $\zeta_1$  and  $u_1$  remain valid.

Therefore, using equations (15) and (16) for equations (5) and (6), respectively, and following the same procedure just used to derive the equation (14), we can obtain the following equation,

$$|K| \exp(i\epsilon) = \frac{\cos \theta (\cot(kd) - kb\alpha) - i(1 - kb\beta \cos \theta)}{\cos \theta (\cot(kd) - kb\alpha) + i(1 + kb\beta \cos \theta)} \dots (17)$$

in which  $\alpha = (1 + \mu_2)/V$ ,  $\beta = (\mu_1/\sigma)/V$ , and  $\epsilon$  is the phase angle of the reflected wave.

Equation (17) gives a relation between the coefficients of the fluid resistances, the reflection coefficient and the phase angle. Since it is a complex equation, the coefficients of the fluid resistances can be determined provided that the reflection coefficient and the phase angle are known. In order to simplify the equation, we introduce the following variables,  $x = kb\alpha (= kb(1 + \mu_2)/V)$ ,  $y = kb\beta (= kb(\mu_1/\sigma)/V)$  and  $m = \cot(kd)$ . Furthermore, we assume that the coefficients  $\mu_1$  and  $\mu_2$  are independent of the incident wave angle. Then, equation (17) can be written as

$$|K| \exp(i\epsilon) = \frac{(m-x) - i(1-y)}{(m-x) + i(1+y)} \dots (18)$$

Separating this into the real part and the imaginary part, we have two equations for x and y,

$$x^2 + y^2 - 2mx - 2\{ (1+\gamma)/(1-\gamma) \} \cdot y + (1+m^2) = 0 \dots (19)$$

$$\delta(x^2 + y^2) - 2(m\delta + 1)x + (\delta m^2 + 2m - \delta) = 0 \dots (20)$$

in which  $\gamma = |K|^2$  and  $\delta = \tan \epsilon$ .

Consequently, solving equations (19) and (20) simultaneously, we have

$$\left. \begin{aligned}
 & \left\{ \begin{aligned}
 y &= \frac{A(\delta^2+1) \pm \sqrt{(\delta^2+1)(A^2-1)}}{(\delta^2 A^2+1)} \\
 x &= \delta A y + (m-\delta)
 \end{aligned} \right. & (\delta \neq 0, \pm\infty) \\
 \\
 & \left\{ \begin{aligned}
 y &= 1/A \\
 x &= m \pm \sqrt{1-y^2}
 \end{aligned} \right. & (\delta = \pm\infty) \\
 \\
 & \left\{ \begin{aligned}
 y &= A \pm \sqrt{A^2-1} \\
 x &= m
 \end{aligned} \right. & (\delta = 0)
 \end{aligned} \right\} \dots\dots\dots (21)$$

in which  $A=(1+\gamma)/(1-\gamma)$ . The radical sign which gives  $|K| \cdot \exp(i\epsilon)$  when  $x$  and  $y$  are substituted into equation (18) should be chosen: the other set of  $x$  and  $y$  gives  $|K| \cdot \exp(i\epsilon+\pi)$ .

3. Theoretical and Experimental results

Before conducting the theoretical calculations and the wave basin experiments, we first made two-dimensional wave tank experiments on wave reflection for a specific wave-absorbing quay to determine the resistance coefficients.

The properties of the model wave-absorbing quay were as follows: The thickness of the perforated wall was 6cm; the length and the width of each water chamber were 10cm and 6cm, respectively; the perforated wall had circular holes (14mm diameter) distributed uniformly and its porosity ratio  $V$  was 0.19.

The model was set at one end of the wave tank (water depth  $h=0.35m$ ) which is 18m long, 0.3m wide and 0.6m deep, with a flap type wave generator at the other end, and the reflection coefficient  $|K|$  and the distance  $x^*$  between the wall and the node were measured. The phase angle can be obtained from  $x^*$  by the relation  $\epsilon=4\pi(x^*/L)-(2n+1)\pi$  ( $n=0, \pm 1, \pm 2, \dots$ ;  $L$  is the wave length). The measured values are shown in figure 3, in which the white circle and the black circle indicate  $|K|$  and  $x^*/L$ , respectively.

Using the measured reflection coefficients and phase angles, we calculated the coefficients  $\mu_1/\sigma$  and  $\mu_2$  through equation (21), and the results are shown in figure 4. Figure 3 shows that the wave absorption characteristic of this model wave-absorbing quay is good for  $kh$  near 1.8, but relatively bad for  $kh$  less than 1.4. This corresponds to the results in figure 4 that both  $\mu_1/\sigma$  and  $\mu_2$  increase rapidly as  $kh$  decreases, and thus the boundary condition (equation (14)) approaches to the solid boundary condition  $\partial\phi/\partial x=0$

which means no wave absorption.

Of course the wave absorption characteristics differ greatly depending on the combination of the values of  $b$ ,  $d$  and  $V$ , but the scope of this investigation is to derive and to verify the boundary condition, and not to investigate the effective wave-absorbing quays, only single model of the wave-absorbing quay was used.

In succession from the two-dimensional wave tank experiments, we conducted theoretical calculations and wave basin experiments for two model harbors with the wave-absorbing quay. The shapes of the model harbors and the locations of the wave-absorbing quay are illustrated in figure 5 (model-1) and in figure 7 (model-2). The wave-basin (20m long 9m wide 0.6m deep) in the laboratory of Civil Engineering Hydraulics, Kyushu University, was used. The water depth was kept 0.35m throughout the experiments. The incident wave height and the wave heights at several points in the model harbors were measured, and Amplification Factor (indicated by  $A$ ), defined as the ratio of the wave amplitude in the harbor basin to the incident wave height, was calculated.

As for the method for solving wave-induced oscillation in harbors, we used the method presented by Yoshida and Ijima (10) only because the computer program was available. The method is based on the direct use of Green's Identity Formula in three-dimension for the expression of the velocity potential of the wave motion in the harbor basin, thus the method itself is applicable to the harbors of arbitrary shape and variable depth.

The comparisons between the theoretical and experimental results on the Amplification Factor are shown in figures 5 and 6 for model 1, and in figures 7 and 8 for model 2. The broken lines and the black circles indicate the theoretical and the experimental values, respectively. In addition, theoretical results in the case of no wave-absorbing quay were also shown for model-1 with solid line. comparison.

Figures 5 and 6 and figures 7 and 8 show very good agreements between the theory and the experiment. This confirms that the boundary condition (equation (14)) and the values of the coefficients  $\mu_1/\sigma$  and  $\mu_2$ , determined through equation (18) and two-dimensional experiments, properly represent the wave absorption effects of the wave-absorbing quay in harbors. The results also show that the boundary condition is practically applicable up to "Intermediate depth waves" inspite of shallow water wave approximation used for the derivation of it.

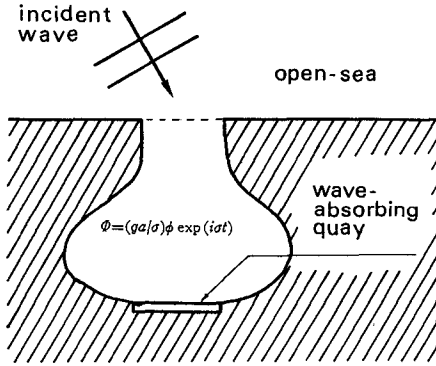


Figure 1. Schematic drawing of the harbor with wave-absorbing quay.

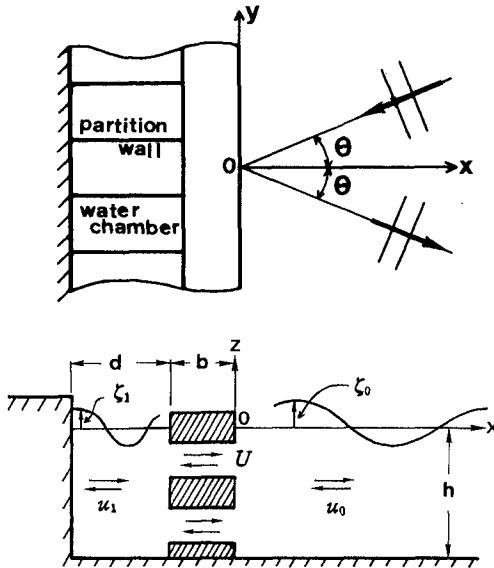


Figure 2. Wave-absorbing quay.

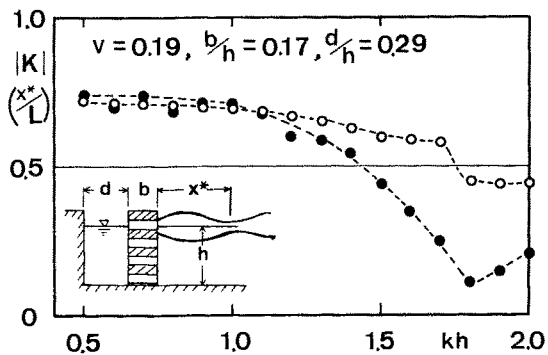


Figure 3. Reflection coefficient and distance between wall and node measured in two-dimensional experiment.

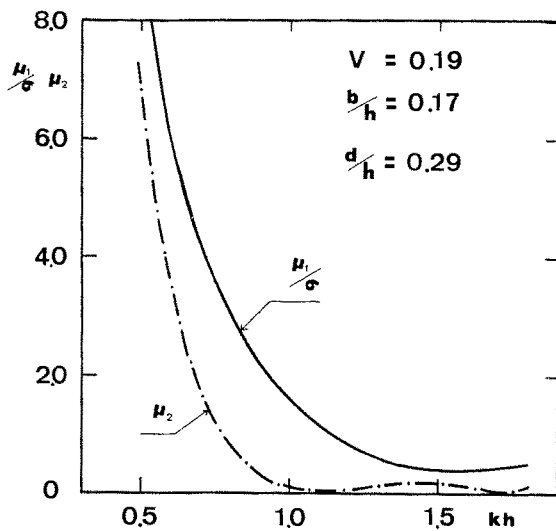


Figure 4. Coefficients of fluid resistances.



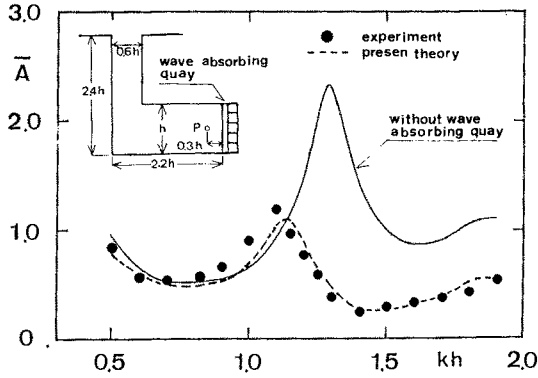


Figure 5. Comparison between theoretical and experimental results for Amplification Factor at point P.

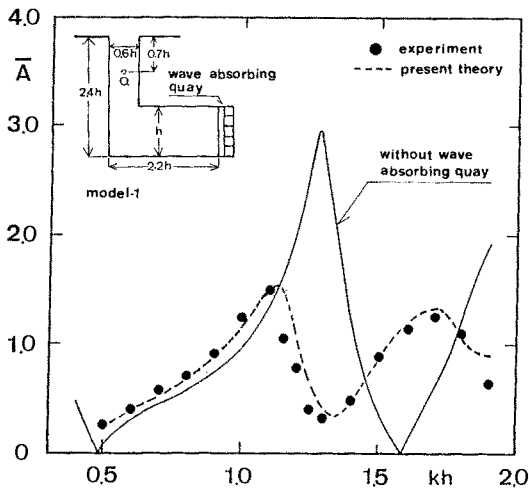


Figure 6. Comparison between theoretical and experimental results for Amplification Factor at point Q.

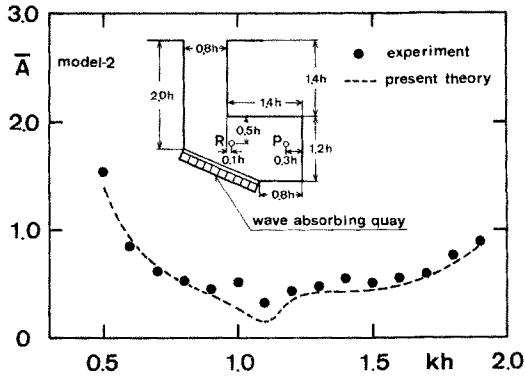


Figure 7. Comparison between theoretical and experimental results for Amplification Factor at point R.

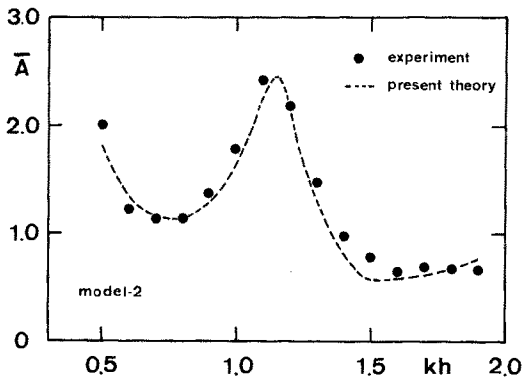


Figure 8. Comparison between theoretical and experimental results for Amplification Factor at point P.

#### 4. Conclusions

To solve wave-induced oscillations in harbors with wave absorbing quays, we have derived a boundary condition on the wave-absorbing quay in the form as  $\partial\phi/\partial x = \Omega\phi$ . The coefficient  $\Omega$  contains two unknown coefficients of the fluid resistances,  $\mu_1$  and  $\mu_2$ . We have further derived a relation between the two coefficients and the complex reflection coefficient of the wave-absorbing quay, and have shown that  $\mu_1$  and  $\mu_2$  can be determined sub-empirically from the relation and the experimental data on wave reflection of the wave-absorbing quay.

The validity of the boundary condition was confirmed by comparing analytical results with the data obtained by wave basin experiments. Scale effects on  $\mu_1$  and  $\mu_2$ , however, have not been considered, thus further investigations on them may be needed to use the boundary condition on actual harbors.

#### REFERENCES

- (1) Hwang, L. S. and Tuck, E. O., "On the Oscillation of Harbors of Arbitrary Shape," J. Fluid Mech. vol.42 part 3, 1970.
- (2) Ippen, A. T. and Goda, Y., "Wave Induced Oscillations in Harbors: The Solution for a Rectangular Harbor connected to the Open-Sea," MIT Hydrodynamics Laboratory Report No. 59, 1963.
- (3) Ijima, T., Tanaka, E. and Okuzono, H., "Permeable Seawall with Reservoir and the Use of 'WAROCK'," Proceedings of the 15th Coastal Engineering Conference, 1976.
- (4) Ijima, T. and Okuzono, H., "Reflection of Normal Incident Waves at Porous or Perforated Quaywall," Memoirs of the Faculty Engineering, Kyushu University, vol.42 No.4, 1982.
- (5) Jarlan, G. E., "A Perforated Vertical Wall Breakwater, -An Examination of Mass-Transport Effects in Gravitational Waves-," The Dock & Harbor Authority, 1961.
- (6) Lee, J. J., "Wave-Induced Oscillation in Harbors of Arbitrary Geometry," J. Fluid Mech., vol.45, part2, 1971.
- (7) Mattioli, F., "Wave-Induced Oscillations in Harbors of variable depth," Computer and Fluids, vol.6, 1978.
- (8) Raichlen, F. and Naheer, E., "Wave Induced Oscillations of Harbors with variable depth," Proceedings of the 15th Coastal Engineering Conference, 1976.
- (9) Terret, F. L., Osorio, J. D. C. and Lean, G. H., "Model Studies of A Perforated Breakwater," Proceedings of the 11th Coastal Engineering Conference, 1968.
- (10) Yoshida, A. and Ijima, T., "Resonance in Harbors of Arbitrary Topography," Proceedings of the 5th International Conference on Boundary Elements, Springer-Verlag, 1983.

## CHAPTER SIXTY FOUR

### The Physical Basis of The Mild-Slope Wave Equation

Lars Behrendt\*

Ivar G. Jonsson\*\*

#### Abstract.

The mild-slope wave equation is derived by demanding minimum in total wave energy.

By demanding conservation of wave energy, two different functionals for the finite element solution of the mild-slope wave equation are constructed. The first functional is based on a finite/infinite element formulation, and the second one is based on a hybrid finite element formulation. Both functionals are constructed in a straight-forward way that leads to a better physical understanding of the functionals and a full understanding of each separate part of them.

#### 1. Introduction.

Waves of arbitrary length propagating in an area of varying depth may be described by the mild-slope wave equation. This equation was first derived by Berkhoff (1972). Later an alternative derivation was given by Smith and Sprinks (1975). A detailed discussion can be found in Jonsson and Brink-Kjær (1973).

Berkhoff (1972) solved the mild-slope wave equation by using the finite element method. Chen and Mei (1974) formulated a hybrid finite element method that, contrary to Berkhoff's formulation, leads to a symmetric stiffness matrix, which is almost a necessity when dealing with larger element grids. Their formulation has later been used in a generalized version by Houston (1981) and Tsay and Liu (1983).

Bettes and Zienkiewicz (1977) solved the mild-slope wave equation by using a simple finite/infinite element method based on a variational formulation different from the one used by Chen and Mei (1974).

In this paper is given a derivation of the mild-slope wave equation based on energy considerations. Then it is demonstrated how — by generalizing the approach used to derive the wave equation — one can construct the functionals used in both the hybrid element and in the finite/infinite element methods when solving the wave equation. General intermediate depth theory will be used, and energy dissipation along an absorbing boundary is included.

\*M.Sc., Postgraduate Student, \*\*Ph.D., Associate Professor, Institute of Hydrodynamics and Hydraulic Engineering (ISVA), Technical University of Denmark, Bldg. 115, DK-2800 Lyngby, Denmark.

## 2. Basic Theory.

When the fluid is assumed to be ideal, it is possible to describe the motion of small amplitude surface gravity waves by the complex velocity potential  $\phi$  :

$$\Phi(x,y,z,t) = \phi e^{-i\omega t} \frac{\cosh k(z+h)}{\cosh kh} \quad (1)$$

where  $x$  and  $y$  are horizontal co-ordinates,  $z$  is the vertical co-ordinate,  $t$  is the time,  $h$  is the local water depth,  $\omega$  is the angular frequency and  $k$  is the wave number. Quantity  $\phi = \phi(x,y)$  is a two-dimensional complex potential function.

The complex wave amplitude  $\eta$  is :

$$\eta = \frac{i\omega}{g} \phi \quad (2)$$

and the instantaneous complex surface elevation  $\xi$  is :

$$\xi = \eta e^{-i\omega t} \quad (3)$$

When one deals with a complex potential, a complex wave amplitude and a complex surface elevation, it is only natural also to introduce complex energies.

The complex potential energy of the wave motion per horizontal unit area is defined by :

$$E_p \equiv \int_0^{\xi} \rho g z \, dz \quad (4)$$

and after some calculations one finds :

$$E_p = -\frac{\rho}{g} e^{-2i\omega t} \frac{1}{2} \omega^2 \phi^2 \quad (5)$$

The complex kinetic energy per horizontal unit area is defined by :

$$E_k \equiv \int_{-h}^0 \frac{1}{2} \rho (\nabla_3 \phi)^2 \, dz \quad (6)$$

$\nabla_3$  being the three-dimensional gradient operator. After some calculations this can be written as :

$$E_k = \frac{\rho}{g} e^{-2i\omega t} \frac{1}{2} [c c_g (\nabla\phi)^2 + \frac{1}{2}(1-G)\omega^2 \phi^2] \quad (7)$$

$c$  being the phase velocity,  $c_g$  the group velocity and  $\nabla$  the horizontal gradient operator.

The total complex wave energy of the wave motion per unit area is the sum of the potential energy (5) and the kinetic energy (7) :

$$E = \frac{\rho}{g} e^{-2i\omega t} \frac{1}{2} [c c_g (\nabla\phi)^2 - \frac{c_g \omega^2}{c} \phi^2] \quad (8)$$

The complex energy flux through a section characterized by normal  $n$  is per unit length :

$$E_f = \int_{-h}^0 p^+ u \, dz \quad (9)$$

where  $p^+$  is the excess pressure :

$$p^+ = -\rho \frac{\partial\phi}{\partial t} \quad (10)$$

and  $u$  is the horizontal particle velocity in the  $n$ -direction :

$$u = \frac{\partial\phi}{\partial n} \quad (11)$$

Inserting (10) and (11) in (9) and integrating one finds :

$$E_f = \frac{\rho}{g} e^{-2i\omega t} i\omega c c_g \phi \frac{\partial\phi}{\partial n} \quad (12)$$

It is noted that the energies (5), (7) and (8) and the energy flux (12) are all functions of time  $t$ . When dealing with the corresponding quantities in ordinary, real-value wave theory one uses the mean value over one wave period. When one deals with a complex energy and energy flux this has no meaning, since these mean values will all be zero. However, after some simple calculations one easily realizes that the absolute values of the complex energies are equal to twice the value of the corresponding real quantities. The same result is found for the energy flux.

### 3. The Wave Equation.

An area of calculation, A, is shown in Fig. 1.

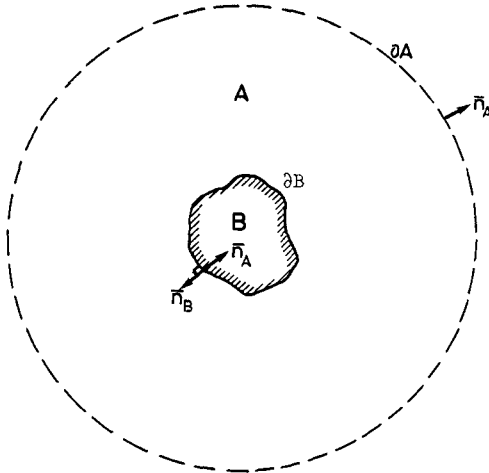


Fig. 1. Area of calculation A in the horizontal plane.

Inside area A some wave scattering structure, area B, is located. The water depth in area A may vary. For simplicity it is assumed in this chapter that the boundary of area B,  $\partial B$ , is fully reflecting leading to the boundary condition :

$$\frac{\partial \phi}{\partial n_B} = 0 \quad \text{along } \partial B \quad (13)$$

It is also assumed that the outer boundary of area A,  $\partial A$ , is lying at infinity. Far away from the central part of area A, the Sommerfeld radiation condition must be fulfilled :

$$\lim_{r \rightarrow +\infty} \sqrt{r} \left( \frac{\partial \phi}{\partial r} - ik \right) \phi^S = 0 \quad (14)$$

where  $\phi^S$  is the velocity potential of the scattered wave field.  $\phi^S$  may be found from the total potential  $\phi$  by the expression :

$$\phi = \phi^i + \phi^S \quad (15)$$

where  $\phi^i$  is the known velocity potential of the incident wave motion. What (14) says is in fact that the scattered wave system should be outgoing at some distance from the central part of area A.

The total complex wave energy in area A,  $E_A$ , can be found from (8):

$$E_A = \frac{\rho}{g} e^{-2i\omega t} \iint_A \left[ cc_g (\nabla\phi)^2 - \frac{c}{g} \frac{\omega^2}{c} \phi^2 \right] dx dy \quad (16)$$

Since the wave motion by definition is stationary  $E_A$  must also be stationary. This means that the first variation of  $E_A$  must vanish, i.e.

$$\delta E_A = 0 \quad (17)$$

Using Green's theorem one finds from (16) :

$$\delta E_A = \frac{\rho}{g} e^{-2i\omega t} \left\{ - \iint_A \delta\phi \left[ \nabla \cdot (cc_g \nabla\phi) + \frac{c}{g} \frac{\omega^2}{c} \phi \right] dx dy + \int_{\partial A + \partial B} cc_g \delta\phi \frac{\partial\phi}{\partial n_A} ds \right\} \quad (18)$$

The line-integral in (18) along  $\partial B$  vanishes by introducing (13). It can be argued that also the integral along  $\partial A$  can be ignored. Hereafter by combining (17) and (18) one gets :

$$\iint_A \delta\phi \left[ \nabla \cdot (cc_g \nabla\phi) + \frac{c}{g} \frac{\omega^2}{c} \phi \right] dx dy = 0 \quad (19)$$

This must hold for any  $\delta\phi$ . Therefore the term in the square brackets must be zero everywhere in area A :

$$\nabla \cdot (cc_g \nabla\phi) + \frac{c}{g} \frac{\omega^2}{c} \phi = 0 \quad (20)$$

This is the mild-slope wave equation.

So, for the total complex wave energy in the area of calculation to be stationary the mild-slope wave equation is the necessary and sufficient demand.

However, from physical reasoning one can tell that for a known incident wave system there will be no stationary situation except the one that represents the minimum in wave energy. Therefore, the mild-slope wave equation is also a consequence of the total wave energy in the area of calculation being minimized.



4. Two Functionals.

4.1. General Remarks.

For many practical purposes it is convenient not to deal with an area of infinite extension as that shown in Fig.1., but instead to split the horizontal plane in an inner area A, and an outer area R reaching to infinity as shown in Fig.2. Thus, it is possible to treat the inner and the outer area in separate ways as will be done in the following sections.

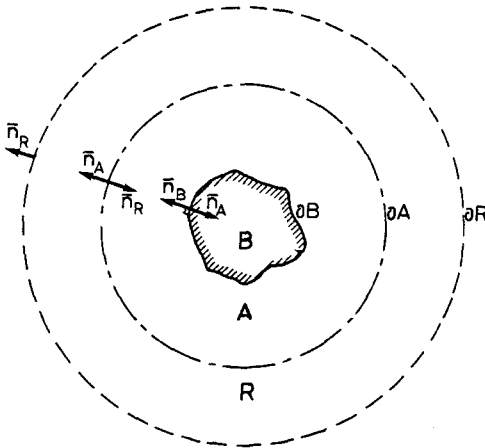


Fig.2. Areas of calculation A and R in the horizontal plane.

Again, inside area A some wave scattering structure B is located. For generality, the boundary of this area, ∂B, may be partially absorbing :

$$\frac{\partial \phi}{\partial n_B} + i k \alpha \phi = 0 \quad \text{along } \partial B \quad (21)$$

where  $\alpha$  is an absorption coefficient. For waves incident at a right angle to the boundary, (21) results in reflected waves with the reflection coefficient  $(1-\alpha)/(1+\alpha)$ . Thus,  $\alpha=1$  corresponds to full absorption of waves incident at a right angle, and  $\alpha=0$  corresponds to a fully reflecting boundary.

Over the boundary ∂A which now is not at infinity, the velocity potential has to be smooth which leads to the boundary conditions :

$$\phi_R = \phi_A \quad \text{along } \partial A \quad (22)$$

$$\frac{\partial \phi_R}{\partial n_A} = \frac{\partial \phi_A}{\partial n_A} \quad \text{along } A \quad (23)$$

where  $\phi_A$  and  $\phi_R$  are the potentials in area A and R respectively.

In the outer area R the velocity potential can be expressed as :

$$\phi_R = \phi^i + \phi^S \quad (24)$$

where again  $\phi^S$  must satisfy the radiation condition (14) leading to the vanishing of  $\phi^S$  and its derivative at the boundary of area R,  $\partial R$ .

4.2. A Simple Element Formulation.

A simple element formulation is here understood as a formulation that only involves element shape functions to describe the solution to the problem. The mild-slope wave equation has been solved by use of such a method by Bettes and Zienkiewicz (1977) where infinite elements were used in the outer area R, and ordinary finite elements were used in the inner area A. Hereby Bettes and Zienkiewicz were able to extend the integration to cover the entire x-y plane.

Using the results from section 2 and 3 will now demonstrate how one in a new and easily understandable way can construct the functional used by Bettes and Zienkiewicz (1977) in their finite/infinite element formulation.

The total complex wave energy in area A is given by (16). In a quite similar way the total energy in area R,  $E_R$ , may be found. Energy is lost along the partially absorbing boundary  ${}^R\partial B$ . This is described by an energy flux through the boundary. Hereby the following equation describing conservation of total complex wave energy arises :

$$\frac{\partial}{\partial t} (E_A + E_R) + \int_{\partial B^A} E_f^A ds + \int_{\partial B^R} E_f^R ds = 0 \quad (25)$$

where  $E_f^A$  is positive as a flux out through the boundary  $\partial B$  meaning the direction  $n$  in (12) should be  $n_A$  ( $=-n_B$ ).  $E_f^R$  is positive as a flux out through the distant boundary  $\partial R^A$ , i.e.  $n$  should be  $n_R$ .

Integrating (25) once with respect to time  $t$  yields :

$$E_A + E_R + \int_{\partial B} \left[ \int E_f^A dt \right] ds + \int_{\partial R} \left[ \int E_f^R dt \right] ds = \text{Constant} \quad (26)$$

Using (12) and (21) the integral along  $\partial B$  in (26) can be calculated :

$$\int_{\partial B} \left[ \int E_f^A dt \right] ds = -\frac{\rho}{g} e^{-2i\omega t} \int_{\partial B} \frac{1}{2} i\omega c_g \phi^2 ds \quad (27)$$

Using (12) and (24) the integral along  $\partial R$  in (26) can be written as :

$$\int_{\partial R} \left[ \int E_R^R dt \right] ds = -\frac{\rho}{g} e^{-2i\omega t} \left\{ \int_{\partial R} cc_g \frac{1}{2} \phi^i \frac{\partial \phi^i}{\partial n_R} ds \right. \\ \left. + \int_{\partial R} cc_g \frac{1}{2} \phi^S \frac{\partial \phi^S}{\partial n_R} ds + \int_{\partial R} cc_g \frac{1}{2} \phi^i \frac{\partial \phi^S}{\partial n_R} ds \right. \\ \left. + \int_{\partial R} cc_g \frac{1}{2} \phi^S \frac{\partial \phi^i}{\partial n_R} ds \right\} \quad (28)$$

As in (18) it can be argued that these integrals along  $\partial R$  can be ignored.

Introducing (24) in the expression for  $E_R$  one gets :

$$E_R = \frac{\rho}{g} e^{-2i\omega t} \left\{ \iint_R \frac{1}{2} [cc_g (\nabla \phi^i)^2 - \frac{c_g \omega^2}{c} (\phi^i)^2] dx dy \right. \\ \left. + \iint_R \frac{1}{2} [cc_g (\nabla \phi^S)^2 - \frac{c_g \omega^2}{c} (\phi^S)^2] dx dy \right. \\ \left. + \iint_R [cc_g \nabla \phi^i \cdot \nabla \phi^S - \frac{c_g \omega^2}{c} \phi^i \phi^S] dx dy \right\} \quad (29)$$

The first integral in (29) is stationary, and it can therefore be discarded. The second integral contains the velocity potential  $\phi^S$  of the scattered wave field which is to be modelled by special shape functions in the outer area  $R$ . The third integral in (29) may be rewritten as follows :

$$\iint_R [cc_g \nabla \phi^i \cdot \nabla \phi^S - \frac{c_g \omega^2}{c} \phi^i \phi^S] dx dy = \\ \int_{\partial R + \partial A} cc_g \phi^S \frac{\partial \phi^i}{\partial n_R} ds - \iint_R \phi^S [cc_g \nabla^2 \phi^i + \frac{c_g \omega^2}{c} \phi^i] dx dy \quad (30)$$

Again the line integral in (30) along  $\partial R$  can be discarded. Furthermore assuming the water depth in the outer area  $R$  to be constant, the second integral on the right hand side of (30) vanishes, since  $\phi^i$  naturally must be a solution to the wave equation.

Hereafter the integrated energy equation (26), with (16), (27) and (29) introduced, gives the functional (omitting the unimportant factor  $\frac{\rho}{g} e^{-2i\omega t}$ ) :

$$\begin{aligned}
F(\phi) = & \iint_A \left[ \frac{1}{2} c c_g (\nabla \phi)^2 - \frac{c_g \omega^2}{c} \phi^2 \right] dx dy \\
& + \iint_R \left[ \frac{1}{2} c c_g (\nabla \phi^S)^2 - \frac{c_g \omega^2}{c} (\phi^S)^2 \right] dx dy \\
& - \int_{\partial A} c c_g \phi^S \frac{\partial \phi^i}{\partial n_A} ds \\
& - \int_{\partial B} \frac{1}{2} i \alpha \omega c_g \phi^2 ds = \text{Constant} \quad (31)
\end{aligned}$$

By taking the first variation of (31) it is found that :

$$\delta F(\phi) = 0 \quad (32)$$

$F(\phi)$  is exactly the functional used by Bettes and Zienkiewicz (1977). By finite/infinite element discretization (32) can be expressed as a system of linear equations, which easily can be constructed and solved on a computer. When solving (32) one finds the function  $\phi$  — or, more precisely, a close approximation to the true  $\phi$ -function — which with the preconditions introduced fulfils the energy conservation equation (25). So, from a physical point of view, what really happens in this finite/infinite element formulation is that the conservation of total complex wave energy in the entire plane is ensured.

#### 4.3. A Hybrid Element Formulation.

A hybrid element method is a combination of a conventional element method and some other method. The mild-slope wave equation was initially solved by Berkhoff (1972,1975) using a hybrid element method. A slightly different hybrid element formulation was introduced by Chen and Mei (1974) solving the shallow water wave equation. Later this formulation in its intermediate depth version has been used by Houston (1981) and by Tsay and Liu (1983). The basic principle of the Chen and Mei method is that while the inner area A (see Fig.2.) is divided into finite elements, a semi-analytical solution to the mild-slope wave equation is used in the outer area R to represent the velocity potential  $\phi^S$ . Hereby integration over the outer area R can be avoided.

Using the same new procedure as in the previous section, a functional for the hybrid element formulation as originally given for shallow water by Chen and Mei (1974) will now be constructed. However, as in the previous section, intermediate depth theory will be used, and an absorbing boundary condition will be included.

Conservation of total complex wave energy is again the starting point. However, since the two areas of calculation are going to be treated in two separate ways, it is necessary to describe the conservation of energy in two separate equations. This leads to the following energy conservation equation for the inner area A :

$$\frac{\partial E_A}{\partial t} + \int_{\partial A + \partial B} E_f^A ds = 0 \quad (33)$$

and for the outer area R :

$$\frac{\partial E_R}{\partial t} + \int_{\partial A + \partial R} E_f^R ds = 0 \quad (34)$$

$E_f^A$  and  $E_f^R$  are energy fluxes positive out of areas A and R, respectively. From (33) and (34) one gets by integration :

$$E_A + \int_{\partial A + \partial B} [ \int E_f^A dt ] ds = \text{Constant} \quad (35)$$

$$E_R + \int_{\partial A + \partial R} [ \int E_f^R dt ] ds = \text{Constant} \quad (36)$$

The integral in (35) along the partially absorbing boundary  $\partial B$  can be calculated according to (27). The integral in (35) along  $\partial A$  can be calculated :

$$\int_{\partial A} [ \int E_f^A dt ] ds = - \frac{\rho}{g} e^{-2i\omega t} \int_{\partial A} \frac{1}{2} cc_g \phi_A \frac{\partial \phi_A}{\partial n_A} ds \quad (37)$$

Using Green's theorem one may write the wave energy in the outer area,  $E_R$ , as :

$$E_R = \frac{\rho}{g} e^{-2i\omega t} \left\{ - \iint_R \frac{1}{2} \phi_R [ \nabla \cdot (cc_g \nabla \phi_R) + \frac{c_g \omega^2}{c} \phi_R ] dx dy + \int_{\partial A + \partial R} \frac{1}{2} cc_g \phi_R \frac{\partial \phi_R}{\partial n_R} ds \right\} \quad (38)$$

Now, introducing the precondition that  $\phi_R$  must fulfil the mild-slope wave equation (20), it is seen from (38) that  $E_R$  may be written as :

$$E_R = \frac{\rho}{g} e^{-2i\omega t} \left\{ \int_{\partial A} \frac{1}{2} cc_g \phi_R \frac{\partial \phi_R}{\partial n_R} ds + \int_{\partial R} \frac{1}{2} cc_g \phi_R^i \frac{\partial \phi_R^i}{\partial n_R} ds \right\} \quad (39)$$

where again integrals along  $\partial R$  containing  $\phi^S$  or its derivative have been discarded.

When in addition assuming the water depth in the outer area R to be constant, it can be shown that :

$$\int_{\partial A} cc_g \phi^S \frac{\partial \phi^i}{\partial n_R} ds = \int_{\partial A} cc_g \phi^i \frac{\partial \phi^S}{\partial n_R} ds \tag{40}$$

The integral along  $\partial A + \partial R$  in (36) can be calculated :

$$\begin{aligned} \int_{\partial A + \partial R} [ \int E_f^R dt ] ds = & - \frac{\rho}{g} e^{-2i\omega t} \left\{ \int_{\partial A} \frac{1}{2} cc_g \phi^S \frac{\partial \phi^S}{\partial n_R} ds \right. \\ & \left. + \int_{\partial A + \partial R} \frac{1}{2} cc_g \phi^i \frac{\partial \phi^i}{\partial n_R} ds + \int_{\partial A} cc_g \phi^i \frac{\partial \phi^S}{\partial n_R} ds \right\} \end{aligned} \tag{41}$$

where (40) has been used and some integrals along  $\partial R$  again have been discarded.

By use of (27) and (37) to (41), energy equation (35) may now be written as :

$$\begin{aligned} \frac{\rho}{g} e^{-2i\omega t} \left\{ \iint_A \frac{1}{2} [ cc_g (\nabla \phi_A)^2 - \frac{c_g \omega^2}{c} \phi_A^2 ] dx dy \right. \\ \left. - \int_{\partial A} \frac{1}{2} cc_g \phi_A \frac{\partial \phi_A}{\partial n_A} ds - \int_{\partial B} \frac{1}{2} i \alpha \omega c_g \phi_A^2 ds \right\} = \text{Constant} \end{aligned} \tag{42}$$

and energy equation (36) may be written as :

$$\begin{aligned} \frac{\rho}{g} e^{-2i\omega t} \left\{ \int_{\partial A} \frac{1}{2} cc_g \phi_R \frac{\partial \phi_R}{\partial n_R} ds - \int_{\partial A} \frac{1}{2} cc_g \phi^S \frac{\partial \phi^S}{\partial n_R} ds \right. \\ \left. - \int_{\partial A} \frac{1}{2} cc_g \phi^i \frac{\partial \phi^i}{\partial n_R} ds - \int_{\partial A} cc_g \phi^S \frac{\partial \phi^i}{\partial n_R} ds \right\} = \text{Constant} \end{aligned} \tag{43}$$

Now it is time to include the matching boundary conditions along  $\partial A$ , (22) and (23). This is done by using (22) in the first integral in (43) and (23) in the second integral in (42). The reason for this choice is that when it comes to actual calculations,  $\phi_A$  will be represented by finite element shape functions, and therefore the derivative of  $\phi_A$  will in general only be an approximation to the true one and should therefore be avoided. On the other hand,  $\phi_R$  will be represented by an analytical series solution containing some unknown constants. The derivative of  $\phi_R$  will therefore be known exactly.

It is noted that the third integral in (43) only contains  $\phi^i$  and its derivative. Thus, it is stationary and therefore unimportant.

Now, by adding the two expressions (42) and (43), omitting the unimportant factor  $(\rho/g)\exp(-2i\omega t)$  and taking advantage of the unimportance of the stationary integral, one gets the 'hybrid functional' :

$$\begin{aligned}
F_H(\phi) = & \iint_A \frac{1}{2} [c c_g (\nabla \phi_A)^2 - \frac{c_g \omega^2}{c} \phi_A^2] dx dy \\
& + \int_{\partial A} c c_g [\frac{1}{2} \phi^S - (\phi_A - \phi^i)] \frac{\partial \phi_R}{\partial n_A} ds \\
& - \int_{\partial A} \frac{1}{2} c c_g \phi^S \frac{\partial \phi^i}{\partial n_A} ds \\
& - \int_{\partial B} \frac{1}{2} i \alpha \omega c_g \phi_A^2 ds = \text{Constant} \quad (44)
\end{aligned}$$

Similarly to (32) one finds by taking the first variation of (44) :

$$\delta F_H(\phi) = 0 \quad (45)$$

$F_H$  is the functional first derived in its shallow water version by Chen and Mei (1974). The present formulation is more general since intermediate depth theory has been used, and an absorbing boundary condition has been included. Again it can be concluded that the basic demand expressed in (45) used in finite element calculations simply ensures conservation of total complex wave energy in the entire horizontal plane.

### 5. Discussion.

Two different functionals, each corresponding to its own element formulation, have been derived. When constructing the functional in section 4.2, constant water depth was assumed in the outer area. When constructing the functional in section 4.3, it was necessary to assume that  $\phi^S$  fulfil the wave equation in the constant water depth outer area. When making the actual calculations, this is ensured by representing  $\phi^S$  by a semi-analytical solution to the Helmholtz equation. This equation is the constant water depth version of the mild-slope wave equation. For practical use the two formulations have the same assumptions behind the functionals. The variational formulation described in section 4.3 is more complicated than the one in section 4.2, but that argument should not be used to downgrade the hybrid element method since this formulation only has to be gone through once. The authors of the present paper believe that when using efficient programming, i.e. mainly sparse-matrix handling techniques, there will be no significant difference in the cost of running the two models.

Finally an example of the results of diffraction calculations that one can get using the finite element method is shown in Fig.3 and Fig.4. Fig.3 shows the relative wave amplitude in and just outside a harbour. The incoming waves are approaching the coastline at a right angle and all boundaries are fully reflecting. Fig.4 shows the instantaneous surface elevation at a chosen time where the sum of the incident and the reflected waves has zero elevation everywhere outside the harbour. Therefore, what is seen outside the harbour at this moment is

alone the surface elevation of the scattered wave field.

More results including absorbing boundary conditions and superposition of waves can be found in Skovgaard et. al. (1984).

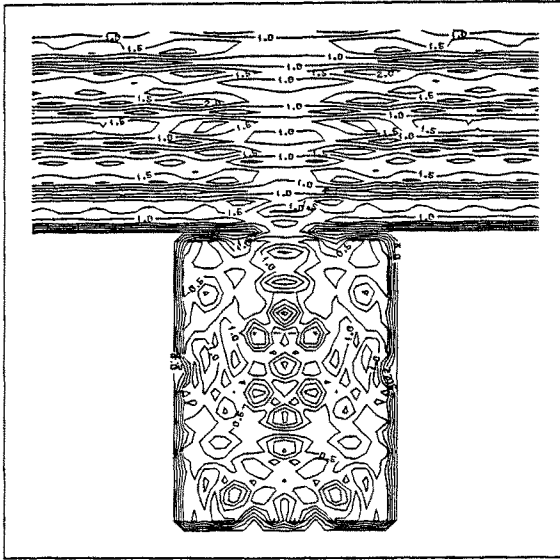


Fig.3. Harbour, relative amplitudes.

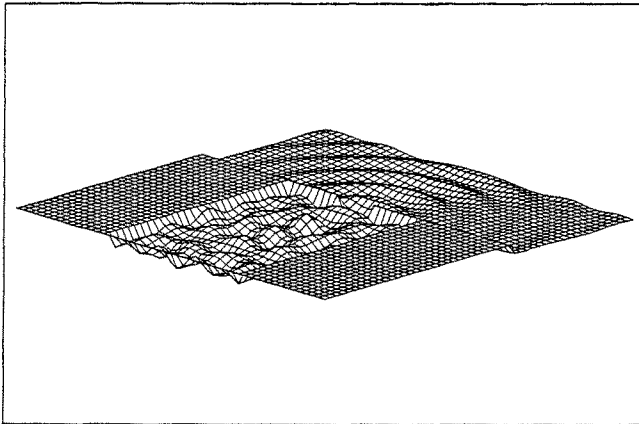


Fig.4. Harbour, relative surface elevation at a chosen time.



## 6. Conclusion.

The mild-slope wave equation has been derived by demanding minimum of total wave energy in the area of interest. This approach provides a new physical understanding of the mild-slope wave equation.

A functional for a simple element method and a functional for a hybrid element method have been derived from a general energy conservation principle. In both cases the procedure is straight-forward, and there is no need for any trial-and-error methods. Hereby a full understanding of each single part of the functionals is obtained and also a better understanding of the physical basis of the finite element method for the calculation of diffraction of small water waves.

## 7. References.

- Berkhoff, J.C.W. (1972). "Computation of combined refraction-diffraction." Proc. 13th. Coastal Engng. Conf., Vancouver 1972, ASCE. New York, Vol. 1, chap. 24, pp. 471-490.
- Berkhoff, J.C.W. (1975). "Linear wave propagation problems and the finite element method." in Finite Elements in Fluids. (Ed. Callagher, R.H., Oden, J.T., Taylor, C. and O. Zienkiewicz), Vol.1, Wiley, Chichester, pp. 251-264.
- Bettes, P. and Zienkiewicz, O.C. (1977). "Diffraction and refraction of surface waves using finite and infinite elements." Int. J. Num. Meth. Engng., Vol. 11, No. 8, pp. 1271-1290.
- Chen, H.S. and Mei, C.C. (1974). "Oscillations and wave forces in an offshore harbor." Massachusetts Institute of Technology. Parsons Laboratory, Rep. No. 190.
- Houston, J.R. (1981). "Combined refraction and diffraction of short waves using the finite element method." App. Ocean Res., Vol. 3, No. 4, pp.163-170.
- Jonsson, I.G. and Brink-Kjær, O. (1973). "A comparison between two reduced wave equations for gradually varying depth." Inst. Hydrodyn. and Hydr. Engng. (ISVA), Techn. Univ. Denmark, Prog. Rep. No. 31, pp. 13-18.
- Skovgaard, O., Behrendt, L. and Jonsson I.G. (1984). "A finite element model for wind wave diffraction." Proc. 19th. Coastal Engng. Conf., Houston 1984, ASCE. New York, in press.
- Smith, R. and Sprinks, T. (1975). "Scattering of surface waves by a conical island." J. Fluid Mech., Vol. 72, part 2, pp. 373-384.
- Tsay, T-K. and Liu, P.L-F. (1983). "A finite element model for wave refraction and diffraction." App. Ocean Res., Vol. 5, No. 1, pp.30-37.

## CHAPTER SIXTY FIVE

### Steep Unsteady Water Waves: An Efficient Computational Scheme

J W Dold and D H Peregrine

School of Mathematics, University of Bristol,  
University Walk, Bristol BS8 1TW, England.

A new method for computing the unsteady motion of a water surface, including the overturning of water waves as they break, has been developed. It is based on a Cauchy theorem boundary integral for the evaluation of multiple time derivatives of the surface motion. The numerical implementation of the method is efficient, accurate and stable.

#### 1. Introduction

Longuet-Higgins and Cokelet [2] first described a means of computing steep surface motions and the overturning of water waves in 1976. Since then their method has been used and modified by various authors ([1] to [8]). A useful discussion of most of the techniques available to date is given by Baker et al [1]. The water motion is assumed to be inviscid and irrotational; the necessary solution of Laplace's equation for the velocity potential is cast into some form of boundary integral; and the free surface boundary conditions are used to advance the calculations in time.

Most of these methods have been found to suffer from a "sawtooth" numerical instability [7], which is usually controlled by some kind of smoothing. They can also be computationally expensive; using an implementation of the method of Longuet-Higgins and Cokelet, New [4] found that about 20 hours of processor time on a Honeywell level 68 (multics system) computer were needed to determine, with reasonable accuracy, the motion of a breaking wave to the

point at which the jet strikes the lower surface.

The method described here uses Cauchy's theorem for analytic functions of a complex variable to formulate the boundary-integral equation in a form suitable for efficient solution by iteration. The same equation is used to find extra time derivatives of the surface motion at each step. For a given accuracy the resulting truncated Taylor series is used to estimate the maximum acceptable time-step, and to perform the time stepping.

The method is found to be both stable and very accurate for steep steadily-propagating waves. Unsteady waves can only be checked against other numerical solutions. Comparisons with solutions obtained using the approach of Longuet-Higgins and Cokelet give clear indications that this method is more accurate. Furthermore the program for this method is found to run an order of magnitude faster, for given accuracy.

## 2. Outline of Method

Incompressible irrotational flow is described by a velocity potential satisfying

$$\nabla^2 \phi = \phi_{xx} + \phi_{yy} = 0 \quad (1)$$

where

$$\underline{u} = \nabla \phi. \quad (2)$$

It is assumed that the fluid is bounded below by an impermeable flat bottom at  $y = -h$ . The appropriate boundary condition for  $\phi$  is

$$\phi_y(x, -h, t) = 0. \quad (3)$$

With these conditions governing the behaviour of the body of the fluid it is possible to focus attention on the fluid surface alone; as described in section 4, a boundary-integral equation can be used to summarise the whole fluid's behaviour in terms of its surface properties. In particular the normal and tangential gradients of  $\phi$  at the surface can be determined, knowing only the surface values of  $\phi$ . This gives the velocity  $\underline{u}$  from (2). The kinematic condition, that a surface particle moves with its

own velocity, shows that the instantaneous movement of the surface is then fully determined; if  $(X, Y)$  marks a particle on the surface then the rates of change of  $X$  and  $Y$  are given by

$$\frac{D}{Dt} (X, Y) = \underline{u} = (\phi_x, \phi_y). \quad (4)$$

To follow the motion of the surface further it is also necessary to know the way in which  $\phi$  varies. Bernoulli's equation gives the rate of change of  $\phi$  on the surface as

$$\frac{D\phi}{Dt} = \frac{u^2}{2} - (P/\rho + gY) \quad (5)$$

where  $P$  takes the value of the surface pressure which for many practical purposes may be taken as a constant, the actual value of which makes no difference to the motion of the fluid.

Most existing numerical schemes for following the movement of the fluid surface make use of this formulation with the following basic algorithm.

Given  $(X, Y, \phi)$  on the surface at the time  $t$ :

- i) solve  $\nabla^2 \phi = 0$  with  $\phi_y(x, -h, t) = 0$  to obtain  $\nabla \phi$  on the surface and hence evaluate  $D(X, Y, \phi)/Dt$
- ii) time-step to obtain  $(X, Y, \phi)$  on the surface at the time  $t + \Delta t$ , and repeat.

### 3. Extended Approach

Equations (1) and (3) can be successively differentiated with respect to time to yield the following equations and bottom conditions:

$$\begin{aligned} \nabla^2 \phi_t &= 0 & \text{with } \phi_{ty}(x, -h, t) &= 0 \\ \nabla^2 \phi_{tt} &= 0 & \text{with } \phi_{tty}(x, -h, t) &= 0 \end{aligned} \quad (6)$$

etc.

Clearly  $\phi_t, \phi_{tt}$  and all similar Eulerian derivatives of

$\phi$  satisfy Laplace's equation and the bottom condition just as  $\phi$  does. In the same way therefore it is possible to solve for the gradients of these derivatives and obtain the corresponding Eulerian rates of change of velocity, for which they are the appropriate potential functions. This can be seen by differentiating (2). Extension of the kinematic condition (4) to obtain  $D^2(X,Y)/Dt^2$  etc. is also straightforward. Similarly, differentiation of Bernoulli's equation (5) gives the corresponding Lagrangian rates of change of  $\phi$  on the surface.

In order to determine these higher derivatives it is necessary to obtain  $\phi_t, \phi_{tt}$  etc. on the surface. By using Bernoulli's equation once again and expressing the result in terms of Lagrangian, rather than Eulerian derivatives of pressure, these can be found in terms of known variables. For example,

$$\phi_{tt} = - \left[ \underline{u} \cdot \left( \underline{u}_t + \frac{D\underline{u}}{Dt} \right) + \frac{DP}{Dt}/\rho + g \frac{DY}{Dt} \right]. \quad (7)$$

Thus the Eulerian derivatives of  $\phi$  are given once  $P, DP/Dt$  etc. are specified. For a constant surface pressure all Lagrangian derivatives of  $P$  at the surface would simply be zero.

The algorithm for calculating the surface motion can thus be extended in the following way

Given  $(X, Y, \phi)$  on the surface at the time  $t$ :

- i) solve  $\nabla^2 \phi = 0$  with  $\phi_y(x, -h, t) = 0$  to obtain  $\nabla \phi$  on the surface and evaluate both  $D(X, Y, \phi)/Dt$  and  $\phi_t$
- ii) similarly use  $\phi_t$  to obtain both  $D^2(X, Y, \phi)/Dt^2$  and  $\phi_{tt}$
- iii) proceed in the same way to calculate up to a chosen order of time derivative
- iv) time-step, using Taylor series in  $X, Y$  and  $\phi$  with some backward differencing, to obtain  $(X, Y, \phi)$  on the surface at the time  $t + \Delta t$ , and repeat.

A scheme using calculations up to  $D^3/Dt^3$  in this algorithm has been implemented numerically.

Some immediate advantages are found with this approach. Firstly, it is possible to take larger time steps for a given accuracy. Secondly, the derivatives are calculated for the same surface profile,  $(X, Y)$ . This means

that the solutions are all obtained using exactly the same boundary-integral kernels. Both of these result in an improvement in numerical efficiency and hence shorter computer running times. It is also useful to have more detailed information calculated about the surface motion at each time step.

4. Integral Equation

For a variety of reasons it was decided to use Cauchy's integral theorem as the means of solving Laplace's equation. Its use leads to a fairly simple formulation in which the singularities in the integral kernels are easily taken into account. This contrasts with the more cumbersome logarithmic singularity found with approaches which use Green's identity. In addition the Cauchy formulation is soluble by iteration which can be a quick method of solution.

(i) Cauchy's Integral Theorem

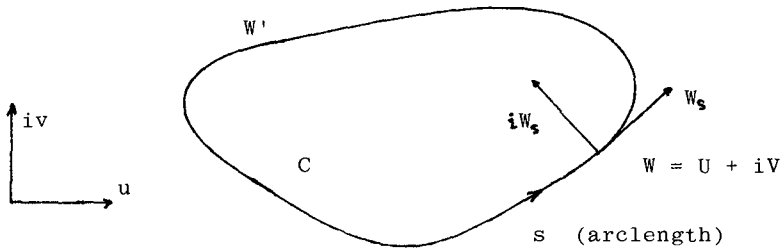


Figure 1: Closed contour

For  $\phi$  satisfying Laplace's equation within the contour C, illustrated in figure 2, the complex potential gradient,  $\phi_u - i\phi_v$ , is an analytic function of the variable,  $w = u + iv$ . The following useful expression of the principal value form of Cauchy's integral theorem is then satisfied.

$$\phi_n = \frac{1}{\pi} \int \text{Im} \left[ \frac{W_s}{W' - W} \right] \phi_n' ds' + \frac{1}{\pi} \int \text{Re} \left[ \frac{W_s}{W' - W} \right] \phi_s' ds'. \quad (8)$$

In this equation the arclength derivative,  $W_s$ , of the surface position,  $W(s)$ , is the complex unit tangent, and

$\phi_s$  and  $\phi_n$  are the tangential and inward normal gradients of  $\phi$ , respectively.

(ii) Application

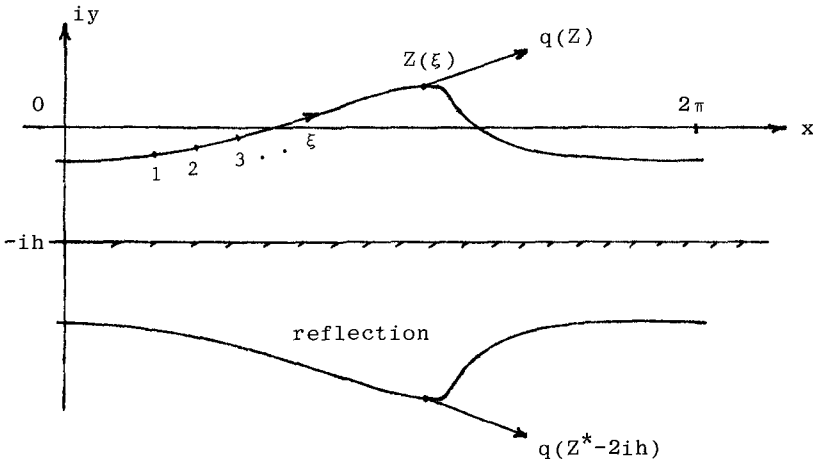


Figure 2: Physical plane

In the complex representation of the physical plane,  $z = x + iy$ , the complex gradient of the potential becomes

$$q = \phi_x - i \phi_y \tag{9}$$

and the bottom condition (3) can be satisfied by adopting the "reflection" condition,

$$q(Z^* - 2ih) = q^*(Z), \tag{10}$$

with the fluid assumed to extend continuously below the bottom to the reflection of the complex surface,  $Z$ , in the bottom.

It is useful at this point to assume that the system is periodic in  $x$  so that only a finite length of surface need be considered. No generality is lost in taking the spatial period to be exactly  $2\pi$ . The periodic surface  $Z(\xi)$  in the  $z$  plane is then transformed to a closed contour  $W(\xi)$  in the  $w$  plane by the conformal

transformation,

$$w = e^{-iz} = u + iv. \tag{11}$$

Applying the formula (8) to this contour and the transformation of the reflected contour leads to the following integral equation

$$\begin{aligned} \phi_v = \frac{1}{\pi} \int \operatorname{Im} \left[ \frac{W_\xi}{W-W'} + \frac{W_\xi}{W-e^{-2h/W'}*} \right] \phi_v' d\xi' \\ + \frac{1}{\pi} \int \operatorname{Re} \left[ \frac{W_\xi}{W-W'} - \frac{W_\xi}{W-e^{-2h/W'}*} \right] \phi_\xi' d\xi' \end{aligned} \tag{12}$$

where  $\phi_\xi$  is simply the derivative of  $\phi$  with respect to the parameter  $\xi$  along the surface, while  $\phi_v$  is the outward normal gradient of  $\phi$  scaled by  $|W_\xi|$ . Supposing that (12) can be solved for  $\phi_v$ , the complex potential gradient of  $\phi$  in the physical plane is then given by

$$\phi_x + i\phi_y = \frac{W^*W_\xi}{|W_\xi|^2} (\phi_\xi + i\phi_v). \tag{13}$$

(iii) Numerical Solution

In order to solve equation (12) numerically it is now convenient to identify  $\xi$  as a point label parameter with  $X(\xi)$ ,  $Y(\xi)$  and  $\phi(\xi)$  defined on the surface for integral values of  $\xi$ . Derivatives with respect to  $\xi$  can be estimated using either central difference or Fourier series methods. By considering a Taylor expansion for  $W'$  the singular part of the integral kernels in (12) can be seen to be of the form

$$\frac{W_\xi}{W-W'} = \frac{1}{\xi-\xi'} + \frac{W_\xi\xi}{2W_\xi} + O(\xi'-\xi). \tag{14}$$

Since  $(\xi - \xi')^{-1}$  is real this makes it clear that only the kernel comprising the real part of  $W_\xi / (W - W')$  is genuinely singular, and since

$$\lim_{\xi' \rightarrow \xi} \frac{\phi_\xi' - \phi_\xi}{\xi - \xi'} = -\phi_{\xi\xi} \tag{15}$$

the effect of this singularity in the integral is easily



determined. It can thus be shown that the formula

$$\int \operatorname{Re} \left[ \frac{W_\xi}{W-W'} \right] \phi'_\xi d\xi' \approx \sum_{\xi' \neq \xi} \operatorname{Re} \left[ \frac{W_\xi}{W-W'} \right] \phi'_\xi + \operatorname{Re} \left[ \frac{W_{\xi\xi}}{2W_\xi} \right] \phi_\xi - \phi_{\xi\xi} \tag{16}$$

can be used to provide a numerical estimate for this integral. Taking account of the other non-singular components of (12) the integral kernels were expressed in matrix form. Given any potential function  $\phi(\xi)$  on the surface, the derivatives  $\phi'_\xi$  and  $\phi_{\xi\xi}$  were estimated numerically and the matrix equations were solved iteratively for  $\phi_v$ .  $\nabla\phi$  was then obtained using equation (13).

5. Accuracy, Stability and Speed

The resulting scheme for following the free surface motion was tested in a number of cases and was found to show no sign of the "sawtooth" numerical instability. Figure 3 shows one such test using 32 points to follow the propagation of a steep steady surface wave in deep water (with  $ak = 13/32$  or about 92% of the highest wave) for ten wave periods. It is interesting to note the particle drift of nearly twice the wavelength,  $\lambda$ , with the triangle  $\Delta$  marking the same particle. The results are just as should be expected to within an accuracy of about  $\lambda/10^4$ . This accuracy reflects an accuracy in the phase speed for the calculated wave of about 0.005%.

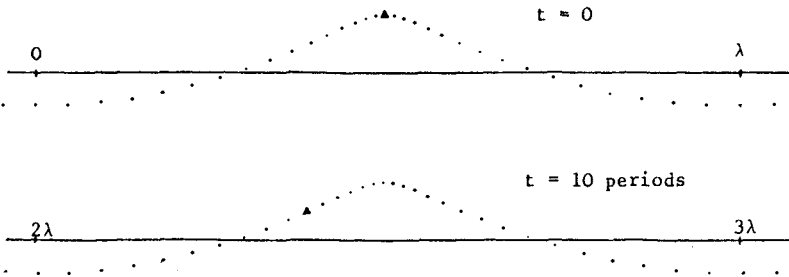


Figure 3: Steep surface wave ( $ak \approx 13/32$ ) after 10 wave periods using 32 points.

On a Honeywell level 68 (multics system) computer the program took about 2 minutes of C.P.U. time per wave period to execute this calculation, a running time which could have been reduced with fewer points and/or larger time steps at the sacrifice of some accuracy. The examples shown in figures 4 to 6 below each took about 20 to 30 minutes of C.P.U. time to calculate, and may be compared with the 20 hours, or so, experienced by New [4].

There are some limitations to the method. It was found that it is not always possible to reliably calculate progressively higher and higher derivatives. This is particularly so in regions of large strain rates, such as under the jet of a breaking wave, where the spreading out of surface particles leads to a reduced ability to resolve the wave profile. Since higher derivatives vary more dramatically in this region they are found to be the first to suffer from a loss of resolution. One can still proceed making use only of lower order derivatives.

Another region where a lack of resolution was encountered is at the tip of a jet such as can be seen in figure 6. The shape of this jet tip reflects a situation in which the point marked with the triangle  $\Delta$  is being accelerated into the fluid while points nearby are being accelerated outwards. Smoothing was used to control the motion in this case. It is not clear whether this observed tendency reflects a growing numerical instability or whether a genuine physical phenomenon, such as a breaking up of the jet tip, is taking place.

6. Some Examples of Results

For the examples presented below the acceleration due to gravity was given the value unity. Except in cases of zero gravity no generality is lost by this choice.

- i) Figure 4 shows the detail of a very small jet formed at the crest of a breaking wave which was generated by suddenly imposing a mean water depth of 2.5 (where the wavelength is  $2\pi$ ) on the otherwise deep water travelling wave of figure 3. After about two wave periods this causes the small jet to form at the crest of the wave. It is interesting to compare the profile at the wave crest with the  $120^\circ$  angle shown by the dotted line in figure 4.

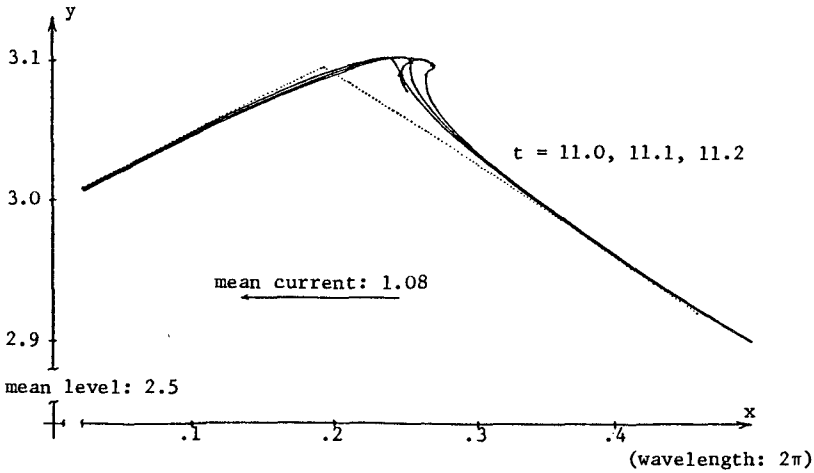


Figure 4: Formation of a "spilling breaker" by introducing finite depth into the wave in figure 3.

ii) By contrast figure 5 shows the development of a very large plunging breaker arising from an initial large amplitude travelling sine wave. Figure 6 shows a detail of the jet tip of this wave taken as far as the computation would allow.

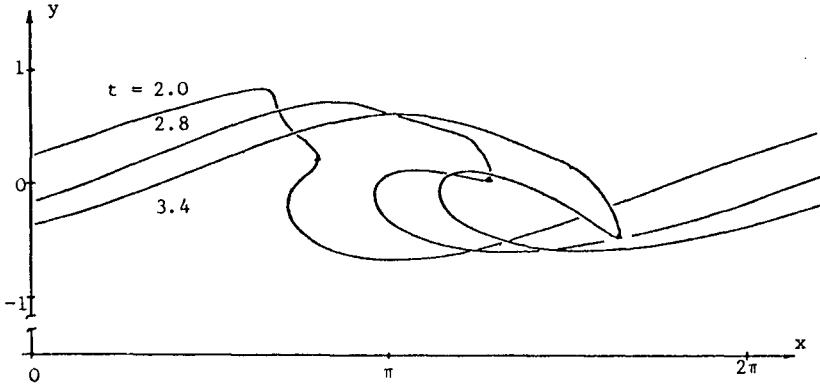


Figure 5: Massive plunging breaker from an initial travelling sine wave of amplitude 0.844, in deep water.

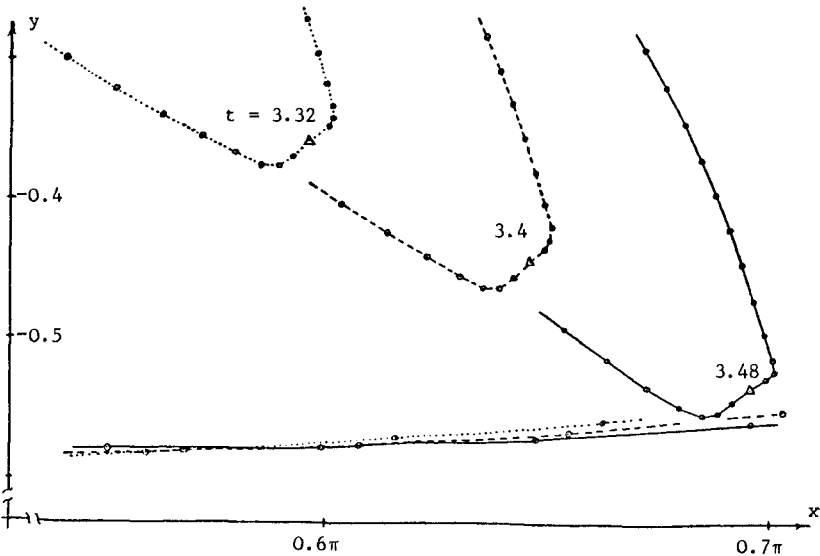


Figure 6: Detail of the tip of the jet in figure 5.

- iii) A curious example of surface motion leading to both the formation of a vertical jet and a plunging breaker is shown in figure 7. The initial conditions leading to this are illustrated by the dotted lines, showing a stretching of the surface in one region and a convergence and focussing of the motion of the surface in another.

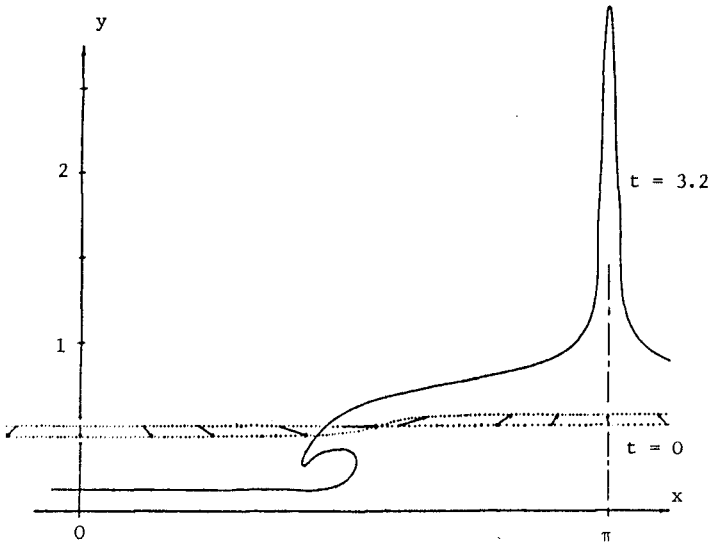


Figure 7: Surface motion arising from the symmetric, periodic, initial conditions in shallow water, of a flat surface with strongly convergent (and divergent) flow, as indicated by the dotted lines.

## 7. Conclusions

The use of higher derivatives and the use of Cauchy's integral theorem have led to an efficient numerical scheme for calculating the motion of steep surface waves. The efficiency of the program means that it can now be used in a wide variety of ways. It is already well suited to fundamental studies of nonlinear wave phenomena such as breaking. With little further development it could be used for assessing forces on structural elements or vessels which are small compared with the dimensions of the wave. This type of computation could replace the "design wave" concept where steep steady waves are currently used. For this application some measure of breaker "strength" should be developed.

## References

- 1 Baker, G R, D I Meiron and S A Orszag, 1982: Generalised vortex methods for free-surface flow problems, *J. Fluid Mech* 123, 477-501.
- 2 Longuet-Higgins, M S, and E D Cokelet, 1976: The deformation of steep surface waves on water; 1. A numerical method of computation, *Proc Roy Soc Lond A* 350, 1-26.
- 3 New, A L, 1983: PhD Thesis, Bristol University.
- 4 New, A L (private communication).
- 5 New, A L, P McIver and D H Peregrine, 1984: Computations of overturning waves, *J. Fluid Mech*, to appear.
- 6 Roberts, A J, 1983: A stable and accurate numerical method to calculate the motion of a sharp interface between fluids, *IMA J. Appl Math* 31, 13-36.
- 7 Srokosz, M (private communication).
- 8 Vinje, T, and P Brevig, 1981: Numerical simulation of breaking waves, *Adv. Water Resources* 4, 77-82.

## CHAPTER SIXTY SIX

### EXPLICIT SOLUTIONS TO PRACTICAL WAVE PROBLEMS

by

Peter Nielsen\*

#### ABSTRACT

Explicit formulae are provided for wave problems covered by linear wave theory. Two goals are pursued. The first is to provide a faster and more flexible tool than usual wave tables. The second is to provide explicit, analytical solutions to problems that have so far demanded time consuming numerical integrations. As an example we solve the problem of wave height variation due to refraction, shoaling and energy dissipation over a soft mud bottom. The obtained explicit solutions are accurate enough for practical purposes and require very little computational effort, in fact they will enable the engineer to solve many wave problems with a handheld calculator. Another advantage of analytical solutions is that they are always much more instructive than numerical results.

#### INTRODUCTION

Determination of local parameters like wave length,  $L$ , celerity,  $c$ , and height,  $H$ , for linear waves involves solution of the dispersion relation

$$k_0 h = kh \tanh kh \quad (1)$$

for finding the local wave number  $k$  at the depth  $h$ ;  $k_0$  is the deep water wave number given by

$$k_0 = 4\pi^2/gT^2 \quad (2)$$

Since (1) is a transcendental equation,  $k$  or  $kh$  has to be found either by an iterative numerical method or by using a wave table. This is a troublesome process considering the limited accuracy with which linear wave theory represents the physical reality. See Figure 1.

On the other hand linear wave theory is often the only practical option so we will still want to use it, but preferably in a

---

\*Assistant Professor, Coastal and Oceanographic Engineering Department, University of Florida, Gainesville, Florida, 32611.

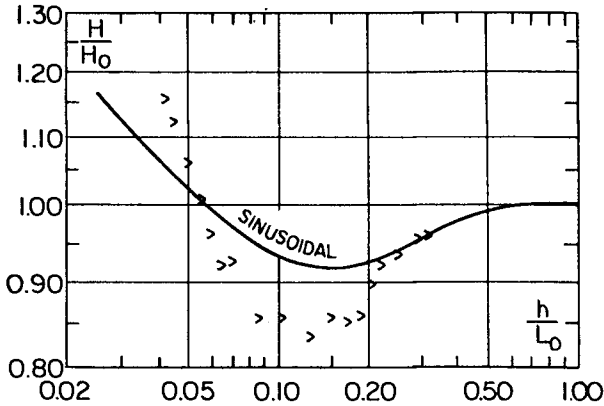


Figure 1: Measured values of the shoaling coefficient  $H/H_0$  compared to linear theory (After Brink Kjaer and Jonsson 1973). The error is of the order 10 percent.

mathematical form which is no more complicated than the accuracy of the theory justifies. In other words, there is no reason to solve equation (1) to seven significant digits every time we need a value of  $kh$ .

In the following we shall see how  $kh$  and many other functions related to linear waves can be expressed very simply in terms of  $k_0h$ , and thus become explicit functions of the water depth.

Not only is it possible to write linear wave functions in terms of  $k_0h$ , but it turns out that these formulae are very simple and adequate for practical use.

Take of example the function

$$F(k_0h) = \frac{1}{\frac{c}{c_0} \cosh^2 kh} \quad (3)$$

which occurs in relation to the problem of wave energy loss over a soft mud bottom. This apparently complicated function becomes

$$F(k_0h) = (k_0h)^{-0.5} [1 - 0.5 k_0h + \dots] \quad (4)$$

the accuracy of which is better than 1 percent for  $k_0h < 0.92$  that is in depths up to 14 meters for an 8 second wave.



The advantage of using the explicit form (4) is not just to make the evaluation of F easier, in fact the main advantage is that the explicit expression makes it possible to evaluate integrals like

$$I = \int_{h_1}^{h_2} Fdh \tag{5}$$

analytically. With this ability we are able to give analytical solutions to many wave problems in intermediate depths, for which explicit solutions have so far only been possible in shallow water.

The improvement of accuracy compared to using shallow water formulae all the way is by no means trivial.

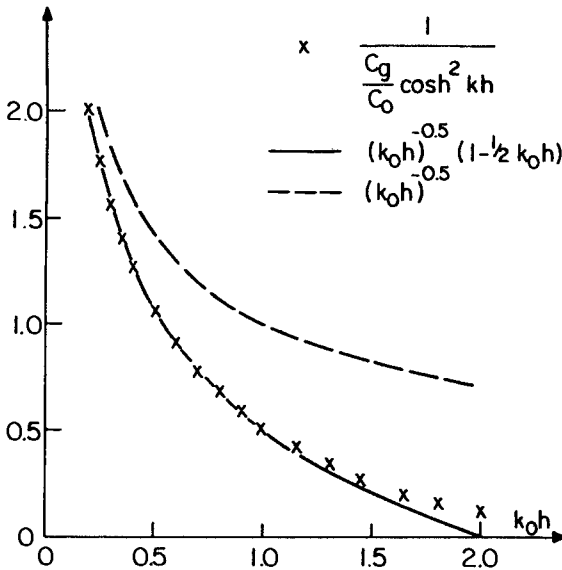


Figure 2: Comparison of the two approximations (4) and (6) to correct values  $F(k_0h)$  given by (3).

Figure 2 shows equation (4) as well as the shallow water expression

$$F_S(k_0h) = (k_0h)^{-0.5} \tag{6}$$

compared to correct values. We see that the improvement by adding just one more term is remarkable. And the accuracy of equation (4) is probably a lot better than the accuracy by which physical parameters of a natural mud bottom can be described.

The efficiency of formulae like (4) as simple and accurate approximations was first pointed out by Nielsen (1982).

AN ALTERNATIVE WAVE TABLE

Most coastal engineers are familiar with the use of wave tables for linear waves.

WAVE TABLE

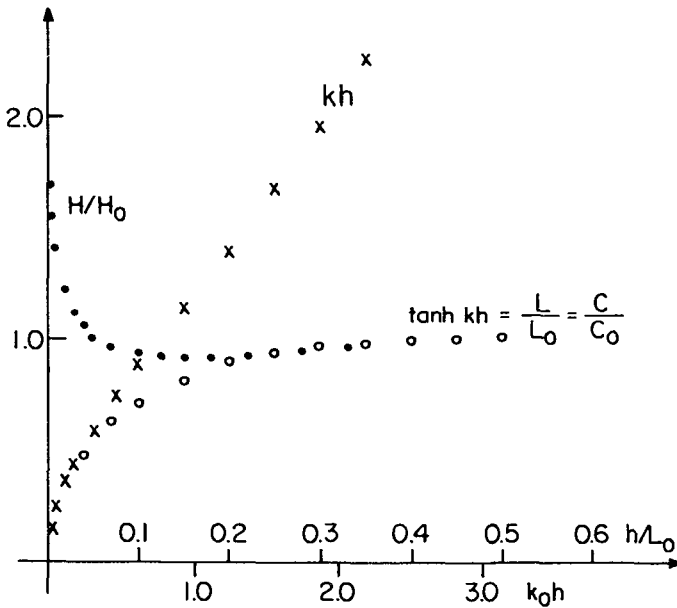


Figure 3: A wave table provides discrete values of commonly used wave parameters in terms of  $k_0h$  or  $h/L_0$ .

The general form of wave tables is illustrated in Figure 3 and is based on the fact that the dependence of linear wave parameters on the depth  $h$  can be expressed in the form

$$P = P_0 F(k_0 h) \tag{7}$$

where subscript "o" denotes deep water properties. For example, the local wave speed is given by

$$c = c_0 \tanh kh = c_0 G(k_0 h) \tag{8}$$

The function  $G(k_0h)$  does not have an exact explicit form in terms of usual functions but it is of course possible to construct explicit approximations to  $G(k_0h)$  with any degree of accuracy. The aim of the following is to suggest a standard method for providing such approximations and give a few examples.

The most commonly used form of approximations to transcendental or implicitly given functions are MacLaurin series or power expansions around zero. For example

$$\tanh x = x - \frac{1}{3}x^3 + \frac{2}{15}x^5 - \dots \quad (9)$$

However, such expansions do not exist for functions like  $G(k_0h)$  in equation (8), because  $G(k_0h)$  is not analytical at  $k_0h=0$ .

It is therefore necessary to use a different form of expansions. We choose the form

$$G(k_0h) = G_s(k_0h)[1 + a_1k_0h + a_2(k_0h)^2 + \dots] \quad (10)$$

where the subscript  $s$  stands for shallow water. The coefficients  $a_1$  are constants.

The shallow water expressions are always power functions of  $k_0h$ , but the power is often not an integer. Still, functions of the form (10) are convenient in the sense that they are easy to integrate.

Let us now consider the most fundamental example:

$$F(k_0h) = kh \quad (11)$$

i.e., we want to write  $kh$  in the form

$$kh = F_s(k_0h)[1 + a_1k_0h + a_2(k_0h)^2 + \dots] \quad (12)$$

The fundamental relation between  $kh$  and  $k_0h$  is the dispersion relation

$$k_0h = kh \tanh kh \quad (1)$$

First we find  $F_s(k_0h)$  by letting both  $kh$  and  $k_0h$  approach zero. We find

$$F_s(k_0h) = \sqrt{k_0h} \quad (13)$$

Next, the coefficients  $a_1$  are found by inserting

$$kh = \sqrt{k_0 h} [1 + a_1 k_0 h + a_2 (k_0 h)^2 + \dots] \tag{14}$$

into the dispersion relation, using the expansion (9) for the hyperbolic tangent. The result is

$$kh = \sqrt{k_0 h} [1 + \frac{1}{6} k_0 h + \frac{11}{360} (k_0 h)^2 + \dots] \tag{15}$$

This formula is accurate enough for most practical purposes. For  $k_0 h < 0.31$  which corresponds to 5 meters of water for an 8 second wave, the relative error is less than 0.01 percent. For  $k_0 h < 0.63$  the error is less than 0.07 percent, and even for  $k_0 h = 2.5$ , corresponding to 40 meters of water for an 8 second wave the relative error is only 0.44 percent.

### ALTERNATIVE WAVE TABLE

	<u>1% Limit <math>k_0 h</math></u>
$kh = \sqrt{k_0 h} [1 + \frac{1}{6} k_0 h + \frac{11}{360} (k_0 h)^2]$	2.72
$\tanh kh = \sqrt{k_0 h} [1 - \frac{1}{6} k_0 h]$	1.62
$C_g/C_0 = \sqrt{k_0 h} [1 - \frac{1}{2} k_0 h + \frac{7}{72} (k_0 h)^2]$	2.09
$K_s = (k_0 h)^{-0.25} [1 + \frac{1}{4} k_0 h + \frac{13}{288} (k_0 h)^2]$	1.34
$\frac{1}{\sinh kh} = (k_0 h)^{-0.5} [1 - \frac{1}{3} k_0 h]$	1.54

Figure 4: An alternative wave table, the column to the right shows the limiting values of  $k_0 h$  below which the accuracy is better than one percent.  $k_0 h = 1.5$  corresponds to a depth of 24 meters for an 8 second wave.

Once we have an expression for  $kh$  it is straightforward to obtain similar expressions for different functions of  $kh$  like

$$\frac{c_g}{c_o} = \tanh kh \left[ 0.5 + \frac{kh}{\sinh 2kh} \right] \tag{16}$$

and

$$K_s = H/H_o = \sqrt{0.5 c_o / c_g} \tag{17}$$

$c_g$  is the local group velocity.

Figure 4 shows five commonly used functions and the limits below which the relative error is less than one percent.

All the formulae shown above are tuned to the needs of nearshore coastal engineering work in that they are exact in the shallow water limit. In deep water it is necessary to use another type of expansion. The small parameter is no longer  $k_o h$  but  $\exp(-k_o h)$  or  $\exp(-kh)$ .

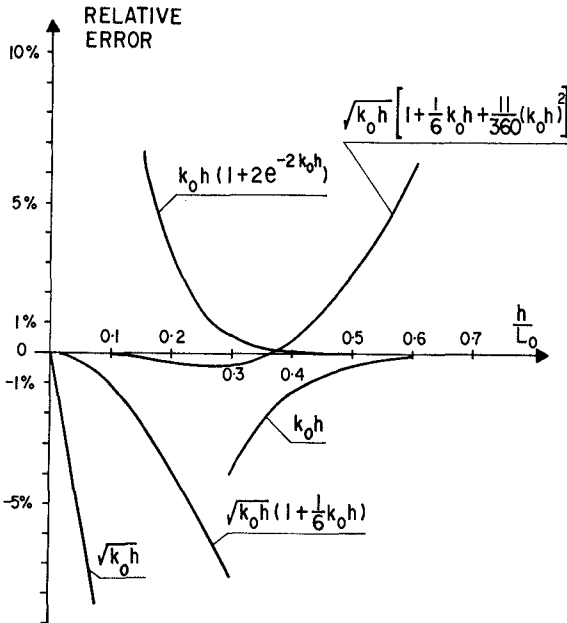


Figure 5: Relative error of (15) and (18), and of some truncated versions.

Again based on the dispersion relation (1) we find the following deep water approximation for kh:

$$kh = k_0 h [1 + 2e^{-2k_0 h}] \tag{18}$$

Figure 5 shows the relative errors of eq. (18) and (15) and of some truncated versions.

DISSIPATION PROBLEMS

Explicit formulae are necessary for analytical evaluation of integrals. For example the integral

$$I = \int_{h_1}^{h_2} \sinh kh \, dh \tag{19}$$

cannot be evaluated analytically because kh is an implicit function of h. Such integrals occur frequently in coastal engineering and the only way of evaluating them has so far been by numerical integration.

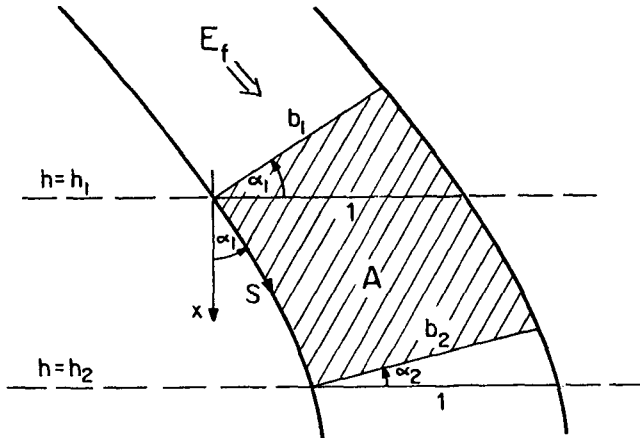


Figure 6: Definition diagram for wave height predictions over straight parallel bottom contours.

One of the most common problems for coastal engineers is to predict wave height variation due to shoaling, refraction and different sorts of energy dissipation. Such calculations are based on energy flux ( $E_f$ ) considerations and if the bed contours can be assumed straight and parallel as in Figure 6, the fundamental differential equation is

$$\frac{d}{ds} (E_f \cos \alpha) = D_E \cos \alpha \tag{20}$$

where  $D_E$  is the energy dissipation per unit area, and  $s$  is the distance measured along the wave orthogonals.

If the sea bed consists of sand and the effects of winds are neglected, most energy dissipation will be due to bed friction and the solution can be based on

$$D_E = \frac{2}{3\pi} \rho f_e u_{b,\max}^3 \quad (21)$$

where  $f_e$  is Jonsson's energy dissipation factor (Jonsson, 1966), and  $u_{b,\max}$  is the wave induced velocity amplitude near the bed.

The solution, as given by Nielsen (1984), is

$$H_2 = \frac{H_1 \sqrt{\frac{c_{g1} \cos \alpha_1}{c_{g2} \cos \alpha_2}}}{1 + H_1 \frac{k_o f_e}{3\pi} \sqrt{\frac{c_{g1} \cos \alpha_1}{c_o}} J} \quad (22)$$

where  $J$  is given by

$$J = \int \frac{k_o h_2}{k_o h_1} \frac{c_o^{1.5} \cos^{-1.5} \alpha}{c_g^{1.5} \sinh^3 kh} \frac{dx}{dh} dk_o h \quad (23)$$

It turns out that the fairly complicated integrand in (23) has a reasonably simple approximation of the form (10) so that the solution can be evaluated on a handheld calculator with sufficient accuracy for practical purposes. In fact the accuracy of the approximate solution which takes about 100 program steps on an HP-15c is probably far better than the accuracy of any available procedure for prediction of the energy dissipation factor  $f_e$ .

Figure 7 shows wave height variation due to refraction, shoaling and friction, calculated with numerical evaluation of  $J$  on a major computer and by the explicit solution

$$J = \frac{k_o^{1-1/p}}{pA^{1/p}} \left\{ \frac{(k_o h_1)^{1/p-2.25}}{\frac{1}{p} - 2.25} \left[ 1 - \left(\frac{h_1}{h_2}\right)^{2.25-1/p} \right] \right\}$$

$$\begin{aligned}
 & + \frac{(\delta - \frac{1}{4})(k_o h_1)^{1/p-1.25}}{\frac{1}{p} - 1.25} \left[ 1 - \left(\frac{h_1}{h_2}\right)^{1.25-1/p} \right] \\
 & + \frac{(\mu - \frac{\delta}{4} - \frac{61}{480})(k_o h_1)^{1/p-0.25}}{\frac{1}{p} - 0.25} \left[ 1 - \left(\frac{h_1}{h_2}\right)^{0.25-1/p} \right] \} \quad (24)
 \end{aligned}$$

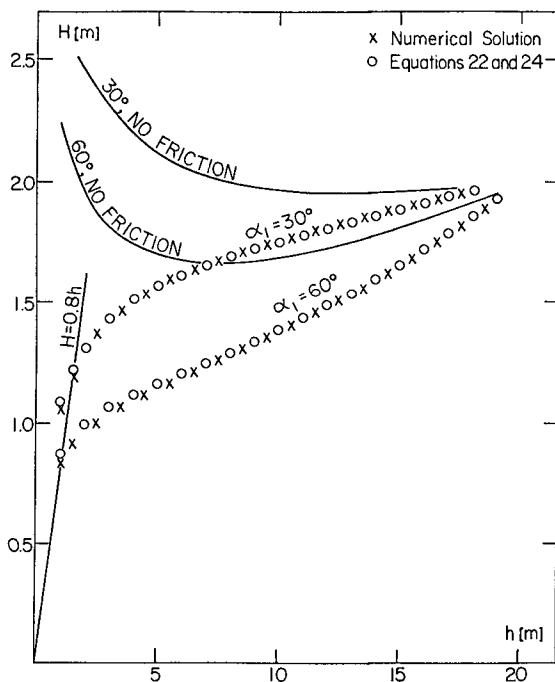


Figure 7: Comparison between the explicit solution (equations 22 and 24) and a numerical solution. The shown example corresponds to \$T = 8s\$, \$f\_e = 0.1\$ and a beach profile given by \$h = 0.1(x\_o - x)^{2/3}\$.

The beach profile is assumed to have the form

$$h = A(x_o - x)^p \quad (25)$$



and the coefficients  $\delta$  and  $\mu$  represent the effects of refraction via Snell's law. They are given by

$$\delta = \frac{0.75 \sin^2 \alpha_1}{k_o h_1 (1 - \frac{1}{3} k_o h_1)} \quad (26)$$

$$\mu = \frac{1.4 \sin^4 \alpha_1}{(k_o h_1)^2} - \frac{1}{3} \delta \quad (27)$$

$\alpha_1$  is the initial angle between wave crests and bed contours.

#### ENERGY DISSIPATION OVER A MUD BOTTOM

Waves propagating over a bed of soft mud will tend to induce a wave motion in the mud and thus feed energy into the mud at a rate of

$$D_M(t) = -p(t) \frac{dn}{dt} \quad (28)$$

where  $p$  is the pressure at the interface and  $n$  is the local elevation of the deformed interface. See e.g., Gade (1958).

If the pressure has the form

$$p(t) = p_o + p_1 \cos \omega t \quad (29)$$

and the interface elevation is given by

$$\eta(t) = \eta_o - \eta_1 \cos(\omega t - \phi) \quad (30)$$

Then the time averaged energy flux downwards through the interface is

$$\overline{D_M} = \frac{1}{T} \int_t^{t+T} -p(t) \frac{dn}{dt} dt \quad (31)$$

$$= \frac{1}{2} p_1 \omega \eta_1 \sin \phi \quad (32)$$

And introducing the mud response parameter (Tubman and Suheyda, 1976)

$$M = \frac{\rho g \eta_1}{P_1} \tag{33}$$

we get

$$D_M = \frac{1}{2} M \sin \phi \frac{\omega p_1^2}{\rho g} \tag{34}$$

For linear waves we have

$$P_1 = \rho g \frac{H}{2} \frac{1}{\cosh kh} \tag{35}$$

and thus the energy flux into the mud can be written

$$D_M = \frac{\pi \rho g M \sin \phi}{4T \cosh^2 kh} H^2 \tag{36}$$

WAVE HEIGHT VARIATION OVER A MUD BOTTOM

For sinusoidal waves propagating over a mud bottom equation (20) becomes

$$\frac{d}{ds} \left( \frac{1}{8} \rho g H^2 c_g \cos \alpha \right) = - \frac{\pi \rho g M \sin \phi}{4T \cosh^2 kh} H^2 \cos \alpha \tag{37}$$

which has the solution

$$\left( \frac{H_2}{H_1} \right)^2 = \frac{c_{g1} \cos \alpha_1}{c_{g2} \cos \alpha_2} \exp(M \sin \phi I) \tag{38}$$

with

$$I = \int_{s_1}^{s_2} - \frac{2\pi}{T} \frac{ds}{c_g \cosh^2 kh} \tag{39}$$

To evaluate this integral we must bring the integrand to an explicit form in terms of the independent variable.

If  $h$  varies monotonically with  $s$ , we can change the variable of integration into  $k_0 h$ . From Figure 6 we get

$$ds = \frac{d k_0 h}{k_0 \frac{dh}{dx} \cos \alpha} \quad (40)$$

and since  $c_0 k_0 = 2\pi/T$  we find

$$I = - \int_{k_0 h_1}^{k_0 h_2} \frac{d k_0 h}{\frac{dh}{dx} \frac{c_g}{c_0} \cos \alpha \cosh^2 kh} \quad (41)$$

Now using the alternative wave table (Figure 4) and a bit of algebra we find

$$\frac{1}{\frac{c_g}{c_0} \cosh^2 kh} \approx (k_0 h)^{-0.5} [1 - 0.5 k_0 h] \quad (42)$$

the accuracy of which is discussed in Figure 2. Since most natural mud bottoms are quite flat it is not very restrictive to assume constant bed slope and straight, parallel contours. Then Snell's law gives

$$\frac{1}{\cos \alpha} = [1 - (\frac{c}{c_1})^2 \sin^2 \alpha_1]^{-0.5} \quad (43)$$

and we use

$$\frac{c}{c_0} = \tanh kh \approx \sqrt{k_0 h} (1 - \frac{1}{6} k_0 h) \quad (44)$$

to get

$$\frac{1}{\cos \alpha} = [1 - \beta k_0 h (1 - \frac{1}{3} k_0 h)]^{-0.5} \quad (45)$$

where

$$\beta = \frac{\sin^2 \alpha_1}{k_0 h_1 (1 - \frac{1}{3} k_0 h_1)} \quad (46)$$

After some algebra we then get

$$I = - \frac{dx}{dh} \int_{k_o h_1}^{k_o h_2} \left[ (k_o h)^{-0.5} + \frac{1}{2} (\beta-1)(k_o h)^{0.5} + \left( \frac{3}{8} \beta^2 - \frac{5}{12} \right) (k_o h)^{1.5} \right] dk_o h \quad (47)$$

and

$$I = - \frac{dx}{dh} \left\{ 2(k_o h_1)^{0.5} \left[ \left( \frac{h_2}{h_1} \right)^{0.5} - 1 \right] + \frac{1}{3} (\beta-1)(k_o h_1)^{1.5} \left[ \left( \frac{h_2}{h_1} \right)^{1.5} - 1 \right] + \left( \frac{3}{20} \beta^2 - \frac{1}{6} \beta \right) (k_o h_1)^{2.5} \left[ \left( \frac{h_2}{h_1} \right)^{2.5} - 1 \right] \right\} \quad (48)$$

This formula together with (38) provides a very simple tool for predicting wave height variation over a soft mud bottom, and because the solution is explicit we can quite easily use it "in reverse", i.e.: If the final wave height,  $H_2$ , is known we can solve directly for  $M \sin \phi$ .

DISCUSSION

A set of simple explicit formulae have been provided (Figure 4) for easy calculation of linear wave properties. These formulae provide a handy alternative to wave tables, thus the basic

$$kh = \sqrt{k_o h} \left[ 1 + \frac{1}{6} k_o h + \frac{11}{360} (k_o h)^2 + \dots \right] \quad (15)$$

can easily be memorized by people who deal with linear waves frequently.

The major advantage of introducing explicit formulae is probably that it makes it possible to give analytical solutions to problems that involve integration. Such a solution to the problem of wave height variation due to shoaling refraction and frictional dissipation was given by Nielsen (1984) and a similar solution has been given above for the case of energy absorption by a soft mud bottom.

The accuracy of the solution (38) and (48) will depend on the depths  $h_1$  and  $h_2$  and on the starting angle  $\alpha_1$ . An error estimate can

be obtained by comparing discrete values of the integrands in (41) and (47).

At the presentation of this paper, Dr. O. Skovgaard of the Technical University of Denmark pointed out that a reduction by 20% or more in computing time could be obtained by using (15) as the first estimate in iterative procedures for determination of  $kh$ . It could be added that extra accuracy gained by iteration is often of no practical consequence because of the limited accuracy with which the physical environment can be described and of the crudeness of other underlying assumptions. - This is a matter of opinion, but it seems reasonable to omit iteration and rely entirely on (15) at least in the "debugging" phase for big wave programs.

#### ACKNOWLEDGEMENT

The present study was supported by the U.S. Office of Naval Research, Coastal Sciences Program, Task No. 388-189, Contract No. N00014-83-K-0198 through the Virginia Institute of Marine Science and University of Florida.

#### REFERENCES

1. Brink-Kjaer, O. and I.G. Jonsson (1973): Verification of cnoidal shoaling: Putnam and Chinn's experiments. Progr. Rep. 28, Institute of Hydrodynamics and Hydraulic Engineering, Tech. Univ. Denmark, pp. 19-23.
2. Gade, H.G. (1958): Effects of a non-rigid, impermeable bottom on plane surface waves in shallow water. Journal of Marine Research, Vol. 16, pp. 61-82.
3. Jonsson, I.G. (1966): Wave boundary layers and friction factors. Proc. 10th International Conference on Coastal Engineering, Tokyo, Chapter 10.
4. Nielsen, P. (1982): Explicit formulae for practical wave calculations. Coastal Engineering, Vol. 6, No. 4, pp. 389-398.
5. Nielsen, P. (1983): Analytical determination of nearshore wave height variation due to refraction, shoaling and friction. Coastal Engineering, Vol. 7, No. 3, pp. 233-251.
6. Nielsen, P. (1984): Wave height variation on straight beaches. A.S.C.E., Vol. 110, WW2, pp. 283-286.
7. Svendsen, I.A. and I.G. Jonsson (1976): Hydrodynamics of Coastal Regions. Den Private Ingenioerfond, Lyngby, Denmark.
8. Tubman, M.W. and J.N. Suheyda (1976): Wave action and bottom movement in fine sediments. Proc. 15th Int. Conf. Coastal Engineering, Hawaii, pp. 1168-1183.

## CHAPTER SIXTY SEVEN

### THE INTERACTION OF SMALL AND FINITE AMPLITUDE LONG WAVES AND CURRENTS

By F. Raichlen,<sup>1</sup> F.ASCE, and J. J. Lee,<sup>2</sup> M.ASCE

#### INTRODUCTION

The interaction of waves and currents is important for many engineering problems. For example, when considering forces on marine structures, the velocity and acceleration field must be defined, and thus the manner in which a current interacts with small and finite amplitude waves must be understood. When the current is large and oblique to the waves, the direction of the force on an offshore structure may change significantly with depth introducing a torsional moment. Wave refraction and the concomitant attenuation or amplification of waves are also affected by offshore currents. An example is the effect on incident waves of offshore currents induced by the discharge of cooling water from coastal-sited power plants. This current can modify the direction and magnitude of approaching waves, and by these changes the breaking waves at the shore and the nearshore sediment transport associated with these waves may be changed.

A number of theoretical studies have been conducted on various aspects of wave-current interactions; see Peregrine (1976). One theoretical study, Thomas (1981), will be used in this investigation. Careful experiments in this area are limited; several are: Iwagaki and Asano (1980), Sarpkaya (1957), and Thomas (1981). Each of these has given attention to certain aspects of small amplitude wave-current interactions. The experiments are difficult to conduct because of the problems inherent in introducing waves into a flume with a steady-uniform current or conversely a current into a wave tank with permanent waves. Certain features of these experimental problems can be seen through the following two examples. If a plunger-wave machine were used and located at one end of a flume in which a steady current is flowing, although the waves would be developing as they interact with the current, the previously steady current would be changed to an unsteady one by the periodic blockage of the flow by the plunger. If the waves are generated at one end of the tank and allowed to develop, and a current is introduced from the bottom of the tank, this current must expand to the full depth of the flow; hence, the waves propagate on a developing current. Therefore, comparisons to theory are, to some extent, difficult to realize, because the theory generally assumes wave-current interactions when each is fully developed.

This study basically had two objectives. The major objective was

---

<sup>1</sup>Professor of Civil Engineering, W. M. Keck Laboratory of Hydraulics and Water Resources, California Institute of Technology, Pasadena, CA.

<sup>2</sup>Professor of Civil Engineering, University of Southern California, Los Angeles, CA.

whether simple linear superposition could be used to describe wave-current interactions with weakly nonlinear finite amplitude waves. In essence, the question raised is: could the water particle velocities measured under a wave without a current be added to those measured with the current alone to yield the total velocity similar to that which was determined experimentally for the combined wave and current. The second was to investigate, using a simple means of introducing a current into the wave tank and withdrawing it, the effect of the configuration of the current inlet/outlet arrangement on the water particle velocities associated with the wave during the interval of wave development. For the possible currents generated in this study, conclusions could be drawn relative to these two questions.

This study is primarily experimental. The numerical method proposed by Thomas (1981) has been applied to the periodic wave measurements; as mentioned, this analysis will not be described herein, and the interested reader is referred to that publication for a discussion of the method. In this paper attention will be devoted to the experimental results and the question of superposition; results obtained using the numerical method proposed by Thomas (1981) will be included only as an adjunct to these.

#### EXPERIMENTAL EQUIPMENT AND PROCEDURES

##### Wave generation and measurement

Experiments have been conducted in a 40 m tilting tank which is 0.60 m deep and 1.10 m wide. The tank has glass sidewalls throughout with a stainless steel bottom which is flat to within approximately  $\pm 0.1$  mm. Circular rails attached to the top of the walls of the tank form precision tracks for an instrument carriage to which a wave gage can be attached. The wave machine used in this study is a vertical bulkhead generator located at one end of the tank and is driven by an electro-hydraulic system. The servo system which controls its motion consists of a servo controller, a function generator, and a feedback device. The function generator is a nonlinear function synthesizer with a microprocessor which stores a list of binary numbers corresponding to an arbitrary signal. The maximum voltage amplitude and the time are divided into 4096 parts; using these data a smooth signal can be obtained.

The motion of the wave machine was programmed for these experiments using the method described by Goring and Raichlen (1980) for the generation of long-nonlinear waves with a bulkhead wave generator. The boundary condition on the face of the plate for this technique is that the wave propagates away from the plate as it moves. Thus, the usual assumption of a negligible plate motion relative to its mean position is not necessary.

The variation of the water surface profiles with time were obtained using a parallel wire, resistance wave gage composed of 0.25 cm diameter stainless steel wire spaced 0.4 cm apart.

##### Inlet and outlet structures

The inlet and outlet structures were each constructed of lucite and were essentially boxes resting on the bottom of the tank extending

across the width of the tank (110 cm), 61 cm in the direction of wave propagation, and 13.75 cm high. Inflow (or outflow) was brought into (or taken from) the flume by means of a 10.2 cm dia. pipe connected to one end of the inlet/outlet box. Straight vanes were used in the box to divide the front of the box and the pipe into six equal areas. Even with this attempt to distribute the flow uniformly across the width of the flume, flow separation occurred within the box leading to non-uniform flow conditions at the box exit. Nevertheless, as it will be shown, the velocity became well distributed through the depth of the tank at the measuring location.

Two pump-piping arrangements were used for these experiments. In the case of periodic waves the discharge was 0.02 cubic meters per second using a pump-piping system that permitted the flow to be reversed. In the experiment with solitary waves, where a larger velocity was desired, a discharge of 0.028 cubic meters per second was realized, but only adverse flows were possible, i.e., the box nearest the wave machine always collected the flow.

In the case of periodic waves the water depth was kept at 30.2 cm for all experiments and for the solitary waves the depth was maintained at 17.42 cm. For the latter, the smaller depth was necessary so that the mean current velocity would be a significant percentage of the water particle velocities in the wave. Considering the physical arrangement the water depth over the boxes was small for the solitary wave case and wave breaking occurred over the box; this will be discussed.

#### Measurement of water particle velocities

A two-dimensional laser-Doppler velocimeter (LDV) employing the reference beam technique was used to measure the water particle velocities at a location 21.6 m from the wave generator for experiments with periodic waves and 23.6 m from the wave generator for the solitary wave investigation. (These two locations are near the middle of the wave tank.) Two reference beams and a scattering beam were generated using a 5 mW helium-neon laser, and these were optically focused near the center of the wave tank. To provide a means for defining the direction of the velocity components the LDV was equipped with a frequency shifter consisting of two Bragg cells (which operate at a nominal frequency of about 40 MHz) and a frequency synthesizer with phase-locked loops. The frequency shift between the reference beams and the scattering beam created by the Bragg cells was 86.92 KHz. The laser and its associated optics were mounted to a carriage which was isolated from the wave tank. This permitted the laser to be moved vertically through the depth and along the wave tank in the direction of wave propagation.

#### PRESENTATION AND DISCUSSION OF RESULTS

In this section the results obtained using the LDV will be presented for both periodic and solitary waves. (The periodic waves generated were weakly nonlinear cnoidal waves.) For periodic waves the experimental results are compared to the velocities obtained from the linear superposition of independently measured velocities and to the numerical theory of Thomas (1981). The comparison of the results of experiments with solitary waves will be made only to the results obtained by the linear superposition of measurements of the wave alone and the current alone.



Cnoidal waves

Velocity profile for steady current alone

Measurements of the current velocity were made at the various depths at the same location where the wave measurements would be taken; 21.6 m (about 71.5 depths) from the wave machine. The velocity distribution is shown in Figure 1 where the abscissa is the velocity and the

ordinate is the relative distance from the bottom. A universal velocity distribution is fitted to the data, for both favorable and adverse currents, with the assumption that the von Karman constant was 0.4. Since the flume was horizontal, the flow must be nonuniform and an independent estimate of boundary shear stress is not possible. Therefore, the coefficient B and the shear stress are obtained from the fitted line in the semi-logarithmic plot, the mean velocity U is obtained from the spacial integration of the velocity distribution. It is recalled that the coefficients in the velocity distribution expression normally used are A = 5.75 and B = 2.5; hence, the velocity distributions measured are in fair agreement with the usual logarithmic profile.

SYMBOL	CURRENT	U (cm/sec)	$\sqrt{\tau_0/\rho}$ (cm/sec)	A	B
—○	FAVOR.	6.16	0.201	5.75	3.02
---●	ADVER.	6.26	0.146	5.75	4.34

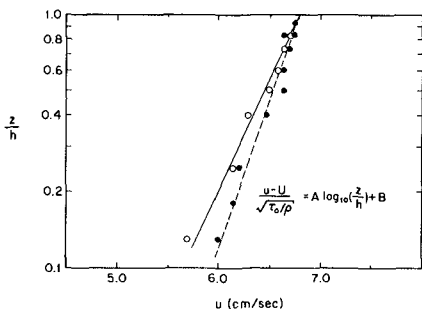


Figure 1 Velocity Distribution of Current Alone with Experiments with Periodic Waves.

(However, the boundary shear stress obtained in this manner gives small values of the Darcy-Weisbach friction factor so that full interpretation of the profile is difficult.)

Velocities for the wave without a current

Two sets of experiments were conducted to investigate the kinematic properties of the cnoidal waves, which were to be used in the current-wave experiments, propagating in the tank without the current. It was realized early in the experimental program that the inflow box near the wave machine could create an effect on the wave even though the velocity and wave measurements were made nearly 72 depths away.

Time histories of the water surface variation, the horizontal velocity, and the vertical velocity at mid-depth for the case without the inflow box are presented in Figure 2. (The cnoidal waves generated were weakly nonlinear with a wave period of 3.015 seconds and the ratio of wave height to depth of about 0.04.) It is noted that although the wave is not highly nonlinear, even with the large wave length to depth ratio (about 17), high frequency components are not apparent in either the water surface-time history ( $\eta$  vs  $t$ ) or the time history of the horizontal velocity ( $u$  vs  $t$ ). This primarily is due to the careful wave generation procedure used. For both the water surface and the horizontal velocity, the second, third, and fourth waves are similar and well formed. The theoretical cnoidal wave profile is shown in the upper

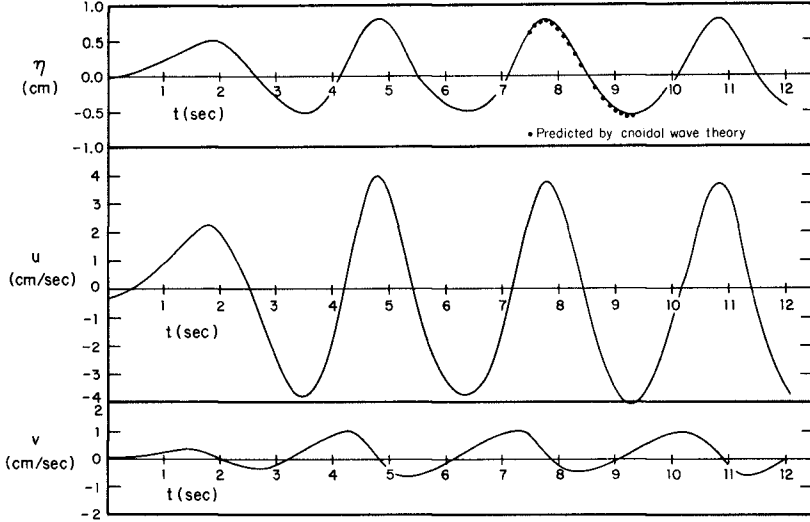


Figure 2 Water Surface, Horizontal, and Vertical Velocity-Time Histories at  $z/h = 0.5$  for No Current (Without inflow box in place).

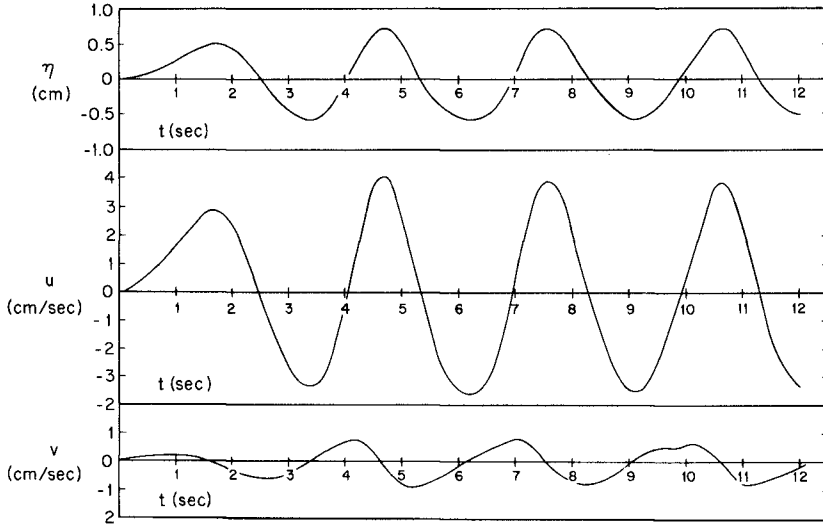


Figure 3 Water Surface, Horizontal, and Vertical Velocity-Time Histories at  $z/h = 0.5$  for No Current (With inflow box in place).

portion of Figure 2, and it agrees reasonably well with the experiments. The magnitude of the vertical velocity,  $v$ , is significantly less than the horizontal velocity, i.e., of the order of about 20%, and its distribution appears skewed. The reason for this is not fully understood.

Similar time histories are presented in Figure 3 at mid-depth for the wave propagating over the inflow box but without a current. The primary effect is the vertical and the horizontal velocities are reduced compared to the corresponding conditions without the box. This may be an effect which is associated with the wave propagating over the box with only about five wave lengths to the measuring station.

In Figure 4 the variation of the maximum water particle velocities with relative depth measured under the crest of the wave is presented for the wave propagating in the bare tank and for the wave propagating in the tank with the inflow box; in the latter no current is imposed.

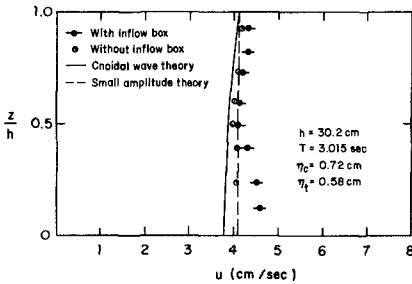


Figure 4 Depthwise Distribution of Maximum Horizontal Velocity Under the Second Crest of a Cnoidal Wave Train.

The most obvious effect of the box occurs at elevations which are between the bottom and mid-depth. In the case with the box the velocities tend to increase as the bottom is approached whereas without the box the velocities remain relatively constant through the depth. Thus, the box seems to have an effect on the wave with regard to the depthwise distribution of its kinematic properties, perhaps more so than its effect on the wave profile. The data are compared to predictions from cnoidal theory and from small amplitude wave theory, and it appears that within the limits of experimental accuracy, the experiments without the box agree with the results of the small amplitude wave theory somewhat better than with those from the cnoidal theory.

#### Waves with a favorable current

In this section experimental results obtained with the waves and the current traveling in the same direction (a favorable current) are presented. Similar to previous figures, the time histories of the water surface and the horizontal and vertical velocities at mid-depth are presented first in Figure 5. A comparison of Figure 5 and Figure 3 show that there is, at most, a difference of about 3% to 4% in the wave amplitude and the wave length between the second and third wave crest for the cases without and with the current. The crest height is reduced and the wave lengths are somewhat longer, as expected. Taken in totality, however, the effect of the current on the wave profile indeed is quite small and within the range of experimental error; results such as those obtained by Jonsson et al. (1970) indicate this also.

The depthwise distributions of the velocities are shown in Figure

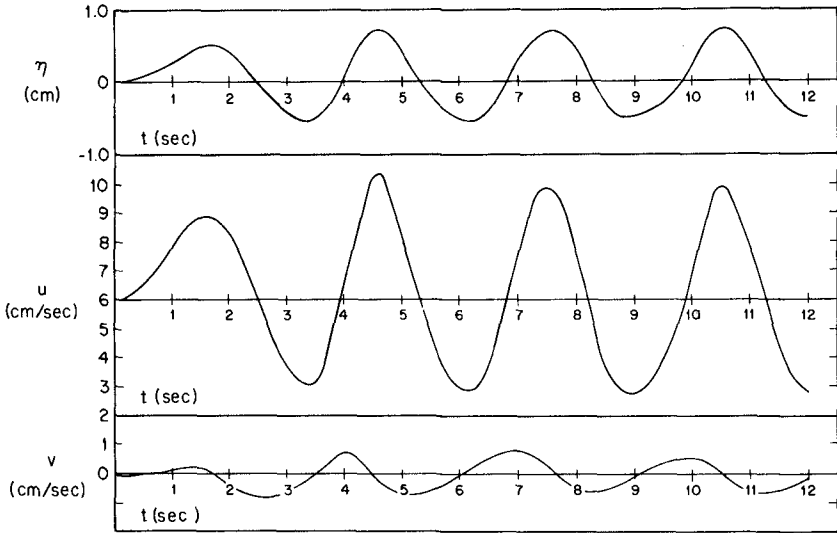


Figure 5 Water Surface, Horizontal, and Vertical Velocity at  $z/h = 0.5$  for Wave and Current in Same Direction (Favorable Current).

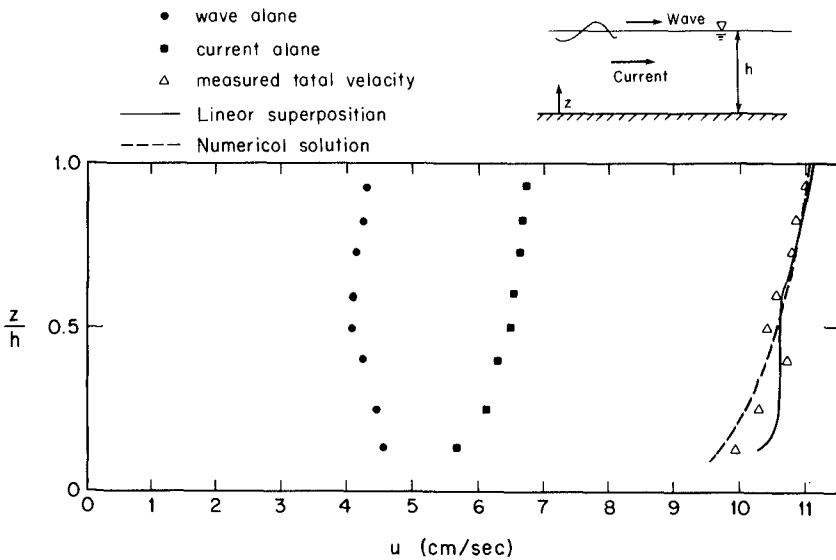


Figure 6 Distribution of the Horizontal Velocity for Wave and Current in Same Direction (Favorable Current).

6; the data are presented for the wave alone, the current alone, and the measured total velocity. The solid curve is obtained from superposing the measured data corresponding to the wave alone and that from the current alone. The dashed curve is the total water particle velocity predicted by the numerical solution proposed by Thomas (1981) which is based on the water particle velocity under the wave obtained from small amplitude wave theory. Above mid-depth the data agree well with each approach, and below it is difficult to establish the better agreement.

#### Waves with adverse current

For these experiments the direction of the current was reversed and is denoted as adverse. Data similar to those obtained for favorable currents are presented in Figure 7 showing the time histories of the water surface and the horizontal and vertical velocities at mid-depth. A close examination of the wave record indicates that the waves are somewhat steeper than they were for waves without the current or for waves traveling on a favorable current (see Figures 3 and 5, respectively). Perhaps more apparent are changes in both the horizontal velocity and the vertical velocity in terms of the steepness of the time history. The greatest differences between the kinematics of the waves propagating on a favorable and adverse current appear to be associated with the variation with time of the vertical velocities. This might be expected due to the small magnitude of the vertical velocity compared to the horizontal velocity for long waves, and hence, its sensitivity to small changes in the wave.

The measured velocity distributions are presented in Figure 8 for the wave alone, the current alone, and the total velocity. As for the case of the favorable current, linear superposition has been used based on the measured values along with the numerical solution proposed by Thomas (1981). In this case, the numerical solution appears to agree better with the data than the results of simple linear superposition. However, the differences are not large enough so that general conclusions can be drawn.

#### Solitary waves

In this section results obtained from experiments with solitary waves under the influence of adverse currents will be presented and discussed. The wave height was determined by the conditions that on the one hand a limited pump discharge was available for the solitary wave-current interaction investigation while on the other wave particle velocities were desired which would be of the same order of magnitude as the available current. The maximum average current velocity possible was 14.9 cm/sec and, to satisfy these conditions, a wave with a relative height (height/depth) of about 0.3 was used. Due to pump and piping restrictions only an adverse current could be generated. The velocity distribution for this current is presented in Figure 9 where the ordinate is the relative distance from the bottom and the abscissa is the velocity. Each data point shown is the result of averaging 10 different velocity samples at that elevation. Since each sample has a duration of one minute, in essence the data point is a temporal average of about 10 minutes of record. The averaging was necessary because of low frequency velocity fluctuations which apparently were caused by the outlet/inlet configuration. The inferred shear stress yields a friction

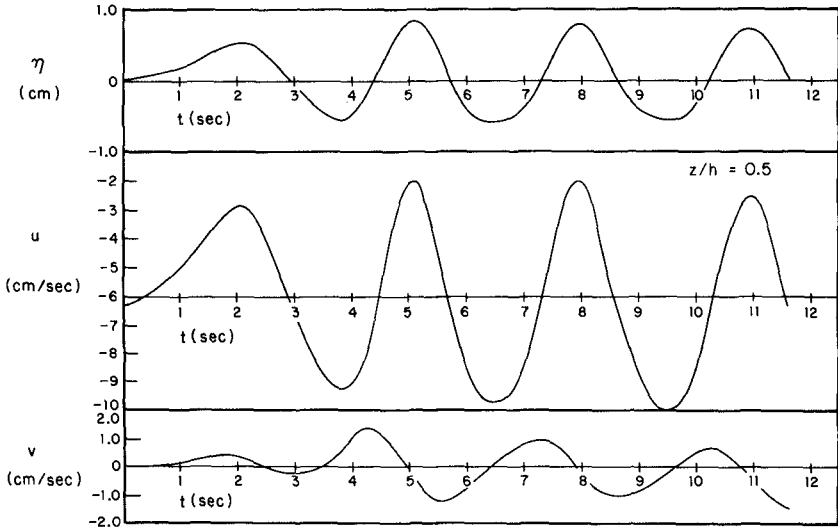


Figure 7 Water Surface, Horizontal, and Vertical Velocity at  $z/h = 0.5$  for Wave and Current in Opposite Directions (Adverse Current).

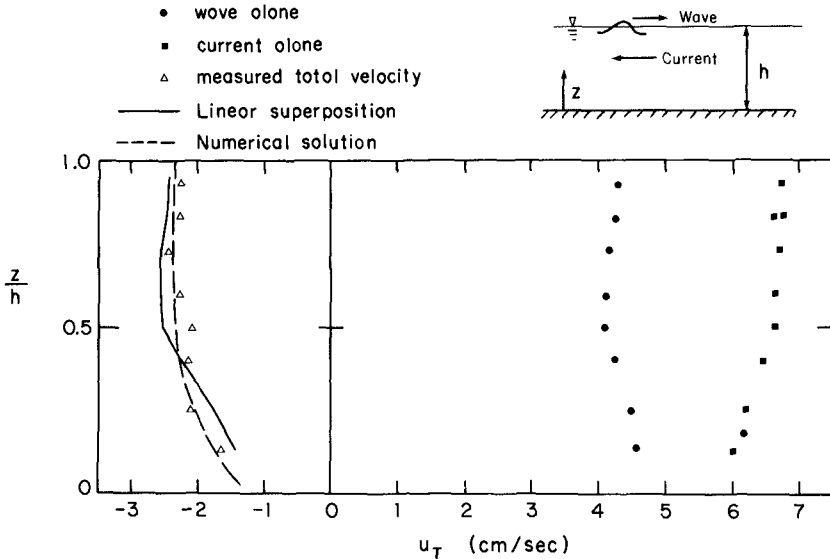


Figure 8 Distribution of the Horizontal Velocity for Wave and Current in Opposite Direction (Adverse Current).

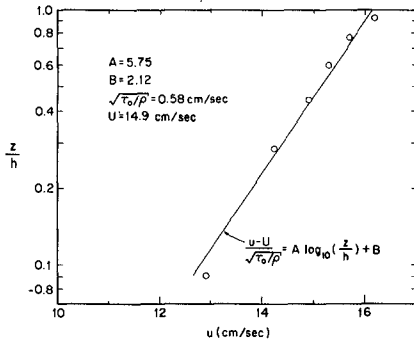


Figure 9 Velocity Distribution of Current Alone for Experiments with Solitary Waves.

factor smaller than predicted by usual means, but this is mitigated by the fact that the flume is horizontal and the current takes some distance to develop.

The solitary wave is generated using techniques developed in other experimental studies where excellently formed waves with a negligible oscillatory tail were realized, e.g., see Lee, Skjelbreia, and Raichlen (1982). Water surface time histories of waves propagating without and with the adverse current have been obtained at relative distances from the wave generation of:  $x/h = 15.5, 75.8,$  and  $135.5$ . In each case the wave broke as it propagated

over the outlet box and then reformed into a lead wave which appeared to be solitary in shape followed by a group of oscillatory waves.

It is important to investigate the reproducibility of the wave generation arrangement used in these experiments, since the LDV is an instrument which can measure velocities only at one point at a given time. Therefore, to obtain the depthwise velocity distribution, the experiments must be repeated relocating the LDV for each measurement. In Figures 10 and 11 the wave profile is shown 135.5 depths from the wave generator (at the velocity measuring station) for the cases without and with an adverse current, respectively. For both current conditions the profile consists initially of a wave similar to a solitary wave followed by an oscillatory tail. Each of these records is for six different experiments, and the reproducibility is evident; even small oscillations in the record generally are reproduced well. It is interesting that in comparing the amplitude normalized with respect to the depth, for the wave with the adverse current the leading wave is about 2% greater in height than for the wave without the current.

Wave profiles were measured at several locations along the tank and the travel times between  $x/h = 15.5$  and  $x/h = 135.5$  were determined to compare wave celerities for conditions without and with the adverse current; these are shown in Table 1. (The experiments with the same last digit in the experiment number should be compared, e.g., WPA1 to WPCL, and etc.) If the mean current (14.9 cm/sec) is subtracted from the measured wave speed without a current the resultant celerity is within about 2% of that measured.

In Figures 12 through 15 time histories of the horizontal velocities are presented as measured at four different elevations and 135.5 depths from the wave generator. In each figure the measured horizontal water particle velocity for the waves propagating on a current is presented along with the water particle velocity time history which has been obtained by subtracting the measured velocity of the mean current from the measured horizontal velocity of the wave alone. Hence, the

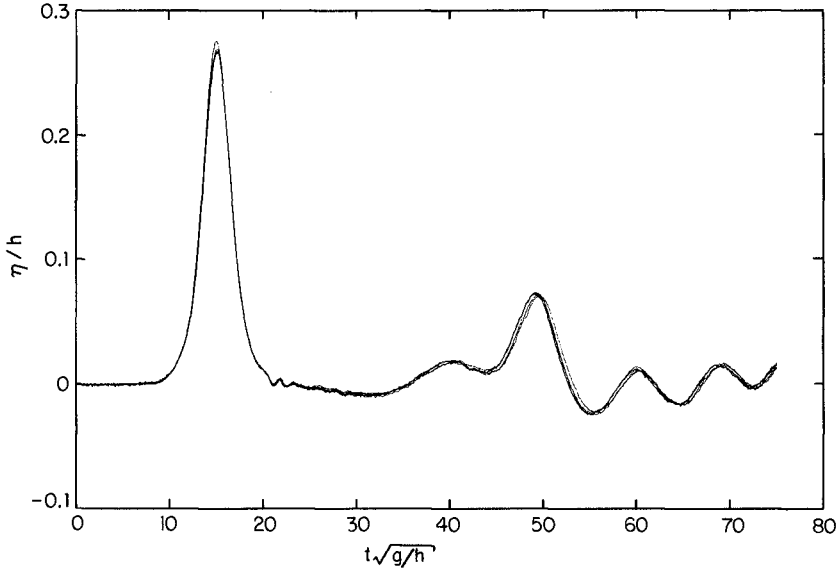


Figure 10 Water Surface-Time History at  $x/h = 135$  with Outlet Box in Place, Without Adverse Current.

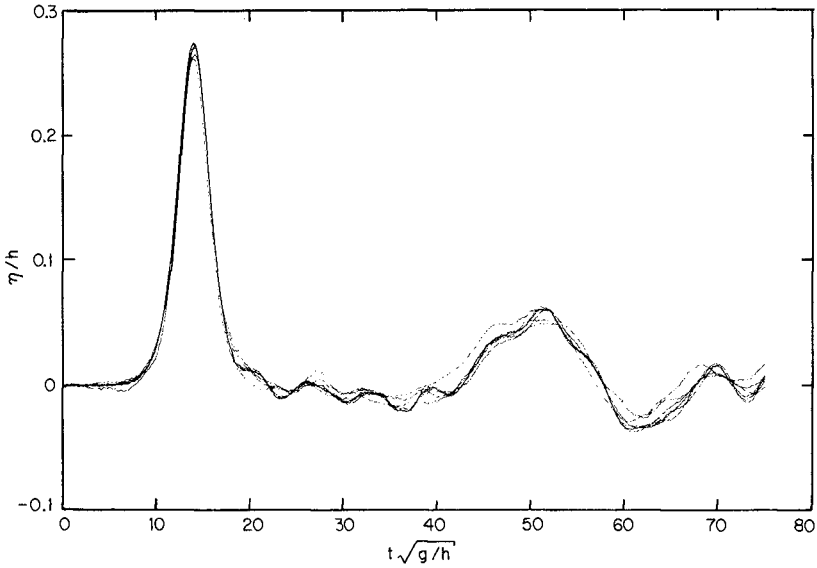


Figure 11 Water Surface-Time History at  $x/h = 135$  with Outlet Box in Place, With Adverse Current.



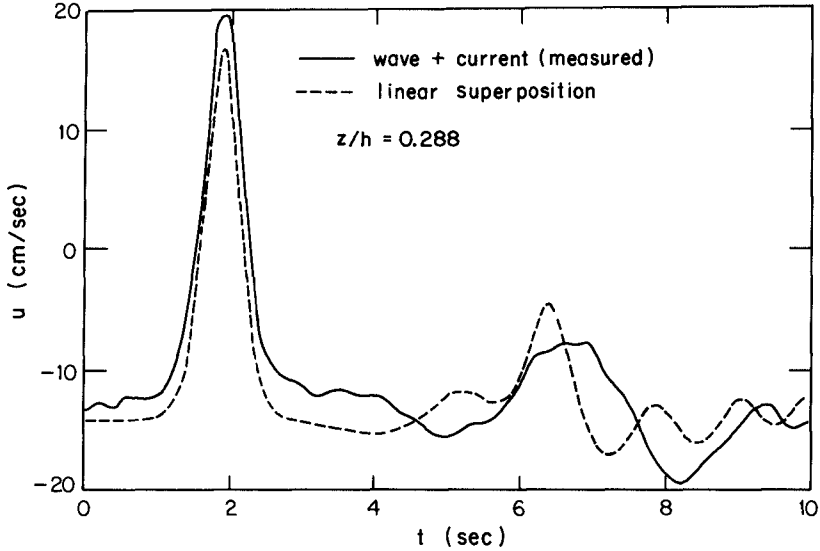


Figure 12 Horizontal Velocity Time History at  $z/h = 0.288$ .

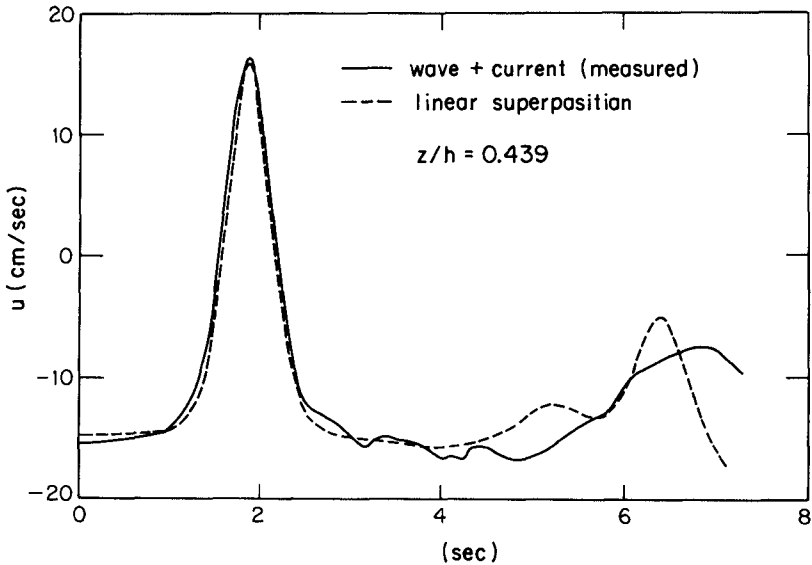


Figure 13 Horizontal Velocity Time History at  $z/h = 0.439$ .

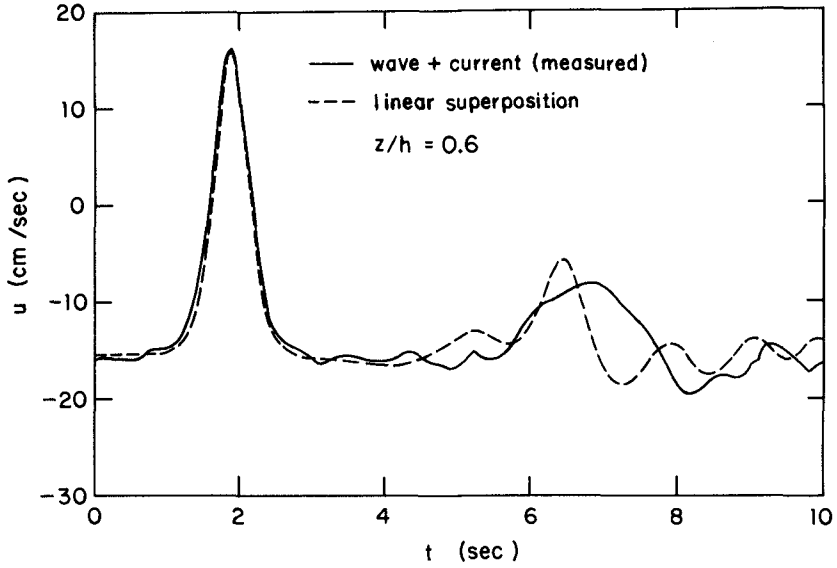
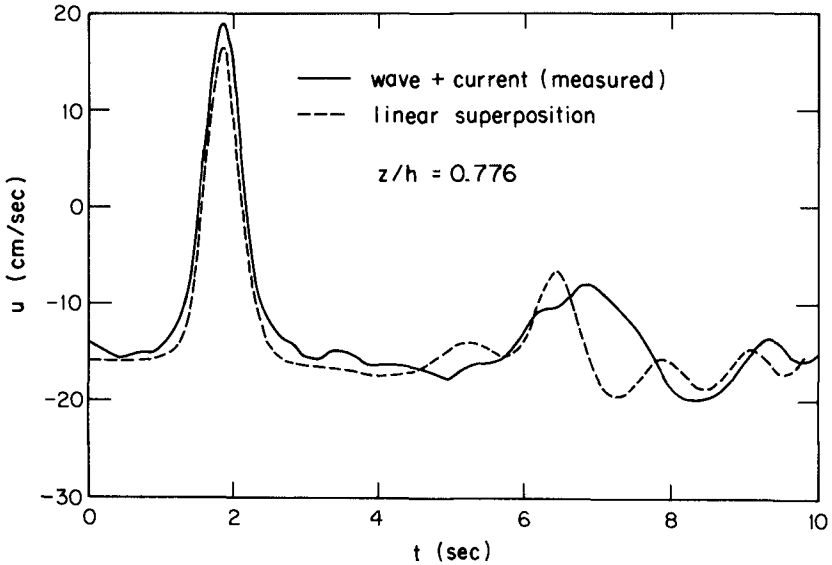
Figure 14 Horizontal Velocity Time History at  $z/h = 0.6$ .Figure 15 Horizontal Velocity Time History at  $z/h = 0.776$ .

Table 1 Celerities of the lead wave with and without a current.

Experiment	Current	C cm/sec
WPA1	no	154.96
WPA2	no	151.59
WPA3	no	149.42
WPC1	yes	140.48
WPC2	yes	138.16
WPC3	yes	134.26

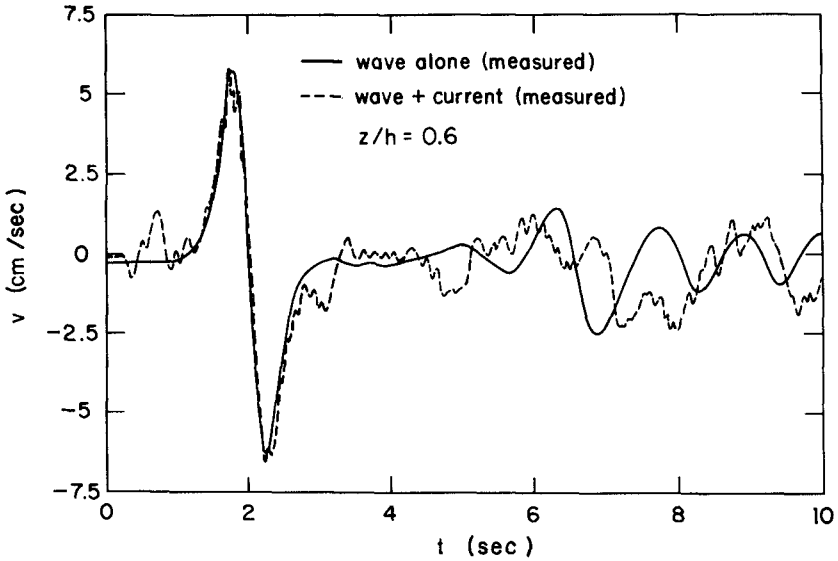
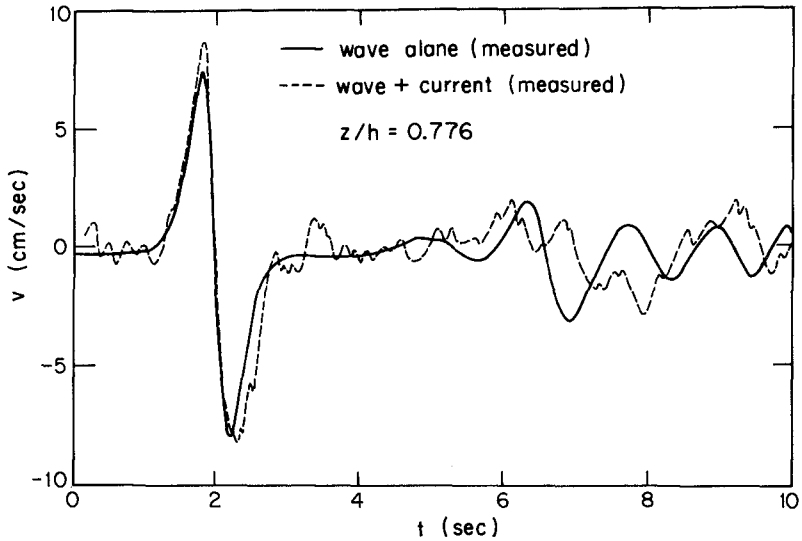
dashed curve corresponds simply to linear superposition. There are differences which are apparent in these comparisons; however, the differences between the results of linear superposition and the measured total velocity for the lead wave are not large. In nearly all cases, the maximum velocity at the wave crest is underestimated by superposition by less than 10% to 15%. However, the trailing waves are significantly affected by the current so that superposition does not define the velocity field well in that region. (It should be noted that results from the method of Thomas (1981) were not compared to the experiments, since inherent to that method is the assumption that the water particle velocities under the wave for the condition without the current can be defined in a linear manner from harmonic components.)

In Figures 10 and 11, in which the variation of the water surface elevation with time was presented, similar differences between the wave profiles without the current and with the current were evident. Since this effect was significant in the trailing region of the wave, in this region differences between the velocities obtained by linear superposition and those measured with the current would be expected. Therefore, it appears the current affects the oscillatory waves which trail the main wave more than it affects the lead wave, and, thus, the velocity for the oscillatory tail cannot be constructed by simple linear superposition.

Examples of the time history of the vertical velocity components are presented in Figures 16 and 17 for relative depths of  $z/h = 0.6$  and  $0.78$  at  $x/h = 135.5$  and in each figure for conditions without and with the current. (Note the vertical scales in Figures 16 and 17 are different.) Several features are apparent. The ratio of the maximum vertical velocities at these two elevations is close to the ratio of the elevations themselves demonstrating the variation with depth of the maximum vertical velocities would be reasonably linear as predicted by linear long wave theory. The vertical velocity time histories at each of these two depths for conditions without and with the current are similar especially with respect to the velocity associated with the leading wave. As with the horizontal velocities most of the effect appears to be related to the velocities corresponding to the oscillatory tail.

#### CONCLUSIONS

The following major conclusions may be drawn from this investigation:

Figure 16 Vertical Velocity Time History at  $z/h = 0.6$ .Figure 17 Vertical Velocity Time History at  $z/h = 0.776$ .

1. Even a very simple means of introducing a current into a wave tank for wave-current interaction studies can yield useful results. Indeed it may not be possible to investigate exactly wave-current interactions in the laboratory as the problem is formulated theoretically, since either the wave is developing on a permanent current or the current is developing while a permanent wave is propagating through it.

2. For engineering purposes, for waves of the order of magnitude investigated, linear superposition appears to adequately describe the maximum horizontal water particle velocities.

3. For the case of solitary waves where the oscillatory tail of the wave caused by the wave propagating over the inflow box was considerably changed by the current, the horizontal and vertical velocities were affected accordingly.

4. This investigation further demonstrates the importance of the LDV for "in situ" measurements of velocities in water waves.

#### ACKNOWLEDGMENT

The study was supported by the Naval Construction Battalion Center with technical coordination provided by Mr. Jerry Dummer. The LDV which was used in this study was developed in connection with an investigation sponsored by the National Science Foundation under NSF Grant CME79-12434. Mr. James Skjelbreia assisted in certain aspects of the data collection.

#### REFERENCES

- Goring, D. and Raichlen, F., "The Generation of Long Waves in the Laboratory," Proceedings of the Seventeenth Coastal Engineering Conference, Sydney, Australia, 1980.
- Iwagaki, Y. and Asano, T., "Water Particle Velocity in Wave Current System," Coastal Engineering in Japan, Vol. 23, 1980.
- Jonsson, I.G., Skougaard, C., and Wang, J.D., "Interaction Between Waves and Currents," Proceedings of the Twelfth Coastal Engineering Conference, Washington, D.C., 1970.
- Lee, J.J., Skjelbreia, J., Raichlen, F., "Measurement of Velocities in Solitary Waves," Journal of Waterway, Port, Coastal and Ocean Division, ASCE, Vol. 108, No. WW2, May 1982.
- Peregrine, D.H., "Interaction of Water Waves and Currents," Advances in Applied Mechanics, Vol. 16, 1976.
- Sarpkaya, T., "Oscillating Gravity Waves in Flowing Water," Transactions, ASCE, Vol. 122, 1957.
- Thomas, G.P., "Wave-Current Interactions: An Experimental and Numerical Study. Part 1: Linear Waves," Journal of Fluid Mechanics, Vol. 110, 1981.

## CHAPTER SIXTY EIGHT

### COMBINED REFRACTION-DIFFRACTION OF NONLINEAR WAVES IN SHALLOW WATER

James T. Kirby,<sup>1</sup> Philip L.-F. Liu,<sup>2</sup> A.M.'s. ASCE

Sung B. Yoon<sup>3</sup> and Robert A. Dalrymple<sup>4</sup>, M. ASCE

The parabolic approximation is developed to study the combined refraction/diffraction of weakly nonlinear shallow water waves. Two methods of approach are taken. In the first method Boussinesq equations are used to derive evolution equations for spectral wave components in a slowly varying two-dimensional domain. The second method modifies the equation of Kadomtsev & Petviashvili to include varying depth in two dimensions. Comparisons are made between present numerical results, experimental data and previous numerical calculations.

#### Introduction

In recent years, the recognition of the need for an improvement on the predictive capabilities of standard refraction methods (for example, Skovgaard, et al., 16) has led to the development of several techniques for computing wave fields modified by the combined effects of refraction and diffraction. Among these methods, the parabolic equation method (PEM) appears to be particularly attractive in the study of wave propagation in open coastal regions since its usefulness depends on a nearly unidirectional propagation of waves with little backscatter. The method was first developed for monochromatic linear waves by Radder (14) and Lozano & Liu (12) and has been extended to include effects such as frictional dissipation (3) and wave-current interaction (1,6,9). Recently, the formulation has been extended to the case of second-order monochromatic Stokes waves (8,11,19). Iterative methods have been developed in order to model the gradual development of reflected wave components, both for the linear (10) and Stokes wave (7) formulations.

Waves in shallow water near the coastline are rarely monochromatic, and are subject to fairly strong nonlinear interactions due to near-resonances as the phase speeds of individual spectral components approach coincidence. In addition, the smallness of the ratio of water

1. Assistant Professor, Marine Sciences Research Center, State Univ. of New York, Stony Brook, NY (presently, Coastal and Oceanographic Engineering Dept., Univ. of Florida, Gainesville, FL 32611).
2. Professor, School of Civil and Environmental Engineering, Cornell University, Ithaca, NY 14853.
3. Graduate Student, School of Civil and Envir. Engrg., Cornell Univ., Ithaca, NY 14853.
4. Professor, Dept. of Civil Engineering, University of Delaware, Newark, DE 19716.

depth to wavelength in such regions invalidates the assumptions underlying the Stokes theory and leads, instead, to a description of the wavefield based on the Korteweg-deVries or Boussinesq equations. For this reason, we have investigated methods for calculating the propagation and evolution of spectral wave components in an arbitrarily varying, two-dimensional domain, with the restrictions of shallow water and the parabolic approximation applied. The results of this study extend the PEM to the case of nonlinear waves in shallow water, and are applicable to the study of harmonic generation and spectral evolution as well as refraction-diffraction.

Two methods of approach are described. First, Boussinesq equations are used to derive evolution equations for spectral wave components in a slowly varying, two-dimensional domain. Secondly, we describe a similar modeling approach based on a version of the weakly two-dimensional Korteweg-deVries equation of Kadomtsev & Petviashvili (5) (hereafter referred to as the K-P equation). The present approach extends the K-P equation to include varying water depth in two dimensions. The resulting systems of coupled nonlinear partial differential equations for spectral wave components from two approaches are quite similar. These equations are written in finite difference form using the Crank-Nicolson method, yielding an initial-boundary value problem for the spatial evolution of each spectral mode.

The present model is used to examine the refraction of a cnoidal wave over a plane slope in a rectangular channel. Numerical solutions agree very well with previous analytical and numerical results. The formation of stem waves along the boundary and the development of a high-frequency modulation are observed and discussed. Comparisons are also made between the predictions of each model and the experimental data of Whalin (18) for his three second wave period case. The agreement between experimental data and numerical results is reasonable but not excellent. Both models predict much higher first harmonic amplitudes along the centerline of the tank. The prediction of the second and third harmonic amplitudes is seen to be better.

#### Nonlinear Shallow-Water Wave Equations and Parabolic Approximation

The Boussinesq equations, which include nonlinearity and dispersion to the leading order, are used as a basis of the first approach. Using  $\omega$  as the characteristic frequency,  $a_0$  as the characteristic wave amplitude and  $h_0$  as the characteristic water depth, we introduce the following dimensionless variables:

$$t = \omega t' \quad , \quad (x, y) = \frac{\omega}{\sqrt{gh_0}} (x', y') \quad , \quad z = z'/h_0$$

$$h = h'/h_0 \quad , \quad \vec{u} = \vec{u}' / \left[ \frac{a_0}{h_0} \sqrt{gh_0} \right] \quad , \quad \zeta = \zeta'/a_0 \quad (1)$$

where  $\zeta$  is the free surface displacement and  $\vec{u}$  represents the depth-averaged horizontal velocity vector. The quantities with prime denote dimensional quantities. If the scale of water depth is small in

comparison with the horizontal length scale and the wave amplitude is small compared with the water depth, i.e.,

$$\mu^2 = \omega^2 h_0 / g \ll 1 \tag{2}$$

$$\epsilon = a_0 / h_0 \ll 1 \tag{3}$$

the Boussinesq equations take the following dimensionless forms:

$$\frac{\partial \zeta}{\partial t} + \nabla \cdot [(h + \epsilon \zeta) \vec{u}] = 0(\epsilon^2, \epsilon \mu^2, \mu^4) \tag{4}$$

$$\begin{aligned} \frac{\partial \vec{u}}{\partial t} + \epsilon \vec{u} \cdot \nabla \vec{u} + \nabla \zeta = \mu^2 \left\{ \frac{1}{2} h \frac{\partial}{\partial t} \nabla [\nabla \cdot (h \vec{u})] - \frac{1}{6} h^2 \frac{\partial}{\partial t} \nabla (\nabla \cdot \vec{u}) \right\} \\ + 0(\epsilon^2, \epsilon \mu^2, \mu^4) \end{aligned} \tag{5}$$

where two small parameters,  $\epsilon$  and  $\mu^2$ , are assumed to be of the same order of magnitude. In the present study we also assume that the variation of water depth is small in a characteristic wavelength, i.e.,  $0(|\nabla h|) \leq 0(\mu^2)$ .

We shall study the propagation of a shallow water wave train which is periodic in time with the fundamental frequency  $\omega$ . The solutions can be expressed as a Fourier series

$$\zeta(x, y, t) = \frac{1}{2} \sum_n \zeta_n(x, y) e^{-int} \quad , \quad n=0, \pm 1, \pm 2, \dots \tag{6}$$

$$\vec{u}(x, y, t) = \frac{1}{2} \sum_n \vec{u}_n(x, y) e^{-int} \quad , \quad n=0, \pm 1, \pm 2, \dots \tag{7}$$

where  $(\zeta_{-n}, \vec{u}_{-n})$  are the complex conjugates of  $(\zeta_n, \vec{u}_n)$ . Substituting eqs. (6) and (7) into eqs. (4) and (5) and collecting the coefficients of different Fourier components yields the set of equations

$$-in \zeta_n + \nabla \cdot (h \vec{u}_n) + \frac{\epsilon}{2} \sum_s \nabla \cdot (\zeta_s \vec{u}_{n-s}) = 0(\epsilon^2, \epsilon \mu^2, \mu^4) \tag{8}$$

$$-in \vec{u}_n + (1 - \frac{\mu^2 n^2}{3} h) \nabla \zeta_n + \frac{\epsilon}{4} \sum_s (\vec{u}_s \cdot \vec{u}_{n-s}) = 0(\epsilon^2, \epsilon \mu^2, \mu^4) \tag{9}$$

where  $s = 0, \pm 1, \pm 2, \dots$ . From these two equations we can find the following lowest order relationships:

$$\vec{u}_n = -\frac{i}{n} \nabla \zeta_n [1 + 0(\epsilon, \mu^2)] \tag{10}$$

$$\nabla \cdot \vec{u}_n = in \zeta_n / h [1 + 0(\epsilon, \mu^2)] \tag{11}$$

for  $n \neq 0$ , and

$$\vec{u}_0 = -\frac{\epsilon}{2h} \sum_s \zeta_s \vec{u}_{-s} + 0(\epsilon^2, \mu^4, \epsilon \mu^2) \tag{12}$$



$$\zeta_0 = -\frac{\epsilon}{4} \sum_s \vec{u}_s \cdot \vec{u}_{-s} + O(\epsilon^2, \mu^4, \epsilon\mu^2) \tag{13}$$

For the case where water depth is a constant,  $h = 1$ , eqs. (8) and (9) reduce to those derived by Rogers & Mei (15).

Using eqs. (10) and (11) in eqs. (8) and (9) and eliminating  $\vec{u}_n$  gives

$$\begin{aligned} \nabla \cdot \left[ \left( h - \frac{\mu^2 n^2 h^2}{3} \right) \nabla \zeta_n \right] + n^2 \zeta_n = \frac{\epsilon}{2h} \left\{ \sum_s (n^2 - s^2) \zeta_s \zeta_{n-s} \right. \\ - h \sum_{s \neq n} \left( \frac{n+s}{n-s} \right) \nabla \zeta_s \cdot \nabla \zeta_{n-s} - 2h^2 \sum_{\substack{s \neq 0 \\ s \neq n}} \frac{1}{s(n-s)} \left( \frac{\partial^2 \zeta_s}{\partial x^2} \frac{\partial^2 \zeta_{n-s}}{\partial y^2} \right. \\ \left. \left. - \frac{\partial^2 \zeta_s}{\partial x \partial y} \frac{\partial^2 \zeta_{n-s}}{\partial x \partial y} \right) \right\} + O(\epsilon^2, \epsilon\mu^2, \mu^4) \end{aligned} \tag{14}$$

which constitutes a system of nonlinear equations for  $\zeta_n$  ( $n = 1, 2, 3, \dots$ ). Since eq. (14) is a differential equation of the elliptic type, appropriate boundary conditions must be assigned along the boundaries. Once  $\zeta_n$  ( $n = 1, 2, \dots$ ) are found, eq. (10) can be used to calculate the velocity vector  $\vec{u}_n$ . The mean free surface set-up or set-down,  $\zeta_0$ , is obtained from eq. (13).

We now consider the cases where the dominant wave propagation direction is known and is in the x-direction. The free surface displacement for the n-th harmonic can be written as

$$\zeta_n = \psi_n(x, y) e^{inx} \tag{15}$$

where  $\psi_n(x, y)$  denotes the amplitude function which takes both refraction and diffraction effects into account. Substitution of eq. (15) into eq. (14) yields

$$\begin{aligned} G_n \left( \frac{\partial^2 \psi_n}{\partial x^2} + \frac{\partial^2 \psi_n}{\partial y^2} \right) + (2in G_n + \frac{\partial G_n}{\partial x}) \frac{\partial \psi_n}{\partial x} + \frac{\partial G_n}{\partial y} \frac{\partial \psi_n}{\partial y} \\ + \left( in \frac{\partial G_n}{\partial x} - n^2 G_n + n^2 \right) \psi_n = \frac{\epsilon}{2h} \left\{ \sum_s [h s(n+s) + (n^2 - s^2)] \psi_s \psi_{n-s} \right. \\ - h \sum_{s \neq n} \left( \frac{n+s}{n-s} \right) \left[ \nabla \psi_s \cdot \nabla \psi_{n-s} + i s \psi_s \frac{\partial \psi_{n-s}}{\partial x} + i(n-s) \psi_{n-s} \frac{\partial \psi_s}{\partial x} \right] \\ - 2h^2 \sum_{\substack{s \neq 0 \\ s \neq n}} \frac{1}{s(n-s)} \left[ \frac{\partial^2 \psi_s}{\partial x^2} \frac{\partial^2 \psi_{n-s}}{\partial y^2} - \frac{\partial^2 \psi_s}{\partial x \partial y} \frac{\partial^2 \psi_{n-s}}{\partial x \partial y} \right. \\ - s^2 \psi_s \frac{\partial^2 \psi_{n-s}}{\partial y^2} + s(n-s) \frac{\partial \psi_s}{\partial y} \frac{\partial \psi_{n-s}}{\partial y} + i(2s \frac{\partial \psi_s}{\partial x} \frac{\partial^2 \psi_{n-s}}{\partial y^2} \\ \left. - s \frac{\partial \psi_s}{\partial y} \frac{\partial^2 \psi_{n-s}}{\partial x \partial y} - (n-s) \frac{\partial^2 \psi_s}{\partial x \partial y} \frac{\partial \psi_{n-s}}{\partial y} \right] \left. \right\} + O(\mu^4, \epsilon\mu^2, \epsilon^2) \end{aligned} \tag{16}$$

where

$$G_n = h - \frac{\mu^2 n^2 h^2}{3} \tag{17}$$

In principle, eq. (16) can be solved as a system of boundary value problems for  $\psi_n$ .

The amplitude function  $\psi_n$  is primarily a function of the water depth due to wave shoaling. Therefore,  $\psi_n$  varies slowly in the direction of wave propagation at the same rate as that of  $h$  in the  $x$ -direction. Thus

$$\frac{\partial \psi_n}{\partial x} \sim \frac{\partial h}{\partial x} \sim O(\epsilon, \mu^2) \tag{18}$$

$$\frac{\partial^2 \psi_n}{\partial x^2} \sim O(\epsilon^2, \mu^4, \epsilon \mu^2) \tag{19}$$

The diffraction effects are considered important. Hence,

$$\frac{\partial \psi_n}{\partial y} \sim O(1) \tag{20}$$

Using eqs. (18-20), we can simplify eq. (16) significantly to get

$$\begin{aligned} 2in \frac{\partial \psi_n}{\partial x} + \frac{\partial^2 \psi_n}{\partial y^2} + \frac{1}{G_n} \frac{\partial G_n}{\partial y} \frac{\partial \psi_n}{\partial y} + \left[ \frac{in}{G_n} \frac{\partial G_n}{\partial x} - n^2 \left( 1 - \frac{1}{G_n} \right) \right] \psi_n \\ = \frac{\epsilon}{2hG_n} \left\{ \sum_s [h s(n+s) + n^2 - s^2] \psi_s \psi_{n-s} - h \sum_{s \neq n} \left( \frac{n+s}{n-s} \right) \frac{\partial \psi_s}{\partial y} \frac{\partial \psi_{n-s}}{\partial y} \right. \\ \left. + 2h^2 \sum_{s \neq n} \frac{1}{n-s} \left[ s \psi_s \frac{\partial^2 \psi_{n-s}}{\partial y^2} - (n-s) \frac{\partial \psi_s}{\partial y} \frac{\partial \psi_{n-s}}{\partial y} \right] \right\} \end{aligned} \tag{21}$$

Significantly, we have converted a set of elliptic equations (16) into a set of parabolic equations, (21), which may be solved with efficient numerical techniques. For later use, we can rewrite eq. (21) in a dimensional form

$$\begin{aligned} 2in k_o \frac{\partial \psi_n}{\partial x} + \frac{1}{G_n} \frac{\partial}{\partial y} \left( \bar{G}_n \frac{\partial \psi_n}{\partial y} \right) + \frac{1}{G_n} \left( in k_o \frac{\partial \bar{G}_n}{\partial x} - n^2 k_o^2 \bar{G}_n + \frac{n^2 \omega^2}{g} \right) \psi_n \\ = \frac{1}{G_n} \left[ \frac{1}{2} \sum_s [k_o^2 s(n+s) + \frac{\omega^2}{gh} (n^2 - s^2)] \psi_s \psi_{n-s} - \frac{1}{2} \sum_{s \neq n} \left( \frac{n+s}{n-s} \right) \right. \\ \left. \frac{\partial \psi_s}{\partial y} \frac{\partial \psi_{n-s}}{\partial y} + \sum_{s \neq n} \frac{g k_o^2 h}{\omega^2 (n-s)} \left[ s \psi_s \frac{\partial^2 \psi_{n-s}}{\partial y^2} - (n-s) \frac{\partial \psi_s}{\partial y} \frac{\partial \psi_{n-s}}{\partial y} \right] \right] \end{aligned} \tag{22}$$

where

$$\bar{G}_n = h \left( 1 - \frac{n^2 \omega^2 h}{3g} \right) \tag{23}$$

is the dimensional form of eq. (17) and

$$k_0 = \frac{\omega}{\sqrt{g h_0}} \quad (24)$$

is the wave number associated with a reference constant water depth  $h_0$ .

The Crank-Nicolson method is used to rewrite the governing differential equations, (21), in a finite difference form. The forward difference scheme is employed in the x-direction, which is a time-like variable, and a centered difference scheme is used in the y-direction. Details are similar to those given by Liu and Tsay (11) and are omitted here.

#### An Alternate Approach Based on the K-P Equation

The application of the parabolic approximation to the more general Boussinesq equations involves an implied restriction to the case of waves with a unidirectional propagation direction and small transverse modulation. In this connection, it is of some interest to examine model equations with time dependence incorporated which embody the same basic assumption. For the case of shallow water and constant depth, an equation of this form has been developed by Kadomtsev & Petviashvili (5). The K-P equation may be written (following Bryant, 2) as

$$\frac{\partial}{\partial x} \left( \frac{\partial \zeta}{\partial t} + \frac{\partial \zeta}{\partial x} + \frac{3\epsilon}{2} \zeta \frac{\partial \zeta}{\partial x} + \frac{\mu^2}{6} \frac{\partial^3 \zeta}{\partial x^3} \right) + \frac{1}{2} \frac{\partial^2 \zeta}{\partial y^2} = 0 (\epsilon^2, \epsilon \mu^2, \mu^4) \quad (25)$$

The connection to the parabolic approximation may be seen by considering only  $O(1)$  terms and making the substitution

$$\zeta = \psi(x, y) e^{i(x-t)} \quad (26)$$

yielding (after assuming  $O(\partial^2 \psi / \partial x^2) \ll O(\partial \psi / \partial x)$ )

$$2i \frac{\partial \psi}{\partial x} + \frac{\partial^2 \psi}{\partial y^2} = 0 \quad (27)$$

which is the parabolic approximation of the Helmholtz equation (Yue & Mei, 19). The K-P equation, which extends the Korteweg-deVries equation to include weak transverse modulations, thus contains the same degree of information as the parabolic approximation.

Based on this correspondence, we may construct a version of the K-P equation for variable depth. Retaining dimensional quantities, the resulting model equation may be written as

$$\begin{aligned} \frac{\partial}{\partial x'} \left( \frac{1}{C'} \frac{\partial \zeta'}{\partial t'} + \frac{\partial \zeta'}{\partial x'} + \frac{1}{4h'} \frac{\partial h'}{\partial x'} \zeta' + \frac{3}{2h'} \zeta' \frac{\partial \zeta'}{\partial x'} + \frac{(h')^2}{6} \frac{\partial^3 \zeta'}{\partial x'^3} \right) \\ + \frac{1}{2h'} \frac{\partial}{\partial y'} \left( h' \frac{\partial \zeta'}{\partial y'} \right) = 0 \end{aligned} \quad (28)$$

where  $C' = \sqrt{gh'}$ . Neglecting  $y$  derivatives, the equation reduces to the form given by Johnson (4) after non-dimensionalization. Retaining only lowest order terms, making the substitution (where we drop primes for convenience),

$$\zeta = \bar{\psi}(x,y) e^{i(\int k dx - \omega t)} \tag{29}$$

$$\omega = C'k \tag{30}$$

and referencing the phase function to a constant value  $k_0$  (following Kirby & Dalrymple, 8) leads to the parabolic approximation

$$2ikh \frac{\partial \psi}{\partial x} + 2 kh(k-k_0)\psi + i \frac{\partial(kh)}{\partial x} \psi + \frac{\partial}{\partial y} (h \frac{\partial \psi}{\partial y}) = 0 \tag{31}$$

which is simply the shallow water limit of the linear approximation

$$2ik C_g \frac{\partial \psi}{\partial x} + 2k C_g(k-k_0)\psi + i \frac{\partial}{\partial x} (k C_g) \psi + \frac{\partial}{\partial y} (C_g \frac{\partial \psi}{\partial y}) = 0 \tag{32}$$

obtained by Kirby & Dalrymple (8). In eq. (32)  $C_g = \partial\omega/\partial k$  is the group velocity.

Before substituting a series expansion for  $\zeta$ , it is advantageous to alter the dispersive term  $\partial^3\zeta/\partial x^3$  by the following substitution

$$\frac{\partial^2 \zeta}{\partial t^2} - g \frac{\partial}{\partial x} (h \frac{\partial \zeta}{\partial x}) = 0(\epsilon, \mu^2) \tag{33}$$

yielding the modified equation

$$\frac{\partial}{\partial x} \left\{ \frac{1}{C} \frac{\partial \zeta}{\partial t} + \frac{\partial \zeta}{\partial x} + \frac{1}{4h} \frac{\partial h}{\partial x} \zeta + \frac{3}{\partial h} \zeta \frac{\partial \zeta}{\partial x} \right\} + \frac{h}{6C^2} \frac{\partial^3}{\partial t^2 \partial x} (h \frac{\partial \zeta}{\partial x}) + \frac{1}{2h} \frac{\partial}{\partial y} (h \frac{\partial \zeta}{\partial y}) = 0 \tag{34}$$

which has approximately the same dispersion relation as the set of equations (4) and (5). The parabolic approximation is obtained in similar fashion to the procedure of the previous section; we proceed using the slightly revised form

$$\zeta = \frac{1}{2} \sum_{n=-\infty}^{\infty} \bar{\psi}_n(x,y) e^{in(\int k dx - \omega t)} \tag{35}$$

to manipulate eq. (34) initially, after which a shift to a reference depth is employed (as in eq. 31) to obtain

$$2in k_0 \frac{\partial \psi_n}{\partial x} + \frac{k_0}{k \bar{G}_n} \frac{\partial}{\partial y} (h \frac{\partial \psi_n}{\partial y}) + \frac{1}{\bar{G}_n} \left[ \frac{in k_0}{2} \frac{\partial \bar{G}_n}{\partial x} - 2n^2 k_0 (k_0 - k) \bar{G}_n \right. \\ \left. + \frac{4}{3} \left( \frac{k_0}{k} \right) \frac{4}{g} \frac{\omega_n}{h} \right] \psi_n = \frac{3n^2 k_0}{4\bar{G}_n} \left[ \sum_{s=1}^{n-1} \psi_s \psi_{n-s} + 2 \sum_{s=1}^{N-n} \psi_{-s} \psi_{n+s} \right]; \\ 1 \leq n \leq N \tag{36}$$

where

$$\zeta = \frac{1}{2} \sum_{n=-\infty}^{\infty} \psi_n(x, y) e^{in(k_0 x - \omega t)} \quad (37)$$

and where  $\bar{G}_n$  and  $k_0$  are defined previously. The difference in the coefficients of  $\psi_n$  in eqs. (22) and (36) is accounted for by the fact that the substitution (37) is used throughout the entire process to obtain eq. (22) rather than the intermediate form, eq. (35).

Comparing eq. (36) to the corresponding equation (22), derived from the Boussinesq equation, we observe that the basic characteristics of these equations are the same. We remark, however, that in the approach using the K-P equation the nonlinearity is localized due to the original form of the equation (no  $y$ -derivatives in nonlinear term), and that the retention of only the lowest-order depth dependence in the  $y$ -derivative term implies a possible error in energy flux conservation and refraction for waves shoaling over a general two-dimensional topography. This latter effect could be alleviated by making the substitution  $\partial(\bar{G}_n \partial \psi_n / \partial y) / \partial y$  for the given term in eq. (36). However, numerical experiments for the case of Whalin's experiment (18) have shown that this effect is not important to the present study.

#### Refraction of Waves over a Plane Slope

Both of the models derived here are strictly applicable to the case of waves propagating over topography which is very slowly varying in comparison to the fundamental wavelength. Experimental data which satisfies this criterion is lacking due to the large wave basin needed. Therefore, we first compare the present model's results to a case for which computational results are available. Such a case has been provided by Skovgaard & Peterson (17), who used the properties of a very slowly-varying train of cnoidal waves to develop a theory for the refraction and shoaling of obliquely incident waves on a plane beach. This situation has also been studied recently by Madsen & Warren (13), who obtained a numerical solution for the case of waves propagating in a rectangular channel containing a plane slope oriented at an angle of  $26.6^\circ$  to the channel side walls. Madsen & Warren used a time-dependent, finite difference solution of a set of conservation laws equivalent to eqs. (4) and (5) to obtain their numerical results. Here, we use the parameters chosen by Madsen & Warren and study the same channel configuration; however, we neglect the lateral boundary damping employed by Madsen & Warren in order to study the details of the reflection process at the vertical, impermeable side walls. The computational domain is given by  $0 < x < 2154.5$ ,  $0 < y < 1534.5$ , with waves normally incident at  $x = 0$ . Slope-oriented coordinates are given by

$$\begin{aligned} x' &= (x - 420) \cos(26.6^\circ) - (y - 775) \sin(26.6^\circ) \\ y' &= (x - 420) \sin(26.6^\circ) + (y - 775) \cos(26.6^\circ) \end{aligned} \quad (38)$$

with water depth given by

$$h(x', y') = \begin{cases} 21 \text{ m} & ; \quad x' < 0 \\ (21 - 0.013 x') \text{ m} & ; \quad 0 \leq x' \leq 1076.9 \text{ m} \\ 7 \text{ m} & ; \quad x' > 1076.9 \text{ m} \end{cases} \quad (39)$$

Wave parameters for the problem are given by

$$\begin{aligned} T &= 17.3 \text{ s} = \text{wave period} \\ H &= 1.74 \text{ m} = \text{wave height at 21 m depth} \end{aligned}$$

which gives a deepwater wavelength  $L_0 = 467.1 \text{ m}$  and an Ursell number  $U_r = (H/2h)/(kh)^2 = 0.13$  in the deepwater portion of the channel. Initial conditions for the calculation are thus specified according to a third order Stokes wave at  $x = 0$ . A total of  $N = 6$  components are retained, and the computational domain is divided into a rectangular grid with  $\Delta x = \Delta y = 15.5 \text{ m}$ .

A plot of the model topography is given in Figure 1 along with a snapshot of the instantaneous water surface elevation, with contour increments of 1 m for bottom topography and 0.4 m for surface elevation. As the wave shoals, refraction effects are apparent in the center of the channel, and the wave develops from nearly sinusoidal form to shallow water profiles with narrow crests and broad troughs. The formation of a "Mach Stem" is apparent on the right boundary, where refraction turns the incident wave towards the wall, inducing a grazing-incidence reflection as in the study of Yue & Mei (19). Also apparent is the development of a high-frequency modulation, possibly consisting of an un-phaselocked higher mode, which evolves in the shallower portion of the tank. This short wave component causes a significant modulation of waveheight  $H(x, y)$  in the shallow ( $h = 7 \text{ m}$ ) portion of the domain.

A plot of normalized waveheight  $H/h$  versus normalized water depth  $h/L_0$  for  $y = 750 \text{ m}$  is given in Figure 2 in comparison to the refraction model of Skovgaard & Peterson (17) and the time-dependent numerical results of Madsen and Warren (13). The evolution of  $H/h$  is seen to be quite smooth up to the shallower depths, with the plotted points (corresponding to every fifth computational point) agreeing quite well with the refraction theory. In the shallow portion of the tank, the short wave modulation causes a significant variation in local wave height about the theoretical value. Wave height  $H$  was obtained by stepping the individual components through time to construct  $\zeta'(x, y, t)$  and then determining  $H(x, y)$  according to  $\zeta'_{\max} - \zeta'_{\min}$ .

Refracted angles of incidence between the wave and slope also agreed quite well with the refraction model and are not shown.

Plots of the water surface profile along the line  $y = 750$  and through the "Mach Stem" region  $y = 0$  are shown in Figures 3a and b, respectively. In both cases, results show the presence of separate peaks in the wave troughs; this was also noted in the results of Madsen & Warren and was attributed to truncation errors. The rapid evolution of a nearly uniform wave train is evident in the Mach-stem region in Figure 1. We remark that, due to the narrowness of the wave

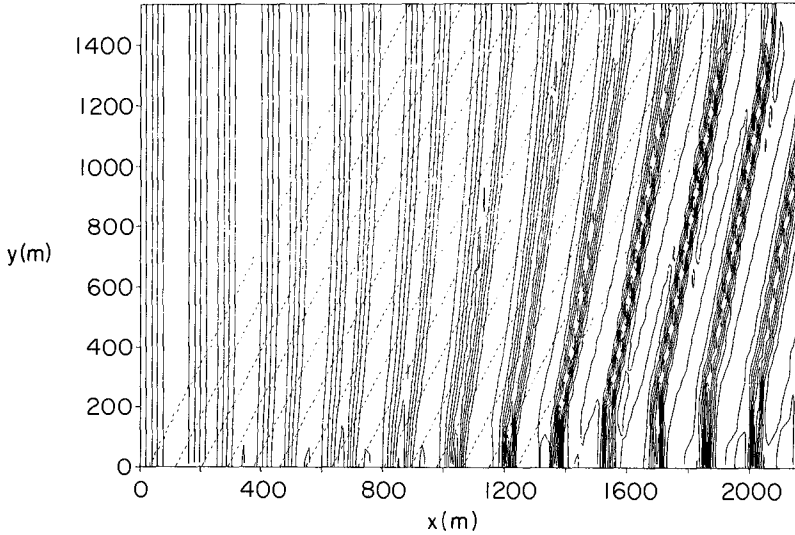


Figure 1. Bottom topography and contours of instantaneous surface elevation at  $t = 0$ ; - - - bottom contours in increments of 1 m,  $7 \text{ m} < h < 21 \text{ m}$ , — contours of free surface elevation in increments of 0.4 m.

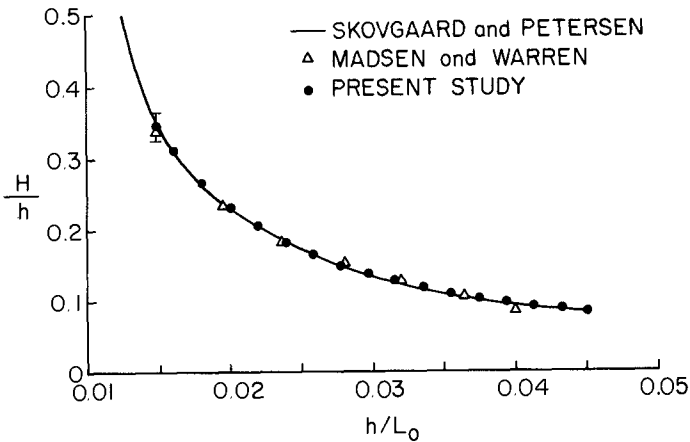


Figure 2. Normalized waveheight  $H/h$  as a function of  $h/L_0$ ; error bar  $\Phi$  at  $h/L_0 = 0.015$  indicates range of  $H$  values in shallow part of tank due to short wave modulation.

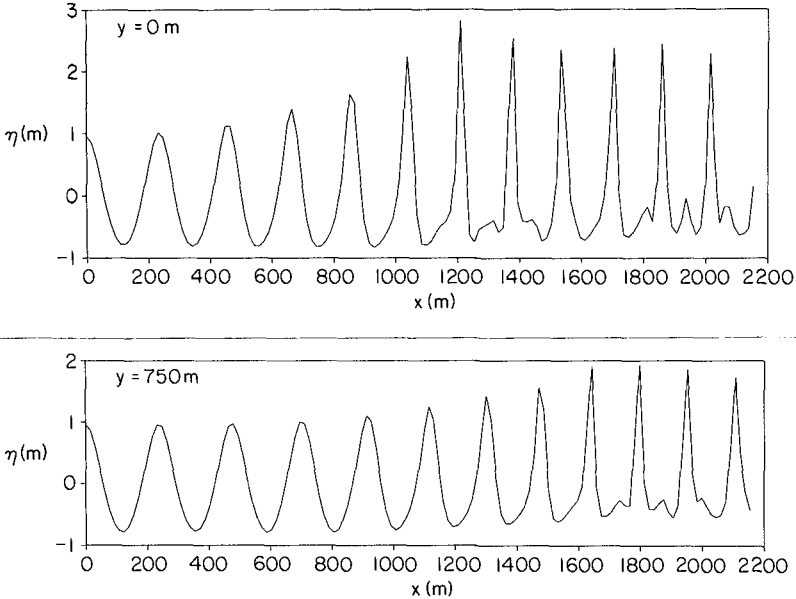


Figure 3. Free surface profiles for cnoidal wave refraction: (a) along  $y = 0$  m, sidewall and through Mach stem region, and (b) along  $y = 750$  m, near the centerline of channel.

crests, displacement of these crests away from actual computational grid points may contribute significantly to the modulation of crest elevations  $\zeta'_{\max}$  which is apparent in the plotted results.

We remark that increasing the number of modes without a further reduction of grid size did not significantly alter the results of this example. Tests with smaller grid size have not yet been conducted.

#### Wave Focusing By a Topographical Lens

Whalin (18) conducted a series of laboratory experiments concerning wave convergence over a bottom topography that acts as a focusing lens. The wave tank used in the experiments has the horizontal dimensions 25.603 m x 6.096 m. In the middle portion of the wave tank,  $7.62 \text{ m} < x < 15.24 \text{ m}$ , eleven semicircular steps were evenly spaced and led to the shallower portion of the channel (Figure 4). The equations approximating the topography are given as follows:



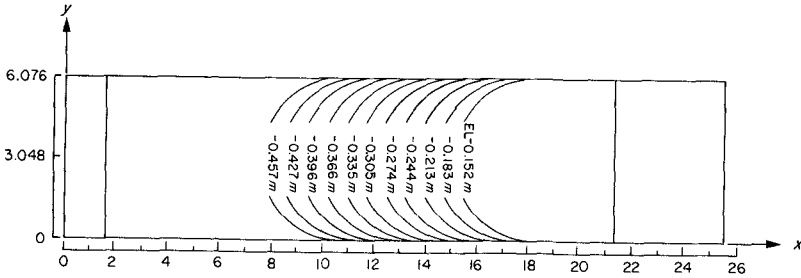


Figure 4. Topographical lens in Whalin's (18) wave tank experiments.

$$h(x,y) = \begin{cases} 0.4572 \text{ m} & (0 \leq x < 10.67 - G(y)) \\ 0.4572 + \frac{1}{25} (10.67 - G - x) \text{ m} & (10.67 - G \leq x \leq 18.29 - G) \\ 0.1524 \text{ m} & (18.29 - G \leq x \leq 21.34) \end{cases} \quad (40)$$

where

$$G(y) = [y(6.096 - y)]^{1/2} \text{ m} \quad (0 \leq y \leq 6.096 \text{ m}) \quad (41)$$

The bottom topography is symmetric with respect to the centerline of the wave tank,  $y = 3.048 \text{ m}$ .

A wavemaker was installed at the deeper portion of the channel where the water depth  $h_0$  is 0.4572 m. Three sets of experiments were conducted by generating waves with periods  $T = 1, 2, \text{ and } 3 \text{ secs.}$ , respectively. Different wave amplitudes were generated for each wave period. For the cases of  $T = 1 \text{ and } 2 \text{ secs.}$ , a second order Stokes wave theory (11) has been shown to describe the combined refraction-diffraction mechanisms adequately. The focusing of water waves by refraction led to a focal region, in which energy was transferred to the second harmonic. For the experimental set with  $T = 3 \text{ s}$  the Ursell parameter,  $U_r = (a/h)/(kh)^2$ , is generally greater than unity in the shallower water region, which indicates that the Stokes wave theory is no longer valid and the present shallow water wave theory should be used. In Table 1, we summarize the experimental data and the corresponding small parameters  $\epsilon$  and  $\mu^2$ . The water depth in the shallower region,  $h_1 = 0.1524 \text{ m}$ , has been used as the water depth scale.

Wave Period	Incident Wave Amplitude			$\epsilon = a_0/h_1$			$\mu^2 = \omega^2 h_1/g$
T(s)	$a_0$ (cm)						
3.0	0.68	0.98	1.46	0.0446	0.0643	0.0958	0.0682

Table 1. Experimental and Numerical Parameters

According to Whalin's report, the second and the third harmonic waves grow rapidly in the focal zone. In fact, the amplitude of the higher harmonics becomes larger than that of the first harmonic (see Figures 5 and 6). To study this problem, we obtain numerical solutions by using both approaches described above. In numerical computations for each model, five harmonics ( $N = 5$ ) are considered.

Owing to the symmetry of the problem with respect to the centerline of the wave tank, only one half of the wave tank is discretized. The computational domain starts from the wavemaker,  $x = 0$ , and ends at  $x = 22$  m. The no-flux boundary conditions are used along the side wall and the centerline of the wave tank, i.e.

$$\frac{\partial \psi}{\partial y} = 0 \quad \text{along } y = 0 \text{ and } 3.048 \text{ m} \quad (42)$$

for all  $n$ . The wave amplitude for the first harmonic waves at the wavemaker ( $x = 0$ ) is prescribed with the values shown in Table 1. The initial conditions for higher harmonic waves are zero.

In numerical computations different grid sizes are tested for the convergence of the numerical scheme. Numerical solutions presented here are obtained by using  $\Delta x = 0.25$  m and  $\Delta y = 0.3048$  m, although no noticeable differences are observed when the grid sizes are doubled.

In Figure 5a, numerical results based on the Boussinesq equation approach for the case with  $\epsilon = 0.0446$ ,  $\mu^2 = 0.0682$  and  $a_0 = 0.0068$  m are presented with experimental data. Wave amplitudes along the centerline of the wave tank are plotted. Since it is assumed that only the first harmonic waves are generated at the wavemaker, the wave energy in the higher harmonic components are sufficiently small over the constant depth region ( $0 < x < 8$  m). However, as waves start to refract over the topography and focus along the centerline of the tank, a significant amount of energy is transferred into higher harmonic components. The agreement between laboratory data and numerical solutions is reasonable. The numerical model overestimates the first harmonic amplitudes. The second and third harmonic wave amplitudes are in good agreement with reported data. (Several experiments with higher values of  $N$  indicated only minor changes for modes 1-3.) Results for the cases  $a_0 = 0.0098$  m ( $\epsilon = 0.0643$ ,  $\mu^2 = 0.0682$ ) and  $a_0 = 0.0146$  m ( $\epsilon = 0.0958$ ,  $\mu^2 = 0.0682$ ) are shown in Figures 5b and 5c, respectively. Again, the model uniformly overpredicts first harmonic amplitude along the channel centerline, although the amplitude of the second harmonic is well-predicted in both cases. The third harmonic amplitude is also well-predicted in Figure 5b. The high-amplitude case of Figure 5c indicates a tendency for the numerical result to undergo a recurrence behavior before the experimental maximum of  $\zeta_3$  is obtained.

Numerical results for the three cases presented above were also obtained using the K-P model with  $N = 5$ . Here,  $h_0$  and  $k_0$  are taken to correspond to the shallow portion of the tank. To compare these

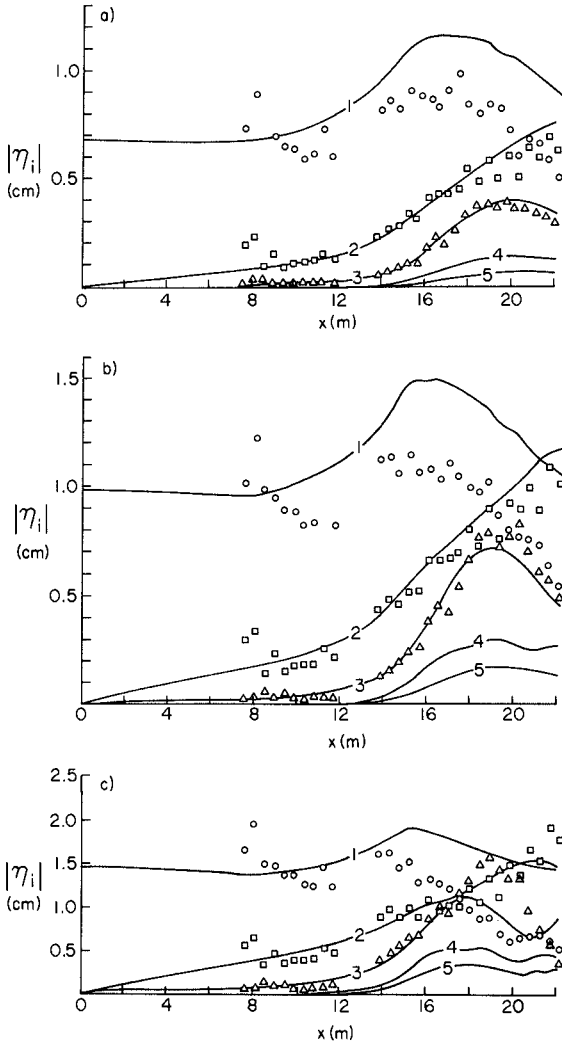


Figure 5. Harmonic amplitudes along centerline of Whalin's channel. a)  $a_0 = 0.68$  cm, b)  $a_0 = 0.98$  cm, c)  $a_0 = 1.46$  cm. Results using equation (21).

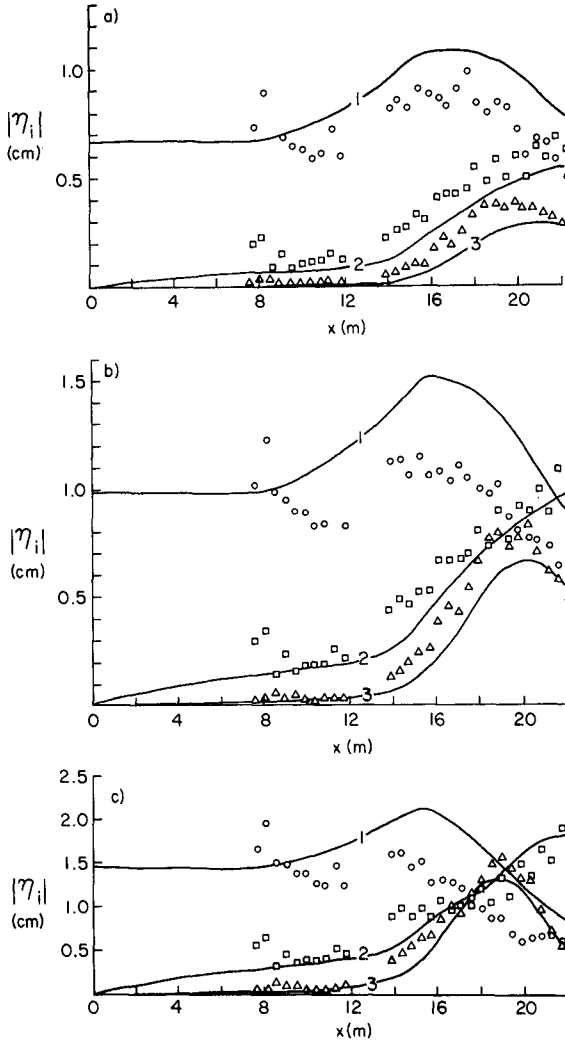


Figure 6. As in Figure 5. Results using equation (36).

two models, numerical solutions for the first three harmonics are shown in Figure 6a-c. For the low amplitude case  $a_0 = 0.68$  cm (Figure 6a), the results from the K-P model show an underprediction of second and third harmonic amplitudes, indicating the possible effect of the lowest-order  $y$  derivative term given in eq. (36). For the higher amplitude case (Figure 6b and c), nonlinearity becomes relatively more important and results of the two models are in closer agreement, with the exception that harmonic amplitudes grow somewhat more slowly in the K-P model. Both models are seen to be capable of predicting the essential features of harmonic generation in the focusing of a nonlinear wave. We remark that results of each model are sensitive to the choice of initial conditions, so that more detailed comparisons than those obtained here are not possible in the absence of detailed data in the vicinity of the wavemaker ( $x < 8$  m).

Finally, the evolution process described in the present cases occurs in the space of about two first harmonic wavelengths, indicating that the theoretical limitation to slowly varying topography and amplitudes is not restrictive in practice.

#### Concluding Remarks

The present study has demonstrated that the parabolic equation method may be successfully applied to the modeling of weakly nonlinear, weakly dispersive wave motions governed by the Boussinesq equations. The present study has been confined to the investigation of the propagation of monochromatic waves together with their nonlinearly-generated harmonics. However, given the necessary computer capacity, the method is directly applicable to the problem of modeling two-dimensional spectral evolution in shallow water.

In this study we have neglected the effects of frictional dissipation and wave breaking; the models in their present form are thus applicable to the region seaward of the surf zone. The inclusion of wave breaking effects in the models may be expected to be a non-trivial extension of the present results, since the models do not directly calculate the total wave height at each computational point.

#### Acknowledgements

This research was carried out with the support of the Office of Naval Research, Coastal Sciences Program (JTK and RAD) and New York Sea Grant Institute (PLFL and SBY). The possible utility of the K-P equation in the study of combined refraction and diffraction was suggested by Dr. J. L. Hammack.

This is contribution No. 434 of the Marine Science Research Center.

## Appendix 1 References

1. Booiij, N., 1981, "Gravity waves on water with non-uniform depth and current," Rept. 81-1, Dept. Civil Engrg., Delft University of Technology.
2. Bryant, P. J., 1982, "Two-dimensional periodic permanent waves in shallow water," J. Fluid Mech. 115, 525-532.
3. Dalrymple, R. A., Kirby, J. T., & Hwang, P. A., 1984, "Wave diffraction due to areas of energy dissipation," J. Waterway, Port, Coastal and Ocean Engineering, ASCE, 110, 67-79.
4. Johnson, R. S., 1972, "Some numerical solutions of a variable-coefficient Korteweg-deVries equation (with applications to solitary wave development on a shelf)," J. Fluid Mech. 54, 81-91.
5. Kadomtsev, B. B. and Petviashvili, V. I., 1970, "On the stability of solitary waves in weakly dispersing media," Sov. Phys. Dokl. 15, 539-541.
6. Kirby, J. T., 1984, "A note on linear surface wave-current interaction over slowly varying topography," J. Geophys. Res. 89, 745-747.
7. Kirby, J. T., 1984, "On the gradual reflection of weakly-nonlinear Stokes waves in regions with slowly varying topography," submitted for publication.
8. Kirby, J. T. and Dalrymple, R. A., 1983, "A parabolic equation for the combined refraction-diffraction of Stokes waves by mildly varying topography," J. Fluid Mech., 136, 453-466.
9. Liu, P. L-F., 1983, "Wave-current interactions on a slowly varying topography," J. Geophys. Res. 88, 4421-4426.
10. Liu, P. L-F. and Tsay, T.-K., 1983, "On weak reflection of water waves," J. Fluid Mech. 131, 59-71.
11. Liu, P. L-F. and Tsay, T.-K., 1984, "Refraction-diffraction model for weakly nonlinear water waves," J. Fluid Mech. 141, 265-274.
12. Lozano, C. and Liu, P. L-F., 1980, "Refraction-diffraction model for linear surface water waves," J. Fluid Mech. 101, 705-720.
13. Madsen, P. A. and Warren, I. R., 1984, "Performance of a numerical short-wave model," Coastal Engineering 8, 73-79.
14. Radder, A. C., 1979, "On the parabolic equation method for water-wave propagation," J. Fluid Mech. 95, 159-176.
15. Rogers, S. R. and Mei, C. C., 1978, "Nonlinear resonant excitation of a long and narrow bay," J. Fluid Mech. 88, 161-180.
16. Skovgaard, O., Jonsson, I. G. & Bertelsen, J. A., 1975, "Computation of wave heights due to refraction and friction," J. Waterways, Port, Harbors and Coastal Engineering Div., ASCE, 101, 15-32.
17. Skovgaard, O. and Petersen, H. M., 1977, "Refraction of cnoidal waves," Coastal Engrg. 1, 43-61.
18. Whalin, R. W., 1971, "The limit of applicability of linear wave refraction theory in a convergence zone," Res. Rep. H-71-3, U.S. Army Corps of Engrs., Waterways Expt. Station, Vicksburg, MS.
19. Yue, D. K. P. and Mei, C. C., 1980, "Forward diffraction of Stokes waves by a thin wedge," J. Fluid Mech. 99, 33-52.

## CHAPTER SIXTY NINE

### PROFILE ASYMMETRY OF SHOALING WAVES ON A MILD SLOPE

Paul A. Hwang\*, A.M., ASCE

#### Abstract

From limited experimental evidence, shoaling monochromatic waves seem to possess certain similarities. Specifically, the harmonic composition follows the trend of solitary or cnoidal waves, and the phase difference of harmonics vary with water depth monotonically. Based on the above observation a similarity model is constructed to study the asymmetric properties of shoaling waves. The implication of wave asymmetry on wave breaking is discussed.

#### Introduction

When the amplitude of a monochromatic wave becomes appreciable, the wave profile becomes asymmetric with respect to the horizontal axis, that is, a higher crest elevation than trough levels (Stokes, 1880). On shoaling water, in addition to the horizontal asymmetry, the wave form is obviously skewed with respect to the vertical axis with a steeper crest front than the crest rear face. Extensive studies have been conducted to study the wave asymmetry, especially for the case of breaking waves (McCowan, 1894; Munk, 1949; Iversen, 1952; Biesel, 1952; Ursell, 1953; Ippen and Kulin, 1955; Eagleson, 1957; Galvin, 1969; Goda, 1970; Hwang, 1982; Kjeldsen, 1981, 1983). Many studies of wave transformation at different stages of shoaling process also presented asymmetric information for nonbreaking waves (Iwagaki, 1968; Iwagaki and Sakai, 1972; Svendsen and Buhr-Hansen, 1978; Flick et al., 1981). The writer is especially interested in the approach of Flick et al. who performed harmonic analysis of the nonlinear shoaling waves. They found that both the amplitude and the phase spectra of a monochromatic shoaling wave vary with water depth in a deterministic fashion from the beach toe up to the breaking point: the amplitude spectrum resembles that of a cnoidal wave of the same height and the phase angle of each harmonic changes monotonically with decreasing water depth. Hwang (1982) applied harmonic analysis on breaking waves at different locations on sloping beaches, a very similar amplitude and phase spectral transformation was observed. It is speculated that certain similarity relationships of shoaling waves exist. The following presents an attempt to construct a similarity model for shoaling waves and to study their asymmetric properties.

\*Air-Sea Interaction Laboratory, College of Marine Studies, University of Delaware, Lewes, Delaware 19958.

## A Similarity Model

Flick et al. (1981) and Hwang (1982) studies wave profiles by Fourier decomposion

$$\eta = \sum_{n=1}^{\infty} a_n \cos(n\sigma t + \phi_n) \quad (1)$$

where  $\eta$  is the surface fluctuation,  $a_n$  the  $n$ -th component,  $\sigma$  the angular frequency,  $t$  the time coordinate and  $\phi_n$  the phase lag of the  $n$ -th component. They found that the variation of  $a_n$  with water depth follows closely the Fourier components of solitary or cnoidal waves (Figure 1a), and the phase of each oomponent changes monotonically with water depth (Figure 1b).

The amplitude spectrum of a cnoidal wave is given by (Cayley, 1895)

$$\frac{a_n}{H} = \frac{8}{3} k^2 h^3 n q^n \frac{1}{1 - q^{2n}} \quad (2)$$

where

$$q = \exp [-\pi K(1-m)/K(m)] \quad (3)$$

and  $K(m)$  is the complete elliptic integral of the second kind. The cnoidal parameter  $m$  is related to the wave parameters by the following relationship

$$m = \frac{3\pi^2 U_r}{4K^2(m)} \quad (4)$$

$U_r$  is the Ursell number defined as

$$U_r = H/k^2 h^3 \quad (5)$$

where  $H$  is wave height,  $k$  the wave number and  $h$  the water depth.

The amplitude spectrum of a solitary wave is given by (Gradshteyn and Ryzhik, 1980)

$$\frac{a_n}{H} = \frac{4n}{3U_r} \left( \sinh \frac{n\pi}{(3U_r)^{1/2}} \right)^{-1} \quad (6)$$

Eqs. (3) and (6) are plotted on Figure 1a along with experimental data. The difference between two theories is found insignificant in the range shown, and both theories agree with the trend of data reasonably well. In the following, we use Eq. (6) to calculate harmonic amplitudes due to its simplicity.



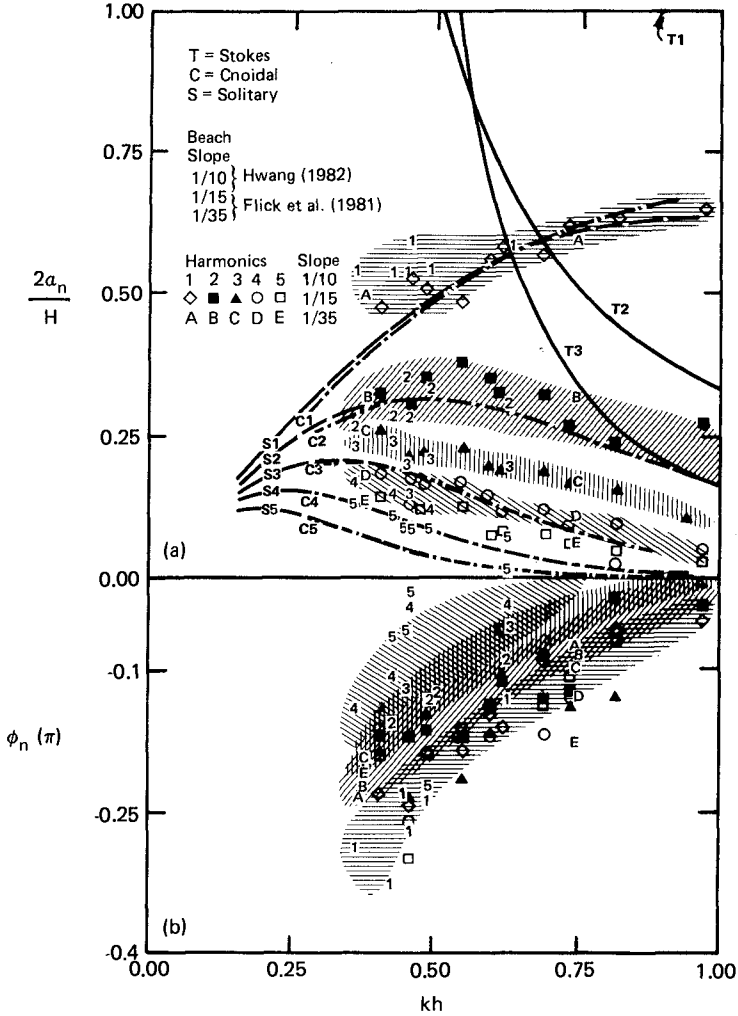


Figure 1 - Variation of (a) amplitude, (b) phase lag, of harmonics vs. kh.

Wave theories developed that considered the bottom slope modulation of the surface profile (Iwagaki, 1968; Chu and Mei, 1970; Iwagaki and Sakai, 1972; Guza and Davis, 1974) generally show poor agreement of the harmonic phase lags. The empirical relationship derived from the data in Figure 1b is used

$$\phi_n = -0.03 - 0.34(kh-1) \quad (7)$$

where  $\phi_n$  is expressed in  $\pi$ -radian. Alternatively,  $\phi_n$  can be expressed in  $Ur$  (Figure 2)

$$\phi_n = -0.05 - 0.052 Ur \quad (8)$$

Calculation shows little difference on the asymmetric properties (discussed in next section) using either equation. Eqs. (7) and (8) did not consider the variation of  $\phi_n$  with bottom slope or the harmonic numbers. From the limited data collected, the effect of bottom slope on  $\phi_n$  is very difficult to distinguish. Trying to establish a complete empirical relationship of  $\phi_n$  from such a small data set is probably not justified. The simplification employed therefore only gives a qualitative description. Eqs. (3) or (6) and (7) or (8) define a wave profile.

#### Wave Profiles and Asymmetric Factors

Figure 3 shows a few examples of the normalized wave profiles defined by Eqs. (6) and (7). For each profile, fifteen harmonics were included (Eq. 6). Due to the superposition of harmonics, the wave form is asymmetric with respect to the horizontal axis. The wave form is also skewed due to different phase lags among harmonics. The degree of asymmetry (both horizontal and vertical) increases with decreasing depth (or increasing  $Ur$ ).

There are many different parameters proposed to define the wave asymmetry (Iversen, 1952; Adeyemo, 1968; Iwagaki and Sakai, 1972; Kjeldsen, 1981, 1983, among others). The parameters  $\epsilon$ ,  $\delta$ ,  $\lambda$ , and  $\mu$  proposed by Kjeldsen (Figure 4) are adopted for the following discussion. The parameter  $\epsilon$  (the crest front steepness) is of special interest to this study since it represents the largest "local" steepness of the wave form and may dominate the wave breaking inception;  $\epsilon$  is related to the "global" wave steepness  $H/L$  (where  $L$  is the wave length) by

$$\epsilon = \eta'/L' = \frac{\eta'}{H} \frac{L}{L'} \frac{H}{L} \quad (9)$$

The factor  $\alpha_F = (\eta'/H)(L/L')$  can be interpreted as a "front steepness amplification factor," which defines the ratio between the crest front and the overall steepness. For a pure sinusoidal wave,  $\alpha_F = 2$ . Similarly, a "rear steepness amplification factor" can be defined as  $\alpha_B = (\eta'/H)(L/L'')$ . For nonlinear symmetric waves  $\alpha_F = \alpha_B > 2$ , and for asymmetric waves  $\alpha_F > \alpha_B > 2$ .

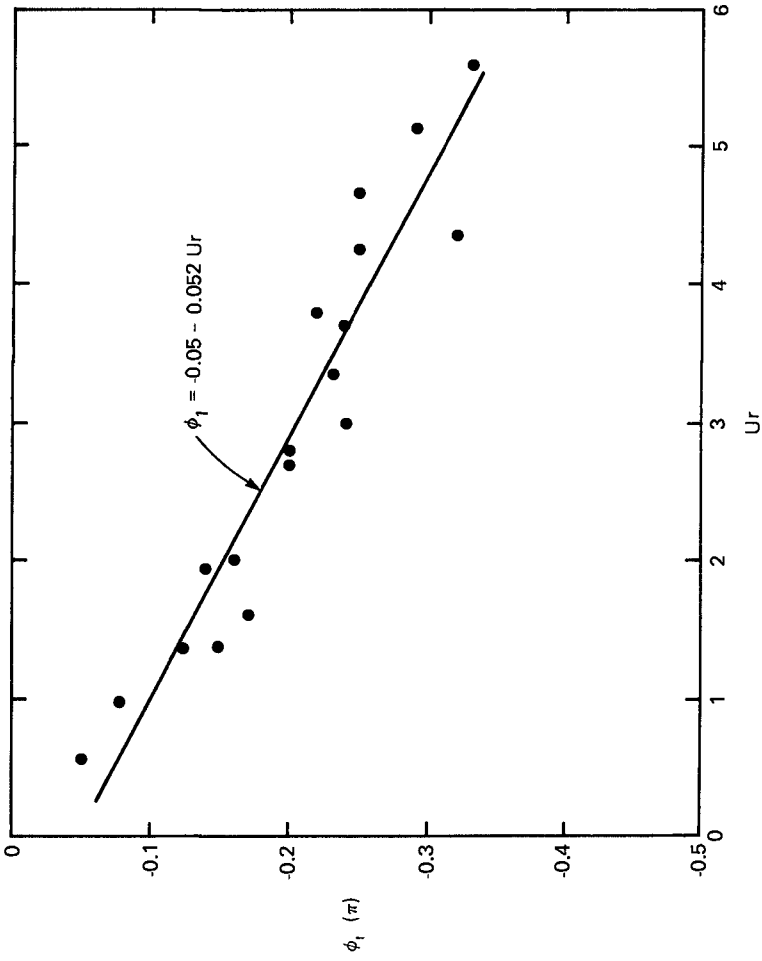


FIGURE 2 —Phase lag of the first harmonic vs.  $Ur$ .

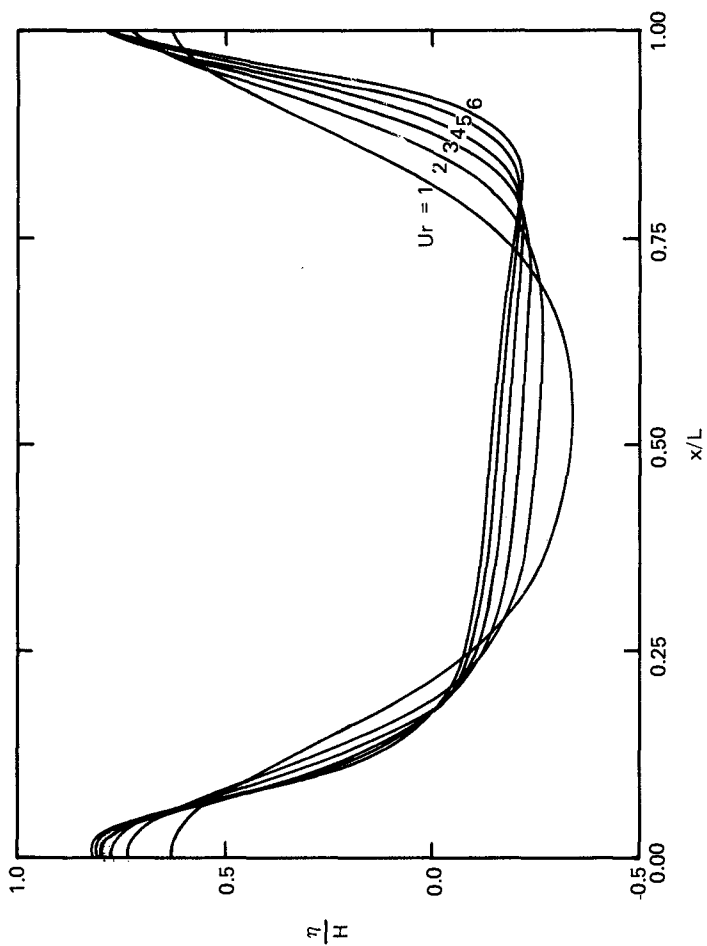


Figure 3 — Normalized wave profile. Waves propagate toward left.

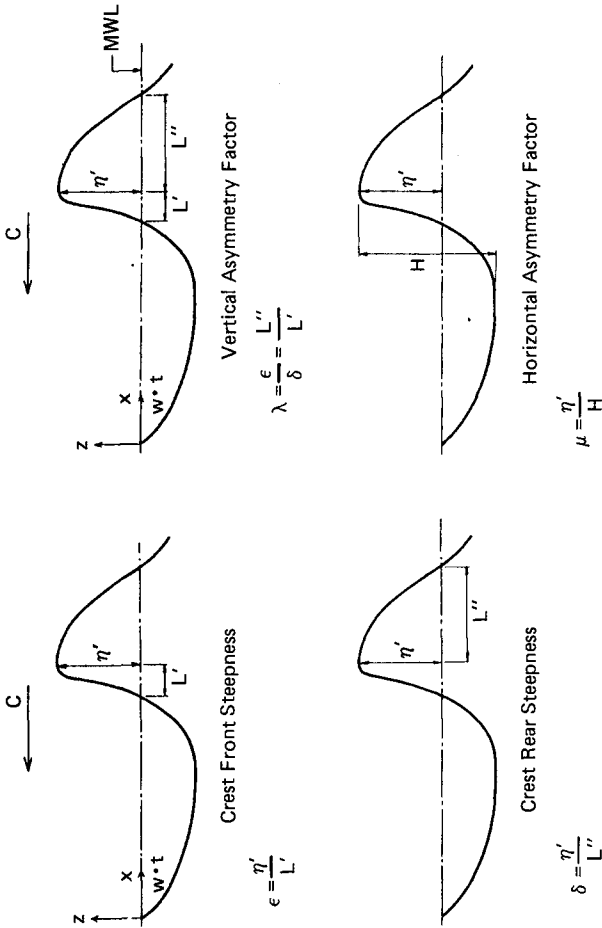


Figure 4 — Definitions of asymptotic parameters (reproduced from Kjeltdsen and Myrhaug, 1979).

Fig. 5 plots the asymmetry factors  $\alpha_F$  and  $\alpha_B$  with respect to the dimensionless water depth  $kh$ . Both vertical and horizontal asymmetry increase toward shallower water. The degree of asymmetry at any given depth ( $kh$ ) increases with wave nonlinearity ( $H/h$ ). The horizontal asymmetry  $\mu$  is found to be smaller than the corresponding symmetric wave of the same amplitude spectrum (compare the solid and the dashed curves of  $H/h=0.5$ , Fig. 5b), at the lowest  $kh$  range calculated, a reduction of 6% was shown. The vertical asymmetry factor  $\lambda$  is identically one for a symmetric wave. The slope amplification factors at the crest front  $\alpha_F$  and crest rear  $\alpha_B$  are plotted in Fig. 5c and d. As mentioned before,  $\alpha_F = \alpha_B = 2$  for a sinusoidal wave. Both  $\alpha_F$  and  $\alpha_B$  increase with wave nonlinearity, in which case, the crest region becomes narrower and trough region is elongated. For a symmetric wave  $\alpha_F = \alpha_B$ . When waves become asymmetric, the crest front becomes steeper and the crest rear becomes milder (compare dashed and solid curves for the case  $H/h=0.5$  in Fig. 5c and d).

Fig. 6 plots  $\lambda$ ,  $\mu$ ,  $\alpha_F$  and  $\alpha_B$  vs.  $Ur$ . Similar conclusions as those of Fig. 5 can be drawn.

#### Discussion and Conclusion

The amplitude and phase spectra of shoaling waves changes continuous with water depth. The former resembles the spectra of either cnoidal or solitary waves. A similarity model was constructed to study the asymmetric properties of shoaling waves using the solitary wave spectrum and an empirical relation of the harmonic phase lags with water depth.

As expected, the resulting wave profiles become more asymmetric both horizontally and vertically as water depth decreases or Ursell number increases. Compared with a symmetric wave of the same amplitude spectrum, the vertically asymmetry factor is always higher but the horizontal asymmetry factor shows a decrease. Due to the skewing of the wave profile, the crest front steepness is considerably greater than the overall wave steepness  $H/L$ .

The wave steepness is closely related to the breaking occurrence. In the classical studies of limiting (symmetric) Stokes' wave in deep water, the enclosing angle at wave crest was found to be  $120^\circ$  (Stokes, 1880). McCowan (1894) proved that the breaking angle of a wave in shallow water is still  $120^\circ$ . These results were confirmed by laboratory experiments and field observations (Gaillard, 1904, see eg. review of Kinsman, 1965). Michell (1893) showed that the corresponding maximum steepness  $H/L=1/7$  in deep water. When a wave moves into shoaling water, the limiting steepness decreases and becomes a function of both relative depth and the beach slope. Although this subject was studied extensively, the mechanism of wave breaking on a sloping beach is not yet clear. Subsequently, the breaking characteristics were generally expressed in terms of the ratio between the breaking wave height and water depth ( $H_b/h_b$ ), or the ratio between the wave height at breaking point and at deep water ( $H_b/H_0$ ). Many empirical formulas were proposed (Iversen, 1952; Galvin, 1969; Goda, 1970 among others). From the above short literature survey, it seems that the breaking angle is one of the rare breaking invariants (another invariant maybe the fluid particle

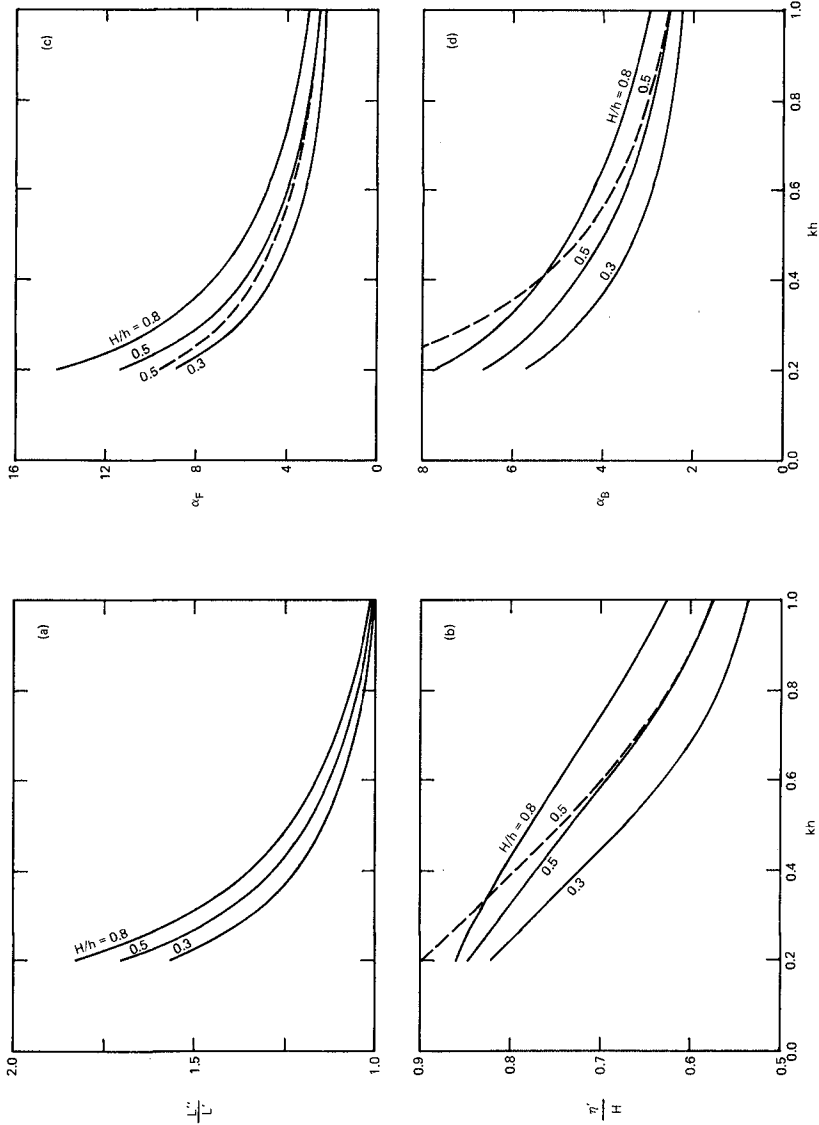


Figure 5 — Calculated asymmetric parameters. (a) Vertical asymmetry, (b) Horizontal asymmetry, (c) Front steepness amplification, and (d) Rear steepness amplification. Dashed line corresponds to the case of symmetric waves.

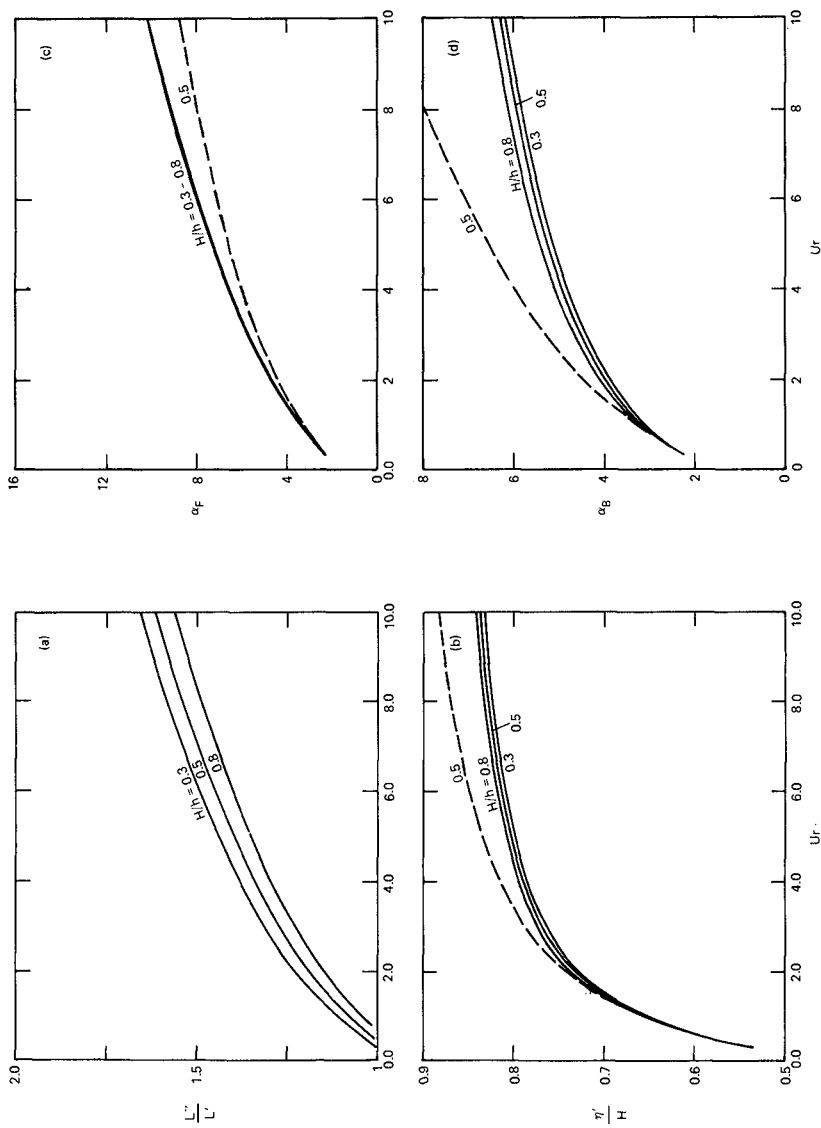


Figure 6 --- Same as Figure 5, except plotted against Ursell number  $U_r$



acceleration but this is very difficult to measure). For waves of vertically asymmetric profiles, the breaking angle is more closely related to the crest front and crest rear steepnesses. The crest front steepness is probably an important geometric index for "local" wave steepness. The local wave steepness was used by Longuet-Higgins and Smith (1983) in measurements of breaking probability.

#### Acknowledgement

The work is supported by a Grant from University of Delaware Research Foundation. The author would like to thank Dr. Kjeldsen for his constructive suggestions.

#### References:

- Adeyemo, M. D., 1968, Effect of beach slope and shoaling on wave asymmetry, Proc. 11th Coast. Eng. Conf., 145-172.
- Biesel, F., 1952, Study of wave propagation in water of gradually varying depth, in Gravity Waves, Circular No. 521, Nat. Bureau of Standards, Washington, D. C.
- Cayley, A., 1895, An Elementary Treatise on Elliptic Functions, George Bell and Sons, London.
- Chu, V. H., and C. C. Mei, 1970, On slowly-varying Stokes waves, J. Fluid Mech., 41, 873-887.
- Flick, R. E., R. T. Guza and D. L. Inman, 1981, Elevation and velocity measurements of laboratory shoaling waves, J. Geophys. Res., 86, 4149-4160.
- Gaillard, D. C., 1904, Wave action in relation to engineering structures, Prof. Paper of the Corps of Engineers, U. S. Army, No. 31.
- Galvin, C. J., Jr., 1969 Breaker travel and choice of design wave height, J. Waterways and Harbor Div., ASCE, WW2, 175-200.
- Goda, Y., 1970. A synthesis of breaker indices, Trans. Japan. Soc. Civil Eng., 2, 227-230.
- Gradshteyn, I. S., and I. M. Ryzhik, 1980, Table of Integrals, Series and Products, Academic Press.
- Guza, R. T., and R. E. Davis, 1974, Excitation of edge waves by waves incident on a beach, J. Geophys. Res., 79, 1285-1291.
- Hwang, P. A., 1982, Wave kinematics and sediment suspension at wave breaking point, Ph.D. dissertation, Dept. of Civil Eng., Univ of Delaware.
- Ippen, A. T., and G. Kulin, 1954, The shoaling and breaking of the solitary wave, Proc. 5th Coast. Eng. Conf., 27-47.
- Iversen, H. W., 1952, Laboratory Study of breakers, in Gravity Waves, Circ. No. 521, Nat. Bureau of Standards, Washington, D. C.
- Iwagaki, Y., 1968, Hyperbolic waves and their shoaling, Proc. 11th Coast. Eng. Conf., 124-144.
- Iwagaki, Y., and T. Sakai, 1972, Shoaling of finite amplitude long waves on a beach of constant slope, Proc. 13th Coast. Engl. Conf., 347-364.
- Kinsman, B., 1965, Wind Waves: their generation and propagation on the ocean surface, Prentice-Hall, Inc.
- Kjeldsen, S. P., 1981, Design Waves, Rep. No. NHL-1-81008, Norwegian Hydrodynamic Laboratories.

- Kjeldsen, S. P., 1983, Determination of severe wave conditions for ocean systems in a 3-Dimensional irregular seaway, VIII Congress of the Pan-Am Institute of Naval Engineering.
- Longuet-Higgins, M. S., and N. D. Smith, 1983, Measurement of breaking by a surface jump meter, J. Geophys. Res., 82, 971-975.
- McCowan, J. 1894, On the highest wave of permanent type, Phil. Mag., Ser. 5, 38, 351-358.
- Michell, J. H., 1893, The highest wave in water, Phil. Mag. Ser. 5, 36, 430-437.
- Munk, W. H., The solitary wave theory and its application to surf problems, Ann. New York Academy of Science, 51, 376-462.
- Stokes, G. G., 1880, On the theory of oscillatory waves, in Mathematical and Physical Papers, Vol. I, Cambridge Univ. Press. 197-229.
- Svendsen, I. A., and J. Buhr-Hansen, 1978, On the deformation of periodic long waves over a gently sloping bottom, J. Fluid Mech., 87, 443-448.
- Ursell, F., 1953, The long wave paradox in the theory of gravity waves, Proc. Cambridge Phil. Soc., 49 (4).

## CHAPTER SEVENTY

### THE EXACT SOLUTION OF THE HIGHEST WAVE DERIVED FROM A UNIVERSAL WAVE MODEL

Yang Yih Chen<sup>1</sup> Frederick L.W. Tang<sup>2</sup>

#### ABSTRACT

The solitary wave is first established in this paper by extending the series solution of periodic gravity wave as the wavelength approaches to infinite. Then, the highest gravity wave of permanent type in finite depth of water is immediately analyzed. The maximum ratio of wave height to water depth is obtained as 0.854654..., and the angle at the crest for the considered highest wave is estimated to be 90°.

#### INTRODUCTION

Since Stokes (1847) developed the theory of oscillatory waves, the analysis for the periodic gravity waves of permanent form in the water has comprehensively been expanded, particularly, a very interested and important problem is the highest waves. However, up to now, all wave theories which have presented are not continuously available to describe the flow field of a wave motion in which both amplitude and wavelength vary from small to possible maximum in any fixed depth of water. Therefore, to solve this highest wave problem, several special wave theories have been employed, for example, as the cnoidal wave by Laitone (1960), the solitary wave by McCowan (1894), Yamada (1957), Lenau (1966) and Longuet-Higgins (1974), and an integral equation of wave motion by Byatt-Smith (1970) etc. The purpose of this paper is to establish a universal model which can adequately be used to analyze the waves motion in arbitrary uniform depth, from deep to shallow water, up to a solitary wave especially, and its wave height from small to just breaking; i.e. this model is adjustable to all the region for the periodic gravity waves of permanent type can be existed.

In §I, we recapitulate to formulate the series solution for the periodic gravity waves of permanent type in water of arbitrary uniform depth, which has been submitted in 19th International Conf. on Coastal Eng. In §II, the solitary wave similar to McCowan's type is established, in §III, §IV and §V, the structure of the highest waves is discussed.

---

1. Associate researcher, Institute of Harbor & Marine Technology, R.O.C.

2. Professor, National Cheng Kung University, Taiwan, R.O.C.

1. THE NEW MODEL OF WATER WAVES

The solution of Laplace equation in water wave motion are to be set as follows:

$$\psi(x,y,t) = \sum_{n=1}^{\infty} C_n e^{-nk d} [e^{nk(d+y)} - e^{-nk(d+y)}] \cos nk(x-ct) \dots (1.1)$$

$$\phi(x,y,t) = \sum_{n=1}^{\infty} C_n e^{-nk d} [e^{nk(d+y)} + e^{-nk(d+y)}] \sin nk(x-ct) \dots (1.2)$$

$\psi(\cdot)$  : Stream function

$\phi(\cdot)$  : Potential

$C_n$  : constants to be worked out

$n$  : 1, 2, 3, .....

$e$  : exponential

$k$  : wave number,  $k=2\pi/L$

$L$  : wavelength

$d$  : water depth under  $x$  - axis

$c$  : wave celerity

The co-ordinate system is illustrated in Fig 1.

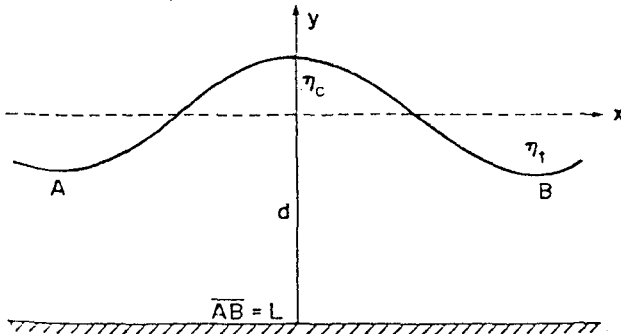


Figure 1 The coordinate system of wave motion

The motion is altered to be steady flow by adding an opposite velocity  $c$ .  $(x-ct)$  in above equations will be replaced by  $x$ , then

$$\psi(x,y) = -cy + \sum_{n=1}^{\infty} C_n e^{-nk d} [e^{nk(d+y)} - e^{-nk(d+y)}] \cos nkx \dots (1.3)$$

$$\phi(x,y) = -cx + \sum_{n=1}^{\infty} C_n e^{-nk d} [e^{nk(d+y)} + e^{-nk(d+y)}] \sin nkx \dots (1.4)$$

The equation of surface elevation is to be obtained by  $\psi(x, \eta) = 0$  as follows

$$\eta(x) = \sum_{n=1}^{\infty} \frac{C_n}{c} e^{-nk d} [ e^{nk(d+\eta)} - e^{-nk(d+\eta)} ] \cos nkx \dots\dots\dots (1.5)$$

$\eta$ : elevation of wave surface with reference to x axis

The constants are worked out by boundary conditions as shown in the previous paper published in Captain conference (19th proc. ICCE page 508-520).

The solution is as follows:

In deep water,  $d \rightarrow \infty$ , when  $n=1$ ,  $\dots\dots\dots (1.6)$

$$\psi(x, y) = -cy + \frac{c\theta}{Ke^\theta} e^{ky} \cos kx \dots\dots\dots (1.7)$$

$$\eta(x) = \frac{\theta}{ke^\theta} e^{k\eta} \cos kx \dots\dots\dots (1.8)$$

$$\theta = \frac{2\pi\delta}{1 + e^{-2\pi\delta}}, \quad \delta = \frac{H}{L}, \quad \text{the wave steepness.}$$

In water area of finite depth, when  $n=1$ ,

$$\psi(x, y) = -cy + c\eta_c \frac{\sin hk(d+y)}{\sin hk(d+\eta_c)} \cos kx \dots\dots\dots (1.9)$$

$$\eta(x) = \eta_c \frac{\sin hk(d+y)}{\sin hk(d+\eta_c)} \cos kx \dots\dots\dots (1.10)$$

and  $\eta_c$  is to be computed through following equation by Newton-Raphson's method

$$\delta = \frac{H}{L} = \frac{\eta_c}{L} \{ [1 + \cosh(2\pi\delta)] - \coth hk(d+\eta_c) \sinh(2\pi\delta) \} \dots\dots\dots (1.11)$$

$\eta_c$ : the elevation of wave crest above x-axis

wave celerity  $c$ , period  $T$  and the difference between still water level and the water depth of  $\psi(x, \eta) = 0$ , namely the depth under x-axis,  $\zeta = d_s - d$  have been worked out ( $d_s$  the depth of still water).

After elaborate experiments, the new model represents the reality very well. (19th Proc. ICCE page 510-520)

II. EXTENSION OF THE MODEL

For extending the new model to the region of solitary wave, the co-ordinate system is set as Fig-2.

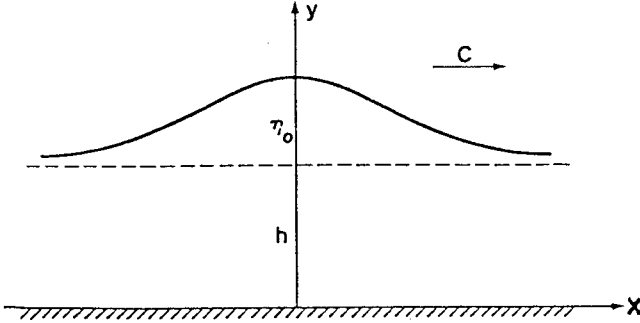


Figure 2 The coordinate system of solitary wave

The equations expressing  $\psi, \phi, \eta$  are changed to be

$$\psi(x, y) = -c(y - h) + \sum_{n=1}^{\infty} C_n^1 (e^{nky} - e^{-nky}) \cos(nkx) \dots\dots (11.1)$$

$$\phi(x, y) = -cx + \sum_{n=1}^{\infty} C_n^1 (e^{nky} + e^{-nky}) \sin(nkx) \dots\dots\dots (11.2)$$

$$\eta(x, y) = \sum_{n=1}^{\infty} \frac{C_n^1}{c} [e^{nk(h+\eta)} - e^{-nk(h+\eta)}] \cos(nkx) \dots\dots\dots (11.3)$$

$$C_n^1 = C_n e^{-nk d}$$

let

$$K_n = \frac{2C_n^1}{c} \sinh[nk(h + \eta_0 + \epsilon_0)] \dots\dots\dots (11.4)$$

$\eta_0$  is the height of wave crest on water level and  $\epsilon_0$  is an constant,  $\epsilon_0 > 0$ .

Above equations become

$$\psi(x, y) = -c(y-h) + c \sum_{n=1}^{\infty} K_n \frac{\sinh(nky)}{\sinh[nk(h + \eta_0 + \epsilon_0)]} \cos(nkx) \dots (11.5)$$

$$\phi(x, y) = -cx + c \sum_{n=1}^{\infty} K_n \frac{\cosh(nky)}{\sinh[nk(h + \eta_0 + \epsilon_0)]} \sin(nkx) \dots\dots (11.6)$$

$$\eta(x) = \sum_{n=1}^{\infty} K_n \frac{\sinh[nk(h + \eta)]}{\sinh[nk(h + \eta_0 + \epsilon_0)]} \cos(nkx) \dots\dots\dots (11.7)$$

While  $L \rightarrow \infty$ ,  $k = \frac{2\pi}{L} \rightarrow 0$ , let  $k = d\tau$ ,  $nk = \tau$ ,  $K_n = K(\tau)$

$$\lim_{L \rightarrow \infty} \sum_{n=1}^{\infty} \frac{K_n \sinh\left(\frac{2n\pi}{L} y\right)}{\sinh\left[-\frac{2n\pi}{L} (h + \eta_0 + \epsilon_0)\right]} \cos\left(\frac{2n\pi}{L} x\right) \dots\dots\dots (11.8)$$

$$= \frac{1}{2\pi} \int_0^\infty LK(\tau) \frac{\sinh(y\tau)}{\sinh[(h+\eta_0+\epsilon_0)\tau]} \cos(\tau x) d\tau \dots\dots (11.8)$$

The integration should be a finite quantity even though the wave-length becomes infinitive, let

$$\lim_{L \rightarrow \infty} \frac{L \cdot K(\tau)}{2\pi} = \beta' \dots\dots\dots (11.9)$$

$\beta'$  will be a constant of finite value, consequently

$$\begin{aligned} & \lim_{L \rightarrow \infty} \sum_{n=1}^\infty \frac{K_n \sinh(nky)}{\sinh[(h+\eta_0+\epsilon_0)\tau]} \cos(nkx) \\ &= \beta' \int_0^\infty \frac{\sinh(y\tau)}{\sinh[(h+\eta_0+\epsilon_0)\tau]} \cos(\tau x) d\tau \\ &= \frac{\beta'}{2} \int_{-\infty}^\infty \frac{e^{i\tau x} \sinh(y\tau)}{\sinh[(h+\eta_0+\epsilon_0)\tau]} d\tau \dots\dots\dots (11.10) \\ & \quad i = \sqrt{-1} \end{aligned}$$

let

$$\tau (h + \eta_0 + \epsilon_0) = \pi \xi \dots\dots\dots (11.11)$$

$$\begin{aligned} & \lim_{L \rightarrow \infty} \sum_{n=1}^\infty \frac{K_n \sinh(nky)}{\sinh[nk(h+\eta_0+\epsilon_0)]} \cos(nkx) \\ &= \frac{\beta'}{2} \frac{\pi}{(h+\eta_0+\epsilon_0)} \int_{-\infty}^\infty \exp\left(-\frac{i\pi x \xi}{h+\eta_0+\epsilon_0}\right) \frac{\sinh\left(\frac{\pi y \xi}{h+\eta_0+\epsilon_0}\right)}{\sinh(\pi \xi)} d\xi \dots\dots (11.12) \end{aligned}$$

A complex integral as follows is invoked here, and which is integrated through the route in Fig. 3.

$$I = \int_{-\infty}^\infty e^{i\lambda_0 u} \frac{\sinh(a_0 u)}{\sinh(\pi u)} du \quad -\pi < a_0 < \pi \dots\dots\dots (11.13)$$

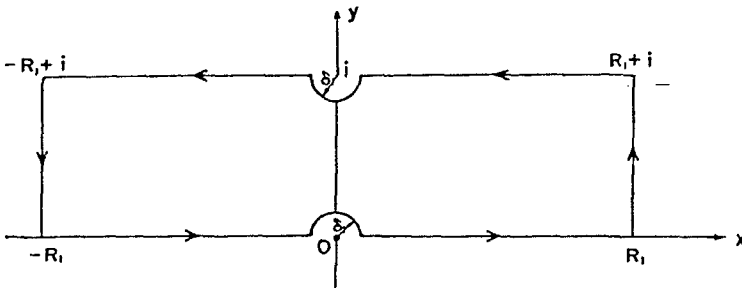


Figure 3 The contour of complex integration  $I, R_1 \rightarrow \infty, \delta_1 \rightarrow 0$

From mathematical operation, the integral is evaluated to be

$$I = \frac{\sin a_0}{\cosh \lambda_0 + \cos a_0} \quad -\pi < a_0 < \pi \dots\dots\dots (11-14)$$

As a result, it is proved that

$$\begin{aligned} & \lim_{L \rightarrow \infty} \sum_{n=1}^{\infty} \frac{K_n \sinh(nky)}{\sinh[nk(h + \eta_0 + \epsilon_0)]} \cos(nkx) \\ &= \frac{\pi \beta'}{2(h + \eta_0 + \epsilon_0)} \frac{\sin\left(\frac{\pi y}{h + \eta_0 + \epsilon_0}\right)}{\cosh\left(\frac{\pi x}{h + \eta_0 + \epsilon_0}\right) + \cos\left(\frac{\pi y}{h + \eta_0 + \epsilon_0}\right)} \dots\dots (11-15) \end{aligned}$$

put

$$\frac{\pi \beta'}{2(h + \eta_0 + \epsilon_0)} = \beta \dots\dots\dots (11-16)$$

The stream function and potential of the wave motion in the case of wave length approaching infinitive are to be obtained as follows:

$$\psi(x, y) = -c(y-h) + c\beta \frac{\sin(my)}{\cosh(mx) + \cos(my)} \dots\dots\dots (11-17)$$

$$\phi(x, y) = -cx + c\beta \frac{\sinh(mx)}{\cosh(mx) + \cos(my)} \dots\dots\dots (11-18)$$

Consequently, the wave profile can be expressed to be

$$\eta(x) = \frac{\beta \sin[m(h + \eta)]}{\cosh(mx) + \cos[m(h + \eta)]} \dots\dots\dots (11-19)$$

$$\text{where } m = \frac{\pi}{(h + \eta_0 + \epsilon_0)} \dots\dots\dots (11-20)$$

These equations identify with McCowen's theory. Therefore, the mathematical model submitted by the authors is proved to be able to represent the waves of symmetrical profile progressing in area of any water depth with any wavelength. So that this model can be nominated to be "universal".



III. EXACT SOLUTION OF FLOW FIELD IN SOLITARY WAVE

From the equations(II.17),(II.18) and (II.19), the partical velocity q can be calculated as follows:

$$q^2 = c^2 \left\{ 1 + \frac{m^2 \beta^2 - 2m\beta(1 + \cosh mx \cos my)}{(\cosh mx + \cos my)^2} \right\} \dots\dots\dots (III.1)$$

Expand and rearrange this equation, then substitute(II.17) to it, following expression is to be obtained.

$$q^2 = c^2 + m^2 [\psi(x, y) + c(y-h)]^2 \cdot \left[ \frac{1}{\sin^2(my)} - \frac{2}{m\beta} \right] - 2mc [\psi(x, y) + c(y-h)] \cot(my) \dots\dots\dots (III.2)$$

The partical velocity on the surface can be evaluated by substituting  $\psi(x, h+\eta) = 0$  to (III.2) and then have

$$(q^2)_{y=h+\eta} = c^2 \left\{ 1 - 2m\eta \cot[m(h+\eta)] + m^2 \eta^2 \cdot \left[ \frac{1}{\sin^2[m(h+\eta)]} - \frac{2}{m\beta} \right] \right\} \dots\dots\dots (III.3)$$

The water elevation in very distant location will have no disturbance, so

$$x \longrightarrow \pm \infty, \quad \eta = 0, \quad (q^2)_{x \rightarrow \pm \infty} = c^2 \dots\dots\dots (III.4)$$

Also from the dynamical boundary condition on the surface, the Bernoulli's constant Q can be evaluated as

$$Q = g(h+\eta) + \frac{1}{2} \left[ \left( \frac{\partial \psi}{\partial x} \right)^2 + \left( \frac{\partial \psi}{\partial y} \right)^2 \right]_{y=h+\eta} = \frac{1}{2} c^2 + gh \dots\dots (III.5)$$

so that

$$\left[ \left( \frac{\partial \psi}{\partial x} \right)^2 + \left( \frac{\partial \psi}{\partial y} \right)^2 \right]_{y=h+\eta} = (q^2)_{y=h+\eta} = c^2 - 2g\eta \dots\dots\dots (III.6)$$

From equations(III.3) and (III.6), another equation of wave profile can be worked out as follows

$$\eta(x) = \frac{2m \cot[m(h+\eta)] - 2g/c^2}{m^2 \left\{ \frac{1}{\sin^2[m(h+\eta)]} - \frac{2}{m\beta} \right\}} \dots\dots\dots (III.7)$$

Use the condition of  $X \rightarrow \pm \infty, \eta = 0$  again, c is to be calculated as follows

$$c^2 = \frac{g}{m} \tan(mh) \dots\dots\dots (III.8)$$

This is just the same as McCowan's theory (1891).

At  $x=0$ ,  $\eta = \eta_0 = H$ ,  $H$  is the wave height of solitary wave, from (III.19)

$$H = \beta \tan \left[ \frac{1}{2} m (h+H) \right] \dots\dots\dots (III.9)$$

and

$$m\beta = mH \cot \left[ \frac{1}{2} m (h+H) \right] \dots\dots\dots (III.10)$$

Substitute (III.8) and (III.10) to (III.7) in the case of  $\eta = H$  at  $x=0$ . Then we obtain

$$H = \frac{2m \cot [m(h+H)] - 2m \cot (mh)}{m^2 \left\{ \frac{1}{\sin^2 [m(h+H)]} - \frac{2 \tan \left[ \frac{1}{2} m (h+H) \right]}{mH} \right\}} \dots\dots\dots (III.11)$$

Rearrange this equation

$$\begin{aligned} & mH \{ 1 + \cos [m(h+H)] \} \\ &= 2 \{ \cot [m(h+H)] - \cot (mh) \} \cdot \sin^2 [m(h+H)] \cdot [ 1 + \cos m(h+H) ] \\ & \quad + 2 \sin^3 [m(h+H)] \dots\dots\dots (III.12) \end{aligned}$$

It is soon seen that, when the wave height  $H$  and the depth  $h$  of water are given,  $m$  can be worked out by solving this equation, then  $c$ ,  $\beta$  are also to be calculated through (III.8) and (III.9). The profile of solitary wave is to be delineated.

In this section, not any approximate calculation is used, so it can be called the exact solution.

IV. ON THE HEIGHT OF CRITICAL WAVE

When the crest particle velocity is equal to the wave celerity, the wave begins to break. The critical wave height is the height of wave just before breaking. In a coordinate system of steady motion the critical condition is that the particle velocity at the wave crest is zero. From (III.6)

$$c^2 = 2g\eta_0 = 2gH \dots\dots\dots (IV.1)$$

From (III.8)

$$c^2 = 2gH = \frac{g}{m} \tan (mh) , \quad mH = \frac{1}{2} \tan (mh) \dots\dots\dots (IV.2)$$

Substitute this equation to (III.12) and rearrange, following equation is obtained

$$\begin{aligned} & \frac{1}{2} \tan (mh) \left\{ 1 + \cos \left[ mh + \frac{1}{2} \tan (mh) \right] \right\} \\ & = 2 \left\{ \cot \left[ mh + \frac{1}{2} \tan (mh) \right] - \cot (mh) \right\} \\ & \quad \times \left\{ \sin^2 \left[ mh + \frac{1}{2} \tan (mh) \right] \right\} \left\{ 1 + \cos \left[ mh + \frac{1}{2} \tan (mh) \right] \right\} \\ & \quad + 2 \left\{ \sin^3 \left[ mh + \frac{1}{2} \tan (mh) \right] \right\} \dots \dots \dots (IV. 3) \end{aligned}$$

Solve this equation

$$mh = 1.070733 \dots \dots \dots (IV. 4)$$

Substitute to equation (IV.2)

$$mH = 0.915106 \dots \dots \dots (IV. 5)$$

Here the ratio of critical wave height to the water depth is worked out as follows

$$\frac{H}{h} = \frac{H}{d} = 0.854654 \dots \dots \dots (IV. 5)$$

This value is very agreement with those results obtained by Yamada (1957), Lenou (1966), Byatt-smith (1970), and Longuet-Higgins (1974). Also not any approximate computation is adopted in this section, this number is reliable and correct.

V. ON THE SHAPE OF CRITICAL WAVE

Substitute (II.19) (III.9) and (III.10) to equation (III.12), after complicated algebraical operation, following relationship in critical wave situation can be worked out.

$$mH = \sin [ m ( h + H ) ] \dots \dots \dots (V.1)$$

Now, to find the shape of the crest of critical wave, differentiate the wave profile with respect to x

$$\begin{aligned} \frac{d\eta}{dx} &= m \beta \left\{ \frac{\cos [ m ( h + \eta ) ]}{\cosh (mx) + \cos [ m ( h + \eta ) ]} + \frac{\sin^2 [ m ( h + \eta ) ]}{\{ \cosh (mx) + \cos [ m ( h + \eta ) ] \}^2} \right\} \\ & \quad + \frac{d\eta}{dx} - \frac{m\beta \sinh (mx) \sin [ m ( h + \eta ) ]}{\{ \cosh (mx) + \cos [ m ( h + \eta ) ] \}^2} \dots \dots \dots (V.2) \end{aligned}$$

Substituting equation (II.19) to this equation and simplifying

$$\frac{d\eta}{dx} = \frac{\frac{m\eta^2}{\beta \sin [ m ( h + \eta ) ]} \cdot \sin h ( mx )}{\{ m\eta \cot [ m ( h + \eta ) ] + \frac{m}{\beta} \eta^2 - 1 \}} \dots \dots \dots (V.3)$$

In critical case, x=0, η=H, using the relationship of (V.1)

$$\lim_{x \rightarrow 0} \left( \frac{d\eta}{dx} \right)_{\eta=H_{\text{critical}}} = \frac{0}{0} \dots\dots\dots (V.4)$$

The wave crest of critical wave is a singular point, using L'Hospital's rule and through some complicated operations, then, we obtain

$$\lim_{x \rightarrow 0} \left( \frac{d\eta}{dx} \right)^2 = \frac{mH}{m\beta \left[ \frac{\cos m(h+H)-1}{\sin m(h+H)} \right] + 2mH} = \frac{mH}{mH}$$

Immediately, we have

$$\lim_{x \rightarrow 0} \left( \frac{d\eta}{dx} \right) = \pm 1 \dots\dots\dots (V.5)$$

This means that the critical wave crest is a branch point, the slopes of left and right side are

$$\left( \frac{d\eta}{dx} \right)_{x=0^-} = -1 \quad \left( \frac{d\eta}{dx} \right)_{x=0^+} = +1 \dots\dots\dots (V.6)$$

Consequently, the crest is a summit where two symmetrical curves intersect, the slope angle of both side is 45°, as a result, the angle of the critical wave crest is 90° in stead of 120° stated by Stokes (1880) and identifies with Rankine's theory (1865).

The shape of the wave is illustrated in Fig. 4

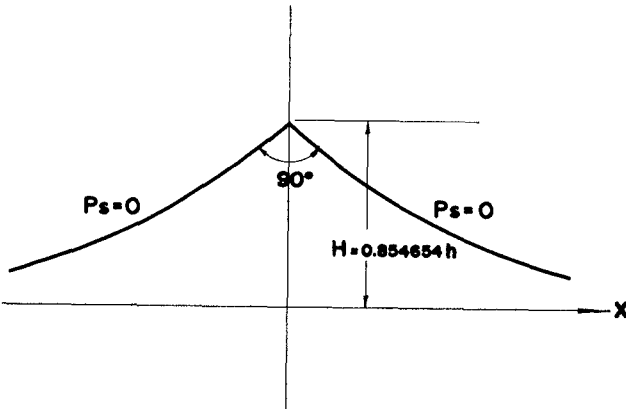


Figure 4 The Structure of highest wave

CONCLUSION

The new model submitted in this paper is proved to be applicable to any wavelength and any water depth so it can be nominated to be "universal model".

The ratio of critical wave height to water depth derived from this model is

$$\frac{H}{d} = 0.8546 \dots$$

and the angle of the critical wave crest is  $90^\circ$ .

No approximate calculation is adopted in this theory, the solution is to be called "exact".

REFERENCE

- Byatt-smith, J.G.B. "An exact integral equation for steady surface waves", Proc. Roy. Soc. Lond. A. 315, 405-418, 1970.
- Chen, Y.Y., Ouyang, Y.C. and Frederick, L.W. Tang, "New equation of surface elevation in wave motion", Proc. 18th Conference on Coastal Engineering, 508-520, 1982.
- Laitone, E.V. "The second approximation to Cnoidal and Solitary waves", Journal of Fluid Mechanics, 9, 430-444, 1960.
- Lenau, C.W. "The solitary wave of maximum amplitude", Journal of Fluid Mechanics, 26, 309-320, 1966.
- Longuet-Higgins, M.S. "On the mass, momentum, energy and circulation of a solitary wave", Proc. Roy. Soc. Lond. A. 337, 1-13, 1974.
- McCowan, J. "On the solitary wave", Philosophic Magazine, Series 5, 32, 45-58, 1891.
- McCowan, J. "On the highest wave of permanent type", Philosophic Magazine, Series 5, 38, 351-357, 1894.
- Rankine, W.J.M. "Supplement to a paper on stream-lines", Philosophic Magazine, Series 4, 29, 25-28, 1865.
- Stokes, G.G. "On the theory of oscillatory waves", Trans. Camb. Phil. Soc., 8, 441-455, 1847.
- Stokes, G.G. "Considerations relative to the greatest height of oscillatory waves which can be propagated without change of form", Mathematical and physical papers, Vol. 1, PP.225-228, Cambridge University Press.

Yamada, H. "On the highest solitary wave", Rep. Res. Inst. Appl. Mech. Kyushu University, 5, 53-67, 1957.

## CHAPTER SEVENTY ONE

### COMBINED REFRACTION-DIFFRACTION CALCULATIONS WITH DIRECTIONAL WAVE SPECTRA

P. Gaillard

SOGREAH, Grenoble, France

#### ABSTRACT

A method of calculation of the combined effects of wave refraction, diffraction and reflection in harbours of arbitrary shape and non uniform water depth, subject to periodic or random waves is presented. Examples of application are given and practical aspects on the wave spectrum discretisation are considered.

#### INTRODUCTION

The study of wave disturbance within harbours at the design stage has for many years been considered in terms of harbour response to various isolated unidirectional periodic waves both in laboratory scale models and numerical models. With the increasing application of wave measurement techniques giving information on the directional wave spectrum, a need is now felt to account for the directional spreading of wave energy, as well as for its frequency-wise distribution, in the design of ocean and coastal structures.

Numerical methods applying either refraction calculations (Collins et al [3]) or diffraction calculations in constant water depth (Goda et al [4], Nagai [6]) to directionally distributed random waves have formerly been published. However, methods involving both refraction and diffraction effects are required for engineering studies.

This paper presents a method of calculation of the combined effects of wave diffraction, reflection and refraction in harbours of arbitrary shape and non uniform water depth, which applies equally to periodic waves and random waves, conforming to a given directional wave spectrum.

This method has been applied since 1977 in studies of harbour projects involving periodic waves as offshore boundary conditions. It has recently been extended to account for prescribed irregular wave characteristics at the model boundaries.

## METHOD APPLIED WITH PERIODIC WAVES OR SPECTRAL COMPONENTS

The area investigated at the harbour site is discretised into a set of connected basins with constant water depths, these generally being unequal and conforming to the sea-bed topography. Within each of these domains, the problem is dealt with by a boundary integral element method as described by Barailler and Gaillard [1], Biesel and Ranson [2]. The refraction effects due to the sea-bed configuration are taken into account at the common boundaries between connected basins.

The excitation of the harbour by a periodic incident wave of angular frequency  $\omega$  induces a steady state dynamic response of the same frequency. The water surface elevation  $\zeta$  and the velocity potential  $\phi$  are accordingly expressed in the form:

$$\begin{aligned}\zeta(x,y,t) &= \text{Re} \left\{ \bar{\zeta}(x,y) e^{-i\omega t} \right\} \\ \phi(x,y,z,t) &= \text{Re} \left\{ \bar{\phi}(x,y,z) e^{-i\omega t} \right\}\end{aligned}\quad (1)$$

The unknown complex function  $\bar{\zeta}$  is, within each basin of constant depth  $h$ , a solution of the Helmholtz equation:

$$\nabla^2 \bar{\zeta} + k^2 \bar{\zeta} = 0 \quad (2)$$

with:

$$\omega^2 = gk \tanh kh \quad (3)$$

The function  $\bar{\phi}$  can be derived from  $\bar{\zeta}$  by the formula:

$$\bar{\phi}(x,y,z) = -i \frac{g}{\omega} \bar{\zeta}(x,y) \frac{\cosh k(z+h)}{\cosh kh} \quad (4)$$

The solution of (2) is expressed in the form of the boundary integral:

$$\bar{\zeta}_0 = -\frac{i}{4} \int_{\Gamma} \frac{\partial \bar{\zeta}}{\partial n} G_2(OM) ds \quad (5)$$

where:

$\Gamma$  is the boundary of the basin considered

$\partial/\partial n$  is the normal derivative taken positive inwards

$G_2(OM)$  the second Green's function associated with an arbitrary internal point  $O$  and a boundary point  $M$ , cf. fig. 1a.

$G_2(OM)$  is the solution of (2), which has a vanishing normal derivative along  $\Gamma$  and a logarithmic behaviour in the vicinity of  $O$ . When the domain is a half-plane, this solution is:

$$G_2(OM) = 2 H_0^{(1)}(kr) \quad (6)$$



$$\bar{\zeta}_0 = -\frac{1}{2} \int_{\Gamma} \frac{\partial \bar{\zeta}}{\partial n} H_0^{(1)}(kr) ds \tag{7}$$

where  $H_0^{(1)}$  is the Hankel function of the first kind and order zero. This formula can be applied to an arbitrarily shaped domain D by considering the combination of solutions associated with a discrete set of half-planes including D and bounded by the tangent to different sections of the boundary  $\Gamma$ . The area under investigation has to be subdivided into several basins of convex shape when necessary.

Furthermore, the normal derivative of  $\bar{\zeta}$  involved in (7) should be related exclusively to the waves entering into the basin considered. These waves may include:

- incoming waves with known characteristics, either given as basic data or derived from preliminary refraction calculations between the open sea and the harbour site. The sections of boundary where this occurs are referred to as main entrances;
- waves with unknown characteristics ab initio, which come from other connected basins or which are reflected from harbour structures. The sections of boundary where this occurs are classified as secondary entrances.

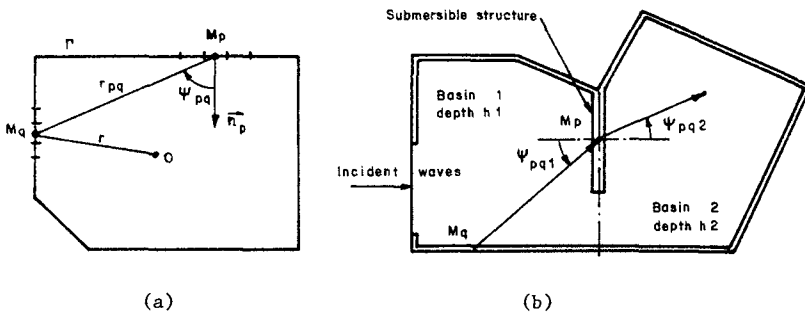


Fig. 1: Definition sketch

The method takes into account partial or total reflection from coastal structures and partial transmission when these are permeable or submersible, provided that the relevant coefficients are given. However, energy dissipation by bottom friction or wave breaking at locations other than these structures is not considered.

In the case of a reflective structure, the following boundary condition holds between the reflected (incoming) wave  $\bar{\zeta}_e$  and the incident (outgoing) wave  $\bar{\zeta}_s$ :

$$\bar{\zeta}_e = C_R \bar{\zeta}_s \tag{8}$$

$$\frac{\partial \bar{\zeta}}{\partial n} \bar{e} = - C_R \frac{\partial \bar{\zeta}}{\partial n} \bar{s} \quad (9)$$

$$\left( \frac{\partial \bar{\zeta}}{\partial n} \right)_p = - i \frac{k}{2} \int_{\Gamma} \left( \frac{\partial \bar{\zeta}}{\partial n} \right)_q H_1^{(1)}(kr_{pq}) \cos \Psi_{pq} ds \quad (10)$$

$$\Psi_{pq} = (\vec{n}_p, \vec{M}_p \vec{M}_q)$$

In the case of a permeable or submersible structure, the physical phenomenon can be complex because of the generation of harmonic wave components. As concerns the transmission of the fundamental component, the relationship between the outgoing wave in basin 1 and the incoming wave in basin 2, as shown in the figure 1b, is:

$$\bar{\zeta}_2 = C_T \bar{\zeta}_1 \quad (11)$$

$$\frac{\partial \bar{\zeta}}{\partial n} = - C_T \frac{\partial \bar{\zeta}}{\partial n} \quad \text{if } h_2 = h_1 \quad (12)$$

$$\left( \frac{\partial \bar{\zeta}}{\partial n} \right)_p = - M_{pq} \left( \frac{\partial \bar{\zeta}}{\partial n} \right)_q \quad \text{if } h_2 \neq h_1 \quad (13)$$

$$M_{pq} = \frac{k_2 \cos \Psi_{pq2}}{k_1 \cos \Psi_{pq1}} C_T \quad (14)$$

When the water depths in the adjacent basins are different, the direction of waves originating from a given boundary source,  $M_q$  varies according to Snell's law of refraction:

$$k_1 \sin \Psi_{pq1} = k_2 \sin \Psi_{pq2} \quad (15)$$

There is total reflection on the boundary if:

$$\Psi_{pq1} \geq \Psi_{1L} \quad \Psi_{1L} = \sin^{-1}(k_2/k_1) \quad (16)$$

This is observed for instance when waves propagating towards the shore encounter a navigation channel with an oblique incidence.

The complex parameters  $C_R$  and  $C_T$  have a modulus equal to the reflection or transmission coefficient of the structure and an argument equal to the phase lag introduced by the phenomenon considered. These parameters have to be derived from theoretical analysis or experimental investigations.

If the actual variation of water depth from one basin to another is gradual, i.e. with a sea-bed configuration of very mild slope which does not give rise to any appreciable wave reflection, the law of conservation of energy flux at the common boundary is applied.

$$\left| \bar{\zeta}_1 \right|^2 C_{g1} \cos \Psi_{pq1} = \left| \bar{\zeta}_2 \right|^2 C_{g2} \cos \Psi_{pq2} \quad (17)$$

This leads to the boundary condition (13) with:

$$M_{pq} = \frac{k_2}{k_1} \left[ \frac{C_{g1}}{C_{g2}} \frac{\cos \psi_{pq2}}{\cos \psi_{pq1}} \right]^{1/2} \quad (18)$$

The numerical calculation involves two steps:

- first, the solution of the system of equations resulting from the discretisation of the basin boundaries, the unknowns being the values of the normal derivative  $\partial \bar{\zeta} / \partial n$  in each basin at the centre of the boundary segments located on secondary entrances;
- then, the calculation of  $\bar{\zeta}$  in an arbitrary network of points by means of the discretised form of (7). This provides information on the spatial distribution of the local wave height  $2a$ , wave phase  $\theta$ , and diffraction coefficient  $K_d$  given by:

$$\bar{\zeta} = a e^{i\theta} \quad K_d = a/a_0 \quad (19)$$

where  $2a_0$  is the reference wave height given offshore or in the vicinity of the harbour entrance.

Additional information on the local wave direction  $\alpha$ , defined as the normal to the local constant phase line, and on the effective local wave number  $k_e$  is given by:

$$\frac{\partial \theta}{\partial x} = k_e \cos \alpha = \text{Im} \left\{ \frac{1}{\bar{\zeta}} \frac{\partial \bar{\zeta}}{\partial x} \right\} \quad (20)$$

$$\frac{\partial \theta}{\partial y} = k_e \sin \alpha = \text{Im} \left\{ \frac{1}{\bar{\zeta}} \frac{\partial \bar{\zeta}}{\partial y} \right\}$$

$$\left\{ \frac{\partial \bar{\zeta}}{\partial x}, \frac{\partial \bar{\zeta}}{\partial y} \right\} = -i \frac{k}{2} \int_{\Gamma} \frac{\partial \bar{\zeta}}{\partial n} H_1^{(1)}(kr) \left\{ \cos \mu, \sin \mu \right\} ds \quad (21)$$

$$\mu = (\vec{OX}, \vec{OM})$$

#### METHOD APPLIED WITH RANDOM WAVES

If the wave disturbance to be considered within the harbour results from random waves conforming to a given directional spectrum offshore, this spectrum is discretised into a finite set of directional and frequency-wise components. The harbour response to the excitation by each spectral component is calculated by the procedure described in the preceding section. This calculation gives:

- the diffraction coefficient  $K_d$  as a function of wave frequency  $f$ , initial wave direction  $\alpha_0$  and wave height  $a_0$ ; if the reflection and transmission coefficients of the structures involved in the study are considered as independent of the incident wave height,  $K_d$  will be independent of  $a_0$ , since the method is based on linear theory;

- . the correspondence between the local wave direction  $\alpha$  and the initial direction  $\alpha_o$  of the spectral component.

From these results, it is possible to derive the local directional spectrum and frequency spectrum at any selected point P, by means of the following expressions:

$$S(f, \alpha, P) = S_o(f, \alpha_o) K_p^2 \quad K_p^2 = \frac{C_{go} C_o}{C_{gp} C_p} \quad (22)$$

$$S(f, P) = \int_0^{2\pi} S_o(f, \alpha_o) [K_d(f, \alpha_o, P)]^2 d\alpha_o \quad (23)$$

where:

$S_o(f, \alpha_o)$  is the reference wave spectrum

$C_o, C_{go}$  are respectively the phase and group velocities at the location where the reference wave spectrum is specified

$C_p, C_{gp}$  are the phase and group velocities at point P

$K_d$  and  $K_p$  are theoretically related by:

$$K_d^2 = K_p^2 \frac{\partial \alpha}{\partial \alpha_o} \quad (24)$$

The spatial distribution within the harbour of various overall spectral properties can be derived from the spectral moments:

$$M_j = \int_0^\infty df \int_0^{2\pi} f^j S_o(f, \alpha_o) K_d^2 d\alpha_o \quad (25)$$

$$M_{pq} = \int_0^\infty df \int_0^{2\pi} k^{p+q} \cos^p \alpha \cos^q \alpha S_o(f, \alpha_o) K_d^2 d\alpha_o \quad (26)$$

The following spectral parameters are considered in the applications of the method which are presented here: the significant wave height  $H_s$ , the mean zero-upcrossing wave period  $T_m$ , the mean wave direction  $\theta_m$  and the mean spreading angle  $\theta_s$ , as defined by Goda, Miura and Kato [5]. These parameters are defined by:

$$H_s = 4 \sqrt{M_o} \quad (27)$$

$$T_m = (M_o/M_2)^{1/2} \quad (28)$$

$$\theta_m = \tan^{-1} (M_{o1}/M_{1o}) \quad (29)$$

$$\theta_s = \tan^{-1} \left\{ \frac{\sqrt{M_{o0} (M_{o1}^2 M_{2o} - 2M_{1o} M_{o1} M_{11} + M_{1o}^2 M_{o2})}}{M_{o1}^2 + M_{1o}^2} \right\} \quad (30)$$

The parameters associated with the reference wave spectrum are represented by  $H_{so}, T_{mo}, \theta_{mo}, \theta_{so}$ .

### EXAMPLES OF APPLICATION

Several examples of application of the above method to complex harbour layouts with periodic and random waves are presented here. Besides, practical aspects on the wave spectrum discretisation techniques are considered in the case of a breakwater gap.

#### Comparison with experimental data

Figure 2 shows the results of a comparative study of the wave disturbance within a harbour performed with a numerical model based on the above method and with a laboratory scale model at a scale of 1/150. The water depth ranges approximately between 31 m at the offshore boundary and 6 m in the nearshore zone of the harbour, and 24 diffraction basins were considered in the numerical model.

The results obtained for 12 s periodic waves are shown in the form of curves of constant relative wave-height, the latter being expressed in percentage of the reference wave-height offshore. The local wave direction, calculated by means of (20) (21), is also shown in figure 2b. A similar wave-height distribution is observed in both models.

#### Harbour access channel effect on wave propagation

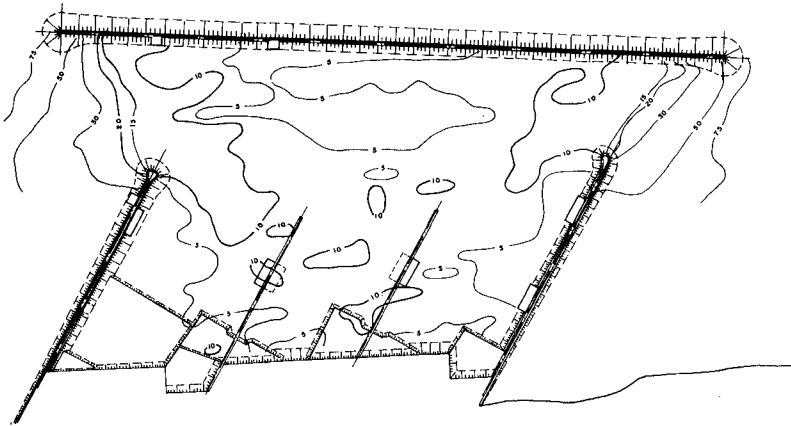
The second example is an application of the numerical method to the study of the impact of a harbour extension scheme on the wave disturbance in Fos harbour (France). This study, performed at the request of the Marseilles Port Authority, is illustrative of the effect of harbour access channels on wave propagation.

Figure 3 shows the area investigated, the location of the harbour entrance channel being indicated by dashed lines. The results obtained for wave periods of 6 and 8 seconds are shown respectively in figure 3a and b, with the same presentation as in figure 2b. An enlarged view of the wave height and wave direction distributions in the harbour area is shown at the left hand side of the figure. A smaller mesh size of the calculation network has been used for this purpose.

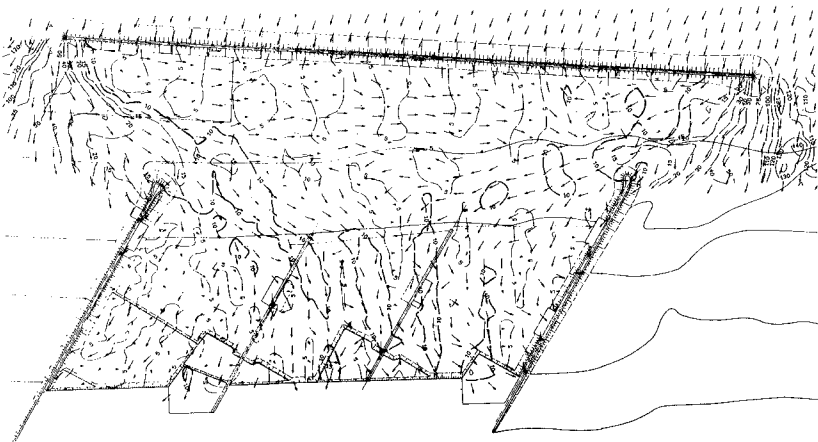
This figure shows a marked effect of the wave period on the wave pattern. The reflection of the incoming waves on the outer side of the harbour access channel is observed with the higher period and this produces a favourable sheltering effect in the harbour area.

#### Wave spectrum discretisation techniques

In order to study the influence of the wave spectrum discretisation technique on the accuracy of results, numerical calculations have been done in the case of a breakwater gap in constant water depth with directional wave spectra representative of wind waves and swell respectively.



(a)



(b)

Fig. 2: Comparison of the wave-height distributions in a harbour obtained respectively with a laboratory scale model (a) and a numerical model (b) for 12 s periodic waves. In the latter model, the local wave direction is indicated by arrows.

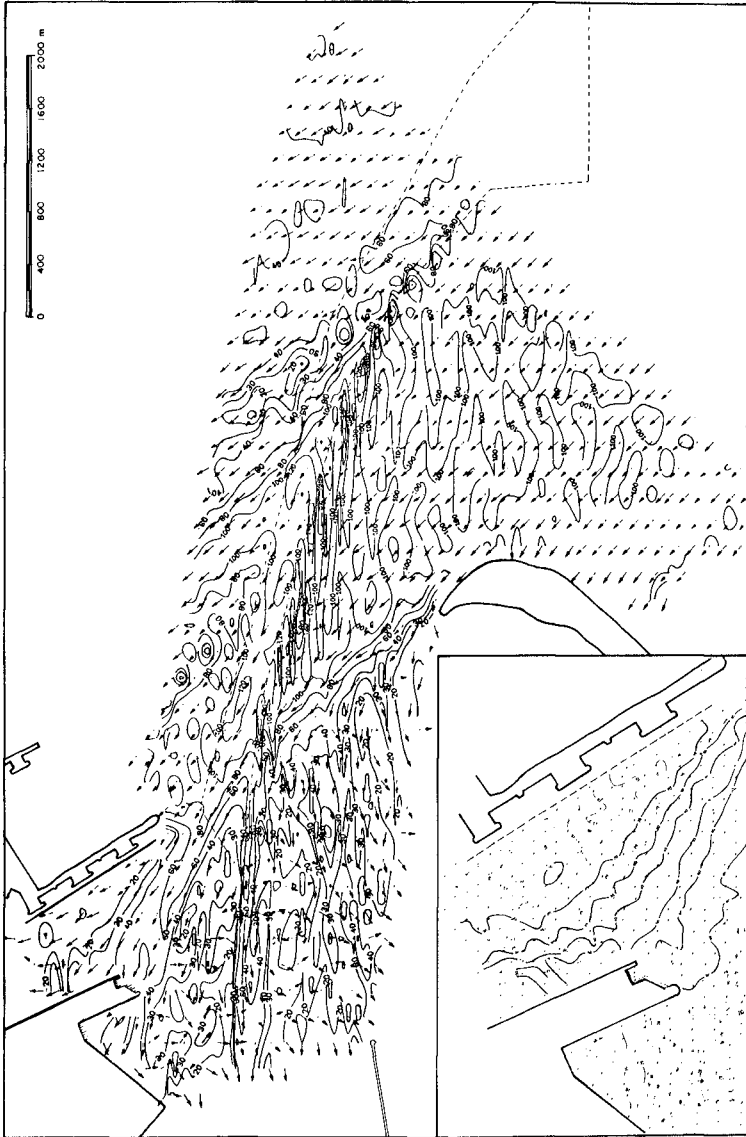


Fig. 3a: Wave-height and wave direction obtained with a numerical model of Fos harbour for waves of period  $T = 6$  s.

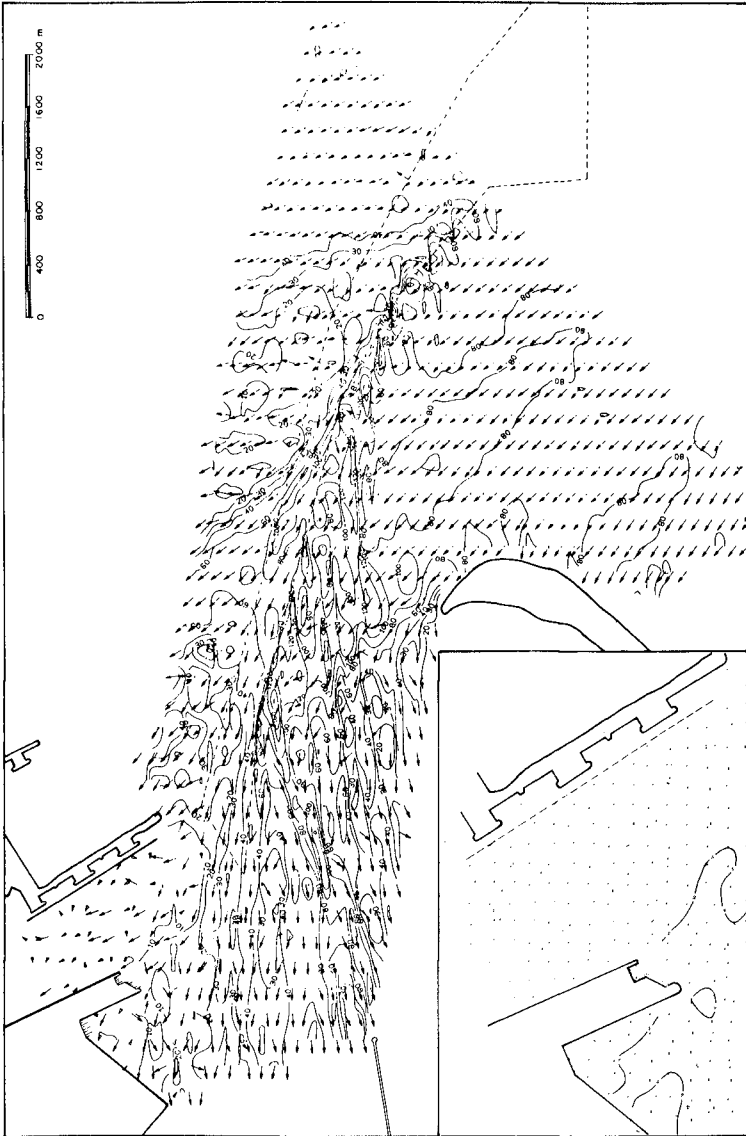


Fig. 3b: Wave-height and wave direction obtained with a numerical model of Fos harbour for waves of period  $T = 8$  s.



The incident wave spectra were chosen of the form proposed by Goda et al [4] :

$$S_o(f, \alpha_o) = \bar{S}_o(f) \cdot D(f, \alpha_o) \quad (31)$$

$$\bar{S}_o(f) = 0.312 H_s^2 T_p^{-4} f^{-5} \exp \left[ -\frac{5}{4} (T_p f)^{-4} \right] \quad (32)$$

$$D(f, \alpha_o) = C \left[ \cos \frac{1}{2} (\alpha_o - \theta_{mo}) \right]^{2s} \quad (33)$$

$$s = \begin{cases} s_{\max} (f/f_p)^5 & f \leq f_p \\ s_{\max} (f/f_p)^{-2.5} & f > f_p \end{cases} \quad (34)$$

where:

$T_p$  and  $f_p$  are the period and frequency of the spectral peak

$C$  is a normalisation constant.

In the example considered, the gap-width to wave length ratio corresponding to the spectral peak is approximately  $B/L_p = 1.81$ .

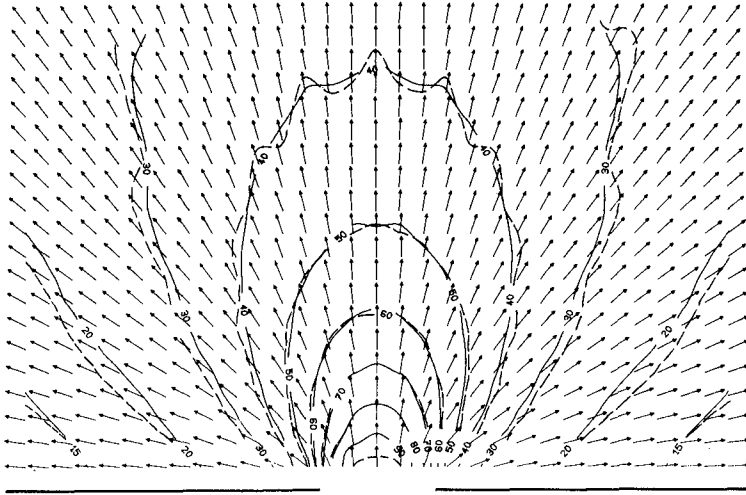
The results of two of the discretisation techniques implemented are reported here:

- The first one consists in a uniform allocation of wave energy to all frequency bands, this energy being lumped up at frequencies chosen in order to conserve the mean period defined by (28). The angular discretisation is done with a constant interval  $\Delta \alpha_o$  in a range of  $\pm \pi/2$  around the mean direction of the spectrum.
- The second technique is the same in the frequency domain. The angular discretisation is done with a constant interval, but the total range is reduced, the actual energy located beyond this range being allocated to the extreme angular components when this energy is lower than a given threshold value.

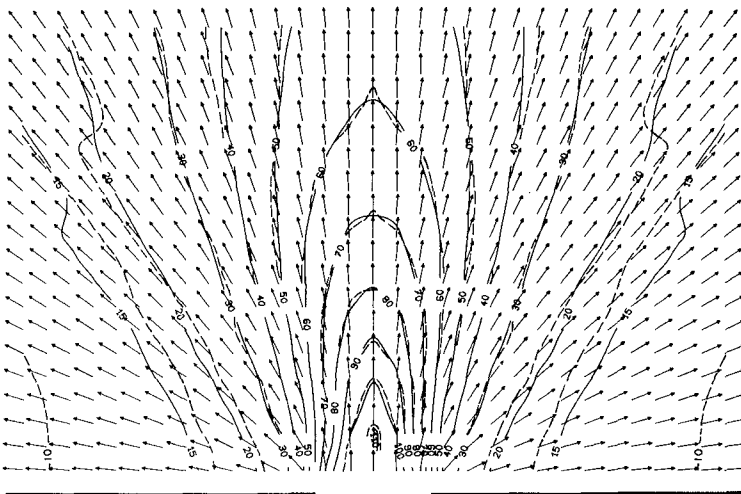
Figure 4 shows the distributions of the relative significant wave height  $H/H_{so}$  for the wave spectra corresponding respectively to  $s_{\max} = 10^0$  and 75. The full lines show the wave-height distribution resulting from the first technique with 204 spectral components, distributed in 12 frequency intervals. The dashed lines result from the second technique, which leads to the computation of 70 and 34 spectral components respectively for the broad and narrow spectra, with 6 frequency intervals. A good agreement of the results is found.

As concerns the mean wave direction  $\theta_m$ , indicated by arrows in figure 4, there is no discernible difference between the two techniques.

Figure 5 shows the distribution of the relative mean wave period  $T/T_m$  for the broad spectrum in the form of level curves. The results obtained with the first and second discretisation techniques are shown on the left and right hand sides of the gap centre-line respectively.



(a)



(b)

Fig. 4: Wave-height and wave direction behind a breakwater gap of relative width  $B/L = 1.83$  for random waves with: (a)  $s = 10$  (b)  $s = 75$ . The solid and dashed lines are related to the first and second discretisation techniques.

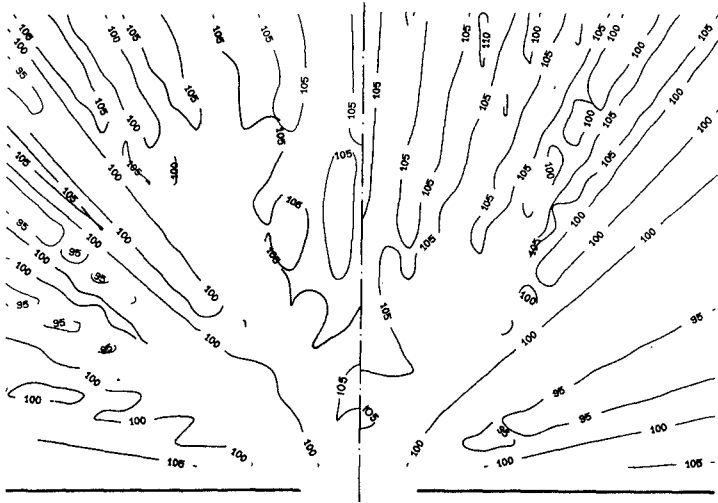


Fig. 5: Distribution of the mean wave period  $T_m/T_{m0}$  behind the breakwater gap for a directional wave spectrum with  $s = 10$ . See also legend of fig. 6.

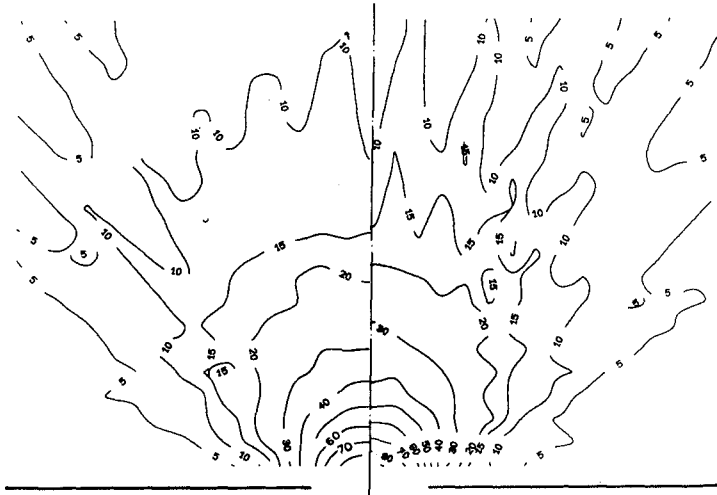


Fig. 6: Distribution of the mean spreading angle  $\theta/\theta_0$  for the same wave spectrum. LHS and RHS show the results of the first and second discretisation techniques (204 and 70 spectral components respectively).

Figure 6 shows the distribution of the ratio  $\theta_s/\theta_{s_0}$  for the same case with a similar presentation.

Differences due to the discretisation technique are more pronounced with the mean wave period and the mean spreading angle than with the significant wave height distribution, although the results are of the same order of magnitude. This sensitivity to discretisation is connected with the presence of higher moments of the wave spectrum in the expressions used for calculating these parameters.

#### Study of a complex harbour layout with random waves

Figures 7 and 8 give an example of study of the wave disturbance in a harbour of complex shape with random wave characteristics given as boundary conditions. In this case, the reference frequency spectrum is of the Jonswap type and the angular dispersion function is of the form (33) (34) with  $s_{\max} = 50$ . This relatively narrow spectrum is discretised into 39 spectral components, distributed over 5 frequency bands, by the second technique just described.

Figure 7a shows the spatial distribution of the diffraction coefficient  $K_d$  associated with one of the spectral components considered, in the form of curves of constant  $K_d$  values. The local wave direction associated with this period is indicated by arrows.

Figure 7b shows the distribution of the relative significant wave height  $H/H_{s_0}$  in the form of level curves and arrows indicate the local mean wave direction defined by equation (29).

Figure 8a shows the distribution of the relative mean wave period  $T_m/T_{m_0}$ , as defined by equation (28) and figure 8b the distribution of the relative mean spreading angle  $\theta_s/\theta_{s_0}$ , defined by equation (30). In this particular case, the wave reflection on the harbour structures tends to increase the angular spread of the locally observed wave spectrum and this effect predominates over the adverse effect of wave diffraction in many parts of the harbour.

#### CONCLUSION

The method described provides an interesting means of evaluation of wave disturbance in harbour projects, in terms of wave spectral properties. The numerical calculations confirm the conclusion of other authors that the directional spreading of wave spectra is an important characteristic to account for in such studies, if sufficient information is available on the local wave climate.

The second wave spectrum discretisation technique presented here is recommended for selecting the spectral components to account for in the calculations. The number of components needed depends on the type of input wave spectrum and on the wave parameters required.

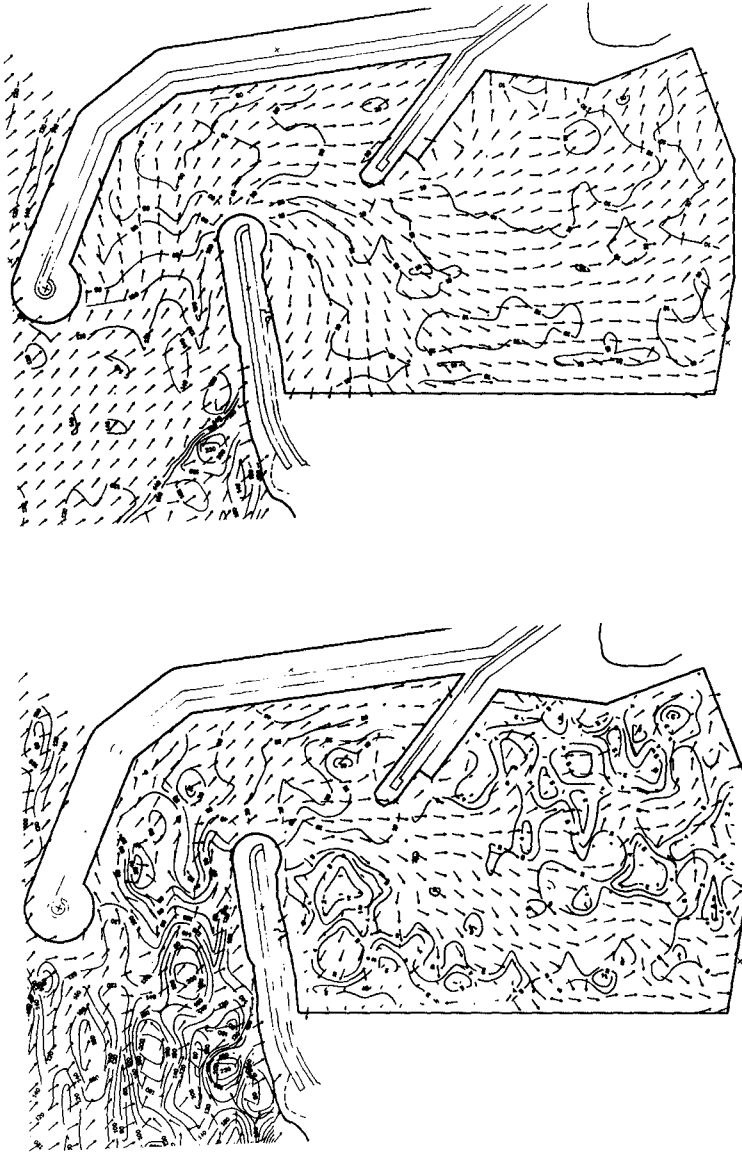


Fig. 7: Spatial distribution of: (a) coefficient  $K_d$  and wave direction  $\alpha$  for one spectral component, (b) significant wave height  $H_s/H_{s0}$  and mean wave direction  $\theta_m$  in a harbour of complex shape.

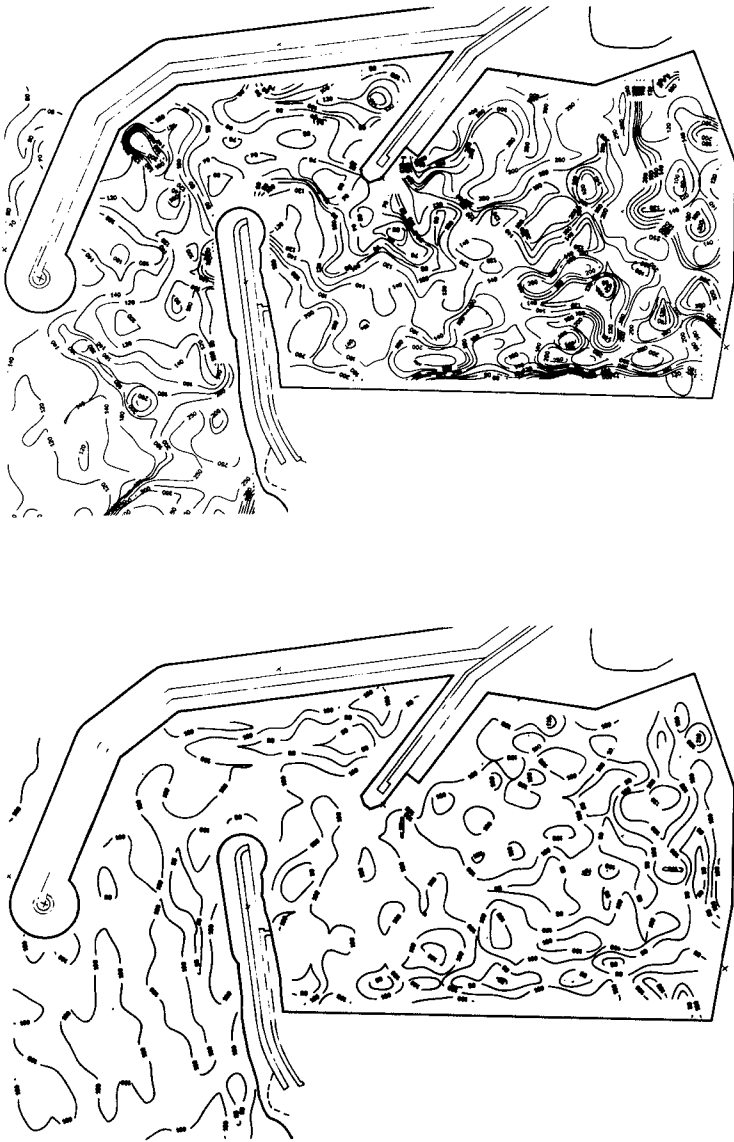


Fig. 8: Spatial distribution of (a) mean wave period  $T_m/T_{m0}$ , (b) mean dispersion angle  $\theta_s/\theta_{s0}$  in the harbour of figure 7.

The sensitivity analysis performed shows that the significant wave-height and mean wave direction are much less sensitive to the spectrum discretisation than the mean wave period and the mean spreading angle.

In practical applications, a careful choice of the reference directional wave spectrum is necessary, because of the marked influence of the angular distribution of energy on the wave pattern in sheltered areas and on the computer time required for these calculations.

#### REFERENCES

- [1] L. Barailler and P. Gaillard, 1964: Exemples de réalisation de modèles mathématiques à Sogreah pour des études de propagation de houle. Proc. 9th Coastal Engineering Conf., Lisbon, pp. 41-54.
- [2] F. Biesel and B. Ranson, 1961: Calculs de diffraction de la houle. IAHR Conference, Dubrovnik, pp. 688-699.
- [3] J.I. Collins, W.L. Chiang and F. Wu, 1981: Refraction of directional spectra. Proc. Conference on directional wave spectra applications, Berkeley, ASCE, pp. 251-268.
- [4] Y. Goda, T. Takayama and Y. Suzuki, 1978: Diffraction diagrams for directional random waves. Proc. 16th Coastal Engineering Conf., Hamburg, pp. 628-650.
- [5] Y. Goda, K. Miura and K. Kato, 1981: On-board analysis of mean wave direction with discus buoy. Int. Conf. on wave and wind directionality, Paris, Editions Technip, pp. 339-359.
- [6] K. Nagai, 1972: Diffraction of the irregular sea due to breakwaters. Coastal Engineering in Japan, JSCE, vol. 15 pp. 59-67.

## CHAPTER SEVENTY TWO

### A NUMERICAL SOLUTION OF BOUSSINESQ TYPE WAVE EQUATIONS

H. SCHAPER

W. ZIELKE

Institut of Fluid Mechanics  
University of Hannover  
Fed. Republic of Germany

#### 1. INTRODUCTION

Numerical models of short waves in shallow water, which are of particular interest for the calculation of the wave climate in harbours and coastal areas, have been presented by Abbott et al. (1978) and by Hauguel (1980). These models are based on the solution of the Boussinesq or Serre type equations. A recent discussion of the range of application for the equations has been presented by McCowan (1982).

Nevertheless, there is some uncertainty as to which terms in the differential equations are of importance, and how they are to be approximated. Therefore, no final judgement can presently be made on the accuracy and credibility of the solutions. Research on such models is still in progress and is of high theoretical and practical interest.

Some of the aspects of current research relate to the handling of nonlinear terms, the non-reflecting boundary conditions and the transfer capability of the models for spectral input. This paper will reflect on these points.



## 2. BASIC EQUATIONS

For simplicity, we will restrict ourselves to the one-dimensional case, for which the Boussinesq type equations read

$$(1) \quad \frac{\partial p}{\partial t} + \frac{\partial}{\partial x} \left( \frac{p^2}{h} \right) + g h \frac{\partial \zeta}{\partial x} = \frac{D}{2} \frac{h}{\partial x^2} \frac{\partial^3}{\partial t} \left( \frac{dp}{h} \right) - \frac{D^2 h}{6} \frac{\partial^3}{\partial x^2 \partial t} \left( \frac{p}{h} \right)$$

$$(2) \quad \frac{\partial \zeta}{\partial t} + \frac{\partial p}{\partial x} = 0$$

with  $D$  = mean water depth,  $\zeta$  = surface elevation,  $h = D + \zeta$   
 $p$  = flux per unit width,  $g$  = acceleration due to gravity.

For the actual calculation with a finite difference method, the third order terms on the right hand side of (1) have to be rewritten such that each term contains only derivatives of either  $p$  or  $\zeta$ . Two third order terms remain, as well as some 15 other terms with products of first and second order derivatives:

$$(1') \quad \dots = \frac{D^2}{3} \frac{\partial^3 p}{\partial x^2 \partial t} - \frac{D^2}{3} \frac{p}{h} \frac{\partial^3 \zeta}{\partial x^2 \partial t} + \text{product terms}$$

We assume that the product terms are small in comparison to the third order terms (Abbott et al., 1978). Equations (1') and (2) can be collected in matrix form

$$(3) \quad \frac{\partial w}{\partial t} + A \frac{\partial w}{\partial x} + B \frac{\partial^3 w}{\partial x^2 \partial t} = R$$

with

$$w = \begin{bmatrix} p \\ \zeta \end{bmatrix} \quad A = \begin{bmatrix} \frac{2p}{h} & gh - \frac{p^2}{h^2} \\ 1 & 0 \end{bmatrix} \quad B = \begin{bmatrix} -\frac{D^2}{3} & \frac{D^2 p}{3h} \\ 0 & 0 \end{bmatrix} \quad R = \begin{bmatrix} \frac{D^2}{h^2} D, x \\ 0 \end{bmatrix}$$

## 3. NUMERICAL APPROXIMATION

In order to implement the third order terms of (3), a two level scheme with central differences is used, the difference star being given in Fig. 1. The finite difference approximations of the partial derivatives are given by equations (4.a) - (4.c).

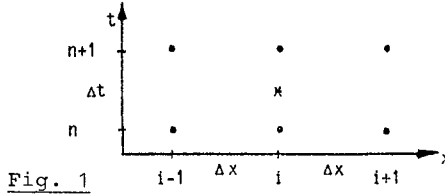


Fig. 1

$$(4.a) \quad \left. \frac{\partial w}{\partial t} \right|_i^{n+1/2} = \frac{w_i^{n+1} - w_i^n}{\Delta t} - \frac{\Delta t^2}{24} \frac{\partial^3 w}{\partial t^3} + O(\Delta^3)$$

$$(4.b) \quad \left. \frac{\partial w}{\partial x} \right|_i^{n+1/2} = \frac{w_{i+1}^{n+1} - w_{i-1}^{n+1} + w_{i+1}^n - w_{i-1}^n}{4\Delta x} - \frac{\Delta t^2}{8} \frac{\partial^3 w}{\partial x \partial t^2} - \frac{\Delta x^2}{6} \frac{\partial^3 w}{\partial x^3} + O(\Delta^3)$$

$$(4.c) \quad \left. \frac{\partial^3 w}{\partial x^2 \partial t} \right|_i^{n+1/2} = \frac{(w_{i+1}^{n+1} - 2w_i^{n+1} + w_{i-1}^{n+1}) - (w_{i+1}^n - 2w_i^n + w_{i-1}^n)}{\Delta x^2 \Delta t} + O(\Delta^3)$$

The third order correction terms are detected by Taylor series expansion of the used grid points.

At the boundary nodes 0 and N one sided difference stars have to be used and one coefficient of the correction terms is changed

$$(4.d) \quad \left. \frac{\partial w}{\partial x} \right|_0^{n+1/2} = \frac{(-3w_0 + 4w_1 + w_2)^{n+1} + (-3w_0 + 4w_1 - w_2)^n}{4\Delta x} - \frac{\Delta t^2}{8} \frac{\partial^3 w}{\partial x \partial t^2} + \frac{\Delta x^2}{3} \frac{\partial^3 w}{\partial x^3} + O(\Delta^3)$$

$$(4.e) \quad \left. \frac{\partial w}{\partial x} \right|_N^{n+1/2} = \frac{(w_{N-2} - 4w_{N-1} + 3w_N)^{n+1} + (w_{N-2} - 4w_{N-1} + 3w_N)^n}{4\Delta x} - \frac{\Delta t^2}{8} \frac{\partial^3 w}{\partial x \partial t^2} + \frac{\Delta x^2}{3} \frac{\partial^3 w}{\partial x^3} + O(\Delta^3)$$

Clearly all the correction terms cannot be approximated with the used 6-point star, because only a derivative of the kind  $\partial^3/\partial x^2 \partial t$  is possible. So the correction terms needed to be transformed into this form. As pointed out in literature (Peregrine, 1967, Abbott et al., 1978) the linearised equations (5) can be used and the transformations are given in (5.a) - (5.c).

$$(5) \quad \frac{\partial w}{\partial t} + L \frac{\partial w}{\partial x} = 0 \quad \text{with} \quad L = \begin{bmatrix} 0 & gD \\ 1 & 0 \end{bmatrix}$$

$$(5.a) \quad \frac{\partial^3 w}{\partial t^3} = L^2 \frac{\partial^3 w}{\partial x^2 \partial t}$$

$$(5.b) \quad \frac{\partial^3 w}{\partial t^2 \partial x} = -L \frac{\partial^3 w}{\partial x^2 \partial t}$$

$$(5.c) \quad \frac{\partial^3 w}{\partial x^3} = -L^{-1} \frac{\partial^3 w}{\partial x^2 \partial t}$$

Substitution of the finite difference approximations into equation (3) leads to

$$(6) \quad w_{,t} - \frac{\Delta t^2}{24} L^2 w_{,xxt} + A w_{,x} + \frac{\Delta t^2}{8} \underbrace{A L}_{L^2} w_{,xxt} + \frac{\Delta t^2}{6} \underbrace{A L^{-1}}_I w_{,xxt} + B w_{,xxt} = R$$

The product  $AL^{-1}$  can be replaced by the unit matrix, because  $L$  is the linearised form of  $A$ . The product  $AL$  is linearised to  $L^2$ , and all third order terms can be collected in matrix  $C$ .

$$(7) \quad w_{,t} + A w_{,x} + \underbrace{\left( B + \frac{\Delta x^2}{12} L^2 + \frac{\Delta x^2}{6} I \right)}_C w_{,xxt} = R$$

Now equation (7) can be rearranged with respect to the used grid points

$$(8) \quad \left[ -\frac{\Delta t}{4\Delta x}A + \frac{1}{\Delta x^2}C \right] w_{i-1}^{n+1} + \left[ I - \frac{2}{\Delta x^2}C \right] w_i^{n+1} + \left[ \frac{\Delta t}{4\Delta x}A + \frac{1}{\Delta x^2}C \right] w_{i+1}^{n+1}$$

$$= \left[ \frac{\Delta t}{4\Delta x}A + \frac{1}{\Delta x^2}C \right] w_{i-1}^n + \left[ I - \frac{2}{\Delta x^2}C \right] w_i^n + \left[ -\frac{\Delta t}{4\Delta x}A + \frac{1}{\Delta x^2}C \right] w_{i+1}^n + \Delta t R$$

and the coefficients of the unknowns can be collected in the matrices D, E, F, while the right hand side of (8) is collected in the vector G.

$$(9) \quad D_i w_{i-1}^{n+1} + E_i w_i^{n+1} + F_i w_{i+1}^{n+1} = G_i$$

Equation (9) is applied to all internal grid points 1...N-1. Similar equations can be performed for the boundary nodes 0 and N.

Neglecting the nonlinearity and the implementation of boundary conditions, which are described in detail later, a linear equation system of the following form arises.

$$\begin{bmatrix} D_0 & E_0 & F_0 & & & & & & & & \\ D_1 & E_1 & F_1 & & & & & & & & \\ & D_2 & E_2 & F_2 & & & & & & & \\ & & D_3 & E_3 & F_3 & & & & & & \\ & & & & & & & & & & \\ & & & & & & & & & & \\ & & & & & & D_{N-1} & E_{N-1} & F_{N-1} & & \\ & & & & & & D_N & E_N & F_N & & \end{bmatrix} * \begin{bmatrix} w_0 \\ w_1 \\ w_2 \\ w_3 \\ \vdots \\ \vdots \\ w_{N-1} \\ w_N \end{bmatrix} = \begin{bmatrix} G_0 \\ G_1 \\ G_2 \\ G_3 \\ \vdots \\ \vdots \\ G_{N-1} \\ G_N \end{bmatrix}$$

This system is solved very efficiently by a double sweep algorithm, taking into account the matrices  $F_0$  and  $D_N$ .

## 4. NONLINEAR TERMS

The differential equations are solved in the points  $*(i, n+1/2)$ . The matrices A and B, therefore, have to be evaluated at the time level  $n+1/2$ . A linearization by using the time level  $n$  can only be accepted, when calculating sufficiently long and shallow waves. The unknown values of  $W^{n+1/2}$ , arising in A and B, can be calculated explicitly from a Taylor series expansion

$$(10) \quad w_i^{n+1/2} = w_i^n + \frac{\Delta t}{2} \left( A \frac{\partial w}{\partial x} + B \frac{\partial^3 w}{\partial x^2 \partial t} - R \right) + \frac{\Delta t^2}{8} \frac{\partial^2 w}{\partial t^2} + \dots$$

by substitution of the differential equations (3) for  $\partial w / \partial t$ .

Some remarks should be made to this point:

- the third order terms of (3) are negligible, because of less influence;
- the second order term in (10) can also be neglected
- the convective parts of the first order terms of (3) cannot be neglected, especially in the calculation of high waves.

## 5. BOUNDARY CONDITIONS

It is of great interest for the practical application of numerical wave models, to introduce the waves at the boundary of the model using a time serie of the water elevation.

Such a condition is introduced by substitution of

$$(11) \quad \zeta_0 = f(t)$$

for either the momentum or the continuity equation at the node 0.

In this case, for example, the coefficient matrices will take the following form, where the coefficients of the remaining original equation are denoted by  $x$

$$\begin{matrix} \begin{bmatrix} x & x \\ 0 & 1 \end{bmatrix} w_0^{n+1} & + & \begin{bmatrix} x & x \\ 0 & 0 \end{bmatrix} w_1^{n+1} & + & \begin{bmatrix} x & x \\ 0 & 0 \end{bmatrix} w_2^{n+1} & = & \begin{bmatrix} x \\ f \end{bmatrix}^{n+1} \\ D_0 & & E_0 & & F_0 & & G_0 \end{matrix}$$

In the same way, a condition of total reflection may be introduced at the node N, which means

$$(12) \quad p_N = 0$$

$$\begin{matrix} \begin{bmatrix} 0 & 0 \\ x & x \end{bmatrix} w_{N-2}^{n+1} & + & \begin{bmatrix} 0 & 0 \\ x & x \end{bmatrix} w_{N-1}^{n+1} & + & \begin{bmatrix} 1 & 0 \\ x & x \end{bmatrix} w_N^{n+1} & = & \begin{bmatrix} 0 \\ x \end{bmatrix} \\ D_N & & E_N & & F_N & & G_N \end{matrix}$$

If waves are reflected from within the domain, non reflecting boundary conditions have to be used, which allow waves to leave the domain undisturbed. In this case, we use the equation given by Hanguel (1980), which he adopted from long wave theory.

$$(13) \quad p_n - c \zeta = -2c f(t)$$

with  $p_n$  flux normal to the boundary,  $\zeta$  water elevation,  $c$  wave celerity,  $f(t)$  water elevation of the incoming wave

Equation (13) may be slightly changed for simulation of partial reflection, occurring at breakwaters, for example. Naturally  $f(t)$  is equal to zero in this case, and with a reflection coefficient  $\gamma$  we get:

$$(14) \quad p_n - (1-\gamma) c \zeta = 0$$

Both conditions (13) and (14) are as well easily introduced as (11) and (12).

6. NUMERICAL RESULTS

Regular as well as irregular waves may be input, using the time function  $f(t)$ . For test calculations waves of permanent form, cnoidal waves, as well as their limiting case, solitary waves, are of particular interest.

Figures 2 and 3 show calculations of solitary waves where the coefficients are based only on the old time level  $n$ . As shown in Fig.2 for waves with an amplitude of 1 m, the errors due to the nonlinearity may be suppressed by using a very small time step (Fig. 2b). This was not possible for 2 m waves (Fig. 3).

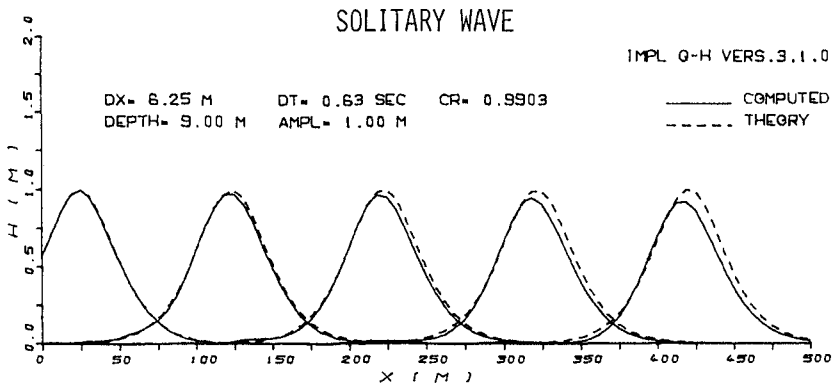


Fig. 2 a

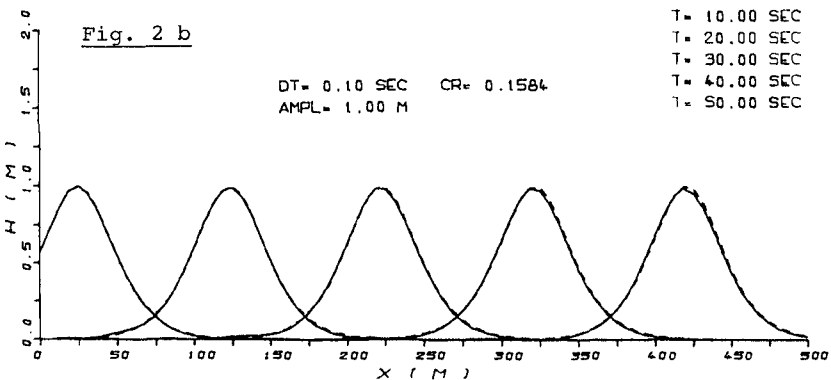


Fig. 2 b

## SOLITARY WAVE

IMPL Q-H VERS.3.1.1.0

DX= 6.25 M    DT= 0.63 SEC    CR= 0.9903  
 DEPTH= 8.00 M    AMPL= 2.00 M

———— COMPUTED  
 - - - - - THEORY

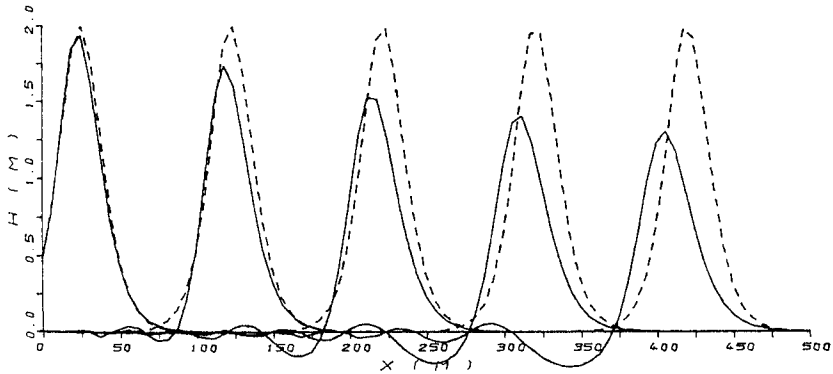


Fig. 3 a

DX= 6.25 M    DT= 0.10 SEC    CR= 0.1584  
 DEPTH= 8.00 M    AMPL= 2.00 M

T= 10.00 SEC  
 T= 20.00 SEC  
 T= 30.00 SEC  
 T= 40.00 SEC  
 T= 50.00 SEC

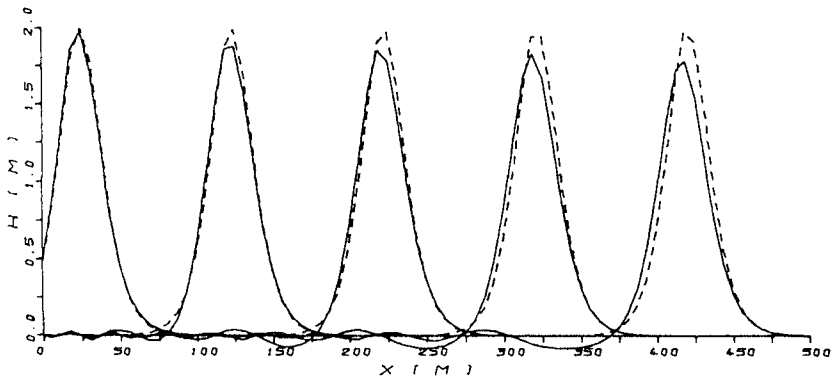


Fig. 3.b



The advantage of determining the coefficients from the time level  $n + 1/2$  (equation (10)) is shown in Fig. 4, for the case of 2 m waves and a time step of 0,625 sec.

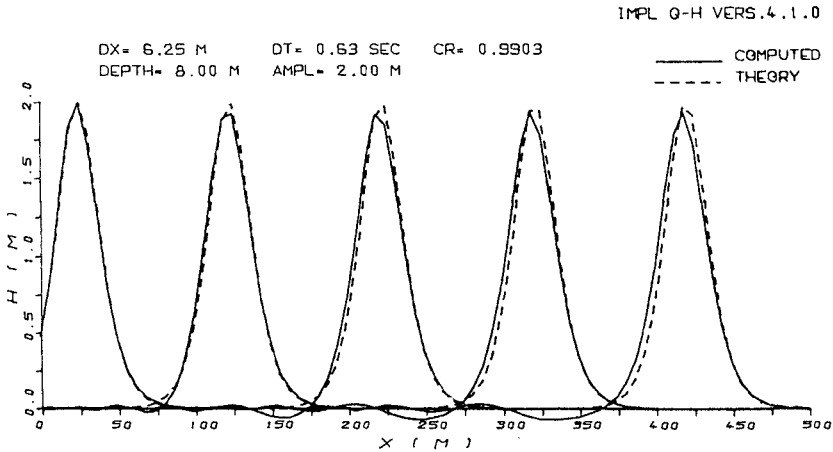


Fig. 4

Fig. 5 shows calculations for a solitary wave of limited height. Again it should be noted, that the wave is fed into the system using a time function for the water elevation only.

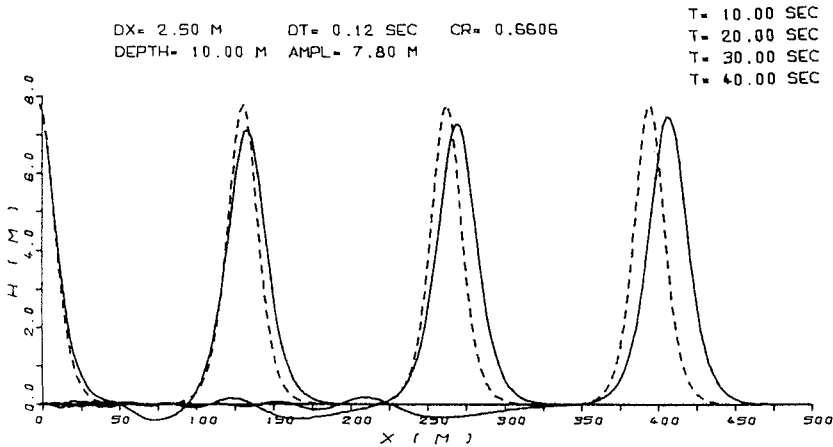
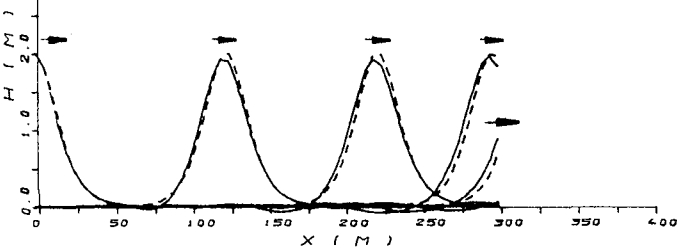


Fig. 5

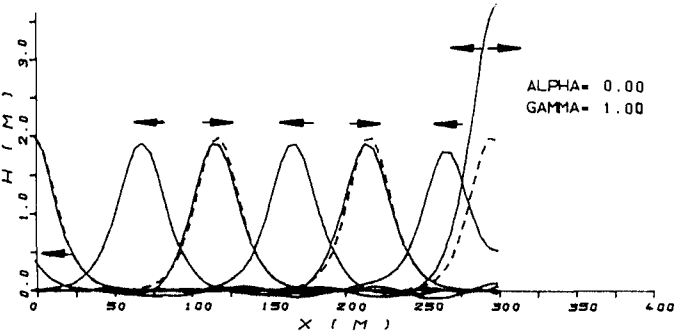
The behavior of the non-reflecting boundary conditions is shown in Fig. 6. In case (a) the reflection coefficient is zero and the wave leaves through the right boundary, located at  $x = 300$  m. In case (b) where  $\gamma$  is equal to one, the wave is totally reflected at the boundary and leaves the solution domain through the left boundary. In case (c) the reflection coefficient is 0,7 and the wave is partially reflected.

DX= 5.00 M    DT= 0.50 SEC    CR= 0.9903    ALPHA= 0.00    \_\_\_\_\_ COMPUTED  
 DEPTH= 8.00 M    AMPL= 2.00 M    GAMMA= 0.00    - - - - - THEORY



T= 7.50 SEC  
 T= 20.00 SEC  
 T= 30.00 SEC  
 T= 37.50 SEC  
 T= 40.00 SEC  
 T= 42.50 SEC  
 T= 50.00 SEC

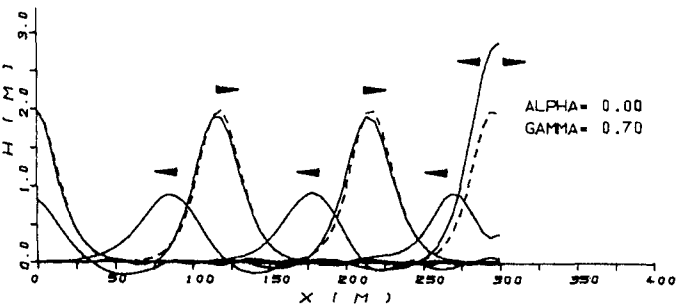
Fig. 6 a



ALPHA= 0.00  
 GAMMA= 1.00

T= 8.00 SEC  
 T= 20.00 SEC  
 T= 30.00 SEC  
 T= 38.00 SEC  
 T= 42.00 SEC  
 T= 52.00 SEC  
 T= 62.00 SEC  
 T= 72.00 SEC

Fig. 6 b



ALPHA= 0.00  
 GAMMA= 0.70

T= 8.00 SEC  
 T= 20.00 SEC  
 T= 30.00 SEC  
 T= 38.00 SEC  
 T= 42.00 SEC  
 T= 52.00 SEC  
 T= 62.00 SEC  
 T= 72.00 SEC

Fig. 6 c

Figure 7 shows the transformation of a solitary wave into several waves, due to its passing over a sloped bottom onto a shelf. These results are in good agreement with those of Hauguel (1980).

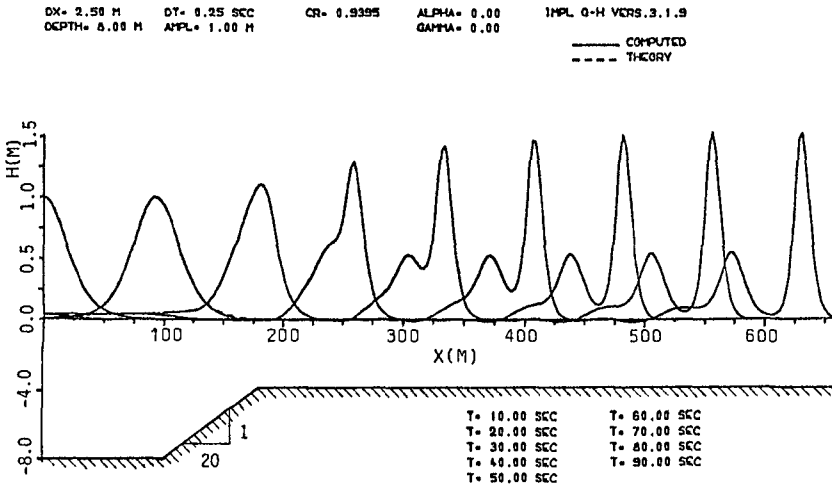
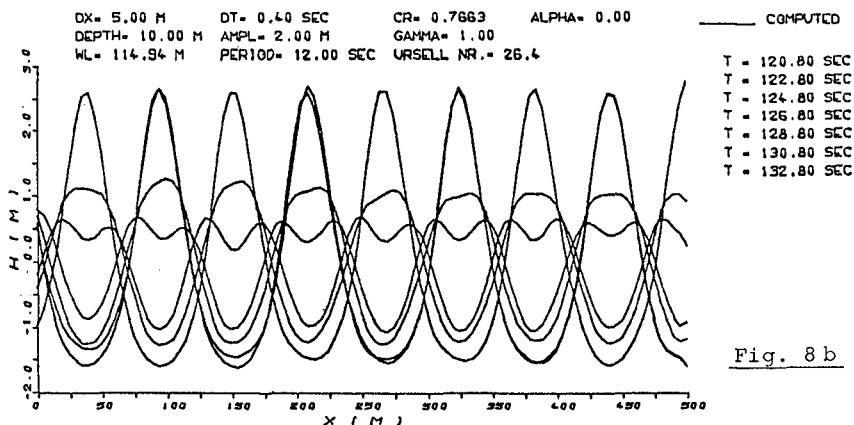
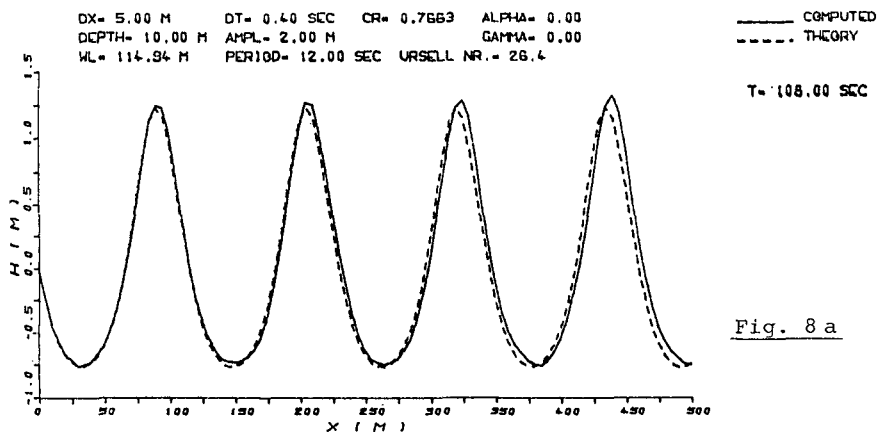


Fig. 7

Figures 8 a, b show the calculation of a cnoidal wave with a wave height of 2 m and a period of 12 sec. The water depth was held constant at 10 m.

Case (a), with a zero reflection coefficient, is again a test for the radiation condition at the right boundary.

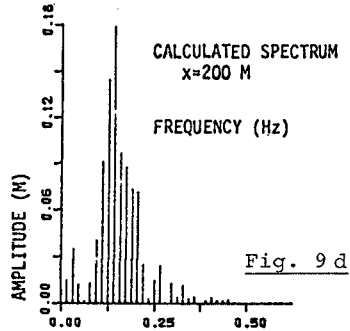
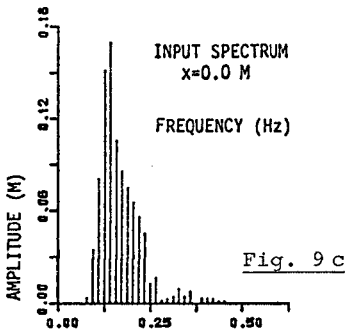
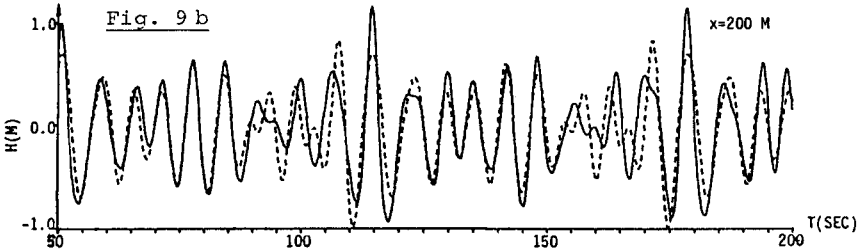
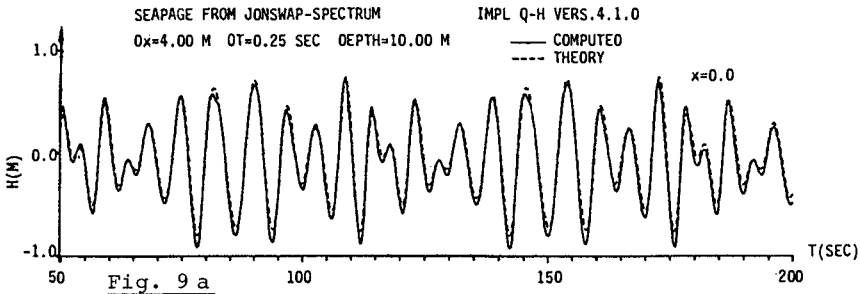
In case (b), with total reflection, a standing wave results with a wave height of 4.30 m. The period of 12 sec and the wave length of 115 m remain unchanged. This example is a severe test of the left boundary condition.



One of the attractive features of a Boussinesq type wave model is the ability to calculate nonlinear irregular waves.

The transformation of a Jonswap spectrum into a time series is used as input to the numerical model (Fig. 9 a, c). The wave length at the peak frequency was approximately 50 m and the shortest components less than 30 m. The water depth was held constant at 10 m. Figure 9 b shows the water elevations at  $x = 200$  m and Figure 9 d the spectra, calculated with Fast Fourier Transformation.

The dotted lines in Figs. 9 a, b are obtained analytically from a superposition of the single frequency components. One can observe that some interaction between frequencies occurs in the numerical model. The results can be better understood, however, if one considers the frequency domain, which includes lower frequencies (Fig. 9 c). Only a comparison with experimental data can verify, whether these frequencies are physically meaningful. Experiments to obtain such data are planned for the near future.



The last test illustrates the essential differences between the results of a Boussinesq type wave equation and a shallow water wave equation. Fig.10 shows, that a hydraulic surge, under certain conditions, is transformed into a moving undular hydraulic jump.

These undulations are a result of the vertical accelerations included in Boussinesq type wave equations. Shallow water wave equations, which neglect vertical accelerations, would produce only a step in the water elevation, as indicated by the dotted line in Fig.10.

The frequencies, as well as the amplitudes of the undulations, are in good agreement with experimental results given by Favre (1935).

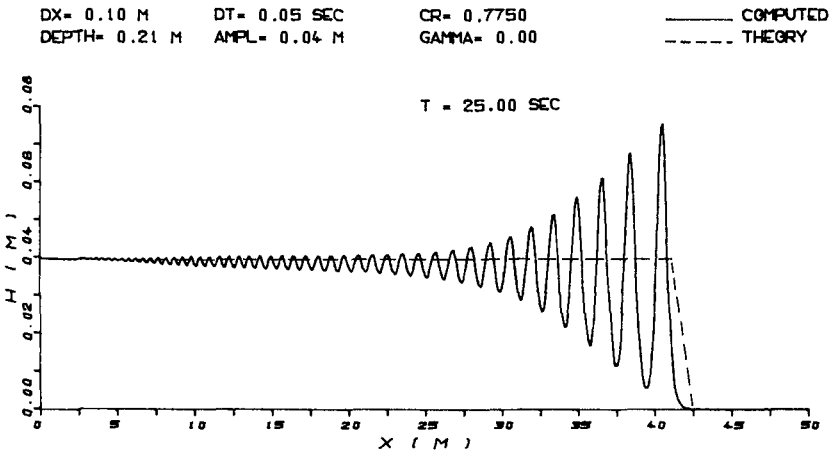


Fig. 10

## 7. CONCLUSIONS

Numerical solutions of Boussinesq type wave equations provide a powerful tool for the prediction of short waves in shallow water. They cover a wide range, including intermediate depth conditions and wave heights just before breaking.

Solitary and cnoidal waves, as well as irregular waves have been calculated. The necessary boundary conditions, such as total reflection, partial reflection and non-reflection have been successfully incorporated in the model.

The results presented in this paper are limited to the one dimensional case. Fig. 11 shows a result of the two dimensional version, currently under investigation.

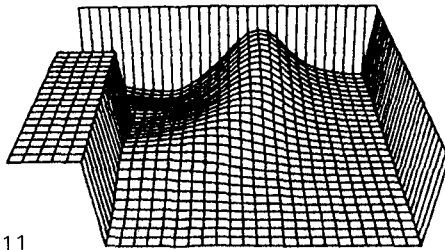


Fig. 11

## 8. REFERENCES

- Abbot, M.B., Petersen, H.M. and Skovgaard, O. (1978): On the numerical modelling of short waves in shallow water. J.Hyd.Res., Vol. 16, No. 3.
- Favre, H. (1935): Etude théorique et expérimentale des ondes de translation. Dunod, Paris.
- Hauguel, A. (1980): Adaption of tidal numerical models to shallow water wave problems. Proc. 17th Conf. on Coastal Eng., Sydney.
- McCowan, A.D. (1982): Numerical short wave modelling - an evaluation. Abstracts 18th Conf. on Coastal Eng., Cape Town.
- Peregrine, D.H. (1967): Long Waves on a Beach. J.Fluid Mech., Vol. 27, No. 4.

The authors gratefully acknowledge the financial support of the " Deutsche Forschungsgemeinschaft", which sponsored the work within the "Sonderforschungsbereich 205, Küsteningenieurwesen".

## CHAPTER SEVENTY THREE

### INTERACTION OF NON-UNIFORM CURRENTS AND SURFACE WAVES

By Nabil M. Ismail, A. M. ASCE\*

#### ABSTRACT

Modifications of surface gravity waves and opposing nonuniform currents due to their interaction in coastal waters were experimentally and theoretically investigated. The flow field is modelled as a steady turbulent jet heads directly into the surface waves. Experimental results show that the net waves momentum flux is decreased as waves propagate into the jet which gives rise to mean water set-up towards the jet source. Opposing waves increase the spreading rate of the jet and causes vertical upwelling of the mean flow, near the bottom, towards the free surface. Theoretical predictions of the increase of the jet spreading rate and wave set-up agree with the experimental data. Wave-current interaction modifies significantly waves bottom flow pattern by focusing ambient nearshore waters on the jet outlet.

#### INTRODUCTION

Over a large portion of the world's oceans and seas, the spatial distribution of surface currents generated by winds, tides and ocean circulation is so great that an understanding of wave propagation on currents is very important. An example of these nearshore ocean processes is the interaction of surface waves, propagating towards the coast, with tidal flows out of bays, river flows, and cooling water discharges from power plants. Currents in coastal waters influence wave propagation significantly due to the strong current shear and in turn the waves modify the current. These wave and current modifications play an integral role in defining the near shore dynamic characteristics. In addition, the modifications have important implications in regard to prediction of coastal sediment transport, and mixing of materials dispersed into the surf zone. Furthermore, knowledge of changes of mean water level due to wave-current interaction is necessary for numerous engineering endeavors.

The present study is directly related to the interaction of waves coming from offshore and tidal flows out of bays. There has been very limited experimental work reported in the literature on the interaction of non-uniform currents with surface gravity waves which necessitates performing of a detailed experimental study on the subject.

\*Sr. Engr., Pipeline & Production Technology Division, Bechtel Petroleum, Inc., San Francisco, Calif.



The main purpose of this study is to explore experimentally and theoretically modifications of waves and non-uniform currents due to their interaction in coastal waters. The experiments were carried out for the more general of a steady turbulent jet heads directly into the surface waves. Experiments were limited to those cases for which the wave's particle oscillatory velocities are much larger than turbulent velocity fluctuations associated with the jet flow. Experimental measurements of velocity were made primarily along the longitudinal axis of the jet. The theoretical analysis and experimental work performed in this investigation were directed towards achieving the following objectives:

- o To determine experimentally modifications of the surface gravity waves; specifically, wave amplitudes and wave oscillatory water particle velocities
- o To determine experimentally and theoretically the modifications of the non-uniform flow (jet); specifically the distribution of the mean flow velocity profile over the water column, the change in the spreading rate of the turbulent jet, and mean water level
- o To assess, using a photographic system, the modifications of the bottom flow pattern resulting from either the waves forward mass transport or the jet bottom entrainment due to the interaction of one (waves or jet) with each other (jet or waves)

#### THEORETICAL BACKGROUND

The effect of large-scale fluid motion on wave propagation has been the subject of a number of relatively recent studies. The dynamics of these wave trains can be expressed in terms of the "wave action conservation principle" established by Bretherton and Garrett (2). It is given by

$$\frac{\partial}{\partial t} \left( \frac{E}{\omega_r} \right) + \nabla \cdot [(\vec{U} + \vec{C}_g) \frac{E}{\omega_r}] = 0 \quad \dots(1)$$

where  $\vec{U}$  is the nonuniform current velocity,  $\vec{C}_g$  is the vector wave group velocity,  $E$  is the wave energy density, and  $\omega_r$  is the waves intrinsic frequency.

Longuet-Higgins and Stewart (10) investigated two special cases of the general case considered by Bretherton and Garrett (2) using a perturbation expansion form for the solution. The first case is when the nonuniform current velocity  $\vec{U}$  in the direction of wave propagation and the horizontal variation of  $\vec{U}$  is compensated for by vertical upwelling from below. The second case is when the horizontal variation in  $\vec{U}$  is compensated for by a small horizontal inflow from the sides. The results of their work were a crucial advance in the theory of wave-current interaction.

Among the theoretical approaches followed is one which is a direct integration of the equations of motion with respect to the water depth and averaging over the phase of the fluctuating motion [Phillips (11)].

Crapper (3) considered the interaction of nonlinear deep water gravity waves and a steady nonuniform current, using the average Lagrangian method due to Whitham (12). His theoretical results showed that the rate of amplification of large waves is less than that of the essentially linear theory of Longuet-Higgins and Stewart (10).

Determining the back interaction of the wave field on the current mean flow is fraught with little difficulties. Hasselmann (5) and Garrett (4) emphasized that Phillips' approach yields the force exerted by the waves on the complete flow, consisting of the mean flow plus the wave field. Part of this force causes a change in the wave momentum rather than the momentum of the mean flow. Therefore, the rate of change of the wave momentum should be subtracted from the total force, in order to obtain the net force exerted by the waves on only the current flow. However for the purpose of analysis of the experimental results obtained in this study, a momentum balance of the complete flow is appropriate for the theoretical representation of the flow field.

#### Parameters Scaling

For the case of surface gravity waves propagating on a steady nonuniform flow, it is natural to consider the ratios of the independent parameters of the waves to those of the turbulent jet. Take  $L$ ,  $b$  the longitudinal and transverse distances, and  $U_*$ , the longitudinal surface velocity at  $y = b$ , as the characteristic lengths and velocity scales of the turbulent jet (Fig. 1). Take  $L$ , the wave length, and  $C$ , the wave phase speed as the characteristic length and velocity scales of the waves. These scales lead to non-dimensional group [Ismail (6)]

$$G = \frac{b}{L} \frac{L\sqrt{g\pi/L}}{U_*} = \frac{b}{L} \frac{C}{U_*} = \frac{r}{L} \quad \dots(2)$$

This group corresponds to the ratio of the radius of curvature,  $r$ , of the wave rays due to the refraction by the vorticity of the horizontal shear flow  $\xi$ , to the incident wave length  $L$ . The ranges of wave and current independent variables employed in the experiments were selected in a manner to keep the value of the parameter  $G$  larger than one. This restriction was done to focus on the direct dynamical aspects of interaction between the waves and the current.

Taking  $\alpha$  as number characterizing the ratio of the wave velocity fluctuation  $\tilde{u}_*$  to the jet characteristic surface mean velocity  $U_*$

$$\tilde{u}_* = \alpha U_* \quad \dots(3)$$

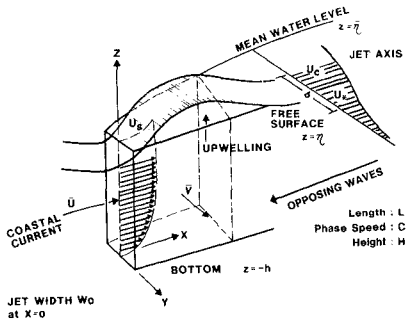


FIG. 1 Definition Sketch

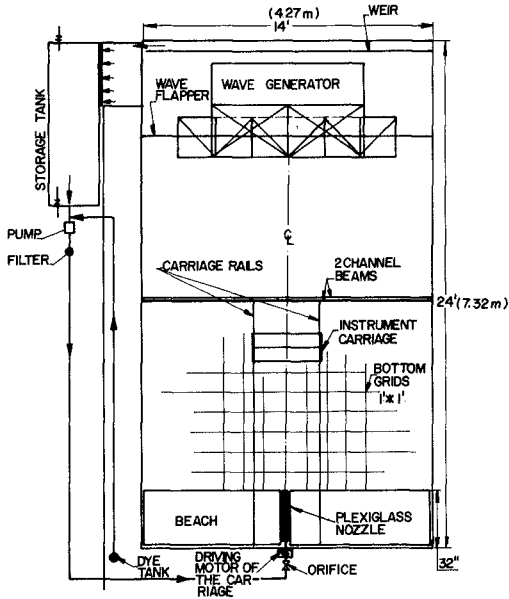


FIG. 2 Plan View of the Experimental Arrangements

For the case of waves propagating on currents in coastal waters,  $\alpha$  is roughly of the order 0.5-1.0.

Taking  $\beta$  as a number characterizing the ratio of the velocity scales of the turbulent fluctuations and the time mean longitudinal surface velocities can be written as

$$u'_* = (\overline{u'_i u'_i})^{1/2} = \beta U_* \quad \dots(4)$$

in which  $U_*$  is defined as  $U$  at  $y = b$ . On a spatial average,  $\beta$  is roughly of the order of 0.25.

Taking  $\epsilon$  as a number characterizing the relative water depth  $kh$  where  $k$  is the surface wave number and  $h$  is the water depth. Wave and current parameters are assumed to be uniformly distributed over the water depth for the range of the parameter  $\epsilon \approx 0.5-1.0$  considered in this analysis.

#### Momentum Balance of the Wave Current Flow

The equation describing the momentum balance of the complete flow follows that of Phillips (11), except we will be including the bottom shear stresses into the momentum considerations. Further, we expand the time mean horizontal velocity of the complete flow  $\bar{u}_i$  into the time average of the mass flux due to the current  $U_i$  and the wave mass transport velocity  $U_{mi}$  into the momentum balance for steady or quasi-steady complete flow to yield (9).

$$\begin{aligned} \frac{\partial}{\partial x_j} \int_{-h}^{\bar{\eta}} \rho U_i U_j dz &= -\rho g(\bar{\eta} + h) \frac{\partial \bar{\eta}}{\partial x_j} - \frac{\partial}{\partial x_j} S_{ij} - \\ &\frac{\partial}{\partial x_j} \int_{-h}^{\bar{\eta}} \rho (U_i U_{mj} + U_j U_{mi}) dz - \frac{\partial}{\partial x_j} \int_{-h}^{\bar{\eta}} \rho \overline{U'_i U'_j} dz + \bar{\tau}_j^B \dots(5) \end{aligned}$$

where the subscripts  $i$  and  $j$  refer to horizontal components of parameters. The terms of the right hand side of Eq. (5) represent parameters which could exert a force by the wave on the complete flow. These forces which contribute to the divergence of the current flow momentum  $\rho U_i U_j$  are respectively, the horizontal force due to the slope of the mean surface water level  $\bar{\eta}$ , the spatial gradients of the wave radiation stress  $S_{ij}$ , the convective momentum flux  $\rho U_i U_{mj}$ ;  $\rho U_j U_{mi}$  and the turbulent momentum flux  $\rho \overline{U'_i U'_j}$ . The last term,  $\bar{\tau}_j^B$ , represents the bottom shear stress.

Expressing each term of Eq. (5) in the scales introduced earlier one can approximate the momentum balance of the complete flow and partition it into separate mean flow and wave momentum balances. For the mean water level  $\bar{\eta}$ , one can argue that it is the sum of a wave

contribution  $\bar{\eta}_w$  and of a jet mean flow contribution  $\bar{\eta}_c$ . The approximate x-components of the momentum balance are as follows.

#### Mean flow momentum

$$\frac{\partial}{\partial x} \rho \bar{u}^{-2} + \frac{\partial}{\partial y} \rho \bar{u} \bar{v} = -\rho g \frac{\partial \bar{\eta}_c}{\partial x} - \frac{\partial}{\partial y} \rho \bar{u} \bar{v} - \frac{\partial}{\partial y} \rho \overline{u'v'} + \frac{1}{2} \rho \bar{f} u^{-2} \quad \dots(6)$$

The above equation, which governs the mean flow momentum in the stream wise direction, appears similar to the classical x-momentum equation for nonbuoyant jets in shallow water. However, there is a distinction which is manifested by the appearance of the second term on the r.h.s. of the equation. This term, which is due to wave refraction, represents the dominant force on the longitudinal momentum of the jet mean flow.

#### Wave momentum flux

$$\rho g \frac{\partial \bar{\eta}_w}{\partial x} + \frac{\partial}{\partial x} \rho (\bar{u}^2 - \bar{w}^2) + \rho g \frac{\partial}{\partial x} \frac{\bar{\eta}^2}{\bar{\eta} + h} = 0 \quad \dots(7)$$

In the above equation, the force due to the slope of the free surface  $\bar{\eta}_w$  would balance the difference between the two longitudinal gradients of the variance of the free surface and the isotropic waves momentum flux.

#### Jet spreading rate

The change of the spreading rate of the turbulent mean flow is determined by extending the scale analysis to the y-momentum equation to seek a relation between forces causing the spreading and the mean flow inertial terms (9). The increase of the spreading rate of the jet due to opposing waves is given by

$$\left(\frac{dB'}{dx}\right)_e = \frac{\frac{1}{2} \rho a_0^2 g / (C_0 - U_e) \cdot U_e}{0.122 \rho U_e^2 W_0} \quad \dots(8)$$

The numerator of the above expression can be thought of as the momentum action of the wave flow field on the jet flow, and is represented by the waves momentum density  $\frac{1}{2} \rho a_0^2 g / (C_0 - U_e)$  times the convection jet flow velocity  $U_e$ . The denominator of this expression is proportional to the initial jet momentum flux (at the efflux point).

#### EXPERIMENTAL STUDY

The ranges of the undisturbed design parameters  $a_0/L_0$ ,  $h_0/L_0$ ,  $W_0/L_0$ ,  $x/W_0$ , and  $U_e/C_0$  were selected in a manner such that the secondary circulation flow of the jet and due to the waves do not cause the deflection of the jet, and the turbulent intensities are smaller than the values of the wave-induced particle velocities. According to the scale analysis performed in the last

section, and also to the pilot experiments which were carried in the wave tank the ranges of the design parameters to be used were determined. These ranges are shown in Table 1.

TABLE 1. RANGE OF WAVE-CURRENT PARAMETERS

Experimental Design	Parameter (still water)	Range
wave amplitude/wave length:	$a_0/L_0$	0.0025-0.02
wave length/water depth:	$L_0/h_0$	4-12
nozzle width/wave length:	$W_0/L_0$	0.10-0.03
jet efflux velocity/wave phase speed:	$U_e/C_0$	0.07-0.10
longitudinal distance/nozzle width:	$X/W_0$	0-80

#### Experimental Arrangements

The series of laboratory experiments which were performed in this study used an idealized model in which a steady turbulent jet heads directly into surface waves. The water depth was kept constant (0.114 m). The location and orientation of the mechanical wave generator, the beach (with a slope of 1:7) and the alignment of the discharge nozzle were the same for all of the experiments. An overall plan view of the experimental arrangement is given in Fig 2.

The turbulent jet was generated by pumping water from the reservoir through a plexiglas nozzle which had inside dimensions of 3.8 cm wide by 11.0 cm high, 76.0 cm in length. Excess water in the wave tank flowed over a sharp-crested weir upstream of the wave generator. Using this weir allowed a closed system to form for circulating the water and maintaining steady-state flow conditions. The experimental facility is located at the Hydraulic & Coastal Engineering Laboratory, University of California, Berkeley.

#### Data Acquisition System:

The data acquisition system can be divided into three subsystems:

a. A photographic system consisted of a camera mounted on a movable base above the longitudinal axis of the wave tank. The camera was used to take a series of color photographs of the jet, which was made visible by dye injected into the flow. It was also used to take a sequence of photographs of the bottom flow pattern in the tank. This was done using the flow-visualization technique of dropping dye crystals (potassium permanganate particles, 0.50 mm-0.59 mm) to the bottom of the tank, and photographing the resulting dye streaks.

b. Parallel wire wave gages were used in conjunction with a Sanborn (Series 150) recorder in order to measure the surface water elevations as a function of time at a specific location in the wave tank. A Sanborn Carrier Preamplifier (Model 150-1100 AS) was used to

supply the 2400 CPS/4.5 volt excitation for the gages. The full bridge was provided by an isolation transformer to prevent electrical interference between neighboring wave gages.

c. A Cushing Inc. Model 612-P "velmeter" converter was used in conjunction with a miniature electromagnetic cylindrical sensor (Model 600-40). These were mainly used to measure the jet velocity at several locations along the centerline of the wave tank. The sensor was 0.74 cm in diameter, with its electrodes 0.8 cm away from its tip. The minimum time constant of the "velmeter" converter is 0.1 second.

#### Experimental Procedures

- a. Surface wave parameters were measured without the jet being discharged. Wave measurements included the time history of the water surface elevations at several points along the wave travel. No cross waves were found to exist for the range of waves generated, so that the waves were purely two dimensional. Dye crystals were dropped into the tank, near the bottom, for flow visualization of the waves bottom mass transport, and a time sequence of color photographs was taken.
- b. A turbulent jet was also generated separately. Sufficient time was allowed to pass for steady conditions of the jet to be developed. Dye was usually inserted in the jet for flow visualization. As for the case of the waves, color photographs were taken for the growth of the dye crystals on the bottom. Velocity measurements, using electromagnetic flow meter and the hot film sensor, were made at several locations along the longitudinal axis of the jet.
- c. Data on the wave-jet flow pattern was obtained by generating the waves followed by the jet flow opposing the waves. A steady state of the flow field was usually reached within a few minutes. As before, color photographs were taken for the bottom flow pattern.

#### Analog to Digital Conversion:

The analog outputs from the measuring devices were recorded, digitized, and then processed on a CDC 6400 computer. Tests with data samples of both the water surface elevations and instantaneous particle velocity, showed that the time series obtained in these experiments proved to be a weakly stationary ergodic random process. Choice of digitization time interval and record length requires a knowledge of the frequency range of interest for the particular parameter measured in the experiments. For water surface elevations the analog signal was digitized at a rate 10 samples per second. The time interval chosen for the velocity analog signal to be digitized was 20 samples per second. This was done as most of the energy within a spectrum lies generally within the low frequency band. It

has been found that over the range of wave frequencies generated in this study (0.8 - 1.4 Hz), approximately 100 seconds were sufficient for accurate estimate of time mean and spectral quantities.

## RESULTS

### Current Modifications

In this section, experimental results regarding the effect of opposing wave motion on the horizontal shear of the current  $\xi$  and on the modification of the rate of spreading of the jet are presented.

The experimental data taken along the longitudinal axis of the jet show that in the presence of waves mean velocities of the current near the bottom are decreased with a tendency of the current shear near the water surface to increase. As wave frequency and amplitude increase, the decrease of the mean velocities near the bottom becomes more prominent with an increase of the mean velocities near the water surface [Ismail, (6,8)].

The experimental data also indicate that there is a net decrease in the momentum density of the current along the jet longitudinal axis which is accompanied by an increase in the spreading rate of the jet. The increase of spreading rate of the jet was deduced experimentally using a photographic means and was compared with that derived theoretically (Eq. 8). The comparison shows that for linear waves the agreement between the theory and experiment is excellent for a distance less than  $2X/W_0 \approx 64$  [Ismail (9)].

### Surface Waves Modifications

Surface waves modifications due to the opposing non-uniform current are presented in the following subsections. First, the effect of the jet on the modification of wave amplitudes is presented. Second, modifications of the wave particle velocities by the current are presented, followed by modifications of the wave bottom mass transport.

### Wave amplitudes

The experimental results show that waves were decreased in length and increased in height as waves propagated into the jet. Waves were also shown to be refracted as they propagated into the jet. However, the degree of refraction was slight as the dimensionless parameter  $G$  was kept large in the design of experiments in order to focus on the direct dynamical aspects of the interaction.

Figures 3 and 4 show respectively the spectrum of the wave energy potential density for three waves of different characteristics in case of waves on still water and waves in the presence of the current. The results shown on Fig. 4 show that for waves of higher Ursell number the second and higher harmonics have larger normalized energy density. The amplification of wave amplitude due to the



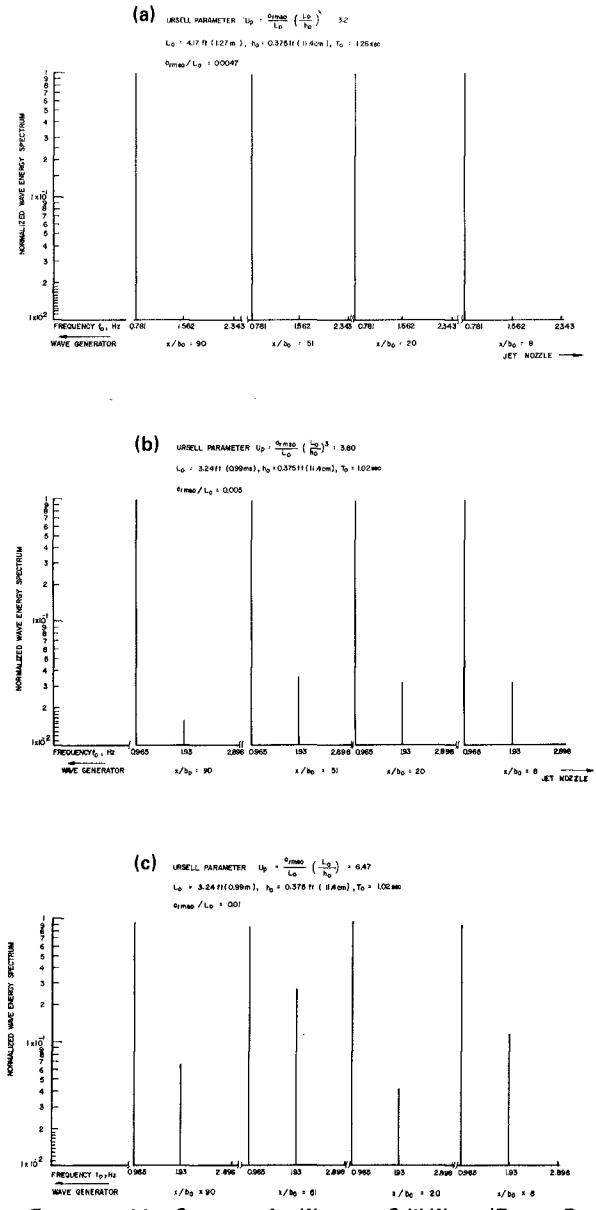


FIG. 3 Frequency Line Spectrum for Waves on Still Water (Energy Density is normalized by the Variance  $\overline{\eta^2}$ )

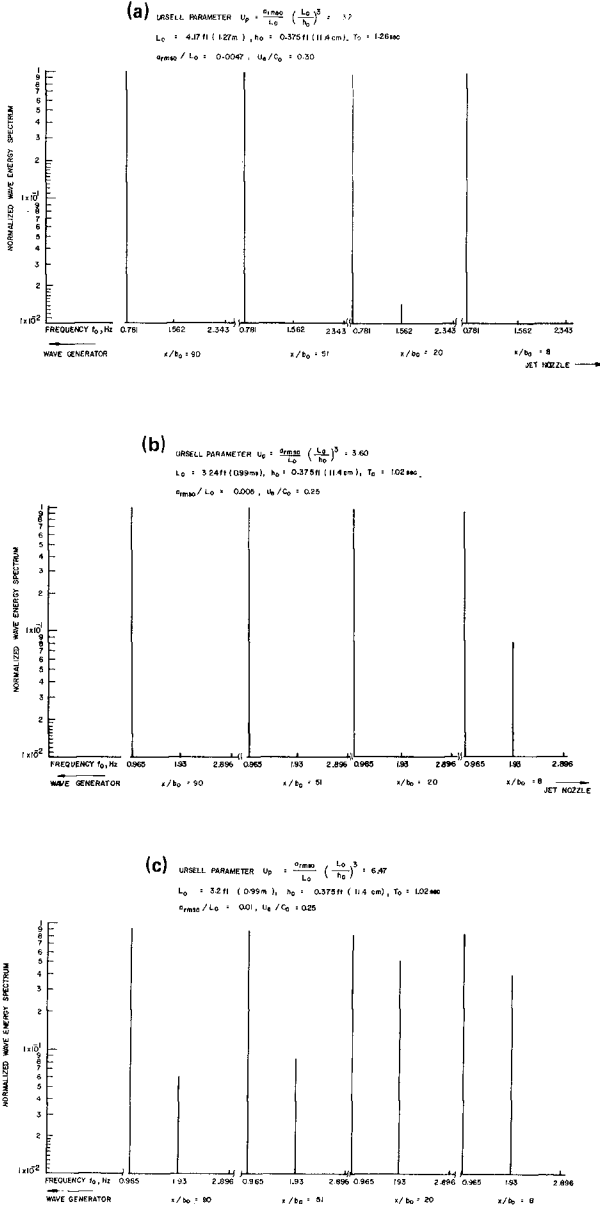


FIG. 4 Frequency Line Spectrum of Waves on a Jet (Energy Density, Normalized by the Variance  $\eta^2$ )

opposing current, represented by the rms of water surface elevation, along the jet axis for the same three runs is shown in Fig. 5. The variation of the dimensionless center line surface velocity  $U_c/U_e$  is plotted also on the same figure.

#### Wave particle velocities

The Eulerian particle velocities of waves  $\tilde{u}_i$  were obtained by subtracting the time mean of the measured instantaneous velocity  $\tilde{u}_i(x)$  from the phase averaged instantaneous velocity  $\langle u_i(x,t) \rangle$ . The process of phase averaging has the effect of rejecting the background turbulence and extracting the organized motion  $(\tilde{u}_i + \tilde{u}_i)$  and is defined by

$$\langle u_i(x,t) \rangle = \lim_{N \rightarrow \infty} \frac{1}{N} \sum_{n=1}^N u_i[(x,t) + nT] \quad \dots(9)$$

where T is the wave period and N is the number of waves examined.

The experimental results of velocity measurements along the jet longitudinal axis show that the wave particle velocities were increased in the presence of the opposing current. However, the magnitude of increase diminishes as the opposing waves approach the jet efflux point which results in having a gradient of wave momentum flux opposite to that induced by the variance of the free surface. Fig. 6 shows representative data of the gain of wave horizontal momentum flux at two Longitudinal positions on the jet axis.

#### Wave set-up

Theoretical predictions of change of mean water level due to wave set up  $\bar{\eta}_w$  were obtained by integrating Eq. (7) and making use of the experimental data of wave amplitudes in the presence of current. Theoretical values of wave particle velocities in the presence of opposing waves were obtained using a wave-current model which approximate the shear current by a constant vorticity current. The dispersion relation is given by Biesel (1) for small amplitude waves as

$$(U_s - C)^2 = \{[g + s(U_s - C)] \tanh kh\}/k \quad \dots(10)$$

where C is the wave phase speed and s the constant vorticity of the current. The dispersion relation was solved by iteration, for the wave number k, once the surface velocity  $U_s$  and the constant vorticity s of the current were determined from the measured current velocity profile. The wave particle velocities were obtained by a direct differentiation of the stream function of the combined wave-current flow. Fig. 7 shows the comparison between the theoretical predictions and experimental data of the change of the mean water level  $\bar{\eta}_w$  due to opposing waves.

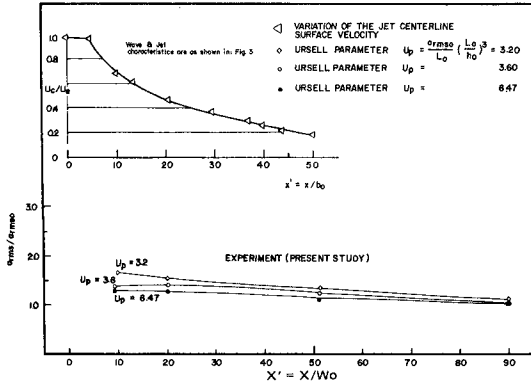


FIG. 5 Amplification Factor  $a_{rms}/a_{rms0}$  For Shallow Water Waves on Opposing Steady Non-uniform Current

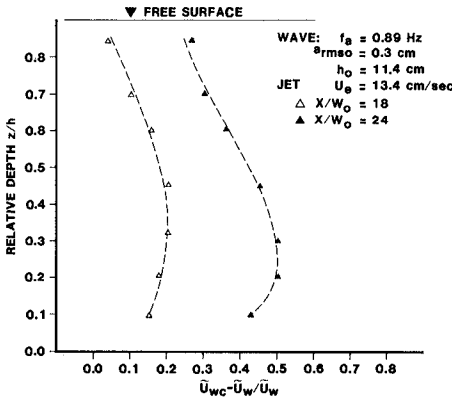


FIG. 6 Relative gain of R.M.S. Wave Horizontal Particle Velocity

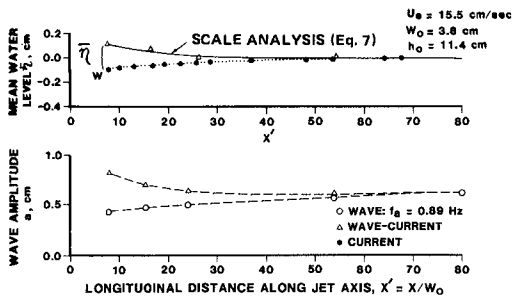


FIG. 7 Wave Set-up in the Presence of Opposing Non-uniform Current

### Wave bottom mass transport

The data obtained using the photographic system show that mass transport due to wave motion on the bottom and across the tank is in the direction of wave propagation. This can be seen in Fig. 8.a from the growth of the dye crystal vectors on the bottom. Here the waves are moving from under the clock in the photographs towards the lower front of the photo. Fig. 8.b shows a sample of the photographs taken for the jet and associated bottom secondary circulation.

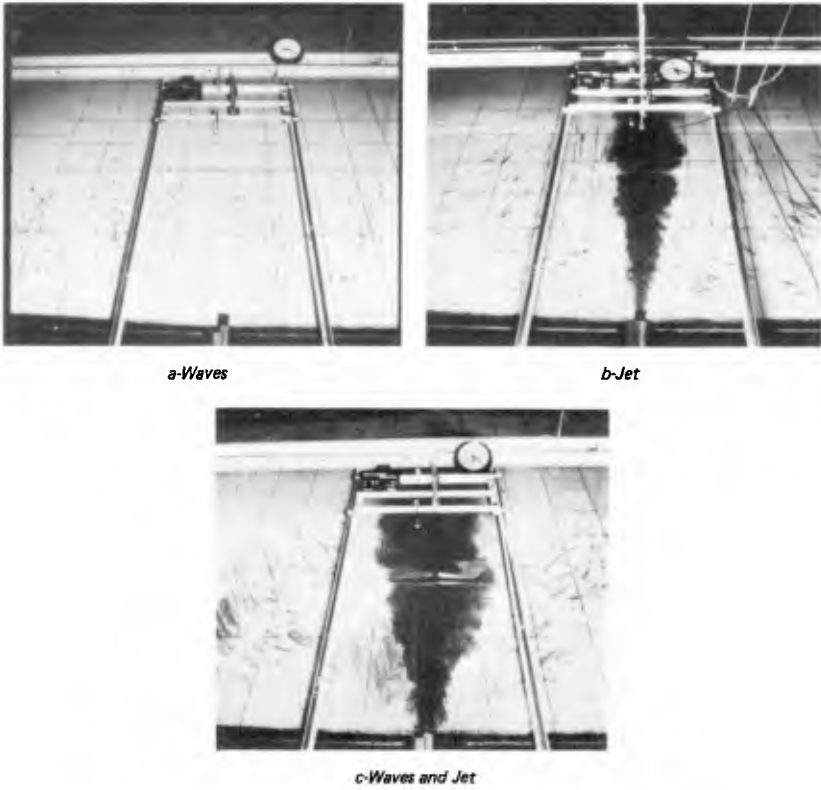
The combined bottom mass transport pattern of the wave-jet flow system is shown in Fig. 8.c. It can be seen that the pattern of the waves forward mass transport at the bottom has been changed, due to the jet bottom flow. Within the jet zone of vertical shear it is found that the direction of the dye vector growth is dependent upon the relative strength of the waves to the jet. On the other hand, the mass transport pattern on the bottom and in the ambient water is directed towards the point of jet discharge. This modification of the flow pattern is induced by the jet secondary circulation. Thus, in prototype situations the jet secondary circulation derives bottom flow from the offshore zone towards the jet outlet.

### SUMMARY AND CONCLUSIONS

The major objective of the present study has been to investigate experimentally and theoretically the modifications of surface gravity waves and steady nonuniform current (jet) when they are propagated against one another in coastal waters. The design of the experiments allowed the turbulent velocity fluctuations associated with the current flow to be much smaller than the wave particle velocities.

The experimental results show that wave amplitudes, hence the wave potential energy, are increased as waves propagate into the jet. Also, wave particle velocities were increased. The longitudinal spatial gradient of the waves momentum flux due to particle velocity was found to be opposite and larger than that induced by the variance of the free surface. The net balance of wave momentum fluxes gave rise to a wave set-up at the jet source. These experimental results agree with the theoretical findings of Crapper (3) in that the rates of growth of large waves, on opposing nonuniform currents, are less than those rates for small amplitude waves. The difference in the rate of growth is a result of the fact that changes in energy propagate at a different speed from changes in wave number.

The experimental results indicate that the depth-averaged mean velocity of current, at the jet longitudinal axis, decreases in the presence of waves. This decrease is accompanied by an increase of the rate of spreading of the jet. Also the vertical velocity profile of the current is modified by the wave motion. While the mean velocity is decreased near the bottom, the mean velocity near the water surface is increased.



**FIG. 8** Photographs of the Bottom Flow Pattern in a Wave, a Jet, a Wave-Jet Flow.

Flow visualization of bottom flow pattern showed that in the presence of opposing waves the direction of the dye vector growth, within the jet zone of vertical shear, is dependent upon the relative strength of waves to the jet. On the other hand, the mass transport pattern on the bottom and in the ambient is focused on the jet outlet.

Scale analysis on the depth-averaged momentum equations yielded theoretical expressions of the increase of the jet spreading rate in the presence of waves and the wave-setup induced by the current's longitudinal rate of strain. Theoretical predictions obtained agree with the experimental data.

Wave-current interaction, through increasing the jet spreading rate and focusing the ambient bottom water on the jet outlet, have significant implications in regard to predicting mixing of thermal discharges in the marine environment and in analyzing the sediment budget at tidal inlets and river mouths.

#### ACKNOWLEDGMENT

The major part of this work constitutes a thesis presented by the author to the University of California at Berkeley, Calif., in 1981, in partial fulfillment of the requirements for the degree of Doctor of Philosophy. The author expresses his deepest appreciation to Robert L. Wiegel of the University of California, Berkeley, and to Joseph L. Hammack of the University of Florida, Gainesville, for their guidance.

#### APPENDIX I - REFERENCES

- 1) Biesel, F., "Etude Theoreque de la Houle en Eau Courante," La Houille Blanche, No. 5A, 1950, pp. 279-285.
- 2) Bretherton, F. P. and Garrett, C. J. R., "Wave trains in Inhomogeneous Moving Media," Proc. Roy. Soc., A302, 1969, p. 529.
- 3) Crapper, G. D., "Nonlinear Gravity Waves on Steady Non-uniform Current," Journal of Fluid Mechanics, Vol. 52, Part 4, 1972, p. 713.
- 4) Garrett, C., "Generation of Langmuir Circulations by Surface Waves - a Feedback Mechanism," Journal of Marine Research, Vol. 34, No. 1, 1976, pp. 117-130.
- 5) Hasselmann, K., "On the Mass and Momentum Transfer between Short Gravity Waves and Larger-Scale Motions," Journal of Fluid Mechanics, Vol. 50, part 1, 1971, pp. 189-205.

- 6) Ismail, N. M., "Wave-Current Interaction," thesis presented to the University of California, Berkeley, CA, in 1981, in partial fulfillment of the requirements for the degree of Doctor of Philosophy (also, Technical Report HEL 27-7, Hydraulic & Coastal Engineering Laboratory, University of California, Berkeley, CA, Oct. 1980).
- 7) Ismail, N. M., "Effects of Opposing Waves on the Mixing of a Horizontal Surface Momentum Jet," Technical Report 27-9, Hydraulic & Coastal Engineering Division, University of California, Berkeley, CA, June 1981, 49 pp.
- 8) Ismail, N. M., "Effects of Wave-Current Interaction on the Design of Marine Structures," Proc. Offshore Technology Conference, Houston, TX, May 2-5, 1983.
- 9) Ismail, N. M. and Wiegel, R. L., "Effects of Opposing Waves on Momentum Jets Spreading," Journal of the Waterway, Port, Coastal and Ocean Division, ASCE, Vol. 109, No. WW4, Proc. Paper 18384, Nov. 1983, pp 465-483.
- 10) Longuet-Higgins, M. S. and Stewart, R. W., "The Changes in Amplitude of Short Gravity Waves on Steady Non-Uniform Currents," Journal of Fluid Mechanics, Vol. 10, Part 4, June 1961, pp. 529-549.
- 11) Phillips, O. M., The Dynamics of the Upper Ocean, Cambridge University Press, Cambridge, England, 1977.
- 12) Whitham, G. B., "Mass, Momentum, and Energy Flux in Water Waves," Journal of Fluid Mechanics, Vol. 21, Part 1, Jan. 1962, pp. 135-147.



## CHAPTER SEVENTY FOUR

### A Finite Element Model for Wind Wave Diffraction

Ove Skovgaard\*   Lars Behrendt\*\*   Ivar G. Jonsson\*\*\*

#### Abstract

The applicability of a hybrid finite element model for the calculation of combined diffraction-refraction of small time-harmonic water waves is demonstrated. The model is valid for arbitrary water depths and wave lengths, i.e. it is based on intermediate depth theory (IDT). The model includes arbitrarily varying partial reflection along the boundaries. Superposition of waves (to simulate a spectrum approach) with different incident directions is demonstrated, and CPU-times and core memory requirements are given.

The model is verified and documented with respect to sensitivity of the model parameters in detailed tables, using the classical Homma island on a parabolic shoal. The wave period is here chosen in such a way that a small number of elements (larger than 500 and less than 2,000) is enough to get an accurate solution.

For a new simple, but realistic harbour geometry many detailed and accurate graphical results are given. The wave period ( $T = 9$  sec.) is here chosen so that it is representative for natural wind waves, and the size of the harbour is selected, so that the model gets a fairly large number of elements (of the order 10,000).

#### 1. Introduction

Small-amplitude time-harmonic waves of arbitrary length propagating in an area of varying depth may be described by the mild-slope wave equation. This equation was first derived by Berkhoff (1972). He solved the mild-slope wave equation by using a finite element method based on sources placed along the open boundaries. Chen and Mei (1974) formulated a hybrid finite element model (FEM) based on shallow water theory (SWT). This model was generalized to intermediate depth theory (IDT) by Houston (1981). Houston's hybrid FEM is restricted to full reflection along solid boundaries. In Behrendt and Jonsson (1984) a new derivation of the fundamental functional is presented. This new method includes partially absorbing boundaries and makes it straightforward also to include bottom friction.

In the present paper the hybrid functional by Behrendt and Jonsson (1984) (hereafter denoted by Paper I) is implemented, verified by comparison with exact solutions, and investigated for sensitivity of model parameters. The computational requirements and many detailed and accu-

\* Ph.D., Assoc. Prof., Laboratory of Applied Mathematical Physics (LAMF), Bldg. 303; \*\* M.Sc., Postgrad. Stud.; \*\*\* Ph.D., Assoc. Prof., Institute of Hydrodynamics and Hydraulic Engineering (ISVA), Bldg. 115,

Technical University of Denmark  
DK-2800 Lyngby, Denmark.

rate results are illustrated for a new simple but realistic harbour geometry. In this harbour we demonstrate that partial reflection can be specified arbitrarily varying along solid boundaries (e.g. rubble mound breakwaters). This property is crucial for realistic modelling of wind wave diffraction in harbours. Another crucial property for practical applications is that superposition of waves with different directions and periods is computationally feasible.

2. The Hybrid Finite Element Model and its Implementation

This hybrid FEM is a combination of a simple finite element approach in area A (see Figs. 1 and 2) and a semi-analytical expansion in the outer area R (see Figs. 1 and 2), where we assume a constant water depth.

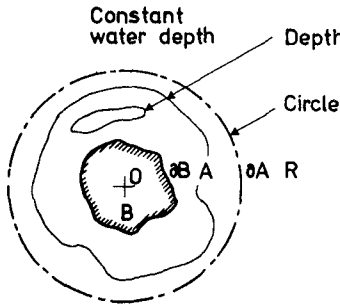


Figure 1. Sketch of model in the horizontally plane, infinite ocean.

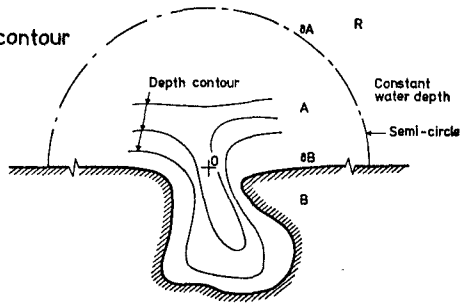


Figure 2. Sketch of model in the horizontally plane, semi-infinite ocean.

Inside the circle or semi-circle  $\partial A$  the depth contours can be specified arbitrarily, but the change in depth over a wave length of the water waves has to be moderate. Along the "solid" boundary  $\partial B$  energy may be absorbed by specifying an arbitrarily varying absorption coefficient  $\alpha$  ( $0 \leq \alpha \leq 1$ ). Thus,  $\alpha = 1$  corresponds to full absorption of waves incident at a right angle, and  $\alpha = 0$  corresponds to a fully reflecting boundary. The partially absorbing boundary condition is the well-known Eq. (21) in Paper I.

The semi-analytical expansion in the outer area R of constant water depth is a solution to the classical Helmholtz wave equation (which is the constant water depth version of the mild-slope wave equation, see Paper I Eq. (20)) satisfying the Sommerfeld radiation condition (see Paper I Eq. (14)) at infinity. For the infinite ocean in Fig. 1 the expansion is:

$$\phi^S = \sum_{n=0}^{\infty} H_n^{(1)}(kr) [\alpha_n \cos(n\theta) + \beta_n \sin(n\theta)] \tag{1}$$

where  $\phi^S$  is the velocity potential of the scattered wave field (see Paper I Eq. (15)),  $H_n^{(1)}$  is the Hankel function of the first kind of order n, k is the wave number, and r and  $\theta$  are polar co-ordinates in the horizontal plane. The coefficients  $\alpha_n$  and  $\beta_n$  are determined by matching this solution with the solution in area A.

For the semi-infinite ocean in Fig. 2 the expansion is the same as in Eq. (1) with  $\beta_n \equiv 0$ ,  $n = 0, 1, \dots, \infty$ . Now  $\theta$  equals  $0^\circ$  or  $180^\circ$  along the infinite, fully reflecting straight coastline in area R. In the model the expansions are truncated at  $n = n_{\max}$  which is an input parameter to the model. The number  $n_{\max}$  depends on the desired accuracy of the solution and on the maximum distance  $r$  from the origo 0. For the classical Homma island, see Homma (1950), the necessary number  $n_{\max}$  has been studied in Appendix I in Skovgaard and Jonsson (1981).

The basic principle in the present finite element method is the minimization of a functional  $F_H(\phi)$ , see Eq. (44) in Paper I. This minimization is expressed in Eq. (45) in Paper I. The functional is discretized using finite elements in area A and using the expansion (1) describing  $\phi^S$  along  $\partial A$ . The finite elements chosen are simple triangular three-node elements with linear shape functions. This procedure results in a system of complex linear equations with a quadratic banded sparse symmetric coefficient matrix  $\{K\}$ . The maximum semi-bandwidth depends strongly on the chosen numbering of the nodes in the finite element grid. In the pioneering study by Chen and Mei (1974) the semi-bandwidth was also much dependent on the number of nodes along  $\partial A$ , and on 'nmax'.

### 3. An Example of Verification and Sensitivity: Homma's Island

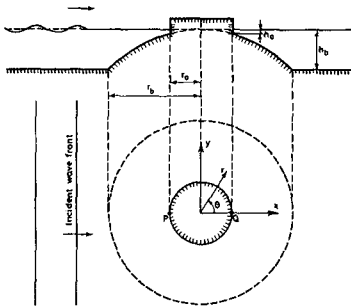


Figure 3. Sketch of an idealized island on a parabolic shoal; (a) vertical; (b) horizontal.  $r_a = 10,000$  m,  $r_b = 30,000$  m,  $h_b = 4,000$  m,  $h_a = h_b(r_a/r_b)^2 = 4,000/9$  m.

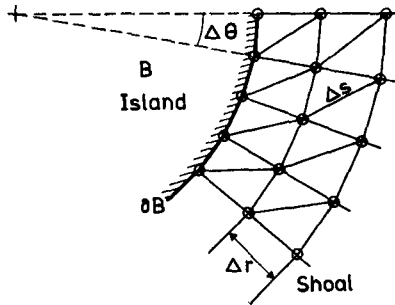


Figure 4. Horizontal sketch of finite element grid over part of the shoal in Fig. 3. The grid covers the shoal for  $0^\circ \leq \theta < 360^\circ$  and  $r_a \leq r \leq r_b$ .

As an example from the verification program we have considered the classical Homma island surrounded by a parabolic shoal in an infinite ocean of constant water depth, see Fig. 3, and Jonsson et al. (1976), Table 1 and Eq. (1.1). A detail of the finite element grid is shown in Fig. 4.

The boundary  $\partial B$  is fully reflecting in this example. The boundary  $\partial A$  has been placed along the outer boundary of the shoal, i.e. area A is

Table I. Text: see next page, top.

	$\theta = 0^\circ$	$\theta = 30^\circ$	$\theta = 60^\circ$	$\theta = 90^\circ$	$\theta = 120^\circ$	$\theta = 150^\circ$	$\theta = 180^\circ$	$ \text{line} $
$(A/A_1)_{r=r_a}$	2.3708	1.7663	1.5067	2.6885	3.3686	3.4553	3.4193	
	-0.324	-0.0213	+0.0050	-0.0176	-0.0222	-0.0115	-0.0050	0.1150
	-0.0981	-0.0644	+0.0202	-0.0424	-0.0553	-0.0234	-0.0042	0.3080
$(\varphi)_{r=r_a}$	151.69	134.42	60.33	16.40	355.95	341.70	335.92	
	-1.30	-1.69	-0.92	-0.56	-0.58	-0.45	-0.28	5.78
	-4.00	-5.28	-2.96	-1.67	-1.66	-1.21	-0.69	17.47
$(A/A_1)_{r=2r_a}$	1.8330	1.2805	1.0478	1.8636	1.9754	1.6535	1.4924	
	-0.138	-0.064	+0.041	-0.0079	-0.0071	+0.0003	+0.0040	0.0436
	-0.0342	-0.0127	+0.0132	-0.0177	-0.0134	+0.0069	+0.0164	0.1145
$(\varphi)_{r=2r_a}$	170.97	152.55	64.80	18.54	353.78	332.71	322.61	
	-0.81	-1.05	-0.35	-0.42	-0.59	-0.52	-0.34	4.08
	-2.33	-2.91	-0.83	-1.08	-1.57	-1.44	-1.03	11.19
$(A/A_1)_{r=3r_a}$	1.5372	0.9995	0.8037	1.3281	0.9573	0.4871	0.4960	
	+0.028	+0.063	+0.058	+0.0047	+0.0098	+0.0092	+0.0022	0.0408
	+0.0077	+0.0180	+0.0171	+0.0135	+0.0273	+0.0272	+0.0083	0.1191
$(\varphi)_{r=3r_a}$	195.95	176.09	70.91	21.01	344.19	282.12	242.10	
	-0.66	-0.75	+0.06	-0.33	-0.53	+0.45	+0.91	3.69
	-1.85	-2.11	+0.19	-0.89	-1.48	+1.13	+2.57	10.22
$(A/A_1)_{r=9r_a}$	1.2238	0.5617	1.0683	0.9848	1.0639	0.8277	1.1541	
	+0.010	+0.069	-0.025	-0.0019	+0.0040	-0.0061	-0.0079	0.0303
	+0.0019	+0.0187	-0.0063	-0.0058	+0.0112	-0.0161	-0.0226	0.0826
$(\varphi)_{r=9r_a}$	31.14	337.87	162.99	347.78	206.96	41.13	357.80	
	-0.55	-0.35	-0.07	+0.13	-0.18	+0.35	-0.05	1.68
	-1.43	-0.97	-0.11	+0.34	-0.56	+0.99	-0.15	4.55

Table I.

Calculated non-dimensional wave amplitudes  $A/A_i$  and phase angles  $\varphi$  for plane time-harmonic (of period  $T = 480$  sec.) incident waves around the Homma island in Fig. 3. Dimensionless radius  $r/r_a = 1, 2, 3,$  and  $9$ .  $\theta = 0^\circ, 30^\circ, \dots, 180^\circ$ . The values of phase angle  $\varphi$  are chosen in the interval  $0^\circ \leq \varphi < 360^\circ$ . For each of the 28 pairs of  $(r/r_a, \theta)$  three results are given in a column. The upper number is the exact solution, the middle number is the difference with a sign between the exact solution and our FEM-solution Nr. I. The lower number is the difference with a sign between the exact solution and our FEM-solution Nr. II. The rightmost column contains for each line a summation of the absolute values of the differences mentioned above.

the area covering the shoal. The geometry is symmetrical and it could be modelled by a semi-infinite ocean, but the finite element grid (Fig. 4) is not symmetrical, so we have to introduce an infinite ocean model.

Exact solutions using an orthogonal collocation method and IDT wave theory for this problem have been published in tabular form earlier, see Jonsson et al. (1976) and Skovgaard and Jonsson (1981). Here an exact solution for a new wave period ( $T = 480$  sec.) is given in Table I.

In Table I we have compared two finite element solutions (denoted by No. I and No. II) with the exact solution. FEM solution No. I is based on a very fine grid:  $\Delta\theta = 6^\circ$ , i.e.  $\theta = 0^\circ, 6^\circ, \dots, 360^\circ$ , and  $\Delta r/r_a = 0.1$  for  $1 \leq r/r_a \leq 2$ , and  $\Delta r/r_a = 0.2$  for  $2 \leq r/r_a \leq 3$ ,  $n_{\max} = 16$  (see Section 2). FEM solution No. II is based on a rather coarse grid:  $\Delta\theta = 10^\circ$ , i.e.  $\theta = 0^\circ, 10^\circ, \dots, 360^\circ$ , and  $\Delta r/r_a = 0.25$  for  $1 \leq r/r_a \leq 3$ ,  $n_{\max} = 11$ . The total number of elements is 1.800 and 576 in models No. I and II respectively.

Solution Nr. I was constructed in order to verify our model, i.e. verify the hybrid formulation, verify the functional, verify the discretization, and finally verify the implementation. Here the maximum distance (dimensionless with respect to local wave length,  $L_a = 31,648$  m and  $L_b = 93,959$  m) between neighbouring vertices of the triangular elements was of the order 0.05 for  $r/r_a = 1$  and 0.04 for  $r/r_a = 3$ , i.e. minimum  $20 \Delta s$  (see Fig. 4) per local wave length.

Solution No. II was constructed in order to measure the sensitivity of the finite element discretization. Here the maximum distance (dimensionless with respect to local wave length) between neighbouring vertices of the triangular elements was of the order 0.10 for  $r/r_a = 1$  and 0.06 for  $r/r_a = 3$ , i.e. minimum  $10 \Delta s$  per wave length near  $\partial B$  and minimum  $16 \Delta s$  per wave length near  $\partial A$ .

Solution No. I has a maximum error in  $A/A_i$  of  $-0.0324$  (corresponding to 1.37%) at  $r/r_a = 1$  and  $\theta = 0^\circ$  (point Q in Fig. 3, the centrepoint at the island in the shadow region). For the 28 results in Table I the mean error ( $1/28 \sum |\text{error}|$ ) is 0.0082, or relative mean error ( $1/28 \sum |\text{error}| / (A/A_i)_{\text{exact}}$ ) 0.58%. The rightmost column informs us that the sum of the errors along  $r/r_a = 1$  equals approximately the sum of the errors along the other three semi-circles  $r/r_a = 2, 3,$  and  $9$ . Note that for all considered 28 points there is no distinct pattern of the signs of the errors. The maximum error in phases  $\varphi$  is  $-1.69^\circ$  and it is found at  $r/r_a = 1$  and  $\theta = 30^\circ$  (which is not where the maximum error in  $A/A_i$  was found). The mean error in  $\varphi$  ( $1/28 \sum |\text{error}|$ ) is  $0.54^\circ$  for the 28 results.

These results for solution No. I did not change when  $n_{\max}$  was increased. This is in accordance with Skovgaard and Jonsson (1981), Fig. 24,

which showed that  $n_{\max} \gtrsim 12$  was enough for  $1 \leq r/r_a \leq 9$ . To describe our *hybrid* finite element solution we present the calculated expansion coefficients  $\alpha_0$ ,  $\alpha_n$ , and  $\beta_n$  for  $n = 1, 2, \dots, n_{\max}$  in Table II. First, in accordance with the reference mentioned above it was checked that the expansion coefficients in the table were in fact invariant to any increase in the number 'nmax'. Secondly, note that the largest  $\beta_n$ -coefficient is of the order of magnitude  $10^{-15}$  (the magnitude of the largest  $\alpha_n$ -coefficient is of the order of magnitude 1); this is in agreement with the fact that if a symmetrical grid had been used, all the calculated  $\beta_n$ -values should have been approximately zero, because for a semi-infinite ocean (Fig. 2) they are identically equal to zero.

Table II

Calculated expansion coefficients  $\alpha_0$ ,  $\alpha_n$ , and  $\beta_n$  for  $n = 1, 2, \dots, n_{\max} = 16$  in Eq. (1).  $T = 480$  sec., FEM-solution No. I.

n	$\alpha_n$		$\beta_n$	
	Re	Im	Re	Im
0	(-01)-1.9036	(-02)-3.7654		
1	+1.5557	(-01)-8.3137	(-15)+3.4083	(-15)-4.4021
2	(-01)+7.2245	(-01)+3.0857	(-16)+3.4004	(-16)-6.6716
3	(-03)-2.2846	(-02)+6.7557	(-16)-9.3783	(-16)-6.2251
4	(-03)-3.7408	(-06)-6.9968	(-16)+4.3754	(-16)+2.0117
5	(-09)+8.5146	(-04)-1.3050	(-17)+8.6204	(-18)+8.3134
6	(-06)+2.7177	(-12)+3.6930	(-18)-8.9236	(-18)+4.3720
7	(-16)-3.3380	(-08)+2.5711	(-19)-2.9753	(-19)+4.7180
8	(-10)+2.8321	(-19)-2.6609	(-19)+1.9747	(-20)+9.4608
9	(-20)-4.9453	(-11)+1.5208	(-20)+1.0105	(-20)+1.9679
10	(-13)-3.0731	(-21)-2.3659	(-21)+1.2234	(-22)+2.9296
11	(-22)-1.8402	(-15)-4.1857	(-22)-1.6817	(-23)+1.0816
12	(-17)+4.3363	(-23)-1.3715	(-23)+4.0399	(-23)+1.6757
13	(-24)-3.5198	(-19)+3.6025	(-24)+3.4282	(-24)+1.5503
14	(-21)-2.4754	(-26)+1.5796	(-25)+1.7842	(-26)+2.3390
15	(-26)-1.4705	(-23)-1.4367	(-27)+4.3157	(-27)+4.9126
16	(-26)+7.0580	(-29)+2.3355	(-28)+7.2292	(-28)+1.6390

We here ought to mention that the entire implementation was done on an IBM 3081 using double precision floating point numbers, which corresponds to approximately 16 floating point digits.

Solution No. II has a maximum error in  $A/A_1$  of -0.0981 (corresponding to 4.14%) at  $r/r_a = 1$  and  $\theta = 0^\circ$  (i.e. same point Q as for solution No. I). If we compare with Houston (1981), Figs. 7 and 9, which has a similar comparison but for another period ( $T = 120$  sec.), it is seen that the largest error is found on the 'illuminated' side of the island (around point P in Fig. 3). From this we can draw the conclusion that the location of the largest error is very much dependent on the wave period. For the 28 results in Table I the mean error for  $A/A_1$  is 0.0223, or relative mean error 1.63% (which is about three times larger values than what was found for solution No. I). The rightmost column informs us that also for this solution (No. II) the sum of the errors along  $r/r_a = 1$  equals approximately the sum of the errors along the other three semi-circles  $r/r_a = 2, 3,$  and  $9$ . Note that for all considered 28 points the signs of the errors in solutions No. I and II are the same, and the magnitude is roughly a factor three larger in case II than in case I.

The maximum error on the phases in solution No. II is  $-5.28^\circ$  and it is found in the same point as the maximum phase error in solution No. I. The mean error in  $\varphi$  in solution No. II is  $1.55^\circ$  for the 28 results presented. Again this mean error is approximately about three times larger than the corresponding mean error for solution No. I. A calculation similar to case No. II with the same finite element grid but  $n_{\max}$  increased from 11 to 20 was performed. Over the shoal there was no change in the solution for the five digits shown in Table I. However, for  $r/r_a = 9$  minor changes in the errors were noticed, but these modifications were so small that the mean errors in  $A/A_i$  and  $\varphi$  given above did not change. Again, this is in agreement with Skovgaard and Jonsson (1981), where it was shown that for  $r/r_a = 9$ ,  $n_{\max} = 11$  is just about too small to yield five digits of accuracy.

A contour plot of the  $A/A_i$  solution in model No. I is shown in Fig. 5. A three-dimensional plot of an instantaneous surface elevation around the island is shown in Fig. 6.

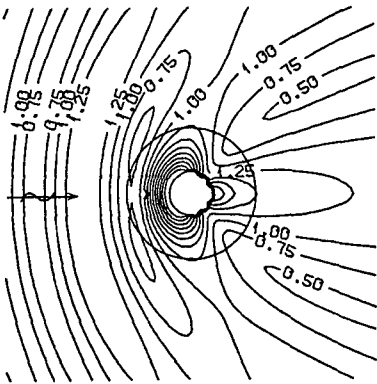


Figure 5. Contours for the relative amplitude around the Homma island,  $T = 480$  sec. The interval between  $A/A_i$ -curves is 0.25.

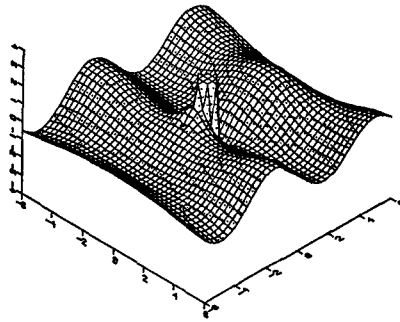


Figure 6. Relative surface elevation around the Homma island,  $T = 480$  sec.

Finally, we stress that in this section we have investigated a rather difficult bottom geometry giving rise to combined shoaling, refraction, and diffraction in an infinite ocean model.

#### 4. An Example of Absorption and Superposition: Rectangular Harbour

In this section we will demonstrate the effect of energy absorption along boundaries, the effect of obliquely incident waves, and finally the effect of superposition of incident waves of different angles and amplitudes. The presentation will be restricted to the simple harbour geometry shown in Fig. 7, left.

In Section 3 we considered an example of an infinite ocean (Fig. 1). Here we consider an example of a semi-infinite ocean (Fig. 2). The layout of the finite element grid and the location of the boundary  $\partial A$  between the finite element area  $A$  and the outer region  $R$  is given in Fig. 7, right. In Fig. 8 an enlarged sketch of the finite element grid around the tip of one of the breakwaters is shown.

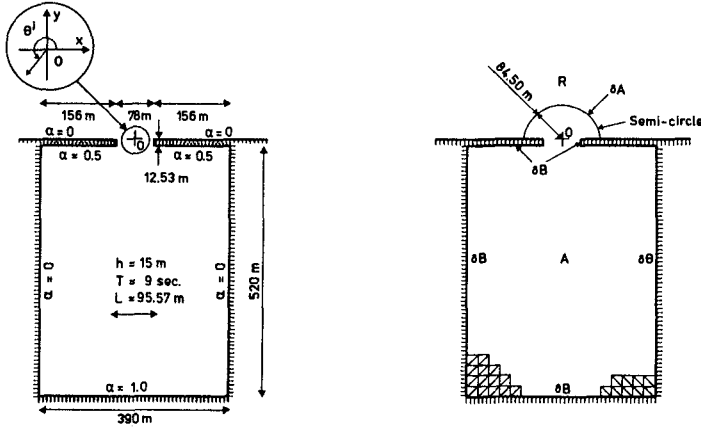


Figure 7. Left: Sketch of harbour geometry. Constant water depth in- and outside the harbour. Right: Sketch of finite element grid and boundary  $\partial A$  between finite element area A and semi-infinite ocean R.

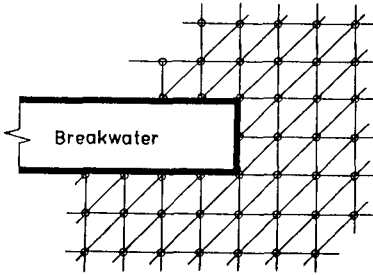


Figure 8. Detail of finite element grid around breakwater.

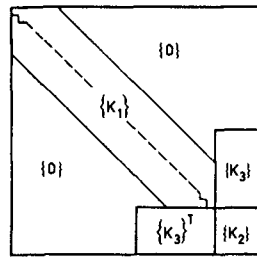


Figure 9. The coefficient matrix  $\{K\}$  and its three submatrices  $\{K_1\}$ ,  $\{K_2\}$ , and  $\{K_3\}$ .

The total number of nodal points in the finite element grid is 5,445 and the total number of elements is 10,556. Along the left and right boundaries inside the harbour there are 83 element sides, i.e. the short and long sides are 6.26 m and 9.02 m respectively. Along the innermost boundary of the harbour there are 60 element sides, i.e. the short and long sides are 6.50 m and 9.02 m respectively. In all the following figures a representative short wave period of  $T = 9$  sec. has been used corresponding to a wave length in the entire area (constant water depth in the whole area for simplicity) of  $L = 95.57$  m. This corresponds to a ratio of maximum side length in the elements to wave length of  $9.02/95.57 = 0.0944$  or minimum 10.6 element sides per wave length. This resolution is representative of what a practical engineer would use. Referring to the previous section one would expect a relative mean error in  $A/A_i$  and  $\phi$  of



the magnitude 1-2% and  $1^{\circ}$ - $2^{\circ}$  respectively. All figures were first calculated using  $n_{max} = 20$ . Hereafter all calculations were repeated with  $n_{max} = 24$  (i.e. an increase of 4). No change could be detected in any figure.

The nodal points were numbered starting at the left-hand corner and going right on the innermost boundary of the harbour, i.e. the numbering was done along lines parallel to the x-axis (see Fig. 7, left). This principle has been used in the entire grid, also in the minor part of area A outside the entrance of the harbour. This was done to minimize the bandwidth in the coefficient matrix  $\{K_1\}$ , which is by far the largest of the coefficient matrix  $\{K\}$ , see Fig. 9.

The submatrix  $\{K_1\}$  is stored in packed form giving it the dimensions: the number of nodal points (5,445) times the largest difference in nodal point numbers found in any element plus 1 (here  $62 + 1 = 63$ ), i.e.  $5,445 \times 63 = 343,035$  complex numbers. The quadratic submatrix  $\{K_2\}$  has the side length equal to the number of expansion coefficients, i.e.  $n_{max} + 1 (= 21)$ , i.e.  $21 \times 21 = 441$  complex numbers in the full matrix.

The submatrix  $\{K_3\}$  has the dimensions of the largest difference in nodal point numbers of the nodes on  $\partial A$  (here equal to 283) times  $n_{max} + 1 (= 21)$ , i.e.  $283 \times 21 = 5943$  complex numbers.

The programming was done using the IBM OS PL/I Optimizing Compiler, release 4.0, see IBM (1981a) and IBM (1981b). All the programming was done in double precision, which with our machines is approximately 16 digits (8 bytes per real number and 16 bytes per complex number). The program was compiled and executed with VM/CMS on an IBM 3033 and with MVS/TSO on an IBM 3081 (16 M bytes of core memory on each machine). The CPU-times given below are from executions on the IBM 3081, which is a dual-processor machine. In the timings only one processor was used.

After testing, all debugging facilities were removed from the code and all programs were recompiled with the REORDER and OPTIMIZE(TIME) options. In the execution of this relatively modest harbour the whole code could reside in core memory during execution. For one single period (no superposition) the execution time was approximately 140 CPU-seconds (i.e.  $2\frac{2}{3}$  min.) and the memory size 6 M bytes. Houston (1981) reported for a model of the same size (10,560 elements) an execution time of less than 1 min. on a CRAY-1. He used single precision in his FORTRAN program, which is approximately 15 floating point digits on a CRAY-1. When the CRAY-1 vector-computer is being used as a scalar computer, it is approximately 4-5 times as fast as a single processor of the scalar IBM 3081 computer. So we can conclude that our implementation is at least twice as fast as Houston's implementation. Note that the two implementations use approximately the same number of digits in the floating point calculations, viz. 16 and 15.

In Paper I, Figs. 3 and 4, an example of contours of relative amplitude and three-dimensional surface elevation at a specific time has been given in the case of normal incidence (in Fig. 7, left,  $\theta^i = 270^{\circ}$ ) and all boundaries being fully reflecting. To further illustrate these two figures we here show the relative wave amplitudes in three cross-sections parallel to the y-axis (see Fig. 7) in Fig. 10 and three cross-sections parallel to the x-axis in Fig. 11.

The first example is rather academic due to all boundaries being fully reflecting. In the following examples partial reflection is included in accordance with the  $\alpha$ -values in Fig. 7, left. To be very precise, the  $\alpha$ -value of 0.5 was used along the inner side of the breakwaters, around

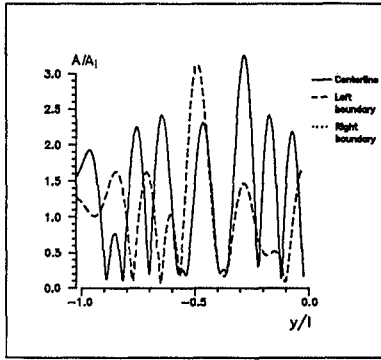


Figure 10. Relative wave amplitudes  $A/A_i$  for  $T = 9$  sec. in three cross-sections:  $x = -195$  m,  $0$  m,  $+195$  m. All boundaries are fully reflecting, i.e.  $\alpha = 0$  everywhere.  $\theta^i = 270^\circ$ .

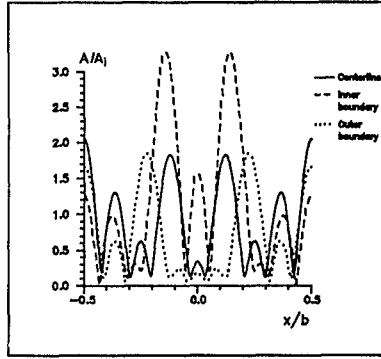


Figure 11. Relative wave amplitudes  $A/A_i$  for  $T = 9$  sec. in three cross-sections:  $y = -532.53$  m,  $-269.40$  m,  $-12.53$  m. All boundaries are fully reflecting, i.e.  $\alpha = 0$  everywhere.  $\theta^i = 270^\circ$ .

the tip of the breakwaters, and on that part of the outer side of the breakwaters that is inside area A.

In Figs. 12, 13, and 14 the results are shown for  $\theta^i = 270^\circ$  with the absorbing boundary conditions.

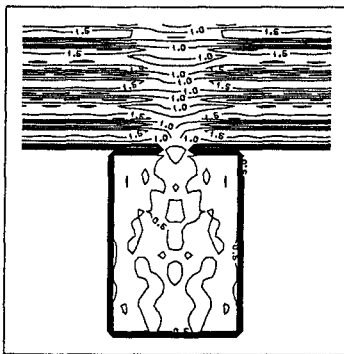


Figure 12. Harbour, contours of relative amplitudes  $A/A_i$ .  $T = 9$  sec.,  $\theta^i = 270^\circ$ . Partial absorption as defined in Fig. 7, left.

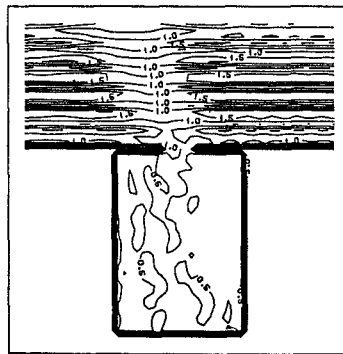


Figure 15. Same as Fig. 12, except that  $\theta^i = 247.5^\circ$ .

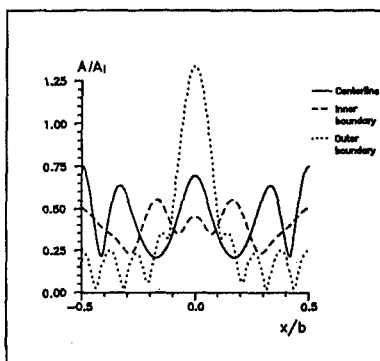
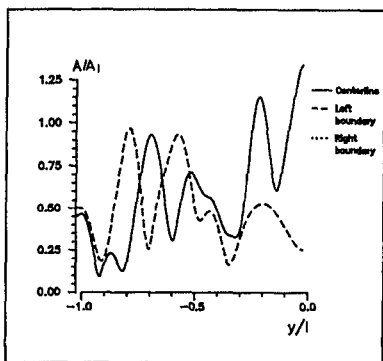


Figure 13. Same as Fig. 10, except for partial absorption as defined in Fig. 7, left.

Figure 14. Same as Fig. 11, except for partial absorption as defined in Fig. 7, left.

In Figs. 15, 16, 17, 18, and 19 the results are shown for  $\theta^i = 247.5^\circ$  with absorbing boundary conditions.

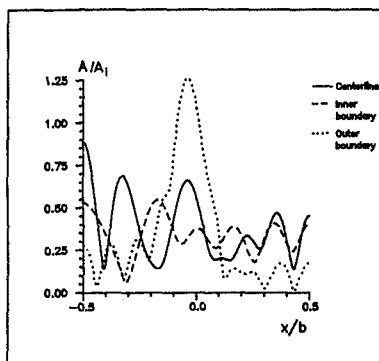
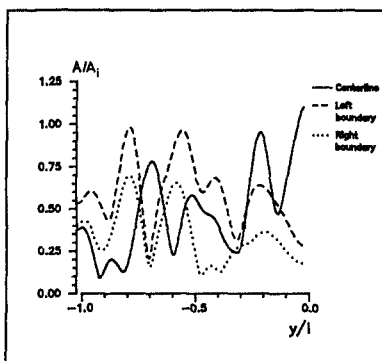


Figure 16. Same as Fig. 13, except that  $\theta^i = 247.5^\circ$ .

Figure 17. Same as Fig. 14, except that  $\theta^i = 247.5^\circ$ .

In Figs. 18 and 19 the results are shown for superposition of three different angles of incidence ( $\theta^i = 225.0^\circ, 247.5^\circ, \text{ and } 270.0^\circ$ ) with  $A/A_i = 1/\sqrt{6}, \sqrt{2}/3, 1/\sqrt{6}$  respectively (i.e.  $A/A_i \approx 0.41, 0.82, \text{ and } 0.41$ ). Note that  $\Sigma(A/A_i)^2 = 1$  for the three incident wave systems.

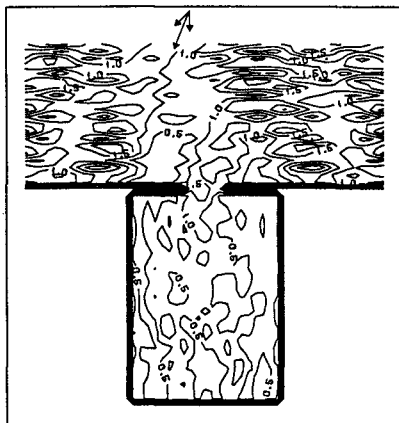


Figure 18. Harbour, contours of relative amplitudes  $A/A_i$ . Superposition of three incident wave systems,  $\theta^i = 225.0^\circ$ ,  $247.5^\circ$ , and  $270.0^\circ$ .  $T = 9$  sec. Partial absorption as defined in Fig. 7, left.

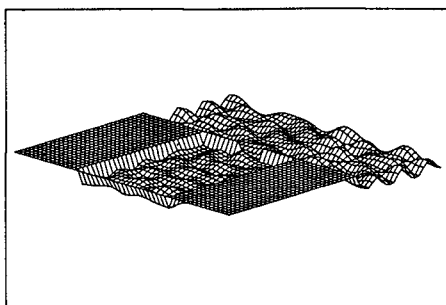


Figure 19. Harbour, relative surface elevation at a specific time corresponding to the example in Fig. 18.

#### 5. Discussion and Conclusion for the Harbour Example

The first set of figures (Figs. 10, 11 and Figs. 12, 13, and 14) demonstrated in detail the effect of full reflection vs. partial absorption.

The next set of figures (Figs. 12, 13, and 14 and Figs. 15, 16, and 17) demonstrated in detail the effect of normal incidence vs. oblique incidence (same partial absorption in both cases).

The final set of figures (Figs. 15, 16, and 17 and Figs. 18 and 19) demonstrated in detail the effect of one direction of incidence with all the wave energy vs. the same amount of energy spread over three directions of incidence. The dominant direction in the superposed wave fields is the same as in Figs. 15, 16, and 17.

We notice that in the cases with normal wave incidence ( $\theta^i = 270^\circ$ ) there is full symmetry, which is illustrated by Figs. 10-14.

The conclusions which can be drawn from all the sets of figures are not surprising: partial absorption diminishes the wave amplitudes drastically; the distribution of the same total wave energy among several directions has some diminishing effect on the wave amplitudes.

The execution time for calculating the wave field for a single period was earlier given to be  $2\frac{1}{3}$  min. The code is still a research code, and if, in the future, consulting engineers are going to superpose many directions and many periods for each lay-out of the harbour geometry a more optimized code has to be developed.

A more promising alternative to decrease the execution time would be to develop and implement the model on a vector-processor like CRAY-X-MP, CYBER 205, NEC SX-2, FUJITSU VP-200, or HITACHI S-810. The first three machines are strictly FORTRAN-machines, but the last two have IBM-compatible sets of machine instructions and should therefore be able to run IBM PL/I, which has vector operations built into the language itself.

#### References

- Berkhoff, J.C.W. (1972). "Computation of combined refraction-diffraction." Proc. 13th Coastal Engng. Conf., Vancouver, 1972, ASCE. New York, Vol. 1, Chap. 24, pp. 471-490.
- Behrendt, L. and Jonsson, I.G. (1984). "The physical basis of the mild-slope wave equation." Proc. 19th Coastal Engng. Conf., Houston, 1984, ASCE. New York, in press. (Paper I.)
- Chen, H.S. and Mei, C.C. (1974). "Oscillations and wave forces in an off-shore harbor." Massachusetts Institute of Technology. Parsons Laboratory, Rep. No. 190.
- Homma, S. (1950). "On the behaviour of seismic sea waves around circular island." Geophys. Mag., 21, pp. 199-208.
- Houston, J.R. (1981). "Combined refraction and diffraction of short waves using the finite element method." App. Ocean Res., Vol. 3, No. 4, pp. 163-170.
- IBM (1981a). "OS and DOS PL/I Language Reference Manual", Order number GC26-3977-0. White Plains, New York.
- IBM (1981b). "OS PL/I Optimizing Compiler: Programmer's Guide", Order number SC33-0006-5. White Plains, New York.
- Jonsson, I.G., Skovgaard, O. and Brink-Kjaer, O. (1976). "Diffraction and refraction calculations for waves incident on an island." J. Mar. Res., 34, pp. 469-496.
- Skovgaard, O. and Jonsson, I.G. (1981). "Computation of wave fields in the ocean around an island." Int. J. Num. Meth. Fluids. Vol. 1, pp. 237-272.

## CHAPTER SEVENTY FIVE

### CURRENT DEPTH REFRACTION OF REGULAR WAVES

Ivar G. Jonsson<sup>1</sup> and John B. Christoffersen<sup>2</sup>

#### ABSTRACT

The complete set of equations for the refraction of small surface gravity waves on large-scale currents over a gradually varying sea bed is derived and presented. Wave lengths, direction of propagation and wave heights are all determined along the so-called wave rays as solutions to ordinary, first-order differential equations.

Dissipation due to bed friction in the combined current wave motion is included. The ray tracing method is used in an example. A method for the calculation of current depth refraction of weakly non-linear waves is proposed.

#### 1. INTRODUCTION

When water waves propagate over an area with a variable water depth and current velocity, the ensuing gradients together with the current wave interaction can cause drastical changes in the direction, length and height of the waves, see e.g. Mallory (1974). In this transformation of the waves, diffraction effects are often negligible, and the phenomenon is termed current depth refraction.

This phenomenon is a significant physical process in many coastal and offshore areas, for instance near river mouths and tidal inlets, in the surf zone along a beach, and where wind waves meet major ocean currents. The refraction is of great importance for erosion and deposition in coastal areas, forces on offshore structures, and ship navigation.

Current depth refraction is a complex problem of wave propagation in an inhomogeneous, anisotropic, dispersive, dissipative and moving medium. Attempts to solve the general case have therefore been scarce. Noda et al. (1974) are probably the first to try this. They employed a global finite difference scheme for solving the governing partial differential equations and experienced so many difficulties that they advocated a search for a method which made integration along characteristic curves possible. Later Iwagaki et al. (1977) tried such an approach, but since they mixed different kinds of characteristic curves and furthermore did not introduce wave action conservation, they did

---

<sup>1</sup> Institute of Hydrodynamics and Hydraulic Engineering (ISVA), Technical University of Denmark, Bldg. 115, DK-2800 Lyngby, Denmark.

<sup>2</sup> Laboratory of Applied Mathematical Physics (LAMF), Technical University of Denmark, Bldg. 303. Present address: Christiani & Nielsen Ltd., Vester Farimagsgade 41, DK-1606 Copenhagen V., Denmark.

not really succeed in creating a practical model.

For wave height calculations on a current field the so-called wave action is important. Independently of each other this concept was found by Bretherton and Garrett (1968) for a rather general class of waves and by Hayes (1968) for acoustic waves. Jonsson et al. (1970) introduced the similar concept for water waves on a current, see their eq. (5.6).

Peregrine (1976), Phillips (1977), Jonsson (1978a), Peregrine and Jonsson (1983), and Peregrine et al. (1983) have given detailed reviews of waves on currents.

While today efficient and accurate models exist for the calculation of pure depth refraction, see e.g. Skovgaard et al. (1975), a similar model for the calculation of current and depth refraction does not exist. It is the main purpose of this paper to introduce the complete mathematical framework for such a model, which also takes bed friction and dissipation into account. It will be shown that the existence of a phase function, combined with a dispersion relation and a wave action conservation equation (which will be shown to be just a manipulated energy principle), lead to ordinary (first-order) differential equations along so-called wave rays for all wave quantities.

Small, regular waves are assumed; however, also non-linear waves are briefly dealt with.

Also an example of the practical use of a current depth refraction model will be presented. It is based exclusively on ray theory.

## 2. ASSUMPTIONS AND BASIC CONCEPTS

In most of this study small (and regular) progressive gravity waves are considered. Fluxes of mass, momentum and energy are integrated over depth and averaged over absolute period  $T_a$ , in that order. The problem is therefore formulated in two horizontal dimensions  $x_i, i = 1, 2$ .

A pure wave motion is defined as one with no net drift; thus the average - over-depth current velocity  $U_1$  is a zeroth order quantity. For a further discussion of this subject, see Jonsson (1978b), p. 228, and Jonsson and Wang (1980), pp. 157-158. The current velocity is assumed constant over depth.

Bed shear and accompanying dissipation is included. However, shear stresses in vertical sections are neglected. The bed slope is assumed small, so that the horizontal bed expressions are valid locally, i.e.  $|\nabla h| \ll kh$ , where  $\nabla$  is the horizontal gradient operator ( $\partial/\partial x_1, \partial/\partial x_2$ ), and  $k$  is the magnitude of the wave number vector  $k_i$ , so that  $k = 2\pi/L$ ,  $L$  being wave length. Furthermore, only large-scale currents in space and time are considered, i.e.  $|\nabla U| \ll kU$  and  $|\partial U/\partial t| \ll \omega_a U$ , where  $U$  is current speed,  $t$  is time, and  $\omega_a = 2\pi/T_a$  is the absolute angular frequency.

The study is within the framework of geometrical optics, i.e. wave fronts of small curvature are assumed thus excluding diffractive effects.

Two frames of reference are introduced. One is a coordinate system fixed in space; this is the absolute frame of reference, in which is used subscript 'a'. The other is a Galilean transformation of the first where the transformation velocity is the current velocity. Observations in this moving system are termed 'relative', and subscript 'r' is used here.

Referring to Fig. 1 the following relation exists between absolute and relative phase velocities

$$c_a = c_r + U \cos(\delta - \alpha) \quad (1)$$

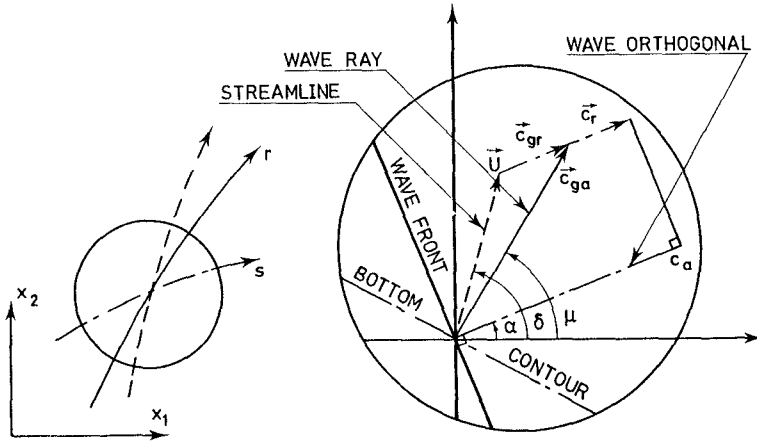


Fig. 1 - Horizontal sketch for characteristic curves, angles and velocities.

where angles  $\delta$  and  $\alpha$  are explained in the figure. (Note that by definition  $c_a$  is at right angles to the wave front, and that the vector  $U_i + (\hat{c}_r)_i$  has no physical meaning). Multiplying (1) by wave number  $k$  yields the Doppler relation

$$\omega_a = \omega_r + k_i U_i \tag{2}$$

in which the tensor summation notation is used, i.e.  $k_i U_i = k_1 U_1 + k_2 U_2 = kU \cos(\delta - \alpha)$ . The relative angular frequency is  $\omega_r = 2\pi/T_r$ ,  $T_r$  being relative period. The dispersion relation is

$$\omega_r^2 = g k \tanh kh \tag{3}$$

with  $g$  being gravity acceleration. Relative phase speed is found from  $c_r = \omega_r/k$ . Note that while  $\omega_a = \omega_a(h, k_i, U_i)$  we have  $\omega_r = \omega_r(h, k)$ .

In Fig. 1 three sets of curves are distinguished, streamlines, wave orthogonals and wave rays. The new concept is the wave ray, which goes in the direction of the absolute group velocity

$$(c_{ga})_i = c_{ga} (\cos\mu, \sin\mu) \tag{4}$$

The wave ray is not a unique concept. In the general (i.e. non-steady) case one must distinguish between *ray paths*, analogous to particle paths in conventional hydrodynamics, and *ray lines*, analogous to streamlines. In steady flow these curves are identical. The term wave ray will in the general case normally be used for the ray path, and in steady flow for ray line. The differential equation for the wave ray is



$$\frac{dx_i}{dt} = (c_{ga})_i \quad i = 1, 2 \quad (5)$$

in which in general  $(c_{ga})_i$  is a function of  $x_i$  and  $t$ .

In Fig. 2 ray paths and ray lines are illustrated together with the concepts of ray tube element and ray tube, which will be introduced in connection with the wave height calculation.

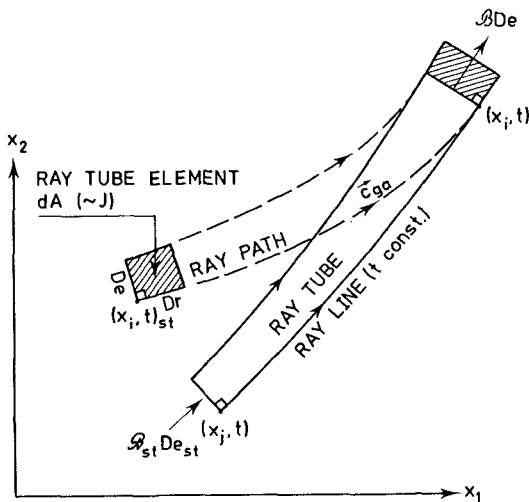


Fig. 2 - Horizontal sketch showing ray path, ray line, ray tube element and ray tube.

From (2) we find the relation between the absolute group velocity and the relative ditto  $(c_{gr})_i$

$$(c_{ga})_i \equiv \frac{\partial \omega_a}{\partial k_i} = \frac{\partial \omega_r}{\partial k_i} + U_i = (c_{gr})_i + U_i \quad (6)$$

which is illustrated in Fig. 1. The relative group velocity goes in the direction of the wave orthogonal and is given by

$$(c_{gr})_i = c_{gr} (\cos \alpha, \sin \alpha) \quad (7)$$

with the relative group speed

$$c_{gr} = \frac{1}{2} c_r (1 + G) \quad (8) \quad G = \frac{2kh}{\sinh 2kh} \quad (9)$$

Also the relative phase velocity goes in the orthogonal direction:

$$(c_r)_i = c_r (\cos \alpha, \sin \alpha) \quad (10)$$

The time derivative 'seen' by an observer moving along a wave ray with speed  $c_{ga}$  is

$$\frac{d}{dt} = \frac{\partial}{\partial t} + (c_{ga})_i \frac{\partial}{\partial x_i} = \frac{\partial}{\partial t} + c_{ga} \frac{D}{Dr} \quad (11)$$

where 'r' is the length along the ray. This operator ( $d/dt$ ) turns out to be extremely important.

### 3. PROBLEM FORMULATION

In an environment with waves and currents the coastal and ocean engineer is primarily interested in the effect of the fluid flow on structures, the sea bed and vessels. To achieve this goal one must know the wave length ( $L$ ), direction of propagation ( $\alpha$ ), wave height ( $H$ ), as well as the mean water level ( $b$ ) and the current vector ( $U_i$ ), all as functions of space and time ( $x_i, t$ ). This enables a calculation of the total water particle velocities and pressures and thus the forces.

The length and time scales for the waves are most often very much smaller than the corresponding scales for the current. Because of these contrasting scales it is natural to solve the wave field and the current field in two separate steps; this so-called two-level approach was suggested by Skovgaard and Jonsson (1976). Another good reason for this approach is that only at the current level one has to deal with partial differential equations. At the wave level, it turns out that only ordinary differential equations have to be solved. This is done by integration from initial (i.e. one point) boundary conditions along the wave rays. There is naturally, a coupling between the two levels (through bed shear and radiation stress), and an iterative procedure will in principle be necessary.

The known quantities in a water area will be the 'geometrical depth'  $D(x_i)$  (see Fig. 3) describing the bathymetry, and the Nikuradse roughness  $k_{N_i}(x_i)$  of the bed. Also certain lateral boundary conditions must be specified for the current field; for the waves, input data must be specified where the waves 'enter' the calculation area. Details of calculation for the current field will not be presented here; reference is made to Christoffersen (1982).

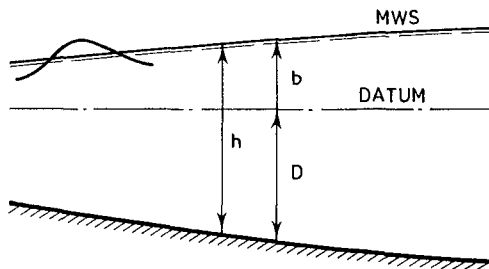


Fig. 3 - Vertical sketch. Definitions of geometrical depth  $D$ , mean surface elevation  $b$ , and mean water depth  $h$ .

In refraction calculations one normally assumes a steady state. In this paper, however, we shall present the general non-steady formulae, since the derivation of these is not more complicated than the steady ones. The steady state is hereafter considered as a special case.

#### 4. THE KINEMATICS

The basic assumption of ray theory (kinematic wave theory) is that changes in wave characteristics are so slow that locally plane waves can be assumed, see Hayes (1970). This means that *locally* we can introduce a phase function

$$\theta = \omega_a t - k_i x_i + \theta_0 \quad (13)$$

By differentiation of (13) we obtain

$$\frac{\partial \theta}{\partial t} = \omega_a \quad (14) \quad \frac{\partial \theta}{\partial x_i} = -k_i \quad (15)$$

These two quantities are then allowed to vary on a larger scale, and by further differentiation we find the so-called consistency relations

$$\frac{\partial k_i}{\partial t} + \frac{\partial \omega_a}{\partial x_i} = 0 \quad (16) \quad \frac{\partial k_i}{\partial x_j} = \frac{\partial k_j}{\partial x_i} \quad (17)$$

Equation (16) expresses conservation of waves, and (17) that the wave number vector is irrotational. On this basis it becomes possible to find the wave number vector, and thus the wave length and propagation direction, since  $L = 2\pi(k_1^2 + k_2^2)^{-1/2}$  and  $\tan \alpha = k_2/k_1$ . (A further consequence of the assumption of locally plane waves is the Doppler relation (3)).

Using the operator (11) on  $k_i$ , and for  $\partial k_i/\partial t$  inserting (16) yields

$$\frac{dk_i}{dt} = -\frac{\partial \omega_a}{\partial x_i} + (c_{ga})_j \frac{\partial k_i}{\partial x_j} \quad (18)$$

Since  $\omega_a = \omega_a(h, k_j, U_j)$  one obtains

$$\frac{\partial \omega_a}{\partial x_i} = \frac{\partial \omega_a}{\partial h} \frac{\partial h}{\partial x_i} + \frac{\partial \omega_a}{\partial k_j} \frac{\partial k_j}{\partial x_i} + \frac{\partial \omega_a}{\partial U_j} \frac{\partial U_j}{\partial x_i} \quad (19)$$

Using (2) to give  $\partial \omega_a/\partial h = \partial \omega_r/\partial h$  and  $\partial \omega_a/\partial U_j = k_j$ , further introducing (17) and (6), (18) and (19) finally yield

$$\frac{dk_i}{dt} = -\frac{\omega_r G}{2h} \frac{\partial h}{\partial x_i} - k_j \frac{\partial U_j}{\partial x_i} \quad (20)$$

Here it is used that  $\partial \omega_r/\partial h = \omega_r G/2h$ , see Christoffersen and Jonsson (1980). Since  $d/dt$  is given by (11), the important result is achieved that through (20) the rate of change of the wave number vector is found along a ray.

In conclusion, the ray path  $x_i$  and the wave number vector  $k_i$  along this path, are determined by the 4 ordinary, first-order differential

equations (5) and (20), with proper initial conditions.

The absolute angular frequency can be determined either from the algebraic Doppler relation (2) or from (Christoffersen, 1982)

$$\frac{d\omega_a}{dt} = \frac{\omega_r G}{2h} \frac{\partial h}{\partial t} + k_j \frac{\partial U_j}{\partial t} \tag{21}$$

It appears that for a steady medium,  $\omega_a$  remains constant for a 'ray tube element', see Fig. 2.

Similarly, an equation for  $d\omega_r/dt$  along a wave ray can be found, see Christoffersen (1982), chapter 4. The relative angular frequency can also be found from the algebraic expression (3).

In the next chapter it will be found that the evolution of the so-called ray tube element (Fig. 2) must be known in order to calculate the wave height along a ray. Since this is a kinematic problem, it will be dealt with in the present chapter.

A ray tube element is a differential concept, to be visualized as an infinitesimally short 'tube' made up of neighbouring rays. Its area being  $dA$ , the 'Jacobian'  $J$  is introduced as

$$J = \frac{dA}{dA_{st}} = \frac{De}{De_{st}} \frac{c_{ga}}{c_{ga,st}} \tag{22}$$

since  $dA = De Dr$  (Fig. 2), and  $Dr = c_{ga} dt$ . In (22) suffix 'st' stands for 'start' or initial value.

Knowledge of how a ray tube element changes as it moves is found in Aris (1962), pp. 83-84. The so-called Euler expansion formula simply states that

$$\frac{1}{J} \frac{dJ}{dt} = \frac{\partial (c_{ga})_i}{\partial x_i} \tag{23}$$

Using (6) and (2) to evaluate the right hand side of (23) (the divergence of  $(c_{ga})_i$ ) it is found that

$$\frac{1}{J} \frac{dJ}{dt} = \frac{\partial^2 \omega_r}{\partial k_i \partial k_j} \frac{\partial k_j}{\partial x_i} + \frac{\partial^2 \omega_r}{\partial k_i \partial h} \frac{\partial h}{\partial x_i} + \frac{\partial U_i}{\partial x_i} \tag{24}$$

The second order derivatives in (24) are

$$\frac{\partial^2 \omega_r}{\partial k_i \partial h} = \frac{\partial^2 \omega_r}{\partial k \partial h} \frac{k_i}{k} \tag{25}$$

$$\frac{\partial^2 \omega_r}{\partial k_i \partial k_j} = \left( \frac{\partial^2 \omega_r}{\partial k^2} - \frac{1}{k} \frac{\partial \omega_r}{\partial k} \right) \frac{k_i k_j}{k^2} + \frac{1}{k} \frac{\partial \omega_r}{\partial k} \delta_{ij} \tag{26}$$

where  $\delta_{ij}$  is the Kronecker delta.

The evaluation of  $\partial k_j / \partial x_i$  in (24) is quite tricky. Playing around with the consistency relations and the Doppler relation finally yields the 'derived ray equation' (Hayes, 1970).

$$\begin{aligned} \frac{d}{dt} \left( \frac{\partial k_j}{\partial x_i} \right) = & - \frac{\partial k_k}{\partial x_i} \left[ \frac{\partial^2 \omega_r}{\partial k_k \partial k_\ell} \frac{\partial k_\ell}{\partial x_j} + \frac{\partial^2 \omega_r}{\partial k_k \partial h} \frac{\partial h}{\partial x_j} + \frac{\partial U_k}{\partial x_j} \right] - k_k \frac{\partial^2 U_k}{\partial x_i \partial x_j} \\ & - \frac{\partial k_k}{\partial x_j} \left[ \frac{\partial^2 \omega_r}{\partial k_k \partial h} \frac{\partial h}{\partial x_i} + \frac{\partial U_k}{\partial x_i} \right] - \frac{\partial^2 \omega_r}{\partial h^2} \frac{\partial h}{\partial x_i} \frac{\partial h}{\partial x_j} - \frac{\partial \omega_r}{\partial h} \frac{\partial^2 h}{\partial x_i \partial x_j} \end{aligned} \quad (27)$$

in which  $\partial \omega_r / \partial h = \omega_r G / 2h$ . This equation contains three ordinary differential equations, determining the symmetrical tensor  $\partial k_j / \partial k_i$  along rays. For details see Christoffersen (1982), and Jonsson and Christoffersen (1982).

## 5. THE DYNAMICS

The mass conservation equation is simply

$$\frac{\partial}{\partial t} (\rho h) + \frac{\partial}{\partial x_i} (\rho h U_i) = 0 \quad (28)$$

The momentum conservation equations (Phillips, 1977, eq. 3.6.11), with the mean bed shear stress  $(\tau_b)_i$  added, read

$$\frac{\partial}{\partial t} (\rho h U_i) + \frac{\partial}{\partial x_j} (\rho h U_i U_j + S_{ij}) + \rho g h \frac{\partial b}{\partial x_i} + (\tau_b)_i = 0 \quad (29)$$

Standard sign convention is adopted for shear, i.e. the shear stress acting on the *bed* is taken positive in the positive  $x_i$ -direction. Phillips' bed shear stress appears with the opposite sign (his p. 65).

The energy conservation equation (Phillips, 1977, eq. 3.6.18) with the total dissipation per unit area  $E_d$  added reads

$$\begin{aligned} \frac{\partial}{\partial t} \left( \frac{1}{2} \rho h U_j^2 + E + \frac{1}{2} \rho g (b^2 - D^2) \right) \\ + \frac{\partial}{\partial x_i} \left( \frac{1}{2} \rho h U_i U_j^2 + \rho g h U_i b + E (c_{ga})_i + S_{ij} U_j \right) + E_d = 0 \end{aligned} \quad (30)$$

Note that there is some ambiguity in Phillips' definition of dissipation, see Christoffersen and Jonsson (1980). In the above equations  $S_{ij}$  is the radiation stress tensor given by

$$S_{ij} = \delta_{ij} S_p + \frac{k_i k_j}{k^2} S_m \quad (31)$$

where  $S_p$  and  $S_m$  are the pressure and momentum parts of the radiation stress given by

$$S_p = \frac{1}{2} E G \quad (32) \quad S_m = \frac{1}{2} E (1 + G) \quad (33)$$

Here  $E$  as usual is the wave energy density,  $1/8 \rho g H^2$ .

Christoffersen and Jonsson (1980) derived the wave action equation for a dissipative steady medium. The wave action equation for a general unsteady dissipative medium is here derived in a simpler and more straightforward way.

Eliminating first the mean surface height  $b$  by multiplying (29) by  $U_i$  and subtracting the result from (30) yields

$$\frac{\partial E}{\partial t} + \frac{\partial}{\partial x_i} \left( E (c_{ga})_i \right) + S_{ij} \frac{\partial U_j}{\partial x_i} + E_d - (\tau_b)_i U_i = 0 \tag{34}$$

Dividing by  $\omega_r$  and using also (11) gives

$$\begin{aligned} \frac{\partial}{\partial t} \left( \frac{E}{\omega_r} \right) + \frac{\partial}{\partial x_i} \left( \frac{E}{\omega_r} (c_{ga})_i \right) + \frac{E_d - (\tau_b)_i U_i}{\omega_r} \\ + \frac{1}{\omega_r} \left( \frac{E}{\omega_r} \frac{d\omega_r}{dt} + S_{ij} \frac{\partial U_j}{\partial x_i} \right) = 0 \end{aligned} \tag{35}$$

Here, the variation of  $\omega_r$  along a ray can be expressed in terms of the radiation stress tensor as (Christoffersen, 1982)

$$\frac{E}{\omega_r} \frac{d\omega_r}{dt} = - S_{ij} \frac{\partial U_j}{\partial x_i} \tag{36}$$

Inserting (36) in (35), the last term vanishes, and the new general wave action equation emerges as

$$\frac{\partial \mathcal{A}}{\partial t} + \frac{\partial}{\partial x_i} \left( \mathcal{A} (c_{ga})_i \right) + E_w = 0 \tag{37}$$

in which wave action  $\mathcal{A}$  and 'wave action dissipation'  $E_w$  are by definition

$$\mathcal{A} = \frac{E}{\omega_r} \tag{38} \quad E_w = \frac{E_d - (\tau_b)_i U_i}{\omega_r} \tag{39}$$

Note that all terms in (37) vanish for a vanishing wave motion. Thus the energy equation (30) for the total flow has been transformed into a neat energy equation for the wave motion. This can be further simplified, though. Introducing (23) in (37) yields

$$\frac{d}{dt} (\mathcal{A} J) + E_w J = 0 \tag{40}$$

This means that wave action  $\mathcal{A}$  - and thus wave height  $H$  - can be calculated along a wave ray by solving the ordinary differential equation (40). By introducing (22), an alternative version of (40) appears as

$$\frac{d}{dt} (\mathcal{B} De) + E_w c_{ga} De = 0 \tag{41}$$

with wave action flux  $\mathcal{B} \equiv \mathcal{A} c_{ga}$ .

### 6. WAVE HEIGHT CALCULATION

The wave height equation is most easily found by looking at the steady case. With  $\partial/\partial t = 0$  we find from (11) and (41),  $D(\mathcal{B}De)/Dr + E_w De = 0$ , where 'r' is distance along the ray, and 'e' is distance at right angles to this (Fig. 2). It thus appears that wave action propagates between neighbouring rays and is dissipated through wave action dissipation. The wave action flux through the ray tube is  $\mathcal{B}_{st} De_{st}$  at one end ('st' stands for start), and  $\mathcal{B} De$  at an arbitrary

point (Fig. 2). Taking the square root of the ratio between these two quantities yields the wave height equation

$$\frac{H}{H_{st}} = \sqrt{\frac{\omega_r}{\omega_{r,st}}} \sqrt{\frac{c_{ga,st}}{c_{ga}}} \sqrt{\frac{De_{st}}{De}} \sqrt{\frac{\mathcal{A}_J}{\mathcal{A}_{st,Jst}}} \quad (42)$$

$$= K_C \times K_S \times K_{ra} \times K_f$$

in which  $K_C$  is the 'Doppler coefficient',  $K_S$  the 'shoaling coefficient',  $K_{ra}$  the 'refraction coefficient', and  $K_f$  the 'friction coefficient'. It can be shown that (42) also is valid in the non-steady case, see e.g. Jonsson (1982). The three first coefficients are determined by the kinematics of the current-wave field, and it is immediately seen from (22) that  $J = (K_S K_{ra})^{-2}$ , i.e.

$$\frac{H}{H_{st}} = K_C J^{-1/2} K_f \quad (43)$$

By dividing (40) with  $\mathcal{A}_{st} J_{st}$  ( $J_{st} \equiv 1$ ) and introducing the expression for  $K_f$  in (42), we find for the friction coefficient

$$\frac{d}{dt} (K_f^2) = - \frac{E_w}{\mathcal{A}_{st}} J \quad (44)$$

i.e. yet another ODE to be solved along the rays.

There remains the calculation of  $E_w$  in (44). From (39) it appears that this calls for the determination of bed shear  $(\tau_b)_i$  and dissipation  $E_d$ . In Christoffersen and Jonsson (1984) a detailed calculation procedure is presented for the calculation of these quantities. The method is based on two-layer models for the current-wave boundary layer, one for 'small roughnesses' and one for 'large roughnesses'. In general the following approximate result was obtained:  $E_d = (\tau_b)_i U_i + \langle (\tau_{wb})_i (u_{wb})_i \rangle$ , whereby from (39) we find  $E_w = \langle (\tau_{wb})_i (u_{wb})_i \rangle / \omega_r$ . Here  $(\tau_{wb})_i$  is the wave part of the bed shear stress and  $(u_{wb})_i$  the wave particle velocity just outside the wave boundary layer at the bed.

## 7. SUMMARY OF RESULTS

The procedure for the calculation of the wave field ( $k_i, H$ ) is hereafter. The wave ray - along which all other quantities can be calculated - and the wave number vector are determined by the four differential equations (5) and (20) with proper initial conditions, assuming water depths and current velocity known. Note that operator  $d/dt$  is given by (11).

The wave height is then determined by (43). Doppler coefficient  $K_C$  is found from its definition in (42), and the Jacobian  $J$  by the four differential equations (24) and (27). Finally  $K_f$  is found from (44).

The above procedure is generally valid. In practise a steady situation is often assumed, and simpler equations emerge, see Christoffersen (1982), and Jonsson and Christoffersen (1982). A discussion of the possible calculation of the current field, and of the interaction between the waves and the currents through radiation stress and bed shear is given in the former reference.

8. EXAMPLE

To illustrate the effect of currents on waves, we look at conditions outside an inlet with a 'jet' ebb flow as shown in Fig. 4.

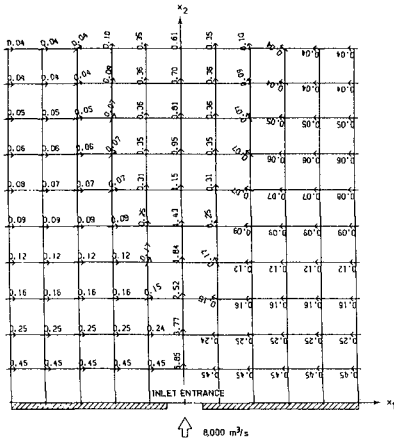


Fig. 4. Horizontal plan. Ebb current velocities (m/s) outside inlet. Arrows indicate current direction and numbers are current speed. The current is symmetrical about the  $x_2$ -axis. Grid spacing is 200 m, and water depth is  $h = 10\text{ m} + 0.02 x_2$  ( $x_2 > 0$ ), i.e. bed slope 1:50. The inlet entrance is 200 m wide, with water depth  $h_0 = 10\text{ m}$ . Discharge through inlet is  $Q = 8,000\text{ m}^3/\text{s}$ , giving an average-over-width current velocity  $U_0 = 4\text{ m/s}$ .

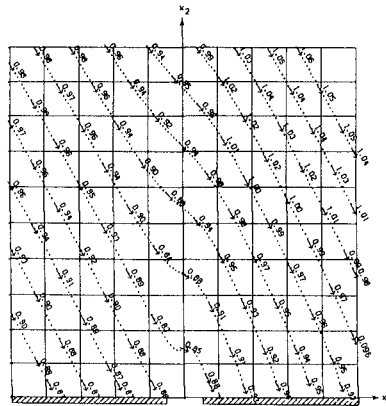


Fig. 5. Horizontal plan. Wave rays (...) on ebb current in Fig. 4. Arrows indicate orthogonal direction, and numbers are wave heights (m) (no dissipation). The thirteen computed rays start at  $x_2 = 5,000\text{ m}$  ( $h = 110\text{ m}$ ). The corresponding  $x_1$ -values vary from  $x_1 = -3,600\text{ m}$  to  $x_1 = -1,200\text{ m}$ , with 200 m spacing. The angle of incidence is here  $30^\circ$ . Initial wave height is  $H_{st} = 1\text{ m}$ , and absolute wave period is  $T_a = 8\text{ s}$ .

With angle of incidence  $30^\circ$  far from the inlet, the computed orthogonal directions and wave heights (no dissipation) are presented along the rays in Fig. 5. The fact that wave rays and orthogonals do not coincide (when currents are present), is most clearly seen near the inlet entrance, where current velocities are large. The most striking - and perhaps unexpected - result of our calculations as presented in Fig. 5, is the marked reduction in wave height in the central part of the ebb current. The reason for this is that the oblique incidence of the waves on the opposing current in ques-



tion, in this area generates a sharp reduction in refraction coefficient. This is a result of the obvious increase in ray spacing here.

9. NON-LINEAR WAVES

In Shen and Keller (1973) and Shen (1975) (considering non-linear wave propagation in shallow water without a current) it was found that the kinematics to a first approximation was governed by linear theory, i.e.  $\omega_r = k \sqrt{gh}$ , which is the shallow water version of (3). This meant that non-linearity only played a role in the calculation of the dynamics, which was governed by a Korteweg-DeVries equation. This equation is known to have cnoidal wave solutions, see Svendsen and Hansen (1978) where the energy flux has been calculated for cnoidal waves.

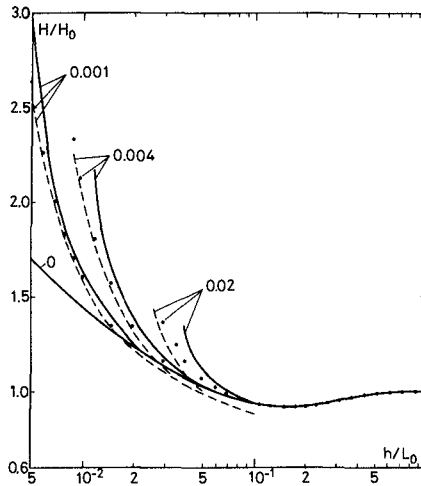


Fig. 6 - Shoaling curves. Full lines: Cokelet's theory. Dashed lines: Svendsen and Brink-Kjær (1972). (From Sakai and Battjes, 1980) Dots: Present study. Values of  $H_0/L_0$  are shown.

Further Ryrie and Peregrine (1982), considering refraction of numerically exact finite-amplitude waves, found that linear wave theory normally proved quite accurate for predicting the wave directions. These observations really indicate that a first simple extension to include weakly non-linear waves, could be to keep the linear-wave kinematics unaltered, and only take non-linearity into account in the wave action equation (40). This means that one just replaces the linear wave energy density in (38) with the non-linear wave energy density  $E = B(m) \rho g H^2$  where

$$B(m) = \frac{1}{3m^2} \left[ \frac{E}{K} (2 + 2m_1 - 3 \frac{E}{K}) - m_1 \right] \tag{45}$$

see e.g. Sarpkaya and Isaacson (1981), p. 185.

Here  $m_1 = 1-m$ , and further  $K(m)$  and  $E(m)$  are the complete elliptic integrals of the first and second kind, respectively. The parameter  $m$  is determined from  $HL^2/h^3 = (16/3) m K^2$ .

Because of  $B(m)$  ( $= 1/8$  for linear waves), a fifth factor  $K_n = \sqrt{B_{st}/B}$  is introduced in (42), to account for non-linearity.

To illustrate the applicability of this new and simple approach, we show in Fig. 6 the results of shoaling without a current.

In the figure, the Sakai and Battjes (1980) results for shoaling of finite amplitude waves (using Cokelet's theory) have been compared with our model, and with the results of Svendsen and Brink-Kjær (1972), showing that our model yields encouraging results for the wave heights, also giving a smooth transition from deep to shallow water. The smaller the steepness, the better the agreement with the Cokelet theory.

The proposed extension does not only give improved results, (as compared with linear theory), but it is also easy to implement in a refraction program capable of treating arbitrary bathymetries and current fields.

## 10. CONCLUSIONS

The assumption of *locally* plane waves, combined with a dispersion relation and wave action conservation, have led to the complete set of equations for current and depth refraction of regular water waves. These are ordinary, first-order differential equations for all wave quantities, when formulated along the so-called wave rays. Bed friction and accompanying dissipation is included. The ray equations form the basis of a computer program, which is applied to a case of refraction on an ebb current outside an inlet. A method to incorporate non-linear waves in the system is proposed.

Dr. Ove Skovgaard, Laboratory of Applied Mathematical Physics, is acknowledged for his unfaltering interest and good advice on the computational problems.

## REFERENCES

- Aris, R., 1962. Vectors, Tensors and the Basic Equations of Fluid Dynamics. Prentice-Hall Int., London. ix + 286 pp.
- Bretherton, F.P., and C.J.R. Garrett, 1968. Wavetrains in inhomogeneous moving media. Proc. Roy. Soc., A, vol. 302, 529-554.
- Christoffersen, J.B., 1982. Current Depth Refraction of Dissipative Water Waves. Inst. Hydrodyn. and Hydraulic Engng. (ISVA), Techn. Univ. Denmark, Series Paper 30, v + 179 pp.
- Christoffersen, J.B., and I.G. Jonsson, 1980. A note on wave action conservation in a dissipative current wave motion. App. Ocean Res., vol. 2, 179-182.
- Christoffersen, J.B. and I.G. Jonsson, 1984. Bed friction and dissipation in a combined current and wave motion. Manuscript submitted for publication.
- Hayes, W.D., 1968. Energy invariant for geometric acoustics in a moving medium. Physics of Fluids, vol. 11, no. 8, 1654-1656.

- Hayes, W.D., 1970. Kinematic wave theory. *Proc. Roy. Soc. London, A*, vol. 320, 209-226.
- Iwagaki, Y., T. Sakai, T. Tsuda and Y. Oka, 1977. Wave refraction and wave height variation due to current. *Bull. Disas. Prev. Res. Inst.*, Kyoto Univ., vol. 27, part 2, no. 248, 73-91.
- Jonsson, I.G. 1978a. Combinations of waves and currents. In: *Stability of Tidal Inlets*, by Per Bruun. Elsevier, Amsterdam, 162-203.
- Jonsson, I.G., 1978b. Energy flux and wave action in gravity waves propagating on a current. *J. Hydr. Res.*, vol. 16, 223-234.
- Jonsson, I.G., 1982. Current depth refraction: A heuristic particle approach. *Inst. Hydrodyn. and Hydraulic Engng. (ISVA)*, Tech. Univ. Denmark, Prog. Rep. 57, 3-11.
- Jonsson, I.G., and J.D. Wang, 1980. Current-depth refraction of water waves. *Ocean Engng.*, vol. 7, 153-171.
- Jonsson, I.G., and J.B. Christoffersen, 1982. The complete equations for current depth refraction of water waves. *Inst. Hydrodyn. and Hydraulic Engng. (ISVA)*, Tech. Univ. Denmark, Prog. Rep. 57, 13-24.
- Jonsson, I.G., C. Skougaard, and J.D. Wang, 1970. Interaction between waves and currents. *Proc. 12th Coastal Engng. Conf. Washington, D.C.*, Sep. 1970, Am. Soc. Civ. Engrs., New York, vol. 1, 489-507.
- Mallory, J.K., 1974. Abnormal waves on the South East coast of South Africa. *The International Hydrographic Review*, Monaco, vol. LI, No. 2, 99-129.
- Noda, E.K., C.J. Sonu, V.C. Rupert, and J.I. Collins, 1974. Near-shore circulations under sea breeze conditions and wave-current interactions in the surf zone. Rep. TC-P-72-149-4, Tetra Tech., Pasadena, Cal., AD 776643, 205 pp.
- Peregrine, D.H., 1976. Interaction of water waves and currents. In: *Advances in Applied Mechanics*, ed. C.-S. Yih, Academic Press, New York, vol. 16, 9-117.
- Peregrine, D.H. and I.G. Jonsson, 1983. Interaction of Waves and Currents. Coastal Engineering Research Center, Virginia, USA, Misc. Report No. 83-6, 88 pp.
- Peregrine, D.H., I.G. Jonsson and C. Galvin, 1983. Annotated Bibliography on Wave-Current Interaction, Coastal Engineering Research Center, Virginia, USA, Misc. Report No. 83-7, 82 pp.
- Phillips, O.M., 1977. *The Dynamics of the Upper Ocean*. 2nd ed. Cambridge University Press. viii + 336 pp.
- Ryrie, S. and D.H. Peregrine, 1982. Refraction of finite-amplitude water waves obliquely incident on a uniform beach. *J. Fluid Mech.*, vol. 115, 91-104.
- Sakai, T. and J.A. Battjes, 1980. Wave shoaling calculated from Cokelet's theory. *Coastal Engng.*, vol. 4, 65-84.
- Sarpkaya, T. and M. Isaacson, 1981. *Mechanics of Wave Forces on Off-shore structures*. Van Nostrand Reinhold Co., New York, vii + 651 pp.

- Shen, M.C., 1975. Ray method for surface waves on fluid of variable depth. *SIAM Review*, Vol. 17, No. 1, 38-56.
- Shen, M.C. and J.B. Keller, 1973. Ray method for non-linear wave propagation in a rotating fluid of variable depth. *Physics of Fluids*, vol. 16, No. 10, 1565-1572.
- Skovgaard, O., I.G. Jonsson, and J.A. Bertelsen, 1975. Computation of wave heights due to refraction and friction. *Proc. Am. Soc. Civ. Engrs., J. Waterways, Harbors and Coastal Engng. Div.*, vol. 101, 15-32. (Closure: 1976, vol. 102, 100-105).
- Skovgaard, O., and I.G. Jonsson, 1976. Current depth refraction using finite elements. *Proc. 15th Coastal Engng. Conf., Honolulu, Am. Soc. Civ. Engrs., New York*, vol. 1, 721-737.
- Svendsen, I.A. and O. Brink-Kjær, 1972. Shoaling of cnoidal waves. *Proc. 13th Conf. Coastal Engng., Vancouver*, vol I, 365-383.
- Svendsen, I.A. and J. B. Hansen, 1977. The wave height variation for regular waves in shoaling water. *Coastal Engineering*, vol. 1, 261-284.

## CHAPTER SEVENTY SIX

### A Numerical Model For Refraction Of Linear And Cnoidal Waves

John R. Headland<sup>1</sup>, A.M. ASCE  
Hsiao-Ling Chu<sup>2</sup>, M. ASCE

#### Abstract

A numerical model for refraction of linear and cnoidal waves over an arbitrary bottom is presented. The model, which is based on the ray theory of refraction (11), utilizes linear theory in deep and intermediate water and cnoidal theory in shallow water. The model permits one to determine nearshore wave properties using a nonlinear wave theory. Nearshore wave properties such as wave height, celerity, and wave angle determined using the linear-cnoidal refraction model may vary considerably from those determined using a linear refraction model. In general, cnoidal waves refract less, travel faster, and shoal higher than linear waves. This result can have a considerable effect on coastal engineering design, particularly in the areas of coastal structure design and longshore transport computations.

#### Introduction

Linear theory is generally used for wave shoaling and refraction computations despite its well-documented inability to accurately predict shallow water wave characteristics (6). Several investigators (6, 8, 14) have used nonlinear theories to analyze wave refraction over straight and parallel bottom contours but have not extended the work to an arbitrary bottom. Crowley et. al. (5) have developed a nonlinear refraction model for an arbitrary bottom utilizing vocoidal wave theory. This paper presents a numerical model for wave refraction over an arbitrary bottom which incorporates linear theory in deep and intermediate water but uses cnoidal theory in shallow water.

The numerical model presented herein is based on the ray theory of refraction. Ray theory suffers from several shortcomings, especially the inability to provide realistic solutions in areas of strong convergence and caustics. A variety of refraction-diffraction models have been developed in recent years (1, 2, 12) to overcome problems associated with ray theory. These models may utilize either linear (2, 12) or nonlinear theory (1). Refraction-diffraction models are clearly an improvement over ray theory, but use of these models requires substantial computer time even for a

<sup>1</sup>Coastal Engineer, Moffatt and Nichol Engineers, Suite 107, 3717 National Drive, Raleigh, North Carolina 27612 and Graduate Student,

<sup>2</sup>Department of Civil Engineering, Duke University, Durham, NC 27706.  
<sup>2</sup>Professor of Civil Engineering, California State University, Long Beach, California 90840.

relatively small geographical area (2). Ray models are therefore indispensable at the present state-of-the-art and are often used as input to a refraction-diffraction model or to a physical model. Ray models were recently used on two major coastal engineering projects (9, 10).

The objective of this paper is to present the governing equations for wave refraction, present the linear and cnoidal equations used in them, and discuss their numerical solution. Application of the model to straight and parallel bottom contours and an idealized shoal are presented and discussed. Differences in nearshore wave characteristics based on cnoidal versus linear wave refraction are emphasized.

Wave Refraction Equations

Figure 1 illustrates the nomenclature and coordinate system for the wave refraction problem. The wave ray (orthogonal) travels with celerity,  $c$ , makes an angle,  $A$ , with the  $x$ -axis, and its position at a given time,  $t$ , is defined by the coordinates,  $x$ , and  $y$ . The wave ray separation factor,  $\beta$ , which is related to the refraction coefficient by  $K = \sqrt{1/\beta}$ , is also defined in Figure 1. The governing equations for wave refraction used in the model are those presented by Skovgaard et. al. (13) with time,  $t$ , as the independent variable. Wave ray paths are governed by the following equations:

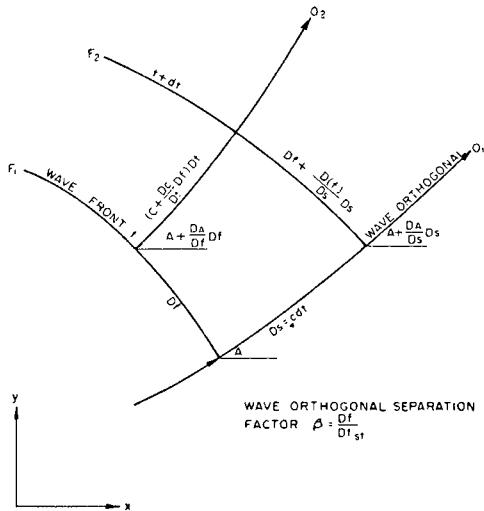


Fig. 1 Wave refraction nomenclature .

$$\dot{x} = c \cos A \quad (1)$$

$$\dot{y} = c \sin A \quad (2)$$

$$\dot{A} = \frac{dc}{dh} (h_x \sin A - h_y \cos A) \quad (3)$$

Where the subscripts on  $h$  denote a partial derivative (i.e.,  $h_x = \partial h / \partial x$ ) wave separation is determined using the following equation:

$$\ddot{\beta} + p_t \dot{\beta} + q_t \beta = 0 \quad (4)$$

where

$$p_t = -2 \frac{dc}{dh} (h_x \cos A + h_y \sin A) \quad (5)$$

$$q_t = c \frac{dc}{dh} (h_{xx} \sin^2 A - h_{xy} 2 \sin A \cos A + h_{yy} \cos^2 A) + c \frac{d^2c}{dh^2} (h_x \sin A - h_y \cos A)^2 \quad (6)$$

Equations 1 through 6 are valid for both linear and cnoidal theories (14). These equations require determination of the wave speed,  $c$ , and its first and second derivatives with water depth (i.e.,  $dc/dh$ ,  $d^2c/dh^2$ ) according to a particular wave theory. This is done readily for linear theory because one can uncouple the wave speed and wave height computations. On the other hand, the cnoidal wave speed depends on wave height and thus the wave separation factor,  $\beta$ . This complicates evaluation of the wave speed derivatives with depth because other variables such as wave height also vary with depth.

### Linear Theory

Linear theory is used when the relative depth  $d/L > .10$  or when the Ursell parameter,  $U = HL^2/h^3 < 15$ , (15,16). Equations for the linear wave celerity,  $c$ , and its derivatives with depth are as follows, (13):

$$c = \frac{gT}{2\pi} \tanh kh \quad (7)$$

$$\frac{dc}{dh} = \frac{c}{h} \frac{G}{1+G} \quad (8)$$

$$\frac{d^2c}{dh^2} = -\frac{dc}{dh} \frac{2g}{c^2 (1+G)^2} \quad (9)$$

$$G = \frac{2kh}{\sinh 2kh} \tag{10}$$

where T = wave period, h = water depth, k = wave number = 2π/L, and L = wave length. Wave heights in the linear region are computed as follows:

$$H = H_0 K_R K_S \tag{11}$$

where H = local wave height, H<sub>0</sub> = the deepwater wave height, K<sub>R</sub> = the refraction coefficient, and K<sub>S</sub> = the shoaling coefficient. The shoaling coefficient according to linear theory is as follows:

$$K_S = \sqrt{\frac{1}{\tanh(kh) (1 + G)}} \tag{12}$$

Cnoidal Theory

Cnoidal theory is used when the relative depth, d/L<sub>0</sub> <.10 and/or the Ursell parameter, U > 15. The cnoidal equations used are those reported by Svendsen and Brink-Kjaer (15). These equations represent first-order cnoidal theory.

$$c^2 = gh (1 + \frac{H}{h} A_C) \tag{13}$$

$$U = \frac{16}{3} m K^2 = \frac{HL^2}{h^3} \tag{14}$$

$$E_f = \rho g H^2 c B_C \tag{15}$$

where  $A_C = \frac{2}{m} - 1 - \frac{3E}{mK} \tag{16}$

$$B_C = \frac{1}{m^2} \left[ \frac{1}{3} (3m^2 - 5m + 2 (4m-2) \frac{E}{K}) - (1 - m - \frac{E}{K})^2 \right] \tag{17}$$

Where m = elliptic parameter, ρ = mass density of water, K = complete elliptic integral of the first kind, E = complete elliptic integral of the second kind, and E<sub>f</sub> = the wave energy flux. Wave speed derivatives dc/dh and d<sup>2</sup>c/dh<sup>2</sup> are determined by adjusting Equations 13 through 15 for refraction and combining them to give the following:



$$\lambda = c^2 - gh - gA_c E_{f0}^{1/2} B_c^{-1/2} c^{-1/2} \beta^{-1/2} = 0 \quad (18)$$

$$\begin{aligned} \Omega = E_{f0}^{-1/2} B_c^{-1/2} c^{3/2} \beta^{-1/2} - \frac{16}{3} K^2 \frac{h^3}{T^2} \\ + \frac{16}{3} m' \frac{K^2 h^3}{T^2} = 0 \end{aligned} \quad (19)$$

where  $m'$  = the complementary elliptic parameter ( $1 - m$ ) and  $E_{f0}$  is the reference value of energy flux. The first derivative of the wavespeed with depth,  $dc/dh$ , is determined by applying the chain rule to equations 18 and 19:

$$\lambda_h + \lambda_c \frac{dc}{dh} + \lambda_{m'} \frac{dm'}{dh} + \lambda_\beta \frac{d\beta}{dh} = 0 \quad (20)$$

$$\Omega_h + \Omega_c \frac{dc}{dh} + \Omega_{m'} \frac{dm'}{dh} + \Omega_\beta \frac{d\beta}{dh} = 0 \quad (21)$$

$$\text{where} \quad \frac{d\beta}{dh} = \frac{1}{c} \frac{d\beta}{dt} (h_x \cos A + h_y \sin A)^{-1} \quad (22)$$

The subscripts on  $\lambda$  and  $\Omega$  denote a partial derivative e.g.,  $\partial\lambda_h = \partial\lambda / \partial h$ . Equations 20 through 22 are solved simultaneously for  $dc/dh$ ,  $dm'/dh$  and  $d\beta/dh$ . The second derivative of wave celerity with depth,  $d^2c/dh^2$ , is determined by applying the chain rule to equations 20 and 21 to give:

$$\begin{aligned} \lambda_{hh} + 2 \lambda_{hc} \frac{dc}{dh} + \lambda_{hm'} \frac{dm'}{dh} + \lambda_{h\beta} \frac{d\beta}{dh} + \\ 2\lambda_{m'c} \frac{dc}{dh} \frac{dm'}{dh} + 2\lambda_{\beta m'} \frac{d\beta}{dh} \frac{dm'}{dh} + 2\lambda_{\beta c} \frac{dc}{dh} \frac{d\beta}{dh} \\ + \lambda_{cc} \left(\frac{dc}{dh}\right)^2 + \lambda_c \frac{d^2c}{dh^2} + \lambda_{m'm'} \left(\frac{dm'}{dh}\right) + \lambda_{m'} \frac{d^2m'}{dh^2} \\ + \lambda_{\beta\beta} \left(\frac{d\beta}{dh}\right)^2 + \lambda_\beta \frac{d^2\beta}{dh^2} = 0 \end{aligned} \quad (23)$$

$$\begin{aligned}
 &\Omega_{hh} + 2\Omega_{hc} \frac{dc}{dh} + \Omega_{hm'} \frac{dm'}{dh} + \Omega_{h\beta} \frac{d\beta}{dh} + \\
 &2\Omega_{m'c} \frac{dc}{dh} \frac{dm'}{dh} + 2\Omega_{\beta m'} \frac{dm'}{dh} \frac{d\beta}{dh} + 2\Omega_{\beta c} \frac{dc}{dh} \frac{d\beta}{dh} \\
 &+ \Omega_{cc} \left(\frac{dc}{dh}\right)^2 + \Omega_c \frac{d^2c}{dh^2} + \Omega_{m'm'} \left(\frac{dm'}{dh}\right)^2 + \Omega_{m'} \frac{d^2m'}{dh^2} \\
 &+ \Omega_{\beta\beta} \left(\frac{d\beta}{dh}\right)^2 + \Omega_{\beta} \frac{d^2\beta}{dh^2} = 0
 \end{aligned} \tag{24}$$

where

$$\frac{d^2\beta}{dh^2} = \frac{d^2\beta}{ds^2} \left(\frac{d^2h}{ds^2}\right)^{-1} \tag{25}$$

$$\begin{aligned}
 \frac{d^2\beta}{ds^2} &= \frac{1}{c^2} \frac{dc}{dh} (h_x \cos A + h_y \sin A) \frac{d\beta}{dt} - \frac{dc}{dh} \\
 &\frac{1}{c} (h_{xx} \sin^2 A + h_{xy} 2 \sin A \cos A + h_{yy} \cos^2 A) -
 \end{aligned} \tag{26}$$

$$\begin{aligned}
 &\frac{d^2c}{dh^2} \frac{1}{c} (h_x \sin A - h_y \cos A)^2 \beta \\
 \frac{d^2h}{ds^2} &= -\sin A \frac{dA}{ds} h_x + \cos A (\cos A h_{xx} + \sin A h_{xy}) \\
 &+ \cos A \frac{dA}{ds} h_y + \sin A (\cos A h_{xy} + \sin A h_{yy})
 \end{aligned} \tag{27}$$

$$\frac{dA}{ds} = \frac{1}{c} \frac{dc}{dh} (\sin A h_x - \cos A h_y) \tag{28}$$

Equations 23 through 28 are solved simultaneously for  $d^2c/dh^2$ .

Numerical Solution of the Linear and Cnoidal Equations

The linear dispersion equation (Eq. 7) is solved by the Newton-Raphson method. The cnoidal wave equations (Eq. 13 through 15) are combined to form the cnoidal shoaling equation (15):

$$M f_1 (U) + N f_2 (U) = 1 \tag{29}$$

where  $f_1 (U) = -B_c^{-2/3} U^{-1/3} A_c \tag{30}$

$$f_2 (U) = B_c^{2/3} U^{4/3} \tag{31}$$

$$M = (H_r B_r L_r)^{2/3} / h^2 \tag{32}$$

$$N = M^{-1} h/gT^2 \tag{33}$$

The reference values of  $H_r$ ,  $L_r$  and  $B_r$  may be given in deep water according to linear theory or in shallow according to cnoidal theory; the choice depends on where refraction computations are started. Eq. 29. is solved numerically using the Newton-Raphson Method. However, several precautions are necessary to ensure a proper solution. The Newton-Raphson procedure is formulated in terms of the complementary elliptic parameter,  $m'$ , instead of the elliptic parameter,  $m$ . This is necessary because, as the elliptic parameter,  $m$ , approaches 1 (i.e.,  $m'$  approaches zero), the numerical computations cannot be computed with accuracy.

The elliptic functions E and K are evaluated using the Arithmetic/Geometric Mean (AGM) scale presented in (7). The following AGM scale is used to evaluate the elliptic functions:

$$\begin{array}{lll}
 a_0 = 1 & b_0 = \sqrt{m'} & c_0 = \sqrt{1 - m'} \\
 \\
 a_1 = \frac{1}{2} (a_0 + b_0) & b_1 = \sqrt{a_0 b_0} & c_1 = \frac{1}{2} (a_0 - b_0) \\
 \text{---} & \text{---} & \text{---} \\
 \text{---} & \text{---} & \text{---} \\
 \text{---} & \text{---} & \text{---} \\
 \\
 a_N = \frac{1}{2} (a_{N-1} + b_{N-1}) & b_N = \sqrt{a_{N-1} b_{N-1}} & c_N = \frac{1}{2} (a_{N-1} - b_{N-1})
 \end{array} \tag{34}$$

The coefficients  $a_n$ ,  $b_n$ , and  $c_n$  are computed using nine steps ( $N=9$ ) which give accurate estimates (i.e.  $c_9 < 10^{-6}$ ). From the AGM scale, E and K are computed as follows:

$$K = \pi/2a_N \tag{35}$$

$$E = K(1 - \frac{1}{2} (c_0 + 2c_1 + 2^2 c_2^2 + \text{---} + 2^N c_N^2)) \tag{36}$$

A second difficulty encountered in solving the cnoidal shoaling equation by the Newton-Raphson Method is that the equation has two roots (14, 15). Skovgaard and Petersen (14) conclude that the correct root corresponds to the smallest value of  $m'$  or the highest value of  $m$ . The Newton-Raphson interaction is started at a sufficiently low value of  $m'$  (i.e.,  $m' = 1 \times 10^{-37}$ ) to assure convergence to the correct root. Iterations are continued until the value of  $m'$  is determined within an accuracy of  $1 \times 10^{-6}$ .

The cnoidal shoaling equation describes the variation of a wave of given energy flux and wave period in the cnoidal region. Originally, Svendsen and Brink-Kjaer (15) solved the cnoidal shoaling equation assuming a continuity in energy flux between linear and cnoidal theories at the matching point of  $h/L_0 = 0.10$ . However, this results in a discontinuity in wave height. Svendsen and Buhr-Hansen (16) compared the shoaling characteristics of laboratory waves to shoaling predicted by cnoidal theory and found that cnoidal theory predicted shoaling more accurately if wave height instead of wave energy is matched at  $h/L_0 = 0.10$ . This presents some difficulties for wave refraction computations because there are discontinuities at the linear-cnoidal interface not only in wave height and/or wave energy, but also in wave celerity, separation, and other variables. This problem is of secondary importance for practical applications.

Numerical Solution of the Refraction Equations

The governing equations for wave refraction (i.e. 1 through 6) are solved as an initial value problem in a manner similar to Skovgaard et. al. (13). Equation 4 for the wave separation is rewritten as two first order differential equations and the governing equations are solved as a system of ordinary differential equations:

$$\dot{Z} = \dot{\beta} \tag{37}$$

$$\dot{Z} = -p_t Z - q_t \beta \tag{38}$$

with the following initial conditions:

$$\begin{aligned} x &= x_0 \\ y &= y_0 \\ A &= A_0 \\ \beta &= \beta_0 \\ Z &= Z_0 \end{aligned} \tag{39}$$

The integration is carried out using a combination of the Runge-Kutta-Gill and Adams-Moulton methods for initial value problems.

### Evaluation of Water Depth and Water Depth Derivatives

Water depth values are stored in a bathymetry grid. The partial derivatives of water depth are computed using central difference finite difference formulas. Values of water depth (and/or its derivatives) at a point which is not on a grid point are interpolated using the following formula (4):

$$f_{i+p, j+q} = (1-p)(1-q)f_{i,j} + p(1-q)f_{i+1,j} \\ + (1-p)qf_{i,j+1} + pqf_{i+1,j+1} \quad (40)$$

where  $i$  and  $j$  denote the  $x$  and  $y$  grid point respectively, and  $p$  and  $q$  define the  $x$  and  $y$  position within a grid space and  $f$  denotes the water depth and/or one of its derivatives.

### Verification for Straight and Parallel Contours

Calculations were performed for straight and parallel bottom contours. The results were compared to analytical solutions based on Snell's Law. Snell's Law is expressed by the following:

$$\text{Ray Paths: } \frac{\sin \alpha}{c} = \text{constant} \quad (41)$$

$$\text{Ray Separation: } \beta = \frac{\cos \alpha}{\cos \alpha_0} \quad (42)$$

In the above equations  $\alpha$  = the wave ray angle with the shore normal. The bathymetry grid for the verification runs was arranged so that  $\alpha = A$  (the wave ray angle with the positive  $x$ -axis).

Problems in matching linear and cnoidal theories preclude complete verification of the model for straight and parallel contours. For this reason, the model was verified for the linear and cnoidal ranges separately. Accuracy of the linear portion of the model was similar to that reported by (4) and (13) for both Eq. 41 and Eq. 42. Typically, linear refraction computations deviated from Snell's Law results only about 1 part in 10,000 per time step for a variety of conditions.

The numerical model was tested in the cnoidal region for straight and parallel contours by using initial conditions appropriate for cnoidal theory. To avoid erroneous results accurate initial conditions must be specified; these values include:

$$x, y, A, Z, \beta \\ \text{and } c, dc/dh, d^2c/dh^2, B_c, L, h, U, H, A_c$$

The initial values for  $\beta$ , and  $Z$  are given by the following according to (13):

$$\beta = \frac{\cos \alpha}{\cos \alpha_{st}} \tag{43}$$

$$Z = \frac{\sin \alpha}{\cos \alpha_{st}} (-h_x \sin A + h_y \cos A) \frac{dc}{dh} \tag{44}$$

where  $A = \alpha$  for the test cases, and  $st$  denotes the starting value.

Figure 2 shows the bathymetry grid, initial conditions, and wave rays for both cnoidal and linear theory for one of the test runs. In general, computational accuracy is less for cnoidal theory than linear theory. Typically, the results deviate from the Snell's Law results about 5 parts in 1000 per time step. This error stems from a variety of factors such as grid size, time step, and initial wave conditions, but primarily results from round-off error in the computation of the elliptic functions and more importantly in computation of the derivatives of the elliptic functions. Effort is presently underway to improve the accuracy of these computations. In the meantime, the verification results show the numerical scheme to be adequate for engineering applications. Uncertainties in incident wave conditions, bathymetry, and subjectivity associated in bathymetric smoothing, overshadow the small round-off error present in the model.

Fig. 2 shows that the cnoidal wave rays refract less than the linear rays, (i.e. the wave ray separation is less and the nearshore wave angle is higher for the cnoidal rays). Not evident from Fig. 2 is the fact that the cnoidal rays shoal significantly higher than the linear rays. These results are summarized in Table 1 which compares the cnoidal and linear wave rays at an equal nearshore depth. The above findings are consistent with those of Skovgaard and Petersen (14) who investigated cnoidal wave refraction over straight and parallel contours. A direct comparison to Skovgaard and Petersen (14) is not possible because computations performed for this paper were started in the cnoidal region whereas the results of Skovgaard and Petersen were related to deepwater values.

Table 1. Typical Results for Straight and Parallel Contours  
Wave Characteristics at  $h = 2.5$  feet (0.76 meters)

Theory	$K_S$	$K_R$	C feet per second (meters per second)	A (degrees)	H, feet
Linear	1.32	0.793	9.06 (2.76)	34.3	0.96 (0.29)
Cnoidal	1.56	0.787	10.25 (3.12)	38.7	1.15 (0.35)

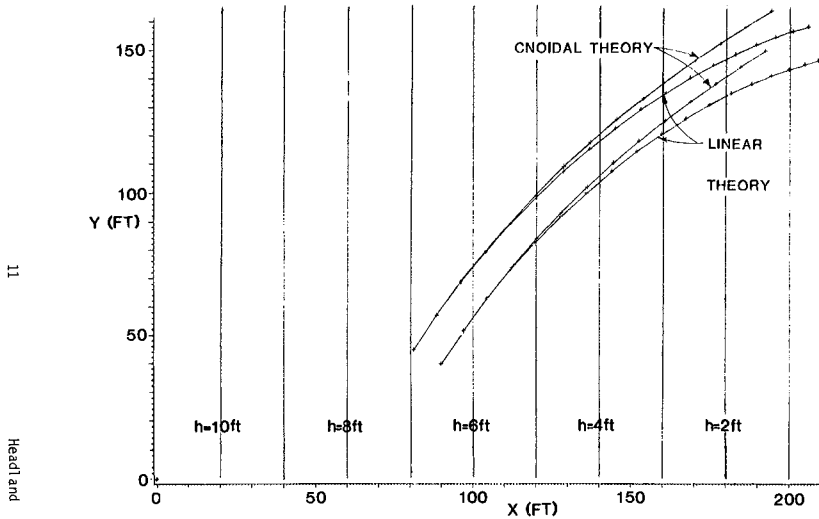


Fig. 2 Refraction over straight and parallel contours.

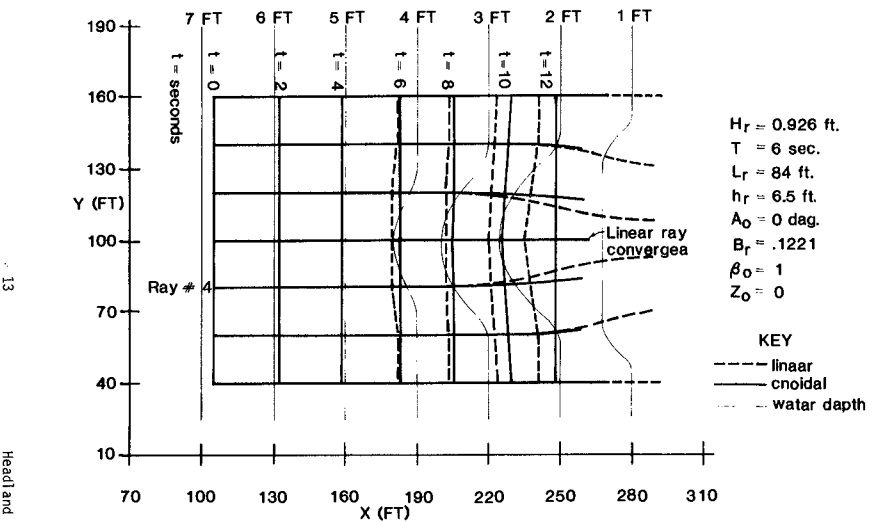


Fig. 3 Refraction over an idealized shoal.

11

Headland

13

Headland

Results For An Idealized Shoal

Refraction of cnoidal waves over an arbitrary bottom is illustrated by applying the model to an idealized shoal, similar to that used by Walker (17). The idealized shoal and bathymetry grid is shown in Fig. 3. Fig. 3 also shows the initial conditions and wave rays for a series of linear and cnoidal rays. Qualitatively, the refraction pattern for the cnoidal rays differs significantly from the linear rays as the cnoidal rays converge less over the shoal. The results are analogous to those for straight and parallel contours. Table 2 provides a comparison of linear and cnoidal results for ray number 4 at nearly equal depths. Table 2 indicates that the linear rays bend more and converge more than the cnoidal rays (i.e. higher wave angle and higher refraction coefficient). Table 2 also indicates that, despite the higher refraction coefficient for linear theory, the resulting wave height is higher for the cnoidal ray. This suggests that wave shoaling, rather than refraction, dominates the wave height growth. In summary, the cnoidal rays travel faster, propagate further, refract less, and shoal higher than linear rays.

Table 2. Typical Results For An Arbitrary Bottom

Wave Characteristics for Ray No. 4

Theory	A degrees	$\beta$	h feet (meters)	$K_s$	$K_R$	C feet per second (meters per sec.)	H, feet (meters)
Linear	8.28	0.9406	1.90 (.579)	1.42	1.031	7.75 (2.36)	1.41 (.43)
Cnoidal	3.65	0.9673	2.04 (.622)	1.85	1.017	10.38 (3.16)	1.74 (.53)

Summary

A numerical model for the refraction of linear and cnoidal waves is presented. The numerical model provides an engineering solution to the refraction of cnoidal waves. The model shows that cnoidal waves refract less and shoal higher than linear waves. Problems associated with matching linear and cnoidal theories require further research but the present model can be used until such research is available. The numerical approach is a general procedure which provides framework for incorporation of other nonlinear theories, such as third order Stokes waves in deep and intermediate water. Present effort is directed towards improving the numerical accuracy of the elliptic function and elliptic function derivatives.



The results shown in Fig. 3 for an idealized shoal are indicative of the differences between cnoidal and linear refraction for prototype applications. Clearly, nearshore waveheights based on cnoidal theory will vary considerably from those based on linear theory. This could have a considerable impact on coastal structures located in an area of divergence subjected to nonbreaking or near breaking waves. Higher nearshore wave heights and more importantly wave angles would have an impact on longshore transport calculations.

#### References

1. Abbott, M.B., Skovgaard, O., and Petersen, H.M., "On the Numerical Modelling of Short Waves in Shallow Water," *Journal of Hydraulic Research*, 16 (3), 1978.
2. Berkhoff, J.C.W., "Mathematical Models for Simple Harmonic Linear Waves; Wave Diffraction and Refraction," Delft Hydraulics Laboratory, Publication No. 163, 1976.
3. Berkhoff, J.C.W., Booy, N., and Radder, A.C., "Verification of Numerical Wave Propagation Models for Simple Harmonic Linear Water Waves," *Coastal Engineering*, Vol. 6, 1982, pp. 255-279.
4. Coudert, J. and Raichlen, F., discussion of "Wave Refraction near San Pedro Bay, California," by Yuan Jen, *Journal of the Waterways, Harbors and Coastal Engineering Division, ASCE*, Vol. 96, No. WW3, Proc. Paper 7443, Aug., 1970, pp. 737-747.
5. Crowley, J.B., Fleming, C.A., and Cooper C.K., "Computer Model for the Refraction of Nonlinear Waves," Proc. 18th Conference on Coastal Engineering, Cape Town South Africa, 1982, pp. 384-403.
6. Dean, R.G., "Evaluation and Development of Water Wave Theories for Engineering Application," Special Report No. 1, U.S. Army Corps of Engineers, Coastal Engineering Research Center, Vol. 1 and 2, 1974.
7. Goring, D.G., "Tsunamis--The Propagation of Long Waves Onto a Shelf," Report No. KH-K-83, W.M. Keck Laboratory of Hydraulics and Water Resources, California Institute of Technology, Pasadena California, 1978.
8. LeMehaute, B., and Wang, J.D., "Transformation of Monochromatic Waves from Deep to Shallow Water," U.S. Army Corps of Engineers Coastal Engineering Research Center, Technical Report No. 80-2, 1980.
9. Lillevang, O.J., Raichlen, F., Cox, J.C., and Behnke, D.L., "A Detailed Model Study of Damage to a Large Breakwater and Model Verification of Concepts for Repair and Upgraded Strength," Proc. 19th Conference on Coastal Engineering, Houston, Texas, 1984.
10. Mynet, A.E., de Voogt, W.J.P., and Schmeltz, E.J., "West Breakwater-Sines Wave Climatology," Coastal Structures Conference, Washington, D.C., 1983, pp. 17-30.
11. Munk, W.H., and Arthur, R.S., "Wave Intensity Along a Refracted Ray," *Gravity Waves*, National Bureau of Standards Circular 521, Washington, D.C., Nov., 1952, pp. 95-109.
12. Radder, A.C., "On the Parabolic Equation Method for Water Wave Propagation," *Journal of Fluid Mechanics*, 95, 1979, pp. 159-176.

13. Skovgaard, O., Jonsson, I.G., and Bertelsen, J.A.; "Computation of Wave Heights Due to Refraction and Friction," ASCE Journal of the Waterways, Harbors and Coastal Engineering Division, Vol. 101, WW1, 1975, pp. 15-32.
14. Skovgaard, O. and Petersen, M. H., "Refraction of Cnoidal Waves," Coastal Engineering, Vol. 1, 1977, pp. 43-61.
15. Svendsen, I.A., and Brink-Kjaer, O., "Shoaling of Cnoidal Waves," Proc. 13th Conf. on Coastal Engineering, Vancouver, Canada, 1972.
16. Svendsen, I.A. and Buhr-Hansen, J., "The Wave Height Variation For Regular Waves in Shoaling Water," Coastal Engineering, 1, 1977, pp. 261-284.
17. Walker, J.R., "Wave Transformations over a Sloping Bottom and over a Three Dimensional Shoal," James K.K. Look Lab. of Oceanogr. Eng., Rep., 75-11. Dept. of Ocean Eng. University of Hawaii, 1974.

## CHAPTER SEVENTY SEVEN

### EFFECTS OF OPPOSING CURRENT ON WAVE TRANSFORMATION

#### ON SLOPING SEA BED

by

Shigeki Sakai\* and Hiroshi Saeki\*\*

#### ABSTRACT

The transformation and the breaking of waves affected by an opposing current on the sloping sea bed were discussed. It was found that the characteristics of wave transformation before breaking point can be determined by the deep water wave steepness and the dimensionless unit width discharge. Concerning the wave decaying due to breaking, the characteristics of the change in the wave height depend only on the slope of the sea bed.

Fourth order solutions of Stokes wave on a uniform current were calculated based on the first and second definition of the wave celerity, respectively. The theoretical solutions for wave transformation by the energy flux method were presented. Comparisons between the theoretical solutions and the experimental results gave the criteria of the applicability of our solutions corresponding to the dimensionless unit width discharge. In the calculation of energy flux, it was pointed out that the change in the mean level of the free surface should be taken into account. It was made clear that the change in the mean level of the free surface can be evaluated by Bernoulli's equation, and the energy flux in which the change in the mean level of the free surface was taken into account was proposed.

The criteria of breaking corresponding to the dimensionless unit width discharge were clarified, experimentally.

#### 1. INTRODUCTION

The river mouth blocking is a very serious problem for coastal engineers. The goal of the study is to clarify how the sand is piled up at the river mouth by waves and currents. And for the first step to this problem, the transformation and breaking of waves affected by an opposing current on the sloping sea bed were investigated.

\* Instructor, Department of Civil Engineering, Iwate University, Morioka, Japan

\*\* Professor, Department of Civil Engineering, Hokkaido University, Sapporo, Japan

Various studies about the wave transformation without an opposing current have been presented by many researchers, and it has been clear that the characteristics of wave transformation can be determined by the slope of the sea bed and the deep water wave steepness. But no systematical experiment for the transformation of waves affected by an opposing current has been carried out.

Concerning the theoretical approach to this problem, Longuet-Higgins and Stewart(1960) and Jonsson, Skovgaard and Wang(1970) presented the attractive papers, and their treatments were the second order of approximation.

With respect to the wave breaking affected by an opposing current, Yu(1952) presented the paper about the breaking due to a current in deep water, and Iwagaki, Asano et al(1980) showed the characteristics of breaking due to a current in shallow water. Authors(1981) proposed relationships between the breaker indexes and the characteristics of wave in deep water, however an equation for criteria of breaking affected by an opposing current on the sloping sea bed has not been obtained.

In this paper, the characteristics of wave transformation was described throughout a number of experiments. Fourth order solutions of Stokes wave on a uniform current were calculated. The theoretical solutions for wave transformation by applying the energy flux method to our solutions were presented, and were compared with the experimental results to examine an applicability of our solutions. And criteria of breaking were clarified by experiments. In the calculation of the energy flux, it was pointed out that a change in a mean level of a free surface should be taken into account.

2. EXPERIMENTAL RESULTS

2-1. Experimental Equipment and Procedure

Our experiments were conducted with the general setup as shown in Fig.1. This wave channel had a length of 26m, a width of 36cm and a depth of 1m. A pump and a flap-type wave generator were located at one

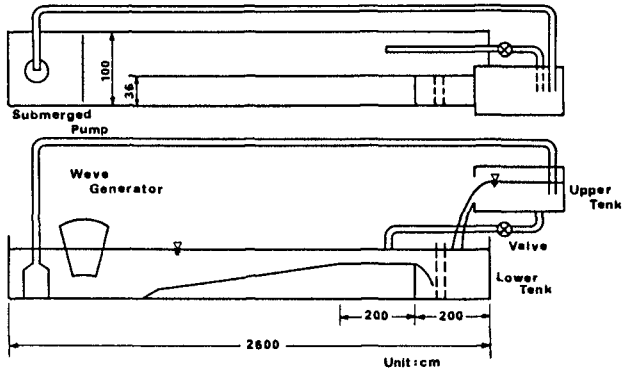


Fig.1 General setup

end of the channel. The water which was transported by the pump was received by an upper tank and the discharge was controlled in this tank by a valve. The turbulence of falling water into a lower tank was dissipated by screens in the lower tank, and the water flowed onto a sea bed as an opposing current. The slopes of the sea bed were 1/15, 1/30 and 1/50.

The water level was determined so that the hydraulic jump would not appear and the water surface on the sea bed would not be disturbed. In the experiments for wave transformation, wave profiles were measured by six wave gauges at intervals of 50cm. In the experiments for wave breaking, five wave gauges were placed at every 15cm intervals in order to measure accurately the breaking points and the wave height and wave celerity at those points. The wave period  $T$ , the wave height in deep water  $H_0$  and the unit width discharge  $q$  were varied as in Table 1.

Table 1

$T$	: 0.85 ~ 2.76	( s )
$H_0$	: 1.1 ~ 28.3	( cm )
$q$	: 100.0 ~ 790.0	( $\text{cm}^3/\text{s}/\text{cm}$ )

2-2. Wave Transformation before Breaking

It has been clear that the characteristics of wave transformation without an opposing current are determined by the slope of the sea bed  $S$  and the deep water wave steepness  $H_0/L_0$ . But when waves are affected by an opposing current, the characteristics will depend on the unit width discharge of current  $q$ . Figure 2 shows the effects of  $q$  on the shoaling coefficients. The horizontal axis gives the dimensionless water depth  $h^*$ ,  $h^*$  is  $h$  divided by  $gT^2$ , where  $h$  is a water depth,  $g$  is

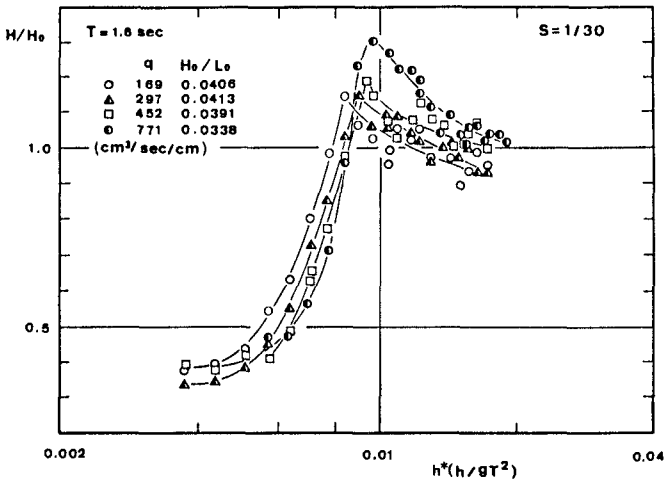


Fig.2 Effects of the unit width discharge on the shoaling coefficients

the gravity acceleration and  $T$  is a wave period. The vertical axis indicates the shoaling coefficients. In this figure, there are four kinds of data, and all of them have the same  $S$ , the same  $T$  and the almost same  $H_0/L_0$ . From this figure it is shown that a wave with a larger  $q$  has larger shoaling coefficients, in other words, the characteristics of wave transformation vary with  $q$ . Figure 3 is a comparison of the shoaling coefficients of waves which have a different  $T$ , but have the same  $S$ , the same  $q$  and the almost same  $H_0/L_0$ . This comparison gives the fact that a wave with a shorter  $T$  has larger shoaling coefficients. Consequently, it can be concluded that the effects of an opposing current on wave transformation depend not only on the unit width discharge but also on the wave period.

When a dimensionless unit width discharge as a parameter which indicates the effects of an opposing current on wave transformation is introduced as follows;

$$q^* = q / g^2 T^3 \quad \text{----- (2-1)}$$

we can arrange the data using this parameter as shown in Fig.4, and it is verified that the shoaling coefficients of waves which have the same  $S$ , the same  $H_0/L_0$  and the same  $q^*$  are identical to each other, and that waves with a larger  $H_0/L_0$  and a larger  $q^*$  have larger shoaling coefficients before breaking points.

Concerning the change of the wave length, Fig.5 shows that the change of a ratio of wave length to wave length in deep water  $L/L_0$  can be also determined by  $S$ ,  $H_0/L_0$  and  $q^*$ , and that waves with a larger  $H_0/L_0$  and a larger  $q^*$  have smaller  $L/L_0$ . Therefore, it is clear that the characteristics of wave transformation before breaking point are determined by the slope of the sea bed, the deep water wave steepness and the dimensionless unit width discharge.

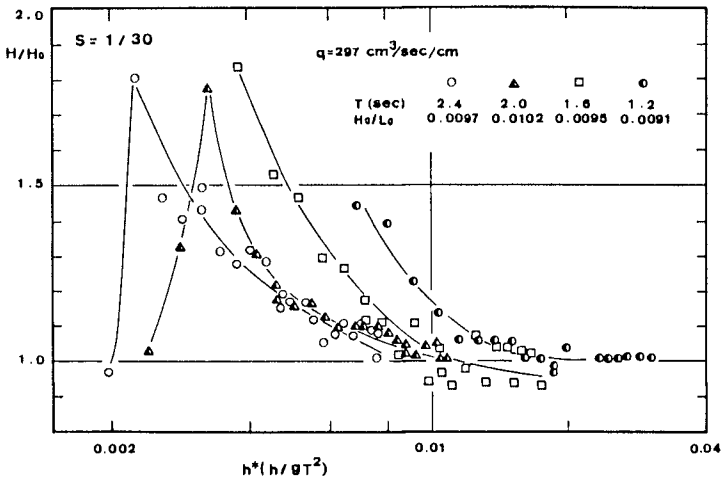


Fig.3 Effects of the wave period on the shoaling coefficients

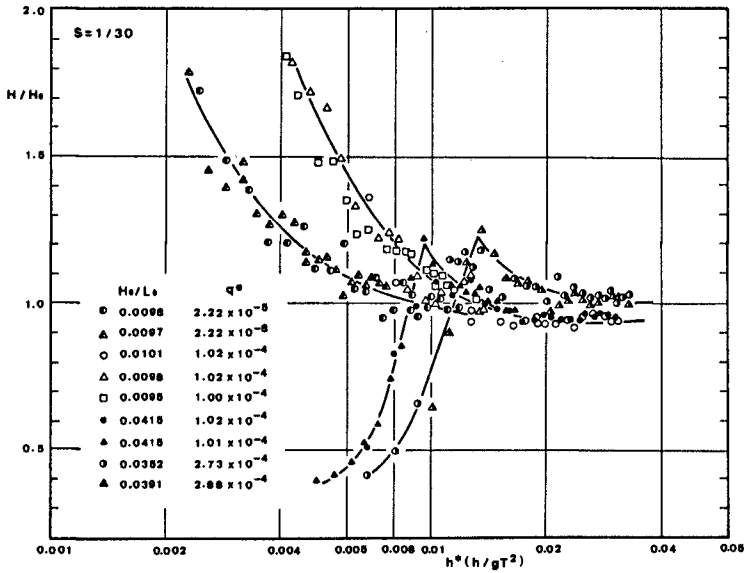


Fig.4 Effects of the dimensionless unit width discharge and the deep water wave steepness on the shoaling coefficients

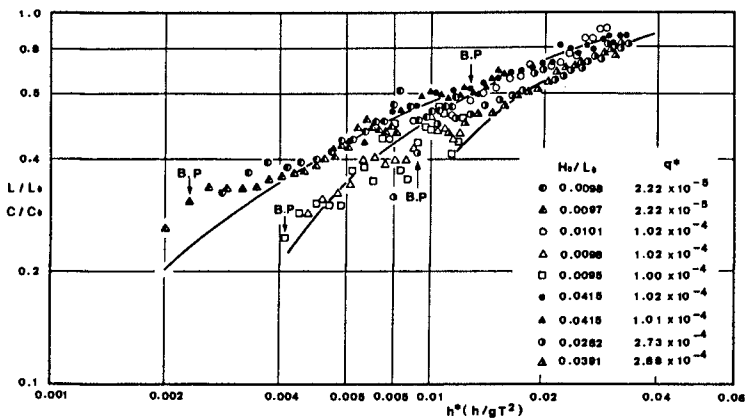


Fig.5 Effects of the dimensionless unit width discharge and the deep water wave steepness on the change of wave length

Next, the effects of the slope are examined. Figure 6 gives a comparison of the shoaling coefficients on three kinds of the slope, and all of them have the almost same  $H_0/L_0$  and the same  $q^*$ . Though the breaking depth and the breaking wave height depend on  $S$ , the shoaling coefficients before breaking points are similar to each other. Then it is found that the effects of the slope on the wave transformation before breaking points can be ignored, when the slope is between 1/15 and 1/50.

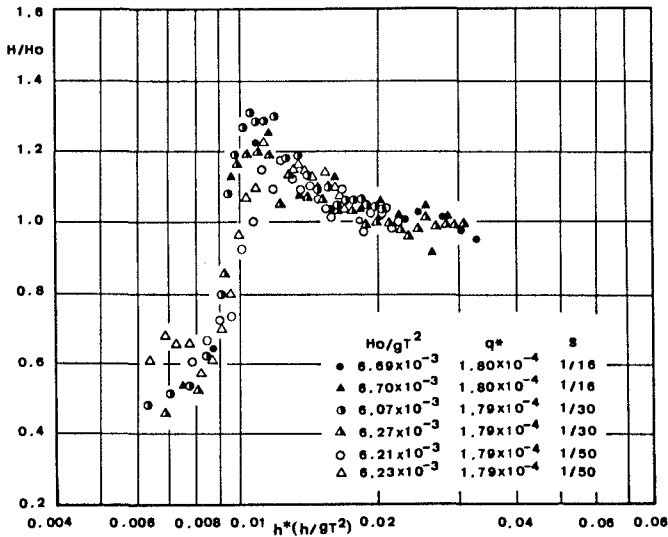


Fig.6 A comparison of the shoaling coefficients on different kinds of the slope

2-3.Wave Decaying due to Breaking

With respect to wave decaying due to the breaking, it has been clear that the changes of wave height without an opposing current depend only on the slope of the sea bed  $S$ . Though our experiments show that a ratio of wave height to water depth at the breaking point has a small influence on the change of wave height, it can be regarded as a whole that the change of wave height with an opposing current depends only on  $S$ . In Fig.7, the broken lines indicate the results without an opposing current which were presented by Saeki and Sasaki(1974), and the solid lines give our results. The decaying of wave height with an opposing current is larger than a wave without an opposing current on all kinds of the slope. And the decaying of wave height becomes milder as the slope becomes steeper. The characteristics of decaying on  $S=1/50$  is different from the other, by reason that waves on  $S=1/50$  were reformed after progressing a certain distance, and decayed by the second breaking again. This phenomenon is peculiar to waves on the mild slope.



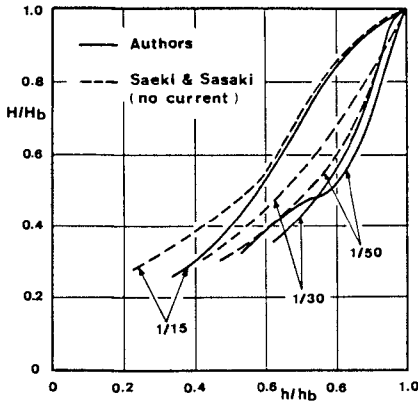


Fig.7 Effects of the current and the slope on the decaying due to the breaking

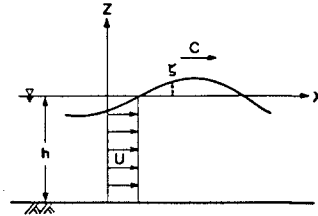


Fig.8 Coordinates system

It is remarkable that the slope is a most important parameter for wave decaying due to the breaking even when waves are affected by an opposing current, while the most important parameters for wave transformation before breaking are the deep water wave steepness and the dimensionless unit width discharge.

3. THEORETICAL APPROACH

3-1. Fourth Order Solutions of Stokes Wave on a Uniform Current

It has been pointed out that the solutions of wave theory vary with the definition of the wave celerity, by some researchers. First and second definition of the wave celerity are defined as Eqns. (3-1) and (3-2), respectively.

$$C = \int_0^L (C + u) dx / \int_0^L dx \quad \text{----- (3-1)}$$

$$C = \int_0^L \int_{-h}^{\zeta} (C + u) dz dx / \int_0^L \int_{-h}^{\zeta} dz dx \quad \text{----- (3-2)}$$

where C is a wave celerity, u is a horizontal velocity, L is a wave length, h is a water depth and zeta is a wave profile.

In the coordinates system as shown in Fig.8, Laplace's equation and the boundary conditions are expressed as follows:

$$\nabla^2 \phi = 0 \quad \text{----- (3-3)}$$

$$\phi_t + gz + \frac{1}{2} (\nabla \phi)^2 = B \quad z = \zeta \quad \text{----- (3-4)}$$

$$\phi_z - \phi_x \zeta_x - \zeta_t = 0 \quad z = \zeta \quad \text{----- (3-5)}$$

$$\phi_z = 0 \quad z = -h \quad \text{----- (3-6)}$$

where phi is a velocity potential and g is the gravity acceleration.

According to the perturbation method of the fourth order of approximation,  $\phi$ ,  $\zeta$ ,  $B$ ,  $C$  are assumed as follows:

$$\begin{aligned} \phi = & U \cdot x + (C - U) \{ \lambda^2 A_{02} + \lambda^4 A_{04} \} \cdot x \\ & + \frac{(C - U)}{k} \{ (\lambda A_{11} + \lambda^3 A_{13}) \cosh k(h+z) \sin \theta \\ & + (\lambda^2 A_{22} + \lambda^4 A_{24}) \cosh 2k(h+z) \sin 2\theta \\ & + \lambda^3 A_{33} \cosh 3k(h+z) \sin 3\theta \\ & + \lambda^4 A_{44} \cosh 4k(h+z) \sin 4\theta \} \end{aligned} \quad \text{----- (3-7)}$$

$$\begin{aligned} \zeta = & \frac{1}{k} \{ \lambda f_{11} \cos \theta + (\lambda^2 f_{22} + \lambda^4 f_{24}) \cos 2\theta \\ & + \lambda^3 f_{33} \cos 3\theta + \lambda^4 f_{44} \cos 4\theta \} \end{aligned} \quad \text{----- (3-8)}$$

$$B = B_0 + \lambda^2 B_2 + \lambda^4 B_4 \quad \text{----- (3-9)}$$

$$\{ C - U \}^2 = \{ C_0 - U \}^2 \{ 1 + \lambda^2 C_2 \} \quad \text{---- (3-10)}$$

where  $U$  is a velocity of steady uniform current,  $k=2\pi/L$ ,  $L$  is a wave length,  $\theta=k(x-Ct)$  and  $\lambda$  is an expansion parameter. After Eqns.(3-7), (3-8), (3-9) and (3-10) are substituted into Eqns.(3-3), (3-4), (3-5) and (3-6), the coefficients in  $\phi$ ,  $\zeta$ ,  $B$ ,  $C$  are finally calculated as:

$$\begin{aligned} A_{11} &= \frac{1}{s^*} \quad , \quad A_{13} = -\frac{1}{8} \frac{C^*2}{s^{*5}} \{ 5C^*2 + 1 \} - \frac{A_{02}}{s^*} \\ A_{22} &= \frac{3}{8} \frac{1}{s^{*4}} \\ A_{24} &= \frac{1}{768} \frac{1}{s^{*10}} \{ 192C^*8 - 424C^*6 - 312C^*4 + 480C^*2 - 17 \} - \frac{3}{8} \frac{A_{02}}{s^{*4}} \\ A_{33} &= -\frac{1}{64} \frac{1}{s^{*7}} \{ 4C^*2 - 13 \} \\ A_{44} &= \frac{1}{1536} \frac{1}{s^{*10}} (6C^*2 - 1) \{ 80C^*6 - 816C^*4 + 1338C^*2 - 197 \} \end{aligned} \quad \text{---- (3-11)}$$

$$\begin{aligned} f_{11} &= 1 \quad , \quad f_{22} = \frac{1}{4} \frac{C^*}{s^{*3}} \{ 2C^*2 + 1 \} \\ f_{24} &= \frac{1}{384} \frac{1}{s^{*9}} \{ 272C^*9 - 504C^*7 - 192C^*5 + 322C^*3 + 21C^* \} \\ f_{33} &= \frac{3}{64} \frac{1}{s^{*6}} \{ 8C^*6 + 1 \} \\ f_{44} &= \frac{1}{384} \frac{1}{s^{*9}} (6C^*2 - 1) \{ 768C^*11 - 448C^*9 - 48C^*7 + 48C^*5 \\ & \quad + 106C^*3 - 21C^* \} \end{aligned} \quad \text{---- (3-12)}$$

$$\begin{aligned} B_0 &= \frac{U^2}{2} \quad , \quad B_2 = \frac{g}{4k} \frac{1}{s^* C^*} + U \{ C_0 - U \} A_{02} \\ B_4 &= -\frac{g}{64} \frac{1}{k} \frac{1}{s^{*7} C^*} \{ 4C^*6 + 16C^*4 - 38C^*2 + 9 \} \\ & \quad + \frac{1}{16} U \{ C_0 - U \} \frac{1}{s^{*4}} \{ 8C^*4 - 8C^*2 + 9 \} A_{02} \\ & \quad + \frac{1}{2} \{ C_0^2 - U^2 \} A_{02}^2 + U \{ C_0 - U \} A_{04} \end{aligned} \quad \text{---- (3-13)}$$

$$\begin{aligned} \{ C_0 - U \}^2 &= \frac{g}{k} \tanh kh \\ C_2 &= \frac{1}{8} \frac{1}{s^{*4}} \{ 8c^{*4} - 8c^{*2} + 9 \} + 2 A_{02} \end{aligned} \quad \text{---- (3-14)}$$

where  $c^* = \cosh kh$ ,  $s^* = \sinh kh$ .

And a relationship between  $\lambda$  and a wave steepness is as follows:

$$\frac{H}{L} = \frac{1}{\pi} \left\{ \lambda + \frac{3}{64} \lambda^3 \frac{1}{s^{*6}} ( 8c^{*6} + 1 ) \right\} \quad \text{---- (3-15)}$$

Applying the first definition of the wave celerity expressed by Eqn. (3-1), the coefficients  $A_{02}$  and  $A_{04}$  become as:

$$A_{02} = A_{04} = 0 \quad \text{---- (3-16)}$$

The coefficients based on the second definition are calculated as:

$$\begin{aligned} A_{02} &= - \frac{1}{2} \frac{c^*}{kh s^*} \\ A_{04} &= \frac{1}{32} \frac{c^*}{kh s^{*7}} \{ 4c^{*6} - 20c^{*4} + 16c^{*2} - 9 \} - A_{02}^2 \end{aligned} \quad \text{---- (3-17)}$$

### 3-2. Change in Mean Level of Free Surface

In order to calculate a wave transformation by using our solutions of Stokes wave on a uniform current, the energy flux method is applied.

As regard with the energy flux of a wave on a uniform current, Eqn. (3-18) which was presented by Longuet-Higgins and Stewart (1960) is well known.

$$R_x = ECg + EU + SxU + \frac{1}{2} \rho h U'^3 \quad \text{---- (3-18)}$$

This equation was derived from the following equation.

$$R_x = \int_{-h}^{\zeta} \left\{ p + \frac{1}{2} \rho u^2 + \rho g z \right\} u dz \quad \text{---- (3-19)}$$

where  $u = U + u'$ ,  $U$  is a velocity of a steady uniform current,  $u'$  is a horizontal velocity of wave motion,  $u^2 = u'^2 + v^2$ ,  $v$  is a vertical velocity,  $p$  is a pressure and  $\rho$  is a density of fluid. In their derivation, a mean level of a free surface was set on an origin of Z-axis, then a potential energy  $gz$  was measured from the mean level of the free surface. When energy fluxes expressed by Eqn. (3-18) are compared at various water depth and current, and if the mean level of the free surface change depending on the water depth and the current, the change in the mean level of the free surface results in the change of the basis of the potential energy. Therefore Eqn. (3-18) can not be applied directly to calculate the transformation of wave progressing over varying depth.

Jonsson, Skovgaard and Wang (1970) introduced a conception named "mean energy level", from which the potential energy was measured. They took the change in the mean level of the free surface into account, and indicated that the conservation of the energy flux of wave on a non-uniform current should be expressed as follows:

$$\frac{d}{dx} \left\{ \left( 1 + \frac{U}{C} \right) ( U + Cg ) E \right\} = 0 \quad \text{---- (3-20)}$$

This equation is effective for the second order of approximation.

In order to apply fourth order solutions of Stokes wave on a uniform current to calculate the wave transformation on non-uniform current with varying depth, some more consideration about the change in the mean level of the free surface is needed. For this purpose, we use Bernoulli's equation as:

$$\phi_t + \frac{p}{\rho} + gz + \frac{1}{2} (\nabla\phi)^2 = c(t) \quad \text{---- (3-21)}$$

In the derivation of our solutions, the mean level of the free surface was set on the origin of the Z-axis, and the potential energy was measured from this origin of the Z-axis, in other words from the mean level of the free surface. When this coordinate is named Z'-axis, Bernoulli's equation with respect to such coordinates system is expressed as follows:

$$\phi'_t + \frac{p'}{\rho} + gz' + \frac{1}{2} (\nabla\phi')^2 = B' \quad \text{---- (3-22)}$$

B' has a value particular to the basis of the potential energy besides a water depth, a wave height and a wave length. Now, we define that the origin of Z-axis and the basis of the potential energy are set on the mean level of the free surface in deep water, and that Δh is a difference between the origin of Z-axis and the Z'-axis which was used for the derivation of wave solutions in an arbitrary water depth, as shown in Fig.9. When Z'-axis is transformed like Eqn.(3-23), Eqn.(3-22) becomes as follows:

$$z = z' - \Delta h \quad \text{---- (3-23)}$$

$$\begin{aligned} \phi_t + \frac{p}{\rho} + gz + \frac{1}{2} (\nabla\phi)^2 = c(t) = B' \text{ deep} \\ = B' - g\Delta h \quad \text{---- (3-24)} \end{aligned}$$

Because Bernoulli's equation is satisfied over all region of water depth, and B' in deep water calculated by Stokes wave theory vanishes, a relationship between B' and Δh is verified as:

$$\Delta h = B'/g \quad \text{---- (3-25)}$$

Therefore it becomes clear that B'/g calculated with respect to the Z'-axis is identical to the change in the mean level of the free surface. Using Eqn.(3-24) and (3-23), the energy flux can be calculated as:

$$W = -\rho \int_{-h}^{\zeta} \phi_t \cdot \phi_x dz = -\rho \int_{-h}^{\zeta'} \phi'_t \cdot \phi'_x dz' \quad \text{---- (3-26)}$$

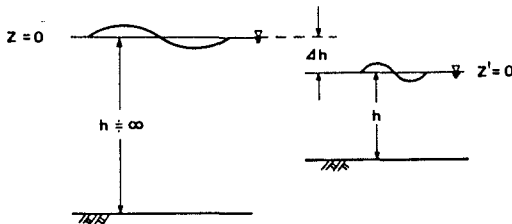


Fig.9 Coordinates systems and Δh

Thus, we can obtain the energy flux in which the change in the mean level of the free surface is taken into account, by using the velocity potential  $\phi'$  described with respect to  $Z'$ -axis.

If Airy wave theory is applied to Eqn.(3-26), the energy flux is identical to that in Eqn.(3-20) by Jonsson, Skovgaard and Wang. And if the second order theory is used for Eqn.(3-25), the change in the mean level of the free surface is identical to the wave set-down due to radiation stress given by Longuet-Higgins and Stewart(1964). And our treatment about the change in the mean level of the free surface is more general.

Substituting our fourth order solutions into Eqn.(3-26), the energy flux  $W$  are finally calculated as

First definition;

$$W = \rho \frac{C}{k} \{ U \cdot (C-U) \cdot Q_{11} + (C-U)^2 \cdot Q_{12} \} \quad \text{---- (3-27)}$$

where

$$Q_{11} = \lambda^2 \frac{1}{s^{*2}} \left\{ \frac{1}{2} s^* c^* + \frac{\lambda^2}{32} \frac{c^*}{s^{*5}} (-4c^{*6} + 20c^{*4} - 16c^{*2} + 9) \right\}$$

$$Q_{12} = \lambda^2 \frac{1}{s^{*2}} \left[ \frac{1}{4} (s^* c^* + kh) + \frac{\lambda^2}{8} \left\{ \frac{1}{8s^{*6}} (s^* c^* + kh) \cdot \right. \right.$$

$$\left. \left. (-20c^{*6} + 16c^{*4} + 4c^{*2} + 9) \right. \right.$$

$$\left. \left. + \frac{c^*}{4s^{*3}} (16c^{*4} + 2c^{*2} + 9) \right\} \right]$$

Second definition;

$$W = \rho \frac{C}{k} \{ U \cdot (C-U) \cdot kh \cdot Q_{21} + (C-U)^2 \cdot Q_{22} \} \quad \text{---- (3-28)}$$

$$Q_{21} = \lambda^2 \left[ \frac{1}{2} \frac{c^*}{kh s^*} - \lambda^2 \left\{ \frac{C-U}{U} \frac{1}{4} \frac{c^{*2}}{(kh)^2 s^{*2}} \right. \right.$$

$$\left. \left. + \frac{1}{32} \frac{c^*}{kh s^{*7}} (4c^{*6} - 20c^{*4} + 16c^{*2} - 9) \right. \right.$$

$$\left. \left. - \frac{1}{4} \frac{c^{*2}}{(kh)^2 s^{*2}} \right\} \right]$$

$$Q_{22} = \lambda^2 \frac{1}{s^{*2}} \left[ \frac{1}{4} (s^* c^* + kh) + \frac{\lambda^2}{8} \left\{ \frac{c^{*3}}{2s^{*3}} (2c^{*2} + 1) \right. \right.$$

$$\left. \left. + 3 s^* c^* + \frac{3}{s^{*3}} (2c^{*2} - 1) \right. \right.$$

$$\left. \left. + \left( 2 \frac{c^*}{s^*} \frac{1}{kh} - \frac{c^{*2}}{2s^{*4}} (5c^{*2} + 1) \right) (s^* c^* + kh) \right. \right.$$

$$\left. \left. + \frac{9}{8} \frac{1}{s^{*6}} ((2c^{*2} - 1) s^* c^* + kh) \right\} \right]$$

### 3-3. Applicability of Solutions

In order to examine an applicability of the theoretical solutions of wave transformation calculated by our solutions, the theoretical solutions are compared with the experimental results. Figure 10 is an example of the comparison between the experimental results and the theoretical solution based on the first definition of the wave celerity. The theoretical solution illustrated as a solid line agrees with the

experimental results from deep water to the breaking points. Thus, the solution can be regarded as a fairly good approximation. In some cases, the theoretical solutions have larger values than the experimental results in the region of shallow water, and the difference becomes larger as the dimensionless water depth  $h^*$  becomes smaller. And it seems that the extent of  $h^*$  in which the theoretical solution is applicable depend on a parameter  $H_0/gT^2$ , which means the deep water wave steepness, and the dimensionless unit width discharge  $q^*$ .

We took points where the experimental result intercepts with a range of  $\pm 5\%$  of the theoretical solution, and defined criteria of the applicability. Figures 11 and 12 show relationships between a ratio of water depth to wave length  $h/L$  and a ratio of wave height to wave length  $H/L$  at the criteria of the applicability of the solutions based on the first and second definition of the wave celerity, respectively. In these figures, the results for all kinds of the slopes are included, and classified by  $q^*$ . The average lines corresponding to a similar  $q^*$  can be drawn as shown as the solid lines in Fig.11 and 12.

The effects of  $H_0/gT^2$  on the criteria were examined, and the effects could be ignored compared with the effects of  $q^*$ .

Then, it was found that the criteria of the applicability of the theoretical solutions depend on  $q^*$ , and the extent of the applicability based on the first definition of the wave celerity is wider than the extent based on the second definition with larger  $q^*$ .

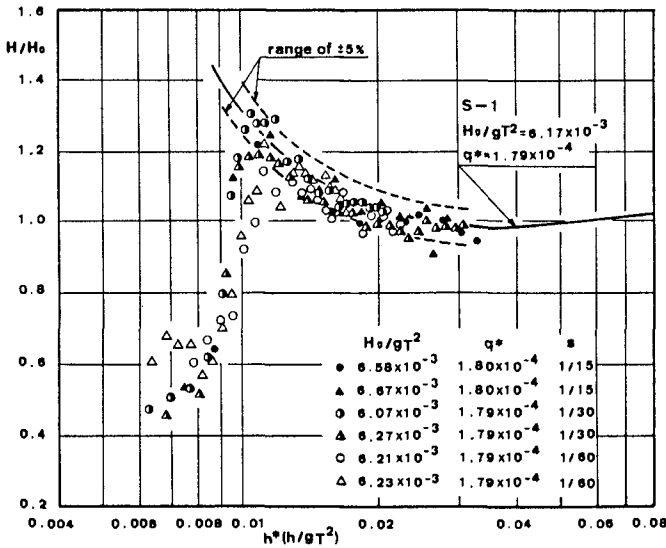


Fig.10 A comparison between experimental results and a theoretical solution based on the first definition of the wave celerity

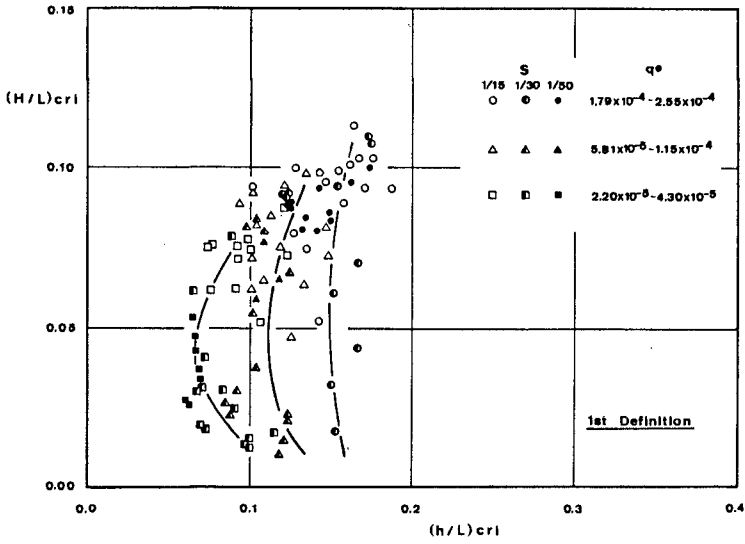


Fig.11 Criteria of the applicability of solutions based on the first definition of the wave celerity

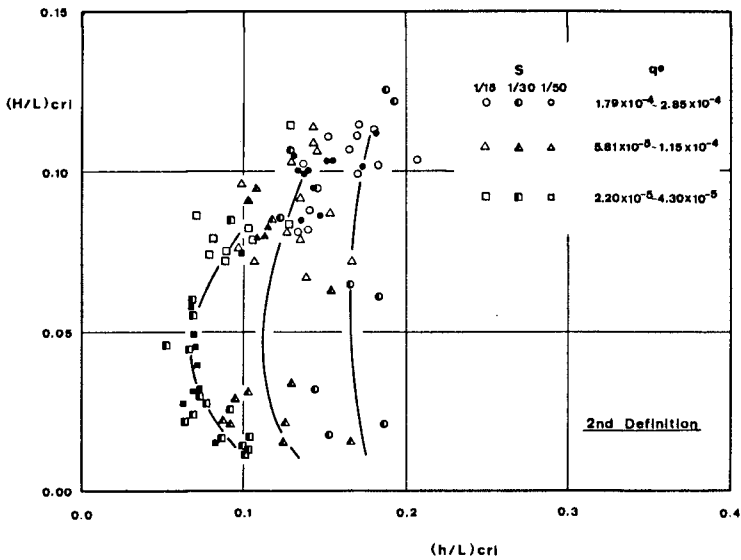


Fig.12 Criteria of the applicability of solutions based on the second definition of the wave celerity

Next, the applicability of the theoretical solutions for the change of wave length is examined. Figure 13 is a comparison between the experimental results and the theoretical solutions. L, S-1 and S-2 indicate the solution by Airy wave theory, our solution of Stokes wave theory based on the first definition of the wave celerity and our solution based on the second definition, respectively. Figure 13 shows that L and S-2 are good approximations for the experimental results in deep water, and S-1 and S-2 are good in shallow water. Therefore it is concluded that S-2 is a best approximation, as a whole, for the change of the wave length on an opposing current.

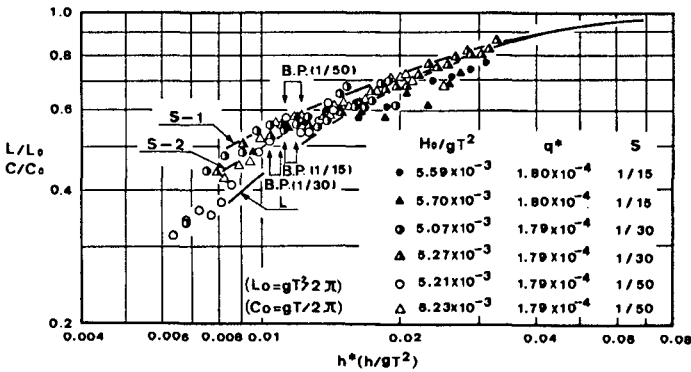


Fig.13 A comparison between experimental results and theoretical solutions for changes of wave length

4. CRITERIA OF BREAKING

In order to clarify the criteria of breaking on an opposing current, relationships between a ratio of wave height to wave length  $(H/L)_b$  and a ratio of water depth to wave length  $(h/L)_b$  at breaking points are shown in Fig.14. The experimental results are classified by the dimensionless unit width discharge  $q^*$ . S-1 and S-2 indicate theoretical criteria of breaking calculated by applying Rankine-Stokes' breaking condition to our fourth order solutions. The theoretical criteria give larger values than the experimental results. This disagreement can be explained by the fact that the theoretical breaking depth is shallower and the theoretical breaking wave height is larger than the experimental results, even when the theoretical wave transformation before breaking point agrees with the experimental results, as shown in Fig.10.

The theoretical criteria shows a relationship like as :

$$\left(\frac{H}{L}\right)_b = \alpha \tanh\left(\frac{2\pi h}{L}\right)_b \quad \text{---- (4-1)}$$

Iwagaki, Asano, Yamanaka and Nagai presented that Miche's equation which is expressed as Eqn.(4-2) was a relatively good approximation for wave breaking due to the current on a flat bed.



$$\left(\frac{H}{L}\right)_b = 0.142 \tanh\left(\frac{2\pi h}{L}\right)_b \quad \text{----- (4-2)}$$

While Miche's equation agrees with our results for no current and smaller  $q^*$ , this equation shows an upper limit of the experimental results, and in particular this can not approximate experimental results for larger  $q^*$ .

Experimental results show that one average line can be drawn as a whole, but the difference of the relationship due to  $q^*$  can be recognized. We assumed that Eqn.(4-1) expresses criteria of breaking affected by an opposing current on a sloping sea bed, and we obtained the proportional coefficient  $\alpha$  corresponding to  $q^*$  as shown in Fig.15. When  $q^*$  is small,  $\alpha$  is similar to Miche's coefficient, and as  $q^*$  becomes larger,  $\alpha$  becomes smaller than Miche's coefficient and approaches a certain value gradually.

By the experimental results and the theoretical approaches, the criteria of the applicability of our solutions on an opposing current and the criteria of wave breaking corresponding to each  $q^*$  are found in Fig.16.

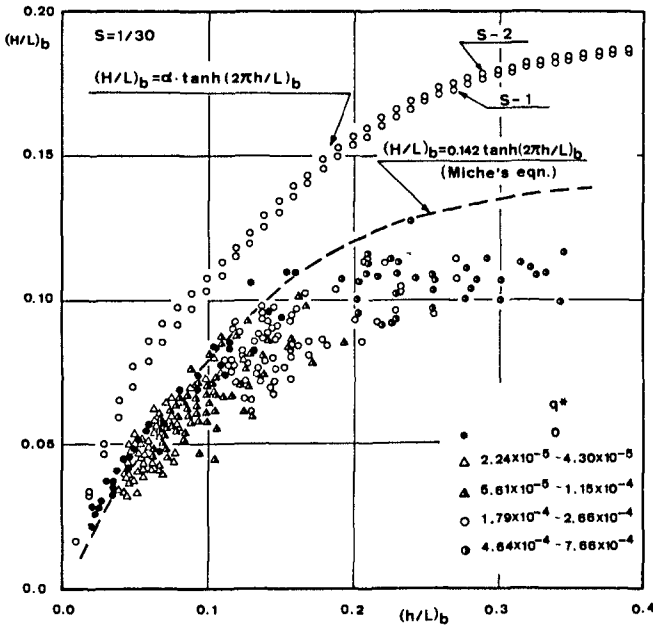


Fig.14 Relationships between a ratio of wave height to wave length and a ratio of water depth to wave length at breaking point

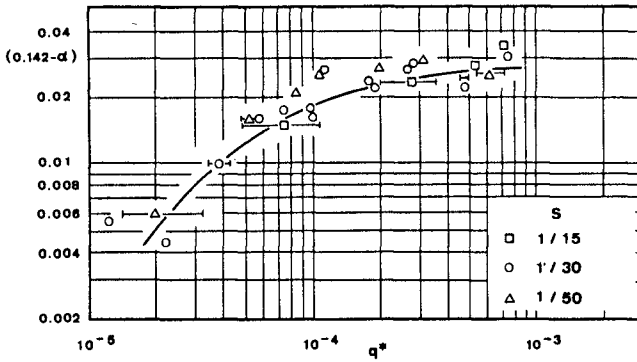


Fig.15 Relationships between  $\alpha$  and  $q^*$

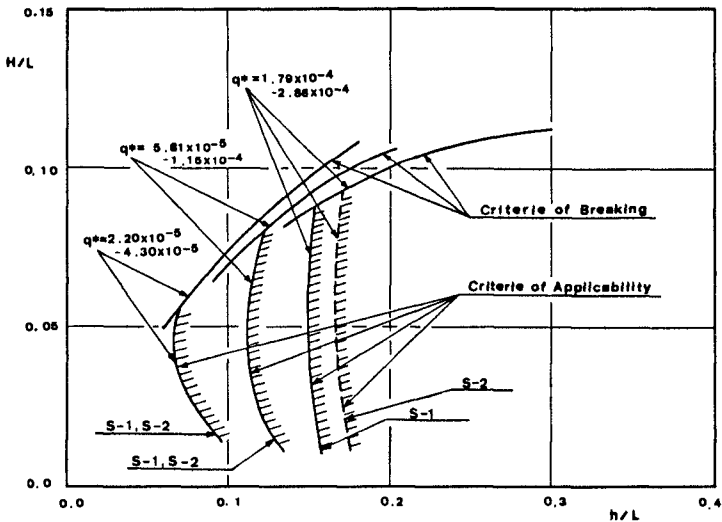


Fig.16 Criteria of the applicability of theoretical solutions and criteria of the breaking, corresponding to  $q^*$

5. CONCLUSIONS

The transformation and breaking of waves affected by an opposing current on a sloping sea bed were discussed, experimentally and theoretically. Main conclusions in this paper are as follows:

- (1) The characteristics of wave transformation before breaking points can be determined by  $H_0/gT^2$  and  $q^*$ . Waves with larger  $H_0/gT^2$  and larger  $q^*$  have larger  $H/H_0$  and smaller  $L/L_0$ .

- (2) Wave decaying due to breaking depends only on the slope of the sea bed. Wave height decaying with an opposing current is larger than the decaying without an opposing current for all kinds of the slope, and it becomes milder as the slope becomes steeper.
- (3) The solutions of Stokes wave on a uniform current were calculated based on the first and second definition of the wave celerity, respectively.
- (4) It was clarified that the change in the mean level of the free surface due to the variation of the water depth and the current can be evaluated by Bernoulli's equation, and the energy flux in which the change in the mean level of the free surface are taken into account was presented.
- (5) Comparisons between the theoretical solutions for wave transformation and the experimental results yielded the criteria of applicability of our solutions, corresponding to each  $q^*$ .
- (6) The criteria of wave breaking corresponding to  $q^*$  were proposed, experimentally.

## REFERENCES

- Iwagaki, Y., T. Asano, T. Yamanaka and F. Nagai(1980): Fundamental study on breaking of waves due to currents ( in Japanese ), Proc. of 27th J.C.C.E., pp. 30-34.
- Jonsson, I.C., C. Skovgaard and J.D. Wang(1970): Interaction between waves and currents, Proc. of 12th I.C.C.E., pp. 489-507.
- Saeki, H and M. Sasaki(1974): Study on wave transformation after breaking ( in Japanese ), Proc. of 21st J.C.C.E., pp. 39-44.
- Sakai, S., N. Otsuka, H. Saeki and A. Ozaki(1981): Interaction between finite amplitude waves and opposing current on sloping sea bed, International Symposium on Hydrodynamics in Ocean Engineering, Vol.1, pp. 367-391.
- Tsuchiya, Y. and M. Yamaguchi(1972): Some considerations on water particle velocities of finite amplitude wave theories, Coastal Engineering in Japan, Vol.15, pp. 43-57.
- Longuet-Higgins, M.S. and R.W. Stewart(1960): Changes in the form of short gravity waves on long waves and tidal currents, J.F.M., Vol.8, pp. 565-583.
- Longuet-Higgins, M.S. and R.W. Stewart(1964): Radiation stresses in water waves; a physical discussion, with applications, Deep-sea Res., Vol.2, pp. 529-562.
- Yu, Y.Y.(1952): Breaking of waves by an opposing current, Trans. A.C.U., Vol.33, No.1, pp. 39-41.

## CHAPTER SEVENTY EIGHT

### Measurements of Mass Transport over a Rough Bed

by J.F.A. Sleath\*

Measurements have been made with a laser doppler anemometer of the time-mean velocity of the fluid close to the bed in a wave flume. Both a rough bed, consisting of gravel of median diameter 11 mm, and a smooth bed were investigated. With the rough bed the time-mean velocity at a given height was found to be strongly dependent on position relative to prominent roughness elements. At one point the time-mean drift at a given height might be in the direction of wave propagation while, at another, in the opposite direction. Significant variation in time-mean drift with horizontal position was observed at all values of Reynolds number tested. The effect of bed roughness on the average value of the time-mean velocity at a given height was found to be most marked at low Reynolds numbers: the maximum near bed value with this gravel bed was about 3 times that for a smooth bed at the lowest Reynolds numbers tested. At the highest Reynolds numbers there was no clear difference between the rough and smooth bed values even though the boundary layer over the rough bed was fully turbulent whereas that over the smooth bed was laminar. However, at these high Reynolds numbers both the rough and the smooth beds showed a reduction in drift velocity below that predicted by Longuet-Higgins (9) because of the increased importance of higher harmonics in the flow.

#### INTRODUCTION

It is well known that water waves induce a steady drift of fluid particles in addition to an oscillatory motion. Although this steady drift, which is usually referred to as the 'mass transport' velocity, is weak compared with the oscillatory component of velocity it has a significant effect on the dispersion of pollutants in the sea. It is also important in any study of the transport of sediment, particularly in the onshore-offshore direction.

Despite its engineering importance, rather little is known about the mass transport velocity under the sort of conditions encountered on site. Longuet-Higgins (9) has obtained a theoretical solution for the mass transport produced by waves over a smooth bed in laminar flow. Laboratory tests (e.g. ref. 2) show that for smooth beds and constant depth there is good agreement between theory and experiment in the boundary layer at the bed provided allowance is made for higher harmonics under more extreme wave conditions (see refs. 4, 11). However, most beds on site are far from smooth and the flow is usually turbulent. Longuet-Higgins (10) suggested that the mass transport velocity just outside the boundary layer would be the same in turbulent flow as for laminar flow. On the other hand, Johns (5) calculated that the maximum

\* Lecturer, Cambridge University Engineering Department, Trumpington Street, Cambridge, England

value of the time-mean component of the Eulerian velocity in a turbulent boundary layer was less than half that for laminar flow.

It might seem that all that would be required to settle this question would be a few well-chosen experiments. The problem is that the observation of dye traces or neutrally buoyant beads, which is the method traditionally used for laminar flows, is not reliable in turbulent flows. When the flow is turbulent dye traces are rapidly diffused and neutrally buoyant beads are hurled from one fluid layer to another so that their final displacement is the result of velocities at many different heights. Some rough bed measurements were made by Brebner et al (1) using dye traces and neutrally buoyant beads. These suggested that the mass transport velocity was increased by bed roughness when the flow was laminar but decreased when the flow was turbulent. However, for the reasons outlined above there is clearly a need to confirm and extend these tests using some other measuring technique. In addition, since Brebner et al's tests could not extend far into the turbulent regime, there is a need for tests with significantly higher levels of turbulence.

The objectives of the present work were thus to make new measurements of the drift velocity, using a different method from that of Brebner et al, and to study flows in which the boundary layer really was fully turbulent.

#### EXPERIMENTAL APPARATUS AND LAYOUT

The experiments were carried out in the 17.5 m wave flume of the Cambridge University Engineering Department. This wave flume is 0.58 m wide internally, has a flap type wave generator at one end and a pebble beach at a slope of 1:20 at the other. The test section is of constant depth and approximately 9 m long.

The test conditions are shown in Table 1. In this Table  $T$  is period,  $H$  is wave height,  $d$  is mean water depth,  $\theta$  is water temperature,  $k$  is wave number and  $a$  is the theoretical value of the orbital amplitude of the fluid just outside the boundary layer at the bed. Both  $k$  and  $a$  have been calculated from first-order small-amplitude wave theory. For the larger wave heights and smaller values of  $kd$  this small-amplitude theory is not a good approximation and consequently the quoted values should be treated with caution. In no test did wave breaking occur in the test section.

Most of the tests were carried out with a single layer of gravel of median diameter 11.0 mm and  $\phi$ -standard deviation 0.14 spread uniformly over the bed for a distance of 8 m near the middle of the flume. However, for purposes of comparison, a number of tests were carried out with a smooth bed. This consisted of a sheet of plate glass of length 3 m backed up at each end by steel sheets, each of length 2 m, with a gloss paint finish.

The fluid velocities were measured with a laser doppler anemometer mounted on a milling machine base so that it could be traversed vertically and horizontally. The anemometer consisted of a 5 mW Helium Neon laser with DISA optics and frequency shifter and either a Cambridge

Test No.	T (sec.)	H (mm)	d (mm)	$\theta$ ( $^{\circ}$ C)	kd	$(\bar{u})_{\max}$ (m/s)	a (mm)
smooth bed							
1	1.79	82	336	12.8	0.699	8.0	54
2	1.89	94	372	12.9	0.696	2.0	62
3	1.84	42	366	21.2	0.711	-0.46	27
4	1.87	88	366	21.0	0.698	7.4	58
5	0.99	14	375	12.8	1.66	0.18	2.8
6	0.96	12	373	12.4	1.75	0.13	2.1
7	0.96	113	365	21.5	1.71	-1.4	21
8	0.95	47	366	20.3	1.73	2.2	8.7
rough bed							
9	1.74	29	334	12.6	0.697	0.80	19
10	1.88	38	334	13.4	0.659	2.6	27
11	1.92	85	334	13.7	0.643	2.6	62
12	1.90	77	333	14.0	0.650	2.6	55
13	1.86	73	333	14.8	0.665	-3.0	51
14	1.92	92	333	13.0	0.644	-1.8	67
15	0.98	72	364	12.0	1.64	10.5	14
16	0.97	109	364	12.5	1.69	11.1	21
17	0.98	26	364	12.9	1.64	1.7	5.2
18	0.98	89	358	12.0	1.62	9.1	18
19	0.96	60	359	11.2	1.68	3.6	12
20	0.98	28	333	12.2	1.55	2.4	6.2
21	0.99	22	362	14.3	1.62	1.5	4.5
22	0.96	15	362	15.1	1.69	0.50	2.8
23	0.98	52	362	15.3	1.65	5.8	10
24	0.97	11	361	14.1	1.66	0.40	2.1
25	0.93	115	330	20.7	1.65	-2.2	23
26	0.94	11	331	20.6	1.63	0.46	2.4
27	0.97	55	331	21.0	1.56	10.3	12
28	0.96	85	193	22.9	1.07	-2.7	33
29	0.97	29	194	13.5	1.06	4.5	11

Table 1. Test conditions

Consultants or a DISA frequency tracker. Apart from the different frequency shifter the system and mode of operation were the same as that described by Du Toit & Sleath (3). Most of the measurements were made with the Cambridge Consultants tracker but occasionally the DISA tracker was used as a check. Analogue output from the frequency tracker was stored on an FM instrumentation tape recorder and subsequently re-played via an analogue-to-digital converter into a computer for analysis. With the aid of a phase marker, recorded at the same time as the anemometer output, the computer calculated the mean velocity over 60 wave cycles. The velocity harmonics for the mean cycle obtained by superimposing the 60 individual cycles and the root-mean-square fluctuation in velocity from the mean cycle were also calculated. Each channel from the tape recorder was sampled 400 times per wave cycle.

Calibration of this equipment was carried out in two ways. First of all, the frequency trackers were checked at intervals during the test programme by feeding sinusoidal signals of known frequency from a signal generator into the input terminal and measuring the output with a digital voltmeter. This provided a check on the frequency/voltage conversion factor quoted by the manufacturers and also on the stability and linearity of these instruments. Secondly, with still water in the wave flume but sufficient seeding particles in the measuring volume to provide a reasonable signal, the output from the trackers was recorded with a variety of known voltage offsets provided by a variable voltage source. These recordings were then analysed by the computer in the normal way. This allowed the conversion factor between tracker voltage and computer output to be determined as well as the zero corresponding to no flow. This second calibration was also repeated at intervals throughout the test programme.

Measurements were also made of the wave reflection from the beach and of the three-dimensionality of flow in the flume. In none of the tests did the reflected wave height exceed 3% of the incident wave height. Significant three-dimensionality of the time-mean drift was observed very close to the walls of the flume and also in the body of the flow near the water surface. However, in the immediate vicinity of the bed three-dimensionality was negligible for the smooth bed over most of the width of the flume. For the rough bed, any variation across the flume in the vicinity of the bed was insignificant compared with the much larger perturbations caused by the individual roughness elements.

The normal test procedure was for the still water level to be measured, the laser switched on and then the wave generator started up at the required stroke and frequency. After approximately one hour the water temperature was recorded, the wave period was measured with a stopwatch, and the wave height with hook and pointer gauges which were removed from the water as soon as the measurement had been made. Next the required velocity measurements were made. Finally, wave height, period and water temperature were measured again and the wave generator and laser were switched off. All electronic equipment other than the laser was left running continuously day and night. Normally only one test was carried out each day in order to ensure that no residual drifts remained from previous tests. Seeding of the flow was provided by adding small quantities of milk as required.

## TEST RESULTS AND DISCUSSION

Fig. 1 shows a comparison between the amplitude of the measured and theoretical velocities  $U_{\infty}$  just outside the boundary layer at the bed. In addition to the tests listed in Table 1, Fig. 1 also includes results for a number of preliminary tests in which drift velocity was not measured. The quantity  $(U_{\infty})_{\text{meas}}$  is the amplitude of the fundamental component of velocity obtained by Fourier analysis of the velocity record and the 'theoretical' velocity  $(U_{\infty})_{\text{theor}}$  is that calculated from first-order small-amplitude wave theory for the given test conditions. On the whole, the agreement between theory and experiment is quite good. The main reason for discrepancy is that, as pointed out above, many of the waves are not well represented by small-amplitude theory.

Bed roughness also introduces uncertainties into any comparison between theory and experiment. With very coarse roughness, as in the present case, the boundary layer is no longer negligibly thin compared with the depth of water. Thus a velocity measured outside the boundary layer is too far from the bed to be equal to the theoretical bed velocity whereas, closer to the bed boundary layer and bed geometry effects may be significant.

The effect of bed geometry is particularly important for the drift velocity. Fig. 2 shows an example of the way in which the time-mean velocity varies with distance across the flume at various heights above the grain crests. According to Kamphuis (7), the Nikuradse roughness length  $k_s$  is equal to  $2D_{90}$ . In the present case that would give a roughness length of 24.5 mm. This is comparable with the lateral distance between peaks in the drift velocity shown in Fig. 2. In fact, it was observed that the time-mean velocity in the direction of wave propagation was strongest in the troughs between roughness elements and decreased as the measuring point approached a protruding grain. This is not surprising since it is well known that individual roughness elements on the bed set up their own re-circulating drift currents which can significantly alter the mean drift produced by wave action.

If the perturbation in drift velocity is associated with individual roughness elements it should decay at large distances from the bed like  $\exp(-2\pi y/k_s)$  with  $k_s = 25.4$  mm in the present case. Fig. 3 shows the way in which the perturbation  $\bar{u}'$  varies with height at three positions (A,B,C) across the wave flume in two different tests. In each case the amplitude of the perturbation at height  $y$  has been normalised in terms of its value at the level of the grain crests ( $y = 0$ ). The experimental points in Fig. 3 do seem to be tending towards the predicted curve at large values of  $y$ .

Another example of the way in which the perturbation in velocity decays with height is shown in Fig. 4. In this Figure,  $x$  is the horizontal distance from the centreline of the flume. It is clear that only a small shift in horizontal position can produce a dramatic change in the measured time-mean velocity  $\bar{u}$ .

In many situations it is the mean drift velocity, averaged across the wave flume, which is of most interest. Fig. 5 shows how the



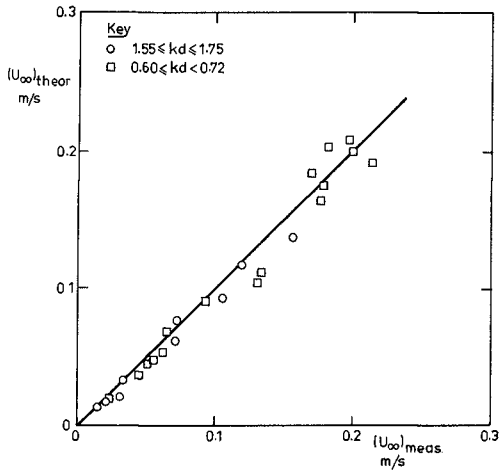


Fig. 1 Comparison of measured and theoretical values of the velocity amplitude just outside the boundary layer

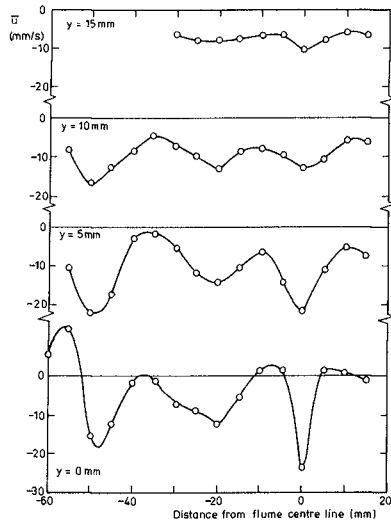


Fig. 2 Variation of the time-mean velocity in the direction of wave propagation with position across the wave flume and height  $y$  above the bed (Test no. 25)

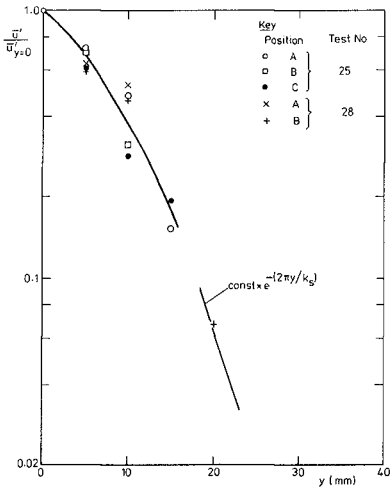


Fig. 3 Variation of perturbation in drift velocity with height for Tests 25 and 28

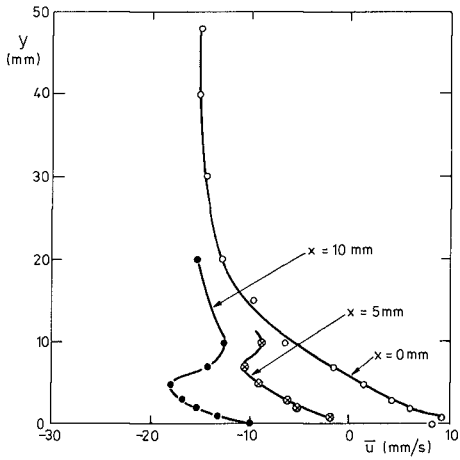


Fig. 4 Variation of the time-mean velocity  $\bar{u}$  with height  $y$  at three positions across the flume (Test no. 13)

spatial-mean value of  $\bar{u}$  at the level of the grain crests varies with the ratio of fluid orbital amplitude  $a$  to grain size  $D$  for the rough bed. In each case the spatial-mean value of  $\bar{u}$  at the level of the grain crests was also the maximum measured value of this mean drift in the direction of wave propagation, which is why it is denoted by  $\bar{u}_{\max}$  in Fig. 5 (and also in Table 1). It is possible that the mean velocity in the troughs between crests might be even higher but even with the laser tilted at an angle to the horizontal detailed measurements could not be made much below the mean crest level so it was not possible to investigate this point. Also shown in Fig. 5 are the smooth bed results, for which  $D$  should be interpreted as a numerical constant equal to 11.0 mm. For the smooth beds it was, of course, possible to determine the actual maximum value of  $\bar{u}$  in the direction of wave propagation.

At first sight the results shown in Fig. 5 are somewhat confusing. This is because the drift velocity is affected both by the bed roughness and by wave harmonics. Collins (2) found that for a smooth bed the mass transport velocity was reduced from Longuet-Higgins' theoretical value when wave conditions became severe. Sleath (11) and Isaacson (4) have shown that this reduction is due to the effect of higher harmonics on the solution (Longuet-Higgins' theory is only a first approximation). Thus, in assessing the effect of bed roughness it is necessary to compare the rough bed results with those for the smooth bed under similar conditions. When this is done, we see that for values of  $a/D$  less than about 1.5 bottom roughness increases  $\bar{u}_{\max}$  whereas at large values of  $a/D$  there is little difference between the results for rough and smooth beds.

A possible reason for the increase in the mean drift velocity at low values of  $a/D$  is the effect of wave asymmetry on the formation of vortices by individual roughness elements on the bed. If vortices were formed more vigorously during one half cycle than during the other some change in the mean drift might be expected. The reduced effect at high  $a/D$  may be attributed to less clearly defined vortex formation with increasing turbulence and the relatively smaller influence of wave asymmetry when well away from the conditions at which vortices only just form. The parameter  $a/D$  is proportional to the Keulegan Carpenter number  $Kc$ . It is well known that force coefficients for isolated bodies in oscillatory flow are strongly dependent on  $Kc$  at low values of this parameter but relatively independent at high  $Kc$ . This behaviour is usually attributed to the effect of vortex formation.

Fig. 5 shows results for two quite different values of  $kd$ . This is because the existing equipment did not allow a very wide range of  $a/D$  to be covered at a single value of  $kd$ . Low values of  $a/D$  were inaccessible at  $kd \approx 0.7$  because the waves became too small for meaningful measurements whereas at  $kd \approx 1.7$  wave breaking prevented the investigation of large  $a/D$ . It should be borne in mind that the effect of wave harmonics on  $\bar{u}_{\max}/(U_{\infty}^2 k/\omega)$  is different for different values of  $kd$  and consequently the two sets of points do not necessarily follow the same curve when plotted against  $a/D$ . However, in both cases the smooth bed results should tend to  $\bar{u}_{\max}/(U_{\infty}^2 k/\omega) = 0.87$  in the limit as  $a/D$  tends to zero. Fig. 5 shows that this is the case, at least for the  $kd \approx 1.7$  results.

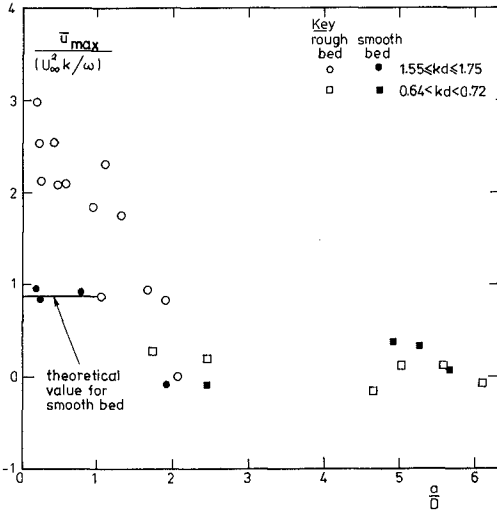


Fig. 5 Variation of the maximum value of the mean drift velocity with  $a/D$ . (For the smooth bed tests take  $D = 11.0$  mm)

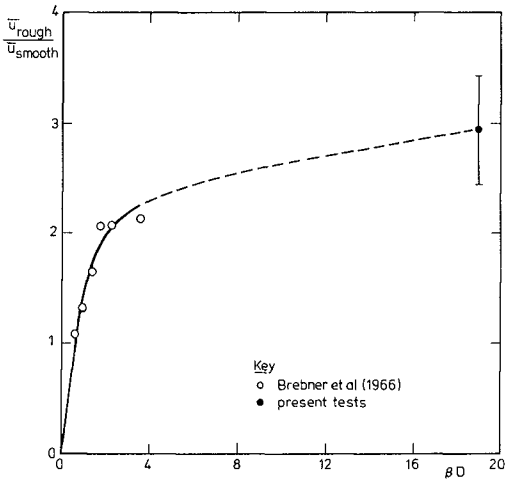


Fig. 6 Comparison of the maximum drift velocity measured for rough beds in the limit as  $a/D \rightarrow 0$  with that for smooth beds under similar wave conditions

Various criteria for transition to turbulence over rough beds have been put forward. For example, Kajiura (1968) suggested that the process of transition to turbulence begins when  $U_{\infty} D/\nu$  exceeds 104 and that the flow is fully turbulent when  $U_{\infty} D/\nu$  exceeds 1000. For the present bed roughness and wave conditions this would mean that fully developed turbulence occurred with the rough bed for  $a/D > 1.3$  when  $kd \doteq 1.7$  and  $a/D > 2.4$  when  $kd \doteq 0.7$ . The first signs of turbulence would be apparent with the rough bed for  $a/D > 0.13$  when  $kd \doteq 1.7$  and  $a/D > 0.25$  when  $kd \doteq 0.7$ . Although it is possible to argue about the exact limits for transition to turbulence it is clear that at the larger values of  $a/D$  in Fig. 5 the boundary layer over the rough bed would certainly be fully turbulent. In fact, observations with dye traces showed significant dispersion in all of the rough bed tests.

As mentioned above, the fluctuation in velocity from the average cycle obtained by superimposing the 60 recorded cycles was also calculated. The variation in the root-mean-square value of this fluctuation was qualitatively similar to that described by Kemp & Simons (8). However, background noise was too great for more detailed study.

#### COMPARISON WITH OTHER RESULTS

As far as the writer is aware, the only published measurements of the effect of bed roughness on the mass transport velocity are those of Brebner et al (1). At low values of  $a/D$  they also observed that bed roughness tended to increase the maximum forward drift near the bed. Fig. 6 shows the ratio of the maximum drift velocity measured for the rough bed in the limit as  $a/D \rightarrow 0$  to that for a smooth bed under the same wave conditions. It should be emphasised that since Brebner et al's tests were carried out with dye and neutrally buoyant beads they refer to the Lagrangian velocity whereas the present measurements were of the Eulerian velocity. Consequently the results are not directly comparable even though the appropriate expression was used for the smooth bed velocity in each case. Nevertheless it is clear that the present results are not inconsistent with those of Brebner et al in the limit as  $a/D \rightarrow 0$ . In Fig. 6,  $\beta$  is equal to  $(\omega/2\nu)^{1/2}$ . Thus  $\beta D$  is a measure of the ratio of bed roughness size to viscous boundary layer thickness.

At high values of  $a/D$  Brebner et al observed the mass transport velocity over their rough beds to be less than that given by Longuet-Higgins' (9) theory. However, Collins (2) also observed a similar reduction with smooth beds in the same wave flume under equivalent conditions. Once again, these results are not inconsistent with what was observed in the present tests.

Finally, it is of interest to compare the present findings with the predictions of Longuet-Higgins (10) and Johns (5) for turbulent boundary layers. In each case the theory assumes a fully turbulent boundary layer so that the comparison ought to be with the test results at large  $a/D$ . Under these conditions the present measurements show no clear difference between the spatial-mean values for the rough bed tests, for which the boundary layer was fully turbulent, and those for the smooth bed, for which the flow was laminar. The test results would thus seem to support Longuet-Higgins' suggestion that turbulence does not affect the value of the drift velocity at the outer edge of the boundary layer.

However, because of the experimental scatter and because the drift velocity at large  $a/D$  is relatively weak (because of the effect of higher harmonics) Johns' prediction of a reduction in drift due to turbulence cannot be totally excluded.

#### CONCLUSIONS

The laser doppler anemometer measurements of the drift velocity in a wave flume with rough and smooth beds show the following results:

(1) over a rough bed the time-mean velocity at a given height is critically dependent on position relative to prominent roughness elements on the surface of the bed. At one point the mean drift may be in the direction of wave propagation while, at another, in the opposite direction. These perturbations were found to be significant close to the bed for all values of  $a/D$  tested. They do, however, decrease with height above the bed.

(2) If the time-mean drift at a given height is averaged across the wave flume it is found that bed roughness produces a significant increase in the maximum drift velocity near the bed at small values of  $a/D$ . At large values of  $a/D$  there was no clear difference between the maximum mean drift velocities above rough and smooth beds even though the boundary layer was fully turbulent for the rough bed and laminar for the smooth bed.

#### REFERENCES

- 1 Brebner, A., Askew, J.A. & Law, S.W. Effect of roughness on mass transport of gravity waves. Proc. 10th Conference on Coastal Eng. Tokyo, pp.175-184, 1966
- 2 Collins, J.I. Inception of turbulence at the bed under periodic gravity waves. J. Geophys. Res. Vol. 68, No. 21, pp.6007-6014, 1963
- 3 Du Toit, C.G. & Sleath, J.F.A. Velocity measurements close to rippled beds in oscillatory flow. J. Fluid Mech. Vol. 112, pp.71-96, 1981
- 4 Isaacson, M. The second approximation to mass transport in Cnoidal waves. J. Fluid Mech. Vol. 78, pp.445-457, 1976
- 5 Johns, B. Residual flow and boundary shear stress in the turbulent bottom layer beneath waves. J. Physical Oceanography, Vol. 7, pp.733-738, 1977
- 6 Kajiura, K. A model of the bottom boundary layer in water waves. Bull. Earthquake Res. Inst., Vol. 46, pp.75-123, 1968
- 7 Kamphuis, J.W. Friction factors under oscillatory waves. Proc. ASCE, J. Waterway Harbor & Coastal Eng. Div. Vol. 101, No. WW2, pp.135-144, 1975

- 8 Kemp, P.H. & Simons, R.R. The interaction between waves and a turbulent current: waves propagating with the current. *J. Fluid Mech.* Vol. 116, pp.227-250, 1982
- 9 Longuet-Higgins, M.S. Mass transport in water waves. *Phil. Trans. Roy. Soc. Series A*, No. 903, Vol. 245, pp.535-581, 1953
- 10 Longuet-Higgins, M.A. The mechanics of the boundary layer near the bottom in a progressive wave. *Proc. 6th Conference on Coastal Eng. Miami*, pp.184-193, 1957
- 11 Sleath, J.F.A. A second approximation to mass transport by water waves. *J. Marine Research*, Vol. 30, No. 3, pp.295-304, 1972.

## CHAPTER SEVENTY NINE

### NEAR BOTTOM VELOCITIES IN WAVES WITH A CURRENT; ANALYTICAL AND NUMERICAL COMPUTATIONS

W.G.M. van Kesteren<sup>1)</sup> <sup>by</sup> and W.T. Bakker<sup>2)</sup>

#### ABSTRACT

In this paper, starting from the Prandtl hypothesis a three-dimensional numerical bottom boundary layer model has been developed, which allows to calculate bottom friction by a combination of waves and currents. The model has been compared with two-dimensional analytical computations which gave similar results. The bottom friction values found are comparable to the ones, found by Lundgren (1972), however in the most relevant cases somewhat less. Furthermore in the two-dimensional case the model has been compared with measurements of Bakker and Van Doorn (1978). With respect to the oscillatory motion, still some minor deviations occur between theory and measurements, due to deficiencies of the Prandtl theory.

#### 1 Introduction

Investigation of the bottom boundary layer is primary of importance because it reveals the stirring mechanism of the sand in the surf zone. This is one of the most important factors, determining the sand transport in the surf zone and therefore coastal erosion and sedimentation.

Furthermore, the boundary layer determines the bottom friction and therefore the velocity of, for instance, the longshore current and the wave energy loss.

From the present paper may be expected:

- . insight in the internal flow field, when waves and currents make an angle with each other;
- . insight in the turbulent viscosity;
- . a formula for bottom friction for waves and currents, making an angle with each other.

For this, the old, well-known Prandtl mixing-length theory is used.

From the data, presented by Bakker and Van Doorn (1978) it appears, that this theory overestimates the turbulent viscosity in the higher layers somewhat. Figure 1 shows a characteristic set of velocity profiles as measured by Van Doorn and as presented according to the Prandtl hypothesis. The general picture tallies, but the overshoot in reality is somewhat larger than theory predicts.

- 1) Project engineer, Delft Hydraulics Laboratory, the Netherlands (formerly: Delft University of Technology, the Netherlands).
- 2) Principal scientific officer Delft University of Technology; Scientific Coordinator Coastal Research of the Ministry of Transport and Public Works - Rijkswaterstaat.



2 Instantaneous velocity field

Assuming uniform flow in horizontal direction and the Prandtl/Von Karman hypothesis for the shear stress in Appendix A an equation is developed for the intrusion of the shear stress into the fluid:

$$\frac{\partial \tau}{\partial t} = \underline{\underline{S}} v_t \frac{\partial \tau}{\partial z^2} \quad (1) \quad \text{wherein: } v_t = \kappa z \sqrt{|\underline{\underline{I}}|/\rho} \quad (2)$$

Here  $\tau$  stands for the shear stress with components  $(\tau_x, \tau_y)$ ,  $x$  and  $z$  are the horizontal and vertical coordinate respectively,  $t$  = the time,  $\rho$  = the specific density,  $v_t$  the turbulent viscosity,  $\kappa$  = the Von Karman constant, and  $\underline{\underline{S}}$  a second-order tensor, specified in Eq. (A9).

Eq. (1) is analogous to the famous diffusivity equation, where the viscosity  $\nu$  replaces the turbulent viscosity, and in which  $\underline{\underline{S}}$  can be omitted. Tensor  $\underline{\underline{S}}$  accounts for the difference in direction between  $\partial \tau / \partial t$  and  $\partial^2 \tau / \partial z^2$ .

Furthermore, in appendix A an equation (A11), similar to (1) for the defect velocity  $\underline{u}_d$  has been derived; the defect velocity is the difference  $\underline{u} - \underline{U}$  between the velocity  $\underline{U}$  far from the bottom and the local velocity  $\underline{u}$  in the boundary layer (Fig. A1). This equation (A11) is solved numerically. Figure 1 gives a solution for the two-dimensional case, compared with data of Bakker and Van Doorn (1978). It shows, that the Prandtl hypothesis overestimates the turbulent viscosity in the higher layers somewhat. The general picture tallies, but the overshoot in reality is somewhat more than the theory predicts. Figure 2 shows the standard deviation (theory compared with measurements) as function of the height above the bottom. The figure demonstrates, that the present model is more accurate than the one, presented in 1978 (Bakker and Van Doorn), mainly because the upper boundary can be fulfilled without approximation.

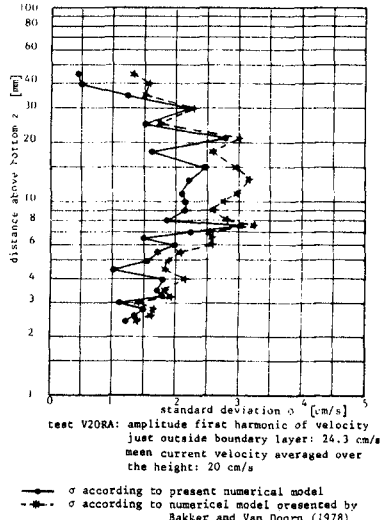
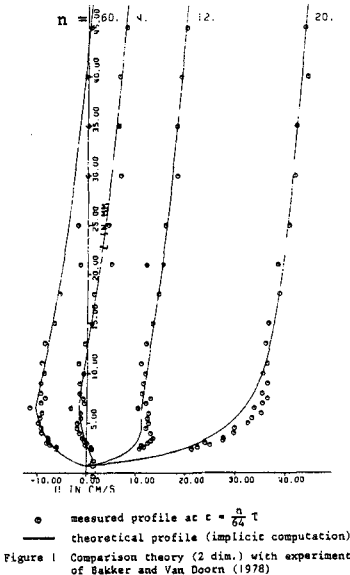


Figure 1 Comparison theory (2 dim.) with experiment of Bakker and Van Doorn (1978)

Figure 2 Standard deviation between numerical theory and experiment of Bakker and Van Doorn (1978)

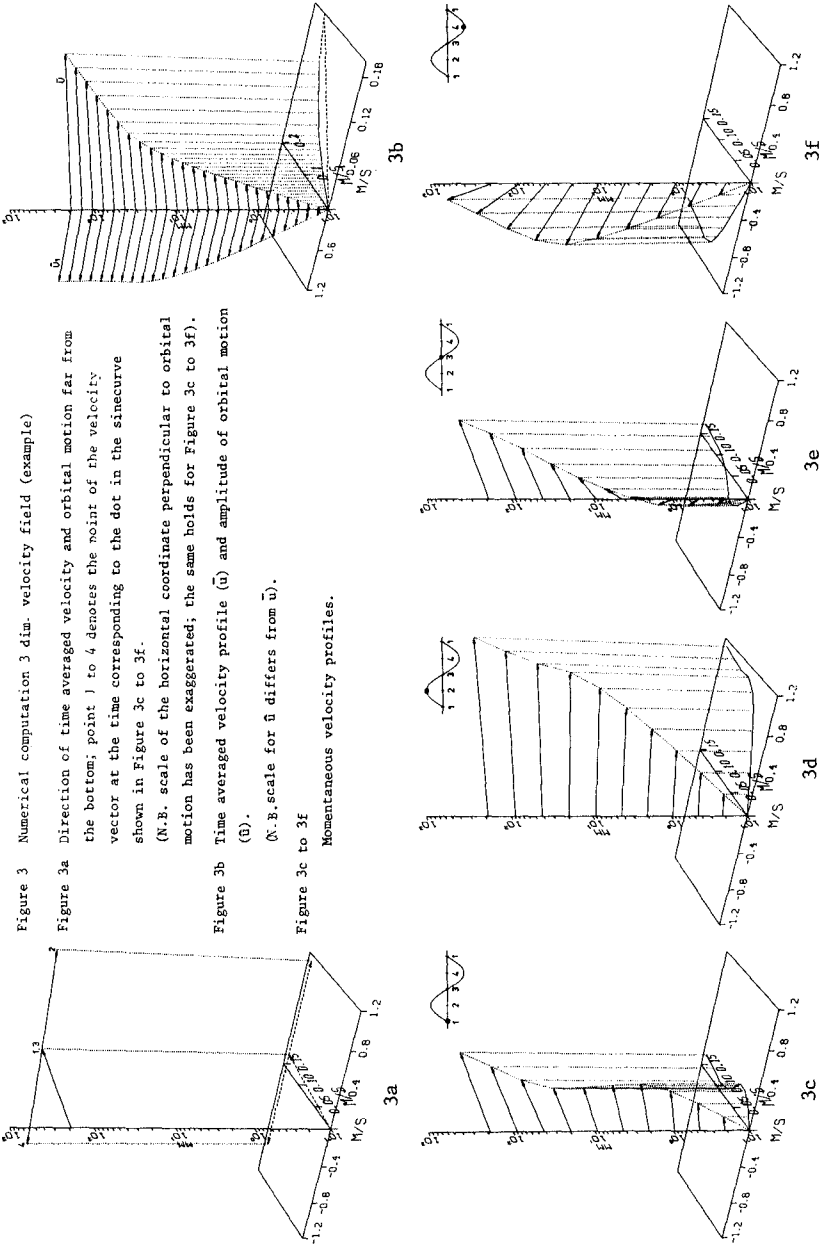


Figure 3 Numerical computation 3 dim. velocity field (example)

Figure 3a Direction of time averaged velocity and orbital motion far from the bottom; point 1 to 4 denotes the point of the velocity vector at the time corresponding to the dot in the sinecurve shown in Figure 3c to 3f.

(N.B. scale of the horizontal coordinate perpendicular to orbital motion has been exaggerated, the same holds for Figure 3c to 3f).  
Figure 3b Time averaged velocity profile ( $\bar{u}$ ) and amplitude of orbital motion ( $\bar{v}$ ).

(N.B. scale for  $\bar{v}$  differs from  $\bar{u}$ ).

Figure 3c to 3f Momentaneous velocity profiles.

Figure 3 shows the solution in a three-dimensional case.

In Figure 3a the direction of the current far from the bottom is equal to the direction of the pressure gradient. The direction of the orbital motion is given by the points 1, 2 etc., representing the point of the current vector far from the bottom at successive times,  $1/4$  wave period apart. Figure 3c to 3f show these velocity profiles for 4 successive times. All the vectors are in a horizontal plane; the direction changes when going from upward to downward. In Figure 3b the resulting profile for the mean velocity and the amplitude of the first harmonic are shown. From this figure it appears that the direction of the mean velocity near the bottom differs considerable from the direction of the mean velocity outside the boundary layer, which asymptotically approaches the direction of the mean pressure gradient, or, which is the same, the mean shear stress. This effect should be taken into account in cases with for instance sandtransport near the bottom. The kink in the mean velocity profile will be treated in the next chapter.

Similar to the viscous boundary layer a unique relation can be expected in the turbulent case between horizontal velocity just outside the boundary layer and the shear stress acting on the bottom. However when the Prandtl hypothesis is used for determining the turbulent shear stresses in terms of the local velocity field it appears from analytical considerations (Appendix B) and numerical computations that only a unique relation can be obtained when the shear stress velocity  $p_b$  is used instead of the shear stress near the bottom  $\tau_b$ . The shear stress velocity  $p$  in the three dimensional case is defined as:

$$\underline{\tau} = \rho \underline{p} |\underline{p}| \quad (5)$$

The shear stress velocity can be expressed in terms of the local velocity field according to the Prandtl hypothesis (see Appendix B):

$$p = \kappa z \frac{\partial u}{\partial z} \quad (6)$$

The relation (5) has been treated more elaborate in Appendix B in order to make analytical computations of the instantaneous velocity field by linearizing Eq. (1) (see Appendix B) and of the time-averaged velocity field (see next chapter).

The amplitude of the first harmonic of the shear stress velocity  $\hat{p}_b$  at the bottom is related to the amplitude of the first harmonic of the oscillation  $\hat{U}$  far from the bottom. For moderate currents<sup>1)</sup> (time-averaged shear stress  $\bar{\tau}$  smaller than  $0.01 \rho \hat{U}^2$ ) there exists a unique relation between  $\hat{p}_b/\hat{U}$  and the ratio strouhalength  $a$  ( $= \hat{U}T/2\pi$  where  $T$  is the wave period) over bottom roughness  $r$ , which is shown in Figure 4 and can be approximated by:

$$\frac{\hat{p}_b}{\hat{U}} = \exp \left[ \sum_{n=0}^3 k_n \{\ln(a/r)\}^n \right] \quad (7)$$

wherein:  $k_0 = -1.092$ ;  $k_1 = -.3364$ ;  $k_2 = +.01876$ ;  $k_3 = -4.621 \cdot 10^{-4}$   
Using  $\hat{p}_b$  as basis for mathematical modeling, Figure 5 represents a dimensionless plot of the amplitude and phase of the first harmonic of the defect velocity  $\hat{u}_d^*$  ( $= \hat{u}_d/\hat{p}_b$ ) as function of the dimensionless

1) For larger currents is referred to Appendix B.

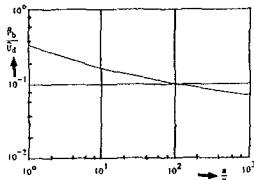


Figure 4 Relation between  $\hat{p}_b/\hat{U}$  and  $a/r$

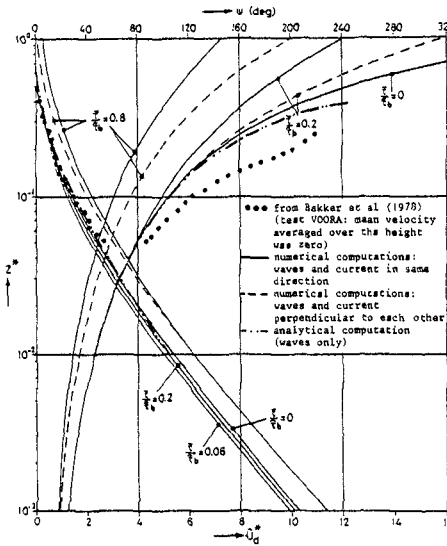


Figure 5 Dimensionless amplitude and phase of the defect velocity

height  $z^*$  above the bottom; here the height  $z$  above the bottom has been made dimensionless with a characteristic height  $Z$ , which refers to the intrusion depth of the instantaneous shear stresses i.e. the boundary layer thickness coherent with the oscillatory motion. Based on analytical considerations (see Appendix B)  $Z$  is expressed as:

$$Z = \kappa \hat{p}_b T \quad (8)$$

In Figure 5 curves are given for waves and current codirectional and perpendicular to each other and for several values of mean shear stress over amplitude of the first harmonic of the bottom shear stress ( $\bar{\tau}/\hat{\tau}_b$ ). The increasing numbers at the lines refer to these rates and give an increasing effect of current with respect to the oscillation. Here  $\bar{\tau}$  denotes the time-averaged shear stress and  $\hat{\tau}_b$  the amplitude of the first harmonic of the shear stress at the bottom. Increasing the mean shear stress results (after an initial small decrease) in an increase of the amplitude of the defect-velocity; for moderate currents

( $\bar{\tau} < 0.01 \rho \hat{U}^2$ ) the effect of magnitude and direction of the mean shear stress is small. The phase is more sensible for mean current changes. The dash-dot-lines in Figure 5 are the results of analytical computations, which are treated in Appendix B. For clearness' sake only the case without current is shown.

The dots in Figure 5 representing measurements of Bakker and Van Doorn show, that although the amplitude is rather well produced, the phase of the calculated oscillatory motion still has discrepancies with respect to measurements, due to deficiencies of the Prandtl model.

### 3 Time-averaged velocity field

Consider the time-averaged velocity field. The equation of motion reads (see also Appendix A and B):

$$\frac{\partial u}{\partial t} = - \frac{1}{\rho} \text{grad } P + \frac{1}{\rho} \frac{\partial \tau}{\partial z} \quad (9)$$

wherein: grad P = horizontal pressure gradient

Averaging over the wave period, the acceleration term cancels out. For a flow with confined depth  $h$ , the shear stress increases linearly with the depth. Furthermore, the mixing length  $l$  should be:

$$l = \kappa z \sqrt{(1-z/h)} \tag{10}$$

From Eq. (9) and (10), for stationary flow a logarithmic velocity distribution would result. However, this distribution would be found also from the assumptions made in this paper: a mixing length  $\kappa z$  and a uniform shear stress over the depth.

The period mean velocity field can be derived from the internal shear stress velocity  $p$ , and a given mean shear stress by using Eq. (5) and (6) time averaged.

If, for simplicity in the two-dimensional case, only the mean  $\bar{p}$  and first harmonic  $\hat{p}$  of the shear stress velocity are considered, the shear stress according to Eq. (5) equals ( $\omega$  being the angular velocity):

$$\tau = \rho(\bar{p} + \hat{p} \sin \omega t) |\bar{p} + \hat{p} \sin \omega t| \tag{11}$$

Hence  $\bar{\tau}$  is larger than  $\rho \bar{p}^2$ .

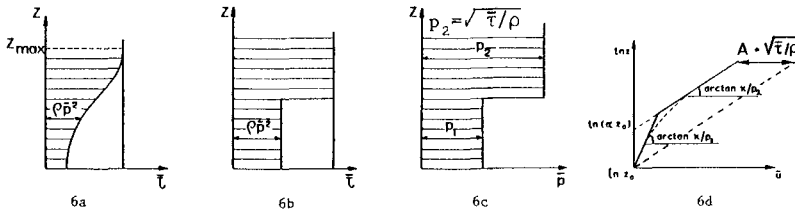


Figure 6 Computation mean velocity schematically

The nearer to the bottom, the larger the fluctuations of the shear stress and therefore, the larger the contribution of these fluctuations to the total shear stress. Thus the hatched part in Figure 6a shows the contribution of the mean shear stress velocity to the shear stress and the blank part the contribution of the variable part. One may schematize this picture to Figure 6b. The same figure is depicted in Figure 6c, however now the time-averaged shear stress velocity  $\bar{p}$  is plotted on the horizontal axis instead of the mean shear stress  $\bar{\tau}$ .

The time averaged velocity can be found from integration the time-averaged Eq. (6) over the depth:

$$\bar{u} = \int_{z_0}^z \frac{\bar{p}}{\kappa z} dz \quad \text{wherein: } z_0 = r/33 \tag{12}$$

Thus integrating Figure 6c over the depth, on logarithmic paper a broken line will come to being. This is shown schematically in Figure 6d. The gradient on the upper part is the same as one would have had without the effect of waves, but with the same pressure gradient (i.e.  $\bar{\tau}$ ).

In fact, the lower part of the line in Figure 6d is not too important. One might extend the upper part in downward direction, thus finding an increase of the apparent roughness with a factor  $\alpha$ . Lundgren (1972) presents this feature in the following way:

$$\bar{u}(z) = \sqrt{\bar{\tau}/\rho} \left( \frac{1}{\kappa} \ln \frac{z}{z_0} - A \right) \tag{13} \text{ wherein: } A = \frac{1}{\kappa} \ln \alpha \tag{14}$$

In Eq. (13),  $\bar{\tau}$  can be found from the waterlevel gradient <sup>1)</sup>. This parameter A implies a reduction of the velocity u with A times the shear stress velocity (see Fig. 6d). The same is found for the depth-averaged velocity, as A does not depend on the level z. For example: if the mean velocity is 1 m/s, corresponding with a shear stress velocity of 4 cm/s, a value A of 1 corresponds with a velocity reduction of 4 cm/s.

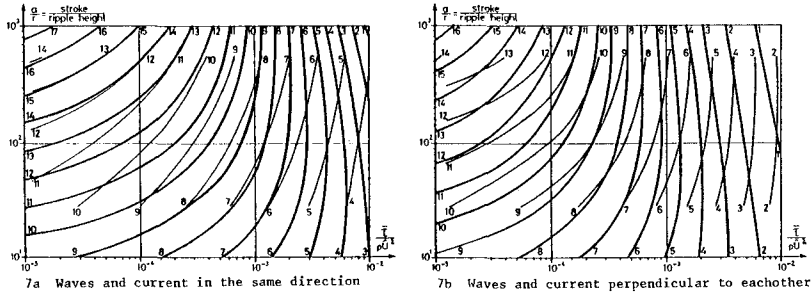


Figure 7 Comparison A-values according to Lundgren (1972) and analytical theory

In Figure 7 the values of A are plotted as function of  $\bar{\tau}/(\rho \hat{U}^2)$  and a/r. Figure 7a shows the case, that waves and currents are codirectional, Figure 7b that waves and currents are perpendicular to each other. The thin lines refer to Lundgren (1972), the thick lines to the present theory. Differences in A between both theories are not more than 2 in the relevant area.

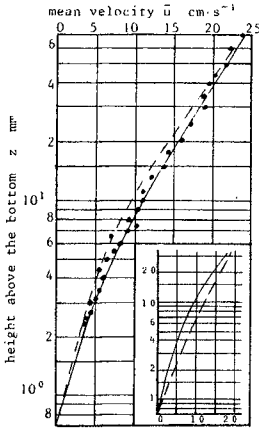
When waves and current are perpendicular to each other, the variations of p during the wave period are less than when waves and current are in the same direction. Thus  $\rho \hat{p}^2$  will differ less from  $\bar{\tau}$  (Fig. 6a) and therefore in the first case the factor A will be smaller (Fig. 7).

If one wants to implement the friction factors in a mathematical model, the use of graphs is inconvenient. For this goal the following formula for A may be useful:

$$A = \frac{1}{\kappa} (K_1 - K_2 \ln z_0^* + K_3 z_0^*) \tag{15}$$

where  $K_1$ ,  $K_2$  and  $K_3$  are given functions (see (C7)) of the ratio  $\bar{\tau}/(\rho \hat{p}_b^2)$ ; the ratio  $\hat{p}_b/\hat{U}$  is found from Eq. (7). The constants  $K_1$ ,  $K_2$  and  $K_3$  also depend on the angle  $\alpha_{wc}$  between waves and currents (appendix C). Furthermore, A is a function of the dimensionless  $z_0^*$  given in Eq.(C8) where  $z_0$  (equal to  $r/33$ ) has been made dimensionless with the reference height Z (see Eq. (8)). Analytical calculations concerning A and the constants  $K_1$ ,  $K_2$  and  $K_3$  are given in Appendix C.

1) In the case of breaking waves from the onshore gradient of the "shear stress" component of the radiation stress.



• From Bakker et al (1978) (test V20RA: mean velocity averaged over the height was  $20 \text{ cm.s}^{-1}$ ; amplitude first harmonic just outside boundary layer was  $24.3 \text{ cm.s}^{-1}$ )  
 --- numerical computation  
 ——— analytical computation  
 inset: numerical computation:  
 waves // current (—)  
 waves  $\perp$  current (---)

Figure 8 Mean velocity; theory compared with experiment of Bakker and Van Doorn (1978)

Figure 8 shows the velocity profile as result of measurements (Bakker and Van Doorn, 1978) and computations in a two-dimensional case. The inset shows the same velocity profile again, in combination with the case that waves and current are perpendicular to each other. One observes, that the apparent roughness in the case with waves and current perpendicular to each other is smaller than for parallel wave- and current direction; for this extend the upper part of the lines in the inset in downward direction. N.B. When using Eq. (13) for cases with combined waves and currents, it should be kept in mind, that the non-linear transport of water in the area above the wave trough falls outside the scope of this paper. This transport can be considerable.

4 Coastal engineering history

Very schematically, the history of science about the combination of waves and currents is the following (see Fig. 9). In the past one did not realize oneself, that waves additional to current effect this current (Fig. 9a). In 1967 for a given discharge Bijker pointed out the increase of shear stress by waves (Fig. 9b). This inversely includes the reduction of current by waves, given a mean water level gradient. In present time we realize ourselves, that waves change the vertical velocity distribution and therefore, that the reduction in discharge is not as drastically as Bijker predicts (Fig. 9c).

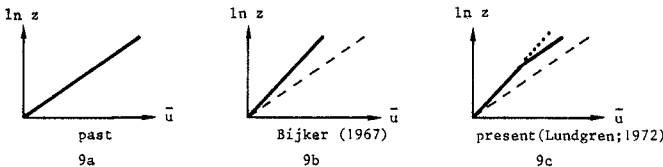


Figure 9 History of computation of mean velocity

5 Notation

$\lambda$	stroklength ( $=\lambda T/2\pi$ )	(m)
A	factor determining the influence of waves on the time-averaged velocity-profile according to Lundgren (Eq.(13))	(-)
A, B	complex constants in hypergeometric functions (Eq.(B16))	(-)
a,b,c,d	constants in approximation K(z) (Eq.(B12) and (B13))	(-)
C <sub>1,2,3,4</sub>	complex integration constants in Eq. (B16) to (B18)	(-)
E	complete elliptic integral of the second kind	(-)
k <sub>i=0,1...</sub>	coefficient of power-series-expansions	(-)
ker <sub>i</sub> , kei <sub>i</sub>	Kelvin functions of order i	(-)
ber <sub>i</sub> , bei <sub>i</sub>		(-)
K	complete elliptic integral of the first kind	(-)
K <sub>1,2,3</sub>	coefficients in Eq. (15) for A - value of Lundgren	(-)
K(z)	coefficient in differential equation analytical theory (Eq. (B4) and (B5))	(m <sup>2</sup> s <sup>-1</sup> )
l	turbulent mixing length (Eq.(10))	(m)
m, n	constants in approximation influence $\alpha_{wc}$ on A-value Lundgren (Eq.(C2))	(-)
N <sub>0</sub> , $\phi_0$	modulus and phase of zero order Kelvin' functions	(-)
p	internal shear stress velocity	(ms <sup>-1</sup> )
P	internal fluid pressure	(Pa)
r	Nikuradse roughness	(m)
S	second order tensor (Eq.(A9))	(-)
T	wave period	(s)
t	time	(s)
u	horizontal velocity	(ms <sup>-1</sup> )
U	horizontal velocity far from the bottom and boundary condition for the velocity field	(ms <sup>-1</sup> )
u <sub>d</sub>	defect-velocity ( $=u-U$ ; see also Fig. A1)	(ms <sup>-1</sup> )
x, y	horizontal coordinates	(m)
z	vertical coordinate	(m)
z <sub>0</sub>	height above the bottom where the horizontal velocity is zero ( $=r/33$ )	(m)
Z	reference height for the boundary layer thickness coherent with the oscillatory motion (Eq.(8))	(m)
$\alpha$	factor determining the increase of apparent bottom roughness (Eq.(14))	(-)
$\alpha_{wc}$	angle between wave-propagation and current far from bottom	(deg)
$\beta_{wc}$	tangent modulus in approximation of p*	(-)
$\gamma$	Euler's constant	(-)
$\delta$	direction of first derivative of horizontal velocity	(deg)
$\zeta$	argument in analytical solution (Eq.(B16))	(-)
$\theta$	phase of u <sub>d</sub> (Eq.(B19))	(rad)
$\kappa$	Von Karman's constant	(-)
$\Lambda$	sum of digamma functions (Eq.(B16))	(-)
$\nu$	kinematic viscosity	(m <sup>2</sup> s <sup>-1</sup> )
$\nu_t$	turbulent viscosity	(m <sup>2</sup> s <sup>-1</sup> )
$\xi$	factor for influence $\alpha_{wc}$ in analytical theory (Eq.(B11))	(-)
$\rho$	specific density	(kgm <sup>-3</sup> )
$\tau$	internal shear stress	(Pa)
$\phi$	phase of p (Eq.(B2))	(rad)
$\chi_{1,2}$	hypergeometric functions (Eq.(B16))	(-)
$\psi$	digamma function	(-)
$\omega$	angular velocity (2 $\pi$ /T)	(s <sup>-1</sup> )

Other symbols added to a variable x:

$\vec{x}$	vector
$\bar{x}^*$	dimensionless value
$\bar{x}$	time-averaged value
$\tilde{x}$	amplitude first harmonic
$\hat{x}$	first harmonic
$x_b$	value at the bottom

6 References

Bakker, W.T., 1973  
 Bottom friction and velocity distribution in an oscillatory flow,  
 Memo 72-23, Rijkswaterstaat, Directorate for Watermanagement and Hydraulic Research,  
 Department for Coastal Research.

Bakker, W.T. and Van Doorn, Th., 1978  
 Near bottom velocities in waves with a current,  
 Proc. 16th. Int. Conf. on Coastal Eng. Hamburg, ASCE, vol. II, pp. 1394-1414 (also: Publication 208,  
 Delft Hydraulics Laboratory, Delft, The Netherlands).

Bijker, E.W., 1967  
 Some considerations about scales for coastal models with movable bed,  
 Doctorate Dissertation, Delft University of Technology (also: Publication 50,  
 Delft Hydraulics Laboratory, Delft, The Netherlands).

Lundgren, H., 1972  
 Turbulent currents in the presence of waves,  
 Proc. 13th. Int. Conf. on Coastal Eng. Vancouver, ASCE, vol. II, pp. 623-634.



Appendix A: Numerical computations

Assumptions:

a. Only horizontal velocities, uniform in horizontal direction, are considered i.e. pressure gradient grad P uniform in vertical direction

b. The shear stress  $\tau$  can be found from the Prandtl hypothesis:

$$\tau = \rho v_t \frac{\partial u}{\partial z} \quad (A1)$$

$$v_t = \kappa^2 z^2 \left| \frac{\partial u}{\partial z} \right| \quad (A2)$$

wherein:  $\left| \frac{\partial u}{\partial z} \right| = \sqrt{\left( \frac{\partial u_x}{\partial z} \right)^2 + \left( \frac{\partial u_y}{\partial z} \right)^2}$  (A3)

c. The time averaged shear stress  $\bar{\tau}$  is uniform in vertical direction (cf ch.3).

Derivation of Eq. (1) and numerical solution:

According to assumption a the equation of motion reads:

$$\frac{\partial u}{\partial t} = -\frac{1}{\rho} \text{grad } P + \frac{1}{\rho} \frac{\partial \tau}{\partial z} \quad (A4)$$

Define  $\underline{U}$  and  $\underline{u}_d$  in the following way:

$$\frac{\partial \underline{U}}{\partial t} = -\frac{1}{\rho} \text{grad } P \quad (A5)$$

$$\underline{u}_d = \underline{u} - \underline{U} \quad (A6)$$

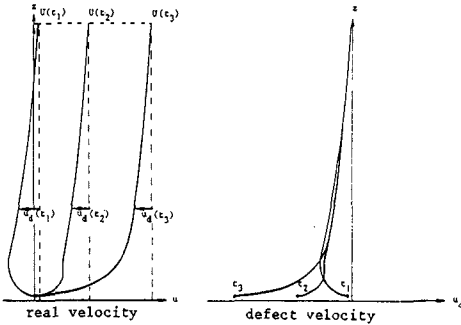


Figure A.1 Definition defect-velocity.

The velocity  $\underline{U}$  (only a function of  $t$ , cf. assumption a) denotes the velocity at a depth, to be chosen arbitrary, however far enough above the bottom to attenuate the periodical changes of  $\tau$ . This can be seen from Eq. (A4) by taking the 2nd term on the right handside equal to zero (assumption c). The velocity  $\underline{u}_d$  denotes the defect-velocity (see Fig. A1).

Substitution of Eq. (A5) and (A6) into (A4) yields:

$$\frac{\partial \underline{u}_d}{\partial t} = \frac{1}{\rho} \frac{\partial \tau}{\partial z} \quad (A7)$$

Write  $\tau$  as  $(\tau_x, \tau_y)$ , and  $\underline{u}$  as  $(u_x, u_y)$ , then differentiation of  $\tau_x$  to  $t$  gives, using Eq. (A1) to (A3):

$$\begin{aligned} \frac{\partial \tau_x}{\partial t} &= \rho \left\{ \frac{\partial v_t}{\partial t} \frac{\partial u_x}{\partial z} + v_t \frac{\partial^2 u_x}{\partial t \partial z} \right\} \\ &= \rho v_t \left\{ (1 + \cos^2 \delta) \frac{\partial^2 u_x}{\partial z \partial t} + \sin \delta \cos \delta \frac{\partial^2 u_y}{\partial z \partial t} \right\} \end{aligned}$$

wherein:  $\cos \delta = \frac{\partial u_x}{\partial z} / \left| \frac{\partial u}{\partial z} \right|$  and  $\sin \delta = \frac{\partial u_y}{\partial z} / \left| \frac{\partial u}{\partial z} \right|$

Computation of  $\partial \tau_y / \partial t$  in a similar way yields:

$$\frac{\partial \tau}{\partial t} = \rho v_t \underline{S} \cong \frac{\partial^2 u}{\partial z \partial t} \tag{A8}$$

wherein: 
$$\underline{S} = \begin{vmatrix} 1 + \cos^2 \delta & \cos \delta \sin \delta \\ \cos \delta \sin \delta & 1 + \sin^2 \delta \end{vmatrix} \tag{A9}$$

Differentiation of Eq. (A7) to z, multiplication with  $v_t \underline{S}$  and substitution of Eq. (A8) results in Eq. (1), because  $\partial u / \partial z$  equals  $\partial u_d / \partial z$ .

With a similar derivation as the one for  $\partial \tau / \partial t$  one finds:

$$\frac{\partial \tau}{\partial z} = \frac{\rho}{\kappa z} v_t \underline{S} \cong \frac{\partial}{\partial z} \left\{ \kappa z \frac{\partial u}{\partial z} \right\} \tag{A10}$$

Substitution of Eq. (A2) into (A10) and Eq.(A10) into (A7) yields an equation for the defect-velocity:

$$\frac{\partial u_d}{\partial t} = \kappa z \frac{\partial u_d}{\partial z} \cdot \underline{S} \cong \frac{\partial}{\partial z} \left\{ \kappa z \frac{\partial u_d}{\partial z} \right\} \tag{A11}$$

Eq. (A11) has been solved numerically using a finite difference method based on the Crank-Nicholson implicate integration scheme with the boundary conditions:

- $\frac{u_d}{z} = 0$  at the upper end
- $\frac{u_d}{z} = -U$  near the bottom at a height  $z_0$  which is proportional to the dimension of the bottom roughness  $r$  ( $z_0 = r/33$ )
- $\underline{U} =$  imposed velocity at the upper boundary

Appendix B: Analytical computations

In this appendix only relations will be derived, on one hand for parallel direction of oscillation and current (i.e.  $\alpha_{wc} = 0^\circ$ ) and on the other hand for oscillation and current perpendicular to each other (i.e.  $\alpha_{wc} = 90^\circ$ ).

Differentiation of the equation of motion (A4) to z using assumption a, multiplication with  $\kappa z$  and substitution of (6) gives:

$$\frac{\partial p}{\partial t} = \frac{1}{\rho} \kappa z \frac{\partial^2 \tau}{\partial z^2} \tag{B1}$$

When only the first harmonics are taken into account for the linearized approximation the shear stress  $\tau$  and shear stress velocity  $p$  can be written as:

$$\begin{aligned} p &= \bar{p} + \tilde{p}; & \tilde{p} &= \hat{p} \sin(\omega t + \phi) \\ \tau &= \bar{\tau} + \tilde{\tau}; & \tilde{\tau} &= \hat{\tau} \sin(\omega t + \phi) \end{aligned} \tag{B2}$$

wherein:  $\phi =$  phase of  $\tilde{p}$  and equals in an approximation upto the first harmonic the phase of  $\tilde{\tau}$

Because  $\tilde{p}$  and  $\tilde{\tau}$  are in phase, derivation to  $t$  yields in the case of  $\alpha_{wc} = 0^\circ$  and  $90^\circ$ :

$$\frac{\partial \tilde{p}}{\partial t} = \tilde{\tau} \cdot \frac{\partial \tilde{\tau}}{\partial t} \tag{B3}$$

wherein:  $\hat{p}, \hat{\tau}$  the modulus of  $\tilde{p}$  and  $\tilde{\tau}$

Evidently Eq. (B3) is only relevant in the plane of oscillation. Only considering this plane in the following, the vector-sign (underlining) may be skipped.

After substitution of (B3) into (B1) and using assumption c an equation, similar to (1) is found<sup>1)</sup>:

$$\frac{\partial \tilde{\tau}}{\partial t} = K \frac{\partial \tilde{\tau}}{\partial z} \tag{B4} \quad \text{wherein: } K = \kappa z \frac{\hat{\tau}/\rho}{\hat{p}}$$

For  $\alpha_{wc} = 0^\circ$  from Eq. (5) and (B2) can be derived:

$$\frac{\hat{\tau}}{\rho \hat{p}^2} = \frac{4}{\pi} \frac{\bar{p}}{\hat{p}} \arcsin \frac{\bar{p}}{\hat{p}} + \frac{4}{3\pi} \left( 2 + \frac{\bar{p}^2}{\hat{p}^2} \right) \sqrt{1 - \frac{\bar{p}^2}{\hat{p}^2}} \quad \text{for } \bar{p} < \hat{p}$$

$$\frac{\hat{\tau}}{\rho \hat{p}^2} = 2 \frac{\bar{p}}{\hat{p}} \quad \text{for } \bar{p} > \hat{p} \tag{B6}$$

$$\frac{\bar{\tau}}{\rho \bar{p}^2} = \frac{2}{\pi} \left( \frac{1}{2} + \frac{\bar{p}^2}{\hat{p}^2} \right) \arcsin \frac{\bar{p}}{\hat{p}} + \frac{3}{\pi} \frac{\bar{p}}{\hat{p}} \sqrt{1 - \frac{\bar{p}^2}{\hat{p}^2}} \quad \text{for } \bar{p} < \hat{p}$$

$$\frac{\bar{\tau}}{\rho \bar{p}^2} = \frac{1}{2} + \frac{\bar{p}^2}{\hat{p}^2} \quad \text{for } \bar{p} > \hat{p} \tag{B7}$$

These keep their validity in dimensionless shape, wherein  $\bar{p}, \hat{p}, \bar{\tau}$  and  $\hat{\tau}$  are made dimensionless with the value of  $\beta$  at the bottom (i.e.  $\hat{p}_b$  for  $\bar{p}$  and  $\hat{p}$ , and  $\rho \hat{p}_b^2$  for  $\bar{\tau}$  and  $\hat{\tau}$ ). In the following these dimensionless values are denoted with an asterisk.

- 1) Eq. (B4) is quite similar to (1). Generally it should be kept in mind, that Eq. (B4) is a linearized equation, where (1) has general validity, and therefore the coefficient K is not equal to  $v_t^2$ . However for parallel oscillation and current  $\delta$  equals 0,  $v_t$  and therefore in the plane of oscillation Eq. (1) and (A9) yields:

$$\frac{\partial \tau}{\partial t} = 2 v_t \frac{\partial \tau}{\partial z} \quad \text{wherein: } v_t = \kappa^2 z^2 \left| \frac{\partial u}{\partial z} \right|$$

For large  $z$  the value of  $|\partial u/\partial z|$  approaches  $\bar{p}/\kappa z$ , and therefore  $2v_t + 2\kappa z \bar{p}$ . As  $\hat{\tau}/\rho$  will be  $2 \bar{p}\hat{p}$  for large value of  $z$  (see Eq. (B6)), the value of K according to Eq. (B5) equals  $2 v_t$ . This demonstrates the similarity between Eq. (1) and (B4) in this case.

- 2) Even, generally, the time-independent K is not equal to the time-averaged  $\sum v_t$ .

In Figure B1 is displayed a dimensionless  $K^* = K/(\kappa^2 \hat{p}_b^2 T)$  versus a dimensionless height  $z^* = z/(\kappa \hat{p}_b T)$ . Furthermore the value of  $K^*$  depends on  $\bar{\tau}/\hat{\tau}_b$ . For the relation  $\hat{p}^* = \hat{p}/\hat{p}_b$  an exponential decay is assumed (Bakker, 1973):

$$\hat{p}^* = e^{-(3\pi^3/16) z^*} \tag{B8}$$

The rate of decay according to Eq. (B8) is coherent with the choice of the reference height  $Z$ , defined as  $Z = \kappa \hat{p}_b T$ . A relation between  $\bar{\tau}^*/\hat{\tau}_b^*$  and  $\hat{p}^*$  follows from division of (B7) by (B6). Given the value of  $\bar{\tau}^*/\hat{\tau}_b^*$  using Eq. (B8) the value of  $\hat{p}^*$  can be found. From (B7) results  $\bar{\tau}^*$ . For a certain level  $z^*$ , the value of  $\hat{p}^*$  follows from Eq. (B8). As  $\bar{\tau}^*$  remains constant in the vertical sense, the value of  $\bar{\tau}^*/\hat{p}^{*2}$  is known. Substitution of this value in Eq. (B7) yields a value of  $\bar{p}^*/\hat{p}^*$ , which further can be substituted in Eq. (B6) yielding  $\tau^*/\hat{p}^{*2}$  and therefore  $K^* (= z^* \hat{\tau}^*/\hat{p}^*)$ . For  $\alpha_{wc} = 90^\circ$  a similar approach can be chosen. Instead of Eq. (B6) and (B7) is found:

$$\frac{\hat{\tau}}{\rho \hat{p}^2} = \frac{4}{3\pi} \sqrt{1 + \frac{\bar{p}^2}{\hat{p}^2}} \left[ (2 + \frac{\bar{p}^2}{\hat{p}^2}) E \left\{ \frac{1}{1 + \frac{\bar{p}^2}{\hat{p}^2}} \right\} - \frac{\bar{p}^2}{\hat{p}^2} K \left\{ \frac{1}{1 + \frac{\bar{p}^2}{\hat{p}^2}} \right\} \right] \text{ for } \bar{p}/\hat{p} > 0 \tag{B9}$$

$$\frac{\bar{\tau}}{\rho \hat{p}^2} = \frac{2}{\pi} \frac{\bar{p}}{\hat{p}} \sqrt{1 + \frac{\bar{p}^2}{\hat{p}^2}} E \left\{ \frac{1}{1 + \frac{\bar{p}^2}{\hat{p}^2}} \right\} \text{ for } \bar{p}/\hat{p} > 0 \tag{B10}$$

wherein:  $K \{ \} =$  complete elliptic integral of the first kind  
 $E \{ \} =$  complete elliptic integral of the second kind

For the analytical computations of the time-dependent velocity field the coefficient  $K^*$  is approximated in 3 sections (see Fig. B1): Above the intersection of the straight line and the curve valid for waves only, the straight line is assumed i.e.:

$$\text{upper part: } K^* = \xi \cdot z^* \sqrt{\bar{\tau}^*} \tag{B11}$$

wherein:  $\xi = 2$  for  $\alpha_{wc} = 0^\circ$  ;  
 $\xi = 1$  for  $\alpha_{wc} = 90^\circ$

Eq. (B11) follows from substitution of Eq. (B6) ( $\alpha_{wc} = 0^\circ$ ) or Eq. (B9) ( $\alpha_{wc} = 90^\circ$ ) into Eq. (B5) for the limiting case of  $\bar{p}/\hat{p} \rightarrow 0$  and  $\bar{p} \rightarrow \sqrt{\bar{\tau}/\rho}$ . Below the intersection of the straight line and the curve for waves only, the curve is assumed, which is approximated by:

$$\text{middle part: } K^* = ae^{-bz^*} \quad ; \quad a = 0.111 \quad b = 3.267 \tag{B12}$$

$$\text{lower part: } K^* = cz^* - dz^{*2} \quad ; \quad c = 0.849 \quad d = 2.817 \tag{B13}$$

The intersection of lower and middle part is situated at  $z^* = 0.186$ . The influence of the current on the time-dependent solution is restricted to the upper part where Eq. (B11) is valid. As long as the straight line in Figure B1 intersects the curve I + II for waves only, the influence of the current on the time-dependent velocity field is negligible near the bottom. This can also be seen from nu-

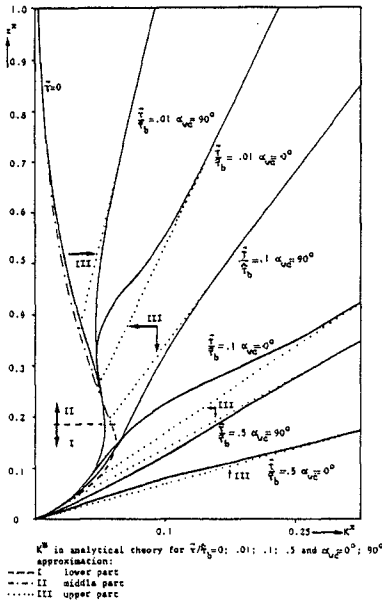


Figure B.1 Coefficient  $K^*$  as function of  $z^*$   $C_1, C_2, C_3$  en  $C_4$ :  
(analytically and approximation)

lower part: the solution consists of hypergeometric functions, which in the following already are expressed in power-series-expansions

$$\hat{u}_{dc}^* = \frac{d}{kc} [C_1 \{ 1 + \chi_1(\zeta) \} + \frac{\hat{\tau}_b^*}{d} \{ 1 + \ln \zeta + \chi_2(\zeta) \}] \quad (B16)$$

wherein:  $c, d$  are given in Eq. (B13)

$$\chi_1(\zeta) = \sum_{n=1}^{\infty} \frac{(A+1)_n (B+1)_n}{(n+1)! n!} \cdot n \cdot \zeta^{n-1}$$

$$\chi_2(\zeta) = \sum_{n=1}^{\infty} \frac{(A+1)_n (B+1)_n}{(n+1)! n!} \cdot n \cdot \zeta^{n-1} \Lambda(n)$$

$$(A+1)_n = (A+1) (A+2) \dots (A+n)$$

$$\Lambda(n) = \psi(A+1+n) - \psi(A+1) + \psi(B+1+n) - \psi(B+1) - \psi(n+2) + \psi(2) - \psi(n+1) + \psi(1)$$

$$\psi(m) = \text{digamma function} = -\gamma + \sum_{n=1}^{m-1} \frac{1}{n}$$

1) Mind that (exact) the same solution is found for waves and current codirectional and perpendicular to each other, if in the last case the time-averaged shear stress is four times as large as in the first case (because then part III is the same; see Eq. (B11)).

merical computations in Figure 5.1) The intersection disappears for large currents, when the slope of the straight line exceeds the tangent of the basic curve at the origin (Fig. B1) i.e.:

$$\xi \sqrt{\frac{a}{\tau}} > \frac{8}{3\pi} \quad (B14)$$

With above given approximations for  $K^*$ , Eq. (B4) can be solved analytically with the boundary conditions:

$$z = 0: \underline{\tau} = \frac{\bar{\tau}}{\tau} + \frac{\hat{\tau}_b}{\tau} \sin \omega t \quad (B15)$$

$$z \rightarrow \infty: \underline{\tau} \rightarrow \bar{\tau}$$

When the time dependent shear stress  $\bar{\tau}$  is found, with Eq. (A7) the time-dependent defect velocity  $\hat{u}_d$  can be computed. The analytical solutions for the amplitude and phase of the first harmonic of  $u_d$  (in complex form; suffix  $c$  denotes 'complex') are determined apart from complex integration constants

$$\begin{aligned} \gamma &= .57722 \text{ (Euler's constant)} \\ A, B &= \text{complex constants restricted by} \\ & \quad A + B = -1; A \cdot B = 2\pi i/d \\ & \quad \text{(as } d = 2.817: A = 0.617 - 0.999 i \\ & \quad \quad \quad \quad \quad \quad \quad \quad B = -1.617 + 0.999 i) \\ \zeta &= \frac{d}{c} \cdot z^* \end{aligned}$$

middle part: the solution consists of Kelvin functions:

$$\hat{u}_{dc}^* = \frac{b \zeta}{\kappa} [C_2 \{ \ker_1(\zeta) + i \cdot \text{kei}_1(\zeta) \} + C_3 \{ \text{ber}_1(\zeta) + i \cdot \text{bei}_1(\zeta) \}] \quad (B17)$$

wherein:  $\zeta = 2\pi \sqrt{\frac{2}{\pi a}} e^{\frac{1}{2}bz^*}$

$\ker_1(\zeta)$ ,  $\text{kei}_1(\zeta)$ ,  $\text{ber}_1(\zeta)$  and  $\text{bei}_1(\zeta)$  are Kelvin functions  
upper part:

$$\hat{u}_{dc}^* = C_4 [ \ker_0(\zeta) + \text{kei}_0(\zeta) + i \{ \text{kei}_0(\zeta) - \ker_0(\zeta) \} ] \quad (B18)$$

wherein:  $\zeta = 2 \sqrt{\frac{2\pi z^*}{\xi \sqrt{\tau^*}}}$

For large currents, when only the upper part can be applied, Eq. (B18) becomes:

$$\hat{u}_d^* = \frac{2\hat{\tau}_b^*}{\xi \sqrt{\tau^*}} \cdot \frac{1}{\kappa} N_0(\zeta) \quad ; \quad \theta = \phi_0(\zeta) \quad (B19)$$

wherein:  $N_0(\zeta) = \sqrt{\ker_0^2(\zeta) + \text{kei}_0^2(\zeta)}$   
 $\phi_0^0(\zeta) = \arctan \{ \text{kei}_0(\zeta) / \ker_0(\zeta) \}$   
 $\phi^0 = \text{phase of } \hat{u}_d^0 \text{ defined by } \hat{u}_d = \hat{u}_d \sin(\omega t + \theta)$

For clearness' sake only the analytical solution for the case of waves only is presented in Figure 5. The analytical solution then consists only of the combination of Eq. (B16) and (B17).

From Eq. (B19) a simple relation can be derived between the ratio  $\hat{\tau}_b / (\rho \hat{U}^2)$  and the ratio stroklength over bottomroughness  $a/r$ . Replace in Eq. (B19) the dimension operator  $\hat{p}_b$  (denoted by a asterisk) by  $\hat{U}$ , and consider Eq. (B19) at a level  $z = z_0$ , where  $\hat{u}_d = \hat{U}$ . The result is:

$$\frac{\hat{\tau}_b}{\rho \hat{U}^2} = \frac{\kappa \xi}{2} \sqrt{\frac{\tau}{\rho \hat{U}^2}} N_0^{-1}(\zeta) \quad (B20)$$

wherein:  $\zeta = \frac{2}{\sqrt{33 \kappa \xi a/r \sqrt{\tau/\rho \hat{U}^2}}}$

This equation is only valid when Eq. (B14) can be applied. Practically Eq. (B19) and (B20) differ only slightly from the numerical solution in the range of  $a/r > 1$  and  $\tau/(\rho \hat{U}^2) >> 0.1$ .

Appendix C: Analytical calculation of Lundgren's A-value

In this appendix the analytical solution for the time-averaged velocity field will be treated. With Eq. (12) this field can be found from the time-averaged shear stress velocity. The last can be found from the definition of the shear stress velocity by Eq. (5) in the following way<sup>1)</sup>

As described in Appendix B, the ratio  $\bar{p}^*/\hat{p}^{*2}$ ) can be found as function of the dimensionless height  $z^*$  above the bottom using Eq. (B7) when  $\alpha_{WC} = 0^\circ$  and Eq.(B10) when  $\alpha_{WC} = 90^\circ$ . From Eq. (B8) the dimensionless  $\bar{p}^*$  can be derived. For various values of  $\bar{\tau}/\hat{\tau}_b$  those curves are plotted in Figure C1, in the case of  $\alpha_{WC} = 0^\circ$ .

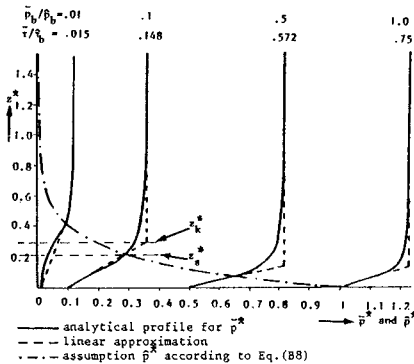


Fig. C.1 Profile for  $\bar{p}^*$  and  $\hat{p}^*$  (anal. and approx.)

For integrating over the depth according to Eq. (12) the curves for  $\bar{p}$  are approximated by a vertical and an oblique line (see Fig. C1). The vertical line corresponds with the value of  $\bar{p}^* = \sqrt{\bar{\tau}^*}$ , the oblique line connects the bottom point  $\bar{p}^* = \bar{p}_b^*$  with the point, where  $\bar{p}^* = \hat{p}^*$ :

$$\bar{p}^* = \bar{p}_b^* + \beta z^* \tag{C1}$$

This approximation can only be applied, when  $\bar{p}_b^* < 1$ . As will be shown later this restriction covers the cases where the influence of waves on a current becomes significant. As the dash-dot line in Figure C1 denotes  $\hat{p}^*$  (given by Eq. (B8)), the intersection point of the drawn line and the dash-dot line is also a point of the oblique line.

From Eq. (B7) and (B10) it shows, that in the intersection points, ( $z^* = z_s^*$ ), where  $\bar{p}^* = \hat{p}^*$  the value of  $\bar{\tau}^*/\hat{p}^{*2}$  equals 1.5, when  $\alpha_{WC} = 0^\circ$  and  $2\sqrt{2}/\pi E\{\frac{1}{2}\} = 1.216$  when  $\alpha_{WC} = 90^\circ$ . Generally it can be derived that:

$$\hat{p}^* = \sqrt{\frac{\bar{\tau}^*}{1 + (m + n \cos^2 \alpha_{WC})^2}} \tag{C2}$$

wherein:  $m^2 = \frac{2\sqrt{2}}{\pi} E\{\frac{1}{2}\} - 1 \approx 0.216$

$$n = \frac{1}{2}\sqrt{2} - m$$

$E\{\}$  = complete elliptic integral of the second kind.

Using Eq. (B8) for  $\hat{p}^*$  from Eq. (C1) the height of the intersection level  $z_s^* = z_s^*$  is found:

$$z_s^* = -\frac{8}{3\pi} \ln \left\{ \frac{\bar{\tau}^*}{1 + (m + n \cos^2 \alpha_{WC})^2} \right\} \tag{C3}$$

1) In an approximation, up to the first harmonic.

2) The asterisks have the same meaning as in Appendix B.

Then from Eq. (C1)  $\beta$  can be derived:

$$\beta = (\hat{p}^* - \bar{p}_b^*) / z_k^* \tag{C4}$$

The level  $z_k^*$ , where the vertical line and the oblique line intersect equals:

$$z_k^* = (\sqrt{\bar{\tau}^*} - \bar{p}_b^*) / \beta \tag{C5}$$

From integration, according to Eq. (12), the velocity  $\bar{u}_k^*$  at the level  $z_k^*$  can be found. For  $z^* > z_k^*$  a logarithmic velocity profile is found (Fig. 6d) i.e. a straight line on logarithmic paper through the point  $(z_k^*, \bar{u}_k^*)$  under the inclination  $\arctan(\kappa / \sqrt{\bar{\tau}^*} / \rho)$ . Extension of this line, in downward direction yields the level  $\alpha z_0^*$  where  $\alpha$  is the magnification of the apparent bottom roughness (Fig. 6d):

$$\ln \alpha = (1 - \frac{\bar{p}_b^*}{\sqrt{\bar{\tau}^*}}) \ln \frac{z_k^*}{z_0^*} - \frac{\beta}{\sqrt{\bar{\tau}^*}} (z_k^* - z_0^*) \tag{C6}$$

Using Eq. (14) this gives the A-value of Lundgren according to Eq. (15) wherein:

$$K_1 = K_2 \ln z_k^* - K_3 z_k^* ; K_2 = 1 - \frac{\bar{p}_b^*}{\sqrt{\bar{\tau}^*}} ; K_3 = \frac{\beta}{\sqrt{\bar{\tau}^*}}$$

( $\beta$  and  $z_k^*$  according to Eq. (C4) and (C5))  
 The coefficient  $K_1$ ,  $K_2$  and  $K_3$  can be written as function of  $\bar{\tau} / (\rho \hat{p}_b^2)$  and  $\alpha_{wc}$ . These functions are approximated with power-series-expansions for the cases  $\alpha_{wc} = 0^\circ$  and  $\alpha_{wc} = 90^\circ$ :

$$K_i = \sum_{n=0}^4 k_{in} \{ \ln(\frac{\bar{\tau}}{\rho \hat{p}_b^2}) \}^n \quad (i = 1, 2, 3) \tag{C7}$$

The coefficients  $k_{in}$  are listed in the table below.

	$\alpha_{wc} = 0^\circ$					$\alpha_{wc} = 90^\circ$				
	$k_0$	$k_1$	$k_2$	$k_3$	$k_4$	$k_0$	$k_1$	$k_2$	$k_3$	$k_4$
$K_1$	-0.914	.623	.159	.0110	-	-0.3921	.2264	-.1325	-.00410	-.002850
$K_2$	.284	-.285	-.0416	-.00214	-	.1120	-.0858	.0737	.0175	.001092
$K_3$	2.654	-.511	-.408	-.0761	-.00464	1.3845	.1398	.3302	.0883	.006240

The values of the coefficients for  $0^\circ < \alpha_{wc} < 90^\circ$  can be approximated by linear interpolation.

Eq. (C7) and (15) relate A to  $\bar{\tau} / (\rho \hat{p}_b^2)$  and  $z_0^*$ ; this relationship can be easily converted to the presentation according to Lundgren (Fig. 7). Here  $\bar{\tau} / (\rho \hat{U}^2)$  replaces  $\bar{\tau} / (\rho \hat{p}_b^2)$ . Evidently these dimensionless variables can be converted to each other with the aid of the ratio  $\hat{p}_b / \hat{U}$ , given in Eq. (7) as function of the ratio  $a/r$ . Furthermore in Lundgren's presentation the variable  $a/r$  replaces  $z_0^*$ ; these variables are related in the following way (using Eq. (8)):

$$z_0^* = \frac{z_0}{\kappa \hat{p}_b T} = \frac{1}{66 \kappa \pi} \frac{\hat{U}}{\hat{p}_b} \frac{1}{a/r} \tag{C8}$$



## CHAPTER EIGHTY

### FIELD AND LABORATORY VERIFICATION OF THE WAVE PROPAGATION MODEL CREDIZ

M.W. Diggemans<sup>1)</sup>, M.J.F. Stive<sup>1)</sup>, A.J. Kuik<sup>2)</sup>, A.C. Radder<sup>3)</sup> and N. Booij<sup>4)</sup>

#### ABSTRACT

Both the effects of refraction and diffraction may be efficiently modeled in wave propagation models by introduction of the parabolic approximation. The performance of the model CREDIZ, which is based on this parabolic approximation, was investigated in three verification studies. Two of these studies concern laboratory situations, i.e. one having a simple geometry and one having a more complicated geometry. The third study concerns a field situation, i.e. a shoal dominated area in an estuary mouth. It is found that despite the schematization to monochromatic, nearly linear wave propagation, the model CREDIZ performs remarkably well for engineering purposes.

#### 1.0 INTRODUCTION

For the prediction of wave behaviour in coastal regions numerical wave propagation models are common engineering practise nowadays. The majority of the models are based on linear wave propagation. The physical processes usually accounted for are: shoaling, refraction and diffraction. The various approximations can be derived from the now well-known mild slope equation in which refraction and diffraction effects are both modeled. Because of the elliptic nature of this equation the numerical solution is quite involved. Neglecting the diffraction altogether in the mild slope equation results in the wave ray (geometric optics) approximation. An intermediate case is obtained by neglecting the diffraction only in the main wave propagation direction and maintaining it in the transverse direction, which results in the so-called parabolic approximation.

A wave propagation model, frequently used in the current Dutch advisory practice, is CREDIZ. This numerical model is based on the parabolic approximation and determines the combined effect on a monochromatic wave field of arbitrary bottom topographies and current patterns, including energy dissipation effects due to wave breaking and bottom friction (Radder, 1979, Booij, 1981). To assess the accuracy of CREDIZ, two verification studies in laboratory wave basins have been carried out. Recently, a field study in a coastal region in the SW part of the

---

1) Delft Hydraulics Lab., Delft, the Netherlands

2) Rijkswaterstaat, Delta Department, The Hague, the Netherlands

3) Rijkswaterstaat, Department of Data Processing, Rijswijk, the Netherlands

4) Delft University of Technology, Delft, the Netherlands.

Netherlands, offshore the Haringvliet sluices, was conducted. Results of these verification studies are reported here.

2.0 MATHEMATICAL FORMULATION OF CREDIZ

Without sources and sinks, the mild slope equation, including currents reads

$$\nabla \cdot (cc_g \nabla \phi) + 2i\omega \vec{U} \cdot \nabla \phi - (\omega_r^2 - \omega^2 - k^2 cc_g) \phi = 0, \tag{1}$$

where terms with  $\nabla \cdot \vec{U}$  and  $\vec{U}^2$  are neglected.  $\vec{U}$  is the (steady) current velocity,  $\nabla$  is the horizontal gradient operator,  $\phi(x_1, x_2)$  is the complex wave potential function,  $k$  is the wave number,  $\omega$  is the absolute angular frequency and  $\omega_r$  is the relative angular frequency. The absolute and the relative frequency are related by

$$\omega = \omega_r + \vec{k} \cdot \vec{U}, \tag{2}$$

where  $\omega_r$  fulfils the linear dispersion relation

$$\omega_r = [gk \tanh kh]^{\frac{1}{2}} \tag{3}$$

with  $g$  being the gravity acceleration and  $h$  the local depth.

In the parabolic approximation the assumption is made that the waves propagate mainly into a specific direction  $s$ . Introducing the coordinate  $n$ , which is orthogonal to  $s$ , an operator  $M$  can be defined by

$$M\phi = (\omega^2 - \omega_r^2) \phi + \frac{\partial}{\partial n} (\beta \frac{\partial \phi}{\partial n}) + 2i\omega U_n \frac{\partial \phi}{\partial n} \tag{4}$$

where  $\beta = cc_g$  and  $U_n$  is the current component in the direction  $n$ . The parabolic approximation to (1) is then given by

$$\left( \frac{i\omega U_s}{\beta} + \frac{\partial}{\partial s} \right) [\sqrt{\beta k} \phi + \frac{p_1}{k\sqrt{\beta k}} M\phi] - ik\sqrt{\beta k} \phi - i \frac{p_2}{\sqrt{\beta k}} M\phi = 0, \tag{5}$$

where the coefficients  $p_1$  and  $p_2$  result from the approximation of pseudo operators by differential operators and are related by

$$p_2 = p_1 + 1/2, \quad 0 \leq p_1 \leq 1/2 \text{ (optimal, } p_1 = 1/4). \tag{6}$$

Because of the intended use in coastal areas, wave dissipation is also modeled in CREDIZ, i.e. both dissipation due to bottom friction and dissipation due to wave breaking are accounted for. Introduction of dissipative terms leads to the addition of the following expression to the left-hand side of (5)

$$\left( \frac{i\omega U_s}{\beta} + \frac{\partial}{\partial s} \right) p_1 \frac{i\omega W}{k\sqrt{\beta k}} \phi + p_2 \frac{\omega W}{\sqrt{\beta k}} \phi. \tag{7}$$

where  $W = W_b + W_f$ , and  $W_b$  and  $W_f$  are the contributions due to wave breaking and bottom friction respectively. For the dissipation due to bottom friction is used

$$W_f = \frac{s_o^2}{2g} \left( \frac{8}{3\pi} f_w s_o H + 2f_s \dot{U} \right), \quad s_o = \omega_r / \sinh(kd). \quad (8)$$

where  $f_w$  and  $f_s$  are coefficients for the wave-induced and the wave-current induced parts of the shear stress. Standard values are  $f_w = 0.01$  and  $f_s = 0.005$ . The dissipation due to wave breaking is modeled according to the model of Battjes and Janssen (1978) (see also Battjes and Stive (1984) in these proceedings).

The influence of the wave amplitude  $a$  on the propagation velocity is taken into account in an approximate way, following Walker (1976): for the depth  $h$  in the dispersion relation (3) is taken

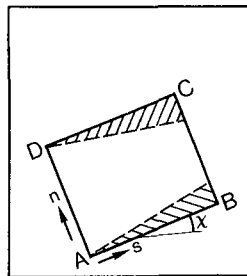
$$h = d + p_v * a,$$

where  $d$  is the actual mean water depth and  $p_v$  is an adjustable parameter, with a standard value of 1. It is noted that in the limit for shallow water the wave celerity of a solitary wave from the KdV equation results for  $p_v = 1$ . In the deep water limit the linear expression for  $c$  is recovered.

The solution of (5) requires the availability of initial and boundary conditions. The initial values can be derived from the incoming wave field, which may be (weakly) non-uniform with regard to amplitude and direction. For the lateral boundaries, one has to deal with the presence of open boundaries on which the wave field is generally not known. A simple boundary condition is

$$\cos\chi \frac{\partial\phi}{\partial s} + \sin\chi \frac{\partial\phi}{\partial n} = ik\phi,$$

which ensures the absorption of waves with local wave number  $k$  approaching under an angle  $\chi$  exactly, and waves in other directions are absorbed partially. A zone along the lateral boundaries in which the results are less accurate is indicated in the sketch.



### 3.0 VERIFICATIONS

#### 3.1 Laboratory

In the laboratory both a simple and a realistic bottom topography were used; both periodic and random, unidirectional waves without currents were applied. In the simple situation, consisting of a parabolic shoal on a sloping bottom, small amplitude waves were applied to study the purely linear part of CREDIZ only: results are given by Berkhoff et al. (1982). Here we report results of a computation in which amplitude effects are taken into account. The more realistic situation pertained to a coastal topography at the NW coast of Spain. In this case also finite-amplitude waves were applied resulting in breaking waves in the model.

The shoal situation.

The simple laboratory situation consisted of a parabolic shoal (elliptic in the plane) placed on a 1/50 shoaling bottom, see Figs. 1 and 2. The measurements were conducted in a wave basin of 30 by 35 m in extent and a 20 by 20 m measuring areas was taken in which a measuring grid of at least .5 by .5 m was taken: locally this grid was reduced to .25 by .25 m. The comparison of the computed and measured wave field is specifically carried out along five sections tranverse to and three sections in the wave propagation distance, see Fig. 1. A comparison of the iso-amplitude contours for the situation of regular waves (incoming wave amplitude 2.32 cm and wave period T = 1 s) is given in Fig. 3. Here purely linear wave propagation in the computation is considered, see also Berkhoff et al. (1982) from which this case is taken. The iso-amplitude contours show a satisfactory agreement, but locally, in the convergence zone, some deviations in lateral extent of the convergence region can be noticed. This is mainly due to the linear nature of the computation, as confirmed by Kirby and Dalrymple (1984) who took non-linearity into account. Because CREDIZ also allows the incorporation of an amplitude effect on the wave propagation characteristics by choosing  $p_v \neq 0$ , we recomputed the shoal situation at the end of September 1984, taking  $p_v = 1$ . The iso-amplitude contours for this situation are shown in Fig. 4, giving indeed a better correspondance with the measurements behind the shoal. The difference between the two computations ( $p_v = 0$  versus  $p_v = 1$ ) can be most clearly seen by considering sections 5 and 6. The results are given in Fig. 5 for both  $p_v = 0$  and  $p_v = 1$ . For both sections 5 and 6 a much better correspondance with the measurements is obtained for the  $p_v = 1$  case compared to the  $p_v = 0$  case, although even in the purely linear situation a satisfactory correspondance is obtained. For both situations the rms deviations  $\epsilon_{rms}$  and the bias b are defined by

$$b = n^{-1} \Sigma (a_c - a_m) / [n^{-1} \Sigma a_m]$$

$$\epsilon_{rms} = [n^{-1} \Sigma (a_c - a_m)^2]^{1/2} / [n^{-1} \Sigma a_m]$$

We have for section 5 and 6 separately and for all sections together the following results (taken from Dingemans and Radder, 1984)

section	$p_v = 1$		$p_v = 0$	
	b	$\epsilon_{rms}$	b	$\epsilon_{rms}$
5	0.9	10.6	2.5	35.8
6	-1.2	10.8	10.2	36.7
all	3.0	10.2	3.0	22.5

Table 1 Bias b and rms deviation  $\epsilon_{rms}$  in %

The realistic laboratory situation.

The realistic bottom geometry concerns a coastal region near San Ciprian (NW Spain), built in a wave basin for other purposes, see Fig. 6. The region of interest is also shown in the Figure. Notice the cape just seawards from the proposed breakwater alignment. The measuring grid is

shown in Fig. 7. Of the several tests in which the significant wave period, wave height, etc. were varied, the cases of run 6 with very high initial wave height and run 3 with moderate initial wave height are discussed here; in both tests random waves were applied. For the other cases reference is made to Stive and Dingemans (1983). The iso-wave height lines for both the measurement and the computation of run 6 are shown in Fig. 8, together with contour lines of the normalized difference (in %). The comparison is done point by point. The rms deviation is 16% with a bias of 9%. Along the breakwater the comparison is shown in Fig. 10. It is seen that the computed wave heights are essentially higher than the measured ones, but the trend is nearly the same. For this case much wave breaking occurred in the model experiment. For run 3 the results are shown in Figures 9 and 11; the rms deviation is 10.8% and the bias is 5.3%. Both computations for runs 3 and 6 were carried out with  $p_v = 1$  and  $\gamma = 0.8$ , while no bottom friction effects were taken into account. For run 3 wave breaking is of no importance, but for run 6 it is (breaking waves were observed in the physical model). Estimating  $\gamma$  with the formula given by Battjes and Stive (1984) yields for run 3  $\gamma = 0.70$  and for run 6  $\gamma = 0.83$ ; therefore the deviation along the breakwater alignment for run 6 (Fig. 10) cannot be explained by differences in wave breaking characteristics (the value for  $\gamma$  used is lower than the optimal one and with the latter the deviation would become larger). It seems that the computed results are somewhat smeared out in CREDIZ; this is presumably due to an overemphasis of the diffraction effect. This can also be observed from Figs. 12 and 13 in which scatter plots of the results are given. The variation in computed wave heights is less than it is in the measured ones. From the other cases studied in Stive and Dingemans (1983) it was found that the correspondance of CREDIZ is closer in the random wave tests than it is in the periodic wave tests, which is fortunate because CREDIZ is meant to be applied in the field. The present measurements applied random wave without directional spreading so that it may be expected that the correspondance between computations with the monochromatic model CREDIZ and measurements becomes even more close in situations in which tests are conducted with a two-dimensional spectrum.

### 3.2 Field

For the field measurements a region offshore the Haringvlietsluices was chosen. The area is characterized by a shallow shoal which falls partly dry during low tide, a region with nearly straight isobaths offshore the shoal, and a complicated bottom geometry inshore of the shoal, see Fig. 14. A measurement campaign was especially set up in order to assess the applicability of CREDIZ in realistic field situations. At the start of the project the results of the shoal experiment (see Berkhoff et al. (1982)) were available and therefore the main attention was directed to those aspects not yet studied, i.e. the dissipation processes and the effect of non-linearity on the wave celerity. Six waverider buoys were placed more or less around the Hinderplaat; the one available directional buoy (a WAVEC buoy) was especially used to obtain good initial conditions for the computations. Furthermore, two wave staffs were present in the region. Further offshore also wave information was available from the platform LEG and the waverider EURO-3. The measurement campaign was conducted in Fall 1982 and lasted 13 weeks of which during the first 8 weeks the directional buoy was available.

The method of comparison in this case of a relatively small number of point measurements is done as follows. From the file of measurements, given in the form of wave parameters, measurements under specific conditions were selected. Several wave registrations meeting these conditions are usually found, sometimes several weeks apart. A computation is performed for the averaged boundary condition, usually provided by the WAVEC. The comparison is based on the averaged wave parameters at each sensor location. Another method concerns a hindcast in which single measurements are used. Computed wave heights are averaged afterwards over some spatial region because the wave measurement at a sensor location is taken to be characteristic for some region of space; here a region of 250 by 250 m is used.

One measurement condition was called "the ideal condition" because of the fact that a wave condition was selected for which the mathematical model may be expected to give reasonable results. The selection criteria consisted of: 1) registrations of good quality, 2) not too low water levels (water levels between 1.25 and 1.60 m with respect to chart datum (NAP)), 3) not too low waves ( $H_{mo} > .50$  m), 4) waves from the North-West (principal wave direction between  $300^\circ$  and  $330^\circ$ ), being the direction which is nearly perpendicular to the isobaths offshore the Hinderplaat, 5) not too much directional spreading, and 6) old waves, giving swell-type of waves. Five wave registrations were found to comply with these criteria, two on September 22 and three on October 16. Since not all sensors were sampled simultaneously, a time window was applied in order to obtain approximately simultaneous wave registrations at the various sensors. As time window was taken  $t - 25 \text{ min} \leq t_o \leq t + 35 \text{ min}$ , where  $t_o$  is the start time of the wave registration at either the WAVEC or at the staff Ha-1, which were samples starting at each whole hour (the WAVEC for one half hour duration and Ha-1, as were all other sensors, for 20 minutes).

The mean values of  $H_s (=H_{mo})$ ,  $T_p$ , the principal wave direction  $\theta$  and the water level, WST, at the WAVEC are  $\langle H_s \rangle = 133 \text{ cm}$ ,  $\langle T_p \rangle = 7.02 \text{ s}$ ,  $\langle \theta \rangle = 321.4^\circ$  and  $\langle \text{WST} \rangle = 143 \text{ cm}$ ; the standard deviations are  $s(H_s) = 11.0 \text{ cm}$ ,  $s(T_p) = 0.2 \text{ s}$ ,  $s(\theta) = 3.2^\circ$  and  $s(\text{WST}) = 11.5 \text{ cm}$ . The results of computation T26, with parameters  $p_v = 1$ ,  $\gamma = 0.70$ ,  $f_w = 0.005$  are compared with the measurements in the Table below.

sensor	measurement		computation	
	$\langle H_s \rangle$	$s(H_s)$	$\langle H \rangle$	$s(H)$
WR1	133.7	8.4	130.0	5.4
WR2	127.5	20.5	126.2	7.1
WR3	133.3	21.2	135.3	2.6
WR4	52.0	7.7	54.4	22.0
WR5	108.9	9.5	103.6	7.5
WR6	124.3	4.7	115.8	8.5
Ha-1	137.5	17.7	134.4	7.7
E-75	59.0	1.4	34.2	6.1

Table 2 Comparison of ideal condition with CREDIZ computation T26.  
Wave heights in cm

A quite satisfactory correspondance is obtained at all sensor locations, except at location E-75, close to the sluices. At E-75 a relatively large discrepancy is found; the principal reason is that the location is far behind the breaker zone (visible in Fig. 15 for the iso-amplitude contours) and the characteristic wave period T differs much before and behind a strong dissipation zone. The relative error is defined by  $\delta = (\langle H \rangle - \tilde{H}_s) / \tilde{H}_s$ . Taken over all sensors we have  $\langle \delta \rangle = 7.4\%$ , where as for E-75 alone we have  $\delta = -42\%$ ; without E-75 one has  $\langle \delta \rangle = 3.0\%$  and  $s(\delta) = 2.1\%$ .

#### The hindcast.

The period of 14 and 15 October 1982 was selected for the hindcast; wind and water level time histories are shown in Fig. 16. In the hindcast period a rather constant wind direction from North-Westerly directions is present. An example of a wave spectrum of the directional buoy is shown in Fig. 17 and a nearly simultaneous spectrum of WR4 (behind the Hinderplaat) is given in Fig. 18. The results of the hindcast is shown in Figs. 19-21 in which the crosses denote the computed wave heights and the points the ones measure ( $H_{mo}$ ). A scatter plot of all pairs computed and measured wave heights is given in Fig. 22. Especially E-75 is seen to give unsatisfactory results, and for low water levels, also WR4. In terms of the bias and the rms deviation the results as given in the following Tables are obtained. The bias b and the rms deviation  $\epsilon_{rms}$  are defined by

$$b = n^{-1} \Sigma (\langle H \rangle - \tilde{H}_s) / [n^{-1} \Sigma \tilde{H}_s]$$

$$\epsilon_{rms} = [n^{-1} \Sigma (\langle H \rangle - \tilde{H}_s)^2]^{1/2} / [n^{-1} \Sigma \tilde{H}_s]$$

test	T27	T32a	T29	T28	T30	T31
time	17:00	20:00	22:00	23:00	02:00	04:00
WST	-10	20	85	170	150	45
all sensors	-1.5	-2.4	+1.9	+6.9	-3.2	+0.5
not E-75	+3.6	+5.4	+6.1	+8.6	+0.9	+1.8
not E-75, WR4	+7.5	+11.8	+8.7	+9.4	+1.0	+5.1

Table 3 Bias b in %

test	T27	T32a	T29	T28	T30	T31
time	17:00	20:00	22:00	23:00	02:00	04:00
WST	-10	20	85	170	150	45
all sensors	19.2	26.1	16.5	12.4	15.3	13.4
not E-75	13.3	18.9	13.2	12.8	11.0	12.8
not E-75, WR4	8.7	13.4	11.7	12.4	10.7	9.9

Table 4 Deviation  $\epsilon_{rms}$  in %

test	T27	T32a	T29	T28	T30	T31
time	17:00	20:00	22:00	23:00	02:00	04:00
WST	-10	20	85	170	150	45
all sensors	29.6	37.2	18.9	8.6	16.0	22.3
not E-75	21.3	27.6	13.9	7.9	9.5	22.7
not E-75, WR4	8.2	12.5	8.9	8.5	7.3	13.5

Tabel 5 Overall error  $\langle \delta \rangle$  in %

Because of the before mentioned fact that CREDIZ is not suited to predict the wave height at E-75, the station far behind the dissipation zone, with reasonable accuracy and because for low water levels the predicted wave height at WR4, just behind the Hinderplaat is not accurate, the figures for the case that both E-75 and WR4 are excluded have most significance. Notice that the shallowest part of the Hinderplaat is only 10 cm below chart datum and that the bottom soundings at the Hinderplaat are relatively less accurate than elsewhere in the region. It thus follows from the hindcast that wave heights are predicted with an accuracy of at least 15%.

#### 4.0 CONCLUSION

Despite the schematization to monochromatic waves and nearly linear wave propagation the model CREDIZ performs remarkably well for engineering purposes in a variety of conditions in coastal areas, as indicated by both the laboratory and the field verification studies. The findings may be stated as follows.

- For those situations in which the (random) wave field can be characterized by a single frequency and a single wave height measure, CREDIZ gives quite accurate results for the wave height in coastal areas, typically better than 15% deviation. For regions far behind a dissipation zone the results are less accurate, but then the wave field can hardly be characterized by a single frequency.
- From the laboratory studies it followed that the computed wave height field is smoother than the measured one for periodic waves. CREDIZ is more suited for application to random wave fields for not too broad spectra.
- The field comparisons are carried out without accounting for current due to lack of simultaneous current measurements. Currents are typically less than 1 m/s maximum.
- Better results may be obtained by choosing input parameters such as  $\gamma$  for the breaking process and the friction coefficient more carefully than was done here. As an example serves the ideal condition for which deviations of less than 5% were obtained after a short sensitivity study.

#### ACKNOWLEDGEMENT

The performance and analysis of the field experiments has been carried out by the Advisory Branch Hellevoetsluis of Rijkswaterstaat, under the direction of Mr. W.R. Abels. For the numerical computations we were assisted by Mr. P. v.d. Bosch of Delft Hydraulics Laboratory and Mr. G.M. Visser of the Delta Department of Rijkswaterstaat.



REFERENCES

BATTJES, J.A. and J.P.F.M. JANSSEN, 1978: Energy loss and set-up due to breaking of random waves. Proc. 16th Coastal Eng. Conf., Hamburg 1978, pp. 569-587

BATTJES, J.A. and M.J.F. STIVE, 1984: Verification of a dissipation model for random breaking waves. Proc. 19th Coastal Eng. Conf., Houston 1984

BERKHOFF, J.C.W., N. BOOIJ and A.C. RADDER, 1982: Verification of numerical wave propagation models for simple harmonic linear water waves. Coastal Engineering 6, 1982, pp. 255-279

BOOIJ, N., 1982: Gravity waves on water with non-uniform depth and current. Ph.D. thesis, Delft Univeristy of Technology

DINGEMANS, M.W., 1983: Verification of numerical wave propagation models with field measurements; CREDIZ verification Haringvliet. Delft Hydraulics Laboratory, Report W488 part 1, December 1983

DINGEMANS, M.W. and A.C. RADDER, 1984: Note on the verification of the parabolic wave propagation model CREDIZ: a simple non-linear extension; preprint, Oct. 1984

KIRBY, J.T. and R.A. DALRYMPLE, 1984: Verification of a parabolic equation for propagation of weakly-nonlinear waves. Coastal Engineering 8, 1984, pp. 219-232

RADDER, A.C., 1979: On the parabolic equation method for water-wave propagation, J. Fluid Mech. 95, pp. 159-176.

STIVE, M.J.F. and M.W. DINGEMANS, 1983: Verification of the refraction-diffraction wave propagation model CREDIZ in a realistic laboratory situation. Delft Hydraulics Laboratory, Report S581, December 1983

WALKER, J.R., 1976: Refraction of finite-height and breaking waves. Proc. 15th Coastal Eng. Conf., Hawaii 1976, pp. 507-524

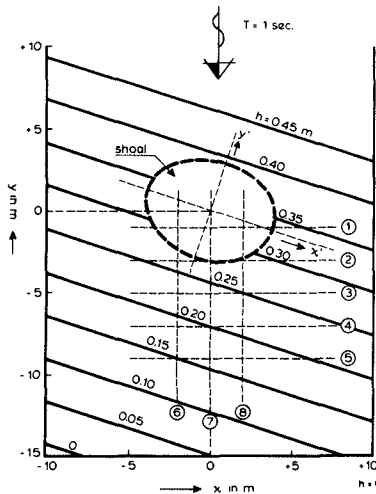


Fig. 1

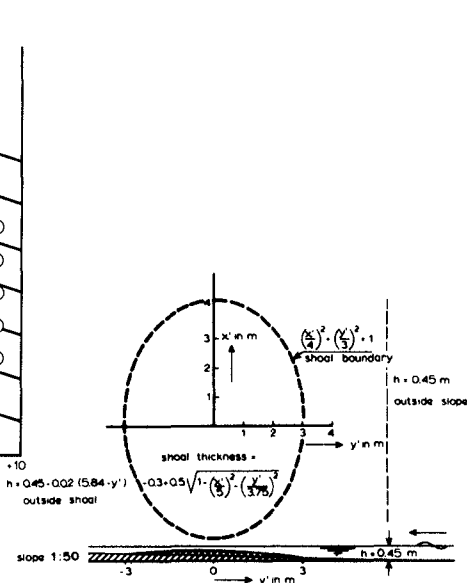


Fig. 2

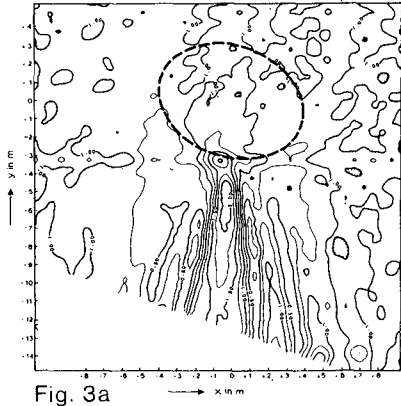


Fig. 3a

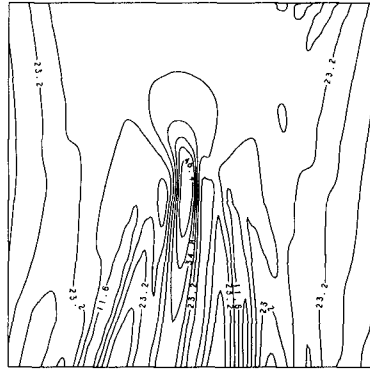


Fig. 3b

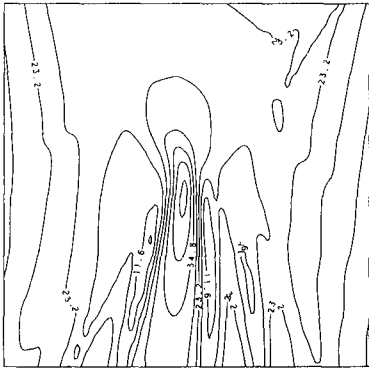


Fig. 4

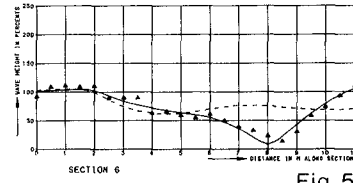
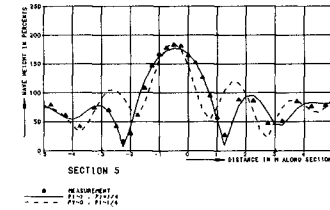


Fig. 5

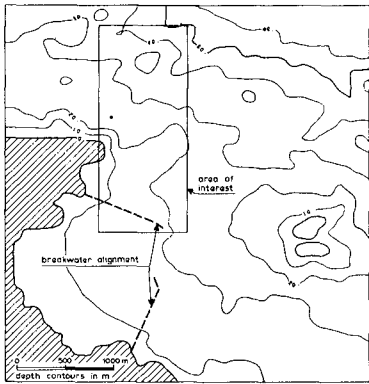


Fig. 6

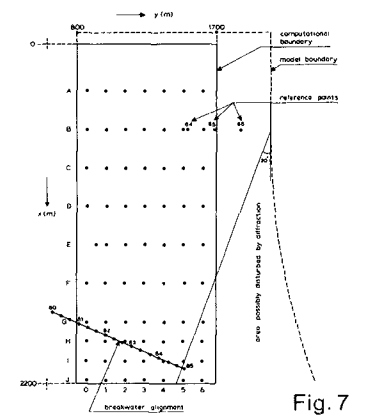


Fig. 7

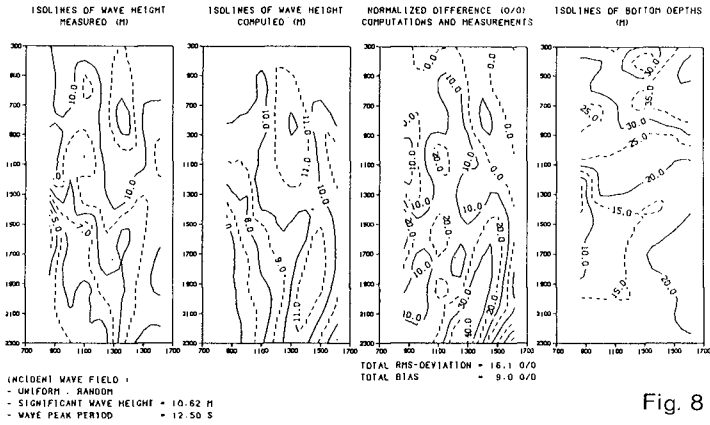


Fig. 8

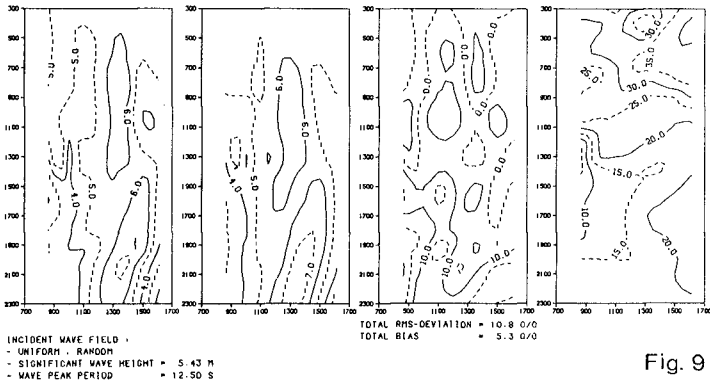


Fig. 9

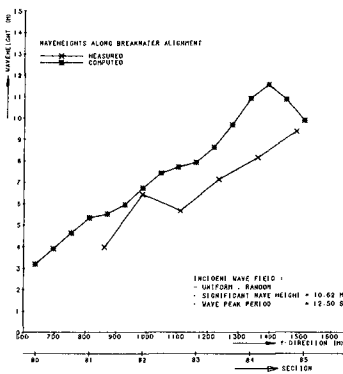


Fig. 10

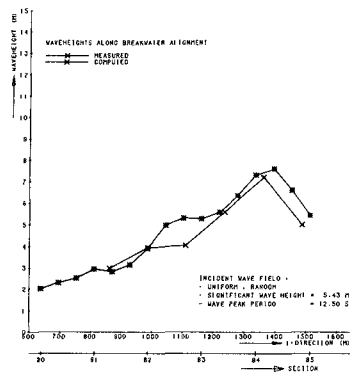


Fig. 11

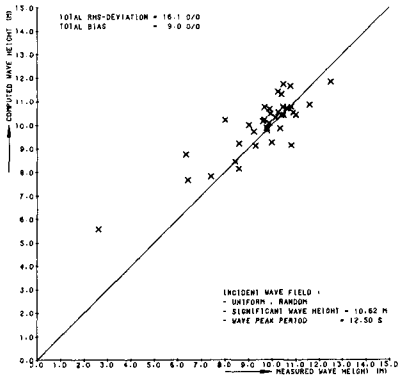


Fig. 12

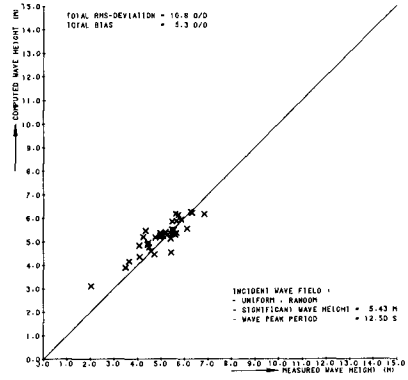


Fig. 13

Bottom contours 1981 bottom, 500 m mesh, with STROBO

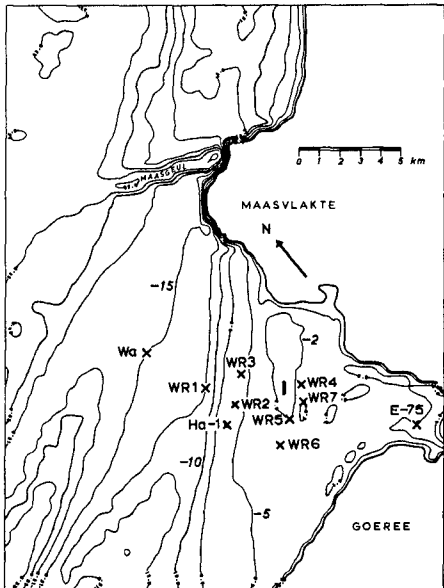


Fig. 14

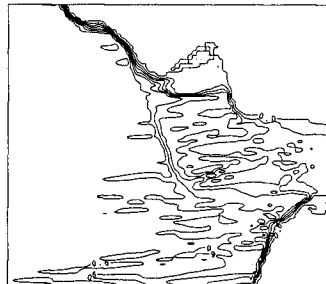


Fig. 15

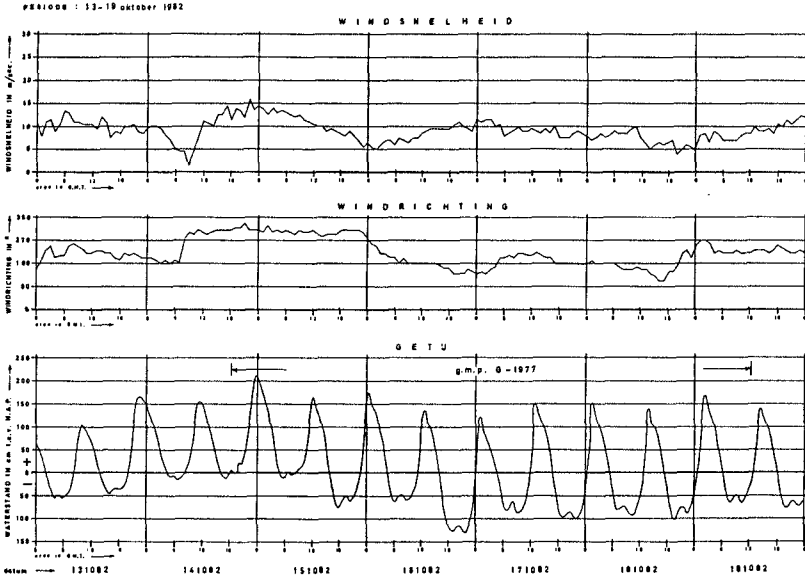


Fig. 16

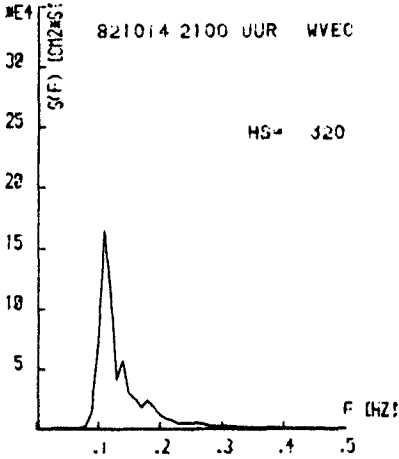


Fig. 17

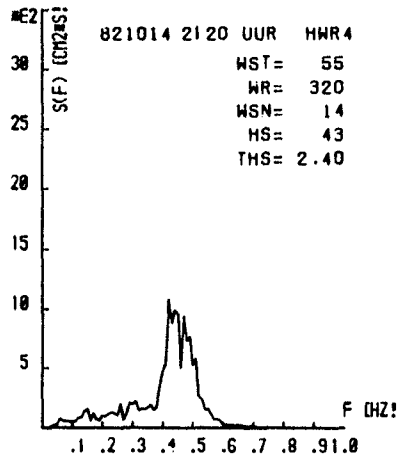


Fig. 18

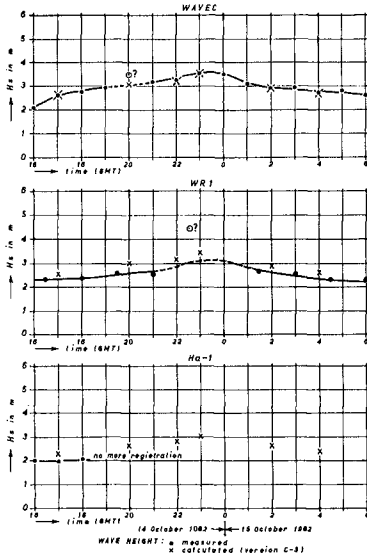


Fig. 19

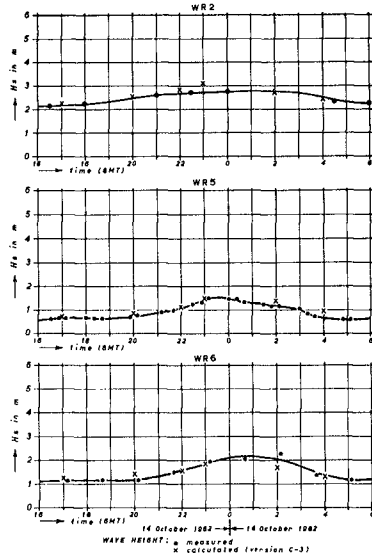


Fig. 20

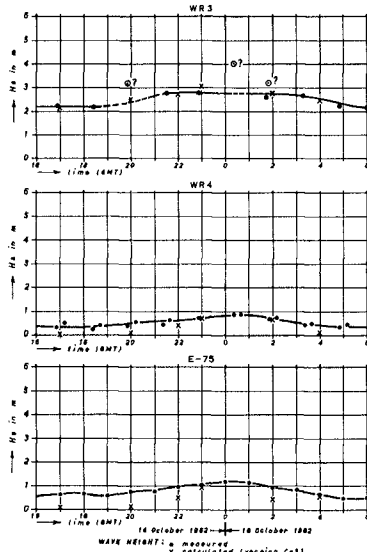


Fig. 21

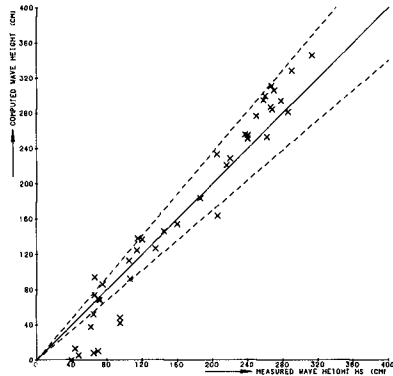


Fig. 22

## CHAPTER EIGHTY ONE

### CONFORMAL MAPPING SOLUTION OF A WAVE FIELD ON THE ARBITRARILY SHAPED SEA BOTTOM

by

Kazuo Nadaoka and Mikio Hino

Dept. Civil Eng., Tokyo Institute of Technology  
2-12-1, Meguro-ku, Tokyo, Japan.

#### ABSTRACT

A new wave equation has been derived for the full nonlinear dispersive waves propagating over an arbitrarily shaped sea bed. The method of the derivation of the equation uses a conformal mapping technique by which the original domain can be transformed onto a domain with a uniform depth to make the basic equation easily integrable vertically. By taking an inverse Fourier transform, the velocity potential obtained by the integration can be expressed in the form which can construct the exact wave equation from the water surface boundary conditions. An algorithm for the numerical integration of the equation is presented with some examples of the solution.

#### 1. INTRODUCTION

Nearshore wave deformation is characterized mainly by the effects of nonlinearity and dispersivity of waves, and non-uniformity of bottom topography. So far there have been many studies on the wave deformation by using the well known KdV equation or Boussinesq equation ( e.g., Peregrine, (1967), Madsen and Mei(1969) ). Although these equations have been modified to include the bottom effect by Kakutani(1972), Shuto(1974), Peregrine (1967) and others, their applicability is limited to slowly varying bottom topography. Furthermore, these wave equations can describe only weak nonlinearity and dispersivity of waves.

The present study derives a new wave equation which may be applied to full nonlinear-dispersive waves propagating over a sea bottom with an arbitrary topography. The method of the derivation of the equation uses a conformal mapping technique by which the original domain can be transformed onto a uniform depth region. The mapping does not change the form of the basic equation, i.e., Laplace's equation on a velocity potential, and simplifies bottom boundary condition so that the basic equation becomes easily integrable. The velocity potential function obtained by the integration includes all components of a time-varying wave number spectrum. Further, the velocity potential function so obtained may be expressed as a function with a convolutional integral by an inverse Fourier transform technique. Hence, the water surface boundary conditions can yield the exact wave equation by using the representation of the velocity potential at the water

surface. An algorithm of the numerical integration of the equation is presented with some examples of the solution. In the appendixes, some descriptions on an analytical method to obtain an approximate solution by using a WKB perturbation technique are presented with a method to estimate wave reflection coefficients.

2. FORMULATION OF EQUATIONS

2.1 Basic Equation and Boundary Conditions in a Mapped Space

Physical plane denoted by  $z = x+iy$  may be transformed conformally onto a  $\zeta$ -plane by an analytical complex function,

$$\zeta = f(z). \tag{1}$$

The function  $f$  can be chosen as that which transforms the domain  $D$  with an arbitrarily shaped bottom topography in the  $z$ -plane onto the domain  $D'$  with a uniform depth  $\beta_0$  in the  $\zeta$ -plane as shown in Fig.1. If we denote  $\zeta$ -plane as  $\zeta = \alpha+i\beta$ , Eq.(1) can be written as

$$\begin{aligned} \alpha &= \phi_1(x,y), \\ \beta &= \phi_2(x,y), \end{aligned} \tag{2}$$

or inversely,

$$\begin{aligned} x &= \psi_1(\alpha,\beta), \\ y &= \psi_2(\alpha,\beta). \end{aligned} \tag{3}$$

The function  $f$  defines the curvilinear coordinates system  $(\alpha,\beta)$  in the original domain. From another point of view, it can be said that the function  $f$  is just a complex velocity potential function so that the constant  $\alpha$  and  $\beta$  lines correspond to equi-potential lines and stream lines, respectively. Therefore, we can utilize the usual potential flow theory to construct the function  $f$  in which one of the stream lines forms the bottom boundary and another stream line coincides with the still water surface. For example, the region over a uniformly sloping beach can be transformed into a constant depth region by the complex function

$$\zeta = \ln z. \tag{4}$$

This is a velocity potential function for the flow due to a point source with a unit strength located at the intersection of bottom line and the still water surface (Fig.2). For the more general case of the bottom topography, we can use a numerical method proposed by, e.g., Chenin and Schwartz (1982).

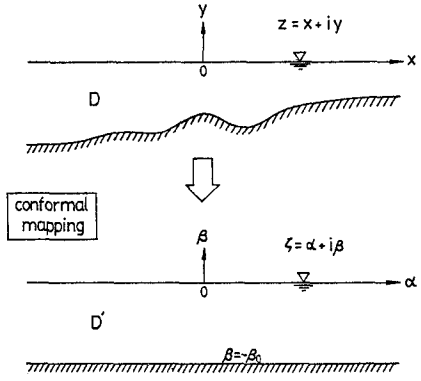


Fig.1 Conformal mapping of wave field



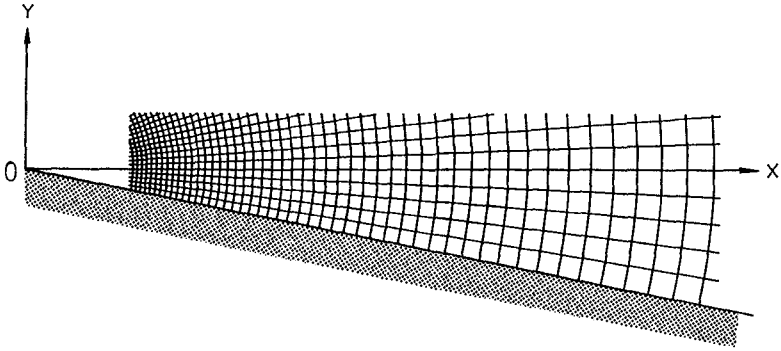


Fig. 2 Orthogonal curvilinear grid system for uniformly sloping beach

The basic equation and the boundary conditions in the z-plane may be written as follows.

$$\frac{\partial^2 \Phi}{\partial x^2} + \frac{\partial^2 \Phi}{\partial y^2} = 0, \tag{5}$$

$$\frac{\partial \Phi}{\partial y} = - \frac{\partial \Phi}{\partial x} \cdot \frac{\partial h}{\partial x}, \quad y = -h(x) \tag{6}$$

$$\frac{\partial \eta}{\partial t} + \frac{\partial \Phi}{\partial x} \cdot \frac{\partial \eta}{\partial x} - \frac{\partial \Phi}{\partial y} = 0, \quad y = \eta(x, t) \tag{7}$$

$$\frac{\partial \Phi}{\partial t} + \frac{1}{2} \cdot \left[ \left( \frac{\partial \Phi}{\partial x} \right)^2 + \left( \frac{\partial \Phi}{\partial y} \right)^2 \right] + g\eta = 0, \quad y = \eta(x, t) \tag{8}$$

where  $\Phi$  is a velocity potential,  $h$  is a water depth,  $\eta$  is a water surface elevation, and  $g$  is the gravitational acceleration.

In the  $\zeta$ -plane, the boundary conditions become

$$\frac{\partial \Phi}{\partial \beta} = 0, \quad \beta = -\beta_0 \tag{9}$$

$$\frac{\partial \tilde{\eta}}{\partial t} + s^2 \cdot \left[ \frac{\partial \Phi}{\partial \alpha} \cdot \frac{\partial \tilde{\eta}}{\partial \alpha} - \frac{\partial \Phi}{\partial \beta} \right] = 0, \quad \beta = \tilde{\eta}(\alpha, t) \tag{10}$$

$$\frac{\partial \Phi}{\partial t} + \frac{s^2}{2} \cdot \left[ \left( \frac{\partial \Phi}{\partial \alpha} \right)^2 + \left( \frac{\partial \Phi}{\partial \beta} \right)^2 \right] + g \cdot \psi_2(\alpha, \tilde{\eta}) = 0, \quad \beta = \tilde{\eta}(\alpha, t) \tag{11}$$

where  $s$  is a scale factor related with the mapping defined as

$$s = \left| \frac{d\zeta}{dz} \right|. \tag{12}$$

In the water surface boundary conditions (10) and (11), the scale factor  $s$  is coupled with the nonlinear terms. Hence it can be said that the scale factor  $s$  directly affects the nonlinearity of waves. Further, the scale factor  $s$  represents nonuniformity of the gravity as will be shown later.

In contrast with the boundary conditions, the basic equation remains its form unchanged through the mapping by the nature of the conformal transform, i.e.,

$$\frac{\partial^2 \Phi}{\partial \alpha^2} + \frac{\partial^2 \Phi}{\partial \beta^2} = 0. \tag{13}$$

Therefore, the basic equation can be easily integrable vertically on the  $\zeta$ -plane with the simplified bottom boundary condition (9).

2.2 General Solution of the Basic Equation

The Fourier transform of Eq.(13) with regard to  $\alpha$  becomes

$$\frac{\partial^2 \bar{\Phi}}{\partial \beta^2} + k^2 \bar{\Phi} = 0, \tag{14}$$

where  $\bar{\Phi}$  is the Fourier transform of  $\Phi$  with respect to  $\alpha$  defined as

$$\bar{\Phi}(k, \beta, t) = \frac{1}{2\pi} \int_{-\infty}^{\infty} \Phi(\alpha, \beta, t) \cdot e^{-ik\alpha} \cdot d\alpha. \tag{15}$$

Eq.(14) can be integrated with the bottom boundary condition

$$\frac{\partial \bar{\Phi}}{\partial \beta} = 0,$$

to yield

$$\bar{\Phi}(k, \beta, t) = A(k, t) \cdot \frac{\cosh k(\beta + \beta_0)}{\cosh k\beta_0}. \tag{16}$$

Therefore,  $\Phi$  is represented by the inverse Fourier transform of  $\bar{\Phi}$

$$\Phi(\alpha, \beta, t) = \int_{-\infty}^{\infty} A(k, t) \cdot \frac{\cosh k(\beta + \beta_0)}{\cosh k\beta_0} \cdot e^{ik\alpha} \cdot dk, \tag{17}$$

where  $A(k, t)$  is a time varying wave number spectrum to be determined by the water surface boundary conditions, Eqs.(10) and (11).

From Eq.(17),  $\Phi_\alpha$ ,  $\Phi_\beta$  and  $\Phi_t$  can be represented as

$$\frac{\partial \Phi}{\partial \alpha} = i \int_{-\infty}^{\infty} k \cdot A(k,t) \cdot \frac{\cosh k(\beta + \beta_0)}{\cosh k\beta_0} \cdot e^{ik\alpha} \cdot dk, \tag{18}$$

$$\frac{\partial \Phi}{\partial \beta} = \int_{-\infty}^{\infty} k \cdot A(k,t) \cdot \frac{\sinh k(\beta + \beta_0)}{\cosh k\beta_0} \cdot e^{ik\alpha} \cdot dk, \tag{19}$$

$$\frac{\partial \Phi}{\partial t} = \int_{-\infty}^{\infty} \frac{\partial}{\partial t} A(k,t) \cdot \frac{\cosh k(\beta + \beta_0)}{\cosh k\beta_0} \cdot e^{ik\alpha} \cdot dk. \tag{20}$$

To execute the inverse Fourier transform of the right hand side of the above equations, we may introduce a new variable  $\chi(\alpha,t)$  defined as

$$\chi(\alpha,t) = \int_{-\infty}^{\infty} A(k,t) \cdot e^{ik\alpha} \cdot dk, \tag{21}$$

and use the following inverse Fourier transform formula ( e.g., Erdélyi, 1954 ),

$$F^{-1} \left[ \frac{\cosh k(\beta + \beta_0)}{\cosh k\beta_0} \right] = - \frac{2\pi}{\beta_0} \left\{ \frac{\sin(\frac{\pi\beta}{2\beta_0}) \cdot \cosh(\frac{\pi\alpha}{2\beta_0})}{\cosh(\frac{\pi\alpha}{\beta_0}) - \cos(\frac{\pi\beta}{\beta_0})} \right\} \equiv K_1(\alpha,\beta), \tag{22}$$

(  $-\beta_0 \leq \beta < 0$  )

$$F^{-1} \left[ \frac{\sinh k(\beta + \beta_0)}{\cosh k\beta_0} \right] = i \cdot \frac{2\pi}{\beta_0} \left\{ \frac{\cos(\frac{\pi\beta}{2\beta_0}) \cdot \sinh(\frac{\pi\alpha}{2\beta_0})}{\cosh(\frac{\pi\alpha}{\beta_0}) - \cos(\frac{\pi\beta}{\beta_0})} \right\} \equiv i \cdot K_2(\alpha,\beta), \tag{23}$$

(  $-\beta_0 \leq \beta < 0$  )

where  $F^{-1}[\cdot]$  is the operator to take inverse Fourier transform. From the above equations and the convolution formula (24) on the inverse Fourier transform,

$$F^{-1}[\bar{f}_1(k) \cdot \bar{f}_2(k)] = \frac{1}{2\pi} \int_{-\infty}^{\infty} f_1(\xi) \cdot f_2(\alpha - \xi) \cdot d\xi. \tag{24}$$

we can express the velocity potential  $\Phi(\alpha,\beta,t)$  and its partial derivatives with respects to  $\alpha$ ,  $\beta$  and  $t$  as follows.

$$\Phi(\alpha,\beta,t) = \frac{1}{2\pi} \int_{-\infty}^{\infty} K_1(\xi,\beta) \cdot \chi(\alpha - \xi,t) \cdot d\xi, \tag{25}$$

$$\frac{\partial \Phi}{\partial \alpha} = \frac{1}{2\pi} \int_{-\infty}^{\infty} K_1(\xi,\beta) \cdot \frac{\partial}{\partial \alpha} \chi(\alpha - \xi,t) \cdot d\xi, \tag{26}$$

$$\frac{\partial \Phi}{\partial \beta} = \frac{1}{2\pi} \int_{-\infty}^{\infty} K_2(\xi,\beta) \cdot \frac{\partial}{\partial \alpha} \chi(\alpha - \xi,t) \cdot d\xi, \tag{27}$$

$$\frac{\partial \Phi}{\partial t} = \frac{1}{2\pi} \int_{-\infty}^{\infty} K_1(\xi,\beta) \cdot \frac{\partial}{\partial t} \chi(\alpha - \xi,t) \cdot d\xi. \tag{28}$$

Hence the water particle velocity in the  $\zeta$ -plane can be calculated through these equations by prescribing the value of  $\chi$ . However it should be noted that the region in which the above equations are valid is  $-\beta_0 \leq \beta < 0$ .

2.3 Derivation of Linear Full Dispersive Wave Equation

For linear waves, the water surface boundary condition on  $\Phi$  becomes

$$\frac{\partial^2 \Phi}{\partial t^2} + g \cdot s_0(\alpha) \cdot \frac{\partial \Phi}{\partial \beta} = 0, \quad \beta = 0. \tag{29}$$

where  $s_0(\alpha)$  is the scale factor at  $\beta = 0$ . In the above equation, the gravitational acceleration  $g$  is coupled with the scale factor  $s_0(\alpha)$ . Hence, it can be said that, for the linear waves, the mapping replaces the effect of the water depth variation in the  $z$ -plane with that of non-uniformity of the gravity in the  $\zeta$ -plane.

The limit values of  $\Phi_\beta$  and  $\Phi_t$  represented as Eqs.(26) and (27) when  $\beta \rightarrow -0$  are

$$\lim_{\beta \rightarrow -0} \frac{\partial \Phi}{\partial \beta} = \frac{1}{2\beta_0} \int_{-\infty}^{\infty} K(\xi) \frac{\partial}{\partial \alpha} \chi(\alpha - \xi, t) d\xi,$$

$$\lim_{\beta \rightarrow -0} \frac{\partial \Phi}{\partial t} = \frac{\partial}{\partial t} \chi(\alpha, t),$$

where  $K(\xi)$  is a kernel function defined as

$$K(\xi) = \operatorname{cosech}\left(\frac{\pi}{2\beta_0} \xi\right). \tag{30}$$

Substituting these equations into Eq.(29) and using the relation  $\chi_t = g \cdot \eta$ , we can obtain the following linear wave equation to describe evolution of water surface elevation  $\eta$ .

$$\frac{\partial^2}{\partial t^2} \eta(\alpha, t) + \frac{g}{2\beta_0} \cdot s_0(\alpha) \cdot \int_{-\infty}^{\infty} K(\xi) \frac{\partial}{\partial \alpha} \eta(\alpha - \xi, t) d\xi = 0. \tag{31}$$

In the second term of the above equation, the non-uniformity of the gravity expressed as  $g \cdot s_0(\alpha)$  represents the effect of bottom topography in the original  $z$ -plane and the convolutional integral includes the effect of wave dispersivity. For long waves, Eq.(31) becomes

$$\frac{\partial^2}{\partial t^2} \eta(\alpha, t) - g \cdot s_0(\alpha) \cdot \beta_0 \cdot \frac{\partial^2}{\partial \alpha^2} \eta(\alpha, t) = 0. \tag{32}$$

2.4 Derivation of Full Nonlinear-Dispersive Wave Equation

Nonlinear wave equation may be derived by the almost same manner as the case of linear waves. In this case, however, Eqs.(26) to (28) on  $\Phi_\alpha$ ,  $\Phi_\beta$  and  $\Phi_t$  are not applicable in the region of  $\beta \geq 0$  as already mentioned. This limitation is originated from the formula (22) and (23) on the kernel functions  $K_1$  and  $K_2$ . Therefore, alternative methods must be developed to evaluate the value of those kernel functions at the water surface boundary.

The one method is to reevaluate  $K_1$  and  $K_2$  by replacing the denominator of Eq.(16) with  $\cosh k(a_0 + \beta_0)$  where  $a_0$  is a parameter chosen as  $a_0 > \tilde{\eta}_{\max}$ . The other method is to take Taylor expansion of the functions to be transformed in Eqs.(22) and (23) around  $\beta = 0$ . The results by the latter method become as follows.

$$K_1(\alpha, \beta) = 2\pi \sum_{n=0}^{\infty} (-1)^n \frac{\beta^{2n}}{(2n)!} \cdot \delta^{(2n)}(\alpha) + \frac{\pi}{\beta_0} \int_{-\infty}^{\infty} K(\xi) \cdot \sum_{n=0}^{\infty} (-1)^n \frac{\beta^{2n+1}}{(2n+1)!} \cdot \delta^{(2n+1)}(\alpha - \xi) d\xi, \tag{33}$$

$$K_2(\alpha, \beta) = \frac{\pi}{\beta_0} \int_{-\infty}^{\infty} K(\xi) \cdot \sum_{n=0}^{\infty} (-1)^n \frac{\beta^{2n}}{(2n)!} \cdot \delta^{(2n)}(\alpha - \xi) d\xi - 2\pi \sum_{n=0}^{\infty} (-1)^n \frac{\beta^{2n+1}}{(2n+1)!} \cdot \delta^{(2n+1)}(\alpha), \tag{34}$$

where  $\delta^{(n)}(\alpha)$  is the n-th derivative of Dirac's delta function. From Eqs. (33) and (34),  $\Phi_\alpha$ ,  $\Phi_\beta$  and  $\Phi_t$  can be expressed as

$$\frac{\partial \Phi}{\partial \alpha} = \chi^{(1)}(\alpha, t) + \frac{\beta}{2\beta_0} \int_{-\infty}^{\infty} K(\xi) \cdot \chi^{(2)}(\alpha - \xi, t) d\xi + \dots, \tag{35}$$

$$\frac{\partial \Phi}{\partial \beta} = \frac{1}{2\beta_0} \int_{-\infty}^{\infty} K(\xi) \cdot \chi^{(1)}(\alpha - \xi, t) d\xi - \beta \cdot \chi^{(2)}(\alpha, t) + \dots, \tag{36}$$

$$\frac{\partial \Phi}{\partial t} = \frac{\partial}{\partial t} \chi(\alpha, t) + \frac{\beta}{2\beta_0} \int_{-\infty}^{\infty} K(\xi) \cdot \frac{\partial}{\partial t} \chi^{(1)}(\alpha - \xi, t) d\xi + \dots, \tag{37}$$

where the superscripts (n) for  $\chi$  indicate the n-th order partial derivative with respect to  $\alpha$ .

Substitution of Eqs.(35) to (37) into the surface boundary conditions (10) and (11) leads to the following integro-differential equations on  $\tilde{\eta}$  and  $\chi$ .

$$\frac{\partial \tilde{\eta}}{\partial t} + \frac{1}{2\pi} \cdot s^2(\alpha, \tilde{\eta}) \cdot \left[ \int_{-\infty}^{\infty} K_1(\xi, \tilde{\eta}) \frac{\partial}{\partial \alpha} \chi(\alpha - \xi, t) d\xi \cdot \frac{\partial \tilde{\eta}}{\partial \alpha} - \int_{-\infty}^{\infty} K_2(\xi, \tilde{\eta}) \frac{\partial}{\partial \alpha} \chi(\alpha - \xi, t) d\xi \right] = 0, \tag{38}$$

$$\int_{-\infty}^{\infty} K_1(\xi, \tilde{\eta}) \frac{\partial}{\partial t} \chi(\alpha - \xi, t) d\xi + \frac{1}{4\pi} \cdot s^2(\alpha, \tilde{\eta}) \cdot \left[ \left\{ \int_{-\infty}^{\infty} K_1(\xi, \tilde{\eta}) \frac{\partial}{\partial \alpha} \chi(\alpha - \xi, t) d\xi \right\}^2 + \left\{ \int_{-\infty}^{\infty} K_2(\xi, \tilde{\eta}) \frac{\partial}{\partial \alpha} \chi(\alpha - \xi, t) d\xi \right\}^2 \right] + 2\pi g \cdot \psi_2(\alpha, \tilde{\eta}) = 0. \tag{39}$$

Since the equations are derived without any assumptions and constraints, they constitute a set of exact wave equations on  $\tilde{\eta}$  and  $\chi$ . Therefore they can essentially express arbitrary degree of nonlinearity, dispersivity and the effect of non-uniformity of the water depth.

Fenton & Rienecker (1980) proposed a numerical method for the accurate solution of nonlinear equations for water waves over a horizontal bed. The method uses the finite Fourier series approximation on the velocity potential  $\phi$  and predicts the evolution of water surface elevation  $\eta$  with that of the Fourier coefficients. On the contrary, the wave equations (38) and (39) include all components of the continuous wave number spectrum  $A(k, t)$ , and they can describe directly the evolution of  $\tilde{\eta}$  and  $\chi$  in the physical space.

### 3. NUMERICAL SOLUTION OF WAVE EQUATIONS

#### 3.1 Algorithm of the Numerical Integration of the Equations

The kernel function  $K(\xi)$  included in the linear wave equation (31) and the nonlinear wave equations (38) and (39) has a singularity at  $\xi = 0$  such as

$$\lim_{\xi \rightarrow \pm 0} K(\xi) = \pm \infty.$$

To avoid this singularity the following procedure has been developed.

If the interval of integration of a convolutional integral  $I(\alpha, t)$  for  $K(\alpha)$  and a continuous function  $f(\alpha, t)$  is divided into the three parts as

$$\begin{aligned} I(\alpha, t) &= \int_{-\infty}^{\infty} K(\xi) \cdot f(\alpha - \xi, t) d\xi \\ &= \left( \int_{-\infty}^{-\Delta\xi} + \int_{-\Delta\xi}^{\Delta\xi} + \int_{\Delta\xi}^{\infty} \right) \cdot K(\xi) \cdot f(\alpha - \xi, t) d\xi \\ &= I_1 + I_2 + I_3, \end{aligned} \tag{40}$$

then the singularity is included in the second integral  $I_2$ . Substitution of the Taylor expansion of  $f(\alpha - \xi, t)$  around  $\xi = 0$  into the second integral  $I_2$  leads to

$$I_2(\alpha, t) = \sum_{n=0}^{\infty} \int_{-\Delta\xi}^{\Delta\xi} (-1)^n \frac{\xi^n}{n!} \operatorname{cosech}\left(\frac{\pi}{2\beta_0}\xi\right) d\xi \cdot \frac{\partial^n}{\partial \alpha^n} f(\alpha, t).$$

When  $n$  is an even number, the value of the integral becomes zero in the sense of Cauchy principal value because the kernel function  $K(\xi)$  is an odd function. Thus, if  $\Delta\xi$  is taken to be enough small to neglect the higher order terms,  $I_2(\alpha, t)$  can be evaluated by

$$\begin{aligned} I_2(\alpha, t) &\cong - \int_{-\Delta\xi}^{\Delta\xi} \xi \cdot \operatorname{cosech}\left(\frac{\pi}{2\beta_0}\xi\right) d\xi \cdot \frac{\partial}{\partial \alpha} f(\alpha, t) \\ &= -2 \cdot \left(\frac{2\beta_0}{\pi}\right)^2 \cdot \operatorname{Shi}^* \left(\frac{\pi}{2\beta_0}\Delta\xi\right) \cdot \frac{\partial}{\partial \alpha} f(\alpha, t), \end{aligned} \quad (41)$$

where

$$\begin{aligned} \operatorname{Shi}^*(x) &= \int_0^x \frac{\xi}{\sinh \xi} d\xi = \sum_{k=0}^{\infty} \frac{(2-2^{2k})B_{2k}}{(1+2k)(2k)!} x^{1+2k} \\ &= x - \frac{x^3}{3 \cdot 3!} + \frac{7x^5}{15 \cdot 5!} - \frac{31x^7}{21 \cdot 7!} + \frac{127x^9}{15 \cdot 9!} - \dots, \end{aligned} \quad (42)$$

(  $|x| < \pi$  )

and  $B_n$  is Bernoulli numbers.

Using the above procedure, we can obtain an alternative representation of the linear wave equation.

$$\begin{aligned} \frac{\partial^2}{\partial t^2} \eta(\alpha, t) &= -\frac{g}{2\beta_0} s_0(\alpha) \int_{-\infty}^{-\Delta\xi} K(\xi) \frac{\partial}{\partial \alpha} \eta(\alpha - \xi, t) d\xi \\ &\quad + \left(\frac{2}{\pi}\right)^2 \beta_0 g \cdot s_0(\alpha) \cdot \operatorname{Shi}^* \left(\frac{\pi}{2\beta_0}\Delta\xi\right) \cdot \frac{\partial^2}{\partial \alpha^2} \eta(\alpha, t) \\ &\quad - \frac{g}{2\beta_0} s_0(\alpha) \cdot \int_{\Delta\xi}^{\infty} K(\xi) \frac{\partial}{\partial \alpha} \eta(\alpha - \xi, t) d\xi. \end{aligned} \quad (43)$$

Since the above equation has no singularity, it may be easily solved by a usual finite difference scheme.

For the nonlinear wave equation, the almost same procedure as the linear case can be used except that the nonlinear wave equation includes higher order derivatives of the unknown variable  $\chi$ .

3.2 Examples of Numerical Solutions

(1) Linear waves

As an example of the numerical solution for the linear wave equation (43), a calculation has been made for waves propagating over a stepped sea bed with a slope of arbitrary inclination as shown in Fig.3. The scale factor  $s_0(\alpha)$  for this case becomes

$$s_0(\alpha) = \frac{\beta_0}{h} e^{\theta 1/(2\beta_0)} \cdot \left[ \cosh\left(\frac{\pi 1}{2\beta_0}\right) - \tanh\left(\frac{\pi \alpha}{2\beta_0}\right) \cdot \sinh\left(\frac{\pi 1}{2\beta_0}\right) \right]^{-\theta/\pi}, \quad (44)$$

where

$$1 = \frac{\beta_0}{\theta} \cdot \ln\left(\frac{h}{b}\right). \quad (45)$$

The above equation may be obtained by using the Poisson-Schwartz's integral formula. The solid lines in Fig.3 represent the constant  $\alpha$  and  $\beta$  lines. The initial conditions for the integration adopted here are

$$\eta(\alpha, 0) = a \cdot \exp\left[-(\alpha - \alpha_0)^2 / (2\beta_0)^2\right], \quad (46)$$

with  $a = 1.5m, \quad \beta_0 (= h) = 10m,$

and

$$\frac{\partial}{\partial t} \eta(\alpha, 0) = 0.$$

The inclination of the slope  $\theta$  and the water depth ratio  $b/h$  are chosen as the value of  $45^\circ$  and  $1/4$ , respectively. The upper figure in Fig.3 shows the scale factor  $s_0$  as a function of  $x$ . From the meaning of the scale factor as previously mentioned, we can say that, in the  $\zeta$ -plane, the gravitational acceleration for the shallower region is four times as great as that for the large depth region.

The result of the computation is shown in Fig.4 where the full lines represent the solution for the linear full-dispersive wave equation (31), while the broken lines show the solution for the linear long wave equation (32). The full-dispersive wave solution shows that, in contrast with the non-dispersive wave solution, the longer waves propagate faster than the shorter waves. This is a direct manifestation of the wave dispersivity. The figure also shows that the right going waves divide into reflected waves and transmitted waves on the slope.

(2) Nonlinear waves

Nonlinear wave solution has been obtained for the same stepped bottom topography as the above. For the reason of simplicity, only the first terms in the power series of Eqs.(35) to (37) are taken for the calculation here. The initial condition for  $\tilde{\eta}$  is chosen as the same as Eq.(46) but with  $a = 2.0 m$ . The initial condition for  $\chi$  is taken as  $\chi(\alpha, 0) = 0$  which means that there is no fluid motion at the initial stage.



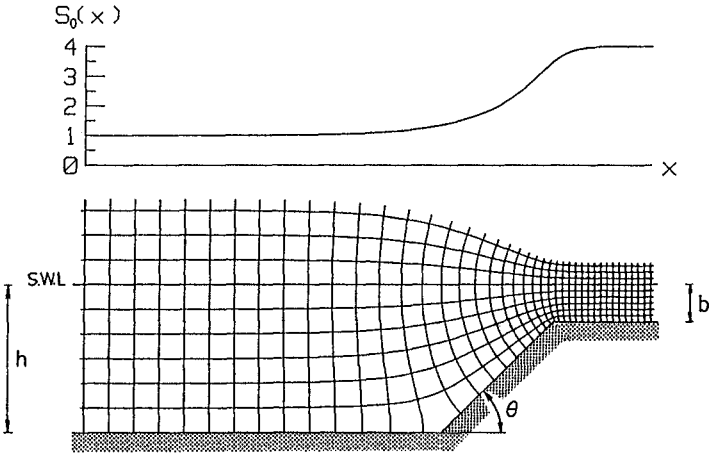


Fig.3 Orthogonal curvilinear grid system and scale factor  $s_0(x)$  for a stepped bottom profile.

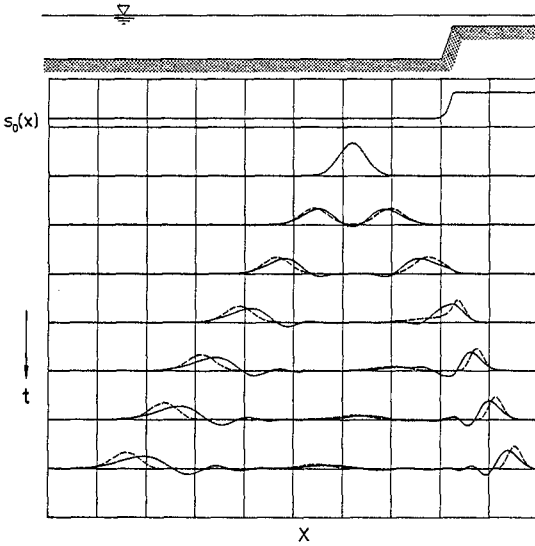


Fig.4 Linear wave evolution over a stepped sea bed.

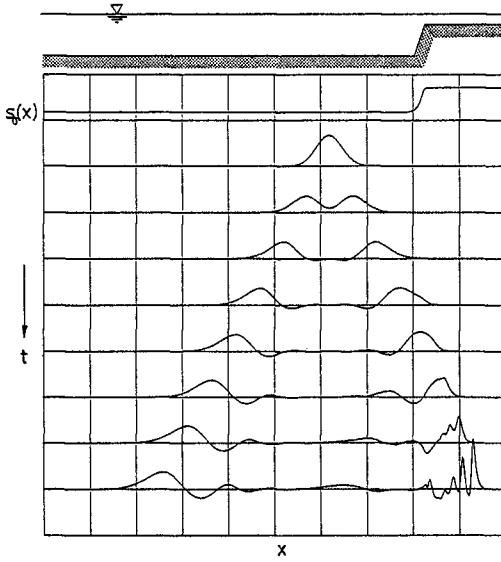


Fig.5 Nonlinear wave evolution over a stepped sea bed.

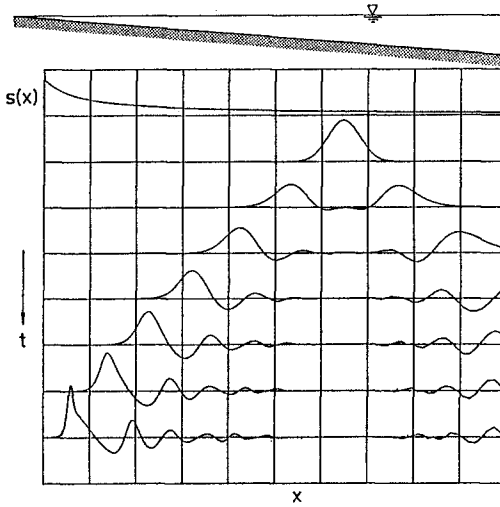


Fig.6 Nonlinear wave evolution over a uniformly sloping beach.  
 (  $\tan\beta_0 = 1/30$  )

Figure 5 shows the result of the computation and indicates that the dispersion and reflection of waves take place as in the case of linear waves. The figure also reveals that the right going waves steepen their front face as they propagate over the slope and give rise to fission into the several solitons on the step. This phenomena of solitons has been already reported by Madsen and Mei (1969) and is considered to be due to the combined effects of nonlinearity and dispersivity of waves and bottom topography. Figure 6 shows another example for waves on a uniformly sloping beach for which the mapping function  $f$  is defined as Eq.(4).

From these examples, it may be concluded that the wave equation derived in the present study is effective to describe the wave evolution under the combined effects of nonlinearity and dispersivity of waves and nonuniformity of the water depth.

#### REFERENCES

- Bellman, R. and Kalaba, R.: Functional equations, wave propagation and invariant imbedding, *Jour. Math. Mech.*, Vol.8, No.5, pp.683 ~ 704, 1959.
- Chenin, M.I. and Schwartz, S.: Generation of an orthogonal curvilinear computational grid for a finite difference method, *International Symposium on Refined Modelling of flows*, sponsored by IAHR, Paris, 1982.
- Chu, V.H. and Mei, C.C.: On slowly-varying Stokes waves, *Jour. Fluid Mech.*, Vol.41, part 4, pp.873 ~ 887, 1970.
- Erdélyi, A. (ed.): *Tables of integral transforms*, Vol.1, McGraw-Hill, New York, 1954.
- Fenton, J.D. and Rienecker, M.M.: Accurate numerical solutions for nonlinear waves, *Proc. 17th Conf. on Coastal Eng.*, pp.50 ~ 69, 1980.
- Hamanaka, K. and Kato, K.: Perturbation analysis of finite amplitude waves with slowly varying depth, *Proc. 29th Japanese Conf. on Coastal Eng.*, pp.65 ~ 69, 1982 (in Japanese).
- Ijima, T. and Sakai, T.: Theoretical study on the effects of submerged breakwater, *Proc. 18th Conf. on Coastal Eng.*, pp.141 ~ 147, 1971 (in Japanese).
- Kakutani, T.: Effect of an uneven bottom on gravity waves, *Jour. Phys. Soc. Japan*, Vol. 30, No.1, pp. 272 ~ 275, 1972.
- Madsen, O.S. and Mei, C.C.: The transformation of a solitary wave over an uneven bottom, *Jour. Fluid Mech.*, Vol.39, part 4, pp.781 ~ 791, 1969.
- Peregrine, D.H.: Long waves on a beach, *Jour. Fluid Mech.*, Vol.27, part 4, pp.813 ~ 827, 1967.
- Shuto, N.: Non-linear long waves in a channel of variable section, *Coastal Eng. in Japan*, Vol.17, pp.1 ~ 12, 1974.

APPENDIX A. WKB Solution for Progressive Waves over a Gradually Varing Bottom

If the bottom variation is gradual, the use of the conformal mapping technique becomes not so essential and an approximate solution can be obtained by a usual WKB method ( e.g., Chu and Mei, 1970 ). However, for the problems such as sediment transport, conformal mapping solutions gives more usefull estimation of bottom velocity field compared with other methods because the conformal mapping solution satisfies exactly the bottom boundary condition.

This appendix describes an approximate method to obtain an analytical conformal mapping solution. The method uses a WKB perturbation technique developed by Hamanaka and Kato (1982).

Introducing a small parameter  $\delta$  which characterizes the horizontal scale of the bottom variation, we can normalize the variables as

$$\begin{aligned} (\alpha', \beta') &= (\delta\alpha, \beta) \cdot \frac{\omega^2}{g}, & t' &= \omega t, \\ (\tilde{\eta}', \beta'_0) &= (\tilde{\eta}, \beta_0) \cdot \frac{\omega^2}{g}, & \Phi' &= \Phi \cdot \frac{\omega^3}{g^2}. \end{aligned} \tag{A-1}$$

For convenience the primes will be dropped from here on. From this normalization the linearized governing equations become

$$\delta^2 \frac{\partial^2 \Phi}{\partial \alpha^2} + \frac{\partial^2 \Phi}{\partial \beta^2} = 0, \tag{A-2}$$

$$\frac{\partial \tilde{\eta}}{\partial t} - s_0^2(\alpha) \cdot \frac{\partial \Phi}{\partial \beta} = 0, \quad \beta = 0 \tag{A-3}$$

$$\tilde{\eta} + s_0(\alpha) \cdot \frac{\partial \Phi}{\partial t} = 0, \quad \beta = 0 \tag{A-4}$$

$$\frac{\partial \Phi}{\partial \beta} = 0, \quad \beta = -\beta_0. \tag{A-5}$$

In the next step, let us introduce a local wave number  $k$  and transform the independent variables as

$$(\alpha, \beta, t) \rightarrow (\alpha, \beta, \xi), \quad \xi = \delta^{-1} \int k d\alpha - t. \tag{A-6}$$

Then Eqs.(A-2) to (A-5) become

$$k^2 \frac{\partial^2 \Phi}{\partial \xi^2} + \frac{\partial^2 \Phi}{\partial \beta^2} = -\delta^2 \frac{\partial^2 \Phi}{\partial \alpha^2} - \delta \left( \frac{\partial k}{\partial \alpha} \cdot \frac{\partial \Phi}{\partial \xi} + 2k \cdot \frac{\partial^2 \Phi}{\partial \alpha \cdot \partial \xi} \right) \tag{A-7}$$

$$s_0^2(\alpha) \cdot \frac{\partial \Phi}{\partial \beta} + \frac{\partial \tilde{\eta}}{\partial \xi} = 0, \quad \beta = 0 \tag{A-8}$$

$$\tilde{\eta} - s_0(\alpha) \cdot \frac{\partial \Phi}{\partial \xi} = 0, \quad \beta = 0 \tag{A-9}$$

$$\frac{\partial \Phi}{\partial \beta} = 0, \quad \beta = -\beta_0. \tag{A-10}$$

The unknown variables  $\Phi$ ,  $\tilde{\eta}$ , and  $k$  may be expanded by  $\delta$  as

$$\begin{aligned} \Phi &= \Phi_0 + \delta\Phi_1 + \delta^2\Phi_2 + \dots, \\ \tilde{\eta} &= \tilde{\eta}_0 + \delta\tilde{\eta}_1 + \delta^2\tilde{\eta}_2 + \dots, \\ k &= k_0 + \delta k_1 + \delta^2 k_2 + \dots. \end{aligned} \tag{A-11}$$

Substituting (A-11) into Eqs. (A-7) to (A-10) and separating the orders we obtain a set of systematically solvable equations. The solutions can be summarized as follows.

At  $O(\delta^0)$ :

$$\begin{aligned} \Phi_0 &= a \cdot \cosh k_0 (\beta + \beta_0) \cdot \sin \xi, \\ \tilde{\eta}_0 &= a \cdot s_0(\alpha) \cdot \cosh k_0 \beta_0 \cdot \cos \xi, \\ s_0(\alpha) \cdot k_0 \cdot \tanh k_0 \beta_0 &= 0. \end{aligned} \tag{A-12}$$

At  $O(\delta^1)$ :

$$\begin{aligned} \Phi_1 &= - \left\{ \frac{1}{2} a (\beta + \beta_0) \frac{\partial k_0}{\partial \alpha} \cosh k_0 (\beta + \beta_0) + \frac{\partial a}{\partial \alpha} (\beta + \beta_0) \sinh k_0 (\beta + \beta_0) \right\} \cdot \cos \xi, \\ \tilde{\eta}_1 &= s_0(\alpha) \cdot \left\{ \frac{1}{2} a \beta_0 \frac{\partial k_0}{\partial \alpha} \cosh k_0 \beta_0 + \frac{\partial a}{\partial \alpha} \beta_0 \sinh k_0 \beta_0 \right\} \cdot \sin \xi, \\ k_1 &= 0. \end{aligned} \tag{A-13}$$

⋮

For nonlinear waves, the solution can be obtained by the almost same manner as the above by introducing another small parameter  $\epsilon$  which characterizes nonlinearity of waves and by representing the unknown variables in the form of double perturbation with respect to  $\delta$  and  $\epsilon$ .

APPENDIX B. Reflection Coefficients for Linear Steady Waves

For the case of the steady waves with angular frequency  $\omega$ , the linear wave equation (31) becomes

$$\hat{\eta}(\alpha) = \frac{g}{2\beta_0\omega^2} \cdot s_0(\alpha) \cdot \int_{-\infty}^{\infty} K(\xi) \cdot \frac{d}{d\alpha} \hat{\eta}(\alpha - \xi) d\xi, \tag{B-1}$$

where  $\hat{\eta}(\alpha)$  is an amplitude of the water surface fluctuation and defined as

$$\eta(\alpha, t) = \hat{\eta}(\alpha) \cdot e^{i(\omega t - \pi/2)}. \tag{B-2}$$

Although Eq.(B-1) can be used to calculate reflection coefficients for linear steady waves, a simpler and more direct method can be developed with an approximation on  $\Phi$ . At first, the assumption is made on the velocity function  $\Phi$  such as

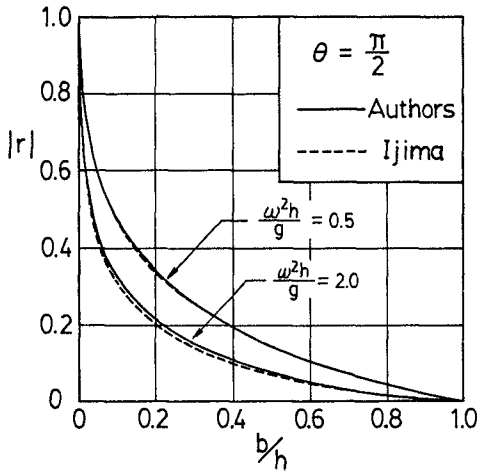


Fig. B1

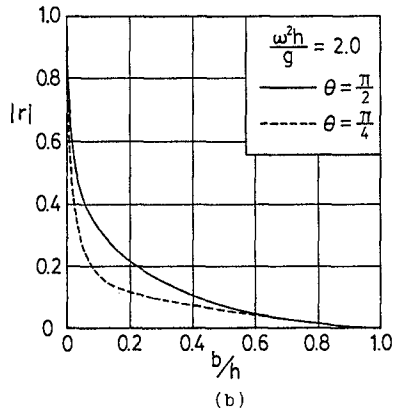
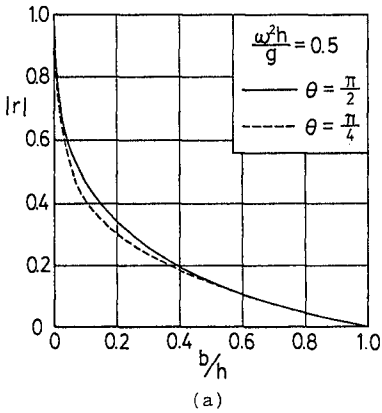


Fig. B2

$$\Phi = F(\alpha) \cdot \frac{\cosh\{k(\alpha)(\beta + \beta_0)\}}{\cosh\{k(\alpha)\beta_0\}} \cdot e^{i\omega t}, \quad (\text{B-3})$$

which satisfies the bottom boundary condition (9). This equation is valid for the case of  $\Phi_{\alpha\alpha} \ll \Phi_{\beta\beta}$ . In particular Eq.(B-3) becomes exact for long waves.  $k(\alpha)$  in the above equation must hold the following relation from the surface boundary condition (29) on  $\Phi$ .

$$\omega^2 = g \cdot s_0(\alpha) \cdot k(\alpha) \cdot \tanh\{k(\alpha)\beta_0\}. \quad (\text{B-4})$$

From the linearized boundary condition and Laplace's equation on  $\Phi$ , Eq. (B-3) yields the following differential equation on  $\hat{\eta}(\alpha)$ .

$$\frac{d^2}{d\alpha^2} \hat{\eta}(\alpha) + k^2(\alpha) \cdot \hat{\eta}(\alpha) = 0. \quad (\text{B-5})$$

The reflection coefficient  $|r(\alpha)|$  for the wave field expressed by the above equation can be calculated from the following Riccati's equation derived by the invariant imbedding method (Bellman and Kalaba, 1959).

$$\frac{d}{d\alpha} r(\alpha) = -2ik(\alpha) \cdot r(\alpha) - \frac{k'(\alpha)}{2k(\alpha)} \cdot \{1 - r^2(\alpha)\}. \quad (\text{B-6})$$

The reflection coefficient to be obtained is the value of  $|r(\alpha)|$  at  $\alpha = -\infty$ . Therefore, it is more convenient to change the independent variable from  $\alpha$  to  $\xi$  by the function  $\xi = \tanh \alpha$ . From this transform, the domain of the independent variable becomes  $[-1 < \xi < 1]$ .

The reflection coefficient can be obtained by a numerical integration using a usual integration scheme such as Runge-Kutta-Gill method. The integration is to be performed backward from  $\xi = 1$  to  $\xi = -1$  under the initial condition,  $r = 0$  at  $\xi = 1$ .

As an example, the calculation was carried out for the stepped bottom shown in Fig.3. Figure B1 shows the results for the case of  $\theta = \pi/2$ . In this special case, the reflection coefficient can be also estimated accurately by, e.g., Ijima's method (1971) in which the velocity potential is found by matching conditions at the junction of sea bed. The full lines in the figure indicate the result by the present method, while the broken lines show the result by the Ijima's method. It is shown that, for the case of  $\omega^2 h/g = 0.5$  corresponding to shallow water waves, the result by the present method shows fairly good agreement with the Ijima's result, and even for the case of  $\omega^2 h/g = 2.0$  corresponding to almost deep water waves, the present method gives still good results.

The effect of the inclination of the slope has been investigated by the present method. The results are shown in Figs. B2 (a) and (b). From these figures, it is found that the effect of the inclination on the reflection coefficients is more significant for the case of the large value of  $\omega^2 h/g$ . This is considered to be due to the difference of the ratio of the horizontal scale of the slope to the wave length.

## CHAPTER EIGHTY TWO

### A FINITE ELEMENT METHOD FOR STORM SURGE AND TIDAL COMPUTATION

by

Y.COEFFE (1), S.DAL SECCO (2), P.ESPOSITO (3), and B.LATTEUX (4)

#### Abstract

The paper reports the current progress in developing a finite element method for the shallow water equations. Some recent developments as the implementation of a semi implicit scheme or the use of an incident wave condition are described. Different realistic applications are presented concerning tidal and storm surge simulations.

#### Introduction

Long waves in coastal areas, when water depth is small compared to the wave length, can be numerically simulated by the resolution of the shallow water equations. The use of a finite element method is then specially well fitted when the shape of the domain to deal with is rather complex, as it often occurs in the field of maritime hydraulics, or when some areas of particular interest require a finer description (entrance of a harbour, for example).

Such a model has been developed, using a special procedure to reduce the storage requirement by deriving from the basic equations separate problems on each of the scalar variables. The implementation of a semi-implicit scheme makes it possible to avoid wave damping when simulating wave propagation on broad areas with a limited number of nodes in a wave length. Finally the possible use of an incident wave condition, the consideration of the atmospheric forcing terms, as well as the use of spherical coordinates, qualify the model to examine the generation and propagation of storm surges.

- 
- (1) Head of the Maritime Hydraulic Division, Laboratoire National d'Hydraulique, E.D.F., Chatou, France.
  - (2) Research Engineer, Laboratoire National d'Hydraulique, E.D.F., Chatou, France.
  - (3) Research Engineer, Laboratoire National d'Hydraulique, E.D.F., Chatou, France.
  - (4) Research Engineer, Laboratoire National d'Hydraulique, E.D.F., Chatou, France.



Equations and general description of the method

The shallow water equations are the following (\*):

$$\frac{\partial z}{\partial t} + \text{div } \bar{Q} = 0 \quad (1)$$

$$\frac{\partial Q_i}{\partial t} + \text{div} (Q_i \bar{u}) + gh \frac{\partial z}{\partial x_i} - K \Delta Q_i = F_i \quad (i = 1, 2) \quad (2)$$

where

$$\left\{ \begin{array}{l} g = \text{acceleration due to gravity} \\ h = \text{depth of water} \\ K = \text{dispersion coefficient} \\ \bar{Q} \left\{ \begin{array}{l} Q_1 = \text{flow rate per unit length} \\ Q_2 \end{array} \right. \\ \bar{u} \left\{ \begin{array}{l} u_1 = \text{velocity field} \\ u_2 \end{array} \right. \\ z = \text{free surface elevation} \\ \bar{F} \left\{ \begin{array}{l} F_1 = \text{forces (Coriolis, bottom} \\ F_2 \text{ friction, wind, atmospheric} \\ \text{pressure gradient)}. \end{array} \right. \end{array} \right.$$

Fractional step algorithm for the convection terms

Taking a simple first order time discretisation of equations (1) and (2) between two time steps  $t^n$  and  $t^{n+1}$ , the discretised unknown fields  $\bar{Q}^n$ ,  $z^n$ ,  $\bar{u}^n$  and  $\bar{Q}^{n+1}$ ,  $z^{n+1}$ ,  $\bar{u}^{n+1}$  are introduced.

Then, using an auxiliary unknown field  $\bar{Q}^*$ , equations (1) and (2) can be decomposed into a pure convection system and the remainder.

$$\begin{aligned} \text{* convection step : } & \frac{\partial Q_i}{\partial t} + \text{div} (Q_i \bar{u}^n) = 0 \quad (i=1,2) \quad (3) \\ & \text{this step gives } \bar{Q}^* \end{aligned}$$

\* diffusion and propagation step :

$$\left\{ \begin{array}{l} \frac{\partial z}{\partial t} + \text{div } \bar{Q} = 0 \\ \frac{\partial Q_i}{\partial t} - K \Delta Q_i + gh \frac{\partial z}{\partial x_i} = F_i \quad (i=1,2) \end{array} \right. \quad (4)$$

with initial conditions  $z^n$ ,  $\bar{Q}^*$  at  $t^n$ .

The convection step is solved using characteristics method.

---

(\*) These equations are written in cartesian coordinates, but spherical coordinates can also be used in the model.

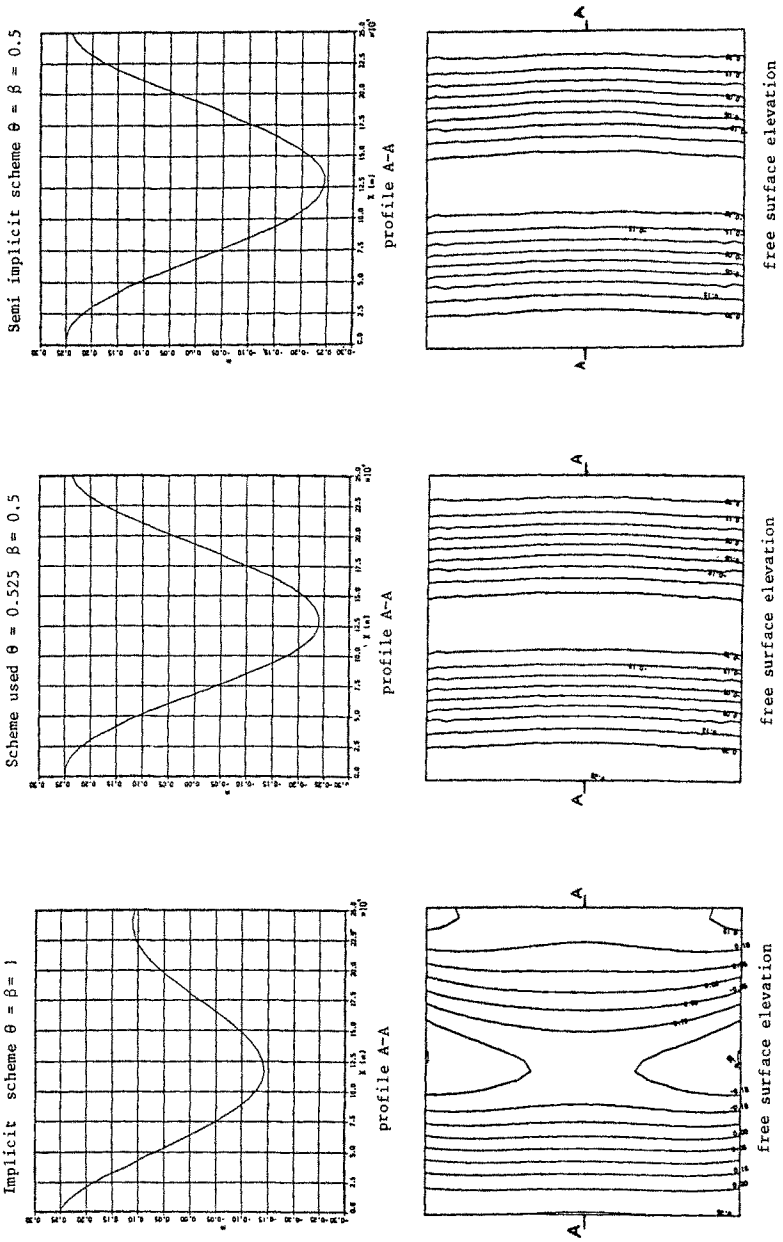


FIGURE 1 : Influence of semi-implication. A plane wave moves from left to right in a square vessel with 17 nodes per wave length.

The main advantages of this method are :

- unconditional stability
- no non-symmetric system to assemble and solve at each time step
- good accuracy (reduced numerical diffusion) when using quadratic shape functions (at least).

The main drawback of classical characteristic method is probably the fact that conservativity is not ensured by the scheme. But a new approach using a weak formulation of equations (3) can be used in order to achieve conservativity [2]. However the results presented in this paper are rather good as for conservativity.

#### Diffusion-Propagation step

A semi-implicit discretisation has been chosen for system (4) because it has been shown that pure implicit schemes have poor propagation characteristics when used on a coarse mesh (figure 1 and [4]).

The non linear term  $g h \text{grad} z$  is first splitted up into two terms :

$$g h_m \text{grad}(z) + g(h - h_m) \text{grad}(z)$$

$h_m$  being a reference depth of water dependant on the location of the point but independent of the time.

Then introducing 
$$\left\{ \begin{array}{l} C = \sqrt{gh_m} : \text{celerity of waves} \\ \alpha = \frac{1}{\Delta t} \\ \theta, \beta \in [0.5, 1] \text{ two coefficients} \end{array} \right.$$

the following discretisation :

$$\left\{ \begin{array}{l} \frac{\partial z}{\partial x_i} = \beta \frac{\partial z^{n+1}}{\partial x_i} + (1 - \beta) \frac{\partial z^n}{\partial x_i} \end{array} \right. \quad (5)$$

$$\left\{ \begin{array}{l} \frac{\partial Q_j}{\partial x_i} = \theta \frac{\partial Q_j^{n+1}}{\partial x_i} + (1 - \theta) \frac{\partial Q_j^n}{\partial x_i} \end{array} \right. \quad (6)$$

leads to the system to be solved :

$$\left\{ \begin{array}{l} \alpha^2 z^{n+1} - K\theta\alpha\Delta z^{n+1} - \theta \text{div}(C^2 \beta \text{grad} z^{n+1}) = W \end{array} \right. \quad (7)$$

$$\left\{ \begin{array}{l} \alpha \bar{Q}^{n+1} - K\theta\Delta \bar{Q}^{n+1} + C^2 \beta \text{grad} \bar{Q}^{n+1} = \bar{T} \end{array} \right. \quad (8)$$

where equation (7) comes from  $\alpha(1) + \theta \text{div}(4)$  and  $(W, \bar{T})$  are known at each time step.

It must be noticed that equation (7) can be solved easily if  $z^{n+1}$  is given on the boundary. Then,  $\bar{Q}$  can be computed from equation (8) where the term  $C^2 \beta \text{grad } z^{n+1}$  is now a known function and can be rejected into the right hand side.

The problem then amounts to the determination of the trace of  $z$  on the boundary. The procedure used for this purpose is an extension of the technique proposed by Glowinski-Pironneau [3] for the Stokes problem. It is described in detail in [1] and [8].

#### Finite Element Discretisation

All the numerical results presented in this paper have been carried out using a quadratic triangular mesh for the flow rate  $\bar{Q}$  and for the surface elevation  $z$ . The elliptic problems of equations (7) and (8) lead to the resolution of 3 symmetric definite matrix problems (one for  $z$  and one for each component of the flow rate). At each time step the boundary conditions for  $z$  is computed through the resolution of 3 problems (similar to the 3 previous one) and the resolution of a boundary problem (the size of its definite matrix being the number of boundary points).

This technique is advantageous on the point of view of computational efficiency. Two "domain" matrices have to be stored, one for the variable  $z$ , another for each component of  $\bar{Q}$  (it is the same matrix for the two components). They are symmetric and sparse and small enough to be processed by an in-core solver such as an incomplete Choleski preconditioned conjugate gradient. In addition, the matrix of the boundary operator has to be factorized and stored.

#### Boundary conditions

On the coast a simple prescribed flux condition can be prescribed :  $\bar{Q} = \bar{0}$ .

On the open boundaries, a specified flux condition (both components) could be too reflexive. In order to specify a wave rather than a flow rate and above all to let waves generated inside leave the domain easily, an incident wave boundary condition may be used. Such a condition, described in details in LABADIE and LATTEUX [8], is written in the following way :

$$\left\{ \begin{array}{l} - C^2 z + K \frac{\partial \bar{Q}}{\partial n} \cdot \bar{n} + c \bar{Q} \cdot \bar{n} = (\bar{n} \cdot \bar{u} - 1) c^2 \psi \quad (9) \\ K \frac{\partial \bar{Q}}{\partial n} \cdot \bar{\tau} + c \bar{Q} \cdot \bar{\tau} = (\bar{\tau} \cdot \bar{u}) c^2 \psi \quad (10) \end{array} \right.$$

Where  $\bar{n}$  and  $\bar{\tau}$  denote boundary exterior normal and tangent vectors,  $\bar{u}$  is a unit vector indicating the direction of the wave to specify and  $\psi$  is a scalar function of space and time describing the incident wave entering the domain through the open boundary ( $z$  and  $\bar{Q}$  must be discretised by equations (5) and (6)). The conditions (9) and (10) allow any wave normal to the boundary to leave the domain

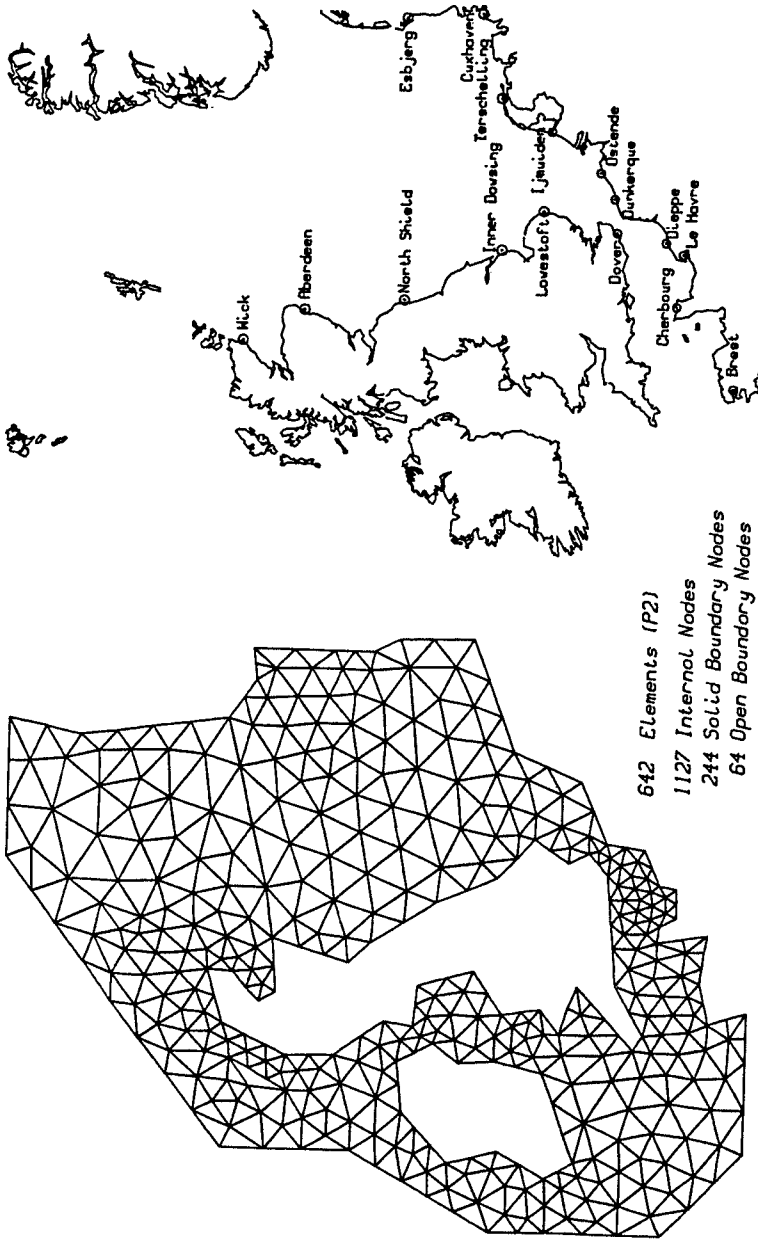


Figure 2 : Finite Element Mesh of the North-West European continental shelf and position of ports

without any reflexion. In the simple study of storm surges described further,  $\psi$  can be chosen as follows :

$$\psi = \psi_0 = \frac{P - P_0}{\rho g}$$

with  $P$  : atmospheric pressure  
 $P_0$  : reference atmospheric pressure : 1013 mb

This expression denotes simple static equilibrium at the edge of the continental shelf. But, as we shall see further, taking  $\psi = 0$  seems to give better results. Other terms may be added in order to take into account tidal forcing.

#### Numerical results

A previous paper [6] reported a first realistic computation concerning the tidal flow pattern in the vicinity of the new outer harbour of Dunkirk.

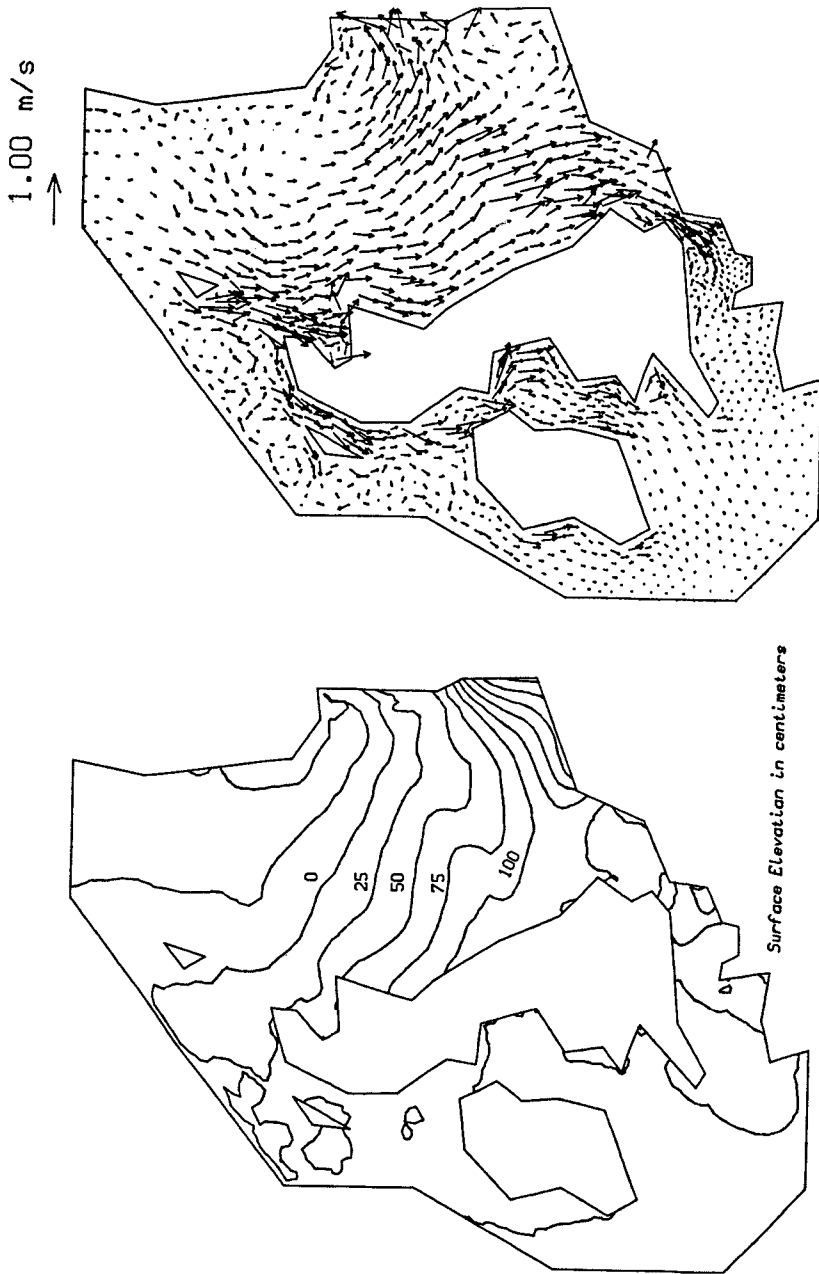
The present one gives the results of simulation of storm surges on the North-West European Continental Shelf and of tide in the English Channel.

#### The November 1973 storm surge

A series of storm surge computation models of the North-West European Continental Shelf has been developed since 1969 at the I.O.S. (Institute of Oceanographic Sciences, BIDSTON, UK) using finite difference discretisations and a review of this work is given by HEAPS [7]. As a test for an extended prediction covering a period of 44 days, FLATHER [5] computed the surges from 4 november to 18 december 1973 by means of an improved model including tidal influence. Using our model on the spherical coordinate mesh of figure 2 and taking meteorological data from a tape furnished by JONSMOD (JOINT NORTH SEA MODELLING GROUP) we computed the surge of 19 and 20 november.

Figure 3 presents an exemple of surface elevation and currents just before the very high surge of 19 november 13 h TU. It is an instant when the currents reach their maxima. Although the meteorological data have different origins, the results of this computation and previous results from FLATHER [5] are very similar. The comparison between measurements, FLATHER's results and this finite element computation is done by means of the plots of figure 4a and 4b. In order to simulate the surge of 19-20 november, the computation was started 3 days before (16/11/73 at 3 h).

It can be shown that the behaviour of the finite element model is rather good in general and that the two peaks of 16 and 19 November are very well reproduced, although interaction with the tide was not considered in this simulation.



Surface Elevation in centimeters

Figure 3 : Surface Elevation and Currents - 19/11/73 at 13H

Dot Line : Observed surges  
Fine Line : Results from FLATHER (I.O.S.)  
Thick Line : Finite element computation

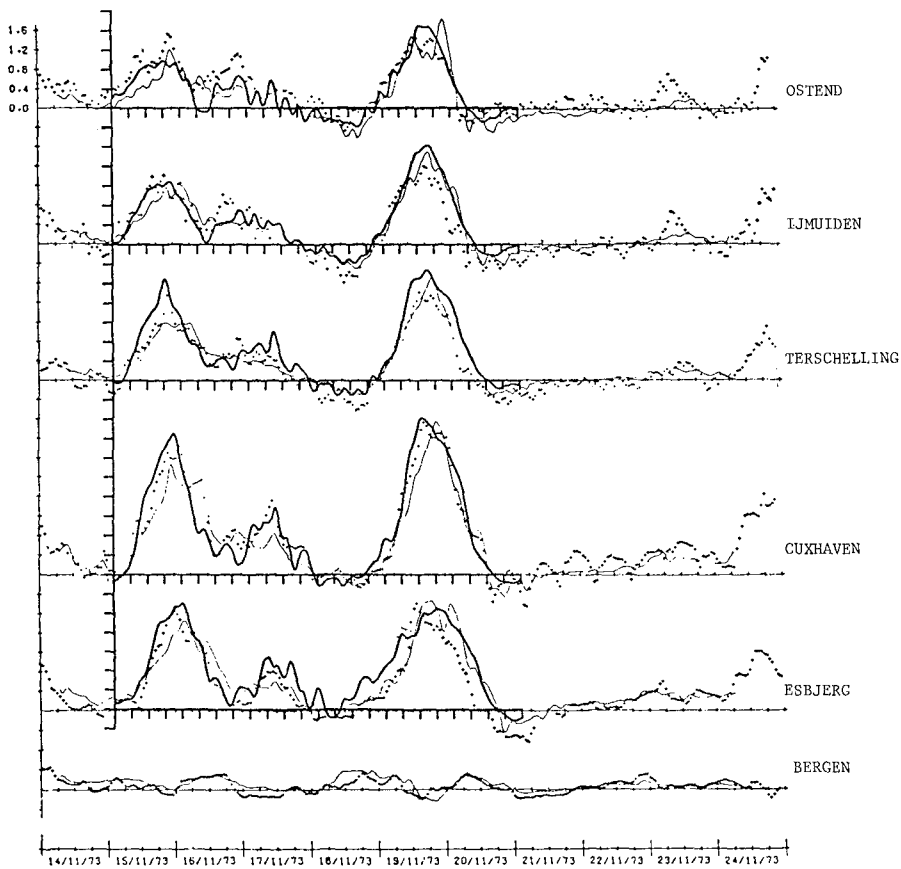


Figure 4 a: STORM SURGES AT CONTINENTAL PORTS



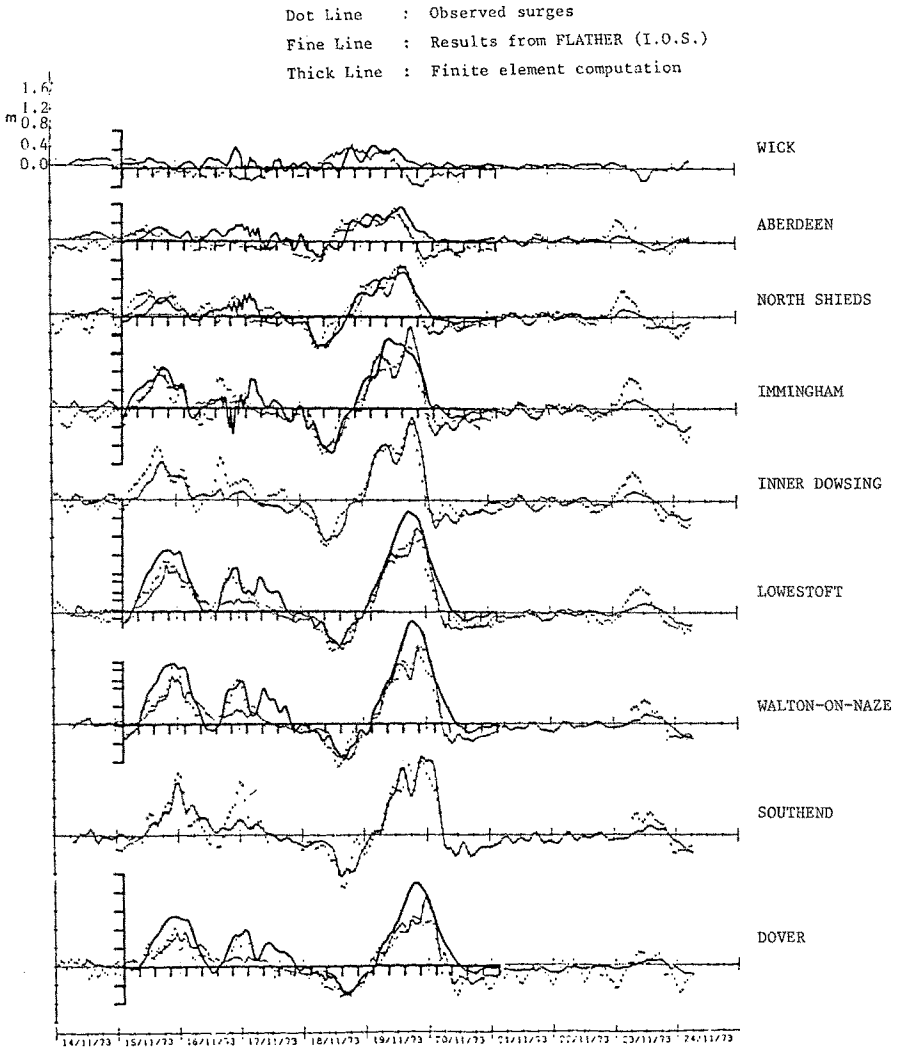


Figure 4b : STORM SURGES AT BRITISH PORTS

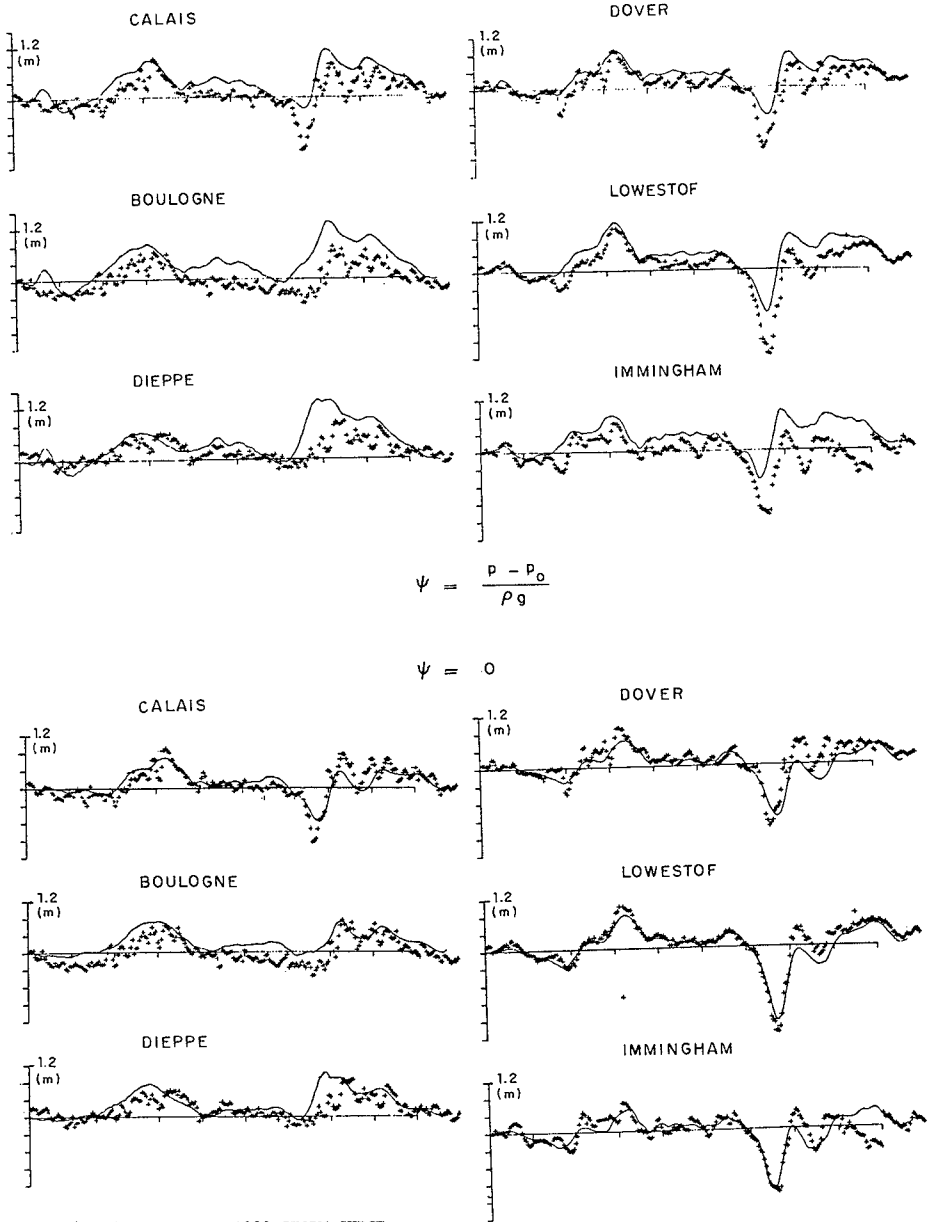


Fig. 5 : DECEMBER 1982 STORM SURGE

#### The December 1982 storm surge

The November 1973 storm surge was mostly what we should call a North Sea storm surge. Indeed, the depression moved approximately East-South-East from somewhere between Iceland and the Faroes, subsequently crossing southern Scandinavia, and was therefore located far away from the English Channel.

The December 1982 storm surge was different because two large depressions successively joined the English Channel while crossing the North Sea. Our first results obtained using the "incident wave condition" and taking  $\Psi = (P-P_0)/\rho g$  showed overestimations of water levels in almost every port. Taking  $\Psi = 0$ , i.e. without generating external waves, but only letting internal waves leave the domain, the results obtained were much better (see figure 5). The reason is that taking  $\Psi = (P-P_0)/\rho g$ , an important external wave normal to the boundary is generated and that was probably not the case in the reality.

Two other storm surges similar to the previous one were simulated and the incident wave condition with  $\Psi = 0$  always gave better results than with  $\Psi = (P-P_0)/\rho g$ . Our conclusion is that the hydrostatic approximation doesn't reproduce correctly an external surge. In particular the effects of the wind are omitted in the expression of  $\Psi$ . Some investigation has to be made on the subject. However the good agreement between observed and computed elevations is very encouraging since we can improve our model using tidal influence, better meteorological data, optimised mesh...

#### Tidal simulation in the English Channel

The tidal phenomenon in the English Channel can be considered as an interesting case for the application of the model on a large domain : tide and currents are rather well known, and the high tide ranges, small depths and strong currents provide a good test for the treatment of the non-linearities of the equations (propagation and friction terms).

The domain extends westwards till to the edge of the continental shelf, and covers on the north-east a small part of the North Sea.

Computation has just begun, under simple conditions : flow discharge prescribed on the boundaries, corresponding to a mean spring tide, and totally implicit numerical scheme. Besides, the advection step is not considered here.

The mesh is rather coarse for this first trial on the English Channel (fig. 6) : there are 220 triangular elements, and 521 nodes of discretization for the quadratic approximation. This rough discretization allows a very fast computation : the whole tide is simulated within less than 10 minutes C.P.U. on a CRAY 1 computer.

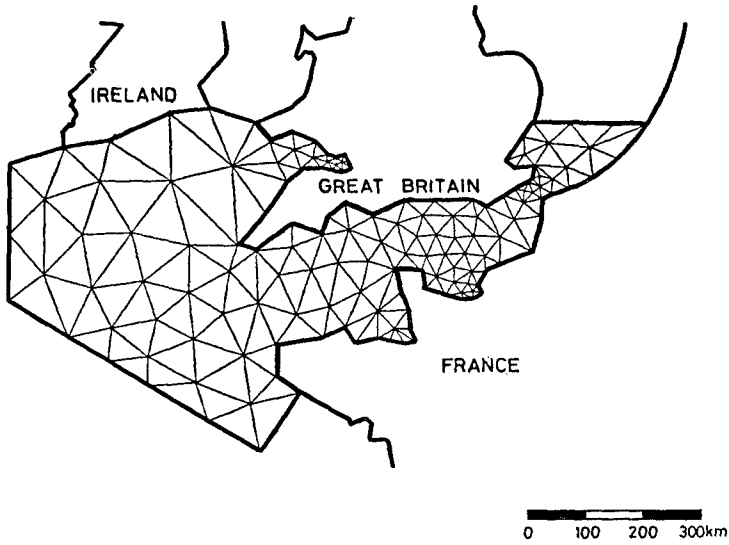


Fig.6- Finite element grid of the English Channel

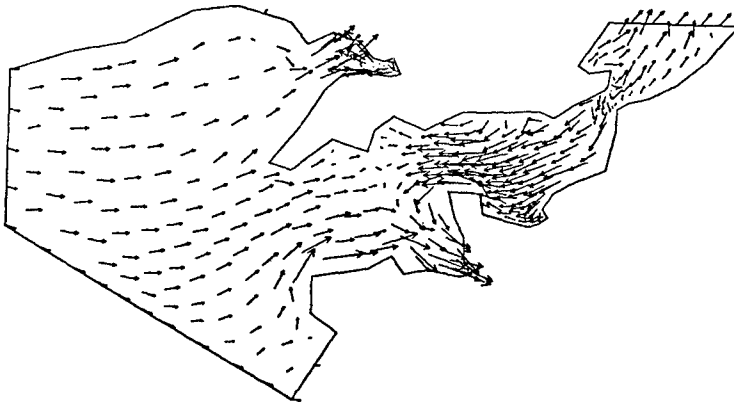
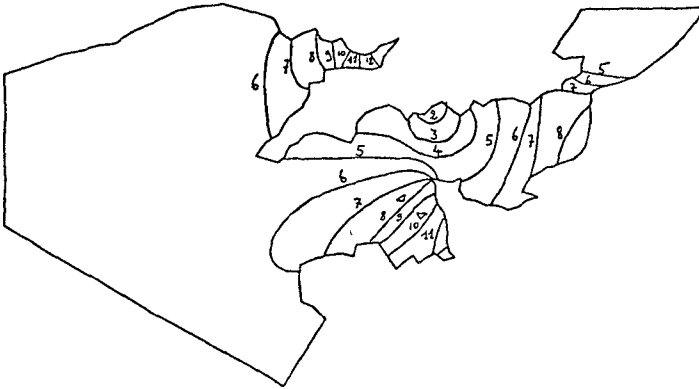
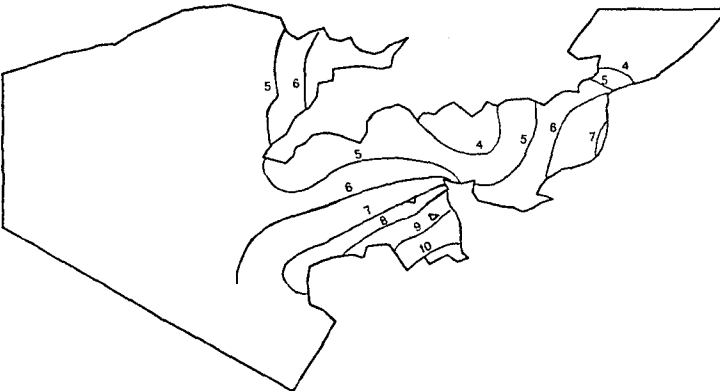


Fig.7- Computed tidal currents at HW. at BREST



b) Measured co - tidal lines



a) Computed co-tidal lines

Fig.8 \_Comparison between computed and measured tide ranges in the English Channel (Mean Spring Tide)

Fig. 7 displays the tidal current pattern at High Water (Brest). Fig. 8 exhibits the comparison between computed and measured tide range over the English Channel. The main features of the complex tidal pattern in this region, as the significant difference between english and french coast, due to the rotation of the Earth, and the wave amplification in the Gulf of Saint-Malo, are qualitatively well reproduced. However a damping of the computed tidal wave is obvious, coming from the use of an implicit scheme : with only 40 nodes in a wave length, the tide range has generally been weakened by 10 to 20 %.

Further computations performed with a semi-implicit scheme, and possibly with a finer mesh, will probably strongly improve these results.

#### Conclusion

A finite element method has been developed to solve the shallow water equations, and has proved to be particularly well fitted for the simulation of hydrodynamics in complex shaped domains, whatever their size, with reasonable in core memory requirements.

It is the feeling of the authors that, thanks to the advantages of a grid of finite element type (large elements far away, small elements near the region of interest) which decreases the number of required unknowns, the cost of such a model becomes comparable to the one of a classical finite difference model.

The use of a semi-implicit scheme enables the model to avoid wave damping even with a coarse discretization of a wave length ; the implementation of an incident wave condition and the consideration of the atmospheric forcing terms make it quite convenient for the study of the generation and propagation of storm surges on broad areas, just as the North-West European Continental Shelf ; first results concerning the simulation of a measured storm surge has turned to be very satisfactory.

Next steps will concern the tuning of the model on other observed storm surges, the examination of tide-storm surge interaction and, thanks to a better model of turbulence, a better modelling of 2 D boundary layers developped near obstacles and of associated boundary conditions.

#### References

1. J.P. Benque, G. Labadie, B. Latteux  
A finite element method for the shallow water equations. 2nd International Conference on numerical methods for laminar and turbulent flow, VENICE, Italy, July 13-16, 1981.
2. J.P. Benque, G. Labadie, J. Ronat  
A finite element method for the Navier Stokes equations coupled with temperature equation, submitted to the International Journal for Numerical Methods in Fluids, 1983.

3. M.O. Bristeau, R. Glowinski, J. Periaux, P. Perrier, O. Pironneau, G. Poirier.  
Application of optimal control and finite element methods to the calculation of transonic flows and incompressible viscous flows. Rapport de recherche 78-294. INRIA LABORIA, 78150 LE CHESNAY, FRANCE, 1978.
4. P. Esposito  
Utilisation des éléments finis pour le calcul des surcotes en Manche. Rapport E.D.F. HE/41/82.55, 1983.
5. R.A. Flather  
Results from a storm surge prediction model of the North-West European Continental Shelf for April, November and December 1973. Report n° 24. Institute of Oceanographic Sciences, BIDSTON, U.K, 1976.
6. A. Hauguel, G. Labadie, B. Latteux  
A finite element method for the shallow water equations. 18th International Conference on Coastal Engineering, Capetown, South Africa, November 14-19, 1982.
7. N.S. Heaps  
Storm surges 1967-1982 Geophys J.R. Astr. Soc. 74, 331-376, 1983.
8. G. Labadie, B. Latteux  
Résolution des équations de St Venant par une méthode d'éléments finis. Rapport E.D.F. HE/41/82.15 and HE/42/82.34, 1982.



*Cape Cod National Seashore, MA*

**PART II**

**COASTAL PROCESSES AND SEDIMENT TRANSPORT**

*Great Egg Harbor Inlet, Ocean City, N.J.*







## CHAPTER EIGHTY THREE

### ADDED EVIDENCE ON NEW SCALE LAW FOR COASTAL MODELS

Robert Hallermeier\*

#### Abstract

*Further positive results on appropriate scaling of movable-bed models support an analytical expression developed in 1983. That development examined a simple parameter for a profile view of nearshore sedimentation, making a distinction between small and large situations by the incorporated threshold of sand motion. The resulting scale laws proved fairly consistent with various empirical results, including those by E. Noda and P. Vellinga.*

*The focus here is on full utilization of 25 available tests of profile development in large wave tanks. Seven published small tests are found to be notably accurate as unintended models of various large tests, giving support to the new scale law. Also, the occurrence of shore erosion or accretion in all large tests is seen to be in accordance with the basic sedimentation parameter.*

#### INTRODUCTION

Two distinct approaches to predictive capability for nearshore changes are mathematical and physical modeling. In mathematical models, the appropriate level of detail seems a fundamental quandary: relatively simple treatments using some overall conditions offer intuitive appeal but have not yet managed impressive results in correlating measured beach changes (Seymour and King, 1982), while intricate computer models are still subject to fundamental questions about advisable numerical techniques and adequately detailed physics (McDowell and O'Connor, 1982). It is well known that prediction of average sand transport rates by waves is subject to large uncertainties, and this places limits on the present potential of mathematical models.

On the other hand, physical models are subject to criticism because of known differences in sand-bed processes in large prototype and small laboratory situations. However, scale effects do not preclude accurate reproduction of natural nearshore changes, if important transport mechanics are clearly enough identified that the model's design permits it to function as a meaningful physical analog for the prototype. Identification of dominant

\*Visiting Coastal Scientist, Cyril Galvin, Coastal Engineer, Box 623, Springfield, Virginia 22150, U.S.A.

transport mechanisms is a central topic of the present research on physical modeling (and conclusions might also be pertinent to adequate mathematical models).

This paper is the last in a series of three concerning laboratory models for sandy nearshore regions dominated by wave action. All considerations have been based on distinct thresholds in wave-sand interactions, with quantitative deductions about accurate modeling compared to empirical evidence. The first paper (Hallermeier, 1984) examined two types of wave-cut features occurring outside the breakers, and concluded that practical models should omit the extensive region of moderate bed agitation and be confined mainly to the surf zone. The second paper (Hallermeier, 1985) developed a new analytical viewpoint for accurate profile modeling, and showed it to be supported by many published empirical results and by a new test program. This paper presents additional evidence on the validity of the new design guidance for physical surf-zone models.

Examining literature on coastal models from the past 15 years, actual treatments seem to separate into categories somewhat different from the three given by Keulegan (1966). Customary approaches to design guidance for physical models with sand and waves might be classified according to three types of basis, here called formal, empirical and parametric. The first type considers basic principles for replicating flows in terms of conserving force ratios (Froude, Reynolds, Archimedes, etc., numbers) between model and prototype. This formal approach is exemplified by modeling guidance presented by Yalin (1971) and Kamphuis (1975, 1982). A judgment on relative importance of various processes must enter such developments if they provide practical guidance about compromises always necessary between the contradictory formal requirements for physical modeling.

The empirical approach to model design recommendations proceeds solely from correlation of actual successes and failures, as in guidance by Noda (1972) and Vellinga (1982). Although disguised by usual expressions of results in generalized form, such conclusions strictly pertain only to prototype and model conditions actually investigated.

Fundamental limitations of formal and empirical routes has led to model design guidance based on preserving some parameter(s) judged most crucial to coastal processes. One example is research examining the sediment excursion ratio  $H/wT$ , where  $H$  is wave height,  $w$  is sediment fall velocity, and  $T$  is wave period (Dean, 1973). However, investigations to date (Noda, 1978; Vellinga, 1978; Gourlay, 1980; Sayao and Guimaraes, 1984; Hallermeier, 1985) have indicated that preserving  $H/wT$  between model and prototype is neither sufficient nor necessary to reproduce nearshore profiles.

The development pursued here is based on a different parameter meant to indicate sand movement in the surf zone: sand mobility is measured in terms of the threshold of sand motion rather than the fall velocity. To some extent, this corresponds to considering the stage of bedload or total sand transport rather than suspended sand movement alone.

#### NEW VIEWPOINT OF NEARSHORE SEDIMENTATION

The new parameter treating sedimentation on nearshore profiles is defined by characteristic flow velocities:

$$\psi = (V_h/U_o)/V_v \quad (1)$$

where  $V$  is peak wave-induced velocity,  $U_o$  is the threshold (horizontal) velocity for sediment motion, and subscripts  $h$  and  $v$  indicate horizontal and vertical components. The postulate is that planar similarity between model and prototype exists when identical values of  $\psi$  occur. Development of model design guidance proceeds (Hallermeier, 1985) by noting that these peak velocities share a common time scale, the wave period  $T$ , so their ratio can be given by the ratio of characteristic length scales  $L_h/L_v$ . The other step is to invoke convenient asymptotic expressions (Hallermeier, 1980) for sand motion thresholds in small and large situations, i.e., with laminar shearing of the boundary layer (for relatively high frequency waves) versus with a thoroughly mixed boundary layer (for lower frequency waves).

Preservation of  $\psi$  in an overall sense between small model and large prototype requires a scale ratio of

$$N_v/N_h = 0.0494 (T_m)^{0.5} (s_m)^{0.75} (gD_m)^{0.25} (s_p D_p)^{-0.5} \quad (2)$$

$N$  indicates (fairly large) length scale between the two situations; subscripts  $p$  and  $m$  refer to prototype and model;  $D$  is sediment grain diameter;  $s$  is relative immersed sediment density in the fluid; and  $g$  is acceleration due to gravity. Besides Eq. (2), customary Froude scaling of waves requires time scale between prototype and model to be

$$N_t = (N_v)^{0.5} \quad (3)$$

giving a dynamic and a kinematic requirement for accuracy.

Perhaps the most encouraging evidence regarding the proposed scaling law in Eq. (2) is its quantitative similarity to the empirically-based conclusion by Vellinga (1982). That result was expressed using the scale between sediment fall velocities, and omitted any independent effect of wave period as in Eq. (2), but values for appropriate model distortion  $\Delta = (N_h/N_v)$  by the two approaches show generally fair agreement in common open-coast conditions with quartz sands. Thus, Eq. (2) is supported by

many of the Vellinga test results on dune erosion by extreme storm events on The Netherlands coast. The present relationship also appears to help correct the weakness noted by Vellinga (1982) in his recommended modeling law.

Another persuasive item of general evidence is that the present approach can nearly recover an empirical scaling law given by Noda (1972). In his laboratory investigations, all tests were evidently small in an absolute sense so the identical (laminar) asymptotic expression for sand motion is applicable to each. In that case, preservation of between two situations requires

$$\frac{N_h}{N_v} = \left[ \frac{D_p T_p^2 S_p^3}{D_m T_m^2 S_m^3} \right]^{0.25} = (N_D N_V)^{0.25} (N_S)^{0.75} \text{ (small replicas; 4)}$$

using Eq. (3) and introducing the scales of sand diameter and immersed density between the two cases. Noda's results were given as two independent equations yielding

$$N_h/N_v = (N_v)^{0.25} (N_D)^{0.127} (N_S)^{-0.151} \quad (\text{E. Noda; 5})$$

or, if  $N_S$  is eliminated because the major empirical emphasis was on  $N_S = 1$  with quartz sediment in both situations,

$$N_h/N_v = (N_v)^{0.205} (N_D)^{0.209} \quad (\text{E. Noda; 6})$$

There is a striking similarity between Eqs. (6) and (4) for the case of  $N_S = 1$ , so the present viewpoint seems to point out the mistaken nature of the scaling law deduced by Noda (1972): that it pertains to appropriate design giving profile replication between a pair of small situations, and not to the design of an accurate model for a large prototype.

The opposite case of replication consists of two large profiles. Then sand motion is governed by the same equation in each situation, that for a thoroughly mixed boundary layer. This yields for the preservation of  $\psi$

$$N_h/N_v = (N_D N_S)^{0.5} \quad (\text{large replicas; 7})$$

a form quite different from Eqs. (2) or (4).

From the present viewpoint, scale relations are not continuous. Distinction between models and either small or large replicas seems necessary for consistent treatment of scaled profile development. The idea that models and replicas are fundamentally different concepts has never received proper emphasis, but some evidence is apparent in a recent empirical analysis by Ito and Tsuchiya (1984).

The present approach and results on accurate scaling are entirely consistent internally, including an objective

classification of "small" and "large" situations in terms of sand motion initiation. An intermediate range of transitional situations must be expected, but "small" has an upper size bound related to cessation of laminar boundary flow while "large" has a lower size bound related to onset of thoroughly-mixed flow in the boundary layer (Sleath, 1974, 1984). These size bounds are sensibly consistent with usual laboratory models being small and natural coastal situations of engineering interest being truly large.

#### **MODELS OF LARGE-SCALE PROFILE CHANGES**

New test results reported in Hallermeier (1985) gave some support for present guidance on accurate models, and clearly contradicted preservation of  $H/wT$  as a scaling law. Positive evidence consisted of only a few accurate models from a program of about 50 tests, each aiming to reproduce some profile developed in a large wave tank at the Beach Erosion Board, U.S. Army Corps of Engineers (Saville, 1957). Successful models were in fair accord with Eq. (2), whereas unsuccessful tests were usually not;  $H/wT$  had about the same value in most pairs of situations.

Reproduction of profile development from an initially plane sand slope provides a stringent test of modeling guidance: success indicates that the spatial pattern of net transport through corresponding times was identical on model and prototype profiles. Successful models do not imply that nearshore transport processes have been reproduced, but do demonstrate that net effects have been accurately scaled in a sensitive situation. Besides scale effects, possible laboratory effects on test results should be considered: for example, there are start-up effects in mechanical wave generation (Madsen, 1970) and the artificial borders to the sand bed can affect transport processes, as when a bulkhead eventually becomes exposed to waves. Some care was taken in the test program described by Hallermeier (1985) to reproduce steady wave durations in meaningful situations, but undesirable laboratory complications must be present in an additional data base on models assembled here.

The following results pertain to unintended models of the 25 available tests in large wave tanks, so timing of wave stops and fully consistent scales are quite unlikely. The large-scale data base includes 15 BEB tests mentioned above, and 10 recent tests at CRIEPI, Japan. Full documentation of the two BEB test series has never been published, but original test data are available at the Waterways Experiment Station (WESCR), Vicksburg, Mississippi. A brief report by Kajima, et al. (1982) on CRIEPI tests does not provide full details such as stopping times or intermediate profiles. Together the 25 large tests of profiles developed by steady wave action include  $H$  between 0.5 and

Table 1. CONDITIONS FOR SMALL-TANK TESTS TREATED AS UNINTENDED MODELS OF LARGE-TANK PROTOTYPES.

Test I.D.*	$H_0$ , cm	$T$ , sec	$H_0/L_0$	$d$ , cm	$D$ , mm	Sand $s$	Time, $t$ , hr	Start Slope	$N_H$	$N_T^2$	$N_d$	$N_t^2$	Distortions: test Eq.(2)
Model test by Shinohara et al. (1958)													
a. S/901	147	7.87	0.015	396	0.4	1.65	50	1/15					
b. Fig.2a	3.84	1.40	0.0127	35	0.2	1.66	6	1/10	38.7	31.6	11.3	69	1.50 1.43
Model test by Fairchild (1959)													
e. K/3-2	105	6.0	0.019	450	0.27	1.71	98.1	1/20					
f. 530	10	1.8	0.02	38.1	0.22	1.65	31.5	1/18	10.5	11.1	11.8	9.7	1.11 1.03
Model test by Ijima and Aona (1959)													
i. S/101	100	11.33	0.0050	457	0.4	1.65	(15.0)	1/15					
j. Fig.3b	6.8	3.00	0.0048	40	0.28	1.9	(4.0)	1/20	13.7	14.3	11.4	14.1	0.75 0.81
Model test by Nicholson (1968)													
k. S/801	83	3.75	0.0377	457	0.4	1.65	50	1/15					
l. 78	5.8	1.00	0.0365	40	0.42	1.61	15	1/10	14.3	14.3	14.3	11.1	1.50 1.44
Model test by Monroe (1969)													
n. S/301	118	11.33	0.0059	427	0.4	1.65	50	1/15					
q. 3Qrtz	13.85	3.58	0.0069	42.7	0.26	1.58	16	1/15	8.5	10.0	10.0	9.8	1.00 0.87
Model test by Paul et al. (1972)													
r. K/2-1	176	6.0	0.0313	350	0.47	1.69	35	3/100					
u. Fig.2d	3.9	0.91	0.03	19	0.52	0.6	6	1/10	45.1	43.5	18.4	34.0	3.33 3.28
Model test by Chesnutt and Stafford (1977)													
e. K/3-2	105	6.0	0.019	450	0.27	1.71	98.1	1/20					
x. 72D-06	11.8	1.9	0.021	71	0.22	1.65	(30.0)	1/20	8.9	10.0	6.3	10.7	1.00 1.10

\*First of pair is prototype, distinguished by S for Saville (unpub.) or K for Kajima et al. (1982).

Table 2. SUMMARY OF MAJOR PROFILE FEATURES DEVELOPED IN PROTOTYPE AND UNINTENDED MODEL TESTS.

SUBAERIAL BEACH	INSHORE REGION	SEAWARD PROFILE	OVERALL COMPARISON
<p>a. Accreted; peak to 0.4m at 10m from start shoreline                      b. Accreted sharp peak to 5 cm at 35cm from shoreline</p>	<p>1.5m shore retreat; eroded to 0.8m deep, 2.5m offshore                      7cm shore retreat; eroded to 2.5cm deep, 1m offshore.</p>	<p>Double bar; main peak 1.1 m high at 40m offshore                      Muted bar; peak 1.6cm high at 125cm offshore</p>	<p>Features mostly similar but scale appears to be about 20 to 30 rather than <math>N_v = 40</math>, <math>N_h = 60</math></p>
<p>f. Accreted; sharp peak to 5 cm at 1m from shoreline                      e. Accreted; peak 20cm high at 8m from shoreline                      x. Accreted; peak 3cm high at 1m from shoreline</p>	<p>45cm shore retreat; eroded to 7cm deep &amp; 3.7m offshore                      2m shore retreat; eroded to 50cm deep &amp; 24m offshore                      Neutral shoreline; eroded to 7cm deep &amp; 4m offshore</p>	<p>Thin deposit on slope toe &amp; more on tank floor                      Large double bar, thin erosion along slope toe                      Deposition to 4cm thick out to 8.5m offshore</p>	<p>Nearshores similar but variable smaller scales than deduced 11 or 12                      Major nearshore changes all scale appropriately near about <math>N_v=N_h=7</math></p>
<p>i. Accreted; peak 80cm high at 9m from shoreline                      j. Accreted; sharp peak 16cm high, 15cm from shoreline</p>	<p>3m shore advance; slight erosion to 21m offshore                      65cm shore advance; major erosion to 4.3m offshore</p>	<p>Erosion along slope toe, thin deposit landward                      Variable relatively thin accretion and erosion</p>	<p>Similarity limited to large shore accretion; detailed features and sand sources different</p>
<p>k. Mixed slight changes; eroded high, accreted low                      l. Mixed slight changes; accreted high, eroded low</p>	<p>0.6m shore advance, broad accretion from offshore                      6cm shore retreat, some accretion from offshore</p>	<p>35cm high bar out at 14m &amp; trough to 35m offshore                      3cm high bar out at 60cm &amp; trough to 1.4m offshore</p>	<p>Bar and seaward trough, dominant features, have scale near <math>N_v=15</math>, <math>N_h=25</math>; differences elsewhere</p>
<p>n. Accreted; broad peak to 1m high at 7m onshore                      q. Accreted; peak to 10cm high 1.2m from shoreline</p>	<p>1m shore advance; neutral just beyond shore bulge                      15cm shore advance; 11cm deep trough 2m offshore</p>	<p>Deeply eroded slope toe, some accretion landward                      Mainly slope erosion and deposition on tank floor</p>	<p>Beach features nearly scale at intended <math>N=10</math>, but subaqueous features are radically different</p>
<p>r. Deposit to 25cm thick, up to 11m onshore                      u. Deposit to 1cm thick, up to 20cm onshore</p>	<p>Low deposits out to 23m, erosion to 55m offshore                      Low deposit out to 35cm, erosion to 1m offshore</p>	<p>Sizable bar and trough near slope toe                      Nearly no development</p>	<p>Small nearshore changes scale at <math>N_v=30</math>, <math>N_h=60</math>, rather than deduced values of <math>N_v=40</math>, <math>N_h=130</math></p>



1.8 m,  $T$  between 3 and 16 sec, three initial slopes, and four fine to medium quartz sands; a wide range of conditions is represented but coverage is not intensive.

Potential unintended models for these 25 prototypes can be sought in over 50 reports documenting profile development in small situations. For the present search, attention was limited to 20 accessible recent reports, which include about 150 profile development tests. The search for unintended models began by requiring a good match between a small and large test in deep-water wave steepness ( $H_o/L_o$ ) as required by Eq. (3). Then fairly consistent scaling in wave height, water depth, wave period, and duration of profile development was sought. In this way, seven model/prototype pairs listed in Table 1 were located; model slope distortion relative to the prototype is in each case fairly consistent with the requirement of Eq. (2). (Besides space limitations here, full comparison of all small and large profiles is not provided because the present partial search aimed only at extending the scant data base of successful models, and definitive contradiction of present modeling guidance would be doubtful, in that laboratory effects are unknown.)

Table 2 provides a summary of profile features arising in model/prototype pairs. There is a distinct similarity in nearshore profile development for each case, with matches tending to be more quantitative than qualitative in pairs of situations with more consistent overall scaling. Given the startling variety of profile developments which can occur on an initial plane slope, in terms of number, location, and dimensions of major features, these seven cases distinctly provide support for Eq. (2) as a scale law.

To give a quantitative indication of Eq. (2) guidance, Figure 1 presents a nomogram constructed by standard means (Levin, 1946). Taking the prototype to be  $s_p = 1.6$  (quartz in saltwater), remaining parameters are arranged by like exponents into three ratios:  $D_p/T_p$ ,  $N_v/D_m$ , and  $N_h/N_v$ . The dual central axis of Figure 1 shows necessary distortion for either quartz or coal in water as model materials.

Figure 1 also indicates some of the range of validation provided by models newly described here or in Hallermeier (1985). Conditions for all 9 models shown by dashed lines include quartz sand. This display of various cases supporting Eq. (2) may be deceptive in exaggerating the range of model conditions: individual values of five parameters rather than three ratios actually gives the empirical basis for the new scaling law. However, this indicated basis excludes other published model tests whose support for Eq. (2) was discussed previously (Hallermeier, 1985).

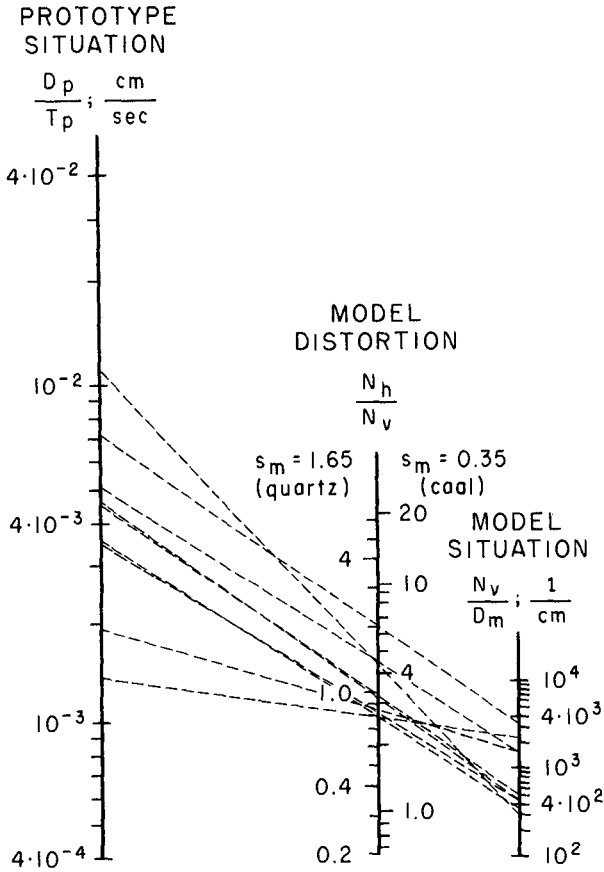


Figure 1. Nomogram for sedimentation similitude with either quartz or coal as model material, based on Eqs. 2 and 3, along with presumption that prototype has  $s_p = 1.6$  [quartz in saltwater]. Support for this scale law, related here or in Hallermeier (1985), is indicated by dashed lines showing approximate conditions for quartz models of large tank tests.

The overall range of verification with radically different prototype situations provides extensive corroboration for the new parametric viewpoint of sedimentation.

#### SOME BASIC EFFECTS IN LARGE PROFILE CHANGES

Situations in large tests of profile development have been idealized, but the present viewpoint indicates scale effects are absent so recorded changes should be exactly pertinent to net onshore/offshore sand transport in large field waves. Results in large tests can be directly applicable to several cases of engineering interest. One example is immediate adjustment of a beach fill which might be placed as a direct berm extension into the usual surf zone. Another example is erosion of a simple accreted beach profile by relatively steady storm waves.

The latter case can be illustrated using results of a BEB test along with the well-documented (Gable, 1981) storm event which occurred during a Nearshore Sediment Transport Study experiment at Santa Barbara, California. Quartz sand of 0.227 mm diameter and foreshore slope about 1 on 15 at Leadbetter Beach matched the first series of large tank tests, so Eq. (7) shows a relationship is possible between field and laboratory events. Representative wave conditions may be approximated as  $H = 1.25$  m and  $T = 14$  sec for the 5-day California storm during February 1980; near this is laboratory test number 7 with steady waves of  $H = 1.6$  m and  $T = 16$  sec. This yields a match in wave steepness, so the tank test can be an undistorted replica of the Leadbetter Beach event, at about 30% linear magnification. Such a viewpoint is seen to be consistent with recorded shore effects (Figure 2) which include fairly steady shoreline retreat totaling 40 m over the 5-day storm.

In the laboratory, waves ultimately exposed a concrete wall behind the sand slope so only the first 20 hours of testing should be considered; in that time, the still-water shoreline retreated 10 m (Caldwell, 1959). Mean-sea-level shoreline at Leadbetter Beach retreated 9 m during the first storm day, exactly consistent with laboratory effects being at the stated magnification. Agreement of recorded shore changes persists into finer details: in each case the foreshore steepened with lesser retreat at higher elevations up to the berm crest; also, behind the berm crest there was slight sand deposition. These effects indicate marked similarity of shore hydraulics and net sand transport in the two cases. However, the laboratory situation was in fact much simpler: nearly two-dimensional with no alongshore transport and with steady waves and no tide on a plane slope.

Still, this example reveals a fundamental congruence of large-tank profile development to natural effects, and encourages classification of basic results from large lab-

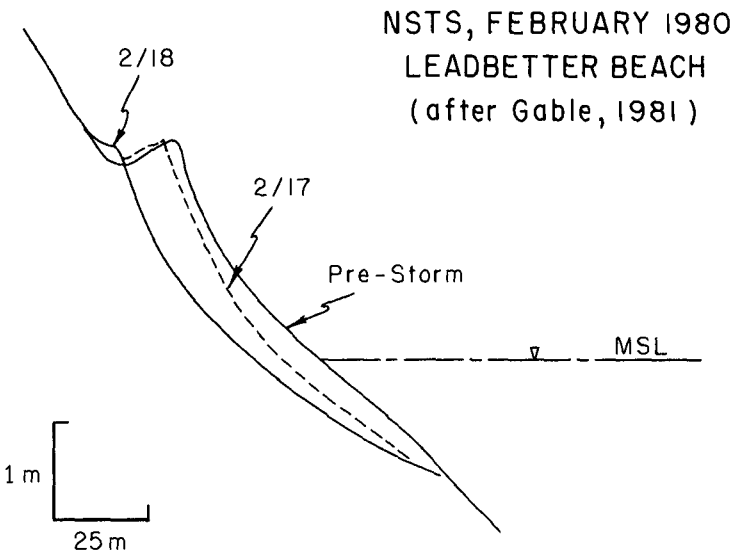
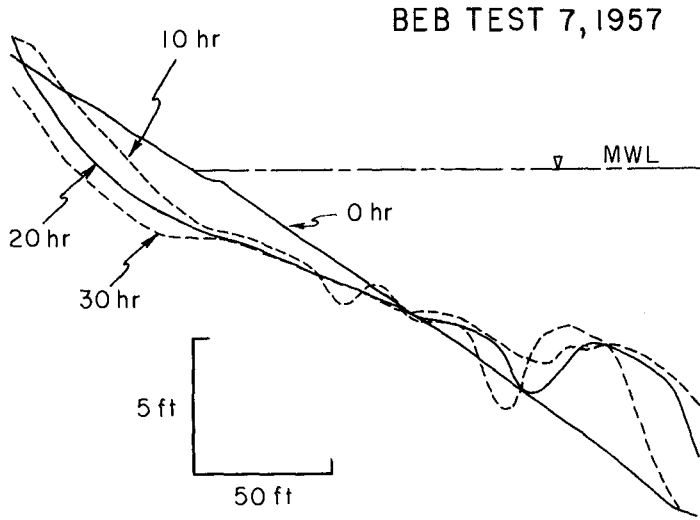


Figure 2. Similar shore changes recorded in large tank test and during storm at Leadbetter Beach, California.

oratory tests. The occurrence of shore erosion or accretion at large scale will be examined in terms of two published treatments and the present viewpoint.

The two treatments of profile modification considered here are those by Dean (1973), who introduced sediment fall velocity as a crucial parameter, and Sunamura and Horikawa (1974), who developed a more detailed parametric model for net sand transport. Dean (1973) reported a successful break of storm/eroded vs. normal/accreted profiles for 184 (mainly small) tests by a linear relationship between  $H_o/L_o$  and  $w/gT$  (parameters combined in  $H/wT$ ). Sunamura and Horikawa (1974) distinguished shore erosion or accretion in terms of a linear relationship between  $H_o/L_o$  and a semi-empirical parameter including  $D$ ,  $L_o$ , and initial slope; their main data base was about 75 long-term small tests but the same functional result was judged pertinent to shore changes in 23 large situations. (In each treatment results indicated marked change between small and large situations in the numerical coefficient of the relationship, and those changes can be shown to be roughly consistent with Eqs. (4) and (7) for usual conditions; however, the present viewpoint indicates a different correlating parameter should arise for changes in small and large situations.)

For the 25 available tests in large wave tanks, Figures 2a and 2b display types of shore change (above still water line) in terms of those two relationships. Conditions in terms of those parameters provide a useful demarcation of test results, although the originally proposed relationships ( $45^\circ$  lines in this format) cannot be retained. The dashed lines shown provide a clear break between shore erosion and accretion, with only one outlier in Figure 2a and none in Figure 2b. Close examination reveals the break in Figure 2b to be somewhat more clear, with better ordering of marked erosion through neutral development to marked accretion. This verifies the importance of initial slope  $M$ .

The third panel of Figure 2 evaluates the usefulness of sedimentation similitude considerations in attempting such a demarcation of conditions for shore erosion or accretion. The Appendix develops from Eq. (1) the abscissa

$$\psi' = \pi(8sD)^{0.5}/(TM'g^{0.5}) \quad (8)$$

where  $M'$  denotes initial slope divided by 1 on 15, slope for a majority of the tests. Results in Figure 2c upon close inspection show a somewhat clearer break of actual effects than is obtained in the other panels. The major difference in the third plot is that the Eq. (8) parameter has a stronger dependence on initial slope (derived from the requirements for sedimentation similitude in large-scale replications). Empirical results of Sunamura and

SHORE CHANGES IN 25 LARGE WAVE-TANK TESTS WITH PLANE SLOPES

$\Delta$  BEB } Filled = Accretion, Open = Erosion, Slash = Balance or Neutral,  
 $\circ$  CRIEPI } Doubled Symbol Indicates Marked Change

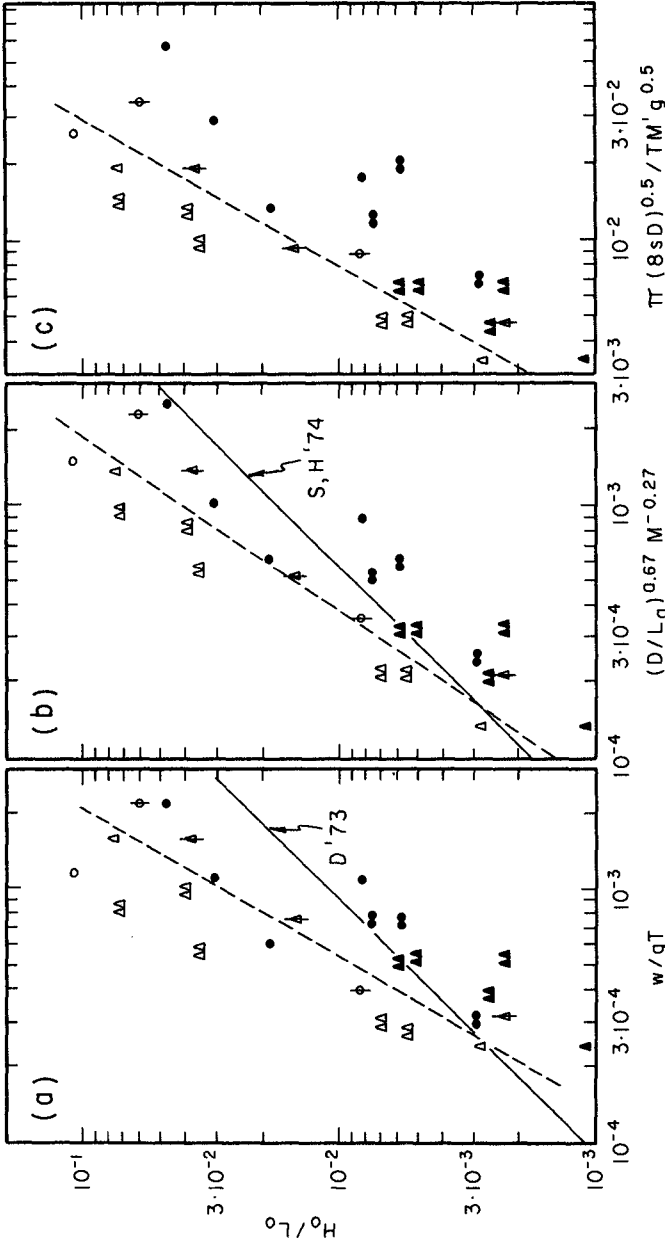


Figure 3. Three classifications with erosion at left and accretion at right of dash lines: a. Dean (1973); b. Sunamura and Horikawa (1974); c. new sedimentation parameter.

Horikawa (1974) indicating a relatively weak slope dependence were primarily from small-scale profile developments, where the independent effects of slope and wave steepness, when combined into the surf-similarity parameter, apparently tend to cancel (Hallermeier, 1984).

Although only large-scale data have been considered, these findings definitely support the new viewpoint of nearshore sedimentation and thus of appropriate model design. Note that preceding examinations do not exhaust the usefulness of available large tests. The few situations exhibiting little profile development or a switch in shoreline movement seem worth special study. Also, inshore and offshore profile changes remain of basic interest, even though profile forms developed in large tanks may be somewhat unnatural due to the steep initial slopes, i.e., the marked distortion of natural surf zones.

#### CONCLUDING REMARKS

Evidence presented above and in Hallermeier (1985) is favorable rather than definitive regarding the accuracy of the proposed scaling law for coastal models. The approach yielding Eq. (2) has been shown to explain various previously reported empirical results including fairly successful movable-bed models. However, the new modeling relation has not yet been subjected to a stringent test program designed to define its usefulness and limitations.

Several unverified aspects of the guidance in Eq. (2) should be mentioned. If a model is to use prototype sediment for convenience and accuracy in size distribution, and to be undistorted for accurate wave patterns near structures, the new scale law provides no free choices: one value of  $N_v$  will be appropriate. Whether or not distortion of a chosen magnitude can be successfully imposed on a sand model remains unanswered. Also largely unknown is the usefulness of Eq. (2) with lightweight model sediments and in design of three-dimensional models. Finally, with prototype wave period figuring in basic model design (because of the sand motion process in the laboratory), a representative period must be determined.

One way to evaluate present guidance further would be review of the designs for three-dimensional models documented to have been either accurate or erroneous. Preliminary examination of some successful models reveals that it is possible to find designs basically agreeing (Fried, 1976) or disagreeing (Noda, 1966) with Eq. (2). However, detailed consideration of prototype sites with regard to littoral drift, dominant structures, etc., would be required for firm assessments. Also needing consideration are different procedures and informal approaches to the "modeling art" arising in various laboratories.

To summarize available evidence, Eq. (1) gives a direct and rational viewpoint of nearshore sand movements on the profile. Horizontal flow velocity divided by the threshold velocity for sand motion is a primary indicator of transport stage, and  $\psi$  seems a more fundamental sedimentation indicator than a parameter with sediment settling velocity can be. Also, settling velocity for common sands depends on fluid viscosity, so its absence for present guidance prevents an awkward requirement to control water temperature in laboratory models. Although limited, empirical results give clear support to the new viewpoint of modeling.

#### APPENDIX - DERIVATION OF EQUATION (8)

The fundamental definition of Eq. (1) is invoked along with linear wave theory at mid-depth in shallow water and the threshold for sand motion in large situations, giving

$$V_h = 0.5 H (g/d)^{0.5} \quad (A1)$$

$$V_v = 0.5 \pi H/T \quad (A2)$$

$$U_o = (8sgD)^{0.5} \quad (A3)$$

$$\psi = T/\pi(8sdD)^{0.5} \quad (A4)$$

where  $d$  is nearshore water depth. To measure profile changes by a meaningful dimensionless form, the last expression is multiplied by wave celerity  $c = (gd)^{0.5}$ , propagation rate of mobilizing impulses. For comparable dependences with other sedimentation parameters used in Figure 3, the present measure must be inverted.

Adjustment is needed for effect of varying initial slope since Eq. (7) indicates large tests are related by

$$N_h/N_v = (N_M)^{-1} = (N_D N_S)^{0.5} \quad (A5)$$

where  $M$  is bed slope. This indicates the functional trade-off, e.g., between a steeper slope and a finer, less dense sediment, with respect to replicating some standard large situation. Choosing test conditions with the most common slope ( $M = 1/15$ ) to remain unadjusted, a parameter for profile changes based on Eq. (1) may thus be written as

$$\psi' = \pi(8sD)^{0.5}/(TM'g^{0.5}) \quad (A6)$$

where  $M' = (15M)$ . This is the form provided in Eq. (8).

#### ACKNOWLEDGEMENTS

This research began at "CERC North", Fort Belvoir, Virginia, in the summer of 1983, and thanks are due those responsible for that unique research environment. I appreciate support provided by Cyril Galvin, Coastal Engineer, for attendance at the Houston Conference and final preparation of this paper.



## REFERENCES

- J.Caldwell, 1959: "Shore erosion by storm waves," Misc. Pap. 1-59, Beach Erosion Board, Washington, D.C.
- C.B.Chesnutt & R.P. Stafford, 1977: "Laboratory effects in beach studies: Movable-bed experiments with  $H_o/L_o = 0.021$  (1971/2)," Misc. Rep. 77-7, Vols. III, IV, Coastal Engineering Research Center, Fort Belvoir, Va.
- R.G.Dean, 1973: "Heuristic models of sand transport in the surf zone," Proc. Conf. Engng. Dynam. Surf Zone (Sydney, Australia), pp. 208-214.
- J.C.Fairchild, 1959: "Suspended sediment sampling in laboratory wave action," Tech. Memo. 115, Beach Erosion Board, Washington, D.C.
- I.Fried, 1976: "Protection by means of offshore breakwaters," Proc. 15th Coastal Engng. Conf., pp. 1407-1424; and 1983 personal communication to R.P. Savage.
- C.G.Gable, Ed., 1981: "Report on data from the Nearshore Sediment Transport Study Experiment at Leadbetter Beach, Santa Barbara, California," IMR Reference No. 80-5, Scripps Institution of Oceanography, LaJolla, California.
- M.R.Gourlay, 1980: "Beaches: Profiles, processes and permeability," Proc. 17th Coastal Engng. Conf., pp. 1320-1339.
- R.J.Hallermeier, 1980: "Sand motion initiation by water waves: Two asymptotes," ASCE Waterways Journal, Vol. 106, pp. 299-318.
- R.J.Hallermeier, 1984: "Wave cuts in sand slopes applied to coastal models," ASCE Waterways Journal, Vol. 110, pp. 34-49.
- R.J.Hallermeier, 1985: "Unified modeling guidance based on a sedimentation parameter for beach changes," to appear in Coastal Engineering.
- I.Ijima and N. Aona, 1959: "On the effect of shore materials on beach accretion," Proc. 6th Japan. Coastal Engng. Conf., pp. 49-56 (in Japanese).
- M.Ito and Y. Tsuchiya, 1984: "Scale-model relationship of beach profile," to appear in Proc. 19th Coastal Engng. Conf., 17 pp.
- R.Kajima, T. Shimizu, K. Maruyama and S. Saito, 1982: "Experiments on beach profile change with a large wave flume," Proc. 18th Coastal Engng. Conf., pp. 1385-1404.
- J.W.Kamphuis, 1975: "The coastal mobile bed model," C.E. Rep. 75, Queen's University at Kingston, Ontario, Canada.
- J.W.Kamphuis, 1982: "Coastal mobile bed modelling from a 1982 perspective," C.E. Rep. 76, Queen's University at Kingston, Ontario, Canada.
- G.H.Keulegan, 1966: "Model laws for coastal and estuarine models," in Estuary and Coastline Hydrodynamics, A.T. Ippen, Ed., McGraw-Hill, New York, pp. 691-710.
- A.S.Levin, 1948: Nomography, Wiley, New York.

- O.S.Madsen, 1970: "Waves generated by a piston-type wave-maker," Proc. 12th Coastal Engng. Conf., pp. 589-607.
- D.M.McDowell and B.A. O'Connor, 1982: "Numerical analysis of sediment transport in coastal engineering problems," in Hydraulic Modelling in Maritime Engineering, (Conf. Proc.), Thomas Telford, London, pp. 79-86.
- F.F.Monroe, 1969: "Oolitic aragonite and quartz sand: Laboratory comparison under wave action," Misc. Pap. 1-69, Coastal Engineering Research Center, Washington, D.C.
- J. Nicholson, 1968: "A laboratory study of the relationship between waves and beach profiles," Proc. 3rd Australasian Conf. on Hydr. and Fluid Mech. (Sydney, Australia), pp. 33-37.
- E.K.Noda, 1972: "Equilibrium beach profile scale-model relationship," ASCE Waterways Journal, Vol. 98, pp. 511-528.
- H.Noda, 1966: "Model study on the filling up of a fishery harbor by drifting sand," Proc. 10th Coastal Engng. Conf., pp. 564-594.
- H.Noda, 1978: "Scale relations for equilibrium beach profiles," Proc. 16th Coastal Engng. Conf., pp. 1531-1541.
- M.J.Paul, J.W. Kamphuis, and A. Brebner, 1972: "Similarity of equilibrium beach profiles, Proc. 13th Coastal Engng. Conf., pp. 1217-1236.
- T.Saville, Jr., 1957: "Scale effects in two-dimensional beach studies," Proc. 7th I.A.H.R. Cong., pp. A3/1-8.
- O.S.F.J.Sayao and J.C. Guimaraes, 1984: "Experimental verification of similarity criteria for equilibrium beach profiles," to appear in Proc. 19th Coastal Engng. Conf.
- R.J.Seymour and D.B. King, Jr., 1982: "Field comparisons of cross-shore transport models," ASCE Waterways Journal, Vol. 108, pp. 163-179.
- K.Shinohara, T. Tsubaki, M. Yoshitaka, and C. Agemori, 1958: "Sand transport along a model sandy beach by wave action," Coastal Engineering in Japan, Vol. I, pp. 111-130.
- J.F.A.Sleath, 1974: "Stability of laminar flow at seabed," ASCE Waterways Journal, Vol. 10, p. 105-122.
- J.F.A.Sleath, 1984: Sea Bed Mechanics, Chap. Two, Wiley, New York.
- T.Sunamura and K. Horikawa, 1974: "Two-dimensional beach transformation due to waves," Proc. 14th Coastal Engng. Conf., pp. 920-938.
- P.Vellinga, 1978: "Movable bed model tests on dune erosion," Proc. 16th Coastal Engng. Conf., pp. 2020-2039.
- P.Vellinga, 1982: "Beach and dune erosion during storm surges," Coastal Engineering, Vol. 6, pp. 361-387.
- M.S.Yalin, 1971: Theory of Hydraulic Models, Macmillan, London.

## CHAPTER EIGHTY FOUR

### Onshore-Offshore Sediment Transport Numerical Model

A. Swain<sup>1</sup> and J. R. Houston<sup>2</sup>, A. M. ASCE

#### Abstract

A numerical model is presented for calculating beach profile development due to offshore sediment transport and tested with laboratory and field data. The model allows variable wave conditions, water level fluctuations due to tide and storm surge, arbitrary bathymetry, and arbitrary sediment size. The agreement between calculated and measured beach profile erosion is good.

#### Introduction

The interactions of waves and currents with beaches are not well understood. The complexities of the phenomena do not allow useful closed-form solutions. On the other hand, hydraulic models designed to simulate these phenomena are subject to fundamental limitations of laboratory test and scale effects. Various numerical models have been developed (e.g. 1,2) to describe beach profile development due to wave attack. Although some of these models provide reasonable qualitative results, none have been shown to produce good quantitative predictions. This paper describes a numerical model based upon concepts developed by Swart (3), to calculate beach profile development. The model was tested by comparison with laboratory experiments and field data. The response of beach profiles during a period of extreme tides and storm surge also was investigated and results are presented.

#### Governing Equations

The numerical model developed in this study uses the governing equations obtained by Swart (3). Swart (4) conducted model studies and used regression analysis to obtain equations governing development of beach profiles (4). The readers may refer to references 3 and 4 for details.

The beach profile development during a time step was calculated according to the following equation from Swart (3) (See Fig. 1):

$$h_{ti} = h_{1i} \exp(-X_b t) + \delta_{Ai} (1 - \exp(-X_b t)) \quad (1)$$

<sup>1</sup>Research Hydraulic Engineer, Research Division, Coastal Engineering Research Center, U. S. Army Engineer Waterways Experiment Station, P. O. Box 631, Vicksburg, MS 39180-0631

<sup>2</sup>Chief, Research Division, Coastal Engineering Research Center, U. S. Army Engineer Waterways Experiment Station, P. O. Box 631, Vicksburg, MS 39180-0631

in which  $h_{ti}$  = depth of profile measured from the water level (MSL + Tide) at time  $t$  and at location  $i$  on the profile;  $h_{li}$  = depth of initial profile measured from the water level (MSL + Tide) at time  $t=0$  and at location  $i$  on the profile;  $\delta_{Ai}$  = depth of the equilibrium profile measured from the same reference at location  $i$ ; and  $X_b$  is a time factor (rate coefficient) (5).

Method of Calculation

The method of calculation is as follows: first an initial profile ( $h_{li}$ ) is selected. Then, from the known wave characteristics (height, period, and angle), sediment size, and time-varying tide,  $h_o$ ,  $X_b$ , and  $\delta_{Ai}$  are calculated according to the method of Swart. Equation 1 is then solved to calculate  $h_{ti}$  during the first time step. At the beginning

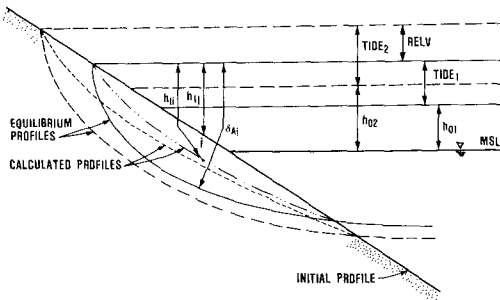


Figure 1. Definition Sketch of Various Numerical Parameters

of the second time step, a new set of wave and tide conditions is input. Equation 2 is then used to calculate the new position of the developed profile with respect to the new datum (MSL + Tide),

$$h_{li} = h_{ti} - RELV \tag{2}$$

in which

$$RELV = (h_o + Tide)_t - (h_o + Tide)_{t+\Delta t} \tag{3}$$

where  $h_o$  = elevation from the MSL to the upper boundary of developed profile, and  $\Delta t$  is the time step. A one-hour time step was used throughout the entire study. It should be noted that the elevation  $h_o$  corresponds to the most shoreward location that waves reach on the beach.

In the numerical model this location varied with time, because the tide datum and wave climate varied. Figure 1 presents a definition sketch showing the various parameters involved in Eqs. 1, 2, and 3. The governing equations (3) for  $X_b$ ,  $h_o$ , and  $\delta_{Ai}$  were calculated and Equation 1 was then numerically solved. The above procedure was repeated during each time step, until the desired number of iterations for the final beach profile development was attained.

#### Model Testing

The accuracy of the numerical model was tested by comparison of calculations with laboratory experiments and with prototype measurements. Figure 2 shows a comparison of the beach profile measured in hydraulic model tests by Eagleson et al. (6), and calculations of the profile response numerical model. The parameters used in the numerical model calculations were identical to those of the laboratory tests (initial profile, wave height, wave period, diameter of testing material, and length of time of the test). Figure 2 shows that the major features of the measured profile were reproduced by the numerical model. Additional comparisons of hydraulic scale model tests with the results of the numerical model are given in Swain and Houston (5).

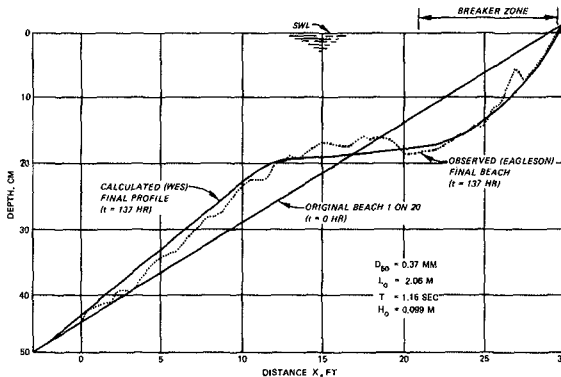


Figure 2. COMPARISON BETWEEN EXPERIMENTAL (EAGLESON, 1963, TEST 3) AND CALCULATED ONSHORE-OFFSHORE PROFILES

Figure 3 presents a comparison between numerical model calculations and measured profile change in the prototype. The field data include a 16-21 February 1980 storm off the west coast of the United States, at Leadbetter Beach, Santa Barbara, California. The Nearshore Sediment Transport Study (NSTS) documented daily profile measurements in addition to complete directional spectral wave data during the storm (7). This was a large storm that produced approximately 40 m (122 ft) of shoreline erosion. The inputs to the numerical model were sand grain size, initial profile, and hourly values of significant wave height, period, direction, and tide level. Figure 3 shows good agreement between measured profiles and the numerical calculations over the 5-day period of the storm. An important result found in the numerical calculations was that tidal fluctuations were a first-order effect in the mechanism of offshore sediment

transport (8). The sensitivity of the numerical model to other important parameters is discussed by Swain (9).

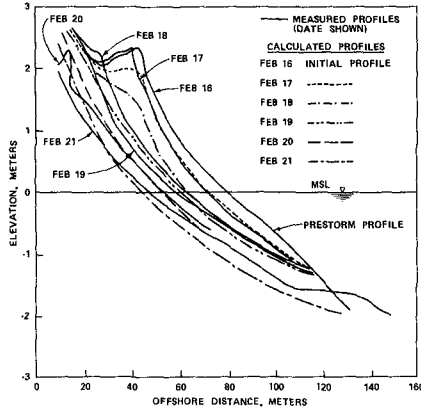


Figure 3. COMPARISON OF CALCULATED AND MEASURED BEACH PROFILES  
LEADBETTER BEACH, CALIFORNIA, 1980, NEARSHORE SEDIMENT TRANSPORT STUDY

An additional comparison between measured profile modification during the Currituck Sand-Bypass Study (10), and the profile response numerical model calculations was made. This study involved placement of 26,750 cu m (34988 cu yd) of sediment on the coast near New River Inlet, North Carolina, using the split-hull dredge CURRITUCK. A profile was chosen through the center of the dump to avoid "end effects." Wave characteristics were obtained during the study using the Littoral Environment Observation (LEO) technique. The mean diameter of the disposal

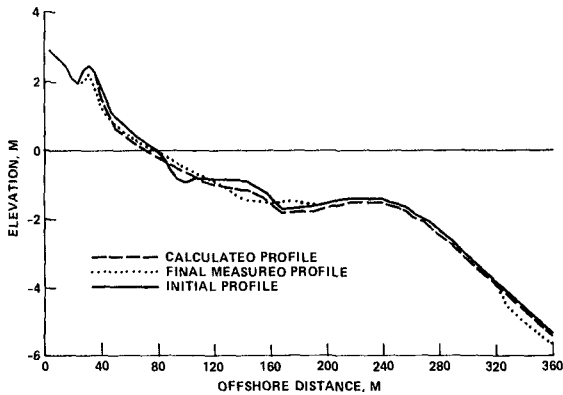


Figure 4. COMPARISON OF CALCULATED AND MEASURED SHORE-NORMAL PROFILE  
NEW RIVER INLET, NORTH CAROLINA  
(DREDGED DISPOSAL SAND MOVEMENT)

material was 0.23 mm. Figure 4 shows the initial profile measured after the dump was completed, and measured and calculated profiles after 36 days. The numerical calculations predicted that there would be little modification in the profile over the time period except for some erosion of the break point bar and filling of the adjacent trough. The measured profile confirms the numerical prediction. Figure 4 shows the calculated and measured profiles differ at most by a few tenths of a meter in elevation. This difference is within the level of accuracy of the profile measurements.

As a final test for the model, beach erosion caused by the 1962 Ash Wednesday storm along the Outer Bank Barrier Islands of North Carolina on the east coast of the United States was simulated. This study area includes the vicinity of the Oregon Inlet which is presently the only inlet along the Outer Banks between Cape Hatteras and Chesapeake Bay. Bodie and Pea Islands border the north and south sides of the Oregon Inlet respectively. Figure 5 presents a portion of the barrier islands system. Wave characteristics were obtained from the U. S. Army Engineer Waterways Experiment Station (WES) Wave Information Study (11). Tide and surge elevations were obtained from the WES Implicit Flooding Model, a tidal circulation and storm surge model (12). Wave conditions were available at three-hour intervals for a period of 4 days. However,



Figure 5. **AERIAL PHOTOGRAPH OF OREGON  
INLET BEFORE AND AFTER THE  
1962 ASH WEDNESDAY STORM**

tidal and surge elevations were generated at intervals of one hour for the same number of days. Thus the tide and surge level was updated each time step and the wave conditions updated every third time step. Figure 6 shows a comparison of the calculated and the measured shore-normal erosion along Bodie Island. Measurements show that beach erosion varied from a few hundred feet along much of the island to approximately 1500 ft near the north spit. The north spit was a low-lying area that was

inundated during the storm. The numerical calculations predict a similar trend. Figure 7 presents a similar plot along the Pea Island. It is seen that the calculated erosion agrees well with the measurements.

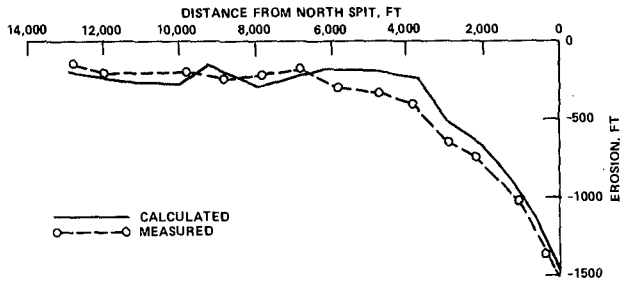


Figure 6. COMPARISON OF CALCULATED AND MEASURED SHORE-NORMAL EROSION OREGON INLET, NORTH CAROLINA (BODIE ISLAND, 1962 ASH WEDNESDAY STORM)

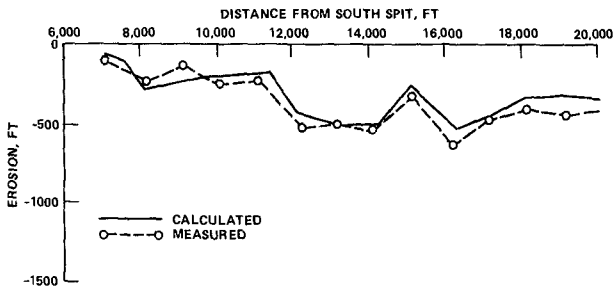


Figure 7. COMPARISON OF CALCULATED AND MEASURED SHORE-NORMAL EROSION OREGON INLET, NORTH CAROLINA (PEA ISLAND, 1962 ASH WEDNESDAY STORM)



However, the comparison is not a rigorous test of the model since there was a constraint that stopped further erosion. The storm produced large waves over such long duration that erosion continued until stopped by the large sand supply of the high dunes. The north spit did not have high dunes and the erosion distance shown in Fig. 6 is the width of the barrier island since the spit was completely eroded.

#### Conclusions

A time-dependent numerical model to predict beach profile erosion was developed. The accuracy of the model was tested with laboratory experiments and with prototype measurements. It was found that the beach response model can accurately predict profile response to waves and fluctuating water levels.

#### Acknowledgments

The authors wish to acknowledge the U. S. Army Engineer District, Wilmington, for funding the study on which this paper is based and the Office, Chief of Engineers, U. S. Army Corps of Engineers for authorizing publication of this paper.

#### Appendix.—References

1. Dally, W. R., and Dean, R. G., "Suspended Sediment Transport and Beach Profile Evolution," *Journal of the Waterway, Port, Coastal and Ocean, Div.*, ASCE, February 1984.
2. Seymour, R. J., and King, D. B., "Field comparison of Cross-Shore Transport Models," *Journal of the Waterway, Port Coastal and Ocean Div.*, ASCE, May 1982.
3. Swart, D. H., "A Schematization of Onshore-Offshore Transport," *Proceeding of the 14th Coastal Engineering Conference, Copenhagen, Denmark, June 1974.*
4. Swart, D. H., "Predictive Equations Regarding Coastal Transports," *Proceedings of the 15th Coastal Engineering Conference, Honolulu, Hawaii, 1976.*
5. Swain, A., and Houston, J. R., "A Numerical Model for Beach Profile Development," *Proceedings of the 6th Canadian Hydrotechnical Conference, CSCE, Ottawa, Canada, June 1983.*
6. Eagleson, P. S., Glenne, B., and Dracuq, J. A., "Equilibrium Characteristics of Sand Beaches," *Proceedings, ASCE, Hyd. Vol. 89, June 1963.*
7. Gable, C. G., "Report on Data from the Nearshore Sediment Transport Study Experiment at Leadbetter Beach, Santa Barbara, California, January-February, 1981, IMR Ref. No. 80.5, Scripps Institution of Oceanography, La Jolla, California 92093.
8. Swain, A., and Houston, J. R., "Discussion to the Proceeding Paper 17749 by Richard J. Seymour, The Nearshore Sediment Transport Study," *ASCE, Port, Coast and Ocean, Div.*, February 1984.

9. Swain, A., "Additional Results of a Numerical Model for Beach Profile Development," Proceedings of the Annual Conference, CSCE, Halifax, Nova Scotia, Canada, May 1984.
10. Schwartz, R. K., and Musialowski, F. R., "Nearshore Disposal: Onshore Sediment Transport," Coastal Sediment 77, ASCE, Charleston, South Carolina, November 1977.
11. Jensen, R. E., "Atlantic Coast Hindcast, Shallow Water Significant Wave Information," WIS, Report No. 6, 1983, U. S. Army Engineer Waterways Experiment Station, Vicksburg, MS.
12. Leenknecht, D. A., Erickson, J. A., and Butler, H. L., "Numerical Simulation of Oregon Inlet Control Structures, Effects on Storm and Tide Elevations in Pamlico Sound," Tech. Report CERC-84-2, April 1984, U. S. Army Engineer Waterways Experiment Station, Vicksburg, MS.

## CHAPTER EIGHTY FIVE

### MEASUREMENTS OF BEDLOAD TRANSPORT IN THE NEARSHORE ZONE USING RADIOISOTOPIC SAND TRACERS.

by

Georges Drapeau and Bernard Long\*

#### ABSTRACT

A field study was conducted on the North Coast of the Gulf of St. Lawrence in Eastern Canada to evaluate sediment transport processes in a coastal area that would be affected by the modification of river regimes for hydropower production. Radioactive tracers were used to evaluate the mobility of coastal sediments. Three injections were carried out using Neodymium 147 (half-life 11.1 days), at 450, 550 and 2200 m. from the shoreline at depths from 3 to 10 m. The high sensitivity of the detection system allowed to monitor the study area for 44 days. The tagged sediments responded to waves and tidal currents and were sensitive to minor changes. Comparison of the patterns of evolution of the three injections permitted to evaluate the relative mobility of bottom sediments as a function of water depth and distance from shore. Bedload transport rates were calculated but they are related to specific events such as storms within the Gulf of St. Lawrence more than to steady state conditions.

#### INTRODUCTION

Among the long term hydropower developments on the North Shore of the Gulf of St. Lawrence, one project would divert part of the Saint-Jean River into the Romaine River (Figure 1). This modification of the Saint-Jean River drainage basin would decrease the sediment supply to the coastal zone and aggravate coastal erosion. Coastal erosion in this area is enhanced by the directional wave attack from the South West while the coast is protected from eastern fetches by a series of coastal islands (Figures 1 and 2). A research program was initiated to evaluate sediment transport processes in the coastal area that would be most affected by the modification and regulation of river regimes. Radioactive tracers were used to define

---

\* Professors, INRS-Océanologie, Université du Québec, Rimouski, Qc, Canada G5L 3A1.

the mobility of coastal sediments and contribute to the study of sediment transport processes in that portion of the coastal zone of the Gulf of St. Lawrence.

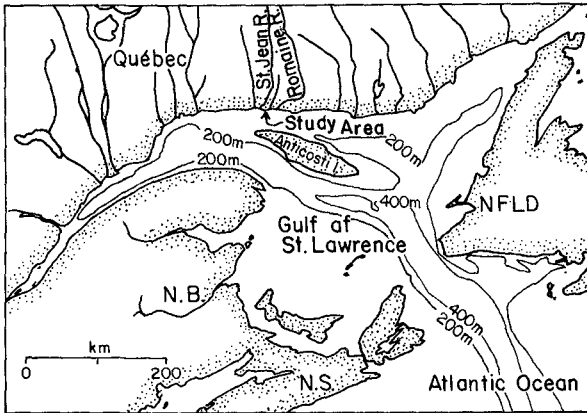


Figure 1. Location map of the study area.

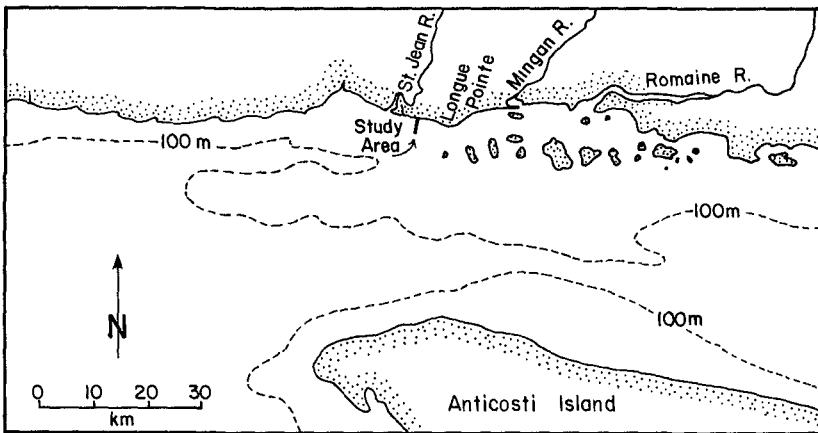


Figure 2. Regional map of the study area. This map in conjunction with figure 1 outlines that the study site is exposed to waves from SW and W and is protected from storms from other directions by Anticosti Island and a series of coastal islands. Longue Pointe is lined up with the western extremities of Anticosti Island and the coastal archipelago and it demarcates westward an erosional coastline and eastward an accretional coastline.

This paper describes the results obtained with radioactive tracers with some emphasis on the theory and methodology used, because they differ from other radioactive tracer experiments carried out in North America, namely those of Duane and his colleagues on the coast of California (Duane and James, 1980) and Lavelle and his colleagues on the New York continental shelf (Lavelle et al., 1978).

The study area is located 5 km East of the St. Jean River on the North Coast of the Gulf of St. Lawrence (Figure 2). This region is characterized by the fact that the coastline is erosional westward from Longue Pointe and accretional eastward from that point, because of the directional wave approach along that coast. The main fetch for that area is from the South-West as shown on figure 1. Figure 2 outlines with more detail that the study area is exposed to fetches from the South-West and that the window of wave propagation is quite narrow because of the protection offered by Anticosti Island and a series of coastal islands. West of Longue Pointe the present shoreline cuts through shorelines formed at higher sea levels from 1660 BP to present (Long et Drapeau, 1983). The shoreline is accretional East of Longue Pointe because of the protection offered by the coastal islands.

The study area is subjected to the combined action of waves and tidal currents. The tide is semi-diurnal and ranges between 1.7 and 2.9 m. Four Aanderaa current meters were deployed during the survey and measured reversing tidal currents of 24 to 50 cm/s during flood tides and 15 to 28 cm/s during neap tides. Long term records are not available to define yearly wave climates. During the fall of 1982, waves occasionally reached a height of 1.5 m and periods of 5 to 6 seconds in response to winds blowing from the South-West.

The nearshore zone in the study area is characterized by a shallow platform that reaches a depth of 10 m, 2.3 km offshore (figure 4). The surficial sediments are composed of well sorted 0.2 to 0.4 mm sand. Sources for these sediments are on one hand the material eroded from the coastline and on the other hand the input from the North Shore rivers (Cataliotti-Valdina et Long, 1983). Nearshore sand bars are developed on the shallow inshore platform. These bars are aligned parallel to the shoreline although they are discontinuous. Karakiewicz et al. (1983) relate the formation of this sand bar system to progressive gravity waves in the presence of tides.

#### BEDLOAD TRANSPORT EQUATION

The bedload transport rate  $Q$  is based on the mean velocity  $V_m$  of the mobile bedload layer of width  $L$ , usually taken as unit width, and the thickness of the mobile layer  $E$ . This volume rate is multiplied by the density  $\rho$  of the sediment to determine the transport in terms of mass per unit time for a unit width.

$$Q = \rho V_m L E$$

The unknowns are then  $V_m$  and  $E$ .  $V_m$  is determined by measuring the movement of the centroid of the tracer cloud as it is done currently with radioactive as well as luminescent tracers.

The estimation of the thickness of the mobile sediment layer is more problematic. The approach used for this study was developed by Sauzay (1967) at the Université de Toulouse and used extensively in France, particularly by the Centre d'Études Nucléaires de Saclay (Tola, 1982).

Sauzay based his analysis on the principle that if the total amount of radioactive material used for injection is measured precisely and if the detections that follow the tracer injection account for all the tracer used, then a relationship exists between the amount of tracer used  $A$ , the total count of detected radiation  $N$  and the thickness of burial of the tracer  $E$  (Figure 3).

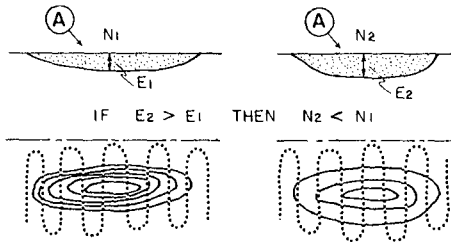


Figure 3. Schematic of the concept of count rate balance. «A» is the amount of tracer energy. «N» is the amount of tracer detected and «E» is the thickness of the tracer in the mobile sediment layer.

The probe is calibrated to conform to the penetrating power law for a point source:

$$f(z) = f_0 e^{-\alpha z} \tag{1}$$

where  $f_0$  and  $\alpha$  are calibration constants.

As the sand tracer is not a point source and is rather scattered within the sediment from the seafloor (depth = 0) to a maximum depth  $E$ , equation 1 is integrated.

$$f(z) = \int_0^E f_0 e^{-\alpha z} dz \tag{2}$$

The count rate recorded by the probe is also a function of the tracer concentration with depth  $C(z)$  and should also be part of the integration process.

$$f(z) = \int_0^E f e^{-\alpha z} C(z) dz \quad (3)$$

We analyse first a hypothetical case where the concentration of the tracer is uniform for the whole depth  $E$ , then

$$C(z) = C_m \quad (4)$$

The radiation count rate  $N$  is then easily determined by integrating equation 3 for the interval 0 to  $E$ .

$$N = C_m f_0 \frac{1}{\alpha} \left[ 1 - e^{-\alpha E} \right] \quad (5)$$

The initial amount of radioactivity injected  $A$  being known as well as its half-life, the remaining activity at the time of a given survey  $A(t)$  can be determined. The hypothetical uniform tracer concentration per unit  $C_m$  used in the preceding equation can be expressed as:

$$C_m = \frac{A(t)}{E} \quad (6)$$

and by substitution of equation 6 in equation 5 we obtain:

$$N = \frac{A(t)}{E} f_0 \frac{1}{\alpha} \left[ 1 - e^{-\alpha E} \right] \quad (7)$$

Remains to be reconsidered the initial hypothesis of constant tracer concentration with depth. The distribution of radioactive tracer within the mobile sediment layer can take different configurations. Sauzay (1967) has analysed different tracer distributions as a function of depth and he has integrated these data to obtain what is termed the equivalent concentration  $C_c$ .

$$C_c = \int_0^E C(z) dz \quad (8)$$

The approach taken by Sauzay is to introduce the coefficient:

$$\beta = \frac{C_c}{C_m} \quad (9)$$

The maximum depth  $E$  is then obtained implicitly by solving the equation

$$N = \beta \frac{A(t)}{E} f_0 \frac{1}{\alpha} \left[ 1 - e^{-\alpha E} \right] \quad (10)$$

Experience has shown (Tola, 1982) that a parabolic tracer distribution is the most realistic and the use of a constant value of 1.15 for  $\beta$  has produced consistent results.

## FIELD DEPLOYMENTS

The radioactive element used for that series of experiments on the North Shore of the Gulf of St. Lawrence is Neodymium 147 whose half-life is 11.1 days. The radioactive tracer used is made of specially prepared glass containing neodymium. This glass was radioactivated at the Centre d'Études Nucléaires de Saclay. For the purpose of this experiment, the granulometry of the glass was chosen between 0.2 and 0.4 mm to coincide with that of the natural sediment.

The radioactive tracers were injected at three locations in the study area (see Figure 4). Two injections were deployed nearshore, one on each side of a sand bar located 450 m offshore at a depth of 3 m. The third injection was located at the edge of the flat platform, 2.2 km offshore. Five hundred grams of glass radioactivated at the level of 2.9, 2.2 and 1.7 Curies were spread on the seafloor surface at each location.

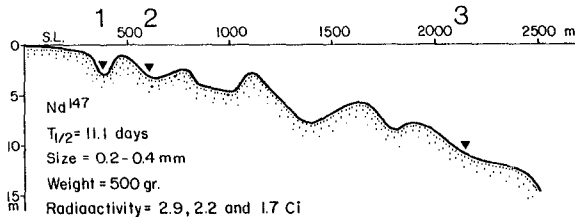


Figure 4. Seafloor profile of the study area. The location of the three injection points is indicated by black triangles. The characteristics of the tracer are summarized on the figure.

The detection equipment used was developed at the Centre d'Études Nucléaires de Saclay. It is composed of a NaI scintillation probe which is connected to two parallel systems of detectors, counters and plotters, one system working on a linear scale and the other on a logarithmic scale. This combination permits to follow with the same precision the response of the tracer at low as well as high levels of radioactivity.

The scintillation probe used is miniature as compared with the RIST probe (Duane, 1970; Lavelle et al., 1978). It is contained within a waterproof stainless steel cylinder 5.3 cm in diameter by 36 cm long that weighs only 2 kg. The probe is mounted on a sled that maintains the center of the probe at a constant height of 5 cm above the seafloor (Figure 5).



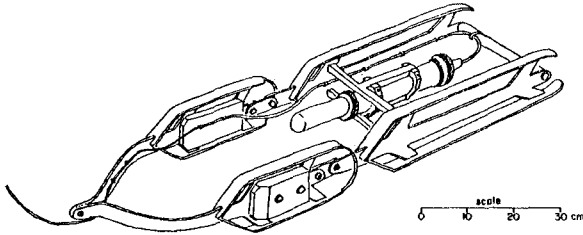


Figure 5. Drawing of the scintillation probe mounted on a sled that maintains the probe at a constant height of 5 cm above seafloor (after Anguenot, Caillot et Courtois, 1968).

It is essential that each survey completely covers the radioactive cloud as schematized on figure 3. As explained previously, the evaluation of the thickness  $E$  of the mobile sediment layer is based on the assumption that each survey detects all the tracer initially injected. The survey lines are oriented perpendicular to the direction of sediment transport and are prolonged to ascertain that the limits of the survey extend well beyond the radioactive cloud.

Radiation count rates are integrated for each transect and totalled for the whole survey. Calculations are based on a towing velocity of 1 m/sec because the probes are calibrated for radiation count rates in counts per second with reference to radioactive material uniformly covering one square meter. Sauzay (1967) has shown that towing the detection system at a constant velocity of 1 m/sec produces the same results as if count rates per second were measured at fixed grid locations. It was possible during the surveys in the Gulf of St. Lawrence to maintain a survey velocity of 1 m/sec and to correct for departures using a Trisponder system for positioning.

## RESULTS

Contours of the radiation levels and locations of the centroid of the labelled zones are shown on figure 6. The contours of radiation levels outline how the initial 500 gram release of radioactive glass mixes with the indigenous sediment and spreads on the seafloor. The lowest contour is 50 counts/sec above background and the other contours are for 150, 500, 1500, 5000, 15 000, and 50 000 counts/sec. In the case of these experiments on the North Coast of the Gulf of St. Lawrence, all three injections show that the highest tracer concentration has moved and that the tracers have spread during the 44 days that the experiment lasted.

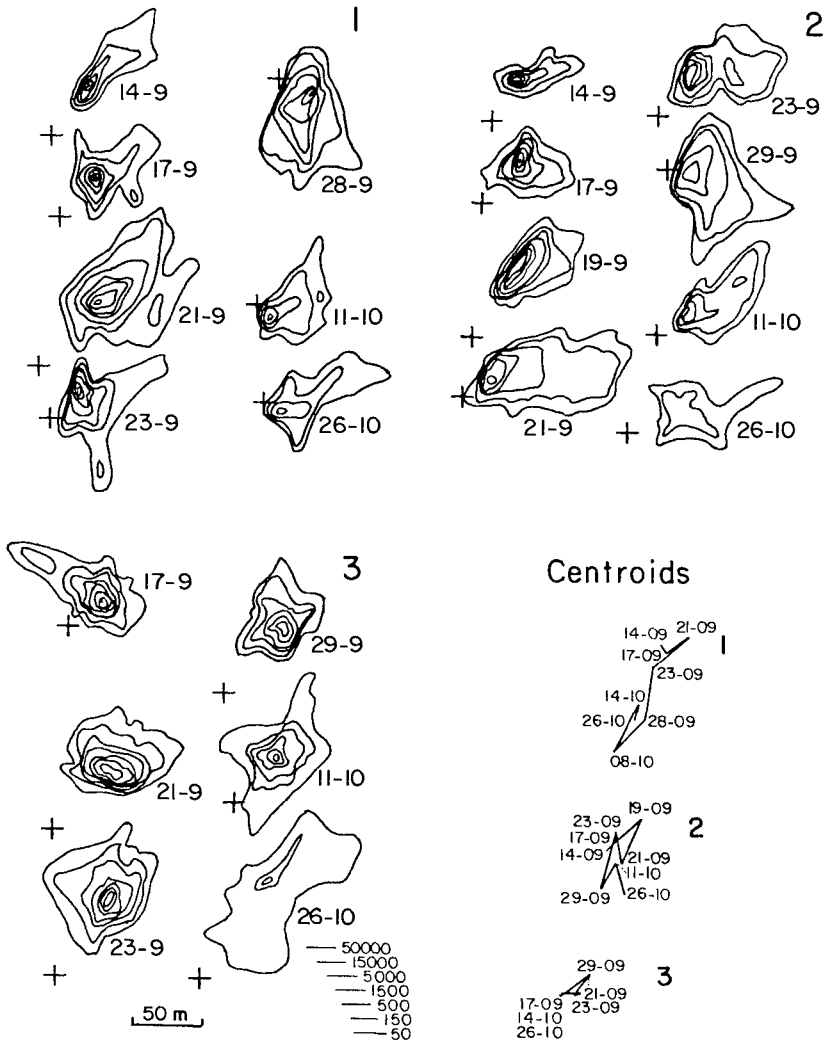


Figure 6. Evolution of tracer patterns for the three experimental sites. Each site is identified by a bold figure and each survey is identified by date-month. A cross is drawn as a fixed reference for each site to evaluate the movement of the tracer cloud. The outer countour is always 50 counts/sec and the others are 150, 500, 1500, 5000, 15000, and 50000 counts/sec. The movement of the centroids is shown in the lower right portion of the figure.

The movement of the centroid of the tagged sediments is used to calculate the mean velocity of the mobile sediment layer. It is apparent on figure 6 that the movement of the centroid, although alike, does not coincide with the highest tracer concentration.

Experiment number one was the closest to the seashore, that is 350 m from the high tide line in a slight depression on the shore side of the first sand bar (Figure 4). The first survey on September 14, two days after injection, shows that the tagged sediments have spread towards the North-East. As the sea was calm during these two days, the spreading pattern of the tagged sediments outlines the influence of the ebbing tidal currents that prevailed during and immediately following the injection of the tracer on the seafloor. The survey on 17 September outlines the influence that 0.5 m waves had on the labelled sediments. Tidal currents reached 41 cm/sec for a period of two hours between 14/9 and 17/9. The survey on 21/9 shows the result of a 30 hour storm that produced 5 to 6 second waves that reached 1 m heights. The following surveys show the evolution with time of the tagged sediments, but it should be kept in mind that the contours of radiation levels are not compensated for radioactive decay and by 26 October only 6.5 percent of the initial radioactivity was left.

The second injection site was located between the first and the second sand bar, 600 metres from the shoreline. The first survey on September 14 outlines essentially the same characteristics as for the first site that the tracer two days after injection has spread towards the North-East but is still concentrated within a 40 by 70 meters area. Comparison of surveys 19/9 and 21/9, before and after the storm mentioned previously, indicates that the movement of sediments on the seafloor has been somewhat more intense at that second location. Tidal currents were stronger: flood currents reached 20 cm/sec and ebb currents of 52 cm/sec were measured during the storm. After that storm, the tagged sediments at that location evolved in a similar manner as those of the inshore location.

The third experiment took place beyond the sand bars, 2.2 km offshore at a depth of 10 meters. The distance offshore and the greater water depth explain that the tracer was less mobile at that location. The elongation of the radioactive cloud towards the North-West is a response to flood tidal currents of 37 cm/sec. The survey 21/9, when compared with those of experiments 1 and 2 for the same date, indicates that the disturbance of the seafloor by storm waves was less intense at that third location because of the greater water depth. Tidal currents reached 41 cm/sec during the storm that preceded that survey. The comparatively large area covered by the 50 counts/sec outside contour on 26/10 could be explained by the fact that the radioactive tracers were less dispersed at that location further offshore and could yield a uniform signal above 50 counts/sec after 44 days.

The movement of the centroid of each radioactive cloud is also shown on figure 6. As explained previously, the movement of the centroid is not identical to that of the highest tracer concentration. The figure 6 outlines the relative mobility of each cloud of radioactive sediments. Sediments from experimental site 1 were closest to

shore and also the most mobile. By contrast, the centroid of the tagged sediment from experimental site 3, 2.2 km offshore, only moved back and forth a distance of some 25 m.

## DISCUSSION

Bedload sediment transport rates have to be identified with the time scale of interest, be it that of waves, tides or seasonal storms. For instance, direct methods that measure grain-to-grain movement respond to all modes of excitation of the seabed and particularly to the oscillatory movement of waves. The experiments with radioactive tracers on the North Shore of the Gulf of St. Lawrence responded to tidal and storm events and they outlined that the net movement of sediments after 44 days is of comparable amplitude to the movements linked to tides and storms. Ideally, the rate of movement of the radioactive tracers would reach an asymptotic value as the tracer becomes more homogeneously integrated to the seabed. This asymptotic value would be representative of the yearly rate of transport. This «steady-state» was not reached during these experiments with Neodymium 147 on the North Shore of the Gulf of St. Lawrence: a longer half-life tracer would be needed.

Bedload sediment transport rates were calculated however for the main storm on September 20th. The centroid of the tagged sediments moved a distance of 36 m during a period of 48 hrs, that is  $V_m = 0.75$  m/hr. Using the algorithm described above, the thickness of the mobile layer was determined as  $E = 2.95$  cm for the 19/9 survey before the storm and  $E = 13.06$  cm for the 21/9 survey after the storm. A mean value of 5 cm was used for the bedload calculations. These data yielded a bedload transport rate of 60 kg/m/hr in the direction 163 degrees from North. These results are compared with calculations based on the bedload sediment transport model developed by Vincent, Young and Swift (1982). Nearbed current velocities were obtained from Aaderaa current meters fixed upsidedown on the seafloor to measure currents 50 cm above bottom. Records from these current meters are reproduced on figure 7 and they show a very good signature from the tidal currents, but they also indicate that Savonius-type current meters are not suitable to monitor wave-dominated conditions. To obviate the problem of not having current measurements during the storm itself, current data for September 19th were used because the records show that tidal currents are not varying much from one day to the next one (see Figure 7). Calculations for different wave conditions, that is wave periods of 5 seconds and wave heights of 0.5, 0.7, 0.9, and 1.0 meter are shown on figure 7. The transport model predicts 58.3 kg/m/hr for 1 m waves which corresponds to the waves conditions that prevailed in the study area on September 20th.

The good agreement between the tracer experiment and the calculated sediment transport rate has its merits but it could be anticipated. The model developed by Vincent, Young and Swift (1982) is based on linear wave theory which implies that even the highest waves would not produce the slightest net residual transport component. In the study area, on the North Shore of the Gulf of St. Lawrence, tidal

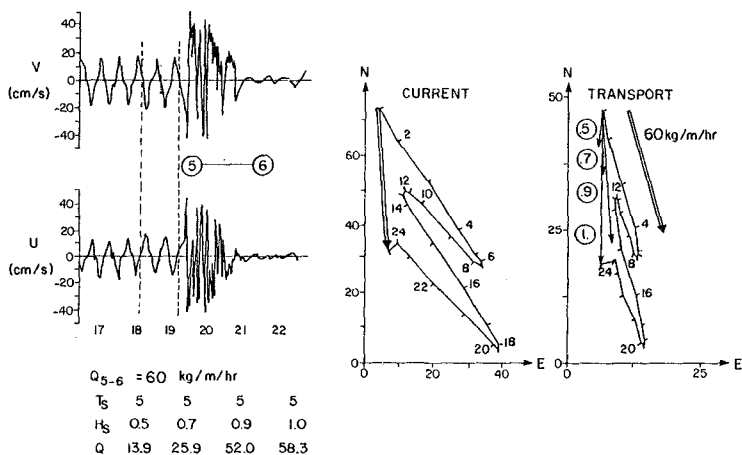


Figure 7. Experimental site 2. A time series of a portion of current meter deployment is shown on the upper left. The V(North) and U(East) components outline the semidiurnal tidal currents. A progressive current vector diagram for the diurnal tide of 19 September, delineated by dotted lines on the time series, is drawn in the center of the figure. A sediment transport progressive vector diagram appears on the right side of the figure. This diagram reproduces the progressive vector for sediment transport resulting from the combined effect of the tidal currents and 1 m high waves. Resulting transport vectors for 0.5, 0.7 and 0.9 m waves are also shown on the same diagram. A vector representing the transport rate measured with radioactive tracers (60 kg/m/hr) is also drawn at the extreme right for comparison. The results of transport calculations for different combinations of wave heights with the tidal current are tabulated on the lower left side of the figure.

currents are important and the application of a linear wave theory model reflects this phenomenon. The good agreement between the field measurements and the calculations is also interesting because the model is used at the limits of applicability. On one hand the model developed by Vincent and his colleagues uses bottom friction concepts developed by Grant and Madsen (1978) for waves in the presence of weak currents; in the present study the tidal currents are comparable to the nearbed wave orbital velocities. On the other hand the water depth versus wave height is also a limiting factor in this study that uses a linear wave theory. The latter problem is presently investigated by Boczar-Karakiewicz (1981). For many sediment tracer studies in the nearshore zone a non-linear wave model combined with nearbed

currents of comparable amplitude to the bottom wave orbital velocities would provide a more realistic representation of the environmental conditions.

The rate of sediment transport (60 kg/m/hr) determined with radioactive tracers for the moderate storm conditions of September 20th are of the same order of magnitude as results obtained in other areas. Lavelle and colleagues (1978) used radioactive sediment tracers on the Long Island inner shelf and obtained sediment flux estimates of 61.2 kg/m/hr (0.17 gm/cm/sec) for winter storm conditions. The approach taken by Lavelle and colleagues to determine the sediment flux is basically different from that of the present study however, as they assumed that the points of highest tracer concentration were stationary and used an advection-diffusion equation to obtain flux estimates of the tagged sediments. Vincent, Young and Swift (1982) used their model to calculate bedload transport at a 10 m water depth 1 km from the Long Island coastline where they estimated bedload transport peaks of 316 kg/m/hr (3160 gm/cm/hr).

#### SUMMARY AND CONCLUSIONS

To summarize, this study shows that radioisotopic sand tracers were used successfully in the nearshore environment of the North Coast of the Gulf of St. Lawrence. The main conclusions drawn from these experiments are:

1. The compactness and lightweight of the scintillation probe and support equipment facilitated the logistics. It was then possible to improve the precision of the surveys using a highly maneuverable small fishing boat.
2. Radioisotopic sand tracers are very effective because they can be surveyed accurately without disturbing the sediment with which they intermix. The labelled sediments were sensitive to waves and tidal currents. It was possible to relate the evolution of the radioactive cloud patterns to specific events such as peak tidal currents and storm generated waves.
3. The use of three tracer injections permitted to evaluate the relative mobility of the seabed. Ideally, the rate of movement of the radioactive tracers would reach an asymptotic value as the tracer becomes more integrated with seabed. These experiments with Nd 147 did not last long enough to reach that steady state.
4. Estimates of sediment transport rates of 60 kg/m/hr during a storm compare with other radioisotopic sand tracer measurements particularly on the Long Island Shelf. Comparison of storm transport rates using tracers also shows a very good coherence with a linear wave analytical model.

#### ACKNOWLEDGMENTS

This research was supported by grants from the National Sciences and Engineering Council of Canada, the Ministère de l'Éducation du Québec and Hydro-Québec. The authors would like to express their thanks to Dr. A. Caillot for his collaboration to the radioactive

tracers study, to Dr. R.A. Young for his assistance with the transport model and to Mr. M. Gagnon for processing the current meter data.

#### REFERENCES

- Anguenot, M., A. Caillot and G. Courtois, 1968. Utilisation de traceurs radioactifs à l'étude sédimentologique du Lac de Maracaibo: CEA Internal Report DR/SAR.S/68-7/GC/JJ.
- Boczar-Karakiewicz, B. and J.L. Bona, 1981. Über die Riffbildung an sandigen Küsten durch progressive Wellen. Mitteilungen des Leichtweiß-Instituts für Wasserbau der Technischen Universität Braunschweig 7D, p. 380-42D.
- Boczar-Karakiewicz, B., B.F. Long et G. Drapeau, 1983. Formation and modification of a system of sand bars by progressive gravity waves in the presence of tides (an example from the North Coast of the St. Lawrence Gulf). Proc. Can. Coastal Conf., 1983, NRC, p. 37-51.
- Cataliotti-Valdina, D. et B.F. Long, 1983. Évolution du débit liquide et de la charge solide d'un estuaire sub-boréal: rivière St-Jean, Québec. Jour. Can. Sc. Terre, V. 2D, p. 184-194.
- Duane, D.B., 197D. Tracing sand movement in the littoral zone: progress in the radioisotopic sand tracer (RIST) study, July 1968 - February 1969. US Army Corps of Engineers, Coastal Engineering Center, MP4-7D.
- Duane, D.B. and W.R. James, 198D. Littoral transport in the surf zone elucidated by an eulerian sediment tracer experiment. Jour. Sed. Pet., V. 5D, p. 929-942.
- Grant, W.D. and D.S. Madsen, 1978. Bottom friction under waves in the presence of a weak current. Tech. Rept. ERL-MESA, NOAA, Boulder, Colo.
- Lavelle, J.W., D.J.P. Swift, D.E. Gadd, W.L. Stubblefield, F.N. Case, H.R. Brashear and K.W. Haff, 1978. Fair weather and storm sand transport on the Long Island, New York, inner shelf. Sedimentology, V. 25, p. 823-842.
- Long, B.F. and G. Drapeau, 1983. Évolution du transport sédimentaire par traceurs radioactifs sur la zone infralittorale de la Basse Côte Nord du Saint-Laurent. Comptes rendus Conf. Can. Littoral, 1983. CNR, p. 201-215.
- Sauzay, G., 1967. Méthode du bilan des taux de comptage d'indicateurs radioactifs pour la détermination du débit de charriage des lits sableux. Thèse Doc. Toulouse, 162 p.
- Toia, F., 1982. The use of radioactive tracers in dynamic sedimentology. CEN de Saclay. Note CEA-N-2261, 42 p.
- Vincent, C.E., R.A. Young and D.J.P. Swift, 1982. On the relationship between bedload and suspended sand transport on the Inner Shelf, Long Island, New York. Jour. Geophys. Res., V. 87, no. 66, p. 4163-417D.

## CHAPTER EIGHTY SIX

### SAND TRANSPORT BY WIND ON A WET SAND SURFACE

Shintaro Hotta<sup>1</sup>, Susumu Kubota<sup>2</sup>

Sadakazu Katori<sup>3</sup> and Kiyoshi Horikawa<sup>4</sup>

#### ABSTRACT

Using those results which were judged to be reasonable among various experiments, an equation predicting the threshold shear velocity on a wet sand surface was obtained. Then, based on a literature survey, results from fundamental experiments, and information obtained from a series of field observation carried out by the authors, a hypothesis to explain the blown sand phenomena on a wet sand surface was developed. Experiments with a well-sorted sand having a median diameter of 0.3 mm showed that the prediction was valid if the water content of the sand layer was less than 8 %.

#### I INTRODUCTION

One of the important problems in coastal engineering in recent years has been the unraveling of the processes of beach change. Extensive studies have been carried out on this topic throughout the world. Most research has been concerned with the study of waves on beaches and the resultant beach change due to wave action. However, on beaches where a strong seasonal wind blows, the sand transport by wind will be an important factor affecting beach change. In such a case, the transport by wind should be included in the sand budget on beaches. Therefore, we undertook comprehensive field investigations and laboratory studies to establish calculation methods for the transport of sand by wind on beaches (Horikawa, Hotta and Kubota, 1982; Kubota, Horikawa and Hotta, 1982; Horikawa, Hotta, Kubota and Katori, 1983; Horikawa, Hotta, Kubota and Katori, 1984).

- 
- 1 M.E., Research Assoc., Dept. Civil Engg., Tokyo Metropolitan Univ., Fukasawa 2-1-1, Setagaya-ku, Tokyo, 158 Japan
  - 2 Research Engineer, INA Civil Engineering Consultants Co., Ltd., 22-1 Suido-cho, Shinjuku-ku, Tokyo, 162 Japan (formerly Research Engineer, Nearshore Environment Research Center)
  - 3 M.E., Research Engineer, INA Civil Engineering Consultants Co., Ltd., 22-1 Suido-cho, Shinjuku-ku, Tokyo, 162 Japan (formerly Research Engineer, Nearshore Environment Research Center)
  - 4 Dr. Eng., Dean of the Faculty of Engineering, University of Tokyo, Hongo 7-3-1, Bunkyo-ku, Tokyo, 113 Japan



At the first stage of this study, the troublesome fact was encountered that sand transport by wind on beaches often occurs during seasons when the sand surface is wet with rain or snow, e.g., beaches on the Japan Sea Coast in winter. Few studies of blown sand on a wet sand surface have been carried out, in contrast to the considerable number of studies of blown sand on a dry plane sand surface.

In order to fully evaluate the contribution of transport by wind in the sand budget, the problem of blown sand on a wet sand surface should not be neglected. As a first step in grappling with this problem, a literature survey was made and the present state of knowledge was summarized. To fill in various information gaps, two simple fundamental experiments were performed for 1) the threshold shear velocity of sand with high water content and 2) the sand transport rate by wind on a wet sand surface. These results are described in Horikawa, Hotta and Kubota (1982). The purpose of the present paper is to describe the work performed subsequent to the above work.

## II DISCUSSION OF SELECTED PREVIOUS WORKS

For convenience in later discussion, we will first give a brief summary of the present state of blown sand on a wet sand surface, based on our previous work (Horikawa et al., 1982). That is:

1. A considerable amount of laboratory and field data exists on the threshold wind speed or threshold shear velocity of sand grains on a wet sand surface. However, the definition of the critical condition at which grains begin to move, the elevation from the sand surface at which the wind speed as an external force was measured, and the sand characteristics varied among the experiments. Therefore it is difficult to quantitatively compare the relationships obtained.

Figure 1 shows the experimental results of threshold wind speed obtained by various workers. Generally speaking, with a water content up to 10% the threshold wind speed increases linearly with an increase in the water content of the sand surface. Also, the larger the median diameter of the sand the higher the threshold wind speed will be.

Theoretical and empirically-based equations for the threshold wind speed or the threshold shear velocity have been proposed by Belly (1962), Kawata and Tsuchiya (1976), and Nakashima and Suematsu (1976). They are:

$$u_{*c} = A \sqrt{\frac{\rho_s - \rho_a}{\rho_a}} g d (1.8 + 0.8 \log_{10} w) \quad (\text{Belly}) \quad (1)$$

$$\begin{aligned} \tau_{*c} &= \frac{u_{*c}^2}{((\rho_s/\rho_a) - 1) g d} \\ &= A^2 \left\{ \frac{\sin(\varphi - \theta)}{\cos \varphi} \right\} \left\{ 1 + \frac{2\sqrt{3}}{5} \sqrt{\alpha_1} \alpha_2 \sqrt{n_0} \frac{\sin 2\varphi}{\sin(\varphi - \theta)} T_k \right\} \end{aligned}$$

$$T_k = \sqrt{\frac{\rho_s}{\rho_w}} \frac{T \sqrt{w} \cos \xi}{(\rho_s - \rho_a) g d^2} \quad (\text{Kawata \& Tsuchiya}) \quad (2)$$

$$u_{15f} = \sqrt{\frac{B'}{A'}} \sqrt{g \cdot d \cdot \frac{\rho_s}{\rho_a}}$$

$$A' = -2.0 \times 10^{-7} + 22.0 \times 10^{-7} \exp(0.39w)$$

$$B' = 1.0 \times 10^{-5} \exp(-0.34w) \quad (\text{Nakashima \& Suematsu}) \quad (3)$$

where  $u_{*cw}$  is the threshold shear velocity on a wet sand surface,  $\rho_s$ ,  $\rho_a$  and  $\rho_w$  are the densities of sand, air and water,  $A$  is a constant with an approximate value 0.1,  $g$  is the acceleration of gravity,  $d$  is the grain diameter and  $w$  is the water content which is defined by the ratio of water weight contained in sand and dry sand weight. The quantity  $\varphi$  is the friction angle of a sand grain at rest,  $\theta$  is the average angle of the sand surface slope,  $T$  is the surface tension,  $n_0$  is the number of contact points of a grain in the sand layer,  $\sqrt{\alpha_1}$  and  $\alpha_2$  are constants,  $\xi$  is the angle of contact between sand grain and water,  $u_{15}$  and  $u_{15f}$ , are the wind speed and the threshold wind speed at a height of 15 cm, and  $A'$  and  $B'$  are constants.

The curves for Eqs. 1, 2, and 3 are drawn in Fig. 2 for comparison. Figure 2 will be explained a later. Otherwise, the threshold shear velocity on a dry sand surface is given by

$$u_* = A \sqrt{\frac{\rho_s - \rho_a}{\rho_a} g d} \quad (\text{Bagnold, 1954}) \quad (4)$$

2. The sand transport rate by wind on a wet sand surface is as yet an unsolved problem. The empirical coefficient value obtained various worker on a wet sand surface is small compared with the case of a dry sand surface, if the Bagnold formula is assumed. Also, there is no evidence that the Bagnold formula is applicable. The mechanism of sand movement on a wet sand surface has not been theoretically formulated and developed. However, equations empirically obtained for predicting the sand transport rate by wind on a wet sand surface have been presented by Iwagaki (1950), and Nakashima and Suematsu (1976):

$$q = 0.3 (u_{100} - 6) \quad (\text{Iwagaki}) \quad (5)$$

$$q' = A' \frac{\rho_s}{g} u_{15}^2 (u_{15} - u_{15f}) \quad (\text{Nakashima \& Suematsu}) \quad (6)$$

where  $q$  and  $q'$  are the transport rate and  $u_{100}$  is the wind speed at a height of 1 m. Here  $q$  is given in  $\text{tf/m/day}$  and  $u_{100}$  in  $\text{m/s}$ . The coefficient  $A'$  is given in Eq. 3.

The above is a brief summary. Now, Eqs. 1, 2, 3, 5 and 6 are discussed and examined in more detail.

First, we shall examine Eq. 1, due to Belly. It is questionable as to whether we may discuss this equation on the same level as the other equations, because the way of moistening the sand layer was different than in the other experiments. In his experiment, the air was saturated and the sand layer was moistened by absorption from the air. Therefore, there was no evaporation to the air and the layer under the surface was

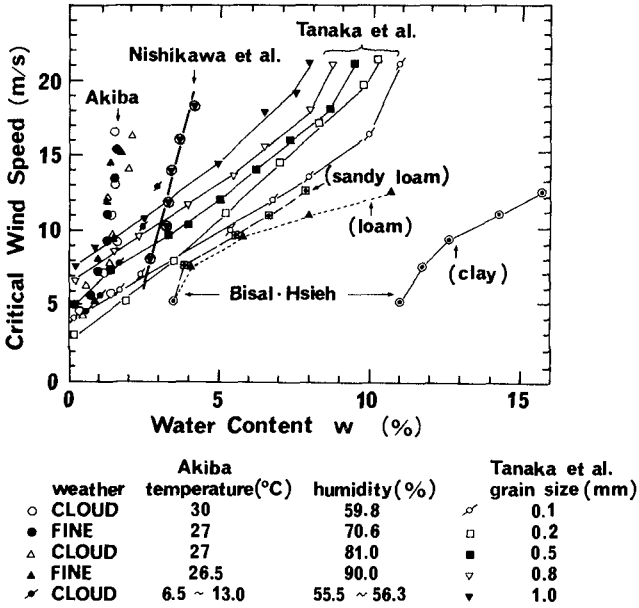


Fig. 1 Relationship between threshold wind speed and water content. (Redrawn by writers from data of original papers)

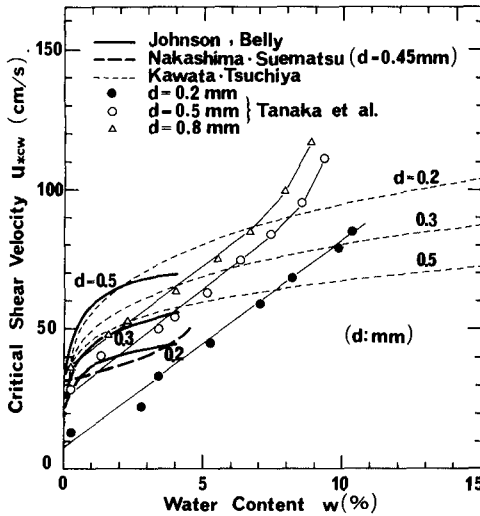


Fig. 2 Comparison of threshold shear velocities.

presumably dry. In all other experiments under discussion, the sand layer was moistened by directly spraying on water. Therefore, evaporation from the surface probably occurred to some degree. Putting this problem aside, we shall examine Eq. 1. We can see that the threshold shear velocity for a wet sand surface is given by adding an amount of increase due to the water to the threshold shear velocity for a dry sand surface. The curves given by Eq. 1 for the grain diameters of 0.2, 0.3 and 0.5 mm are drawn in Fig. 2. This equation is of the same type as Eq. 2. The amount due to the water is proportional to  $\log_{10} w$ . Therefore, the rate of increase of the shear velocity is large until 1% of the water content is reached. At a water content higher than 1%, the rate becomes gentler. This behavior does not agree with other experimental results.

Next, Eq. 2, obtained theoretically by Kawata and Tsuchiya (1976), is examined. Converting the shear stress to the shear velocity, and considering the condition of  $\varphi = 45^\circ$  and  $\theta = 0^\circ$  for simplicity, Eq. 2 becomes

$$u_{*cw} = A \sqrt{\frac{\rho_s - \rho_a}{\rho_a} gd} \sqrt{1 + D} \quad (7)$$

$$D = \frac{2\sqrt{6}}{5} \sqrt{\alpha_1 \alpha_2} \sqrt{n_0} \sqrt{\frac{\rho_s}{\rho_w}} \frac{T\sqrt{w} \cos \xi}{(\rho_s - \rho_a)gd}$$

The amount of increase due to the water,  $D$ , is directly proportional to the square root of the water content and is inversely proportional to the sand grain diameter. This means that  $D$  increases rapidly to unity and the rate of increase of  $D$  becomes small when the water content is greater than unity. In addition,  $D$  will be greater for smaller grain sizes. Therefore, this formulation predicts that for a given water content the threshold shear velocity of small grains is greater than that of large grains.

These characteristics of Eq. 7 are completely contrary to the experimental facts, i.e., the threshold shear velocity increases linearly with increases in the water content of the sand surface; it also increases with the median diameter of the sand, and the threshold shear velocity increases suddenly at a certain water content of the sand surface.

Now we will move to a discussion of Eqs. 3 and 6. The definition of the threshold condition by Nakashima and Suematsu as expressed in Eqs. 3 and 6 was quite reasonable if their experiments were carried out correctly. Their results were given as a function of the wind speed at the height of 15  $\mu$ m. To compare to the other equations and experimental results, the threshold wind speed in Eq. 3 was converted to the threshold shear velocity using a method proposed by Horikawa and Shen (1960). The results expressed in terms of the shear velocity are drawn in Fig. 2. The results are limited to less than 4% in the water content. The applicability of the constants  $A'$  and  $B'$  to other grain diameters has not been examined yet. In addition, the sand transport rate given by Eq. 6 becomes rather small if we accept this result. Equation 6 cannot explain the experimental results of Nishikawa, Tanaka

and Ikeda (1975) nor the results of the our observation carried out on January 1983, described Horikawa et al. (1984), namely that the sand transport rate on a wet sand surface is comparable to that on a dry sand surface when the wind speed is sufficiently high. Sand will be blown off when evaporation rate is high enough even though the sand layer has high water content. Equation 6 cannot explain this phenomenon. Thus Eqs. 3 and 6 are not applicable to calculation of the sand volume on a wet sand surface.

Finally, Eq. 5, due to Iwagaki (1950), is examined. Equation 5 was obtained from a field measurement of sand transport. In the process of determination of the empirical Eq. 5, the threshold wind speed of 6 m/s at a height of 1 m was assumed. But the threshold wind speed of 6 m/s is too small for a wet sand surface. Due to experimental limitations, Eq. 5 cannot be applied for wind speeds over 12 m/s. In addition, the same argument as for Eq. 6 pertains to Eq. 5. Therefore, Eq. 5 cannot be used for practical applications.

The conclusion of this discussion is that, at present, there are no appropriate general formulas for the threshold shear velocity and the sand transport rate by wind on a wet sand surface.

### III FORMATION OF THRESHOLD SHEAR VELOCITY

In the next section, a mechanism of blown sand on a wet sand surface is proposed according to laboratory results and field observation. The threshold shear velocity for a wet sand surface is required. Therefore, using the experimental results of Tanaka, Sano and Kakinuma (1954), the threshold shear velocity will be formulated.

As described in Section II, it was concluded that Eqs. 1, 2 and 3, which express the threshold shear velocity or the threshold wind speed on a wet sand surface, could not be applied under general conditions. This was due to the fact that there were considerable differences in the threshold shear velocity, or the threshold wind speed, obtained in previous experiments, because the criteria defining the threshold condition and the experimental method differed from one another. Therefore, the above experiments offer no way to reliably estimate the threshold shear velocity on a wet sand surface. To extend our results to include blown sand on a wet sand surface, it is necessary to formulate an expression for the threshold shear velocity.

Among the several experiments previously conducted, the authors judged that the experiment performed by Tanaka, Sano and Kakinuma (1954) was conducted under the most suitable conditions and that the results obtained were reliable. Therefore, using the experimental results of Tanaka et al., a formulation of the threshold shear velocity on a wet sand surface is attempted in this section.

Figure 2 will again be considered. As previously described, Eqs. 1, 2 and 3 are also drawn in this figure. A portion of the results of Tanaka et al. for the grain sizes under consideration are also drawn. The results of Tanaka et al. for the critical condition were expressed in terms of the wind speed at a height of 7 cm. The data in Fig. 2 were converted from wind speed to shear velocity using a logarithmic law for

the vertical wind speed distribution and the empirical formula for the roughness length by Zingg (1952), as proposed by Horikawa and Shen (1960).

In Fig. 2, for the water content of 0 % (which means the threshold shear velocity on a dry sand surface), the shear velocity is about 8 cm/s for 0.2 mm, 25 cm/s for 0.5 mm and 35 cm/s for sand 0.8 mm in diameter. Furthermore, for the water content of 0.5 %, the threshold shear velocity becomes 12 cm/s for 0.2 mm, 30 cm/s for 0.5 mm and 40 cm/s for 0.8 mm in diameter. The threshold shear velocity calculated from Eq. 4 on a dry sand surface is 22 cm/s for 0.2 mm, 32 cm/s for 0.5 mm and 41 cm/s for sand 0.8 mm in diameter. The values for the water content of 0 % given by the experiment of Tanaka et al. are smaller than the calculated values from Eq. 4.

However, the values for the water content of 0.5 % roughly agree with those values calculated by Eq. 4, except for the 0.2 mm-diameter sand. The water content is seldom zero percent and normally the water content is about 0.2 to 0.6 % when we measure sand under natural conditions (air dry condition). An experimental error of about 0.2 to 0.6 % in the measurement of the water content may exist, but it is reasonable to believe that sand absorbs water from the atmosphere as assumed by Belly (1962). In the experiments previously conducted to determine the threshold shear velocity on a dry sand surface, we may consider that the sand had in fact absorbed moisture from the air and the sand had about a 0.2 to 0.6 % water content. Therefore, we may accept the threshold shear velocity at around 0.5 % of water content in the experiment by Tanaka et al. as equivalent to that on a natural dry sand surface. Furthermore, we find another remarkable fact in the experiments, namely, that the gradient of the threshold shear velocity with respect to the water content is almost constant, 7.5 (cm/s)/%, for water contents lower than about 8 %, independent of the sand grain size.

From the above considerations and experimental results, an equation expressing the threshold shear velocity must have the properties (1) at 0.0% water content, the threshold shear velocity must correspond to that of a dry sand surface and (2) the gradient should be 7.5 (cm/s)/% for water content lower than 8 %, independent of the grain size. Therefore, the threshold shear velocity on a wet sand surface is taken to be given by

$$u_{*cw} = A \sqrt{\frac{\rho_s - \rho_a}{\rho_a} g d} + 7.5w \quad \begin{array}{l} 0.0 < w < 8.0 (\%), \\ 0.2 \text{ mm} < d < 0.8 \text{ mm} \end{array} \quad (8)$$

where  $w$  is the water content (%).

It is a matter of course that Eq. 8 will be replaced by a new equation in the future according to the results of further well-controlled experiments and theoretical considerations.

Finally, we shall consider why the experimental results of Tanaka et al. showed a linear increase in the threshold shear velocity with increase in the water content irrespective of the grain diameter. In the model developed before, the sand grain was assumed to be spherical. Now we consider real sand. The diameter of a sand grain will be defined

by the longest diagonal line as schematically shown in Fig. 3. The angles of the edges on the surface will be distributed depending on the history of how the sand grain was produced and on how it weathered. In the sand layer, it might be the case that certain sand grains in contact with each other will have sharp edges as for S in Fig. 3(a). It is natural to consider that as a contact configuration of adjoining grains, a sharp edge of a certain grain will touch the flat part of an adjacent grain as shown by A, B and C in Fig. 3(a). If so, the following model to explain the experimental results by Tanaka et al. might be valid (see Fig. 3(b)).

We assume that the representative angle of a sand grain edge is independent of the grain diameter. Then, at low water content (lower than about 8%), the condition of adhering water is independent of the grain diameter. Therefore, an increase in additional cohesive resistance force due to adherence of water at the contact point will be independent of the sand grain size, and a constant increase as given by Eq. 8 results. The above model helps us to understand the experimental results of Tanaka et al.

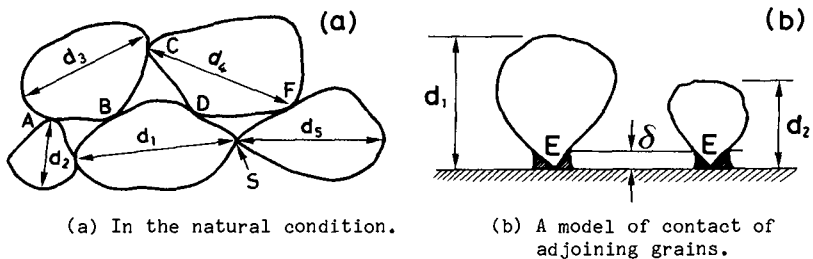


Fig. 3 Schematic diagram of the contact condition of sand grains.

#### IV SUMMARY OF INFORMATION AND DEVELOPMENT OF A HYPOTHESIS FOR BLOWN SAND ON A WET SAND SURFACE

From the literature survey, and from the fundamental experiments and field observations conducted in our work, much information concerning blown sand on a wet sand surface was obtained. The following gives a summary of the more important results:

- (1) The blown sand transport rate observed on a natural beach where a wet sand surface was exposed was almost the same as that measured on a dry sand surface (Kawata, 1950).
- (2) The water content of the blown sand caught by a trap and generated on a wet sand surface which contained about 9 % water content in the upper 10 cm of the surface was about 2.5 %. The empirical coefficient ranged from 0.065 to 0.116 if the Bagnold formula is assumed (Iwagaki, 1950).

- (3) The coefficient of the Bagnold formula was 0.25 on an open beach section and 0.0025 at a location behind a dune if the Bagnold formula is applicable (Aramaki, 1969).
- (4) With elapsed time, the sand transport rate decreased when the wind blew on a wet sand surface. The sand transport rate per 5 min with 0.5 % and 4.2 % water content on the surface was about 1/10 and 1/1000 of that on a dry surface (Nakashima, Sue and Nagasawa, 1973).
- (5) The sand transport rate observed on a wet sand surface with 6 % water content was almost the same as that on a dry sand surface when the wind speed at a height of 1 m was 15.8 m/s, even though it rained, (Nishikawa, Tanaka and Ikeda, 1975).
- (6) Within a few hours after rain stopped, the sand surface reached the air-dry condition when a strong wind blew (Nishikawa et al., 1975).
- (7) The sand transport rate suddenly increased when the water content of the surface sand became lower than 0.3 % and the rate of increase was proportional to the wind speed (Nishikawa et al., 1975).
- (8) There was a certain water content for which the sand transport rate suddenly decreased under a constant wind speed (Nakashima and Suematsu, 1976).

The above results were obtained from previous studies. From the our experimental study in a laboratory wind tunnel and a series of the field observations, we list:

- (9) When a constant wind speed (shear velocity of 42 cm/s) blew on the saturated sand surface,
  - (a) The blown sand on the surface with water content greater than 11 % was negligible, independent of the evaporation rate.
  - (b) The sand transport with a range of water content between 11 % and 6 % was a strong function of the evaporation rate, which was mainly controlled by the air conditions.
  - (c) The sand transport rate was high when the water content of the surface was below 6 %.
- (10) As soon as a rain stopped, blown sand was violently generated under recorded 10 minute-average wind speeds of about 15 m/s at a height of 5 m.
- (11) Within about 18 hr after a rain stopped, the sand volume accumulated in a trench was almost the same as that blown off a dry sand surface.
- (12) The sand volume blown off from a wet sand surface of about 3 or 4 % water content was the same as that trapped by a trench from a dry sand surface when the wind was strong, but the former was about



80 % of the latter when the wind was rather weak.

- (13) The blown sand dislodged from a wet sand surface with about 3 or 4 % of water content which moved downstream reached an equilibrium condition within about 10 m from the boundary where the sand was able to dislodge and the sand surface appeared to be dry. The water content of the flying sand grains was also lower than 1 %.

The above is the main information collected. By linking these fragments together, we become aware of three important matters with relation to the sand blown on a wet sand surface. That is,

- (1) The generation of blown sand on a wet sand surface will be strongly affected by the evaporation rate.
- (2) Concerning the water content, the sand transport rate on a wet sand surface is comparable to that on a dry sand surface when the water content of the surface is small. However, the transport rate decreases suddenly when the water content reaches a certain value.
- (3) Concerning the wind speed, the sand transport rate on a wet sand surface is low when wind speed is low. However, the transport rate becomes comparable to that on a dry sand surface when the wind speed is high even if the sand layer has water content of a few percent.

To explain the above phenomena for the blown sand on a wet sand surface, the following mechanism will be considered. When the sand layer is moist, the threshold shear velocity increases and should be given by an appropriate function of water content in the sand layer. The blown sand on a wet sand surface will then be generated under the same conditions as on a dry sand surface when the shear velocity exceeds the threshold shear velocity. However, even at a condition lower than the threshold shear velocity, sand will be blown when the evaporation rate, controlled by weather conditions, is high, since with a high evaporation rate the sand surface will rapidly dry and the threshold shear velocity of grains on the surface will become lower than that of the underlying sand layer. In this case, the transport rate at a given position depends on the evaporation rate.

The above can be expressed by modifying the Kawamura formula. Thus we write,

$$q = K \frac{\rho_a}{g} (u_* + u_{*cw})^2 (u_* - u_{*cw}) \quad (9)$$

$$u_{*cw} = A \sqrt{\frac{\rho_s - \rho_a}{\rho_a} g d} + 7.5 w I_w$$

$$0.0 < w < 8.0 (\%), 0.2 \text{ mm} < d < 0.8 \text{ mm} \quad (10)$$

where  $u_{*cw}$  is the threshold shear velocity on a wet sand surface and an appropriate function of the water content, and  $I_w$  is an appropriate function of the evaporation rate. The coefficient  $I_w$  has the value 1.0 when the shear velocity exceeds the threshold shear velocity on a wet sand surface and takes a value ranging from 0.0 to 1.0 depending on the

evaporation rate when the shear velocity is higher than the threshold shear velocity on a dry surface but lower than that on a wet surface. This condition is schematically described in Fig. 4. For example, the transport  $q_{w_s}$  in a case when  $I_w$  becomes meaningful is calculated by substituting  $u'_{*cw}$  into Eq. 9 and  $u'_{*cw}$  is an apparent threshold shear velocity given by Eq. 10 taking a value of  $I_w$  between 0.0 and 1.0 depending on the evaporation rate. It is considered that  $I_w$  is a coefficient which converts the drying speed of the wet sand surface by evaporation and a lowering of  $u_{*cw}$ , e.g., to  $u'_{*cw}$ . The coefficient  $I_w$  will be discussed further in Section VI.

The next task is to examine the sand transport rate on a wet sand surface when the shear velocity exceeds the threshold shear velocity on a wet surface.

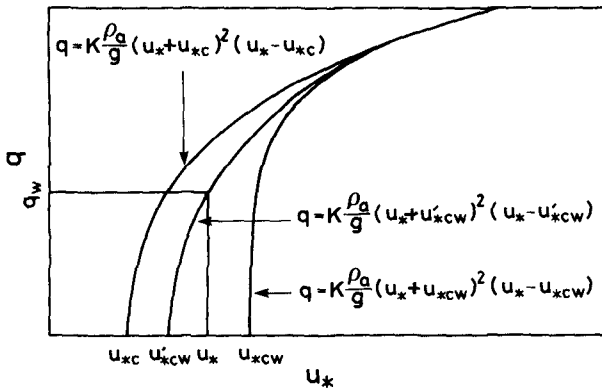


Fig. 4 Schematic explanation of the point at which the coefficient  $I_w$  becomes important.

## V EXPERIMENT FOR THE SAND TRANSPORT RATE ON A WET SAND SURFACE UNDER HIGH SHEAR VELOCITY

### 5.1 Purpose

A hypothesis for the blown sand on a wet sand surface was given in Section IV. To examine this hypothesis, an experiment on a wet sand surface under high shear velocity was carried out. The results are described here.

### 5.2 Facilities (Wind tunnel and Anemometers)

Experiments were carried out using a blowoff type wind tunnel which was specially designed for studying blown sand at the Central Research Institute of Electric Power Industry. The wind tunnel has a test section 110 cm high, 100 cm wide and 20 m long. The bottom is tapered with a gradient of 1/10 at both ends and the cross section of the tunnel

is 100 x 100 cm on which sand can be placed to a thickness of 10 cm. A side wall of glass allows visual observation of the tunnel interior. The wind speed is variable from 3 to 30 m/s, controlled by the frequency of the rotary fan. A sand collecting chamber lies on the end opposite the blower.

For the wind speed measurement, a hot-film anemometer array consisting of four probes and one ultrasonic anemometer was used. The vertical distribution of the wind speed was measured at a location 16 m from the upstream end of the test section in the tunnel. The elevations at which the wind speed measurements were usually made were 5, 10, 20, 30 and 40 cm above the sand surface. These elevations were sometimes changed when some of the anemometers malfunctioned.

The output of the wind speed was recorded on a pen chart recorder with six channels, because a constant wind speed was applied. The wind speed was directly read from the chart. The shear velocity was calculated from the vertical distribution of the wind speed by Eq. 11.

$$u_* = (u_{10} - u_1)/5.75 \quad (11)$$

The sand used in the experiment was taken from Yonezu Beach, the site of our field investigations. The sand was well sorted with a median diameter of 0.3 mm and a uniformity coefficient of approximately 1.7.

### 5.3 Procedure

Sand was spread over the test section of the 20-m long tunnel. The sand surface was carefully flattened and water was gently applied without disturbing the surface until about one-third of the sand layer from the surface was wet. Then, in a period ranging from 10 to 25 days, the sand layer was left to dry until it reached a certain specified water content. The experiment was carried out when the overall sand layer achieved the suitable water content. On the sand surface, partially dried and dried portions of the surface appeared here and there in the tunnel. In this case, a preliminary burst of strong wind at the beginning of the experiment was applied and the dried sand layer on the surface was blown off. Then the experiment was executed.

For measuring the water content of the sand surface, 5-mm samples of sand were scraped from the surface. Immediately after scraping, the samples were weighed and dried and the water content was calculated. Four samples were scraped, two from the upstream side of the tunnel and two from the downstream side. Sampling was done before and after a run and an average value of the eight samples was employed for defining the water content of that run.

The most difficult procedure of the experiment was to achieve a certain specified water content over the sand bed. The tunnel is constructed out of doors. One side of the tunnel is directly exposed to the outside. The sand bed is strongly affected by the weather, such as the sunlight through the glass wall, the local wind flow passing the mouth and end opening of the tunnel, and shading of the tunnel roof by trees. In order to prepare a sand bed of constant water content, many

attempts by trial and error had to be made. In the end, we could not succeed in establishing a reliable method of making a sand bed of constant water content. However, the experiment runs were carried out only under conditions of constant water content of the sand bed.

#### 5.4 Experiment results and discussion

Figure 5 shows an example of the vertical distribution of the wind speed obtained on a wet sand surface for a constant water content of the sand bed. Figure 5 shows that the logarithmic law for the vertical distribution of wind speed was satisfied on the wet sand surface when blown sand was generated. The focal point is given by  $z' = 0.5$  cm and  $u' = 300$  cm/s and this value is of the same order as that for a dry sand surface. The difference is judged to be within experimental error.

Figure 6 shows the sand transport rate on a wet sand surface. Data for which the average water contents of the bed at the upstream side and downstream side of the tunnel before and after a run differed by more than  $\pm 1.0\%$  were not plotted in Fig. 6.

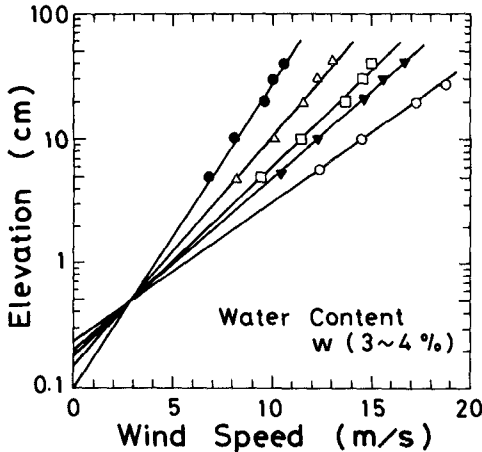


Fig. 5 Example of the vertical distribution of wind speed on a wet sand surface.

The experimental results shown in Fig. 6 for the sand transport rate agree fairly well with Eq. 9 for the values  $K = 1.0$  and  $I_w = 1.0$  when Eq. 10 is substituted into Eq. 9, although the data at high water content were limited. The shortage of data in the high water content range is due to the difficulty in preparing a bed of constant water content. A considerable scatter in the data is recognized in the low shear velocity region. This may be depend not only on experiment error and unsuitability of Eqs. 8 or 10, but also on the rate of evaporation.

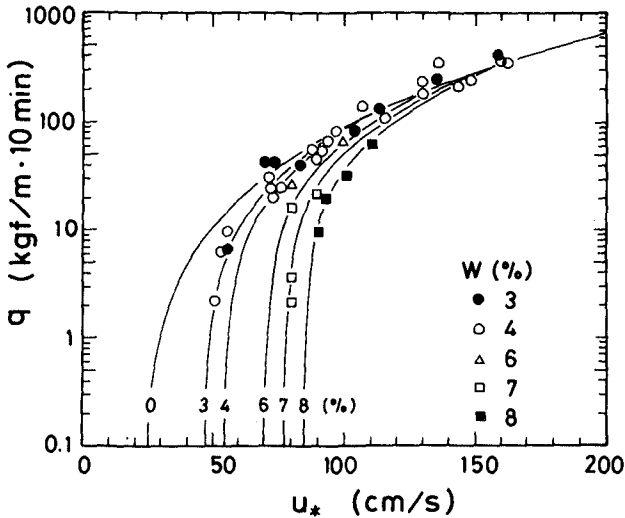


Fig. 6 Sand transport rate under high shear velocity on a wet sand surface.

We conclude that sand will be blown off of a wet sand surface as well as off a dry sand surface when the shear velocity exceeds the threshold shear velocity under a certain water content of the sand surface, although the upper limit of the water content could not be determined from the present experiments.

#### VI FURTHER CONSIDERATION ON THE FACTOR $I_w$ AND THE THRESHOLD SHEAR VELOCITY ON A WET SAND SURFACE

The coefficient  $I_w$  will become meaningful when the shear velocity falls below the threshold shear velocity on a wet sand surface but is higher than that on a dry sand surface.

Considering  $I_w$  further,  $I_w$  is related to the sand transport rate from the upstream area and the water content of the sand surface, i.e., the threshold shear velocity. As described in Section IV, the sand dislodged from a wet sand surface rapidly loses its adhering water when blown downstream and the transporting sand volume increases (the sand transport rate becomes larger with downstream distance from the generation area). At a certain location under consideration, this transported sand volume from the upstream must be added to that which will be generated at that location by the evaporation rate. Thus the distance from the boundary from which the blown sand will be generated to the particular location enters into the determination of  $I_w$ . Furthermore, the sand blown off the downstream affects the water content, i.e., the threshold shear velocity on a wet sand surface. Eventually  $I_w$  and the water content on the wet sand surface become

interconnected. However, the relationship between  $I_w$  and the water content of the sand surface cannot be determined analytically because they are related to each other in a complicated way. Therefore, we have to search for approximate expressions for  $I_w$  and the water content of the surface after a rainfall.

## VII CONCLUSIONS AND SUGGESTIONS FOR FUTURE STUDIES

The important conclusions obtained from this study for the calculation of the sand transport on a wet sand surface are:

1. The threshold wind speed and the threshold shear velocity obtained in previous experiments differed considerably due to differences in experimental methods and the definition of the critical condition. It was difficult to decide which of the results were valid. No acceptable equations could be found for the prediction of the threshold shear velocity on a wet sand surface.

However, using those experimental results which were judged to be reasonable among the various experiments, an empirical equation predicting the threshold shear velocity was obtained (Eq. 8).

2. The sand transport rate will be given by Eqs. 9 and 10.

This equation should be applicable for water contents lower than 8 % on a wet sand surface.

3. The blown sand dislodged from a wet sand surface of 3 or 4 % water content rapidly lost its adhering water. Within about 10 m from the boundary where the sand was generated, the dislodged sand achieved the air-dry condition and the sand transport rate reached equilibrium.

Therefore, no experiment on sand transport may be made on a wet sand surface if there is a distance greater than 10 m at the upstream from the position for which the blown sand would be calculated, and if the water content of the same surface is lower than 4 %.

4. Whether it is raining or not, effective blown sand will be generated if the water content of the sand surface is relatively low or if the wind is strong.

5. In the field, the sand surface may rapidly achieve the air-dry condition due to a high evaporation rate, percolation to the underground and dried sand blown from upstream. In addition, after a rain stops, the sand volume trapped in a trench trap within 18 hr was comparable to the volume trapped corresponding to a dry sand surface.

Therefore, special consideration to rainfall may not be necessary for beaches such as Yonezu Beach where a series of field observation was carried out by the authors, and where blown sand is usually generated under fine weather and only occasionally under rain.

The above are the main conclusions obtained from this study concerning the topic of blown sand on a wet surface. Many other characteristics of blown sand on a wet sand surface were revealed, but

they were not deemed suitable for a quantitative discussion. An intensive effort should be made to investigate the characteristics of blown sand on a wet sand surface.

In particular, the following subjects should be studied.

1. How deep is the sand layer wetted by a rainfall? What relationships are there between the water content, amount of rainfall, median grain diameter and the sand diameter distribution?
2. What processes are involved in the drying of the sand surface? What are the roles of air temperature, humidity, wind speed and solar radiation? Is it possible to predict the water content of the surface at a given time after a rainfall?
3. What is the functional form of  $I_w$  ?
4. Is it possible to improve the equation for the threshold shear velocity, Eq. 8?

To solve the above problems, systematic field observations and well-controlled laboratory experiments are needed. In particular, it is recommended to perform field observations on a rainy beach such as a beach facing to the Japan Sea in winter. For the above studies, the development of new electronic instruments for the rapid measurement of the water content in the sand layer, for the continuous measurement of the blown sand rate, and for the exact measurement of the threshold wind speed are necessary.

#### ACKNOWLEDGMENTS

The support of The Central Research Institute of Electric Power Industry over the course of this work is greatly appreciated. We are also indebted Dr. N.C. Kraus for critically reading and refining the English manuscript, and also for supervising the typing, performed by Miss T. Kohno.

#### REFERENCES

- Aramaki, M. (1969): Blown sand at a northern beach on the Niigata Coast, The Geophysical Review in Japan, Vol. 42, pp. 170-175. (in Japanese)
- Bagnold, R.M. (1954): The Physics of Blown Sand and Desert Dunes, Methuen & Co. Ltd., London, 265 p.
- Belly, P.Y. (1962): Sand movement by wind, Tech. Rept. of Univ. of Calif., Berkeley, Inst. Eng. Res., Series 72, Issue 7, 91 p.
- Horikawa, K. and H.W. Shen (1960): Sand movement by wind action (on the characteristics of sand traps), U.S. Army, Corps of Engrs., BEB, Tech. Memo., No. 119, 51 p.

- Horikawa, K., S. Hotta and S. Kubota (1982): Experimental study of blown sand on a wetted sand surface, Coastal Eng. in Japan, Vol. 25, JSCE, pp. 177-195.
- Horikawa, K., S. Hotta, S. Kubota and S. Katori (1983): On the sand transport rate by wind on beach, Coastal Eng. in Japan, Vol. 26, JSCE, pp. 100-120.
- Horikawa, K., S. Hotta, S. Kubota and K. Katori (1984): Field measurement of blown sand transport rate by trench trap, Coastal Engineering in Japan, Vol. 27. (in press)
- Iwagaki, Y. (1950): On the effect of the sand-drift on the coast by wind for the filling up with sand in Ajiro-Harbor, Journal of JSCE, Vol. 35, No. 6, pp. 265-271. (in Japanese)
- Kawamura, R. (1950): Study on blown sand by wind, Rept. of the Inst. of Science and Technology, Univ. of Tokyo, Vol. 5, No. (3/4), pp. 95-112. (in Japanese)
- Kawata, S. (1950): Field investigation of blown sand on beaches, Forestry Conservation Rep. No. 2, Forestry Agency, Ministry of Agriculture and Forestry of Japanese Govt., pp. 1-22. (in Japanese)
- Kawata, Y. and Y. Tsuchiya (1976): Influence of water content on the threshold of sand movement and the rate of sand transport in blown sand, Proc. of JSCE, Vol. 249, pp. 95-100. (in Japanese)
- Kubota, S., K. Horikawa and S. Hotta (1982): Blown sand on beaches, Proc. 18th Coastal Eng. Conf., ASCE, pp. 1181-1198.
- Nakashima, Y., K. Sue and T. Nagasawa (1973): Effect of surface sand moisture on blown sand (Preliminary Report), Sand Dune Research, Vol. 20, No. 1, The Sand Dune Research Society of Japan, pp. 67-73. (in Japanese)
- Nakashima, Y. and T. Suematsu (1976): Effect of moisture content of sand surface layer on blown sand (III); On the rate of sand movement, threshold velocity, and median diameter of blown sand, Proc. 87th Conf. Japan Soc. of Forestry, pp. 361-362. (in Japanese)
- Nishikawa, M., K. Tanaka and S. Ikeda (1975): Studies on the fixation of drifting sand (3) - Relation between sand surface moisture control and drifting sand -, Bull. of Tottori Univ., Forests, No. 8, pp. 63-82. (in Japanese)
- Tanaka, T., H. Sano and S. Kakinuma (1954): Study on the control of wind erosion, Agricultural Meteorology, Vol. 10, (1-2), pp. 24-30. (in Japanese)
- Zingg, A.W. (1952): Wind tunnel studies of the movement of sedimentary material, Proc. 5th Hydraulics Conf., pp. 111-135.



## CHAPTER EIGHTY SEVEN

### TRANSPORT OF NILE SAND ALONG THE SOUTHEASTERN MEDITERRANEAN COAST

Zev Carmel\*, Douglas L. Inman\*\* and Abraham Golik\*

#### ABSTRACT

The potential for longshore sediment transport (LST) is estimated from a three-year set of directional wave data measured off Haifa, Israel. The resulting annual cycle of LST, together with an analysis of the wave and shore characteristics, suggests a wave-induced sediment transport mechanism with a uni-directional annual transport that gradually decreases along the transport path from the source (Nile delta) to the sink (Haifa Bay). Existing estimates of the rates of transport of Nile sediment are in good agreement with this result.

#### Introduction

Mineralogical studies of coastal sediments from Alexandria eastward to the Sinai and Israel show that the Nile River has been the source of sediment for beaches and coastal dunes as far north as Akko, a shoreline length of about 700 km (Shukri, 1950; Emery and Neev, 1960; Shukri and Philip, 1960; Nachmias, 1969).

This suggests the coastline from the Nile delta through Akko (Fig. 1) to be a classical "littoral cell," i.e., a complete sedimentary compartment that includes the sediments' sources, transport paths and sinks (e.g. Inman and Brush, 1973). The Nile littoral cell thus begins with the Nile River as the original source of fine quartzitic sand whose path leads along the coasts of Sinai and Israel. The cell terminates near Akko, in the Haifa Bay sink (Emery and Neev, 1960; Nir, 1973; Inman et al., 1976; Goldsmith and Golik, 1980; Nir, 1982a). Since the construction of the High Aswan Dam, the Nile no longer brings sediment to the coast, and erosion of the Nile delta now constitutes the sediment source for the Nile littoral cell (Inman et al., 1976; Inman, 1984).

At source, the Nile material may be carried eastward by either the prevailing westerly waves, or the counterclockwise Mediterranean gyre, or both (Inman et al., 1976). Here, the large angle of wave attack (westerly waves on an east-west beach), coupled with the existence of rather high waves (Lowe and Inman, 1983), suggests a very high rate of wave-induced transport. Also, the existence of eastward currents outside of the breaker zone (Manohar et al., 1974; Inman, 1984) indicates the existence of a steady current (the east Mediterranean gyre). This current may also be instrumental in the eastward transport of the Nile material.

---

\* Israel Oceanographic and Limnological Research, P. O. Box 8030, Haifa, Israel

\*\* Center for Coastal Studies, Scripps Institution of Oceanography, La Jolla, California 92093.

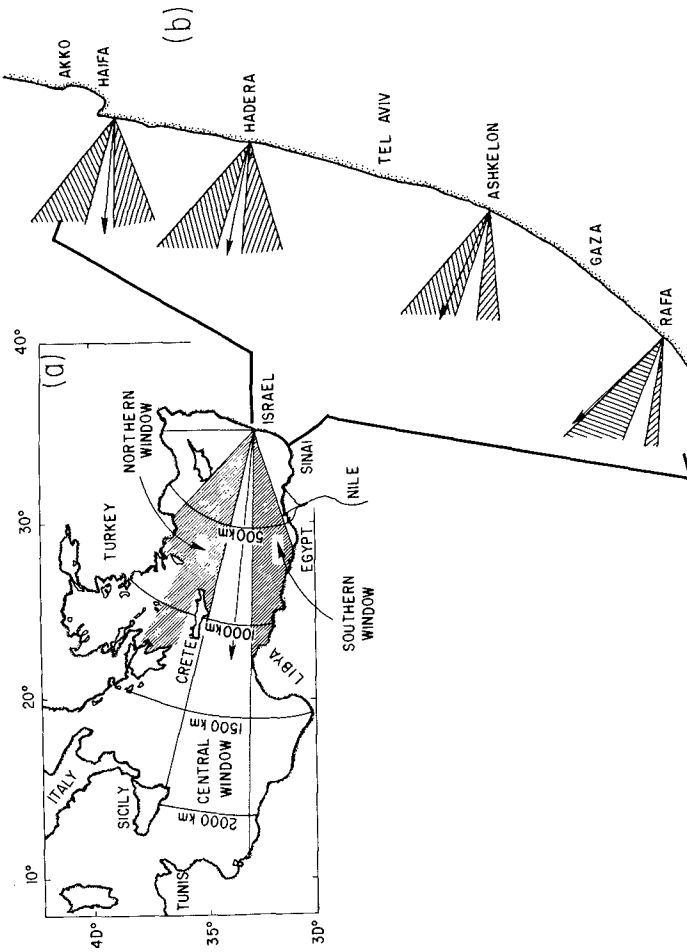


Figure 1. A general map (a) and detailed map (b) of the Eastern Mediterranean region showing the three windows for approach of deep-water waves. The detailed map shows the central window (open), the northern and southern windows (hachured)

Farther east, toward the Sinai and especially along the Israeli coast, the rate of wave-induced transport must obviously be reduced due to the change in shore orientation vis-a-vis the approach directions of deep-water waves (Fig. 1a). It is unclear whether a wave-induced transport ("longshore sediment transport" or LST) or a current-induced transport ("shelf transport") is the main mechanism for moving the Nile sand along the cell.

In this paper we consider the mechanism of sediment transport along the Nile cell, making use of some recent results from a directional wave measuring system off Haifa.

#### Previous Studies of Sediment Transport Along the Israeli Coast

The study of Emery and Neev (1960) is a pioneer work, and classical paper. The observed presence of quartzitic sand with a distinctive suite of heavy minerals, and the gradual decrease in sand size, led these authors to conclude that the beach sands of Israel are derived mainly from the Nile River. This sand is transported, they claim, by both the wave-induced longshore current and by the fringe of the offshore Mediterranean circulation current. During a three-day survey Emery and Neev measured the wave-induced current and found that it is northward directed and decreases in size as one moves along the coast from Sinai through Bat Yam (south of Tel Aviv), but reverses direction and gradually increases north of this nodal point.

Using some theoretical arguments on the beach orientation relative to an assumed dominant direction of wave approach, and the above experiment as an example, Emery and Neev generalize the above findings into the following conclusion. A supposed change in the net LST direction occurs near Tel Aviv, hence a significant amount of current-induced transport must be present to account for the abundance of Nile sediments north of Tel Aviv.

Although the Emery-Neev study deserves much credit for many of its pioneer findings, we feel that it errs in the above general conclusion. In particular, the three-day survey - conducted in the summer - is probably indicative of the summer LST trend, but certainly not of the winter and net annual trends (see later).

Using wave refraction diagrams for various combinations of wave period and direction, Goldsmith and Golik (1980) proposed a slightly different pattern for the LST along the Israeli coastline. According to their study the gross LST is equal or very close to the net transport and is directed eastward along the Sinai coast as far east as Rafa. From Rafa to Haifa sand is transported both northward and southward according to wave direction. Generally, the northward component is larger than the southward in the southern part of the coast, decreases as one goes northward along the coast, and is smaller than the southward component in the northern part of Israel. Again, as with the Emery-Neev study, Goldsmith-Golik invoke a nodal point of zero net-LST in the center of Israel and, consequently, require a large amount of current-induced transport.

Like the preceding Emery-Neev study, the Goldsmith-Golik study lacks adequate ground-truth wave data for proper evaluation. With the recent deployment of directional wave systems off the Israeli coast, we are now in a better position to understand the mechanism and rates of sediment transport along this coast.

#### An LST cycle at Haifa

A directional wave station at Haifa, Israel, provides long-term measurements of both wave energy and direction. It offers an opportunity for estimating the direction and rate of sediment transport within the eastern portion of the Nile littoral cell. Moreover, conclusions can be drawn regarding the sediment transport along the cell.

The following results are based on three years of twice daily wave measurements. Details on the measuring system, procedures, and analysis techniques are given in Carmel et al., 1984a,b.

The monthly-average significant wave height is shown in Fig. 2a. It indicates a bi-modal climate, with a primary (winter) cycle whose monthly average wave height peaks around December-January at about 1.1m, and a secondary (summer) cycle that peaks around July-August at about 0.8m. Further investigations reveal that the winter peak is caused by westerlies (eastward-moving low fronts) which move over southern Europe or northern Africa and generate big storm waves over the eastern Mediterranean (Carmel et al., 1984a). On the other hand, the summer peak consists of rather steady waves which are generated over the eastern basin of the Mediterranean by the seasonal trough of low pressure (Carmel, 1984).

The directional wave data may be used for estimating the potential for longshore sediment transport. This is done through the use of equation (1) (e.g., Inman and Bagnold, 1963; Komar and Inman, 1970; Inman et al., 1976):

$$Q_1 = \frac{K}{(\rho_s - \rho) g N_0} (E C_n \cos \theta \sin \theta)_b \quad (1)$$

where  $Q_1$  is the volume sediment transport rate,  $K = 0.77$  is a dimensionless constant (Komar and Inman, 1970),  $\rho_s = 2.65$  and  $\rho = 1 \text{ gm/cm}^3$  are the densities of the quartzitic grains and water, respectively,  $N_0 = 0.6$  is the "at rest" volume concentration of grains,  $E$  is the wave energy density,  $C_n$  is the group velocity,  $\theta$  is the angle between the wave crest and the beach, and the subscript  $b$  indicates the breaker point.

We use the bi-monthly accumulative wave data to estimate the bi-monthly LST rates from equation (1). The resulting net average LST rates are shown in Figure 2b. The net monthly transport shows an annual cycle with a northward peak of  $75 \times 10^3 \text{ m}^3/\text{month}$  in mid-winter and a southward steady rate of approximately  $-25 \times 10^3 \text{ m}^3/\text{month}$  in summer. Thus, the high winter waves generate a large northbound transport, while the smaller summer waves cause a smaller flow of sediments in the opposite direction. The net annual transport rate is  $110 \pm 100 \times 10^6 \text{ m}^3/\text{yr}$ .

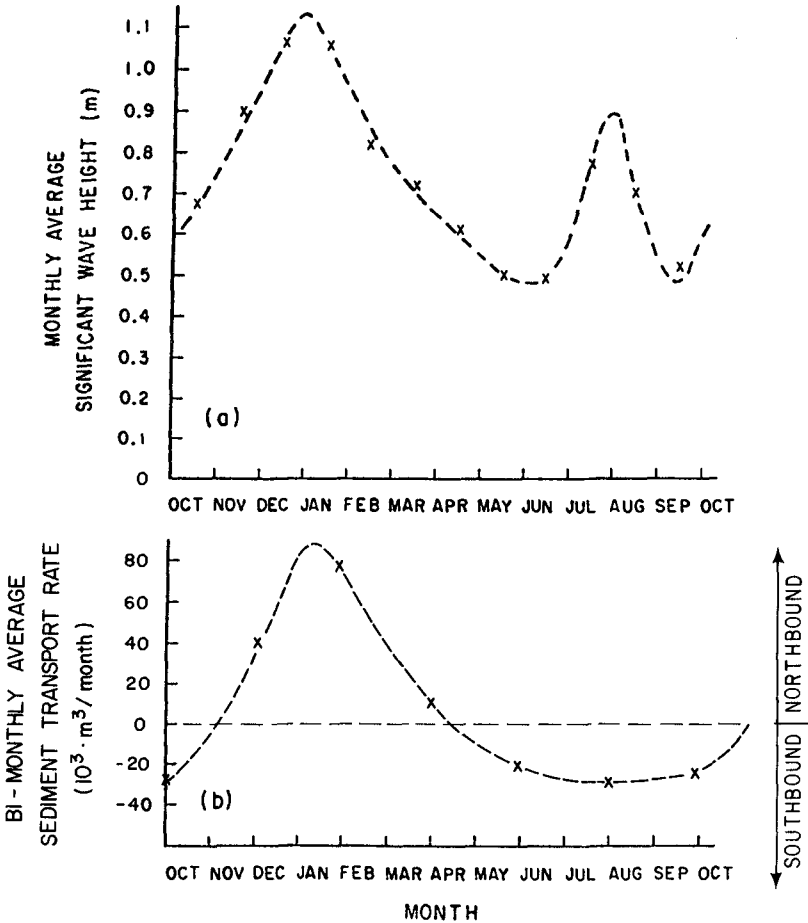


Figure 2. The monthly average significant wave height at Haifa (a); the bi-monthly average sediment transport rates at Haifa, computed from the directional wave data (b).

Projections on the Longshore Transport Rates along the Nile Cell

The winter westerlies and the summer seasonal trough are the dominant meteorological phenomena to govern the wind and wave generation in the Eastern Mediterranean. One thus expects the wave climate along the entire Nile littoral cell to be highly correlative and basically similar.

The deep water waves arrive at Haifa from three windows of deep water wave approach (Fig. 1a). While the stormy winter waves arrive solely from the central and southern windows (Carmel et al., 1984a), the summer waves arrive only from the central and northern windows (Carmel, 1984).

Now, compare for instance the localities of Haifa, Hadera, Ashkelon and Rafa, arbitrarily picked along the Israeli coast (Fig. 1b). The beach normal is denoted by arrows, the wave approach windows, determined as in Fig. 1a by the protruding headlands of Egypt, Libya, Crete and Turkey, are shown by the open and hatched sectors. It is clear from Fig. 1b that the net transport must remain northbound and gradually increase with the southward distance from Haifa. This is a result of the gradual change in beach orientation.

The above presents a consistent picture, where the sediment transport is wave-induced, and the net annual transport is unidirectional and gradually diminishing along the sediment path, thus allowing for the buildup and maintenance of the abundant Nile-sand beaches and coastal sand dunes.

#### Estimates of LST at various locations along the Nile cell

Inman et al. (1976) use a 10-year data set of marine wave observations to compute the LST rate at various locations along the Nile delta. Because of the wide angle of wave attack, this method is considered reliable here. The computed results are "higher" than  $860 \times 10^3 \text{ m}^3/\text{yr}$  for the net (eastward) transport at the Rosetta and Damietta promontories. Only the main wave component was considered here. Quelenec and Manohar (1977), taking all wave components into account, indeed obtained higher rates;  $0-1.5 \times 10^6 \text{ m}^3/\text{yr}$  in between the two promontories, up to  $3 \times 10^6 \text{ m}^3/\text{yr}$  immediately on their eastern sides.

Inman et al. (1970; 1976) also estimate from the entrapment of sand at the entrances of the Bardawil Lagoon, that the net LST rate is about  $500 \times 10^3 \text{ m}^3/\text{yr}$  and eastward at this location in Sinai.

The huge breakwater of the Ashdod harbour in southern Israel has yielded diversified estimates of the LST rate there. Dornhelm (1972) studied the annual bathymetric maps and concluded that the breakwater has interrupted some 80% of the northward sand transport, yielding a rather low estimate of  $50,000 \text{ m}^3/\text{yr}$  northbound net transport. On the other hand, Finkelstein (1981), reanalyzing the same maps, found a large offshore sand accumulation and thereby arrived at a rather large estimate of  $560,000 \text{ m}^3/\text{yr}$  northbound net transport.

An excellent survey of the various estimates of LST along the Israeli coast is given by Nir (1982b), from which the following paragraph is quoted:

"On the basis of theoretical studies Migniot (1974), Sauzay et al. (1974) and Manoujian and Migniot (1975) show that the annual resultant sediment transport is always directed to the north and  $\text{m}^3$  reaches about  $400,000 \text{ m}^3$  at Gaza,  $215,000 \text{ m}^3$  at Ashdod,  $100-150,000 \text{ m}^3$  at Hadera and only  $80,000 \text{ m}^3$  at Atlit."

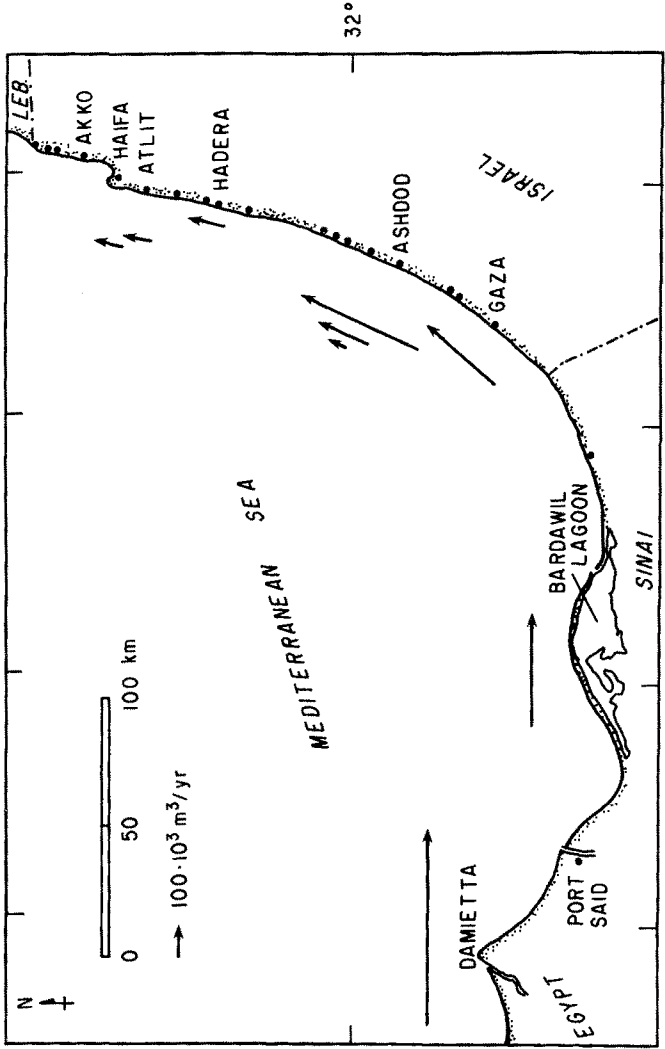


Figure 3. Existing estimates of the net annual LST rate (solid arrows) along the Nile littoral cell.

A summary of the above estimates, including that given by us for Haifa ( $110 \times 10^3 \text{ m}^3/\text{yr}$ ), is given by the direction and length of the solid arrows in Figure 3.

Several features are evident in Figure 3:

1. All estimates yield a counter-clockwise direction for the net transport, i.e., unidirectional along the way from source to sink.
2. Big discrepancies occur between the three estimates made at Ashdod, probably a result of the complicated path and entrapment of sediments around the harbour's breakwater. We take the average of these three estimates ( $275 \times 10^3 \text{ m}^3/\text{yr}$ ) to represent the true transport rate at this locality.
3. The LST estimates begin with a maximum at the Nile source ( $860 \times 10^3 \text{ m}^3/\text{yr}$ ), are gradually diminishing along the sediment pathway, and reach a final low near the Haifa sink ( $80\text{--}110 \times 10^3 \text{ m}^3/\text{yr}$  at Atlit and Haifa, respectively).

Hence, all existing estimates are in good agreement with our result on a wave-induced sediment transport, with a unidirectional and gradually decreasing rate from source to sink.

#### REFERENCES

- Carmel, Z., 1984, "Summer waves off the Mediterranean coast of Israel", In preparation.
- Carmel, Z., D. L. Inman, and A. Golik, 1984a, "Characteristics of storm waves off the Mediterranean Coast of Israel", Coastal Engineering, in press.
- Carmel, Z., D. L. Inman, and A. Golik, 1984b, "Directional wave measurement at Haifa and sediment transport along the Nile Littoral Cell", Coastal Engineering, in press.
- Dornhelm, R. B., 1972, "Determination of the longshore sand transport rate in the vicinity of Ashdod Port", Geol. Surv. Israel, Mar. Geol. Div. Rep., 45 pp.
- Emery, K. O. and D. Neev, 1960, "Mediterranean beaches of Israel", Israel Geol. Surv. Bull., v. 26, p. 1-23.
- Finkelstein, A., 1981, "Sedimentological developments around Ashdod Harbour", 2nd Symposium on Beach Problems, Tel-Aviv, May 25, 1981, 6 pp.
- Goldsmith, V. and A. Golik, 1980, "Sediment transport model of the southeastern Mediterranean coast", Mar. Geology, v. 37, p. 147-175.
- Inman, D. L. and R. A. Bagnold, 1963, "Littoral processes", pp. 529-553, in M. N. Hill (ed.), The Sea; Ideas and Observations, v. 3, The Earth Beneath the Sea, Interscience Publishers, New York and London, 963 pp.
- Inman, D. L. and R. W. Harris, 1970, Preliminary report on the inlets of Bardawil Lagoon, letter report to National Council for Research and Development, Haifa, Israel, 13 pp.
- Inman, D. L. and B. M. Brush, 1973, "The Coastal Challenge", Science, v. 181, p. 20-32.



- Inman, D. L., D. G. Aubrey, and S. S. Pawka, 1976, "Application of nearshore processes to the Nile Delta", p. 205-255 in, UNDP/UNESCO Proc. of Seminar on Nile Delta Sedimentology, Academy of Scientific Res. and Tech., 257 pp.
- Inman, D. L., A. A. Khafagy, Z. Carmel, and A. Golik, 1982, Progress report, September 1981 - February 1982 for coastal management and shore processes in the southeastern Mediterranean, Project II of Agency for International Development, Project AID/NE-CA-1706, 52 pp.
- Inman, D. L., 1984, "The Nile Littoral Cell and Man's Impact on the Coastal Zone of the Southeastern Mediterranean", (see paper, these proceedings).
- Komar, P. D. and D. L. Inman, 1970, "Longshore sand transport on beaches", Journ. Geophys. Res., v. 75, n. 30, p. 5914-27.
- Kran, N., 1980, "Analysis of bathymetric data and sedimentation near Ashdod Harbour (1964-1971)", Rep. Geol. Surv. Israel, Mar. Geol. Div., MG/6/80, 9 pp.
- Lowe, R. and D. L. Inman, 1983, "Wave parameters, Abu Quir Array, Egypt", Center for Coastal Studies, Scripps Inst. of Oceanography, 5 pp., tbl., figs.
- Manohar, M., I. E. Mobarek, and A. Marcos, 1974, "Longshore currents and waves at Burullus Coast", Proc. Fourteenth Coastal Engineering Conference, Amer. Soc. Civil Engin., v. 2, p. 685-698.
- Manoujjan, S. and C. Migniot, 1975, "Sedimentological study in three dimensional model", Lab. Cent. Hydrol. France, Report, 57 pp.
- Migniot, C., 1974, "Creation of a new power station north of Hadera cooling water basin; natural phenomena study and sediment movement study with radioactive and fluorescent tracers", Int. Atomic Energy Agency, Report, 34 pp. with appendix.
- Nachmias, J., 1969, "Source rocks of the Saqiye group sediments in the coastal plain of Israel - a heavy mineral study", Jour. Earth-Sci., v. 18, p. 1-16.
- Nir, Y., 1973, "Geological history of recent and subrecent sediments of the Israel Mediterranean shelf and slope", Geol. Surv. Israel, Report No. MG/73/2, 179 pp.
- Nir, Y., 1982a, "Asia, Middle East, Coastal Morphology: Israel and Sinai", pp. 86-98, in M. L. Schwartz (ed.), Encyclopedia of Beaches and Coastal Environments, v. XV of Encyclopedia of Earth Sciences, Hutchinson Ross Publ. Co., Stroudsburg, PA., 940 pp.
- Nir, Y., 1982b, "Offshore artificial structures and their influence on the Israel and Sinai Mediterranean Beaches", Proc. 18th Coastal Engr. Conf., Amer. Soc. Civil Engr., p. 1837-1856.
- Queleennec, R. E. and M. Manohar, 1977, "Numerical wave refraction and computer estimation of littoral drift; application to the Nile Delta coast", p. 408-433 in, UNDP/UNESCO Proc. Seminar Nile Delta Coastal Processes, Academy Scientific Res. and Tech., Cairo, 624 pp.
- Sauzay, G., C. Gilat, M. Meltzer, G. Courtois, J. Frenkel, A. Lenin, and S. Blit, 1974, "Study of sediment transport on the bed and on the beach at the site of the Hadera power plant", Report, Israel Atomic Energy Comm., 40 pp.
- Shukri, N. M., 1950, "The mineralogy of some Nile sediments", Quart. J. Geol. Soc. London, n. 105, p. 511-534.
- Shukri, N. M. and G. Philip, 1960, "The mineralogy of some recent deposits in the Arish-Gaza area", Cairo Univ. Bull., v. 35, p. 73-85.

## CHAPTER EIGHTY EIGHT

### FLUCTUATIONS IN LITTORAL DRIFT

Richard Silvester<sup>(1)</sup>

#### ABSTRACT

The long assumed uniform movement of sand along the coast produced by wave action can be disputed when the interaction of storm sequences and swell is considered. Storm waves form a protective bar, which essentially puts material back into circulation for the oblique swell to work upon. The resulting longshore transport is swift whilst the bar exists but decreases to negligible proportions once it is denuded and the normal swell-built beach profile recurs. This impulsive drift has many implications for engineers and geomorphologists and to researchers attempting to predict annual rates of transport.

#### WAVE CLIMATE

In oceans a distinction can be made between storm waves and swell. The former are in the fetch, where winds are still generating them or maintaining a fully arisen sea. Swell is the term for waves that are dispersing across the sea outside the fetch. Since the energy concentrated in the relatively small storm zone is now spread over vast areas downwind of generation the wave heights must necessarily decrease (Silvester 1974). The characteristics of these two systems are specific in their influence on a mobile bed at the shoreline.

Storm waves are multi-directional from their mode of generation and due to the many fetches encompassed by a cyclone as it passes near or across the coast. They are continually breaking as the shorter waves steepen on the crests of longer waves, to pour down their front faces and so aid their growth. (Longuet-Higgins and Stewart 1960). Their optimum steepness implies that all waves contain much water above the SWL. Another characteristic of distinct importance is their short duration as on any coast a storm lasts for a few days only, with few repetitions annually.

Swell at any point in the dispersal area consists of waves propagating within a small fan of directions, encompassed by orthogonals to the side boundaries of the fetch. Thus swell waves arrive on a coast from persistent directions, certainly within the same quadrant, from the storm zones which are repetitive from month to month and year to year. In so spreading they take longer to arrive at a given shoreline, as recorded by Snodgrass et al (1966). On most western margins of continents swell arrives continually from the constant generation zones between 40° and 60° latitudes where cyclones travel from west to east. On eastern margins swell is more variable in direction throughout the year.

---

1. Department of Civil Eng., University of W.A. Nedlands, W.Aust.

Storm waves are variable in time until the fully arisen state is achieved and then vary at different points along the fetch. Swell, on the other hand, varies with distance from fetch and also continually with time. As components of the storm spectrum pass any point so the height and period change. The long low waves arrive first, followed by the high medium band of the spectral peak, after which the low period end of the spectrum arrives. It is therefore difficult for researchers to choose some mean wave condition for correlation with sediment transport over an annual period.

### SHORELINE PROCESSES

If there is a sedimentation problem on a section of coast it is due to longshore transport which results in either siltation or erosion, or generally both. It is axiomatic that the persistent swell waves, which effect this movement, are arriving obliquely to the coast, in order that there is a longshore component of energy on breaking.

In crossing the continental shelf these waves are refracted and steepened as they travel into shallower water. The water particles at the bed oscillate and hence disturb the bed but they also suffer a net movement in the direction of wave motion, known as mass-transport. This varies throughout the water column, as seen in Figure 1, with the depth ratio, but for long period swell it is maximum at the bed. (Longuet-Higgins 1953). It may take weeks for this distribution to diffuse from the bed and sea surface for any wave train but is **immediately**

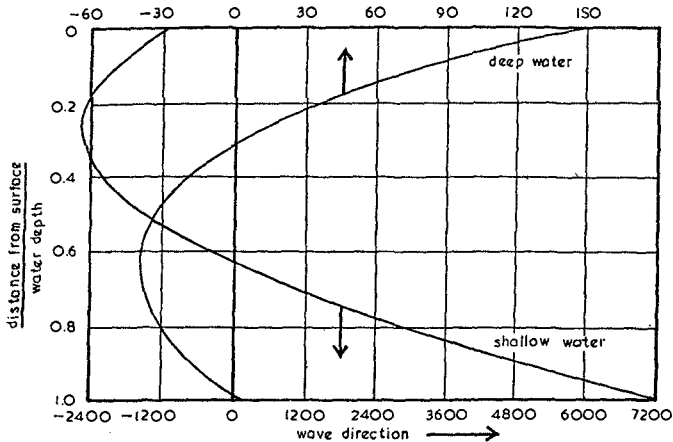


Fig 1. Mass transport due to waves, where  $X$  is net movement per wave period  $T$  for height  $H$ , and  $g$  is accelerative due to gravity assuming a flat bed and laminar boundary layer.

available at the bed. Thus a sweeping motion is exerted on the sedimentary particles towards the shore, and along it, beyond the breaker zone.

When these swell waves are steepened to an unstable steepness they break and then proceed as a bore towards the beach, thus forming the surf zone. Much sediment is suspended by the bore which then carries it up the face of the beach, as seen in Figure 2. The water carried in this uprush percolates through the berm down to a water table at about mean sea level. This is possible whilst there is a reasonable time between each wave, which is the case for swell.

This percolation reduces the volume of downwash so causing the sand carried up to be stranded on the beach, which results in accretion. Such build-up continues so long as there is sufficient material offshore to be fed to the breaking waves. Freshly deposited sand is loose which aids percolation. After persistent swashing by waves the beach face becomes well compacted.

When storm waves arrive to this swell-built profile a crest breaks almost every second, resulting in large volumes of water running up the beach face. This saturates the beach, as seen in Figure 2,

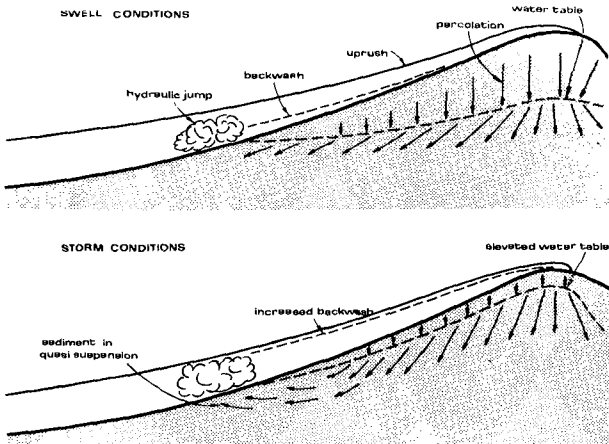


Fig 2. Beach processes for swell and storm conditions.

causing the water table to become almost coincident with the face. The downrush equals the uprush which drags sand down the slope, forming a larger than normal hydraulic jump at the toe. This occurs in the zone where ground water is rising almost vertically in returning to the sea. This sets up a liquefaction or "quick-sand" condition which results in swift erosion and consequent collapsing of the beach face. This creates a near vertical face against which waves reflect. It is little wonder that the beach is eroded metres in a matter of minutes.

The mass of water thrown onto the beach must return to the sea, in this case laden with sand. This runs as a density current hugging the bed, aided by the strong shoreward current at the surface due to the

storm wind shear force. As deeper water is reached the velocity is reduced, so causing the sediment load to be dropped. A mound is formed some distance offshore which grows during the storm until the depth over it is sufficiently small for incoming waves to break over it. (See Figure 3). This breaking is also assisted by the seaward current from excess water returning to the sea. At this stage the major erosion ceases.

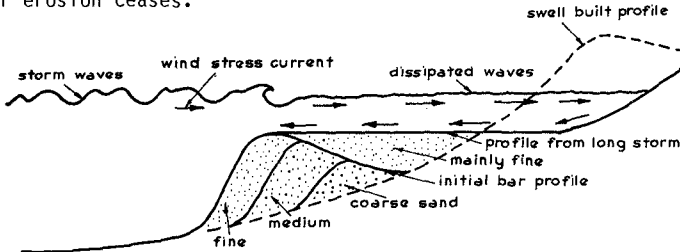


Fig 3. Offshore bar profiles during formation showing sediment sorting.

The first storm of the winter season exerts the greatest influence on the beach when the recession can be accepted as the maximum for the year. Only two situations can cause greater erosion. If a second storm is accompanied by a higher water level, due to a storm surge, or spring tide height, the bar must be elevated to break the waves. Also, if a subsequent storm is of longer duration the attenuated waves reaching the receded new vertical beach face can remove further material which fills the swale between bar and beach with the aid of the circulating current, as seen in Figure 3. An almost horizontal platform could result (Silvester 1979).

This natural sequence of forming a protective bar by storm waves is beautiful to behold. If it did not occur the previously accreted shoreline might be spread evenly over the seabed. It is a mechanism man cannot hope to emulate due to the large volume of material involved. Suggestions that a permanent bar be constructed by rubble-mounds is to no avail since the oblique swell waves would reflect from this submerged structure and scour the bed adjacent to it, so causing costly remedial measures. (Silvester 1977).

#### RETURN OF BAR

Part of this exciting phenomenon of coastal defense is the dismantling of the bar when it is no longer required. This is accomplished by the swell following the storm, either immediately or perhaps some weeks later. These break over the bar causing excessive suspension of sand which is redeposited on the beach. The berm is rebuilt up to the uprush of the waves. This is small initially as waves are well attenuated in traversing the bar and the wide surf zone. As the bar is lowered and the surf zone decreases in width so the run-up increases and hence the height of the berm. This is why the back berm can be lower than the seaward edge and shallow pools exist on it. The present discussion omits any influence of tides, which will have

little effect until they exceed 2 m range.

The seaward slope of the offshore bar could be steeper than the swell built beach as it results from deposition by a seaward current and opposing mass-transport of waves. As swell waves traverse this face their ratio of breaking to deep-water wave height increases, which must result in a stronger littoral current, which is dependent on the square of the breaking wave height. This current is therefore magnified concurrently with enlarged suspension and so results in a great pulse of drift alongshore. This is aided by the larger surf zone width since the total transport is the summation of rates across this normal to the beach, even extending beyond the breaker line. (Andersen and Fredsøe 1983). As sand is pushed shorewards the surf zone becomes very flat.

This excessive littoral drift exists whilst the bar is being returned to the beach, which may take two to three weeks with reasonable swell input. Japanese engineers have concluded that 90% of this transport can take place over two weeks and 10% over the remainder of the year. As can be imagined, the rate is optimum directly after the storm but reduces as the bar recedes and the normal parabolic profile is approached. This is due to the diminishing effect of the bar slope on the waves and the decreasing width of the surf zone. The suggested distribution over time is depicted in Figure 4, which requires

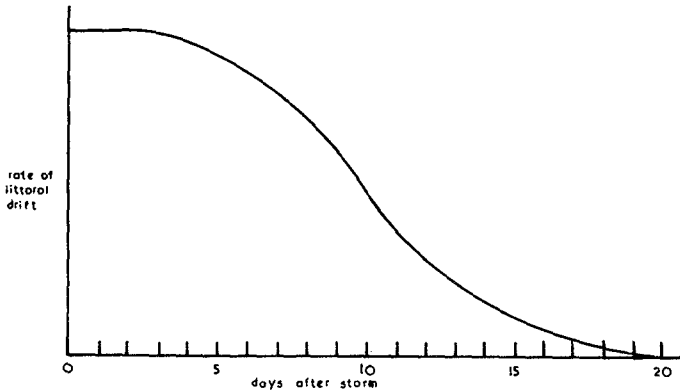


Fig 4. Suggested variation in littoral drift as bar material is replaced on beach.

verification from field measurements. To measure these peaks in drift it would be necessary to monitor accretion in sand spits or against some structures at daily intervals over the two or three weeks until the bar had disappeared, which would require profiling of the bar to ascertain its state.

### FLUCTUATIONS IN LITTORAL DRIFT

The importance of this phenomenon of pulses in longshore transport warrants a little more discussion of the reasons for it. As stated earlier the seaward slope of the bar could be steeper than the bed approaching the swell built profile where the surf zone exists. Whilst this mound could be spread widely by the storm waves and outgoing current during the storm the swell waves could quickly steepen it by their mass-transport in these shoaling conditions. It may be inferred that water entering the valley between bar and beach will inhibit this steepening, but this seaward flow is generally accomplished by rip currents forming at weak spots in the bar. It is well known that these dangerous currents occur just after storms, and hence flow is minimal over most of the bar.

The ratio of breaker height to deep-water height ( $H_b/H_0$ ) varies with deep-water wave steepness, but for any value of this ratio varies with the bed slope as in Figure 5 (Goda 1970). The ratio of crest height to deep-water wave height is decreased tending to make surging rather than plunging breakers. Another trend is for the wave front to become steeper (Adeyemo 1968) with increasing slope, again improving the ability to generate a littoral current through greater mass-transport. There is also the possibility of refraction lagging that from a mildly sloped bed thus increasing the angle at breaking, but this phenomenon has not been reported to the author's knowledge.

Once the waves have broken at the apex of the bar they then traverse obliquely either a swale or even two or three such depressions before arriving at the beach. As noted already these valleys may be filled with sediment if the storm duration is long. In any case they could well be smoothed out by the transport of sediment from the peaks before material is finally replaced on the beach. The resultant bed within the surf zone therefore could be very mildly sloped. This causes the broken waves to reduce more slowly in height as they proceed to the beach face. This again creates better conditions for a strong littoral current.

Another factor to be taken into consideration is the partial reflection of the swell waves from this relatively steep slope of the bar. Battjes (1974) has shown that when the surf similarity parameter  $[ = \tan\alpha / \sqrt{H_b/L_0} ]$  has a value of 2.3 it "corresponds to a regime about half way between complete reflection and complete breaking." These reflected waves, which must necessarily be angled to the bar, interact with the incident waves to establish a short-crested system (Silvester 1974) whose orbital motions are conducive to sediment suspension with a large mass-transport alongshore. This action will cause an excessive drift on the face of the bar beyond the breaker line, which could exceed values estimated from the littoral current expanding from the surf zone.

To show the possibility of this parameter being of this order consider a storm system with a wind speed ( $U_{19.5}$ ) of 30 knots in which case the component with most energy has a period of 10 seconds (Silvester 1974). The steepest bed slope as the swell arrives could be 1:6. If

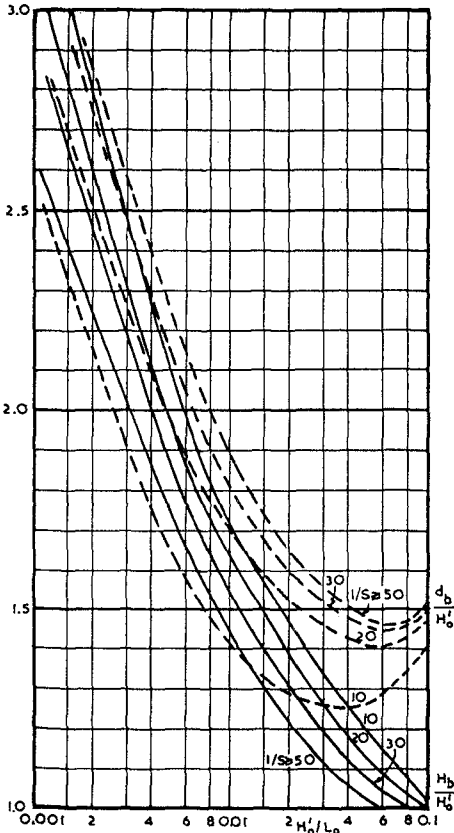


Fig 5. Parameters of breaking waves as presented by Goda (1970).

these waves arrive from a distant fetch their deep water height is of the order of 0.5 m, which near breaking could be doubled to 1.0 metre. Substitution in the above parameter gives a value of 2.07. If 12 seconds were used it becomes 2.5, so that the critical value of 2.3 could readily occur.

Andersen and Fredsøe (1983) have computed littoral drift along a barred beach and compared it to that on an equivalent uniformly sloped profile. Figure 6 is taken from this reference where it is seen that the three bars in (a) cause local increases in  $H/h$  as in (b), from which values of  $q$  have been derived as in (c). The distribution of transport for the equivalent uniform slope is dotted in (c). Areas under these curves give the total rate of transport, which are essentially the same for barred and uniformly sloping beaches. An

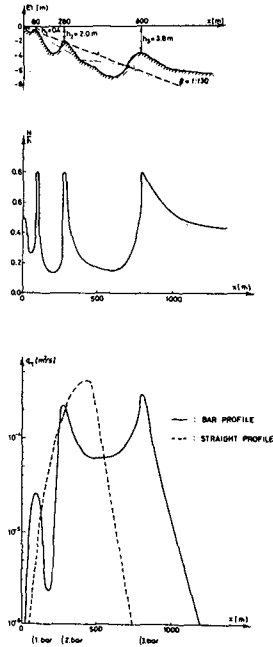
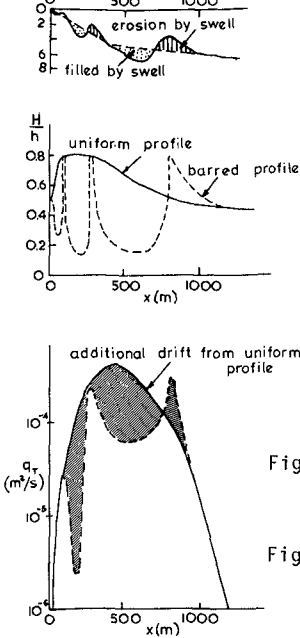


Fig 6. (a) Measured coast profile at the Danish west coast.  
 (b) Variation in wave height towards the coast.  
 (c) Computed sediment transport at the coast depicted in (a).  
 Taken from Andersen and Fredsøe (1983).



alternative progression is illustrated in Figure 7, where the swales are filled by bars seaward of them. This could result in two uniform slopes as shown in (a) which could result in the H/h curve as in (b). The  $q_T$  curve in (c) is based upon relationships indicated in Figure 6, which could result in greater overall transport. Taking in all the inaccuracies of these suppositions there is indicated the propensity for excessive drift whilst sand is being transported back to the beach.

Verification in models should be carried out on the littoral current generated on a barred beach, a uniform slope and the parabolic shape produced by swell waves. Realistic profiles could be formed in a fixed bed to confirm whether littoral current velocities differ greatly in distribution and overall discharge.



**SORTING OF SEDIMENT**

Another process worthy of consideration is the sorting that takes place of sand during the formation and ultimate replacement of Nature's protective bar. When the density current, at the initiation of erosion, slows down the first sand particles to be dropped are coarse, followed seawards by the median and fine components. As seen in Figure 3, the bar will comprise coarse sand at its landward base, median material in the middle, whilst the top and seaward face consist of the smallest grains.

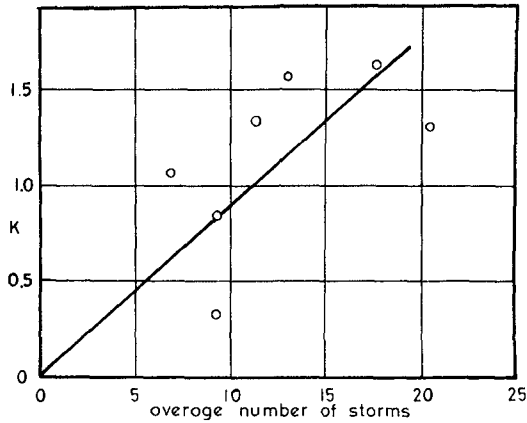


Fig 8. Values of k (Dean et al 1982) versus number of storms during periodic assessment of littoral drift.

Fig 7. Modified transport distribution for a saturated bar with equivalent uniformly sloped beach from Fig 6.

When the swell commences to return the bar to the beach it is the finer material that is acted upon first. This is the stage when breakers are greatest, turbulence is optimum and the current is maximum. This small diameter sand is suspended more readily so that it is moved well downcoast from its original position by the time it is deposited on the back of the berm. Thus distribution aids the sorting in the next bar that is formed.

The median sand will be replaced somewhere in the centre of the berm with less longshore displacement. By the time the coarse material is shifted a short distance back to the outer berm the swell built profile almost exists with its reduced longshore transport capacity. Thus the coarse grains move very little downcoast. This is why measurements of fineness along the coast are taken as indicative of drift direction.

#### LITTORAL DRIFT CALCULATIONS

It is salutary to look at what variables are included in formulae for longshore drift and compare the assumptions with the conditions discussed above. It is normal to correlate volumes of accretion taken over a year with some average swell condition for the same period. As noted already, swell waves vary in height and period from hour to hour and hence the selection of some meaningful average, including direction of approach, is in the realms of fantasy.

As seen above the fluctuations in littoral drift are severe, the bulk of this transport taking place two or three weeks after each storm. If three storms occur during a year instead of one the drift can be trippled. No account appears to be taken of these events even though measured accretions vary tremendously for little apparent reason. Take, for example, the data gathered by Dean et al (1982) at Santa Barbara which recorded the filling of a dredged hole over a period of 380 days. Eight surveys were analysed which resulted in data as listed in Table I. The longshore wave energy was computed two different ways giving P and S. These were then divided into the immersed transport rate to give correlation constants K and  $K_*$ . The ratio of these was computed and listed to illustrate the sensitivity of the mode of deriving this input energy. They give factors varying from 1.78 to 2.94.

But accepting perhaps the usual constant K it is seen that this ranges from 0.32 to 1.63. The authors commented: "However the smallest value which exhibits the greatest deviation from the norm is associated with the fourth intersurvey period which is characterized by a very small value of I. If this one point is not included, the ratio of the largest to the smallest of the remaining K values is less than two, which appears reasonable for this type of measurement." (author's underlining). No mention is made in the article of storm sequences during these surveys but the extra high storm waves would have been included in the energy calculation without reference to the changing directions of these locally generated waves. But averaging of such coefficients, which in this case was 1.23, as distinct from the previously accepted value of 0.77 (U.S. Army Coastal Eng. Res.

Centre 1977) reduces confidence in such formulae.

Inspection of the U.S. Navy Marine Climate Atlas (1977) for the North Pacific Ocean shows the average number of storms for each month for the 10° square adjacent to the California coast near Santa Barbara. These were interpolated for the survey periods in Table I as used by Dean et al (1982) and this is graphed against K as in Figure 8. In spite of the scatter a relationship is indicated of K increasing with the number of storms. It would have been preferable to use the actual number of storms during the 1970-80 period of drift measurement but this was not possible from the wave data available. However, it would appear that this variable should be included in any future assessments of littoral drift.

**Table I** Field results from Santa Barbara (Dean et al 1982)

No. of days	Total Vol Change(m) <sup>3</sup> Rate I(N/S)	Immersed wt Transport Rate I(N/S)	Component Wave Energy Flux at breaking P (N/S)	K=I/P	Component of mmtm S(N/m)	K <sub>*</sub> =I/S (m/s)	K <sub>*</sub> /K
48	32,820	85.3	52.2	1.63	27.8	3.06	1.90
51	65,070	159.1	101.4	1.57	45.4	3.50	2.13
35	82,810	295.0	352.4	0.84	119.5	2.47	2.94
53	10,290	24.2	76.6	0.32	37.9	0.64	2.0
82	22,220	33.8	31.7	1.07	17.6	1.91	1.78
57	38,760	84.8	63.8	1.33	32.6	2.60	1.95
54	35,640	84.6	64.4	1.31	34.2	2.47	1.89

Another example is given of variations in computed drift, model verification, and actual measurements in a sand trap. (Pratte et al 1982). Two previous estimates were 120,000 and 205,000 m<sup>3</sup>/yr. whilst the model suggested 30,000 m<sup>3</sup>/yr. The actual accumulation to date of publication averaged 110,000 m<sup>3</sup>/yr., indicating the need for "a permanent dredging plant." Even though waves from the most severe annual storms were used in the model it is doubtful that a proper bar profile would have formed in the model. These large discrepancies point to some missing link in the chain of events, which is herein suggested as the impulsive movement after each storm. It is stated in this reference that "it took approximately 12 hours to fill in the entrance during storms", which could be taken to mean just after such sequences.

If it is accepted that the bulk of transport occurs during the removal of the bar the greatest concern is the difference in profile used in computations (a uniform slope) from the changing bed structure of this active period. Another important aspect is the assumption of uniform sand size. As noted above the fine sediment on the bar is moved first when turbulence and longshore current is optimum. As the swell-built

profile is approached it is the coarse material being returned a short distance to and along the shore.

#### GEOMORPHOLOGICAL CONSEQUENCES

The author has wondered for many years why sand spits are formed across deep embayments of the coast or why lagoons are enclosed parallel to the shoreline. Why, for example, should such indentations not be silted up completely by the slow uniform supply from littoral drift? The reason now seems to be available, of pulsational supply of sediment by waves that can only deposit it at the tip of the spit. In essence, too much material is fed for them to handle.

At the extremity of a spit, as seen in Figure 9, the waves refract sharply and lose their longshore transporting capacity. Deposition results at this point so that the spit is enlarged parallel to the shoaled wave crests. Sudden spit formation after storms has been observed by many but not monitored scientifically with simultaneous profiling of the disappearing bar associated with it. Such daily records over 2 to 3 weeks would require a large team of workers on stand-by, to go into action immediately after a storm event.

A model verification could be made by having a beach end abruptly as seen in Figure 10. Initially oblique monochromatic waves could break on a profile comprising a bar. Once this has been returned to the beach the bar could be reformed with the aid of wire templates shaped as a mound. A spit should emerge from this condition and could then be compared to the form of accretion when a swell profile is maintained along the upcoast beach. The templates should be extended as the spit elongates.

In natural conditions there could be periods of the year with little drift, in which case the tip of the spit could be rounded off, as indicated in Figure 10. But after the next storm and another pulse the spit will suddenly enlarge and the process continued. Aerial photographs of newly formed spits should exhibit such variations in width, with perhaps semi-circular beaches on the leeward side.

These spits, or barrier beaches as they are termed, occur the world over and vary greatly in magnitude. If conditions permit the shoreline can accrete extensively in front of an initially narrow spit. In this context it should be remembered that sediment transport in past geologic ages could have been much greater than today, because many rivers are now harnessed for water supply or to prevent flooding, thus diminishing the supply of material to the coast. Such barrier beaches will not form unless there is significant oblique swell energy for transport plus a good supply of sediment from rivers debouching upcoast. In some cases spits have formed from either side of an indentation due to swell energy arriving from two quadrants during different seasons of the year. This must be accompanied by storm cycles for impulsive drift to occur, which is a basic requirement for spit formation.

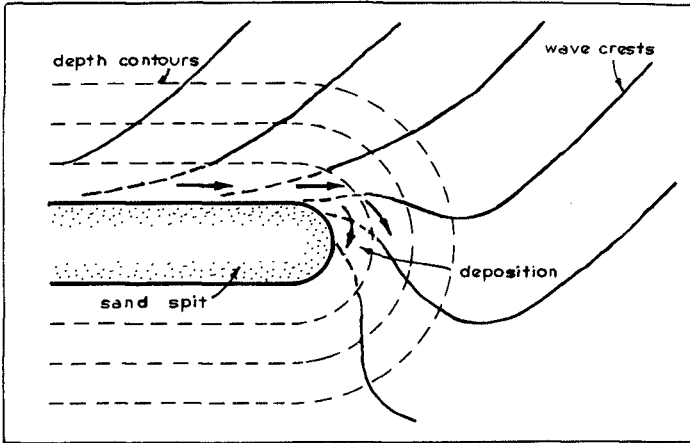


Fig 9. Accretion at the end of a spit during a pulse of littoral drift.

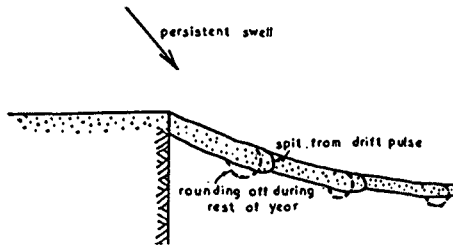


Fig 10. Spit construction at the extremity of a beach with pulsative drift.

Examples of barrier beaches are illustrated in Figure 11, being respectively from the Australian and Atlantic coasts. (Melville 1984). It can be seen that they run for tens of kilometres. These features are ubiquitous and very important commercially. Because of changed supply conditions many of these areas are now being eroded as Nature sculpts them to balance the existing wave climate (Converse 1982). Kaufman and Pilkey (1971) blame solely mans' actions on these adverse developments, but his influence is very modest and local compared to natural trends in longshore sediment distribution.

#### ENGINEERING IMPLICATIONS

Coastal engineers' for some decades have been trying to analyse why littoral drift and concomitant shoreline changes occur so continually and so swiftly. They certainly do not fit into the concept of a nice uniform process. This view of "A river of sand" has distracted research into this mammoth transporting mechanism resulting from severe meteorological fluctuations experienced over millions of years.

These spectacular changes are not only due to the processes described above but also result from other natural and man-made influences. Fluctuating sediment input from rivers, the predominant supply of material to the coast, can effect long-term fluctuations. Concentration of storm wave energy on specific lengths of shoreline can produce larger than normal bars and hence humps of sand traverse

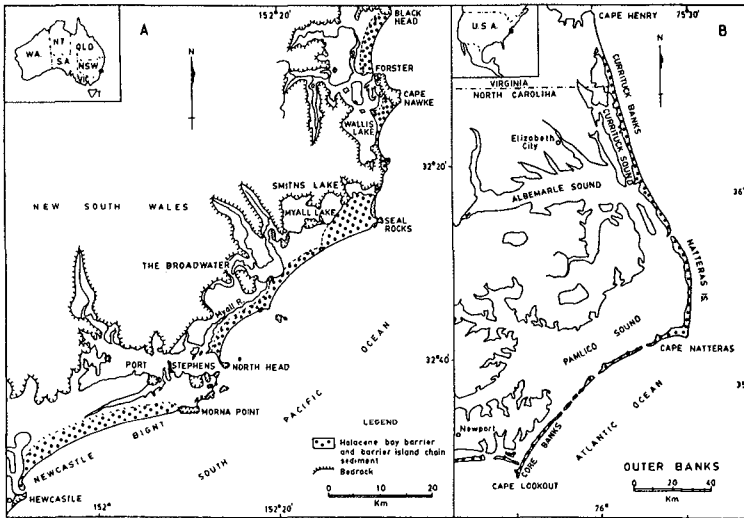


Fig 11. Barrier beaches formed on A: the NSW coast of Australia and B: the east coast of the USA (From Melville 1984).

the coast. Whilst the construction of breakwaters and groin fields can provide a transient interruption to longshore drift a much greater influence is exerted by channels dredged across the continental shelf to a port. This can cause cessation of sediment movement across this line as effectively as if a structure were built along the length of the channel. Material deposited in this trench is dredged and deposited well out to sea. Thus the offshore region downcoast is scoured. The bed is deepened and the profile to the beach steepened which then demands more sand for construction of the protective bar. Some of this will remain offshore to make up the deficiency there and hence the beach recedes. The rate of filling of the channel will vary with distance from shore but will fluctuate more near the surf zone, with peaks just after each storm. This knowledge should help in the surveying and planning of remedial dredging. The formation of shoals and even spits at river and harbour mouths will also be swift after a storm sequence. This affects navigation through these areas and hence recognition of the times of peak supply and perhaps verification of rates during these critical periods can assist by-passing operations. The action of weir-type jetties to accumulate drift for later disposal downcoast could be put in jeopardy by sudden silting of the structure to the outer full height segment.

The engineers' role should be to observe Nature on this precious margin of land and sea, accept these prodigious forces but not try to work against them. Nature achieves an admirable result in protecting the shorelines by her construction of the offshore bar. In this she can be helped by providing the volume of material required for this task. It is possible that this placement of material back into circulation need not be accompanied by longshore movement, if headlands are installed for Nature to sculpture bays of equilibrium shape. (Silvester and Ho 1972). In this case the persistent swell arrives normal to the beach around the complete periphery of the bay and hence places the bar material back from whence it came ready for the next storm.

### CONCLUSIONS

1. Storm waves and swell have denuding and accreting effects respectively on beaches, the former placing beach material in the sea for the latter to transport.
2. The action of storm waves in constructing an offshore bar is Nature's way of protecting the coastlines, which should be used and aided by man.
3. Whilst swell waves return the bar to the beach, over a very short period, the excessive littoral current and suspension of material causes a pulse of littoral drift far greater than on the swell built profile.
4. The reasons for this optimum drift are the increase in breaker height, enlargement of surf zone width, maintenance of broken wave height in this zone, perhaps greater obliquity of breakers, and partial wave reflection on the seaward face of the bar.
5. Sediment sorting during bar formation causes fine particles to be moved more readily alongshore than median sizes, with coarse material being least affected.
6. Formulae for littoral drift vary drastically in their predictions due to their non-recognition of the part played by storm sequences, as instanced in many reports.
7. Impulsive littoral drift can explain why sand spits have formed naturally across deep indentations of the coast to form barrier beaches.
8. Besides the transient peaks of drift from bar formation other longer term influences can vary sediment supply on any coast, the understanding of which should aid the coastal engineer in planning by-passing measures and coping with siltation.
9. Littoral drift can be minimised by headland control which entails sculpturing of equilibrium shaped bays between them, around which the persistent swell arrives normally and hence lacks a longshore component to generate a littoral current.

### REFERENCES

- Adeyemo M.D. (1968) Effect of beach slope and shoaling on wave asymmetry. Proc. 11th Conf. Coastal Eng. Vol. I 145-172.
- Andersen O.H. and J. Fredsøe (1983) Transport of suspended sediment along the coast. Inst. Hydrodynamics and Hyd. Eng., Denmark, Prog. Rep. No. 59, 33-46.

- Battjes J.A. (1974) Computation of set-up, longshore currents, run-up and overtopping due to wind-generated waves. Delft, Uni.Tech. Rep. No. 74-2.
- Converse H. (1982) Barrier beach features of California. Proc. 18th Conf. Coastal Eng., Vol.II, 1008-1027.
- Dean R.G. et al (1982) Longshore transport determined by an efficient sand trap. Proc. 18th Conf. Coastal Eng. Vol.II: 954-968.
- Goda Y. (1970) A synthesis of breaker indices. Trans. Japan Soc. Civil Engrs. 2(2): 227-230.
- Kaufman W. and O. Pilkey (1971) The beaches are moving. Anchor Press, New York.
- Longuet-Higgins M.S. (1953) Mass transport in water waves. Phil. Trans. R.Soc. A245: 535-581.
- Longuet-Higgins M.S. and R.W. Stewart (1960) Changes on the form of short gravity waves on long waves and tidal currents. J.Fluid Mechs., 8: 565-583.
- Melville G. (1984) Headlands and offshore islands as dominant controlling factors during late quarternary barrier formation in the Forster-Tuncurry area, New South Wales, Australia. Sedimentary Geology 39, 243-271.
- Pratte et al. (1982) Harbour sedimentation-comparison with model. Proc. 18th Conf. Coastal Eng. Vol.II, 1119-1126.
- Silvester R and S.K. Ho (1972) Use of crenulate shaped bays to stabilize coasts. Proc. 13th Conf. Coastal Eng. Vol.II, 1347-1365.
- Silvester R. Coastal Engineering Vol.I Elsevier Publ. Co., Amsterdam, 1974.
- Silvester R. (1977) The role of wave reflection in coastal processes. Proc. Coastal Sediments ASCE, Charleston Conf., 639-654.
- Silvester R. (1979) A new look at beach erosion control. Disaster Prevention Res. Inst., Kyoto, Ann. Rep. 22A: 19-31.
- Snodgrass F.E. et al. (1966) Propagation of ocean swell across the Pacific. Phil. Trans. R. Soc. Lond. A259: 431-497.
- U.S. Army Coastal Eng. Res. Centre (1977) Shore Protection Manual, Washington O.C.
- U.S. Navy Marine Climate (1977) Atlas of the World Vol.II, North Pacific Ocean, Naval Weather Service, Washington D.C., Navain 50-16-529.



## CHAPTER EIGHTY NINE

### FLOW RESISTANCE DUE TO INTENSE BEDLOAD TRANSPORT

Daniel M. Hanes \*

#### Introduction

When water flows over a stationary bed the fluid motion is retarded by both skin the friction and local pressure gradient forces related to the roughness of the bed. If the bed itself is composed of discreet movable grains, the boundary is less clearly defined and the dynamics poorly understood (see Gust and Southard, 1983). Owen (1964) proposed that saltating grains (grains which lift off the bed, move through the fluid, and fall back to the bed without colliding with other grains) have the effect of increasing the frictional resistance of the bottom.

At higher flow stages, Hanes and Bowen (1984) have suggested a model for bedload transport which is based upon the dynamics of collisional grain flows following Bagnold (1954, 1956). In such a collision dominated flow, it appears that the resistance of the bed to the overlying flow can be less than the resistance of a fixed bed to the same overlying flow. This result is consistent with the dynamics of rapid granular-fluid flows, as will be discussed below.

#### Drag relation for rapid granular-fluid flows

In a collision dominated granular-fluid flow the relation between the shear stress and the flow parameters for rectilinear shear flow is given by Bagnold (1954) as:

$$U_*^2 = C \frac{\rho_s}{\rho} (\lambda D)^2 (dU/dz)^2 \quad (1)$$

where  $U_* = (\tau/\rho)^{1/2}$ ,  $D$  is the grain diameter,  $\rho$  is the fluid density,  $\rho_s$  is the grain density, and  $\lambda$  is the linear concentration.  $\lambda$  is related to the volume concentration  $N$  by:

$$\lambda = [(N_*/N)^{1/3} - 1]^{-1}, \quad (2)$$

---

\*Assistant Professor, Division of Applied Marine Physics, Rosenstiel School of Marine and Atmospheric Science, University of Miami, 4600 Rickenbacker Causeway, Miami, Florida 33149

where  $N_*$  is the maximum possible concentration of the granular material. The relation (1) has been experimentally verified with differing materials and apparatus by Bagnold (1954), Savage and Sayed (1984), and Hanes and Inman (1984a).

Equation (1) appears similar in form to the analagous relation for a wall bounded turbulent shear flow as given by:

$$u_*^2 = (\kappa z)^2 (du/dz)^2 \quad (3)$$

where  $\kappa$  is von Kármán's coefficient and is approximately 0.4. We can define "resistance coefficients" for equations 1 and 3 as:

$$\epsilon_g = C \frac{\rho_s}{\rho} D^2 \lambda^2 \quad (4a)$$

$$\epsilon_t = \kappa^2 z^2 \quad (4b)$$

where the subscript g refers to granular-fluid and the subscript t refers to turbulent clear fluid. The ratio of these two terms is given by:

$$\epsilon_g / \epsilon_t = \frac{C \rho_s D^2 \lambda^2}{\rho \kappa^2 z^2} \quad (5)$$

Equation 5 represents the ratio of the stress in a granular-fluid layer of thickness  $z$  to the stress in a wall bounded turbulent shear flow at a distance  $z$  away from the wall, where both flows have the same shear rate at  $z$ . Using values of  $C = 0.013$  (Bagnold, 1954),  $\rho_s = 2.65\rho$ , and  $\kappa = 0.4$ , equation 5 is shown in Figure 1 for differing values of  $\lambda$ . The natural limits on  $\lambda$  are 1 and 20. For  $\lambda < 1$  the concentration is too low to apply a collisional model, and for  $\lambda > 20$  the grains are so tightly packed the granular assembly takes on solid behavior. A typical value for  $\lambda$  is 5, corresponding to a volume concentration  $N$  of approximately 0.38. Clearly if  $z$  is greater than only a few grains diameters, the stress for the granular-fluid less than the stress for the turbulent fluid.

#### Observational evidence

There have been very few observations of flow resistance under conditions of intense bedload transport. The most comprehensive data set is Williams (1970). Williams varied the flume width and discharge independently. He was therefore able to evaluate and correct for side wall friction in estimating the bottom stress.

Williams data for flat bed conditions are shown in Figure 2, where  $(u_* / \bar{u})^2$ , representing a quadratic drag coefficient, has been plotted

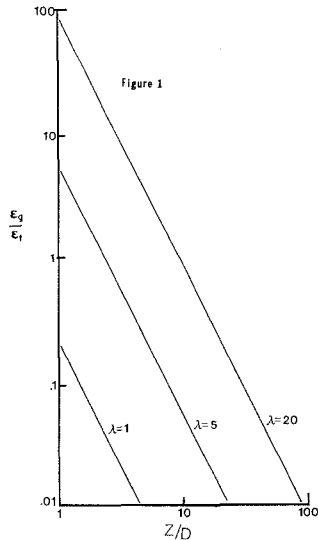


Figure 1: The ratio of granular-fluid flow resistance to clear turbulent fluid flow resistance indicates the granular-fluid has lower resistance for flows thicker than a few grain diameters over the range of possible concentrations.

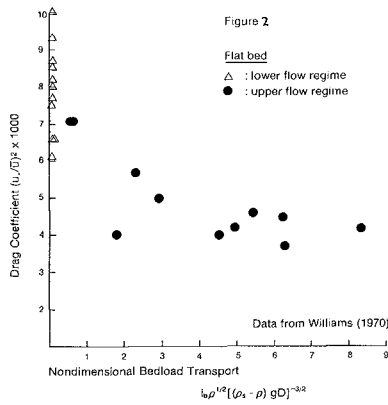


Figure 2: Drag coefficients from Williams (1970) data indicates lower flow resistance under high transport conditions. All data displayed are from flat bed experiments.

against nondimensional bedload transport. The lower flow regime occurs near the threshold for sediment motion, while the upper flow regime occurs at high flow stage after ripples disappear. The drag coefficients for the lower flow regime are clearly higher than those for the intense bedload upper flow regime. There appears to be a trend toward decreased resistance with increasing bedload transport.

#### Discussion

The largest uncertainty in this presentation is proof of the existence of the granular-fluid layer during intense bedload transport. If such a layer exists, it is not difficult to conceptualize the system as two fluid layers, where the lower (granular-fluid) layer is less viscous than the upper (turbulent fluid) layer.

Observations of intense bedload are inherently difficult to make. Horikawa et. al.(1982) used photographic and electro-resistance wires to measure sediment concentration near the bed under large oscillatory flows. They found a thin layer (10 to 20 grain diameters thick) of highly concentrated grains undergoing rapid shear. These observations are strongly supportive of a thin granular-fluid layer.

Other evidence comes from the laboratory shear cell experiments of Hanes and Inman (1984b), who suggest a dynamic Coulomb yield criterion applies at the boundary between the stationary bed and the moving grains. Unless there is a downward normal stress to counteract the shear stress, stationary grains will be mobilized into the flow. As argued by Bagnold (1956), the normal stress must arise from the immersed weight of the grains in the granular-fluid layer.

The applicability of these concepts to situations involving waves is unclear. During the peak phase of velocity the stress may be high enough to cause a granular-fluid layer. Because the motion is oscillatory, though, the system must pass through a stage of zero shear stress at which time there would not be a granular-fluid layer. The flow resistance and energy dissipation related to the mobilization and formation of the granular-fluid layer are unknown. It is therefore uncertain whether the net energy dissipation under large waves on a movable bed will be greater or less than the energy dissipation resulting from the interaction of same waves with a fixed bed.

#### Conclusions

The effects of intense bedload transport are shown to decrease the resistance of the bed to the overlying fluid. This is because the grain-to-grain collisions dominate the dynamics in the granular-fluid layer, which acts somewhat like a boundary layer of less viscous fluid. The adaptation and extrapolation of Owens (1964) saltation model to

intense bedload transport conditions will result in an overestimation of the drag coefficient.

## REFERENCES

- Bagnold, R. A., 1941, "The physics of blown sand and desert dunes", William Morrow & Co., N.Y., 265 pp.
- Bagnold, R. A., 1954, "Experiments on a gravity-free dispersion of large solid spheres in a Newtonian fluid under shear", Royal Society London, Proceedings, Series A, v 225. pp. 49-63.
- Bagnold, R. A., 1956, "The flow of cohesive grains in fluids", Royal Society London, Proceedings, Series A, v 249, pp. 235-297.
- Gust, G. and J.B. Southard, 1983, "Effects of weak bedload on the universal law of the wall," Journal Geophysical Res., v 88, No. C10, p. 5939-5952.
- Hanes, D. M. and Bowen, A. J., 1984, "A momentum based granular-fluid model for intense bedload transport", In review.
- Hanes, D.M. and D.L. Inman, 1984a, "Observations of rapidly flowing granular-fluid materials", Journal of Fluid Mechanics, In press.
- Hanes, D. M. and Inman, D. L., 1984b, "A dynamic yield criterion for granular materials", Journal of Geophysical Research, In review.
- Horikawa, K., Watanabe, A., and S. Katori, 1982, "Sediment transport under sheet flow condition", Proc. 18th Intl. Conf. Coast. Eng.
- Owen, P.R., 1964, "Saltation of uniform grains in air", Journal of Fluid Mechanics, 20(2), p. 225.
- Williams, G. P., 1970, "Flume width and water depth effects in sediment transport experiments", Geological Survey professional paper 562H.

## CHAPTER NINETY

### A Laboratory Experiment of Beach Cusps

Arata Kaneko\*

Beach cusps with a longshore spacing of 20 to 150 cm have been built by the continuous action of incident waves on a steep laboratory beach. In the formation stage of beach cusps, all bed materials on the beach moved shoreward. The backwash vortex, which was found first by Matsunaga and Honji (16,18) on a laboratory beach, gave a good explanation of the shoreward movement of bed materials. Beach cusps formed when the value of a dimensionless parameter  $H_b^2 L_b / h_b^2 L$ , which controls swash motion on a steep beach, became larger than 1.12;  $H_b$  is the height of the breaking wave,  $L_b$  its wavelength,  $h_b$  the water depth at the breaking point and  $L$  the horizontal distance from the shoreline for still water level to the breaking point. The observational spacing of beach cusps formed regularly were in quite good agreement with half a wavelength of the zero-mode subharmonic edge wave generated on a sloping flat beach. As a result of this study, the contribution of edge waves on cusp formation becomes more undoubted.

#### Introduction

Beach cusps have been known as a prominent sedimentary feature on beaches with a quasi-uniform longshore spacing less than several tens meter. Since the first extensive field observation of Shepard (20), many works have been attempted to clarify the dynamics of beach cusps. Although there is still some controversy as to the cause of beach cusps (12), it seems natural to relate their formation to edge waves which generate on a beach and have a longshore periodicity. Also recent field observations provide evidence that shows the close correlation between beach cusps and edge waves (5,6,8,11,19).

In this study, beach cusps are observed in detail through each stage of formation on a steep laboratory beach. Vortices generated on the beach by swash motion are visualized and the vortex-induced mass transport flows are related to cusp formation. The criterion controlling cusp formation and the role of edge waves in the formation are also examined.

\* Associate Professor, Research Institute for Applied Mechanics, Kyushu University 87, Kasuga, Fukuoka 816, Japan.

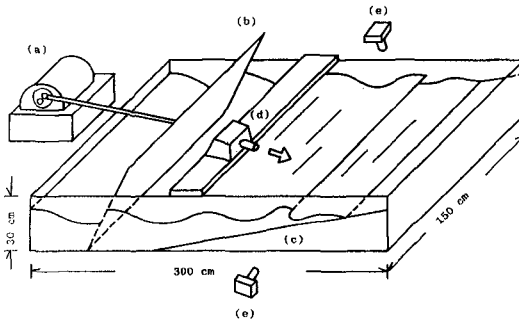


Figure 1. Sketch of experimental set-up:  
 (a) motor; (b) wave generator;  
 (c) model beach; (d) projector;  
 (e) camera.

### Experiments

Experiments were carried out using a wave tank 300 cm long, 150 cm wide and 30 cm deep, equipped with a beach floor 200 cm long (Fig.1). The side walls of the tank were made of transparent plastic to enable observation of bed features and flows on the beach floor. Incident waves on the model beach were formed by oscillating a wave-paddle-type generator with a motor-crank system. The beach slope ( $s$ ) and the period of incident waves ( $T_1$ ) were adjustable in the range of 0.081–0.141 and 0.5–2.4 s, respectively. Glass beads of mean diameter ( $D$ ) 0.028 cm and density ( $\rho_s$ )  $2.43 \text{ g cm}^{-3}$  were used as an erodible bed material instead of natural sands. In the experiment of cusp formation, the beach floor was initially covered with a thin bed of glass beads. The surface of the floor was also painted black to view clearly the movement of glass beads against the dark background. The direction of mass transport flow close to the bed could be estimated by following the movement of glass beads on the beach. Flow visualization was made by tracing the paths of polystyrene beads of  $D=0.15 \text{ cm}$  and  $\rho_s=1.04 \text{ g cm}^{-3}$ , which were suspended in water from the bed by the action of breaking waves. The bed surface and a vertical slice of the flow field were illuminated with a 1-kw light projector and photographed by a 35-mm camera from the positions shown in Fig.1.

### Formation of Cusps

When surface waves climb on a steep beach, the wave steepness increases continuously with the growth of the wave-height and the sharpened water surfaces break down rapidly at a short distance from the shore. We shall define the breaking point as the position where the

height of waves climbing on a beach becomes maximum and the plunging point as the position where the forward face of breaking waves impinges on the water surface ahead. For convenience, we shall use the terms offshore and nearshore zone, respectively, for the seaward and the shoreward sides of a breaking point. The nearshore zone is further divided into breaker and swash zones at a plunging point. It should be noted that no surf zone exists on a steep beach. In all photographs presented later, the right-hand direction indicates shoreward.

Figure 2 shows the formation process of typical beach cusps formed at the condition of  $s=0.081$ ,  $T_1=1.15$  s,  $H_b=3.5$  cm and  $h_b=4.0$  cm, where  $H_b$  is the height of breaking waves and  $h_b$  the water depth at a breaking point. Photographs were taken obliquely over a side wall of the tank after the wave generator was stopped temporarily at each stage of cusp formation. Figure 2a shows the initial feature of the glass-bead bed with 0.2 cm thick over the nearshore zone of 49 cm wide. A dotted line indicates the shoreline for still water level, and a bar at top right is 10 cm. After breaking waves begin to attack the beach, all glass beads gradually move shoreward forming a sedimentary zone parallel to the shore just at the seaward side of the plunging point (Fig.2b). As a result, the amounts of glass beads piled up on the beach face increases continuously. The sedimentary zone begins to diminish with decrease of offshore glass beads, and the ridge of glass beads on the beach face becomes cut by a series of narrow channels equi-spaced in the longshore direction. Finally a clear ridge-channel system, as seen in Fig.2c, forms. The run-up length of water becomes maximum at the central point of the ridges and minimum at the channels. Therefore, water running up on the ridges turns back along the channels, forming strong rip currents. The geometry of the ridge-channel system and the pattern of water circulation are sketched in Fig.3. The same bed and

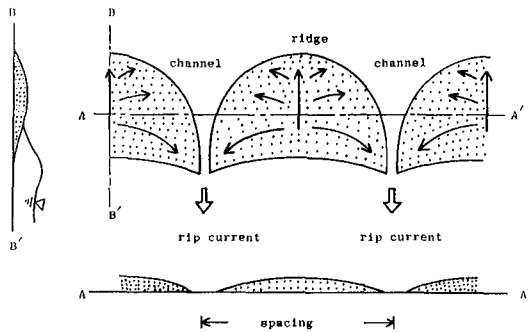


Figure 3. Sketch of the ridge-channel system. The bed profiles of sections A-A' and B-B' are presented at the lower and the left parts, respectively.



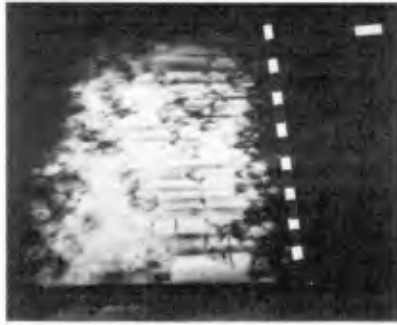
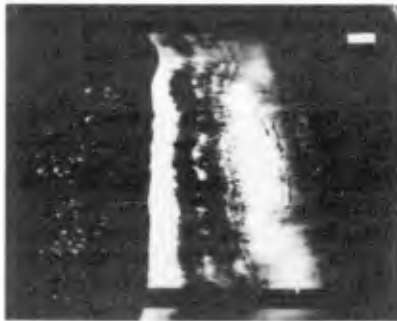
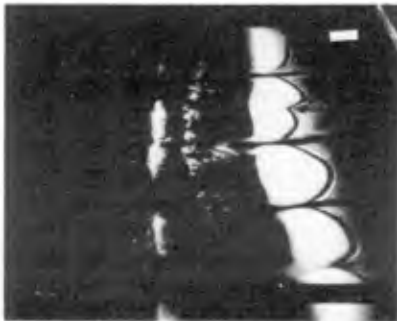
(a)  $t = 0$  s(b)  $t = 223$  s(c)  $t = 784$  s

Figure 2. Formation process of typical beach cusps.  
 $t$  denotes the elapsed time from the start of the experiment.

flow features have often been observed in wave tanks (17,21). In the field, Sallenger (19) observed that a similar ridge-channel system generated in flood-tide changes to ordinary beach cusps after the mouth of the channels was eroded widely on ebb-tide. It will, therefore, be reasonable to call such a ridge-channel system the beach cusp. Kaneko (9) showed through a numerical experiment that horizontal circulation systems are induced by the nonlinear effect of swash motion due to edge waves. This circulation may also play a role in the initiation of beach cusps.

#### Flows on a Steep Beach

Figure 4 shows the anticlockwise-rotating vortex induced near a plunging point immediately after breaking waves forming beach cusps impinged on the forward water surface just beneath a horizontal scale of 4 cm. The experimental condition was at  $s=0.081$ ,  $T_i=1.68$  s,  $H_b=3.7$  cm and  $h_b=3.9$  cm. The vertical slice at a distance of 10 cm from a side wall was illuminated by a light projector and photographed through the side wall. This vortex, called the backwash vortex, was first found by Matsunaga and Honji (16) to form on a highly steep beach in a wave tank. The backwash from water running up on a beach face is responsible for the vortex formation. The backwash vortex is also known to make up a step-like bed profile, composed of a steep seaward face and a nearly horizontal top and called the backwash step (16). Taking into account flow fields induced by the backwash vortex, we can sketch the overall pattern of mass transport flow forming beach cusps and a backwash step, as in Fig.5. The piling-up of bed materials on the beach face, as seen in Fig.2, can also be well explained by the vortex-induced mass transport flow. The wave-induced mass transport flow of Longuet-Higgins (13) may play a role in the shoreward transport of offshore sands.

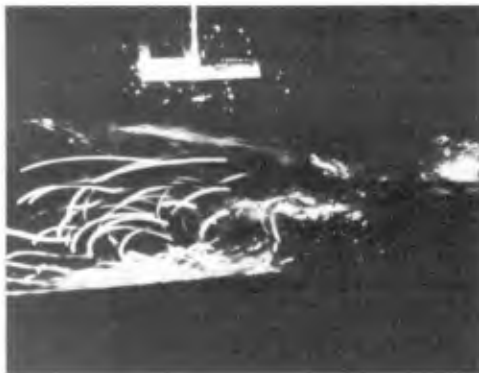


Figure 4. Flows beneath the breaking wave forming beach cusps.

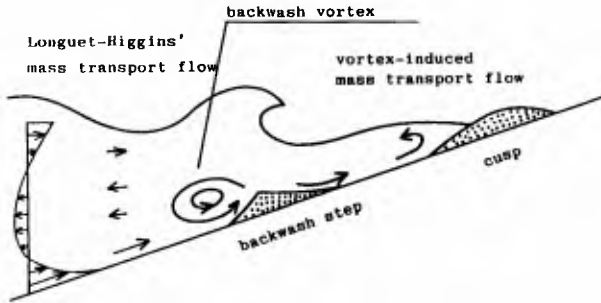


Figure 5. Sketch of mass transport flow forming beach cusps and a backwash step.

Figure 6 shows the flow field near a plunging point photographed immediately after breaking waves forming a longshore bar impinged on the forward water surface just beneath a horizontal scale of 4 cm. The method of photography and light projection was the same as in Fig.4. The experimental condition was at  $s=0.081$ ,  $T_i=0.62$  s,  $H_b=3.3$  cm and  $h_b=4.3$  cm. Notice that  $T_i$  is remarkably reduced in comparison with that for Fig.4. Under such a condition, the period of breaking waves became shorter than that of swash motion. As a result, weak swash motion and prominent wave set-up took place. Flows near the plunging point construct a pair of vortices, a clockwise, shoreward vortex and an anticlockwise, seaward one. The paired vortex may be induced by that the wave-induced mass transport flow of Longuet-Higgins (13) and the undertow due to wave set-up proposed by Longuet-Higgins(15) meet near the plunging point. The longshore bar was observed to form on the bed between these vortices (10). We can also sketch the overall pattern of mass transport flow forming a longshore bar, as in Fig.7.

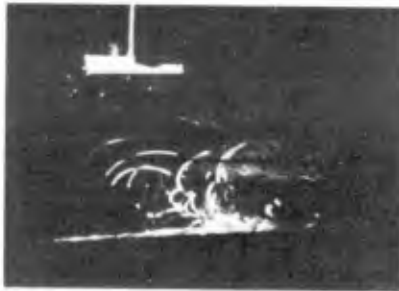


Figure 6. Flows beneath the breaking wave forming a longshore bar.

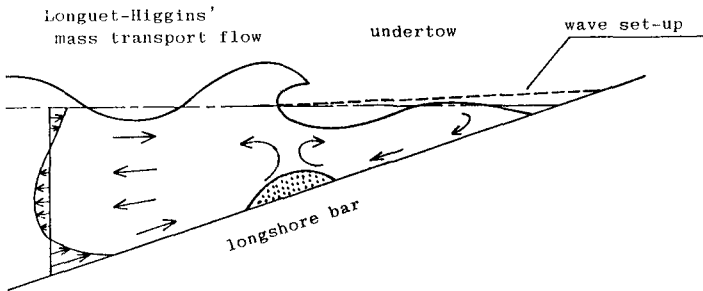


Figure 7. Sketch of mass transport flow forming a longshore bar.

Criterion for Cusps

In the present experiment, beach cusps developed from a thin glass-bead bed on a beach floor. Because of the small amount of glass beads used, the resulting bed deformation could not grow sufficiently to change the initial conditions of incident waves, the height of breaking waves and the breaking point. Under such a situation, the formation region of beach cusps may be determined by the wave conditions on a rigid plane beach.

As mentioned in the previous section, the backwash vortex generated by strong swash motion is responsible for the movement of bed materials to form beach cusps. We shall analyse the swash motion on a steep beach, making use of the terminology as sketched in fig.8. Let  $L_r$  and  $L$  denote the run-up length and the horizontal distance from a shoreline for still water level to a breaking point, respectively.

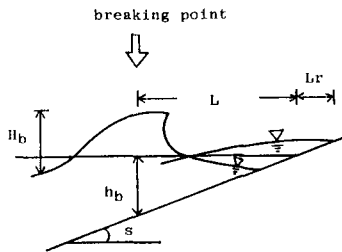


Figure 8. Sketch of the swash motion on a steep beach.

When we simulate a breaking wave by a progressive long wave with wave-height  $H_b$  and wavelength  $L_b$ , its energy over a wavelength may be estimated as proportional to  $\rho g H_b^2 L_b$ , where  $L_b = T_i \sqrt{g h_b}$ . We also simulate swash motion by a standing wave with maximum wave-height  $2L_r s$  at a shoreline for still water level and estimate its energy over a nearshore zone as proportional to  $\rho g (L_r s)^2 L$ . Since a part of energy of the breaking wave is transferred to the swash motion, both the energies may be correlated as follows:

$$\rho g H_b^2 L_b \propto \rho g (L_r s)^2 L \tag{1}$$

Rearranging eq.1 and using  $h_b = sL$ , we can obtain the following relation:

$$\frac{L_r}{L} \propto \left( \frac{H_b^2 L_b}{h_b^2 L} \right)^{1/2} \tag{2}$$

The observational values of  $L_r/L$  are plotted in Fig.9 against those of  $H_b^2 L_b / h_b^2 L$ . In Fig.9, the line for eq.2

$$\frac{L_r}{L} = 0.35 \left( \frac{H_b^2 L_b}{h_b^2 L} \right)^{1/2} \tag{3}$$

best fitting into the plotted data is also drawn. The dimensionless parameter  $H_b^2 L_b / h_b^2 L$  controlling swash motion on a steep beach is called the swash parameter here. Some deviation of the plotted data from eq.3 seems due to that the energy transferred to nearshore mass transport flow and wave set-up are neglected in this analysis. The deviation at the region of large  $H_b^2 L_b / h_b^2 L$  may also be influenced by the excitation of edge waves. The swash parameter can be rewritten as:

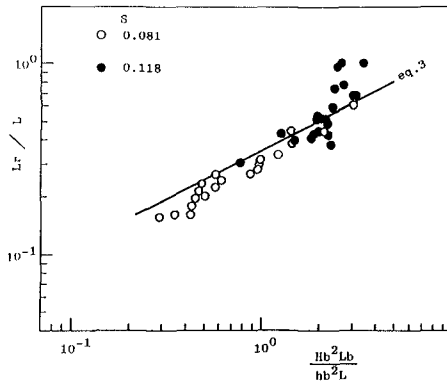


Figure 9. Run-up length.

$$\frac{H_b^2 L_b}{h_b^2 L} = \left( \frac{H_b}{s^2 g T_1^2} \right)^{-1/2} \left( \frac{H_b}{h_b} \right)^{5/2} \tag{4}$$

The values of  $H_b/h_b$  for the present experiment are plotted in Fig.10 against those of  $(H_b/s^2 g T_1^2)^{1/2}$ . Most of the plotted data are grouped by the critical line

$$\frac{H_b^2 L_b}{h_b^2 L} = 1.12 \tag{5}$$

or

$$\left( \frac{H_b}{h_b} \right)^{5/2} = 1.12 \left( \frac{H_b}{s^2 g T_1^2} \right)^{1/2} \tag{5}'$$

into two regions of the beach cusp and the longshore bar, where the dimensionless parameter  $(H_b/s^2 g T_1^2)^{1/2}$  has been called the surf similarity parameter by Battjes (2). According to Battjes' study, the generation regions for surging, plunging and spilling breakers are, respectively,  $(H_b/s^2 g T_1^2)^{1/2} < 0.2$ ,  $0.2 < (H_b/s^2 g T_1^2)^{1/2} < 1.0$  and  $1.0 < (H_b/s^2 g T_1^2)^{1/2}$ . It should be noted that the beach cusp is transferred to the longshore bar at a nearly central part of the generation region for plunging breakers.

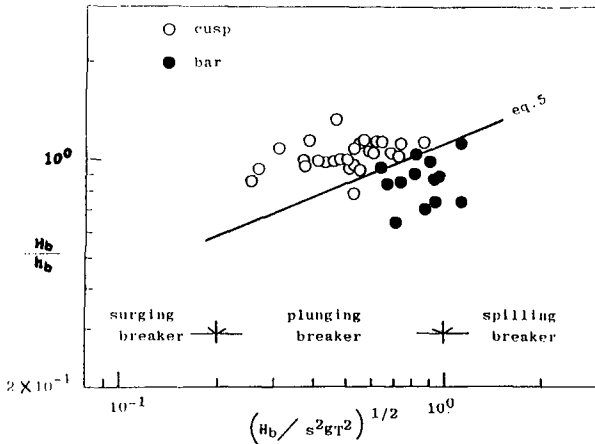


Figure 10. Formation region of cusps.

## Edge waves

According to Ursell's theory (24), the wavelength of edge waves ( $L_e$ ) can be expressed as:

$$L_e = gT_e^2 \sin \{(2n+1)s\} / 2\pi \quad (6)$$

where  $T_e$  and  $n$  are the period and the offshore modal number of the edge wave, respectively. Edge waves on a beach may be classified into two types of subharmonic and synchronous depending on whether the period of edge waves is twice or the same as that of incident waves. Guza and Davis (4) predicted theoretically that the zero-mode ( $n=0$ ) subharmonic edge wave can most easily be excited by incident waves. Huntley and Bowen (7) and Guza and Bowen (6) also found that in the power spectra of nearshore currents, the zero-mode subharmonic edge wave takes place on real beaches. When the longshore undulation of small amplitude due to edge waves is superimposed on the uniform swash motion due to incident waves, the compound swash motion is known to have the longshore spacing of half a wavelength of subharmonic edge waves or a wavelength of synchronous ones (3,10). Equating the spacing of swash motion and beach cusps and using eq.6 and  $T_i$  instead of  $T_e$ , we can express the calculated spacing of cusps ( $L_{cal}$ ) as:

$$L_{cal} = L_e/2 = gT_i^2(\sin s)/\pi \quad (7)$$

for the zero-mode subharmonic edge wave and:

$$L_{cal} = L_e = gT_i^2(\sin s)/2\pi \quad (8)$$

for the zero-mode synchronous edge wave.

Other examples of beach cusps formed regularly are showed in Figs.11a to e. In all the figures, a bar at top right is 10 cm.



(a)



(b)

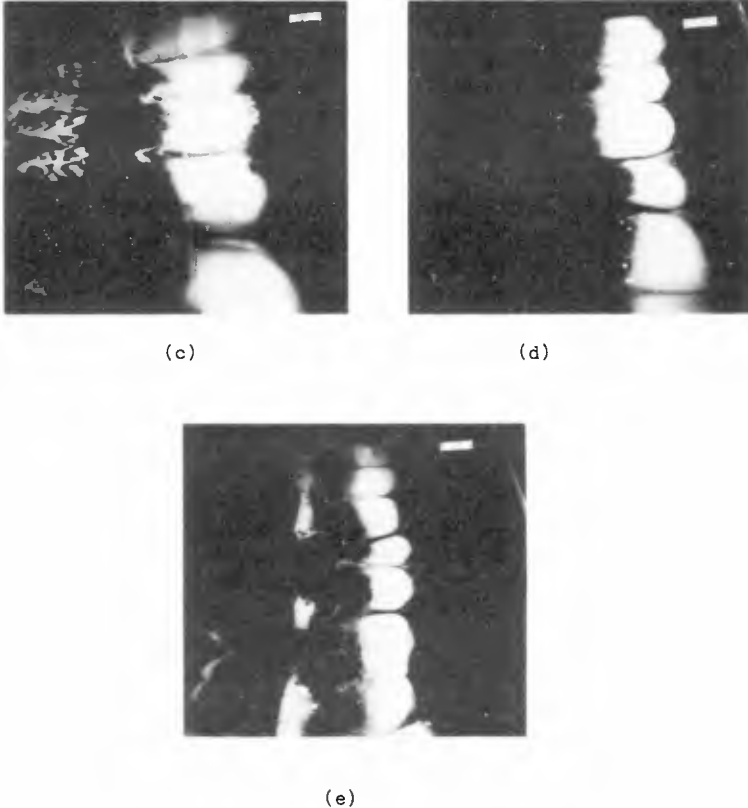


Figure 11. Five examples of beach cusps formed regularly.

Similarly to Fig.2, these beach cusps are composed of ridge-channel systems. Using the width of the wave tank ( $B$ ) and the total number of the ridges ( $N$ ), we can obtain the observational spacing of cusps ( $L_{\text{Obs}}$ ) as:

$$L_{\text{Obs}} = \frac{B}{N - 1} \quad (9)$$

The numerical data of these beach cusps are presented in Table 1. The value of  $L_{\text{Obs}}$  is in quite good agreement with that of  $L_{\text{Cal}}$  based on subharmonic edge waves. It seems that beach cusps become regular when the resonance condition of zero-mode subharmonic edge waves is satisfied with good accuracy. If edge waves occur on a beach, it will be expectable to find them in the longshore undulation of swash motion.



Table 1. Numerical data of beach cusps formed regularly.

Fig.11	s	T <sub>i</sub> (s)	H <sub>b</sub> (cm)	h <sub>b</sub> (cm)	$\frac{H_b^2 L_b}{h_b^2 L}$	L <sub>cal</sub> (cm)	L <sub>obs</sub> (cm)
a	0.081	2.38	3.4	3.1	4.08	143	150
b	0.081	1.72	3.1	3.1	2.42	74	75
c	0.141	0.98	4.2	3.2	4.30	42	38
d	0.107	0.98	3.4	2.9	2.85	32	30
e	0.107	0.76	3.5	3.1	2.20	19	21

Such a property of swash motion was visible only in the experiment for Figs.11a and b with the large cusp spacings. In other cases, edge waves excited may be too weak to be found in swash motion. The values of L<sub>obs</sub> for the laboratory experiments of Ann (1), Tamai (22) and the author, and the field observations of Longuet-Higgins and Parkin (14), Komar (11), Sallenger (19), Guza and Bowen (6) and Takeda and Sunamura (23) are plotted in Fig.12 against that of  $gT_i^2(\sin s)/\pi$ . The value of L<sub>cal</sub> for subharmonic and synchronous edge waves are also drawn with solid and dotted lines, respectively. Although all the laboratory data and most of the field data have a best fit with the solid line, there are some data of Longuet-Higgins and Parkin, Komar and Sallenger which show a scatter around the dotted line. The critical condition, at which synchronous edge waves are transferred to subharmonic ones, may exist.

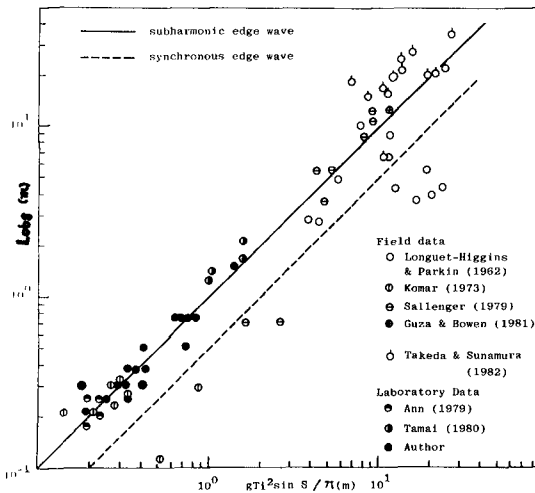


Figure 12. Spacing of cusps.

## Conclusions

Main results obtained in the present study are summarized as follows:

- (1) Beach cusps develop at the beach face when all bed materials on a beach move shoreward, forming a backwash step along the plunging point.
- (2) When all bed materials on a beach assemble near the plunging point, beach cusps can not develop and instead a longshore bar forms along this point.
- (3) Vortices induced beneath the breaking waves by the action of swash motion or wave set-up control the movement of bed materials at the swash zone.
- (4) The transition from the beach cusp to the longshore bar takes place at  $H_b^2 L_b / h_p^2 L = 1.12$ . This dimensionless parameter controlling swash motion on a steep beach is called the swash parameter.
- (5) The observational spacing of beach cusps obtained in the laboratory experiment agrees well with half a wavelength of the zero-mode subharmonic edge wave. A relatively large scatter of the field data may be explained consistently by considering the existence of beach cusps generated by the zero-mode synchronous edge wave.

## Acknowledgments

I would like to thank Prof. H. Honji for valuable suggestions and criticism and Mr. Y. Shiraishi for technical assistance.

## References

1. Ann, K., Experimental study on the formation of rhythmic shorelines, Unpublished Master's Thesis, University of Tokyo, Tokyo, in Japanese, 1979, p.1-135.
2. Battjes, J.A., Surf similarity, Proc. 14th Conf. Coastal Eng., Copenhagen, 1974, p.466-480.
3. Bowen, A.J., Edge waves and the littoral environment, Proc. 13th Conf. Coastal Eng., London, 1972, p.1313-1319.
4. Guza, R.T. and Davis, R.E., Excitation of edge waves by waves incident on a beach, J. Geophys. Res., 79, 1974, p.1285-1291.
5. Guza, R.T. and Inman, D.L., Edge waves and beach cusps, J. Geophys. Res., 80, 1975, p.2997-3012.
6. Guza, R.T. and Bowen, A.J., On the amplitude of beach cusps, J. Geophys. Res., 86, 1981, p.4125-4132.
7. Huntley, D.A. and Bowen, A.J., Field observations of edge waves, Nature, 243, 1973, p.160-162.
8. Inman, D.L. and Guza, R.T., The origin of swash cusps on beaches, Mar. Geol., 49, 1982, p.133-148.
9. Kaneko, A., A numerical experiment on nearshore circulation in standing edge waves, Coastal Eng., 7, 1983, p. 271-284.
10. Kaneko, A., Formation of beach cusps in a wave tank, Coastal Eng., in press, 1985.
11. Komar, P.D., Observations of beach cusps at Mono Lake, California, Geol. Soc. Am. Bull., 84, 1973, p.3593-3600.

12. Komar, P. D., Beach Processes and sedimentation, Prentice-Hall, Englewood-Cliffs, N. J., 1976, p.263-274.
13. Longuet-Higgins, M. S., Mass transport in water waves, Philos. Trans. R. Soc. London, A245, 1953, p.535-581.
14. Longuet-Higgins, M. S. and Parkin, D. W., Sea waves and beach cusps, Geogr. J., 128, 1962, p.194-201.
15. Longuet-Higgins, M. S., Wave set-up, percolation and undertow in the surf zone, Proc. R. Soc. London, A390, 1983, p.283-291.
16. Matsunaga, N. and Honji, H., The backwash vortex, J. Fluid Mech., 99, 1980, p.813-815.
17. Matsunaga, N. and Honji, H., A petal-like sand pattern along the shoreline, Rep. Res. Inst. Appl. Mech., 29, 1981, p.1-12.
18. Matsunaga, N. and Honji, H., The steady and unsteady backwash vortices, J. Fluid Mech., 99, 1983, p.189-197.
19. Sallenger, A. H., Beach-cusp formation, Mar. Geol., 29, 1979, p. 23-37.
20. Shepard, F. P., Gravel cusps on the California coast related to tides, Science, 82, 1935, p.251-253.
21. Tamai, S., Study on the formation of beach cusps, Proc. 21st Japanese Conf. Coastal Eng., Sendai, 1974, in Japanese, p.115-120.
22. Tamai, S., Study on the characteristics of beach cusps and the prediction of shoreline changes, Doctor's Dissertation, Kyoto University, Kyoto, 1980, in Japanese, p.1-179.
23. Takeda, I. and Sunamura, T., Formation and wavelength of beach cusps, Proc. 29th Japanese Conf. Coastal Eng., Sendai, 1982, in Japanese, p.319-322.
24. Ursell, F., Edge waves on a sloping beach, Proc. R. Soc. London, A214, 1952, p.79-97.

## CHAPTER NINETY ONE

### CALCULATION OF THE RATE OF NET ON-OFFSHORE SEDIMENT TRANSPORT ON THE BASIS OF FLUX CONCEPT

Ichiro Deguchi

Assistant Professor, Department of Civil Engineering  
Osaka University, Osaka, Japan

and

Toru Sawaragi

Professor, Department of Civil Engineering  
Osaka University, Osaka, Japan

#### Abstract

Time and spatial variations of sediment concentration of both bed load and suspended load in the process of two-dimensional beach deformation were investigated experimentally. At the same time, the relation between the velocities of water-particle and sediment migration was analyzed theoretically. By using those results, a net rate of on-offshore sediment transport in the process of two-dimensional model beach deformation  $\bar{q}_f$  was calculated on the basis of sediment flux. It is found that  $\bar{q}_f$  coincides fairly well with the net rate of on-offshore sediment transport calculated from the change of water depth.

#### 1. Introduction

The rate of sediment transport has been formulated in various ways and a variety of formulas have been proposed. Some of them deal with only bed load (Einstein(1972), Madsen et al.(1976)) and others are formulated by assuming that the most of sediment is transported in suspension (Bakker(1974), Nielsen et al.(1978), Kana et al.(1977)).

Generally, sediment is brought into suspension from the bed load layer by wave action and the bed load layer plays a role as a boundary condition for the suspended load. Therefore, bed load can exist but suspended load can not exist by itself. On the basis of this fact, some formulas to estimate the rate of suspended sediment transport are proposed by relating bed load to suspended load (Bijker(1971), Walton(1979)).

However, in most of the previous studies, the time averaged rate of sediment transport over one or one-half wave cycle is directly dealt with and only in a few studies (Bakker(1974), Nielsen et al.(1978)), phase variations of the rate of sediment transport are taken into account.

Further, bed load and suspended load differ in the speed of migration and sediment concentration each other. In a two-dimensional beach

deformation process, it is also said that the directions of sediment transport in bed load and suspended load do not always coincide. Consequently, two different expressions have been prepared to estimate the rates of bed load and suspended load.

The rate of sediment transport  $q(t)$  is universally expressed by using the sediment flux as a function of the phase as follow:

$$q(t) = \int_{-(h+\delta)}^{\eta(t)} C(z,t) U_s(z,t) dz \quad (1)$$

where  $C(z,t)$  is the volumetric concentration of sediment,  $U_s(z,t)$  is the velocity vector of sediment migration,  $\eta(t)$  is the surface elevation,  $h$  is the water depth defined as the distance from the still water level to the upper bed load layer and  $\delta$  is the thickness of the bed load layer. So,  $h+\delta$  is the depth where no sediment movement takes place.  $z$ -axis is taken upward from the still water level as shown in Fig.1.

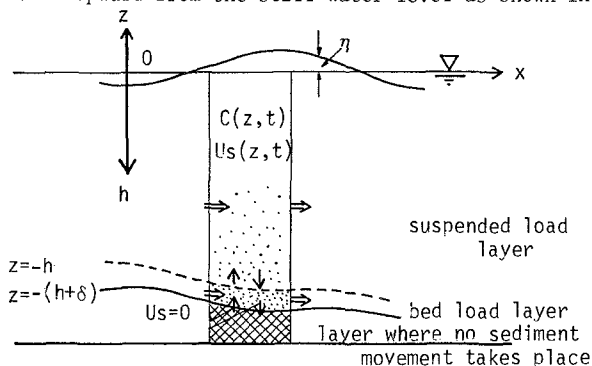


Fig.1 Definition sketch

The aim of this study is to estimate the on-offshore sediment transport rate including both bed load and suspended load according to Eq.(1) systematically. To calculate  $q(t)$  from Eq.(1), it is necessary to estimate time and spatial variations of sediment concentration of both bed load and suspended load as well as the migration speed of sediment.

The authors, first, investigated the characteristics of bed load and suspended load concentration by measuring them in two-dimensional model beach experiments. Then, the relation between water-particle velocity and speed of sediment migration was investigated by analyzing the motion of sediment particle at various sediment concentration. Finally, the net rate of on-offshore sediment transport was calculated on the basis of Eq.(1) by using the measured sediment concentration and analyzed speed of sediment. The results are discussed by comparing with the on-offshore sediment transport rate calculated from the change of water depth.

2. Characteristics of time and spatial variation of sediment concentration

2.1 Previous works

A lot of studies on the suspended sediment have been conducted. Their objectives are to determine the vertical profile of time averaged suspended sediment concentration by applying an one-dimensional diffusion theory, that is, to determine the so-called height of reference level, concentration at the reference level and a diffusion coefficient  $\epsilon_z$ . Some attempts have been made to simulate the phase variation of suspended sediment concentration by assuming the constant  $\epsilon_z$  and the phase dependent concentration at the reference level (Bakker(1974), Nielsen et al. (1978)).

As for the concentration of bed load, only the experimental results measured by Horikawa et al.(1982) are reported. However, at present, it is impossible to quantitatively estimate the time variation of sediment concentration of both bed load and suspended load.

2.2. Measurement of sediment concentration of both bed load and suspended load

A resistance type sediment concentration measuring system devised by Horikawa et al.(1982)(see Fig.2) was used to measure sediment concentration of bed load and suspended load.

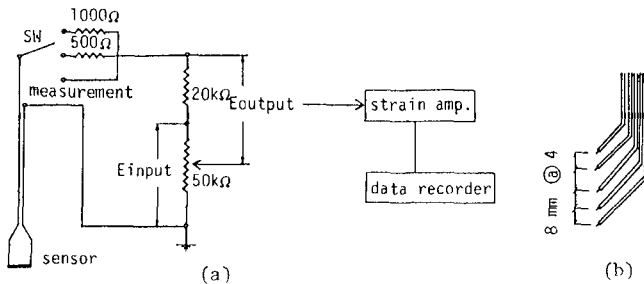


Fig.2 Resistance type sediment concentration measuring system

This system, first, measures the difference of electric resistance between clear water and sediment laden water and then transfers it to the concentration by using a calibration curve. The sensor was made of two enamel coated wires of 5cm long and 0.3mm diameter. Five sensors fixed vertically at a distance of 8mm were used to measure sediment concentration at five different levels simultaneously as shown in Fig.2(b).

Sediment concentration  $C(z,t)$  was measured in four different types of beach deformation processes as shown in Table 1 together with the experimental conditions. In Table 1,  $H_0$  is the deep water wave height,  $T$  is the wave period,  $i$  is the initial beach slope and  $d$  is the mean grain size of the bed material. Concentration measuring points covered whole littoral zone and were distributed vertically from the bed load layer and suspended load region.

Table 1  
Two-dimensional model beach experiments  
and their experimental conditions

	$H_0$ (cm)	T (s)	i	d (cm)	deformation types
Case 1	11	1.20	1/10	0.02	erosion type
Case 2	11	1.28	1/20	0.02	transition type
Case 3	18	1.28	1/20	0.05	transition type
Case 4	12	1.28	1/20	0.05	acretion type

From measured sediment concentration  $C(z,t)$ , time averaged concentration  $\bar{C}(z)$  and phase averaged concentration  $C_p(z,t)$  over 60 waves were calculated. Beach profiles and wave heights were also measured at definite time intervals.

### 2.3. Time variations of sediment concentration

Fig.3 shows examples of measured sediment concentration  $C(z,t)$  in the erosion type beach deformation. In Fig.3(a), measured beach profiles and 6 concentration measuring points (s-1 to s-6) are shown. Fig.3(b) is a result measured at s-4 (inside wave breaking point) and Fig.3(c) is a result obtained at a ripple crest (s-2) in the offshore region. Fig.(i) in each figure shows the surface elevation, Fig.(ii) indicates the concentration in the bed load layer ( $z \approx 0$ ) and Figs.(iii) and (iv) are the suspended sediment concentration at different heights ( $z \approx 0$ ) where  $z^*$  is measured upward from the bottom surface.

It can be seen from these figures that the concentration in the bed load layer in both the surfzone (Fig.3(b)(ii)) and the offshore region (Fig.3(c)(ii)) decreases when a wave crest passes and this indicates that at this phase, an intense sediment transport takes place in the bed load layer. Suspended sediment concentration near the bottom in the surfzone (fig.3(b)(iii)) increases corresponding to the decrease of concentration in the bed load layer and has one peak during one wave cycle. However, in the upper region (Fig.3(b)(iv)), concentration of suspended sediment no longer shows any correspondence with the surface elevation. While in the offshore region (Figs.3(c)(iii) and (iv)), concentration of suspended sediment has two apparent peaks during one wave cycle and this coincides with the results measured by Nakato et al.(1977) and others on a horizontal bottom with bed formations.

On the other hand, as can be seen from Figs.3(c)(iii) and (iv), the maximum concentration of suspended sediment appears almost at the same time without phase lag regardless of the height from the bottom. This indicates that the diffusion of suspended sediment takes place not only in the vertical direction but also in the horizontal direction. Therefore, one-dimensional diffusion theory can not apply to estimate the time variation of suspended sediment concentration. The authors analyzed time variations of suspended sediment concentration by assuming that suspended sediment diffuses from an instantaneous point source according to Ornstein-Uhlenbeck process with constant  $\epsilon_z$  (Soong(1973)). It is found that the procedure gives a good prediction of the time variation of suspended sediment concentration provided that the water-particle velocity due to waves is known.

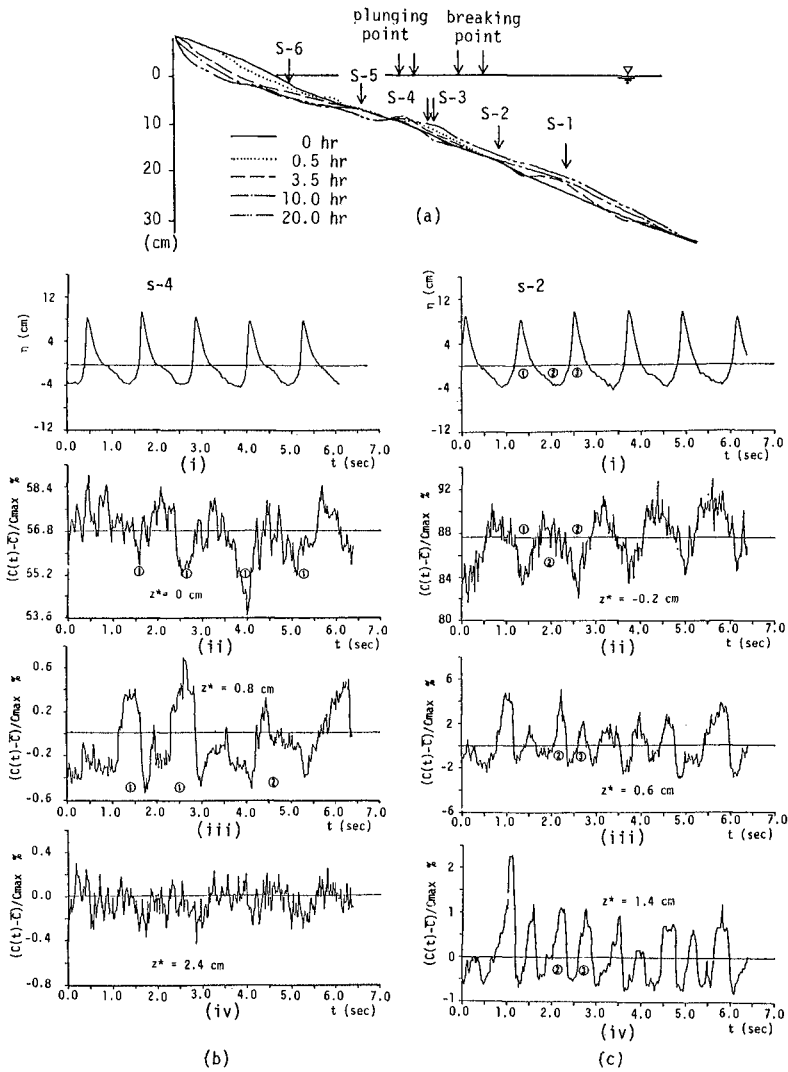


Fig.3 Time variation of sediment concentration  
(erosion type beach deformation)



#### 2.4. Vertical distribution of time-averaged sediment concentration

For reference, some examples of vertical distributions of time-averaged concentration of sediment  $\bar{C}(z^*)$  measured in the erosion type beach deformation process are shown in Fig.4.

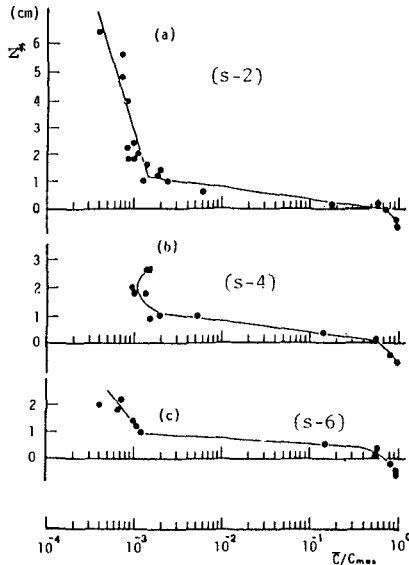


Fig.4 Vertical distribution of time averaged sediment concentration (erosion type beach deformation)

Fig.4(a) is the result obtained in the offshore region s-2 (corresponding to Fig.3(c)) showing that  $\log \bar{C}$  is proportional to  $z^*$ . Fig.4(b) is the result measured near the wave breaking point s-4 (corresponding to Fig.3(b)) and shows that  $\log \bar{C}$  is not directly proportional to  $z^*$ , that is, the concentration near the water surface is larger than that in the middle of water depth. This kind of  $\bar{C}$ -distribution have also been measured by Kana et al. (1977) in the field under plunging wave breaking.  $\bar{C}$ -distribution in Fig.4(c) was measured in the nearshore zone s-6 where the strong turbulence brought by plunging waves already attenuated. In this region,  $\log \bar{C}$  again becomes proportional to  $z^*$ .

From these figures together with the results measured in the other beach deformation processes, it is found that for the vertical distribution of time averaged suspended sediment concentration, one-dimensional diffusion theory with constant  $\epsilon_z$  is applied in appearance except for the region near the wave breaking point.

3. Relation between the migration speed of sediment and water-particle velocity

The motion of the particle suspended in a fluid is usually analyzed by Lagrangian method (Hinze(1959)). Namely, the linearized equation which subjects the motion of the particle in a fluid is expressed by

$$\frac{dU_s}{dt} + BU_s = BU_f + A\frac{dU_f}{dt} + C \tag{2}$$

$$A=3\rho/(2\rho_s+\rho), B=36\mu/((2\rho_s+\rho)d^2), C=(0,0,-2(\rho_s-\rho)g/(2\rho_s+\rho))$$

where  $\rho$  and  $\rho_s$  are the densities of fluid and particle,  $d$  is the diameter of particle,  $\mu$  is the fluid viscosity,  $g$  is the gravitational acceleration and  $U_s$  and  $U_f$  are the velocities of suspended particle and water particle. When the fluid motion is purely oscillatory in the direction of x-axis,ie,  $U_f=(\widehat{U}_{f0}\exp(-i\sigma t),0,0)$ , the solution which satisfies an initial condition at  $t=0,U_s=0$  becomes

$$U_s = \widehat{U}_{f0}G^{1/2} (\cos(\sigma t+\theta) - \exp(-Bt)\cos\theta) \tag{3}$$

$$G=(A^2\sigma^2+B^2)/(\sigma^2+B^2), \theta = \tan^{-1}((B\sigma(1-A))/(A\sigma^2+B^2))$$

where  $\sigma=2\pi/T$ .

Figs.5 and 6 show the amplitude ratio of water-particle velocity and the velocity of suspended particle  $\widehat{U}_s/\widehat{U}_{f0}$  and the phase shift  $\theta$  as a function of the diameter of particle  $d$ .

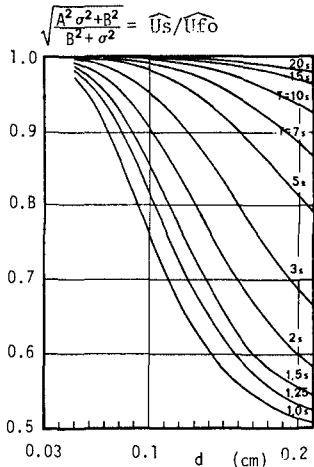


Fig.5 Relation between  $\widehat{U}_s/\widehat{U}_{f0}$  and  $d$

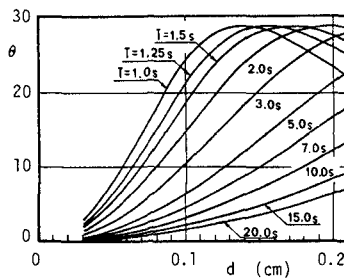


Fig.6 Relation between  $\theta$  and  $d$

From these figures, it is found that  $\widehat{U}_s/\widehat{U}_{f0} \approx 1$  and  $\theta \approx 0$  for the particle which is usually seen in suspension in the laboratory experiments( $d \leq 0.5mm$ ). So, the velocity of suspended sediment  $U_s$  is approximated by water-particle velocity  $U_f$ .

The same procedure can apply to the motion of a projected particle on the bottom (Eagleson et al.(1958)). However, the motion of bed load in a region where an intense sediment transport in high concentration takes place can not be analyzed by this method. Therefore, the authors analyzed the motion of bed load sediment in such regions by solving a boundary layer equation in the Eulerian system of coordinates shown in Fig.7 under the following assumptions:

- 1) the bed load layer is a Newtonian fluid with a hypothetical viscosity  $\mu_s$ ,
- 2) the flow on the bottom is a laminar, for simplicity,
- 3) the bottom sediment layer is moved by the boundary shear and the pressure in the bottom sediment layer.

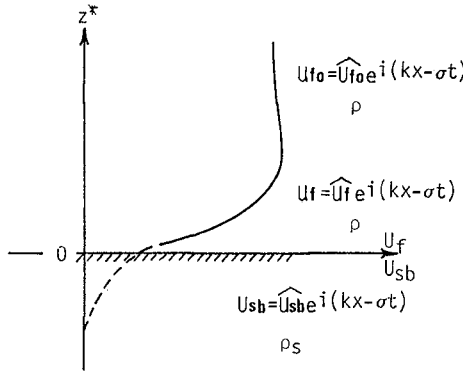


Fig.7 Definition sketch of the coordinates.

According to Bagnold(1956), the first assumption is true when the concentration of the bottom sediment  $C_b$  is less than 0.53. Then, the equation of motion for  $z^* = \infty$  (main flow),  $z^* \geq 0$  (flow within the boundary layer) and  $z^* \leq 0$  (sediment motion in the bed load layer) are expressed as follows:

$$\begin{aligned} \frac{\partial U_{fo}}{\partial t} &= -\frac{1}{\rho} \left( \frac{\partial p}{\partial x} \right) & z^* = \infty \\ \frac{\partial U_f}{\partial t} &= -\frac{1}{\rho} \left( \frac{\partial p}{\partial x} \right) + \frac{\mu}{\rho} \left( \frac{\partial^2 U_f}{\partial z^{*2}} \right) & z^* \geq 0 \\ \frac{\partial U_{sb}}{\partial t} &= -\frac{1}{\rho'_s} \left( \frac{\partial p_s}{\partial x} \right) + \frac{\mu_s}{\rho'_s} \left( \frac{\partial^2 U_{sb}}{\partial z^{*2}} \right) & z^* \leq 0 \end{aligned} \tag{4}$$

where  $\rho'_s = (1-C_b) + \rho_s C_b$  is the density of the bottom sediment layer,  $p$  and  $p_s$  are the pressures in water and the bottom sediment layer and  $U_{sb}$  is the velocity of the bottom sediment layer.

For the pressure  $p_s$  in the bottom sediment layer, the following expression proposed by Sleath(1978) is used:

$$\begin{aligned} P_s &= P_0 \frac{\cosh(k(\kappa x / \kappa z) (z^* + \delta b'))}{\cosh(k(\kappa x / \kappa z) \delta b')} \exp(i(kx - \sigma t)) \\ P_0 &= \rho g H / (2 \cosh kh) \end{aligned} \tag{5}$$

where  $k$  is the wave number,  $\kappa_x$  and  $\kappa_z$  are the coefficients of permeability of the bottom sediment layer in  $x$  and  $z$  directions,  $\delta_b'$  is the thickness of the bottom sediment layer and  $H$  is the wave height at the water depth  $h$ .

For  $\mu_s$  in Eq.(4), the authors use the following relation proposed by Eilers(1941):

$$\mu_s/\mu = (1 + (2.5C_b/2(1 - 1.35C_b)))^2 \tag{6}$$

It is said that this relation remains valid for the wide range of  $C_b$ .

Boundary conditions are given as follows:

$$\begin{aligned} \text{at } z^* = \infty \quad U_f &= U_{f0} = \widehat{U}_{f0} \exp(i(kx - \sigma t)) \\ \text{at } z^* = 0 \quad U_f &= U_{sb} \\ &\text{and} \\ \mu(\partial U_f / \partial z^*) &= \mu_s(\partial U_{sb} / \partial z^*) \\ \text{at } z^* = -\delta_b \quad U_{sb} &= 0 \end{aligned} \tag{7}$$

$\delta_b$  in Eq.(7) is the thickness of the bed load layer and is determined as the largest integer  $\delta_b/d$ , i.e, the number of the bed load layer which satisfies the following inequality:

$$\mu_s(\partial U_{sb} / \partial z^*) \geq d(\rho_s - \rho)gC_b \tan\phi (\delta_b/d) \tag{8}$$

where  $\phi$  is the angle of repose of the bed material in water.

In the calculation, at first,  $\delta_b$  was assumed to be  $\delta_b'$  as a first approximation and the calculations were repeated until the boundary condition Eq.(7) and Eq.(8) were satisfied.

Fig.8 shows an example of calculated vertical distribution of  $U_{sb}$  as a function of the phase. The calculated conditions are also shown in the figure. The vertical distribution of the water-particle velocity obtained from an ordinarily laminar boundary layer equation under the boundary condition that at  $z^*=0$ ,  $U_f=0$ , that is,

$$\begin{aligned} U_f &= \widehat{U}_{f0}(\cos \sigma t - \exp(-\beta z^*) \cos(\sigma t - \beta z^*)) \\ \beta &= \sqrt{\sigma/2\nu} \end{aligned} \tag{9}$$

is also shown in the figure by dotted lines where  $\nu = \mu/\rho$ .

By comparing these two vertical profiles, it is found that the effect of the moving boundary remains in a so-called boundary layer ( $z^* = \sqrt{\nu T/\pi} \approx 0.2\text{mm}$ ). Further, the thickness of the bed load layer is also found to change within one wave cycle and it becomes only 1mm, in other words, only 3 layers move as a bed load at the maximum in the case shown in Fig.8.

Fig.9 shows the relation between the amplitude ratio  $\widehat{U}_{sb}/\widehat{U}_{f0}$  at the bottom surface ( $z^*=0$ ) and sediment concentration  $C_b$ . As can be seen from this figure,  $\widehat{U}_{sb}/\widehat{U}_{f0}$  decreases with increasing  $C_b$  and with decreasing Reynolds' number  $Re (= \widehat{U}_{f0}^2 T/\nu)$ . However, in the region where  $Re$  is larger than  $25 \times 10^4$ , the increase of  $\widehat{U}_{sb}/\widehat{U}_{f0}$  with increasing  $Re$  becomes less significant.

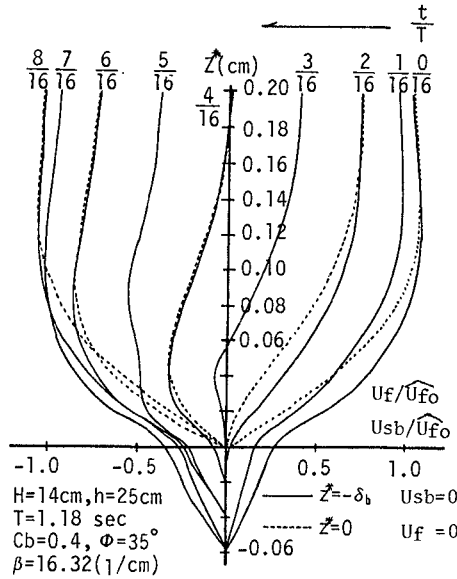


Fig.8 Vertical distribution of  $U_{sb}/\widehat{U}_{fo}$  and  $U_f/\widehat{U}_{fo}$

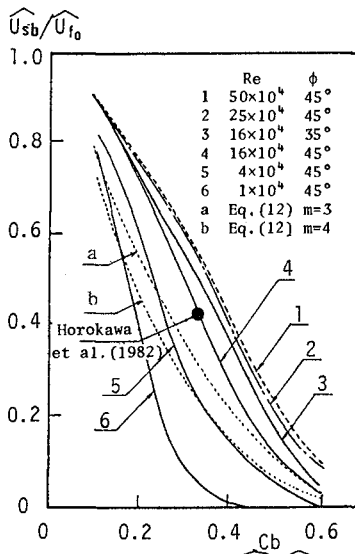


Fig.9 Relation between  $\widehat{U}_{sb}/\widehat{U}_{fo}$  and  $C_b$

An experimental result measured by Horikawa et al.(1982) under the sheet flow condition caused by the oscillatory flow is also shown in the figure. Although this value can not be directly compared with the calculated values, calculated results are judged to give a little larger value of  $\widehat{U}_{sb}/\widehat{U}_{fo}$  than the measured one when compared at the same  $Re$  and  $C_b$ .

However, the procedure to relate  $\widehat{U}_{sb}/\widehat{U}_{fo}$  to  $C_b$  mentioned above is little bit complicated to use in Eq.(1). Therefore, the authors tried to simplify this process. Bagnold(1956) derived the following relation between the drag coefficient  $f'$  of the sediment laden flow and sediment concentration  $C_b$ :

$$f'/f \propto (1 - C_b)^{-m} \quad , \quad m = 3 \text{ to } 4 \tag{10}$$

where  $f$  is the drag coefficient in the clear water defined by

$$f = \tau / (\rho U_f^2 / 2) \tag{11}$$

and  $\tau$  is the drag force acting on a particle and  $U_f$  is the velocity of the unidirectional flow. By using this relation, the ratio of the velocity of the particle in flow  $U_s$  and  $U_f$  can be expressed in term of only  $C_b$  as follow:

$$U_s/U_f = (1 - C_b)^{m/2} \tag{12}$$

However, in general, no sediment movement takes place when all particles in the bed layer are in static contact.  $C_b$  in the bed layer in this state corresponds to  $C_b=C_{max}=0.74$  for uniform spheres perfectly piled. Therefore, it seems reasonable to replace  $C_b$  in Eq.(12) with  $C_b/C_{max}$  as

$$U_s/U_f = (1 - C_b/C_{max})^{m/2} \tag{13}$$

Assuming that this relation holds in the case of sediment movement by waves,  $U_s/U_f$  calculated from Eq.(13) are also shown in Fig.9 for  $m=3$  and 4 by dotting lines. By comparing these with the results obtained from Eqs.(4) to (8), it is found that  $m$  in Eq.(13) depends on  $Re$  and  $m=3$  and 4 correspond to  $Re=16 \times 10^4$  and  $4 \times 10^4$  in the region where  $C_b$  is larger than 0.4. Therefore, in the calculation of Eq.(1), Eq.(13) is used as an approximation of Eqs.(4) to (8).

4. Calculation of the net rate of on-offshore sediment transport

4.1. Vertical distribution of the net sediment flux

In this section, the net rate of on-offshore sediment transport in four kinds of beach deformation processes(see Table 1) are calculated by using Eq.(1). In advance of the calculation of Eq.(1), the time averaged rate of local on-offshore sediment flux  $\overline{q}_f(z^*)$  defined by

$$\overline{q}_f(z^*) = \overline{U_s(z^*,t) C(z^*,t)} \tag{14}$$

was calculated. In this equation,  $U_s(z,t)$  was estimated from Eq.(13) in which  $U_{fo}(z^*,t)$  was calculated by using a linear wave theory,ie,

$$U_{fo} = \sqrt{g(h+\overline{\eta})} \frac{\eta(t) - \overline{\eta}}{h+\overline{\eta}} \tag{15}$$

where  $\overline{\eta}$  is the time averaged surface elevation and  $m$  in Eq.(13) was determined to be 4 for simplicity, although  $Re$  in the experiment ranged between  $10^4$  and  $5 \times 10^4$ . Because Eqs.(4) to (8) seems to overestimate  $U_{sb}/U_{fo}$ .

For  $C(z, t)$ ,  $\bar{C} + C_p$  calculated from the measured sediment concentration in the two-dimensional model beach experiments mentioned in § 2 within 3hrs. after waves began to incident.

Fig.10 shows some examples of the vertical distributions of  $\bar{q}_f(z)$  in the process of erosion type beach deformation. Concentration measuring points are again shown in Fig.10(a) together with beach profiles. As can be seen from Figs.10(b) and (c), in the offshore region, net bed load flux is in the direction of wave propagation (onshore direction) and net flux of suspended sediment is in the offshore direction. This means that the net rate of on-offshore sediment transport in these region is brought about by the difference of two large quantities, i.e. bed load in the onshore direction and suspended load in the opposite direction. While, in the surf zone shown in Figs.10(d), (e) and (f), both bed load and suspended load are in the offshore direction and suspended load apparently surpasses bed load.

Fig.11 shows the vertical distribution of  $\bar{q}_f(z)$  in the process of accretion type beach deformation. Beach profiles and concentration measuring points are shown in Fig.11(a). Being different from the case shown in Fig.10, there is no significant offshore suspended sediment transport throughout: the littoral zone and the maximum sediment flux appears on the bottom surface or in the bottom sediment layer. This means that in the process of accretion type beach deformation, onshore bed load transport is apparently surpasses offshore suspended sediment transport.

In the transition type beach deformations, it is found that there exist two regions, one is the region where onshore bed load transport surpasses and the other is the region where offshore suspended sediment transport surpasses.

As reported by the authors previously (Sawaragi et al. (1980)), whether bed load surpasses suspended load or not at an arbitrary point on a beach can be determined by the ratio of shear velocity  $U^*$  and settling velocity of sediment in still water  $w_0$ . That is, in the region where  $U^*/w_0$  is smaller than 1, onshore bed load transport surpasses offshore suspended load and in the region where  $U^*/w_0$  is larger than 1, suspended load becomes dominant. In which,  $U^*$  is defined by  $\sqrt{fUf_0^2/2}$  and  $f$  is estimated from Jonsson's formula (Jonsson (1980)) assuming that the roughness height is equal to the sediment diameter  $d$ . This criterion is reconfirmed by the present experiments.

#### 4.2 Calculation of the net rate of on-offshore sediment transport

Figs.12 and 13 show the comparisons of the net rate of on-offshore sediment transport  $\bar{q}_f$  obtained by integrating  $\bar{q}_f(z)$  shown in Figs.10 and 11 vertically with  $\bar{q}_h$  calculated from the measured change of water depth. In the integration,  $\bar{q}_f(z)$  was approximated by the dotted lines drawn in the figures.

As can be seen from these figures,  $\bar{q}_f$  calculated from the measured sediment concentration agrees with  $\bar{q}_h$  calculated from the change of water depth. Judging from these, the proposed procedure to calculate the net rate of on-offshore sediment transport provides a good estimate if only the time and spatial variations of sediment concentration and

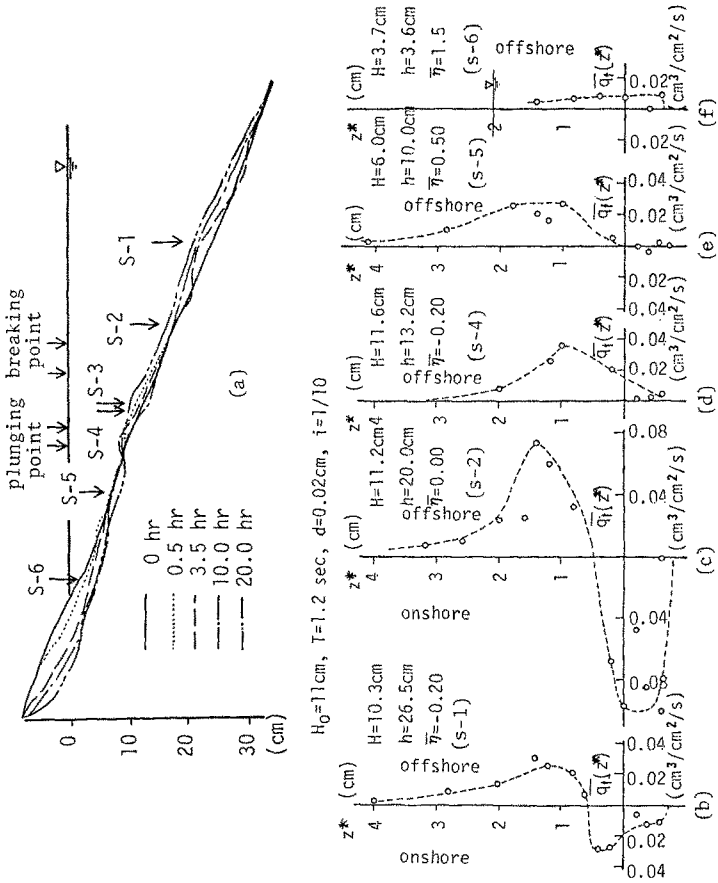


Fig.10 Vertical distribution of sediment flux  
(erosion type beach deformation)



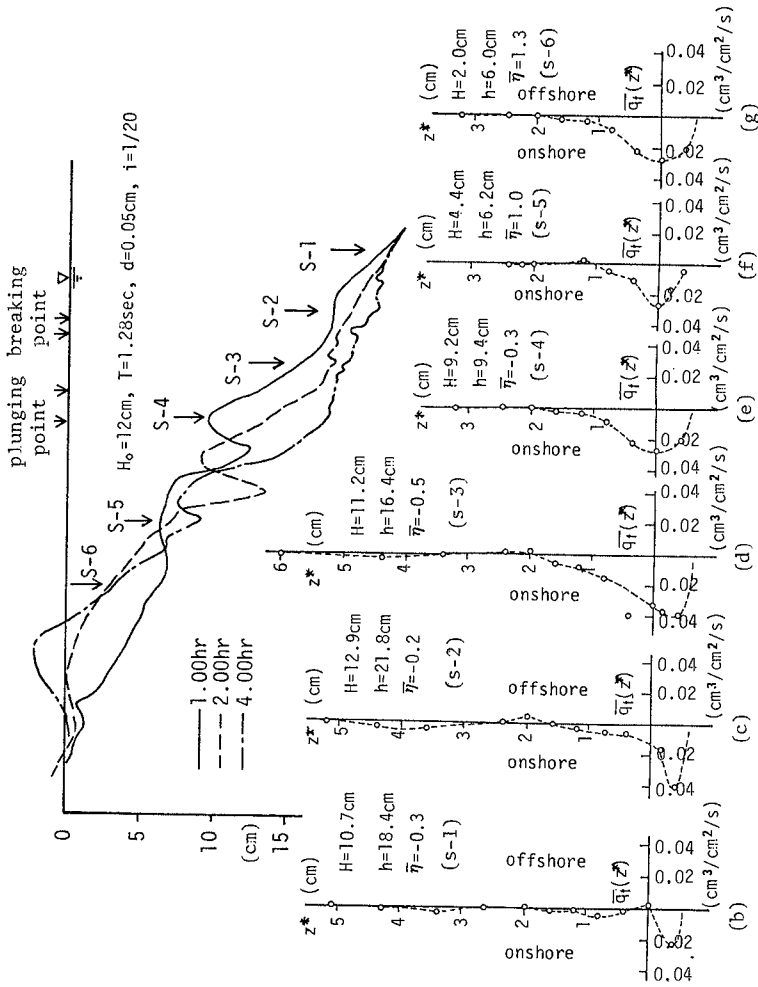


Fig.11 Vertical distribution of sediment flux (accretion type beach deformation)

water-particle velocity are known.

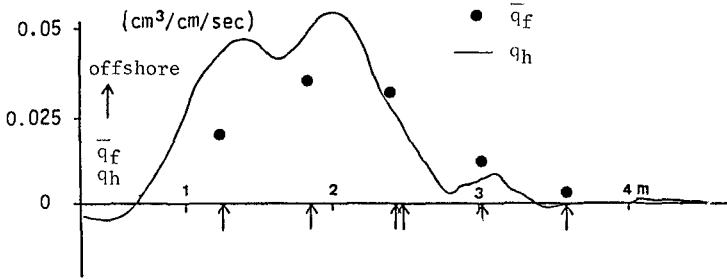


Fig.12 On-offshore sediment transport rate (erosion type beach deformation)

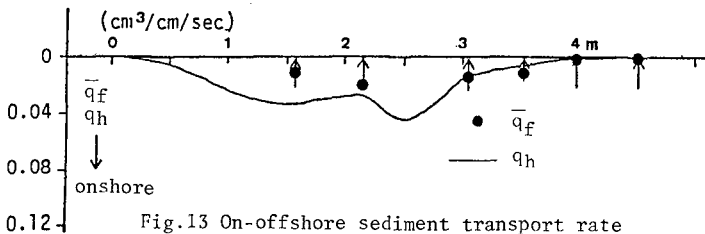


Fig.13 On-offshore sediment transport rate (accretion type beach deformation)

4.2. Attenuation of the net rate of on-offshore sediment transport

It is well known that the net rate of on-offshore sediment transport in the two-dimensional model beach deformation process decreases exponentially with increasing wave running time (Sawaragi et al. (1980)). There seems to exist three mechanisms of this decay of net on-offshore sediment transport. One is the decay of an agitational force of the fluid acting on the bottom sediment as a result of the interaction between the beach deformation and wave deformation. In this case, time averaged sediment concentration decreases with increasing wave running time inevitably. However, time averaged concentration did not change its magnitude and vertical profile in our experiments.

Another two mechanisms are as follows:

- 1) net onshore sediment transport by bed load decreases owing to the change of local bottom profile and consequently, the net offshore sediment transport in suspension decreases with increasing wave running time,
- 2) net rate of onshore bed load transport and net rate of offshore suspended sediment transport become the same, that is, the closed loop is attained between bed load and suspended load.

Fig.14 shows the comparison of  $q_{f0.5-1.5}$  with  $q_{f20-21}$  which are calculated from the measured sediment concentration during 0.5 and 1.5hrs. and during 20 and 21hrs. after waves began to incident in the process of erosion type beach deformation.

At point s-6 in the surf zone shown in Fig.(d), the decrease of net on-offshore sediment transport seems to be brought about by the latter mechanism mentioned above in 2) and at another points, net on-offshore sediment transport rates appear to decay by the former mechanism mentioned above in 1).

However, further detailed investigations about the time and spatial variations of sediment concentration are required to quantitatively estimate the decay of the net rate of on-offshore sediment transport.

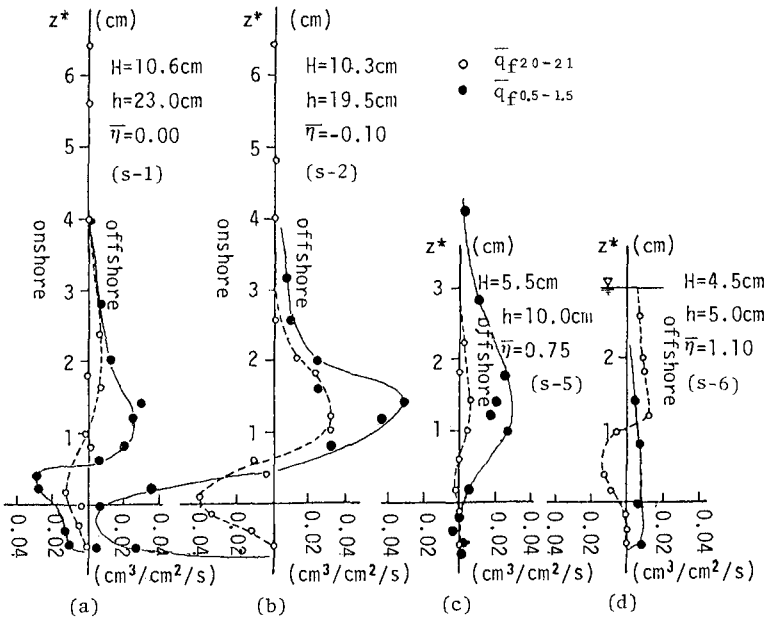


Fig.14 Decay of net on-offshore sediment transport (erosion type beach deformation)

## Concluding remarks

The net rate of on-offshore sediment transport was calculated on the basis of sediment flux by using the measured sediment concentration in two-dimensional model beach experiments and analyzed relation between water-particle velocity and the speed of sediment migration. The results coincide fairly well with the net rate of on-offshore sediment transport calculated from the change of water depth.

In that, interesting, though unverified at present, results about the velocity of the bed load layer and the thickness of the bed load layer are obtained. Some possible mechanisms which attenuate the net rate of on-offshore sediment transport are also pointed out.

The authors are proceeding further investigations about the water-particle velocity in the surfzone and the detailed mechanism of sediment movement to quantitatively predict the time and spatial variation of sediment concentration.

## References

- Bagnold, R.A. (1956) The flow of cohesionless grains in fluid: Proc. Roy. Soc., A, 964, Vol. 249, p. 235-297.
- Bakker, W.T. (1974) Sand concentration in an oscillatory flow: Proc. 14th ICCE, p. 1129-1148.
- Bijker, E.W. (1971) Longshore transport computations: Jour. Waterways, Harbor and Coastal Eng. Div., ASCE, p. 678-781.
- Eagleson, P.S., Dean, R.G. and Peralta, L.A. (1958) The mechanics of the motion of discrete spherical bottom sediment particles due to shoaling waves: Tech. Memo., No. 104, BEB.
- Einstein, H.A. (1972) A basic description of sediment transport on beaches: in Waves on beaches and resulting sediment transport, Academic Press, p. 53-95.
- Eilers, H. (1941) Die Viskosität von Emulsionen hochviskoser Stoffe als Funktion der Konzentrationen: Kolloid, Z., 97, p. 313.
- Hinze, J.O. (1959) Turbulence, McGraw-Hill.
- Horikawa, K., Watanabe, A. and Katori, S. (1982) Sediment transport under sheet flow condition: Abstract of 18th ICCE, p. 260-261.
- Kana, T.K. (1977) Suspended sediment transport at Price Inlet, S.C.: Proc. Coastal Sediment 77', ASCE.
- Madsen, O.S. and Grant, W.D. (1976) Quantitative description of sediment transport by waves: Proc. 15th ICCE, p. 1093-1112.
- Nakato, T., Locher, F.A., Glover, J.R. and Kennedy, J.F. (1977) Wave entrainment of sediment from ripple surface: Jour. Waterway Port Coastal and Ocean Div., ASCE, p. 81-99.
- Nielsen, P., Svendsen, I.A. and Staub, C. (1978) Onshore-offshore sediment movement on beaches: Proc. 16th ICCE, p. 1475-1492.
- Sawaragi, T. and Deguchi, I. (1980) On-offshore sediment transport rate in the surf zone: Proc. 17th ICCE, p. 1194-1214.
- Soong, T.T. (1973) Random differential equation in science and engineering: Academic Press.
- Walton, T.L. Jr. (1979) Littoral sand transport on beaches: Thesis Presented to the Univ. of Florida, Gainesville, in partial fulfillment of the requirement for the Degree of Ph.D.,

## CHAPTER NINETY TWO

### EXPERIMENTAL VERIFICATION OF SIMILARITY CRITERIA FOR EQUILIBRIUM BEACH PROFILES

Otávio S.F.J.Sayão<sup>1</sup>, M.ASCE and José Carlos Guimarães<sup>2</sup>

#### ABSTRACT

This paper presents an attempt towards the determination of the geometric distortion for beach mobile bed models. At first, a derivation of a scaling law for modelling equilibrium beach profiles is given, based on Valembois' (1961) work. Further, an experimental verification of some criteria presented in literature for the reproduction of beach profiles in coastal mobile bed models (e.g. Noda, 1971; Yalin, 1971 and Vellinga, 1982) is carried out, leading to a comparison with the criterion developed herewith.

Model experiments were undertaken in a two-dimensional wave flume with regular waves in an attempt to verify the validity of the four similarity criteria for the reproduction of beach profiles.

For fine sand as model material, the experimental results proved valid the modified criterion based on Valembois (1961), among all criteria used. The use of this similarity criterion showed that the beach profiles were correctly reproduced in the model.

The use of cellulose acetate as model material did not give good results, and none of the similarity criteria used were verified. The use of this lightweight material should be avoided for modelling beach processes.

Further testing with finer sand is recommended to analyse the influence of the dimensionless fall time parameter (Dean, 1973) and to confirm its use for the prediction of equilibrium beach profiles.

#### INTRODUCTION

Wave sediment transport in the nearshore zone is an important factor in the achievement of engineering solutions

---

<sup>1</sup> Associate Professor of Ocean Engineering, COPPE/UFRJ, Universidade Federal do Rio de Janeiro, Brazil; Post Doctoral Fellow, Dept. of Civil Engrg., Queen's University, Kingston, Canada.

<sup>2</sup> Engineer, CODESA, Companhia Docas do Estado do Espírito Santo, ES; Brazil. Formerly, Research Engr., INPH/PORTOBRÁS, Empresa de Portos do Brasil S.A., RJ, Brazil.

to beach erosion problems. The determination of sediment transport rates along the shore and on-offshore is a subject of continuing research efforts all over the world. Usually, these studies are developed with the aid of Coastal mobile bed models. Of particular interest is the study of beach profiles, its formation due to wave action and its equilibrium form.

A beach profile is shaped depending on the interaction of the waves and the beach material. It has been reported in literature that the beach reaches an 'equilibrium profile', defined as a beach profile which maintains its geometrical form in time, see for instance, Eagleson et al (1963), Wiegél (1964), Nayak (1970), and Swart (1974).

A coastal mobile bed model is necessarily distorted. The actual value of this distortion is imposed by the model grain size, i.e. cannot be freely chosen. Bijker (1967) stated that the mobile bed model distortion should be equal to the ratio between the equilibrium beach slopes in the model and prototype. This was later endorsed by Fan and Le Méhauté (1969) and Kamphuis (1975).

Hence, it is common practice in littoral transport model investigations to select the model distortion by conducting preliminary flume tests to determine the equilibrium beach slope of different sand grain sizes under the action of the scaled down waves.

#### SCALE DEFINITIONS

For the rectangular coordinate system, the general model scale  $n$  is given by the vertical scale value

$$n = n_z \quad (1)$$

where the scale  $n$  is defined as the ratio of prototype value over the model value.

In an undistorted small scale hydraulic model all geometric scales are the same. In a geometrically distorted model, the two horizontal scales  $n_x$  and  $n_y$  are identical but differ from the vertical scale  $n_z$ . The geometric model distortion  $N$  may thus be defined as

$$N = \frac{n_x}{n_z} = \frac{n_y}{n_z} \quad (2)$$

A beach slope  $m$  may be defined by the ratio between a characteristic depth at the surf zone and a horizontal distance perpendicular to the beach. If, for instance, the depth of water at the breaking point  $d_b$  is taken as a characteristic depth, then the beach slope becomes

$$m = \frac{d_b}{\lambda_b} \quad (3)$$

where  $\lambda_b$  is the breaker distance, measured horizontally between the breaking point and the shoreline.

The model distortion may be written according to its definition as

$$N = \frac{m_m}{m_p} \quad (4)$$

where  $m_m$  is the model equilibrium beach slope and  $m_p$  is the prototype beach profile. The scale of the beach profile is then given as

$$n_m = \frac{m_p}{m_m} = N^{-1} \quad (5)$$

or

$$\left(\frac{d_b}{\lambda_b}\right)_m = N \left(\frac{d_b}{\lambda_b}\right)_p \quad (6)$$

As  $N > 1$  by definition, then it is clear that the beach profile in the model is steeper than the prototype one, i.e. exaggerated by a factor equal to the model distortion.

#### REVIEW OF PREVIOUS SCALING LAWS

Scaling laws for modelling equilibrium beach profiles have been previously proposed in literature. A review of some published similarity criteria is presented herewith.

Valembois (1961)

Both Valembois (1961) and Goddet and Jaffry (1960) have put forward similarity criteria that include in their expression a distortion of the wave height, which is not reasonable for modelling beach processes. Their work have been discussed in detail in Paul (1972) and Kamphuis (1975).

Valembois (1961) also presented a theoretical derivation of the geometric distortion for beach models based on the mechanism of bed material suspension by wave breaking. For the correct reproduction of equilibrium beach profiles, he stated that similarity of the following ratio is required:

$$\frac{\text{fall velocity/depth}}{\text{mass transport velocity/horizontal distance}} \quad (7)$$

This concept for similarity of Eq.(7) was further developed by Guimarães (1983) and will be discussed in a later chapter.

Noda (1971)

With the work of Fan and Le Méhauté (1969) as a basis,

Noda (1971) has conducted wave flume beach experiments, to find scaling laws on beach profile formation by breaking waves. Sand and several lightweight material were used as model material. Based on the experimental results, Noda (1971) proposed the following similarity criteria

$$n_D \cdot n_{(\gamma_s/\gamma)}^{1.46} = n_z^{0.55} \quad (8)$$

and

$$n_x = n_z^{1.32} n_{(\gamma_s/\gamma)}^{-0.35} \quad (9)$$

where  $n_D$  is the scale of the sediment grain size,  $n_{(\gamma_s/\gamma)}$  is the scale of the relative submerged unit weight of sediment, where

$$\gamma_s = (\rho_s - \rho) g \quad (10)$$

is the underwater unit weight of sediment.

Yalin (1971)

Based on dimensional analysis for sediment transport under the combined influence of short waves, long waves and unidirectional flow, Yalin (1971) developed expressions for nine dimensionless variables controlling bed phenomena for such flow regimes. These may be regarded as criteria for similarity. He also illustrates that similarity of only two out of the nine dimensionless variables proposed can be maintained for practical model design.

For the same fluid in model and prototype and considering unidirectional flow experimental data, Yalin (1971) proposed the following relationship

$$n_x = n_z^{3/2} \quad (11)$$

which may be written as

$$N = n_z^{1/2} \quad (12)$$

and agrees with the regime theory recommendation. Eq.(12) may also be found in Le Méhauté (1970), which derived it in a different manner, when studying similarity of sediment motion for littoral transport models, for sand models with prototype material only. Yalin (1971) suggests that Eq.(12) holds for tidal flow models rather than beach models.

Vellinga (1978, 1982)

Beach and dune erosion during storm surges have been



studied by Vellinga (1978; 1982) based on two-dimensional model experiments. Only fine sand of different grain sizes was used as model material. He considered the importance of the dimensionless fall time parameter  $P$  (Dean, 1973) for the reproduction of beach profiles, where

$$P = \frac{H}{wT} \quad (13)$$

and  $w$  is the fall velocity of the sand grains;  $H$  is the wave height and  $T$  is the wave period.

Vellinga (1978; 1982) proposed the following scaling relationships

$$\frac{n_x}{n_z} = \left( \frac{n_z}{n_w^2} \right)^\alpha \quad (14)$$

and

$$n_t = n_z^{1/2} \quad (15)$$

where the wave conditions were scaled down according to the Froude condition

$$n_H = n_T^2 = n_z \quad (16)$$

$n_w$  is the scale of the fall velocity of the sand grains  $n_H$  is the wave height scale,  $n_T$  is the wave period scale and  $n_t$  is the time scale for hydrodynamical and morphological process.

The empirical coefficient  $\alpha$  was found earlier (Vellinga, 1978) to vary with sand grain size, ranging from 0.5 to 0.3 with  $\alpha = 0.5$  recommended for very fine sand of  $D_{50}$  of the order of 0.1 mm. In a re-analysis of the data, Vellinga (1982) concluded that it should be taken as constant and equal to  $\alpha = 0.28$ . Hence, Eq.(14) becomes

$$\frac{n_x}{n_z} = \left( \frac{n_z}{n_w^2} \right)^{0.28} \quad (17)$$

Vellinga (1982) has compared his scaling law with data from three-dimensional model tests, from large-scale two-dimensional tests with irregular waves up to significant wave heights of 2 m, and from field experiments, and Eq.(17) was favorably verified. Also, a computer model for the prediction of dune erosion was developed, see Vellinga (1983).

#### DERIVATION OF A SIMILARITY CRITERION

The derivation of a scaling law for modelling equilibrium beach profiles is based on Valembois' (1961) work which was

further developed by Guimarães (1983).

Valembois' (1961) expression, see Eq.(7), must be made equal in prototype and model. This requirement becomes

$$\frac{w_p/d_p}{U_p/\lambda_p} = \frac{w_m/d_m}{U_m/\lambda_m} \quad (18)$$

which leads to

$$\frac{d_p}{d_m} \cdot \frac{U_p}{U_m} = \frac{w_p}{w_m} \cdot \frac{\lambda_p}{\lambda_m} \quad (19)$$

yielding in terms of model scales (prototype value/model value) the following relation

$$n_z = \frac{n_w}{n_U} \cdot n_x \quad (20)$$

where  $n_z = n_d$  is the vertical scale and  $n_x = n_\lambda$  is the horizontal scale of the model. Also,  $n_w$  is the scale of the fall velocity of the grains and the scale of the mass transport velocity is  $n_U = U_p/U_m$ .

On the other hand, similarity of the Froude number in model and prototype gives

$$\frac{v_p}{v_m} = \left(\frac{d_p}{d_m}\right)^{1/2} \quad (21)$$

or

$$n_v = n_z^{1/2} \quad (22)$$

in which the scale of the horizontal velocity is  $N_v = v_p/v_m$ .

Considering  $n_U = n_v$ , substitution of Eq.(22) into Eq.(20) gives the following scaling law

$$n_z = (n_w \cdot n_x)^{2/3} \quad (23)$$

Valembois' similarity concept has been transformed into a similarity criterion, i.e. a scaling relationship, see Eq.(23). For a given prototype situation where the bed material is known and considering given the model material and the horizontal scale, which may be determined according to the prototype geometry and laboratory dimensions, the scaling law of Eq.(23) would permit to determine the correct vertical scale

of the model and thus the model distortion. For the particular situation where prototype sand is used in the model, Eq.(23) reduces to Eq.(11).

Le Méhauté (1970) proposed a kinematic similarity condition for both fluvial and coastal modelling

$$\frac{n_x}{n_z} = \frac{n_u}{n_w} \quad (24)$$

where  $n_u$  is the scale of the horizontal orbital velocity. Vellinga (1978) showed that Eq.(24) may be written as

$$\frac{n_x}{n_z} = \left( \frac{n_z}{n_w Z} \right)^{0.5} \quad (25)$$

and this expression for the model distortion, which is the same as Eq.(14) with  $\alpha = 0.5$ , gave good results for his experimental data with finer sands.

It may be seen that Eq.(23) and Eq.(25) are the same but where derived differently. Vellinga (1978) calls  $\alpha = 0.5$  the 'theoretical' value and in later work he proposes the use of  $\alpha = 0.28$  and Eq.(17) for a distortion relationship.

Another different derivation of the same Eq.(23) may be found in Hughes (1983) where the modelling law was proposed based on distortion of the morphological time scale, deviating from the Froude similarity criteria by a factor of  $N$ .

The physical significance of Eq.(23) may be reasoned as follows. Let  $t_s$  be the fall time of the sediment grain, in still water, from the water surface to the bed. Thus  $t_s = d/w$  and the scale of the fall time of the grains is

$$n_{t_s} = \frac{n_d}{n_w} = \frac{n_z}{n_w} \quad (26)$$

Let  $t$  be the time for wave propagation. Hence, in shallow water  $t = \lambda/C_{gr} = \lambda/C$  where  $C_{gr}$  is the celerity of the wave group and  $C$  is the wave celerity. The Froudian time scale for wave propagation is thus

$$n_t = \frac{n_\lambda}{n_C} = \frac{n_x}{n_z^{1/2}} \quad (27)$$

If Valembois' (1961) similarity concept is written as follows

$$\frac{n_w/n_d}{n_U/n_\lambda} = 1 \quad (28)$$

then, considering  $n_U = n_V$ , substitution of Eqs.(22), (26)

and (27) into Eq.(28) gives

$$n_t = n_{t_s} \quad (29)$$

which means that the scale of the fall time of the sediment grain in still water must be equal to the Froudian time scale for wave propagation, or in other words, the fall time of the sediment grains in the model must be reduced in the same proportion as the breaking wave propagation time.

#### EXPERIMENTAL PROCEDURE AND RESULTS

The proposed scaling law of Eq.(23) may be experimentally verified if model tests designed according to it give a good reproduction (in the model) of the prototype beach profiles. By good reproduction of the prototype profiles it is meant that the scale of the beach profiles should be given by Eq. (4) or Eq.(5), i.e, the model distortion is obtained when dividing model beach profile by prototype beach profile.

It is considered in this paper that the coastal mobile bed model is distorted, even though some researchers have proposed to develop model studies in geometrically undistorted coastal models based on the concept of equality of the dimensionless fall time parameter in model and prototype (Dalrymple and Thompson, 1976; Vellinga, 1982; Kamphuis, 1983) or of a similar parameter (Hallermeier, 1984).

Two-dimensional model tests were performed in a wave flume at INPH/PORTOBRÁS, Instituto de Pesquisas Hidroviárias, Empresa de Portos do Brasil S.A., Rio de Janeiro. Detailed information on the experimental equipment and procedure may be found in Guimarães (1983).

#### Sediment Characteristics

Two model bed materials were readily available for testing, fine sand, mined from Cabo Frio dunes, Rio de Janeiro, and cellulose acetate, a lightweight material commonly used for modelling in INPH/PORTOBRÁS.

Model beaches were formed with the two different bed materials (fine sand or cellulose acetate) and were submitted to different monochromatic wave climate. Model tests were run maintaining constant the horizontal scale, and for several vertical scales. The simulated prototype beach profile is composed of fine sand grains and is located in Sergipe State, northeast of Brazil, see Figure 1.

Two sand samples were collected in the field and analysed in the laboratory with the purpose of obtaining the necessary information on the prototype bed material. Table 1 gives the sediment characteristics for both model and prototype materials and Figure 2 gives the grain size distribution curves.

The prototype average beach slope was defined based on 12 shore-normal profiles spaced at 500m intervals, covering both the beaches north and south of the Sergipe river inlet, see Figure 1. For an appraisal of the beach profiles evolution, nautical charts of the region were used with surveys from 1970, 1976 and 1979. The average beach slope obtained was approximately 1/400. This value was considered constant and was used as the prototype equilibrium beach slope, i. e.  $m_p \approx 1/400 = 0.25\%$ .

#### Horizontal Scale Definition

The definition of the horizontal scale was based on the design of a three-dimensional mobile bed model of Sergipe river inlet, presently (1984) underway at INPH/PORTOBRÁS. This model study is related to future port expansions inside the Sergipe river, the inlet behaviour and the sedimentation of the access channel to be dredged through the offshore bar. It was considered that a 200m wide channel in the prototype should be reproduced with a model width of 0.40m, to permit measurements of the small scale parameters with the available equipment at INPH. These dimensions lead to a horizontal scale of  $n_x = n_y = 500$ .

#### Fall Velocity Scales Selection

The fall velocity of the sediment grains was obtained through laboratory measurements. A 2m long glass tube with 3cm diameter was used to measure the fall time of several small sized sediment samples, considering the grain size distribution curves. For each diameter the fall time was recorded 6 times and an average value was found, see Table 2. The distribution curves for the fall velocity were then found (percent finer versus fall velocity curves) for the different materials, see Figure 3, based on the measured data as a function of grain diameter and also on the grain size distribution curves.

Using Figure 3 it was possible to find the scales for the fall velocity of the sediment grains, calculating an average ratio for each given constant value of percent finer as follows

$$\frac{w_1}{w_{1m}} = \frac{w_2}{w_{2m}} = \dots = \frac{w_i}{w_{im}} = \text{constant} = n_w \quad (30)$$

For the model with sand material, the fall velocity scale was found to be  $n_w = 0.671$ . For lightweight material in the model,  $n_w = 1.449$ . These values are also shown in Table 3. It is interesting to note that these values include the effect of the grain size distribution curves and different scale factors would be obtained if median diameter values for the fall velocity would be used.

### Vertical Scales Selection

In order to define the vertical scales to run the model tests, a preliminar calculation was made for the similarity criteria of Noda (1971), Eq.(9), Yalin (1971), Eq.(11), Vellinga (1982), Eq.(17) and modified Valembois, Eq.(23). The results are presented in Table 3.

Based on the variation of vertical scales results shown in Table 3, the tests programme was defined with  $n_z = 40, 50, 75$  and 100 for sand models and with  $n_z = 50, 75$  and 100 for lightweight material. These would provide the experimental verification of the similarity criteria if good reproduction of beach profiles are obtained in the model.

### Wave Flume Tests and Results

A total of 69 tests were performed in the two-dimensional wave flume of INPH/PORTOBRÁS, of which 42 with sand in the model and 27 with cellulose acetate in the model.

The wave flume is 45.5m long and 0.80m wide at the test section. Initial water depth in the model was 1.05m and the mean sea level was adjusted in the flume according to each vertical scale. A glass window 6.0m long permitted observation of the beach profile development. Regular waves were generated by a flap-type wave paddle, 1.5m wide and 2.0m high. Waves were recorded by a resistance type wave probe located in the flume at a depth corresponding to  $\sim 20$ m in the prototype. A one-channel Watanabe recorder gave a permanent recording of the measured wave heights on chart paper. Wave periods were recorded with a digital stop-watch.

The prototype wave climate was reproduced in the model based on measurements presented and analysed in Motta (1965) and Bandeira (1972) Tables 4 and 5 show wave and sea level parameters for both model and prototype, according to the several vertical scales used.

Prior to the start of each test the beach profile was planed and compacted to a uniform slope, calculated with Eq.(4), which would reproduce in scale the prototype beach profile (see Table 5). At the beginning of each test an exaggerated model wave height was produced in the flume for some minutes, in order to form ripples everywhere on the sloping model beach ensuring that a turbulent boundary layer was formed in the model, as suggested by Motta (1967).

During each test the beach profile would develop itself with the continuous action of the regular waves. Equilibrium was reached after 30 hours of testing for sand as the model material. The lightweight model beaches would reach an equilibrium profile after 5 hours of continuous testing. These model times for profile development are in accordance with the ones reported by Paul (1972), which were 24 hours for sand and 6 hours for bakelite beach profiles.

The monitoring of the equilibrium beach profiles in the flume was

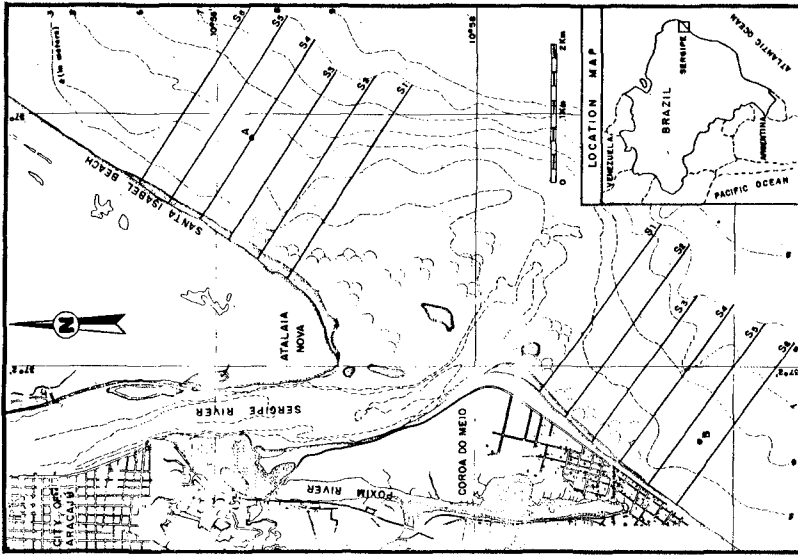


FIGURE 1 - LOCATION OF PROTOTYPE BEACH IN SERGIPE STATE, BRAZIL

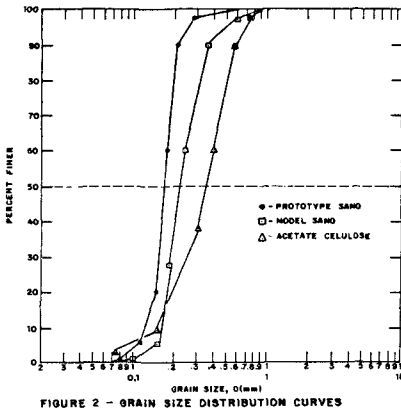


FIGURE 2 - GRAIN SIZE DISTRIBUTION CURVES

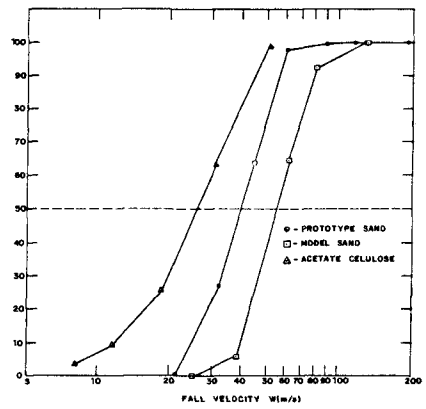


FIGURE 3 - FALL VELOCITY DISTRIBUTION CURVES

done visually after 20 hours of model testing for sand and 3 hours for cellulose acetate. Every beach profile was traced on the window of the flume and whenever no considerable changes would be detected with the continuation of the tests, the profile was then considered to be in equilibrium and the test stopped. An example of the model profile development is shown in Figure 4.

At the end of each test the flume was drained, as slowly as possible, and the beach profile coordinates were recorded through the glass window. Up to 58 depth measurements were taken every 10cm along the profile seawards from the berm crest of the beach. The model beach

TABLE 1. Sediment Characteristics for Model and Prototype

Sediment Characteristic	Prototype	Sand	Model	Sand	Celulose Acetate
$D_{50}$	0.17 mm	0.22 mm	0.22 mm	0.37 mm	0.37 mm
$\rho_s$	2630 kg/m <sup>3</sup>	2650 kg/m <sup>3</sup>	2650 kg/m <sup>3</sup>	1340 kg/m <sup>3</sup>	1340 kg/m <sup>3</sup>
$\gamma_s/\gamma$	1.558	1.65	1.65	0.34	0.34

Note: sea water density was taken as 1028 kg/m<sup>3</sup>.

TABLE 2. Fall Velocity Measured Data

Sediment Grain Size (mm)	Fall Velocity w (mm/s)		Calculated values of w (mm/s) SPM curves for 20°C (1)
	Prototype	Model	
0.074	21	25	8
0.149	32	39	12
0.250	61	62	19
0.420	90	83	31
0.840	120	133	51
2.0	190	-	290
$D_{50}$ (2)	40	59	27

(1) See U.S.Army Corps of Engineers (1977).

(2) Prototype sand  $D_{50} = 0.17$  mm; model sand  $D_{50} = 0.22$  mm; cellulose acetate  $D_{50} = 0.37$  mm; see Figures 2 and 3.

TABLE 5. Testing Data

$n_z$	N	$m_p$	$m_m(1)$	(MSL) P (2) (m)	(MSL) P (3) (cm)
40	12.5	1/400	1/32	+ 1.5	+ 3.75
50	10	1/400	1/40	+ 1.5	+ 3.0
75	6.67	1/400	1/60	+ 1.5	+ 2.0
100	5	1/400	1/80	+ 1.5	+ 1.5

- (1) Initial model beach slope, calculated with Eq.(4).
- (2) Above the zero reference level of the nautical charts.
- (3) Above the initial water depth at the model.

TABLE 3. Calculation of Vertical Scales according to Similarity Criteria

Similarity Criteria	Equation No.	$n_x$		$n_y/\gamma$		$n_w$		Vertical Scale $n_z$	
		SM	LWM	SM	LWM	SM	LWM	SM (1)	LWM (2)
Moda (1971)	Eq.(9)	500	0.944	4.583	-	-	-	100	165
Talin (1971)	Eq.(11)	500	-	-	0.671	1.449	63	63	63
Vellinga(1982)	Eq.(17)	500	-	-	0.671	1.449	108	108	108
This study	Eq.(23)	500	-	-	0.671	1.449	48	48	81

- (1) SM: Sand model
- (2) LWM: Lightweight model, with cellulose acetate
- (3) Eq.(17) was empirically developed for sand models only

TABLE 4. Wave Parameters

$n_z$	$T_p$		$T_m$		$R_p$ (m)	$R_m$ (cm)	
	(s)	(s)	(s)	(s)			
40	8	10	12	1.26	1.58	1.0	2.5
						1.5	3.75
						2.0	5.0
50	8	10	12	1.13	1.41	1.0	2.0
						1.5	3.0
						2.0	4.0
75	8	10	12	0.92	1.15	1.0	1.33
						1.5	2.0
						2.0	2.67
100	8	10	12	0.8	1.0	1.0	1.0
						1.5	1.5
						2.0	2.0



profile slope was defined as the best fit straight line through the experimental data.

The experimental results obtained during the tests are shown in Tables 6 and 7.

#### DISCUSSION

The model experiments were designed in accordance to the calculated vertical scales, see Tables 3 and 5. Given the values of  $n_z$  and knowing the prototype beach slope  $m_p$  for the selected horizontal scale  $n_x = 500$ , it is possible to calculate the beach slope to be expected to form in the model  $m'_m$ , using Eqs. (2) and (4) as follows

$$m'_m = m_p \cdot N = m_p \cdot \frac{n_x}{n_z} \quad (31)$$

From simple comparison of the values for  $m_p$  and  $m'_m$  (see Tables 6 and 7) it can be verified if the prototype beach profile  $m_p$  was well reproduced in the model.

#### Results with Lightweight Material

As it can be seen from Table 6, the use of cellulose acetate as model material did not give good results, and none of the similarity criteria used was verified.

For  $n_z = 50$  the results were very different than the calculated value. For  $n_z = 75$  the results did not depart so much from the calculated beach slope when the model wave height was small. This was due to the fact that not much sediment was moved by such small model waves and the measured profile would retain the influence of the initial beach slope. The same tendency was seen for the  $n_z = 100$  test results, as shown in Figure 5.

#### Results for the Sand Model

For fine sand as model material the experimental results for beach slope agreed well with the profile calculated values when the vertical scale tested was  $n_z = 50$ , see tests numbers 10 to 18 in Table 7. This vertical scale value ( $n_z = 50$ ) is approximately the same than the one calculated with Eq. (23), see Table 3.

Hence these experimental results proved valid the similarity criterion based on the work by Valembois (1961). The use of this scaling law Eq. (23) showed that the beach slopes were correctly reproduced in the model.

For  $n_z = 40$  the beach slope results presented in Table 7 (tests no. 1 to no. 9) did not depart much from the calculated value.

For  $n_z = 50$  and high waves in the model (tests no. 19 to no. 24) the measured beach slope values shown a deviation from the calculated one. This may be explained by the fact that the prototype beach profile was kept constant throughout the analysis and its value was taken from nautical charts which are based on calm weather site surveys, during the summer months.



FIGURE 4. Model Profile Development

When using Eqs. (9) and (17), the predicted values for the vertical scale are  $n_z = 100$  and  $n_z = 108$  respectively (see Table 3). For  $n_z = 75$  and  $n_z = 100$  the measured values for beach slope did not agree with the calculated values, see Table 7, tests no. 25 to no. 42. This seems to indicate that both Eqs. (9) and (17) do not give valid predictions for beach profiles when they are used as scaling laws.

If Eq. (11) is used, the predicted value for the vertical scale ( $n_z = 63$ ) falls between the tested values of  $n_z = 50$  and  $n_z = 75$  and it may be noticed that Eq. (23) is an improved version of Eq. (11) because it takes into account the influence of the fall velocity scale.



FIGURE 5. Test with Cellulose Acetate

Table 7. Experimental Results with Sand in the Model

Acetate in the Model				Model Measured Calculated			
Test No	Scale	Wave Height $H_m$ (cm)	Wave Period $T_m$ (s)	Beach Slope $m_m$ (%)	Beach (Expected)	Beach Slope*	$m_m$ (%)
1	2.0	1.41	1.80	2.5	1.33	3.16	3.16
2	50	3.0	1.41	3.40	1.41	1.80	2.5
3	50	3.0	1.70	2.69	1.70	3.71	3.71
4	50	3.0	1.13	3.18	1.13	3.18	3.18
5	50	3.0	1.41	3.40	1.41	3.40	2.5
6	50	3.0	1.70	2.69	1.70	2.69	2.69
7	50	4.0	1.41	4.65	1.13	6.76	6.76
8	50	4.0	1.41	4.65	1.41	4.65	2.5
9	50	4.0	1.70	3.69	1.70	3.69	3.69
10	75	1.3	1.15	1.68	0.92	1.77	1.67
11	75	1.3	1.15	1.68	1.3	1.77	1.67
12	75	2.0	1.15	1.95	1.39	1.10	1.67
13	75	2.0	1.15	1.95	1.15	1.95	1.67
14	75	2.0	1.15	1.95	1.39	1.03	1.67
15	75	2.7	1.15	2.76	1.15	2.76	1.67
16	75	2.7	1.15	2.76	1.39	1.65	1.67
17	75	2.7	1.15	2.76	1.15	2.76	1.67
18	100	1.0	1.0	0.96	0.8	1.19	1.25
19	100	1.0	1.0	0.96	1.0	1.14	1.25
20	100	1.5	1.0	0.76	0.8	1.16	1.25
21	100	1.5	1.0	0.76	1.2	1.03	1.25
22	100	2.0	1.0	1.46	1.0	1.59	1.25
23	100	2.0	1.0	1.46	1.2	1.66	1.25

$$* m_m^a = m_p \cdot \frac{r_k}{n_z}$$

Table 8. Fall Time Parameter for Sand

Test No	$n_z$	N	$P_m$	P	$n_p$
1	40	12.5	0.336	3.125	9.29
2	40	12.5	0.268	2.5	9.32
3	40	12.5	0.223	2.083	9.34
4	40	12.5	0.504	4.687	9.29
5	40	12.5	0.402	3.75	9.32
6	40	12.5	0.334	3.125	9.34
7	40	12.5	0.673	6.25	9.29
8	40	12.5	0.536	5.0	9.32
9	40	12.5	0.446	4.167	9.34
10	50	10	0.30	3.125	10.42
11	50	10	0.24	2.5	10.40
12	50	10	0.199	2.083	10.45
13	50	10	0.45	4.687	10.42
14	50	10	0.361	3.75	10.40
15	50	10	0.299	3.125	10.45
16	50	10	0.60	6.25	10.42
17	50	10	0.481	5.0	10.40
18	50	10	0.399	4.167	10.45
19	50	10	0.75	7.812	10.42
20	50	10	0.601	6.25	10.40
21	50	10	0.499	5.208	10.45
22	50	10	0.90	9.375	10.42
23	50	10	0.721	7.5	10.40
24	50	10	0.598	6.25	10.45
25	75	6.7	0.239	3.125	13.05
26	75	6.7	0.192	2.5	13.05
27	75	6.7	0.158	2.083	13.14
28	75	6.7	0.368	4.687	12.72
29	75	6.7	0.295	3.75	12.72
30	75	6.7	0.244	3.125	12.81
31	75	6.7	0.497	6.25	12.57
32	75	6.7	0.398	5.0	12.57
33	75	6.7	0.329	4.167	12.66
34	100	5	0.212	3.125	14.75
35	100	5	0.169	2.5	14.75
36	100	5	0.141	2.083	14.75
37	100	5	0.318	4.687	14.75
38	100	5	0.254	3.75	14.75
39	100	5	0.212	3.125	14.75
40	100	5	0.424	6.25	14.75
41	100	5	0.339	5.0	14.75
42	100	5	0.282	4.167	14.75

## Influence of the Fall Time Parameter

Sayão and Kamphuis (1983) have shown that the dimensionless fall time parameter (see Eq. 13) gives an indication of whether or not a shoreline is receding or progressing, being  $P \approx 1$  a critical value as shown in the Shore Protection Manual (US Army Corps of Engineers, 1977). For  $P > 1$  recession of the shoreline occurs, while for  $P < 1$  progression results.

Table 8 shows the values of the dimensionless fall time parameter for the tests where sand was used as model material. The scale of  $P$  is by definition given as

$$n_p = \frac{n_H}{n_w n_T} = \frac{n_z^{1/2}}{n_w} \quad (32)$$

and if Eq. (23) is used

$$n_p = \frac{n_x}{n_z} = N \quad (33)$$

and from Table 8, it is found that for tests with  $n_z = 50$  the values of  $n_p$  are approximately the same as the model distortion values.

It may be seen also from Table 8 that all  $P$ -values in the model are smaller than the critical value, whereas all prototype  $P$ -values are greater than the critical value. This indicates that there is a progressing beach in the model and a receding one in the prototype which will cause similarity problems if coastal sediment transport and coastal erosion are under investigation.

For almost all measurements of beach slope in the model it was noticed that the resulting type was a berm (summer) profile and the shoreline was progressing, as can be seen for example in Figure 4.

As the prototype values for the dimensionless fall time parameter are  $P > 1$ , the site beach should be a receding one. Bandeira (1972) has  $P$  calculated littoral drift along the Sergipe shoreline to be of the order of 800,000 cubic meters / year, with a southward direction. Hence, if the beach profiles are far enough south from the mouth of Sergipe river they would be expected to show a receding trend. No further conclusions could be made due to lack of measured prototype beach profiles.

## CONCLUSIONS AND RECOMMENDATIONS

The use of lightweight material cellulose acetate did not give good reproduction of beach profiles in the model, hence this material should not be used for modelling beach processes.

For fine sand as model material the experimental results proved valid the similarity criterion based on Valembois (1961), see Eq.(23), among all criteria used. The use of Eq. (23) showed that the beach profiles were correctly reproduced in the model, as far as beach slope is concerned.

The use of Eq.(23) means in fact that Vallinga (1982) coefficient is  $\alpha = 0.5$ , which also agrees with the theoretical value proposed by Le Méhauté (1970).

To design a model investigation of beach processes, where the fine sand grain size distribution curve to be used in the model is known, the vertical scale may be calculated with the aid of Eq.(23) and the scale of the fall velocity of the sand grains should be measured in the laboratory. It is to be noted the discrepancy between measured and calculated values of  $w$  (see Table 2).

To improve the data base of the present experiments further testing with finer sand (say  $D_{50} \approx 0.1\text{mm}$ ) would be required, so that the dimensionless fall time parameter in the model would be greater than the critical value. For further empirical research it is recommended that P-values for both model and prototype could be maintained in the same region, i.e., above or below the critical value. That may be sufficient, rather than preserving full similarity for the dimensionless fall time parameter between model and prototype as suggested by other researchers. Also, it would give more flexibility for model material selection.

#### ACKNOWLEDGEMENT

The authors respectfully acknowledge, in memoriam, the cooperation of Professor Victor F. Motta (1931-1982).

#### REFERENCES

- Bandeira J V (1972): "Estimativa do Transporte Litoraneo em torno da Embocadura do Rio Sergipe"; M.Sc. thesis, Federal University of Minas Gerais, Brazil, November.
- Bijker E W (1967): "Some Considerations about Scales for Coastal Models with Movable Bed"; Delft Hydraulics Laboratory, Publication No. 50, November.
- Dalrymple R A and Thompson W W (1967): "Study of Equilibrium Beach Profiles"; Proc. XV Coastal Engineering Conference, Honolulu, Hawaii, USA, ASCE, pp.1277-1296.
- Dean R G (1973): "Heuristic Models of Sand Transport in the Surf Zone" ; Proc. 1st Australian Conference on Coastal Engineering, Sydney, Australia, pp.208-214.
- Eagleson P S, Glenne B and Dracup J A (1963): "Equilibrium Characteristics of Sand Beaches"; Journal of the Hydraulics Division, ASCE, Vol. 89, HY1, pp.35-57.
- Fan L N and Le Méhauté B (1969): "Coastal Movable Bed Model Technology" ; Tetra Tech Inc., Report No. TC-131.
- Goddet J and Jaffry P (1960): "La Similitude des Transports de Sédiments sous l'Action Simultanée de la Houle et des Courants"; La Houille Blanche No.2, pp.136-147.
- Guimarães J C (1983): "Perfis de Equilibrio de Praia, Determinação de Escalas Verticais"; M.Sc. thesis, COPPE/UFRJ, Federal University of Rio de Janeiro, Brazil, May.
- Hallermeier R J (1984): "Wave Cuts in Sand Slopes applied to Coastal Models"; Journal of Waterway, Port, Coastal and Ocean Engineering,

- ASCE, Vol.110, No.1, pp.34-49, February.
- Hughes S A (1983):"Movable Bed Modelling Law for Coastal Dune Erosion"; Journal of Waterway, Port, Coastal and Ocean Engineering, ASCE, Vol. 109, No.2, pp.164-179, May.
- Kamphuis J W (1975):"The Coastal Mobile Bed Model"; C.E. Research Report No.75, Dept. of Civil Engrg., Queen's University, Kingston, Canada.
- Kamphuis J W (1983):"Preliminary Discussion of Scale Effects Tests on Large Coastal Mobile Bed Models"; Proc. Canadian Coastal Conference 1983, Vancouver, BC, pp.237-251, May.
- Le Méhauté B (1970):"Comparison of Fluvial and Coastal Similitude";Proc. XII Coastal Engrg. Conference, Washington, USA, ASCE, pp.1077-1096.
- Motta V F (1965):"Projeto de Estudos na Natureza e em Modelo Reduzido para a Manutenção do Canal de Acesso através da Barra de Aracaju"; Final Report of the Instituto de Pesquisas Hidráulicas, Federal University of Rio Grande do Sul, presented to Petrobrás Oil Company.
- Motta V F (1967):"O Estudo em Modelo Reduzido para a Regularização da Embocadura Lagunar de Tramandaí"; Proc. II Congresso Brasileiro de Transportes Marítimos, SOBENA, Rio de Janeiro, Brazil, September.
- Nayak I V (1970):"Equilibrium Profiles of Model Beaches"; Technical Report HEL-2-25, University of California, Berkeley, USA, May.
- Noda E K (1971):"Coastal Movable-bed Scale-model Relationship"; Tetra Tech Inc., Final Report No.P-71-191-1, March.
- Paul M J (1972):"Similarity of Bed Evolution and Sediment Transport in Mobile Bed Coastal Models"; Ph.D thesis, Queen's University, Canada.
- Sayão O S F J and Kamphuis J W (1983):"Breaking Waves on a Movable Bed Model"; Proc. International Conference on Coastal and Port Engrg. in Developing Countries, Colombo, Sri Lanka, Vol.1, pp.74-88, March.
- Swart D H (1974):"Offshore Sediment Transport and Equilibrium Beach Profiles"; Delft Hydraulics Laboratory, Publication No.131.
- US Army Corps of Engineers (1977):"Shore Protection Manual"; Coastal Engineering Research Centre, 3rd Edition, Washington.
- Valembois J (1961):"Estude Sur Modele Du Transport Littoral, Condictions de Similitude"; Proc. VII Coastal Engineering Conference, The Hague, The Netherlands, ASCE, pp.277-307.
- Vellinga P (1978):"Movable Bed Model Tests on Dune Erosion"; Proc. XVI Coastal Engrg. Conference, Hamburg, West Germany, ASCE, pp.2020-2039.
- Vellinga P (1982):"Beach and Dune Erosion during Storm Surges"; Coastal Engineering, Vol.6, pp.361-387, Elsevier.
- Vellinga P (1983):"Predictive Computacional Model for Beach Dune Erosion during Storm Surges"; Proc. Coastal Structures Conference, Arlington, Virginia, ASCE, pp.806-819, March.
- Wiegel R L (1964):"Oceanographical Engineering"; Prentice-Hall Inc.,USA.
- Yalin M S (1971):"Theory of Hydraulic Models"; MacMillan Press, London.

## CHAPTER NINETY THREE

### Stability of Multiple Inlets

Jacobus van de Kreeke\*

#### Abstract

A computational framework is presented to evaluate the stability of two inlets connecting the same bay to the ocean. It is assumed that both inlets are scoured in alluvial material. The main ingredients in the stability analysis are the closure surface and the equilibrium stress surface. The closure surface of an inlet is defined as the relation between the tidal maximum of the bottom stress and the cross-sectional areas of both inlets. The equilibrium stress surface of an inlet is the relation between the tidal maximum of the bottom stress and the cross-sectional area of that inlet at the time the inlet is in equilibrium with its hydraulic environment. The method is applied to Pass Cavallo and the entrance to the Matagorda Shipping channel further referred to as Matagorda Inlet. Both inlets connect Matagorda bay to the Gulf of Mexico.

#### Introduction

Over a period of decades, many inlets exhibit a change in morphology. These changes are often caused by a gradual increase in length resulting from the deposition of sediment at the ocean-and bay side of the inlet. This in turn leads to a gradual decrease in conveyance and cross-sectional area. Superimposed on this trend are sudden changes in inlet dimensions associated with storms, changes in bay surface area (diking) and the opening or closure of companion inlets. The inlet will respond to these sudden changes by either closing or returning to the old or a new equilibrium morphology. The time for the inlet to adapt depends on whether the inlet is in a shoaling or scouring mode. When in a shoaling mode, the response time depends on the supply of sediment, i.e. the littoral drift, and could vary from weeks to years. On the contrary when in a scouring mode the response time will be short, i.e. less than a few weeks.

If as a result of a sudden change in inlet dimensions or hydraulic conditions the inlet tends to close, the inlet is said to be unstable. If instead the inlet returns to the original or a new equilibrium morphology, the inlet is said to be stable. The

---

\* Professor, Division of Ocean Engineering, RSMAS, University of Miami, 4600 Rickenbacker Causeway, Miami, Florida 33149

extent to which the inlet dimensions or the hydraulic environment can be altered before the inlet tends to close determines the degree of stability of the inlet.

In general stability analysis of inlets deal with the response of an inlet to 1) sudden changes in its dimensions resulting from storms, 2) a reduction in bay surface area and 3) the opening of a companion inlet, either by dredging or extreme events. In this paper, emphasis is on the response of an inlet to the opening of a companion inlet.

The stability analysis as presented in this paper basically deals with the conveyance of an inlet. Therefore the analysis does not yield a definite answer with regard to the navigability of the inlet. For this, more detailed information on cross-sectional areas and depths along the entire channel axis is needed.

Inlet Hydraulics; Closure Curve and-Surface

In analysing the stability, inlets are schematised to prismatic channels. The channel has a cross-sectional area A, (usually taken equal to the cross-sectional area of the gorge), a hydraulic radius R, a length L and a friction coefficient F. The sum of exit and entrance losses are represented by a coefficient m. A coefficient  $\mu$  is introduced to account for contraction of the flow. In terms of the foregoing parameters the cross-sectionally averaged velocity, u in the inlet follows from

$$u = \pm K' \sqrt{2g|\eta_o - \eta_b|} \tag{1}$$

$$\text{with } K' = \mu \sqrt{\frac{R}{mR + 2FL}}$$

In Eq. (1)  $\eta_o$  is the ocean tide and  $\eta_b$  is the bay tide. For a given head difference  $|\eta_o - \eta_b|$ , inlets with the same K' factor have the same current speed.

The bottom shear stress,  $\tau$ , in the inlet is related to the cross-sectionally averaged velocity by

$$\tau = \rho F u |u| \tag{2}$$

in which  $\rho$  is the density of water. In this paper, the friction factor F is related to the hydraulic radius and bottom roughness k by the Colebrook-White expression

$$F = g \left[ 18 \log \frac{12R}{k} \right]^{-2} \tag{3}$$

When considering a relatively short and deep bay connected to the ocean by more than one inlet the condition of continuity may be expressed as



$$\sum Q_i = A_b \frac{d\eta_b}{dt} \tag{4}$$

in which Q is the rate of flow in the inlet,  $A_b$  is the bay surface area and the summation is over the number of inlets.

For a given ocean tide, bay surface area and shape of the cross-section and using Eqs. (1)-(4) it can be shown that for a single inlet bay system the tidal maximum of the bottom shear stress  $\hat{\tau}$ , is a strong function of A and a weak function of L, k and m.

$$\hat{\tau} = \hat{\tau}(A; L, k, m) \tag{5}$$

Here it is assumed that the hydraulic radius R is uniquely determined by the cross-sectional area A. The general shape of the closure curve  $\hat{\tau} = \hat{\tau}(A)$  is indicated in Fig. 1. For small values of A,  $\hat{\tau} \propto A$  and for large values of A,  $\hat{\tau} \propto A^{-2}$ .

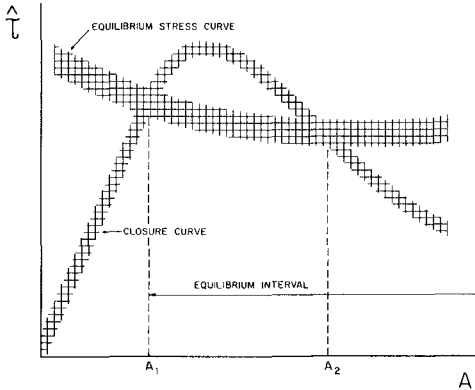


Fig. 1 Closure curve and equilibrium stress curve

For a two inlet bay system

$$\hat{\tau}_I = \hat{\tau}_I[A_I, A_{II}; L_I, F_I, m_I, L_{II}, F_{II}, m_{II}] \tag{6}$$

$$\hat{\tau}_{II} = \hat{\tau}_{II}[A_I, A_{II}; L_I, F_I, m_I, L_{II}, F_{II}, m_{II}] \tag{7}$$

The subscripts I and II refer to the respective inlets. The general shape of the closure surface  $\hat{\tau}_{II} = \hat{\tau}_{II}(A_I, A_{II})$  is indicated in Fig. 2.

In practice, difficulties in calculating the closure curves and closure surfaces might be encountered because of the uncertainties in the values of the inlet lengths, the bottom roughness and the energy loss coefficients.

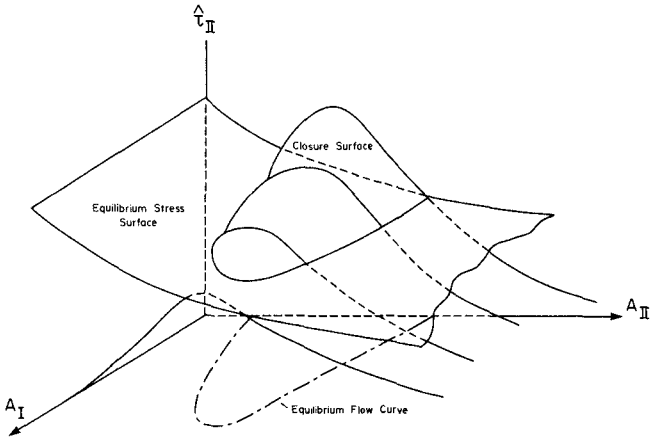


Fig. 2 Closure surface and equilibrium stress surface

The Equilibrium Bottom Shear Stress; Equilibrium Shear Stress Curve and - Surface.

It is postulated that inlets in alluvial material will adjust their dimensions until a bottom shear stress  $\hat{\tau}_{eq}$  is reached, Bruun [1978]. In general  $\hat{\tau}_{eq}$ , referred to as the equilibrium shear stress, will be a function of the littoral drift, wave climate and the dimensions of the inlet cross-section.

In principle for a given coast, and assuming that the littoral drift and wave climate are relatively uniform, the relation between equilibrium shear stress and inlet dimensions can be derived from the tidal prism-cross-sectional area relationships given by among others O'Brien [1969] and Jarrett [1976]. Unfortunately the correlation functions used to derive these relationships lack a physical basis and especially for the region of interest, i.e. the Gulf of Mexico coast, show considerable scatter. Therefore in the application to Pass Cavallo and Matagorda Inlet rather than making use of the tidal prism-area relationships, the value of  $\hat{\tau}_{eq}$  will be determined from the observation that in 1959 Pass Cavallo and in 1971-1972 Matagorda Inlet was in equilibrium with the hydraulic environment.

In a qualitative sense the shape of the equilibrium shear stress curve (pertaining to a one-inlet bay system) and the equilibrium shear stress surface (pertaining to a two-inlet bay system) are presented in respectively Figs. 1 and 2.

### Stability of a Single-Inlet Bay System

Referring to Fig. 1, a condition for the existence of an equilibrium flow area is that the closure curve and equilibrium stress curve intersect. The cross-sectional area  $A_1$ , represents an unstable inlet. The cross-sectional area  $A_2$  pertains to a stable equilibrium flow area. The equilibrium interval of  $A_2$  extends from the value of  $A_1$  to infinity, Escoffier [1940].

### Stability of a Two-Inlet Bay System

To delineate the stability of a two inlet-bay system, for each of the inlets the intersection of its closure surface and equilibrium stress surface is projected in the  $A_I, A_{II}$  plane; see Fig. 3. These curves are referred to as equilibrium flow curves. The equilibrium flow curve for inlet I is the loci of the set of values  $(A_I, A_{II})$  for which  $\tau_I = \tau_{eqI}$  and similarly for inlet II. The enhanced part of the equilibrium flow curves represent stable equilibrium flow areas. Therefore a condition for the simultaneous existence of stable equilibrium flow areas for both inlets is that the enhanced parts of the equilibrium flow curves intersect. In that case the cross-hatched area represents the equilibrium interval. If the actual values of the inlet cross-sections  $(A_I, A_{II})$  are outside the equilibrium interval, one or both inlets will close. For details on the stability of a two-inlet bay system, see van de Kreeke [1985].

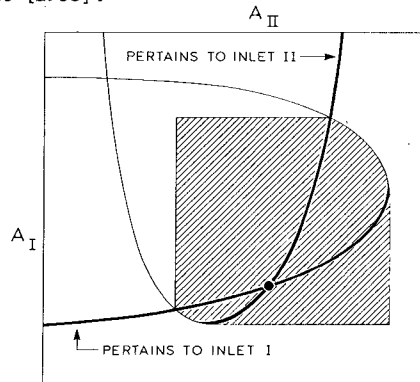


Fig. 3 Equilibrium flow curves for Inlets I and II

### Application to Pass Cavallo and Matagorda Inlet, Texas

The data used in this section is derived from Ward [1982], [1983] and Bruun, [1983]. Until 1963 Pass Cavallo was the only inlet connecting Matagorda Bay and the Gulf of Mexico. A second inlet was added in 1963; this inlet constitutes the entrance to the Matagorda shipping channel. For the location of the inlets and a plan view of the bay, see Fig. 4.

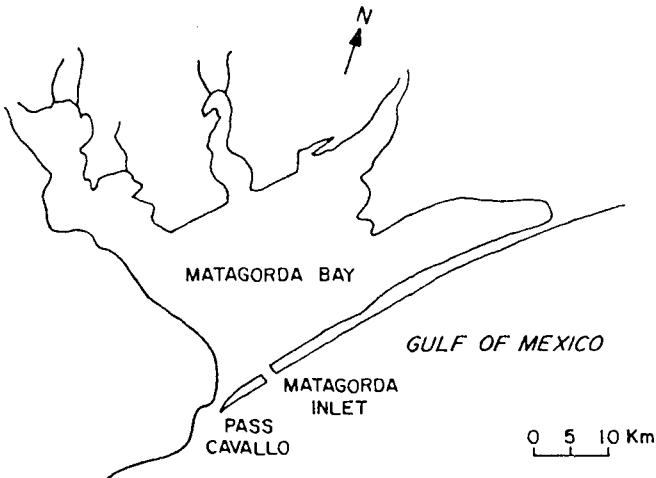


Fig. 4 Matagorda Bay and inlets

Matagorda Bay is a shallow bay with an average depth of 3 m. The Bay surface area is  $1100 \text{ km}^2$ . As a result of the shallow depth and the relatively large horizontal dimensions, the time it takes for the tidal wave to traverse the Bay is on the order of a few hours. Consequently in a strict sense Eq.(4) does not apply and to properly calculate the closure curve and closure surfaces, the propagation of the tide in the bay would have to be accounted for. Because this goes beyond the scope of this study, an approximate solution is sought in which the bay surface area is allowed to fluctuate uniformly. To arrive at realistic current speeds and tidal prisms a reduced bay surface area of  $350 \text{ km}^2$  is introduced.

Tides off Matagorda Bay are mixed. Maximum current speeds occur during spring tide conditions at which diurnal tides are prevalent. The spring tidal range is approximately 1 m.

During a 1959 hydrographic survey the following pertinent inlet characteristics were observed,  $A = 8000 \text{ m}^2$ ,  $R = 4 \text{ m}$ ,  $L = 2350 \text{ m}$ . An average value of the friction coefficient derived from observed velocity profiles is  $F = 5 \cdot 10^{-3}$ . Taking  $\mu = 1$  and  $m = 1$ , it follows that for Pass Cavallo in 1959,  $K' = 0.4$ . Using the approximate solution presented by Keulegan [1951], Eqs. (1) and (4) with  $A_b = 350 \text{ km}^2$  yield  $\hat{u} = 0.94 \text{ m/sec}$  and a tidal prism equal to  $2.5 \cdot 10^8 \text{ m}^3$ . This is close to the observed values of respectively approximately 1 m/sec and  $2.5 \cdot 10^8 \text{ m}^3$ . Furthermore it follows from Eq.(3),  $k = 0.17 \text{ m}$ .

During the years preceding the 1959 survey the geomorphology of Pass Cavallo changed little and it seems reasonable to assume that at the time of the survey the inlet was in equilibrium with the hydraulic environment. It then follows from Eq. (2) with  $F = 5 \cdot 10^{-3}$  and  $u = 0.94$  m/sec that  $\tau_{eq} = 4.4$  N/m<sup>2</sup>. This value is in the middle of the range of equilibrium shear stress values, 3.5-5.5 N/m<sup>2</sup>, suggested by Bruun [1978].

Making use of Eqs. (1)-(4) and the data listed in Table I, the closure curve for Pass Cavallo, Eq. (5), was calculated. The result is presented in Fig. 5. The relation between R and A used in the calculations, see Fig. 6, was established by assuming the inlet to have a parabolic shape and a constant width to maximum depth ratio equal to the value of 333 observed in the 1959 survey.

Table I

Values of pertinent parameter used in calculating the closure curve for Pass Cavallo prior to the opening of Matagorda Inlet.

L = 2350 m	2H = 1 m	$A_b = 3.5 \cdot 10^8$ m <sup>2</sup>
k = 0.17 m	T = 86,400 sec	
m = 1		
R = R(A) see Fig. 6	$A_c = 8000$ m <sup>2</sup> (from previous page)	

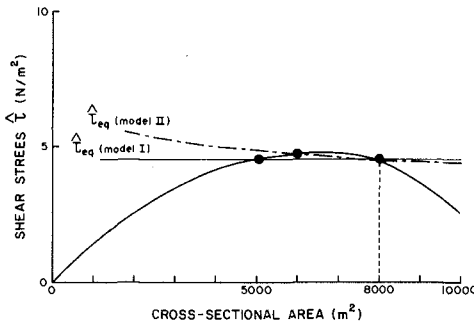


Fig. 5 Closure curve and equilibrium stress curves for Pass Cavallo prior to the opening of Matagorda Inlet

Two models are used for the equilibrium stress curves. In the first model the equilibrium shear stress is assumed constant and equal to the value observed in 1959 i.e.  $\tau_{eq} = 4.4$  N/m<sup>2</sup>. In the second model the current speed,  $u$ , is assumed constant and equal to 0.94 m/sec. The equilibrium shear stress follows from Eq. (2) with  $F$  given by Eq. (3). Equilibrium shear stress curves resulting from the two models are presented in Fig. 5. Note that in the second model  $\hat{\tau}_{eq}$  varies with  $A$ .

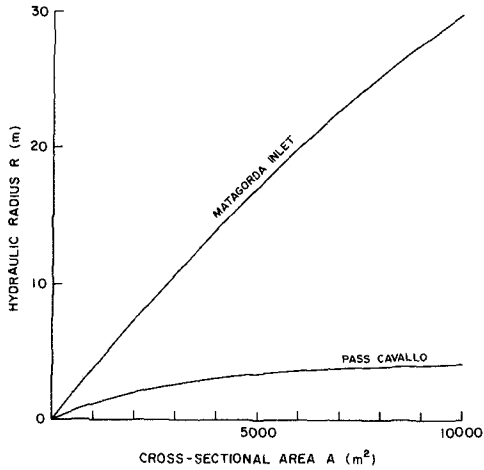


Fig. 6 Relation between hydraulic radius and cross-sectional area for Pass Cavallo and Matagorda Inlet

It follows from the closure curves and equilibrium shear stress curves presented in Fig. 5 that for both equilibrium shear stress models Pass Cavallo is stable. However the degree of stability especially when using the second shear stress model is at best marginal.

In 1963 a second inlet, Matagorda Inlet, was added. The sides of this inlet are protected by rubble and therefore in the stability calculations the width of the inlet is assumed constant and equal to the present width of 300 m. Furthermore a parabolic cross-section is assumed. The resulting relation between R and A for Matagorda Inlet is presented in Fig. 6. Other values of pertinent parameters used in calculating the closure surfaces of Pass Cavallo and Matagorda Inlet, i.e. Eqs. (6) and (7), are presented in Table II.

From observations it follows that after the opening of Matagorda Inlet, Pass Cavallo entered a shoaling mode, whereas Matagorda Inlet continued to scour. Surveys carried out in 1971-1972 yielded  $A_I = 7,500 \text{ m}^2$  and  $A_{II} = 3,600 \text{ m}^2$ . Using the data in Table II, it follows from Eqs. (1) and (4) that in 1971-1972  $\hat{u}_I = 0.75 \text{ m/sec}$  and  $\hat{u}_{II} = 1.2 \text{ m/sec}$ . These values agree with the observation that compared to the 1959 survey, current speeds in Pass Cavallo in 1971-1972 had considerably decreased and were well over 1 m/sec in Matagorda Inlet. The calculated values of

the maximum bottom shear stresses are  $\hat{\tau}_I = 2.8 \text{ N/m}^2$  and  $\hat{\tau}_{II} = 5 \text{ N/m}^2$ . Because of the relatively rapid response to scouring it may be assumed that during the 1971-1972 survey Matagorda Inlet was in equilibrium with its hydraulic environment and therefore  $\hat{\tau}_{eqII} = \hat{\tau}_{II} = 5 \text{ N/m}^2$ . This value is still within the range of equilibrium shear stress values suggested by Bruun [1978]. The values of the K' factor pertaining to the 1971-1972 conditions are  $K_I' = 0.38$  and  $K_{II}' = 0.65$ .

Table II

Values of pertinent parameters used in calculating the closure surfaces for Pass Cavallo and Matagorda Inlet

Pass Cavallo (I)	Matagorda Inlet (II)
L = 2350 m	L = 2150 m
k = 0.17 m	k = 0.17 m
m = 1	m = 1.5
R = R(A) see Fig. 6	R = R(A) see Fig. 6
2H = 1 m	$A_b = 3.5 \cdot 10^8 \text{ m}^2$
T = 86,400 sec	

The two models used to construct the equilibrium shear stress surface for Pass Cavallo are the same as before. The equilibrium shear stress model for Matagorda Inlet corresponding to Model I of Pass Cavallo is  $\hat{\tau}_{eqII} = 5 \text{ N/m}^2$ . The slightly higher value of the equilibrium shear stress for Matagorda Inlet is in agreement with the observation that jettied inlets require a somewhat larger tidal prism and thus larger bottom shear stress to maintain a certain cross-sectional area than unjettied inlets, Jarrett [1976]. The equilibrium shear stress model for Matagorda Inlet corresponding to model II of Pass Cavallo is  $\hat{\tau}_{eqI} = \rho F (1.2)^2$ .

The equilibrium flow curves (i.e. the projection of the intersection of the closure surfaces and equilibrium shear stress surfaces) using model I are presented in Fig. 7. Similarly for Model II the equilibrium flow curves are presented in Fig. 8. In these figures, the subscript I refers to Pass Cavallo and the subscript II refers to the Matagorda Inlet.

Because the enhanced parts of the equilibrium flow curves do not intersect, a combination  $(A_I, A_{II})$  for which both inlets are in equilibrium with the flow conditions does not exist. In 1971-1972, the cross-sectional area for Pass Cavallo and Matagorda Inlet were respectively  $A_I = 7,500 \text{ m}^2$  and  $A_{II} = 3,600 \text{ m}^2$ . Obviously, at that time, Pass Cavallo was in a shoaling mode. Since then the cross-sectional area of Pass Cavallo has gradually decreased leading Matagorda Inlet into a scouring mode. It is expected that this trend will continue. Because of the relatively fast response of an inlet to scouring the values of  $(A_I, A_{II})$  are expected to closely follow the enhanced part of the equilibrium flow curve for Matagorda Inlet.

In the absence of tropical storms and hurricanes, Pass Cavallo will ultimately close and the cross-sectional area of Matagorda Inlet will take on a value between 8,000 and 9,000 m<sup>2</sup>.

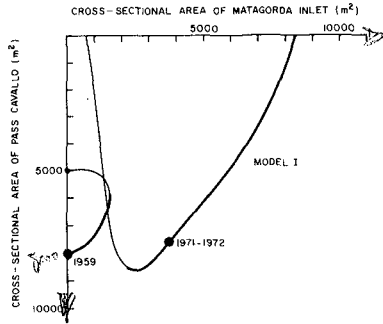


Fig. 7 Equilibrium flow curves for Pass Cavallo and Matagorda Inlet using equilibrium shear stress Model I.

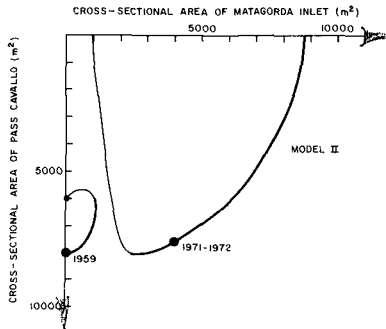


Fig. 8 Equilibrium flow curves for Pass Cavallo and Matagorda Inlet using equilibrium shear stress Model II

Concluding Remarks

In applying the stability analysis, problems as to how to define the length of the inlet, how to estimate values of energy loss coefficients and bottom roughness and what to assume for the shape of the inlet will be encountered. In addition, if the inlet is in a shoaling or scouring mode, the question as to how the shape, the energy loss coefficients and the friction coefficient will change need to be addressed. Because the answers to many of these questions are not known, the proper evaluation of inlet stability requires calculating closure curves (surfaces) and equilibrium stress curves (surfaces) for a large range of inlet dimensions, energy loss coefficients, friction coefficients,



shapes of cross-sectional areas and closure scenarios.

Because of time and financial constraints the number of calculations in this study had to be limited. Also, the simplifying assumption of a uniformly fluctuating bay level is not justified. Therefore the final conclusion with regard to Pass Cavallo should be interpreted cautiously. However so far, all calculations point at a closure of the inlet barring the occurrence of tropical storms and hurricanes.

#### Acknowledgment

This article was developed under the auspices of the Florida Sea Grant College with support from the National Oceanic and Atmospheric Administration, Office of Sea Grant, U.S. Brian Emmett, graduate research assistant, participated in this study and was responsible for most of the calculations.

#### References

- Bruun, P. 1978. Stability of tidal inlets. Elsevier Scientific publishing Company, p. 510.
- Bruun, P. 1983. Discussion of Pass Cavallo, Texas: Case study of tidal prism capture, Journal of the Waterway, Port, Coastal and Ocean Division, ASCE Vol. 109, no. 4. pp. 500-503.
- Escoffier, F.F. 1940. The stability of tidal inlets. Shore and Beach, Vol. 8, No. 4, pp. 114-115.
- Jarrett, J.T. 1976. Tidal prism-inlet area relationships. GITI Report 3, U.S. Corps of Engineers, Waterways Experiment Station, Vicksburg, Miss.
- Keulegan, G.H. 1951. Third Progress Report on tidal flow in entrances. Water level fluctuations of basins in communication with seas. Report No. 1146, National Bureau of Standards, U.S. Department of Commerce, Washington, D.C. p. 32.
- O'Brien, M.P. 1969. Equilibrium flow areas of inlets on sandy coasts. ASCE, J. Waterw. Harbors Div., 95 (WW1): pp. 43-51.
- van de Kreeke, J. 1985. Stability of tidal inlets; Pass Cavallo, Texas. Estuarine, Coastal and Shelf Science. In Press.
- Ward, G.H. 1982. Pass Cavallo, Texas: Case study of tidal prism capture. Journal of the Waterway, Port, Coastal and Ocean Division, ASCE, Vol. 108, No. WW4, pp. 513-525.
- Ward, G.H. 1983. Closure of Pass Cavallo, Texas: Case study of tidal prism capture, Journal of the Waterway, Port, Coastal and Ocean Divisions, ASCE Vol. 109, no. 4. pp. 503-503.

## CHAPTER NINETY FOUR

### Sediment Dynamics Field Experiment: Sunday's River

D H Swart\*

#### ABSTRACT

A field exercise was performed on a high-energy beach east of the Sunday's River in Algoa Bay on the east coast of the Republic of South Africa in the latter half of April 1983. Recorded data include nearly continuous wave data at 7 stations within the breaker zone with simultaneous waverider recordings in a water depth of 10 m, suspended sediment data gathered by means of 'bamboo' poles and instantaneous bottle samplers, daily topographical measurements of the beach and inshore area, data on rip current intensity and spacing for a 10 km coastal strip, more than 3 000 bottom sediment sample analyses and visual observations of wave height and longshore current velocity at hourly intervals through the recording period. Analysis of the data has been completed and interpretation and correlation of various measured phenomena are underway. A second exercise was performed in August 1984, when the emphasis was on nearshore circulation patterns.

#### 1. INTRODUCTION

The Departments of Botany and Zoology of the University of Port Elizabeth (UPE), South Africa, are studying the surf zone energetics in the Sunday's River mouth area. Surf diatom blooms occur very frequently in this area. One of the aspects which specifically needs attention is the physical mechanism which maintains these surf diatom blooms. Clarification of this aspect will help in establishing an energy balance for this area. The Sediment Dynamics Division (SDD) of the National Research Institute for Oceanology (NRIO) was approached to co-operate in the study. As a result two intensive field experiments were undertaken, one in April 1983 and the other in August 1984.

The exercise described here were undertaken jointly by the NRIO and the UPE, with the NRIO concentrating on physical aspects and the UPE on biological aspects. McLachlan and Bate (1984) have reported on certain aspects of the UPE work. The co-operation and support of the UPE were essential for the success of these field exercises. Although only one author is mentioned for this paper, the whole Sediment Dynamics Division co-operated in all aspects of the study.

#### 2. OBJECTIVES

The data gathered during these two field exercises serve a multiple purpose:

\* Head, Sediment Dynamics Division, National Research Institute for Oceanology, CSIR, Republic of South Africa.

- (1) It aids research on coastal sediment dynamics being undertaken by the SDD, in particular various aspects of breaking wave characteristics, nearshore wave dynamics and interaction between waves and currents on the one hand and nearshore suspended sediment motion on the other hand;
- (2) it will provide a physical description of the area to serve as a basis for the biological research carried out by UPE; and
- (3) it will allow the calibration of a 2D finite-element mathematical flow model for the nearshore region, which can then be used to generate a set of possible flow conditions for various wave conditions and nearshore topographies. These can then be used to compute energy budgets for the biota in the nearshore region.

The collaboration with the UPE determined the site for the exercise, as the UPE has for the last ten years been studying various aspects of the biota at the Sunday's River site. Figure 1 shows the position of Port Elizabeth on the South African coastline, whereas Figure 2 shows that the site is situated in a south-facing crenulate-shaped bay with its control point at Cape Recife in the west. The surf zone is of an intermediate type between dissipative and reflective and is characterized by rapidly changing bars, channels and rip currents which are in sympathy with the incident wave climate. The breaker zone slope is relatively mild at 1 in 60 but the seaward face of the bars is frequently as steep as 1 in 10 (see, for example, Figure 3, which was measured by lead line from a helicopter in August 1984). The dominant wave direction according to VOS data is the sector  $225^{\circ}$  to  $255^{\circ}$ . The median incident deepsea wave height in the area is about 3 m.

The Sediment Dynamics Division of the NRIO intends to start instrumenting a measuring site closer to its base at Stellenbosch. It is intended to establish a permanent measuring site at Yzerfontein, 80 km north of Cape Town on the west coast of South Africa (see Figure 1). The field exercise performed at the Sunday's River therefore also have an important secondary aim, namely, to aid in the development of equipment which can withstand the hostile surf on a high-energy coastline. At all times the emphasis was on low-cost experiments.

### 3. EXPERIMENTAL DESIGN

A measuring grid with three onshore-offshore measuring lines 50 m apart was set out and measuring devices were attached to measuring stands.

Fig 1: LOCALITY MAP

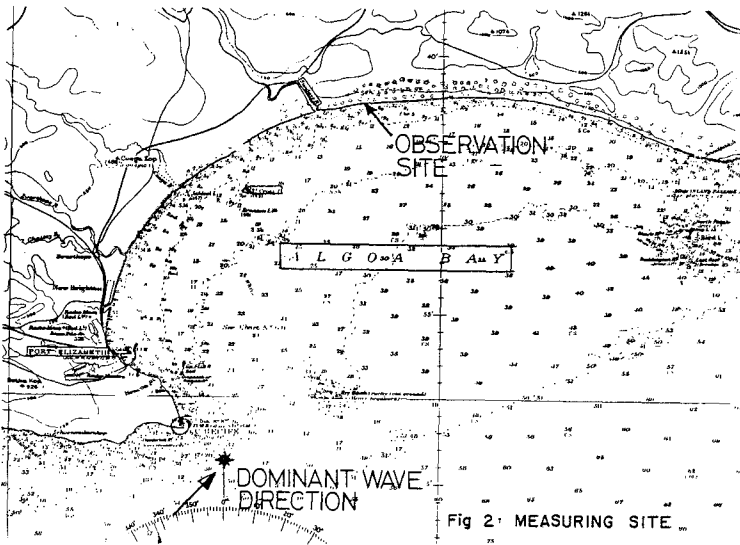
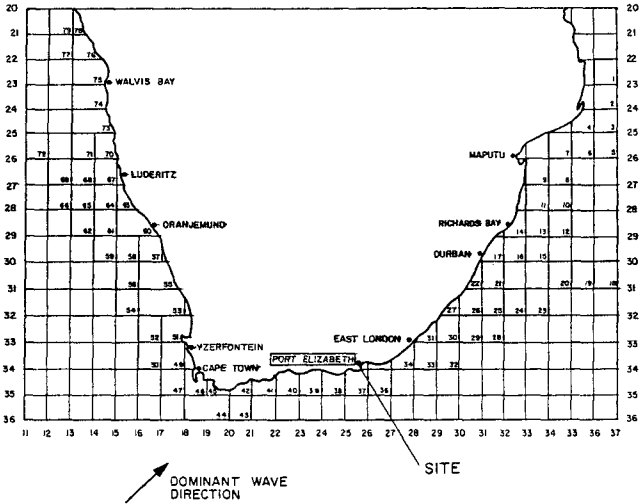
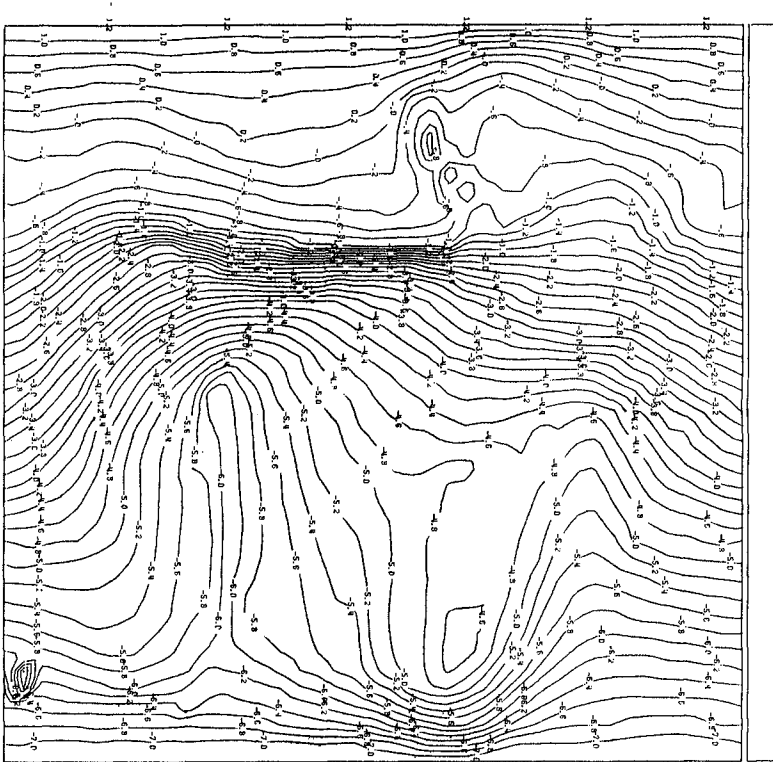
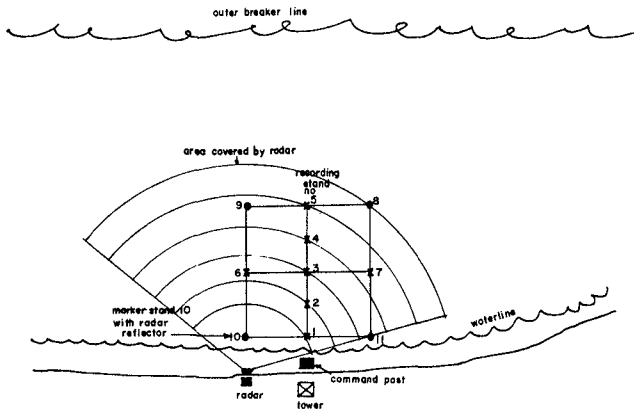


Fig 2: MEASURING SITE



SIZE OF GRID = 400m x 400m

Fig 3: SEA BED TOPOGRAPHY SUNDAY'S MEASURING SITE AUGUST 1984



The following aspects of the experimental set-up are particularly noteworthy:

- A measuring stand was designed after numerous trials. It has a base of 3 m x 3 m and a height of 4 m, and proved to be extremely stable in the surf zone (see Figures 4 and 5). It was placed loosely on the sandy bed and after settling some 5 to 10 cm did not move again, even though no formal anchoring was employed. It is thought that the open piped structure of the base was the reason for its stability. Various instruments were attached to the measuring stands.
- A 15 cm diameter segmented PVC "bamboo tube" with a length of 1,4 m (14 segments of 10 cm each) was designed as a sand trap in such a way that it could be easily attached to and removed from the measuring stand (Figure 6) and could be cleaned of its sand load as soon as possible (Figure 7). One half of the tube was continuous and the front half consisted of 10 cm wide semi-circular lids coinciding with the segments. The pairs of holes which allowed the sand to enter the segments were staggered by 90° at adjacent segments. Alternate pairs thus had the same orientation. Holes of 10 mm diameter were mostly used for 1 hour deployments. During longer deployments (up to 10 hours) holes of 5 mm diameter were used. To allow the transformation of the mass of sand caught in each segment to sediment concentrations, the bamboo tube was calibrated in the laboratory against known sediment concentrations.



Figure 4. Central line of measuring stand



Figure 5.  
Measuring stand  
in surf, note  
wave staff



Figure 6. Replacing bamboo sampler at measuring stand



Figure 7. Cleaning of bamboo sampler



- A 3,5 m long resistance wave height probe was designed and built by the Electronics Systems Division of the NRIO for the determination of water level fluctuations. Results were relayed from each measuring stand to shore by cable where it was recorded at 0,5 s intervals on digital dataloggers. Synchronous data were obtained from 7 wave probes. Data capture was continuous but analysis of the data was performed in 1024s blocks.
4. PRELIMINARY RESULTS

The analysis of the raw data obtained in both experiments has just been completed and the interpretation of the analysed data has commenced. A brief summary of the methods employed and some preliminary results are given below.

During the 1983 Exercise (PE83) the following observations were made:

**Incident waves:** Waves were measured continuously for a week by wave-rider in 10 m water depth directly opposite the measuring site. The measuring interval was 0,5 s. The significant wave height varied between 0,7 m and 1,4 m during this period, while the peak wave period always exceeded 10 s. Observations were also made with a graded telescope mounted on a 15 m high tower which was placed on top of the 10 m high primary dune. In the past this instrument, the so-called clinometer, was used extensively in South African waters for the estimation of wave height, period and direction. It has practically fallen into disuse because the results are observer-dependent.

**Surf zone waves:** Continuous, synchronous wave recordings were made for 4 days at up to 7 locations. More than 700 usable records, each with a length of 1024s, were obtained at these surf zone stations in water depths between 0,7 m and 2 m. Visual estimates of wave height and period at each stand were also made hourly. Wave directions in the surf zone were determined hourly by radar. Extremely consistent results were obtained. The dominant wave direction during the exercise was consistently just west of the normal to the beach.

The surf zone water elevations were analysed in two ways: by normal Fourier techniques as well as by the higher-order Vocoidal Fourier analysis developed by Swart and Fleming (1980) and Swart (1982). In the higher-order analysis vocoidal component waves are extracted instead of sinusoidal waves as in a normal Fourier analysis.

The results indicate that the representative height calculated from the higher-order analysis is always higher than for the customary first-order analysis (see Figure 8). This is in accordance with the earlier theoretical findings (Swart, 1982). Use of the first-order analysis leads to an underestimation of the representative wave height in shallow water. A similar conclusion is found to apply to the peak wave period, which again confirms an earlier theoretical conclusion (Swart, 1982). The wave records show the presence of energy of appreciably low frequency energy, with a peak period which is normally in the range 30 s to 100 s. The rms height in the low-frequency range ( $f < 0,038 \text{ s}^{-1}$ ) is typically about 0,1 to 0,2 m, which can be as high as 25 per cent of the rms height in the gravity wave range ( $f < 0,038 \text{ s}^{-1}$ ).

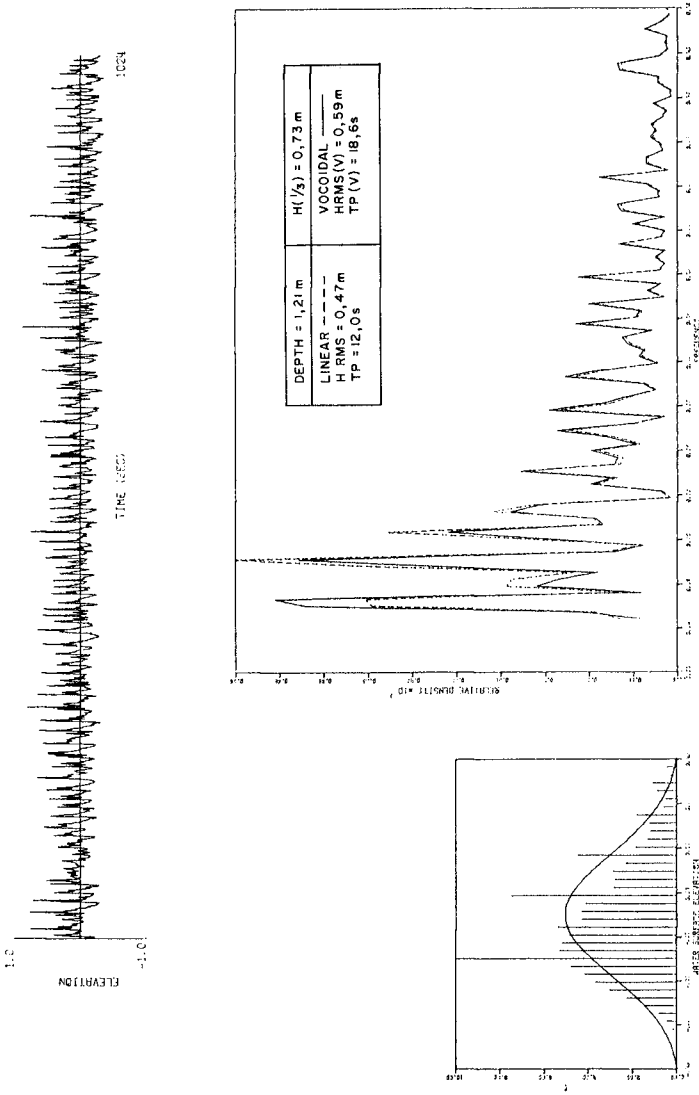


Fig. 8: TYPICAL LINEAR AND VOCOIDAL FOURIER ANALYSIS FOR SURF ZONE WAVES: 28 APRIL 1983; STAFF 4

Cross-sectional analyses are being done to differentiate between edge waves which essentially propagate alongshore and bound waves which essentially travel on-offshore. Figure 9 shows the coherency squared obtained by comparing the surface elevations at the outer (5) and central (3) wave staff in the central measuring line (staff 5 and 3 were 40 m apart) during both high and low tide. The coherency is more significant during high tide when the wave propagation is less affected by the irregularities in the topography. Figure 10 shows the accompanying phase diagram. The results indicate that bound waves in the low frequency band are more prevalent at high tide whereas edge waves are most prevalent at low tide. Analysis is still underway but this conclusion seems to be substantiated by the other analyses.

**Topography:** The nearshore topography from the upper beach to about 1 m below low tide level was determined daily over a distance of 500 m to each side of the central measuring line.

**Current patterns:** Longshore current velocities at the various measuring stands and nearshore current patterns were determined regularly by means of drogues and Rhodamine B dye. During the whole exercise an oblique rip current was situated across the central measuring line in a south-easterly direction. Mean current velocities of up to 5 m/s were measured in this reasonably confined (~ 20 m wide) rip current which pulsed with a period of 1 to 2 minutes and which was always stronger during low-tide.

In future exercises currents will be measured with ducted propellers and overall current patterns will again be determined by using dye.

**Aerial photographs:** A 10 km coastal strip to the east of the Sunday's River, with the measuring site situated about 2 km from the western end of the strip, was flown regularly during the week. Two overpasses were made each day during low tide and another two during high tide. On Friday, 29 April 1983 a total of 20 overpasses were made at roughly 15 minute intervals. The aerial photographs were combined into a mosaic for each overpass, which was then used to study the occurrence of rip currents. These currents were clearly visible on the photographs, while the extent of the surf circulation patterns could also be clearly discerned. The results show that the median surf cell width during the exercise varied between 250 m and 350 m, depending on the state of the tide and the incident wave conditions. The maximum width of the surf circulation cells, measured relative to the mean water line, was about 650 m.

**Sediment in suspension:** More than 100 sets of suspended sediment data were gathered during the week with the aid of bamboo poles and a further 20 sets of instantaneous suspended sediment data by means of sampling bottles. Figure 11 shows a typical correlation between the bottle sampler results and the bamboo sampler results. The 'bamboo' poles were usually removed after a deployment of one hour. Analysis of the sand weight caught in each 10 cm segment above the bed indicates that a sediment concentration based on any one of the following three assumptions would yield a goodness of fit to the data of nearly equal quality, namely a vertical diffusion coefficient which varies linearly or quadratically with distance above the bed or which is constant over the

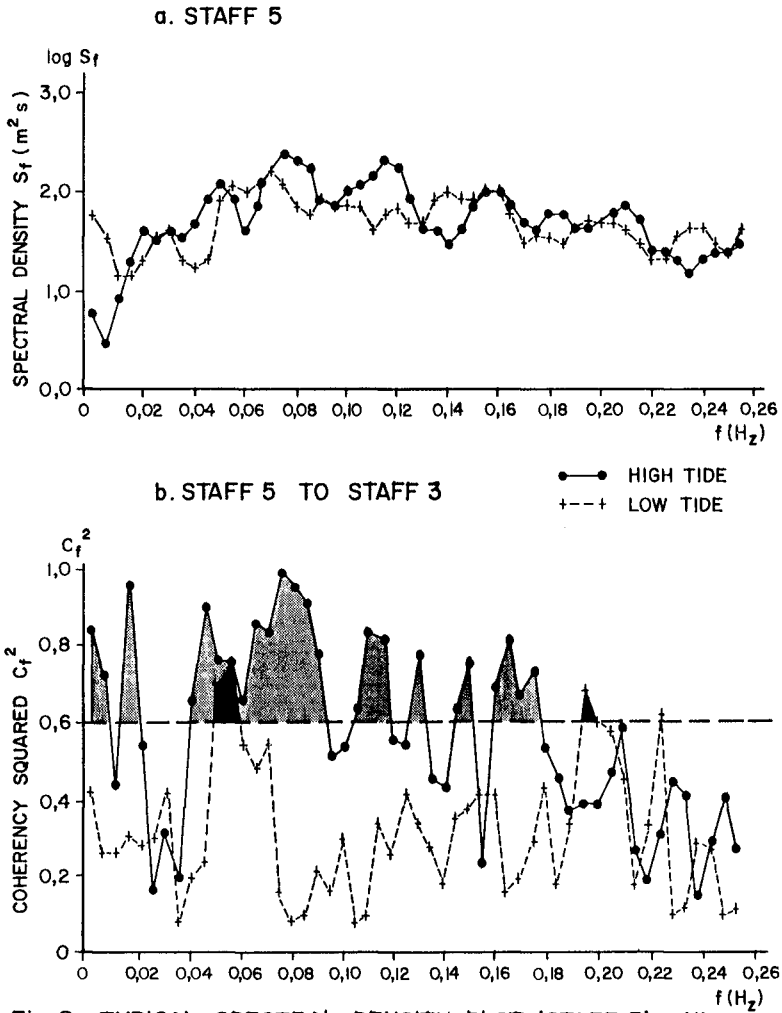
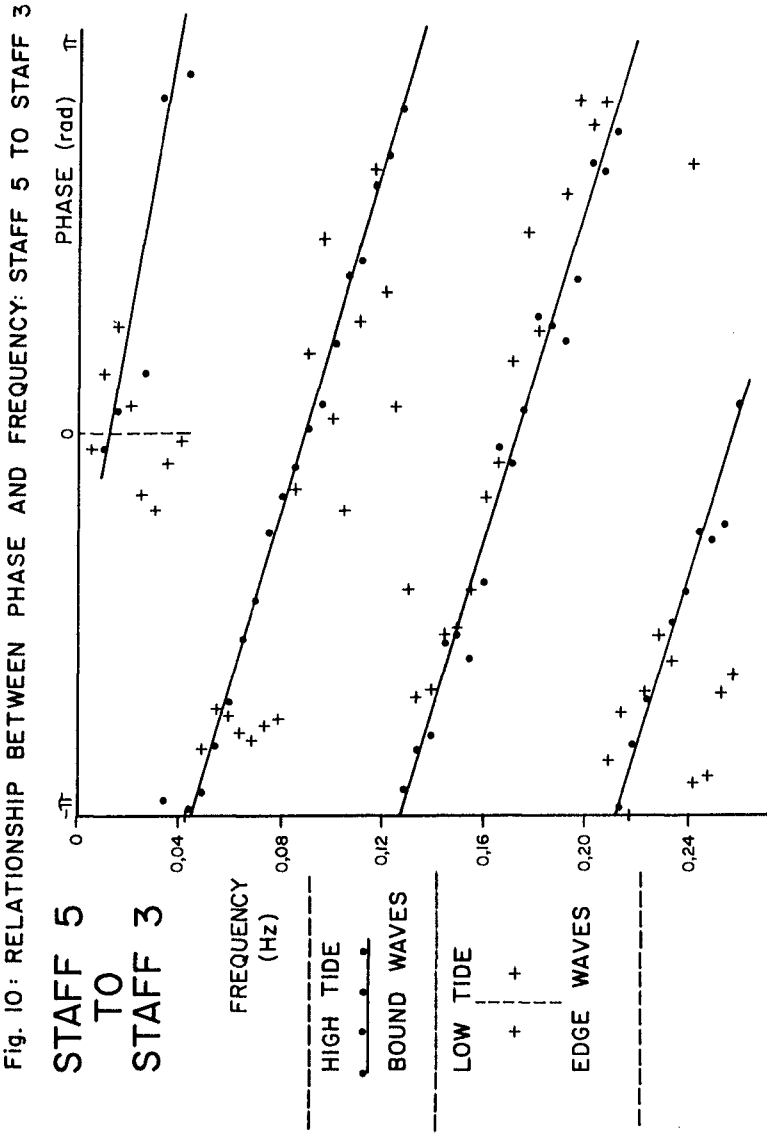


Fig. 9 TYPICAL SPECTRAL DENSITY PLOT (STAFF 3) AND COHERENCY (STAFF 5 TO STAFF 3)



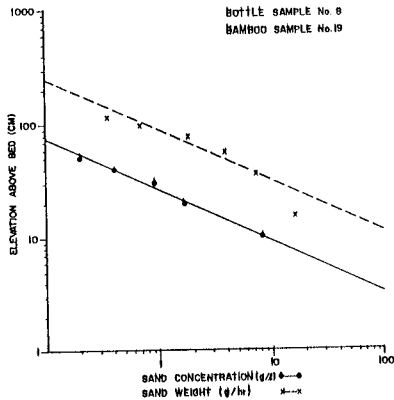


Fig. 11 TYPICAL CORRELATION BOTTLE SAMPLER / BAMBOO SAMPLER

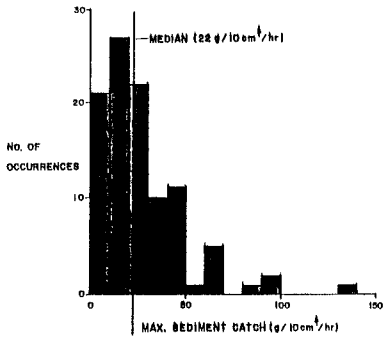


Fig. 12 VARIATION IN MAX. SEDIMENT CATCH

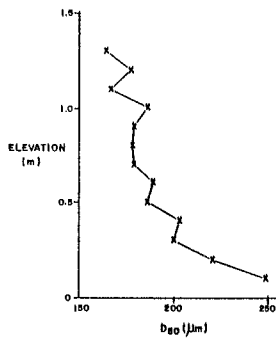


Fig. 13 TYPICAL VARIATION OF GRAIN SIZE WITH DISTANCE ABOVE BED

water column. This is in accordance with earlier findings by Swart (1976) and others, for example, Das (1972). The highest average concentration measured over a one-hour period in the first 10 cm above the bed was 27,1 g/l.

The variation in the maximum sediment load trapped in any segment (in all but a few cases this occurred in the bottom segment) is shown in Figure 12, which shows that the maximum load was 140 g/10 cm segment/hr, whereas the median load was 22 g/10 cm segment/hr. The data were also analysed for grain size variation with distance above the bed. Exponential decay of grain size was found (see Figure 13).

The magnitude of the total suspended load was found to be related strongly and uniquely to the relative position within the surf zone. A peak exists about halfway through the surf zone. It is intended to measure sediment concentration by optical or acoustical backscatter methods in future exercises, in parallel with the samplers employed to date.

**Bottom samples:** More than 3 000 bottom sediment samples were gathered on a regular grid in the measuring area as part of an investigation into the statistical distribution of bed material. The results indicate that longshore variations in grain size over a distance of 100 m are insignificant when compared to the onshore-offshore variations, which indicate a peak at the significant breaker line in both median grain size and the standard deviation of all measurements at a certain distance offshore. The standard deviation peaks at 10 per cent of the median grain size. The results give a preliminary indication about a representative sampling strategy to determine bed material characteristics.

In total 18 NRIO staff members and between 10 and 20 casual helpers participated in this exercise. The total running and capital expenditure was about US\$30 000.

The 1984 Exercise (PE84) was geared to the simultaneous recording of nearshore topography and current patterns.

The following techniques were used:

**Topography:** Conventional survey techniques were employed for daily surveys of 1 km coastal strip in the same manner as discussed for PE83. In addition, two surveys were made by lead line from a helicopter in a 0,4 km x 0,4 km area (see Figure 3). The lead line had a marker attached to it which was triangulated in from shore stations. Survey accuracies are estimated at about 10 cm. The technique supplied topographical information in the central surf zone under relatively high wave conditions (incident significant wave height between 1,5 m and 3 m) when other techniques currently employed in South Africa such as echo-sounding from a skiboat could not be used.

**Currents:** Current patterns were determined on three occasions from the observation of dye distribution after surf zone releases. Extremely complex current patterns were observed, with strong rip currents being concentrated in the channels shown in Figure 3.

**Aerial photographs:** Aerial strips were again done four times daily as in PE83. Data analysis is still underway.

During this 1984 exercise, the staff involvement on the NRIO side was 5, with support from 1 to 2 casual helpers at times. The emphasis in this exercise was more on biological responses than was the case during PE83. The total running and capital expenditure for NRIO was about US\$7 000.

## 5. SUMMARY

The following is a summary of the main conclusions from the two exercises and the results obtained to date.

(1) Extremely useful simultaneous, synchronous recordings at up to 7 wave staffs in the breaker zone and at a waverider in 10 m water depth were obtained. Interpretation of the data is shedding new light on the relative importance of edge waves and bound waves on high-energy intermediate beaches. In the barred beaches observed during the exercises edge waves predominated at low tide and bound waves at high tide.

(2) "Calibrated" data on sediment in suspension in the surf zone and good quantitative data on sediment sorting in the vertical under surf zone conditions were obtained.

(3) The bottom topography and flow patterns in a rough, wide surf zone were determined from a helicopter and by aerial photographs.

It is concluded that it is possible to run a prototype field exercise relatively inexpensively and still obtain very useful simultaneous wind, wave, current and sediment data.

The programme will be extended in the near future to include measured onshore-offshore and longshore current velocity components. A second site for future field exercises is being considered. It is situated in the centre of a 30 km long, flat crenulate bay about 80 km north of Cape Town.

## REFERENCES

DAS, M M (1972). Suspended sediment and longshore sediment transport data review. Proc. 13th ICCE, Vancouver.

McLACHLAN, A and BATE, G C (1984). Preliminary carbon budget for a high-energy surf zone. submitted for publication.

SWART, D H (1976). Coastal sediment transport-computation of longshore transport. Delft Hydraulics Laboratory Report R968.

SWART, D H (1982). The nature and analysis of random waves in shallow water, parts 1 and 2. CSIR Research Report 388.

SWART, D H and FLEMING C A (1980). Longshore water and sediment movement. Proc. 17th ICCE, Sydney.



## CHAPTER NINETY FIVE

### SCALE-MODEL RELATIONSHIP OF BEACH PROFILE

by

Masahiro Ito<sup>1</sup> and Yoshito Tsuchiya<sup>2</sup>

#### 1. ABSTRACT

This paper presents a scale-model relationship for the similarity between large and small scale-models in two-dimensional equilibrium beach profiles. Taking large scale-models using large scale equipment as prototypes, the experimental scale of a medium-sized model was gradually varied keeping the grain size ratio of model to prototype constant. A similarity-comparison between large and small scale beach profiles is made by considering the degree of experimental errors. Judgement results are graphically shown, and a scale-model relationship is proposed. It is found that the scale-model relationship proposed agrees with the ones derived from the empirical formulae expressing the properties of beach profiles. Additionally, the applicability of this scale-model relationship to the reproduction test of natural beaches is examined.

#### 2. INTRODUCTION

The similitude on the beach changes has often been studied experimentally and theoretically by several investigators. As an experimental method, the similitude of two-dimensional beach change was earlier studied using a regular wave flume in the Beach Erosion Board (presently, Coastal Engineering Research Center, US Army) in 1947. Saville (1957) and Iwagaki & Noda (1961) pointed out the scale effect as the reason that the beach profile in the model is not always in agreement with the prototype, when the wave height, wave length and grain-size scale of model are scaled down geometrically by the Froude law for the prototype. Noda (1972)

- 
- 1 Associate Professor, Department of Civil Engineering, Meijo University, Tempaku-ku, Nagoya, Japan.
  - 2 Professor, Disaster Prevention Research Institute, Kyoto University, Uji, Kyoto, Japan.

discussed how the scale-distortion among vertical and horizontal scales, sand grain-size and specific gravity of beach material of the model has an effect on the similitude relationship. Similitudes proposed with these methods are significant only within the specialized experimental conditions, and not clearly confirmed by the verification test on a natural beach.

This paper presents a scale-model relationship for the two-dimensional equilibrium beach profiles. The scale-model relationship proposed is examined by its applicability to the verification test on the natural beach at Ogata in Niigata, Japan.

### 3. EXPERIMENTAL ERROR IN REPRODUCTION TEST

If a laboratory experiment on beach processes is performed several time under initially the same conditions, in general, the properties of beach profiles and breaking waves vary considerably as seen in Fig. 1, in which position and height of  $\downarrow$ -symbol show breaking point and relative wave height, respectively. They happen independently of with wave duration time  $t$ . It is considered that the scatter of properties depends on (i) systematic error, (ii) accidental error and (iii) mistakes. In this study the scatter of data, namely experimental error, is investigated, using the mean error  $\epsilon'$  defined as

$$\epsilon' \Delta x = \frac{1}{n} \sum_{i=1}^n |x_i - \bar{x}| \quad (1)$$

where  $\epsilon \Delta x$  is the experimental error of shoreline change relating to beach profiles and waves,  $n$  the number of replications,  $x_i$  the measured value at the  $n$ -th, and  $\bar{x}$  the mean value.

The relationship between the experimental error of shoreline change evaluated with Eq. (1) and the wave steepness in deep water  $H_0/L_0$  is shown in Fig. 2 including the other data. In this figure, a parameter  $H_0/sd$  usually describing a measure of the scale effect in beach profile is shown. In the parameter,  $H_0$  is the wave steepness in deep water,  $s$  the specific gravity of beach sediment in water, and  $d$  the grain size. From Fig. 2 it is recognized that the parameter does not effect the experimental error of shoreline change. Since the values plotted in Fig. 2 scatter considerably, the solid line is drawn to envelop the highest values plotted. The solid line, namely the dimensionless experimental error of shoreline change  $\epsilon \Delta X_{s1}/L_0$ , is expressed as

$$\epsilon \Delta X_{s1}/L_0 = \pm 5.7 (H_0/L_0)^{1.2} \quad (2)$$

Also, the dimensionless experimental errors of position of berm crest  $\epsilon' \Delta B_x/L_0$  and breaking point  $\epsilon' \Delta X_b/L_0$  derived in the same manner are shown in Fig. 2 with broken and dotted lines, respectively.

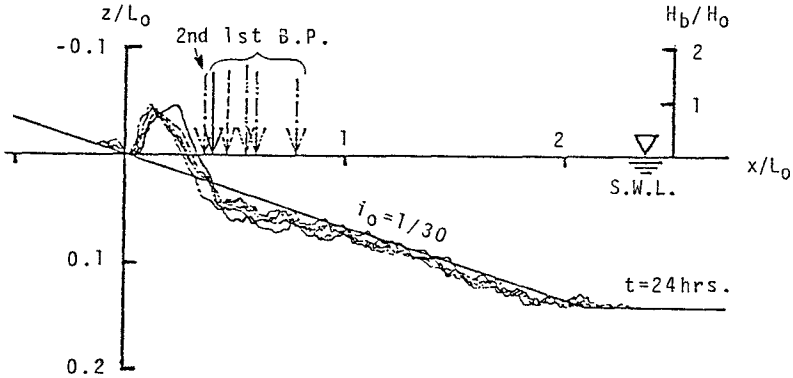


Fig. 1 Experimental error of repeating runs at the wave operation time of 24 hours in Run No. 3M-28 in Table 1.

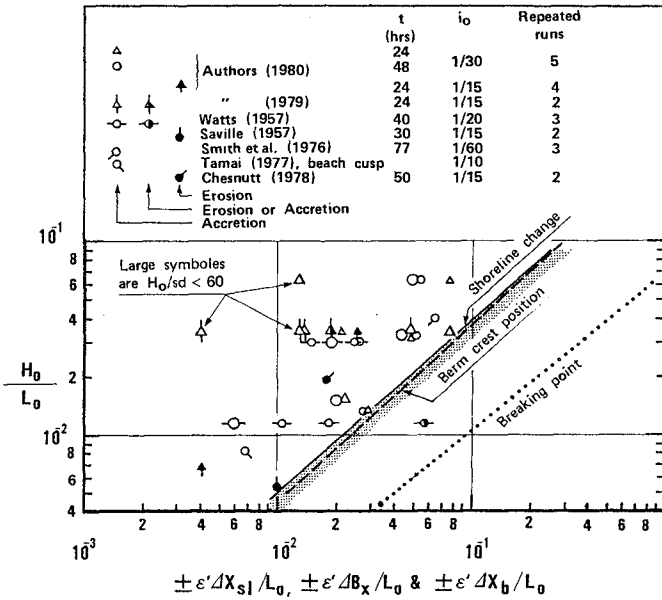


Fig. 2 Experimental errors of shoreline change berm crest position and breaking point .

#### 4. CRITERION OF SIMILARITY

To ensure the similarity of beach processes between the prototype (i. e., large-scale model) and the model (i. e., small-scale model), phenomena such as beach profile, breaking waves and sediment transport by waves have to be similar in both cases. The comparison of the similarity between the two must be judged while considering the experimental error proposed. By the degree of agreement between the two, therefore, the following three criteria are employed:

a) Similitude : The difference in the beach processes, such as changes in shoreline and breaking point, is less than twice the experimental error. The judgement in this case is designated by circles.

b) Dissimilitude : Beach profiles to be compared are substantially different in type such as "bar type" and "step type", and the difference in the beach processes is more than four times the experimental error. This is designated by dark squares.

c) Quasi-similitude : This case is an intermediate situation between a) and b), and designated by triangles.

#### 5. EXPERIMENTS

We performed a number of laboratory experiments in order to determine the scale-model relationship of two-dimensional beach change under the following conditions :

(1) The vertical and horizontal length scales, such as beach profile and water depth in the wave tank, are to be the same (i. e., undistorted), and both scales are to be subject to the Froude law.

(2) Wave characteristics such as wave height  $H$  and wave period  $T$  are determined by the Froude law. The wave generator operated until beach profiles reach equilibrium.

(3) The beach sediment of the small-scale models is sand or silica-sand with the same specific gravity as the sand used in the large-scale models. The grain size of the beach sediment in the model, i. e. the grain-size scale, is to be chosen independently of the experimental scales above-mentioned (1) and (2).

A large-scale model was carried out using a large-size two-dimensional wave flume of 78m long, 1m wide and 1.2m deep, and waves were generated for 60 hours on an initially even-sloping beach. We took the equilibrium beach profile and its experimental conditions to be the prototype. Additionally, those of the prototype-size experiment performed by Saville were also taken to be the prototype.

For comparison, experiments with small-scale models were carried out using the medium-sized wave flume of 28m long, 0.5m wide, and 1m deep. The grain size of the sand or silica-sand used in the model beach sediment was chosen independently of the experimental scale. The experimental scale was gradually varied keeping the grain size ratio of model to prototype constant. The initial beach slope of the model was identical to the prototype. Table 1 is an example of experimental conditions, in which  $d_{50}$  is

the medium size of the beach sediment,  $H_0$  the wave height in deep water,  $L_0$  the wave length in deep water,  $h$  the water depth in the wave tank,  $g$  the acceleration of gravity,  $\nu$  the kinematic viscosity of water and  $t$  the duration time in total. The grain size distribution of the beach sediment used in the prototype and the model is shown in Fig. 3. Median sizes of the beach sediment were used 0.15, 0.30, 0.42, 1.62mm in the model and 0.22, 0.94mm in the prototype, respectively.

Table 1 An example of experimental conditions for prototype and model.

Scale	Run No.	$d_{50}$ (mm)	T (sec)	$H_0$ (cm)	h (cm)	$H_0/L_0$	$d_{50}/H_0$	$h/L_0$	$\frac{\sqrt{gH_0 \cdot d_{50}}}{\nu}$	t/T	Remarks
Proto.	3	0.94	3.00	20.6	100.0	0.015	$5.0 \times 10^{-3}$	$7.0 \times 10^2$	925	$7.2 \times 10^4$	} $\lambda_0 = 1/30$
1/1.82	3M-30	0.42	2.22	11.8	55.0	0.015	3.6	7.2	391	3.9	
1/2	3M-29	0.42	2.12	9.6	50.0	0.014	4.4	7.1	361	4.1	
1/3	3M-28	0.42	1.73	6.8	33.3	0.015	6.2	7.1	296	5.0	
1/4	3M-27	0.42	1.50	4.8	25.0	0.014	8.8	7.0	258	5.8	
1/5	3M-28	0.42	1.34	4.6	20.0	0.017	9.1	7.1	250	6.4	
1/6.7	3M-25	0.42	1.16	3.5	15.0	0.017	12.0	7.2	215	7.4	
1/2.9	3M-23	1.62	1.76	7.2	34.5	0.015	22.4	7.1	1194	0.1	
										7.2	
Proto.	T-22	0.22	11.33	138.2	426.7	0.0069	0.16	2.1	664	1.3	
1/10	T-27	0.15	3.57	13.4	42.7	0.0067	1.1	2.1	200	1.3	
1/20	T-28	0.15	2.53	6.5	21.3	0.0065	2.3	2.1	134	1.3	
1/30	T-29	0.15	2.06	4.4	14.2	0.0066	3.4	2.1	86	1.3	
1/40	T-29'	0.15	1.79	3.4	10.7	0.0068	4.4	2.1	76	1.3	

$d_{50} = 1.62$ mm, sorting coef. = 1.12, specific gravity = 2.55  
 1.15 } sand  
 0.94 }  
 0.42 }  
 0.15 }  
 2.68 }  
 2.77 } silica-sand

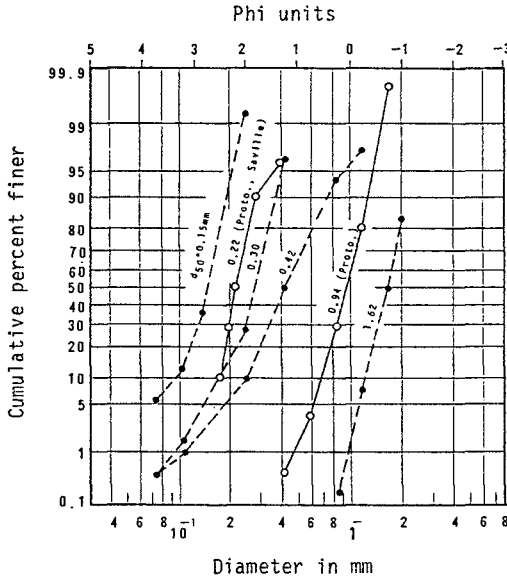


Fig. 3 Grain size distributions of beach sediments used in the model and prototype.

6. EXPERIMENTAL RESULTS AND ANALYSIS

Fig. 4 (a) shows the properties of beach profiles and breaking waves which resulted from the experiment, and expresses similarity-comparisons between the prototype (Run No. 3 in Table 1) and the models (for example, Run No. 3M-30 ~ 3M-25). In this figure, P, S and SP indicate breaker types, such as plunging breaker surging breaker and spilling breaker. The comparison shown in Fig. 4 (a) was made gradually varying the experimental scale  $S=1/n$  [ $= \lambda_{H_0} = (H_0)_m / (H_0)_p = 1/1.82 \sim 1/6.7$ ], keeping the grain-size scale of the model to prototype,  $\lambda_d$  [ $= (d)_m / (d)_p = 0.45$ ] constant. Also, the comparison between the prototype by Saville's experimental result (Run No. T-22) and the models (Run No. T-27 ~ T-29) is also shown in Fig. 4 (b). The degree of experimental error in the experiments is recognized from check run of the Run No. T-28. The judgement of the similarity-comparison between the prototypes and models was made using the criteria a), b) and c) defined already, and the judgement results are shown on the left side of the figure, respectively. Only prototypes in which the ratio of grain size to wave height satisfied the condition that  $(d)_p / (H_0)_p \leq 0.01$  are used for comparison with the models. The results judged are arranged in Fig. 5 of which ranges of

experimental conditions of prototype cover  $H_o/L_o = 0.007 \sim 0.025$ ,  $d/H_o < 0.01$ , and  $i_o = 1/10 \sim 1/30$ , giving the inverse ratio of grain-size scale  $1/\lambda_d [(d)_p / (d)_n]$  the ordinate and the inverse ratio of experimental scale  $1/\lambda_{H_o} (1/S = n)$  the abscissa, respectively. Fig. 5 also includes the results which satisfy the range of the initial beach slope ranging  $1/10$  to  $1/30$  and of the deep water wave steepness ranging  $0.007$  to  $0.025$  among the experimental data from previously investigators.

It is possible to classify the data shown in Fig. 5 into three zones such as "Similitude", "Quasi-similitude" and "Dissimilitude". In Fig. 6, results in the case where  $H_o/L_o = 0.031 \sim 0.042$ , which are similarly classified, are superimposed on those of Fig. 5. In Fig. 6, ranges of experimental conditions of prototype cover  $d/H_o < 0.01$  and  $i_o = 1/10 \sim 1/30$ . A common similitude zone extends over both ranges  $1/\lambda_d > 1$  and  $1/\lambda_d < 1$  of the grain-size scale. The central position of the common similitude zone is shown with a dot-dashed line. The scale-model relationship indicated by the dot-dashed line within the range  $1/\lambda_d > 1$  is expressed by

$$\frac{1}{\lambda_d} = 1.7 \left(\frac{1}{H_o}\right)^b \tag{3}$$

which is transformed to

$$\frac{(d)_n}{(d)_p} = \left(\frac{1}{1.7}\right)^a \left(\frac{1}{n}\right)^b \tag{4}$$

where  $(d)_n / (d)_p$  is the grain-size scale,  $1/n$  the experimental scale, and the values of  $a$  and  $b$  are indicated in Table 2. From Fig. 6, it is seen that the scale-model relationship of Eqs. (3) and (4) shifts slightly from the Froude law stating that  $1/\lambda_d = 1/\lambda_{H_o}$  which is drawn by a dotted line.

Table 2 Values of  $a$  and  $b$  in Eqs. (3) and (4)

Experimental scale / Exponent	$1 > \frac{1}{n} > \frac{1}{2.2}$	$\frac{1}{2.2} > \frac{1}{n}$
a	0	1
b	0.83	0.2

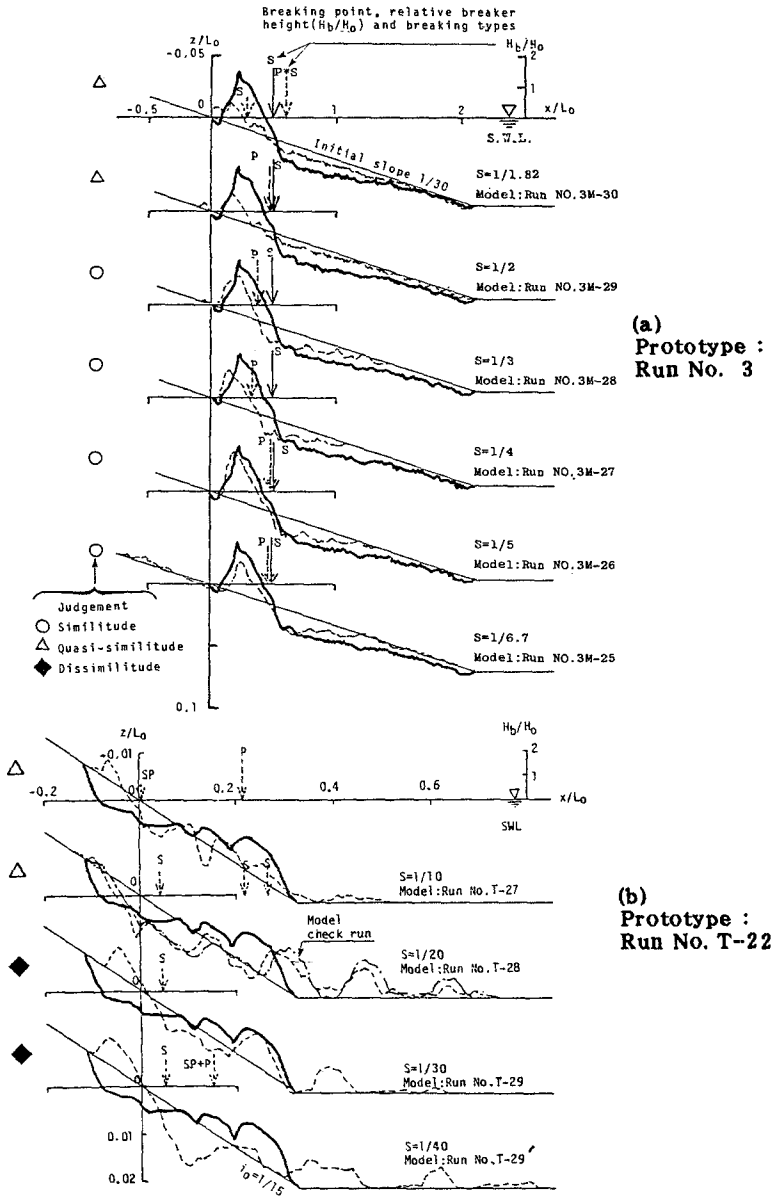


Fig. 4 Similarity-comparison between prototype (solid line) and model (broken line).



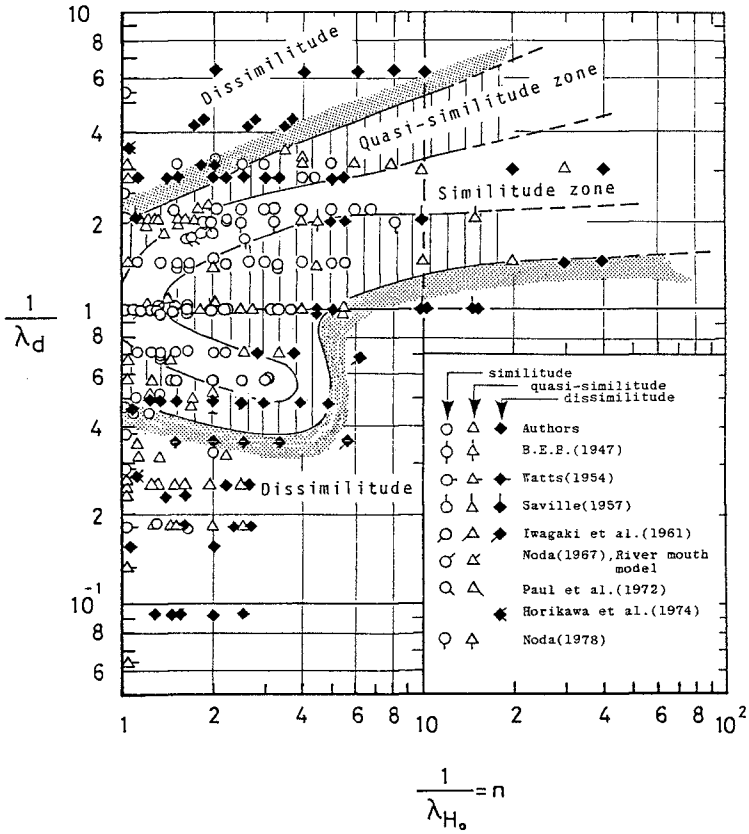


Fig. 5 Graphical representation of similitude of beach profiles.

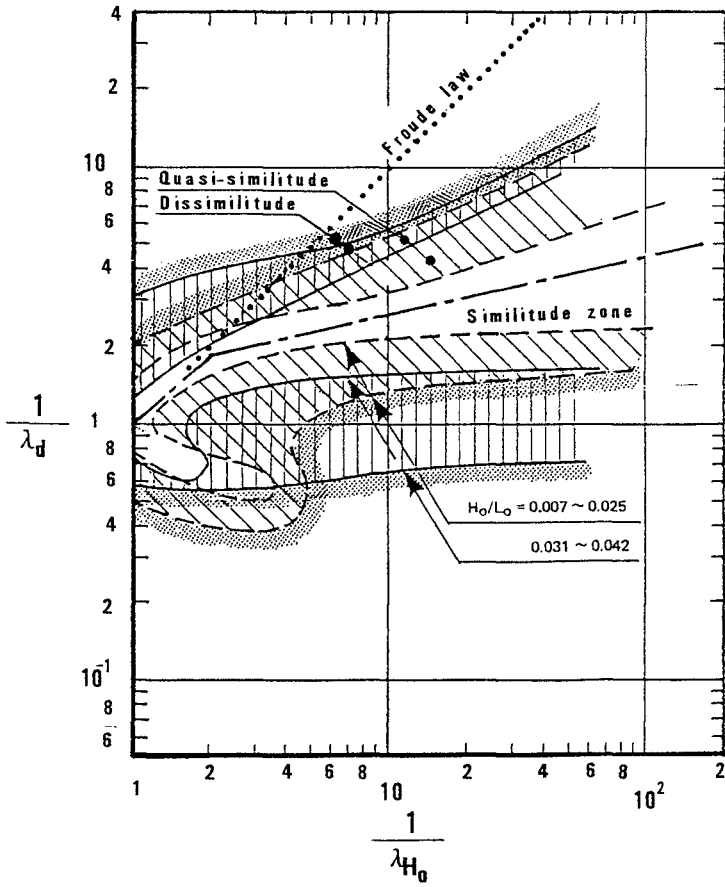


Fig. 6 Similitude of beach profile within range of  $H_0/L_0=0.007 \sim 0.042$ .

## 7. COMPARISON

Let us compare the scale-model relationship indicated in Fig. 6 or Eqs. (3) and (4) with those derived by other investigators. Previous studies of the beach processes are summarized in column No. ③ in Table 3. In table 3,  $d_n$  is the mean diameter of beach sediment,  $w$  the fall velocity of the sediment,  $L_o$  the deep water wave length,  $i_o = \tan \beta$  the initial beach slope,  $l$  the typical length,  $\lambda_x$  the horizontal scale,  $\lambda_y$  the vertical scale,  $\sigma$  the density of beach sediment,  $\rho$  the water density and other notations were explained already. Now, arranging the relationship of column No. ③ using the definition,

$$\lambda \text{ parameter} = \frac{\text{model parameter}}{\text{prototype parameter}} \quad (5)$$

scale-model relationships as shown in column No. ④ are obtained. When the experimental conditions are restricted by the conditions (1), (2) and (3) described in 5, we may make the assumptions that  $\lambda_x = \lambda L_o = \lambda_y = \lambda H_o$ ,  $\lambda i_o = \lambda \tan \beta = 1$ ,  $\lambda t = 1$  and  $\lambda_s = 1$  as well as the water temperature and acceleration of gravity are the same between model and prototype,  $\lambda_v = 1$  and  $\lambda_g = 1$ , respectively.

Substituting these similitude conditions into the scale-model relationships of column No. ④, the relationships of column No. ⑤ are finally derived. Using the same coordinate ( $1/\lambda_d$ ,  $1/\lambda_{H_o}$ ) as Fig. 6, it is possible to describe relationships of column No. ⑤. Similitudes of Nos. A, B and C shown in Fig. 7 (a). The scale-model relationship of Nos. D, E and F is expressed using only the fall velocity of beach sediment  $w$ . Now, we consider the scale-model relationship between the fall velocity and the grain size of material. There are theoretical formula of Stokes, and empirical ones of Allen, Kármán and Newton for the fall velocity of sediment as reported by Tsurumi (1932). The applicable ranges of the four formulae depend on the Reynolds number  $Re = wd/\nu$ . Using the restricted conditions of this study,  $\lambda_s = 1$ ,  $\lambda_v = 1$  and  $\lambda_g = 1$ , the relationships of  $\lambda_w$  and  $\lambda_d$  are eventually obtained as,

Stokes' formula (In this formula, when  $s=1.65$ ,  $\rho=1.0\text{g/cm}^3$  (water density) and  $Re < 4.5$  are given, the applicable sediment size to the formula is  $d < 0.15\text{mm}$ .)

$$\lambda_w = \lambda_d^2 \lambda_s^{-1} \lambda_v \lambda_g^2 = \lambda_d^2 \quad (5)$$

Allen's formula (similarly,  $Re=4.5 \sim 300$ ;  $d=0.15 \sim 1.1\text{mm}$ )

$$\lambda_w = \lambda_d^{2/3} \lambda_s^{-1/3} \lambda_v^{2/3} \lambda_g = \lambda_d \quad (6)$$

Kármán's formula (similarly,  $Re=300 \sim 3200$ ,  $d=1.1 \sim 5.8\text{mm}$ )

$$\lambda_w = \lambda_d^{2/3} \lambda_s^{5/9} \lambda_v^{-1/9} \lambda_g^{5/9} = \lambda_d^{2/3} \quad (7)$$

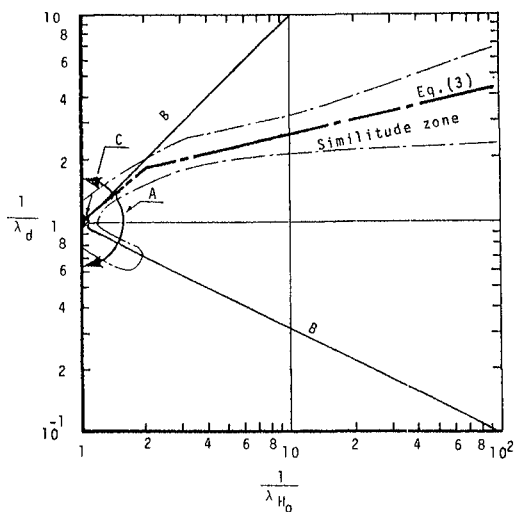
Newton's formula (similarly,  $Re=3200 \sim 10000$ ,  $d > 5.8\text{mm}$ )

$$\lambda_w = \lambda_d^{1/2} \lambda_s^{1/2} \lambda_g^{1/2} = \lambda_d^{1/2} \quad (8)$$

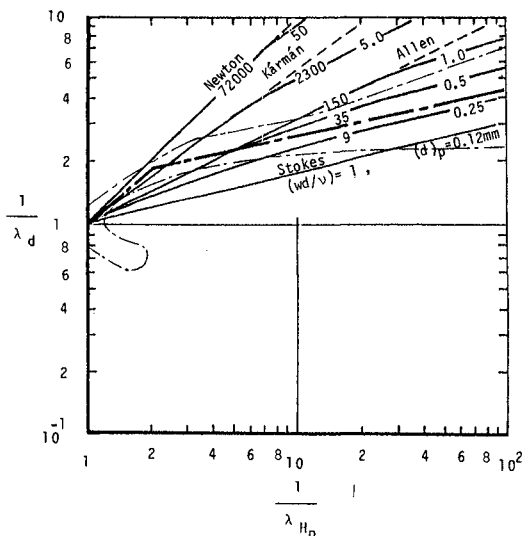
In Table 3 all the relationship of No. D, E and F in column No. ⑤ can be expressed in Fig. 7 (b) taking the Reynolds number of the prototype as a parameter. Since the scale-model relationship in Fig. 6 is comparable with those shown in Fig. 7, it can be seen that the scale-model relationship proposed in this study agrees well with those derived from the relationships which express the properties of beach processes using the fall velocity of beach sediment.

**Table 3 List of similitudes derived from characteristics of beach profile.**

① No.	② Investigator	③ Equation or figure expressing the properties of the beach profile.	④ Similitude-relationship derived from ③.	⑤ Relationship of column No. ④ when $\lambda_x = \lambda_y = \lambda_{H_0} = \lambda_{L_0} = 1$ , $\lambda_s = 1$ , $\lambda_{i_0} = \lambda_{\tan\beta} = 1$ , $\lambda_T = \lambda_x^{1/2}$ , $\lambda_v = 1$ and $\lambda_g = 1$ .	⑥ Remarks
A	J.W.Johnson (1949)	$\frac{H_0}{L_0} > 0.03$ (Storm beach) $\frac{H_0}{L_0} = 0.025 \sim 0.03$ (Transition) $\frac{H_0}{L_0} < 0.025$ (Ordinary beach)	$\lambda_{H_0} \lambda_{L_0}^{-1} = 1$	Relationship between $\lambda_d$ and $\lambda_{H_0}$ is satisfied always.	* The effect of grain-diameter is not considered.
B	Iwagaki & Noda (1961)	$\frac{1}{L_0} = f\left[\frac{H_0}{L_0}, \frac{d_m}{H_0}, \frac{t}{T}, \left(\frac{\sigma}{\rho} - 1\right), \frac{v}{d_m \sqrt{g H_0}}, i_0\right]$	$\lambda_{H_0} \lambda_{L_0}^{-1} = 1$ , $\lambda_d \lambda_{H_0}^{-1} = 1$ , $\lambda_t \lambda_T^{-1} = 1$ , $\lambda_s = 1$ , $\lambda_d^{-1} \lambda_{H_0}^{-1/2} \lambda_v \lambda_g^{-1/2} = 1$ , and $\lambda_{i_0} = 1$	$\lambda_d = \lambda_{H_0}$ $\lambda_d = \lambda_{H_0}^{-1/2}$	
C	E.K.Noda (1972)		** $\lambda_d \lambda_s = 1.85 = \lambda_y$ $\lambda_x = \lambda_y = 1.32 \lambda_s = 0.386$	Only the prototype satisfies in these conditions.	** Similitude-relationship can apply only in the vicinal region of a shoreline.
D	R.G.Dean (1973)	$\frac{H_0}{L_0} > 1.7 \frac{w}{gT}$ (Storm beach) $\frac{H_0}{L_0} < 1.7 \frac{w}{gT}$ (Ordinary beach)	$\lambda_w \lambda_{H_0}^{-1} \lambda_{L_0}^{-1/2} \lambda_g^{-1/2} = 1$	$\lambda_w = \lambda_{H_0}^{1/2}$	
E	R.A.Dairymple (1976)	Similitude-relationship derived from $H_0/L_0$ , Froude law and the equation of fall velocity	$\lambda_x = \lambda_y$ $\lambda_T = \lambda_y^{1/2}$ $\lambda_w = \lambda_y^{1/2}$	$\lambda_w = \lambda_y^{1/2}$	Seven kinds of similitude relationships were proposed. This is one selected from among the seven.
F	Hattori & Kawamata (1980)	$\frac{(H_0/L_0) \tan\beta}{wgT} > 0.5$ (Accretive profile) $\frac{(H_0/L_0) \tan\beta}{wgT} = 0.5$ (Equilibrium P.) $\frac{(H_0/L_0) \tan\beta}{wgT} < 0.5$ (Erosive P.)	$\lambda_w \lambda_{H_0}^{-1} \lambda_{L_0}^{1/2} \lambda_{\tan\beta}^{-1} = 1$ $\lambda_g^{-1/2} = 1$	$\lambda_w = \lambda_{H_0}^{1/2}$	Beach processes within the breaker zone.

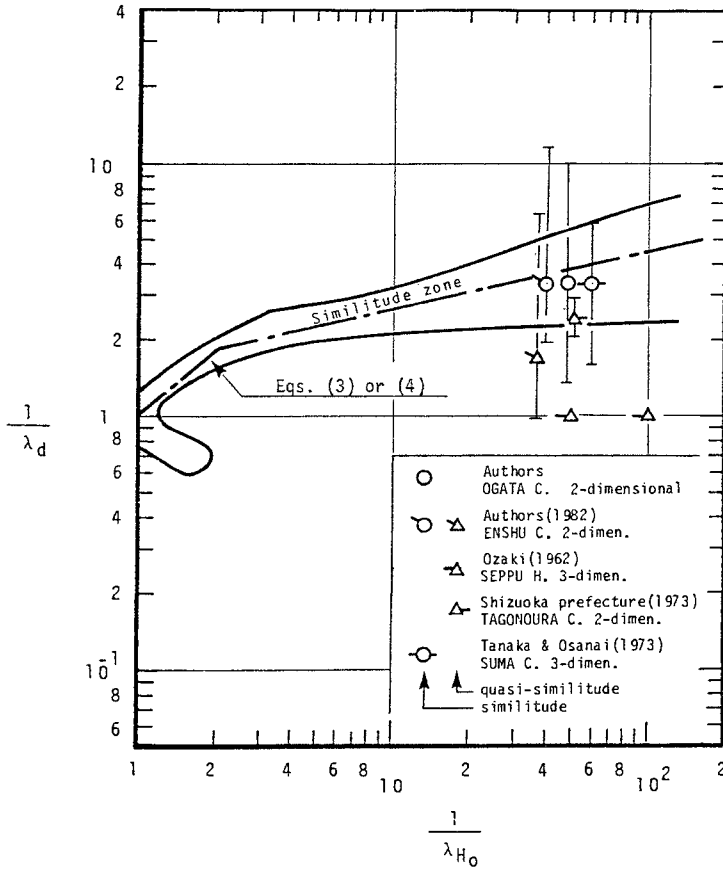


(a) Nos. A, B and C



(b) Nos. D, E and F

Fig. 7 Comparisons of scale-model relationship proposed with those in column No. ⑤ in Table 3.



**Fig. 8** Verification of proposed scale-model relationship by reproduction of natural beaches in scale models.

## 8. VERIFICATION TEST

To verify the scale-model relationship proposed in this study, experiments with a two-dimensional beach model of the Ogata coast in Niigata were carried out. On this coast, the predominant waves strike the shore orthogonally. Therefore, it may be considered that the coast has a two-dimensional property. The experimental conditions of the verification test were set with an experimental scale of  $S=1/50$  and a grain-size scale of  $\lambda_d \approx 1/3.2$  using the scale-model relationship. The properties of waves in the model reproduced the significant waves off Ogata, and the temporal wave change was chosen according to the Froude time scale. It was found that the verification test well reproduced the beach change at the coast. The grain-size scale and the experimental scale used in the verification test agree well with the similitude zone shown in Fig. 8. This figure, as a comparison, also includes other results of two-dimensional wave flume experiments by the first authors (1982) and Sizuoka prefecture (1973), and of the three-dimensional wave basin by Ozaki (1962) and by Tanaka-Osanai (1973). Consequently, it is concluded that the model can reproduce very well beach changes when the experimental conditions are set so as to be contained within the similitude zone proposed.

## 9. CONCLUSIONS

The main conclusions are summarized as;

- 1) The experimental errors of the shoreline change, berm crest position and breaking point in the two-dimensional beach processes are shown as a function of wave steepness in deep water. The tendencies of the three experimental errors on it are similar.
- 2) The three criteria for classifying the degree of similarity between prototype and model are defined from the degree of experimental error.
- 3) The similarity-comparison between prototype and model is made with reference to the similarity criteria. The scale-model relationship of beach changes is proposed from the Fig. 6 showing the result of similarity-comparison.
- 4) The scale-model relationship proposed agrees well with the one derived from the relationship expressing the properties of beach changes using the fall velocity of beach sediment.
- 5) It is found that the proposed scale-model relationship is applicable to reproduce changes in natural beaches in laboratory experiments.

## 10. ACKNOWLEDGMENTS

This study was supported by the Research Grant of Meijo University. The authors would like to express their gratitude to the personnel at the Research Section of Coastal Disaster, Disaster Prevention Research Institute, Kyoto University, and the students in the first author's laboratory, for their assistance during the study.



## REFERENCES

- Beach Erosion Board (1947) : A study of comparative action of waves on model beaches of different scales, *The Bulletin of BEB*, Vol. 1, No. 2, pp. 8-12.
- Dalrymple, R. A. and Thompson, W. W. (1976) : Study of equilibrium beach profiles, *Proc. 15th Coastal Engineering Conf.*, pp. 1277-1296.
- Dean, R. G. (1973) : Heuristic models of sand transport in the surf zone, *Conf. on the Engineering Dynamics in the Surf Zone*, Sydney, pp. 208-214.
- Hattori, M. and Kawamata, R. (1980) : Onshore-offshore transport and beach profile change, *Proc. 17th Coastal Engineering Conf.*, pp. 1175-1193.
- Iwagaki, Y. and Noda, H. (1961) : A study of scale effects in experiments for beach processes, *Proc. 8th Japanese Conf. Coastal Engineering*, pp. 139-143 (In Japanese).
- Ito, M. (1982) : Applicability of the similitude of two-dimensional beach change, *Proc. 29th Japanese Conf. Coastal Engineering*, pp. 311-315 (In Japanese).
- Ito, M. and Tsuchiya, Y. (In contribution) : On the similitude in two-dimensional beach change, *Proceedings of JSCE*, (In Japanese).
- Johnson, J. W. (1949) : Scale effects in hydraulic models involving wave action, *Trans. AGU*, Vol. 30, pp. 517-525.
- Noda, E. K. (1972) : Equilibrium beach profile scale-model relationship, *Jour. Waterways, Harbors and Coastal Engineering Divi. ASCE*, pp. 511-528.
- Ozaki, A. (1964) : On the effect of an offshore breakwater on the maintenance of a harbor constructed on a sandy beach, *Proc. 9th Coastal Engineering Conf.*, pp. 323-345.
- Saville, T. Tr. (1957) : Scale effects in two-dimensional beach studies, *Proc. 7th General Meeting, IAHR*, pp. A3. 1-8.
- Sizuoka prefecture, Japan (1973) : Erosion control on Tagonoura coast, *Report of Laboratory scale model*, 211p. (In Japanese).
- Tsurumi, K. (1932) : Settling velocity; theory and experiments, *Journal of JSCE*, Vol. 18, No. 10, pp. 1059-1094, (In Japanese).
- Tanaka, N. and Osanai, H. (1979) : The stability of artificial beaches; investigations on the project of construction of the artificial beach along Suma Coast by mobile bed model, *Tech. Note of the PHRIMI*, No. 326, 50p. (In Japanese).

## CHAPTER NINETY SIX

### FORMATION OF TOMBOLO AT THE WEST COAST OF IWO-JIMA

By

Toshiyuki SHIGEMURA\*

Jouji TAKASUGI\*\*

and

Yoshihiro KOMIYA\*\*\*

#### Abstract

This paper intends to clarify why and how such a huge tombolo having a surface area of 1,700,000 m<sup>2</sup> has been formed at the west coast of Iwo-jima for relatively short period of 33 years after 1945.

Analyses are performed on various data obtained through literature survey and field measurements to determine the growth rate of tombolo and variation rate of shore and sea floor surrounding the island. Model tests are also made on the formation of tombolo.

The followings are the conclusions derived through the analyses:

- (1). Source of the sediments is the one produced at the northern part of island where sea floor has been lifting at a rate exceeding 30 cm per year.
- (2). Waves with dominant direction of N to NE which appear in fall and winter erode the northern coast and currents induced by these waves carry these sediments southward along both coasts of the island.
- (3). Waves with dominant direction of S to SE which appear in summer and their induced currents carry the sediments northward along both coasts of the island.

#### 1. Introduction

Iwo-jima is a small volcanic island located in the Pacific ocean at a location which is approximately 1250 km southward from Tokyo (24°45'N to 24°49'N in latitude and 141°17'E to 141°21'E in longitude). This island is situated at the southern tip of Izu-Ogasawara volcanic arc.

Figure 1 shows the present topography of Iwo-jima. Surface area and length of shoreline of the island are 23.2 km<sup>2</sup> and 24.3 km, respectively. Geologically, the island consists of the following three parts:

- (1). Motoyama area which is a broad dome or a truncated strato-volcano situating at the northern half of the island.
- (2). Suribachi-yama which is a pyroclastic cone locating at the southern tip of the island.

\* M.ASCE, Professor, Civil Engineering Dept., National Defense Academy  
1-10-20 Hashirimizu, Yokosuka, Kanagawa, Japan

\*\* Lt.s.g., Engineering Dept., Japan Maritime Self Defense Force

\*\*\* 1st Lt., 101 Topographic Battalion, Japan Ground Self Defense Force

(3). Chidoriga-hara area which is a gentle slope locating between Motoyama area and Suribachi-yama, formed by the fill of loose volcanic ashes and fine cinders<sup>1,5</sup>).

This island is relatively flat except for Suribachi-yama and most surface is covered by considerably thick vegetation. There are no rivers in this island, and a few cliffs eroded seriously by waves are found at northern coast. Judging from these features, it seems unnatural to anticipate that sediments are either produced in the island or transported from elsewhere in the vicinity of the island. Nevertheless, Iwo-jima is surrounded by relatively wide sandy beach except for northern part of the island. Further, the shoreline keeps advancing toward seaward year by year.

One of the remarkable characteristics of Iwo-jima is the continuous upheaval of island. This fact can be substantiated by the existence of numerous treads of marine terraces which are found all over the island. Especially for the past few decades, this island has kept lifting at the rate exceeding 30 cm per year at the northern part although upheaval rate at the southern part is smaller considerably<sup>6,10</sup>). This remarkable upheaval seems to have caused the continuous advancement of shoreline toward seaward.

Advancement of the shoreline has been quite remarkable especially at the west coast of Iwo-jima. Nautical chart published by US Navy in 1945 indicates that a group of rocks named kama-iwa was situated approximately 1 km off the west coast of Iwo-jima and the isthmus between kama-iwa and west coast used to be a navigable channel whose maximum depth was 36 m at that time. This channel got narrower and narrower since 1945, and in June 1968 when the island was returned to Japan, kama-iwa has finally touched with the tip of west coast to form a huge tombolo there.

This paper intends to clarify the following questions as quantitatively as possible by analyzing maps, charts and aerial photos of Iwo-jima which are available at the present stage and by performing both field surveys and model tests:

- (1). Where and how were the abundant sediments produced in this island ?
- (2). Why and how was the tombolo formed at the present location ?
- (3). Is the present topography of the island stable in future ?

## 2. Collection of Basic Data

### 2-1. Collection of data through literature survey

#### (1). Topographic data of Iwo-jima

To check the variation of both surface and bottom topographies, maps

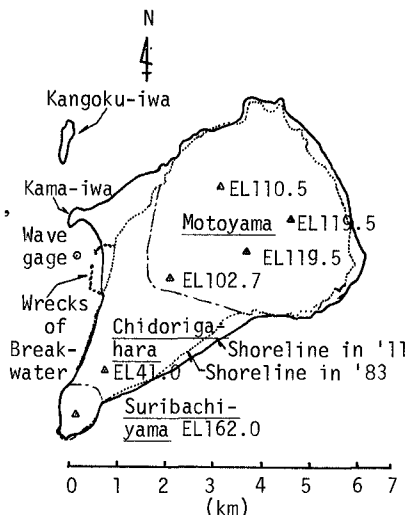


Fig.1. Topography of Iwo-jima.

and charts published and photos taken so far of Iwo-jima were all collected. Table 1 summarizes these collected materials.

Table 1. Source of data used for the analysis of topographic features of Iwo-jima.

No	Source of data	Office of publication	Year	Scale
1	Topographic map	Land Survey Dept., Japanese Imperial Army(Iwo To, No.12)	1911	1/50000
2	Chart	Hydrographic Dept., Japanese Imperial Navy (Iwo To, No.220-3003)	1934	1/30000
3	Chart	Hydrographic Office, US Navy (IO JIMA,DMA97BHA97562)	1945	1/20000
4	Map & Chart	US Army (IWO-JIMA,ST632II NW)	1952	1/25000
5	Topographic map	Geographical Survey Inst., Japan (Iwo To, NG-54-17-12-3)	1968	1/25000
6	Topographic map	National Research Center for Disaster Prevention,Japan (Volcanic Phenomena of Iwo-jima)	1972	1/10000
7	Chart	Hydrographic Dept., Japan Maritime Safety Agency (Chart of the surrounding Sea of Iwo jima)	1981	1/50000
8	Topographic map	Geographic Survey Inst., Japan (Iwo To, NG-54-17-12-1-3-4)	1982	1/50000
9	Aerial photo	Japan Maritime Self-Defense Force	1983	

Each of these materials was enlarged into the pictures with scale of 1/10000. Positions of the shoreline in each picture was determined at every increment of 5 mm or 5 m in real scale by tracing the shoreline with a device or an A-D convertor which converts the position of tracer into digital figures and punches them on data cards automatically. Depth data was determined in the following way, based on the enlarged pictures of the charts published by US Navy in 1945 and of the one published by the Hydrographic Department of Japan Maritime Safety Agency(JMSA) in 1981;

- (a). Provide a common area of 1.4 m in the direction from west to east, be 1 m in the direction from north to south on both enlarged pictures so that the island could be contained in the common area.
- (b). Divide the common area into 3500 square subsections each of which has the area of 2 cm by 2 cm.
- (c). Determine the depth at each corner of the subsections based on the depth data available in their vicinity.

#### (2). Meteorological data in Iwo-jima

Since 1968, a contingent troop of Japan Maritime Self Defense Force (JMSDF) has stationed in Iwo-jima and has been taking meteorological data every 3 hour. The data recorded during the period from 1968 to 1977 will be used for the analysis of meteorological features in Iwo-jima.

#### (3). Upheaval data in Iwo-jima

Kaizuka et al<sup>7)</sup> have pointed out in their paper that Iwo-jima is a top portion of a strato-volcano rising roughly 1500 m to 2000 m above the seabed on which foot of volcano is expanding about 40 km in diameter.

Ouyagi and Kumagai<sup>9)</sup> made <sup>14</sup>C dating test of carbonized wood pieces and corals sampled at various elevation of Iwo-jima and derived the following conclusions:

(a). Geological history of the island might be in the order of 3000 years at most.

(b). Average upheaval rate in the past would be 19 cm per year in Motoyama area and 3 cm per year in Suribachi-yama.

Tsuji et al<sup>10)</sup> compared the elevations of several points shown in the topographic map published by US Army in 1952 with the ones of the corresponding points which they got through their levelling performed in 1968. As a result, they found that outer edge of Motoyama area has upheaved roughly 9 m although Suribachi-yama has upheaved less than 2 m for the past 16 years after 1952.

Kosaka et al<sup>8)</sup> collected old maps and charts of Iwo-jima published after 1911. They also performed levelling at Iwo-jima four times in the period from 1968 to 1978. By analyzing these data, they found that mean upheaval rate in Motoyama area reached roughly 30 cm per year after 1952 although it was 11 cm per year before 1952.

## 2-2. Collection of data through field surveys

### (1). Wave data at Iwo-jima

Wave data has never been measured in Iwo-jima until lately.

On July 7, 1981, the authors installed a supersonic type wave meter about 450 m off the shoreline of west coast where the depth was roughly 12 m. Figure 2 shows the bottom topography in the vicinity of installation point. Bottom slope around there was roughly 1/40.

A mound made of 5 m steel pile with a diameter of 20 cm was driven 3.5 m in depth into the seabed. The sensor was mounted on the top of the mound and was connected to a penoscillograph in an observatory which was built on the shore, through a marine cable whose diameter is 39 mm. This wave meter can record only the fluctuation of water surface at the measuring point. Thus, information of the wave direction can not be obtained from the record. Due to the limitation of recording paper, the recorder was set so that wave data could be recorded for 10 minutes every two hour.

Unfortunately, cable was cut and washed away on August 19, 1981 when

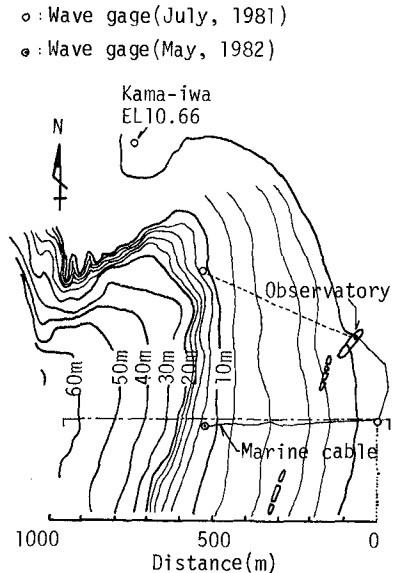


Fig.2. Installation point of wave meter

typhoon #15 hit the island. The record taken just before the incident indicated that the maximum height of the swells was roughly 10 m.

The same wave meter was installed again on May 10, 1982 at the location which is about 500 m south from the former position where the depth is also roughly 12 m (see fig.2). This meter survived for 19 months after the installation although it was also washed away on November 7, 1983 while typhoon #17 was hitting the island. For these 19 months, the recorder had kept recording wave data for 10 minutes every 2 hour. These data was processed by the A-D convertor mentioned previously at a sampling interval of 0.5 second and was punched on data cards automatically.

#### (2). Upheaval data on the backshore of Iwo-jima

Previous works have revealed that upheaval in Iwo-jima is dominant in Motoyama area and that it becomes greater and greater as it goes from the central portion to the shore of the island where the engineers are most interested in. Thus, it was planned to get more reliable upheaval data along the whole backshore of the island. Levelling have been performed three time for 19 months after August 1982, by using 50 measuring stations placed at almost equi-interval on the whole backshore of the island.

#### (3). Physical properties of sands along the shoreline of Iwo-jima

In order to see if the physical properties of sands around the shoreline will vary both seasonally and regionally, sands were sampled on June 1983 and on February 1984 at 50 locations along the shoreline where the lines each of which contain one of the 50 stations intersect perpendicularly to the shoreline. Both sieve analysis and specific gravity test were performed on all of these sands to determine their physical properties.

### 3. Analysis of Collected Data

#### (1). Meteorological features in Iwo-jima

JMSDF made an intensive statistical analysis on the meteorological data recorded in Iwo-jima for the past 10 years after 1968<sup>2)</sup>. Through these analyses together with the author's analysis, the following features were revealed on the meteorological characteristics in Iwo-jima:

##### (i). Temperature in Iwo-jima

(a). Mean monthly temperature is approximately 27°C through summer and fall although it is about 19°C in winter. From spring to summer, temperature rises from 19°C to 27°C almost linearly.

(b). Daily variation of temperature is less than 5°C through the year.

##### (ii). Rainfall in Iwo-jima

(a). Monthly rainfall exceeds 100 mm during the period from May to December although it is less than 70 mm in the rest of the months.

(b). Rainy days count approximately 145 days per year and yearly rainfall is roughly 1300 mm.

##### (iii). Winds in Iwo-jima

Figures 3 shows seasonal wind roses in Iwo-jima. In these roses, rigid lines indicate mean frequency of occurrence in each direction

which was determined from whole data of winds, and do the dotted lines the one determined through the data of winds whose velocities are greater than 10 m/s. From these wind roses, the following features were found on the wind characteristics in Iwo-jima:

(a). East winds are dominant in spring, summer and fall although north winds are dominant in winter. After east winds, south winds are dominant in spring and summer.

(b). West winds are quite few through the year.

(c). Only 3.5 % of total winds are the high winds whose velocities exceed 10 m/s.

(d). Dominant direction of high winds ranges from SE to SSE during summer although it ranges from NNW to NE in fall and winter. High winds also blow from the direction ranging from W to N in winter.

(iv). Typhoons in Iwo-jima

Figure 4 shows the yearly cumulative number of typhoons generated at the north Pacific after 1945<sup>3)</sup>. In this figure, rigid lines indicates cumulative number of whole typhoons generated at the north Pacific and do the dotted and chain lines the ones which hit Iwo-jima, respectively.

From this figure, the following facts were found on the typhoons in Iwo-jima:

(a). 20 to 40 typhoons are generated each year at the north Pacific.

(b). At least one fifth of them hit Iwo-jima every year.

(c). Typhoons with central pressure less than 960 mb possibly hit Iwo-jima at least once a year.

(2). Wave characteristics in Iwo-jima

Each of the 10 minutes records of wave data recorded for 19 months after May, 1982 was processed at a sampling interval of 0.5 second by an A-D convertor to yield 1200 data

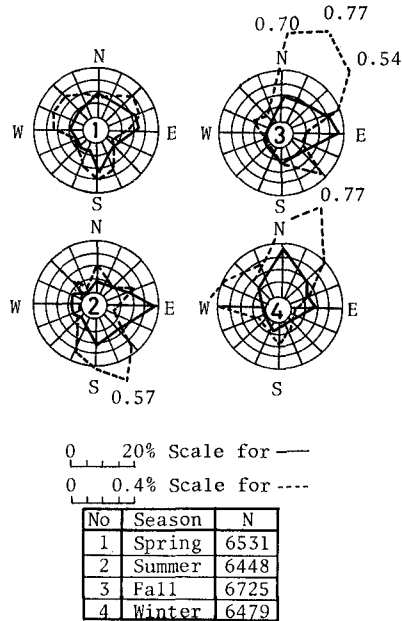


Fig.3. Seasonal wind roses in Iwo-jima.

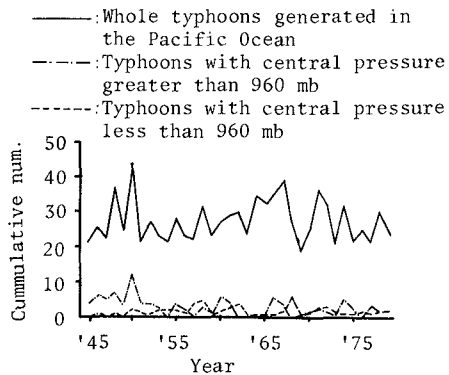


Fig. 4. Typhoon statistics in the north Pacific and Iwo-jima.

from it. These processed data were analyzed by means of the zero up crossing method to determine the heights and periods of waves.

Figure 5 shows an example of the analytical results. Huge peak appeared around the righthand edge are the swells which hit Iwo-jima when typhoon #10 with central pressure of 940 mb passed about 350 km off the west coast of Iwo-jima on July 31, 1982.

The maximum height and its significant period of the swells determined from the record taken at 8 AM of July 31 were 9.2 m and 19.0 seconds, respectively.

Table 2 summarizes seasonal distribution rate of significant waves whose height and period are in the given ranges of magnitude.

Table 2. Seasonal distribution rate of significant height and period of waves in Iwo-jima.

	$H_{1/3}$ (m)				$T_{1/3}$ (s)			
	0-1	1-2	2-3	<3	6	6-8	8-10	<10
Spring	62	36	1	1	29	51	16	4
Summer	70	20	4	6	21	42	21	16
Fall	73	14	7	6	8	43	27	22
Winter	59	35	6	0	31	49	16	4

From this table, it can be seen that dominant waves in Iwo-jima are those whose significant heights are less than 1 m and whose significant periods are less than 8 seconds except for the waves appearing in summer and winter.

Table 3. Values of  $H_{max}$  and  $T_{1/3}$  of the waves recorded while typhoons were hitting Iwo-jima.

No	Date	Time	$H_{max}$	$T_{1/3}$	Pres.	Location	$V_{max}$	$\theta$
#4	May 23, '82	0200	8.4 m	18.5 s	980 mb	NNW 150 km	27.5m/s	ENE
#5	Jun 26, '82	1000	5.4 m	11.1 s	975 mb	NW 250 km	32.5m/s	N
#10	Jul 31, '82	0800	9.2 m	19.0 s	940 mb	WNW 350 km	50.0m/s	NNW
#13	Aug 24, '82	2100	Lack of data		940 mb	W 850 km	45.0m/s	NNW
#15	Aug 30, '82	0900	Lack of data		945 mb	W 300 km	45.0m/s	NW
#18	Sep 11, '82	1000	5.3 m	12.0 s	965 mb	WNW 600 km	35.0m/s	NW
#19	Sep 19, '82	0000	5.2 m	8.3 s	940 mb	WSW1400 km	45.0m/s	WNW
#21	Oct 7, '82	1600	9.8 m	11.5 s	920 mb	WSW 600 km	50.0m/s	NNW
#5	Aug 13, '83	0600	9.8 m	13.3 s	915 mb	WSW1040 km	55.5m/s	NNE
#13	Oct 11, '83	1000	1.8 m	8.1 s	980 mb	NNW1050 km	25.3m/s	ENE
#17	Nov 2, '83	0200	Lack of data		985 mb	NNE1030 km	30.0m/s	NNW

Table 3 summarizes the values of the maximum height and the corresponding significant period of waves recorded for 19 months after May,

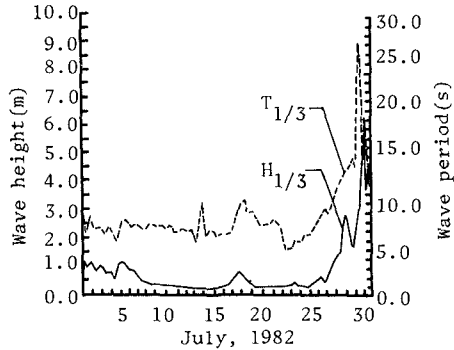


Fig. 5. Variation of significant height and period of waves in July, 1982.



1982 at the west coast of Iwo-jima while typhoons were hitting the island. In this table, location means the direction of and distance to the typhoon measured from the location of wave meter, does  $V_{max}$  the maximum velocity of the wind at the center of typhoon, and does  $\theta$  the advancing direction of the typhoon.

From this table, it can be noticed that swells whose maximum height is roughly 10 m and whose significant period is greater than 12 seconds will approach to the west coast of Iwo-jima when typhoons whose central pressure is less than 940 mb pass within a circle with semi-diameter of 400 km in which Iwo-jima is situated at its center.

Correlation analysis was performed among the characteristic values of the highest waves of each class. Table 4 summarizes correlation coefficients found among these characteristic values.

Table 4. Correlation coefficients among the characteristic values of waves.

	$H_{max}$	$H_{1/10}$	$H_{1/3}$	$H_{mn}$	$T_{max}$	$T_{1/10}$	$T_{1/3}$	$T_{mn}$	$T_{max}^2$	$T_{1/10}^2$	$T_{1/3}^2$	$T_{mn}^2$
$H_{max}$	1.00	0.98	0.97	0.95	0.44	0.52	0.54	0.56	0.31	0.48	0.54	0.61
$H_{1/10}$	0.98	1.00	1.00	0.98	0.47	0.55	0.58	0.59	0.33	0.51	0.58	0.64
$H_{1/3}$	0.97	1.00	1.00	0.99	0.46	0.55	0.57	0.59	0.32	0.51	0.58	0.64
$H_{mn}$	0.95	0.98	0.99	1.00	0.43	0.51	0.53	0.55	0.48	0.49	0.54	0.61

This table indicates that there exists quite high correlation among the wave heights of each class and among the wave periods of each class, respectively although correlation between height and period is quite low.

Table 5 summarizes results of the regression analysis performed among the wave height of the highest waves of each class. In this table,  $a_T$  means the regression coefficient determined through the data in Iwo-jima and does R the correlation coefficient, and does  $a_R$  the regression coefficient predicted through Rayleigh distribution.

These results clearly indicate that distribution of wave height agree quite satisfactorily with Rayleigh distribution.

As mentioned previously, no information was obtained from the records of waves on their directions. However, visually observed data is available on the direction of seas and swells.

Figure 6 shows the seasonal distribution of seas and swells in each direction which were determined on the basis of visually observed data by ships at the area in north Pacific in which Iwo-jima is included <sup>4)</sup>. In these figures, rigid lines indicate the distribution rate of seas and swells determined through the whole data observed in the period from 1973 to 1979. Comparison of figure 6 with figure 3 clearly indicates that distribution pattern of seas and swells are quite similar to those of the wind roses which were made based on the wind data measured at Iwo-jima.

(3). Physical properties of sands sampled along the shoreline of Iwo-jima

To see whether the physical properties of sands near the shoreline

Table 5. Results of the regression analysis performed among heights of the maximum waves of each class.

	$a_T$	R	$a_R$
$H_{max}/H_{1/10}$	1.21	0.98	---
$H_{max}/H_{1/3}$	1.51	0.97	---
$H_{max}/H_{mn}$	2.31	0.95	---
$H_{1/10}/H_{1/3}$	1.25	0.97	1.27
$H_{1/10}/H_{mn}$	1.94	0.98	2.03
$H_{1/3}/H_{mn}$	1.55	0.99	1.60

vary regionally and seasonally, sieve analysis and specific gravity test were performed on the sands sampled in June 1983 and in February 1984, respectively at 50 locations along the whole shoreline of Iwo-jima.

Figure 7 shows the distribution of median diameter ( $D_{50}$ ) and specific gravity ( $G_s$ ) of sands sampled along the shoreline of four coasts (see figure 9). In this figure, abscissa indicates the distance measured southward along the shoreline on each coast from its northern end.

From these figures, the following features were found on the physical properties of sands along the shoreline of Iwo-jima:

- (a). Sands sampled in both N-E and N-W coasts have fairly constant values of  $D_{50}$  ranging from 0.3 mm to 0.7 mm through the year.
- (b). Sands in both S-E and S-W coasts have larger values of  $D_{50}$  through the year in comparison to those in N-E and N-W coasts. Especially, sands sampled at S-W coast in June 1983 have the value of  $D_{50}$  which is greater than 5.0 mm.
- (c). Sands sampled in June 1983 at each coast have the values of  $D_{50}$  which tend to become greater slightly along the shoreline as it goes southward.
- (d). Specific gravity of sands is fairly constant through the year ranging from 2.3 to 2.8 except for that of the sands sampled at N-E coast. However, sands sampled in June 1983 at N-E coast have the values of  $G_s$  which are greater than 3.0.
- (e). Distinct tendency is not found in both regional and seasonal variation of the value of  $G_s$ .

Judging from these findings together with wind

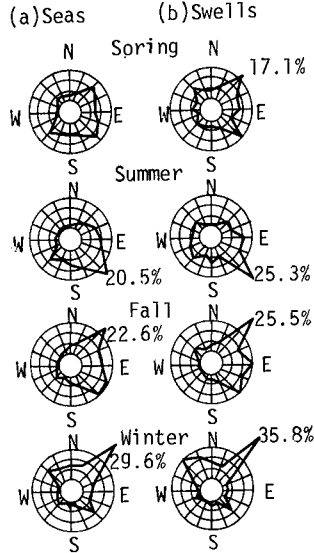


Fig. 6. Distribution of seas and swells in north Pacific near Iwo-jima. (a) Distribution of  $D_{50}$  (b) Distribution of  $G_s$

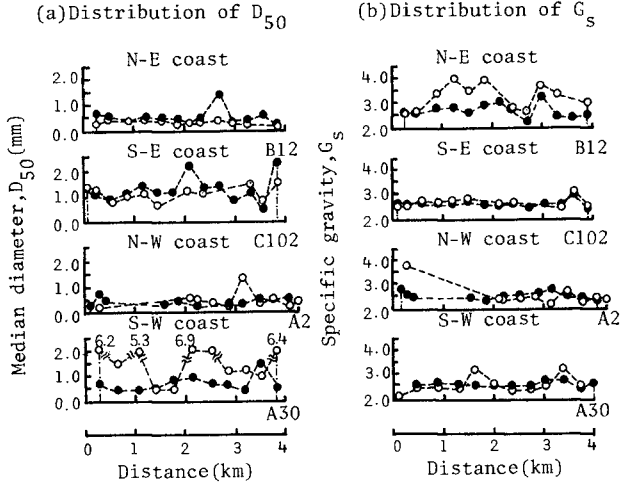


Fig. 7. Variation of median diameter and specific gravity of sands sampled along the shoreline of Iwo-jima.

and wave characteristics in Iwo-jima, it can be anticipated that littoral currents may flow southward in winter but northward in summer along both coasts of the island.

#### (4). Upheaval phenomena in Iwo-jima

Figure 8(a) shows the iso-upheaval lines in Iwo-jima which were presented by Tsuji et al in 1969. These lines were determined by comparing the elevations of several points shown in the map published by US Army in 1952 with the ones of the corresponding points which were obtained by Tsuji et al through their levelling performed in 1968.

Figure 8(b) on the other hand, shows the mean upheaval rate and cumulative upheaved height of Iwo-jima which were presented by Kosaka et al in 1979. They determined these values by comparing the elevations of several points in Motoyama area shown in older maps and charts published after 1911, and by analyzing their own data of the levelling which they performed four times in the period from 1968 to 1978.

These findings indicate the following facts on the upheaval phenomena in Iwo-jima:

- (a). Upheaval rate is not constant over the island but varies remarkably from place to place.
- (b). Upheaval rate in Motoyama area is roughly 30 cm per year recently and cumulative upheaved height has reached roughly 12 m since 1945.

The authors have also performed levellings on the backshore of Iwo-jima in August 1982, June 1983 and February 1984, respectively by using 50 measuring stations which have been placed along the whole backshore of the island. A bench mark was placed at the foot of Suribachi-yama where upheaval might be smallest in this island.

Figure 9 shows the relative values of upheaval height in each station which were determined on the basis of the elevation of each station measured in August 1982. From this figure, the following facts were revealed:

- (a). Stations in N-E coasts had sunk at the rate of roughly 25 cm to 30 cm per year for the first 10 months although they began to upheave at the rate of 30 cm per year after June 1983.
- (b). Northern stations in N-W coast began to upheave at a remarkable rate of roughly 1.5 m per year after June 1983 although southern stations near Kamaiwa area sank at the rate of 15 cm per year in the same period.
- (c). Stations placed in S-E coast kept upheaving at the rate of roughly 35 cm to 40 cm per year after August 1982.

These findings indicate that Iwo-jima keeps upheaving at present in an order of 30 cm to 40 cm per year as a whole although upheaving does not occur at a constant rate over the island but fluctuates from place

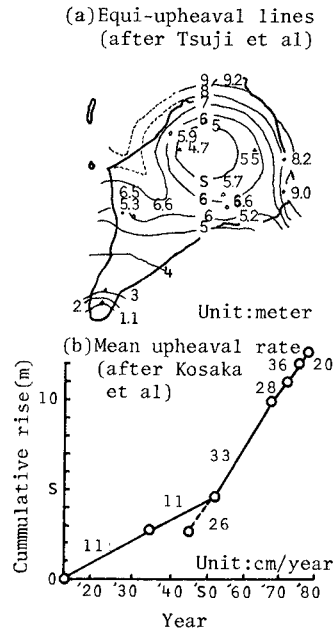


Fig.8. Upheaval phenomena in Iwo-jima.

not occur at a constant rate over the island but fluctuates from place to place and from time to time.

(5). Variation of the shore in Iwo-jima

Figure 10 shows the shorelines of Iwo-jima in 1911, 1952 and 1983, respectively. It can be clearly seen from this figure that shoreline of the island has kept advancing seaward since 1911. Further, it can be noticed that advancement of shoreline is quite remarkable at the west coast of Iwo-jima.

To see the variation of shore more quantitatively, length of the shoreline and shore area were calculated by using the processed data of the shorelines in each year which was stated previously.

Figure 11 shows the variation of both length of the shoreline and shore area which were the relative values determined by comparing those values with the their corresponding values in 1911.

From this figure, the following facts were revealed:

(a). Shoreline in the west coast was elongated continuously until 1972 at mean rate of 60 m per year although it began to be shorten at mean rate of 120m per year after 1972. Shoreline in the east coast, on the other hand has been repeating elongation and shortening since 1911 until present.

(b). Shoreline in the northern tip of the island kept advancing seaward until 1968 at mean rate of 6 m per year although it began to retreat landward at mean rate of 16 m per year after 1968.

(c). Shore area in the west coast kept increasing at mean rate of 3200 m<sup>2</sup> per year until 1972 although it began to decrease at mean rate of 39000 m<sup>2</sup> per year after 1972.

(d). Shore area in the east coast kept decreasing at mean rate of 35000 m<sup>2</sup> per year until 1934 although it has kept increasing at mean rate of 46000 m<sup>2</sup> per year after 1934.

(e). Shore area in northern tip of the island kept increasing until 1968 at mean rate of 5200 m<sup>2</sup> per year although it began to decrease at mean

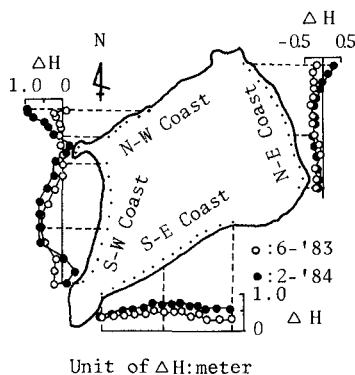


Fig. 9. Upheaval phenomena on the backshore of Iwo-jima.

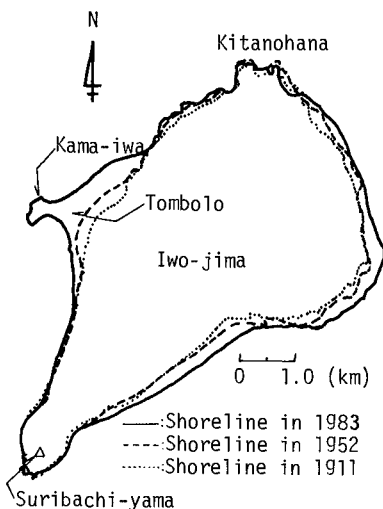


Fig. 9. Upheaval phenomena in the backshore of Iwo-jima.

rate of 18000 m<sup>2</sup> per year after 1968.

(f). Shore area in the whole coast has kept increasing after 1911 until 1968. Increasing was drastic especially after 1952 until 1968. In this period, mean rate of increasing reached 141000 m<sup>2</sup> per year. After 1968 however, shore area in this island has kept almost constant value until present.

Similarly, volumetric variation occurred on the sea floor was also calculated by using depth data in 1945 and 1981, respectively. Here, calculation was made within the zone surrounding the shoreline in 1945 with width of 1 km extended seaward.

Figure 12 shows the result of calculation. In this figure, abscissa indicates the distance measured from the northern edge of the considering area, and do the ordinate either eroded or the deposited volume of the sediments over the subsectional area of 1 km by 200 m in the considering zone.

From this figure, the following facts were revealed:

(a). On the sea floor off the west coast, sediments have been deposited on its most part although sea floor down the southern edge of tombolo has been eroded seriously over the range extending roughly 1.4 km along the shoreline.

(b). On the sea floor off the east coast, sediments have also been deposited on its most part although sea floor has been eroded seriously at the northern part of Suribachi-yama over the range of couple hundred meters along the shoreline.

(c). Total amount of sediments deposited on the sea floor off the west coast is roughly 57.6x10<sup>6</sup> m<sup>3</sup> although the one deposited on the sea floor off the east coast is roughly

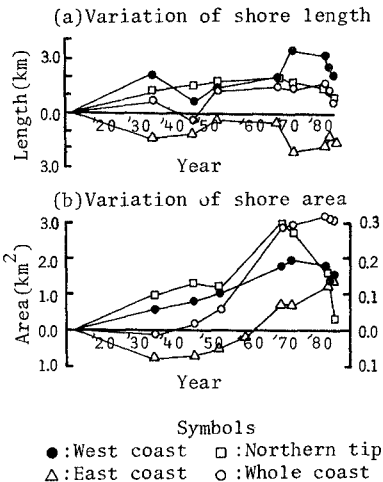


Fig. 11. Variation of shoreline length and shore area in Iwo-jima.

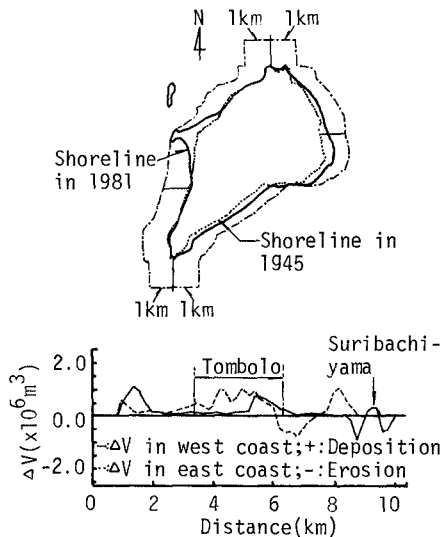


Fig. 12. Volumetric variation of sediments occurred on the sea floor of Iwo-jima.

$36.1 \times 10^6 \text{ m}^3$ . Further, variation pattern appeared on the sea floor are quite similar in both east and west coasts.

These findings together with the results of the analyses done so far possibly indicate that these huge amount of sediments might be the one produced due to the continuous eroding action of dominant waves exerted on the upheaved sea floor, and that these eroded sediments might have been transported by the wave induced currents to form the present bottom configuration in this island.

To examine the suitability of this assumption, similar analysis was made by assuming that the following four types of upheaval have occurred in Iwo-jima for the past 36 years:

Type 1: Island has upheaved 12 m uniformly.

Type 2: Island has upheaved 10 m uniformly.

Type 3: Island has upheaved with an inclination as shown below:

Upheaved 12 m in the northern edge and 2 m in southern edge of the island.

Type 4: Island has upheaved with an inclination as shown below:

Upheaved 10 m in northern edge and 1 m in southern edge of the island.

Table 6 summarized analytical results.

Table 6. Balance of sediments on the sea floor of Iwo-jima.

	West coast			East coast			Unit of $V_e$ and $V_d$ $: \times 10^6 \text{ m}^3$
	$V_e$	$V_d$	R(%)	$V_e$	$V_d$	R(%)	
Case 1	39.177	12.416	31.7	29.025	4.470	15.4	
Case 2	31.087	14.802	47.6	22.423	7.386	32.9	
Case 3	23.254	18.635	80.1	20.104	13.639	67.8	
Case 4	15.098	22,547	141.7	14.352	20.127	140.2	

In this table,  $V_e$  indicates imaginary volume of sediments which was produced by eroding the imaginary sea floor upheaved by adding one of four types of upheaval shown above on the sea floor in 1945 until it gets to the sea floor in 1981. Similarly,  $V_d$  means the imaginary volume of sediments which was deposited on the imaginary sea floor until it gets to the sea floor in 1981. Further, R is the ratio of  $V_d$  to  $V_e$ . From this table, the following facts were revealed:

(a). Source of the sediments which contributed to form the present shoreline and sea floor is the one produced by the erosion of upheaved sea floor.

(b). Upheaval assumed in Type 3 might be the most reasonable one which might have occurred in Iwo-jima for the past 36 years after 1945.

#### 4. Formation of Tombolo at the west coast of Iwo-jima

##### (1). Growth and variation of tombolo at the west coast of Iwo-jima

As stated previously, the channel existed between kamaiwa and west coast had got narrower and narrower since 1945 due to the continuous advancement of west coast and was finally closed in 1968 to form there a huge tombolo.

Figure 13 shows the decreasing rate of the channel width and growth rate of shore area at the west coast before the channel was closed and growth rate of tombolo's width at its neck or the narrowest section of

tombolo and of the shore area after the channel was closed.

Through this figure, following facts were revealed:

(a). After 1945, west coast began to advance seaward drastically at mean rate of roughly 50 m per year until 1968 when kamaui was touched by the tip of the west coast. During this period, shore area at the west coast kept increasing at mean rate of 42000 m<sup>2</sup> per year.

(b). After the channel was closed, both tombolo's width at its neck and the area of tombolo kept increasing at mean rate of roughly 20 m and 8200 m<sup>2</sup> per year, respectively until 1978.

(c). After 1978, tombolo has been in almost equilibrium state having the width of 200 m and area of 1.7x10<sup>6</sup> m<sup>2</sup> although these values have been fluctuating around the respective values stated above.

(2). Experimental verification of the formation of tombolo

Through the results of analyses done so far, the authors derived the following inferences on the formation of tombolo at the west coast of Iwo-jima:

(a). Dominant waves in Iwo-jima which have the direction ranging from N to NE have produced huge amount of sediments by their continuous eroding action on the sea floor of mainly northern part of the island which had been lifted by the inclined upheaval.

(b). Currents induced by these dominant waves have transported sediments southward along both coasts of the island although the currents induced by huge swells which hit Iwo-jima in summer and early fall have transported sediments northward along both coasts of the island.

(c). Sea floor off the west coast has had the topography which helped form tombolo there.

To verify these inferences, it was decided to perform model tests as follows:

Figure 14 shows the experimental zone and observation area chosen off the west coast of Iwo-jima. Based on the depth data in 1945, model of this zone was built with horizontal scale of 1/1000 and vertical scale of 1/500, by using mortar. This model was placed in a wave tank of 12.5 m long by 4.5 m wide by 1.2 m deep and crushed coals with median diameter of 0.27 mm and specific gravity of 1.72 were lain on its surface in 2 cm thick.

In the observation area of 3.0 m long by 1.75 m wide, a base line was placed for the measurement of various terms. On this base line, 25 measuring stations were provided at every 10 cm interval. Further, a model of breakwater built by US Navy in 1945 was also placed at the corresponding location.

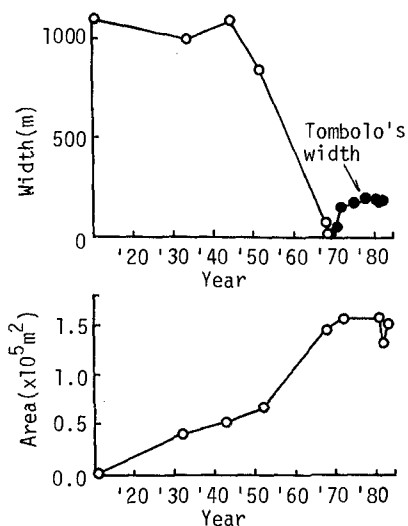


Fig. 13. Growth of the shore at the west coast of Iwo-jima.

Capacitance type wave gage was installed off the northern end of observation area to measure incident waves. Video camera was also hung down from the ceiling to get continuous records of wave refraction and direction of shore currents.

Because of the difficulty in handling model floor, it was decided to perform experiments only for the limited case when stormy waves are loaded from a direction ranging from N to NE on the shore of the island which is upheaved uniformly at a constant rate per year.

Further, it was decided to perform experiments in accordance with the following procedures:

(a). Crushed coals are supplied at a certain rate manually off the northern end of observation area whenever supplied coals are washed away.

(b). Effect of upheaval is given by lowering water level up to 2 cm in total at a constant rate.

(c). Special dye is injected manually off the northern end of observation area.

Since it is impossible to hold similarity law in such a model test as this, only the wave conditions were determined by referring to Froude law of similarity. The rests of conditions were all determined through the primary runs which were done by changing conditions by trial and error method so that shoreline on the model shore may agree most satisfactorily with the one shown on the chart in 1981.

Here, agreement was evaluated by the values of the standard deviation of shoreline on the model shore from the corresponding one shown on the chart in 1981. Standard deviation,  $\Delta S$  was calculated by using the data measured at every 30 minute along each line which was extended seaward from each station on the base line so that it might be perpendicular to the base line.

Seven different conditions were tried in primary runs. As a result, it was found that shoreline at the northern shore of tombolo could be reproduced quite satisfactorily on the model shore if the test was kept performed for 9 hours successively under the conditions shown in table 7.

Table 7. Test conditions determined through primary runs.

Incident waves			Upheaval rate	Supply rate of crushed coals
Height	Period	Dir.ec		
2.2 cm	0.5 sec	NNE	0.25cm/hr	6000 cm <sup>3</sup> /hr

Test was done again under the conditions shown in table 7. Due to the limit of space, variation of shoreline will be described here mainly. Variation of shoreline was measured every 30 minute. Figure 15 shows the

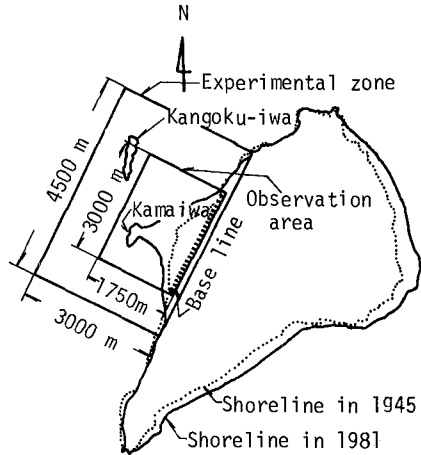


Fig. 14. Experimental zone and observation area chosen for model test.



shorelines measured at every 90 minute. Tip of the west coast began to advance rapidly when it passed roughly 270 minutes after starting the experiment, and finally reached Kamaiwa one hour later. The tip of west coast advanced along the northern slope of a saddle shaped mound which had originally existed along the sea-bed connecting Kamaiwa and west coast. Existence of this saddle resulted in blocking littoral currents there and diverting the course of it into northern tip of Kamaiwa.

As it can be seen from figure 15, shoreline at the northern shore of tombolo has shown quite good agreement with the one in 1981. However, shoreline at the southern shore of tombolo has advanced seaward considerably in comparison to the one in 1981. Further, a sand spit has been formed at the southern lee of Kamaiwa. These might have been formed because waves with the direction of only NNE had been loaded on the model shore.

Figure 16 shows the variation of  $\Delta S$  in the northern shore of tombolo with the lapse of time. In this figure, line with circles mean the values of  $\Delta S$  determined on the basis of whole data measured in the observation area, and do the rests of lines, the values of  $\Delta S$  which were determined on the basis of data measured in each of the 5 subsectional areas which were provided by dividing the observation area at an interval of 500 m to, see regional variation in the values of  $\Delta S$ .

From this figure, it can be seen that values of  $\Delta S$  become small suddenly at every subsectional area if 5 hours have passed after starting the run, and that model shore reaches almost equilibrium state if it has passed 9 hours after starting the run. The values of  $\Delta S$  in each subsectional area are less than 6 cm at the equilibrium state.

This test also indicates that one hour in the run under the conditions corresponds to 4 years in the field. If this time scale is true, upheaval rate and supply rate of crushed coals in table 7 become 31 cm and  $7.5 \times 10^5 \text{ m}^3$  per year, respectively, which are quite reasonable values. Further, it should be noted that the test clearly reproduced on the model floor that it took 23 years for the west coast to reach Kamaiwa and that it took 33 years for the west coast to get to an equilibrium state since 1945. These facts clearly indicates that the author's inferences on the formation of

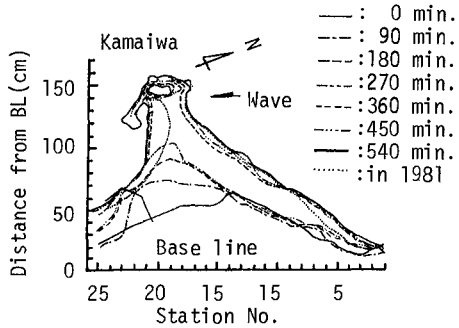


Fig. 15. Variation of shoreline with the lapse of time.

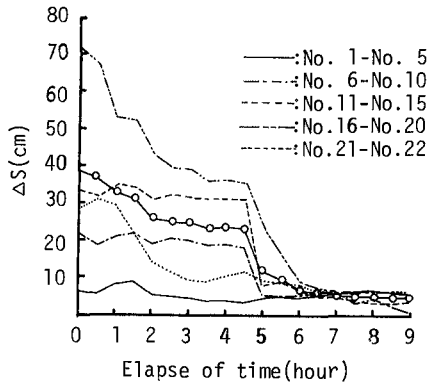


Fig. 16. Variation of  $\Delta S$  with the lapse of time.

tombolo were verified to be mostly true.

## 5. Conclusion

Growing process of tombolo formed at the west coast of Iwo-jima were investigated by analyzing various data obtained through both literature & field surveys. Inferences for the formation of tombolo derived through the analyses were examined by performing model test, which verified that these inferences were mostly true.

## Acknowledgement

The authors are indebted greatly to the 4th Aviation Group of JMSDF and to the 101 Topographic Battalion of JGSDF for their devoted cooperations which were given in various stages in accomplishing this study.

## References

- 1). Isshiki, N.:Geology and Petrography of Iwo-jima(Sulphur Island), Volcano Islands. Research Notes of the National Research Center for Disaster Prevention, No.23, 1976, pp.5-16(in Japanese).
- 2). Japan Port Consultants, Ltd.:Feasibility Study for Building Oil and Cargo Handling Facilities in Iwo-jima, 1982, p.4(in Japanese).
- 3). Same report as reference 2), p.5.
- 4). Same report as reference 2), pp.12-13.
- 5). Kaizuka,S., T. Miyauchi and S. Nagaoka:Marine terraces, active faults and tectonic history of Iwo-jima. Ogasawara Research Committee of Tokyo Metropolitan University, 1983. pp.13-45(in Japanese).
- 6). Kosaka, J et al:Investigation Report of the Volcanic Action in Ogasawara-Iwo-jima. Santama Office for isolated islands, Tokyo Metropolitan Government, No.1, 1972, pp.1-35(in Japanese).
- 7). Same as reference 5).
- 8). Kosaka, J. et al:Investigation Report of the Volcanic Action in Ogasawara-Iwo-jima. Santama Office for isolated islands, Tokyo Metropolitan Government, No.3, 1979, pp.1-89(in Japanese).
- 9). Ouyagi,N. and T. Kumagai:Carbon Fourteen Age of Iwo-jima(Sulphur Island), Volcano Island. Research Notes of the National Research Center for Disaster Prevention, No.25, 1977, pp.5-18(in Japanese).
- 10). Tsuji, S., M. Kuriyama and E. Tsurumi:Investigation Report of Ogasawara Islands. Report of Geological Survey Institute, Japan, No. 37, 1969, pp.1-18(in Japanese).
- 11). Same as reference 10).

## CHAPTER NINETY SEVEN

### A MODEL FOR OFFSHORE SEDIMENT TRANSPORT

M.J.F. Stive\* and J.A. Battjes\*\*

#### ABSTRACT

Observation of the two-dimensional breaking of random waves on a beach suggests that under conditions of active surf an important mechanism in the process of offshore sediment transport is the transport by the undertow or return flow, induced by the breaking of waves. It is found that a model incorporating this mechanism exclusively is able to describe the local sediment transport and the resulting bottom variation of a beach under random wave attack to a first approximation. A laboratory verification is made based on measurements of both the dynamics of the water motion and the bottom profile. Finally, a realistic equilibrium state is shown to result from the model.

#### 1. INTRODUCTION

The particular role of a nearly two-dimensional wave motion in the movement of sediment normal to the shore is poorly understood. It is generally assumed that a number of interaction mechanisms between this wave motion and the sediment motion contribute to the formation of the beach profile, also in the three-dimensional topographies that occur on a natural coast. Full account of all mechanisms can be taken if a description of both the horizontal velocity field,  $u(x,z,t)$ , and the sediment concentration field,  $c(x,z,t)$ , in space and time is available, so that the net cross-shore sediment transport,  $\bar{q}(x)$ , may be calculated from

$$\bar{q}(x) = \int_d u(x,z,t) \cdot c(x,z,t) dz \quad (1)$$

where the integration is performed over the instantaneous depth  $d$  and the overbar indicates time averaging. From the cross-shore variation of  $\bar{q}(x)$  the bottom changes may be derived.

Visual and experimental observation of random waves on a two-dimensional beach indicate that one of the more important mechanisms under active surf conditions may be the transport of sediment by the time mean, seawards directed flow near the bottom induced by the breaking of waves. It is shown that this mechanism is so dominant that a model incorporating this mechanism alone describes the bottom variations in the surf zone to a satisfactory, first approximation. This paper describes the properties of this one-mechanism model and its verification based on laboratory measurements both of the wave

---

\* Delft Hydraulics Laboratory, Delft, the Netherlands

\*\* Delft University of Technology, Delft, the Netherlands

motion and of the bottom profile. Furthermore, the equilibrium consequences of the model formulation are investigated.

In the elaboration of the present model simple, available formulations for the model elements have been used. Improved formulations can easily be incorporated without affecting the principle of the model. Extension of the model with other transport mechanisms is a logical step towards a more complete cross-shore sediment transport model. In this respect transport due to the asymmetry of the wave motion should be considered first.

## 2. MODEL FORMULATION

In principle the net cross-shore sediment transport may be calculated from Eq. (1). However, insufficient knowledge of the velocity and concentration field forces us to rely on a simplified form of Eq. (1), using the following observations and assumptions:

- (a) The sediment load,  $s$  ( $= \int_d c dz$ ), is mainly contained in the region near the bottom and as such locally determined.
- (b) The horizontal velocity field,  $u$ , is depth-uniform in the region near the bottom.

With the introduction of mean and (wave-induced) fluctuating components in the sediment load and the near-bottom horizontal velocity, i.e.  $s = \bar{s} + s'$  and  $u = \bar{u} + u'$ , the net sediment transport may be calculated as

$$\bar{q} = \overline{u \cdot s} = \overline{u \cdot \bar{s}} + \overline{u' \cdot s'} \quad (2)$$

Although this result reduces the problem to one which is potentially solvable on basis of our present knowledge we found it useful to reduce the problem further using the following assumptions:

- (c) The contribution due to the correlation between the fluctuating sediment load and horizontal velocity is small compared to that due to the mean (return) flow, i.e.  $\overline{u' \cdot s'} \ll \overline{u \cdot \bar{s}}$ .
- (d) The seawards directed, near-bottom mean flow velocity induced by a breaking wave is large compared to the mean flow velocity induced by a non-breaking wave of the same height, so that in a random wave field  $\bar{u}_{br} \gg \bar{u}_{nonbr}$ .

Based on these assumptions result (2) is simplified further to

$$\bar{q} = \bar{u}_{br} \cdot \bar{s} \quad (3)$$

In this approximation the net sediment transport in the surf zone is directed offshore. Simple, first approximations to the return flow,  $\bar{u}_{br}$ , and the mean sediment load,  $\bar{s}$ , may be as follows.

### the mean return flow in random breaking waves

It is assumed that in a random wave field breaking on a beach the majority of the breaking waves has a quasi-steady depth-similar flow field as described by Stive and Wind (1982) for breaking, periodic waves. Based on the dimensionless flow field presented there and adopting the observation that the flow profile is rather uniform over

the lower depths the return flow velocity in a periodic, breaking wave field is simply modelled as:

$$\bar{u}_{br,periodic} = 1/8 (g/d)^{1/2} H_b \quad (4)$$

where  $g$  is the acceleration of gravity,  $d$  the water depth and  $H_b$  the breaking wave height. The net mass flux below the level of the wave troughs becomes

$$M = 1/8 \rho (g/d)^{1/2} H_b d_t \quad (5)$$

where  $d_t$  is the water depth up to the trough level. This result corresponds closely to the net mass flux result above the level of the wave troughs for a steady, linear wave train on a horizontal bottom:

$$M = E/c \quad (6)$$

where  $E = 1/8 \rho g H^2$  is the wave energy density and  $c$  denotes the wave speed. After introducing the shallow water approximation to  $c$ :

$$M = E/c \approx 1/8 \rho (g/d)^{1/2} H^2 \quad (7)$$

In random waves on a beach the fraction of waves breaking at a point ( $Q_b$ ) varies with position. Battjes and Janssen (1978) have presented an implicit expression for  $Q_b$  as a function of the ratio of the rms wave height ( $H_{rms}$ ) to a local breaking height, which in turn is primarily depth-controlled. A simple, explicit approximation qualitatively close to this relation and quantitatively well in accordance with laboratory observations is:

$$\tilde{Q}_b = 20(H_{rms}/d)^5 \quad (8)$$

The return flow velocity in a random, breaking wave field is simply modelled here as

$$\bar{u}_{br,random} = \bar{u}_{br,periodic} \cdot \tilde{Q}_b \quad (9)$$

#### the mean sediment load in random breaking waves

A reliable, predictive model for the mean sediment concentration or even for the mean sediment load due to random, breaking waves is not available yet. For the present purposes a prediction method is derived based on the sediment concentration measurements and theoretical analyses presented by Nielsen et al (1978, see also Nielsen, 1979) for non-breaking waves and Bosman (1982) for breaking waves. The method is broadly described below and details are given in an Appendix.

Laboratory measurements of time- and bed-averaged concentration profiles under breaking, random waves conducted by Bosman (1982) indicate that (a) in the near-bottom layer the upward decay of the concentration is exponential and (b) the sediment load is mainly confined to and determined by the bottom layer, so that

$$\bar{s} = C_0 \cdot \lambda_1 \quad (10)$$

where  $C_0$  is a reference concentration at the bottom and  $\lambda_1^{-1}$  is the relative concentration gradient in the bottom layer. The bottom reference concentration is found to be nearly linearly proportional to a Shield's type parameter  $\theta'$  (see Appendix Eq. 23...25). Adoption of a diffusion-type model with a constant turbulent viscosity,  $\epsilon_1$ , and sediment fall velocity,  $w_1$ , for the bottom layer region leads to

$$\lambda_1 = \epsilon_1 / w_1 \quad (11)$$

which indicates that  $\lambda_1$  closely corresponds to a characteristic turbulent length scale. In fact  $\lambda_1$  is found to be linearly proportional to the ripple height in the ripple regime and to the wave boundary layer thickness in the sheetflow regime. Since the bottom layer is only weakly influenced by surface breaking, Nielsen's (1979) formulations for the bottom reference concentration and the viscosity coefficient were used for the situation of random, breaking waves, i.e. on basis of Bosman's measurements Nielsen's parameterizations of  $C_0$  en  $\epsilon_1$  were quantitatively adapted. The resulting prediction method for the mean sediment load covers the region of initiation of motion to sheetflow conditions for median grain diameters of say 100  $\mu\text{m}$  to 500  $\mu\text{m}$ . However, the parameterizations were only checked in a very limited region, so the results should be applied with caution. It is stressed that there is an urgent need to conduct and analyse sediment concentration measurements under surf conditions close to reality.

#### practical calculations

With the undertow and the mean sediment load known as functions of the local hydrodynamic conditions and the sediment properties the offshore sediment transport can be calculated. In practical computations the sediment properties may be assumed constant. The hydrodynamic conditions, however, are a function of the horizontal distance from the shore and the offshore wave parameters. These conditions can be derived from numerical calculations with the wave height decay model presented by Battjes and Janssen (1978). This may be regarded as the first discrete step in a practical calculation procedure, illustrated in Fig. 1. The rms wave height,  $H_{\text{rms}}$ , the breaking wave height,  $H_b$ , and the fraction of breaking waves,  $\bar{Q}_b$ , follow directly from the decay model. The local kinematics are calculated in the second step, where the rms orbital velocity,  $u_{\text{rms}}$ , is derived from linear theory and  $\bar{u}_{br}$  from Eq. (9). In the third step the sediment transport is calculated according to Eq. (3) where a proportionality constant,  $b$ , is introduced which should be of order unity if the model is right. It is noted that the sediment transport is locally determined only. Finally, the bottom changes are calculated through application of the mass balance equation for the sediment. This procedure may be repeated for the new beach profile.

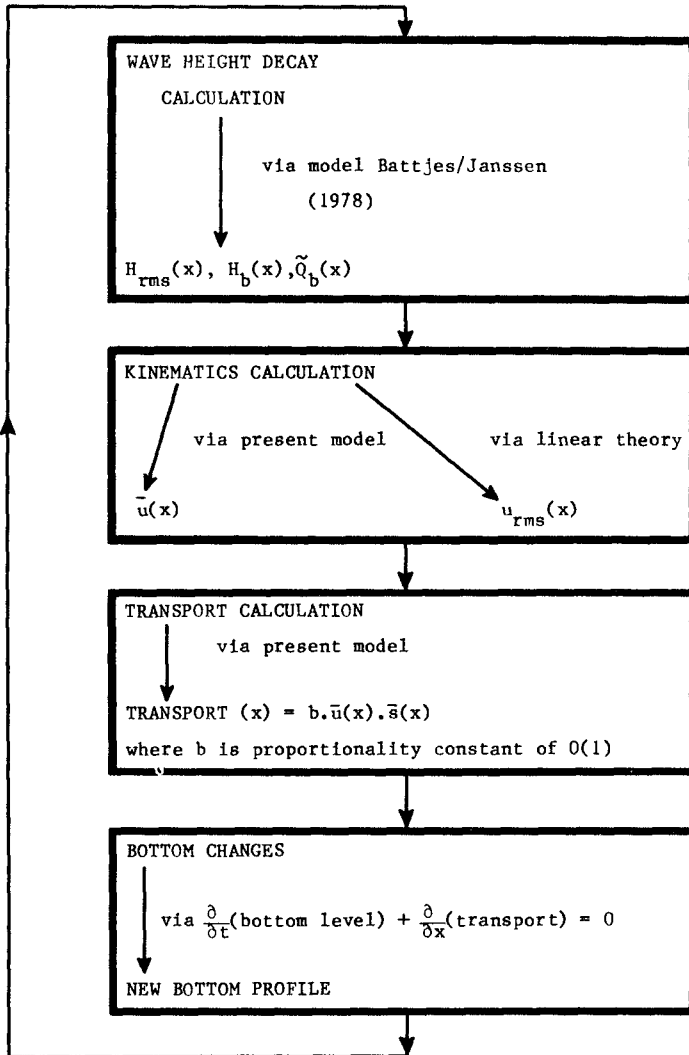


Fig. 1 Computation procedure

In the numerical evaluation of the above procedure a second order Runge-Kutta algorithm is used in the wave decay model and a modified Lax scheme in the bottom change calculations.

As a boundary condition on the waterline the present formulation yields  $\bar{q} = 0$ . To simulate the smoothing effect of swash motion on the sediment transport near the waterline  $\bar{q}(x)$  was damped starting from a depth of approximately half the initial wave height in proportion to the mean water depth.

### 3. MODEL VERIFICATION

A laboratory measurement programme aimed at verification of the present model has not yet been initiated. Therefore we rely on available measurement results of which some examples are presented here.

Firstly, model calculations of the wave kinematics on a beach of nearly constant slope (1:40) are compared with measurements in a large scale wave facility (see Fig. 2). The ability of the model to predict the wave height decay is extensively discussed by Battjes and Stive (1984). Here we are interested in the prediction of the return flow and the rms orbital velocity, which were measured 0.2 m above the bottom. The prediction appears to be sufficiently close for our purposes. It is noted that the trend of some theoretical overprediction of  $u_{rms}$  in the outer breaking regime towards negligible overprediction in the actual surf zone is similar to that found and partly explained by Van Heteren and Stive (1984).

Secondly, calculations of bottom changes are compared with measurements on three different beach profiles. The first case concerns a barred profile of relatively fine sediment in a small scale flume. The second case concerns a parabolic profile of somewhat coarser sediment in a small scale flume. The third case concerns the earlier mentioned nearly 1:40 profile of medium sized sediment in a large scale flume. Some characteristic parameters of these three cases are collected in Table 1, where the mean water depth is denoted by  $h$ , the rms wave height by  $H_{rmsr}$ , and the peak frequency by  $f_p$  with the subscript  $r$  denoting reference value in the horizontal part of the flume. In case 2 the initial wave conditions were varied to simulate a wave climate. This variation was accounted for in the computations.

case	source	profile	grain diameter ( $\mu\text{m}$ )	$h_r$ (m)	$H_{rmsr}$ (m)	$f_{pr}$ (Hz)
1	Van Overeem (1983)	barred	100	0.80	0.21	0.39
2	Boer (1984)	parabolic	145	0.80	0.11-0.19	0.40-0.53
3	Stive (1984)	plane	225	4.19	1.00	0.19

Table 1 Characteristic parameters of laboratory experiments



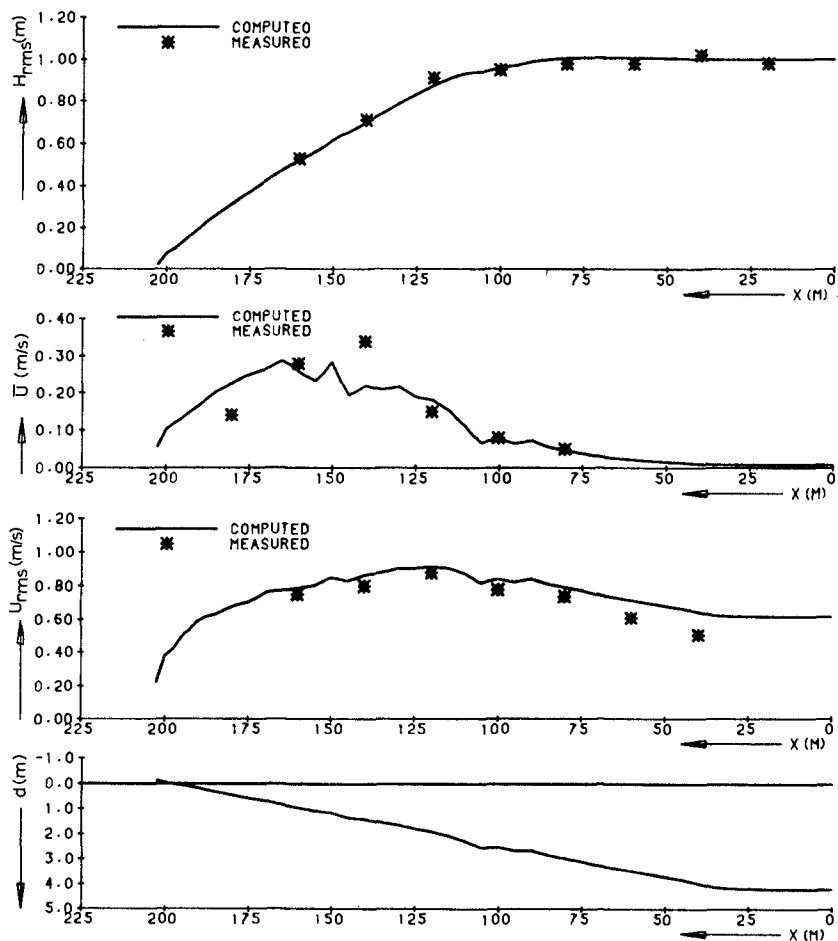


Fig. 2 Measured and computed wave height ( $H_{rms}$ ), return flow velocity ( $\bar{U}$ ) and rms orbital velocity ( $U_{rms}$ ) on a large scale, laboratory beach

The comparison between measurements and computations is presented in Figs. 3...5. In case 1 the resultant profiles themselves are compared, while in the other cases it was judged more informative to compare the actual bottom changes. In general, the relative profile activity and distinct features, such as the offshore movement of a step and the formation of a bar, are predicted well by the computations. The actual quantitative changes are simulated reasonably (although sometimes somewhat shifted in space), if the proportionality constant  $b$  is made to vary between 0.25 and 1.0. The qualitative

predictions of details is surprisingly good at some locations. Apparently, the modelling of the sediment transport as function of the wave conditions is insufficiently accurate to yield a universal value for  $b$ . If, however, for prediction purposes a value  $b = 0.5$  is applied the bottom changes are at most overestimated or underestimated by a factor of two.

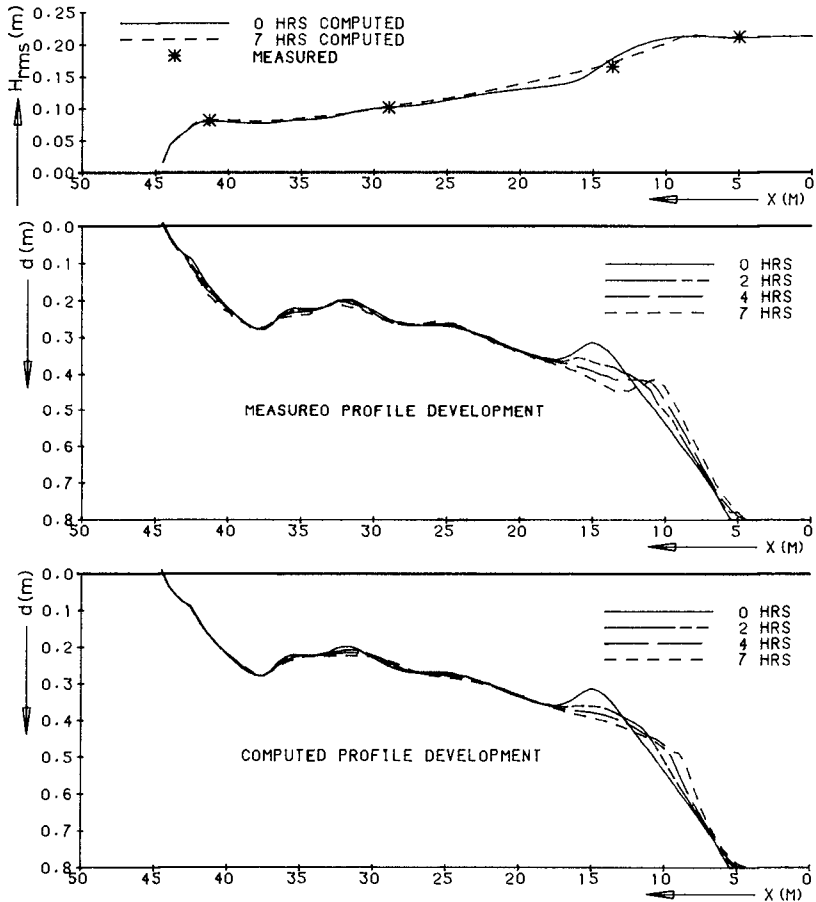


Fig. 3 Measured and computed ( $b = 0.25$ ) profile development on a small scale, laboratory beach: case 1

Finally, a preliminary comparison is presented of calculated and measured bottom changes of a beach acting as a foreshore of a protected dune (see Fig. 6). The dune revetment prohibits sediment transport, so that the sudden increase of sediment transport at the dune foot

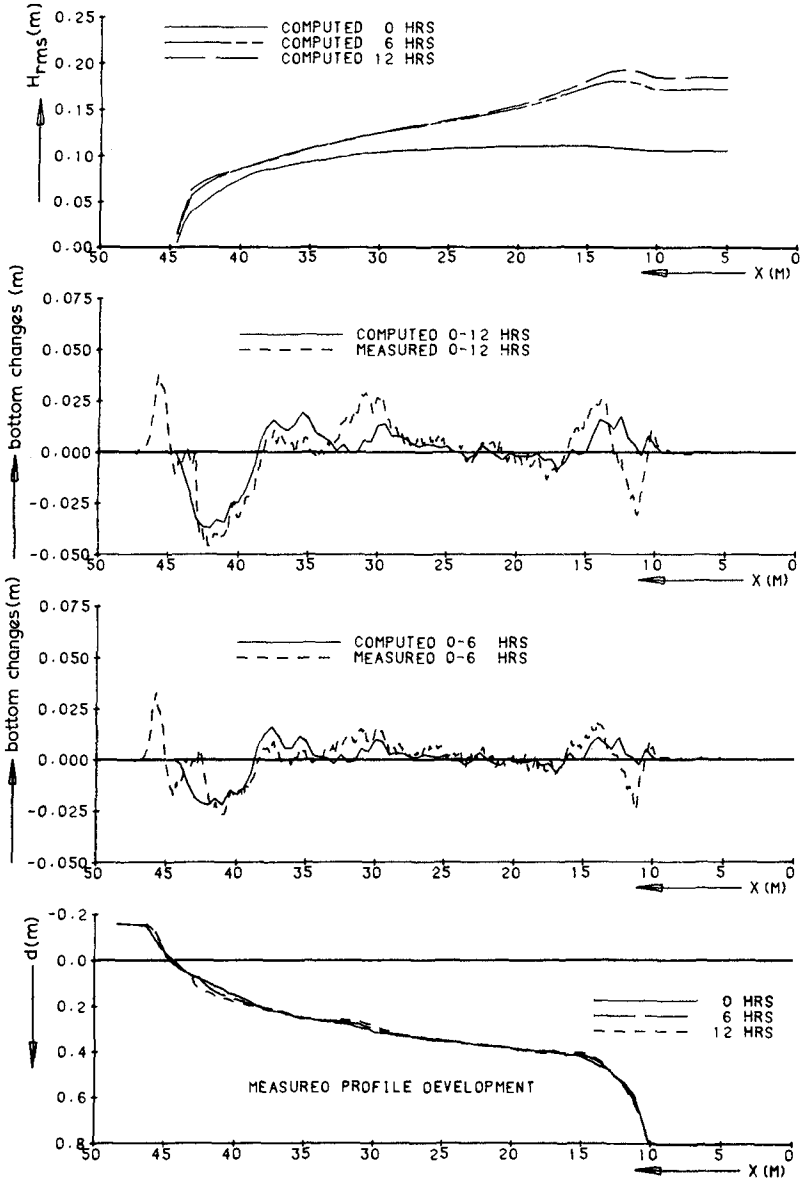


Fig. 4 Measured and computed ( $b = 1.0$ ) bottom changes on a small scale, laboratory beach: case 2

causes an erosion hole. The hydraulic conditions during the experiments simulated the conditions of a design storm surge, so that both the water level and the wave conditions varied in time. The variation of the conditions was taken into account in the calculations. It appears that the erosion at the foot is well predicted applying a value of  $b = 0.5$ . This indicates that the presently modelled return flow mechanism plays an important role in the dune erosion process.

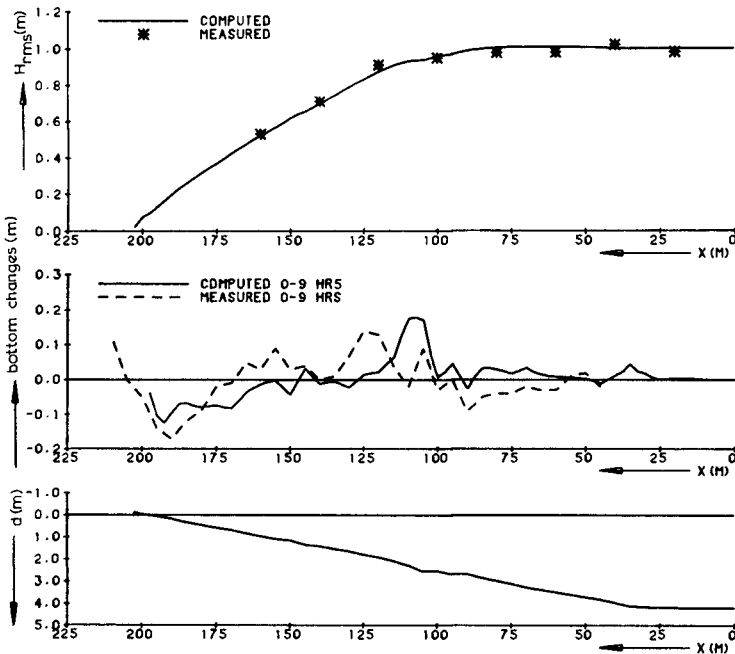


Fig. 5 Measured and computed ( $b = 0.25$ ) bottom changes on a large scale, laboratory beach: case 3

4. EQUILIBRIUM STATE

An important aspect in the verification of the present model is the reality of the profile equilibrium state which results from the model formulations. A state of equilibrium is said to be reached when gradients in the sediment transport are absent so that the profile shape is stable. This definition implies that a two-dimensional surf zone is assumed to have a sediment source on the shoreside and a sediment sink at the seaside. The consequences with respect to natural beaches are described below.

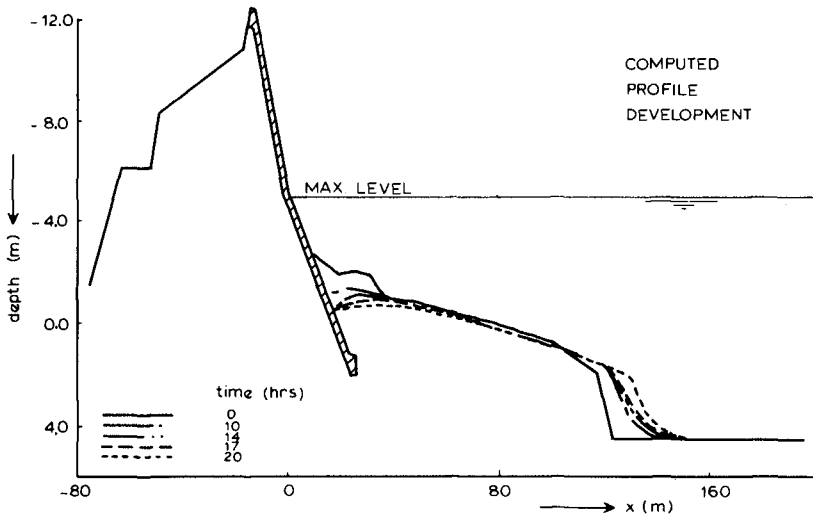
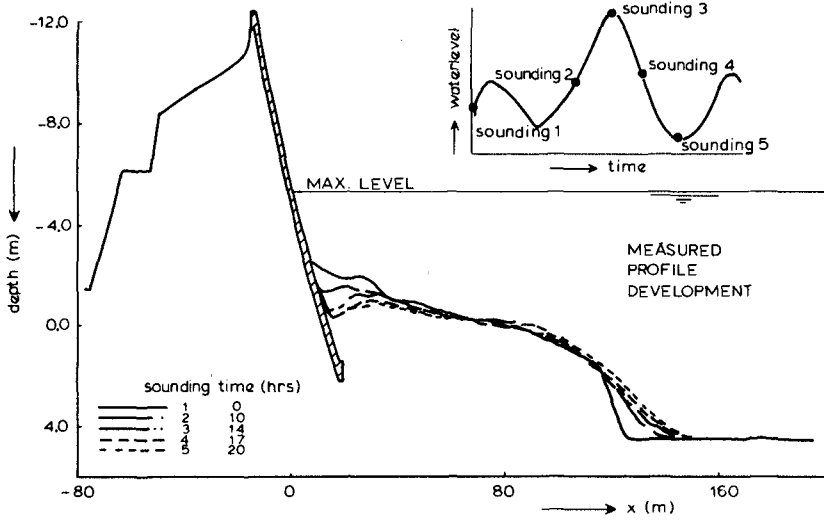


Fig. 6 Measured and computed ( $b = 0.5$ ) profile development on a beach at the foot of a protected dune

In order to perform our analysis it is necessary to introduce simplified relations for the model parameters. Firstly, the shallow water approximations to the breaking wave height,  $H_b$ , the orbital velocity,  $u_{rms}$ , and the orbital amplitude,  $a_{rms}$ , are adopted, i.e.

$$\begin{aligned} H_b &= \gamma' d & (\gamma' = \text{constant}) \\ u_{rms} &= \frac{1}{2} H_{rms} (g/d)^{\frac{1}{2}} & (12) \\ a_{rms} &= \frac{1}{2} H_{rms} (g/d)^{\frac{1}{2}} (2\pi f_p)^{-1} \end{aligned}$$

Secondly, in the  $\theta'$ -range relevant to surf zone conditions ( $\theta' \approx 1.0 - 1.5$ ) the mean sediment load,  $\bar{s}$ , is approximately proportional to the orbital amplitude,  $a_{rms}$ , and to the Shields parameter,  $\theta'$ , (see Figs. 8 and 9 of the Appendix), i.e.

$$\bar{s} :: a_{rms} \theta' \quad (13)$$

where  $\theta'$  is defined by Eq. (24). Inserting the results in Eq. (3) yields the following proportionality relation for the offshore sediment transport,  $\bar{q}$ :

$$\bar{q} :: H_{rms}^6 d^{-6} f_p^{-1} D^{-1} \quad (14)$$

where  $D$  is a characteristic grain diameter. For the transport to be constant it is a necessary condition that

$$H_{rms} :: d^{3/4} f_p^{1/8} D^{1/8} \quad (15)$$

The relation between wave energy and water depth may further be elaborated by use of the energy balance equation, i.e.

$$\frac{d}{dx} (E.c_g) + \text{Diss} = 0 \quad (16)$$

where the dissipation term due to wave breaking following Battjes and Janssen (1978) is proportional to:

$$\text{Diss} :: Q_b f_p H_b^2 \quad (17)$$

An approximation to Battjes and Janssen's implicit equation for  $Q_b$  yields

$$Q_b :: (H_{rms}/d)^6 \quad (18)$$

where it is noted that this result differs from Eq. (8) (used in the derivation of Eq. (14)), since here an accurate approximation is sought to  $Q_b$  in the wave decay model.

Using the results (17) and (18) and again adopting shallow water approximations, the energy balance equation gives

$$\frac{d}{dx} (H_{rms}^2 d^{\frac{1}{2}}) :: H_{rms}^6 f_p d^{-4} \quad (19)$$

Combining the governing Equations (15) and (19) and integration yields

$$d \propto \hat{x}^{2/3} f_p D^{1/3} \quad (20)$$

where  $\hat{x}$  is the horizontal distance from the water line. With respect to the dependence of  $d$  on  $\hat{x}$  this result is well in accordance with empirical findings first noticed by Bruun (1954). Also the other dependencies are found to be in at least qualitative accordance with observations (see e.g. Dean, 1984, whose results indicate a quantitative similar grain diameter dependence). These results lend support to the present model.

## 5. DISCUSSION AND CONCLUSION

The present offshore transport model incorporates only one of the mechanisms responsible for cross-shore sediment movement that is expected to exist on beaches under nearly two-dimensional wave attack, i.e. sediment transport due to breaking wave induced return flow. The model is applied to some laboratory beaches exposed to random breaking wave action. Realistic, first order predictions of the bottom changes are obtained. These laboratory findings indicate that in the active surf zone the return flow mechanism dominates others mechanisms. The predictions may be improved by including other mechanisms, e.g. such as due to the asymmetry of the wave motion.

Natural beaches are only confronted with an active surf zone during a relatively small period of time. Moreover, the position of the surf zone varies with the tidal level. Obviously a realistic prediction of the beach profile response under general, natural conditions requires the inclusion of more sediment transport mechanisms than the return flow mechanism alone. If, however, one is interested in the relatively large response of beaches under storm conditions (when the surf zone is extended significantly offshore) the present model is expected to perform satisfactorily. This is confirmed by the fact that the equilibrium profile shape following from the model is in good accordance with field observations.

## ACKNOWLEDGEMENT

This work was done as a part of the TOW Study Programme for Coastal Sediment Transport in the Netherlands. The Programme is financed by the Dutch Government and jointly carried out by the Ministry of Transport and Public Works (Rijkswaterstaat), Delft University of Technology and Delft Hydraulics Laboratory. Thanks are due to J. v. Overeem for making available the results presented in Fig. 6.

APPENDIX: The Mean Sediment Load

As shown by Bosman (1982) sediment concentration distributions in random, breaking waves may be satisfactorily described by a "double layer" or "double first order" model for a rather wide variety of laboratory situations, such as horizontal and sloping bottom, no and net currents, non-breaking and breaking random waves. Based on a diffusion type description for each layer the model leads to an exponential concentration distribution as follows (see also Fig. 7):

$$C(z) = \begin{cases} C_0 e^{-z/\lambda_1} & \text{for } z < A \\ C(A) e^{-(z-A)/\lambda_1} = C_0 e^{-A/\lambda_1} e^{-(z-A)/\lambda_2} & \text{for } z > A \end{cases} \quad (21)$$

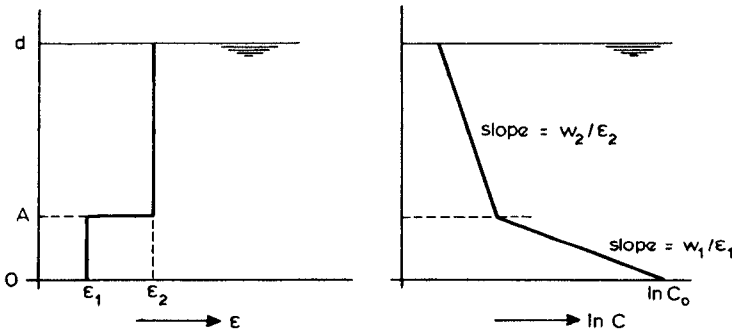


Fig. 7 "Double first order" model for the sediment concentration distribution in random, breaking waves (after Bosman, 1982)

where A is the bottom layer thickness. Each layer has a constant turbulent viscosity,  $\epsilon$ , and a fall velocity, w, for the sediment in that layer such that  $\lambda_1 \equiv \epsilon_1/w_1$  and  $\lambda_2 \equiv \epsilon_2/w_2$  (based on diffusion). Bosman's measurements show that the upward exponential decay of the concentration is so strong that the total sediment load,  $\bar{s}$ , is mainly confined to and determined by the bottom layer as follows:

$$\bar{s} = C_0 \cdot \lambda_1 \quad (22)$$

where  $C_0$  is the bottom concentration and  $\lambda_1^{-1}$  is the relative concentration gradient in the bottom layer.

These laboratory flume measurements only cover a limited range of conditions, for instance only one median grain diameter was used. To generalize the results we follow the work of Nielsen (1979). Nielsen gives no explicit formulation for the sediment concentrations or the total load due to random waves and certainly not due to random, breaking waves. He does present semi-empirical expressions for the ripple height,  $\xi$ , and the bottom reference concentration,  $C_0$ , due to random waves. With respect to the effects of breaking we adopt the observation that the sediment concentrations near the bottom and the



geometry of the bottom due to breaking waves do not differ essentially from those due to non-breaking waves. This implies that we may rely on formulations for non-breaking, random waves.

#### bottom reference concentration

As in steady flow the bottom reference concentration is assumed to be determined by the Shields parameter, i.e. the dimensionless bed shearstress, and Nielsen suggests also for random waves:

$$C_o = K(\theta' - 0.05) \frac{2}{\pi} \arccos(0.05/\theta')^{\frac{1}{2}} \quad (23)$$

where K is a constant and the Shields parameter  $\theta'$  is defined as

$$\theta' = \frac{f_w u_{rms}^2}{\Delta g D} \quad (24)$$

where  $f_w$  is a friction factor,  $u_{rms}$  is the rms orbital velocity,  $\Delta$  is the relative sediment density ( $\rho_s/\rho_w - 1$ ) and D is a characteristic grain diameter. The friction factor is given as (Swart, 1974):

$$f_w = \exp[5.2(2.5 D/a)^{0.2} - 6.0] \quad (25)$$

where a is the orbital amplitude. The "arccos" term in Eq. (23) accounts for the fraction of time that the critical stress value of 0.05 is exceeded. Confrontation of expression (23) with Bosman's bed-averaged measurements confirms Nielsen's suggestion. The constant K has a best value of 0.028, the same value as found at the ripple crests under periodic waves.

#### ripple height

Semi-empirically Nielsen derived the following expression for the ripple height due to random waves:

$$\xi/a = 21(\psi)^{-1.85} \quad \text{for } \psi > 10 \quad (26)$$

$$\xi/a = 0.3 \quad \text{for } \psi \leq 10$$

$$\text{where } \psi = \frac{u_{rms}^2}{\Delta g D}$$

#### turbulent viscosity coefficient

Semi-empirically Nielsen derived for periodic waves that the viscosity coefficient made dimensionless by the length scale ripple height,  $\xi$ , or boundary layer thickness,  $0.4 \delta$ , and the velocity scale  $gT$  is a complicated function of the parameter  $a\omega/w_1$ , so

$$\epsilon_1 / [(\xi + 0.4\delta) gT] = f(a\omega/w_1) \quad (27)$$

where  $\omega$  is the angular velocity and T the wave period.

In the length scale quantity  $(\xi+0.4\delta)$  the ripple height,  $\xi$ , dominates in situations with noticeable ripples and the boundary layer thickness,  $0.4\delta$ , dominates in the absence of ripples. The latter is defined as (Jonsson and Carlsen, 1976):

$$\delta/a = 0.072 (2.5D/a)^{0.25} \tag{28}$$

From a comparison with the measurements of Bosman we have found that also in the region  $aw/w_1 > 20$  the lower asymptote (Eq. 6.112) of the expression (Eq. 6.111) suggested by Nielsen (1979) for periodic waves coincides best with the random wave measurements. This asymptote is given as:

$$\varepsilon/[(\psi+0.4\delta) gT] = 0.35 \cdot 10^{-3} (aw/w_1)^{0.68} \tag{29}$$

results

The present prediction method is based on the above described findings. In summary, for the prediction of the mean sediment load,  $\bar{S}$ , expressions (23), (26), (28) and (29) are used. Logically Bosman's measurements correspond well with this formulation (see Fig. 8a). The sensitivity of the method for a variation in grain diameter is shown in Fig. 8b.

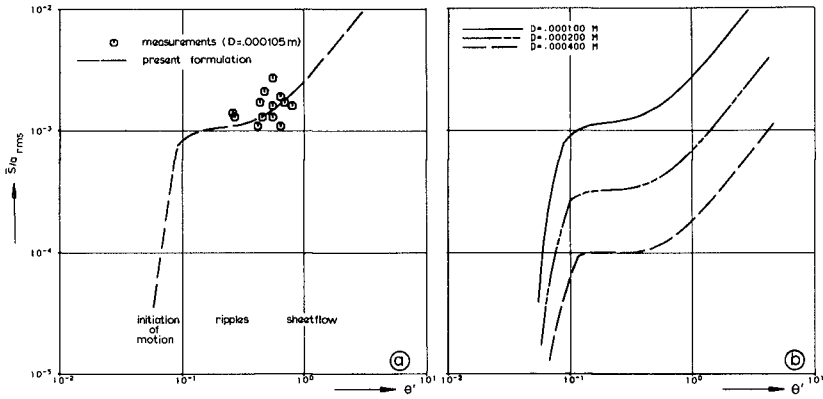


Fig. 8 Non-dimensional sediment load as a function of the Shields parameter for  $f_p = 0.5 \text{ Hz}$

## REFERENCES

- Battjes, J.A. and J.P.F.M. Janssen, Energy loss and set-up due to breaking of random waves, in Proceedings 16th International Conference Coastal Engineering, pp. 569-587, ASCE, New York, 1978.
- Battjes, J.A. and M.J.F. Stive, Calibration and verification of a dissipation model for random breaking waves, in Proceedings 19th International Conference Coastal Engineering, ASCE, New York, 1984.
- Boer, S., Coastal protection scheme Lido di Ostia, Report M 2027, Delft Hydraulics Laboratory, 1984.
- Bosman, J.J., Sediment concentrations under waves and currents (in Dutch, publication in preparation), Report M 1875, Delft Hydraulics Laboratory, 1982.
- Bruun, P., Coast erosion and development of beach profile, Techn. Memo No. 44, CERC, 1954.
- Dean, R.G., Applications of equilibrium beach profile concepts, in Proceedings 19th International Conference Coastal Engineering, ASCE, New York, 1984.
- Jonsson, I.G. and N.A. Carlsen, Experimental and theoretical investigations in an oscillatory turbulent boundary layer, J. Hydraulic Research, Vol. 14, No. 1, pp. 45-60, 1976.
- Nielsen, P., Some basic concepts of wave sediment transport, Series paper No. 20, Institute of Hydrodyn. and Hydr. Eng., Techn. Univ. of Denmark, 1979.
- Nielsen, P., I.A. Svendsen and C. Staub, Onshore-offshore sediment movement on a beach, in Proceedings 16th International Conference Coastal Engineering, pp. 1475-1492, ASCE, New York, 1978.
- Stive, M.J.F., A scale comparison of waves breaking on a beach, accepted for publication in J. Coastal Eng., 1984.
- Stive, M.J.F., and H.G. Wind, A study of radiation stress and set-up in the nearshore region, J. Coastal Eng., 6: 1-25, 1982.
- Swart, D.H., Offshore sediment transport and equilibrium beach profiles, Publication No. 131, Delft Hydraulics Laboratory, 1974.
- Van Heteren, J. and M.J.F. Stive, Wave kinematics and wave directionality in the surf zone, in Proceedings 19th International Conference Coastal Engineering, ASCE, New York, 1984.
- Van Overeem, J., Morphologic behaviour of beach fill with underwater dam, Report M 1891, Delft Hydraulics Laboratory, 1983.

## CHAPTER NINETY EIGHT

### A SYSTEM OF MATHEMATICAL MODELS FOR THE SIMULATION OF MORPHOLOGICAL PROCESSES IN THE COASTAL AREA

S. Boer\*, H.J. de Vriend\* and H.G. Wind\*

#### ABSTRACT

A compound mathematical model (COMOR) for the simulation of morphological changes in the coastal area is being developed. The model is very flexible; it can be composed according to the specific demands of the problem which is considered. So far the model is being applied in the advisory practice to predict initial morphological changes. Recent experiences have shown that the model is quite useful, although at present the knowledge of the individual coastal processes and their interactions is still insufficient to utilize it optimally. However, it is foreseen that in the near future such mathematical models will become a powerful tool in coastal engineering.

#### 1 INTRODUCTION

Numerous physical processes, often at different time and length scales, play a part in coastal morphology. When attempting to understand these processes and their mutual interactions, computer simulations can be of great help, especially if the second horizontal dimension is involved.

The progress in mathematical modelling and the increased capabilities of modern computers have contributed substantially to the application of numerical models in coastal research. In the field of simulation of coastal morphological evolution this started with the strongly schematized single-line models (Grijm, 1964; Le Méhauté and Soldate, 1978), but via an extension to multiple-line models (Bakker, 1968; Boer, 1983) the second horizontal dimension came into the picture (Flemming and Hunt, 1976; O'Connor et al, 1981; Watanabe, 1982; Coeffé and Péchon, 1982; McAnally et al., 1984). Although most of these models were developed primarily for research purposes they have proved to be a useful tool in hydraulic advisory practice, as well.

Within the framework of the Coastal Research Group of the applied hydraulic research programme TOW, the Ministry of Transport and Public Works (Rijkswaterstaat), the Delft Hydraulics Laboratory and the Delft University of Technology are developing a system of computer programs (COMOR) which provides the possibility to compose compound mathematical models for the simulation of horizontally two-dimensional morphological changes in the coastal area. The basic idea of the COMOR-system

---

\* Delft Hydraulics Laboratory, the Netherlands

is to assemble the presently available knowledge on the individual physical processes in morphological models.

COMOR-models, so far without time-dependency in the bottom topography, are being applied in hydraulic advisory practice at the Delft Hydraulics Laboratory. They have proved a good support of the usual investigation techniques (desk studies, scale models). Besides, experience with these applications helps to identify and weigh the needs for further research and hence to steer the future development of mathematical modelling in this field.

After a brief description of COMOR and some aspects of the modeling technique the present paper goes into some representative applications. Finally a discussion on the practical applicability is given.

## 2 DESCRIPTION OF COMOR

In order to meet the requirement of maximum flexibility COMOR was given a modular structure. This means that a model consists of a series of computer programs describing the waves, the net currents, the sediment transports and the bottom changes and that these programs are coupled in a neutral way, such that each of them can easily be replaced by another one. Thus it is possible to compose a model according to the specific demands of the problem to be considered. The neutral coupling of the constituent models is realized by using one central data base for all of them. Each model draws its input data from this file and adds its results to it. In practice this means that each computer program suited as a module in COMOR-models needs its own interface (input and output) with the central data base in order to be actually applicable.

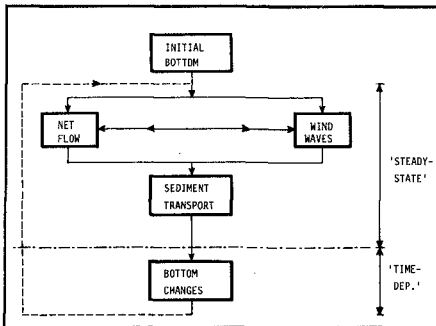


Fig.1 Computation procedure COMOR

logical evolutions the bottom level is changed after a certain time interval. Subsequently waves, currents and transports are computed for the new bottom. In some practical applications it is not necessary to predict the morphological evolution over a long period. The "initial" rate of change of the bottom level (considered at the morphological

Figure 1 outlines the computation procedure underlying COMOR. Starting from the initial bottom configuration in the area of interest and a given set of (boundary) conditions, the waves, the net current field, the sediment transport and the bottom level changes are computed, basically in a quasi-stationary procedure. This implies, that all kinds of composite wave, current and transport computations are allowable but that in any of them the bottom level is kept constant. In the computation of time-dependent morpho-

time scale) then gives sufficient information, provided that it is computed on the basis of a "mixture" of flow and wave conditions that is representative for the period considered. This implies that the effect of the bottom evolution on the waves, currents and transport is left out of consideration. In doing so a number of problems (stability, accuracy, computer-expenses) attending time-dependent computations can be avoided.

3 MODELLING TECHNIQUE

The scheme in Figure 1 outlines the computational procedure followed in COMOR-models, reduced to its basic form. It gives no information, however, on how a model is composed, how it is used and how its results are combined and interpreted. These activities, denominated "modelling technique" here, determine to a large extent the quality of a model application. As a discussion in detail on this modelling technique, however important, would go beyond the scope of this paper, only some of the most relevant aspects will be discussed briefly.

The COMOR-models for initial changes applied so far refer to situations in which, within the area of interest, the morphological changes are influenced by wave-induced as well as tidal currents. This leads to a wide variety of length scales which have to be considered. The area of interest of the morphological models is usually rather small (length scale a few kilometres) compared with the tidal wave length and the distance along which the wave propagation is influenced by the limited water depth. For economical reasons smaller and more refined models are often nested into larger models in order to arrive at a sufficiently accurate description of the tidal motion and the wave field in the area of interest. If this area is small compared with the tidal wave length, the tidal motion can be approximated by a series of unsteady rigid-lid or even steady flow models, with the flow rate imposed at the boundaries. In such cases the tidal model only serves to generate the boundary conditions for the tidal flow component in the detailed flow model covering the area of interest. This leads to a composed model as indicated in Figure 2, with separate modules for the computation of the overall tidal motion, the wave field, the combined wave- and tide- induced flow in the region of interest and the sediment transport there, in this sequence and without feedback. In practice it is not always feasible to follow this procedure throughout. Especially the largest

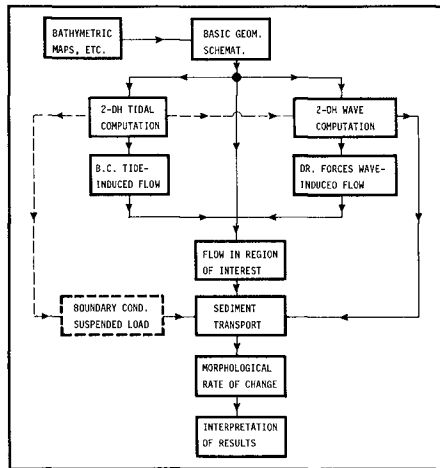


Fig. 2 Flow chart "initial" models

feasible to follow this procedure throughout. Especially the largest

tidal and wave models are rather expensive to be built and calibrated, whence in smaller projects existing models are used as far as possible. As these existing models have usually been developed for other purposes, they will not always fit in with the project objectives. Therefore these largest models are linked up with the detailed models via one or more intermediate sized models.

The selection of the computation methods for the currents, waves and transport to be used should be based on the ability to deal with the physical phenomena involved and the order of accuracy and reliability required. At this point the modellers have to rely heavily on experience, as systematic estimation methods for the relevance of elementary physical phenomena are hardly available. In general the models simulating the wave field, the coastal currents and the sediment transport in the region of interest should be in keeping with each other as well as with the geometrical schematization. At present a variety of computation methods and computer codes is available to describe waves, currents and transport rates. However, little is known yet about the morphological impact of the underlying elementary physical processes. Especially the state of knowledge on the sediment transport under the combined action of waves and currents is such that an accurate sediment transport model is still far from being available. The transport formulae presently applied in coastal morphology are based on the assumption of local equilibrium and relate the sediment transport to local time-mean parameters only. In view of the inaccuracy of the sediment transport model it may seem inappropriate to use highly sophisticated models for the simulation of the waves and coastal currents, as they will hardly increase the accuracy of the morphological computation.

The schematization of the wave climate (deep water wave heights, wave periods and directions) and the tidal motion (tidal cycle and modulation) is one of the major problems in modelling coastal processes, since Monte-Carlo or real-time simulations are far from feasible yet. Even when considering "initial" morphological changes the wave climate and the tidal motion have to be schematized to a limited number of conditions in order to obtain bottom change rates that are representative for the "initial" time span. In the applications so far a single tidal cycle is schematized to a small number of steady state conditions, which are combined with a series of wave conditions during that individual cycle. The horizontally two-dimensional morphological models contain many interactions some of which are non-linear. Therefore the criteria imposed at present on these schematizations, viz. a correct representation of the average annual longshore transport for the waves and the mean flood and ebb-phase transports for the tide, still contain a great deal of arbitrariness and should be applied with caution. The selected schematization of the tidal motion and the wave climate specifies a series of production runs from the results of which the expected net morphological changes in the area of interest are to be derived. To that end a weighting procedure has to be established, in accordance with the schematization procedure.

A practical point of concern is the conformity of the geometrical schematizations in the various constituent models. As a rule these models make use of different computational grids and hence their

geometrical schematizations will show differences. In order to limit these differences as much as possible the original bathymetric data are reduced to a basic geometrical schematization, representing the relevant properties of the actual bathymetry and disregarding irrelevant details. It may be remarked that this choice is by no means always simple. The geometrical schematizations in all constituent models are derived from this basic schematization rather than from the original bathymetric data.

A specific aspect of compound models is the processing of the intermediate model results. The sensitive interaction of waves, current and transport in the computation of the rate of bottom changes poses heavier demands on their accuracy and reliability than in the case of separate application. Besides, additional output quantities are often needed. The wave model for instance has to produce not only wave heights and directions, but also orbital velocities near the bottom and whatever other parameters are needed to model wave effects on the net current and the sediment transport. Similarly, the flow model has to yield not only the magnitude and direction of the net flow velocity, but also other parameters needed for the transport model such as the bottom shear stress.

The last aspect mentioned here concerns the computational procedures applied in the numerical models for the region of interest. Usually only a finite-element procedure or a curvilinear finite-difference procedure provides the possibility to deal with the capriciously shaped coastlines and structures encountered in practice. Moreover these procedures allow for local grid refinements such that the morphological processes in the breakerzone, which is usually rather narrow compared with the total area of interest can be reproduced with sufficient accuracy.

#### 4 PRACTICAL APPLICATIONS

COMOR has been applied in different studies with the following fields of interest:

- design of artificial coastal extensions and islands
- design of sea water intakes and outfalls
- analysis of autonome coastal changes
- design of coastal protection schemes.

Some representative applications in the advisory practice as well as in research projects will be treated hereafter. For each of the applications the problem statement, the predominant physical processes, the simulation of these processes and the principal conclusions are considered.

#### Morphological aspects of an artificial storage basin for the disposal of dredged spoil near Rotterdam, the Netherlands

In the morphological study of a storage basin for the disposal of dredged spoil, reclaimed from the sea by means of a sanddam (see Figure 3), COMOR has been applied to estimate the amount of regular beach nourishment which will be necessary to compensate for the erosion of the sea-exposed dam. The region of interest is a fairly



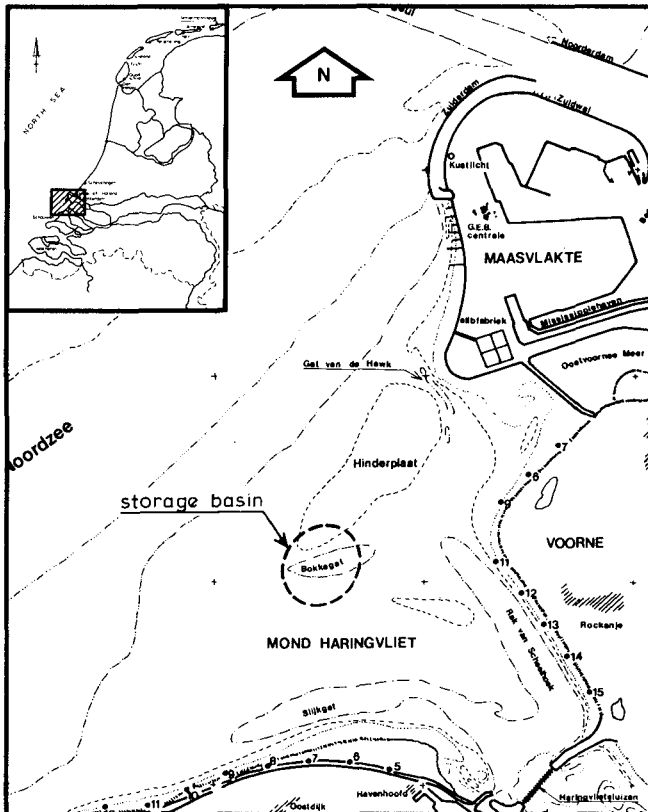


Fig. 3 Future situation

shallow area with a shoal, the Hinderplaat, falling partly dry at low tide. The foreshore shows almost straight and parallel depth contours. The storage basin is projected just at the southernmost edge of the Hinderplaat. The coastal area is exposed to deep water waves coming from directions between N and SW. The wave height distribution near the Hinderplaat is dominated by wave breaking. As such the transport by wave-induced currents is an important phenomenon in the erosion of the sanddam. However, the transport by tidal currents is expected to be important as well as the basin is situated in the immediate vicinity of a tidal gully, the Bokkegat. For this reason, the detailed flow model describes the combined wave-induced and tidal current.

Figure 4 shows the sequence of the constituent models of COMOR for this application. Existing calibrated models have been used for the simulation of the "far field" tidal motion and the wave propagation there. The tidal computations are based on the numerical solution of the vertically integrated two-dimensional long wave equations, discretized on a grid of square meshes (for instance, see Langerak,

1978). Figure 5 shows the tidal flow pattern at the moment of maximum flood flow, computed with the small tidal model.

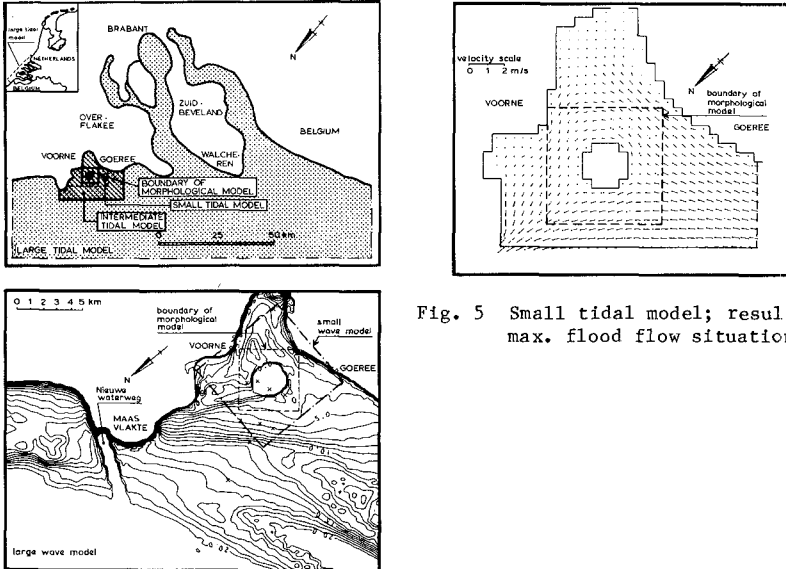


Fig. 5 Small tidal model; results max. flood flow situation

Fig. 4 Constituent tidal and wave models

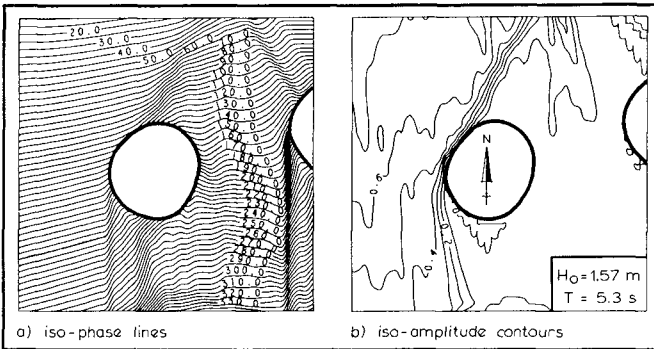


Fig. 6 Small wave model; results for waves from the North

The wave field has been computed with a model based on the parabolic approximation for the propagation of time-harmonic water waves (see Radder, 1979). In the model shoaling, refraction, diffraction and energy dissipation due to bottom friction, currents and wave breaking are included (see Dingemans et al., 1984). In Figure 6 the wave field for waves from the North computed with the small wave model are shown. To simulate the combined wave-induced and tidal flow in the area of interest, a finite element model for friction dominated steady flow (see Wind and Perrels, 1982) is applied. Figure 7 shows the

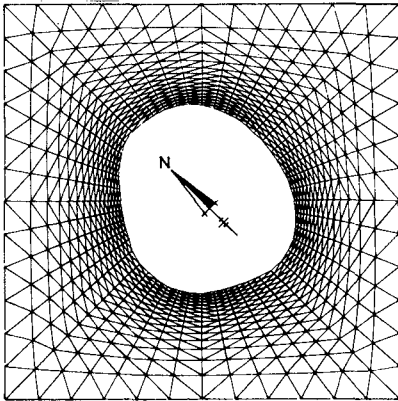


Fig. 7 Finite-element mesh

finite-element mesh used here. In the detailed flow model the tidal constituents of the flow are imposed via boundary conditions prescribing the inflow and/or the outflow velocities. The wave-induced current is driven by forces inside the area derived from the radiation stresses in the wave field (Longuet-Higgins, 1970; Battjes, 1974). The sediment transport model is based on the local equilibrium transport formulation due to Bijker (Bijker, 1967; Bijker, 1971). The bottom change rates follow from the conservation of sediment mass.

In Figure 8 the results of the computation of the detailed models for the waves from a Northern direction and maximum flood flow are outlined. The current pattern shows a longshore current along the seaward side of the dam, directed to the South-west. Around the basin contraction of the tidal currents takes place. Additional calculations have shown that, as a result of this phenomenon, the longshore current is strongly counteracted by the flood flow. The sediment transport pattern shows no significant transport rates in the sheltering area of the basin. Here the pronounced influence of the wave heights on the transport rates is expressed. Around the basin the bottom changes in a small strip are mainly determined by the longshore current, whereas at higher waterdepths the influence of the tidal motion is predominant: erosion occurs where the tidal flow accelerates and sedimentation where it decelerates. The contour plot of the bottom change rate in Figure 8 exhibits a rather irregular pattern with alternating sedimentation and erosion zones, which is hard to interpret qualitatively. For this reason the initial bottom contours have also been compared with the ones after a given time interval.

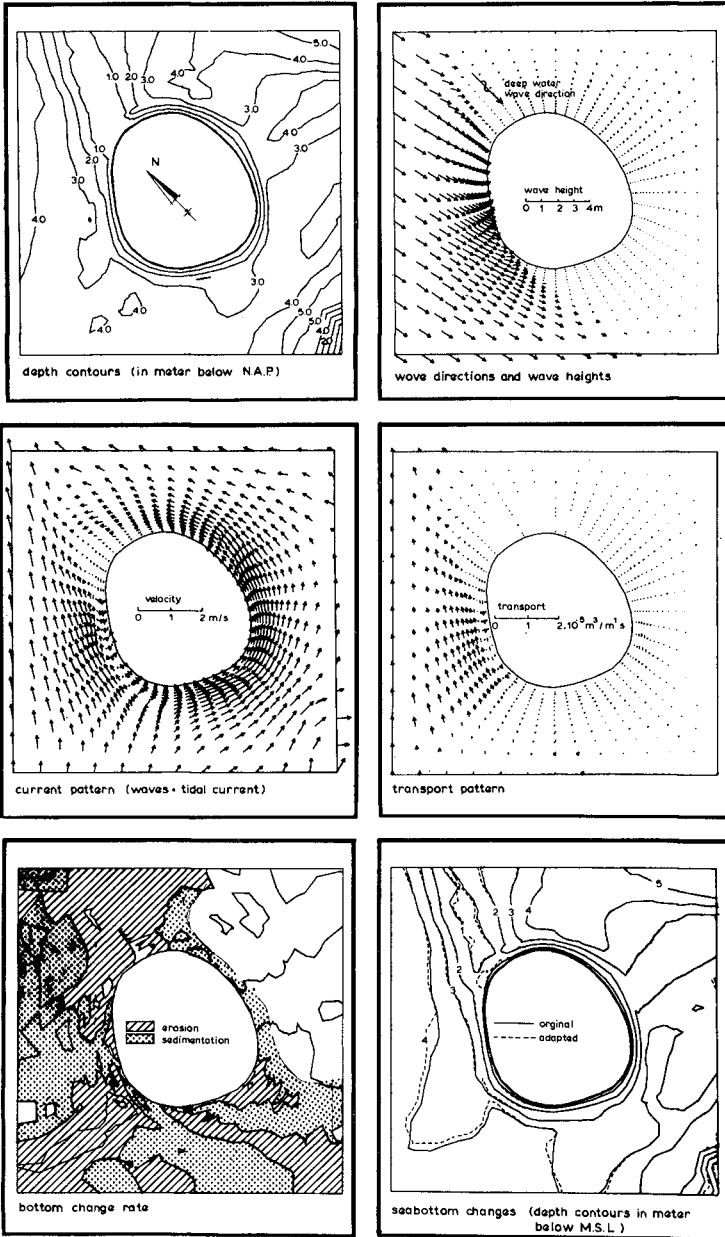


Fig. 8 Detailed models; results at moment of maximum flood and waves from the North

The final computational results of COMOR indicate that the resulting sediment transport pattern and the amount of beach nourishment is strongly influenced by onshore and/or offshore directed sediment transport resulting from the interaction between longshore current and tidal flow. The traditional computation methods viz. the computation of the resulting longshore sediment transport rates for successive cross sections, generally disregard this aspect. As such the COMOR model has contributed considerably to the understanding of the relevant phenomena for this situation.

Sedimentation study of sea water intake for the West Coast Steam Power and Desalination Complex, Umm al Qaiwain, United Arab Emirates

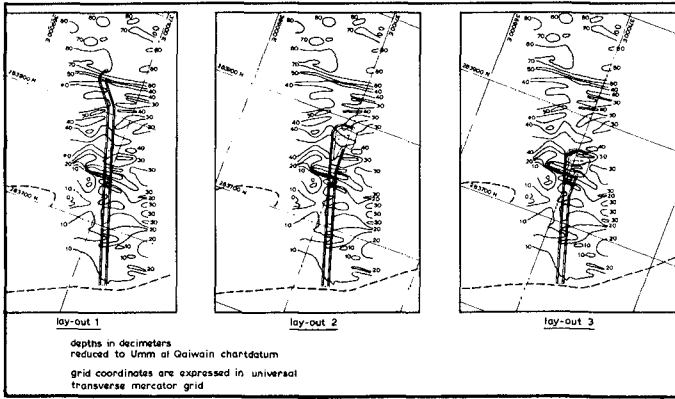


Fig. 9 Evaluated intake layouts

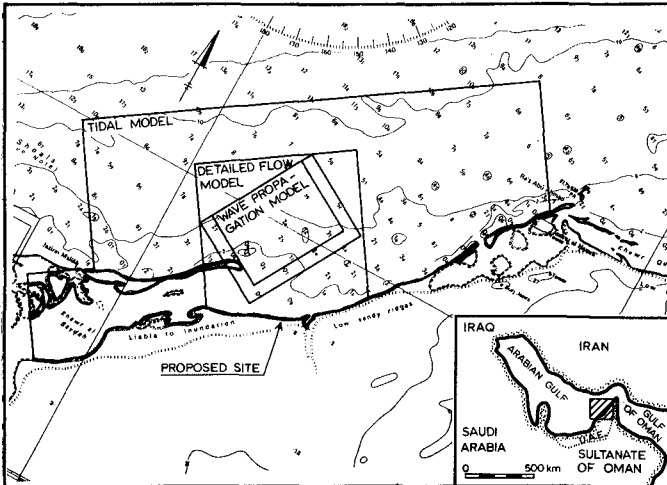


Fig. 10 Site location and constituent models

The sedimentation study was made to select the technically and economically optimal intake layout enabling the continuous withdrawal of up to  $53 \text{ m}^3/\text{s}$  of seawater. Three different intake layouts all consisting of two more or less parallel breakwaters forming a protected intake channel, have been evaluated (see Figure 9). COMOR is applied to determine the general morphologic changes after the construction of the seawater intake. The proposed site of the intake channel is a coastal stretch with a relatively wide and flat beach (Figure 10) exposed to predominant wave action from directions between W and NW. Along this coast a net Eastward longshore transport occurs, forming a spit at the extremity of the island Jazirat-Mallah. In addition, tidal and wave-induced currents carry a significant part of the longshore transport from Jazirat-Mallah towards the Chor Umm al Qaiwain. Part of this sediment is settling down in the area in front of the proposed site. Another part is transported North-east by the ebb current and picked up by the wave-induced longshore current East of the site.

The COMOR model applied in this project includes wave-induced as well as tidal currents. Figure 10 also shows the constituent models, varying in size between  $5 \times 17 \text{ km}^2$  for the tidal model to  $3 \times 5 \text{ km}^2$  for the wave propagation model. The numerical solution procedures in the various models are identical to those in the former application. Tidal computations were carried out for an average tidal situation of which the boundary conditions were derived from field measurements. For the deep water boundary conditions of the wave field, the predominant wave direction was used in combination with the annual extreme wave height. Special attention was given to the reproduction of the diffraction of waves around the head of the intake structure. To reduce computer costs the wave diffraction model covers only part of the detailed model area. In the remaining parts, simple refraction and shoaling computations were performed. The computations with the detailed flow model and the morphological model were carried out for two steady state conditions representing the mean ebb and flood currents. As an illustration, Figure 11 shows the computed wave field and the combined wave-induced and ebb current pattern, for the medium size inlet configuration.

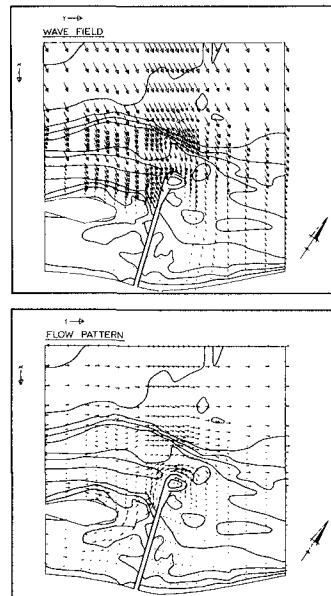
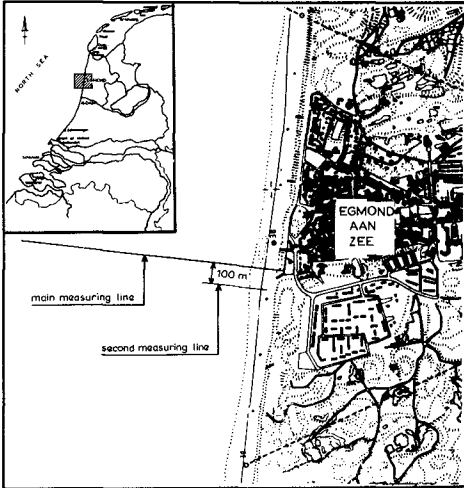


Fig. 11 Computed wave field and current pattern

The principal result of the application of the COMOR-model in this case was the indication that, depending on the layout of the construction, the tidal current and the wave-induced circulation in the

shadow zone could interact in a very unfavourable way, meeting just in front of the inlet (layout 1 in Figure 9) or the inlet could be situated entirely in the longshore transport zone (layout 3 in Figure 9). This indication, rather than the quantitative predictions of the morphological changes resulting from the model, has been used in the advice.

Current and sediment transport analysis at Egmond, the Netherlands



Recently within the framework of TOW two field campaigns on the Dutch Coast near Egmond (see Figure 12) have been conducted. The aims of the field measurements were the following

- to test instruments for the measurements of wave heights, currents and sediment transport in the surf zone;
- to collect data of hydraulic and morphologic phenomena in the near-shore zone.

For details of the 1982 campaign reference is made to Stive and Derks (1984). The location near Egmond was selected because of its longshore uniformity of

Fig. 12 Site location at Egmond

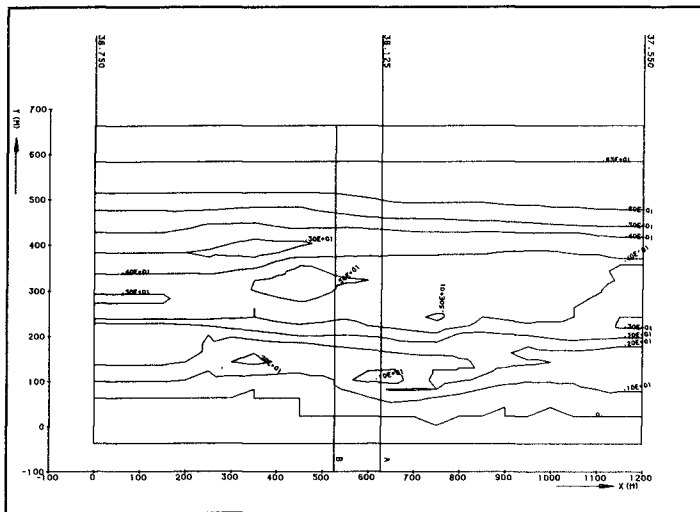


Fig. 13 Geometrical schematization

bottom topography and hydraulic conditions. During both campaigns data on wave heights, currents, vertical tide, suspended sand concentration, wind velocity and -direction, seawater temperature and bottom topography were gathered for conditions ranging from calm weather to 9 Beaufort. Here the COMOR system was applied to study the sensitivity of the measuring data to the "overall" nearshore conditions of the project site. The area covered in the COMOR model is  $700 \times 1200 \text{ m}^2$ . As can be seen in Figure 13 the depth contours are fairly straight and parallel. In the coastal profile a bar can be distinguished at a distance of approximately 400 m offshore.

The wave, current and sediment transport modules in COMOR are identical to those described for the first application. Figure 14 shows the wave field, current pattern and bottom changes resulting from deep

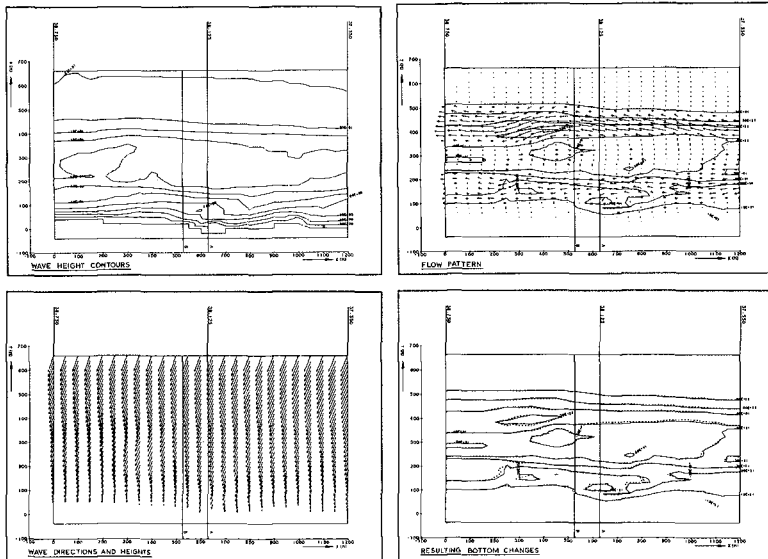


Fig. 14 Computed wave field, current pattern and bottom changes

water waves of North-westerly direction, with a significant wave height  $H_s = 3.88 \text{ m}$  and a peak frequency of  $T_p = 8.5 \text{ s}$ . The current pattern shows two longshore current lanes, one on the bar and the second current close to the shore. Note that the mild variation in the bottom topography has a pronounced influence on the current pattern. It is expected that the influence of the bottom topography on the current pattern will reduce if convection is included. The bottom topography appears to migrate in current direction due to gradients in sediment transport.

Although the analysis of the results is by no means completed, the COMOR model has already contributed considerably to the understanding of the nearshore morphology.



Tidal current and sediment transport analysis at IJmuiden, the Netherlands

For the onset of a study of morphological changes under tidal conditions, the geometry of the port of IJmuiden has been selected. IJmuiden is the gateway to Amsterdam (Figure 15). The tidal period for IJmuiden is on average 12.37 hours. The maximum velocity at a depth of 10 m is in the order of 0.6 m/s. The bottom roughness has been estimated at 0.2 m.

For the computation of the flow field a model for the solution of the Navier-Stokes equations has been used. This model has been developed in cooperation with the Laboratoire National d'Hydraulique, Chatou, France. For details, see Officier, Vreugdenhil and Wind (1985). The turbulent viscosity field is obtained by solving the  $k-\epsilon$  equations. The inflow boundary condition has been assumed to vary sinusoidally with time. The variation in mean water level has not been taken into account (rigid lid approximation) as it is not expected to have a dominant effect on the development of the flow pattern.

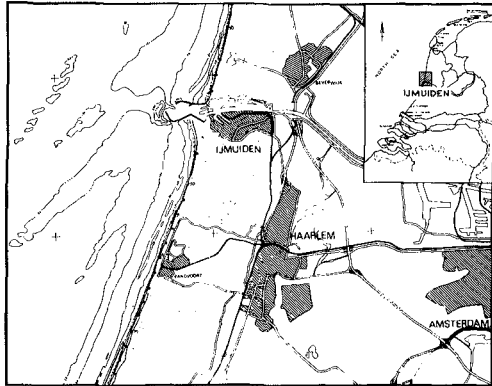


Fig. 15 Site location at IJmuiden

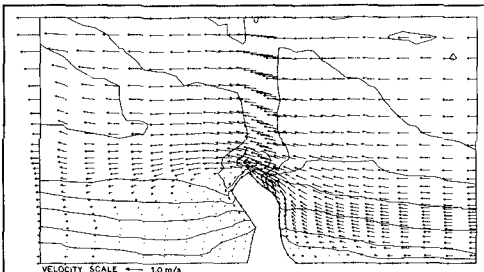


Fig. 16 Computed flow field

The flow field shown in Figure 16 results 3.30 hours after slack tide. Near the harbour entrance a flow contraction can be noticed, while downstream of the harbour moles an eddy is visible. A preliminary comparison of the computed flow field with float tracks indicates similar characteristics. For a more detailed comparison field measurements are a prerequisite. It will be clear

that the flow field is by no means stationary. According to a simple rule of thumb the length of the eddy parallel to the shore should be, for a stationary condition, in the order of six times the length of the harbour mole. Due to the tide reversal the growth of the eddy is stopped and the eddy moves towards deeper water. The time dependency of the flow field has implications for the sediment transport. For instance any morphologic study for IJmuiden based on stationary current fields seems not to be warranted.

A first estimate of the sediment transport can be obtained if a sediment transport formula is combined with the flow field. The resulting sediment transport rate is formed by the small difference between the large sediment transport quantities during the ebb and flood cycle. In nature the resulting sediment transport is among others also determined by the net tidal flow and the rate of suspension of the sediment. These effects are under investigation. As a preliminary result in Figure 17 the change in bottom topography is shown if the sediment transport is calculated using the Engelund-Hansen transport formula. The artificial time scale for the change in bottom topography is 24 hours. It is interesting to note that the gully in front of the harbour is moving in current direction. The wave like character of the bottom change is inherent to the local sediment transport concept.

Although the analysis of the tidal morphology is just started, the model performance is positive. It appeared that the Navier-Stokes current model could model could easily be included resulting in predictions of the evolution of the eddies near the port entrance. The effect of evolution of the flow field on the morphology is presently under investigation.

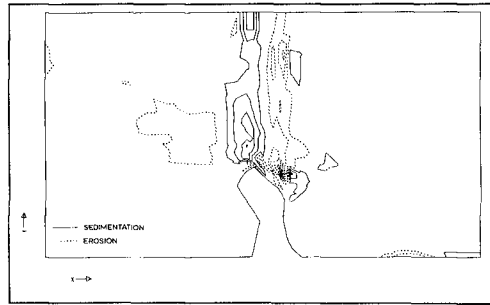


Fig. 17 Computed change in bottom topography

## 5 EVALUATION

Despite the accumulation of a substantial knowledge of the individual morphological processes, the simulation of coastal morphological evolution by mathematical modelling is still in an early stage of development. It is realized that a considerable amount of knowledge, insight and experience remains to be gathered before COMOR may be used as a fully independent quantitatively predictive model. For instance:

- the validity of the depth averaged description of the flow is not satisfactorily verified for coastal currents;
- the transport formulae presently applied in coastal morphology are rather inaccurate;
- little is understood of the time-dependent interaction of waves, currents and transports on the one hand and bottom changes on the other hand;
- the criteria imposed on the schematization of the wave climate and tidal motion contain a great deal of arbitrariness;
- the verification of the compound morphological model is still lacking, hampered as it is by insufficient experimental information.

The aforementioned aspects may suggest that the application of the COMOR model for coastal engineering advisory purposes is at present rather questionable. However the way COMOR is applied so far is

not essentially different from the procedures which are widely used in desk calculations for isolated points of the field. So far the practical applications of COMOR concern only initial morphological changes. The reliability of the model is determined to a high extent by the reliability of the constituent models. In most cases these models have been verified individually, so the reliability of their results can be estimated. Nevertheless the final computational results of the COMOR model must be interpreted with caution. This interpretation is primarily a matter of physical insight and awareness of the model limitations. The results of COMOR must be considered as a support of advice just as the traditional computation methods which are already used in desk studies for years. Applied in this way, COMOR models for initial changes appear to be quite useful in coastal advisory practice, especially in comparative studies (investigation of alternative plans, response to an abrupt change in conditions, etc.) or as a qualitative support of other well calibrated tools (coastline models, scale models, etc.).

## REFERENCES

- BAKKER, W.T., (1968): The dynamics of a coast with a groyne system. Proc. 11th ICCE, London: 492-517.
- BATTJES, J.A., (1974): Computation of set-up, longsh. currents, run-up and overtopping due to wind generated waves. Doct. thesis, Delft Univ. of Techn., 244 pp.
- BOER, S., (1983): A num. model for the computation of coastline changes under the influence of tidal and wave-driven currents. Delft Hydr. Lab., TOW-rep. R 1605-IV (in Dutch), 39 pp.
- BIJKER, E.W., (1967): Some consideration about scales for coastal models with movable bed. Doct. thesis, Delft Univ. of Techn., 142 pp.
- BIJKER, E.W., (1971): Longshore transport computations. Proc. ASCE J. of Waterw. Harb. and Coast. Eng. Div., WW 4, Nov. 1971.
- COEFFE, Y. and PECHON Ph., (1982): Model. of sea-bed evolution under wave action. Proc. 18th ICCE, Capetown, 1149-1160.
- CRAILE, A.D.D., (1982): The drift velocity of water waves. J. Fluid Mech., 116, 187-205.
- DERKS, H. and STIVE, M.J.F., (1984): Field invest. in the TOW Study Progr. for Coastal Sed. Transp. in the Netherlands. Proc. 19th ICCE, Houston.
- DINCEMANS, M.W., STIVE, M.J.F., Kuik, A.J., Radder, A.C. and Booij, N. (1984): Field and lab. verific. of the wave propag. model CREDIZ. Proc. 19th ICCE, Houston.
- FLEMMING, C.A. and HUNT, J.N., (1976): Application of a sed. transp. model. Proc. 15th ICCE, Honolulu: 1184-1202.
- CRUICKSHANK, W., (1964): Theoretical forms of shorelines. Proc. 8th ICCE, Lisbon: 219-235.
- LEEUWENSTEIN, W. and WIND, H.G., (1984): The comp. of bed shear in a numerical model. Proc. 19th ICCE, Houston.
- LE MÉHAUTE, B. and SOLDATE, M., (1978): Math. modelling of shoreline evolution. Proc. 16th ICCE, Hamburg: 1163-1179.
- LONCQUET-HICCINS, M.S., (1953): Mass transport in water waves. Phil. Trans. Roy. Soc. Lond., A 245(903): 535-581.
- LONCQUET-HICCINS, M.S., (1970): Longsh. currents generated by obliquely incident sea waves. J. Geophys. Res. 75: 6778-6789 & 6790-6801.

- LONGUET-HIGGINS, M.S., (1983): Wave set-up, percolation and undertow in the surf zone. Proc. Roy. Soc. Lond., A 390: 283-291.
- McANALLY, W.H., LETTER Jr., J.V., STEWART, J.P., THOMAS, W.A. and BROGDON, N.J. (1984): Appl. of Columbia hybrid modeling system. J. Hydr. Engrg., 110(5): 627-642.
- O'CONNOR, B.A., MORCOS FANOS A. and CATHERS, B. (1981): Sim. of coast. sed. movements by comp. model. Proc. 2nd Int. Conf. Eng. Software, London; Adey, R.A. (ed), CML Publ. Ltd., Southampton, 1981, 554-568.
- OFFICIER, M.J., VREUGDENHIL, C.B., and WIND, H.G., (1985): Appl. in hydr. of num. solutions of the Navier-Stokes equations. Recent adv. in Num. Fluid Dyn., Vol. V, Taylor, C. (ed.).
- WATANABE, A., (1982): Num. models of nearsh. currents and beach deformation. Coastal Engrg. in Japan, 25: 147-161.
- WIND, H.G. and PERRELS, P.P., (1982): FRIMO a finite el. model for coast. currents dominated by bottom friction. Delft Hydr. Lab., TOW-rep, W 439-1, 18 pp.

## CHAPTER NINETY NINE

### A SIMPLIFIED MODEL FOR LONGSHORE SEDIMENT TRANSPORT

by

James A. Bailard

Naval Civil Engineering Laboratory  
Port Hueneme, California 93043

#### ABSTRACT

An energetics-based longshore sediment transport model is developed which takes the form of a modification to the wave power equation. Instead of being constant, the wave power coefficient is a function of the breaker angle and the ratio of the orbital velocity magnitude and the sediment fall velocity. This modification extends the range of application of the wave power equation to include both field and laboratory conditions.

#### INTRODUCTION

Waves, breaking at an angle to the shore, cause sand to be moved laterally along the beach. On a straight beach with parallel contours, the longshore sand transport is spatially uniform and no planform changes in the beach will occur. If, however, the longshore sand transport is interrupted by a groin or a jetty, sand will accumulate on the updrift side of the structure and erosion will occur on the downdrift side. Coastal engineers are often required to predict the rate of accretion and erosion associated with a structure, thus there is a need for an accurate and easily applied longshore transport model.

Although the wave power equation was developed more than 20 years ago (Inman and Bagnold, 1963), this equation remains the most widely accepted method today for predicting the longshore sediment transport rate (SPM, 1977). The wave power equation linearly relates the spatially-integrated immersed weight longshore sediment transport rate,  $I_{\ell}$ , to what has been termed the longshore component of wave energy flux,  $P_{\ell}$ , i.e.

$$I_{\ell} = K P_{\ell} \quad (1)$$

where the wave power coefficient,  $K$ , is generally assumed to

be a constant equal to 0.77 (Komar and Inman, 1970). The factor  $P_{\rho}$  can be expressed as

$$P_{\rho} = (E C_n)_b \sin \alpha_b \cos \alpha_b \quad (2)$$

where  $E$  is the energy of the incident waves,  $C_n$  is the group velocity of the waves,  $\alpha$  is the incident wave angle, and the subscript  $b$  denotes the value at breaking.

In spite of its widespread application, the wave power equation accurately predicts the longshore sediment transport rate only over a narrow wide range of conditions. For example, laboratory measurements of  $K$  suggest a value of approximately 0.2, while field measurements suggest a value closer to 0.8 (see Figure 1). This difficulty is in part the result of the relative simplicity of the wave power equation. For example, the assumption of a constant wave power coefficient prevents any differentiation between the bedload and the suspended load transports, nor does it allow any accounting of the sediment grain size or the beach slope.

More complex, analytically-based longshore sediment transport models have been proposed which predict the distribution of the longshore transport rate across the surfzone. These models are based on adaptations of stream-based sediment transport models, and include traction-based models (eg. Ostendorf and Madsen, 1976; Swart, 1976), and energetics-based models (e.g. Komar, 1971, 1977; Thornton, 1973; Bowen, 1980; Bailard, 1981). In order to predict the distribution of the longshore sediment transport rate across the surfzone, all of the above models incorporate some form of a breaking wave model and a longshore current model. The resulting equations are generally cumbersome, incorporating a number of undetermined coefficients, and require numerical solution. As a result of the added complexity of these models, none have had widespread application.

The objective of this study was to develop a sediment transport model which preserves the general form and simplicity of the wave power equation, but which extends its range of application. The basis for the model was a simplification of Bailard's (1981) energetics-based longshore transport model. Simplifying assumptions used in the model development were based on an analysis of Nearshore Sediment Transport Study (NSTS) field data (see Gable, 1979, 1980). Both laboratory and field measurements of longshore sediment transport rates were used to calibrate the model.

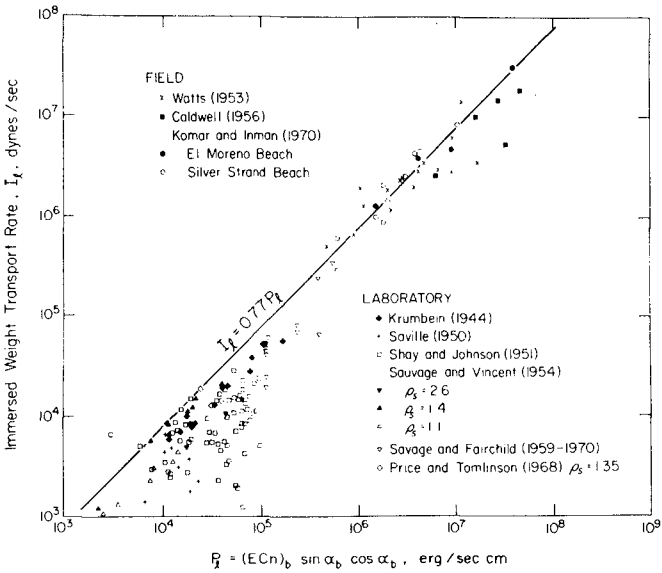


Figure 1. The wave power equation, shown by the solid line, overpredicts laboratory measurements of longshore transport rate when a constant wave power coefficient is assumed (from Komar and Inman, 1970).

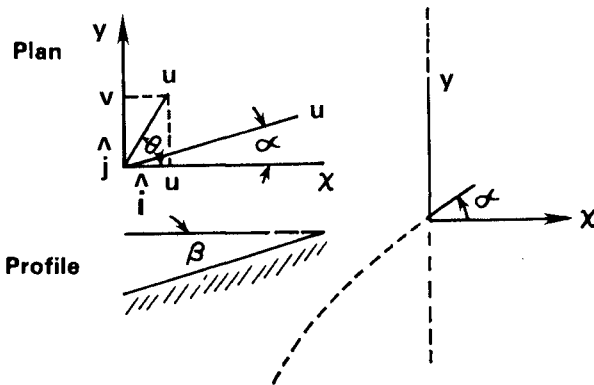


Figure 2. Schematic diagram showing the velocity field parameters in the surfzone.

## THEORY

## Generalized Transport Equation

The basis for the model development was a generalized form of Bagnold's (1963, 1966) sediment transport model for streams. Bagnold's model assumes that sediment is transported in two modes, bedload and suspended load. The bedload transport is assumed to occur as a thin granular-fluid layer which is supported by the bed via grain to grain collisions. The suspended load transport is assumed to take place above the bedload layer, with the sediment supported by fluid turbulence. In both cases, energy is expended by the stream in transporting the sediment. Bagnold assumed that the rate of sediment transport was proportional to the rate of energy dissipation in the stream, with separate proportionality constants, termed efficiency factors, associated with the bedload and suspended load transports respectively.

Bailard (1981) generalized Bagnold's energetics-based stream model for time-varying flow over an arbitrarily sloping bottom. The resulting sediment transport equation was

$$\begin{aligned} \langle \vec{i}_t \rangle = & \rho c_f \frac{\epsilon_B}{\tan \phi} \left[ \langle |\vec{u}_t|^2 \vec{u}_t \rangle - \frac{\tan \beta}{\tan \phi} \langle |\vec{u}_t|^3 \rangle \hat{i} \right] \\ & + \rho c_f \frac{\epsilon_S}{W} \left[ \langle |\vec{u}_t|^3 \vec{u}_t \rangle - \frac{\epsilon_S}{W} \tan \beta \langle |\vec{u}_t|^5 \rangle \hat{i} \right] \end{aligned} \quad (3)$$

where  $\vec{i}_t$  is the instantaneous sediment transport rate vector,  $\vec{u}_t$  is the instantaneous nearbottom velocity vector,  $\rho$  is the density of water,  $c_f$  is the drag coefficient of the bed,  $\epsilon_B$  is the bedload efficiency factor,  $\epsilon_S$  is the suspended load efficiency factor,  $\phi$  is the internal angle of friction of the sediment,  $\tan \beta$  is the bedslope,  $W$  is the fall velocity of the sediment,  $\hat{i}$  is the unit vector directed downslope, and  $\langle \rangle$  indicates a time-averaged quantity.

An important feature of the above equation is that the bedload transport (first bracketed quantity) and the suspended load transport (second bracketed quantity) both consist of a primary component directed parallel to the instantaneous fluid velocity vector, and a secondary component directed downslope. The latter is associated with the downslope component of the sediment load.

## Local Surfzone Transport Equations

In order to predict the sediment transport rate in the surfzone, the local surfzone velocity field must first be specified. Figure 2 depicts a plane contour beach with the x-axis directed shoreward and the y-axis directed parallel to the beach. The slope of the beach is  $\tan \beta$  and the local



wave angle is  $\alpha$ .

For simplicity, the nearbottom velocity field was assumed to be composed of an oscillatory component  $\tilde{u}$ , oriented at angle  $\alpha$  to the x axis, and steady velocity components  $u$  and  $v$ , directed parallel to the x- and y-axes respectively. The total velocity vector,  $\vec{u}_t$ , becomes

$$\vec{u}_t = (\tilde{u} \cos \alpha + u) \hat{i} + (\tilde{u} \sin \alpha + v) \hat{j} \quad (4)$$

where  $\hat{i}$  and  $\hat{j}$  are the unit vectors associated with the x- and y-axes. In addition, the oscillatory velocity component was assumed to be composed of a primary component  $u_m$  with frequency  $\sigma$ , and higher harmonic  $u_{2m}$  with frequency  $2\sigma$ , etc, so that

$$\tilde{u} \cong u_m \cos \sigma t + u_{2m} \cos 2\sigma t + \dots \quad (5)$$

Substituting Equation 4 into Equation 3 and assuming that

$$u/u_m \ll 1; \quad v/u_m \ll 1; \quad \cos \alpha \cong 1; \quad \langle i_x \rangle \ll \langle i_y \rangle \quad (6)$$

the local time-averaged longshore sediment transport rate becomes

$$\begin{aligned} \langle i_y \rangle = & \rho c_f u_m^3 \frac{\epsilon_B}{\tan \phi} \left[ \delta_v + \delta_v^3 + \frac{\tan \beta}{\tan \phi} u_3^* \tan \alpha \right] \\ & + \rho c_f u_m^4 \frac{\epsilon_s}{W} \left[ \delta_v u_3^* + \frac{u_m}{W} \epsilon_s \tan \beta u_5^* \tan \alpha \right] \end{aligned} \quad (7)$$

where

$$\zeta_v = v/u_m; \quad u_3^* = \langle |\vec{u}_t|^3 \rangle / u_m^3; \quad u_5^* = \langle |\vec{u}_t|^5 \rangle / u_m^5 \quad (8)$$

With the exception of  $c_f$ ,  $\epsilon_B$ , and  $\epsilon_s$ , all of the parameters in Equation 8 can be predicted from one of the several breaking wave and longshore current models available (e.g. Longuet-Higgins, 1970). In its full complexity, this procedure results in a complex expression for the cross-shore distribution of the longshore sediment transport rate (Baillard, 1981). Spatial integration of the distribution yields an expression similar in form to the wave power equation except that the wave power coefficient is a complex function of the incident wave, beach, and sediment properties. The complexity of this expression, and

the fact that it requires numerical evaluation has prevented any widespread use of the model.

#### Spatially-Integrated Longshore Transport Equation

The principal obstacle to obtaining a closed-form solution for  $K$  in Bailard's (1981) model were the complex expressions for the wave velocity moments  $u_3^*$  and  $u_5^*$ . Guza and Thornton (1981) have shown, however, that for weak mean currents and a gaussian orbital velocity distribution,  $u_3^*$  and  $u_5^*$  are constants equal to 0.58 and 1.13 respectively. Estimates from NSTS field data generally support these findings except that measured values are closer to 0.60 and 1.25. Based on these findings, one of the simplifying assumptions used in the present model development was that  $u_3^*$  and  $u_5^*$  are constants equal to 0.60 and 1.25.

The longshore current model used in the present development was the radiation stress-based model by Ostendorf and Madsen (1979). In order to keep the solution as simple as possible, a number of simplifications were made with relationship to the model's provisions for finite breaker height and longshore current strength. The resulting expression for the longshore current,  $v$ , is as follows

$$v = v_c v^* \quad (9)$$

where  $v_c$  is a characteristic longshore current strength and  $v^*$  is the dimensionless longshore current distribution expressed as follows (P#0.4)

$$v^* = C_1 \left( \frac{1 - C_2}{C_2 - C_3} \right)^{C_3} x^* + C_1 x^* \quad x^* \leq 1$$

$$v^* = C_1 \left( \frac{1 - C_3}{C_2 - C_3} \right)^{C_2} x^* \quad x^* > 1 \quad (10)$$

The parameters  $C_1$ ,  $C_2$ , and  $C_3$  are the following functions of the lateral mixing parameter,  $P$ ,

$$C_1 = (1 - 2.5 P)^{-1}$$

$$C_2 = -\frac{1}{8} - \left( \frac{1}{64} + \frac{1}{P} \right)^{1/2}$$

$$C_3 = -\frac{3}{4} + \left( \frac{9}{16} + \frac{1}{P} \right)^{1/2} \quad (11)$$

and the dimensionless surfzone position,  $x^*$ , is defined as

$$x^* = \frac{x - x_s}{x_b - x_s} \quad (12)$$

where  $x_s$  and  $x_b$  are the positions of the shoreline and the break-point on the x-axis respectively.

The characteristic longshore current strength,  $v_c$ , is defined as

$$v_c = \delta_c u_{mb} \quad (13)$$

where  $u_{mb}$  is the oscillatory velocity magnitude, obtained from shallow water wave theory, i.e.,

$$u_m = \frac{\gamma}{2} \sqrt{g h} \quad (14)$$

and  $\delta_c$  is the relative longshore current strength parameter defined as

$$\delta_c = \frac{5 \pi \tan \Delta \sin \alpha_b}{8 c_f} \quad (15)$$

The parameter  $\tan \Delta$  is equal to the average beach slope,  $\tan \beta$ , modified for wave setup, i.e.

$$\tan \Delta = \frac{\tan \beta}{1 + \frac{3}{8} \gamma_b^2} \quad (16)$$

The parameter  $\gamma$  is defined as the ratio of the surfzone wave height,  $H$ , to the water depth,  $h$ , and is assumed to have the following distribution

$$\begin{aligned} \gamma &= \gamma_b & x^* \leq 1 \\ \gamma &= \gamma_b \left( \frac{h_b}{h} \right)^{5/4} & x^* > 1 \end{aligned} \quad (17)$$

where  $\gamma_b$  is assumed to be equal to 0.8

Combining Equations 8 and 9 and assuming that Snells Law applies, the following equation was obtained for the cross-shore distribution of the longshore transport rate

$$\begin{aligned}
 \langle i_y \rangle = & \rho c_f u_{mb}^3 \frac{\epsilon_B}{\tan \phi} \left[ \frac{1}{2} \left( \frac{Y}{Y_b} \right)^2 \delta_c v^* x^* + \delta_c^3 v^*{}^3 \right. \\
 & \left. + \frac{\tan \beta}{\tan \phi} \left( \frac{Y}{Y_b} \right)^3 u_3^* x^*{}^2 \tan \alpha_b \right] \\
 & + \rho c_f u_{mb}^4 \frac{\epsilon_s}{W} \left[ \left( \frac{Y}{Y_b} \right)^3 \delta_c u_3^* v^* x^*{}^{3/2} \right. \\
 & \left. + \tan \beta \frac{u_{mb}}{W} \epsilon_s \left( \frac{Y}{Y_b} \right)^5 u_3^* x^*{}^3 \tan \alpha_b \right]
 \end{aligned} \tag{18}$$

The spatially integrated longshore transport rate,  $I_\ell$ , was obtained by spatially integrating Equation 18, i.e.

$$I_\ell = \frac{h_b}{\tan \Delta} \int_0^\infty \langle i_y \rangle dx^* \tag{19}$$

Noting that  $K = I_\ell/P_\ell$ ,  $\tan \alpha_b \approx \sin \alpha_b$ , and

$$\rho c_f \frac{h_b}{\tan \Delta} u_{mb}^3 \delta_c = \frac{5 \pi}{8} \gamma_b P_\ell \tag{20}$$

then the wave power coefficient  $K$  can be expressed as

$$K = \epsilon_B K_1 + \epsilon_s K_2 + \epsilon_s^2 K_3 \tag{21}$$

where

$$\begin{aligned}
 K_1 = & \frac{5 \pi}{8} \left( \frac{\gamma_b}{\tan \phi} \right) \left\{ \frac{c_1}{2(c_2 - c_3)} \left[ \frac{1 - c_2}{c_3 + 2} + \frac{c_2 - c_3}{3} - \frac{1 - c_3}{c_2 - \frac{1}{2}} \right] \right. \\
 & + \frac{25 \pi^2}{256} \left( 1 + \frac{3}{8} \gamma_b^2 \right)^{-2} \left( \frac{\tan \beta}{c_f} \right)^2 \sin^2 2 \alpha_b c_1^3 \left[ \frac{\left( \frac{1 - c_2}{c_2 - c_3} \right)^3}{3 c_3 + 1} \right. \\
 & \left. + \frac{3 \left( \frac{1 - c_2}{c_2 - c_3} \right)^2}{2 c_3 + 2} + \frac{3 \left( \frac{1 - c_2}{c_2 - c_3} \right)}{c_3 + 3} + \frac{1}{4} - \frac{\left( \frac{1 - c_3}{c_2 - c_3} \right)}{3 c_2 + 1} \right] \\
 & \left. + \frac{8}{15 \pi} \left( \frac{\tan \beta}{\tan \phi} \right) \left( \frac{c_f}{\tan \beta} \right) \left( 1 + \frac{3}{8} \gamma_b^2 \right) u_3^* \right\}
 \end{aligned} \tag{22}$$

$$K_2 = \frac{5 \pi}{8} \gamma_b u_3^* \frac{u_{mb}}{W} \left( \frac{c_1}{c_2 - c_3} \right) \left[ \frac{1 - c_3}{c_3 + \frac{5}{2}} + \frac{c_2 - c_3}{7/2} - \frac{1 - c_3}{c_2 - \frac{5}{4}} \right] \tag{23}$$

and

$$K_3 = \frac{25}{36} \gamma_b \tan \beta \left( \frac{c_f}{\tan \beta} \right) \left( 1 + \frac{3}{8} \gamma_b^2 \right) u_5^* \left( \frac{u_{mb}}{W} \right)^2 \quad (24)$$

Equations 22 through 24 were further simplified using the results of Komar (1976). Komar analyzed laboratory and field measurements of longshore currents and found that  $P$  was approximately equal to 0.2 and the ratio  $\tan \beta / c_f$  was approximately equal to 7. Introducing these assumptions into Equations 22 through 24, the following results were obtained

$$K_1 = 0.385 + 20 \sin^2 2 \alpha_b + 0.074 \tan \beta \quad (25)$$

$$K_1 = 0.228 u_{mb} / W \quad (26)$$

$$K_3 = 0.123 \tan \beta (u_{mb} / W)^2 \quad (27)$$

#### MODEL CALIBRATION

The remaining free parameters in Equation 21 which need to be specified are the bedload and suspended load efficiency factors. Bagnold (1966) found that for stream flow,  $\epsilon_B$  and  $\epsilon_S$  were equal to 0.13 and 0.01 respectively. In the present case, these factors were estimated from laboratory and field measurements of  $K$ .

The laboratory data used to estimate  $\epsilon_B$  and  $\epsilon_S$  were selected data from Saville (1949, 1950) and Shay and Johnson (1951). The field data were from Bruno et. al. (1980), Dean et. al. (1983), Komar and Inman (1970), Kraus et. al. (1983), and Moore and Cole (1960). Average characteristics of these data sets are summarized in Table 1.

Initially, a nonlinear least squares procedure was used to estimate  $\epsilon_B$  and  $\epsilon_S$ , however, it was quickly found that the contribution of  $K_3$  to  $K$  was negligible in relationship to  $K_1$  and  $K_2$ . When  $K_3$  was eliminated from Equation 21, the resulting equation was linear in  $\epsilon_B$  and  $\epsilon_S$ , thus a multiple linear regression technique could be used. The resulting estimates for  $\epsilon_B$  and  $\epsilon_S$  and their 95% confidence intervals were

$$\begin{aligned} \epsilon_B &= 0.13 \pm 0.009 \\ \epsilon_S &= 0.032 \pm 0.004 \end{aligned} \quad (28)$$

Combining these estimates with Equation 21, the desired

Table 1. Characteristics of laboratory and field data sets used to calibrate the present longshore transport model.

Laboratory					
Source	#OBS	W(cm/sec)	Umb/W	$\theta$ (deg)	Kobs
Saville	7	4.0	8.3	6	0.16
Shay & Johnson	3	4.0	8.5	6	0.22

Field					
Source	#OBS	W(cm/sec)	Umb/W	$\theta$ (deg)	Kobs
Bruno et. al	7	2.5	113	0.2	0.87
Dean et. al	7	2.7	31	15	1.15
Komar & Inman					
El Moreno	10	9.5	11	9	0.82
Silver Strand	3	2.0	72	4	0.66
Kraus et. al					
Ajigaura	2	3.2	38	4	0.31
Hirono	2	9.5	16	2.5	0.11
Shimokita	1	2.7	48	6.0	0.61
Moore & Cole	1	20.5	9.3	12	0.19

equation for the wave power coefficient,  $K$ , was obtained

$$K = 0.05 + 2.6 \sin^2 2 \alpha_b + 0.007 u_{mb}/W \quad (29)$$

Figure 3 shows a plot of the observed values of  $K$  versus the values estimated by Equation 29. With the exception of the data from El Moreno Beach (Komar and Inman, 1970), and the single data point from Moore and Cole (1960), the fit is relatively good.

#### DISCUSSION

The advantage of the present model over the wave power equation is that it can be used to predict the longshore sediment transport rate over a wider range of input conditions. Using a constant wave power coefficient equal to 0.77, the wave power equation does an adequate job of predicting the longshore transport rate provided the grain size is between 0.15 and 0.25 mm and the wave height is between 0.5 and 2.0 m. Outside of this range, particularly, under laboratory conditions or for large sand sizes in the field, the power equation is significantly in error.

The present model corrects the above mentioned shortcoming of the wave power equation by separately accounting for the bedload and suspended load transports. As a result, the wave power coefficient becomes a function of the incident breaker and sediment characteristics. Nevertheless, the resulting equation for  $K$  involves only parameters which are already available from the usual longshore transport calculations.

The present longshore transport model has a number of limitations which must be mentioned. First, the energetics sediment transport equations which are used in the model development are vertically integrated and ignore the vertical structure of the sediment concentration and velocity fields. Recent field measurements of vertical distributions of these parameters, substantiate their importance, particularly in relationship to cross-shore sediment transport (Jaffee et. al., 1984). Their importance in relationship to longshore transport processes is unknown.

A second limitation of the model is that the rate of energy dissipation (to which the transport rate is proportional) is computed directly from the drag at the bed. Contributions associated with the breaking wave at the surface are neglected, in spite of their overall dominance (Thornton and Guza, 1983). The implicit assumption is that the bottom boundary layer is the primary factor controlling the upward flux of sediment from the bottom, however, this is only

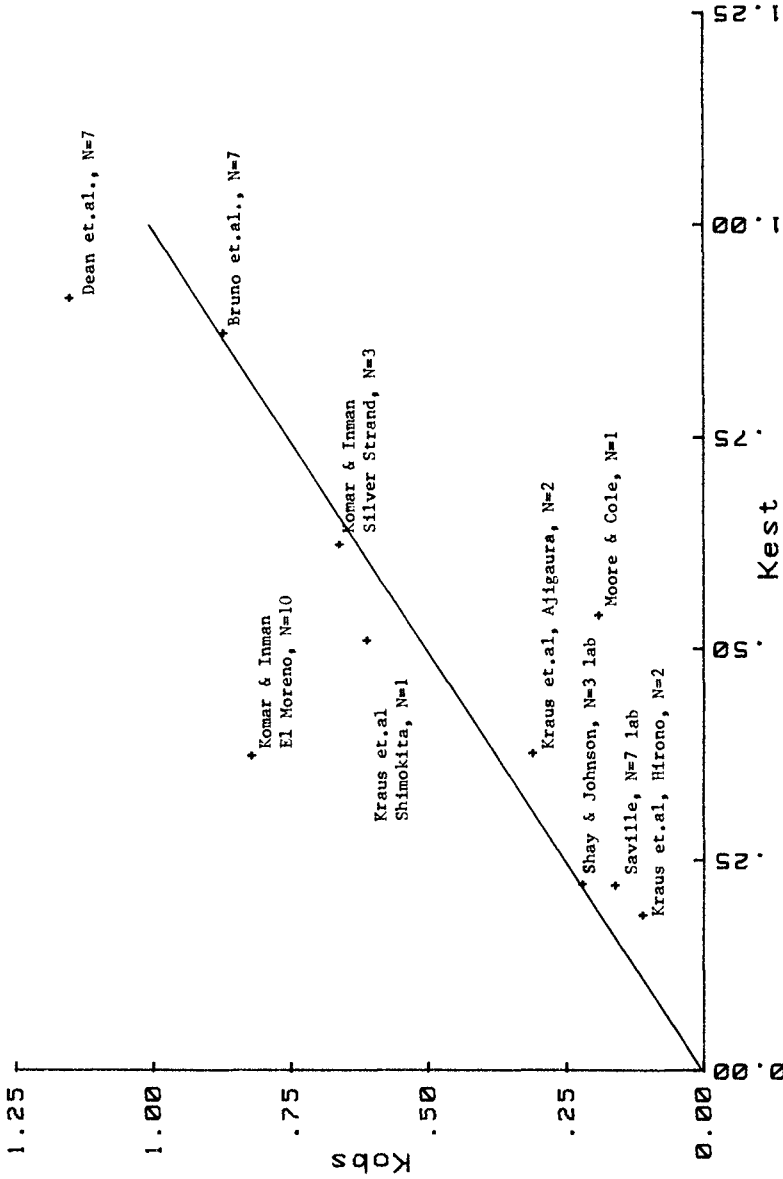


Figure 3. A comparison of measured wave power coefficients with wave power estimates generated from Equation 29.



conjecture. A possible improvement to the model might be to incorporate a variable drag coefficient to partially account for the energy dissipation of the breaking waves. Alternatively, the rate of energy dissipation could be directly associated with the local gradient in the energy flux (e.g. Thornton, 1973 and others).

A third limitation of the model is that threshold of motion effects for the sediment have been neglected. Seymour (1983) has shown that under most field conditions, threshold effects are not significant, while under laboratory conditions they are significant. Threshold effects could be incorporated into the present model using the statistical method developed by Seymour (1983), but the resulting equations would be more complex.

Additional limitations of the model can be summarized as follows. The distribution of the longshore transport rate was derived from the usual breaking wave assumptions. Analysis of NSTS field data has shown that some of these assumptions are clearly incorrect. For example, one common assumption is that the total velocity variance monotonically decreases towards the shore. Field measurements on dissipative beaches show instead that the velocity variance is nearly constant across the surfzone (Guza and Thornton, 1981; Bailard, 1983). This result has important ramifications concerning the distribution of the longshore current and the longshore sediment transport rate.

A related problem is that beach profile shapes have been shown to have a significant effect on the distribution of the longshore current (McDougal and Hudspeth, 1984). Moreover, proper characterization of the lateral mixing of momentum is still an unanswered question. As a result, the distribution of the longshore transport rate specified in the present model should be considered as only approximate.

The overall effect of the above mentioned limitations on the present model is not known. To some degree, many of these effects have been hidden by the processes of integration as well as by the least squares estimation procedure for determining the bedload and suspended load efficiency factors.

#### CONCLUSIONS AND RECOMMENDATIONS

The following conclusions were reached as a result of this study.

1. A simple modification to the wave power equation has been developed through a systematic application of Bagnold's energetics sediment transport concepts. Instead of being

constant, the wave power coefficient is found to be a function of the incident breaker angle and the ratio of the orbital velocity at the break point divided by the sediment fall velocity.

2. The above modification was found to extend the range of application of the wave power equation. Longshore transport rates under laboratory conditions can be predicted with the same equation used for field conditions. The equation can also be applied to beaches with larger sediment sizes.

3. Although the model describes the distribution of the longshore transport rate across the surfzone, this distribution should be applied with caution. Recent measurements of surfzone waves and currents suggest that a number of the common assumptions used to develop the present model and most longshore current models are not very accurate.

4. There may be a limit to the extent that vertically-integrated energetics-based sediment transport models can be used to describe surfzone sediment transport processes. Vertical distributions of cross-shore velocities and sediment concentrations are clearly important in determining on-offshore sediment transport rates. Their importance in longshore transport processes is unknown.

5. The present model might be improved by including sediment threshold of motion effects, a variable drag-coefficient, and a different formulation for the rate of energy dissipation. While these modifications will probably provide a more accurate prediction of the longshore sediment transport rate, they will also increase the complexity of the model. Most likely, however, significant improvements in modeling surfzone sediment processes will come only through an increased understanding of the vertical structure of the sediment concentration and velocity.

Based on these findings, it is recommended that future work be focused on measuring the vertical structure of the sediment concentration and fluid velocity fields. A parallel effort should focus on developing improved models for wave bore dynamics, surfzone boundary layer dynamics, bedload, and suspended load mechanics, and time-averaged longshore and on-offshore currents in the surfzone.

#### REFERENCES

Bagnold, R.A., 1963, "Mechanics of marine sedimentation," in *The Sea: Ideas and Observations*, vo. 3, Interscience, New York.

- Bagnold, R.A., 1966, "An approach to the sediment transport problem from general physics," U.S. Geological Survey Prof. Paper, 422-I.
- Bailard, J.A., 1981, "An energetics total load sediment transport model for a plane sloping beach," J. Geophysical Res., vol. 86, no. c11, pp 10938-10954.
- Bailard, J.A., 1983, "Modeling on-offshore transport in the surfzone," 18th Conf. on Coastal Engineering, ASCE, pp 1419-1438.
- Bowen, A.J., 1980, "Simple models of nearshore sedimentation: Beach profiles and longshore bars," in Coastline of Canada Geological Society of Canada, Halifax.
- Bruno, R.O., Dean, R.G., and Gable, C.G., 1980, "Longshore Transport Evaluations at a Detached Breakwater," 17th Conf. on Coastal Engineering, ASCE, pp 1453-1475.
- Dean, R.G., Berek, E.P., Gable, C.G., and R.J. Seymour, 1983, "Longshore transport determined by an efficient trap," 18th Conf. on Coastal Engineering, ASCE, pp 954-968.
- Gable, C.G., 1979, Report on data from the Nearshore Sediment Transport Study experiment at Torrey Pines Beach, CA, IMR Ref. 79-8, Inst. of Mar. Res., La Jolla, CA.
- Gable, C.G., 1980, Report on data from the Nearshore Sediment Transport Study experiment at Leadbetter Beach, CA, IMR Ref. 80-5, Inst. of Mar. Res., La Jolla, CA.
- Guza, R.T., and E.G. Thornton, 1981, "Velocity moments in the surfzone," Contract Report to the Naval Civil Engineering Laboratory, November, 1981, 56pp.
- Hudspeth, R.T. and W.G. McDougal, 1984, "Evaluation of planar and nonplanar composite beaches," 19th Conf. on Coastal Engineering, ASCE.
- Inman, D. L. and R.A. Bagnold, 1963, "Littoral Processes", in The Sea: Ideas and Observations, vol. 3, 529-533, Interscience, New York.
- Jaffe, B., Sternberg, R., and A. Sallenger, 1984, "The role of suspended sediment in shore-normal beach profile changes," 19th Conf. on Coastal Engineering, ASCE.
- Komar, P.D., 1971, "The mechanics of sand transport on beaches," J. Geophysical Research, vol. 76, pp 713-721.
- Komar, P.D., 1976, Beach Processes and Sedimentation, Prentice Hall, New Jersey, 429 pp.

Komar, P.D., 1977, "Beach sand transport: Distribution and total drift," ASCE Waterways, Harbors and Coastal Eng., WW4, pp 225-239.

Komar, P.D., and D.L. Inman, 1970, "Longshore sand transport on beaches," Journal of Geophysical Research, vol 75, pp 5914 -5927.

Kraus, N.C., Isobe, M., Igarashi, H., Sasaki, T.O., Horikawa, K, 1983, "Field measurements on longshore sand transport in the surfzone," 18th Intern. Conf. on Coastal Engineering, ASCE, pp 969-988.

Louguett-Higgins, M.S., 1970, "Longshore currents generated by obliquely incident sea waves," J. Geophysical Res., vol. 75, pp 6790-6801.

Moore, G.W. and J.Y. Cole, 1960, "Coastal processes in the vicinity of Cape Thompson, Alaska," Geologic Investigations in Support of Project Chariot in the Vicinity of Cape Thompson, North-Western Alaska-Preliminary Report, U.S. Geol. Survey Trace Elements Investigation, Report no. 753.

Ostendorf, D.W., and O.S. Madsen, "An analysis of longshore currents and associated sediment transport in the surfzone," Rep. 241, Ralph M. Parsons Lab., Dept. of Civil Engineering, Mass. Inst. of Tech., Cambridge, Mass.

Saville, T., 1949, Preliminary Report on Model Studies of Sand Transport Along an Infinitely Long Straight Beach, Rep. HE-111-305, Fluid Mech. Lab., University of Calif., Berkeley.

Saville, T., 1950, "Model study of sand transport along an infinitely long, straight beach," Eos Trans. AGU, vol 31, pp 555-565.

Seymour, R.J., unpublished manuscript, "A similtude model for longshore sand transport."

Shay, E.A. and J.W. Johnson, 1951, Model Studies on the Movement of Sand Transported by Wave Action Along a Straight Beach, Ser. 14, Inst. of Eng. Res., Dept. of Engineering, Univ. of Calif., Berkeley.

SPM, 1977, "Shore Protection Manual, U.S. Army Coastal Engineering Research Center, 3 volumes.

Swart, D.H., 1976, "Predictive equations regarding coastal transports," 15th Intern. Conf. on Coastal Engineering, ASCE.

Thornton, E.B., 1973, "Distribution of sediment transport across the surfzone," 12th Intern. Conf. on Coastal

Engineering, ASCE, pp 1049-1068.

ACKNOWLEDGEMENT

This research was supported by the Independent Research Program at the Naval Civil Engineering Laboratory.

## CHAPTER ONE HUNDRED

### AN ASSESSMENT OF BEACH NOURISHMENT SEDIMENT CHARACTERISTICS

D.K. Stauble<sup>1</sup>, M. Hansen<sup>2</sup> and W. Blake<sup>1</sup>

#### ABSTRACT

An important component of beach nourishment design is to assess the compatibility of the borrow material with the native beach sediment. One avenue to judge the "success" of a project is the amount of fill retained over a specific period of time after fill placement. Presumably, if the fill material placed on the eroded beach is compatible with the energy of the coastal processes, it will be resorted along the profile but be retained within acceptable limits in the vicinity of the project area.

At present the selection of suitable borrow material is based only on theoretical criterion. Specifically, the Fill Factor and Renourishment Factor are based on models developed by Krumbein (1956), Krumbein and James (1965), James (1974), Dean (1974), James (1975) and Hobson (1977). These methods of judging borrow area suitability have not been fully tested in the field and the Shore Protection Manual (U.S. Army, 1977) warns that they should only be used as a general indication of possible fill behavior.

A review of monitoring reports on selected recent beach restoration and sand by-pass projects revealed a lack of standardization on data collection and analysis. Little evaluation of the actual behavior of fill material on the nourished beach had been carried out. To assess the suitability of the fill material, projects with adequate data were investigated and the short (one year) and long term (two to three years) behavior of actual fill data was described. Detailed collection of native sediment before nourishment, representative borrow material at time of placement and samples at specific times after fill placement were used to determine the redistribution of fill grain size characteristics and determine the accuracy of the present beach fill models.

It was found that present models do not take into account non-normal grain size distributions found at the projects studied or  $\text{CaCO}_3$  shell material. A safety factor assuming loss of fine material from the borrow should be used with the Adjusted Shore Protection Manual Fill Factor Method to give more accurate results. The delta variable in the Renourishment Factor was found to vary between projects and should be calculated for each project. At the present time use of the entire grain size distribution is necessary to understand the sediment redistribution after fill placement.

-----  
<sup>1</sup>Department of Oceanography and Ocean Engineering, Florida Institute of  
Technology, Melbourne, Florida 32901 USA

<sup>2</sup>Coastal Eng. Res. Center, Vicksburg, MS 39180 USA

## INTRODUCTION

Beach Nourishment as a technique for shoreline stabilization and storm protection has become increasingly popular over the past decade. Beaches widened by artificial fill placement act to dissipate erosive wave energy, provide upland property storm protection and supply additional sediment to a usually sediment starved sand budget area. Aesthetically, renourished beaches are also of recreational value to an important coastal tourist industry.

The rapidly rising cost of beach restoration and inlet sand by-passing projects have led opponents to question the long term value of such a "soft" coastal structure. In the past, many projects have been poorly monitored and inadequately documented. This has resulted in a dearth of scientific and engineering data for design and permitting officials to assess project success; and has contributed to costly project delay and redesign.

The high cost of beach restoration projects requires that we be able to predict how the sediment placed on the beach is going to respond to the physical forces acting upon it. The present theoretical beach-fill models have only been tested on a limited basis. Therefore, a more accurate understanding of beach-fill redistribution using actual field data from past projects would be a major contribution to our knowledge of beach erosion control.

Engineering monitoring reports and field collection from several recent beach nourishment projects provided the sediment data used in this study. It was difficult to find projects that had enough usable sediment data to make a comparison study possible. At present, there is no standardization in project monitoring and it was sometimes difficult to compare projects directly since the data provided were obtained in various ways and presented in different formats. The projects selected for this study had minimal similarity in data and were from locations that provided variation in both sediment characteristics and wave climate. The locations used to evaluate monitoring techniques, accuracy of the current beach fill models and to develop monitoring and analysis guidelines for future projects, included beach nourishment projects at Indialantic/Melbourne Beach, Delray Beach, and Hollywood/Hallandale located on the moderate to high wave energy (Tanner, 1960) East Coast of Florida. The Captiva Island project was located on the low to moderate Gulf Coast of Florida and the Ocean City project was located on the high wave energy Atlantic Coast of Southern New Jersey (Figure 1).

## SEDIMENT SAMPLING AND ANALYSIS CONSIDERATIONS

To evaluate a beach for nourishment, one must be able to obtain representative native beach and borrow sediment samples. The question of what is a representative sample arises. There are noticeable differences in the grain size distribution as one proceeds from the dune base, across the beach and continues offshore as described by Bascom (1959). The largest grains are usually found in an area just seaward of the backwash/surf interaction zone, an area of much turbulence. The summer berm crest area also contains significant coarse material due to runup sediment transport dynamics. Finer material is found in the dune area owing predominantly to wind transport processes. Seaward of the mean low water area sediments become finer with increasing distance seaward of the breaker zone. When determining the grain size

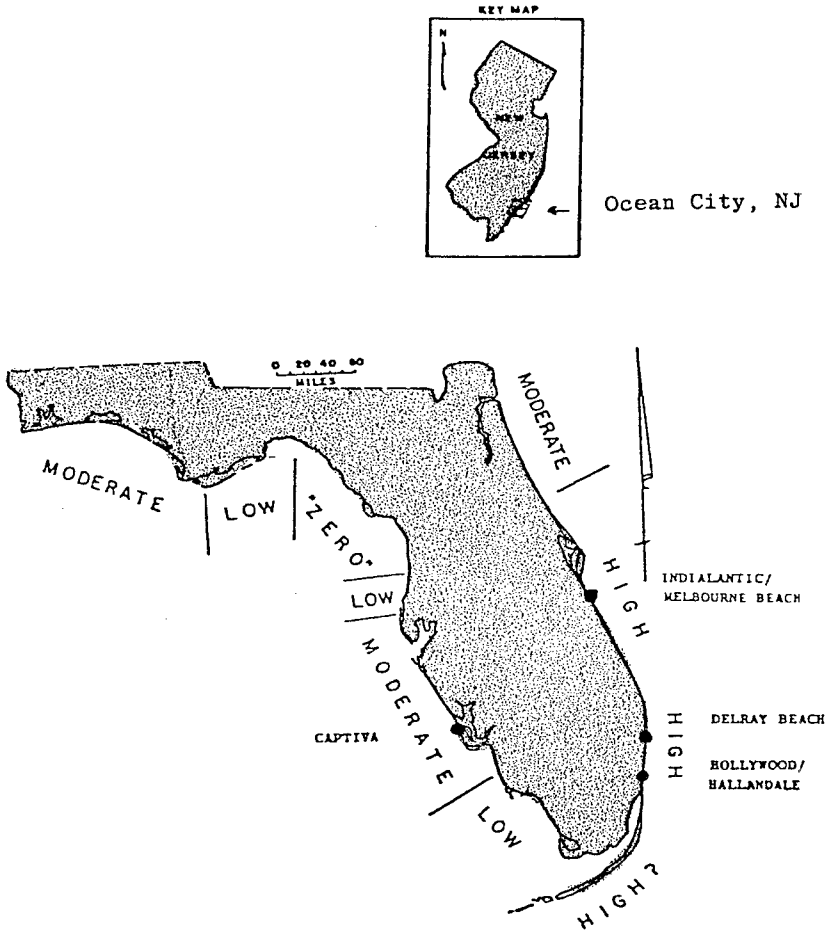


Figure 1. Locations of beach nourishment projects used in this study. Wave energy zones after Tanner (1960).



distribution of the native beach, it has been found that by combining samples from across the beach and nearby offshore areas, the variability in grain-size is reduced (Hobson, 1977). The grain size distribution of these composite samples will vary depending on the location of the included samples.

Analysis of some of this unique field data indicates that location of sediment sampling is critical to give a true picture of the native beach sediment characteristics and post-nourishment fill redistribution. A variety of sampling designs were used in the projects with little standardization (Table 1). A minimal requirement for inclusion in this study was data on the native beach, borrow area and a reasonable interval of post-nourishment monitoring sediment samples. Most monitoring reports used fixed distances from a benchmark, or fixed elevations about NGVD for collection of samples independent of the dynamic coastal processes. It was found that choosing sampling sites along the profile based on hydrodynamic zonation on the beach (ie. area of maximum runup, mid-tide area and mean low tide area) gives the best representative picture of grain size distribution. These zones change over the course of any study depending on tide, wave and profile shape parameters.

Location of sediment sampling is critical to give a picture of the true fill redistribution. A wide variety of sampling designs were used with differences in location, number and frequency of sampling. To reduce variability between the various sampling intervals, a mathematical composite was constructed from data generated after the individual samples have been analyzed either from graphic representation in project monitoring reports or actual field collection. The samples were all sieved at either 1/2 or 1/4 phi intervals. The percentage of sediment in each size class of the different samples was then combined and an average grain size distribution was calculated. This method preserved information on individual samples for later use and allowed for various combinations of composites.

Several types of composite samples, as described by Hobson (1977), were examined to determine which of these samples eliminated the variability and provided the best comparison of behavior over time. Two basic types of composites were chosen after an examination of various combinations of samples available from each project, the intertidal composite and the profile composite:

- 1) The intertidal composites consist of samples from within the intertidal zone, (Figure 2) between mean hightide to mean lowtide, collected around the time of lowtide. This composite gave a good picture of the behavior of the beach-fill since this is the area of fill placement and most of the subsequent reworking.
- 2) The profile composites consist of intertidal samples plus samples collected seaward of the swash zone to approximately a 12 foot depth (Figure 2). This is a common type of composite used on most past projects.

The borrow area sediment sampling and analysis also varied from project to project (Table 1). Some of the projects reported composite samples of cores taken from the borrow area, summarizing vertical and horizontal distributions while others used composites or individual samples from the area of fill placement. The borrow material was obtained from various environments. Indialantic/Melbourne Beach had borrow material with a similar mean grain-size but was more poorly sorted and was sediment dredged from a barrier island to

PROJECTS	SEDIMENT SAMPLE TYPES							
	NATIVE	BORROW	3 MO.	6 MO.	9 MO.	1 YR.	18 MO.	LONG TERM
INDIANLAWTIC/ MELBOURNE BEACH	(HT, MT, LT) 200, 300/400	FROM DUMP TRUCK 3 LOCATIONS	X	X	X	X	X	X
CAPTIVA	ENTIRE PROJECT COMPOSITE ONLY	FROM CORES COMPOSITE	(+6, +3, 0) -3, -6, -9, -12	-	X	X	X	X
DELRAY	+15, +12 (+9, +6, 0) -3	FROM CORES COMPOSITE		-	-	-	-	X
HOLLYWOOD/ HALLENDALE	(+7, +4, 0) -3, -6, -9, -12 FT.	NO BORROW	-	X	X	X	-	-
OCEAN CITY, N.J.	(HT, MT, LT) NO OFFSHORE	FROM PIPE	X	X	X	X	X	X

Table 1. Variation in sediment sampling location on beach and time interval between sample collection. Sample locations within parentheses were collected in the intertidal area, others below NGVD. HT = high tide, MT = mid tide and LT = low tide area.

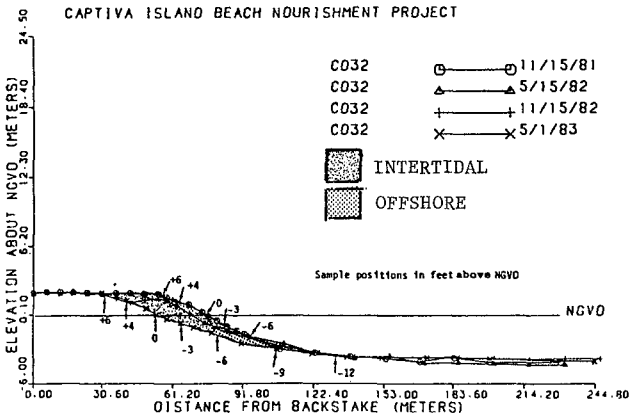
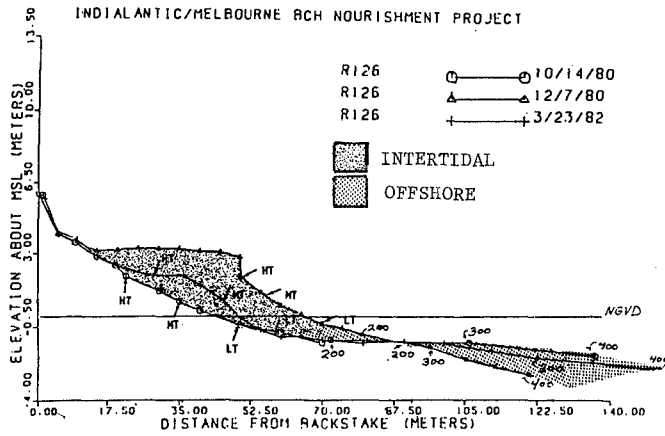


Figure 2. Sediment sampling locations on two of the projects thru time showing the change in intertidal and offshore samples with change in profile shape.

produce a harbour area. Delray Beach had much finer borrow material whose sorting was slightly poorer than the native beach and was from an offshore source area. Hollywood/Hallendale had a borrow that was slightly better sorted and contained finer material owing to its offshore origin. The borrow at Captiva Island was almost identical to the native beach and was obtained from an ebb tidal shoal. At Ocean City, NJ, the borrow was slightly finer and better sorted than the native beach and was dredged from a flood tidal bay source. When comparing native and borrow materials, there was more variation in the sorting values than there was in the mean grain-size. Table 2 summarizes the characteristics of each project.

Ideally, borrow material should have a grain size distribution congruent only with the intertidal samples where the fill is to be placed (Figure 3). The inclusion of offshore samples, however, results in a skewness to the finer grain-sizes and may not provide a true representative picture of the hydrodynamic effects on the native beach in the area of fill placement. A comparison of the borrow to native frequency curve of figure 3b) shows the standard practice of using the profile composite of the native sediment (including both intertidal and nearshore samples) vs. borrow sample, showing a reasonable match in distribution at all grain sizes. Figure 3a) shows a composite of only the intertidal samples, which gives a better picture of a borrow sediment that is deficient in the medium to coarse sand range, with an excess of fine material.

An examination of the various project data shows a distinct difference in grain size distributions landward and seaward of the low tide area. Sediment collected from the intertidal area (where most fill was placed on the projects examined) was found to be most representative of native beach material and gave a better picture of fill redistribution after placement (Stauble, et. al., 1983). Samples collected seaward of the low tide zone exhibited a distinctly different grain size distribution, tending to be composed of finer, better sorted material. This offshore area post-fill sediment grain size redistribution behaved differently from the intertidal area (Figure 4) in that the offshore sediments remained fined grained with little change in the mean and sorting. The intertidal composites, however, changed their mean and sorting as the coastal processes resorted the sediment and changed the profile shape.

At the present time, the difference between the native and borrow grain size distributions is one of the major determining factors for the project's success. From the data analyzed in this study, it was found that excess fine-grained material in the borrow was quickly winnowed away and transported offshore and/or downdrift of the nourished area. The standard practice of including the finer grained nearshore sediment samples into native beach composites appears to give a false picture on which to compute suitability of borrow material.

#### FILL MATERIAL COMPATIBILITY

Once sediment data is obtained for the native beach and the prospective borrow material, a method is needed to determine how suitable the material will be for placement on the beach. Several beach-fill models have been established to calculate an "overflow ratio" or fill factor which is defined as the volume

PROJECT	VOLUME OF FILL PLACED	LENGTH OF PROJECT	SOURCE AND METHOD OF PLACEMENT	SAMPLING INTERVAL	PROFILES WITH SEDIMENT SAMPLES	SAMPLES ALONG PROFILES	COMMENTS
Indiantic/ Melbourne Beach, FL	195,060m <sup>3</sup>	3.38km	upland source dumped from truck onto beach	1 per week for 2 months, then gradually reduced to every 3 months	3 within project profiles, plus 2 control profiles	dune base, RT, HT, Swash, + 3 offshore samples at 200, 300, 400 meters of high tide line	project completed Jan. 1981
Hollywood/ Hilandale, FL	1,514,432m <sup>3</sup>	8.46km	offshore source 1500 - 300m. 7 borrow sites dredge.	Pre-Construction every 3 months increaser to 1 year	6 profiles	+7, +4, 0, -3, -6, -9, -12ft.	project completed Nov. 1979
Delray Beach FL	1,269,749m <sup>3</sup> (1973) 536,180m <sup>3</sup> (1978) (two areas)	4.93km	offshore source dredged/trucked from stockpile source	Pre (6-73) Borrow (6-73) Post (7-81)	3 profiles	+15 to -3ft (3ft intervals)	project completed July 1978
Captive Island, FL	501,155m <sup>3</sup>	3.05km	source: ebb tidal dredge	Pre, post, 6, 12 18 months	4 within, 1 outside	+6 to -12ft (3ft intervals)	project completed Oct. 1981
Ocean City, NJ	917,520m <sup>3</sup>	3.6km	source: flood tidal delta/ bay area dredge	Pre, post, 2 weeks, each 3 months until 15 months	3 profiles	HT, MT, LT	project completed Aug. 1982

Table 2. Project characteristics showing design variations and lack of standardization in data collection.

NATIVE VS. BORROW

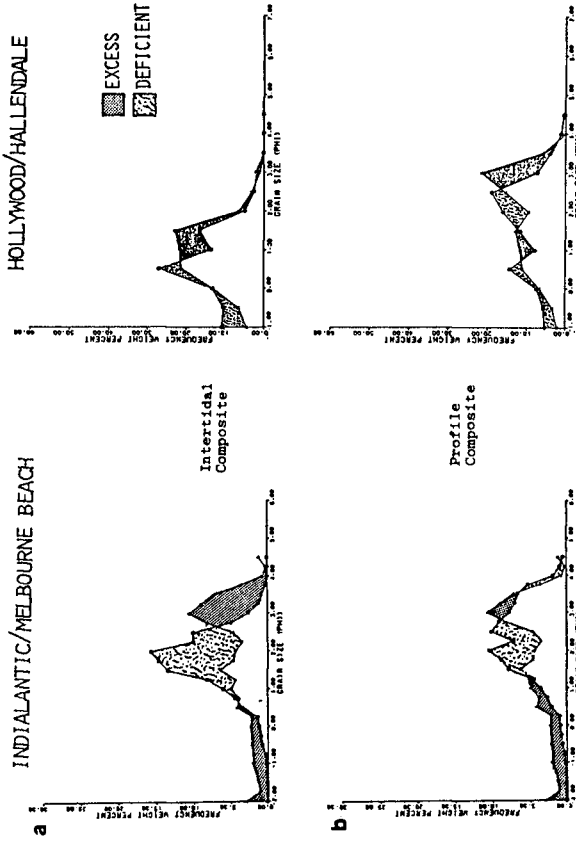


Figure 3. Comparison of grain size distribution frequency curves of borrow vs. native sediment using a) composite of just the intertidal samples and b) composite of the entire profile including the offshore samples. Intertidal composites give truer picture of size variation.

INTERTIDAL VS. OFFSHORE COMPOSITE COMPARISON

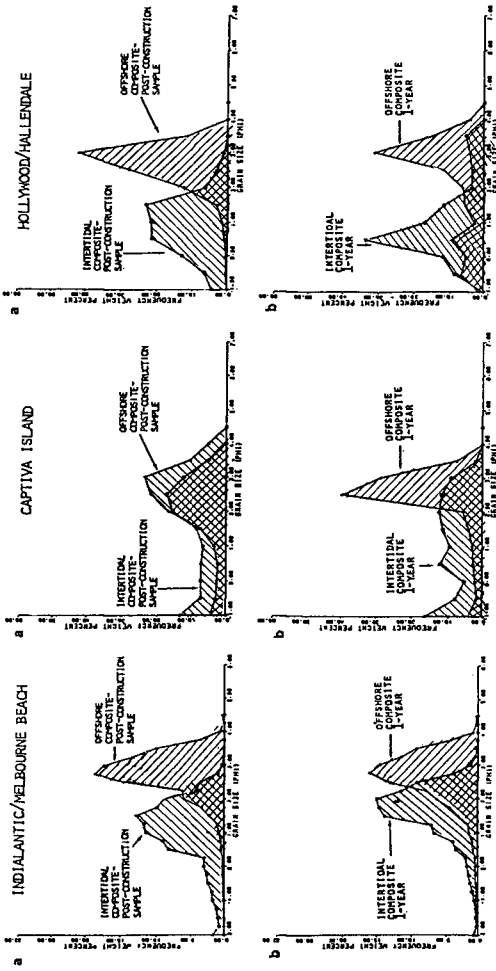


Figure 4. Comparison of intertidal vs. offshore composite grain size distribution frequency curves from three projects a) immediately after fill placement and b) one year after construction. Intertidal sample composites show the largest resorting.

of borrow material required to produce a unit volume of usable fill material with the same grain size distribution as the native material (James, 1975, Hobson, 1977). These beach-fill models require two parameters for calculations: the mean grain-size which is a measure of the central tendency and the sorting which is a measure of the spread of the grain sizes about the mean.

Currently there are three beach-fill models described by the Shore Protection Manual (U.S. Army, 1984): (1) The Shore Protection Manual (SPM) Method proposed by Krumbein and James (1965), (2) The Dean Method (Dean, 1974) and (3) The Adjusted Shore Protection Manual (Adjusted SPM) Method developed by James (1975).

The SPM method, developed by Krumbein and James (1965), compares the ratios of weight percentages of the native-to-borrow composites across the range of observed grain-sizes to determine the grain-size at which the ratio is a maximum (critical grain-size). One major problem with this method is the assumption that the coarse, more stable fraction will be winnowed away to create the compatible grain size distribution.

To overcome problems with the SPM method, Dean (1974) proposed a second method to calculate a fill factor. His approach assumes that selective sorting will winnow fine materials from the fill until the mean of the modified fill equals the native mean. A major problem is that the model predicts stability for all grain-sizes when the borrow materials are coarser and more poorly sorted than native sediments, even though the finer grain-sizes will be removed by winnowing. The SPM method implies that selective sorting will occur in both coarse and fine size fractions, whereas Dean's method implies only removal of material in the finer size classes.

James (1975) created a third fill factor model to correct the basic problems of the first two. This model, known as the Adjusted SPM method (Adjusted SPM), assumes the fill factor to be equal to the "critical ratio" of the SPM method, except when the borrow is coarser than the native sediments. This results in a modified grain size distribution which is as close as possible to the proportions of the native distribution in the finer size classes, but retains the borrow characteristics of the coarser size classes. Typically, the Adjusted SPM method produces fill factors less than the SPM method but greater than Dean's method (Hobson, 1977).

Each of fill factor approaches use many of the same assumptions:

- (1) Sediments native to the beach are considered to be the most stable for the environment.
- (2) Local sorting processes act upon the entire volume of fill to achieve a GSD similar to the native sediments sometime after fill placement.
- (3) Sorting processes change the fill material into native-like sediments by winnowing out a minimum amount of the original fill.
- (4) GSD's of the native and borrow sediments are assumed to be normally distributed for the purposes of simplifying calculations. (Hobson, 1977).

There is some question as to the validity of these assumptions. The native and borrow sediment distribution was not found to be normally distributed in the projects studied. A typical borrow vs. native frequency



curve shows that there was usually excess material in the coarse fraction consisting mostly of carbonate shell and in the fine fraction due to the lower energy environment of the borrow area. Most of the fill was deficient in the medium sand sizes typically found on the native beach (Hansen,1982).

A post-nourishment fill estimate provides a technique to determine the accuracy of the various beach fill models. The fill factor is the volume of borrow material required to produce a unit volume of stable fill material. A fill factor of 2 would mean that 1/2 of the borrow material was unstable, so twice the design volume of sediment would have to be placed on the beach to result in the design beach. The post-nourishment fill estimate is the reverse of this calculation. If 50% of the fill is lost from a project after one year, then a post-nourishment fill estimate of 2 is calculated. By comparing what actually happened to the fill with what the models predict, one can get a better idea of each model's accuracy.

With these values of actual fill behavior estimates, a comparison of the three fill factor models was undertaken to see which one estimates fill behavior the best. Hobson (1977) suggested using a safety factor with the Adjusted Shore Protection Manual Method to account for the proportions of material finer than sand ( $>4 \phi$ ), since these sizes are considered unstable on the beach and are lost soon after fill placement. The safety factor, G, can be calculated to account for these unstable sizes, using:

$$G = \frac{100\%}{\beta \phi} \times R(a) \quad (1)$$

where:  $\beta$  = % of sediment expected to remain (in  $\phi$  units)

Hobson, 1977 suggests  $<4 \phi$  or % sand size contained in sample, this study suggests  $<3 \phi$  or %  $>$  very fine sand.

The use of G has the effect of increasing the Adjusted fill factor when there are percentages of sediment finer than sand ( $>4 \phi$ ) or as found in this study material finer than fine sand. These values still fall between the Dean and SPM fill factors as predicted.

It was found in all of the study projects that the borrow material contained a maximum of only 3% mud-size particles and the cut off point of 4  $\phi$  was insignificant when using the safety factor G. After analyzing the post nourishment fill behavior it was discovered that most of the material finer than 3  $\phi$  was winnowed from the fill on most of the projects. A calculated safety factor using the 3  $\phi$  cut off was used and gave results close to the post-nourishment fill estimates. Table 2 summarizes the fill factor calculations and compares them to the post fill loss estimate.

James (1974) established a technique to predict how often renourishment will be needed and to evaluate the long-term performance of different fill materials. This technique involves the use of a mass-balance equation which compares material going into and out of the nourishment area. This equation is:

$$R_j = e^{-\Delta \left[ \frac{\mu_b - \mu_n}{\sigma_n} \right] - \frac{\Delta^2}{2} \left[ \frac{\sigma_b^2}{\sigma_n^2} - 1 \right]} \quad (2)$$

Site	Post-Hour. Fill Est.	R(s) SPH F.F.	R(d) Dean F.F.	R(a) Adj. F.F.	R(a) with G 4 phi 3 phi
I/MB profile	2.17	1.65	1.00	1.10	1.11 1.40
inter- tidal	2.17	2.20	1.00	1.38	1.40 2.10
Delray Beach	1.7	>10	15	>10	---- ----
Hol/Hal	1.09	-----	----	1.09	---- ----
Captive Island	1.22	1.02	1.00	1.01	1.01 1.20
Ocean City N.J.	No Volume Lost Estimates Available	unstable	----	1.75	1.75 2.3

Table 3. Comparison of post nourishment fill estimates with the Shore Protection Manual (R<sub>s</sub>), Dean (R<sub>d</sub>), Adjusted Shore Protection Manual (R<sub>a</sub>) fill factor models and the Adjusted Shore Protection Manual model with the safety factor G using the 4 phi and 3 phi size cut off for each project. The G of 3 phi gave "overflow" ratios closest to post nourishment estimates.

where:  $R_J$ —relative retreat rate (renourishment factor)  
 $\mu$  and  $\sigma$ —phi mean and phi sorting parameters  
 b and n—subscripts referring to borrow and native sediments  
 $\Delta$ —dimensionless parameter related to selective sorting  
 (winnowing) in the environment.

James suggests that the range of delta values may be from 0.5 to 1.5. He recommends that calculations of the renourishment factor use a value of 1.0 for the delta parameter and that the calculated values should be regarded as only approximate (James, 1975). The "delta" value can be computed from the following equation:

$$\Delta = \frac{\mu_n - \mu'_n}{\sigma_n} \quad (3)$$

where:  $\mu_n$  = the native mean before an erosional event.  
 $\mu'_n$  = the native mean after an erosional event.  
 $\sigma_n$  = the sorting of the native material, where  
 $\sigma_n = \sigma'_n$  is assumed true (James, 1974).

The delta value was computed for the projects from data obtained before and after erosional events as best that can be determined for projects where data was available. This value gave a better estimate of fill behavior than an assumed value of 1.0. It is recommended that a delta value should be calculated for each nourishment project to accurately apply this model. Usually, a beach requiring nourishment is undergoing an erosional period, so by taking sediment samples several times prior to nourishment, the delta value can be determined using equation (2).

### LONG TERM GRAIN SIZE REDISTRIBUTION

An examination of long term grain size characteristics of the fill material has lead to a complex picture of project grain size redistribution. The projects used in this study exhibited a wide range of native-to-borrow grain size distributions and coastal wave energy distributions. A method was developed, using a "post-nourishment fill estimate", based on volume of fill stabilized over a year or longer and the changes in grain size distribution over time, to graph fill behavior.

The inclusion of the safety factor, G, seems to predict more accurate fill factors than the Adjusted fill factors alone. Our findings indicate that safety factor calculations should be shifted to the fine limit of native sediment, not the 4 phi limit suggested by Hobson (1977). Figure 5a-d depicts the grain-size excesses and deficiencies in the borrow material as compared to the native beach at the top half of each figure and actual gains and losses one year later (8 years later for Delray Beach) at the bottom of each figure. If there was excess fine material in the borrow, the intersecting grain-size is shown by the dashed line. In the lower half of each figure, the solid line indicates the 3 phi grain-size at which the G values were calculated. The grain-size at which actual losses of fines occurred (if any) are shown with the crossed line. The 3 phi cut off point was used for the ease of obtaining percent sand at that point. Use of the 3 phi cut off point for calculating G

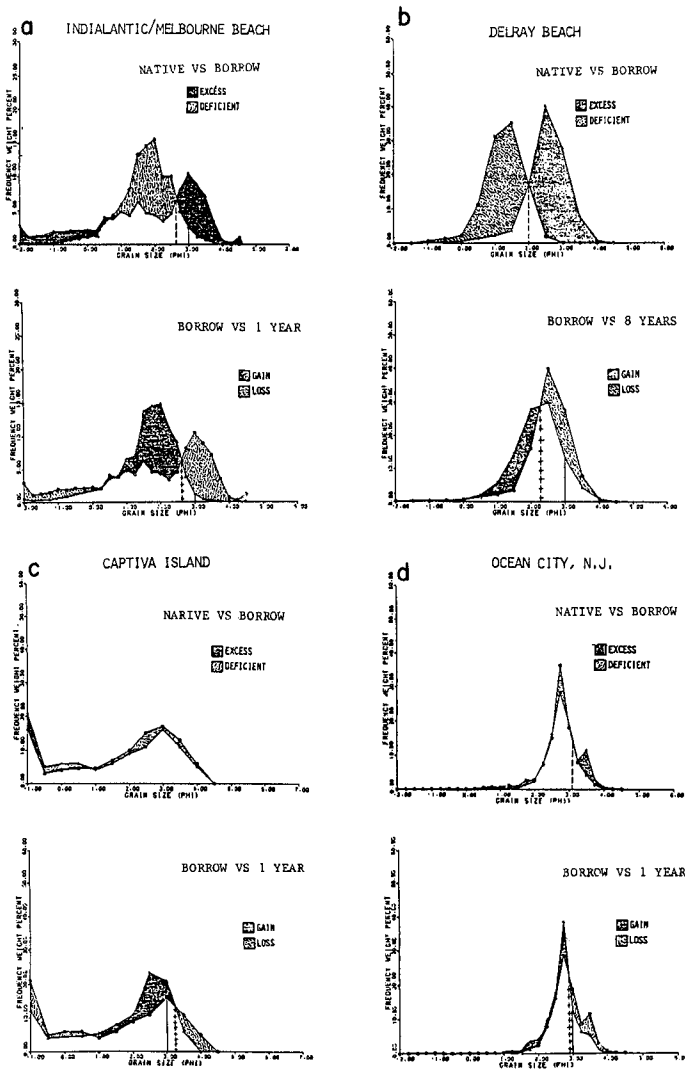


Figure 5. Grain size frequency curves from the four projects comparing 1) the borrow with the native showing the 3 phi cut off and the actual excess fine grain material and 2) the borrow with the one year (8 year for Delray Beach) showing the calculated 3 phi cut off with the actual loss of fine material.

and actual losses correlate well at Indialantic/Melbourne Beach (Fig. 5a), Captiva Island (Fig. 5c) and Ocean City (Fig. 5d). For the projects that had a reasonably good match between borrow and native or borrow that was for the most part slightly finer than native in areas of moderate to high wave energy the 3 phi adjustment gave a reasonable prediction of fill behavior. The correlation was not as good at Delray Beach (Fig. 5b) which had such a large grain-size difference between the borrow and native and resulted in a significant long term change in the grain size distribution. No borrow information was available for Hollywood/Hallandale, but analysis using sediment collected three months after fill placement showed that the native material contained coarser material than the borrow that replaced it even though the borrow was composed of medium sand. From three months to one year later, the beach gained a significant amount of fine material not found in either the native or borrow sediment.

### CONCLUSION

From this study it can be concluded that:

1. Composite samples are needed to remove the variability in sediment distribution across a beach and in a borrow area. Intertidal composite samples are more suitable for use in the models. Offshore sediments include fine sizes and changed little in their grain size distribution over the project life. Fill was placed in the intertidal area in all projects studied and this area had the greatest redistribution of sediment grain sizes.
2. The Adjusted Shore Protection Manual method (recommended in the majority of cases by U.S. Army, 1984), gave the best calculation of actual fill behavior, provided a safety factor (G) was used. A safety factor of 3.0 Phi has been found to give the best results for the projects studied.
3. Fill factor models commonly use only the sediment mean and standard deviation values. The sample mean and sorting alone are not sufficient to describe the variability of the native, borrow and post-fill sediment behavior because natural sediment distributions are not normally distributed as assumed in the models. Frequency distribution plots provide the best means of showing the differences between the native and borrow grain sizes over the entire sediment distribution.
4. Renourishment Factor calculations using computed  $\Delta$  values gave the best match to actual fill behavior.
5. Standardization of collection, analysis and presentation of beach nourishment sediment data is needed for better understanding of project behavior.

It must be noted that grain size information alone is not sufficient to predict success of a project. Compatibility of the borrow material is but one of the factors to be considered in project planning, along with fill placement techniques, knowledge of coastal processes and interaction with other coastal structures (Dean 1983). New guidelines are in the process of being developed (Stable and Nelson, 1984) for monitoring all aspects of a nourishment project. More projects with adequate data need to be examined and a standard data collection and reporting system established. We will then have a better basis

for understanding fill behavior and development of new predictive methods for project success.

#### ACKNOWLEDGMENTS

Portions of this research have been supported by the U.S. Army Corps of Engineers, Jacksonville District; Florida Sea Grant; and the Florida Department of Natural Resources, Division of Beaches and Shores.

#### REFERENCES

- Bascom, W.N., 1959. The relationship between sand size and beach-face slope: American Geophysical Union Transactions, V.32(6), pp. 886-874.
- Dean, R.G., 1974, Compatibility of Borrow Material for Beach Fills. Proc. 14th International Conf. on Coastal Eng., ASCE, Vol. II, pp. 1319-1330.
- Dean, R.G., 1983, Principles of Beach Nourishment. in: CRC Handbook of Coastal Processes and Erosion, P.D. Komar, ed., CRC Press, Boca Raton, Fl., pp. 217-231.
- Hansen, M.E., 1982. Evaluation of Beach Fill models and the effect of carbonate material on beach fill. Unpublished Masters Thesis, Florida Institute of Technology, Melbourne, FL., 107P.
- Hobson, R.D., 1977, Review of Design Elements for Beach Fill Evaluation. TP 77-6, U.S. Army Corps of Engineers, Coastal Eng. Res. Center, 42 p.
- Krumbein, W.C., 1957, A Method for Specification on Sand for Beach Fill Evaluation. TM 102, U.S. Army Corps of Engineers, Beach Erosion Board.
- Krumbein, W.C., and W.R. James, 1965, A Lognormal Size Distribution Model for Estimating Stability for Beach Fill Material TM-16, U.S. Army Corps of Engineers, Coastal Eng. Res. Center, 17 p.
- James, W.R., 1974, Beach Fill Stability and Borrow Material Texture. Proc. 14th International Conf. on Coastal Eng., ASCE, Vol. II, pp. 1334-1344.
- James, W.R., 1975, Techniques in Evaluating Suitability of Borrow Material for Beach Nourishment. TM-60, U.S. Army Corps of Engineers, Coastal Eng. Res. Center, 81 p.
- Stauble, D.K., M. Hansen, R. Hushla and L. Parsons, 1983, Beach Nourishment Monitoring, Florida East Coast: Physical Engineering Aspects and Management Implications. Proc. Third Symposium on Coastal and Ocean Management, ASCE, pp. 2512-2526.
- Stauble, D.K. and W.G. Nelson, 1984, Beach Restoration Guidelines: Prescription for Project Success. In: The New Threat to Beach Preservation, L. Tate, ed., Fl. Shore and Beach Pres. Soc., Tall., Fl., pp. 137-155.
- Tanner, W.F., 1960, Florida Coastal Classification. Trans. Gulf Coast Assoc. of Geol. Soc., Vol. X, pp. 259-266.
- U.S. Army, 1984, Shore Protection Manual, 4th. ed., Coastal Eng. Res. Center.

## CHAPTER ONE HUNDRED ONE

### LONGSHORE SEDIMENT TRANSPORT ON DEAN BEACH PROFILES

William G. McDougal,<sup>1</sup> A.M., ASCE  
Robert T. Hudspeth,<sup>1</sup> M., ASCE

#### Abstract

Natural beaches exhibit an equilibrium profile that is planar nearshore and non-planar, concave-up offshore. The longshore current on these Dean equilibrium beaches is shown to depend on the location of the intersection between the planar and non-planar profiles and on the dimensionless mixing strength parameter if the eddy viscosity coefficient is linearly dependent on the distance offshore. The effect of the profile intersection on the longshore sediment transport rate is demonstrated for two energetics based sediment transport models; viz. the Bagnold and energetics stress models.

#### Nomenclature

a	local wave amplitude;
A	dimensionless coefficient for Dean profile;
b (B)	dimensional (dimensionless) horizontal distance offshore to profile intersection;
c ( $C_g$ )	wave celerity (group celerity);
$C_f$	dimensionless friction coefficient for bottom stress;
d (D)	dimensional (dimensionless) total water depth including wave setup/down;
g	gravitational constant;
$G_{p(np)}$	dimensionless constant for planar (non-planar) beach profile;
h (H)	dimensional (dimensionless) still water depth;
$i_{1(2)}$ ( $I_{1(2)}$ )	dimensional (dimensionless) sediment transport rate for Bagnold (stress) model;
$I_v(\cdot)$ ( $K_v(\cdot)$ )	modified Bessel function of the first (second) kind of order $\nu$ ;
k	linear wave theory wave number;
K	dimensionless longshore sediment rate coefficient;
L	wave length;
m	roots for planar beach solution;
n	linear wave theory group velocity ratio;
N	dimensionless constant for eddy viscosity;
$P_{p(np)}$	dimensionless mixing strength parameter for planar (non-planar) beach;

<sup>1</sup> Ocean Engineering Program, Department of Civil Engineering, Oregon State University, Corvallis, OR 97331.

$\hat{A}$	dimensionless transport rate coefficient;
$s, S$	planar beach slope;
$s_{xy}$	radiation stress;
$T$	wave period;
$u_o$	magnitude of linear wave theory bottom velocity;
$v(V)$	dimensional (dimensionless) longshore current;
$x, y, z$	Cartesian coordinate system with $z$ positive up from the still water level;
$x_o$	horizontal distance offshore to origin of concave-up profile;
$\zeta$	dimensionless argument;
$\eta$	water surface elevation;
$\theta$	local wave angle of incidence;
$\kappa$	dimensionless wave height to water depth ratio;
$\mu_e$	dimensionless eddy viscosity coefficient;
$\pi$	constant;
$\rho$	fluid mass density; and
$\tau_{by}$	bottom shear stress.

## Introduction

Analytical solutions for longshore currents have been obtained using the concepts of radiation stresses developed for planar beaches (Bowen, 1969; Thornton, 1970; Longuet-Higgins, 1970a,b) and for non-planar, concave-up beaches (McDougal and Hudspeth, 1983a,b). In the nearshore zone inside the breaker line, the non-planar, concave-up type of beach profile seems to be generally more applicable to storm or to other high wave energy conditions. However, Dean's analysis (1977) of a total of 502 different non-storm beach profiles along the Atlantic and Gulf coasts of the United States seems to support Bruun's earlier postulation (1954, 1962) that beach profiles are typically non-planar, concave-up and vary as the horizontal distance offshore raised to the two-thirds power. Unfortunately, the Bruun type of non-planar, concave-up beach profile exhibits a mathematical singularity in the beach slope at the origin which is usually located in the swash zone. Evidently, the offshore bathymetry analyzed by Dean (1977) did not contain enough bathymetric data sufficiently close inshore to this swash zone to better resolve this concern for the mathematical singularity in the beach slope for a concave-up profile. In contrast, the nearshore observations of Komar (p.c.) seem to support the theory that non-storm beach profiles do not exhibit a singularity in beach slope near the swash zone and are often planar for the nearshore portion of the surf zone. One possible resolution of these two apparently conflicting observations is that typical non-storm beach profiles are planar nearshore and non-planar, concave-up offshore. Dean (p.c.) has recently derived a physical explanation for a planar nearshore profile. This type of composite beach profile that is planar nearshore and non-planar, concave-up offshore is probably more realistic of the actual type of beach profiles that exist during non-storm conditions and will be called a Dean beach profile.



An analysis is presented for a Dean beach profile that is planar nearshore and non-planar,  $x^{2/3}$  concave-up offshore. The analysis utilizes the radiation stress concepts and incorporates an integrated, turbulent Reynolds stress tensor that is approximated by an eddy viscosity model. Although there has been some concern expressed about the justification for the various mathematical forms used to represent the turbulent eddy viscosity coefficient in the dynamic equations of motion (Battjes, 1975), the analysis by McDougal and Hudspeth (1984) of seven different mathematical expressions for the turbulent eddy viscosity coefficients demonstrated that numerical results are relatively insensitive to the exact form of the mathematical model used for non-planar, concave-up beach profiles. For this analysis, the mixing length scale of the turbulent eddy viscosity coefficient is assumed to vary linearly (Longuet-Higgins, 1970a) with the total water depth (i.e., still water depth plus wave setup/setdown). This assumed mathematical form for the mixing length scale of the turbulent eddy viscosity coefficient results in a relatively more tractable analytical model for both the planar (Longuet-Higgins, 1970a) and for the non-planar,  $x^{2/3}$  concave-up Dean beach profiles (McDougal and Hudspeth, 1983a). The effects of the location of the intersection between the planar nearshore profile and the non-planar, concave-up offshore profile (i.e.,  $x = b$ ) is examined in some detail by varying the location of this intersection between the two profiles. Specifically, the profile intersection is located inside, at, and outside of the breaker line. Both the Bagnold and an energetics stress model for the longshore sediment transport (McDougal and Hudspeth, 1983b) are used to demonstrate the effects of the location of the profile intersection on the longshore sediment transport rates.

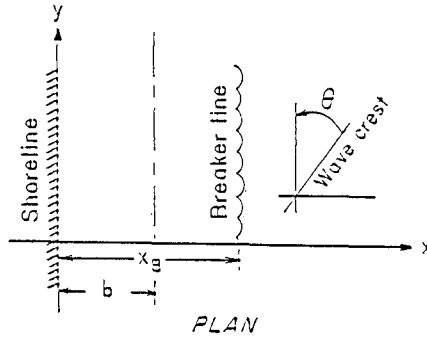
#### Dean Beach Profile

Figure 1 illustrates a Dean beach profile that is planar nearshore and non-planar, concave-up offshore. The horizontal distance to the intersection between the planar and non-planar profiles is located at  $x = b$ . Although the intersection between the planar nearshore profile and the non-planar, concave-up offshore profile is shown in Fig. 1 to be located inside the breaker line ( $x = b < x_B$ ), it may also, in general, be located either at ( $x = b = x_B$ ) or outside of the breaker line ( $x = b > x_B$ ). The still water depth,  $h(x)$ , for the composite beach shown in Fig. 1 is given by

$$h(x) = \begin{cases} s_h x & ; x < b & (1a) \\ \alpha_h (x-x_0)^{2/3} & ; x > b & (1b) \end{cases}$$

where  $s_h$  is the planar bottom slope;  $\alpha_h$  is a dimensional coefficient of proportionality having dimensions of length raised to the one-third power; and  $x_0$  is the location at the still water level of the origin of the non-planar profile. The horizontal distance offshore to the origin of the non-planar profile,  $x_0$ , and to the

Fig. 1 Definition sketch for Dean profile.



intersection between the planar and non-planar profile,  $b$ , may be related to the planar slope,  $s_h$ , and the dimensional coefficient of proportionality,  $\alpha_h$ , by requiring continuity of depth,  $h(b)$ , and of profile slope,  $dh(b)/dx$ , at  $x = b$ , i.e.,

$$b^3 \zeta^3 = (b-x_0)^2 \quad (2a)$$

$$9 (b-x_0) \zeta^3 = 4 \quad (2b)$$

where

$$\zeta = (s_h / \alpha_h) \quad (2c)$$

which gives

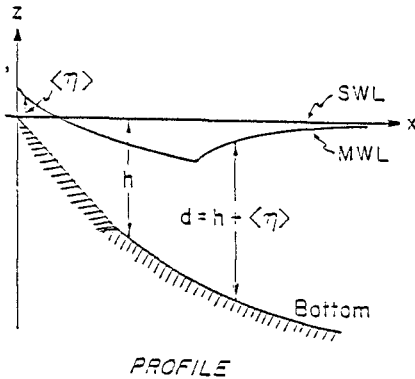
$$b = 4/9 \zeta^3 \quad (3a)$$

$$x_0 = 4/27 \zeta^3 = 1/3b \quad (3b)$$

McDougal and Hudspeth (1983a) have shown that the wave-induced setup/setdown,  $\langle \eta(x) \rangle$ , profiles are given by

$$\langle \eta(x) \rangle = \begin{cases} \frac{3\kappa^2}{(8+3\kappa^2)} [h_B - h(x)] - \frac{\kappa^2 h_B^2}{16} & ; x < x_B \end{cases} \quad (4a)$$

$$\langle \eta(x) \rangle = \begin{cases} -\frac{a(x)ka(x)}{2\sinh 2kh(x)} & ; x > x_B \end{cases} \quad (4b)$$



where  $\langle \cdot \rangle$  = time averaging operator;  $a(x)$  is the local wave amplitude;  $\kappa = 2a(x)/[h(x) + \langle \eta(x) \rangle]$  is the constant of proportionality inside the breaker line between the local wave amplitude,  $a(x)$ , and the total water depth,  $d(x) = h(x) + \langle \eta(x) \rangle$ ; and the local radian wave number,  $k = 2\pi/L$ , is determined from linear wave theory according to

$$(2\pi/T)^2 = gk \tanh kh \quad (5)$$

where  $T$  = the wave period and  $L$  = the wave length. In addition, it can be shown that the total water depth,  $d(x)$ , for the non-planar Bruun  $x^{2/3}$  profile may be modeled in a best least-squares sense by a total water depth profile that is proportional to the horizontal distance offshore raised to the one/half power with a partial correlation coefficient of 0.986 for  $0 < x < x_B$ . Consequently, the total local depth profiles [i.e., still-water-depth,  $h(x)$ , plus setup  $\langle \eta(x) \rangle$ ] for both the planar nearshore and the non-planar offshore profiles will be represented by

$$d(x) = \begin{cases} s_d x & ; x < b \\ \alpha_d (x - x_o)^{1/2} & ; x > b \end{cases} \quad (6a)$$

$$(6b)$$

where  $s_d$  is the slope of the total water depth. Again, continuity of the two profiles and of the two profile slopes at the location of the profile intersection,  $b$ , gives

$$b = 0.5 \lambda^2 \quad (7a)$$

$$x_o = 0.25 \lambda^2 = 0.5 b \quad (7b)$$

Nondimensionalizing all length scales by the dimensional surf zone width,  $x_B$ , (dimensional variables will be denoted by lower case letters), the following dimensionless variables (denoted by upper case letters) are introduced:

$$A = \alpha_d / \sqrt{x_B} \quad (8a)$$

$$B = b/x_B \quad (8b)$$

$$D(x) = d(x)/x_B \quad (8c)$$

$$H(x) = h(x)/x_B \quad (8d)$$

$$X = x/x_B \quad (8e)$$

$$X_o = x_o/x_B \quad (8f)$$

$$S_d = b/d(b) \quad (8g)$$

which gives the dimensionless total water depth profile as

$$D(x) = \begin{cases} S_d X & ; X < B & (9a) \\ A(X-X_o)^{1/2} & ; X > B & (9b) \end{cases}$$

Equation of Motion

The dimensional longshore depth- and time-averaged equation of motion given by Liu and Mei (1974) reduces to

$$-\frac{d}{dx} s_{xy} + \tau_{by} + \frac{d}{dx} [\mu_e d \frac{d}{dx} v] = 0 \tag{10}$$

where  $\mu_e$  is the turbulent eddy viscosity coefficient;  $\tau_{by}$  is the longshore component of bottom stress;  $v$  is the depth- and time-averaged longshore current component; and  $s_{xy}$  is the onshore-longshore component of the radiation stress tensor given by linear wave theory as

$$s_{xy} = -0.5 \rho g a^2 n \sin \theta \cos \theta \tag{11a}$$

$$n = 0.5 (1 + 2kh/\sinh 2kh) \tag{11b}$$

where  $\theta$  is the local angle of wave incidence (vide, Fig. 1).

The gradient of the onshore-longshore component of radiation stress may be approximated by

$$\frac{d}{dx} \{s_{xy}\} = \begin{cases} -\frac{5}{16} \rho g \kappa^2 \frac{\sin \theta_B}{\sqrt{d_B}} d^{1/2} \frac{d}{dx} \{d\} & ; x < x_B & (12a) \\ 0 & ; x > x_B & (12b) \end{cases}$$

where  $\rho$  is the fluid mass density;  $g$  is the gravitational constant; and  $\theta_B$  is the local angle of wave incidence at the breaker line.

The bottom shear stress is approximated by

$$\tau_{by} = -\frac{C_f}{\pi} \kappa \rho \sqrt{gd} v \tag{13}$$

where  $C_f$  is an empirically determined friction coefficient of the order of 0.01. The turbulent eddy viscosity coefficient is assumed to vary linearly with the horizontal distance offshore (McDougal and Hudspeth, 1984) according to

$$\mu_e = N \rho x \sqrt{gd} \tag{14}$$

in which  $N$  = a numerical constant. Substituting Eqs. (12) - (14) into Eq. (10) yields

$$\frac{N\pi}{\kappa C_f} \frac{d}{dx} \left\{ d^{5/2} \frac{dv}{dx} \right\} - d^{1/2} v = \begin{cases} -\frac{5}{16} \frac{\kappa\pi d^{3/2}}{C_f} \sin\theta_B \left(\frac{g}{d_B}\right)^{1/2} \frac{d}{dx}\{d\} & ; x < x_B \\ 0 & ; x > x_B \end{cases} \quad \begin{matrix} (15a) \\ (15b) \end{matrix}$$

Nondimensionalizing Eqs. (15) by the following dimensionless variables

$$S_B = d_B/x_B \quad (16a)$$

$$V = v/v_B \quad (16b)$$

where the component of the planar beach longshore current at the breaker line with no mixing is given by (Longuet-Higgins, 1970a)

$$V_B = \frac{5}{16} \frac{\kappa\pi}{C_f} \sin\theta_B \sqrt{gd_B} s_B \quad (16c)$$

reduces Eqs. (15) to

$$\frac{\pi N}{\kappa C_f} \frac{d}{dX} \left\{ D^{3/2} \frac{dV}{dX} \right\} - D^{1/2} V = \begin{cases} -\Delta D^{3/2} \frac{dD}{dX} & ; X < 1 \\ 0 & ; X > 1 \end{cases} \quad \begin{matrix} (17a) \\ (17b) \end{matrix}$$

where

$$\Delta = (x_B/d_B)^2 \quad (17c)$$

Equations (17) may be further expanded for each of the two beach profiles by substituting for the total water depth,  $D(X)$ , using Eqs. (9).

Planar Beach Solutions. The dynamic equations of motion for the longshore current may be obtained from Eqs. (17) by substituting Eq. (9a) to obtain

$$P_P \frac{d}{dX} \left\{ X^{5/2} \frac{dV}{dX} \right\} - X^{1/2} V = \begin{cases} -G_P X^{3/2} & ; X < 1 \\ 0 & ; X > 1 \end{cases} \quad \begin{matrix} (18a) \\ (18b) \end{matrix}$$

where the nondimensional strength of lateral mixing on a planar beach is defined by

$$P_p = \frac{\pi N S_B^2}{\kappa C_f} \tag{18c}$$

and

$$G_p = \begin{cases} B \frac{1}{(2-B)} & ; B < 1 \\ 1 & ; B > 1 \end{cases} \tag{19a}$$

$$\tag{19b}$$

The solutions to Eqs. (18) are (Longuet-Higgins, 1970a)

$$V = \begin{cases} C_{11} X^{m_1} + C_{12} X^{m_2} + \xi G_p X & ; X < 1 \\ C_{21} X^{m_1} + C_{22} X^{m_2} & ; X > 1 \end{cases} \tag{20a}$$

$$\tag{20b}$$

where

$$\xi = \frac{2}{2-5P_p} \tag{20c}$$

$$m_{1,2} = -\frac{3}{4} \pm \left( \frac{9}{16} + \frac{1}{P_p} \right)^{1/2} \tag{20d}$$

provided that  $P_p \neq 0.4$ .

Non-planar Beach Solutions. The dynamic equations of motion for the longshore component of current may be obtained from Eqs. (17) by substituting Eq. (9b) according to

$$P_{np} \frac{d}{dx} \left\{ \chi^{5/4} \frac{dV}{dx} \right\} - \chi^{1/4} V = \begin{cases} -\frac{G_{np}}{2} \chi^{1/4} & ; \chi < 1 - X_0 \\ 0 & ; \chi > 1 - X_0 \end{cases} \tag{21a}$$

$$\tag{21b}$$

where  $\chi = (x-x_0)$  and the nondimensional strength of lateral mixing on a non-planar beach is defined by

$$P_{np} = \frac{\pi N A^2}{\kappa C_f} \tag{21c}$$

and

$$G_{np} = \begin{cases} \frac{2}{2-B} & ; B < 1 \\ 2B & ; B > 1 \end{cases} \tag{22a}$$

$$\tag{22b}$$

p. 152) having solutions given by

$$v = \begin{cases} a_{11}\phi_1(Z) + a_{12}\phi_2(Z) + 0.5G_{np} & ; X < 1 & (23a) \\ a_{22}\phi_1(Z) & ; X > 1 & (23b) \end{cases}$$

where

$$\phi_1(Z) = Z^{-1/8} I_{1/4}(\gamma Z^{1/2}) \quad (23c)$$

$$\phi_2(Z) = Z^{-1/8} K_{1/4}(\gamma Z^{1/2}) \quad (23d)$$

$$Z = X - B/2 \quad (23e)$$

$$\gamma = \frac{2}{\sqrt{P}_{np}} \quad (23f)$$

Evaluation of the longshore component of velocity,  $v$ , on a Dean beach requires solving Eqs. (18) for the planar nearshore component when  $X < B$  and Eqs. (21) for the non-planar offshore component when  $X > B$ . Since both Eqs. (18) and (21) are of second-order, continuity of the magnitude and the slope of the current will be required at  $X = B$  in order to quantify these unknown constants of integration. In order to evaluate the effect of the location of the intersection of the planar and non-planar profiles at  $X = B$ , the unknown constants of integration in Eqs. (20) and (23) will be determined for each of the three separate locations; viz. 1) inside the breaker line ( $B < 1$ ); 2) at the breaker line ( $B = 1$ ); and 3) outside the breaker line ( $B > 1$ ). The matching conditions to be used at the intersection of the two profiles are: 1) continuity of longshore current magnitudes

$$V_{<} = V_{>} ; X = B \quad (24a)$$

and 2) continuity of the gradient of the longshore currents

$$\frac{d}{dX} V_{<} = \frac{d}{dX} V_{>} ; X = B \quad (24b)$$

where  $V_{<}$  is the current for  $X < B$  and  $V_{>}$  is the current for  $X > B$ .

B < 1 Solutions. When the profile intersection is located inside the breaker line,  $B < 1$ , the solutions are given by

$$v = \begin{cases} C_{11} X^m + \xi G_p X & ; X < B & (25a) \\ a_{11}\phi_1(Z) + a_{12}\phi_2(Z) + G_{np}/2 & ; B < X < 1 & (25b) \\ a_{22}\phi_2(Z) & ; X > 1 & (25c) \end{cases}$$

where  $Z$  is defined by Eq. (23e) and

$$a_{11} = G_{np} Z^{3/2} \phi_3(\zeta) \quad ; \quad \zeta = 1 - B/2 \quad (26a)$$

$$a_{12} = \frac{a_{11} [m_1 \phi_1(\zeta) - B \phi_4(\zeta)] - \xi G_p B^{(m_1-1)} + 0.5 m_1 G_{np}}{B \phi_3(\zeta) - m_1 \phi_2(\zeta)} \quad ; \quad \zeta = B/2 \quad (26b)$$

$$a_{22} = \frac{a_{11} \phi_1(\zeta) + 0.5 G_{np}}{\phi_2(\zeta)} + a_{12} \quad ; \quad \zeta = 1 - B/2 \quad (26c)$$

$$C_{11} = B^{-m_1} [a_{11} \phi_1(\zeta) + a_{12} \phi_1(\zeta) + 0.5 G_{np} - \xi G_p B] \quad ; \quad \zeta = B/2 \quad (26d)$$

$$\phi_3(\zeta) = -\frac{\zeta^{-9/8}}{4} [K_{1/4}(\gamma \zeta^{1/2}) + 2\gamma \zeta^{1/2} K_{-3/4}(\gamma \zeta^{1/2})] \quad (26e)$$

$$\phi_4(\zeta) = -\frac{\zeta^{-9/8}}{4} [I_{1/4}(\gamma \zeta^{1/2}) - 2\gamma \zeta^{1/2} I_{-3/4}(\gamma \zeta^{1/2})] \quad (26f)$$

**B = 1 Solutions.** When the location of the profile intersection coincides with the location of the breaker line,  $B = 1$ , the solutions are given by

$$v = \begin{cases} C_{11} X^{m_1} + \xi G_p X & ; X < 1 \quad (27a) \\ a_{22} \phi_2(Z) & ; X > 1 \quad (24b) \end{cases}$$

where  $Z$  is defined by Eq. (23e) and

$$a_{22} = \frac{(m_1-1) \xi G_p}{m_1 \phi_2(\zeta) - \phi_3(\zeta)} \quad ; \quad \zeta = 1 - B/2 \quad (28a)$$

$$C_{11} = a_{22} \phi_2(\zeta) - \xi G_p \quad ; \quad \zeta = 1 - B/2 \quad (28b)$$

**B > 1 Solutions.** When the profile intersection is located outside the breaker,  $B > 1$ , the solutions are given by

$$v = \begin{cases} C_{11} X^{m_1} + \xi G_p X & ; X < 1 < B \quad (29a) \\ C_{21} X^{m_1} + C_{22} X^{m_2} & ; 1 < X < B \quad (29b) \\ a_{22} \phi_2(Z) & ; X > B > 1 \quad (29c) \end{cases}$$

where  $Z$  is defined by Eq. (23e) and



$$C_{22} = \frac{(m_1 - 1) \xi G_p}{m_1 - m_2} \tag{30a}$$

$$C_{21} = \frac{C_{22} [m_2 \phi_2(\zeta) - B \phi_3(\zeta)] B^{(m_2 - m_1)}}{B \phi_3(\zeta) - m_1 \phi_2(\zeta)} \quad ; \quad \zeta = B/2 \tag{30b}$$

$$C_{11} = C_{21} + C_{22} - \xi G_p \tag{30c}$$

$$C_{22} = \frac{C_{21} B^{m_1} + C_{22} B^{m_2}}{\phi_2(\zeta)} \quad ; \quad \zeta = B/2 \tag{30d}$$

Figures 2 and 3 demonstrate the effects of the offshore distance to the profile intersection  $X = B$ , on the longshore current profile,  $V$ , for mixing strengths  $P_p = P_{np}$  equal to 0.1 and 1.0, respectively. Two longshore current profiles are shown for  $B < 1.0$  (viz.  $B = 0.1$  and  $0.5$ ) and one profile each for  $B = 1$  and for  $B > 1$  (viz.  $B = 1.95$ ). These profiles demonstrate that the magnitude of the longshore current profile decreases with increasing magnitude of the dimensionless mixing strength parameter  $P_p$  [cf. Eq. (18c)] for planar beaches and  $P_{np}$  [cf. Eq. (21c)] for non-planar beaches. The horizontal offshore distance,  $X$ , to the maximum longshore current decreases with decreasing values of the horizontal distance to the profile intersection,  $B$ , for  $B < 1$ . However, the magnitude of the maximum longshore current increases with increasing values of the horizontal distance to the profile intersection,  $B$ , for  $B < 0.8$ . The magnitudes then decrease with increasing values of  $B$  for  $0.8 < B < 1.0$ .

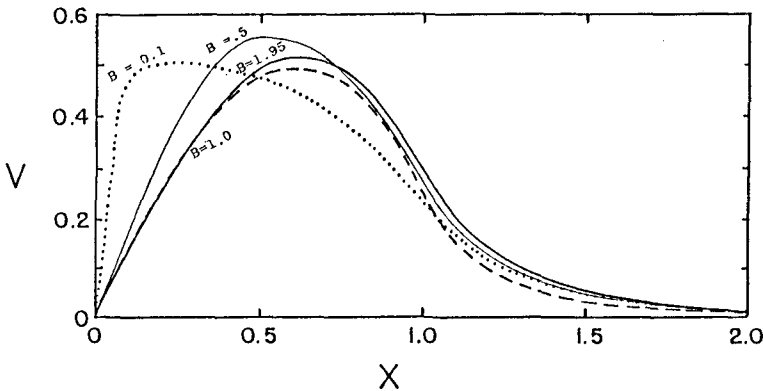


Fig. 2 Effect of profile intersection,  $B$ , on the longshore current profile,  $V$  ( $P_p = P_{np} = 0.1$ ).

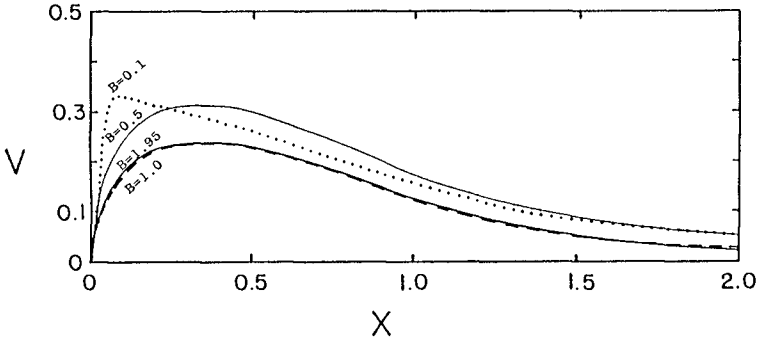


Fig. 3 Effect of profile intersection,  $B$ , on the longshore current profile,  $V$   $\{P_p = P_{np} = 1.0\}$ .

Figure 4 demonstrates the effect of the location of the profile intersection,  $B$ , on the magnitude of the maximum longshore component of velocity,  $V_{max}$ , for two values of the dimensionless mixing strength parameters.

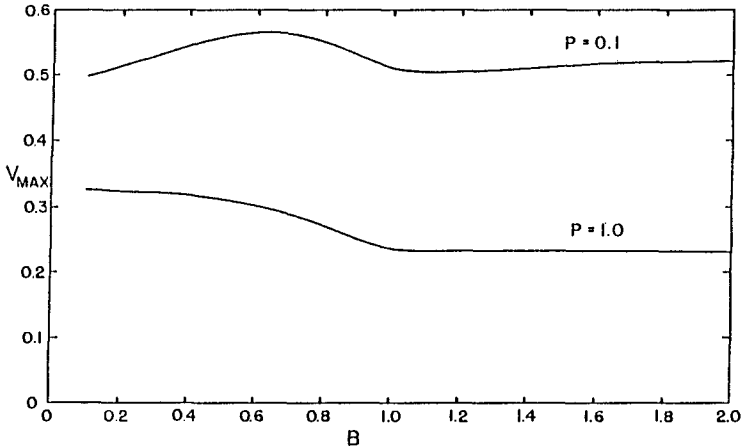


Fig. 4 Effect of profile intersection,  $B$ , on the maximum magnitude of the longshore current,  $V_{max}$ .

### Energetics Sediment Transport Models

The magnitude of the longshore current is required for the evaluation of the longshore transport of sand. Since the current profiles for the Dean beach profiles differ significantly from those predicted analytically for planar beaches, the corresponding sediment transport profiles should also be expected to differ. The longshore transport profiles of sand are developed using the following two energetics-based transport models: (1) the Bagnold-type model (Bagnold, 1963) which has been widely used in surf zone applications (cf. Inman and Bagnold, 1963; Komar and Inman, 1970; Komar, 1971, 1975, 1977; Thornton, 1973; Bowen, 1978; Walton and Chiu, 1979); and (2) an energy-dissipation model based on the total stress exerted on the sand by the mean wave-induced current (cf. Komar, 1971; Bailard and Inman, 1981; McDougal and Hudspeth, 1983b). The energetics stress model has been calibrated with the Bagnold model for a planar beach in which the dimensionless transport rate coefficient,  $K$ , for the Bagnold model has previously been evaluated by Komar (1975).

#### Bagnold Model

Bagnold (1963) proposed a sand transport model which includes both bed load and suspended load. This model assumes that the orbital wave motion mobilizes the beach sand and wave power is then expended maintaining the sand in motion. The presence of a mean current, regardless of how small, transports the sand. The Bagnold immersed-weight transport rate per unit width of surf zone,  $i_1$ , for small angles of wave incidence is (cf. Thornton, 1973):

$$i_1 = K \frac{d}{dx} \left( \frac{1}{2} \rho g a^2 c_g \right) \frac{v}{u_o} \quad (31)$$

in which  $K$  is a dimensionless transport rate coefficient;  $a$  is the local wave amplitude;  $c_g$  is the wave group velocity; and  $u_o$  is the magnitude of the near-bottom orbital wave velocity. Assuming that shallow-water, linear wave conditions exist ( $c_g = \sqrt{gd}$ ) and that the local wave amplitude is proportional to the total water depth,  $d$ , (i.e.,  $2a = \kappa d$ ), the immersed transport rate in the longshore direction shoreward of the breaker line reduces to:

$$i_1 = \frac{5}{8} K \rho g \kappa d v \frac{d}{dx} d \quad ; x < x_B \quad (32)$$

Nondimensionalizing the longshore transport rate by the breaker line sand transport on a planar beach due to the no-mixing longshore current (cf. Longuet-Higgins, 1970a),  $i_{BL1}$ , the dimensionless longshore transport profile is given by:

$$I_1 = \frac{i_1}{i_{BL1}} = \begin{cases} v \frac{D}{D_B} \frac{d}{dX} \left( \frac{D}{D_B} \right) & ; X < 1 & (33a) \\ 0 & ; X > 1 & (33b) \end{cases}$$

in which

$$i_{BL1} = \frac{5}{2} K \frac{\rho g}{\kappa} \frac{a_B^2}{x_B} v_{LH} \tag{33c}$$

$$v = v/v_{LH1} = v/\frac{5}{16} \frac{\pi \kappa}{C_f} s_d \sqrt{gd_B} \sin \theta_B \tag{33d}$$

where  $\pi$  is a numerical constant and  $C_f$  is a dimensionless friction coefficient of order 0.01.

For a planar beach, the Bagnold model sediment transport profile is given by

$$I_1 = \begin{cases} XV & ; X < 1 \tag{34a} \\ 0 & ; X > 1 \tag{34b} \end{cases}$$

For a concave-up  $x^{1/2}$  beach profile, the Bagnold sediment transport model becomes

$$I_1 = \begin{cases} \frac{1}{2} V & ; X < 1 \tag{35a} \\ 0 & ; X > 1 \tag{35b} \end{cases}$$

Figure 5 demonstrates the effect of the dimensionless profile intersection,  $B$ , as the longshore sediment transport rates,  $I_1$ , computed by the Bagnold model for two extreme values of the dimensionless mixing strength parameter  $\{P_p = P_{np} = 0.1 \text{ and } 1.0\}$ .

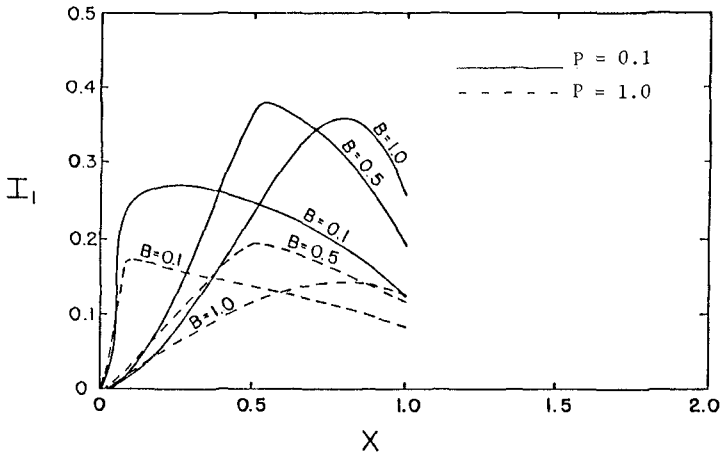


Fig. 5 Effect of profile intersection,  $B$ , on Bagnold longshore sediment transport rates,  $I_1$ .

Stress Model

Komar (1971) proposed a swash sediment transport model based on the energy dissipation associated with the bottom stress. Bailard and Inman (1981) also developed an energetics stress model using the bottom stress to estimate the time-dependent bedload transport in the surf zone. These models are both Bagnold-type models conceptually; but since the energy dissipation rate or available power for mobilizing sediment is based on the bottom stress, these models are termed stress models. The immersed-weight transport rate per unit width of surf zone,  $i_2$ , for the stress model for small angles of incidence is (cf. McDougal and Hudspeth, 1983a)

$$i_2 = c_5 \rho |u_o| v^2 \sin\theta \quad (36a)$$

in which  $c_5$  is a constant for a given sediment and

$$u_o = a \frac{k}{\omega} \operatorname{sech}(kd) (\hat{i} + \sin\theta \hat{j}) \quad (36b)$$

in which  $\omega$  = the radian wave frequency.

Note that in Eq. (36a), no shallow-water wave assumptions have been invoked and no restrictions have been placed on the mechanism which generates the longshore current. This model may be used for high wind- or tide-induced flows as well as for wave-induced long-shore currents.

As in Eqs. (33), the transport rate is nondimensionalized by the transport rate at the breaker line from a stress model on a plane beach using the no-mixing velocity determined by Longuet-Higgins (1970a). The dimensionless transport,  $I_2$ , is given by

$$I_2 = \frac{\sin\theta}{\sin\theta_B} \frac{u_o}{u_{oB}} v^2 \quad (37a)$$

in which

$$I_2 = i_2/i_{BL2} = i_2 / (c_5 \rho |u_{oB}| v_{LH}^2 \sin\theta_B) \quad (37b)$$

Employing Snell's law for refraction, the transport rate reduces to

$$I_2 = \frac{a}{a_B} v^2 \quad (38)$$

in which the hyperbolic cosines have been approximated by unity in the surf zone. This transport relationship applies for any type of beach profile and mean current.

Komar (1975) has determined the transport coefficient for the Bagnold model on a planar beach by comparison with observed total transports. The total transport is defined by

$$I_T = \int_0^{\infty} I \, dX \quad (39)$$

The stress model is calibrated by equating the total transport on a planar beach with that for the calibrated Bagnold model. This yields a dimensionless transport coefficient for the stress model,  $R$ ,

which is a function of the lateral turbulent mixing strength parameter,  $P_p$ .

Figure 6 demonstrates the dependence of the dimensionless transport rate coefficient on the dimensionless mixing strength parameter.

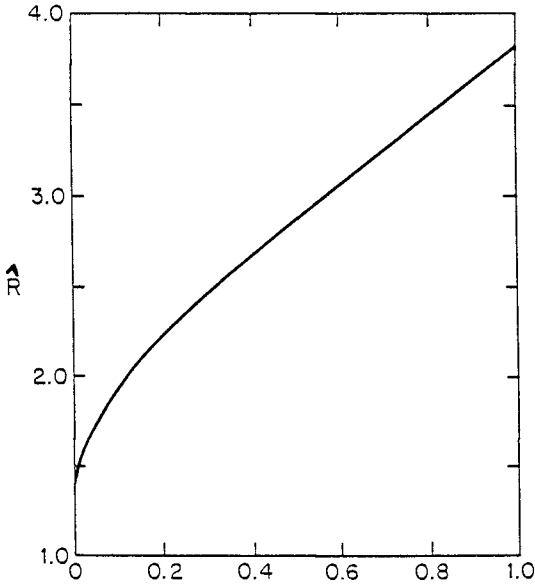


Fig. 6 Dimensionless stress transport rate coefficient calibrated with a Bagnold transport rate for a planar beach.

The longshore transport rate given by the stress model for a planar beach (including the calibration coefficient) is

$$I_2 = \begin{cases} \hat{R} X V^2 & ; X < 1 & (40a) \\ \hat{R} V^2 & ; X > 1 & (40b) \end{cases}$$

The longshore transport rate given by the stress model for a concave-up beach is

$$I_2 = \begin{cases} \hat{R} X^{1/2} V^2 & ; X < 1 & (41a) \\ \hat{R} V^2 & ; X > 1 & (41b) \end{cases}$$

Figure 7 demonstrates the effect of dimensionless profile intersection,  $B$ , on the longshore sediment transport rates,  $I_2$ , computed by a stress model for two extreme values of the dimensionless mixing strength parameters.

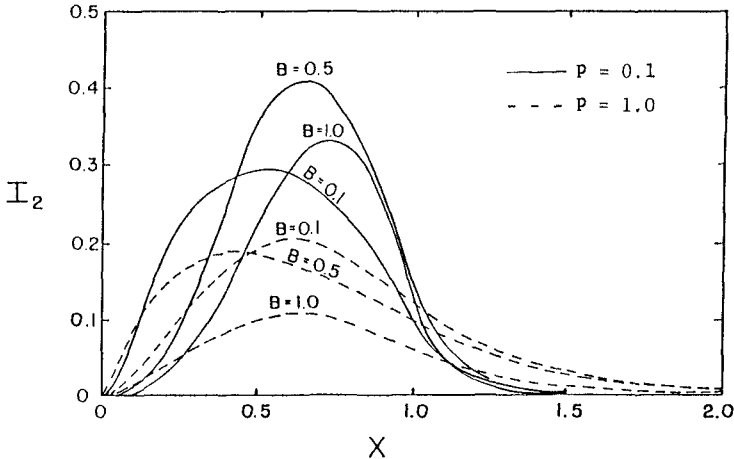


Fig. 7 Effect of profile intersection,  $B$ , on stress-type longshore sediment transport rates,  $I_2$ .

### Conclusions

Dimensionless longshore current profiles,  $V$ , on equilibrium Dean beach profiles depend on both the location of the dimensionless horizontal distance offshore to the profile intersection,  $B$ , and the dimensionless mixing strength parameters,  $P_n$  and  $P_{np}$ . The maximum dimensionless longshore current,  $V_{max}$ , occurs near a value of  $B = 0.8$ . The dimensionless longshore current profiles,  $V$ , are essentially independent of  $B$  for  $B > 1$ . The longshore current,  $V$ , decreases with increasing values of dimensionless mixing strength,  $P$ . The effect of the dimensionless profile intersection,  $B$ , and mixing strength parameter,  $P$ , is similar for both Bagnold and stress type longshore sediment transport rates.

### Acknowledgements

This research was supported by the Oregon State University Sea Grant College Program, National Oceanic and Atmospheric Administration Office of Sea Grant, Department of Commerce, under Grant No. NA81AA-D-00-086 (Project NO. R/CE-13). The U.S. government is authorized to produce and distribute reprints for governmental purposes, notwithstanding any copyright notation that may appear hereon.

## References

1. Bagnold, R.A., 1963. Beach and nearshore processes, Part I. In: Mechanics of Marine Sedimentation. The Sea, M.N. Hill (Editor), pp. 507-528.
2. Bailard, J.A. and Inman, D.L., 1981. An energetics bedload model for a plane sloping beach: Local transport. J. Geophys. Res., 86, pp. 2035-2043.
3. Battjes, J.A., 1975. Modeling of turbulence in the surf zone. Proc. Symp. Modeling Techniques, pp. 1050-1061.
4. Bowen, A.J., 1969. The generation of longshore currents on a plane beach. J. Mar. Res., 27, pp. 206-214.
5. Bowen, A.J., 1978. Simple models of nearshore sedimentation, beach profiles and longshore bars. Proc. Conf. Coastlines of Canada.
6. Bruun, P., 1954. Coast Erosion and Development of Beach Profiles. Beach Erosion Board, Tech. Memo. No. 44, 82 pp.
7. Bruun, P., 1962. Sea-level rise as a cause of shore erosion. J. Waterways Harbors Div., Am. Soc. Civ. Engrs., 88, pp. 117-130.
8. Dean, R.G., 1977. Equilibrium Beach Profiles: U.S. Atlantic and Gulf Coasts, Univ. of Delaware, Ocean Engineering Report No. 12, 45 pp.
9. Hildebrand, F.B., 1976. Advanced Calculus for Applications (Second Edition), Prentice-Hall, Englewood Cliffs, NJ, p. 152.
10. Inman, D.L. and Bagnold, R.A., 1963. Beach and nearshore processes. Part II. Littoral processes. In: The Sea, M.N. Hill (Editor), pp. 529-553.
11. Komar, P.D., 1971. The mechanics of sand transport on beaches. J. Geophys. Res., 76, pp. 713-721.
12. Komar, P.D., 1975. Longshore currents and sand transports on beaches. Proc. Civil Eng. in the Oceans/III, 1, pp. 333-354.
13. Komar, P.D., 1977. Beach sand transport: Distribution and total drift. J. Waterway, Port, Coast Ocean Div., Am. Soc. Civ. Eng., 103, pp. 225-239.
14. Komar, P.D. and Inman, D.L., 1970. Longshore sand transport on beaches. J. Geophys. Res., 75, pp. 5914-5927.
15. Liu, P.L.-F. and Mei, C.C., 1974. Effects of a Breakwater on Nearshore Currents due to Breaking Waves. Ralph M. Parson Laboratory, Department of Civil Engr., Massachusetts Inst. of Tech., Report No. 12, 243 pp.
16. Longuet-Higgins, M.S., 1970a. Longshore currents generated by obliquely incident sea waves, 1. J. Geophys. Res., 75, pp. 6778-6789.
17. Longuet-Higgins, M.S., 1970b. Longshore currents generated by obliquely incident sea waves, 2. J. Geophys. Res., 75, pp. 6790-6801.
18. McDougal, W.G. and Hudspeth, R.T., 1983a. Wave setup/setdown and longshore current on non-planar beaches. Coastal Eng., 7, pp. 103-117.



19. McDougal, W.G. and Hudspeth, R.T., 1983b. Longshore Sediment Transport on Non-Planar Beaches. Coastal Eng., 7, pp. 119-131.
20. McDougal, W.G. and Hudspeth, R.T., 1984. Comparison of turbulent lateral mixing models. J. Mar. Res. (in review).
21. Thornton, E.B., 1970. Variation of longshore current across the surf zone. Proc. 12th Coastal Engrg. Conf., ASCE 291-308.
22. Thornton, E.B., 1973. Distribution of sediment transport across the surf zone. Proc. 13th Conf. Coastal Eng., pp. 1049-1068.
23. Walton, T.L. and Chiu, T.Y., 1979. A review of analytical techniques to solve the sand transport equation and some simplified solutions. Proc. Spec. Conf. Coastal Structures, pp. 809-837.

## CHAPTER ONE HUNDRED TWO

### TIME SCALES OF NEARSHORE PROFILE CHANGES

William A. Birkemeier, A. M. ASCE\*

**Abstract:** Time scales of nearshore profile change are examined using a unique set of highly accurate surveys collected over a 3½ year period at CERC's Field Research Facility. The data are analyzed in terms of the formation and movement of the nearshore bars and with empirical eigenfunctions. The largest and most rapid changes in the profiles occurred during storms. The inner bar (depth of -0.6 to 1.5 m, 1.6 to 4.5 ft) moved offshore during even minor storms and recovered relatively quickly. The outer bar (depth of 3 to 4 m, 9 to 13 ft) formed during the largest storms and recovery was considerably slower, requiring six months or longer. The eigenvector analysis confirmed the importance of storms but identified a seasonal shift of material from the beach and inner bar to the offshore.

#### Introduction

Though it is well known that beach and nearshore changes occur rapidly during storms, and that post-storm recovery occurs more slowly, there is a general lack of field data, particularly from the nearshore zone, to quantify these processes. The objective of this paper is to examine the magnitude and temporal scales of profile change using over three years of highly accurate repetitive nearshore surveys (out to a depth of 8 m, 26 ft, MSL) collected at the Field Research Facility (FRF) of the U. S. Army Engineer Waterways Experiment Station, Coastal Engineering Research Center (CERC). The FRF is located on the Atlantic Ocean in Duck, North Carolina (Figure 1) and is described in detail by Birkemeier, et al (4).

#### Field Data

The survey data were collected using the Coastal Research Amphibious Buggy (CRAB), a motorized, 3-wheeled tripod capable of operating to depths of 9 m (30 ft) and in waves up to 2 m (6.4 ft). During the first six months of surveys, which began in January 1981, the position and elevation of the CRAB were determined using a level to read a 12.3 m (40 ft) high stadia board. All surveys subsequent to June 1981 were conducted using a Zeiss Elta-2s Electronic Total Station. The combined CRAB-Zeiss system (5) is unique because it permits highly accurate surveying of the zone of greatest profile activity. The data set includes over 105 surveys each of profile lines 62 and 188, which are located approximately 500 m (1650 ft) on either side of the FRF

---

\*Hydraulic Engineer, U. S. Army Engineer Waterways Experiment Station, Coastal Engineering Research Center, Field Research Facility, SR Box 271, Duck, NC 27949-9762

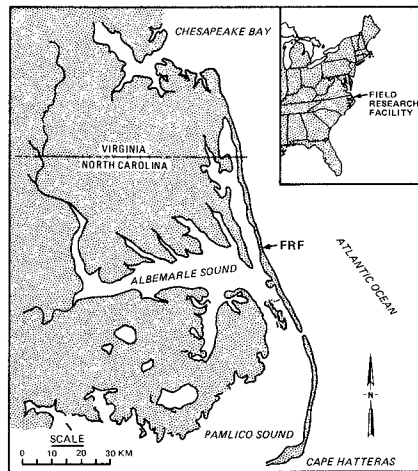


Figure 1. Location of the Field Research Facility

research pier (Figure 2). Based on monthly surveys of the bathymetry around the pier, these lines are located in a region of shore parallel offshore contours and are sufficiently removed from known pier effects (8). Surveys were generally conducted biweekly and after storms, with actual survey intervals varying from 1 to 44 days. The data provide a detailed record of profile evolution including periods of erosion, recovery and stability. The profile lines are characterized by a beach of poorly sorted, coarse-to-medium size sand and a nearshore zone composed of better sorted medium-to-fine sand. Table 1 summarizes general profile characteristics.

TABLE 1.-Profile Characteristics

Dune Height -	6 to 7 m (20 to 22 ft)
Beach Width -	20 to 45 m (65 to 148 ft)
Foreshore Slope -	1:12.5
Offshore Slope (based on 7.5 to 8 m contours) -	1:164
Maximum Shoreline Variation -	25 m (80 ft)
Maximum Volume Variation -	235 m <sup>3</sup> /m (93.7 yd <sup>3</sup> /ft) of beach

For the purposes of this report, the shoreline is defined as the distance to the mean sea level (MSL) intercept and profile volume changes are computed as cross-sectional changes multiplied by a unit width (1 m or 1 ft) of beach. The volume change given in Table 1 is the cumulative net volume change computed between successive surveys over the entire profile length (900 m, 3000 ft). All of the surveys of

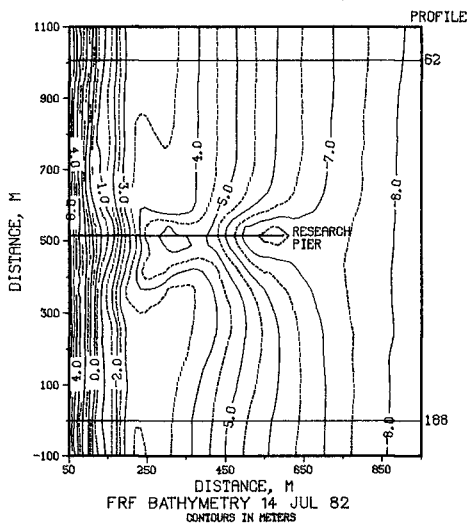


Figure 2. Location of study profile lines

line 188 are overplotted in Figure 3. As can be seen by the plot of maximum vertical change shown in the upper half of Figure 3, most profile activity is restricted to depths less than 7 m (23 ft) with little measurable vertical variation at deeper depths (only 15 cm, .5 ft, maximum variation at 8 m, 26 ft, depth). Because of this tendency for the surveys to "close out" near their offshore terminus, most of the overall volume variation given in Table 1 is attributed to longshore movement of material onto and off of the profiles.

#### Field Observations

Although changes occurred in both cross-shore and longshore directions, this study concentrates only on cross-shore changes resulting from the movement of material between the beach and nearshore; and the formation, movement, and disappearance of bar/trough features. The lack of detailed longshore data is important since rhythmic bar/trough and beach features frequently occur in the study area and undoubtedly affect the profile data and their interpretation. Mason, et al (7) address the formation and rapid movement of a rhythmic inner bar monitored during a detailed nearshore experiment, DUCK82, conducted around profile line 62.

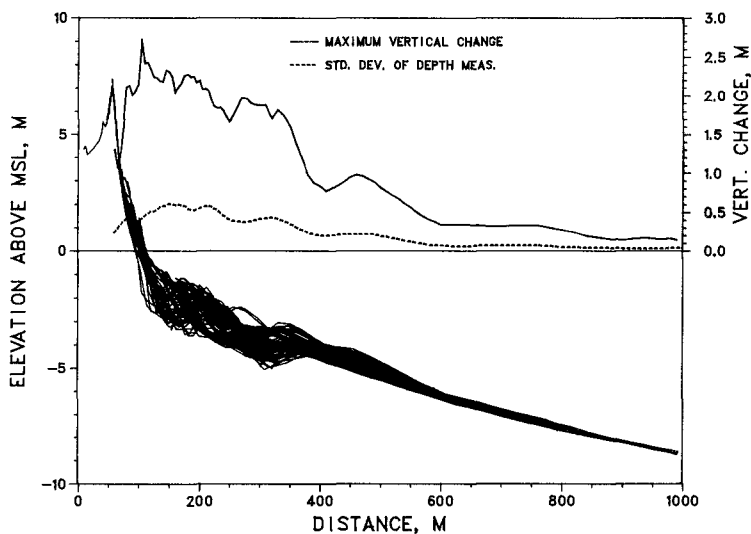


Figure 3. Envelope of 155 surveys of profile line 188 collected between January 20, 1981 and July 27, 1984

Profile changes at the study site occur at time scales ranging from swash periods (6) to annual cycles and longer. Time scales resolvable with the present data vary between a few days and one to two years. Though the profiles have varied in configuration from nearly unbarred to triple barred, they typically exhibit a double bar configuration with a narrow inner bar and a wide outer bar. Figure 4 illustrates five configurations. Most significantly, after 3.5 years the profile configurations have begun to repeat themselves. Though the reoccurrence of nearly similar profile shapes, such as those shown in Figure 5 taken nearly three years apart, is rare, the fact that they reoccur at all is most intriguing.

One of the best indicators of profile configuration and activity is the location and horizontal movement of the bar crest. Large changes to the profile, in terms of volume movements, always resulted in significant bar movement. Bar crest depth, though important, was less useful as an indicator of activity, since large bar movements occurred with little or no change in crest depth.

Figure 6 traces the time history of the shoreline and bar crest positions for both profile lines. This figure shows three major features of the data including: the relative stability of the shoreline, the formation and frequent oscillations of the inner bar, and the long period oscillations of the outer bar. Though the outer bar position has an apparent offshore trend superimposed on a seasonal-like oscillation, it is believed that this is actually the result of storm erosion/recovery sequences at varying time periods of one to two years. The

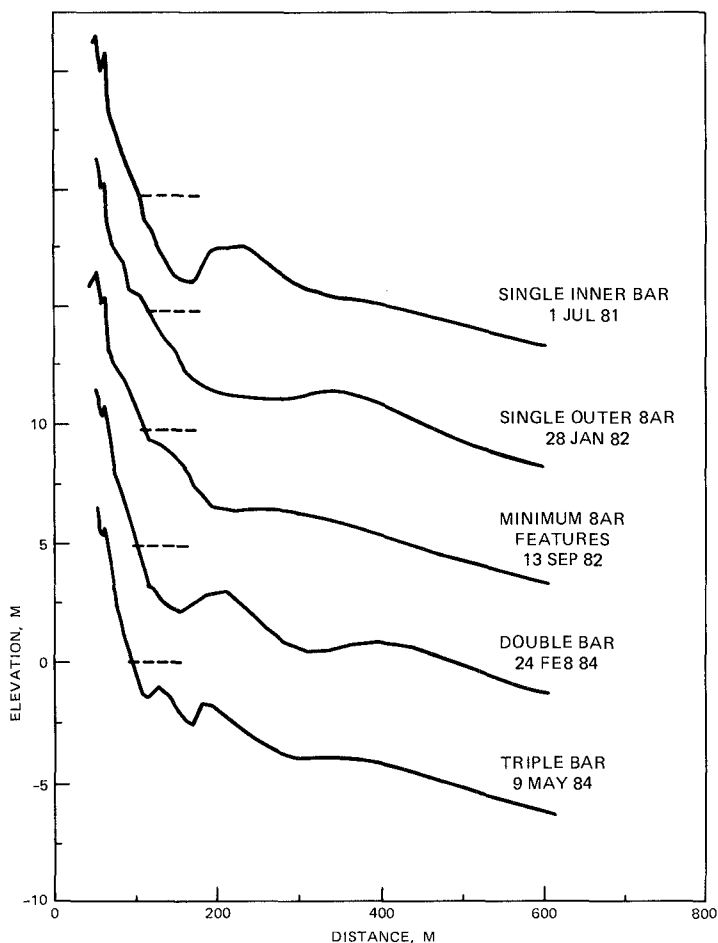


Figure 4. Typical profile configurations for profile line 62

development and slow movement of the outer bar can be better visualized with Figure 7 which is a perspective view of the data shown in Figure 3.

Minor storms affected the inner bar causing it to move offshore, while larger storms produced major changes in configuration, moving both bars offshore, and depositing sand in deeper water. Storm changes were rapid, occurring over periods of one to five days. Onshore bar movement which occurred during periods of low waves was also found to be post-storm related. The speed and amount of recovery which occurred

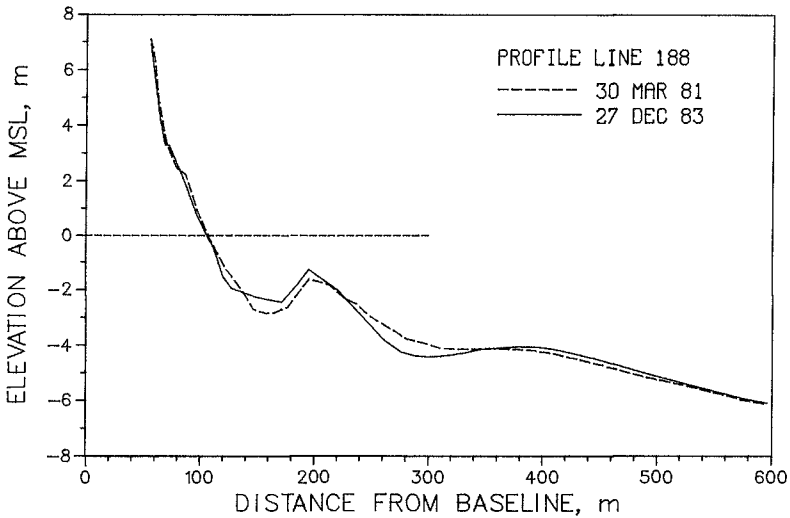


Figure 5. Similar profile shapes for surveys nearly three years apart at profile line 188

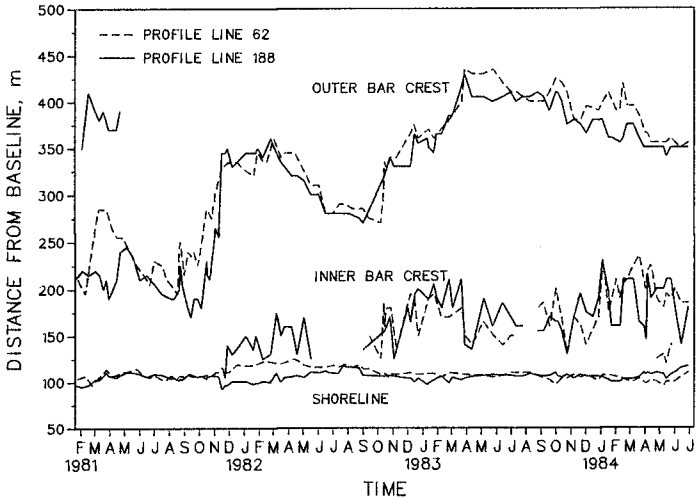


Figure 6. Variation in shoreline and bar crest positions

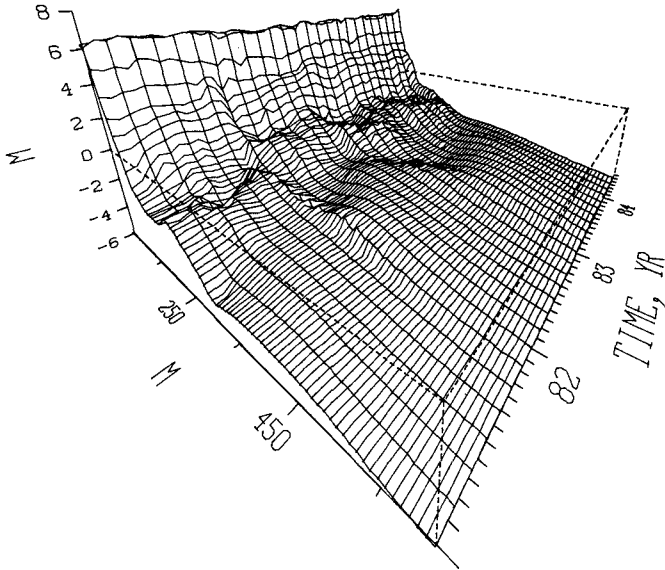


Figure 7. Perspective view of profile line 188 through time

were affected by the wave conditions and by the post-storm configuration of the profiles. All bar features tended to disappear during extended periods of low wave conditions (six months or longer).

An example of the rapid modifications caused by storms is shown in Figure 8. The surveys bracket a series of three storms with the final and most severe storm occurring November 13-15, 1981. This sequence of storms shifted the bar crest 165 m (540 ft) offshore and ultimately caused the profile to change from single to double barred. The November 13-15 storm, which produced 3.5 m (11.5 ft) waves and the highest water level of the study (1.6 m above MSL), also caused the greatest profile changes of the study, resulting in a major rearrangement of the nearshore zone. During this three-day event, the bar shifted 90 m (295 ft) offshore, at a rate that probably exceeded 30 m/da (100 ft/da), with  $150 \text{ m}^3/\text{m}$  ( $60 \text{ yd}^3/\text{ft}$ ) of material moving offshore. Interestingly, the two profile lines never returned to the same single bar configuration that existed prior to the November storm.

In contrast, the slow recovery from the changes caused by the Fall 1981 storms occurred during six months of relatively calm conditions from February to August, 1982 (Figure 9). During this period, the outer bar migrated onshore a distance of 85 m (280 ft) at an average rate of 0.47 m/da (1.5 ft/da). Depth over the bar remained nearly constant at -3.3 m (-10.8 ft) with a total shift of material of approximately  $100 \text{ m}^3/\text{m}$  ( $40 \text{ yd}^3/\text{ft}$ ). The configuration of the profile at the



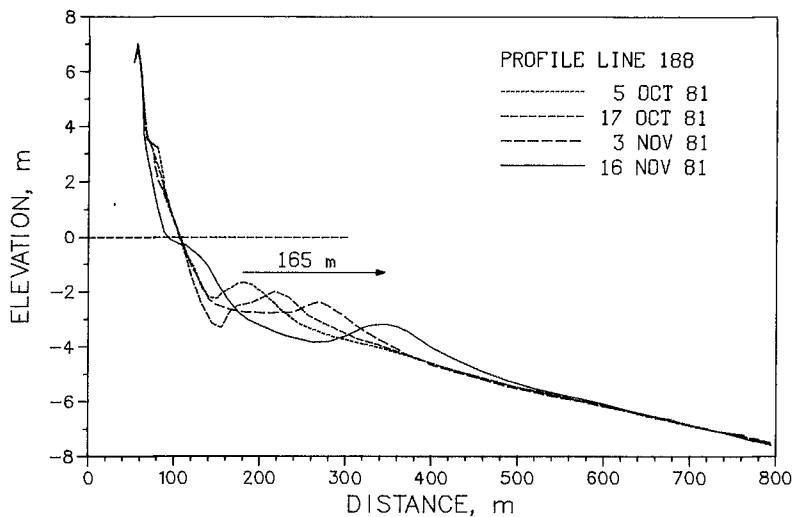


Figure 8. Rapid offshore movement of sediment resulting from three Fall 1981 storms

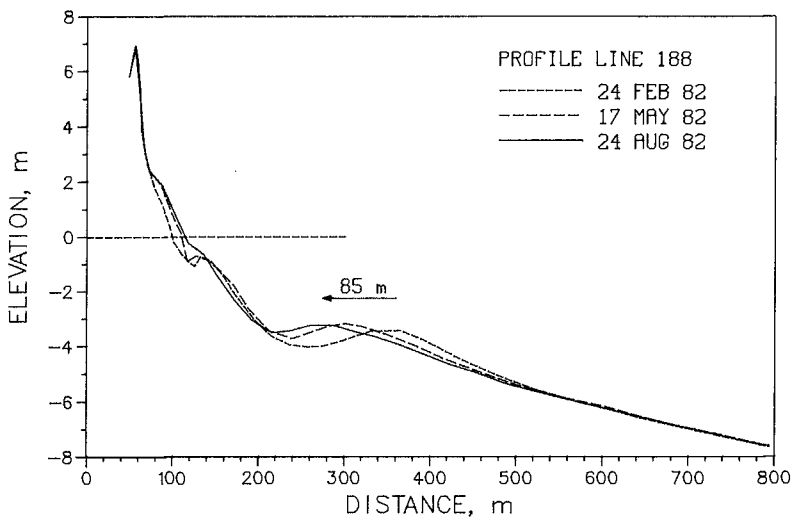


Figure 9. Slow onshore migration of the outer bar during a six month period of low wave conditions

end of the period was reflective, as defined by Wright, et al (12), with no inner bar and only a minor outer bar.

A different cross-shore sequence occurred in 1983. As shown in Figure 6, offshore movement during the fall reoccurred in 1982, but, from October 1982 to March 1983, the outer bar moved farther offshore into deeper water (-4.2 m, -13.8 ft). Though no single storm during this period exceeded the intensity of the November, 1981 storm, there were over 11 minor storms, 5 with significant wave heights in excess of 3 m (10 ft). Onshore movement of the outer bar from this deeper depth did not occur until late fall of 1983 and continued through the end of the study period in July 1984 when the outer bar nearly disappeared.

It is important to note that the observed patterns of bar formation and offshore movement always occur well within the surf zone. For example, the surf zone during the November, 1981 storm extended more than 250 m (820 ft) seaward of the post-storm outer bar position (approximately 600 m, 1970 ft, from the survey baseline, Figure 9). Based on results from DUCK82 (9) and work by Short (10), and others, bar position at these distances from the shoreline is not a function of incident wave periods but of long period, infragravity waves (0.5 to 5 min) with bars forming at either the nodes or antinodes of the infragravity wave.

Onshore movement of the outer bar, in the study area, occurred only when the bar was seaward of the surf zone. This rule does not necessarily hold for the shallow inner bar, as onshore movement of 1.2 m/hr (3.9 ft/hr) has been recorded near line 62 in October 1982 during a storm when the bar was well within the surf zone and waves were 2 m (6.4 ft) high with a 14 sec period.

#### Eigenvector Analysis

One technique which has found recent popularity in analyzing variation in profile shape is that of empirical eigenfunctions. In simplified terms, this statistical procedure separates the variation in a rectangular matrix of data into two sets of orthogonal functions. For the present data, one function (the set of eigenvectors) is spatially dependent, while the other (the eigenvector weightings) is dependent only on time. By requiring each successively higher eigenvector to explain, in a least squares sense, the variance remaining in the data set, only a few eigenvectors are required to explain a high percentage of the variation. Random noise in the data which is uncorrelated with the data set as a whole is filtered out to higher order eigenvectors. Since only a few vectors are usually required to reconstruct the original data, the results of the analysis provides a compact representation of the original data. The procedure is similar, and often compared, to fourier analysis where data are separated into linear combinations of sines and cosines. However, the eigenvector analysis does not assume, a priori, any functional shape.

Detailed discussions of the eigenvector analysis procedure are given by Aubrey (1,3), and by Vincent and Resio (11). Aubrey used the technique to parameterize beach and nearshore profile data and different

wave-based variables. Vincent and Resio used a slightly different procedure to parameterize wave spectra. This study uses the procedure of Vincent and Resio where the eigenvectors are derived from a covariance matrix which is based on departures from the mean.

Though the eigenvector technique has been used by many different investigators to analyze nearshore profile data, it does have a number of significant limitations. First, since it is a statistical technique, the different vectors (modes of variation) do not necessarily have any physical significance, though it may be possible to attribute significance to them. For instance, Aubrey (2) found that his second eigenvector was related to seasonal sediment exchange between the nearshore bar and the beach berm. Secondly, the analysis assumes that every survey is equally spaced in time and that all cases are equally weighted, an assumption that is not usually the case with field data, including the present data set. Finally, when analyzing data from a single profile line, the eigenfunction analysis does not separate cross-shore effects from longshore effects.

Even with these limitations, an eigenvector analysis can be a powerful aid in identifying and parameterizing the major spatial and time dependent variations in a particular data set. The rectangular matrix in our case is an M by N matrix of depths, at 37 specific distances (N) along profile line 188 and for each of 115 surveys (M). The actual survey data were digitized at 17 m (55.77 ft) intervals from a distance of 70 m (229.7 ft) on the profile out to 682 m (2237.5 ft). This offshore limit was chosen because it contains most of the variation (see Figure 4) and because most of the surveys extend at least this far. Surveys which did not reach this limit were either deleted or extended using averaged data from the prior and following surveys. Data extensions were usually less than 100 m (300 ft).

Table 2 summarizes the variance explained by the first five eigenvectors which together account for 91.4 per cent of the variance in the data set. Eigenvectors 1 and 2 explain nearly equal amounts of variance suggesting that there are two basic profile configurations in the data set (in fact, these two eigenvectors are reversed on profile line 62).

TABLE 2.-Variance explained by first 5 eigenvectors

<u>Vector</u>	<u>Variance Explained</u> (per cent)	<u>Cumulative Variance</u> (per cent)
1	37.6	37.6
2	27.2	64.8
3	13.3	78.1
4	10.0	88.1
5	3.3	91.4

The results of the analysis are shown in Figures 10 and 11, which plot the eigenvectors and temporal weightings, respectively. These figures are most easily interpreted by first determining the effect of positive and negative weightings on the different eigenvectors when

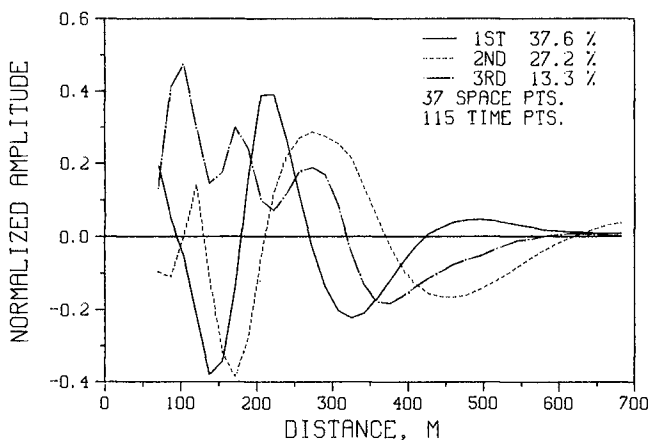


Figure 10. First 3 eigenvectors for profile line 188

combined with the mean profile, and then examining the temporal weightings for any significant trends. To determine the effect of a particular vector, multiply the amplitude of the vector at a particular distance on the profile by the weighting on that vector for a particular survey and add the result (which is in meters) to the mean depth at that distance. This has been graphically done for the first three eigenvectors in Figure 12, which shows the mean profile shape and the effect of positive and negative weightings.

From Figures 10 and 12, it can be seen that eigenvector 1 describes the change of the profile from a single bar configuration (when positively weighted) to a double bar shape (when negatively weighted) with a well-defined outer bar and an inner bar just seaward of the shoreline. By examining the weightings on the first eigenvector (Figure 11), vector 1 is of greatest importance (highest and most consistent weightings) during early 1981 and following the November, 1981 storm. This vector then accounts for the shift in profile configuration shown in Figure 8 and describes the relative stability of the profile following the Fall 1981 storms.

When negatively weighted, eigenvector 2 also describes a double bar configuration but the resulting shape is different than that described by vector 1. Both the inner and outer bars are farther offshore (Figure 12). From Figure 11, it can be seen that the weightings on the second vector are positive in early 1981 and negative in 1983. In fact, the second vector has a very low weighting during 1982 when the weighting on the first vector is high. Eigenvector 2 is of greatest importance from October, 1982 to March, 1983, the period corresponding to

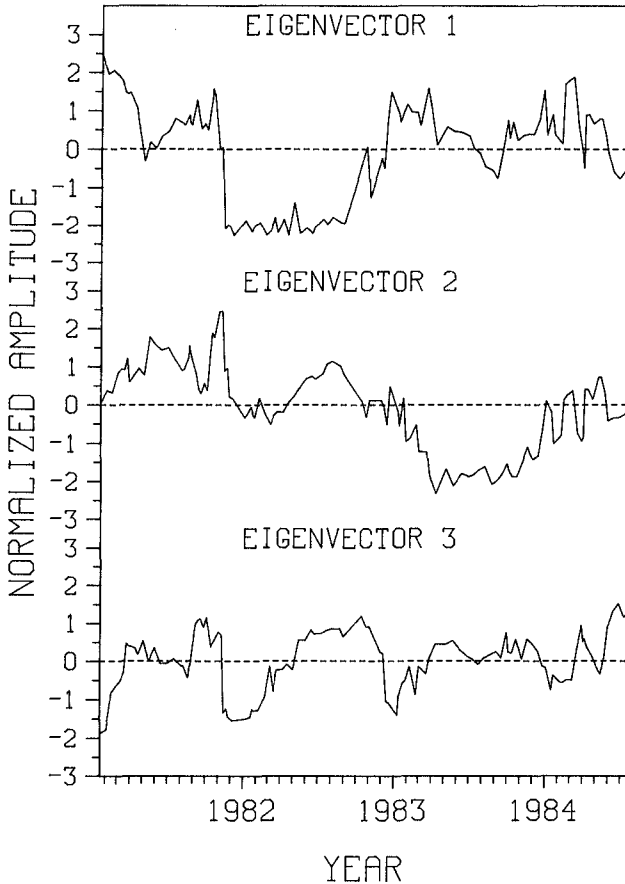


Figure 11. Temporal weightings on the first 3 eigenvectors for profile line 188

the second sequence of offshore movement of the outer bar described earlier.

Together, eigenvectors 1 and 2 describe the major cross-shore movements on the profile. Rather than being seasonally controlled, they appear to result from two unique sequences of storm/recovery activity.

Though the third eigenvector explains only 1/2 of the variance explained by vector 2, its weightings have the most well-defined annual cycle, having a negative peak every year around January and February. From Figure 12, the third eigenvector describes a shift of sediment

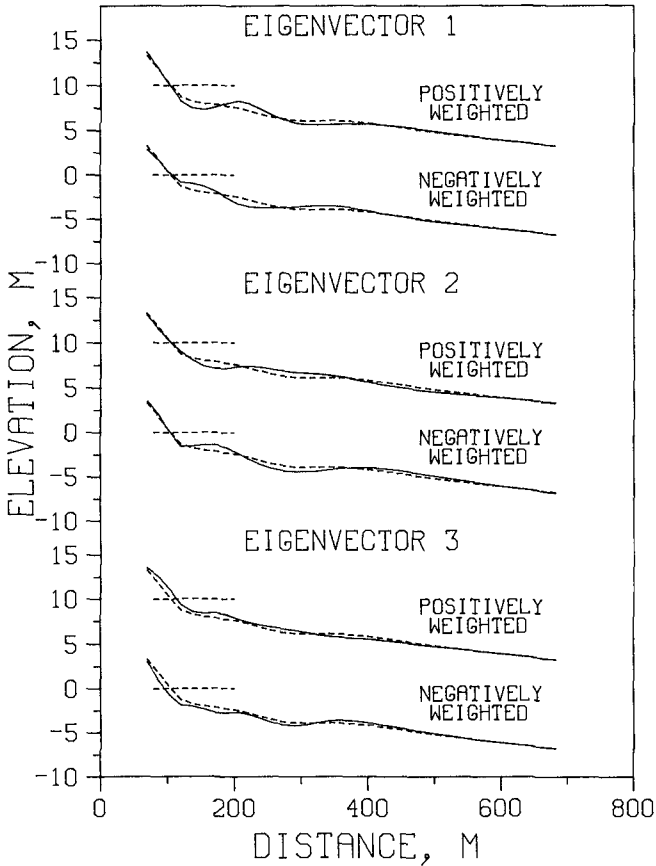


Figure 12. Effect of the first 3 eigenvectors on the mean profile using a unit weighting

from the beach and nearshore to the offshore (feeding the outer bar) when the weightings change from positive (summer) to negative (winter). The material shifts around a point 308 m (1010 ft) from the baseline at a mean depth of 3.9 m (12.8 ft). While this is a node for the third vector, both eigenvectors 1 and 2 have antinodes near this distance.

#### Summary

This paper uses a unique set of field data to examine the cross-shore movement of sediment. Rapid and major changes to profile shape occurred during significant storms and generally stormy periods. Minor storms caused changes only to the inner bar. The post storm recovery

of the outer bar required in excess of six months of relatively low wave conditions. An eigenvector analysis of the data confirmed these findings. The first two eigenvectors, which combined account for 64.8 per cent of the variance, were attributed primarily to two different double bar configurations which resulted from storm sequences in 1981 and 1982-1983. The third vector accounted for a well-defined annual cross-shore shift of material.

The rate and quantity of material moved has implications for: the frequency and coverage of nearshore surveys, the siting of instruments, and the design of shore perpendicular structures including cable crossings and ocean outfalls. In addition, study results indicate that in order to nourish a beach, fill material must be placed in water depths less than 2 to 3 m (6 to 10 ft), the region of the inner bar, and that the timing of the placement is critical. Placement of material prior to a period of storms will result in offshore movement.

#### Acknowledgments

The data used for this study resulted from the combined efforts of the small but dedicated staff of the Field Research Facility and their tireless hours spent, under usually less than ideal conditions, collecting and processing the data. Results presented herein, unless otherwise noted, are based on research conducted at the Coastal Engineering Research Center, Waterways Experiment Station, under the Shore Protection and Restoration Program, Coastal Engineering Functional Area, Civil Works Research and Development, U. S. Army Corps of Engineers. Permission to publish this information was granted by the Chief of Engineers.

## Appendix 1.-References

1. Aubrey, D. G., "Statistical and Dynamical Prediction of Changes in Natural Sand Beaches," PhD dissertation, University of California, San Diego, 1978.
2. Aubrey, D. G., "Seasonal Patterns of Onshore/Offshore Sediment Movement," *Journal of Geophysical Research*, 84, 1979, pp. 6347-6354.
3. Aubrey, D. G., "The Statistical Prediction of Beach Changes in Southern California," *Journal of Geophysical Research*, 85, 1980, pp. 3264-3276.
4. Birkemeier, W. A., DeWall, A. E., Gorbics, C., and Miller, H. C., "User's Guide to CERC's Field Research Facility," MR 81-7, U. S. Army Corps of Engineers, Coastal Engineering Research Center, Fort Belvoir, Oct. 1981.
5. Birkemeier, W. A., and Mason, C., "The CRAB: A Unique Nearshore Surveying Vehicle," *Journal of Surveying Engineering, ASCE*, Vol. 110, No. 1, pp. 1-7.
6. Howd, P. A., and Holman, R. A., "Beach Foreshore Response to Long Waves in the Surf Zone," *Proceedings of the Coastal Engineering Conference, ASCE, Houston, 1984.*
7. Mason, C., Sallenger, A. H., Holman, R. A., and Birkemeier, W. A., "DUCK82 - A Coastal Storm Processes Experiment," *Proceedings of the Coastal Engineering Conference, ASCE, Houston, 1984.*
8. Miller, H. C., Birkemeier, W. A., and DeWall, A. E., "Effects of CERC Research Pier on Nearshore Processes," *Proceedings of the Coastal Structures '83 Conference, ASCE, 1983, pp. 765-784.*
9. Sallenger, A. H., Holman, R. A., and Birkemeier, W. A., "Storm Induced Response of a Nearshore Bar System," *Journal of Marine Geology*, in press.
10. Short, A. D., "Multiple Offshore Bars and Standing Waves," *Journal of Geophysical Research*, September 20, 1975, pp. 3838-3840.
11. Vincent, C. L., and Resio, D. T., "An Eigenfunction Parameterization of a Time Sequence of Wave Spectra," *Coastal Engineering*, 1, 1977, pp. 185-205.
12. Wright, L. D., Thom, B. G., and Chappel, J., "Morphodynamic Variability of High Energy Beaches," *Proceedings of the Conference on Coastal Engineering, ASCE, Hamburg, 1978, pp. 1180-1194.*



## CHAPTER ONE HUNDRED THREE

### BEACH RESPONSE TO COASTAL WORKS

#### GOLD COAST, AUSTRALIA

H.V. Macdonald\* and D.C. Patterson\*

#### ABSTRACT

The paper outlines the results of comprehensive beach surveys carried out over more than 20 years showing the effects of seawalls, groynes and beach nourishment on the beaches of the beach resort city of Gold Coast, Australia. Beach profile changes and, in particular, quantification of the overall extent of accretion and erosion resulting from groynes which interrupt the longshore movement of sand are outlined. The paper confirms the already known principles of behaviour of these coastal works and documents clearly the full detrimental impact that inappropriate structures can have on a natural sand beach system.

#### 1.0 INTRODUCTION

The city of Gold Coast, one of Australia's richest and most popular tourist centres, extends in a relatively narrow strip along 30 kilometres of predominantly sandy coastline immediately north from Queensland's state border (Figure 1). The city is an amalgamation of several townships originally settled early this century as resorts where the climate, beaches and surf conditions were all highly suited to public recreation. Today the city's economy still depends on tourism, which in turn depends on the existence of adequate beaches.

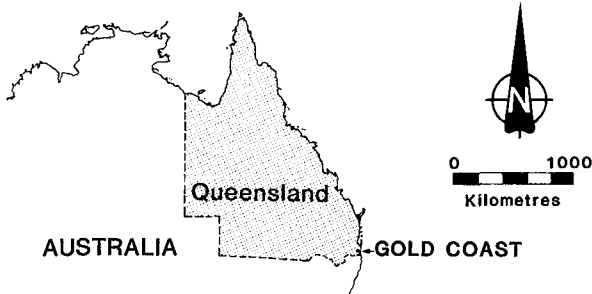


Figure 1(a). General Locality Plan

\*Engineers, Department of Harbours and Marine, G.P.O. Box 2195, Brisbane, Queensland Australia. 4001.



Figure 1(b). Gold Coast City

1.1 Erosion Problems and Coastal Works

Over the years, residential development located close to the beach has increased substantially in extent and value. The threat of damage to this property from beach erosion caused by the effects of cyclones which regularly affect the area has led to the construction of protective rock seawalls along most of the city's foreshore. Initially the problems were the result only of locating the development too close to the sea within the zone of natural beach movements. However, over the past 20 years, these problems have been exacerbated in some areas by groyne structures constructed at various locations along this coastline which experiences a relatively strong longshore sand transport. Some beach replenishment has been carried out in several badly eroded or more popular recreational areas. A summary of the major coastal engineering works carried out in the area is shown in Figure 2.

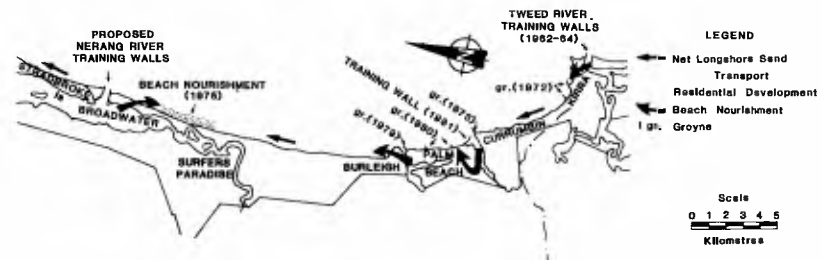


Figure 2. Summary of Coastal Works, Gold Coast.

## 1.2 Coastal Management

The principal components of investigation and planning for management of Gold Coast beaches are listed below.

- (a) Commencing in 1964, the Queensland State Government collected field data relating to beach processes and in 1968 commissioned the Delft Hydraulics Laboratory, Netherlands to evaluate the data and report on the erosion problems. In 1970 the laboratory presented its report containing detailed recommendations for beach restoration by sand nourishment and other accompanying works.
- (b) In 1968 the Queensland Government passed its Beach Protection Act and established the Beach Protection Authority to investigate and provide advice to local governments on beach erosion problems. In Queensland, financial responsibility for implementing beach restoration works rests essentially with the various local governments including the Gold Coast City Council.
- (c) The Authority and the State Government adopted the Laboratory's recommendations and the Gold Coast City Council was advised accordingly through extensive discussion and through the provisions of the legislation.
- (d) The Authority has continued its programme of wave recording, beach surveys, aerial photography and daily beach readings (COPE) in the Gold Coast area with particular emphasis being given to those areas affected by works carried out from time to time. Recently, the Authority's engineers reassessed the rates of sand transport along the coast based on the extended wave data record. As well, the survey data was used to identify changes to the beach system since 1962 including the effects of coastal works carried out during that time. This information is passed to the Gold Coast City Council to assist in planning and implementation of appropriate beach protection works in accordance with the approved scheme.

## 1.3 Aims and Objectives

The aim of the paper is to document the coastal protection measures used at Gold Coast in terms of their effects on beaches and on property as well as a comparison of the benefits which accrue in the immediate vicinity of the works with the effects on the coastline as a whole. The ultimate objective is that the decisions on works to be implemented at Gold Coast and other beach areas be based on a full and clear understanding of the impact that some works can and have had on the beach system as a whole.

## 2.0 GOLD COAST BEACH PROCESSES

Analyses of the results of beach surveys together with calculations based on the measured wave climate for the area have been used to provide a good understanding of the natural beach processes along the Gold Coast. In the broader view, the Gold Coast beaches form part of an extensive system of longshore moving sand having its origins up to 150 kilometres to the south. The entire supply of sand to the beaches comes from this longshore movement of sand.

### 2.1 Delft Hydraulics Laboratory Report (Reference 2)

The fundamental conclusions of the 1970 report by the Delft Hydraulics Laboratory were -

- (a) onshore/offshore transfers of up to about 400 cubic metres per metre can be expected during and subsequent to severe cyclone erosion events. However there is no net loss of sand from the beach system during this process.
- (b) because development has been located over the former natural dune system, the beaches contain insufficient sand reserves seaward of the development to accommodate severe cyclone erosion events and require restoration by nourishment of 10 - 15 million cubic metres of sand.
- (c) there is a differential in the longshore transport rates along the Gold Coast, leading to a persistent long term erosion of the beaches of 0.3 million cubic metres of sand per year. The Laboratory's assessed longshore transport rates were -
  - (i) Letitia Spit : approx 0.5 million m<sup>3</sup>/year
  - (ii) Kirra area : approx 0.2 million m<sup>3</sup>/year
  - (iii) Nerang River area : approx 0.5 million m<sup>3</sup>/year

It can be seen that there is an assessed corresponding "loss" to deep water of 0.3 million cubic metres per year between Letitia Spit and Kirra. There is no evidence available to support an accumulation of such an amount of sand offshore in this area.

- (d) construction in 1962-64 of training walls at the Tweed River mouth would trap about 4 million cubic metres of sand on Letitia Spit. Because not all of this effect would have passed to the Gold Coast, this groyne effect would result in a loss of 1.7 million cubic metres of sand from the beaches at the southern end of the Gold Coast.

## 2.2 Beach Protection Authority Report (References 1 and 4)

The recent study of longshore transport rates carried out by the Beach Protection Authority of Queensland concluded that -

- (a) there is little or no longshore transport differential along the Gold Coast and, correspondingly, there would be little or no loss of sand to deep water between Letitia Spit and Kirra. The net longshore rate is uniform at approximately 500,000 m<sup>3</sup>/year.
- (b) any significant changes to the beaches over the past 20 years have been the direct result of coastal works. Specifically, essentially all of the sand trapped on Letitia Spit by the Tweed River training walls would have moved northward to the Gold Coast beaches and therefore represents a loss of sand from those beaches.

## 3.0 BEACH RESPONSE TO COASTAL WORKS

Each beach section of the Gold Coast has a different history of coastal management and therefore has responded uniquely to the coastal works affecting it. It is convenient to consider the coast in three broad units based on both geographic and management considerations. These units are-

- (i) Southern Region - Letitia Spit to Currumbin, affected predominantly by the Tweed River training walls and seawalls.

- (ii) Central Region - Currumbin to Burleigh, affected predominantly by groynes and seawalls.
- (iii) Northern Region - Burleigh to Nerang River, with extensive development protected by seawalls and limited beach nourishment.

Each of these three coastal units are discussed separately below.

### 3.1 Southern Region (incorporating Tweed River Training Walls).

The groyne works undertaken in this region are shown in Figure 3 and include the Tweed River training walls (aimed at improving navigation to the river) and groynes at Kirra (aimed at offsetting erosion caused by the training walls). The river mouth was trained originally around 1900, however the strong longshore transport subsequently re-established the entrance bar. The training walls were extended a further 400 metres during 1962-1964 by the New South Wales Government.

The beaches both updrift and downdrift of the river training works have been monitored in detail since 1962, providing a good understanding of the effects of these works. The beach monitoring has included -

- (i) regular aerial photography including low level work used for photogrammetric contouring during 1962 and 1963.

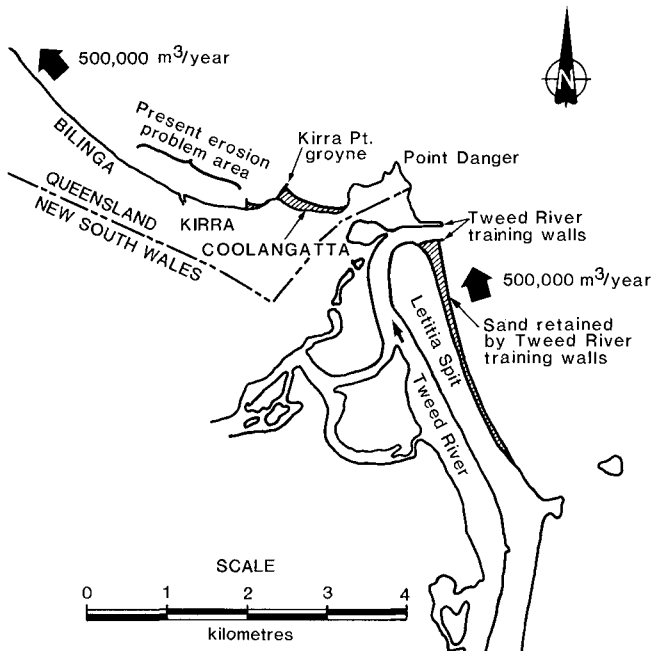


Figure 3. Groyne Works – Southern Gold Coast Region

- (ii) beach and hydrographic surveys by the New South Wales Government (available for 1962 to 1965), the Gold Coast City Council (1984) and the Beach Protection Authority over the period 1964 to 1984.
- (iii) an Authority's COPE station established at Coolangatta in 1982.

**Accretion updrift of Tweed River Training Walls**

To 1983, the coastline immediately south (updrift) of the training walls had accreted by a distance of 250 to 300 metres since wall construction in 1962, with changes to the near-shore profile extending to the 18 metre depth contour (Figure 4). The quantity of accretion varies from a maximum of 4000 m<sup>3</sup>/m near the walls to essentially nil at Fingal about 3 kilometres to the south, totalling 4.8 million cubic metres south of the walls (Figure 5). As well, a new bar has formed across the river entrance, involving the accretion of an additional 1.6 million cubic metres to date.

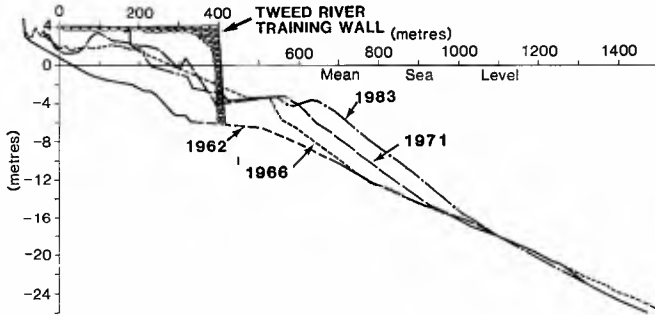


Figure 4. Accretion Adjacent to Tweed River Training Walls.

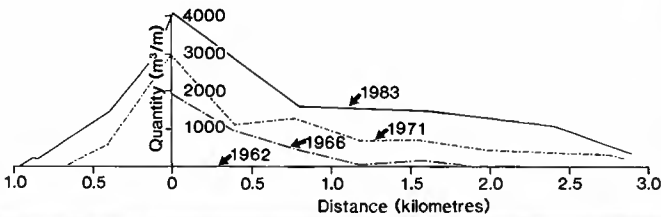


Figure 5. Distribution of Accretion Along Letitia Spit.

The time history of total accretion, including that along Letitia Spit and in the new entrance bar, is shown in Figure 6, reaching a total of 6.4 million cubic metres in 1983. The accretion trend indicates that further sand accumulation in this area can be expected, although the rate of such accumulation should decrease as the rate of natural sand bypassing to the Gold Coast beaches increases.

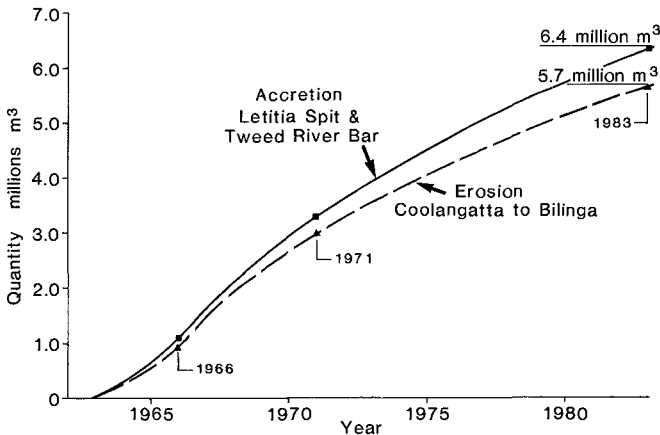


Figure 6. Time History of Updrift Accretion and Downdrift Erosion Resulting From Tweed River Training Walls.

#### Erosion Downdrift of Tweed River Training Walls

The downdrift erosion measured to 1983 extends along about 4.5 kilometres of coastline from Point Danger to Bilinga (Figure 7). The erosion trend indicates that this loss is propagating further downdrift with time. The time history of erosion (Figure 6) indicates a trend similar to that of the updrift accretion, although somewhat (about 10%) less. While this difference may be the result of a minor reduction in the longshore transport capacities between Letitia Spit and the southern Gold Coast beaches, it is considered more likely to be attributable to the limitations of the survey procedures. The measured total downdrift erosion had reached 5.7 million cubic metres by 1983. It should be noted that this quantity, based on the surveyed changes at 21 profile locations, exceeds but is more reliable than the preliminary estimate of 3.5 million cubic metres of erosion outlined in Reference 4 based on only 4 profile locations. This emphasises the need for comprehensive surveys for such analyses.

The measured downdrift erosion has occurred across some 1200 metres width of the nearshore profile, out to depths of about 15 metres (Figures 8 & 9). Sand levels have dropped by up to 5 metres near the beach in the worst eroded area with general erosion by 1 to 2 metres over a broad offshore area in water depths formerly of the order of 5 to 9 metres.

Rock seawalls were constructed at Coolangatta and Kirra to limit the beachline recession there. In 1972 a groyne was constructed at Kirra Point in order to restore Coolangatta's recreational surfing beach (Figure 3).

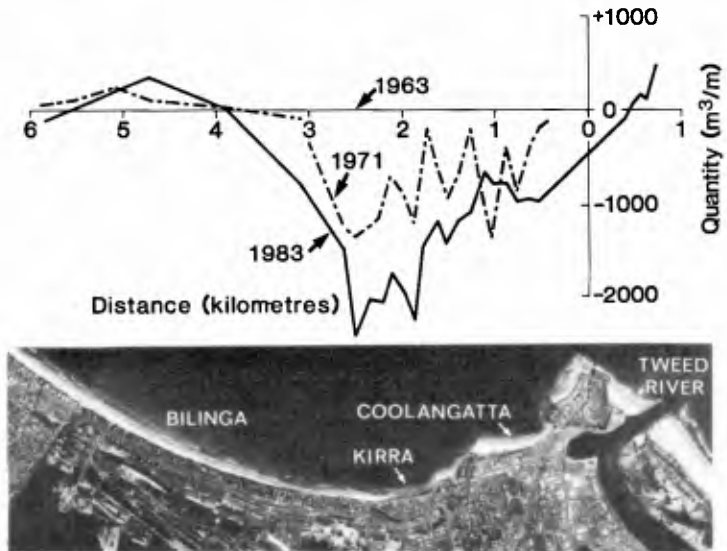


Figure 7. Distribution of Downdrift Erosion – Point Danger to Bilinga.

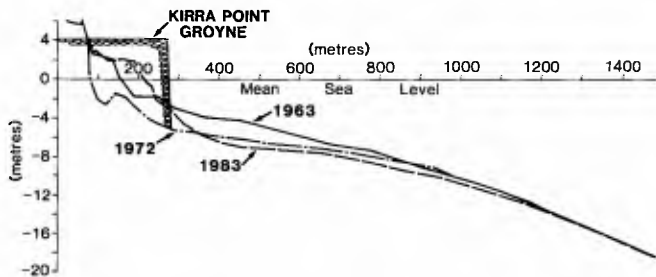


Figure 8. Sequence of Surveyed Profiles Updrift of Kirra Point Groyne.

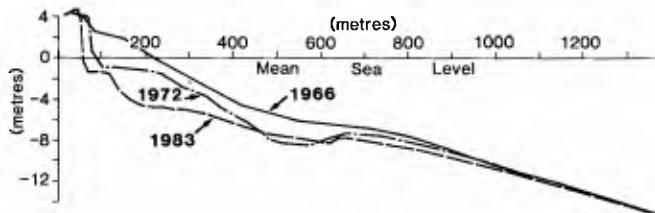


Figure 9. Sequence of Surveyed Profiles Downdrift of Kirra Point Groyne.



### Effects of Kirra Point Groyne

Details of the design and effects of the Kirra Point groyne are outlined in Reference 5 (Robinson & Patterson 1975). The influence of the Kirra Point groyne in accumulating sand extends seawards to about the 6 metre depth contour. Some 300,000 cubic metres of sand have been accumulated on Coolangatta beach above that level. In the deeper parts of the offshore profile unaffected by the groyne, erosion caused by the Tweed River training walls continued progressively (Figure 8) such that there remains an overall net erosion of these profiles (Figure 7).

The trapping of sand by the Kirra Point groyne exacerbated the erosion effects of the Tweed River training walls at Kirra, immediately downdrift, where massive erosion of the beach and dune occurred during storms in 1974. As a result, a rock seawall was destroyed and a camping park area was eroded away as the coastline receded by up to 80 metres. A new seawall was constructed along the new eroded dune alignment to protect roads and facilities.

A second groyne was constructed at Kirra during 1974 (the Miles Street groyne - Figure 3) in an attempt to retain a usable beach in front of the Kirra Surf Lifesavers' Clubhouse. Approximately 1 million cubic metres of sand were pumped from the Tweed River to Kirra Beach to offset the erosion. However, the benefits of this nourishment were temporary because -

- (a) the rate of longshore supply of sand to the nourished area downdrift of the various groyne structures was, at the time, substantially less than the longshore transport capacity which distributed the nourished sand along the coast towards the north.
- (b) the quantity pumped was small in relation to the total quantity eroded in the Kirra area.



*The Tweed River training walls have trapped on Letitia Spit 6.4 million cubic metres of sand that would otherwise have moved northward to the Gold Coast beaches. The construction of groynes at Kirra in an attempt to overcome the resulting beach erosion problem has further interrupted the flow of sand, and has moved the problem area further north.*

- (c) the sand was taken from the zone of beach sand transport within the river which subsequently has progressively infilled with sand from the beaches (Reference 3). Hence the long term benefit to the beaches would be small.

The downdrift beach at North Kirra has never recovered from the combined erosion effects of the training walls and groynes. The sand loss is presently concentrated in this area where erosion of the beach profile by about  $2500 \text{ m}^3/\text{m}$  to 1983 has been surveyed. A rock seawall there is preventing further erosion of roads and property, but at the same time is also preventing the re-establishment of a beach.

### 3.2 Central Region (Currumbin/Palm Beach/Burleigh)

The Currumbin/Palm Beach area is characterised by residential development and associated roadways located close to the beach. At Currumbin, the esplanade road was constructed along the foredune. This road was eroded repeatedly until a rock seawall was constructed to protect it in the 1950's. The frequent lack of a usable beach led to groyne construction connecting Currumbin Rock to the mainland in 1973 (Figure 10).

Palm Beach has experienced long-standing erosion problems largely as a result of residential development being located too close to the beach. Some freehold allotments were originally established on bare areas of dune sand. As a result of periodic dune erosion, rock seawalls have been constructed over the years to protect what remains of the properties. Worsening erosion and the threat of damage to properties led to construction of three groynes over the period 1977 to 1980. A training wall was constructed at Currumbin Creek in 1981 to control the natural cyclical migration of the entrance.

Burleigh Beach extends 2 kilometres between two rocky headlands. A 250 metre long seawall was constructed in 1956 to protect car park and surf lifesaving facilities in the southernmost section. The remaining 1.75 kilometres of esplanade land was left undeveloped, although the natural dunes was levelled after mining for heavy minerals, mown and recreational park facilities installed.

From time to time, sand has been dredged from the creek estuaries at Currumbin and Tallebudgera to the beaches, including some  $0.3 \text{ million m}^3$  to Palm Beach in 1980 to accompany groyne construction. These estuaries form part of the active beach sand transport system.

Monitoring of the beaches and estuaries in this region has been carried out through regular aerial photography and beach and hydrographic surveys by the Beach Protection Authority over the period 1966 to 1983, with intense coverage since 1980. An Authority COPE station has operated at Burleigh since 1980.

#### Currumbin Rock Groyne (1973)

This groyne connected Currumbin Rock to the mainland, thereby preventing the longshore transport of sand through the intermediate area. As a result, about 0.79 million cubic metres of sand accreted on Currumbin Beach (Figure 10) and the entire longshore transport now passes around the seaward side of Currumbin Rock.

Immediately downdrift, within about a kilometre of Currumbin Rock, while the beach line receded, the nearshore profile accreted to carry the longshore transport. Works have been carried out effectively removing sand from the creek estuary and moving the beach line seawards in this area. These combined effects are shown on Figure 10 as a net gain

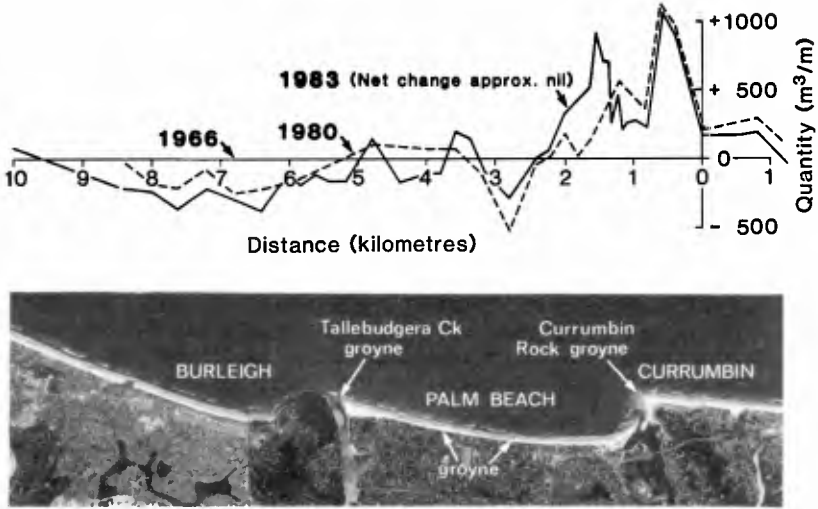


Figure 10. Distribution of Accretion / Erosion – Currumbin to Burleigh.

of sand to the beach system amounting to about 0.5 million cubic metres to 1983. Of this, a net quantity of about 0.2 million has come from the estuary which will tend to infill again with sand from the beaches unless repeated dredging is undertaken to keep the sand on the beaches.

Further downdrift, erosion has occurred along some 5 kilometres of coast at both Palm Beach and Burleigh. At Palm Beach where beaches were already in poor condition in front of seawalls protecting property, sand levels dropped still further, in some areas, to below the low tide level. A nearshore gutter some 200 metres wide and 2 to 3 metres deep, often carrying strong longshore currents, developed adjacent to the seawalls and persisted through to 1980 (Figure 11).

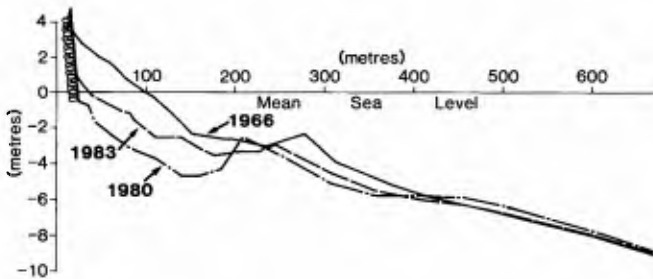


Figure 11. Effect of Seawall on Beach Profile, Palm Beach.



*Palm Beach in 1980 with residential development protected by rock seawall and no usable beach.*

The Tallebudgera Creek groyne, built in stages between 1977 and 1979, stabilised the northern section of Palm Beach against progressive erosion and is expected to have had the effect of transferring sand losses further downdrift to Burleigh. The groynes built on Palm Beach in 1980 are relatively short in relation to the width of the zone of longshore transport. They have held small quantities of the nourished sand in their immediate vicinity.

Overall, there was a surveyed net erosion of some 1.1 million cubic metres of sand along the downdrift areas of Palm Beach and Burleigh between 1966 and 1983. This is comparable with the total net gain to the beaches of 1.29 million cubic metres adjacent to the Currumbin Rock groyne, of which some 0.2 million has been obtained from the Currumbin Creek estuary. Hence, there is a balance in the overall quantities, with a redistribution leading to accretion in some areas and erosion in others as a result of groyne construction.

The losses of sand along Burleigh Beach occurred first in the offshore parts of the beach profiles, and manifested as significant beachline recession only during and after storms which served to re-establish the normal profile shape but at a more landward location. The net erosion at Burleigh since 1966 had reached typically  $300 \text{ m}^3/\text{m}$  by 1983 with recession of the duneline of up to 20 metres. Despite this, where erosion into the dune has occurred unobstructed by seawalls, the beach itself remains in good condition as a recreational amenity.

### 3.3 Northern Region (Burleigh to Nerang River)

This section of the Gold Coast is characterised by an almost continuous strip of residential development located on the main dune. Properties along most of this coastal section have periodically been subjected to erosion during cyclones. As a result, a seawall extends along almost the entire 14 kilometre length of beach.

The Nerang River entrance is located at the northern end of the Spit. The entrance has migrated progressively northwards for at least 4.4 kilometres over the past 80 years accompanied by growth of the Spit and erosion of Stradbroke Island. In the process, sand transported into the river entrance has been left deposited in the Broadwater and alienated from the active beach system. As well, the groyne effect of the entrance bar has moved progressively northwards with the entrance.

**Beach Nourishment**

In 1974, some 1.4 million cubic metres of sand were dredged from the sand reserves in the Broadwater to Surfers Paradise beach to improve its recreational amenity. The sand was placed on a limited beach length of about 3.5 kilometres at an average rate of 400 m<sup>3</sup>/m creating a new dune and berm in front of the seawall. It would be expected that the effect of this nourishment would distribute progressively in both directions along the coast while the benefit in the central nourishment area would reduce over time.

Figure 12 shows a plot of the time history of the distance to the mean monthly edge of berm from the seawall line over the period 1974 to 1984. This data was obtained from the COPE station at Surfers Paradise. Despite the expected redistribution of the nourished sand, these works have clearly provided a substantial benefit in terms of the usable beach width over this entire period. Recent storms in 1983 and 1984 have eroded the beach significantly as shown in Figure 12 and the profiles of Figure 13, however the erosion has been accommodated within the dune system and a usable recreational beach continues to exist. No detrimental effects resulting from the beach nourishment works have been noted either within the beach system or at the sand source area.

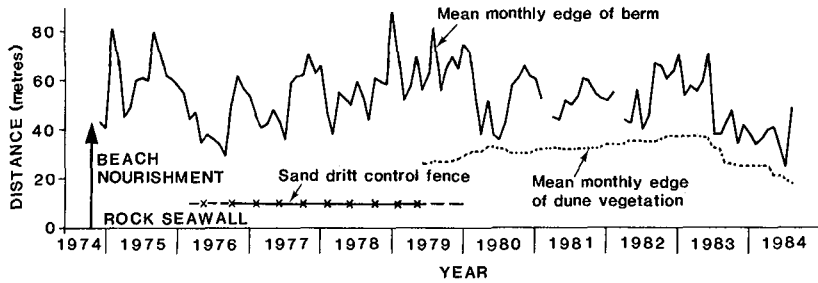


Figure 12. Time History of Berm Width at Surfers Paradise Following Beach Nourishment in 1974.

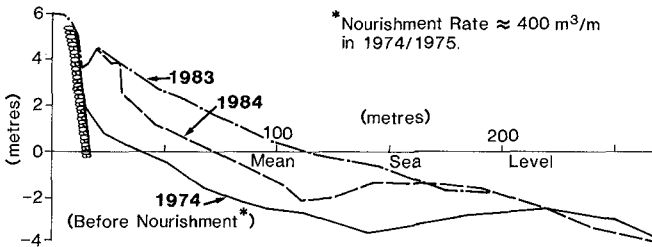


Figure 13. Behaviour of Beach Nourishment, Surfers Paradise.



*All of the Gold Coast beaches were substantially eroded by cyclones in 1967. Severe problems were experienced where development was located close to the beaches, such as in the Surfers Paradise area (pictured).*



*Beach nourishment to Surfers Paradise in 1974 has established a new beach and dune system in front of the seawall. The photo shows the beach in 1983 in good condition.*



*All of the Gold Coast beaches were substantially eroded by cyclones in 1967. Severe problems were experienced where development was located close to the beaches, such as in the Surfers Paradise area (pictured).*



*Beach nourishment to Surfers Paradise in 1974 has established a new beach and dune system in front of the seawall. The photo shows the beach in 1983 in good condition.*

#### 4.0 CONCLUSIONS

The variety and magnitude of works carried out along the Gold Coast and the comprehensive monitoring of the effects of these works over some 20 years have allowed a good understanding of their effects on the coastal system to be obtained. In general, the effects of these works on the beaches of the Gold Coast conform with the already known principles of behaviour. These are summarised below.

##### Groyne Structures

Groynes interrupting the net longshore sand transport have trapped sand on the updrift side and caused an equivalent quantity of erosion on the downdrift side. The extent and time scale of these effects depends on the effective length of the groyne and the total longshore transport intercepted by the groyne. It is apparent that the effective groyne length of river training walls is greater than for equal length groynes on a continuous beach, presumably because of the additional effects of the river flow. Entrance bar development may add significantly to the total quantity accumulated by such training walls, as appears the case at the Tweed River. The quantity of sand accumulated by these walls now exceeds 6 million cubic metres.

The approximate equality of the surveyed quantities of accretion adjacent to the Tweed River training walls and of erosion along the southern Gold Coast beaches supports the conclusions of the recent longshore transport study for the area. That is, that essentially all of the longshore transport along Letitia Spit would normally have passed to the Gold Coast beaches had the training walls not been constructed. Theoretical groyne accretion calculations together with the trends in the surveyed results indicate that the training walls may ultimately trap of the order of 7 million cubic metres of sand and that the majority of the longshore transport is currently bypassing the walls naturally to the beaches to the north. It is expected that this natural bypassing will be restored to at least 90% of its original rate by 1990.

Other groynes along the coast have affected the beaches to varying degrees, depending on their effective lengths and the proportion of the total longshore transport intercepted. Of these, the Kirra Point groyne which intercepted about 70% of the transport, trapping some 0.3 million cubic metres, and the Currumbin Rock groyne which has accumulated about 1.1 million cubic metres, have had the most impact on the beaches.

##### Seawalls

Seawalls serve to restrict the horizontal recession of the beachline resulting from erosion occurring either during storm events or as a persistent trend such as at beaches downdrift of groynes. Their impact on the beaches is largely dependent on their location on the beach profile. The further seaward they are constructed, the greater their influence and the less likely will a usable beach be maintained in front.

On the persistently eroding beaches at North Kirra and Palm Beach, the receding beachline has effectively placed the seawall progressively further and further seaward on the beach profile until no beach exists at all in front of the wall. Clearly, the establishment of fixed seawall alignments on persistently eroding sections of beach will lead eventually to loss of the beach as a useful recreational amenity.

It has been noted at Coolangatta, Kirra and Palm Beach that, once the waves impinge on the seawalls for a significant proportion of the time, wave reflections and accelerated longshore currents can lead to increased scour adjacent to the walls.



### Beach Nourishment

Beach nourishment to Surfers Paradise beach using the native sand derived from a source remote from the active beach system has been highly effective. Despite the fact that the nourishment was limited in its extent and would be expected to distribute along the coast over time, the benefit of these works has persisted for over 10 years and storm erosion continues to be accommodated within the nourished dune system in most areas.

Sand pumping to the beaches from areas such as estuaries within the zone of natural movements of beach sand will provide no lasting benefit to the beaches unless repeatedly carried out.

Restoration of the beaches in the Kirra area and re-establishment of the normal flow of sand along the coast could be achieved by beach nourishment, but would require nourishment to the eroded beaches by a quantity of sand equal to that trapped by the training walls, the source of such sand being remote from the active beach system.

### Beach Management

The Gold Coast erosion problems, namely the threat of property damage and the loss of the adjacent beaches, are the result of inappropriately located development (leading to the construction of seawalls) exacerbated by works (groynes) intended to overcome these problems together with the construction of the Tweed River training walls aimed at improving navigation to the river.

The future beach management policy at Gold Coast will be influenced by the needs of the tourist industry. The variety of works undertaken to date, their obvious effects and those reported from survey results provide the decision-makers with positive evidence of their impact on the coast and allow future works to be undertaken with a clear understanding of these impacts.

The present state of the Gold Coast beaches as a whole is such that the fundamental recommendation of the Delft Hydraulics Laboratory in 1970, namely restoration of the beaches by extensive sand nourishment, is still appropriate despite the expenditure of millions of dollars on coastal works in the area.

## 5.0 REFERENCES

1. BEACH PROTECTION AUTHORITY (1981). Gold Coast Longshore Transport. Beach Protection Authority, Queensland.
2. DELFT HYDRAULICS LABORATORY (1970). Gold Coast, Queensland, Australia – Coastal Erosion and Related Problems, R257. Delft Hydraulics Laboratory, Netherlands.
3. DRUERY B.M. and CUREDALE J.W. (1978). Tweed River Dynamics Study. Department of Public Works, New South Wales.
4. PATTEARSON C.C. and PATTERSON D.C. (1983). Gold Coast Longshore Transport. Proc. Sixth Australian Conference on Coastal and Ocean Engineering, Gold Coast, Queensland.
5. ROBINSON D.A. and PATTERSON D.C. (1975). The Kirra Point Groyne, A Case History. Proc. Second Australian Conference on Coastal and Ocean Engineering, Gold Coast, Queensland.

## CHAPTER ONE HUNDRED FOUR

### METHOD FOR ASSESSING STORM DAMAGE TO BEACH HOUSES

BY LYNN C. DOYLE, MEMBER ASCE, & WILLIAM L. FOX\*

**ABSTRACT:** Methods and procedures for the assignment of the pro rata share of damages caused by rising water and high winds arising from natural weather phenomena were virtually non-existent following Hurricane Frederic in 1979. Damages to beach front structures were often assumed to be caused by high water. Frederic marked the first natural weather disaster to strike a heavily populated area since the formation of the National Flood Insurance Program in 1970. The damages caused by the winds and rising water from Hurricane Frederic, therefore, created an economic incentive to attempt to distinguish between wind and rising water contributions. This paper presents a method and outlines procedures followed in damage assessments following Hurricane Frederic in an effort to minimize the difficulties insurance carriers and adjustors may have following future similar phenomena. It may, additionally, serve to promote improved design and/or building codes where such phenomena are probable.

#### INTRODUCTION

Houses located on ocean beaches usually incur considerable damage from storms of hurricane strength. This damage may be caused by wind forces, flood water forces, or a combination of these two forces. Insurance companies and adjustors, both wind and flood insurance carriers, sometimes have a difficult problem in assessing the cause of damage and, therefore, prorating costs to these beach houses.

Such difficulties were encountered by adjustors, insurance carriers, governmental agencies and others following the extensive property damage caused by Hurricane Frederic. Frederic, a force 3 hurricane, whose center passed through Mobile, Alabama on September 12, 1979, caused a reported \$2 billion in property damage. Winds were clocked at 140 MPH at Dauphin Island at the entrance to Mobile Bay and rising water was estimated to have been 15 feet above MSL. Hurricane Frederic was the first natural disaster causing both wind and water damage since the birth of the National Flood Insurance Program in 1970. Consequently methodology and procedures to be followed in determining probable cause and in apportioning costs were virtually non-existent. The task of those concerned with the assessment of damages and costs was to develop usable and acceptable criteria and procedures.

This paper outlines a method and provides guidelines which may be used to assess the cause of damage to pile supported beach houses.

\*President and Controller, respectively, Geotechnical Engineering Testing, Inc., 904 Butler Drive, Mobile, AL 36609.

### RATIONALE

The rationale used was that careful observation and documentation of damages as evidenced by erosion of foundation soils, water marks, building orientation, elevations, wind surface area and other material factors would yield a logical and equitable basis for assigning dollar values to the respective causal wind and rising water forces.

### PROCEDURE

In our approach, we observed and recorded data relative to the way in which wind and water loads affected the pile loads and/or capacities. The two forces, quite obviously directly increased the loads on the piles. Less obvious, however, was the diminished load-bearing capacity of the piles due to the erosion of foundation soils.

Our field observations were directed toward the determination and measurement of the following factors:

1. wind velocity and direction
2. still water depth
3. location of the structure relative to wave protection features such as sand dunes and other structures.
4. size of structure
5. orientation of structure
6. pre-storm elevation of structure
7. soil erosion around structure foundation
8. bracing system used (x-bracing or a concrete floor slab fixed to the piles at ground levels, etc.)
9. type of damage to the structure
10. condition of surrounding structures and the general type of damage sustained.

Using the field data as developed for each given case, we were able to hypothesize the magnitude of loads due to wind and water forces and the change in pile capacities due to erosion of foundation soils.

The rising water could affect the piles both through increased loads and through diminished bearing capacity due to erosion. Consequently the contribution of water toward structure damage was considered to be the sum of the absolute values of load and of pile capacity change. Wind contributed to the damage was assumed to be through increased loading only. The contribution of wind and water forces were totalled and each force then was expressed as a percentage of that total.

Damage proration to wind and water forces (and by extension to wind and flood insurance carriers) was made in accordance with those percentages.

### WIND LOADING

Wind loads acting upon the beach houses during storms of hurricane produced a very high lateral force on the structure—especially the foundation piles that are usually used to support beach

houses. The force from wind may be computed from the standard formula:

$$f = V^2k$$

where  $f$  = the unit force from the wind in psf

$V$  = the velocity of the wind in mph

$k$  = a constant usually taken as .003

A plot of unit wind load force vs. the wind velocity is shown by Figure 1. The unit wind force for a storm having a given wind velocity can be multiplied by the vertical projected area of the structure which the wind acts upon to estimate the total load acting on the structure.

FIGURE 1

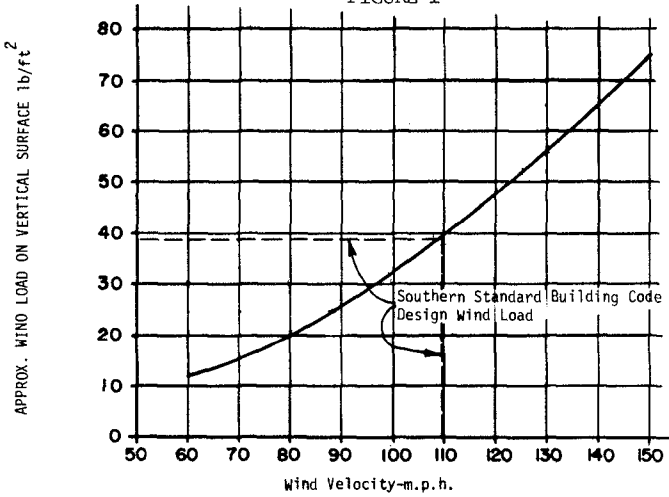
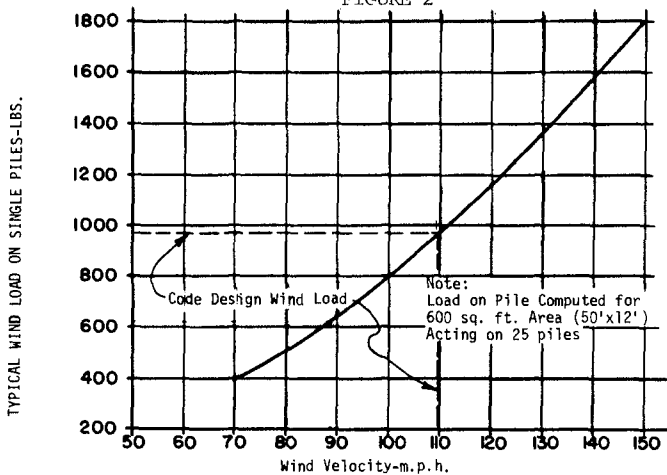


FIGURE 2



The formula to be used for this load determinations is:

$$P = f A$$

where P= Total load on structure

f= Unit Force from wind

A= Structure surface area perpendicular to the wind.

For a pile supported structure where all the piles are securely fixed to it, the total wind load will be distributed nearly evenly to each pile and this load is computed as:

$$fp = P/\text{No. of Piles} = \text{horizontal force on top of pile}$$

A plot showing the load on single piles (for a given size structure and number of piles) vs. the wind velocity is shown on Figure 2.

FIGURE 3

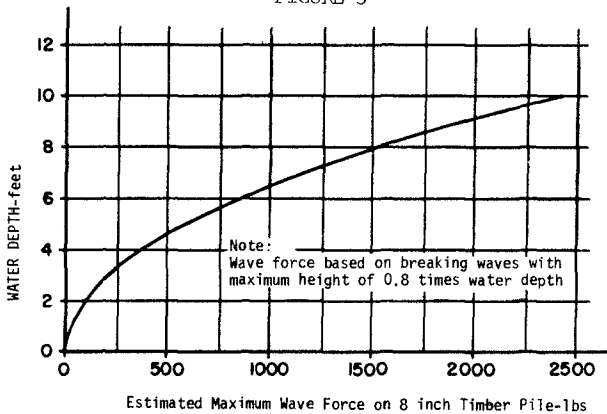
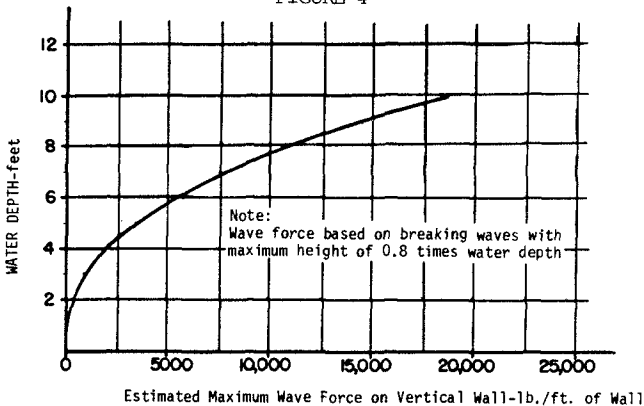


FIGURE 4



**WAVE LOADING**

Forces from waves acting upon structures are considerably more variable than are the wind loads during a storm of hurricane intensity. Many factors are to be considered for determining wave heights and thus forces from the storm. Some of the significant factors are:

1. Wind Velocity
2. Duration of wind
3. Distance wind travels over water (fetch)
4. Changing direction of wind
5. Water Depth
6. Sea bottom characteristics
7. Wave protection features-jetties, sand dunes etc.
8. Particular theory used for estimating wave heights and forces

For the evaluations made, generally a worst case condition was assumed where load forces for breaking waves were estimated to act on the structure. It was assumed in computations that the waves would have a maximum height of 0.8 times the still water depth. Therefore, if the still water depth could be determined, an estimate of wave height and wave forces could be made. Using methods published in the U. S. Army Coastal Engineering Research Center Shore Protection Manual, estimates were made of maximum wave loads on typical 8 inch timber piles. This water depth load relationship is shown by Figure 3.

The load would act on the pile at about the still water depth. For other size piles the loads would be directly proportional to the pile width. It is our opinion that a breaking wave would only act on a few piles at a single instant when it breaks with the most number of piles being one row of piles that support the structure. A portion of this horizontal load would be transferred to the structure and distributed to the other piles - the amount depending on the location of load application at about the still water depth.

Estimates were also made of the maximum wave force that would act on a vertical solid stationary wall for various water depths. This relationship is shown on Figure 4.

It can be seen from Figure 4 that very high wave loads are placed on the vertical solid wall of a structure and this load may act on all or a portion of the wall at an instant. It is our opinion that most beach house structures located at elevations where waves break upon the vertical walls could not stand up to the very high forces. This is verified by the very heavy seawall structures or jetties that are often constructed where waves break against the wall.

### EROSION OF SOILS AROUND PILES

During flooding of the coastal areas from the storm the water with wave and tidal actions usually move back and forth around the fixed structure. This water movement around fixed objects causes an increase in the water velocity and while this increased velocity does not exert a significant force on the structure, it does erode or scour the soil (usually sand along the beach) away from the foundation or pile. For footing foundations supporting the structure on the soil, erosion below the foundations will cause it to settle and thus the structure would settle and may collapse if the erosion is deep enough. For pile supported structures the erosion around the pile tends to decrease the load supporting ability of the piles— both axial load and lateral load capacity. Our surveys after Frederic indicated that a loss of axial pile capacity was not a significant cause of damage to beach houses. Table 1 shows typical axial pile capacities for a range of pile tip penetrations that may be evaluated if necessary to assess damage to a structure.

The lateral load capacity of piles may be significantly affected by the erosion of supporting soil from around the piles. Not only is the soil resistance on the pile decreased by the loss of soil but the moment or level arm at which the horizontal loads are applied to the soils are increased.

Estimates have been made of the lateral load capacity of typical 8 inch diameter piles having various embedment depths in typical sands we have found along the coast. These lateral load estimates based on one inch of deflection at the ground line are for two conditions. One is for piles having all the lateral load acting at the top of the piles such as a pile without any bracing and this capacity— embedment depth relationship is shown on Figure 5. The other condition analyzed is for a pile with the horizontal load acting on the pile at about eight ft from the top such as a well braced pile and this capacity relationship is shown on Figure 6.

It is noted that the braced pile should have two to three times the lateral load capacity of the unbraced piles regardless of the pile embedment depth.

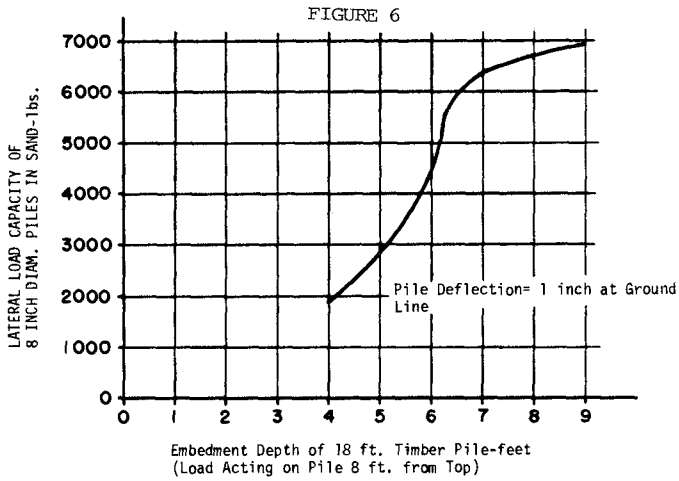
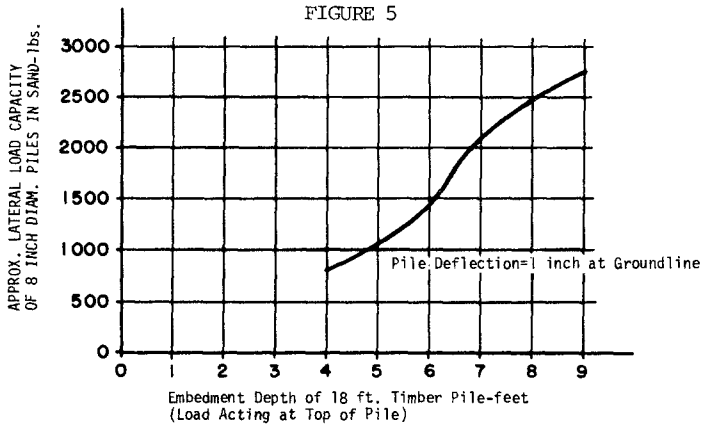




TABLE NO. 1

TABLE OF ESTIMATED ULTIMATE STATIC PILE CAPACITIES  
FOR 8 INCH TIMBER PILES

BEACH HOUSE STRUCTURES  
LOCATED IN COASTAL AREAS

APPROXIMATE GROUND ELEVATION: 0

SUBSURFACE SOIL PROPERTIES  
\*\*\*\*\*

LAYER NO.	LAYER TOP DEPTH	UNIT WT, PCF	FRICT ANG, DEG	CONST K	ADHESION PSF	POINT BRG FACTOR, NO
*****	*****	*****	*****	*****	*****	*****
1	0	60	33	1	0	30

ESTIMATED ULTIMATE CAPACITIES-TONS  
\*\*\*\*\*

TIP DEPTH	TIP ELEV.	SKIN FRICT.	POINT CAPACITY	SHORT-TERM CAPACITY	LONG-TERM CAPACITY	TENSION CAPACITY	POTENTIAL DRAG LOAD
*****	*****	*****	*****	*****	*****	*****	*****
2	-2	.1	.6	.7	.7	.1	0
4	-4	.3	1.3	1.6	1.6	.2	0
6	-6	.7	1.9	2.6	2.6	.5	0
8	-8	1.3	2.5	3.8	3.8	.9	0
10	-10	2	3.1	5.2	5.2	1.4	0
12	-12	2.9	3.8	6.7	6.7	2.1	0
14	-14	4	4.4	8.4	8.4	2.8	0
16	-16	5.2	5	10.2	10.2	3.7	0
18	-18	6.6	5.7	12.3	12.3	4.6	0
20	-20	8.2	6.3	14.4	14.4	5.7	0

**EROSION + WAVELOAD SUM VS WIND LOAD**

The method suggested to proportion this damage is to add the average wave load on a pile (estimate number of piles in one row that wave might act on in a given instant and multiply by the individual pile load for the given water depth and divide by the total number of piles supporting the structure to determine the average wave load on each pile) to that lateral load capacity which might be lost by the decrease in embedment depth from erosion for the given pile condition. This load change could be attributed to the water while the wind loading placed on each pile would be attributed to the wind. These loads would be used to obtain a causal percent.

**CONCLUSION**

The estimates of storm load forces that might be applied to a beach house structure during a hurricane may provide a basis for assessing the cause of damage for a particular structure. A survey of the structure after the storm, some basic design data for the structure, and factual data about the storm will be needed. Generally the data needed will be:

1. The wind velocity and direction.
2. The still water depth.
3. The location of the structure relative to wave protection features such as sand dunes and other structures.
4. The size of structure and its orientation.
5. The elevation of the structure before the storm.
6. The amount of soil erosion around the structure foundation.
7. The bracing system used for piles-( X bracing or a concrete floor slab fixed to the piles at ground level etc.)
8. The type of damage that the structure sustained.
9. The condition of surrounding structures and the general type of damage which they sustained.

Using these data and the utilization methods that we have discussed, one should be able to make good judgments as to the cause of the damage-whether it be water or wind.

This method for assessing storm damage to beach houses may be used by insurance companies or adjustors to make realistic judgements of the relative cause of damage to structures which are subjected to both high winds and rising waters during natural weather phenomena. The factors presented and their potential for causing damage to beach house structures may be used to improve the initial design or to strengthen existing structures where such weather conditions are probable.

**EXAMPLES OF DAMAGE ASSESSMENT**

1. For waves breaking against the main beach house structure the very high loads would probably demolish the structure-flood water would be the primary cause of damage.
2. For erosion below foundations of a structure, the beach



Photographs of structure torn from its foundation. Wave and wind loads probably caused the damage.



Photograph of "X" braced structure that has received very little damage at ground level. Erosion of soils was approximately three feet.



Photographs of structure that was originally enclosed at ground level. Wave forces obliterated the ground level enclosure and the water eroded approximately four feet of sands from below the concrete slab. The wind loads, wave loads, and sand erosion probably caused the horizontal deflection of the supporting piles.



Photograph of piles that supported a structure that are broken. Excess wind loading probably caused these piles to break.



Photograph of leaning piles that supported a structure. Excess wind loading and loss of soil resistance from erosion probably caused this failure of the foundation.



Photograph of structure that is essentially undamaged except for leaning piles and obliterated stairs. The leaning piles were probably caused by a combination of excess wind loading and loss of soil resistance due to erosion of about two feet of sands. The obliteration of the stairs was probably caused by wave forces.



Photograph of structure foundation that is essentially undamaged. The wind forces probably tore the structure from the foundation leaving the floor attached to the piles. Most of this damage was caused by the wind forces.

house would probably collapse—flood water would be the primary cause of damage.

3. For a beach house elevated or located where waves did not reach the main structure and the foundations remain undamaged or where piles may be broken but that portion in soil remains plumb and undamaged—wind would be the primary cause of damage.

4. For a beach house where soil erosion occurred and/or waves broke against the piles plus wind loading on the piles— add the loss of pile capacity from erosion for decrease in embedment depth to the wave loading and compare that sum to the total wind load per pile to proportion the cause of damage to wind and water.

5. For some beach house locations where little to no evidence or data remains about the structure to make judgments about the cause—we suggest splitting the cause 50-50 between wind and water.

6. In all cases, use common sense along with as much analytical judgment as possible to assess damages.

## CHAPTER ONE HUNDRED FIVE

### NUMERICAL MODEL FOR DUNE EROSION DUE TO WAVE UPRUSH

J. S. Fisher (1), M ASCE  
M. F. Overton (2), AM ASCE

#### ABSTRACT

The objective of the work presented herein is to quantitize dune erosion as a function of the swash mechanics. In order to achieve this aim, a numerical model is developed which solves the one dimensional continuity and momentum equations for depth and velocity of the swash at the face of the dune. These parameters are then used as input to the dune erosion model which predicts the extent of toe retreat of the dune as a function of time. Since the model is formulated in real time, both short and long term events may be simulated. This is particularly important in terms of understanding the short term event in which the dune and beach face do not achieve an equilibrium profile.

#### INTRODUCTION

The prediction of dune retreat due to storm processes is the subject of increasing concern in coastal engineering. Dunes are often used as the primary defense to coastal erosion and flooding. Previous efforts at predicting the rate of dune erosion have generally depended upon the development of a post-storm equilibrium profile, where the volume of sand lost from the dune is determined by the quantity of sand required to establish this profile, Hughes and Chiu (4), and Vellinga (7). Therefore, if the beach does not reach an equilibrium condition due to the specifics of the storm parameters, ie. storm duration, wave height, and/or storm surge, this method will over-predict the amount of dune retreat.

(1) Associate Professor, Department of Civil Engineering,  
North Carolina State University, P.O. Box 7908, Raleigh, NC  
27695-7908

(2) Assistant Professor, Department of Civil Engineering,  
North Carolina State University



The model described in this paper is being developed to predict the dune erosion for a single storm, and does not require that there be an equilibrium profile established at the end of the event. The model considers the size and position of the dune on the beach, the degree vegetated, and the strength and duration of the storm swash.

This somewhat unique approach to dune erosion modeling (where time is a true variable) depends upon an estimate of the actual volume of sand eroded from the base of the dune for each individual swash uprush. While there is a large body of literature dealing with the mechanism for beach erosion by wave swash, Dean and Maurmeyer (1), there is virtually no literature dealing with the scour of the dune.

#### METHODOLOGY

In order to quantitize the erosion due to the short term event, it was felt that the interaction between the mechanics of wave swash and sediment scour at the dune toe was of primary importance. A schematic of the idealized model is presented in Figure 1.

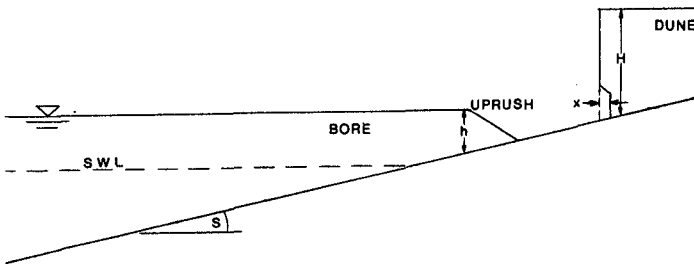


FIGURE 1. Schematic of the model components.

Important geometric considerations are the bore height, water depth, still water level, beach slope, dune height, and dune position on the beach. In addition to these geometric factors, the sand grain size and the density of plant roots are input parameters to the erosion model.

The uprush is modeled as a bore on a frictionless inclined beach following the work of Hibberd and Peregrine (3). The one dimensional equations for continuity and momentum are solved using a Lax-Wendroff solution technique yielding the velocity and depth of the bore as it moves up the beach to the dune. The Hibberd and Peregrine model was modified to include as a boundary condition on the landward side, the position of the dune. The dune acts as an impermeable vertical boundary to the uprush. Therefore, the numerical restraint is that the velocity is held to zero at the dune face. The initial conditions within the fluid are that the bore height is 1.6 times the water depth at the seaward boundary, a relationship shown in the data presented by Svendsen Madsen and Hansen (5), and with a velocity determined by the equations of equilibrium for a moving hydraulic jump. Elsewhere in the fluid domain the water depth is the still water level and the velocities are zero. As the equations are integrated in time, the bore propagates uniformly over the water and then decreases in height as it moves up the beach. As the swash hits the dune a reflected wave is formed and propagates seaward combining with the still advancing uprush. Eventually the bore recedes as the natural backwash.

The specific discharge of the uprush (depth times velocity) is considered to be the key parameter in determining the dune scour. Numerical results of the discharge versus time are presented in Figure 2 for three positions of the dune relative to the intersection of the still water level and the beach. The discharge is characterized by a rapid rise in magnitude, a period of relatively constant value (depending on the location of the dune), and a rapid decrease. The general trends are that the maximum value of the discharge decreases rapidly and the length of time that the bore is attacking the dune increases slightly as the distance of the dune toe up the beach increases.

The erosion at the base of the dune is then estimated by relating the volume eroded to the characteristics of the uprush. This is done on a 'per uprush' basis so that the time of uprush attack as well as the storm duration become important parameters in the estimation of the total amount of dune erosion per storm. This approach has been qualitatively evaluated using laboratory data from our 17 m wave flume. The assumption that the volume of scour at the base of the dune (per unit time) is a function of the specific discharge of the uprush appears to be a good first approximation, and is consistent with relationships derived for sediment transport in rivers, Vanoni (6). We are initiating a series of field experiments with prototype dunes at the U. S. Army Corps of Engineers Field Research Facility, at Duck, North Carolina, in order to more thoroughly evaluate this hypothesis.

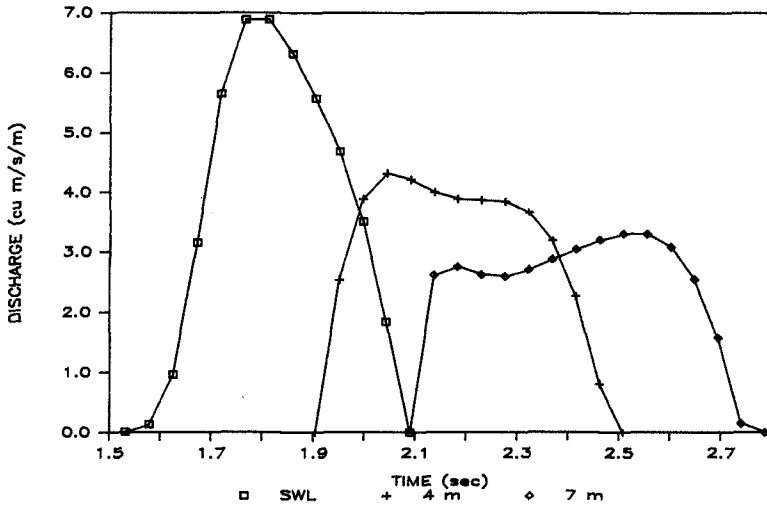


FIGURE 2. Specific discharge at the toe of the dune versus time for three positions of the dune relative to the intersection of the still water level and the beach face.

The scour at the base of the dune will ultimately cause the dune to fail. The depth of scour necessary to undermine the dune is a function of the properties of the dune sand, the degree of water saturation, and the density of plant roots. The latter can be significant, as shown in the work of Gray and Leiser (2).

This maximum scour is computed as:

$$D = c/ws + (w/ws)(H/2(\tan(\phi)))$$

where  $D$  = maximum depth of scour before the dune fails, m,  
 $c$  = sand cohesion, Pa (function of root density, as shown by Gray and Leiser (2)),  
 $ws$  = specific weight of the sand, N/cu m,  
 $w$  = specific weight of the water, N/cu m,  
 $H$  = dune height, m,  
 $\phi$  = friction angle.

The current model assumes that the volume of sand that fails is distributed at the toe of the dune and that the process of attack of the swash on the face of the dune is repeated. The dune is said to retreat when the volume of sand eroded exceeds that in a column of sand equal to the depth of the scour times the original height of the dune. At this point, the specific discharge of the swash is recalculated given the new position of the dune. This procedure is summarized in Figure 3, a flow chart of the model.

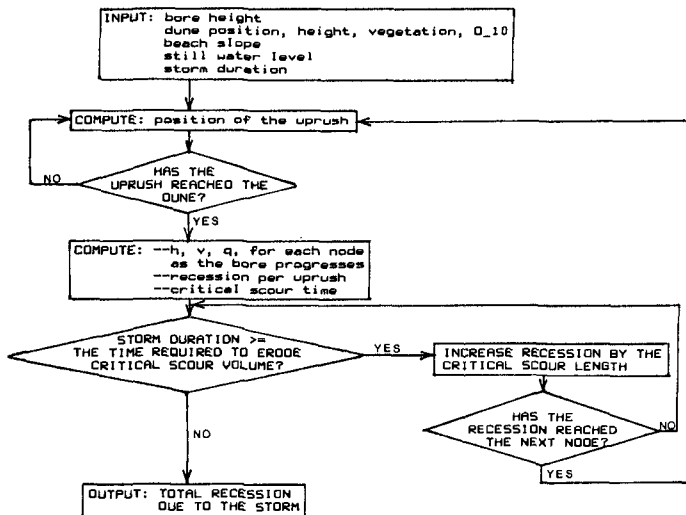


FIGURE 3. Flow chart of the uprush/dune erosion model.

#### SUMMARY

The model described in this discussion is still in the early stages of development. The additional laboratory and field data which will be collected in the next phase of this research will result in changes and refinements to the present form of the model. The ultimate objective of this work is to develop a dune erosion model which can be coupled to a shoreline erosion model such as the one described by Dean and Maurmeyer (1). Thus, the dune model would serve as an erodable landward boundary for the shoreline model.

## ACKNOWLEDGEMENT

This research is being supported with a grant from the University of North Carolina Sea Grant Program.

## REFERENCES

1. Dean, R.G. and E.M. Maurmeyer, 1983. Models of Beach Profile Response, Handbook of Coastal Processes and Erosion, ed. P.D. Komar, CRC Press, Inc., Boca Raton, Florida.
2. Gray, D.H. and A.T. Leiser, 1982. Biotechnical Slope Protection and Erosion Control, Van Nostrand Reinhold Company, N.Y., N.Y.
3. Hibberd, S. and D.H. Peregrine, 1979. Surf and run-up on a beach: a uniform bore. Journal of Fluid Mechanics, 95 (2): 323-345.
4. Hughes, S.A. and T.Y. Chiu, 1981. Beach and Dune Erosion During Storms. Coastal and Oceanographic Engineering Department, University of Florida.
5. Svendsen, I.A., Madsen, P.A., and J. Buhr Hansen, 1978. Wave characteristics in the surf zone, Sixteenth Coastal Engineering Conf., Vol. 1, 520-539.
6. Vanoni, V.A. (ed.) 1975. Sedimentation Engineering, American Society of Civil Engineers, Headquarters of the Society, N.Y., N.Y.
7. Vellinga, P., 1983. Predictive computational model for beach and dune erosion during storm surges. Coastal Structures '83: 806-819.

## CHAPTER ONE HUNDRED SIX

### A NEW OSCILLATORY FLOW TUNNEL FOR USE IN SEDIMENT TRANSPORT EXPERIMENTS

David B. King Jr., A.M.ASCE 1  
John D. Powell 2  
Richard J. Seymour, A.M.ASCE 3

#### ABSTRACT

The details of a new oscillatory flow tunnel at Scripps Institution of Oceanography are discussed. The flow tunnel has a large cross-section and large water excursion distance. The piston motion is programmable. The test bed can be tilted. These, and other aspects, make the facility useful to a wide variety of oscillatory flow sediment transport experiments.

#### INTRODUCTION

A new research facility, an oscillatory flow sediment transport tunnel, has recently been completed at the Hydraulics Laboratory, Scripps Institution of Oceanography, University of California, San Diego. The facility simulates many aspects of sediment transport on beaches, and its primary purpose is to be used in experiments which increase the understanding of granular-fluid mechanics in oscillatory flows. The facility is shown in Figure 1. It is built in the shape of a flat U-tube with a long, rectangular, center section and cylindrical risers on either end. When being operated, the facility is completely filled with water, and a piston in one of the vertical risers creates an oscillatory flow which moves sediment in the test section (the center portion of the horizontal section). The main components of the facility, as shown schematically in Figure 2 from right to left, are:

- 1) a hydraulic ram which drives the piston,
- 2) the piston and piston cylinder,
- 3) a flow straightener and turbulence decay section,

- 
- 1 Research Assistant, Scripps Institution of Oceanography, California, USA
  - 2 Development Engineer, Scripps Institution of Oceanography, La Jolla, California, USA
  - 3 Associate Research Engineer, Scripps Institution of Oceanography, California, USA



FIGURE 1: Photograph of the Oscillatory Flow Tunnel at Scripps Institution of Oceanography.

- 4) a sediment trap,
- 5) the test section,
- 6) a pivot with jack to tilt the entire facility,
- 7) a recirculating pump,
- 8) a second trap, decay section and flow straightener, and
- 9) a reservoir.

### DESCRIPTION OF THE FLOW TUNNEL

#### TEST SECTION

The maximum oscillatory water particle displacement in the test section is 1.75 meters. At a minimum period of 3.5 seconds, the maximum sinusoidal velocity is 1.6 m/s. A maximum steady flow of 0.2 m/s, driven by the recirculating pump, can be superimposed upon the oscillatory flow. The steady flow can be run in either direction.

The test section is 39 cm wide by 40 cm high. The working cross-section with a 10 cm deep sand bed is 39 cm by 30 cm. The test section is 7.0 meters long (four water particle excursion lengths). The test section has clear acrylic plastic side walls (3.2 cm thick) and top wall (5.0 cm thick). These are externally reinforced by steel I-beams. The thick sides and lid were designed to minimize deflection and consequent attenuation of the water column velocity.

At the center of the test section, there is a window on each side that is unobstructed by external supports for 1.75 meters (a maximum excursion length). This can be used for photography or other visual observations. The other windows vary in length from 50 to 75 cm. The bottom (also I-beam reinforced) is made of fiberglass coated plywood.

The top of the entire test section is hinged and sealed with an O-ring. It can be opened with a hand-operated worm screw winch to allow easy access to the test bed. Between experiments, the bed is re-leveled by means of a cart, which rides on the top surface of the side walls (the O-ring sealing surface). The cart has an adjustable wiper blade which extends down to plane the bed. When in operation, the lid is clamped shut at each vertical I-beam support. The lid has a series of small ports which can be used to inject dye into the tunnel and to purge trapped air bubbles.

The test section is an integral part of a deep steel truss framework which was designed for minimum structural deflection with a full water load. When filled with water and unsupported at the ends, the maximum deflection of the truss is approximately 3mm. During construction, an initial camber was fabricated into the truss so that when loaded, the test section would become flat.

#### TRAP AND TURBULENCE DECAY SECTIONS

There are identical sediment traps at each end of the test section. These sections are 1.75 meters long (an excursion length) by 39 cm wide



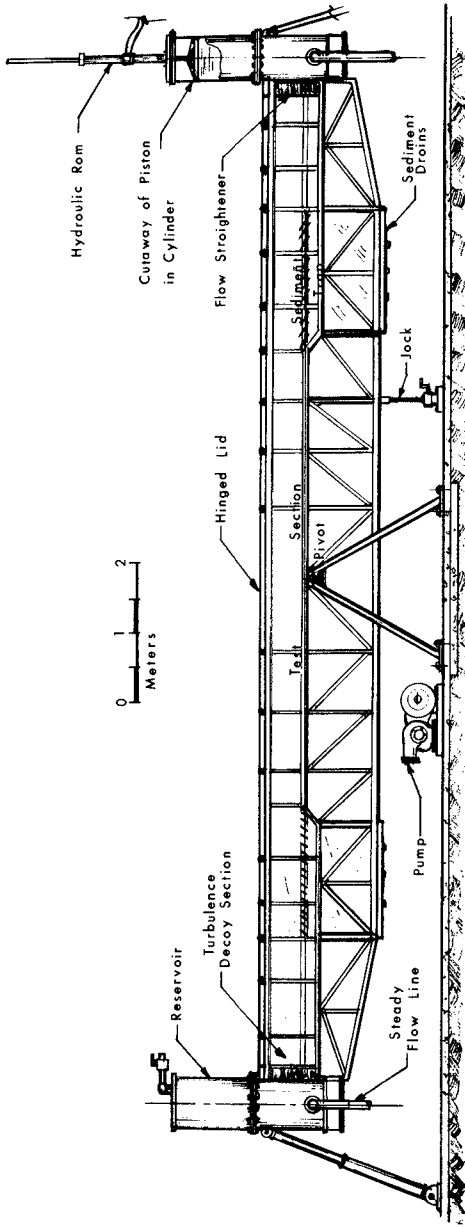


FIGURE 2: Schematic of the Oscillatory Flow Tunnel showing the important sections.

by 1.41 meters deep. Between each trap and vertical riser, there is a turbulence decay section. The turbulence decay sections are 1.75 meters long, by 39 cm wide by 57 cm deep. One of the two side walls of the trap and decay sections is made of I-beam reinforced clear acrylic plastic (3.2 cm thick). The other side and the bottom are made of I-beam reinforced, fiberglass coated plywood. The top of the trap and decay section is also a hinged clear acrylic plastic lid (5.0 cm thick), sealed in the same manner as the test bed lid. The three lids allow easy access to the entire horizontal portion of the facility.

The sediment traps have servo actuated, horizontal, louvered covers. When a trap is the upstream trap, the louvers close, and the water flows past a flat plate boundary. When the flow reverses and a trap becomes the downstream trap, the louvers open to allow the sand to enter the trap. The louvers are actuated by the same electronics that control the piston motion. An offset can be added to account for a superimposed steady flow.

The sediment is both carried into the trap by gravity and by a small current. This current exits the trap through a one-way valve and then flows beneath a false bottom in the turbulence decay section and finally into the vertical riser. The one-way valve stops any return current when the flow reverses.

The top of the trap covers are nominally 2 cm below the level of the sand bed (32 cm from the top of the channel). However, this elevation has been made adjustable to allow for changes in the sand bed thickness or the distance between the top of the bed and the top of the louvers. The louvers can be set anywhere between 27 and 37 cm from the top of the channel.

There are nine rectangular funnels which cover the bottom of each trap (arranged 3 x 3) with a drain valve beneath each. These allow the sediment to be removed. The three center funnels (on the lengthwise axis of the facility) are each 10 cm wide and are the only ones used to collect data. The sediment that collects in the outside funnels are affected in unknown ways by the side walls of the channel and trap covers. The bottom of the trap is bolted to the sides and sealed with an O-ring. The bottom, with the funnels and drains attached, can be dropped out to allow further access to the trap area.

The turbulence decay section has a false bottom whose elevation is adjustable to match the elevation of the louvers. Beneath the false bottom is the one-way flow section described above. In each turbulent decay section next to the vertical riser, there is a flow straightener. This consists of a cloth screen sandwiched between two pieces of honeycomb. The screen is a fine mesh plankton net (nominal 0.05 mm mesh size opening) which stops sand from reaching the vertical risers (and the piston O-ring). The honeycomb nearest the vertical riser has 4.7 mm (3/16th inch) stainless steel cells. Its primary purpose is to support the screen. The honeycomb on the test section side supports the screen and also (along with the screen) acts to eliminate the large scale turbulence created by the elbow in the flow. This honeycomb is made of packed soda straws (double hole coffee stirrers) 12.5 cm long by nominally 1.5 mm in diameter.

## PISTON

The piston is driven by a hydraulic ram mounted directly above it. The ram moves the piston in response to an electronic input signal which modulates a 2.5 liter per second (40 gpm) Moog electro-hydraulic servo valve. Hydraulic fluid is supplied by a 22 kW, 21 MPa (3000 psi) hydraulic power supply. This system allows the piston to be moved in any reasonable manner, not only sinusoidally as would be the case with a piston rod mounted eccentrically on a flywheel. Thus, Stokes wave motion or random wave motion are easily produced.

Oscillatory water motions are created digitally on an IBM PC XT computer. The computer is equipped with a MetraByte Dascon-1 board that provides the digital to analog converter (DAC), producing a varying +/- 5 VDC signal. This signal is converted to a modulated 2 kHz signal by a Vetter FM Recorder Adaptor and recorded on a standard audio cassette tape. The cassette tapes are then available for repeated use as an input signal for the piston.

During operation, the recorder outputs the demodulated +/- 5 VDC signal. A pair of 10 turn pots (for redundancy), attached to a gear rack on the piston rod, track the piston position. A servo amplifier sums the recorder signal with the negative feedback signal from the position pots. As the input signal changes, the output of the servo amp tends to move away from zero. This signal is fed to the servo valve which opens one of two high pressure hydraulic ports, moving the ram in the appropriate direction and thus changing the feedback voltage which decreases the magnitude (absolute) of the servo amp signal. In this way, the position of the piston is an accurate analog of the input signal. The servo system also allows manual adjustment of the piston position for use during filling and other system checkout. A sight gauge, attached to the outside of the piston cylinder, allows accurate manual positioning.

The piston has a working stroke length of 0.75 meters and a diameter of 0.62 meters giving a displacement volume of 0.22 cubic meters. The piston head is fabricated from clear acrylic plastic to allow for observation of trapped air. The air can be removed by a purge valve in the piston face. The piston cylinder is made from heavy wall steel tubing, precisely machined, coated with aluminum metal spray, and top coated with sprayed fused teflon. The seal is a teflon coated O-ring.

If the piston were to accidentally travel too far in either direction, the hydraulic ram would stop the piston abruptly at the end of the ram's excursion length. Under operation, this could easily cause a water hammer of serious proportions. To avoid this problem, both mechanical and electronic safeguards were installed in the system. An electronic safety circuit automatically shuts the system down if any of a number of conditions occur. These include the piston going outside a specified range, the piston traveling at too high a velocity, the pressure in the tank exceeding a specified limit, or the two feedback pots not agreeing on the piston position. The position feedback pots provide the position signal which is differentiated to obtain the

velocity. The pressure limit is provided by a pressure switch set at 62 kPa (9 psi). The safety circuit uses a series of comparators to monitor these signals. When an unsafe condition is sensed, an electric dump valve to the main hydraulic power supply is opened which bypasses the hydraulic flow to the piston servo system.

Should this safeguard system fail, a passive mechanical system would disconnect the piston face from the water column, and still avoid a water hammer. If traveling upward, before the ram reaches the end of its stroke, the piston will unseat from the piston cylinder. If the piston is traveling downward, before the ram reaches the limit of its stroke, the piston will push out a blow-out plug by shearing four restraining pins. The blow-out plug is the entire bottom of the vertical riser. Thus, water will drop out of the vertical riser, avoiding the over pressure of a waterhammer. Water pressure on the face of the blow-out plug will cause the pins to shear at pressures exceeding +/- 88 kPa (12.7 psi). Along with the piston face, the blow-out plug is made of steel braced clear acrylic plastic for visual inspection of the interior of the vertical cylinder.

#### RESERVOIR

The other vertical riser acts as a reservoir and has the only air-water interface in the system. The air in the reservoir is open to the atmosphere through a quarter turn PVC valve. This valve is open when the tank is being filled and can be opened or closed during operation. If closed, the air in the reservoir acts as an air spring which decreases the power requirements on the piston. By initial adjustment of the water level in the airspring before closing the vent valve, the midpoint of the alternating pressure range can be offset with respect to atmospheric pressure. There is a sight gauge on the reservoir to monitor the water level during filling and experimentation. A second blow-out plug, identical to the one beneath the piston, forms the bottom of the reservoir.

#### STEADY FLOW

A 15 hp, high head centrifugal pump is used to superimpose a steady flow on the oscillatory flow in the facility. The steady flow system is shown schematically in Figure 3. A 35 meter long inertia section is used to reduce pressure from the high head pump. Consequently, the oscillating pressures in the tank cause only a small change in the total head seen by the pump. Since the pump has a relatively flat pressure vs flow curve, the changing pressures in the tank cause a negligible change in the pump flow.

The flow goes through a bank of five different sized valves connected in parallel. This allows a large number of flow velocities (32) in the tank to be easily and reliably reproduced. The flow then goes through a four-way valve which directs the flow to and from either end of the tank. The steady flow enters and leaves the tunnel in the vertical risers and so the water flows through the flow straighteners before reaching the test bed.

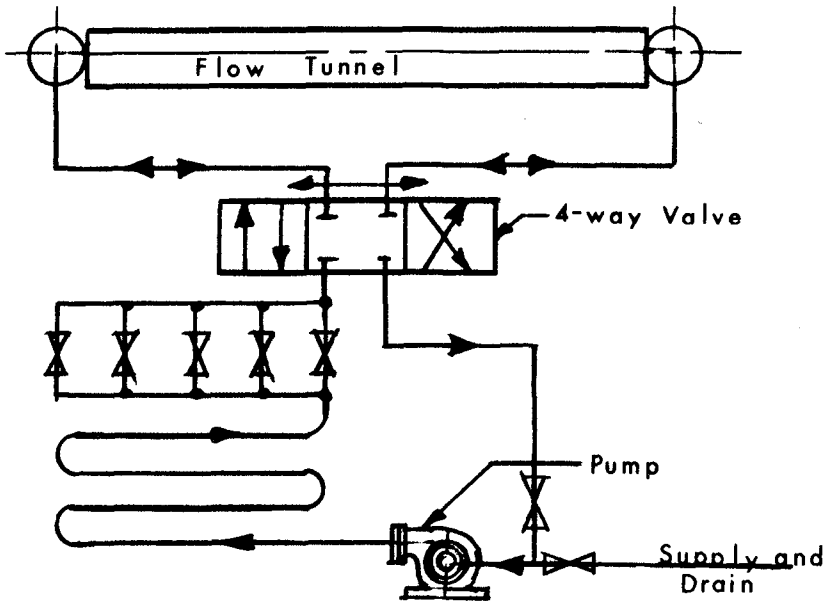


FIGURE 3: Schematic of the steady flow system.

The same pump is also used to fill the tunnel. Water is drawn from a wave basin, another facility at the Hydraulics Laboratory. The wave basin has a large expanse of shallow water. Since this acts as a settling basin, the water used in the oscillatory flow tunnel is free of both fine sediment and air bubbles.

#### TILT

In order to simulate the effects of cross-shore sediment transport on a sloping beach, the entire facility can be tilted between  $-5.7$  degrees and  $+9.1$  degrees from the horizontal. The pivot point is located at the bottom of the center of the test section. A hand-operated worm screw jack, which changes the tilt, is located near one of the sediment traps. One degree of tilt is produced by 40 crank handle turns. There are adjustable braces at the ends of each vertical riser to help support the facility and to minimize vibrations.

Physically, the facility is nearly symmetrical about the pivot point. Thus, experiments can be duplicated by completely reversing the flow, tilt, etc., to check for any bias in the system. The only asymmetries are that the facility tilts above 5.7 degrees only in one direction and that there is a piston only at one end. The piston causes larger pressure excursions at one end than the other. However, the flow is driven by the derivative of pressure,  $dp/dx$ , not the magnitude of the pressure itself.

#### FLOW FIELD IN THE WATER TUNNEL

In the water tunnel, the fluid is oscillated in a closed rectangular tube over a test bed. There is no free surface and thus waves are not formed. In the test section, there are thin boundary layers along each wall. The rest of the fluid (the core region) moves irrotationally. The boundary layers do not grow to meet in the middle as they do in steady pipe flow.

The flowfield does not entirely duplicate wave motion in that there are no vertical oscillatory velocities and no horizontal oscillatory variations in velocities. Longshore currents, turbulence associated with breaking waves, percolation flow, etc., are also not produced. However, the horizontal flowfield produced by an Airy wave can be exactly reproduced in the water tunnel, both in the boundary layer and in the core region. The horizontal fluid velocities of a Stokes wave can be exactly reproduced in the core region or at any one elevation in the boundary layer. The flow at all other elevations is closely approximated.

The turbulence generated in this facility is a factor that has been carefully considered. Since the turbulent structure of the surfzone is very poorly known, an attempt has been made to isolate the test bed from all turbulence sources except the turbulence generated at the bed boundary layer. Thus the sediment transport in this facility most closely resembles the cross-shore bed load transport seaward of the breaker zone on a beach. The design requirement has been that the rms artifact turbulence level in the sediment test section should be much much less than the fall velocity of the sediment. The fall velocities of the sediments (grain diameters of .1 to 1 mm) are on the order of 1 to 10 cm/s.

Artifact turbulence could be convected or diffused to the test bed from the flow straighteners. Also the turbulence produced by the side and top wall boundary layers of the test section could diffuse to the bed. The flow straighteners are located two excursion lengths from the ends of the test section. Theory and observation have shown that the turbulence generated by these structures decays before it can diffuse or be convected to the test section. Likewise, theory and observation have shown that the turbulence generated by the side walls of the test section do not influence the test bed other than at the very edges. Since sediment from only the middle 10 cm of the 39 cm wide test bed is used in data collection, results are not affected by the turbulence created by the side (or top) wall boundary layers.

TABLE I: COMPARISON OF OSCILLATORY FLOW TUNNELS

	1	2	3	4	5	6	7	8	9
Type of design	U tube	loop	U tube	U tube	loop	dbble U	U tube	U tube	U tube
Driving mech	cmp air	hyd ram	cmp air	cmp air	ecc fly	ecc fly	hyd ram	ecc fly	hyd ram
Type of flow	sinu	random	sinu	sinu	sinu	sinu	random	sinu	random
Max Amp (m)	3.5	2.4	.46	.41	2.0	1.2	.34	.75	.80
Mean flow (m/s)	0	0.6	0	0	0.6	0	0.2	0	0.2
Tot Length (m)	17.	13.	5.0	4.0	15.	5.0	12.	6.0	16.
Bed Length (m)	10.0	9.1	1.8	3.0	12.	2.5	2.0	2.0	7.0
Flow Height (m)	.31	2.3	.31	.048*	1.0	.30	.40	.25	.30
Bed Width (m)	.41	.51	1.2	.025*	.50	.21	.30	.25	.39
Meas Sed Trans	no	no	no	no	no	no	no	yes	yes
Max Bed Slope	flat	flat	flat	flat	flat	flat	flat	flat	9.1 deg

\* 51 mm diameter circular pipe

1 Technical University, Denmark. Lundgren and Sorenson (1958), Jonsson (1963), Jonsson and Carlsen (1976), Staub, Svendsen, and Jonsson (1983).

2 Wallingsford, England. Dedow (1966), Rance and Warren (1968).

3 Georgia Institute of Technology. Carstens (1966), Carstens and Neilson (1967), Carstens, Neilson and Altinbilek (1969).

4 McMaster University, Hamilton, Canada. Chan, Baird and Round (1972).

5 Queens University, Kingston, Canada. Morgridge and Kamphuis (1972), Reidel, Kamphuis and Brebner (1972), Brebner and Reidel (1973), Kamphuis (1975), Brebner (1980).

6 National Bureau of Standards, Washington, D.C. Lofquist (1975), Lofquist (1977), Lofquist (1978), Lofquist (1980).

7 Delft Hydraulics Laboratory, The Netherlands. Hulsbergen and Bosman (1980).

8 University of Tokyo, Japan. Horikawa, Watanabe, and Katori (1982).

9 Scripps Institution of Oceanography, University of California, San Diego.

COMPARISON WITH OTHER WATER TUNNELS

A number of other water tunnels have been reported in the literature. The characteristics of these are shown in Table 1. Some of these tunnels have been used without sediment to study the nature of fluid boundary layers. Others have had sand beds and have been used to study the initiation of sediment motion and or the structure and growth of ripples. Only one tunnel, reported in Horikawa, et al, 1983, has been used thus far to measure sediment transport.

As can be seen from Table I, the Scripps tunnel is one of the larger tunnels that have been built and one of the more versatile. It is unique in that it is the only tunnel with a test bed whose slope can be adjusted.

REFERENCES

- 1 Brebner, A., 1980, "Sand Bed-Form Lengths Under Oscillatory Flow," Proc 17th Coastal Eng Conf, ASCE, Chap 81. pp1340-1343.
- 2 Brebner, A., and P.H. Reidel, 1973, "A New Oscillating Water Tunnel," J Hydraulic Res., 11:2, pp107-121.
- 3 Carstens, M.R., 1966, "Similarity Laws for Localized Scour," J Hydraulics Div., ASCE, 92, HY3, May, pp13-36.
- 4 Carstens, M.R. and F.M. Neilson, 1967, "Evolution of a Duned Bed Under Oscillatory Flow," J Geophys Res., 72:12, June, pp3053-3059.
- 5 Carstens, M.R., F.M. Neilson, and H.D. Altinbilek, 1969, "Bed Forms Generated in the Laboratory Under an Oscillatory Flow: Analytical and Experimental Study," TM-28, CERC, U.S.Army Corps of Engineers, June, 83pp.
- 6 Chan, K.W., M.H.I. Baird, and G.F. Round, 1972, "Behavior of Beds of Dense Particles in a Horizontally Oscillating Liquid," Proc Royal Soc of London, Series A, 330, pp537-559.
- 7 Dedow, H.R.A., 1966, "A Pulsating Water Tunnel for Research in Reversing Flow," Houille Blanche, 7, pp837-841.
- 8 Horikawa, K., A. Watanabe and S. Katori, 1983, "Sediment Transport Under Sheet Flow Condition," Proc 18th Coastal Eng Conf., ASCE, pp1335-1352.
- 9 Hulsbergen, C.H. and J.J. Bosman, 1981, "A Closely Responding, Versatile Wave Tunnel," Proc 17th Coastal Eng Conf., ASCE, pp310-317.
- 10 Jonnson, I.G., 1963, "Measurements in the Turbulent Wave Boundary Layer," Proc 10th IAHR Congr., 112:85-92.



- 11 Jonsson, I.G., 1978, "A New Approach to Oscillatory Rough Turbulent Boundary Layers," Series Paper 17, ISVA, Tech Univ Denmark, 87pp.
- 12 Jonsson, I.G. and N.A. Carlsen, 1976, "Experimental and Theoretical Investigations in an Oscillatory Turbulent Boundary Layer," J of Hydraulic Res., 14:1, pp45-60.
- 13 Kamphuis, J.W., 1975, "Friction Factor Under Oscillatory Waves," J Waterways, Harbors and Coastal Eng Div., ASCE, 101:WW2, May, pp135-144.
- 14 Lofquist, K.E.B., 1975, "An Effect of Permeability on Sand Transport by Waves," CERC TM-62, U.S.Army Corps of Engineers, 74pp.
- 15 Lofquist, K.E.B., 1977, "A Positive Displacement Oscillatory Water Tunnel," CERC MR 77-1, U.S.Army Corps of Engineers, 26pp.
- 16 Lofquist, K.E.B., 1978, "Sand Ripple Growth in an Oscillatory-Flow Water Tunnel," CERC, TP 78-5, U.S.Army Corps of Engineers, 103pp.
- 17 Lofquist, K.E.B., 1980, "Measurements of Oscillatory Drag on Sand Ripples," Proc 17th Coastal Eng Conf., ASCE, Chap 186, pp3087-3106.
- 18 Lundgren, H. and T. Sorensen, 1958, "A Pulsating Water Tunnel," Proc 6th Coastal Eng Conf, ASCE, pp356-358.
- 19 Mogridge, G.R. and J.W.Kamphuis, 1972, "Experiments on Bed Forms Generated by Wave Action," Proc 13th Coastal Eng Conf., ASCE, pp1123-1142.
- 20 Rance, P.J. and N.F. Warren, 1968, "The Threshold Movement of Coarse Material in Oscillatory Flow," Proc 11th Coastal Eng Conf., ASCE, pp487-491.
- 21 Riedel, H.P., J.W. Kamphuis and A. Brebner, 1972, Measurement of Bed Shear Stress Under Waves," Proc 13th Coastal Eng Conf., ASCE, Chap 31. pp587-603.
- 22 Staub, C., I.A. Svendsen and I.G. Jonsson, 1983, "Measurements of the instantaneous Sediment Suspension in Oscillatory Flow by a New Rotating-Wheel Apparatus," Progress Report 58, Inst. Hydrodyn. and Hydraulic Engrg., Tech Univ Denmark, pp41-49.

## CHAPTER ONE HUNDRED SEVEN

### BEACH RESPONSE TO LONG PERIOD LAKE-LEVEL VARIATION

by

William L. Wood<sup>1</sup> and Lee L. Weishar<sup>2</sup>

#### ABSTRACT

A 4-year set of beach and offshore profiles, measured at monthly intervals, is evaluated to determine the effect of wind-wave forcing and long period (1 year or greater) lake-level variation on beach profile change in the "tideless" Great Lakes. This evaluation indicates two distinct regions of change in the beach and nearshore area of these profiles. The beach-berm region responds directly to lake-level modulation of wind-wave forcing. This response occurs on two time scales (seasonal and long period), but always in direct relation to mean lake-level variation. The inner-bar actively changes under the influence of wind-waves, but appears to lack a well-defined seasonal pattern. Empirical eigenfunction analysis is applied to these data in order to statistically quantify the significance of these observed changes. This analysis provides confirmation of a hypothesized long-period (years) variation of the beach and berm in direct response to lake-level variation.

#### INTRODUCTION

Changes in beach profile are caused by variations in incident wave energy conditions and by changes in mean water level position. The seasonal onshore-offshore movement of beach sediment, caused by variations in incident wave conditions, has been discussed by numerous investigators [Shepard (9), Bascom (4), Sonu and Van Beek (10), and Aubrey et al. (1)]. Quantification of seasonal beach profile changes has been achieved by Winant et al. (13) and Aubrey (2)

---

<sup>1</sup>Department of Civil Engineering, Purdue University, West Lafayette, Indiana 47907; current address Chief/Engineering Development Division, Coastal Engineering Research Center, Vicksburg, Mississippi 39180-0631.

<sup>2</sup>Coastal Processes Branch, Research Division, Coastal Engineering Research Center, Vicksburg, Mississippi 39180-0631.

for oceanic coasts. Similar quantification of offshore and beach changes on a tideless coast has been carried out by Weishar and Wood (12).

Beach profile changes caused by variation in mean water level position occur on two time scales. Short-term changes (30 days or less) result from both tidal fluctuations and storm wave set-up. Long-term changes (1 year or greater) are related to eustatic or hydrologic changes along a coast. Bruun (5) developed a conceptual model which assumed that beach and offshore profile slope and position is maintained in direct response to a rise or fall in mean sea-level. This concept, known as equilibrium beach theory, is of special interest for the Great Lakes where annual and longer term variations in mean lake-level range from 50 to 200 cm. Hawley and Judge (8) and Hands (6 and 7) evaluated changes in offshore and beach profile in response to rising lake-level in Lake Michigan. Hands (7) discussed a "general sequence of response to increased water levels" which included shoreward migration of longshore bars and shore recession. Weishar and Wood (12) were able to quantify a relationship between offshore profile adjustment and lake-level rise and fall. Specifically, they showed that profile changes offshore from the inner bar (approximately 100 m offshore) were directly related to the mean annual variation in lake-level. However, Weishar and Wood (12) were not able to find a similar direct relationship between beach recession and advance and, respectively, rise and fall in lake-level. This result seems contrary to expectation from physical reasoning concerning the coastal process-response system.

The primary objective of this paper is to show how wind-wave forcing and long-term lake-level variations affect seasonal and long-term changes in beach profile of sandy "tideless" coasts of the Great Lakes. A 4-year set of precisely measured offshore and beach profiles has been collected at monthly intervals from the southern end of Lake Michigan (Figure 1). Empirical eigenfunction analysis is used to statistically quantify annual and long-term mean lake-level variation influences on beach profile adjustment. Short-term (30 days or less) variability is identified in this paper, but attention is focused primarily on long-term (1 year or greater) variability.

#### PHYSICAL SETTING

This study was conducted along the southeastern shore of Lake Michigan within the Indiana Dunes National Lakeshore, Indiana (Figure 1). This region is characterized by straight, medium-grained sand beaches, with coarse-sand and pebble-sized deposits intermittently present at the beach step and in the swash zone. The beach slopes gently offshore and is terminated onshore by glacial ridges or sand dunes ranging from 10 to 40 m in height. Figure 2 shows a generalized cross section of the beach and offshore region which is characterized by at least two well-defined submarine bars. The outer bar is located approximately 160 m offshore in 2.5 to 3.0 m of water. This bar is relatively stable but may be destroyed

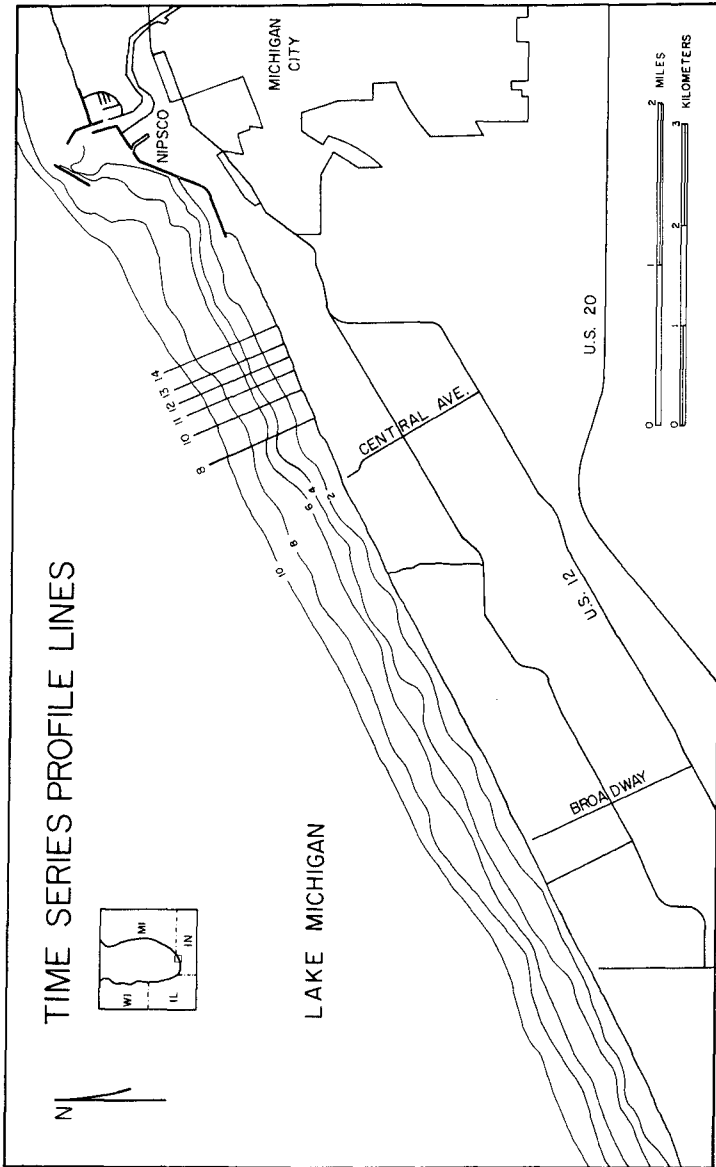


Figure 1. Study site location map.

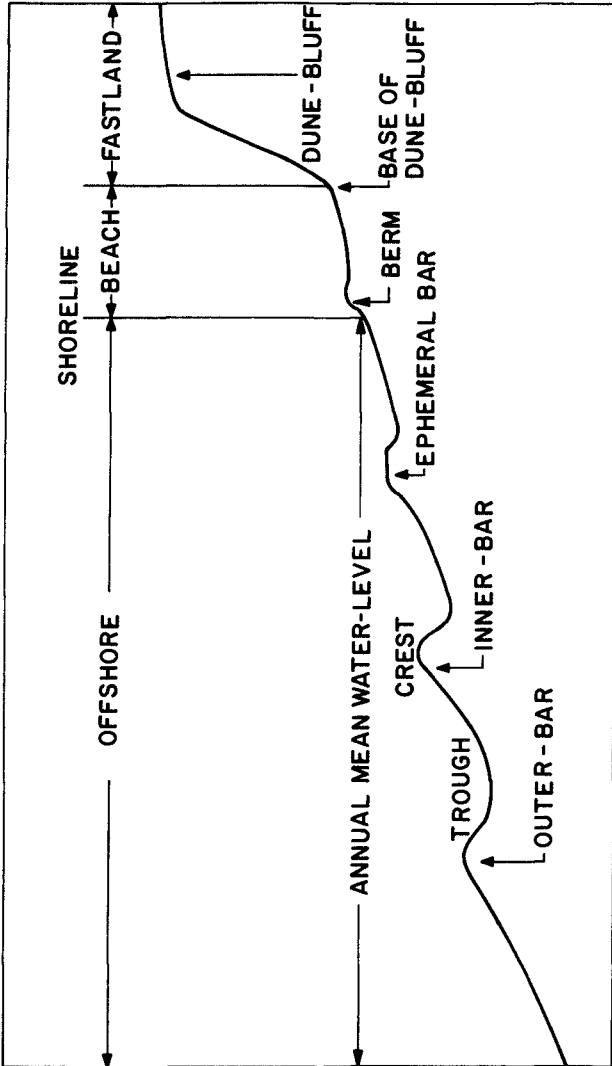


Figure 2. Beach profile showing characteristic features.

intermittently during passage of high-intensity storm events. The inner bar is located 60 to 90 m from shore in 1.0 to 1.5 m of water. This bar is more active than the outer bar because of frequent occurrence of waves breaking over its crest.

The study area lies within a closed littoral cell approximately 20 km in extent [Corps of Engineers (11)]. This cell is bounded by the Michigan City breakwater updrift (shown in Figure 1) and Burns Harbor breakwater downdrift. Sediment is supplied to this cell from the coastal ridge and dune system shoreward and to a much lesser extent from small streams located within the cell. Predominate wave activity is from the north, which causes a net longshore transport of sand towards the southwest. Net littoral-transport rates along this length of coastline are approximately  $4.6 \times 10^4$  m<sup>3</sup>/yr [Corps of Engineers, (11)].

The beach in this region responds to seasonal variation in incident wave climate. During summer, average wave heights are less than 1.0 m, which results in a gradual onshore buildup of the beach profile. Late fall and winter storm waves reach heights in excess of 3.0 m at the outer limits of the offshore zone. These storm waves overtop the entire back-beach profile, which results in direct erosion of beach ridge and dune slopes. From late December until early April the offshore and beach zones are either covered with ice and snow or protected from wave activity by nearshore ice ridges. Small amounts of fine sediment are deposited along the profile as this ice melts in early spring. Most of this fine sediment is redistributed across the foreshore by initial wave activity following ice melting. In spring, following ice melting, ephemeral bars are observed between the inner bar and beach. These bars migrate shoreward under the influence of waves and eventually attach to shore, forming ridge-and-runnel systems. This migration of sediment initiates change from the eroded winter profile to onshore buildup of the summer beach profile.

The coastlines of the Great Lakes are essentially tideless. Variation in mean still-water level does occur on an annual cycle with a range from 0.2 to 1.0 m. Long-period (4 to 22 years) lake-level variations with a maximum range of nearly 2.0 m are also present on all the Great Lakes.

#### FIELD EXPERIMENT

A series of topographic surveys was initiated in the spring of 1976 to monitor changes in offshore and beachface profiles. Survey data were collected at monthly intervals from May through November of 1976, 1977, 1978, and 1979 along six range lines in southeastern Lake Michigan (Figure 1).

Elevation measurements were taken from dune base to offshore depths in excess of 10.0 m. A conventional theodolite and rod survey was used to measure elevations across the beach at 3.0-m

intervals. The shallow offshore region (0-3.0 m) was surveyed using a combination of rod soundings and fathometer soundings.

For those unfamiliar with the Great Lakes, it is important to note that early-morning lake-surface conditions can be "glassy" calm (no swell or local wind-waves present). Therefore, offshore surveys were conducted only during periods of essentially calm lake surface. Recognition of this condition helps to understand the reproducibility claimed in the following paragraphs.

A fathometer was used to profile the bottom from a depth of approximately 1.0 m to depths in excess of 10.0 m. These fathometer surveys overlapped the rod surveys by about 100 m in the shallow offshore region. All hydrographic surveys were conducted with a Raytheon Model DE-719-RTT precision survey fathometer. This instrument is capable of recording underwater topography in water depths between 0.5 and 125 m with an accuracy of  $\pm 0.5$  percent (of measured depth).

Prior to each run, the unit was calibrated to adjust for temperature effect on the speed of sound in water. Still-water level was measured and recorded so that all bathymetric profiles could be reduced to Low Water Datum (LWD) and changes in water-level elevation would not be misinterpreted as topographic changes.

The method for determining boat position during the fathometer runs utilized base stations set up on the beach. A theodolite was placed directly over a base station and the range line was established by turning a predetermined horizontal angle from an adjacent base station. Three to five buoys were positioned at fixed intervals along each range line. The distance from each buoy to the base station was measured with a Hewlett-Packard Model 3805A Distance Meter. The HP 3805A has a range of 1600 m and is accurate to within .02 m at a distance of 1000 m. A rod sounding was taken at each buoy to provide additional calibration checks.

The hydrographic survey was recorded as a continuous profile while the boat maintained a "constant" speed over the range line. The boat was kept on line by a shore observer siting through the theodolite and communicating with the boat driver by walkie-talkies. Tick marks were placed on the fathometer chart paper as each buoy was passed. Using this procedure, the maximum boat deviation was less than 2.0 m off the range line and maximum offshore deviation was  $\pm 3.0$  m.

#### OBSERVED SEASONAL PROFILE CHANGES

Four years of monthly beach and offshore bathymetric profile data were initially evaluated in order to identify dominant areas of profile change. This evaluation indicated three distinct areas of profile change: the beach-and-berm, the inner-bar, and the

outer-bar regions. Each of these regions was observed to vary independently of the other two.

The beach-and-berm region, in early spring, is typically found in a highly eroded, winter-beach configuration. Ephemeral bars are usually present in shallow water immediately adjacent to the beach. Beach-and-berm buildup begins in late spring and early summer. Ephemeral bars migrate shoreward under the influence of locally generated wind-waves and attach themselves to the beach. The beach-and-berm region continues to accrete throughout the summer months. This accretion results in a widening of the beach and a lakeward movement of the berm crest. This observed sequence of profile change is similar to that described by Bajorunas and Duane (3) for their beach and shallow-water bar region in Lake Superior.

The beach-and-berm region begins to erode in late fall and early winter because of the increase in frequency and intensity of local storms. As this region erodes, the berm crest shifts toward the back-beach while the overall slope of the beach decreases. It is not possible to monitor the offshore region during the late winter months (January-March) because of extensive ice cover. However, the beach-and-berm region remains in an eroded state until the following spring.

The inner-bar region shows no well-defined pattern of seasonal migration. During the 4 years of monitoring, the inner bar was observed to shift onshore and offshore apparently in response to local storms. Although a sequential shoreward migration of the inner bar was observed in summer 1976 (Figure 3), most movement in this region was less well ordered (Figure 4). The monthly movement of the inner bar appears to be independent of movements in the beach-and-berm or outer-bar regions. It is possible that the monthly survey interval was too long to be able to properly characterize inner-bar movement. This possibility is evaluated more thoroughly in the statistical results section of this paper.

The outer-bar region of the bathymetric profile exhibits a consistent seasonal migration pattern. The outer bar migrates onshore from early spring to early winter (Figure 3 and 4). In the following early spring, after ice breakup, the outer bar is observed to be offshore from its early-winter position. Apparently, the outer bar must move offshore during the period from early ice formation to ice breakup. This regular pattern of onshore-offshore migration of the outer bar is observed in each of the four survey years.

#### STATISTICAL ANALYSIS

Empirical eigenfunction analysis results in a set of eigen-vectors (empirical functions) and eigenvalues (mean square amplitudes) of a matrix of data thought to be composed of uncorrelated modes of variability. The primary reasons for using empirical eigen-functions to evaluate beach and offshore profile data are: (1) they



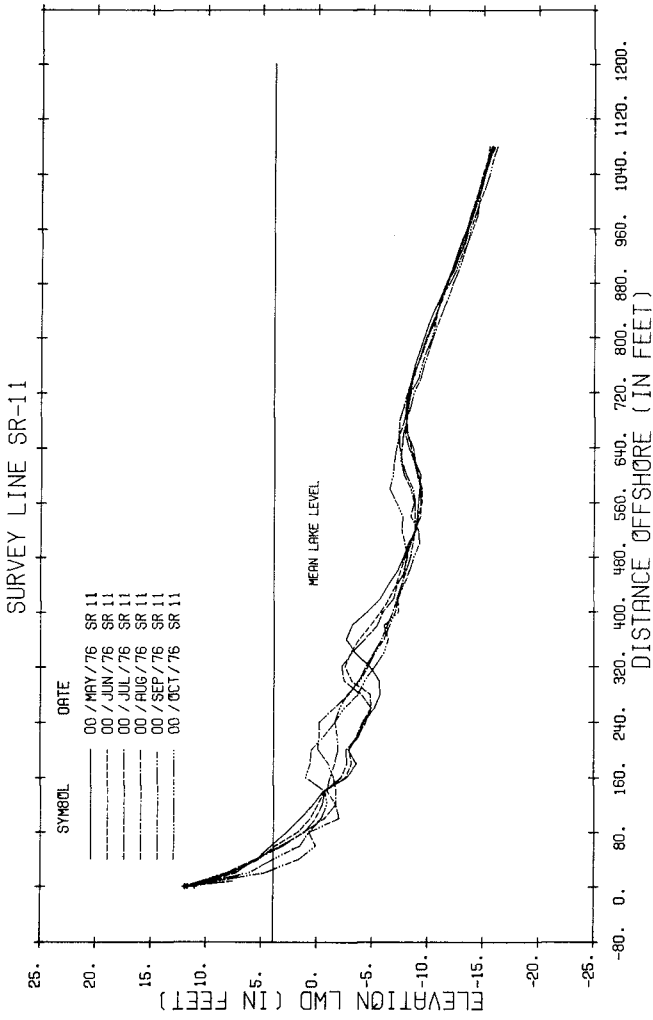


Figure 3. Sequential monthly profiles showing regular migration of the inner-bar.

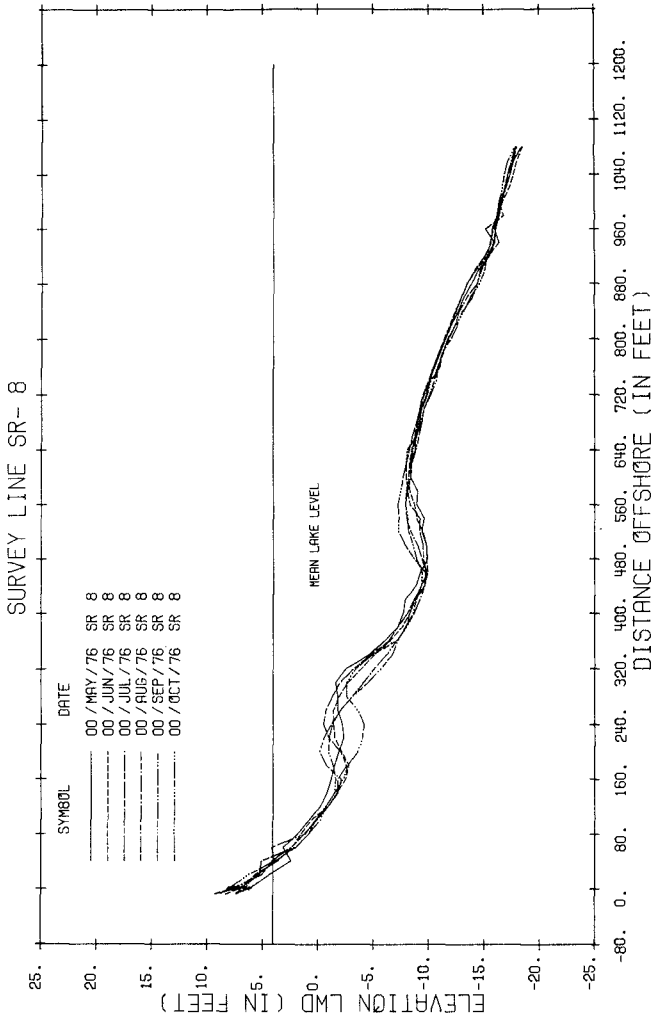


Figure 4. Sequential monthly profiles showing irregular movement of the inner-bar.

are assumed to be uncorrelated modes of variability of the data field, (2) they afford the most efficient method for compressing a data field, and (3) they simplify understanding procedures of minimum mean square error estimation. The details of this method can be found in many of the references mentioned earlier (see Winant et al. (13)).

In an earlier study Weishar and Wood (12) were successful in establishing a direct relationship between lake-level rise or fall and respectively an advance or retreat of the outer bar. However, they were unable to establish a similar direct relationship between beach recession and advance and respectively rise and fall in lake-level. This result is contradictory to Weishar and Wood's (12) model of beach and offshore profile response to long-term lake-level variation. The reason for this seeming contradiction is that sediment volume changes in the offshore bar system are large compared to beach volume changes. Beach response is, therefore, relatively insignificant in an empirical eigenfunction analysis of an entire cross-sectional profile of the beach and offshore zone. This analysis biasing should be rectified by simply truncating the cross-sectional profile data at a position shoreward of the outer bar trough.

A 4-year set of monthly beach and nearshore profiles, truncated on the offshore side of the inner bar (see Figure 2) was used to generate sets of empirical eigenfunctions. Each set of profile data began at the base of dune-bluff on the back beach and extended down the offshore side of the inner bar to a point where the same number of data points were included in each profile. Analysis of this data set should support the hypothesis that beach response on the "tideless" Great Lakes varies as a direct function of lake-level rise and fall.

## RESULTS

Statistical analysis of the monthly data sets using empirical eigenfunctions resulted in three primary eigenfunctions whose eigenvalues accounted for over 91 percent of the total mean square variance contained within the data (Table 1). The eigenfunction with the largest eigenvalue accounted for approximately 72 percent of the mean square value. This eigenfunction essentially reflects the mean of the beach and nearshore profile and is referred to as the mean-beach function. The time dependence of the mean-beach function shows little variation over the 4-year data interval.

The eigenfunction with the second highest eigenvalue accounted for approximately 9 percent of the total mean square value or 28 percent of the residual variance from the mean-beach function. This function shows a broad undulating minimum extending across the berm and beach and is identified as the beach-berm function. The time dependence of this function shows an annual trend with maxima in spring and early fall and a minimum in July. This

temporal trend corresponds directly with annual lake-level variation which reaches a maximum in July and a minimum in January-February.

The time dependence of the beach-berm function has a pronounced trend, across the zero amplitude line, which is continuous over the 4-year data interval 1976 to 1979. Such variation is characteristic of long period lake-level change. A comparison between the long period (annual) lake-level variation and the mean annual temporal variation of the beach-berm function tends to support the hypothesized relationship presented earlier in this paper. The cross-correlation coefficient between the mean temporal dependence of the beach-berm function and mean lake-level variation is 0.85 which is significant at a level of  $E = 0.01$ .

Table 1. Results of Composite 4-Year Empirical Eigenfunction Analysis

	SR-8	SR-10	SR-11	SR-13	SR-1
Eigen- value 1	74.6	68.5	72.9	64.3	70.5
Eigen- value 2	10.3(40.4)	12.4(39.3)	10.0(37.0)	16.4(45.9)	10.4(35.2)
Eigen- value 3	6.4(25.3)	9.6(29.0)	8.0(29.6)	9.7(27.3)	9.2(31.2)
Eigen- value 4	4.8(18.7)	5.8(18.5)	5.8(21.6)	6.0(16.9)	5.6(19.0)
Eigen- value 5	4.0(15.7)	3.7(11.9)	4.8(17.6)	3.5(9.8)	4.3(14.5)

NOTE: Number in parenthesis is percent of residual mean square variation after removing the first eigenfunction.

#### CONCLUSIONS

The preceding quantitative analysis has shown that long-term (1 year and greater) lake-level variation is a significant source of physical forcing on beach-berm topographic changes. It should be clarified that mean lake-level changes do not physically transport sediment in the beach erosion of the beach and offshore profile. Sediment transport in this region is related to long-term modulation of local wind-wave energy by mean lake-level change. The best correlation between the temporal response of the beach-berm function and lake-level response occurs on an annual time scale.

However, there also appears to be a weaker but significant correlation between monthly variation in lake-level and beach-berm function response. Conversely, temporal response of the inner-bar function has no coherent trend throughout the 4-year monthly data sets. This may be a result of aliasing of data in the inner-bar region. It is reasonable to assume that the inner-bar, located in relatively shallow water (1.0-2.0 m) would be influenced by relatively small wind-wave events. The time scale of meteorologic system movement through the lower Great Lakes (3 to 7 days) is clearly less than the 30-day sampling interval.

As a direct result of this analysis the beach-berm portion of beach and offshore profiles on the "tideless" Great Lakes can be modelled using the same approach suggested by Weishar and Wood (12). However, their model should now have greater sensitivity of predicted response in the beach-berm region. Predictions of long-term coastal adjustment to lake-level and seasonal wave climate can now be extended to the entire beach and offshore profile of a Great Lakes coastline.

#### REFERENCES

1. Aubrey, D. G., Inman, D. L., and Nordstrom, C. E., 1976, Beach Profiles at Torrey Pines, California: Proc. Fifteenth Int. Conf. on Coastal Eng., Am. Soc. Civil Engineers, p. 1297-1311.
2. Aubrey, D. C., 1979, Seasonal Patterns of Onshore/Offshore Sediment Movement: Jour. Geophys. Res., v. 84, p. 6347-6354.
3. Bajorunas, L. and Duane, D. B., 1967, Shifting Offshore Bars and Harbor Shoaling: Jour. Geophys. Res., v. 72, p. 6195-6205.
4. Bascom, W. H., 1954, Characteristics of Natural Beaches: Proc. Fourth Conf. on Coastal Eng., Am. Soc. Civil Engineers, p. 163-180.
5. Brunn, P., 1962, Sea-Level Rise As a Cause of Shore Erosion: Jour. Waterways, Harbors, and Coast Eng. Div., v. 88, p. 117-130.
6. Hands, E. G., 1976, Observations of Barred Coastal Profiles Under Influence of Rising Water Levels, Eastern Lake Michigan: Fort Belvoir, Virginia, U. S. Army Corps of Engineers, Coastal Engineering Research Center, pub. TR76-4, p. 1967-1976.
7. Hands, E. B., 1980, Prediction of Shore Retreat and Nearshore Profile Adjustments to Rising Water Levels on the Great Lakes: U. S. Army Corps of Engineers Technical Paper 80-7, 119 p.

8. Hawley, E. F. and Judge, C. W., 1969, Characteristics of Lake Michigan Bottom Profiles and Sediments from Lakeside, Michigan to Gary, Indiana: Proc. Twelfth Conf. Great Lakes Res., Int. Assoc. Great Lakes Res., p. 198-209.
9. Shepard, F. P., 1950, Beach Cycles in Southern California: Washington, D.C., U. S. Army Corps of Engineers Beach Erosion Bd., Technical Memorandum 20, 26 p.
10. Sonu, C. J. and Van Beek, J. L., 1971, Systematic Beach Changes on the Outer Banks, North Carolina: Jour Geology, v. 79, p. 416-425.
11. U. S. Army Corps of Engineers, 1971, Section III reconnaissance report--Michigan City Harbor, Indiana: Internal Report, Chicago District, U. S Army Corps of Engineers.
12. Weishar, L. L. and Wood, W. L., 1983, An Evaluation of Offshore and Beach Changes on a Tideless Coast: Jour. Sed. Petrology, v. 53, p. 847-858.
13. Winant, C. D., Inman, D. L., and Nordstron, C. E., 1975, Description of Seasonal Beach Changes Using Empirical Eigenfunctions: Jour. Geophys. Res., v. 80, p. 1979-1986.

## CHAPTER ONE HUNDRED EIGHT

### Beach and Dune Response to Severe Storms

David L. Kriebel and Robert G. Dean

#### ABSTRACT

A numerical model is developed and applied to estimate the frequency distribution of severe erosion events. The proposed method is an extension of existing Monte Carlo storm surge simulation models. Hurricane and tropical storm meteorological parameters are randomly selected to generate a series of synthetic storms; the storm surge for each storm is estimated using a Bathystrophic storm surge model. The storm surge hydrograph is then used as input to a numerical erosion simulation model which determines beach profile response for each storm based on wave energy dissipation per unit volume as a general erosion forcing mechanism. Five 100-year random simulations are performed from which the return periods of storm surge and erosion, i.e. volume eroded and dune recession, are estimated.

#### INTRODUCTION

While major advances have been made in recent years in the development of frequency distributions for storm surge elevations, little progress has been made with regard to forecasting the probabilities of extreme erosion events. Detailed estimates of storm surge frequencies are now commonly made through numerical simulation of the governing equations based ultimately on historical probabilities of the meteorological characteristics of severe storms. For erosion events, on the other hand, it has not been possible to utilize this combined probabilistic-deterministic approach, since little is known concerning the equations or boundary conditions that govern storm erosion.

The goal of this study is to develop a general methodology to forecast the frequency distribution of severe erosion events based on severe storms expected over a wide range of return periods. The proposed methodology includes two phases: 1) the development of a computational method for predicting erosion due to a severe storm of given characteristics, and 2) the incorporation of this method into a larger model which accounts for the probabilities of occurrence of severe storm events. The results of the study are pertinent to current efforts to estimate the extent of erosion expected during a major storm, say with a 100-year return period, which may be required for coastal insurance, zoning, construction regulation, or structural

---

Coastal and Oceanographic Engineering Department, University of Florida, Gainesville, FL 32611.

design. Likewise, an estimate of the frequency distribution of erosion events will aid in the interpretation of the severity of particular erosion events relative to other possible erosion events.

The most widely used techniques for predicting single-storm erosion are schematic or geometric methods that are adaptations of the so-called Bruun's Rule (Bruun (1962)), which was originally proposed for estimating erosion due to sea level rise. The schematic method most often cited in the literature is that of Edelman (1968); although similar procedures have been proposed by Dean (1984) and others. Typical assumptions used by these methods for predicting storm-induced erosion include: 1) longshore transport gradients are spatially averaged, therefore, beach response is governed by a conservation of the sand volume perpendicular to shore, 2) offshore sand transport is effectively limited by the breakpoint of incident waves, and 3) the post-storm profile is in a dynamic state of equilibrium relative to the peak storm surge level. This last assumption implies that the profile has sufficient time to reach equilibrium during the peak surge. Comparisons of these methods to field data, however, suggest that these methods typically overpredict erosion in some cases by more than a factor of five. In effect, these methods predict the maximum erosion potential of the peak surge, a value that is seldom realized in nature due to the relatively slow response of beaches to changing water levels.

Several researchers, including Swart (1974), Vellinga (1983), and Hughes (1983) have developed more realistic predictive methods based on empirical results of small and large scale laboratory tests. The most useful computational methods, of Swart and Vellinga, use the general schematic arguments of Edelman's method; however, through derived model laws and experimental results, the effects of almost all of the most important parameters in the dune erosion process are quantified.

At present, the literature includes only two general methods for estimating erosion frequencies. Vallianos (1974) applied peak storm surge levels associated with various return periods to estimate beach fill requirements for the same return periods, based on a modified form of Edelman's methods. In a more detailed approach, van de Graaff (1983) used the computational method of Vellinga to predict dune erosion probabilities as the result of seven parameters, each with a known or assumed probability distribution. Two methods are presented for estimating these probabilities; one is a complete integration of seven probability distributions, the other is an approximate method in which mean dune recession is estimated based on water level and wave height distributions. Variability of this estimate is then given by a normal distribution with a standard deviation defined by the other five parameters.

The overall objectives of the present study are the same as those of van de Graaff, namely to obtain a rational estimate of the erosion frequency distribution by combining a computational erosion model with the probabilistic components of forcing parameters. However, the specific methods proposed in this study are quite different



in several aspects. First, the erosion model proposed for estimating single-storm beach response is more deterministic and based on a numerical simulation of simplified governing equations including a proposed process-based sediment transport equation and the equation for continuity of sand. Therefore, the entire time-history of profile response is predicted directly, based on the time-history of the storm surge. The method is based on the equilibrium beach profile theory described by Dean (1984), and, like other methods, it is intended to be simple and schematic and does not attempt to represent many important surf zone processes. Finally, the estimation of erosion frequency distributions is accomplished through a Monte Carlo simulation procedure, which is a logical extension of existing methods for predicting storm surge frequencies. The Monte Carlo procedure has the advantages of simulating nature as realistically as possible and of being based on historical probabilities of meteorological parameters which are well defined in most areas.

Existing Monte Carlo storm surge simulation models, for example Fallah, et al. (1976), generally employ the following steps:

- Input consists of probability distributions of meteorological parameters and astronomical tide amplitudes.
- Artificial storms are assembled through random statistical sampling of the historical probability distributions.
- A deterministic model is used to generate hurricane, wind and pressure fields.
- A second deterministic model is used to generate storm surge.
- The storm surge and astronomical tide are randomly combined to give the total storm tide for each synthetic storm.
- When a sufficient number of storms have been simulated, the distribution of storm tide elevations is estimated through an extreme value analysis.

With the development of an efficient beach and dune erosion model, the methodology is easily extended as depicted in Figure 1. The storm tide for each storm is estimated based on a randomly assembled set of storm parameters. In this study, a simple Bathystrophic storm surge model initially proposed by Freeman, Baer, and Jung (1957) is used for efficiency. Breaking wave heights are also estimated for each storm. The deterministic erosion model is then used to generate the time-dependent erosion for each storm, relative to a common pre-storm profile, based on the time-histories of the storm tide and breaking wave heights. Finally, a frequency analysis is performed on the maximum erosion characteristics to give the frequency distribution of eroded volumes and dune recession.

#### EROSION MODEL - DEVELOPMENT

The beach erosion model is based on the premise that a beach profile will always move toward its most stable, equilibrium form in response to given input or forcing conditions. There is considerable empirical evidence to suggest that the general equilibrium form of beach profile may be approximated by a monotonic curve of the form

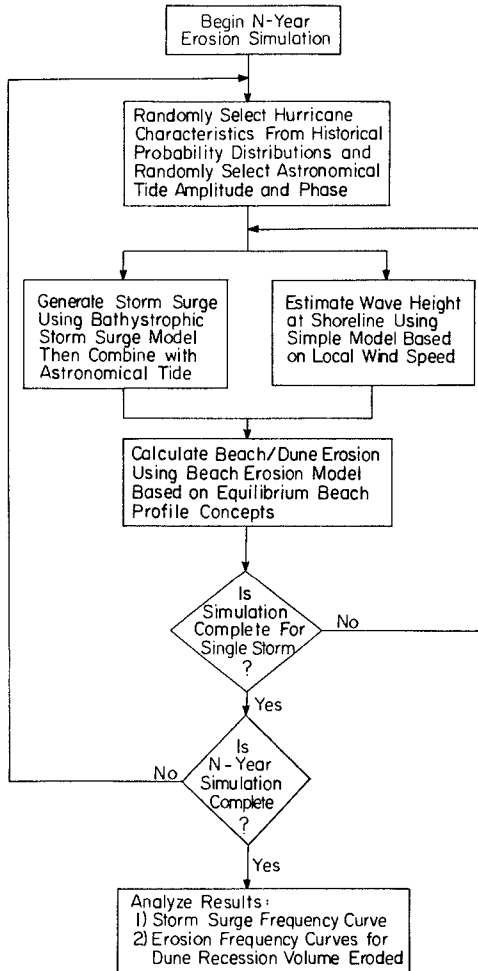
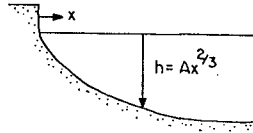


Figure 1. Flow Chart for Monte Carlo Storm Surge and Erosion Simulation.

$$h = Ax^{2/3} \tag{1}$$

which is the result of the uniform dissipation of wave energy per unit volume due to spilling breakers. As shown in Figure 2, the scaling parameter, A, may be theoretically related to a unique value of the energy dissipation per unit volume,  $D_*$ , which exists at all

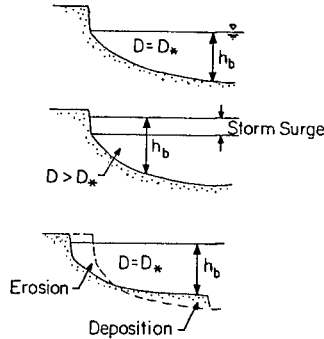
I. EQUILIBRIUM BEACH PROFILE FORM



based on uniform energy dissipation per unit volume where A is related empirically to sediment size and can be related to  $D_*$  by:

$$A = \left[ \frac{24}{5} \frac{D_*}{\gamma K^2 g^{1/2}} \right]^{2/3}$$

II. ENERGY DISSIPATION PER UNIT VOLUME  $D = \frac{1}{h} \frac{\partial F}{\partial x}$



III. SEDIMENT TRANSPORT EQUATION  $Q = K(D - D_*)$

Figure 2. Basic Concepts for Erosion Model.

points in the surf zone when the profile is in equilibrium. Analysis of over 700 beach profiles has provided an empirical relationship between sediment size and the equilibrium profile characteristics A and  $D_*$  as discussed by Dean (1984).

During a severe storm, the increased water level initially permits waves to break closer to shore. This effectively reduces the width of the surf zone and at the same time increases the energy dissipation per unit volume at all points in the surf zone. The profile is therefore "out of equilibrium" since actual energy dissipation levels are greater than the stable value,  $D_*$ . Based on the assumption that the profile will respond back toward equilibrium, the final result must be a widening of the surf zone until the actual energy dissipation equals  $D_*$ . This result can only be achieved by a net redistribution of sand over time, with erosion occurring nearshore and deposition pushing the breakpoint offshore.

Bakker (1968) and Swart (1974) have previously proposed that the net offshore sediment flux could be represented in terms of the

disequilibrium of geometric profile lengths. In a similar fashion, if energy dissipation per unit volume is assumed to be the general forcing mechanism, then the offshore sediment transport rate may be related to the excess energy dissipation per unit volume as:

$$Q = K(D - D_*) \quad (2)$$

in which K is a proportionality factor to be determined. In a concurrent study, Moore (1982) found K to be on the order of  $10^{-6} \text{ m}^4/\text{N}$ .

For numerical simulation of time-dependent profile response, the equation for sediment flux is coupled with the equation for continuity of sand in the onshore-offshore direction

$$\frac{\partial x}{\partial t} = - \frac{\partial Q}{\partial h} \quad (3)$$

which is then solved numerically. Details of the numerical simulation are presented by Kriebel and Dean (1984). As a brief summary, the surf zone is represented by a series of elevation contours of uniform width,  $\Delta h$ , with the distance,  $x$ , defined from a reference baseline to the center of each contour. The solution proceeds by raising the water level and establishing the offshore limit of the active profile at the breakpoint of incident waves. The energy dissipation per unit volume,  $D$ , and the sediment transport rate,  $Q$ , are then calculated throughout the surf zone. An implicit, linearized finite-difference scheme is used which yields a tridiagonal matrix relating the change in position,  $\Delta x$ , of three adjacent contours. This system is then solved by the so-called double-sweep procedure to determine the change in contour location,  $\Delta x$ , over each time step.

#### EROSION MODEL - RESULTS

General characteristics of the numerical solution appear to be consistent with natural and laboratory beach profile response. If an initial equilibrium profile with linear beach face slope and a distinct berm is subjected to an instantaneous increase in water level which is held steady as the system responds toward equilibrium, then the general solution for either berm recession or volumetric erosion exhibits nearly exponential behavior, approaching equilibrium asymptotically. This behavior agrees quite well with laboratory results of Saville (1957), Swart (1974), Vellinga (1983), and Hughes (1983). Numerical results for 0.2 to 0.3 mm sand and wave heights of 1 to 5 meters indicate that natural erosion time scales are on the order of 10 to 100 hours, thus indicating that equilibrium is probably not attained during typical storm conditions.

For practical application to single storm erosion simulation, the time-history of erosion may be estimated simply by inputting new water level and wave height conditions at each time step over the duration of the storm surge. In the example in Figure 3, the time-dependent erosion is predicted for an idealized storm surge hydrograph applied to a representative beach profile as discussed by

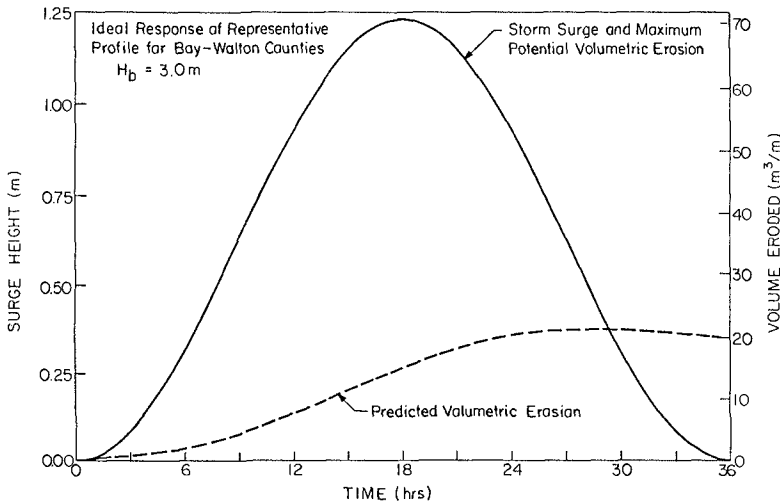


Figure 3. Time-Dependent Erosion Prediction for Idealized Storm Surge.

Kriebel and Dean (1984). In this case the right axis is scaled to the maximum erosion potential of the peak surge - a value that requires the peak surge level to be held steady for almost 300 hours.

This idealized example illustrates the general characteristics of the time-dependent erosion solution and reveals several features that seem representative of nature. First, the erosion potential of the peak surge is not realized during most storm events. Based on idealized cases with peak surge elevations of up to 3.6 m and 36 hour durations, only 14% to 36% of the maximum erosion potential is attained. Second, the erosion rate is maximum at about the time of the peak surge. Offshore transport processes respond at a slow rate relative to changing water levels, thus energy dissipation per unit volume, spatial gradients in sediment flux, and the erosion rate are all maximum at the time of the peak surge. Finally, the maximum erosion lags the peak storm surge. As the water level recedes, energy dissipation remains greater than equilibrium for some time causing erosion to continue.

A preliminary verification of the erosion model is obtained from a hindcast of erosion associated with Hurricane Eloise in the Florida Panhandle. The calibrated, Bathystrophic storm surge model is used to estimate the open coast storm surge and the predicted peak surge of 3.2 meters compares favorably to predictions of 3.2 meters by the National Weather Service (Burdin (1977)) and 2.9 m by Dean and Chiu (1982). This hydrograph is then applied to a schematic profile which is considered representative of the area of interest. A total of 20

test runs are made to simulate various combinations of beach slope, dune slope, wave heights, and water levels - both to test model sensitivity and since exact values cannot be specified for all parameters.

In a summary of results for all 20 test cases in Table 1, predicted volumetric erosion ranges from 20.8 to 38.4 m<sup>3</sup>/m with best estimates of 27.1 to 30.1 m<sup>3</sup>/m based on the parameters that best describe pre-storm and storm conditions. For comparison, Chiu (1977) gives average eroded volumes of 23.3 to 30.1 m<sup>3</sup>/m. Both observed and predicted erosion are in close agreement, especially when compared to the maximum erosion potential of 113 to 289 m<sup>3</sup>/m associated with steady-state peak surge levels.

Table 1. Comparison of Numerical Solution to Observed Erosion

	Volume Eroded m <sup>3</sup> /m	Dune Recession m
Range Predicted	20.8 to 38.4	4.8 to 9.5
Best Estimates	27.1 to 30.1	6.8 to 7.0
Observed (Chiu)	23.3* to 30.1*	2.7 to 6.1 (4.6 m contour) 7.2 to 12.8 (3.0 m contour)
Maximum Potential	112.9 to 288.6	33.5 to 76.2

\*Includes 5m<sup>3</sup>/m to reflect maximum erosion before recovery

As discussed by Kriebel and Dean (1984) dune steepening is not simulated in the model and this is evident in a comparison predicted and observed dune recession values. Predictions range from 4.8 to 9.5 m with best estimates of 6.8 to 7.0 m. Observed dune recession varies depending on the elevation contour and varies from 2 to 13 m with the 3.0 meter contour eroding about twice as far as the 4.6 m contour. However, predicted values are of the correct order of magnitude; this is further evidenced by the 33 to 76 m estimates of the maximum erosion potential of the same dunes.

It is emphasized that the predicted post-storm profiles such as shown in Figure 4 are not in equilibrium relative to the peak surge level and do not have the equilibrium  $Ax^{2/3}$  shape consistent with the 0.26 mm sand in the profile. The true equilibrium profile is attained only after the peak storm surge is maintained for about 1,000 hours after which equilibrium erosion values are up to 10 times the erosion predicted by the time-dependent storm surge.

#### ESTIMATION OF EROSION FREQUENCIES

As noted, the proposed erosion model is incorporated into a general Monte Carlo simulation model, as depicted in Figure 1, to obtain estimates of the frequency distribution of erosion events. Required input parameters include the probability of a hurricane or tropical storm occurring in a given year and the probability

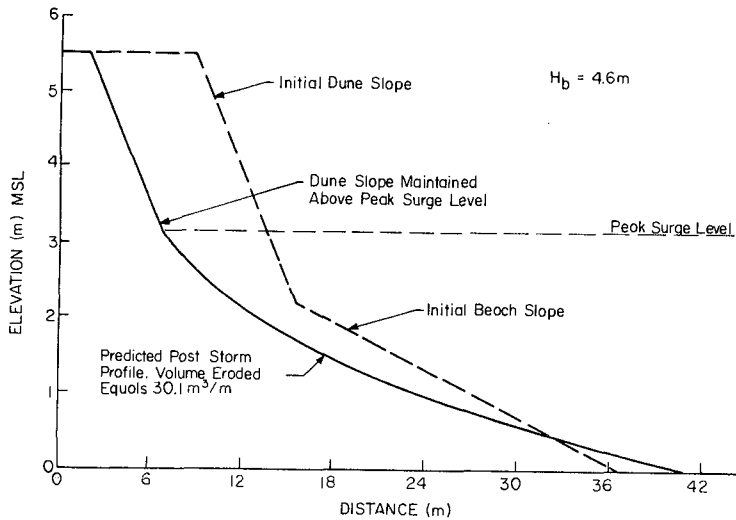


Figure 4. Example of Predicted Post Storm Profile, Hurricane Eloise.

distributions of various storm parameters which include the central pressure, radius of maximum wind, forward speed, direction of motion, and location of the storm track. Synthetic storms are assembled by selecting each parameter based on a separate uniformly distributed random number between 0 and 1. Once a storm is randomly assembled, the surface wind speed, pressure field, and storm surge are simulated at one-half hour time-steps. In this study, a one-dimensional Bathystropic storm surge model is chosen for simplicity and is calibrated through the bottom friction coefficient as described by Marinou and Woodward (1968), or Bodine (1971). The storm surge is then combined with a randomly-phased astronomical tide to produce the total storm tide.

While the storm tide serves as the principle driving mechanism in the numerical solution, an estimate of the breaking wave height is needed to serve as a boundary condition governing the surf zone width. A procedure similar to that used by Dean and Chiu (1982) is employed in which the maximum deepwater significant wave height of the hurricane is first determined according to the method of Bretschneider (1957). The local breaking wave height is then estimated by scaling the maximum deep water wave height according to the ratio of local wind speeds at the shoreline to maximum wind speeds in the storm. With the water surface elevation and breaking wave height at each time-step, the profile change over each time-step may then be determined with the erosion model. This is repeated for

each synthetic storm over the N-year period. Results of the procedure include the peak storm surge, maximum volumetric erosion, and maximum dune recession for each storm. Frequency curves are then determined for each variable based on a simple plotting position formula.

#### APPLICATION OF MONTE CARLO STORM SURGE - EROSION MODEL

As an example of the Monte Carlo procedure, five 100-year simulations have been carried out for Bay County, Florida. The five simulations include 63, 74, 67, 69, and 70 hurricanes and tropical storms respectively for an average of nearly 69 storms per 100 years over the 300 nautical miles of coastline considered. For each storm, the initial profile, representative of pre-Eloise conditions, is re-established so results may then be compared to observed erosion from Hurricane Eloise.

In Figure 5, the storm surge frequency curves of all five runs are presented and show the expected natural variability obtained from the Monte Carlo procedure. Storm magnitudes for lower return periods are well-defined; however, the 100-year storm surge estimate varies by about 1 meter. In order to reduce this variability, the five individual curves are averaged in Figure 6. While this average curve could also be bounded by confidence limits based on observed variability between different Monte Carlo simulations, several more runs would be required to obtain stable estimates of the standard deviations of each return period. The predicted average frequency curve is compared to the results of two other numerical estimates for the same area, indicating the validity of the procedure for estimating storm surge frequencies.

The frequency distributions for volumetric erosion from each of the five 100-year simulations are plotted in Figure 7. As expected, there is some variation between the five curves at 50 to 100 year return periods; however, the erosion curves are closely grouped at all return periods. Again, the five curves are averaged and the mean volumetric erosion, as well as dune recession, are extended to 500-year levels in Figures 8 and 9. Without empirical data on historical storm related erosion events, it is difficult to verify these randomly generated erosion frequency curves. However, the predicted values are in general agreement with guidelines for storm-related erosion given by the U.S. Army Corps of Engineers (1977) where the severity of open coast erosion is broadly classified as:

moderate storm	10 - 25 m <sup>3</sup> /m
extreme storm	25 - 25 m <sup>3</sup> /m
rare storm	50 - 125 m <sup>3</sup> /m

An interesting comparison can be made between the predicted frequency curves, in Figures 6, 8, and 9, and the observed storm surge and erosion characteristics of Hurricane Eloise. Although there is no data to firmly establish the peak storm surge level of Hurricane Eloise for the area of interest, if the predicted value of 3.2 m is accepted then it appears that Eloise may be associated with



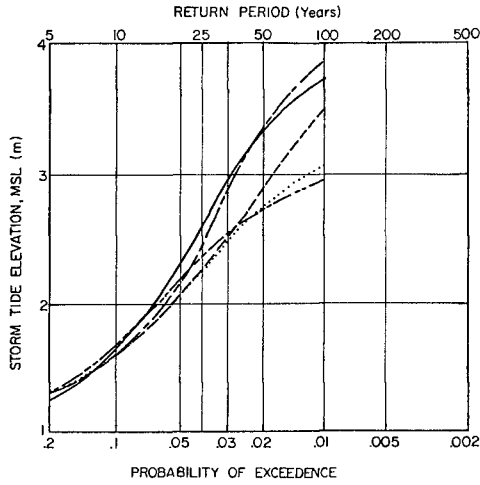


Figure 5. Results of Five 100-Year Simulations for Peak Storm Surge.

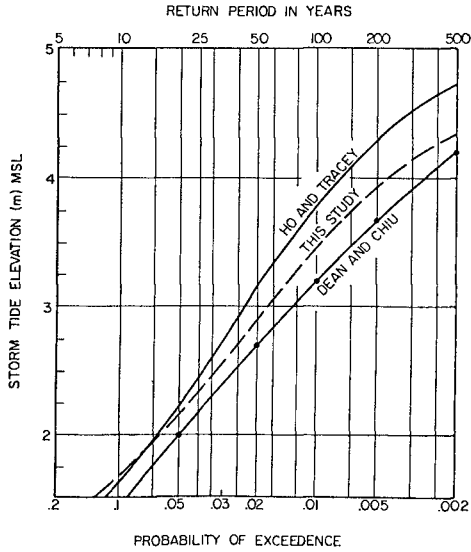


Figure 6. Comparison of Predicted Storm Surge Frequency Curves.

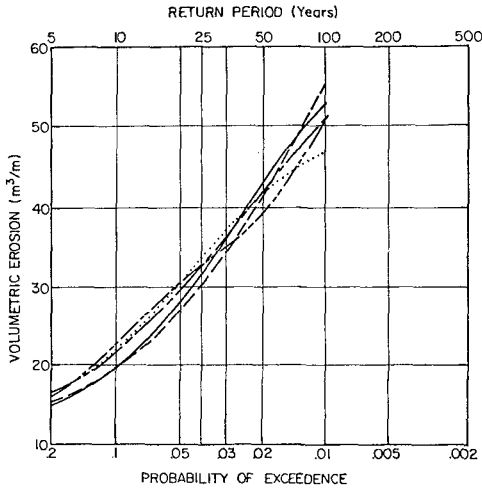


Figure 7. Results from Five 100-Year Simulations for Volume Eroded.

a return period of about 75 years. However, if observed erosion characteristics with a 9 m dune recession and an eroded volume of  $30.1 \text{ m}^3/\text{m}$  are considered, then from Figures 8 and 9, Hurricane Eloise should probably be classified as a 25 to 50 year storm in terms of its erosion damage. Since Hurricane Eloise was a rapidly moving storm of short duration, a relatively small percentage of its erosion potential was realized.

This conclusion is reinforced in Figure 10 where the peak storm surge is plotted against the predicted maximum volumetric erosion for all storms in one simulation run. It is evident that the largest storm surge levels do not always produce the greatest erosion. Likewise, several relatively small storms can produce significant erosion due to longer durations. The range of erosion values associated with Hurricane Eloise clearly fall below what would normally be expected for a storm of the same magnitude, i.e. peak surge. Certainly, storm duration and magnitude, not just magnitude alone, are important considerations when estimating erosion frequencies.

CONCLUSIONS

A numerical model has been developed which allows a first-order estimate of: 1) the time-dependent beach and dune erosion associated with tropical or extra-tropical storm surge and 2) the frequency distribution of extreme erosion events based ultimately on historical meteorological parameters of severe storms. The proposed erosion model is certainly in the developmental stages. Current research is being directed toward incorporating wave runup, variable beach slopes, and the formation of dune scarps. Also, a detailed

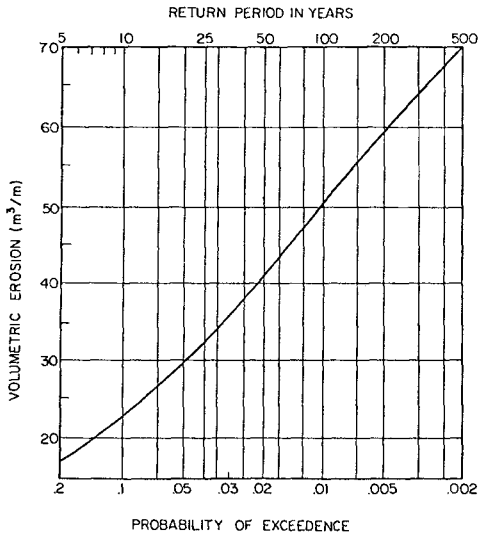


Figure 8. Predicted Frequency Curve for Volume Eroded.

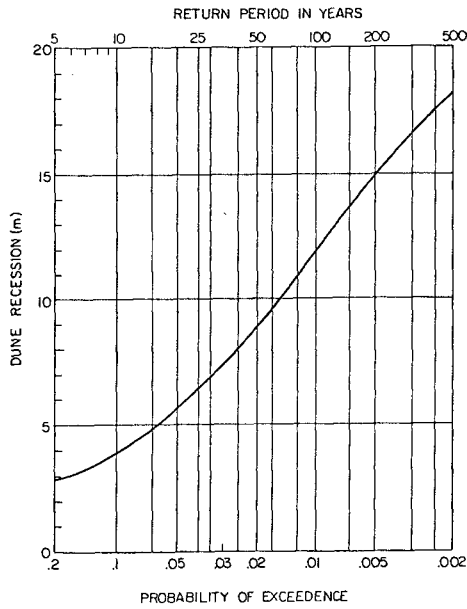


Figure 9. Predicted Frequency Curve for Dune Recession.

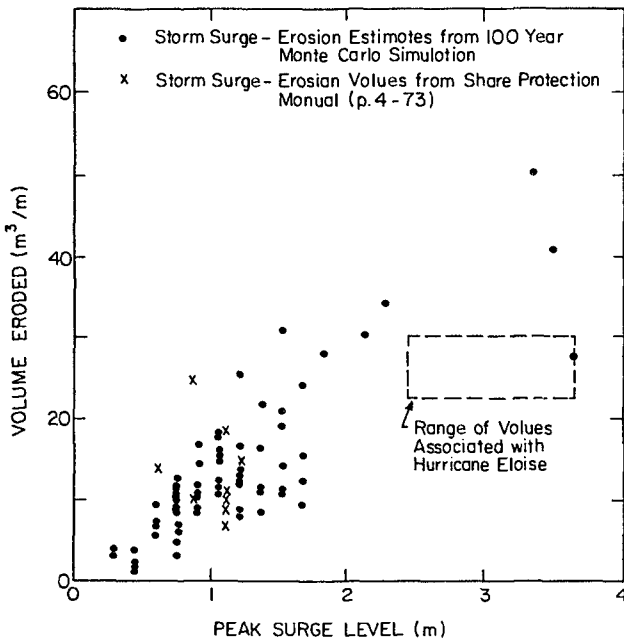


Figure 10. Comparison of Predicted Storm Surge and Volume Eroded for One 100-Year Monte Carlo Simulation.

calibration and verification of the model is being performed based on available field data on pre- and post-storm beach profiles from Hurricane Eloise.

Numerical estimates of erosion frequency distributions appear reasonable although verification is impossible without extensive field data on storm erosion. In general, however, the Monte Carlo procedure is well-verified for predicting storm surge probabilities. The method presented is a logical extension of the Monte Carlo technique that may permit the development of erosion frequency distributions for any open coast location in which historical meteorological parameters of severe storms are available.

#### ACKNOWLEDGEMENTS

The support of the National Oceanic and Atmospheric Administration, the University of Delaware Sea Grant College Program, and the Florida Department of Natural Resources is gratefully acknowledged. Ms. Cynthia Vey and Ms. Lillian Pieter provided excellent secretarial and drafting support, respectively.

## REFERENCES

- Bakker, W.T., "The Dynamics of a Coast with a Groyne System," Proc. 11th Conf. on Coastal Engineering, London, 1968.
- Bodine, B.R., "Storm Surge on the Open Coast: Fundamentals and Simplified Prediction," U.S. Army Corps of Engineers, CERC Tech. Memo No. 35, 1971.
- Bretschneider, C.L., "Hurricane Design Wave Practices," ASCE, Journal of Waterways and Harbors Div., WW2, May, 1957, p. 1-33.
- Bruun, P., "Sea-Level Rise as a Cause of Shore Erosion," Journal of Waterways and Harbors Division, ASCE, Vol. 88, WW1, Feb. 1962, p. 117-130.
- Burdin, W., "Surge Effects from Hurricane Eloise," Shore and Beach, Vol. 45, No. 2, April 1977.
- Chiu, T.Y., "Beach and Dune Response to Hurricane Eloise of September 1975," Coastal Sediments '77, ASCE, 1977, p. 116-134.
- Dean, R.G., "Application of Equilibrium Beach Profile Concepts," Proc. 19th Conf. on Coastal Engineering, Houston, 1984.
- Dean, R.G. and Chiu, T.Y., "Combined Storm Tide Analysis for Walton County, Florida," Florida Dept. of Natural Resources, Tallahassee, 1982.
- Edelman, T., "Dune Erosion During Storm Conditions," Proc. 11th Conf. on Coastal Engineering, London, 1968, p. 719-722.
- Fallah, M.H., Sharma, J.N., and Yang, C.Y., "Simulation Model for Storm Surge Probabilities," Proc. 15th Conf. on Coastal Engineering, Honolulu, 1976, p. 934-940.
- Freeman, J.C., Baer, L., and Jung, G., "The Bathystrophic Storm Tide," Journal of Marine Research, Vol. 16, No. 1, 1957, p. 12-22.
- Ho, F.P. and Tracey, R.J., "Storm Tide Frequency Analysis for the Gulf Coast of Florida from Cape San Blas to St. Petersburg Beach," National Weather Service, U.S. Dept. of Commerce, NOAA Tech. Memo. NWS HYDRO-20, 1975.
- Hughes, S.A., "Movable-Bed Modeling Law for Coastal Dune Erosion," Journal, Waterway Port Coastal and Ocean Engineering, Vol. 109, No. 2, May, 1983, p. 164-179.
- Kriebel, D.L. and R.G. Dean, "Numerical Simulation of Time-Dependent Beach and Dune Erosion," Submitted to Journal of Coastal Engineering for Publication Consideration, 1984.

- Marinos, G. and Woodward, J.W. "Estimation of Hurricane Surge Hydrographs," ASCE, Journal of Waterways and Harbors Division, Vol. 94, No. WW2, May, 1968, p. 189-216.
- Moore, B., "Beach Profile Evolution in Response to Changes in Water Level and Wave Height," M.S. Thesis, University of Delaware, 1982.
- Saville, T., "Scale Effects in Two-Dimensional Beach Studies," Trans. 7th Meeting of Intl. Assoc. of Hydraulic Research, Lisbon, 1957, p. A3-1 to A3-10.
- Swart, D.H., "Offshore Sediment Transport and Equilibrium Beach Profiles," Publication No. 131, Delft Hydraulics Lab., Delft University of Technology, 1974.
- U.S. Army Corps of Engineers, Coastal Engineering Research Center, Shore Protection Manual, U.S. Govt. Printing Office, 1977.
- Vallianos, L., "Beach Fill Planning-Brunswick, County, North Carolina," Proc. 14th Conf. on Coastal Engineering, Copenhagen, 1974, p. 1350-1369.
- van de Graaff, J., "Probabilistic Design of Dunes," Proceedings, Coastal Structures '83, April 1983, p. 820-831.
- Vellinga, P., "Predictive Computational Model for Beach and Dune Erosion During Storm Surges," Proceedings, Coastal Structures '83, April 1983, p. 806-819.

## CHAPTER ONE HUNDRED NINE

### THE NILE LITTORAL CELL AND MAN'S IMPACT ON THE COASTAL ZONE OF THE SOUTHEASTERN MEDITERRANEAN

by

Douglas L. Inman and Scott A. Jenkins

#### INTRODUCTION

Man's intervention with coastal processes takes many forms. However, the most serious large scale, long term coastal erosion results from the interception by dams of rivers supplying sediment to the coast. This loss of sediment may have catastrophic effects along coasts where streams discharge directly into coastal waters. The Nile littoral cell is an impressive example of the effect of dams on coastal erosion.

The Nile littoral cell is located in the southeastern Mediterranean Sea and extends 700 km from Alexandria, Egypt in the south to Akko, Israel in the north. The sediment load from the Nile River was deposited along the submerged portion of the delta, where it was sorted and transported to the east by the prevailing waves and by currents of the counterclockwise east Mediterranean gyre that commonly flows at about 50 cm sec<sup>-1</sup> over the delta. Prior to 1964, the turbid plume of the flood waters of the Nile River could be traced along the Mediterranean coast for over 700 km to the shores of Lebanon. Fine silt and clay sized material were carried easterly and into deeper water, while sand is carried easterly along the shelf and shore as far as Haifa Bay.

Until 1964, the major sediment source of the littoral cell was the Nile River. Construction of the High Aswan Dam, which began filling in 1964, has resulted in a near absence of Nile River flow into the Mediterranean and a corresponding complete loss of the Nile River as a source of nutrients to coastal waters, and as an active sediment source for the delta and the coastline of the Nile littoral cell. As a result, the Nile Delta is now subject to severe erosion in a number of localities.

#### GEOLOGIC SETTING

The physiography of the Mediterranean basin is best understood in terms of the tectonics of the moving plates of the lithosphere. The complex Mediterranean region results from the collision between the African and the Eurasian plates, a process that is gradually closing the Mediterranean Sea. In the eastern portion of the sea, under-thrusting of Mediterranean seafloor under the Eurasian continental plate has formed a broad zone of plate collision extending from the foot of Italy, eastward and to the south of Greece, Crete and Cyprus. The plate collision has resulted in a mountainous, volcanic belt north of and parallel

---

Center for Coastal Studies, Scripps Institution of Oceanography, La Jolla, California, 92093

to the zone of under-thrusting. The plate collision also has produced a series of transform faults caused by the adjustment of interplate continental fragments (e.g. Nur and Ben-Avraham, 1978; Ben-Avraham, 1978; Jongsma and Mascle, 1981). The tectonics is complicated locally by a spreading center in the Red Sea and its transform faults which includes the major Levant rift zone that cuts through the Gulf of Aqaba and the Dead Sea. Local adjustment faults occur in the Akko region that probably determine the location of Haifa Bay and Akziv submarine canyon.

#### Sea Level Changes

Fluctuations in the level of the Mediterranean Sea have been important factors in the cutting and filling of the Nile Valley, the formation of the delta, and the distribution of Nile River sediments. The Nile valley was cut to its maximum depth during the great Miocene desiccation about 24 m.y. (million years) ago when the Mediterranean was isolated from the world oceans, causing the sea to dry and become a salt pan. At that time the river cut a gorge deeper than the Grand Canyon of the Colorado. The valley began filling over its ancient delta when the Mediterranean filled during the Pliocene about 10 m.y. ago. The present Nile Delta has a sediment thickness of over 3.5 km along the continental shelf, and a sediment volume estimated to be  $350$  to  $387 \times 10^3 \text{ km}^3$  (Said, 1981; Ross and Uchupi, 1977; respectively).

There were many sea level fluctuations during the Pleistocene that resulted in Nile valley cut and fill and in different positions in the delta shoreline. Sea level rose from about -140 m, 15,000 years ago and is still rising at a rate of about 15 cm per century. The present sea level rise is a factor in coastal erosion, possibly accounting for a shoreline retreat of 10 to 15 m per century.

#### Distribution of Recent Sediments

Two major and distinct sediment types are found on the beaches and shelves of the southeastern Mediterranean Sea. A calcareous suite of sediments that consists of shell fragments and other organic detrital material, usually found near its origin, or of carbonate oolites thought to be brought as windblown sand from the western desert (Hilmy, 1951). Off the Nile Delta and elsewhere on the shelf, mounds of living coralline algae contribute coarse debris to the surrounding sediments (Coleman, et al., 1981).

The second sediment type consists of sand, silt and clay brought to the sea by the Nile River before the High Aswan Dam. The clay minerals include montmorillonite, kaolinite and illite. In the past, fine sediments from the Nile River have provided a major portion of the sediment fill of the eastern portions of the Levantine Basin between Cyprus and Lebanon (Venkatarathnam and Ryan, 1971; Nir, 1982a). The sand size fraction of this sediment consists predominantly of quartz with a distinctive admixture of heavy minerals. Amphibole (hornblende) and pyroxene (augite) are dominant and in nearly equal abundance; while the unique yellow-green and brown-violet varieties of augite are diagnostic for Nile sands (Shukri and Philip, 1960).

The Nile River is the only abundant source of sediment in the



eastern Mediterranean, and wherever these sediments are transported they have overwhelmed the sparse supply of calcareous sediment. During floods through the Rosetta mouth some Nile sediment has gone as far west as Ahu Quir headland. However, the prevailing winds, waves and currents of the east Mediterranean gyre have resulted in an easterly and northeasterly transport of Nile sediment. Nile sediment is dominant from Ahu Quir headland for 700 km to Akko on Haifa Bay.

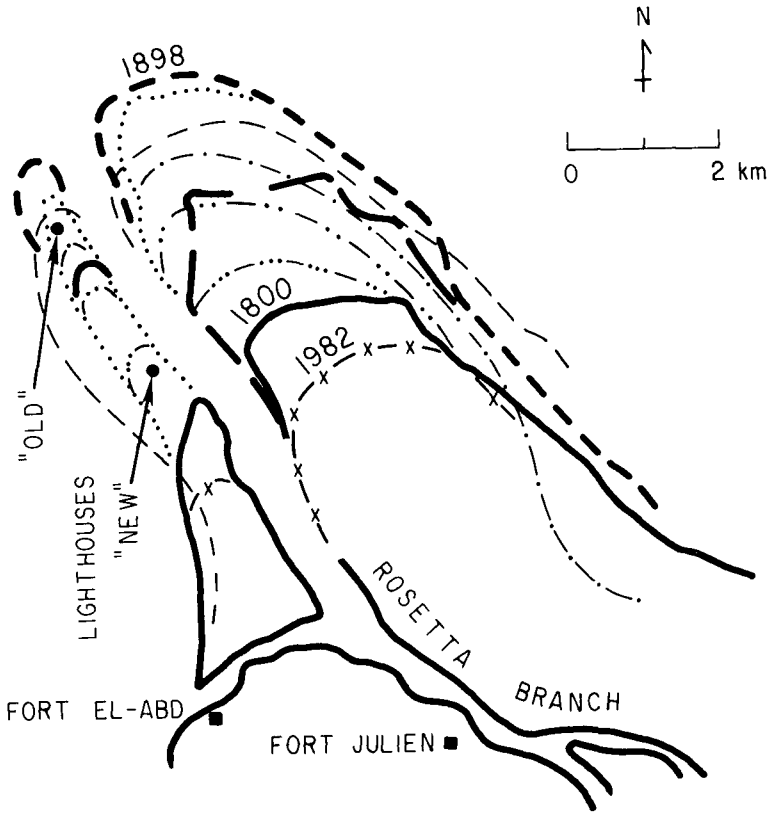
The beach sands from west of Mersa Matruh for 300 km to Ahu Quir headland are calcareous oolites and shell fragments (Hilmy, 1951; El-Wakeel and El-Sayed, 1978). From Ahu Quir Bay to Haifa Bay the beach and shelf sediments are predominantly from the Nile as shown by many studies of mineral distribution (Rim, 1950; Shukri and Philip, 1960; Pomeranchlum, 1966; Nir, 1982a).

A detailed study by Nir (1980) of the sediments in the vicinity of Haifa Bay shows that the quartz sand from the Nile divides into two distinct paths, separated by a series of submarine kurkar ridges. A shallow (out to 15 m depth) band of Nile sand follows the coast around Carmel Head and into the bay forming the beaches and wind blown sand dunes of Haifa bay. Beach accretion and dune formation at Haifa appear to be the sink for the shallow water Nile sand. A deeper (25 m and over) band of Nile sand and silt parallels the coast and appears to extend north of Akko. The transport and final sink for this sediment is not clear. At a lower sea level Akziv submarine canyon may have been the sink for sand bypassing Haifa Bay.

#### SHORELINE CHANGES

Historically the position of the coastline of the Nile Delta has been determined by the relative importance of deposition of sediments during the annual floods of the Nile River which build the delta seaward, versus the action of waves and currents which transport the sediments and erode the delta. Generally, until the beginning of this century the discharge of sediment has exceeded the potential for erosion, and the delta built seaward (Figure 1). However, man's intervention, beginning with construction of barriers in the lower reaches of the Rosetta and Damietta branches and with the construction of the Low Aswan Dam in 1902, changed the pattern to one of erosion. Construction of the High Aswan Dam, which began filling in 1964, has resulted in a complete loss of the Nile River as an active sediment source for the delta. As a consequence, the action of waves and currents, which have remained undiminished, are in the process of eroding and changing the configuration of the coastline of the Nile Delta.

There appears to have been significant accretion of the Nile Delta from at least 1600 to 1898. During that time Rosetta promontory probably extended seaward about 8 or 9 km (Sestini, 1976). The promontory extended 3.6 km (37 m/yr) between the surveys of 1800 and 1898, then remained nearly stationary from 1898 to 1909. From the turn of the century to the present the seaward portion of the promontory has eroded at a progressively more rapid rate. The erosion rates for the periods preceding the surveys of 1926, 1965, 1973 and 1982 being 18, 20, 125 and 211 m/yr, respectively (Figure 1). The "new" Rosetta Lighthouse which was 1 km inland in 1970, became an offshore island in 1976 (Niel-



ACCRETION

EROSION

1800 ———

1909 ·····

1965 -·-·-

1857 - - -

1926 - - -

1973 -·-·-

1898 - · - · -

1945 - · · -

1982 - x -

Figure 1. Historical shorelines of Rosetta Promontory (data from Sestini, 1976; Misdorp, 1977; Khafagy, 1981).

sen, 1977; Khafagy et al., 1981).

The establishment in 1971 of a series of beach profiles extending from Abu Quir Bay to east of Ras El Bar was an essential part of the erosion study. Repeated surveys along these profiles has proved to be the most effective means of monitoring the erosion. Comparison of beach profiles show that the coastline has retreated off the delta promontories averaging 160 m between 1971-1972 and 211 m/yr between 1973 and 1982 off the Rosetta branch and 143 m/yr between 1943 and 1973 on the Damietta promontory east of Ras El Bar (ARE/UNESCO, 1973). In contrast there has been a modest shoreline advance (accretion) in the embayments, e.g., 8 m/yr (1947-1965) at the Gamasa outlet (Kadib, 1969; Mobarek, 1972; Orlova and Zenkovich, 1974). Although beach profiles have been conducted since 1971 there are few printed details. Hammad et al (1979) give the average loss of sediment from the shoreline to 6 m depth as  $19 \times 10^6 \text{ m}^3/\text{yr}$  for the period 1972 to 1976. Manohar (1981) graphs results for this same period and others that clearly show the rate of erosion is accelerating.

Inman et al (1976), using only the principal wave component from surface marine observations obtained longshore sand transport rates of about  $860,000 \text{ m}^3/\text{yr}$  to the east near Rosetta and Damietta promontories and somewhat lower values between promontories. QueIennec and Manohar (1977) estimate the net transport rate near the promontories to be more than  $3 \times 10^6 \text{ m}^3/\text{yr}$  with lower rates between promontories. Comparisons of photographs of the entrances to Bardawil Lagoon, about 140 km east of Ras El Bar, show that the volume of sand trapped on the west side of jetties and eroded from the east side gives easterly transport rates of about  $500,000 \text{ m}^3/\text{yr}$  (Inman and Harris, 1970; Inman et al., 1976).

Numerous structures have been built along the coast of Israel. Most were built to widen beaches for recreational use and prevent cliff erosion, and others to provide harbors. Ashdod Harbor diverts sand offshore in amounts that suggest longshore transport rates of 215-560,000  $\text{m}^3/\text{yr}$ . Other studies indicate longshore sand transport rates of 400,000, 125,000, and 80,000  $\text{m}^3/\text{yr}$  at Gaza, Hadera and Atlit respectively (Nir, 1982h). from wave measurements Carmel et al (1984b) estimate the transport at Haifa to be about 110,000  $\text{m}^3/\text{yr}$ . These various estimates of longshore transport are discussed further and plotted in Carmel et al (1984c).

#### NILE RIVER DISCHARGES

The Nile River derives its waters from the Lake Plateau of Tanzania and Kenya (White Nile) and from the Ethiopian highlands (Blue Nile). It has a drainage basin of about  $3 \times 10^6 \text{ km}^2$  and a length of 6800 km. The Nile traverses 35 degrees of latitude in its long northerly flow from its source in Tanzania to the Mediterranean Sea. Before the High Aswan Dam, the river discharged annually  $86 \times 10^9 \text{ m}^3$  of water (Hurst, 1952; Said, 1981).

Man's intervention in the flow of the Nile dates back at least to pharaonic times when Senusret had a canal built from the ancient Pelusiac branch of the Nile to the Red Sea (circa 1900 BCE). Modern intervention began with construction of the Delta Barrage below Cairo in

1861. The barrage sluices opened to pass flood waters, of which about 70 percent flowed out the Rosetta mouth and 30 percent through the Damietta. The barrage was the beginning of perennial versus basin irrigation, and the extensive use of Nile silts and clays as nutrients in agriculture. This use continued with the Low Aswan Dam built in 1902, up until the High Dam was completed in 1964, which trapped all of the sediment load.

The Low Aswan Dam was increased in height in 1907 and again about 1929 to a total height of 38 m. The dam is 2 km across and raised the river level for 350 km upstream to the Second Cataract near Wadi Halfa. The Low Aswan Dam was specially provided with sluices to pass the flood waters and their sediment load. However, because of its height and extensive back-up of water, it is not surprising that it trapped some sediment (Hammad et al., 1979). Calculations show that about 60% of the fresh water discharged at the Low Aswan Dam was lost to irrigation and evaporation on its way to the Mediterranean (Sharaf El Din, 1977).

Before 1861, probably much of the fine load and most of the sand was carried during the flood months, and deposited off the Mediterranean delta of the Nile. The erosion of Rosetta promontory which began about the turn of the century was probably in part due to a decreased supply of sediment caused by the Low Aswan Dam (Figure 1).

The flood months of the Nile River are usually taken as July through November, with the maximum monthly discharge of about 17 and  $21 \times 10^9 \text{ m}^3$  during August and September respectively. However, measurements show that the rising phase of the flood in August carries the highest percentage of suspended load. A minimum water discharge of  $1.5 \times 10^9 \text{ m}^3$  occurs in May. The sand content of the suspended load appears to have been about 30% for the free Nile above the dams, and was about 25% at Gaafra below the Low Aswan Dam. This difference would be expected if the Low Aswan Dam trapped sediment, as sand is more sensitive to changes in river gradient behind dams than is the wash load.

The peak flood water level of the Nile has been monitored for millennia, providing the longest time series of annual floods known (Hurst, 1957; Van Atta and Helland, 1977). The levels were accurately recorded because they provided a reliable method of taxing the people for the irrigation and growth of crops. Unfortunately there has been but little measurement of suspended sediments and no measurement of bedload. According to Queleennec and Kruk (1976) there were two series of suspended load measurements separated by several breaks, including one of 17 years, centered around World War II. Series 1 included the years 1928-1931 and 1938, while series 2 spanned the period from 1955-1969. Suspended load measurements for the free Nile flood above the low dam were made at Halfa only during series 1; while measurements for the Nile at Gaafra below both the low and high dams were made during both series 1 and 2. Series 1 measurements occurred during a period of low river flow (1913-1931) while series 2 included a period of high flow (1953-1963).

There have been a number of studies of suspended sediment discharge of the Nile River. All are based on series 1 and 2 data except for Simaika (1970; see Hammad et al, 1979) who seems to have extended the

series 2 data above the Low Aswan Dam from 1955 to some unspecified date by moving measurements from Halfa to Kajnarty. The effect of this move on the quality of data is not discussed. The data of Simaika (1970) and Fahmy (1974) appear to be based on averages of data taken during the relatively short periods of measurement (i. e. 5 and 14 years respectively), and thus do not include a long series of data nor the highest or lowest flow years.

In order to obtain a longer, more representative data base Quelenec and Kruk (1976) correlated the series 1 and 2 suspended sediment data with water discharge for both rising and falling water levels. This gave them a sediment rating curve so that suspended load could be simulated from water discharge, for which there is extensive data. In this way they found that the average annual suspended load of the Nile at Gaafra for the 60 years from 1904 to 1963 to be  $160 \times 10^6$  tons/yr. The lowest sediment load was less than  $50 \times 10^6$  tons/yr in 1913 and the highest was greater than  $300 \times 10^6$  tons/yr in 1954. No sediment has passed the High Aswan Dam since it began filling in 1964. The sediment is deposited and is rapidly filling the headwaters of Lake Nasser behind the dam.

For the sediment budget needed in this study it is necessary to estimate the total load of the free flowing Nile for this century. The data from Simaika has too few years to be representative while that from Quelenec and Kruk (1976) includes the effects of the Low Aswan Dam. Hammad et al (1979) use the data of Simaika and Fahmy to show that the Low Aswan Dam trapped suspended sediment at the rate of  $10.5 \times 10^6$  tons/yr. Thus none of the data is entirely satisfactory for our purposes, and none includes bedload. From standard text such as Schumm (1977) and Richards (1982) it would appear that for rivers with the channel and suspended load characteristics of the Nile, the bedload is between 1% and 10% of the total load.

In lieu of a longer data base, that of Quelenec and Kruk is used here as the best estimate of the long term suspended load of the free Nile. From this the total load is estimated in Table 1 and compared with the measured erosion rate of the Nile delta out to depths of 6m. Since the erosion extends beyond 6m depth, and the erosion rate is increasing with time (Manohar, 1981), the erosion rate of sand must be greater than the measured rate of  $19 \times 10^6 \text{ m}^3/\text{yr}$  along the delta. On the other hand it may not be as great as the  $41 \times 10^6 \text{ m}^3/\text{yr}$  assuming a Nile bedload of 10%. Therefore for purposes of this study it is assumed that the total annual yield of sand of the free Nile was between 20 and  $41 \times 10^6 \text{ m}^3/\text{yr}$ , and was probably about  $30 \times 10^6 \text{ m}^3/\text{yr}$ .

#### DRIVING FORCES: WINDS, WAVES AND CURRENTS

The circulation in the Mediterranean Sea is both geostrophic and thermohaline with salinity, due to an excess of evaporation over precipitation and runoff, increasing to the east where it reaches 39 ‰ in the Levant Sea off Israel. The surface circulation of the east Mediterranean is dominated by the counterclockwise flow of the east Mediterranean gyre that carries water from the straits of Sicily past the Nile delta, into the Levant Sea, to the north and west of Cyprus, and into the Cretan Sea (Sverdrup et al., 1942, p. 649; Orin, 1971;

Table 1. Estimated sediment yield of the Nile River at Gaafra compared with Nile Delta erosion.

Location and Source of Data	Sediment Rate →	10 <sup>6</sup> tons/yr	10 <sup>6</sup> m <sup>3</sup> /yr <sup>†</sup>
<u>Nile River Load at Gaafra, 1904-1963</u>			
1. Average suspended load (sand and wash) (Quélenec and Kruk, 1976)		160	
2. Sand in suspended load 0.3 x (1) (Simaika, 1970)		48	30.2
3. Bedload (sand) (1% of total load)* (10% of total load)**		1.6 17.8	1.0 11.2
4. Total sediment load	1% * 10% **	161.6 177.8	
Washload (silt and clay (0.7 x (1) (Simaika, 1970)		112	
Sand load (2) + (3)	1% * 10%**	49.6 65.8	31.2 41.4
<u>Nile Delta Erosion, 1972-1976</u>			
Shore to 6 m depth, 200 km of delta shore- line (Hammad et al., 1979; Manohar, 1981)		30.2	19
Sand yield of Nile before High Aswan Dam			19-41

\* Assuming bedload to be 1% of total load. \*\* Assuming bedload to be 10% of total load. † Assuming "at rest" volume ratio (solid/whole space) of 0.5;  $\rho_s = 1.59 \text{ tons/m}^3$

Sharaf El Din, 1977; Bethoux, 1980). Surface currents of the gyre impinge upon the shallow Nile delta and sweep across it with velocities of 20 to 100 cm/sec and locally up to 2 m/sec. Prior to the closure of the High Aswan Dam in 1964, the turbid plume from the floodwaters of the Nile River could be traced along the Mediterranean coast for over 700 km from Ahu Quir headland to the shores of Lebanon (Hecht, 1964; Orin, 1969; Sharaf El Din, 1977).

The Damietta promontory of the Nile interacts with the east Mediterranean gyre to form a large eddy that begins at Damietta, extends offshore for up to 35 km and eastward along the coast for about 70 km. The seaward portion of the eddy is a high speed jet over 5 km wide that forms off the promontory and flows northeasterly and then easterly with

measured surface to bottom velocities of over 60 cm/sec (Murray et al., 1981). The eddy drives a field of actively migrating sand ridges easterly over a smooth mud plain. The sand belt begins in depths of 10 m flows northeasterly, turns easterly and finally arcs southeasterly towards the coast between Port Said and Bardawil Lagoon (Coleman et al., 1981). This appears to be a major transport path and sink for Nile sand.

The currents of the east Mediterranean gyre dissipate energy as they flow over the shallow shelf of the Nile delta. There is insufficient current data to make detailed calculations. However the energy loss may be approximated from the drag relation,

$$\text{energy loss/area} = \tau u = c_f \rho u^3$$

where  $\tau$  is the drag force per unit area (newtons/m<sup>2</sup>),  $u$  is the mean current velocity (m/sec),  $c_f = 2 \times 10^{-3}$  is the drag coefficient and  $\rho$  is the density of sea water. Assuming that an average current of 50 cm/sec flows over a shallow (<50 m) area of  $10^4 \text{ km}^2$ , the above relation gives an overall energy dissipation rate of about  $2.5 \times 10^6 \text{ kW}$ .

Tidal ranges are about 30 cm along the coast of the southeastern Mediterranean. The effect of tides is negligible except near large lagoons, where together with wind and evaporation they control water exchanges through the entrances. Tides will not be further considered here.

### Waves

The most common winter storms contain low pressure areas which move from west to east over Southern Europe and the Mediterranean. The track of the storm centers pass progressively over Italy, Greece and southern Turkey, so that the cyclonic winds in the lower quadrants of the storm blow from west to east, progressively covering most of the 2200 km fetch between Sicily and Israel. The storms may occur every 6 to 7 days and their centers are often fast moving, with migration velocities of 900 to 1000 km/day. This migration rate is comparable with the speed of the waves, causing the wave height to be enhanced. The waves typically have deep water heights of 3 to 6 m and periods of 8 to 10 sec and sometimes up to 15 sec (Carmel et al., 1984a). The waves arrive off Abu Quir about one-half day before reaching the Israel coast.

The details of wave directional climate from measurements along the coasts of Israel and Egypt are given in a series of recent reports (Inman et al., 1982; Lowe and Inman, 1983; Carmel et al., 1984a,h,c; Elwany, et al., 1984). Along the Israel coast near Haifa these measurements reveal a bimodal distribution of wave height and energy flux with the winter storm waves approaching from south of the beach normal and the lower summer waves from north of the beach normal. The magnitude of the monthly averaged energy flux ranged from 1 to 7 kW/m with an average annual energy flux of 3.3 kW/m. Thus the Mediterranean coast of Israel is a moderately high-energy coast with a bimodal annual cycle (Carmel et al., 1984h,c).

Because of the shorter fetch, the Nile delta coast of Egypt has a slightly lower wave energy, but a more pronounced, unidirectional flux of energy along the coast. The average annual flux of wave energy incident on the Nile delta coast is about 2.5 kW/m (Lowe and Inman, 1983; Elwany et al., 1984). Correcting for refraction, a deepwater energy flux of 2.5 kW/m, results in a total energy dissipation rate due to waves along the 200 km from Abu Quir to Port Said of about  $0.5 \times 10^6$  kW.

Longshore Sand Transport by Wave Action

Theory and field measurements of waves and the resulting longshore transport of sand show that the sand transport is directly proportional to the longshore power factor of the waves (e.g. Komar and Inman, 1970; Inman et al., 1980).

$$I_1 = K [P \sin \alpha \cos \alpha]_b = K [CS_{yx}]_b \tag{1}$$

where  $K \cong 0.8$  is a dimensionless constant,  $P = EC_n$  is the energy flux of the waves (watts/m),  $E$  is the wave energy per unit area ( $\text{joules/m}^2$ ),  $C_n$  is the wave group velocity (m/sec),  $S_{yx} = E n \sin \alpha \cos \alpha$  is the longshore radiation stress,  $\alpha$  is the angle the breaking wave makes with the shoreline, and the subscript  $b$  indicates that all properties are measured at the breakpoint of the waves. In the above relation,  $Q_1$  is the immersed weight longshore transport rate (newtons/sec) and may be expressed in terms of the "at rest" volume transport rate  $Q_1$  ( $\text{m}^3/\text{sec}$ )

$$Q_1 = I_1 / (\rho_s - \rho) g N_0 \tag{2}$$

where  $\rho_s$  and  $\rho$  are the densities of the solid grains and the water respectively,  $g$  is the acceleration of gravity and  $N_0$  is the volume concentration of sand, equal to about 0.6 for well sorted sand at rest. For quartz sand in seawater the factor  $1/(\rho_s - \rho) g N_0$  has the value of  $1 \times 10^{-4} \text{ m}^3/\text{newton}$ .

The potential for the longshore transport of sand by waves can be calculated from relations (1) and (2) when the wave characteristics at the breakpoint are known. This requires that waves be refracted from deep water to the breakpoint. Application of Snell's law to the refracted waves, and the assumption that the energy flux  $P = EC_n$  is conserved between wave rays gives the relation between deep water and the breakpoint as

$$P_b = P_\infty \cos \alpha_\infty / \cos \alpha_b \tag{3}$$

where the subscript  $\infty$  refers to waves in deep water. Limited studies of wave refraction along the Nile delta coast were made by Inman et al (1976) and Quelennec and Manohar (1977) using wave data from marine observations. A more comprehensive study is in progress by Elwany et al (1984) based on measurements from wave directional arrays. These measurements show that the prevailing deep water direction for storm waves is from about  $N60^\circ W$ , and that the waves commonly have periods of 8 to 10 sec.



A refraction diagram for 8 sec waves from  $N60^{\circ}W$  (Figure 2) shows pronounced zones of wave convergence and divergence that result in strong gradients of wave height and breaker angle along the coast. This means that the longshore transport rate  $Q_l$  is not constant but varies with distance along the coast as shown in the central graph of Figure 2. This variation in  $Q_l$  results in areas of erosion and accretion along the coast. The rates of erosion and accretion are given by the divergence of the drift  $\partial Q_l / \partial l$  (eg Inman et al, 1976) as shown in the lower graph of Figure 2. It is to be noted that positive values of  $\partial Q_l / \partial l$  indicate erosion while negative values indicate accretion.

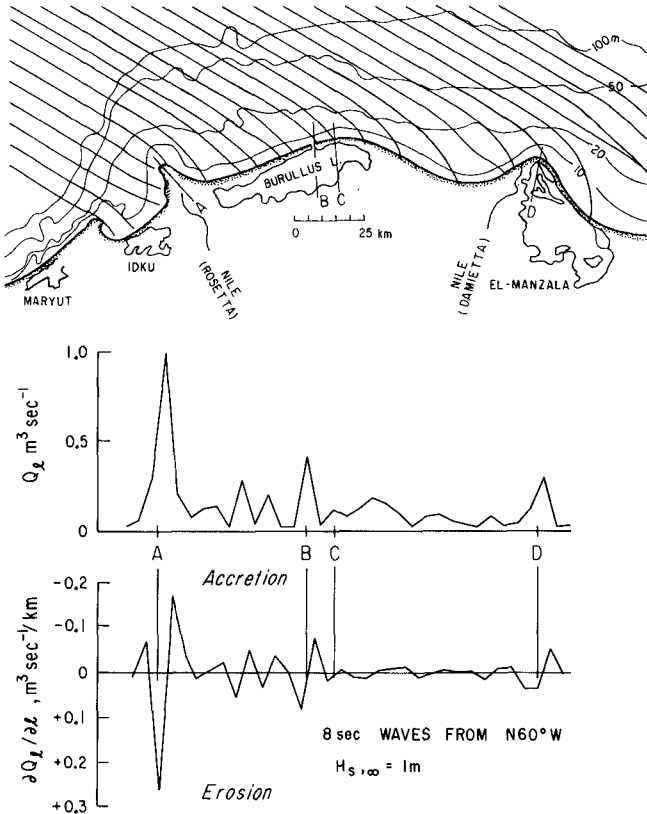


Figure 2. Wave refraction and variation of longshore sand transport (LST) along the Nile delta coast for a 1 m high, 8 sec wave coming from  $N60^{\circ}W$ . Note that the LST (center) is everywhere to the east even though the divergence  $\partial Q_l / \partial l$  shows local zones of erosion (+) and accretion (-) (data from Elwany et al., 1984).

Although Figure 2 is for a single wave condition it illustrates several fundamental aspects of delta morphology. First, there are three general zones of pronounced erosion, that occur off the promontories of Rosetta, Burullus and Danietta. Zones of accretion occur to the east of each erosion zone. Finally, a net easterly longshore transport of sand occurs in the presence of alternate zones of accretion and erosion as  $Q_1$  is everywhere positive and to the east. Several previous studies have wrongly concluded that the presence of alternate zones of erosion and accretion indicated coastal compartments that were closed to net uni-directional transport of material.

The variations in wave intensity and direction and the resulting complex pattern of wave refraction along the delta coast preclude simple interpretations of the wave potential for a net annual longshore transport of sediment. Therefore, for the present it is useful to take a more aloof view and consider the transport potential that the estimated deep water wave energy flux of  $P_\infty = 2.5 \text{ kW/m}$  would produce along the coast. Inspection of relations (1), (2) and (3) show that the longshore sand transport is proportional to the product  $\cos \alpha_\infty \sin \alpha_b$ , which varies along the delta coast. However inspection of the refraction diagrams for prevailing waves (e.g. Figure 2) show that  $\alpha_\infty$  commonly varies between  $45^\circ$  and  $60^\circ$  while  $\alpha_b$  is most commonly between  $20^\circ$  and  $45^\circ$ . Thus the product  $\cos \alpha_\infty \sin \alpha_b$  commonly falls between 0.17 and 0.5, and the longshore transport will commonly fall between 1 and  $3 \times 10^6 \text{ m}^3/\text{yr}$ . Thus a conservative estimate of the net annual longshore transport due to wave action along the delta coast is  $1 \times 10^6 \text{ m}^3/\text{yr}$  to the east.

#### Wind and Cliff Erosion

Wind storms, and the prevailing winds produce significant sand transport along the Nile littoral cell. Some windblown sand is lost to sea, but most is deposited in coastal sand dunes as evidenced by the many dune fields along the coast. The most important fields are the Baltim dunes between Burullus and Ras El Bar, the coastal dunes of the Sinai (Tsoar, 1974), and the smaller dune fields along the Israel coast (Nir, 1982a). The rates of sand loss to dunes has not been carefully monitored.

Nir (1982a) points out that the extensive quarrying of beach sand for construction purposes that lasted through the mid 1960's caused a deficit of about one-third of the total beach resources in Israel. Israel beaches still show a deficit of sand that has indirectly accelerated the erosion at Kurkar seacliffs. Sand quarrying has considerably complicated quantitative sand transport studies along the coast of Israel.

#### BUDGET OF SEDIMENT FOR THE NILE LITTORAL CELL

The littoral cell is a coastal sedimentation compartment that contains a complete cycle of littoral sedimentation including sources, transport paths and sediment sinks (e.g. Inman and Chamberlain, 1960; Inman and Brush, 1973). When transport rates (fluxes) are assigned to the sources, paths and sinks, the cell can be evaluated in terms of the "budget" of sediment which is subject to the usual constraints associated with the conservation of mass. Evaluation of the transport rates

is further constrained by the laws of thermodynamics which govern the partitioning of energy fluxes associated with the forces that drive the sediment. Thus application of the driving forces to the budget of sediment within the framework of the littoral cell permits critical evaluation of the "goodness of fit" of the processes at work in the cell.

The Nile littoral cell extends from Alexandria, Egypt to Akko on Haifa Bay, Israel. The driving forces are the waves and currents associated with the east Mediterranean gyre. The forces transport Nile River sediment from the delta to Haifa Bay. Although many details remain to be clarified, this paper makes clear a number of aspects important to understanding the budget of sediment in the Nile littoral cell. These are stated below in the form of tentative conclusions:

1. Mineralogical studies show that the principal source of sand for the beaches and shelf from Alexandria to Akko was the Nile River. The Nile was also the source of much of the finer sediments on the outer shelf and in the Levant basin (Figure 3).
2. A decline in sediment supply from the Nile to the Mediterranean Sea coast coincided with the construction of the Low Aswan Dam in 1902. Completion of the High Aswan Dam in 1964 resulted in a total loss of Nile River sediment.
3. The net average supply of sand size material to the sea by the "free" Nile appears to have been about 20 to 40 million  $m^3/yr$ . The total supply of all particulate material in the bedload and suspended load was about 160 million tons/yr.
4. Waves and currents associated with the east Mediterranean gyre are the principal driving forces that transport sediment to the east and northeast along the coast. It is estimated that the energy dissipation due to current action over the sediment bottom of the Nile delta is about  $2.5 \times 10^6$  kW, while that associated with wave action nearshore is about  $0.5 \times 10^6$  kW. The relative importance of waves and currents in transporting sediment is not clear.
5. Observations near structures show that the longshore sand transport rates by waves is greatest in the vicinity of the Nile delta ( $\sim 1 \times 10^6$   $m^3/yr$ ), decreases to about one-half off Bardawil ( $\sim 0.5 \times 10^6$   $m^3/yr$ ), and to about one-tenth near Haifa ( $\sim 0.1 \times 10^6$   $m^3/yr$ ). Longshore sand transport rates based on models using measured wave energy fluxes are in general agreement with these transport rates.
6. There is over an order of magnitude difference between the rates of erosion measured from the shoreline to 6 m depth along the Nile delta ( $\sim 20 \times 10^6$   $m^3/yr$ ) and the longshore sand transport by waves ( $\sim 1 \times 10^6$   $m^3/yr$ ). This suggests that currents sweeping across the shallow shelf of the Nile delta are important in transporting sand to the east. The strong eddy off the Damietta promontory appears to be a transport mechanism that moves about  $19 \times 10^6$   $m^3/yr$ . Accordingly, there must be a number of "modern", local sediment sinks within the overall cell. One appears to be between Port Said and Bardawil, the other between Bardawil and El Arish (Figure 3).

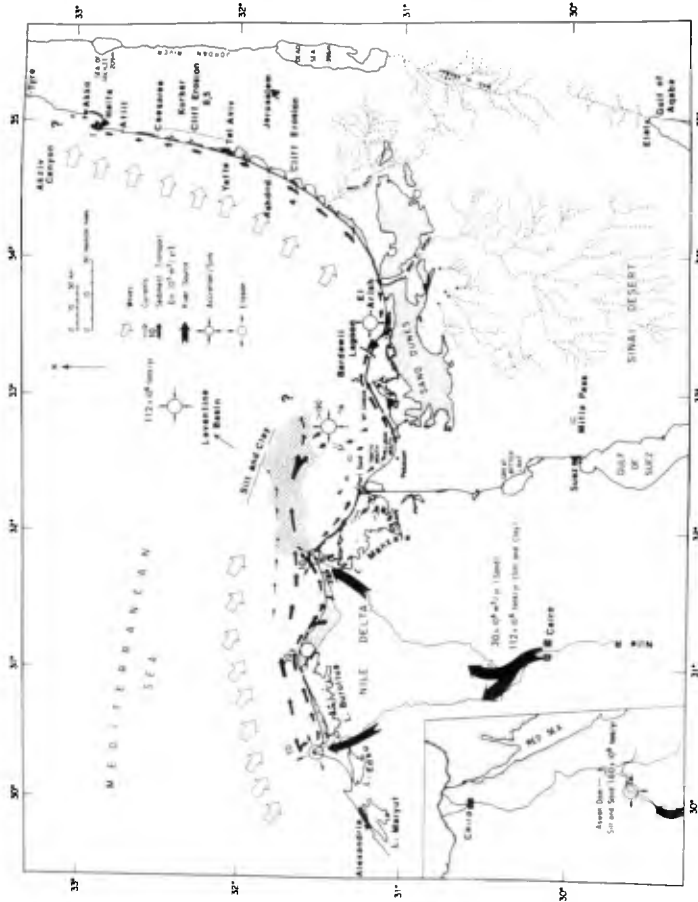


Figure 3. Budget of sediment for the Nile Littoral Cell.

The term "modern" is applicable because as the Damietta promontory erodes back, the intensity of the eddy will decrease, causing the sediment transport capacity to decrease.

7. Windblown sand causes a loss of sand from the beaches of the cell as indicated by the many coastal dune fields. Unfortunately, the rates of loss have not been carefully monitored. However, loss by windblown sand may help to explain the absence of widening beaches that otherwise would occur under the overall negative gradient in the longshore sand transport with distance to the east.

8. Cliff erosion is not generally important to the budget of sediment except locally in Israel where it may contribute to the beach sediments north of Tel Aviv.

The above tentative conclusions regarding the driving forces, the sediment sources and sinks, and the sediment transport paths have been placed in the framework of the budget of littoral sediment for the Nile littoral cell in Figure 3. It is apparent that much more detailed study is needed to further quantify the budget. However, Figure 3 should serve as a useful framework for the guidance of future studies.

#### ACKNOWLEDGEMENTS

This report presents the results of an AID sponsored study "Coastal Management and Shore Processes in the southeastern Mediterranean" which is part of the "Cooperative Marine Technology Program for the Middle East." Many people aided in its preparation. We express our gratitude and indebtedness to A. A. Khafagy and M. H. S. Elwany of Egypt and to Z. Carmel, A. Golik, and Y. Nir of Israel.

#### REFERENCES

- ARE/UNESCO, 1973, "Coastal erosion studies", Arab Republic Egypt/UNESCO Project, EGY/70/581, Technical Rept. No. 1, Alexandria.
- Ben-Avraham, B., 1978, "The Structure and Tectonic Setting of the Levant Continental Margin, Eastern Mediterranean", Tectonophysics, v. 46, p. 313-331.
- Bethoux, J.-P., 1980, "Mean water fluxes across sections in the Mediterranean Sea...", Oceanologica Acta, v. 3, n. 1, p. 79-88.
- Carmel, Z., D. L. Inman, and A. Golik, 1984a, "Characteristics of storm waves off the Mediterranean Coast of Israel", Coastal Engineering, in press.
- Carmel, Z., D. L. Inman, and A. Golik, 1984b, "Directional wave measurement at Haifa and sediment transport along the Nile Littoral Cell", Coastal Engineering, in press.
- Carmel, Z., D. L. Inman, and A. Golik, 1984c, Transport of Nile sand along the southeastern Mediterranean coast, (see paper these proceedings).
- Coleman, J. M., H. H. Roberts, S. P. Murray, and M. Salama, 1981, "Morphology and dynamic sedimentology of the eastern Nile delta shelf", Marine Geology, v. 42, p. 301-326. (also some pages in Nittrouer, C. A., ed., 1981).

- El-Wakeel, S. K. and M. K. El-Sayed, 1978, "The texture, mineralogy and chemistry of bottom sediments and beach sands from Alexandria region, Egypt", Marine Geology, v. 27, p. 137-160.
- Elwany, M. H. S., D. L. Inman, and A. A. Khafagy, 1984, Wave climate and sand transport along the Nile delta, (in preparation, 1984).
- Fahmy, A., 1974, A note on the effect of sediment on the capacity of the High Dam Reservoir, Research and Experimental Station, Ministry of Irrigation, Cairo (Arabic text).
- Hammad, H. Y., A. A. Khafagy, I. Mobark, and S. Sidky, 1979, "A short note on the sediment regime of the Nile River", Bull. Inst. Ocean. and Fisheries, A. R. Alexandria, v. 7., p. 314-322.
- Hecht, A., 1964, On the turbulent diffusion of the water of the Nile floods in the Mediterranean Sea, Bull. of the Sea Fisheries Res. Station, Haifa, n. 36, p. 1-24.
- Helland, K. N. and C. W. VanAtta, 1978, "The Hurst phenomenon in grid turbulence", Jour. Fluid Mech., v. 85, pt. 3, p. 573-589.
- Hilmy, M. E., 1951, "Beach sands of the Mediterranean coast of Egypt", Jour. Sedimentary Petrol., v. 21, n. 2, p. 109-120.
- Holeman, J. N., 1968, "The sediment yield of major rivers of the world", Water Resources Res., v. 4, n. 4, p. 737-741.
- Hurst, H. E., 1952, The Nile, Constable Pub., London.
- Hurst, H. E., 1957, "A suggested statistical model of some time series which occur in nature", Nature, v. 180, n. 4584, p. 494.
- Inman, D. L. and T. K. Chamberlain, 1960, Littoral sand budget along the southern California coast, Report of the Twenty-First Int. Geol. Cong., Copenhagen, v of abstracts, p. 245-246.
- Inman, D. L. and R. W. Harris, 1970, Preliminary report on the inlets of Bardawil Lagoon, letter report to National Council for Research and Development, Haifa, Israel, 13 pp.
- Inman, D. L. and B. M. Brush, 1973, "The Coastal Challenge", Science, v. 181, p. 20-32.
- Inman, D. L., D. G. Aubrey, and S. S. Pawka, 1976, "Application of nearshore processes to the Nile Delta", p. 205-255 in, UNDP/UNESCO Proc. of Seminar on Nile Delta Sedimentology, Academy of Scientific Res. and Tech., 257 pp.
- Inman, D. L., J. A. Zampol, T. E. White, D. M. Hanes, B. W. Waldorf, and K. A. Kastens, 1980, Field measurements of sand motion in the surf zone, Proc. of the 17th Engineering Conf., Amer. Soc. Civil Engin., New York, v. 2, p. 1215-34.
- Inman, D. L., A. A. Khafagy, and Y. Ben-Nun, 1981, "Coastal Management and Shore Processes in the Southeast Mediterranean", p. 35-67 in AID, Cooperative Marine Technology Program for the Middle East, Progress Report 1, Progress Report for January-June 1981, 152 pp.
- Inman, D. L., A. A. Khafagy, and A. Golik, 1982, "Coastal Management and Shore Processes in the Southeast Mediterranean", p. 60-109 in AID, Cooperative Marine Technology Program for the Middle East, Progress Report 2, Annual Report 1981, 412 pp.
- Jongsma, D. and J. Masche, 1981, "Evidence for northward thrusting south-west of the Rhodes Basin", Nature, v. 293, n. 5827, p. 49-51.
- Kadib, A. A., 1969, "Sand movement along a portion of the northern coast of U.A.R.", 22nd Int. Navigation Congress, Section 2, p. 273-87.

- Khafagy, A. A. et al, 1981, "Autumn hydrographic profiles along the Egyptian coast from Abu Quir to Port Said; 1974-1979", Coastal Research Institute, Alexandria, Cooperative Marine Technology Program for the Middle East, CMSP/81/81, 23 pp.
- Komar, P. D. and D. L. Inman, 1970, "Longshore sand transport on beaches", Jour. Geophys. Res., v. 75, n. 30, p. 5914-27.
- Lowe, R. and D. L. Inman, 1983, Wave parameters, Abu Quir Array, Egypt", Center for Coastal Studies, Scripps Inst. of Oceanography, 5 pp., tbl., figs.
- Manohar, M., 1981, "Coastal Processes at the Nile Delta Coast", Shore and Beach, v. 49, n. 1, p. 8-15.
- Misdorp, R., 1977, "The Nile promontories and the Nile continental shelf", p. 456-551 in, UNDP/UNESCO Proc. Seminar Nile Delta Coastal Processes, Academy Scientific Res. and Tech., Cairo, 624 pp.
- Mobarek, I. E., 1972, "The Nile delta coastal protection project", Proc. Thirteenth Coastal Eng. Conf., Amer. Soc. Civil Eng., v. 2, p. 1409-26.
- Murray, S. P., J. M. Coleman, and H. H. Roberts, 1981, "Accelerated currents and sediment transport off the Damietta Nile promontory", Nature, v. 293, n. 5827, p. 51-54.
- Nielsen, Ev., 1977, "Shore evolutions", pp. 15-59, UNDP/UNESCO Proc. Seminar Nile Delta Coastal Processes, Academy Scientific Res. and Tech., Cairo, 624 pp.
- Nir, Y., 1980, "Recent sediments of Haifa Bay", Geol. Surv. Israel, Report No. MG/11/80, 8 pp., 4 figs.
- Nir, Y., 1982a, "Asia, Middle East, Coastal Morphology: Israel and Sinai", pp. 86-98, in M. L. Schwartz (ed.), Encyclopedia of Beaches and Coastal Environments, v. XV of Encyclopedia of Earth Sciences, Hutchinson Ross Publ. Co., Stroudsburg, PA., 940 pp.
- Nir, Y., 1982b, "Offshore artificial structures and their influence on the Israel and Sinai Mediterranean Beaches", Proc. 18th Coastal Engr. Conf., Amer. Soc. Civil Engr., p. 1837-1856.
- Nir, Y., 1984, "Recent sediments of the Israel Mediterranean Continental Shelf and Slope", Univ. of Gotteborg, Ph.D. Thesis, Dept. of Marine Geology, 211 pp.
- Nur, A. and Z. Ben-Avraham, 1978, "The Eastern Mediterranean and the Levant: Tectonics of Continental Collision", Tectonophysics, v. 46, p. 297-311.
- Oren, O. H., 1969, "Oceanographic and biological influence of the Suez Canal, the Nile and the Aswan Dam on the Levant Basin", pp. 161-167, in M. Sears (ed.), Progress in Oceanography, v. 5, 191 pp.
- Oren, O. H., 1971, "The Atlantic water in the Levant Basin and on the shores of Israel", Cah. Oceanogr., v. 23, n. 3, p. 291-297.
- Pomerancblum, M., 1966, "The distribution of heavy minerals in...continental shelf of Israel", Jour. Sedimentary Petrol., v. 36, n. 1, p. 162-174.
- Queleennec, R. E. and C. B. Kruk, 1976, "Nile suspended load and its importance for the Nile Delta morphology", p. 130-144, in, UNDP/UNESCO Proc. Seminar on Nile Delta Sedimentology Academy Sci. Res. and Tech., Alexandria, 257 pp.
- Queleennec, R. E. and M. Manohar, 1977, "Numerical wave refraction and computer estimation of littoral drift; application to the Nile Delta coast", p. 408-433 in, UNDP/UNESCO Proc. Seminar Nile Delta Coastal Processes, Academy Scientific Res. and Tech., Cairo, 624 pp.

- Richards, K., 1982, Rivers, form and process in aluvial channels, Methuen, London and New York.
- Rim, M., 1950, "Sand and soil in the coastal plain of Israel", Israel Exploration Journal, v. 1, n. 1, p. 33-48, with 4 plates.
- Ross, D. A. and E. Uchupi, 1977, "Structure and sedimentary history of southeastern Mediterranean Sea - Nile cone area", Amer. Assoc. Petrol. Geol. Bull., v. 61, p. 872-902.
- Said, R., 1981, The geological evolution of the River Nile, Springer-Verlag, New York and Berlin, 151 pp. and sheets.
- Schumm, S. A., 1977, The fluvial system, John Wiley and Sons, 338 pp..
- Sestini, G., 1976, "Geomorphology of the Nile Delta", p. 12-24, in, UNDP/UNESCO Proc. Seminar on Nile Delta Sedimentology Academy Scientific Res. and Tech., Alexandria, 256 pp.
- Sharaf, El Din, 1977, "Effect of the Aswan High Dam on the Nile flood and on the estuarine and coastal circulation pattern along the Mediterranean Egyptian coast", Limnology and Oceanography, v. 22, n. 2, p. 194-207.
- Shukri, N. M. and G. Philip, 1960, "The mineralogy of some recent deposits in the Arish-Gaza area", Cairo Univ. Bull., Faculty of Science, v. 35, p. 73-85.
- Simaika, Y. M., 1970, "Degradation of the Nile bed due to the interception of silt in the High Aswan Reservoir", Commission Internationale des Grandes Barrages, Dixieme Congress, Montreal.
- Sverdrup, H. U., M. W. Johnson, and R. H. Fleming, 1942, The Oceans, Prentice-Hall, New York, 1087 pp.
- Tsoar, H., 1974, "Desert dunes morphology and dynamics, El Arish, Northern Sinai", Zeitschrift fur Geomorphologie, Neue F., suppl. Bd. 20, p. 41-61.
- UNDP/UNESCO, 1976, Proceedings of Seminar on Nile Delta Sedimentology, held in Alexandria 25-29 October 1975, organized by UNDP/UNESCO and Alexandria Univ., published by the Egyptian Academy of Scientific Research and Technology, 257 pp.
- VanAtta, C. W. and K. N. Helland, 1977, "A note on the Hurst Phenomenon in turbulent flows", Water Resources Res., v. 13, n. 6, p. 1003-5.
- Venkatathnam, K. and W. B. F. Ryan, 1971, "Dispersal patterns of clay minerals in the sediments of the eastern Mediterranean Sea", Marine Geology, v. 11, p. 261-282.



## CHAPTER ONE HUNDRED TEN

### GRADING EFFECTS IN CONCENTRATION MEASUREMENTS

---

by:  
J. van de Graaff <sup>1)</sup> &  
J.A. Roelvink <sup>2)</sup>

#### ABSTRACT

In analysing measured sediment concentration distributions the effect of the non-uniformity of the bottom material is frequently not taken fully into account. Examples of calculations are given to clarify the grading effect on the parameters that determine the concentration distribution (e.g. diffusion coefficient distribution). Results of a preliminary test series indicate that the particle size affects the diffusion coefficient involved. [ $c(\text{sediment}) = \beta c(\text{fluid})$ ;  $\beta$  size dependent].

#### 1 INTRODUCTION

The CERC formula is an example of an over-all description of the longshore sediment transport rate. A limited range of problems can be solved with the help of this formula since it only describes sediment transports due to wave-driven currents. In more general coastal engineering problems not only wave driven currents but also currents like tidal currents, ocean currents and wind driven currents play an important role. To be able to tackle the latter type of problems, one needs a transport formula to calculate the transport as a function of boundary conditions like water depth ( $h$ ), wave height ( $H$ ), wave period ( $T$ ), current velocity ( $v$ ) and bottom particle size ( $D_{50}$ ). The sediment transport rate for currents more or less perpendicular to the orbital plane of the waves can be simply described as:

- 
- 1) Senior Scientific Officer  
Delft University of Technology, The Netherlands  
2) Student Assistant  
Delft University of Technology, The Netherlands

$$S = \int_0^h v(z) * c(z) dz \quad (1.1)$$

where: S : sediment transport rate  
 v(z) : current velocity (function of z)  
 z : height above the bottom  
 c(z) : time averaged sediment concentration  
 h : water depth

As far as the authors know, only the so-called Bijker formula (Bijker 1971; Van de Graaff and Van Overeem 1979) describes the transport in a physical sense according to Eq. (1.1) and can be used generally in coastal engineering problems. However, although a ready made formula is available, tests have been carried out all over the world in measuring the time average sediment concentration distribution over the water column under wave and current conditions. (Among many others : MacDonald 1977; Nielsen 1979; Bosman 1982.) Such experiments are carried out since it is felt that the concentration distribution as proposed by Bijker is not valid under all conditions.

By analysing concentration measurements one tries to find the underlying 'mechanism' which holds the particles in suspension and causes the measured distribution. Since the suspension mechanism is most likely diameter dependent, it is necessary to take fully into account the grading, the non-uniformity, of the bottom particles.

## 2 SUSPENSION MECHANISM AND 'THEORETICAL' DISTRIBUTIONS

Fig. 1 shows an example of a so-called time and bed averaged sediment concentration distribution over the waterdepth due to (random) waves running over a sloped beach profile. The samples have been taken by suction in a direction perpendicular to that of wave propagation. The 'time and bed averaged' procedure has been developed by Bosman 1982; it means that the suction time is long with regard to the wave period ( $\approx 100 T$ ) and that the suction pipe's intake nozzle is moved to and fro by a carriage over a few ripple lengths ( $\approx 5 \lambda$ ). By this procedure local effects (just above a ripple top quite different concentrations do exist than do above a ripple trough) are smoothed out. In the example of Fig. 1, as well as in the other examples of this paper, the several measuring points have been measured simultaneously.

A distribution like in Fig. 1 is typical for random- as well as for regular waves. The fact that close to the (mostly) rippled bed high concentration rates are found, is caused by the scraping effect of the orbital motion of the waves over the bed.

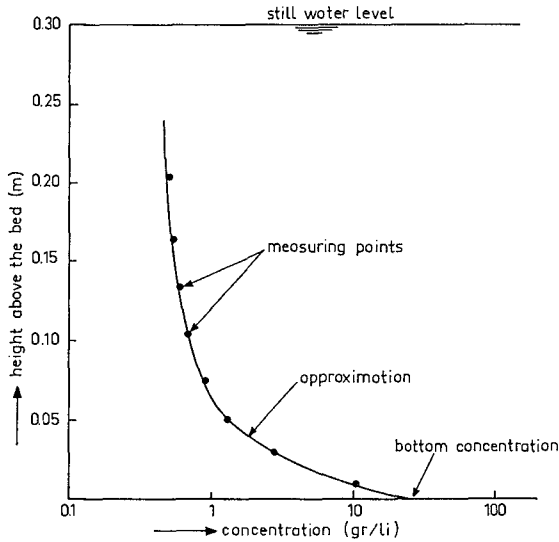


Fig. 1 Concentration Distribution over Water Depth

Why and how the particles can reach the higher levels in the vertical, is not clear yet. The vertical orbital motion in the waves plays a convective role probably.

Whatever the mechanism may be, in this paper a simple diffusion mechanism is assumed. Assuming a steady state condition, in general the concentration distribution over the depth can be described by the expression:

$$w * c(z) + \epsilon(z) * dc(z)/dz = 0 \quad (2.1)$$

where:  $w$  : fall velocity  
 $c(z)$  : average concentration at level  $z$  above the bed  
 $\epsilon(z)$  : eddy diffusion coefficient  
 $z$  : vertical upward directed ordinate; the bottom being  $z=0$

Assuming uniform material ( $w = \text{constant}$ ) the distribution of  $\epsilon(z)$  over the waterdepth defines the shape of the concentration distribution line over the water depth. The bottom concentration profile fixes the actual position of the concentration profile shape.

As a final aim, the concentration distribution's characterizing parameters ( $\epsilon(z)$  distribution) and the bottom concentration should be related to the boundary conditions. In this paper, however, a more modest aim will be pursued: analysing the effects of non-uniform material on the apparent  $(z)$  distribution.

In the literature some basic  $\epsilon(z)$  distributions have been suggested all leading, in case of uniform bottom material, to typical concentration distributions. Three of those  $\epsilon(z)$  distributions will be mentioned, according to their names as found in literature.

- a) Coleman type
- b) Rouse type
- c) Bhattacharya type

In Table 1 the characteristics of the  $\epsilon(z)$  distributions are given together with the resulting concentration distributions.

	$\epsilon(z)$ distr.	$\epsilon(z)$	$c(z)$	
Coleman	constant	$\epsilon(z)=\text{const.}=\epsilon$	$c(z)=c_b \exp\left(-\frac{w \cdot z}{\epsilon}\right)$	*
Rouse	parabolic	$c(z)=4c_{\text{max}} \frac{z}{h} \left(\frac{h-z}{h}\right)$	$c(z)=c_a \left(\frac{h-z}{z} \frac{a}{h-a}\right)^{4\frac{w \cdot h}{\epsilon_{\text{max}}}}$	**
Bhattacharya	triangular	$c(z)=\frac{z}{h} c_{\text{max}}$	$c(z)=c_a \left(\frac{h}{z} \frac{a}{h}\right)^{w \cdot h/\epsilon_{\text{max}}}$	**

\*  $c_b$  : bottom concentration ( $z=0$ )

Table 1. \*\*  $c_a$  : concentration at reference level  $z=a$   
(  $c(z) \rightarrow \infty$  for  $z \rightarrow 0$  )

The  $\epsilon(z)$  distributions as given in Table 1 hold for sediment. In river flow sediment studies, a distinction is made frequently between  $\epsilon_s$  (sediment) and  $\epsilon_f$  (fluid). In general a simple direct relation between  $\epsilon_s$  and  $\epsilon_f$  is assumed:

$$\epsilon_s = \beta * \epsilon_f \tag{2.2}$$

where:  $\beta$  : a proportionality factor.

A widespread discussion is going on concerning the actual  $\beta$ -value; values  $<1$  as well as  $>1$  have been mentioned. The case  $\beta > 1$  seems to get the greater support at the moment. (See for instance Van Rijn 1982). Furthermore it seems most likely that  $\beta$  is particle size dependent. For coarser material larger  $\beta$  values can be expected.

In a unidirectional flow the relation between  $\epsilon_f$  and  $\epsilon_s$  seems clear. It is felt that the turbulence in the masses of water is also the working agent in holding the particles in suspension (micro-scale). Under wave action a still less understood situation exists. Most likely the micro-scale turbulence is less important than the orbital motion induced processes (macro-scale). However, as

mentioned already, in the wave action case also a simple diffusion process is assumed. With respect to  $\beta$  values a similar approach is chosen as for unidirectional flow, whatever the real meaning of a  $\beta$  value may be under wave action.

In section 5 some results of preliminary tests are reported concerning probable  $\beta$  values.

### 3 RELEVANCY OF GRADING EFFECTS

Trying to fit the real concentration measurements of figures like Fig. 1 with the distributions as predicted by the standard cases of Table 1, leads to large differences. In reality none of the given types holds for most of the measured concentration distributions. A more appropriate  $\epsilon(z)$  distribution should be found and is therefore one of the ultimate aims of concentration analysis studies. The 'theoretical'  $\epsilon(z)$  distributions of Table 1 can, however, be used fruitfully to clarify the effect of the grading of the bottom material. Because of its simple behaviour a Coleman type  $\epsilon(z)$  distribution is chosen in the next example.

Starting from an arbitrary bottom concentration, the resulting concentration distribution over the water depth has been calculated for 5 different graded bottom materials. Fig. 2 gives the particle size distributions involved; standard log-normal distributions have been chosen.

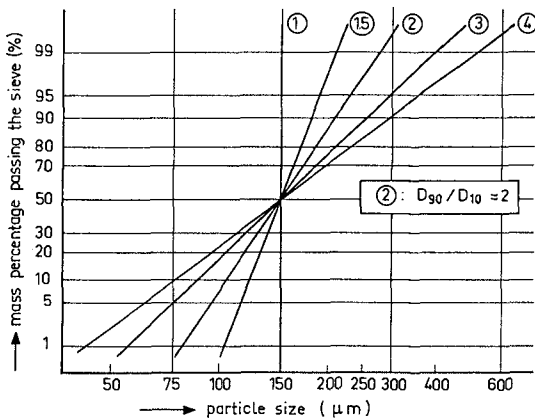


Fig. 2 Particle Size Distributions

In the calculation it is assumed that the particles in suspension close to the bed (bottom concentration) have the same particle size distribution as the original bottom material. Furthermore that amount of sand is assumed to exist of  $k$  fractions, all equal in weight. In each fraction only particles between narrow limits are present in conformity with the particle size distribution. If  $k$  is large enough, the particle size distribution within a certain fraction can be assumed to be constant. For  $k=10$  the characteristic particle size  $D(i)$  of the  $i$ -th fraction ( $1 < i < 10$ ) becomes:

$$D(i) = D(10 \cdot i - 5) \tag{3.1}$$

The fall velocity  $w(i)$  belonging to the particle size  $D(i)$  can be computed with:

$$w(i) = \frac{1}{10} (0.475 \log^2 D(i) + 2.180 \log D(i) + 3.226) \tag{3.2}$$

Formula (3.2) holds for salt water with a temperature of 5° C.

Assuming a constant  $\epsilon(z)$  value  $\epsilon$  over the water depth, the concentration distribution over the depth of each fraction can be computed with:

$$c(z,i) = c(b,i) \exp\left(\frac{-w(i) z}{\epsilon}\right) \tag{3.3}$$

For each fraction the same  $\epsilon$  value is assumed (thus in this calculation  $\beta=1$  for each particle size).

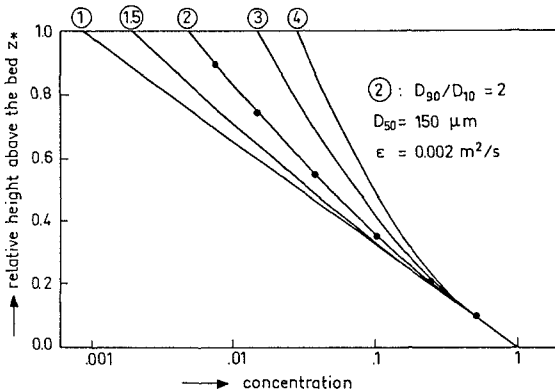


Fig. 3 Concentration Distribution

The ultimate concentration  $c(z)$  at height  $z$  above the bottom yields:

$$c(z) = \sum c(z,i) \quad (3.4)$$

Fig. 3 shows the result for  $\epsilon = 0.002 \text{ m}^2/\text{s}$ ,  $k = 10$  and the diameter distributions of Fig. 2, all with a  $D_{50}$  of  $150 \mu\text{m}$ . Depending on the rate of grading, characterized by the  $D_{90}/D_{10}$  ratio, a variety of concentration curves can be found. For normal beach material the  $D_{90}/D_{10}$  ratio ranges from 2 to 3.

From the calculated contributions of the fractions to the ultimate concentration at level  $z$  above the bottom, the apparent size distribution at that level can be computed. Fig. 4 gives the  $D_{50}$  distribution for some rates of grading.

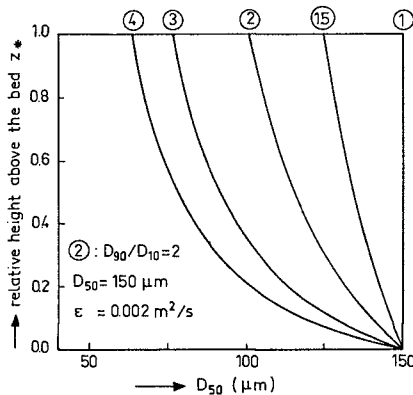


Fig. 4  $D_{50}$  Distribution over Water Depth

A quick, but rough, idea of the order of magnitude of the mistake made when one does not take into account the non-uniformity of the bottom material in analysing measured concentration distributions, can be found as follows.

Assume one has actual measuring points as indicated in Fig. 3 (see on line (2)). Assume moreover that one does not take into account the grading effect and one is focussed on finding the constant  $\epsilon$  value that explains the position of the measured points as well as possible. So one fits a straight line through the measuring points in Fig. 3. From the slope of that line the apparent (but wrong)  $\epsilon$  value can be found. The ratio  $\epsilon(\text{apparent})/\epsilon(\text{actual})$  is then a measure of the mistake made. In Fig. 5 some results are given. To find  $\epsilon(\text{apparent})$  not a complete fit calculation has been

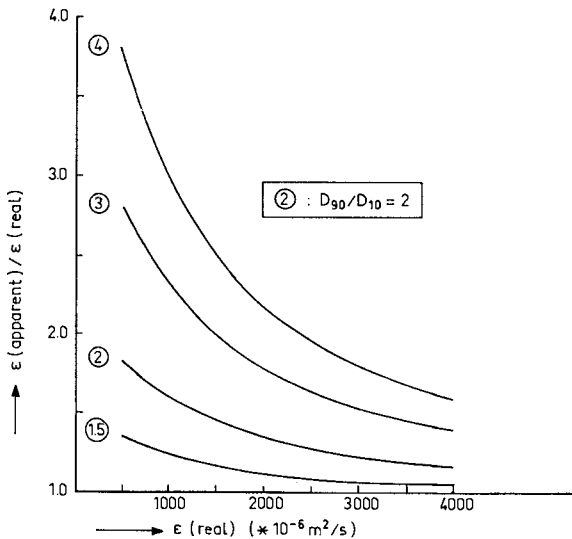


Fig. 5 Mistakes in  $\epsilon$  Prediction

made, but quite simply, only the real concentrations  $c(0.85)$  and  $c(0.15)$  have been taken into account [  $c(0.85)$  means concentration at elevation  $z=0.85$  h ]. From Fig. 5 it can be seen that, depending on the rate of grading and on the actual  $\epsilon$  value a variety of mistakes can be found. It seems clear that it is absolutely necessary to take grading effects into full account in analysing measured concentration distributions.

#### 4 ACTUAL CONCENTRATION MEASUREMENTS

In Fig. 6 a measured concentration distribution is given as found during a test in a wave flume of the Fluid Mechanics Laboratory of the Delft University of Technology. The boundary conditions are as follows:

- horizontal bed with natural ripples
- water depth  $h = 0.30$  m
- wave conditions:  $H = 0.10$  m;  $T = 1.7$  s
- $D_{50} = 97 \mu\text{m}$ ;  $D_{10} = 75 \mu\text{m}$ ;  $D_{90} = 126 \mu\text{m}$

The measured points have been approximated according to the procedure as briefly described in Appendix I. Starting with the (extrapolated) bottom concentration and taking into account 20 fractions the  $\epsilon(z)$  distribution which describes the approximating curve precisely, can be computed. Fig. 7 presents the resulting  $\epsilon(z)$  curve.



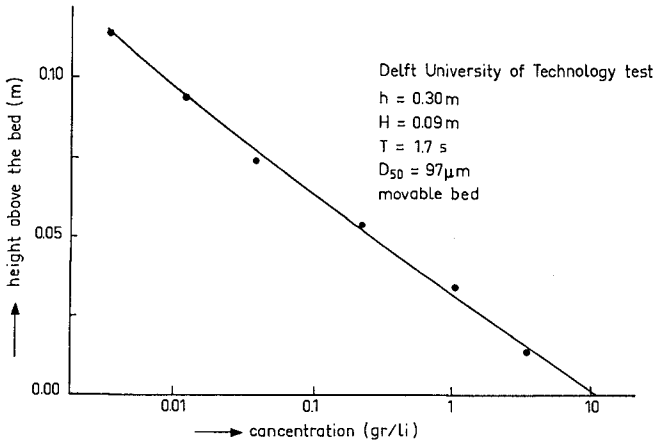


Fig. 6 Concentration Distribution Movable Bed

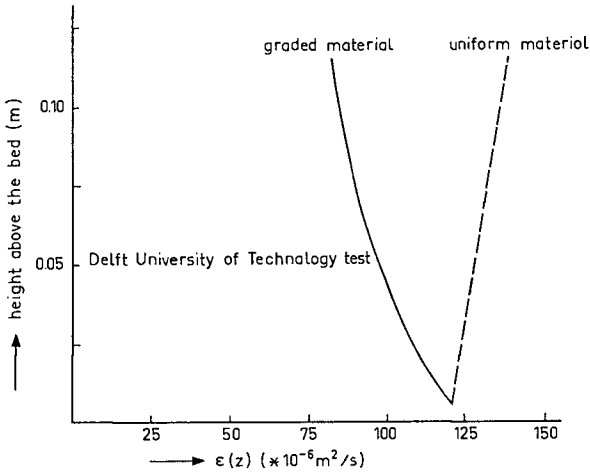


Fig. 7  $\epsilon(z)$  Distribution

(In the same figure the result is given when one does not take into account the non-uniformity of the bottom material; again large differences can be found.) The size distribution of the samples caught at the various heights above the bottom has been analysed with the help of the Delft University Settling Tube (see for details Slot and Geldof 1984) of the Fluid Mechanics Laboratory. Also the distribution according to calculations has been determined. Fig. 8 gives the comparison between measurements and calculations. Although some differences are found, the conclusion is that the general trend is a rather good fit.

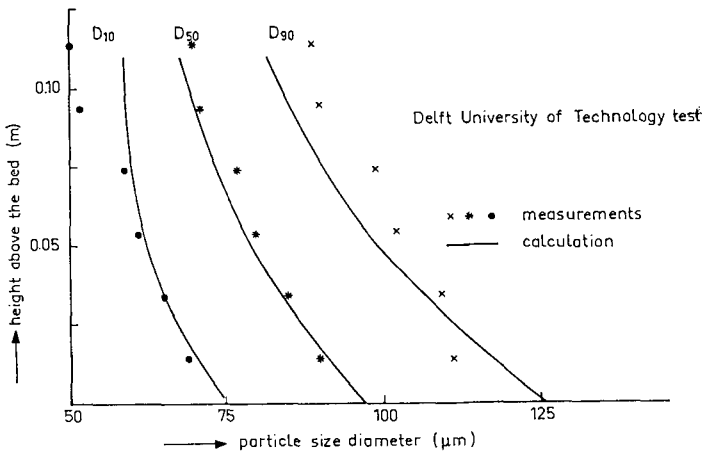


Fig. 8 D10 - D50 - D90 Distribution

In the calculations as described in this section,  $\beta=1$  has been assumed. The suggestion of size dependent  $\beta$  values being greater than 1 as briefly discussed in section 2, may be an explanation of the fact that, especially at greater heights above the bed, the D90 values are underestimated by the calculations and the D10 values slightly overestimated.

In order to gain some insight into possible  $\beta$  values a preliminary test has been carried out in one of the flumes of the Delft Hydraulics Laboratory.

##### 5 EFFECT OF GRAIN SIZE ON $\beta$ -VALUES

The research on concentration distributions is one of the main topics of the 'Sediment Transport' working group of the Dutch Applied Research Program Rijkswaterstaat - Coastal Research (TOW). This TOW program is carried out in

close cooperation between the Public Works Department, the Delft Hydraulics Laboratory, the Delft University of Technology and the Royal Dutch Meteorological Institute. In the framework of the 'Sediment Transport' group a single series of tests has been carried out by the Delft Hydraulics Laboratory in order to get a first idea of the effect of grain size on  $\beta$ -values. The results have been analysed by the authors.

Normal movable bed tests are unsuitable to clarify the mechanism involved. The rate of 'diffusion coefficient production' in an actual case does not depend on the boundary conditions (to be kept constant) like water depth, wave height and wave period only, but also on the form (height and length) of the bed ripples. These bed ripples are, given the boundary conditions, highly diameter dependent. A constant rate of wave and bed induced diffusion activity, equal for several grain sizes, can only be achieved with a fixed rippled bed, covered with such a small amount of particles, that the original bed form is not disturbed. In the tests with a horizontal bottom, wooden fixed ripples have been applied; ripple height: 0.017 m; ripple length: 0.07 m. Seven tests have been carried out with nearly uniform sand; D50-values of 87, 112, 170, 192, 221, 280 and 346  $\mu\text{m}$  respectively. Although uniform material was desired, it turned out from fall velocity tests in the settling tube, that some variations existed. The D90/D10 ratio actually ranged from 1.3 to 1.5. A single test was carried out with well-graded material: D50 = 217  $\mu\text{m}$ ; D90/D10 = 2.15.

In the tests one set of boundary conditions was maintained. Water depth  $h = 0.30$  m; (regular) wave height  $H = 0.08$  m; wave period  $T = 2$  s. In each test a restricted amount of sand was thrown into the flume. Two to five series of simultaneously sucked samples in 4 points were gathered for each material tested. Fig. 9 shows an example of the vertical concentration distribution. Mark the quite similar distribution shape of the curves (1) and (2), despite the fact that for curve (1) the concentrations are approximately a factor 15 less than for curve (2). In case (1) less sand was thrown into the flume.

In a first analysing round, real uniformity was assumed for the 'uniform' material tests. Since in all cases nearly straight lines were found for the concentration distribution over the water depth (see Fig. 9), pointing to a Coleman-type distribution, constant  $\epsilon$  values can be calculated with the help of the proper formula of Table I. Fig. 10a represents the results, showing a distinct dependency of the calculated  $\epsilon$  values on the settling velocity. A nearly linear relationship is found. By extrapolation ( $\rightarrow w=0$ ) an (fluid)-value can be calculated. For the tested materials  $\beta$ -values up to 1.8 can be found for  $w = 0.04$  m/s (D50  $\approx 300$   $\mu\text{m}$ ).

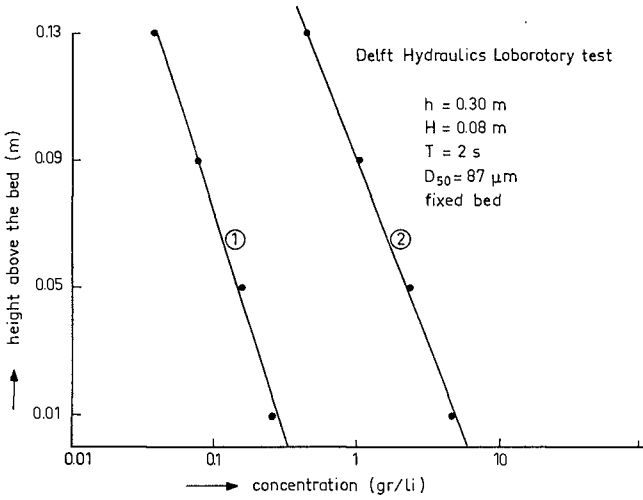


Fig. 9 Concentration Distribution

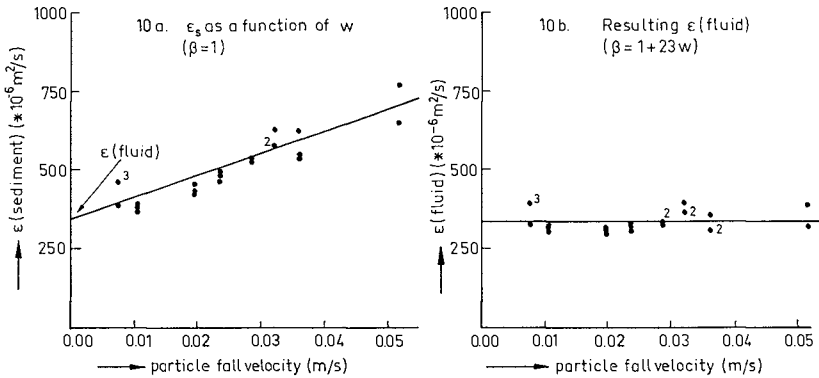


Fig. 10 Diffusion Coefficient vs. Fall Velocity

In a second analysing round, the real grading of the 'uniform' materials was taken into account. As a hypothesis a linear relationship (to be stated) between  $w$  and  $\beta$  was assumed. The fit procedure described in Appendix I was applied. Due to the grading and the applied fit procedure, a non-constant  $\epsilon$  distribution over the water depth is found this time. The variation over the water depth, however, is not very large. An average value over  $0 < z < 0.09$  m has been calculated. By an iteration process the most appropriate  $\epsilon$ (fluid) value and the  $\beta$ -slope value  $m$  were calculated. Fig. 10b shows the ultimate result.

$$\epsilon \text{ (fluid)} = 0.000337 \text{ m}^2/\text{s}; \beta = 1 + 23.0 * w$$

(5.1)

The relationship that was found to exist between  $\beta$  and  $w$  holds for the set of boundary conditions during the test series.

As long as a similar relationship has not been derived for other sets of boundary conditions, the  $\beta - w$  relationship cannot be used generally. Tests with different boundary conditions, to be carried out in the Fluid Mechanics Laboratory of the Civil Engineering Department of the Delft University of Technology, are being prepared. Since a general  $\beta - w$  relationship is not yet available, the calculations as presented in section 4 cannot be refined at this moment.

## 6 CONCLUSIONS

- The non-uniformity of the bottom material strongly affects the concentration distribution over the water depth under wave action.
- When the concentration distribution is described with the help of a diffusion equation, the diffusion coefficient seems to be particle-size dependent;  $\epsilon$  (sediment) =  $\beta \epsilon$  (fluid), the  $\beta$  coefficient being approximately a linear function of  $w$ .
- However, it is not clear yet whether a similar  $\beta - w$  relationship holds for quite different boundary conditions or not. Further research will have to clarify that topic.

## 7 REFERENCES

- Bijker, E.W. (1971)  
'Longshore transport computations'  
Proc. ASCE, Journal of the Waterways, Harbors and Coastal  
Engineering Division, WW 4, November 1971
- Bosman, J.J. (1982)  
'Concentration measurements under oscillatory water  
motion'  
Delft Hydraulics Laboratory / TOW  
Report on model investigation M.1695 part II  
Delft, February 1982
- Graaff, J. van de and J. van Overeem (1979)  
'Evaluation of sediment transport formulae in coastal  
engineering practice'  
Coastal Engineering 3 pages 1-32  
Elsevier Scientific Pub. Comp. Amsterdam 1979
- MacDonald, T.C. (1977)  
'Sediment suspension and turbulence in an oscillating  
flume'  
TP 77-4 U.S. Army Corps of Engineers  
Coastal Engineering Research Center, Fort Belvoir, Va.  
April 1977
- Nielsen, P. (1979)  
'Some basic concepts of wave sediment transport'  
Series paper 20, Inst. Hydrodynamics and Hydraulic  
Engineering (ISVA) Technical University of Denmark
- Rijn, L.C. van (1982)  
'Computations of bed load and suspended load transport'  
Delft Hydraulics Laboratory  
Research Report S 487 part II  
Delft, September 1982
- Slot, R.E. and H.J. Geldof (1984)  
'An improved settling tube system for sand'  
Journal of Hydr. Res. (in preparation)

## Appendix I

## FIT PROCEDURE MEASURED CONCENTRATION DISTRIBUTIONS

In behalf of the calculation procedures of this paper (e.g.  $\epsilon$ - and D50- distributions over the water depth) one needs a mathematical description of the concentration distribution over the water depth. Mostly -compare Fig. 1- a restricted amount of measuring points is available. Besides that the measuring points show some scattering. When applying fit procedures with many degrees of freedom, unrealistically high bottom concentrations and strange curves in the upper section of the vertical can be found frequently.

This is unacceptable for the aims, stated in this paper, and when the bottom concentrations have to be related to the boundary conditions also.

The described fit procedure seems rather objective and holds true for tests on model scale at least.

From Fig. 1 ( $z^*$  vs.  $\ln c(z)$ ) it can be seen that:

- highest concentrations occur near the bed
- a gradual decrease in concentration occurs towards higher levels above the bottom.

Looking at the gradients as a function of  $z^*$  for arbitrary concentration distributions, one can schematize the gradients in curves according to Fig. A1. (In Fig. A1 a 'standard' square is assumed. The vertical axis ( $z^*$ ) ranges from 0 to 1 and the horizontal axis ( $d \ln(c)/dz^*$ ) also from 0 to 1. The actual gradients can be found by multiplying with a negative factor). It seems to be better -and easier- to impose some restrictions on the gradient curve than to do so on the original concentration curve.

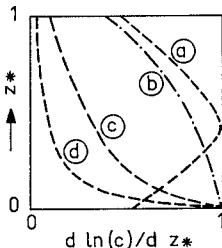


Fig. A1

Standard Square

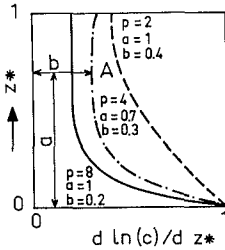


Fig. A2  
Possible Fillings

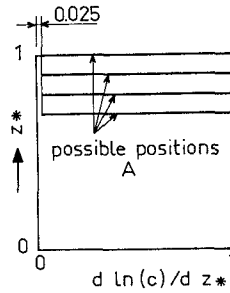


Fig. A3  
Extreme Positions  
Point A

REQUIREMENTS OF GRADIENT CURVES IN STANDARD SQUARE

1) For  $z^*=0$ , the gradient is 1 and at its maximum. At the bottom the largest gradients are assumed to occur. So curves like curve (a) in Fig. A1 are not acceptable.

2) No negative gradients. A negative gradient in the standard square at a certain level above the bottom means that the concentration increases towards higher distances from the bottom. That seems quite unlikely; experiments never showed any clear evidence to that. Also zero-gradients are unlikely. In the standard square minimal  $b$  values (see Fig. A2) of 0.025 are assumed. The value of 0.025 is subjective; however, slightly different values hardly affect the total result as it turned out after analysing a number of test cases.

3) No large gradients close to the bed in the standard square. In Fig. A1 curve (b) seems attractive. At the bed the largest gradient occurs; nevertheless close to the bed also rather large gradients occur. A distribution like curve (b) will never lead to unrealistically high bottom concentrations. However, from actual measurements it turned out that curves like (c) and (d) in Fig. A1 are more likely in some cases. However, with curve (d) extremely high bottom concentrations can be found. So it seems appropriate to make some restrictions. In Fig. A2 and A3 some possible filling-ups of the standard square are given. By assuming a maximum value of 8 for  $p$  (see next section), very high bed concentrations can be avoided.



## RESULTS

The curves in Fig. A2 can be described by:

$$d(\ln(c))/dz^* = q [ b + (1-b) [(a-z^*)/a]^p ] \quad (A.1)$$

where: q : (negative) scale factor  
 b : horizontal ordinate point A ( $0.025 < b < 1$ )  
 a : vertical ordinate point A  
 (in the procedure proposed a can be 1 or 0.9 or 0.8 or 0.7; these values are rather subjective).  
 p : exponent of fit parabola for gradient curve (p can be 2; 4; 6 or 8)

Integration of Eq. (A.1) yields:

$$\ln(c) = q [ bz^* - (1-b)(a-z^*) / (p+1) [(a-z^*)/a]^p + d ] \quad (A.2)$$

where: d is the integration constant

In a computer program the procedure starts with  $a=1$  and  $p=8$ . The 'best' values of the parameters q, b and d are determined with a least squares method. If it turns out that  $b < 0.025$  or  $b > 1.0$ , then b is fixed at 0.025 or 1.0 respectively and the procedure is restarted. The parameters q and d are determined now. In the next step it is checked whether a better result is found with  $a=1$  and  $p=6$ , and so on. Next the procedure starts with  $a=0.9$  and  $p=8$  again. As stated the least a-value is taken to be 0.7.

From test series it turned out that the fit procedure proposed seems to be rather objective. (Compare Fig. 1)

## CHAPTER ONE HUNDRED ELEVEN

### REDESIGN OF ENTRANCE STRUCTURES FOR TWO SMALL CRAFT HARBORS IN OHIO

Rilly L. Edge, Cubit Engineering Limited  
Ren L. Sill, Cubit Engineering Limited  
James A. Swartzmiller, Ohio Department of Natural Resources  
John S. Fisher, Cubit Engineering Limited  
Charleston, S.C.

#### 1.0 INTRODUCTION

Wildwood Harbor and Chagrin River are two areas on Lake Erie at which intensive boating activities occur throughout the recreational months of April through October. At Wildwood Harbor (Figure 1) an enclosed basin exists with a relatively open mouth which allows excessive wave activity to enter. These waves often focus directly on the launch ramp opposite the entrance. At Chagrin River (Figure 2) a major project was recently completed to stabilize the river entrance which had experienced substantial shoaling, and to help prevent winter ice blockage. The jetties and associated spending beach in the River worked well to prevent continuous shoaling and allow the river to flood and carry the ice lakeward; however, significant reflected waves resulted from this construction affecting navigation through the entrance and boats in the adjacent Yacht Basin.

#### 2.0 HYDRAULIC MODEL CONSTRUCTION

Physical models were constructed of both sites to simulate present conditions, and to evaluate solution alternatives. Since the construction technique developed by Cubit is unique, it is described briefly below. For relatively short (6 months) model life expectancies, models are constructed from 2 ft x 8 ft sheets of styrofoam insulation board. This material is light, and easily cut and assembled, thus minimizing model construction time. The procedure used is as follows:

- (a) First, contour maps of the area to be modelled are developed with contour intervals appropriate to the styrofoam thickness. In this case the 1:24 vertical scale for Wildwood meant that a 1 inch thickness corresponds to 2 ft of depth in the prototype. For Chagrin River, the 1:48 vertical scale meant that 1 inch corresponded to 4 ft of depth in the prototype.
- (b) Based on the horizontal scales selected (1:100 for Wildwood, 1:48 for Chagrin River), equivalent 2 ft x 8 ft rectangles are drawn on the bathymetric maps of the site.
- (c) Overhead projection transparencies of the contour map are prepared.

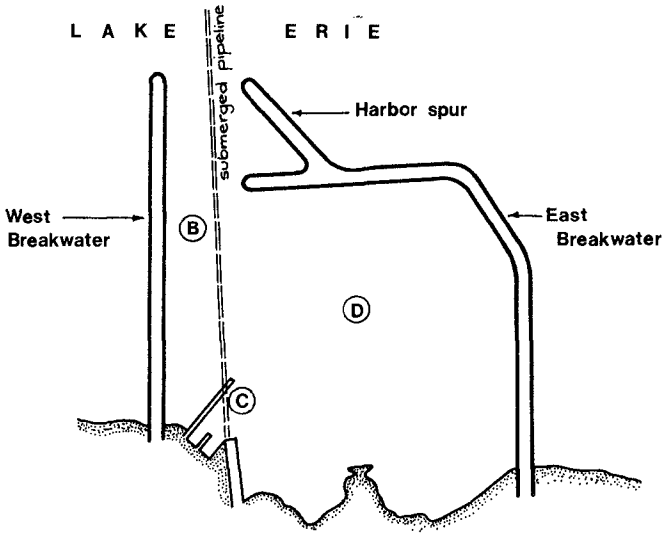


FIGURE 1. MODEL LAYOUT OF EXISTING FACILITIES WITH DATA COLLECTION POINTS INDICATED

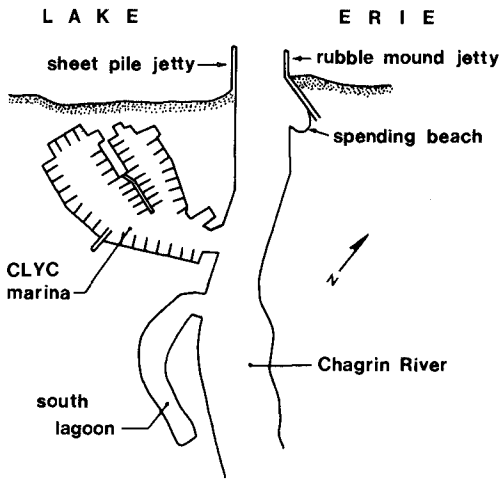


FIGURE 2. MODEL LAYOUT OF EXISTING FEATURES IN THE CHAGRIN RIVER AREA

- (d) These transparencies are projected onto the styrofoam sheets for each contour interval.
- (e) Each individual sheet is marked and cut.
- (f) Pieces are assembled in the basin using a butyl caulk to secure their location.
- (g) The stairstep edges are smoothed with a hot nichrome wire.
- (h) Finish sanding the edges smooth.
- (i) Coat the entire model surface with a veneer of a mortar surface bonding compound (e.g. Surewall brand).

This completes the construction of the model substrate. With the addition of wave maker and plumbing for riverine flow the model is ready for instrumentation and testing.

### 3.0 WILDWOOD HARBOR

A physical hydraulic model was constructed for the Wildwood Park vicinity located within the Cleveland Lakefront State Park and on the shoreline of Lake Erie. The harbor was constructed in the 1950's to protect construction equipment laying a 12 ft diameter pipeline into Lake Fria for the City of Cleveland's raw water supply. Since that time the area has become a major recreational area for swimming, boating and fishing. The pipeline however still poses a problem for the final design since it runs through the mouth of the harbor.

#### A. The Model

Data obtained from the physical model were analyzed with the purpose of reducing the wave problem within the harbor, and in particular, near the location of the boat launching ramp. This study examined the current configuration of the harbor and tested design alternatives designed to reduce the wave action within the marina. The designs which showed the most promise were examined in further detail. Following these analyses, conclusions as to the best alternatives were evaluated based on their impact on the wave conditions in the harbor, constructability, and navigation.

A horizontal scale of 1:100 and a vertical scale of 1:24 were used in constructing the model of the harbor and the immediate offshore area to a depth of 14 ft. Distorted model scaling was utilized to insure adequate depths in the model. The model was 24 ft long and 14 ft wide. To produce the desired wave effects, a wave generator consisting of a rotating offset cylinder was employed. Wave periods from 6 to 8 seconds were used with approach directions and wave heights taken from Resio and Vincent [1976]. This resulted in a prototype wave height of approximately 12 ft and directions varying between normal to the entrance to N 25 degrees W.

The testing program proceeded through several different phases. The initial phase consisted of producing waves with prototype periods of 5 and 8 seconds. Many different design alternatives were tested and both subjective and quantitative data were collected. Visual observations were made of the waves as they traveled from the deeper offshore water between the present breakwaters and into the marina. Observations of the wave activity within the marina itself were also made. The quantitative phase of the data collection process consisted of obtaining wave heights at three separate locations within the marina. These collection points were designated as B, C, and D and are shown in Figure 3. Data were collected through the use of capacitance wave gauges and displayed on a strip chart recorder.

Following the analysis of the results from the preliminary phase, several alternatives were chosen for more in-depth study. Also, wave periods of 6 and 8 seconds were used during this phase. During this stage, varying structure lengths of the selected design alternatives were tested in an attempt to determine the optimum length.

Finally, to observe the effect of the wave approach angle on the selected design alternatives, the wave generator was placed such that it produced waves which approached the marina from a direction of N 25 degrees W. During this third stage, wave periods of 6 and 8 seconds were again tested.

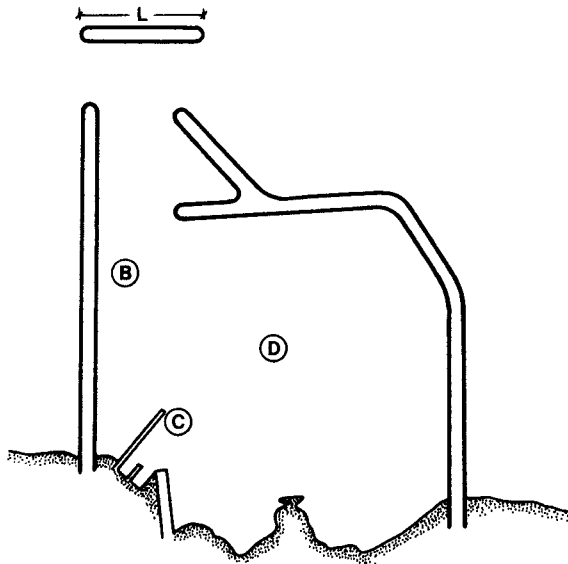


FIGURE 3. MODEL LAYOUT OF ALTERNATIVE 1: OFFSHORE BREAKWATER

## R. Results

The initial testing phase involved thirteen different layouts of the breakwaters and possible additions surrounding Wildwood Park. The first test condition was that of the facilities as they presently exist and this test will be referred to as the "existing conditions" throughout the remainder of this paper.

In distorted physical models of harbors, such as this, it is impossible to effectively scale the wave heights. Because of this fact and also for ease of comparison, the wave data were non-dimensionalized with the existing wave height at each station.

Twelve alternatives were tested, however only three geometries are shown here:

- 1) offshore breakwater,
- 2) spur on west breakwater, and
- 3) west breakwater spur in combination with an east breakwater extension.

In Figures 3, 4, and 5, the geometries are self explanatory without need for additional comment. These conceptual designs exhibited significant wave height reductions, and were studied in some detail.

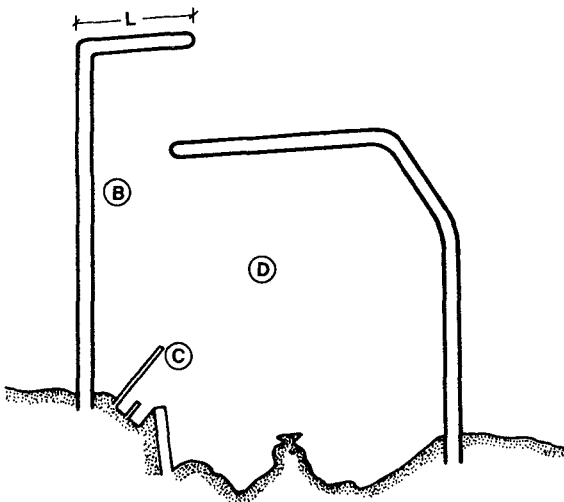


FIGURE 4. MODEL LAYOUT OF ALTERNATIVE 10: L-SHAPED WEST BREAKWATER

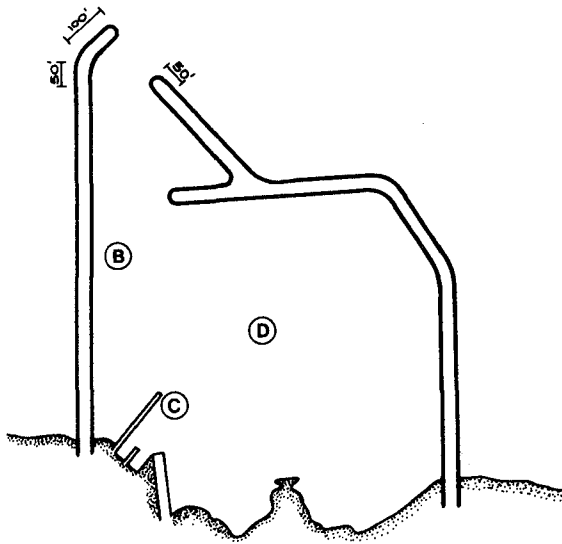


FIGURE 5. MODEL LAYOUT OF ALTERNATIVE 14: ANGLED EXTENSION OF WEST BREAKWATER

Following the initial testing of all alternatives, the three previously mentioned designs were selected for additional testing. One of the original restrictions placed on the project was the requirement that no construction take place over the water supply pipeline. The alternatives that met this requirement were generally less effective in reducing the wave activity within the harbor when compared to some of those that extended over the pipeline. As would be expected, in order to most effectively reduce the wave action, the best solution was found to be the prevention of the majority of the waves from directly entering the marina with a detached breakwater. Once the waves were allowed in the harbor, they were difficult to dissipate without taking up substantial harbor space. On the other hand, the alternatives that were laid over the pipeline and more or less shadowed the harbor entrance prevented waves from entering the harbor directly. Thus, the waves were dissipated before they entered the harbor. Because of the success obtained during the initial phase of testing, it was decided to further examine two alternatives which prevented the waves from entering the marina directly even though they called for construction to take place over the in-place pipeline.

### C. The Second Tasting Phase

The next phase of the testing program consisted of the use of 6 and 8 second wave periods. From the initial testing phase, the arrangements shown in Figure 3 and 4 were determined to be the most feasible solutions to the wave problem. In an attempt to determine the optimum length of the two alternatives, the two structures were tested and examined under the above wave conditions. The various lengths tested for the offshore breakwater and for the L-shaped west breakwater are given below.

<u>Offshore Breakwater</u>	<u>L-Shaped Extension</u>
150'	50'
200'	100'
250'	150'
300'	200'
350'	250'
	300'

The offshore breakwater was positioned such that the water supply pipeline was located in the center of the new breakwater. Consideration was given in the design to a removable center section to give access to the pipeline.

Non-dimensionalized wave heights are plotted as a function of structural length in Figures 6 and 7. The results indicated that for both the alternatives the best reductions in wave activity took place when the length of the added structure equalled or exceeded the width of the harbor entrance channel. Additional lengths of the structure provided diminishing benefits once this length was achieved relative to costs.

The tests also showed that the offshore breakwater had to be slightly longer than the L-shaped west breakwater to achieve the same level of effectiveness within the harbor. Thus, for the same structure length, the west breakwater modification appeared to do a slightly better job of reducing the wave action than the offshore breakwater alternative.

This may be due to the fact that the L-shaped west breakwater allows the waves to enter from only one end whereas the offshore breakwater permits waves to diffract around both ends. Also, with the removal of the harbor spur in the west breakwater modification, this stone could be used in the construction of the new L-shaped west breakwater. Therefore, at a first glance, the volume of new stone required for alternative ten appeared to be less than that for alternative one.

### D. Selection of Concept For Design

The conceptual designs developed from the modal study were evaluated by the Ohio Department of Natural Resources. Their evaluation procedure considered both engineering and non-engineering considerations. They have authorized final design for a minor variation



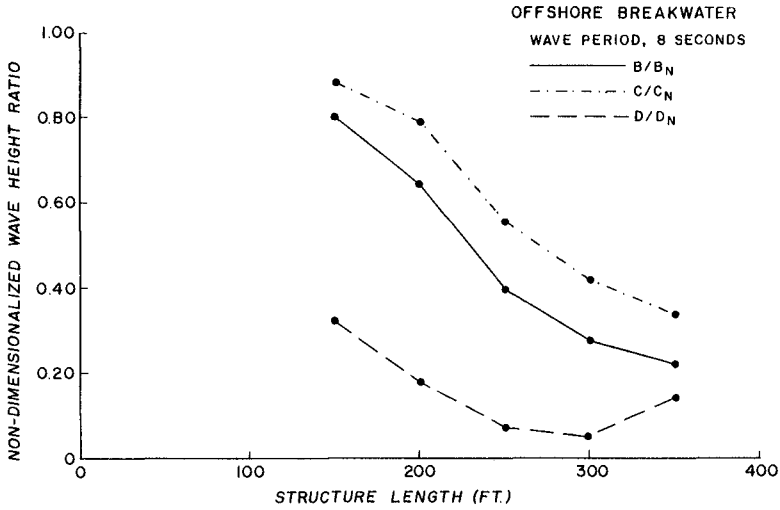


FIGURE 6. SECOND PHASE NON-DIMENSIONALIZED WAVE HEIGHTS vs. STRUCTURE LENGTH FOR OFFSHORE BREAKWATER

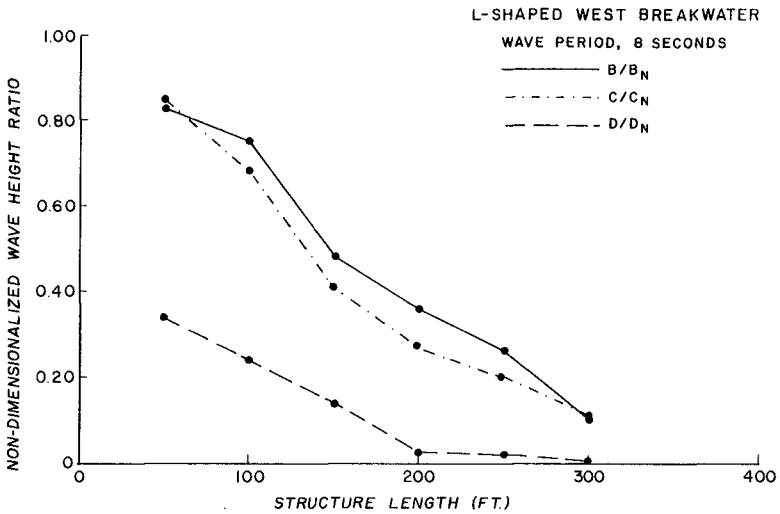


FIGURE 7. SECOND PHASE NON-DIMENSIONALIZED WAVE HEIGHTS vs. STRUCTURE LENGTH FOR L-SHAPED WEST BREAKWATER

of the breakwater configuration shown in Figure 5. This design is a necessary compromise between the most effective concept and the need to maintain access to the 12 ft diameter water supply pipe.

#### 4.0 CHAGRIN HARBOR

##### A. Introduction

The Chagrin River (see Figure 2) which discharges approximately 16 miles east of Cleveland, Ohio, is stabilized on both banks with revetments, sheet piling and a spending beach. Lakeward of the spending beach are parallel rubble mound and sheet pile jetties on the east and west, respectively, which have been constructed to stabilize the shoreline and river channel. The entrance to the Chagrin River is exposed to wind and storm generated waves originating mainly from the north and northwest. These waves approach and enter the Chagrin River between the two jetties and proceed to travel upstream whereupon they enter two inland lagoons where small craft are moored. The waves entering lagoons produce a situation that is unfavorable for the berthing of boats. In fact, numerous mooring lines have broken with the subsequent damage of several boats. The sinking of one vessel has resulted from excessive wave activity within the basin.

As a part of the design to alleviate the wave problem a hydraulic model study was to examine the existing conditions in the Chagrin River and the two lagoons, to confirm model performance, and to evaluate various design configurations and modifications to determine possible solutions for protection of the two lagoons from wave action damage. The possible solutions as well as the existing condition were tested using waves of varying direction and period in an attempt to arrive at a solution that performed well under various conditions.

The Chagrin River model was constructed to an undistorted linear scale of 1:4R, model to prototype. Selection of this scale was based on reducing the effects of bottom friction, the size of the indoor laboratory facility to house the model, flow from the Chagrin River, and the need to properly simulate wave reflection in the two lagoons. To ensure accurate reproduction of reflected wave patterns, a geometrically undistorted model was deemed necessary using Froude's model law.

Available bathymetric data indicate that the harbor is uniformly six (6) feet in depth at the low water design level. In order to best simulate the actual prototype conditions with storms, the water level in the model was raised a scaled amount to represent an increase in depth of one (1) foot so that the depth of water in the main lagoon used for testing procedures was approximately seven (7) feet.

The selection of wave conditions was based on three sources of information. One was the U.S. Army Engineers report on Vermilion Harbor (1970). This report indicated that the storm waves had periods from 4 to 8 seconds with most wave action occurring with the 4 to 5 second waves. These waves generally originate from the north or northeast. A report obtained from the Chagrin Lagoons Yacht Club (3) compiled the wave conditions on the Lake, the river, and the lagoons at various times from December, 1982 through May, 1983. This was used for obtaining

predominant wave directions as well as a comparative analysis of wave heights at the various locations. A report from Stanley Consultants (1979) showed the worst wave conditions occurring in the Chagrin River area had wave periods of four to five seconds.

#### R. Test Program

With this available data, waves with periods of five (5) to ten (10) seconds were chosen to start the testing procedure. After examining the quantitative data and the qualitative comparisons, waves with a 5-second period were selected to best represent the conditions that create a major problem in the two lagoons. Further testing was primarily based on this wave period.

The test data obtained during the testing program included the measurement of wave heights in Lake Erie, the river channel and the lagoons. A schematic of the selected locations where wave heights were recorded is shown in Figure 8. The encircled letters indicate points where wave data were collected throughout the testing program. The letters not encircled are additional data points that were added during the testing program to give a more complete picture of the wave activity in the two lagoons.

The base tests were performed with existing prototype conditions simulated in the model and are termed "present conditions" hereafter. Preliminary tests were conducted with waves varying in period from five (5) to ten (10) seconds to test the model's response and to aid in producing worst case conditions. These results indicated that a wave period of five seconds created substantial wave activity in the lagoons. The wave attenuation in the model as the waves traveled from the lake into the lagoons was found to compare favorably with the observed wave data (3). Additionally, the wave generator was positioned directly in front of the river channel to produce waves that would travel directly up the river. It was reasoned that if a given set of test conditions can be determined to be the worst or more critical in the model, a solution that alleviates this problem should, with minor revisions, solve the problem for the lesser conditions.

The alternatives tested in the model ranged from offshore breakwaters to various spending beaches to the partial and complete closure of the lagoon entrances. For the most part, the alternatives were designed to either prevent the excessive wave energy from entering the river and lagoons or to dissipate the wave energy along the river channel. Brief descriptions of the various alternatives are given in the following subparagraphs. Alternative 1 was that of leaving the existing facilities in their present condition.

Alternative 2 consisted of the placement of a wave absorbing material along the east bank. This represented the removal of the rubble and gabion revetments in that location and the establishment of a smooth sloping beach in its place.

Alternative 3 considered the installation of a rubble mound offshore breakwater. The breakwater spanned the distance of the river channel between the two existing jetties.

Alternatives 4 and 5 involved additions to the present jetties. The two reduced the entrance channel width to reduce the amount of wave energy entering the river channel.

Alternatives 6, 12, 13, 17, and 18 considered the placement and combination of various spending beaches. The spending beaches were located on both sides of the river channel and functioned to dissipate the wave energy at those locations.

Alternatives 7 and 10 consisted of the placement of wave tripping structures along the vertical bulkhead located on the west bank. These structures served to disrupt the waves traveling along the bulkhead and in turn dissipate the wave energy.

Alternatives 8, 9, and 11 involved reductions in the entrance widths to the two lagoons. A reduction in the entrance width should lead to a corresponding reduction in the wave energy that is allowed to enter the lagoons.

Alternative 15 consisted of the placement of wave absorbing material along the entire length of the vertical bulkhead lining the west bank. This simulated the installation of a continuous wave dissipating structure.

Alternative 16 combined two of the previously mentioned alternatives. It utilized the reduction of the lagoon entrances as well as a new spending beach located on the eastern shoreline.

Alternative 19 involved the complete closure of the entrance to the main lagoon. To achieve access to the main lagoon, a channel connecting the main and south lagoons was constructed.

Alternatives 20 and 21 consisted of the placement of riprap along the vertical bulkhead on the western shore. This was intended to disrupt wave travel along the bulkhead and into the lagoons. Additionally, alternative 21 included the installation of a spending beach on the east bank.

Alternatives 24 and 25 involved the cutting of "tooth-like" indentions along the vertical bulkhead as shown in Figure 9. To reduce the reflection and increase the energy dissipation, the cuts were filled with riprap. Also, a spending beach on the east bank was included in alternative 24.

Tests involving the present conditions along with all of the alternatives were conducted during the testing program. In order to appropriately derive the effectiveness of each of the alternatives, the collected wave data were non-dimensionalized by the existing wave heights at each station. The values recorded during the existing condition were used as the denominator in the non-dimensionalization. Therefore, the non-dimensionalized value is an indication of how much wave activity will occur at a particular location as compared to that of the present condition.

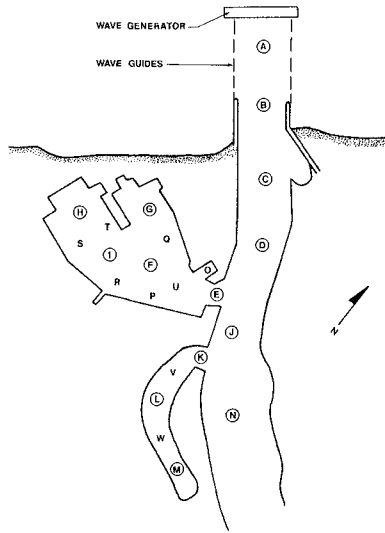


FIGURE 8. SCHEMATIC OF THE WAVE DATA COLLECTION POINTS

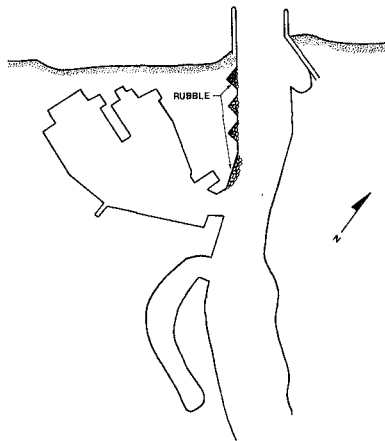


FIGURE 9. MODEL LAYOUT OF ALTERNATIVE 24: TOOTH-LIKE CUTS ALONG THE BULKHEAD WITH RUBBLE FILL

### C. Results

The most striking observation made during the testing phases was the progression of waves along the vertical bulkhead lining the west bank (the deep side of the river channel) and leading into the two lagoon entrances. As the waves entered the Chagrin River between the jetties, a portion of the wave was dissipated very effectively by the existing spending beach. On the other hand, that portion of the wave traveling down the deeper western side encountered no such interference. Thus, a large amount of the wave energy was able to reach and enter the two lagoons.

Once the waves and their accompanying energy entered the lagoons, various oscillations and formations resembling standing waves were established at numerous locations. The basic reason for such activity is that once inside the lagoons the waves had no place to effectively dissipate their energy. This is due to the fact that the lagoons are lined by a vertical bulkhead which serves to reflect the waves with little energy dissipation.

Tests were also conducted in which the flow in the Chagrin River was simulated. The effects of the river flow were tested in most of the previously mentioned scenarios and for various wave periods. The results indicated that the waves in the river were steepened, and in general, the wave heights measured in the lagoons during the flow tests were the same or less when compared to the tests without flow. The wave activity in the south lagoon was significantly reduced because the river flow assisted in dissipating the wave energy in the river. Therefore, in order to create worst case conditions as far as the wave activity in the lagoons was concerned, particular attention was paid to the results of the tests with no flows.

The majority of the alternatives in varying degrees functioned to produce a reduction in wave activity in the two lagoons. Results for non-dimensional wave heights are given in Table 1 for the 5 sec condition in the main lagoon. Following the tests, it was possible to eliminate most of the alternatives based on several criteria:

1. poor overall performance or poor performance in either lagoon;
2. economically unattractive;
3. structures exposed to winter ice flows in river; and
4. potential navigation problems.

Following performance evaluations and utilizing the above criteria, Alternative 24 was considered the best overall for the Chagrin Harbor system. Since the saw tooth cuts do not extend into the river, they will not be subject to ice damage. Further, the size of the harbor entrances do not have to be reduced and thus the alternative poses no additional navigation difficulties. Finally, the solution is economically more attractive than the offshore breakwater, Alternative 3 and most importantly tests indicated that wave heights were reduced substantially.

TABLE 1  
 PRELIMINARY TEST RESULTS FOR THE MAIN LAGOON, 5-SECOND PERIOD

Non-Dimensionalized Wave Height					
Alternative	$E/E_n$	$F/F_n$	$G/G_n$	$H/H_n$	$I/I_n$
2	0.97	1.00	0.80	1.30	1.13
3	0.14	0.08	0.11	0.02	0.38
4	1.18	1.08	1.07	0.80	0.50
5	0.21	0.31	0.13	0.30	0.13
6	0.35	0.23	0.53	0.40	0.63
7	0.17	0.18	0.07	0.06	0.25
8	1.04	1.08	0.24	0.40	0.25
9	0.90	0.77	0.07	0.40	0.50
10	0.75	0.20	0.20	0.35	0.08
11	0.43	0.00	0.36	0.10	0.14
12	0.23	0.50	0.18	0.25	0.29
13	0.14	2.25	0.18	1.00	0.09
15	0.06	0.14	0.27	0.22	0.33
16	0.87	0.07	0.27	0.11	0.17
17	0.25	0.17	0.07	0.67	0.17
18	0.62	0.21	0.14	0.55	0.33
19	0.19	0.00	0.00	0.00	0.03
20	1.11	0.29	0.16	0.14	0.31
21	0.27	0.01	0.07	0.08	0.11
24	0.11	0.04	0.03	0.04	0.01
25	0.18	0.03	0.02	0.01	0.06

## 5.0 CONCLUSION

In both cases the models produced several alternatives which were presented to the Ohio Department of Natural Resources as potential solutions to the wave problems. Representatives of the local yacht clubs were invited to work with the model in confirming the natural conditions and identifying acceptable solutions. Based on various design constraints presented by the local officials and State government a single solution was selected for each site. Both projects are now in final design stage and construction should be completed for the 1985 boating season. At that time, prototype results will be available to compare with the results of the model studies.

## REFERENCES

1. Resio, Donald T. and Charles L. Vincent, "Design Wave Information for the Great Lakes," Technical Report H-76-1, 1976, U.S. Army Engineer Waterways Experimental Station, Vicksburg, Mississippi.
2. Stanley Consultants, "Chagrin River Sedimentation and Stabilization Analysis," A report prepared for the Ohio Department of Natural Resources, July 1979.
3. Unpublished data from the Chagrin Lagoons Yacht Club addressing the existing surge problem. Data delivered to ODNR on May 18, 1983. A copy of this sent to Cubit Engineering Limited on May 19, 1983.
4. Brasfield, C. W., "Wave Action and Breakwater Location-Vermilion Harbor, Ohio," Technical Report H-70-5, 1970, U.S. Army Engineer Waterways Experiment Station, Vicksburg, Mississippi.



## CHAPTER ONE HUNDRED TWELVE

### Coastal Changes at Bethany Beach, Delaware

Jennifer E. Dick<sup>1</sup>  
Robert A. Dalrymple<sup>2</sup>

#### Introduction

The coastal processes affecting Bethany Beach, Delaware were studied and the short-term and long-term trends in coastal changes were determined in order to develop recommendations for protecting Bethany against coastal erosion (Dick and Dalrymple, 1983). Bethany Beach is located on the Delaware Atlantic coastline which is a wide sandy bay-mouth barrier beach distinguished by highlands at Rehoboth Beach and Bethany Beach. The shoreline is straight, with only minor bulges and indentations (see Figure 1).

Bethany Beach is a residential and resort community. Privately-owned properties front the publicly-owned beach. Construction of new motels and summer homes is anticipated along with the continued growth of commercial activities to accommodate the increased number of visitors. Bethany is protected by a series of nine groins built between 1934 and 1945. Many of these groins have deteriorated, and are flanked at the landward end. Winter storms severely erode the beach and damage shorefront property. The beach is generally narrow (approximately 45 m wide), especially along the southern portion, and is backed by low dunes (about 15-45 m above NGVD). A timber bulkhead extends along most of the backshore.

#### Wave Climate

The majority of the waves emanate from the northeast to east; higher waves are from east-northeast during winds of 6.7 m/s or greater. Smaller waves predominate during months of southerly winds with speeds less than 6.7 m/s. Wave heights off the coast of Delaware average 1.2 meters from October to March, and 0.3 meter for the remainder of the year (Polis and Kupferman, 1973). The mean swell direction offshore Delaware Bay is from the southeast during the summer months and from the northeast during the winter (Mauer and Wang, 1973). Ocean waves under severe storm conditions have been estimated to be nine meters high in the surf zone (U.S. Army Corps of Engineers, 1956). The recurrence intervals of extreme waves in the offshore area are summarized below:

<sup>1</sup>Civil Engineer, New England Div., Army Corps of Engineers,  
Waltham, MA 02154.

<sup>2</sup>Professor, Dept. of Civil Engineering, Univ. of Del., Newark,  
DE 19716.

recurrence interval (years)	<u>5</u>	<u>10</u>	<u>25</u>	<u>50</u>
maximum significant wave height (meters)	11	12	14	15
extreme wave height (meters)	18	21	26	29

(Polis and Kupferman, 1973).

Long-Term Trends

The long-term trends in coastal changes were investigated through comparison of a series of historical aerial photographs. Five photographs dating from 1938 to 1977 were selected for study, three from the U.S. Department of Agriculture, one from NASA and one from the Delaware Department of Natural Resources and Environmental Control (DNREC). In

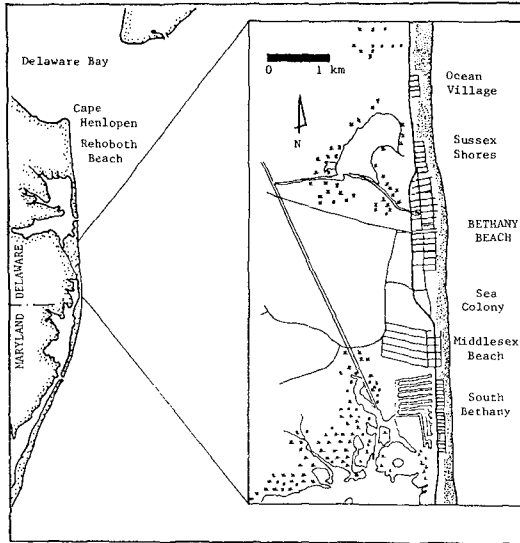


Figure 1: Location Map of Bethany Beach, Delaware.

May, 1938 (the date of the earliest photograph) the groin field had just been enlarged by four groins constructed north and south of the original four groins. Figure 2 clearly illustrates the effects of the groin field on the beach planform. At the time the first photograph was taken the littoral drift was to the north. As the sediment was transported north, the orientation of the shoreline in each groin compartment shifted.

Between May, 1938 and May, 1973, the shoreline straightened out by filling in the groin compartments resulting in slow accretion throughout most of the study area. Before 1968, the rates of change were gradual, in most cases less than a meter horizontally per year. Between 1968

and 1973 the rates increased to between one and five meters per year, averaging about two meters per year.

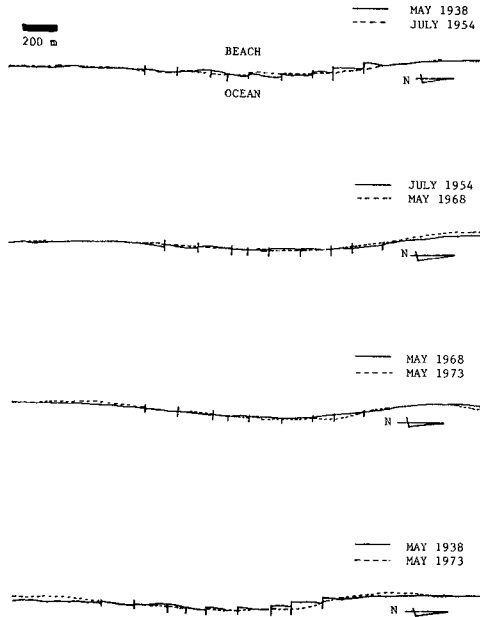


Figure 2: Position of Shoreline at Bethany Between May 1938 and May 1973

The aerial photogrammetric study of Bethany Beach indicates that the historical trend of shoreline change is slow accretion. It is clear from the early photographs that the groins accumulated sediment, thereby widening the beach. The photographs show that the area of the beach protected by the groins has remained relatively constant; however, there is a possibility that the area north and south of the groins (particularly south) have suffered from increased erosion since the construction of the groins. The irregularities in the shoreline at Bethany do not appear to be caused by the groin field. The indentation just north of the groins is the relict of an inlet located there around 1690 (Kraft et. al., 1976). The convexity of Bethany Beach is identifiable on U.S.G.S. charts from 1918; however, the bulge has become more prominent to the south since the construction of the groins.

#### Annual Trends

The short-term changes for one year were determined from periodic

surveys of the beach face and coastal zone. Thirteen nearshore profiles, both north and south of Bethany Beach as well as within the town proper were surveyed 11 times from May, 1982 to May, 1983 by the DNREC (dates are shown in Figure 4). The exposed beach was measured using standard surveying techniques and the offshore portion was measured using a tathometer and triangulation. According to the DNREC (Williams, 1983) the dry land elevations were measured to within 3.0 cm and the offshore soundings were measured to 6.0 cm. The bathymetric surveys constituted the raw data from which the changes in beach profiles as well as sand volumes were examined.

The survey location stretched from 110 meters south of Bethany proper to about 152 meters north of the corporate limits (see Figure 3). From a baseline on Bethany Beach 13 profile lines were established, separated by 152.4 meters and extending offshore to the -9-meter contour, which is usually considered the depth of closure.

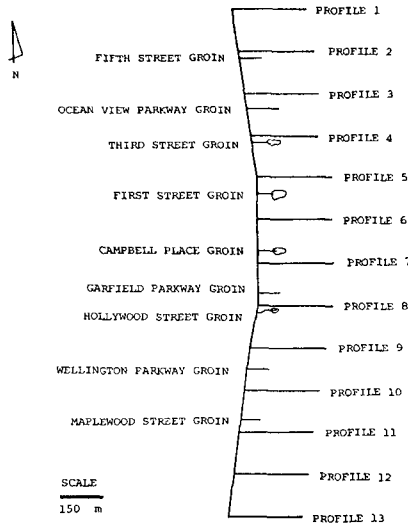


Figure 3: Location of Croins and Profile Lines

Spring to summer profile changes (May 4 - October 18)

It is commonly assumed that sediment shifts seasonally between the berm and the bar so the volume of sand involved remains relatively constant; however, the survey data reveals that the volume of sand did not remain constant at Bethany. Figure 4 illustrates the variations in beach sand volume during the study period. Figure 5 represents the shape of the beach at the time of the first survey. Between May 4 and September 15, 1982, the volume of sand over the survey area increased by  $9.7 \times 10^4$  cubic meters. The change in beach sand volume between

surveys was found by subtracting the elevation of each survey point of the earlier survey from that of the later survey and multiplying by the area between survey points. Between early May and mid-October erosion was generally limited to between the National Geodetic Vertical Datum (NGVD) and the -3-meter contour (see Figure 6). The majority of the survey stations experienced a net accretion of sediment. (The shoreline in Figure 6 has been artificially straightened. This was done so onshore-offshore changes would not be masked by longshore variations due to the convexity of the shoreline at Bethany.) Significant changes in elevation detected offshore could be a result of survey error; however, repetition of the surveys show that survey errors are likely to be smaller than the offshore changes shown in Figure 6. For instance, changes of nearly 55 cm were observed on profile 7 at -9 meters (NGVD).

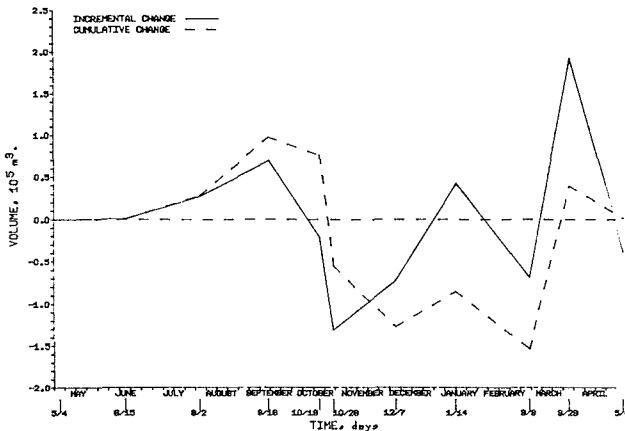


Figure 4: Incremental and Cumulative Change in Volume of Beach Sand over the Survey Area. (Survey Dates Denoted by Vertical Bars on Abscissa.)

#### Impact of October storm (October 18 - October 29)

An intense low pressure system moved northeastward from the Virginia Capes to southern New England on October 24-26, 1982. The storm, with steady winds of 18-22 m/s and gusts up to 37 m/s, was one of the worst storms on the Delaware Coast in the past 20 years. Wave heights exceeding six meters were observed off Indian River Inlet (10 km to the north) and tides were 0.5 meters above normal.

The profiles were surveyed one week before and three days after the storm. Comparison of the two surveys indicates that  $13 \times 10^4$  cubic meters of sediment were transported out of the survey area (see Figure 4). The gross sediment transport (the absolute value of the changes between surveys) was over  $24 \times 10^4$  cubic meters. Figure 7

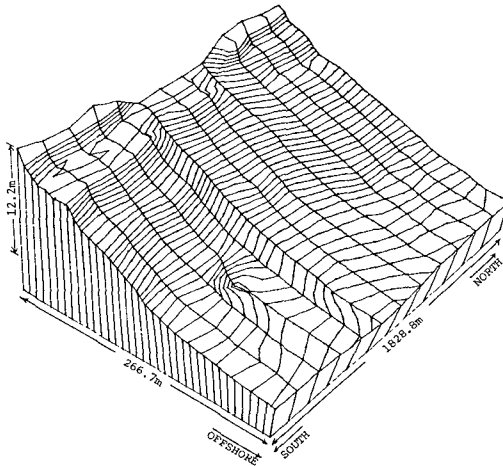


Figure 5: Three-dimensional Representation of Bethany Beach at the Time of the First Survey, May 4, 1982. (Exaggerated Scale)

represents the locations of erosion and accretion due to the storm. All 13 profiles experienced a net loss of sand, transforming the overall shape of the beach from slightly convex to concave. The beach face was severely eroded during the storm. The waterline retreated landward an average of 14.8 meters along the survey reach. The maximum retreat was nearly 28 meters on profile six. Figure 8 illustrates the effects of the storm on the beach profile. (Because of the heavy seas it was impossible to obtain closure between the dry land and the bathymetric surveys, so a gap in the survey data exists. All the data points within this gap were interpolated between known values; therefore, the width of the offshore bars in the surf zone is uncertain.) Significant erosion was observed from the bar region to the seaward limit of the survey area. One profile eroded nearly 52 cm at a depth of 8.3 meters.

Extrapolation of the profile data indicates that the profiles would need to be extended an additional 127 meters seaward to reach the depth of closure which is likely to be -10 m. The volume of sediment that would be accounted for if the profiles had been extended out to this depth is estimated to be one fourth of the volume of sand lost from the survey area during the storm.

Winter profile changes (October 29 - March 3)

The October storm began the transformation of the beach into the winter profile configuration. By early December, the beach showed signs of recovery from the storm, but remained in the winter

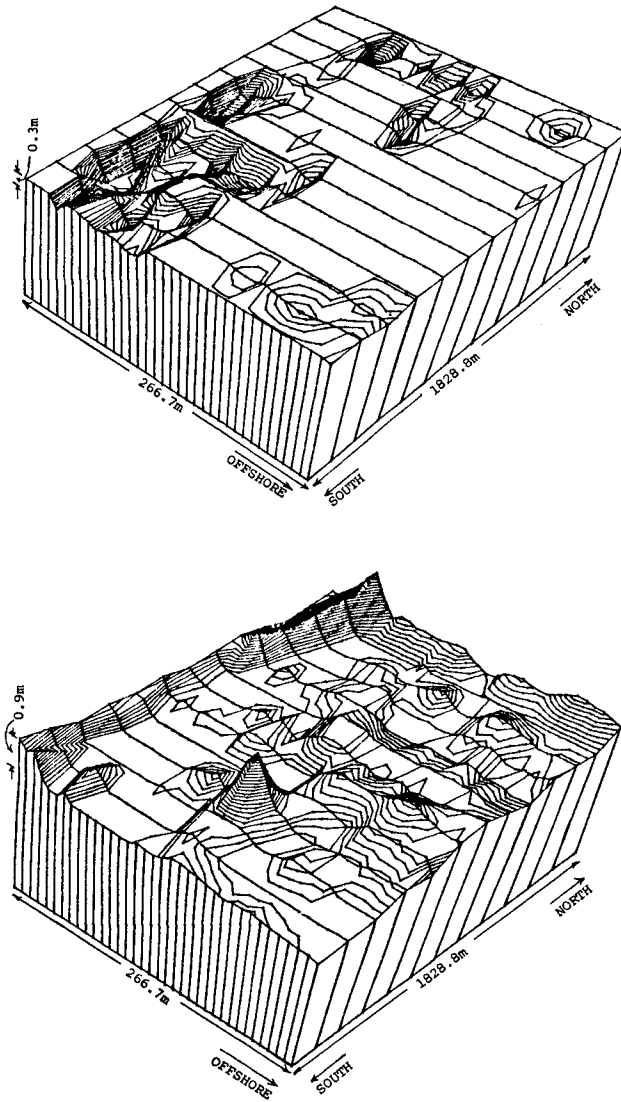


Figure 6: Location of Erosion and Accretion Along the Profiles Between May 4 and October 18, 1962. (Straightened Waterline, Exaggerated Scale)

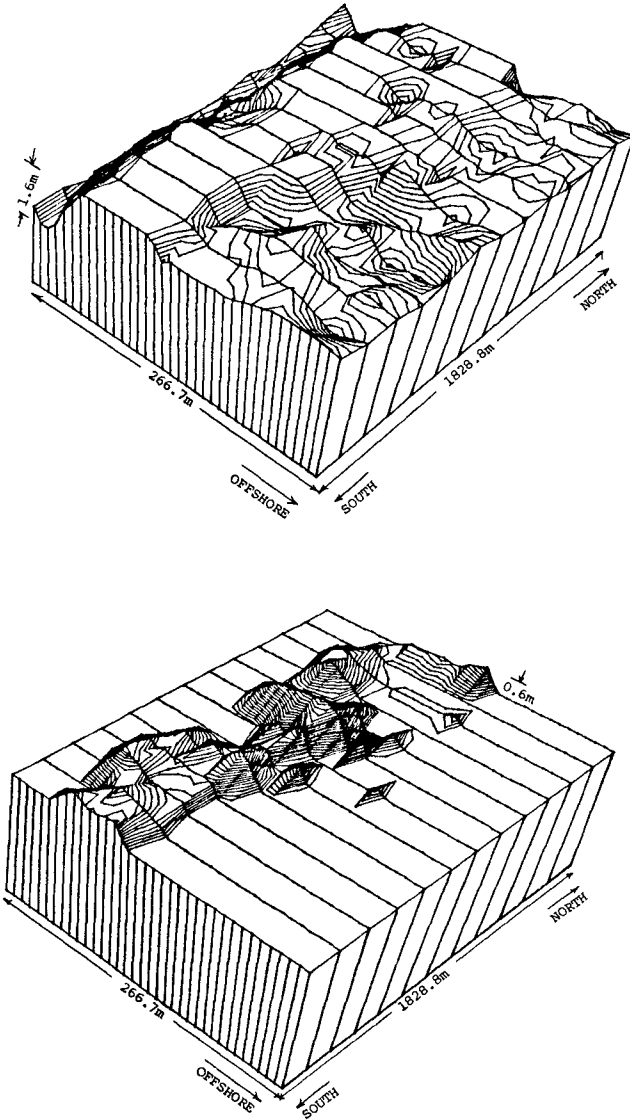


Figure 7: Location of Erosion and Accretion due to October Storm. (Straightened Shoreline, Exaggerated Scale)



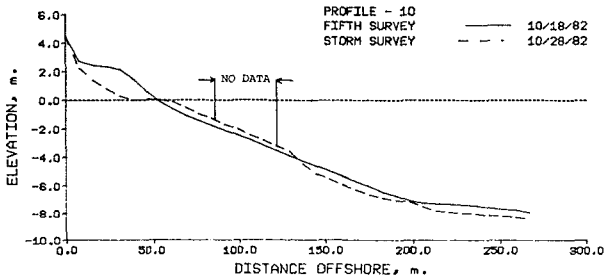


Figure 8: Profile 10 Before and After October Storm

configuration. The area between the landward limit of the survey and the NGVD which was severely eroded during the storm, experienced universal aggradation during the recovery; however, the foreshore did not return to its pre-storm profile. Although the foreshore accreted, the berm remained lower and narrower than it was prior to the October storm.

Bethany Beach suffered a severe winter in 1983, especially during February when a series of storms occurred. The direction of sediment transport is toward the south during the winter, so the northern seven profiles accreted. By trapping the sediment transported from the north, the northern groin compartments starved the south end of Bethany, causing the southern profiles to erode. This erosion/accretion pattern caused a rotation of the waterline about the middle of the groin field. The waterline moved seaward in the northern half of the study area and landward in the southern half.

During February, the berm and foreshore were eroded and the sediment moved offshore to form longshore bars. Since early May 1982,  $15.4 \times 10^4$  cubic meters of sediment had been transported out of the survey area reducing the volume of sand on the beach to its lowest point for the year. By early March the winter profile was fully developed.

#### Changes in profiles during spring (March 3 - May 5)

At the end of March the volume of beach sand had increased significantly. In one month the volume of sand increased by  $19.3 \times 10^4$  cubic meters, most of which was deposited in the offshore region. It appears that the sand accreted offshore and then moved landward between the end of March and early May, when the beach was beginning the transition from the winter to the summer profile configuration. Material from below the NGVD was transported shoreward creating a higher and wider berm. Increases in berm elevation of nearly two meters were recorded.

A full year passed between the first and last survey. The volume of sand was only slightly greater in May 1983 than in May 1982, of

which most of the difference was offshore. Because of the severe winter and late spring, the beach in May 1983 was seasonally behind the May 1982 beach. The foreshore and berm had not yet developed in May 1983.

Eigenfunction Analysis

Previous studies of beach changes and other phenomenon have been conducted using the empirical orthogonal function (EOF) method. The EOF method is an efficient way to describe beach profile changes; however, it should be emphasized that it is a descriptive process and therefore does not reveal any information regarding the governing processes. The reader is referred to Winant et. el. (1975) for a derivation of the technique.

Winant et. al. (1975) has shown that when the EOF method is applied to beach profile data, the eigenfunctions have a physical interpretation. The first eigenfunction, corresponding to the largest eigenvalue is called the "mean beach function" and represents the average profile. The second eigenfunction, termed "berm-bar function", has a large maximum at the location of the summer berm and a minimum at the location of the winter bar. The third eigenfunction, the "terrace function", has a maximum at the location of the low tide terrace. Higher order eigenfunctions account for a very small percentage of the variance of the profile configuration.

Figure 9 is a schematic representation of the decomposition of a beach profile by the empirical eigenfunction method. The original profile can be described by the summation of each eigenfunction multiplied by its corresponding coefficient. The weight of the coefficient defines the degree of variation from the statistical mean.

Three types of eigenfunctions were calculated on the profile data: the "usual" temporal analysis (Winant et. al., 1975; Aubrey, 1979); spatial analysis of the variations along the beach during each survey; and spatial analysis of the variations along the beach for the changes between surveys.

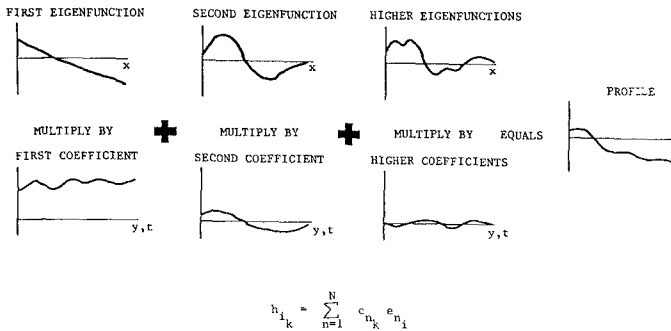


Figure 9: Eigenfunction Decomposition of the Profiles

### Temporal Analysis

Temporal eigenfunction analysis of beach profile data identifies the seasonal variations along a particular profile during the survey period. The first eigenfunction described the mean profile, accounting for about 99.7% of the variance. The second largest eigenfunction accounted for about 0.2% of the mean square value of the data, or about 70% of the variance with the mean beach function removed. The third largest eigenfunction accounted for less than 0.1% of the mean square value of the data.

The maximum and minimum of the second eigenfunction denote the locations of the greatest change. Figure 10 shows the first three eigenfunctions and the corresponding coefficients for the temporal analysis of profile 2. As expected, the second eigenfunction identified the berm and bar as regions with the most deviation from the mean. The coefficients for the second eigenfunction are consistent for all of the profiles, which indicates that the seasonal variations are described well by the temporal eigenfunction analysis. In Figure 10 the large positive eigenvalue at the berm means that the berm was enlarging during the summer and early fall. The negative second coefficient (see Figure 11) during the winter months indicates that the berm was eroding and the bar region accreting. Temporal analysis revealed berm changes extended from the landward end of the survey about 55 m to just seaward of mean sea level. A bar region about 100 m wide was also identified. Significant values at the offshore end of the second eigenfunctions for all of the profiles signifies that this is an area of considerable change rather than the depth of closure. It is unlikely that survey error would result in such consistent values.

Since the third function identifies the location of the low-tide terrace, it is probable that significant changes in the level of the low-tide terrace can take place in only a few days. This would cause aliasing in data from six-weekly surveys (Winant et. al., 1975).

### Spatial Analysis

Spatial eigenfunctions identified the variations along the beach at a particular time. As expected, the eigenfunction associated with the largest eigenvalues represented the mean profile, accounting for about 99.6% of the total variance. The second eigenfunction usually accounted for about 0.3% of the mean square value of the data, or 70% of the variance of the data with the mean beach function removed. The third eigenfunction accounted for about 0.1% of the mean square value of the data, or 20% of the variance with the mean beach function removed.

The mean beach function identified the major trends along the beach at a particular time. Figure 12 shows the first three eigenfunctions computed for the straightened profile data from 3 March 1983. The mean beach function revealed that the beach was in the winter profile. The berm was indistinct and a small bar can be identified between 45 m and 120 m offshore.

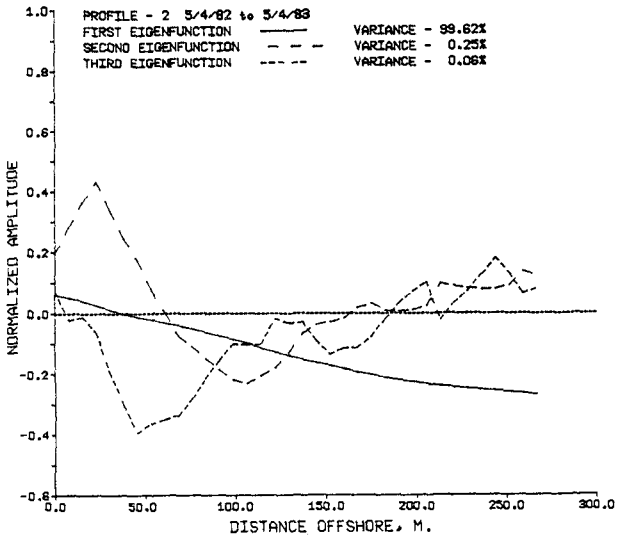


Figure 10: The First Three Eigenfunctions for the Profile Data for Profile 2

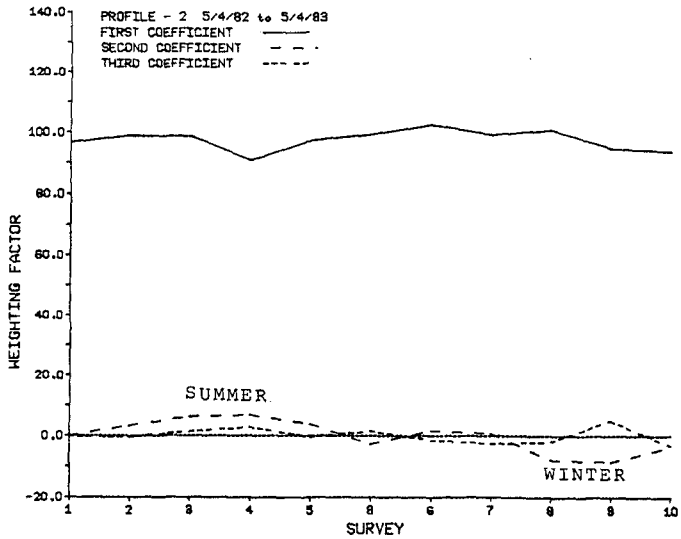


Figure 11: The Coefficients Corresponding to the Eigenfunctions from Profile 2 Data

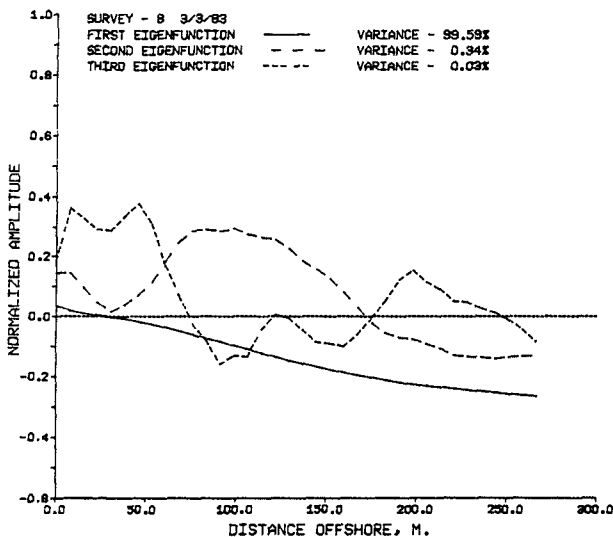


Figure 12: The First Three Eigenfunctions for Profile Data from March 3

The second eigenfunction identified the bar region as an area of substantial variation along the beach. The eigenfunction also described the berm and seaward limit of the survey area as locations with considerable deviations from the mean. The value of the second eigenfunction is nearly zero at the location of the waterline because straightened beach profile data was used. In Figure 13, the coefficients of the second function are positive for the northern four profiles, so in the northern section of the beach the berm and bar were more developed than the mean. The coefficients for the middle five profiles are nearly zero. For this area, the mean function closely described the beach profile configuration. Since the coefficients corresponding to the southern profiles are negative, the berm and bar in the south end of the study area were less distinct.

For most of the surveys, the second coefficient changed signs between the eighth and tenth profiles. The coefficients of the middle region are frequently zero, implying that these profiles are shaped similar to the mean. The reversal in sign indicates that the beach is "rotating" about the middle or mean region. The beach face in the southern end of the survey is steeper with more sediment deposited offshore of the bar region than at the northern end. More sediment is deposited in the berm and bar regions on the northern profiles resulting in a steeper offshore profile. For this reason, the second eigenfunction for the spatial variations along the beach will be called the rotation function.

Although in Figure 12 the shapes of the second and third eigenfunctions are very similar, and in Figure 13 the third

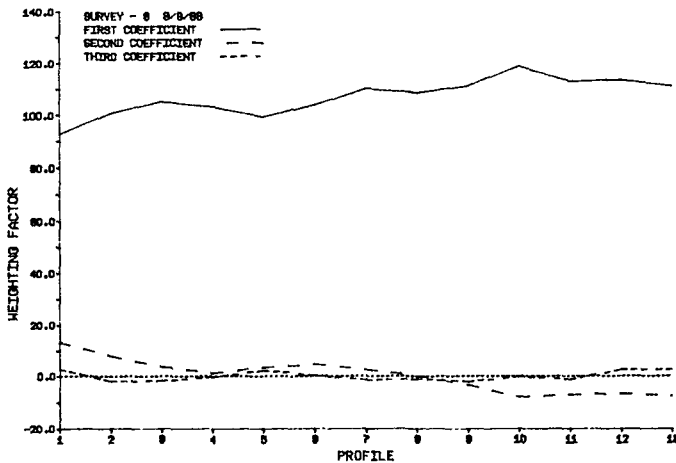


Figure 13: The Coefficients Corresponding to the Eigenfunctions Obtained from March 3rd Data

coefficients resemble the second coefficients, this was not typical for all of the surveys. Because the third eigenfunction accounts for such a small percent of the total variance, it describes weaker deviations from the mean so the configurations of the third eigenfunction and the corresponding coefficients are, in general, less consistent along the beach than the configurations of the second eigenfunctions and coefficients.

#### Difference Eigenfunctions

Spatial eigenfunctions were also computed on matrices formed of the differences in elevation between two surveys. The first eigenfunction in this analysis describes the mean changes along the beach between two surveys. The development of the beach into the summer profile is described by the first eigenfunction with a large maximum at the berm and a minimum at the bar. Because the storm altered the beach profile from its summer to winter configuration, in specifying the areas of greatest change between surveys, the eigenfunction analysis of the difference matrix identified the seasonal variations along the beach which are represented by a maximum at the berm and a minimum at the location of the bar. This describes the same variation as the berm-bar function of the temporal analysis. Therefore, the first eigenfunction of the difference matrix between a summer and a winter survey represents the seasonal changes in the profile, and in fact, it is really the berm-bar function of the temporal analysis. Comparison of the second eigenfunction in Figure 10 and the first eigenfunction in Figure 14 confirms this finding.

Between August 1982 and March 1983 the mean eigenfunctions indicate that there was significant change at the seaward limits of the

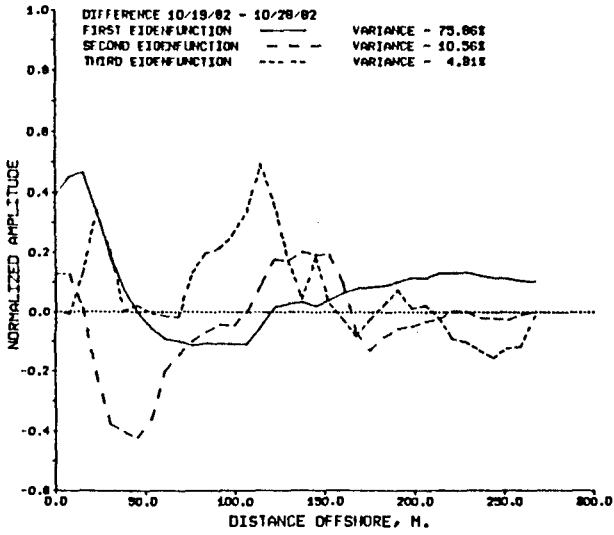


Figure 14: The First Three Eigenfunctions for the Difference Matrix for October 19 and October 28

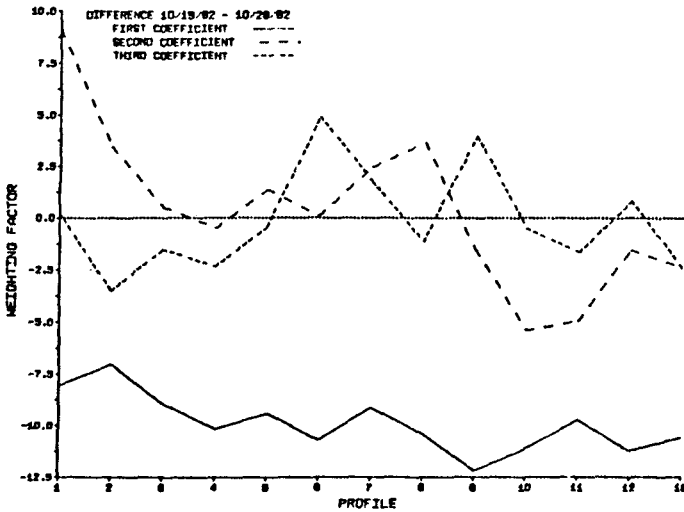


Figure 15: The Coefficients Corresponding to the Eigenfunctions Above

profiles. In half of these: between August and September, December and January, and early and late March, this was the location of the greatest change. Although the mean function accounted for about 60% of the variance, it accounted for a greater percent of the variance during the months with the worst storms, October and February. The second and third functions accounted for 15% and 10%, respectively. Higher order eigenfunctions accounted for a much larger percentage of the variance than in the previous analyses.

The coefficients associated with the mean beach function of the difference matrix reversed sign between the fifth and seventh profiles on several of the surveys. Since the waterline also shifts about the same location it is probable that the sand was transported alongshore between the northern and southern sections. Between mid-October and May, the coefficients associated with the first eigenfunction are consistent along the survey area. This signifies that the predominant process was the same over the survey area during the winter.

#### Conclusions

Although erosion has long been considered a serious problem at Bethany Beach, the shoreline has not changed significantly since the groins were constructed nearly fifty years ago. Historical aerial photographs show that the groins accumulated sediment, thereby widening the beach. Between 1938 and 1977, the shoreline within the groin field accreted an average of 0.4 meters/year. These rates include the artificial beach fill that the State of Delaware placed on the beach between 1954 and 1961. The fill was eroded by the March 1962 storm but then replaced by the U.S. Army Corps of Engineers (U.S. Army Corps of Engineers, 1971). The areas north and south of the groins (particularly south) may have suffered from a reduced rate of accretion or even erosion since the construction of the groins.

Examination of the survey data revealed that substantial changes in beach sand volume occurred during the year, but the annual change in volume was very small. Between June and September, the volume of beach sand increased gradually. A severe storm in October transported  $13 \times 10^4$  cubic meters out of the survey area. The total transport, or the absolute value of the volumes of erosion and accretion, was over  $24 \times 10^4$  cubic meters. In early March, the beach sand volume reached its lowest point for the year. Since early May,  $15.4 \times 10^4$  cubic meters of sediment had been transported out of the survey area. In 3 1/2 weeks, the volume of beach sand increased by  $19.3 \times 10^4$  cubic meters, to the highest volume for the year. Despite the large changes that occurred during the year, the net change in volume over the study period was only 1150 cubic meters.

Considerable changes in elevation were observed in depths previously thought to be below the depth of closure. Changes of up to a meter were detected in water depths of 8-9 meters. Because of the experience of the survey crew and the consistent trends between profiles both temporally and spatially, it is assumed that these are actual offshore changes and not a result of survey error.



During the survey period the position of the shoreline varied by around 30 meters. The shoreline and sediment deposition pattern rotated seasonally about the middle profiles. During the summer months when the sediment transport was northward, the southern profiles accreted and the northern profiles eroded. During the winter, the direction of sediment transport reversed causing the northern profiles to accrete and the southern profiles to erode.

The EOF method efficiently produced quantitative results describing changes in the beach profiles. The usual temporal eigenfunction analysis identified the seasonal transition between the summer and winter profiles as the predominant process affecting Bethany. It also revealed the significance of the changes at the offshore end of the profiles. By employing the EOF method spatially to examine the variations along the beach at a particular time, a rotation function was found that identifies the seasonal rotation of the sedimentation patterns about the middle profiles. The first eigenfunction of the spatial analysis of the differences between surveys identifies the same seasonal variations as the berm-bar function of the temporal analysis. The implication of this finding is that the seasonal movement of the beach can be determined from two surveys, one taken of the summer profile and one of the winter, instead of repeated surveys that are necessary for a temporal eigenfunction analysis.

#### Acknowledgement

The authors would like to express their thanks to the Delaware Department of Natural Resources and Environmental Control for the funding of this research. Special thanks go to Robert Henry and Charles Williams of the DNREC for supplying the field data.

#### References

- Aubrey, D.G., 1979, Seasonal patterns of onshore/offshore sediment movement. *J. of Geophysical Research*, 84: 6347-6354.
- Dick, J.E. and Dalrymple, R.A., 1983, Coastal engineering study of Bethany Beach, Delaware, Research Report No. CE-83-38, Ocean Engineering Program, University of Delaware, Newark, DE, 185 pp.
- Kraft, J.C., Allen, D.A., Belknap, D.F., Chacko, J.J., and Maurmeyer, E.M., 1976, Delaware's changing shoreline, TR-1, Delaware Coastal Zone Management Program, Dover, DE, 319 pp.
- Mauer, D. and Wang, H., 1973, Environmental vulnerability of the Delaware Bay area to supertanker accommodation, Vol. III: chemistry, engineering, geology, and physical oceanography, Report on the Council on Environmental Quality, Newark, DE, 331 pp.
- Polis, D.F. and Kupferman, S.L., 1973, Delaware Bay Report Series, Vol. 4 - Physical Oceanography, University of Delaware, Newark, DE, 170 pp.
- U.S. Army Corps of Engineers, 1956, Delaware coast from Kitts Hummock to Fenwick Island, beach erosion control study, U.S. Army Corps of Engineers, Philadelphia District, 47 pp. and appendices A-H.
- U.S. Army Corps of Engineers, 1971, The National Shoreline Study: Regional Inventory Report, North Atlantic Region, Vol. I, U.S. Army Corps of Engineers, New York, NY, 120 pp.

- Williams, C., 1983, Personal communication, Delaware Dept. of Natural Resources and Environmental Control, Soil and Water Division.
- Winant, C.D., Inman, D.L., and Nordstrom, C.E., 1975, Description of seasonal beach changes using empirical eigenfunctions. J. of Geophysical Research, 80: 1979-1986.

## CHAPTER ONE HUNDRED THIRTEEN

### Procedure for Determining Dredging Requirements in Coastal Inlet Channels

James W. Forman, Jr., M. ASCE <sup>1</sup> and  
Limberios Vallianos, M. ASCE <sup>2</sup>

#### Abstract

In order to assess the technical feasibility of a long term maintenance dredging plan at Oregon Inlet, a simple procedure was devised to evaluate the capabilities of existing ocean going hopper dredges to maintain an ocean entrance channel in an inlet environment characterized by wave climate and resulting influx of littoral material as severe as any Atlantic coast location. The dredging analysis procedure described in this paper was used to evaluate dredge plant capabilities under the operational constraints imposed by depth limitations resulting from the continuous influx of sediment into the project channel, the wave climate, and dredging production capacity in terms of actual hopper capacity and cycle times for different disposal schemes. The shoaling and dredging simulation procedure is described in terms of its application to the proposed navigation project at Oregon Inlet, NC.

#### Introduction

The natural geometry of an inlet's ebbtide delta or ocean bar is the end product of the integrated effects of tidal currents, wave action and the associated sediment transport and deposition. Of particular concern here is the natural elevation of the ocean bar, which represents both the limiting elevation of sediment accumulation resulting from the influx of littoral materials contributed by the adjacent shores and the level below which littoral sediments will assuredly collect if the ocean bar is entrenched by a navigation channel. In this regard, the rate of sediment accumulation increases with increasing channel depths so that, at some depth, the channel is capable of effecting total interdiction of the sediments entering the inlet environment. Therefore, a rational evaluation of a dredging plan requires establishing the rate of sediment influx to the general inlet environment, the rate of sediment accumulation within the channel at specific depths, and the net rate of sediment removal by a floating

(1) Civil Engineer, Coastal Engineering Branch, U.S. Army  
Corps of Engineers, Wilmington District, Wilmington, NC 28402

(2) Civil Engineer, Chief, Coastal Engineering Branch, U.S.  
Army Corps of Engineers, Wilmington District, Wilmington, NC 28402

dredge plant having certain production capabilities. The general procedure described herein develops these factors in terms of daily time periods in order to develop a day-to-day simulation of siltation processes and dredging effects.

Daily Littoral Materials Transport Volumes

The volume of littoral materials transported toward Oregon Inlet on a given day depends on the characteristics of incoming waves occurring on that particular day. The alongshore transport of sediment is a function of the wave height squared, the wave period, and the angle at which waves break relative to the shoreline. However, an adequate estimate of the relative magnitude of alongshore sediment transport can be obtained simply on the basis of wave height squared in accordance with the relationship:

$$Q_i = Q_g \left[ \frac{H_i^2}{\sum_{i=1}^n H_i^2} \right] \quad (i=1,2,3\dots n) \quad (1)$$

where:

- i = number of the day during the year
- Q<sub>i</sub> = littoral transport occurring on day i (cu. yds.)
- Q<sub>g</sub> = total volume of alongshore sediment transport to the inlet each year (cu. yd s.)
- H<sub>i</sub> = average wave height for the i<sup>th</sup> day of the year
- n = total number of days during the year (taken as 360 days on the basis of twelve 30-day months)

The total average annual rate at which sand is transported toward Oregon Inlet, Q<sub>g</sub>, has been computed as 2,105,000 cu. yds., see reference (1).

Day-to-day variations in the height of the waves required in the above daily transport equation were obtained by analyzing the wave data recorded by the Coastal Engineering Research Center's wave gage at Nags Head between 1963 and 1977. These data were synthesized into the average duration of waves falling within seven wave height classes given in table 1.

Table 1  
Wave Height Classes

<u>Wave Height Class</u>	<u>Wave Height Range (ft)</u>	<u>Average Wave Height in Range (ft)</u>
1	$0 < H < 1.0$	0.5
2	$1 < H < 1.5$	1.3
3	$1.5 < H < 2.5$	2.0
4	$2.5 < H < 4.0$	3.3
5	$4.0 < H < 6.0$	5.0
6	$6.0 < H < 10.0$	8.0
7	$10.0 < H$	10.0

The probability that waves within each of the seven wave height classes would occur during a given month was obtained by:

$$\left[ \text{Probability } H = H_{m,n} \right] = \frac{(Ovbs)_{m,n} (Dura)_{m,n}}{\sum_{m=1}^7 \sum_{n=1}^{12} \left[ (Ovbs)_{m,n} (Dura)_{m,n} \right]} \quad (2)$$

where:

- m = wave height class (m=1, 2, ..., 7)
- n = Number of month
- (Ovbs)<sub>m,n</sub> = Number of observations of waves within class m during month n
- (Dura)<sub>m,n</sub> = Average duration of waves within class m during month n (in days)

The number of days that a particular wave height class would occur during a given month was computed by multiplying the probability of occurrence of that wave class by the number of days in the month. For simplicity, all months consisted of 30 days, and wave durations were in whole day increments. The end product of the wave data analysis was a wave height-time matrix representing day-to-day variations in wave heights throughout the year, including periods of relatively calm sea conditions and moderate storm events.

#### Channel Sedimentation

A method developed by Galvin (see reference (2)) was adopted as the means of computing the volume of sediments expected to deposit within a channel of given depth. This method relates the sediment transport potential within the dredged channel to that existing on the ocean bar in its natural state. Galvin developed what is termed the "transport ratio" (equation 3), the ratio of the sediment transport capacity of the dredged channel to that of the natural ocean bar channel.

$$\text{Transport Ratio} = \left( \frac{d_1}{d_2} \right)^{5/2} \quad (3)$$

Galvin defines the predredging depth ( $d_1$ ) as the minimum controlling depth that exists over the ocean bar prior to any dredging, whereas  $d_2$  is the depth of the dredged bar channel. Both of these depths, which are defined schematically on figure 1, are measured relative to mean tide level (MTL). For the case in which  $d_1 = d_2$ , no shoaling would occur in the channel; however, if  $d_1/d_2 = 0.5$ , the transport ratio would equal 0.18, which means that for every 100 cu. yds. of sediment that enters the channel domain, only 18 cu. yds. would be flushed out by the currents, leaving 82 cu. yds. as the volume of deposited material. Since the dredging analysis is concerned with the material that remains in the channel, the sediment retention factor is defined as simply:

$$\text{Sediment Retention Factor} = 1 - \left( \frac{d_1}{d_2} \right)^{5/2} \quad (4)$$

Four hydrographic surveys of the ocean bar of Oregon Inlet made in the 1950's, or prior to the initiation of dredging, were used to determine the natural controlling depth of the bar ( $d_1$ ) for use in this dredging analysis. The average controlling depth obtained from these four surveys was 9.5 feet MLW or about 10.5 feet MTL.

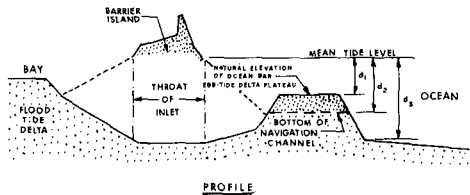


FIG. 1  
DEFINITION SKETCH

On a daily basis, the amount of material that would be retained in the ocean bar channel of the inlet would be:

$$\text{Daily Shoal Volume} = c Q_g \frac{H_1^2}{\sum_{i=1}^{360} H_i^2} \left[ 1 - \left( \frac{d_1}{d_2} \right)^{5/2} \right] \quad (5)$$

where all the terms in this equation have been previously defined except for the factor  $c$  which is designated here as the "potential shoaling factor". As stated previously, the rate of sediment accumulation in the bar channel increases with the depth of the cut.

However, until sufficient channel depth is attained to intercept all materials moving into the inlet environment, some material will continue to bypass the inlet via the sloping seaward face of the ocean bar below the bottom of the channel cut. Accordingly,  $c$  is defined as the proportion of the gross alongshore transport entering channel, of which a portion is deposited in accordance with the above equation.

In order to assess the magnitude of the potential shoaling factor, a regression analysis was conducted to establish a basic relationship between inlet bar channel siltation and those factors judged to be most influential in the filling and flushing of the channel. Basic data for the analysis was obtained from information available on four unstabilized, dredge-maintained inlet bar-channel projects (including Oregon Inlet) under the jurisdiction of the Wilmington District.

#### Regression Analysis

Three basic factors were selected as being dominant in terms of influencing the magnitude of shoaling at a particular inlet site having a dredge-maintained ocean bar.

- o Ebbtide flow energy is the primary factor acting to flush littoral materials from the inlet environment and, by so doing, serves to maintain the inlet as a viable coastal feature. Its influence in the analysis is represented by the symbol  $E_{DT}$ , the difference of the mean ebbtide flow energy flux across the ocean bar at its natural elevation and the mean ebbtide flow energy flux through the cross section of the dredged ocean bar channel. It is assumed that the tidal discharge is not significantly altered from one condition to the other. The basic concept reflected in the tidal energy flux difference is that the tidal flow velocities directed seaward over the ocean bar at its natural elevation, in combination with wave agitation, are sufficiently rapid to prevent accumulation of sediments above the natural bar level. Conversely, if a section of the ocean bar is deepened by a navigation channel, the related average local flow velocity is diminished resulting in sediment deposition.

- o The magnitude of wave energy reaching the littoral zones adjacent to the inlet is the primary factor controlling the quantity of littoral material moving toward the inlet and, is the fundamental element influencing the shoaling characteristics of an ocean bar navigation channel. In the analysis, the unrefracted wave energy flux per unit width of wave crest offshore of the area of interest, designated  $E_w$ , is used as the basic measure of the magnitude of sediment transport toward the inlet.

- o The depth of an ocean bar channel determines, in large measure, the degree to which a channel will interdict the littoral sediments entering the inlet environment. In the analysis the measure of sediment entrapment potential, is taken as  $D_R$ , the ratio of the depth of the channel to the depth at which the seaward slope of the ocean bar closes or intersects with the sea bottom. Each of these depths is measured from the natural elevation of the ocean bar or ebbtide delta plateau; therefore,

the ratio  $D_R$  represents the extent to which the ocean bar's seaward slope has been incised by the channel.

The channel sedimentation potential increases or decreases as each of the three factors,  $E_{\Delta T}$ ,  $E_W$ , and  $D_R$  becomes larger or smaller, respectively. Accordingly, the factors were combined to establish a normalized, independent variable  $F_I$  for the regression analysis. The value  $F_I$  will be referred to as the "Filling Index" where:

$$F_I = \left( E_{\Delta T} \times E_W \times D_R \right) \div 10^{14} \quad (6)$$

The denominator  $10^{14}$  is employed so that only the mantissa of the product's true value is used.

A normalized, dependent variable for the analysis was selected as the ratio of the volume of channel filling to the computed volume of the total alongshore sediment influx to the inlet multiplied by 100. This percentage value is referred to as the "volume ratio",  $V_R$  and as explained:

$$V_R = \frac{\text{Volume of Channel Sedimentation}}{\text{Volume of Gross Alongshore Sediment Transport}} \quad (7)$$

The regression analysis was based on data related to four dredge-maintained inlets within the boundaries of the Wilmington District: Oregon, Beaufort, Masonboro (prior to jetty construction) and Lockwoods Folly Inlets. The conditions at these inlets provided for a wide range of  $F_I$  and  $V_R$  values. Specifically, information available consisted of: (a) measured tidal discharges (Oregon, Beaufort, and Masonboro Inlets) or inlet throat cross sectional areas (Lockwoods Folly Inlet) which permitted tidal discharge computations by means of tidal prism-inlet area relations; (b) site wave statistics representing one or more years of wave gage records; (c) detailed alongshore sediment transport analyses for the shorelines adjacent to each of the inlets; and (d) one or more sets of inlet hydrographic surveys, each consisting of a first and second survey taken at different dates. This permitted measurement of the volume of sediment filling within the navigation channels in the time periods between surveys. The criterion for selection of sequential inlet hydrographic surveys was that the navigation channel in the second survey of any set was in the same location as the channel in the first survey. It could then be assumed that the channel was horizontally stable between surveys and that the only changes occurring were decreases in depth resulting from sediment deposition. From the records of inlet surveys, a total of 12 sets (24 hydrographic surveys) was selected that fulfilled the survey criterion, thus establishing 12 primary data points for the analysis.

For Beaufort Inlet, 10 surveys were used spanning the period February 1964 to May 1974, during which the authorized navigation project depth was 36.5 feet at mean tide level. This provided five data points for channel depths exceeding 36.5 feet at mean tide level. However, an additional data point was developed for



Beaufort Inlet by considering the dredging record for that inlet between 1937 and 1960, during which the authorized project depth was 31.5 feet at mean tide level. This additional data point was based on the average annual sediment volume removed from the ocean entrance channel, the average daily wave energy flux over the year, and an average channel depth of 34.0 feet below mean tide level, assuming that the average depth of the channel between dredging operations was 2.5 feet below authorized project depth. With this additional information, a total of 13 data points was available for analysis.

For each inlet selected, the basic tidal energy parameter,  $E_{\Delta T}$ , was developed. This parameter defined by equation 8, represents the difference in the daily ebb flow energy flux between the natural and dredged channel conditions. A detailed development of this parameter is presented in reference (1).

$$E_{\Delta T} = \frac{4T}{3\pi} q_{\max}^3 \left[ \frac{d_2^2 - d_1^2}{d_1^2 d_2^2} \right] \quad (8)$$

where  $T$  = Period of tidal wave  
 $q_{\max}$  = maximum instantaneous discharge  
per unit width of ebb flow area.

The next basic parameter of the independent variable is  $E_w$ , the average daily wave energy flux per unit width of wave crest offshore of the site of interest. This parameter represents the intensity of sediment transport from the adjacent beaches to the inlet environment. A basic formulation of wave energy flux can be found in reference (3). Daily wave energy flux can be expressed in a reduced form as:

$$E_w = 1.769 \times 10^6 (H'_o)^2 T \quad \text{ft. lbs.} \quad (9)$$

where  $H'_o$  = Deepwater wave height  
equivalent to observed  
shallow water wave unaffected  
by refraction and friction,  
given in feet  
 $T$  = Wave period in seconds

The wave data used for each site had been obtained from nearshore wave recordings near each inlet site.

Throughout the evaluation it was assumed that the wave records represented the average wave climates for the various sites. The average monthly significant wave heights were converted to deep water equivalent wave heights ( $H_o$ ) based on wave periods, water depths at the respective wave gages, and computed deep water wave lengths ( $L_o$ ).

The computed daily wave energy flux for each month's average daily deepwater equivalent wave height was multiplied by the number of days in the associated month to arrive at monthly energy flux values. If the quantity of channel fill was being measured, for example, by a first survey dated 15 June and a second survey dated 31 October, the average daily wave energy flux associated with that rate of channel sediment filling was computed as the summation of half of the June energy flux and all the monthly energy values for July, August, September and October, divided by the number of days in the whole period.

The last parameter of the independent variable, the depth ratio,  $D_R$ , is a measure of the degree to which channel depths influence the entrapment of sediments. With reference to figure 1, the depth ratio is given as:

$$D_R = \frac{d_2 - d_1}{d_3 - d_1} \quad (10)$$

The dependent variable,  $V_R$ , is, as previously defined, the ratio of the volume of channel fill ( $V_F$ ) to the volume of alongshore sediment transport ( $V_{ST}$ ). The volume of fill ( $V_F$ ) was determined simply by computing the accumulation of channel fill between the first and second hydrographic surveys in each set of surveys. For the additional Beaufort Inlet data point, representing the average conditions in the period 1937-1960, the volume of fill was computed as the average annual volume of material dredged from the inlet entrance channel. The annual alongshore sediment transport volumes for the various sites were available from detailed sediment budget analysis conducted by the Wilmington District. The annual quantities for each site and published references wherein the analyses can be found are as follows: Oregon Inlet - 2.11 million cubic yards, reference (1); Beaufort Inlet - 0.86 million cubic yards, reference (4); Masonboro Inlet - 1.15 million cubic yards, reference (5); and Lockwoods Folly Inlet - 0.60 million cubic yards, reference (6). The independent and dependent variables were computed for each inlet case. The resulting data points are plotted on the diagram shown on figure 2. Tests of several regression equations and related curves revealed that the best fit of the data points was attained by "Hoerl's" special function distribution given in general form by:

$$V_R = a r_I^b e^{CFI} \quad (11)$$

where:

- a, b and c are coefficients
- $V_R$  = volume ratio
- $r_I$  = filling index

In accordance with this generalized form, the regression analysis provided the following relationship:

$$V_R = 10.036686F_I^{-0.000387} e^{0.108489F_I} \quad (12)$$

which is valid for  $F_I$  values equal to or greater than 2 and has the curvilinear form shown on figure 2.

In order to display the expected channel sediment filling in a dredge-maintained navigation channel through the ocean bar at Oregon Inlet, the regression equation was solved for filling index,  $F_I$ , values corresponding to various channel depths. Channel low water depths corresponding to the  $F_I$  scale are shown along the bottom of figure 2. The daily deepwater equivalent wave energy flux used to compute the  $F_I$  values was derived from a nearshore wave height and period of 3.0 feet and 8.6 seconds, respectively. These represent the mean significant wave characteristics synthesized from the record of wave measurements by a gage located in a water depth of 17 feet at Nags Head, N.C., over the period July 1964 - April 1976. In reference to figure 2, it is readily evident that ocean bar channel depths in Oregon Inlet at and below the authorized channel depths of 20 feet MLW datum have corresponding  $F_I$  values well within the domain of 100 percent entrapment of the alongshore sediment transport from the adjacent beaches.

The results of the regression analysis would fully justify adopting a c factor of 1.0 for the "Daily Shoal Volume" equation selected for the dredging analysis.

In the case of Oregon Inlet, the shoaling dredging simulation was run using C values of 0.5, 0.75, and 1.0 in order to determine the sensitivity of the basic procedure with respect to the magnitude

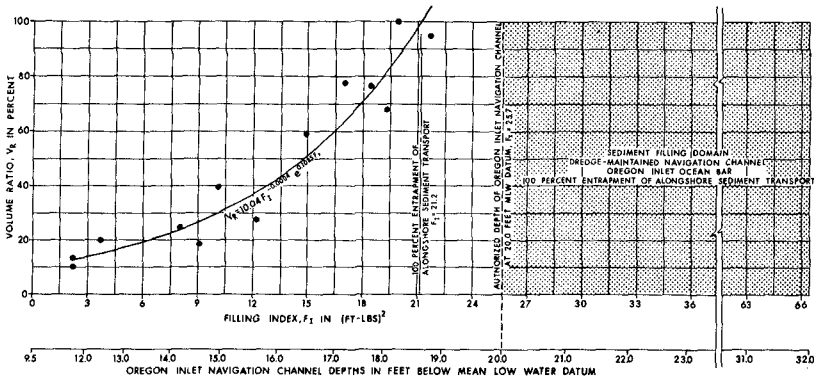


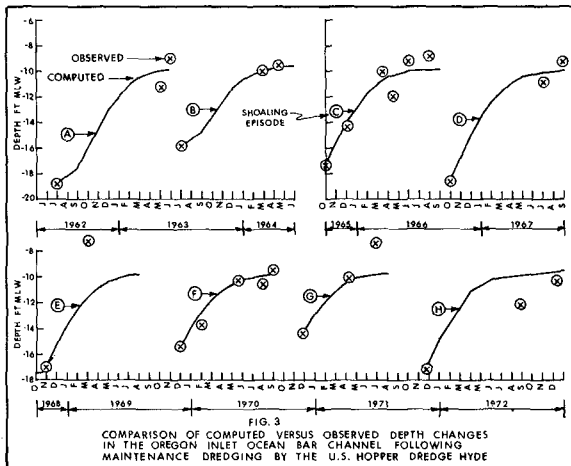
FIGURE 2  
REGRESSION ANALYSIS  
CHANNEL DEPTH - SEDIMENT FILLING RELATIONSHIPS  
DREDGE-MAINTAINED NAVIGATION CHANNEL  
OREGON INLET OCEAN BAR

of dredging resulting from the analysis. In all cases, the results indicated that an intensive dredging effort would be required to maintain the project channel dimensions requiring a channel having a width of 400 feet and a depth of 20 feet below MLW. It was decided to perform the dredging analyses for Oregon Inlet with a c factor of 0.75. This provided a degree of conservability in the analysis and recognized that there were other processes not accounted for that could cause some increased tidal flushing of the channel.

Verification of the Shoaling Rate Simulation Procedure

The method adopted for computing shoaling in the ocean bar channel was compared to actual shoaling rates experienced following eight maintenance dredging operations at Oregon Inlet by the U.S. Hopper Dredge HYDE. The eight shoaling episodes are designated by the letters A through H on figure 3. Controlling depths, rather than average depths were used in the comparison during the time in which the HYDE was employed at Oregon Inlet. Since the computational method utilizes average depths in the channel, the computed and controlling depths are not comparable on a one-to-one basis. However, the rate of change in the controlling depths is directly related to the rate of change in the average depths.

Controlling depths in the ocean bar channel immediately after each dredging operation ranged from about 14.5 and 18.8 feet below MLW, whereas depths at the end of each shoaling episode varied between 7.2 and 10.3 feet below MLW. The average controlling depth in the channel during the shoaling episodes was 12.8 feet below MLW computed by averaging the after-dredging and end-of-episode controlling depths. Since the average controlling depth was only 3.3 feet below the average natural elevation of the ocean bar (9.5



feet below MLW), the proportion of total littoral drift entering the channel domain would be small in comparison to conditions under which minimal depths of 20 feet below MLW would be permitted. In reference to the line of regression displayed on figure 2, channel depths of 12 to 13 feet below MLW would result in volume ratios,  $V_R$ , of 13 to 17 percent. With reference to figure 3, it is evident that, in general, depths less than the average of 12.8 feet existed for longer periods of time than the depths which were greater than average. Therefore, a volume ratio  $V_R$  amounting to about 13 percent was selected as being representative of the past conditions. On the basis of this, the potential shoaling factor  $c$ , adopted for the verification procedure, was 0.25.

#### Dredging Simulation

Removal of sediment from the inlet ocean bar channel by dredging is represented in the procedure by a daily dredging production rate. The production rate is the volume of material that can be removed from the channel during a single working day. This daily volume is the product of the effective hopper capacity for the dredge being evaluated and the number of dredging and disposal cycles that can be accomplished during a working day. A single dredging and disposal cycle time is determined by:

$$\text{Cycle Time} = \text{Dredging Time} + \text{Haul Time} + \text{Disposal Time} + \text{Return Time} + \text{Turning Time}$$

These times are determined by the operational and physical characteristics of the dredge vessel: the light and loaded speeds and the hopper capacity and filling rate.

In the procedure, a dredge is said to operate on a given day if sufficient depth exist in the channel for safe operations, the wave heights do not exceed allowable levels, and operational and maintenance schedules are met. The safe operating depth is defined by:

$$\text{Safe Operating Depth} = \frac{\text{Loaded Vessel Draft} + 1.2 H}{1} \quad (13)$$

where H is the wave height as previously defined. The vessel draft is the actual loaded draft plus a margin of safety of 1-1/2 to 3 feet. Half the wave height is added to allow for vessel motions when underway.

Wave height limitations were determined through discussions with vessel captains and by comparison of dredge logs and wave records for the Corps of Engineers dredge HYDE and the Gulf Coast Trailing Company dredge MERMENTAU. The HYDE performed channel maintenance dredging during the period 1962 to 1971. Comparison of daily operating logs to wave data collected at the Nags Head Pier, located approximately 25 miles north of Oregon Inlet, showed that

when wave heights reached or exceeded 4.0 feet, the HYDE did not operate. Comparison of wave records from the Field Research Facility at Duck, NC, located approximately 60 miles north of Oregon Inlet, and operating records of the MERMENAU operating at the inlet in 1983, showed the operations were terminated when wave heights exceeded 3.5 feet at Duck. These limiting wave height values were used as a guide in establishing limitations for other dredge vessels considered in dredging studies at Oregon Inlet.

In studies of dredging feasibility at Oregon Inlet, intensive dredging and disposal operations with continuous operations 21 hours per day and 7 days per week were evaluated. In order to account for dredge vessel down time required for scheduled and unscheduled maintenance and taking on fuel, water and provisions, dredging operations were permitted 6 out of 7 days. Together with down time due to wave conditions the average down time per month averaged about 20 percent. This agrees with down time experienced by MERMENAU operations in Oregon Inlet in 1983.

#### Dredging Shoaling Evaluation Procedure

The depth computed by the shoaling - dredging simulation is the net result of shoaling and dredging in the inlet channel. It is assumed that depth changes occur uniformly over the length and width of the channel. Channel length is measured between the 20 foot contours inside and outside the inlet. Channel width and depth are specified project dimensions. In the case of Oregon Inlet the project channel depth and width were 20 feet and 400 feet respectively. The measured channel length was 3,280 feet. From the daily variation of channel depths provided by the shoaling and dredging simulation, monthly minimum and maximum depths are taken to obtain a time history of monthly channel depth variation over the period of analysis.

The simulation also provides an accounting of simulated dredging operations in terms of the number of days per month the dredge operates, the number of dredging days lost due to weather (waves), and quantities of material dredged in cubic yards.

Several alternative dredging schemes for maintenance of an ocean entrance channel at Oregon Inlet were evaluated using the dredging and shoaling simulation. The various schemes varied in terms of the method of disposal and type of dredge vessel considered.

The first alternative considered involved dredging of the channel by trailer suction hopper dredge and pumping the dredged material to adjacent beaches much like conventional beach nourishment techniques. The direct pumpout scheme was evaluated for three different floating dredge plants representing a range of capacities and vessel drafts. Two Corps of Engineers dredges and a class of privately owned split hull hopper dredges with direct pumpout capabilities were evaluated. The shoaling and dredging simulation was applied to evaluate the capabilities and efficiency of each plant to maintain the project

channel at Oregon Inlet. Evaluated were the Corps dredge MARKHAM, a medium sized hopper dredge with a total bin capacity of 2,000 cubic yards and a loaded draft of 23 feet; the Corps dredge HAINS with a total bin capacity of 330 cubic yards and a loaded draft of 13 feet; and the split hull hopper dredge ATCHAFALAYA operated by Gulf Coast Trailing Company with a total bin capacity of 1,000 cubic yards and a loaded draft of 14.5 feet.

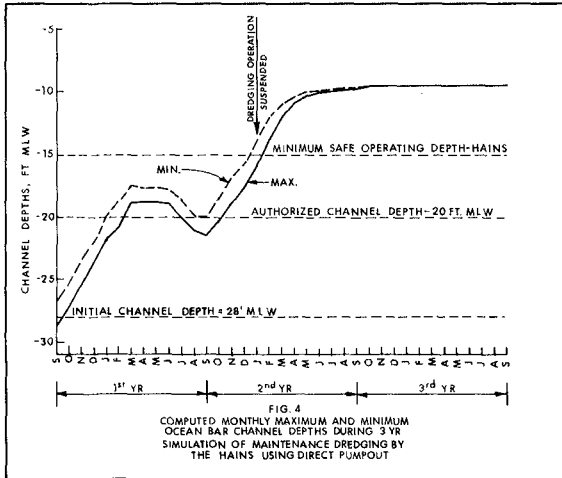
Dredging cycle times were determined by:

$$\text{Direct Pumpout Cycle Time} = \text{Dredging Time} + \text{Haul Time} + \text{Hookup and Pumpout Time} + \text{Return Time} + \text{Turning Time}$$

Production rates were based on a working day of 21 hours, a 26 day working month, and wave height limitations of 5 feet for the MARKHAM and ATCHAFALAYA and 4 feet for the HAINS. It was assumed that sufficient initial channel depths existed in the bar channel to allow for safe operations of each dredge at the initiation of maintenance dredging operations. In each case, maintenance dredging was assumed to begin in September, the beginning of the period of highest wave energy and associated alongshore transport to Oregon Inlet. The basic results of the analyses of the various dredges is presented below as an example of the application of the shoaling and dredging simulation procedure.

The production rate of the HAINS, when utilizing the direct pumpout technique is 3,980 cubic yards/day. The average daily influx of sediment to the channel, assuming that only 75 percent of the total littoral drift reaches the channel domain, is 4,330 cubic yards/day. Though the shoaling-dredging simulation accounts for a portion of the daily sediment influx being flushed from the channel by ebb tide currents, the number of days during the year that the HAINS could not work in the inlet due to normal downtime or inclement conditions would make it impossible for this particular dredge to maintain the channel below 20 feet MLW using direct pumpout. In evaluating the HAINS for direct pumpout, initial channel depths of 24 to 28 feet MLW were considered. However, even with the initial depth of 28 feet MLW, the depth in the channel decreased to slightly less than 20 feet MLW by the end of the first year of dredging. With the HAINS continuing to operate at its maximum rate into the second year, the shoaling-dredging simulation predicted that the channel depth would decrease to less than the 15-foot MLW maximum safe operating depth for the HAINS by January. The time variations of the computed minimum and maximum monthly depths in the Oregon Inlet ocean bar channel during direct pumpout maintenance dredging operations by the HAINS are shown on figure 4.

The direct pumpout capacity of the MARKHAM is 14,000 cubic yards/day which is more than three times the average daily influx of sediment to the channel; therefore the MARKHAM would not have to be committed to Oregon Inlet on a year-round basis. However, the channel developed by the MARKHAM at the end of an operation



would have to be of sufficient depth to store materials depositing in the channel during nondredging months to a depth at or below 24 feet MLW. Otherwise, a dredge of smaller draft of shallower draft would have to be used to reestablish the 24-foot MLW depth required by the MARKHAM on its return to the project site.

Though the MARKHAM is capable of dredging to a maximum depth of 45 feet, the practical limit on the dredge of the inlet channel was set at 32 feet MLW or slightly below the toe of the seaward slope of the ocean bar at Oregon Inlet. In evaluating the MARKHAM, various limits were set on the number of months that the dredge would work in Oregon Inlet and on the maximum depth that the dredge would be allowed to cut into the bar. The number of months ranged from 4 to 8, whereas the maximum channel depths considered were 28, 30, and 32 feet MLW. A total of 15 combinations of dredge time and maximum depth were considered. Of the 15 alternatives tested, only two yielded predicted channel depths greater than 24 feet MLW at the end of the 12-month evaluation period. An alternative involving a 7-month commitment of the MARKHAM to Oregon Inlet and a maximum channel depth of 32 feet MLW was selected for the purpose of comparison with other alternative schemes.

The selected maintenance dredging operation for the MARKHAM was simulated over a 3-year period to determine if the dredge would be able to maintain adequate depths over an extended period of time. A plot of the monthly maximum and minimum channel depths for this 3-year simulation is given on figure 5. The depths for a particular month remained fairly constant from year to year, and the channel depth never decreased to less than 24 feet MLW. Thus, it is evident that the MARKHAM could, without difficulty, maintain the Oregon Inlet ocean bar channel using direct pumpout.



The evaluation of the ATCHATALAYA, which has a direct pumpout production rate of 5,900 cu. yds./day, considered five initial depths in the bar channel, namely 20, 24, 26, 28, and 30 feet MLW. Plots of the minimum monthly depths in the inlet channel for each of the five initial depths considered for the ATCHAFALAYA are shown on figure 6. For the 20-foot MLW initial depth, there was not a sufficient depth buffer in the channel to accommodate the difference between the rate of shoaling and dredging that would occur between September and January. Consequently the depth in the channel decreases below the 16-foot MLW safe operating depth for the ATCHAFALAYA. This would result in a cessation of the dredging activity in January. With an initial depth of 24 feet MLW, the ATCHAFALAYA was able to work in the bar channel throughout the year; however, the minimum depth in the channel did decrease to slightly less than 20 feet MLW during the months of January through April. For all the other initial depths considered, i.e., 26, 28, and 30 feet MLW, the shoaling-dredging simulation indicated that the ATCHAFALAYA would be able to maintain channel depths deeper than 20 feet MLW throughout the year. Additionally, the depth in the channel at the end of the yearly dredge cycle was slightly deeper than at the beginning for initial depths of 26 and 28 feet MLW; therefore, during normal littoral transport years the ATCHAFALAYA would be able to maintain the 20-foot MLW bar channel from year to year. Since all of the initial channel depths equal to or greater than 26 feet MLW resulted in acceptable channel depths during the year, the 26-foot MLW initial channel depth was selected.

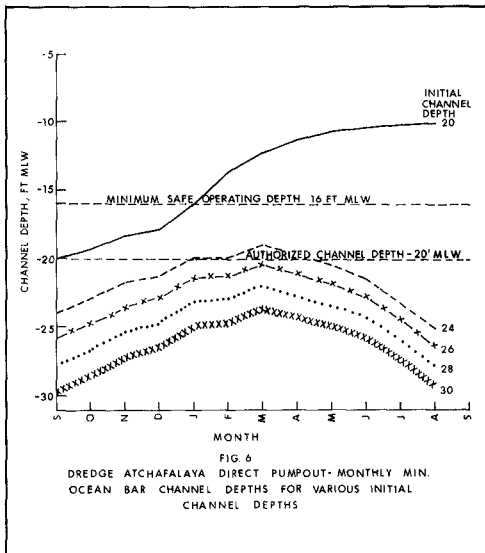
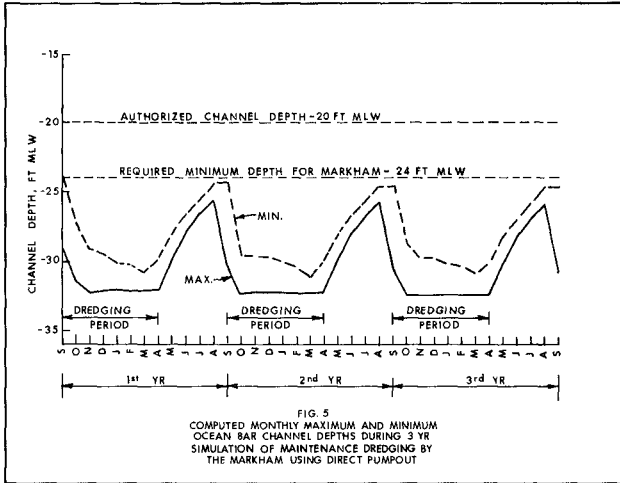
#### Summary

The procedure discussed in this paper provides a simple method for evaluating the capabilities of different dredge plants for maintaining a channel through the ebb tidal bar of Oregon Inlet, NC. The information required for its application includes the natural controlling depth of the ocean bar, the project channel width and length, the dredge plant capacities and operational characteristics, and a wave record covering the period of analysis.

The results of the procedure provide a time history of channel depths over the period of analysis and a means of evaluating the efficiency of a given dredge plant operating in the inlet. A dredging plan can be optimized by varying the length of the dredging period and the initial channel depths.

#### Acknowledgements

The procedure described by this paper is the product of extensive dredging studies conducted by the Wilmington District in connection with the Manteo (Shallowbag) Bay project. The studies were conducted by the Engineering Division, Coastal Engineering Branch. The District Engineer during the studies was COL. Robert Hughes. Chief of the Engineering Division was Mr. Jaman Vithalani. The Chief of the Coastal Engineering Branch was Mr. Limberios Vallianos.



## References

- (1) Manteo (Shallowbag) Bay, North Carolina, Design Memorandum 2, U.S. Army Engineer District, Wilmington, September 1980
- (2) Galvin, Cyril, "Shoaling Rate at Moriches Inlet," Report prepared for the New York District, U.S. Army Corps of Engineers, 25 July 1979.
- (3) "Shore Protection Manual" Vol. I, U.S. Army Coastal Engineering Research Center, 1977.
- (4) Morehead City Harbor, N.C., General Design Memorandum, U.S. Army Engineer District, Wilmington, May 1976.
- (5) Masonboro Inlet, N.C., General Design Memorandum, U.S. Army Engineer District, Wilmington, October 1977.
- (6) Brunswick County Beaches, N.C., General Design Memorandum, U.S. Army Engineer District, Wilmington, 1973.

## CHAPTER ONE HUNDRED FOURTEEN

### The Computation of Bed Shear in a Numerical Model

W. Leeuwenstein\* and H.C. Wind\*\*

#### 1. Introduction

Obstructions located in coastal and offshore waters usually disturb the natural flow pattern. This disturbed flow will, in general, cause local morphological changes in the position of the erodable boundary.

Often these changes should not be allowed to exceed certain limits, for example, when local scour around an offshore construction may endanger foundations.

Local morphological changes result from changes in the local sediment balance, brought about by the flow disturbance.

In the present paper a mathematical model is described which gives the bottom shear stresses and the configuration of the seabed around an obstruction using a computation of the two dimensional turbulent flow field. The obstruction considered is a submarine pipeline laid uncovered on a seabed consisting of non-cohesive sediment. A research project on the local scour near submarine pipelines is being carried out at the Delft University of Technology. Part of the project is the application and extension of an advanced numerical flow model for scour development near pipelines on the seabed exposed to current action. This work is being carried out in cooperation with the Delft Hydraulics Laboratory. The code of the flow model has been developed in a joint venture between the Delft Hydraulics Laboratory and the Laboratoire National d'Hydraulique in France.

The turbulent flow field is computed taking into account the influence of turbulence generated at the bed and by the pipe. The bed shear stresses are assumed to play the key role in the interaction between the flow and the seabed. In the computer model the bed shear is related to the flow through the "law of the wall". The model operation is schematized in the diagram below in which the first loop represents the evolution of the velocity field through a series of hydraulic time steps. After the velocity field is stabilized, in the second loop one morphological time step can be used for the computation of the local seabed changes. In this second loop the computed bed shear is applied together with a sediment transport formula.

After the morphological time step a new bed topography is obtained and a new grid is generated for the next flow computation.

---

\* Delft University of Technology, The Netherlands

\*\* Delft Hydraulics Laboratory, The Netherlands

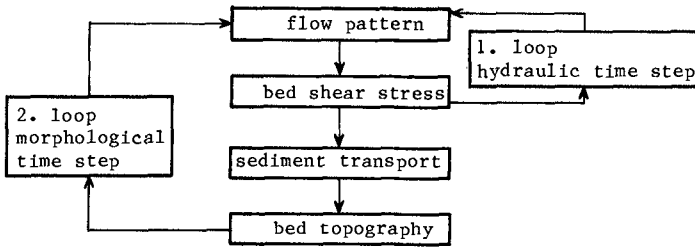


Fig. 1 Flow diagram of model operation

## 2. Theory

### 2.1 Flow Field

A detailed computation of the flow pattern is a prerequisite for the calculation of small scale changes of the seabed. In the present example the changes in the seabed are of the same magnitude as the pipe diameter which is, in general, small relative to the flow depth.

The basic equations describing the flow are the equations of motion and continuity for the fluid. The two dimensional unsteady Navier-Stokes equations for the mean flow are written as:

$$\frac{\partial u}{\partial t} + u \frac{\partial u}{\partial x} + v \frac{\partial u}{\partial y} + \frac{1}{\rho} \frac{\partial p}{\partial x} - \frac{1}{\rho} \left( \frac{\partial \tau_{xy}}{\partial y} + \frac{\partial \sigma_{xx}}{\partial x} \right) = 0$$

$$\frac{\partial v}{\partial t} + u \frac{\partial v}{\partial x} + v \frac{\partial v}{\partial y} + \frac{1}{\rho} \frac{\partial p}{\partial y} - \frac{1}{\rho} \left( \frac{\partial \tau_{xy}}{\partial x} + \frac{\partial \sigma_{yy}}{\partial y} \right) = 0 \quad (1)$$

where  $u$  and  $v$  are the horizontal ( $x$ ) and vertical ( $y$ ) velocity components respectively,  $p$  is the pressure and  $\sigma_{xx}$ ,  $\sigma_{yy}$ ,  $\tau_{xy}$  are the shear stresses in the fluid,  $\rho$  is the density of the fluid. The equation of continuity is:

$$\frac{\partial u}{\partial x} + \frac{\partial v}{\partial y} = 0 \quad (2)$$

In the equations of motion the viscous and turbulent shear stresses appear together as

$$\sigma_{xx} = \rho \nu 2 \frac{\partial u}{\partial x} - \rho \overline{u'^2}$$

$$\tau_{xy} = \rho \nu \left( \frac{\partial u}{\partial y} + \frac{\partial v}{\partial x} \right) - \rho \overline{u'v'}$$

$$\sigma_{yy} = \rho \nu 2 \frac{\partial v}{\partial y} - \rho \overline{v'^2} \quad (3)$$

where  $\nu$  is the kinematic viscosity of the fluid,  $u'$  and  $v'$  are the turbulent fluctuations associated with the time-averaged velocities  $u$  and  $v$  respectively.

Using Boussinesq's hypothesis the turbulent stresses in Eq. (3) can be written as:

$$-\overline{u'v'} = \nu_t \left( \frac{\partial u}{\partial y} + \frac{\partial v}{\partial x} \right) \quad (4)$$

where  $\nu_t$  is the turbulent equivalent of  $\nu$  and is commonly known as the turbulent eddy viscosity.

In the present model the eddy viscosity,  $\nu_t$ , is written in terms of the turbulent kinetic energy  $k$  and its dissipation rate  $\varepsilon$ :

$$\nu_t = c_\mu \frac{k^2}{\varepsilon} \quad (5)$$

where  $c_\mu$  is a universal constant with a value of  $c_\mu = 0.09$ .

The kinetic energy,  $k$ , and its dissipation rate,  $\varepsilon$ , are solved from two partial differential equations in  $k$  and  $\varepsilon$ , both containing  $\nu_t$ , and referred to as energy transport equations. For a detailed description of these equations for the standard  $k$ - $\varepsilon$  model, see Rodi (1980).

## 2.2 Boundary Conditions

In the present model the the law of the wall is used at the bed:

$$\frac{u_t}{u_*} = \frac{1}{\kappa} \ln \frac{y_1}{y_0} \quad (6)$$

where:

- $u_t$  = the tangential velocity at a distance  $y_1$ , which is the distance of the first grid line, from the bed,
- $u_*$  = the shear velocity
- $\kappa$  = the von Karman constant
- $y_0$  =  $r_N/33$  with  $r_N$  being the equivalent Nikuradse roughness length

The following boundary conditions are used with respect to the bed in the equations of the  $k$ - $\varepsilon$  model:

$$k = \frac{u_*^2}{\sqrt{c_\mu}} \quad (8)$$

$$\varepsilon = \frac{|u_*|^3}{\kappa y} \quad (9)$$

At the upstream boundary the standard distribution functions for uniform open channel flow are applied with regard to  $u$ ,  $v$ ,  $k$  and  $\varepsilon$ .

A rigid lid is applied along the free surface. The pressure distribution against the lid, which in fact is a fixed boundary without shear, acts on the fluid similarly to the pressure resulting from the free surface elevations, see Alfrink (1982).

## 2.3 Sediment Concentration Field

A spatial distribution of sediment exists as a result of the exchange of sediment between the flow field and the bed and due to further vertical exchanges caused by flow turbulence. Due to gravity forces acting on the grains the sediment concentration, in general, tends to increase towards the bed. In the present model the variation in bottom topography is found using the computed flow field.

The following unsteady equation describing the conservation of sediment is used in the model to derive the bottom boundary condition:

$$\frac{\partial c}{\partial t} + u \frac{\partial c}{\partial x} + (v - v_s) \frac{\partial c}{\partial y} - \frac{\partial}{\partial x} (D_x \frac{\partial c}{\partial x}) - \frac{\partial}{\partial y} (D_y \frac{\partial c}{\partial y}) = 0 \quad (10)$$

where:

$c$  = the sediment concentration  
 $v_s$  = the fall velocity of the sediment in still water  
 $D_x$  and  $D_y$  = the coefficients of sediment diffusion in the  $x$  and  $y$  direction respectively

Combining Eq. (10) with the equation for continuity, Eq. (2), it follows that:

$$\frac{\partial c}{\partial t} + \frac{\partial}{\partial x} (uc - D_x \frac{\partial c}{\partial y}) + \frac{\partial}{\partial y} \{ (v - v_s) c - D_y \frac{\partial c}{\partial y} \} = 0 \quad (11)$$

and that the horizontal and vertical transport through a unit area can be defined respectively as:

$$s_x = u c - D_x \frac{\partial c}{\partial y} \quad (12)$$

$$s_y = (v - v_s) c - D_y \frac{\partial c}{\partial y} \quad (13)$$

Boundary conditions with respect to the concentration field at the free surface ( $y = y_s$ ) for the sediment and for the fluid are, respectively:

$$s_y = s_x \frac{\partial y_s}{\partial x} + c \frac{\partial y_s}{\partial t} \quad \text{and} \quad (14)$$

$$v = u \frac{\partial y_s}{\partial x} + \frac{\partial y_s}{\partial t} \quad (15)$$

leading, with Eqs. (12) and (13) to

$$v_s c + D_y \frac{\partial c}{\partial y} = D_x \frac{\partial c}{\partial y} \frac{\partial y}{\partial x} \quad (16)$$

Similar boundary conditions apply for the bed ( $y = y_b$ ) and assuming a constant porosity,  $p'$ , for the bed thus leads to:

$$s_y = s_x \frac{\partial y_b}{\partial x} + c \frac{\partial y_b}{\partial t} - (1 - p') \frac{\partial y_b}{\partial t} \quad (17)$$

$$v = u \frac{\partial y_b}{\partial x} + \frac{\partial y_b}{\partial t} \quad (18)$$

$$v_s c + D_y \frac{\partial c}{\partial y} = (1 - p') \frac{\partial y_b}{\partial t} + D_x \frac{\partial c}{\partial y} \frac{\partial y_b}{\partial x} \quad (19)$$

From Eq. (19) it is obvious that the term for vertical diffusion, which is in general negative near the bed, will hinder sedimentation.

Assuming that the coefficients of diffusion for water,  $\nu_t$ , (eddy viscosity) and for sediment,  $D_y$ , are equal, sedimentation will be hindered where the eddy viscosity field shows high values for  $\nu_t$ .

Combining Eq. (11) for the concentration field with definitions of the horizontal and vertical transport,  $s_x$  and  $s_y$ , given in Eqs.

(12), (13), respectively, gives, after integration over the flow depth, the equation of continuity of sediment

$$\int_{y=y_b}^{y=y_s} \left( \frac{\partial c}{\partial t} + \frac{\partial s_x}{\partial x} + \frac{\partial s_y}{\partial y} \right) dy = 0 \quad (20)$$

Using Eqs. (13), (16) and (17) leads to

$$\frac{\partial}{\partial t} \left( \int_{y_b}^{y_s} c \, dy \right) + \frac{\partial}{\partial x} \left( \int_{y_b}^{y_s} s_x \, dy \right) + (1-p') \frac{\partial y_b}{\partial t} = 0 \quad (21)$$

The total sediment transport capacity can now be written as:

$$S = \int_{y_b}^{y_s} s_x \, dy \quad (22)$$

Using  $S$  according to Eq. (22) in Eq. (21) gives an alternative formulation with regard to the bottom boundary condition for cases where total sediment load is considered:

$$\frac{\partial}{\partial t} \left( \int_{y_b}^{y_s} c \, dy \right) + \frac{\partial S}{\partial x} + (1-p') \frac{\partial y_b}{\partial t} = 0 \quad (23)$$

For the computation of the bottom changes use has been made of Eq. (23) assuming a stationary concentration field ( $\partial/\partial t = 0$ ). The objective of the study is to analyze the evolution of scour beneath a pipeline. The bottom changes will be restricted to the characteristics of bottom changes due to bed load.

#### 2.4 Bed Load Transport

For cases with bed load transport a suitable bed load transport formula is used to compute  $S$ . The transport capacity  $S$  is calculated using the computed bed shear  $u_*$  and the threshold value  $u_{*c}$ . The value of  $u_{*c}$ , indicating the initiation of bed load transport, has been determined experimentally by many investigators, for instance Shields (1936). In the course of this study three bed load formulae will be considered. The first formula is similar to the Meyer-Peter Müller formula:

$$\Phi = a (\theta - \gamma_s \theta_c)^b \quad (24)$$

where

$$\Phi = \frac{S}{(g\Delta D^3)^{\frac{1}{2}}} \quad \text{and} \quad \theta = \frac{u_*^2}{\Delta g D} \quad (25)$$

The values of the parameters  $a$  and  $b$  have been chosen 13.3 and 1.5 respectively. The parameter  $\gamma_s$  represents the influence of the local bed slope  $dy_b/dx$  on the threshold value  $u_{*c}$  and is defined, using  $\psi$  the angle of internal friction of the sediment, as:



$$\gamma_s = \sin\{\psi - \arctg(dy_p/dx)\} (\sin\psi)^{-1} \tag{27}$$

An example of an empirical formula describing in particular conditions with minor sediment transport is the formula of Paintal (1971):  

$$\Phi = 6.56 * 10^{18} \theta^{16} \tag{28}$$

De Ruyter (1982) has elaborated upon the stochastic description of sediment transport. He has expressed the sediment transport rate as a function of the pick up rate  $N_p$  and the saltation length  $\lambda$ . In dimensionless terms this formula can be expressed as:

$$\Phi = \Pi \Lambda \tag{29}$$

where

$$\Pi = \frac{\pi D^3}{6} \frac{N_p}{\sqrt{\Delta g D}} \text{ and } \Lambda = \frac{\lambda}{D} \tag{30}$$

The formula of  $N_p$  is given in the Appendix by (A3). An important parameter is the dimensionless saltation length  $\lambda/D = a' \theta$ . For  $\theta < \theta_c$  it has been assumed that  $a'$  approaches  $550 \theta_c/\theta$ . For  $\theta > \theta_{cr}$  the value of  $a'$  has been assumed to be equal to 550. The ratio of  $\sigma_\tau/\tau$  and  $\theta_c$  have been estimated at a value of 0.4 and 0.1 respectively. It should be emphasized that the transport rate described by (A1) has been reduced with a factor of 3 for calibration purposes.

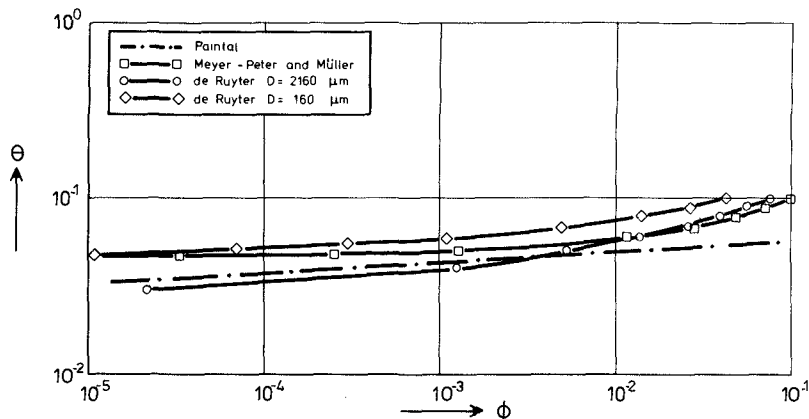


FIG. 2 COMPARISON OF BED LOAD TRANSPORT FORMULAE

The tendency of all the transport rates in Fig. 2 is similar, i.e. a rapid decrease in transport rate near the critical Shields value. This implies that for a given shear stress distribution, the transport distributions for the presented transport formulae will also be similar of shape even as the resulting bottom changes. This conclusion will be used in the analysis of the scour underneath the pipe. Finally it may be remarked that although the shape of the bottom changes is similar, the magnitude depends among others on the choice of the transport formula.

3. Examples

As an example has been chosen the scour beneath a submarine pipeline. Characteristic features of the scour hole obtained from laboratory experiments can be found in Figs. 3 and 4. First the equilibrium scour hole will be treated followed by the evolution of a scour hole with time.

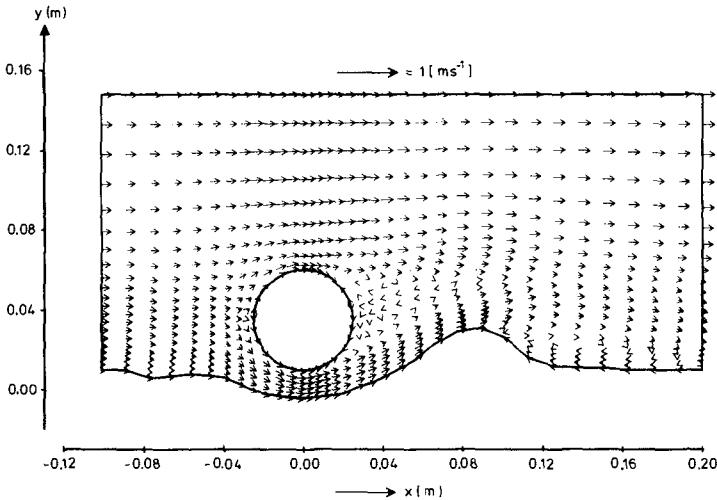


FIG. 3a FLOW PATTERN

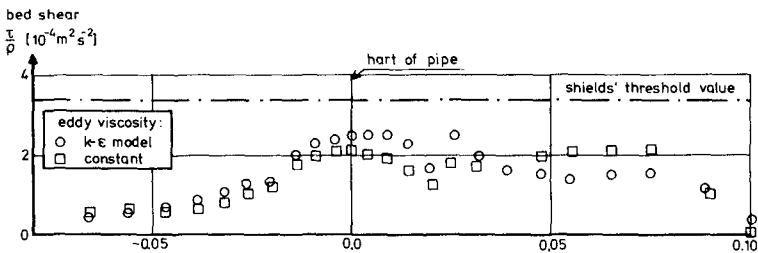


FIG. 3b COMPUTED BEDSHEAR

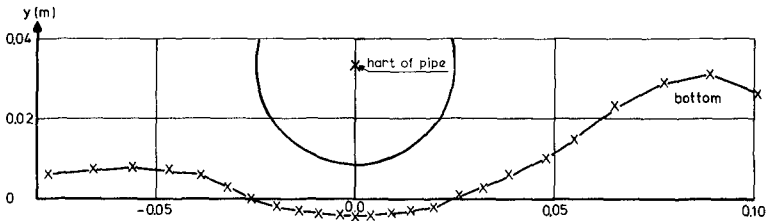


FIG. 3c CONFIGURATION OF SCOURHOLE

3.1 Equilibrium Scour Hole

The bed shear has been computed along the bottom of a scour hole for a situation with clear water scour, when the sediment supply towards the area of scour is zero. Although minor movement of individual grains was observed occasionally in the small scale scour test in the laboratory the scour hole can be assumed to show its equilibrium shape. The minor grain movement occurred on the rising slope and was due to fluctuations in the bed shear. The flow field is shown in Fig. 3a. Fig. 3b shows the computed bed shear for a constant viscosity of  $10^{-4} \text{ [m}^2\text{s}^{-1}\text{]}$  and also for an eddy viscosity computed by the  $k-\epsilon$  model. The computed time mean bed shear downstream of the pipe is a little below Shields' mean threshold value which is approximately  $u_*^2/(\Delta gD) = 0.03$  for the grain diameter used in the test. This is in agreement with the observation that the scour hole is in an equilibrium state. The test data of the example are:

- pipe diameter : 50 mm,
- mean current velocity:  $0.25 \text{ ms}^{-1}$
- grain size :  $D_{50} = 700 \text{ }\mu\text{m}$

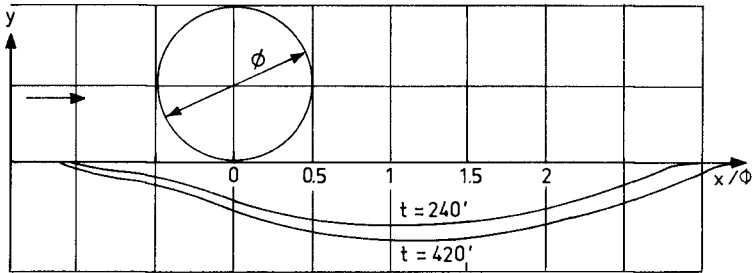


FIG. 4a SCOUR EVOLUTION

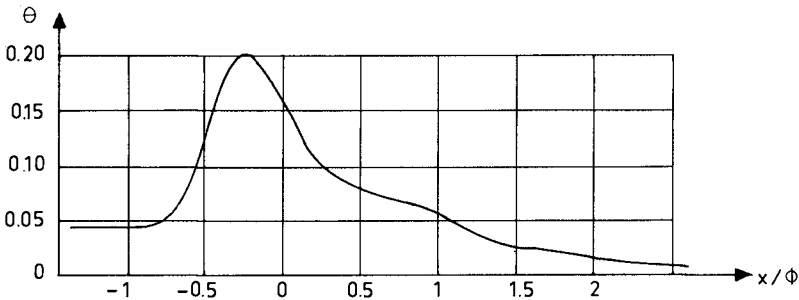


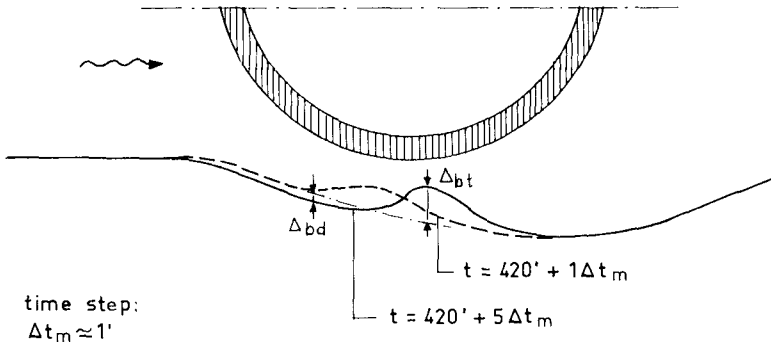
FIG. 4b COMPUTED BED SHEAR

3.2 Scour Development with Time

In this example the evolution of the scour hole has been computed starting with the geometry of a partially developed scour hole.

Five morphological time steps have been made each preceded by a series of hydraulic time steps, covering a total time interval of 5 minutes of the scour process. The computed bed shear is shown in Figs. 4a and 4b together with scour hole configurations as observed during the small-scale test after 240 and 420 minutes scouring respectively. Fig. 4a shows the further evolution of the scour hole, during the 5 minutes after  $t = 420$  minutes, as computed using the bed load concept of the model.

A propagating bed wave or ripple appears as a direct consequence of the use of a transport formulation relating the bed load transport to the bed shear. Its propagation velocity,  $c_b$ , is approximately 0.36 [m/hour] and the height of the crest,  $\Delta_{bt}$ , and the depth of the trough,  $\Delta_{bd}$ , converge to values of 0.014 and 0.007 m respectively, see Fig. 5b. Because of the persistence of the ripple the computations have been terminated after 5 minutes. In order to analyse these bed



time step:  
 $\Delta t_m \approx 1'$

FIG. 5a COMPUTED EVOLUTION OF SCOUR HOLE DUE TO BED LOAD TRANSPORT

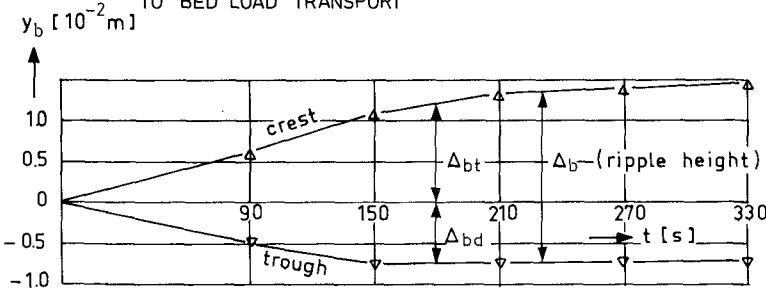


FIG. 5b RIPPLE DEVELOPMENT RELATIVE TO LOCAL INITIAL BED

features the computed sediment transport,  $S_b$ , is given in Fig. 6a together with the mean sediment transport,  $S_m$ , during the 3 hour time interval between the two scour hole configurations shown in Fig. 4a. It will be clear from Fig. 6a that the computed bed load transport capacity at  $t = 420$  deviates considerably from the mean value computed over the three hourst time preceding  $t = 420$ . In Section 4 this discrepancy will be further analyzed.

The test data are:

- pipe diameter : 140 mm,
- mean current velocity:  $0,40 \text{ ms}^{-1}$ ,
- grain size :  $D_{50} = 100 \text{ } [\mu\text{m}]$

sediment transport capacity  $[10^{-6} \text{ m}^3 \text{ s}^{-1} \text{ m}^{-1}]$

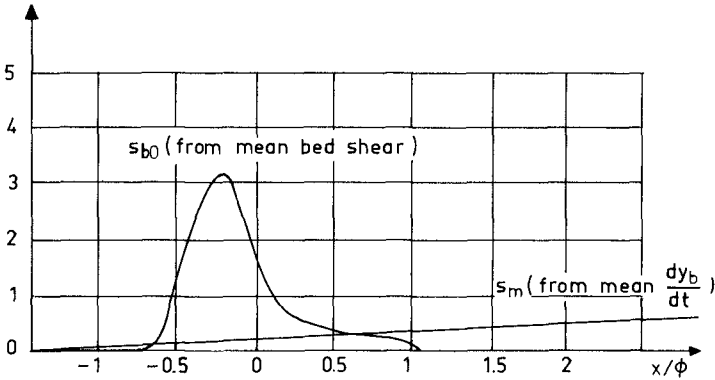


FIG. 6a COMPUTED AND OBSERVED SEDIMENT TRANSPORT DISTRIBUTIONS

gradient of transport  $[\text{ms}^{-1}]$

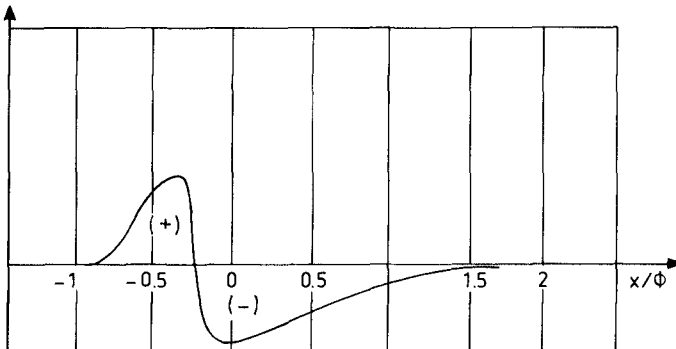


FIG. 6b COMPUTED SEDIMENT TRANSPORT GRADIENTS

#### 4. Analysis at the Results and Discussion

In view of the results in the examples treated in Sections 3.1 and 3.2 a first assessment can be made of the role that can be ascribed to bed shear with regard to local seabed morphology.

For the development and the equilibrium state of scour underneath submarine pipelines it can be assumed that the leading parameter is the bed shear. An increasing scour depth can be assumed to be closely related to an increasing bed shear in the direction of flow at least for cases with dominating bed load transport. In line with this assumption an equilibrium scour hole occurs when the bed shear remains constant along the bed provided that the threshold value is exceeded.

The example in Section 3.1 clearly confirms the assumption for an equilibrium scour hole in coarse sediment where the sediment supply upstream of the pipe equals zero. On the rising slope downstream it was observed that minor movement of individual grains still occurred even though the scour depth was practically in equilibrium. This observation is in agreement with the computed bed shear on the slope which in the scour hole is nearly constant and just below the mean threshold value of  $\theta_c = u_{*c}^2/(\Delta gD) = 0.03$  according to Shields (1936).

The example given in Section 3.2, in which the evolution of the scour hole with time was treated, demonstrated the unsatisfactory description of the sediment transport given by formulae like Eq. (24), even though bed load transport has been observed to contribute predominantly to the scour development. The appearance of a wave in the bed is inherent to the transport formulae like Eq. (24), where the sediment transport is so directly related to the bed shear. Fig. 6 clearly demonstrates the reason for the bed wave or ripple developing in the model. This reason is not numerical, but is a direct consequence of the sediment transport concept chosen and the sign of  $\partial S/\partial x$ .

During 5 minutes computing time the wave or ripple propagates in the direction of the flow while a mean degradation of the bed is being computed. All the sediment being transported by means of ripple propagation, the net loss of sediment from the scour hole, is determined by the propagation velocity and the height of the ripple.

Fig. 4b indicates that the ripple converges to a certain height,  $\Delta_b$ , which may enable a computation of the time averaged loss of sediment using:

$$dA = \xi \Delta_b c_b \quad (31)$$

where

- $dA$  = the increase in scour volume per unit width and per unit time and
- $\xi$  = a coefficient depending on the ripple configuration, representing the effective ripple height.

Using Eq. (31) with the computed values for  $c_b$  and the effective ripple height  $\xi\Delta_b$  the scour volume corresponding with the ripple propagation is of the same order as the observed mean scour from  $t = 240'$  to  $t = 420'$  (Fig. 4a).

In the small-scale laboratory scour tests a gradual degradation

of the bed has been observed at the time interval of 180 minutes. In the bed load concept a constant  $dy_b/dt$  means, that during that time,  $\partial s/\partial x$  is approximately constant and  $s$  increases gradually along the bed in the direction of the flow (the theoretical curve  $s_m$  for the transport capacity). Using the bed load concept the computed transport confirms with the curve  $s_b$  which in turn conforms to the bed shear in Fig. 3b. Both curves for the transport deviate considerably, indicating that the concept of bed load as a direct function of the time averaged bed shear is not unconditionally sufficient to describe local scour. Four reasons for this insufficiency are discussed below. These reasons are a) suspended transport, b) stochastic bed shear, c) bed-form roughness and d) transport formulation.

a) Suspended transport

It is obvious that with increasing bed shear sediment will be brought into suspension and a concentration field will develop resulting in additional convective and diffusive sediment transport in addition to the bed load transport. Ripples, appearing as a result of strong bed shear gradients as shown in the example, will, in the very initial phase, be in suspension. Suspended sediment transport will be included in a more extended version of the present program and will be based upon the equations given in Par. 2.3.

b) Introduction of stochastic bed shear

In turbulent flow the bed shear has a stochastic character and consists of a constant time averaged value  $\bar{\tau}$ , which follows directly from the present model, and a fluctuating component  $\tau'$ . Using only  $\bar{\tau}$  for the computation of the bed load transport capacity according to Eq. (24) the contributions of instantaneous bed shear values  $\tau$  (or  $u_*$ ) with a probability  $p(\tau)$ , or  $p(u_*)$ , can be neglected.

Instantaneous values of  $\tau > \bar{\tau}$ , even though their probability may be low, can contribute considerably to the sediment transport capacity.

Laboratory measurements have demonstrated that the significant turbulence downstream of pipelines which can be practically expressed in standard deviations,  $\sigma_u$ , of the flow velocity.

Once the turbulent kinetic energy,  $k$ , is known and assuming  $v' \ll u'$  the standard deviation  $\sigma_u$  follows from:

$$\sigma_u = \sqrt{2k} \quad (32)$$

In the appendix a method is given which, starting with  $\sigma_u$ , through  $\sigma_\tau$  results in an amplification factor,  $A$ , for the sediment transport capacity.  $A$  is a function of the mean bed shear level,  $\beta$ , and the relative level of turbulence,  $\alpha/\alpha_0$ . By multiplying the sediment transport capacity,  $S_{b0}$  and using only the mean bed shear  $\bar{\tau}$  (or  $\bar{u}_*$ ), by  $A$  the sediment transport capacity,  $S_b$  is obtained which also includes the effect of variation of turbulence. In case of  $\bar{\tau} < \bar{\tau}_c$  the Meyer-Peter Müller formula (24) yields a zero transport rate independent of the variation of turbulence. Fig. 7 shows  $A$  as a function of  $\alpha/\alpha_0$  and  $\beta$  and is further explained in the Appendix. Fig. 8 shows the effect of the measured relative turbulence,  $\alpha/\alpha_0$ , for the pipeline example discussed in Section 3.2. Above  $x/\theta = 1.0$  the computed amplification factor increases rapidly due to the low bed shear level,  $\beta = \bar{\tau}/\bar{\tau}_c$ , (see Fig. 7), and, finally,  $\beta$  arrives at values where the

approach leading to a value of the amplification factor is no longer applicable.

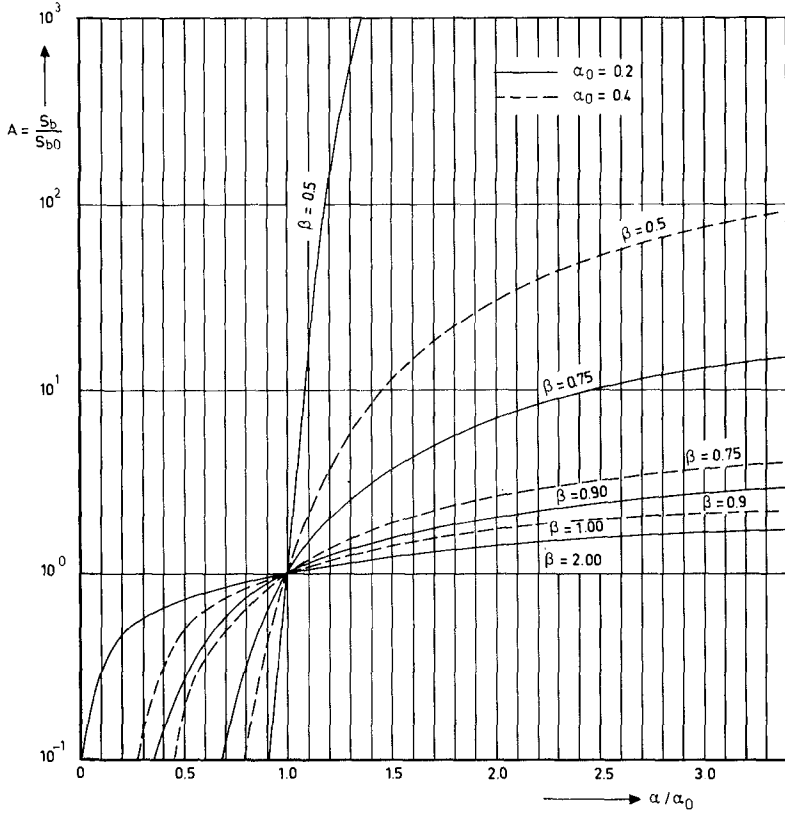


FIG. 7 AMPLIFICATION OF SEDIMENT TRANSPORT AS A FUNCTION OF SHEAR STRESS LEVEL  $\beta$ . AND RELATIVE TURBULENCE INTENSITY  $\alpha/\alpha_0$

According to Fig. 8 the amplification factor beneath the pipe is one. This means that introduction of stochastic bed shear does not influence the ripple height. On the lee side locally the amplification factor increases rapidly (Fig. 8). This increase is caused partly by the decrease in  $S_{b0}$  in Eq. (A6). Due to the local effect in the present example it is not expected that introduction of stochastic bed shear will in this case lead to a more uniform erosion on the lee side of the pipe.

c) Varying bed roughness

In the small-scale scour tests with movable bed it has been observed that, in general, the bed becomes smooth underneath the pipe and that the ripple pattern is restarted on the downstream slope.



Although this phenomenon will be less pronounced for larger scale scour its influence on the bed shear, Eq. (6), and the related transport (mechanism) should be taken into account.

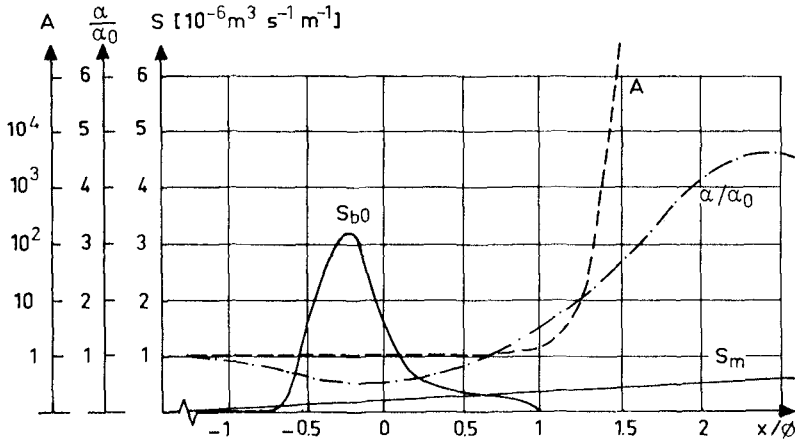


FIG. 8 OBSERVED TURBULENCE INTENSITY AND AMPLIFICATION FACTOR

d) Flexible transport formulation

Relaxation of the rigidly formulated (bed load) formulae, Eq. (24) and Eq. (28), by introducing variable coefficients  $a$  and  $b$  indeed makes sense physically. It is known that the value of  $b$ , in particular, decreases when  $\theta$  and, therefore, the transport,  $S$ , increases.

The various influences on the redistribution of sediment transport mechanisms underneath the pipe and downstream will without doubt change the type of transport and its formulation.

The use of a flexible formulation for the sediment transport, though physically justified and even required, is not warranted at present, because of lack of knowledge about the variation of the parameters.

5. Summary and Conclusions

The local morphological changes beneath pipelines originating from hydraulic conditions show variations which are on a relatively small scale compared to the water depth. A numerical model to compute these very local hydraulic conditions is essential for the study of scour problems as for example can occur with a submarine pipeline. A detailed computation of bed shear and turbulence characteristics, as provided by the present model, has been used to obtain the sediment transport capacity along the bed near a pipeline. Although the bed shear is the leading parameter for the sediment transport a combination of the latter with an empirical bed load formula seems to result in a rather rigid schematization of the complex sediment transport for the presented examples of local scour. The computed bed changes include ripple development, at least when a bed load concept is used,

which excludes sediment suspending under the influence of high values of local bed shear. The example with a computation on a flow field around a pipe with an equilibrium scour hole has proved the value of the present model for appreciating the morphological stability of local seabed configurations.

Implementation of the suspended load concept is the next step which will be taken in the further development of the present model.

## 6. Acknowledgements

The authors acknowledge the contributions of Mr. de Ruyter on Fig. 2 and on the Appendix. Discussions with Dr. de Vriend and Mr. van Rijn have appeared to be very fruitful.

## 7. References

- ALFRINK, B.J., 1982: "Value of refined modelling for the flow over a trench". Proceedings of the International Symposium on Refined Modelling of Flows, Paris.
- EINSTEIN, H.A., 1950: "The bed load function for sediment transportation in open channel flows". Technical Bulletin No. 1026, U.S. Dept. of Agriculture, Washington D.C.
- PAINTAL, A.S., 1971: "Concept of critical shear stress in loose boundary open channels". Journal of Hydraulic Research, No. 1 91-107.
- RODI, W., 1980: "Turbulence Models and their application in hydraulics". International Association for Hydraulic Research, Delft.
- RUYTER, J.C.C. de, 1982: "The mechanics of sediment transport on bed forms". Euromech 156 Mechanics of Sediment Transport, Istanbul.
- YALIN, M.S., 1977: "Mechanics of sediment transport". Oxford, Pergamon Press.

## 8. List of Symbols

A	amplification factor	[-]
a	coefficient transport formula	[-]
a'	coefficient saltation	[-]
b	coefficient transport formula	[-]
	index: bed	[-]
c	sediment concentration	[-]
	index: critical	[-]
c <sub>b</sub>	propagation celerity of bed forms	[ms <sup>-1</sup> ]
c <sub>μ</sub>	constant in k-ε model	[-]
D	grain diameter	[m]
D <sub>x</sub> , D <sub>y</sub>	coefficients of diffusion	[m <sup>2</sup> s <sup>-1</sup> ]
dA	scour area	[m <sup>2</sup> ]
F	function symbol	[-]
g	acceleration of gravity	[ms <sup>-2</sup> ]
k	kinetic energy	[m <sup>2</sup> s <sup>-2</sup> ]
N <sub>p</sub>	pick-up rate	[s <sup>-1</sup> ]
p	pressure	[Nm <sup>-2</sup> ]
	probability	[-]
p'	porosity of sediment	[-]
r	excess bed shear	[-]
r <sub>N</sub>	Nikuradse roughness	[m]

S	sediment transport capacity	$[m^2 s^{-1}]$
s	sediment transport capacity	$[ms^{-1}]$
t	time	[s]
u	velocity in x-direction	$[ms^{-1}]$
u*	shear velocity	$[ms^{-1}]$
v	velocity in y-direction	$[ms^{-1}]$
v <sub>s</sub>	fall velocity of grains	$[ms^{-1}]$
x	horizontal coordinate	[m]
y	vertical coordinate	[m]
y <sub>b</sub>	bed level	[m]
y <sub>s</sub>	water surface level	[m]
α	turbulence level, $\sigma_\tau/\bar{\tau}$	[-]
β	bed shear level, $\bar{\tau}/\tau_c$	[-]
γ <sub>s</sub>	slope factor	[-]
Δ	relative density of grains	[-]
Δ <sub>b</sub>	ripple height	[m]
Δt	time step	[s]
ε	energy dissipation rate	$[m^2 s^{-3}]$
η	coefficient	[-]
θ	Shields bed shear parameter	[-]
κ	von Karman constant	[-]
λ	saltation length	[m]
ν <sub>t</sub>	turbulent eddy viscosity	$[m^2 s^{-1}]$
ξ	coefficient	[-]
ρ	density of water	$[kgm^{-3}]$
σ <sub>u</sub>	standard deviation of u	$[ms^{-1}]$
σ <sub>τ</sub>	standard deviation of τ	$[Nm^{-2}]$
τ	(bed) shear	$[Nm^{-2}]$
∅	pipe diameter	[m]
Φ	transport parameter	[-]
ψ	friction angle	[-]

APPENDIX: Increase of Bed Load Transport Capacity due to Turbulence

A method is described below to account for the effect of turbulent fluctuations in the bed shear on the bed load transport capacity. In general the instantaneous bed shear will contribute to the bed load transport as soon as the threshold value,  $u_{*c}$ , (or correspondingly  $\tau_c$  or  $\theta_c$ ) is exceeded. The approach starts with a sediment transport formulation based upon the displacement of an individual grain with diameter  $D$ . Let  $N_p$  be the number of grains picked up by the flow per unit of time and of the bed surface. Furthermore let  $\lambda$  be the saltation length of a grains picked up by the flow. When the bed consists of spheres with a volume of  $1/6\pi D^3$ , the bed load transport capacity can be written as

$$S_b = \frac{1}{6} \pi D^3 N_p \lambda \tag{A.1}$$

The saltation length is assumed to be proportional to both the grain size,  $D$ , and the dimensionless bed shear,  $\theta$ , for  $\theta > \theta_c$ , so that

$$\lambda = a' D \theta \tag{A.2}$$

where  $a'$  is a dimensionless constant which, according to de Ruyter (1982), has a value of  $a' \approx 300$  to 800. In the computation the values shown in Section 2 have been used.

According to Ruyter (1982) the pick-up rate,  $N_p$ , can be expressed as

$$N_p = \frac{4\eta}{\pi D^2} \sqrt{\frac{\rho g \Delta t g \phi}{\rho_s D \tau_c}} \sqrt{\sigma_\tau} F_p(r) \tag{A.3}$$

where

- $\eta$  = coefficient
- $tg\phi$  = the friction coefficient for the grains
- $\sigma_\tau$  = the standard deviation of bed shear
- $r$  =  $(\bar{\tau} - \tau_c) / \sigma_\tau$  a measure of the excess bed shear

$$F_p(r) = \frac{1}{\sqrt{2\pi}} \int_0^\infty \sqrt{x} \exp\left\{-\frac{1}{2}(x - r)^2\right\} dx \tag{A.5}$$

The definition of the function,  $F_p(r)$ , originates from the assumption that  $\tau$  is Gaussian distributed with a mean  $\bar{\tau}$  and a variance  $\sigma_\tau^2$ .

An amplification factor,  $A$ , can be defined as the ratio of the bed load transport capacities,  $S_b$  and  $S_{b0}$ , both at the same mean bed shear,  $\bar{\tau}$ , but with different fluctuations,  $\sigma_\tau$ . Here  $S_{b0}$  is used as a reference transport capacity at a "reference turbulence"  $\sigma_{\tau 0}$ .

Combining Eqs. (A.3), (A.4) and (A.5) results in

$$A = \frac{S_b}{S_{b0}} = \sqrt{\frac{\sigma_\tau}{\sigma_{\tau 0}}} \frac{F_p(r)}{F_p(r_0)} \tag{A.6}$$

It is obvious that the relative change in bed load transport capacity due to turbulence is a direct function of  $\sigma_\tau$  and even though the mean bed shear  $\bar{\tau}$  remains constant, its absolute value has an

indirect effect through the function  $F_p$ . The actual value of the constant,  $a'$ , in the formulation of the saltation length,  $\lambda$ , Eq. (A.2), appears to vanish in Eq. (A.6).

For any location along the bed the amplification factor,  $A$ , for the bed load transport can be found with Eq. (A.6) given a value for  $\sigma_\tau$ . Assuming the instantaneous bed shear  $\tau$  to be proportional to the square of the instantaneous velocity  $u$  near the bed one can express  $\sigma_\tau/\bar{\tau}$  as:

$$\frac{\sigma_\tau}{\bar{\tau}} = \frac{\sigma_u}{\bar{u}} \frac{\sqrt{4+2(\sigma_u/\bar{u})^2}}{1+(\sigma_u/\bar{u})^2} \quad (\text{A.7})$$

The variations,  $\sigma_u$ , of the total velocity  $u$  around its mean value  $\bar{u}$  have been measured in a physical model but can also be derived from the turbulent kinetic energy,  $k$ , computed by the present model.

The influence of  $\sigma_\tau$  on the bed load transport capacity can be shown conveniently by defining two parameters,  $\alpha$  and  $\beta$ , which represent the levels of turbulence and mean bed shear respectively.

$$\bar{\tau} = \beta \tau_c \quad (\text{A.8})$$

$$\sigma_\tau = \alpha \bar{\tau} \quad (\text{A.9})$$

Combining Eqs. (A.8), (A.9) with Eq. (A.4)  $r$  is written as

$$r = \frac{\beta - 1}{\beta} \frac{1}{\alpha} \quad (\text{A.10})$$

Given a value for  $r$  the value of  $F_p(r)$  can be found numerically. The values of the amplification factor,  $A$ , according to Eq. (A.6), have been computed and plotted in Fig. 7 for various values for the relative turbulence  $\alpha/\alpha_0$  and at a number of values for the bed shear level,  $\beta$ .

Values of 0.2 and 0.4 have been chosen as examples for the reference turbulence level,  $\alpha_0$ . Measurements of the velocity upstream of the pipe at a distance of 0.01 m from the bed indicate  $\sigma_u/\bar{u} \approx 0.10$ , leading, with Eq. (A.7), to  $\sigma_\tau/\bar{\tau} = 0.2$ . Most of the classical empirical (bed load) transport formulae originate from test conditions with uniform flow conditions with a turbulence  $\sigma_\tau/\bar{\tau} \approx 0.4$ .

The bed load transport capacity computed with empirical formulae should, therefore, be amplified with a factor  $A$  using  $\alpha_0 = 0.4$  as a reference and the actual mean bed shear as the bed shear level  $\beta$ .

The approach given here is limited practically by the extend of the function  $F_p(r)$ . For  $r < -5$ ,  $F_p(r)$  tends to approach zero. With Eq. (A.10) the limits can be indicated in terms of  $\alpha_0$  and  $\beta$  through  $\beta = 1/(1+5\alpha_0)$ .

## CHAPTER ONE HUNDRED FIFTEEN

### Nearshore Sediment Transport: Estimates From Detailed Measurements Of The Nearshore Velocity Field

A.J. Bowen and J.C. Doering\*

#### Abstract

A very wide variety of conceptual models has been used to explain the movement of sediment in the nearshore region. While there is general agreement that the incident waves are primarily responsible for the mobilisation of sediment, many processes have been proposed as the transport agents, for example, wave drift velocities, wave asymmetry, longshore and rip currents, undertow, the downslope component of gravity. As it is currently difficult to make reliable point measurements of sediment transport, many of these ideas can not be tested directly. However, in many cases, detailed measurements of the velocity field in the water can be used to examine at least the relative importance of these possible processes. The situation is complicated by the lack of accepted formulae for sediment transport. The result is that the velocity measurements are also being used to examine the 'reasonability' of the various formulations.

#### Introduction

A major obstacle to further understanding of nearshore sediment dynamics is the lack of instruments which directly measure sediment transport. Although various types of instrumentation are under development, at present the velocity field in the water can be determined much more accurately than any parameter directly related to sediment movement. We now have large data sets from flowmeters at various vertical and horizontal positions on a wide variety of beaches. It is not, however, altogether clear how this data can be best used. The classical approach in coastal engineering is to relate such sedimentary parameters as can be measured, for example accretion rates on a growing spit, to general properties of the incident waves, often properties which only involve measurements offshore in deep water.

\*Dept. of Oceanography  
Dalhousie University  
Halifax, N.S.  
B3H 4J1 Canada

A number of specific models have recently been proposed which can make use of detailed current data, Grant and Madsen (1979), Bowen (1980a) Bailard and Inman (1981). These models, however, raise fundamental questions not only about the nature of the flow, for example, the vertical structure and particularly the scale of the boundary layer, but also about the relative importance of the various possible physical processes. The recent interest in undertow nicely illustrates both sets of problems as the measurement of undertow requires vertical resolution of a quasi-steady flow pattern over an appropriate vertical scale for sedimentary processes. As few appropriate observations exist from the field the significance of undertow is unclear although its possible importance can readily be demonstrated in two-dimensional laboratory experiments.

The overall problem is that there is no single, conceptual model to describe the important processes in any particular nearshore environment; there is no unique hypothesis to test. For example, there is no general agreement as to whether the downslope component of gravity (a physical force whose existence can not be denied) plays any significant role on sandy beaches. One way of using the current meter data that now exists is as the input for simple models based on a variety of assumptions about the relative importance of various processes. The result will be a set of predictive models for the sediment transport in the particular environment in which measurements were made. However, these predictions are not meant to be taken too seriously, the primary objective is to identify the most important processes operating in a particular environment. An initial step is, therefore, to examine the general properties of the velocity fields that have been observed and, in particular, to look at the contrast between the measurements in different coastal environments.

#### Properties of the Flow Field

In terms of sediment transport, the more obvious flow properties of interest are the mean, the variance (a measure of wave energy) and the skewness (a measure of wave asymmetry). Other parameters which might be derived from a record of the instantaneous horizontal velocity vector  $u(t)$  at a given point are, for example, estimates of the bottom stress  $u|u|$  and the sediment transport given by the velocity to some high power  $u|u|^n$  (or a formula in which a velocity  $u_c$  related to a critical stress for movement is subtracted).

A more complex formulation, of particular interest in examining the possible role of gravity, is that of Bagnold

(1966) which explicitly includes the bottom slope. For example, Bailard and Inman (1981) define the bedload transport  $i_b$  as

$$i_b = K(u^3 + \alpha u^2 |u| \nabla h) \quad (1)$$

where  $h$  is the water depth and  $\alpha^{-1}$  the friction angle of the sediment. The basic result expressed is that the sediment is transported more easily downslope than upslope. In the absence of good measurement techniques, the prediction of an instantaneous transport rate is not a result that can readily be assessed. However, the net transport over a long period of time (at least several wave periods) is a prediction of considerable practical interest, focussing attention on the factors that determine the magnitude of terms such as  $\langle u^3 \rangle$ ,  $\langle u^2 |u| \rangle$  where the bracket denotes the time average over a timescale  $T$ .

Note that in this particular model  $u$  is the total velocity and includes any mean,  $u^3$  is then not skewness as normally defined. In other models, more cautious discrimination between the waves and the mean may be necessary (Grant and Madsen, 1979).

Interest in parameters such as  $u^3$  focusses attention on three particular points:

(i) the statistical behaviour of the parameter as a function of time  $t$  and averaging time  $T$ ; the probability distribution of  $u^3$  and relative variation of this parameter, compared to  $u^2 |u|$  for example.

(ii) the factors that contribute to the value and variation of  $u^3$ ; is it primarily the mean and low frequency variation in the 'mean' or is skewness arising from asymmetry in the shape of the velocity distribution?

(iii) theoretical models to examine the variation of these parameters as functions of time and space (particularly space in the sense of water depth). Simple models in which the theoretical distribution of the wave field is either sinusoidal or Gaussian can be readily compared to the scalar moments  $u^2$ ,  $u^2 |u|$  etc.

#### Field Measurements of the Flow Field

In practice observation are made with a limited set of current meters at specific positions in the nearshore region. In the Nearshore Sediment Transport Study (NSTS) on the west coast of the United States the horizontal variation of the flow field was of primary interest and only one flowmeter was deployed at any position (about



0.50 m above the bed). This leads to considerable uncertainty about the relevance of the measurement, particularly that of the mean flow, to conditions close to the bed. Consequently in our recent experiments on the Canadian east coast, at Queensland, Nova Scotia (Bowen, 1980b) and Pte. Sapin, New Brunswick (Canadian Coastal Sediment Study), vertical arrays of three or four electromagnetic flowmeters have been deployed at a single point. This enables us to address some of the uncertainties about our ability to measure flow parameters, such as the high order moments, which have been underlined by Aubrey, Spencer and Trowbridge (1984). These data sets can be used as a basis for a number of fundamental questions: -

(i) How well do we measure  $u$ ,  $u^3$  etc; do the vertical and horizontal distributions of various parameters make any sense?

(ii) Do the simple theoretical models provide guidance as to the quality of measurements necessary?

(iii) Where should measurements be made? In deeper water, a height of 1 m is often used as a standard (but not without problems).

(iv) Does the combination of data and models suggest that any factors can be neglected? For example, a critical stress ( $u_c$ ) or the downslope component of gravity.

Figure 1 shows the on-offshore component of velocity  $u$  at three positions 0.10, 0.45 and 0.80 m above the bed in a depth of 1.40 m of water at Queensland, N.S. The significant wave height is approximately 0.7 m. The obvious result is the very high coherence between the measurements. When the small, and vertically variable, mean flows are removed the statistical properties of the records are essentially identical. This is encouraging. The various sensors have different locations on a support frame which necessarily provides some obstruction to the flow, the lowest sensor is held downwards, the mean flows are slightly different etc. Despite these differences the estimates of velocity are very similar. There is, however, no obvious way of estimating the validity of the measurement of the mean flow, some vertical structure is expected.

The general nature of the statistical distribution of flow speed is shown in Figure 2. Negative values are onshore. The observations are sufficiently close to the Gaussian distribution. (the Gaussian curve of equal variance is shown for comparison) that the ratios of even

moments  $\langle u^4 \rangle / \langle u^2 \rangle^2$ ,  $\langle u^2 |u| \rangle / \langle u^2 \rangle^{3/2}$  are close to that expected for a Gaussian distribution. A similar result was found in the NSTS results (Guza and Thornton, in press).

For a Gaussian distribution the odd moments are zero. In the data, contributions to  $u^3$  arise from two sources, the mean flow and the skewness associated with the stronger onshore velocity under the wave crest, particularly evident in the record QE151BX.

Figure 3 shows low-passed records of  $u^3$ ,  $u^2|u|$  and the ratio  $u^3/u^2|u|$ , the filter removing the variation at the incident frequency. The light lines running horizontally show the mean values over this record. These parameters show a very obvious variability associated with the beat structure of the incident waves. This strong variability at relatively low frequency suggests that rather long records will be required to obtain stable estimates of the values of these high moments.

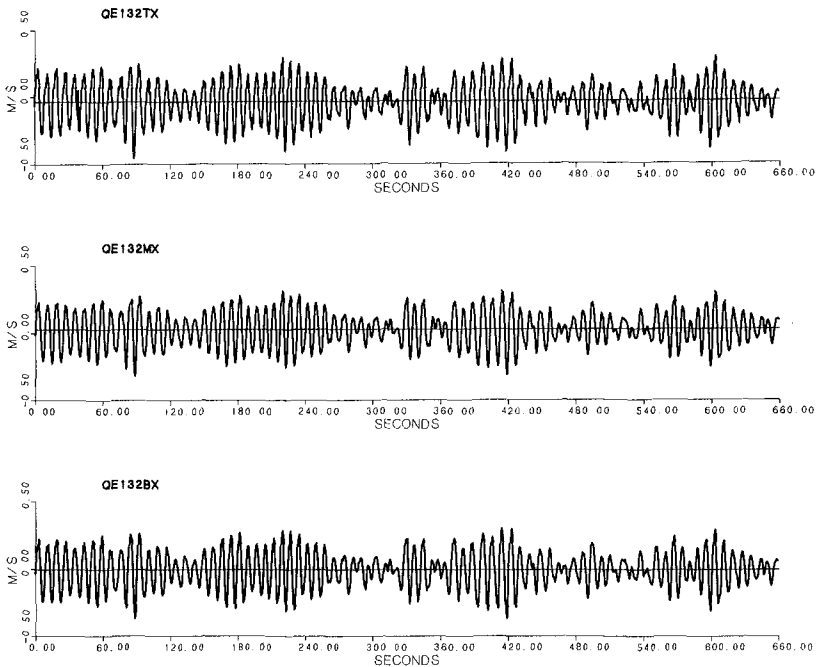


Figure 1. The on-offshore component of velocity  $u$  at 0.10 (bottom), 0.45 (middle) and 0.80 (top) m at Queensland Beach N.S.

Now Equation 1 can be considered in terms of an equilibrium condition. If the beach profile did not change appreciably during the experiment, which was in fact the case,  $i_b \approx 0$ . Then if the longshore velocities  $v$  are much smaller than  $u$  (again observationally confirmed), from (1)

$$\alpha \frac{dh}{dx} \sim \frac{\langle u^3 \rangle}{\langle u^2 |u| \rangle} \quad (2)$$

For this data set, the ratio is approximately  $-0.013$  so with  $\alpha^{-1}$  of order of  $0.63$  the estimate for the beach slope is  $0.080$  very much of the order of the observed slope of  $1:15$ . This does not imply the model is a complete

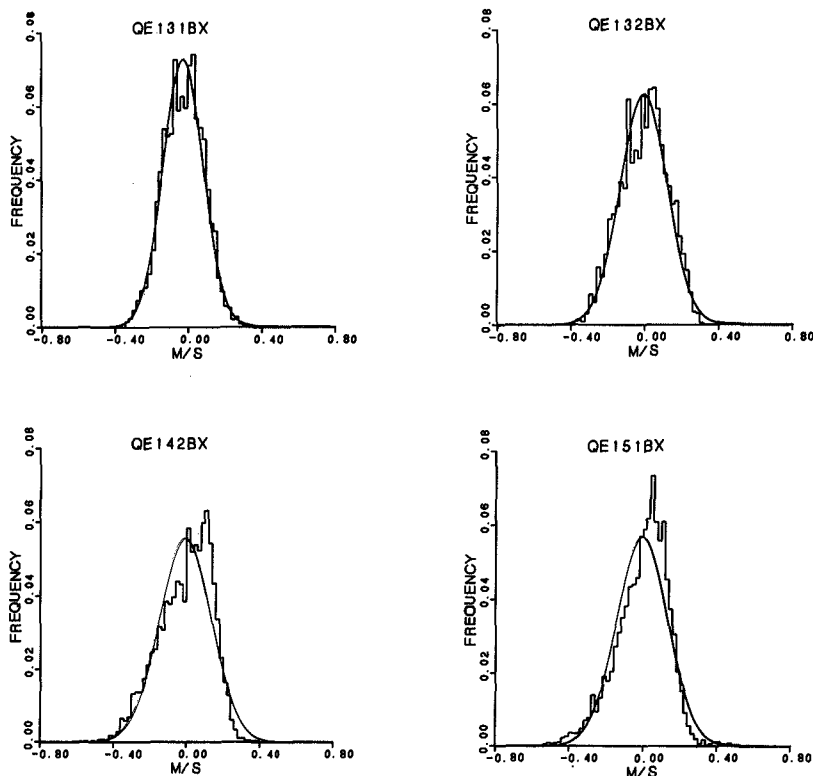


Figure 2. Statistical distribution of  $u$  for the bottom sensor, water depths 1.40 (131), 1.28 (132) 0.70 (142) and 0.55 (151) m at Queensland Beach. Observations at one station as the tide ebbed. Negative values are onshore.

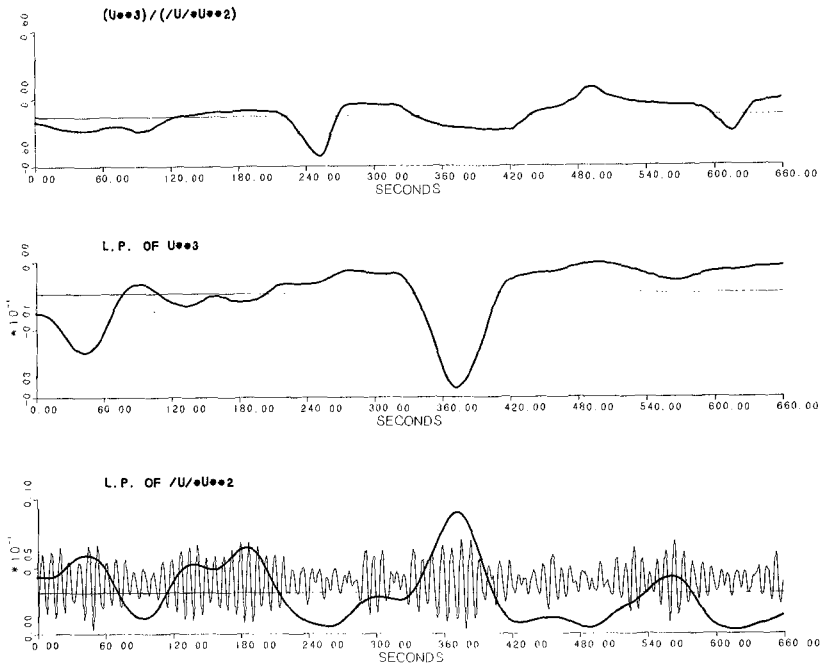


Figure 3. Parameters  $u^2|u|$  (bottom),  $u^3$  (middle) and their ratio (top), from the bottom record of Fig. 1. The results have been low passed to remove the variation at the incident frequency. The original record is shown for comparison.

description of the dynamics. Later in the tidal cycle, as the water becomes shallower, the onshore tendency is stronger (Figure 2). As the "equilibrium" is defined in terms of two surveys at successive low tides, an exact model should be the integral of the local sediment transport over the tidal cycle. However, the results do suggest that the effect of gravity can not be excluded from any discussion of sedimentary dynamics.

This model can readily be expanded to include the effects of the critical velocity  $u_c$  needed to move a sediment particle, the appropriate form of Equation (2) is

$$a \frac{dh}{dx} = -\langle u|u^2 - u_c^2| \rangle / \langle |u||u^2 - u_c^2| \rangle \text{ for } u > u_c \quad (3)$$

In Figure 4, the change in the predicted equilibrium slope is shown as a function of  $u_c / \langle u^2 \rangle^{1/2}$  where  $\langle u^2 \rangle^{1/2}$  is the r.m.s. value of  $u$ . Two representative data sets both show that the effects of  $u_c$  are not likely to be

evident until  $u_c > \langle u^2 \rangle^{1/2}$ . Orbital velocities near the shoreline are typically of the order of 0.25 → 1.00 ms<sup>-1</sup> so the effect of critical stress is likely to be important only for particles substantially larger than sand. Figure 4 is, in effect, another version of the explanation for the shoreward movement of large stones on a sandy beach. When  $i_b \approx 0$  for the smaller sizes,  $i_b$  will be onshore for all larger particles as  $\langle |u| |u^2 - u_c^2| \rangle$  is always increased relative to  $\langle |u| |u^2 - u_c^2| \rangle$ .

A rather different approach to the field data is to examine the spatial distribution of parameters relating to sediment transport. To do this sensibly, it is useful to remove the mean flow  $\bar{u}$  from the data and define a velocity  $u_1$  where

$$u_1(t) = u(t) - \bar{u} \tag{4}$$

Mathematically, the higher moments will depend on both the value of the mean  $u$  and the skewness of  $u_1$ . However, in different depth and horizontal positions the relative

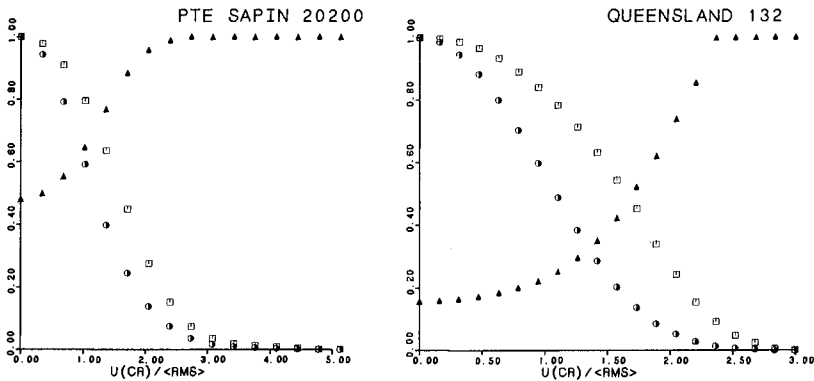


Figure 4. The parameters  $\langle |u| |u^2 - u_c^2| \rangle$  (□),  $\langle |u| |u^2 - u_c^2| \rangle$  (●) normalized by their value at  $u_c = 0$  and  $\alpha dh/dx$  (▲).

contributions will vary significantly. In Figure 1, the data suggests that  $u_1(t)$  does not vary greatly with depth (in shallow water)<sup>1</sup> and a comparison between data from different horizontal positions and separate experiments should be of interest.

Figure 5 shows the skewness, defined in the normal statistical sense as  $\langle u_1^3 \rangle / \langle u_1^2 \rangle^{3/2}$ , as a function simply of water depth. The data from<sup>1</sup> inside the surf zone from the NSTS and UK experiments tends to lie on a straight line increasing from zero at the shoreline to a maximum (negative) value in the breaker region with skewness decreasing offshore. However the data for Queensland cuts right across the general trend, but again increases onshore to a maximum close to the break point.

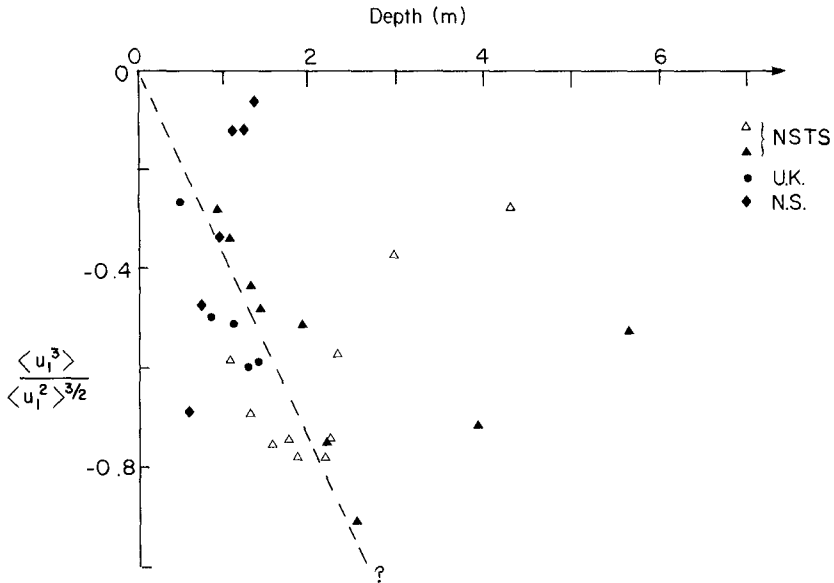


Figure 5. Skewness as a function of depth for data for NSTS (Guza and Thornton, in press), U.K. (Huntley and Bowen, 1975) and Queensland, N.S.

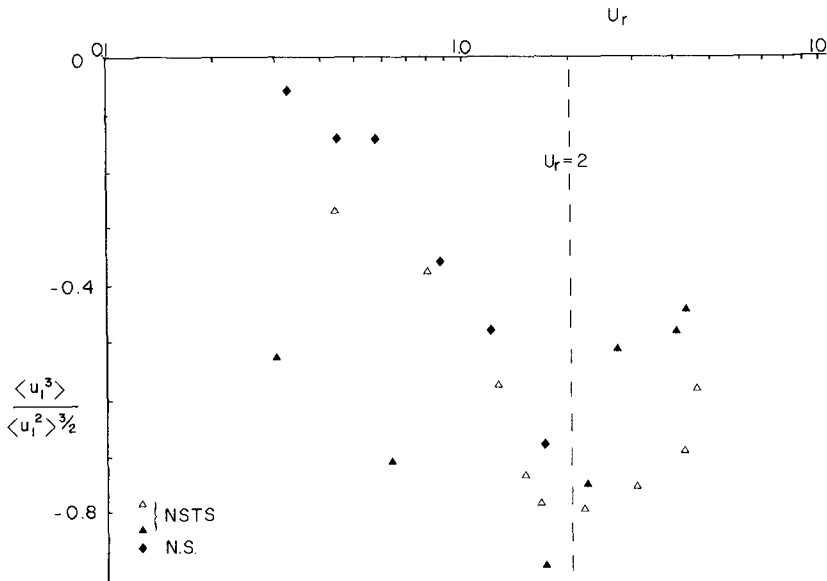


Figure 6. Skewness as a function of the Ursell Number,  $U_r$ .

It is not clear how to normalize this data, there are no simple theoretical models for wave skewness that adequately explain the observed phase shift between the first harmonic and the fundamental. However, the size of the first harmonic relative to the fundamental is given for a Stokes wave by the Ursell Number,  $U_r$  where

$$U_r = ak/(kh)^3 \quad (5)$$

$a$  being the wave amplitude,  $k$  the wavenumber. In Figure 6, the skewness is plotted against  $U_r$  which brings the Queensland data much more in line with that of the NSTS. This is encouraging but the development of a predictor for the skewness is not likely to be a simple matter particularly as it obviously depends on the breaking process.

## Conclusions

The existence of substantial sets of current meter data allows a much more realistic examination of the various ideas and formulae that have been proposed to describe nearshore sediment dynamics than would be possible using any idealized wave theory. Actual observation of the mean flow, the variance and the higher harmonics, both inside and outside the surf zone, provide an immediate assessment of the relative importance of some of the possible processes. As an example, Figure 7 shows the dependence of two transport measures,  $\langle u \rangle$ , representing bed load,  $\langle u^3 | u \rangle$  suspended load (Bagnold, 1966) on the strength of the mean velocity  $\langle u \rangle$ , positive offshore. Here real data from the Queensland experiment has been used to define  $u_i(t)$  and the various mean values added. This defines, for this particular environment, the relative importance of the mean flow and the uncertainty in the transport parameters which will arise from uncertainties in its measurement.

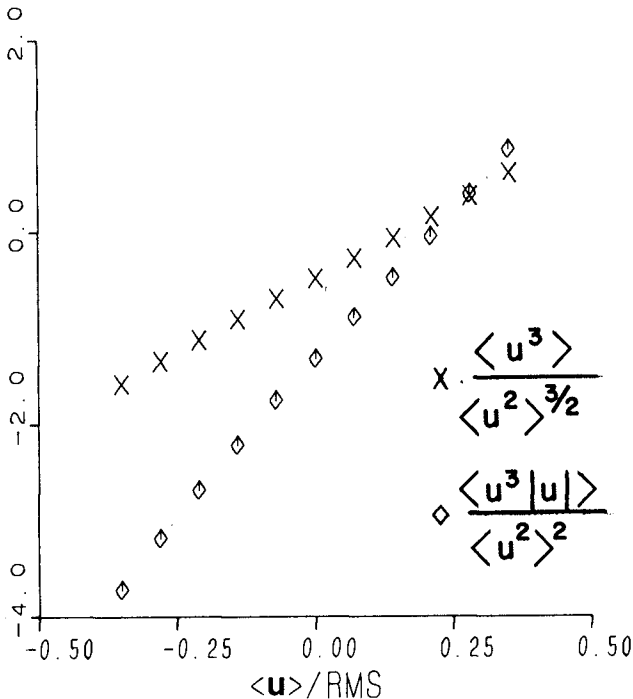


Figure 7. The parameters  $\langle u^3 \rangle$  and  $\langle u^3 | u \rangle$  as a function of the normalized mean flow  $\langle u \rangle / \langle u^2 \rangle^{1/2}$ .



The existing data suggest that the measurement of skewness and high moments of the velocity field are rather more consistent than might have been expected. However, the mean flow is uncertain and only measured with difficulty close to the sea bed. Figure 7 suggests that small velocities do play a significant role in contributing to the moments and good estimates of the mean flow are necessary. As this flow is generally an increasing function of wave height, the strongest signals are expected in severe conditions. As the sediment transport processes are themselves likely to be of most interest in severe conditions, this is convenient but suggests the likelihood of some distinctly uncomfortable moments in future field experiments. The Canadian Coastal Sediment Study has, for example, focussed on measurements in October–November in 1983, October in 1984.

#### References

1. Aubrey, D.G., Spencer, W.D. and J.H. Trowbridge. 1984. Dynamic response of electromagnetic current meters. Woods Hole Oceanographic Institute. Tech. Rept. 84.20, 150 pp.
2. Bagnold, R.A. 1966. An approach to the sediment transport problem from general physics. U.S. Geol. Survey Prof. Paper 422-1, 37 pp.
3. Bailard, J.A. and D.L. Inman 1981. An energetics bedload model for a plane sloping beach: local transport. *Journal of Geophysical Research* 86, 2035-2043.
4. Bowen, A.J. 1980: A simple model of nearshore sedimentation: beach profiles and longshore bars. *in* *The Coastline of Canada*. S.B. McCann (ed.). Geological Survey of Canada, Ottawa 1-11.
5. Bowen, A.J. 1980b. Nearshore velocity measurements and beach equilibrium. *Proc. Canadian Coastal Conf.* 1980. NRC Canada, 21-29.
6. Grant, W.D. and O.S. Madsen, 1979. Combined wave and current interaction with a rough bottom. *J. Geophys. Res.* 84, 1797-1808.
7. Guza, R.T. and E.B. Thornton. (in press). Velocity moments in the nearshore. *J. Waterways, Ports, Coastal and Ocean Engr., ASCE*.
8. Huntley, D.A. and A.J. Bowen (1975). Comparison of the hydrodynamics of steep and shallow beaches. *in* *Nearshore Sediment Dynamics and Sedimentation eds. J. Hails and A. Carr.* John Wiley, 69-109.

## CHAPTER ONE HUNDRED SIXTEEN

### LABORATORY REPRODUCTION OF SEABED SCOUR IN FRONT OF BREAKWATERS

by

Isao Irie\*, Kazuo Nadaoka\*\*

#### ABSTRACT

Mechanism of scour in front of breakwaters by standing waves in two and three dimensions has been studied theoretically and experimentally to clarify the experimental conditions by which the prototype behavior could be best reproduced in laboratory. The phenomenal reproduction of scour in laboratory is satisfactory if some conditions on the characteristics of waves and bed materials are fulfilled. This enables experimental approach to find out the optimum protection methods against scour in front of breakwaters.

#### INTRODUCTION

Extensive prolongation of breakwaters in many ports in Japan has sometimes caused severe scouring in front of breakwaters. In some crucial cases, the size of scour has developed up to 6 meters in scour depth and almost a hundred meters in scour length measured normal to breakwaters, threatening stability of breakwaters.

To work out the most effective protection methods against those problems, model experiment could be an effective measure. However, no confirmation has been made so far as to whether the phenomena in prototype could be properly reproduced in laboratory.

The objective of the present study is to make clear the mechanism of two and three dimensional scour in front of breakwaters by standing waves through detailed measurement of velocities and bed material movement, to find out the experimental conditions by which the prototype behavior could be best reproduced in laboratory, and to examine the reproducibility of model experiments.

The type of breakwaters constructed at deeper water depth is mostly of caisson type composite breakwater. It has the advantages of experiencing lesser wave pressures because they reflect waves in the form of standing waves and also lesser wave forces upon rubble mounds due to their lower crown height. In the composite breakwater, however, the stability is frequently threatened by scour in front of breakwaters.

---

\* Chief of Littoral Drift Laboratory, Hydraulic Engineering Division, Port & Harbour Research Institute (PHRI), 1-1, Nagase 3, Yokosuka, Kanagawa, Japan

\*\* Assistant, Department of Civil Engineering, Tokyo Institute of Technology, 12-1, Ohokayama 2, Meguro, Japan

The process in which structural destruction due to scour is transmitted would be in falling dominos manner as illustrated in Fig. 1. The process must be checked at some stages so that countermeasures which will be taken against scour are most effective and economical.

In order to achieve the above purposes experimentally, the conditions required for satisfying phenomenal similarity are examined first of all by investigating the mechanism of bed material movement on a flat bed, an artificially roughened bed and a movable bed.

Based upon the required conditions for phenomenal similarity, it is examined whether the size of scour large enough to affect on the stability of breakwaters could be reproduced in laboratory.

BED MATERIAL MOVEMENT ON A FLAT BED BY STANDING WAVES

When progressive waves are reflected by a vertical wall perfectly, a standing wave is produced resulting in the surface oscillation containing loop at the wall and node at  $L/4$  apart from the wall where  $L$  is the wave length. In order to obtain the basic idea on the mechanism of scour by standing waves, characteristics of bed material movement on a flat bed are studied theoretically and experimentally first of all.

A knowledge of the fluid velocity distribution close to the bed is of considerable importance. Figure 2 shows the results of the measurement of the Eulerian drift velocity distribution with a laser-doppler anemometer. It is clearly seen that there exists a thin layer drift from node to loop near the bed and the opposite drift in the upper layer, and this seems to coincide with the theoretical distribution of a second order mean velocity by standing waves given by Longuet Higgins.

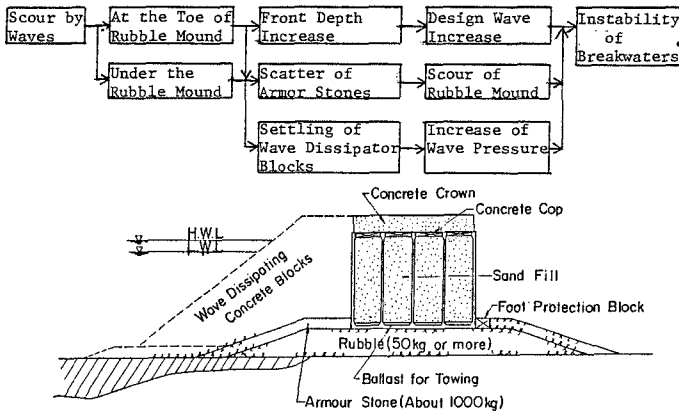


Fig. 1 The process in which structural destruction is transmitted up to the main body of breakwater.

If bed materials are to move according to the drift near the bed, bed materials placed on a flat bed should move from nodes to loops according to Fig. 2, however, every materials whose specific gravity is 2.65 were observed to move from loops to nodes.

In order to clarify those contradictory phenomena, a theoretical consideration has been made as follows. Sand particles on a flat bed are not necessarily in the state of motion during a wave period but at a stand still at a certain moment because of the bottom friction. If the oscillatory movement of water particles is completely sinusoidal, no residual shift of sand particles would result after a wave period.

Actually, the motion of water particles is not sinusoidal because of the non-linearity of waves and a net shift of sand particles would result after a wave period.

The following equations of motion are formed;

$$dx_s/dt = u_s \quad (1)$$

$$du_s/dt = 3C_d |u - u_s| \cdot (u - u_s) / 4d(s + C_m) + 1/(s + C_m) \cdot du_0/dt \\ C_m / (s + C_m) \cdot du/dt \pm (s - 1) / (s + C_m) \mu_f \quad (2)$$

where,

$x_s$ : Horizontal position of sand particles.

$u_s$ : Velocity of sand particles.

$u$ : Velocity of water particles in the boundary layer.  
( at  $z = d/2$  )

$u_0$ : Velocity of water particles just outside of boundary layer.

$d$ : Diameter of sand particles.

$s$ : Specific gravity of sand particles.

$C_d$ : Drag coefficient.

$C_m$ : Virtual mass coefficient.

$\mu_f$ : Friction coefficient with the bottom.

The moment at which sand grains start to move from the rest is obtained by judging whether the sum of the first three terms in the right hand side of equation (2) exceeds the fourth term. Here, the coefficients were selected so that  $\mu_{fs} = 0.5$ ,  $\mu_{fm} = 0.1$ ,  $C_d = 0.5$  and  $C_m = 0.5$ .

The velocity  $u$  of water particles is calculated by the following equation;

$$\partial u / \partial t = \partial u_0 / \partial t + \nu \cdot \partial^2 u / \partial z^2 \quad (3)$$

where,

$\nu$ : Kinematic viscosity.

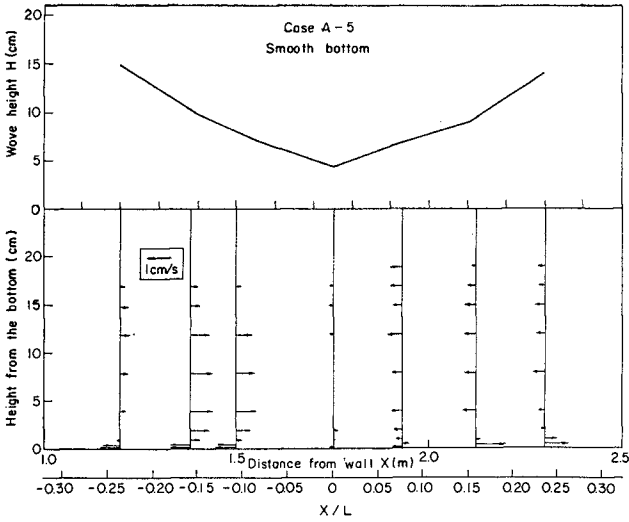


Fig. 2 The Eulerian drift velocities measured by a laser-doppler anemometer.

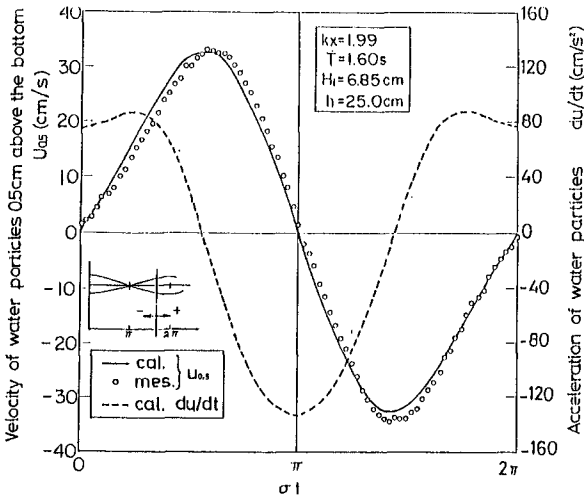


Fig. 3 Periodical change of velocity and acceleration of water particles 0.5 cm above the bottom.

- $u_0$  : Velocity of water particles just outside the boundary layer.
- $z$  : Height from the bottom.

Figure 3 shows the periodical change of velocity and acceleration of water particles 0.5 cm above the bottom calculated by third order finite amplitude theory. The result of the measurement of water particle velocity is also shown in the figure. The velocity curve is symmetric about zero point whereas the acceleration curve is not symmetrical. It is seen that acceleration inbetween nodes and loops exhibits much higher value in the direction from loops to nodes. This results in the net shift of sand particles toward nodes from loops if the particles are moved having bottom friction because initiation of motion after a stand still is much earlier in this direction.

The results of calculation of net shift of sand grain after a wave period utilizing equation ( 1 ), ( 2 ) and ( 3 ) are shown in Fig. 4. The velocity  $u$  of water particles in the boundary layer calculated by equation ( 4 ) is distorted so that amplitude toward node is higher than opposite phase. Furthermore, acceleration just outside the boundary layer  $\partial u_0 / \partial t$  is distorted as already explained. As the result of these distortions, velocity of sand grains  $u^s$  toward node is always higher than the opposite direction, and this results in the residual shift  $\Delta X$  toward nodes as seen in the figure.

Movements of sand particles on a flat bed were followed by a movie camera and the results are compared with theory as shown in Fig. 5. The rate of shift of sand particles in a wave period has coincided fairly well with the theory.

#### BED MATERIAL MOVEMENT ON AN ARTIFICIALLY ROUGHENED BED

Mechanism of bed material movement on the movable bed for which the scour problems actually occur may be of much difference from that of a flat bed because of the roughness due to sand ripples. In order to examine the effect of the roughness on the movement of bed materials, experiments on the mechanism of bed material movement on the artificially roughened bed were carried out . As shown in Fig. 6, two kinds of roughness were utilized; obstacles of 1.0 cm and 0.5 cm in height were placed at the equal intervals of 5.0 cm and 3.0 cm respectively so that the steepness of artificial roughness is of 1/5 to 1/6 which is the steepness of sand ripples commonly found. Bed materials of various settling velocities were placed at the trough of artificial roughness in the place between nodes and loops of standing waves.

Figure 7 shows the results of the measurement of the Eulerian drift velocities with a laser-doppler anemometer when the height of artificial roughness is 1.0 cm. If the velocity distribution is compared with that in Fig. 2 in which the same wave condition is applied, it is clearly seen that the thickness of drift layer near the bottom has remarkably developed in Fig. 7. In such a velocity field, bed materials once suspended would tend to move from nodes to loops, however, bed materials having the influence of bottom friction would still tend to move in the reverse direction due to non-linearity of waves as already mentioned. Thus, characteristics of net bed material movement would

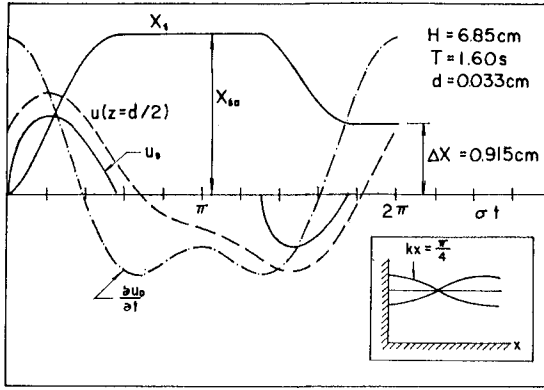


Fig. 4 Theoretical calculation of net shift of sand grains during a wave period.

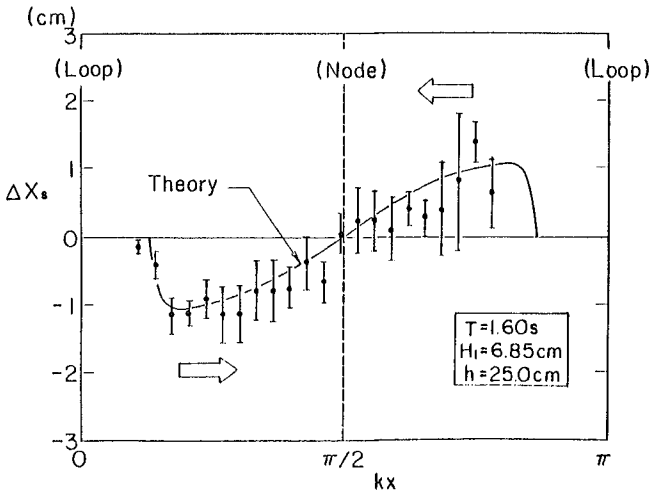


Fig. 5 Comparison of experiment with theory on the net shift of sand grains during a wave period.

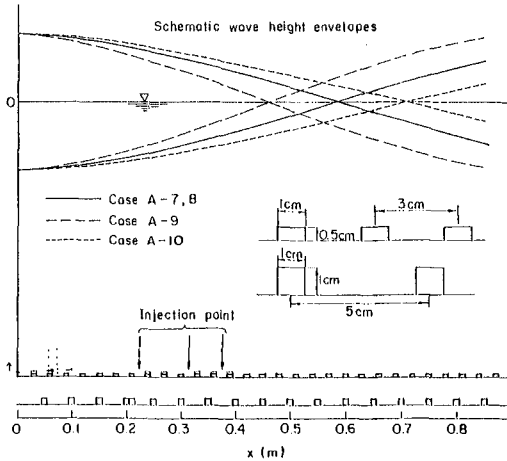


Fig. 6 Dimensions of artificial roughness.

depend on the relative importance between suspended load and bed load and this was examined experimentally.

Figure 8 shows the results of experiments on the movement of various bed materials, that is, coal grains, finer sand and coarser sand whose median diameters are 0.27 mm ( specific gravity  $\approx 1.58$  ), 0.20 mm ( s.g. = 2.65 ) and 0.33 mm ( s.g. = 2.65 ) respectively.

After the wave action of almost two minutes, the volumes of those materials in each trough of artificial roughness were measured. The volume  $V_L$  of the portion which moved toward loops and the volume  $V_N$  of the portion which moved toward nodes were calculated, and the direction of net movement of bed materials was judged by examining whether the value of  $V_L/V_N$  exceeded one or not. If  $V_L/V_N > 1$ , it means that the direction of net movement is from nodes to loops and this is called L-type movement, and if  $V_L/V_N < 1$ , it means that net movement direction is from loops to nodes and this is called N-type movement.

L-type movement will appear when suspended load is predominant and transported due to the drift from nodes to loops as already seen in Fig. 7. Therefore, relative velocity of water particles  $u_b/w$  will be a dominant parameter for the appearance of L-type movement where  $u_b$  is the amplitude of water particle velocity at the bottom for incident waves and  $w$  is the settling velocity of bed materials.

The reason for the appearance of N-type movement could be considered as follows. As already explained, bed materials on a flat bed are moved from loops to nodes so long as the bed materials experience the effects of bottom friction and this will also applicable in the present case. Another reason for the appearance of N-type movement will be the difference of the vortex formation in the wakes of the obstacles of artificial roughness. Vortices are carried back over the obstacles



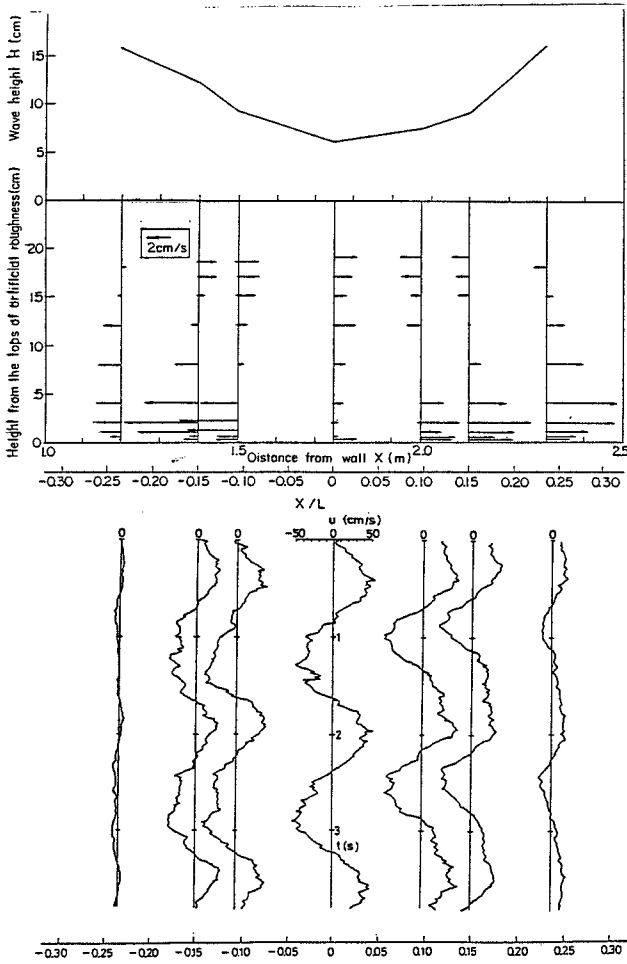


Fig. 7 ( Top ) Eulerian drift velocities when artificial roughness is 1.0 cm.  
 ( Bottom ) Change of water particle velocity with time at each corresponding position.

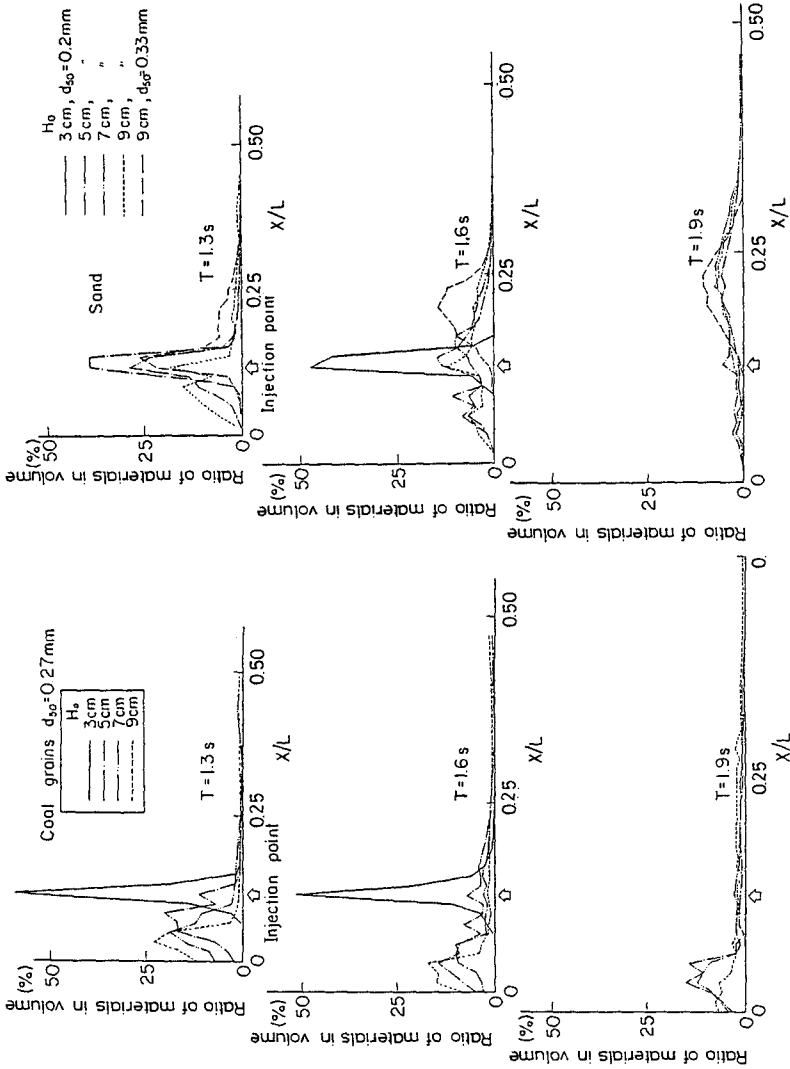


Fig. 8 Movement of various bed materials injected at the trough of artificial roughness.

and then out over the trough when the flow reverses and this process is repeated under the oscillatory motion of water particles. If the motion of water particles is sinusoidal, development of vortices on the both sides of obstacles will be the same and there will be no contribution to the net material movement onshoreward or offshoreward. As seen in Fig. 3 and Fig. 7 in which the changes of water particle velocities with time between nodes and loops of standing waves are illustrated, however, the time from a zero velocity to a maximum velocity is actually longer when the flow is toward loops than toward nodes whereas the amplitudes of the velocity is almost the same in both directions. It is apparent that more vortex development will take place if the time for development is longer on the premise that the amplitudes in both directions are the same. Consequently, vortex development is always greater in the loop side of the obstacles than the other side and much materials will be enrolled in the vortices of loop side and carried out over the obstacles toward nodes when the flow reverses. This would lead to a net bed material movement from loops to nodes resulting in N-type movement.

Thus, at any rate, appearance of N-type depends on the  $U^2/V$ -linearity of waves and this is expressed in the Ursell Number  $U = HL^2/h$  where, H, L and h are wave height, wave length and water depth respectively.

The experimental results of the relations between  $V_L/V_N$  versus  $u_b/w$  are plotted with  $U = HL^2/h$  in parameter as shown in Fig. 9. From the figure, L-type tends to appear when the relative velocity  $u_b/w$  increases for a given Ursell Number and N-type tends to appear when the Ursell Number increases for a given relative velocity. Those characteristics of the appearance of L-type movement and N-type movement seem to endorse the understanding on the mechanism of bed material movement described above.

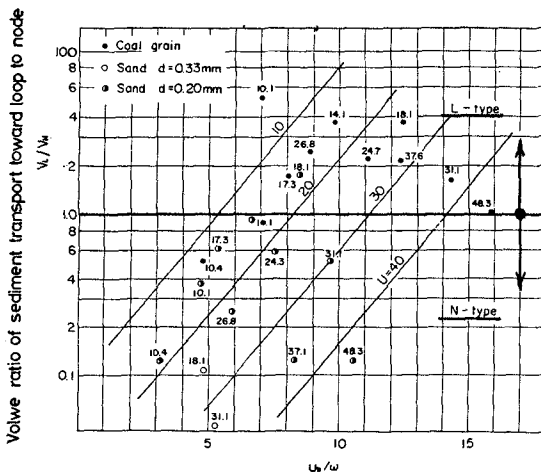


Fig. 9 L-type and N-type appearance in the bed material movement on a fixed bed. The parameters show the Ursell Number.

## TWO DIMENSIONAL SEABED SCOUR BY STANDING WAVES

If L, N-type movement of bed materials as observed in artificially roughened fixed bed exists also for the movable bed, two types of seabed scour will appear accordingly.

Figure 10 shows the results of experiments of sea bed scour when coal grains ( median diameter  $d_{50} = 0.27$  mm, specific gravity s.g. = 1.58) are utilized as bed materials. Waves from 3.0 to 6.5 cm in wave height and 1.6 sec in wave period were acted on the breakwater wall for 6 hours in the cases from (B-1) to (B-6). Since the rubble mound of breakwater had the berm width of 10 meters ( 25 cm in the model as model scale was 1/40 of the prototype ), only the offshore side from the toe of rubble mound is illustrated in the figure.

Comparison of bottom profiles with wave envelopes depicts that accumulation of bed materials takes place at nodes and erosion takes place inbetween nodes and loops when wave height is smaller than 5.5 cm, that is, in the cases of ( B-1 ) to ( B-5 ), whereas accumulation takes place at loops and erosion takes place at nodes when wave height is much higher, that is, in the cases of (B-6) and (B-7). A geometrical consideration of the balance of volumes of bed materials would indicate that the cases of (B-1) to (B-5) are the consequences of N-type movement and the cases of (B-6) and (B-7) are the consequence of L-type movement.

Similar experiments on the mode of seabed scour was carried out utilizing finer sand (  $d_{50} = 0.20$  mm, s.g. = 2.65 ) and coarse sand (  $d_{50} = 0.33$  mm, s.g. = 2.65 ). In the finer sand, sea bed scour due to both

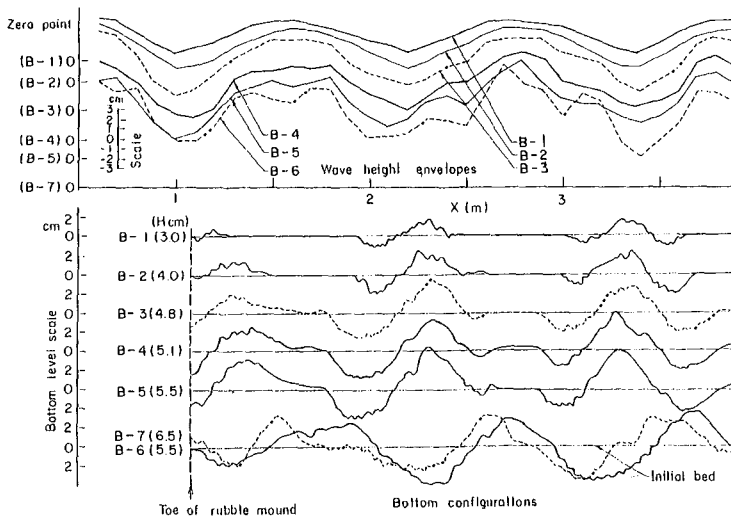


Fig. 10 Bottom configurations under standing waves of various wave heights.

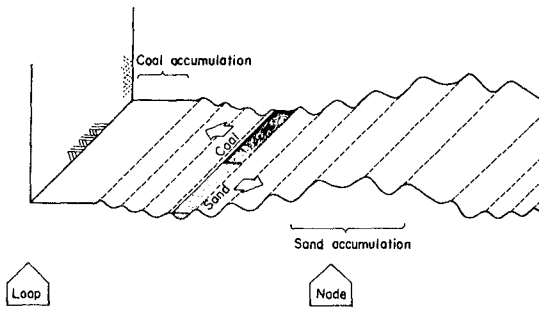


Fig. 11 Difference of the direction of movement between coal grains and coarser sand in the same velocity field.

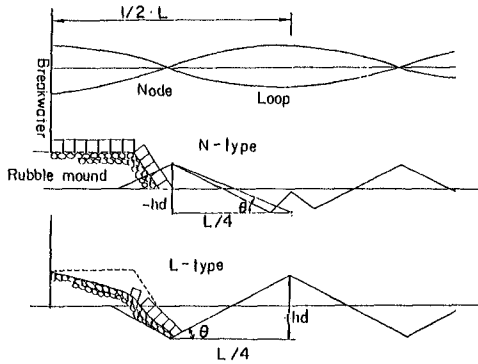


Fig. 12 Schematic illustration of two types of scour.

L-type movement and N-type movement appeared whereas in the coarser sand, seabed scour of only N-type movement appeared. The mechanism of the appearance of N-type movement and L-type movement in the movable bed could be considered similar to that in the artificially roughened fixed bed. An interesting experiment was carried out for a better understanding of the appearance of two types of scour mode in the movable bed. As shown in Fig. 11, sand ripples were formed first of all by acting waves of 7 cm in height and 1.6 sec in period for 50 minutes with the water depth of 25 cm and then the movable bed was fixed hard with glue so that no deformation would take place any more. In a trough of sand ripples between nodes and loops, sand of 0.33 mm in median diameter and 2.65 in specific gravity, and also coal grains of 0.27 mm in median diameter and 1.58 in specific gravity were placed half in half within the flume width as shown in the figure and waves were again acted. As seen in the figure, coal grains which are the lighter materials moved toward loop exhibiting L-type movement whereas the coarser sand moved toward node exhibiting N-type movement. In the present case, the drift distribution must have been the same and the only difference is the settling velocity between coal grains and coarser sand. This fact seems to endorse that the mechanism for the artificially roughened bed is also applicable for the movable bed.

Thus, existence of two types of scour, that is, L-type scour due to L-type movement and N-type scour due to N-type movement has been confirmed as shown in Fig. 12. A simple geometric inspection of scour shape with respect to the size of the rubble-mound of usual breakwaters would indicate that the scour of L-type is more critical for the stability of breakwaters.

Figure 13 shows the experimental results of the critical appearance of L, N-type scour in the movable bed where ordinate and abscissa show the relative velocity and the Ursell Number respectively. The numbers attached on the circles and triangles in the figure show the comprehensive slope of the score holes, that is,  $\tan \theta = (h_b / (L/4))$ .

The results of experiments by Xie are also shown in the figure. The relative velocity is more critical for the appearance of L-type or N-type scour than the Ursell Number where those parameters were equally important in the fixed bed.

The most important fact in the figure will be that L-type scour appears when the relative velocity  $u_b/w$  exceeds more or less the value of ten. Since the relative velocity normally exceeds tens or twenties in the prototype, the scour in prototype would have the scheme of L-type scour and thus, the model experiments of scour in front of breakwaters by standing waves cannot be reproduced unless  $u_b/w > 10$  is satisfied.

Utilization of finer materials would reproduce more remarkable scour which is indispensable for the examination of effective protection methods.

Figure 14 shows an example of scour which is reproduced utilizing fine sand of 0.06 mm in median diameter. The scale of the model was 1/50 and waves of 12 cm in height and 1.4 sec in period were acted on the composite type breakwater at the depth of 30 cm.

A remarkable damage of rubble mound would take place when the node of standing waves comes near the toe of rubble mound. It will have a lesser effect of scour if wave period is very long so that the first node of standing waves comes much offshore of the toe of rubble mound.

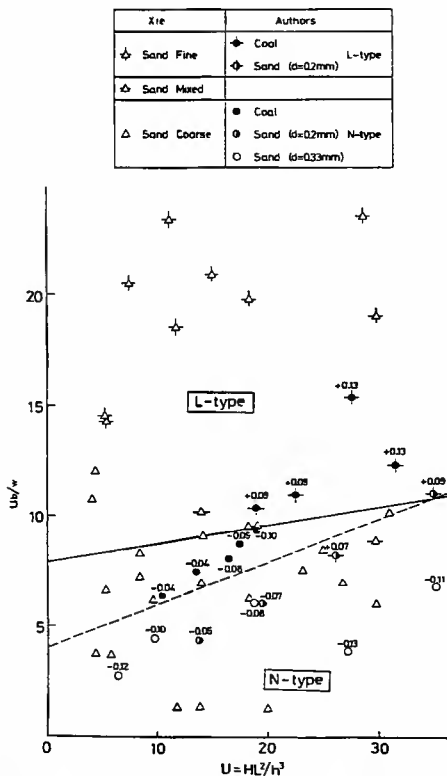


Fig. 13 Critical appearance of N,L-type scour in the movable bed



Fig. 14 An example of two dimensional scour

## THREE DIMENSIONAL SEABED SCOUR

Diagonal action of waves on breakwaters would result in the drift parallel to the breakwaters and this will affect on the scour. Many researchers have studied on the mass-transport by diagonal standing waves experimentally and theoretically. Authors have also made calculations of three dimensional mass-transport by diagonal partial standing waves in the similar manner and confirmed quantitative validity of the theory through laboratory study.

Those results indicated that mass-transport diverges at nodes and converges at loops forming converged flow parallel to the breakwaters. With roughened bottom, the thickness of the drift due to mass-transport near the bottom was observed to increase having no basic change of directions. Those results depicts that in three dimensional scour under diagonal waves, bed materials at nodes are transported from nodes to loops and also toward downstream parallel to breakwaters so long as suspension is predominant.

Actually, in three dimensional experiments with regular waves, scour took place at nodes as observed in two dimensional cases. The definite difference from two dimensional cases was that the average elevation of the bottom was eroded down due to the transportation of bed materials downstream along the breakwater. This resulted in the remarkable scour near the tip of breakwater and somewhat heavier accumulation in the downstream area along the breakwater.

Figure 15 illustrates the example of scour near the tip( upstream area ) of breakwater with the model scale of 1/40 when waves of 15 cm in height and 1.6 sec in period were acted for 16 hours at 30 degrees to the normal line of breakwater. The bed materials was sand of 0.13 mm in median diameter. The downstream bottom topography became much complicated because of the effects of oscillations in the model basin and also variation of wave height along the breakwater.

Those difficulty of producing uniform scour along the breakwater which is the common feature found in prototype was considerably improved when irregular waves are utilized.

Figure 16 illustrates the result of experiments in which waves of 8 cm and 1.3 sec in significant wave height and period respectively were acted for 11 hours at 30 degrees to the normal line of breakwater. It is seen that the scour took place at nodes of irregular standing waves and no significant scour took place in the offshore area. Furthermore, the scour is most remarkable near the tip of breakwater and gradually diminishes toward downstream area along the breakwater.

In the figure, bottom topography in front of breakwater of Fukui Port facing to Japan Sea is illustrated. Comparison of the scour shape between model and prototype would depict that reproduction of scour in front of breakwater by standing waves is quite satisfactory.

## CONCLUSIONS

1. Due to the non-linearity of waves, bed materials placed on a flat bed move from loops to nodes of standing waves so long as the materials have the effects of bottom friction.





Fig. 15 An example of seabed scour near the tip of breakwater.

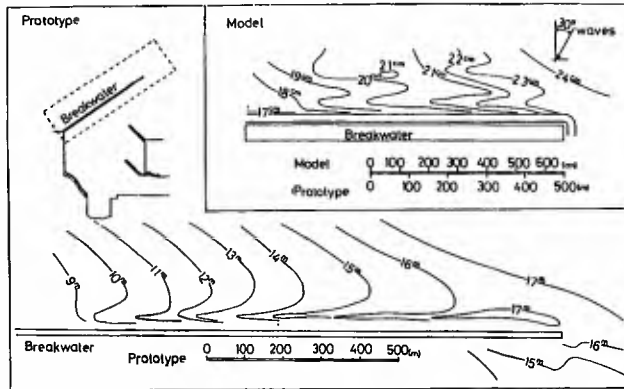


Fig. 16 Comparison of scour shape between model and prototype.

2. There are two modes of bed material movement under standing waves when the bottom has the artificial roughness, that is, L-type movement in which bed materials move from nodes to loops and N-type movement in which bed materials move from loops to nodes. Criteria of appearance of those types depend on the relative velocity  $u_b/w$  and the Ursell Number  $U(=HL^2/h^3)$ .
3. In the movable bed, two types of scour due to standing waves exist accordingly, that is, L-type scour in which bottom is scoured at nodes and accumulated at loops and N-type scour in which bottom is scoured inbetween nodes and loops and accumulated at nodes.
4. In order to reproduce the prototype scour in laboratory, it is required that the relative velocity  $u_b/w$  exceeds the value of ten.
5. The scour whose size is large enough to affect on the stability of breakwater can be reproduced if fine materials are utilized.
6. Reproduction of three dimensional scour is satisfactory if irregular waves are utilized.

## REFERENCES

- 1) Hideaki Noda: Mass Transport in Wave Boundary Layer and Seabed Scour, Proc. of 17th Japanese Conf. on Coast. Eng, 1970, pp.59-66.
- 2) Isao Irie. et al.: Two Dimensional Scour in Front of Breakwaters by Standing Waves---A Study from the Standpoint of Bedload Movement--- Rept. of PHRI, Vol.23 No.1, 1984, pp.3-52.
- 3) Longuet-Higgings: Mass Transport in Water Waves, Phil. Trans. of Royal Soc., London Series A, No.903, Vol.245, 1953, pp. 535-581.
- 4) Norio Tanaka, Isao Irie & Hiroaki Ozasa: A Study on the Velocity Distribution of Mass Transport Caused by Diagonal, Partial Standing Waves, Rept. of PHRI, Vol.11, No.3, 1972, pp.111-140.
- 5) Xie Shi-Leng: Scouring Patterns in Front of Vertical Breakwaters and Their Influence on the Stability of the Foundations of the Breakwaters, Technische Hogeschool, Delft (Netherland), 1981, 61p.

## CHAPTER ONE HUNDRED SEVENTEEN

### NUMERICAL SIMULATION ON THE CHANGE OF BOTTOM TOPOGRAPHY

#### BY THE PRESENCE OF COASTAL STRUCTURES

by

Masataka Yamaguchi<sup>1</sup> and Yōichi Nishioka<sup>2</sup>

#### ABSTRACT

This paper presents a numerical model for predicting the change of bottom topography caused by coastal structures placed on a sandy beach. The model consists of three sub-models of wave transformation by varying topography and coastal structures, nearshore current and change of bottom topography. The computation of nearshore current patterns induced by the presence of a detached breakwater shows qualitative agreement with the experiment. The effects of wave and structure characteristics on current pattern and topographical change are investigated by consideration of model computation with several configurations of coastal structures such as detached breakwaters or groins. The main conclusions are that the model produces the general features of erosion and deposition caused by coastal structures and that drastic change of current pattern and bottom topography occur when reflected waves from the structures cover a large area.

#### 1. INTRODUCTION

In recent years, shoreline models for predicting the changes in the plane shape of beach following the construction of coastal structures have been extensively used for practical applications. But, there are many limitations such that they neglect onshore-offshore sediment transport and assume parallel movement of the beach profile. In order to solve these problems, a more rational model, in which the effect of waves and nearshore currents in surf zone on sediment transport is explicitly included, is required. At the present stage of study, there are few works done from this point of view except for a numerical model by Fleming and Hunt (1976).

- 
- 1) Prof., Dept. of Ocean Eng., Ehime Univ., Bunkyocho 3, Matsuyama 790, Ehime Pref., Japan
  - 2) Engineer, Ōsaka Prefectural Office, Ōtemaenomachi 2, Higashiku, Ōsaka 540, Ōsaka Pref., Japan

Their model may be useful for practical applications. But, the assumptions made in their model regarding nearshore current and so on seem to be too simplified.

A mathematical model to predict the topographical change caused by coastal structures was developed at our laboratory in 1981 and since then, much effort has been devoted to improving the model (1983a, 1983b and 1984). The model consists of three kinds of submodels of wave transformation by varying topography and coastal structures, wave-induced nearshore current and topographical change of the seabed. This paper presents the description of the latest model and the model computations of the characteristics of nearshore current patterns and bottom modifications caused by detached breakwaters or groins.

## 2. MODEL DESCRIPTION

### (1) Wave transformation model

Wave transformation is computed by the wave ray method, in which the wave ray equation and wave intensity equation are solved simultaneously. The determination of wave direction along a ray is made by solving the wave ray equation expressed by time  $t$ ,

$$\frac{d\alpha}{dt} = \cos\alpha \frac{\partial c}{\partial x} - \sin\alpha \frac{\partial c}{\partial y} \quad (1)$$

in which  $\alpha$  is the wave direction and  $c$  the wave celerity. The computation of wave refraction is made by the wave intensity equation,

$$\frac{d^2\beta}{dt^2} + p_t \frac{d\beta}{dt} + q_t \beta = 0, \quad \beta = K_r^{-2} \quad (2)$$

in which  $\beta$  is the ray separation factor,  $K_r$  the refraction factor, and  $p_t$  and  $q_t$  are the functions of  $\alpha$  and the derivatives of  $c$ . The shoaling factor  $K_s$  is estimated by the well-known formula.

$$K_s^2 = c_{gM} / c_g \quad (3)$$

in which  $c_g$  is the group velocity and subscript 'M' means offshore wave characteristics.

In the model, bottom friction, diffraction, reflection and energy dissipation by wave breaking are approximately taken into account. But, wave-current interaction is not included. The Bretschneider-Reid formula on uniform depth is applied step by step to evaluate wave damping due to bottom friction. The diffraction effect of coastal structures is approximated by applying the Sommerfeld solution for semi-

infinite breakwater or its superposed solution to individual point on each wave ray. The Goda criterion (1975) is used to test whether wave breaking is occurring on each point along a wave ray or not. This is expressed as

$$\frac{H_b}{L_0} = 0.17 \left\{ 1 - \exp \left\{ -1.5 \frac{\pi D_b}{L_0} (1 + 15i^{4/3}) \right\} \right\} \quad (4)$$

in which  $H$  is the wave height,  $L$  the wave length,  $D (=h+\eta)$  the total depth including wave set-up or wave set-down  $\eta$ ,  $h$  the still water depth,  $i$  the bottom slope and subscripts '0' and 'b' mean deep water and wave breaking respectively. It is assumed that the waves break at a depth  $D$  if the wave height  $H$  is greater than  $H_b$  and that the wave height exceeding  $H_b$  does not exist in the surf zone.

The first step in the computation of wave transformation is to determine wave direction and wave height at each point along a wave ray and to cover the entire domain of interest with a great number of wave rays. Wave rays of not only incident waves but also diffracted waves from breakwater tip and reflected waves from structure wall are followed in succession.

The second step is to make linear interpolation of three kinds of wave data separately into each grid point prepared for the computation of nearshore current and topographical change, and to obtain single data of wave direction and wave height on each grid point through the energy composition of these data. Then, the radiation stress is estimated in the usual manner from the assumption of pure progressive waves.

## (2) Nearshore current model

In order to compute nearshore current and wave set-up or set-down induced by waves, vertically integrated conservation of water mass and momentum are used. The conservation equation of water mass is given as

$$\frac{\partial D}{\partial t} + \frac{\partial DU}{\partial x} + \frac{\partial DV}{\partial y} = 0 \quad (5)$$

in which  $U$  and  $V$  are the nearshore current velocity components in  $x$  direction and in  $y$  direction respectively. The momentum equations are as follows.

$$\left. \begin{aligned} \frac{\partial DU}{\partial t} + \frac{\partial DU^2}{\partial x} + \frac{\partial DUV}{\partial y} &= -gD \frac{\partial \eta}{\partial x} \\ + \frac{1}{\rho} \left\{ \frac{\partial}{\partial x} (D\mu \frac{\partial U}{\partial x}) + \frac{\partial}{\partial y} (D\mu \frac{\partial U}{\partial y}) \right\} &- \frac{1}{\rho} \left( \frac{\partial S_{xx}}{\partial x} + \frac{\partial S_{xy}}{\partial y} + \tau_{bx} \right) \end{aligned} \right\} (6)$$

$$\left. \begin{aligned} \frac{\partial DV}{\partial t} + \frac{\partial DUV}{\partial x} + \frac{\partial DV^2}{\partial y} &= -gD \frac{\partial \eta}{\partial y} \\ + \frac{1}{\rho} \left\{ \frac{\partial}{\partial x} (D\mu \frac{\partial V}{\partial x}) + \frac{\partial}{\partial y} (D\mu \frac{\partial V}{\partial y}) \right\} - \frac{1}{\rho} \left( \frac{\partial S_{xx}}{\partial x} + \frac{\partial S_{yy}}{\partial y} + \tau_{by} \right) \end{aligned} \right\}$$

in which  $\rho$  is the density of fluid,  $\mu_e$  the lateral mixing factor and  $S_{xx}$ ,  $S_{xy}$ ,  $S_{yx}$  and  $S_{yy}$  are the radiation stress tensor defined by Longuet-Higgins.

The Longuet-Higgins expression (1970) is used as lateral mixing factor.

$$\mu_e = \kappa \rho l \sqrt{gD} \tag{7}$$

in which  $l$  is the distance measured from the real shoreline and  $\kappa(0.01)$  the constant. The bottom friction is assumed proportional to the squared velocity, taking into account the wave orbital velocity.

$$\left. \begin{aligned} \tau_b = (\tau_{bx}, \tau_{by}) &= \frac{\rho c_f}{T} \int_0^T |w| w dt \\ w &= (-u_{\max} \sin \alpha \cos \sigma t + U, -u_{\max} \cos \alpha \cos \sigma t + V) \\ u_{\max} &= \pi H / T \sinh kD \end{aligned} \right\} \tag{8}$$

in which  $c_f$  is the bottom friction coefficient in the wave-current system and  $\sigma$  the angular frequency. Eq. (8) is estimated by the Nishimura approximation formula (1982) to save the computation time without losing numerical accuracy. It can be written as

$$\left. \begin{aligned} \tau_{bx} &= \rho c_f \left\{ \left( w + \frac{\bar{u}^2}{w} \cos^2 \theta \right) U + \frac{\bar{u}^2}{w} \sin \theta \cos \theta V \right\} \\ \tau_{by} &= \rho c_f \left\{ \frac{\bar{u}^2}{w} \sin \theta \cos \theta U + \left( w + \frac{\bar{u}^2}{w} \sin^2 \theta \right) V \right\} \\ w &= \left( \sqrt{U^2 + V^2 + \bar{u}^2 + 2W\bar{u}} + \sqrt{U^2 + V^2 + \bar{u}^2 - 2W\bar{u}} \right) / 2 \\ W &= U \cos \theta + V \sin \theta, \quad \bar{u} = 2u_{\max} / \pi \end{aligned} \right\} \tag{9}$$

This formula approximates eq. (8) with high accuracy, as far as the wave orbital velocity of the small amplitude wave theory is used.

A finite difference model has been established to solve these equations. Fig. 1 is the coordinate system used in the nearshore current and topographical change computation, in which  $x$  axis and  $y$  axis are taken in the offshore direction and in the longshore direction respectively. Fig. 2 shows the configuration of variables in the finite difference model. Velocity components and bottom friction are defined on the grid sides and all other variables are given at the grid center.

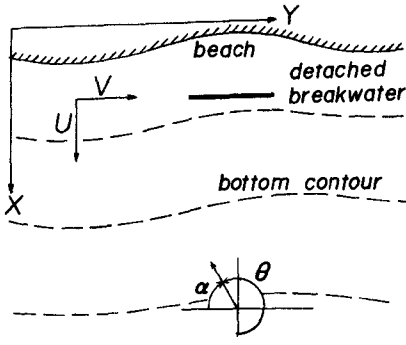


Fig. 1 Coordinate system used in nearshore current computation.

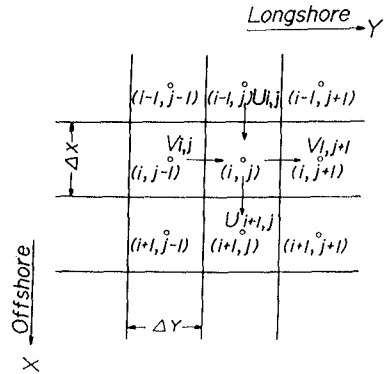


Fig. 2 Configurations of variables in finite difference model.

(3) Topographical change model

The two-dimensional continuity equation of sediment transport may be written as

$$-\frac{\partial h}{\partial t} + \frac{1}{(1-\lambda)} \left( \frac{\partial q_x}{\partial x} + \frac{\partial q_y}{\partial y} \right) = 0 \tag{10}$$

in which  $\lambda$  (0.3) is the bottom sediment porosity, and  $q_x$  and  $q_y$  are the local sediment transport rate components in  $x$  direction and in  $y$  direction respectively.

The Tsuchiya model (1982) is extensively applied to the evaluation of local sediment transport rate  $q$  in a two-dimensional flow field. The model was derived from the assumption that waves are responsible for the stirring up of bottom materials and that currents transport sediments in their direction. It can be expressed as

$$q = c_0 \frac{\rho}{\rho_d} \left( 1 - \frac{\tau_c^*}{\tau^*} \right) D \sqrt{U^2 + V^2} \tag{11}$$

in which  $c_0$  (0.02) is the average concentration of sediments,  $\rho_d/\rho$  (2.65) the specific weight of sediments,  $\tau^*$  the Shields parameter and  $\tau_c^*$  the value at the critical stage of sediment movement.

The finite difference method used in the numerical integration of eq. (10) is the same as that of eq. (6). In this case, local sediment transport rate components are estimated by redistributing the local sediment transport rate evaluated

at the grid center to the grid sides which define nearshore current components.

#### (4) Boundary condition and computational procedure

The initial condition and conditions for an offshore fixed boundary and an onshore moving boundary used in the model are the usual ones. In the longshore direction, the periodic boundary condition proposed by E. Noda (1974) is imposed on all the variables relevant to the computation. Moreover, no-flow condition is assumed at the structure boundary.

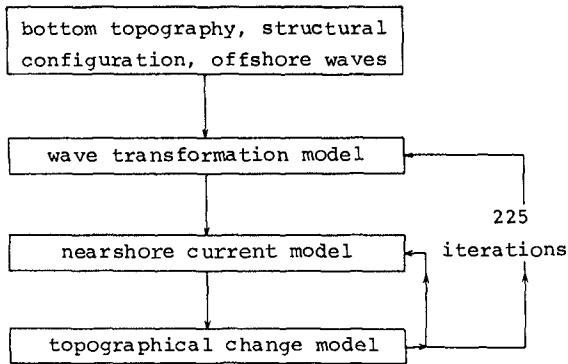


Fig. 3 Schematic diagram of computation flow.

The computer program starts with the determination of the spatial distribution of wave characteristics under the given conditions of offshore waves, bottom topography and structure configuration, and then nearshore current computation is carried out by using radiation stress estimated from the wave transformation model. A steady state solution of the nearshore current was obtained by 1260 iterations. Subsequently, alternating computation between the nearshore current and topographical modification was initiated. During the computation, the wave characteristics were recalculated every 225 iterations in order to take into account the effect of topographical change. The schematic diagram of computation flow is shown in Fig. 3.

### 3. EXPERIMENTAL VERIFICATION OF NEARSHORE CURRENT MODEL

The computation of the nearshore current pattern is compared with the Isobe experiment (1980) for the purpose of verifying the applicability of the present model. The experiment was conducted on a plane beach with the slope of  $i = 0.05$  and



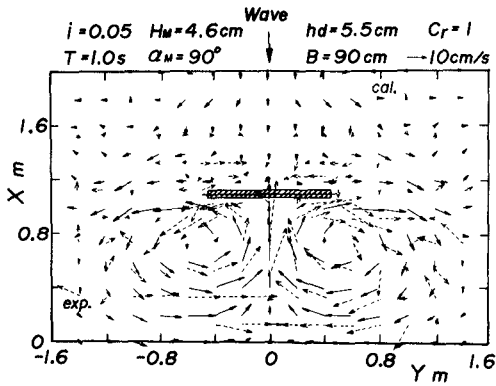


Fig. 4 Comparison of model computation with experiment for nearshore current pattern.

constant water depth of  $h = 25.8$  cm in the offshore region. In the wave basin, an iron plate detached breakwater with the length of  $B = 90$  cm was placed parallel to the shoreline at the water depth of  $h_d = 5.5$  cm. The incident wave height, wave period and incident wave angle of waves used in the experiment were  $H_M = 4.3$  cm,  $T = 1$  s and  $\alpha_M = 90^\circ$  respectively.

The comparison of the computed nearshore current pattern with the experiment is indicated in Fig. 4, in which  $C_r$  is the reflection coefficient of the breakwater. The overall characteristics of the current pattern, such as the formation of a pair of circulation currents with the opposite direction of rotation behind the breakwater, are in qualitative agreement with the experiment. But, the current pattern in the upside of the breakwater is slightly different from the experiment. Further testing is needed to verify the applicability of the present model.

#### 4. NUMERICAL SIMULATION OF BOTTOM MODIFICATION

##### (1) Conditions used in model computation

As shown in Fig. 5, the configurations of coastal structures used in the model computation are from six cases; i) one detached breakwater placed parallel to the shoreline, ii) two detached breakwaters placed parallel to the shoreline, iii) one groin placed perpendicular to the shoreline, iv) two groins placed perpendicular to the shoreline, v) one groin placed oblique to the shoreline, and vi) two groins placed oblique to the shoreline.

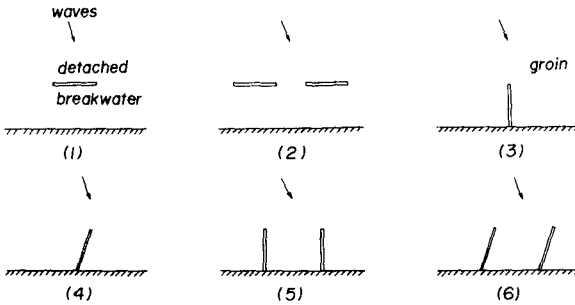


Fig. 5 Configuration of coastal structure used in computation.

The nearshore current pattern and change of the bottom topography are computed after 1 to 3 hours of constant wave action. The initial topography is taken as a plane beach with constant slope, although the present model is applicable to arbitrary bottom topography. The study area is divided into 15 points in the offshore  $x$  direction and 54 points in the longshore  $y$  direction with the grid distance of  $\Delta x = \Delta y = 10$  m. The maximum water depth is  $h_{max} = 4$  m and the time step used in the finite difference model is  $\Delta t = 1$  s. The fixed conditions in the computation are the incident wave height ( $H_M = 1$  m), wave period ( $T = 3.5$  s) and beach slope ( $i = 0.04$ ). The variable conditions are the incident wave angle ( $\alpha_M$ ), water depth of the structures ( $h_d$  or  $h_g$ ), reflection coefficient of the structures ( $C_r$ ), action time of waves ( $t$ ), number of structures (1 or 2), length of the structures ( $B$ ), distance between the structures ( $D_d$  or  $D_g$ ) and the angle of structures to the shoreline ( $\beta_H$ ).

The effects of these parameters on current pattern and bottom modification are investigated by comparison with the computed results for the standard condition, but only some of the examples are presented in this paper.

(2) Topographical change caused by detached breakwaters

Fig. 6 is the nearshore current pattern and the resulting topographical change after 1 hour of wave action for the standard conditions in the case of a detached breakwater. A large circulation current with clockwise rotation is formed on the downwave side behind the breakwater. But, a small circulation current found on the upwave side behind the breakwater before the beginning of topographical change computation disappears with the progress of bottom modification. Contourlines in the left side region behind the breakwater advance and bottom topography reveals the tendency of

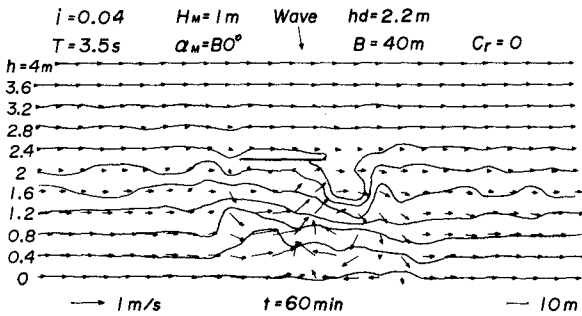


Fig. 6 Topographical change caused by a detached breakwater.

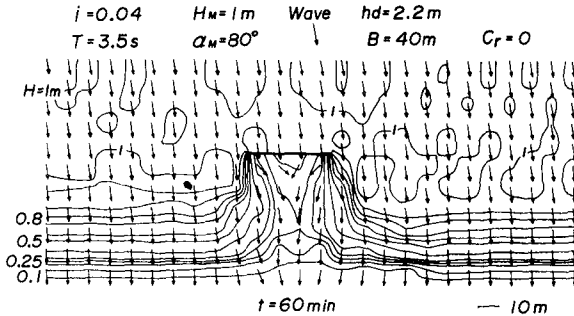


Fig. 7 Spatial distribution of wave height and wave direction in the case of a detached breakwater.

accretion in this area. On the other hand, contourlines in the area close to the right side of the breakwater retreat, and this results in the tendency of marked erosion in the region. However, the present model does not adequately produce the shoreline change, because swash transport of sediments is not included.

Fig. 7 is the spatial distribution of wave height and wave direction. Wave height decreases in the surf zone and in the shadow zone of the breakwater because of wave breaking and wave diffraction and in the offshore zone, it increases and decreases in space through the effect of diffracted waves.

Fig. 8 indicates the results after 3 hours of wave action. Meandering of the longshore currents is amplified with the progress of topographical modification. Accreting tendency on the left side reduces with the passage of time and the topographical change of the sea bottom approaches a state of

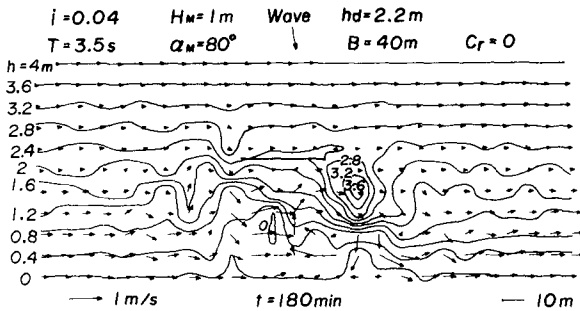


Fig. 8 Effect of action time of waves on topographical change in the case of a detached breakwater.

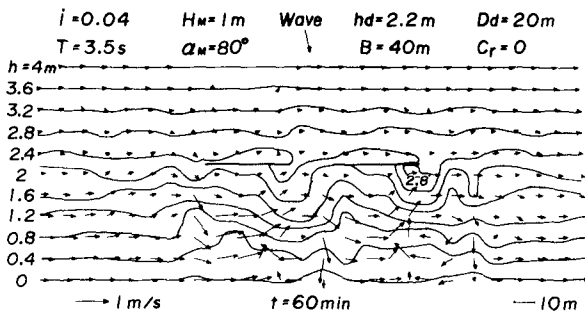


Fig. 9 Topographical change caused by two detached breakwater.

equilibrium. On the contrary, the eroding tendency on the right side continues and a scoured hole and the local advance of the shoreline are observed.

The results in the case of two detached breakwaters are given in Fig. 9. On the leeside of each breakwater, circulation currents are formed respectively, but their shapes are different from each other because of the effect of mutual interference between the two breakwaters. When the distance between the two breakwaters is longer, the interference effect becomes weaker and the circulation currents take a more similar shape. The feature of bottom modification is a similar situation. Contourlines behind each breakwater reveal slightly different changes. For instance, the scoured hole in the vicinity of the right edge of the right breakwater is deeper than the one on the right edge of the left breakwater.

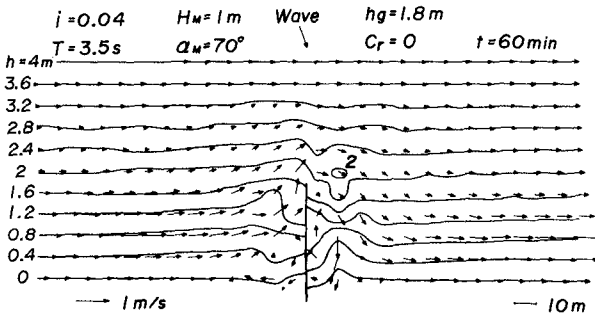


Fig. 10 Topographical change caused by a perpendicular groin.

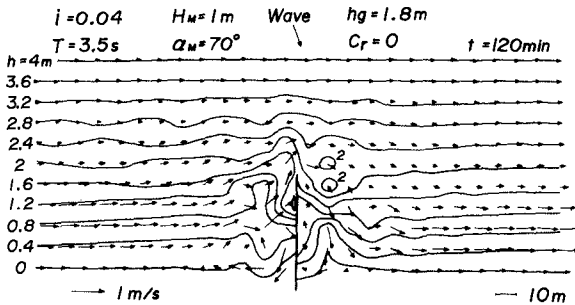


Fig. 11 Effect of action time of waves on topographical change in the case of a perpendicular groin.

### (3) Topographical change caused by perpendicular groins

This section describes the bottom modification caused by groins placed perpendicular to the shoreline. Fig. 10 is the current pattern and bottom topography after 1 hour of wave action. In addition to the predominant longshore current moving around the groin tip, a small circulation current and a larger one are found in the frontal region of the groin and in the sheltered region respectively. The former current with the progress of topographical change. As a general feature of bottom modification, contourlines outside the surf zone advance on the left side of the groin and retreat on the right side. The contrary tendency is observed in the surf zone.

After 2 hours of wave action, the variation of nearshore current and bottom topography grows more and more as given

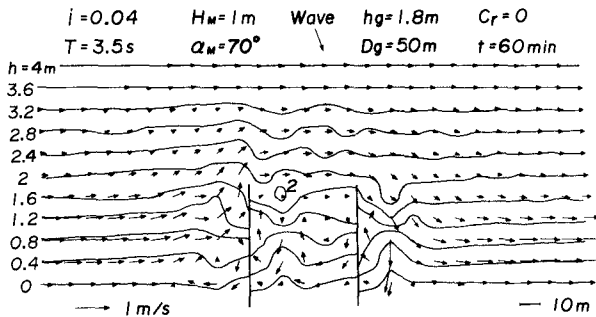


Fig. 12 Topographical change caused by two perpendicular groins.

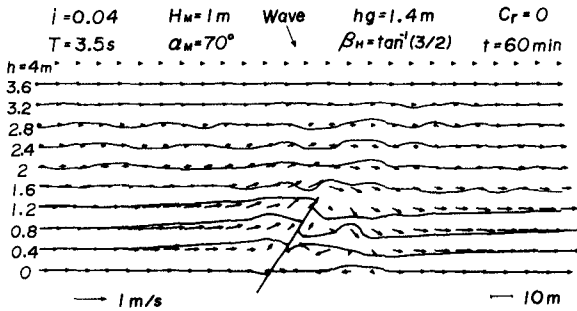


Fig. 13 Topographical change caused by an oblique groin.

in Fig. 11. As a result, we can see the overturning of contourlines in the vicinity of the groin tip.

The results computed for two perpendicular groins are plotted in Fig. 12. Four circulation currents are formed on both sides of the groins, but the corresponding circulation currents are different from each other in their shape and magnitude because of the mutual interference effect between the two groins. This current characteristics produce slightly different pattern of contourline change in the corresponding region of each groin, compared to the case of one perpendicular groin.

(4) Topographical change caused by oblique groins

Fig. 13 is the current pattern and contourline plots of modified bottom topography in the case of an oblique groin.

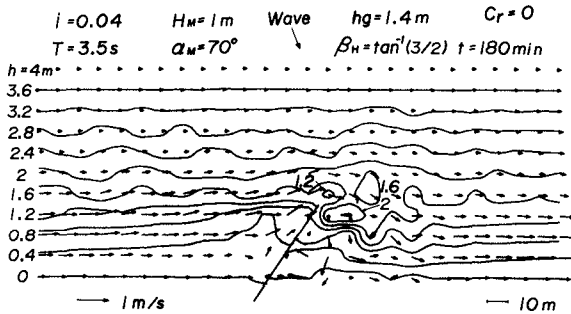


Fig. 14 Effect of action time of waves on topographical change in the case of an oblique groin.

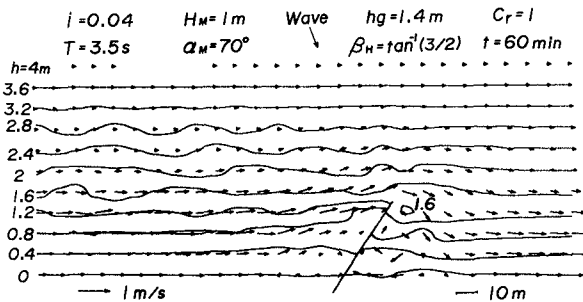


Fig. 15 Effect of wave reflection on topographical change in the case of an oblique groin (1).

The predominant longshore current passing around the groin and a clockwise circulation current in the sheltered region of the groin are observed as the case of a perpendicular groin, but a small circulation current in the upwave region of the groin toe is no longer formed. Contourlines in the upwave region advance and contourlines in the vicinity of the groin tip retreat, similar to those produced by a perpendicular groin. The difference is that the time for variation of bottom topography becomes slower compared to the case of a perpendicular groin.

After 3 hours of wave action, the current pattern and bottom topography are modified as shown in Fig. 14. The tendency mentioned above is promoted with the passage of wave action time, and isolated bars and locally-scoured holes are formed in the vicinity of the groin tip.

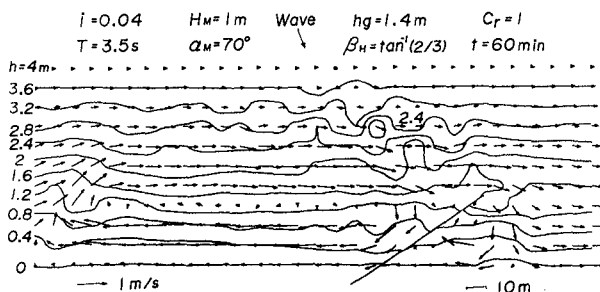


Fig. 16 Effect of wave reflection on topographical change in the case of an oblique groin (2).

Fig. 15 shows the effect of waves reflected from the groin, in the case where reflection coefficient is taken as 1. A small circulation current is formed at the toe of the groin on the upwave side by the influence of reflected waves. However, the overall characteristics of current pattern and bottom topography are not so different from Fig. 13, although the undulation of contourlines in the upwave region becomes greater by the influence of diffracted waves associated with reflected waves. This is because the region of reflected waves is confined in a smaller area for the present configuration of a groin.

In the case where the region of reflected waves is larger, the current pattern and bottom topography are drastically altered in the upwave region, as illustrated in Fig. 16. A clockwise circulation current with a large scale is formed in the upwave region and remarkable modifications of bottom topography take place.

Fig. 17 and Fig. 18 are the results computed after 1 to 3 hours of wave action in the case of two oblique groins. We can see the current pattern with the predominant longshore current going around the oblique groins and a circulation current with a slightly different scale formed behind each groin, as in the case of two perpendicular groins. The difference of the circulation current pattern was brought about by the mutual interference between the two groins and this affects the topographical change of the sea bottom in the area enclosed by the two groins. As a general feature, it can be said that the topographical change in this area is slower compared to that in the other area. Moreover, the progress of bottom modification tends to give rise to the reinforcement of nearshore current velocity and the greater variation of its direction in space at most sites investigated.



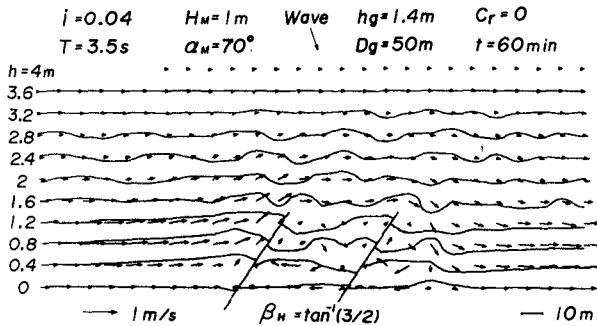


Fig. 17 Topographical change caused by two oblique groins.

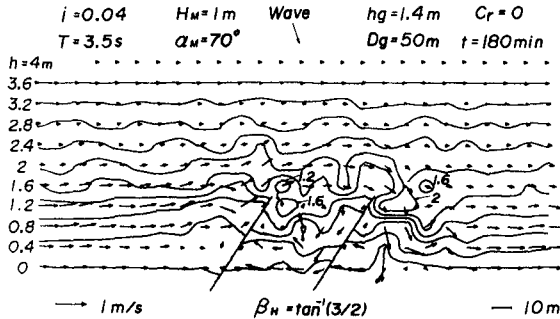


Fig. 18 Effect of action time of waves on topographical change in the case of two oblique groins.

## 5. CONCLUSIONS

The main conclusions of this study are summarized as follows.

- i) A numerical model for predicting the change in bottom topography caused by the presence of coastal structures was proposed by combining three submodels of wave transformation, nearshore current and topographical change of the sea bottom.
- ii) The model produces the general characteristics of erosion and deposition caused by the presence of coastal structures.
- iii) Drastic changes of current patterns and bottom topography occur when the reflected waves from coastal structures cover a large area.
- iv) Experimental verification of the computed results is needed to check the applicability of the proposed model.

and to improve the model.

## 6. ACKNOWLEDGEMENT

A part of this study was accomplished with the support of the Scientific Research Fund of the Ministry of Education, for which the authors express their appreciation.

## 7. REFERENCES

- Fleming, C.A. and J. N. Hunt (1976): Applications of a sediment transport model, Proc. of 15th Conf. on Coastal Engg., Vol. II, pp. 1184 - 1202.
- Gōda, Y. (1975): Deformation of irregular waves due to depth-controlled wave breaking, Rept. of Port and Harb. Res. Inst., Vol. 14, No. 3, pp. 57 - 106 (in Japanese).
- Isobe, M. (1980): Cooperative study on the dynamics in surf zone (II) - natural beach and breakwater-defensed coast -, Nearshore Environment Research Center, Rept. 10, pp. 130 - 145 (in Japanese).
- Longuet-Higgins, M.S. (1970): Longshore current generated by obliquely incident sea waves, Jour. of Geophys. Res., Vol. 75, No. 33, pp. 6778 - 6789.
- Nishimura, H. (1982): Numerical simulation of nearshore circulation, Proc. of 29th Japanese Conf. on Coastal Engg., pp. 333 - 337 (in Japanese).
- Noda, E.K. (1974): Wave-induced nearshore circulation, Jour. of Geophys. Res., Vol. 79, pp. 4097 - 4106.
- Tsuchiya, Y. (1982): The rate of longshore sediment transport and beach erosion control, Proc. of 18th Conf. on Coastal Engg., Vol. II, pp. 1326 - 1334.
- Yamaguchi, M., S. Ōtsu and Y. Nishioka (1981): Numerical simulation of three-dimensional beach change caused by a detached breakwater, Abstract of 36th Annual Meeting of JSCE, pp. 849 - 850 (in Japanese).
- Yamaguchi, M., Y. Nishioka and S. Ōtsu (1983a): Numerical simulation on the change of bottom topography by the presence of coastal structures, Memoirs of the Faculty of Engg., Ehime Univ., Vol. X, No. 2, pp. 275 - 283 (in Japanese).
- Yamaguchi, M. and Y. Nishioka (1983b): Computational method of three-dimensional beach change caused by detached breakwaters or groins, Proc. of 30th Japanese Conf. on Coastal Engg., pp. 239 - 243 (in Japanese).

Yamaguchi, M. and Y. Nishioka (1984): Numerical simulation on the change of bottom topography by the presence of coastal structures (2) - cases for two detached breakwaters or two jetties -, Memoirs of the Faculty of Engg., Ehime Univ., Vol. X, No. 3, pp. 399 - 406 (in Japanese).

## CHAPTER ONE HUNDRED EIGHTEEN

### NORTH SEA TIDE AND STORM SURGE INVESTIGATION

Prof. Dr.-Ing. Winfried Siefert<sup>+)</sup>

#### Abstract

An extensive investigation of tide and storm surge measurements in the coastal waters of the southeastern North Sea (German Bight) is now being concluded, giving new hints to tidal behaviour in a complex area, consisting of extended tidal flats, interrupted by islands, sand banks, estuaries and gullies. The analysis was promoted by the "German Coastal Engineering Board" (KFKI) and will be the basis of further investigations of the storm surge conditions in tidal estuaries.

Tidal records and high and low water values of 130 gauges in an area of 12.000 km<sup>2</sup> (5.000 sq.mi.) were used to evaluate

- cotidal lines in the German Bight
- mean tide curves
- regressions between different locations
- neap and spring tide conditions
- secular changes over the last 80 years
- storm surge development.

#### Tidal Character in the German Bight

The tidal motion in this area is induced by the amphidromic tide in the southeastern North Sea (fig. 1). It was believed that the tides in the triangle off the German coast proceed from the West to the East and then to the North, but it turned out that this is not the case: Coriolis and centri-

<sup>+) Strom- und Hafengebäude Hamburg, Lentzkaai, 2190 Cuxhaven,</sup>

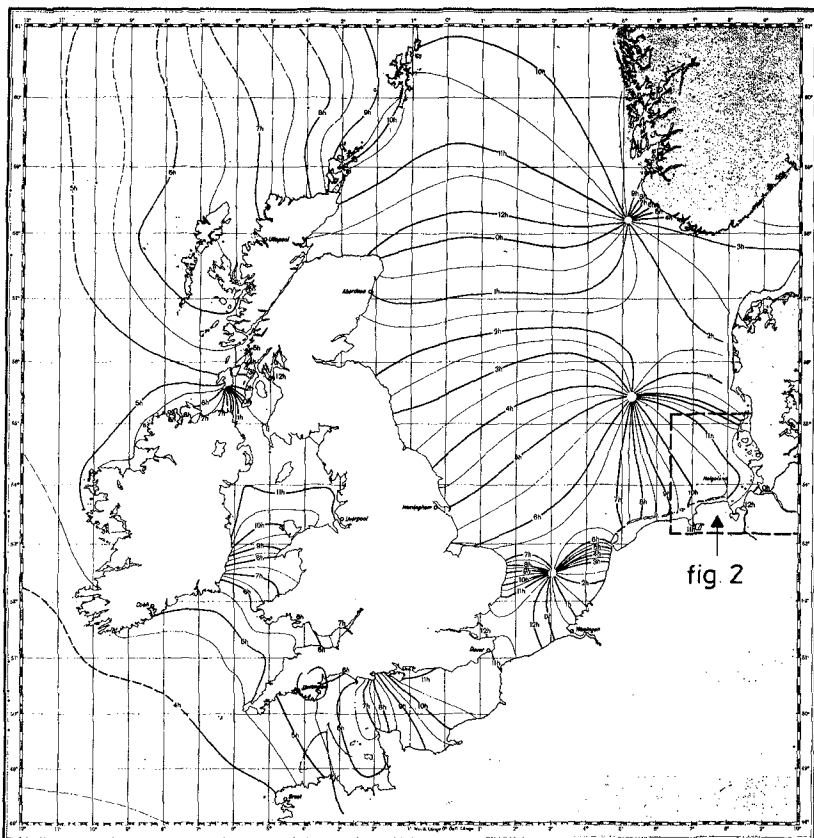


Figure 1. Cotidal Lines in the North Sea for Mean HW Conditions (Deutsches Hydrographisches Institut, 1982)

fugal forces lead to deformations of surface gradients resulting in a motion mainly from the West to the East, so it will be shown that the general conditions of fig. 1 are not realistic near the coastlines.

The area of investigation is given on fig. 2, including the long-term and seasonal tide gauges, indicated by black dots. They cover an area of  $80 \times 80 \text{ km}^2$  ( $50 \times 50 \text{ sq.mi.}$ ), most of them in the three estuaries and on the tidal flats in a zone, 10 to 20 km wide. Fig. 3 to 8 show some of the results

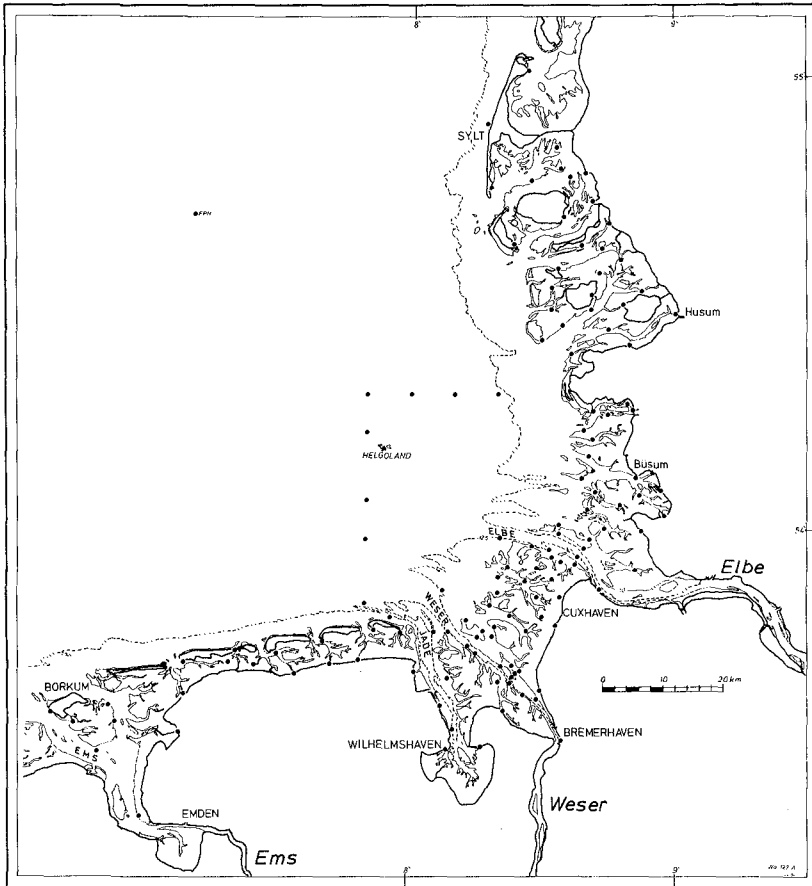


Figure 2. Long-term and Seasonal Tide Gauges in the South-eastern North Sea

that are to be published in the near future in detail (3).

Fig. 3 indicates the lines of mean HW occurrence from 20 to 20 minutes, showing no full agreement with fig. 1: HW time is more or less propagating from the West to the East, signs of a rotation (due to an amphidromic point) cannot be realized. There is another very interesting result: The tide curves off the coast are usually asymmetric with values

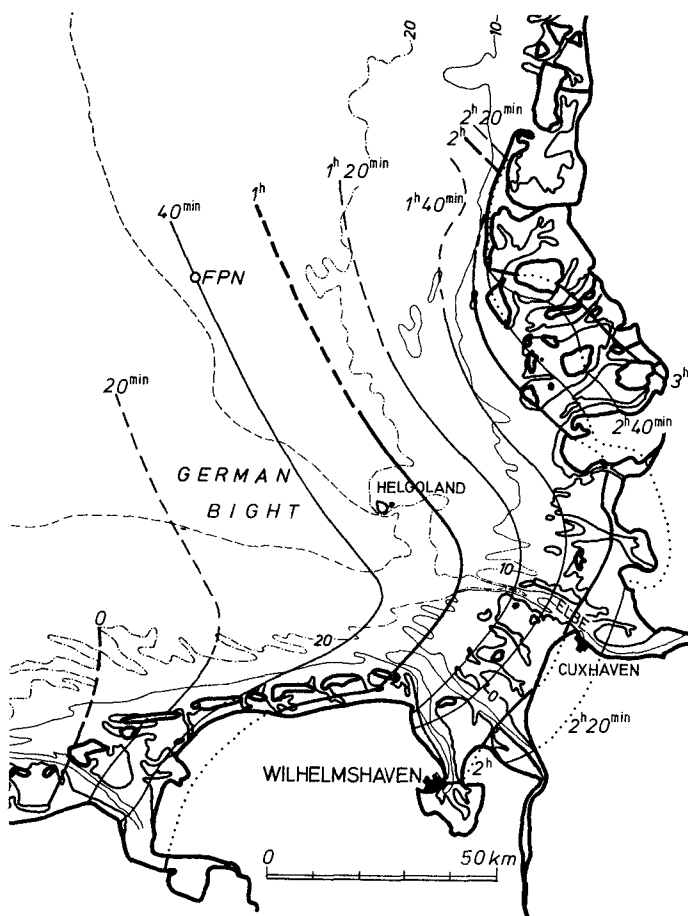


Figure 3. Cotidal Lines in the German Bight for Mean HW Conditions; Measurements 1975/79

$T_F/T_E$  between 0.8 and 1.0 (fig. 4). It has to be taken into account that the curves in the North Sea - at least in water depths between 30 and 50 m - are not symmetric and that the asymmetry does not increase with the propagation to the coast, but decrease. An expected decrease is found in the estuaries; in some areas we even find longer ebbs than floods! Moreover, we are able to define the flats and

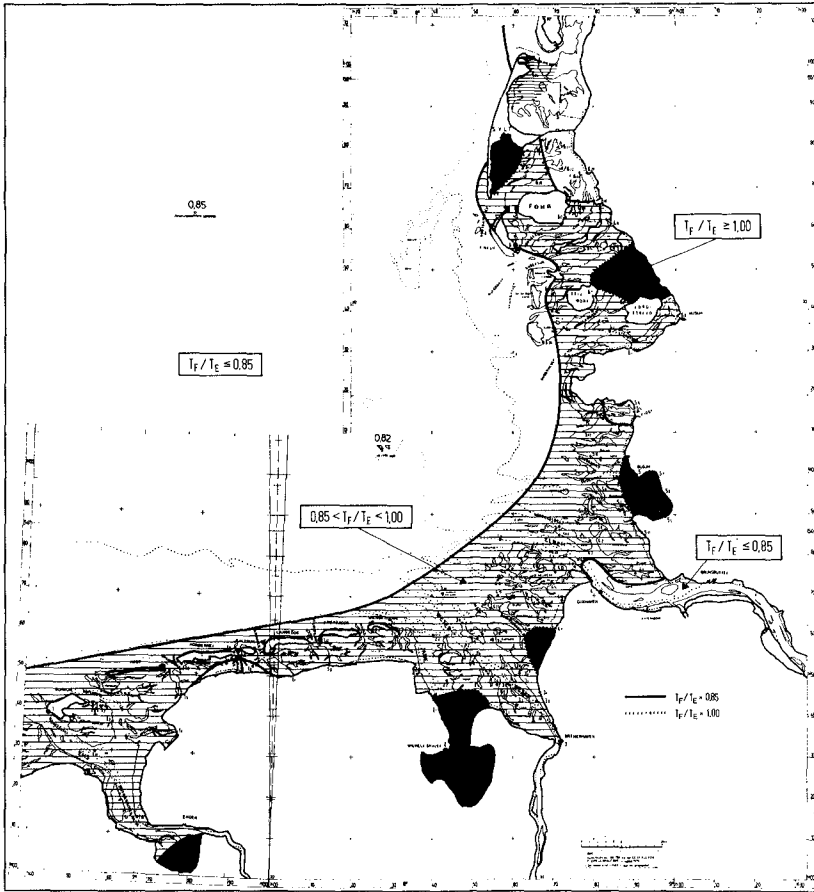


Figure 4. Flood Duration  $T_F$  over Ebb Duration  $T_E$  in the German Bight for Mean (Semi-diurnal) Tides

gullies as a system of neighbouring flood- and ebb-dominated areas (see fig. 5). The former are characterized by longer flood than ebb duration ( $T_F > T_E$ ) and coastwards decreasing low water levels, combined with residual currents across the tidal flats towards the latter. The lines of mean HW levels, computed for 1975/79 and given in cm above gauge datum on fig. 6, rise with 10 cm/10 km from the Northwest to the



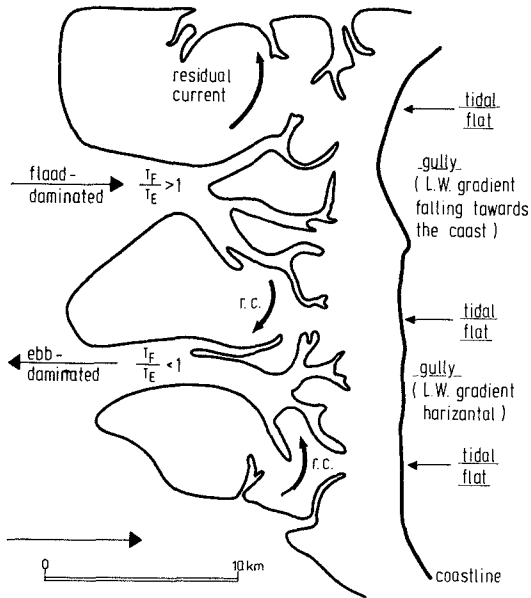


Figure 5. Array of Tidal Flats with Typical Pattern of  $T_F/T_E$  and Residual Currents

Southeast, becoming very complex in the eastern tidal flats and in the estuaries of Weser and Elbe. The highest mean HW levels are found in the bights west of the Weser and north of the Elbe estuaries. The mean tidal range on fig. 7 increases significantly from the deeper water zones towards the coastline (measurements from 1.3 m to 3.8 m with remarkable gradients in the northernmost wadden sea. Near-coast spring tidal range is about 60 cm higher.

The mean tide curves differ a lot. Fig. 8 gives some examples: Different heights and shapes, due to the topographical and current conditions. These curves of 130 tide gauges enabled us to calculate lines of constant water levels in the German Bight for all tide phases. As far as we know it is the first time that this could be done by such an amount of field data. And the result stated what had to be expected

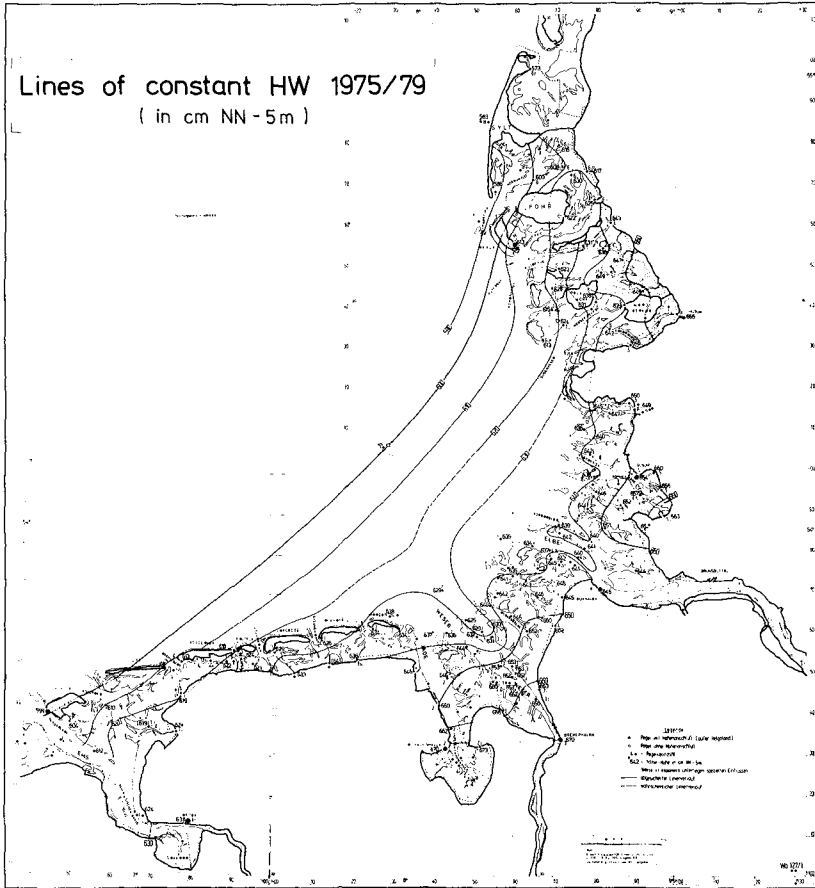


Figure 6. Mean HW Levels in the German Bight for 1975/79

by the cotidal lines on fig. 3: The amphidromic tide in the southeastern North Sea (fig. 1) does not rule the movements in the German Bight in a strong manner as was believed: We can assume a border of main influence (sketch on fig. 9). In the area between that border and the coastline, the tidal movement is stimulated from the West, and there should be only weak interactions across the assumed border. That

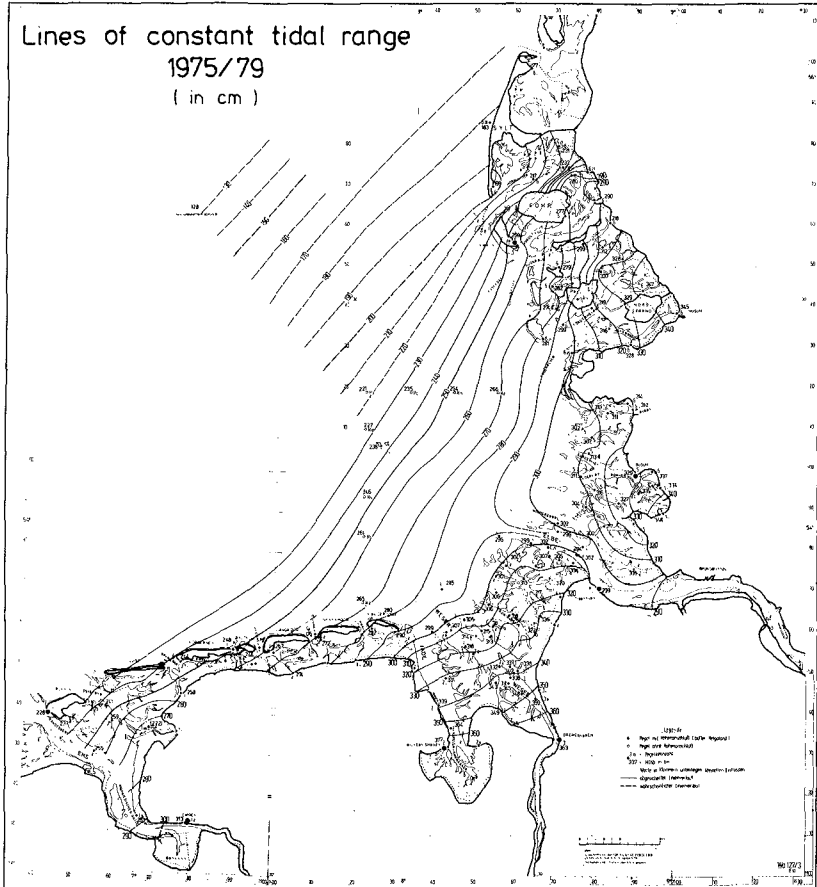


Figure 7. Mean Tidal Range in the German Bight for 1975/79, Given in cm

leads to a predominant west-east tidal motion (and south-west-northeast for the northern area), in agreement with current measurements and ice tracer observations. This is underlined by the effect that we can define a zone of about 6.000 km<sup>2</sup> (2.500 sq.mi.), where the water levels behave in an interesting way: During LW time at Borkum (BOR on fig. 9) the indicated zone is characterized by constant water levels

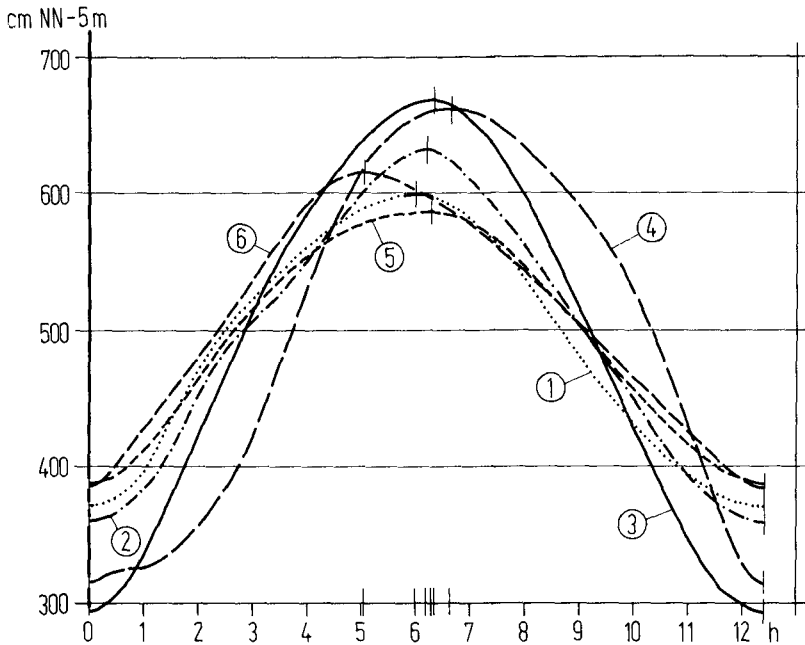


Figure 8. Examples for Different Mean Tide Curves in the German Bight (See Fig. 2):

- 1: Borkum: outside tidal flats
- 2: Bensersiel: straight coastline, protected by islands
- 3: Wilhelmshaven: bight effect
- 4: Steertloch: bight effect, south of Büsum
- 5: Hörnum: southern tip of Sylt, island effect
- 6: Osterley: east of Hörnum, island and tidal flat effects

(variances only within 10 cm), and they are the lowest in the whole German Bight at this tide phase. At HW time in Borkum the same area can be defined as of constant water level, being the highest at that phase. Conclusions are:

- Water is "pumped" into the inner bight during flood phases, building up a ridge with slopes to the North

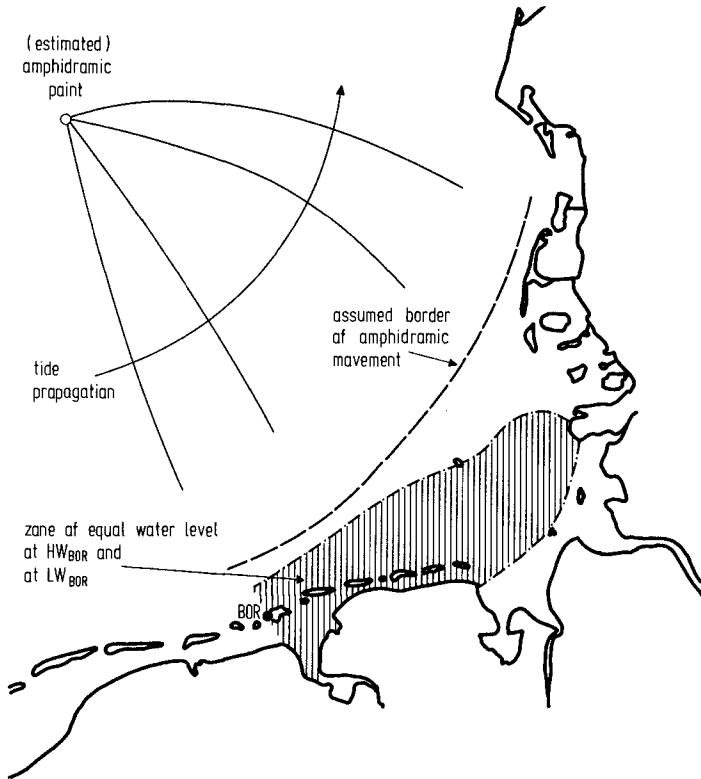


Figure 9. Mean Amphidromic Behaviour in the Southeastern North Sea and Zone of Special Conditions

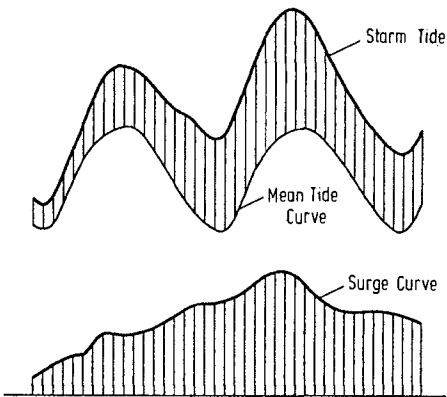


Figure 10. Definition Sketch, Mean Tide Curve and Storm Surge

- and to the Southeast;
- water is moving out of the indicated zone, finally forming a trough;
  - wind induced currents from westerly directions can easily fill up this trough; so storm surges usually start somewhere around  $LW_{BOR}$ , and constant wind conditions lead to higher surge values during LW than during HW (surge being defined as on fig. 10);
  - no conservative tidal wave profil appears near the coast; consequently linear wave theory should not be applied to coastal tides.

In this context it is very interesting that computations of the Danish Hydraulic Institute in its numerical North Sea model show that the origin of the discussed trough lies west of the Dutch coast, i.e. in the sphere of the neighbouring (southern) amphidromic tide, migrating along the coast into the German Bight, thereby steadily deepening.

#### Recent HW and LW Changes

During the last decades tide and storm surge investigations along the German North Sea coast and in the estuaries have rapidly been intensified. But there are some gauges with records of more than 100 years as well, and two of them will have their bicentennial jubilee in 1986 (Cuxhaven and Hamburg). So much historic data is available. On the other hand the development of the last 15 years is to be of high interest: We can evaluate distinct changes in water levels since 1970 recognizable both in HW and LW. Three typical examples for the German Bight are given for the islands Bor-kum (BOR) and Helgoland (HEL) (fig. 11) and for Cuxhaven (CUX) at the seaward boundary of the Elbe estuary (fig. 12):

- HW BOR: rising until 1970, the constant
- HEL: rising until 1950 (?), then constant
- CUX: rising until today, with an increase during the last decade.

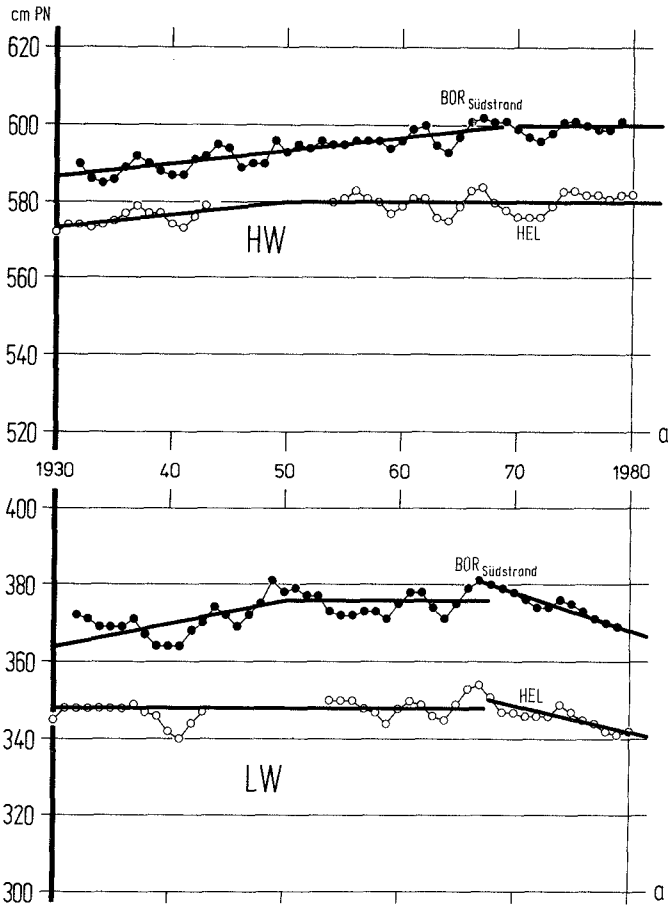


Figure 11. HW and LW Developments (3 Years Running Means) at Helgoland (HEL) and Borkum (BOR)

LW BOR: rising until 1950, constant until late 1960ies, the falling

HEL: constant until late 1960ies, then falling

CUX: rising until 1950, then slowly falling, with an increase in the late 1960ies.

The result is: at the islands 10 to 50 km in front of the coast HW has been constant since 1970, while at the coast (CUX is typical!) HW is rising remarkably. At the same time

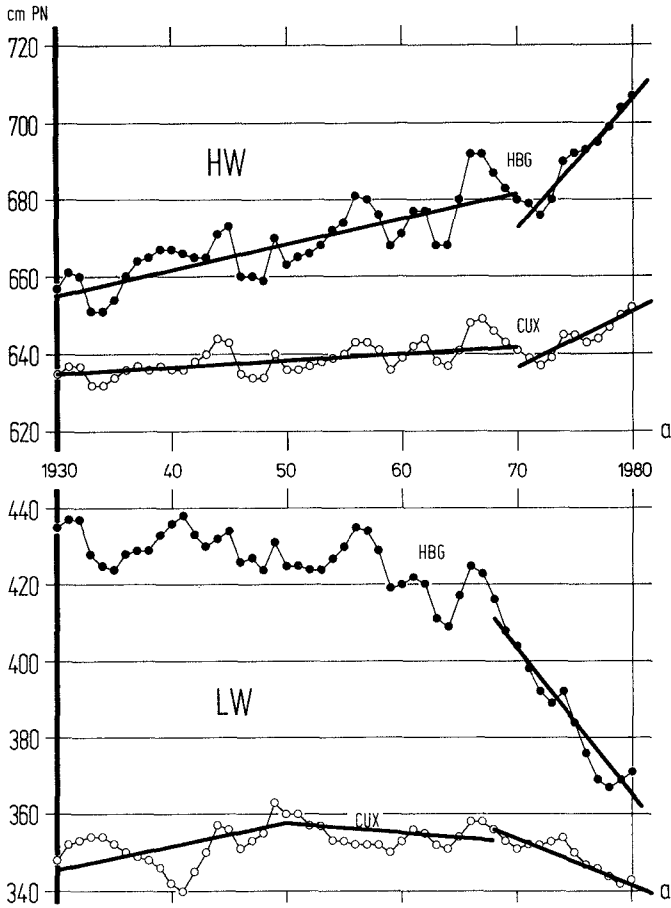


Figure 12. HW and LW Developments (3 Years Running Means) at the Elbe Estuary (Cuxhaven, CUX) and 100 km (60 mi.) upstream (Hamburg, HBG)

LW is falling at the islands and at the coast; so the tidal range increases rapidly.

In the tidal estuaries the HW and LW developments are governed by seaward and regime conditions. The seaward influence in the Elbe is shown in fig. 12. Hamburg (HBG) is situated 100 km upstream from Cuxhaven, and qualitatively



the developments are the same as in CUX. Especially the LW data also seems to show strong effects of deepening of fairway. The same is realized in other estuaries in Europe.

So this yields two conclusion: either all estuaries have been deepened since 1970 resulting in round about the same amount of LW-change, or something must have happened outside the estuaries. The latter idea was first published by the author in 1976 and emphasized later (2).

During the last years the number of indications about changes of tidal characteristics in the North Sea is rising:

- At the German coast we measure tidal ranges that have never occurred before;
- tidal current velocities in the outer parts of the estuaries (seaward of fairway improvements) increased;
- shapes of mean tide curves have changed distinctly.

The question is, whether the amphidromic tide in the southeastern North Sea is constant or not, and if not: why? This problem can not yet be solved, but we are trying to find a solution.

#### Storm Surge Tendencies

The coasts of the southeastern North Sea had to be protected against severe storm surges with high dikes and other defence constructions. The heights of these events steadily rose during the last 500 years due to secular water level increase of about 20 cm/100 years.

During the same period since 1960, when the mean tide conditions changed in front of the coast, the heights and frequencies of storm surges increased, as indicated by fig. 13 and 14: Ten years overlapping means have risen by 20 to 30 cm within a period of 30 years at stations 10 to 20 km off the coast (BOR, AW) and at the coast (CUX) as well (fig. 13), the main portion being during the last 20 years, accompanied by a distinct increase of the storm surge num-

ber (fig. 14): 10 events in three years until 1960 to 15 up to 20 since 1965. So this development is in phase with the rise of mean HW levels in this area (fig. 11, 12). The reasons are different, of course: Storm surge growth is the result of two developments: the number of storm has been increasing during the last decade, as has at the same time the frequency of the critical wind directions (e.g.  $270^{\circ}$  for the Ems,  $280^{\circ}$  to  $290^{\circ}$  for the Weser and Elbe).

All these tendencies, concerning mean tidal conditions at all gauges as well as storm surge heights and frequencies,

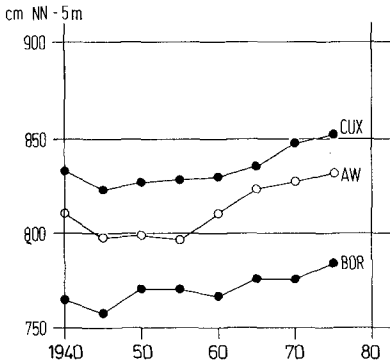


Figure 13. Mean Heights of Storm Surges Higher than 1.5 m above HW at the Entrances of Ems (BDR), Weser (AW) and Elbe (CUX) (10 Years Overlapping Means)

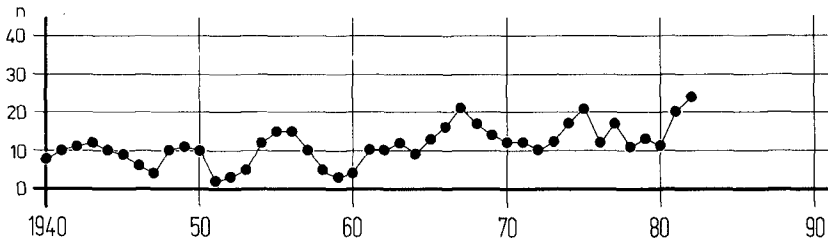


Figure 14. Number of Storm Surges in Cuxhaven Higher than 1.5 m above HW or Surge Heights above 2.0 m (Running Sums over 3 Years)

result in a rising danger for the coast of the south-eastern North Sea and especially for the estuaries including for instance Bremen and Hamburg (1).

#### Outlook

The detailed evaluation of field tide data of an area in front of the coast resulted in a number of new experiences and helps to improve explanations for certain proceedings. So we are encouraged to intensify the studies, starting in 1985, with

- more detailed investigations within the area of fig. 2,
- extension to the Dutch and Danish coasts and - if data is available - into the North Sea, both for the mean situation of 1975/79,
- a second evaluation of data of 1982/86 for the whole enlarged area,
- a comparison of the tide conditions in both periods to find hints about possible changes.

#### References

- (1) Rohde H., 1984. New Aspects Concerning the Increase of Sea Level on the German North Sea Coast. Proc., 19th ICCE, Houston, Tx. 1984
- (2) Siefert W., 1982. Bemerkenswerte Veränderungen der Wasserstände in den deutschen Tideflüssen. Die Küste, Vol. 37
- (3) Siefert W., Lassen H., 1985. Gesamtdarstellung der Wasserstandsverhältnisse im Küstenvorfeld der Deutschen Bucht nach neuen Pegelauswertungen. In preparation for Die Küste. Vol. 42

## CHAPTER ONE HUNDRED NINETEEN

### Suspended Sand Transport on a Dissipative Beach

John P. Downing\*

#### ABSTRACT

Field studies were conducted in November 1979 to measure suspended sand transport on Twin Harbor Beach, Washington U.S.A. This beach has an average slope of 0.02 and is composed of well-sorted sand with a mean diameter of 0.21mm. The significant height of breaking swells approaching the beach at small angles can be estimated from variance spectra of water level by  $4.36 \sigma_{\eta}$ . In the surf zone significant wave heights are linearly related to the local mean water depth by  $\gamma = H_s/h = 0.45$ . Variance,  $\sigma_{\eta}^2$ , in the gravity wave band (0.048 to 1.0 Hz) is proportional to water depth squared. Low-frequency variance (less than 0.048 Hz) although not systematically related to water depth, is usually largest in the inner surf zone where breakers are small.

Sand suspension is correlated with strong offshore flows that recur at about one-fifth the incident wave frequency. Vertical mixing of sand in the water column by these water motions rather than turbulence generated by shear at the bed associated with individual wave oscillations is a key mechanism in sand transport on dissipative beaches.

The largest sediment loads occur in the inner surf zone where low-frequency motions dominate the breakers. Maximum longshore transport rates, however, were measured in the middle of the surf zone because of the higher longshore current speeds there. The suspended load probably accounts for as much as 45 percent of the litoral drift on a dissipative beach exposed to moderately-high swells approaching the shore at small angles.

#### INTRODUCTION

Sand transport by shoaling waves and nearshore currents in the surf zone is a key process controlling the plan and profile of sandy shores. Nearshore circulation and sand transport vary from one coastal area to another depending upon beach morphology, sediment size, and wave climate. These variations form a continuum of surf dynamics between steep reflective beach systems and gently-sloped dissipative ones. Reflective beaches have narrow surf zones with plunging and collapsing breakers whereas dissipative beaches have wide surf zones with spilling breakers, low frequency current and water level oscillations, and bar-trough morphologies. Several intermediate states of surf dynamics have been scaled with a parameter:

$$\epsilon = A_1 \omega_1^2 / g \tan^2 \beta \quad (1)$$

\* Northern Technical Services, Inc., 14715 N.E. 95th St., Redmond, WA 98052. Formerly: School of Oceanography, University of Washington

(1, 6, 19, 20 and 21) where:  $A_i$  = breaker amplitude,  $\omega_i$  = incident wave radial frequency;  $g$  = gravitational acceleration, and  $\tan \beta$  = beach slope. Dissipative beaches are in the range  $33 < \epsilon < \sim 400$  (20).

The Nearshore Sediment Transport Study (NSTS), begun in 1977, was designed to expand the data base on nearshore sediment dynamics for engineers and coastal managers. As part of NSTS an instrumentation system consisting of: 1) an array of optoelectronic sensors, 2) an electromagnetic current meter, 3) a resistance wave gauge, and 4) a portable data acquisition system was installed on Twin Harbors Beach, Washington U.S.A. (4) in November 1979. Water level, current and sediment concentration data were acquired to characterize the fields of suspended sand and horizontal water motions across a dissipative open-ocean beach.

#### SITE DESCRIPTION

Twin Harbors Beach is on the exposed part of a large barrier spit that forms the seaward margin of Grays Harbor, (Figure 1). The coastline follows a beach ridge complex formed by rapid marine and eolian accretion in the past 5,000 years (2).

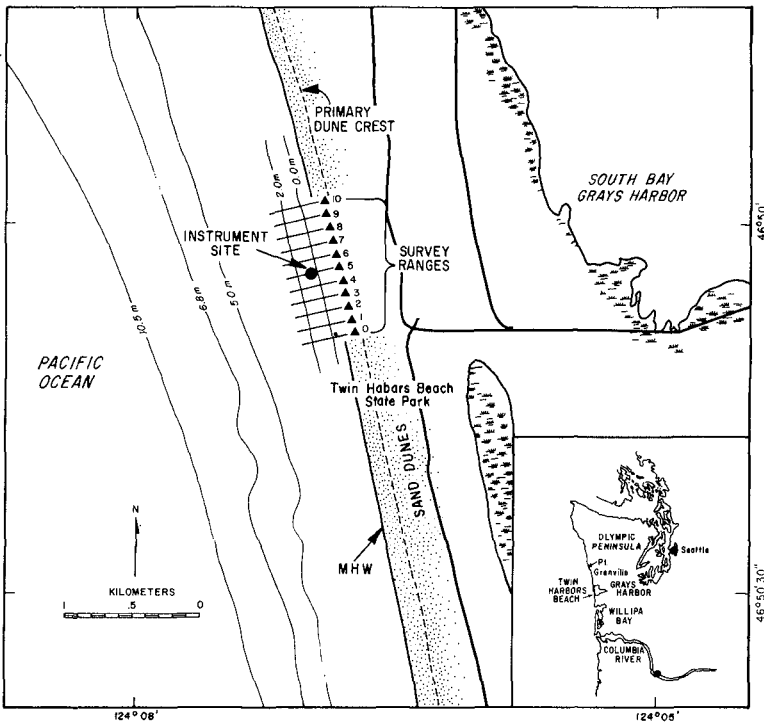


Figure 1 Twin Harbors Beach location map and bathymetry of the study area.

The nearshore bathymetry at the experiment site was determined from 14 rod and level surveys conducted between January and November 1979 along the rangelines shown on Figure 1. The beach is divisible into three zones. The upper beach face has no berm and is relatively steep,  $0.06 < \tan \beta < 0.15$ . In the zone between 25 and 200 m, the profile is featureless and concave up with constant slope (0.01-0.03); see Figure 2. Mean beach slope is irregular seaward of about 200 m because longshore bars and troughs form there during storms. Fluctuations in beach elevation, during the survey period were largest in the outer zone, where 2.0 m fluctuations were measured. Sand level fluctuations landward ranged from 0.2 to 0.3m during the year.

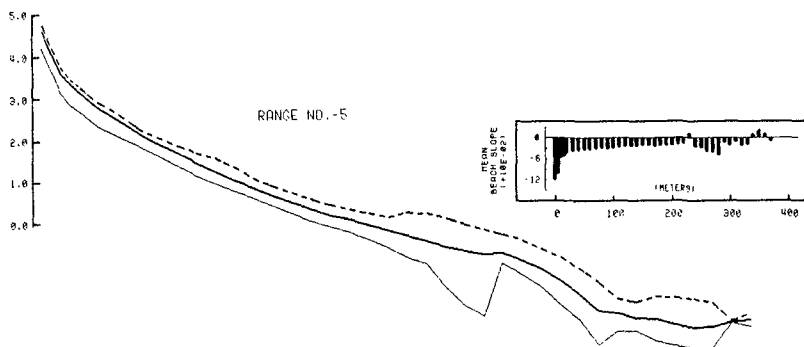


Figure 2 Mean beach profile at range 5 January through November 1979.

The mean grain size and sorting coefficient of sand at the experiment site are 0.21 mm (2.22 Phi) and 0.05 mm (0.38 Phi), respectively (15).

Twin Harbors Beach is exposed to the swell and wind wave regime of the northeast Pacific. The net longshore transport rate near the site estimated by the U.S. Army Corps of Engineers (18), is  $2.2 \times 10^6$  cubic yards per year to the north. This exceeds the net transport rates on all California and east coast beaches for which historical data exist by a factor of 2 to 4 (17). In accordance with the scheme applied to exposed Australian beaches by Wright et al. (19), Twin Harbors Beach has a very dissipative surf zone with  $\epsilon$  values between 80 and 240.

#### INSTRUMENTATION

Figure 3 shows the instrumented mast used for this investigation. Detailed descriptions of individual sensors are given by Downing in (3 and 4). Water level was determined with a surface piercing resistance wave sensor; horizontal current velocity was measured with a MARSH-McBIRNEY electromagnetic current meter and suspended sand concentrations were detected with an integrating infrared back-scatterometer. Analog voltage signals from these sensors were sampled at the rate of  $10 \text{ Hz}$ , digitized with 12-bit resolution, and recorded on floppy disks with a portable data acquisition system. Twelve-bit digitization produces nominal resolution of one part in 4096 for each measured parameter.

The sensor array was installed on survey range no. 5, 180 m from benchmark-BM 5 (Figure 4). The sensors were mounted on a rigid mast held in place by three guy wires attached to anchor stakes driven into the beach sand. The vertical positions of the sensors were measured relative to the sea bed at the instrument mast. The orientation of the current meter probe was established with a magnetic compass and spirit level and is accurate to  $\pm 2^\circ$  of azimuth and  $\pm 0.5^\circ$  relative to vertical. The X axis of the probe was aligned with the local isobaths as determined by the beach surveys. Table 1 lists the vertical positions of the sensors with respect to the beach face.

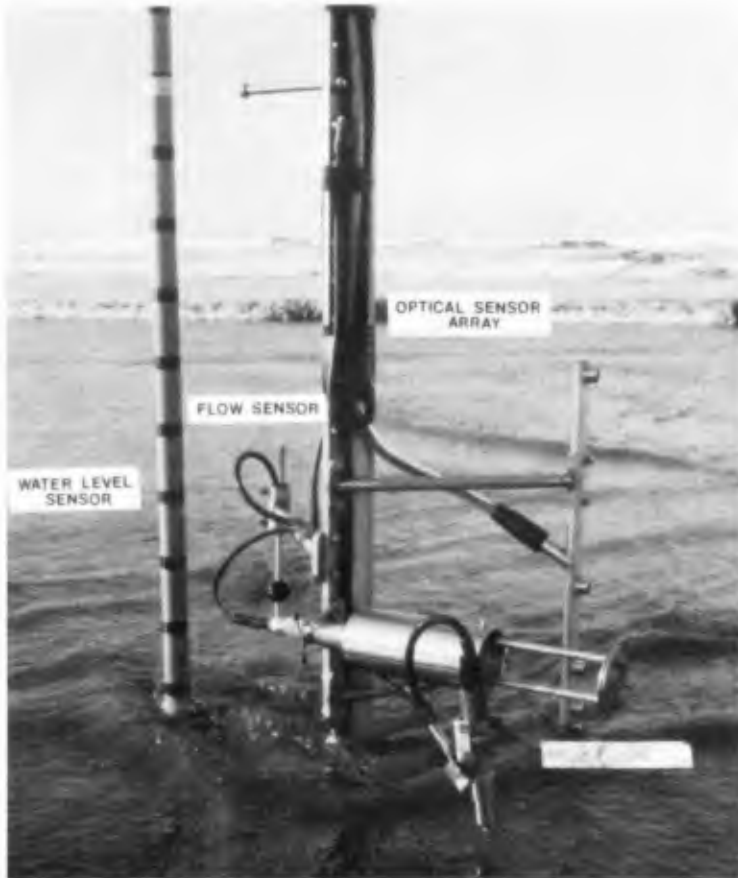


Figure 3 Sediment transport instrument installation.

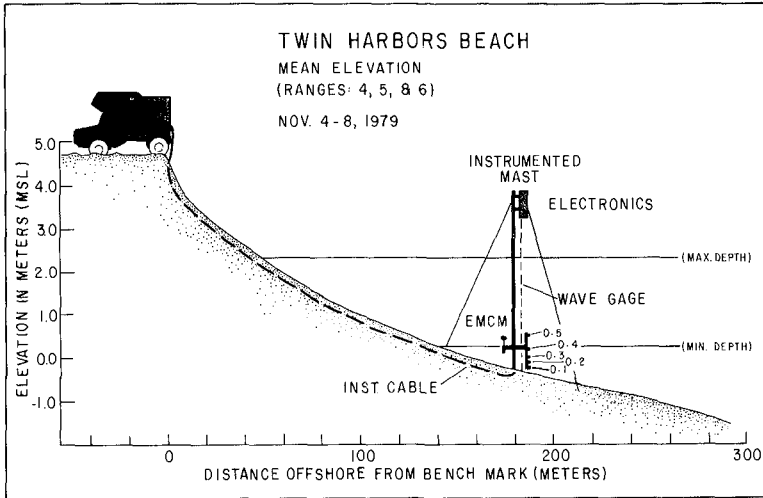


Figure 4 Location of instrumentation on range No. 5.

Table 1. Sensor Locations.

Sensor	Range	Parameter	x (m)	z (m)
EMCM	5	U V	180.2	0.18
Water Level	5	h	180.0	0-3.5
OBS-1	5	C <sub>s</sub>	180.2	0.025
OBS-2	5	C <sub>s</sub>	180.2	0.055
OBS-3	5	C <sub>s</sub>	180.2	0.115
OBS-4	5	C <sub>s</sub>	180.2	0.235
OBS-5	5	C <sub>s</sub>	180.2	0.535

Notes:

x = Distance offshore from survey baseline.      V = Shore-normal velocity.  
 z = Elevation above sea bed.                      h = Water Depth.  
 U = Alongshore velocity.                          C<sub>s</sub> = Suspended sand concentration.

DATA PROCESSING

The coordinate system for computations consists of an X axis, positive onshore; an alongshore Y axis, positive to the north; and a Z axis which is positive up. The origin of the Z axis is the bed elevation at the instrumentation mast.

The binary data were block-averaged over a 0.4-second time window to reduce the bandwidth from 5.0 to 1.25 Hz. The block-averaged time series of  $\langle t \rangle$ , U and V(t), and C<sub>s</sub>(t) were Fourier transformed using a



Cooley-Tukey algorithm to determine the distribution of variance with frequency. Prior to the transformation, records of 1024 points were demeaned, linearly detrended, and tapered with a cosine window. The raw spectral estimates of four sequential non-overlapping records were ensemble averaged and then smoothed by averaging over a four point spectral window. The resulting spectral estimates have 32 degrees of freedom and represent the mean variance in a bandwidth of 0.0098 Hz.

For the purpose of comparing wave heights across the surf zone, a statistic,  $H_s$ , called the significant breaker height was computed from the spectral density functions (SDF),  $S_\eta(f)$ , for each record. This statistic represents  $4\sigma_\eta$  ( $\sigma_\eta$  equals the square root of the variance) in the frequency band from 0.047 to 1.25 Hz. The variance in this frequency band was computed from the SDFs of  $\eta(t)$  by summing the estimates,  $S_\eta(f_n)$ , from  $n = 20$  to 512:

$$\sigma_\eta^2 = \sum_{n=20}^{512} S_\eta(f_n) \quad (2)$$

This is equivalent to computing  $\sigma_\eta$  from a band-passed record of  $\eta(t)$ .

Conversions of voltage levels to scientific units were made with the instrument gains and offsets determined from laboratory calibrations made before and after the experiment (4). Computations of instantaneous suspended sand flux in kg/m/s were made by evaluating the integrals:

$$Q_x(t) = U(t) \int_0^h C_s(z,t) dz \quad (3)$$

$$Q_y(t) = V(t) \int_0^h C_s(z,t) dz \quad (4)$$

where the units of  $C_s$  are mass per unit volume and  $h$  is the instantaneous water depth.

Several assumptions were made to simplify these computations. First, it was assumed that sand concentration varied linearly between sensors. At the bed, the concentration was estimated by extrapolating the gradient between the lowest two sensors to the bottom.  $C_s$  at the surface was set equal to zero. This assumption results in under estimation of the suspended load since the vertical gradients are exponential. It was further assumed that horizontal velocity was vertically uniform. As will become clear later, this assumption was not valid when applied to the computations of shore-normal transport rates. The assumption was unavoidable, however, because only one current meter was deployed.

## RESULTS

Wave, current and suspended sand data were acquired during five periods (runs) on the 6th, 7th and 8th of November, 1979. The duration of runs ranged from 1 to 3.5 hrs. and with the exception of Run no. 4, all were completed during ebbing tides.

The surf during this period originated from a large low-pressure disturbance that occurred in the Northeast Pacific Ocean between the 2nd and 4th of November. Sustained winds of 40 knots blew over a fetch more than 4,000 miles long during the most intense part of the storm. Twelve to fifteen second swells began to break on Twin Harbors Beach during the afternoon of November 4th and continued to produce a moderate surf until the afternoon of November 7th.

#### Wave Conditions

The results of spectral analyses of the water level records are summarized in Table 2 which gives the frequencies and corresponding periods of maxima and minima of the smoothed SDFs. Examples of time series of water level and SDFs representative of conditions in the outer, middle, and inner surf zone are shown in Figures 5 and 6. Spectral density decreases with frequency as  $f^{-3}$  to  $-7/3$  and the primary spectral peak is between 0.0093 and 0.0267 Hz (37.5 and 107 s). A secondary peak associated with the incident swell occurs between 0.067 and 0.105 Hz (9.5 and 15 s). Periods associated with these spectral peaks averaged over all the records are 13.3 and 67 seconds.

Minima are consistently present in the SDFs of  $(t)$  at about 0.048 Hz ( $T = 21.5$  s). This is considered to be the low frequency limit of free surface and velocity fluctuations associated with the incident waves. Water motions and free surface oscillations with frequencies less than 0.047 Hz are called low frequency oscillations. The maximum significant wave height of 1.0 m was measured during the first part of Run no. 2 in a mean water depth of 2.17 m and a corresponding offshore distance of 114 m. About half of the waves early in Run no. 2 were unbroken and the offshore distance of 114 m is taken as the width of the surf zone ( $x_b$ ) during the experiment. Wave heights are linearly proportional water depth and ranged from 0.21 m at  $x/x_b = 0.35$  to 1.0 m at  $x/x_b = 1.0$ .

#### Currents

The longshore current, during 94 percent of the experiment was towards the south with an average speed 0.27 m/s. During two 13.7 min periods it reversed direction and flowed to the north usually less than 0.01 m/s. The maximum 6.83-minute average longshore current was 0.66 m/s.

The persistent southerly longshore current indicates that waves approached the beach from the northwest throughout the experiment and that cellular circulation, rip currents, and large horizontal eddies did not occur during most of the study. Shore-normal current components were offshore during all runs with mean and maximum speeds 0.15 and 0.37 m/s respectively. The implications of a net offshore flow are discussed in a later section.

#### Suspended Sand Concentrations and Transport

Measured transport rates varied between 0.01 and 1.00 Kg/m/s during the experiments and are representative of offshore distances ranging from  $X = 0.35-1.0$ . Figure 6 shows time series of sand concentrations in

the water column at three locations across the surf zone. Sand suspension on this beach is a transient phenomena which occurs at time intervals much longer than the period of the incident waves. The duration and number of sand suspension events increases with decreasing water depth, and they are associated with prolonged periods of offshore flow.

The vertical distribution of suspended sand in the water column has two distinct forms. During quiescent intervals between suspension events, the water column is lightly charged with sediment and the concentration of sand is vertically uniform; see Figure 7. During suspension events, when large quantities of sand are mixed in the water column, there is a strong concentration gradient to about 10 cm above the bed. Above this level sand concentration is more vertically uniform.

Table 2 Summary of time-averaged water level, current and sand transport data.

Run No.	Date (Time)	$\bar{X}$	$\bar{h}$	$\bar{T}_1$	$\bar{H}_g$	$\bar{T}_w$	$\bar{U}$	$\bar{V}$	M	$\bar{Q}_x$	$\bar{Q}_y$
		(m)	(m)	(s)	(m)	(s)	(m/s)	(m/s)	(kg/m <sup>2</sup> )	(kg/m.s)	(kg/m.s)
1	6-Nov. (01:53)	.82	1.65	93.8	.72	13.2	-.20	-.44	.336	-.071	-.159
1	6-Nov. (02:21)	.81	1.58	75.0	.65	13.2	-.20	-.56	.508	-.138	-.266
1	6-Nov. (02:48)	.76	1.46	53.6	.63	12.9	-.18	-.46	.398	-.045	-.191
1	6-Nov. (03:16)	.69	1.25	85.0	.55	13.3	-.19	-.31	.639	-.067	-.251
1	6-Nov. (04:04)	.55	.88	78.8	.42	15.0	-.24	-.31	2.074	-.995	-.561
RUN MEANS		.73	1.36	76.4	.59	13.9	-.20	-.42	.791	-.263	-.286
2	6-Nov. (13:06)	.98	2.15	50.0	1.04	13.2	-.28	-.38	.271	-.074	-.117
2	6-Nov. (13:33)	.95	2.05	75.2	.93	12.9	-.17	-.41	.211	-.028	-.088
2	6-Nov. (14:01)	.90	1.89	75.2	.83	12.9	-.20	-.38	.176	-.028	-.069
2	6-Nov. (14:28)	.84	1.69	50.0	.72	12.9	-.18	-.09	.124	-.017	-.013
2	6-Nov. (14:55)	.75	1.42	56.7	.60	13.0	-.17	-.04	.113	-.013	-.005
RUN MEANS		.88	1.84	64.0	.82	13.0	-.20	-.26	.179	-.032	-.058
3	7-Nov. (01:56)	.80	1.58	50.0	.73	11.7	-.13	-.27	.250	-.026	-.066
3	7-Nov. (02:23)	.80	1.57	83.3	.70	11.5	-.10	-.25	.166	-.011	-.037
3	7-Nov. (02:51)	.47	.70	52.7	.47	12.9	-.16	-.05	8.508	-.715	-.282
RUN MEANS		.69	1.28	59.2	.63	12.3	-.13	-.19	2.975	-.251	-.128
4	7-Nov. (12:40)	.86	1.74	37.5	.79	12.7	-.12	-.30	.090	-.006	-.027
4	7-Nov. (13:07)	.88	1.84	50.0	.84	10.3	-.09	-.28	.074	-.006	-.021
4	7-Nov. (13:35)	.90	1.87	53.0	.86	15.1	-.13	-.23	.069	-.012	-.160
RUN MEANS		.88	1.82	46.8	.83	12.7	-.11	-.27	.078	-.008	-.069
5	8-Nov. (05:47)	.82	.82	50.0	.39	13.2	-.05	-.25	.423	-.020	-.106
5	8-Nov. (06:14)	.66	.66	93.8	.32	NS	-.08	-.04	.502	-.028	-.010
5	8-Nov. (06:42)	.50	.55	107.0	.23	NS	-.07	-.09	.865	-.012	-.051
5	8-Nov. (07:09)	.39	.39	50.0	.19	11.8	-.06	-.04	1.900	-.134	-.030
RUN MEANS		.59	.61	75.2	.28	12.5	-.07	-.11	.923	-.049	-.049
GRAND MEANS		.75	1.38	64.3	.63	12.9	-.14	-.25	.989	-.121	-.118

Notes:

- NS Not significant.  
 $X = x/x_b$   
 $x_b =$  width of surf zone)
- $T_1 =$  Period of spectral density peaks.  
 $T_w =$  Period of spectral density peak associated with incident waves.

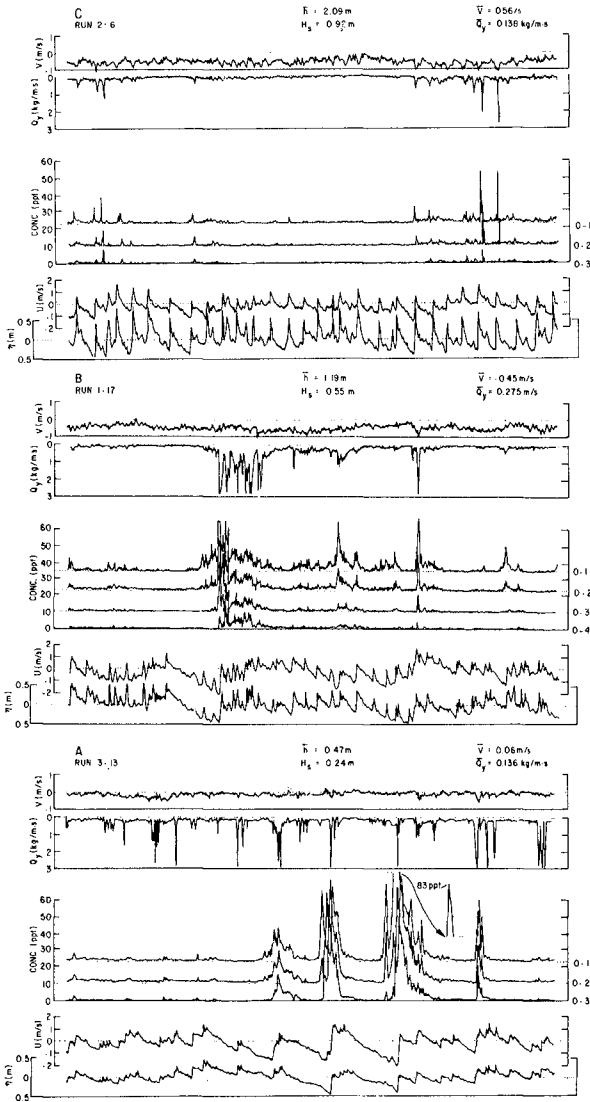


Figure 5 Time series of water level, currents, suspended sand concentrations, and longshore sand transport in the A) inner, B) middle, and C) outer surf zone.

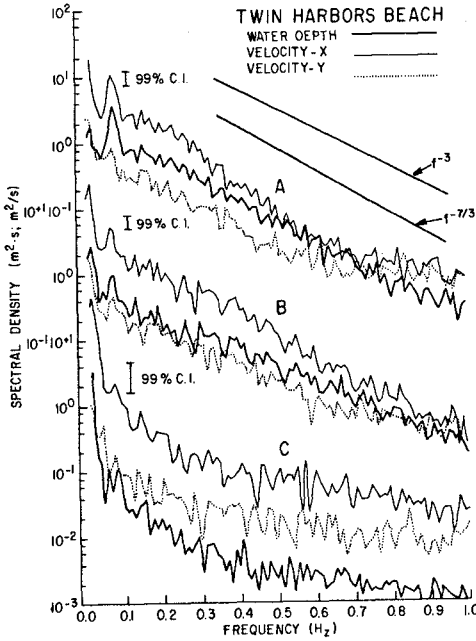


Figure 6 Wave and current spectra for A) outer, B) middle, and C) inner surf zone.

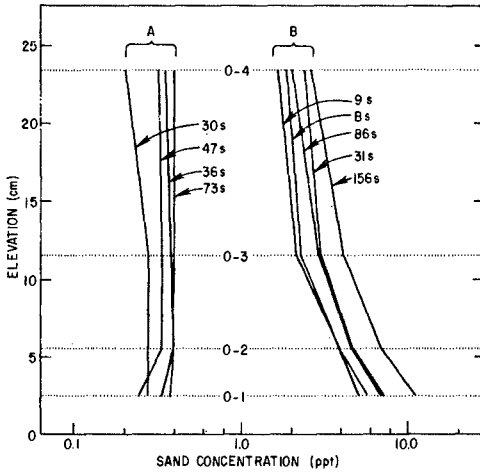


Figure 7 Suspended sand concentration profiles  
 A. During quiescent conditions  
 B. During suspension events  
 Profile annotations indicate the averaging time in seconds.

DISCUSSION

The variance spectrum of water level is convenient to compute, and an empirical check was made to determine how closely measured significant breaker heights can be approximated from the total variance in the gravity wave band. Measurements of the crest to trough heights of 434 spilling breakers across the surf zone indicate that  $H_s$  is best approximated by  $4.36 \sigma$ . This approximation is probably site specific but indicates that a useful wave height parameter can be easily computed from the variance spectrum.

The variation of  $H_s$  with local depth is linear, and the breaking criteria,  $\gamma$ , is  $0.45 \pm 0.05$ . Because several formulas for computing orbital velocities, setup and runup, include the "constant,"  $\gamma$ ; a comparison of field-determined breaking criteria is given in Table 3. These data indicate that  $\gamma$  varies with beach and surf conditions and should be selected cautiously.

Table 3. Wave breaking criteria.

Beach Slope ( $\tan \beta$ )	$\gamma$	Beach	Reference
0.011	0.42	Goolwa, Aust.	(20)
0.014	0.6	Saunton, G.B.	(7)
0.02	$0.45 \pm 0.05$	Twin Harbor Beach, WA	This study
0.13	1.2	Slapton, G.B.	(7)

In Figure 9 computed values of wave energy,  $E_w$ , and total energy,  $E_t$ , have been plotted versus water depth to illustrate possible wave energy decay processes. A least squares fit is drawn through the  $E_w$  values to indicate the trend of wave decay. The distance between this curve and the plotted values of  $E_t$  provides an estimate of the energy associated with low frequency motions. A gradient of wave energy is developed across the surf zone and dissipation is manifested in the growth of low frequency oscillations in water level with attendant fluctuations in the shore-normal current. The energy transfer from high to low frequency, revealed by the present analysis, is not systematic. There is considerable variability in low-frequency energy across the surf zone which cannot be characterized by a convenient parameter such as  $H_s$ . High values of total energy are more likely in the outer surf zone but are not restricted there. Peak values appear at regularly spaced intervals across the surf zone suggesting a standing wave with antinodes at  $h = 0.80$  m and  $h = 1.60$  m ( $X = 0.53$  and  $0.82$ ).

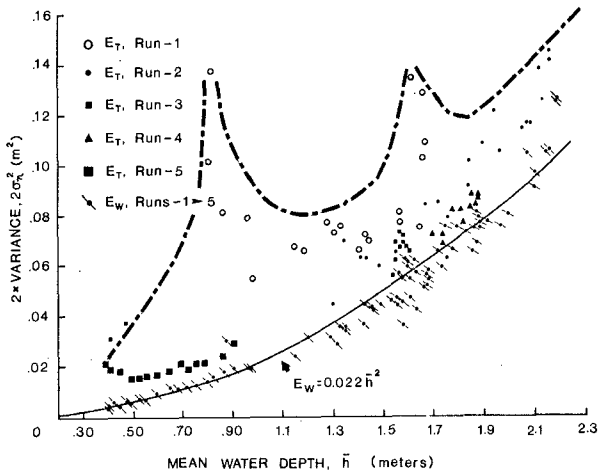


Figure 8 Graph of wave energy,  $E_w$ , and total energy,  $E_t$ , versus water depth.

The mean shore-normal velocity component at  $Z = 18$  cm is 0.15 m/s offshore. Offshore flow at mid-depth is predicted by some theories and laboratory experiments (12 and 16), but is not consistent with most other field data (6) except that from Goolwa Beach, Australia (20). It appears that the mass transport under shoaling waves on highly dissipative beaches can be balanced by nearshore circulation other than eddies and rip currents (10). The total loss of sand from the beach on a weekly basis computed from the profile data (5 to 8 November) was only  $0.06 \text{ m}^3$ . This is nearly three orders of magnitude less than the sand loss of  $50 \text{ m}^3$  per week calculated from the shore-normal transport data, a large discrepancy. In order to balance the sand budget, it appears there must be onshore sand transport near the bed since there is rarely enough suspended sand above  $z = 18$  cm to balance the loss at mid-depth. This result underscores the importance of measuring velocities at several elevations, especially nearer the bed, when monitoring total transport.

#### Variation of Sand Transport and the Total Load

The changing character of the wave induced water motions and sand suspension across the surf zone, Figure 5, and their effect on longshore sand transport is more evident when time and space averaging of the currents and suspended load is done. The 6.8-minute average values of  $V$ ,  $M$  and  $Q_y$  for all runs were grouped according to their location across the surf zone into bins 10 meters wide. Average values for these parameters in each of the bins were normalized by their respective maxima, and their variation across the surf zone is shown on Figure 9.

In the mid- to outer surf zone,  $x = 75-115$  m, the longshore current is large and decreases linearly to 1/10 of the maximum value in the inner surf zone. The suspended sand load is uniformly low in the outer surf zone,  $x = 85-115$  m, and increases near shore. Longshore sand flux is low in the outer zone, primarily because there is little suspended sand available for transport by the high currents there.  $Q_y$  peaks in the mid- to inner zone where the suspended load is moderately high and longshore current speeds are nearly maximum. Near shore the sediment load reaches a maximum but the longshore current is minimal, producing only moderate transport. This general trend of high longshore transport in the mid-surf zone with decreased rates both on and offshore supports Komar's (9) model for the total longshore transport.

Komar (9 and 10) has reviewed the energetics approach to sand transport prediction and indicates that equation 4 represents the longshore transport resulting from radiation stresses as well as nearshore currents from the tides and winds. The total longshore transport is given by:

$$Q_s = 2.5 (EC_n)_b \frac{\bar{V}_l}{U_m} \quad (4)$$

where  $Q_s$  is the at-rest volume of sand transported per day ( $m^3/day$ );  $EC_n$  is the wave energy flux at the breaker zone;  $\bar{V}_l$  is the mean longshore current in the middle of the surf zone and  $U_m$  is maximum orbital velocity under the breakers. The advantage of this equation is that breaker angles which are difficult to measure do not appear explicitly. Maximum orbital velocity is given by (10):

$$U_m = \gamma/2 [g (\bar{\eta} + h)]^{1/2} \quad (5)$$

A comparison of total measured advective sand transport with total predicted longshore transport was made to estimate the contribution of the suspended load. The total transport estimate is made with the wave conditions observed during the early part of Run no. 2, since the instrument was located in the zone of initial wave breaking. The quantity  $(\bar{\eta} + h)$  is replaced by the measured mean water depth  $\bar{h}$  which includes setup  $\bar{\eta}$ , and the breaking parameter,  $\gamma$ , is taken as 0.7 times the measured value since RMS wave heights are used in Komar's formula. Likewise the wave energy flux is computed with

$H_{rms} = 0.7 H_s$ ; so  $EC_n = \frac{1}{8} \rho g H_{rms}^2 \sqrt{gh}$ . The longshore current velocity



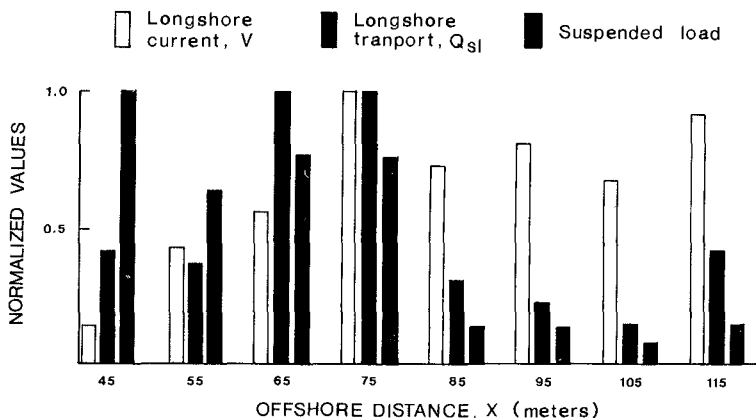


Figure 9 Variation of longshore current speed, suspended load, and sand transport across the surf zone.

at the mid-surf position is given by the average of the longshore velocities measured in water depths between 0.7 and 1.0 m. The values used for computing  $Q_s$  are:  $H_{rms} = 0.59$  m;  $\bar{h} = 2.1$  m;  $\bar{V}_1 = 0.25$  m/s and  $U_m = 0.64$  m/s. The predicted total longshore transport rate is 1,930 m<sup>3</sup>/day.

In making the estimate of advective sand transport, the surf zone was subdivided into twelve shore-parallel bands, 10 meters wide. Transport rates in each band are equal to the average of measured values in the band. Values in the inner surf zone are obtained by linear extrapolation of the innermost measurements to zero at the shoreline. In this way, a value of 915 m<sup>3</sup>/day was estimated for the suspended load transport during the experiment. This comprises 47 percent of the total load predicted above.

#### Wave-sediment Interaction

Suspension events appear to be the major process which makes sand available for advective transport on Twin Harbors Beach. More than 190 suspension events were recorded during the ten hours of measurements. These events nearly always occurred during offshore flow that persists for several wave periods (Figure 6). Three of these events have been selected for description and are illustrated in Figure 10.

For each event, the time histories of sand concentration at the lowest four sensors and horizontal current speed are shown with a sequence of  $C_s$  profiles. The suspension events occur as follows:

- 1) The water column is relatively clear during initial offshore acceleration of the flow.

- 2) High concentrations and gradients develop near the bed and sand is mixed into the water column as bores propagating shoreward interact with the seaward flowing current. There is usually a lag of several seconds between the occurrence of high sand concentrations near the bed

and their occurrence in the upper water column ( $z > 24$  cm). Maximum sediment loads usually lag peak offshore current speeds and the passage of the larger bores.

3) The decay of suspension events is most often characterized by a loss of suspended load with a uniform decrease of concentration at all levels.

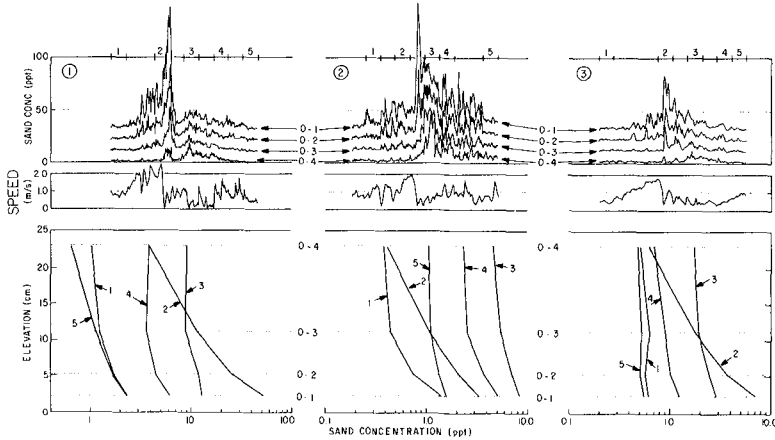


Figure 10 Sequential suspended sand profiles during suspension events. Numbered intervals on upper axis are six seconds long; current speeds are the resultant of X and Y-velocity components. Concentration profiles are six-second averages.

Several important aspects of the water motion producing these suspension events could not be measured for the present study. These include the vertical velocity component and the local convective accelerations. These respects of water motion appear to be critical to our full understanding of the suspension process (8). Further it appears that the approach to the problem of suspended sand transport taken in previous investigations (11 and 13) may not be productive on natural dissipative benches since wave by wave sand suspensions are a small part of the total load.

CONCLUSIONS

At Twin Harbors Beach:

1) The significant height of breaking swells approaching the beach at small angles can be estimated from variance spectra of water level by  $4.36\sigma_\eta$ . In the surf zone significant wave heights are linearly related to the local mean water depth by  $\gamma = H_a/h = 0.45$ . Variance,  $\sigma_\eta^2$ , in the gravity wave band (0.048 to 1.0 Hz) is proportional to water depth squared. Low-frequency variance (less than 0.048 Hz) although not systematically related to water depth, is usually largest in the inner surf zone where breakers are small.

2) Sand suspension is correlated with strong offshore flows that recur at about one-fifth the incident wave frequency. Vertical mixing of sand in the water column by these water motions rather than turbulence generated by shear at the bed associated with individual wave oscillations is a key mechanism in sand transport on dissipative beaches.

3) The largest sediment loads occur in the inner surf zone where low-frequency motions dominate the breakers. Maximum longshore transport rates, however, were measured in the middle of the surf zone because of the higher longshore current speeds there. The suspended load probably accounts for as much as 45 percent of the littoral drift on a dissipative beach exposed to moderately-high swells approaching the shore at small angles.

#### ACKNOWLEDGMENTS

I thank Professors Dick Sternberg and Clive Lister for their insight and productive suggestions about this research. Rex Johnson and Stan Woods were the skilled craftsmen who made the instruments. Harvey Smith provided energetic support in the field. Financial support was provided by a NOAA grant administered by the National Sea Grant College Program and the Nearshore Sediment Transport Study, a multi-institutional effort (#SGNOAA NAB1 KA-D-0030).

#### REFERENCES

1. Battjes, J. 1975. Surf similarity. Proc. 14th Coastal Eng. Conf., ASCE, pp. 466-479.
2. Cooper, W. S. 1958. Coastal sand dunes of Washington and Oregon. Geol. Soc. Amer. Memoir 72, 169 p.
3. Downing, J. P., R. W. Sternberg and C. R. B. Lister. 1981. New Instrumentation for the Investigation of Sediment Suspension Processes in the Shallow Marine Environment. In Nittrouer, C. A. (ed.), Sedimentary Dynamics of Continental Shelves: 19-34. Mar. Geol. 42 (Special Issue).
4. Downing J. P. 1983. Field Studies of Suspended Sand Transport, Twin Harbor Beach, Washington. Ph.D. Dissertation, University of Washington, Seattle, Washington.
5. Guza, R. T. and A. J. Bowen. 1976. Finite amplitude edge waves. J. Mar. Res. 34(1): 269-293.
6. Guza, R. T. and E. B. Thornton. 1980. Local and shoaled comparisons of sea surface elevations, pressures, and velocities. J. Geophys. Res. 85(C3): 1526-1530.
7. Huntley, D. A. and A. J. Bowen. 1975. Comparison of the hydrodynamics of steep and shallow beaches. In: Nearshore Sediment Dynamics and Sedimentation--an Interdisciplinary Review (eds. J. Hails and A. Carr). John Wiley & Sons, New York.

8. Johns, B. 1980. The modeling of the approach of bores to a shoreline. *Coastal Engineering* 3: 207-219.
9. Komar, P. D. 1977. Beach Processes and Sedimentation. Prentice-Hall, New Jersey, 429 p.
10. Komar, P.D. 1983. Nearshore currents and sand transport on beaches. In: Coastal and Shelf Dynamical Processes, B. Johns [ed.], Elsevier Press.
11. Kumaya, M. and H. Nishimura. 1980. Variation of suspended sediment with wave energy. Proc. 27th Japanese Conf. Coastal Eng., pp. 235-239.
12. Longuet-Higgins, M.S. 1953. Mass transport in water waves. Phil. Trans. Roy. Soc. (London), Series A, 245(903): pp. 535-581.
13. Nielsen, P. 1979. Some basic concepts of wave sediment transport. Series Paper 20, Inst. of Hydrodynamics and Hydraulic Eng., Tech. Univ. of Denmark, Lyngby, 160 p.
14. Phipps, J. B. and J. M. Smith. 1978. Pacific Ocean Beach Erosion and Accretion. State of Washington Dept. of Ecology Unpublished Report, 75 p.
15. Plopper, C. S. 1978. Hydraulic sorting and longshore transport of beach sand, Pacific coast of Washington. Ph.D. thesis, Syracuse Univ., 185 p.
16. Russell, R. C. H. and J. D. C. Osorio. 1958. An experimental investigation of drift profiles in a closed channel. Proc. 6th Coastal Eng. Conf., ASCE, pp. 171-193.
17. U.S. Army Coastal Engineering Research Center. 1977. Shore Protection Manual.
18. U.S. Army Corps of Engineers--Seattle District. 1973. Grays Harbor and Chehalis River and Hoh River, Washington North Jetty Rehabilitation. Unpublished report.
19. Wright, L. D., J. Chappell, B. G. Thom, M. P. Bradshaw, and P. Cowell. 1979. Morphodynamics of reflective and dissipative beach and inshore systems: southeastern Australia. *Mar. Geol.* 32(1/2): pp. 105-140.
20. Wright, L. D., R. T. Guza and A. D. Short. 1982. Dynamics of a high-energy dissipative surf zone. *Mar. Geol.* 32: pp. 105-140.
21. Wright, L. D., P. Nielsen, A. D. Short, F. C. Coffey and M. O. Green. 1982. Nearshore and surf zone morphodynamics of a storm wave environment. Eastern Bass Strait, Australia, Coastal Studies Unit, Univ. of Sydney Tech. Rep. No. 82/3, 153 p.

## CHAPTER ONE HUNDRED TWENTY

### Field Investigations of Suspended Sediment Transport in the Nearshore Zone

R.W. Sternberg\*, N.C. Shi†, and John P. Downing††

#### ABSTRACT

The suspended sediment distribution and longshore sediment transport characteristics at Leadbetter Beach, Santa Barbara, California were investigated using a series of miniature optical backscatter sensors which can measure particle concentrations as high as 180 gm/l and have 10 Hz frequency response. Vertical arrays of sensors were maintained at up to four positions across the surf zone during 7-25 February 1980 and were operated concurrently with pressure sensors and current meters. Data were collected on a daily basis over 2-4 hour periods.

The data were analyzed to reveal concentration profiles of suspended sediment, the average suspended sediment loads, and the longshore particle flux in relation to varying wave conditions. Results show that sediment transport occurs as individual suspension events related to incident wave motions and infragravity motion oscillations within the surf zone; suspended sediment concentration decreases approximately logarithmically away from the seabed; the maximum values of longshore transport rates occur in the mid-surf zone; and the measured suspended sediment longshore transport rate is equal to the total longshore transport rate as predicted by existing transport equations.

#### INTRODUCTION

As part of the Nearshore Sediment Transport Study (NSTS) carried out at Leadbetter Beach, Santa Barbara, California, in January-February 1980 (7), an extensive series of suspended sediment measurements were made concurrently with observations of wave motions (currents and water level fluctuations), sediment characteristics, and beach profiles. The total NSTS experiment was broad in scope, integrating a wide variety of research objectives (20,21,22). This project emphasized suspended sediment transport, with major objectives of characterizing the temporal and spatial suspended sediment distribution across the surf zone and investigating the relationship between surf zone physical processes and the littoral transport of suspended sediment. In addition, the longshore transport models of (16,17) were evaluated with respect to the longshore component of suspended sediment flux measured during a range of incident wave conditions.

\* School of Oceanography, University of Washington, Seattle, WA 98195

† Virginia Institute of Marine Science, Gloucester Point, VA 23062

†† Northern Technical Services, 117 Lake Street South, Kirkland, WA 98033

STUDY AREA

Leadbetter Beach is a relatively straight sandy beach located directly updrift from the breakwater-harbor area of Santa Barbara, California (Fig. 1). It was selected as a study site because the approaching wave direction is reasonably constant due to the narrow window between the offshore Channel Islands and because the high angle of wave incidence provides a nearly unidirectional longshore current from west to east, i.e., from the study site towards the Santa Barbara breakwater which represents a total sediment trap. Semidiurnal tides have a mean range of 110 cm and a mean tide level of 85.3 cm (MLLW). The beach has a steep slope and the surf zone is narrow. The textural properties of the beach sand indicate that it is fine to medium (mean = 0.236 mm) with a sorting coefficient of 0.40.

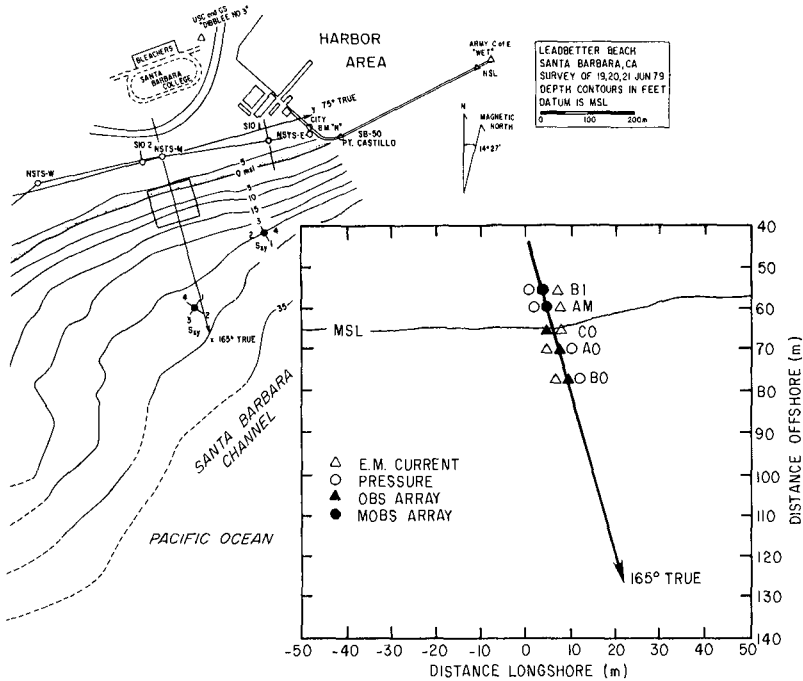


Fig. 1. Study site, including main cross-shore transect and expanded view showing instrument locations.

## TECHNIQUES

## Suspended sediment sensors

Suspended sediment concentration was measured with an optical backscatter sensor (OBS) developed at the University of Washington (4). An OBS sensor consists of a stainless steel housing 19 mm in diameter by 11 mm in length (Fig. 2). It houses an infrared emitting diode (IRED) with peak radiant intensity at 950 nm, a silicon photo-voltaic cell with peak spectral response at 900 nm, and an appropriate filter to limit transmittance from incident light. The optical components are encapsulated in the sensor head with clear epoxy resin. When operating, a scattering volume of 1.3 cc is irradiated through a 5.6 mm aperture at the geometric center of the photo-detector by a IR-beam with a half-cone angle of  $14^\circ$ . Backscattered radiation ( $110\text{-}165^\circ$ ) is converted to photocurrent by the detector oriented in a plane normal to the emitter beam axis and located close to it.

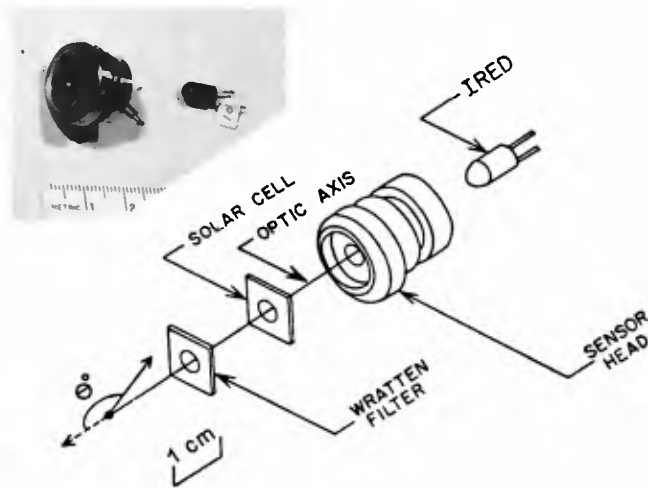


Fig. 2. OBS sensor and cut-away view.

A representative calibration curve for an OBS sensor using a beach sand with median diameter of 0.165 mm is shown in Figure 3. The response of the instrument is linear in the concentration range of 0.1 to 100 ppt by weight. The response of the instrument is minimal to air bubbles injected into the calibration tank (indicated in Fig. 3 by arrows). Each optical sensor was individually calibrated with Leadbetter Beach sediment before and after the Santa Barbara experiment. The instrument response was linear in the concentration range from 0.1 to 150 ppt and 0.1 ppt is the threshold of detection.

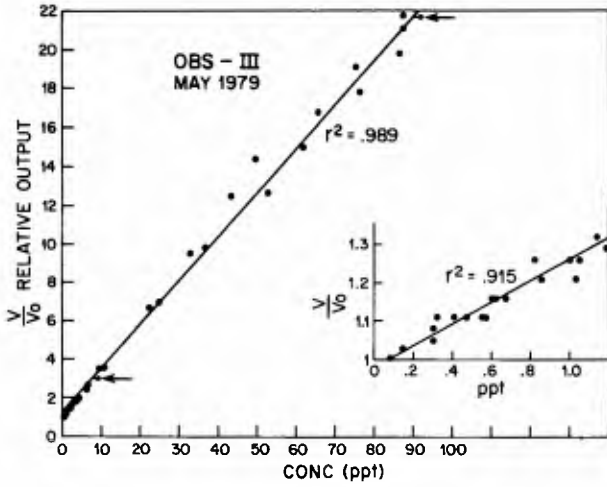


Fig. 3. Calibration curve and expanded scale for values <1.2 ppt.

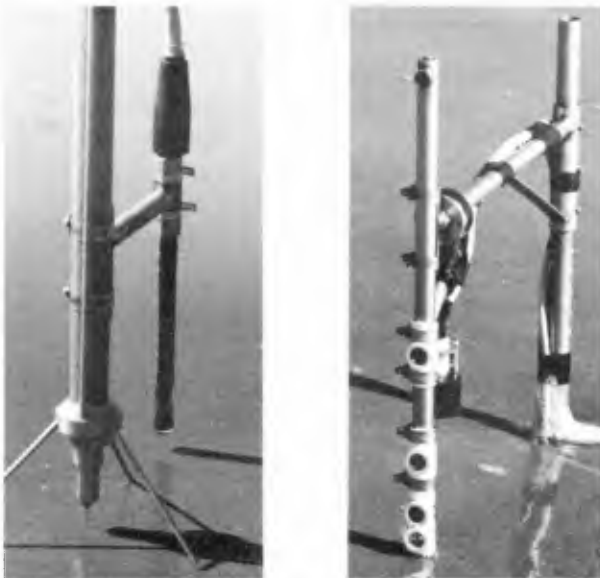


Fig. 4. MOBS (left) and OBS sensor arrays.



### Sensor arrays

To meet the program objectives vertical arrays of OBS sensors were placed on a transect across the surf zone; vertical arrays were constructed in two sizes. An OBS array consists of five sensors mounted in a steel tube with a logarithmic spacing between sensors (Fig. 4). The total length of the array is 51 cm and the spacings between sensors is 3, 6, 12, and 30 cm. This configuration was used in the outer surf zone where water depths were  $>0.5$  m. Plastic "shields" were fitted on the lower sensors to minimize damage from moving cobbles in the surf zone resulting from storm conditions.

A miniaturized version of the OBS array was used in the inner surf zone where water depths were generally  $<0.5$  m. The miniature array (MOBS) consists of five OBS sensors mounted on a structural rod and encapsulated in plastic. The length of the MOBS array is 16 cm and the spacings between sensors is 3, 3, 5, and 5 cm (Fig. 4).

Up to five suspended sediment sensor arrays (OBS and MOBS) were deployed in proximity to current meters and pressure transducers placed along a primary cross-shore range line (Fig. 1). The OBS sensor arrays were cantilevered into the flow from pipes jettied into the bottom. Sensor electronics were buried in the seabed beneath each OBS sensor array and connected to the shore laboratory with a multiconductor cable. The MOBS sensor arrays were suspended from a tripod structure jettied into the upper beach face. A current meter and pressure gauge or wave staff also were mounted on each tripod. Sensor electronics were strapped on the tripod well above the sea surface and the multiconductor cable connecting the sensor electronics to the shore was buried.

All arrays were mounted vertically with the lowest sensor 3.5 cm off the seabed and the highest sensor located at 64.5 cm and 19.5 cm above the seabed for OBS and MOBS arrays, respectively. The elevation of each array was monitored before and after each data series.

OBS arrays (AO, BO, and CO) were located 6 m west of the main range line and on the same isobath as an EM current meter ( $z \approx 45$  cm) and a pressure sensor ( $z \approx 20$  cm); MOBS arrays (AMO, BMO) were located within 50 cm of an EM current meter positioned at  $z = 4$  cm (Fig. 1). All sensor output signals were transmitted continuously to the shore station and subsequently scanned and recorded in the NSTS data system.

### Data collection

The basic strategy of the sampling program was to maintain a cross-shore transect of OBS and MOBS arrays over as wide a range of wave conditions as possible. Data were collected on a daily basis between 7 and 24 February 1980. Each data series consisted of a time series of approximately 2-4 hours duration with one or more of the sensor arrays operating. Figure 5 shows the data series collected by individual sensor arrays relative to significant wave height ( $H_s$ ), which varied from about 0.3 to 1.8 m over the duration of the experiment.

LEADBETTER BEACH

80	-	-	-		-	-	-	-	-			-	-	-
AO	-	-	-		-	-	-	-	-			-	-	-
CO					-	-	-	-	-			-	-	-
AMO	-	-										-	-	-
BMO		-										-	-	-

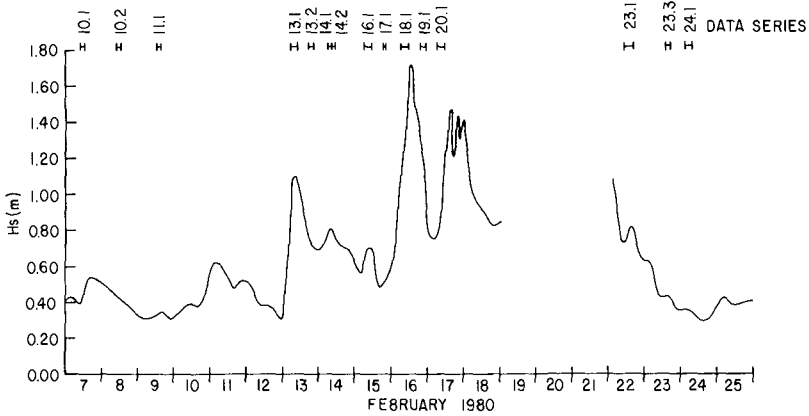


Fig. 5. Data series collected by individual sensor arrays (shown above) relative to significant wave height over the duration of the experiment.

ANALYSIS

Data set

During the experiment, 15 suspended sediment data series were collected (Fig. 5). Each consisted of continuous sampling of all operational sensor arrays, along with measurements of velocity, water level, and beach profiles (made by other NSTS investigators). For a variety of reasons it was not possible to analyze all of the data collected. Several data series were collected during periods of very low tides when sensors were not continually submerged. Also, some suspension events of nearshore sand were obscured in data collected during a severe storm because the quantity of very fine sediment in the surf zone due to storm drain flooding in Santa Barbara increased the background signal levels.

After inspecting all of the data records a data quality index was used to choose the data series that were analyzed. The primary considerations were that the data series spanned a range of wave conditions, had low background signals from washload, provided reasonable coverage

across the surf zone, and required a minimum amount of editing. Six data series (13.1, 13.2, 14.1, 14.2, 23.3, 24.1, Fig. 5) were chosen for analysis. Within these six data series, thirty segments representing different tide levels were chosen arbitrarily for averaged data analyses (34-min averages). For a tabulation of this data set see (24).

#### Suspended sediment

Three categories, high frequency data analysis, averaged data analysis, and sediment transport calculations and predictions, were employed. Initially, the raw data from all sensor outputs were block averaged to a 2 Hz sampling rate and converted to scientific units. An example of a 6 1/2-min data series is shown in Figure 6. Data included

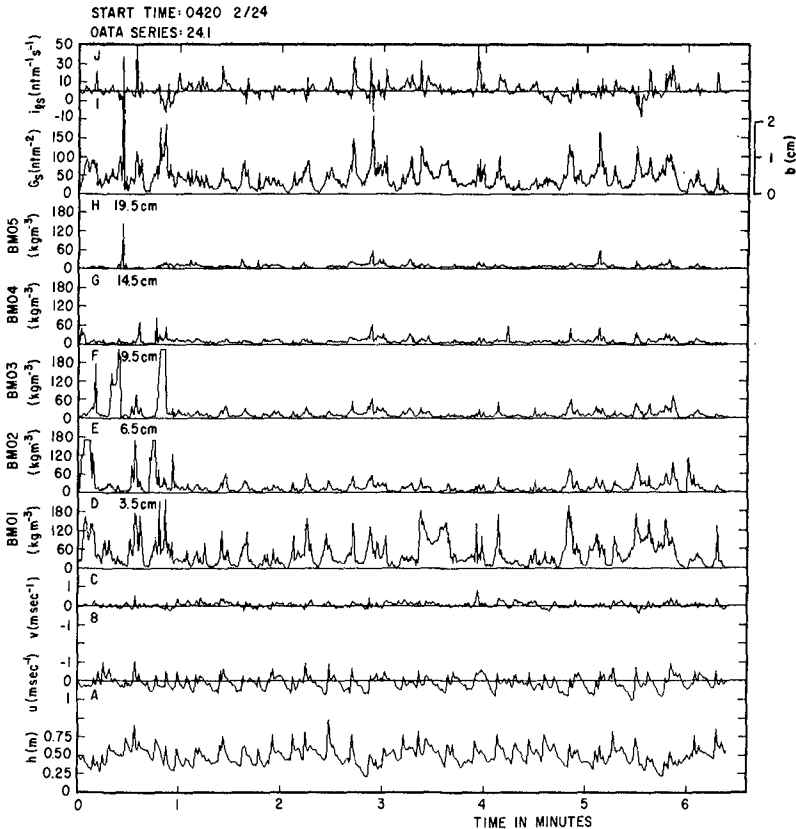


Fig. 6. A 7-min time series during data series 24.1.

are (A) water depth  $h$ , (B) on-offshore velocity component  $u$ , (C) longshore velocity component  $v$ , (D-H) suspended sediment mass concentration at five levels above the seabed, (I) total immersed weight suspended sediment load  $G_s$  and depth of erosion required to supply the suspended load  $b$ , (J) immersed weight suspended sediment longshore transport per unit width of seabed  $i_{\ell s}$ . The values of  $(G_s)$ ,  $(b)$ , and  $(i_{\ell s})$  were computed every 1/2 s using the following equations:

$$G_s = \frac{\rho_s - \rho}{\rho_s} g \int_0^h C dz \tag{1}$$

$$b = \frac{\int_0^h C dz}{\rho_s C_b} \tag{2}$$

$$i_{\ell s} = G_s v \tag{3}$$

where  $\rho_s$  and  $\rho$  are sediment and fluid density;  $g$  is acceleration of gravity,  $C$  is suspended sediment mass concentration,  $h$  is total depth, and  $C_b$  is the volume concentration of the seabed (0.6), and  $v$  is longshore component of velocity.

The second category of analysis involved the computations of mean values of various sediment parameters. The averaging period for these computations was taken as 2048 s or approximately 34 min. This period is thought to be sufficiently long to give stable averages and yet short enough to minimize tidal variations during the averaging period. The mean suspended sediment concentration at each level above the bed  $(\bar{C})$  and the mean immersed weight suspended sediment load  $(\bar{G}_s)$  were determined by averaging the values of  $C$  and  $G_s$  over 2048 s.

The third category of analysis included computations of immersed weight suspended sediment transport rate from the field measurements and the prediction of the total longshore transport rate using the methods of (16,17). The local immersed weight longshore transport rate of suspended sediment  $(\bar{i}_{\ell s})$  occurring at each sensor array was computed as shown in equation (4) and the total longshore transport rate of suspended sediment  $(I_{\ell s})$  was determined by summation of the individual measurements of  $\bar{i}_{\ell s}$  made across the surf zone (eq. 5). Equations 6 and 7 outline the computational methods for predicting the total longshore transport rate of sediment as developed by (16,17):

$$\bar{i}_{\ell s} = \bar{G}_s v \tag{4}$$

$$I_{\ell s} = \sum \bar{i}_{\ell s} \Delta X \tag{5}$$

$$I_{\ell} = KP_{\ell} \quad \text{where } K = 0.77 \text{ and } P_{\ell} = (EC_n)_b \sin \alpha_b \cos \alpha_b \tag{6}$$

$$I_{\ell} = K'(EC_n)_b \frac{\bar{v}_{\ell}}{u_m} \quad \text{where } K' = 0.28 \tag{7}$$

where  $X$  is distance from shoreline,  $(EC_n)_b$  is the wave-energy flux at the breaker,  $\alpha_b$  is the breaker angle,  $v_l$  is the longshore current velocity at the mid-surf position,  $U_m$  is the maximum horizontal orbital velocity evaluated at the breaker zone,  $K$  and  $K'$  are dimensionless coefficients determined empirically, and other terms are as defined above.

Because of the small number of sensor arrays deployed, measurements of  $\bar{I}_{1s}$  made at different stages of the tide (and hence for different values of  $X/X_b$ ) during a data series were combined to increase data coverage across the surf zone.

#### Waves and currents

Various characteristics of the waves at breaking are required to calculate the littoral transport rate (eqs. 6 and 7). These include breaker height, breaker depth, breaking angle, and bottom oscillatory velocity. As all the variables were not measured throughout the experiment (e.g., angle of breaking), predictions of breaker characteristics for each data series were made using offshore pressure data. Waves measured at the offshore wave array (see Fig. 1) were subjected to computer analysis that included considerations of refraction and breaking. Where possible the predicted breaking characteristics were compared to the observed breakers to test the methods; however, the predicted breaker characteristics were used for calculations of littoral transport. The detailed procedure for this analysis and a data tabulation is given in (24). The measured longshore velocity used in eq. 7 was estimated by plotting values of  $\bar{v}$  obtained from the current meters placed across the surf zone and interpolating between points to  $X/X_b = 0.5$ . The values of  $P_1$  and  $(EC_n)_b \bar{v}_1 / u_m$  (eqs. 6 and 7) were computed using rms rather than significant wave conditions to be consistent with other studies.

### RESULTS AND DISCUSSION

#### Suspended sediment

Some general observations of suspended sediment characteristics from data series 24.1 are summarized as follows:

- 1) The suspended sediment concentration near the seabed ( $z = 3.5$  cm) varied over a wide range and reached  $180 \text{ kg m}^{-3}$  during individual suspension events (Fig. 6D). The depth of erosion ( $b$ ) required to supply the measured suspended load is approximately 1-2 cm and is comparable to the mixing depth evaluated in various sand tracer studies (9,18).
- 2) The concentration decreased systematically away from the seabed (Fig. 6D-H).
- 3) Individual suspension events were in phase with bores propagating across the surf zone. Where the offshore directed flow prior to an incoming bore attained significant magnitude (i.e., the threshold of grain motion was exceeded), a sediment suspension event was initiated and then reinforced by the passage of a bore propagating shoreward.

4) The frequency and duration of sediment suspension events were strongly correlated with incident wave conditions. Low frequency oscillations of onshore/offshore velocity and water level were observed in many data records. Large temporal variations in the magnitude of suspension events also occurred; they appear to be of greatest magnitude in relation to major offshore flows of water corresponding to troughs in the low frequency signals.

Four representative suspended sediment profiles from data series 24.1 are shown in Figure 7. Two are from the breaker region ( $X/X_b = 0.84, 0.96$ ) and two are from the mid-surf zone ( $X/X_b = 0.49, 0.60$ ). The position of the lowest sensor in these profiles was 3.5 cm above the seabed which is over 150 grain diameters above the boundary ( $Md = 0.23$  mm); thus any particles measured by the sensors are considered as suspended load (6,23). The dominance of suspended load transport at  $z = 3.5$  cm is also suggested by the maximum measured volume concentration of solids being 0.07 which is below the minimum volume concentration (0.08 or 0.09) considered necessary to produce a bedload transport layer supported by intergranular collisions (1,2,8). A generalized suspended sediment profile (11,12), collected shoreward of the breaking point, which was considered to be representative of suspended sediment profiles

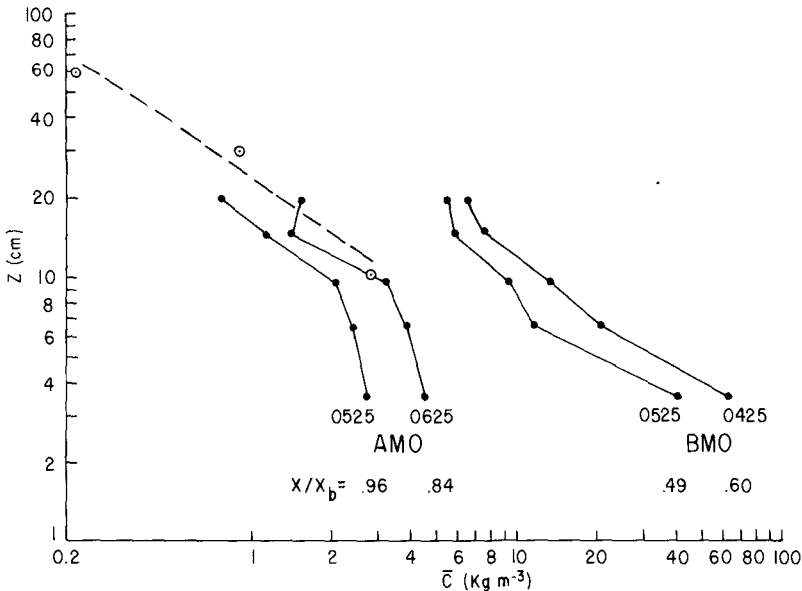


Fig. 7. Vertical profiles of mean values of suspended sediment from two sensor arrays during data series 24.1. Time of day indicates beginning of each averaging period and  $X/X_b$  indicates relative position across the surf zone where  $X_b$  equals breaking point. Open circles and dashed line are explained in the text.

associated with plunging breakers, is included (Fig. 7). The profiles plotted from data series 24.1 generally are similar to previous results (11,12). The mean concentration measured at  $z = 10$  cm for data series 24.1 ranges from approximately  $2\text{--}12 \text{ kg m}^{-3}$ , compared to  $3 \text{ kg m}^{-3}$  reported by (11,12), and the concentration increases logarithmically toward the seabed.

Sediment transport

The longshore transport rate of suspended sediment ( $I_{\ell s}$ ) was determined for each of the six data series (Fig. 8). Values of  $I_{\ell s}$  were plotted according to their relative position within the surf zone ( $X/X_b$ ), and the area encompassed by the points is proportional to  $I_{\ell s}$ .

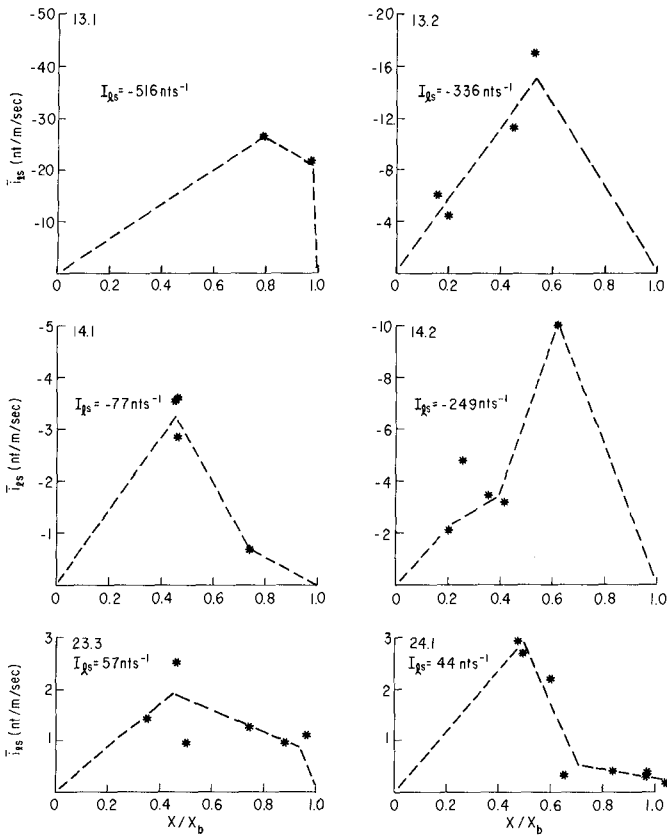


Fig. 8. Cross-shore distribution of  $I_{\ell s}$ . The total longshore transport rate ( $I_{\ell s}$  from eq. 3) is noted for each curve.

The curves have been extended to zero at the positions of  $X/X_b = 0$  and 1.0. Thus, any swash zone transport or transport beyond the breaker point was not considered. The shapes of the curves, although irregular, follow a general pattern, with maximum longshore transport approximately in the mid-surf position. The data points tend to be grouped on either the shoreward or the seaward side of  $X/X_b = 0.5$ , and no single data series spanned the width of the surf zone. Nevertheless, visual inspection of the six data series appears to justify the way in which the curves are extrapolated to zero. This general distribution of  $I_{\ell s}$  suggested by previous field measurements (3,11), laboratory measurements (19), and theoretical predictions (14). The area under each curve multiplied by the width of the surf zone represents the measured value of  $I_{\ell s}$  (Fig. 8 and Table 1).

Table 1. Longshore transport calculations.

Data Series	Average $P_{\ell}$ (nt/s)	Average $(ECn)_b v_{\ell}/u_m$ (nt/s)	Width $X_b$ (m)	Beach slope $\beta$	Measured $I_{\ell s}$ (nt/s)	K	K'
13.1	-203	-1470	34	0.041	-516	2.54	0.35
13.2	-374	-2360	48	0.041	-336	0.90	0.14
14.1	-229	-462	55	0.037	-77	0.34	0.17
14.2	-278	-618	60	0.037	-249	0.89	0.40
23.3	19	207	55	0.022	57	3.00	0.28
24.1	17	75	35	0.021	44	2.59	0.59
Average				0.033		1.71	0.32

It is also of interest to know how the longshore transport rate of suspended sediment compares with the estimated total littoral transport rate. Assuming that equations 6 and 7 predict the total longshore transport rate ( $I_{\ell}$ ), as discussed by (16), the ratio of  $I_{\ell s}$  to  $I_{\ell}$  represents the contribution of suspended sediment to the total. In Figures 9A and B the values of  $I_{\ell s}$  from this study (solid circles) have been superimposed on a plot from (16).

In Figure 9A the data from this study tend to fall above the predictive line while the agreement in Figure 9B is excellent. The average value of K is 1.71, approximately twice the value determined from previous studies (eq. 6,  $K = 0.77$ ), whereas that of K' is 0.32 which is within 14% of the value determined previously (eq. 7,  $K' = 0.28$ ).

According to (16), equation 7 (Fig. 9B) is the more fundamental of the two sand transport relationships and should be applicable regardless of the origin of the longshore current ( $\vec{v}_1$ ), e.g., tide or wind generated, and currents of the cell circulation, or of oblique wave approach. It was also pointed out by (16) that it is usually easier to measure the longshore current than the breaker angle needed in the evaluation of  $P_{\ell}$  in equation 6. Further, it was demonstrated (18) that equation 7 is applicable where the longshore current was the net result of two opposing currents. The close agreement between the results of this study and previous studies (Fig. 9B) suggests that all of the longshore transport at Leadbetter Beach can be accounted for by suspended



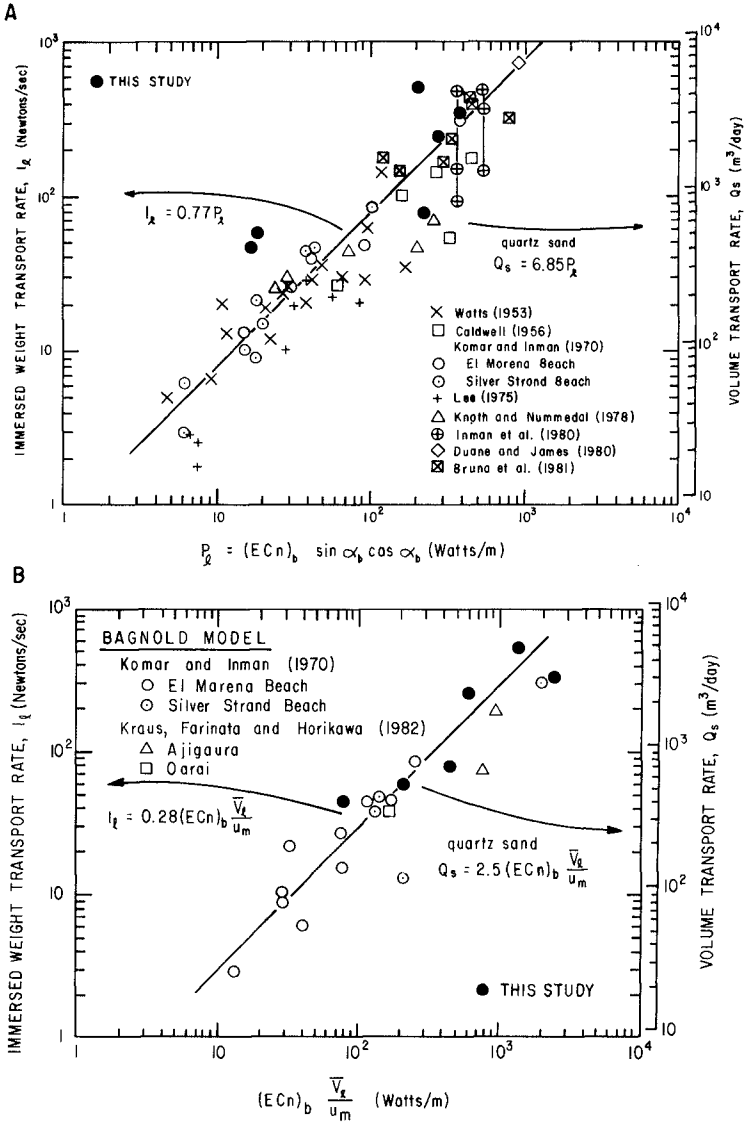


Fig. 9. Measurements of sand transport rates on beaches compared with wave conditions expressed as  $P_x$  of eq. 6 (A); eq. 7 (B) (16). Data from this study are superimposed on each curve.

sediment transport and that equation 7 adequately predicts the total immersed weight longshore transport rate of suspended sediment in the surf zone.

The ratio of  $I_{ls}$  to  $I_l$  is significantly higher than has been generally measured or estimated by other investigators (Table 2).

Table 2. Ratio of suspended sediment to total longshore sediment transport rate.

Study	Lowest Measurement (cm)	$\frac{I_{ls}}{I_s}$
Komar (1978) (15)	7.6-10	0.07-0.26
Inman et al. (1981) (9)	10	0.15-0.20
Kana and Ward (1981) (13)	5	1.0
		storm post-storm
Downing (1983) (3)	3.5	0.30
This study	3.5	0.47
		1.0

Although it would be expected that physical processes in the surf zone would have a major influence on sediment suspensions and hence might account for the differences observed above, there are also major differences in sampling techniques that play an important role.

The relative quantities of suspension transport versus bedload transport was analyzed by (15) who developed an equation to estimate the ratio  $I_{\text{susp}}/I_{\text{total}}$  ( $= I_{ls}/I_l$ ). The important parameters in this equation are the mean volume concentration ( $\bar{c}$ ), beach slope ( $\tan \beta$ ), and ratio of breaker height to breaker depth ( $\gamma$ ). The analysis included pump data (5,25) and diver collected data (10). Sediment samples were collected no closer than 7.6 cm from the seabed and the results suggest that the value of  $I_{ls}/I_l$  is  $<0.26$ .

In another study (9) using diver-operated samplers, suspended sediment samples were not collected within 10 cm of the seabed; the ratio of  $I_{ls}/I_l$  was 0.15-0.20. Bulk water samplers (13) were mounted from a pier with the lowest 5 cm above the seabed. During storm conditions the ratio of  $I_{ls}$  to  $I_l$  was high, similar to our results. During post-storm conditions, however, the value of  $I_{ls}/I_l$  decreased to 0.30.

A study (3) using sensors and methods similar to the present study obtained a much lower  $I_{ls}/I_l$  ratio (0.47). Except for the experimental site being a wide dissipative beach rather than a narrow, reflective beach, the two studies were similar; the difference in  $I_{ls}/I_l$  is quite possibly related to dynamic processes.

For the present study the mean values of  $c$  for all data (average of  $G_s$  converted to volume concentration) is  $1.46 \times 10^{-3}$ ,  $\tan \beta = 0.033$ , and  $\gamma = 0.53$ . Using these values in the equation of (15) gives an estimate of  $I_{ls}/I_l \approx 0.92$  which is in agreement with the results shown in Figure

9B. This further suggests that our observations are consistent with previous analyses (15) and that  $I_{\ell s}/I_{\ell}$  is predictable on the basis of mean volume concentration, beach slope, and the breaker height to breaker depth ratio.

#### CONCLUSIONS

1. Sediment transport in the nearshore zone occurs as individual suspension events associated with bores propagating landward. Sediment concentrations as high as  $180 \text{ kg m}^{-3}$  are measured at 3.5 cm off the seabed under passing bores and may be greater than  $50 \text{ kg m}^{-3}$  at 55 cm elevation. Individual suspension events occur abruptly and may last only seconds. Temporal variations of the magnitude of suspension events are observed in most data records. These variations in magnitude appear to be related to the bore amplitude and low frequency oscillations of the velocity component within the surf zone.

2. Mean concentration profiles show an approximately logarithmic decrease away from the bed.

3. Maximum erosion depths required to supply each suspension event are approximately 1-2 cm, comparable to the mixing depth evaluated in various sand tracer studies.

4. The longshore transport rate of suspended sediment is maximum within the mid-surf region and decreases towards both the breaking point and the shore. Suspended sediment transport appears to be high in the swash-backwash region of the shore; however, detailed data analysis has not been completed.

5. The total immersed weight longshore transport rate of suspended sediment accounts for all of the total longshore transport rate as predicted by the equations developed by (16,17). The suspended sediment transport rate as measured during the experiments at Leadbetter Beach can be predicted by equation 7.

#### ACKNOWLEDGEMENTS

We would like to thank S. Woods and R. Johnson for their expert advice and fine craftsmanship in fabricating the instrumentation used for this study. H. Smith provided energetic assistance in gathering the field data and B. Jaffe assisted in the early stage of data analysis. This research was supported in part by a National Sea Grant (NOAA) contract #SGNOAA NA81 KA-D-0030 and Office of Naval Research Contract N00014-84-C-0111.

## REFERENCES

1. Bagnold, R.A.: 1963. "Mechanics of Marine Sedimentation." In Hill, M.N. (ed.), *The Sea* 3: 507-528. Wiley-Interscience, New York, NY.
2. Bailard, J.A. and D.L. Inman: 1979. "A Reexamination of Bagnold's Granular-Fluid Model and Bedload Transport Equation." *J. geophys. Res.* 84: 7827-7833.
3. Downing, J.P., Jr.: 1983. "Field Studies of Suspended Sand Transport, Twin Harbors Beach, Washington." Ph.D. Dissertation, University of Washington, Seattle, Washington.
4. Downing, J.P., R.W. Sternberg, and C.R.B. Lister: 1981. "New Instrumentation for the Investigation of Sediment Suspension Processes in the Shallow Marine Environment." In Nittrouer, C.A. (ed.), *Sedimentary Dynamics of Continental Shelves*: 19-34. *Mar. Geol.* 42 (Special Issue).
5. Fairchild, J.C.: 1973. "Longshore Transport of Suspended Sediment." Proc. 13th Coastal Engineering Conference: 1069-1088.
6. Francis, J.R.D.: 1973. "Experiments on the Motion of Solitary Grains Along the Bed of a Water-Stream." *Proc. R. Soc. Lond. A.* 332: 443-471.
7. Gable, C.G. (ed.): 1981. "Report on Data from the Nearshore Sediment Transport Study Experiment at Leadbetter Beach, Santa Barbara, California, January-February, 1980." 314 p.
8. Inman, D.L.: 1963. "Sediments: Physical Properties and Mechanics of Sedimentation." In Shepard, F.P., *Submarine Geology*: 101-151. 2nd Ed., Harper & Row Publishers, Inc., New York, New York.
9. Inman, D.L., J.A. Zampol, T.E. White, D.M. Hanes, B.W. Waldorf, and K.A. Kastens: 1981. "Field Measurements of Sand Motion in the Surf Zone." Proc. 17th Coastal Engineering Conference: 1215-1234.
10. Kana, T.W.: 1976. "A New Apparatus for Collecting Simultaneous Water Samples in the Surf Zone." *J. sedim. Petrology* 46: 1031-1034.
11. Kana, T.W.: 1979a. "Surf Zone Measurements of Suspended Sediment." Proc. 16th Coastal Engineering Conference: 1725-1743.
12. Kana, T.W.: 1979b. "Suspended Sediment in Breaking Waves." Tech. Rep. No. 8-CRD, Coastal Research Division, Department of Geology, University of South Carolina, Columbia, South Carolina.
13. Kana, T.W. and L.G. Ward: 1981. "Nearshore Suspended Sediment Load During Storm and Post-Storm Conditions." Proc. 17th Coastal Engineering Conference 2: 1158-1174.

14. Komar, P.D.: 1977. "Beach Sand Transport: Distribution and Total Drift." *J. Wat Way Port Coast. Ocean Div. Am. Soc. civ. Engrs* **103(WW2)**: 225-239.
15. Komar, P.D.: 1978. "Relative Quantities of Suspension Versus Bed-Load Transport on Beaches." *J. sedim. Petrology* **48**: 921-932.
16. Komar, P.D.: 1983. "Nearshore Currents and Sand Transport on Beaches." In Johns, B. (ed.), *Physical Oceanography of Coastal and Shelf Seas*: 67-109. Elsevier Science Publishers B.V., Amsterdam, Netherlands.
17. Komar, P.D. and D.L. Inman: 1970. "Longshore Sand Transport on Beaches." *J. geophys. Res.* **75**: 5914-5927.
18. Kraus, N.C., R.S. Farinato, and K. Horikawa: 1981. "Field Experiments on Longshore Sand Transport in the Surf Zone." *Coast. Engng Japan* **24**: 171-194.
19. Sawaragi, T. and I. Deguchi: 1979. "Distribution of Sand Transport Rate Across a Surf Zone." *Proc. 16th Coastal Engineering Conference*: 1596-1613.
20. Seymour, R.J. (ed.): In press. "Nearshore Sediment Transport Study." Plenum Press, New York.
21. Seymour, R.J. and D.B. Duane: 1979. "The Nearshore Sediment Transport Study." *Proc. 16th Coastal Engineering Conference*: 1555-1562.
22. Seymour, R.J. and C.G. Gables: 1980. "Nearshore Sediment Transport Study experiments." *Proc. 17th International Conference on Coastal Engineering*: 1402-1415.
23. Smith, J.D. and T.S. Hopkins: 1972. "Sediment Transport on the Continental Shelf Off of Washington and Oregon in Light of Recent Current Measurements." In Swift, D.J.P., D.B. Duane, and O.H. Pilkey (eds.), *Shelf Sediment Transport: Process and Patterns*: 143-180. Dowden, Hutchinson and Ross, Inc., Stroudsburg, Pennsylvania.
24. Sternberg, R.W.: In press. *Suspended Sediment Measurements. A. Continuous Measurements.* In Seymour, R.J. (ed.), *Nearshore Sediment Transport Study.* Plenum Press, New York.
25. Watts, G.M.: 1954. "Field Investigation of Suspended Sediment in the Surf Zone." *Proc. 4th Conference on Coastal Engineering*: 181-199.

## CHAPTER ONE HUNDRED TWENTY ONE

### SEDIMENT RESPONSES TO NATURAL WAVES

Alexander F. Nielsen and Angus D. Gordon\*

#### ABSTRACT

This paper is concerned with wave-induced seabed forcing functions and sediment responses on the Australian South East Continental Shelf. The transfer of surface displacement energy to near-bed oscillatory water movement energy is examined with respect to linear and second order wave theories. Seabed sediment responses are examined by comparing field bedform size data to laboratory data with a view to determining characteristic spectral parameters that may be applied with existing theories to predict sediment responses under natural wave spectra. A rippled bed incipient motion criterion incorporating the contribution to boundary shear stress made by the presence of bedforms as well as particle size is developed empirically from field data using dimensional analysis techniques.

#### 1. INTRODUCTION

Continental shelves are a rich source of consumables including food, minerals, oils and aggregate sands. Increasingly, they are being seen as a resource also in terms of wastes disposal, typically including dredge spoil, toxic substances and sewage. As advances in technology allow expansion in shelf resource utilisation the need to further the understanding of shelf processes increases. Of particular interest are the interactions between shelf sediments and sea bed mounted structures.

The present understanding of shelf sediment movement is based mainly on theoretical studies and laboratory experiments. While these studies have produced considerable advances in the understanding and theoretical description of sediment movement in a wave and current environment, they have mostly been carried out only for periodic, progressive, near-sinusoidal wave motions. The superposition of steady currents, where relevant, is normally based on a wholly theoretical approach. The theoretical treatment of natural wave spectra is complex and laboratory data are not readily available as random wave generators for flume and water tunnel experiments have only recently been developed.

---

\* Coastal Branch, New South Wales Public Works Department, 140 Phillip Street, Sydney, 2000, Australia.

To meet the challenge of providing sound advice on proposed continental shelf developments off South East Australia, the application of monochromatic, theoretical and laboratory work to field conditions was studied with respect to three areas of particular interest:

- . the synthesis of natural sea surface displacements and seabed water motions;
- . the determination of characteristic parameters from natural wave spectra which enable the application of monochromatic theories of sediment motion to situations where finite spectral bands exist;
- . the threshold of sediment movement under natural wave spectra on a rippled bed.

## 2. FIELD DATA

Concurrent studies off Sydney being carried out for various projects by the authors made available field data sets in 24, 60 and 80 metres water depth (Figure 1). At each site a Marsh McBirney 585 adaptive recording electromagnetic current meter was installed on the seabed in a metal frame with the sensor 1 metre above the bed. Details of the recording and calibration data are given in Gordon and Hoffman (in prep) and Nielsen (1984). Three years of data were collected at the 24 metre site while 6 months data were taken at the two deeper sites.

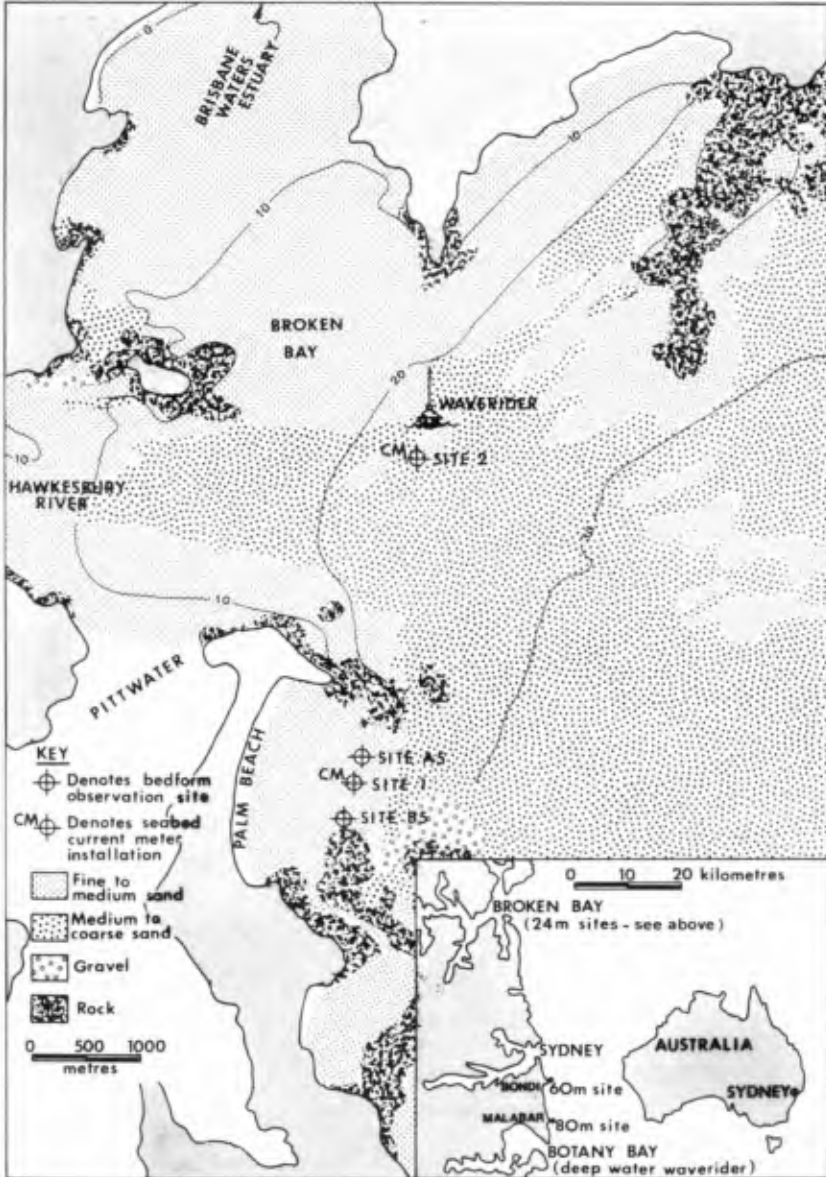
Two Datawell 700 mm diameter waverider buoys were used. One buoy had been operating for some 13 years in deep water off Botany Bay, 7 km south of the 80 metre site (Youll, 1981). The other was installed adjacent to the 24 metre site (Site 2, Figure 1).

Seabed surface features were mapped using an Atlas Deso 20 Fathometer and Klein side-scan sonar equipment calibrated by sediment sampling, bottom photography and diver observation (Gordon and Hoffman, 1984, and in prep.). Seabed observations at the 60 and 80 metre sites were made using a time lapse camera system synchronised with the current meter recording program. Seabed observations at the 24 metre sites were made by divers. The sediment characteristics at each site are given in Table 1.

TABLE 1

SEDIMENT GRAIN SIZE PARAMETERS

Site	Depth (m)	D16 (mm)	D50 (mm)	D84 (mm)	% Shell	% Fines
1	24	0.30	0.24	0.17	-	2
2	24	0.64	0.45	0.32	6	3
A5	24	0.36	0.32	0.25	-	2
B5	24	0.27	0.22	0.16	-	2
BON	60	0.33	0.26	0.18	26	14
MAL	80	0.35	0.21	0.15	33	32



**STUDY AREA**  
(AFTER HOFFMAN ET AL., 1980)

**FIGURE 1**



### 3. RESULTS

#### 3.1 Synthesis of Sea Surface Displacements and Near-bed Wave-induced Water Motions

Sea surface displacement energy spectra were compared with seabed wave-induced current velocity spectra utilising wave theories to examine the modification with depth that occurs to the spectral energy distribution and to develop a technique for generating seabed spectra at sites remote from the sea surface wave data collection point.

For each waverider and current meter record a spectral energy/frequency distribution was obtained using a fast Fourier transform technique. Spectral estimates were made at 0.1 Hz frequency intervals and cross-spectral correlations were carried out at the three water depths as follows (see Nielsen (1984) for detailed discussion of these parameters):

$$\left[ \frac{u}{H} \right]_f = \frac{1}{2} \cdot \left[ \frac{M_c(o)}{M_w(o)} \right]^{1/2} \cdot \left[ \frac{S_c(f)}{S_w(f)} \right]^{1/2} \quad \text{Eqn. 1}$$

where:

(u)f = maximum, wave-induced, near-bed horizontal water particle velocity with period 1/f;

(H)f = wave height with period 1/f;

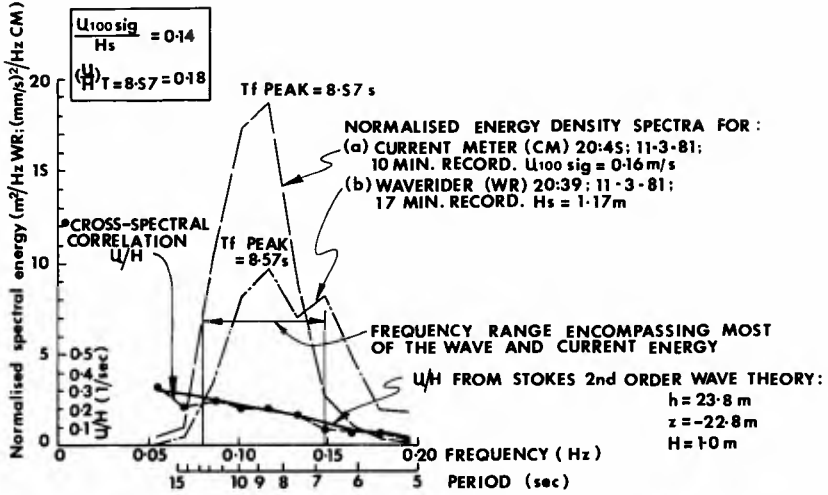
M(o) = is the area under the spectral energy/frequency distribution graph;

S(f) = is the normalised spectral estimate at frequency band f;

Subscript c = current meter; and

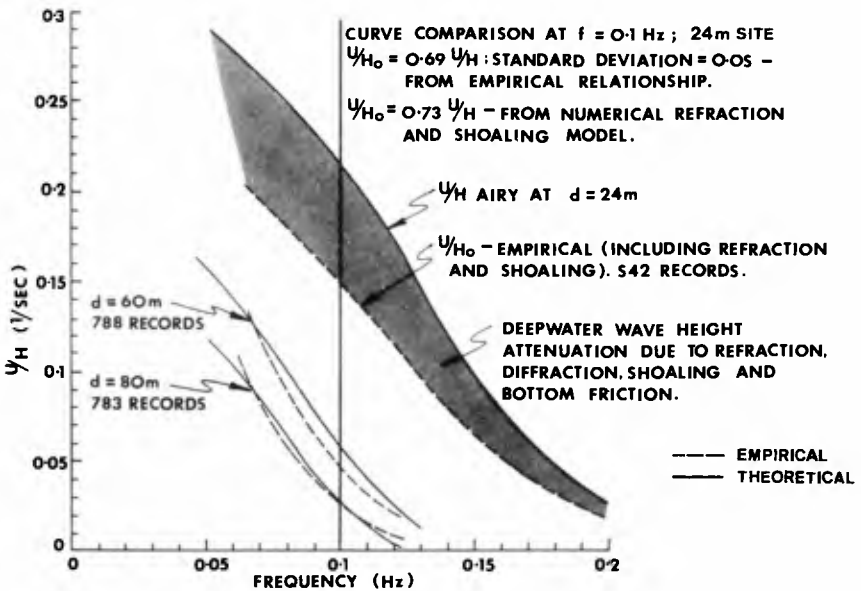
subscript w = waverider.

These empirical values were compared with theoretical computations based on both Stoke's 2nd Order and Airy theories at the 24 metre site and with Airy theory at the 60 and 80 metre sites. A typical cross-spectral correlation for a set of concurrent waverider and adjacent current meter records at the 24 m site is shown in Figure 2. Here the correlation was virtually exact compared with Stoke's 2nd Order wave theory over the frequency range encompassing most of the current energy. Some two thousand current meter records were correlated with the deepwater waverider data, and statistically analysed and compared to Airy Theory (Figure 3). In general it can be seen that Airy theory applied to the deepwater waverider data over-estimates near-bed velocities, particularly at the shallower depths. This effect at the 24 metre site is attributable to wave height attenuation through wave refraction and shoaling. Further attenuation can be attributed to friction and diffraction. These results and other factors are discussed in more detail in Gordon and Hoffman (in prep.) and Nielsen (1984).



CROSS-SPECTRAL CORRELATION BETWEEN SELECTED NEARBY WAVERIDER AND CURRENT METER RECORDS

FIGURE 2



ACROSS SHELF CROSS-SPECTRAL CORRELATIONS BETWEEN DEEPWATER WAVERIDER AND CURRENT METER RECORDS

FIGURE 3

The results of the analyses showed that a reasonable approximation of wave-induced seabed current energy can be made by spectral transfer of waverider data to the seabed using monochromatic wave theories to obtain values of the velocity/wave height ratio in Equation 1. Where refraction, diffraction, shoaling and the effects of bottom friction are significant, the theoretical values of the velocity to wave height ratio may be adjusted on the basis of numerical modelling. However, where wave height attenuation is severe the application of simple numerical models may not be appropriate (Nielsen, 1984).

### 3.2 Characteristic Spectral Parameters for Sediment Motion

To apply the existing understanding of sediment transport processes to natural field situations it was first necessary to examine the appropriateness of characterising natural energy spectra in terms of displacement and frequency parameters. It was considered that an examination of bedform response to near-bed velocity spectra could be used to indicate and evaluate such characteristic parameters if appropriate; there being considerable data available from flume and oscillating water tunnel experiments concerned with bedform response to periodic, progressive, near-sinusoidal water movements.

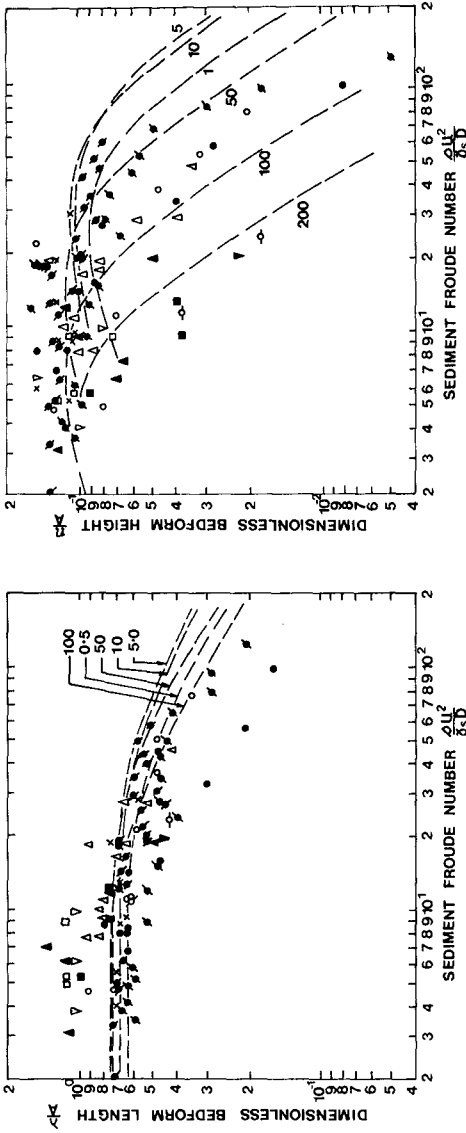
Laboratory data were examined and it was found that the bedform curves of Mogridge and Kamphuis (1972) described and quantified well the existing understanding of bedform generation and degeneration under monochromatic wave conditions (Figure 4). Also, Nielsen (1984) reviewed the field data of Inman (1957) and compared them to the bedform curves of Mogridge and Kamphuis. To obtain a good agreement between these data and the laboratory results it was necessary to increase Inman's calculated significant hydraulic parameters by a factor of 1.5. Inman's hydrodynamic data were based on fathometer records and that, coupled with the considerations of depth effect on surface displacement energy, is considered to have resulted in his over-estimation of near-bed velocities and displacements.

At the 80 metre site no bedform generation was observed during the 6 month deployment period. The film indicated that sheet flow rapidly followed the onset of transport. This is believed to be due to the high fines content (Table 1) and the high level of biogenic activity at the site which together produced a partly cohesive bed (Gordon and Hoffman, in prep.).

While at the 60 metre site some bedform activity was noted these bedforms were poorly developed and the resolution of the film was such that no accurate measurements of bedform size could be made (Gordon and Hoffman, in prep.).

The most reliable field data set comprised forty-three separate events for which bedform geometric data were obtained at four locations adjacent to the 24 metre site (Figure 1).

The bedform observations were taken by divers and included measurements of ripple wavelength, height, and crest orientation, assessments of ripple asymmetry, general bedform configurations and whether the sand grains on the bed were active or inactive. The data



LEGEND :

symbol	$\frac{\omega D}{g_s T^2} \times 10^6$	symbol	$\frac{\omega D}{g_s T^2} \times 10^6$	symbol	$\frac{\omega D}{g_s T^2} \times 10^6$
•	1.0	∇	136	∇	500
•	1.4 - 2.6	◻	242	◻	600
•	3.1 - 6.5	Δ	350	—	850

— Bedform height curves modified after Mogridge & Kamphuis (1972); numbers to each curve are values of  $\frac{\omega D}{g_s T^2} \times 10^6$

COMPARISON OF DATA FROM INMAN & BOWEN (1963), KENNEDY & FALCON (1965), HORIKAWA & WATANABE (1967), CARSENS ET AL. (1969) & LOFQUIST (1980) WITH BEDFORM CURVES MODIFIED AFTER MOGRIDGE & KAMPHUIS (1972) FIGURE 4

are summarised in Table 2 and detailed in Nielsen (1984). The ripple wavelengths were measured by placing a scaled ruler over and normal to the ripple crests. Most of the wavelength measurements over 100 mm were made to the nearest 50 mm. The accuracy of wavelength measurements is considered to be  $\pm 25$  mm for those measurements recorded to 50 mm, and  $\pm 10$  mm for measurements recorded to 10 mm. Ripple heights were measured by placing a second scale vertically and normal to the ruler across the ripple crests, measuring down to the ripple troughs. In most cases, these measurements were taken to 10 mm (or in inch, equivalent to 25 mm) and the accuracy of these measurements is considered to be  $\pm 10$  mm. Ripple orientations were measured by diver compass sightings along the ripple crests. Measurements were made to magnetic north with an estimated accuracy of  $\pm 15^\circ$ . It is to be noted that the bedform patterns on the seabed where measurements were taken were not always uniform. The divers assessed the bedform distributions and took measurements where "average" bedform characteristics prevailed. The accuracies quoted above do not apply to the variations in bedform size parameters observed at the measurement sites.

The water particle velocity measurements could not necessarily be taken simultaneously with the bedform measurements. As bedform measurements were made at meter servicing times, most (70%) of the bedform measurements were made within seven hours of the velocity readings. As waverider data were generally available every six hours, bottom velocities and bedform data could be related through the waverider records, using the method for bottom transfer (section 3.1), when there were large elapsed times between the two.

As reported by Inman (1957), the sand ripples observed in this study varied widely in size, shape and duration. Some ripples were uniform with long parallel crests, others occurred in complex patterns. During some observations the ripples, while active, appeared not to change much in time, whereas during other observations the ripple bed erupted and disappeared under large wave surges only to rapidly reform following the passage of the surge. It was difficult in most cases to ascertain if the ripples measured were formed by the waves present at the time of measurement. One reason for this was that to avoid decompression procedures the divers had a limited bottom time to observe the ripple behaviour. If the ripples were active it was not necessarily clear if they were changing to a new equilibrium with the wave forces or whether they had attained a stable form. In some cases, a judgement could be made as to whether the ripples were in equilibrium with the wave climate by comparing ripple orientations to wave directions. In other cases this was not possible. In the main the divers, including the authors, were experienced investigators.

A convenient way of describing ripple geometry is by the ripple steepness  $\eta/\lambda$ . The bedform curves of Mogridge and Kamphuis indicate that there is a maximum attainable value of ripple steepness. They found that while this maximum value varied according to the specific gravity of the sand particles, for quartz sand under the range of natural field hydraulic conditions pertaining to this study, 0.16 is the maximum attainable value of steepness for wave-generated ripples (based on regular, near-sinusoidal, periodic fluid motion). This result is generally in agreement, albeit at the lower end of the

TABLE 2

REF. NO.	DATE	TIME (hrs:mins)	DEPTH (m)	$\lambda$ (mm)	$\eta$ (mm)	CURRENT METER (site no; time)	WAVERIDER (I=Inshora O=Offshore;times)	COMMENTS (A=active;I=inactive; S=asymmetrical; N=not in equilibrium with wave climate)
<b>SITE 1</b>								
1	19:6:81	12:20	23.7	350	60	1;2030	I; 0854 ,1446	A , S
2	27:7:81	14:30	24.0	225	35	-	I; 1446	I , S
3	12:10:81	11:00	23.4	100	60	1;0445	I; 0845 ,1445	I , S
4	12:11:81	13:15	23.0	250	50	1;0945 , 1645	-	I , S
5	3:2:82	07:45	23.5	500	100	-	O:0600, 1200	A , S
6	11:3:82	14:15	23.0	500	50	1;1550	O: 1200,1800	A , S
7	4:5:82	10:30	23.4	250	70	1;0750	O: 0600	I , S
8	14:9:82	10:00	24.0	250	70	1;0740	I; 0711 , 1311	A , -
<b>SITE 2</b>								
9	23:11:79	08:30	24.5	250	20	2;1136	O:0900	A , -
10	29:11:79	07:20	24.0	380	75	2;0630	-	A , S
11	14:12:79	14:00	24.0	450	185	2;0630,1830	O:0828,1426,2030	A , -
12	14:1:80	09:30	23.9	1000	200	2;1136	O:0900,1458	A , S
13	28:3:80	10:20	24.2	900	170	2;1536	O:0852,1449,2053	I , -
14	29:4:80	10:00	24.0	1000	160	-	I:0900 ,1500	A , S
15	18:5:80	11:04	24.1	600	70	2;1000	O:0846 ,1443	I , asymmetrical
16	23:6:80	11:30	23.4	900	200	-	O:0842 ,1438	A , S
17	21:8:80	11:00	23.6	800	150	2;1400	O:0600,1200,1800	A , S
18	16:9:80	10:00	24.0	600	100	-	I: 0900	I , S
19	30:10:80	10:20	24.0	700	150	-	I: 0900	A , S
20	4:12:80	10:00	23.7	400	100	2;0940	I: 0900	A , N , S
21	16:12:80	09:40	23.6	400	100	-	I: 0900	I , S
22	22:1:81	11:40	24.3	500	70	2;0605	I:0900,1500	A , N , S
23	3:3:81	11:00	23.5	750	150	2;1940	I; 0848,1448	A , S
24	11:3:81	10:30	23.9	500	150	2;2045	I; 0839,1439	A , S
25	17:6:81	13:00	23.5	600	100	2;0215	I; 2055,0303	A , S
26	27:7:81	12:30	23.8	800	150	2;1545,1845	I: 0854 ,1446	- , -
27	19:11:81	10:30	23.5	400	80	2;2345	-	A , S
28	22:12:81	12:15	23.5	700	80	2;0845,2245	-	A , N , -
<b>SITE A5</b>								
29	15:1:80	12:50	22.8	500	50	2;1136 ,1536	-	A , S
30	29:4:80	13:30	22.4	400	30	-	I:0900, 1500	A , S
31	16:5:80	14:10	22.4	300	75	2;0900,1600	-	A , S
32	4:9:80	11:45	22.0	400	80	2;0700,1400	I:0900 ,1500	A , S
33	16:9:80	14:05	22.6	300	100	-	I: 1500	- , -
34	3:3:81	14:30	23.0	400	100	2;1940	I; 1448	A , asymmetrical
35	8:10:81	13:20	23.4	300	70	1; 0945 ,1645	I; 0845,1445	A , S
<b>SITE B5</b>								
36	29:2:80	11:10	24.0	250	50	2;1136	O:0856 ,1406	I , N , S
37	1:4:80	12:30	23.5	200	50	2;1136	I: 0900 ,1500	I , N , S
38	29:4:80	12:30	22.8	80	30	-	I: 0900 ,1500	A , S
39	16:5:80	12:15	23.0	300	70	2;0900,1600	-	A , S
40	4:9:80	12:15	22.5	150 & 300	25 & 50	2;0700 ,1400	I: 0900 ,1500	I , N , S
41	11:3:81	13:35	22.8	200	25	2;2045	I; 1439 ,2039	A , -
42	30:7:81	12:00	22.8	100	40	2;1345	I; 0854 ,1446	A , S
43	8:10:81	12:30	23.0	220	25	1; 0945 1645	I; 0845 ,1445	I , S

TABLE 3

REF. NO.	Tm (s)	Um,100 (m/s)	Am,100 (m)	$\frac{\lambda}{A}$	$\frac{\eta}{A}$	$\frac{\partial D}{\partial s T^2 m}$ (10 <sup>-6</sup> )	$\frac{\partial U^2_{m,100}}{\partial s D}$	$\frac{\partial U^2_{m,0}}{\partial s D}$	Um,0 D	Um,100 D	DATA ASSESSMENT	ORTHOGONAL DIRECTIONS (°T.N.) WAVES	RIPPLE CRESTS	
1	15.1	0.35	1.66	0.21	0.036	0.07	30.9	44.5	99	20800	P-poor	167.4	169.5	
2	15.1	0.20	0.95	0.24	0.039	0.07	10.1	14.6	58	6900	F-fair	-	102.0	
3	15.1	0.18	0.86	0.12	0.068	0.07	8.5	12.2	52	10900	F	154.3	147.0	
4	16.9	0.26	1.42	-	-	0.05	18.0	26.0	75	13200	G-good	166.4	102.0	
5	13.1	0.51	2.09	0.24	0.049	0.09	67.5	97.2	147	51200	F	-	124.5	
6	10.4	0.20	0.67	0.74	0.075	0.14	10.1	14.6	58	9900	G	138.4	124.5	
7	12.4	0.22	0.82	0.30	0.084	0.11	12.0	17.3	62	15000	F	145.7	127.0	
8	15.1	0.22	1.03	0.24	0.067	0.07	12.0	17.3	62	15000	G	156.0	127.0	
9	0.8	0.20	0.62	0.40	0.032	0.21	5.5	7.9	107	4000	F	87.0	102.0	
10	9.9	0.17	0.52	0.73	0.146	0.30	3.8	5.5	89	12400	G	127.7	102.0	
11	12.9	0.30	1.16	0.39	0.160	0.18	12.0	17.3	161	55000	P	112.2	-	
12	12.9	0.26	1.05	0.95	0.190	0.18	9.6	13.8	143	52900	F	118.2	124.5	
13	11.4	0.18	0.67	1.35	0.255	0.22	4.6	6.7	99	30900	P	95.3	132.0	
14	12.4	0.35	1.35	0.74	0.118	0.19	16.4	23.6	188	55500	F	-	147.0	
15	12.1	0.33	1.23	0.49	0.057	0.20	15.0	21.6	179	23100	F	114.5	222.0	
16	14.2	0.50	2.15	0.42	0.093	0.14	33.6	48.4	268	99200	P	-	102.0	
17	18.8	0.18	1.08	0.74	0.140	0.08	4.6	6.7	99	27300	F	102.8	147.0	
18	14.4	0.25	1.14	0.53	0.088	0.14	8.5	12.2	135	24800	F	-	124.5	
19	13.0	0.35	1.42	0.49	0.106	0.17	16.4	23.6	188	52100	F	120.1	147.0	
20	11.2	0.20	0.69	-	-	0.24	5.5	7.9	107	19800	G	76.9	147.0	
21	10.8	0.20	0.67	0.60	0.150	0.25	5.5	7.9	107	19800	G	112.0	102.0	
22	13.7	0.23	0.99	-	-	0.16	7.4	10.6	125	16200	G	80.1	147.0	
23	12.1	0.28	1.08	0.70	0.140	0.20	10.9	15.7	153	42200	G	78.7	102.0	
24	12.1	0.30	1.14	0.44	0.132	0.20	12.0	17.3	161	44600	F	114.1	102.0	
25	Naar-simultaneous hydrodynamic data not available											P	115.6	147.0
26	15.1	0.17	0.80	1.00	0.188	0.13	3.8	5.5	89	24800	G	111.0	124.5	
27	Naar-simultaneous hydrodynamic data not available											P	106.3	147.0
28	12.9	0.17	0.67	-	-	0.18	3.8	5.5	89	13200	G	88.5	34.5	
29	11.2	0.15	0.52	0.97	0.097	0.17	4.4	6.3	58	7400	F	108.9	102.0	
30	13.0	0.31	1.29	0.31	0.023	0.12	19.1	27.5	121	9400	F	-	147.0	
31	Hydrodynamic data outside range of refraction analysis											P	66.7	107.0
32	12.9	0.20	2.13	0.48	0.095	0.12	7.7	11.0	75	15900	F	121.5	147.0	
33	Hydrodynamic data not available; dual ripple trains observed											P	-	-
34	12.9	0.30	1.20	0.33	0.083	0.12	17.2	24.8	115	29800	F	78.7	102.0	
35	12.9	0.17	0.67	0.45	0.105	0.12	5.2	7.5	63	35900	G	132.1	147.0	
36	Hydrodynamic data outside range of refraction analysis											P	75.3	112.0
37	Badforms not in equilibrium with wave climate											P	121.7	-
38	13.0	0.35	1.42	0.06	0.021	0.08	33.7	48.6	91	10400	P	-	102.0	
39	Hydrodynamic data outside range of refraction analysis											P	66.7	102.0
40	Badforms not in equilibrium with wave climate											P	116.7	147.0
41	11.2	0.35	1.23	0.16	0.020	0.11	33.7	48.6	91	8800	P	114.1	102.0	
42	12.9	0.45	1.83	0.06	0.022	0.09	56.0	80.7	117	17900	P	131.2	147.0	
43	12.9	0.17	0.67	0.33	0.038	0.09	11.2	16.0	44	4100	G	132.1	124.5	

range, with results from other studies (Nielsen, 1984).

The data on ripple steepness are presented in Figure 5. These data portray a scatter around an average value of  $\eta/\lambda = 0.18$ . For most of the data the maximum measured value of  $\eta/\lambda$  was 0.25. However, a few extreme values of  $\eta/\lambda = 0.4$  were measured. Measurement error in part may account for the scatter portrayed. It is significant to note that the scatter reduced with increasing ripple wavelength. This tendency was observed also by Inman (1957, see his Figure 14); the higher values of  $\eta/\lambda$  reported by Inman were associated with the smaller ripple wavelength measurements. Inman also observed less scatter for data obtained from coarser sediments, a tendency also suggested in these data.

To determine the characteristic spectral parameters, the field data were plotted initially against the bedform curves of Mogridge and Kamphuis using significant hydraulic spectral parameters with Tf peak (not presented). It was found that the dimensionless wavelengths and wave heights of the field data points were considerably larger, on average by a factor of 2.15, than those of the laboratory data. The reason for the departure from the laboratory results was considered to lie in the choice of the velocity and displacement parameters used in the calculations of the data point co-ordinates. Consideration of the authors' diving observations while collecting the seabed data and the consistency with Inman's results suggested that maximum rather than significant spectral parameters would be more appropriate.

Goda (1974) showed that the ratio of maximum to significant wave height parameters has a mean value of 1.65 and a standard deviation of 0.26. He also showed that the ratio of the period parameter associated with the maximum wave to the period associated with the peak spectral

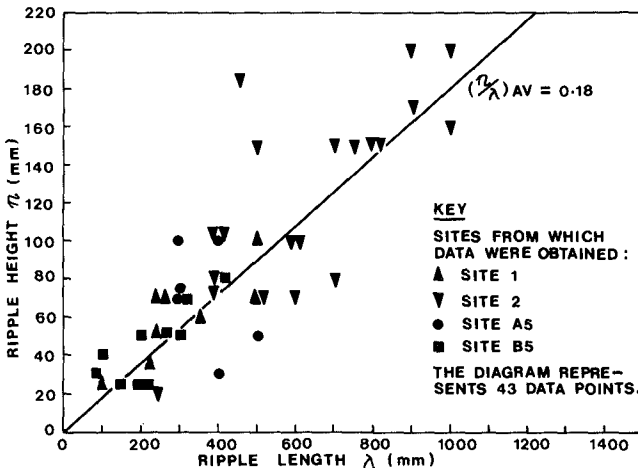


FIGURE 5



estimate lies in the range of 0.5 to 1.4. Adopting maximum spectral velocity parameters, it was found by iterative procedures that a period parameter of value 1.3  $T_{peak}$  produced a reasonable agreement between the field data and the bedform curves of Mogridge and Kamphuis (Figure 6).

The bedform investigation, therefore, suggested that maximum spectral hydraulic parameters should be used when applying existing theories based on monochromatic wave studies to shelf bed response under natural wave action; the inference being that these maximum spectral parameters should be used also for sediment entrainment and transport calculations.

### 3.3 Incipient Motion on a Rippled Bed

There are very little laboratory data and virtually no field data on the threshold of sediment movement on a rippled bed; most of the experimental work has been directed towards evaluating incipient motion criteria on flat beds.

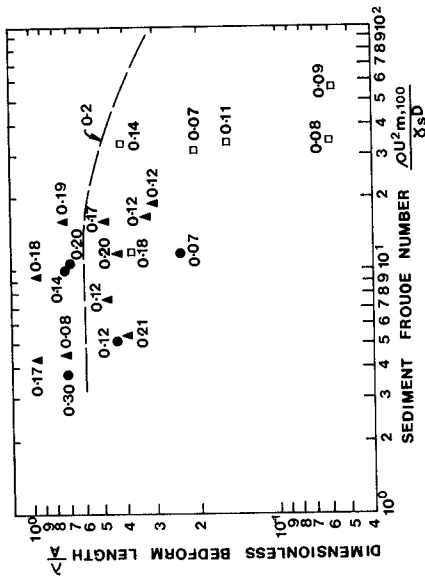
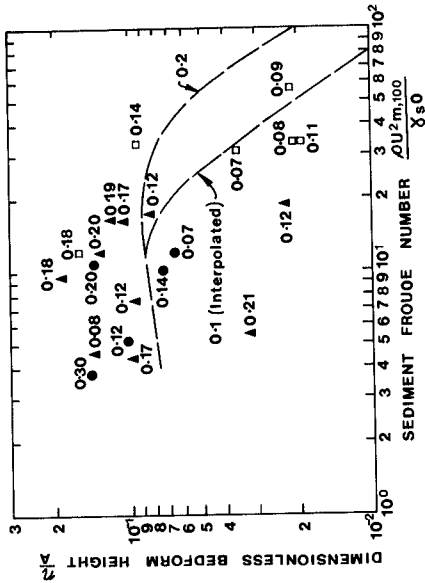
Eagleson and Dean (1959) and Carstens et al. (1969) analytically considered the general condition of the threshold of motion. Their analyses were based on the hydrodynamic forces of drag and lift and the submerged weight on a typical protruding particle. Additional surface forces arising from the inertial reaction of the particles and of the fluid around the particles were not included because initial movement under wave action was observed to occur at the maximum, horizontal, near-bed velocity; that is, when acceleration in the flow is negligible.

The difficulty in applying the method, however, lies in the calibration of the constants. Where boundary layer effects become significant with oscillating flow over a duned bed, the analytical solution to the incipient motion criterion becomes very complex. It was therefore considered practical to determine empirically a threshold criterion using dimensional analysis techniques.

It was considered that for flow over a rippled bed, the important dimensionless variables were:

- (1)  $\frac{\rho u^2}{\gamma_s D}$  The sediment Froude number, being derived from the ratio of hydrodynamic surface forces on the sediment to the submerged weight of the sediment, which is essentially Shields parameter.
- (2)  $\frac{u D}{\nu}$  The particle Reynolds number upon which the sediment Froude number is dependent.
- (3)  $\frac{u R}{\nu}$  The bedform Reynolds number; a dimensionless variable introduced to take account of the effect of bedform height on bed roughness and, hence, the shear stress on the bed.

This set of dimensionless variables includes all the relevant characteristic parameters proposed by Mogridge and Kamphuis (1972) except for  $\rho_s$ , which was considered constant as the only relevant data found were observations made on quartz sand beds.



LEGEND  
 ● GOOD  
 ▲ FAIR  
 □ POOR

DATA ASSESSMENT. DATA ARE PRESENTED IN TABLES 2 AND 3.

— BEDFORM CURVES MODIFIED AFTER MOGRIDGE AND KAMPHUIS (1972) FOR  $\frac{\rho D}{\gamma_s T^2} = 0.2 \times 10^{-6}$ .

CO-ORDINATES OF FIELD DATA POINTS CALCULATED USING  $U_{m,100}$  AND  $T_{max} = 1.3 T_{peak}$ .

NUMBERS TO EACH DATA POINT ARE VALUES OF  $\frac{\rho D}{\gamma_s T^2} \times 10^6$ . A = NEAR-BED ORBITAL DIAMETER

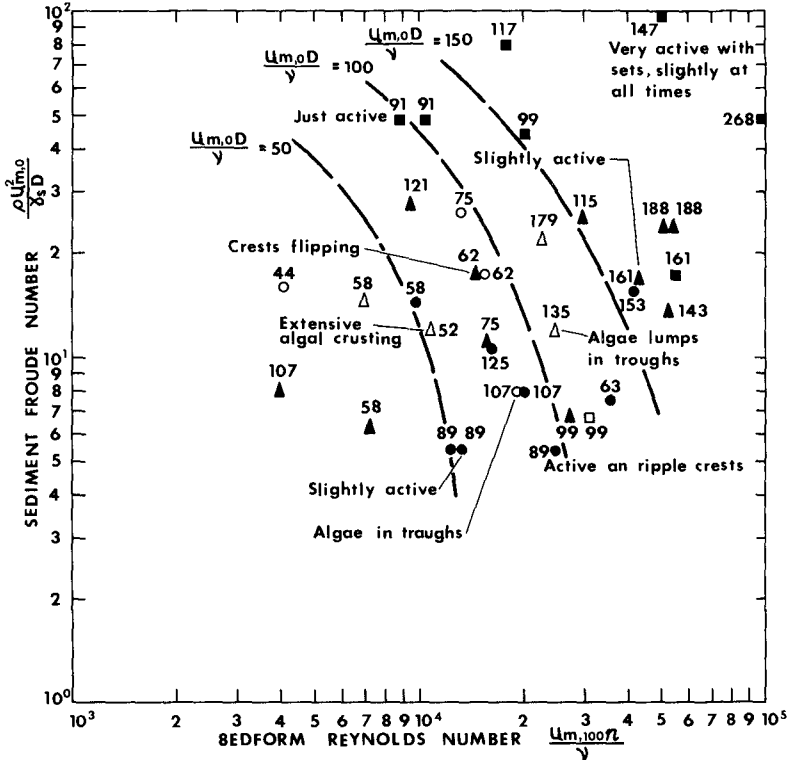
COMPARISON OF DIMENSIONLESS BEDFORM SIZE DATA WITH BEDFORM CURVES OF MOGRIDGE & KAMPHUIS (1972) FIGURE 6

The field data from the 24 metre site are plotted on Figure 7 using maximum spectral velocity parameters to determine the co-ordinates of the field data points. Unfortunately, insufficient data of good quality were available to confidently define curves of constant particle Reynolds number at incipient motion. Dashed curves, therefore, have been interpolated from these data to highlight the conceptual understanding of the relationship between the sediment Froude number, particle Reynolds number and bedform Reynolds number at incipient motion and to indicate the inaccuracy in determining this relationship from these data.

These curves not only take account of those observations where the sediment was described as being at the threshold of movement, such as "just active" or "crests flipping", but also of both the "inactive" and "active" observations. For a particular curve of constant particle Reynolds number, all data lying to the upper right hand side of the curve represent a seabed condition which is either "active", with higher or lower values of particle Reynolds numbers than the curve, or "inactive" with particle Reynolds numbers higher than the value of the curve. On the lower left hand side of a particular curve, active seabed conditions occur when the particle Reynolds number is of a lower value than that of the curve, and for an inactive seabed condition that falls within this region of the graph, the particle Reynolds number may have any value.

For small bedform Reynolds numbers, that is, for small bedform heights approaching a flat bed, the interpolated bedform curves suggest values of sediment Froude number for incipient motion in the order of 100, which values are two orders of magnitude higher than would be calculated following the method of Komar and Miller (1974). However, the behaviour of the curves is not known for conditions approaching a flat bed as the hydraulic conditions near a flat bed are quite different to those of a rippled bed. For a flat bed there is no flow separation or vortex formation as observed on rippled beds, therefore, the nature of the respective boundary layers must be quite different (Carstens et al., 1969).

Additional factors considered to be important with respect to defining the location of the curves of the critical particle Reynolds numbers at incipient motion include the adopted grain size parameter and the value of bedform height. Incipient motion occurs at ripple crests. While grain size data for the ripple crests were not taken, the divers observed that the grain size on the ripple crests was different to that in the troughs. Inman (1957) and Cook and Gorsline (1972) found that the crest grain size is in the order of 0.05 mm coarser than the average grain size for sands finer than 0.5 mm. The grain size adopted will affect the values of particle Reynolds number and sediment Froude number. Bedform height data are much more difficult to measure than bedform length data, which is reflected in the wider range of scatter in bedform height data in Figure 6. In addition to bedform height being more difficult to measure, there is a greater spectral variability in bedform height than in bedform length under natural wave motion. Both of these factors will affect the determination of the proposed bedform Reynolds number and hence the accuracy to which the curves of constant particle Reynolds number defining incipient motion can be determined.



NOTES :  $U_{m,100}$  = Spectral maximum, near-bed (100 cm above), wave-induced, maximum horizontal orbital velocity.  
 $U_{m,0} = 1.2 U_{m,100}$ ; the maximum velocity at dune crest (after Corstens et al., 1969).  
 Numbers to each data point are particle Reynolds numbers.  
 Comments to data points are additional diver observations not included in Tables 2 and 3.

LEGEND :

<u>Inactive</u>	<u>Active</u>	} Assessment of data accuracy
○ good	● good	
△ fair	▲ fair	
□ poor	■ poor	

----- Interpolated curves of constant particle Reynolds number defining incipient motion.

RELATIONSHIP BETWEEN SEDIMENT FROUDE NUMBER, PARTICLE REYNOLDS NUMBER AND BEDFORM REYNOLDS NUMBER DEFINING INCIPENT MOTION ON RIPPLED BEDS  
 FIGURE 7

#### 4. CONCLUSIONS

The cross-spectral correlation analysis showed that by using an appropriate wave theory, it was possible to synthesise spectra of seabed oscillatory water particle motions with those of sea surface displacements. Further, this could be achieved at stations remote from the wave data collection site by applying suitable wave refraction, attenuation and shoaling factors obtained by monochromatic theories.

An examination of seabed response to natural wave spectra suggested that for applying monochromatic sediment entrainment and transport theories, calibrated to laboratory results, to shelf bed sediment transport studies, the appropriate characteristic spectral parameters are:

$$H_m = 1.65 H_s; u_m = 1.65 u_s; T_m = 1.3 T_p$$

This assumed that the bedform response mechanism was indicative and therefore typical of sediment movement mechanisms including incipient motion and entrainment. That the data were limited to a single water depth, a narrow band of slight wave conditions due to diving safety provisions, limited variation in quartz sand grain sizes and the difficulty of taking precise diver measurements, dictates that in the definition of these characteristic parameters, the constants 1.65 and 1.3 be seen as preliminary figures only. Further, it must be recognised that the overall aim was to develop a method of calculating sediment movements on the Continental Shelf for engineering projects.

The incipient motion investigation indicated that incipient motion on a rippled bed occurs at considerably lower energy conditions than on a flat bed for fine to coarse sands. The criteria for incipient motion on a duned bed include both particle roughness and bedform roughness, both affecting the level of shear stress at the bed. While trends in the field data are apparent, further data are required to confidently define the relationships between the Shields parameter, particle Reynolds number and bedform Reynolds number for incipient motion on a rippled bed.

#### 5. ACKNOWLEDGEMENTS

This paper is published with the permission of the New South Wales Public Works Department. The authors are indebted particularly to the following Departmental officers who also performed diving duties and made bedform measurements; Bandu Sena, John Hoffman, Doug Lord, Mike Nolan, Mike Geary, Bob Sneddon, Jim Lawler and Bruce Fidge.

#### 6. REFERENCES

Carstens, M.R., Neilson, F.M. and Altinbilek, H.D. (1969). Bedforms generated in the laboratory under oscillatory flow: analytical and experimental study. TM-28, U.S. Army Corps of Eng., CERC June, 1969.

- Cook, D.O. and Gorsline, D.S. (1972). Field observations of sand transport by shoaling waves. *Marine Geology*, 13: 31-55.
- Eagleson, P.S. and Dean R.G. (1959). Wave-induced motion of bottom sediment particles. *Jnl. Hydraulics Div., A.S.C.E.*, proc. paper 2202.
- Gordon, A.D. and Hoffman, J.G. (1984). Sediment transport on the South-East Australian Continental Shelf. *Proc. 19th I.C.C.E. Houston, Texas*. Sept. 3-7, 1984.
- Gordon, A.D. and Hoffman, J.G. (in prep). Report in preparation on sand transport processes relating to proposed seabed sewage outfall diffuser installations. N.S.W. Public Works Department, Coastal Branch.
- Hoffman, J.G., Gordon, A.D., Nielsen, A.F. and Lord, D.B. (1980). Assessment of environmental impact; marine aggregate project, Broken Bay, N.S.W., New South Wales Public Works Department, Coastal Branch, Rpt. No. 80022.
- Horikawa, K. and Watanabe, A. (1967). A study on sand movement due to wave action. *Coast. Eng. Japan*, Vol. 10, 1967. pp 39-57.
- Inman, D.L. (1957). Wave generated ripples in nearshore sands. Beach Erosion Board, TM-100.
- Inman, D.L. and Bowen, A.J. (1963). Flume experiments on sand transport by waves and currents. *Proc. 8th Int. Conf. on Coast. Eng., Mexico City, Mexico*.
- Kennedy, J.F. and Falcon, M. (1960). Wave generated sediment ripples. *Mass. Inst. Tech., Dept. Civil Eng. Hyd. Lab., Rpt. No. 86*, August, 1965.
- Komar, P.D. and Miller, M.C. (1974). Sediment threshold under oscillatory waves. *Proc. 14th Coast Eng. Conf., Copenhagen, June 24-28, 1974*.
- Lofquist, K.E.B. (1980). Measurements of oscillatory drag on sand ripples. *Proc. 17th Int. Conf. Coast. Eng., Sydney, Australia, March 23-28, 1980*.
- Mogridge, G.R. and Kamphuis, J.W. (1972). Experiments on bedform generation by wave action. *Proc. 13th Coast. Eng. Conf., Vancouver, B.C. Canada, July 10-14, 1972*.
- Nielsen, A.F. (1984). Sand Ripples Under Natural Waves. *M. Eng. Sc. Thesis, Univ. of New South Wales, February 1984*.
- Youll, P.H. (1981). Botany Bay waverider systems - ten years of records. *Proc. 5th Aust. Conf. Coast & Ocean Eng., Perth, Western Aust., November 25-27, 1981*.

## CHAPTER ONE HUNDRED TWENTY TWO

### Shore Approach at the Danish North Sea Coast, Monitoring of Sedimentation in a Dredged Trench

Karsten Mangor\*  
Torben Sørensen\*\*  
Erling Navntoft\*\*\*

#### 1. Introduction

The Danish Natural Gas and Oil Transmission system included the landing of a 30' Gas pipeline and a 20' Oil pipeline in a common shore approach at the Danish North Sea Coast. The location of the site is shown in Figure 1.1.

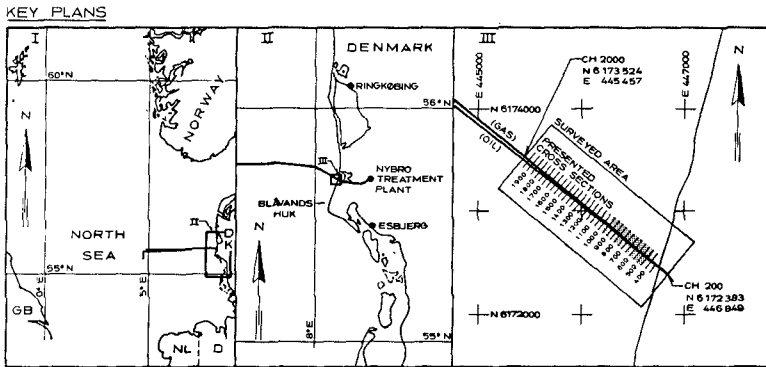


Figure 1.1 Key plans of the North Sea Shore Approach Site.

The two pipes were pulled ashore in a common pre-dredged trench into a sheet piled cofferdam across the beach. The trench was 1600 m long and had a volume of about 600,000 m<sup>3</sup>. The dredging and the backfilling were monitored closely together with wind, wave, and current conditions over the four months dredging and installation period. After termination of the pulls and backfilling the trench was left for natural backfilling. The backfilling was monitored for one year together with the environmental conditions.

\* K. Mangor, Senior Hydraulic Engineer, Danish Hydraulic Institute (DHI), Agern Allé 5, DK-2970 Horsholm, Denmark.

\*\* T. Sørensen, Director, DHI.

\*\*\* E. Navntoft, Senior Hydraulic Engineer (Ph.D.), DHI.

The monitoring during the construction period was performed by the contractor Saipem/Volker Stevin and by the client, Danish Oil and Natural Gas Company, (D.O.N.G. A/S) with assistance from the Danish Coast Authority (KI). The monitoring activities, which continued after the final check of the backfilling within the construction contract, were initiated by DHI and partly financed by the Danish Council for Industrial and Scientific Research (STVF). The monitoring was performed in co-operation between D.O.N.G. A/S, KI and DHI.

All data from the monitoring program are presented in the report:

North Sea Shore Approach  
Monitoring of Sedimentation in a Dredged Trench  
August 1984  
Prepared by DHI for STVF.

## 2. General Description of the Site

### 2.1 Site Conditions

The sandy coastal area at the shore approach site appears as follows: Backland with heather covered dunes, foredunes being partly covered with beach grass, a 150 m wide sand beach and a 1200 m wide breaker zone with three bars.

This appearance together with geological and historical evidence shows that the beach at the landfall site has accreted and is now largely in dynamic equilibrium with long term rates of supply and loss and sediments being equal.

During severe storms the coast profile will be smoothed resulting in beach erosion and seawards movements of the bars. After the storm the coast profile will normally restore again after some time.

The project exploited ten years of yearly coast profiling every kilometre performed by the Danish Coast Authority. Combining 10 x 10 profiles located symmetrically around the pipeline using the foot of the dunes as the common reference point, the low envelope was established. As the profiles represent calm weather conditions a storm erosion of 1,2 m and the required wall time cover of 1,0 m was added to the low envelope in order to obtain the top of pipe profile, see Figure 2.1.

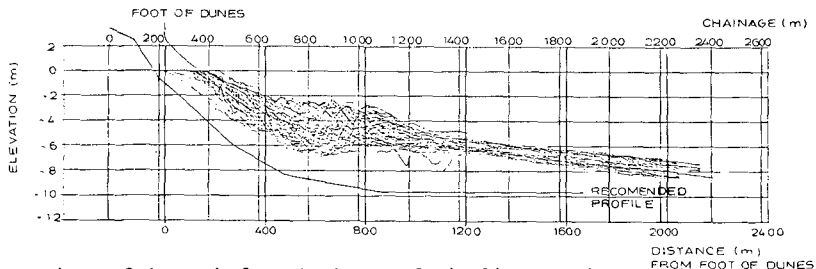


Figure 2.1 Seabed Variations and Pipeline Profile.



The required minimum distance between the gas pipe and the oil pipe was 5 m out to chainage 800, whereafter the minimum distance increased 1 m per 100 being 17 m at chainage 2000 at the end of the trench. The gas pipeline is located towards north with a straight alignment in the direction  $310^{\circ}$ . The normal to the coast is  $285^{\circ}$ , thus the trench formed an angle of  $65^{\circ}$  with the coast.

## 2.2 Environmental Conditions

The Shore Approach site is fully exposed to the North Sea environment. Because of the extremely high longshore sediment transport in the area the Shore Approach was considered one of the major challenges of the entire Danish Natural Gas and Oil Transmission system.

The gross longshore sediment<sub>3</sub> transport in the area has been evaluated at approximately 1.5 mio. m<sup>3</sup> per year, with an average during the spring and summer months of approx. 100,000 m<sup>3</sup> per month. The net longshore transport is southgoing. Variations with factors of 2-3 should not be considered as unnormal. During the worst day a transport exceeding 100,000 m<sup>3</sup> may be expected.

On basis of the environmental conditions the construction period for the sea bound Shore Approach works were selected to March through June.

## 3. Collected Data

The collected data consists of bathymetric surveys, bottom samples, wind, wave and water level data. A summary of the data collection programme is presented in Table 3.1.

YEAR MONTH	1982												1983						
	FEB.	MAR.	APR.	MAY	JUNE	JULY	AUG.	SEPT.	OCT.	NOV.	DEC.	JAN.	FEB.	MAR.	APR.	MAY	JUNE	JULY	
COMPLETE SOUNDINGS																			
DREDGING + SOUNDINGS																			
BOTTOM SAMPLES																			
WIND																			
WAVES																			
CURRENT																			
ORBITAL VELOCITY																			
WATER LEVEL $\leftarrow$ , H.+L. WATERS $\rightarrow$																			

Table 3.1 Summary of the data collection programme.

### 3.1 Soundings

All soundings were performed by echo sounder combined with various types of electronic positioning systems.

The complete sounding campaigns of the dredged area have consisted of three longitudinal profiles, one in the gas pipe centre line and one on each side spaced 2-300 m. Moreover cross-sections perpendicular to the gas pipe alignment with a distance of 25 to 50 m and a length of 3-400 m on each side of the centre line were performed.

Beyond above-mentioned complete sounding campaigns the Contractor performed soundings currently during the dredging period March through June 2, 1982.

On basis of the described sounding campaigns, sounding plans have been prepared at a scale of 1:1000. On the basis of the sounding plans cross-sections for every 50 m have been prepared. These cross-sections have formed the basis for the calculations of the sedimentation, which is described in Section 4.

### 3.2 Bottom Samples

Bottom samples have been collected before the dredging of the trench. After the dredging of the trench samples have been collected in and off the trench in connection with some of the mentioned surveys, see the summary in Table 3.1. All bottom samples were collected by a grab sampler which penetrates 10-15 cm into the bottom.

The sea bed soils consist of alternating layers of fine and medium to coarse sand covering sandy gravel.

Fine sand: Mean Grain Size :  $d_{50} = 0.14-0.21$  mm  
Uniformity Ratio :  $d_{60}/d_{10} = 1.27-1.47$

Medium to coarse sand: Mean Grain Size :  $d_{50} = 0.28-0,80$  mm  
Uniformity Ratio :  $d_{60}/d_{10} = 2.17-2.78$

The samples taken in the trench are of two different categories:

Category 1 : Dark greyish green MUD with varying contents of fine sand and silt and shell fragments.  
Mean Grain Size :  $d_{50} = 0.02$  to 0.1 mm  
Organic Content : 3- 14%.

Category 2 : SAND, fine to medium, grey, varying small contents of mud.  
Mean Grain Size :  $d_{50} = 0.14-0.23$  mm

Category 1 is found at the bottom of the trench in areas where practically no backfilling has taken place. Category 2 is found at the bottom and to the sides in areas which have experienced considerable backfilling. It is assumed that the trench finally was filled completely with Category 2 varying with thin layers of Category 1.

### 3.3 Wind measurements

Wind measurements from the nearby Blåvandshuk Light House have been collected for the total monitoring period.

3.4 Wave Measurements

Waves were measured from March 13, 1982 to June 20, 1983 at 12 m water depth about 2 km north of the Shore Approach site. The measurements were performed by a Datawell Waverider buoy. In periods where wave records are missing, see Table 3.1, the wave heights have been estimated from the wind data using correlations between  $H_s$  and the wind speed for various direction intervals. The correlations were established from the periods with simultaneous recordings of waves and wind.

The wind direction was used as offshore wave direction. Refraction calculations was performed using the DHI wave refraction model - SPEC-FRAC - in order to obtain wave conditions at breaking,  $H_{s,b}$ ,  $\theta_b$ . The breaking criteria  $H_{s,b} = 0.8 h_b$  was used, where  $h_b$  is the water depth at the breaking point.

The distribution of the breaking waves in the six periods in which backfilling has been measured, ref. Section 4, are presented in Figure 3.1.

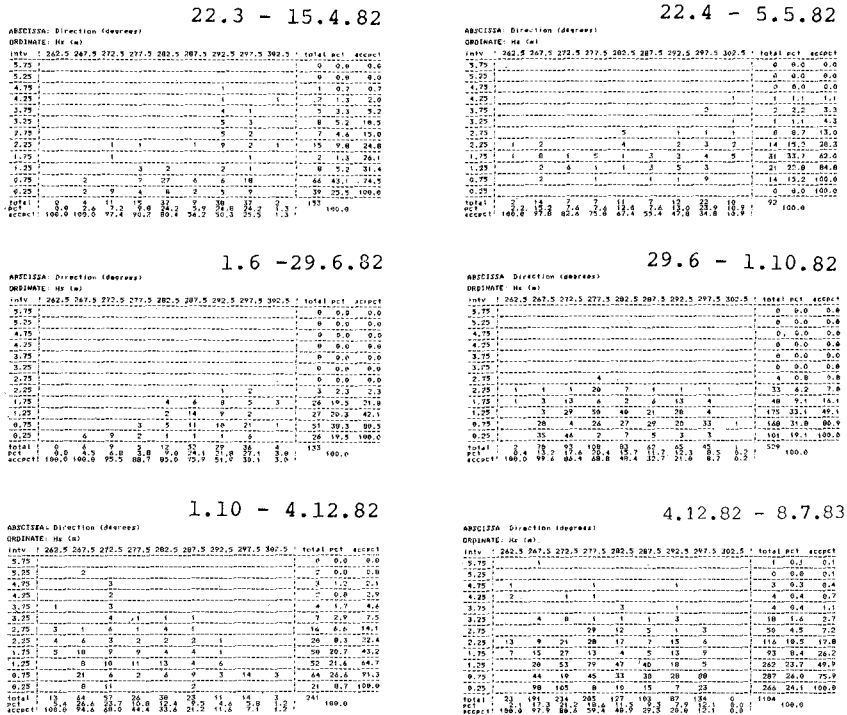


Figure 3.1 Distribution of breaking waves in six periods.

### 3.5 Current and Wave Induced Orbital Velocity

Current and wave induced orbital velocities have been measured by an electromagnetic current recorder of the type Marsh McBirney. The recorder was mounted in a rack which was placed at the sea bed at the same position as the wave recorder. The sensor of the Marsh McBirney recorder was situated 1.5 m above the sea bed.

Because of combination of financial, technical and weather-caused difficulties the wanted continuous time series of above-mentioned parameters were not obtained. The periods of data coverage are presented in Table 3.1. It was originally planned that the direction of the orbital velocities should be used as the wave direction at 12 m water depth, however, for above-mentioned reasons the wave directions were established by the refraction calculations.

The current outside the breaking zone has two main components: tidal and storm surge currents. The main directions of the tidal currents are directed N-S and the maximum tidal currents at mean spring are approx. 0.2 m/s. The storm surge currents are also directed N-S with the north-going being the dominating. The following exceedance frequencies have been estimated.

Exceedance percentage	Storm surge current
1%	0.25 m/s
5%	0.17 m/s
50%	0.07 m/s

### 3.6 Water Level Conditions

The tide is semi-diurnal with a mean tidal range of approx. 1.0 m.

The following relation between the storm surge and the wind speed for westerly winds may be used as a good first estimate: storm surge =  $7 \times U_{\text{wind}}$ , the wind speed  $U_{\text{wind}}$  in m/s gives the surge in cm.

## 4. Measured Sedimentation

Sedimentation or backfilling in the trench during a certain period has been calculated by multiplying the backfilling area for a cross-section  $A_3$ , by the distance between the cross-sections, see Fig. 4.1. By this method the sedimentation distribution along the trench, i.e., approximately perpendicular to the coast, has been calculated.

The sedimentation and other profile characteristics have been calculated according to the sketch presented in Figure 4.1.

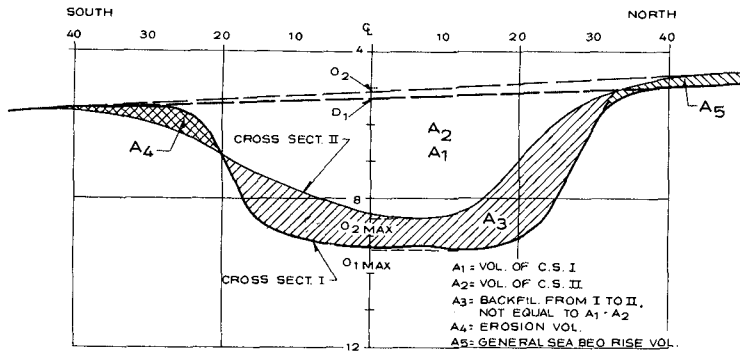


Figure 4.1 Definition of Cross-Section Characteristics.

Cross-sections of some characteristic areas for the available periods are presented in the Figures 4.2, 4.3 and 4.4, see summary Table 4.1.

Period	Charac. Area Chainage	2nd bar 700	Trough 2nd to 3rd bar 1000	3rd bar 1150-1200	Offshore 3rd bar 1700
22.3 to 15.4.82		Not dredged	Partly dredged	Fig. 4.2	Fig. 4.2
22.4 to 05.5.82		Not dredged	Not dredged	Fig. 4.3	Fig. 4.3
01.6 to 29.6.82					
29.6 to 1.10.82					
1.10 to 3.12.82	Fig. 4.4		Fig. 4.4	Fig. 4.4	Fig. 4.4
3.12.82 to 8.7.83					

Table 4.1 Summary over presented cross-sections.

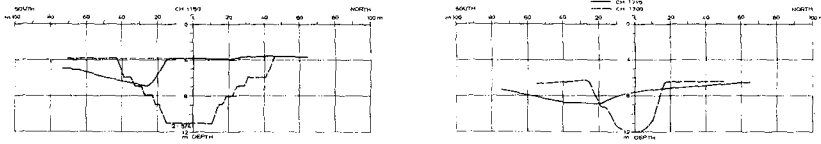


Figure 4.2 Cross-sections from 3rd and offshore 3rd bar, period 23.3 to 15.4.82.

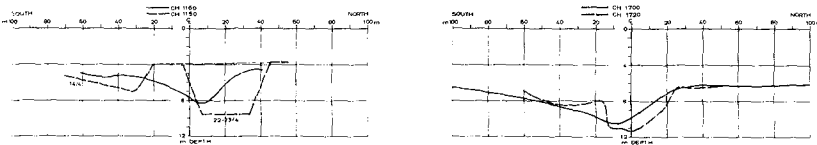


Figure 4.3 Cross-sections from 3rd and offshore 3rd bar, period 22.4 to 5.5.82.

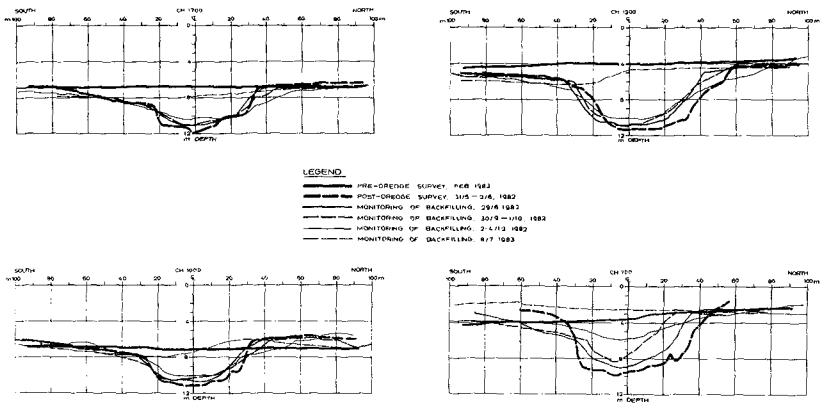


Figure 4.4 Cross-sections from 2nd bar, trough between 2nd and 3rd bar, 3rd bar and offshore 3rd bar, four periods.

The mean sea bed profile, the profiles of the trench in the beginning and the end of the periods, the distribution of the trench volume at the beginning of the periods and the distribution of the measured backfilling during the periods are presented in Figure 4.5.

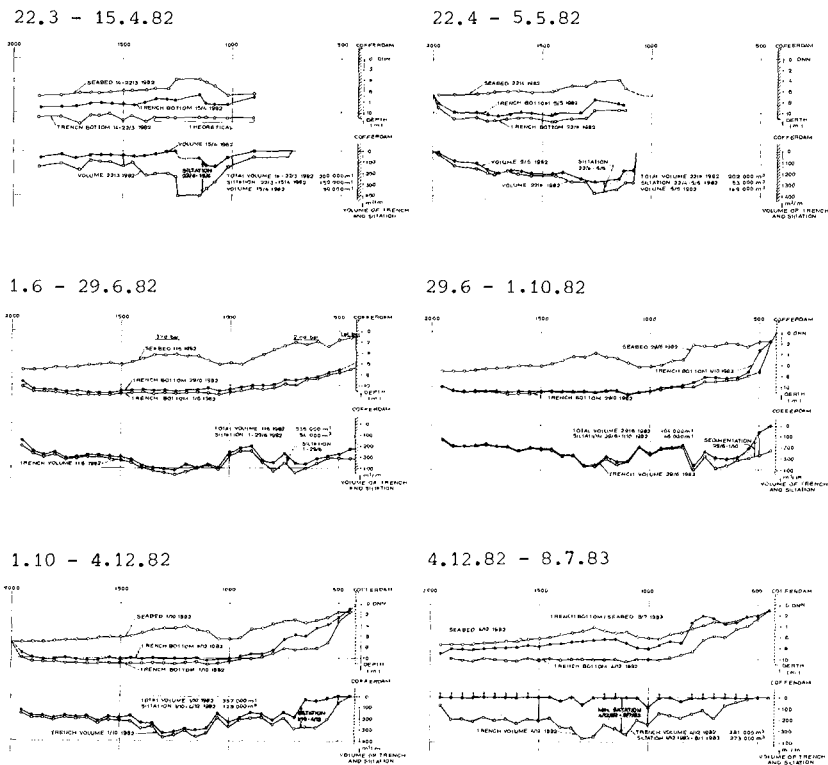


Figure 4.5 Seabed and trench bottom profiles and distributions of trench volume and siltation for six periods.

The backfilling distribution in the profiles is varying considerably because of variations of the wave conditions in the backfilling period. The backfilling is concentrated in the bar areas, in rough weather at the outer bar, see f.ex. the distribution in the period 23.3 to 15.4.82 in Figures Nos. 4.2 and 4.5, in mild periods at the two minor bars, see f.ex. the distribution in the period 29.6 to 1.10.82 in Figures Nos. 4.4 and 4.5.

5. Calculated Longshore Transport by CERC-Formula

The gross longshore transport in the backfilling periods have been calculated inserting the three hourly breaking wave parameters ( $H_{s,b}$ ,  $\alpha_b$ ), see in Figure 3.1, in the CERC-formula:

$$Q = 1228 H_{s,b}^{5/2} \sin 2\alpha_b$$

$H_{s,b}$  in m gives  $Q$  in  $m^3/3 h$ .

By assuming the bulk of the transport in the profile taking place between the depths  $0.7 h_b$  and  $1.3 h_b$  a simplified theoretical distribution of the longshore transport in the profiles has been evaluated. This distribution fits reasonably well with the measured distributions of backfilling. By subtracting the transport which takes place in areas with no trench from the calculated gross transports, one obtain corrected transport amounts, which should be directly comparable with the total measured backfilling amounts. It has been assumed that all longshore transport are trapped in areas with an intact or partly filled trench.

The corrected longshore transport is presented as function of the measured backfilling in Figure 5.1.

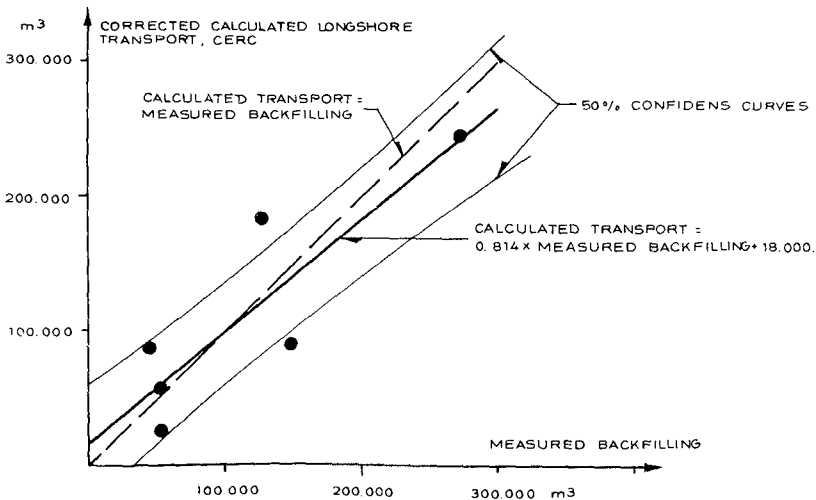


Figure 5.1 Calculated Longshore Transport (CERC) versus Measured Backfilling.



## 6. Improved Calculation of Longshore Transport

Finally the measured backfilling rate for the period March 22, 1982 to April 15, 1982 has been compared to the gross longshore sediment transport for the same period calculated by a method recently presented by J. Fredsøe, /1/. This method enables the calculation of the sediment transport - bed load as well as suspended load - in the combined flow field of a steady current superimposed by waves. Briefly the method considers the wave boundary layer at the flow bed as it grows up and collapses cyclically with the wave motion in the combined flow. By application of the momentum equation to the boundary layer and a few additional simple principles the temporal variation of the layer is calculated and subsequently the temporal variation in the bed shear stress and eddy viscosity distribution over the depth. The bed load transport rate is immediately related to the bed shear stress as is the concentration of suspended load at the bed and both respond with zero time lag to the variations in the bed shear stress. The concentration distribution over the depth is assumed to be described by the one-dimensional diffusion equation with the sediment diffusivity equal to the eddy viscosity. This equation is solved numerically with depth and time yielding the cyclic variation of the suspended load concentration at any particular depth. The corresponding instantaneous suspended load transport rate is the product of flow velocity and suspended load concentration integrated over the flow depth and is thus cyclic as well. The instantaneous transport rates - bed load as well as suspended load - are averaged over a wave cycle and added to yield what is termed the sediment transport rate. All calculations are carried out by automatic computer. For further details reference is made to /1/.

The steady current is the longshore current which is assumed to be exclusively wave generated. As an approximation it is calculated as proposed by Longuet-Higgins, /3/, for a coast with no bars but with the following modifications :

- The reference velocity  $V_o$  is determined as for a coast with no bars but with the coastal slope equal to the bed slope at the point of breaking
- The velocity distribution across the surf zone is calculated as for a coast with slope 1:130 and no bars, see Fig. 6.1.b.
- Only the outermost breaking line is taken into account, even though wave breaking may occur up to three times before reaching the coastline.

After breaking at wave height  $H_B$  the wave height  $H$  is assumed to be modified with the distance  $\Delta x$  from the breaking lines as,

$$H/H_B = 0.35 + 0.65 \exp(-0.12 \Delta x/H_B)$$

see e.g. /2/. As the decayed wave runs up the front slope of the following bar the wave height increases again with diminishing depth and breaking occurs once again and so forth until the coastline is reached.

In this way the steady current as well as the wave agitation are calculated at a number of points across the surf zone for the wave conditions occurring during the period 22.3 - 15.4.82.

The sediment transport rate at each point is calculated corresponding to each significant wave height and angle of incidence at breaking as depicted on Fig. 3.1 using that the normal to the coast has the direction  $285^{\circ}$  and assuming the sediment grain size to be 0.2 mm and the water temperature  $5^{\circ}\text{C}$ . With the duration of each wave condition as shown on Fig. 3.1 the gross transport rate has been calculated for each point. The results are shown on Fig. 6.1.a and compared to the measured backfilling during the same period. The calculated longshore transport comes out in volume solid material during the period whereas the backfill is measured as volume of material in deposit. It has been converted to volume solid material by assuming a porosity of 40%. It is noted that the measured backfill is about 2 times the calculated gross transport. In this connection it should be mentioned that:

- The measured backfill has not been reduced by the volume originating solely from the deformation of the trench and is therefore not equal to the gross longshore transport.
- Longshore currents from other sources than obliquely incident breaking waves have been ignored and may not be so, especially during and after a stormy period as occurred within the period considered.

With this in mind the discrepancy between the calculations and the measurements is not really that discouraging. Efforts continue to improve the method of calculations, primarily by improving the method of calculating the longshore currents.

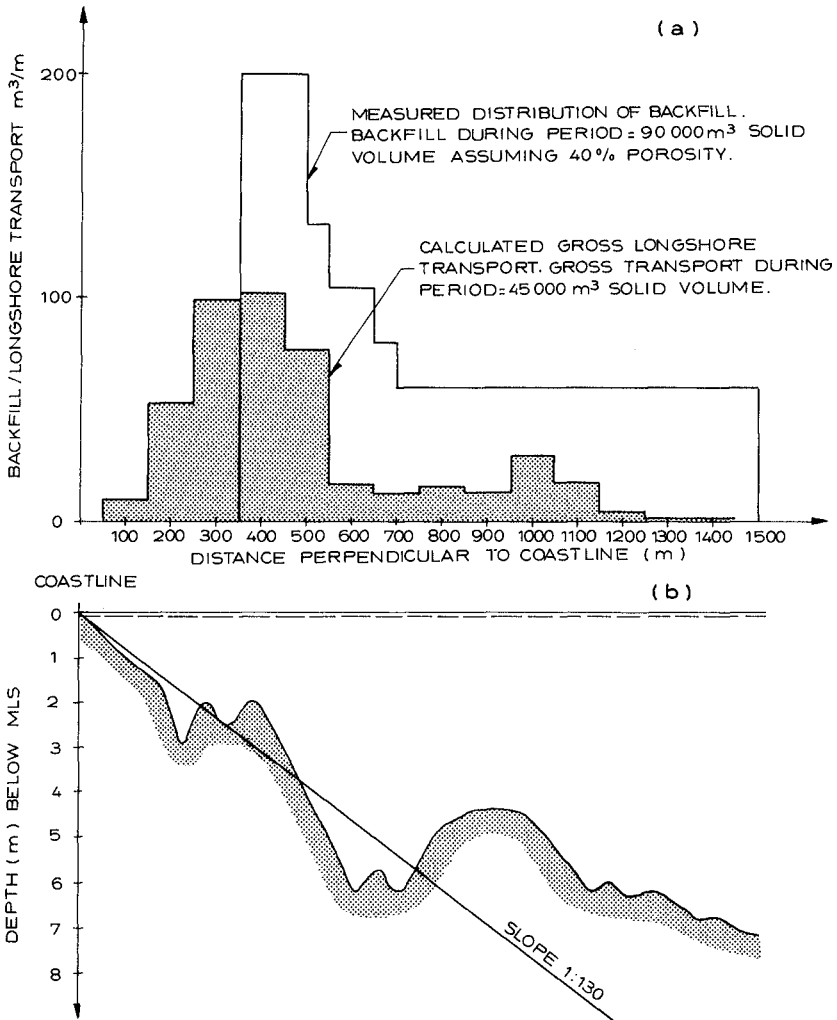


Fig. 6.1 (a) Longshore transport for period 22.3-15.4, 1982 by J. Fredsøe's model /1/ and natural backfill during the same period.

(b) Coast profile as observed during same period.

References

- /1/ J. Fredsøe : 'Sediment Transport in Current and Waves'.  
ISVA Series Paper No. 35, Technical University of Denmark,  
June 1984.
- /2/ Ole Holst Ander & J. Fredsøe : 'Transport of Suspended Sediment  
along the Coast'. ISVA Progress Report No. 59, Technical Univer-  
sity of Denmark, Nov. 1983.
- /3/ M. S. Longuet-Higgins : 'Longshore Currents Generated by  
Obliquely Incident Sea Waves, 1 & 2'.  
J. Geo. Res., Vol. 75, No. 33, Nov. 1970.

1006/KM/PM/YBR/jer/PA1

## CHAPTER ONE HUNDRED TWENTY THREE

### FIELD INVESTIGATIONS IN THE TOW STUDY PROGRAMME FOR COASTAL SEDIMENT TRANSPORT IN THE NETHERLANDS

H. Derks\* and M.J.F. Stive\*

#### ABSTRACT

Field campaigns were conducted in 1981 and 1982/83 on the Dutch coast near Egmond. Measurements were made of surface elevations, water velocities and sediment concentrations in 3 to 8 surf zone locations and 2 to 5 offshore locations simultaneously. A total of 50 measurement series was obtained under a variety of weather conditions, resulting in offshore wave heights of 0.2 to 4.6 m. A description is given of the field set-up, the instruments and measurements, and the collected data. The quality of the various measurement systems and the data produced has been investigated extensively by intercomparison of instruments and devices in the field. The results are reported here.

#### 1.0 INTRODUCTION

The TOW Study Programme for Coastal Sediment Transport in the Netherlands aims to improve our knowledge of the phenomena governing the sediment transport in the coastal zone in order to develop methods for a detailed and accurate prediction of the coastal morphology. The TOW Programme is financed by the Dutch Government. The organization of the Programme is a joint effort of the Public Works Department (Rijkswaterstaat), the Delft University of Technology and the Delft Hydraulics Laboratory. The Programme includes theoretical studies, laboratory investigations and investigations in the field. The different subjects are covered by 8 task groups.

Within the above framework the Field Experiments Task Group has so far conducted two field campaigns on the Dutch coast. In this paper a summary is given of the objectives, the set-up of the campaigns, the instruments involved, the measurements, the collected data, the data analysis and the quality of the data as measured by the instruments under different conditions.

#### 2.0 OBJECTIVES

The collection of simultaneous data on waves, currents and sand transport phenomena in the nearshore area requires an extensive measurement system. No sufficient information was available on the requirements for the well functioning of such a system as a whole. A general objective of the present study was to test such a measurement system in nature in order to study the functioning of the different

---

\* Delft Hydraulics Laboratory, Delft, the Netherlands



Photo 1 Surf zone measurement stations 1982/83 campaign



Photo 2 Close-up of surf zone measurement station

parts of the systems. Execution of measurements had to be possible during conditions of windforce 8 Beaufort and higher. The constructional provisions had to be sufficient for the safe exposure of the measurement set up to the conditions present at the Dutch coast during the winter season. Occurrence of storms of windforce 10-11 Beaufort is normal then.

In detail the objectives of the field investigations can be distinguished as follows:

- collection of data to study the hydraulic and morphologic phenomena in the nearshore areas of the coast.
- collection of data to study the functioning of devices and instruments for the measurement of wave heights, waterlevels, currents, sediment concentrations and bottom configuration under various conditions inside and outside the surfzone.
- testing of the system for data acquisition and data analysis at the site.
- testing of the various constructional provisions.
- collection of experience in the execution of field campaigns.

The latter 4 objectives were covered by the Field Experiments Task Group. The study of the hydraulic and morphologic phenomena is being covered by the other task groups in the TOW programme.

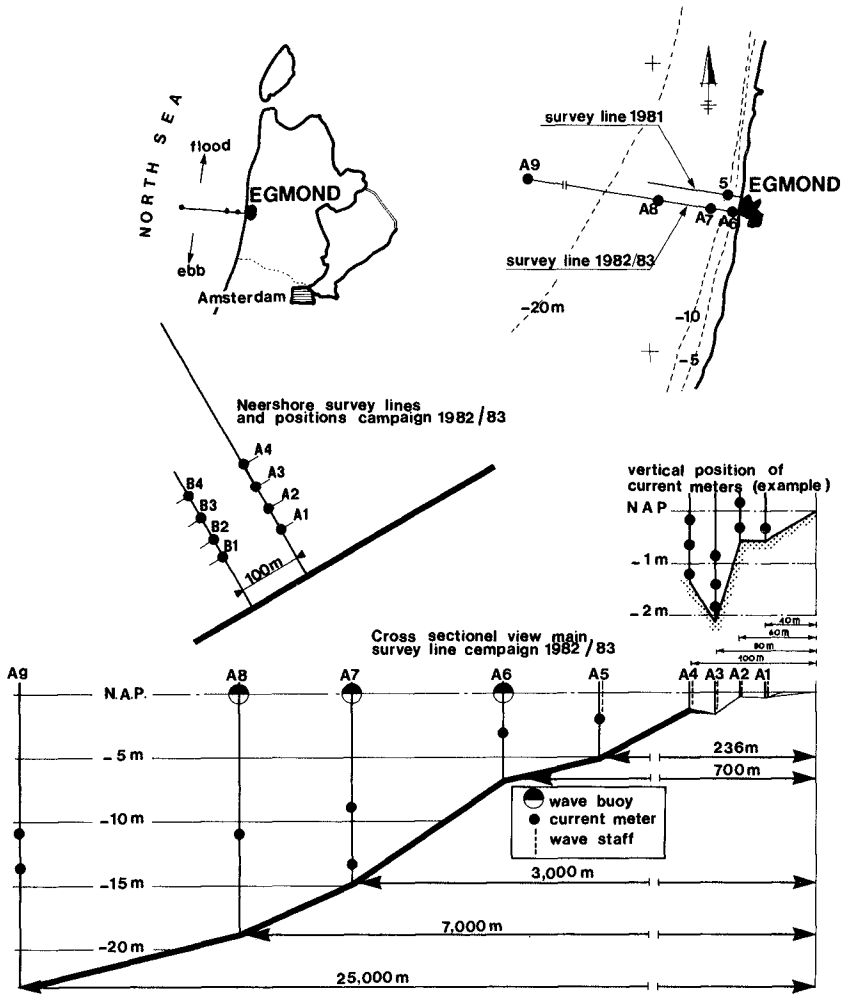


Fig. 1 Location and measurement set-up

### 3.0 FIELD CAMPAIGNS

#### 3.1 Set-up

Both field campaigns were conducted on the Dutch coast near Egmond. The location near Egmond was selected because of its relative uniformity in bottom topography and hydraulic conditions alongshore. The first campaign was held in May and June 1981 during relatively calm weather conditions. The second campaign was held from September 1982 to January 1983 when weather conditions were relatively rough.

Simultaneous measurements of surface elevations, velocities and sand concentrations were carried out along a main survey line perpendicular to the coast. In the 1981 campaign 3 surf zone stations and 2 offshore stations were present. In the 1982/83 campaign 4 surf zone stations and 5 offshore stations were installed, while also a second survey line was added 100 m south of the main line with 4 additional surf zone stations (see Fig. 1). The surf zone stations consisted of a working platform on scaffolding, lightly constructed of steel pipes that had been driven into the bottom by fluidizing the sand. From the platforms the instruments could be installed on sensor piles. The platforms were mutually connected by a foot jetty, which was also used for the cable connections with the shore. An impression may be obtained from Photos 1...4. In the offshore region instruments were either placed on or moored to the bottom. In this case signals were transmitted to the shore by radio, with the exception of self-recording tidal current meters. Data acquisition was done directly inshore of the main survey line in a facility of portable cabins by means of a HP 1000 computer and subsystem.

#### 3.2 Instruments and Measurements

Whether an instrument meets the measurement requirements, in general, will have to be judged on the data produced by that instrument under the desired conditions. In this respect a problem arises when no representative data measured by other instruments are available, such as is the case with data collected in the surf zone during a severe storm. By means of theory the order of magnitude of a phenomenon can be estimated. It is also possible to calibrate instruments under controlled conditions which are a close approximation of reality. However, the confidence that a signal produced by a device is sufficiently representative can only be based on information provided by the measuring practice itself.

Therefore the instrumental set-up is chosen in such a way that the data collection is done under a great variety of external conditions, whereby the variety of positioning is small and the signals are measured simultaneously by as many instruments as possible.

By intercomparison of signals collected by identical instruments the variability of a certain phenomenon with place can be determined. Hereafter intercomparison of signals collected by non-identical instruments can give information about the influence on the representation of signals caused by other factors specifically those related to the measuring principle of the instrument. Finally, the general review





Photo 3 Surf zone stations under storm conditions at intermediate tidal level



Photo 4 Surf zone stations under storm conditions and at high tidal level

of the results of all measurements of this kind provides an impression of the reliability of the representation of a signal by a measuring device under certain conditions.

The phenomena of interest in the conducted field campaigns of 1981 and 1982/83 are:

- surface elevations;
- mean waterlevels;
- instantaneous water velocities in the surf zone;
- mean current velocities outside the surf zone;
- sand concentrations in the surf zone;
- bottom topography.

Surface elevations were measured by means of Plessey wave staffs and Data Well waveriders. Common aspects of the functioning of both instruments are unexpected disturbances of the measuring signal, zero stability, response of instruments under several wave conditions. With respect to the Plessey wavestaff the effect of the presence of a protective pipe mounted around the staff was studied also.

Absolute values of the mean water level were measured by means of Plessey wave staffs, Vega pressure sensors and a TPD tidal recorder. Point of interest is the inter-exchangeability of the values. Relative values of the mean waterlevel were measured by DAG 6000 self contained pressure meters.

Instantaneous water velocities were measured by means of the following instruments

- Marsh McBirney (USA) - electromagnetic current meter
- Colnbrook (UK) - electromagnetic current meter
- NSW (GFR) - electromagnetic current meter
- Vector Akwa (Neth) - acoustic pulse travel time current meter
- ASTM (Neth) - acoustic doppler shift current meter.

The following aspects being characteristic for the functioning of the instruments in the surf zone were studied:

- representation of velocities by different meters under various conditions
- effects on the representation of velocities under high concentrations of entrained air and sand particles
- characteristics of the represented velocities in situations when the sensor is subject to sudden transitions of air to water and vice versa (measurements in passing wave crests)
- representation of velocities during measurements in one vertical in 5 points simultaneously
- effects on the measurement of the horizontal velocity signals caused by interaction of the vertical velocity component and the shape of the probe.

Mean current velocities outside the surf zone were measured by NBA and Flachsee underwater current meters usually in one point in the vertical. In one location the distribution of the mean velocity in the vertical was studied by means of two current meters.

Sand concentrations were measured by means of a suction sampler system and the ASTM acoustic backscatter meter. One point of interest is to know the conditions for the correct functioning and calibration of both instruments. A large number of practical aspects of the functioning still has to be cleared. Another important aspect is to have sufficient knowledge of the processes involved in the variation of the sand concentration over time and depth. The ASTM is capable of producing instantaneous values of the sand concentration measured in a point.

The bottom configuration was measured periodically by levelling (by foot) and echosounding (by boat). From this system no detailed information about instantaneous changes of the bottom topography in time and place is obtained. Therefore, echosounding equipment of 1 MHz working frequency was installed in the measuring locations in the surf zone and its capability of producing additional information about the instantaneous local bottom elevation was studied.

Directions of wave crests inside the surf zone were measured by video recording the wave field in the surf zone using a reference system for the wave crest positions. Information about the direction of breaking wave crests can be obtained from the images by determining the angles made by the passing wave crests.

#### 4.0 COLLECTED DATA AND DATA ANALYSIS

Data acquisition was done at the site by means of a HP 1000 computer and subsystem. This computer was implemented with facilities for data analysis techniques. Also facilities for plotting of the results were available. The availability of data analysis and plotting facilities at the site proved to be an essential part in checking the quality of the measured data. Already at the site a start was made with a selected number of time series analysis which serve as an inventory of the collected data. The total volume of work involved in making this inventory was such that the greater part was done at Delft Hydraulics Laboratory on the same HP system after the ending of the measurements.

The total number of instruments used during the 1982/83 campaign was 34. The total number of measurement series of both campaigns amounts 52. The measurement series are varying in duration from 40 minutes to 13 hours. The weather conditions vary from calm weather to windforce 9 Beaufort, and there is variation in the number of instruments and their distribution over the different measuring positions. The collected data are inventorized in Derks (1982, 1983). A summary of the collected data is given in the table below.

campaign	number of measurement series	duration of measurement series	number of parameters	offshore significant wave height
1981	5	5 hours	20-25	0.2-1.5 m
1982/83	20	30-45 minutes	10-20	0.3-2.5 m
	17	1- 3 hours	10-20	0.3-2.5 m
	10	3-13 hours	35-45	0.2-4.6 m

Table 1 Collected data

Analysis of the collected data is principally carried out by and under responsibility of the different task groups. Current study aspects are wave energy decay between 3 km offshore and the beach (see Battjes and Stive, 1984), low frequency velocity characteristics (see Gerritsen and Van Heteren, 1984), wave driven currents and sediment transport in the horizontal plane (see Boer et al, 1984) and wave kinematics and directionality (see Van Heteren and Stive, 1984). An important aspect is the assessment of the quality of the data as measured by the various measurement systems. Since there are no absolute standards, in general, a judgement of the performance of instruments and devices must be made by intercomparison of signals. As described above this aspect was covered in the set-up of both campaigns. The evaluation was conducted by the Field Experiments Task Group and is reported in Derks (1982, 1984). A summary of the results is given in the following section.

## 5.0 PERFORMANCE OF MEASUREMENT SYSTEMS

### 5.1 Surface Elevations

In deep water, at distances of 700, 3,000 and 7,000 m offshore, surface elevations were measured by means of Data Well wave riders, floating vertical accelerometer buoys moored by an elastic cable. During the Egmond measurements it was noted that disturbances of the signal occurred during high sea. Under these conditions the radioconnections could be interrupted by capsizing of the buoy. No data are available for intercomparison of the buoys with other measurement systems.

In shallow water up to distances of 250 m offshore, surface elevations were measured by means of Plessey wave staffs, resistance staffs mounted at fixed positions. The signal produced by this instrument showed a lot of irregularities during the measurements. Spurious peaks of large steepness and amplitude and sudden changes of the mean signal level occurred. During the 4 months measurements the calibration factors also showed a significant variability. In general wave height distributions and spectra could be determined by careful screening of the signals and by eliminating the peaks on basis of their steepness. Intercomparison of the results determined by the Plessey wave staff and the Vega pressure meter at positions with a local depth of 1-2 m showed that the pressure is not hydrostatic. Cross spectral analysis shows that the coherence value is very close to 1 at the frequency range from 0-0.5 Hz, while the gain value over this range drops almost

linearly from 1 to 0. The presence of the perforated protection pipe resulted in 10% lower values of the significant wave height ( $H_{1/3}$ ) although the total variance of the signal is not influenced.

## 5.2 Mean Water Level

Comparative measurements were made with the Plessey wave staff - Vega pressure sensor and the Plessey wave staff - TPD tidal recorder in combined positions. As a consequence of the irregularities shown by the wave staff signal and the large variability of the calibration factors, no correct water levels could be determined from the Plessey wave staff signal.

Other combinations of instruments were not studied. The signals measured by the TPD tidal recorder, the Vega pressure sensor and the DAG 6000 pressure sensor individually showed no irregularities.

## 5.3 Instantaneous Water Velocities inside the Surf zone

### Criteria for intercomparison of signals

The functioning of a number of current meters in the surf zone was studied by intercomparison of signals produced by pairs of instruments. The instruments were placed on the same elevation. The mutual horizontal distance between the two instruments was varied up to a range of 2.50 m. The signals were measured in two or three orthogonal directions whose orientation was according to the direction of the main survey lines of the measurement set-up. The differences between a pair of signals produced by instruments in two different positions however, are not fully due to the functioning of the instruments, but partially due to the spatial variability of the velocity signal. In order to be able to make a correct judgement this spatial variability was studied. This was done by intercomparison of signals produced by pairs of identical instruments.

The measurements were carried out with a pair of electromagnetic Marsh McBirney current meters and a pair of acoustic Vector Akwa current meters under a variety of conditions of wave height and water depth. As a consequence the differences in the concentrations of sand and air were relatively large.

The results of the measurements showed that the signals of the water velocity inside the surf zone in general have the following characteristics:

- (1) the time averaged value of the velocity component parallel to the coast is relatively large while the variance of the signal is relatively small. In other words the velocity signal parallel to the coast has a relatively large static component and a relatively small dynamic component. The velocity signal perpendicular to the coast has just reverse characteristics.
- (2) From the measurements with pairs of identical current meters it appears that the spatial variability of the velocity signal in the surf zone within a horizontal distance of 2.50 m is as follows (see also Fig. 2 for an example):

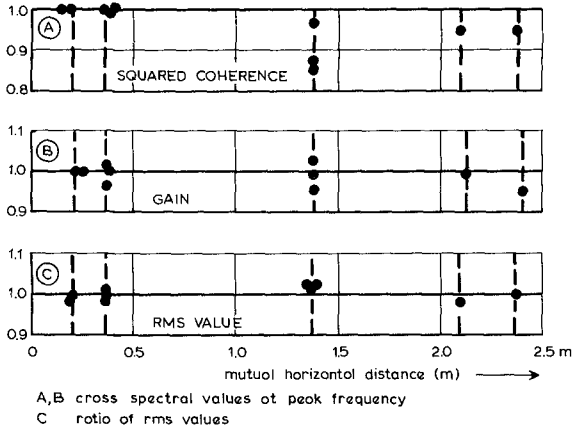


Fig 2 Spatial variability of onshore velocity derived from two closely spaced, identical Marsh McBirney current meters

basic characteristics	velocity component parallel to the coast	velocity component perpendicular to the coast
mean value	relatively small variation	relatively large variation
variance	relatively small variation	relatively small variation
coherence and gain between signals in the same direction	relatively small	relatively large

Most suitable for the intercomparison of signals produced by closely spaced current meters in the surf zone are those characteristics that show the least spatial variability with distance and the highest coherence and gain mutually. In this sense the coherence and gain of the velocity signals perpendicular to the coast, the mean value of the velocity signal parallel to the coast as well as the variance of the signals in both directions are the most suitable criteria.

The comparison of velocity signals provides a relative measure of the similarity between two velocity signals. Influences that affect both instruments equally, are not detected. A more absolute judgement of the quality of the measured signals can be obtained by means of the intercomparison of the separate velocity signals and the signal of the local surface elevations.

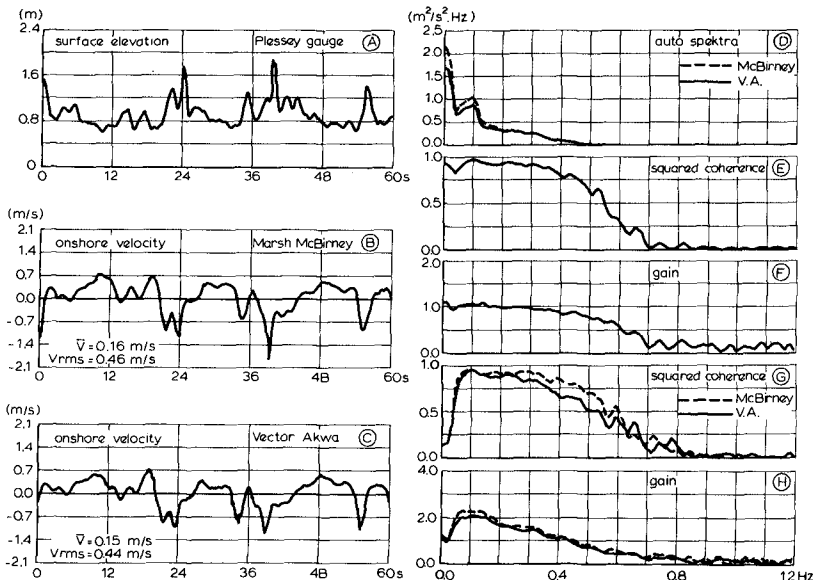
Representation of the velocity signals in the surf zone by different currentmeters

(1) In the present study information on the quality of the velocity signal in the surf zone, as represented by the different currentmeters, is obtained in two ways:

- a) directly from cross spectral analysis between two velocity signals,
- b) indirectly from cross spectral analysis between the separate velocity signals and the local surface elevation.

From a) it appears that although the measuring principles of the inspected currentmeters in some cases may be very different, the represented signals are quite similar. It appeared that unless special conditions are present, the difference between two signals produced by non identical currentmeters is of the same order of magnitude as the difference between two signals produced by identical instruments.

The results of b) indicate that the currentmeters also in a quantitative sense give a good representation of the velocity signal. An example is given in Fig. 3. An illustration of the results that may be obtained is given in Fig. 4.



A,B,C recorded time series of surface elevation and onshore velocities  
 D,E,F cross-spectra between onshore velocities  
 G,H cross-spectra between surface elevation and onshore velocity

Fig 3 Intercomparison of closely spaced (1.70 m apart) current meters

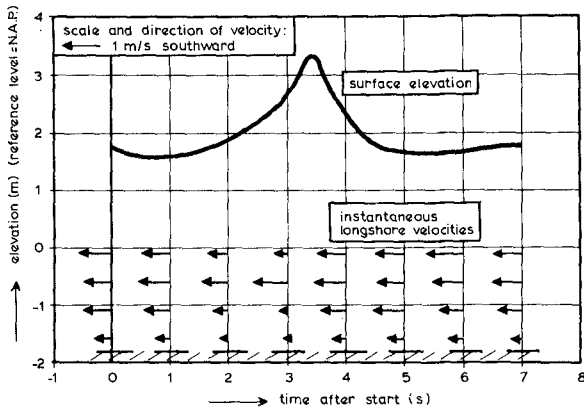


Fig. 4 Instantaneous longshore velocities and surface elevation

- (2) Of the inspected current meters the Marsh McBirney electromagnetic current meter gives the best representation of the velocity signal in the depth region 0,2 m away from the bottom up to the wave trough level. The influence of high concentrations of entrained air and sediment in the water appears to be small. Disturbances of the signal were observed when the sensor was close to the sand bottom ( $< 0.2$  m). Unless the instrument is provided with a special proximity execution (optional), disturbance of the measured velocity signal happens when the electromagnetic field of another electromagnetic current meter comes too close (distance  $< 0.50$  m). When the sensor is positioned above the level of the wave troughs of the Marsh McBirney current meter seems to respond reliably.
- (3) The representation of the velocity signal by the NSW electromagnetic current meter is equivalent to that of the Marsh McBirney current meter, however no data are available about characteristics of the represented signal when the sensor is positioned above the level of the wave troughs.
- (4) The representation of the velocity signal by the Colnbrook electromagnetic current meter is not equivalent to that of the Marsh McBirney current meter. Although the coherence values calculated in the intercomparison of Colnbrook signals and Marsh McBirney signals are equivalent to the values calculated in intercomparison of signals from identical instruments, mean values, gain values and the variances show systematic differences. This may be caused by the instability of calibration factors. It is also recommended to check the exact position of the volume of measurement of the Colnbrook probe, since the disc-shaped Colnbrook probe, being different from the spherical probe of the Marsh McBirney, may generate an electromagnetic field of different



shape. From the calculated coherence values it could be seen that the shape of the signal represented by the Colnbrook current meter is hardly influenced by highly concentrated entrained air and sediment. When the probe is positioned above the level of the passing wave troughs disturbance of the Colnbrook signal occurs so the characteristics of the signal are not suited for measurement of velocity in passing wave crests. Also disturbances of the signal occur when the Colnbrook probe is positioned close to the bottom or close to the electromagnetic field of other instruments.

- (5) The Vector Akwa acoustic current meter gives the best representation of the velocity signal in the depth region near the bottom. In the upper depth region the quality of representation is somewhat less compared to the Marsh McBirney current meter. This is probably caused by the presence of air bubbles. The influence of high concentrations of sediment on the representation of the signal by the Vector Akwa current meter is negligible. Strong disturbances of the signal occur during measurements in breaking waves when the sensor is positioned above the level of the wave troughs. Compared to the Marsh McBirney currentmeter, the instrument's response seems less reliable in this region.
- (6) The representation of the velocity signal by the ASTM acoustic (doppler shift) current meter in general is equivalent to the Marsh McBirney current meter. It appears from the available data that the representation of the velocity signal by the ASTM current meter is not influenced by entrained air and sediment in the water. The applied range of measurement positions extends from 0.20 m above the bottom up to the surface level. In comparative conditions the ASTM current meter does not show any disturbances of the signal like the Marsh McBirney current meter in positions close to the bottom or like the Colnbrook current meter in positions close to the water surface. No information is available about the characteristics of the represented signal when the sensor position is above the wave trough level.

#### 5.4 Mean Current Velocities outside the Surf Zone

Mean current velocities and direction of current outside the surf zone were measured by means of Flachsee and NBA automatic current meters. Comparative measurements between the instruments were not made. The mean current velocity was determined every 10 minutes. By means of the NBA current meter both mean values and instantaneous values of the current direction were recorded. By means of the Flachsee current meter only instantaneous values of current direction could be measured. Rupture of mooring constructions during rough weather conditions may cause loss of instruments. In the present study 3 NBA current meters were lost this way.

#### 5.5 Sand Concentrations in the Surf Zone

From the present study no clear conclusions appear whether the pumping system or the ASTM can be used for determining representative figures on the sand concentration in the surf zone. This was mainly

caused by the fact that during the measurements the knowledge about the sand concentration governing processes was insufficient. As a consequence it was not possible to indicate the requirements that had to be put on the measurement system. In the present study measurements were only done in single points. Intercomparison between results produced by the ASTM and the pumping system could not be made as it is presently known that only values obtained by averaging over the bed are useful for this purpose.

Generally it can be said that the pumping system in principal seems to offer a useful method for determining sand concentration values in the surf zone. From the point of view of measuring technique the system in its actual shape is not easily manageable during extensive measurements especially when the weather is rough. Under these conditions it is desirable to have a continuous analog electric signal of the measured sand concentration. Also it is necessary to improve the reliability of the functioning of the pumping system. In its present shape the functioning of the system is too vulnerable.

From the present study it appears that concentration values over  $100 \text{ kg/m}^3$  have to be measured. For the functioning of the pumping system these values are not critical. The ASTM however also needs to be adjusted for measurement of similar values. Unlike the pumping system the ASTM is capable of producing instantaneous values of sand concentration.

#### 5.6 Bottom Topography

The present system for measurement of bottom topography consists of periodically levelling and echo sounding (by boat) of the beach profile in fixed lines. This system offers rather limited results. A dense net of highly accurate bottom positions determined at short time intervals cannot be obtained by this system. A structural improvement of the measuring system for bottom topography is not expected to be possible at short terms.

A contribution to improve the existing system is offered by using 1 MHz echo sounding equipment in fixed positions inside the surf zone. With this equipment the bottom elevation can be monitored instantaneously offering possibilities to study short term relations between local bottom elevation and other parameters. It appeared from the measurements that this system effectively can be used for detecting locally instantaneous bottom elevation in the surf zone at a higher accuracy than is possible by means of leveling or echo sounding by boat. Also, with this system measurements can be performed under conditions when the other systems can not be applied.

#### 5.7 Wave Crest Directions in the Surf Zone

From the 1981 measurements it appeared that indeed it is possible to obtain information about the wave crest directions in the surf zone by means of the applied system (3.2). However, the system is selective as in the wave field only the crests of breaking waves can be distinguished. This implies that only information is obtained about

the direction of the breaking wave crests. Of course wave directions in the surf zone also can be obtained from the horizontal velocity vector and the surface elevation.

## 6.0 CONCLUSIONS

The 1981 and 1982/83 campaigns together yielded a total number of more than 50 measurements. The collected data are being studied in order to enlarge the existing knowledge and to improve theories of the surf zone processes.

In addition to the above mentioned study purposes the data have been used to investigate the accuracy of the representation of the measured signals collected by the different measurement systems. The conclusions of the latter study are as follows:

- (1) On basis of the results of the present study it is possible to select and design systems for accurate measurement of instantaneous water particle velocities in the surf zone under conditions up to windforce 10-11 Beaufort. The measurement positions in the horizontal and vertical plane (including positions above the level of the wave troughs) can be freely chosen. It is necessary to check some minor matters concerning the functioning of the available current meters.
- (2) The results of the present study are not sufficient to design a system capable of producing accurate values of the sand concentration in the surf zone that are representative for a certain time and place. In order to achieve such a system it will be necessary to improve the reliability of the functioning of the pumping system. Moreover it is necessary to have sufficient knowledge of the processes determining the sand concentration. The study on these aspects and the comparative study between the pumping system and the ASTM should be continued.
- (3) The available system for the measurement of bottom topography produces periodic readings of bottom positions by means of echo sounding and levelling. Sufficiently detailed readings in time and place presently cannot be obtained by this system. The available 1 MHz echo sounding equipment can produce valuable additional information on instantaneous bottom elevation in a number of measurement positions. The study of the use of this equipment should be continued.
- (4) It is recommended to study the accuracy of the available systems for the measurement of mean water levels.
- (5) In the used system for measurement of surface elevations, consisting of moored Data Well wave riders and Plessey wave staffs mounted in fixed positions, disturbances of the signals occur. Problems related to the wave buoys possibly can be solved in combination with the selection of a measurement system for wave directions. It is recommended to use other wave staffs.

## ACKNOWLEDGEMENT

This study was carried out under responsibility of the Field Experiments Task Group in the TOW programme. The field work was done as a joint effort of Adviesdienst Hoorn of Rijkswaterstaat (Public Works Department) and Delft Hydraulics Laboratory. Thanks are due to the numerous people involved in the execution of the measurements. Special thanks are due to Mr. F.J. Keuper and Mr. Th. Kos of Adviesdienst Hoorn for their invaluable efforts and kind cooperation in organizing and conducting the measurements.

## REFERENCES

- Battjes, J.A. and M.J.F. Stive , 1984  
Verification of a dissipation model for random breaking waves  
19th International Conference on Coastal Engineering, Houston
- Boer, S., H.J. de Vriend and H.G. Wind, 1984  
A mathematical model for the simulation of morphological processes in the coastal area  
19th International Conference on Coastal Engineering, Houston
- Derks, H., 1982  
Inventory of measurements of the 1982/83 campaign and investigation of performance of instruments (in Dutch)  
Delft Hydraulics Laboratory, report R1597-II
- Derks, H., 1983  
Inventory of measurements of the 1982/83 campaign (in Dutch)  
Delft Hydraulics Laboratory, report R 1597-IV
- Derks, H., 1984  
Investigation of performance of instruments during the 1982/83 campaign (in Dutch)  
Delft Hydraulics Laboratory, report R 1597-VII
- Gerritsen, F. and J. van Heteren, 1984  
The effect of low frequency oscillations on coastal morphology  
19th International Conference on Coastal Engineering, Houston
- Van Heteren, J. and M.J.F. Stive, 1984  
Wave kinematics and wave directionality in the surf zone  
19th International Conference on Coastal Engineering, Houston

## CHAPTER ONE HUNDRED TWENTY FOUR

### Field Observation on Suspended-load in the surf zone

Kazumasa KATOH<sup>1</sup>, Norio TANAKA<sup>2</sup> and Isao IRIE<sup>3</sup>

#### ABSTRACT

Both the concentration of suspended-load and the current velocity have been measured continuously in the surf zone. In order to measure the concentration of the suspended-load in the surf zone, a optical densitometer has been developed. The current velocity was measured by means of electromagnetic current meters. According to data analyses, the mean concentration of the suspended-load is high in the final breaking zone and in the breaker zone. In the final breaking zone, the concentration fluctuates with the period of the incident waves. On the other hand, it fluctuates with the period longer than 40 seconds in the breaker zone and it becomes high when the current is offshoreward. The directions of the net transport of the suspended-load in the middle layer in and near the surf zone are offshoreward.

#### 1. INTRODUCTION

The surf zone is a very complicated field with respect to fluid motion owing to the breaking waves, the long period waves, the nearshore currents and the strong turbulences due to wave breaking. The scale and internal structure of this velocity field are being revealed gradually in the field and in the laboratory with the developments of current meters such as electromagnetic current meters and laser doppler velocimeters. The surf zone is also a very important field for sand movement. Scale of fluctuations and structures of sand transport should be corresponding to those of fluid motion. For examples, the sands suspended by the action of the incident waves or its breaking are transported by the nearshore currents. The fluid motion due to long period waves may affect on the sand transport to form the nearshore rhythmic topography such as multiple longshore bars, large cusps and crescentic bars.

---

1) Chief of Storm Surge and Tsunami Laboratory, 2) Director of Marine Hydrodynamics Division, 3) Chief of Littoral Drift Laboratory, Port and Harbour Research Institute, Ministry of Transport, 1-1,3-Chome, Nagase, Yokosuka, Japan.

The relationships between the sand movement and the characteristics of fluid motion in the surf zone, however, are not satisfactorily known so far, since in most of the cases the sand movement in the surf zone were measured as the time averaged values, which were difficult to be connected with the features of fluid motion. In order to understand these relationships between the sand movement and fluid motion, they must be measured continuously in the surf zone at the same time.

Therefore, both the concentration of suspended-load and the current velocity have been measured continuously in the surf zone at Ooarai Beach in Japan and the relationships between them are examined in this paper.

2. INSTRUMENTS USED IN THE FIELD OBSERVATION

\* **Densitometer** : In order to continuously measure the concentration of suspended-load in the surf zone, a densitometer was developed ( see Fig. 1 ). This consists of ten pairs of luminous and photo-electric cells mounted vertically and separated 5 centimeters apart each other. The vertical interval of these pairs of cells is 5 centimeters at the lowest part and becomes larger upward, being 20 centimeters at the highest part as seen in Fig. 1. The distance from the lowest pair of cells to the highest one is 1.20 meters. The pairs of cells are numbered upward from the lowest one, that is, the n-th pair of cells is denoted by the symbol of  $C_n$  (  $n = 1, 2, 3, \dots, 10$  ). A time constant of response of each pair is 0.1 second and ten pairs of cells are controlled periodically in order with a period of 0.03 second. After the field observation, a calibration of the densitometer was carried out in the laboratory, with the sand taken from the beach under the condition of the water

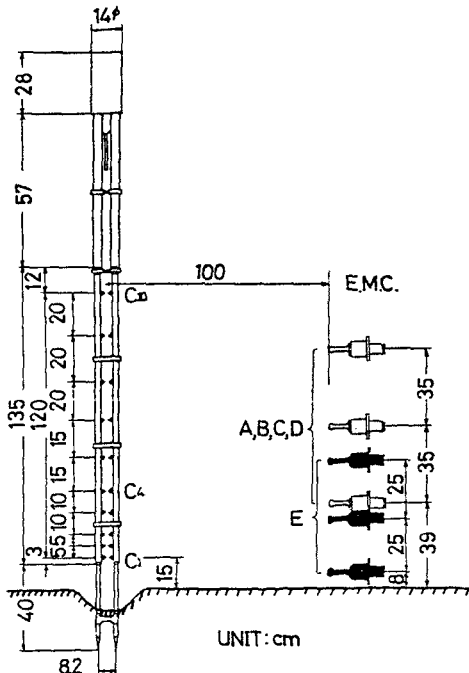


Fig. 1 Densitometer and its arrangement with electromagnetic current meters.

temperature as same as that of the field. The range of calibration was from 0ppt to 20ppt. Figure 2 shows the typical result of the calibration for  $C_3$ . The relation between the output voltage and the concentration can be approximated by a dashed curve as shown in Fig. 2. The same tendency was obtained for the other pairs of cells. In the data analysis, however, a linear relation for each pair, e.g. shown by a straight line in Fig. 2, is utilized in order to convert the output voltage into the concentration.

\* Current meters : Three electromagnetic current meters of two-components type were used to measure the current velocities.

\* Wave meters : Two capacitance type wave meters were used to measure the wave profiles.

\* Set of instruments : The densitometer was installed outside a tower which was constructed with members of steel pipe of 5 centimeters in diameter shown in Photo. 1. Three electromagnetic current meters were vertically installed inside the tower to measure the on-offshore and vertical components of velocity. A horizontal distance from the densitometer to the electromagnetic current meters was 1.0

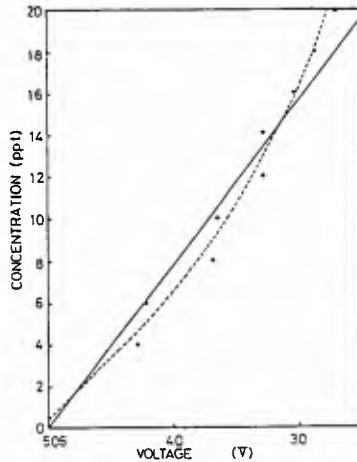


Fig. 2 Typical result of calibration for densitometer ( $C_3$ ).



Photo. 1 Observation tower

meter. After installing these instruments to the tower on the land, the frog-men carried the tower into the surf zone, and put it on the sea bed by adjusting the direction from the densitometer to the electromagnetic current meters to be parallel to that of the shoreline.

3. SITE OF FIELD OBSERVATION ( OARAI BEACH )

The field observation was carried out at Oarai Beach in Japan during the periods of August 26 to 27, 1982. This beach is located in the north end of a sandy coast of about 70 kilometers long facing to the Pacific Ocean ( see Fig. 3 ), and is adjacent to Oarai Port. The observation point was located about 220 meters south from the jetty which has a function of preventing the sand from entering Oarai Port. The observation point was almost the same level as the datum line ( see Fig. 4. ). The characteristics of the beach materials ( sand ) are that the medium diameter is  $d_{50}=0.24$  millimeter; the sorting coeffi-



Fig. 3 Location of Oarai Beach.

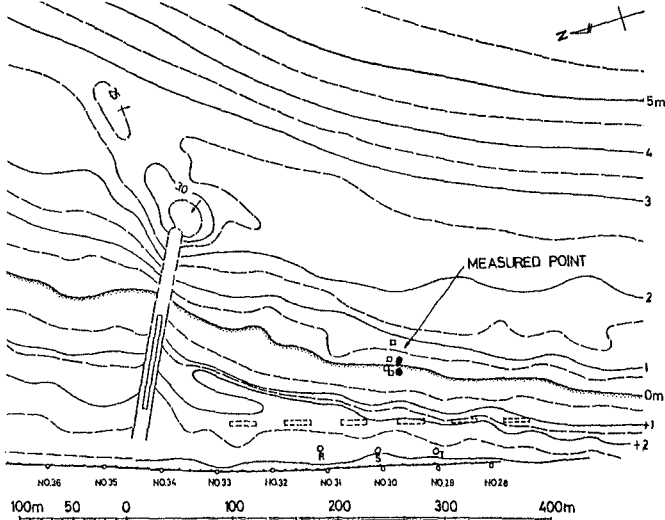


Fig. 4 Beach topography of investigated site relative to datum line and measurement points.



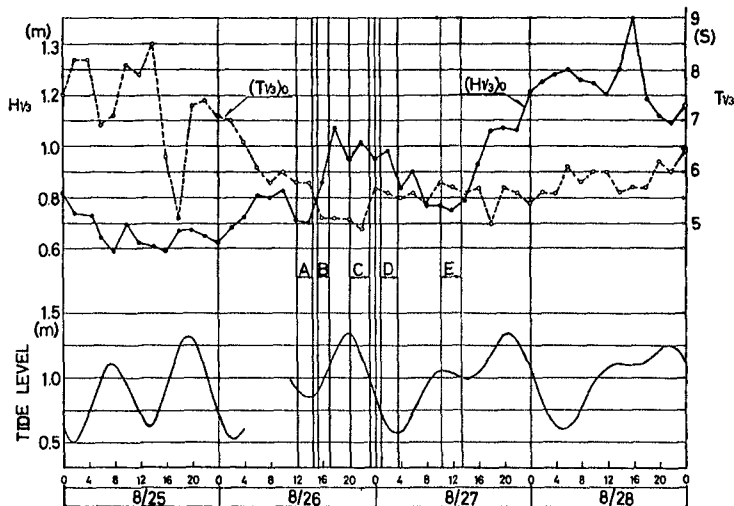


Fig. 5 Significant wave height, wave period and tidal level during the field observation.

cient is  $S_0=1.34$ ; the skewness parameter, which indicates the degree of asymmetry of grain size distribution, is  $S_k=1.12$ .

Figure 5 shows the significant wave height, wave period (measured at the depth of 30 meters under the datum line) and the tidal level (measured inside Ooarai Port) during four days, in which the field observation of two days is included. In this figure, symbols of A - E indicate the times while the field observation was carried out (hereinafter referred to as A - E). During these observations, the significant wave height was 0.7-1.0 meter and the wave period was around 5.5 seconds in deep water. The direction of the incident waves at the measurement points was nearly normal to the shoreline and the longshore currents could not be noticed as far as the visual observation could be made.

A detail of the measurement points are shown in Fig. 6, in which opened marks indicate the measurement points of A, B, C, D and closed marks indicate those of E. The arrangement of the densitometer and the electromagnetic current meters is shown in Fig. 1. The beach profile along the measurement line shown in Fig. 6 was surveyed just after the final observation of E, and is shown in Fig. 7. In this figure, the highest and the lowest water levels and the water level in each observation time are also shown.

When the tidal level was relatively low, the pairs of cells from  $C_7$  to  $C_{10}$  and the upper two current meters frequently emerged above the water surface. Then, the data obtained at the lower part are analyzed.

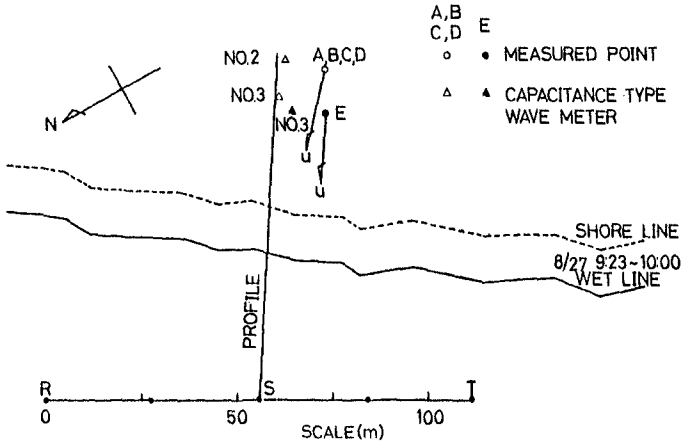


Fig. 6 Detail of measurement points.

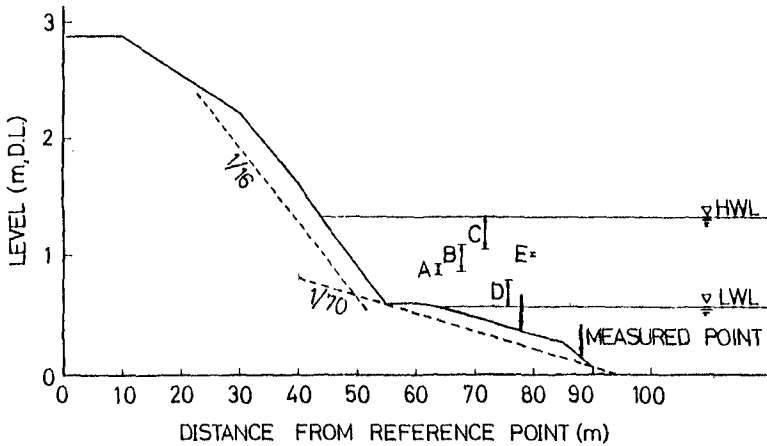


Fig. 7 Beach profile, tidal level during the field observation and measurement points.

4. RELATIONSHIP BETWEEN CONCENTRATION OF SUSPENDED-LOAD AND TIDAL LEVEL

Figure 8 shows the typical examples of the concentration of suspended-load, which were measured at C<sub>1</sub> to C<sub>3</sub> ( in the region of 15 to 25 centimeters above the sea bottom ) in B and D. One more example will be shown in Fig.13. When the concentration is low in B, the concentration of C<sub>1</sub> is negative, that of C<sub>3</sub> is about 8ppt and that of C<sub>2</sub> is

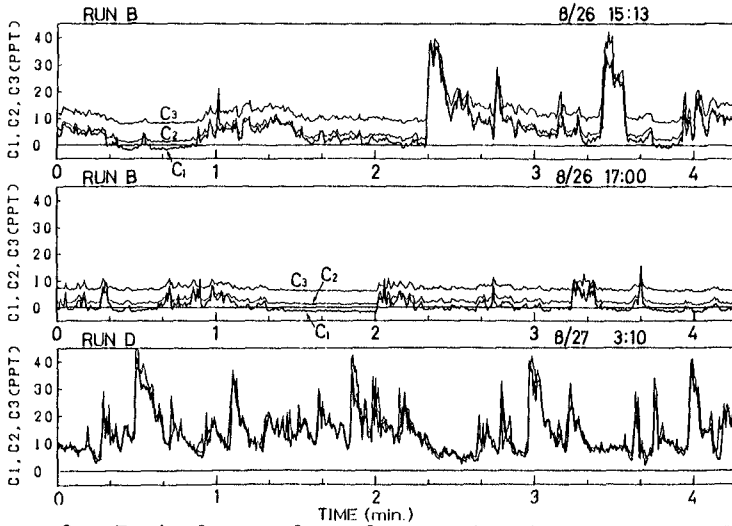


Fig. 8 Typical examples of concentration of suspended-load ( C<sub>1</sub> - C<sub>3</sub> in B, D )

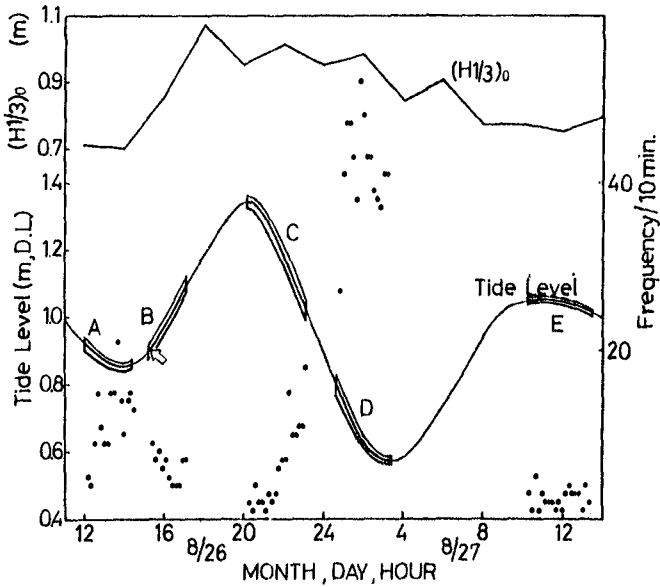


Fig. 9 Relationship between tidal level and occurrence frequency of concentration of suspended-load exceeding 20ppt.

reasonable, although these concentrations fluctuate similarly. This might have been due to that the surface conditions of the luminous and photo-electric cells were different from those in calibration, e.g. the surface of glass was blurred, which yielded the bias voltage in the output signal.

As seen in Fig. 8, the concentration of suspended-load in the region of 15 to 25 centimeters from the sea bottom frequently becomes more than 20ppt, even if we don't take the above errors into account. The high concentration occurs three times in the upper figure, zero time in the middle figure and many times in the lower figure. That is to say, the occurrence frequency of the high concentration depends on the case. Then, the occurrence frequency of the concentration exceeding 20ppt per 10 minutes are examined in the analog record of every ten minutes, and the results are plotted in Fig. 9. In this figure, the significant wave height and the tidal level are also shown. The high concentration occur most frequently of about 40 times in D with the lowest tidal level, whereas it is rare of several times in E and the first half of C during which the tidal level is higher. In A, B and the second half of C with medium tidal level, the frequency is around ten times. Generally speaking, the high concentration is rare at a high tide and is frequent at a low tide. In short, there is a negative correlation between the occurrence frequency of the high concentration and the tidal level. This situation is considered to be related to the position of a wave breaker zone which shifted with the tidal level.

The relative position of the observation points shifted from the inside of the surf zone to the out side of it, and vice versa due to the change of the tidal level. Then taking into account the relative distance from the shoreline to the observation point, the occurrence frequencies of the high concentration exceeding 20ppt are plotted in the upper part of Fig. 10. In this figure, a mean velocity and a distribution of the breaking point of the incident waves are also shown. A method of measurement of the breaking point will be mentioned in the next section. The bottom slope of 1/70 shown with dashed line in Fig. 7 is considered for estimating the relative distance. Based on this result, the on-offshore distribution of the occurrence frequency are shown with a curve after considering the followings:

(1) As seen in Fig. 9, the significant wave height is about 0.9 meter in B, D and E, while it is 0.7 meter in A and 1.1 meters in C.

(2) The difference of the incident wave height induced the displacement of the wave breaker zone, that is, the incident waves broke in the surf zone relatively nearer to the shoreline in A and relatively farther from the shoreline in C.

(3) Therefore, in order to obtain the standard on-offshore distribution of the occurrence frequency, the positions of the occurrence frequency in A and in C must be shifted in

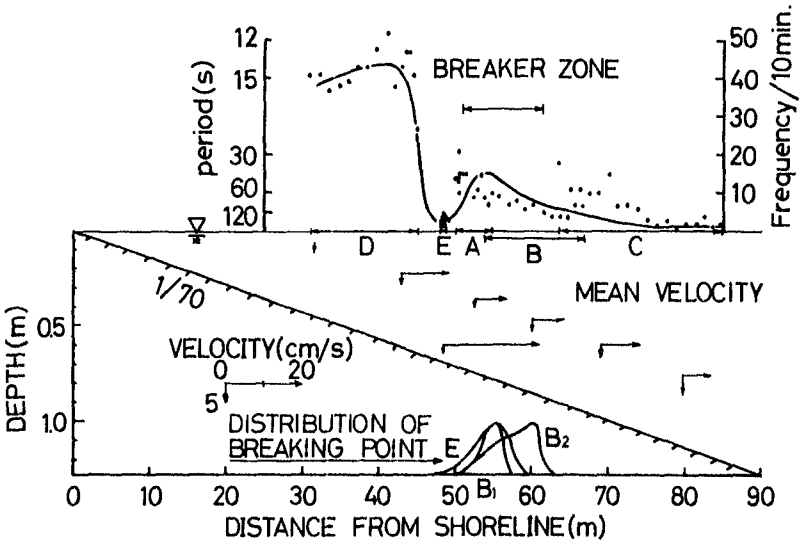


Fig. 10 On-offshore distribution of occurrence frequency of high concentration and mean velocity.

the offshore direction and in the onshore direction, respectively.

As seen in Fig. 10, the on-offshore distribution of the occurrence frequency has two peaks. The onshore-side peak, represented by the data obtained in D, indicates that the mean period of the occurrence of the high concentration is 12 to 16 seconds. The significant wave period, which is calculated by the zero down-crossing method by using every 17 minutes' wave profile data measured at the point of No.2, is  $14.2 \pm 1.6$  seconds. That is, the mean period of the occurrence of the high concentration is almost the same as the significant period of the incident waves. Although the visual observation on the situation around the observation point in D could not be made because it was the middle of the night, the final wave breaking may have occurred there since the water depth at the observation point was about 50 centimeters. The other peak of the occurrence frequency is located at the breaker zone. The mean period of the occurrence at the breaker zone is longer than 40 seconds, which is obviously longer than the period of the incident waves.

#### 5. LONG PERIOD FLUCTUATION OF SUSPENDED-LOAD IN THE SURF ZONE

It has been reported that the concentration of the suspended-load becomes high with the period longer than that

of the incident waves in the breaker zone ( Brenninkmeyer 1974, Wright et al. 1982 ). In this section, the long period fluctuation of the concentration of the suspended-load will be examined.

Figure 11 shows the result of a cross-spectral analysis between the on-offshore velocity component and the concentration of the suspended-load which were measured at  $C_1$  in B, during which the observation point was located in the breaker zone. For this analysis, the analog data are digitalized with the interval of 0.1 second, which yield the digital data of 1 second interval by being calculated the mean value of every series of 10 digital data. A sampling interval and a number of data used in the cross-spectrum analysis are  $\Delta t=1$  second and  $N=2048$  ( about 34 minutes ), respectively. The equivalent degree of freedom with a filter used for smoothing is  $r=16$ . The vertical coordinate in the upper figure is for the values of spectral density of

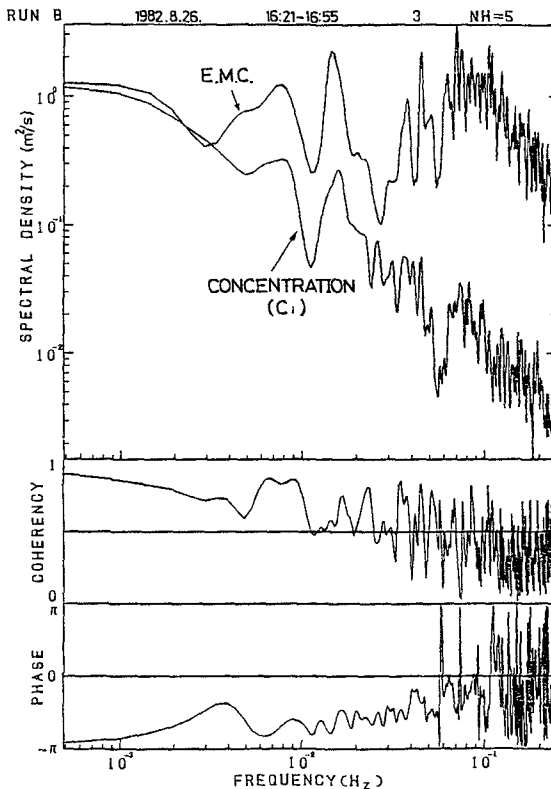


Fig. 11 Cross-spectrum between on-offshore velocity and concentration (  $C_1$  ).

the velocity. In order to show the spectral density of the concentration in the same figure, the concentration data ( ppt ) have been divided by 50 in advance.

As seen in Fig. 11, there are two pronounced spectral peaks in both the velocity and the concentration at the frequencies of 0.015Hz ( 67 seconds ) and 0.008Hz ( 125 seconds ). At these frequencies, the coherences of the velocity versus the concentration are high and the phase differences between them are nearly 180 degrees. Therefore, it can be said that the concentration of the suspended-load becomes high when the velocity is negative, i.e. the direction of the current is offshoreward. There is, however, no spectral peak in the concentration at the frequency of the incident waves.

The breaking positions and the breaking types of the incident waves were visually observed in B, and the results were recorded with a voice on a magnetic-tape, on which the velocity and the concentration of the suspended-load were also recorded at the same time by means of a Data Recorder. Figure 12 shows the wave breaking type and the on-offshore distribution of the wave breaking position. In this case, the mean period of wave breaking is about 19 seconds, which is calculated by dividing the visual observation time by a total number of waves observed, being longer than that of the incident waves. Then, the waves of small size may have been ignored in the visual observation since the rate of the spilling type is low. As seen in Fig. 12, the measurement position was located inside the breaker zone and at its position the incident waves broke most frequently.

Figure 13 shows the typical example of the records; the upper figure is the on-offshore velocity; the lower figure is the concentration of the suspended-load. The arrows in the middle part of Fig. 13 show the time when the incident waves broke. The opened arrows indicate that the incident waves broke at the offshore-side of the observation point,

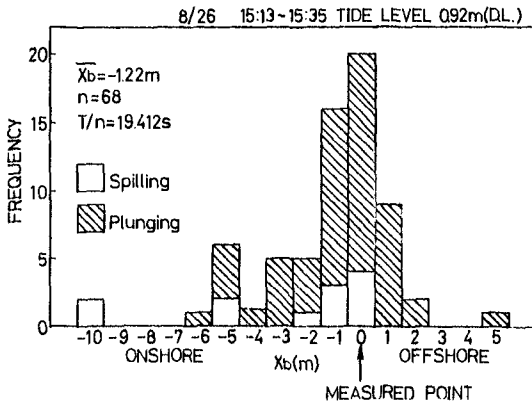


Fig. 12 Wave breaking type and on-offshore distribution of wave breaking position.

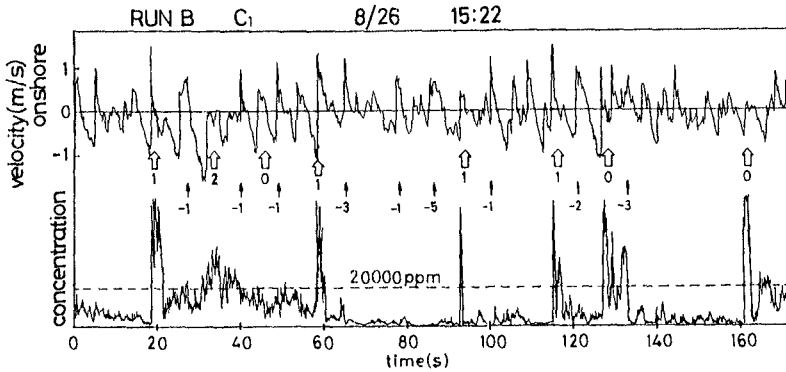


Fig. 13 Typical example of on-offshore velocity, concentration and breaking position.

while the black arrows indicate that they broke at the onshore-side. Moreover, the figure under the each arrow is the distance in meter from the observation point to the breaking point. All the breaking type in Fig 13 were judged as plungings. According to Fig.13, whenever the concentration of the suspended-load exceeded 20ppt, the incident waves broke at the offshore-side of the observation point which is indicated with the opened arrow. At these times, the concentration suddenly increased, and rapidly decrease except a period of 20 to 60 seconds. This evidence can be explained as follows: The abundant suspended-load due to the wave breaking at the offshore-side of the observation point is transported in forming the suspended-load cloud to the observation point by the onshoreward current under the wave crest. Subsequently it is transported to the offshore direction by the offshoreward current under the wave trough. Since the concentration of the suspended-load rapidly decrease in the second stage, the state of the suspended-load cloud should be maintained without enough diffusion during this process. Almost all of the suspended-load, however, deposit by the time when the following wave crest passes through the observation point without breaking.

During the period of 20 to 60 seconds, the concentration of the suspended-load gradually increased to be more than 20ppt and gradually decreased to be a low level. The condition of the incident waves, which broke at the offshore-side and at the onshore-side of the measurement position alternatively, is different from that of the other periods. Furthermore, the maximum offshoreward velocity occurred at nearly 30 seconds and the duration of the onshoreward velocity was relatively short. Then, the followings are inferred: The tendency of transportation of the suspended-load from the offshore to the observation point is weak due to the short duration of the onshoreward velocity. In this case, the suspended-load due to the wave



breaking at the onshore-side likely to be transported to the observation point. The repetitive wave breakings in a short period has an effect of maintaining the sand in suspension over a long time.

#### 6. NET TRANSPORT OF SUSPENDED-LOAD

At first in this section, the mean velocity is examined. As seen in Fig. 1, the height of the electromagnetic current meters from the sea bottom differed from case to case, e.g. that of the lowest one was 8 centimeters in E and 39 centimeters in the other. The electromagnetic current meters in the upper part occasionally emerged above the water surface when the wave trough passed at the observation point during the relatively low tidal level. Therefore, the records obtained by the lowest current meter in level are used for calculating the mean velocity. Figure 14 shows the changes of the mean velocity of the on-offshore component in 5 minutes during each observation case. The onshore direction of the velocity is defined as positive.

The mean velocity in A, B, C are almost constant of 10 cm/s offshoreward. In the first half of D the mean velocity is 15 cm/s offshoreward, while it is nearly zero in the second half of D. In E the mean velocity gradually changes from about 40 cm/s offshoreward to about 25 cm/s offshoreward.

Taking into account the relative distance from the shoreline to the observation point, these mean velocities are shown together with the vertical mean velocities in Fig. 10. A number of data shown is not enough to give the whole

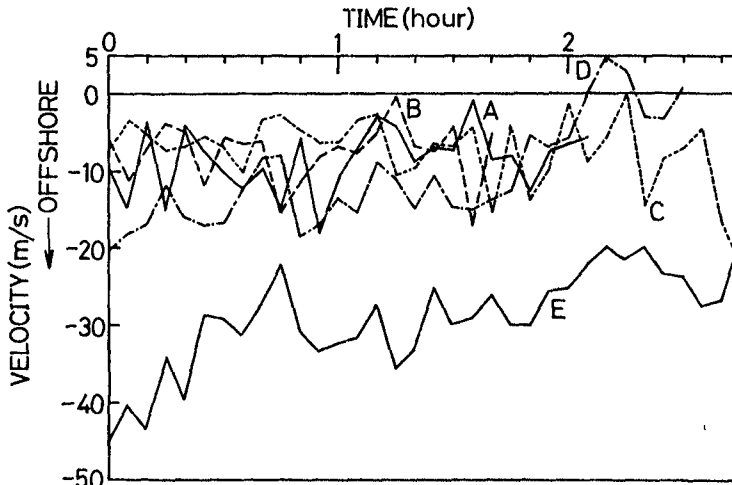


Fig. 14 Changes of mean velocity of on-offshore component in 5 minutes.

structure of the mean velocity in the surf zone. However, comparing with the experimental results of the mean velocity on the constant sloping beach which were measured by means of a laser doppler velocimeter ( Nadaoka et al. 1982 ), we can see the feature of that the horizontal and vertical mean velocities below the trough level of the incident waves are offshoreward and downward respectively everywhere.

If we assume that the suspended-load will be transported with the same velocity as fluid particles, a net transport of the suspended-load  $Q_{snet}$  passing through a vertical cross section can be estimated as follow:

$$Q_{snet} = \int_0^t \int_{-h}^{\eta} cu \, dz \, dt \tag{1}$$

where  $c$  is the concentration of suspended-load and  $u$  is the horizontal velocity. Since the vertical arrangement of the three electromagnetic current meters were limited, only the time integration is considered hereinafter. In the calculation of the net transport of the suspended-load, the concentration measured at  $C_3$  is used because it is judged based on the analog record of  $C_3$  that there is almost no effect of the entrainment of air bubbles due to the wave breaking on the concentration measured. As seen in Fig. 8, the bias voltage has been considered to be contained in the record of  $C_3$ . Then in the calculation, the concentration is corrected as that the minimum concentration becomes to be 0ppt in each observation case.

The time integration in eq.(1) is conducted numerically with the digital data of both the horizontal velocity component and the concentration of 0.5 second interval which is the mean values of every 5 digital data of 0.1 second interval. The solid lines in Fig. 15 show the accumulation of the net transport of the suspended-load in each

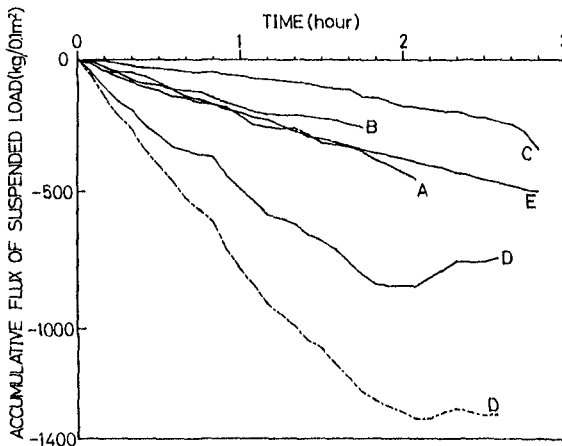


Fig. 15 Accumulation of net transport of suspended-load

observation case. A horizontal axis is for a lapse time and a vertical one is for the accumulation of the net transport passed through the vertical cross section of 1 meter in longshore length and 0.1 meter in height. The accumulation of the net transport was negative, offshoreward, in all cases and the absolute value of it became large in the order of C, B, E, A, D. In the case of D, the onshore net transport occurred in the final 40 minutes because the absolute quantity decreased.

By using the mean velocity and the mean concentration in 5 minutes, the time integration is conducted for D and the result is shown with a dashed line in Fig. 15. The absolute quantity of the dashed line for D is larger than that of the solid line for D. This difference in the final accumulation is considered to be due to that the concentration of the suspended-load is higher when the direction of the current is onshoreward. The same tendency of the difference between the results of the different calculations is also noticed in the case of A, but the difference is small, being about 10 percent. In the remaining cases, the results of the different calculations are almost the same each other.

The net transports of the suspended-load per one minute, which can be estimated by the slope of the tangent to the solid curves in Fig. 15, are shown with closed arrows in Fig. 16, by taking into account the relative distances from the shoreline to the observation point. In the upper part of Fig. 16, the mean concentrations at  $C_3$  during 10 minutes are

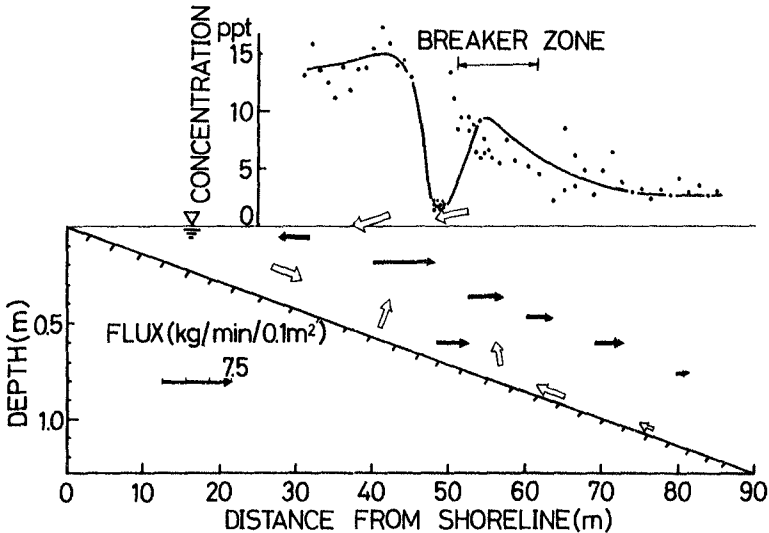


Fig. 16 Mean concentration at  $C_3$  in 10 minutes and net transport of suspended-load.

also shown. As seen in this figure, the directions of the net transport of the suspended-load are offshoreward except at the location nearest to the shoreline. These offshoreward net transport should cause the considerable change of the bottom profile. The bottom profile, however, scarcely changed during the field observation. Then, we cannot help considering the onshoreward transport at the other points of the observation point.

Let's examine the location where the onshoreward net transport of the sand occurs. In the outside of the surf zone where the bed-load is predominant, the skewness of the velocity fluctuation becomes greater to the breaker zone from the offshore due to the wave shoaling, which makes the tracers on the sea bottom to move onshoreward ( Nadaoka et al. 1982 ). Therefore, it is considered that the bed-load should be transported in the onshore direction in the outside of the surf zone.

In the surf zone, the skewness of the velocity fluctuation becomes smaller to the shoreline and the direction of the mean velocity is offshoreward near the sea bottom, and the tracers on the sea bottom are transported to the breaker zone ( Nadaoka et al. 1982 ). Therefore it is difficult to consider the onshoreward transport of the bed-load near the sea bottom. The onshoreward net transport of the suspended-load in the upper layer seems to be rather the most probable. This is because the concentration of the suspended-load in the upper layer becomes higher when the wave crest passes ( Tanaka et al. 1979 ) and the detailed measurement in the flume by means of a laser doppler velocimeter shows that the mean velocity above the level of the wave trough is onshoreward ( Nadaoka et al. 1982 ). As seen in Fig. 16, the net transport of the suspended-load is onshoreward at the location nearest to the shoreline or nearest to the mean water surface which located at the onshore-side of the final breaking zone. This evidence supports the above consideration. By considering the positions of both the breaker zone and the final breaking zone, the directions of the net transport of the sand inferred are shown with opened arrows in Fig. 16.

The mean concentration of the suspended-load is about 7 to 8ppt in the breaker zone and about 15ppt in the final breaking zone, respectively. These results agree approximately with the former ones obtained by the direct sampling of the suspended-load in the field ( Tanaka et al. 1979 ). The mean concentration around the offshore-side peak of it distributes asymmetrically with respect to the breaker zone, decreasing gradually offshoreward. This is considered to be because the sand suspended in the breaker zone is transported in the offshore direction by the mean velocity of the same direction.

## 7. CONCLUSIONS

The field observation was carried out at Ooarai Beach in

Japan, in order to understand the relationships between the fluid motion due to the incident waves and the concentration of the suspended-load. Both the fluid motion and the concentration have been continuously measured at the same time in the surf zone. The main two conclusions obtained in this paper are as follows:

The mean concentration of the suspended-load is high in the final breaking zone and in the breaker zone. In the final breaking zone, the concentration fluctuates with the period of the incident waves. On the other hand, it fluctuates with the period longer than 40 seconds in the breaker zone and it becomes high when the current is offshoreward.

The directions of the net transport of the suspended-load measured in the middle layer in and near the surf zone are offshoreward. For this transport of the sand, the compensatory transport of the sand is inferred such as that the bed-load is onshoreward at the outside of the breaker zone and the suspended-load is onshoreward in the upper layer in the surf zone.

In the field observation, the fluid motion and the concentration of the sand were measured only at one fixed point. In order to examine the relationships between them in more detail, it is necessary to measure them at many points at the same time. The effect of the longshore currents on the suspended-load and the mechanism of the suspension of the sand from the sea bottom are subjects for a future study.

In the field observation, the authors received kind assistances from Mr. Kazuo Nadaoka, Tokyo Institute of Technology, and the member of the Littoral Drift Laboratory, Port and Harbour Research Institute. The authors should like to express their grateful thanks to them.

#### REFERENCES

- 1) Brenninkmeyer, B. M., 1974 : Mode and period of sand transport in the surf zone, Proc. 14th Int. Conf. on Coastal Eng., pp.812-827.
- 2) Nadaoka, K. and T. Kondoh, 1982 : Laboratory measurement of velocity field structure in the surf zone by LDV, Coastal Eng. in Japan, 25, pp.125-145.
- 3) Tanaka, N., K. Katoh and K. Nadaoka, 1979 : Distribution of suspended-load in the surf zone, Proc. of 26th Conf. on Coastal Eng. in Japan, pp.182-186 ( in Japanese ).
- 4) Wright, L. D., R. T. Gusa and A. D. Short, 1982 : Dynamics of a high-energy dissipative surf zone, Marine Geology, 45, pp41-62.

## CHAPTER ONE HUNDRED TWENTY FIVE

### SEDIMENTATION IN DREDGED CHANNELS AND BASINS.

#### PREDICTION OF SHOALING RATES

C.M.Vicente <sup>1)</sup> and L.P.Uva <sup>2)</sup>

#### 1 - ABSTRACT

A method is presented for predicting shoaling in dredged channels and basins where deposition of finer sediment fractions carried in suspension by tidal currents occurs.

The method is based on the analysis of hydrographic surveys of different dates, which show the hydrographic evolution of dredged areas located in the site or in its vicinity. It can also be applied to experimental dredged pits.

Results obtained from the analysis of surveys are worked out by using mathematical expressions deduced from a simplified hypothesis, empirically based. Parameters are determined which can be used to predict shoaling either when new dredgings are made or when previously dredged sites are deepened.

#### 2 - DESCRIPTION OF METHOD

The basic assumption, of empirical nature, considers that the shoaling rate is proportional to the relative bottom elevation. This proportionality is expressed by

$$dC/dt = K(C_e - C) \quad 1)$$

where:

$C$  is a variable that represents the different bottom elevations at instant  $t$ ;  $C_e$  is a constant that represents the bottom natural equilibrium elevation in the zone studied, and  $K$  is a constant sedimentation coefficient that expresses the proportionality already mentioned.

---

1) Research Officer, Laboratório Nacional de Engenharia Civil, Av. do Brasil, 101; 1799 Lisboa Codex, Portugal.

2) Research Assistant, Laboratório Nacional de Engenharia Civil, Lisboa, Portugal.

To establish this assumption three aspects were considered which experience in the field of the maintenance of dredged zones in estuaries has shown to be very general:

- Sedimentation occurs whenever dredging is carried out to make deeper a zone previously in natural equilibrium;
- The sedimentation rate increases as a function of the thickness of the dredged layer;
- The bottom tends to shoal back to its natural equilibrium elevation corresponding to the situation prior to the first dredging operation whenever maintenance dredging is discontinued for a sufficient number of years.

When applying the method it is assumed that the natural equilibrium elevation  $C_e$  and the sedimentation coefficient  $K$  are constant throughout the zone under analysis and do not significantly vary in the course of time. So that this may be true, the following conditions seem to be required:

- The zone analysed must not be too large so that there can be approximate uniformity of the characteristics of sediments in suspension and of hydrodynamic conditions, concentrations and salinities.
- The time interval between two surveys must not be less than one year so that the semidiurnal and fortnightly tidal variations as well as the seasonal variations which hydrodynamic conditions, concentrations and salinities ordinarily present can be eliminated or markedly filtered.

By integrating equation 1), one obtains:

$$C = C_0 + (C_e - C_0) \cdot (1 - e^{-Kt}) \quad 2)$$

This expression is graphically represented by a family of curves, each one giving the time variation of a point of the bottom with the initial generic elevation  $C_0$  (Fig. 1).

The existence of a curve for each initial elevation  $C_0$  enables expression 2) to describe the evolution of a zone with different bottom elevations. The shoaling rate decreases as elevation  $C$  increases, the evolution of erosion prone zones located above natural equilibrium elevation ( $C > C_e$ ) being also reproduced.

The family curves have the elevation  $C_e$  as asymptote.  $C_e$  represents the elevation to which all points at different depths will tend if they are let to evolve naturally during a sufficiently long period.

From expression 2) it may be deduced that, if the evolution of each point in a set follows a family curve, then the mean elevation of that set will also be represented by one of the curves.

It is of interest to compare expressions 1) and 2) with other expressions and empirical methods described in the technical literature on this subject.

A) Lyakhnitsky and Smirnov [2] presented a shoaling coefficient similar to  $K$ . It was defined by

$$\epsilon = \frac{S}{\Delta h}$$

where  $S$  is the mean thickness of the silt layer settled to the bottom of the channel during one year, and  $\Delta h$  is the thickness of the dredged layer.

B) The Balanin formula presented by Djunkovski and Smirnov [1] describes the time variation of shoaling in a dredged channel. It can be expressed through

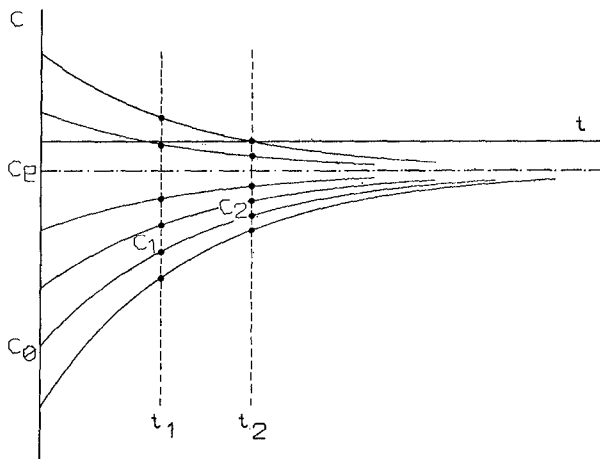


Fig. 1 Family of curves  $C=C_0+(C_e-C_0)(1-e^{-Kt})$



$$h_t = \frac{1 - (1-p)^t}{(1-p)^t} \cdot (H - H_0)$$

where

$h_t$  is the thickness of the sediment deposit after  $t$  years;  
 $H_t$  is the channel depth;  
 $H_0$  is the initial natural depth;  
 $p^0$  is a coefficient characteristic of sedimentation at the place in question.

If  $t=1$  year, we obtain

$$\frac{h}{H - H_0} = \frac{p}{1-p}$$

which shows that with Balanin's formula the shoaling rate ( $h$ ) is proportional to the thickness of dredging, that is, to its depth with reference to the bottom natural equilibrium elevation ( $H - H_0$ ), as established in 1).

C) Perestrelo [3] in his studies of shoaling of dredged basins in the Tagus estuary empirically fitted exponential curves expressed as in 2), to the points that showed the time evolution of the mean bottom elevation.

This author used this expression only to characterize dredged zones of approximately constant depth. He also considered that, contrary to the present method, the shoaling coefficient depends on the dredged depth.

D) One of the empirical procedures used in USA and cited by Trawle [4] considers the shoaling rate to be proportional to the area of the dredged channel section, measured below the bottom natural equilibrium elevation. This procedure agrees with expression 1) if the section can be considered nearly rectangular, i. e., when the channel bottom width is much larger than the width of its side slopes.

From the analysis of expression 2) it can be concluded that there are two procedures to obtain the values of  $K$  and  $C_e$  which characterize the family of curves (Fig. 1):

- a) From the evolution of mean elevation of a deep zone;
- b) From the variation between times  $t_1$  and  $t_2$ , of the elevation of a set of points of a zone with varied depths.

Using procedure a) one immediately extracts parameters  $K$  and  $C_e$  from the exponential equation which best fits the evolution of bottom mean elevation.

Using procedure b) parameters are obtained as follows: let  $t_1$  and  $t_2$  ( $t_1 < t_2$ ) be the dates of the two surveys, and  $C_1$  and  $C_2$  elevations at times  $t_1$  and  $t_2$  respectively. Then from 2) we have:

$$C_2 = C_1 + (C_e - C_1) \cdot (1 - e^{-K(t_2 - t_1)}) \quad \text{i.e.}$$

$$(C_2 - C_1) = A C_1 + B$$

In case the basic assumption holds, the straight line indicated should fit shoaling at different depths. The straight line coefficients are:

$$A = e^{-K(t_2 - t_1)} - 1$$

and

$$B = (1 - e^{-K(t_2 - t_1)}) \cdot C_e$$

From coefficients  $A$  and  $B$  one obtains parameters  $K$  and  $C_e$ .

### 3 - APPLICATIONS

Both procedures were applied. Procedure a) was applied to the evolution of the mean elevations of two zones. Data concerned Macao outer harbour in the south coast of China (Fig. 2) and a dredged basin in the Tagus estuary in the west coast of Portugal.

Both sets of data correspond to periods during which no main tenance dredging was carried out. To these data could be fitted exponential regression curves such as those already mentioned, and high correlation coefficients were obtained (Figs. 3 and 4). Data used in Fig. 4 were taken from Perestrelo's work [3] referred to above.

Procedure b) was applied in three sites: three applications in a channel of Aveiro lagoon (Mira channel) located in the west coast of Portugal (Fig. 5); one in a dredged channel in the Tagus estuary (Fig. 6); one in Macao, in the Ka-Ho experimental dredged pit (Fig. 2).

The calculation was as follows: a mesh was established with about one thousand points, equally located in the two hydrographic surveys of dates  $t_1$  and  $t_2$  to be compared; the points were grouped according to the elevation ranges of the earlier survey; in each range the mean values of elevations  $C_1$  and of the corresponding shoaling ( $C_2 - C_1$ ) were determined; the regression line best fitting the set of points so defined was determined; parameters  $K$  and  $C_e$  were determined from the coefficients of the lines following the expressions indicated.

In Figs. 7 to 11 the results of instances of application corresponding to such grouping are presented. The amplitude of each range is 0.20 m.

The number of points in each range varied; that is why weighted values were considered in the linear regression. This aspect is clearly shown in the example of Table 1. Notice that the largest deviations from the fitted line were found in ranges to which corresponded a small number of bottom points.

The hydrographic surveys were made at time intervals varying between 1 and 6 years. During those intervals no maintenance dredging was made.

Linear regression was also established between variables  $C_1$  and  $(C_2 - C_1)$  by considering the points not grouped (Examples in Figs. 12 and 13).



Fig. 2 Location map of Macao - Macao outer harbour and Ka-Ho experimental dredged pit.

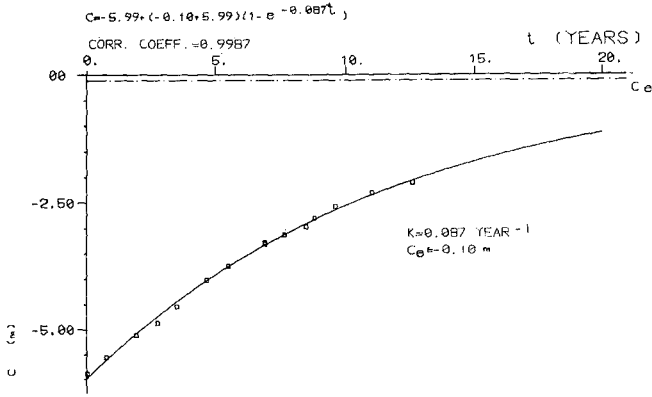


Fig. 3 Application of procedure a). Macao outer harbour.

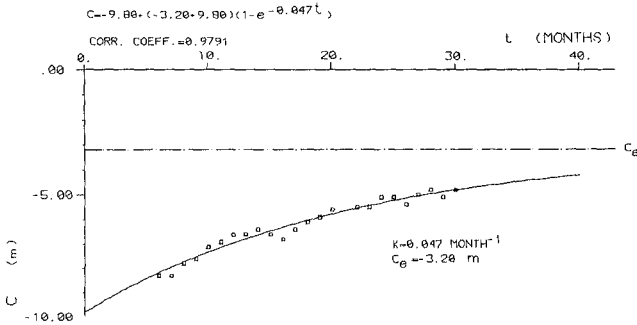


Fig. 4 Application of procedure a) to a dredged basin in the Tagus estuary.

Application of the procedure b) brought to light the following aspects:

- It was always possible to establish a good linear correlation between the mean values of depth  $C_1$  and shoaling ( $C_2 - C_1$ ). From the line obtained one could deduce with close approximation the mean shoaling for sets of points contained in each depth range.
- Higher correlations were obtained when surveys were made at larger time intervals.
- In the case of Aveiro lagoon for which three surveys of the same zone were available,  $K$  and  $C_e$  were found to take very close values in the two successive time intervals defined by these three surveys. In the periods 1975-80 and 1980-81,  $K$  values were found to amount to 0.108 and 0.121  $\text{year}^{-1}$ , whereas  $C_e$  values were 1.39 and 2.00 m.

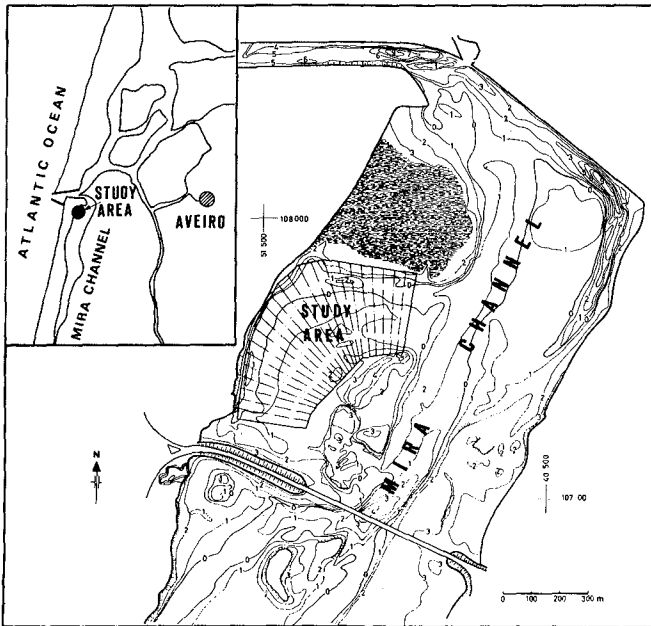


Fig. 5 Location map of Mira channel - Aveiro lagoon.

- A study of the distributions of deviations between shoaling values observed and those calculated by the regression line, considering points not grouped, showed that distributions were similar in all cases analysed regardless of the place and of the time interval between two surveys (Examples in Figs. 14 and 15).

Ninety per cent of the deviations fell in a range of  $\pm 50$  cm. It is assumed that  $\pm 25$  cm is the range of deviations corresponding to inaccuracies in surveys and in their comparison. The remainder is believed to be due to the approximations inherent in the basic assumption which disregards the influence of other variables besides depth influencing the shoaling rate.

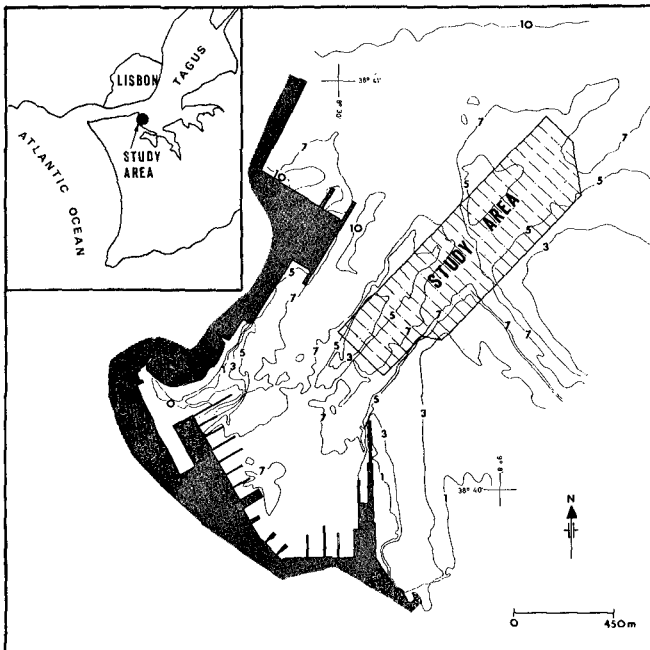


Fig. 6 Location map of a dredged channel in the Tagus estuary.

Table 1 Application of procedure b). Mi-  
ra channel (Aveiro lagoon). Sur-  
veys: Sep.-Oct.1975 and Sep.1981.  
Range 0.20 m.

ELEVATION RANGE FIRST SURVEY (M)	MEAN ELEVATION FIRST SURVEY (M)	MEAN ELEVATION SHOALS (M)	NUMBER OF POINTS
-3.40	-3.85	3.31	1
-3.20	-3.09	1.93	1
-2.80	-2.71	1.72	4
-2.80	-2.71	1.72	0
-2.60	-2.59	2.11	0
-2.40	-2.27	1.58	4
-2.20	-2.08	1.62	11
-2.00	-1.91	1.71	13
-1.80	-1.69	1.53	27
-1.60	-1.50	1.44	22
-1.40	-1.39	1.44	27
-1.20	-1.09	1.29	39
-1.00	-0.92	1.22	31
-0.80	-0.71	1.11	41
-0.60	-0.54	1.09	41
-0.40	-0.31	0.94	35
-0.20	-0.12	0.82	33
0.00	0.09	0.75	33
0.20	0.28	0.65	39
0.40	0.49	0.59	37
0.60	0.71	0.46	46
0.80	0.90	0.33	82
1.00	1.11	0.18	73
1.20	1.30	0.14	88
1.40	1.48	0.04	66
1.60	1.69	0.06	96
1.80	2.00	-0.06	38
2.00	2.08	-0.21	38
2.20	2.27	-0.27	8
2.40	2.44	-0.31	8
2.60	2.60	-0.13	4
2.80	2.87	-0.58	6
3.00	3.32	-0.80	2
3.20	3.52	-0.59	0
3.40	3.65	-0.25	0
3.60	3.80	-0.00	0
3.80	3.80	-1.00	1

TOTAL NUMBER OF POINTS 1025

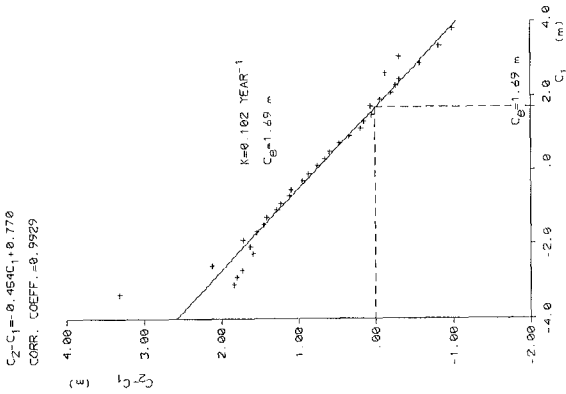


Fig.7 Application of procedure b). Mi-  
ra channel (Aveiro lagoon). Sur-  
veys: Sep.- Oct.1975 and Sep.1981.  
Range 0.20 m.

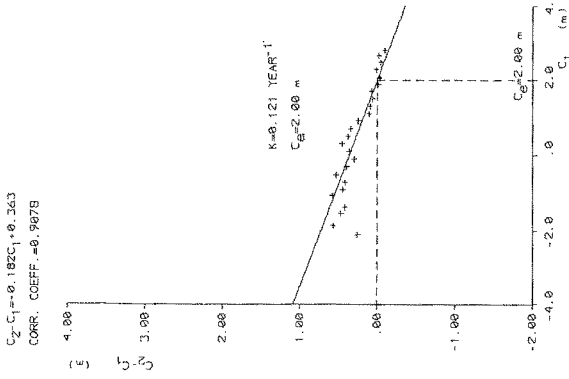


Fig.8 Application of procedure b). Mira channel (Aveiro lagoon). Surveys: Sep.- Oct., 1975 and Jan., 1980. Range 0.20 m.

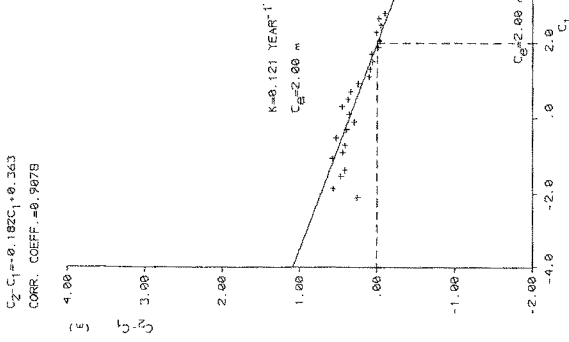
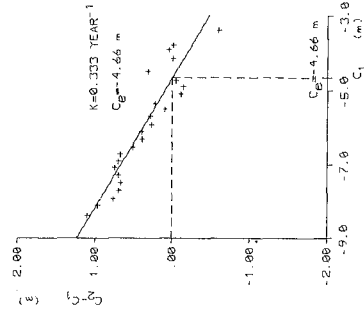


Fig.9 Application of procedure b). Mira channel (Aveiro lagoon). Surveys: Jan. 1980 and Sep. 1981. Range 0.20 m.



$C_2 \cdot C_1 = -0.281 C_1 - 1.321$   
 CORR. COEFF. = 0.8991



$C_2 \cdot C_1 = -0.069 C_1 - 0.316$   
 CORR. COEFF. = 0.8388

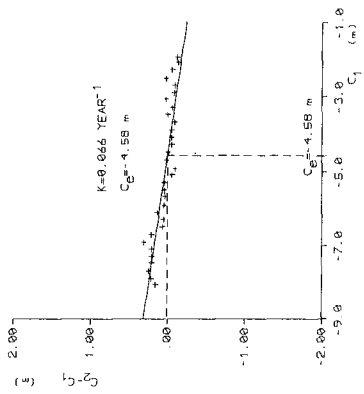
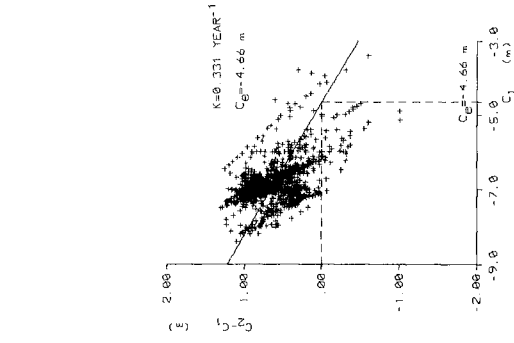


Fig.10 Application of procedure b) to a dredged channel in the Tagus estuary. Surveys: Oct. 1978 and Nov. 1979. Range 0.20 m.

Fig.11 Application of procedure b). Ka-Ho (Macao). Surveys: Apr. 1974 and Apr. 1975. Range 0.20 m.

$C_2 \cdot C_1 = 0.282C_1 - 1.312$   
 CORR. COEFF. = 0.5259



$C_2 \cdot C_1 = 0.282C_1 - 1.312$   
 CORR. COEFF. = 0.5259

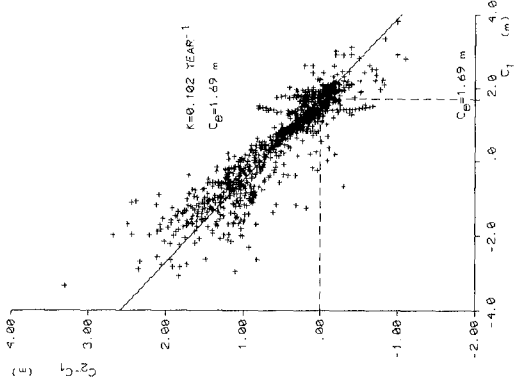


Fig.12. Application of procedure b). Mira channel (Aveiro lagoon). Surveys: Sep.-Oct. 1975 and Sep. 1981. Points not grouped.

Fig.13 Application of procedure b). Ka-Ho (Macao). Surveys: Apr. 1974 and Apr.1975. Points not grouped.

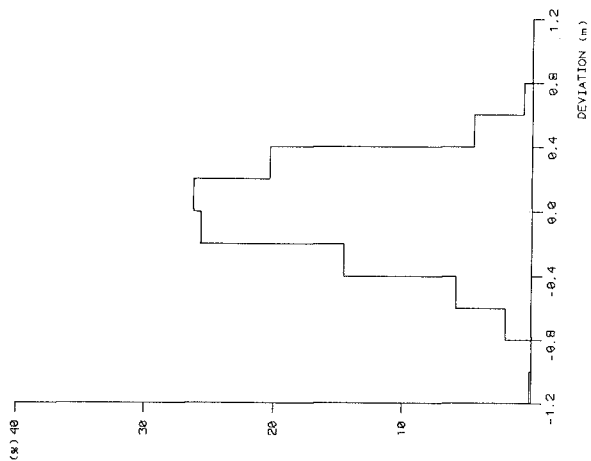


Fig. 15 Deviation histogram. Ka-Ko (Macao). Surveys: Apr. 1974 and Apr. 1975. Points not grouped.

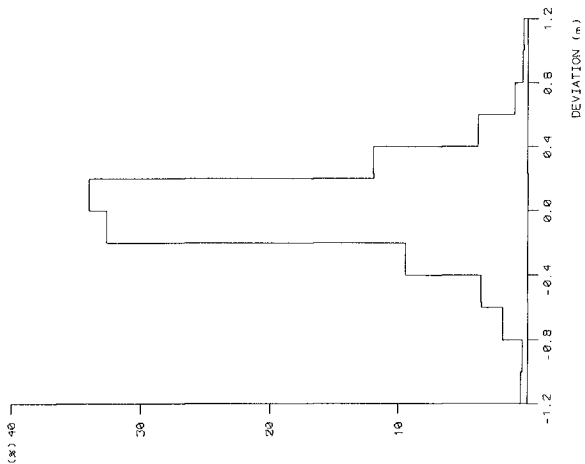


Fig. 14 Deviation histogram. Mira chanel (Aveiro lagoon). Surveys: Sep. Oct. 1975 and Sep. 1981. Points not grouped.

The occurrence of identical deviation distributions in all the cases analysed explains why the correlation coefficient improved as the time interval between two surveys increased. With large time intervals shoaling takes higher values, and the relative value of deviations decreases. This aspect is shown in Figs. 12 and 13.

- The fact that high correlations are usually not found except when referred to mean values of the two variables will not permit as a rule to predict shoaling accurately enough at a given point but only in a zone or at a numerous set of points of the bottom. This limitation does not seem to be very inconvenient since the practical purpose of the method is to predict the evolution either of reaches only or of the whole of dredged channels and basins.

#### 4 - CONCLUSIONS

High correlations could be established between mean values of depth and of shoaling in different dredged zones where deposition of finer sediment fractions carried in suspension by tidal currents occurs. In every case data were fitted by empirically based expressions that were worked out to represent the variation of bottom elevations with space and time.

The results of the comparison of surveys can be used to predict volumes of maintenance dredging of channels and basins to be established or deepened in the zone under study. It is assumed that this zone will not be subjected to long term variations of sedimentation characteristics.

The procedure to be used for this prediction consists in the definition of the sedimentation coefficient  $K$  and equilibrium elevation  $C_0$ , based on the analysis of two or more surveys. Once these parameters are known, annual maintenance rates for different alternative dredging elevations  $C_0$  can be estimated by using the expression derived from 2), with  $t = 1$  year.

It is worth mentioning that procedure b) requires only two surveys provided they are carried out within an interval of at least one year during which no dredgings are made. Such a feature makes it largely adequate to practical use due to ordinary limitations as regards field data to characterize shoaling conditions.

## 5 - REFERENCES

[1] - Djunkovski, N.N. and Smirnov, G.S., 1957: XIX International Navigation Congress. London. 1957. Section II. Communication 3.

[2] - Lyakhnitsky, V.E. and Smirnov, G.S., 1961: XX International Navigation Congress. Baltimore, 1961. Section II. Subject 2.

[3] - Perestrelo, J.F., 1971: Comportamento de canais e bacias dragados em fundos lodosos de estuários. Instituto Superior Técnico. Lisboa.

[4] - Trawle, M.J., 1981: Effects of depth on dredging frequency. Report 2. Methods of estuarine shoaling analysis. U.S. Army Waterways Experiment Station. Technical report H-78-5.

## CHAPTER ONE HUNDRED TWENTY SIX

### SURVEY TECHNIQUES USED TO MEASURE NEARSHORE PROFILES

Christopher G. Gable (1) and Jerome R. Wanetick (2)

#### Abstract

The three most common survey techniques used to measure nearshore profiles are (1) conventional boat-sonic depth sounder; (2) hydrostatic pressure profiler; and (3) the self powered Coastal Research Amphibious Buggy (CRAB). Theory of operation and methodology used for each technique are summarized and evaluated. Three separate field tests using survey data from each technique are evaluated for system repeatability. Data reduction, sea surface correction, and filtering methods for boat-depth sounder survey data are examined.

#### 1. Introduction

The measurement of nearshore profiles is extremely important to coastal engineers concerned with navigation and shore protection structures, cross and longshore sediment transport, and seasonal shoreline changes. Accurately surveying the nearshore region between a relatively stable point on the beach to a depth of little or no elevation change is a frequent problem to the coastal engineer. As described by Seymour (1984), in many coastal engineering applications of nearshore surveying, the absolute elevation is not as important as the changes in elevation since the previous profile. Wave orbital velocities responsible for mobilizing the sediment decrease with increasing water depth, thus the amount of change in sand elevation is expected to decrease with distance offshore. In general, the bottom slope decreases with offshore distance such that the small changes in deeper water are integrated over a large area resulting in very significant sand volume changes. For example, a net change of 30,000 cubic meters over approximately one kilometer of beach represents an average change in depth of only 3 cm. This results in the paradox that the greatest accuracy of measurement is required at the greatest distance away from the known reference elevation.

Surveying the dry portions of the beach to a depth of 1 meter use conventional land surveying methods, using rod, level, and chain techniques with sufficient accuracy of plus or minus 1 cm. Surveying the underwater portion of nearshore beach profiles (-1 to -10 meters) has presented significant accuracy problems. The boat-depth sounder

- (1) Associate Development Engineer, Ocean Engineering Research Group, Scripps Institution of Oceanography, University of California, La Jolla, CA 92093
- (2) Development Technician, Ocean Engineering Research Group, Scripps Institution of Oceanography, University of California, La Jolla, CA 92093

method is unable to operate thru the active surf zone region (-1m to -3m depth) and uses the sea surface as the vertical datum. Surface waves with a broad range of frequencies must be filtered out of the profile. Two other recently developed survey systems eliminate the sea surface reference uncertainty by measuring the bottom profile directly. The Hydrostatic Profiler, developed at Scripps Institution of Oceanography, is a portable system using the hydrostatic pressure principle to measure vertical differences between a pressure sensor that follows the profile on the ocean bottom and a reference sensor on the shoreline. The two pressure sensors are connected by a fluid filled tube and horizontal distance determined by measuring the extension of the tube. The Coastal Research Amphibious Buggy (CRAB) of the U.S. Army Coastal Engineering Research Center (CERC) is a self-powered stable platform that traverses the ocean bottom carrying a laser reflector above water. A total station survey instrument located over a known bench mark on land, shoots the reflector at discreet points to obtain precise X,Y,Z data from the dry beach to a depth of 10 meters.

This paper will briefly summarize and evaluate each of these survey techniques. Theory of operation, methodology, advantages, limitations, accuracy in repeatability, and depth sounder data filtering methods using actual field data are discussed.

## 2. Boat-Depth Sounder Method

### 2.1 Theory of Operation and Field Techniques

Surveys of the dry beach out to wading depth use the conventional rod, level, and chain technique. By selecting times of low tide, wave, and current conditions, it is possible to extend the rod and level technique seaward to a depth of about 1 meter with an accuracy of plus or minus 1 cm. The nearshore bathymetry (-1 to -10 meters) is usually measured by some type of Automated Bathymetry System (ABS). An ABS consists of state-of-the-art electronic equipment including a sonic depth sounder, depth digitizer, range-range positioning navigation system, printer, data logger, and cassette recorder. The ABS is secured to a small survey boat (Figure 1) and requires one boat operator, one field electronic engineer, and a minimum of two experienced surveyors for proper operation. Boat-depth sounder surveys are best performed during the highest possible tide to provide both overlap and data quality control with the rod and level survey. The general procedure for conducting these overlapping surveys is described in Nordstrom and Inman (1975) and shown in Figure 2.

Both the depth sounder and digitizer measure and record the elapsed time interval between transmission of an acoustic pulse and receipt of a return echo from the seafloor. To precisely relate this time interval to water depth, a speed of sound adjustment is made at the survey site. This adjustment is accomplished by conducting "bar" checks, a process of lowering a target ("bar") on a calibrated line to known depths below the depth sounder transducer. Both the depth sounder and digitizer are adjusted to display the proper depth precisely.

To assure that the survey boat remains on the correct range azimuth and to duplicate each survey line monthly or seasonally; a transit and



Figure 1 Automated Survey System

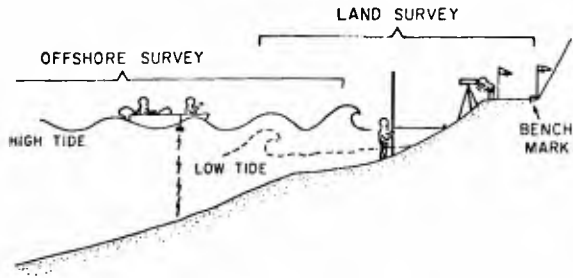


Figure 2 Survey Overlapping Procedure  
(from Nordstrom and Inman, 1975)



electronic positioning responder is set over each profile bench mark. The transit operator gives course corrections to the boat operator via FM radio as shown in Figure 3. Two range survey targets are placed on-range on the beach to provide the boat operator a visual line. Offshore distance is measured directly from the responder located over the bench mark. The second positioning responder is located over a bench mark a sufficient distance up or down the beach to provide an accurate measure of the distance off-line at each position fix.

An Automated Bathymetry System used for an extensive series of nearshore surveys for the Nearshore Sediment Transport Study (NSTS) in Santa Barbara, California, is described in detail by Dean et al. (1982) and Gable (1981).

Bruno and Gable (1976) describe a series of nearshore surveys made at Channel Islands Harbor, California, using a more primitive but widely used "standard" survey method. For this method the survey boat operator is directed along the profile azimuth visually with on-line targets and course corrections updated via FM radio from an on-shore sextant operator. Every ten seconds, the analog depth strip recorder is marked and vessel position recorded on a plane sheet via plane table and alidade as shown in (Figure 4).

These boat supported survey systems, which use the sea surface as the vertical datum, suffer from the presence in the analog and digital record of surface waves with a broad range of frequencies. The measurement of the instantaneous sea level needed to adjust the depth sounder record is subject to numerous errors. These errors include the measurement of tide levels at locations several miles away, high frequency wind driven waves causing water level set-up, and waves of longer period (1-15 minutes) associated with surf beat and trapped edge waves.

## 2.2 System Evaluation

The advantages of using the boat-depth sounder techniques include: (1) the ability to survey over the sand-rock interface; (2) precise X,Y position with plus or minus 3 meter accuracy using microwave positioning equipment; (3) continuous depth sounder, analog and/or digital record; (4) proven electronic and survey equipment readily available for purchase or lease; and (5) after initial set up, rapid successive profile data is collected.

The disadvantages include: (1) wave and sea level uncertainties; (2) the inability to detect small relief features due to wave motion and data filtering techniques; (3) the inability to accurately survey thru the active surf zone; (4) the technique is highly labor and capital intensive; and (5) vertical motions of the boat relative to mean sea level, caused by waves of any frequency, introduce errors that are difficult to remove objectively.

## 2.3 Repeatability Test and Filtering Techniques

To determine the system accuracy of the depth sounder survey method, a series of three repetitive surveys were run over the same range line on the same day. An Automated Bathymetry System of the type described previously was used to collect the depth sounder data. All data was collected from Range W-8 at Leadbetter Beach, Santa Barbara,



Figure 3 Course Correction Procedure



Figure 4 Plane Table Survey Procedure

California, on 25 February, 1980. within a 45 minute period. All depth sounder data presented in Figures 5-9 have been corrected for tide. The three depth sounder repeatability runs presented in Figure 5 is the raw digital depth data. The variance in the raw data increases with distance offshore and is very close to the measured sea surface variance with a significant wave height of 41 cm. The average range at the indicated distances is 20.1 cm. The general trend of the beach slope can be seen; however, all bottom detail is lost due to the high signal to noise ratio. If a running mean filter is used on each survey run (Figure 6), this signal to noise ratio and variance is significantly reduced. The average vertical range is decreased by almost a factor of three. Varying the number of points to be averaged over each iteration determines the best fit for each data set. Fifteen points per iteration provided the best fit for this particular data set. Most high frequency noise has been filtered; however, some low frequency noise still remains masking small bottom features that may actually exist. The variance can be reduced even further with a corresponding loss of bottom detail by averaging more points per iteration. In Figure 7, a classical least squares has been applied to the digitized distance-elevation pairs to fit a polynomial curve to each raw survey data run. A seventh order polynomial was found to best fit this data set. The variance at distance 200, 300, 400, and 500 meters is smaller than that of the running mean fit. The average range of the polynomial fit is half that of the running mean. Taking the simple average over a specified distance interval of all three raw data runs is a technique also routinely used by some investigators in an attempt to filter out the sea surface changes. As seen in Figures 8 and 9, the averaged survey data is more coherent but the signal to noise ratio is still quite large compared with the running mean and polynomial fits of these averaged data.

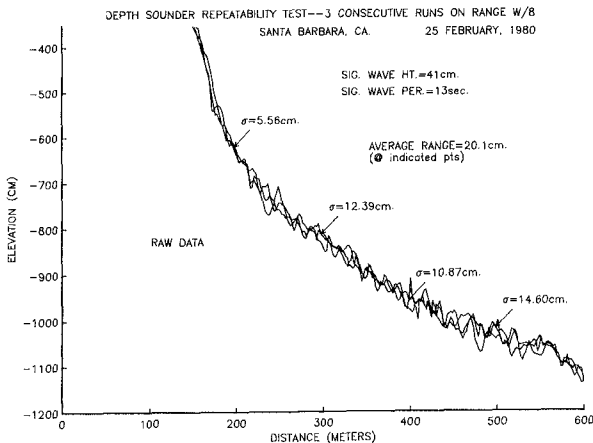


Figure 5 Raw Digital Depth Data

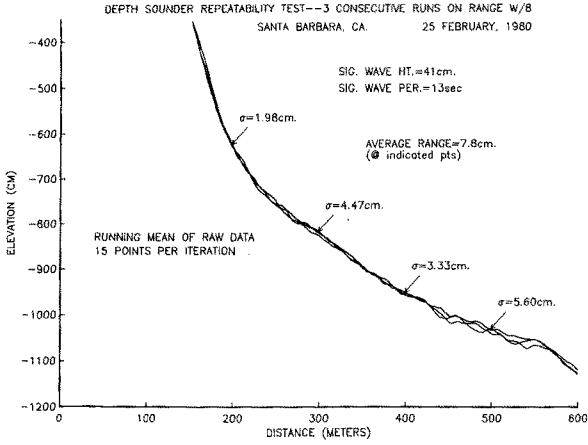


Figure 6 Running Mean of Raw Data

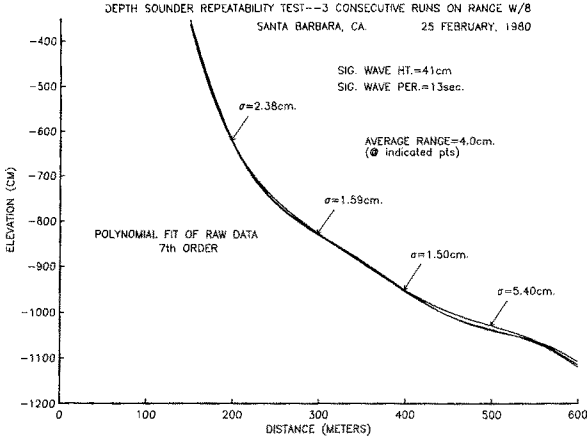


Figure 7 Polynomial Fit of Raw Data

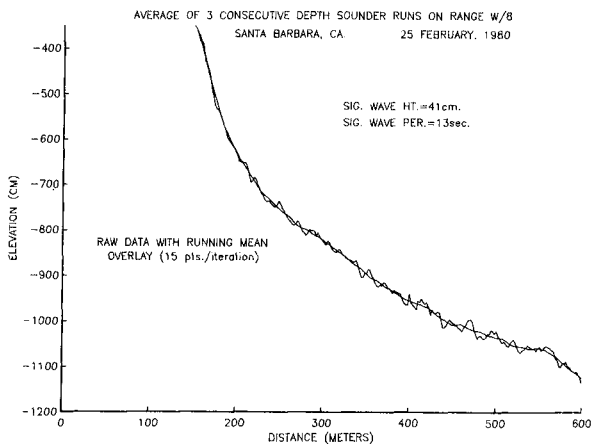


Figure 8 Averaged Raw Data with Running Mean Overlay

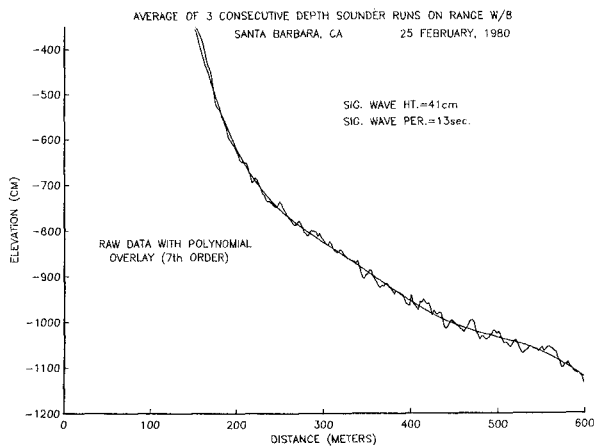


Figure 9 Averaged Raw Data with Polynomial Overlay

### 3. Hydrostatic Profiler Method

#### 3.1 Theory of Operation and Field Techniques

The hydrostatic profiler is a profiling system which uses the hydrostatic pressure principle to measure vertical differences between a pressure sensor that follows the ocean bottom and a stationary reference sensor on the beach. The two pressure sensors are connected by a fluid filled tube and the horizontal (offshore) distance determined by measuring the extension of the tube. A schematic of the profiler configuration and theory of operation is provided in Figure 10. The hydrostatic profiler has six main components: (1) a highly sensitive pressure transducer and thermistor assembly at each end of the cable; (2) a cable containing the necessary electrical conductors, strength members, and a fluid filled tube that provides a hydraulic path between the transducers; (3) a winch mounted into the bed of a four wheel drive truck to house the reference sensor and to store and retrieve cable (Figure 11), (4) a pinch wheel distance counter (Figure 12); (5) a sled to carry the profiling transducer (Figure 13); and (6) a portable data logger to record data from all sensors. Visual target cones are set on the beach designating the range azimuth to be followed. The profiler sled is towed offshore using an inflatable surf rescue boat (Figure 14). The boat must stay on the correct range azimuth while pulling the sled and cable out to maintain an accurate horizontal (longshore) position. The profiler sled is lowered to the ocean bottom at the desired offshore position or depth. The data logger is activated and the sled is automatically winched shoreward at specified increments (usually every 5 meters). At each distance increment the profiler sled is stopped and remains stationary for a 1 to 2 minute period. This stationary period is needed to average out pressure fluctuations in the tube caused by acceleration of the fluid while winching. The profiler is finally stopped at an offset point on the beach which was previously surveyed horizontally and vertically to a known bench mark. This offset point is the initial point from which the entire profile is referenced. The theory of operation, design specifications, calibrations, operational deployment, signal processing, and performance evaluation of the profiling system is described in detail by Seymour and Bothman (1984).

#### 3.2 System Evaluation

The advantages of using the hydrostatic profiler to measure nearshore profiles include: (1) the total elimination of sea surface elevation uncertainties by measuring the ocean bottom directly; (2) the ability to survey discreetly from deep water (~10m) through the active surf zone; (3) precise offshore distance measurements of plus or minus 1 meter and depth data of plus or minus 5 cm. (4) the profiling system is highly mobile, requires minimum manpower to operate, and can be easily transported to remote survey sites; and (5) small relief features (bars, troughs, etc.) are easily detected with very high resolution.

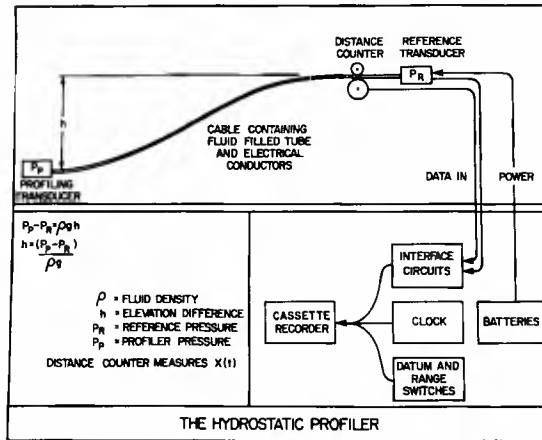


Figure 10 Schematic of Profiler Configuration (from Seymour and Bothman, 1984)



Figure 11 Cable Winch System on Four Wheel Drive Truck



Figure 12 Pinch Wheel Distance Counter and Winch System



Figure 13 Profiling Transducer Sled





Figure 14 Profiler Deployment

The disadvantages include: (1) the longshore position of the profiler is very dependent on the skill and quality of deployment; (2) the profiler sled and cable is dragged over the ocean bottom and can be easily caught on obstructions such as rock, reef, wreckage, or debris; (3) data quality decreases with high waves, strong currents, and steep beaches due to cable strumming and high signal to noise ratio; (4) the offshore distance is limited by a fixed cable length and (5) equipment set-up and surveying time for one profile line takes a minimum of two hours.

### 3.3 Repeatability Test

To determine system accuracy, a series of three repetitive surveys were run over Range 181 at the CERC Field Research Facility at Duck, North Carolina, on 25 July, 1984, within a six hour period. The environmental conditions were ideal for such a test with low wave and current conditions. The hydrostatic profiler sled was deployed offshore each time by CERC's CRAB. There was no attempt to reoccupy identical positions. Therefore, elevations were compared by linearly interpolating data at five meter distances.

As shown in Figure 15, the variance at distance 200 and 400 meters for the three runs is quite small. The variance of 8.54 cm at distance 300 meters is due to actual elevation change of the offshore bar-trough system. The average range for all three distances is 7 cm.

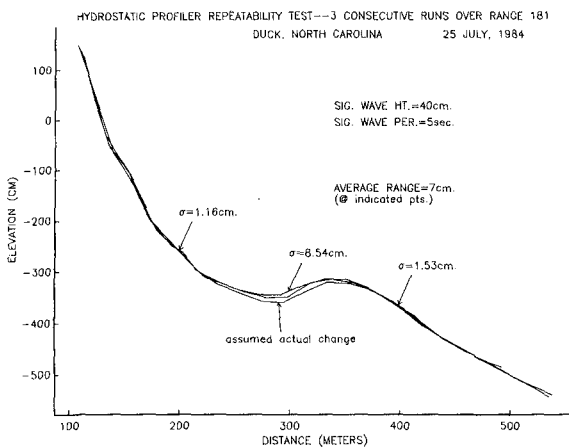


Figure 15 Hydrostatic Profiler Repeatability Test

#### 4. Coastal Research Amphibious Buggy (CRAB) Method

##### 4.1 Theory of Operation and Field Techniques

The CRAB is a 10.6 meter high vehicle which uses three hydraulically driven tires on the legs of a tall tripod (Figure 16). Power is supplied by an automobile engine on the platform above the maximum waterline. This vehicle, when combined with an electronic total survey station, allows rapid, accurate surveying of the surf zone and nearshore waters out to depths of 9 meters. The primary function of the CRAB is to support a prism cluster above water. The exact distance from the prism cluster to the bottom of the tripod wheels is measured precisely before each survey. Visual range targets are set on the beach designating the range azimuth the CRAB operator is to follow. A Zeiss Elta-2 electronic total survey station is set up over a known bench mark. This compact instrument contains an electronic distance meter, a self-reading electronic theodolite, a micro-processor, a rechargeable power supply, and an interchangeable solid-state memory. The instrument is aimed at the prism cluster mounted on the CRAB to obtain a data point (Figure 17). Within seconds the distance to the CRAB and the horizontal and vertical angles are automatically measured. The micro-processor instantaneously calculates the X,Y,Z coordinates of the position under the CRAB and stores them into memory. Direct instrument read-out allows the surveyor on-shore to help guide the CRAB operator in maintaining accurate horizontal position. Data points are measured discreetly along the profile range approximately every 10 meters. Each data point takes about 10 seconds to measure and one entire profile about 45 minutes to complete. A detailed description of the CRAB specifications, data processing, and system evaluation is provided in Birkemeier and Mason (1984).



Figure 16 CERC's Coastal Research Amphibious Buggy (CRAB)



Figure 17 Zeiss ELTA-2 Survey Instrument Sighting on CRAB

#### 4.2 System Evaluation

The advantages of using the CRAB profiling system include: (1) the total elimination of sea surface elevation uncertainties by measuring the ocean bottom directly, (2) the ability to survey discreetly from deep water (-10m) through the active surf zone; (3) precise instantaneous X,Y,Z data at discreet points; (4) ability to operate in high wave and strong longshore current conditions; (5) ability to conduct surveys with reduced long term cost, minimum manpower, and high accuracy of plus or minus 5 cm.

The disadvantages include: (1) the CRAB traverses over the ocean bottom and can easily be caught or damaged on obstructions such as rock, reef, wreckage or debris. (2) depth of profile is limited by fixed superstructure CRAB height of 11 meters; (3) high initial expense in CRAB construction and instrumentation purchase; (4) the size of the CRAB and cost of transportation make the system highly immobile and must be used for long periods within a limited geographic area; and (5) small relief features are not always detected due to wide wheel base.

#### 4.3 Repeatability Test

To determine system accuracy, a series of three repetitive CRAB surveys were run over Range 183 at the CERC Field Research Facility at Duck, North Carolina, on 8 July, 1982, within a 4 hour period. Environmental conditions were moderate with 70 cm significant wave height and 9 second significant period. Longshore current velocities were low. The CRAB made no attempt to reoccupy identical positions. Therefore, elevations were compared by linearly interpolating data at five meter distances. As shown in figure 18, the variance at distance 200, 400, and 700 meters is quite small. The variance of 15.52 cm between distance 100 and 200 meters is due to actual elevation change of the berm. The average range for all four distances is 11.5 cm.

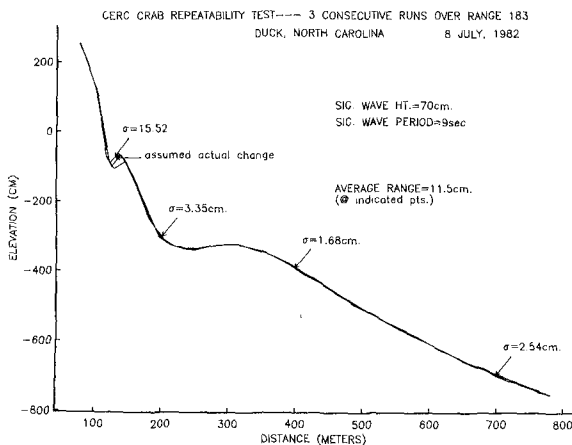


Figure 18 CRAB Repeatability Test

## 5. Discussion and Conclusion

The three survey techniques most frequently used to measure nearshore profiles are: (1) boat-depth sounder; (2) Hydrostatic Pressure Profiler; and (3) the Coastal Research Amphibious Buggy (CRAB). The sea sled technique, discussed by Sallenger et al. (1983), is presently used for special studies and not routine nearshore surveys. The sea sled is identical in principle to that of the CRAB; however, it is not self powered and is physically much smaller. Repeatability data from sea sled surveys was not available to include in this paper and therefore not discussed.

The boat-depth sounder technique is the most widely used and accepted method. All equipment is electronically proven and readily available worldwide. The field data collection and data processing techniques will vary with investigator. For example, surveys conducted to support Sea Grant's Nearshore Sediment Transport Study (NSTS) used a highly electronic automated survey system. To help filter out the effects of waves and low frequency oscillations, each profile line was surveyed three times and the depth and distance determined by averaging the values obtained over a five meter interval. The Army Corp of Engineers generally use electronic navigation equipment or a standard plane table technique for positioning with an analog or digital depth recorder. Each profile is surveyed only once and the raw data tabulated with no sea surface filtering whatsoever, or is manually hand smoothed. The classical least squares fit, running mean, and averaging techniques in filtering tide corrected depth sounder data, remove all bias and subjectivity that is inherent to the normal hand smoothing and manual digitizing techniques. However, due to the continual problem of using sea level as the vertical reference and correcting for both high and low frequency noise, depth sounder data will always possess a degree of uncertainty and ocean bottom detail will always be masked by sea level fluctuations. A highly controlled repeatability test conducted during small wave conditions using an automated survey system shows that the average range in digital depth was 20 cm.

As a result, depth sounder surveys are adequate for profile studies where gross seasonal changes or shoreline erosion trends are the goal. However, if confident measurements are required with fine detail and low volume error, such as sediment transport and bedform studies, the Hydrostatic Pressure Profiler or CRAB is highly recommended. The repeatability test for both of these survey systems show that the average range was less than 10 cm while all bottom detail was preserved. These systems follow the ocean bottom directly producing highly accurate detailed maps of the nearshore region.

Finally, it is acknowledged that the field data presented in this paper is not the ideal data set. Survey data from each technique was collected at different locations, times, and conditions. A future experiment has been designed to specifically address the repeatability of each technique simultaneously on the same beach.

## 6. Acknowledgements

The financial support provided by the Sea Grant Program and the Army Corps of Engineers is greatly appreciated. The authors would also like to thank W.A. Birkemeier of the CERC Field Research Facility for providing CRAB survey data and S.L. Elgar of Scripps Institution of Oceanography for providing valuable ideas on filtering depth sounder data.

## 7. References

Birkemeier, W.A., and C. Mason, 1984. "THE CRAB: A Unique Nearshore Surveying Vehicle", Journal of Surveying Engineering, Volume 110, No. 1, March, 1984.

Bruno, Richard O. and Christopher G. Gable: 1976. "Longshore Transport at a Total Littoral Barrier," Proceedings, 15th Coastal Engineering Conference, Honolulu, Hawaii, July 11-17, 1976.

Bruno, Richard O., Robert G. Dean, and Christopher G. Gable, 1980. "Longshore Transport Evaluations at a Detached Breakwater," Proceedings, 17th Coastal Engineering Conference, March 23-28, 1980, Sydney, Australia, Vol. II, pp. 1453-1475.

Dean, R.G., E.P. Berek, C.G. Gable, and R.J. Seymour, 1983. "Longshore Transport Determined by an Efficient Trap," Proceedings, Eighteenth Coastal Engineering Conference, 14-19 November, 1982, Cape Town, Republic of South Africa, Vol. II, pp. 954-968.

Gable, C.G., Ed., 1981. "Report on Data from the Nearshore Sediment Transport Study Experiment at Leadbetter Beach, Santa Barbara, California, January-February 1980. University of California, Institute of Marine Resources, IMR Ref. No. 80-5, 314 pp.

Sallenger, A.H., P. Howard, C. Fletcher, P. Howd, 1983: A system for measuring bottom profile, waves and currents in the high-energy nearshore environment. Marine Geology 51, pp. 63-76.

Seymour, R.J. and D.P. Bothman: 1984. "A Hydrostatic Profiler for Nearshore Surveying." Coastal Engineering, 8:1-14.

## CHAPTER ONE HUNDRED TWENTY SEVEN

### LONGSHORE VARIABILITY OF WAVE RUN-UP ON NATURAL BEACHES

R. A. Holman\* and A. H. Sallenger, Jr.\*\*

#### ABSTRACT

The longshore variability of wave run-up from a natural beach is examined using data from a large field experiment at the Field Research Facility in Duck, North Carolina, in October, 1982. Two particular runs were selected for intensive analysis. These were chosen to represent a dissipative and a reflective surf zone condition, so have Iribarren numbers 0.97 and 1.81 respectively. The dissipative data run showed much more uniform statistics in the longshore than did the reflective run. Also, the dissipative run was dominated by the infragravity band energy while the reflective run was dominated by the incident band. Selection of several important frequency bands for frequency-domain EOF analysis showed that the lower frequency peaks appeared to be associated with leaky modes (very long longshore wavelengths) and the pier had little influence. On the other hand, higher frequencies were clearly influenced by the pier in both amplitude and phase. An interesting subharmonic peak from the reflective run appeared to be a low (but not zero) mode standing edge wave.

A new technique, time exposure photography, is introduced. It allows the quick determination of longshore variability such as would be produced by a dominant standing edge wave. It can also be used to image offshore bathymetry and sand bar systems.

#### INTRODUCTION

Wave run-up, the time-varying motion of the water's edge relative to still water level, is generally considered composed of two components, the set-up and the swash. If we denote the time series of run-up as  $\eta_R(t)$ , then

$$\eta_R(t) = \bar{\eta} + R(t),$$

where  $\bar{\eta}$ , the time average of the time series, is the set-up and

\* Associate Professor, College of Oceanography, Oregon State University, Corvallis, OR, 97331.

\*\*United States Geological Survey, Menlo Park, CA, 94025.

$R(t)$  is the swash. Both of these quantities are of considerable interest to engineers. The combination of set-up and swash must be considered for the determination of safe set-back distances for structures on a coast. The velocities of the swash may provide the major erosive force on sediment or artificial structures.

While run-up at a point is a useful quantity to measure, it is longshore gradients of run-up which provide clues to some of the most interesting nearshore dynamics. Bowen (1969) showed how longshore gradients in set-up would force longshore currents, and so could generate rip currents at set-up minima. For the swash, it is the longshore phase relations which are most useful in that they can be used to define a longshore wavenumber,  $k_y$ , of the motion. This is particularly relevant to the understanding of the infragravity band in nearshore wave spectra (frequencies from 0.003 to 0.05 Hz). There has been a great deal of recent debate whether these long period motions are in the form of discrete free waves trapped to the shoreline, called edge waves, or alternately in non-trapped waves called leaky modes. For a particular frequency,  $\sigma$ , these possibilities are distinguished by

$$\begin{aligned}\sigma^2 &\leq gk_y && \text{- edge waves} \\ \sigma^2 &\geq gk_y && \text{- leaky modes.}\end{aligned}$$

The wave for which the equality holds is called the cutoff mode. Thus measurement of the longshore structure, hence longshore wavenumber, of the motions is the most direct way to resolve the controversy.

It is the intention of this paper to examine the longshore variability of run-up from a natural beach based on an extensive dataset obtained at Duck, North Carolina in October, 1982. We will first describe the general experimental layout and the field techniques used. Two runs, representing very different incident wave conditions, are then selected for intensive study. These data are analyzed both in terms of their general statistics and in terms of frequency through frequency-domain EOF analysis. In the final section we present a new technique, time-exposure photography, to quickly describe longshore variability in swash statistics. The technique also has application to the remote sensing of offshore bathymetry.

#### THE FIELD EXPERIMENT

In October 1982 a large field experiment was carried out at the CERC Field Research Facility (FRF) at Duck, North Carolina (Mason et al, in press). The FRF is located in the middle of 100 km stretch of barrier islands with the only topographic perturbation in the longshore being the pier itself which extends 560 m offshore and causes some interruption of the natural contours (Miller et al, 1983). The average beach face slope was approximately 1:10 although this value varied significantly through the experiment and on several



occasions (when the shoreline was very rhythmic) in the longshore. A bar system was present approximately 50 m offshore although the position and amplitude of the bar varied in response to storms. Bar morphology varied from linear to crescentic. A typical example of morphology in the vicinity of the pier is shown in Figure 1.

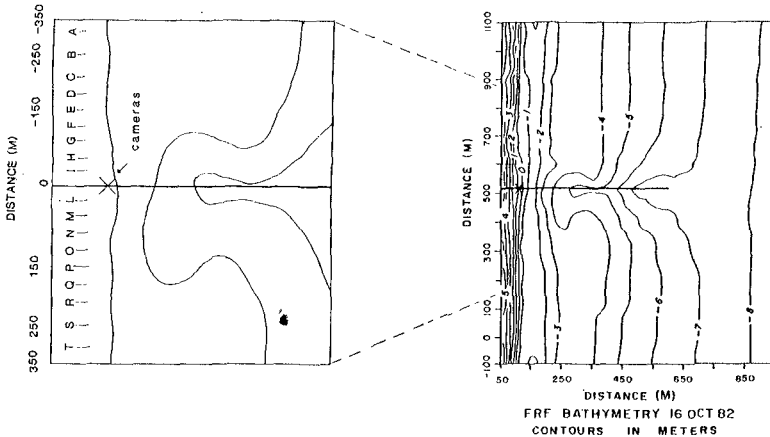


Figure 1. Typical bathymetry in the environment of the pier for October, 1982 (right hand figure). On the left is a blow-up of the beach immediately surrounding the pier, showing the longshore locations of ranges referred to later.

Run-up data were collected using longshore-looking time-lapse photography from super 8 movie cameras mounted on scaffolding on the pier, approximately 13 m above mean sea level. Large markers were placed in pairs, spaced 10m in the cross-shore direction, every 50 m down the beach for 300 m on either side of the pier. Additional single markers were placed at odd multiples of 25 m. The markers served as a reference for the beach profile grid and provided scale for the film images.

A data run usually consisted of running two movie cameras synchronously, one pointed to the north and one to the south. A frame was shot every second for a total run length of 35 min, or 2100 frames. Slight differences in the digitizing interval were corrected by carefully timing the length of each run, counting the number of frames taken, and calculating the average  $\Delta t$ . Laboratory studies have shown no noticeable drift in this number through a 35 min period.

Digitization of the film data for any of the longshore locations is accomplished with a computer-assisted digitization scheme described in Holman and Guza, 1984. Replicate digitizations by different operators, performed on a number of films, showed the standard deviation on set-up and significant swash height measurements presented here to be approximately 10%. Inter-calibration of the film technique with the dual resistance wire runup sensor on a low-slope beach showed some systematic differences in measured means and standard deviations, with the film technique registering a slightly higher mean, and a 35% larger standard deviation (83% larger variance) than the wire sensor (Holman and Guza, 1984). This is partly related to the sensitivity of the wire sensor to the height of the wire above the beach, and partly to the subjective interpretation of rundown of the films.

Beach surveys were carried out using the FRF Zeiss Elta-2 electronic total station system. This gives profile data, corrected to mean sea level, with an accuracy of better than 0.5 cm over the area of filming. These data were used to transform the raw cross-slope runup data to a vertical signal. All data presented in this paper will be in terms of the vertical component of runup. The profile data were also used to define a foreshore beach slope,  $\beta$ , as the mean slope over the 5m width of beach surrounding the mean sea level at the time of the run. Profile data were collected at least every two days and up to twice per day when the profiles were changing rapidly.

Incident wave data were collected from a waverider buoy positioned 3 km offshore in approximately 20 m depth. Incident significant wave height is calculated as  $H_0 = 4\sigma$ , where  $\sigma$  is the standard deviation of a twenty minute time series. Incident period is the period associated with the peak energy in the spectrum. Tide data is provided by a NOAA tide gauge attached to the end of the pier. Raw tide gauge data, consisting of spot measurements of sea surface elevation every six minutes, showed a standard deviation of 0.04 m during storms. Mean sea level was estimated from the average of the 6 consecutive measurements corresponding to the data run. The tide gauge was outside the surf zone for all but the largest storms.

#### OBSERVATIONS

Figure 2 shows the incident wave height and period statistics for the month of October, 1982, and indicates the duration of the experiment. Through the three weeks of the experiment, more than 80 films were exposed. Given the wealth of data available, it was decided to select two particular runs for intensive analysis for this paper. The two runs chosen were picked to represent different sorts of surf zone conditions. Run 19, shown in figure 2 as occurring near the beginning of the first major storm, is representative of dissipative conditions, with a wide surf zone of spilling breakers.

The deep-water incident wave height was 2.4 m with a peak period of 12 seconds. The longshore average beach slope was 0.10. By contrast, run 56 represents fairly reflective surf zone conditions. The incident wave height was 0.7 m, period 12.5 seconds, and average beach face slope 0.10.

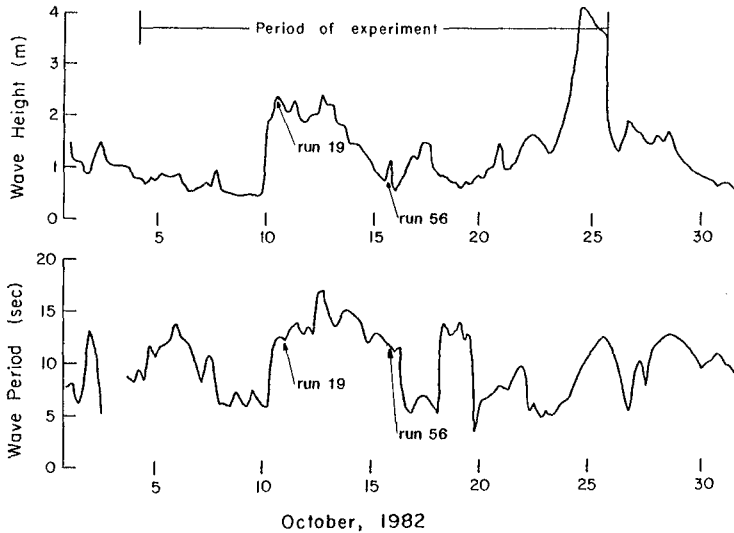


Figure 2. Significant wave height and peak period measured at the offshore waverider in 20 m depth. Noted are the duration of the entire experiment and the times of the two runs selected for intensive analysis.

Several non-dimensional measures exist which express the degree to which a surf zone is dissipative or reflective. One of these, the Iribarren number  $\xi_0$ , is given by

$$\xi_0 = \frac{\beta}{(H_0/L_0)^{1/2}}$$

where  $H_0$  is the deepwater significant wave height and  $L_0$  the deepwater wavelength associated with the peak period in the incident spectrum. For run 19 the Iribarren number was 0.97, while for run 56 it was 1.81. Previous papers had shown that  $\xi_0$  or a similar parameter is an important parameter in swash dynamics (Guza and Inman, 1975; Holman and Sallenger, in press). Thus it is of interest

to look for systematic differences between these two data runs.

Figure 3 shows the significant swash height and the set-up statistics for runs 19 and 56 as a function of longshore distance. Several general observations can be made from these figures. The first is regarding the influence of the FRF pier, located at  $y=0$ . For run 19 there are systematic differences in both these quantities across the pier with the significant swash height changing from  $1.49 \pm 0.13$  (error bars being one standard deviation) to the north of the pier to  $2.01 \pm 0.22$  to the south, and set-up changing from  $1.24 \pm 0.18$  to the north to  $0.80 \pm 0.14$  to the south. Interestingly, the incident waves approached from  $20^\circ$  north of the local beach normal, so the higher swash was actually in what should have been a shadow zone. We can only speculate that this arises from refraction over the complicated bathymetry associated with the pier.

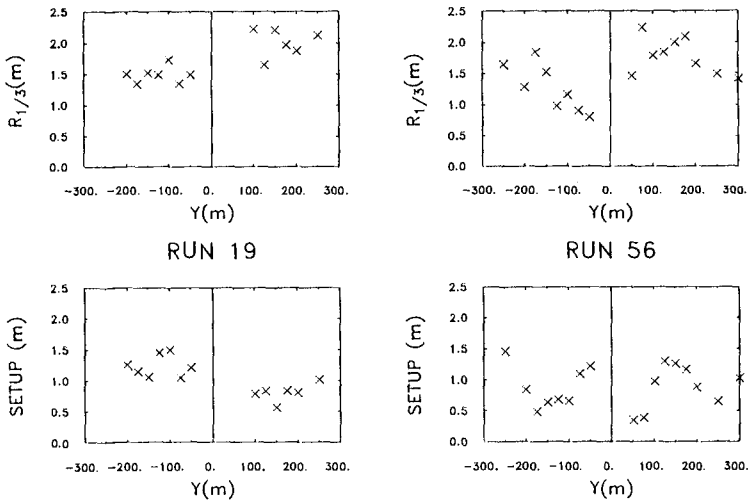


Figure 3. Significant swash height and set-up statistics for runs 19 and 56 as a function of longshore distance. The solid line at  $y=0$  is the FRF pier.

For run 56 the swash height varies from  $1.27 \pm 0.37$  north of the pier to  $1.78 \pm 0.30$  to the south. Again the larger swash is to the south despite an angle of incidence  $8^\circ$  to the north of local normal. The set-up data for this run show uniform statistics across the pier, from  $0.89 \pm 0.34$  to the north, to  $0.89 \pm 0.36$  to the south.

The second general observation regarding this figure is that if we consider the sides of the pier separately, the statistics associated with the dissipative conditions are a great deal more uniform in the longshore than those associated with the reflective conditions. The average standard error (standard deviation divided by the mean) for run 56 was 31.1%, about 2.4 times the value, 13.1%, for run 19. While one cannot make a conclusion about longshore uniformity based on two examples, the trend of reduced longshore variability during dissipative conditions has been noted by others including Wright and Short, 1983, and Garrow, 1985. Note that a small longshore variability in bulk statistics does not indicate that longshore dependent processes such as edge waves are not operating, just that their statistics vary little when averaged through all frequencies. The frequency dependency of these data will be examined in the next section of the paper.

The final point to note regarding figure 3 is that despite a large difference in the incident wave height between these two runs (2.4 versus 0.7m), the set-up and swash statistics are not strongly different. In other words, the relative set-up and swash (normalized by the incident wave height) for the high Iribarren number day is much larger than for the low Iribarren number day. This dependence of non-dimensional run-up statistics on Iribarren number was noted also in Holman and Sallenger, in press (not surprisingly, since that paper was based on the same dataset).

#### FREQUENCY-DEPENDENT ANALYSIS

To understand the longshore variability of statistics in greater detail, it was necessary to resolve the data into the frequency domain and perform frequency-dependent analysis. Figures 4 and 5 show the spectra for each longshore range for runs 19 and 56, respectively. Spectra for individual ranges are plotted according to the indicated axes but are each displaced vertically 0.615 orders of magnitude from the previous. Spectra labels correspond to the longshore locations shown in figure 1. Also shown are the frequency bands, labelled at the bottom of the figure, which will be used for subsequent frequency-domain EOF analysis. These frequency bands are 0.005 Hz wide for the infragravity band (20 dof) and 0.01 Hz wide for higher frequencies (40 dof).

Systematic differences are evident between the spectra for the two days. For the reflective day, run 56, the single dominant peak is at the incident frequency and is just the standing wave component of the incident waves. For lower frequencies, the infragravity band is low energy and without significant structure. On the other hand, the spectra for the dissipative day, run 19, are dominated by the infragravity band. The spectral peak associated with the incident band, while still present, is of lower energy. There is also some structure through the infragravity band.

Analysis for each data run proceeded on a frequency band by frequency band basis. The results from only the three most important bands for each run will be presented in this paper. For run 19, band C (0.07-0.08 Hz) was taken to represent the incident waves. Band 8 (0.035-0.040 Hz) was selected since it appeared particularly energetic, especially in the north end of the array. Finally, band 4 (0.015-0.02 Hz) showed some signs of a significant peak, but, more

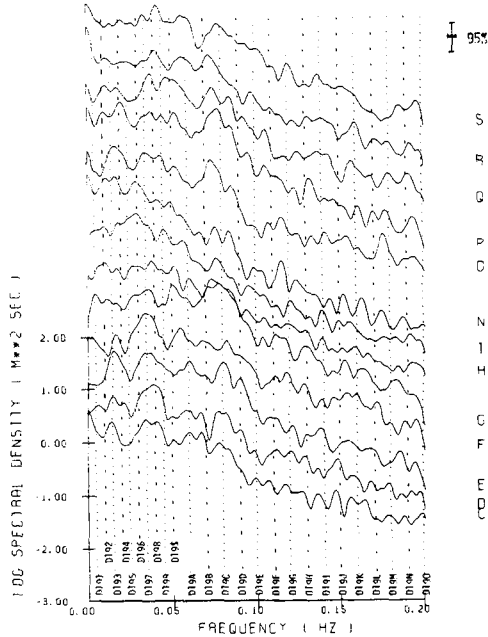


Figure 4. Displaced spectra for all longshore ranges digitized for run 19. Each spectrum is displaced 0.625 orders-of-magnitude above the previous. Letters at right refer to longshore ranges indicated in figure 1, labels at bottom refer to individual frequency bands marked by the dotted lines (labels mark the upper limit of their band).

importantly, was found to be significant in data taken by offshore sensors described in this volume by Sallenger and Holman, in press. For the reflective day, run 56, the incident peak (band C, 0.07-0.08 Hz) was clearly important. Also common to all sensors was a low-frequency hill (band 1, 0.000-0.005 Hz). Finally, in a number of the spectra there are suggestions of a small peak at the

subharmonic frequency (band 8, 0.035-0.040 Hz, one half of the incident band frequency). Since Guza and Inman, 1975, have suggested the importance of the subharmonic on reflective beaches, further investigation of this band was indicated.

The longshore structure of each band was found using the technique of frequency-domain empirical orthogonal functions or EOFs (Wallace and Dickenson, 1972; Wang and Mooers, 1977; Holman and

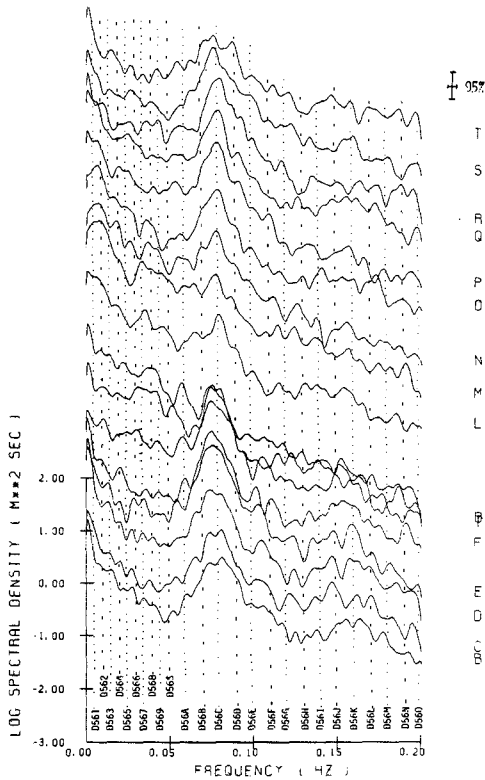


Figure 5. Same as figure 4, but for run 56.

Bowen, 1984). If the cross-spectra between pairs of ranges  $j$  and  $k$  for a particular frequency range is given by

$$U_{jk} = C_{jk} + iQ_{jk} \quad j, k = 1, N$$

where  $C$  and  $Q$  are the cospectral and quadrature spectral estimates

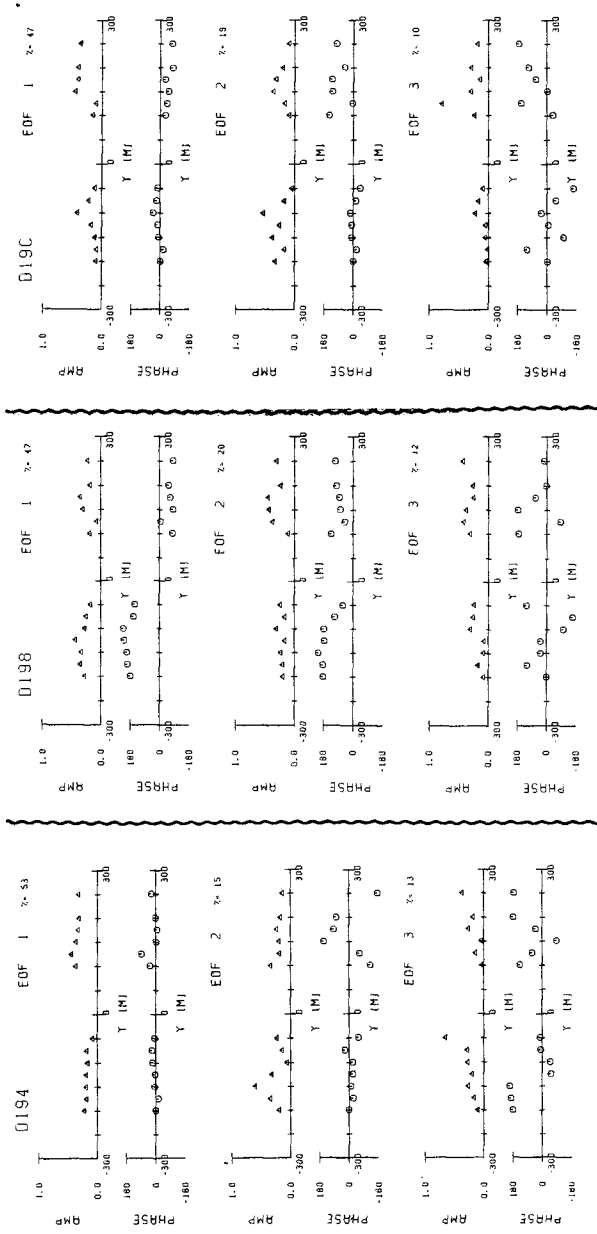


Figure 6. Frequency-domain EOFs for three dominant frequency bands for run 19. The band labels, at the top of each set of EOFs, correspond to figure 4. Band D194 is 0.015-0.020 Hz, band D198 is 0.035-0.040 Hz, and band D19C is the incident peak at 0.07-0.08 Hz. The amplitude and phase functions for the first three EOFs are slow in each case, along with the percent of the band variance explained by each.



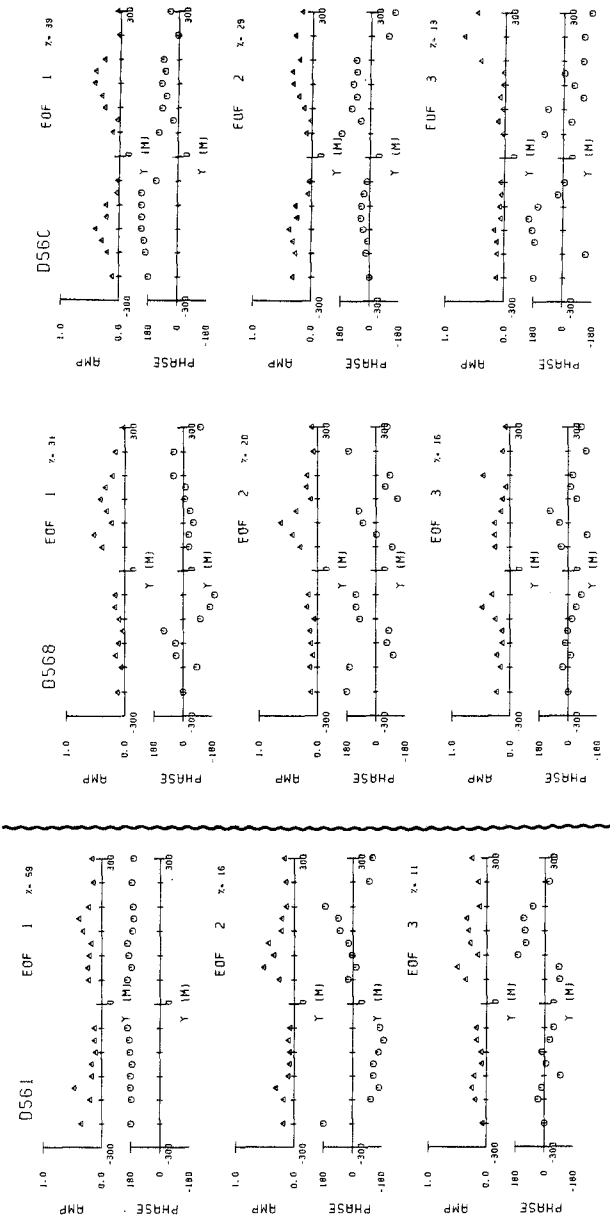


Figure 7. Same as figure 6 but for run 56. Band D561 is from 0.000-0.005 Hz, band D568 is 0.035-0.040 Hz, and band D56C is 0.07-0.08 Hz.

and  $N$  is the number of ranges, the EOFs are just the eigenvectors of  $U_{ij}$ . The eigenvectors will be complex, so can be expressed in terms of an amplitude and a phase. The amplitude is generally normalized to unit vector length and the phase expresses the relative phase amongst the ranges.

Figures 6 and 7 show the results of this analysis for the selected bands for runs 19 and 56 respectively. The first three EOFs, along with the percentages of the variance for the frequency band explained by each EOF, are shown in each case. We will examine each band in turn.

Band 4 of run 19 is dominated by the first EOF, with 53% of the variance being explained. The amplitude for this mode shows a definite change across the pier. However, the phase (with the exception of one point) is uniform alongshore. Thus the energy in this band is associated with a very small longshore wavenumber, possibly zero. The cutoff wavelength separating the edge wave and leaky mode regimes is approximately 5 km for this band. For the 500 m length of this array this is equivalent to a  $36^\circ$  phase shift over the array length. While the present data cannot exclude the possibility that this is a very high mode edge wave, the phase information seems to indicate a leaky mode.

Band 8 of run 19 shows a rather more interesting picture. Again, the first mode dominates with 47% of the variance. For this mode, the amplitude shows more variability. Moreover, the phase shows a dramatic jump across the pier. A phase jump of  $180^\circ$  is suggestive of a wave standing in the longshore, possibly a standing edge wave. However, without indications of a second zero crossing away from the pier, the wavelength cannot be estimated and the edge wave hypothesis confirmed. Also it is interesting to note that if the pier, with its related pilings and bathymetry discontinuities, is thought to be a potential reflector of longshore-propagating wave motions, then the pier should be associated with a zero-crossing in longshore velocity, not in elevation.

Band C of run 19 represents the incident wave band. All EOFs indicate the localized effect of the pier on the wave amplitude. The phase of the first mode is relatively uniform although there is some indication that the wave arrives first near the pier (waves propagate "down-phase" in this analysis). This may be due to the greater water depths surrounding the pier. Note that there is no indication of southward progression expected from the  $20^\circ$  north angle of incidence.

Band 1 of run 56 corresponds to the very low frequency hill in most of the run 56 spectra. While there are some indications of variability in amplitude (the shoreface was also rhythmic), the phase of the first mode is uniform longshore. This is expected since these low frequencies are associated with long wavelengths. Since the wavelength of the cutoff edge wave is of the order of 62 km, these



Figure 8. Normal photograph of Short Sands Beach. Swash and breakers from such a snapshot give just one realization of dissipation in the swash or over a sand bar.



Figure 9. Ten-minute time exposure of the same scene taken immediately after Figure 8. Longshore variability of swash dissipation is obvious, but did not reproduce well from color slide.

data can say little to distinguish between edge waves and leaky modes at this frequency. However one can probably conclude that this mode is not a mode 0 or 1 edge wave, whose wavelengths would be less than a few kilometers.

Band 8 for run 56 represents the subharmonic band of the incident peak. Interestingly the energy contained in this band is much more evenly distributed among the EOFs. While the first EOF provides a somewhat confusing picture in phase, the second EOF is rather intriguing. The phase for this mode appears to make  $180^\circ$  phase jumps about every third point. This seems particularly apparent to the north of the pier (not in the shadow zone). This phase behaviour is consistent with a standing wave motion with a wavelength of 150 m. The wavelength of the cutoff mode for this band is 1100 m, so this motion lies clearly in the edge wave regime. While the appropriate beach slope for use in the edge wave dispersion relation is unclear, one can conclude that this motion is probably a standing edge wave of mode number that is low but greater than zero. This bears on the work of Guza and Davis, 1974, who predicted a mode zero edge wave based on theoretical and lab work.

Finally, band C of run 56 shows the incident wave behaviour. This band clearly shows the rather confusing effect of the pier on the incident waves. For all modes, the amplitude and phase show a strong variation away from the pier and on either side of the pier.

#### TIME EXPOSURE PHOTOGRAPHY

The analysis of time series taken from different longshore locations reveals a great deal about the nature of wave motions in the nearshore. However it is often very difficult to collect suitable datasets, and the analysis can be somewhat long. An intriguing objective was to find a technique which could quickly show longshore variability in bulk wave statistics. Such a technique could resolve a dominant standing edge wave, for example, if one were present. A technique that does fill these needs is time-exposure photography. While a single snapshot provides only one realization of the wave field, a time exposure over a long period of time will average the image. For the case of waves in the nearshore the time exposure will be dominated by the white foam of breaking waves, so will essentially be an image of average breaking dissipation. The appropriate averaging time will depend on the time scales of variability. For normal incident waves, modulations generally occur on the time scale of minutes, so it was felt that a ten minute exposure would give an adequate averaging.

Figures 8 and 9 show an example of this technique. Figure 8 is a snapshot of an 800 m long bounded beach on the Oregon coast, Short Sands Beach. Individual wave breaking and run-up are easily distinguished. Figure 9 shows a ten minute time exposure of the same scene taken from the same vantage immediately following the snapshot.

The individual swashes now contribute to a broad white blur. Intriguingly, the width of this blur on the foreshore seems to vary in the longshore direction. Near the center of the beach the swash signal is its widest, while at points approximately  $1/4$  and  $3/4$  along the length of the beach, there are indications of a narrow swash zone. Beach surveys show little longshore variability, so the photographic signal appears to be the signature of a standing wave motion with two half-wavelengths trapped in the bay.

As a sidelight, it appears that this same technique can be used to effectively image offshore bathymetry. An offshore bar system is suggested by figure 8, but its structure is obscured by the complicated breaking pattern. However, in figure 9 the averaging of the time exposure has greatly simplified the apparent image of the bar system allowing one to easily distinguish the extent of the bar and the shoreward trough. The rather sharp delineation of the recommencement of breaking on the foreshore may indicate a step in the profile. It is apparent that this technique can be used to good advantage to map at least the general morphology and possibly, with further research, actual depths. The time exposure technique should be a very useful tool in the study of morphology changes during storms.

#### CONCLUSIONS

This paper presents data on the longshore variability of wave run-up on natural beaches. From the simplest point of view this variability can be viewed as noise, showing uncertainty in run-up data collected at a single point. However it is through the phase relationships of this variability that a number of important questions can be answered about wave motions in the nearshore. The most important application is in the distinction between edge waves and leaky modes as the agents of fluid motion in the surf zone.

The longshore variability of swash was examined for two data runs selected from a much larger dataset collected at Duck, North Carolina, in October, 1982. The runs were selected as examples of dissipative and reflective surf zones. The data are all from within 300m of a pier.

The bulk run-up statistics of set-up and significant swash height were clearly influenced by the presence of the pier and its associated bathymetric discontinuities, being significantly different on either side of the pier. Interestingly, the swash height was higher on what should have been the shadow side of the pier, indicating odd refractive effects over the complex bathymetry. The longshore variability of these statistics was much larger for the reflective day (the higher Irribarren number).

Frequency-domain EOF analysis was used to examine the structure of three dominant energy peaks for each of the two data runs. This

analysis tended to reinforce the importance of the pier to phase and amplitude, although for low enough frequencies the dominant modes tended to show very long wavelengths, probably associated with leaky modes. An interesting peak at the subharmonic frequency of the reflective day appeared to be a standing edge wave with wavelength 150 m.

A new technique of time-exposure photography is shown capable of pointing out dominant variabilities in wave statistics such as would be associated with a standing edge wave. The technique also shows a great deal of promise for imaging offshore sand bar morphologies. Ease of logistics would allow the evolution of morphologies to be monitored through storms.

#### ACKNOWLEDGEMENTS

Data collection for this paper was carried out under contract 12-08-0001-A-0022 from the U.S. Army Engineers Waterways Experiment Station, Coastal Engineering Research Center and the U.S. Geological Survey. The analysis work and development of the time exposure technique was supported by the Office of Naval Research, Coastal Sciences program under contract NR 388-168. Special thanks go to Aage Gribskov, Sara Culley and Eric Grann for help with the acquisition and digitization of the film data. Also, thanks to Harriet and her pals at the pier for donuts and other support.

#### REFERENCES

- Bowen, A. J. (1969). Rip currents. 1. Theoretical investigations. *J. Geophys. Res.*, 74(23): 5467-5478.
- Garrow, H. C. (1985). Shoreline rhythmicity on a natural beach. M.S. thesis, Oregon State University, pp189.
- Guza, R. T. and R. E. Davis (1974). Excitation of edge waves by waves incident on a beach. *J. Geophys. Res.*, 79(9): 1285-1291.
- Guza, R. T. and D. L. Inman (1975). Edge waves and beach cusps. *J. Geophys. Res.*, 80(21):2997-3012.
- Holman, R. A. and A. J. Bowen (1984). Longshore structure of infragravity wave motions. *J. Geophys. Res.*, 89(C4):6446-6452.
- Holman, R. A. and A. H. Sallenger, Jr. (in press). Set-up and swash on a natural beach. *J. Geophys. Res.*.
- Mason, C., Sallenger, A. H., Jr., Holman, R. A., and W. A. Birkemeier (1984). A comprehensive experiment on storm-related coastal processes. in Proc. 19th Conf. on Coastal Engineering, ASCE, in press.

- Sallenger, A. H., Jr. and R. A. Holman (1984). Infragravity waves on a barred profile during a storm. in Proc. 19th Conf. on Coastal Engineering, in press.
- Wallace, J. M. and R. E. Dickenson (1972). Empirical orthogonal representation of time series in the frequency domain, I, Theoretical considerations. J. Appl. Meteorol., 11:887-892.
- Wang, D. P. and C. N. K. Mooers (1977). Long coastal-trapped waves off the west coast of the United States, summer 1973. J. Phys. Oceanogr., 7:856-864.
- Wright, L. D. and A. D. Short (1983). Morphodynamics of beaches and surf zones in Australia. in CRC Handbook of Coastal Processes and Erosion, ed. P. D. Komar, CRC Press, Boca Raton, 35-64.

## CHAPTER ONE HUNDRED TWENTY EIGHT

### DUCK82 - A COASTAL STORM PROCESSES EXPERIMENT

Curtis Mason,<sup>1</sup> Asbury H. Sallenger,<sup>2</sup>  
Robert A. Holman,<sup>3</sup> and William A. Birkemeier<sup>4</sup>

**Abstract:** In October, 1982, a multi-agency nearshore processes experiment was conducted at Duck, NC to measure the nearshore morphological response to storm-induced waves and currents. The experimental setting for a series of companion papers is described, as are the oceanographic and meteorological characteristics of the storms. Rapid changes to the nearshore bar system occurred during the early stages of the first storm, and the bar developed a pronounced crescentic configuration during subsequent periods of high waves. Much of this activity is attributed to the effects of infragravity waves having periods greater than 30 seconds.

#### Introduction

Background. In recent years, several field experiments have been conducted to define nearshore processes and sediment transport patterns under "normal" wave and wind conditions. Large arrays of wave and current measuring sensors, combined with bathymetric surveys, have provided preliminary evidence of complex relationships between forcing processes and sediment response. To date, however, lack of both rugged instrumentation and a means to survey nearshore areas during high wave conditions have precluded measurements of storm-related nearshore processes.

To document the response of a typical East Coast site to extra-tropical storms (northeasters), a cooperative experiment known as DUCK-82, was conducted in October, 1982 at the Field Research Facility (FRF) of the U. S. Army Engineer Waterways Experiment Station, Coastal Engineering Research Center, Vicksburg, Miss. Participating in the experiment were investigators from the FRF, the U. S. Geological Survey, Oregon State University, and the University of Washington. Newly developed sensors and equipment were deployed which, for the first time, allowed a comprehensive analysis of the processes affecting the magnitude and time scale of short-term nearshore response.

The objectives of the experiment were to define the two and three-dimensional response of a coastal area extending from a well developed

---

1 Oceanographer, U. S. Army Engineer Waterways Experiment Station, Coastal Engineering Research Center, Field Research Facility, Duck, NC.

2 Oceanographer, U. S. Geological Survey, Office of Energy Resources and Marine Geology, Menlo Park, CA.

3 Assistant Professor, Oregon State University, College of Oceanography, Corvallis, OR.

4 Hydr. Engineer, U. S. Army Engineer Waterways Experiment Station, Coastal Engineering Research Center, Field Research Facility, Duck, NC.



fore-dune system to about the 7 m (22 ft) water depth; to measure the waves, currents, winds, and other forces producing this response; and to determine the relative importance of these forces in controlling the observed sedimentary response.

This paper discusses the experimental setting and methods, the meteorological and oceanographic characteristics of two storms affecting the study area, and the resulting nearshore morphological response. Finally, five ICEE-84 papers addressing other aspects of the experiment are introduced. Birkemeier (3) provides perspective for these short-term studies by describing long-term changes to selected profiles at the same site.

#### Experiment Description

Site. The Field Research Facility is located near Duck, NC on the northern end of North Carolina's Outer Banks (Figure 1), a long narrow string of barrier islands fronting the Atlantic Ocean. Offshore contours (6 to 15 m, 19 to 49 ft, water depths) in the vicinity of the FRF are generally straight and shore-parallel, although there is a deep trough in the immediate vicinity of the FRF research pier (1). Along the beaches and in water depths less than about 6 m (19 ft), changes in morphology can be large and rapid.

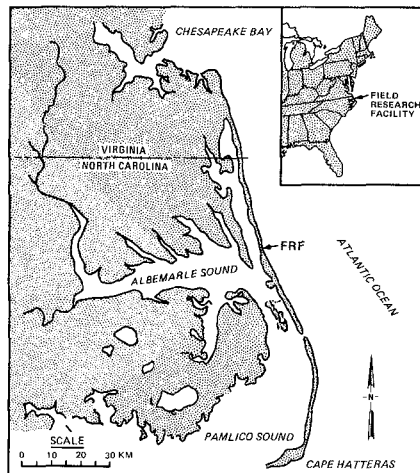


Figure 1. Location of study area

Sediments in the area vary greatly in size. The foreshore typically exhibits a bi-modal size distribution comprised of a coarse (~1 mm) fraction interspersed with finer (~0.3 mm) sands, with a median size of about 0.75 mm. Offshore, sands decrease in median size from about 0.2 mm on the nearshore bar to less than 0.1 mm in 20 m (65 ft) of water.

#### Experimental Design

Nearshore Process Data Collection. The experimental design required

a wide variety of instrumentation to be operated simultaneously and at frequent intervals during storms. Four Marsh-McBirney electromagnetic current meters and seven Baylor staff wave gages were located on the FRF pier (Figure 2), and a Waverider<sup>®</sup> buoy wave gage was located 3 km (2 mi) offshore in 20 m (65 ft) of water. A Weathermeasure anemometer located on the FRF building at an elevation of +19 m (+62 ft) MSL provided wind speed and direction information.

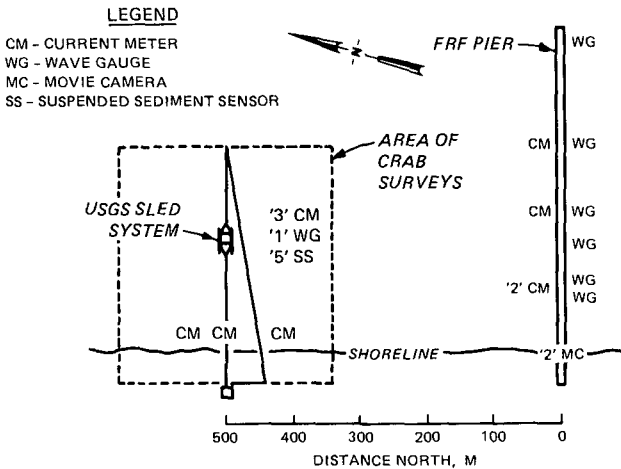


Figure 2. Experiment configuration

A large sea sled specially designed for storm use (9), Figure 3, was towed by a double-drum winch and triangular line arrangement along a shore-normal transect about 457 m (1485 ft) north of the pier to measure storm-induced waves, currents, and suspended sediment. Mounted on the sled was a vertical array of electromagnetic current meters (0.5, 1.0 and 1.75 m, 1½, 3 and 5½ ft, above the bottom), a pressure wave gage, and an optical suspended sediment meter. Data from these instruments were telemetered to a shore-based data collection system. Movie cameras at the shore end of the pier provided data for measurement of wave runup (5).

**Nearshore Surveys.** Fifteen profile lines were established within the survey area near the north boundary of the FRF (Figure 2) to determine the three-dimensional morphological response to storms. The profiles were 23 m (75 ft) apart, over 300 m (975 ft) long, and extended over a longshore distance of 320 m (1040 ft). The southernmost profile was 340 m (1105 ft) north of the FRF pier, sufficiently distant to be outside any pier influence. The center profile was surveyed with the USGS sled system using a Hewlett-Packard infrared total station and optical prisms on top of the sled's 10 m (33 ft) mast. Approximately 20 minutes were required to measure each profile. Since the sled had



Figure 3. USGS sea sled

previously operated in plunging breakers in excess of 5 m (16 ft), it was anticipated that profiles could routinely be obtained throughout any storm expected to occur at the site.

The other 14 profiles were measured using the FRF's Coastal Research Amphibious Buggy (CRAB), Figure 4, and Zeiss Elta-2 total station system (2). The CRAB is a motorized 10.6 m (35 ft) high wheeled tripod supporting an operating platform and a set of optical prisms which reflect the Zeiss' infrared beam. Vertical and horizontal accuracy of this system is about  $\pm 5$  cm, and about five hours were required to measure the three-dimensional morphology. CRAB operations were suspended when wave heights exceeded 2 m (6½ ft), and strong longshore currents occasionally prevented the CRAB from crossing the triangular tow line of the sea sled to obtain data near the sled profile line.

To define micro-scale processes of foreshore deposition and erosion, a tightly-spaced grid of steel pins was emplaced for high-frequency sampling of bed elevations within a small portion of the main survey area (6).

#### Storm Characteristics

Figure 5 shows the time history of waves and winds prevailing at the FRF site during October. Fortuitously for the experimental plans, two northeasters provided typical storm conditions in mid and late



Figure 4. Coastal Research Amphibious Buggy (CRAB)

October, 1982. The first of these storms began to affect the study area early on the morning of 10 October. Northeast winds reached a maximum sustained speed of 13 m/s (30 mph), and wave heights rapidly increased to over 2 m (6½ ft) by 1000 on the 10th. As the storm moved offshore, winds slowly abated, and within 24 hours had decreased to only about 7 m/s (16 mph). However since the storm center moved almost due east (Figure 6), it continued to generate large waves, and significant wave heights in excess of 2 m (6½ ft) were measured by the Waverider<sup>R</sup> buoy until 0200 on the 13th. The maximum height of 2.6 m (8½ ft) occurred at 1200 on the 12th.

Peak wave periods during the early part of the storm averaged about seven seconds (Figure 5), reflecting the locally-generated nature of the waves. As the storm moved offshore, a gradual shift in the peak period to higher values occurred. On the evening of the 11th, the peak period was 13 seconds, and by noon on the 12th it had reached 17 seconds. Wave spectral plots (Figure 7) clearly show the shift in peak period that occurred between the 10th and 11th, as well as the concurrent change from a multi-modal to a uni-modal spectra.

Longshore currents measured along the sled line were southward during the storm, reaching a maximum of about 1 m/sec (3 ft/sec) on the 10th. As the storm moved eastward, the wave approach angle changed from northeast to southeast, producing a change in the longshore current direction such that by the 12th, currents were directed northward.

The second storm of the season, between 23 and 25 October, was considerably more severe than the first. Winds from the northeast increased gradually to a maximum sustained speed of 23 m/sec (51 mph) on the evening of the 24th (Figure 5), with a concurrent increase in significant wave height to a maximum of over 4 m (13 ft) shortly thereafter. Peak periods remained between 6 and 9 seconds (Figure 7), with

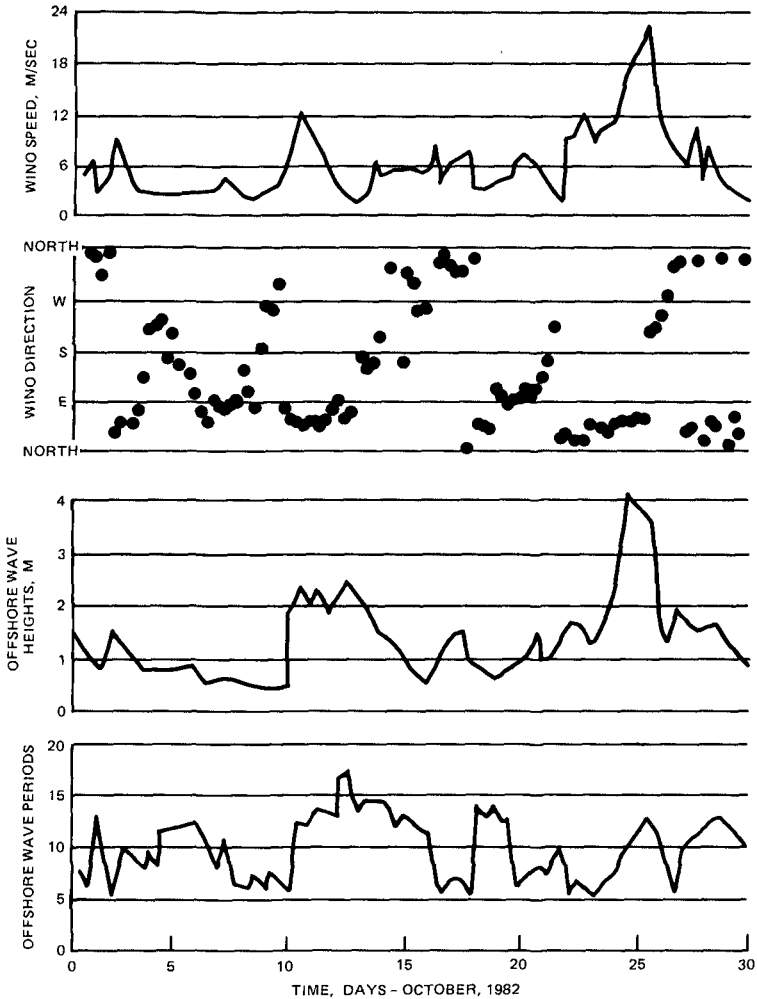


Figure 5. Wind and wave conditions, Oct 82, Duck, NC

only slight indications of energy at longer periods.

Longshore currents were directed southward at about 0.5 m/sec ( $1\frac{1}{2}$  ft/sec) during most of the storm, but reversed direction at about 2200 on the 24th, reaching a maximum northward speed of 0.7 m/sec (2 ft/sec) at 0500 on the 25th. Radar images obtained during the storm clearly show that the direction of wave approach changed gradually from a northeast angle on the 24th to a southeast angle by 0730 on the 25th,

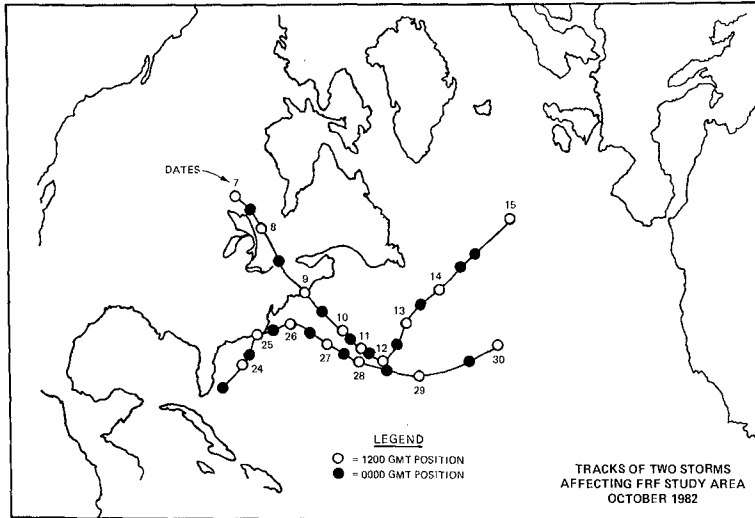


Figure 6. Storm tracks, Oct 82 (after NWS)

and wind data indicate a similar shift in direction (Figure 5) as the storm center moved northward past the site (Figure 6).

#### Morphological Response

This section describes the two and three-dimensional response of the nearshore study area to the storm of 10-15 October 1982, and the two-dimensional response to the storm of 23-25 October.

The first three-dimensional survey was completed on 7 October prior to the first storm. The next was completed on 13 October, when wave conditions had subsided sufficiently to allow deployment of the CRAB. Full surveys were also completed on the 15th and 19th. Profile data from the single sled profile line were obtained twice daily throughout the first storm and the subsequent recovery period, but a severely abraided tow line precluded sled operations during the second storm. Therefore, CRAB profiles were used for interpreting late-October nearshore profile changes.

#### Inner Bar Changes

Prior to the first storm, nearshore morphology was characterized by a well-developed berm and relatively small nearshore bar (Figure 8a). The bar crest was about 0.3 m (1 ft) above the trough level, and was positioned only 13 m (42 ft) offshore. The bar was relatively linear and shore-parallel, although some irregularities were apparent at the northern end of the survey area (Figure 9a).

During the storm, the bar crest at the sled line migrated offshore 57 m (185 ft), Figure 8a. Thirteen meters (42 ft) of this migration

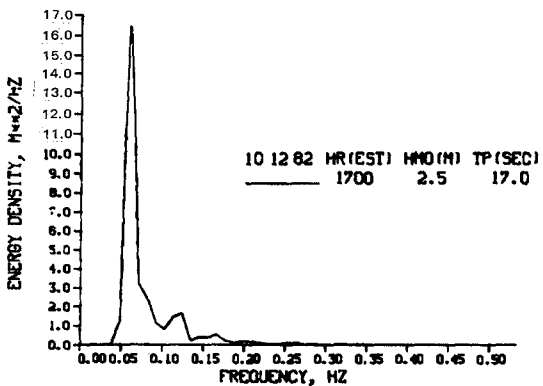
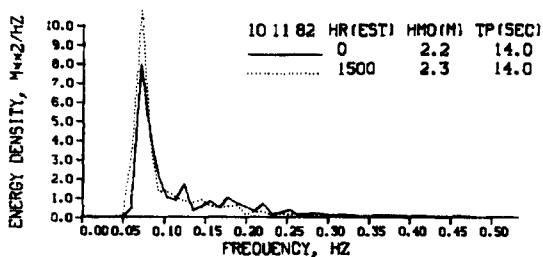
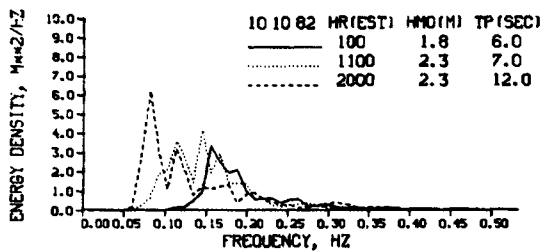
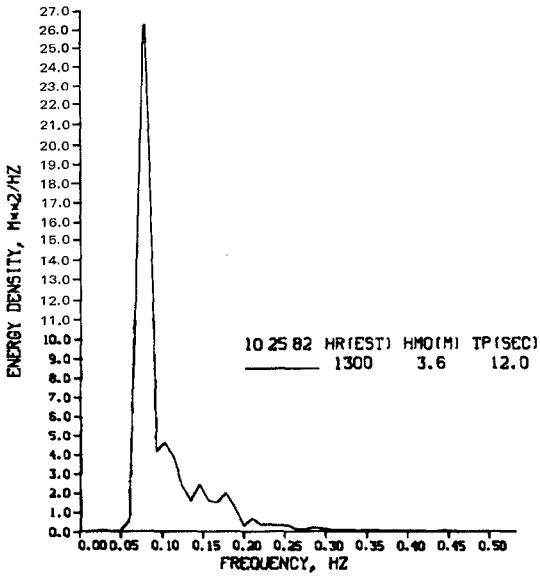
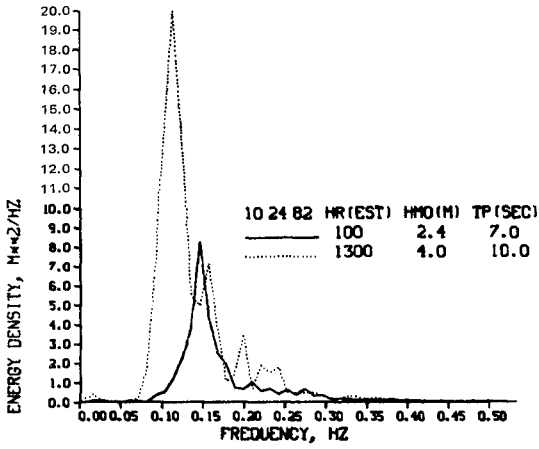


Figure 7. Wave spectra, FRF offshore Waverider<sup>R</sup>, October 1982





occurred over a six hour period on the 10th, yielding a very rapid migration rate of 2.2 m/hr (7 ft/hr). Between the 10th and 11th, the bar was stable, while between the 11th and 12th, it again migrated off-shore, at a rate of 1.4 m/hr (4½ ft/hr). Since the CRAB could not operate due to high waves, the three-dimensional characteristics of the inner bar during the storm could not be determined, although seaward movement of the entire bar crest is hypothesized.

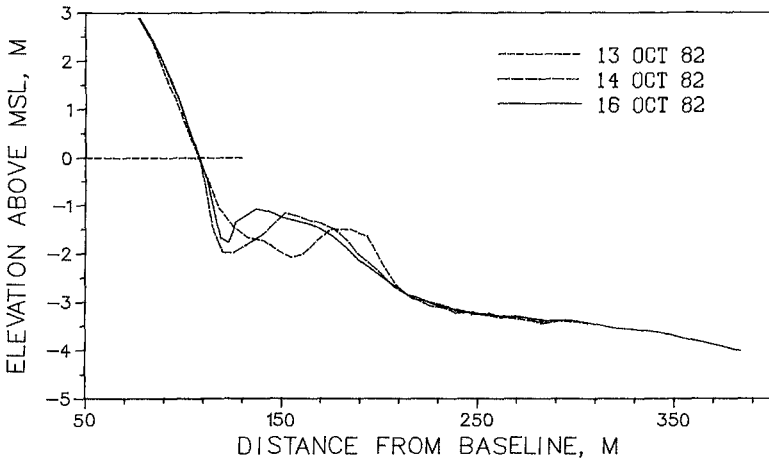
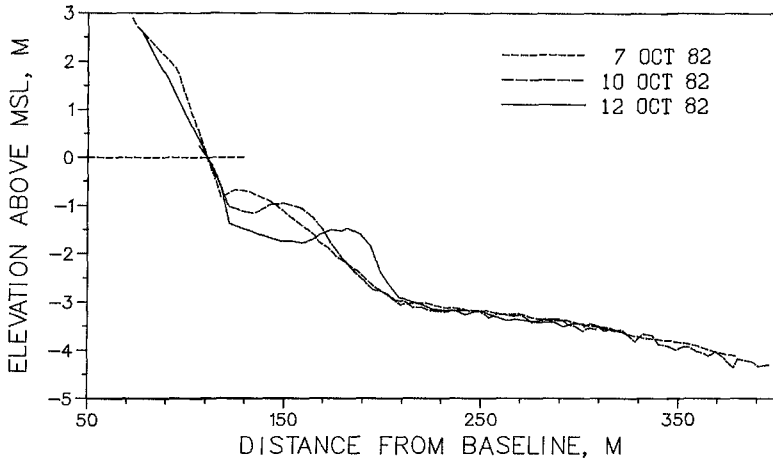


Figure 8. Sea sled profiles, 7-16 October 1982

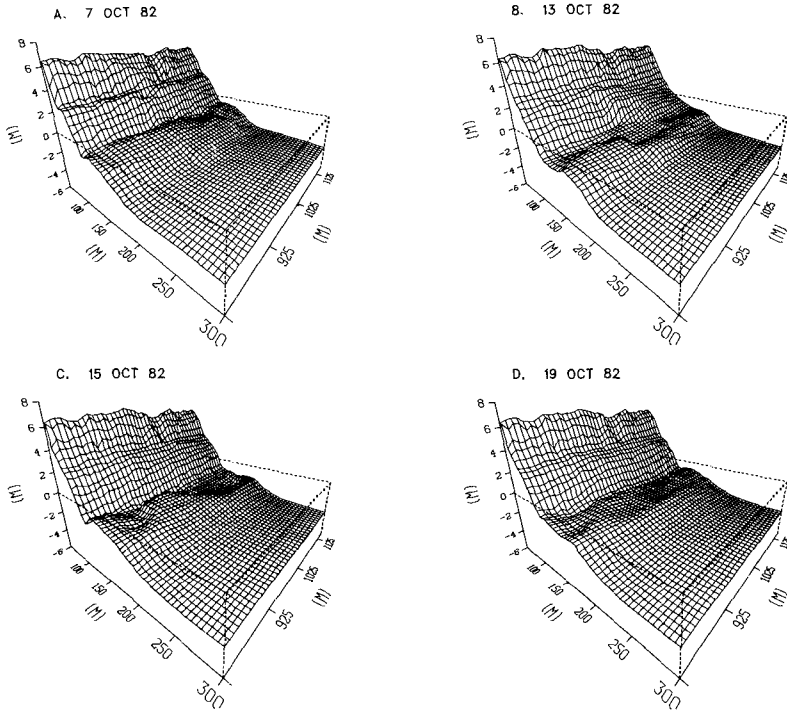


Figure 9. Three-dimensional plots of nearshore bathymetry

On the 13th, the day after the period of peak incident energy, the nearshore bar appeared to be roughly crescentic (Figure 9b). Between the 13th and 15th, the crescentic shape became better developed and by the 15th had reached a classic crescentic configuration. The longshore wave length was approximately 205 m (666 ft) and the cross-shore distance to the crescentic bar crest was about 70 m (227 ft).

In addition to becoming better developed, the bar system also appeared to have migrated northward about 40 m (130 ft), Figures 9b and 9c. This migration and the developing crescentic form caused nearshore profiles to change very differently depending upon longshore location. For example, between the 13th and 15th, the bar at the sled line showed an apparent landward migration of 36 m (117 ft), whereas during the same period only 69 m (224 ft) northward the bar migrated offshore 18 m (58 ft). These changes were occurring very rapidly even though wave energy was decreasing. For example, over a 24 hour period on the 13th and 14th, the bar crest on the sled line migrated onshore at the rate of 1.2 m/hr (5 ft/hr). Between the 14th and 16th, this rate decreased to 0.5 m/hr (1½ ft/hr), Figure 8b.

Between 15 and 19 October, the inner bar migrated landward, and by the 19th had disappeared, leaving a platform similar to that of 7 October.

#### Outer Bar Changes

Prior to the first storm, there was no indication of an outer bar on the profile. However, during that storm a small amount of deposition occurred about 350 m (1137 ft) seaward of the baseline (Figure 10). During the second storm, the trough deepened and widened, and the bar crest rose and migrated farther offshore. The net result of both storms was the formation of an outer bar about 360 m (1170 ft) from the baseline. The bar remained stable between storms, and did not acquire a crescentic configuration during storms.

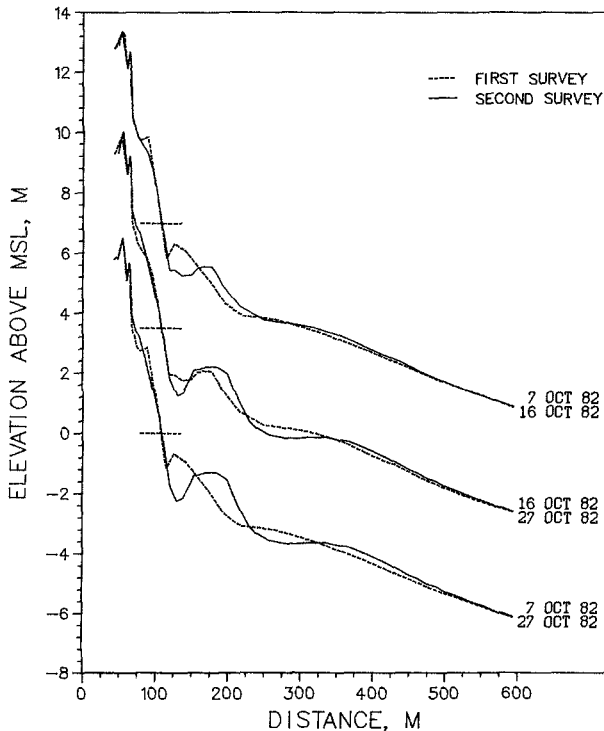


Figure 10. CRAB profile 62 - 7-27 October 1982

## Discussion

Figure 11 shows the significant breaker locations and bar crest distances throughout the storm. The surf zone width reaches 900 m (2925 ft), whereas the bar migrated no farther than 70 m (227 ft) from the shoreline. It is important that during the storm, waves were breaking continually across the surf zone, and were not reforming and breaking on the bar crest. Therefore, it is clear that the inner bar could not have formed according to a plunging breaker hypothesis, where a bar is formed at the breaker position by scouring of a trough by the breaker. The inner bar (located within the landward 10 percent of the surf zone) became better developed and migrated offshore in the presence of spilling breakers. The outer bar was also well inside the surf zone during the storm.

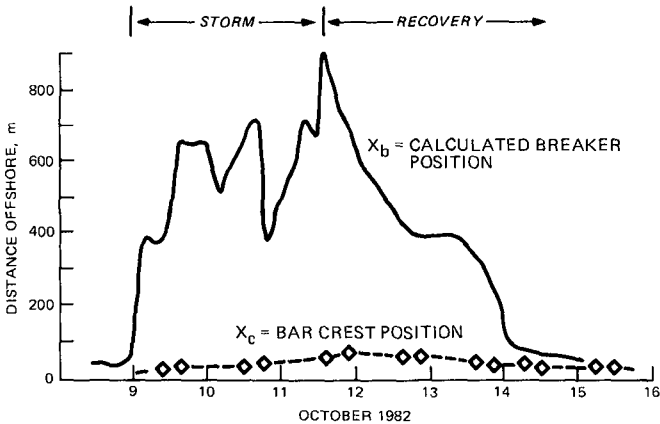


Figure 11. Time history of bar crest and breaker positions and depths

Sallenger, et al (11) indicate that the inner bar movement could have been caused by a standing infragravity wave with a period between 55 and 75 seconds. The inner bar would have formed at either the first node or antinode of the standing wave pattern as described by Bowen (4). Sallenger, et al (11) also hypothesized that crescentic development of the inner bar may have been forced by standing infragravity edge waves as the storm waned. Sallenger and Holman (10) provide evidence that infragravity waves were indeed very important during the storm. However, additional analysis of the wave and current data is required before the relationship between infragravity waves and bar response can be confirmed.

### Related Results

Since the DUCK82 experiment consisted of several related areas of investigation, the ICCE-84 proceedings contain papers summarizing results to date, which are introduced below. Two of these papers concern wave characteristics measured during the storms, while the three remaining papers discuss cross-shore and/or beach face sediment transport processes.

As mentioned previously, Sallenger and Holman (10) confirmed the existence of significant currents associated with infragravity waves during the first storm. RMS cross-shore flows due to waves with periods greater than 20 sec exceeded 0.5 m/sec (1½ ft/sec) over the bar crest. Holman and Sallenger (5) also investigated infragravity wave activity during the second storm, when surface water level setup and significant swash heights exceeded 1.5 and 2.5 m (5 and 8 ft) respectively. Although offshore wave periods were less than 10 seconds, runup data collected on the shoreface indicated that dominant oscillations were of much longer periods, with approximately 75 percent of the variance in the infragravity band.

Using data collected from the sled-mounted current meters and optical suspended sediment meter, Jaffe, et al (7) concluded that suspended sediment transport played a major role in the cross-shore profile changes. A strong coupling was found to exist between material suspended high in the water column and the onshore phase of wave-induced flows such that a net onshore flux of particles occurred even though the mean flow was offshore. Richmond and Sallenger (8) found that during the first storm, different sediment sizes could be transported in opposite cross-shore directions under the same incident wave field. The field data corroborated sediment transport patterns predicted by Bowen's (4) equations as derived from Bagnold's theory on sediment transport. Finally, Howd and Holman's (6) high frequency sampling of swash zone bed elevations showed coherent perturbations to the fore-shore slope with RMS heights of nearly 5 cm which were progressive upslope, with periods of 8 to 10 minutes.

### Summary and Conclusions

A comprehensive nearshore processes experiment was conducted which, for the first time, documents detailed temporal and spatial storm-related processes and morphological response. Two-dimensional profile response measurements indicate that large and rapid changes occurred. As wave heights increased, the inner bar became better developed and migrated offshore at very rapid rates (>2 m/hr, >6 ft/hr). Development of the outer bar also showed a dependence upon wave heights, with minor changes when offshore waves were less than 2.5 m (8 ft), and significant changes when heights exceeded 3.5 m (11 ft). During the waning stages of the first storm, the inner bar rapidly developed a crescentic morphology, with parts of the bar migrating onshore at rates of over 1 m/hr (3 ft/hr). Neither the inner nor outer bars appeared to be related to breaking wave processes, since both bars were well within the storm surf zone. Rather, based on frequent quantitative measurements of wave and current conditions, the inner bar formation seems to be better explained by the effect of infragravity waves, which appear to play the leading role in controlling the response of nearshore sedimentary features to storms.

The rapid response of bar morphology to changing wave conditions indicates the need for more rapid sampling of surf zone morphology. It appears that previously held concepts of a slowly responding system may be erroneous. Only with a much-improved spatial and temporal sampling scheme can this be verified, since even with the frequent sampling conducted during this experiment, there is no guarantee that the dominant time scale of bar response was captured. The problem is further complicated by the apparent ease with which natural bar systems become three-dimensional. The development of instrumentation to measure three-dimensional morphology during storm conditions should be given high priority in the future.

#### Acknowledgment

Results presented herein are based on research conducted by the Coastal Engineering Research Center, Waterways Experiment Station, under the Coastal Flooding and Storm Protection Program, Coastal Engineering Functional Area, Civil Works Research and Development, U. S. Army Corps of Engineers, and the Office of Energy Resources and Marine Geology, U. S. Geological Survey. Permission to publish this information was granted by the Chief of Engineers.

## Appendix 1.—References

1. Birkemeier, W. A., DeWall, A. E., Gorbics, C., and Miller, H. C., "User's Guide to CERC's Field Research Facility," MR 81-7, U. S. Army Corps of Engineers, Coastal Engineering Research Center, Fort Belvoir, VA, Oct., 1981.
2. Birkemeier, W. A., and Mason, C., "The CRAB: A Unique Nearshore Surveying Vehicle," *Journal of Surveying Engineering, ASCE*, Vol. 110, No. 1, March 1984.
3. Birkemeier, W. A., "Time Scales of Nearshore Profile Changes," *Proceedings of the Coastal Engineering Conference, ASCE, Houston, Sept., 1984.*
4. Bowen, A. J., "Simple Models of Nearshore Sedimentation, Beach Profiles, and Longshore Bars," *The Coastline of Canada*, S. B. McCann, Editor, Geological Society of Canada, Paper 80-10, pp. 1-11, 1980.
5. Holman, R. A., and Sallenger, A. H., "Longshore Variability of Wave Runup on Natural Beaches," *Proceedings of the Coastal Engineering Conference, ASCE, Houston, Sept., 1984.*
6. Howd, P. A., and Holman, R. A., "Beach Foreshore Response to Long Waves in the Surf Zone," *Proceedings of the Coastal Engineering Conference, ASCE, Houston, Sept., 1984.*
7. Jaffe, B. E., Sternberg, R. W., and Sallenger, A. H., "The Role of Suspended Sediment in Shore-Normal Beach Profile Changes," *Proceeding of the Coastal Engineering Conference, ASCE, Houston, Sept., 1984.*
8. Richmond, B. M., and Sallenger, A. H., "Cross-Shore Transport of Bimodal Sands in the Surf Zone," *Proceedings of the Coastal Engineering Conference, ASCE, Houston, Sept., 1984.*
9. Sallenger, A. H., et al, "A System for Measuring Bottom Profiles, Waves, and Currents in the High-Energy Nearshore Environment," *Marine Geology*, Vol. 51, 1983, pp. 63-76.
10. Sallenger, A. H., and Holman, R. A., "Infragravity Waves on a Barred Profile During a Storm," *Proceedings of the Coastal Engineering Conference, ASCE, Houston, Sept., 1984.*
11. Sallenger, A. H., Holman, R. A., and Birkemeier, W. A., "Storm Response of a Nearshore Bar System," *Marine Geology*, in press.

## CHAPTER ONE HUNDRED TWENTY NINE

Offshore Breakwater, Wheatley, Ontario

G.T. Beaulieu<sup>1</sup>, M.G. Skafel<sup>2</sup>, W.F. Baird<sup>3</sup>

The safe entry during storms to the fishing harbour at Wheatley on Lake Erie was compromised by breaking waves at the harbour entrance. These waves approach the entrance from a narrow easterly sector due to storm tracks, fetch limitations, and refraction. Using a physical model, a small offshore breakwater was selected as the best solution to eliminate the breaking waves. During the six years since construction, the breakwater has performed satisfactorily and has had a negligible effect on the littoral processes as determined from regular bathymetric surveys.

### Introduction

The harbour at Wheatley, Ontario (Fig. 1) is primarily used by commercial fishing vessels. Prior to 1978, storm waves from easterly directions broke over the bar at the harbour entrance producing hazardous conditions for these vessels. During these storms, fishing vessels returning to port had difficulty maintaining control and entering the harbour safely. In several cases vessels had to seek shelter at other harbours, the nearest being over two hours away.

The objective of this study was to find an entrance configuration that would eliminate wave breaking and reduce the wave height to an acceptable level over the bar at the harbour entrance. The solution was to build an offshore breakwater.

### Wheatley Harbour

Wheatley Harbour (Fig. 2) is the most important freshwater commercial fishing harbour in Canada. The harbour is the home port for approximately 45 fishing tugs and provides berthage for up to four transient tugs. The typical vessel size which utilizes the harbour is about 20 metres in length, 4.2 metre beam and 2.0 metre draft.

The entrance channel is dredged to a depth of 3 metres and has a minimum width of 21 metres. Ice generally restricts fishing activity in January and February.

The shoreline to the east of Wheatley Harbour consists of eroding clay bluffs and sand beaches. The net movement of littoral material is towards the southwest and has been estimated to be about 50,000 m<sup>3</sup>/year (2). As a result of this transport material, about 4,700 m<sup>3</sup> of sand on average had to be dredged from the entrance channel each year.

<sup>1</sup> Small Craft Harbours Branch, Fisheries and Oceans Canada, Burlington, Ontario, Canada L7N 3J1

<sup>2</sup> National Water Research Institute, Burlington, Ontario, Canada L7R 4A6

<sup>3</sup> W.F. Baird and Associates, Ottawa, Ontario, Canada, K2C 3N6



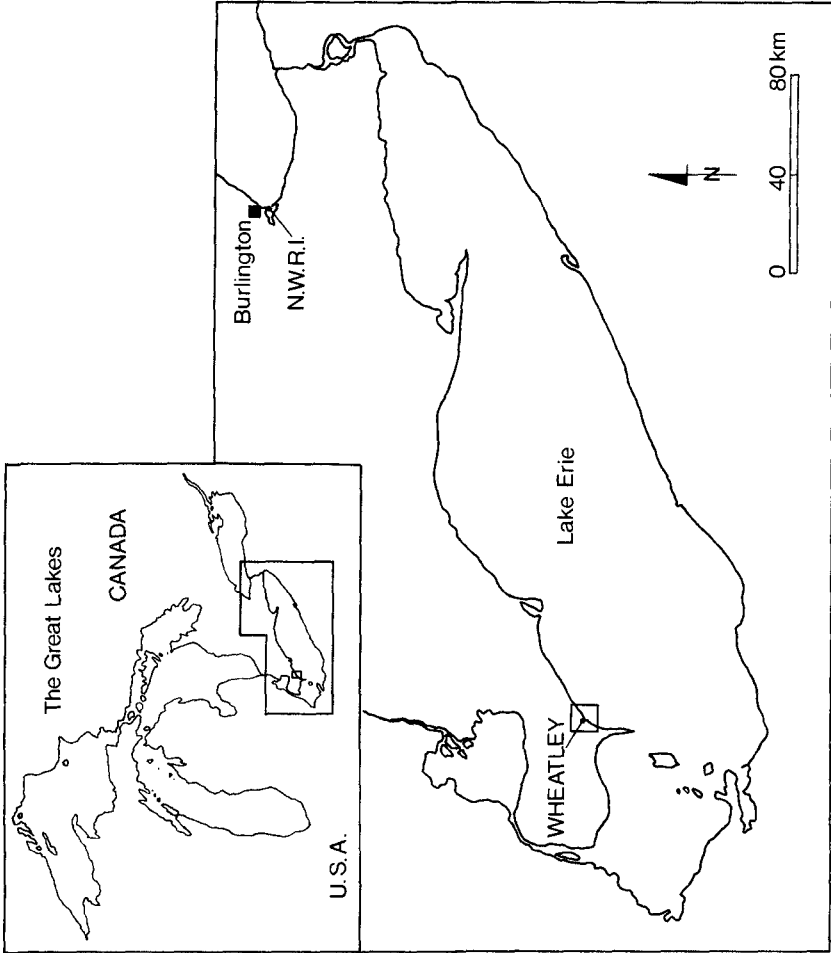


Figure 1. Location Map.

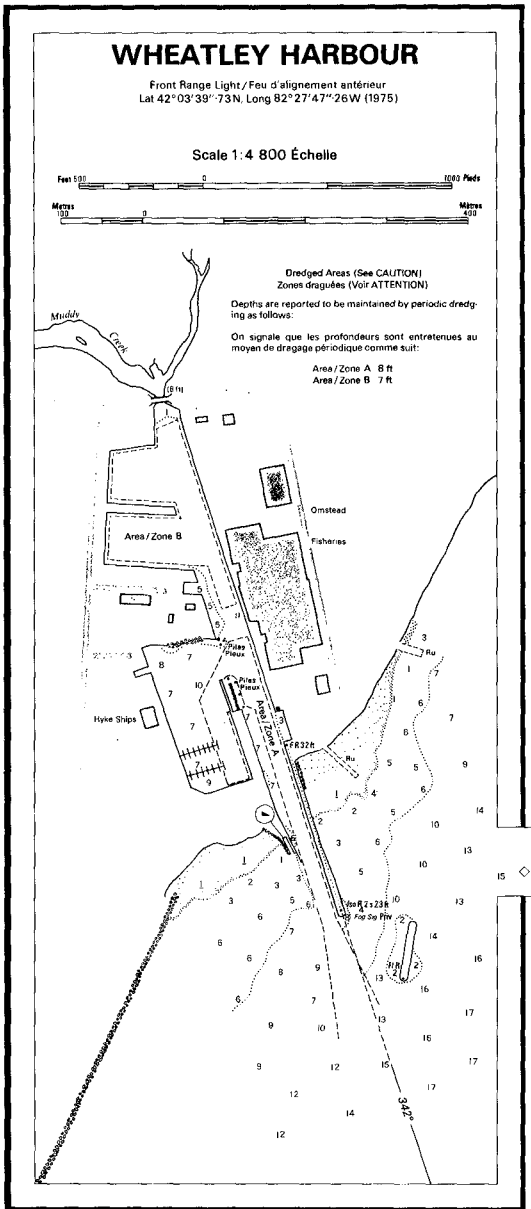


Figure 2. Hydrographic Chart, Wheatley Harbour.

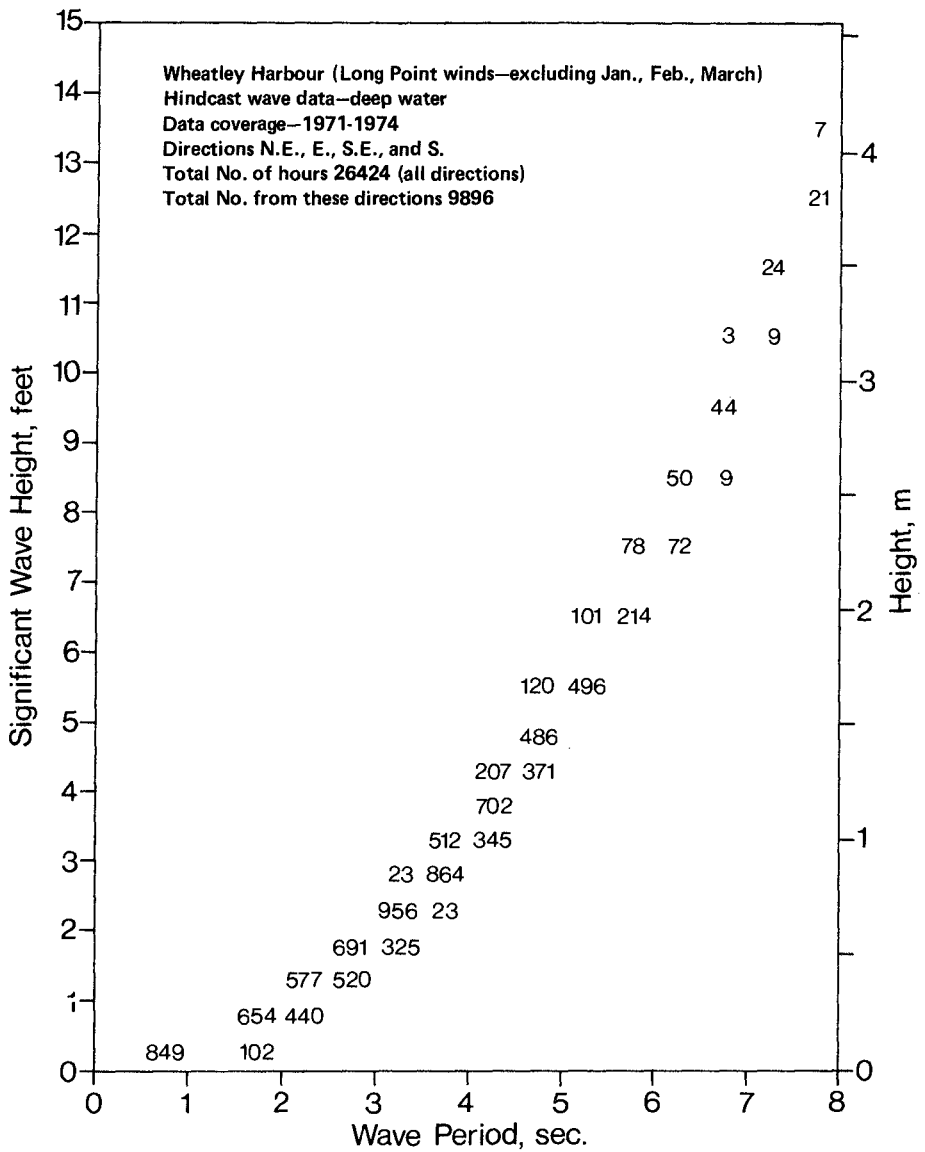


Figure 3

Hindcast scatter diagram



Figure 4. Breaking Wave at Harbour Entrance, Model.

### Wave Climate

The harbour is exposed to waves generated by northeast, east, southeast and south winds. The most severe conditions are from easterly storms which generate waves of from 5 to 7 second periods with deep water significant heights of 6 to 12 feet (1.8 to 3.7 metres). The wave climate was hindcasted (Fig. 3) using a procedure based on Bretschneider's equations (1).

Refraction analysis showed that the large waves, which cause the navigation problem, approach the harbour entrance from a small sector of 90° to 105° true.

### Model Study

A fixed bed model of the harbour and its approaches to the 4 metre contour was constructed to a geometric scale of 1 to 60 in the Hydraulics Laboratory at the National Water Research Institute (3). Irregular waves were used to simulate prototype waves from the east sector. A refraction analysis was used to define the wave direction at the model boundary.

The model tests, combined with the wave climate, indicated that severe breaking wave conditions could be expected during four storms in an "average" year. This conclusion was verified in discussion with the local fishermen. Reproduction in the model of the severe breaking condition is shown in Figure 4.

It was established that the significant wave height should be less than 1.2 metres to prevent breaking and to ensure safe entry and exit from the harbour. By keeping the waves as large as possible, but under this limit of 1.2 metres, the structure would have a minimal effect on the littoral processes.

Numerous offshore breakwater configurations were studied in the model until a suitable configuration was determined.

The variable design features in each breakwater configuration were length, distance from the harbour entrance structures, and orientation.

### Recommended Solution

The structure that was recommended met the following design criteria:

- it was sufficiently far from the entrance not to represent a hazard to navigation;
- it provided protection during easterly storms to eliminate breaking waves (reduced the significant wave height to less than 1.2 metres);
- it did not reduce the wave height more than necessary, to interfere as little as possible with littoral processes;

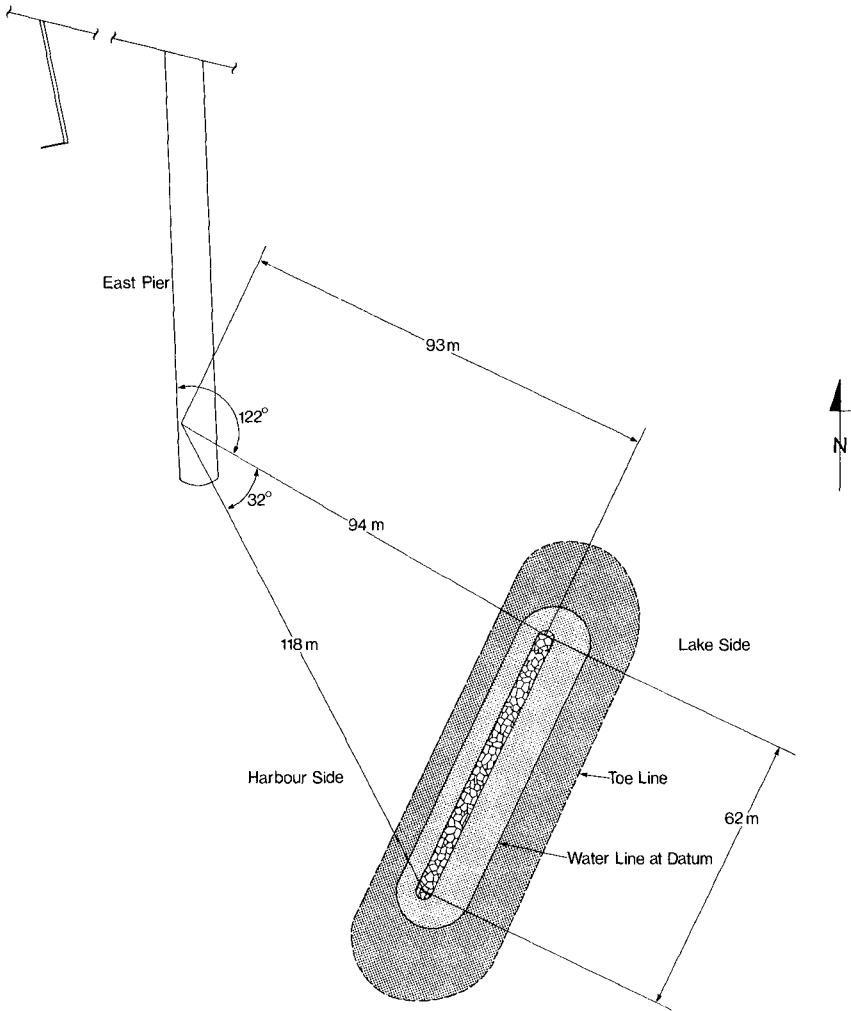


Figure 5 Layout plan, recommended solution

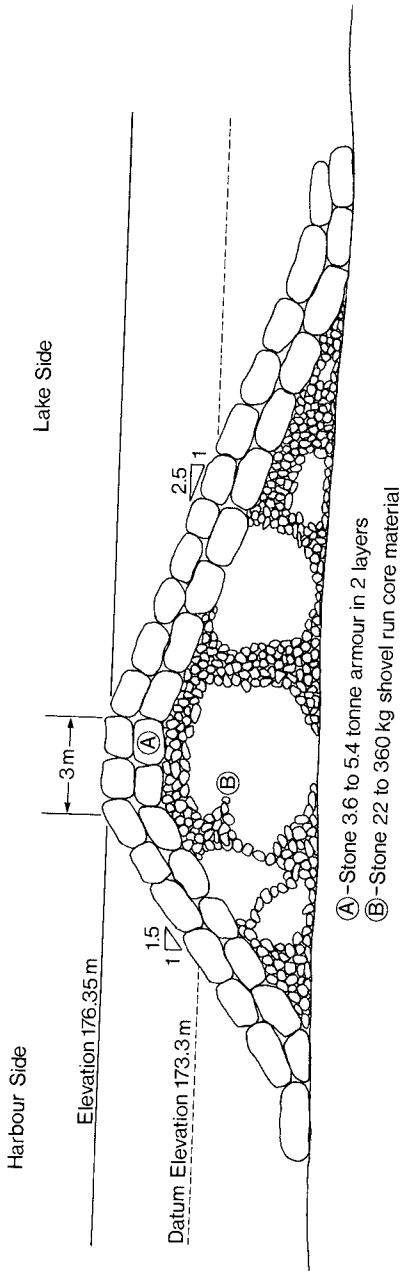


Figure 6. Cross-Section of Recommended Breakwater.



Figure 7. Oblique Aerial Photo of Wheatley Harbour.



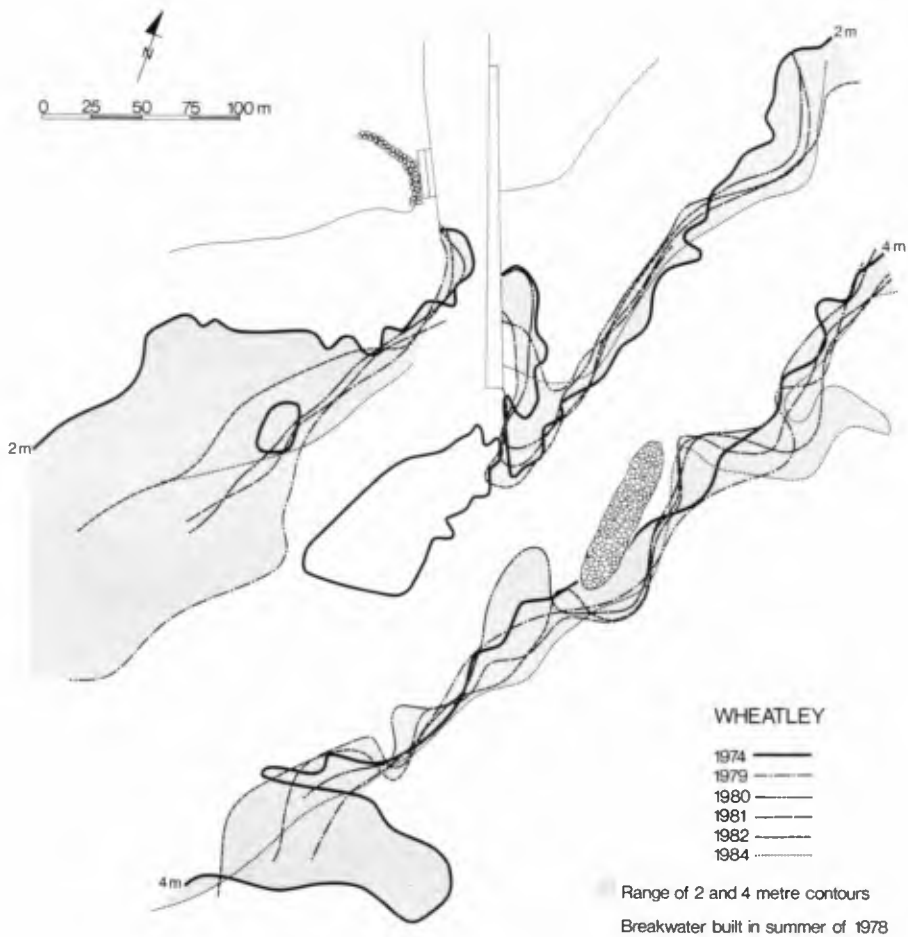


Figure 8 2 and 4 metre contours

- it represented the least cost of all structures meeting the above criteria.

A breakwater approximately 62 metres long was selected, located as shown in Figure 5 and Figure 7. It consists of a rubble mound core protected by two layers of armour stone. The core material is 22 kg to 360 kg shovel quarry run material, with 50 percent greater than 225 kg. The armour stone is 3.6 - 5.4 tonnes with 70 percent of the stone greater than 4.5 tonnes (Figure 6).

The top elevation of the breakwater is at 3 metres above datum which is about 2.5 metres above average lake level and about 1.5 metres above the all-time average monthly high.

The breakwater was constructed in the summer of 1978 at a cost of \$320,000 (Canadian). During its six years of existence, wave breaking has been reduced so that fishing vessels are now able to return to the harbour under storm conditions. The fishermen of Wheatley Harbour are entirely satisfied with the structure.

#### Changes to the Nearshore

The major uncertainty with the offshore breakwater as a solution to the navigation problem was the effect on the movement and deposition of littoral material. Hydrographic surveys have been conducted regularly since the construction in 1978. To illustrate the changes that have occurred, the 2 metre and 4 metre contours from the various surveys have been reproduced in Figure 8. The location of the contours has remained relatively stable since 1978. There has been minimal shoaling behind the breakwater and in the channel.

#### Summary

A relatively small offshore breakwater has been precisely positioned off Wheatley Harbour to provide protection from breaking waves approaching from a narrow easterly sector. This solution allows fishing tugs to enter the harbour safely during storm conditions. Little or no interference with the movement of sediment in the littoral zone has been observed since the breakwater was constructed six years ago.

#### Acknowledgements

The authors are grateful to Ms. D.A. Hempel and Mr. D. Ellis for their assistance in the preparation of this paper.

#### References

1. Bretschneider, C.L. 1970. Forecasting Relations for Wave Generation. Look Laboratory, Quarterly No. 3, Vol. 1, July, P. 90.
2. St. Jacques, D.A. and N.A. Rukavina. 1976. Lake Erie Nearshore Sediments, Port Burwell to Point Pelee, Ontario. National Water Research Institute, Burlington, Ontario.
3. Skafel, M.G. 1977. Wheatley Harbour Model Study. National Water Research Institute, Burlington, Ontario.

## CHAPTER ONE HUNDRED THIRTY

### ON PREDICTING INFRAGRAVITY ENERGY IN THE SURF ZONE

Asbury H. Sallenger, Jr.\* and Robert A. Holman\*\*

#### Abstract

Flow data were obtained in the surf zone across a barred profile during a storm. RMS cross-shore velocities due to waves in the infragravity band (wave periods greater than 20 s) had maxima in excess of 0.5 m/s over the bar crest. For comparison to measured spectra, synthetic spectra of cross-shore flow were computed using measured nearshore profiles. The synthetic spectra were calculated assuming a white runup spectrum of mode-4 edge waves of unit amplitude, although the results would be essentially the same for standing waves or any edge-wave mode above 2. The structure, in the infragravity band, of these synthetic spectra corresponded reasonably well with the structure of the measured spectra. Total variances of measured cross-shore flow within the infragravity band were nondimensionalized by dividing by total infragravity variances of synthetic spectra. These nondimensional variances were independent of distance offshore and increased with the square of the breaker height. Thus, cross-shore flow due to infragravity waves can be estimated with knowledge of the nearshore profile and incident wave conditions.

#### Introduction

Waves in the infragravity band, usually defined as wave periods greater than 20 s, can be energetic in the surf zone when offshore waves are large (for example, Holman et al., 1978; Wright et al., 1979; Guza and Thornton, 1981; Holman, 1981; Holman and Sallenger, in press). In fact, within the swash and inner surf zones, energy in the infragravity band has been observed to exceed, sometimes greatly, the energy of waves in the incident band, wave periods less than 20 s. In view of the significance of energy in the infragravity band, flows caused by infragravity waves are likely important to sediment transport in the surf zone (Bowen and Inman, 1971; Short, 1975; Wright et al., 1979; Wright et al., 1982; Sallenger et al., in press). In this paper, we focus on the prediction of the magnitude of cross-shore flows due to infragravity waves.

\* U.S. Geological Survey, Menlo Park, CA 94025

\*\*Oregon State University, Corvallis, OR 97331

Several studies have tried to quantify the relationship between the magnitude of waves in the infragravity band and parameters characterizing offshore wave conditions. Guza and Thornton (1981) found that significant swash oscillations due to infragravity waves increased with increasing offshore wave height. Using a much larger data set, Holman and Sallenger (in press) showed that infragravity swash oscillations could be predicted better by the Iribarren Number

$$\xi_o = \tan\beta (H_o/L_o)^{-0.5} \quad (1)$$

where  $\beta$  is foreshore slope and  $H_o/L_o$  is deep-water wave steepness.

Runup data, such as used by the two studies discussed above, are particularly useful in determining the relationship between the magnitude of infragravity waves at the shoreline and offshore wave characteristics. This is because infragravity waves in the surf zone have the cross-shore structure of standing waves or high-mode edge waves (Suhayda, 1974; Holman, 1981). Measurements at the shoreline, such as runup, are not affected by offshore decay of energy or by offshore nodal positions which vary with frequency. To use offshore measurements, such as measurements of flow, we must account for the effects of the standing wave structure.

In the present study, cross-shore flow data were obtained across the surf zone during a storm. To account for offshore position of the flow measurements, we nondimensionalized measured variances of cross-shore flow in the infragravity band by computed variances based on a white runup spectrum of edge waves (or standing waves) of unit amplitude. We will show that the nondimensional variances are predictable by incident wave characteristics.

In the following section, we discuss the significance of nondimensional flow variances and how the variances were calculated. After presenting the experimental methods and setting, we discuss measured cross-shore flow data and how flow varied over the barred profile during the storm. Next, we show how well synthetic infragravity spectra, based on the white runup spectrum, matched the measured spectra, and, similarly, how well total variances in the infragravity band of the synthetic spectra matched that of the measured spectra. Finally, we show how nondimensional variances varied with incident wave conditions.

### Theory

As discussed above, a difficulty of interpreting data from fixed locations in the surf zone is that the waves in the infragravity band appear to be standing. The shape of the infragravity part of the spectrum is strongly dependent upon the cross-shore position at which the record was obtained. In order to interpret the offshore flow data, we have calculated synthetic spectra based on a white runup spectrum of mode-4 edge waves with unit shoreline amplitude. The results would be essentially the same for standing waves or edge

waves of any mode above 2. The calculations were performed as described in Holman (1981). Cross-shore flow variances were found numerically for different distances offshore and for different frequencies within the infragravity band. Using these calculated variances, synthetic spectra were computed for distances offshore corresponding to measured spectra. These synthetic spectra offer a means to interpret the measured infragravity spectra in that valleys and peaks associated with standing wave motions can be directly compared to measured spectra.

For a particular distance offshore, we can also compare total variances in the infragravity band of measured and synthetic spectra. A nondimensionalized infragravity variance is given by

$$\lambda^2 = \frac{\int_0^{\zeta} U_{vr}^m(f) df}{\int_0^{\zeta} U_{vr}^c(f) df} \quad (2)$$

where  $U_{vr}^m(f)$  and  $U_{vr}^c(f)$  are measured and computed cross-shore velocity spectra respectively, and  $\zeta$  is the frequency separating incident and infragravity bands. As mentioned above,  $\zeta$  is usually taken rather arbitrarily as 0.05 Hz. Here, we have defined  $\zeta$  for each incident wave condition by determining, visually, the low frequency side of the dominant incident wave peak. Periods of incident wave peaks varied from 10 to 18 s. Using a 20 s (0.05 Hz) cutoff for the spectrum with the 10 s dominant incident wave may underestimate the amount of energy in the infragravity band.

$\lambda^2$  is a measure of the level of energy in the infragravity band, and is independent of position offshore and profile configuration. Thus,  $\lambda^2$  can be directly compared to offshore wave parameters. However,  $\lambda^2$  assumes a white runup spectrum and would not be a useful quantity if the runup spectrum had only one, or a few, energetic frequencies in the infragravity band. It is possible that if a broad band of infragravity energy is forced when offshore waves become large,  $\lambda^2$  may be a useful quantity even if the runup spectrum is not uniformly white. Below we find reasonable correspondence, for data obtained during a storm, between  $\lambda^2$  and a parameter characterizing incident wave conditions.

#### Experiment Setting and Methods

The experiment, known as DUCK82, was conducted during October 1982 at the Field Research Facility (FRF) of the US Army Corps of Engineers in Duck, North Carolina. The FRF is located on a long straight beach of a barrier island. Mason et al. (this volume) present details of the experiment setting, and introduce papers on other investigations conducted during the DUCK82 experiment.

Flow data were obtained using the USGS sled system (described in detail in Sallenger et al., 1983). The system consists of an instrumented sled that was towed along the bottom, both offshore and onshore, with a double-drum winch and triangular-line arrangement. Three electromagnetic current meters (Marsh-McBirney model 512) in a

vertical array and a pressure sensor were mounted onto the frame of the sled and the data were telemetered to a shore receiving station. The nearshore profile was measured using an infrared rangefinder on the beach and optical prisms mounted on top of the sled's mast. The sled system was set up 500 m north of the FRF pier, presumably outside the influence of the pier (Mason et al., this volume).

The flow data discussed here were obtained with a current meter mounted on the sled 1 m above the bottom. For a given day, records were obtained at five to eight locations across the surf zone. Each record was 34.1 minutes long. A set of records was obtained around high tide to minimize depth variations during the runs.

### Results

Much of the cross-shore flow data discussed here were taken during a storm, October 10-12, 1982. The remainder of the data were taken immediately following the peak of the storm, Oct. 13, and on a relatively calm day when nearshore morphology was not highly three-dimensional, Oct. 20. Details of the meteorological and wave characteristics of the storm and post-storm period are given in Mason et al. (this volume). An example of the bar response during the storm is shown in Fig. 1A. The bar migrated offshore at rates up to 2.2 m/hr. Following the storm, the bar morphology developed into a classic example of a crescentic bar. Mason et al. (this volume) and Sallenger et al. (in press) discuss the storm-induced response of the nearshore morphology.

RMS cross-shore flows due to waves in the infragravity band exceeded 0.5 m/s (Fig. 1B). We defined infragravity RMS cross-shore flow as

$$U_{rms\_ig} = \left( \int_0^{\zeta} U_{vr}^m(f) df \right)^{0.5} \quad (3)$$

Note that maxima in cross-shore flow occurred at the crest of the bar. These flow maxima are evidently the result of mass transport over the shallow water of the bar crest.

Relative magnitudes of cross-shore flows due to infragravity waves and incident waves are shown in Figure 1C. At places within the inner surf zone, cross-shore flow variances in the infragravity band approached or exceeded variances in the incident band. Note that for everywhere on the profile, ratios of variances in the infragravity band to those in the incident band for October 12 are greater than ratios for October 10. Since variances in the incident band are limited by wave breaking (the breaker zone occurring several hundred meters farther offshore than our seawardmost measurement location), Figure 1C indicates that infragravity energy became increasingly important during the two days. Below, we will try to quantify a relationship between infragravity energy and characteristics of offshore waves.

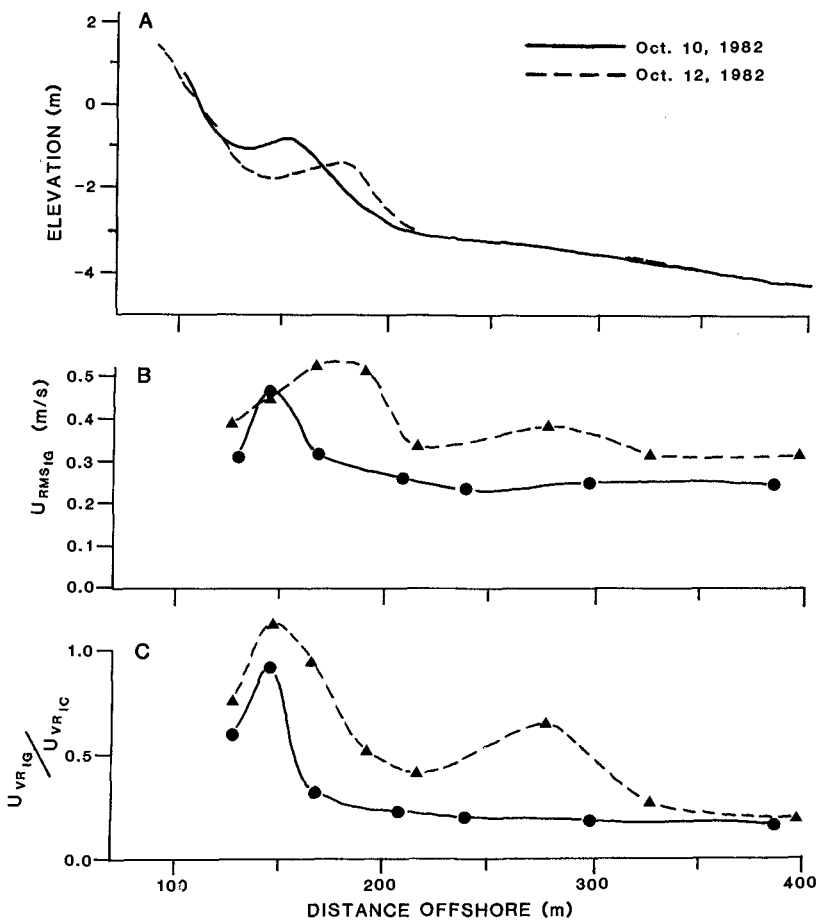


Figure 1. A. Nearshore profiles measured with the USGS sled system for two of the storm days. B. Measured RMS cross-shore flows of the infragravity band. C. Ratios of variances of the infragravity band to variances of the incident band.

We present four spectra from a single day (Figs. 2 and 3) to illustrate the correspondence between measured and synthetic spectra. The locations of each measurement station on the nearshore profile are shown in Figure 4. As discussed above, the synthetic spectra are based on a white runup spectrum of unit amplitude. The measured spectral structures agree reasonably well with the synthetic structures. For example, spectral valleys, which indicate positions of zero crossings (nodes), of the measured spectra coincide closely with valleys of synthetic spectra. Energy levels of synthetic spectra were adjusted by moving the spectra vertically in order to fit the lower energy peaks of the measured spectrum. For a given set of records, all obtained on the same day under basically the same incident wave conditions, the calculated spectra are moved vertically the same amount. Any dominant peaks in the measured spectra would rise above the synthetic spectra. (Alternatively, the energy levels of synthetic spectra could have been adjusted by multiplying by the mean of  $\lambda^2$  for a given day which would yield a best fit between the measured and synthetic spectra). Much of the infragravity energy in the measured spectra fits the synthetic spectra; however, at some frequencies energy in the measured spectra exceeds the energy in the synthetic spectra. At these frequencies, there should be peaks in the runup spectrum, that is, the runup spectrum was not white. These dominant peaks appear to have been induced by the bar offshore; their significance will be discussed elsewhere.

For a particular distance offshore, we define a synthetic infragravity variance as

$$U_{vr,ig}^c = \overline{\lambda^2} \int_0^{\zeta} U_{vr}^c(f) df \tag{4}$$

where the overbar indicates that  $\lambda^2$  is averaged for all offshore positions for a given day. A measured infragravity variance is given by the numerator of equation 2. In Figure 5, we compare measured and synthetic infragravity variances for different distances offshore. Only two days are shown, but the correspondence is similar for all days. Since the shapes of the curves for each day are nearly the same,  $\lambda^2$  (equation 2) is roughly constant for a given day and independent of distance offshore.

For five different days with greatly varying incident wave conditions, values of  $\lambda^2$  were calculated. In Figure 6 we show how mean  $\lambda^2$  for a given day varied with the square of the offshore significant breaker height,  $H_b$ .  $H_b$  was calculated from offshore wave characteristics using Komar and Gaughan (1973). There is good correspondence between  $H_b^2$  and  $\lambda^2$ . Linear regression gives

$$\overline{\lambda^2} = 0.45 H_b^2 - 0.60 \tag{5}$$

with  $r = 0.99$ . For equation 4 to be dimensionally correct, a factor of unity with dimensions of  $m^{-2}$  is multiplied times the slope.



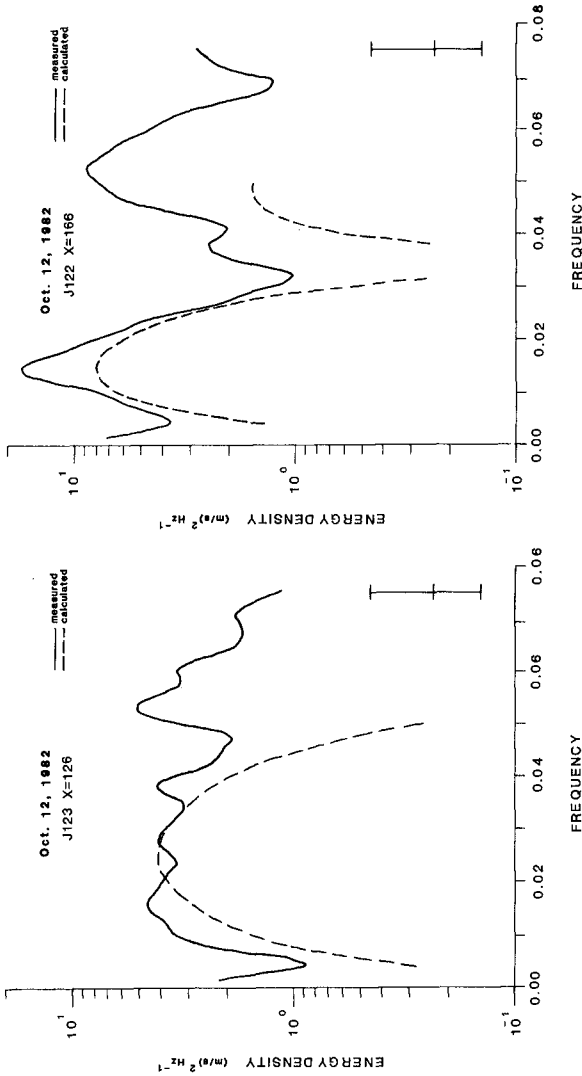


Figure 2. Surf-zone spectra from October 12, 1982. X indicates distance offshore in meters from a baseline; the shoreline relative to this baseline is about 110 m. The number preceded by the J is the run number. 95% confidence limits are shown. The location of each measurement station is shown in Fig. 4.

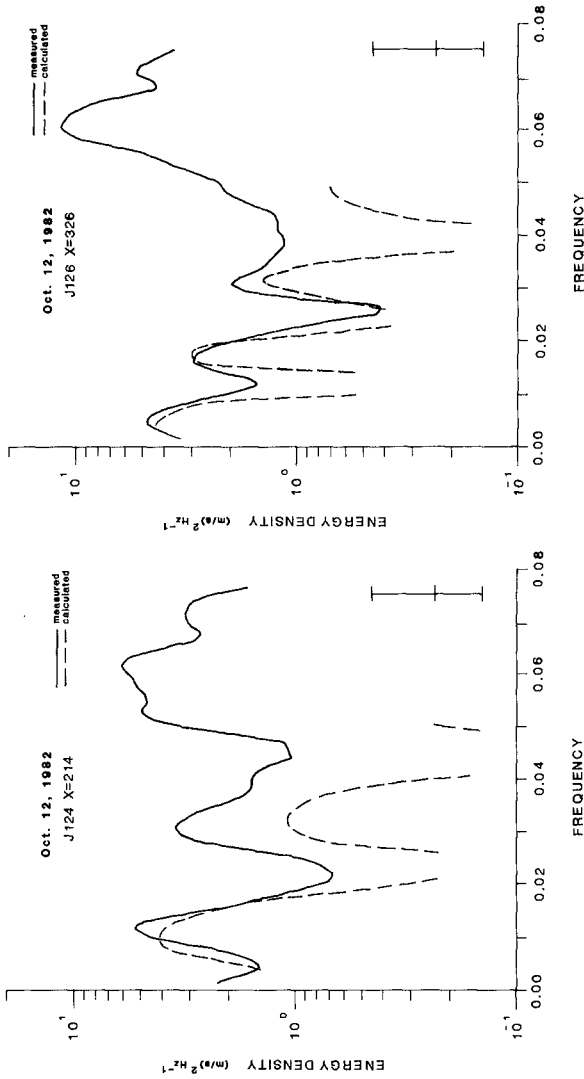


Figure 3. Surf-zone spectra from October 12, 1982. X indicates distance offshore in meters from a baseline; the shoreline relative to this baseline is about 110 m. The number preceded by the J is the run number. 95% confidence limits are shown. The location of each measurement station is shown in Fig. 4.

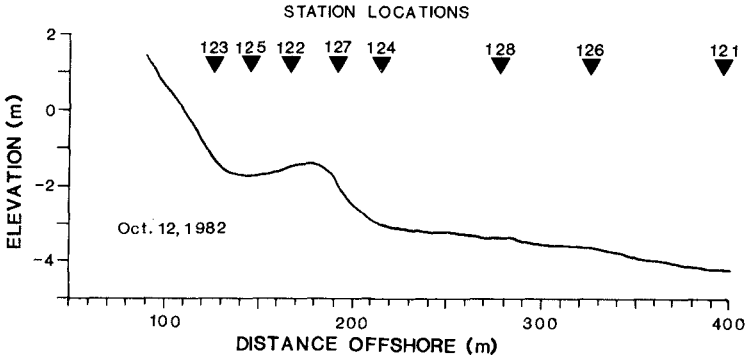


Figure 4. Station locations for October 12. The numbers refer to the J numbers shown on the spectra of Figures 2 and 3.

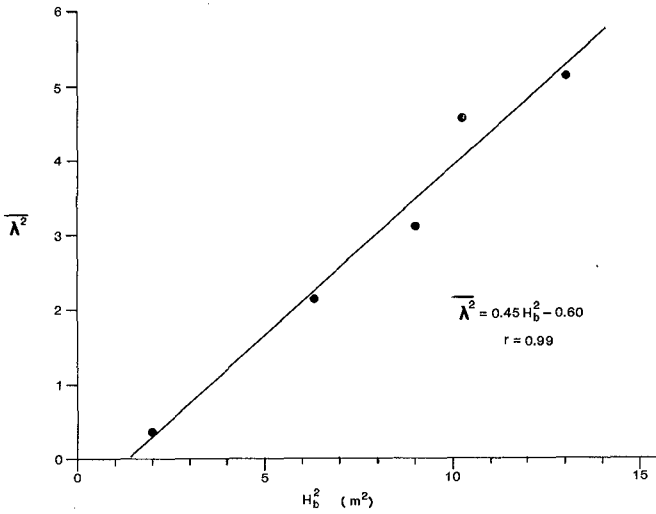


Figure 6. Nondimensional cross-shore flow variances of the infragravity band,  $\lambda^2$  equation 2, averaged for all offshore positions for a given day are dotted against the square of the breaker height.

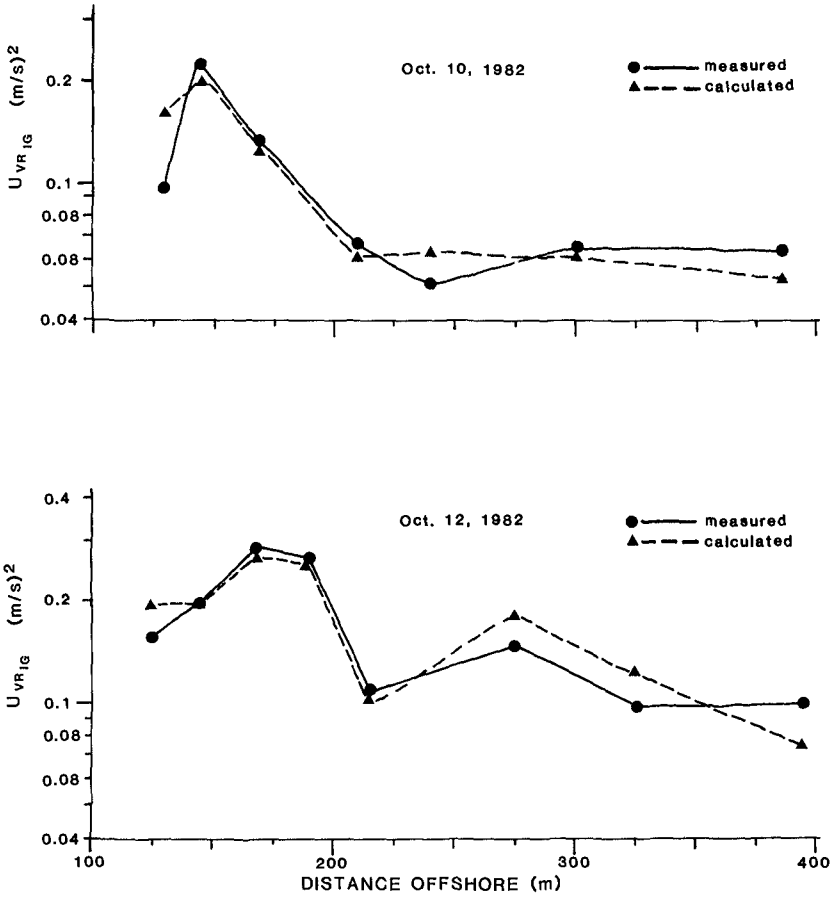


Figure 5. Measured and synthetic variances of the infragravity band. Synthetic variances are defined by equation 4. Measured variances are defined by the numerator of equation 2.

### Discussion

Recall that for  $\lambda^2$  to be applicable, the shoreline spectrum should be white, although we have shown in the discussion of the spectra that the runup spectrum was not white. The implication is that nondimensionalizing cross-shore flow variance, as done in equation 2, is reasonable when the runup spectrum has significant energy across the infragravity band even when that energy is not perfectly white.

It should be interesting to add additional data to Figure 6 to determine whether the relationship is similar for other morphologies and other beaches. However, since we plot against a dimensional quantity in Figure 6 the universal applicability of equation 4 is probably limited. As an alternative, we have plotted the dimensionless Iribarren number,  $\xi_0$  (equation 1) which seems to parameterize many surf zone processes, against  $\lambda^2$ , but the correspondence is not as good as with  $H_b^2$  (correlation coefficient of 0.56 compared to 0.99).

Knowing the shape of the profile and the breaker height, one can calculate reasonably well the flow due to infragravity waves in the surf zone, at least for the location studied. Since we can also calculate the RMS cross-shore flow in the incident band, incident waves being limited by depth in the surf zone, we can estimate the total oscillatory velocity field. The calculation of total oscillatory flow should be useful for numerical modelers who usually focus on modeling only incident band flows and waves. It should also be useful for sediment transport applications.

### Conclusions

1.  $U_{rms}$  due to infragravity waves was maximum over the bar crest where it exceeded 0.5 m/s. Cross-shore flow variance due to infragravity waves approached or, in places, exceeded variance in the incident band.

2. As in some earlier studies, calculated spectra, based on a white runup spectrum compared reasonably well with measured spectra.

3. Cross-shore flow variance due to waves in the infragravity band were nondimensionalized by dividing by computed variances based on a white runup spectrum. The nondimensional variances increased with the square of the offshore breaker height.

### Acknowledgments

We thank the many persons who contributed to the success of the DUCK82 experiment including Jeff List, Tom Reiss, Peter Howd, Bruce Richmond, Bruce Jaffe, Beth Laband, and the U.S. Army Corps of Engineers crew at the Field Research Facility. We thank David Barnes for doing most of the calculations reported in this paper. Our part of the experiment and the data analysis were funded jointly by the

U.S. Geological Survey and the U.S. Army Corps of Engineers Waterways Experiment Station.

#### References

- Bowen, A. J., 1980, Simple models of nearshore sedimentation: beach profiles and longshore bars. In: S. B. McCann (Ed.), *Coastline of Canada, Littoral Processes and Shore Morphology*, Geol. Surv. Can., Pap. 80-10, p. 1-11.
- Bowen, A. J., Inman, D. L., 1971, Edge waves and crescentic bars, *J. Geophys. Res.* 76, 8662-8671.
- Guza, R. T. and Thornton, E. B., 1981, Wave setup on a natural beach, *J. Geophys. Res.* 86(c5), 4133-4137.
- Holman, R. A., 1981, Infragravity energy in the surf zone, *J. Geophys. Res.* 86(c7), 6422-6450.
- Holman, R. A., Huntley, D. A., and Bowen, A. J., 1978, Infragravity waves in storm conditions, *Proc. 16th Coastal Eng. Conf.*, p. 268-284.
- Holman, R. A. and Sallenger, A. H., in press, Setup and swash on a natural beach, *J. Geophys. Res.*
- Komar, P. D. and Gaughan, M. K., 1973, Airy wave theory and breaker height prediction, *Proc. 13th Conf. Coastal Eng., Am. Soc. Civ. Eng.*, p. 405-418.
- Mason, C., Sallenger, A. H., Holman, R. A., and Birkemeier, W. A., in press, DUCK82 - A coastal storm processes experiment, *Proc. 19th Coastal Engineering Conference, Am. Soc. Civ. Eng.*
- Sallenger, A. H., Holman, R. A., and Birkemeier, W. A., in press, Storm response of a nearshore bar system, *Marine Geology*.
- Sallenger, A. H., Howard, P. C., Fletcher, C. H., and Howd, P. A., 1983, A system for measuring bottom profile, waves and currents in the high-energy nearshore environment, *Marine Geology*, 51, p. 63-76.
- Suhayda, J. N., 1974, Standing waves on beaches, *J. Geophys. Res.* 72, 3065-3071.
- Wright, L. D., Chappell, J., Thom, B. G., Bradshaw, M. P., and Cowell, P., 1979, Morphodynamics of reflective and dissipative beach and nearshore systems: southeastern Australia, *Marine Geology*, 32, 105-140.
- Wright, L. D., Guza, R. T., Short, A. D., 1982, Dynamics of a high energy dissipative surf zone, *Marine Geology*, v. 45, p. 41-62.

## CHAPTER ONE HUNDRED THIRTY ONE

### SEDIMENT TRANSPORT ON THE SOUTH-EAST AUSTRALIAN CONTINENTAL SHELF

Angus D. Gordon and John G. Hoffman\*

#### ABSTRACT

Engineering projects on the continental shelf off Sydney, Australia, have stimulated investigation into the sediment transport system of the shelf. Investigation activities associated with these projects have included: definition of sea bed morphology, sediment distribution and bedform characteristics; monitoring of steady and wave induced currents; wind data collection; suspended sediment sampling; bottom camera sediment movement investigations and analytical studies of sediment reaction to sea bed forcing functions. Sea bed velocity exceedence relationships for both wave oscillations and steady currents have been determined at depths of 24 m, 60 m and 80 m. Thresholds of sediment movement have been defined. Relative sediment transport computations have been undertaken and studies of suspended sediment concentration profiles are in progress so that absolute transport rates can be determined. The prevailing conditions, which include a mainly south bound current, are seldom sufficient to induce entrainment of shelf sediments. Transport events mainly result from major storms in the Tasman Sea which produce both high energy waves and north bound currents. Although these events are rare and short lived, the combined wave and current shear produced at the sea bed during the events gives rise to entrainment conditions which result in their dominance of the shelf sediment transport system.

#### 1. Introduction

The coincidence of a number of engineering studies on the continental shelf off Sydney, Australia, has provided the opportunity to study shelf bed characteristics and sediment transport under the combined action of currents and the prevailing wave spectra. This paper examines the forcing functions on the sea bed outside the surf zone in water depths from 24 metres to 80 metres. It also documents the response of the sediments to the forcing functions. The location of the study area is shown in Figure 1.

#### 2. Physiographic Setting

The S.E. Australian continental shelf off Sydney varies in width from 20 to 40 kilometres. Its surface comprises a mixture of unconsolidated sediments and bedrock reef (Figure 2). Seaward of the

---

\*Coastal Branch, N.S.W. Public Works Department,  
140 Phillip Street, Sydney, N.S.W. 2000, Australia.

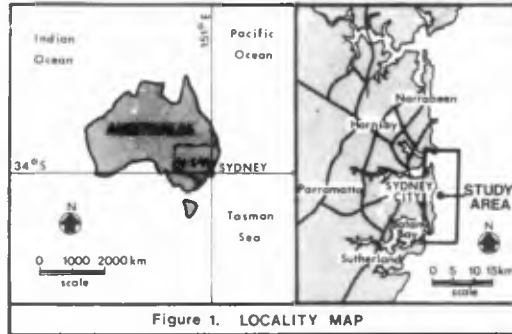


Figure 1. LOCALITY MAP

surf zone, the profile is generally concave up with slopes of 1:50 in 20 metres depth and 1:100 in 80 metres depth. Typically, the 20 metre contour is 1 km and the 80 m contour 10 km offshore. There are locations where the profile is considerably steeper. This occurs where extensive rocky cliff formations are the predominant coastal feature. In these locations the 20 metre contour is often less than 200 metres offshore with the 80 metre contour some 3 km offshore (Figure 2).

Sea bed sediments gradually become finer from medium sands in the surf zone with typical values of  $d_{50}$  of 0.35 mm to a  $d_{50}$  of 0.18 mm in 14 m depth. These fine sands continue out to depths of 25 to 30 m. From 30 m out to about 60 m, a diverse suite of sediments are found. They range from fine sand to coarse sand and gravel. Deeper than 60 m, fine sands with some silt content predominate. Shell contents are highly variable but are generally highest near areas of exposed reef. Shelf sediment types and their distribution are shown in Table 2 and Figure 2.

Morphological anomalies associated with sediment features occur in certain locations. These features include convex upwards sand lobes, cross shelf sand ridges and mid shelf sand bodies with rhythmic asymmetric morphology (Figure 2).

### 3. Shelf Data

Data were obtained from an extensive side scan sonar and sediment sampling survey of the Sydney coast (Gordon and Hoffman, in prep, (a)) and from detailed studies at three sites across the shelf (Nielsen, 1984; Gordon and Hoffman, in prep, (b)). Table 1 summarises the instrumentation used and the data collected at the three sites. All instruments were calibrated before and after deployment and cross spectral checks between the electromagnetic current meters and the waverider buoys were also carried out (Nielsen and Gordon, 1984).



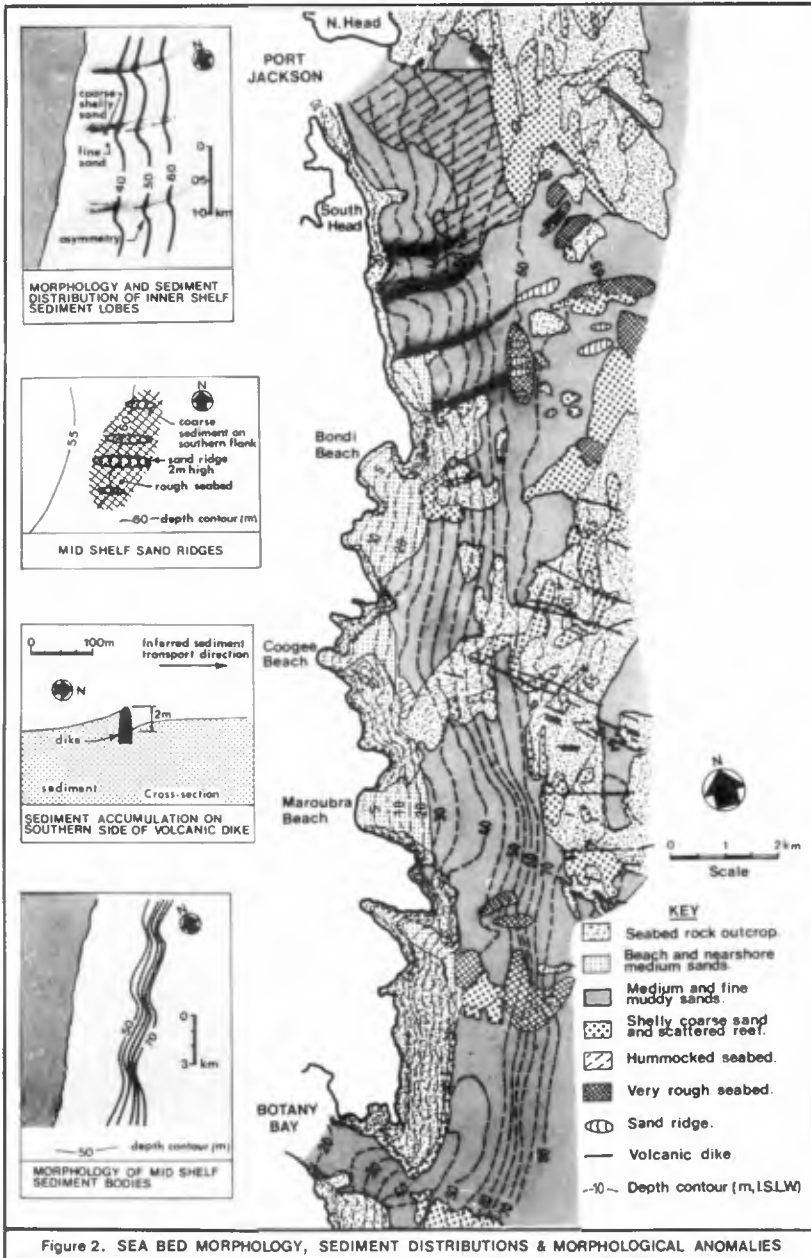


Figure 2. SEA BED MORPHOLOGY, SEDIMENT DISTRIBUTIONS & MORPHOLOGICAL ANOMALIES

TABLE 1. STUDY SITES, INSTRUMENTATION AND DATA COLLECTED.

Water depth	Period of data collection	Instrumentation and sampling schedules *				
		Waves	Currents	Wind	Sediments	Seobed morphology and bedforms
24m	24 months	Waverider buoy. 1/2 s x 18m x 6h.	Marsh M <sup>c</sup> Birney X-Y current meter. 1s x 10m x 7h.	Dynes anemograph. Continuous.	Surface samples, diver and vibro coring.	Side-scan sonar and diver observations.
60m	6 months	Waverider & dynamic pressure sensor. 1/2 s x 18m x 4h	Marsh M <sup>c</sup> Birney X-Y current meter. 1s x 8m x 4h.	Lambrecht anemometer. Continuous.	Surface samples, vibra and box coring, suspended sediment samples.	Side-scan sonar, RCV video & time lapse camera. 32s x 8m x 4h.
80m	6 months	Waverider & dynamic pressure sensor. 1/2 s x 18m x 4h.	Marsh M <sup>c</sup> Birney X-Y current meter. 1s x 8m x 4h.	Lambrecht anemometer. Continuous.	Surface samples, vibra and box coring, suspended sediment samples.	Side-scan sonar, RCV video & time lapse camera. 32s x 8m x 4h.

\* Sampling schedule : As x Bm x Ch = burst sampling at intervals of A seconds continuously for B minutes every C hours

4. Forcing Functions

The forcing functions which may influence sediment transport on the Sydney shelf are:

- steady currents due to -
  - (a) the onshelf component of ocean currents;
  - (b) wind induced currents; and
  - (c) wave induced mass transport;
- tidal currents; and
- oscillatory currents induced by surface gravity waves.

4.1 Ocean Currents

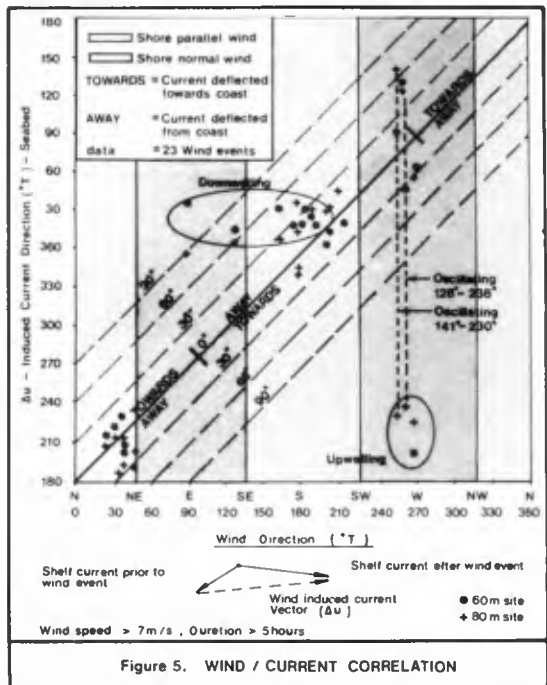
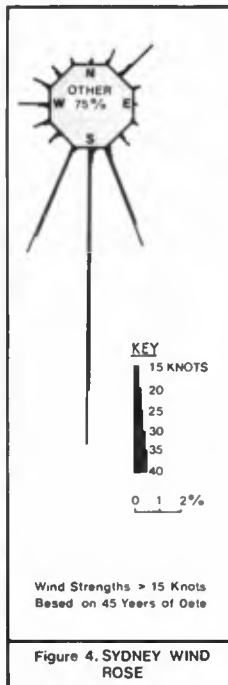
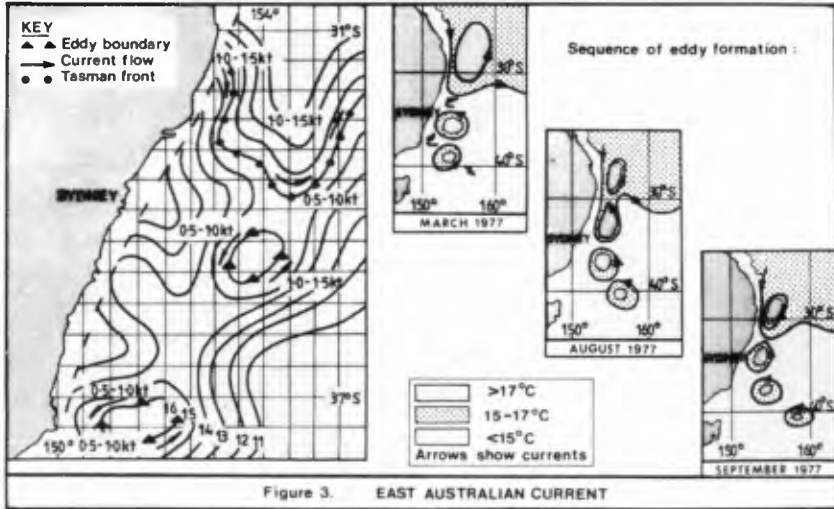
The S.E. Australian shelf is influenced by the offshore East Australian Current. Originally believed to be a southbound flow along the western extremity of the Tasman Sea, it is now known to consist of a complex system of migrating eddies (Nilsson and Cresswell, 1980; see Fig.3).

4.2 Wind Induced Currents

Local winds induce currents which act to modify the prevailing onshelf regime. Rotation of these currents from the prevailing wind direction can occur due to the Ekman effect (to the left in the southern hemisphere). At the shelf bed near the coast, compensating currents in the form of upwellings and downwellings may also be experienced.

Analysis of the study data showed that a direct correlation exists between the anemometer information and the induced change of current behaviour (Figures 4 and 5) for events when the wind speed exceeds 7 m/s for a duration of more than 5 hours. At lesser wind speeds or durations, no clear trend was discernible.

The lag between the commencement of the wind event and the impact on the prevailing current regime is typically between 4 and 24 hours. Prevailing current strength and direction as well as wind strength, direction and duration determine the lag period. Subjective judgement



was required in determining onset of these events. The present data set is considered insufficient to explore the lag question further.

Data for shore parallel wind events with wind speeds greater than 7 m/s and duration greater than 5 hours which produced approximately shore parallel currents were used to compare observed bottom currents with those predicted by Bretschneider's (1967) method:

$$\frac{\bar{V}}{U} = \sqrt{\frac{k}{k^*} \sin\theta} \tanh\left[\frac{Ut}{D} \sqrt{kk^* \sin\theta}\right]$$

- where  $\bar{V}$  = depth averaged current
- $U$  = sustained wind speed
- $k$  = surface stress parameter ( $3 \times 10^{-6}$ )
- $k^*$  =  $n^2 g D^{-1/3}$
- $n$  = Manning factor (0.025)
- $D$  = water depth
- $t$  = duration of wind speed
- $\theta$  = angle between wind and shore normal

The resulting observed and predicted currents, corrected to 1 m above the sea bed, are presented in Figure 6 and show reasonable agreement. Hence, based on the limited data set available, a tentative relationship between wind speed/duration and induced sea bed current magnitude at the 60 m and 80 m sites was determined (Figure 7).

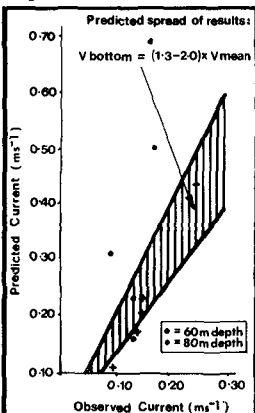


Figure 6. PREDICTED AND OBSERVED BOTTOM CURRENTS

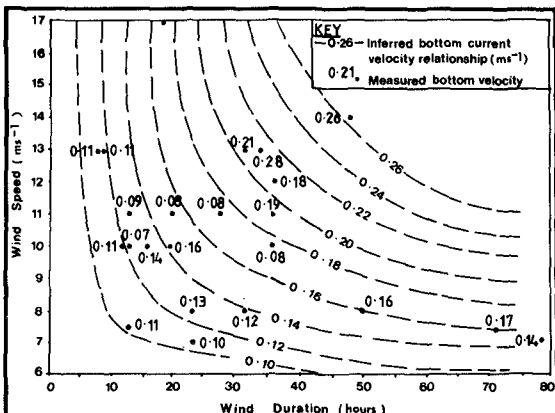


Figure 7. SUGGESTED RELATIONSHIP BETWEEN WIND SPEED / DURATION AND INDUCED SEA BED CURRENT FOR SYDNEY SHELF

### 4.3 Wave Induced Mass Transport

The depth of water in the study area is such that in general the wave induced mass transport is negligible and was therefore neglected. The time series data from the current meter records supported this approach. That is, changing wave conditions produced no discernible change in steady current direction or strength.

### 4.4 Tidal Currents

The steep nearshore slopes, the relatively narrow shelf and the small ocean tidal range (mean value 1.2 m) combine to produce weak tidal currents on the shelf. Hamon (1984) carried out a tidal analysis of the study data. He showed that longshore tidal components are in the order of 1 cm/s and offshore components are negligible. Therefore, as with the wave induced mass transport, tidal currents are not considered to be a significant factor in shelf sediment transport in the study area.

### 4.5 Wave Oscillations

The S.E. Australian continental shelf experiences a moderate to high energy wave environment. Deep water significant wave heights of 1.5 m are exceeded 50% of the time and spectral peak periods are typically between 8 and 12 seconds (Figures 8 and 9). During severe storms however, the significant wave height can reach 10 to 12 metres with peak periods of 14 to 16 seconds. A synoptic chart for a typical storm in the Tasman Sea is shown in Figure 10.

An analysis of the study data and a comparison with 10 years of waverider data at Sydney (Youll, 1981; Figure 8) was undertaken. This showed that the two data sets produced almost identical wave height exceedence curves (Gordon and Hoffman, in prep, (b)), indicating that the study data could be taken to be representative of the long term wave climate.

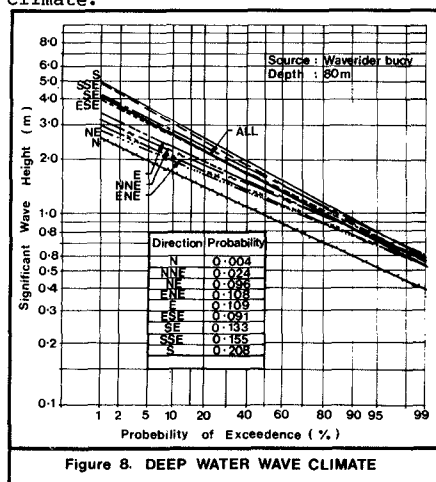


Figure 8. DEEP WATER WAVE CLIMATE

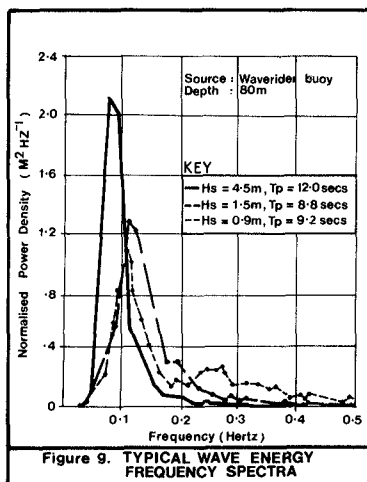
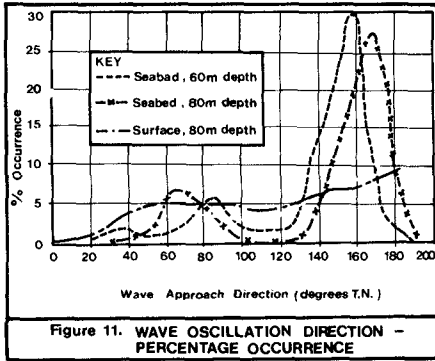
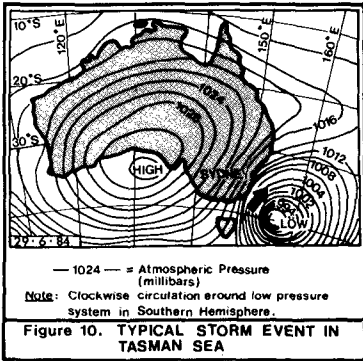


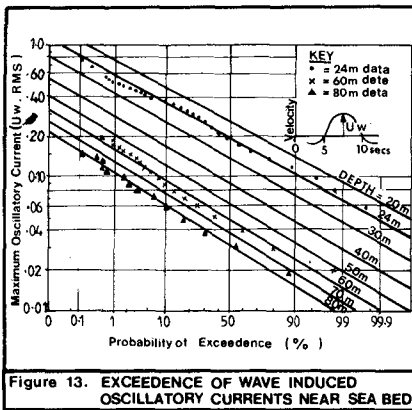
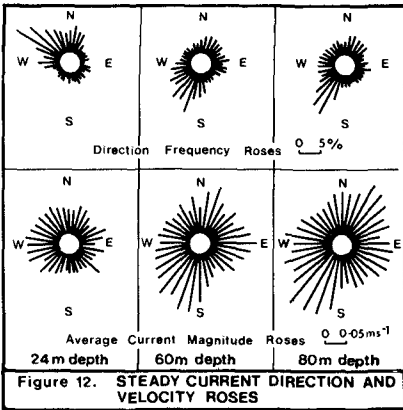
Figure 9. TYPICAL WAVE ENERGY FREQUENCY SPECTRA

Comparison of the directional wave oscillation records from the electromagnetic current meters with the long term directional statistics based on surface observations produced an interesting result. Particularly at the 60 and 80 m sites the depth dependent high frequency filtering showed that the majority of the recorded longer period energy comes from the south-east to south sector; the Lower Tasman Sea generating area. This contrasts with several years of wave directional data obtained at the surface which suggest that there is only a weak bias towards this sector (Fig. 11). It does however explain previously noted anomalies associated with attempts to match surf zone sediment transport calculations on the N.S.W. coast to recorded shoreline changes using the sea surface observations (Gordon et al, 1978).



4.6 Combined Forcing Functions

Seabed wave oscillations combine with steady currents to entrain sediment whilst the steady currents act to transport the suspended material in the direction of the current. The electromagnetic current meters and sampling schedules selected enabled the determination of both the steady currents due to wind and ocean movements (Figure 12) and the wave induced oscillations one metre above the bed (Figure 13).



Exceedence curves of near bed steady and oscillatory currents at depths of 24 m, 60 m and 80 m are shown in Figures 14 to 16. These indicate steady current components ( $U_C$ ) and the root mean square and 1% values of both the maxima of the oscillatory components ( $U_W$ ) and of the vector addition of the steady and oscillatory components ( $U_{C+W}$ ). The latter analysis was undertaken record by record (at one second intervals), taking into account the directions of both the steady and oscillatory components. The wave oscillation velocity parameter  $U_{1\%}$  was selected based on the arguments put forward by Nielsen and Gordon (1984) that this parameter is the most appropriate for determining sediment entrainment under natural wave spectra. The ratio  $U_{1\%}$  to  $U_{rms}$  was investigated over some 70 records. Based on the statistical mean of the results, the relationship adopted was:  $U_{1\%} = 1.75 U_{rms}$ . This suggests that seabed wave oscillatory velocities in this depth of water do not fit a Rayleigh distribution (Rayleigh gives  $U_{1\%} = 2.15 U_{rms}$ ).

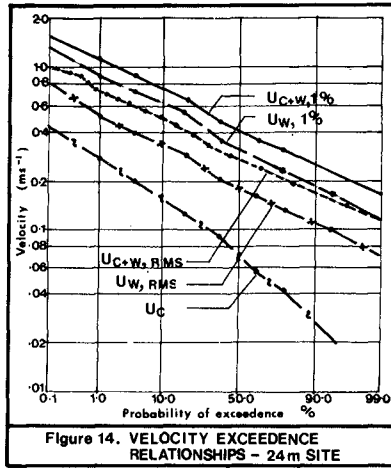


Figure 14. VELOCITY EXCEEDENCE RELATIONSHIPS - 24m SITE

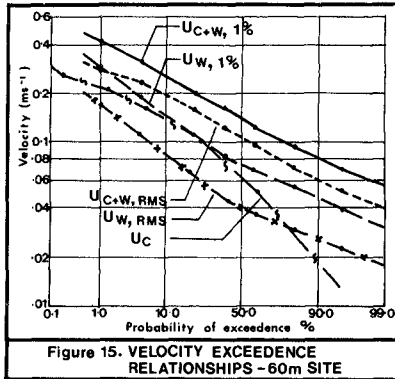


Figure 15. VELOCITY EXCEEDENCE RELATIONSHIPS - 60m SITE

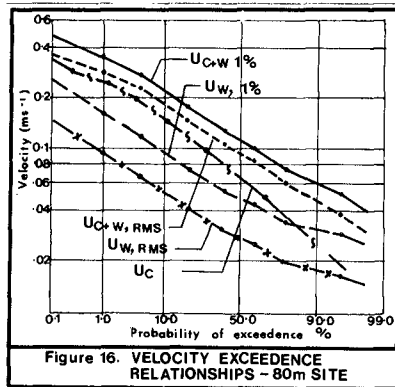


Figure 16. VELOCITY EXCEEDENCE RELATIONSHIPS - 80m SITE

5. Sediment Transport

Sediment transport on the Sydney shelf was analysed by considering the following questions:

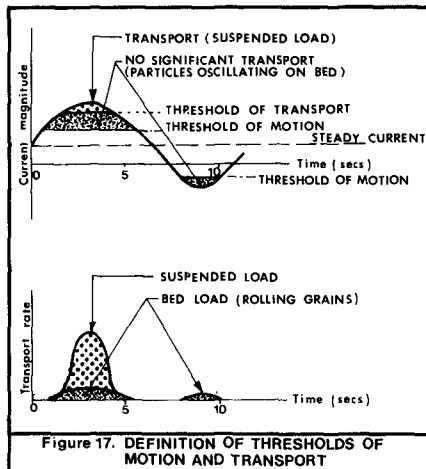
- . What is the availability of sediment, both in terms of areal extent and sediment type?
- . Under what hydraulic conditions do the various sediments move?
- . How often are these conditions exceeded?
- . What is the direction and magnitude of both the gross and net sediment transport?

5.1 Availability

Side scan sonar, fathometer and seismic studies were used to determine the availability of sediments (Figure 2). Surface sediment sampling and R.C.V. video studies provided the detailed surface sediment data. In all, some 650 bottom surface samples and some 41 sub-bottom cores were obtained. Grain size distributions were determined hydraulically in a calibrated fall velocity tube (Gordon and Hoffman, in prep, (a)). Table 2 shows sediment characteristics at various water depths.

5.2 Threshold of Movement

Two thresholds of movement under combined waves and currents are recognised: the threshold of motion and the threshold of transport (Figure 17). The former occurs when the oscillatory shear is sufficient to result in sediment oscillation without net translation, a phenomenon observed in both the R.C.V. and diver studies. The latter (transport) occasionally occurs when the steady currents produce sufficient shear to initiate bed load transport. More commonly on the Sydney shelf however, the threshold of transport is only exceeded when the wave induced motion entrains the sediment. The entrained sediment is then transported by the prevailing steady current.





Entrainment may be caused by boundary layer flow instabilities around bed forms (Nielsen, 1979) or simply result from the combined wave and current shear exceeding that required to lift sediment particles from the bed.

Study site data showed that significant bedforms are present most of the time at the 24 m site (Nielsen and Gordon, 1984); they were also noted from the R.C.V. film and from the side scan survey out to about 40 metres depth. At the 60 metre site, bedforms were only observed on 18 occasions during the 6 months time lapse camera deployment. At the 80 m site no hydraulically induced bedforms were recorded on any of the instruments.

It was noted from the bottom cameras and the samplers that on many occasions fine sediments were in suspension without there being noticeable changes to sea bed conditions. Significant sediment transport events involving major bed changes did, however, occur at all sites. At these times, the current meter data showed that the threshold of motion, as defined by the modified Shields curve (Madsen and Grant, 1976), had been exceeded (Gordon and Hoffman, in prep, (b)). The bed at the deeper sites tended to rapidly progress from a flat bed, pock marked by animal burrows, to a sheet flow condition. During these events, both the coarse and fine fraction of the sediment were captured in the suspended sediment sampler array.

Flume studies under steady flow conditions and mechanical soils tests carried out to examine the progression from no transport to sheet flow indicated that the higher silt content of the sediments at the deeper sites caused them to behave in a semi-cohesive manner until the bed shear was sufficient to directly entrain both the fine and coarse fractions.

It was noted that bedform development and geometry is more marked in the regions where the sediments include significant shell hash (> 5%). This effect appears to be proportional to the coarse shell fragment content of the sediment. It was not, however, a feature of sediments where the shell fraction was medium to fine.

Table 2 presents the results from the threshold of motion studies from flume tests under steady flow and from the bottom camera and diving data. To date, velocity has been used as the parameter for defining thresholds. Although the methods of Madsen and Grant have been used to calculate shear stress, it is recognised that further work is required before meaningful determination of this parameter can be undertaken. In particular, the calculation of both an appropriate friction factor for semi-cohesive flat beds with appreciable biological activity and the determination of the relevant boundary layers and velocity distribution for wave spectra require further research.

It was found that calculations using Jonsson based approaches were sensitive to determination of friction factor and in particular to which velocity parameter was chosen to represent the wave spectra, e.g.  $U_{rms}$  or  $U_{1\%}$ .

TABLE 2. SEDIMENT GRAIN SIZES, THRESHOLDS OF MOTION AND TRANSPORT AND TRANSPORT VELOCITIES

Water depth (m)	Sediment					Comment	Threshold of motion ( $U_{ms}^{-1}$ )		Threshold of transport ( $U_{ms}^{-1}$ )		Transport velocity ( $U_{ms}^{-1}$ ) at activity levels			
	grain size (mm)			silt content	shell content		steady currents	currents* and waves	steady currents	currents* and waves	5	6	7	8
	d <sub>16</sub>	d <sub>50</sub>	d <sub>84</sub>											
24	0.30	0.24	0.16	1%	31%	medium fine sand	0.20	0.14	0.40	0.22				
40	0.75	0.62	0.35	2%	35%	coarse sand with shell fragments	0.26	0.10	0.35	0.18				
60	0.33	0.20	0.16	14%	26%	med fine sand silty fine shell	0.20	0.13*	0.30	0.14*	0.13*	0.14*	0.16	0.24
80	0.19	0.17	0.15	32%	33%	fine silty sand, fine shell fraction	0.30	0.10*	0.38	0.13*	0.10*	0.13*	0.20	

\*  $U_c + U_w$

5.3 Exceedence of Threshold

Diver observations and the time lapse camera data were used to determine the exceedence of threshold. Camera data were subjectively assessed and classed into various activity levels (Figure 18). The hydraulic parameters associated with these levels were then determined. The suspended sediment sampling bottles attached to the current meter frames provided data on the grain size of the sediment being transported at various heights (up to 2.1 m) above the seabed. The camera data and sample bottles indicated that the fine fraction of the sediment tended to be in suspension at activity levels of 4 to 5 whilst activity levels of 6 to 7 were required for the coarser fraction. (Because of the inherent problems of such sampling devices, no attempt was made to use the samples collected in the bottles as a measure of sediment transport or to develop depth/concentration relationships.)

When considered in terms of shear stress, this result contradicts the implications of the Shields curve which suggests that the finer material should be more difficult to entrain. Although the Shields approach was developed for steady flow conditions only, Madsen and Grant (1976) and others have suggested that it can be applied, with suitable choice of parameters, to oscillatory motion.

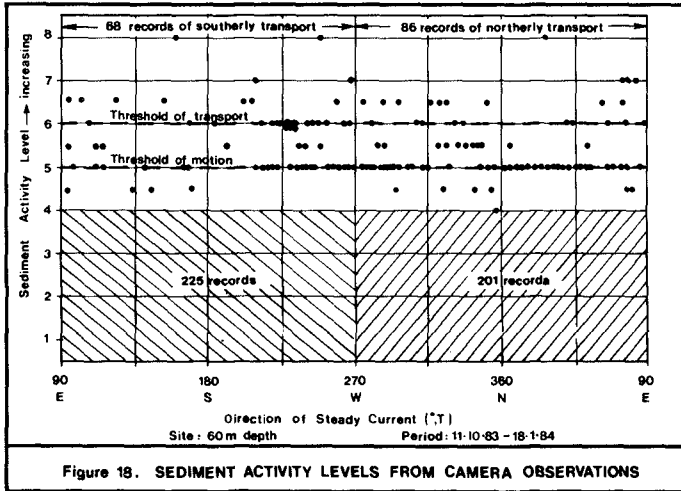


Figure 18. SEDIMENT ACTIVITY LEVELS FROM CAMERA OBSERVATIONS

Two possible explanations for the observed phenomenon are suggested. The first is that fine sediment seen in suspension at low activity levels comes from a remote source; the second is that for the finer fraction, bottom pressure variations associated with wave motion can induce rapid pore pressure fluctuations in this semi-cohesive material. This may result in a bed instability which would effectively lower the shear stress required for entrainment of the finer fraction thus inducing a leaching action. The available data base was insufficient to resolve this matter.

Table 2 presents the threshold data and the estimated velocities associated with the designated activity levels at the 60 m and 80 m sites. The velocity estimates were obtained by taking the statistical mean of  $U_{1\frac{3}{8}}$  velocities associated with each event, at each designated activity level.  $U_{1\frac{3}{8}}$  was selected as the relevant spectral parameter based on bottom observations that the thresholds of motion and transport are associated with extreme spectral parameters (Gordon and Hoffman, in prep, (b); Nielsen and Gordon, 1984).

#### 5.4 Transport

Whilst some bed load transport was observed at the 24 m site, suspended transport was observed to be the dominant mechanism at all sites. For the purposes of this study, the oscillatory motion of sediment without net movement taking place was not considered to constitute sediment transport.

Shelf sediment transport was estimated by considering the time averaged flux of suspended sediment:

$$\bar{Q} \approx \int_0^h U_0(z) \bar{C}(z) dz$$

where  $\bar{Q}$  = time averaged transport

$U_0(z)$  = average velocity at height  $z$  above the bed

$\bar{C}(z)$  = time averaged concentration at height  $z$  above the bed

$h$  = bottom zone thickness

This was applied to each individual record for which it had been determined that threshold had been exceeded (Table 2 and camera data).

Nielsen et al (1982) suggested the relationship:

$$\ln \bar{C} = \ln C_0 - \frac{\bar{w}h}{\sqrt{E_B} E_S} \tan^{-1} \sqrt{\frac{E_S}{E_B}} \frac{z}{h}$$

where  $\bar{C}(z)$  = time averaged suspended sediment concentration at elevation  $z$ .

$C_0$  =  $\bar{C}(0)$

$\bar{w}$  = average settling velocity of sediment

- $h$  = water depth  
 $E_B$  = diffusivity due to boundary layer turbulence  
 $E_S$  = diffusivity due to non boundary layer turbulence

and showed that:

$$C_0 \approx 0.008 \left( \frac{\tau'}{\rho g (s-1)d} \right)^{2.5} \quad \text{for } r = 2.5d$$

Although Nielsen's (1979) work was confined to flume tests and the later work (Nielsen et al, 1982) to prototype measurements in the vicinity of the surf zone, some deep water data exist (Glenn, 1983) which was useful in scaling Nielsen's approach to the deeper shelf sites. This was necessary due to the lack of concentration profile data at these sites.

Absolute values of sediment transport have not been determined; further studies of the concentration profiles are being undertaken. This work is initially being carried out at the 24 m site. At the deeper sites, the six months data show that sediment transport events are rare. For example, at 60 metres, twelve events ranging in duration from 4 to 56 hours occurred where transport is considered to have taken place. At the 80 metre site, only six events of duration 8 to 16 hours were recorded. It should be noted that Figure 18 presents the number of recordings obtained, not the number of continuous events. For each event, a record was taken each four hours.

A significant finding of the study was that resultant net transport on the shelf is to the north and is determined by storms in the Tasman Sea. It had been generally believed that net transport was to the south since the net movement of water on the shelf is in that direction. During Tasman Sea storms, the wave induced seabed shear dominates and results in the entrainment of bed material which is then transported by the prevailing currents. As a majority of storms which impact on the shelf are a product of low pressure systems in the Lower to Central Tasman Sea (Figure 10), a strong coast parallel wind shear to the north is generated. This wind field gives rise not only to the waves which induce entrainment but also a short lived north bound shelf current (see Section 4.2). Near the coast, the Ekman effect rotates this current to produce a set up which is balanced by a downwelling. Hence, whilst the midshelf current during the storms is directly to the north, nearshore there is an additional offshore component at the sea bed due to the downwelling phenomenon. Overall, the net movement of sediment is therefore to the north and offshore near the coast but swings more towards the north further offshore.

The side scan sonar records include features consistent with net northerly sediment transport and with the modifying near-coast downwelling effect (Gordon and Hoffman, in prep (b) and Figure 2).

Sedimentological studies carried out by Roy (1984) suggest that average annual sediment transport is small; his estimates of accretion rates on identified depositional features on the shelf are in the order of 2 to 5 mm/year.

## 6. Conclusions

- . Transport on the shelf off Sydney mainly occurs during storm events in which wave activity produces sufficient seabed shear to cause entrainment. The dominant southerly steady current on the shelf seldom induces sufficient seabed shear to entrain sediment. On the occasions when wave induced shear results in entrainment, the mechanism producing the waves also tends to give rise to a short duration north bound current and hence the net movement of sand sized material is to the north. Near the coast, modification to the current pattern due to downwelling results in movement which is to the north and offshore.
- . Side scan sonar data have identified a number of sediment features which are believed to be related to this movement; the implied stability of these features suggests that transport rates on the shelf are small. This is supported by the sedimentological evidence and by the sediment transport calculations.
- . Estimates of absolute values of sediment transport on the Sydney shelf require further studies on concentration profiles and improved estimates of bottom shear stress.
- . Extreme wave spectral parameters are considered the most appropriate for examination of threshold of movement in these environments.

## Acknowledgements

This paper is published with the permission of the New South Wales Public Works Department. The paper includes information from both Public Works Department offshore investigations and ocean outfall studies carried out by the Department for, and funded by, the Sydney Metropolitan Water Sewerage and Drainage Board.

The authors also wish to gratefully acknowledge the assistance of A. Nielsen, P. Evans, P. Nielsen, N. Lawson, R. Rice and A. Price.

## References

- Bretschneider, C.L. (1967): On the generation of wind-driven currents over the continental shelf. Trans. Third Annual MTS Conference, San Diego, pp. 97-113.
- Glenn, S.M. (1983): A continental shelf bottom boundary layer model: the effects of waves, currents and a movable bed. Sc. D. thesis, Woods Hole Oceanographic Institution, Report No. WHOI-83-6.
- Gordon, A.D. and Hoffman, J.G. (in prep, (a)): Sydney coastal study. N.S.W. Public Works Department, report in prep.
- Gordon, A.D. and Hoffman, J.G. (in prep, (b)): Sea bed and sediment transport studies at outfall diffuser sites, Bondi and Malabar. N.S.W. Public Works Dept, report in prep.
- Gordon, A.D., Lord, D.B. and Nolan, M.W. (1978): Byron Bay-Hastings Point erosion study. N.S.W. Public Works Department, Report No. PWD.78026.
- Hamon, B.V. (1984): Tidal currents off Sydney. University of Sydney, Marine Studies Centre, unpublished manuscript.
- Madsen, O.S. and Grant, W.D. (1976): Sediment transport in the coastal environment. Mass. Inst. of Technol., Ralph M. Parsons Lab., Report No. 209.
- Nielsen, A.F. (1984): Sand ripples under natural waves. M. Eng. Sci. thesis, University of New South Wales, Dept. Civil Eng.
- Nielsen, A.F. and Gordon, A.D. (1984): Sediment responses to natural waves. Proc. 19th Int. Conf. Coastal Engrg., Houston.
- Nielsen, P. (1979): Some basic concepts of wave sediment transport, Technical University of Denmark, Inst. Hydrodynamics and Hydraulic Engineering (ISVA), series paper 20.
- Nielsen, P., Green, M.O. and Coffey, F.C. (1982): Suspended sediment under waves. University of Sydney, Coastal Studies Unit, Tech. Report No. 82/6.
- Nilsson, C.S. and Cresswell, G.R. (1980): The formation and evolution of East Australian Current warm core eddies. Progress in Oceanography, 9, 133-83.
- Roy, P.S. (1984): The geology of marine sediments on the south Sydney inner shelf, S.E. Australia. Dept. Mineral Resources, Geological Survey of N.S.W., Report No. G.S. 1984/158.
- Youll, P.H. (1981): Botany Bay waverider system - ten years of records. Proc. 5th Aust. Conf. Coast and Ocean Engrg., Perth.

## CHAPTER ONE HUNDRED THIRTY TWO

### BEACH FORESHORE RESPONSE TO LONG-PERIOD WAVES

P. A. Howd\* and R. A. Holman\*\*

#### ABSTRACT

A field experiment has been carried out to test the hypothesis that infragravity and lower frequency waves influence patterns of erosion and deposition on the beach foreshore. The data show coherent fluctuations in the foreshore sediment level which can be related to low frequency wave motions. The fluctuations have heights of up to 6 cm with typical time scales of 8 to 10 minute periods. They can be characterized in two ways: by the progression of the fluctuation up the foreshore slope (landward), and by the decrease in the root-mean-square (RMS) height of the fluctuations as they progress landward.

Analysis of runup time series obtained by time-lapse photography concurrent with the sediment level measurements reveals long-period waves of undetermined origin which are positively correlated with the sediment level fluctuations. This strongly suggests that the waves are responsible for forcing the sediment level fluctuations.

#### INTRODUCTION

##### Background

The beach foreshore is a complex environment. There are numerous physical processes which interact to produce the profile observed at any moment in time. The recent works of Bowen (1980), and Holman and Bowen (1982) demonstrate the role of infragravity (and longer) waves in determining surf-zone profiles, but no recent study has been made of the role of long waves in determining the foreshore profile. This paper reports on one aspect of such an influence.

Patterns of foreshore profile response to tidal fluctuations began to be reported after World War II. Grant (1948) hypothesized that the changes in beach foreshore saturation, due to either tides or storm surges, would cause distinctive changes in the profile. He reasoned that saturated beaches would be more apt to erode since backwash would be undiminished by percolation. On unsaturated beaches, backwash should be diminished by percolation and deposition would be favored. Emery and Foster (1948) studied the change in the

\* Graduate Student at Large, College of Oceanography, Oregon State University, Corvallis, Oregon

\*\*Associate Professor, College of Oceanography, Oregon State University, Corvallis, Oregon

foreshore groundwater profile over a tidal cycle and concluded that there was significant exchange of water between the runup and the beach, and that this exchange could influence patterns of erosion and deposition.

Duncan (1964) drew upon these conclusions and produced what has become accepted as the best conceptual explanation of foreshore profile change due to tidally induced changes in the beach groundwater. He found that the beach groundwater level lagged the rise in sea level. The foreshore should then steepen during flood tide as deposition occurs on the unsaturated upper foreshore and erosion occurs on the saturated lower foreshore. During ebb tide the opposite sedimentation pattern holds. The upper foreshore erodes due to the effluence of the groundwater lagging behind the falling tide. His field study supports this hypothesis as do the results of others (Strahler, 1964; Harrison, 1969).

Studies of small scale morphology on the beach foreshore have been carried out intermittantly. Tanner (1965, 1977) and Broome and Komar (1979) discuss the existence and formation of backwash ripples. These low-aspect ripples (wavelength of about 50 cm, height approximately 1 cm) can be formed under hydraulic jumps in the backwash on gently sloping beaches. They are not characterized by active migration.

Waddell (1973) conducted a study of the interaction between runup processes, beach groundwater and the sediment level response on the foreshore. He measured sediment level at two locations, one meter apart, on the upper foreshore of a low-energy, medium-sand beach. Simultaneously, he measured runup and the beach groundwater at a series of locations. He found significant fluctuations in sediment level and presented evidence that the oscillations were sandwaves progressing down the foreshore slope due to bedload transport in the backwash phase of the runup. Waddell (1976), referring to the same data, concluded that standing waves in the inner surf-zone were responsible for periodic fluctuations in the beach groundwater level. These groundwater oscillations created "a zone which was periodically saturated or nonsaturated." He then invoked Duncan's (1964) hypothesis and concluded that nonsaturation, or a low in the groundwater oscillation, encouraged deposition and that the subsequent saturation of the location lead to erosion, the result being the observed periodic oscillations. He did not explain how this theory could account for the apparent seaward progression of the oscillations.

Sallenger and Richmond (in press) conducted a field study in Monterey Bay, California with the aim of characterizing sediment level oscillations on a steep, coarse-grained, high-energy foreshore. They measured the sediment level at a series of locations that stretched across the upper two-thirds of the swash-zone, finding sediment level oscillations at periods of six to fifteen minutes occurring at locations above and below the mean swash position. They reported that the oscillations progressed landward during a period of net seaward transport, thus ruling out the possibility of lower flow



regime bedforms such as sand waves. The width of foreshore monitored allowed them to show a landward decrease in the RMS height of the oscillations.

#### Goals

The purpose of this study was to test two hypotheses regarding foreshore sediment level oscillations with periods on the order of ten minutes. The first of these hypotheses is that infragravity or longer waves are capable of influencing the foreshore profile. The second hypothesis is that the profile response is not limited to the zone of intermittent saturation, groundwater fluctuations playing a lesser role than has been thought.

To test these hypotheses a field experiment was carried out on a high-energy, coarse-grained beach. The location chosen differed from that of Sallenger and Richmond (in press) in that it was on an open coast rather than within a major embayment known to have seiches. The goals of the field study were to document forcing (or non-forcing) of the sediment level oscillations by long period waves, to show that the oscillations are independent of any long term erosional or depositional trends on the foreshore, and that the oscillations are not directly related to the saturation of the foreshore.

#### EXPERIMENT SETTING AND METHODS

The field experiments were conducted during September 1981 and October 1982 at the U.S. Army Corps of Engineers, Coastal Engineering Research Center (CERC), Field Research Facility (FRF) on the outer banks of North Carolina near the town of Duck (Figure 1). The beach is interrupted only by piers for at least 50 km on either side. The nearest pier (belonging to the FRF complex) is 500 m from the experiment location. The surf-zone morphology in the region of the experiment is characterized by a single linear bar during conditions similar to those of the study periods. The average mid-foreshore slope during the studies was approximately 1:10. The foreshore is composed of medium to coarse sand with an average grain diameter of approximately 1 mm (Figure 2). During the two experiments the waves were oblique to the beach and had significant wave heights very close to 1 m as measured at a waverider buoy anchored in 20 m of water. There was little wind and waves were of the swell type. The tide range was approximately 0.9 m and semidiurnal. Figure 3 summarizes the environmental conditions surrounding the experiments.

On September 19, 1981, 19 stakes 1 cm in diameter and 1.5 m long were driven into the foreshore in the locations shown in Figure 4. The foreshore topography was dominated by a series of cusps, one of which is evident from the contours. The primary shore-normal line of eleven stakes had a spacing of 2.0 m.

In October 1982 an array containing eight shore-normal lines of stakes was established on the foreshore (Figure 5). The eight shore-normal lines were spaced 5 m apart. The second line from each

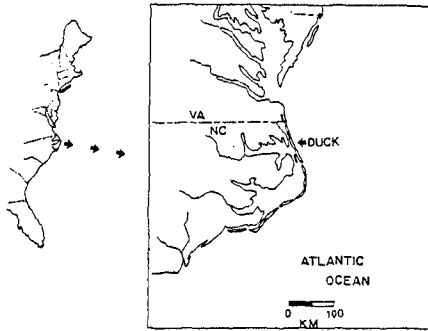


Figure 1. Location map. The field study was conducted at the Coastal Engineering Research Center Field Research Facility just north of the town of Duck, North Carolina. The beach is uninterrupted from Cheseapeake Bay to the north to Oregon Inlet to the south.

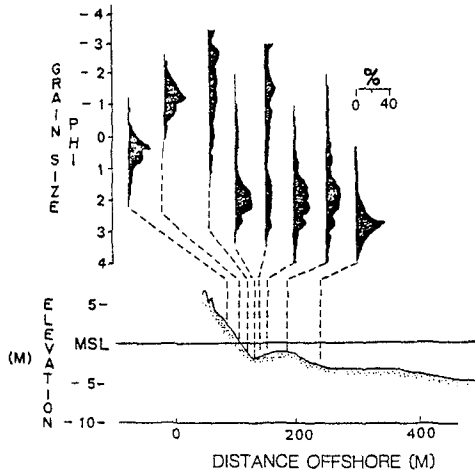


Figure 2. Grain size distribution. Cross-shore grain size distribution on a transect several meters south of the study site on 28 October 1982. The foreshore is composed of sand with an average diameter of approximately 1 mm. Data courtesy of Bill Birkemeier, CERC-FRF.

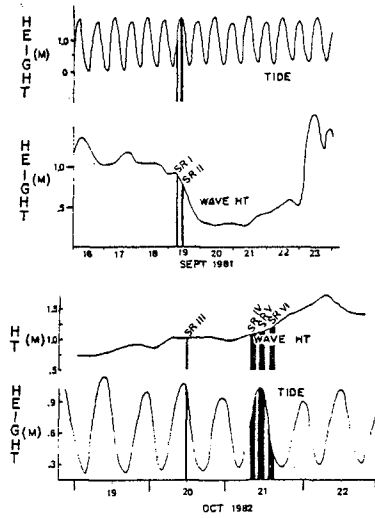


Figure 3. Environmental conditions. The significant wave height was measured by a waverider buoy in 20 m of water. The tides are semidiurnal and have a range of 0.75 to 1.3 meters.

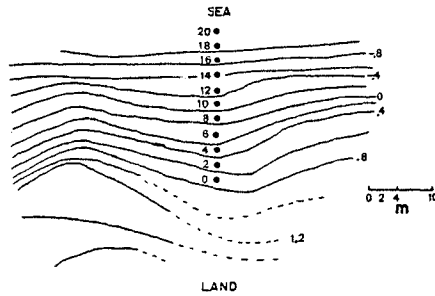


Figure 4. Foreshore topography and stake locations for the 1981 experiment (DS I and DS II). The primary stake transect was located in the trough of a cusp. The stakes are numbered according to their distance seaward from the landwardmost stake and are spaced at 2.0 m intervals.

end of the grid had shore-normal stake spacings of 2.5 m while the remaining lines had 5 m spacings. The foreshore contours show a remnant cusp in the backshore separated from the active, featureless foreshore by a well defined berm crest. A contour map of the surf-zone topography from 19 October 1982 shows a bar approximately 20 m from shore. The mapping, done by the FRF staff using their CRAB (Birkemeier et al., 1981), shows the bar to be linear along shore. There was little evidence to suggest that there was any appreciable change in the topography over the two day period.

Fluctuations in sediment level relative to the stake tops were measured using a modified meterstick. A hinged baseplate approximately 10 cm in diameter was affixed to one end of the meterstick to prevent penetration of the sediment surface. A moveable pointer was fitted to the meterstick and was used to determine the length of stake exposed. The stake tops were referenced to a known elevation using an infrared rangefinder. The resolution of the technique, employing different measurers and different metersticks was  $\pm 1.5$  mm in the upper swash-zone and  $\pm 2.5$  mm in the lower swash-zone. Resolution of the measurements made on stakes not subjected to runup was  $\pm 0.5$  mm. The differences are primarily due to the time available to make the measurement and the saturation of the sediment.

During both the 1981 and the 1982 experiments, time-lapse motion pictures were used to record the wave runup on the foreshore. This method allows for digitization of the runup at a series of longshore locations as well as the identification of the saturated portion of the foreshore. The results of a comparison of the film techniques and a dual-resistance wire runup meter are presented by Holman and Guza (1984).

The 19 September 1981 experiment consisted of two sixty minute segments, one centered on mid-flood tide, DS (Data Segment) I, the second centered on high tide, DS II. The stakes on the primary shore-normal line were measured to the nearest millimeter at approximately 48 second intervals. Measurements were made after the backwash cycle when the stake was either suberial or the velocity of the water covering the location was low. The landwardmost stakes were measured only after they had been exposed to runup action. The times at which the measurements were made were recorded to the nearest 0.2 minute ( $\pm 6$  seconds).

The 1982 experiment consisted of one 35 minute segment near high tide on 20 October (DS III) and three 90 minute segments centered on mid-flood, high, and mid-ebb tides on 21 October (DS IV, DS V, and DS VI, respectively). Again, the stakes in a shore-normal line were measured at approximately 48 second intervals after the backwash cycle. Measurements were recorded to the nearest 0.2 minute. Stakes on the B-line (Figure 5) were those measured most frequently. The number of stakes measured varied according to the number of people measuring and the width of the swash-zone.

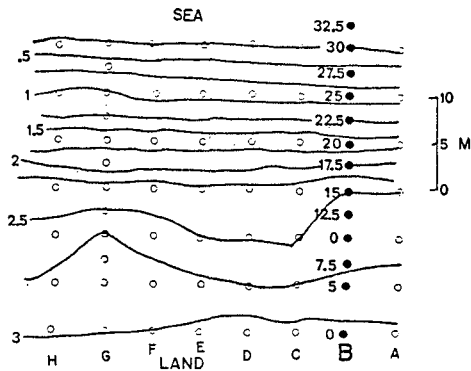


Figure 5. Foreshore topography and stake locations for the 1982 experiment (DS III to DS VI). The B line of stakes were those used in the study. The active portion of the foreshore was seaward of 17.5 m. A remnant cusp was perched landward of the berm crest. The foreshore is linear and has a slope of slightly greater than 1:10.

#### FIELD STUDY RESULTS

All the data show sediment level fluctuations superimposed on longer term trends. Figure 6 shows a representative set of time series of change in sediment level at a location versus time for the primary, shore-normal line of stakes. The stakes are numbered using their distance from the landward baseline, thus higher numbers refer to stakes further seaward. The trends are due either to the tidal cycle sedimentation patterns or to longer scale foreshore evolution such as changes related to storm cycles. On a shorter time scale, the fluctuations are periodic, and decrease in amplitude in a landward direction from a maximum height of greater than 6 cm to near zero. The stake locations on the lower foreshore show fluctuations occurring more rapidly than those at the upper, landward stakes. The fluctuations are visually progressive, and are coherent over at least 15 m in a longshore direction.

Statistical analysis quantifies these visual observations. The records were processed using linear interpolation to give time series with a constant interval of 12 seconds. The trend and mean were then removed so that they would not mask the analysis of the oscillations.

Figure 7 presents the relationship between root-mean-square (RMS) height and the distance from the top of the swash action for the 1982 data. The RMS heights of the fluctuations were computed as

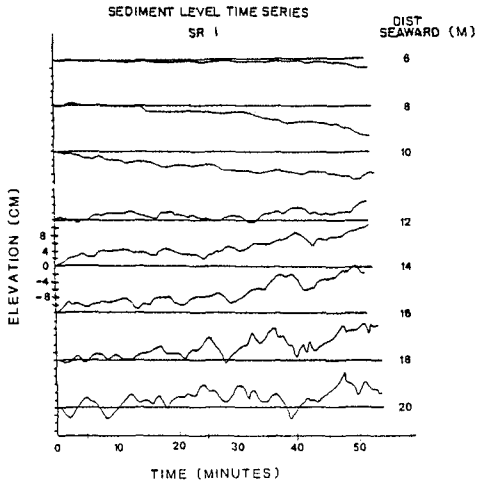


Figure 6. Sediment level time series, DS I. The time series are reported relative to the initial elevation at each location. Several things are obvious. There are trends in the records, the oscillations decrease in amplitude in a landward direction, and they seem to progress.

two times the standard deviation of the record. All segments show the landward decrease in the RMS height of the oscillations, which ranged from a maximum of  $> 4$  cm at the seawardmost stake to near 0 cm for the landward stakes.

Crosscorrelation analysis was used to compare the detrended and demeaned time series. This analysis computes the correlation between two series of data at a series of lag times (Davis, 1973). It is not a frequency specific calculation as is the measure of coherence reported in association with cross spectral analysis. The lag associated with the maximum value in crosscorrelation is a measure of the shift of one series which results in the two series being most alike.

Figure 8 summarizes the results of the analysis as contour plots of crosscorrelation as a function of distance and lag time. Negative lags indicate that events at that location preceded the events at the reference stake. The contours indicate a change from negative lags for stakes below the reference point to positive lags above. This indicates landward progression of the fluctuations.

The flood-tide data, DS I and DS IV, both show lags which indicate landward migration of the oscillations (Figures 8A and 8D). Adjacent stakes in the mid-forshore have crosscorrelation maxima ranging from 0.54 to 0.79 while stakes which are farther from one another have values which range from essentially zero to 0.43. The lowered crosscorrelation values between non-adjacent stakes are

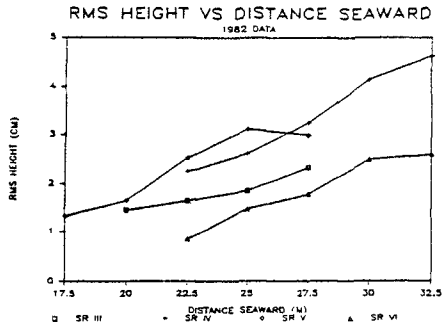


Figure 7. RMS heights of the sediment level fluctuations versus distance seaward for the 1982 data. Note the decrease in the RMS height in a landward direction for all the runs. The RMS height was computed as twice the standard deviation of the run.

primarily due to the loss of the high frequency oscillations present in the records obtained in the lower swash-zone.

The three high-tide segments also have maxima associated with landward migration of the fluctuations (Figures 8B, 8C, and 8E). Again, the values of the maxima are highest between adjacent stakes and decrease for non-adjacent stakes due to the loss of higher frequency fluctuations at the upper swash-zone locations.

Crosscorrelation was also used to compare the runup data to the sediment level fluctuations. Problems were encountered as the result of the large difference in the periods of dominant motion. The dominant runup period was near 8 seconds, while the dominant sediment level oscillations had periods from 2 to 8 minutes. Low pass filtering of the runup records helped alleviate this problem. Figure 9 shows the low-passed runup data along with the sediment level data for segment III. There are three obvious low frequency events in the runup time series that can be directly traced to the sediment level data. In all cases the lag associated with the best fit between the two types of series show motions in the runup precede the motions in the sediment level records. This would have to be the case if the runup is forcing the sediment level response. In general, the cross-correlation values are lower than those between adjacent stakes and sensitive to the characteristics of the filter applied to the runup time series. This is not surprising due to the assumed complexity of the transfer function between the runup and the profile response.

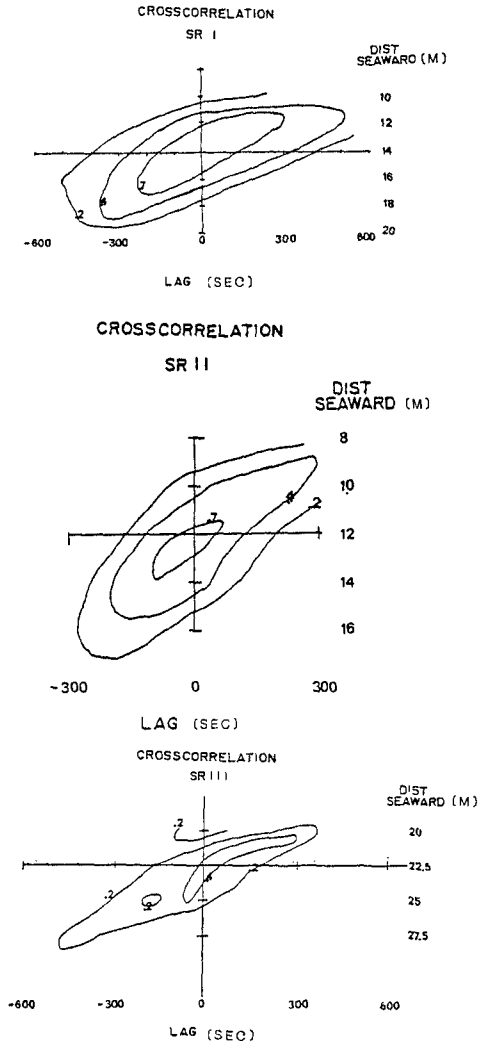
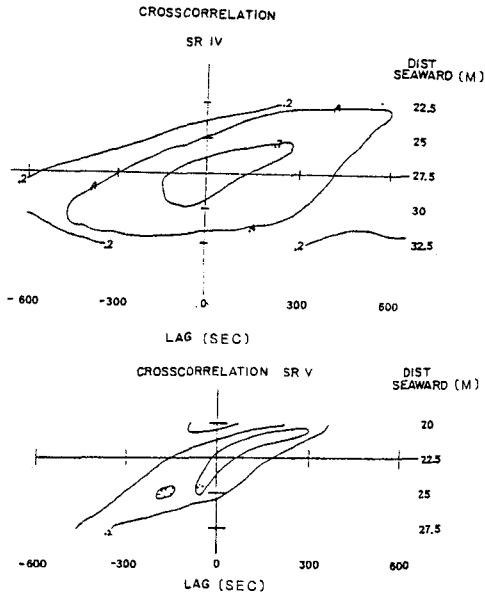


Figure 8. Crosscorrelation vs. time and distance. The crosscorrelation was computed between each time series and a reference time series from near the center of the section of the foreshore monitored during the experiment. Negative lags refer to shifting the reference series back in time, positive lags refer to forward shifts, thus the elongation of the contours from lower left to upper right indicates landward progres-





sion of the fluctuations. Values greater than 0.2 are significant at a minimum of 95% for all the plots at any lag shown. A: DS I, flood tide 19 September 1981. B: DS II, high tide 19 September 1981. C: DS III, high tide 20 October 1982. D: DS IV flood tide 21 October 1982. E: DS V high tide 21 October 1982. The results of DS VI were less characteristic and are discussed elsewhere (Howd, 1984).

Spectral analysis was done to allow specific frequency bands to be examined and compared between simultaneous records. Due to the record length containing as few as three cycles of the sediment oscillations, and the fact that the sampling interval allowed resolution of only those periods greater than 100 seconds, the technique was of limited use. The results are subject to considerable error.

Figure 10 shows a typical spectrum of runup. The distribution of energy is shown over a wider range of frequencies. As is typical for low wave conditions on a steep beach, the incident runup peak is clearly visible at 0.1 Hz. The dominant peak at approximately 0.0625 Hz is the subharmonic of the incident waves ( $f = 0.12$  Hz). The reason for the difference between the incident wave frequency as recorded in the swash zone ( $f = 0.10$ ) and in the inner surf zone ( $f = 0.12$ ) is unknown but has been seen in other data from steep beaches (Sallenger, pers. comm.). Low frequency peaks are also present.

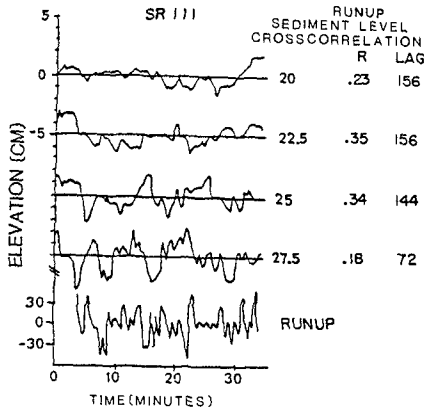


Figure 9. Detrended time series of sediment level and runup. The runup time series has been converted to a vertical excursion using the average foreshore profile and low pass filtered to exclude motions with periods of less than 70 s. The correspondence between the runup series and the sediment level time series at the seawardmost stake is obvious.

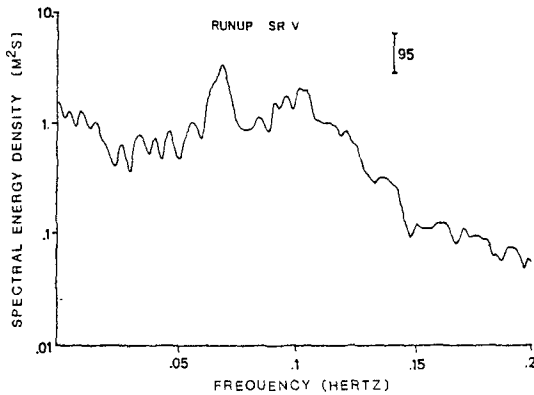


Figure 10. Runup spectrum, DS V. The spectrum shows the incident runup peak near a period of 10 seconds (0.1 Hz.), a peak at 16 seconds (0.0625 Hz.) thought to be the first subharmonic of the 8 second period incident waves (period measured in the surf zone), and several lower frequency peaks.

## DISCUSSION OF FIELD DATA

The sediment level fluctuations maintain their form despite the high energy of the swash-backwash action. This suggests that the forcing of the shape must be continued past the initial formation of the features. The data show that sediment level oscillations do occur on the foreshore of a beach in apparent response to long period waves. The origin of the waves is unknown, but recent work by Lanvon et al. (1982) documents the shoaling of shelf waves with similar periods on beaches in Australia.

The fact that the oscillations are present on all sections of the foreshore subject to swash action discounts the hypothesis presented by Waddell (1976) for the origin of these features. If Waddell's (1976) hypothesis were true, then on a foreshore of the steepness of the beach studied here, the long period wave would need to have an amplitude of greater than 1 m in order to force fluctuations of the saturation line that would extend over the range required. There was no evidence that such high-amplitude, low-frequency waves existed at the time of the study. The oscillations were also measured seaward of the lowest position of the saturation line. It should be noted that the beach on which Waddell did his study was of considerably lesser slope and a wave of smaller amplitude would be required.

An alternative explanation for the formation of the sediment-level oscillations is the formation of antidunes in the lower swash-zone. Antidunes form in supercritical flow, such as may occur during the latter stages of backwash. The migration of the form as an antidune is dependent on maintaining supercritical flow above the bedform. This could not be the case in the upper swash-zone. Furthermore, the direction of antidune migration is opposite to the direction of sediment transport. The observed oscillations migrate landward without regard for the direction of net sediment transport. So while antidunes may explain the initial formation of the oscillation, they do not explain the migration of the form on the foreshore.

A simulation model, presented elsewhere (Howd, 1984 and Howd and Holman, in prep), suggests that the sharp discontinuity in slope at the step-zone is necessary for the formation of the fluctuations. The existence of sharp discontinuities (apparently in equilibrium) in the foreshore slope in this area implies the existence of large local gradients in hydrodynamic characteristics. Thus small horizontal dislocations of the swash zone caused by infragravity waves may induce rapid response and slope adjustments, namely a perturbation which progresses upslope. Sallenger (personal communication) noted that in one experiment the step migrated landward past several of their stakes. The sediment level oscillations present prior to the passage of the step disappeared when the location became seaward of the step. This would suggest that the oscillations are generated in the lowermost foreshore near the vicinity of the step. The magnitude of the oscillation is related to the degree of disequilibrium, that is to the difference between the existing slope and the equilibrium slope, and to the time available for a response.

## SUMMARY AND CONCLUSIONS

The primary objective of this field study was to document the influence of long-period waves on the beach foreshore profile. The data collected show such an influence. Oscillations of sediment level were recorded with maximum heights of up to 6 cm at time scales of 8 to 10 minutes. The oscillations decrease in amplitude as they migrate landward. Cross-correlation analysis showed the landward progression of the fluctuations and suggested that the oscillations in sediment level were the result of corresponding long period waves in the runup.

The fluctuations have been observed over the entire extent of the active swash-zone. Their occurrence below the zone of periodic saturation discounts the theory presented by Waddell (1976) for the origin of these features. An alternative explanation is based on disequilibrium conditions existing in the vicinity of the step-zone. The foreshore response to the disequilibrium is hypothesized to be the formation and migration of the observed fluctuations. It is obvious that the foreshore is capable of responding rapidly and in a very coherent manner to subtle changes in the dynamics of the swash-zone.

## REFERENCES

- Birkemeier, W.A., A.E. DeWall, C.S. Gorbics, and H.C. Miller (1981). A Users Guide to CERC's Field Research Facility. Miscellaneous Report No. 81-7 U.S. Army, Corps of Engineers, CERC, Fort Belvoir, Va.
- Bowen, A.J. (1980). Simple models of nearshore sedimentation; beach profiles and longshore bars. In The Coastline of Canada, ed. S.B. McCann. Geological Survey of Canada.
- Broome, R. and P.D. Komar (1979). Undular hydraulic jumps and the formation of backwash ripples on beaches. Sedimentology 26: 543-559.
- Davis, J.C. (1973). Statistics and Data Analysis in Geology. John Wiley and Sons, New York, NY, 550 p.
- Duncan, J.R. (1964). The effects of water table and tide cycle on swash-backwash sediment distribution and beach profile development. Marine Geology 2: 186-187.
- Emery, K.O., and J.F. Foster (1948). Water tables in marine beaches. Journal of Marine Research 7: 644-654.
- Grant, U.S. (1948). Influence of the water table on beach aggradation and degradation. Journal of Marine Research 7: 655-660.
- Harrison, W. (1969). Empirical equations for foreshore changes over a tidal cycle. Marine Geology 7: 529-551.

- Holman, R.A., and A.J. Bowen (1982). Bars, bumps, and holes: Models for the generation of complex beach topography. Journal of Geophysical Research 87: C1 457-468.
- Holman, R.A., and R.T. Guza (1984). Measuring runup on a natural beach. Journal of Coastal Engineering, 8, 129-140.
- Howd, P.A. (1984). "Beach foreshore response to long-period waves in the swash-zone." M.S. Thesis, Oregon State University, 88 p.
- Howd, P.A. and R.A. Holman (in prep). "A simple model of beach foreshore response to long period waves."
- Lanyon, J.A., I.G. Eliot, and D.J. Clarke (1982). Observations of shelf waves and bay seiches from tidal and beach groundwater-level records. Marine Geology 49: 23-42.
- Sallenger, A.H., and B.M. Richmond (in press). High-frequency sediment level oscillations in the swash zone. Marine Geology.
- Strahler, A.N. (1966). Tidal cycle of changes on an equilibrium beach. Journal of Geology 74: 247-268.
- Tanner, W.F. (1965). High-index ripple marks in the swash zone. Journal of Sedimentary Petrology 35: 968.
- Tanner, W.F. (1977). Froude regimes in the swash zone. In Coastal Sedimentology ed. W.F. Tanner, Geology Department, Florida State University, Tallahassee, FL.
- Waddell, E. (1973). Dynamics of swash and its implications to beach response. Louisiana State University Coastal Studies Institute Technical Report 139. 49 p.
- Waddell, E. (1976). Swash-groundwater-beach profile interactions. In Beach and Nearshore Sedimentation eds. R.L. Davis and R.L. Ethington. Society of Economic Paleontologists and Mineralogists Special Publication 24: 115-125.
- Wright, L.D., J. Chappell, B.B. Thom, M.P. Bradshaw, and P. Cowell (1979). Morphodynamics of reflective and dissipative beach and inshore systems: Southeastern Australia. Marine Geology 32: 105-140.

## CHAPTER ONE HUNDRED THIRTY THREE

### THE ROLE OF SUSPENDED SEDIMENT IN SHORE-NORMAL BEACH PROFILE CHANGES

Bruce E. Jaffe\*, Richard W. Sternberg\*\* and Asbury H. Sallenger\*

#### ABSTRACT

Field measurements of suspended sediment-transport were made across a dissipative surf zone during a storm. A correlation between high suspended mass in the water column and periods of onshore flow caused a net onshore transport of suspended sediment even though the mean near-bottom flow was directed offshore. The observed onshore migration of a nearshore bar was predicted by gradients in the cross-shore suspended-sediment transport.

#### INTRODUCTION

The response of the nearshore profile to cross-shore sediment transport has been the focus of numerous theoretical and laboratory studies (e.g. Bowen, 1980; Watanabe et al., 1980). However, due to measuring difficulties, few field data have been obtained of cross-shore sediment transport and the accompanying beach profile changes. In this study, measurements of cross-shore suspended-sediment transport were made across the surf zone during a storm. Nearshore profiles were taken both before and after the transport measurements. We attempt to relate gradients in the cross-shore transport of suspended sediment to profile changes. We show that a bar migrated onshore due to net onshore suspended-sediment transport even though mean currents were directed offshore.

#### EXPERIMENT SETTING AND METHODS

An extensive field study investigating nearshore processes was conducted in the fall of 1982 at the U.S. Army Corps of Engineers Field Research Facility (FRF) in Duck, N.C. The FRF is located on a long straight beach of a barrier island (Fig. 1). Mason et al. (this volume) provide details on meteorology, deepwater waves and three-dimensional morphology at the FRF during the experiment. Surf-zone data were collected 500 m north of the FRF pier using the U.S. Geological Survey sea sled (Sallenger et al., 1983). The sled is moved both onshore and offshore using a double-drum winch and triangular line arrangement (Fig. 2). As the sled moved, the nearshore profile was measured with an infrared rangefinder on the beach and reflecting prisms mounted on top of the sled's 10 meter mast. The sled was also used to transport instruments to different positions in the surf zone. Instruments mounted on the sled included a pressure sensor, three bidirectional electromagnetic current meters

\* U.S. Geological Survey, Menlo Park, CA 94025

\*\*School of Oceanography, University of Washington, Seattle, WA 98195

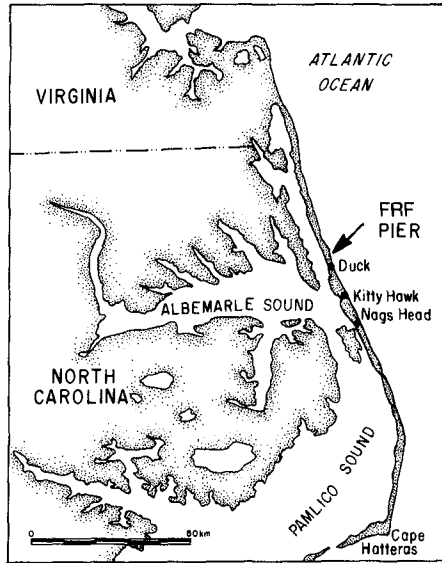


Fig. 1 Location map

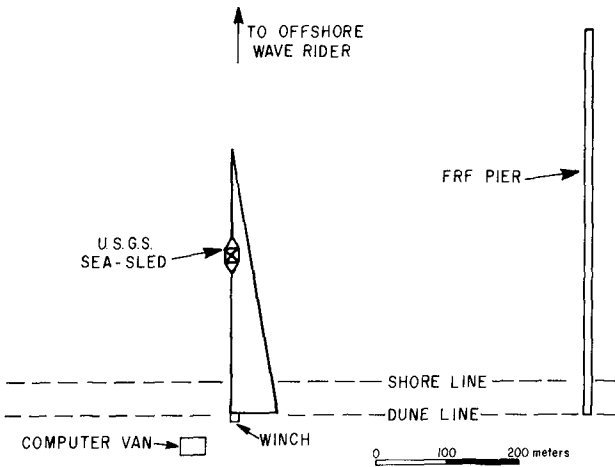


Fig. 2 Experiment set-up at the U.S. Army Corps of Engineers' Field Research Facility.

oriented to measure the cross-shore and longshore flow at 0.5, 1.0, and 1.75 meters above the bed, and a vertical array of five optical backscatter (OBS) sensors (Fig. 3). The OBS sensors measured suspended-sediment concentrations from 0.1 to 80 gm/kg at 0.10, 0.13, 0.19, 0.31, 0.61 m above the bed. The OBS array was mounted on an outrigger extending 0.85 m from the north side of the sled.

Data presented in this paper were collected as follows. First, the nearshore profile was measured. Second, 34.1 minute long records of sled instruments, sampled at 2 Hz, were obtained at seven stations distributed across the surf zone. Sled stations were occupied in a random sequence of offshore distances. Measurements were obtained around high tide to minimize sea level changes. To complete the data set, a second nearshore profile was taken six hours and thirty minutes after the first profile.



Fig. 3 Sled instrumentation. Shown are three current meters (CM), a pressure sensor (PS), and an array of optical backscatter (OBS) sensors (photo courtesy of Bruce Richmond).



The OBS sensors, which were used to measure suspended-sediment concentrations, were developed by John Downing and others at the University of Washington (Downing et al, 1981). The small sensor size (2.2 cm in diameter) allows for measurement of the vertical variation in suspended sediment. The OBS irradiates a 1.3 cm<sup>3</sup> conical volume and detects the intensity of backscattered light. Intensity of backscattered light is a function of sediment concentration and grain size. For a given concentration, smaller grains, with a larger ratio of surface area to volume, will backscatter more light than larger grains. Since backscatter intensity is a function of grain size, OBS sensors were calibrated in the laboratory with sand collected at the FRF 210 meters offshore from the baseline. The calibration sand had a mean diameter of 0.14 mm, typical for sand seaward of the bar at the FRF. Calibrations of the OBS sensors could be described by two linear segments with a break in slope around 2 ppt (Fig. 4). Since the grain size of bed material was coarser in the trough, this calibration would underestimate suspended-sediment concentrations in the trough if all of the bed material was suspended. For a description of the calibration technique see Downing et al, 1981.

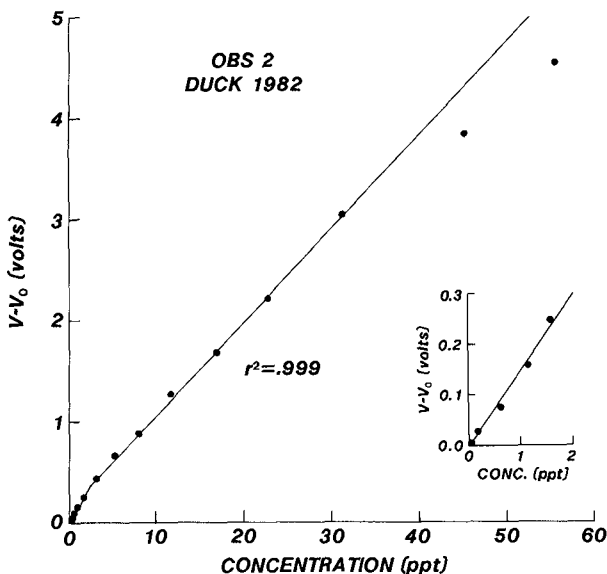


Fig. 4 Calibration curve for the optical backscatter sensor positioned 0.13 m above the bed. The calibration could be described by two least squares fits. The least squares fits only used concentrations below 30 ppt by weight because concentrations exceeded 30 ppt less than five percent of the time.

## OBSERVATIONS

On October 13, 1982, during the final stages of an extratropical storm (northeastern), deepwater significant wave heights at Duck were 1.6 m and peak wave periods were 12 to 15 s (Mason et al, this volume). A surf-zone width ( $X_b$ ) of 350 meters was calculated from a breaker height computed using measured deepwater wave characteristics (Komar and Gaughan, 1973), the nearshore profile, and measured ratios of surf-zone breaker height to depth. Visual observations were consistent with the calculated  $X_b$ . The surf zone was strongly dissipative, with three or four bores present at one time. We made measurements at  $X/X_b$  ranging from 0.1 to 0.65, where  $X$  was the cross-shore distance from the shoreline to the measurement location (Fig. 5E). These positions included three dynamically different regions; 1) the area seaward of the bar 2) the bar 3) the longshore trough. At measurement locations, mean water depths ranged from 2.1 to 4.3 m and RMS wave heights from 0.70 to 1.41 m (Figures 5C and 5D).

Measurements of horizontal water velocities were separated into mean and fluctuating vector components. The mean current speed at 0.50 m above the bed was highest in the longshore trough, 0.46 m/s, and decreased offshore except for sled station 6 where a strong longshore current increased the mean speed (Fig. 5A). Mean currents were directed offshore and to the north at all measurement stations. Standard deviations of current speeds, measures of the combined strengths of the oscillatory and turbulent fluctuations, are shown in figure 5B. The standard deviation calculation included infragravity oscillations.

Time-series measurements of suspended-sediment concentration showed that sand suspension occurred as intermittent events at all measurement positions. Figure 6 presents a 10 minute segment of a data record from sled station 6 ( $X/X_b = 0.5$ ) showing water depth, cross-shore and longshore velocities at 0.5 m elevation and suspended-sediment concentrations at four elevations above the bed. This record is typical in that it shows long periods of low suspended-sediment concentrations interrupted by shorter periods of high concentration. A comparison of records from different stations shows that the high concentration suspension events occurred more frequently and were of shorter duration in deeper water. Since all of the measurement positions were well within the calculated plane-bed regime (Komar and Miller, 1975), suspension events were not due to vortices associated with small-scale bedforms.

Although suspension was intermittent, the time-averaged concentrations systematically varied with distance above the bed and cross-shore position (Fig. 7). Seaward of the bar crest, the mean concentration at 0.13 m above the bed decreased landward from 1.8 gm/kg at sled station 7 to 1.1 gm/kg at sled station 4. Just landward of the bar crest mean concentrations at 0.13 m increased greatly to concentrations equal to that measured at the most seaward station. Lowest concentrations occurred in the longshore trough. At all sled stations, concentrations decreased monotonically from 0.13 to 0.61 m above the bed and concentration gradients generally decreased in shallower water.

DUCK 82  
OCT. 13

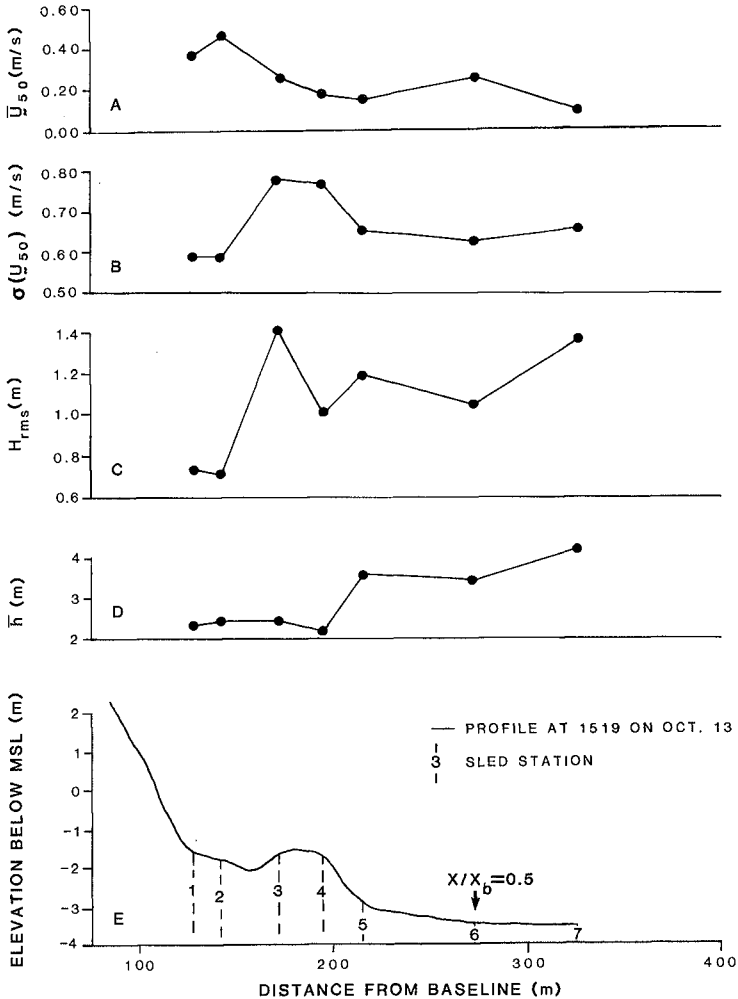


Fig. 5 Surf zone characteristics on Oct. 13th A) Cross-shore variation of the vector mean current speed B) Cross-shore variation of the standard deviation of the current speed C) RMS wave heights across the surf zone D) Water depths across the surf zone E) Shore-normal profile taken by the sled. The data collection sequence was sled station 7, 3, 1, 5, 2, 4.

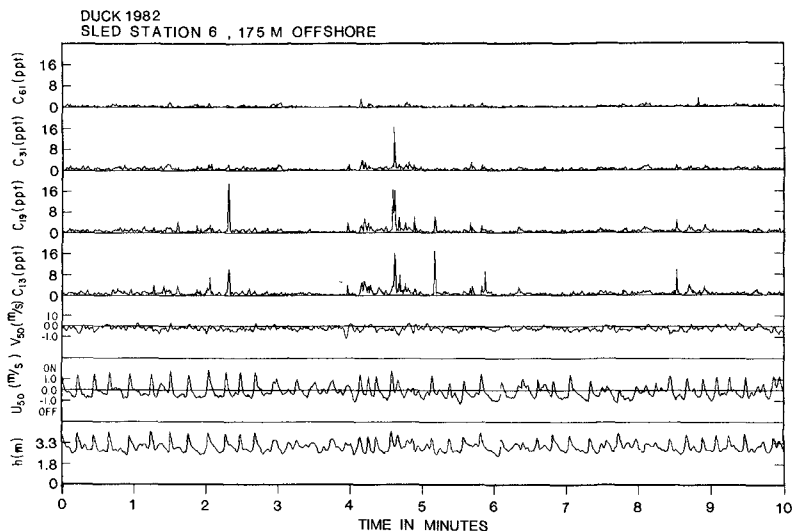


Fig. 6 Data time series from sled Station 6 ( $X/X_b = 0.5$ ). From the bottom, the hydrostatic approximation to sea level ( $h$ ), cross-shore velocity ( $u$ ), longshore velocity ( $v$ ), and suspended-sediment concentrations ( $gm/kg$ ) at four levels above the seabed. Subscripts are elevations above the seabed in centimeters.

Mean concentrations at 0.10 m above the bed (not shown in figure 7) were within 0.1 ppt of the concentrations at 0.13 m. Concentrations were less at 0.10 m than at 0.13 m except at sled station 7. We were unable to find calibration errors for the OBS sensors that would explain the mean concentration decrease between 0.13 and 0.10 m. Still, we thought it unusual that the concentration would decrease towards the bed, so we did not use the 0.10 m readings when calculating suspended masses and fluxes.

The bar migrated onshore between 1519 hours and 2150 hours as its landward flank accreted and the seaward flank and longshore trough eroded (fig. 8D). Maximum vertical changes for the seaward flank, landward flank, and landward side of the longshore trough were -0.21, 0.18, and -0.31 meters, respectively. These profile changes are large compared to the measurement error of the sled system, which has been determined to be 0.045 m (Sallenger et al., 1983). To check the applicability of the 0.045 m figure, we estimated the total measurement error in the system on Oct. 13th. Bed elevations during occupation of a sled station were compared with bed elevations predicted by linearly interpolating the two measured profiles to the time of the occupation. The elevation differences were 0.01 to 0.05, with an average of 0.03 m, which is close to the 0.045 m standard deviation of change calculated by Sallenger et al, 1983.

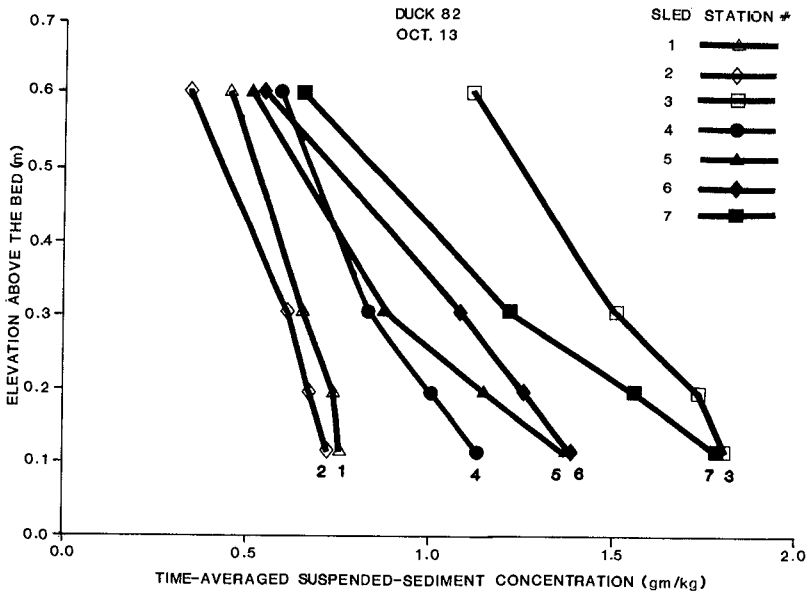


Fig. 7 Time-averaged suspended sediment concentration profiles. Each point represents the average of 4096 concentration measurements (34.1 minutes of data collected at 2 Hz). The data collection sequence was sled station 7, 3, 1, 5, 2, 4.

#### CALCULATIONS AND DISCUSSION

In order to calculate a suspended mass, concentrations were estimated in regions the sensors did not measure. Concentrations were linearly interpolated between sensors. Above the highest sensor, concentrations were estimated from a linear extrapolation from values at 0.31 m and 0.61 m. When the extrapolation produced a concentration greater than zero at the seafloor, the concentration at the seafloor was set equal to zero and concentrations linearly interpolated between the value at 0.61 m and the seafloor. Concentrations below the lowest sensor were also linearly extrapolated from the sensors at 0.13 and 0.19 m. With these estimations, concentrations were integrated over the total water column to obtain a suspended mass. In general, the suspended mass decreased moving onshore in the inner sixty-five percent of the surf zone with the notable exception of the sled station just landward of the bar crest where suspended mass was higher than at each of the other stations (Fig. 8A).

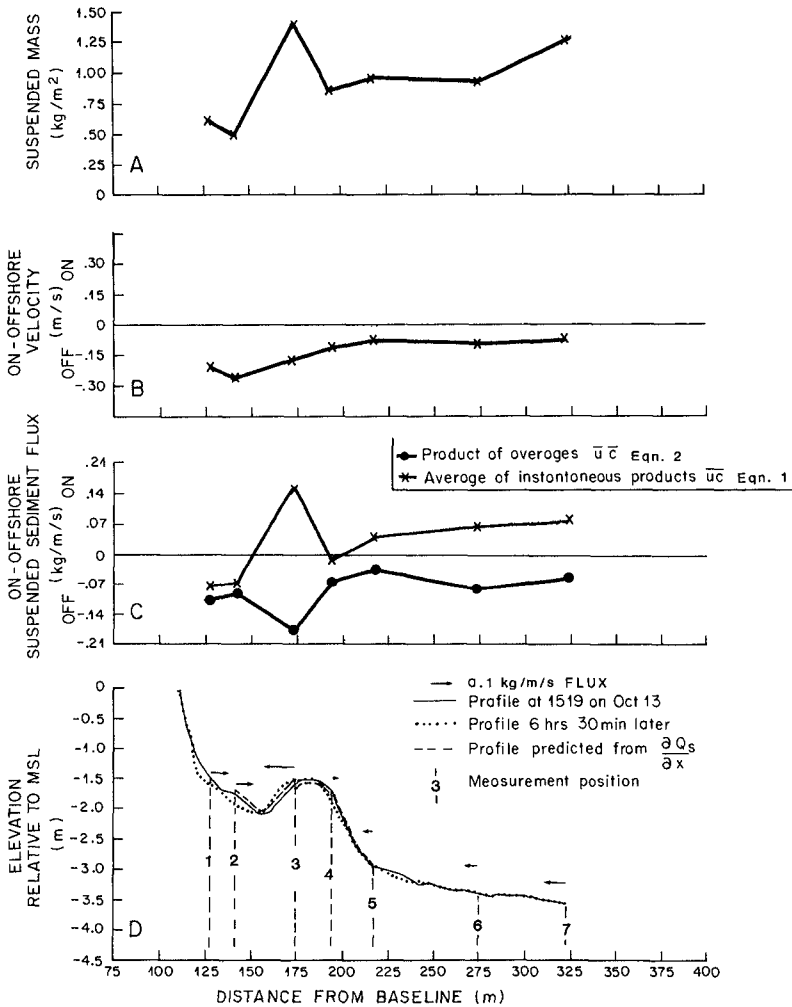


Fig. 8 A) Cross-shore variation in suspended mass B) Cross-shore variation of mean cross-shore velocities at 0.5 m above the seabed C) Comparison of suspended-sediment flux calculated from average and instantaneous quantities (D) Comparison of measured profiles with changes predicted by cross-shore gradients in suspended-sediment flux. The data collection sequence was sled station 7, 3, 1, 5, 2, 4.

Time-average cross-shore suspended-sediment fluxes were calculated for each measurement location in two manners. Fluxes, utilizing the high frequency measurements, were calculated using

$$\bar{c} \bar{u} = \frac{1}{34.1} \int_{t=0}^{t=34.1 \text{ min.}} \int_{z=0}^{z=h} c(z,t) u(z,t) dz dt \quad (1)$$

where  $c$  is suspended-sediment concentration,  $u$  is cross-shore velocity,  $z$  is elevation above the seabed, and  $h$  is the time-varying seasurface. Fluxes, given by the products of the time-average quantities, were also calculated using

$$\bar{c} \bar{u} = \int_{z=0}^{z=h} \left( \frac{1}{34.1} \int_{t=0}^{t=34.1 \text{ min.}} c(z,t) dt \right) * \left( \frac{1}{34.1} \int_{t=0}^{t=34.1 \text{ min.}} u(z,t) dt \right) dz \quad (2)$$

Both calculations were performed using the vertical structure of velocity and concentration. Concentrations were extrapolated in the same manner as they were for suspended mass calculations. We assumed the oscillatory component of the cross-shore velocity was constant with elevation above the bed. This assumption overestimates velocity in the wave boundary layer, but, if the boundary layer was 0.05 m thick, the assumption would increase the flux by less than ten percent. The cross-shore mean current was linearly extrapolated to zero at the bed from the velocity at 0.50 m above the bed. The choice of a linear extrapolation was supported by the shapes of the velocity profiles.

Since near-bottom mean currents were offshore in the inner sixty-five percent of the surf zone, fluxes calculated using equation 2 were offshore at all measurement stations (Fig. 8C). However, fluxes calculated using equation 1 were onshore at four of the seven measurement stations (Fig. 8C).

The different results from the two methods of calculating the cross-shore flux occurred because a correlation existed between velocity fluctuations and concentration fluctuations. Rewriting the equations in terms of mean and fluctuating parts illustrates that eq. 1 includes the fluctuation correlations while eq. 2 does not. In the following analysis, an overbar denotes a time-averaged quantity and a prime denotes a fluctuating quantity.

The concentrations at an instant in time is composed of a mean concentration and a fluctuating concentration

$$c = \bar{c} + c' \quad (3)$$

Likewise, the cross-shore velocity at an instant in time is

$$u = \bar{u} + u' \quad (4)$$

Equation 1 multiplies the concentration and velocity before time averaging. Using the above notation, equation 1 can be written as

$$\overline{cu} = \overline{(\bar{c} + c')(\bar{u} + u')} \quad (5)$$

$$= \bar{c} \bar{u} + \overline{c'u'} + \overline{c'u} + \overline{c'u'} \quad (6)$$

The second and third terms in Eq. 6 drop out because, by definition, the time average of the fluctuations is zero. This leaves

$$\overline{cu} = \bar{c} \bar{u} + \overline{c'u'} \quad (7)$$

In equation 2 the fluctuating quantities vanish before multiplying concentrations and velocities. Following the same procedure as above, equation 2 can be written as

$$\bar{c} \bar{u} = \overline{(\bar{c} + c')(\bar{u} + u')} \quad (8)$$

Subtracting equation 8 from equation 7 gives  $\overline{c'u'}$ , a measure of the correlation of concentration and velocity fluctuations. For lack of a better term,  $\overline{c'u'}$  is referred to as a flux coupling. A low value for the flux coupling indicates a randomness of fluctuations relative to each other while a high value indicates a high degree of correlation.

The cross-shore flux coupling was positive (onshore) at every measurement position and increased with increasing water depth (Fig. 9). Again the position landward of the bar crest, sled station 3, was most active and had the highest flux coupling. The coupling of high suspended-sediment concentration with periods of onshore flow caused a net onshore transport of suspended sediment in the presence of a net offshore transport of near-bottom water.

Bed elevation changes were predicted from the cross-shore variation in the suspended-sediment transport calculated using equation 1. Convergences and divergences of the cross-shore transport contribute to accretion and erosion, respectively, of the nearshore profile. There was a convergence of cross-shore suspended-sediment transport on the bar's landward flank and a divergence on the bar's seaward flank (8D). The cross-shore suspended-sediment transport could account, qualitatively, for the migration of the bar landward in the presence of the mean offshore near-bottom currents. To see how much of the profile change could be attributed to the cross-shore suspended-sediment transport, average profile change between sled stations were calculated using a simplified form of the erosion equation.

$$\Delta\eta = \frac{1}{\phi} \frac{1}{\rho_s} \frac{\Delta Q_{sx}}{\Delta x} \Delta t \quad (9)$$

where  $\eta$  is the bed elevation in meters,  $\phi$  is the porosity of the bed material equal to 0.40,  $\rho_s$  is the density of the sediment in  $\text{kg m}^{-3}$ ,  $Q_{sx}$  is the mass flux of suspended sediment in  $\text{kg m}^{-1} \text{s}^{-1}$ ,  $x$  is the cross-shore distance, and  $t$  is time in seconds. We assumed that



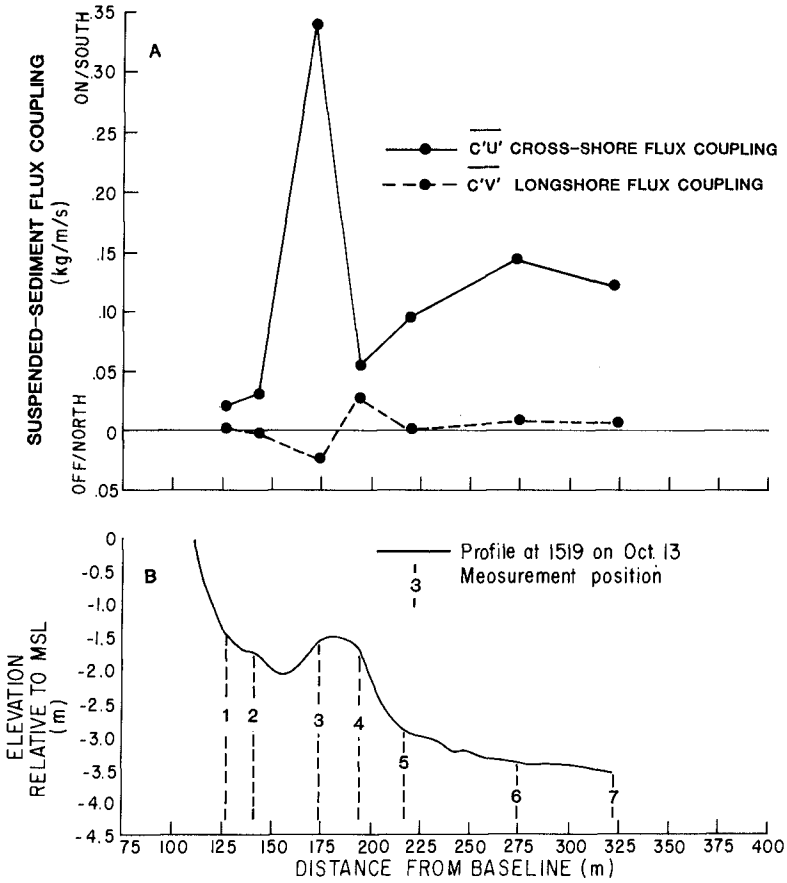


Fig. 9 Cross-shore variation of the longshore ( $\overline{c'v'}$ ) and cross-shore ( $\overline{c'u'}$ ) flux couplings. Flux couplings were calculated by subtracting Eq. 2 from Eq. 1. The data collection sequence was sled station 7, 3, 1, 5, 2, 4.

the 34.1 minute record of flux was representative for the six hour and thirty minute period between profiles. Profile changes calculated using equation 9 were compared to the observed profile changes. Figure 10 shows the relationship between predicted and measured average bed elevation changes between stations. Profile changes were calculated using both the total water column and only the lowermost 0.75 m to indicate the contribution of the flux extrapolations in the upper water column. Away from the bar, the observed erosion is not predicted. Possibly gradients in the longshore suspended-sediment transport or in the longshore and cross-shore bedload transport caused the observed erosion. Accretion was predicted on the landward flank of the bar and erosion on the seaward flank. The measured average profile changes exhibited the same pattern and were of similar magnitude.

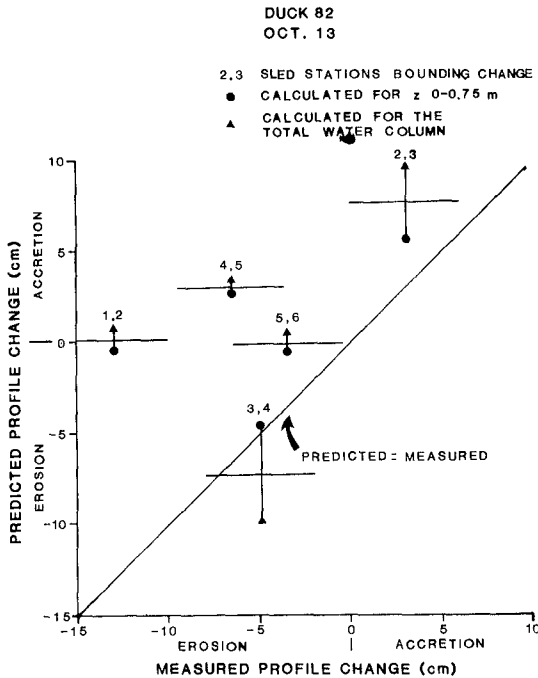


Fig. 10 Comparison of measured average bed elevation changes between sled stations with average changes predicted from convergences and divergences in the cross-shore suspended-

## CONCLUSIONS

Measurements showed that a strong coupling existed between high suspended mass in the water column and periods of onshore flow such that a net onshore transport of sediment occurred even though the mean flow was in an offshore direction. In the vicinity of the bar crest, gradients in the cross-shore suspended sediment transport could account for changes in the nearshore profile. These results suggest suspended sediment is very important in surf zone processes.

## ACKNOWLEDGMENTS

This work was supported by the U.S. Geological Survey and a fellowship while at the University of Washington from Texaco Inc.. We would like to thank the staff of the FRF for excellent field support throughout the experiment. Jim Smith and Arthur Nowell of the University of Washington were instrumental in guiding the early stages of data analysis. Helpful criticism of the manuscript were given by Bruce Richmond, Ed Clifton and Raphael Jaffe. Jeff List and David Barnes contributed many hours of time to brainstorming, wild speculations, and ultimately towards putting the work in its proper perspective. The first author is forever grateful to his wife, Trish, whose warm body and pleasant disposition balanced the cerebral abstractions of research. Lastly, many thanks to Jack.

## REFERENCES

- Bowen, A. J. (1980): Simple models of nearshore sedimentation: beach profiles and longshore bars, in *The coastline of Canada*, S. B. McCann, Editor, Geological Survey of Canada, Paper 80-10, pp. 1-11.
- Downing, J. P., Sternberg, R. W. and Lister, C. R. B. (1981): New instrumentation for the investigation of sediment suspension processes in the shallow marine environment, *Mar. Geol.*, Vol. 42, pp. 19-34.
- Komar, P. D. and Gaughan, M. K. (1973): Airy wave theory and breaker height prediction, *Proc. 13th Coastal Eng. Conf., ASCE*, pp. 405-418.
- Komar, P. D. and Miller, M. C. (1975): The initiation of oscillatory ripple marks and the development of plane-bed at high shear stresses under waves, *J.S.P.*, Vol. 45, pp. 697-703.
- Mason, C., Sallenger, A. H., Holman, R. A., and Birkmeyer, W. A. (in press): A comprehensive experimentation storm-related coastal processes, *Proc. 19th Coastal Eng. Conf., ASCE*.
- Sallenger, A. H., Howard, P. C., Fletcher, C. H., and Howd, P. A. (1983): A system for measuring bottom profile, waves and currents in the high-energy nearshore environment, *Mar. Geol.*, Vol. 51, pp. 63-76.
- Watanbe, A., Riho, Y., and Horikawa, K. (1981): Beach profiles and on-offshore sediment transport, *Proc. Coastal Eng. Conf., ASCE*, pp. 1106-1120.

## CHAPTER ONE HUNDRED THIRTY FOUR

### CROSS-SHORE TRANSPORT OF BIMODAL SANDS

Bruce M. Richmond\* and Asbury H. Sallenger, Jr.\*

#### ABSTRACT

Foreshore sediment level and sediment size were monitored as part of an extensive nearshore processes experiment - DUCK 82. Changes in foreshore texture were compared with computed values of onshore transported material based on current measurements from the surf zone and sediment transport theory (Bag-nold, 1963, 1966). Preliminary results indicate reasonable agreement between predicted size of sediment transported onshore and beach texture changes. It is also demonstrated that coarse sediment may move onshore while finer material may simultaneously move offshore.

#### INTRODUCTION

Theoretical (Bowen, 1980) and field (Murray, 1967) studies have shown the possibility of oppositely directed sediment transport for different sized material under oscillatory flow. As waves shoal, oscillatory water velocities become asymmetric with a strong landward flow followed by a slower and longer seaward return flow. Because of its higher peak flow, the landward-directed current is able to transport coarser material than the seaward current. Zenkovich (1967) discussed a hypothetical situation where 1 mm diameter particles were in equilibrium with the local conditions. Particles finer than 1 mm moved seaward while coarser particles moved landward with particles of 4 mm diameter having the greatest landward thrust. In a tracer study using three different particle sizes, Murray (1967) demonstrated under conditions of shoaling wind waves that finer grain sizes had a greater tendency to move offshore. Bowen (1980) showed theoretically that when a sediment of a given grain size is in equilibrium with a given slope and wave regime (net sediment transport rate is zero for this size) any coarser material should move onshore and finer material offshore.

Sonu (1972) working at Nags Head, N.C. described variations of foreshore profile and beach sediment texture over a period of several months. He discussed a sequence of texture changes associated with storm and recovery cycles which can be summarized as follows: a) The passage of a storm resulted in a foreshore composed of unimodal fine sediment. b) In the early stage of beach recovery, coarse material with a unimodal distribution appeared in the lower foreshore.

\* U.S. Geological Survey, Menlo Park, CA 94025

c) Continued accretion was accompanied by the addition of finer material leading to a strongly bimodal sediment composition. d) At the well-developed accretive state, finer sands were the dominant beach sediment. Sonu proposed that the length of time for the above cycle to occur was on the order of 2-3 months.

In this paper, we present field data from the Outer Banks of North Carolina on beach profile and sediment texture changes. This study was in conjunction with other studies on surf-zone processes during the DUCK 82 experiment (Mason and others, this volume). The experiment site at the Field Research Facility (FRF) of the U.S. Army Coastal Engineering Research Center at Duck, N.C. offered an excellent opportunity to examine mobility of different grain size populations under a variable wave climate. A wide range of sediment sizes is present including a terrigenous (non-biological) pebble fraction (Figure 1). We compared measured foreshore grain size to grain-sizes predicted to move onshore by a sediment transport model (Bagnold, 1963, 1966; Bowen, 1980).

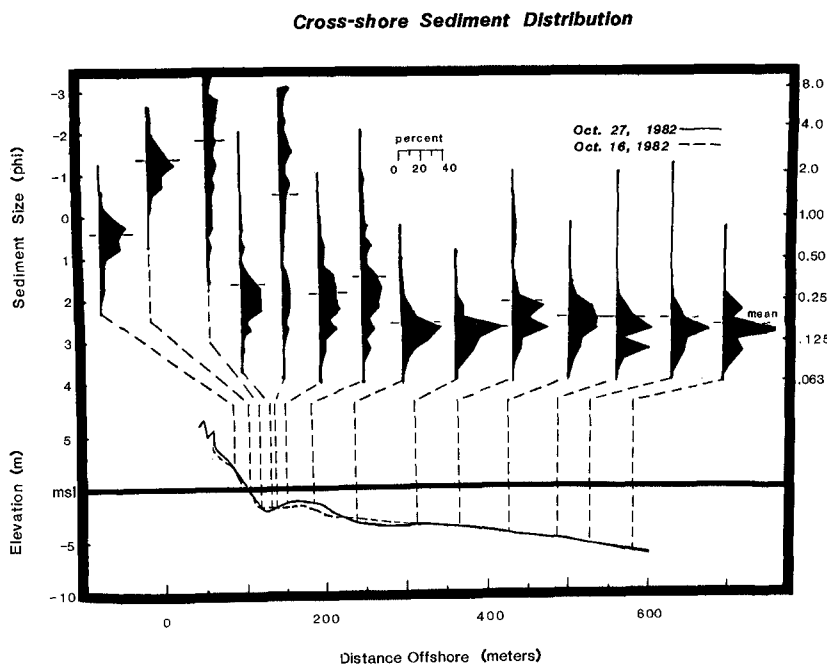


Figure 1. Cross-shore sediment distribution along the USGS sled line.

EXPERIMENT DESIGN AND METHODS

The data collection effort involved sampling foreshore sediments and measuring sediment-level variations while gathering nearshore wave and current measurements (Figure 2). Foreshore sediment levels were measured relative to the tops of 1-cm-diameter aluminum rods spaced 2.5 m apart in a shore-normal line. This line was part of a 35 by 40 meter foreshore grid described more fully in Howd and Holman (this volume). Uniform foreshore sand samples 6 mm thick were collected by a "cheese-slicer" device while beach gravels were hand sampled. Offshore samples were obtained with a grab sampler deployed from the CRAB (Coastal Research Amphibious Buggy). Foreshore sediment and sediment levels were monitored at variable intervals depending on the beach response and the goals of a particular experiment, although measurements were made at least daily.

Twice-daily nearshore profiles were obtained with the USGS sled system (Sallenger and others, 1983). Electro-magnetic flow meters attached to the sled provided current information. The data were telemetered to a shore receiving station. The length of each data run was 34.1-minutes ( see Sallenger and Holman, this volume).

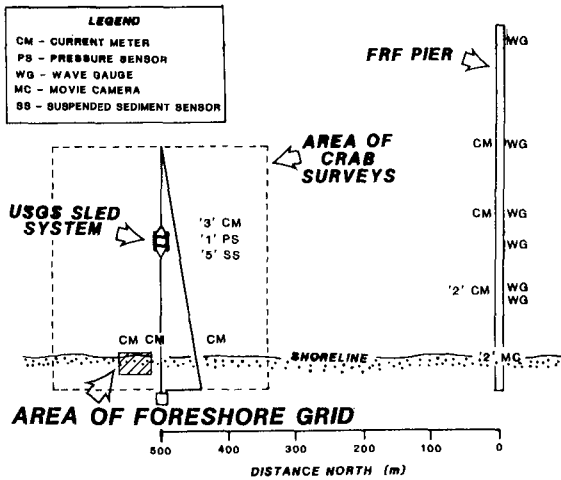


Figure 2. Map showing experimental set-up for the DUCK 82 experiment. The foreshore grid is 35 by 40 meters (it is discussed more extensively in Howd and Holman, this volume). FRF=Field Research Facility, CRAB=Coastal Research Amphibious Buggy. The USGS sled is not drawn to scale.

### Calculation of Sediment Transport

Although the mechanisms of sediment transport and deposition on the beach face differ from those in the nearshore, the sediment moving onshore through the inner surf zone should be an indicator of the material deposited on the foreshore. Bagnold's (1963, 1966) total-load transport model was used to predict at which grain size a reversal in transport direction would occur at an inner surf-zone station close to the swash zone. The reversal size is that size at which coarser material should move onshore and finer material offshore. These predictions were compared with actual changes of foreshore grain size. Bagnold's model was selected because it has been used successfully to explain some characteristics of cross-shore sediment transport (Bowen, 1980).

From Bowen (1980), the total immersed weight transport is

$$i_t = i_s + i_b \quad 1$$

where the suspended load equals

$$i_s = \frac{\epsilon_s C_D \rho u^3 |u|}{W - u\beta} \quad 2$$

and the bedload is given by

$$i_b = \frac{\epsilon_b C_D \rho u^3}{\tan \Phi - \frac{u\beta}{|u|}} \quad 3$$

These equations were simplified as follows:

$$i_s \approx \frac{\epsilon_s C_D \rho}{W} \left( \overline{u^3 |u|} + \frac{\overline{|u^5| \beta}}{W} \right) \quad 4$$

$$i_b \approx \frac{\epsilon_b C_D \rho}{\tan \Phi} \left( \overline{u^3} + \frac{\overline{|u^3| \beta}}{\tan \Phi} \right) \quad 5$$

$$i_t \approx C_D \rho \left( \frac{\epsilon_s}{W} \overline{u^3 |u|} + \frac{\epsilon_s}{W^2} \beta \overline{|u^5|} \right) \quad 6$$

$$+ \frac{\epsilon_b}{\tan \Phi} \overline{u^3} + \frac{\epsilon_b}{\tan^2 \Phi} \beta \overline{|u^3|} \right)$$

Where:

$C_D$  - drag coefficient (0.005; Bowen, 1980),  $i_t$  - total immersed-weight transport rate of solids,  $i_s$  - suspended-load transport rate,  $i_b$  - bedload transport rate,  $u$  - instantaneous cross-shore velocity (from sled measurements),  $W$  - fall velocity of sediment grains (variable),  $\beta$  - local slope (variable),  $\epsilon_s$  - efficiency of suspended-load transport (0.025; Bailard, 1981),  $\epsilon_b$  - efficiency of bedload transport (0.21; Bailard, 1981)  $\rho$  - fluid density ( $1027.0 \frac{kg}{m^3}$ ),  $\tan \Phi$  - friction angle of sediment (0.63).

Input velocities were derived from a current meter at a height of one meter above the bed and local slope was measured from the sled profile taken nearest in time to the current measurements. Sediment settling velocity was varied at 0.005 m/s increments to determine at which "size" a reversal in sediment transport direction would occur.

## RESULTS

Two data sets are discussed; the first considers foreshore texture changes for ten different days in October 1982, and the second examines nearshore profile and texture changes during a storm on Oct. 12th.

In the first example mid-foreshore sediment size was compared to the predicted size of sediment moving onshore past the landwardmost sled position for ten different days (Table I). In all cases the landwardmost sled position was immediately seaward of the swash zone. Significant wave heights determined from a waverider buoy in 18 meters of water three km from shore varied from a low of 0.7 m to a high of 2.3 m. In all cases the beach modal sizes were greater than or equal to the calculated values. Modal size is used because it corresponds to the most frequently occurring particle diameter and represents actual size of sediment present (mean grain size may be a size that is poorly represented in a bimodal sample).

Decreasing wave height was associated with a coarsening of the beach sediments and, conversely, increasing wave heights were followed by a fining of the foreshore. The initial coarsening may be due to the high mobility of the coarse sediments and close proximity to the probable source - the nearshore trough (Figure 1). The predicted reversal size is generally smaller than the actual foreshore sediment size which is consistent with the model because the calculated size represents the finest size which should be moving onshore. This is readily apparent on Oct. 14th where the predicted reversal size is 0.08 mm and the actual middle foreshore size is 4.1 mm. Finer material however, was deposited higher on the foreshore. It should be noted that there is a natural size grading across the foreshore, generally from coarse to fine as one travels landward across



the foreshore, which accounts for some differences between observed and predicted sizes. Although only one sample per day is used in this analysis, there were samples periodically taken at 5 m intervals across the foreshore which confirmed the general fining or coarsening trends reported.

Table I. Variation between predicted and observed (two values indicate a bimodal sample) sediment changes.

Date/1982	Modal Mid-foreshore Sediment Sizes (mm)	Predicted Reversal Size* (mm)	Significant Wave Height (m)
10-10	0.35	0.36	2.2
10-11	0.42	0.36	2.3
10-12	0.71 0.30	0.38	2.1
10-13	1.41	0.39	1.6
10-14	4.10	0.08	1.1
10-15	0.71	0.18	0.7
10-17	0.35	0.08	1.5
10-20	1.41 0.30	0.42	1.2
10-21	0.40	0.30	1.3
10-22	0.71 0.30	0.18	1.5

\*The calculated size at which a reversal in transport direction occurred.

Figure 3 is a photograph of a trench from the upper foreshore on Oct. 15th illustrating alternating coarse and fine laminations and the bimodality of the beach sediment. The upper coarse layer and the overlying finer laminations were deposited during the previous few days and represent a portion of the Sonu sequence discussed earlier. A major difference between these observations and Sonu's is the more rapid development in this study (a matter of days rather than weeks or months).



Figure 3. Foreshore trench from Oct. 15th, displaying variations in texture and planar laminations.

One of the questions from the the first example is what is the source for the coarse sediment-does it represent onshore transported material or is it an erosional lag? In this second example, we compare profile changes to sediment grain-size changes. The observed sediment sizes are then compared to values predicted to move onshore by the sediment-transport model.

October 12, 1982, was the third day of an extra-tropical storm (northeaster). During the storm, northeast winds reached a maximum sustained speed of 13 m/s at the study site, and maximum significant offshore wave heights reached 2.5 m (Mason and others, this volume). On Oct. 10th, the first day of the storm the foreshore underwent severe erosion with vertical losses greater than 1 m locally. Continued erosion occurred on the 11th but at a much reduced rate. By Oct. 12th offshore significant wave height was 2.5 m and peak period was 15.2 s; both foreshore accretion and erosion were occurring although erosion dominated. Available sediment sizes (Figure 1) varied from fine sand (offshore bar) through medium and coarse sand (inner nearshore and beach) to granules and pebbles (trough).

Several profile and sediment-size changes occurred during the rising tide (Figure 4a). The middle and upper foreshore underwent erosion while the lower foreshore accreted. Coarse sand, granules and pebbles were deposited on the lower foreshore while finer sands were removed from the middle and upper foreshore. The size distributions of the sediments (surficial and subsurface) eroded from the upper foreshore were such that they could not have supplied the volume of coarse material deposited on the lower foreshore. This implies that fine material was removed from the foreshore while, simultaneously, coarse material was derived from an offshore source. During this same period the offshore bar, which was composed of fine sand, was migrating offshore (Figure 4b; Sallenger and Holman, this volume; Sallenger and others, in press). The most reasonable interpretation is that coarse material was transported onshore to accumulate on the lower foreshore, while finer material was transported offshore, both from the upper foreshore and in the offshore-migrating bar.

The predicted direction of sediment movement for given size classes at selected locations across the nearshore profile are presented in Figure 4b. From the landwardmost sled position, sediment coarser than 0.4 mm (medium sand) is predicted to move landward. This landward transported coarse material probably contributed to the observed coarsening of the lower foreshore. The granules and pebbles deposited on the lower foreshore were considerably coarser than the 0.4 mm predicted reversal size. However, the reversal size indicates only the finest material moving onshore. Elsewhere along the profile the coarsest material predicted to move offshore was medium sand at a point just seaward of the bar crest. All material coarser than very fine sands was calculated to move onshore at the seawardmost sled position and near the deepest part of the trough. The seaward migration of the bar was presumably the result of offshore-transported medium and finer sands.

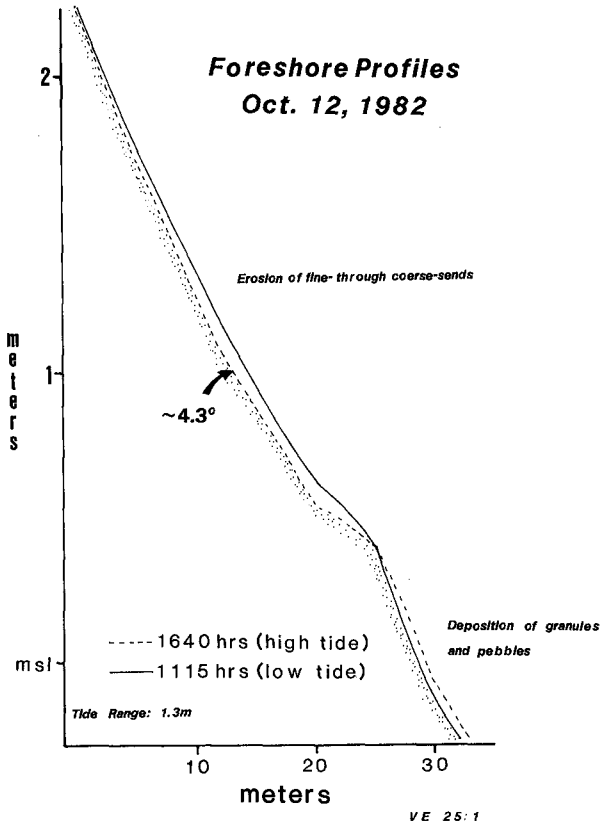


Figure 4a. Foreshore profile and texture changes for Oct. 12th.

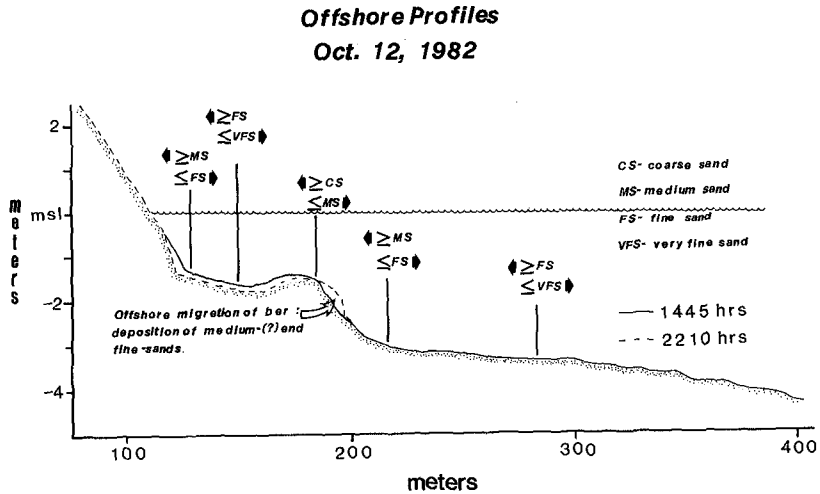


Figure 4b. Offshore profile changes and predicted directions of sediment transport for different grain-sizes at selected sled locations.

#### CONCLUDING REMARKS

Field evidence from a mixed sandy nearshore supports theoretical predictions that different size classes of sediment can be transported in opposite directions under the influence of the same flow field. Using a sediment transport model, coarse sand was predicted to move onshore as coarse sediment was observed to be accumulating on the foreshore.

The two major parameters responsible for variation in the sediment transport direction are the slope and current velocity. Negative slopes (i.e., a landward slope) introduces some inconsistencies. Onshore transport directions for all sizes studied were predicted for a sled position on the landward sloping bar surface on Oct. 12th. This conflicts with field evidence, based on profile change, of offshore sediment transport for this general location. Theoretically, if the mean offshore currents are strong enough, seaward transport should occur over a landward sloping feature.

The Bagnold efficiency factors,  $\epsilon_s$  and  $\epsilon_b$ , are another uncertainty. However, we varied these factors within the limits suggested by Bailard (1981) and these changes resulted in reversal size changes of  $\pm .25 \Phi$  --acceptable variations for this study.

Although the results are strictly applicable only to the experimental conditions, they are significant in terms of the transport of any natural sediment or exotic materials such as dredge spoil or beach nourishment fill.

#### ACKNOWLEDGEMENTS

We would like to thank the entire staff of the FRF for their excellent support in the field. Peter Howd (formerly of OSU) spent many long hours, often under very adverse conditions, measuring sediment levels. David Barnes assisted with the computer programming and Ralph Hunter and Bruce Jaffe made many valuable comments on the manuscript. W. A. Birkemeier (FRF) kindly supplied the sieve data for the offshore samples.

#### REFERENCES

- Bagnold, R. A., 1963: Mechanics of marine sedimentation, in *The Sea*, M. N. Hill ed., Interscience, v.3:507-528.
- Bagnold, R. A., 1966: An approach to the sediment transport problem from general physics. *U.S. Geological Survey Prof. Paper*, 422-I. 37pp.
- Bailard, J. A., 1981: An energetics total load sediment transport model for a plane sloping beach. *Jour. Geophys. Research* 86:10938-10954.
- Bowen, A.J., 1980: Simple models of nearshore sedimentation; beach profiles and longshore bars. in *The Coastline of Canada*, S. B. McCann ed., Geological Survey of Canada, Ottawa, 80-10:1-11.
- Howd, P. A. and R. A. Holman, In press: Beach foreshore response to long period waves. *19th International Coastal Engineering Conference Proceedings*. This volume.
- Mason, C., A. H. Sallenger, R. A. Holman, and W. A. Birkemeier, In press: A comprehensive experiment on storm-related coastal processes. *19th International Coastal Engineering Conference Proceedings*. This Volume.

Murray, S. P., 1967: Control of grain dispersion by particle size and wave state. *Jour. Geology*, 75:612-634.

Sallenger, A. H., P. Howard, C. Fletcher, and P. Howd, 1983: A system for measuring bottom profile, waves and currents in the high- energy nearshore environment. *Marine Geology*, 51:63-76.

Sallenger, A. H., and R. A. Holman, In press: On predicting infragravity energy in the surf zone. *19th International Coastal Engineering Conference Proceedings*. This volume.

Sallenger, A. H., R. A. Holman, and W. A. Birkemeier, In press: Storm-induced response of a nearshore-bar system. *Marine Geology*.

Sonu, C. J., 1972: Bimodal composition and cyclic characteristics of beach sediment in continuously changing profiles. *Jour. Sedimentary Petrology*, 42:852-857.

Zenkovich, V. P., 1967: *Processes of Coastal Development*. Wiley Interscience, N.Y., 738 pp.

## CHAPTER ONE HUNDRED THIRTY FIVE

### DEPOSITIONAL EFFECTS OF OFFSHORE BREAKWATER DUE TO ONSHORE-OFFSHORE SEDIMENT MOVEMENT

Hideaki Noda \*

#### ABSTRACT

Physical parameters controlling the development of tombolo behind offshore breakwaters are clarified on the basis of the results obtained by laboratory tests. Especially, the depositional effects are evaluated by taking a permeable type structure into account. They are wave characteristics, sediment size, the water depth where the structures are to be placed and its dimension. The amount of sand deposition behind the structures is presented by non-dimensional parameters such as the relative distances from the initial shoreline to the structure and to the breaking point of waves, the ratio of the gap width to the wave length in deep water and the ratio of the length of the offshore breakwater to the wave length in deep water.

#### INTRODUCTION

In considering depositional effects of an offshore breakwater by waves and currents on a beach, it is well known that offshore breakwaters act as barriers to littoral drift, blocking the natural sediment movement along the shoreline. However, sand transported from offshore sea beds by onshore-offshore sediment movement is also deposited within the protected lee of an offshore breakwater constructed on a coast where the littoral drift is not predominant, as shown by Toyoshima<sup>2)</sup>.

To gain some insight into the mechanisms, this paper deals experimentally with changes in the shoreline caused by the construction of offshore breakwaters and the amount of sand deposition within the protected lee of the breakwaters.

In addition, the distributions of the wave height and direction are measured and the currents behind the structures are observed by using floats. The results are utilized to estimate the distribution of the radiation stresses and the currents behind the offshore breakwater.

Finally, triangular-shaped groynes placed behind gaps of the structure are experimentally examined as a beach control measure.

\* Professor, Department of Ocean Civil Engineering,  
Tottori University, Tottori, JAPAN



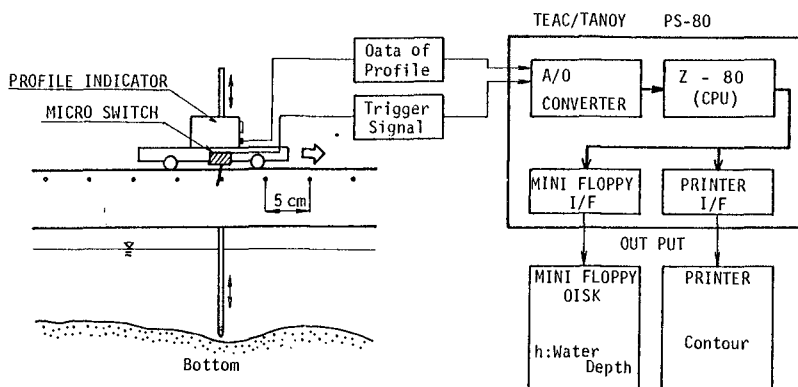


Fig. 1 Schematic diagram of measuring method for bottom configuration

Table 1 Wave conditions

	T (sec)	$L_0$ (cm)	$H_0$ (cm)	$H_0/L_0$	$H_0/d$
Type B	1.20	225	6.90	0.03	400
Type S	1.28	256	2.74	0.01	150

T: wave period,  $H_0$ : deepwater wave height

$L_0$ : deepwater wave length, d: median diameter of sand

LABORATORY EXPERIMENTS

## DESCRIPTION OF TWO MODELS

Two kinds of models were selected as the subject of the study; one was a wave flume which was designed to estimate the amount of sand transported shoreward through the permeable-type offshore breakwater and the other a wave basin which was designed to evaluate the amounts of sand transported shoreward both through the structure and from the gap between adjacent units.

The wave flume equipped with a flat-type wave generator was used; its dimension was 23 m long, 0.5 m wide and 0.6 m deep. The sediment used in the experiments was the well-sorted sand with a median diameter of 0.2 mm and a specific gravity of 2.65. The initial beach profiles constituted by this sand were uniform slope of 1/10.

The methods of the wave flume experiments are to measure the changes of the beach profiles and to estimate the volume of sand intruding into the protected area through the breakwater by using the results of the profile changes. The profiles of beaches were measured by an equipment which was developed to measure a number of depths of the bottom as soon as possible by combining a profile indicator with a personal computer as shown in Fig. 1. After the beach profile was deformed by the wave and reached the equilibrium state, the permeable-type breakwater was installed in the surf zone of the equilibrium profile and shifts in the profile were obtained until the equilibrium profile was reformed again. Table 1 is a list of wave conditions used in the experiments.

The second experiment was made by use of a wave basin measuring 12 m long, 5 m wide and 0.6 m deep. The beach was characterized by the same initial slope and sand as those of the first experiment. In order to examine the relationship between the depositional effects of the offshore breakwater and the wave behavior, the following quantities were measured: the change in shoreline shape, the amount of sand deposited in the protected lee, the distribution of the wave height and the wave direction, the distance from the breaking point to the initial shoreline and the velocity of the current behind the breakwater.

## BEACH PROFILE CHANGE IN TWO-DIMENSIONAL CASE

In the experiments, two types of wave characteristics were selected to study the effect of wave action on the changes of the beach profile. As shown in Table 1, one is the B-type wave which forms a storm profile with a longshore bar and the other the S-type wave which develops a swell profile. The reason for using the two kinds of waves is to investigate the difference of sand volume deposited within the protected area by using the same waves (B-B or S-S) or the

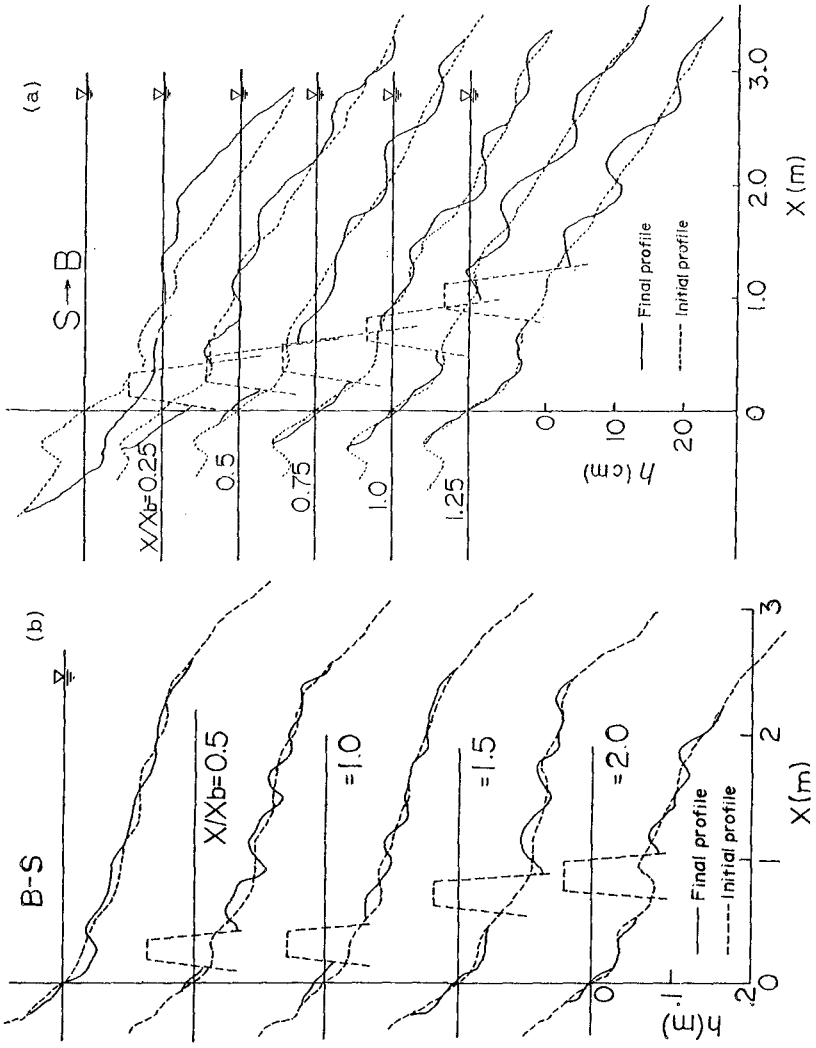


Fig. 2 Changes of beach profiles for various locations of offshore breakwater

different waves (B-S or S-B) before and after placing the structure.

Figs. 2-(a) and (b) show an example of the profile changes obtained from different waves (S-B) before and after installing the breakwater, in which  $X$  and  $X_b$  are the distances from the initial shoreline to the center of the offshore breakwater and that to the breaking point, respectively. The beach profiles at the top of this figure show the equilibrium beach profile (solid line) which was developed by the actions of the B-type wave after the equilibrium profile (dotted line) was formed by the actions of the S-type wave. As an expected result, it was found that the great recession of the final shoreline takes place in the case where there is no breakwater, while the progression of the final shoreline is caused by placing the breakwater. Fig. 2-(b) shows the similar results for B-S waves. Fig. 3 shows the relationship between the amount changes within the protected area and the relative distance of the located offshore breakwater, and  $V$  is the amount of sand deposited after placing the breakwater. In addition, the symbols shown in the upper left of this figure indicate that the experiments were carried out by using the same waves (B-B or S-B) or the different waves (B-S or S-B) before and after placing the breakwater.

This figure summarizes the depositional effects of the sediment intruding shoreward through the permeable breakwater and the amount of sand deposition depends on both the wave characteristics and the values of  $X/X_b$ . The location to maximize the amount of deposition is found when the breakwater is located at  $X/X_b=0.5$  to  $1.0$  for all cases of wave types.

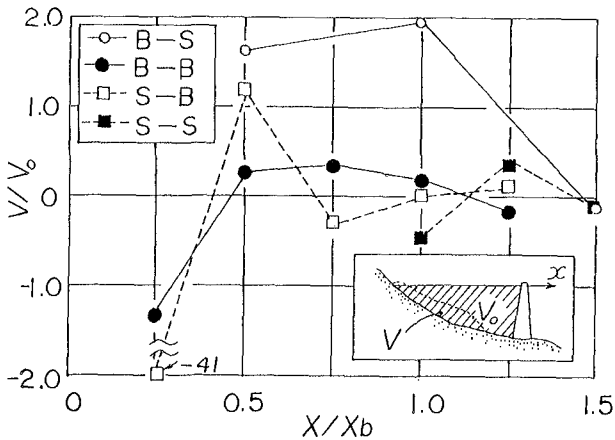


Fig. 2 Measured relationships between  $V/V_0$  and  $X/X_b$

## CHANGE OF BEACH CONFIGURATION IN THREE-DIMENSIONAL CASE

Table 2 is a list of wave conditions used in the wave basin experiments. The method of the experiments was conducted as follows: after having the B-type waves act on the beach with a uniform slope of 1/10 and then installing the offshore breakwaters on the various locations inside the surf zone, the final equilibrium beaches were formed by the actions of the same waves. The waves used in Run A were designed to correspond to those of the two-dimensional experiment (B-B) so that quantitative evaluations can be made by comparing both data. The reason why steeper waves were used in Run B was to emphasize the depositional effects due to the onshore-offshore sediment transport, considering that the wave used in this experiment ( $H_0/L_0 = 0.087$ ) had a tendency to cause greater erosion.

Table 3 is a list of non-dimensional quantities related to the distance from the initial shoreline to the center of the offshore breakwater  $X$ , the length of the breakwater  $l_B$  and the width of gap between the breakwaters  $B$ . Fig. 4 shows the definition sketch for the offshore breakwaters and the beach configuration. Fig. 5-(a) and (b) are the examples of the bathymetry in the initial ( $t=0$  hr.) and the final ( $t=16$  hrs.) states, respectively.

Fig. 6 shows a few examples obtained in these experiments. In these figures, the solid and chain lines show the initial and final shorelines, while the various dotted and broken lines indicate the equi-depositional contour lines (unit cm) obtained from the difference between the final and initial bathymetries. These three figures result from different locations of the structure but correspond to the same wave condition (B-B). It is found that well-developed tombolos and the maximum deposition occur when the offshore breakwater is located at  $X/X_b = 0.56$ . As shown by Shinohara and Tsubaki<sup>1)</sup>, bi-modal tombolo develops in the case of a short distance between the initial shoreline and the location of the structure ( $X/X_b = 0.39$ ).

From the condition of continuity, the total volume of sand deposition,  $Q$ , in the region abb'a' shown in Fig. 4 becomes

$$Q = Q_0 B + V l_B \quad (1)$$

where  $Q_0$  represents the total volume of sand deposition per unit width of the gap transported through the gap and  $V$  the total volume of sand deposition per unit length of the breakwater resulting from sand intrusions through the permeable breakwater. An alternative form of Eq.(1) may read

$$\frac{Q_0}{V} = \frac{Q}{V B} - \frac{l_B}{B} \quad (2)$$

in which  $Q_0/V$  indicates the ratio of the total volume of sand deposition per unit width of the gap transported shoreward from the gap to that of sand deposition resulting from sand intrusions through the permeable breakwater. The

Table 2 Wave conditions in three dimensional experiments

	T (sec)	$L_0$ (cm)	$H_0$ (cm)	$H_0/L_0$	$H_0/d$
Run A	1.19	221	5.70	0.026	335
Run B	0.73	83	7.20	0.086	424

Table 3 Dimension and location of offshore breakwater

		$X/X_b$	$X/l_B$	$l_B/L_0$	$B/L_0$
Run A	1	0.50	0.44	0.724	0.23
	2	0.75	0.66		
	3	1.00	0.88		
Run B	1	0.39	0.44	1.93	0.60
	2	0.56	0.63		
	3	0.78	0.94	2.90	
	4		0.63		

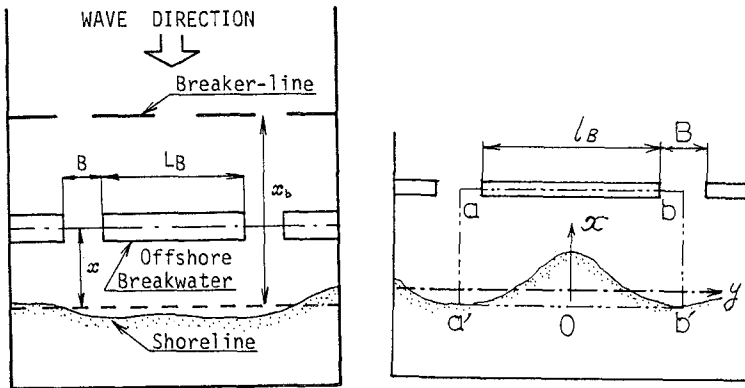
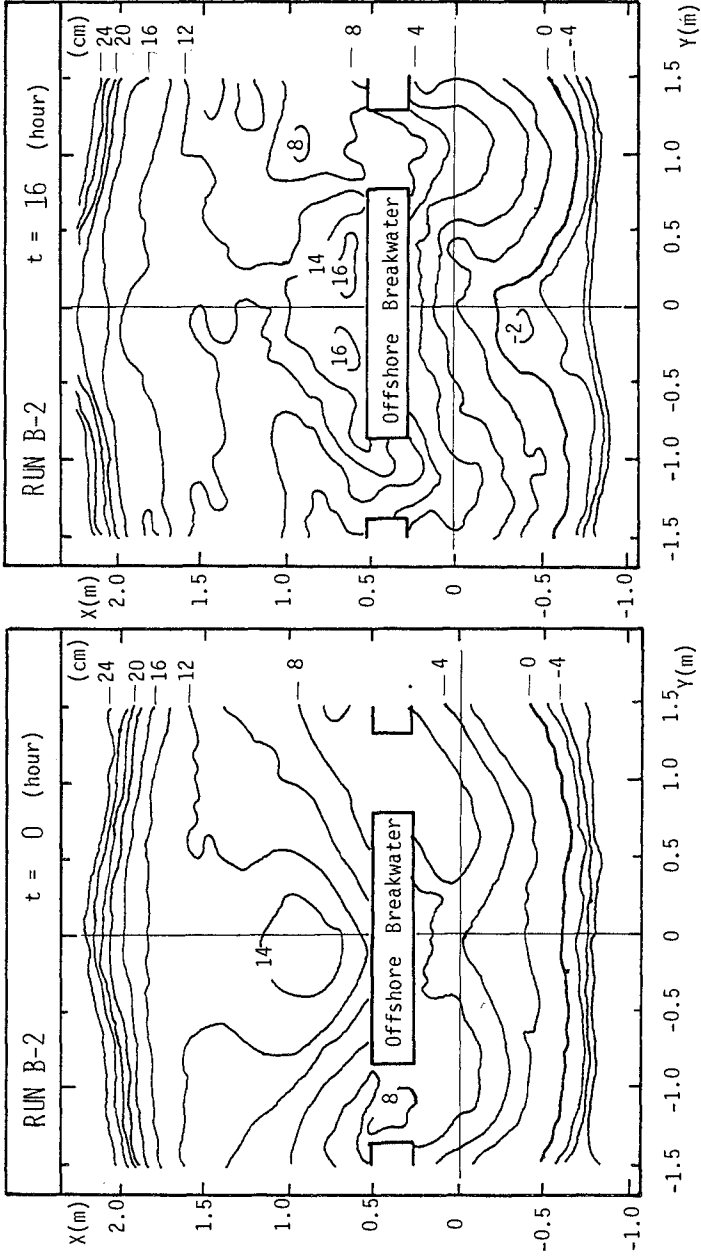


Fig. 4 Definition sketch for offshore breakwater



(a)

(b)

Fig. 5 Bottom topographies at the initial and final state

value of  $Q_0/V$  can be calculated by using the measured values of  $Q$  and  $V$  on the basis of Eq.(2).

Fig. 7 shows the relationship between  $Q/Ad$  and  $X/X_b$  obtained from Runs A and B, and also the same relationship between  $V/Xd$  and  $X/X_b$  obtained from the case of B-B in the two-dimensional experiments, in which A is the area of abb'a' shown in Fig. 4 and  $d$  the median diameter of sand size. A comparison of the results in Run A with those of two-dimensional experiment (B-B) having the same wave condition as that of Run A in this experiment (B-B) and the estimation of  $Q_0/V$  on the basis of Eq.(2) shows that the total amount of sand deposition per unit width of the gap transported shoreward from the gap is about three times that of the sand deposition resulting from the wave intrusion through the permeable breakwater itself. Therefore, the results suggest that the non-dimensional volume of sand deposition directly depends not only on the values of  $X/X_b$  but also on the values of  $l_p/B$ , the ratio of the length of the offshore breakwater to the width of the gap. There is, however, an exception;  $Q_0/V = -0.34$  for  $X/X_b = 0.75$ . This fact indicates that the amount of the sand transported seaward from the gap is about three times that of the sand intruding shoreward through the permeable breakwater, although  $Q/Ad=0$  balances the sand budget within the protected area (see Fig. 7).

Fig. 8 shows two beach profiles, one at the center of the breakwater and the other at the center of the gap for  $X/X_b = 0.75$ . In this figure, it is found that a large amount of sand existing near the shore-

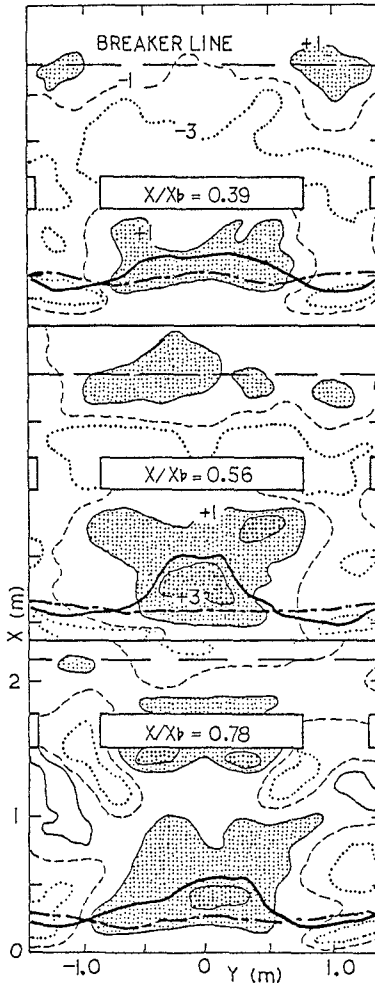


Fig. 2 Changes of shoreline and bottom configuration at various locations of offshore breakwater



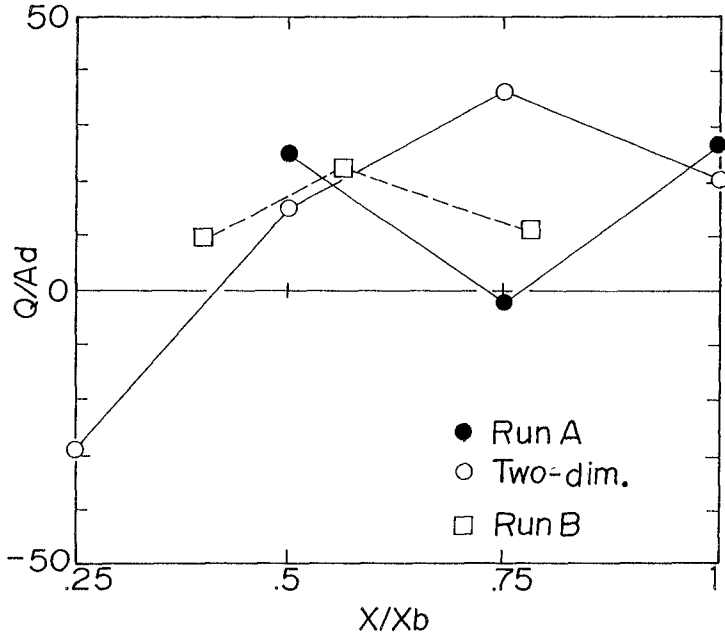


Fig. 7 Relationship between  $Q/Ad$  and  $X/X_b$

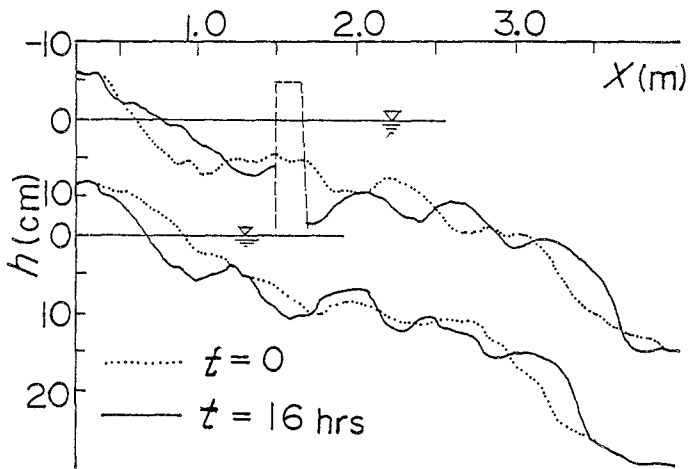


Fig. 8 Changes of beach profiles

line behind the gap is taken away by waves and currents, since the progression of the shoreline takes place and a tombolo is developed near the center of the breakwater but the scour of its lee just behind the offshore breakwater occurs and the regression of the shoreline behind its gap is greatly eroded.

#### MEASUREMENT OF WAVE AND CURRENT CHARACTERISTICS

An attempt was made to investigate the mechanism of sand deposition due to the onshore-offshore sediment transport, the measurements of wave parameters and the resulting currents in the protected area were made under the condition of Run B-2 in which the maximum amount of sand deposition in the area of the protected lee was observed.

Fig. 9 shows the results of measured wave height and direction in various locations. In this figure, the local variation of wave height is expressed by the ratio of wave heights measured in each location,  $H$ , to the incident wave height  $H_I$ . Both the direction and the length of each solid line segment with an arrow head represent the direction of waves and the ratio  $H/H_I$ , respectively. Each contour line corresponds to a certain value of this ratio. The following may be found from this figure : 1) a partial clapotis is developed in the area seaward of the offshore breakwater, 2) diffraction of waves is observed in the vicinity of the gap, and 3) transmitted waves intruding through the breakwater are recognized just behind the offshore breakwater.

By introducing a rectangular co-ordinate system  $(x,y)$ , in which the orientation of the co-ordinate system is chosen so that the x-axis lies roughly perpendicular to the initial shoreline as shown in Fig. 10, the radiation stresses in the measuring points of the wave height are expressed by

$$\begin{pmatrix} S_{xx} & S_{xy} \\ S_{yx} & S_{yy} \end{pmatrix} = E \begin{pmatrix} n \cos^2 \theta + n - 0.5, & -0.5 n \sin 2\theta \\ -0.5 n \sin 2\theta, & n \sin^2 \theta + n - 0.5 \end{pmatrix} \quad (3)$$

where  $\theta$  is the angle between the wave direction and x-axis,  $n$  the ratio of the group velocity to the wave velocity and  $E$  the wave energy. In addition, the non-dimensional friction terms  $(R_x, R_y)$  related to the wave-induced currents are given by

$$\begin{aligned} R_x &= -\frac{1}{\rho gh} \left( \frac{\partial S_{xx}}{\partial x} + \frac{\partial S_{yx}}{\partial y} \right) \\ R_y &= -\frac{1}{\rho gh} \left( \frac{\partial S_{xy}}{\partial x} + \frac{\partial S_{yy}}{\partial y} \right) \end{aligned} \quad (4)$$

in which  $\rho$  is the density of water,  $g$  the acceleration of gravity and  $h$  the water depth. The radiation stresses based on Eq.(3) can be calculated by using the measured wave

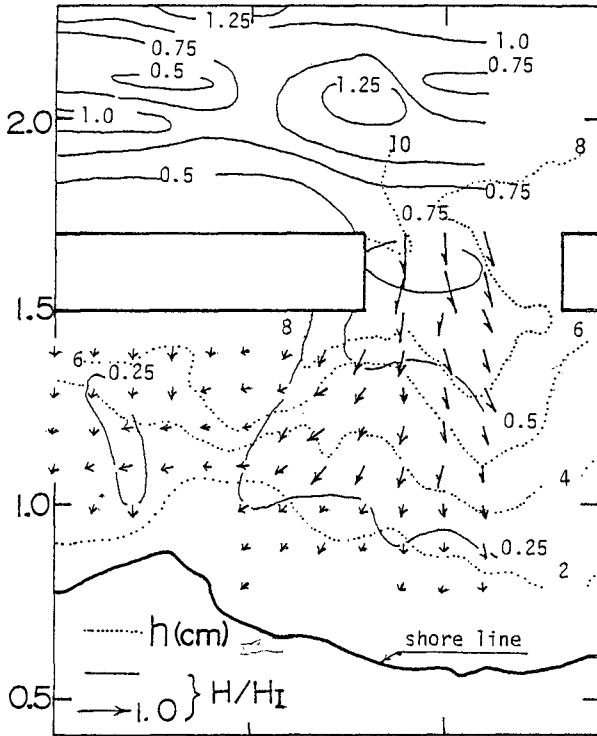


Fig. 9 Distribution of wave height expressed by the ratio of  $H/H_I$

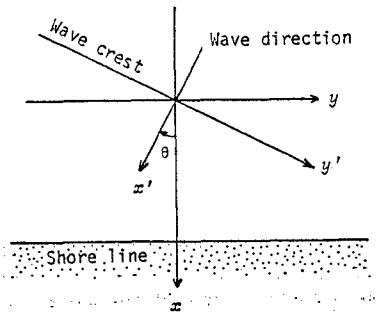


Fig. 10 Definition sketch of co-ordinate system

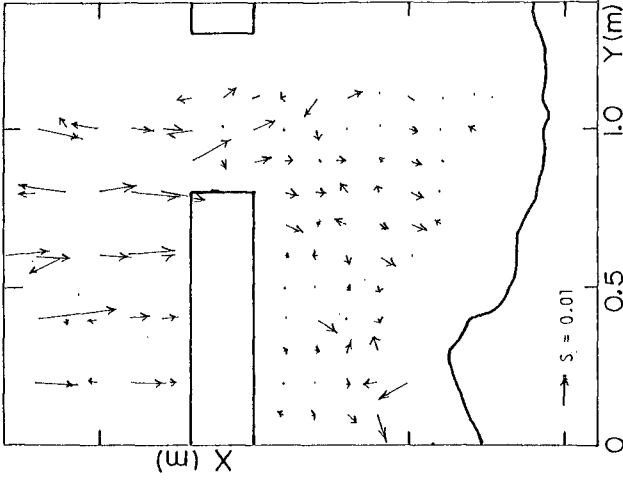


Fig. 11 Distribution of  $S$  estimated by radiation stresses

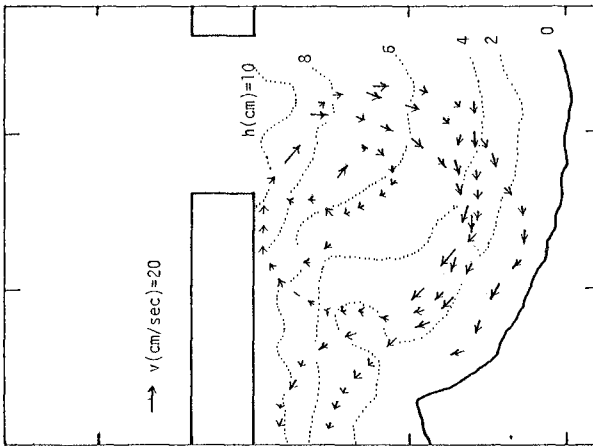


Fig. 13 Current pattern measured by float

parameters and then the friction terms in Eq.(4) can be also computed based on the numerical results of the radiation stresses calculated above and by use of a finite difference numerical method.

Fig. 11 describes the spatial distribution of the vectors  $S$  estimated on the basis of Eq.(4), in which the magnitude

and direction of the vector  $S$  are calculated by  $S = (R_x^2 + R_y^2)^{1/2}$  and  $\theta_s = \tan^{-1}(R_y/R_x)$ , respectively. Fig. 12 shows the observed current pattern in which the velocity and direction of currents are expressed by a segment of a solid line with an arrow head. Comparison of Fig. 11 with Fig. 12 suggests that the circulation estimated in Fig. 11 shows a similar pattern to that of the wave-induced currents in the shoreward region of the gap. It seems that such a numerical method serves for estimating wave-induced currents in the protected area. Furthermore, it appears that the circulation observed in Fig. 12 contributes to the sand accumulation within the protected lee of the breakwater, the development of tombolo and the retreat of the shoreward area of the gap by onshore-offshore sediment movement.

#### SOME MEASURES FOR EROSION IN LANDWARD AREA OF GAP BETWEEN OFFSHORE BREAKWATERS: AN ATTEMPT

Since the offshore breakwater had such a defect that the shoreward area of gap between adjacent units was eroded in all the cases of the experiments, some measures were tested to protect the area from landward retreat. One of the measures was to place triangular-shaped jetties in the area, considering that the jetty is effective from the view-point of preventing the circulation of currents which appears to develop tombolo.

Experiments were made by using the same wave basin as mentioned in the foregoing section. The wave condition was the same as Run B in three dimensional case, and the locations where the offshore breakwaters were placed were the same as Runs B-2 and B-3 (see Tables 2 and 3). Fig. 13 shows a schematic diagram of the triangular-shaped jetty which was placed behind the gap of the offshore breakwaters. Here,  $X_j$  is a distance from the initial shoreline (chain line) to the head of the jetty.

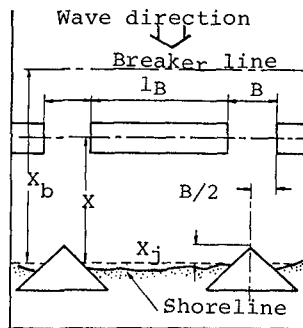


Fig. 14 shows the changes of

Fig. 13 Schematic diagram

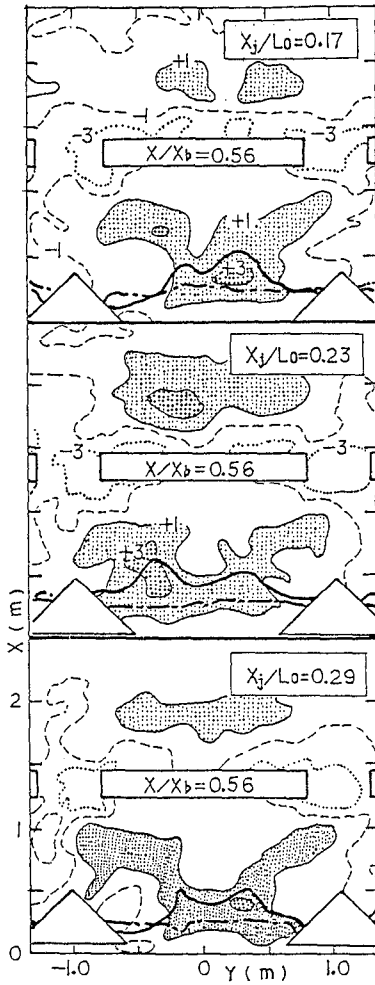


Fig. 14 Comparison of changes in shoreline and Bottom configuration for the cases with jetty

the shoreline form and the bottom topography for various values of  $X_j/L_0$  under the same wave condition as Run B-2 and  $X/X_b=0.56$ .

Comparison between these figures and the middle figure in Fig. 6 (no jetty) indicates that the landward retreat takes place in the tip part of tombolo, while the scour in the surroundings of the gap and the offshore breakwater is reduced considerably. Furthermore, a remarkable fact is that the regression of shoreline in the area can be prevented when the jetties are placed at  $X_j/L_0=0.23$ .

Fig. 15 summarizes the results of the sand volume deposited in the protected area,  $Q/Ad$  vs.  $X_j/L_0$ . In the case of  $X/X_b=0.56$ , the sand volume deposited in the area decreases slightly with increase in the values of  $X_j/L_0$ . Furthermore, a noticeable result is that the non-dimensional sand volume in all cases with the jetty is small compared to those without the jetty, while the landward retreat of the shoreline behind the gap can be prevented in the former cases. Contrastly, in the case of  $X/X_b=0.78$ , the sand volume for the experiments with the jetty always exceed that for the experiments without the jetty.

It is clear that an appropriate location for constructing jetties is largely confined by wave characteristics, width of gap, length and location of the offshore breakwater. It also appears that the relative location of the offshore breakwater and jetty plays an important role in the development of the current pattern.

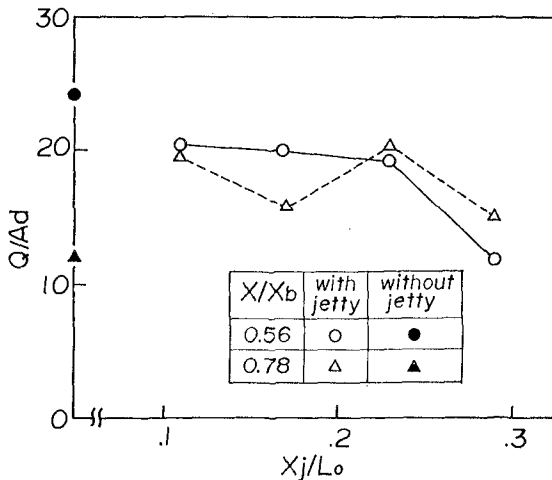


Fig. 15 Relationship between  $Q/Ad$  and  $X_j/L_0$

CONCLUSION

The following may be concluded from the laboratory tests on the depositional effects of the offshore breakwater due to onshore-offshore sand transport:

1. the optimum locations at which the effective deposition of sediment behind the offshore breakwaters develops are at  $X/X_b=0.5$  for B-type waves and at  $X/X_b=1.0$  for S-type waves in the results of two-dimensional tests.
2. there is found no sand that intrudes shoreward through the permeable type of the offshore breakwater when the structures are placed seaward beyond the breaker line of waves. On the contrary, a large amount of sands may be carried away offshore when the offshore breakwaters are placed near the shoreline.
3. the total amount of sand deposition per unit width of the gap transported shoreward from the gap is about three times that of sand deposition intruding through the permeable breakwater, when the dimensions and location of the breakwaters are chosen appropriately.
4. the current pattern induced by the wave action behind the structures may be predicted by applying the concept of radiation stresses.
5. construction of the triangular jetties may be utilized as one of the measures to prevent the scour in the surroundings of the breakwaters or the landward retreat behind the gap.

ACKNOWLEDGMENTS

The author would like to express his appreciation to Mrs. K. Noda, Y. Shimizu and N. Kurose for their assistance in the laboratory experiments, and expresses appreciation for financial support of the Grant-in-aid for Scientific Research of Ministry of Education.

REFERENCES

- 1) Shinohara, K. and T. Tsubaki: Model study on the change of shoreline of sandy beach by the offshore breakwater, Proceedings of 10th Coastal Engineering Conference, 1966, pp.550-563.
- 2) Toyoshima, O.: Design of a detached breakwater system, Proceedings of 14th Coastal Engineering Conference, 1974, pp.1419-1431.



## CHAPTER ONE HUNDRED THIRTY SIX

### PERMEABLE GROYNES: EXPERIMENTS AND PRACTICE IN THE NETHERLANDS

W.T. Bakker\*, C.H. Hulsbergen\*\*, P. Roelse\*, C. de Smit\*\*\*  
and J.N. Svasek\*\*\*

#### ABSTRACT

This paper reports on model experiments and up to 20 years of practice in nature with a permeable groyne system, consisting of single or double permeable rows of wooden piles perpendicular to the beach, without bottom protection. This system costs only 10 to 25% of the impermeable stone groynes which have for centuries been used in the Netherlands.

Model experiments confirm that wave-induced currents in the protected areas are reduced to 65%, and tidal currents even to 50%, depending on the pile screen configuration. Prototype measurements could not lead to straightforward conclusions with statistical significance: the effect of the pile screens on beach evolution is partly merged into natural fluctuations and trends. Wooden pile screens do not prevent the shoreward motion of tidal channels, which can cause washing out of piles. Furthermore, constructional failures, which in the future can be avoided, at some places resulted in negative experience. It is concluded that permeable pile screens deserve serious consideration as a first flexible and cheap phase in combating coastal erosion. Its application however should be based on a thorough analysis of the local coastal current climate.

#### 1 INTRODUCTION

Holland has to defend its low-lying land against the wind-swept waters of the North Sea. Large portions of its natural defence line, the coastal dune ridge, are subject to erosion [Bakker and Joustra, 1970], as a result of long-term or cyclic beach recession and short-term storm-surge dune erosion. In the past centuries many different structures have been applied in order to contribute to the coastal defence system, among which about 500 stone groynes. Traditionally, these structures are founded on willow matting and consist of rubble stone covered by hand-set stones. Especially in the SW province of Zeeland, where the tidal range reaches 4 m, the groynes were heightened by constructing single or double wooden pile rows on their crests. There is good reason to state

---

\* Ministry of Transport and Public Works/Rijkswaterstaat, the Netherlands  
\*\* Delft Hydraulics Laboratory, the Netherlands  
\*\*\* Svasek B.V. Engineering, Rotterdam, the Netherlands

that the recession of the coastline is indeed retarded by these massive groynes; their effectiveness has been studied in practice [Bakker and Joustra, 1970], theoretically [Bakker, 1968] and experimentally [Hulsbergen, Bakker, and van Bochove, 1976].

However, four main disadvantages of massive groynes are obvious, viz.:

- They are very expensive.
- They tend to induce deep erosion pits seaward of the groyne-head because of locally increased currents.
- They may stimulate rip-currents and seaward loss of sand.
- Extensive lee-side erosion may occur on the adjacent unprotected coastline.

Since 1965 a new type of groyne has been applied in the Netherlands in order to cope with these problems: it merely consists of wooden piles driven into the beach with mutual distances of about one pile diameter, so that permeable pile screens are formed, aligned perpendicularly to the beach, without bottom protection. These "permeable groynes" will further be referred to as "pile screens" or simply "screens", whereas traditional massive structures will be indicated as "groynes". The purpose of the pile screens is discussed in chapter 2.

The pile screens were initially constructed as an experiment, and different geometrical variations (length, height, distance, single or double rows, etc.) have been applied. In 1972 analytical and laboratory studies were performed in order to gain a better understanding of their effect in various hydraulic and geometrical settings; the results are outlined in chapter 3. Design and cost aspects are discussed in chapter 4.

Some of the pile screen projects, which were implemented since 1965, have been a success; others failed. This is discussed in chapter 5. In some cases it is difficult to distinguish the proper screen effect from the large-scale background morphologic development. Chapters 6 and 7 aim to analyze and summarize the experience gained so far.

## 2 PURPOSE OF PERMEABLE PILE SCREENS

In contrast to massive groynes, which seek to form a complete obstruction to the longshore current and to the longshore sediment transport, permeable pile screens are meant as an artificial hydraulic resistance in order to reduce the longshore current velocity and thus reduce the rate of longshore sediment transport. This may be explained as follows.

The longshore sediment transport concept [Bijker, 1971] is based on the notion that sediment is stirred up from the bottom by a shear stress which is produced by the combined action of waves and currents; the currents may be a combination of wave-induced and tidal currents. Once stirred up, the sediment is transported by the currents while being kept in suspension by waves and currents for some time. Hence, by reducing the current velocity (by means of the screens), both the stirring-up and the transporting phases of the sediment transport mechanism will be reduced, virtually without directly reducing the primary wave action.

With respect to the disadvantages of massive groynes as mentioned in chapter 1, the purpose and the expectation of permeable pile screens

can be summarized as follows:

- low cost structures
- less pronounced current concentration seaward of the head, provided that the permeability is adapted along the screen length
- reduced tendency to form rip-currents, for the same reason
- the ability to reduce the longshore sediment transport in a gradual way is an important asset in order to reduce the lee-side erosion behind massive structures: by an adequate screen field lay-out the total sediment deficit of the lee-side area will be distributed over a larger distance, thus decreasing the rate of recession.

### 3 LABORATORY EXPERIMENTS

Preliminary calculations, taking into account the bed shear stress and the estimated hydraulic resistance of the pile screens, showed that velocity reductions of 30% would result for 50 to 75% open screens, 200 m long and 400 m apart; a further reduction would require progressively more piles per unit beach length [Hulsbergen and ter Horst, 1973]. In view of the uncertainty involved in the underlying assumptions, and because of the lack of detail in terms of the resulting current pattern, in 1972 fixed-bed laboratory tests were deemed necessary in order to find out to what extent pile screens of various geometrical forms reduce the coastal currents under different hydraulic boundary conditions.

The model set-up is shown in Figs. 1 and 2. Horizontal and vertical scales are both 40, and the velocity scale is 6.32 according to Froude. The coastal profile is typical for Zeeland, where tidal currents of 1 m/s occur in a water depth of 10 m close to the beach, and where the tidal range is appr. 4 m. The model bed consists of smooth concrete and has straight parallel depth contours. A variety of prefab model pile screen configurations (Fig. 3) have been installed in grooves which are 1.25 m apart. (All units in this chapter are in model measures unless otherwise indicated).

The model piles are 6 mm in diameter and their mutual clearance varies from 6 mm at the landward end to 19 mm near the seaward tip. The piles may be combined to short screens (3.5 m long) or long screens (5 m long), either as a single row, or in double rows 8.75 cm apart. The mutual screen distance varies from 3.75 m to 10 m.

Several hydraulic conditions have been installed, of which the most important are:

- H.W. and current only (most of the tests)
- H.W., a current, and a wave generated current in the same direction as the tidal current; regular wave period  $T = 1.04$  sec, wave height at (spilling) breaking  $H_{br} = 3.0$  cm, angle of incidence at breaking  $\alpha_{br} = 8^\circ$ .

For a variety of special velocity measurements with screen configurations and hydraulic conditions different from those mentioned above, reference is made to [Hulsbergen and ter Horst, 1973].

The main test results for the present purpose are expressed in terms of the relative velocity  $V_{rel}$ , i.e. the ratio of the longshore current velocity with screens over the longshore current velocity without screens, measured on the same spot and with the same hydraulic condition. Combining some of these results, the following conclusions are drawn.

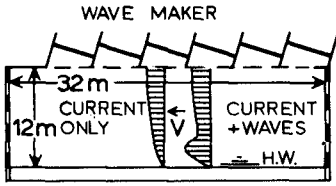


FIG.1 Model basin

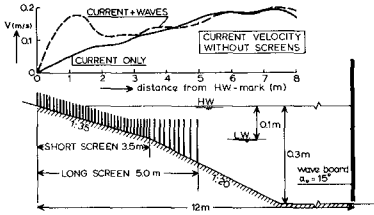


FIG.2 Cross-section of model

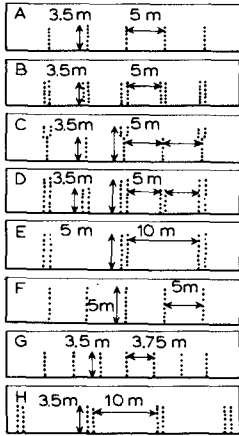


FIG.3 Screen configurations

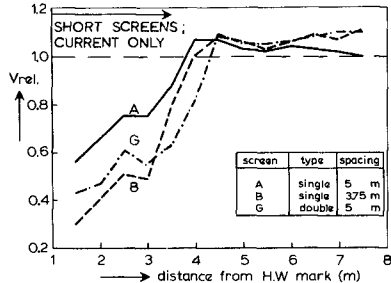


FIG.4 Effect of more screens

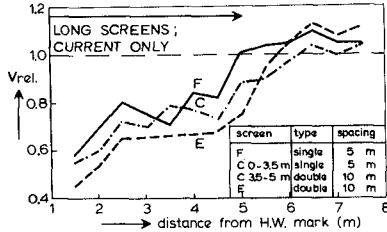


FIG.5 Effect of screen concentration

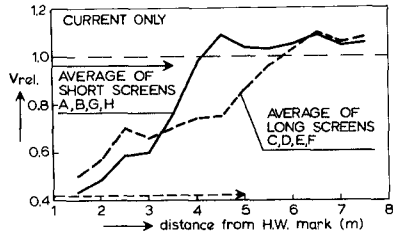


FIG.6 Effect of screen length

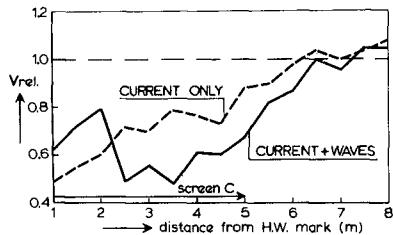


FIG.7 Effect of waves

For current only:

- a. In general the investigated screens cause an appreciable reduction of the longshore current velocity; near the beach  $V_{rel}$  is only 50%, but further seaward  $V_{rel}$  increases, and even grows up to 115% just seaward of the tip.
- b.  $V_{rel}$  diminishes, but not proportionally, as the number of screens per unit length of beach is increased (Fig. 4, short screens).
- c.  $V_{rel}$  diminishes as the screens are concentrated (e.g. double rows at 10 m intervals instead of single rows at 5 m intervals), without increasing the amount of material per unit length of beach (Fig. 5, long screens).
- d. Lengthening of screens causes a reduction in current velocity at that depth, but this is partly at the expense of the reduction as it existed in the short screen range (Fig. 6, average  $V_{rel}$  values for short and long screens).
- e. The aforementioned screen effects cause an increase of the perpendicular gradient in the longshore current profile which may lead to an increasing offshore sediment transport. Especially short screens have this disadvantage.

For a current and a wave-generated current in the same direction:

- f. As compared to current only there are important differences; one must discriminate between the areas inside and outside the surf zone (the waves start breaking at approximately 2 m from HW mark).
- g. Outside the surf zone, concentration of screens without increasing the amount of material per unit length of beach causes  $V_{rel}$  to decrease, just as for current only. Inside the surf zone, however, concentration of screens causes  $V_{rel}$  to increase (for explanation see point i).
- h. Outside the surf zone, the value of  $V_{rel}$  is lower than for current only (Fig. 7, screen type C). This can be explained by noting that orbital motion in the plane of the pile screens effectively hinders the tidal current to flow through the openings between the piles.
- i. Inside the surf zone, the value of  $V_{rel}$  is larger than for current only (Fig. 7). This can be explained by the different mechanism of generation of a tidal current and a wave-generated current:
  - a tidal current, once hindered by a screen, restarts slowly by the gradual diffusion of mass and momentum from the outside main stream towards the retarded water near the coast;
  - a wave-generated current on the other hand, once slowed down by a screen, is fed immediately with momentum and mass by the breaking waves themselves which travel right into the retarded zone.

One overall conclusion is that it makes a great deal of difference to the efficacy of permeable pile screens whether there are waves, and if so, from what direction. Perpendicularly incident waves increase the velocity reduction of the screens; obliquely incident waves, however, generate a longshore current to which the screens form only a limited hindrance. For the test conditions it seems that screens of type C show an overall good performance. With an adequate formula, e.g. [Bijker and Svasek, 1969] or [Bijker,

1971], the above hydraulic results may be transferred to longshore sediment transport quantities, and thence into predictions for coastal development without and with screens.

#### 4 DESIGN, CONSTRUCTION AND COSTS

The functional design of pile screens should be based on the required reduction of the longshore sediment transport, and thus on the required reduction of the current velocity parallel to the coast. So, one should start with a careful analysis of the natural coastal current climate, and one should well discriminate between tidal and wave generated currents (see chapter 3). Starting from such analysis, and taking into account the computational and experimental results as outlined in chapter 3, for a particular location an optimum is found for the screen geometry in terms of pile screen length, mutual distance of screens and piles, and height of piles.

Obviously, aspects of local materials, construction operations and costs may interfere with the ideal functional design. In the Netherlands only wooden piles (oak or tropical) with round or square cross-section (0.25 - 0.30 m) have been used. Piles of square cross-section may be placed in a diamond pattern rather than orthogonally in order to save material for the same hydraulic resistance. These piles may be subject to borers and/or marine growth; concrete may be an alternative.

The toplevel of the piles is partly determined by the workability conditions (waves and tides). The total length of the piles must allow for natural variations in local bed elevation; as a rule 60% of the total length is in the bed. A typical screen is shown in Fig. 8. When a double screen is applied (which is cheaper than 2 single rows), their mutual distance is 3 m. In order to allow traffic on the beach an oblique opening is provided. The piles may be jettied or rammed with a conventional rig on the dry beach. Beyond the low water line there are several options, viz. working from a floating barge, from a mobile platform (Fig. 8), from a temporary jetty, or working over the top of the finished part (double screens only). The costs of screens increase rather fast if they extend seaward of the low water line. A rough idea is given in Fig. 9, where three screen configurations are shown with their cost per 1000 m<sup>1</sup> of beach length as compared to typical traditional massive groynes.

#### 5 APPLICATIONS OF PILE SCREENS IN NATURE

Since 1965 permeable pile screens have been applied on ten locations in the Netherlands (Fig. 10).

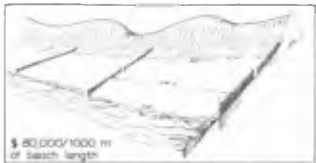
- On the SW coast of Walcheren, the recreational beach of Flushing (Fig. 10, ①) is situated at the leeside of a protruding remnant of an old dike, and is since long subject to leeside scour. Additional to periodical sand supply (1952, 1966 and 1975), in 1975 the old deteriorated groyne system was replaced by three double pile screens. It is hard to specify their effect because of the many artificial changes of this beach. There are slight indications that the rate of sand loss is decreasing.
- On the SW coast of Walcheren near the village of Zoutelande (Fig.



FIG.8 Construction of screens



\$ 2,500,000/1000 m beach length



\$ 80,000/1000 m of beach length



\$ 600,000/1000 m. of beach length

FIG.9 Costs of groynes and screens

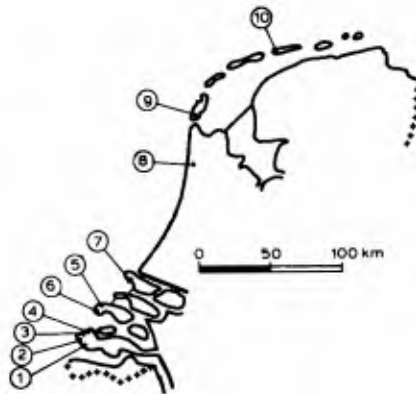


FIG.10 Locations of screens

10, ②), in 1968 the existing coastal protection (consisting of heavy massive groynes with piles on top) was extended in SE direction by means of three long double screens and two short single screens (Fig. 11, and lower photo on Fig. 8). Since then the discontinuity in the coastline, caused by the leeside scour resulting from the original system, was evened out. Even some accretion occurred directly southward of the former end of the groyne system. The leeside scour shifted to the end of the new screen system. This project indicates that these pile screens do have the expected effect.

- The NW coast of Walcheren borders the estuary of the Eastern Scheldt (Fig. 10, ③, ④, and Fig. 12), and reacts intensely upon the dynamic behaviour of its tidal channels. Although generally eroding, accretion may also occur during long-term fluctuations. In 1968 the deteriorated groynes near the village of Domburg (Fig. 12, ③ and Fig. 13a) were replaced by pile screens. Originally the landward part of the screens consisted of a single row of piles (Fig. 13b), whereas the seaward part was double. As mussel growth on the seaward piles increased the flow resistance even more (Fig. 14), unfavourable current concentrations resulted both seaward and landward of the dense sections (Fig. 15). The resulting current velocity during H.W. on the beach was even higher than before the screens were there. Therefore, in 1977-1978 all screens were doubled, and at the SW end some extra screens were placed. At the SW end the beach accreted, but in the NE part the beach receded. An explanation has not been found. An overall picture of beachline behaviour since 1920 in this area is given in the lower part of Fig. 13. For a number of ranges perpendicular to the coast, the position of the point half way between the H.W. line and the L.W. line is indicated as a function of time. Further, in Fig. 13 is indicated: the moment of the landward extension of the old groyne stone heads with pile screens, the moment of construction of new screens, and the moment of doubling these screens. From Fig. 13 a diminution of the erosion in the last decade can be observed; however, long-term fluctuations may have played a role.
- The first application of pile screens in the Netherlands dates from 1965, near the village of Oostkapelle on the NW coast of Walcheren (Fig. 10, ④ and Fig. 12, ④). The existing row of stone groynes with horizontal crowns had caused leeside erosion in northward direction; therefore a row of short screens was built in 1965 (Fig. 16). These screens and their effects were drastically affected by large scale autonomous morphological developments in this area (Fig. 16). Between the main tidal channel "the Roompot" of the Eastern Scheldt estuary and the local near-shore flood channel "the Urk", a shoal developed right in front of the beach with screens. This shoal urged the "Urk" channel closer inshore, and seaward extension of the screens could not prevent this development. Later on, the shoal even merged with the beach (Fig. 16, 1981), and some more additional screens were built. This could not prevent that during the last phase of the shoreward moving "Urk" channel heavy damage occurred to the screens, and even some 12 m long piles were washed out.
- The development of the west coast of the island of Schouwen is de-



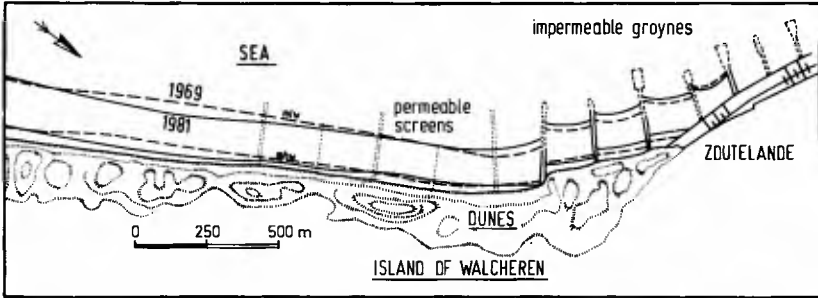


FIG.11 Screens near Zoutelande ②

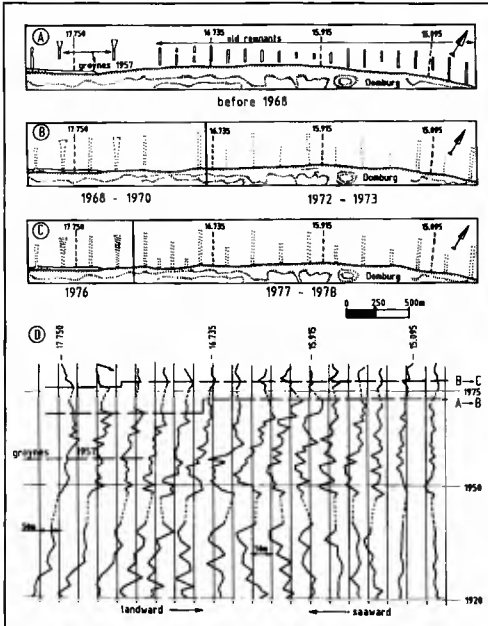


FIG.13 Screens near Domburg ③

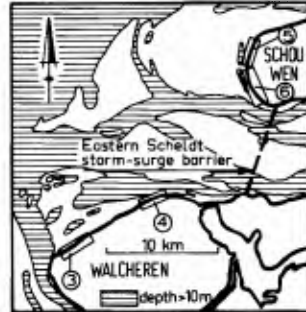


FIG.12 Screens near Eastern Scheldt estuary



FIG.14 Mussel growth

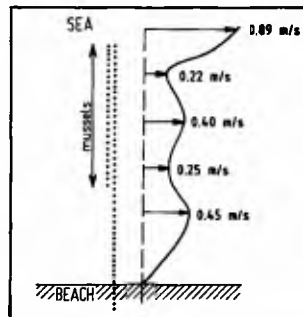


FIG.15 Effect of mussels

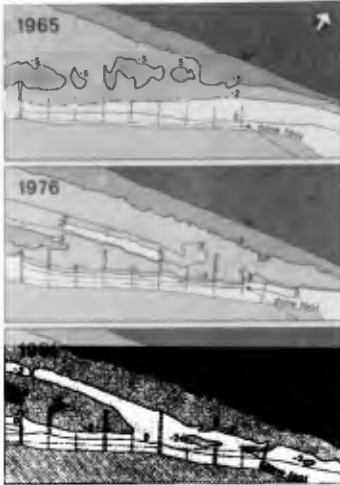


FIG.16 Screens near Oostkapelle (4)

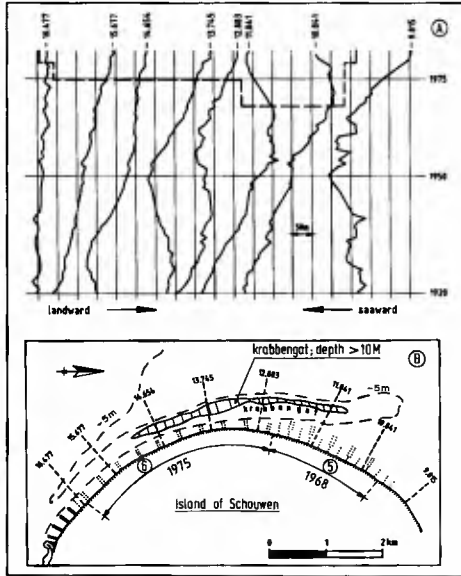


FIG.17 Screens on Schouwen (5), (6)



FIG.18 Pulled piles



FIG.19 Outflanking



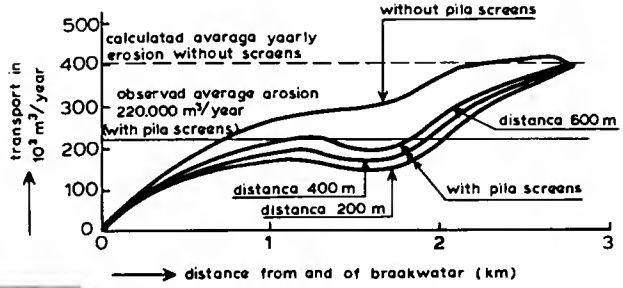
FIG.20 Rip channel near screen

terminated by the secondary tidal channel "the Krabbengat" (Figs. 12 and 17), which moves landward during the last centuries. Periods of erosion and accretion alternate, under the influence of changes in the tidal estuaries of the Eastern Scheldt to the South of Schouwen, and the Brouwershavense Gat to the North. In 1968 long screens were erected along the northern part of the beach (Fig. 10 (5), Fig. 12 (5), and Fig. 17), and soon a spectacular accretion occurred, even with new dune formation on the beach. The landward piles were consequently pulled somewhat (Fig. 18) because they tended to disappear under the sand. It is not clear, however, to what extent this accretion is due to the pile screens alone. The original recession of the beach stopped about 5 years before the screens were placed: probably the areas of accretion and erosion tended to shift under the influence of "the Krabbengat". Furthermore, the estuary of the Brouwershavense Gat was closed in 1972, of which the effects cannot accurately be assessed.

- In 1975 the above mentioned row of screens was extended southward with short double screens (Fig. 10 (6), Fig. 12 (6) and Fig. 17). The long-term trend of erosion however did not change. Also out-flanking behind the landward end of the screens near the dunes occurred (Fig. 19). Another negative aspect was observed in that rip-currents tended to concentrate along the screens (Fig. 20).
- Just south of the new entrance to Europort (Fig. 10, (7)) a new coastal defence system was necessary in order to protect the reclaimed harbour area [Svasek and de Nekker, 1977]. Instead of the original design, which consisted of a section of 4000 m of rubble mound breakwater, an artificial beach and dune combination was proposed, saving about 80 million dollars on construction costs. In order to maintain the artificial beach, an artificial sand supply of 400,000 m<sup>3</sup>/yr would be required [Svasek and Versteegh, 1977]. Further optimization calculations resulted in a project with seven pile screens (Fig. 21) plus a limited sand supply of 200,000 m<sup>3</sup>/yr [Bijker et al., 1981]. Four double pile screens extended to the depth contour of MSL - 3 m, and three short single screens down to MSL - 0.5 m were placed in between. The 0.3 m diameter piles were spaced 0.3 m apart. To determine the pile length, a seasonal depth variation of 1 m was assumed. As the planned sand supply of 200,000 m<sup>3</sup>/yr was not effectuated, a local erosion of about this same rate should be expected. Based on frequent detailed soundings and beach levelings in the area concerned, a comparison was possible (Fig. 22) between the calculated erosion (with pile screens but without sand supply), and the observed erosion which amounted to 220,000 m<sup>3</sup>/yr. This is in good agreement, taking into account the feasible accuracy of the levelings and soundings. As the area concerned is approximately 600,000 m<sup>2</sup> large, the average erosion in 2 years was about 0.6 m with local scour of more than 1 m. About 2½ years after construction, the most southern two long screens lost about 30% of their piles (mainly in the deepest section) during a severe storm.

The main causes for this failure are:

- Artificial feeding was omitted, causing the bed to be eroded locally below the storm season profile, for which an overdepth of 1 m was designed.
- The tidal channel "Gat van Hawk", which was shoaling and stable



← pila screens above MSL -3m →

FIG.22 Calculated screen effect near Europort (7)



FIG.21 Screens near Europort (7)

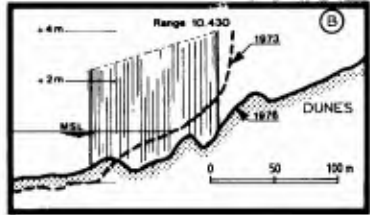
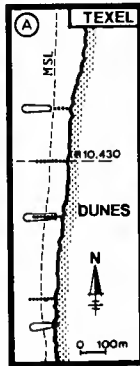


FIG.24 Screens on Texel (9)

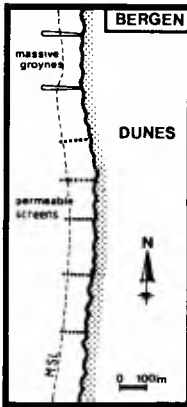


FIG.23 Screens near Bergen (8)

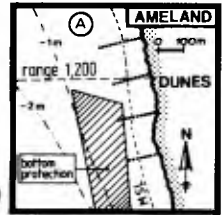
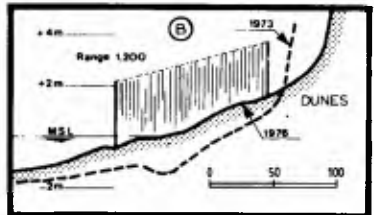


FIG.25 Screens on Ameland (10)



in position at the time of design, moved unexpectedly in shoreward direction.

- Some of the washed-out piles did not meet the design length requirements.

Later on, this pile screen project was abandoned.

- In 1974 near Bergen (Fig. 10, ⑧) five single short screens were erected with mutual distances of 150 to 200 m (Fig. 23). These screens, only covering the beach width of 120 m, were designed to mitigate the leeside scour just south of a long row of stone groynes. Afterwards the general beach elevation increased with 0.5 to 1.0 m. The proper screen effect is hard to tell, because in the same time windscreens of reed were placed and reshoveling of the beach occurred.

From regular levelings it appeared that just seaward and landward of the screens erosion occurred, the latter caused by outflanking.

- The island of Texel suffers from severe erosion, and has been extensively defended with stone groynes. The area under consideration (Fig. 10, ⑨) is subject to heavy erosion, the dune foot receding at a rate of 15 m/yr. The classical groynes, with a flat crown at about MSL, are extended in landward direction if the coast keeps eroding; furthermore in that case the system is extended with more groynes (short ones in first design) along the beach.

In 1973, some of the relatively recent stone groynes were extended in landward direction (following further dune foot recession) with pile screens instead of stone groynes; furthermore some intermediate pile screens were constructed (Fig. 24a). Rather strong outflanking occurred near the dune foot, probably boosting the dune foot erosion rather than stopping it (Fig. 24b). For this reason the pile screens were removed in 1980.

- Also in 1973, on the island of Ameland (Fig. 10, ⑩) four single pile screens were constructed. These screens - in combination with other coastal defence systems - link the continuous bottom protection along the main tidal channel "the Borndiep" with the beach (Fig. 25a). The coastal erosion in the area covered by the screens stopped indeed, whereas in the vicinity erosion proceeded. Just as on Texel however outflanking occurred near the dune foot (Fig. 25b).

## 6 EVALUATION OF THE EFFECT OF PILE SCREENS IN NATURE

With respect to reporting on experience with coastal defence systems the general difficulty remains how to tell the proper effect from the background noise.

With respect to impermeable groynes some proof is available of its potential to combat erosion [Bakker and Joustra, 1970]. However, the system presently under investigation is a "softer" system and its effect may easily merge into the effect of nature. This so much the more as essentially where groynes are applied, nature shows either heavy fluctuations or heavy erosion. In the case of heavy erosion the present system failed in the sense that without these screens the same or maybe a more favourable effect could have been achieved (Oostkapelle; Texel). Therefore only the cases with heavy natural fluctuations remain to be analyzed, yielding the results mentioned in chapter 5.

Besides it is a fascinating thought that the use of impermeable groynes near Oostkapelle probably would have given worse results: the contraction and the turbulence near the head of the groyne could have prevented the favourable incorporation of the migrating shoal with the beach.

Having no statistically significant evidence regarding the screen effect, the question still remains: should the use of pile screens be advised for coastal defence?

In the first place, as long as no really predictive mathematical (large-scale) coastal models are available, the words of Schijf regarding coastal protection plans still apply: "Postpone till tomorrow what not necessarily has to be done today".

However, given the fact that something should be done at a certain site applying the best available knowledge, pile screens might come in the picture. First checkpoint should be an evaluation of the risk of washing out of piles by shoreward motion of tidal channels. One might face situations that even the maximum practical pile length will not be enough to guarantee constructional stability. It should be kept in mind, that pile screens cannot prevent this channel motion.

If this risk is acceptable, or if it can be eliminated (for instance by periodical sand supply), the authors feel, that the use of pile screens deserves serious consideration.

- Based on theoretical and experimental evidence (chapter 3) positive effects can be expected; especially in areas with a large tidal range, piles have effect during a longer part of the tidal cycle than stone groynes with flat berms.
- Most of the negative experience can be attributed to constructional failures, which in the future can be avoided. For instance, in Oostkapelle and Europort the piles were too short at the site where the washing-out occurred, because at these locations no heavy erosion had been foreseen. It seems to be of much importance that the screens are well incorporated in the dunes, implying some temporary removal of sand. At present, mussels are regularly removed from the screens.
- Although an objective financial balance of the use of pile screens is hard to make (as the effects are not clear and a financial value can hardly be assigned), the feeling exists, that this balance is positive and that, for instance, it has been a wise decision to protect the Schouwen area with pile screens instead of impermeable groynes.
- Pile screens form a much more flexible construction than stone groynes: piles can be added, lifted or removed, and in the case of very heavy erosion one can make - if absolutely necessary - stone berms in a later stage, thus postponing the expense. Furthermore a combination of pile screens and sand supply is feasible.

## 7 CONCLUSIONS

### I Advantages of permeable pile screens are:

- a. Low cost (Fig. 9).
- b. Reduced longshore current velocity, as demonstrated by model tests (Figs. 4, 5, 6, 7).
- c. Flexible construction, which may easily be adapted to changing

beach elevation (Fig. 18).

- d. A more continuous beach line (as compared to the saw-tooth beach line with impermeable groynes). This is an advantage, in the sense that the point of most erosion determines the safety of the coastal protection.
- e. A more gradual velocity gradient and less turbulence near the seaward end (as compared to impermeable groynes).

#### II Problems encountered are:

- a. Failure on the seaward side: washing-out of piles.
- b. Failure on the landward side: outflanking near the dune foot. (Fig. 19).
- c. Mussels, often causing a diminution of the permeability of the outer region of the screens. Where the inner region consists of a single screen this may lead to higher local current velocities than before the screens were constructed (Figs. 14, 15).
- d. Attraction of rip-channels, with consequent seaward sand loss (Fig. 20).

#### III Proposed remedies against the problems are:

- a. Careful analysis with respect to morphological changes in the coastal area (are tidal channels moving to the coast? Does lee-side erosion occur?). Piles should be embedded for 60 percent of the total length below the lowest beach level to be expected.
- b. Pile screens should be sufficiently extended landward of the existing dune foot, even if this includes a temporary removal of much sand
- c. Regular removal of mussels.

#### REFERENCES

- Bakker, W.T., 1968: The dynamics of a coast with a groyne system. London, Proc. 11th Coastal Engineering Conference, Chapter 31, pp. 492-517
- Bakker, W.T., and D.S. Joustra, 1970: The history of the Dutch coast in the last century. Washington, Proc. 12th Coastal Engineering Conference, Chapter 43, pp. 709-728
- Bijker, E.W., and J.N. Svasek, 1969: Two methods for determination of morphological changes induced by coastal structures. Paris, Proc. 22nd International Navigation Congress, Section II, Subject 4, pp. 181-202
- Bijker, E.W., 1971: Longshore transport computations. Proceedings American Society of Civil Engineers, Vol. 97, WW4, November, pp. 687-701
- Bijker, E.W., J.P. van der Leijé, J.J. Pilon, J.N. Svasek, J.K. in 't Veld, and H.J. Verhagen, 1981: Coastal changes due to the reconstruction of artificial harbour entrances and practical solutions, including beach replenishment.

Edinburgh, Proc. 25th International Navigation Congress, Section II, Volume 5, pp. 853-875

- Hulsbergen, C.H., and W. ter Horst, 1973: Effect of permeable pile screens on coastal currents.  
Delft Hydraulics Laboratory report M 1148, (in Dutch).
- Hulsbergen, C.H., W.T. Bakker, and G. van Bochove, 1976: Experimental verification of groyne theory.  
Honolulu, Proc. 15th Coastal Engineering Conference, Chapter 85, pp. 1439-1458.
- Svasek, J.N., and J. de Nekker, 1977: Recent developments in harbour building at sea.  
Terra et Aqua, no. 14, pp. 2-7
- Svasek, J.N. and J. Versteegh, 1977: Mathematical model for quantitative computations of morphological changes caused by man-made structures along coasts in tidal estuaries.  
Baden-Baden, Proc. 17th IAHR Congress, Vol. 4, paper C 25, pp. 189-198



## CHAPTER ONE HUNDRED THIRTY SEVEN

### Study of the Evolution of Dredged Material Discharges by Means of Radioactive Tracers

F. Tola, A. Caillot, G. Courtois, P. Gourlez, R. Hoslin, J. Massias,  
M. Quesney, G. Sauzay\*

#### Abstract

The choice of a dumping area for dredged materials must be carried out taking into account the general movement of sediments in order to evaluate the risk they represent for the zone itself, the harbour-works and the coastal area.

The use of radioactive tracers allows to study, in situ, transfer properties under tidal currents of fine sediments resuspended during the release, the distribution over the sea-bed of coarse particles and their future evolution due to currents and waves.

In this way, parameters such as transport axis, mean velocity, dispersion, dilution and bed-load transport rates are determined.

Four experiments which took place at OCTEVILLE, ANTIFER (FRANCE), SINGAPORE and ZEEBRUGGE (BELGIUM) during the ten past years illustrate the method.

#### I - Introduction

The construction or enlargement of a harbour and its access channel and future keep up need voluminous and expensive dredging work. In France, keep up itself represent per year, 40 million cubic meters of dredged materials at a total cost of 600 M.F. (about 70 millions U.S. dollars).

These operations modify the sedimentologic equilibrium of the environment and generate an increase of turbidity because of fine sediments removal. Besides, the discharge of dredged spoils on a dumping area next to the dredging site rise this problem of an eventual return of silt sediments to the harbour or the littoral and thus induce silting and pollution leading to additional tasks which may be avoided.

In order to forecast the effects of such discharges on the environment a good knowledge of sediments behaviour concerning both suspension and bed-load transport, is necessary. Yet up to now, the wide range of parameters, the complexity of liquid-solids interactions and the more or less cohesive nature of bed materials make almost impossible pure

\* Commissariat à l'Energie Atomique, Service d'Applications  
des Radioéléments, (S.A.R.), Centre d'Etudes Nucléaires de Saclay,  
B.P. 21 - 91190 Gif sur Yvette, France.

theoretical calculations and hydraulic model simulations. Thus, to be reliable such models must at least be calibrated by measures in nature, carried out on the future dumping area and for conveniently chosen and well known hydrological conditions.

Such in situ measures are possible thanks to RADIOACTIVE TRACERS. The technology, developed and improved throughout almost 250 experiments during the last 30 years has give rise to numerous publications (A. Caillot, 1970; G. Courtois, 1970; F. Tola, 1982). Only the principal features will be therefore recalled, the purpose of the present paper being mainly to illustrate the method by typical examples.

## 2. Methodology

A small quantity of labelled particles representative of natural sediments (similar granulometric distribution and hydrodynamic properties) is introduced in the medium, either directly or mixed to some hundreds of tons of dredged materials contained in a hopper (Fig. 1).

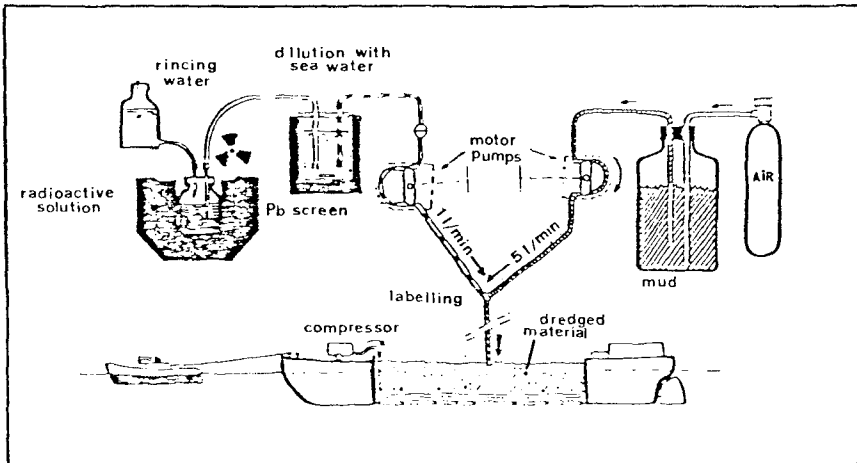


Figure 1 - Labelling and Injection of Silt Sediments.

The transport of radioactivity is used to determine sediments movement in the course of time. Material carried away in suspension is measured by means of vertical arrays of radiation probes attached to two tracking vessels which perform longitudinal and transversal detection of the plume. For bed measures, a single probe is fixed on a sledge which is then towed over the bed (Fig. 2). A location device allows regular plot of fix on a 1/5000 scale chart.

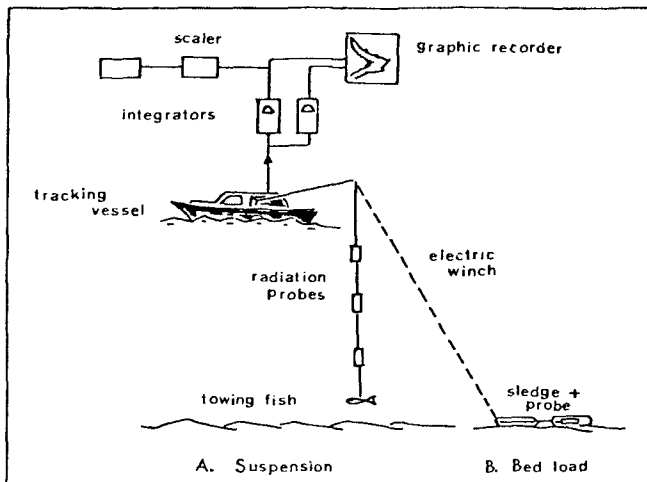


Figure 2 - Detection Equipment of Tracking Vessels.

When studying dredged material discharges we are interested on the following points:

- behaviour of fine sediments (silt and very fine sand) carried away in suspension,
- distribution of sand particles over the sea-bed,
- disposal efficiency,
- future evolution of deposited materials.

Sediments in suspension are followed during 3 to 4 hours. We proceed to bed detection 18 to 24 hours after release takes place in order to allow mixing of the radioactive tracer to natural sediments.

5 to 9 Ci of gold 198 (half life 2.7 days,  $\gamma$  energy of 410 keV) are sufficient to label 1 kg of silt sediments or 0.5 to 1 kg of crushed glass simulating sand particles.

Information collected during this type of experiment is completed by measures carried out from point injections of small quantities of labelled materials in several points of the site and for different hydrological conditions. A clear scheme of the general movement of dredged spoils is thus obtained.

In order to study transfer properties of a silt suspension, sediments are labelled with gold 198 as previously. The following parameters are determined:

- trajectory of the center of gravity,
- mean transport velocity,

- vertical concentration profiles,
- horizontal dispersion (which may be represented by the longitudinal and transversal standard deviations  $\sigma_x$  and  $\sigma_y$ ),
- dilution, that is maximum concentration in function of time,
- particles sedimentation, when it takes place.

To study the evolution of deposited materials we use glass labelled with iridium 192 (half life 74 days,  $\gamma$  complex spectrum of energy 296 to 885 keV), allowing experiments lasting 5 to 6 months and thus increasing considerably the amount of data obtained. Only 0.5 to 1 Ci of iridium 192 is sufficient to label 0.25 to 1 kg of glass, per point; that is ten times less than the maximum activity permitted (G. Courtois, R. Hours, 1964). Such low quantities allow easy preparation, transport and manipulation of radioactive products as well as a rapid integration of the tracer to natural sediments.

Qualitative and semi quantitative informations are obtained, such as:

- main transport axis and, eventually, secondary ones,
- mean velocity of particles gravity center,
- dispersion parameters, dimensions of the spot,
- tidal currents and waves effects (bed-load transport, saltation, resuspension),
- burying (sedimentation), mostly during slack water,
- presence of morphological factors (sand banks, deeps, channels) which will either act as a trap of particles or canalize them in a privileged direction.

Lastly, the mean transport thickness is determined thanks to the "total count rate balance" method (G. Sauzay, 1968), thus allowing to quantify the entrainment rate.

Radioactive tracers experiments are completed by intensive hydraulic and meteorological measurements such as currents and wind direction and intensity, waves height, period and direction and tides amplitude. In this way, data concerning sedimentary movements can be linked to local conditions.

### 3. Illustration of the Method by S.A.R. Main Studies

Four experiments which made use of radioactive tracers techniques and took place respectively at OCTEVILLE, ANTIFER (FRANCE), SINGAPORE and ZEEBRUGGE (BELGIUM), have been selected to illustrate the method. Their detailed description is available in a recent publication (F. Tola, 1984) from which we reproduce the most striking features.

#### 3.1 - Evolution of dredged material discharges off OCTEVILLE

Dredged materials resulting from the upkeep of LE HAVRE harbour are discharged off OCTEVILLE at a depth of 14 m. They are mainly composed of silt sediments ( $< 40 \mu\text{m}$ ) and fine sands (60 to 350  $\mu\text{m}$ ), improperly incorporated to sedimentologic equilibrium, recirculation of which may affect the coastal environment and ANTIFER oil installations located 15 km N.N.E of the dumping area. On request of LE HAVRE authorities, several radioactive tracers experiments were carried out in order to appraise the real risks:

1°) Transport in suspension and sea-bed distribution of dredged spoils discharges

70 tons of dredged material contained in a hopper at an initial concentration of 150 g/l (73% silt, 27% fine sand) were discharged during a spring tide flood. Fine particles, mainly silt sediments less than 40 μm, form a suspension subject to dispersion due to turbulence, swell and velocity gradients, conveyed Northwards towards ANTIFER and covering almost 7 km in 3 h without settling (Fig. 3). By that time the cloud is spread over an elliptical surface 1 km and 250 m main axis (± 26), with uniform vertical concentration profiles less than 16 g/l.

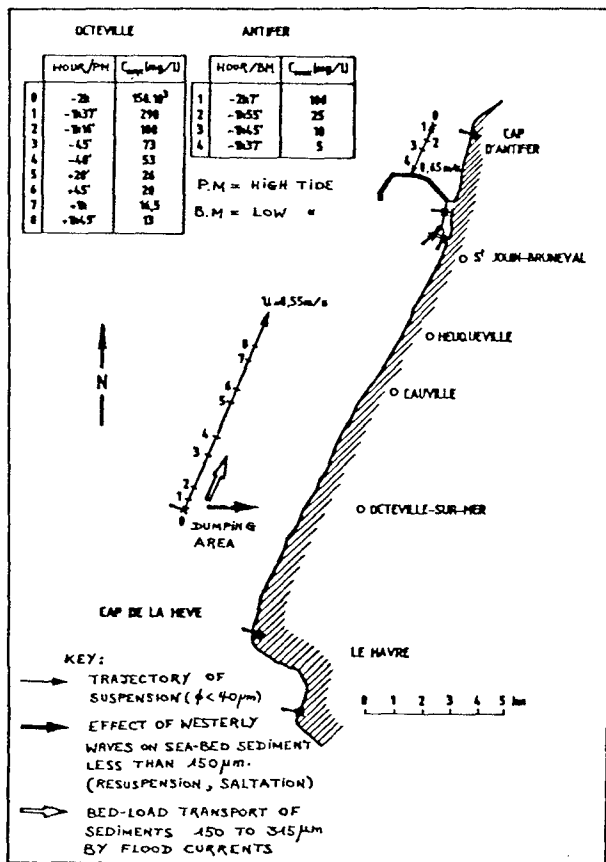


Figure 3. Sedimentary Movements at OCTEVILLE and ANTIFER

However, materials discharged off OCTEVILLE may be highly concentrated and therefore have an initial rigidity which will oppose to dilution when released. Mud with a rigidity greater than some  $N/m^2$  would settle next to the point of immersion.

Detection performed 18 h later shows that sand particles are superficially distributed over the sea-bed, up to 1 km N.N.E, the distance covered before settling depending on the grain size (Fig. 4):

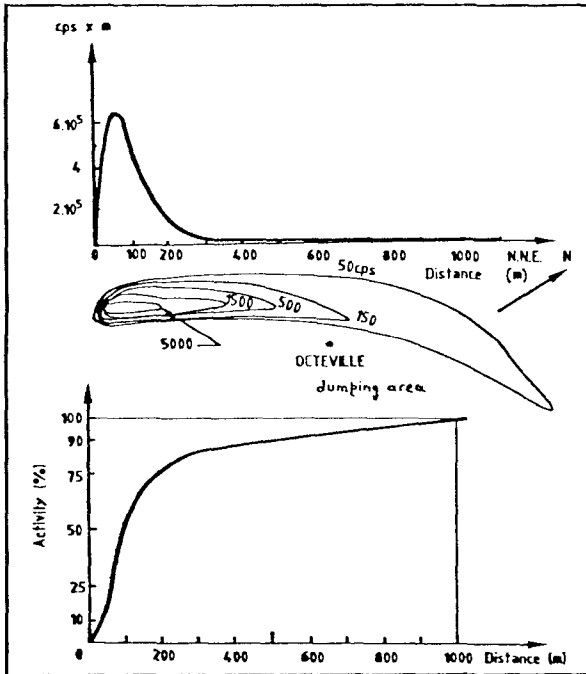


Figure 4. Distribution of Sand Particles over the Sea-bed 18 h after Immersion: Lines of Equal Concentration and Transport Diagrams.

- 50% of sand particles ( $\phi > 105 \mu m$ ) lay at less than 100 m from the point of immersion, - 75% of them ( $\phi < 80 \mu m$ ), at less than 200 m,
- only particles less than  $80 \mu m$  settle at more than 200 m and reach the limits of the spot (1000 m). Mean fall velocity corresponding to  $d_{50} = 105 \mu m$  is 0.7 cm/s, while it is found to be equal to 1.1 cm/s in calm water.

### 2°) Evolution of deposited materials

Two injections of glass particles labelled with iridium 192 were performed next to OCTEVILLE dumping area and a third one in front of CAUVILLE. In the first case the granulometric distribution of the tracer is close to that of dredged materials (80 to 315  $\mu\text{m}$ ), while in the last one it is close to that of natural sea-beds sediments (170 to 1000  $\mu\text{m}$ ).

Compared to sea-bed sediments which are rather motionless, dredged materials seem quite movable under the same hydrological actions (Fig. 3):

- W to N.W. waves ( $H_s = 2$  to 4.5 m) developed during storm periods ensure resuspension of fine particles which are then conveyed and dispersed in the coastal direction. 70% of sand ( $\phi < 150 \mu\text{m}$ ) cover in this way more than 500 m in 3 1/2 months;
- spring tide currents disperse particles less than 350  $\mu\text{m}$  in a N.N.E. direction (flood predominance);
- by calm weather, N.W. waves disperse sand particles towards the coast (S.E.).

### 3.2 - Evolution of ANTIFER dredging material discharges

About 30 million cubic meters of dredged materials derived from the construction of ANTIFER oil terminal installations are discharged 2.5 to 6 km North, at a depth of 17 to 22 m.

According to their nature, initial concentration and intensity of currents, which during spring tides may exceed 2 m/s in flood and 1.4 m/s in ebb, sediments will either deposit where release takes place or, on the contrary, be conveyed in suspension, bed-load or saltation. Transport in a Southwards direction would lead to the silting up of the channel access and the harbour-works as well as pollution of the coastal area.

Radioactive tracers experiments allowed to estimate the risk of recirculation of sand spoils.

### 1°) Transport in suspension and sea-bed distribution of sandy material discharges

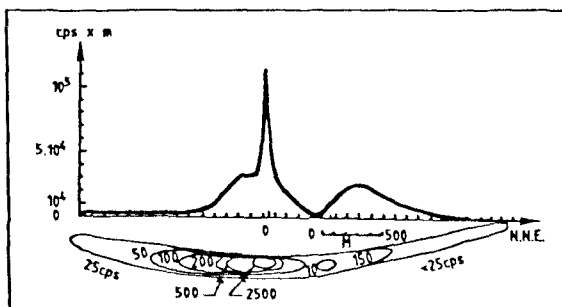
About 100 tons of sediments (10% silt and 90% 50 to 550  $\mu\text{m}$  sand) were released from a hopper dredger, off Cape of ANTIFER, by maximum spring ebb currents, since such hydraulic conditions exhibit a high risk for the harbour-works.

The tracer, representative of fine sand 50 to 350  $\mu\text{m}$ , was followed in suspension immediately after release took place and its distribution over the sea-bed measured 18 h later.

Only sand particles less than  $125 \mu\text{m}$ , which represent 15% of the total mass, is carried away in suspension. But contrarily to silt sediments, they will cover at the most 1600 m before settling (Fig. 3), since 40 min after immersion takes place there is no tracer in suspension at detectable concentrations ( $4 \text{ mg/l}$ ).

Thus, within 40 min time, the almost entire mass of sand spoils is distributed over the sea-bed up to 1600 m S.S.W. from the immersion point. 18 h later, that is after two floods the following evolution is observed (Fig. 5):

- only 30% of the total mass still remains on the sea-bed: sand particles less than  $200 \mu\text{m}$  (critical entrainment velocity  $u_* \leq 1.25 \text{ cm/s}$ ) have been resuspended by flood currents, transported N.N.E. and dispersed beyond the limits of the spot at non detectable concentrations,



- sediments lying on the bed are distributed along a S.S.W.-N.N.E. axis, 1/3 of them are still up to 1600 m S.S.W. from the point of immersion while the remaining 2/3 were retrieved up to 1800 m N.N.E.

Figure 5. Distribution of Sand Particles over the Sea-Bed 18 h after Immersion at ANTIFER.

On the whole, flood currents have entrained 90% of dredged materials N.N.E. (70% at more than 1800 m), that is, a transport ten times greater in regards to ebb.

## 2°) Evolution of deposited materials

Two immersions of glass particles labelled with iridium 192 were performed at a depth of 20 m and the tracer followed during 113 days. These experiments confirmed previous results, mainly, flood predominance next to ANTIFER dumping area.

Therefore, sand spoils released at more than 2.5 km North from ANTIFER oil installations represent a fairly low danger for the harbour-works.



### 3.3 - Study of transfer properties of a suspension of silt sediments at SINGAPORE

At SINGAPORE, ground levelling and littoral extension for urbanization purposes lead to sea disposal of some million cubic meters of silt sediments near the shore. CHANGI airport was built in this way over a site of 660 ha constituting an artificial beach 12 km long. Actually, 15 million m<sup>3</sup> of materials coming from the interior (LOYANG and TAMPINES) are discharged through a pipeline 750 m off BEDOK (Fig. 6).

Such procedure will undoubtedly increase the turbidity of the surrounding areas and could create potential danger to the environment. Besides, transfer and settling of fine particles during a west going tide may pollute recreational areas and generate considerable siltation in the port.

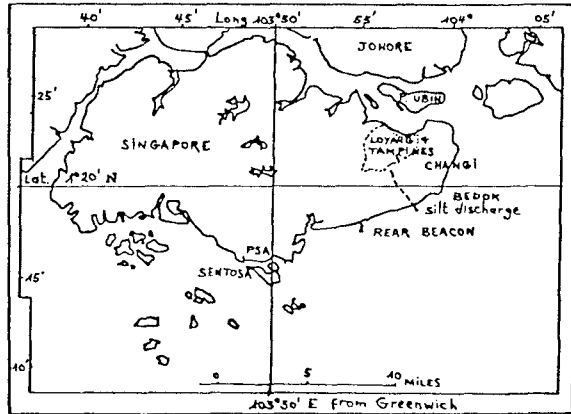


Figure 6. General Map of SINGAPORE

On request of P.S.A. authorities and A.I.E.A. financial support radioactive tracers experiments were carried out in order to study the behaviour of silt sediments in suspension and determine the risk they represent for the coastal area and the harbour-works. Thus, two punctual and instantaneous injections of mud labelled with gold 198, at an initial concentration of 18 g/l, were performed off BEDOK during a west going tide (lasting 16 h, with velocities 0.4 to 0.5 m/s). The cloud so formed was followed during 3 1/2 h over a distance of 6.5 km, by that time dilution being of a  $2.5 \times 10^{-6}$  factor.

These experiments were completed by local velocity measures and float-tracking. They allowed to determine the trajectory and mean transport velocity of sediments, dispersion parameters and dilution (Fig. 7).

For fully established tidal conditions, a lowly concentrated suspension of silt sediments ( $\phi < 40 \mu\text{m}$ ) has very similar transfer properties as fluid particles. They are conveyed by currents over large distances with negligible retard and without settling, while turbulence effects ensure uniformity of vertical concentration profiles over a depth of 10 m within 30 min.

Below a critical threshold, depending on sediments physico-chemical properties and concentration, the energy of turbulence is no longer sufficient to maintain particles in suspension and sedimentation takes place. Indeed, this mainly occurs at the on-coming of tide turn since then velocities decrease and vanish.

Results derived from radioactive tracers experiments were extrapolated to a continuous discharge of silt sediments during ebb and lasting at least 9 hours (Fig. 8): The plume would reach the shore and the harbours entry respectively 4 1/2 and 9 hours after the beginning of injection, followed by siltation during slack water.

- It follows a double risk:
- pollution of the sea-shore by mud particles,
  - silting-up of harbour works during slack water.

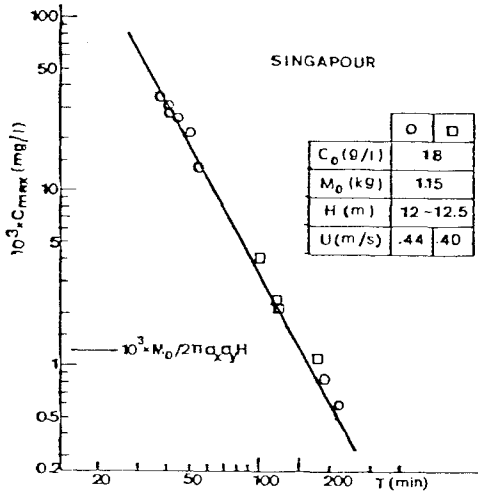
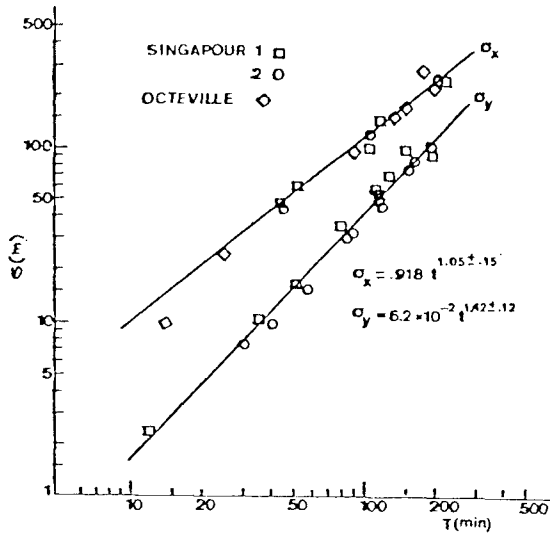


Figure 7. Evolution of Horizontal Dispersion Parameters and Maximum Concentration of a silt Sediment Suspension ( $\phi < 40 \mu m$ ).

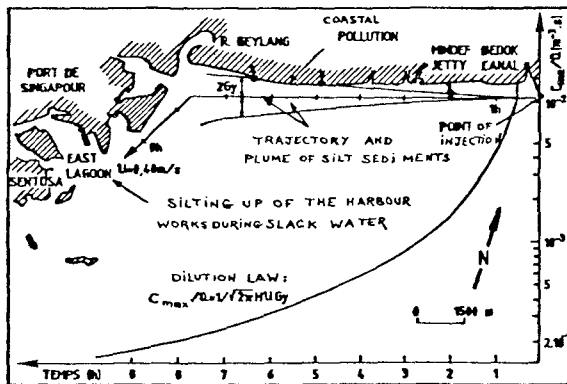


Figure 8. Trajectory, Mean Velocity, Dispersion and Dilution of a Continuous Release of Silt Sediments off BEDOK (SINGAPORE).

#### 3.4 - Sedimentary movements along the Belgian littoral

In 1974, the Belgian government planned to equip ZEEBRUGGE with a modern harbour and a new channel allowing access of greater ships. In order to limit its effects on littoral sedimentologic equilibrium, this task was carried out considering results of a wide research program including radioactive tracers measures. On the whole, 17 injections were decided by HAECON N.V - GHENT both for optimization of dredging operations as well as studying the behaviour of fine sediments resuspended during the discharge and the evolution of spoil disposals (Fig. 9).

##### 1° Dredging disposals at SIERRA VENTANA

In order to forecast the risk of siltation of the future channel because of recirculation of dumped spoils, labelled sediments (60% silt and 40% glass particles simulating sand) previously mixed to 2250 tons of dredged materials of density 1.49 were discharged from a suction hopper dredger during a spring tide ebb. Sediments carried away in suspension were followed during almost 3 1/2 h, while distribution of deposited materials was measured 24 h later.

Silt sediments and a fraction of fine sands (33%) form a lowly concentrated suspension convected and dispersed southwards towards the future channel (Fig. 9, point D5). Sand particles will most probably deposit before reaching it, contrarily to silt sediments which covered 7 km in 3 h with a mean velocity of 0.6 m/s. The experience was unable to put forward their sedimentation. However, this seems rather unlikely, at least during spring tides, given the absence of slack in the area concerned and the intensity of currents which may reach 1.5 m/s. Thus, silt sediments will be carried away by flood currents and dispersed Northwards. Further experiments (D3-4) confirmed such presumptions.

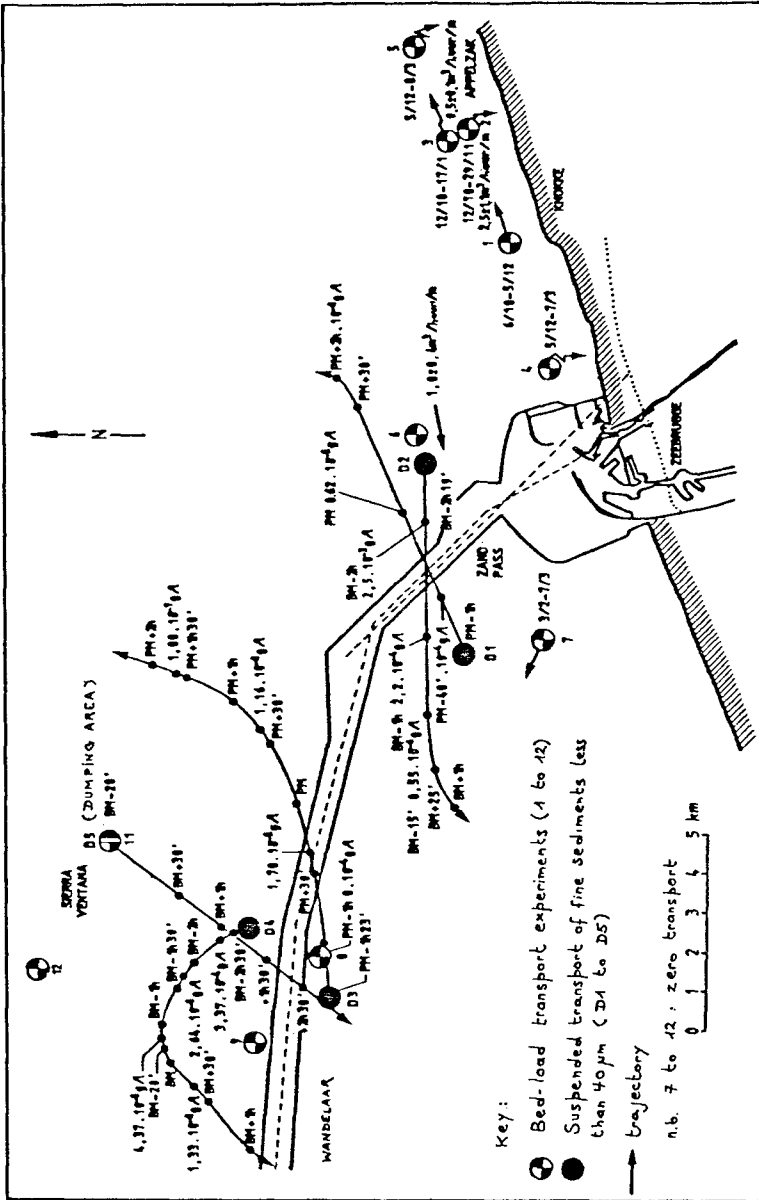


Figure 9. Radioactive Tracers Studies of Sedimentary Movements at ZEEBRUGGE.

About 27% of dumped spoils, that is, 67% of sands settle at less than 1000 m from the point of immersion and over 400 m width (Fig. 10) without any further evolution, sediments being almost insensitive to currents and waves even during storms ( $H_s = 5.5$  m).

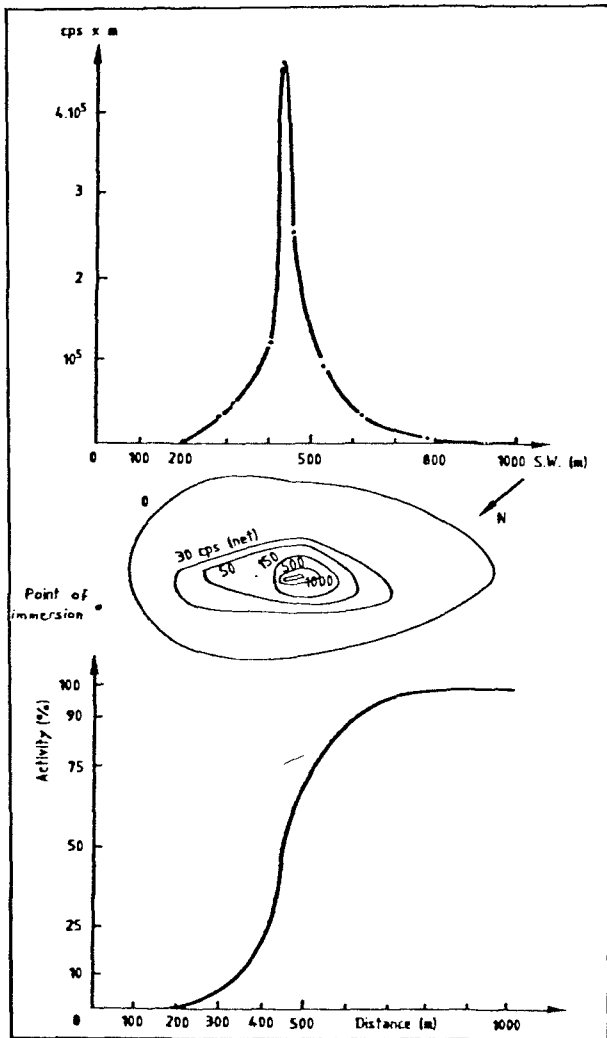


Figure 10. Seabed Distribution of Dumped Spoils at SIERRA VENTANA 24 h after Release Takes Place.

2°) General movement of sea-bed materials off ZEEBRUGGE

12 immersions of glass labelled with iridium 192 were carried out in different points from 5 to 18 m depth, and the tracer followed for a period of 4 months during which violent storms alternated with spring tides.

These experiments allowed to study the behaviour of sea-bed sediment of 160 to 315  $\mu\text{m}$  mean diameter and quantify their transport (Fig. 9, points 1 to 12). Their movement is not identical in every point nor occasionated by the same hydraulic actions:

- near the littoral and by less than 5 m depth (points 2 and 4), swell effects ( $H_s = 5.5$  m) ensure resuspension, dispersion and transport towards the coast of sediments less than 250  $\mu\text{m}$ ,
- between 5 and 10 m depth, added to wave effects during storms as previously, spring tide currents give rise to a rapid but superficial bed-transport: respectively 35 and 22 m/day with a mean transport thickness of 7 to 8 cm in points 1 and 6 (Fig. 11). The resulting movement is oblique relative to the coast-line. At APPELZAK (points 1 and 3), there is flood predominance with a net transport Eastwards of 0.5 to 2.5  $\text{m}^3/\text{day}/\text{m}$ . Next to the ZAND PASS (points 6 and 7), there is ebb predominance, with a net transport of 1.8  $\text{m}^3/\text{day}/\text{m}$  towards the channel east from it,
- beyond 15 m depth (points 8 to 12), sand particles are unaffected by waves but dispersed along a S.W.-N.E. axis, by alternate effects of flood and ebb currents, although the resulting transport is negligible (less than  $2 \times 10^{-3}$   $\text{m}^3/\text{day}/\text{m}$ ). Resuspension is not significant, excepted North from the future channel (point 9) where spring tide currents give rise to resuspension of sediments less than 300  $\mu\text{m}$  including 30% of cohesive materials ( $\phi < 40 \mu\text{m}$ ). The corresponding critical entrainment velocity is equal to 1.4 cm/s.

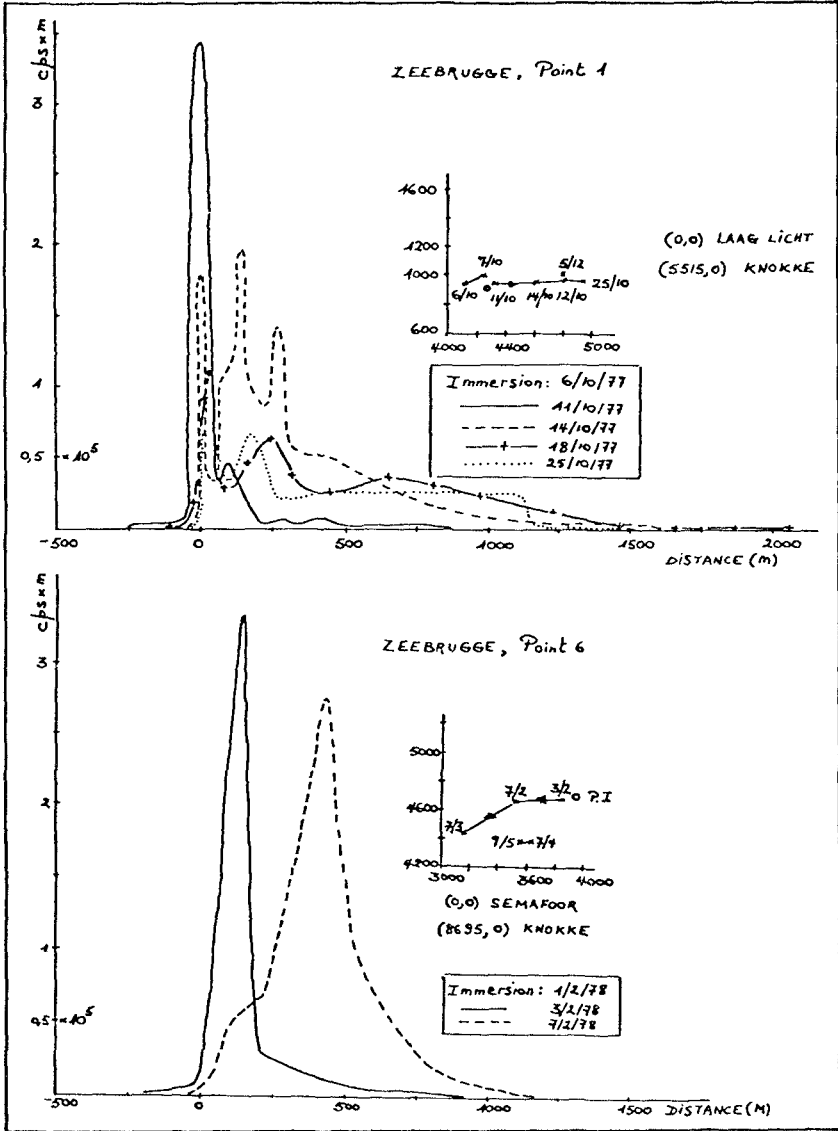


Figure 11. Evolution of Transport Diagrams and Gravity Center. ZEEBRUGGE, Points 1 and 6.

Main quantitative results are summarized on the following table:

Bed-load Transport and Resuspension of Fine Sands off ZEEBRUGGE

Measure Point (see figure 9)	1	2	3	4	6	7
Tracer grain size ( $\mu\text{m}$ )	160-315					
Period of observation before resuspension (days)	19	14	49	61	34	34
Mean transport thickness (cm)	7	8	6	5	8	3
Mean transport velocity (m/day)	35	6	2	1	22	1.4
Entrainment rate ( $\text{m}^3/\text{day}/\text{m}$ )	$2.5 \pm 1.1$	$0.5 \pm 0.1$	$0.1 \pm 0.03$	$0.05 \pm 0.01$	$1.8 \pm 0.4$	$0.04 \pm 0.03$
Transport direction	E	S	E	S	W.SW	W.SW
% of sediments resuspended by waves	95	84	56	40	75	80
Waves magnitude $H_s$ (m)	3.2	5.5				
Maximum grain size of particles resuspended ( $\mu\text{m}$ )	300	250	220	220	250	250
Depth (m)	5	5	5	5	9	5 to 6



3°) Transport of silt sediments in suspension

Four punctual and instantaneous immersions of mud labelled with gold 198, at an initial concentration of 20 g/l, were performed on both sides of the ZAND PASS and the futur channel for flood and ebb spring tide conditions (Fig. 9, points D1 to D4).

The suspension so formed was tracked over a distance of 7 to 10 km within 3 h preceding tide reversal, during which there is no significant sedimentation. Besides a dilution of a  $10^5$  factor a few minutes after injection, spring tide currents 0.5 to 1.5 m/s are sufficient to maintain sediments in suspension at concentrations close to natural turbidity and transport them over large distances.

Yet, next to the ZAND, and more generally, close to the coast, tide turn is accompanied by slack water which may last almost 1 h during which sedimentation takes place. Even if the possibility of resuspension must not be set aside, there is still a risk of silting up of the channel. On the contrary, at WANDELAAR or more generally, as we go away from the coast, slack water is less pronounced and the risk of siltation slighter.

Sediments transport is accompanied of vertical diffusion and horizontal dispersion. As it was the case at SINGAPORE, vertical concentration profiles become rapidly uniform after what, for constant depths and permanent current conditions, maximum concentration evolution follows the classical two-dimensional law:

$$C_{max} = M_0 / 2\pi \sigma_x \sigma_y$$

(Figs. 7 and 12).

Horizontal dispersion is represented by standard deviations  $\sigma_x$  and  $\sigma_y$  of longitudinal and transversal activity profiles (Fig. 13a and b). These parameters are found to be independent from the depth of the point of measure and not only functions of time, but also of velocity, acceleration and their time and space variations.

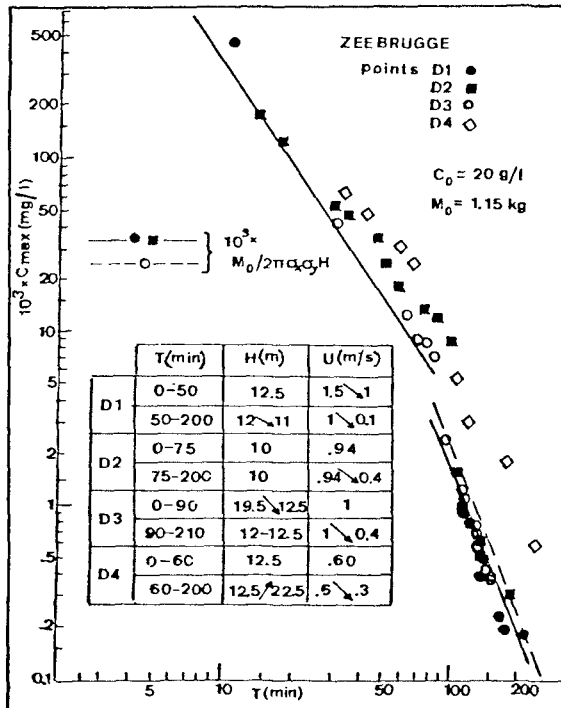


Figure 12. Dilution of a Suspension of Silt Sediments off ZEEBRUGGE.

A comparison of results from different experiments is given in figure 14. Since hydraulic conditions vary from one experiment to another, so does dispersion parameters when expressed in function of time.

For permanent current conditions, values of  $\sigma_x$  and  $\sigma_y$  are well fitted by a power law:

$$\sigma_i = k_i \cdot t^{n_i}, \quad i = x, y,$$

where coefficients  $k_i$  and  $n_i$  are constant but differ according as  $i = x$  or  $y$ . This is the case for SINGAPORE and OCTEVILLE. Velocity variations will affect coefficients  $k_i$  and  $n_i$ , inducing an increase of exponent  $n_i$  and a decrease of  $k_i$ , as it is the case for ZEEBRUGGE experiments.

Lastly, horizontal dispersion seems to increase with currents intensity and velocity variations, being greater in points D1, D2 and D3 of ZEEBRUGGE then it is in point D4 or at SINGAPORE.

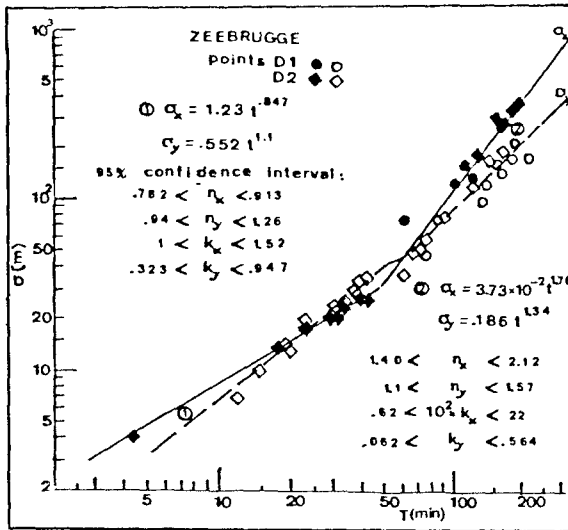


Figure 13a. Horizontal Dispersion Parameters of a Suspension of Silt Sediments off ZEEBRUGGE.

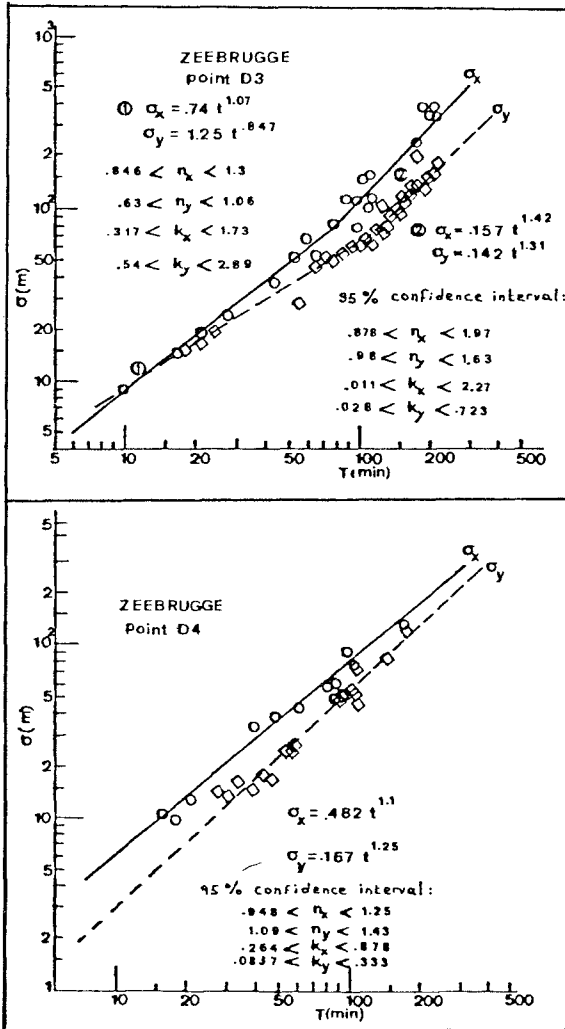


Figure 13b. Horizontal Dispersion Parameters of a Suspension of Silt Sediments off ZEEBRUGGE.

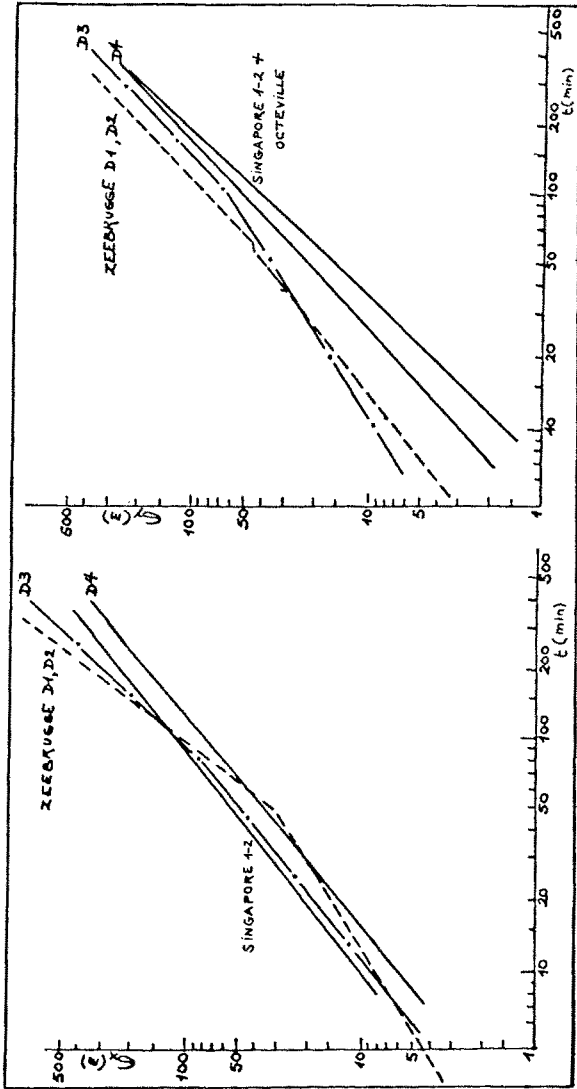


Figure 14. Horizontal Dispersion Parameters of a Silt Sediment Suspension. Comparison of Results.

## 4 - Conclusion

In the past, dredging operations and dumping conditions were mainly based on local habits and empirical experience. Nowadays, the necessity of practicing voluminous spoil discharges at least prices, yet limiting environmental pollution and the risk of recirculation of materials, requires quantitative evaluation of dredging efficiency. Experience shows that radioactive tracers are well suited for such a task. Besides, our present knowledge on dynamic properties of sediments is improved.

## References

- A. CAILLOT (1970) - Méthodes de marquage des sédiments avec des indicateurs radioactifs. La Houille Blanche. N.S.7.
- G. COURTOIS (1970) - Dynamique des sédiments et traceurs radioactifs : l'expérience française. La Houille Blanche. N.S.7.
- G. COURTOIS, R. HOURS (1964) - Propositions concernant les conditions particulières d'emploi des radioéléments artificiels pour étudier les mouvements des sédiments. CEA/SAR S 64-13 Internal Report.
- G. SAUZAY (1968) - Méthode du bilan des taux de comptage d'indicateurs radioactifs pour la détermination du débit de charriage des lits sableux. Thèse Univ. Toulouse, Rep. CEA-R 3431.
- F. TOLA (1982) - The Use of Radioactive Tracers in Dynamic Sedimentology. Note CEA-N-2261.
- F. TOLA (1984) - Etude des rejets des produits de dragage à l'aide de traceurs radioactifs. CEA/SAR S 84-03-T 21 Internal Report.

## CHAPTER ONE HUNDRED THIRTY EIGHT

### A PRE-DREDGING SAND MOBILITY STUDY USING A RADIOISOTOPE TRACER

A DAVISON\*

#### ABSTRACT

The wave-driven movement of sand across the alignment of a proposed navigation channel was investigated using radioactive chromium-51 labelled tracer sand. The mean particle velocity and thickness of the mobile layer were determined over a two-month period, and an annual infill rate estimated.

Wave height and period were measured concurrently. Despite two storms, during which near-bed oscillating velocities of  $1.5 \text{ m s}^{-1}$  were calculated, the sand transport at 10 m (BMWL) appears to occur within the wave boundary layer. Onshore transport in the direction of wave propagation, due to mass transport velocity and wave asymmetry effects, was easily identified.

Tidal currents up to  $1.2 \text{ m s}^{-1}$  (at 3 m above bed) had less than the expected effect on the tracer dispersion pattern.

#### 1. INTRODUCTION

The operating economics of modern bulk carriers demand that vessels be able to enter and leave ports at full capacity under most tidal conditions. Navigation channels must provide a minimum underkeel clearance of one metre. The potential of any port, in terms of size or draught of vessels which can enter, can be limited by the water depths in the approach channels, critical sections of which may be at some distance from the berths. [1] Maintenance dredging operations to keep these channels open must not be excessive.

At present, the main shipping channel for deep draught vessels entering and leaving the Port of Brisbane follows a long and complex path through Moreton Bay to avoid the extensive sand shoals which block the northern approaches. The Port of Brisbane Authority (PBA) has proposed that a new channel be dredged which could provide an alternative and more direct access (Figure 1(a)(b)). This channel would

---

\* Australian Atomic Energy Commission, Isotope Applications Research Group, Private Mail Bag, Sutherland, NSW, Australia 2232.

effectively "cut the corner", reduce the distance travelled by ships to and from the south by 40 km and require only 15 km of maintenance dredging as opposed to 30 km on the old route.

The new route would involve upgrading an existing tidal channel which is presently used by shallower draught vessels and constructing a shorter (3 km) section through a sand bar to link it with the open sea. In this critical section, water depth on the bar at low tide is 9 m, but a depth of 17 m is required for deep draught vessels.

### 1.1 Regional Sand Migration

In this region of the east coast of Australia, it is generally recognised that there is a northward movement of sand. Extensive studies carried out by the Delft Hydraulics Laboratory [2] and the Queensland Department of Harbours and Marine (QHM) Coastal Protection Branch [3] revealed that  $5 \times 10^5$  t of sand moves past the nearby Gold Coast each year, pushed by currents in the surf zone generated by the predominantly south-easterly swell which, in southern Queensland, strikes the coast at an oblique angle. Evidence of this northward littoral drift can be seen where the training walls extending seaward of the entrance to the Tweed River have interrupted the sand flow. In the 16 years since their construction, approximately  $8 \times 10^6$  t of sand has been trapped behind the southern wall, starving the upstream Gold Coast beaches of their normal sand supply, and resulting in heavy beach erosion.

It is likely that similar quantities of sand are moving on the seaward side of Moreton Island and that the sand shoals in the northern reaches of Moreton Bay are the result of centuries of littoral drift. Sand has moved around Cape Moreton, along the northern beaches of Moreton Island, and has been deposited across the bay entrance. Tidal currents and wave action have moulded the 400 km<sup>2</sup> deposit into an ebb and flood delta cut by several deep tidal channels. Each tidal channel has its own smaller but identifiable ebb and flood fan. It is uncertain whether the deposit is now simply a "sink" for the sand or whether the shoals provide a bypass for all or some of the sand to beaches near Caloundra and further north. If bypassing is occurring, the critical section of the proposed navigation channel would cut across the sand migration route at right angles.

### 1.2 Sand Mobility at Channel Site

The hydrodynamics over the shoal system are complex. Local wind waves up to 2 m with 3 to 5 second periods can be generated in the bay; swell waves up to 5 m with 8 to 12 second periods resulting from storms at sea can cross the site; the diurnal tidal range is  $\approx 2$  m and generates reversing tidal currents with velocities up to  $1.2 \text{ m s}^{-1}$ . The

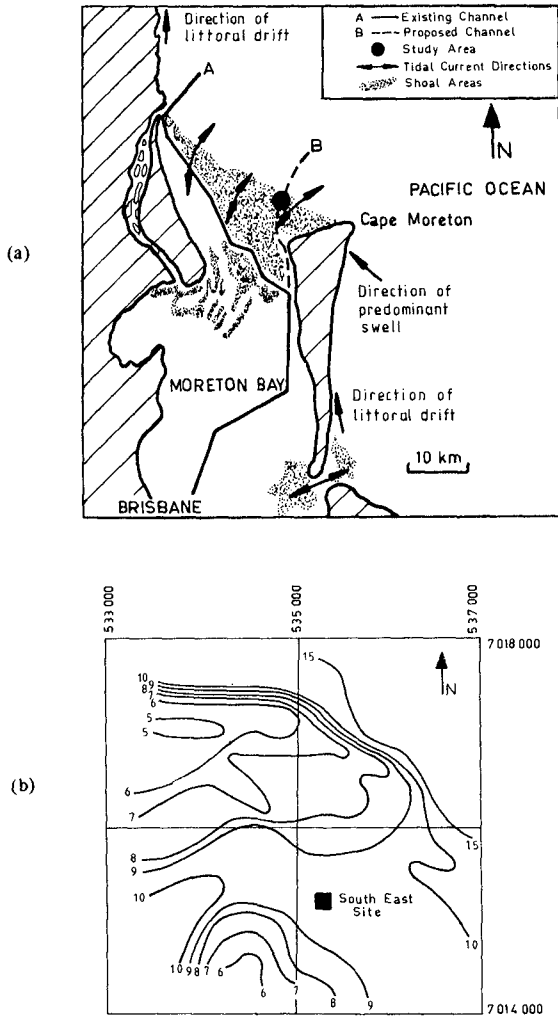


Figure 1. (a) Existing and proposed navigation channels through the Moreton Bay shoals. (b) Depth contours over the ebb fan of the North East tidal channel.



conditions indicate a high bed mobility but the many variables involved make calculation or mathematical modelling of sand migration rates from hydrodynamic data difficult. Ebb oriented dune-forms exist in the deeper regions of the tidal channel. Some lower bed-forms occur on the fan itself but no clear indication of the major direction of sand migration can be defined.

Determination of siltation rates using a mobile bed hydraulic model equipped with tide and wave generators is expensive and some preliminary field data are required for precise tuning. Radioactive tracer techniques provide an alternative method to acquire qualitative and quantitative on-site data. The PBA contracted the AAEC Isotope Application Research Group to carry out on-site tracing tests. These were carried out between 26 April 1983 - 1 July 1983.

## 2. AIMS OF THE INVESTIGATION

Although there are many factors which could cause channel infill, and recognising that construction of the channel could radically alter the sediment movement pathways in the location, a possible cause of siltation would be the littoral-drift/bay-bypass mechanism. The radiotracer study was designed to investigate the presence of this mechanism.

The principal aims of the investigation were:

- (i) To determine the direction of sand movement
- (ii) To determine the rate of sand movement
- (iii) To determine the rate of channel infill caused by any identified sand movement normal to the channel alignment.

## 3. SEDIMENT TRANSPORT RATES BY RADIOACTIVE TRACER TECHNIQUES

Quantitative sediment transport rates by the spatial integration method may be determined from

$$Q = 2VD \text{ td}^{-1}\text{m}^{-1}$$

where V = mean particle velocity ( $\text{md}^{-1}$ )

D = mobile bed thickness (m)

and a bulk density factor of 2 is assumed.

Radioactive sand tracer is released onto the ocean floor. The spatial distribution of tracer is determined at suitable time intervals. The centroid of each complete scan is calculated. Shift in centroid location over the corresponding time interval gives the mean particle velocity (V).

The mathematical concept of bed-load movement is applied even though the actual particle movement may be a series of 'hops' in suspension followed by long periods in

which the particle remains buried in the sediment layer. This mobile layer has a thickness in ocean waters which depends on wave climate, particle size, ripple height and particle roughness. Its thickness (D) is determined from the vertical dispersion of tracer into the sea bed, measured by the count recovery method or by coring.

### 3.1 Choice of Tracer

Chromium-51 ( $t_{1/2} = 27$  days;  $\gamma = 0.32$  MeV) was chosen as the most suitable radioisotope for preliminary investigations in Moreton Bay. Direct underwater detection is possible but the energy is low enough to reduce the need for bulky shielding during transport and tracer release procedures.

### 3.2 Tracer Sand Preparation

Two kilograms of sand were taken from the shoals, washed, graded (0.2 mm median diameter), nitric acid-washed, to remove shell grit (5%), etched in hydrofluoric acid to remove iron and manganese oxides, and dried. Ammonium dichromate solution was added until the sand was just moistened. The ammonium dichromate was decomposed by heating to 600°C; this produced an even coating of green chromium sesquioxide on the sand. Wet and dry self-abrasion followed by repeated washing removed all loose oxide and oxide deposited on the high spots on the grains. Microscopy showed that the residual oxide was extremely well attached on fissures and etched pits. Laboratory tests showed negligible levels of chromium in supernatant water after extended periods of violent agitation. It is therefore unlikely that any label would detach under marine conditions. No significant density change is involved since residual chromium content is 0.35%.

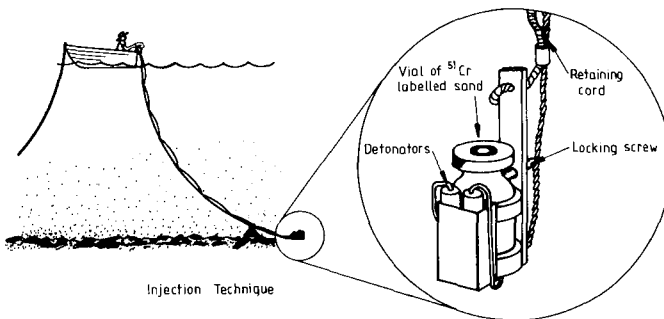


Figure 2. Tracer release technique. Vials of chromium-51 labelled sand are transferred from lead delivery pots into brass holders preloaded with two electric detonators. Detonation on the sea bed breaks the vials and releases the tracer sand.

Neutron activation of the label to chromium-51 was carried out in the X-202 bulk irradiation facility in the AAEC's materials testing reactor HIFAR.

### 3.3 Tracer Release

For preliminary tests a site, located 1 km south-east of the proposed channel line (Figure 1b) was chosen as representative of the area.

Mean water depth at this site was 10 m BMWL. The detonation technique was used to inject tracer sand into the sea bed (Figure 2) over a slack water period on 28 April 1984. Twelve vials, with a total activity of 1.45 Ci 50 (GBq) were used. Total mass of tracer was 0.6 kg. This technique is quick and simple. Release was complete in 30 minutes. The incorporation of tracer into the bed material.

### 3.4 Tracer Monitoring and Determination of Mean Particle Velocity $V$

The subsequent lateral movement of the tracer was followed over a period of two months. A waterproof scintillation detector was mounted on a sledge and dragged over the sea bed on fixed lines. The sledge position was fixed using HIFAR navigation equipment, and shore stations at Caloundra and Woorum as reference points. Usually, the tracks ran along fixed arcs of  $\approx 27$  km radius with Caloundra as the central point. The navigation equipment is accurate to  $\pm 3$ m. Count rates were corrected for radioactive decay and superimposed over the tracks provided by the PBA surveyors. Isoactivity contours were drawn and centroid and lateral movements of the tracer determined. In tracer studies, in an ocean environment, tracer advection in one direction can be masked by tracer diffusion in all directions. Successive scans show considerable overlap and centroid shifts are often tens of metres. Recently the very accurate navigation systems available have made it possible to track on a 10 m grid spacing at up to 30 km from shore stations, and to reveal these small shifts. By endeavouring to limit the initial area of the labelled zone, tracing on such a tight grid does not become arduous and most complete scans can be accomplished in one day of fair weather.

The areal disposition of the tracer relative to two reference points connected by a line parallel to the proposed channel alignment for the period 4 May to 1 July 1983 is shown in Figure (3). Tidal action stretched the concentration contours in the ebb and flood directions. There is also an identifiable movement in a north-westerly direction along the wave orthogonal and across the line of the proposed channel. This movement, attributed to wave generated mass transport velocity and wave asymmetry

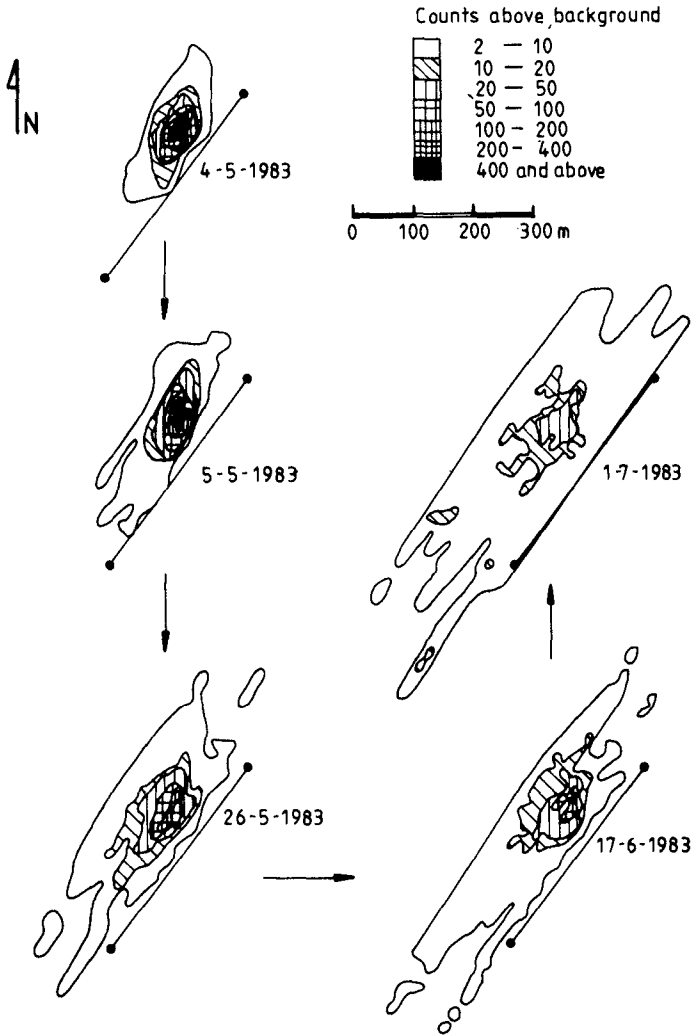


Figure 3. Lateral dispersion of labelled zone over the two month test period. Movement is shown relative to two reference points joined by a line parallel to the channel alignment.

effects, can be regarded as "onshore" transport.

The movement normal to the direction of the tidal currents and across the channel alignment is plotted as a function of time in Figure 4 (a). The integrated count along the lines at 10 m intervals from the reference line are plotted on the vertical axis for each complete scan. The Lateral shift of the centroid position is plotted as a function of time in Figure 4 (b) and indicates a steady movement towards the north-west.

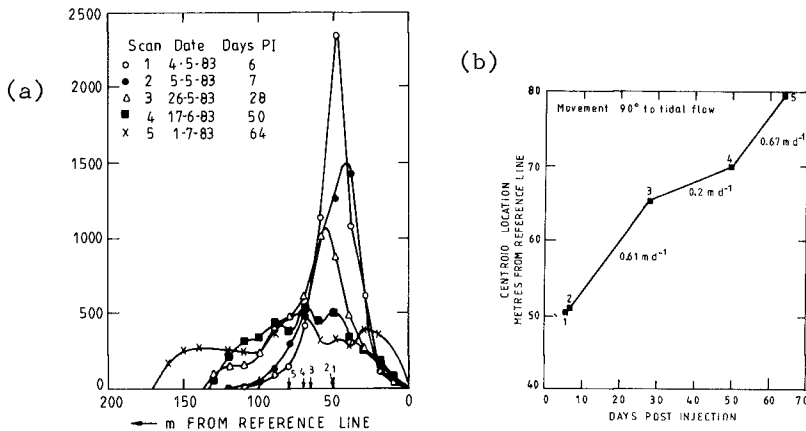


Figure 4. (a) Lateral distribution of tracer  
(b) Centroid location as a function of time after tracer release. Mean particle Velocities are indicated.

During the 56 days, following an initial 7-day period of tracer incorporation, there was a lateral shift of 28.8m, resulting in a mean particle velocity ( $V$ ), normal to the channel alignment, of  $0.52 \text{ m day}^{-1}$ :

### 3.5 Thickenss of the Mobile Layer (D)

As tracer sand becomes incorporated into the bed material the total activity which is apparent to a sledge mounted detector falls absorption by bed material of the  $\gamma$ -ray emission from tracer particles.

The ratio of apparent activity : injected activity (% recovery) is a function of the  $\gamma$  energy of the isotope employed and the incorporation thickness.

The detector response to buried tracer is described by the equation

$$\frac{\alpha ND}{\beta f_0 A} = 1 - e^{-\alpha D}$$

where  $\alpha$  is the absorption coefficient at the relevant  $\gamma$ -energy for a sandwater mix;  $N$  is the number of counts recovered;  $f_0$  is the detector response where tracer is a surface layer only;  $A$  is the total activity injected;  $D$  is the depth of tracer incorporation; and  $\beta$  is a non-homogeneous distribution factor [4]. The factors  $\alpha$  and  $f_0$  were determined in a laboratory tank from the count rate reduction observed when a plane source of chromium-51 was buried under increasing thicknesses of sand. Under these circumstances

$$f = f_0 e^{-\alpha d}$$

where  $f$  is the observed count rate and  $d$  is the covering thickness;  $d$  can also be regarded as the mean depth of tracer incorporation. The total thickness depends upon the vertical distribution factor  $\beta$ . A value of  $\beta = 1.25$  was used in this study. The value of  $\alpha$  and  $f_0$  for chromium-51 and the detector used was found to be  $17.9\text{m}^{-1}$  and  $2.8$  counts  $\text{s}^{-1} \mu\text{Ci}^{-1}\text{m}^{-2}$  respectively.

Figure 5 shows the measured mean tracer particle depth ( $d$ ) and the derived total thickness of the mobile layer ( $D$ ) as the ratio of apparent activity : released activity expressed as percentage.

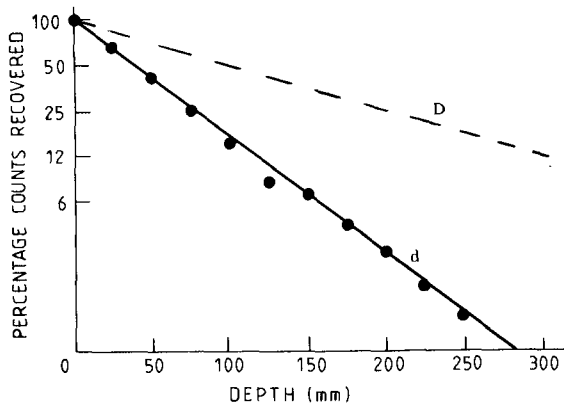


Figure 5. Calibration curves used in the determination of the mean particle burial depth ( $d$ ) and overall thickness of the mobile layer ( $D$ ).

The percentages of total possible counts recovered per complete scan, together with the mobile bed thickness calculated from these values, are plotted as a function of time

in Figure 6. After an initial period of seven days, incorporation was apparently complete and remained constant at a depth (D) averaged over the whole labelled zone of 0.25 m. A similar period for full tracer penetration was found during tests in Swansea Bay, Wales [5].

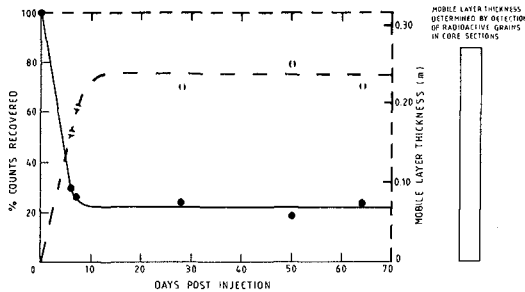


Figure 6. % Counts recovered and derived thickness of mobile layer (D) plotted against time after tracer release. The mobile layer thickness determined from cores is shown to the right.

Cores were taken from the labelled zone after 50 days using a vibration corer powered by compressed air. These cores were sliced into 0.02 m sections and the chromium-51 content measured in the laboratory (NaI crystal with multi-channel analysis). Active particles were found evenly distributed over the range shown in Figure 6. The deepest particle was 0.27 m below bed level, corroborating the value of 0.25 m found by the count recovery method.

Unlike tracer tests involving mud, relatively few active particles are employed during sand tracer tests. A prohibitive number of cores would be necessary to obtain a complete vertical distribution profile.

### 3.6 Sand Transport Rate

The wave driven transport rate normal to the tidal current and channel alignment can be calculated from the values of  $V$  and  $D$ .

$$\begin{aligned}
 Q &= 2VD \\
 &= 2(\text{tm}^{-3}) \times 0.52 (\text{md}^{-1}) \times 0.25 (\text{m}) \\
 &= 0.26 \text{ tonnes d}^{-1} \text{ m}^{-1}
 \end{aligned}$$

Based on this transport rate a 3000 m channel cut through the fan will intercept  $2.85 \times 10^5$  tonnes of sand per year. This preliminary value, calculated from data acquired over only a two-month period and a single central downstream location, appears reasonable and equivalent to  $\approx 60\%$  of the

known littoral drift rate.

An extended study is in progress using iridium-192 labelled tracer sand ( $t_{1/2} = 74$  days) which has been released as a 2000 m line source.

3.7 Current and Wave Data

Sections of the record of velocity and direction of the diurnal tidal current measured 3 m above the bed are shown in Figure 7. The region is ebb dominated. Both ebb velocity and duration exceed that of the flood tide. The ebb-flood and flood-ebb current direction change occurs through the south-eastern seaward sector.

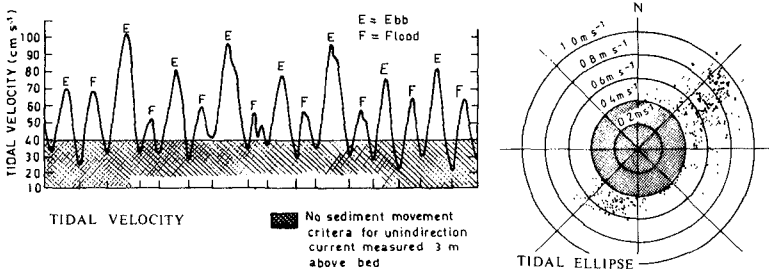


Figure 7. section of tidal current velocity and direction record.

Wave height ( $H_g$ ) wave period ( $T_g$ ) and the near bed maximum oscillating current velocity ( $U_b$ ), calculated from linear wave theory, are shown in Figure 8. A period of "heavy" weather ( $S_1$ ) and two storms ( $S_2, S_3$ ) are indicated. A value for  $U_b$  of  $1.55 \text{ m s}^{-1}$  was calculated for the peak of both storms  $S_2$  and  $S_3$ .

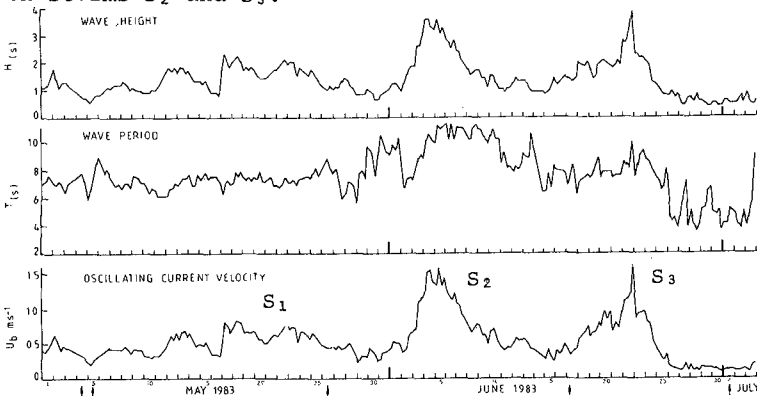


Figure 8. Wave height, wave period and calculated oscillating near bed current during test period.



The deepwater wave climate for the area, from data accumulated over several years [ 3 ], is compared with the slightly more energetic climate recorded during the study in Figure 9.

The records indicate that criteria for the initiation of movement for 0.2 mm sand under steady (tidal) or oscillating (wave generated) currents were exceeded at all times.

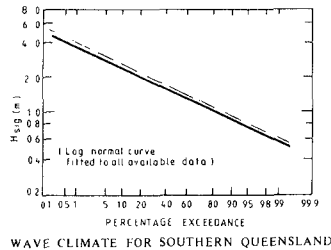


Figure 9. Annual wave climate ———, and wave climate recorded during test period -----.

#### 4. CONCLUSIONS

Movement of sand towards the north-west and across the proposed channel alignment has been identified.

The values found for the mean particle velocity ( $V = 0.52 \text{ m d}^{-1}$ ) and thickness of the mobile layer ( $D = 0.25 \text{ m}$ ) result in a sand transport rate of  $0.26 \text{ tm}^{-1}\text{d}^{-1}$ . This value is strictly only applicable to the central 600 m of channel and for the two months during which sand movement was monitored. Variation in water depth over the fan is small and the wave climate during the test period was representative of the annual average. It is therefore not unreasonable to extrapolate the measured value in both time and space. On this basis a 3000 m channel will intercept  $2.85 \times 10^5$  tonnes of sand per year, equivalent to 60% of the known littoral drift rate.

On first examination a remarkable feature of the study is the relatively low advection rate of the 0.2 mm bed material, and deserves further comment. The labelled zone remained compact throughout and exhibited little stretching in the direction of the tidal currents. No offshore transport could be detected but onshore transport in the direction of wave propagation and across the line of tidal flow was apparent.

Behaviour of this kind is characteristic of transport processes occurring very close to the bed where steady current velocities are weakest and where wave mass transport velocities supplemented by wave asymmetry effects are strongest, and in the direction of wave advance.

During the storm events  $S_2$  and  $S_3$  maximum near-bed orbital velocities calculated from linear wave theory were  $1.5 \text{ m s}^{-1}$  which would have eliminated bed ripples and caused a sheet flow condition similar to that observed by Jonsson (6) utilising equivalent velocities in wave tunnel studies.

Considerable quantities of sand would have been mobilized in oscillating motion both as bedload and suspension in agreement with the measured mobile layer thickness of 0.25 m. However the superimposed steady (tidal) current has little advective effect on this dense slurry apparently trapped in the wave boundary layer. Weakening of the steady current velocities within the wave boundary layer has been predicted by Fredsøe (7) and measured by Bakker and Doorn (8) in a flume. Under these circumstances steady current velocity profiles with roughness lengths of the order of the wave boundary layer thickness are obtained. Similar effects have been observed in field studies (9).

Upward transfer of sediment to heights above the bed, where the steady current could cause advection, is suppressed by the steep density gradient between the near bed slurry or rheological layer (10) and the water immediately above.

It is of interest to note that, while the depth of water at the study site was 10 m (BMWL), the beach profile closure depth is 9.5 m (BMWL) on this part of the east coast of Australia (11). This value should be compared with the water depth at the boundary between near shore and shoal zones as defined by Hallermeier. This boundary is at the deepest water depth where "suspension" processes can occur under extreme wave conditions, and is calculated to be 9.0 m (BMWL) (12).

## 5. REFERENCES

1. Langhorne D N (1978) Offshore Engineering and Navigational Problems. Technical Note published by Institute of Oceanographic Sciences and the Society for Underwater Technology UK.
2. Bijker, E W (1968) - Littoral drift as a function of waves and currents. Delft Hydraulics Laboratory Publication No. 58.
3. Pattearson C C and Patterson D C (1983) Gold Coast Longshore Transport. Sixth Australian Conference on Coastal and Ocean Engineering, Gold Coast Queensland pp 251-256.

4. Sauzay G (1967). The count rate balance method of measuring transport rates. CEA Report No CEA-R-3431.
5. Heathershaw A D, Carr A P (1977) - Measurements of sediment transport rates using radioactive tracers. 5th Symposium of Waterway, Port, Coastal and Ocean Division, American Soc. Civil Eng., Charleston, South Carolina, p 399.
6. Staub C, Jonsson I G and Svendsen I A (1984) Time Variation of Sediment Suspension in Oscillatory Flow. 19th International Conference on Coastal and Ocean Engineering (Houston, USA).
7. Fredsøe J (1981) Mean Current Velocity distribution in Combined Waves and Current. Progress Report Coastal Eng. Lab. (ISVA) pp 21-26.
8. Bakker W T and Doorn Th V (1978) Near bottom Velocities in waves with a current. 16th Int. Conf. on Coastal and Ocean Engineering (Hamburg) pp 1394-1413.
9. Cacchione D A and Drake D E (1982) Measurement of Storm generated bottom stresses on the Continental Shelf. J Geophys. Res 87, 1952-1960.
10. Moss A J (1972) Bed-load Sediments. Sedimentology, 18, 159-219.
11. Chapman D M, Smith A W (1983) - Gold Coast Swept Prism - Limits. Proc. 6th Australian Conf. on Coastal and Ocean Engineering, Gold Coast, pp 132-138.
12. Hallermeier, J R (1981) - A profile zonation for seasonal sand beaches from wave climate. Coastal Eng. 4, 253-277.

## CHAPTER ONE HUNDRED THIRTY NINE

### DEVELOPMENT OF A SEDIMENT TRANSPORT MEASURING SYSTEM

Eberhard Renger \*

#### ABSTRACT

A new method for continuously recording sediment concentrations with high accuracy has been developed. It is proposed to apply the method for in-situ measurements in connection with investigations of tidal control and sediment transport induced by shipping traffic.

The operating principle is as follows: at the measurement location, sediment laden water is continuously sucked-in by means of a pump and is forced under pressure into a hydrocyclone ( solid bowl centrifuge ) through a delivery pipe of varying length. Here the extracted sediment flux (particle size  $\approx 5 \mu\text{m}$ ) is delivered by the shortest route to a settling tank and continuously weighed under water (wet-weighing). Following calculation and appropriate adjustment to the sample discharge (  $Q$  ) the weight increase for selected time intervals (  $\Delta G (\Delta t)$  ) yields the mean concentration for the time interval (  $\bar{c} (\Delta t)$  ) in weight / unit volume (  $\text{mg/l}$  ) (direct measurement, calibration not required ).

Details and experiences of the 3 major development stages will be described. A fully-automatic instrument for continuously measuring nonsteady sediment movement is now available. The instrument may be installed above as well as below water as desired.

#### 1. INTRODUCTION AND PROBLEM DEFINITION

In connection with investigations of tidal control to reduce sedimentation and of sediment transport induced by shipping traffic in the inner German Bight / North Sea, it is necessary to continuously record instationary sediment transport over long periods at different measuring stations. Owing to a lack of information concerning the spatial distribution and temporal variation of sediment

---

\*Senior Research Engineer, Landesamt für Wasserhaushalt und Küsten Schleswig-Holstein, Kiel - Germany

movement in the investigation areas, it was necessary to develop an overall concept which was realised in practice according to the following stages:

1. Selection and partial development of a suitable method of continuously recording sediment concentrations and the specification of a minimum performance
2. Preliminary experiments concerning the measurement of the instationary nature of sediment movements at a single point of measurement. This was necessary in order to estimate the most appropriate measurement frequency and measurement duration.
3. Simultaneous test recordings at various depths in the same cross-section in order to assess the importance of vertical variations in the transport (number of instruments !)
4. Simultaneous test recordings at various measuring points in a horizontal plane at the same cross-section in order to assess the importance of horizontal variations in the transport (number of instruments !)
5. Further development of the measuring technique in order to obtain optimal conformity with the overall objective with due consideration of the above-mentioned experimental tests

Since each stage of the investigation depended to a large extent upon the results of the experiments, it was necessary at the outset to ensure a high degree of flexibility in research planning and conduct. In accordance with the latter, the following basic principles were specified:

- a) Adoption of uncomplicated and readily available instrument components as building blocks
- b) On-the-spot evaluation of test results in order to ensure an optimal progress of the experiments
- c) Well-conceived stage planning in order to ensure overall optimisation of the investigation aim and solution possibilities

In this paper, attention will be mainly confined to the development stages of the measuring technique.

## 2. SELECTION CRITERIA FOR THE MEASURING TECHNIQUE

In order to prescribe the measuring technique, a study of existing investigations was first carried out (1),(2),(3). The following basic information led to constraints regarding the technical problems of measurement concerned with here:

- 1) Existing data concerning grain-size distributions for suspended sediment and bed samples reveal mean frequency maxima ranging between about 50 and 100  $\mu\text{m}$ .
- 2) At the present time, existing indirect recording techniques require extensive calibration by means of sampling and laboratory analyses (weighing), especially under consideration of particle dependence.
- 3) The determination of sediment balances (residual transport) depends predominantly upon the number of instruments used.

For these reasons, the continuous partial flux analysis with sediment weighing was selected as the most suitable method of investigation ((4), and Fig.1).

With the aid of a pump and a suitable extraction and feed system, a sample discharge is continuously forced under pressure through a hydrocyclone (solid bowl centrifuge). The separated particle stream falls within seconds by gravity into a settling tank and is continuously weighed. Following calculation and appropriate adjustment to the sample discharge ( $Q$ ), the weight increase for selected time intervals ( $\Delta G (\Delta t)$ ), directly yields the mean sediment concentration for the time interval ( $\bar{c} (\Delta t)$ ) in weight / unit volume ( $\text{mg/l}$ ).

The development of the measuring technique and the corresponding instrumentation took about 2 years. This essentially involved 3 major stages of development (see Fig.3).

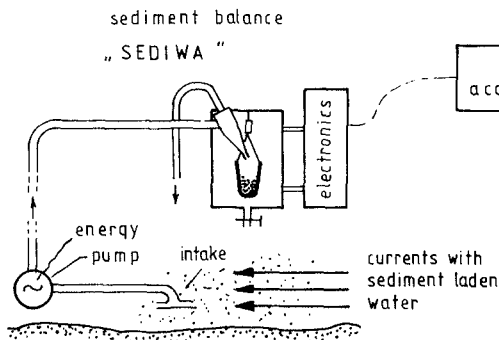


Fig. 1 :  
schematic drawing  
showing mean  
components of  
suspended sediment  
measuring device  
(SEDIWA, submersible)

### 3. HYDROCYCLONES AS SOLID BOWL CENTRIFUGES

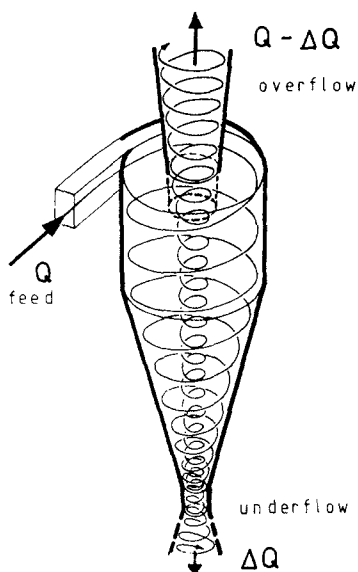


Fig. 2 :

Hydrocyclone flow diagram

As described by TRAWINSKI in (5) the hydrocyclone can be regarded as operating as a solid bowl centrifuge in which the casing is not rotated, but rotation of the suspension is produced by its being fed into the cyclone tangentially under pressure. Depending on the degree of solids recovery to the underflow, the cyclone can act either as clarifier or as classifier. The rejects are thickened in any case.

Fig.2 demonstrates schematically the working of a hydrocyclone. The suspension fed into it forms a primary vortex along the inside surface of the cylindrical and conical wall, aiming to leave the cone apex. As this is throttled, only part of the stream is discharged as underflow, carrying the coarse particles or even all of the solids with it. The bulk of the liquid - being cleaned by the residual fine particles with it - is forced to leave the cyclone through the overflow nozzle by

forming an upward-spinning secondary vortex surrounding the core of the casing. Inside the core, a low pressure is generated, collecting all the air that has been carried in as bubbles or dissolved in the feed water. Even vapor will enter this visible air core. Because of the increase in circumferential speed in the secondary vortex, higher centrifugal forces are generated, resulting in a highly efficient secondary separation. The rejected fine particles settle radially and join the primary vortex, from which most of them are discharged finally through the spigot formed by the cone apex. The separation inside a hydrocyclone therefore takes place as a result of two process stages, the final cut point being determined mainly by the acceleration of the inner secondary vortex.

### 4. SELECTION OF MEASUREMENT CYCLONES

The separation efficiency of hydrocyclones is mainly determined by the cyclone geometry (diameter, length) and the discharge. The normal measurement specifications for standard cyclones require information regarding concentrations,

particle distribution as well as discharge for the feed. These three design parameters must be estimated by theoretical or empirical methods before instrument construction and specified for the selection of the cyclone. In respect of this, following relationships must be considered:

1. The natural particle distribution of between 0 and approximately 500  $\mu\text{m}$ , with a mean maximum of between 50 and 100  $\mu\text{m}$ , lies within the optimum working range of hydrocyclones. The smaller number of large particles occur very seldom and may therefore be legitimately excluded by means of a prefilter so as to protect the equipment from blockage. Parts of the equipment susceptible to blockage include the slot-shaped inlet nozzle ( $\text{max } d < \text{slot-width}$ ) and the circular underflow nozzle ( $d \leq 1/5$  nozzle diameter). Other than this, no strict requirements are necessary for optimal performance of the equipment.
2. The natural concentration of the sample discharge ( Q ) of between about 0 and 10 g/l maximum, with a predominant peak between 50 and 500 mg/l, results in an optimum degree of selectivity in the separation process. The absolute magnitude of the latter, as related to the frequency of occurrence, is a decisively important factor for the dimensioning of the sediment scale. For optimal performance, the accuracy of weighing, measurement frequency, size of the settling tank and flushing frequency must be counterbalanced.
3. The discharge ( Q ) is essentially proportional to the diameter of the hydrocyclone. Since the size of the separated material also increases with the diameter of the hydrocyclone the sediment stream to be weighed becomes less representative owing to the restricted range of particle size. The fine-grained fraction ( $< d_p$ ) of the residual turbidity in the hydrocyclone overflow increases, and since this cannot be measured at the present time, it must be treated as an error in instrument measurement. Consequently, the optimisation demands a minimization of the discharge ( Q ).

It should be noted that the sub-optimization of the hydrocyclone and the magnitude of the sample discharge ( Q ) as a function of the sediment scale both play a predominant role. Owing to the unknown sediment fluxes, further development of the method in the hydraulics laboratory was not undertaken. By adopting readily available instrument components, initial tests and measurements in the field were immediately carried out. By this means, first impressions of actual sediment movements, as referred to in section 1, could be obtained simultaneously.



## 5. OVERALL OPTIMISATION OF THE MEASURING SYSTEM

### 5.1 Components of the measuring technique

The in-situ measuring instrument with on-line facilities is comprised of the following sub-units (compare with Fig.1 , Fig.3 and Table 1 ):

- a) Extraction and feed equipment with intake arrangement, delivery pump, feed pipe, support, power supply, positioning facility
- b) Hydrocyclone and disposal unit with discharge measurement, overflow pipe, inlet regulation, pressure controls
- c) Settling tank and sediment scale with tank adjustment, filling equipment, flushing device, constraining fixtures
- d) Instrument control and data recording with underflow regulation, tank flushing, operation monitor, data acquisition, data storage, concentration computations, in-situ data logging

As indicated in Table 1 , the three development stages involve different dimensions of the sample discharge ( Q ) and weighing apparatus. Accordingly, the instrument components listed under a) to d) are differently dimensioned. A detailed technical description will be avoided here.

### 5.2 Determination of sediment concentrations

As described in Sections 3 to 5 , only the sediment stream in the hydrocyclone underflow is continuously weighed at present. All fine particles (smaller than the separation grain diameter  $d_T$  ) as well as organic material enter the hydrocyclone overflow and are only occasionally monitored by manual sampling (discontinuously) followed by laboratory analysis.

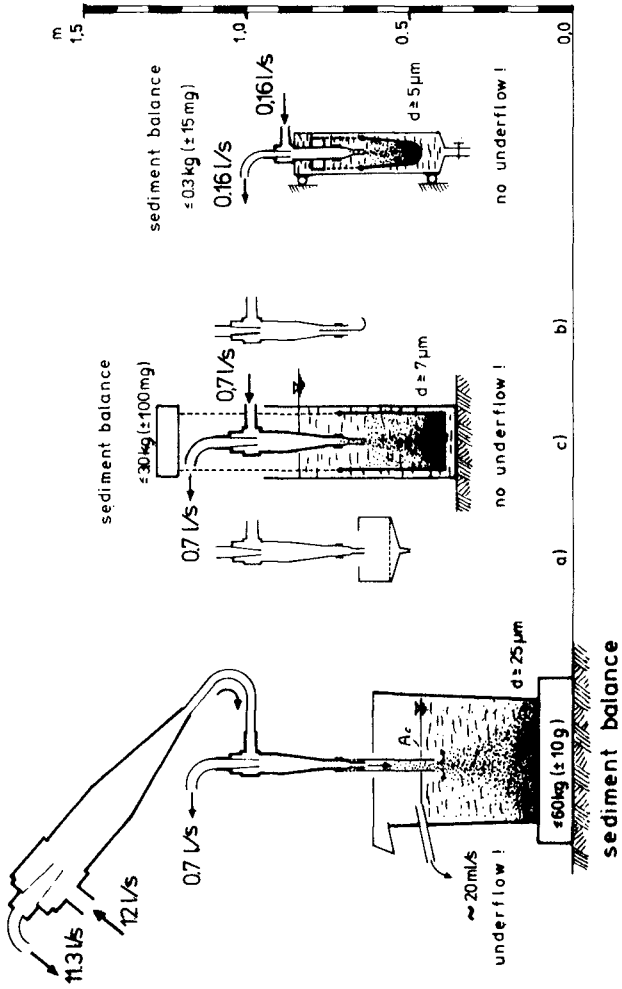
The sediment concentration for particles larger than (  $d_T$  ) is calculated as follows:

$$\bar{c} (> d_T) = \frac{\Delta G}{\Delta t \cdot Q} \quad (\text{mg/l}) \quad (1)$$

where:  $\bar{c} (> d_T)$  = mean sediment concentration for particles ( $> d_T$ ) in the time interval ( $\Delta t$ )

$\Delta G$  = weight increase in the time interval ( $\Delta t$ )

$\Delta t$  = time interval for computing mean sediment concentrations (  $\bar{c}$  ) (held constant during a sequence of measure-



**STAGE I                      STAGE II                      STAGE III**

Fig. 3 : most significant stages ( I to III ) of the development of the sediment transport measuring system

	COMPONENTS OF OPTIMIZATION	TENDENCY min, max.	dim.	STAGES OF DEVELOPMENT		
				stage I	stage II	stage III
instrument.	1.1 geometry (length, diameter)	x	[m]	10 / 0.2	0.6 / 0.1	0.3 / 0.05
	1.2 weight	x	[kg]	200	60	10
operation	2.1 energy	x	[KW]	≈ 10.0	≈ 1.0	≈ 0.5
	2.2 discharge ( feed )	x	[ l/s ]	12.0	0.70	0.16
	2.3 pressure	x	[ bar ]	5.0	3.5	2.5
	2.4 reliability	x				
	2.5 maintenance costs	x				
	2.6 degree of automation	x				
separation	3.1 separation mesh (cut point)	x	[ μm ]	25	7	5
	3.2 volume split ratio [ $\alpha = Q_f / Q_z$ ]	x	—	≈ 1.500	≈ 1.0	≈ 1.0
	3.3 moss recovery [ $\Theta = M_0 / M_z$ ]	x	—			
accuracy	4.1 time steps of measurement	x	[ min ]	5	0.5	0.5
	4.2 weight increase	x	[ g ]	min. ± 10.0	± 0.1	max. ± 0.02
	4.3 accuracy of measurement	x	[ h ]	≈ 5	≈ 2	≈ 2
	4.4 flushing intervals	x	[ min ]	≈ 5	≈ 2-5	≈ 1
	4.5 flushing duration	x				

Table 1 : Optimization of the sediment transport measuring system S E D I W A

ments, however may be arbitrarily chosen up to the maximum filling - time of the settling tank )

Q = magnitude of the sample discharge

According to the particular stage of development I to III, these measurement parameters vary. Beyond stage II, wet weighing must take account of buoyancy forces (compare with Table 1). The different combinations of hydrocyclone and weighing apparatus are shown to scale in Fig.3 .

### 5.3 Stage I - Trial tests with a large-scale equipment

In order to become acquainted with the handling and performance of hydrocyclones and the measuring technique as well as the variance of the particle discharges, a full-scale instrument was installed for trial tests (compare with Fig.3,I ). Owing to the present inability to control the underflow discharge of about 20 ml/s, a through-flow settling tank with a free surface was selected. With a realisable settling area (  $A_c$  ) of about 12 dm<sup>2</sup> together with the corresponding volumetric capacity (  $V \approx 40$  l ), a separation grain-size of about 25  $\mu$ m was specified. All finer particles were already eliminated from the measurements by means of an exterior large cyclone. The large sample discharge ( Q ) of about 12 l/s ensured a relatively large sediment delivery to the settling tank. Despite hydraulic related disturbances of the scale, measuring intervals of 5 minutes were possible. The test results yielded detailed information concerning the particle flux (  $d > d_T$ ,  $d_T = 25 \mu$ m ). Data was recorded by means of a simple printer.

### 5.4 Stage II - Trial tests with a mobile instrument

In order to quickly obtain information regarding the spatial distribution of sediment movements over a cross-section, the simultaneous operation of three mobile sediment measuring instruments was necessary (types due to stage II, see Fig.3 ). Corresponding considerations concerning a minimization of instruments led to a drastic reduction of the required sample discharge ( Q ) from 12 to 0.7 l/s. This was achieved by regulating the hydrocyclone underflow. Following preliminary tests with filters (stage IIa) and special valves (stage IIb), hydraulic regulation of the underflow by means of pressure control was eventually adopted. By immersing the lower part of the hydrocyclone beneath the free surface of the settling tank, the underflow (water) was completely choked. The sediment (  $> d_T$  ) escaped with negligible delay due to density currents alone. By this means, the free surface-area of the settling tank could be reduced by a factor of 10 to 3 dm<sup>2</sup>.

The improved selectivity (separation grain-size  $d_T=7\mu\text{m}$ ) obtained with the smaller sample discharge of  $0,7 \text{ l/s}$  considerably increased the measurement range in the direction of fine sediments. Owing to the reduced sample discharge, however, the sediment flux in the underflow decreased by about one-tenth. In order to maintain the same accuracy of measurements ( resolution, measurement frequency ), it was necessary to reduce the weighing range by the same factor (one-tenth).

By taking advantage of the above-mentioned instrument reductions, a completely submerged suspension of the weighing container was possible. As a result, hydrodynamic disturbances during weighing were eliminated. In addition, the accuracy of measurement could be increased by a further order of magnitude (see Table 1) by taking advantage of buoyancy forces during weighing. The weighing was carried out with high precision laboratory scales and a hand-held-computer was used for data acquisition.

With this instrument configuration, which may be termed semi-automatic, several dozen tides were monitored ( see Fig.4 ). The measurements revealed large spatial and temporal variations in sediment concentrations. Correspondingly, the filling times of the settling tank to maximum capacity also differed ( from about 0.5 to 5 hrs in the EIDER Estuary / North Sea ). Changing of the settling-tank, followed by underflow stabilization for the next period of measurement, lasted on average between about 2 to 5 minutes.

### 5.5 Stage III - Fully-automatic sediment concentration measuring instrument SEDIWA

---

The valuable experiences gained in instrument handling, precision and measured results during the development stages I and II led to a further optimisation of the equipment ( Fig.3, Stage III and Table 1 ). The long-term installation of several instruments, especially on poorly accessible and submerged mountings, necessitated a further minimisation of instruments, improved operating stability and full automation (compare with Fig's 3 and 5 ).

The selection of a mini-cyclone with a discharge capacity of  $0,16 \text{ l/s}$  reduced the separation grain-size (  $d_T$  ) to  $5 \mu\text{m}$ . Due to the new reduction in the sample discharge of about one-fifth, a corresponding increase in the weighing accuracy of around  $\pm 20 \text{ mg}$  will be necessary. This can only be justified, however, provided the hydraulic disturbances for the instrument and environment are relatively small. Owing to the fact that underflow pressure was several tenths of a bar, the hydraulic regulation of the underflow had to be abandoned. The corresponding effects of oper-

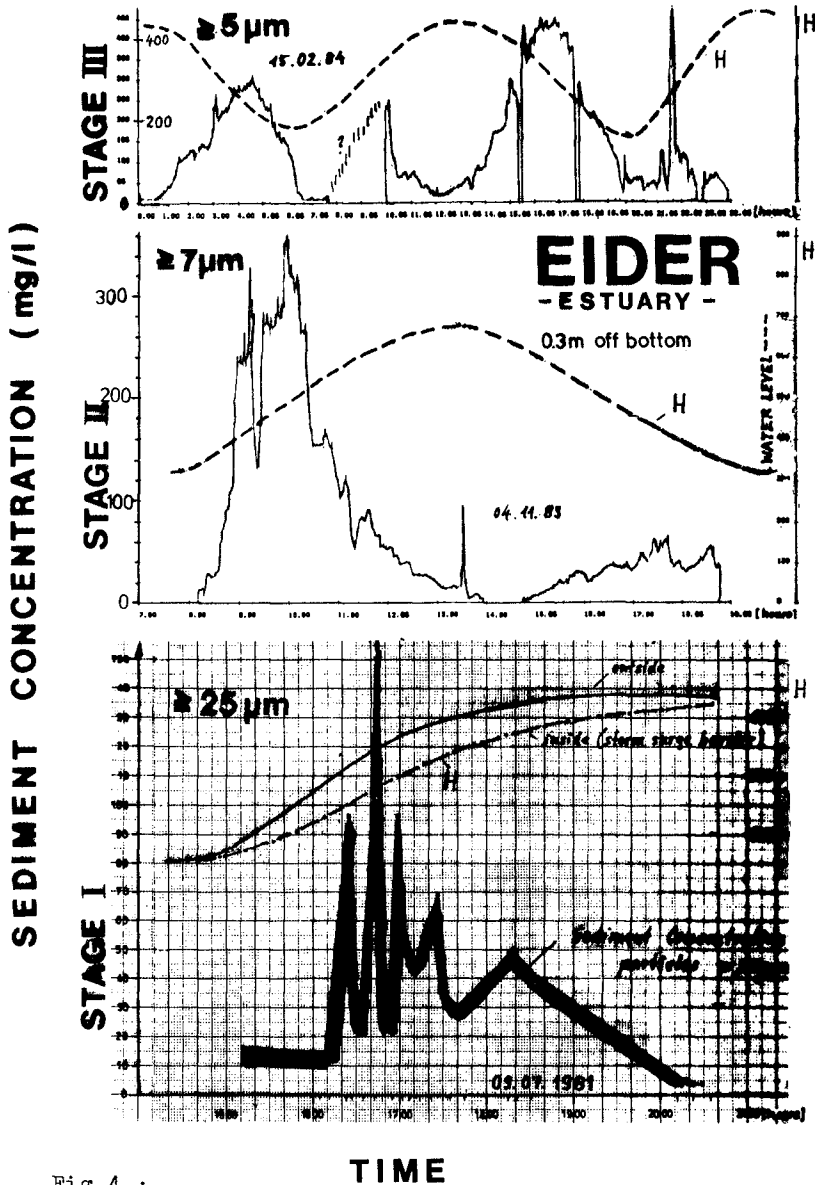


Fig.4 :  
 Simultaneous records of suspended sediment concentration and water level (tidal curve)

ating pressure fluctuations upon the several meters high water column of a free-surface buoyancy tank would adversely affect the separation process.

The necessity of including a submerged scale in a pressure-stabilized instrument configuration required a transition to a closed excess-pressure chamber in the hydrocyclone underflow. By this means, a highly sensitive underwater weighing cell ( $\pm 15 \text{ mg}$ ) could be developed and installed. The weighing container, which is about the size of a beaker, has a maximum filling capacity of approximately 200 g of sediment ( $> 5 \mu\text{m}$ ). Depending on the rate of sediment accumulation, the filling time is of the order of several hours.

Emptying of the container (compare with Fig. 5 c) is achieved by simply opening the flushing valve located at the base of the chamber. By choking the overflow, the excess pressure of about 1 bar in the chamber falls drastically. This leads to a strong flushing jet in the cyclone underflow which re-empties the full settling tank within about 1 minute. Following the flushing phase, the valve is closed again. The chamber pressure and the underflow discharge immediately stabilize and the measuring procedure resumes without delay.

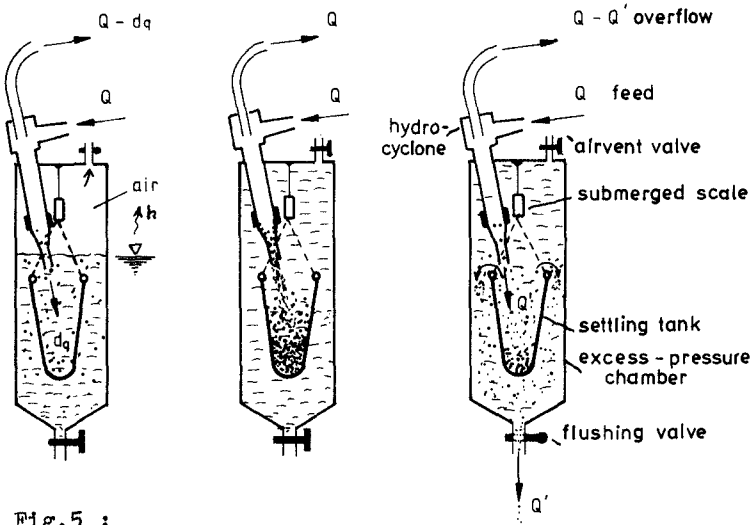


Fig. 5 :  
 a) filling ...      b) operation ...      c) flushing .. of SEDIWA  
 - submersible sediment measuring system -

For fully-automatic operation, a control unit with data acquisition is provided. Together with time and weight measurements, the magnitude of the sample discharge (in general constant) is continuously monitored by means of a discharge meter in the return-flow line behind the cyclone overflow. The calculation of sediment concentrations (according to Equation (1), section 5.2), including processing of the measured data, is achieved by means of simple software.

With this type of instrument, several series of measurements lasting a number of days have already been successfully carried out in the absence of personnel (compare with Fig.4). The continuous recording over several tides provided valuable information for the subsequent analysis of the wide-ranging data relating to instationary sediment movement.

#### 6. MERITS OF SEDIWA AND CONCLUSIONS

1. Flow sampling, i.e. delivery of the total material to be investigated (water with contents) for further detailed examination
2. Continuous extraction, i.e. the possibility of detecting special events (eg. detection of transient peaks)
3. Sediment sample collector, i.e. availability for subsequent (eg.) sediment-petrographical analysis
4. Accumulative weight method, i.e. especially for temporally dependent analysis and evaluation (integration, balances), the relative influence of errors becomes increasingly less
5. Minimum time discretization, i.e. optimum suitability to highly instationary sediment movement
6. Absolute measurement technique, i.e. recordings in weight / unit volume (avoids calibration)
7. Larger range of material, i.e. weighing of all particles greater than  $d_{\pi} = 5 \mu\text{m}$  (separation grain-size of the hydrocyclone = cut point)
8. High precision, i.e. by minimising the sample discharge ( $Q$ ) and with pressure-stable isolation of the hydrocyclone underflow, including weighing unit as well as weighing under buoyancy, a highly sensitive weighing cell may be employed
9. Immersed installation, i.e. minimisation of support and serving facilities
10. On-line measurement technique, i.e. as a consequence of cyclonisation followed by immediate submerged weighing of sediment, complete availability of the com -



puted concentration values only a few seconds after sampling (also later, as desired)

11. Full automation, i.e. hydraulic delivery technique, reduction of mechanical parts to only a flushing valve, waterproof electrics and electronics, presence of personnel not required

## 7. ACKNOWLEDGEMENTS

This work was carried out as part of two coastal engineering research programs of the Landesamt für Wasserhaushalt und Küsten Schleswig-Holstein by request of the Ministry of Food, Agriculture and Forests. Support for this study was provided by the KFKI (Kuratorium für Forschung im Küsteningenieurwesen) and the BMFT (Bundesministerium für Forschung und Technologie), which is greatly acknowledged by the author. The firm ME (Meerestechnik + Electronic) contributed to this work by optimizing the technical layout of the prototype SEDIWA.

## REFERENCES

- (1) Christiansen, Hermann , 1974 - Über den Transport Suspenderter Feststoffe in Ästuarien am Beispiel der Elbmündung bei Neuwerk. Hamburger Küstenforschung Heft 28
- (2) Göhren, Harald , 1973 - Ein automatisches Schwebstoff-Dauermeßgerät für den Einsatz im Wattenmeer und in Brandungszonen. Die Küste, Heft 24, S.8-19
- (3) Renger, Eberhard ,and Partenscky, H.-W., 1980 - Sedimentation processes in tidal channels and tidal basins caused by artificial constructions. 17th Int. Conf. on Coastal Engineering, Proc.Vol. II, pp 2481 - 94
- (4) Renger, Eberhard , 1982 - Dauermessungen des suspendierten Feststoffgehaltes im Tidegebiet mit Hilfe von Durchlaufzentrifugen. Int. conf. on marine research, ship technology and ocean engineering, IMT 82-418, Hamburg
- (5) Trawinski, Helmut , 1976 - Theory, applications and practical operation of hydrocyclones. Engineering and Mining Journal (E/M), pp 115-127
- (6) Trawinski, Helmut , 1981 - Sind die Anwendungsgrenzen des Hydrozyklons konstruktiv zu erweitern ? - Sonderdruck aus MM - Maschinenmarkt, 87.Jahrgang, Heft 34 und 52 (S. 684-87, 1069-72)

## CHAPTER ONE HUNDRED FORTY

### EFFECT OF RIP CURRENT BARRIER ON HARBOR SHOALING

by

Tamio O. Sasaki\*, M. ASCE and Hiroshi Sakuramoto\*\*

#### ABSTRACT

Prototype experiments on rip currents and sediment transport around structures were conducted at two fishery harbors on microtidal high energy beaches facing the Pacific Ocean. The purpose of the experiments was to examine the performance and mechanism of rip current barrier structures on harbor shoaling. Based on the results of five experiments, the wave breaker heights during which varied from 1.1 m to 3.0 m, it is concluded that shore-parallel rip current barriers are effective if their length is greater than the surf zone width and if they are located outside the surf zone. When the above conditions are satisfied, the rip current barrier is a cost-effective measure against shoaling of small craft harbors.

#### 1.0 INTRODUCTION

Two case studies are presented which demonstrate the mitigating effect of rip current barrier structures on the shoaling of small craft harbors. A rip current is a fast and narrow current that carries sediment offshore. One of the major reasons why harbor breakwaters and jetties cause beach erosion on adjacent beaches, offshore sediment loss to form rip head bars, and shoaling inside of harbors is the formation of rip currents induced by and adjacent to the structures (Fig. 1a). The construction of sand traps is often adopted as a protection measure where the longshore drift dominates, (e.g., at Channel Island Harbor, Bruno and Gable, 1976; Pointe Sapin Harbor, Pratte et al., 1982). However, the detailed functioning of a sand trap is not well understood, and a large amount of maintenance dredging may be necessary.

The present paper focuses on the role of rip currents in the shoaling process, based on field observations. Then the rip current barrier concept to block rip currents is presented as a possible cost-effective solution (Fig. 1b). The study sites, Taito Katagai Fishery Harbors, are respectively located on the southern end and middle of the Kujukuri Coast, facing the Pacific Ocean (Fig. 2).

---

\* Chief Engineer, INA Civil Engineering Consultants, Co. Ltd., 22-1 Suido-cho, Shinjuku-ku, Tokyo, 162 Japan.

\*\* Senior Engineer, INA Civil Engineering Consultants, Co. Ltd.

## 2.0 STUDY SITES AND RESULTS

Kujukuri Coast is a 55 km-long, very shallow coast bounded at both ends by eroding sea cliffs, Byobugaura and Taito Point (Fig. 3), 10 km and 2 km long, respectively. The average beach slope up to the 20 m depth is about 1/100. The dominant drift of sand is from both ends to the middle of the coast (Sunamura and Horikawa, 1977). The beach consists of fine sand (0.2 - 0.3 mm). The tidal range is 1.0 - 1.5 m.

## 2.1 Taito Fishery Harbor

An extreme case of harbor shoaling occurs at Taito Fishery harbor (Figs. 3 & 4). Taito Fishery Harbor originally had two shore-normal breakwaters that extended about 150 m seaward. As seen in Fig. 4, the harbor was totally filled with sediment soon after construction. To recover harbor functioning, extension of the breakwaters and construction of "wing-like" breakwaters which stop rip currents from flowing directly offshore was tried (Figs. 5 & 6). As a result, accretion at the root of the north breakwater has increased and sediment shoaling has been mitigated.

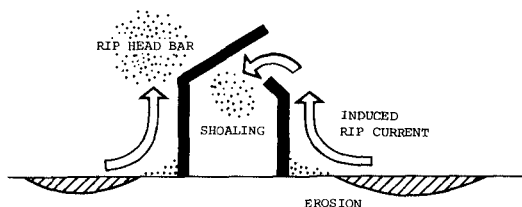


Fig. 1a Schematic diagram of induced rip current and harbor shoaling due to presence of a breakwater.

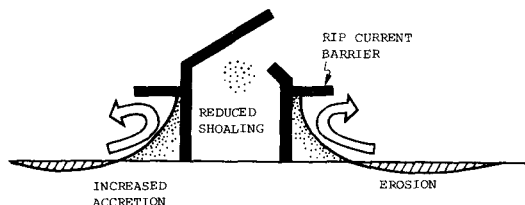


Fig. 1b Schematic diagram of a rip current barrier. Accretion at the feet of the breakwaters increased and shoaling in the harbor decreased.

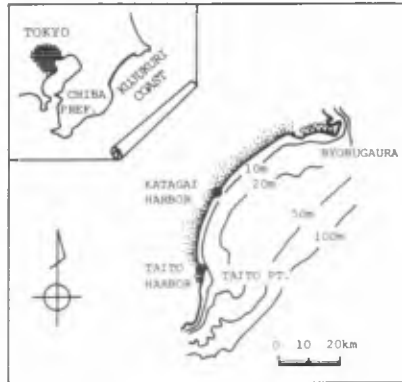


Fig. 2 Location map of Kujukuri Coast, and Taito and Katagai Fishery Harbors.



Fig. 3 Overview of Taito Fishery Harbor and the vicinity to the northwest.



Fig. 4 Taito Harbor totally filled with sediment.



Fig. 5 Recovered Taito Harbor after rip current barrier construction.

### Field Observation of Rip Currents

Observations of the rip currents at the site were conducted in November and December 1979, and January 1980. The breaker heights were 3.0, 1.1 and 1.7 m, respectively. The circulation patterns shown in Fig. 7 were obtained from photographs of successive dye patch dispersion patterns (Fig. 8). The photographs were taken with a Hasselblad 500EL camera mounted on a hovering helicopter. A total of 10 - 20 kg of fluorescent dye was released at 6 - 12 points within and outside of the surf zone.

Several very regular nearshore circulation patterns and barrier-induced rip currents were found on the north side of the harbor during the Dec. 1979 and Jan. 1980 experiments (middle and bottom of Fig. 7). However, at the east side, a typical blocked rip current as shown in Fig. 1b was not found except in the Jan. 1980 experiment, due to the size and orientation of the south rip current barrier. In CASE-791124, the eastern rip current barrier was ineffective, and thus a rip current developed seaward. The wave height was large in this case, so that most of the harbor structures were inside the surf zone.

### 2.2 Katagai Fishery Harbor

Another example is Katagai Fishery Harbor, located about 30 km north of Taito harbor. Sediment transported alongshore on the neighboring beaches arrives at both sides of the harbor. Therefore, the entrance jetties had to be extended year by year before 1974 due to accretion (Fig. 9). The length of the jetties reached 600 m; the total entrance channel length is about 1 km. This harbor was originally built to have a common entrance with the Sakuta river. The annual rate of shoreline advance was about 6 m/year at both sides of the jetties. The annual rate of accretion estimated by Sunamura and Horikawa (1977) for the central part of the Kujukuri coast is  $494,000 \text{ m}^3/\text{year}$ .

Figure 10 shows the change in nearshore topography from 1974. Major accretion occurred at depths less than 4 - 5 m; however, significant accretion took place deeper than 6 - 7 m as well. Angled plan shape breakwater construction started in 1975. The breakwaters are connected to the jetties by piers. This structure plan shape was designed based on results of laboratory experiments to maintain the entrance by a flushing. (A similar concept and shape appear in Maza et al. (1977) as a convergent jetty.) This angled breakwater did not give a good solution under prototype conditions. As shown in Fig. 10, large accretion occurred on the lee side of the breakwater and thus the amount of required maintenance dredging increased.

### Field Observation of Rip Current and Sediment Transport

Field observations of the nearshore current and sediment transport were conducted on October 1978 and March 1980 to study the underlying mechanism of the barrier (Table 1) before and after the rip current barrier construction. Several plan shape alternatives were compared by numerical modeling of the nearshore current system (Sasaki, 1975). As a result, rip current barriers as seen in Fig. 11 were finally adopted.

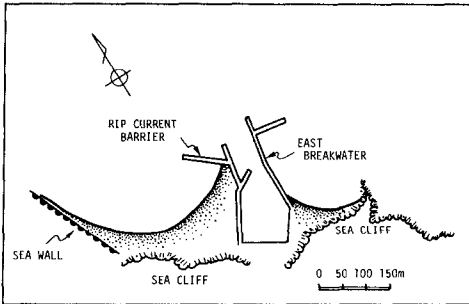


Fig. 6 Plan of Taito Harbor.

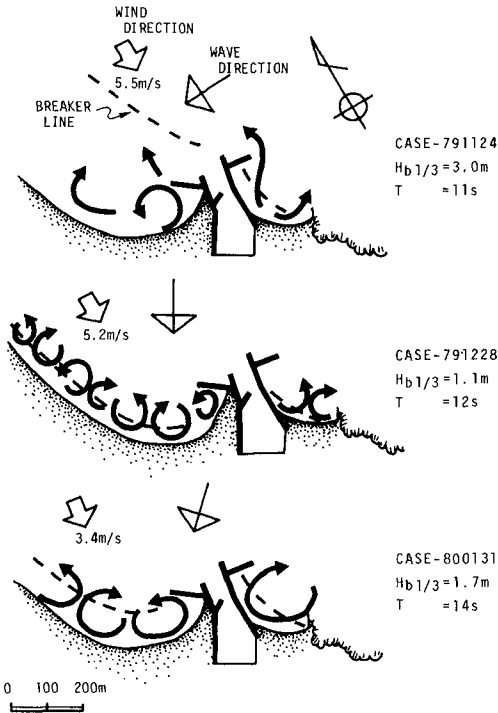


Fig. 7 Nearshore circulation patterns in the vicinity of rip current barriers.

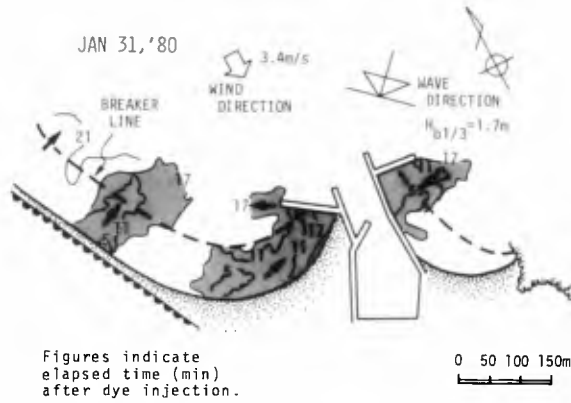


Fig. 8 Dispersion of dye patches around rip current barriers.

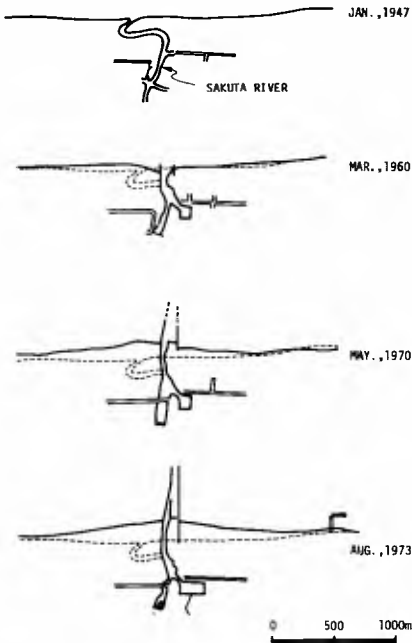


Fig. 9 History of shoreline evolution associated with jetty construction at Katagai Fishery Harbor.



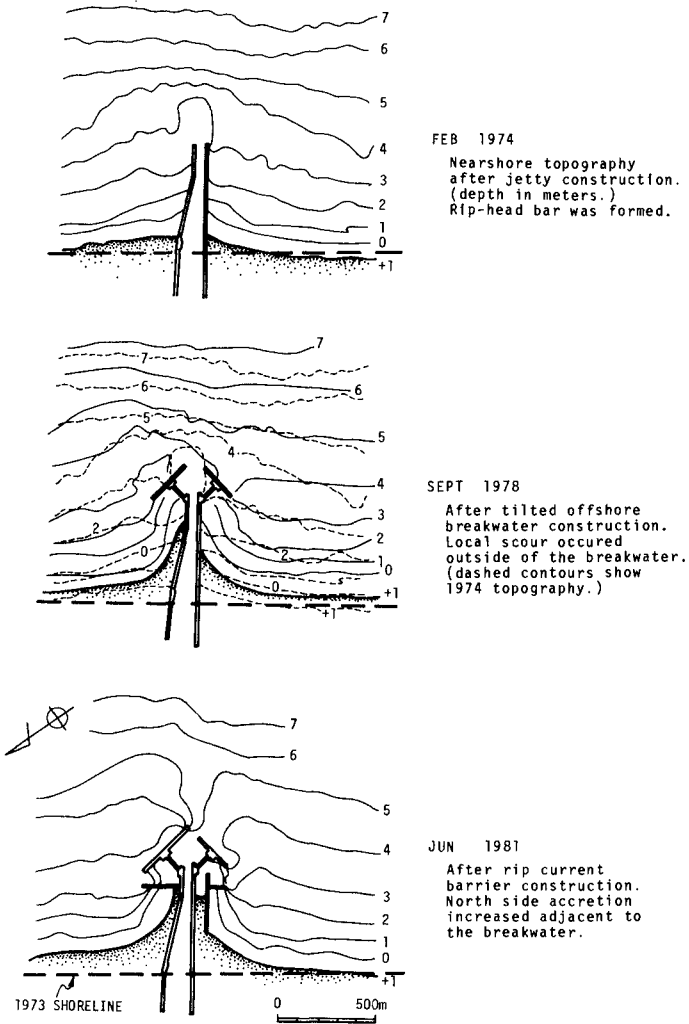


Fig. 10 History of nearshore topography around jetties and breakwaters after 1974.

Table 1 Wind and wave climates of field observations at Katagai Harbor.

Date	Time	Wind Direction	Wind Speed (m/s)	Wave Direction	Wave Period (s)	Signif. Breaker (m)	Surf Zone Width (m)
13 Oct. 1978	7:00	NNW	2.5	N73°E	9.6	1.5	300
	10:00	N	3.4	N75°E	10.3	1.6	300
	17:00	N	1.7	N76°E	10.0	1.8	400
14 Oct. 1978	6:30	NNW	2.4	N75°E	10.8	1.2	150
	12:30	ENE	5.0	N74°E	9.5	1.3	130
	15:30	NE	1.4	N75°E	9.6	1.3	130
25 Mar. 1980	13:10	ENE	7.2	S65°E	9.8	1.6	280

Rip currents were observed by a tethered balloon system (Sasaki et al., 1976) on 14 Oct. 1978. The dispersion of dye patches was obtained from time-lapse photography (Fig. 12). The associated current velocity is given in Fig. 13. Dye released at the foot of the north jetty moved along the jetty, then reached the harbor entrance. The dye patches on the south side also moved with the rip current then formed rip heads underway to the harbor entrance. The maximum velocity of the rip currents was 40 - 50 cm/s. The dye northward from the injection point dispersed in the bore.

Sediment movement was observed with fluorescent tagged sand tracer. One thousand kg of tracer was injected on both sides of the jetties, and samples were taken 2, 4, 6, 8, and 24 hr after injection. The distribution of tracer numbers (Fig. 14) shows very similar patterns to the current (Fig. 13). The tracer study was conducted the day before the current measurement; however, the incident wave directions were almost the same on 13 and 14 October (Table 1). The maximum drift velocities on both sides of the jetties were 7 cm/s and 1 cm/s, respectively.

One major empirical conclusion of this prototype experiment is that the sediment movement pattern is predictable based on current measurements. Thus, current measurement were conducted to determine the sediment movement after the construction of the rip current barriers.

#### Current around Rip Current Barrier

Nearshore current measurements were made on 25 March 1980 by using a helicopter-mounted camera instead of the balloon. Fluorescent dye was released at 7 points, 3 kg at each point in the surf zone and 2 kg at each point outside the surf zone. Figure 15 shows the dispersion of the dye patches around the vicinity of the rip current barriers. The rip current barriers block the rip currents effectively and produce forced circulation cells (Fig. 16). The velocity field is given in Fig. 17.

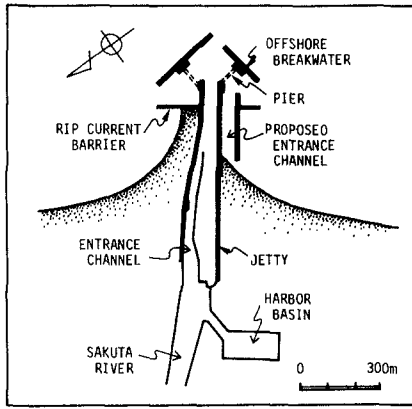


Fig. 11 Plan of Katagai Harbor. Harbor basin is located about 1 km inland from the entrance.

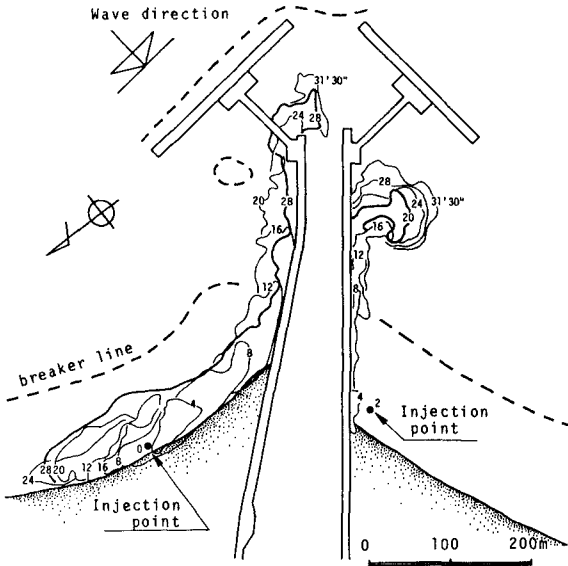


Fig. 12 Dispersion of dye released at the feet of the jetties. Numbers denote elapsed time in min. after injection. Rip heads are outlined.

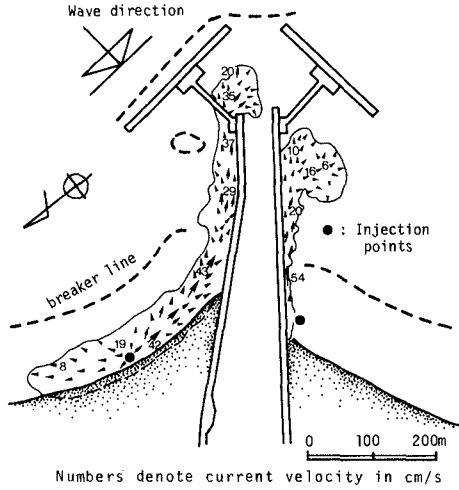


Fig. 13 Velocity distribution of rip currents derived from dye patch movement on 14 Oct. 1978.

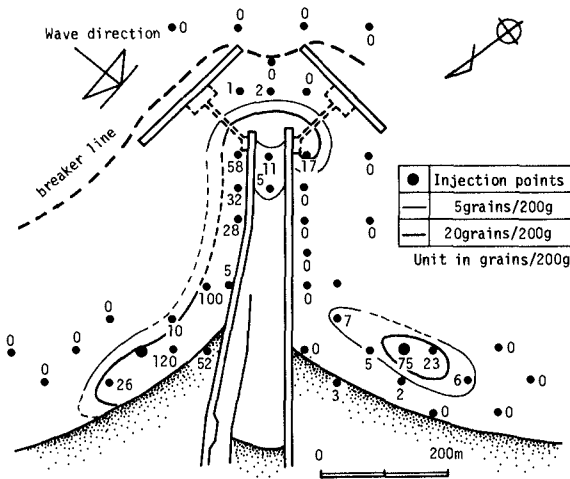


Fig. 14 Tracer movement 6 hr after injection on 13 Oct. 1978. Tracer entered the channel mouth.

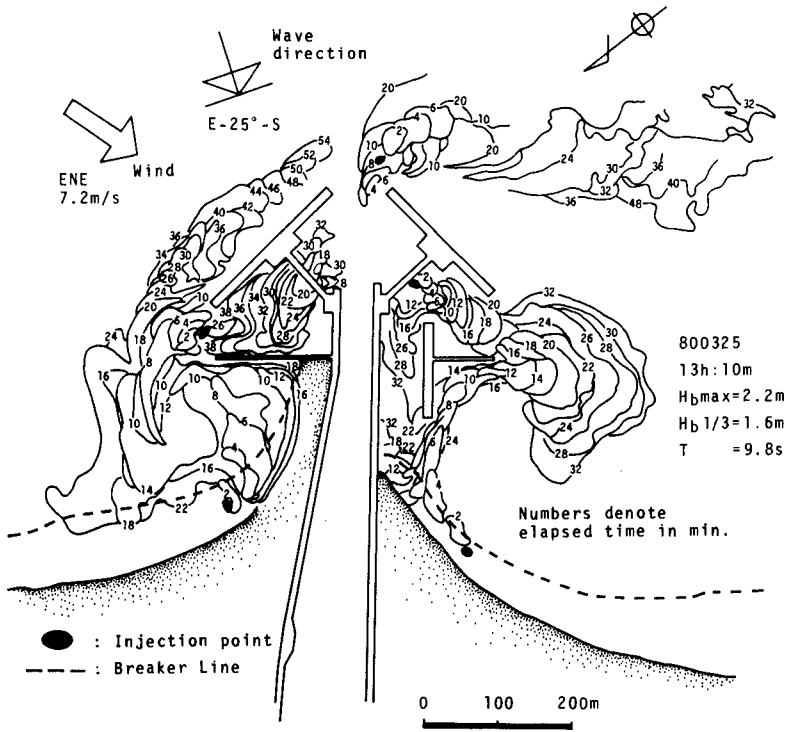


Fig. 15 Dispersion of dye patches around rip current barriers.

Because the south rip current barrier is short compared with the north barrier, the effectiveness of the barrier is limited. The shore-normal structure attached to the barrier is a portion of the proposed jetty to the separate harbor entrance channel from the Sakuta river.

#### Effect of Rip Current Barrier on Mitigation of Harbor Shoaling

Sounding charts were compared for surveys taken before and after rip current barrier construction (Fig. 18). General accretion is seen offshore and north of the harbor. On the other hand, an eroded area appears on the south side of the harbor. The offshore accretion may be the result of rip head bar formation during storms. Several sounding charts (e.g., bottom of Fig. 10) show huge rip channels. This tendency is consistent with the action of angled breakwaters and indicates that rip current barriers of this size are not effective in storms.

In the lee of the north barrier, accretion continues to take place, and thus the rate of accretion at the harbor entrance is decreasing. At the south, due to the geometry of the barrier, the mitigation effect is imperfect, and further extension of the barrier is deemed necessary.

### 3.0 CONCLUDING DISCUSSION

Prototype experiments on the rip currents and sediment transport at two fishery harbors on the Kujukuri coast, Japan, were conducted to test the effect of rip current barriers for mitigating shoaling. Rip currents are always induced along shore-normal structures, and they carry sediment offshore to form rip head bars as well as deposit sediment inside harbors to cause harbor shoaling.

To mitigate harbor shoaling and sediment loss offshore, some control of rip currents is needed. A rip current barrier is defined as a shore-parallel structure that blocks the path of a rip current. It reduces the current velocity and turns the current direction shoreward to form a forced cellular circulation (Fig. 1b).

Field observations of the breakwater-induced rip currents at Taito Fishery Harbor under conditions of a 3 m breaker height suggest that if the barrier is outside the surf zone, it will be effective in blocking rip currents (Fig. 7). Field observations of induced-rip currents and sediment transport without a rip current barrier and of rip currents with a rip current barrier carried out at Katagai Fishery Harbor suggest that the rip current barrier is effective only under moderate wave conditions. Rip head bars under storm conditions were still formed after the rip current barrier construction.

A rip current barrier can be regarded as a cost-effective solution to mitigate harbor shoaling; however, to make it a final solution, deeper and longer structures to act as a total sand trap are required. The minimum length of a proposed rip current barrier should be greater than the radius of the induced design nearshore circulation cells, that is, approximately the surf zone width. In the case of Katagai Fishery Harbor, rip current barriers would be effective under wave conditions of 2 - 3 m breaker wave heights, which at this beach correspond to a 200 to 300-m surf zone width.



Fig. 16 Rip current barriers at Katagai Fishery Harbor. Arrows show measured rip currents.

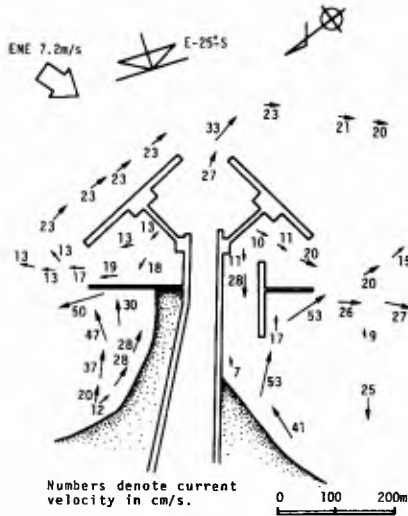


Fig. 17 Flow field derived from dye dispersion.

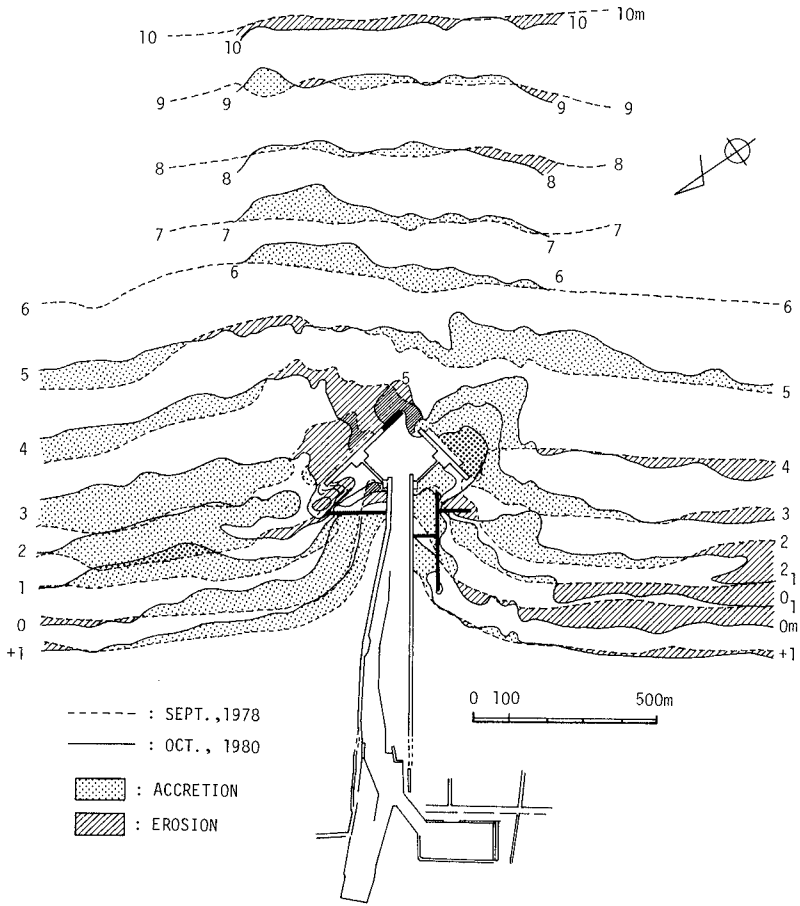


Fig. 18 Comparison of bottom contours before and after rip current barrier construction.



Because the Kujukuri coast has an exceptionally gentle beach slope, it would be very expensive to build barriers extending to the deep offshore. For such situations, an "island-type" fishery harbor has been proposed, where the harbor is located far offshore like an island and connected to the mainland by a bridge (Sakai, 1984). However, rip current barriers are feasible on moderately sloped or steep beaches.

#### 4.0 ACKNOWLEDGEMENTS

This study was performed as part of a contract with the Chiba Prefectural Government. The authors acknowledge permission to publish given by the Fishery Harbor Division, Fishery Department of Choshi Fishery Harbor Office of Chiba Prefecture, and T. Sugawara, Chief of the Second Fishery Engineering Laboratory, Agricultural Engineering Research Station, Ministry of Agriculture, Forestry and Fishery. Also thanks are due to proofreading by Dr. N.C. Kraus of the Nearshore Environment Research Center, Tokyo.

The findings in the present paper are not to be construed as an official Chiba prefectural government position.

#### REFERENCES

- Bruno, R.O. and C.G. Gable (1976): Longshore transport at a total littoral barrier, Proc. 15th Coastal Eng. Conf., ASCE, 1203-1222.
- Bruno, R.O., G.M. Watts and C.G. Gable (1977): Sediments impounded by an offshore breakwater, Proc. Coastal Sediments '77, ASCE, 1006-1025.
- Horikawa, K. and T. O. Sasaki (1972): Field observations of nearshore current system, Proc. 13th Coastal Eng. Conf., ASCE, 635-652.
- Maza, J.A., M.L. Munoz and M. Porraz (1977): Jetties studies contribution, Proc. Coastal Sediments '77, ASCE, 248-266.
- Pratte, B.D., D.H. Willis and J. Ploeg (1982): Harbor Sedimentation-comparison with model, Proc. 18th Coastal Eng. Conf., ASCE, 1119-1126.
- Sakai, I. (1984): A proposal on island-type fishery harbor, J. Japan Soc. Civil Eng., JSCE, 69 (4), 31-35.
- Sasaki, T.O. (1975): Simulation of shoreline and nearshore current, Proc. Civil Eng. in the Oceans/III, ASCE, 179-196.
- Sasaki, T.O., K. Horikawa and S. Hotta (1976): Nearshore current on a gently sloping beach, Proc. 15th Coastal Eng. Conf., ASCE, 626-644.
- Sunamura, T. and K. Horikawa (1977): Sediment budget in Kujukuri coastal area, Proc. Coastal Sediment '77, ASCE, 475-487.

## CHAPTER ONE HUNDRED FORTY ONE

### SHORELINE CHANGE AT OARAI BEACH: PAST, PRESENT AND FUTURE

Nicholas C. Kraus<sup>1</sup>, Hans Hanson<sup>2</sup> and Soichi Harikai<sup>3</sup>

#### ABSTRACT

Large breakwaters and groins are being constructed at Oarai Harbor, Japan. As a result the beach is significantly deforming. The first part of this paper documents past and recent shoreline change at Oarai. The general characteristics of the offshore waves, breaking waves, and longshore current pattern are described and used to explain qualitative features of the observed shoreline change. The second part presents results of numerical simulations of shoreline change at the site which occurred over different time periods. The model includes three sources of wave diffraction, a rigorous formulation of the seawall boundary condition, and sand bypassing at groins. The modeling of historical shoreline change was reasonably successful. As an exercise in investigating problems associated with prediction, the model was used to forecast the shoreline position at the site five years from now. The prediction of the wave history was the main problem encountered. A simple intuitive method was devised to estimate the probable range in variation of the wave history, and the results are discussed in connection with the shoreline forecast.

#### 1. INTRODUCTION

Since 1977, the fishing harbor at Oarai, Ibaraki Prefecture, Japan, has been undergoing expansion for conversion to a ferry and cargo port, to be completed around 1990. Figure 1 shows past and planned construction. Extension of the harbor breakwater and construction of the large detached breakwater for improvement of navigation have resulted in considerable changes along the sandy beach to the south.

- 
1. M. ASCE; formerly, Senior Engineer, Nearshore Environment Research Center, Tokyo, Japan; presently, Research Physical Scientist, Coastal Engineering Research Center, U.S. Army Engineer Waterways Experiment Station, P.O. Box 631, Vicksburg, MS 39180, USA.
  2. Lecturer, Department of Water Resources Engineering, Univ. of Lund, Fack 725, Lund S-220-07, Sweden.
  3. Research Engineer, INA Civil Engineering Consultants Co., Ltd., 22-1 Suido-cho, Shinjuku-ku, Tokyo 162, Japan.

Oarai Harbor suffers from chronic and troublesome accretion of sediment. To describe it, we can do no better than to quote from an article by Hiroi (1921): "A small harbor at Isohama (presently Oarai), in Ibaraki Prefecture, built in 1911 - 1916, is an instance of failure to keep off the inroad of drifting sands. The breakwaters (see Fig. 1 here), when built, had enclosed a water surface of about 30 acres, nearly all of which is now dry ground. The entrance, which is 240 ft in width, had a depth of 13 ft at the low water of ordinary spring tide. The prevailing winds are from NE, raising waves which cause the travel of sand and shingle along the beach lying to the east of the harbor. Accumulation of the sand began to take place as the breakwaters progressed, and by the time the latter were completed, nearly 370,000 cu. yds. of sand were found deposited in the harbor, which makes the yearly inroad of sand 74,000 cu. yds. The harbor has since been entirely invested by sand . . ."

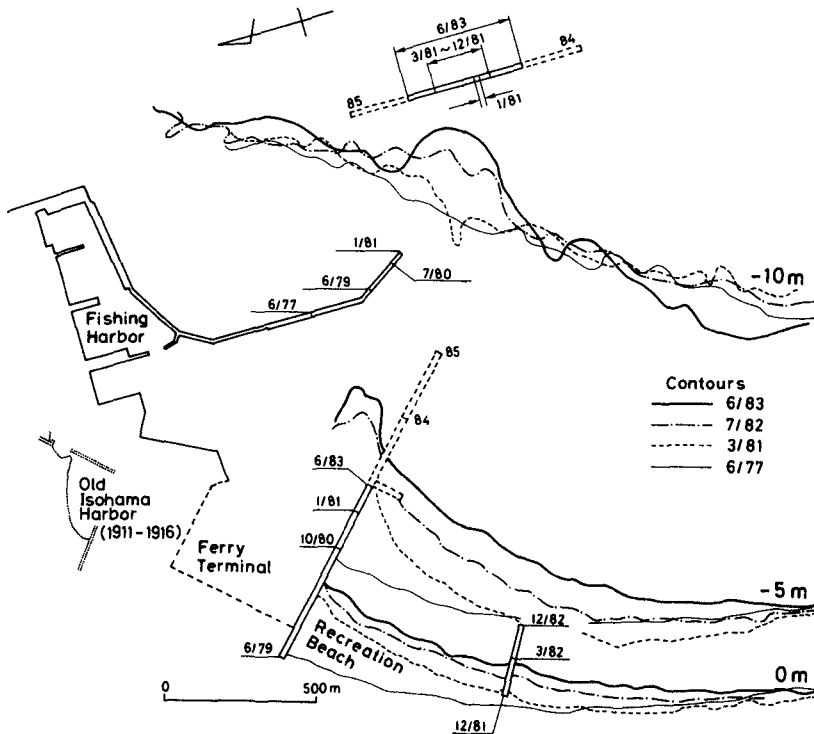


Fig. 1 Construction and contour change at Oarai.

In modern times, prior to construction of the detached breakwater and short groin, long-term sediment-related problems took the form of harbor shoaling and rapid shoreline advance at the long groin, together with erosion along the beach 1 to 3 km to the south of the harbor. Construction of the detached breakwater and short groin (Fig. 2) appear to have had a positive effect in reducing the rate of shoreline advance near the long groin. An apparent negative effect has been the gradual movement of the area of maximum erosion further south. The area of maximum erosion is presently located about 3 km to the south of the long groin, along what had once been a fairly wide sandy beach. The beach within 5 km to the south of the harbor contains two large seawalls (north seawall, approx. 1.5 km long; south seawall, 800 m long), two large impermeable groins, and numerous groups of armor blocks positioned in rows along the beach to provide shore protection and footing protection for the seawalls.

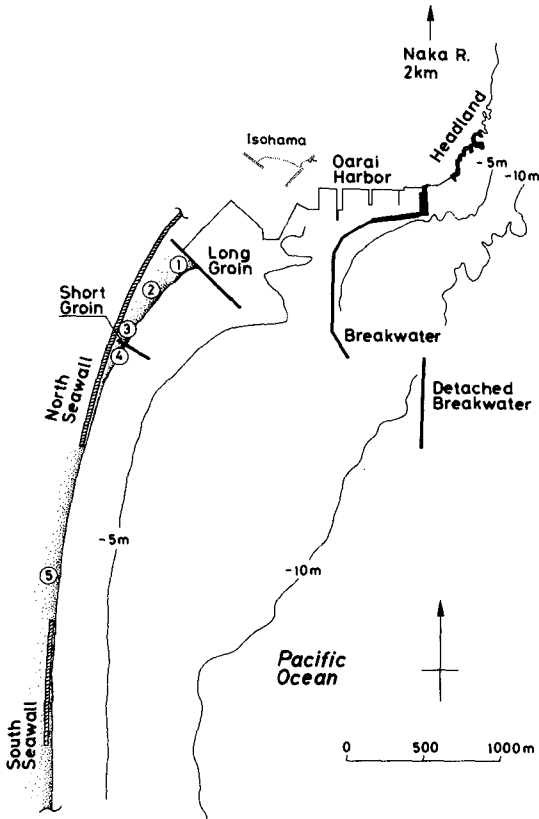


Fig. 2 Oarai harbor and the beach to the south.

The present paper, a continuation of the study of Kraus & Harikai (1983), consists of two parts. The first part presents a case study documenting the wave climate, currents, and past and present shoreline positions. The general features of the long-term shoreline change are then related to construction of the harbor breakwaters and groins. The second part presents results of simulations of the shoreline change.

## 2. CASE STUDY

### 2.1 Background

Oarai Harbor lies on a north-south-oriented coast about 150 km north of Tokyo. The area has served fishermen since ancient times owing to the shelter given by the rocky Oarai Headland against the predominant NE and ENE incident waves. The harbor has a long history of sediment shoaling. Hiroi (1921) and Ijima et al. (1961) report the complete burial of early harbor structures shortly after their construction in 1916 (Fig. 1). Using radioactive tracers, Ijima et al. (1961) found that a large portion of the infiltrating sand comes from the discharge of the Naka River, 2 km to the north. Through a series of hydraulic model experiments, Arakida et al. (1978) concluded that sand is also transported north toward the harbor due to the circulation cell produced by diffraction at the harbor breakwater tip (see also Mizumura, 1982).

### 2.2 Waves

The Oarai Harbor Management Office operates an ultrasonic wave gage and a strain gage, located at a depth of 20 m and connected to shore by cable. The strain gage, which measures the wave direction, does not function if the significant wave height falls below about 40 cm. Statistics for 100 waves are computed and recorded automatically at 2-hr intervals. Figure 3 gives a histogram plot of the frequencies of the significant wave height, direction, and energy flux for a 4-yr period.

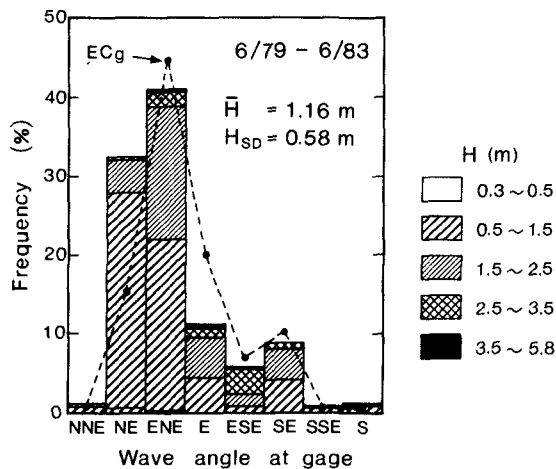


Fig. 3 Wave height, direction, and energy flux ( $EC_g$ ).

A wave data set covering four years at 6-hr intervals was formed from the records. This data set, termed the RDS (Raw Data Set) consists of triplets of values of the significant wave height, direction, and period ( $H$ ,  $\theta$ ,  $T$ ). The RDS contains gaps due to instrument down-time and limitations of the strain gage. For the numerical modeling, a data set without gaps was required. This data set, termed the CDS (Complete Data Set) was fabricated by first separating the available data from the RDS by month, giving four sets of 120 triplets, including blanks, for a 30-day month. Values were then randomly selected from the triplets available in the four sets for each month, and the gaps filled. The random selection and placement was done by computer and the results slightly 'cleaned' by hand. The respective distributions of  $H$ ,  $\theta$ , and  $T$  of the CDS closely approximate those of the RDS.

As part of the NERC project (Horikawa and Hattori, 1984), the breaking wave height was measured at five locations alongshore (circled Nos. 1-5 in Fig. 2). Measurements were made weekly for periods of about 30 months (Nos. 1, 2, 3) and 18 months (Nos. 4, 5) between May 1980 and Dec. 1982. The significant breaking wave height,  $H_b$ , was measured by sighting over a graduated staff placed at the mean water shoreline; the average of ten of the higher waves was used. The frequency distributions of the average long-term breaking wave height at the five stations is shown in Fig. 4. The frequency of smaller wave heights increases with approach to the long groin, i.e., with penetration into the wave shadow zone produced by the headland and harbor structures.

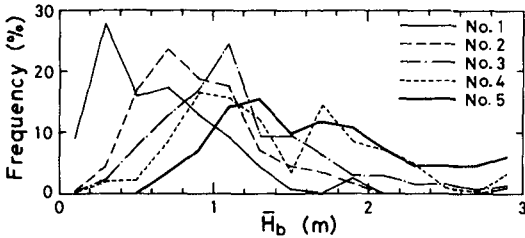


Fig. 4 Frequency distributions of significant breaking wave height alongshore (locations given in Fig. 2).

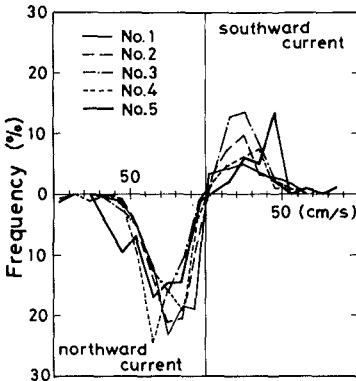


Fig. 5 Frequency distributions of longshore current magnitude alongshore.

### 2.3 Longshore Current and Sand Movement

The direction and speed of the longshore current were measured with floats, performed together with measurement of the breaking wave height. The frequencies according to direction are shown in Fig. 5. The longshore current is directed more often to the north than to the south and this tendency increases with approach to the long groin.

Waves incident at the site, arriving mainly from the northern sector, should produce a current moving to the south. The observed northward-moving longshore current is evidence of the large circulation cell produced by the headland and harbor structures. At some location near the edge of the diffraction shadow zone on the beach, the current reverses direction: at this location the beach will erode. The area of erosion is expected to move south with enlargement of the shadow zone due to extension of the detached breakwater. The northward-moving longshore current weakens deep inside the shadow zone, and sand is deposited there.

### 2.4 Shoreline Change

Shoreline positions on survey charts were digitized at 25-m intervals for plotting, analysis, and use in the shoreline simulations. The shoreline positions measured in summer and winter surveys are displayed in Figs. 6a & b. It is seen the shoreline near the long groin has steadily advanced, independent of season, if the interval of one year is selected as the time scale. Figure 6c shows the shoreline position during the four seasons of 1982. Although a general trend for accretion near the long groin is observed, the pattern of shoreline change is masked by short-term fluctuations such as those caused by sequences of storms and calm weather, and by changes in wave direction.

From Figs. 6a & b, it is seen that the north seawall served an important function in protecting the residential area behind it during the 1970's. With construction of the long groin (which blocks the northward-moving littoral drift) and extension of the harbor breakwater and detached breakwater (which increases the area of the diffraction zone where sand will be deposited), an expansive sandy beach has formed in front of the seawall. In contrast, on a recent inspection of the site in April 1984, the beach approximately 3 km south of the long groin was found to be severely eroding. Rubble mound blocks and the 800-m long south seawall in this area were being undercut and flanked.

Figure 7 plots the mean rate of change of the shoreline position for surveys taken before and after start of construction of the detached breakwater, based on 17 and 13 surveys, respectively. After start of construction, the rate of shoreline advance decreased by 50% near the long groin; the rate of advance increased somewhat in the region 1-2 km from the groin, and the formerly stable section of beach roughly centered at the 3-km mark began to erode (necessitating wider coverage in the shoreline surveys). The reduced rate of increase near the long groin is attributed to the low waves (weak longshore current) in this area deep in the shadow of the harbor breakwaters and to reduction of transport onshore through trapping by the detached breakwater. Trapping seems apparent, as judged by the change in 10-m contours in Fig. 1.

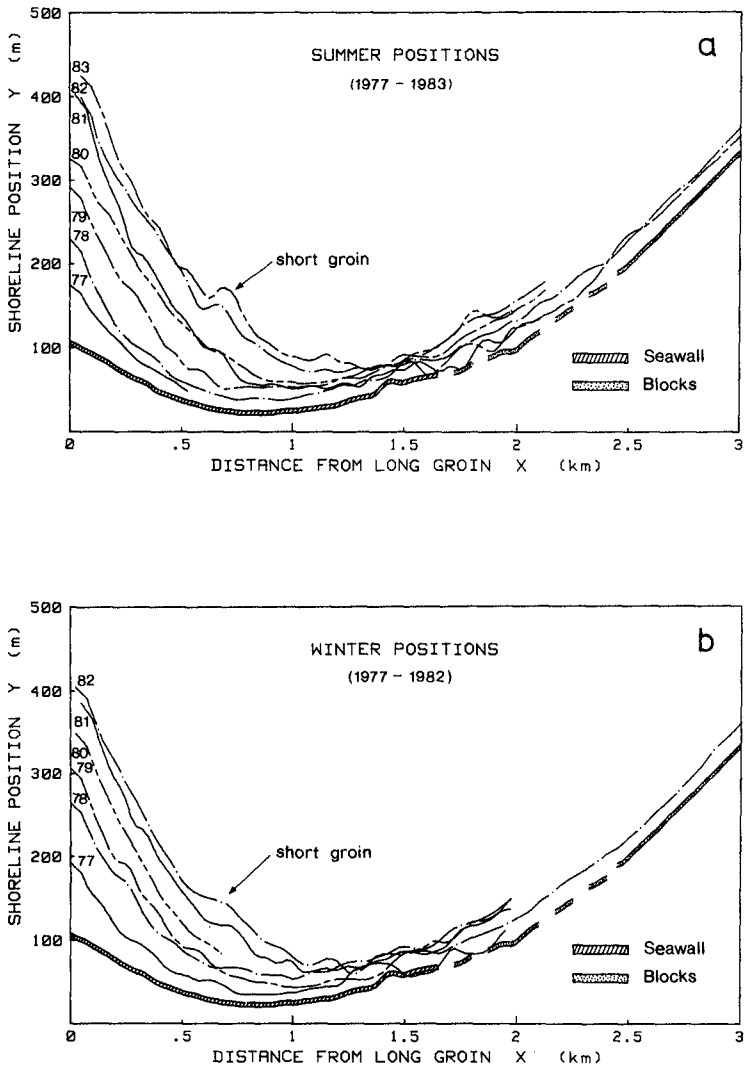


Fig. 6 Shoreline positions at Oarai Beach: (a) in the summer, (b) in the winter. (cont'd)



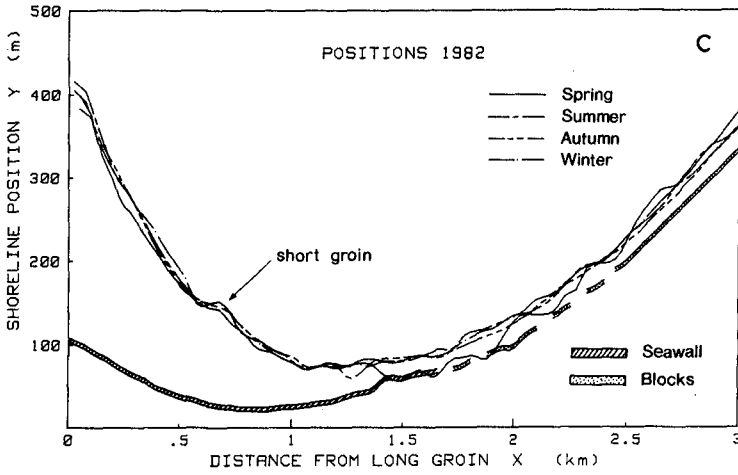


Fig. 6 Shoreline positions at Oarai Beach (c) during the four seasons of 1982.

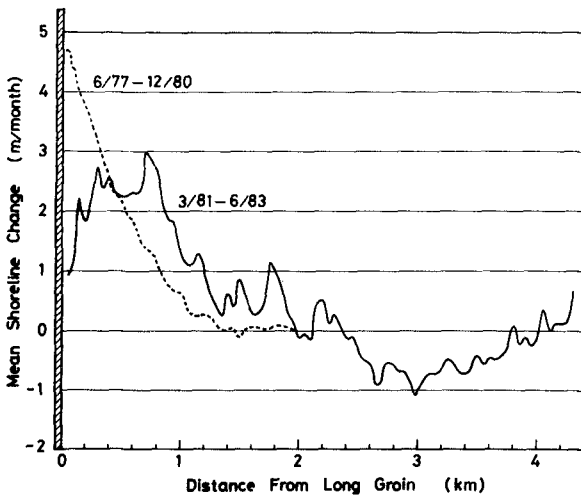


Fig. 7 Measured mean rate of shoreline change for periods before and after construction of the detached breakwater.

### 3. NUMERICAL MODEL

#### 3.1 Background

The 1-line (shoreline) numerical model was used to simulate changes in the beach planform at Oarai. The purpose of the 1-line model is to reproduce the large-scale features of shoreline change that take place over a relatively long period. The temporal and spatial scales of the major types of beach change numerical models are discussed by Kraus (1983). In the present case, application of the 1-line model for periods of several months to several years is justified by the clear trend in shoreline movement shown in Figs. 6a & b.

The basic model used is that of Kraus and Harikai (1983), who modeled shoreline evolution at the site for the period between 1977 and 1980. A number of refinements to and extensions of the model were made for carrying out the present study. We plan to present a description of the numerical model in another paper. Here we simply list the major improvements and changes: (1) The calculation procedure for the breaking wave height and angle alongshore was refined (Kraus, 1983, 1984) and extended to account for three sources of diffraction -- at the tip of the harbor breakwater and at both tips of the detached breakwater. (2) A seawall boundary condition which conserves sand volume and preserves transport direction was incorporated (Hanson and Kraus, in press). (3) The angle of the groins to the shoreline was taken into account (Perlin and Dean, 1978), and a simple prescription was introduced to permit sand bypassing at the groins. The changes in the model necessitated recalibration and verification.

#### 3.2 Shoreline Model

The governing equation for the shoreline position  $y$  is given by

$$\frac{\partial y}{\partial t} + \frac{1}{D} \left( \frac{\partial Q}{\partial x} \mp q \right) = 0 \quad (1)$$

in which  $x$  is the longshore coordinate,  $t$  is the time,  $D$  is the depth of closure (beyond which the profile is assumed not to move),  $Q$  is the longshore sand transport rate, and  $q$  is the cross-shore transport rate onshore (-) or offshore (+). The predictive expression for the longshore transport rate is taken as

$$Q = \frac{H_b^2 C_{gb}}{16(\rho_s/\rho - 1)(1-p)} \left( K_1 \sin 2 \theta_{bs} - 2K_2 \frac{\partial H_b}{\partial x} \cot \beta \cos \theta_{bs} \right) \quad (2)$$

in which  $C_{gb}$  is the wave group velocity at the breaker line,  $\rho_s$  ( $\rho$ ) is the sand (water) density,  $p$  is the sand porosity,  $\theta_{bs}$  is the angle of the breaking wave crests to the shoreline and  $\tan \beta$  is the beach slope. The coefficients  $K_1$  and  $K_2$  are treated as parameters in calibration of the model.

The first term in Eq. (2) corresponds to the CERC formula (CERC, Chap. 4, 1977) and describes the sand transport due to obliquely incident waves. The second term describes the transport due to a systematic variation in wave height alongshore. The second term has been found to be of importance for describing the shoreline change near structures, where diffraction dominates (Ozasa and Brampton, 1980; Kraus and Harikai, 1983; Mimura et al., 1983; Kraus, 1983). Gourlay (1982) gives a review of various derivations of Eq. (2).

The Shore Protection Manual (CERC, 1977, Chap. 4) recommends a value equivalent to  $K_1 = 0.77$  for root-mean-square height. Several theoretical evaluations of  $K_2$  have been given, resulting in different values, depending on the assumptions made (Gourlay, 1982). Experience of the authors in shoreline modeling, results of the NERC tracer experiments (Kraus et al., 1982), and other reports (Gourlay, 1982) indicate that  $K_1$  is more likely to be in the range 0.1 to 0.6.

Considering the uncertainty in the values of  $K_1$  and  $K_2$  and the multitude of approximations and simplifications in the model, it is appropriate to treat  $K_1$  and  $K_2$  as site-specific parameters to be determined by calibration. Modeling experience indicates that the ratio  $K_2/K_1$  lies in the range 0.5 to 1.5. The parameter  $K_1$  acts principally as a time scale adjustment factor. The parameter  $K_2$  controls the relative strength of the two terms in Eq. 2.

The depth of closure  $D$  in Eq. (1) also acts to adjust the time scale of shoreline movement. This characteristic depth in the model is related to the width of the beach through which sand is transported alongshore. Hallermeier (1983) has given expressions for calculating the depth of the seaward boundary where significant longshore transport and intense on-offshore transport take place. The simplest version has been found suitable for use with the shoreline model (Kraus and Harikai, 1983). It is

$$\frac{D}{H_s} = 2.28 - 10.9 \frac{H_s}{L_s} \quad (3)$$

in which  $H_s$  and  $L_s$  are the significant wave height and wavelength of waves in the shoaling zone, here assumed to be equivalent to those of the deepwater wave. In the simulations,  $D$  is recalculated at each change in the wave input.

The cross-shore transport rate,  $q$ , is the final quantity remaining to be specified before calculations can begin. Unlike the longshore transport rate, there are no predictive expressions available. Reflecting this situation, there have been only a few attempts to model shoreline change including cross-shore transport (Komar, 1973; Ozasa and Brampton, 1980; Kraus and Harikai, 1983). In the present case, we are faced with the need to account for the sand that moves around the harbor breakwater from the north. The amount, its time dependence, and its distribution are complicated functions of the discharge at the Naka River, wave conditions, and stage of construction of the detached breakwater. We described the onshore transport with the following convenient utilitarian expression:

$$q = q_0 / (1 + ((x - 2 \cdot x_0) / x_0)^{p_0}) \quad (4)$$

in which  $q_0$  (units:  $m^3/s-m$  alongshore) is used as a fitting parameter together with  $K_1$  and  $K_2$ .

### 3.3 Breaking Wave Model

The wave model for one diffraction source has already been described (Kraus, 1983, 1984). The introduction of three sources required additional assumptions to define the local breaking wave direction and wave height; we plan to present the procedure elsewhere. In essence, the wave model consists of solving the following equation:

$$\frac{H_b}{h_b} = \frac{K_D K_R K_S}{h_b} H_{tip} = \gamma \quad (5)$$

in which  $h_b$  is the depth at breaking,  $K_D$ ,  $K_R$ , and  $K_S$  are respectively diffraction, refraction, and shoaling coefficients for linear waves,  $H_{tip}$  is the incident wave height at the tip of the structure and  $\gamma$  is a breaking wave index. A multiple iteration is performed over  $h_b$  and either one or two angles entering in  $K_D$  and  $K_R$ , depending on the level of approximation desired and run time considerations. At convergence, both the breaking wave height and angle are determined at a given point alongshore. The model was favorably compared with laboratory measurements and with measurements made at Oarai prior to construction of the detached breakwater (Kraus, 1983, 1984).

## 4. RESULTS OF SHORELINE SIMULATION

### 4.1 Recalibration of the 1-Diffraction Source Model

In order to examine the extent to which the various refinements altered the model, the model was recalibrated for the same period used by Kraus & Harikai (1983) (11 Jul 79 - 21 Feb 80) and with the same wave conditions. Best results were obtained with values of the transport parameters ( $K_1$ ,  $K_2$ ,  $q_0$ ) of (0.1, 0.1,  $4.0 \cdot 10^{-6} m^3/s-m$ ) as opposed to the previously determined values of (0.3, 0.4,  $2.5 \cdot 10^{-6} m^3/s-m$ ). The reduction in  $K_1$  and  $K_2$  is mainly due to (1) the improved calculation of the breaking wave angle, which causes an increase in magnitude of the angle (an increase in  $\theta_{bs}$  requires a decrease in  $K_1$  to maintain the same time scale) and (2) the improved, volume-conserving seawall boundary condition. The results of this exercise demonstrate the fact that the transport parameters depend on the model used as well as on the characteristics of the particular site.

#### 4.2 Calibration & Verification of the 3-Diffraction Source Model

For modeling periods after start of construction of the detached breakwater (Jan. 81), three sources of wave diffraction had to be used. Also, it was found during calibration runs that the distribution of onshore transport,  $q(x)$ , appeared to have a different character than for the pre-1981 period. Inspection of the outputs of many runs with different combinations of transport parameters indicated a visual best fit with  $K_1 = K_2 = 0.1$ ,  $q_0 = 4.5 \cdot 10^{-6}$   $m^3/s\text{-m}$ , and  $x_0 = 300$  m,  $p_0 = 4$ .

Verification runs with these and other values were made for the 2 1/4-year period from 11 Mar 81 to 15 Jun 83. Figure 8 shows results for the final shoreline position obtained with the calibrated model, together with the shorelines computed using other values of the transport coefficients. The simulated final shoreline obtained with the calibrated model agrees well with the actual shoreline up to 2 km from the long groin, but it shows too much advance along the beach 2 to 4 km from the long groin. The results of the calibrated model are far superior to those obtained using the other values of the transport coefficients.

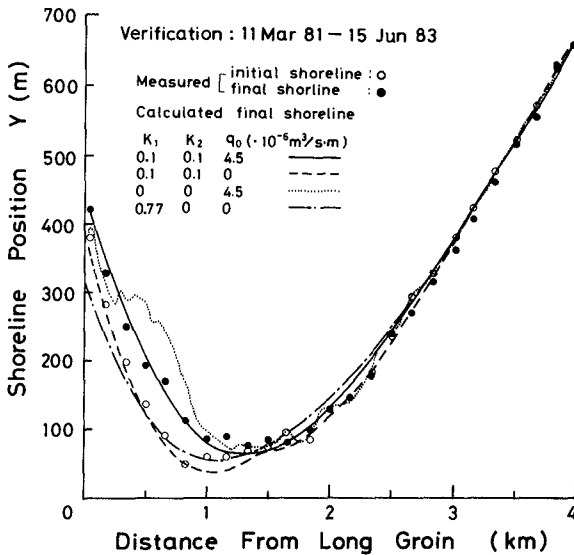


Fig. 8 Measured and calculated shoreline change for the verification interval.

The calculated mean rate of shoreline change along the beach is shown in Fig. 9. It can be compared with the measured rate for the same period, the solid curve in Fig. 7. The rate of shoreline change up to 1 km from the long groin is well reproduced. However, the location of the calculated maximum rate of erosion is at about the 1.5-km point, instead of at 3 km, and the calculation gives an essentially stable shoreline from about the 3-km point. The lack of agreement suggests the need to use a more sophisticated refraction routine for the irregular bottom topography for the region far from the harbor structures, where diffraction is no longer the dominant wave transformation.

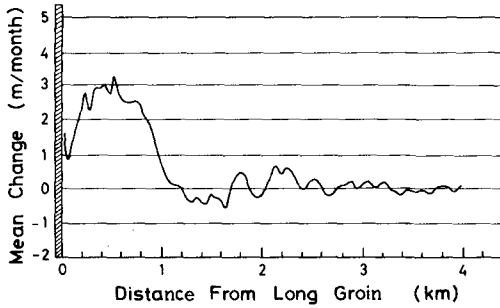


Fig. 9 Calculated mean rate of shoreline change for the verification interval 11 Mar 81 - 15 Jun 83.

Figure 10 compares calculated shoreline positions using the calibrated model and different averaging intervals of the wave input over the verification period (energy flux-weighted averages at the gage). In general, for the region near the long groin, the agreement deteriorates with increase in the averaging interval defining the representative wave conditions. The calculated shoreline in the region distant from the groin appears to be governed by the location of the eroded sector, which, in turn, is produced by the relatively fixed distribution of the breaking wave angle alongshore. Although recalibration of the model for a given averaging interval may improve the result somewhat, because of the sensitivity of the wave calculation to the incident wave angle, the result is expected to be inferior to that obtained by updating the wave information at simulated 6-hr intervals (cf., Le Mehaute et al., 1983, Kraus & Harikal, 1983).

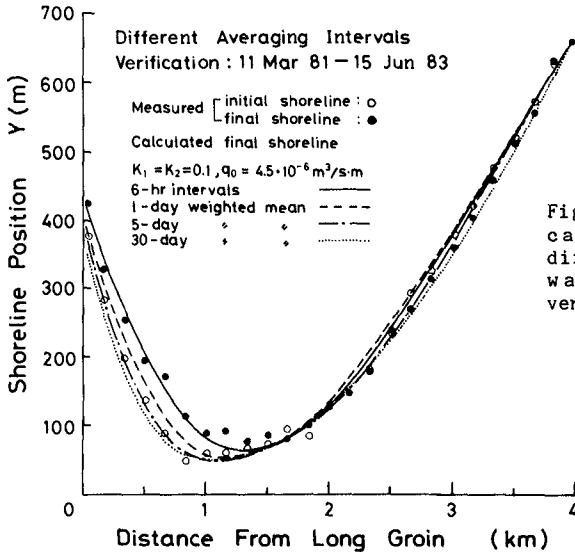


Fig. 10 Shoreline change calculated by using different time-averaged wave inputs for the verification period.

### 4.3 Forecast Shoreline Change

Although the verification simulation had a mixed outcome of success, it was decided to use the model to predict future shoreline change as an exercise for investigating problems associated with forecast-type simulations. Engineering-oriented forecasts of shoreline change cannot be found in the open literature, probably because of the legal aspects involved. The main technical problem is the treatment of the wave input, i.e., how the time history of the waves should be forecast.

In the present work, two additional problems emerged. First, due to active construction at the site, the construction schedule and structure positions had to be estimated for automatic update in the model. (These affect the location of the diffraction sources and bypassing at the groins.) The second problem concerned the possible trapping function of the detached breakwater of sediment that would normally move south around the harbor breakwater and then onshore. We speculate that the detached breakwater traps most of this sediment. To investigate the potential trapping function,  $q_0$  was varied in different series of forecast runs.

Treatment of the the wave time history in shoreline numerical modeling has been considered by Le Mehaute, Wang & Lu (1983) and Kraus & Harikai (1983). In the former study it was demonstrated that the results of shoreline modeling depend on both the interval at which the wave data are input and the order of the input. In the latter study it was shown that time averaging of the wave data for Oarai for intervals greater than about 5 days gave rather poor results. The acceptable interval for updating wave information in a model will depend on the steadiness of the waves at the site in question, in particular, for wave direction.

In forecasting shoreline change, the assumption is made that the time sequence of wave events and the wave conditions in the future will have much the same character as in the past. It is valuable to have a long wave record with which to accurately describe the average and time-varying wave conditions. One must also keep in mind possible long-term cycles in the wave climate (e.g., Kuhn and Shepard, 1983), as well as infrequent extreme events.

Noting that the exact time history of wave events is not predictable, Le Mehaute et al. (1983) introduced a Monte Carlo procedure to provide measures for the possible deviation. Their approach is a sound conceptual solution to the problem. However, our experience gives us the impression that direct application of the Monte Carlo method might yield a range of shoreline change which is too narrow.

Basically, we would like to estimate the maximum range of shoreline movement resulting from wave histories which do not differ "too greatly" from the past time history. The "not too great" differences should incorporate variations in both wave conditions (energy flux) and sequence of wave events. In other words, how can we estimate limits of variations in the future wave data set? We took the direct approach of manipulating the individual distributions of wave height and direction, while leaving the period distribution unchanged for simplicity.

For a simple estimation of the limits of the maximum range of deviation of the forecast waves, it was assumed that wave height and direction distributions would be shifted by a certain amount from the past distribution (given by the CDS). As a limit of the shift, we took one half of the standard deviation of the respective distributions, i.e.,  $H$  was allowed to vary between  $H \pm H_{SD}/2$ , and similarly for  $\theta$ , where the subscript SD denotes the standard deviation. This procedure provides deviations in the energy flux. To estimate the effect of sequencing, the CDS was ordered with respect to increasing and decreasing  $H$  and  $\theta$ . In all data sets generated, only one quantity was manipulated and the other two quantities were left unchanged to form a new triplet of values of  $H$ ,  $\theta$ , and  $T$  at 6-hr intervals.

The transport parameters  $K_1$  and  $K_2$  were held at 0.1 as determined in the calibration, but  $q_0$  was varied to produce different series of runs. The resultant shorelines for the 5-yr forecast period using  $q_0 = 2.0 \cdot 10^{-6}$  are shown in Fig. 11. The heavy line denoted by  $H$ ,  $\theta$ ,  $T$  gives the result using the CDS. The greatest deviation from the CDS prediction occurs for the runs with  $H \pm H_{SD}/2$ , corresponding to severe and mild wave conditions, respectively (neglecting the correlation with wave period and direction). All runs gave a shoreline advance near the groin. The amount of advance is less than that which occurred over recent 5-yr periods. Except for the run with decreasing  $\theta$ , all runs produced an eroded beach starting from about 2 km from the long groin. Other series with different  $q_0$  had much the same qualitative features.

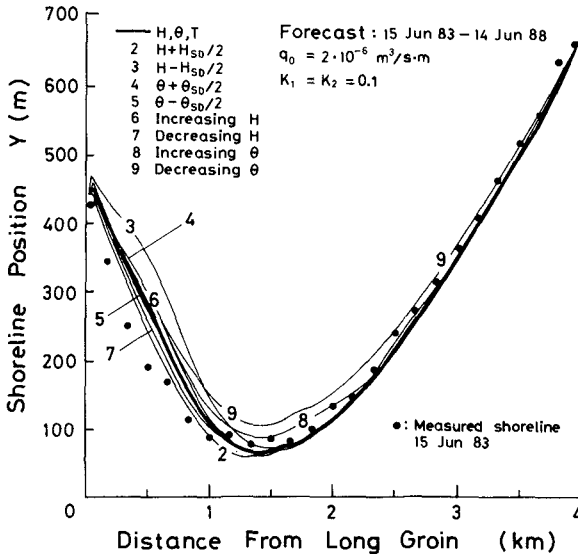


Fig. 11 Results of shoreline forecast simulations.

The forecast shoreline changes both near and far away from the long groin are in general agreement with recently observed trends at the site. However, the inability to predict the time-dependent behavior of  $q_0$  introduces a great uncertainty into the forecast, and the results should be interpreted appropriately in light of that uncertainty.



## 5. CONCLUDING DISCUSSION

The large harbor breakwaters being built at Oarai for the purpose of improving navigation exert a great effect on the near and distant sandy beach. The observed shoreline change can be well understood on the basis of long-term measurements of the waves and currents. The 1-line numerical model was reasonably successful in simulating the observed shoreline change in spite of the complications of multi-sources of wave diffraction, the wide area of coverage including a seawall and two groins, and problems with estimating onshore sand transport. The forecast shoreline change for the next five years was in general agreement with the present trend in evolution of the shoreline.

In order to make more accurate predictions of shoreline change for Oarai, the following four topics should be addressed. (1) The necessity of including a 2-dimensional refraction routine for the region far from the long groin should be investigated. (2) The south seawall should be included in the model and the model range should be extended well past the south seawall. (3) The trapping efficiency of the detached breakwater should be empirically estimated (as from bottom surveys, and possibly tracer experiments). (4) The expected limits of variation of the wave time history should be more objectively determined from the statistical properties of the CDS, and the joint probability distribution of wave height, direction, and period should be utilized.

## ACKNOWLEDGMENTS

We would like to express our deep appreciation to the staff of the Oarai Harbor Management Office for making available the wave and shoreline data, and for kindly providing other information and assistance. We would also like to thank Prof. M. Hom-ma, Director of NERC, for bringing the interesting article of Hiroi to our attention. Finally, NCK would like to thank Prof. M. Hattori of Chuo University for arranging a hospitable 2-month stay at his institution, during which time this paper was completed.

## REFERENCES

- Arakida, T., Y. Tsurukawa and K. Mizumura (1978): Currents and shoreline change behind a breakwater, Proc. 25th Japanese Conf. on Coastal Eng., pp. 199-203. (in Japanese)
- CERC (1977): Shore Protection Manual, U.S. Army, Corps. of Engineers, Coastal Eng. Res. Center, 3V., U.S. Govt. Printing Office.
- Gourlay, M.R. (1982): Nonuniform alongshore currents and sediment transport - a one dimensional approach, Res. Rep. No. CE31, Dept. of Civil Eng., Univ. of Queensland, Australia, 67 pp.
- Hallermeier, R.J. (1983): Sand transport limits in coastal structure design, Proc. Coastal Structures '83, ASCE, pp. 703-716.

- Hanson H. and N.C. Kraus (in press): Seawall constraint in the shoreline numerical model, *J. of Waterway, Port, Coastal and Ocean Eng.*, ASCE.
- Hiroi, I. (1921): On the nature of drifting sands as affecting harbor construction on sandy coasts, *J. of the College of Eng., Tokyo Imperial Univ.*, Vol. XI, No. 3, pp. 47-82 + figures.
- Horikawa, K. and M. Hattori (1984): Achievements of the NERC project, *Proc. 19th Coastal Eng. Conf.*, ASCE, (in press).
- Ijima, T., S. Sato, H. Aono and Y. Tsurukawa (1961): Littoral transport at the Isohama Coast, *Proc. 8th Japanese Conf. on Coastal Eng.*, pp. 168-175. (in Japanese)
- Komar, P.D. (1973): Computer models of delta growth due to sediment input from rivers and longshore transport, *Geol. Soc. Am. Bull.*, Vol. 84, pp. 2217-2226.
- Kraus, N.C. (1983): Applications of a shoreline prediction model, *Proc. Coastal Structures '83*, ASCE, pp. 632-645.
- Kraus, N.C. (1984): Estimate of breaking wave height behind structures, *J. of Waterway, Port, Coastal and Ocean Eng.*, ASCE, Vol. 110, No. 2, pp. 276-282.
- Kraus, N.C. and S. Harikai (1983): Numerical model of the shoreline change at Oarai Beach, *Coastal Eng.*, Vol. 7, No. 1, pp. 1-28.
- Kraus, N.C., M. Isobe, H. Igarashi, T.O. Sasaki and K. Horikawa (1982): Field experiments on longshore sand transport in the surf zone, *Proc. 18th Coastal Eng. Conf.*, ASCE, pp. 969-988.
- Kuhn, G.G. and F.P. Shepard (1983): Beach processes and sea cliff erosion in San Diego County, California, in (P.D. Komar, ed.) *Handbook of Coastal Processes*, CRC Press, Boca Raton, Florida, pp. 267-284.
- Le Mehaute, B., J.D. Wang and C.-C. Lu (1983): Wave data discretization for shore line processes, *J. of Waterway, Port, Coastal and Ocean Eng.*, Vol. 109, No. 1, pp. 63-78.
- Mimura, N., T. Shimizu and K. Horikawa (1983): Laboratory study on the influence of detached breakwater on coastal changes, *Proc. Coastal Structures '83*, ASCE, pp. 740-752.
- Mizumura, K. (1982): Shore line change estimates near Oarai, Japan, *J. Waterways, Port, Coastal and Ocean Eng.*, ASCE, Vol. 108, No. WW1, pp. 65-80.
- Ozasa, H. and A.H. Brampton (1980): Mathematical modelling of beaches backed by seawalls, *Coastal Eng.*, Vol. 4, No. 1, pp. 47-64.
- Perlin, M. and R.G. Dean (1978): Prediction of beach planforms with littoral controls, *Proc. 16th Coastal Eng. Conf.*, ASCE, pp. 1818-1838.

## CHAPTER ONE HUNDRED FORTY TWO

### MECHANISM OF BEACH PROFILE DEFORMATION DUE TO ON-OFFSHORE SAND DRIFT

BY

Wi-Gwang Pae<sup>1)</sup> and Yuichi Iwagaki M. ASCE<sup>2)</sup>

#### ABSTRACT

In the present study, two-dimensional laboratory experiments were performed to investigate the sediment transport due to waves on a fixed sloping beach. Polystyrene particles and glass balls were used as tracers to determine the mass transport velocity near the bottom and the net transport velocity of sediment moving on an impermeable slope. Relationships between the mass transport velocity of water and the net sediment transport velocity are investigated experimentally. The mechanism of two-dimensional beach deformation from an initial uniform slope toward an equilibrium profile due to bed-load movement is discussed on the basis of spatial distributions of the net sediment transport velocity. In addition, some results of experiments using a movable bed are presented to confirm the validity of a beach deformation model derived from the discussion of the tracer experiments.

#### 1. INTRODUCTION

Hydraulic characteristics in the on-offshore direction on a beach are very complicated; fluid forces which cause sediments to move vary with time, and the direction of the net transport velocity of water (mass transport velocity) is spatially changed. Moreover, the value of the mass transport velocity is dependent upon both space and time. Owing to these complexities in the hydraulic characteristics on the beach, the mechanism of sediment transport in the on-offshore direction due to waves is not so easy to understand as that in the longshore direction.

In general, the beach profile deformation is caused by the spatial difference of the net transport rate of the bottom sediment. When the net transport rate of the bottom sediment is spatially uniform, the bottom configuration does not change even if the instantaneous velocity of water particles is large. In this study, a model of the beach profile

1) M. Eng., Postgraduate, Dept. of Civil Eng., Kyoto University, Kyoto 606, Japan

2) Dr. Eng., Professor, Dept. of Civil Eng., Kyoto University, Kyoto 606 Japan

deformation is presented on the basis of the spatial distribution of the net transport velocity of bottom sediments.

Stokes (1847) is the first one who pointed out that a steady second order drift velocity (mass transport velocity) exists in an inviscid irrotational wave field. Longuet-Higgins (1953) treated the problem on the mass transport in a finite-length channel with due consideration of fluid viscosity. In his solution, the whole flow field was divided into three regions; the interior, the surface, and the bottom boundary layers. The boundary conditions are no-slip at the bottom, zero-stress on the surface, and zero net mass transport in the whole field. In the bottom boundary layer, the mass transport velocity is given as the sum of both the second order Eulerian mass transport velocity and the Lagrangian drift resulting from the first order irrotational motion inside the boundary layer. In the interior region, the mass transport velocity is derived by using the classical matching principles of standard boundary layer problem; that is, the limit value of the boundary layer solution equals the boundary value of the interior solution.

The mass transport velocity on a sloping beach is considered to play an important role in the transport of bottom sediments. Rijker, Kalkwijk and Pieters (1974) modified Longuet-Higgins' solution in the uniform depth by incorporating the shoaling effect. The theoretical values, however, are found to be considerably larger than those obtained in their experiments. Wang, Sunamura and Hwang (1982) investigated the drift velocity at the breaking point under different types of breaking waves on a rigid, plane beach. According to their results, independently of breaker types, the drift velocity profile at the breaking point is similar to that of Longuet-Higgins, but the offshore drift velocity in the main flow column shows a more uniform vertical distribution than that in the offshore region. Iwagaki, Pae and Moriguchi (1982) investigated the net transport velocity of solid particles on a smooth sloping beach to determine the relationship between the mass transport velocity of water and the net transport velocity of bottom sediments. Their experimental results show that there are distinct correlations between the net transport velocities of glass balls and of polystyrene particles for the regions shoreward and seaward of the breaking point.

## 2. EXPERIMENTAL APPARATUS AND PROCEDURE

### 2.1 Experimental Apparatus

The wave tank used is 30 m long, 50 cm wide, and 75 cm deep. One side of the wave tank has a glass wall 15 m in length. A rigid impermeable bottom of two different surface conditions, smooth and rough, was used. The slope of beach was 1/20 only. In case of the rough slope, the surface was uniformly roughened with spherical particles of 3 mm in diameter. The wave height was measured by using two wave gauges of capacitance type. One wave gauge was installed at a location in the region of uniform water depth to measure incident waves. The other gauge

was installed at a point on the slope where two holes were opened to feed solid tracer particles slowly onto the bottom.

Polystyrene particles and glass balls with four different diameters were used as tracers. The properties of these particles are shown in Table 1. Polystyrene particles with a diameter of approximately 3 mm were coloured with paint. The glass balls were also coloured for each diameter.

Pairs of these tracer particles were simultaneously lifted up onto the sloping bottom through the two holes at a speed of 0.05 cm/sec by means of an apparatus devised by the authors. Fig. 1 shows this device of a constant speed feeder of tracer particles, which has three rods moved vertically by a small-sized variable speed motor. By the upward motion of the two short rods, tracer particles are lifted up and injected onto the bottom surface.

## 2.2 Experimental Procedure

Typical waves with three kinds of deepwater wave steepnesses were generated. Table 2 shows the characteristics of the waves and the water depth in the experiment.

Pairs of holes, through which the tracer particles were fed as mentioned before were made in the bottom plate at intervals of 40 cm in line with the direction of wave propagation. Movements of the polystyrene particles and glass balls, slowly pushed out on the bottom surface, were filmed by using a 16 mm movie camera (Bolex, H-16, EBM Electric) at a speed of about 24 frames/sec. Colour film was used to obtain informations from the coloured tracers. Trajectories of the particles moving on the bottom were traced from the film with the aid of a film motion analyzer (Motion Analyzer 160, NAC). To reduce the error caused by picture distortion, the particles were traced within the region of  $\pm 10$  cm from the center of each hole in the direction of wave propagation and within the region of  $\pm 1.5$  cm in the transverse direction. The error in reading the instantaneous location of tracers under these conditions was found to be about 3-4%. Transport distances of tracers during one wave cycle were divided by the wave period to obtain net transport velocities.

## 3. EXPERIMENTAL RESULTS AND DISCUSSIONS

### 3.1 Mass Transport Velocity on Bottom of Sloping Beach

Fig. 2 shows the mass transport velocity of polystyrene particles on the bottom of a roughened sloping beach with a nonlinear parameter of waves proposed by Goda(1983). In this figure, the dotted line denotes the theoretical values of the mass transport velocity at the edge of the bottom boundary layer by Longuet-Higgins i.e.  $(5/4)\sinh^2 kh$ . Symbols denote experimental data. A family of curves were determined by the

Table 1 Properties of tracer particles.

No.	Material	Mean Diameter (cm)	Fall Velocity (cm/sec)	Specific Gravity	Reynolds No. on Slope ( $Vs \cdot d/\nu$ )
1	Polystyrene	0.324	3.58	1.03	24
2	Glass	0.230	25.9	2.23	103
3	Glass	0.300	34.2	2.35	174
4	Glass	0.414	42.5	2.47	206
5	Glass	0.491	48.4	2.49	392

Table 2 Experimental conditions.

(a) in case of smooth slope

Wave Height $H_o$ (cm)	Wave Period $T$ (sec)	Depth (uniform) $h_o$ (cm)	Depth (on slope) $h$ (cm)	Wave Steepness $H_o/L_o$	Slope
2.73 ~ 3.02	1.68 ~ 1.70	40.0	1.90 ~ 30.5	0.006 ~ 0.007	1/20
5.97 ~ 6.88	1.41 ~ 1.43	40.0	1.90 ~ 30.5	0.021 ~ 0.024	1/20
8.09 ~ 8.94	1.10 ~ 1.12	40.0	1.90 ~ 30.5	0.046 ~ 0.050	1/20

(b) in case of roughened slope

Wave Height $H_o$ (cm)	Wave Period $T$ (sec)	Depth (uniform) $h_o$ (cm)	Depth (on slope) $h$ (cm)	Wave Steepness $H_o/L_o$	Slope
2.80 ~ 3.26	1.66 ~ 1.70	40.0	0.0 ~ 29.2	0.006 ~ 0.007	1/20
6.42 ~ 7.04	1.40 ~ 1.44	40.0	0.0 ~ 29.2	0.021 ~ 0.022	1/20
9.16 ~ 9.72	1.10 ~ 1.14	40.0	0.0 ~ 29.2	0.047 ~ 0.050	1/20

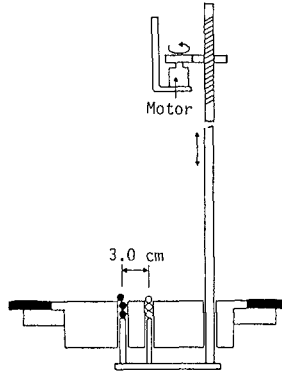


Fig. 1 Equipment for feeding tracer particles.

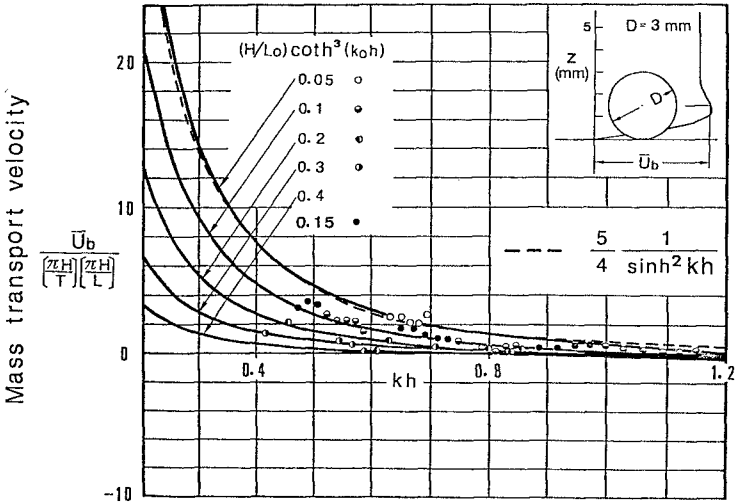


Fig. 2 Mass transport velocity of water on bottom of a sloping beach with a nonlinear parameter of waves proposed by Goda(1983).

method of least squares on the basis of the experimental data.

According to the paper by Goda(1983), the larger the value of the nonlinear parameter becomes, the more the nonlinearity of waves becomes remarkable. It is shown in Fig. 2 that the mass transport velocity on the bottom becomes small with an increase in the value of this parameter. In this connection, it is said that the mass transport velocity on the bottom of a sloping beach becomes small with an increase in the nonlinearity of waves.

3.2 Relationship between Mass Transport Velocity and Net Transport Velocity of Glass Balls

Figs. 3(a) and (b) show the relationships between the mass transport velocity and the net transport velocity of glass balls on a roughened beach of 1/20 slope. Assuming that the relationship is linear, it is expressed as follows:

$$(\bar{U}_b/\sqrt{gH_0})g = a(\bar{U}_b/\sqrt{gH_0})p + b \tag{1}$$

in which  $(\bar{U}_b/\sqrt{gH_0})g$  denotes the non-dimensional net transport velocity of glass balls and  $(\bar{U}_b/\sqrt{gH_0})p$  that of the polystyrene particle, and both  $a$  and  $b$  are constants. The values of  $a$  and  $b$  in case of the roughened beach of 1/20 slope are listed in Table 3 and Table 4, in which  $k_s$  denotes the roughness height (3mm), and  $D$  the diameter of a glass ball.

Table 3

Values of best-fit parameters  $a$  and  $b$  in the region of Fig. 3(a).

$k_s/D$	$a$	$b$
1.30	0.68	2.35
1.00	0.41	1.25
0.73	0.27	0.94
0.61	0.50	1.65
0.00*	0.56	0.50

Table 4

Values of best-fit parameters  $a$  and  $b$  in the region of Fig. 3(b).

$k_s/D$	$a$	$b$
1.30	1.42	0.06
1.00	0.68	0.79
0.73	0.24	0.92
0.61	0.28	0.40
0.00*	0.67	2.05

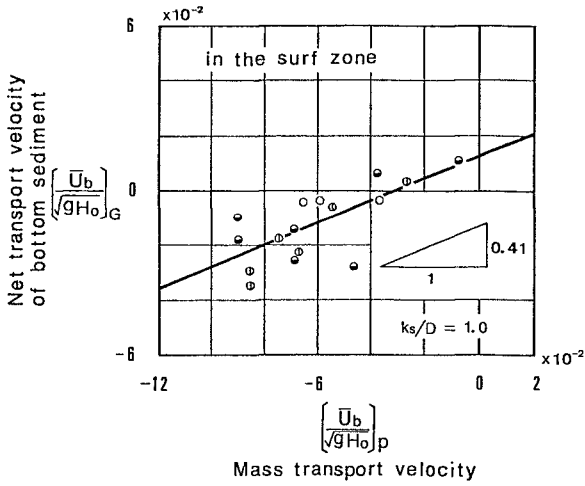
\* : Data on a smooth sloping beach.

In the region offshore from the breaking point, the value of  $a$  becomes large with an increase in  $k_s/D$ . In the surf zone,  $a$  does not change so much as in the offshore region.

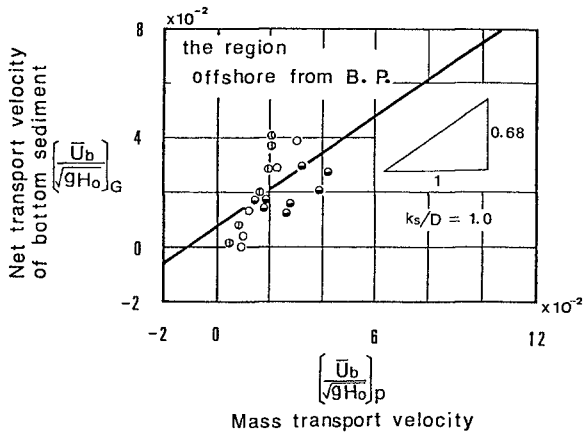
3.3 Spatial Distribution of Net Transport Velocity of Glass Balls

Figs. 4(a) and (b) show the spatial distributions of the net transport velocity of glass balls with a parameter of  $k_s/D$ . In these figures, the abscissa is the ratio of still water depth on the slope to





(a) in the surf zone



(b) in the region offshore from Breaking point

Fig. 2 Relationship between mass transport velocity and net transport velocity of glass balls ( $H_o/L_o$ :  $\circ$  0.007,  $\phi$  0.022,  $\bullet$  0.040).

that at the breaking point, and the ordinate is the non-dimensional net transport velocity of glass balls. The positive component of  $(\bar{U}_b/\sqrt{gH_0})g$  indicates the onshore transport. The data on a smooth sloping beach are plotted for reference.

From Fig. 4, it is shown that firstly, the position where  $(\bar{U}_b/\sqrt{gH_0})g$  becomes zero appears at three or four locations in case of the roughened slope, and at two locations in case of the smooth slope. Secondly, a dynamic equilibrium point near the plunging point of breaking waves where  $h/h_b$  is 0.6-1.1 appears independently of both the bottom surface condition, smooth or rough, and the bottom sediment condition, relatively large or small to the bottom roughness. Thirdly, this dynamic equilibrium position corresponds to the place where sediment accumulates because the transport direction of bottom sediments offshore from this position is onshore and that onshore from this place is offshore. Fourthly, the position where the net transport velocity becomes zero in the offshore region has a qualitative difference due to the existence of roughness. That is to say, in case of the smooth surface, this position becomes a dynamic equilibrium point which corresponds to the "Null point" defined by Cornaglia(1889), Eagleson and Dean(1961), and other investigators. However, in case of the roughened surface, this position means a static place corresponding to a critical water depth for sediment movement.

#### 3.4 Effect of Wave Steepness on Depth of Dynamic Equilibrium Point

Fig. 5 illustrates the effect of the deepwater wave steepness on the water depth in the dynamic equilibrium position. From this figure, two main points are found; the first is that the offshore equilibrium position appears in all cases of  $H_0/L_0$ , and the second is that the water depth of the offshore equilibrium position becomes shallow with a decrease in the deepwater wave steepness. On the other hand, the water depth in the onshore one is also affected by the deepwater wave steepness as well as in the offshore position.

### 4. MECHANISM OF ON-OFFSHORE SEDIMENT TRANSPORT

#### 4.1 Discussions on Mechanism of Beach Profile Change

In this section, the mechanism of on-offshore transport of sediment as bed-load by wave action is discussed on the basis of the present experimental results. In addition, an attempt is made to explain the change of beach profile obtained in the existing experiment.

Considering the specific gravity of the tracers, it may be assumed that the net transport velocity of the polystyrene particles during a wave period closely approximates the mass transport velocity of water, and that the velocity of the glass balls represents the net transport velocity of bottom sediments induced by wave action. As shown in Tables 3 and 4, there exists a clear correlation between the mass transport

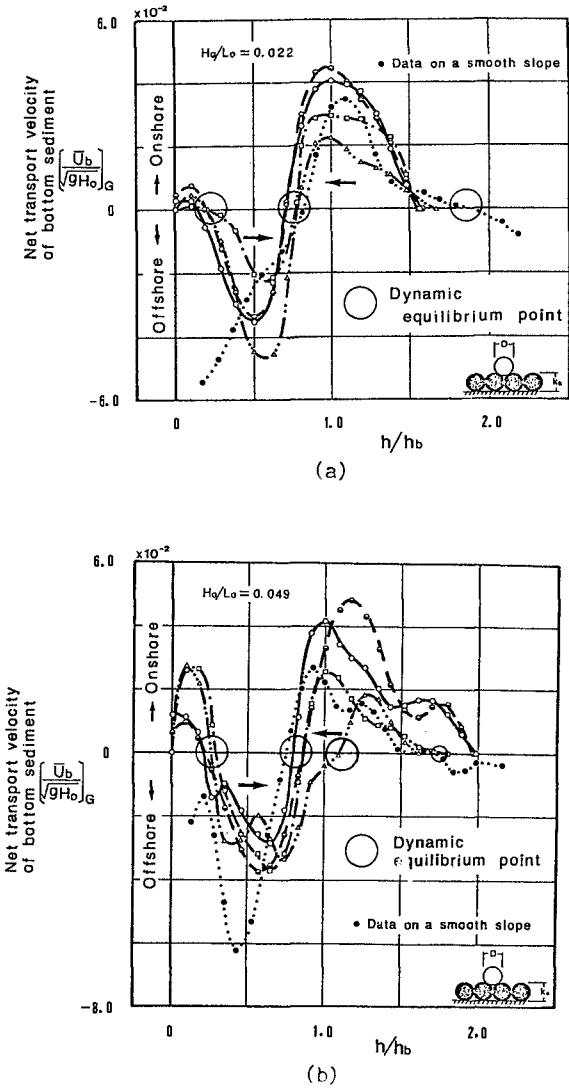


Fig. 4 Spatial distribution of net transport velocity of glass balls,  $(U_b/\sqrt{gH_0})_G$  ( $ks/D$ :  $\bullet$  1.30,  $\circ$  1.00,  $\square$  0.73,  $\triangle$  0.67).

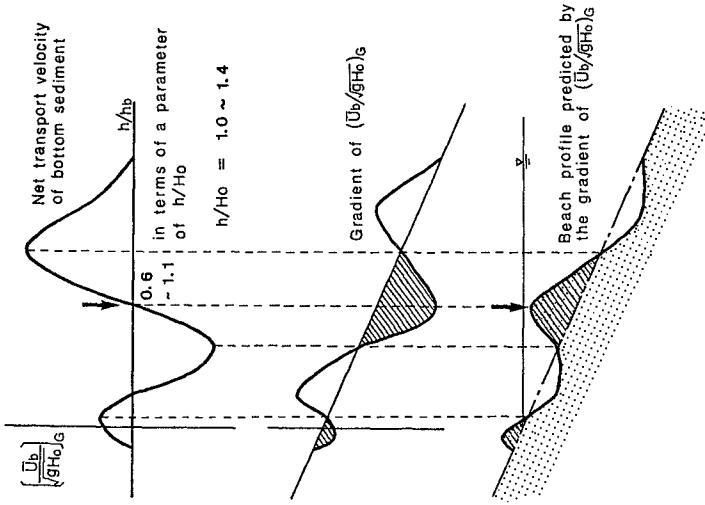


Fig. 6 Mechanism of beach profile deformation on basis of spatial distribution of net transport velocity of glass ball.

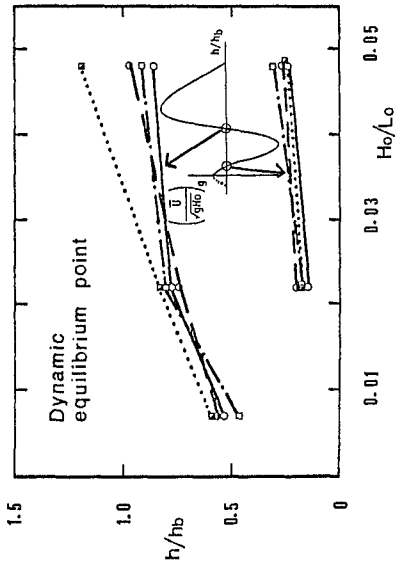


Fig. 5 Effect of deepwater wave steepness on water depth of dynamic equilibrium position ( $ks/D$ :  $\bullet$  1.30,  $\square$  1.00,  $\triangle$  0.73).

velocity of water near the bottom and the net transport velocity of the bottom sediments moving probably by rolling on a sloping bottom.

Here the mechanism of beach profile deformation is discussed on the basis of the spatial distribution of the net transport velocity of glass balls because the glass balls used in the present experiment have almost the same specific gravity as that of sand grains. Fundamental assumption in this model is that the bottom sediment is moved as bed-load.

Fig. 6 illustrates the mechanism of beach profile deformation on the basis of the spatial distribution of the net transport velocity of bottom sediments. The upper figure in Fig. 6 is the typical spatial distribution of the net transport velocity of sediments. This distribution is necessary to discuss the beach profile change, because the spatial difference of the net transport velocity of sediments causes beach profile deformation. The middle figure in Fig. 6 is the spatial distribution of the gradient of  $(\bar{U}_b/\sqrt{gH_0})g$ . This gradient is directly related to the change of bottom profile configuration. The lowest figure in Fig. 6 is the beach profile predicted by the continuity relationship between the time variation of the bottom elevation and the spatial variation of the net transport rate of bottom sediments.

From the upper and the lowest figures in Fig. 6, two points are found; the first is that the region offshore from the breaking point will be always eroded, and the second is that the offshore position of two dynamic equilibrium points represents the place where sediments accumulate. These two characteristics always appear in the beach profile evolution, independently of both the deepwater wave steepness ( $H_0/L_0$ ) and the condition of bottom sediments ( $ks/D$ ).

To elucidate the mechanism of sediment transport by wave action on a movable bed, an attempt is made to explain the process of beach profile change in model tests by considering the mass transport obtained for the spherical particles moving on a roughened slope. Beach deformation from an initial uniformly sloping beach to a final equilibrium profile can be classified into three types as shown in Fig. 7 according to Sawaragi and Deguchi (1980). In Type I, accumulation occurs in the offshore region and erosion on the beach face, so that a bar is formed. In Type II, erosion occurs on the beach face and accumulation both on the back beach and in the offshore region, but the bottom in the region deeper than the place where the accumulation occurs in the offshore region has two different profiles, either accretive or erosive. In Type III, accumulation occurs on the beach face and erosion in the offshore region, so that a step is often formed.

The behaviour of the glass balls in the present experiment may correspond to that of coarse sediment transported as bed-load. As far as the present results are concerned, accumulation takes place near the location where the value of  $h/h_b$  is 0.6-1.1, and the region offshore from the breaking point is eroded, independently of the deepwater wave steepness. Accordingly, when sediments are transported as bed-load, a uniformly sloping beach may probably change in the process of Type II-2 in Fig. 7 at the initial stage regardless of wave characteristics.

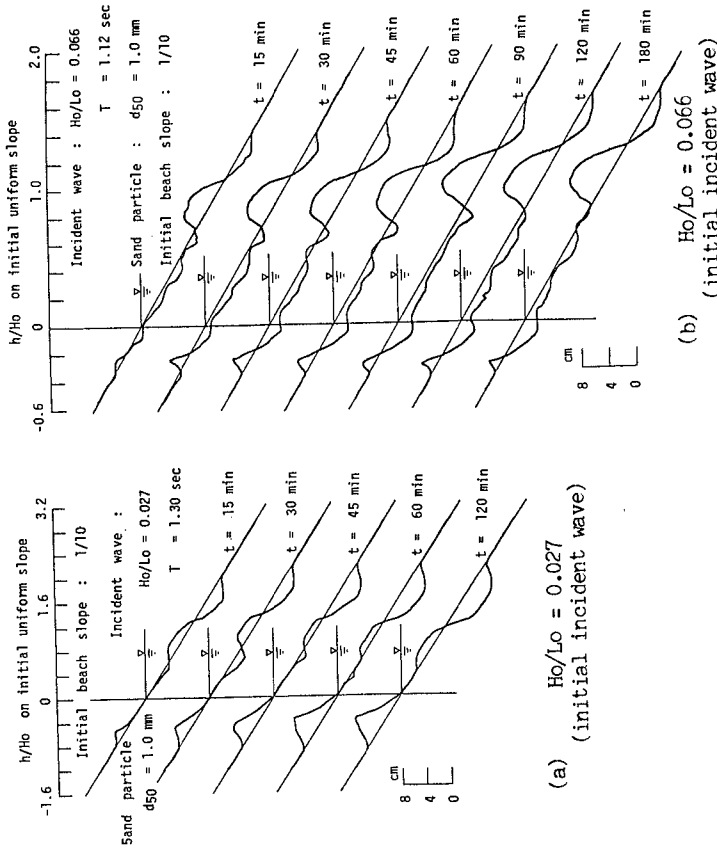


Fig. 8 Examples of beach profile deformation ( $d_{50} = 1.0$  mm, initial uniform slope:  $1/10$ ).

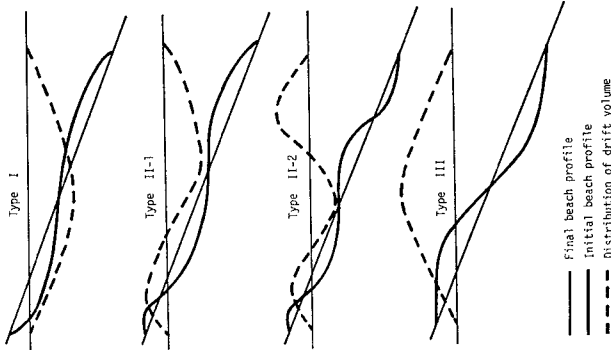


Fig. 7 Classification of beach process from uniformly sloping beach to equilibrium beach (Sawaragi and Deguchi, 1980).

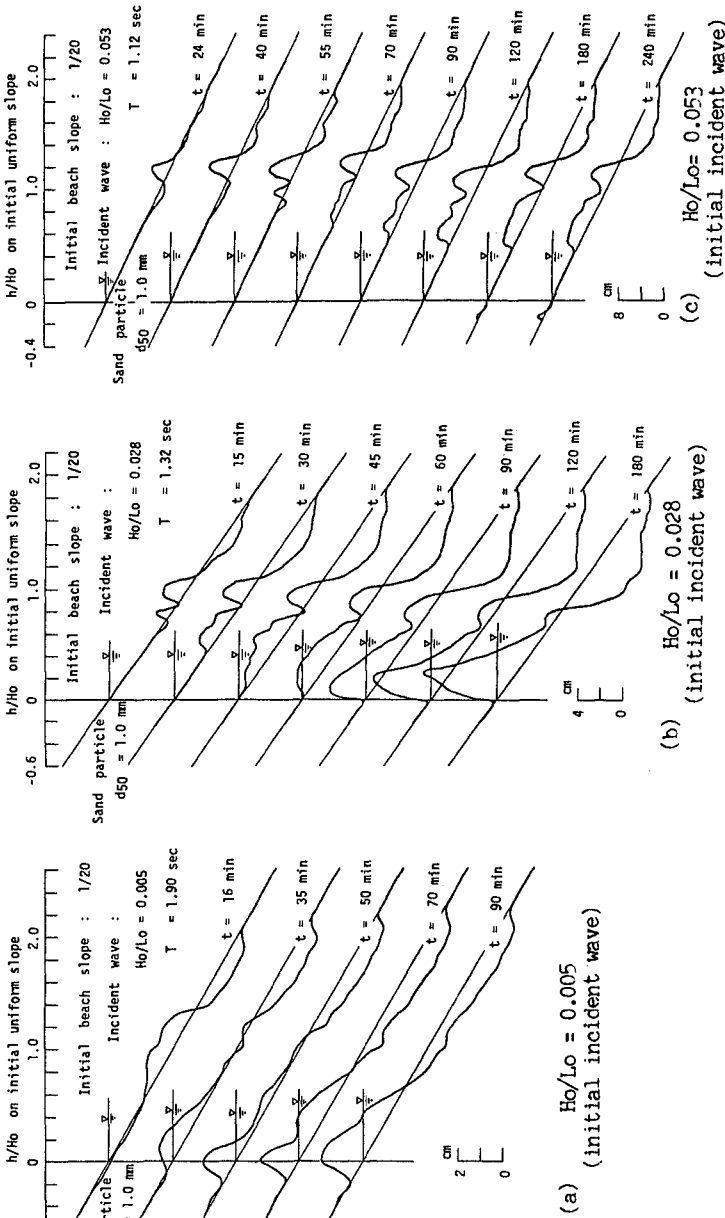


Fig. 9 Examples of beach profile deformation ( $d_{50} = 1.0$  mm, initial uniform slope:  $1/20$ ).

On the other hand, when sediments are transported mainly in suspension, the beach profile is expected to change in the process of Type I or II-1, because the mass transport of water on a sloping beach is in the offshore direction in a middle layer above the bottom, and hence the suspended sediment is easily transported offshore. This explains the reason why fine sediments are easily transported offshore and form a large longshore bar.

#### 4.2 Some Results of Model Beach Profile Deformation

In terms of a parameter of the still water depth to deepwater wave height ratio  $h/H_0$ , the region where  $h/h_b$  is 0.6-1.1 corresponds to the region where  $h/H_0$  is 1.0-1.4.

Figs. 8 and 9 show some results of the beach profile deformation in case of initial uniform slopes 1/10 and 1/20 for each deepwater wave steepness. Sand of 1 mm in  $d_{50}$  was used in these movable bed tests in order to get the condition of bed-load movement of bottom sediments. To investigate the beach process in detail, the beach profile was measured at short time intervals.

From these results of movable bed tests under the same wave condition as in the fixed plane roughened beach, two main points are found; that is, the first is that a uniformly sloping beach with sand of relatively large diameter of 1 mm begins to change into the profile which has an accretive portion at the location where  $h/H_0$  is 1.0-1.2 at the initial stage. At the first stage toward an equilibrium state, this profile is formed in all cases, independently of both the deepwater wave steepness and the initial uniform slope. However, at the next stage, the beach profile changes under the influence of the wave steepness. The effect of the initial beach slope is seemed to be related to the speed of beach profile change, namely the deformation speed of the beach profile becomes rapid rather in case of 1/10 initial beach slope than in case of 1/20 initial beach slope. The second is that under the condition of bed-load movement of bottom sediment, in the process of the beach profile deformation the region offshore from the breaking point is always eroded independently of both  $H_0/L_0$  and the initial beach slope.

#### 4.3 Discussions on Validity of Present Model

Fig. 10 shows the system of interactions among fluid characteristics, sediment movement and bottom configuration in the beach process. Each relationship clarified mainly in the unidirectional flow is briefly described as follows: relation (1) means the effect of the fluid field on the movement of bottom material, i.e. the fluid forces acting on the bottom sediments. In case of the wave field, the representatives in the relation (1) are considered to be the bottom shear stress, the mass transport velocity of water and the turbulence intensity by wave breaking. Relation (2) shows that for example, the von Karman constant diminishes as the concentration of suspended particles increases, Hino(1963). Relation (3) is the continuity condition of bottom sediment represented by the relation between the spatial gradient



of the sediment transport rate and the time variation of the bottom elevation. Relation (4) means the effect of the gravity force on the sediment movement, that is to say, the on-offshore component of the gravity force of the bottom sediment becomes large with an increase in the slope of beach. Relation (5) shows that the fluid field is affected by the bottom configuration, i.e. the energy loss becomes different due to the bottom configuration. Relation (6) is not clear at present.

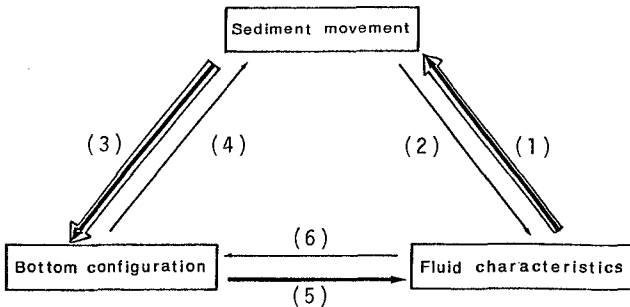


Fig. 10 System of interactions among fluid characteristics, sediment movement and bottom configuration.

From the results of the present investigation, when the sediment is transported as bed-load, the mechanism of beach profile deformation at the first stage from an initial uniform slope to an equilibrium state will be determined by the interaction between fluid characteristics and sediment movement and, therefore, can be explained on the basis of the spatial distribution of the net transport velocity of glass balls on a uniformly sloping beach.

However, at the second stage from a uniform slope to an equilibrium state, the mechanism of beach profile deformation will be governed by various interactions among fluid characteristics, sediment movement and bottom configuration.

## 5. CONCLUSIONS

In the limit of the present investigation, the following conclusions are drawn.

The mass transport velocity of water near the bottom on a roughened beach of  $1/20$  slope becomes small with an increase in the nonlinearity of waves.

The linearity between the mass transport velocity of water and the net transport velocity of bottom sediment is made clear by using tracers of polystyrene particle and glass balls.

When the sediment is transported as bed-load, the mechanism of

beach profile deformation at the first stage from a uniform slope to an equilibrium state can be predicted on the basis of the spatial distribution of the net transport velocity of glass balls.

At the second stage from a uniform slope to an equilibrium state, the mechanism of sediment transport has to be investigated on the basis of hydraulic characteristics of flow fields for the deformed bottom configuration.

Under the condition of bed-load transport of sediment, in the process of the beach profile deformation, the region offshore from the breaking point is always eroded independently of both the deepwater wave steepness and the initial slope of a beach.

#### REFERENCES

- Bijker, E.W., J.P.Th. Kalkwijk and T. Pieters: Mass transport in gravity waves on a sloping bottom, Proc. 14th Conf. Coastal Eng., 1974, pp. 447-465.
- Cornaglia, P., this was translated for Benchmark volume by W.N. Felder, University of Virginia, from "Delle Spiagge" in *Accad. Naz. Lincei Atti Cl. Sci. Fis., Mat. e Nat. Mem.* 5, ser. 4: 284-304 (1889), Benchmark Papers in Geology, Vol. 39, Dowden, Hutchinson and Ross, Inc., 1977, p. 382.
- Eagleson, P.S. and R.G. Dean: Wave-induced motion of bottom sediment particles, *Trans. ASCE*, Vol. 126, Part 1, 1961, pp. 1162-1189.
- Goda, Y.: A unified nonlinearity parameter of water waves, Report of the Port and Harbour Research Institute, Vol. 22, No. 3, 1983, pp. 3-30.
- Hino, M.: Turbulent flow with suspended particles, *Journal of the Hydraulics Division, ASCE*, Vol. 89, No. HY4, Proc. Paper 3579, 1963, pp. 161-185.
- Iwagaki, Y., W.-G. Pae and O. Moriguchi: Mechanism of sediment transport by waves on an impermeable slope, *Coastal Eng. in Japan*, Vol. 25, 1982, pp. 51-63.
- Longuet-Higgins, M.S.: Mass transport in water waves, *Phil. Trans. Roy. Soc. London, A*, No. 903, Vol. 245, 1953, pp. 535-581.
- Sawaragi, T. and I. Deguchi: On-offshore sediment transport rate in the surf zone, Proc. 17th Conf. Coastal Eng., 1980, pp. 1195-1214.
- Stokes, G.G.: On the theory of oscillatory waves, *Trans. Cambridge Phil. Soc.*, Vol. 8, 1847, pp. 441-455.
- Wang, H.T., T. Sunamura and P.A. Hwang: Drift velocity at the wave breaking point, *Coastal Eng.*, Vol. 6, No. 2, 1982, pp. 121-150.

## CHAPTER ONE HUNDRED FORTY THREE

### BEACH FILL BY TURNING THE COURSE OF SANDBARS

BY

Heie Focken Erchinger \*

#### ABSTRACT

The paper describes the littoral drift along the Eastfrisian Islands. The inlets between the islands are crossed by offshore bars which migrate round the deep channel of the inlet northwards on a bow. Their point of approaching the next island scatters. That causes periods of accretion during the approach of the bars on the beach and of erosion in certain beach sections without bar approach and sand supply.

When an offshore bar approaches a beach it moves a swash channel ahead as a rule. This causes a rising beach erosion by currents and wave wash and hinders the settling of the bar on that beach section. This paper reports a field study on influencing the migration of a bar by building a sand dam through such a swash channel. It was intended to feed the eroded section of the beach by the steered approach of the bar. The accretion by the desired approach of the bar on the eroded beach section was higher than expected and measured more than 270 m<sup>3</sup>/m.

#### 1.0 Introduction

On sandy coasts the littoral drift often crosses inlets as bars. Their point of approaching the beach of the next islands is important for the natural nourishment of the beach. The scattering approach causes periods of beach erosion in sections passed by offshore bars without approach. In case of severe erosion of the beach and the front dune expensive protective measures are often necessary.

In 1982 on the Isle of Langeoog, one of the Eastfrisian Islands on the German North Sea coast (Fig. 1), the winter storms effected a severe erosion of the beach and the barrier dune.

#### \* Address:

Bauamt für Küstenschutz

Postbox 102, D 2980 Norden, F. R.-Germany

Current employment:

Coast Protection Department of Lower Saxony, Public works on Beach- and Dune Protection, Dune Conservation, Dyke Construction and Land Reclamation

As an offshore bar was passing that section we looked for a possibility to steer the bar directly onto the beach. We imagined it could be reached by a sand dam through the swash channel as a connection from the beach to the offshore bar. That should interrupt the currents in the swash channel and influence the wave climate as a refraction groyne.

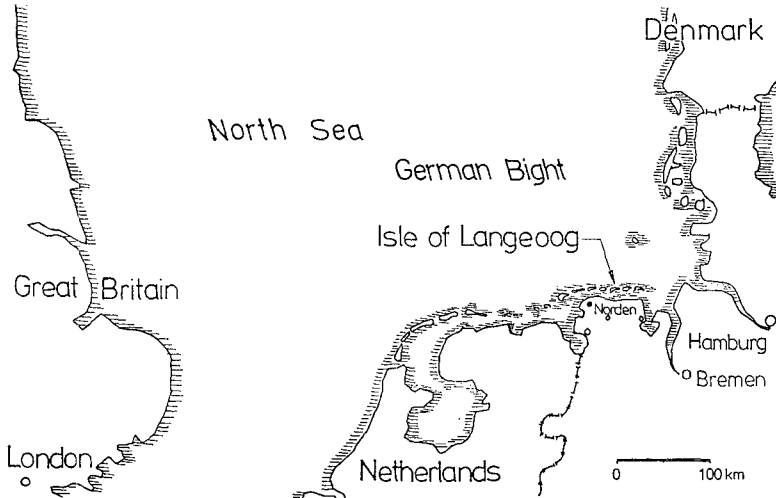


Fig. 1: The Isle of Langeoog - one of the Eastfrisian Islands on the Southern North Sea Coast -

## 2.0 LOCAL CONDITIONS

### 2.1 Littoral drift along the Eastfrisian Islands

Along the seven Eastfrisian Islands the littoral drift moves from west to east. The tidal inlets between the single islands are passed by sand bars migrating round the deep channel of the inlet northwards on a bow. When the bars leave a western island at first the influence of the strong ebb current in the deep channel of the inlet dominates and pushes them far to the north. Then the effect of the wave wash increases and moves the bars across the channel and towards the beach of the next island (Fig. 2). The point of the approaching that island depends on the inlet and sea conditions.

The migration of the bars depends on tidal currents as well as on storm conditions and wave action. In average they move about 430 m per year (6). Their volume and their point of approaching the beach is scattering (Fig. 3). As the beach is heightened and widened by

an approaching bar, the strenght of the dune-beach-system against wave action rises after the bar approach and on the further way of the littoral drift from that section (3). But on the opposite side of this section without sand supply erosion of the beach and the front dune takes place. That happened 1982 near beach profile 24 on the isle of Langeoog.

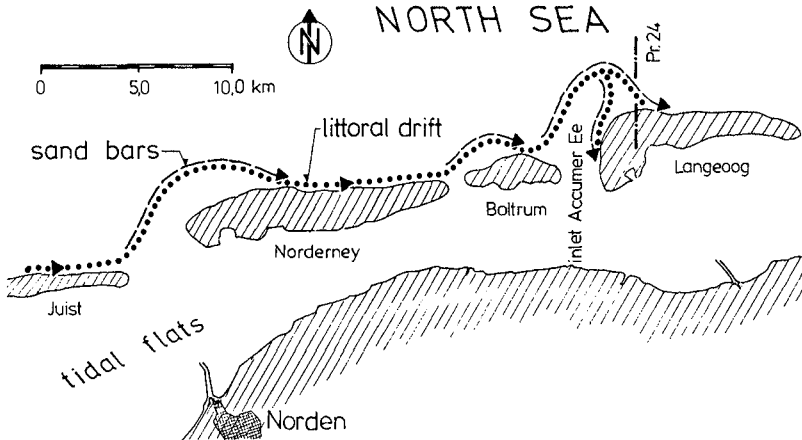


Fig. 2: Littoral drift along the Eastfrisian Islands.

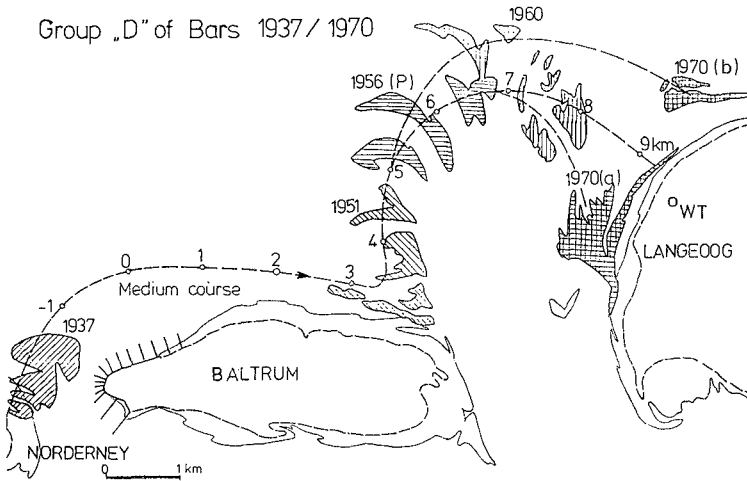


Fig. 3: Island to island migration of offshore bars and scattering of beach approach (6).

## 2.2 Beach conditions on the Isle of Langeoog

The Isle of Langeoog is a dune island with natural beaches and barrier dunes as natural protective structures against flooding the low lying land and the village during storm surges. This function of the barrier dunes is important, as the storm surge water level can increase to 3.8 m higher than MHW. The barrier dunes must be wide enough to keep a sufficient strength after very severe storm surges, when the extremely strong wave attack might have eroded a 10 to 20 m wide strip of the frontdune.

On the Isle of Langeoog the sand bars approach the beach on its west end. That normally effects an overall sand balance on this beach(7). But in spring 1982 we found the barrier dunes near the village eroded by wave attack during the winterly storm surges. The beach in front of them was steep and narrow, so further erosion had to be expected. To prevent the slight barrier dune from further erosion and from breaking through protective measures had to be carried out. Normally sand bars feed the beach, but in 1982 the bar passed the eroded beach section near Profile 24 in a distance of 350 m. Its approach could be expected in an acute angle further to the east.

The following solutions seemed to be conceivable:

- a construction of a revetment and groynes,
- an artificial beach fill,
- a nourishment of this beach-section by turning the migration of the bar directly onto the beach.

A revetment and groynes could not be taken into consideration seriously as the erosion would be temporary until the next bars approach the beach. Besides such constructions would have infavourable effects by lee-erosion and reflexion and also by disturbing the natural dune-beach-landscape and its development according to nature. Last not least they would be very expensive.

An artificial beach fill in the normal manner must include the fill of the swash channel to prevent a high rate of erosion by the rising velocity of the currents in the partly filled narrow channel. Such a fill needs 600 m<sup>3</sup>/m sand, that is a volume of 600,000 m<sup>3</sup> on the about 1 km long beach section.

As the creation of a dam through the swash channel and the fill of the backbeach was calculated only to need less than 40 % of that volume of sand it was decided to try the turning of the migration of the bar.



Fig. 4: Aerial view of the newly created connection of the offshore bar to the beach of the Isle of Langeoog by means of a sand dam.

### 3.0 SAND MOVEMENT

#### 3.1 Movement of the bar

Under wave action the sand of the bar moves on its outer slope in easterly direction and deposits at its end. During higher tide water levels another part of the eroded sand is washed across the surface of the bar by wave wash and deposits on the landward steep slope. This material might be moved further by tidal and wave currents in the swash channel mainly to the east end of the bar (1). That effects the approach of the bar in an acute angle further to the east.

#### 3.2 Currents in the swash channel

No tidal currents faster than 0.4 m/s were measured in this swash channel which is 100 m wide and 1.8 m deep at half-tide- water level.

During wave attack they would be higher and more effectively. But the currents in the swash channel hindered the deposit on the beach as the currents move the sand to the end of the bar. Therefore it should be favourable for the deposit of the bar to stop the currents in the swash channel. This could be effected by filling a dam across the channel.

During constructing the dam by hydraulic dredging the sand loss by the tidal currents had to be calculated. In the swash channel the rate of sandtransport was found as

0.1 m<sup>3</sup>/h by a current of 0.4 m/s and as  
2.2 m<sup>3</sup>/h by a current of 1.0 m/s (2,4).

These dates show, that it is possible to build the dam across the channel by hydraulic dredging with a usual capacity of the dredger pump of more than 500 m<sup>3</sup>/h.

#### 4.0 THE DAM AND ITS EFFECT

##### 4.1 Fill of the backbeach and the dam

In July 1982 the 300 m long dam was filled with 120 000 m<sup>3</sup> sand, medium grain size 0.2 mm, with a shape of a groyne (fig. 6) with a 20 m wide crest 80 cm above MHW. The dam should close up the swash channel and put an end to the currents as well as effect an influence on the wave climate by this type of a refraction groyne a discribed by FÜHRBÖTER (4) on the ICCE 1974 in Copenhagen.

But not only the dam but also the backbeach at the toe of the barrier dune was filled by 100 000 m<sup>3</sup> sand. As the approach of the bar would last a while, which depends on the storm conditions and the wave action, the backbeach was filled to prevent a rupture of the slight dune during the early winterly storm surges.

To get sand with the same grain size it was taken from the forebeach 5 m below MHW and 2.5 km to the east.

##### 4.2 Approach of the bar and the dam

During the following winter 1982/83 37 storm surges have been registered. That means more than three times the normal number of about 11 storm surges per year. During the autumn happened a severe erosion of the artificial fill of the backbeach. But during the further stormes after December accretion began and rose by the approaching bar just in the desired beach section.

Fig. 7 shows, that five months after building the dam the bar had moved 75 m right onto the beach. The dam had turned to the east round its root at the beach and still kept its function as a refraction groyne. In February 1983 after long lasting strong wave attack the bar and the dam had been deposited on the beach totally, so that



the beach has become wide and strengthened. After the winter storms the further accretion has continued, but not with such high rates as during the wave attack of the storm surges (5).

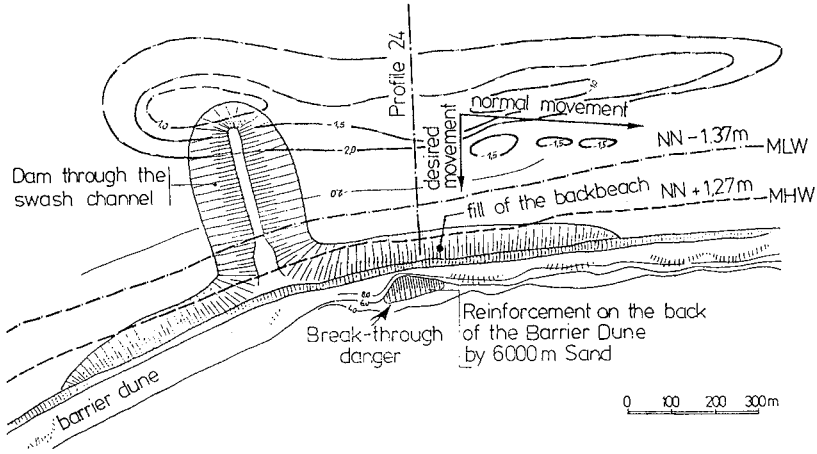


Fig. 5: Sand dam through the swash channel from the beach to the offshore bar and fill of the backbeach.

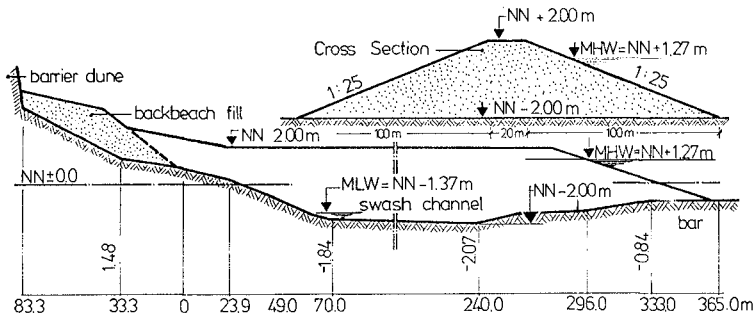


Fig. 6: Dam through the swash channel

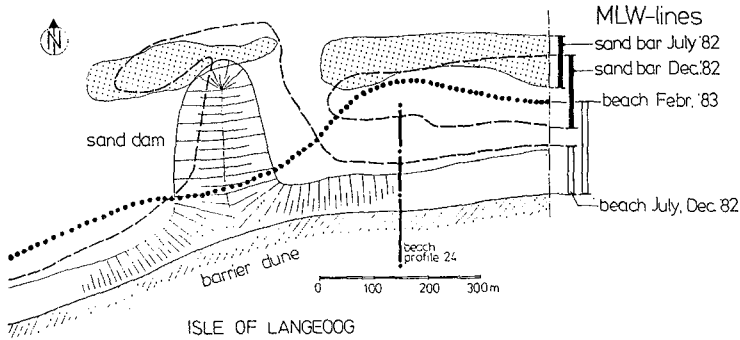


Fig. 7: Approach of the bar and accretion of the beach after steps of measurement in July 82, Dec. 82, Febr. 83.

The development of the beach was observed in beach profile 24 (Fig.8). The following dates have been registered compared with the original profile of July 1982:

	accretion (+) or erosion(-) m <sup>3</sup> /m	result m <sup>3</sup> /m
July 1982 artificial beach fill	+ 93	93
Dec. 1982 erosion of the back-beachfill	- 63	30
Febr.1983 accretion	+ 232	262
July 1983 accretion	+ 44	306

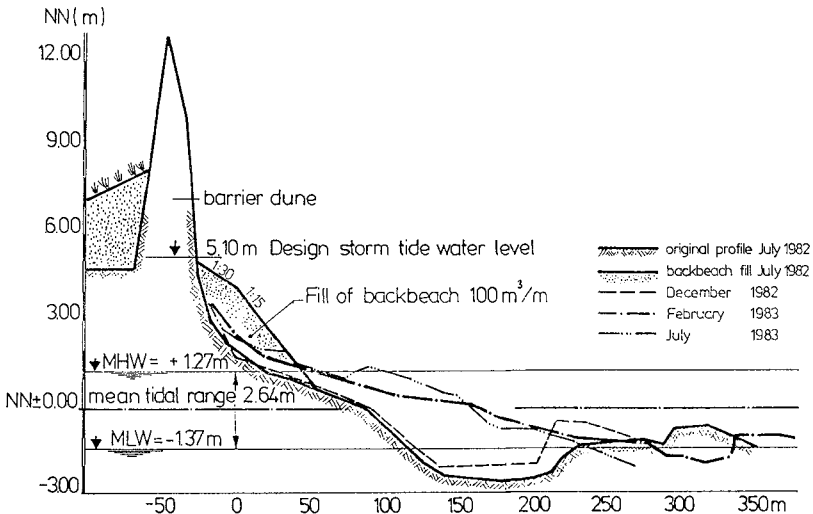


Fig. 8: Cross section of the beach and the fore beach with the approaching offshore bar after measurements in July 82, Dec. 82, Febr. 83 and July 83 in beach profile 24.

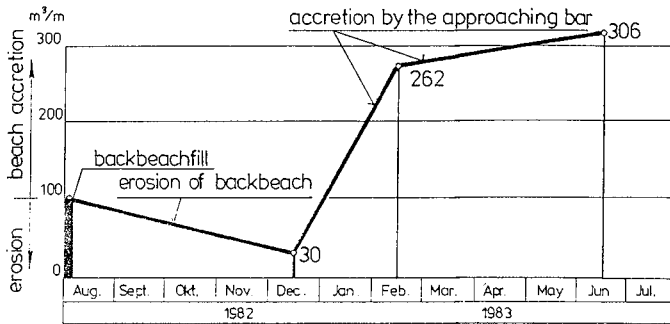


Fig. 9: Development of beach profile 24 - Erosion and, since Dec. 82, accretion of the beach by the approaching bar regarding to the original cross section -.

The accretion by the approach of the bar was higher than expected and measured more than 270 m<sup>3</sup>/m. This succes shows, that it is possible to influence the migration of the bar and to accelerate its approach by the combined effect of interrupting the currents in the swash channel and influencing the waves by a refraction groyne.

## References:

1. Dette, HH., 1974: Über Brandungsströmungen im Bereich hoher Reynolds-Zahlen - About Longshore Currents at high REYNOLDS-Numbers -. Mitt. d. Leichtweiß-Instituts der Technischen Universität Braunschweig, H.41,1974
2. Dillo, 1960: Die Sandwanderung in Tideflüssen - Migration of Sand in tidal Rivers - Mitt. d. Franzius-Instituts der Technischen Universität Hannover, H. 17, 1960.
3. Erchinger, H.F.,1974: Protection of Sandy Coasts in Dependence of the Dune-Beach-Type. Proceedings of the 14th ICCE in Copenhagen, Vol. II, New York, 1974
4. Führböter, A., 1974: A Refraction Groyne built by Sand. Proceedings of the 14th ICCE in Copenhagen, Vol. II, New York 1974
5. Führböter, A., 1979: About the Duration of Storm Surges and the connected Wave Energies. Mitt. d. Leichtweiß-Instituts der Techn. Universität Braunschweig, H. 65, 1979.
6. Homeier, H. u. Luck, G., 1971: Untersuchung morphologischer Gestaltungsvorgänge im Bereich der Accumer Es als Grundlage für die Beurteilung der Strand- und Dünenentwicklung im Westen und Nordwesten Langeoogs. Jahresbericht der Forschungsstelle für Insel- und Küstenschutz, Band XXII, Norderney, 1971.
7. Lüders, K., Führböter, A., Rodloff, W., 1972: Neuartige Dünen- und Strandsicherung im Nordwesten der Insel Langeoog. Die Küste, H. 23, Heide 1972.

## CHAPTER ONE HUNDRED FORTY FOUR

### BEACH AND SURF ZONE EQUILIBRIA AND RESPONSE TIMES

L. D. Wright<sup>1</sup>, S. K. May<sup>2</sup>, A. D. Short<sup>3</sup>, and M. O. Green<sup>1</sup>

#### ABSTRACT

Analyses were performed on a 6½ year time series of daily wave data, daily beach state data and monthly beach and surf zone profile data. Beach state changes, which involve the relatively rapid redistribution of sediment already stored locally, are predictable in terms of Dean's (3) simple parameter  $\Omega = H_b / (w_s T)$  where  $H_b$  is breaker height,  $w_s$  is sediment fall velocity and T is wave period. Each of the six beach states has a different equilibrium range of  $\Omega$  values and the direction of change (erosion or accretion) depends on the departure from the equilibrium association. Empirical eigenvector analyses performed on the profile data permitted separation of different response components. The lower order vectors expressing the grosser aspects of the profile features such as beach volume and surf zone gradient displayed maximum variance at periods in excess of 2 years whereas much shorter response times characterized the higher order components such as bar-trough shapes and asymmetries. We infer that the fast response, and more predictable, components of beach and surf zone change largely involve smaller scale sediment exchanges between the beach and surf zone whereas the slower responses are related to larger scale exchanges between the surf zone and the inner continental shelf.

#### INTRODUCTION

Beach changes can involve changes in beach volume or beach state or both. Beach state, as used here, refers to the six common beach states (5, 6, 8, 9, 10, 11; Fig. 1). These include the reflective (steep) and dissipative (flat) extremes as well as 4 intermediate states which are (in order of decreasing surf energy): longshore bar-trough (LBT); rhythmic bar-and-beach (RBB); transverse bar-and-rip (TBR); and ridge-and-runnel/low tide terrace (LTT). Each state is dominated by a different set of hydrodynamic mechanisms. At a

---

<sup>1</sup>Virginia Institute of Marine Science, School of Marine Science, College of William and Mary, Gloucester Point, Virginia, 23062.

<sup>2</sup>U.S. Army Corps of Engineers Waterways Experiment Station, Vicksburg, Mississippi, 39180.

<sup>3</sup>Coastal Studies Unit, University of Sydney, Sydney, Australia.

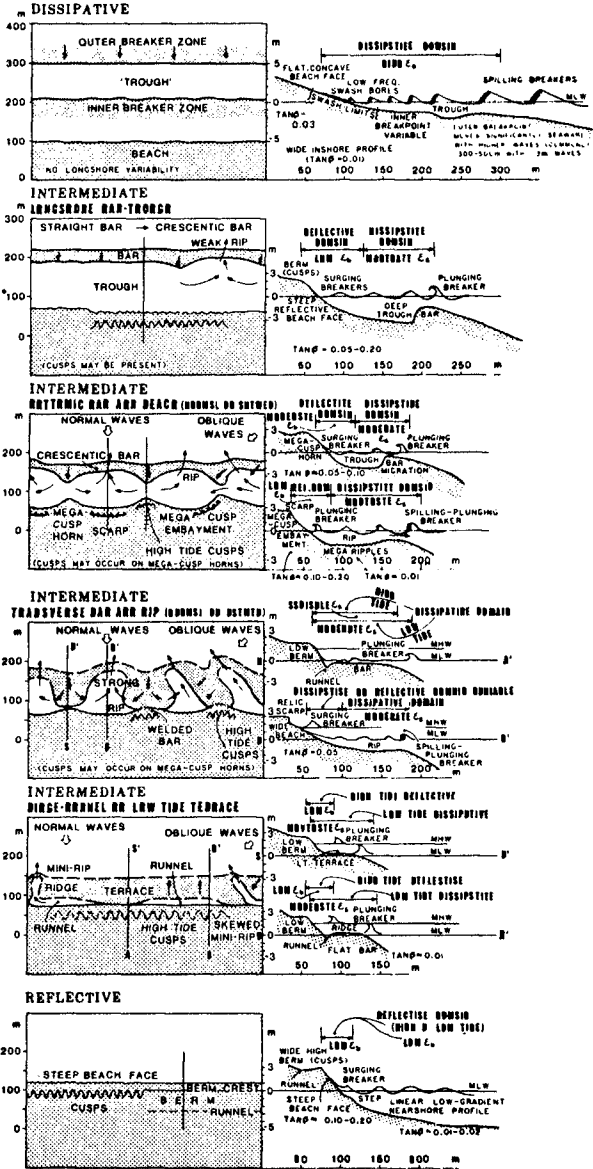


Figure 1. Plan and Profile Characteristics of the Six Common Beach States.

somewhat crude, first order level beach state exhibits a reasonable degree of dependence on Dean's (3) parameter  $\Omega = H_b / (w_s T)$  where  $H_b$  is breaker height,  $T$  is wave period and  $w_s$  is sediment settling velocity (9). However, variations in  $\Omega$  can only partially explain the short term temporal variations in beach state or in beach profiles. Rates and directions of beach response are governed not only by the short-term history of  $\Omega$ , but equally by antecedent beach state. Long-term (> 1 year) cycling of sediment between the inner shelf and the surf zone add further complexity to attempts at gaining short-term predictability.

The purpose of this paper is to present the most recent results in the development of a general model for predicting short-term changes in beach and surf zone morphodynamics, emphasizing moderate to high energy natural systems. To this overall end, we have examined the equilibrium relationships between beach state and  $\Omega$ ; rates of change of both beach state and beach volume as functions of disequilibrium; and response times and frequency-response characteristics for different types and scales of change.

#### TECHNIQUES

Time series spanning 6½ years of daily wave data and beach state observations, and biweekly to monthly beach and surf zone leveling transects at 8 locations on the moderate to high energy Narrabeen Beach near Sydney in southeastern Australia, supplemented by shorter time series from other beaches, provided the basic data set of our analyses. The daily data were subjected to harmonic and spectral analyses to identify dominant response cycles. Using smoothed time series, time derivatives of  $\Omega$ , beach state and beach volume were estimated. To evaluate the degree to which beach state can be predicted in terms of  $\Omega$ , discrete discriminant analyses were performed utilizing a record of 1,545 cases. Empirical eigenvector analyses were performed on the beach profile data to characterize the time-varying profile features. Weightings on the dominant eigenvectors were subjected to spectral analyses to determine the dominant frequencies of variation of each vector.

#### SHORT-TERM CHANGES IN BEACH STATE

A 20-month section of the time series of daily significant wave height,  $H_s$ , daily estimated  $\Omega$  values, daily beach state, and subaerial beach volume,  $V_b$ , as observed on mid-Narrabeen Beach is shown in Figure 2. From Figure 2, it is apparent that wave conditions and beach state change rapidly whereas subaerial beach volume responds much more slowly. In addition, any given state can occur at any time of the year regardless of whether subaerial beach volume is normal, accreted, or eroded.

The time interval required for a full-state (i.e. one complete state) response to changing wave conditions averaged 7 days for Narrabeen Beach. Harmonic and spectral analyses show that the largest amount of beach change is associated with 'cycles' of 70 to 120 days.

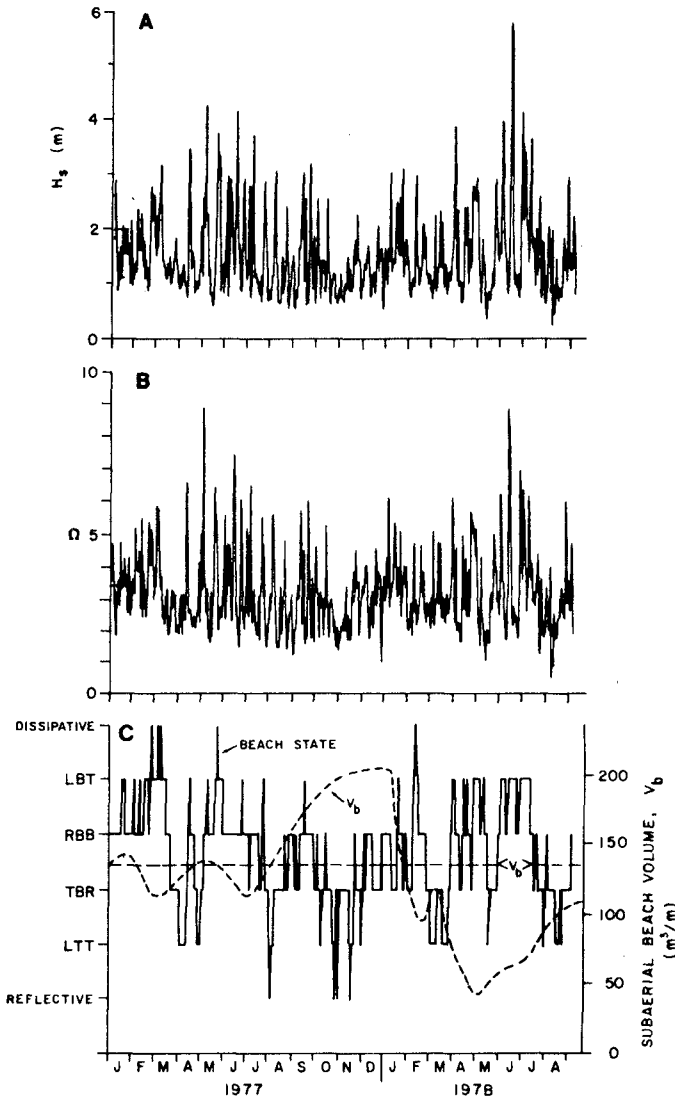


Figure 2. Time series of daily significant deepwater wave height (A), daily  $\Omega$  values (B), and daily beach state (C). Subaerial beach volume is also shown in C.  $\langle V_b \rangle$  indicates the long-term mean subaerial beach volume.



However, a pronounced secondary peak in amplitude of beach state change occurs in the period band of 15-20 days. This response results from the normal passage of pressure systems. In this response band, beach state changes lag changes in  $\Omega$  by 4 days.

Discrete discriminant analyses were used to test the degree to which day-to-day variability in beach state can be predicted in terms of  $\Omega$ . Two  $\Omega$  values were used in the analyses: the immediate value occurring on the day the particular state was observed and a weighted mean value  $\bar{\Omega}$  expressing recently antecedent conditions. The weighted mean value was computed from

$$\bar{\Omega} = \left[ \begin{array}{c} D \\ \sum_{i=1}^{D} 10^{-i/\phi} \end{array} \right]^{-1} \sum_{i=1}^{D} (\Omega_i 10^{-i/\phi}) \quad (1)$$

where  $i=1$  on the day before state observation and  $i=D$  on  $D$  days before observation. The parameter  $\phi$  depends on the rate of memory decay; the weighting factor decreases to 10% at  $\phi$  days before observation. The immediate value of  $\Omega$  made a negligible contribution to explaining daily beach state changes. However, the antecedent conditions as expressed by  $\bar{\Omega}$  showed a very strong association when  $\phi=5$  days and  $D=30$  days.

Table 1 summarizes the means and standard deviations of  $\bar{\Omega}$  associated with each state. Although the means of  $\bar{\Omega}$  differ significantly between states, the overlap between similar states (e.g. rhythmic bar and beach and transverse bar and rip) is too large to permit highly successful prediction of all six states. Predictability, in terms of discriminant functions which are overwhelmingly dominated by  $\bar{\Omega}$ , is substantially increased when adjacent and similar pairs of states are combined into fewer classes. To produce three broader groups we combined the reflective extreme with the low-tide-terrace/ridge and runnel state, the transverse bar and rip state with the rhythmic bar and beach state, and the longshore bar-trough state with the dissipative extreme. The rationale for this simplification is discussed more fully by Wright et al. (12). The central tendencies of  $\bar{\Omega}$  for each of the three recombined groups are presented in Table 2. The probability distributions of  $\bar{\Omega}$  for each class are shown in Figure 3 from which clear separation can be seen. Predicted state corresponded to the observed state in 68.5% of the 1,545 cases examined when the simplified classification was used. The success rates of predicting the reflective and dissipative end members were 85% and 78% respectively.

By examining cases where the time derivatives of both state and  $\Omega$  were near zero, it was possible to define the equilibrium conditions associated with each state. The equilibrium values,  $\Omega_e$ , of each state are summarized in Table 3. Directions of change (erosional or accretionary) are predicted in terms of "instantaneous" or short-term time averaged departures of  $\Omega$  from the equilibrium value appropriate to the inherited beach state prevailing at the time change begins.

Table 1

Average Associations Between Beach State,  $\bar{\Omega}$ , and  $\bar{\Omega}$  for Narrabeen Beach

<u>Beach State</u>	<u>Number of Occurrences</u>	<u>Mean <math>\bar{\Omega}</math></u>	<u>Mean <math>\bar{\Omega}</math></u>	<u>Stan. Dev. <math>\bar{\Omega}</math></u>	<u>Stan. Dev. <math>\bar{\Omega}</math></u>
Reflective	38	2.33	2.18	0.60	0.32
LTT	233	2.52	2.35	0.80	0.49
TBR	691	3.15	3.16	0.98	0.67
RBB	402	3.34	3.38	1.00	0.65
LBT	170	4.64	4.74	1.55	1.04
Oissipative	11	5.42	5.46	1.47	0.93

Table 2

Average Associations Between Merged Beach State Classes,  $\bar{\Omega}$ , and  $\bar{\Omega}$  for Narrabeen Beach

<u>Merged Beach States</u>	<u>Number of Occurrences</u>	<u>Mean <math>\bar{\Omega}</math></u>	<u>Mean <math>\bar{\Omega}</math></u>	<u>Stan. Dev. <math>\bar{\Omega}</math></u>	<u>Stan. Dev. <math>\bar{\Omega}</math></u>
Ref. & LTT	271	2.50	2.36	0.77	0.46
TBR & RBB	1093	3.22	3.24	0.99	0.67
LBT & Diss.	181	4.69	4.86	1.56	1.05

Table 3

Equilibrium Associations Between Beach State and  $\bar{\Omega}_e$

<u>Beach State</u>	<u><math>\bar{\Omega}_e</math> Mean</u>	<u>Stan. Dev.</u>
Reflective	< 1.5	----
LTT	2.40	0.19
TBR	3.15	0.64
RBB	3.50	0.76
LBT	4.70	0.93
Dissipative	> 5.5	----

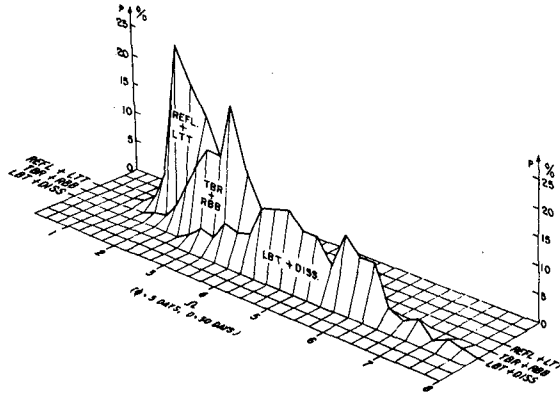


Figure 3. Frequencies of association between  $\bar{\Omega}$  values and the three merged beach state classes.

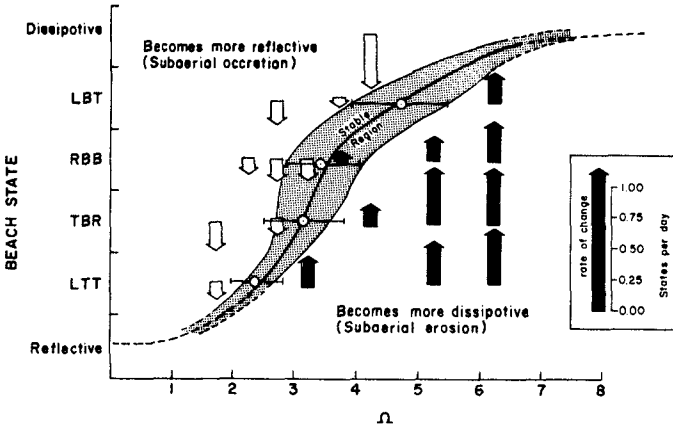


Figure 4. Beach State Equilibria and Directions and Rates of Change. The central curve indicates the mean equilibrium associations between state and  $\Omega$ . If a beach lies to the right and below the stable region in terms of the combination of preexisting state and prevailing  $\Omega$ , subaerial erosion will take place to produce more dissipative conditions. If the combination is above and to the left, then subaerial accretion can be expected.

The inferred equilibrium associations and directions of change are indicated by Figure 4. In general, it is possible to predict probable states in terms of recently antecedent wave conditions with reasonable success. Furthermore, the direction of change can be predicted when the instantaneous combination of state and  $\Omega$  is in sufficient disequilibrium as to lie outside the "stable region" of Figure 4.

VARIATIONS IN BEACH AND SURF ZONE PROFILES

The same 6½ year data set includes monthly beach and surf zone profiles which provide a relatively long time series of subaerial beach volume and profile shape. In contrast to the relatively fast changes in beach state, beach volume changes are slow and involve sediment exchanges across the inner shelf. The largest changes in the subaerial beach volume of Narrabeen Beach have amplitudes in excess of  $100 \text{ m}^3 \text{ m}^{-1}$  and occur over time intervals of 2 to 4 years. Changes in profile dimensions and shape express in part the relatively rapid changes in state and in part the much slower changes in gross sediment volume.

Empirical eigenvector analyses provided an objective, quantitative characterization of changing profile shapes. Basically, the analysis transforms a set of intercorrelated variables into a new coordinate system in which the axes are linear combinations of the original variables and are mutually orthogonal. Two types of analyses were conducted: (1) in the first ("fixed datum") the eigenvectors express profile variability referenced to a fixed datum; (2) in the second ("floating datum") the profile variability is referenced to the instantaneous position of the shoreline and is independent of absolute degree of accretion or erosion. The latter analyses best express profile shape and can be related to beach state. The lower order eigenvectors ( $E_1, E_2$ ) express the grosser aspects of the profile such as beach volume, width and gradient. More complex profile features such as bar-trough configurations, asymmetries, and steps are expressed by progressive addition of higher vectors ( $E_3, E_4, E_5$ ). The additive properties of the vectors are illustrated by Figure 5.

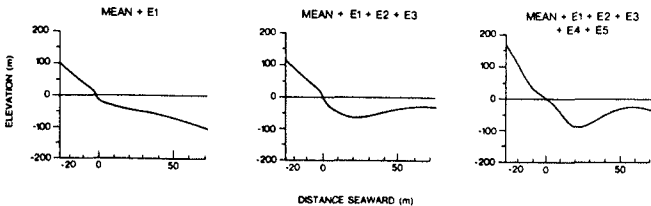


Figure 5. Additive Properties of the Eigenvectors (Floating Datum Case).

The physical meanings of the first four fixed datum eigenvectors are illustrated in Figure 6. Most of the variance in the profile of Narrabeen Beach is accounted for by eigenvector 1 which expresses beach width and sediment volume; that is, in essence, a sand storage function. As illustrated by Figure 6, a positive weighting on eigenvector 1 indicates an accreted profile (relative to the mean) whereas a negative weighting indicates an eroded profile. The amplitudes of profile changes associated with eigenvectors 2-4 are small relative to those associated with eigenvector 1. However, these higher modes of profile behavior are more closely related to profile shape. A positive weighting on eigenvector 2 indicates a steeper beach with a well developed berm fronted by bar-trough topography. A negative weighting corresponds to overall profile flattening.

Figure 7 shows power spectra of the weightings on the four fixed datum eigenvectors. The maximum and only consequential variance in eigenvectors 1 and 2 is seen to occur at periods of two or more years. Temporal variations in eigenvector 1 directly parallel variations in subaerial beach volume (Fig. 2); the weightings on this vector are coherent and in phase between all profiles along Narrabeen Beach indicating that a shore-normal rather than a longshore redistribution of sediment is responsible for the changes.

The floating datum modes of profile variation are independent of absolute sand storage volume and beach width and are therefore better able to describe the behavior of profile shape. Figure 8 shows the nature of the profile shape effects described by the first five floating datum eigenvectors. Table 4 indicates the profile shape "signatures" of each of the six beach states (Fig. 1) expressed in terms the signs of the weightings on the eigenvectors. The first eigenvector expresses the overall flattening (+ weighting) and steepening (- weighting) of the surf zone and beach and thus characterizes the relative degree of dissipativeness or reflectivity of the system. This mode of variation is most effective in discriminating between the two extreme beach states (Table 4). Pronounced bar-trough topography yields positive weightings on both eigenvectors 2 and 3 (Figs. 8 and 5); the absence of bars is expressed by negative weightings on both of these vectors. Accordingly, the strongly barred states (LBT, RBB) are distinguished from the other states on the basis of the weightings on eigenvectors 2 and 3 in combination. Adjacent (in Fig. 1) and somewhat similar intermediate states are discriminated between in terms of the higher vectors. For example, eigenvector 4 distinguishes between the longshore bar trough state (+ weighting) and the rhythmic bar and beach state (- weighting) while eigenvector 5 distinguishes the rhythmic bar and beach state from the transverse bar and rip state.

The results of spectral analyses performed on the time series of the weightings on the floating-datum eigenvectors are shown in Figure 9. The power spectrum of the weightings on eigenvector 1 shows the dominant peak to be centered at periods between 24 and 42 months. This suggests that the largest amplitude variations in overall profile gradient or "dissipativeness" are related to the same long-period processes that produce the major variations in gross sand storage. The existence of a secondary but significant peak at about 2.3 months

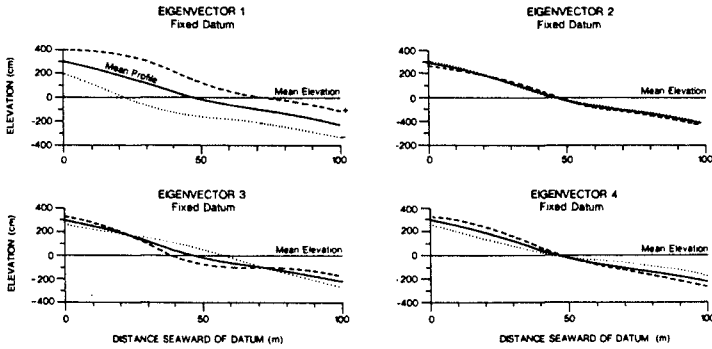


Figure 6. Fixed-datum modes of profile variation for Narrabeen Beach. Positive and negative weightings on the eigenvectors are indicated respectively by the dashed and dotted curves. The solid curve indicates the time-averaged mean profile.

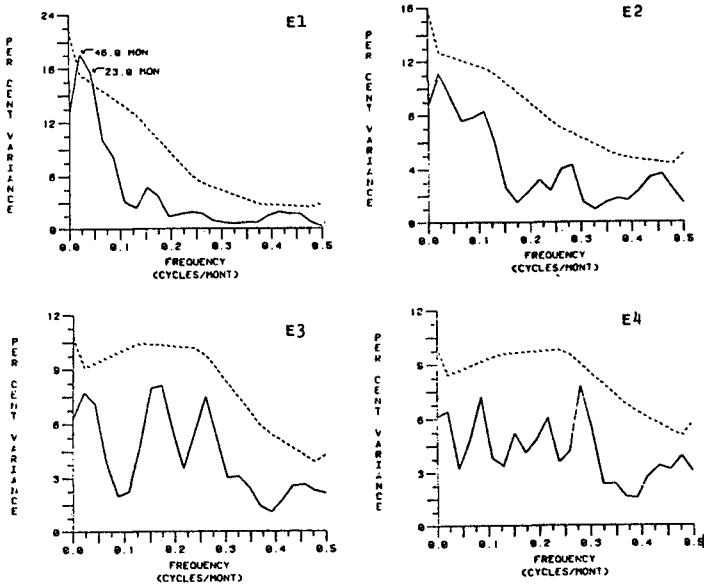


Figure 7. Power spectra of the weightings on the four fixed-datum eigenvectors. The dashed curve indicates the 95% confidence level for spectral peaks.

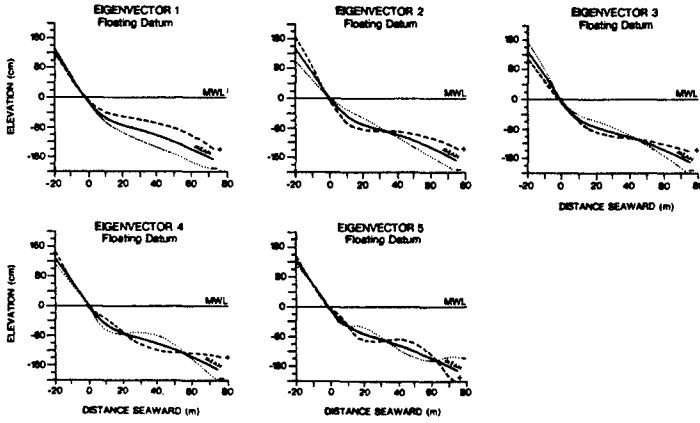


Figure 8. Floating-datum modes of profile variation. Positive and negative weightings are indicated respectively by the dashed and dotted curves.

Table 4. Relationships Between Beach State and the Signs of Weightings on the Five Floating Datum Eigenvectors.

Floating Datum Eigenvector No.	Beach State					
	Refl.	LTT	TBR	RBB	LBT	Diss.
E1	-- *	-	~0	~0	-	++ *
E2	-	-	+	+	+	-
E3	-	-	~0	+	+	+
E4	+	~0	~0	-	+	~0
E5	+	+	+	-	~0	-

\*Extreme negative and extreme positive weightings are indicated by -- and ++ respectively.

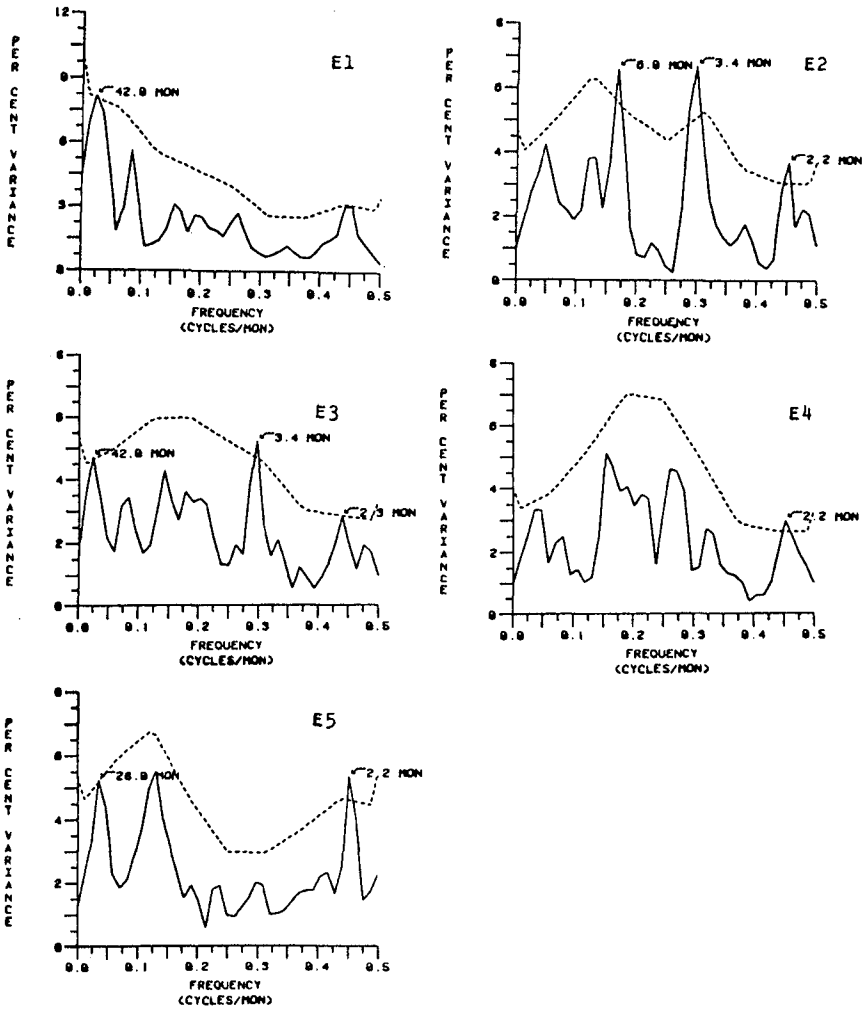


Figure 9. Power spectra of the weightings on the five floating-datum eigenvectors.



indicates that profile gradient is also responsive to higher frequency forcings. The dominant variations in eigenvectors 2 through 5 occur at periods of 2 to 6 months. This corresponds to the period band of the largest amplitude fluctuations in beach state as discussed earlier. However, it must be noted that eigenvectors 2-5 all exhibit appreciable variance at periods of 2 years or more. We can infer from this that even the higher-order aspects of profile shape --and hence beach state-- are significantly overprinted by slow oscillations in inshore sediment storage.

#### DISCUSSION AND CONCLUSIONS

The state, profile configuration, and sand storage of a beach and surf zone system as observed at any given time are consequences of the time integration of numerous antecedent processes having different space and time scales. We have attempted to deal, albeit superficially, with part of the complexity of this problem by separating the total response into components, each of which has its own characteristic space scale and temporal frequency. Others before us have performed similar analyses on beach profiles with the aim of elucidating seasonal (e.g. 1, 4, 7) as well as tidal cycle (e.g. 2) responses. We are concerned not only with the temporal behavior of the profile and of the volume of sediment stored therein but equally with the temporal behavior of the three-dimensional beach and surf zone state. Our interest in beach state lies in the fact that beach state is an indicator of the dominant surf zone process signature (9) and influences the mechanisms and probability of beach erosion or accretion (8). Furthermore, changes in beach state permit at least short-term quasi-equilibrium with changes in wave conditions to be achieved, by virtue of surf zone process modification, without major changes in the gross sand storage properties of the beach. This has the potential of temporarily arresting or impeding the large-scale response of the profile to larger scale (larger than scale of surf zone) and longer term disequilibrium. Conversely, however, beach state is subject to changes induced by large scale, low frequency sediment fluxes. For example, the introduction of sediment into a surf zone from alongshore or from seaward of the surf zone can cause a reflective or intermediate beach which is in equilibrium with low to moderate waves to become dissipative.

The range, rate and frequency of response of a particular mode of beach variability depends in part on the frequency and intensity of the forcing involved, in part on the degree of disequilibrium induced by changing morphodynamic conditions, and in part on the scale and associated "time constant" of the mode of variability. Modes of change which involve the redistribution of relatively small quantities of sediment over relatively small distances have short response times in comparison to modes, such as the sand storage function for example, which involve large exchanges of sediment and require more total work. Beach state changes can take place, at least within a limited range of intermediate states, by means of localized short-range redistribution of the sediment already contained in the surf-zone and intertidal beach. Accordingly, and as illustrated by Figure 2, beach state can change rapidly and frequently and, for this reason, can be roughly predicted in terms of recently antecedent wave conditions. Major

shifts in state from fully dissipative to fully reflective or vice versa are more closely linked to total inshore sand storage and to overall flattening and steepening and are thus much lower in frequency.

In the case of the moderate energy Narrabeen Beach dealt with in this paper, we see that beach state and the associated higher modes of profile change respond quickly whereas gross sediment storage and overall inshore gradient respond slowly. Changes in the fixed-datum sand storage function and to some extent in the floating datum gradient function (eigenvector 1) involve the import and export of large quantities of sand to and from the beach and surf zone system. Since Narrabeen Beach is headland-bounded, these sediment transfers must occur in the cross-shore dimension and must thus involve exchanges between the surf zone and the inner shelf. As illustrated conceptually by Figure 10, we infer that the slow-response modes of variability involve large-scale cycling of sediment across the inner shelf. On the Australian east coast the "closure" depth to which the sediment exchange is active is probably between 20 m and 30 m. It is obviously shallower on less energetic coasts. The actual physical processes responsible for alternating shoreward and seaward transport over the inner shelf remain to be identified.

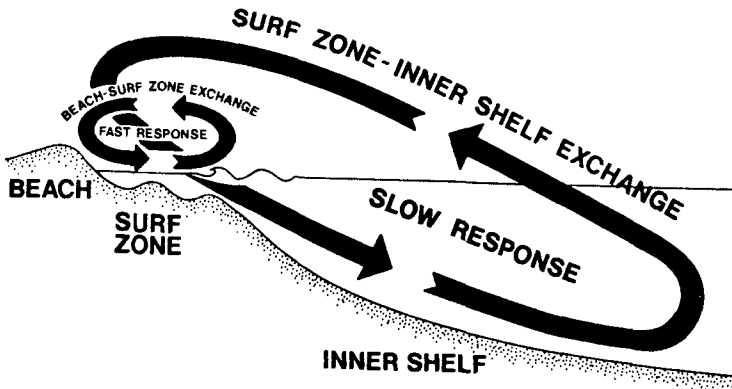


Figure 10. Scales and frequencies of beach, surf zone, and inner shelf responses. Rapid, relatively high frequency temporal changes in beach state and higher-order modes of profile variability largely involve the short-range redistribution of sediment already contained within the beach/surf-zone system. Low-frequency variability in sand storage and associated effects involves large-scale and slow exchanges of sediment between the surf zone and the inner shelf.

## ACKNOWLEDGEMENTS

This study has been supported by the Office of Naval Research, Coastal Sciences Program, Task NR 388-189. The collaboration of Drs. B. Hayden and P. Nielsen is gratefully acknowledged.

## REFERENCES

1. Aubrey, D.G., 1979. Seasonal patterns of onshore-offshore sediment movement. *J. Geophys. Res.*, vol. 84, pp. 6347-6354.
2. Clarke, D.J., Eliot, I.G. and Frew, J.R., 1984. Variation in subaerial beach sediment volume on a small sandy beach over a monthly lunar tidal cycle. *Mar. Geol.* vol. 58, pp. 319-344.
3. Dean, R.G., 1973. Heuristic models of sand transport in the surf zone. *Proc. Conf. on Engineering Dynamics in the Surf Zone*, Sydney, N.S.W., 1973, pp. 208-214.
4. Eliot, I.G. and Clarke, D.J., 1982. Temporal and spatial variability of the sediment budget of the subaerial beach at Warilla, New South Wales. *Aust. J. Mar. Freshwater Res.*, vol. 33, pp. 945-969.
5. Short, A.D., 1979a. Wave Power and Beach Stages: A Global Model. *Proc. Int. Conf. Coastal Eng.*, 16th, Hamburg, 1978, pp. 1145-1162.
6. Short, A.D., 1979b. Three Dimensional Beach Stage Model. *J. Geol.*, vol. 87, pp. 553-571.
7. Winant, C.D., Inman, D.L. and Nordstrom, C.E., 1975. Description of seasonal beach changes using empirical eigenfunctions. *J. Geophys. Res.*, vol. 80, pp. 1979-1986.
8. Wright, L.D., 1981. Beach Cut in Relation to Surf Zone Morphodynamics. *Proc. Int. Conf. Coastal Eng.*, 17th, Sydney, 1980, pp. 978-996.
9. Wright, L.D. and Short, A.D., 1984. Morphodynamic Variability of High Energy Surf Zones and Beaches: A Synthesis. *Mar. Geol.* vol. 56, pp. 93-118.
10. Wright, L.D., Chappell, J., Thom, B.G., Bradshaw, M.P. and Cowell, P., 1979a. Morphodynamics of Reflective and Dissipative Beach and Inshore Systems: Southeastern Australia. *Mar. Geol.*, vol. 32, pp. 105-140.
11. Wright, L.D., Thom, B.G. and Chappell, J., 1979b. Morphodynamic Variability of High Energy Beaches. *Proc. Int. Conf. Coastal Eng.*, 16th, pp. 1180-1194.
12. Wright, L.D., Short, A.D. and Green, M.O., 1985 (in press). Short-Term Changes in the Morphodynamic States of Beaches and Surf Zones: An Empirical Predictive Model. *Mar. Geol.* vol. 62.

## CHAPTER ONE HUNDRED FORTY FIVE

### Quantification of Shoreline Rhythmicity

Holly C. Garrow\*

#### Abstract

The study of beach morphology, for example, its changes with wave and tide conditions, is facilitated by the development of simple numerical values which characterize the morphology. Multivariate (EOF) analysis of topographic contour data is a means for determining important morphologic components which vary independently. If these components correspond to familiar shoreline features the researcher considers important, then the development of each component can be quantified by its significance, or weighting, in each sample. Alternatively, the components may be complicated and not useful in quantifying beach morphology. A study of these morphologic components, however, can provide insights into the dynamics of the beach system.

If multivariate analysis produces complicated components, an alternative approach, of subjectively identifying shoreline characteristics of interest, can be taken. The characteristics may be the same as those frequently used in past studies, such as beach slope or sand volume. It is likely, though, that EOF analysis of topographic data will suggest more sophisticated characteristics which should be used. Some of these, for example, mean shoreline position or amplitude of a rhythmic shoreline, may be easily quantified, whereas, others such as longshore position of rhythmic features or cusp width relative to embayment width, may be more difficult to quantify.

Both of these analysis approaches were applied to beach survey data obtained over a period of ten months (including the El Niño winter of 1982/83) on Siletz Spit, Oregon. The shoreline was rhythmic with an 800-850 m wavelength throughout the duration of the study. Rhythmic topography has been associated with significant past beach and dune erosion at this site. Hence, it is of interest to describe the beach morphology quantitatively, and relate three dimensional beach changes to wave and tide conditions.

Field observations and EOF analysis determined three important characteristics of shoreline morphology: overall accretion/erosion of the shoreline, amplitude of the rhythmic topography, and longshore position of the rhythmic features. EOF analysis was not able to separate these three morphologic components. They were quantified, respectively, by mean distance offshore to a specified contour, the standard deviation of a contour about that distance, and the weights of the first eigenvector calculated by EOF analysis of topographic contour data normalized to the same mean and standard deviation.

Mean shoreline position was shown to move onshore with increasing wave height, as expected. Rhythmicity amplitude varied inversely

\*College of Oceanography, Oregon State University, Corvallis, OR  
97331

with the wave height, but there is evidence to believe this is not the case for all winters on Siletz Spit. Rhythmic topography formed and increased in amplitude under depositional conditions during the ten months of this field study. Due to differences between the rates of change of mean shoreline position (up to 5 m/2 wks) and of rhythmicity amplitude (up to 10 m/2 wks), rhythmic topography should be able to develop under erosional conditions as well.

In many beach systems, EOF analysis of topographic contour data should not be expected to produce simple morphologic components which correspond to familiar shoreline features. EOF analysis can be an aid in furthering one's understanding of the dynamics of a beach system and can be a useful guide in subjectively identifying important shoreline characteristics. In some instances, EOF analysis of a modified data set may allow one to quantify one or more of these characteristics.

### Introduction

Simple numerical values are needed to describe beach morphology before three dimensional beach changes can quantitatively be related to wave, tide, or other 'environmental' forces. In general, two approaches can be taken to determine useful values which characterize the beach morphology. Both require data documenting beach topography in three dimensions.

One approach is a multivariate analysis of beach profile data collected at different longshore locations and/or different times (Winant et al., 1975; Aubrey et al., 1980; Wright et al., in press). This provides an objective determination of important and independent components of beach morphology. It also weights each component, depending on its importance. Ideally, the components correspond to familiar features such as a straight beach profile with an offshore bar (if beach profiles are analyzed) or perhaps a shoreline with cusped protrusions (if topographic contours of the beach are analyzed). The weightings then provide a measure of how well developed that feature was at the time of the survey. However, depending on the field site, numbers of samples taken, and duration of the study, the components may be complicated and not represent morphologies of interest.

An alternative analysis approach is to determine, subjectively, characteristics of the topography which are of interest, such as foreshore beach slope or average surf zone beach slope, beach volume, or the horizontal or vertical amplitude of cusps. Many such characteristics are easily quantified, but others, for example, longshore positions and spacing of a rhythmic shoreline pattern, can prove to be more elusive.

The goal of the present investigation was to apply both of these approaches to examine the origin and development of large scale rhythmic shoreline forms. In particular, much attention was given to determine the applicability of multivariate analysis of topographic contour data to studies of three dimensional beach topography. To this end, a ten-month long field study was undertaken on the Oregon

coast to document changes in beach topography. The field site was an 830 m long stretch of beach on Siletz Spit, 30 km north of Newport, Oregon (Fig. 1). Eleven evenly-spaced beach profiles were obtained at two-week intervals during times of low Spring tides. Other data utilized in analyses of the observed beach topography changes include direct measurements of the incident waves (obtained every six hours), continuous tidal measurements, and local weather conditions, all measured at Newport.

This study was part of a larger effort to improve our understanding of rhythmic topography. Also included in the larger study, but presented elsewhere (Garrow, 1985), were the analyses of 24 historical air photo mosaics, more extensive statistical analyses of the survey data, evaluations of the proportions of infragravity and incident wave energy on the foreshore (from time-lapse films of wave run-up), and the development of a model for the formation of rhythmic topography at this site.

#### Field Techniques and Observations

Eighteen beach surveys, each consisting of eleven evenly-spaced beach profiles, were carried out on a bi-weekly basis between September 1982 and June 1983. Beach profile locations were constant throughout the study with all elevations referenced to a local base line and datum. Profiles were determined using 'Emery Boards' (Emery, 1961). The absolute x,y,z, coordinate system was established using an Omni-1 Total Station. Because of the high energy winter wave conditions on the Oregon coast, beach profiles often extended only 5 to 10 m seaward of estimated MLLW.

Seven storms, with deep-water significant wave heights greater than 5 m, occurred during the study. This period of time is especially interesting due to the El Niño phenomenon and its associated anomalous environmental conditions. Sea level anomalies up to 1.1 m occurred, associated with thermal and shelf wave phenomena (Huyer et al., 1983; Enfield and Allen, 1980), and up to 0.28 m due to low barometric pressures. Normal tides on the Oregon coast range from 2 to 4 m.

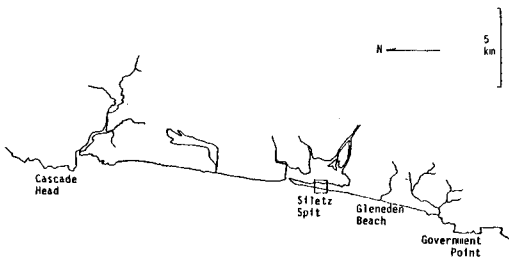


Figure 1. The field site was located on Siletz Spit, Oregon. It was approximately 2 km south of the Siletz Inlet and 8 km north of Government Point.

Contour maps from the survey data show the cycle of beach response to winter storms. Initial surveys showed a typical summer profile which rapidly eroded in early October. While there were moderate-scale fluctuations throughout the winter, significant accretion did not occur until near the end of the field program in June.

A common feature throughout the study period was a large scale rhythmicity in the shoreline. While the amplitude of the rhythmicity varied, statistical analyses showed that the wavelength was stable at 800-850 m. Additional characteristics of the rhythmic topography are: 1) localization of the rhythmicity to 3-4 km south of Siletz Inlet, and 2) variations in the longshore locations of rhythmic features, including longshore migration of a well developed rhythmic morphology (Garrow, 1985).

Important to the problem of understanding variations in beach morphology is the ability to quantify these variations in simple terms. Our visual and survey observations suggested that beach variability was composed of three components; average accretion or erosion, variations in the amplitude of rhythmicity, and variations of the longshore position or phase of the rhythmicity (as noted, the wavelength appeared stable). Empirical orthogonal eigenfunction analysis, a multivariate technique of data analysis, was applied in an attempt to separate these components of beach morphology variations.

#### Multivariate Analysis of Topographic Data

Empirical orthogonal eigenfunction (EOF) analysis is a mathematical technique which may simplify one's original data by reducing the number of variables which need to be considered. Explanations of the details of EOF analysis (also referred to as R-mode analysis) can be found in most texts considering mathematical analyses of multivariate data (ex. Davis, 1973). Aubrey (1979) provides brief reviews of the mathematics involved.

This technique has two main goals, both attained through simple, though voluminous, matrix algebra. First, one must realize that the variables in the original data set are not linearly independent and, hence, are redundant. That is, if one calculated the correlation between all pairs of variables, it is unlikely that all correlations would be zero. With this in mind, one goal is to determine a new set of variables (eigenfunctions or eigenvectors) which are independent. For example, if the original data set (or data matrix) had four variables, perhaps  $\beta_f$  (beach foreshore slope),  $\beta_s$  (average beach surf zone slope),  $H_{1/3}$  (significant wave height), and  $T$  (incident wave period), then each of the new variables would have four elements. A new variable may look like [-2 -5 4 0.5], indicating that it is composed of 'a lot' of  $H_{1/3}$ , and 'a lot of the opposite (-)' of  $\beta_s$ , since 4 and -5 are large, relative to 2 and 0.5. This particular example indicates the typically moderate correlation between increasing wave height and decreasing average beach slope in the surf zone.

The second goal is to define the fewest new variables possible, which will completely describe the original data, such that all sam-

ples can be written as the linear sum of the new variables. Mathematically, the phrase 'completely describes,' means that the new variables must account for all of the variance in the original data set. The importance of each new variable can be considered as how necessary it is in reconstructing the original data set. It is described by the percentage of the total variance (in the original data) for which it accounts. If four new variables were determined by EOF analysis, then one may explain 80% of the variance, another 15%, another 4.99%, and the fourth, only 0.01%. In this case, it could be said that three new variables could be used to describe the original data. In fact, for many applications, only two new variables would suffice. In addition to the percentage of total variance explained by each factor, EOF analyses also evaluate the importance of each new variable to the individual samples. Thus, if one wished to reconstruct sample #6 from the new variables, they may need to 'weight' one new variable by 85%, another by 12%, and the others by 2% and 1%, respectively. However, the 'weightings' for reconstruction of sample #7 may be 70%, 25%, 5%, and 0%. These weightings can be useful in that they show the change in importance of a new variable (or synonymously of a certain relationship between the original variables) from sample to sample.

This technique can be applied to the analysis of beach profile data if one evisions a topographic data set from the study site in which each variable represents one of the 11 profile ranges. EOF analysis of this matrix will produce 11 or fewer eigenvectors, each with 11 elements, which account for all of the variance in the data. Each vector will represent an alongshore topographic pattern or morphology. The hope is that most of the variance in the data set will be accounted for by several dominant morphologies which may be associated with known or hypothesized nearshore processes.

In deciding to perform such an analysis, the question arose as to what the actual elements of the data matrix should be. A number of possibilities were tried and evaluated with the specific goal of better understanding the nature of shoreline rhythmicity at the field site. As noted in the previous paragraph, the variables in all of the matrices evaluated represented longshore position. Several different types of elements were evaluated and discarded. These included: 1) elevations at different offshore distances, 2) local beach slope at different offshore distances, and 3) local alongshore beach slope at different offshore distances. An inverse approach of using the offshore distance to particular topographic contours proved successful.

Cross-shore distances to a particular contour as a function of time, therefore, were used to study the variability of rhythmicity through the 18 separate surveys. If the changes in beach morphology through time are relatively simple, then the mean contour calculated from such a matrix should describe a reasonable longshore topography and EOF analysis of such a matrix should produce one or two meaningful eigenvectors to account for most of the variance.

One's understanding of the results of this analysis on the Siletz Spit data set is enhanced by first examining results of this



analysis approach on hypothetical data matrices representative of ideal beach topographies. The first, and simplest, case is that of a straight beach extending different distances offshore at different times (accreting and eroding). The mean contour is straight, and EOF analysis determines a single dominant eigenvector. This vector is straight alongshore, and the weightings indicate the amount of accretion (positive weights), or erosion (negative weights), about the mean contour location at each time. An additional eigenvector is present in this, and all of the following cases, though it accounts for less than a few percent of the variance. This vector represents noise in the data.

A more interesting case for the study of longshore rhythmicity is that of a cusped shoreline exhibiting sinusoidal topographic contours. One can imagine a number of changes such a shoreline might experience, including variations in amplitude and longshore phase, as well as combinations of these with general erosion and accretion.

If the sinusoidal pattern remains stable in the longshore, but varies in amplitude, the analysis produces a sinusoidal mean and a single sinusoidal eigenvector 180 degrees out of phase with the mean (Fig. 2a). The vector weightings describe 'how much' of the vector must be added to, or subtracted from, the mean to regain the original data. In this simple beach environment, the vector weights can be used directly to describe the amplitude of the rhythmicity present at the time of each survey.

Results from a rhythmic shoreline exhibiting changes in both on/offshore position and amplitude through time is just a combination of the above cases. There is a sinusoidal mean and two dominant eigenvectors (Fig. 2b), one representing variations in amplitude, the other representing erosion or accretion. The percentage variance explained by each of these vectors depends on the relative magnitudes of amplitude variation and changes in on/offshore position.

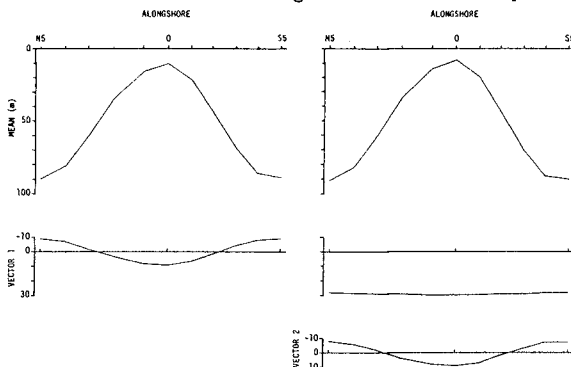


Figure 2. a) Mean contour and first eigenvector of data depicting a stable longshore rhythmic pattern with amplitude variations; b) Mean contour and first and second eigenvectors of data depicting a stable longshore pattern with amplitude variations and overall on/offshore movement.

The previously discussed characteristics of rhythmicity at the study site suggest that a still more realistic hypothetical set of circumstances would include longshore migration, or phase shifting, of the sinusoidal contours. Three cases will be explored using random phase variations within 90, 180, and 360 degree ( $1/4$ ,  $1/2$ , and full wavelength, respectively) envelopes. One-hundred synthetic contour lines were generated in each case. No on/offshore migration of the beach is included in the analyses discussed here; inclusion of this signal does not alter the basic results.

The mean contour and the first and second eigenvectors calculated by the EOF analyses for the 90 degree, 180 degree, and 360 degree phase variation cases are shown in Figures 3a, b, and c, respectively. Any apparent distortion of the mean contour from a perfect sinusoid occurs because the wavelength is not an even multiple of the spacing between variables (beach profiles). It can be noted that the amplitude of the mean decreases with increasing phase shift envelope. Eigenvectors 1 and 2 are sinusoidal and exactly 90 degrees out of phase in all instances. They are also out of phase with the mean by approximately 25 and 205 degrees. This phase offset from the mean accounts for the longshore phase shifting in the data. As phase variation in the data increase, the second vector becomes increasingly important. The 90, 180, and 360 degree phase envelope examples, respectively, have eigenvector 2 to eigenvector 1 ratios, of percents of variance accounted for, of approximately 0.07, 0.14, and 0.06. With longshore migration of a rhythmic shoreline, factor scores still indicate 'how much' of a vector must be added to the mean to regain the original data. However, they now include the longshore location of rhythmic features relative to the mean. When analyzing real data, the meaning of the vector weights must be evaluated subjectively, based on the shapes of the mean and dominant eigenvectors, and the phase relations between them.

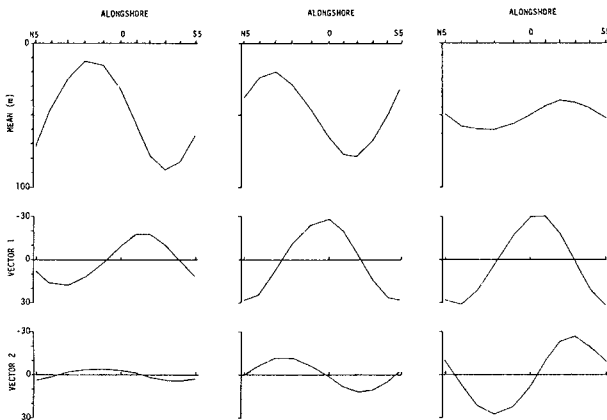


Figure 3. Mean contours and first and second eigenvectors for data depicting a longshore rhythmic pattern with amplitude variations, and a) 90° envelope phase shifting; b) 180° envelope phase shifting, c) 360° envelope phase shifting.

Finally, the influence of noise in the data was investigated. For the case of a matrix consisting solely of random noise, the mean contour is a straight line. EOF analysis produces the same number of eigenvectors as there are variables, all accounting for approximately equal amounts of variance. The vectors themselves are irregular when plotted. In an effort to determine how much noise could be present in a matrix based on a longshore rhythmic beach system and still yield interpretable results, many analyses were run on matrices similar to those just discussed, but including amplitude variations, on/offshore variations in beach position, and varying amounts of noise. It was determined that noise can hinder interpretations of the mean and eigenvectors when it is of the same order of magnitude, or larger than the amplitude of the rhythmic signal. In general, this condition can be identified by the need for more than two or three eigenvectors to account for more than 90% of the variance.

#### EOF Analysis of the Field Data

For analysis of the Siletz Spit topographic data, EOF analysis was run for seven different elevation contours spaced 0.5 m apart. Plots of the means and eigenvectors are shown in Figure 4. All mean contours appear rhythmic with approximately the same lengthscale of 800-850 m. For higher elevation contours, those nearest the dunes, the first eigenvectors show lower amplitude rhythmicity and account for less of the total variance in their matrices than do the first eigenvectors for contours further offshore.

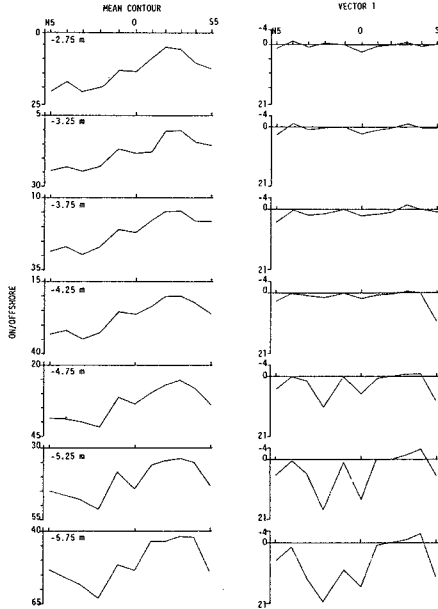


Figure 4. The mean contours and first eigenvectors for each of the seven Siletz Spit contour data sets.

The results of EOF analysis of the seaward-most data are shown more fully in Figure 5. The alongshore patterns are more irregular than those of the synthetic analyses, as would be expected in a natural system, but they definitely reflect some characteristics of the shoreline rhythmicity. The mean contour is obviously rhythmic with a longshore wavelength of 800-850 m and an amplitude of approximately 20 m. Two eigenvectors account for 83% of the variance in the data suggesting that although there is some noise in the system, it is probably much less than the amplitude of the rhythmicity signal. The shapes of the first two vectors are reassuringly similar to those determined in analyses of the hypothetical rhythmic shoreline with amplitude variations and phase shifting of the pattern. Eigenvector 1 departs from the expected phase relation with the mean for this model in the southern part of the area. The nature of the departure suggests that phase shifting at this site was possibly accompanied by small changes in the wavelength of the rhythmicity. Eigenvector 2 also departs from the expected phase relation with the mean, but it is 90 degrees out of phase with vector 1 for most of its length and this is consistent with the model. The amplitudes of the mean, first eigenvector and second eigenvector are 20 m, 25 m, and 15 m, respectively. This is very reminiscent of the synthetic data set with 180 degree phase shifting. The percentages explained by the first two vectors from the Siletz data are also similar to this hypothetical case. The ratio of percent explained by eigenvector 2 to that explained by eigenvector 1 de-emphasizes the noise in the natural system. The ratio for the hypothetical example with a 180 degree phase envelope is 0.15, and for the Siletz field site is 0.17.

Examination of eigenvector 1 shows it to have a mean of 6.4 m, implying an associated on/offshore movement of the contour. Sites labelled S1, S2, S3, and S4 have values near zero, while sites to the north have larger values indicating a greater on/offshore fluctuation in position. Figure 6 shows plots of the sum of the mean contour and

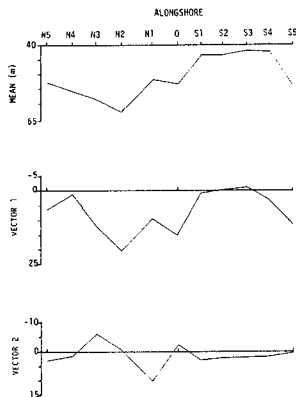


Figure 5. The mean contour and the first and second eigenvectors for the seaward-most contour of the Siletz Spit data set.

the most positively and most negatively weighted first eigenvectors in the data set. From these it is concluded that a change from large positive to large negative for vector weights would describe erosion in the north, a broadening of the embayment in the south, and migration of the cusp to the north with a concurrent decrease in amplitude. Though examination of vector 1 alone suggests that it might describe variation in the wavelength of the rhythmicity, it does not appear to do so within this data set. Eigenvector 2 has a mean near zero and shows most variation in the northern half of the study area. Figure 7 shows plots of the most positively and most negatively weighted second vector in the data set added to the mean contour. A transition from large positive to large negative second eigenvector weights represents a straightening of the beach to the south, a large increase in topographic complexity to the north, and a concurrent decrease in amplitude and northward migration of the southernmost embayment. Vector by vector reconstructions of the data, such as this, can prove extremely enlightening in understanding both the significance of the vectors and the dynamics of the beach system.

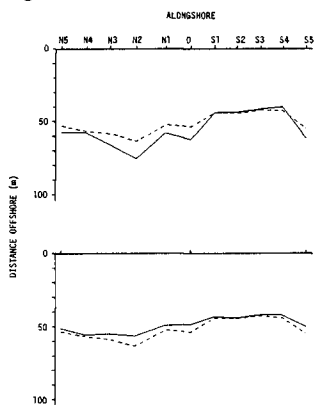


Figure 6. The sum of the mean contour and the most positively weighted (top) and most negatively weighted (bottom) first eigenvectors (solid lines). For reference, the mean contour is shown as a dotted line.

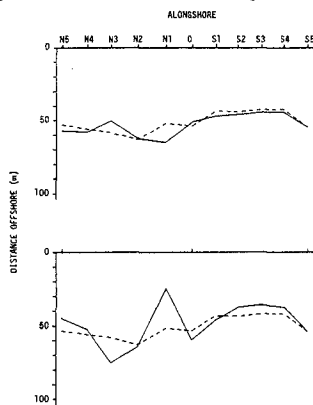


Figure 7. The sum of the mean contour and the most positively weighted (top) and most negatively weighted (bottom) second eigenvectors (solid lines). For reference, the mean contour is shown as a dotted line.

This analysis confirms the visual and survey observations that there are three primary components in the beach variability data. These are general accretion or erosion of the shoreline, amplitude of a dominant 800-850 m wavelength rhythmic pattern, and longshore location or phase of the rhythmic pattern through approximately 180 degrees (or 400 m). EOF analysis is useful in verifying the importance of these components, as demonstrated here and in the analyses of the synthetic data. Furthermore, it is capable of separating accretion/erosion and rhythmicity amplitude variations in a simple two-component system where these morphologies are independent.

Unfortunately, in an interdependent multiple component system, or a phase varying sinusoidal system (both of which apply to the Siletz data), the resulting eigenvectors fail to provide a simple separation of the three topographic parameters.

#### Quantification of the Components of Beach Morphology

To study the relationships between topography and wave and tide conditions, it is desirable to separate the three morphologic components and express each by a meaningful numerical parameter. On/offshore position, and amplitude of rhythmicity, can be described by the mean and standard deviation of the distance offshore to a contour at a given time (Fig. 8). For a truly sinusoidal pattern, the standard deviation of a contour produces a low estimate of rhythmic amplitude. In light of the variations found in natural systems, however, it seems to be a satisfactory descriptor. One possibility for quantification of longshore position of the signal would be longshore location of extrema. The signal produced by the real data is sufficiently noisy to preclude this approach. Recall that for any rhythmic shoreline exhibiting less than about 200 degrees of longshore phase shifting, EOF analysis produces a single eigenvector which describes much of the topographic variation. Vector weights for each excursion are meaningful numerical descriptors of the overall topography. In this instance, if the on/offshore movements of the shoreline and amplitude variation signals can be removed from the data, then the first eigenvector calculated by EOF analysis should describe only the phase shifting, or longshore migration of the rhythmic pattern.

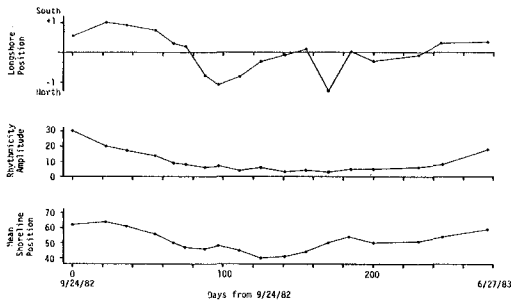


Figure 8. On/offshore position of the shoreline and amplitude of rhythmicity can be described by the mean and standard deviation of the distance offshore to a contour at a given time. The weightings of the first eigenvector of the normalized data matrix can be used as quantitative descriptors of longshore position of the rhythmic pattern.

To this end, the seaward-most contour data was normalized to the same mean and standard deviation. This normalization results in varying amounts of noise for different excursions, increasing the noise in low amplitude (mid-winter) data sets relative to higher amplitude data sets. Figure 9 shows plots of the mean contour, first, second, and third eigenvectors from EOF analysis of the normalized data. Because of the increased noise, 5 vectors are necessary to account for 90% of the variance. For the non-normalized data, the same amount of variance is explained by only 3 vectors. Longshore migration of the rhythmic pattern is described mostly by eigenvector 1. Eigenvectors 2 and 3, primarily 'fine-tune' the shape of the topographic features by narrowing cusps and broadening embayments. Comparison of the first vector weights of the normalized data (Fig. 8) to topographic maps of the beach for each excursion (Garrow, 1985), confirms that these weights can be used as quantitative descriptors of longshore position of the rhythmic pattern. Large negative weightings describe a number of the winter beaches when the embayment was located in the north central part of the site.

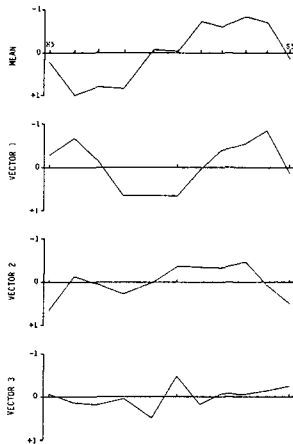


Figure 9. The mean contour and the first, second, and third eigenvectors from EOF analysis of the normalized  $-5.75$  m contour matrix.

Careful analysis of the topographic data reveals three primary components of topographic change on Siletz Spit and suggests three independent and quantitative parameters to describe them. On/off-shore position of the shoreline is best described by the mean distance offshore to a predetermined contour for each excursion. The amplitude of rhythmic topography is most simply and accurately described by the standard deviation of a contour about its mean offshore distance. The longshore position of rhythmic features is best expressed by the weights of the first eigenvector as calculated by EOF analysis of the contour data set in which each sample is normalized to the same mean and standard deviation.

### Waves, Weather, and Topography

Relationships between parameters which represent important characteristics of shoreline morphology and the wave, tide, or weather conditions permit us to: 1) improve our understanding of which variables are important in producing rhythmic topography, 2) make estimates of the response times for the beach morphology components, and 3) learn something about the way in which rhythmic topography forms. Regression analysis between the available topographic and environmental variables confirms some well established trends, but also provides new insights and surprises. The values used to represent wave and weather conditions in this investigation are the means for the time periods between surveys.

Though the linear correlation between mean significant wave height and the position of the mean shoreline is not high ( $-0.720$ ), the expected relationship exists (Fig. 10). As significant wave height increases, the mean shoreline position moves onshore (decreases) as a result of beach erosion. It is suggested that the correlation is as low as it is due to the rather slow response time of the mean shoreline to changes in incident wave conditions. Although the bi-weekly sampling precludes comments on very rapid responses, the mean shoreline position changed, at most, five meters between surveys.

Of interest, the amplitude of the rhythmicity also shows a negative correlation ( $-0.614$ ) with mean significant wave height (Fig. 11). This is opposite to the relationship observed previously during major episodes of erosion on Siltz Spit. At those times, erosion resulted from embayments impinging on the foredune during storms with incident wave heights exceeding six or seven meters (Rea, 1975; Komar and Rea, 1976; McKinney, 1977; Komar, 1983).

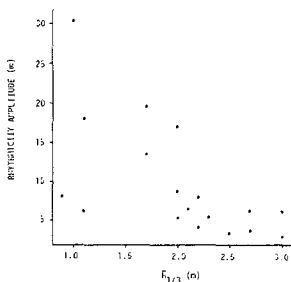


Figure 10. Mean Significant wave height versus mean shoreline position showing a negative correlation between these variables.

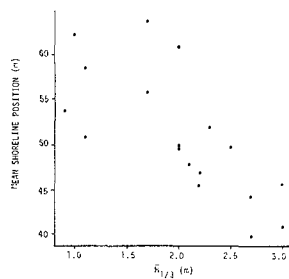


Figure 11. Mean significant wave height versus rhythmicity amplitude. The negative correlation between these variables differs from a positive correlation observed during major erosional episodes of the 1970's.



The winter of 1982/83 was characterized by anomalous weather and tide conditions due to El Niño. Consideration of three well documented periods of significant dune erosion on Siletz during the 1970's (McKinney, 1977), reveals a fundamental difference in conditions between those periods and the 1982/83 winter. First, incident wave conditions do not differ appreciably between the 'erosive' winters and the winter of 1982/83. Incident wave periods during the three major erosive storms varied from 9 to 17 sec. and significant breaking wave heights ranged from 6 to 7 m. However, barometric pressures in the winter of 1982/83 were anomalously low. Monthly mean barometric pressures for January through April were the lowest since sometime before 1971 (Huyer et al., 1983). This difference reflects that storm centers were closer to the Oregon coast in 1982/83, being located off the central California coast, than during the periods of major erosion when they were located in the North Pacific, just south of the Aleutian Islands in the Gulf of Alaska (McKinney, 1977). It is speculated, then, that incident wave characteristics related to the proximity of a storm center may be important in determining the amplitude of rhythmic topography on Siletz Spit.

Of interest, the amplitude of the rhythmicity in the 1982/83 winter showed larger responses to incident wave conditions than did the mean shoreline position. Up to 10 m of change occurred during any two-week period. The relationship between mean shoreline position and rhythmicity amplitude can reveal whether the rhythmic topography is erosional or depositional in origin. The correlation between these two morphology components is +0.841, indicating that the amplitude increased as the shoreline prograded (Fig. 12). However, spectral analyses of the high water lines on air photo mosaics obtained in previous years (Garrow, 1985) suggest a possible negative correlation between these same two variables. The photographs showing significant spectral peaks were taken during August, September, October, February, and April of the several years of photo availability. The high spectral energy found on the fall and mid-winter

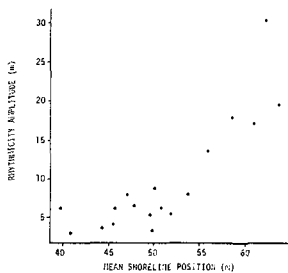


Figure 12. Mean shoreline position versus rhythmicity amplitude. The positive correlation indicates rhythmic topography was of a depositional origin during the time of this study.

photographs indicate that the rhythmic topography may also form, as well as show rapid growth under erosional conditions. It is probable, however, that the development of rhythmicity to very large amplitudes is most likely to occur under erosional conditions. This seems likely, given the more rapid response of rhythmicity amplitude than of mean shoreline position to changes in significant wave height.

### Conclusions

Empirical orthogonal eigenfunction analysis of a matrix containing offshore distances to an elevation contour provides a means for determining the important morphologic variables in an area. These may not correspond to single morphologies deemed important by the researcher if these morphology components do not behave completely independently over the period represented by the measurements. They will also not correspond if longshore migration of a sinusoidal pattern occurs during the time of study. Reconstruction or partial reconstruction of the original data by summing weighted eigenvectors or 'new variables' with the mean can provide insights into the significance of the vectors and the dynamics of the beach system.

Three important morphologic components were identified on Siletz Spit: overall accretion or erosion of the shoreline, amplitude of an 800-850 m wavelength rhythmic topography, and longshore position or phase of the rhythmic features. EOF analysis was useful in verifying the importance of these components but was not able to provide a simple separation of them.

It was determined that the mean shoreline position and rhythmicity amplitude can be quantified, respectively, by the mean distance offshore to a specified contour and the standard deviation of the contour about that distance. Longshore position or phase of the rhythmic pattern can be described by the weights of the first eigenvector, calculated by EOF analysis, of a contour data matrix in which each contour is normalized to the same mean and standard deviation. This should also apply for other, similar systems showing less than about 200 degrees of longshore migration.

This quantification permitted evaluation of the effects of various wave and weather conditions on the shoreline morphology. As expected, the mean shoreline position moved onshore as wave height increased. The amplitude of the rhythmicity was inversely correlated with wave height, though there is some question as to whether this is true for all winters on Siletz Spit. During the winter of 1982/83, rhythmic topography formed and increased in amplitude under depositional conditions. Again, there is some question as to whether this is always the case at this site. Mean shoreline position was shown to change, at most, 5 m during a two-week period, whereas, rhythmicity amplitude changed by as much as 10 m. This difference in rates of change should make formation and development of rhythmic topography possible under erosional conditions, as well as under the depositional conditions observed during this study.

### Acknowledgments

The author wishes to thank R.A. Holman and P.D. Komar for their advice throughout the study and for their critical and rapid review of the manuscript. This work is a result of research sponsored by the NOAA Office of Sea Grant, Department of Commerce, under Grant No. NA81AA-D-00086 (Project No. R/CP-17). The U.S. Government is authorized to produce and distribute reprints for governmental purposes, notwithstanding any copyright notation that may appear hereon.

### References

- Aubrey, D.G. (1979). Seasonal patterns of onshore/offshore sediment movement. *J. Geophys. Res.*, 84, no. C10:6347-6354.
- Aubrey, D.G., D.L. Inman and C.D. Winant (1980). The statistical prediction of beach changes in Southern California. *J. Geophys. Res.*, 85, no. C6:3264-3276.
- Davis, J.C. (1973). *Statistics and Data Analysis in Geology*. Wiley and Sons, New York, 550 pp.
- Emery, K.O. (1961). A simple method of measuring beach profiles. *Limnol. Oceanogr.*, 6, no. 1:90-93.
- Enfield, D.D. and J.S. Allen (1980). On the structure and dynamics of monthly sea level anomalies along the Pacific coast of North and South America. *J. Phys. Oceanogr.*, no. 10:557-578.
- Garrow, H.G. (1985). Shoreline rhythmicity on a natural beach. Oregon State Univ. Master's thesis, 170 pp.
- Huyer, A., W.E. Gilbert and H.L. Pittock (1983). Anomalous sea levels at Newport, Oregon, during the 1982-83 El Niño. *Coastal Oceanogr. Climatol. News*, 5, no. 4.
- Komar, P.D. (1983). The erosion of Siletz Spit, Oregon. In: the CRC Handbook of Coastal Processes and Erosion, P.D. Komar (ed). CRC Press, Boca Raton, pp. 65-76.
- Komar, P.D. and C.C. Rea (1976). Erosion of Siletz Spit, Oregon. *Shore and Beach*, 44, no. 1:9-15.
- McKinney, B.A. (1977). The spring 1976 erosion of Siletz Spit, Oregon, with an analysis of causative wave and tide conditions. Oregon State Univ. Master's thesis, 66 pp.
- Rea, C.C. (1975). The erosion of Siletz Spit, Oregon. Oregon State Univ. Master's thesis, 105 pp.
- Winant, C.D., D.L. Inman and C.E. Nordstrom (1975). Description of seasonal beach changes using empirical eigenfunctions. *J. Geophys. Res.*, 80, no. 15:1979-1986.
- Wright, L.D., S.K. May, A.D. Short and M.O. Green (in press). Prediction of beach and surf zone morphodynamics: Equilibria, rates of change and frequency response. In: Proceedings, 19th Conf. on Coastal Engineering, 1984.

## CHAPTER ONE HUNDRED FORTY SIX

### Modelling of the Depositional Patterns in Hangzhou Bay

Su Jilan\* and Xu Weiwei\*\*

Prediction of depositional patterns in estuaries is one of the primary concerns to coastal engineers planning major hydraulic works. For a well-mixed estuary where suspended load is the dominant transport mode, we propose to use the divergence of the distribution of the net suspended load to predict the depositional patterns. The method is applied to Hangzhou Bay, and the results agree well qualitatively with measured results while quantitatively they are also of the right order of magnitude.

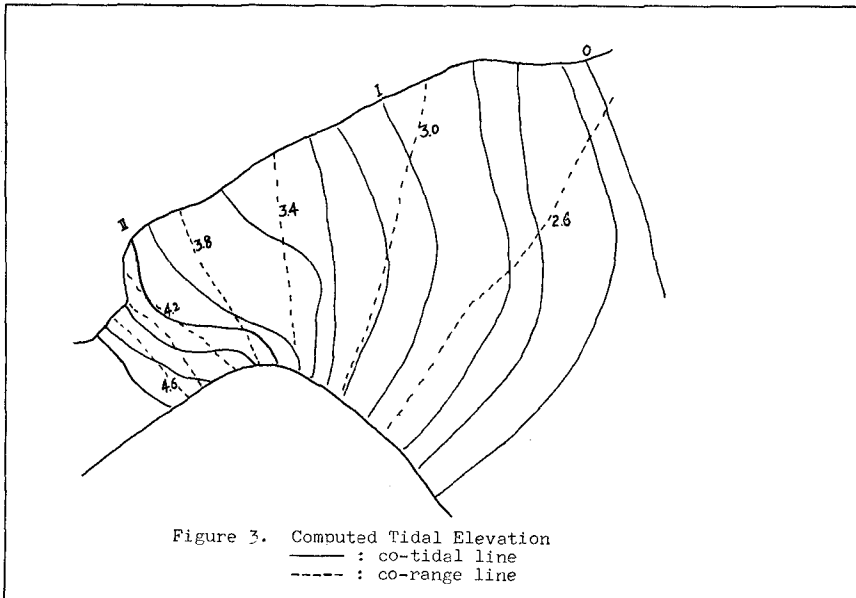
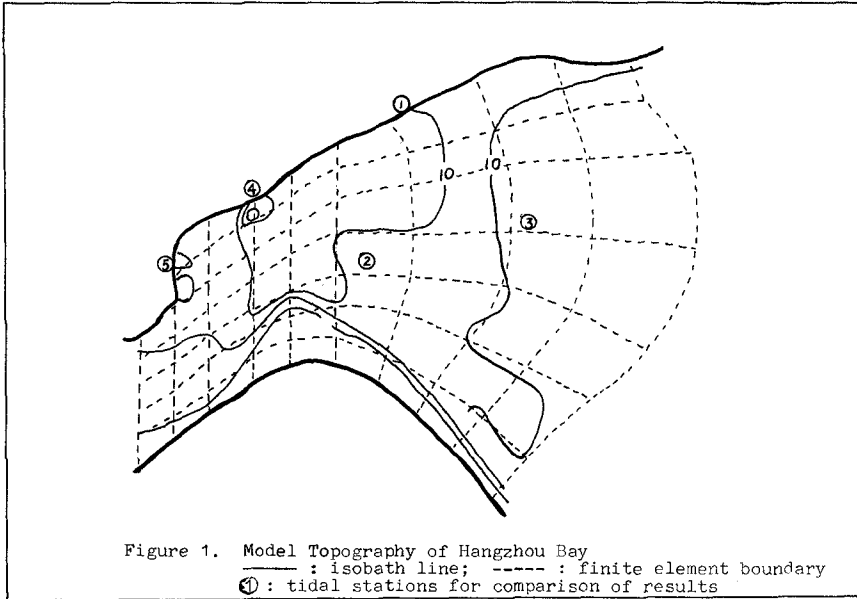
#### Introduction

Hangzhou Bay is the outer part of the Qiantangjiang Estuary. It is about 100 km long and is funnel-shaped such that the width decreases from 90 km at the mouth to 20 km at the western end (Fig. 1). The famous Qiantang bore starts to form at about 10 km further upstream of the Hangzhou Bay. In order to improve the resources management of the estuary several alternative major reclamation projects have been proposed. One of the primary concerns to the engineers studying the feasibilities of these projects is the effect of the hydraulic works on the depositional patterns in the Qiantangjiang Estuary. Because of the complicated nature of sediment transport in tidal situations, so far no successful modelling of the depositional patterns of the estuary has been published.

The annual sediment load of Qiantangjiang is about seven million tons. However, because of its proximity to the Changjiang river, suspended sediment from Changjiang plays a very important role in this estuary. Sediment in Hangzhou Bay is predominantly fine and medium silt. The median size of the suspended load ranges from 10  $\mu\text{m}$  to 13  $\mu\text{m}$  while that of the bed material is 16  $\mu\text{m}$  with only small percentage of clay size particles (Feng Yinjun and Xie Qin-chun, private communication). Since Hangzhou Bay is shallow (Fig. 1) and its tide is strong, the principal mode of sediment transport there is through suspended load. We were thus motivated to use the divergence of the vector field of the suspended load as a measure of the depositional

\*Professor, Second Institute of Oceanography, National Bureau of Oceanography, Hangzhou, China

\*\*Assistant Research Scientist, Second Institute of Oceanography, National Bureau of Oceanography, Hangzhou, China



patterns. This approach avoids the complication, as well as uncertainty, associated with solving the sediment transport equation.

#### Formulation of Problem

The tidal range at the mouth of the Hangzhou Bay is around 3 m and the average discharge of Qiantangjiang is only about 920 cubic meters per second. The Bay is thus a well-mixed estuary. Salinity in the Bay is rarely lower than 10 ‰ and it is usually less than 30 ‰ at the mouth because of the influence of the Changjiang discharge.

For the study of sediment transport in a well-mixed estuary like Hangzhou Bay where the bed material may be regarded as noncohesive, it is appropriate to choose the suspended load formula by Bagnold. According to Yalin (5), for uniform bed material of a specific size, Bagnold's equation can be written as

$$\vec{q} = 0.01 |\vec{\tau}| |\vec{U}| \vec{U} / w \quad (1)$$

where  $\vec{\tau}$  is the bed stress,  $\vec{U}$  is the vertically averaged velocity, and  $w$  is the settling velocity of the grains. The bed stress is related to the Chézy coefficient  $C$  as

$$\vec{\tau} = \rho g |\vec{U}| \vec{U} / C^2 \quad (2)$$

where  $\rho$  is the water density and  $g$  is the gravitational acceleration. Combining Eqs. 1 and 2 we obtain

$$\vec{q} = 0.01 (\rho g / C^2 w) |\vec{U}|^3 \vec{U} \quad (3)$$

The net suspended load of a uniform-sized bed is

$$\langle \vec{q} \rangle = 0.01 (\rho g / C^2 w) \langle |\vec{U}|^3 \vec{U} \rangle \quad (4)$$

where  $\langle \rangle$  denotes averaging in time over a tidal period  $T$ .

The current in Hangzhou Bay is dominated by the semi-diurnal tidal component. Hunter (3) showed that  $\vec{q}$  is dominated by contributions from both the residual current and the quarter diurnal tidal current component, the former being about 1.7 times as large as the latter if both current are of the same magnitudes. Since the amplitude of  $M_4$  is about 5 per cent of that of  $M_2$  in the Hangzhou Bay, a good prediction of the distribution of  $M_4$  current, as well as residual current, will likely serve our purpose except during storms when the wind-driven currents may be dominant. The average river discharge gives a residual current of the order of only  $5 \times 10^{-3}$  m/s, and hence we will ignore the river discharge. Residual currents due to other sub-tidal sources are also ignored. The only part of the resi-

dual current considered in this study will be that due to the  $M_2$  tidal action.

The vertically integrated equations describing the tidal motion in a homogeneous sea are

$$\zeta_t + \nabla \cdot [(h + \zeta) \vec{U}] = 0, \quad (5)$$

$$\vec{U}_t + \vec{U} \cdot \nabla \vec{U} + f \vec{k} \times \vec{U} = -g \nabla \zeta - \vec{\tau} / \rho (h + \zeta), \quad (6)$$

where terms like wind stress and lateral friction have been neglected.  $\vec{k}$  is the unit vector in the upward direction;  $f$  is the Coriolis parameter;  $\zeta$  is the free surface elevation;  $h$  is the mean water depth. For our study the flooding and drying of the tidal flats was not modelled. We simply increased the water depth there somewhat, and at the same time the bottom friction coefficient was also increased to compensate for the distortion of the topography. At the open boundaries the surface elevations are prescribed for all time. For this study only the  $M_2$  constituent of the surface elevation was forced at the open boundaries.

Analysis of systems of hyperbolic equations by Zhu et al. (6) showed that an additional boundary value has to be given at the open boundary if the flow there is into the domain of interest. However, this is impractical for ocean problems. On the other hand, when numerical methods are used to solve the equations an additional condition is usually imposed at the open boundary because of the requirement of the numerical scheme, which now introduces an over-determinancy during the outflow phase at the boundary. For finite element schemes solutions can be obtained without imposing additional condition at the open boundaries. In any case, the solutions are usually reasonably good in practice because the advective terms, which are responsible for the complicated nature of boundary conditions, are usually of secondary importance in ocean problems.

#### Numerical Method and Solution

We used the explicit finite scheme devised by Gray (1) to solve Eqs. 5 and 6. In this method the Lagrangian quadratic isoparametric elements are used, and the Simpson's rule is used to evaluate integrals over these elements. Leap-frog time differencing is used and the friction terms are evaluated at  $t - \Delta t$ . Because of the forced nature of the tidal flow, time-splitting of the solution is not a problem and no smoothing in time is needed. The combination of element type and numerical quadrature serves to greatly reduce the computational effort. Furthermore, the coefficient matrix is diagonal and computations can easily be done on a small computer.

One drawback of this scheme is the appearance of inter-

nodal oscillations in the computed solution due to the distortion of the dispersion relation of Eqs. 5-6 in their discretized forms(4). For our study these oscillations are negligible as far as the tidal elevation and tidal current are concerned. However, they will have effects on the suspended load computations. To filter out these internodal oscillations we used a nine-point smoothing operator at each time step. This operator was first tried on an example studied by Gray and Lynch(2) and its effectiveness was judged to be good (Fig. 2). The results shown in Fig. 2 are those along the axis of the domain during high water at the mouth. As is well known, this smoothing operation will have damping effects on the solutions, especially for the smaller length scale features. Since the  $M_4$  wavelength is significantly longer than the grid sizes used, the effect of smoothing on the  $M_4$  harmonic is probably not too great.

However, small scale spatial variations of the distributions of both the  $M_4$  current and the residual current associated with topographical features will no doubt be distorted. The good agreement of our results with the actual depositional patterns seems to support this assessment, since, as pointed out in the last section, both the  $M_4$  harmonic and the residual current are responsible for the net suspended load in Hangzhou Bay.

The study area is covered by 61 elements (Fig. 1). Because of the resolution limitation inherent in the choice of grid sizes, several deep narrow troughs along the northern coast have been ignored. To simplify the numerical treatment of the tidal flat along the middle of the southern shore we have modified the bathymetry there such that the water depth will be at least 0.5 m at low tides. The depth contours in Fig. 1 have been so modified. To lessen the distortion due to increased water depth, the value of the Chèzy coefficient over the tidal flat was chosen to be  $45 \text{ m}^{\frac{1}{2}}/\text{s}$  as compared to the value of  $75 \text{ m}^{\frac{1}{2}}/\text{s}$  elsewhere.

At both the east and the west boundaries the surface elevations are forced by the  $M_2$  constituents based on available data. Along the west boundary only one data station was available, and there we let the co-tidal line coincide with the boundary, which is compatible with available information. With a time-step of 1 minute integration of Eqs. 5-6 from zero initial values will yield periodic solutions stable to the third significant digits after three tidal periods. Comparisons are made between the computed surface elevation and the  $M_2$  harmonic constants at five stations (Table 1). The agreements are excellent for stations 1-3. The large error in amplitude at station 4 is probably caused by the neglect of a deep trough nearby, while the large discrepancies in phase at stations 4 and 5 are likely due to the accumulated effects of smoothing of



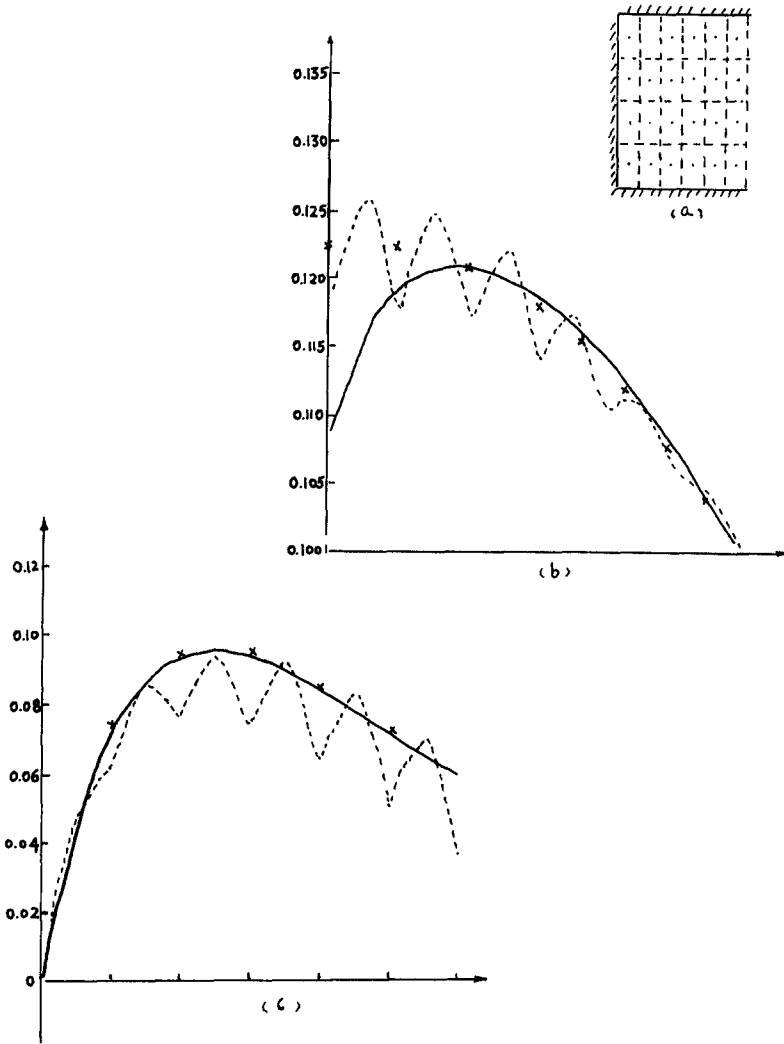


Figure 2. Effectiveness of Smoothing Operation  
 (a) model domain and finite elements;  
 (b) surface elevation; (c) current  
 : exact solution (2)  
 — : with smoothing  
 - - - : without smoothing

Table 1. Comparison of Computed Amplitudes of Surface Elevation vs  $M_2$  Harmonic Constants

Station	1	2	3	4	5
Error					
Magnitude* (%)	-2.4	-3.5	-3.4	-4.1	7.1
Phase** ( $^{\circ}$ )	-1	-0.5	-1	0	10

\*  $100 \text{ (computed - observed)/(observed)}$

\*\* $(\text{computed} - \text{observed})$

Table 2. Maximum Annual Deposition Thickness in Each Subregion

Subregion	Annual Deposition thickness ( $10^{-2}$ m)
1	8.3
2	-0.83
3	-0.16
4	0.05
5	-0.67
6	-1.3
7	1.2
8	-0.33
9	-0.83
10	1.7
11	-8.3
12	3.3

the deep troughs along the northern shore. In Fig. 3 the computed co-tidal lines and co-range lines in Hangzhou Bay plotted. They agree well with the existing measured results. Comparison of computed tidal current at a station in the northeast of the Bay with the harmonic constants of  $M_2$  there based on a 25-hour current measurement showed that the major axis of the computed tidal ellipse is lower by 25 per cent in magnitude and a  $3^\circ$  error in orientation.

As discussed in the last section both the residual current and the  $M_4$  harmonic are important for the suspended transport in Hangzhou Bay. Our computation results showed that, except for the lower corner next to the western boundary where it attains a value close to 0.05 m/s, the (Eulerian) tidal residual current reached a maximum value of about 0.04 m/s over the tidal flat. Elsewhere it is generally less than 0.03 m/s. In the eastern three quarters of the Bay the tidal residual current has an eastward component. In the western quarter of the Bay the residual current is mostly directed towards the west except its eastern area next to the south shore. However, as pointed out earlier in this section, smaller spatial variations are distorted because of the numerical smoothing operation. Therefore, at areas where the tidal residual currents are relatively small, their computed magnitudes and orientations are likely to be unreliable. In addition, no conditions were imposed on the tidal residual elevation at the open boundary, nor, for that matter, were they imposed on the  $M_4$  harmonic. The neglect of these conditions at the western open boundary is more questionable than at the eastern boundary. We have done some rough estimation of the effects on the residual current due to the tidal residual elevation at the western boundary, based on sea level data. The resulting residual current field is probably less than that due to a 7.5 m/s wind.

Eq. 3 implies that the grain-size dependence of the suspended load is through the factor  $w$  only, namely, the settling velocity of the particle. Suppose that  $D$  is the grain size and  $F(D)$  is the size-frequency distribution of the bed material at a station. The net suspended load of this bed material is then

$$\vec{Q} = \int_0^\infty \langle \vec{q} \rangle F \, dD = A \langle |\vec{U}|^3 \vec{U} \rangle, \quad (7)$$

where

$$A = 0.01 \left( \rho g / c^2 \right) \int_0^\infty (F/w) \, dD. \quad (8)$$

It is seen that  $A$  is independent of the tidal dynamics provided that the Chèzy coefficient is constant.

As argued in the Introduction the divergence of the spatial distribution of  $\vec{Q}$  may be used as a measure for the depositional patterns in Hangzhou Bay. In this approach the complication and uncertainty associated with solving

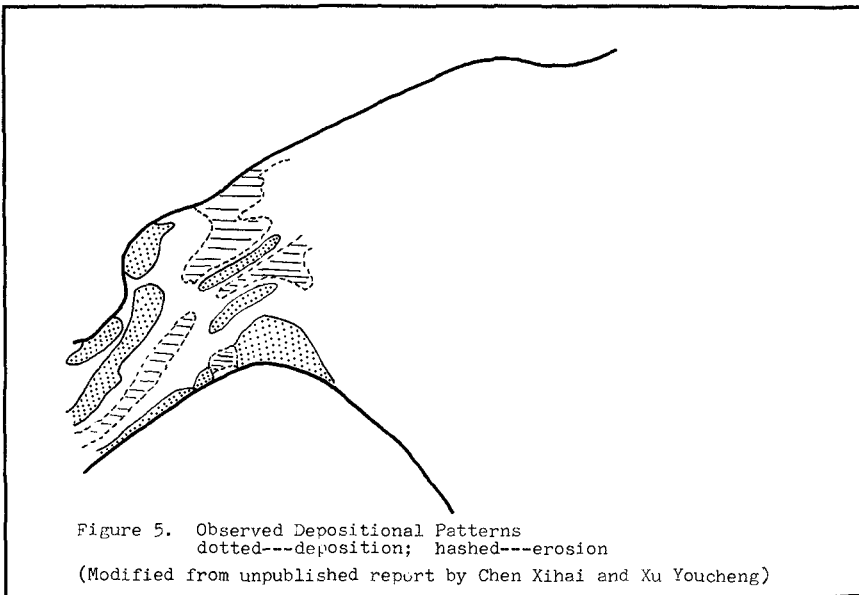
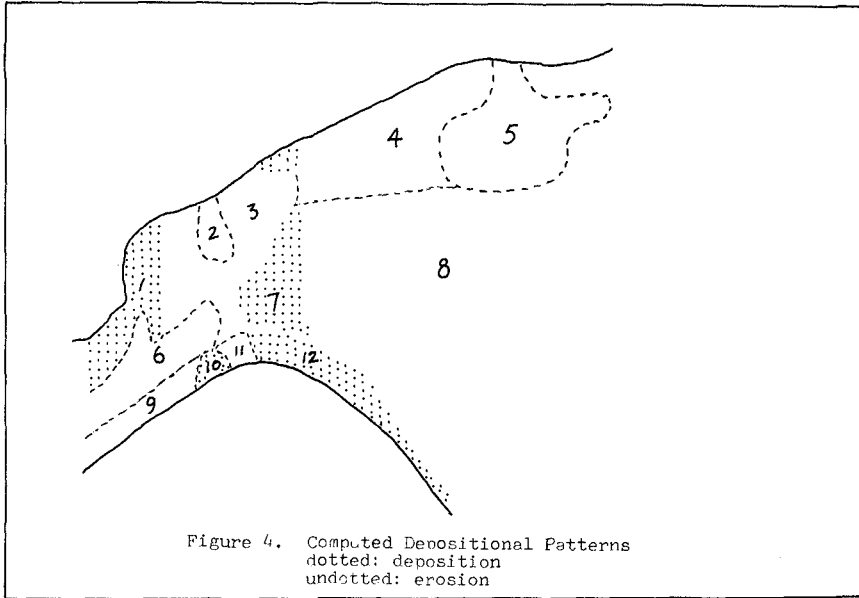
the sediment transport equation are avoided. The results are depicted in Fig. 4. Fig. 5 shows the depositional patterns in the western part of the Bay, based on surveys of topography between 1979 and 1982 during which period the discharge from Qiantangjiang was below normal. It can be seen that the numerical modelling results agree well with the measurements as far as the general patterns are concerned. Findings from other studies also supported our modelling results (Feng Yingjun, private communication). However, as anticipated earlier, the neglect of the deep narrow troughs along the northern coast caused large discrepancy locally.

To have some quantitative estimates of the deposition rate we computed  $\bar{Q}$  by assuming a uniform-size bed material, i.e.,  $\bar{Q} = \langle \vec{q} \rangle$ . Since the median size of the bed material is  $16 \mu\text{m}$  while that of the suspended sediment ranges from  $10$  to  $13 \mu\text{m}$ , we chose  $12 \mu\text{m}$  for computation purpose. Based on the computed results, in Fig. 4 the depositional and the erosional areas are further divided into subregions according to the variation of the value of the divergence. The maximum value of the divergence in each subregion is listed in Table 2. Since the divergence of  $\bar{Q}$  gives the depositional mass rate per unit area, the values listed in Table 2 are derived from the divergence by taking the specific gravity of the sediment to be 2.5. These values of annual depositional thickness are of the same order of magnitude as those estimated from available field study data, except at local areas along the northern coast due to reasons discussed earlier. We believe that refinement of grid sizes will probably improve the model prediction.

The computation also resulted in a net loss of  $1.2 \times 10^8$  ton of sediment from Hangzhou Bay to the ocean annually. Since Qiantangjiang has an annual suspended load of only 7 million tons, the balance has to come from either erosion in the estuary or replenishment of sediment in the upper reach of the Qiantangjiang Estuary from offshore sources. Available information seemed to support the latter mechanism. The Changjiang river discharges close to five hundred million tons of suspended sediment annually north of the Qiantangjiang. It is possible that sediment deposited at the mouth of Hangzhou Bay by Changjiang during summer will be transported upstream of the Bay in winter when the wind is strong.

## Conclusion

Hangzhou Bay is a well-mixed estuary where sediment transport is mainly through the suspended load. It is a shallow estuary with tidal action as the dominant transport mechanism. By using the Bagnold's formula for suspended load and taking the divergence of the distribution of the net suspended transport, a good measure of the depositional patterns in the Bay is obtained. The computed annual depo-



sition-erosion thickness over the Bay is also of the same order of magnitude as that obtained from field studies. Significant discrepancies occur only in small areas where deep narrow troughs have been neglected because of grid resolution limitation. The simple treatment of tidal flats by increasing its water depth and decreasing the Chèzy coefficient seems to be satisfactory.

In this study river runoff, wind effects, and other subtidal effects have been ignored. Only the  $M_2$  surface elevation oscillations are forced at the open boundaries. The results indicate that influence of the suspended sediment from Changjiang seems to be essential to the overall sediment budget in Hangzhou Bay.

#### Acknowledgement

The authors wish to thank Hao Donming and Zhu Tingzhang for their help in the course of computation work. Fruitful discussions with Feng Yingjun and Xie Qinchun are gratefully acknowledged.

#### Appendix: References

1. Gray, W.G., "An efficient finite element scheme for two-dimension surface water computation", Proceedings of the First Conference on Finite Element in Water Resources, 1975, pp 4.33-4.49.
2. Gray, W.G., and Lynch, D.R., "On the control of noise in finite element tidal computations: a semi-implicit approach", Computer and Fluids, Vol. 7, 1979, pp 47-67.
3. Hunter, J.R., "On the interaction of  $M_2$  and  $M_{2n}$  tidal velocities in relation to quadratic and higher power laws", Deutsche Hydrographische Zeitschrift, Vol. 32, 1979, pp 146-153.
4. Walters, R.A., and Carey, G.F., "Analysis of spurious oscillation modes for the shallow water and Navier-Stokes equations", Computer and Fluids, Vol. 11, pp 51-68.
5. Yalin, M.S., Mechanics of Sediment Transport, 2nd edition, Pergamon Press, 1977.
6. Zhu Youlan, Zhong Xichang, Chen Bingmu, and Zhang Zuomin, Finite Difference Methods for Initial Boundary-Value Problems and Flow Around Bodies, (in Chinese), China Science Press, 1980.

## CHAPTER ONE HUNDRED FORTY SEVEN

### UNIFORM LONGSHORE CURRENT MEASUREMENTS AND CALCULATIONS

P.J. Visser\*

#### ABSTRACT

A description is given of laboratory experiments on uniform longshore currents and the comparison of the data with longshore current profiles predicted by a mathematical model. For the mathematical model it is assumed that longshore current generation takes place between the plunge line and the shoreline (instead of shoreward of the breaker line) and Battjes' (2,3) lateral friction model is applied. Good agreement between theory and laboratory data is achieved with realistic values of the bottom roughness.

#### 1. INTRODUCTION

When waves break at an angle to the coast, a mean current is generated parallel to the shoreline (see fig. 1). This longshore current is confined to a zone with a width of order two times the width of the surf zone. Longshore currents and the associated transport of sediment play a significant role in the erosion and deposition of sediment and the dispersion of pollutants.

Since the introduction of the concept of radiation stresses by Longuet-Higgins and Stewart (15), the theory of longshore currents has progressed considerably: Bowen (4), Thornton (18), Longuet-Higgins (13), James (8), Battjes (1), Jonsson, Skovgaard and Jacobsen (10), Liu and Dalrymple (12). In these theories the equations of motion are averaged over the water depth and over the wave period. Then, in a steady state, there is a balance of the longshore driving force, the bottom frictional stress and the lateral friction. The theoretical achievements obtained by these authors are considerable, although some of the assumptions are rather crude, for instance concerning the eddy viscosity outside the surf zone, the dissipation of wave energy inside the surf zone and the bottom friction.

- Measurements of longshore current profiles were done, both
- in the field: in the Nearshore Sediment Transport Study, see Seymour and Gable (16), and in more detail
  - in the laboratory by Galvin and Eagleson (7) and Visser (20,21).

---

\*Scientific Officer, Department of Civil Engineering, Delft University of Technology, P.O. Box 5048, 2600 GA Delft, The Netherlands.

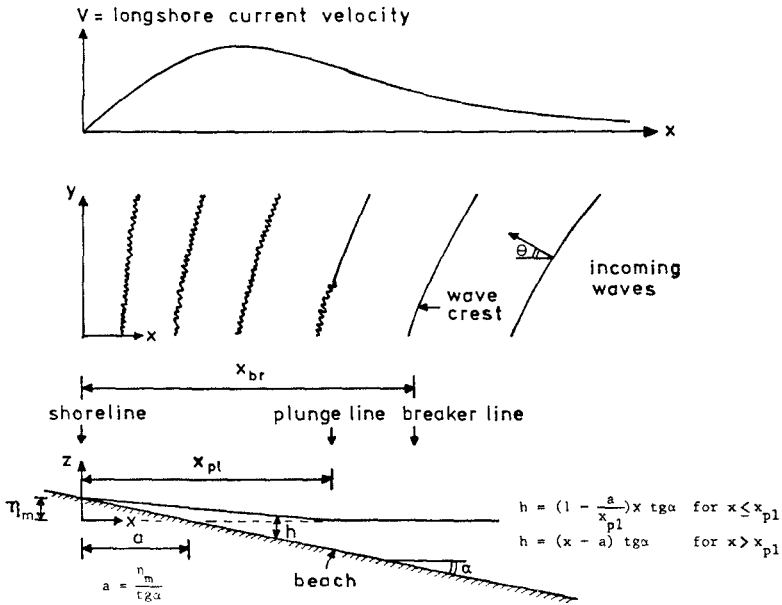


Fig. 1 - The nearshore region.

Care must be taken in comparing Galvin and Eagleson's measurement results with theoretical longshore current profiles, since the measured currents were not uniform along the coast which was caused by the wave basin geometry and the recirculation system.

The measured longshore current profiles, which are compared in this paper with an improved longshore current model, are all uniform along the coast as a result of the application of the method for the adjustment of the proper longshore current in a wave basin proposed by Visser (19), see also Visser (20). In this method the wave basin geometry and the proper recirculation flow through the longshore current openings in the wave guides are determined such that the circulation flow between the wave guides  $Q_c$  (see fig. 2) is minimal.

The aim of the present investigation is to get more insight into the dynamics of longshore current generation by sea waves, i.e. dissipation of wave energy (longshore driving force) and production of turbulence by breaking, diffusion of turbulence and momentum (lateral friction), bottom frictional stress. The principal objective is a mathematical model for calculations of longshore currents being more reliable than the existing ones. The basic assumptions are uniformity in longshore direction, steady state conditions and the bottom contours are straight and parallel to the beach. The investigation is restricted to regular waves.



The scope of the present study is the comparison of longshore currents measured in a wave basin with the current profiles predicted by a mathematical model. In the latter it is therefore assumed that the angle of the beach slope is constant and that the positions of the breaker line, the plunge line and the wave set-up line are known (i.e. following from the measurements). The breaker line is here defined as the line on which the wave height is maximal. The plunge line is the line where the curly crest of a plunging breaker impinges on the preceding wave trough (see also fig. 1).

In the present mathematical model the longshore driving force is modeled taking into account the physical fact that dissipation of wave energy takes place between the plunge line and the shoreline instead of in the whole surf zone (that is shoreward of the breaker line). The bottom friction is modeled by considering the combined orbital and current velocity vector. In fact it is still unclear how to combine the orbital and current velocity near the bottom. Therefore different bottom friction models are applied. The lateral friction is modeled according to Battjes (2,3): it is one of the aims of this investigation to examine the applicability of the ideas proposed by Battjes.

## 2. EXPERIMENTS

### 2.1 Experimental arrangement

The experiments were performed in the 16.60 x 34.00 m<sup>2</sup> wave basin of the Civil Engineering Department of the Delft University of Technology. Opposite to the snake-type wave generator smooth concrete beaches were constructed with slopes 1:10 (fig. 2) and 1:20 (fig. 3), respectively. For the last experiment the 1:20 slope was roughened by bonding 5 - 9 mm gravel with a thin grout on the smooth concrete. The wave guide walls were composed of concrete elements and installed at angles of 15.4 or 31.0 degrees with the normal to the wave board.

To approximate the longshore current flow generated by a uniform wave field on a straight infinitely long and uniform beach, a wave basin configuration was chosen with longshore current openings in both wave guides and with an external recirculation  $Q_r$  which is completely effected by a pump. A distribution system was built in the longshore current opening of the upstream wave guide in order to increase the length along which the longshore current is uniform. The recirculation flow  $Q_r$  was distributed in this system according to the expected distribution of the longshore current flow and was readjusted if that turned out to be necessary. The correct width of the longshore current opening in the downstream wave guide and the proper rate of recirculation flow were determined experimentally, i.e. followed from the application of an experimental method with which it is possible to obtain the uniform longshore current in the present wave basin geometry, (see Visser (20) ).

### 2.2 Experimental procedure

The experimental procedure is given in table 1. Because of the rather fast spreading of dye in the breaker zone, it was not possible to follow the dye in this zone over distances exceeding about 1.0 m. In view of the accuracy, the number of observations per point was

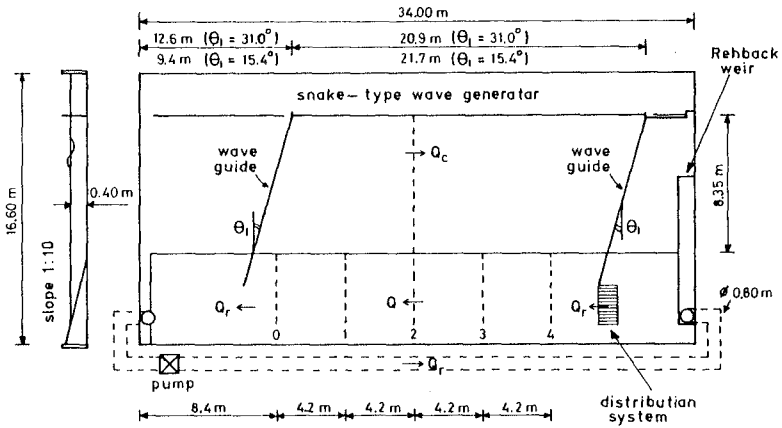


Fig. 2 - Plan view of wave basin (slope 1:10).

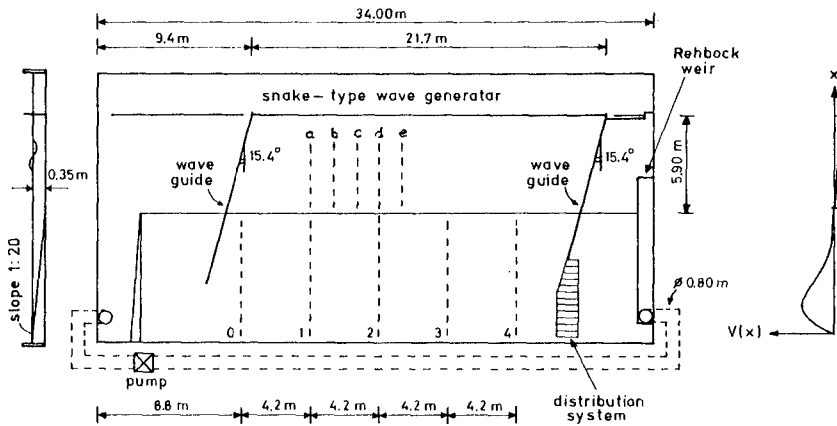


Fig. 3 - Plan view of wave basin (slope 1:20).

measurements of	measuring method	sections (see fig.2 and 3)	hor. distance between two measuring points	number of observations/ observational time
velocity	dye ( $KMnO_4$ ), in the vertical in 3 points (surface, mid-depth <sup>(1)</sup> , bottom)	0, 1, 2, 3, 4	1:10 slope 0.20 m <sup>(3)</sup> 1:20 slope 0.40 m	surf zone:20 <sup>(4)</sup> } outside } surf zone:10 }
wave height	resistance wave probes	1, 2	0.20 m	90 seconds
breaker height and position		a, b, c, d, e	0.20 m (20 points per section)	
		3-5 sections on and near the breaker line <sup>(2)</sup>	0.20 m (29 points per section)	
mean water level	static head in pots connected with tappings flush- mounted in the beach	1, 2	1:10 slope 0.20 m 1:20 slope 0.40 m (in the surf zone also in intermediate points)	
angle of incidence	wave probes  photograph	constant depth part of the basin  breaker line		about 10  about 20
position of plunge line	visually	near 1 and 2		6

(1) except near the water line

(2) near the middle of the beach

(3) 0.20 m near the water line

(4) i.e. 60 observations give a depth-averaged longshore current velocity (40 near the water line)

Table 1 - Experimental procedure.

enlarged to 20 and the measurements were conducted by two persons in this zone. Outside the surf zone, the spreading of dye was rather small and there the measured excursion time of dye was at least 3 seconds (and the excursion distance was 0.30 m or 0.50 m).

exp nr.	beach	$\tan \alpha$	T sec	$d_1$ cm	$\theta_1$ degr	$H_1$ cm	$H_0$ cm	$\theta_0$ degr	$H_{br}$ cm	$d_{br}$ cm	$\theta_{br}$ degr	$\eta_m$ cm	$x_{br}$ cm	p	breaker type
1	smooth	0.101	2.01	39.9	31.1	7.2	9.8	61.5	10.5	10.4	20.9	4.20	145	0.59	pl.
2	smooth	0.101	1.00	39.9	30.5	9.5	10.2	32.5	10.0	10.9	24.0	2.78	136	0.57	pl.
3	smooth	0.101	1.00	40.1	15.4	8.9	9.6	16.4	9.7	11.4	12.1	2.75	141	0.60	pl.
4	smooth	0.050	1.02	35.0	15.4	7.8	8.5	17.0	9.1	11.0	12.5	1.64	251	0.76	pl.
5	smooth	0.050	1.85	34.8	15.4	7.1	7.5	26.4	10.8	11.8	11.5	2.45	279	0.75	pl.
6	smooth	0.050	0.70	35.0	15.4	5.9	6.0	15.5	5.8	8.8	14.3	1.00	194	0.82	sp./pl.
7	smooth	0.050	1.02	35.0	15.4	7.8	8.5	17.0	9.0	12.2	12.2	1.64	275	0.78	pl.

Table 2 - Beach and wave field properties and quantities; the indices 0,1 and br refer to values on deep water, constant depth of the basin and the breaker line, respectively.

2.3 Experimental results

Seven experiments were performed, see table 2 ( $\alpha$  = slope angle, T = wave period). The results of the measurements of wave heights (H), angles of incidence ( $\theta$ ), (still water) breaker depth ( $d_{br}$ ), maximum wave set-up ( $\eta_m$ ), positions of the breaker line ( $x_{br}$ ) and the plunge line ( $p = x_{pl}/x_{br}$ ) with respect to the shoreline ( $x = 0$ ), and breaker types are also listed in table 2, see also fig. 1. The wave height and the angle of incidence on deep water were calculated from the measured values on constant depth part of the basin using linear wave theory and Snell's law.

The results of the mean water level measurements, see Visser (21), indicate clearly that the wave set-up starts at the plunge line instead of the breaker line. This is in conformity with experimental results of other investigators, for instance Bowen, Inman and Simmons (5). Consequently the transfer of momentum from waves to wave set-up and longshore current takes place shoreward of the plunge line, instead of shoreward of the breaker line in the whole surf zone, as often assumed. The mean water level measurements show further that the gradient of the wave set-up is more or less constant, as often observed on slopes with comparable steepnesses. The results of the wave height measurements in sections 1 and 2 indicate that in the breaker zone the wave height remains more or less proportional to the mean water depth, see Visser (21); this is also in agreement with other measurements on comparable slopes.

From the measured current velocities in three points per vertical, the depth-averaged current velocity in that vertical has been calculated. The depth-averaged longshore current velocities in the different sections have been given the present uniform longshore current profiles in the

sections 0,1,2 and 3 (experiments 1,2,3,4 and 7) and in the sections 0,1 and 2 (experiments 5 and 6). The uniformity of these longshore current profiles of each of the seven experiments is very satisfactory, see Visser (20); examples are given in fig. 4 (experiment 2) and fig. 5 (experiment 4). The depth-averaged and longshore-averaged measured current velocities are given in chapter 4 in combination with computed longshore current profiles.

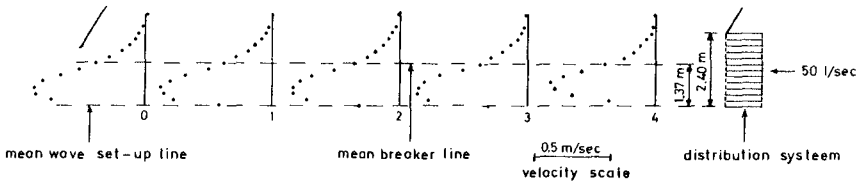


Fig. 4 - Depth-averaged uniform longshore current velocities in experiment 2.

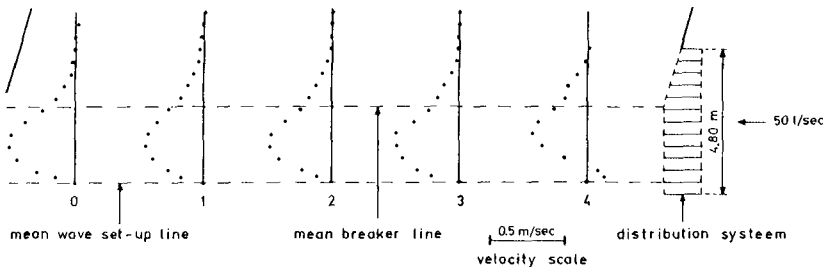


Fig. 5 - Depth-averaged uniform longshore current velocities in experiment 4.

As already described in Visser (19,20), the systematic error of the current velocity measurements is small (order 1%). The random error of the measured velocity in a point (following from 10 or 20 readings) is about  $\pm 4\%$  for the measurements in and near the surf zone. This gives for the depth-averaged velocity in this zone a random error of  $\pm 2.5\%$ . In view of the measuring technique (dye), both the systematic and random error are surprisingly small.

3. MATHEMATICAL MODEL

The equation of motion in longshore direction for the situation under consideration can be written as

$$\frac{dS_{xy}}{dx} - \frac{d}{dx} \left\{ \rho \mu_m h \frac{dV}{dx} \right\} + \tau_{by} = 0, \tag{1}$$

in which

$$\frac{dS_{xy}}{dx} = \frac{\sin \theta}{c} \frac{dF_x}{dx} = - \frac{\sin \theta}{c} D = \text{longshore driving force}, \tag{2}$$

$$\frac{\sin \theta}{c} = \text{constant according to Snell's law (c = phase velocity)}, \tag{3}$$

$F_x$  = flux of wave energy normal to the coast per unit length of shoreline,

$D$  = local rate of wave energy dissipation,

$x, y$  = coordinates in offshore, longshore direction, respectively,

$\mu_m$  = eddy viscosity (momentum),

$h$  = mean water depth,  $V$  = longshore current velocity,

$\tau_{by}$  = mean bottom frictional stress in y-direction.

3.1 Longshore driving force

If it is assumed that for  $x \leq x_{br}$

1. the wave height is proportional to the mean water depth,
2. the gradient of the wave set-up is constant,
3. the shallow water approximation of linear wave theory can be used and
4. the dissipation of wave energy takes place shoreward of the breaker line,

then the following simple model for  $D$ , see Battjes (2), can be derived

$$D = \begin{cases} 0 & \text{for } x > x_{br}, \end{cases} \tag{4}$$

$$D = \begin{cases} \propto x^{3/2} & \text{for } x \leq x_{br}. \end{cases} \tag{5}$$

The assumptions 1 and 2 are in agreement with the present observations. For the present model it is assumed that

1. the dissipation of wave energy takes place for  $x \leq x_{pl} = px_{br}$ ,
2.  $D$  is proportional to  $x^{3/2}$  for  $x \leq x_{pl}$ ,  $D = 0$  for  $x > x_{pl}$ ,
3. the transport of wave energy towards the shore = the transport of wave energy in x-direction on deep water given by linear wave energy =

$$(F_x)_o = \frac{1}{2} E_o c_o \cos \theta_o, \tag{6}$$

where  $E_o = \frac{1}{8} \rho g H_o^2$  = wave energy on deep water per unit area.

Then it follows from eq. (2) that:

$$\frac{dS_{xy}}{dx} = - \underbrace{\frac{1}{4} E_o \sin 2\theta_o}_I \cdot \underbrace{\frac{5}{2} \frac{x}{x_{pl}^{5/2}}}_{II} \quad \text{for } x \leq x_{pl} \quad (7)$$

The first part (I) of eq. (7) is the lateral thrust exerted by the waves on the longshore current. As emphasized by Longuet-Higgins (14), the expression for this total lateral thrust is exact and does not depend on the application of small amplitude theory to waves in the longshore current zone. The second part (II) of eq. (7) denotes the distribution of the lateral thrust across the region in which dissipation of wave energy takes place.

### 3.2 Bottom frictional stress

For the combination of a wave field and a mean current in y-direction, the mean bottom friction in longshore direction can be expressed, see Visser (21), as:

$$\tau_{by} = C \rho V^2 f(\theta, \xi \frac{u_m}{V}), \quad (8)$$

where

$$f(\theta, \xi \frac{u_m}{V}) = \frac{1}{T} \int_0^T \{ 1 + 2 \xi \frac{u_m}{V} \sin \theta \cos \omega t + (\xi \frac{u_m}{V})^2 \cos^2 \omega t \}^{\frac{1}{2}} \times \\ \times (1 + \xi \frac{u_m}{V} \sin \theta \cos \omega t) dt, \quad (9)$$

$C$  = a dimensionless bottom friction coefficient,

$u_m$  = maximum orbital velocity near the bottom,

$\xi$  = a dimensionless factor which depends on how the orbital and mean current velocity near the bottom are combined.

If the orbital velocity near the bottom and the depth-averaged longshore current velocity are combined then  $\xi = 1$ . Bijker (6) has proposed to combine the horizontal orbital and current velocity vector in the (hypothetical) boundary layer and arrives at (8) with (9) in which

$$\xi_B = \frac{p' \kappa}{\sqrt{C}} \approx \frac{0.16}{\sqrt{C}} \quad (p' \approx 0.4), \quad (10)$$

$$\text{where } C = \left( \frac{\kappa}{12 h} \right)^2, \quad (11)$$

with  $r$  = diameter of the bottom roughness elements,  
 is Nikuradse's expression for  $C$  for rough turbulent flow.  
 Bijker's model has been modified by Swart (17):

$$\xi_s = \sqrt{\frac{C'}{C}} = \left[ \frac{0.5}{C} \exp \{ - 5.977 + 5.213 \left( \frac{r}{a_b} \right)^{0.194} \} \right]^{\frac{1}{2}}, \quad (12)$$

in which  $C'$  corresponds with Jonsson's (9) wave friction factor  
 and  $a_b$  = amplitude of water particle excursion near the bottom.  
 For a linear wave theory is applied: this is justified as demonstrated  
 by Lemchauté, Divoky and Lin (11).

3.3 Lateral friction

The eddy viscosity is modelled according to Battjes (2):

$$\mu_m = M q l, \quad (13)$$

in which

$M$  = constant of order 1,

$q$  = characteristic turbulent velocity,

$l$  = characteristic length of turbulence (is set equal to  $h$ ). (14)

The turbulent velocity is calculated from Battjes' (3) balance of  
 turbulent energy

$$\rho h \epsilon - \frac{d}{dx} \{ \mu_e h \frac{d(\frac{1}{2} \rho q^2)}{dx} \} = D, \quad (15)$$

where

$\epsilon$  =  $q^3/h$  = mean rate of turbulent energy dissipation per unit mass, (16)

$D$  = local rate of wave energy dissipation which is set equal to the  
 rate of production of turbulent energy,

$\mu_e$  = eddy viscosity (energy) which is set equal to  $\mu_m$ .

Battjes (3) gives a local solution of eq. (15) in the neighbourhood of  
 the plunge line as defined in this paper. It is, however, possible to  
 give a complete analytical solution, see also Visser (21). Substitution  
 of (13), (14), (16) and the expressions for  $h$  (given in fig. 1) into (15)  
 leads to a differential equation with the following solution

$$q = \{ A_1 \left( \frac{x}{x_{p1}} \right)^{r_1} + \frac{D}{\rho} \}^{1/3} \quad \text{for } x \leq x_{p1}, \quad (17)$$

$$q = \{ A_2 (x - a)^{r_2} \}^{1/3} \quad \text{for } x > x_{p1}, \quad (18)$$

in which



$$A_1 = \frac{(x_{p1} - a) \left(\frac{dD}{dx}\right)_{p1} - r_2 D_{p1}}{\rho (r_2 - r_1) \left(1 - \frac{a}{x_{p1}}\right)}, \quad A_2 = \frac{(x_{p1} - a)^{-r_2} \{x_{p1} \left(\frac{dD}{dx}\right)_{p1} - r_1 D_{p1}\}}{\rho (r_2 - r_1)}, \quad (19)$$

$$r_1 = -0.5 + 0.5 (1 + 4B_1)^{\frac{1}{2}}, \quad r_2 = -0.5 - 0.5 (1 + 4B_2)^{\frac{1}{2}}, \quad (20)$$

$$B_1 = B_2 \left(1 - \frac{a}{x_{p1}}\right)^{-2}, \quad B_2 = 3M^{-1} \text{tg}^{-2} \alpha, \quad (21)$$

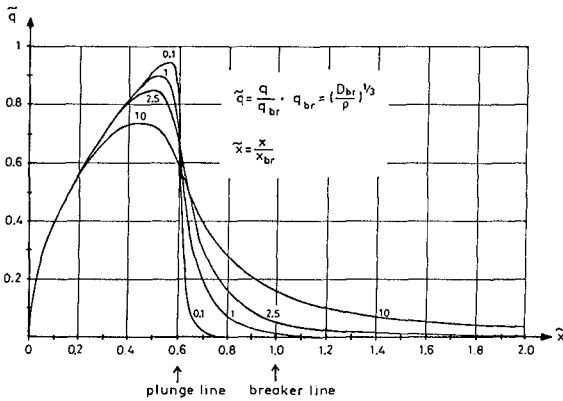


Fig. 6 - Calculated dimensionless turbulent velocity  $\tilde{q}$  as function of  $\tilde{x}$  for different  $M$  (applicable to experiment 3).

As example, fig. 6 shows the theoretical  $\tilde{q}$  for different  $M$  applicable to experiment 3.

3.4 Numerical model

Substitution of (7), (8) and (13) into (1) yields a second order non-linear differential equation which has to be solved numerically, see Visser (21). Because of the non-linearity, this has been done with an iteration procedure.

The boundary conditions are  $V = 0$  at  $x = 0$  and  $V = 0$  as  $x \rightarrow \infty$ . Since for  $x > 2 x_{br}$  the longshore current velocity  $V$  becomes very small, the boundary condition at  $x \rightarrow \infty$  has been rewritten as  $V =$  measured value at  $x \approx 2.5 x_{br}$ .

The numerical program has been checked with the aid of an analytical solution which can be derived for  $p = 1$ ,  $\theta =$  small and  $\xi u_m/V =$  large.

#### 4. COMPARISON OF MEASURED AND COMPUTED LONGSHORE CURRENTS

The rate of agreement between measured and computed longshore currents can be influenced by the choice of two coefficients in the mathematical model, i.e. the bottom friction coefficient  $C$  (through the diameter  $r$  of the roughness elements) and the lateral friction coefficient  $M$ . This is justified to a certain extent because  $r$  and  $M$  are not (exactly) known. But it is to be expected that

for the smooth slopes :  $r \approx 0.001$  m ( $C \approx 0.003$ ),

for the rough slope :  $r \approx 0.01$  m ( $C \approx 0.008$ ).

Further Battjes' (2,3) lateral friction coefficient  $M$  is expected to be of order 1.

The smooth concrete slopes 1:10 and 1:20 were constructed with the same materials, but in principle it is possible that the roughnesses of both slopes differ slightly due to 1) a small difference in workmanship and 2) the fact that the present measurements on the 1:10 slope have been preceded by other experiments on the same slope while the 1:20 slope was constructed especially for the present experiments (the roughness of a concrete slope increases generally in time).

In principle it is also possible to vary the factor  $p$  and to influence in this way the rate of agreement between measured and computed longshore currents; the computations, however, have been carried out with the measured value of  $p$ , see table 2.

The rate of agreement between measured and computed longshore current profiles, has been expressed in a standard deviation, see Visser (21). Thus, optimal values for  $M$  and  $r$  have been determined and the validity of the different bottom friction models (i.e. different expressions for  $\xi$ ) for the present application has been judged.

From the rate of agreement computations it follows that

- $M \approx 2.5 - 3.0$ , which is indeed of order 1,
- both  $\xi = 1$  and  $\xi = \xi_s$  give good agreement between measured and computed longshore current profiles with realistic values of  $r$ ; the general agreement obtained with  $\xi_s$  is somewhat better than with  $\xi = 1$ ,
- the agreement between measured and computed longshore current is very poor with  $p = 1$ .

Figures 7 and 8 show the measured and computed longshore current profiles of the seven experiments; these computed longshore current profiles are based on  $\xi = \xi_s$ , and further on  $M = 3.0$ ,  $r = 0.0012$  m for the smooth concrete 1:10 slope,  $r = 0.0004$  m for the smooth concrete 1:20 slope and  $r = 0.005$  m for the rough 1:20 slope. The agreement between measurements and theory is satisfactory, even very good in experiments 1 through 5, but less in experiments 6 and 7. The longshore current velocities in experiments 6 and 7 are smaller than in the other experiments: the less good agreement between measured and computed longshore current profiles in these experiments is probably caused by the fact that due to  $\xi = \xi_s$  in eq. (8) the bottom friction is over-estimated in the weak current situation, as it is also the case with  $\xi = \xi_b$ , see Visser (21).

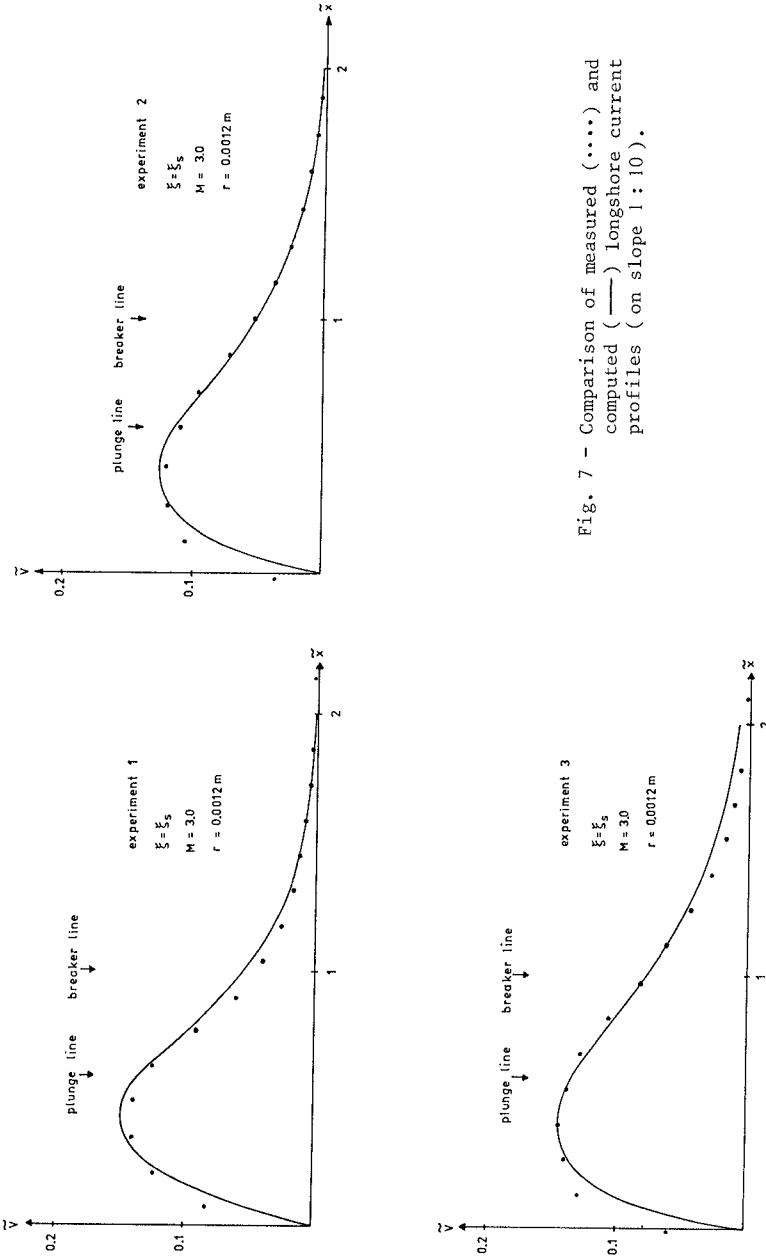


Fig. 7 - Comparison of measured (••••) and computed (—) longshore current profiles (on slope 1 : 10).

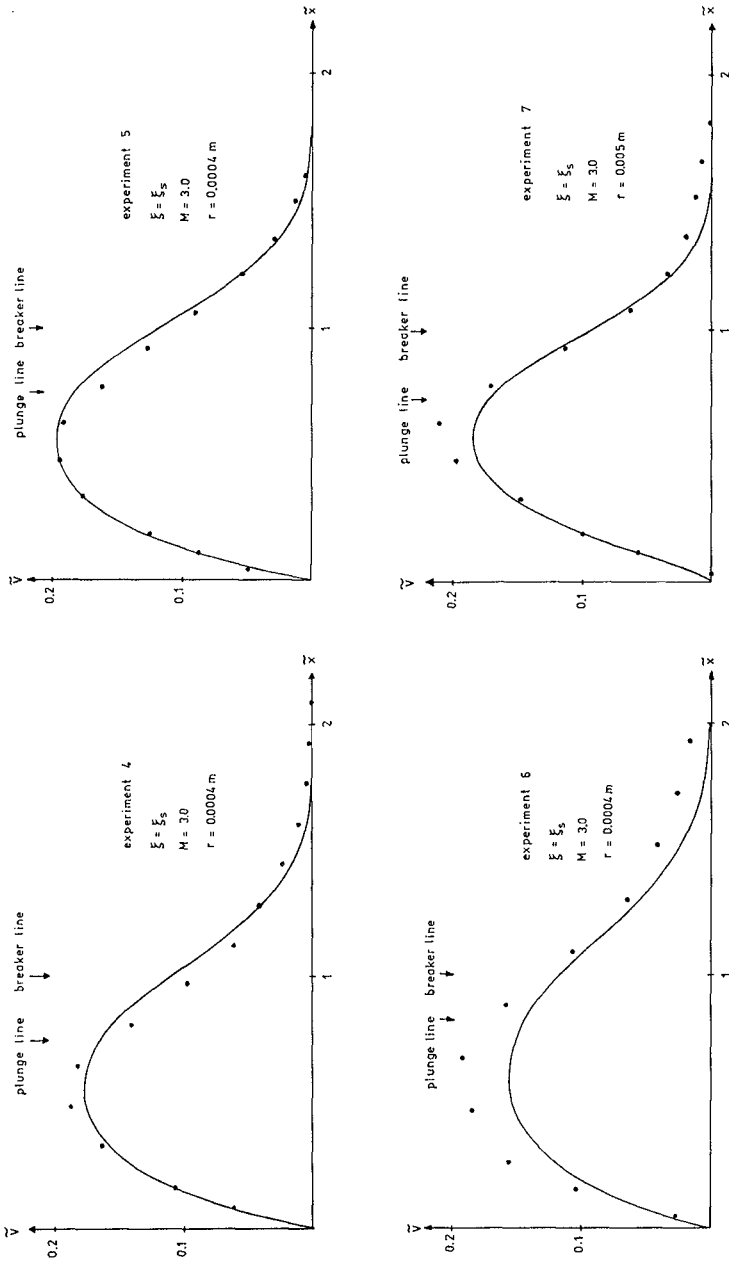


Fig. 8 - Comparison of measured (.....) and computed (——) longshore current profiles (on slope 1:20).

## 5 DISCUSSION AND CONCLUSIONS

The proposed mathematical longshore current model is more plausible on physical grounds than earlier models, in particular the formulation of the longshore driving force (action of this force shoreward of the plunge line) and the application of Battjes' (2,3) lateral friction model (in which the relevant properties of the horizontal turbulent momentum exchange are estimated taking account of the wave energy dissipation by breaking). This mathematical longshore current model has been verified by a number of longshore current measurements in a wave basin. The experimental set-up and execution has been extremely careful in order to obtain reliable results.

The conclusions from this investigation can be summarized as follows:

1. The data obtained from the present longshore current experiments are very usable to check the theoretical results: the rate of accuracy of the measurement results is high, the longshore current profiles are uniform and these were measured in detail.
2. The agreement between the longshore currents predicted by the mathematical model and the experiments is good. This good agreement has been achieved by using realistic values of the bottom roughness.
3. The present investigation confirms the utility of Battjes' (2,3) lateral friction model: best results have been achieved with  $M \approx 2.5-3.0$ , which is indeed of order 1.
4. The longshore current generation takes place between the plunge line and the shoreline (in plunging breakers), instead of in the whole breaker zone.
5. Bottom friction models in which the orbital and mean current velocity are combined, with a depth-dependent bottom friction coefficient and with  $\xi = 1$  or  $\xi = \xi_s$  can be used for the present application.

With respect to the last conclusion it is remarked that more research on this field is necessary because of the uncertainties regarding the real friction in case of combination of wave and current.

## REFERENCES

1. BATTJES, J.A., 1974, Computation of set-up, longshore currents, run-up and overtopping due to wind-generated waves, Comm. on Hydraulics, Dep. of Civil Eng., Delft Univ. of Techn., Rep. no. 74-2, 244 pp.
2. BATTJES, J.A., 1975, Modeling of turbulence in the surf zone, Symposium on Modeling Techniques, California, 1975, A.S.C.E., New York, pp. 1050-1061.
3. BATTJES, J.A., 1983, Surf zone turbulence, Proc. Seminar on Hydrodynamics of waves in coastal areas, I.A.H.R., Moscow, 1983, 4 pp.
4. BOWEN, A.J., 1969, The generation of longshore currents on a plane beach, J. Mar. Res., vol. 27, pp. 206-215.
5. BOWEN, A.J., INMAN, D.L. and SIMMONS, V.P., 1968, Wave "set-down" and set-up, J. Geoph. Res., vol. 73, pp. 2569-2577.

6. BLIJKER, E.W., 1967, Some considerations about scales for coastal models with movable bed, Delft Hydr. Lab., Publ. no. 50, 142 pp.
7. CALVIN, C.J. and EACLESON, P.S., 1965, Experimental study of long-shore currents on a plane beach, U.S. Army Coastal Eng. Res. Center, Tech. Mem. 10, Washington, D.C., 60 pp.
8. JAMES, I.D., 1972, Some nearshore effects of ocean waves, Univ. of Cambridge, Cambridge, diss., 130 pp.
9. JONSSON, I.C., 1967, Wave boundary layers and friction factors, Proc. 10th Conf. Coastal Eng., Tokyo, 1966, pp. 127-148.
10. JONSSON, I.C., SKOVGAARD, O. and JACOBSEN, T.S., 1975, Computation of longshore currents, Proc. 14th Conf. Coastal Eng., Copenhagen, 1974, pp. 699-714.
11. LEMEHAUTE, B., DIVOKY, D. and LIN, A., 1969, Shallow water waves: a comparison of theories and experiments, Proc. 11th Conf. Coastal Eng., London, 1968, pp. 86-107.
12. LIU, P.L-F. and DALRYMPLE, R.A., 1978, Bottom frictional stresses and longshore currents due to waves with large angles of incidence, J. Mar. Res., vol. 36, pp. 357-375.
13. LONCUET-HICCINS, M.S., 1970, Longshore currents generated by obliquely incident sea waves, J. Geoph. Res., vol. 75, pp. 6778-6801.
14. LONCUET-HIGGINS, M.S., 1972, Recent progress in the study of long-shore currents, in "Waves and Beaches", ed. by R.E. Meyer, Academic Press, New York, pp. 203-248.
15. LONGUET-HICCINS, M.S. and STEWART, R.W., 1964, Radiation stresses in water waves: a physical discussion with applications, Deep-Sea Res., vol. 11, pp. 529-562.
16. SEYMOUR, R.J. and CABLE, C.C., 1981, The Nearshore Sediment Transport Study Field Investigations, Proc. 17th Conf. Coastal Eng., Sydney, 1980, pp. 1402-1415.
17. SWART, D.H., 1974, Offshore sediment transport and equilibrium beach profiles, Delft Hydr. Lab., Publ. no. 131, 217 pp.
18. THORNTON, E.B., 1969, Longshore current and sediment transport, Techn. Rep. 5, Dep. of Coastal and Oceanogr. Eng., Univ. of Florida, Gainesville, Florida, 171 pp.
19. VISSER, P.J., 1981, Longshore current flows in a wave basin, Proc. 17th Conf. Coastal Eng., Sydney, 1980, pp. 462-479.
20. VISSER, P.J., 1982, The proper longshore current in a wave basin, Comm. on Hydraulics, Dep. of Civil Eng., Delft Univ. of Techn., Rep. 82-1, 86 pp.
21. VISSER, P.J., 1984, A mathematical model of uniform longshore currents and the comparison with laboratory data, Comm. on Hydraulics, Dep. of Civil Eng., Delft Univ. of Techn., Rep. 84-2.

## CHAPTER ONE HUNDRED FORTY EIGHT

### Modeling of Nearshore Wave Driven Currents

Jon M. Hubertz<sup>1</sup>

#### Abstract

A nearshore current modeling system has been assembled which consists of a shallow water directional spectral wave model, an algorithm to convert directional spectral output from the wave model to radiation stress components and a current model to calculate nearshore wave-driven currents from the radiation stress field.

Wave-driven longshore currents have been hindcast at a coastal site for two wave conditions during a northeaster type storm off Cape Hatteras in October 1982. For one event, when local winds were strong, the calculated longshore current is only a fraction of what was measured. This discrepancy is attributed to a non-wave-driven component of flow which was present but not represented in the model. During the other event, winds were low and long period swell was present. In this case, the calculated and measured longshore flow agree well.

Both measured and calculated shore normal profiles of longshore current in each case show a generally uniform structure across the surf zone. This is in contrast to theoretical profiles based on monochromatic waves which show a maximum in longshore flow near the breaker line.

#### Introduction

The U. S. Army Engineer Waterways Experiment Station, Coastal Engineering Research Center (CERC) is sponsoring research to improve our capability to predict currents in the nearshore area. The prediction techniques which result from this program will then be available to support studies of sediment transport. A workshop held in the summer of 1982 on the subject of modeling nearshore currents provided a forum for discussion of what improvements are most needed to improve nearshore current models. One conclusion of the workshop attendees was that to predict wave-driven currents improvements were needed in transformation of the wave field from the input boundary of a model to the shoreline. It was concluded that acceptable predictions of wave-driven currents were possible only if the distribution of wave parameters in the model region was correct. We have concentrated recently on improving our ability to predict nearshore wave conditions.

Recent research on the transformation of shallow water wave spectra (2) has provided a promising technique to obtain nearshore wave

<sup>1</sup>Research Division, Coastal Engineering Research Center, U. S. Army Engineer Waterways Experiment Station, P. O. Box 631, Vicksburg, MS 39180

conditions. This technique has been incorporated in a two-dimensional directional spectral wave model. Output of the model is a directional spectrum at each grid point over the model region. Each spectrum is a function of wave angle, frequency and depth. These spectra are integrated over frequency and direction to provide an estimate of the three components of radiation stress at each grid point. This field of radiation stress components provides the driving force in a circulation model to predict longshore and cross-shore flows. The wave, radiation stress and current calculations are assembled as a nearshore current modeling system.

Field measurements at CERC's Field Research Facility (FRF) were made in cooperation with the United States Geological Survey (USGS) in the fall of 1982. They provide estimates of longshore and cross-shore flows as well as wave heights along a line normal to shore through the surf zone. Data sets such as these are quite valuable in studying nearshore processes and evaluating models. However, such data may contain the effects of a number of forcing functions such as waves, tides, winds, current fronts, etc. This makes it difficult to isolate particular components for individual study and for comparison to model results where all the processes in nature are not included. Each component in the modeling system is discussed in more detail below, as well as the field measurements and some model results.

#### Nearshore Current Modeling System

Shallow Water Spectral Wave Model.-The basis for the wave model is the model developed by Hsiao (5) to investigate wave energy dissipation in shallow water due to bottom effects. It computes over two horizontal dimensions and allows two-dimensional variation of depth. It is a steady state model which considers the balance of spectral energy among terms for advection of wave energy, refraction and shoaling effects, atmospheric input, bottom friction, percolation and nonlinear wave interactions. The wave number spectral balance equation of the model is:

$$\frac{\partial F(\bar{k}, \bar{x}, t)}{\partial x_i} \frac{dx_i}{dt} = S_A + S_N + S_F + S_P$$

where  $F(\bar{k}, \bar{x}, t)$  is the wave number spectrum and the lefthand side represents refraction and shoaling effects and the righthand side, source terms  $S_A$  - atmospheric input,  $S_N$  - nonlinear wave interaction,  $S_F$  - bottom friction and  $S_P$  - percolation. In addition to these terms, a modification to the model has been made to limit the spectral energy in shallow water by imposing a spectral shape called the TEXEL, MARSEN, ARSLOE (TMA) spectrum. This spectrum provides a favorable fit to about 2800 measured spectra from the three field experiments above. It is related to a quasi-equilibrium deep water spectral shape called the JONSWAP spectrum, (4) by the factor  $\phi$  which results in a quasi-equilibrium shallow water spectral shape. The  $\phi$  factor, (6) varies between zero and one as a function of nondimensional frequency  $W_h$  where  $W_h = 2\pi f \left(\frac{h}{g}\right)^{1/2}$  and  $h$  is depth,  $g$  gravity, and  $f$  is frequency.



A value of zero refers to zero depth and one to deep water. Thus the TMA spectrum can be expressed as:

$$E_{TMA}(f, h) = E_{JSWP}(f) \phi(f, h)$$

with JONSWAP parameters determined from the TMA shallow water data set.

This spectrum appears to account for the distribution of spectral energy in shallow water and with a minor correction even through the surf zone (Vincent, personnel communication). It is not understood at present what physical mechanisms it reflects, only that it approximates the wave spectrum nearshore. If one accepts this, it provides a method to specify spectral energy nearshore and through the surf zone. Thus one no longer has to rely on a monochromatic, single wave direction approach or specify breaking criteria to calculate the distribution of wave energy nearshore.

#### Calculation of Radiation Stresses

Another conclusion of the Nearshore Currents Workshop mentioned above was that the theory of radiation stress, (7) provides a simple and valid mechanism for the generation of nearshore wave driven currents. According to that theory, to second order for a progressive, linear, small amplitude wave, the radiation stress components are:

$$\begin{aligned} S_{xx} &= E \left[ \left( 2n - \frac{1}{2} \right) \cos^2 \theta + \left( n - \frac{1}{2} \right) \sin^2 \theta \right], \\ S_{xy} &= E n \cos \theta \sin \theta, \\ S_{yy} &= E \left[ \left( 2n - \frac{1}{2} \right) \sin^2 \theta + \left( n - \frac{1}{2} \right) \cos^2 \theta \right], \end{aligned}$$

where  $E$  is the wave energy density,  $n$  the ratio of group velocity to wave celerity and  $\theta$  the wave angle. Without recourse to an energy distribution, it has been common to express  $E$  as

$$E = \frac{1}{8} \rho g H^2$$

where  $\rho$  is water density and  $H$  is the root mean square wave height. Thus the radiation stress components depend strongly (as the square) on the distribution of wave height and a mean angle. The wave height in the nearshore has generally been taken as more or less constant up to a breaker line where it decreases rapidly with distance to shore. This results in strong gradients in the radiation stress field near the breaker line and hence strong currents and current shears in this area, if  $\theta$  has some nonzero value (zero indicating waves propagating normal to shore). This approach when combined with some type of lateral eddy viscosity or mixing function to smooth out the velocity field gives comparable results to theory and laboratory observations (1).

In place of the above approach, we have represented the radiation stress components as:

$$S_{xx} = \int_0^{\infty} \int_0^{2\pi} \left[ n \cos^2 \theta + \left( n - \frac{1}{2} \right) \right] E(f, \theta) \, d\theta df,$$

$$S_{xy} = \int_0^{\infty} \int_0^{2\pi} (n \sin \theta \cos \theta) E(f, \theta) \, d\theta df,$$

$$S_{yy} = \int_0^{\infty} \int_0^{2\pi} \left[ n \sin^2 \theta + \left( n - \frac{1}{2} \right) \right] E(f, \theta) \, d\theta df,$$

where in practice the integrals are replaced by summation of the integrands over the frequency and directional domains and  $E(f, \theta, \bar{X})$  is the three-dimensional wave spectrum as a function of position. The three components of radiation stress are calculated at each grid point of the nearshore current model and provide a stress field to generate wave driven currents with a circulation model.

#### Current Model

The wave driven current model was developed by Vemulakonda (8) and is based on the long wave model of Butler (3). In addition to radiation stress, it includes linear bottom friction, advection and lateral mixing terms. A radiation boundary condition is applied at the offshore boundary to permit transients developed during startup of the numerical solution to propagate out of the grid.

The equations for the conservation of mass and momentum, averaged over time (one wave period) and depth are:

$$\frac{\partial u}{\partial t} + u \frac{\partial u}{\partial x} + v \frac{\partial v}{\partial y} + g \frac{\partial \bar{\eta}}{\partial x} + \frac{1}{\rho d} T_{bx} + \frac{1}{\rho d} \frac{\partial S_{xx}}{\partial x} + \frac{\partial S_{xy}}{\partial y} - \frac{1}{\rho} \frac{\partial T_{xy}}{\partial y} = 0,$$

$$\frac{\partial v}{\partial t} + u \frac{\partial v}{\partial x} + v \frac{\partial v}{\partial y} + g \frac{\partial \bar{\eta}}{\partial y} + \frac{1}{\rho d} T_{by} + \frac{1}{\rho d} \frac{\partial S_{xy}}{\partial x} + \frac{\partial S_{yy}}{\partial y} - \frac{1}{\rho} \frac{\partial T_{xy}}{\partial x} = 0,$$

$$\frac{\partial \bar{\eta}}{\partial t} + \frac{\partial}{\partial x} (ud) + \frac{\partial}{\partial y} (vd) = 0,$$

where  $u, v$  are the  $x, y$  horizontal components of velocity,  $\bar{\eta}$  the mean free surface displacement,  $d$  the total depth,  $T_b$  bottom friction stress and  $T_{xy}$  lateral shear stress. These equations are solved using a three time level, alternating direction, implicit, finite difference scheme. The radiation stress field produced by the directional spectral wave model is input to the current model and held fixed while the current model is stepped to a steady state.

#### Model Simulation

A set of wave and current observations in the nearshore zone were obtained in the fall of 1982 at CERC's FRF in cooperation with the USGS.

Mean values of wave and current data were provided by the USGS (Sallenger, personnel communication) for comparison with the results from the near-shore current modeling system described above. These data were obtained along a line normal to shore and 457 m north of the FRF pier. The near-shore region modeled and location of wave and current observations in relation to the pier location are shown in Figure 1. Measurements were made with three electromagnetic current meters and a pressure sensor mounted on a sea sled which was pulled to various positions along the profile line shown in Figure 1. The three current meters were mounted 0.54, 0.99, and 1.74 m from the sea bed. Mean values of longshore and cross-shore flow over 34.1 minute intervals were measured at various distances from shore. Estimates of significant wave height were also made using the current data and pressure data independently.

A summary of mean current components and wave heights for measurements made on 10 October 1982 is shown in Figure 2. Early on the morning of 10 October 1982 a northeaster developed in the vicinity of Cape Hatteras. Winds from the northeast reached a sustained maximum of 13 m/sec at the FRF and waves grew to 2.5 m in the direction of the wind by Noon on October 10. Data shown in Figure 2 were collected from 1200 to 2000 hours Eastern Daylight Time (EDT) on 10 October while wind and wave conditions were approximately constant.

The mean longshore flow from the measured values during this period is about 80 cm/sec toward the south and fairly uniform along the shore normal profile out to the last measurement point at 285 m. Wave heights of 2 m were measured at the offshore station on the profile line and heights of 1 m at the station closest to shore. The profile of measured wave heights is shown in Figure 3 along with the wave heights calculated from the spectral model for the existing wind conditions. In the spectral model application, only Miles' mechanism for energy input from the wind and the TMA limiting spectral shape are imposed. The other options, (Phillips' term for energy input due to pressure fluctuations, bottom friction, percolation and nonlinear interactions) are turned off. A bottom profile as shown in Figure 2 is applied uniformly in the along-shore direction. The assumption of uniform alongshore bathymetry is based on the depth contours of Figure 1 in the model region. Both the wave and current model are capable of simulating arbitrary bathymetry. The upper and lower bars on the measurements of significant wave height indicate independent measures of significant height respectively from pressure and current meters on the sled at each station. The measured variation of wave height normal to shore is reproduced well by the spectral model.

Next, the radiation stress components were calculated as described above using the directional spectra at each grid point. The stress components were input to the current model as the only forcing term. The advective terms and the lateral eddy viscosity terms were turned off and the model was time stepped to a steady state. The alongshore current component as measured and calculated is shown in Figure 4. The general trend of both curves is similar although shifted in magnitude by a significant amount.

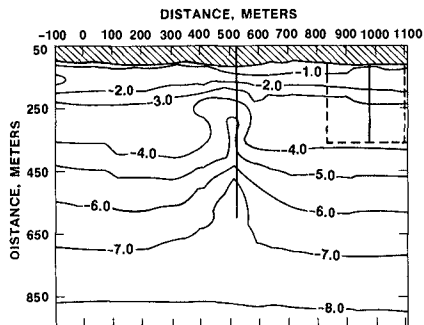


Figure 1. Location of the modeled region (dashed line) in relation to the FRP pier location (solid line over trough). Wave and current observations were made along the solid profile line within the modeled region.

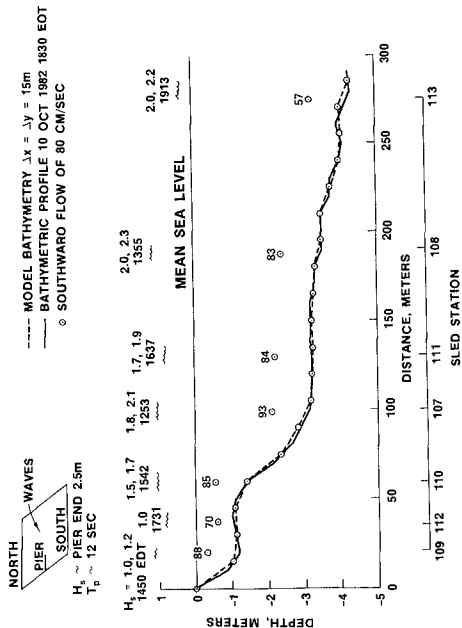


Figure 2. Values of wave height ( $H_s$ ) derived respectively from current and pressure data at stations along the profile line. The time of observation and water level are indicated below values of  $H_s$ . Values of longshore flow shown are averages of values at 0.5, 1.0, 1.75 m above bottom.

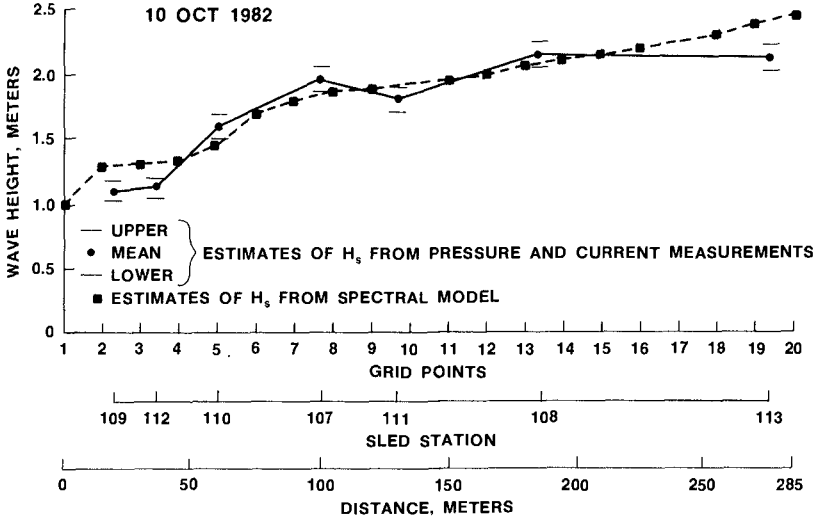


Figure 3. Measured and calculated values of significant wave height along the profile line in the model regions.

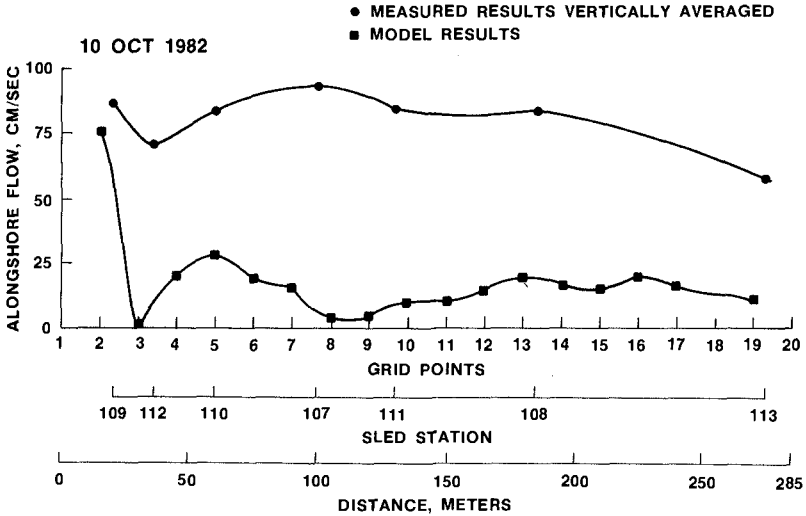


Figure 4. Measured longshore flow and calculated value of the wave-driven component of longshore flow along the profile line in the model region.

Current measurements made from the end of the pier on the morning of 10 October, while the waves were developing, indicate a current toward the south of 55 cm/sec. The surf zone began about 200 m closer to shore than the end of the pier and there was little gradient in wave height near the end of the pier, so this longshore flow was probably not wave induced. There is not enough information to determine the origin of this component of current. A possibility is wind-induced flow. Estimating the surface wind drift as 3 percent of the wind speed would give a value of about 40 cm/sec. If the measured longshore flow in this case is not primarily due to wave driven current, it points out the need to identify and model all of the current generating processes in the nearshore region before one has a generally acceptable nearshore current model.

As this same storm moved offshore, winds at the FRF decreased and large long period waves generated offshore moved toward the pier from the east. On 12 October 1982 waves at the pier end were measured with a significant height of 3 m and peak period of 15 seconds. Such long period waves are extremely unusual on the U. S. East coast. Wave and current measurements were made along the same profile line as on 10 October and are shown in Figure 5. Longshore flow has now shifted northward in response to waves and winds from the southeast quadrant. The average magnitude from the measured values is now about 27 cm/sec. Values are uniform with distance from the shore out to the last measurement station 285 m from shore.

The bathymetric profile has changed from 10 October presumably due to the high wave activity of the previous two days. Figure 6 provides a comparison of the profile changes, showing the bar formation moving deeper and farther offshore.

The spectral wave model was run with the bathymetry appropriate for 12 October 1982. The results are shown in Figure 7. Again, there is good comparison between observed significant wave height and calculated values with a rather uniform decrease in wave height from 2.5 m at the offshore station to 1 m nearshore. The longshore component of flow produced by the current model for this wave height distribution is shown in Figure 8. There is better correlation between measurements and model results in this case leading one to assume that the longshore flow in this case is primarily wave driven.

Note that this longshore flow profile is not typical of theoretical profiles which increase from shore to a maximum inside the "breaker line" and then decrease to zero seaward in a distance about the same as from shore to the "breaker line." The more uniform distribution of longshore flow with distance from shore, as measured and calculated here, is attributed to the uniform decrease in wave height toward shore as observed and modeled in both of the cases considered. The exact physical processes and their relative importance in contributing to the decrease in wave height are unknown. Possibilities would certainly be breaking, white capping, bottom friction and nonlinear interactions. What percentage each of these plays and what other processes are involved remains unknown. It is likely that the key processes will vary

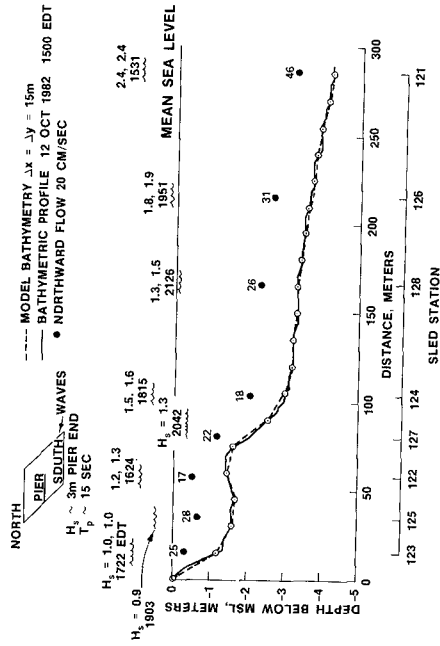


Figure 5. Values of wave height ( $H_s$ ) derived respectively from current and pressure data at stations along the profile line. The time of observation and water level are indicated below values of  $H_s$ . Values of longshore flow shown are averages of values at 0.5, 1.0, 1.75 m above bottom.

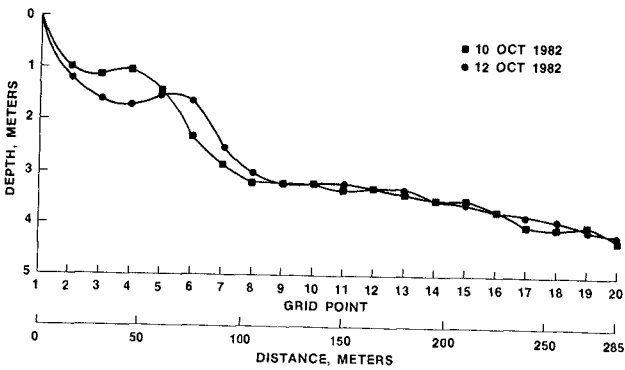


Figure 6. Bathymetric profiles along the profile line in the model.

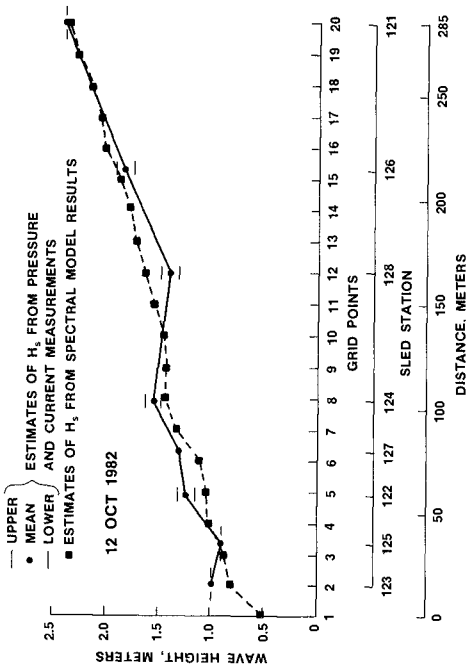


Figure 7. Measured and calculated values of significant wave height along the profile line in the model regions.

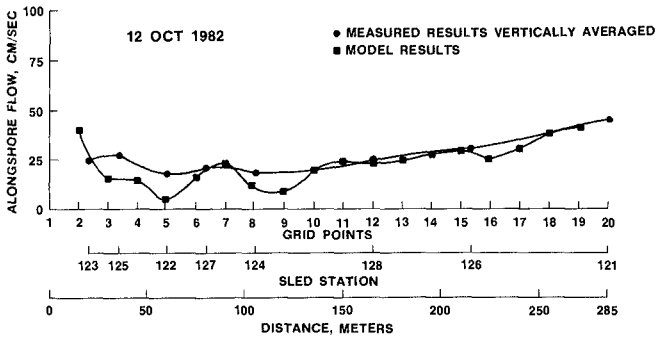


Figure 8. Measured longshore flow and calculated value of the wave-driven component of longshore flow along the profile line in the model region.



for different beach and wave conditions. It is also likely that processes other than wave-driven flow will have to be considered when modeling nearshore currents at a given place and time.

#### Summary

A nearshore current modeling system has been assembled and used to hindcast the wave-driven component of longshore flow for two events at CERC's FRF where wave and current measurements are available. The modeling system is composed of a directional spectral wave model, an algorithm to calculate the components of radiation stress from the spectral wave model and a current model which uses the radiation stress components to calculate the nearshore wave-driven currents.

The first event hindcast was characterized by high winds and local wave generation. Measured longshore flow was relatively uniform in strength and direction from shore to the seaward most measurement station. The computed wave-driven component of flow was also relatively uniform in direction and speed, but only a fraction of the measured value. The discrepancy is attributed to processes other than wave-driven flow which were present but not modeled.

The second event was characterized by low winds and long period waves. The measured and hindcast longshore flow compare well in speed and direction indicating a condition of primarily wave-driven currents. Again, the longshore flow is generally uniform in speed and direction along the measurement profile.

The present nearshore current modeling system shows promise as a tool for studying and predicting nearshore current processes. Employing the directional spectral approach to specify the nearshore wave climate and radiation stress field appears to result in a more uniform cross-shore profile of longshore flow than a monochromatic approach. This is accomplished without resorting to lateral eddy viscosity or mixing parameters to smooth the profile. The more uniform profile is in agreement with the profiles measured at the FRF in October 1982.

A field measurement experiment to support nearshore wave and current model verification and to study nearshore processes is planned for the fall of 1986 at CERC's FRF. Interested investigators are invited to participate in the planning and execution of the experiment. A preliminary set of experiment objectives is available from the author.

#### Acknowledgments

I would like to acknowledge helpful discussions with Dr. Linwood Vincent on the wave model, Dr. Rao Vemulakonda on the current model and Dr. Abby Sallenger on the field measurements. This work was carried out under the Coastal Engineering Research Center's Nearshore Waves and Currents Work Unit, Harbor Entrances and Coastal Channels Program, Coastal Engineering Functional Area of Civil Works Research and Development. The author wishes to acknowledge the Office, Chief of Engineers, U. S. Army Corps of Engineers, for authorizing publication of this paper.

## Appendix.-References

1. Basco, D.R., "Surfzone Currents," Coastal Engineering, Vol. 7, 1983, pp. 331-355.
2. Bouws, E., Gunther, H., Rosenthal, W., Vincent, C.L., "Similarity of the Wind Wave Spectrum in Finite Depth Water, Part 1 - Spectral Form," accepted for publication in the Journal of Geophysical Research, 1984.
3. Butler, H.L., "Evolution of a Numerical Model for Simulating Long Period Wave Behavior in Ocean-Estuarine Systems," Estuarine and Wetlands Processes with Emphasis on Modeling, Marine Sciences Series, Vol. 11, Plenum Press, New York, 1980.
4. Hasselmann, K., Ross, D.B., Muller, P., Sell, W., "A Parametrical Wave Prediction Model," Journal of Physical Oceanography, Vol 6, 1976, pp 201-228.
5. Hsiao, V., "On the Transformation Mechanisms and the Prediction of Finite -Depth Water Waves," Dissertation, University of Florida, 1978.
6. Kitaigorodskii, S.A., Krasitskii, V.P., Aaslavskii, M.M., "On Phillips' Theory of Equilibrium Range in the Spectra of Wind Generated Gravity Waves," Journal of Physical Oceanography, Vol. 5, 1975, pp 410-420.
7. Longuet-Higgins, M.S., Stewart, R.W., "Radiation Stresses in Water Waves: A Physical Discussion with Application," Deep Sea Research, Vol. 11, 1964, pp 529-562.
8. Vemulakonda, S.R., Houston, J.R., Butler, H.L., "Modeling Longshore Currents for Field Situations," Proceedings, 18th Conference on Coastal engineering, 1982, pp 1659-1676.

## CHAPTER ONE HUNDRED FORTY NINE

### Improved Formulas for Estimating Offshore Winds

S. A. Hsu\*

#### Abstract

On the basis of many pairs of simultaneous measurements of wind speed onshore,  $U_{\text{LAND}}$ , and offshore,  $U_{\text{SEA}}$ , in areas ranging from Somalia, near the equator, to the Gulf of Alaska, and under conditions ranging from breeze to hurricane, it was found that for operational use  $U_{\text{SEA}} = 3.93 U_{\text{LAND}}^{1/2}$  for  $U_{\text{LAND}} < 10 \text{ m s}^{-1}$  (or 20 kt); and  $U_{\text{SEA}} = 1.24 U_{\text{LAND}}$  for  $U_{\text{LAND}} \geq 10 \text{ m s}^{-1}$ . These formulas were developed mainly from theoretical considerations and were verified by field measurements.

#### 1. Introduction

Differences in onshore and offshore wind speeds have long been known to exist [see, e.g., (2), (15), (16)]. Marine meteorologists in the weather services are required to forecast offshore winds. Many studies related to coastal marine sciences and engineering require wind data or estimates for offshore regions. Yet in situ measurements over water are often lacking. Traditionally, wind measurements over land, preferably near coasts, have been used to estimate offshore winds. However, because simultaneous onshore and offshore observations do not always exist, systematic studies such as simple comparisons between these two environments are also lacking. Only recently the U.S. National Oceanic and Atmospheric Administration (NOAA) deployed a network of buoys for longer term measurements over the continental shelf as well as farther offshore. All of these buoys are located in or near U.S. coastal waters. However, there are still vast regions in other parts of the world where such a network does not exist.

\*Professor, Coastal Studies Institute, Louisiana State University, Baton Rouge, Louisiana 70803, U.S.A.

It is the purpose of this paper to synthesize various data sources and to provide simple formulas for operational use. Basic developments have been given in (9). Furthermore, because of the availability of wind difference measurements during hurricane conditions, as shown most recently by (12), the formulas originally proposed by (8) have been improved and extended from breeze conditions to hurricane-force winds.

## 2. Formulas

In order to understand and estimate wind speed differences across the coastal zone, two models, one theoretical and another semi-empirical, have been developed and verified using available data sets (9). The following discussion is based mainly on that paper.

Assuming that (1) mean horizontal motion occurs perpendicular to the coast and (2) the geostrophic wind does not change appreciably at the top of the planetary boundary layer (PBL), the equation of motion in the direction of the wind can be reduced so that

$$\frac{U_{SEA}}{U_{LAND}} = \left( \frac{H_{SEA} C_{D LAND}}{H_{LAND} C_{D SEA}} \right)^{1/2} \quad (1)$$

where  $U$ ,  $H$ , and  $C_D$  are wind speed, height of the PBL, and drag coefficient, respectively. Subscripts LAND and SEA stand for onshore and offshore environments, respectively.

Eq. 1 is based on equations of motion, which work fairly well for synoptic weather systems typically more than one day in time scale and at least 1,000 km (1 km = 0.54 nautical miles) in horizontal scale. These systems include anticyclones (high-pressure systems), monsoons, and trades. Their  $U_{LAND}$  values are generally less than  $10 \text{ m s}^{-1}$  ( $1 \text{ m s}^{-1} = 1.94 \text{ kt}$ ).

According to Large and Pond (10), the drag coefficient, reduced to 10-m height and neutral condition,  $C_{D SEA}$ , is independent of stability and fetch (for fetch/height  $> 800$ ) but increases with wind speed above

$10 \text{ m s}^{-1}$ . Using their measurements and many deep-water results of others, Large and Pond (10) obtained

$$10^3 C_{D \text{ SEA}} = \begin{cases} 1.2 & 4 \lesssim U_{10} < 11 \text{ m s}^{-1} \\ 0.49 + 0.065 U_{10} & 11 \lesssim U_{10} \lesssim 25 \text{ m s}^{-1} \end{cases} \quad (2)$$

where  $U_{10}$  is the wind speed at a height of 10 m over the water.

For typical low-relief topography and low mountains on land (peaks  $< 0.5 - 1 \text{ km}$ ), Garratt (4) obtained

$$C_{D \text{ LAND}} = 10 \times 10^{-3} \quad (3)$$

where  $C_{D \text{ LAND}}$  is the drag coefficient at a height of 10 m over the land surface.

According to Hsu (6), variation of  $H_{\text{LAND}}$  is much more pronounced than  $H_{\text{SEA}}$  because of larger diurnal variation in heating and cooling over land than farther offshore. This reasoning shows that the most important variable in Eq. 1 is  $H_{\text{LAND}}$ .

Following Blackadar (1), Plate (11), and many others, during neutral conditions

$$H_{\text{LAND}} = \frac{0.2 U_{* \text{ LAND}}}{f} \quad (4)$$

where  $U_{* \text{ LAND}}$  is the friction (or shear) velocity and  $f$  is the Coriolis parameter.

Note that, by definition,

$$C_{D \text{ LAND}} = \left( \frac{U_{* \text{ LAND}}}{U_{\text{LAND}}} \right)^2 \quad (5)$$

Substituting Eq. 5 into Eq. 4, one gets

$$H_{LAND} = \frac{0.2}{f} \cdot C_{D LAND}^{1/2} \cdot U_{LAND} \quad (6)$$

From Eq. 6, Eq. 1 can be written as

$$\frac{U_{SEA}}{U_{LAND}} = \left( \frac{f \cdot H_{SEA} \cdot C_{D LAND}}{0.2 \cdot C_{D LAND}^{1/2} \cdot U_{LAND} \cdot C_{D SEA}} \right)^{1/2} \quad (7)$$

In other words, for a given coastal zone, if one treats values of  $f$ ,  $H_{SEA}$ ,  $C_{D LAND}$ , and  $C_{D SEA}$  as known factors, as discussed above, then Eq. 7 becomes

$$\frac{U_{SEA}}{U_{LAND}} = A U_{LAND}^{-1/2} \quad (8)$$

where

$$A = \left[ \frac{f \cdot H_{SEA} \cdot C_{D LAND}^{1/2}}{0.2 \cdot C_{D SEA}} \right]^{1/2} \quad (9)$$

For  $U_{SEA} < 11 \text{ m s}^{-1}$  (or  $U_{LAND} \lesssim 10 \text{ m s}^{-1}$ ),  $C_{D SEA} = 1.2 \times 10^{-3}$  (10). In mid-latitudes,  $f \approx 10^{-4} \text{ s}^{-1}$ . Adopting the common value of  $H_{SEA} = 335 \text{ m}$  from Davenport [(12); see also Plate (11)] and  $C_{D LAND} = 10 \times 10^{-3}$  from Eq. (3),

we have

$$A = 3.74 \text{ m}^{1/2} \cdot \text{s}^{-1/2} \quad (10)$$

For weather systems such as hurricanes, the equations of motion do not work well because the centrifugal force is not considered. Under these conditions, the semi-empirical formula based on the power law wind distribution in the PBL [see, e.g., Plate (11)] may be employed. The power law states that

$$\frac{U}{U_H} = \left( \frac{Z}{H} \right)^P \quad (11)$$

where  $U$  at height  $Z$  and  $U_H$  at  $H$  are the velocity within and above the atmospheric planetary boundary layer (PBL), respectively. The thickness of the PBL is  $H$ , and  $P$  is an exponent [for details see, e.g., Sedefian (13)].

If we assume that  $U_H$  on top of the PBL does not change appreciably across the coastal zone and that  $Z = 10$  m, Eq. 11 becomes

$$\frac{U_{SEA}}{U_{LAND}} = \frac{10^{P_{SEA}}}{10^{P_{LAND}}} \times \frac{H_{LAND}^{P_{LAND}}}{H_{SEA}^{P_{SEA}}} \quad (12)$$

Adopting common values from Davenport [(2); see also Plate (11)],  $P_{SEA} = 0.10$  (at sea),  $P_{LAND} = 0.16$  (for flat and open country),  $H_{LAND} = 370$  m, and  $H_{SEA} = 335$  m, we find from Eq. 12 that

$$\frac{U_{SEA}}{U_{LAND}} = 1.25 \quad (13)$$

Eqs. 8 and 13 are our basis for data analyses.

### 3. Data Analyses

Many pairs of onshore and offshore measurements have become available recently [see Hsu (9)]. They are summarized in Table 1. Ratios of  $U_{SEA}/U_{LAND}$  were analyzed as a function of  $U_{LAND}$ . Note that in Hsu (9) wind speeds were below  $18 \text{ m s}^{-1}$ . The most recent data set was provided by Powell (12), who included hurricane-force wind measurements obtained during Hurricane Frederic in 1979. Although there are differences in measuring distances between onshore and offshore stations as well as lateral distance from the eye of the hurricane, the measurements are simplified here as shown in Table 1 for operational use.

### 4. Results

The results are shown in Fig. 1. It is interesting to note that

Table 1. Summary of the Ratio of  $U_{SEA}/U_{LAND}$  as a Function of  $U_{LAND}$  (in  $m s^{-1}$ ) as Measured at Coastal Stations and Offshore Buoys, Ships, and Research Platforms

$U_{LAND}$ Class Interval (1)	$U_{LAND}$ Class Mdpt. (2)	NOAA Buoys vs Coastal Sta. <sup>a</sup> (3)	BNL Buoys vs Onshore Tower <sup>d</sup> (4)	NGSC Platform vs Apalachicola <sup>e</sup> (5)	Ship vs Mogadishu <sup>f</sup> (6)	Ship vs Gardo <sup>g</sup> (7)	Hurricane Frederic, 1979 <sup>h</sup> (8)	Avg. by Region <sup>i</sup> (9)
2.0- 3.9	3	1.51±0.42 <sup>b</sup> (5) <sup>c</sup>	2.30	1.99±0.70 (102)	2.64±0.94 (5)	2.52±1.52 (7)		2.19±0.45 (8) <sup>j</sup>
4.0- 5.9	5	1.34±0.32 (39)	2.02	1.42±0.54 (35)	1.72±0.71 (25)	1.72±1.20 (7)		1.64±0.27 (8)
6.0- 7.9	7	1.36±0.08 (4)	1.59	1.33±0.43 (8)	1.50±0.62 (39)	2.19±1.26 (14)		1.59±0.35 (8)
8.0- 9.9	9		1.35	1.19 (1)	1.38±0.47 (13)	1.52±0.72 (5)		1.35±0.13 (4)
10.0-11.9	11		1.23	1.09 (1)	1.13 (1)	1.31±0.32 (15)		1.19±0.10 (4)
12.0-13.9	13		1.20			1.29±0.21 (7)		1.25±0.06 (2)
14.0-15.9	15		1.20			1.35±0.25 (2)		1.28±0.06 (2)
16.0-17.9	17		1.20				1.32±0.02 (3)	1.26±0.08 (2)



Table 1 continued

U <sub>LAND</sub> Class Interval (1)	U <sub>LAND</sub> Class Mdpt. (2)	NOAA Buoy vs Coastal Sta. <sup>a</sup> (3)	BNL Buoy vs Onshore Tower <sup>d</sup> (4)	NCSC Platform vs Apala- chicola <sup>e</sup> (5)	Ship vs Mogadishu <sup>f</sup> (6)	Ship vs Cardo <sup>g</sup> (7)	Hurricane Frederic, 1979 <sup>h</sup> (8)	Avg. by Region <sup>i</sup> (9)
18.0-19.9	19						1.14	1.14
20.0-21.9	21						(1)	(1)
22.0-23.9	23						1.18	1.18
24.0-25.9	25						(1)	(1)
26.0-27.9	27						1.25	1.25
							(1)	(1)
							1.21+0.02	1.21
							(2)	(1)
28.0-29.9	29							
30.0-31.9	31						1.24	1.24
32.0-33.9	33						(1)	(1)
34.0-35.9	35						1.29	1.29
							(1)	(1)

## Table 1 footnotes

- <sup>a</sup>From four geographic regions ranging from tropical to arctic (see Fig. 1 in Hsu, 1981).
- <sup>b</sup>Mean  $\pm$  standard deviation.
- <sup>c</sup>Total number of observational pairs (onshore and offshore).
- <sup>d</sup>Averaged data pairs between beach tower at Long Island, New York, and offshore Brookhaven National Laboratory buoy (from SethuRaman and Raynor, 1980).
- <sup>e</sup>U.S. Naval Coastal Systems Center platform offshore from Panama City, Florida, and NOAA Apalachicola station (see Hsu, 1979a).
- <sup>f</sup>Merchant ship observations vs. Mogadishu, Somalia (under conditions of general summer monsoon, but away from the Somali jet). For this experiment, see Fein and Kuettner (1980) and Hsu (1981).
- <sup>g</sup>Merchant ship observations vs. Gardo, Somalia (under conditions of Somali low-level jetstream).
- <sup>h</sup>Based on Powell (1982).
- <sup>i</sup>Mean  $\pm$  standard deviation averaged from five columns between (3) and (8)
- <sup>j</sup>Total areas studied. Note four areas already included in Fig. 1 in Hsu (1981).

when  $U_{LAND}$  is below  $10 \text{ m s}^{-1}$  the ratio of  $U_{SEA}/U_{LAND}$  follows the general trend of Eq. 8, whereas this ratio is a constant for  $U_{LAND} \geq 10 \text{ m s}^{-1}$ .

On the basis of Eq. 8, the dashed curve in Fig. 1 indicates that

$$U_{SEA} = 3.93 U_{LAND}^{1/2} \quad (14)$$

Note that the value of  $A$  ( $= 3.93 \text{ m}^{1/2} \cdot \text{s}^{-1/2}$  in Eq. 14) is in good agreement with the typical deduction, as shown in Eq. 10. The large standard deviation under low wind speed conditions is due to large variations in  $H_{LAND}$  and  $H_{SEA}$  because of large temperature differences across the coastal zone [see Hsu (6)]. In addition, averaging time, sampling rate, and heights were not uniformly reported in all pairs.

Under high wind speed conditions, say  $U_{LAND} \gtrsim 10 \text{ m s}^{-1}$ , we have

$$U_{SEA} \approx 1.24 U_{LAND} \quad (15)$$

as shown in Fig. 1. This equation is in excellent agreement with Eq. 13.

##### 5. Concluding Remarks

On the basis of many pairs of simultaneous measurements of onshore and offshore winds in regions ranging from the tropics to the Arctic and under forces ranging from breeze to hurricane, it is found that, for operational use:

For wind speed over land, i.e.,  $U_{LAND} < 10 \text{ m s}^{-1}$ ,

$$U_{SEA} \approx 3.93 U_{LAND}^{1/2}$$

and for  $U_{LAND} \geq 10 \text{ m s}^{-1}$

$$U_{SEA} \approx 1.24 U_{LAND}$$

The above formulas are useful over low-relief ( $< 0.5\text{-}1 \text{ km}$  in height) and open coasts. They may not be applicable for mountainous or cliffy

coast areas. Also, atmospheric mesoscale systems such as low-level jets under special conditions [see Hsu (7)], land- and sea-breeze systems (5), and coastal fronts during the winter season were not taken into account. Although there is still large scatter in the data points as shown in Fig. 1 and many smaller scale meteorological systems were not included because of the different physics involved, it is felt that for engineering applications these simplified formulas should be useful as a first approximation to this complex problem of onshore-offshore wind differences.

Acknowledgments. This study was sponsored in part by the Coastal Sciences Program, Office of Naval Research, Arlington, Virginia. Additional support was provided by the Louisiana Sea Grant College Program, a part of the National Sea Grant College Program maintained by NOAA, U.S. Department of Commerce.

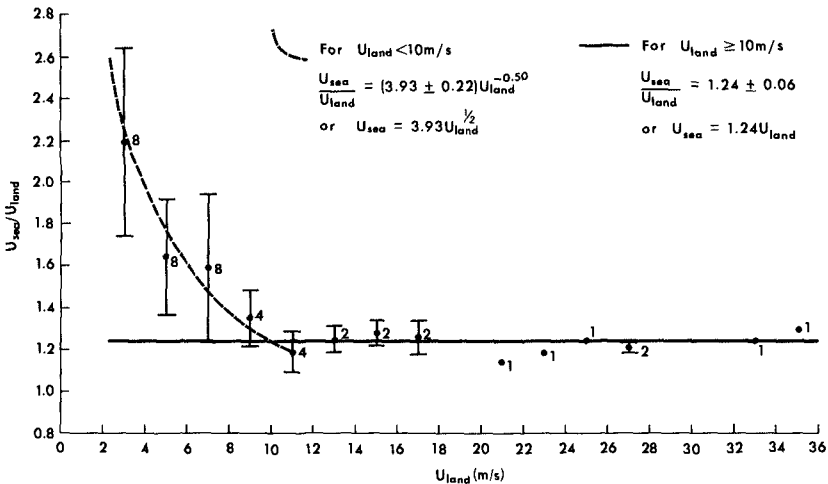


Fig. 1. Ratio of  $U_{SEA}/U_{LAND}$  as a function of  $U_{LAND}$ . Data were based on Table 1. Vertical bars are the standard deviation, and numbers beside the mean point are the areas incorporated in the computations. Values on the right-hand side of the equations are mean and standard deviations, respectively.

## APPENDIX 1.--REFERENCES

1. Blackadar, A. K., "The Vertical Distribution of Wind and Turbulent Exchange in a Neutral Atmosphere," Journal of Geophysical Research, Vol. 67, 1962, pp. 3095-3101.
2. Davenport, A. G., "The Relationship of Wind Structure to Wind Loading," Wind Effects on Buildings and Structures, National Physical Laboratory Symposium No. 16, Her Majesty's Stationery Office, London, 1965, pp. 54-102.
3. Fein, J. S., and Kuettner, J. P., "Report on the Summer MONEX Field Phase," Bulletin of the American Meteorological Society, Vol. 61, 1980, pp. 461-474.
4. Garratt, J. R., "Review of Drag Coefficients over Oceans and Continents," Monthly Weather Review, Vol. 105, 1977, pp. 915-929.
5. Hsu, S. A., "Coastal Air-Circulation System: Observations and Empirical Model," Monthly Weather Review, Vol. 98, 1970, pp. 487-509.
6. Hsu, S. A., "An Operational Forecasting Model for the Variation of Mean Maximum Mixing Height across the Coastal Zone," Boundary-Layer Meteorology, Vol. 16, 1979a, pp. 93-98.
7. Hsu, S. A., "Mesoscale Nocturnal Jetlike Winds within the Planetary Boundary Layer over a Flat, Open Coast," Boundary-Layer Meteorology, Vol. 17, 1979b, pp. 485-495.
8. Hsu, S. A., "On the Correction of Land-Based Wind Measurements for Oceanographic Applications," Proceedings of the 17th Coastal Engineering Conference, American Society of Civil Engineers, Vol. 1, 1980, pp. 708-724.
9. Hsu, S. A., "Models for Estimating Offshore Winds from Onshore Meteorological Measurements," Boundary-Layer Meteorology, Vol. 20, 1981, pp. 341-351.
10. Large, W. G., and Pond, S., "Open Ocean Momentum Flux Measurements in Moderate to Strong Winds," Journal of Physical Oceanography, Vol. 11, 1981, pp. 324-336.
11. Plate, E. J., "Aerodynamic Characteristics of Atmospheric Boundary Layer," Available as TID-25465, National Technical Information Center, Springfield, Virginia, 1971.
12. Powell, M. D., "The Transition of the Hurricane Frederic Boundary-Layer Wind Field from the Open Gulf of Mexico to Landfall," Monthly Weather Review, Vol. 110, 1982, pp. 1912-1932.
13. Sedefian, L., "On the Vertical Extrapolation of Mean Wind Power Density," Journal of Applied Meteorology, Vol. 19, 1980, pp. 488-493.

14. SethuRaman, S., and Raynor, G. S., "Comparison of Mean Wind Speeds and Turbulence at a Coastal Site and Offshore Location," Journal of Applied Meteorology, Vol. 19, 1980, pp. 15-21.
15. Yu, T. W., "Diurnal Variation of Kinetic and Internal Energy in Onshore Winds along the Upper Texas Gulf Coast," Report No. 19, Atmospheric Science Group, University of Texas, Austin, 1970.
16. Zimmerman, J. R., and Burton, W. D., "Late Summer Gale Winds Offshore Coastal Oregon-Washington," National Weather Digest, Vol. 4, 1979, pp. 27-40.

## CHAPTER ONE HUNDRED FIFTY

### ASPECTS OF WAVE CURRENT BOUNDARY LAYER FLOWS

Felicity C. Coffey and Peter Nielsen

#### ABSTRACT

Field measurements of steady current profiles under the influence of waves are described, including a technique for obtaining an extra independent estimate of the friction velocity. Field and laboratory measurements are analysed for the effect on apparent bed roughness by superimposing waves on a current. Finally the applicability of the eddy viscosity concept to combined flows is examined. The conclusion is that in general, different eddy viscosities must be applied to different flow components.

#### INTRODUCTION

The process of sediment transport and the resulting erosion or sedimentation problems in coastal areas is most often the result of a combined effort by waves and steady (or quasi steady) currents. It is therefore desirable for the coastal engineer to be able to model the flow near a movable bed under combined flows. The aim of this paper is to review, what is known today about wave current boundary layer interaction, and what seems to be needed on the experimental side.

Waves and currents interact in two different ways. Firstly, there is the strong and fairly obvious shoaling and refraction effect on waves that propagate through areas with varying current speed. This effect results from interaction throughout the water column, and the current speed near the surface tends to be the most important. Secondly, there is the interaction in the bottom boundary layer, where the waves tend to dominate and modify the current distribution. The present paper deals entirely with the latter process.

Since short periodic flows develop thinner boundary layers in accordance with

$$\delta = \sqrt{\kappa_* T} \quad (1)$$

---

Coastal Studies Unit, Department of Geography, University of Sydney, N.S.W. 2006, Australia.

and thus penetrate better towards the bed, there is a general tendency for the waves to dominate this layer. In equation (1),  $\delta$  is the boundary layer thickness,  $\nu_T$  is the eddy viscosity, and T is the flow period.

The structure of the wave boundary layer is most often unaffected by even a fairly strong current, while the current profile always shows considerable influence from the waves under naturally occurring conditions. Figure 1 is a simplistic resume of the effects of waves on a steady current.

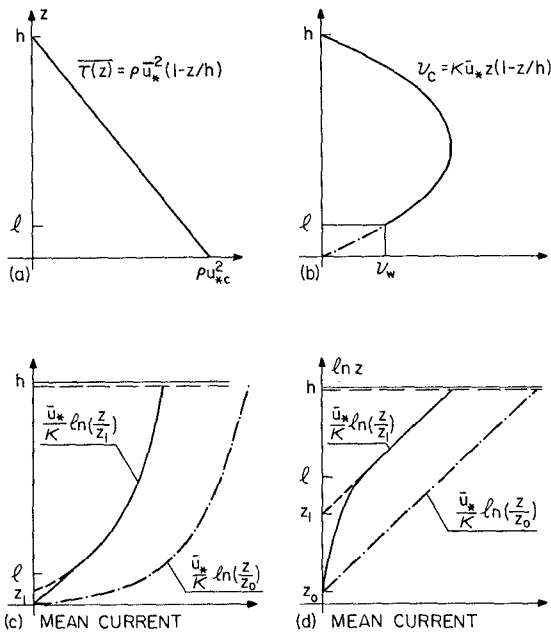


Figure 1: Influence of waves on the steady current profile. (b): The waves create extra eddy viscosity near the bed. (c) and (d): The upper part of the current profile maintains its logarithmic shape, but is shifted towards lower values, and the zero intercept is consequently increased considerably,  $z_1 \gg z_0$ .

It is easier to get a clear idea of what is going on if the steady friction velocity  $\bar{u}_*$  is thought of as a fixed



quantity. That is, we may think of flume experiments where the slope of the mean free surface is kept constant while different wave conditions are enforced.

We assume that the steady shear stress is linearly distributed (Figure 1a),

$$\tau(z) = \rho \bar{u}_*^2 (1-z/h) \quad (2)$$

Deviations from this may occur in the upper layers due to gradients in wave radiation stress, but such deviations will be small in and near the bottom boundary layer. The eddy viscosity induced by the undisturbed steady flow is assumed to have the form

$$\nu_T = \kappa \bar{u}_* z (1-z/h) \quad (3)$$

and (2) and (3) will lead to the familiar logarithmic current profile

$$\bar{u}(z) = \frac{\bar{u}_*}{\kappa} \ln \frac{z}{z_0} \quad (4)$$

where  $\kappa$  is von Karman's constant and  $z_0$  is the zero intercept (Figure 1c,d) of the logarithmic profile. The primary effect of superimposing waves on  $\bar{u}$  comes from increasing the mixing intensity in a thin layer near the bed (Figure 1b), which results in smaller velocity gradients for a fixed  $\bar{u}_*$ .

$$\frac{\partial \bar{u}}{\partial z} = \frac{\tau/\rho}{\nu_T} \sim \frac{\bar{u}_*^2}{\nu_T} \quad (5)$$

Thus the current velocity will grow more slowly with  $z$  through the lower layer when waves are present (Figure 1c,d). Outside the wave boundary layer, the waves will not contribute significantly to the eddy viscosity, and therefore, the shape of the current profile will be unchanged. It can be described by

$$\bar{u}(z) = \frac{\bar{u}_*}{\kappa} \ln \frac{z}{z_1} \quad (6)$$

Hence the only difference from the undisturbed current profile (4) is that  $z_0$  has been replaced by the considerably larger  $z_1$ .

Such changes of the outer steady current profile have been observed in the field by several authors e.g. Cacchione

and Drake (1982) and Grant et al (1983). Laboratory measurements by van Doorn (1981,1982) and by Kemp and Simons (1982,1983) also show this general trend.

The vertical extent of the logarithmic layer is from the top of the wave boundary layer to elevations where the waves or other phenomena start to cause deviations from the linear shear stress distribution, as seen in figure 2.

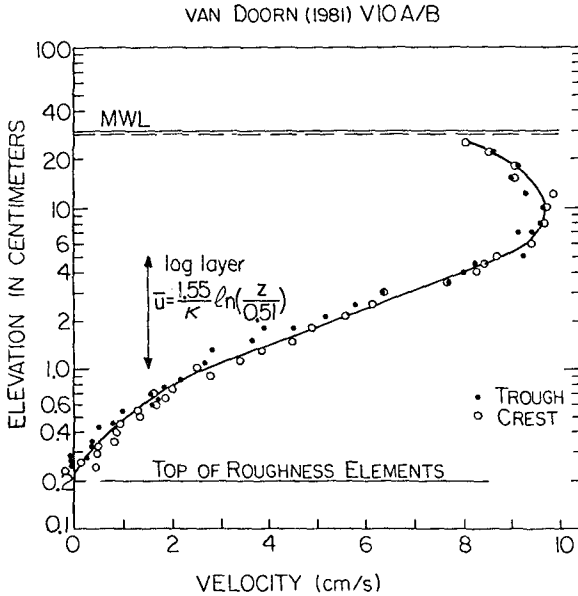


Figure 2: Steady current velocities in the presence of waves. In this case the intercept elevation was increased from  $z_0 = 0.07\text{cm}$  to  $z_1 = 0.51\text{cm}$  due to the presence of waves.

The relative change of the zero intercept ( $z_1/z_0$ ) depends mainly on the relative current strength  $\bar{u}_w/A\omega$ , but also on the relative roughness  $r/A$  and the direction of the currents relative to the waves.  $A$  is the semi excursion in the wave motion just above the wave boundary layer and  $\omega$  is the angular velocity ( $\omega = 2\pi/T$ ),  $r$  is the hydraulic roughness of the bed.

## FIELD EXPERIMENTS

In the literature combined wave current flows are approached from two perspectives. Namely, the influence of waves on a steady flow and the influence of a current on an oscillatory flow. Field observation of oscillatory boundary layers is generally a problem as it is difficult to fit accurate current meters into the thin wave boundary layer. Thus the field experiments presented here were concerned with the measurement of steady flows under the influence of waves.

Normally, the steady flow component in the field, as well as in the laboratory, shows a nicely logarithmic behaviour over a considerable fraction of the depth, (Figure 2) which gives us the friction velocity from the slope and an apparent roughness from the z-intercept, see Figure 1.

In our experiments the steady flow component was measured by an array of five Hales and Rogers propeller flow meters. The flow meters have an inner diameter of 6cm. Simultaneous readings were obtained by storing the voltage output of each flow meter in capacitors and reading alternatively from a digital display. The flow meter output was filtered electronically over a 100s time period and the sampling interval was approximately 1 minute.

Steady flow calibration of each flow meter was performed before and after each field experiment. The flow meters were found to have a very good, linear response. Experiments were also conducted to investigate the effects of waves on the instruments' steady flow response. These effects need to be taken into account when looking at the data.

Field sites with a strong unidirectional current in association with either parallel or normal wave propagation were selected in order to obtain well controlled field experiments. The codirectional and opposing currents to direction of wave propagation were observed in the tidal channel at Port Hacking, South of Sydney, Australia. The water depth ranged between 1.1 to 2.1m and the sediment diameter was approximately 0.28mm. The average wave period and significant wave height ranged between 7 to 10s and 20 to 61cm, respectively. Well rounded ripples were generally observed and were 2-6cm high and 9-40cm long.

To observe perpendicular currents to wave direction, experiments were carried out in rip feeder channels inshore of a bar. Palm Beach, Warriewood Beach and Warri Beach, near Sydney, were selected. During some experiments currents up to 1 m/s were experienced. The water depth was approximately 1.2m and the sediment, slightly coarser than that found in the tidal channel, had an average diameter of 0.46mm. The average wave period and significant wave height ranged between 7 to 11s and 25 to 50cm, respectively. Ripple geometry varied greatly. Large well rounded ripples with height 10cm and length 90cm were observed as well as small, sharp crested, wave generated ripples with height 2cm and length 10cm.

Time averaged values of the bed shear stresses were determined in the field by measuring the mean water surface slope using the so-called "Barometer". The "Barometer", Figure 3, consists of a set of vertical glass tubes which enable us to read the difference in mean water level between different locations. From the bottom of the tubes run plastic hoses out to different locations. The distance between the hose outlets is approximately 50 m. The tubes are connected at the top so that the air pressure is the same in all of them. We use two tubes for each location in order to check that the instrument is working satisfactorily. The water level should be the same in each pair. Water level oscillations within the tubes are not perceptible. The bed shear stresses or the friction velocity can be determined from the surface slope,  $S$ , via

$$\bar{u}_*^2 = -Sgh \quad (7)$$

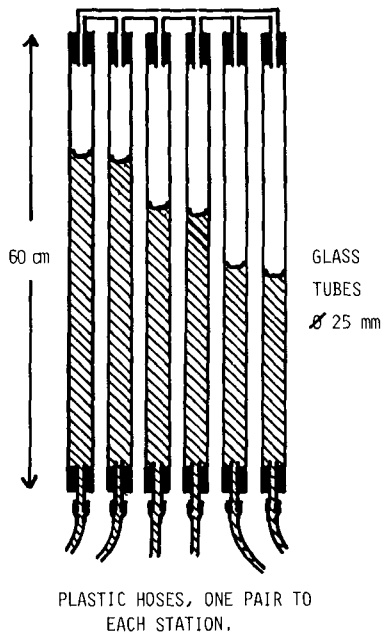


Figure 3: The Barometer. Differences in mean water level between the various stations are shown by the water levels in the vertical glass tubes.

We can compare the friction velocity derived from the "Barometer" measurements with the friction velocity obtained from the observed velocity distribution. This is a valuable check. Note, however, that the "Barometer" can only be used in situations where the surface slope is the sole driving force of the current. In the situation where the waves arrive obliquely to the shoreline the radiation stress becomes a contributing driving force of the longshore current.

#### EMPIRICAL KNOWLEDGE ABOUT THE APPARENT ROUGHNESS, $z$ ,

Figure 4 shows tests 7-19 and laboratory data from the literature plotted for apparent roughness  $z$ , against relative current strength,  $\bar{u}_* / A\omega$ .  $z$  is nondimensionalized by the fixed bed roughness index,  $8\eta^2/\lambda$ , suggested by Nielsen 1983.  $\eta$  is the ripple height and  $\lambda$  is the ripple length. The relative current strength is the ratio between the current friction velocity  $\bar{u}_*$ , and the near bed horizontal velocity due to waves,  $A\omega$ . The results show that with increasing wave dominance  $z$ , increases. This has been observed by Kemp and Simons (1982,83). However, for the current following the waves, marked by the dots, the relationship is not clear and for perpendicular currents (the triangles) this relationship may not hold at all. Thus what we can see from this graph is that the relative orientation of waves and currents is important. More measurements are needed. The fixed bed roughness index appears to be a satisfactory scaling parameter for four of the perpendicular current observations, which flowed over sharp crested ripples. These lie in the vicinity of the laboratory data which used fixed roughness elements. However, the majority of field observations with well rounded ripples lie well below the laboratory data. This indicates that for these cases the relevant scaling parameter is the grain size rather than the ripple geometry.

#### WAVE BOUNDARY LAYER STRUCTURE

The wave induced velocity  $u(z,t)$  inside the wave boundary layer differs from the corresponding free stream velocity  $u_\infty(t)$  with respect to both magnitude and phase. This makes it somewhat complicated to describe the structure of the flow. We shall use the formalism suggested by Nielsen (in prep) which stresses the analogy in form of all oscillatory boundary layers with that of smooth, laminar oscillatory flow. For simplicity, we consider only simple harmonic flow

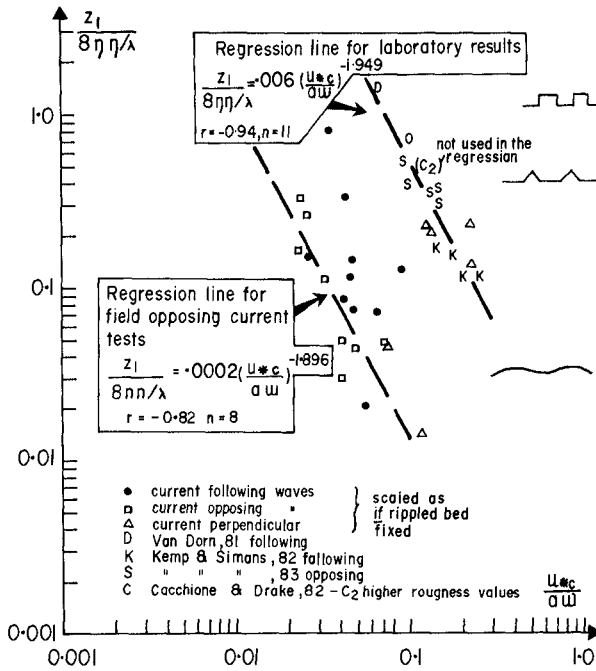


Figure 4: Field and laboratory data plotted for apparent roughness ( $30z_1$ ) against relative current strength,  $\bar{u}_* / A\omega$ .  $z_1$  is nondimensionalized by a fixed bed roughness index,  $8\eta^2/\lambda$ , given by Nielsen 1983, where  $\eta$  is ripple height and  $\lambda$  is ripple length.

With increasing wave dominance  $z_1$  increases. We find two populations of data. The upper set contains laboratory data and four field measurements of perpendicular flows with sharp crested ripples. The lower group consists entirely of field measurements where well rounded ripples were observed. This suggests that when the ripples are rounded, the hydrodynamic roughness is determined by grain size rather than ripple geometry.

or the first harmonic of more complicated flows, and define the non dimensional velocity deficit  $D(z)$  by

$$u(z,t) = [1-D(z)]A\omega e^{i\omega t} \tag{8}$$

$D$  is unity at the bed and zero at infinity, so that the free stream velocity corresponds to  $A\omega e^{i\omega t}$ .

For smooth, laminar flow,  $D$  is given by

$$D(z) = \exp[-(1+i)\frac{z}{\sqrt{2\nu/\omega}}] \tag{9}$$

see e.g. Lamb (1945). Equation (9) shows that argument and magnitude of  $D$  are two sides of the same thing in the sense that

$$\ln D = \text{Arg } D \tag{10}$$

Figure 5 shows the identity (10) for a rough turbulent oscillatory flow measured by van Doorn (1982).

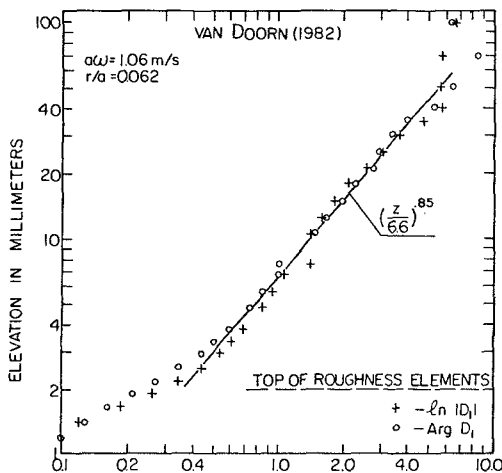


Figure 5: The identity (10) which is an analytical result for smooth laminar flow holds for most turbulent flows as well.

As pointed out by Nielsen (in prep), this identity holds for many turbulent flows as well, with a slight generalisation in the form of D

$$D = \exp[-(1+i) \left(\frac{z}{z_t}\right)^p] \tag{11}$$

where the "Stokes' length"  $\sqrt{2\nu/\omega}$  is replaced by  $z_t$  which is approximately equal to  $0.095\sqrt{\nu A}$ . The slope parameter p varies smoothly from unity for very rough flows ( $A/r < 10$ ), to 0.32 for smooth turbulent flow.

The fact that very rough flows have the same slope parameter as smooth laminar flow, namely unity, is due to the fact that in both of these two cases there is only one vertical length scale involved. For smooth, laminar flow it is the "Stokes' length", and for very rough turbulent flows it is the bed roughness length.

The validity of (10) is not disturbed by superposition of a steady current, and the variation of D(z) changes very little, even with a fairly strong current. See Figure 6.

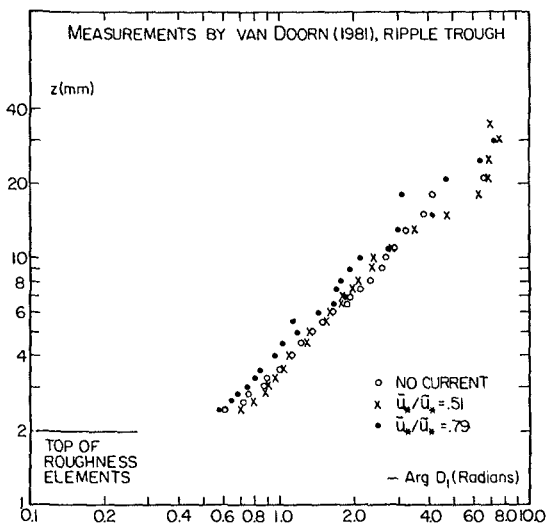


Figure 6: Variation of Arg D with z for different relative strengths of superimposed currents. The steady current induces very little change in the wave boundary layer structure.



## EDDY VISCOSITY IN OSCILLATORY FLOW

Shear stresses and velocity gradients in a turbulent flow are most easily related via an eddy viscosity

$$\nu_T = \frac{\tau/\rho}{\frac{\partial u}{\partial z}} \quad (12)$$

and it is therefore tempting to try and apply eddy viscosity models. It must be remembered however that  $\nu_T$  is only a formal tool without strictly defined physical meaning. This becomes very clear when one considers empirical data on oscillatory flows like the ones shown in Figure 7.

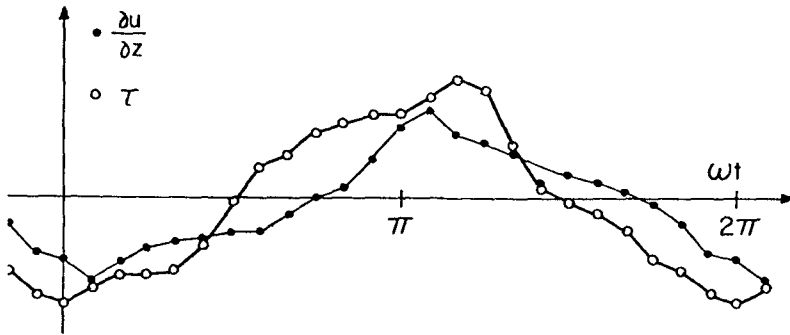


Figure 7: Time dependence of local shear stress and velocity gradient, both phase averaged. From Jonsson and Carlsen (1976) Test 1. The measurements were taken 45mm above a ripple crest.

The fact that the phase averaged values of shear stress and velocity gradients are out of phase (Figure 7) implies a somewhat radical behaviour of the eddy viscosity via the definition (12). Two interpretations are possible. One can either define the eddy viscosity as a real valued function of time, which will then have to vary approximately like  $-\tan \omega t + \text{constant}$ , see Horikawa and Watanabe (1967). The other option is to allow the eddy viscosity be a complex quantity. The latter option leads to a constant  $\nu_T$  if  $\tau$  and  $\frac{\partial u}{\partial z}$  are simple harmonic and the angle  $\text{Arg } \nu_T$  is then the phase shift between the two.

If we apply the second interpretation, measurements like the ones shown in Figure 5 correspond to complex eddy viscosities ( $\text{Arg } \nu_T \neq 0$ ). In fact the form given by eqs. (8) and (11) corresponds to a real valued  $\nu_T$  only when  $p=1$ . In that case the eddy viscosity is a real constant given by

$$\nu_T = \omega z_i^2 / 2 \quad (13)$$

## EDDY VISCOSITIES IN COMBINED FLOWS

Because of its simplicity the eddy viscosity model has been applied to combined flows by several authors in the past: Lundgren (1972), Grant and Madsen (1979) and Christoffersen (1982). All of these authors assumed the existence of a "common" eddy viscosity, which would apply to all flow components.

This assumption seems very reasonable, but it has never been proven. Only very recently, with the publication of the very detailed measurements by van Doorn (1981,1982) has it become possible to test it. The test result is stunning. It is very clearly negative, showing that steady and oscillatory components of the same flow correspond to very different eddy viscosities. See Figure 8.

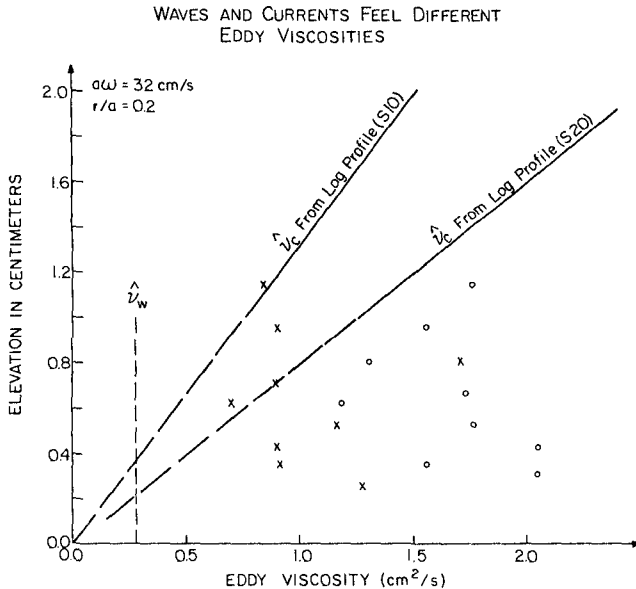


Figure 8: Eddy viscosity estimates derived from steady and oscillatory components of the same flow. The steady component feels 3 times larger eddy viscosities inside the wave boundary layer than do the waves.

The eddy viscosity is estimated from the oscillatory component via equation (13).

The implication of Figure 8 is that future models of combined flows which are based on the eddy viscosity concept, must allow for the use of different eddy viscosities for different flow components.

Some might then say that the use of the eddy viscosity concept is a total over simplification, and that we must turn to other models of the stress strain relation, for example, the von Karman - Prandtl mixing length model

$$\tau = \rho l^2 \left| \frac{\partial u}{\partial z} \right| \frac{\partial u}{\partial z} \quad (14)$$

However the work of van Doorn (1983) and Nielsen (in prep) show that the non linear von Karman - Prandtl model which makes analytical solution impossible, is only marginally better than the linear-eddy-viscosity-model applied by Grant and Madsen (1979). Both models predict the flow phases rather poorly. See Throwbridge (1983) or Nielsen (in prep).

#### CONCLUSIONS

The major effect of waves superimposed onto a current with fixed  $\bar{u}_*$  is to reduce the current gradients inside the wave boundary layer. This leads to a shifting of the upper current profile towards smaller velocities. The shape of the upper current profile is unchanged because there is no wave induced mixing in this layer. One therefore finds (Lundgren, 1972) that the current profile above the wave boundary layer is logarithmic (Figure 2), and defines a friction velocity  $\bar{u}_*$ , by its slope and an apparent roughness ( $30z_i$ ) by its zero intercept  $z_i$ .

The apparent roughness in combined flows is generally found to be an order of magnitude larger than the Nikuradse roughness,  $30z_o$ , defined by a pure current over the same bed. Field and laboratory measurements shown in Figure 4 indicate that the roughness increase  $z_i/z_o$  depends strongly on the relative current strength,  $\bar{u}_*/A\omega$ . The dependence may be roughly described by

$$\frac{z_i}{z_o} \sim \left( \frac{A\omega}{\bar{u}_*} \right)^{1.9} \quad (15)$$

The dependence of  $z_i/z_o$  on the relative direction of waves and currents is so far unresolved. Thus there is a strong need for well controlled experiments with waves running at an angle to the current.

Analysis of high quality laboratory measurements reveals that the eddy viscosity concept can be applied to combined flows only with extreme caution. It is found that we must in general apply different eddy viscosities to different flow components. The measurements of van Doorn (1981,1982) show that the steady flow component feels an eddy viscosity three to four times larger than the one felt by the main oscillatory component.

## REFERENCES

- Cacchione, D A & D E Drake (1982): Measurements of storm-generated bottom stresses on the continental shelf. *J Geophys Res*, Vol 87, pp 1952-1960.
- Christoffersen, J B (1982): Current depth refraction of dissipative water waves. Series Paper 30, ISVA, Tech Univ Denmark.
- Doorn, Th van (1981): Experimental investigation of near-bottom velocities in water waves without and with a current. Delft Hydr Lab, Rep No M1423.
- Doorn, Th van (1982): Experimenteel onderzoek naar het snelheidsveld in de turbulente bodem grenslaag in een oscillerende stroming in een golftunnel. Delft Hydr Lab, Rep No M1562-lb.
- Grant, W D & O S Madsen (1979): Combined wave and current interaction with a rough bottom. *J Geophys Res*, Vol 84, No C4, pp 1797-1808.
- Grant, W D, A J Williams, S M Glenn, D A Cacchione & D E Drake (1983): High frequency bottom stress variability and its prediction in the CODE region. CODE Tech Rep No 15, Woods Hole Oceanographic Inst.
- Horikawa K & A Watanabe (1967): A study on sand movement due to wave action. *Coastal Engrg in Japan*, Vol 10, pp 37-57.
- Jonsson I G & N A Carlsen (1976): Experimental and theoretical investigations in an oscillatory rough turbulent boundary layer. *J Hydr Res*, Vol 14, No 1, pp 45-60.
- Kemp P H & R R Simons (1982): The interaction between waves and a turbulent current: waves propagating with the current. *J Fluid Mech*, Vol 116, pp 227-250.
- Kemp P H & R R Simons (1983): The interaction of waves and a turbulent current: waves propagating against the current. *J Fluid Mech*, Vol 130, pp 73-89.
- Lamb H (1945): *Hydrodynamics*. 6th ed, Dover Pub, New York.
- Lundgren H (1972): Turbulent current in the presence of waves. Proc 13th Int Coastal Engrg Conf, Vancouver, pp 623-634.
- Nielsen P (1983): Analytical determination of wave height variation due to refraction, shoaling, and friction. *Coastal Engrg*, Vol 7, pp 233-251.
- Nielsen P (in prep): On the structure of oscillatory boundary layers. Submitted to *Coastal Engrg*.
- Throwbridge J H (1983): Wave-induced turbulent flow near a rough bed: implications of a time-varying eddy viscosity. PhD thesis, Woods Hole Oceanographic Inst, WHOI-83-40.

## CHAPTER ONE HUNDRED FIFTY ONE

### A THEORETICAL AND EXPERIMENTAL STUDY OF UNDERTOW

J. Buhr Hansen\* and I. A. Svendsen\*

#### ABSTRACT

It is well known that on a three-dimensional beach large volumes of water carried shorewards by the breakers feed longshore currents, which eventually escape back through the breaker line, often as rip currents.

In a steady two-dimensional situation, however, the mass flux represented by (among other things) the surface roller in the breakers returns as a seaward current close to the bottom. This current is called the undertow.

In this paper theoretical results for the undertow are compared with the results of recent laboratory experiments.

#### 1. INTRODUCTION

Although known for years and described quite explicitly in texts on coastal morphology (see e.g Johnson 1919) the undertow seems for a long time to have escaped the attention of coastal engineers and scientists.

Undertow is the name used for the often very strong shore normal mean current which in a surf zone moves seaward below the level of the wave trough.

Clearly such a flow can only be maintained provided a similar flux of water is brought shorewards otherwise. This happens between crest and trough level in the broken surf zone waves. the situation is sketched in Fig. 1.

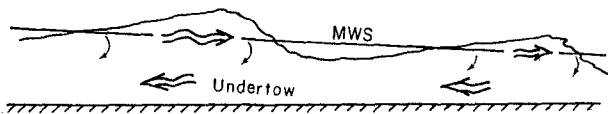


Fig. 1. The circulation flow in the vertical plane.

This circulation in the vertical plane represents a mechanism for maintaining the mass balance in the surf zone of a long beach. Another possible mechanism in the nearshore circulation is the three dimensional pattern of longshore and rip currents, which so far has received much more attention than the two dimensional circulation scheme in Fig. 1.

---

\* Assoc. Prof., Institute of Hydrodynamics and Hydraulic Engineering (ISVA), Technical University of Denmark, DK-2800 Lyngby.

The purpose of the present paper is to discuss the physical processes responsible for the undertow. The discussion is supported by a theoretical model and recent laboratory measurements.

The undertow was observed experimentally by Bagnold (1940) and a qualitative analysis of the phenomenon was given by Dyhr-Nielsen and Sørensen (1970) in a descriptive paper which in essence contained most of the physical ideas pursued quantitatively in the following.

In the last few years the undertow has eventually attracted more attention. Thus Börekci (1982) presented a theoretical model based on the sinusoidal waves for the distribution over depth of this mean circulation, and an almost similar analysis was in fact given by Dally (1980).

Lately Louquet-Higgins (1983a,b) has considered several effects that may be caused by the strong pressure gradient from the set-up which also creates the undertow. In the last of the two papers in terms of convincing experimental demonstrations.

Finally Svendsen (1984b) presented a theoretical model based on the description of surf zone waves developed in Svendsen (1984a).

It may also be mentioned that laboratory values for the undertow can be extracted from the raw data of Stive and Winds experiments and were used by Svendsen (1984b). Also Guza (1984) reports that during the NSTS experiments at Californian beaches all current meters in the surf zone showed uniformly seaward going mean currents. This part of the data, however, has not been processed yet.

The theoretical model for the velocity profile of the undertow developed by Svendsen (1984b) differs from the models of Dally (1980) and Börekci (1982) in the way properties of the broken waves such as radiation stress and mass flux are determined.

The present paper will emphasize the physical aspects rather than mathematical details of the phenomenon, present some new measurements and also discuss the interaction with the bottom boundary layer, a point which was only briefly mentioned in Svendsen (1984b).

For several reasons an eulerian description has been chosen rather than a lagrangian. For one thing it is far simpler. Further all the measurements available are measurements at fixed points (i.e. eulerian descriptions). Most important, however, is the fact that the eulerian description is physically the more informative when mass balance, sedimenttransport etc. is considered.

## 2. THE MECANISM RESPONSIBLE FOR THE UNDERTOW

As mentioned in the introduction the undertow is a (strong) mean current which, superimposed on the oscillatory motion of the surf zone waves, moves seawards.

In this section is shown qualitatively that the undertow represents a balance between three equally important forces acting on the fluid particles.

For a start it is worth to recall that the turbulence created by the breakers spread downwards from the surface, where it was created, so that in the surf zone there is a substantial amount of turbulent kinetic energy present at all levels between bottom and surface. In such an environment a current like the undertow will generate large shear stresses which will tend to stop the current. Thus for the undertow to exist there must be a strong driving mechanism, which yields a seaward directed net force on each fluid particle.

It is well known that the depth- and time-averaged momentum balance

reads:

$$\frac{\partial S_{xx}}{\partial x} = -\rho g(h_0 + b) \frac{\partial b}{\partial x} - \overline{\tau}_b \quad (2.1)$$

where  $b$  is the set-up,  $\overline{\tau}_b$  is the mean bed shear stress, and the radiation stress  $S_{xx}$  is defined as

$$S_{xx} = \int_{-h}^{\eta+b} (\rho u^2 + p_D) dz - \frac{1}{2} \rho g \eta^2 \quad (2.2)$$

The dynamic pressure  $p_D$  is defined by

$$p_D = \rho g(z-b) + p \quad (2.3)$$

In this balance, however, the individual contributions are not equally distributed over depth. In (2.2) both  $u$  and  $p$  will in general vary over the depth and, in surf zone waves in particular, by far the largest contributions to  $S_{xx}$  (including the last term in (2.2) come from the region between trough and crest.

The  $\partial b/\partial x$  term in (2.1) on the other hand represents the pressure gradient from the sloping mean surface, and this contribution is the same at all  $z$ -levels. Fig. 2 shows the situation.

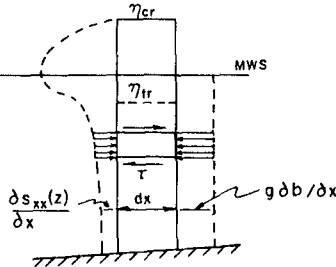


Fig. 2. The distribution of radiation stress and pressure gradients.

Consequently, if we consider a small fluid element at any  $z$ -level below trough level there will (in average over a wave period) be a net (seaward-directed) horizontal force on that fluid element equal to the difference between the local  $S_{xx}$ -contribution and  $g \partial b/\partial x$ . It is this net force which is driving the undertow. In Fig. 2 is also indicated the turbulent shear stress gradients which are responsible for preventing the current from accelerating indefinitely.

Thus a steady undertow establishes a balance between essentially three different forces: the radiation stress the pressure gradient due to set-up and the turbulent shear stresses created by the vertical variation of the undertow velocity in combination with the turbulence already present due to the breaking. The model used in the following is based on this balance. In principle it assumes (in addition to a situation steady in time) uniform conditions at different points in the shore normal direction. Since the depth varies this is clearly not quite true, but applies well to a gently sloping beach. The assumption corresponds to neglecting the convective accelerations in the shore normal direction, and on a steep beach this may not be acceptable.

3. THEORETICAL DESCRIPTION

From the description in Section 2 we realize that the undertow is associated with the strong set-up caused by wave breaking. Hence a proper quantitative description requires that the relevant characteristics of the surf zone waves are modeled suitably (see Svendsen, 1984a).

One of the important features is the mass or volume transport  $Q_s$  which occurs between crest and trough in the waves.  $Q_s$  is defined as (for definition of nomenclature see Fig. 3)

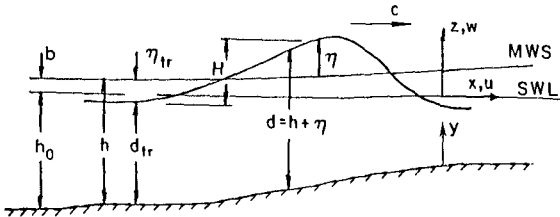


Fig. 3. Definition sketch.

$$Q_s = \overline{\int_{\eta_{tr} + b}^{\eta + b} u \, dz} \quad (3.1)$$

where  $\overline{\quad}$  indicates average over a wave period.

In broken waves this is found to be composed of two contributions (Svendsen, 1984a): one is the ordinary effect of non-linearity known from non-breaking waves. The other is caused by the surface roller which is equivalent to an amount of water directly following the wave as it propagates shorewards. Thus the average particle velocity in the roller equals the propagation speed  $c$  of the wave.

It is therefore assumed that the velocity variation in the waves can be approximated as shown in Fig. 4.

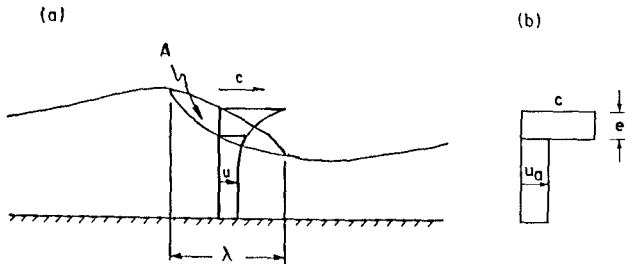


Fig. 4. a. Velocities in a breaker.  
b. Velocity profile used in this paper.

This is combined with the assumption that the change in shape of the waves can be neglected locally which implies that



$$I \equiv \int_{-h_0}^{\eta+b} u \, dz = c\eta \quad (3.2)$$

As written (3.2) also presumes that there is no net mass flux in the waves (two dimensional problem), and that  $\bar{\eta} = 0$  as indicated in Fig. 3.

When substituting these assumptions into (3.1) we get for the total Stokes drift (for derivation see Svendsen (1984 b))

$$Q_s = c \left( \frac{H}{h} \right)^2 \left( B_0 + \frac{A}{H^2} \frac{h}{L} \right) d_{tr} + O \left( \left( \frac{\eta}{h} \right)^3, \dots \right) \quad (3.3)$$

In this expression  $L$  is the "wave length" defined as  $c(x)T$ ,

$$B_0 \equiv \overline{(\eta/H)^2} \quad (3.4)$$

and  $A$  is the area in the vertical plane of the surface roller (see Fig. 4).

Measurements of  $A$  is only available for deep water breaking behind a submerged hydrofoil (Duncan, 1981) where it was found that

$$A \approx 0.9 H^2 \quad (3.5)$$

With no net mass (or volume) flux in the wave we also find the mean velocity  $U_m$  in the region below wave trough to be given by

$$U_m = - \frac{Q_s}{d_{tr}} \quad (3.6)$$

where  $d_{tr}$  is the water depth under the wave trough. With these results we have ensured the conservation of mass in the wave-current motion considered.

The equation of conservation of (horizontal) momentum is used on the form

$$\frac{\partial u}{\partial t} + \frac{\partial u^2}{\partial x} + \frac{\partial uw}{\partial z} = - \frac{1}{\rho} \frac{\partial p}{\partial x} \quad (3.7)$$

where viscous terms have been neglected. The balance described in Section 2 between three contributions then results in the following relation

$$\overline{\frac{\partial u^2}{\partial x}} \approx -g \frac{\partial b}{\partial x} - \frac{1}{\rho} \frac{\partial \bar{\tau}}{\partial z} \quad (3.8)$$

which is the time averaged momentum equation for a fluid particle.  $\bar{\tau}$  is the turbulent shear stress and  $u$  the turbulent mean velocity. (3.8) only applies below the level of the wave trough  $u$  may be divided into a wave part  $u_w$  (with  $u_w = 0$ ) and the undertow component  $U$ . It can then be shown that consistent with assumptions already introduced we have

$$\overline{u_w^2} \gg U^2 \quad (3.9)$$

so that (3.8) may be written as

$$\frac{1}{\rho} \frac{\partial \bar{\tau}}{\partial z} = \frac{\partial}{\partial x} \left( \overline{u_w^2} + gb \right) \tag{3.10}$$

The turbulent shear stress  $\tau$  is described by an eddy viscosity  $\nu_t$  such that

$$\tau = \rho \nu_t \frac{\partial (u_w + U)}{\partial z} \tag{3.11}$$

This is time averaged and we invoke that  $u_w$  to the first approximation can be assumed independent of  $z$ . Then we get

$$\bar{\tau} = \overline{\nu_t(t) \frac{\partial (u_w + U)}{\partial z}} = \overline{\nu_t(t)} \frac{\partial U}{\partial z} = \nu_t(t) \frac{\partial U}{\partial z} \tag{3.12}$$

which means we can apply the time averaged value for  $\nu_t$ . Then (3.10) can be solved directly which yields

$$U(z) = \alpha_1(x) \int \frac{z}{\nu_t(z)} dz + \beta_1(x) \int \frac{dz}{\nu_t(z)} + \gamma(x) \tag{3.13}$$

where

$$\alpha_1(x) = \frac{\partial}{\partial x} \left( \overline{u_w^2} + gb \right) \tag{3.13}$$

and  $\beta_1$  and  $\gamma$  are arbitrary integration functions to be determined by the boundary conditions.

Discussion of boundary conditions

To determine  $\beta_1$  and  $\gamma_1$  we need two conditions.

One seems fairly obvious: that the total volume flux represented by the undertow must equal  $Q_g$ . This can also be expressed as: the mean value of  $U(z)$  between trough and bottom must be  $U_m$ , that is

$$\int_{-h_0}^{\eta_{tr}} U(z) dz = U_m d_{tr} \tag{3.14}$$

As the second condition it will be natural to use the boundary value for  $U$  at the bottom. To do that properly, however, we must recall that at the bottom we have an oscillating boundary layer which averaged over time shows a steady streaming. Thus a consistent choice at this boundary will be either to use as the boundary condition the steady streaming velocity  $U_b$  at the top of the oscillatory boundary layer - and neglect the thickness of that layer so that  $U = U_b$  applies at  $z = -h_0$  - or to include the boundary layer in the solution. The latter necessitates that the boundary layer solution is carried to second order in the perturbation expansion.

Some aspects of this problem is discussed further in section 4 but for the time being it suffice to let

$$U(z) = U_b \text{ for } z = -h_0 \tag{3.15}$$

It may be worth briefly to examine some other possible boundary conditions for  $U(z)$ .

One possibility is to replace (3.14) by a boundary condition at the trough level  $z = \eta_{tr}$  where a proper description of the turbulence can yield a value for  $\bar{\tau}$  i.e. a condition on  $\partial U / \partial z$ .

When using the shear stresses at trough level as a boundary condition it becomes necessary to analyse the magnitude of the  $\partial \overline{uw} / \partial z$ -term in (3.6) ( $u$  and  $w$  being turbulent mean velocities) relative to the turbulent contributions to  $\bar{\tau}$ , and that requires a far more detailed description of the wave motion. The  $\overline{uw}$ -term also includes the convective accelerations caused by the decrease in wave height as the water depth decreases. This will cause  $Q_s$  to decrease shorewards giving a vertical flow downwards proportional (at trough level) to  $\partial Q_s / \partial x$ . The effect represents an enhancement of the horizontal shear stresses. In the present very crude model this effect has been considered included in  $v_t$  but would be necessary elements in a more detailed model.

Dally (1980) and Bökrci (1982) used both (3.14) and a condition for  $\bar{\tau}$  ( $z = \eta_{tr}$ ) and considered in addition the flow between trough and crest. In combination with sinusoidal waves (which they used) this is of limited relevance.

#### Solutions for two $v_t$ -distributions

The simplest possible evaluation of (3.13) is for  $v_t = \text{const}$ . Using the boundary conditions (3.14) and (3.15) thus yields

$$\frac{U(y) - U_b}{c} = \frac{1}{2} \frac{\alpha d_{tr}^2}{c} \left( \frac{y}{d_{tr}} \right)^2 + 2 \left( \frac{U_m - U_b}{c} - \frac{1}{3} \frac{\alpha d_{tr}^2}{c} \right) \frac{y}{d_{tr}} \quad (3.16)$$

where  $y = z + h$  is the distance from the bottom and

$$\alpha \equiv \frac{a_1}{v_t} \quad (3.17)$$

Our knowledge, however, of the turbulence generated by the breakers indicates that it spreads downwards from the surface while decaying. Hence  $v_t$  can be expected to decrease with distance from the surface. To model this we may use a  $v_t$  decreasing exponentially downwards, i.e.

$$v_t = Ne^{a(z - \eta_{tr})} \quad (3.18)$$

With the boundary conditions described above this yields the solution

$$U(z) = - \left( \frac{A_1}{c} + \frac{\alpha_1}{ca^2 N_0} ay \right) e^{-ay} + \frac{\gamma}{c} \quad (3.19)$$

where

$$A_1 = \frac{U_m - U_b}{M_1} - \frac{\alpha_1}{a^2 N_0} \left( 1 + ad_{tr} - \frac{ad_{tr}}{M_1} \right)$$

$$M_1 = \left( e^{-ad_{tr}} - 1 + ad_{tr} \right) / ad_{tr}$$

$$\gamma = U_b + A_1; \quad N_0 = Ne^{-ad_{tr}}$$

4. THE EFFECT OF THE PRESSURE GRADIENT ON THE BOTTOM BOUNDARY LAYER.

The relatively strong mean pressure gradient created by the set-up also changes the momentum balance in the bottom boundary layer. The equation for the mean flow may again be derived from (3.7) but using somewhat different approximations. As before we neglect the effect of the sloping bottom. A perturbation expansion is introduced by

$$u = u^{(1)} + u^{(2)} + \dots, w = w^{(1)} + w^{(2)} + \dots; p = p^{(1)} + p^{(2)} + \dots;$$

After averaging over a wave period and substitution of an eddy viscosity description for  $\tau$  based on a boundary layer viscosity  $\nu_{tb}$  this yields for the second order approximation

$$\frac{\partial}{\partial z} \left( \nu_{tb} \frac{\partial \overline{u^{(2)}}}{\partial z} \right) = \frac{\partial}{\partial z} \left( \overline{u^{(1)} w^{(1)}} \right) + \frac{\partial}{\partial x} \left( \overline{u^{(1)2}} + gb \right) \quad (4.1)$$

Here  $u^{(2)}$  represents the combined undertow and steady streaming in the boundary layer.

This is the equation describing the steady streaming in the bottom boundary layer. The first right term is the usual driving term for this flow (see e.g. Louquet Higgins 1953, 1957). This term tends to zero as we move away from the bottom, and we see that apart from this term the equation is almost the same as (3.8) describing the undertow. The additional differences being that the oscillatory component  $u^{(1)}$  is here  $u^{(1)}(z)$  and  $\nu_{tb}$  will in general be different from  $\nu_t$  for the undertow.

A similar equation (but with some terms included representing the effect of the sloping bottom) was derived by Börekci (1982), and the peristaltic pumping studied by Longuet-Higgins (1983) leads to an equation without the  $\overline{u^{(1)2}}$ -term. The orders of magnitude of the contributions to this momentum balance was discussed by Longuet-Higgins (1983).

Equation (4.1) may in fact be solved directly. For  $\nu_{tb} = \text{constant}$  the solution may be written

$$\overline{u^{(2)}} = \frac{1}{\nu_{tb}} \iint \frac{\partial}{\partial x} \overline{u^{(1)2}}(\xi) d\xi dz + \frac{g}{\nu_{tb}} \frac{db}{dx} \left( \frac{1}{2} z^2 + C_1 z + C_2 \right) + u_s(z) \quad (4.2)$$

where  $u_s$  is the steady streaming without the pressure gradient and with

$\frac{\partial}{\partial x} \overline{u^{(1)2}} = 0$ . Also for variable  $\nu_{tb}$  is the solution straightforward, however.

The boundary conditions to be satisfied by (4.2) is that at  $z = -h$  we have  $\overline{u^{(2)}} = 0$  and at the upper edge of the boundary layer  $\overline{u^{(2)}}$  approaches the undertow velocity  $U$ .

The solution used by Svendsen (1984b) corresponds to assuming the boundary layer infinitely thin and letting  $\overline{u^{(2)}} = U_b = u_s$  at  $z = -h$ . We see that in (4.2) this corresponds to neglecting the first two terms inside the boundary layer.

Equation (4.2) also shows, however, that if  $\nu_{tb}$  is small in comparison with  $\nu_{tb}$  between bottom and trough these terms may become far more important. Comparison of the eddy viscosities  $\nu_t$  found for turbulent

bores by Madsen & Svendsen (1983) with the eddy viscosities in an oscillatory boundary layer corresponding to the wave friction factors determined by Jonsson & Carlsen (1976) indicates that  $v_t$  may be significantly larger than  $v_{tb}$ . Further analysis is needed of this question, and also of the boundary layer under breaking waves rather than ordinary sine waves.

Using, however, a seemingly conservative estimate of  $v_{tb}$  which is 0.2 times a typical value of  $v_t$  in the region between trough and bottom, and constant over the boundary layer, then we get a mean velocity  $u^{(2)}$  at  $z = \delta$  ( $\delta \equiv (2v_{tb}/\omega)^{1/2}$ ) which on a slope  $h_x = 1/34$  is of the same order of magnitude as  $U_{bs}$  given by linear theory but of opposite sign. In other words: in the outer part of the bottom boundary layer the steady streaming is likely to be strongly seawards oriented. As it will be seen this result conforms well to the measurements presented in section 7. In the absence, however, of more precise information about this point we have chosen in the comparison with the measurements to show the effect which different values of  $U_b$  have on the undertow profile. This is done by showing theoretical results corresponding to  $U_b$ -values between + and -  $U_{bs}$  where  $U_{bs}$  is the (Eulerian) value from linear wave theory, i.e.  $U_{bs} = 3/16 c(H/h)^2$ .

#### 5. EXPERIMENTAL SET-UP

The experiments are carried out in a flume 32 m long, 60 cm wide, with a plane beach sloping 1:34.26 (see Fig. 5).

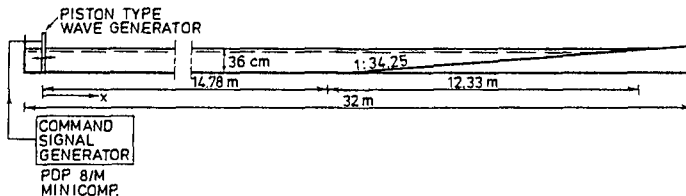


Fig. 5. Experimental set-up.

The motion of the piston type wave generator is controlled by a PDP 8 minicomputer, which generates a command signal of the form

$$\xi = e_1 \sin \omega t + e_2 \sin (2\omega t + \beta)$$

(Buhr Hansen, and Svendsen, 1974).

The water depth in front of the sloping beach is 36 cm, the wave period  $T = 2s$ , and the wave height  $H = 12$  cm. To obtain a stable test situation in the wave flume waves were generated for at least 20 min. before any recordings were taken.

The particle velocities are measured using a bi-directional micro-propeller current meter described in Basco et al, 1982. (see Fig. 6). However, for the undertow measurements special data logging and data-processing programmes were designed.

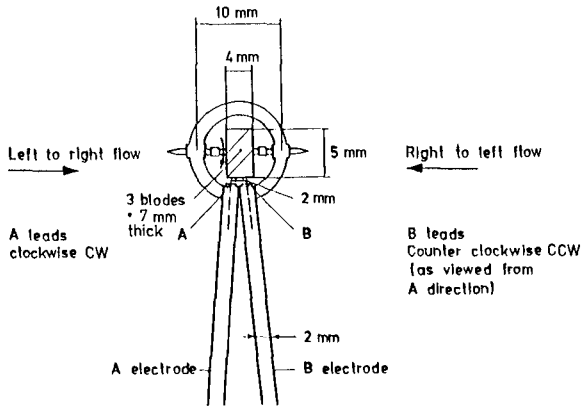


Fig. 5 Schematic illustration of the bi-directional, micro-propeller current meter showing the propeller, mounting, frame, and double electrodes to sense the blade passage for electronic interpretation. (From Basco et al. 1982).

The principle of operation of the current meter is that the propeller blades generate electric pulses when passing either of the electrodes A and B. The speed is determined directly from the length of the time interval between consecutive passages of the same electrode and the direction from the "position" of the pulse from the other electrode recorded in the same time interval.

The propeller is 5 mm diameter with 3 blades equivalent to approximately 5.2 mm peripheral distance between the blades. The propeller blade angle is  $45^\circ$  and the distance between the electrodes is 2 mm.

The time interval between consecutive pulses from one electrode varies from about 200 ms for velocities of 5 cm/s (about the lowest steady flow velocity that may be recorded) to about 15 ms for velocities of 50 cm/s (about the highest velocity observed in these experiments).

The datalogging programme run on a PDP 8/e minicomputer is designed to detect and store both the time of occurrence of pulses from the electrodes (accuracy 1/10 ms) and electrode identification. Notice that it is the leading edge of the pulses that is detected. Simultaneously the analog signal from a wave height meter and the analog output signal from the micro-propeller current meter are sampled. It is important to notice that the samples are triggered by the propeller blade pulses and consequently are unevenly spaced in time.

The analog current meter signal, however, is only used as support in the judging of the velocities calculated from the digital recordings. The reason is, that in oscillating flow - as in the present experiments - the online dataprocessing used to convert the propeller pulses to an analog signal yields a distorted velocity history because the output will always be the mean velocity recorded over the previous time interval, and the correct sign of the output may be delayed further.

The off line data processing programme is designed to convert all time intervals between two consecutive pulses from the same electrode

into water velocities. The speed is inverse proportional to the recorded time intervals (AA and BB respectively in Fig. 7).

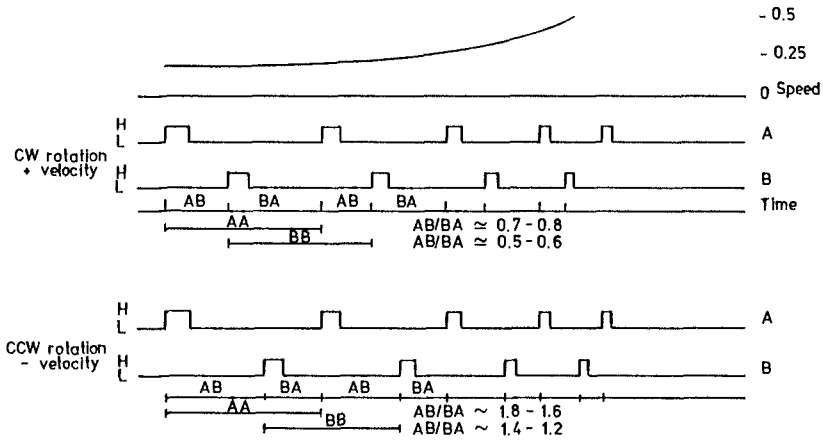


Fig. 7. Timing diagram for propeller pulses under accelerating flow. (In the case of decelerating flow the AB/BA ratios indicated for AA will be valid for BB and vice versa).

The timing diagram in Fig. 7 further shows that the position of the B-pulse between two A-pulses and vice versa yields the sign (or direction) of the velocity: i.e.  $AB/BA \sim .62$  represents positive and  $AB/BA \sim 1.6$  negative velocities under constant speed. However, these well defined AB/BA ratios are found only when the propeller is running at a constant speed. In the case of accelerating/decelerating flow the AB/BA ratio may change considerably. The data processing programme is through a trial-and-error method found to yield the most reliable results when in the computer program we use  $AB/BA > 1.3$  in the AA case and 1.15 in the BB case to determine negative velocities.

When measuring in oscillating flow a special problem arises when the velocities are changing sign (the propeller changes rotational direction), and for some time the velocity remains below the minimum velocity that keeps the propeller running.

When the propeller changes rotational direction it may be observed through the registration of two consecutive pulses from one electrode without any pulse from the other electrode in the same period of time. In this case the velocity is set to zero for this period of time. However, the pulses have a width which is not negligible, and the change in rotational direction will in some cases take place while a pulse is High, and the changing direction of the flow is "only" detected as a sign shift of the calculated velocities. This causes some inaccuracy in the calculated velocity just after a sign shift, but occurs only when the velocities are small. When the velocities are changing rapidly, as it is the case around zero velocity, furthermore, the determination of the correct sign is uncertain. Around zero velocity a number of

obviously erroneous signs are observed.

Both these errors are of minor importance for the determination of the net velocity over the wave period, which is the result we are aiming at here.

Due to the presence of air bubbles in the water - and may be for other reasons as well - a few pulses are not detected by the computer. In the experiments this error occurred with a frequency of 2-4 per 1000 pulses. When appearing during a period of time with considerable velocities ( $> 10$  cm/s) it is corrected by the off-line processing programme. This programme also corrects single velocity values which have been assigned an obviously wrong sign when compared to preceding and following values both  $> 10$  cm/s.

It may be noticed that there is a time lag between the calculated velocities and the recorded surface elevations.

As the velocity measuring method is giving only mean velocities over the time intervals AA and BB respectively it is assumed that the measured velocities are representing the actual velocity in the middle of each time interval. The recorded analog signal from the wave height meter, however, corresponds to the instants of the propeller pulses, and the time series is consequently different from that of the velocities.

Each test comprises 2960 samples equivalent to a recording period in the range of 45 sec (22 wave periods) to 77 sec (38 wave periods).

## 6. DETERMINATION OF NET VELOCITIES AND WAVE DATA

For each test the two simultaneously recorded time series for horizontal particle velocities and surface elevations are analysed independently.

In both time series the individual waves in the recordings are separated through the determination of the zero-up-crossings of the signals and for each individual wave the time average value over the wave period as well as the RMS, maximum and minimum values are calculated. In turn these figures are averaged over the total number of waves included in the time series for each test. Fig. 8 contains a summary of all test results. (Only the experiments in the surf zone are analysed further in this paper).

Each test is associated with a specific horizontal position in the wave flume and a specific depth - or height over the bottom - where the velocity meter is located.

As all tests are performed using the same wave input, the recordings of surface elevations at any of the 6 horizontal positions are repeated a number of times, yielding a possibility of judging the inaccuracies involved in the recordings.

In the surf zone the variations in all surface wave data, e.g.  $\eta_{RMS}$ ,  $H$  and  $b$ , from wave to wave are very significant. Reliable results can consequently only be obtained when the results are averaged over a great number of waves. In these experiments, where one test run comprises 22 to 38 waves, all results are averaged over the total number of waves recorded.



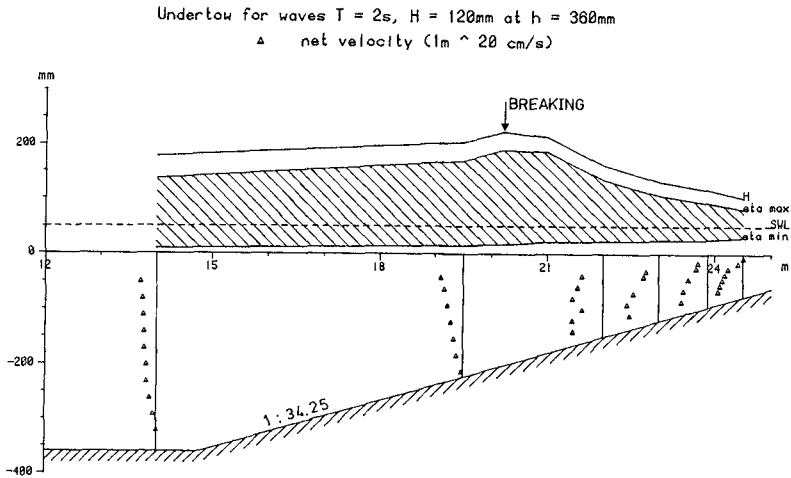


Fig. 8. Summary of test results.

The resulting averaged  $\eta_{RMS}$  values are from test to test reproduced with a standard deviation below 1 mm. Just after breaking the averaged wave heights H are similarly reproduced with standard deviations about 4 mm. Before breaking, and further into the surf zone, however, the standard deviations on H are much smaller (about 1 mm). Similarly the set-down/set-up values are associated with standard deviations of .5-1 mm.

The analysis of the particle velocity measurements clearly reveals the very irregular and strongly turbulent velocity pattern expected after wave breaking. The resulting average net velocities at different positions and depths are given in fig. 8. Each of these net velocities are the averaged values over the 22 to 38 waves included in one test. The single wave net velocities reveal considerable variations, and the average value is within each test associated with a standard deviation about 10 mm/s outside the breaking point and 30-45 mm/s in the surf zone. Nevertheless, two of the tests in the surf zone have been repeated 4 times each, and from test to test the averaged net velocities vary only about  $\pm 5$  mm/s.

7. COMPARISON WITH MEASUREMENTS

To obtain numerical results from (3.16) or (3.19) for comparison with the measurements we first realize that these solutions have the parameters

$$v_t = \text{const.} : \frac{\alpha d_{tr}^2}{c}, \frac{U_m - U_b}{c}$$

$$v_t = Ne^{az} : \frac{\alpha(\eta_{tr}) \cdot d_{tr}^2}{c} = \frac{\alpha_1 d_{tr}^2}{cN}, \alpha d_{tr}, \frac{U_m - U_b}{c}$$

In the following we only consider the latter of the two models.

If we consider  $h$  as the known quantity in stead of  $d_{tr}$  this adds another parameter  $d_{tr}/h$  to the list.

Here the value of  $U_b/c$  has been discussed in Section 4.

For  $\alpha_1 = \partial/\partial x (\overline{u_w^2} + gb)$  we find with  $\frac{H}{h} \sim 0.6$

$$\frac{\partial}{\partial x} \overline{u_w^2} \approx \frac{\partial}{\partial x} c^2 \left( \frac{n}{h} \right)^2 \approx B_0 \left( \frac{H}{h} \right)^2 g h_x \approx 0.027 g h_x$$

$$\frac{\partial}{\partial x} gb \approx g \cdot 0.18 \cdot \frac{H}{h} h_x \approx 0.11 g h_x$$

so that  $\alpha_1 \approx 0.14 g h_x$ . The turbulence model used by Madsen & Svendsen (1983) yields  $v_t$ -values  $\approx 0.005$ - $0.010$   $ch$  depending on the characteristic parameters used. Thus we get for  $\alpha_1 d_{tr}^2 / c v_t$

$$\frac{\alpha_1 d_{tr}^2}{c v_t} \approx \frac{\alpha_1 h^2}{c v_t} \approx 14 - 27 h_x$$

In the present experiments this means

$$A = \frac{\alpha_1 h^2}{c v_t} = 0.4 - 0.8$$

Svendsen (1984b) used  $A = 0.4$  for Stive and Wind's 1982 experiments.

In the comparison with experiments we find that  $A = 0.2$  and  $0.4$  yield the best agreement (Fig. 9) but have shown a comparison including  $A = 1.0$  (Fig 10) which illustrates that the velocity profile is quite sensitive to the value of  $A$ . Clearly further investigations of this problem would be desirable.

The parameter  $ad_{tr}$  represents the decay of the turbulence downwards from the trough level.  $ad_{tr} = 1$  represents a bottom value of  $v_t$  which is 37% of the surface value, and  $ad_{tr} = 2$  similarly represent a reduction to 14% of the surface value.

Figs. 9 and 10 show comparison with the measurements described in section 5 and 6.

A number of observations can be made from the Figs. 9 and 10:

- a) The depth averaged value  $U_m$  of the undertow determined from the shoreward mass flux by (3.6) is generally in good agreement with the measured values
- b) The measurements going closer to the bottom indicates more clearly than those by Stive & Wind (used by Svendsen (1984b)) that the steady streaming in the boundary layer is likely to be in the seaward direction, and with  $U_b = -U_{bs}$  the theoretical results agree quite well with the measurements.
- c) The results appear to be very sensitive to the value of  $A$ ,  $A = 1.0$  being obviously too large. On the other hand the value of  $ad_{tr}$  has been found not to influence the theoretical results nearly as much.

Considering the relatively simple model and the uncertainties

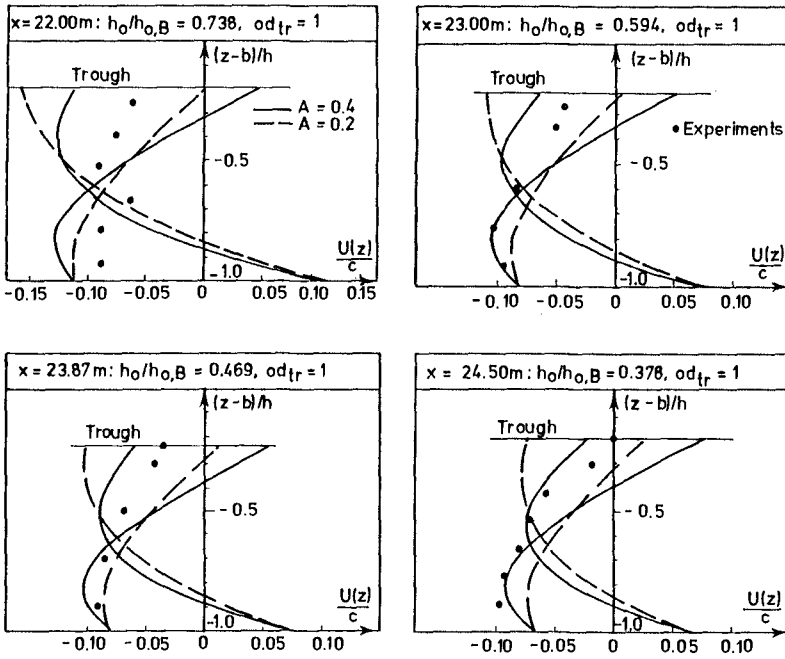


Fig. 9. Comparison between experiments and eq. (3.19) with  $U_b = \pm U_{bs}$  and  $A = 0.2$  and  $0.4$ .

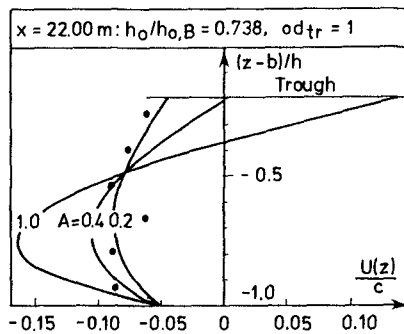


Fig. 10. Comparison between experiments and eq. (3.19) with  $A = 0.2, 0.4$  and  $1.0$ .

regarding at least the two important parameters  $U_b$  and  $v_t$  the agreement must be considered quite satisfactory.

The large seaward velocities near the bottom are considered of significant importance for the erosion of coastlines under storm conditions.

From (3.10) we see that the shear stress  $\tau$  varies linearly with  $z$  irrespective of  $v_t$ . We have for  $\tau$

$$\bar{\tau} = \rho v_t \frac{\partial U}{\partial z} = \rho(\alpha_1 z + \beta_1)$$

The eddy viscosity model also implies that the maximum value of  $U$  corresponds to  $\bar{\tau} = 0$ . In combination with the linear  $\bar{\tau}$ -variation this means that the relative height  $y_0/d_{tx}$  above the bottom of  $U_{max}$  indicates the magnitude of  $\bar{\tau}_b$  relative to the total shear stress variation. Thus the measurements in Figs. 9 and 10 corresponds to very small  $\bar{\tau}_b$ -values, whereas the measurements by Stive & Wind (1980) used by Svendsen (1984b) seem to indicate larger  $\bar{\tau}_b$ -values, though the scattering of the results and the lack of measurements sufficiently close to the bottom make a conclusion at this point uncertain.

#### REFERENCES

- Bagnold, R.A. (1940). Beach formation by waves; some model experiments in a wave tank. *J. Inst. Civ. Eng.*, 15, 27-52.
- Basco, D.R., Ib A. Svendsen and J. Christensen (1982). Measurements with a bi-directional micro-propeller current meter, *Inst. of Hydrodynamics & Hydraul. Eng. (ISVA), Tech. Univ. Denmark, Prog. Rep. 57*, 25-32.
- Börekci, O.S. (1982). Distribution of wave-induced momentum fluxes over depth and application within the surf-zone. Ph. D. Dissertation, Dept. Civil Eng., Univ. of Delaware.
- Buhr Hansen, J. and I.A. Svendsen (1974). Laboratory generation of waves of constant form. *Proc. 14th Coastal Eng. Conf., Copenhagen*, chap. 17, 321-339.
- Dally, W.R. (1980). A numerical model for beach profile evolution, Master's thesis, University of Delaware, Dept. of Civ. Engrg.
- Duncan, J.H. (1981). An experimental investigation of breaking waves produced by a towed hydrofoil. *Proc. R. Soc., London, Ser. A* 377, 331-348.
- Dyhr-Nielsen, M. and Sørensen, T. (1970). Sand transport phenomena on coasts with bars. *Proc. 12th Coastal Eng. Conf., Washington, D.C.*, Chap. 54, 855-866.
- Guza, R.T. (1984). Private communication.

- Johnson, D.W. (1919). Shore processes and Shore line Development.  
Facsimile reproduction 1972, Hafner Publishing Company, New York.
- Longuet-Higgins, M.S. (1953). Mass transport in gravity waves. Philos.  
Trans. R. Soc. London, Ser. A, 245, 535-581.
- Longuet-Higgins, M.S. (1957). The mechanics of the boundary layer near  
the bottom in a progressive wave. Proc. 6th Coast. Engrg. Conf.,  
Chapt. 10, 184-193.
- Longuet-Higgins, M.S. (1983). Peristaltic pumping in water waves.  
J. Fluid Mech., 137, 393-409.
- Madsen, P.A. & I.A. Svendsen (1983). Turbulent bores and hydraulic jumps  
J. Fluid Mech., 129, 1-25.
- Stive, M.J.F., and Wind, H.G. (1982). A study of radiation stress and  
set-up in the near-shore region. Coastal Eng., 6, 1-25.
- Svendsen, I. A. (1984a). Wave heights and set-up in a surf zone.  
Coastal Engineering, 8, 4, 303-329.
- Svendsen, I.A. (1984b). Mass flux and undertow in a surf zone.  
Coastal Engineering, 8, 4, 347-365.

## CHAPTER ONE HUNDRED FIFTY TWO

### SOME TECHNIQUES TO CALCULATE DESIGN CURRENTS IN SHELF AND STRATIFIED COASTAL WATERS

Stephen P. Murray\* and Myron H. Young\*\*

#### I. Introduction

Increasing use of marine environments for (a) petroleum-related structures (both explorational and production), (b) subsea mining (e.g., sulfur and salt), (c) brine disposal from onshore salt domes excavated for oil storage, and (d) offshore waste disposal has necessitated more frequent and more accurate predictions of current speeds and directions in coastal and shelf waters. No analytical techniques for such predictions of wind- and density-driven currents in coastal waters are presented at all in the Shore Protection Manual (1973). Wiegel (1964), however, does discuss wind-driven currents, but offers no modern methodologies for their application to coastal and ocean engineering problems.

Simple predictive models as outlined in this paper are especially valuable in feasibility studies, where the expense of a field measurement program is not yet justified. The prediction of oil spill trajectories is another important application for these procedures.

Three types of models are discussed in turn, all of which incorporate the critically important barrier effect of the coast on the current dynamics: (1) a constant eddy viscosity model, (2) an exponentially decreasing eddy viscosity model, and (3) a constant eddy viscosity model with cross-shore and longshore density gradients. The purpose of this paper is to evaluate these three models in terms of their recommended engineering usage and point out the important gaps for future research.

#### II. The Momentum Equations

As a first step in understanding the mechanics of the processes that drive these nearshore currents, we consider the three-component equations of motion with friction parameterized as a horizontally isotropic eddy viscosity:

\*Coastal Studies Institute, Louisiana State University, Baton Rouge, LA 70803.

\*\*Center for Wetland Resources, Louisiana State University, Baton Rouge, LA 70803.

$$\frac{du}{dt} = fv - \frac{g}{\rho} \int_{-\eta}^z \frac{\partial \rho}{\partial x} dz - g \frac{\partial \eta}{\partial x} + \frac{\partial}{\partial z} \left( K \frac{\partial^2 u}{\partial z^2} \right) \quad (1a)$$

$$\frac{dv}{dt} = -fu - \frac{g}{\rho} \int_{-\eta}^z \frac{\partial \rho}{\partial y} dz - g \frac{\partial \eta}{\partial y} + \frac{\partial}{\partial z} \left( K \frac{\partial^2 v}{\partial z^2} \right) \quad (1b)$$

$$0 = -\frac{1}{\rho} \frac{\partial p}{\partial z} + g \quad (1c)$$

In these equations  $u$  and  $v$  are speed components in the  $x$  and  $y$  directions, respectively,  $z$  is the vertical coordinate positive down,  $g$  is the acceleration of gravity,  $p$  is pressure,  $\rho$  is water density,  $\eta$  is the coordinate of the free surface positive upward from the mean level, and  $f$  is the Coriolis parameter. The term  $du/dt$ ,  $dv/dt$  on the left side of (1a) and (1b), respectively, are the accelerations that result from the forces (per unit mass) on the right-hand side of the same equation. These forces (from left to right in the equations) represent (a) the effect of the rotation of the earth, (b) the baroclinic pressure gradient force arising from horizontal density gradients ( $\partial\rho/\partial x$ ,  $\partial\rho/\partial y$ ) in the water mass, (c) the barotropic pressure gradient force arising from water surface slopes ( $\partial\eta/\partial x$ ,  $\partial\eta/\partial y$ ), and lastly (d) the force of internal friction parameterized with an eddy viscosity ( $K$ ,  $\nu$ , or  $N$ ).

In all three models that follow, the flow is considered quasi-steady, i.e.,  $\partial u/\partial t = \partial v/\partial t \approx 0$ , and locally uniform, such that the convective accelerations are also negligible and thus  $du/dt = dv/dt \approx 0$ .

### III. Constant Eddy Viscosity Model with

#### Negligible Horizontal Density Gradients

If the density gradients in the field are such that the baroclinic pressure gradient terms can be neglected, then (1a, b) can be written

$$K \frac{\partial^2 u}{\partial z^2} = -g \frac{\partial \eta}{\partial x} - fv, \quad (2a)$$

$$K \frac{\partial^2 v}{\partial z^2} = -g \frac{\partial \eta}{\partial y} + fu, \quad (2b)$$

where the coefficient of mixing of momentum (the eddy viscosity)  $K$  has been taken as independent of the vertical coordinate  $z$ . In shallow depths and in waters not strongly stratified in the vertical, this assumption of a three-dimensionally isotropic eddy viscosity is probably not overly restrictive. In this model  $x$  is the direction parallel to shore, positive to the right looking onshore, and  $u$  is the corresponding

speed component;  $y$  is the direction normal to the shore, positive on-shore, and  $v$  is the corresponding speed component;  $z$  is the vertical direction with an origin at mid-depth and positive downward. If the wind field is sufficiently uniform along the coast, we may expect no surface slopes in that direction, i.e.,  $\partial\eta/\partial x \approx 0$ ; then, using the complex velocity  $W = u + iv$ , Eq. (2) may be written

$$\kappa \frac{\partial^2 W}{\partial z^2} - fiW = i f G, \tag{3}$$

where  $G = -(g/f) \partial\eta/\partial y$  is independent of  $z$ .

If the presence of the coast is taken into account by setting

$$\int_{-h/2}^{h/2} v dz = 0 ,$$

i.e., there is no net transport toward or away from the shore, the solution of (3) is

$$W = C + A \sinh jqz + jC \frac{\cosh jqz}{\sinh j\lambda}, \tag{4}$$

where  $\lambda = 1/2 (qh)$ ,  $q^2 = 1/2 (f/K)$ ,  $j = i + 1$ ,  $A$  is a complex constant, and  $C$  and  $G$  are real constants.

The surface boundary condition is the usual quadratic wind stress rule:

$$\tau_s = K \rho \left[ \frac{\partial W}{\partial z} \right]_s = -\kappa_s \sigma Q^2 e^{i\alpha} . \tag{5}$$

The bottom boundary condition is not the usual Ekman "no-slip" condition, which tends to considerably underestimate current speeds in shallow water, but rather a quadratic bottom friction rule:

$$\tau_b = K_b \rho \left[ \frac{\partial W}{\partial z} \right]_b = -\kappa_b \rho R^2 e^{i\gamma}, \tag{6}$$

where  $\kappa_s$  and  $\kappa_b$  are friction coefficients for air-water and water-sea bottom, respectively,  $\sigma$  is air density,  $Q$  is the wind speed blowing at an angle  $\alpha$  to the shoreline, and  $R$  is the current speed making an angle  $\gamma$  to the shoreline.

The methodology of computing the current profile in the vertical (Murray, 1975) follows:



First, the angle  $\gamma$  that the bottom current makes with the shoreline is determined as the root of

$$\begin{aligned} & (\cosh 4\lambda - \cos 4\lambda) \sin \gamma \left( \frac{\rho}{\sigma} \cos \alpha \cos \gamma \right)^{1/2} \frac{g^2 \kappa_s^{1/2} K}{\kappa_s} \\ & + Q \{ \cos \alpha [ \sin (\gamma - \pi/4) \sinh 4\lambda - \cos (\gamma - \pi/4) \sin 4\lambda ] \\ & - 2 \cos \gamma [ \sin (\alpha - \pi/4) \sinh 2\lambda \cos 2\lambda \\ & - \cos (\alpha - \pi/4) \cosh 2\lambda \sin 2\lambda ] \} = 0, \end{aligned} \quad (7)$$

using the Newton-Raphson technique.

Then  $G$  is determined from

$$\begin{aligned} G = R \cos \gamma + \{ & D [ \cos (\gamma - \pi/4) \sinh 4\lambda \\ & + \sin (\gamma - \pi/4) \sin 4\lambda ] \\ & - 2E [ \cos (\alpha - \pi/4) \sinh 2\lambda \cos 2\lambda \\ & + \sin (\alpha - \pi/4) \cosh 2\lambda \sin 2\lambda ] \} \\ & \times (\cosh 4\lambda - \cos 4\lambda)^{-1}, \end{aligned} \quad (8)$$

where

$$R = Q \left( \frac{\kappa_s \sigma \cos \alpha}{\kappa_b \rho \cos \gamma} \right)^{1/2}, \quad (9)$$

$$E = \frac{\cos \gamma}{\cos \alpha} D, \quad (10)$$

$$D = \frac{\kappa_b R^2}{2^{1/2} q K}. \quad (11)$$

Moreover,  $C$ , a wholly real number in (4), is given by

$$C = \frac{-[\kappa_b R^2 \sin \gamma - (\sigma/\rho) \kappa_s Q^2 \sin \alpha]}{4Kq} \quad (12)$$

and the complex coefficient  $A$  may be written

$$A = \frac{-[\kappa_b R^2 e^{i\gamma} + (\sigma/\rho) \kappa_s Q^2 e^{i\alpha}]}{2K j q \cosh j\lambda}. \quad (13)$$

Substituting (8), (12), and (13) in (4) allows the determination of vertical profiles of  $u$  and  $v$  as a function of wind speed and wind direction with respect to the coastline, eddy viscosity, total water depth, latitude, and surface and bottom friction coefficients. Note

that  $\cos\alpha$  and  $\cos\gamma$  must have the same sign, i.e., alongshore components of wind and bottom drift are in the same direction. When winds are from a direction between  $\pi/2$  and  $3\pi/2$ , the sign of  $\gamma$  in (7) must be changed accordingly. The only poorly understood variable in this development is the eddy viscosity, which we calculated from the expression for a well-mixed surface layer (Neumann and Pierson, 1966):

$$K = 0.1825 \times 10^{-4} Q^{5/2} \rho^{-1} , \tag{14}$$

which, for wind speeds  $Q < 700$  cm/sec, is in good agreement with values shown in Munk and Anderson (1948).

The results of the constant eddy viscosity theory are shown compared to three field observations from unstratified coastal water in Figures 1, 2, and 3. The agreement between theory and observation is extremely encouraging for the purpose of practical prediction. Additionally, the

$$W = 8 \text{ m/sec} , \quad \alpha = 30^\circ$$

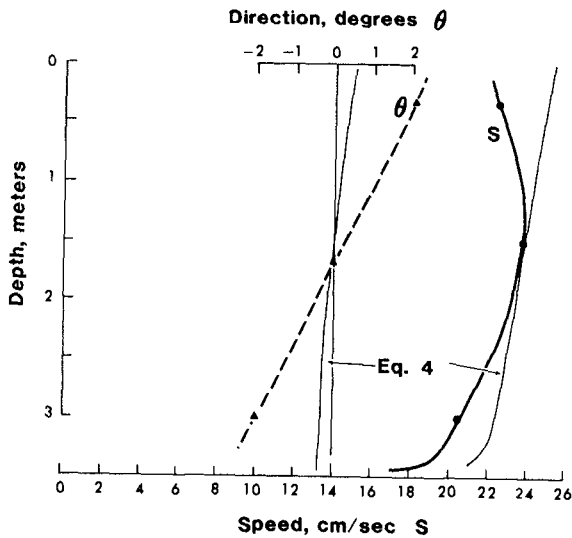


FIG. 1. Speed and direction of currents observed by Saylor (1966) under winds of 8 m/sec at  $30^\circ$  to the coastline compared to prediction of constant eddy viscosity theory, shown as light lines. Current direction is measured from parallel to shore-line, positive onshore.

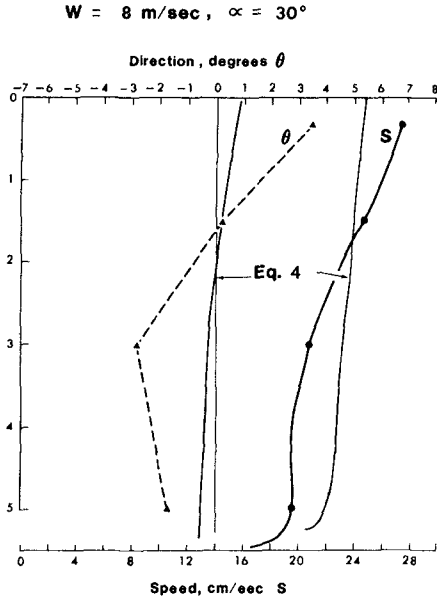


FIG. 2. As in Fig. 1.

constant eddy viscosity model has recently been used by Dr. C. J. Sonu of Tek Marine Inc. to predict the trajectory of icebergs on the Pacific continental shelf ( $h \sim 30 \text{ m}$ ) with quite successful results (Sonu, personal communication, 1984).

An interesting point is the strong dependence of current speed on wind direction with respect to the coast. Figure 4 shows the approximately  $\cos^{1/2}$  response of current speed to wind angle, a result reported earlier by Bretschneider (1967).

#### IV. Variable Eddy Viscosity Theory

In wind-driven current systems the energy driving the current is diffusing downward from the surface, and in moderately stratified water we expect the eddy viscosity to decrease with distance from the surface. Figure 5 shows current speed profiles off the Florida Gulf Coast in moderately stratified water. Note the steep decrease of current speed with depth, suggesting a depth-dependent eddy viscosity, an idea supported by the numerical solutions of equation (2) discussed in Murray

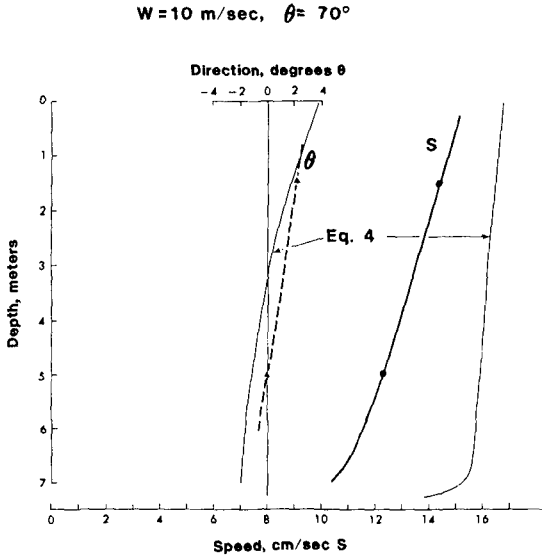


FIG. 3. As in Fig. 1, except for measurements on 11 September under winds of 10 m/sec at  $73^\circ$  to the coastline.

(1975). A practical predictive equation incorporating this effect was not presented, however.

Witten and Thomas (1976) addressed this problem directly with an exponentially decreasing eddy viscosity of the form  $\nu = \nu_0 e^{-az}$ , where  $\nu_0$  is the surface eddy viscosity and  $a^{-1}$  is the e-folding length of the eddy viscosity. Since  $\lambda = ah$  is the ratio of depth to the e-folding length of the eddy, as  $\lambda$  gets smaller the eddy viscosity tends to be more uniform in the vertical. Large values of  $\lambda$  indicate a steep decrease of eddy viscosity with depth. As seen in Figure 6 at  $\lambda = 0.1$ , the surface value of the eddy viscosity is decreased only 5% at mid-depth, at  $\lambda = 0.5$  the decrease at mid-depth is 20%, and at  $\lambda = 1.0$  the decrease at mid-depth is 40%. In this model  $y$  is positive onshore,  $x$  is positive to the right looking onshore, and  $z$  and  $\eta$  are positive up. The complex horizontal momentum equation corresponding to (3) is

$$\frac{\partial}{\partial z} \left[ A \frac{\partial W}{\partial z} \right] - i f W = g \frac{\partial \eta}{\partial n} \tag{15}$$

where  $\partial/\partial n = \partial/\partial x + i \partial/\partial y$ . Witten and Thomas (1976) show that (15) can

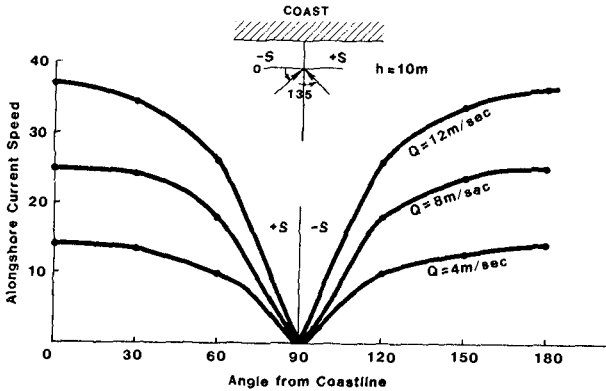


FIG. 4. The effect of changing wind angle to the coast on the alongshore current for three wind speeds (water depth = 10 m) from Eq. (4).

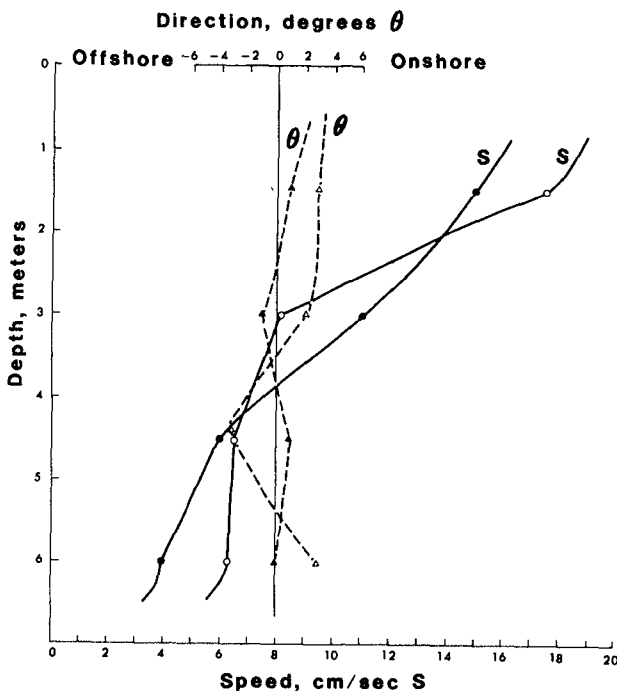
be put into an inhomogeneous form of the modified Bessel equation. The general solution for W then is

$$W = \zeta [AI_1(i^{1/2}\zeta) + BK_1(i^{1/2}\zeta)] + i\frac{\partial\eta}{\partial n}, \tag{16}$$

where  $I_1$  and  $K_1$  are the modified Bessel functions of order one, and A and B are complex constants,  $\zeta = (2\alpha^{1/2}/\lambda) e^{-\lambda z/2}$ ,  $\alpha = fh^2/\nu_0$  is the reciprocal Ekman number, and  $\lambda = ah$  is the ratio of depth to e-folding length of the viscosity. The surface and bottom boundary conditions allow determination of the unknown constants A and B. Using the quadratic wind stress surface boundary condition the same as (5), but a "no slip" condition at the bottom, i.e.,  $W = 0$  at  $z = -h$ , the expressions for A and B are arrived at.

$$A = \frac{-\left\{ \frac{\lambda\tau}{2i^{1/2}} K_1 \left[ \frac{2(i\alpha)^{1/2}}{\lambda} e^{\lambda h/2} \right] + \frac{\lambda i}{2\alpha^{1/2}} e^{-\lambda h/2} K_0 \left[ \frac{2(i\alpha)^{1/2}}{\lambda} \right] \frac{\partial\eta}{\partial n} \right\}}{\left\{ K_0 \left[ \frac{2(i\alpha)^{1/2}}{\lambda} \right] I_1 \left[ \frac{2(i\alpha)^{1/2}}{\lambda} e^{\lambda h/2} \right] + I_0 \left[ \frac{2(i\alpha)^{1/2}}{\lambda} \right] K_1 \left[ \frac{2(i\alpha)^{1/2}}{\lambda} e^{\lambda h/2} \right] \right\}} \tag{17a}$$

$$B = \frac{\left\{ \frac{\lambda\tau}{2i^{1/2}} I_1 \left[ \frac{2(i\alpha)^{1/2}}{\lambda} e^{\lambda h/2} \right] - \frac{i\lambda}{2\alpha^{1/2}} e^{-\lambda h/2} I_0 \left[ \frac{2(i\alpha)^{1/2}}{\lambda} \right] \frac{\partial\eta}{\partial n} \right\}}{\left\{ K_0 \left[ \frac{2(i\alpha)^{1/2}}{\lambda} \right] I_1 \left[ \frac{2(i\alpha)^{1/2}}{\lambda} e^{\lambda h/2} \right] + I_0 \left[ \frac{2(i\alpha)^{1/2}}{\lambda} \right] K_1 \left[ \frac{2(i\alpha)^{1/2}}{\lambda} e^{\lambda h/2} \right] \right\}} \tag{17b}$$



FIC. 5. Current speed (S) and direction ( $\theta$ ) with respect to the coast in moderately stratified water off the Florida Gulf Coast in the morning (solid dots and triangles) and the afternoon (open dots and triangles). Wind speeds are 3-4 m/sec. Note the severe kink in the afternoon speed profile due to decreased afternoon vertical mixing resulting from solar heating of the surface layer.

We solved for A and B by using the relationships between the Bessel functions and the Kelvin functions (Abramowitz and Stegun, 1972, eq. 9.9.1, 9.9.2). Using (14) for the near-surface eddy viscosity, the only unknown in (17) is the complex surface slope,  $\partial\eta/\partial n$ . At this point we call on our continuity condition  $\int_{-n}^{\eta} v dz = 0$ . Our solution procedure is to set the longshore slope  $\partial\eta/\partial x = 0$ , and guess a value for the cross-shore slope  $\partial\eta/\partial y$ , compute the constants A and B, and then compute the velocity profile from (16). Next, test to see if the continuity condition  $\int_{-n}^{\eta} v dz \approx 0$  is satisfied; if it is not, iterate values of the slope

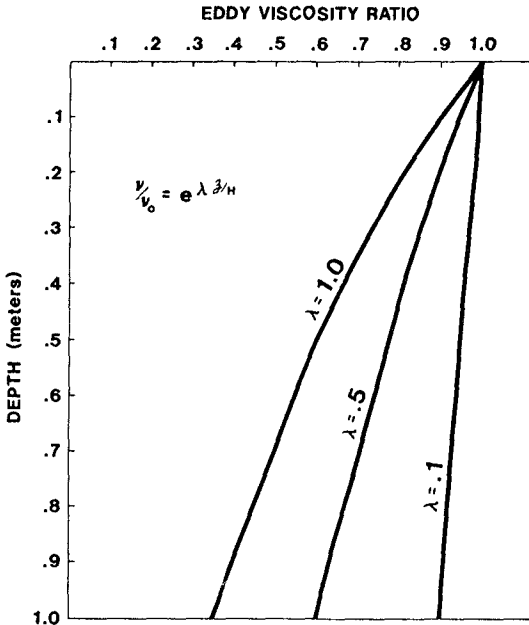


FIG. 6. The effect of  $\lambda$  on the vertical profile of the eddy viscosity.

until the condition is satisfied and accept the values of  $\partial\eta/\partial x$ , A, B, and the velocity profile as the solution.

Figure 7 gives an example of the solution from the exponential eddy viscosity theory with  $\lambda = 0.1$  and  $0.3$ . Speeds are obviously far too low due to the no-slip bottom boundary condition. The constant eddy viscosity solution (4) is also shown for comparison. It gives a correct range of speed, but again the speed is too high near the bottom. In deeper water, Figures 8 and 9 show the two theories are tending to converge. The exponential eddy viscosity model probably gives a better representation of vertical current shear, but the actual magnitudes in the upper half of the water column are better represented by the constant  $\nu$  theory. At this point we recommend the constant eddy viscosity model for shallow water (<20 m) predictions and a judicious combination of both theories for deeper water applications.

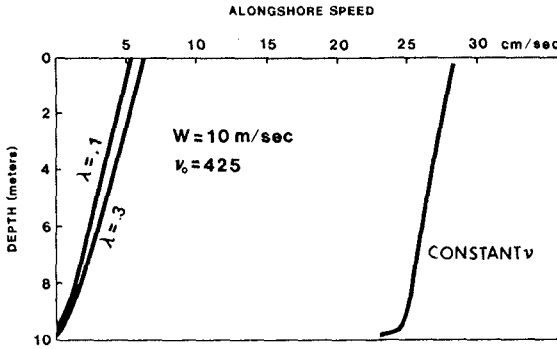


FIG. 7. Current speeds predicted by exponential decaying eddy viscosity theory compared to constant eddy viscosity theory. Wind is 10 m/sec at 45° to coast.

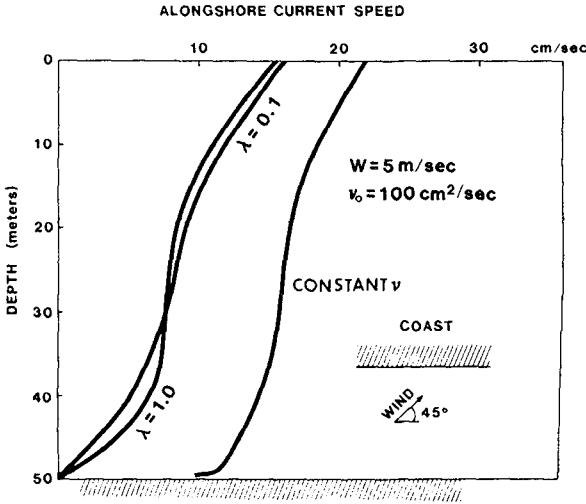


FIG. 8. As in Fig. 7, except wind is 5 m/sec at 45° to coast (deep-water example).

Clearly, the most desirable predictive scheme would incorporate features from both models. We are currently at work on the analytical solution for the wind-driven current problem incorporating both a stress bottom boundary condition and an exponentially varying eddy viscosity.



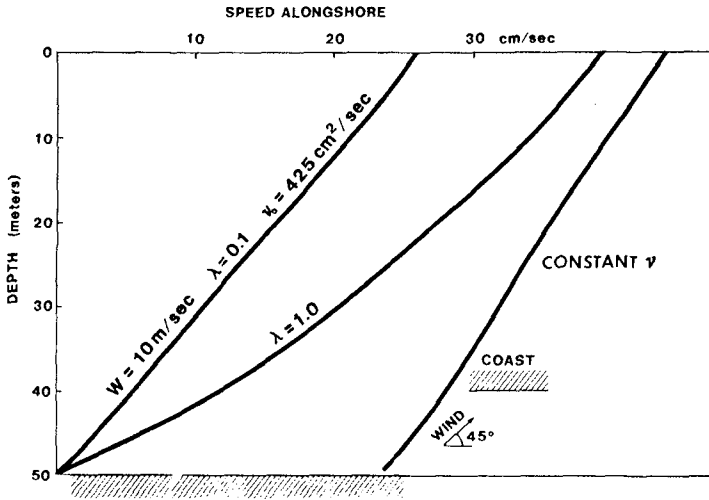


FIG. 9. As in Fig. 8, except wind is 10 m/sec at 45° to the coast (deep-water example).

V. Constant Eddy Viscosity with Horizontal Density Gradient

In many coastal regions, intense rainfall on the local watersheds produces high runoff of fresh water to the coast through a multitude of river input sources that act somewhat as a line source of fresh water along the coast. These freshwater sources typically produce a brackish, turbid band of water that frequently moves at high speeds quasi-parallel to the coast. These baroclinic coastal boundary currents are known from the southeastern coast of the United States (Blanton, 1981), the Louisiana-Texas Gulf Coast (Lewis, 1979), the Alaskan coast (Schumacher and Reed, 1980; Royer, 1979), and the Caribbean coast of Nicaragua (Murray et al., 1982). One or two truly major rivers can also produce a baroclinic coastal current stream, as in the case of the Louisiana-Texas Gulf Coast, cited above, which is the result of the massive discharges from the Mississippi and Atchafalaya Rivers.

The essential difference in the dynamics between this model and the two discussed previously is the inclusion of the baroclinic pressure gradient term. Equation (1a,b) then reduces to

$$0 = fv - \frac{z+\eta}{\rho} \frac{\partial \rho}{\partial x} - g \frac{\partial \eta}{\partial x} + N \frac{\partial^2 u}{\partial z^2} \quad (18a)$$

$$0 = -fu - g \frac{\partial \eta}{\partial y} + N \frac{\partial^2 v}{\partial z^2} \quad (18b)$$

where in this model we take  $z$  positive down,  $\eta$  the sea surface coordinate positive up from the mean level,  $h$  the coordinate of the bottom,  $N$  the eddy viscosity,  $x(u)$  positive in the cross-shore direction toward the shore, and  $y(v)$  positive in the alongshore direction, to the left of an observer looking onshore.

Again defining the complex velocity  $W = u + iv$ , (18a, b) can be put in the complex form

$$\frac{\partial^2 W}{\partial z^2} = \alpha^2 W - \alpha^2 \frac{ig}{f} \left\{ (z+\eta) \frac{1}{\rho} \frac{\partial \rho}{\partial x} + S \right\} \quad (19)$$

where  $S$  is the complex slope  $= \partial \eta / \partial x + i (\partial \eta / \partial y)$  and  $\alpha^2 = if/N$ .

The solution to (19) is

$$W = A \exp \alpha(z+\eta) + B \exp -\alpha(z+\eta) + \frac{ig}{f} \left\{ \frac{z+\eta}{\rho} \frac{\partial \rho}{\partial x} + S \right\} \quad (20)$$

where  $A$  and  $B$  are complex constants to be determined by the boundary conditions. The cross-shore volume flux is given by the real part of

$$\int_{-\eta}^h W dz = \frac{A}{\alpha} (e^{\alpha h} - 1) - \frac{B}{\alpha} (e^{-\alpha h} - 1) + \frac{igh}{2\rho f} \left( \frac{\partial \rho}{\partial x} h + 2\rho S \right) \quad (21)$$

where terms in  $\eta$  are neglected as usual, as they affect the transport by only 0(0.1%).

The complex constants  $A$  and  $B$  and the cross-shore slope  $\partial \eta / \partial x$  are considered unknown in (20). Although often considered negligible, the solution can also include a longshore baroclinic pressure gradient.

The surface boundary condition  $\partial W / \partial z = -\tau_s / N$ , where  $\tau_s$  is complex, determines the first complex constant

$$A = B - \frac{ig}{\alpha f \rho} \frac{\partial \rho}{\partial x} - \frac{\tau_s}{\alpha N} \quad (22)$$

The bottom stress boundary condition

$$N\left(\frac{\partial W}{\partial z}\right)_h + \kappa\rho |W_h| W_h = 0 \quad (23)$$

and the continuity equation close the system by allowing computation of the constant B and the cross-shore slope  $\partial\eta/\partial x$ . For further details, see Murray and Young (1984).

The vertical current profile  $u$  and  $v$  can now be solved from (20) using observed or estimated values of the wind stress, eddy viscosity, water depth, cross-shelf density gradient, and longshore surface slope.

The model is evaluated by comparing our observations taken off the east coast of Nicaragua with the prediction of (20). Figure 10 shows the alongshore speed and salinity distribution in the turbid diluted coastal current found 20-30 km off the coast in this high-rainfall area (Murray et al., 1982). Our measurements of wind stress, water depth, and density structure allow us to compute a predicted velocity distribution and compare it to our field observations of current velocity. Eddy viscosities of  $N = 6 \text{ cm}^2/\text{sec}$  and longshore slopes  $\partial\eta/\partial y \approx 6 \times 10^{-8}$  are also estimated from the data. Pettigrew (1981) reports an eddy viscosity of  $\sim 10 \text{ cm}^2/\text{sec}$  for the east coast of the U.S., so  $5 \lesssim N \lesssim 15$  appears to be a good range for predictions for other coastal areas displaying similar hydrographic conditions. The longshore slope can be set = 0 unless knowledge exists to the contrary.

The distribution of the alongshore velocity component calculated from (20) and (21) under the wind stress, density gradients, and eddy viscosities associated with the field data presented in Figure 10 is given in Figure 11. Although minor details deviate, the agreement between theory and observation is extremely encouraging. For example, the magnitude and location of the current maxima at  $\sim 12$  km offshore and the offshore length scale of 15-20 km are all successfully reproduced. The offshore countercurrent of 5-10 cm/sec in both observations and theory is apparently the result of the slight longshore surface slope opposing the wind.

The theory assumes a density gradient that is constant with depth, and thus predicts significant southerly velocity components throughout the water column. In the observations, however, the density gradient weakens with depth, leading to some overprediction of the near-bottom velocities, but the first-order approximation of the longshore speed

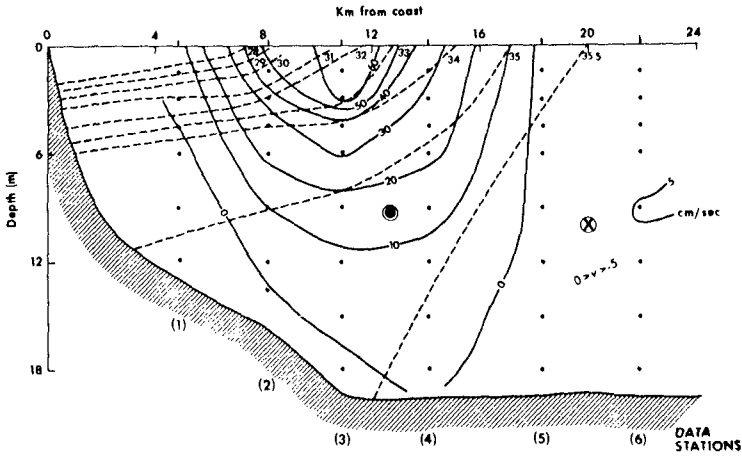


FIG. 10. Alongshore current speeds (cm/sec) observed along east coast of Nicaragua (solid lines) and coincident salinity distribution (dashed lines), which delineate the baroclinic coastal current. Dots indicate data observation points. Basic southerly flow (off page) is bordered by a weak offshore countercurrent.

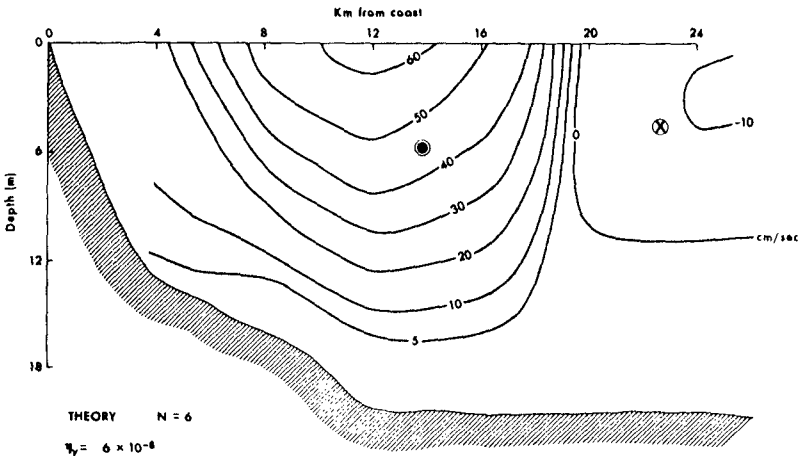


FIG. 11. Prediction of the distribution of alongshore current speeds from the theoretical model (20) under the field conditions shown in Fig. 10.

distribution, the goal of this paper, is clearly a good one.

#### VI. Summary

Three analytical models are presented that can be used to predict vertical profiles of coastal and inner-shelf currents when applied with careful consideration of the pertinent physical parameters in operation. Two of the models are driven solely by wind stress, while the third also incorporates density gradient effects.

An important result suggested by the successful comparison of our field data to theory is the possibility that considerable knowledge of the nearshore velocity distribution along coasts with simple geometry can be obtained, given data on local winds, from routine bathymetric and hydrographic (STD) surveys. An immediate application is the prediction of current structure for offshore petroleum operations and the trajectories of oil spill movements along many subtropical coasts as well as other high-runoff coasts such as the Pacific coast of Alaska.

#### Acknowledgments

This research was supported under a contract between the Coastal Sciences Program of the Office of Naval Research, Arlington, Virginia, and Louisiana State University.

#### References

- Abramowitz, M., and Stegun, I. A., Handbook of Mathematical Functions, National Bureau of Standards Applied Mathematics Series, No. 55, 1972, 1945 pp. (also available from Dover Publishing Company).
- Blanton, J. O., "Ocean Currents along a Nearshore Frontal Zone on the Continental Shelf of the Southeastern United States," Journal of Physical Oceanography, Vol. 11, No. 12, 1981, pp. 1627-1637.
- Bretschneider, C. L., "On the Generation of Wind-Driven Currents over the Continental Shelf," The New Thrust Seaward, Transactions, of the Third Marine Technology Society Conference, San Diego, pp. 96-113.
- Lewis, J. K., "Coastal Frontal Systems as a Pollutant Control Mechanism for Offshore Energy Production," Proceedings of the Marine Technology Society Meeting, New Orleans, 1979, pp. 389-396.
- Munk, W. H., and Anderson, E. R., "Notes on a Theory of the Thermocline," Journal of Marine Research, Vol. 7, 1948, pp. 276-295.
- Murray, S. P., "Trajectories and Speeds of Wind-Driven Current near the Coast," Journal of Physical Oceanography, Vol. 4, 1975, pp. 347-360.

- Murray, S. P., and Young, M. H., "The Nearshore Current along a High-Rainfall, Trade Wind Coast - Nicaragua," Coastal, Estuarine, and Shelf Science (in press).
- Murray, S. P., Hsu, S. A., Roberts, H. H., Owens, E. H., and Crout, R. L., "Physical Processes and Sedimentation on a Broad, Shallow Bank," Estuarine, Coastal, and Shelf Science, Vol. 14, 1982, pp. 135-157.
- Neumann, G., and Pierson, W. J., Jr., Principles of Physical Oceanography, Prentice-Hall, 1966, 454 pp.
- Royer, T. C., "On the Effect of Precipitation and Runoff on Coastal Circulation in the Gulf of Alaska," Journal of Physical Oceanography, Vol. 9, No. 3, 1979, pp. 555-563.
- Saylor, J. H., "Currents at Little Lake Harbor, U.S. Lake Survey Research Report No. 1-1, Lake Survey District, Corps of Engineers, Detroit, Michigan, 1966, 19 pp.
- Schumacher, J. D., and Reed, R. K., "Coastal Flow in the Northwest Gulf of Alaska: The Kenai Current," Journal of Geophysical Research, Vol. 85, No. C11, 1980, pp. 6680-6688.
- Shore Protection Manual, U.S. Army Coastal Engineering Research Center, U.S. Government Printing Office, Washington, D.C., 1973.
- Wiegel, R. L., Oceanographical Engineering, Prentice Hall, New York, 1964, 532 pp.
- Witten, A. J., and Thomas, J. H., "Steady Wind Driven Currents in a Large Lake with a Depth Dependent Eddy Viscosity," Journal of Physical Oceanography, Vol. 6, No. 1, 1976, pp. 85-92.

## CHAPTER ONE HUNDRED FIFTY THREE

### Steady Flows In The Nearshore Zone

John W. Haines\*

#### Abstract

Field measurements using electromagnetic flowmeters on two natural beaches are presented. Mean flows are compared to theory. The horizontal and vertical structure are discussed.

#### Introduction

It has long been suggested that steady nearshore currents redistribute sediment entrained by the more energetic wave motions. This understanding has been the basis for many of the bulk sediment transport formulas developed. Coastal engineers have traditionally been concerned primarily with the shore parallel component of steady flows. Cross-shore flows generally are much smaller in magnitude and do not result in a large net transport of sediment. Nevertheless a large body of work has indicated that steady cross-shore flows generated by low frequency wave motions may generate various barred profiles (3). More recent work has indicated that quite small cross-shore mean flows can be quite significant for profile development and maintenance (2). The spatial structure of these mean flows has obvious implications for sediment transport and nearshore morphology. Theoretical models of the flow due to wind, wind waves and low frequency motions have been developed but field verification is lacking. Until field programs reliably measuring the magnitude and structure of nearshore flow fields are completed, application of these models to sediment transport estimates is unrealistic.

The work described here is a preliminary attempt to describe steady flows in the nearshore zone. Results from two field experiments will be presented. Particular attention will be paid to the vertical structure of such flows. Field measures of vertical structure have previously been neglected due to the expense and, perhaps,

\*Department of Oceanography  
Dalhousie University  
Halifax, Nova Scotia  
B3H 4J1 Canada

the questionable reliability of such measures. Knowledge of vertical structure is important for verification of theory as well as interpretation and use of single point measures. In addition, the offshore spatial structure will be described. Results to date indicate that commonly accepted ideas concerning steady nearshore flows may be difficult to support on all but the simplest of natural beaches.

### Background

Steady nearshore currents may result from a variety of generating mechanisms. Here we shall consider flows averaged on time scales long compared to the group or surf beat period. Wind and tidally forced flows are neglected where possible, although both mechanisms may result in significant flows. Of primary concern here are those currents driven by higher frequency, "wind wave", motions. While it is impossible to rigorously divide measured means into components based on forcing the condition of this study is such that flow associated with other forcing mechanisms should be small.

Measures of shore parallel flows have been more extensively reported than cross-shore flows. Theoretical treatments have been quite successful and are an integral part of longshore sediment transport models. Longshore flows have been modelled and observed to result from longshore gradients in the mean sea level due to low frequency edge wave motions. (5). A more prevalent mechanism is the forcing due to the oblique incidence of wind waves. This mechanism, as described by Bowen (6) and Longuet-Higgins (12) results in forcing due to gradients in the longshore component of the radiation stress. These models, which rely on empirical relations for frictional and lateral mixing effects have been found to compare quite favourably with experimental data (11).

The offshore structure of longshore flows depends primarily on the shore normal gradient of the radiation stress, and thus the wave shoaling and dissipation processes. The theories also describe an offshore dependence due to variation of lateral mixing. Field results seem relatively insensitive to the mixing parameterization chosen; probably because of the smearing effect of a finite bandwidth spectrum (15). The vertical dependence of longshore flows has been largely neglected by the above, depth averaged, treatment. Knowledge of the vertical structure is critical for attempts to estimate stresses acting on the bed. Simple riverine velocity profiles might be applied but in a wave dominated field such models are unlikely to be correct.



Theoretical treatment of cross-shore flows has advanced to levels well beyond our ability to verify in the field (i.e. 9). The theory of Longuet-Higgins (14) and the subsequent lab work of Russell and Osorio (16) has resulted in the commonly accepted picture of two dimensional nearshore flows. Near bed flows are assumed to be onshore outside the surf zone and offshore inside the breaker line (10). These wave generated mean flows result from the presence of viscous boundary layers and the associated production and transport of vorticity. The Longuet-Higgins theory for waves over a horizontal bed predicts, given a time invariant eddy viscosity, flows in the direction of wave propagation at the top of the bottom boundary layer. Above this the flow structure is quite sensitive to conditions at the free surface as well as the particular form of eddy viscosity chosen.

Seaward bottom flow within the surfzone may be attributed to the effects of a mean set-up (10), a mass flux to balance that associated with a translating bore (8) or a surface stress due to breaking waves. If we extend the Longuet-Higgins (13) model to include horizontal gradient terms then:

$$d/dx (\bar{u}^2) + d/dz (uw + u'w') = -d/dx (g\bar{\eta})$$

where  $u$  is the wave motion,  $u'$  the turbulent motion and  $\bar{\eta}$  is the mean change from still water. Further, allowing the depth to be a function of  $x$  and assuming

$$u'w' = -A_v \partial \langle u \rangle / \partial z \quad (\text{where } \langle u \rangle \text{ is the mean velocity})$$

we can solve for the mean flow. By assuming

$$\langle u \rangle = 0 \text{ at the bed, } A_v = \text{constant}$$

and

$$\int_{-h}^{\eta} u \, dz = 0$$

we arrive at

$$\begin{aligned} \langle u \rangle = & F(x) [f(z, z/\delta)]/A_v + A_v d(u_0^2/2)/dz [g(z, z/\delta)]/4\mu^2 \\ & + a_0^2 \sigma k [p(z, z/\delta)]/4 \sinh^2 kd \\ & + a_0 u_0 [q(z)]/d^2 \end{aligned}$$

where  $d = h + \bar{\eta}$      $u_0 = 3/4 \sigma a^2 k / \sinh^2 kh$

$$F(x) = g \frac{\partial \bar{\eta}}{\partial x} + \frac{\partial}{\partial x} (u^2_0 / 2) \quad \mu = (\sigma / 2A_v)^{1/2}$$

$$\sigma = \text{freq.} \quad k = \text{wavenumber} \quad h = \text{depth}$$

Even with the assumption that  $A_v$  is constant a number of solutions may arise depending on  $\frac{dh}{dx}$  and our method of solving for  $F(x)$ .  $F(x)$  represents the loss of energy by the waves. If we assume that  $a = \alpha h$ , where  $\alpha$  is a constant, in the surf zone we may solve for  $F(x)$  by assuming that the momentum flux from the waves results in a stress acting on the free surface. In that case

$$\langle U \rangle(x, z, t) = -3 g \alpha^2 d^2 \frac{dd}{dx} f(z) / (16 A_v)$$

$$+ \alpha^2 g \frac{dd}{dx} g(z) / (32\sigma)$$

$$+ 3\alpha^2 (gd)^{1/2} p(z) / 32.$$

The full solution allows bottom flows in either direction within the surf zone on beaches of realistic slope, with steeper beaches exhibiting offshore flow at the bed. The above solution, while supported by laboratory experiments (6,10), is probably wrong in its simplistic modelling of the bottom stresses, but it does illustrate that almost any velocity profile can be constructed if one manipulates  $A_v$  and the boundary conditions. As of yet there is a paucity of field data to constrain such models.

Quite a number of laboratory experiments measuring cross-shore flows have been completed. Most find the Longuet-Higgins solution to be accurate near the bed and less accurate towards the free surface. Russell and Osorio (16) for example found extremely good agreement for values of  $kd$  between 0.5 and 7.2. No significant effects of a sloping bed of .05 could be seen. Russell and Osorio also saw a reversal of the near bottom flow associated with breaking waves. Further experiments, summarized by Sleath (18) have shown that bed roughness and higher harmonics may decrease the velocity, and in one experiment reverse the flow.

It is readily apparent that the longshore and cross-shore theories of Longuet-Higgins have become quite entrenched. While the longshore current model seems to adequately predict the depth averaged flow little is known about the vertical structure. The laboratory work on cross-shore flows generally supports theoretical conclusions as to the direction of near bed flows but the magnitude of such flows as well as the flow structure above the bed are called into question (18). Reliable tests of the theory on natural beaches still need to be carried out.

Sediment transport models are quite sensitive to the mean velocity (2). Thus it is imperative that we make some effort to evaluate theories predicting mean flows. The spatial structure of this flow field also needs investigation if errors due to the use of point measures are to be estimated.

### Field Experiments

In order to study the vertical structure of mean flows a tripod mounted array of three Marsh-McBirney electromagnetic flowmeters were deployed on two Canadian beaches. The flowmeters were aligned to measure the two horizontal components of the flow. Velocity measures were taken at approximately 35 cm intervals with the bottom sensor ten to fifteen cm above the bed.

The initial experiment took place at Queensland Beach, Nova Scotia, a steep (slope = .1) sheltered pocket beach. Waves at Queensland are long crested and narrow banded in both frequency and direction. Lower frequency motions are quite energetic at times but all indications are that the beach is dominated by two-dimensional motions. Twenty to thirty minute data runs were taken at low and high tide over a two day period. The wave field was fairly stationary with  $kd \sim 0.25$ , wave amplitude about 35 cm and a wave period of 8 sec with pronounced group structure.

A subsequent experiment was carried out at Pte. Sapin, New Brunswick. Pte. Sapin is a fairly steep (.06) beach which quickly gives way to a wide, flat rock platform extending well offshore. Wave conditions are complex with two predominant directions of approach. Waves tend to be obliquely incident, short crested and rather broad-banded in frequency. Longshore transport of sediment is extremely vigorous in storm conditions, as witnessed by the sediment trapping of a breakwater immediately to the south. Any assumptions of two-dimensionality are suspect although no rip systems were observed. Run lengths were an hour in length taken over a variety of conditions. Wave heights ranged from .2 to 1.2 meters at the instrument position with periods from 3 to 8 seconds. Groupiness and angle of incidence varied over a similarly wide range. Ancillary data sets of wind speed and direction, offshore flow, and directional spectra were collected through the efforts of various researchers under the auspices of the National Research Council of Canada as part of the Canadian Coastal Sediment Study (C<sup>2</sup>S<sup>2</sup>).

There are a number of problems with the experiment as described. Working on steep beaches resulted in all data

sets being outside the surf zone. The deployment of only one tripod also prevented simultaneous measures at more than one point along an offshore line. In addition, single point measures yield insufficient information about the lower frequency motions present. These problems have been addressed as we prepare the next  $C^2S^2$  field study but they limit information content of this data set.

The Marsh-McBirney flow meter is a rugged device but it has some limitations. Firstly, it is unclear how near the bed or free surface such an instrument can be deployed. As well, the current meters must be separated by a similarly unknown distance. Our results indicate that ten centimeters is a safe distance; but one that is uncomfortably large for resolving near bed flows. In addition the EM flowmeter measures the Eulerian portion of the flow. For many applications the Lagrangian transport would be more meaningful. Estimates of the Lagrangian velocity indicate it is only slightly different but in cases of small velocities it may be a significant difference.

Recently the response characteristics of Marsh-McBirney flow meters has been questioned (1). Aubrey found that the current meters were unreliable in combined steady oscillatory flows. Errors in the measured mean were 1-6 cm/sec. Problems also arose in areas of large ambient turbulence. Aubrey questioned the reliability of such meters in calculating the higher moments as well. The accuracy of means measured in the field is difficult to estimate but some subjective evaluations can be made. More convincing arguments may be made for the reliability of the moments. The data was approached with some care and the current meter performance checked where possible.

### Results

The mean flows discussed here will be averages over an entire data run. Table 1 shows means averaged over shorter intervals and it is apparent that the means are fairly stationary over time scales of 15 minutes to an hour. The variance is also calculated. Since the records are highly autocorrelated the variance does not allow direct error estimates. Given the length of the data run the statistical uncertainty is nonetheless small with respect to possible sensor errors. The means are small in Table 1 and difficult to evaluate given the problems suggested by Aubrey (1). The variances are heartening with comparable magnitude for the two sensors and showing similar behaviours with time. The higher moments are similarly well behaved indicating that the electromagnetic flow meters are quite well behaved.

Sensor	Direction	Mean/Variance	(cms <sup>-1</sup> /cm <sup>2</sup> s <sup>±2</sup> )				
1	x	1.92/2.51	1.49/2.06	1.35/1.77	1.49/.87	1.54/1.69	
	y	-2.53/.14	-2.60/.13	-2.84/.14	-2.87/.15	-2.59/.14	
2	x	2.07/2.37	2.28/2.18	2.30/1.88	1.49/2.01	1.45/1.85	
	y	1.05/.15	-1.22/.14	-2.23/.14	-2.42/.17	-2.64/.17	

Table 1. Means and variance calculated for consecutive 10 minute data sections on two sensors at different heights. x represents on-offshore flow, positive off-shore.

Near normal wave incidence resulted in small longshore currents at Queensland. The cross-shore flows are plotted in Figure 1. Also plotted is the Eulerian part of the Longuet-Higgins solution. The agreement in the lower two-thirds of the water column is amazingly good. As the data points represent runs separated by up to 24 hours it appears a consistent, long term flow pattern exists. Real values of the velocity range from near zero to approximately 10 cm/sec. The agreement with theory suggests, once again, that the sensors may be quite reliable.

The only systematic deviation from theory is in the top of the water column. This is consistent with lab work (16, 18) and careful analysis of the data suggests it is not a sensor malfunction due to proximity to the free surface. The measured profile indicates, as expected, that the Longuet-Higgins model is inaccurate as one approaches the free surface. This is hardly surprising as the boundary conditions which apply are unknown.

The cross-shore data from Pte. Sapin, similarly plotted, bears no resemblance to the Longuet-Higgins solution (Figure 2). Dimensional velocities ranged from 0 to 9 cm/sec in magnitude. The profiles resulting show no consistency from run to run on the basis of kd values, wave direction or wind direction. In all cases bottom velocities are offshore and maximum velocities are significantly smaller than those predicted by the Longuet-Higgins theory. The question of three-dimensional effects can not be easily addressed. Calculation of the depth averaged flow required to balance the Stokes drift indicates that the measured flow is generally of the right order of magnitude with a tendency to be somewhat smaller. Under any circumstances the indication is strong that the Longuet-Higgins solution for bottom drift is not relevant even 3 to 4 surfzone widths offshore.

Figure 3 shows an indication of two profile types.

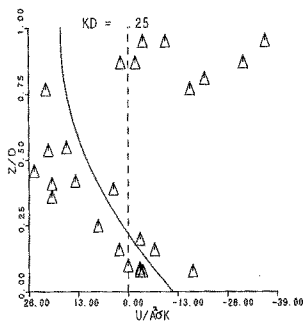


Figure 1. Cross-shore velocities at Queensland Beach. Solid line is the Longuet-Higgins solution for  $kd = 0.25$ . Onshore flows are negative.

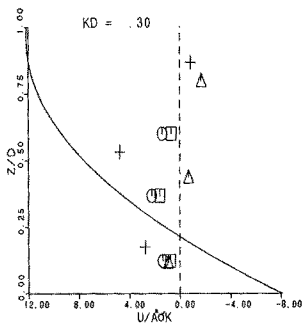


Figure 2. Cross-shore velocities at Pte. Sapin, New Brunswick. Symbols represent different data runs separated by up to three weeks. Onshore flows are negative.

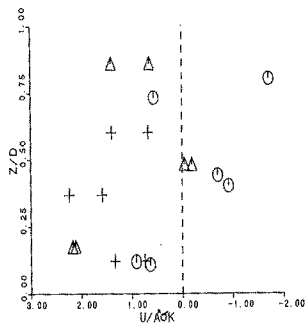


Figure 3. Total data of cross-shore means from Pte. Sapin. Note that all bottom flows are offshore.

This is rather a dangerous trick when working with only three data points in the vertical. The profile represented by the circles has onshore flow in the middle of the water column while the triangle profile exhibits offshore flow accelerated relative to the bottom velocity. The profile types are demonstrably not related to  $kd$  values, wave direction, or wind direction and speed. Figure 4, which shows the bottom velocities indicates that the profiles may be separated on the basis of non-dimensional distance offshore. It should be noted that the three inshore points represent a range of conditions from long waves to small values of dimensional distance offshore and include both extremes in values of  $kd$ . A similar plot could be constructed using the skewness of the velocity distribution rather than distance offshore. Thus it appears that the two profile types reflect some aspect of the shoaling process.

It should be noted in Figure 4 that the bottom velocity itself seems independent of the distance offshore. The profile shape and the direction of flow in the center of the water column are somehow related to wave asymmetry. This is to be expected as mean flows result from the vorticity generation associated with dissipation and shoaling. The data does not allow much speculation about near surface flows.

The cross-shore flows measured seem to change sensibly with wave conditions. Large waves generate large flows. Flows also increase towards the breaker line. The form of the velocity profile is stationary over fairly long time scales. Figure 5 shows results from three pairs of data runs. The pairs represent separations in time of two (crosses), four (circles) and nine hours (triangles). Wave conditions and dimensional velocities changed somewhat but the non-dimensional profile changes very little. Apparently similar conditions separated by longer periods (days to weeks) show quite dissimilar profiles. Figure 5 indicates that flow fields may be stationary over the duration of a storm event. The results again, give us some confidence in the performance of the flow meters.

Longshore flows at Pte. Sapin were variable ranging from 0 to 20 cm/sec. Depth averaged flows are plotted vs. the Longuet-Higgins (11) solution in Figure 6. Measured flows are certainly the right order of magnitude, tending to be somewhat large. This is partially due to wind driven currents also present. Flows are especially large far offshore and these flows probably contain a relatively large wind driven component as they represent small wave conditions. Pte. Sapin waves tend to be locally generated so it is especially difficult to separate wind and wave effects.

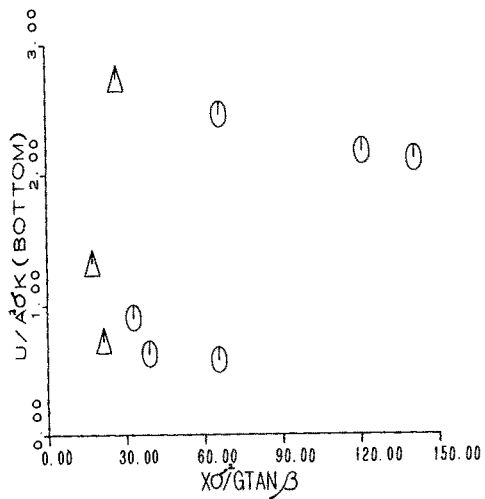


Figure 4 Bottom velocities from Pte. Sapin. Symbols are identical to those in Figure 3.

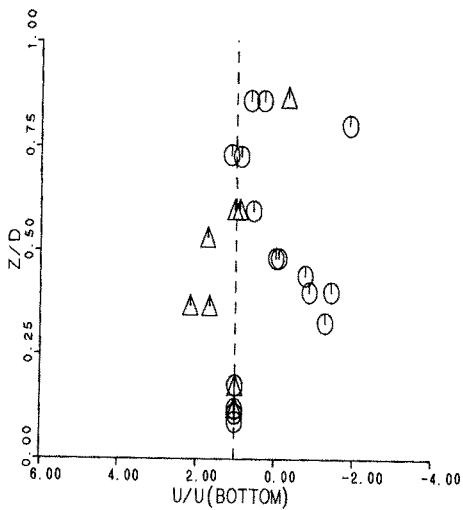


Figure 5 Velocity profiles from Pte. Sapin, see text for description of symbols.



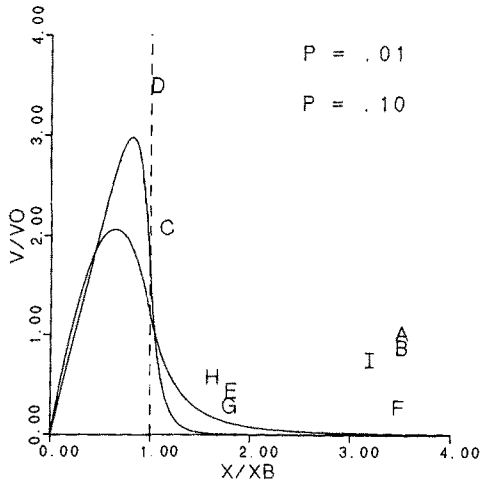


Figure 6 Depth averaged longshore flows where  $V_0$  is the Longuet-Higgins solution and  $X_B$  is the distance to the breaker line.  $P$  is the mixing parameter as described in (12).

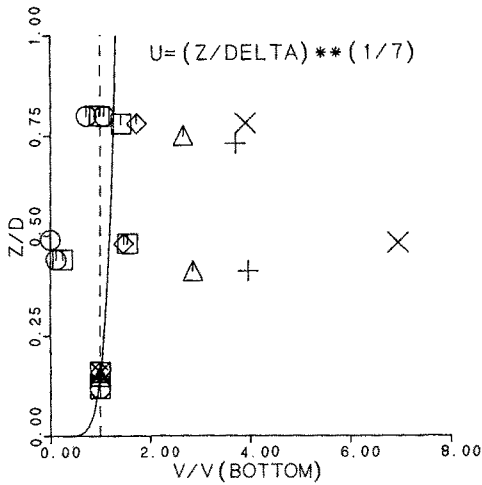


Figure 7 Longshore velocities vs. height above bed where  $\delta$  is the boundary layer thickness. Symbols represent different data runs.

Measured vertical structure is shown in Figure 7. Also plotted is the standard riverine  $Z^{1/7}$  formulation. Such a profile fits only when flows are most vigorous. Otherwise flows are somewhat surface intensified relative to the bottom with the maximum velocity in the middle of the water column. Again this may be due to the relatively greater importance of wind stresses during low wave conditions.

### Conclusion

The data collected so far leads to somewhat negative conclusions. On the simplest of beaches, such as Queensland, prediction of bottom velocities may be made with some measure of confidence. Pte. Sapin suggests that flows on more complex beaches are, at present, unpredictable and point measures of velocity are of questionable value.

Vertical and horizontal profiles are complex but may exhibit some systematic variation on a particular beach. Horizontal changes appear to be closely associated, as expected, with the shoaling process. Changes in the vertical are less well described. For further progress to be made we need to better measure the wave field present as well as gain a measure of the 3-D nature of the system. In addition, Lagrangian measurements, and simultaneous observations along a longshore transect would better constrain our results.

In a very subjective way it appears that EM flowmeters behave in a reasonable manner. Further work needs to be done to address this problem particularly.

Finally, our results are not inconsistent with those found by other researchers. Surf zone flows have been found by a number of researchers to be directed offshore in the lower and middle portions of the water column (7, 17). Our findings, although outside the surf zone, also exhibit offshore flows. Such flows need to be rigorously measured and explained, especially, as their impact on sediment transport raises obvious problems as to the maintenance of the bed profile.

### References

- 1) Aubrey, D.G., Spencer, W.D. and Trowbridge, J.H. (1984). Dynamic response of electromagnetic current meters. Woods Hole Technical Report CRL-B4-3. 150 pp.
- 2) Bowen, A.J. and Doering, J.C. (in press). Nearshore sediment transport: estimates from detailed measure-

- ments of the nearshore velocity field, Proc. 19th Conf. Coastal Eng.
- 3) Bowen, A.J. and Huntley, D.A. (1984). Waves, long waves and nearshore morphology. *In*: B. Greenwood and R.A. Davis, Jr. (eds.), Hydrodynamics and Sedimentation in wave-dominated coastal environments. Mar. Geol., 60: 1.
  - 4) Bowen, A.J. (1980). Simple models of nearshore sedimentation; beach profiles and longshore bars, *in*: The Coastline of Canada, GSC Paper 80-10, 1.
  - 5) Bowen, A.J. (1969a). Rip currents I, J. Geophys. Res., 74: 6638.
  - 6) Bowen, A.J. (1969b). The generation of longshore currents on a plane beach, J. Mar. Res., 37: 206.
  - 7) Hansen, J.B. and Svendsen, I.A. (in press). A theoretical study of undertow, Proc. 19th Conference Coastal Eng.
  - 8) Guza, R. and Thornton, E. (in press). Velocity moments in the nearshore, J. of Waterways, Ports, Coastal and Ocean Eng., ASCE.
  - 9) Liu, Ph. L-F., (1977). Mass transport in water waves propagated over a permeable bed. Coastal Eng. 1: 79.
  - 10) Longuet-Higgins, M.S. (1983). Wave set-up, percolation and undertow in the surf zone, Proc. Roy. Soc. Lond. (A). 390: 283.
  - 11) Longuet-Higgins, M.S. (1972). Recent progress in the study of longshore currents; *in*: Meyer, R.E. (ed.) Waves on beaches and resulting sediment transport. Academic Press, 203.
  - 12) Longuet-Higgins, M.S. (1970). Longshore currents generated by obliquely incident sea waves 1. J. Geophys. Res., 75: 6778.
  - 13) Longuet-Higgins, M.S. (1957) The mechanics of the boundary layer near the bottom in a progressive wave, Proc. 6th Conf. Coastal Eng. 184.
  - 14) Longuet-Higgins, M.S. (1953). Mass transport in water waves, Phil. Trans. Royal Soc. of London, (A) 245.
  - 15) McDougal, W.G. and Hudspeth, R.T. (in press). Comparison of turbulent lateral mixing models, Proc. 19th Conf. Coastal Eng.
  - 16) Russell, R.C.H. and Osorio, J.D.C. (1957), An experimental investigation of drift profile in a closed channel, Proc. 6th Conf. Coastal Eng. 171.
  - 17) Sallenger, A.H., Howard, P.C., Fletcher, C.H. and Howd, P.A. (1983), A system for measuring bottom profile, waves and currents in the high-energy nearshore environment. Mar. Geol., 51: 63.
  - 18) Sleath, J.F.A. (1984) Sea bed mechanics, Wiley Interscience, New York, 335 pp.

## CHAPTER ONE HUNDRED FIFTY FOUR

### OSCILLATORY BOUNDARY LAYER FLOW OVER RIPPLED BEDS

Shinji Sato\* , Nobuo Mimura\*\* and Akira Watanabe\*\*\*

#### ABSTRACT

Characteristics of the oscillatory boundary layer flow above rippled beds were investigated through experiments and numerical calculations. Experiments were conducted in an oscillatory flow tunnel. Velocities above symmetric and asymmetric ripples were measured with split-hot-film sensors under conditions of both sinusoidal and asymmetric oscillations. The stress field in the boundary layer was evaluated based on the distributions of the measured velocity and Reynolds stress. Relations between vortex formation and turbulence were examined, and effects of the asymmetry of oscillatory main flow and of ripple form on the velocity field were discussed. Numerical calculations were carried out by integrating the Navier-Stokes equations with an implicit finite difference scheme. Formation of a lee vortex above ripples was simulated in the calculations. The bottom shear stress and the energy dissipation rate were estimated based on the results of the experiments and calculations.

#### INTRODUCTION

In order to understand the mechanisms of sediment movement as well as wave energy dissipation, it is important to investigate the characteristics of oscillatory boundary layer flow above rippled beds. The oscillatory flow over ripples is complex, since large vortices are formed in the leeside of the ripples and turbulence is produced intermittently. Quantitative understanding of the velocity and the stress field in the boundary layer is essential because of its relevance to various coastal processes such as sand transport, wave damping and mass transport.

Ripples take various shapes depending on the wave condition and the property of bed materials. It has been reported that the asymmetry of

---

\* Research Associate, Dept. of Civil Eng., Univ. of Tokyo, Bunkyo-ku, Tokyo, 113 JAPAN

\*\* Associate Professor, Dept. of Civil Eng., Ibaraki Univ., Hitachi, Ibaraki, 316 JAPAN

\*\*\* Professor, Dept. of Civil Eng., Univ. of Tokyo, Bunkyo-ku, Tokyo, 113 JAPAN

both the ripple shape and the time history of velocity near the bottom exerts a strong influence on the direction and the amount of net sediment transport. In order to accurately estimate the net sediment transport rate, extensive investigations under the conditions of asymmetric oscillations are required.

A number of theoretical and experimental studies have recently been made on the velocity distribution in the oscillatory boundary layer over sand ripples. Some of them are briefly reviewed in the following. Sleath (1974) calculated the flow field by explicit numerical integration of the Navier-Stokes equations and suggested that the flow might remain laminar up to considerably high Reynolds numbers. Longuet-Higgins (1981) applied the inviscid discrete vortex method to the simulation of oscillatory flow over steep ripples. He estimated the value of the drag coefficient of a ripple from the momentum balance of the simulated flow and found the estimated value to be in good agreement with experiments. Toit and Sleath (1982) measured distributions of the horizontal velocity component over rippled beds by using a laser-doppler-anemometer and compared them with those given by available theories. Detailed measurements of the velocity field have been performed by Sawamoto et al. (1982) and by the present authors (1982), with the aids of improvement of measuring technique. However, since the oscillatory boundary layer over ripples involves the complex motion of unstationary inhomogeneous turbulence, a quantitative analysis is not yet satisfactorily accomplished.

The first objective of the present study is to understand the characteristics of the velocity and stress field in the boundary layer through experiments. The second objective is to develop a numerical model to calculate such complicated boundary layer flow with a good accuracy. The third objective is to evaluate the bottom shear stress and the energy dissipation rate based on the measured and calculated results.

#### EXPERIMENTAL FACILITIES, CONDITIONS AND PROCEDURE

Experiments were conducted in an oscillatory flow tunnel, which consists of a loop of closed conduits and a hydraulically-driven piston as illustrated in Fig. 1. The test section is 2m long, 24cm wide and

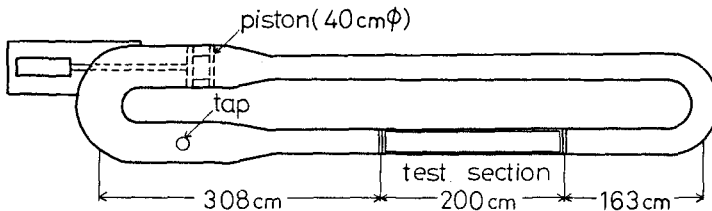


Fig. 1 Plan view of the oscillatory flow tunnel.

31cm in height. The motion of the piston is controlled through an electro-hydraulic servo-system, so that main flows of arbitrary velocity variation can be produced by inputting appropriate voltage signals. The period of flow oscillation is variable from 0.5s to 10.0s, and the maximum amplitude is 70cm at the test section. This facility enables us to make experiments under such realistic conditions as asymmetric back-and-forth motion and irregular oscillation with prototype scales. Preliminary tests were carried out in order to determine the typical size and shape of sand ripples. Well-sorted sand with mean diameter of 0.2mm was used as the bed material. Two-dimensional ripples with sharp crests and rounded troughs were observed for sinusoidal oscillations. The shape of these ripples was found to be well approximated by often adopted following equations.

$$x_0 = X - \left(\frac{\eta}{2}\right)\sin(2\pi X/\lambda) \tag{1}$$

$$z_0 = \left(\frac{\eta}{2}\right)\cos(2\pi X/\lambda) \tag{2}$$

where  $\eta$  is the wave height of a ripple,  $\lambda$  the wavelength,  $X$  an auxiliary parameter, and  $(x_0, z_0)$  represents the surface of ripples. Asymmetric ripples were observed for asymmetric oscillations as illustrated in Fig. 2. We selected several shapes of self-generated sand ripples as the representative geometry. Artificial ripples of the selected ripple geometry, both symmetric and asymmetric, were made of cement mortar for the following experiments.

The artificial ripples were installed on the bottom of the test section, and velocities were measured with split-hot-film sensors at about 100 measuring points close to the bed. Measuring points were arranged systematically in a vertical plane parallel to the main flow. The grid size was 1cm in the horizontal direction and 0.08cm to 2.0cm in the vertical direction.

The split-hot-film sensor consists of two platinum films on a single quartz fiber as shown in Fig. 3. The output from the two films provides a set of data of the magnitude of the velocity component normal to the axis of the fiber,  $U_N$ , and of the component normal to the split plane,  $U_N \sin\theta$ . The magnitude of the velocity component parallel to the split plane is calculated from these two values though its sign cannot be determined.

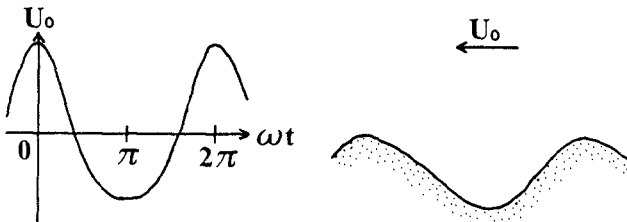


Fig. 2 Asymmetric oscillation and asymmetric ripples.

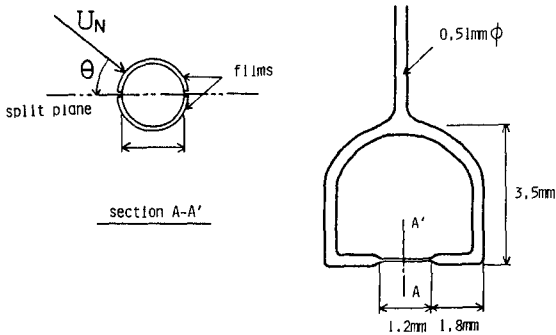


Fig. 3 Schematic diagram of a split-hot-film sensor.

Conditions of the present experiments are listed in Table 1, together with those of the previous experiments (cases H1 and H3) performed by Hamamoto et al. (1982). The period of oscillation is 4s and the wavelength of ripples is 12cm in all the cases. Cases 1 to 6 and H1 are for symmetric ripples under sinusoidal oscillation, and H3 is the case of asymmetric ripples under asymmetric oscillation. Prior to the velocity measurements, flow visualization was made in order to grasp characteristic features of the boundary layer flow of each case. It was found that cases 1 and 2 corresponded to the laminar flow condition. In cases 3 and 4, turbulence was detected in the leeside of a ripple and these cases were considered to be in transition. The flow in cases 5, 6, H1 and H3 was regarded turbulent through a full period.

Table 1 Experimental conditions.

Case	T(s)	$\hat{U}_0$ (cm/s)	$d_0$ (cm)	$\lambda$ (cm)	$\eta$ (cm)
1	4	6.0	7.6	12	1.2
2	4	8.1	10.3	12	1.2
3	4	10.0	12.7	12	1.2
4	4	12.6	16.0	12	1.2
5	4	16.2	20.6	12	1.2
6	4	19.2	24.4	12	1.2
H1	4	28.3	36.0	12	2.0
H3	4	38.5*	36.0	12**	2.0

\* ) asymmetric oscillation

\*\* ) asymmetric ripple

T : period

$\hat{U}_0$ : maximum velocity of the main flow

$d_0$ : orbital diameter of the main flow

DATA ANALYSIS AND EXPERIMENTAL RESULTS

The velocity was decomposed into the mean velocity and turbulent fluctuations. It involves some uncertainty to define turbulence in unstationary flow, for the reason that there exist a number of fluctuating components of various frequency in the turbulent boundary layer. We assumed that the fluctuating components with higher frequency than a critical value might be attributed to turbulence. In order to determine the appropriate cut-off frequency, spectrum of the velocity record was calculated, and it was found that the power spectrum density showed an abrupt increase at 5Hz when the flow became turbulent. The higher frequency component than 5Hz of the velocity record was therefore defined as turbulent fluctuation. Equi-phase mean velocity components  $U$ ,  $W$  and products of turbulent fluctuations  $\overline{u'^2}$ ,  $\overline{w'^2}$ ,  $\overline{u'w'}$  were calculated by averaging equi-phase data over 30 periods.

In the following, discussions are concentrated mainly on case 6 because of space limitation. As stated before, the flow in case 6 was

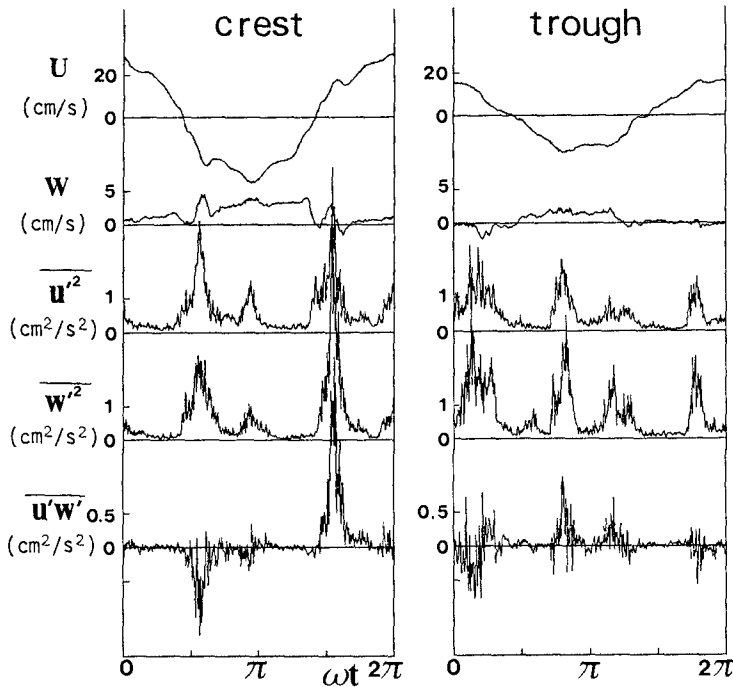


Fig. 4 Time history of  $U$ ,  $W$ ,  $\overline{u'^2}$ ,  $\overline{w'^2}$ ,  $\overline{u'w'}$  measured above a crest and a trough (case 6).



turbulent through a full period. Coherent vortices began to be formed in the leeside of ripples when the velocity of the main flow reached its maximum. These vortices continued to develop until they were ejected after the flow reversal. The ejected vortices were transported over ripples during the next half period for a distance of twice the wavelength of a ripple. Figure 4 shows the time history of mean velocity components  $U$ ,  $W$  and products of turbulent fluctuation  $\overline{u^2}$ ,  $\overline{w^2}$ ,  $\overline{u'w'}$  measured at points about 0.3cm above a ripple crest and a trough. Values of  $\overline{u^2}$  and  $\overline{w^2}$  show two peaks in each half period, which corresponds to the passage of two vortices created in the leeside of the nearest and the neighboring ripples. Values of  $\overline{u'w'}$  above a crest show a strong peak according to the passage of the first vortex but they do not show a peak with the passage of the second vortex. It follows that turbulence maintains a coherent structure just after the vortex ejection and that, as the vortex moves upward, turbulence decays and diffuses to show locally isotropic features.

The stress fields were evaluated by the integration of the two-dimensional momentum equations.

$$\rho \left( \frac{\partial U}{\partial t} + \frac{\partial}{\partial x}(U^2) + \frac{\partial}{\partial z}(UW) \right) = -\frac{\partial P}{\partial x} + \frac{\partial \sigma_{xx}}{\partial x} + \frac{\partial \tau_{xz}}{\partial z} \quad (3)$$

$$\rho \left( \frac{\partial W}{\partial t} + \frac{\partial}{\partial x}(UW) + \frac{\partial}{\partial z}(W^2) \right) = -\frac{\partial P}{\partial z} + \frac{\partial \tau_{xz}}{\partial x} + \frac{\partial \sigma_{zz}}{\partial z} \quad (4)$$

where  $P$  is the equi-phase mean pressure,  $\rho$  is the density of water, and  $\sigma_{xx}$ ,  $\tau_{xz}$  and  $\sigma_{zz}$  are the components of the Reynolds stress tensor defined by

$$\begin{aligned} \sigma_{xx} &= 2\mu \frac{\partial U}{\partial x} - \rho \overline{u'^2} \\ \tau_{xz} &= \mu \left( \frac{\partial W}{\partial x} + \frac{\partial U}{\partial z} \right) - \rho \overline{u'w'} \\ \sigma_{zz} &= 2\mu \frac{\partial W}{\partial z} - \rho \overline{w'^2} \end{aligned}$$

in which  $\mu$  is the molecular viscosity.

The equi-phase mean pressure  $P$  was evaluated by integrating equation (4) with respect to  $z$ . The mean pressure thus evaluated is the sum of the two components as follows.

$$P = P_I + P_D \quad (5)$$

$P_I$  represents the pressure due to the acceleration of the oscillatory main flow and is given by the following relation,

$$P_I = -\rho \int_{x_0}^x \frac{\partial U_0}{\partial t} dx \quad (6)$$

where  $x_0$  is a reference point of which pressure is set to be zero and  $U_0$  is the horizontal velocity of the main flow.  $P_D$  means the component originated from the presence of the wavy boundary and is responsible for drag and lift forces.

Figure 5 shows distributions of the equi-phase mean velocity vector, Reynolds stress and mean pressure ( $P_D$ ) in a half period. The flow is seen to be locally accelerated above a ripple crest and

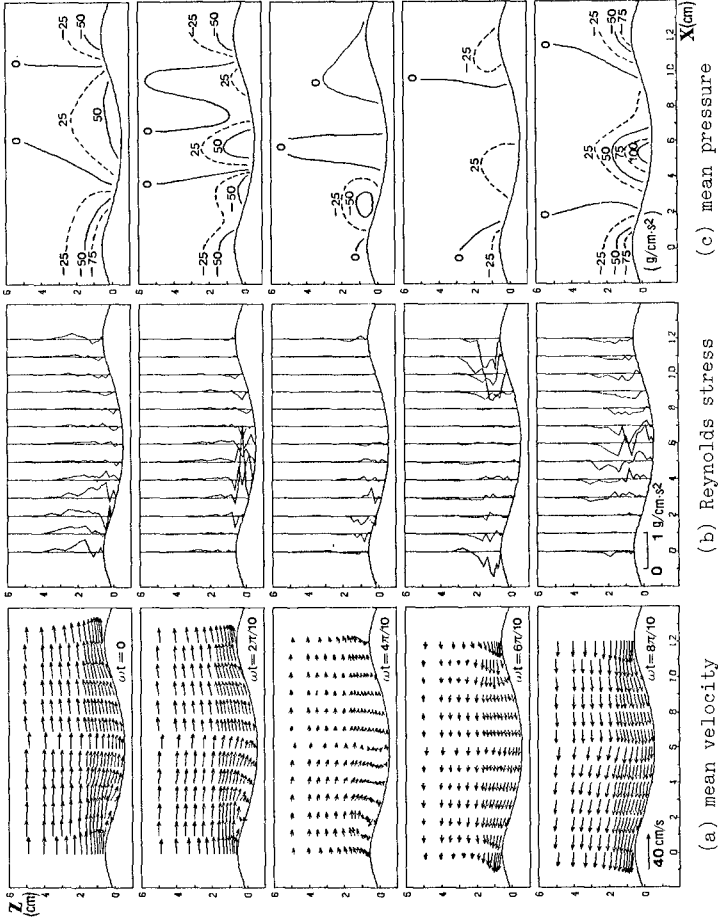
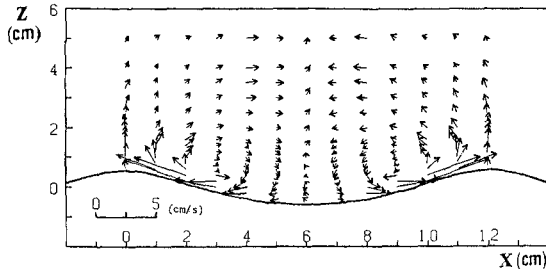


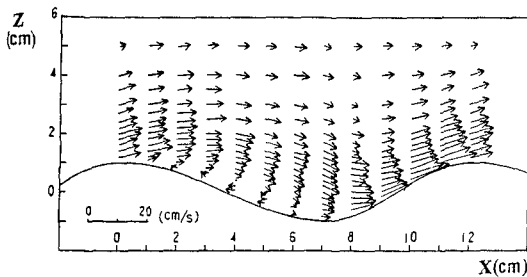
Fig. 5 Distributions of the mean velocity vector, Reynolds stress and mean pressure (case 6).

decelerated above a trough. The process of generation and ejection of a lee vortex is clearly visualized. It is seen that the Reynolds stress is strong in the region of a lee vortex, and that, as the vortex is ejected upward, the area of high turbulence moves with it and then diffuses.  $P_D$  is lower in the vortex core and higher on the upstream side of a ripple crest where the separated flow reattaches to the boundary. Characteristic velocity and stress field is created in the oscillatory boundary layer over ripples through the formation of lee vortices and the local acceleration of the flow.

Time average of the equi-phase mean velocity over one period is not zero in general. Figure 6 gives the residual current in an Eulerian frame. A pair of circulation cells is seen for the case of symmetric ripples and sinusoidal oscillation, whereas a unidirectional flow appears for the asymmetric condition. These patterns of steady streaming seem to be strongly influenced by the formation of lee vortices. Symmetric cells in case 6 are due to the formation of symmetric lee vortices, while the formation of asymmetric lee vortices is responsible for the asymmetric flow pattern in case H3. Quantitative analysis of steady streaming is important because it plays an important role to determine the direction of sediment transport.



(a) symmetric condition (case 6).



(b) asymmetric condition (case H3).

Fig. 6 Velocity distributions of residual current.

NUMERICAL MODELING

The boundary layer flow was calculated by numerically integrating the two-dimensional vorticity equations. The governing equations are the same with those used in the calculation made by Sleath (1974). In the present study, the finite difference scheme and the description of the boundary conditions were improved, so that we could calculate the flow at higher Reynolds numbers with a good accuracy. The governing equations were expressed in an orthogonal curvilinear coordinate system  $(X, Z)$  in order to represent the wavy boundary, i.e. the shape of ripples. In this coordinate system, the two-dimensional vorticity equations are

$$\frac{1}{J} \frac{\partial \zeta}{\partial t} - \frac{\partial \psi}{\partial X} \frac{\partial \zeta}{\partial Z} + \frac{\partial \psi}{\partial Z} \frac{\partial \zeta}{\partial X} = \nu \nabla^2 \zeta \tag{7}$$

$$J \nabla^2 \psi = \zeta \tag{8}$$

in which  $\zeta$  is the vorticity,  $\psi$  the stream function,  $\nu$  the kinematic viscosity,  $J$  the Jacobian of transformation and  $\nabla^2$  the Laplace operator given by  $\nabla^2 = \partial^2/\partial X^2 + \partial^2/\partial Z^2$ . The relation between the coordinate system  $(X, Z)$  and the Cartesian coordinate  $(x, z)$  is defined as

$$x = X - \sum_n a_n e^{-\frac{2\pi}{\lambda} z} \sin \frac{2n\pi}{\lambda} (X - \phi_n) \tag{9}$$

$$z = Z + \sum_n a_n e^{-\frac{2\pi}{\lambda} z} \cos \frac{2n\pi}{\lambda} (X - \phi_n) \tag{10}$$

in which  $a_n$  and  $\phi_n$  are coefficients to be determined so that the curve,  $Z = 0$ , might give a good approximation of symmetric and asymmetric shape of wave-generated ripples.

The boundary conditions at the ripple surface and at the upper boundary are expressed by

$$\frac{\partial \psi}{\partial Z} = \psi = 0 \quad \text{on } Z = 0 \tag{11}$$

$$\psi = \hat{U}_0 \delta \cos \omega t, \quad \zeta = 0 \quad \text{at } Z = \delta \tag{12}$$

in which  $\delta$  is the height of the calculation domain,  $\hat{U}_0$  the velocity amplitude of the main flow, and  $\omega (= 2\pi/T)$  the angular frequency of the oscillation. Values of  $\psi$  and  $\zeta$  along the side boundaries are set to be periodic for the interval of a ripple wavelength.

The numerical integration was carried out by an implicit finite difference scheme, for the conditions of experimental cases 1 to 4 which corresponded to laminar flow or transition. Calculation was also conducted for the asymmetric oscillatory flow over asymmetric ripples, of which wavelength is 12cm and height is 1.7cm, with the value of stream function at the upper boundary given by

$$\psi = \hat{U}_0 \delta (0.8 \cos \omega t + 0.2 \cos 2\omega t) \tag{13}$$

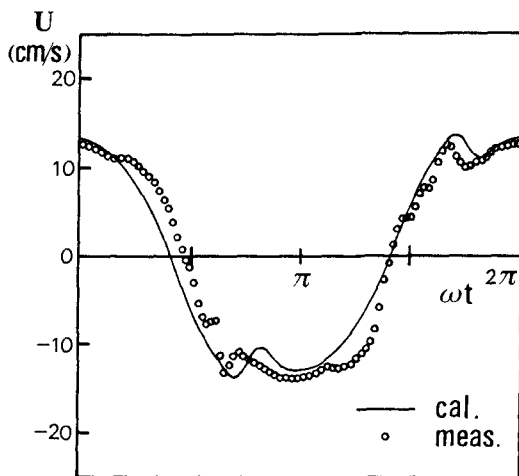


Fig. 7 Comparison of the time history of horizontal velocity above a ripple crest (case 3).

In order to examine the validity of the numerical model, the calculated and experimental results were compared. Figure 7 gives a comparison of the time history of horizontal velocity component at a point 0.3cm above a ripple crest. Agreement between the calculation and the experiment is fairly good.

Figure 8 illustrates the calculated velocity vector in a half period for the case 3. Salient features of the oscillatory flow over rippled bed are reproduced, such as the local acceleration above a ripple crest and the vortex formation in the lee side. The steady streaming was also evaluated from the calculated flow field and it was concluded that characteristic features observed in the experiments were well reproduced for both symmetric and asymmetric conditions. The present model can thus simulate the flow field in which a lee vortex is formed and transition takes place.

The flow structure in a Lagrangian frame is also of interest concerning the sediment transport. In order to study the movement of water particles, a numerical experiment was conducted by using the result of the calculation for the asymmetric condition. Water particles were placed at grid points of the numerical calculation and the movement of the particles which started at the phase of maximum velocity of the main flow was traced in one period. Figure 9 shows an example of trajectories of particles which started from grid points above the steeper flank of a ripple. Figure 10 gives the final displacement of all particles after one period. Some particles were trapped in a lee vortex formed on the steeper flank and were transported leftward and upward with the vortex ejection. There occurred no trapping to a vortex

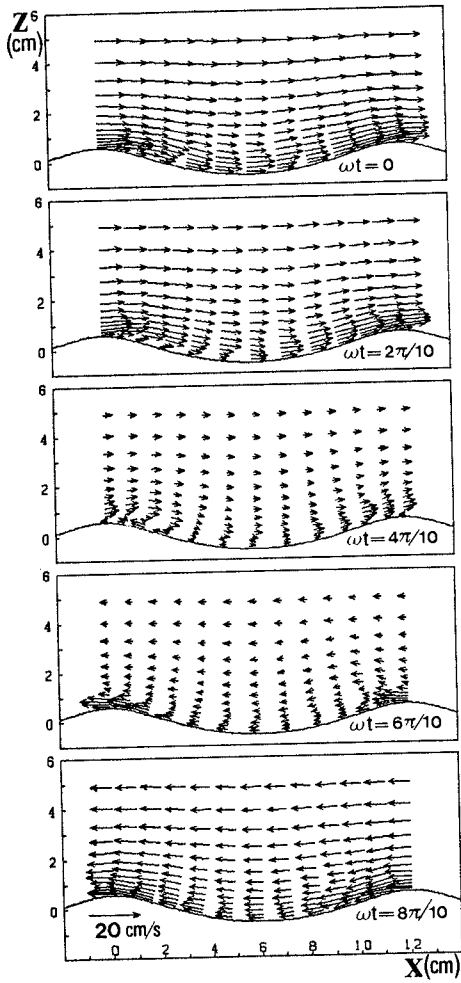


Fig. 8 Calculated flow field (case 3).

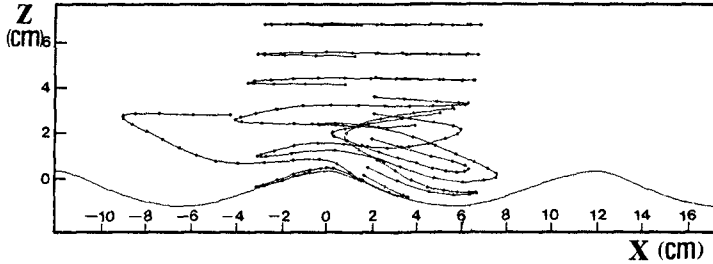


Fig. 9 Trajectories of water particles in one period.

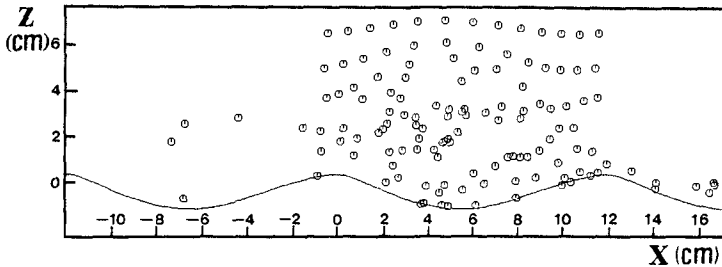


Fig. 10 Final displacement of water particles.

on the milder flank. The resultant net transport of particles near bottom became leftward. Ripples on natural beaches have the steeper flank to the onshore direction and the milder flank to the offshore direction. Although this experiment does not incorporate the effect of the settling of particles nor the interaction between the fluid and particles, the result appears to provide a suggestion on the mechanism of sediment transport to the offshore direction.

#### EVALUATION OF THE BOTTOM SHEAR STRESS

The evaluation of bottom shear stress is essential for the problem of wave damping and sediment transport. The bottom shear stress was estimated by using the results of experiments and numerical calculations. The bottom shear stress was decomposed into following two components.

$$\tau_b = \tau_{bs} + \tau_{bd} \quad (14)$$

where  $\tau_b$  is the total shear stress,  $\tau_{bs}$  is the shear stress due to skin friction and  $\tau_{bd}$  is that due to form drag. The skin friction is

important in the study of sediment transport, while the total shear stress becomes important in the estimation of wave damping.

(1) Bottom shear stress due to skin friction

The skin friction at the bottom was calculated from the results of numerical modeling by the following relation,

$$\tau_{bs} = \mu \left\{ \frac{\partial}{\partial Z} \left( J \frac{\partial \psi}{\partial Z} \right) - \frac{\partial}{\partial X} \left( J \frac{\partial \psi}{\partial X} \right) \right\} = \mu \zeta_b \tag{15}$$

where  $\mu$  is the viscosity and  $\zeta_b$  is the vorticity at the bottom. Figure 11 shows the time history of  $\tau_{bs}$  in case 3 at various points along a ripple surface. Chain lines with two dots indicate the amplitude of the bottom shear stress on a flat plate under the same flow condition. The amplitudes of  $\tau_{bs}$  at a ripple crest (solid line) and at a trough (dotted line) are about 1.6 and 0.7 times the amplitude for a flat plate respectively. These ratios are almost the same with the rates of the local acceleration of the flow. Time mean values of  $\tau_{bs}$  over one period are seen to be negative on a flank of a ripple (broken line and chain line with one dot), which means steady shear stress is exerting in the direction from a trough to a crest.

It is very difficult to estimate the value of bottom skin friction from experimental results, since there is no measurement of velocity in the immediate vicinity of the bottom boundary. We made an attempt to evaluate the bottom skin friction at a crest using the value of shear stress estimated at a measuring point closest to the bottom. The shear stress at the bottom surface was expressed by integrating equation (3) as

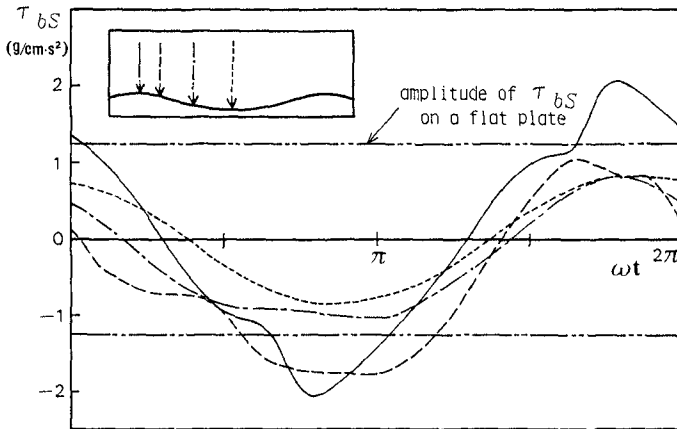


Fig. 11 Calculated history of local bottom shear stresses (case 3).



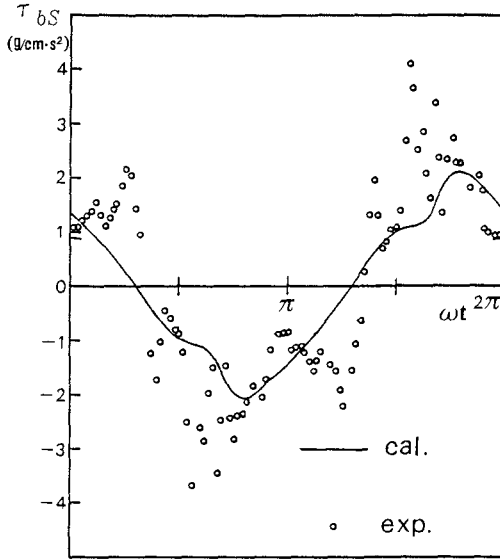


Fig. 12 Comparison of the bottom shear stress at a ripple crest (case 3).

$$\tau_{zx}|_{z'=0} = \tau_{zx}|_{z'=z_1} - \int_0^{z_1} \left\{ \rho \left( \frac{\partial U}{\partial t} + \frac{\partial(U^2)}{\partial x} + \frac{\partial(UW)}{\partial z} \right) + \frac{\partial P}{\partial x} - \frac{\partial \sigma_{zx}}{\partial x} \right\} dz \quad (16)$$

where  $z'$  is the vertical distance from the bed,  $z$ , the height of the point closest to the bed and  $\tau_{zx}|_{z'=z_1}$ , the shear stress estimated at  $z'=z_1$ . The integral was evaluated by means of the trapezoidal rule, where the values of  $\partial U/\partial t$ ,  $\partial(U^2)/\partial x$ ,  $\partial(UW)/\partial z$  and  $\partial \sigma_{zx}/\partial x$  were assumed to be zero at the bottom and to change linearly within the domain of integration. The value of  $\partial P/\partial x$  was assumed to be constant in this domain. Figure 12 shows the time history of the bottom shear stress at a crest evaluated through the experiment (indicated by  $\circ$ ) and the numerical model (solid line). It is found that the bottom shear stress estimated through experiments shows a strong peak when a vortex passes. Scatter of plotted data implies the need to improve the validity of the assumptions and the accuracy of the pressure.

(2) Energy dissipation rate

Consideration of the energy budget of the mean flow leads to the following equation.

$$D = \rho \frac{dU_0}{dt} \psi_0 - \frac{1}{\lambda} \frac{\partial}{\partial t} \int \int \frac{1}{2} \rho (U^2 + W^2) dA \quad (17)$$

where  $D$  is the energy dissipation rate averaged over one wavelength of a

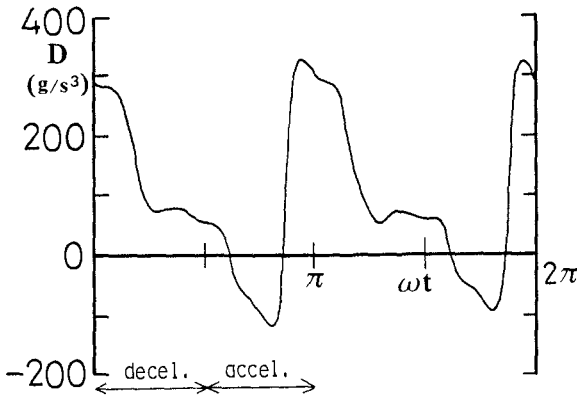


Fig. 13 Time history of the energy dissipation rate (case 6).

ripple and  $\psi_0$  is the value of stream function at the upper edge of the boundary layer.

Figure 13 gives the time history of  $D$  in case 6 evaluated from experimental data. The energy dissipation rate is large positive when the main flow is decelerated ( $0 < \omega t < \pi/2$ ), and becomes negative when accelerated ( $\pi/2 < \omega t < \pi$ ). This means that during the stage of the deceleration of the main flow the energy of the mean flow is dissipated through the generation of turbulence, and that a part of turbulence energy is transferred back to the mean flow during a certain period of the acceleration, which may correspond to the phenomenon of reverse transition.

The time mean value of  $D$  is conventionally related to the velocity of the main flow by

$$\bar{D} = \frac{1}{2} \rho f_e \overline{U_0^2} |U_0| \tag{18}$$

where  $f_e$  is the energy dissipation factor. Evaluation of the energy dissipation factor through experiments was also performed by Bagnold (1946) and Carstens et al. (1969). However, since their experimental conditions are quite different from those of the present experiments, we cannot compare our results with them directly. Values of  $f_e$  estimated through the present experiments and calculations are given in Fig. 14 together with values of friction factor given by Jonsson (1966). The quantity  $k$  represents the value of equivalent roughness and  $a_0$  is the orbital diameter of the main flow. Values of the energy dissipation factor are of the order of 0.05 and independent of the Reynolds number in the domain of the present study. The energy dissipation factor generally differs from the friction factor because there is a phase shift between the main flow velocity and the bottom shear stress. In the turbulent flow, however, this phase shift is so small that the

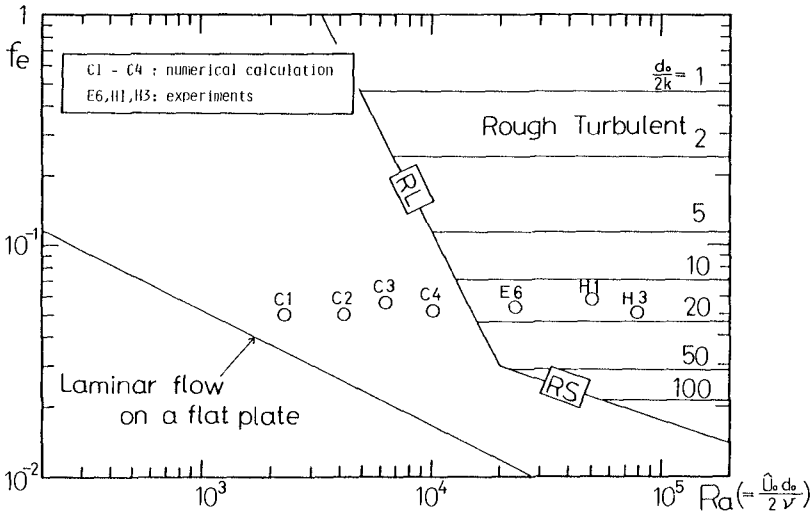


Fig. 14 Values of the energy dissipation factor.

values of  $f_e$  are regarded almost the same with those of the friction factor. By comparing the values of the energy dissipation factor and the friction factor in rough turbulent region of Fig. 14, we can estimate the values of equivalent roughness to be of the same order with the wave height of a ripple. Since there are only three data in rough turbulent region in the present study, more experiments under conditions of oscillatory flow are required to draw a generalized conclusion. It should also be noted that the energy dissipation due to sediment movement has to be taken into account under movable bed condition.

#### CONCLUDING REMARKS

It was concluded through experiments that lee vortices exert a strong influence on the velocity and stress fields of the oscillatory boundary layer above a rippled bed. The relation between the turbulence production and lee vortex evolution was quantitatively discussed based on the results of experiments under both symmetric and asymmetric conditions. The distribution of the residual current velocity was also presented. Using the numerical model developed, the boundary layer flow was accurately simulated up to considerably high Reynolds numbers. The bottom shear stress and the energy dissipation rate were evaluated through the results of experiments and numerical calculations. The authors intend to continue the work on the numerical modeling to make it possible to calculate the flow at higher Reynolds numbers based on the distribution of the measured Reynolds stress.

## REFERENCES

- Bagnold, R. A. (1946): Motion of waves in shallow water. Interaction between waves and sand bottoms, Proc. Roy. Soc. A 187, pp.1-15.
- Carstens, M. R., F. M. Nielson and H. D. Altinbilek (1969): Bed forms generated in the laboratory under oscillatory flow, CERC Tech. Memo. No.28, 39p.
- Hamamoto, K., N. Mimura and A. Watanabe (1982): Laboratory study of oscillatory boundary layer flow above rippled bed (2), Proc. 29th Japanese Conf. Coastal Eng., pp.254-258. (in Japanese)
- Jonsson, I. G. (1966): Wave boundary layers and friction factors, Proc. 10th Coastal Eng. Conf., pp.127-148.
- Longuet-Higgins, M. S. (1981): Oscillating flow over steep sand ripples, J. Fluid Mech., Vol.107, pp.1-35.
- Sawamoto, M., T. Yamashita and T. Kitamura (1982): Measurements of turbulence over vortex-ripple, Proc. 18th Coastal Eng. Conf., pp.282-296.
- Sleath, J. F. A. (1974): Velocities above rough bed in oscillatory flow, Proc. A.S.C.E., Vol.100, No.WW4, pp.287-304.
- Toit, C. G. D. and J. F. A. Sleath (1981): Velocity measurements close to rippled beds in oscillatory flow, J. Fluid Mech., Vol.112, pp.71-96.

## CHAPTER ONE HUNDRED FIFTY FIVE

### VARIATION OF SEDIMENT SUSPENSION IN OSCILLATORY FLOW

Carsten Staub<sup>1</sup> Ivar G. Jonsson<sup>2</sup> Ib A. Svendsen<sup>3</sup>

#### ABSTRACT

Different syphon type suspended load probes were used together with a newly developed 'carousel' sampler for measurements of the instantaneous sediment concentration in turbulent oscillatory flow over a sand bed. Shields parameters were well above the rippled/flat bed transition region, resulting in intense sediment transport over a flat bed. The measurements were performed at different levels in a large oscillating water tunnel. They showed some characteristic features of the temporal concentration variation and of the variation with height of the mean concentration. Also a pronounced effect of the orientation of the suction tube relative to the flow was observed.

#### 1. INTRODUCTION

A large part of the sand in motion under waves on a sandy coast is carried in suspension. Thus, the suspended load plays an important rôle in the net transport of sediment.

Measurements of time-mean sediment concentrations have frequently been published during the last decades. In general, however, such information is not sufficient to determine the net sediment transport due to waves and currents. In a wave motion with a weak current (e.g. the on-shore/offshore problem) the net sediment transport may be caused by the difference between large sediment movements in opposite directions due to the predominantly oscillatory nature of the water flow. Thus, to determine this difference between two large numbers with any accuracy it is necessary to have detailed information about the temporal variation of the sediment concentrations.

The aim of the present experimental study is to provide measurements of the time variation of sediment concentrations above a sand bed under high shear conditions ('sheet flow'). Thus, the sand bed is (almost) plane during the experiments.

---

<sup>1</sup> M.Sc., Institute of Hydrodynamics and Hydraulic Engineering (ISVA), Technical University of Denmark, Building 115, DK-2800 Lyngby, Denmark. Present address: Christiani & Nielsen, Ltd., Vester Farimagsgade 41, DK-1606 Copenhagen V, Denmark.

<sup>2</sup> Ph.D., Associate Professor, ISVA.

<sup>3</sup> Ph.D., Associate Professor, ISVA.

The Shields parameter is defined as

$$\theta = \frac{\tau_{b,\max}}{\rho g (s-1) d_{50}} \quad (1)$$

where  $\tau_{b,\max}$  is the maximum bed shear stress,  $\rho g s$  is the specific gravity of the sand grains,  $\rho$  being the density of water, and  $d_{50}$  is the median grain diameter. When  $\tau_{b,\max}$  is determined by (2) and (3) (see Chapter 3) the situations studied correspond to  $\theta$ -values of about 1.9 - 3.3 (with roughness  $K_N = 2.5 d_{50}$ , see comments in Chapter 3).

Measurements of time variation of sediment concentration have previously been reported by Nakato et al. (1977), Sleath (1982), and Bosman (1982). They all, however, measured the concentrations above a ripple bed corresponding to situations with smaller Shields parameters ( $\sim 0.1 - 0.8$ ), and they used electro-optical equipment.

The measurements presented in the following were carried out in a large oscillating water tunnel, using wave periods of 9.1 s and 6.8 s. The sediment concentrations were measured by letting a syphon probe suck out a sand-water mixture from a fixed point in the tunnel. A horizontal wheel with 18 cups covering the circumference was rotating under the outlet of the syphon, and the rotation was synchronized with the oscillation in the water tunnel. The sand-water mixture in each cup thus represents the concentration averaged over (about) one 18th of the oscillation period, giving a phase interval of  $20^\circ$ .

A limitation of this method compared with electro-optical methods is that rapid concentration fluctuations will not be represented in the results. It also involves some rather complicated phase corrections of measurements.

In Chapters 2 and 3 is given a more detailed description of the experiments, and the test parameters are listed in Table 1.

In Chapter 4 we discuss and analyze the experimental data in order to obtain the results presented in Chapter 5. These include variations of concentration and corresponding variations of the average-over-depth velocity, as well as mean concentration profiles.

## 2. EXPERIMENTAL FACILITIES

The oscillating water tunnel, in which the measurements of sediment concentration were performed, has been described by Lundgren and Sørensen (1958) and Jonsson and Carlsen (1976), but has since been modernized. Briefly, it consists of two cylindrical vertical risers and a horizontal part comprising a 10 m long test section with plexiglass walls and with a rectangular cross section (height  $\times$  width =  $36 \times 39 \text{ cm}^2$ ), see Fig. 1. In the experiments the bottom of the test section was covered with a 7 m long sand field. Thus, the inner height above the sand bed was about 30 cm. The water column was forced to oscillate by varying the air pressure above the water surface in the closed (southern) vertical riser. The air pressure was supplied by a hydraulically driven piston performing a sinusoidal oscillation under the control of an electric signal. The variation of the water level in the open (northern) riser was recorded by a capacitance-type wave gauge. From this record, the average-over-depth velocity,  $u$ , in the test section was determined by differentiating the record signal with respect to time.

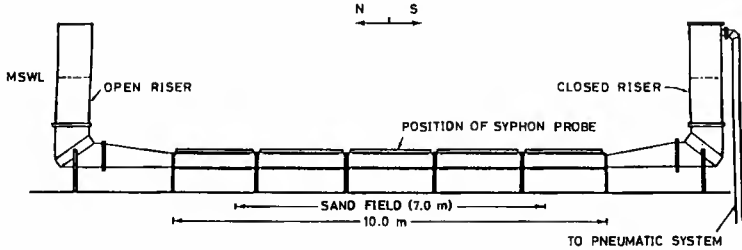


Fig. 1. The oscillating water tunnel.

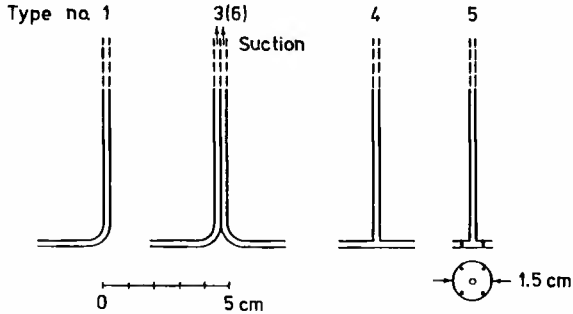


Fig. 2: Syphon probes with different types of intakes used in the experiments. Inner diameter of tubes is 1.6 mm. (Probe no. 6 has inner diameter 2.6 mm, see Table 1).

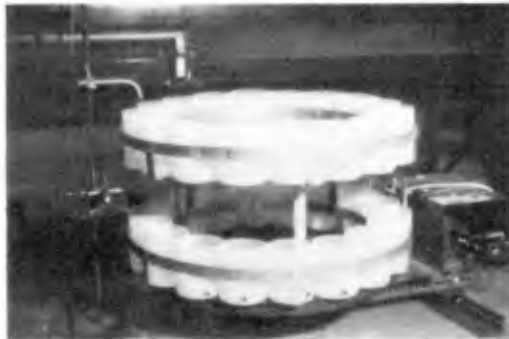


Fig. 3: The 'carousel sampler'. Two sets of cups placed on a horizontal wheel, 18 cups at each level. The outlets from the syphons are seen to the left.

'Wave' periods ( $T$ ) were 9.1 s and 6.8 s, and amplitudes in the test section ( $\alpha$ ) 1.8 to 2.1 m. Maximum flow velocities ( $u_{\max}$ ) were 1.3 to 1.9 m/s.

The probe for the concentration measurements was installed almost at the middle of the test section, see Fig. 1. A number of different probes were used in the experiments. Some of them are shown in Fig. 2. Each probe includes a stainless steel pipe supplied with an extension of plastic tubing with its outlet over the 'carousel sampler', as the horizontal wheel in Fig. 3 has been termed.

During an experiment the excess pressure in the tunnel continuously forced out a sand-water mixture through the probe. The 'carousel sampler' (Fig. 3) actually consists of two levels, each with 18 cups mounted along the circumference and rotating under the outlets of the double syphons used in most of the experiments. The rotation of the wheel was synchronized with the oscillation in the water tunnel. The revolutions of the wheel were recorded by a photo-electric cell, and corrections were made by a feed-back mechanism adjusting the velocity of rotation once every wave period.

Two different types of sand were used with median diameters 0.19 mm and 0.38 mm. Settling velocities at 18°C are about 0.021 m/s for  $d_{50} = 0.19$  mm, and 0.050 m/s for  $d_{50} = 0.38$  mm.

### 3. PROCEDURE

Before each test the level of the sand bed along the test section was measured. Sampling of suspension was begun a few minutes after the start of the oscillations to allow initial disturbances of bed and suspension to vanish, and each test then lasted for 6 - 13 minutes (Table 1). After each test the concentration of sand in the cups was determined by drying and weighing.

Ripples were not observed, but quite often some deviation from a plane horizontal bed was found. However, the associated bed slopes never exceeded 2° and usually were much gentler. The configuration was apparently caused by small irregularities in the flow conditions, perhaps partly related to the asymmetrical way in which the flow was driven. Variations of the bed level in the lateral direction were also recorded and found to be only a few millimetres.

Since the bed level sometimes changed during an experiment, the probe was not exactly at the same height above the sand bed during the whole test. Therefore, the bed level was measured before, during, and after each test, and an 'effective probe elevation' during the test was determined by averaging these three elevations. Both the average value and the range of variation are shown in Table 1 for each test. See also Figs. 8 and 9.

It may also be worth mentioning that there was no observation of local scour in cases where the probe was positioned close to the bottom.

The column 'probe pointing' in Table 1 shows the directions of the probe intakes - which are opposite to the directions of suction velocities. In most of the tests with the coarsest sand wider suction pipes were applied in order to avoid effects of partial or momentaneous blocking of the pipe. However, comparison of results obtained with wide and narrow suction pipes showed no such tendency. In some cases, however, clogging was observed, as demonstrated in the table.



Table 1.

TEST No.	PROBE POINTING	PROBE TYPE (NO)	PERIOD T (s)	EXCURSION $Z_0$ (m)	MAX. VEL. $u_{max}$ (m/s)	SHIELDS PARAMETER $g(c)$	MEDIAN GR. SIZE (mm)	HEIGHT OF PROBE ABOVE BED		WATER TEMP (°C)	TEST DURATION (s)		
								AVERAGE (cm)	RANGE <sup>(a)</sup> (cm)				
820	S	①	9.1	3.6	1.3	1.85		(2.2)	(2.0) - 2.4		634		
823	E	L	-	3.6	-	-	0.19	2.3	2.1 - 2.5		751		
825A	S		-	3.6	-	-		2.5	2.3 - 2.7		724		
825B	N		-	3.6	-	-		2.7	2.7		724		
1	S+(W)	②	9.1	3.64	1.26	1.87		2.0	1.9 - 2.2		581		
2	S+(W)	JL 90°	-	3.68	1.27	1.90	0.19	2.3	2.1 - 2.6		719		
3	N+(S)		-	3.64	1.26	1.87		1.6	1.4 - 1.8		726		
4	W+(S)		-	3.64	1.26	1.86		2.0	1.8 - 2.2		729		
5	N+(E)		-	3.72	1.28	1.93		1.9	(1.6) - 2.0		729		
6	E+(N) <sup>(c)</sup>		-	3.72	1.28	1.93		1.8	1.5 - 2.0		729		
7	N+S		③	9.1	3.72	1.29		1.96		2.4	1.7 - 2.8		606
8	N+S	JL	-	3.78	1.31	2.02	0.19	1.9	1.6 - 2.3		724		
9	N+S		-	3.68	1.28	1.92		1.4	0.8 - 1.7		724(366) <sup>(b)</sup>		
10	N+S		-	3.76	1.30	1.99		1.7	1.5 - 2.2		725		
11	N+S		-	3.80	1.32	2.03		1.2	0.8 - 1.4		734(430)		
12	E+N		②	9.1	3.78	1.31		2.01		1.3	1.1 - 1.6		726
13	E+N	JL 90°	-	3.80	1.32	2.03	0.19	1.8	1.5 - 2.2		725		
14	E+N		-	3.76	1.30	1.98		0.9	0.7 - 1.2		727		
15	-	⑤	9.1	3.74	1.29	1.97		2.0	1.6 - 2.3		726		
16	-	DISC	-	3.78	1.31	2.01	0.19	1.0	0.8 - 1.2		726		
17	N+S	①	6.8	3.62	1.68	3.33		2.1	1.6 - 2.6		678(202)		
18	N+S	JL	-	3.62	1.68	3.33	0.19	1.6	1.3 - 1.8		678(153)		
19	N+S		-	3.62	1.68	3.33		1.9	1.7 - 2.1		678		
20	N+S		-	3.62	1.67	3.30		2.6	2.5 - 2.7	18.6	681		
21	N+S		-	3.62	1.68	3.33		1.2	1.0 - 1.3	18.0	678		
22	N-S		④	9.1	3.72	1.28		1.93		1.7	1.5 - 2.2	16.1	729
23	N-S	JL	-	3.72	1.29	1.94	0.19	2.3	2.2 - 2.5	16.1	727		
24	N-S		-	3.72	1.29	1.94		1.6	1.5 - 1.7	16.4	727		
25	N-S		-	3.78	1.30	2.00		1.4	1.3 - 1.5	16.4	553		
26	N+S		①	9.1	3.72	1.29		1.86		1.7	1.3 - 2.1	13.0	727
27	N+S		JL	-	3.74	1.29		1.96	0.19	0.9	0.7 - 1.2	18.7	727
28	N+S	①	6.8	3.58	1.66	3.26		1.0	0.8 - 1.1	18.6	678		
29	N+S	JL	-	3.54	1.63	3.19	0.19	2.7	2.6 - 2.7	18.9	682		
31	N+S	③	6.8	4.06	1.88	2.37		2.0	1.7 - 2.2	16.6	678		
32	N+S	JL	-	4.08	1.89	2.37	0.38	1.9	1.6 - 2.2	13.8	475		
33	N+S		-	4.08	1.89	2.39		2.4	2.0 - 2.7	14.9	475		
34	N+S		-	4.06	1.88	2.37		2.8	2.7 - 2.9	16.4	678		
35	N+S		⑥	6.8	4.06	1.88		2.36		2.1	1.5 - 2.7	13.2	476
36	N+S	JL	-	4.06	1.88	2.36	0.38	1.1	0.9 - 1.3	15.7	476		
37	N+S		-	4.12	1.90	2.42		1.3	0.5 - 2.0	17.7	340		
38	N+S		-	4.12	1.92	2.44		1.7	1.1 - 2.0	15.1	406		
39	N+S		-	4.14	1.92	2.44		1.3	0.9 - 1.6	18.7	476		
40	N+S		-	4.12	1.91	2.43		2.8	2.4 - 3.0	18.3	509		
41	N+S		-	4.12	1.92	2.44		0.8	0.6 - 1.0	19.0	406		

PROBE TYPE NOS. 1-5:  $\phi_1 = 1.6$  mmPROBE TYPE NO. 6 :  $\phi_1 = 2.6$  mm

(a) Estimated variation of probe level.

(b) One suction tube clogged after time interval in parenthesis.

(c) Directions in parenthesis means that only time-mean concentrations

were measured.

(d) Based on roughness  $k_N = 2.5 d_{50}$ ; see text.

Table 1: Test parameters for suspension measurements. Re directions

N(orth) and S(outh), see Fig. 1. Re details of probes, see Fig. 2.

The Shields parameter listed in the table is defined by (1), where maximum bed shear is determined by

$$\tau_{b,\max} = \frac{1}{2} f_w \rho u_{\max}^2 \quad (2)$$

The wave friction factor is determined from Swart's approximate formula based on the measurements by Jonsson and Carlsen (1976)

$$f_w = \exp\{-5.977 + 5.213 (\alpha/k_N)^{-0.194}\} \quad (3)$$

with the bed roughness  $k_N = 2.5 d_{50}$ . Quantity  $\alpha$  is the water particle amplitude of the oscillation.

The Shields parameters thus determined (Table 1) must be regarded with some reservation. Recent interpretations of the experiments by Carstens et al. (1969), see Grant and Madsen (1982), indicate much higher values for  $k_N/d_{50}$  than 2.5, for oscillatory flow associated with intense sediment transport over a flat bed. From their work one can quote figures as high as 210-240 for  $k_N/d_{50}$ . In this context note that the Shields parameter in Grant and Madsen's work is based on a wave friction factor, where roughness equals grain diameter; thus their Shields parameters - like the ones in Table 1 - are more formal than physical quantities. In conclusion, the 'real' Shields parameters must be expected to be much higher than listed in Table 1.

#### 4. INTERPRETATION OF MEASUREMENTS

The experimental data do not directly provide the information about sediment concentrations which we are aiming at. In the following it is described how the data were analyzed to obtain the experimental results presented in Chapter 5.

The sand-water mixture takes some time to pass through the suction system to the carousel. This phase shift or 'delay' must be accounted for when relating the concentrations to the water velocities in the test section. Also the effect of a varying sand-water mixture velocity in the suction system at  $T = 6.8$  s was considered, and the measurements were corrected accordingly.

Furthermore, the phase shift we are looking for is not just the delay of the water particles, but that of the sediment grains. These two phase shifts are not quite the same because on the non-uniform velocity distribution over the cross section of the pipes and tubes. The centre of the grains cannot get closer than half a grain diameter to the pipe walls where the velocities are lowest. Thus, if the sand grains are uniformly distributed over the remaining pipe cross section the average velocity of the sand through the suction system will be higher than the average velocity of the water. For a quantitative evaluation of this effect, however, we must estimate the velocity profile. From a few simple experiments the 'quickest' sand grains are found to pass through the suction system about 20% faster than the water, that is the maximum sand velocity is approximately 20% larger than the average water velocity. The experiments also indicated that this could be explained by introducing the velocity distribution

$$v = v_{\max} \left(1 - \frac{r}{R}\right)^{1/7} \quad (4)$$

where  $v$  is the velocity,  $r$  is the distance from the centre line, and  $R$  is the inner radius of the pipe (or tube). This well-known expression meets the requirement of a maximum velocity approximately 20% higher than the average velocity. In the tests we have used  $d_{50}/D = 0.10 - 0.13$ ,  $D$  being the inner diameter of the suction system. With the velocity profile given by (4), the difference between the delay of the sand and the delay of the water was found to be between  $2^\circ$  and  $10^\circ$ .

The average velocity,  $u$ , in the test section was determined by differentiating the wave-gauge registrations of the water level in the open vertical leg of the tunnel. As expected for a period of  $T = 9.1$  s, which is close to the natural period of the water column,  $u$  varies nearly sinusoidally (Fig. 4).

At a period of  $T = 6.8$  s, however, the deviation from a sinusoidal velocity variation is appreciable (Figs. 5 and 6). The wave motion corresponding to the flow in the tunnel is defined so that  $\omega t = 0$  ( $\omega = 2\pi/T$ ) at maximum velocity northwards (i.e. towards the open riser).

## 5. RESULTS

Some examples of the measured instantaneous concentrations,  $C_m$ , and the corresponding time variations of water velocities in the tunnel are shown in Figs. 4-6. All are tests with twin suction intakes oppositely directed and parallel to the flow (type 3 in Fig. 2), but located at the same level above the bed. The concentration variation curves are drawn through the measurement points, each corresponding to the sand concentration in one cup. The phase distance between these points is rather variable in Fig. 5 (test no. 28) due to a large variation in suction velocity in this particular test.

As expected the measured concentrations have two maxima during an oscillation period, one for each extreme in velocity. However, there is a considerable difference in magnitude between the two measured concentration maxima. Figs. 4-6 clearly show that the concentration measurements are very sensitive to the direction of the oscillatory flow (typically  $\pm 1.3$  to  $\pm 1.9$  m/s) relative to the suction velocity (typically 0.9 m/s). The effect is probably due to the fact that the heavier sand particles cannot quite follow the water in the large accelerations immediately around the intake of the probe.

Calibration tests for different types of suction probes in a stationary current have been made by Bosman (1982). These calibrations show that for a current directed towards the opening of the probe the true concentrations are up to about 30% larger than the measured concentrations, depending on the ratio between suction and flow velocity. None of Bosman's calibrations, however, were made with the opposite current direction. Qualitative considerations show that in this case concentration measurements will yield a large underestimate of true concentrations, and this is believed to be the reason for the above-mentioned differences between the two measured concentration maxima.

Therefore, in the following we consider measurements made when the current velocity opposes the intake velocity to be unreliable. In the tests with twin suction intakes we consider the at any instant highest of the two  $C_m$ -curves to be the best approximation to the actual concentrations, i.e. we change from one curve to the other one as soon as the

# SEDIMENT SUSPENSION VARIATION

2317

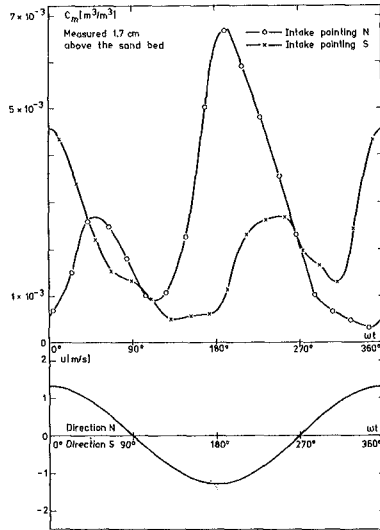


Fig. 4: The temporal variation of the sand concentration  $C_m$ , and the average-over-depth velocity  $u$ , in Test no. 10 (two oppositely directed suction pipes parallel to the flow, type 3 in Fig. 2). Test parameters in Table 1. N and S are North and South.

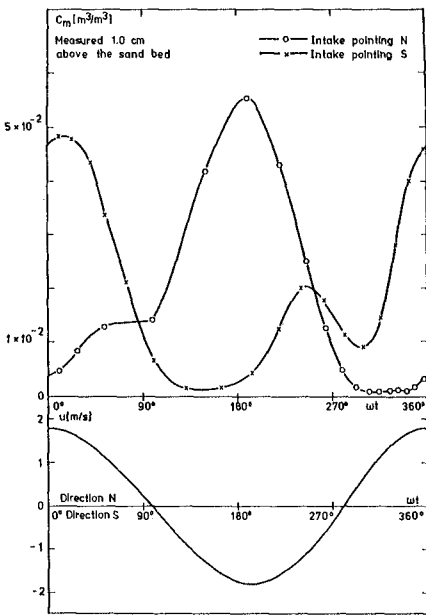


Fig. 5: The temporal variation of the sand concentration  $C_m$ , and the average-over-depth velocity  $u$ , in Test no. 28 (two oppositely directed suction pipes parallel to the flow, type 3 in Fig. 2). Test parameters in Table 1. N and S are North and South.

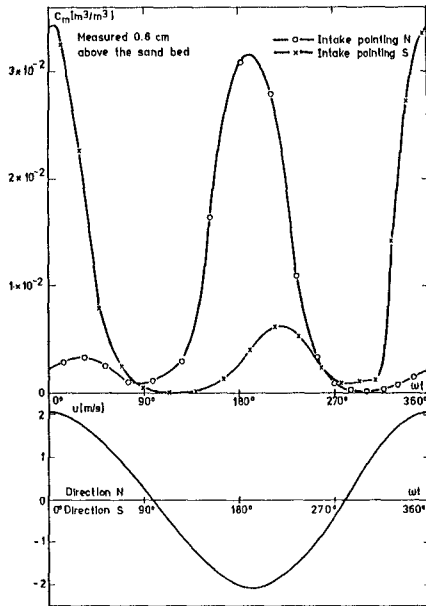


Fig. 6: The temporal variation of the sand concentration  $C_m$ , and the average-over-depth velocity  $u$ , in Test no. 41 (two oppositely directed suction pipes parallel to the flow, type 6 in Fig. 2). Test parameters in Table 1. N and S are North and South.

latter exceeds the former one<sup>4</sup>. This observation puts a question mark to the reliability of time-mean concentrations found in conventional experiments with single, longitudinally directed probe intakes. These should, according to the present experiments, be increased by at least 25-80% to get the actual mean concentrations in the flow (see, e.g. Figs. 4-6). Fig. 7 compares - for all three groups of test parameters - the time-mean concentrations of the actually measured suspension sample,  $\bar{C}_m$ , and the mean concentration,  $\bar{C}$ , determined by time-averaging the highest of two measured concentration variations. In the following only  $\bar{C}$  is considered.

In general, the time variation of concentration was 'peaky', with narrow maxima and broad minima, especially so for the coarse sand.

Mean concentration profiles are shown in Figs. 8 and 9. The range of variation of the height of the probe above the bed during each test is shown as a full line through the measurement point. A special procedure has been applied to determine the mean concentration in the tests with only a single suction tube directed parallel to the flow. The measured concentration variation was shifted 180° to simulate an oppositely directed probe, and the mean concentration was then determined from the at any time highest of the two concentration curves.

In addition to the grain size distribution of bed material a number of samples of suspended sand were analyzed. The median grain sizes for these are plotted in Fig. 10 versus the height of the probe above the sand bed. For the finer sand type, there is a clear tendency towards decreasing grain size at increasing height above bed, whereas no such variation appears in the results for the coarser sand.

## 6. CONCLUSIONS

- a. The time variation of sediment concentration at different heights over bed was measured in a large oscillating water tunnel (Fig. 1). Two types of sand were used with median diameters 0.19 mm and 0.38 mm. 'Wave' periods were 9.1 s and 6.8 s, and amplitudes were 1.8 to 2.1 m. Maximum velocities were 1.3 to 1.9 m/s corresponding to intense sediment transport over an approximately plane bed without ripples.
- b. The 'carousel sampler' (Fig. 3) with the probes in Fig. 2 proved to be well-suited for measuring 'instantaneous' sediment concentration in oscillatory flow (Figs. 4-6), although problems arise with phase corrections and calibration.
- c. The influence of the direction of probe intake relative to the flow on directly measured instantaneous concentration was large (Figs. 4-7). In situations where the flow direction opposed the direction of flow into the probe, the measured concentrations were found to be too small. This was accounted for by using probes with two oppositely directed intakes.

---

<sup>4</sup> Recently, C.H. Hulsbergen, Delft Hydraulics Laboratory, has performed experiments to determine the influence of suction velocity and probe direction on measured concentration (Bosman, 1984). When the report is published, the results will be used in a further adaptation of our measurements.

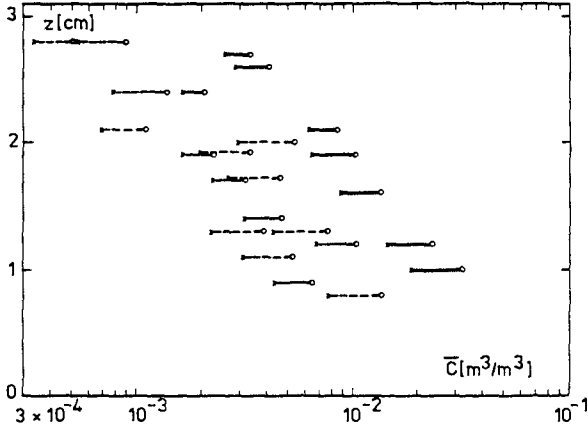


Fig. 7: Comparison of two methods to determine time-mean concentration  $\bar{C}$  in tests with two separate longitudinally directed (N-S) suction intakes.  $\times$ :  $\bar{C}$  determined as the mean concentration for the actually measured suspension sample ( $= \bar{C}_m$ ).  $\circ$ :  $\bar{C}$  determined as the mean value of the at any time highest measured concentration. —:  $d_{50} = 0.19$  mm,  $T = 9.1$  s. ---:  $d_{50} = 0.19$  mm,  $T = 6.8$  s. -·-·:  $d_{50} = 0.38$  mm,  $T = 6.8$  s.

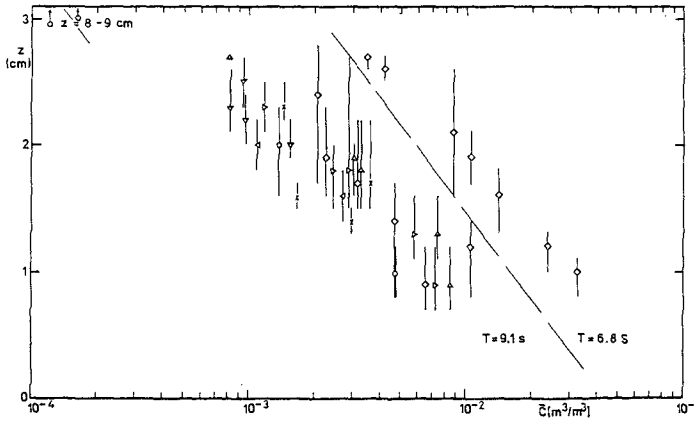


Fig. 8: Time-mean concentrations  $\bar{C}$ , determined from the at any time highest measured concentration.  $d_{50} = 0.19$  mm,  $T = 9.1$  s and 6.8 s. Specifically for single longitudinally directed intakes:  $\bar{C}$  is determined from the at any time highest of curves  $C(\omega t)$  and  $C(\omega t + 180^\circ)$ . The range of variation of the bed level during the tests is marked by a full line through each test point.  $\Delta$ : intake pointing N;  $\nabla$ : intake pointing S;  $\triangleright$ : intake pointing E;  $\triangleleft$ : intake pointing W;  $\diamond$ : two intakes pointing N-S;  $\times$ : T-shaped intake;  $\circ$ : disc-shaped intake.

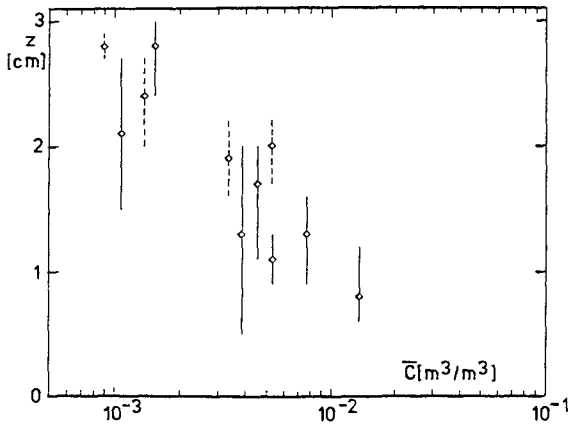


Fig. 9: Time-mean concentrations  $\bar{C}$ , determined from the at any time highest measured concentration.  $d_{50} = 0.38$  mm, and  $T = 6.8$  s. Legend, see Fig. 8.

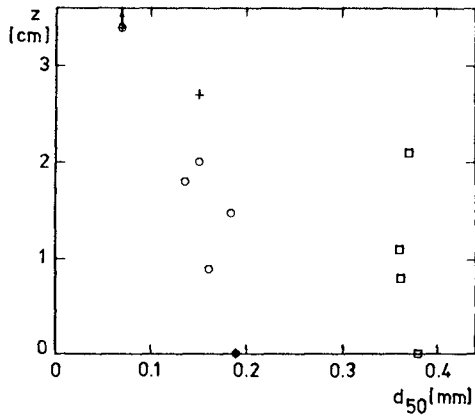


Fig. 10: Median grain diameters of suspended sediment versus height above sand bed. o:  $d_{50}(\text{bed}) = 0.19$  mm,  $T = 9.1$  s. +:  $d_{50}(\text{bed}) = 0.19$  mm,  $T = 6.8$  s. □:  $d_{50}(\text{bed}) = 0.38$  mm,  $T = 6.8$  s.

- d. Also time-mean concentration profiles were found (Figs. 8 and 9).
- e. For the finer sand, grain size was found to decrease with height (Fig. 10).
- f. The time variation of concentration was 'peaky' with narrow maxima and broad minima, especially so for the coarse sand.
- g. The time variation of relative concentration was larger in experiments with coarse sand than with fine sand.

The experiments described in this paper were supported by the Danish Council for Scientific and Industrial Research. The authors also want to thank the staff at ISVA's workshops and laboratory for the skillful rebuilding of the oscillating water tunnel and for great help with the performance of the experiments.

#### REFERENCES

- Bosman, J.J., 1984. Private communication.
- Bosman, J.J., 1982. Concentration measurements under oscillatory water motion. Delft Hydr. Lab., TOW, Report on model investigation M1695, part II, 126 pp.
- Carstens, M.R., F.M. Neilson and H.D. Altinbilek, 1969. Bed forms generated in the laboratory under an oscillatory flow: Analytical and experimental study. Tech. Memo No. 28, U.S. Army Corps of Engineers, Coastal Engrg. Res. Center, Virginia, U.S.A.
- Grant, W.D. and O.S. Madsen, 1982. Movable bed roughness in unsteady oscillatory flow. *J. Geophys. Res.*, Vol. 87, No. C1, 469-481.
- Jonsson, I.G. and N.A. Carlsen, 1976. Experimental and theoretical investigations in an oscillatory turbulent boundary layer. *J. Hydr. Res.*, Vol. 14, No. 1, 45-60.
- Lundgren, H. and T. Sørensen, 1958. A pulsating water tunnel. Proc. 6th Conf. Coastal Engrg., Florida 1957, Ch. 21, 356-358.
- Nakato, T., F.A. Locher, J.R. Glover and J.F. Kennedy, 1977. Wave entrainment of sediment from rippled beds. Proc. ASCE, WW1, Vol. 103, 83-100.
- Sleath, J.F.A., 1982. The suspension of sand by waves. *Journ. of Hydraulic Res.*, Vol. 20, No. 5, 439-452.



## CHAPTER ONE HUNDRED FIFTY SIX

### SCALE EFFECTS IN LARGE COASTAL MOBILE BED MODELS

J.W. Kamphuis\* and R.B. Nairn\*

#### ABSTRACT:

A series of mobile bed model tests of a prototype circular sand island was performed to determine scale effects. It was found that scale effect was largely a function of mobility number with some secondary effects of Reynolds number, bedform and critical profile depth. It was concluded that a model series using prototype sand grain size is necessary at this time to effect successful extrapolation to prototype.

#### 1.0 INTRODUCTION

An extensive series of model tests was performed with circular islands consisting of sand only. The prototype modelled was an artificial island used for drilling purposes in the Canadian Beaufort Sea. It was located in 20 m of water, had a composite slope (mostly 1:12), a drilling platform of 50 m radius and nominally contained  $5 \times 10^6 \text{ m}^3$  of 0.2 mm diameter sand. (Figures 1 and 2 show the model basin and the prototype island profile.) To date 30 different mobile bed models have been built and tested, using scales of 50, 75, 100 and 200 and sand particle sizes of 0.56, 0.18, 0.17 and 0.105 mm. The island models were tested until they were completely submerged.

Erosion volumes were measured at prototype time intervals of 3, 12, 36, 108 and 216 hours, based on hydrodynamic scaling (Froude) relationships. Progression of erosion was also monitored by recording the time to reach several benchmark stations. These were the leading edge of the drilling platform, a post located at the centre of the island, the trailing edge of the platform and the disappearance of the island underwater. Erosion volume was also measured when the test reached the post and when the island became submerged. Thus, erosion rates could be calculated for particular prototype time intervals as well as over the morphological time interval required for erosion to reach the post and for the island to become submerged. In the present paper erosion volumes on the front half of the island only are considered in the analysis.

---

\* Department of Civil Engineering, Queen's University, Kingston, Canada, K7L 3N6

The prototype wave climate was simulated using 8 second monochromatic waves arriving from one single direction. Each model was built twice. One model was subjected to a wave height of 6.5 m, while the other was tested at a wave height of 4.75 m. Both of these are considered to be extreme storm wave conditions. Several models were built more than twice for replication of results, removal of testing errors and for tests with different wave heights.

This paper presents a description of how a series of model tests should be performed and interpreted. This study differs from previous scale effects investigations because a strong longshore sand transport gradient exists in this truly three dimensional problem.

## 2.0 DIMENSIONAL ANALYSIS

The primary objective of coastal mobile bed modeling is to determine prototype sediment transport rates and morphology. A functional relationship between sediment transport and its parameters may be postulated as follows:

$$Q = f(H, L \text{ or } T, D \text{ or } m, \rho, \rho_s, g, \lambda, \nu) \quad [2.1]$$

Here  $Q$  is defined as the volumetric rate of sediment transport. The wave is described by the wave height  $H$  at the toe of the structure and wavelength  $L$  which is a function of wave period  $T$ . Many authors have shown beach slope  $m$  is related to grain diameter  $D$ , therefore  $D$  and  $m$  are not independent parameters. The median grain diameter  $D$  is retained since it was varied in the tests. The geometric parameter  $\lambda$  describes the actual physical size of the model island, for instance the diameter of island. Time  $t$  should be included as a characteristic parameter but since the tests were carried out for distinct prototype time periods (e.g. 0 to 3 hrs. or time for erosion to reach the post) each test can be viewed separately, initially neglecting time effects.

The island tests were performed for storm conditions with plunging breakers which produce much suspended load. Under these conditions bed load moved by shear stress under unbroken waves does not amount to a significant proportion of the sediment transport and hence in the present tests, as well as in the prototype, sediment transport is mainly a result of suspended sediment movement in the surf zone. Since surf zone phenomena are characterized by rough turbulent flow it might be postulated that viscosity should not be included in Equation 2.1. However, as shown in sections 4.2 and 4.4 the morphology of the eroded form of the island is related to viscosity and hence it must be retained as a parameter. The dimensionless relationship for volumetric sediment transport rate  $Q$ , may be written as

$$\frac{Q}{H^3/T} = \phi \left( \frac{gH^2D^2}{L\nu^2}, \frac{H^2}{DL}, \frac{H}{L}, \frac{\lambda}{L}, \frac{\rho_s}{\rho} \right) \quad [2.2]$$

The influence of  $\rho_s/\rho$  has been discussed earlier - Kamphuis (1975a, 1982) and as a result all our coastal models use sand as a mobile bed material. Thus the influence of  $\rho_s/\rho$  was not tested in this series and  $\rho_s/\rho$  was kept the same as in the prototype. The island size  $\lambda/L$  was also kept constant and equal to the prototype value throughout these tests. Wave steepness  $H/L$  was varied in these tests, but in a geometrically similar model this ratio will also be the same as in the prototype.

This leaves the first two parameters which by virtue of the grain size  $D$  cannot be modelled correctly. Thus, these two parameters introduce scale effect. The first parameter is essentially a grain size Reynolds number, expressed in terms of the common wave parameters; the second is a mobility number or Shields parameter. The Reynolds number describes the boundary layer regime. The mobility number represents the ratio of inertia (or disturbing) forces to gravity (or restoring) forces and reflects actual amounts of sediment in motion as well as proportion of sediment in suspension. As scale decreases (larger models), the wave height increases and hence the Reynolds number and the mobility number will both increase resulting in more sediment movement and a larger proportion of material travelling in suspension.

### 3.0 MORPHOLOGICAL DEVELOPMENT

#### 3.1 Description of Morphology

All the island tests with monochromatic waves featured a similar pattern of morphological development. Throughout the tests, the incident waves formed plunging breakers in the vicinity of the radial facing directly into the waves. In most tests sediment agitation and suspension was observed beneath the plunging breakers within the surf zone. Strong longshore currents developed alongside the island forming a longshore trench. The current carried suspended sediment from the zone of plunging breakers and deposited it to form symmetrical wing bars extending out from either side of the back of the island (Figure 3).

Large unidirectional flow dunes clearly defined the location of the longshore current. These dunes abruptly changed to wave induced ripples just outside the breaker line. From the bedform it was apparent that the point of maximum longshore current closely coincided with the zone of greatest bed agitation. This supposition was confirmed with current velocity measurements.

#### 3.2 Rate of Morphological Development

Figure 4A shows cumulative erosion with time for one island test. It reveals that the erosion rate decreases with time as the island approaches dynamic equilibrium form or shape of minimum entropy. Replotting Figure 4A on a log scale as was done in Figure 4B shows a definite change in erosion rate when the leading edge of the erosion scarp infringes on the horizontal drilling platform.

During the erosion process, the waves on the front of the island tend to form an eroding profile which has a relatively constant shape and exhibits a critical depth below which no erosion takes place. The eroding profile has been fully formed at about the time that the erosion reaches the horizontal platform, hence the sudden decrease in erosion rate in Figure 4B. After that time the profile simply erodes back into the island as shown in Figure 5 but since the island is circular, there will be less and less material to erode as the profile approaches the centre of the island. This is reflected in the continuing decrease in erosion rate in Figure 4.

#### 4.0 DIAMETER EFFECTS

The inability to model grain size correctly in the model introduces scale effects as described in Section 2 which may be classified as Inertial Effects (incorrect mobility number) and Viscous Effects (incorrect Reynolds number).

#### 4.1 Inertial Effects

Dimensionless erosion rate is plotted as a function of the mobility number  $H^2/DL$  in Figures 6 and 7. If there were no scale effect, all points for constant sediment size and wave conditions would lie on a horizontal line. If the scale effect were purely a function of  $H^2/DL$ , Figures 6 and 7 would show a straight line. In fact, the lines are curved, indicating that scale effect is largely a function of  $H^2/DL$  but is also influenced by the other parameters. Since  $\rho_s/\rho$  and  $\lambda/L$  were not varied and since along any line in Figures 6 and 7  $H/L$  is constant, the curvature must be a function of the Reynolds number  $gH^2D^2/Lv^2$ . It may be seen in Figure 6 which shows erosion at constant (prototype) time using Froude scaling that as time increases, the curvature of the lines also increases, i.e. there are some secondary considerations. These may be explained directly from Figures 4 and 5. Smaller scale models are at a further state of erosion than larger scale models at any fixed time. This means the average erosion rate over such a period is less as may be inferred from Figure 4. Also the erosion rate is decreased because the constant eroding profile has progressed further into the island for these smaller scale tests, leaving less material to erode.

The latter two effects which may be called "time effects" can be removed by plotting erosion rate for a certain stage of morphological development as was done in Figure 7 where the average erosion rate to the post is plotted. This figure shows less curvature than Figure 6 and essentially the curvature is a result of viscous or Reynolds Number ( $gH^2D^2/Lv^2$ ) effect which is examined further in the next section.

Another way to investigate the effect of the mobility number on island erosion is to plot the time it takes to erode to a certain morphological stage. Figure 8 shows the time required to erode to the post. Once again it is seen that the lines for constant grain size are not straight but curved, reflecting the effect of viscosity.

One reason that sediment transport is highly dependent on mobility number is the fact that the amount of suspended load is closely related to mobility number. Sawaragi and Deguchi (1978) suggest criteria based on the dimensionless parameter  $H/D$  to distinguish between prominence of bed load versus suspended load.

$H/D < 125$	no suspension
$H/D > 200$	sediment is suspended (transition)
$H/D > 300$	suspended load exceeds bed load

The  $H/D$  parameter is identical to  $H^2/DL$  if the model is geometrically similar (then  $H/L$  will be the same in model and prototype). In the island tests  $H/D$  was greater than 300 in most of the finer sand tests (0.105 mm and 0.18 mm) indicating prevalent suspended load. The coarse 0.56 mm sand at all scales and the finer sands at 200 scale were transported almost entirely by bed load, quite unlike the transport mechanism in prototype. The modeling of prototype wave conditions which produce suspended load using typical model scales of 200 to 50 must therefore be performed with a model grain size smaller than 0.2 mm to 0.3 mm ( $H/D > 300$ ) to ensure suspended load is prevalent in the model.

#### 4.2 Viscous Effects

The effects of viscosity are not negligible as often assumed in coastal mobile bed modeling. Because of the flow reversals in wave mechanics often the flow regime in the boundary layer is smooth especially outside the breaking zone. Viscosity effects complicate the analysis in several ways.

Preliminary analysis indicated that the sediment transport increased with an increase in the grain diameter from 0.18 mm to 0.56 mm. It was shown in the previous chapter that bed load is dominant in this grain size range for the scales tested. In order to offer an explanation for this strange variation in sediment transport the boundary layer regime outside the surf zone must be examined. The Shields diagram for unidirectional flow shows that grains become increasingly mobile as the grain size increases from 0.2 mm to 0.6 mm (see Figure 9). This is the region of transition from laminar to turbulent flow in the boundary layer. In this region an increase in grain size intensifies the turbulence within the boundary layer which induces greater sediment mobility. For grain diameters greater than 0.6 mm (for unidirectional flow) the boundary layer flow is fully developed rough turbulent and increases in grain diameter do not cause further increases in sediment mobility. This same phenomenon exists for oscillatory fluid motion. When the island tests with the finer sands are plotted on the flow regime diagram developed by Kamphuis (1975), they indicate smooth flow in the boundary layer which is either laminar or in transition to turbulent. The coarser sand is in the transition region to rough turbulent (see Figure 10), and for the range of scales tested the flow in the boundary layer will be in transition for grain sizes between 0.3 and 4.5 mm. Within this transition zone an increase in grain diameter causes an increase in sediment mobility which translates to greater sediment transport

rates. Similar transition ranges have been suggested by Komar and Miller (1974) and Madsen and Grant (1976).

As the grain size Reynolds number,  $gH^2D^2/Lv^2$  becomes large the boundary layer will become turbulent and the effects of viscosity on bed load may be expected to become negligible. In Figures 7 and 8 there is less curvature through data points corresponding to the tests with smaller scales indicating a reduction in the Reynolds number effect. The remaining curvature is attributable to both remaining Reynolds number effect and secondary influences such as bedform and critical depth.

#### 4.3 Bedform Effect

In the tests with smaller scales and for the two finer sands the existence of bedform indicates that the boundary layer flow is rough turbulent and therefore the effects of viscosity should be minimal. The remaining curvature in Figures 7 and 8 may in part be attributable to bedform since it is a function of the ratio of orbital amplitude to grain diameter which varies with scale. While a varying size of bedform is present in the models, it will be different from the prototype, resulting in scale effect; in fact it is probable that in the prototype under the wave conditions being tested all bedform will be washed out.

The significance of this scale effect may be limited since it has been estimated that the wave energy loss due to the large turbulence brought into the water from the surface by the breaking wave was some hundred times the amount of energy dissipated due to bottom shear stress - (Sawaragi et al (1974)).

#### 4.4 Critical Depth Effect

The critical depth scale effect is important because it has a large impact on the amount of material eroded. Because of the measuring techniques adopted it was difficult to determine the critical depth of erosion accurately. However, if the cumulative erosion on the front half of the island is examined as in Figure 11 a more accurate idea of critical depth effect is obtained.

The cumulative erosion for the profile corresponding to the radial which is perpendicular to the waves displays identical trends observed in cumulative erosion of the front half of the island. This would indicate a variation in cumulative erosion with scale and grain size is largely a two dimensional effect related to critical depth. There is a slight increase in cumulative erosion or critical depth from 200 to 100 scale and then a decrease to the 50 scale. Direct observation of critical depth also confirms it decreases with scale.

Kamphuis (1984) has adapted an equation developed by Hallermeier (1980) for initiation of sediment to describe the critical depth of erosion as follows:

$$H_c = K D^{1/4} T^{3/2} \sinh(kd_c) \quad [4.1]$$

where  $K$  is a constant and  $H_c$  is a wave height which yields critical depth  $d_c$ . The average value<sup>c</sup> of  $K$  found in flume tests by Kamphuis was 0.12 and is identical to the average value of  $K$  for the island tests. This was somewhat fortuitous since the flume tests by Kamphuis were in fact in the middle range of the island tests (i.e. 100 scale). Both flume tests and island tests indicate critical depth is dependent on scale (or  $H^2/DL$ ) and on grain size Reynolds number and therefore  $K$  is not a constant.

The significance of this scale effect would be illuminated if the critical depth in prototype were known. Kamphuis (1984) has fitted a straight line to field results collected by Swart (1974) resulting in the following relation.

$$K = 0.125 + 0.037 H \quad [4.2]$$

Using this equation for  $K$ , the following prototype critical depths are estimated for a wave with an 8 second period using Equation 4.1:

D	Wave Height (m)	K (Eq. 4.2)	Prototype	Laboratory	
			Critical Depth (m) (Eq. 4.2)	Critical Depth (m) 200 scale	Critical Depth (m) 50 scale
0.20 mm	3	0.24	7.6		
	4.75	0.30	10.5	10.0	8.0
	6.5	0.37	12.0	12.0	10.0

The prototype critical depths are very similar to those found in the laboratory. This may indicate that the scale effect from critical depth is small.

## 5.0 THE USE OF REGULAR WAVES

The present tests were performed with regular waves which consistently produced plunging breakers. This very simple artificial wave climate allows a better understanding of the physics involved, but also results in much greater erosion rates than in the prototype case of irregular waves. The regular wave model creates a condition where all waves break at the same point and where the point of maximum longshore current velocity closely coincides with the point of greatest agitation of the bed, resulting in maximum sediment transport rate. For irregular waves, part of the wave spectrum results in spilling breakers, the longshore current velocity distribution is spread over a longer distance perpendicular to the beach and each wave does not break at the point of maximum value of longshore current. Tests which are now underway with irregular waves show that the trough and bar formed by the longshore current as well as the bedform in the

trough are not as pronounced. Also the waves refract further around the island, critical depths remain virtually the same, sediment transport rate is smaller by a factor of 3 to 4 and time to a certain morphological stage is greater by a factor 2.

## 6.0 EXTRAPOLATION TO PROTOTYPE

### 6.1 The Scale Series

The inability to scale down grain size correctly results in the most pronounced scale effect in coastal mobile bed models (Kamphuis 1982, 1975a). A complete understanding of this effect is very difficult because of incomplete theoretical understanding of the sediment transport mechanisms which involve sediment suspension, liquefaction of the bed, percolation and aeration of the surf zone. Also viscous and bedform effects introduce further complexities which are not fully understood. The results from a single physical model test of a previously untested coastal feature cannot therefore reliably describe a prototype e.g. how would one extrapolate from one single point in Figures 6, 7 or 8? One option remaining (until scale effect is fully understood) is a series of tests at different scales. The philosophy of the series of tests is to provide some understanding of the influence of scale effects in the range of scales tested as evidenced by Figures 6, 7 and 8 in the present tests and with this knowledge, attempt to extrapolate to prototype.

### 6.2 Validity of Extrapolation

The present series of tests has revealed the erosion (or sediment transport) rates of the front half of the island for model scales 200 to 50. Any attempt at extrapolation cannot be entirely dependable. However, in some cases extrapolation may be attempted with more confidence than others, for instance extrapolation of the 0 to 3 hr prototype time period (Figure 6A) or the morphological stage to the post, Figures 7 and 8, would be more reliable than longer prototype time periods, (Figures 6B and C) where curvature and differences between the lines of various grain sizes is much more severe. During the shorter prototype time period differences between erosion rates for different grain diameters are not large and the use of smaller grain sizes than the prototype sand aid in extrapolation because the values of  $H^2/DL$  for the finer sands will be greater and closer to the prototype value. It is apparent that the prototype grain diameter should be used in models if longer morphological time segments are used in the extrapolation because of the critical depth effect resulting from differing diameters is large (Figure 8).

Vellinga (1982, 1978) carried out a series of two dimensional dune erosion tests at different scales and grain diameters. In order to establish scaling relationships (based on the fall velocity parameter  $H/Tw$ ) Vellinga built models with different profile distortions and it was discovered that distortion was directly proportional to erosion. Therefore, Vellinga's results can be plotted using the parameters of the present paper by dividing the erosion quantity for a test by the initial profile distortion from a



prototype. The plots for three prototype time periods are shown in Figures 12A, B and C and these figures show the same trends observed for the island tests i.e. the longer time periods show more curvature and a greater difference between the different grain diameters. Vellinga's 5 hr prototype results were enhanced by a test at scale 5 in the Delta flume at Delft. These results have been plotted in Figure 12A and demonstrate that extrapolation is not outside the realm of consideration for shorter prototype time periods.

### 6.3 Extrapolation of Results

An attempt was made at extrapolation using two methods, extrapolating the dimensionless erosion rate for a short prototype time period and extrapolating over a morphological time segment. These two methods were employed to determine the time for the erosion scarp to reach the post at the centre of the island. For the first method an erosion rate was determined for 0 to 3 hrs for the prototype by extrapolation of Figure 6A. The second method was a direct extrapolation of the time to the post (Figure 8). The following results were obtained for regular waves with an 8 second period:

H(m)	time to reach the post (hrs)	
	method 1	method 2
6.5	2-3	3-6
4.75	3-5	5-10

The credibility of extrapolation is demonstrated by the fact that these separate methods yield results of the same magnitude.

The erosion of one prototype island in the Beaufort Sea was monitored by Esso Resources Canada with aerial photographs over the period of three storms in October 1980. During these storms which each lasted less than a day and featured significant wave heights of about 3 m and a wave period of 7 s the island was eroded from the edge of the drilling platform at the top of the 1 in 3 slope to approximately the centre of the island. It is estimated that each storm lasted about 6 hrs, hence the island was effectively subjected to approximately 18 hrs of waves with an approximate significant wave height of 3 m and period of 7 seconds. The extrapolation of model results with 3 m wave height and 8 second period for the morphological time period from the top of the 1:3 slope to the post yield an erosion time of 8 hours for the prototype. Since it was discovered in the model tests with irregular waves that the progression of erosion with the regular wave tests was about twice that with irregular waves, the above number needs to be doubled, giving an approximate estimated prototype erosion time of 16 hours. It must be stressed that both the prototype data and the extrapolation from the models are very approximate but the above comparison looks very promising.

## 7.0 CONCLUSIONS AND RECOMMENDATIONS

1. Scale effects are mainly due to the incorrect simulation of grain diameter.

2. The change in sediment transport rate with scale is primarily due to inertial effects.

3. Viscous effects and the existence of bedform and critical depth scale effects cause secondary influences which make direct extrapolation difficult.

4. To model a previously untested coastal feature, a series of tests must be performed which provides a basis for extrapolation of results to prototype.

5. The influences of the various scale effects have been identified within the scale series but their role in the zone of extrapolation is still relatively unknown. Further research is required at smaller scales.

6. Extrapolation can be performed with some degree of confidence for short prototype time periods and for morphological time segments.

7. Critical depth effects become large between different model grain diameters for the longer prototype times and extrapolation can only effectively be performed from models with the prototype grain size. Over short prototype time periods profile evolution and erosion rates are not much different for the different scales and extrapolation from different grain size curves is possible. Since critical depth effects are minimal in the early time periods finer grain sizes than prototype would help to close the gap on extrapolation to the prototype value of  $H^2/DL$ .

8. At lower values of  $H^2/DL$  or  $H/D$  (Sawaragi and Deguchi suggest a limit of  $H/D = 300$ ) sediment transport will be mainly by bed load in the laboratory and will not resemble a prototype which features predominant suspended load.

## 8.0 ACKNOWLEDGEMENTS

The work presented in this report was supported financially by a grant from the Natural Sciences and Engineering Research Council of Canada (NSERC). The junior author was also supported by an NSERC scholarship during his study at Queen's. The actual model testing involved many individuals and the authors are grateful for the support by this team of dedicated people.

**9.0 REFERENCES**

1. Hallermeier, R.J. (1980) "Sand Motion Initiation by Water Waves: Two Asymptotes", Journal of Waterway, Port, Coastal and Ocean Division, ASCE, Vol. 106, WW3, Aug 1980 pp. 299-318.
2. Kamphuis, J.W. (1975) "Friction Factor Under Oscillatory Waves", Journal of the Waterways, Harbours and Coastal Engineering Division, ASCE, Vol. 101, WW2, May 1975, pp 135-144.
3. Kamphuis, J.W. (1975) "The Coastal Mobile Bed Model", Queen's University Civil Engineering Research Report No. 75, 113 pp.
4. Kamphuis, J.W. (1982) "Coastal Mobile Bed Modelling from a 1982 Perspective", Queen's University Civil Engineering Research Report No. 76, 38 pp.
5. Kamphuis, J.W. (1984) "The Erosional Process along a Till Shoreline", unpublished report to the Deputy Attorney General of Canada, pp. 22-87.
6. Komar, P.D. and Miller, M.C. (1974) "Sediment Threshold Under Oscillatory Waves", Proceedings of the 14th International Conference on Coastal Engineering, Copenhagen 1974, pp. 756-775.
7. Madsen, O.S. and Grant, W.D. (1976) "Quantitative Description of Sediment Transport by Waves", Proceedings of the 15th International Conference on Coastal Engineering, Honolulu 1976, pp. 1093-1112.
8. Mogridge, G.R. (1974) "Scale Laws for Bedforms in Laboratory Wave Models", Proceedings of the 14th International Conference on Coastal Engineering, Copenhagen 1974, pp. 1669-1085.
9. Sawaragi, T. and Iwata, K. (1974) "On Wave Deformation after Breaking", Proceedings of the 14th International Conference on Coastal Engineering, Copenhagen 1974, pp. 481-497.
10. Sawaragi, T. and Deguchi, I. (1978) "Distribution of Sand Transport Rate Across a Surf Zone", Proceedings of the 16th International Conference on Coastal Engineering, Hamburg 1978, pp. 1596-1613.
11. Sayao, O.F.S.J. (1982) "Beach Profiles and Littoral Sand Transport", Ph.D. Thesis, Department of Civil Engineering, Queen's University.

12. Swart, D.H. (1974) "Offshore Sediment Transport and Equilibrium Beach Profiles", Delft Hydraulics Laboratory Publication No. 131, pp. 302.
13. Vellinga, P. (1978) "Moveable Bed Tests on Dune Erosion", Proceedings of the 16th International Conference on Coastal Engineering, Hamburg 1978, pp. 2020-2039.
14. Vellinga, P. (1982) "Beach and Dune Erosion During Storm Surges", Coastal Eng., 6:361-387.

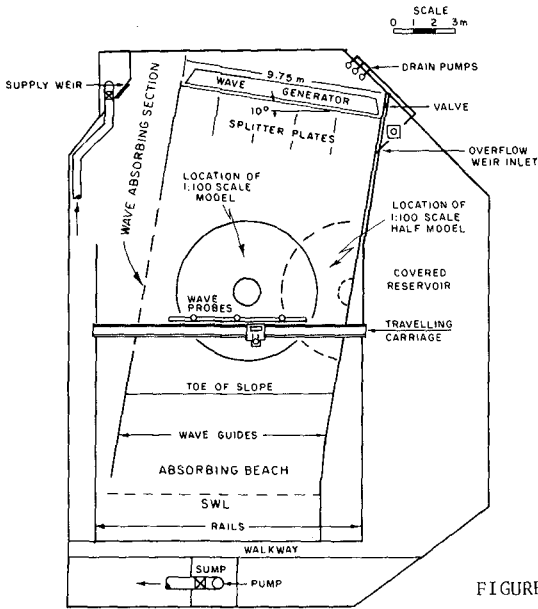


FIGURE 1: MODEL BASIN

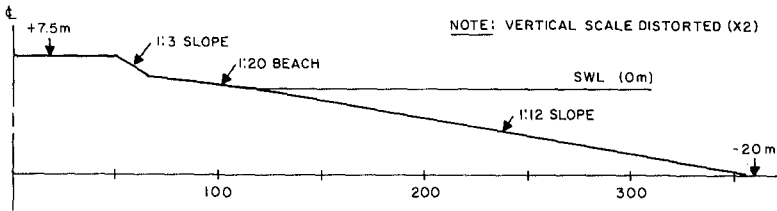
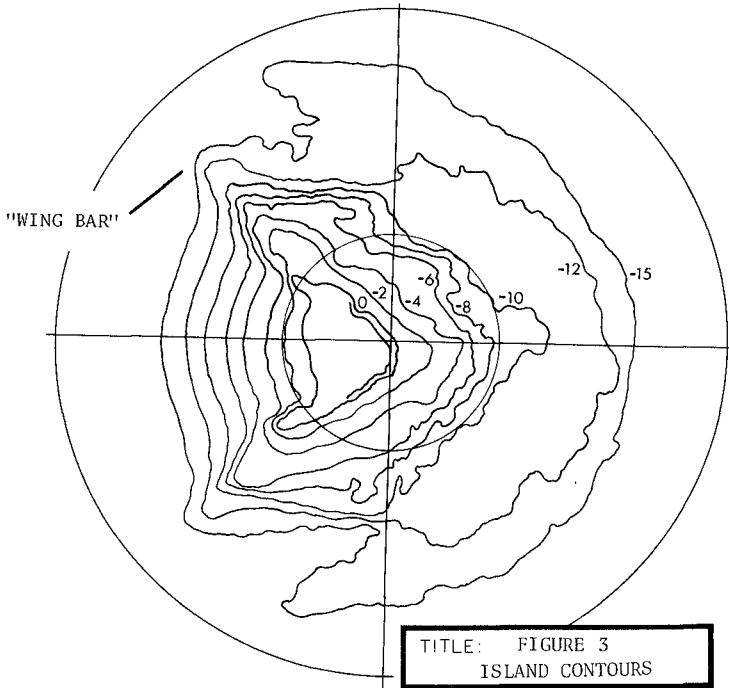
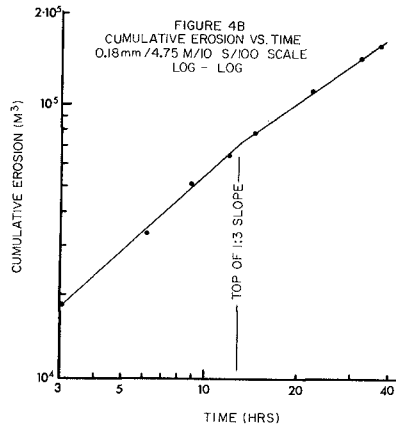
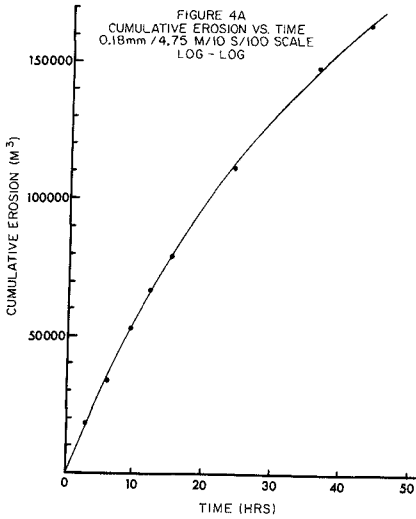


FIGURE 2: PROTOTYPE ISLAND PROFILE



TITLE: FIGURE 3	
ISLAND CONTOURS	
SCALE: 1:100	H: 6.5 m.
TIME: 40 HRS	T: 8 SECS.
D <sub>50</sub> : 0.105 MM	



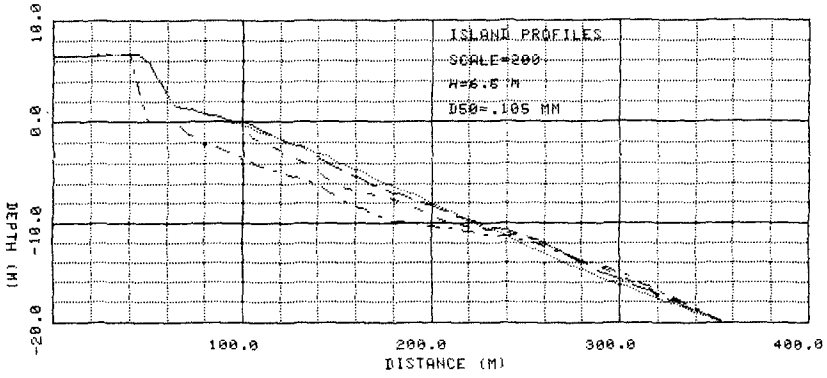
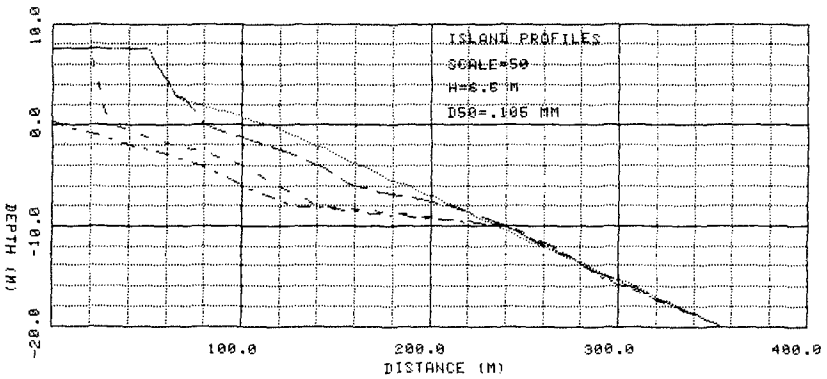


FIGURE 5 A, B: ISLAND PROFILES AT 0, 3, 12, 36 HRS. OR POST



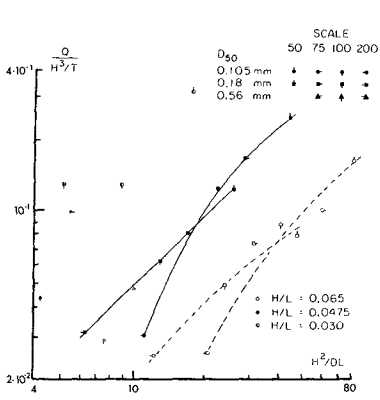


FIGURE 6A: DIMENSIONLESS EROSION VS.  $H^2/DL$   
0-3 HRS. LOG-LOG

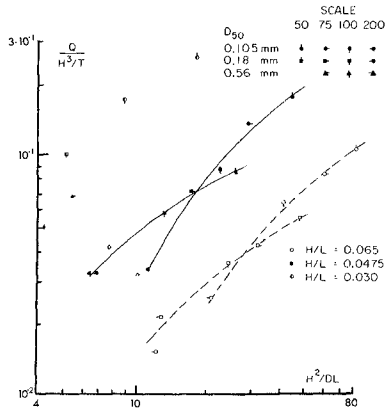


FIGURE 6B: DIMENSIONLESS EROSION VS.  $H^2/DL$   
0-12 HRS. LOG-LOG

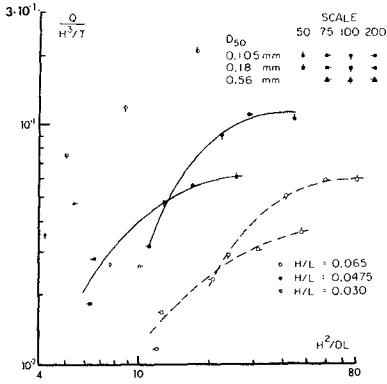


FIGURE 6C: DIMENSIONLESS EROSION VS.  $H^2/DL$   
0-36 HRS. LOG-LOG

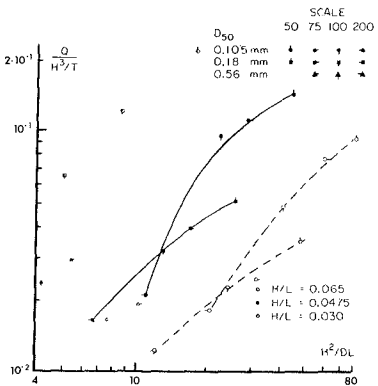


FIGURE 7: DIMENSIONLESS EROSION VS.  $H^2/DL$   
0 HR. TO THE POST LOG-LOG

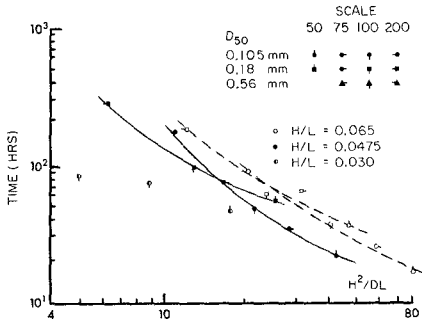


FIGURE 8: TIME TO REACH THE POST VS.  $H^2/DL$  LOG-LOG

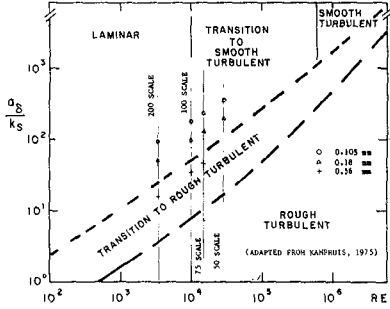


FIGURE 10: FLOW REGIMES

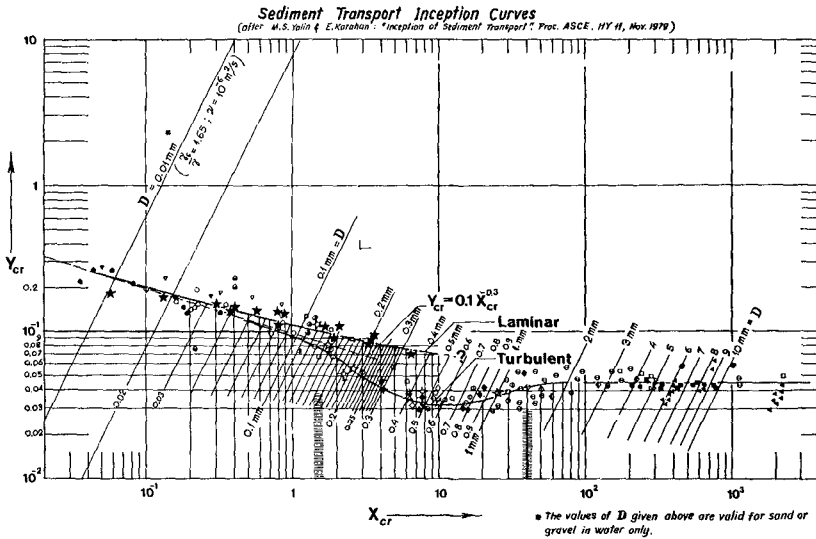


FIGURE 9: SHIELDS DIAGRAM



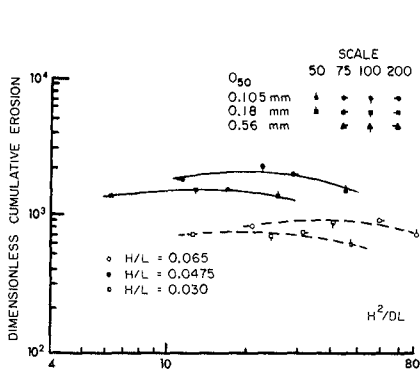


FIGURE 11: DIMENSIONLESS EROSION VS.  $H^2/DL$  0 HR. TO THE POST LOG-LOG

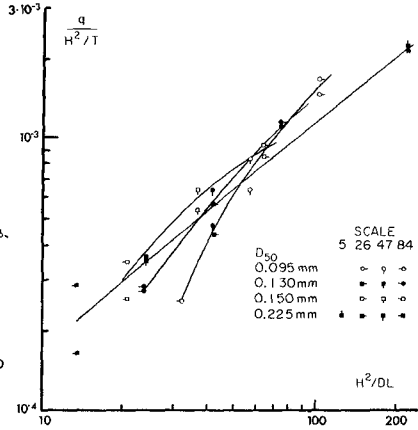


FIGURE 12A: DIMENSIONLESS EROSION RATE VS.  $H^2/DL$  VELLINGA DATA 0 TO 5 HRS. PROTOTYPE

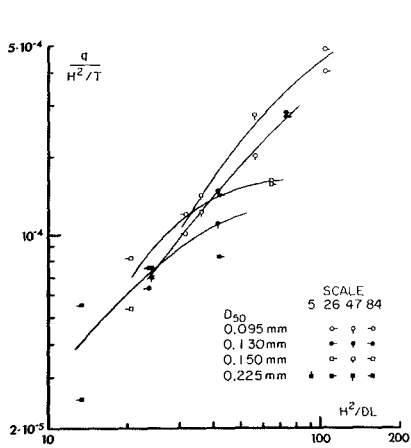


FIGURE 12B: DIMENSIONLESS EROSION RATE VS.  $H^2/DL$  VELLINGA DATA 0 TO 30 HRS. PROTOTYPE

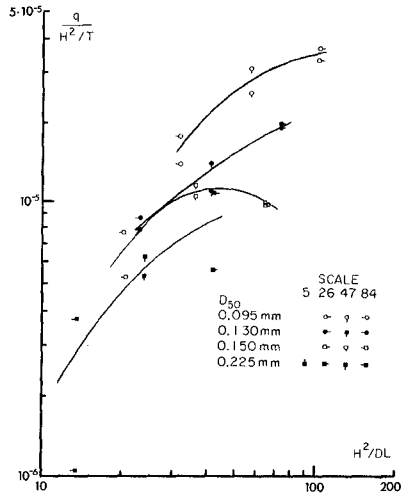


FIGURE 12C: DIMENSIONLESS EROSION RATE VS.  $H^2/DL$  VELLINGA DATA 0 TO 100 HRS. PROTOTYPE

## CHAPTER ONE HUNDRED FIFTY SEVEN

### LOW-PROFILE BARRIER ISLAND OVERWASH AND BREACHING IN THE GULF OF MEXICO

Shea Penland and John R. Suter  
Louisiana Geological Survey  
Coastal Geology Program  
Box G, University Station  
Baton Rouge, La. 70893

#### ABSTRACT

An analysis of 17 tropical cyclone impacts along barrier islands in the Gulf of Mexico has led to the following conclusions: 1) tropical cyclones are the primary mechanism of barrier island overwash and breaching, 2) landward-directed and seaward-directed overwash flow can breach barrier islands, 3) storm track orientation to the shoreline controls the direction of barrier island breaching, 4) shore-normal and right-oblique hurricane impacts breach barrier islands by landward-directed overwash flow, and 5) left-oblique hurricane impacts breach barrier islands by seaward-directed overwash flow.

#### INTRODUCTION

The breaching of low-profile Gulf Coast barrier islands by hurricane impact is controlled by barrier island morphology, storm magnitude, and the type and intensity of other processes that operate on the system (Penland et al, 1980; Simpson and Reihl, 1981; Suter et al, 1982; Penland and Suter, 1984). Due to the asymmetry of the cyclonic wind field and the occurrence of the strongest winds in the northeast storm quadrant, orientation of the storm track to the shoreline controls the direction (landward or seaward) from which barrier island breaching occurs (Figure 1). Analysis of storm orientation and hurricane impacts using historical aerial photographs and tide gauge records of landfalls associated with hurricanes Flossy (1956), Audry (1957), Donna (1960), Carla (1961), Hilda (1963), Betsey (1965), Beulah (1967), Camille (1969), Celia (1970), Carmen (1974), and Eloise (1975) and field investigations of impacts associated with hurricanes Bob (1979), Claudette (1979), Frederic (1979), Allen (1980), Chris (1982) and Alicia (1983) leads to the development of three hurricane process-response models that explain the patterns of low-profile barrier island breaching identified on the Gulf

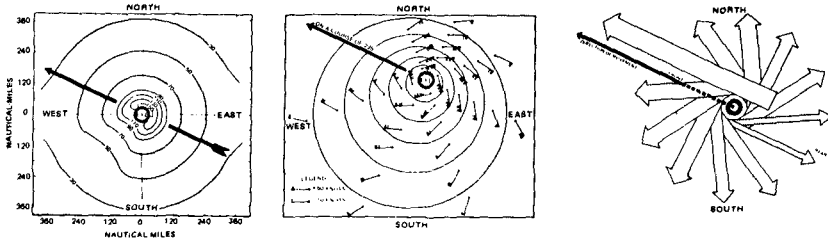


Figure 1. Distribution of pressure, surface winds, and waves within a typical northern tropical cyclone (Crutcher and Quayle, 1974).

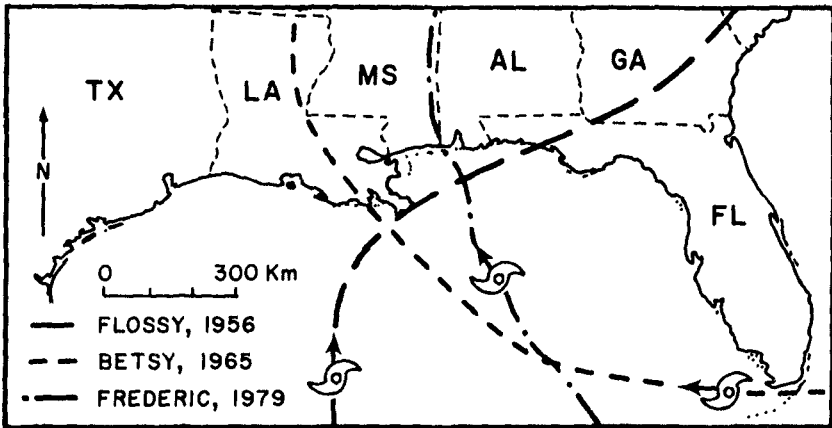


Figure 2. Hurricane Flossy represents a left-oblique impact, Hurricane Betsey represents a right-oblique impact and Hurricane Frederic represents a shore-normal impact.

Coast. These models are:

1. Shore-Normal Hurricane Impact.
2. Right-Oblique Hurricane Impact.
3. Left-Oblique Hurricane Impact.

Case studies for hurricanes Frederic 1979 (shore-normal impact), Flossy 1956 (left-oblique impact), and Betsey 1965 (right-oblique impact) are presented illustrating each type of hurricane impact (Figure 2).

#### LANDWARD-DIRECTED OVERWASH FLOW

For shore-normal hurricane impacts, peak surge and strongest winds occur pre-landfall and are focused onshore to the right side of the storm track. Landward oriented overwash features and barrier island breaches are concentrated to the right of the storm. Left of the storm, somewhat weaker winds are directed offshore. If the lagoon is sufficiently wide and shallow, offshore wind set-up can pile water against the backbarrier, creating the potential for minor seaward overwash, evidence of which may be masked by subsequent landward overwash flow. The breaching associated with hurricane Frederic (1979) at Dauphin Island and Gulf Shores in Alabama and at Perdido Key and Santa Rosa Island in Florida is representative of a shore-normal impact (Figure 3).

For right-oblique hurricane impacts, the peak storm surge precedes the storm and the strongest winds are directed onshore. In this situation major landward overwash and barrier island breaching takes place right of the storm. Because of the orientation of the wind field, the potential exists for minor seaward breaching to occur to the left of the storm. Hurricane Betsey (1965) is representative of right-oblique impact (Figure 4).

#### SEAWARD-DIRECTED OVERWASH FLOW

For left-oblique hurricane impacts, the peak storm surge follows landfall. Due to the orientation of the storm track, the strongest winds are initially directed offshore. This results in a significant water level set-up against the backside of the barrier island and leads to major seaward overwash and breaching left of the storm track. With hurricane passage the direction of overwash switches onshore, enlarging the breaches generated by the earlier seaward overwash. Hurricane Flossy (1956) is representative of a left-oblique impact (Figure 5).

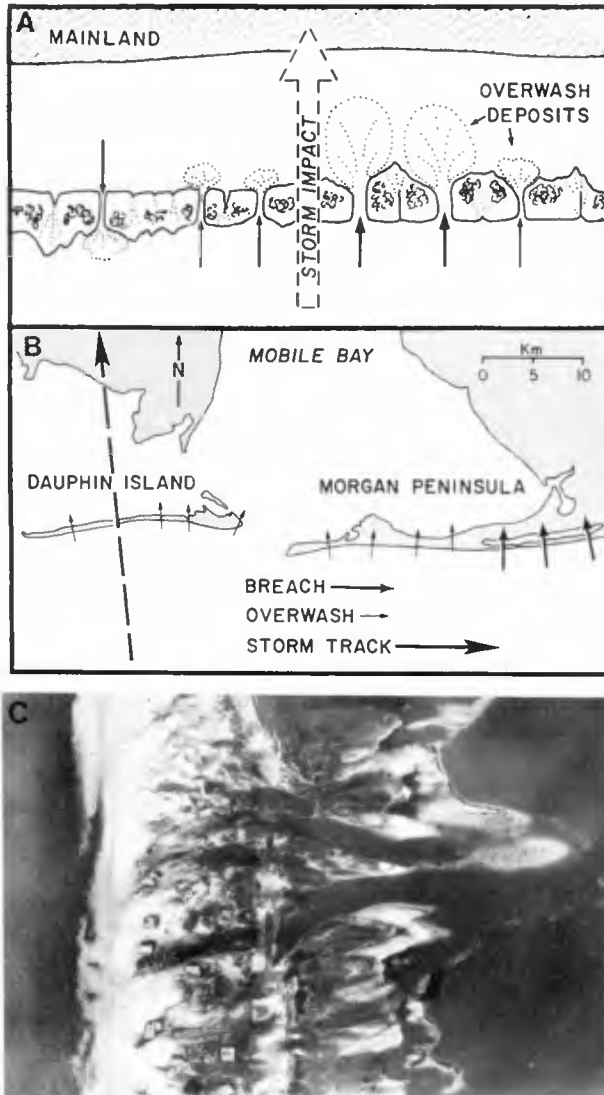


Figure 3. A) Shore-Normal Hurricane Impact Model. B) Hurricane Frederic impact in Alabama. C) An overwash channel associated with hurricane Frederic dissects washover fan spreading into the Mississippi Sound.

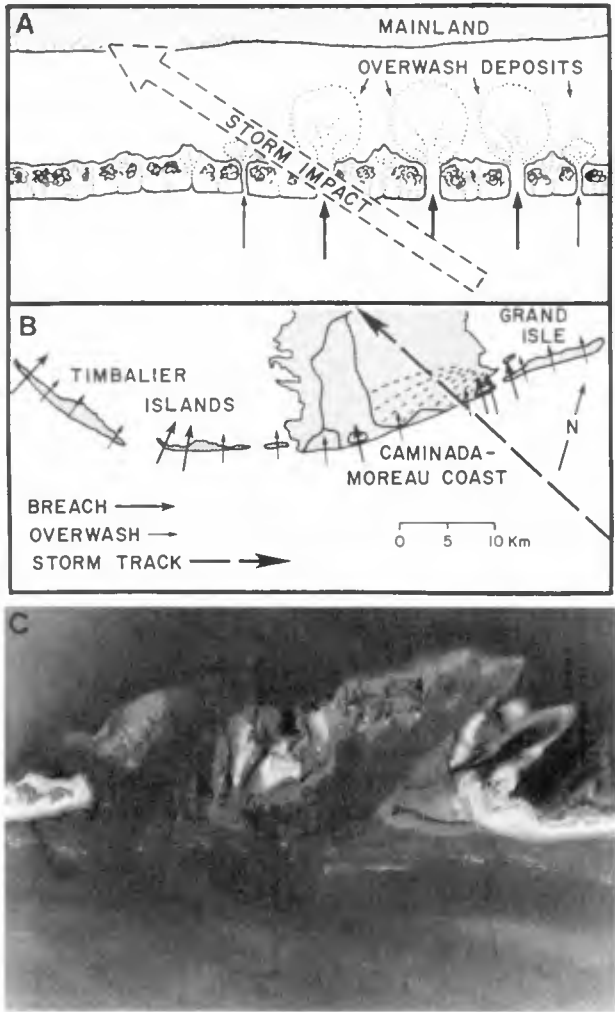


Figure 4. A) Left-Oblique Hurricane Impact Model. B) Hurricane Betsey impact in Louisiana. C) a land-ward oriented beach through Caminada Pass spit. Multiple wash-over fans are deposited in Caminada Bay.

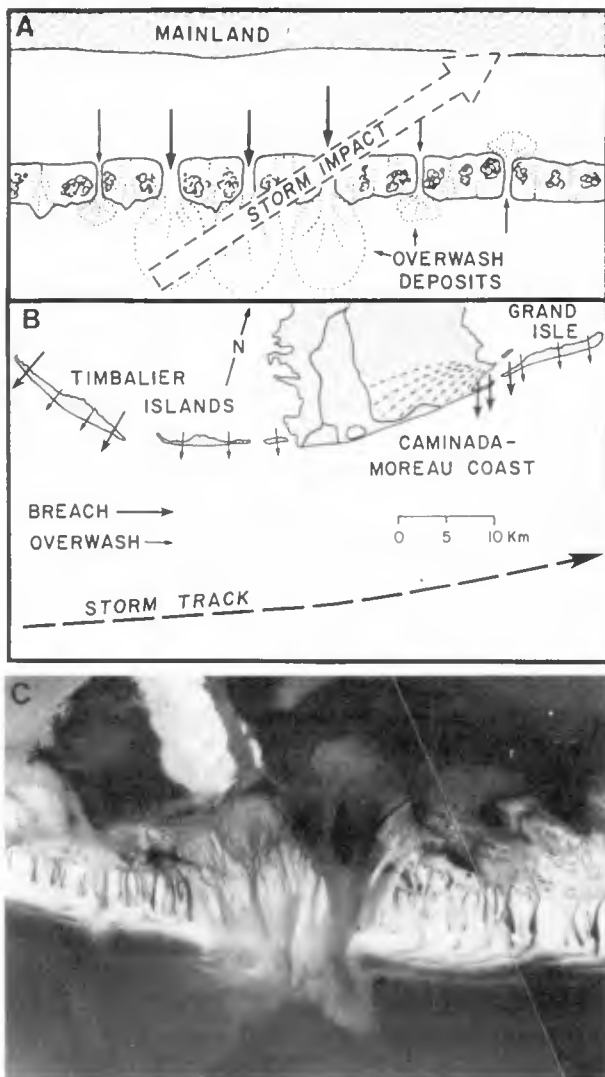


Figure 5. A) Right-Oblique Hurricane Impact Model. B) Hurricane Flossy impact in Louisiana. C) a seaward oriented breach through the western end of Timbalier Island. Note the seaward oriented washover fan spreading across the surf zone into the Gulf of Mexico.

## CONCLUSIONS

The analysis of 17 hurricane and tropical storm impacts along barrier islands on the U.S. Gulf Coast leads to the following conclusions:

1. Storm overwash associated with tropical cyclone impact is the primary mechanism of Gulf Coast barrier island breaching.
2. Barrier islands can be breached by landward-directed or seaward-directed overwash flow.
3. Storm track orientation to the shoreline controls the direction from which barrier island breaching occurs through overwash flow.
4. Shore-normal and right-oblique hurricane impacts breach barrier islands by landward directed overwash flow.
5. Left-oblique hurricane impacts breach barrier islands by seaward directed overwash flow.

## REFERENCES CITED

- Crutcher, H.L., and Quayle, R.G., 1974, Mariners worldwide climatic guide to tropical storms at sea: Naval Weather Service Command, Naval Weather Environmental Detachment, Asheville, NC, 114 p. + 312 charts.
- Penland, S., Nummedal, D. and Schramm, W.E., 1980, Hurricane impact at Dauphin Island, Alabama. Coastal Zone '80, American Society of Civil Engineers, p. 1425-1449.
- Penland, S. and Suter, J.R., 1984, Process-response models for Gulf Coast barrier island breaching. Transactions - Gulf Coast Association of Geological Societies, p. 397-400.
- Simpson, R.H. and Reihl, H., 1981, The hurricane and its impact: Louisiana State University, Press, Baton Rouge, 398 p.
- Suter, J.R., Nummedal, D., Maynard, A., and Kemp, P., 1982, A process-response model for hurricane washover: Proc. 18th Int. Conf. Coastal Eng., American Society of Civil Engineers, p. 1459-1478.



## CHAPTER ONE HUNDRED FIFTY EIGHT

### A NUMERICAL HINDCAST OF STORM CURRENTS ON THE NORWEGIAN SHELF

Cortis K. Cooper, A. M. ASCE\*

#### INTRODUCTION

##### Objectives and Tasks

This paper describes an initial effort to model storm-driven currents and surge in the region indicated in Figure 1. The model results ultimately will be used in the design and operation of offshore oil platforms in the region.

The study consisted of four major tasks: 1) review of the data base and selection of the hindcast storms, 2) hindcast of the selected storms, 3) set-up and testing of the current model, and 4) hindcast of currents for the selected storms.

##### Description of Study Area

Current data were obtained from sites shown as solid circles in Figure 1. Each site consisted of an array of at least four Aanderaa current meters. Meters were typically placed at 50, 100, and 150 m below still water level, and at a few meters above the bottom.

Topographic effects play a major role in the shelf dynamics of the region. The Norwegian Trench is a dominant bathymetric feature with a characteristic depth of 300 m. Its outer edges are indicated by the dashed line in Figure 1. To the west of the trench, lies the Møre Plateau, a flat plane with an average depth of 150 m.

The worst storm conditions occur between late fall and early spring when the water column is generally well mixed. The region intersects the primary wintertime cyclone path and lies close to the average position of the polar front. Hence storms occur almost continuously during the winter season. Major storms in the region are extratropical, lasting for days. The region is too far south to be affected by the "polar low".

The frictional influence on shelf dynamics is relatively small, thus currents exhibit a strong inertial response (50 cm/s) during many storms. Within 50 km of the coast the response is affected by storm-induced alongshore pressure gradients.

The Norwegian Coastal Current is an important flow feature in the area. It flows from south to north through the Trench with a mean speed of 30 cm/s. However, the mean is occasionally interrupted by strongly baroclinic shelf waves which can generate surface currents of 150 cm/s (15).

\*Petroleum Research and Development, Conoco Inc., Ponca City, OK 74603.

Tidal currents are primarily semidiurnal and of order 40 cm/s in magnitude. The banks and submarine canyons are known to affect currents, sometime dramatically in the form of splitting and vortex shedding (12).

### Preview

The next section briefly describes the model formulation. Readers interested in more details should refer to Cooper and Pearce (9,10).

The third section describes the initial application of the model. During this phase of the study it was found that the model solution was dominated by a strong seiche. The seiche was caused by the reflective boundary conditions used in the initial grid system.

Following the difficulty with the boundary conditions, a review of existing techniques for specifying boundary conditions was performed and this is summarized in the fourth section. Readers should find this of general interest since a synthesis is absent in existing literature.

The fifth section describes the final grid system including a brief discussion of model sensitivity, and the sixth section presents some results from the storm hindcast, and discusses some of the reasons for the observed discrepancies between the model and data. The final section summarizes the previous sections, and describes the efforts presently underway to improve these efforts.

### MODEL FORMULATION

The model is based on the primitive barotropic equations. The form on which they are applied in this application is numerically similar to the shallow water wave equations.

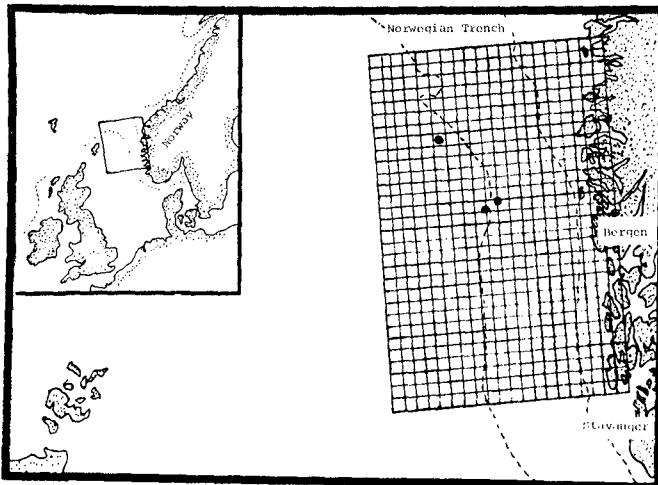


Figure 1: Model grid used in initial runs. Element size is 15.7 km.

### Governing Equations

The model uses the linearized momentum equations:

$$0 = \frac{\partial u}{\partial t} + \frac{\rho_s}{\rho} g \frac{\partial \eta}{\partial x} - N_h (\nabla^2 u) - \frac{\partial}{\partial z} \left( N_v \frac{\partial u}{\partial z} \right) - fv + \frac{1}{\rho} \frac{\partial P_a}{\partial x} + \frac{g}{\rho} \int_0^z \frac{\partial \rho}{\partial x} d\xi,$$

$$0 = \frac{\partial v}{\partial t} + \frac{\rho_s}{\rho} g \frac{\partial \eta}{\partial y} - N_h (\nabla^2 v) - \frac{\partial}{\partial z} \left( N_v \frac{\partial v}{\partial z} \right) + fu + \frac{1}{\rho} \frac{\partial P_a}{\partial y} + \frac{g}{\rho} \int_0^z \frac{\partial \rho}{\partial y} d\xi,$$

where the symbols are defined as follows:

- t the time variable
- x, y the horizontal coordinates in a right-handed Cartesian coordinate system
- z the vertical coordinate, measured as positive downward from SWL
- u, v the horizontal velocity components in the x and y directions, respectively
- $\rho_s$  the density of the fluid, where the s subscript indicates the value at the surface
- g the gravitational constant (9.8 m/s)
- $\eta$  the water height of the free surface above SWL
- $N_h$  the horizontal eddy-viscosity coefficient
- $N_v$  the vertical eddy-viscosity coefficient
- f the Coriolis parameter  $[-2\omega \sin \phi]$  where  $\omega$  is the angular velocity of the earth and  $\phi$  the latitude
- $P_a$  the atmospheric pressure
- $\nabla^2$  the Laplacian operator  $\left[ = \frac{\partial^2}{\partial x^2} + \frac{\partial^2}{\partial y^2} \right]$ .

Note that the vertical velocity is assumed negligible. The density-gradient term was neglected in this application since adequate hydrographic data was unavailable.

The other governing equation used in the model is the continuity equation

$$\frac{\partial U}{\partial x} + \frac{\partial V}{\partial y} = \frac{\partial \eta}{\partial t},$$

where

U and V are the mass fluxes per unit length in the x and y directions, respectively.

### Boundary Conditions

The boundary conditions at the surface are

$$\tau_{sx} = \left[ -\rho N_v \frac{\partial u}{\partial z} \right] \Bigg|_{z=0}, \quad \tau_{sy} = \left[ -\rho N_v \frac{\partial v}{\partial z} \right] \Bigg|_{z=0},$$

where  $\tau_{sx}$  and  $\tau_{sy}$  are the specified shear stresses at the surface in the x and y directions, respectively.

At the bottom a linearized friction law is used

$$\tau_{bx} = [\rho c_b u] \Big|_{z=H}, \quad \tau_{by} = [\rho c_b v] \Big|_{z=H},$$

where  $\tau_{bx}$  and  $\tau_{by}$  are the bottom shear stresses and  $c_b$  is a drag coefficient.

There were insufficient observations to provide boundary conditions on the horizontal boundaries so assumptions had to be made. Initially it was assumed that

- the mass fluxes perpendicular to the coastline were zero;
- the alongshore surface gradient on the cross-shelf boundaries was zero
- the amplitude at the open ocean boundaries was the barometric water rise (i.e. the inverted barometer effect).

#### Numerical Solution Technique

The governing equations and boundary conditions are transformed using the Galerkin technique. A cosine is used as the basis function in this model. The technique explicitly eliminates  $z$  from the transformed equations and greatly simplifies the eventual solution process. The dependence of  $u$  and  $v$  on  $z$  is implicitly retained in the final equations and the  $u$  and  $v$  velocity profiles can be regained whenever desired. A summary of the transformation is given in Cooper and Pearce (9). The method was originally suggested by Heaps (17) and has been used by others (11).

The transformed equations are solved on a staggered finite difference grid system using a "leap-frog" explicit scheme attributed to Lilly (21).

The horizontal grid used in the initial model consisted of 30 X 20 elements of 15.7 km each as shown in Figure 1. The grid was a compromise between the resolution needed to model the steep topographic features in the region, and the long integration times needed to model the regional storms. A more extensive grid was considered but the additional expense was not felt justified given the preliminary nature of the study.

#### INITIAL APPLICATION

##### Model Setup

The model uses three empirical coefficients to parameterize turbulent processes: bottom friction, vertical eddy viscosity, and lateral eddy viscosity. Values for these coefficients were based on equations available in the literature.

The bottom friction coefficient was derived using a Manning's coefficient for "straight and uniform earth". This suggests a value for the model coefficient of roughly 0.2 cm/s.

The vertical eddy viscosity is typically the most influential parameter for relatively deep water areas such as the Norwegian coast. Estimates in the literature for  $N_V$  vary by several orders of magnitude, but many of these estimates can be quickly discarded because of poor quality. Cooper and Pearce (9) successfully used a relationship suggested by Townsend (30) in their application in relatively shallow water. Ramming and Kowalik (25) offer a similar expression for shallow water which gives a value of about one-half that suggested by (30). Both expressions are proportional to the water depth—a reasonable assumption for shallow water. However, as one moves into deeper water it can be soundly argued that  $N_V$  reaches an upper limit which is totally dependent on the primary energy source - in this case wind. Ramming and Kowalik (25) suggest the upper bound for  $N_V$  is given by:

$$N_V = 4.7 \times 10^{-4} W^2/f$$

where  $W$  is the wind speed.

Substituting reasonable values for the Norwegian shelf gives  $N_V = 40 \text{ cm}^2/\text{s}$  for a 10 m/s wind. The good experience with the Townsend relationship (30) suggests the doubling of the constant is in order, giving  $N_V = 80$  - the value used for these initial runs.

The model can include a vertical variation in the eddy viscosity, and this is particularly useful in the case of stratified oceans. There are also physical arguments which suggest the viscosity should vary in the vicinity of a sheared surface. For this application the viscosity was kept constant in the vertical because stratification was negligible during the storms of interest, and because field data has not yet resolved the variation of viscosity near the sea surface.

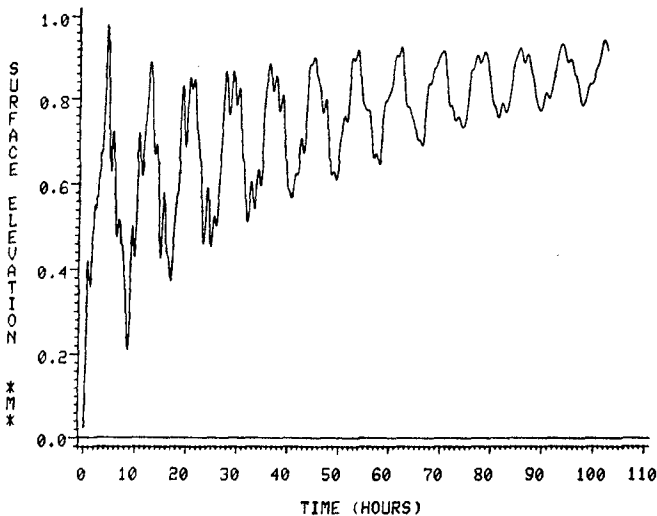


Figure 2: Modeled time series of surface elevation at the coast for initial model grid.

The horizontal eddy viscosity is primarily needed to account for subgrid turbulence, and advective terms. Previous experience by other modelers suggest a value on the order of  $10^8 \text{ cm}^2/\text{s}$  (29).

Since there were inadequate observations along the boundary, it was necessary to make some assumptions. Initially the conditions were specified as described in the previous section. Similar boundary conditions have been used in many shallow water current and surge models.

The model was forced with a spatially constant wind blowing from the south. Wind speed was ramped in time; that is it was increased from zero at model start-up to 10 m/s at 20 hours. No tidal forcing was included.

#### Model Results

Figure 2 summarizes the essential result from the early model runs. The figure shows a time series of surface elevation at a coastal location. An oscillation with a well defined period of 5.5 hours is evident.

The oscillation in the figure corresponds to the seiche period or fundamental free wave mode of the basin in the cross-shelf direction. This is easily shown by substituting the characteristic dimensions of the model basin into the analytic solution given in Lamb (19). Note that the open boundary is a node, and hence the analytic solution in (19) must be doubled.

The seiche is a numerical aberration which results from the ocean boundary conditions. These conditions reflect all incident wave energy (26). Hence, when the wind first starts, it generates free gravity waves within the model domain. These waves eventually impact the ocean boundaries and are reflected back into the model domain. The reflected waves serve to further excite the basin because their frequency is the fundamental mode.

It is clear from these results that a further refinement of the ocean boundary conditions is needed. Some of the alternatives are reviewed in the following section.

#### OVERVIEW OF HORIZONTAL BOUNDARY CONDITIONS

Having adequate data along the outer boundary of a geophysical fluids model is as rare as the proverbial hen's tooth. Thus assumptions must be made. A review of the literature revealed five types of boundary conditions which have been used in shallow water wave models: 1) variable specification, 2) telescoping, nested or stretched grids, 3) energy absorbing elements, 4) Sommerfeld radiation condition, and 5) free/forced wave modes.

Each of these is summarized below including: a description of the method, examples of previous applications, advantages, and disadvantages. It should be kept in mind that the discussion applies only to the shallow water wave equations.

#### Variable Specification

In this technique, one or more of the dependent variables are specified on the boundary. For the initial runs described above,  $\eta$  on the cross-shelf boundary is set to  $\eta$  at the internal element normal to the boundary at each

time step. In other words a one-sided spatial difference across one element is used. On the alongshore boundary,  $\eta$  is set to the inverted barometric rise - in essence a specified constant.

Variable specification has dominated surge modeling. For instance Beardsley and Haidvogel (1) specified  $\eta$  equal to the inverted barometer effect along all ocean boundaries. Forristall et al. (13) specified the flow normal to the boundary equal to zero on the alongshore boundary, and the gradient of the flow equal to zero on the cross-shelf boundaries.

The major advantage of this approach is that it is simple to implement in the code of a numerical model. In addition, the conditions perform reasonably well for forced steady-state flows such as Ekman transport because they will allow realistic alongshore pressure gradients to develop.

The major disadvantage of the approach is that it reflects incident waves. In the case of one-sided spatial differences or constants such as used in this model, the condition is totally reflective as concisely demonstrated by Reid (26).

Fortunately, for many applications reflections are not important. For example, in the case of storm surge models, the grid systems are in predominately shallow water. Two factors work in favor of the modeler: 1) the system is frictionally dominated so reflections are rapidly dampened, and 2) the travel time of long waves is large relative to the model integration time so reflections do not have time to hit the boundary and return to the coast (the primary area of interest). Reflections are also not a problem in quasi-steady or steady-state problems such as (10). Unfortunately, none of these factors apply for the Norwegian Shelf Model. In other words, the system is not frictionally dominated, nor is the integration time short. Furthermore, transient conditions are of major interest.

#### Telescoping, Nested and Stretched Grids

The basic idea common to these approaches is that the element size is a function of space.

In the stretched grid, the size changes smoothly and is "mapped" onto a constant element size using a transformation. Examples include Butler and Sheng (6) and Birchfield (2).

Telescoping grids change the element size suddenly. An example of a telescoping grid using three sizes of elements is given by Greenberg (16). The solution between the grids is coupled in time, allowing waves to propagate across the grid interfaces.

Nested grids solve the system several times. They begin by using a coarse grid, and the resulting solution is used to provide the boundary condition for a smaller "nested", fine scale grid which lies within the large grid. The method does not allow "feedback" from this "nested" grid to the large grid. The earliest example of such an approach is Reid and Bodine (27).

The advantages of these approaches are: 1) the open boundary is moved far away from the area of primary interest thus minimizing the influence of assumptions made at the boundary, and 2) the boundary can be moved to a

region where more reasonable assumptions can be made. Computational costs are minimized by using a larger element size in regions of less interest, or smaller gradients.

There are a number of problems with this approach besides the obvious inelegance and increase in computational cost. For instance, the technique will numerically distort waves as shown by Lewis et al. (20), and Browning et al. (4). In addition the nested grid does not influence the external one, and this is not realistic in general.

#### Energy Absorbing Elements

The basic idea in this approach is to dissipate wave energy when it hits the ocean boundary. This has been done in a number of ways. Busby and Timpson (5) added elements to the outer perimeter of their grid, and they specified large damping coefficients in these elements. These elements are the numerical analogue to "horse hair mats" used in laboratory wave tanks.

The approach is conceptually simple and easy to set up. However, it has a number of disadvantages in that it:

- requires extensive iteration in selecting the model damping parameters. It is not obvious a priori which parameters will minimize reflection and maximize energy absorption;
- is computationally expensive for the study of long wave phenomena because many damping elements will have to be added in order to get effective damping;
- distorts waves running tangentially to the boundary; and
- generates an artificial alongshore pressure gradient for the case of cross-shelf boundaries in the presence of wind forcing. This occurs because the alongshore Ekman transport will encounter undirectional resistance.

#### Sommerfeld Condition

This approach runs a close second in popularity behind the variable specification technique. The Sommerfeld condition can be written as:

$$\frac{\partial \phi}{\partial t} + c \frac{\partial \phi}{\partial x} = 0 \quad [1]$$

where  $\phi$  is either  $U$  or  $\eta$ ,  $c$  is the wave celerity, and the  $x$  direction is assumed normal to the boundary.

The Sommerfeld condition is the proper boundary condition for freely propagating waves at a boundary with infinite extent. Free waves are governed by the wave equation - a hyperbolic equation. The primitive barotropic equations in their full form lie somewhere between hyperbolic and parabolic, but degenerate into the wave equation in the absence of rotation, wind forcing and viscous effects. If these terms are neglected then the Sommerfeld condition does apply to the primitive equations.



An alternative form of the Sommerfield condition has often been used with primitive equation models:

$$U = c \eta + K \quad [2]$$

The equation can be derived by writing the Sommerfield condition for both  $U$  and  $\eta$ , then using the continuity equation to derive two differential equations - one in space and the other in time. The solution to the two equations is of the form [2]. The constant,  $k$ , is usually taken as zero based on physical arguments.

The value for  $c$  in [1] and [2] must be determined, and in general this requires knowledge of the dispersion relationship for the waves in question. Unfortunately, the relationship is not generally known. Orlanski (24), Camerlengo and O'Brien (7), and Miller and Thorpe (22) suggest methods to calculate  $c$  using one-sided differencing methods. However, for homogeneous fluids the value for  $c$  is generally taken as the shallow water wave speed,  $\sqrt{gH}$ , where  $H$  is the local water depth. This of course neglects rotational effects.

Vastano and Reid (40,41) used [1] in the study of tsunami response. They found that the technique was limited by the fact that [1] only radiates waves which hit the boundary at a normal angle - oblique waves will be partially reflected. Mungall and Reid (23) present a modification of [1] which allows radially spreading waves to scatter outward through a rectangularly bounded basin. Additional studies by Hebenstreit et al. (18) show the methods gives satisfactory results.

Reid and Bodine (27) appear to be the first to have used [2]. They studied the free wave propagation of storm surge in Galveston Bay. Wurtele et al. (42) used [2] to compare with the results from Vastano and Reid (40,41). Wurtele et al. (42) looked at the 2-D problem in a rectangular grid, and used the normal component of velocity at an internal grid to calculate  $\eta$  on the boundary. They found only weak reflections and no instabilities.

The obvious advantage of these radiation conditions is that they will allow free waves to propagate out of the model boundaries much as they would in the real world. Previous work clearly indicates that the conditions can be successfully used in the study of many practical free wave problems such as tsunamis.

The technique has some limitations in that it cannot include nonlinearities, rotation, or forced waves.

The last limitation is clearly indicated in the theoretical foundations of the Sommerfield condition; yet many investigators have ignored this fact. For example, Heaps (17) used [2] in the study of wind-driven surge in the Irish Sea. Similarly, Blumberg and Kantha (3) used a form of [1] to study wind-driven synoptic currents on the Eastern U.S. continental shelf.

Application of [1] or [2] to the forced wave problem is not theoretically justified, and can lead to substantial errors particularly in the case of quasi-steady or steady flow. The condition [1] or [2] requires that a pressure gradient be set up in order for flow through the boundary to exist. In the case of wind-driven flow it is clear that flow can occur through the boundary in the

absence of a pressure gradient. Thus when [1] or [2] is used in wind-forced problems, an artificial pressure gradient is established.

The errors which results when [1] or [2] is used for the forced wave problem are illustrated in Figure 3. The figure shows the velocity profiles in an infinitely long channel of constant depth with a constant wind stress. Two different types of models are shown. The linear profile denoted by "Galerkin" is the steady-state result for a constant eddy viscosity model. It can be generated using the Galerkin model by specifying  $\eta=0$  or  $d\eta/dx=0$  at the downwind boundary. The dashed profile denoted by "Galerkin w. rad." is the velocity profile using a radiation boundary condition. Note the velocity has been decreased by roughly a factor of two. This is caused by the artificial pressure gradient generated by the radiation condition. A similar result is found for the vertically averaged model, also illustrated in the figure.

#### Forced/Free Wave Solution

As was pointed out above, the Sommerfield radiation condition is not really appropriate for the study of wind-driven or forced flow. In an effort to remove the forced restriction, Røed and Smedstad (28) developed a method which separates the primitive barotropic equations into two modes: a local or forced mode, and a global or free mode. Using a specialized topography illustrated in Figure 4, Røed and Smedstad (28) were able to eliminate the need for any boundary conditions for the local solution. The boundary condition for the global solution is [1].

The modal approach is theoretically attractive. However, a number of major assumptions regarding topography were made by (28). It remains to be seen whether the technique can be applied to the more general case.

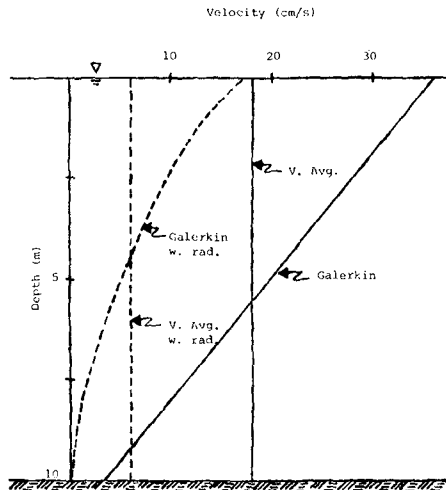


Figure 3: Comparison of profiles from two types of models using different downstream boundary conditions.

## REVISED GRID SYSTEM RESULTS

All of the techniques identified in the previous chapter were considered for this study. Most would have required extensive program recoding or expansion of the existing grid system. The costs associated with these changes could not be justified given the preliminary nature of the study.

A compromise was developed which could be quickly implemented. It consisted of adding 10 columns to the western boundary of the grid shown in Figure 1 resulting in a 30 x 30 grid. No wind stress was imposed on these additional elements, and dissipation parameters in the elements were increased. In addition a radiation condition in the form of [2] was implemented in the model code along the western boundary.

On the lateral boundary,  $dn/dx$  was set to zero as in the initial grid. Adding additional rows on the cross-shelf boundaries as was done on the western boundary would have generated an artificial alongshore pressure gradient for reasons cited in the previous section. Seiching tendencies in the alongshore direction were minimized by eliminating the alongshore bathymetric gradients. This is not unreasonable for this section of the coast.

The model was run using the same forcing as in the initial run (see the third section above). Figure 5 shows representative results using the same empirical coefficients as in the initial run. Comparing this figure to Figure 2 indicates that the radiation condition does substantially reduce the seiche. As indicated in Figure 6, further reduction is achieved by increasing the vertical eddy viscosity and bottom friction by an order of magnitude in the western 10 columns. The figure should be compared to 2 to see the substantial improvement obtained with the revised boundary conditions.

## HINDCAST RESULTS

Once the seiche was removed from the model, it was used to hindcast an actual storm event. Data was available for a major storm which occurred in late October 1974. Cardone (8) provided synoptic wind and pressure fields for the storm at six hour intervals. He used post-synoptic techniques, with data based on land, buoy, and ship data, as well as surface weather maps.

Figure 7 shows the wind vectors hindcasted by (8) near Bergen, on the Norwegian coast. Peak winds reached roughly 20 m/s. Wind direction was primarily from the north, shifting from northeast to northwest during the course of the storm. Spatial wind gradients were generally not large over the scale of the model grid.

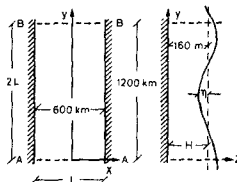


Figure 4: Topography of basin used in the free/forced wave boundary condition studies of Roed and Smedstad

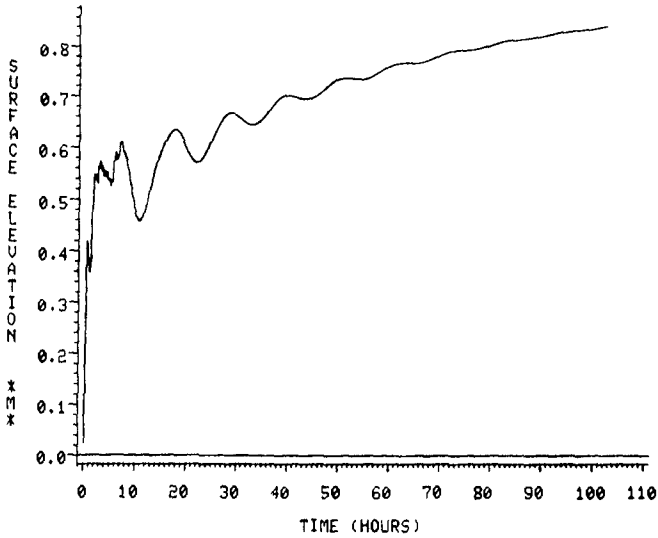


Figure 5: Modeled time series of surface elevation at the coast. Model grid is the same as Figure 2 except five additional columns have been added as well as a radiation boundary condition on western boundary.

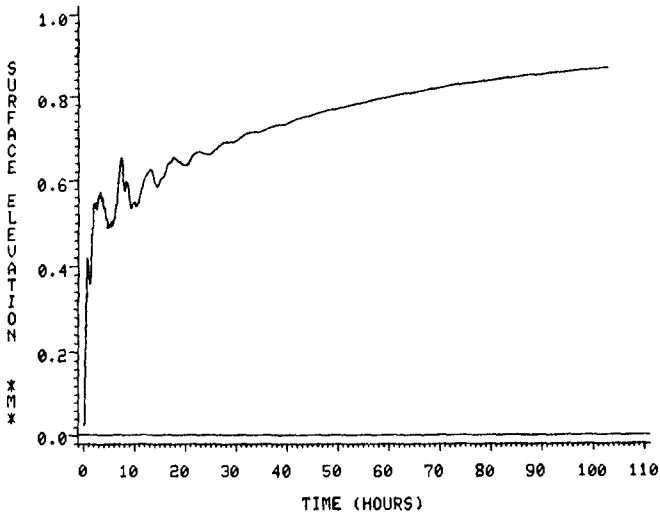


Figure 6: Modeled time series of surface elevation at the coast. Model grid is identical to Figure 5 except five outer columns have been made highly viscous.

The wind and pressure fields were used to force the ocean current model. Everything else was the same as described in the previous section.

Figure 8 shows the comparison at station SN10 marked by the uppermost solid circle in Figure 1. The modeled results are shown as a dashed curve and the data as solid. Both data and model results are taken at 50 m below the still water level. The upper panel in the figure shows the alongshore component with positive indicating a northerly direction. The lower panel shows the cross-shelf component with positive indicating an easterly flow. Comparisons are also available at other depths and sites but these are qualitatively similar to Figure 8, and are not shown.

In general the model predicts the right order of magnitude of the current but there are clearly some major discrepancies. The model results are predominately in the wind direction, while the data are not obviously correlated with the wind. The results can not be substantially improved by varying the model parameters  $N_V$ ,  $c_b$ , or  $N_H$ .

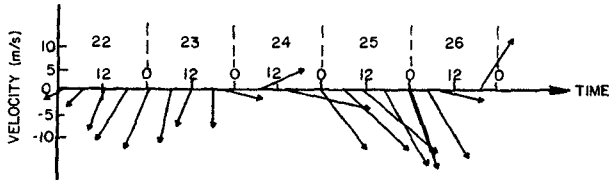


Figure 7: Time series of hindcasted wind vectors at the coast for the storm of October 1974.

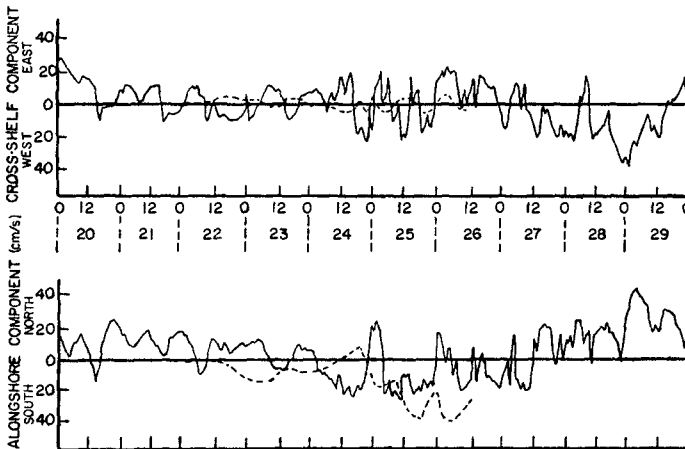


Figure 8: Comparison between modeled and observed currents at station SN10. Data is indicated by solid curve, and model by dashed curve.

The comparison is actually not as bad as it might first seem because the data still contain a relatively strong tidal signal, while the model contains no tidal forcing. An initial attempt was made to filter the tidal signal from the data, but this proved impossible using standard band-pass filters and least-squares or harmonic analysis. The reason for the difficulty is the nearly identical frequency of the inertial and tidal signal. One cannot apply any of these classical techniques without eliminating the inertial component, and of course this is not acceptable since a major portion of storm response of the shelf is inertial.

Figure 9 shows the modeled surface elevation at a central grid element on the coast. Two curves are shown. The dotted curve shows the result using the wind field provided by Cardone (8), whereas the solid curve used the same wind field but winds were updated every 30 minutes by interpolating the six-hour wind field. There are substantial differences between the two curves, indicating the dynamic sensitivity of the system. Much of this is due to the small role of friction in the basin.

Surge data had not been obtained at the time of this study for this particular storm. However, the magnitude of the modeled surge is consistent with other similarly severe storms (14).

#### SUMMARY AND CONCLUSIONS

The objective of the study was to make a first pass at modeling storm-driven currents and surge on the Southern Norwegian Shelf. A linear numerical model based on the barotropic primitive equations was used. Current data were available at several locations from some historical storms, and these were used to assess the model.

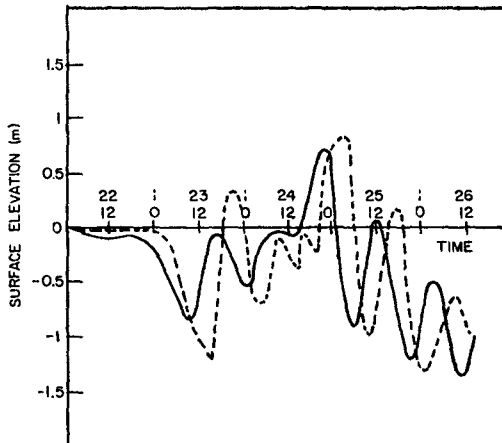


Figure 9: Time series of modeled surface elevation at the coast for storm of October 1974.

Friction was found to be of relatively little importance on the shelf, and storm response was strongly inertial. Stratification was generally negligible during the most severe storms, and hence the barotropic assumption was easily justified.

Preliminary application of the model to the shelf indicated the dominance of a seiche in the cross-shelf direction. The cause was traced to the reflective boundary conditions.

A fairly thorough review of the literature was undertaken in an attempt to find alternative boundary conditions which would eliminate the artificial seiche. Five types of conditions were identified, and examined. None of the conditions are universally applicable. One major finding is that many previous applications have used a radiation condition to study quasi-steady forced flow fields, and it is easily shown that this can generate substantial errors.

Eventually a boundary condition was found which eliminated the seiche. The configuration consisted of: 1) a highly viscous, unforced, outer western boundary, 2) a radiation boundary condition on the western boundary and 3) a simplified bottom bathymetry which eliminated alongshore oscillations.

Finally, the model was applied to hindcast currents during a major storm on the shelf. Results indicated the model gives the proper order of magnitude for both currents and surges. A more quantitative assessment was impossible because the data contained a strong tidal component which could neither be removed nor easily modeled.

Efforts are underway to improve the results described above. These improvements will include: 1) implementation of an improved boundary condition on all ocean boundaries, 2) expansion of the grid system to include the entire Norwegian Sea, 3) further data analysis to remove the tidal signal, or if this is not possible then tidal forcing will be included in the model, and 4) extension of the wind hindcasts to provide adequate model spin up.

#### REFERENCES

- <sup>1</sup>Beardsley, R. C. and D. B. Haidvogel, "Model Studies of the Wind-Driven Transient Circulation in the Middle Atlantic Bight. Part 1: Adiabatic Boundary Conditions," *J. Phys. Oceanogr.*, 11, 3, 355-375, 1981.
- <sup>2</sup>Birchfield, G. E., "Numerical Prediction of Hurricane Movement with the Use of a Fine Grid," *J. Meteorol.*, 17, 406-414, 1960.
- <sup>3</sup>Blumberg, A. F. and L. H. Kantha, "An Open Boundary Condition for Circulation Models," *J. Hydraulics*, ASCE, in press.
- <sup>4</sup>Browning, G., H. O. Dreiss, and J. Olinger, "Mesh Refinement", *Math. Comp.*, 27, 29-39, 1973.
- <sup>5</sup>Busby, F. H., and M. S. Timpson, *Quart. J. Roy Meteor. Soc.*, 93, 1, 1967.
- <sup>6</sup>Butler, H. L. and Y. P. Sheng, "A Wave Separation/Radiation Boundary Condition for Limited Area Modeling of Coastal Project Impact," *Proc. 19th Inter. Conf. on Coastal Engng.*, Houston, ASCE, 1984.

- <sup>7</sup>Camerlengo, A. L., and J. J. O'Brien, "Open Boundary Conditions in Rotating Fluids," *J. Comp. Phys.*, 35, 1, 12-35, 1980.
- <sup>8</sup>Cardone, V., "Hindcast of North Sea Wind and Pressure Fields for Ocean Current Technology Project. Report submitted to Conoco, March 1982.
- <sup>9</sup>Cooper, C. K. and B. R. Pearce, "Numerical Simulations of Hurricane-Generated Currents," *J. Phys. Oceanogr.*, 12, 1070-1091, 1982.
- <sup>10</sup>Cooper, C. K. and B. R. Pearce, "GAL: A 3-D Circulation Model," T. R., MIT Ralph M. Parsons Laboratory, 1977.
- <sup>11</sup>Davies, A. M., "Application of the Galerkin Method to the Formulation of a 3-D Nonlinear Hydrodynamic Numerical Sea Model," *Appl. Math. Model.*, 4, 245-256, 1979.
- <sup>12</sup>Eide, L. I., "Evidence of a Topographically Trapped Vortex on the Norwegian Continental Shelf," *Deep-Sea Res.*, 26, 6A, 1979.
- <sup>13</sup>Forristall, G. Z., R. C. Hamilton and V. J. Cardone, "Continental Shelf Currents in Tropical Storm Delia: Observations and Theory," *J. Phys. Oceanogr.*, 7, 532-546, 1977.
- <sup>14</sup>Gjevik, B., and L. R. Røed, "Storm Surges Along the Western Coast of Norway," *Tellus*, 28, 2, 166-182, 1976.
- <sup>15</sup>Graham, C., "Strong Surface Currents at the Troll Field in the Norwegian North Sea," *Proceedings of Workshop on Joint Probability, E&P Forum, London, 1983.*
- <sup>16</sup>Greenberg, D. A., "Modeling the Mean Barotropic Circulation in the Bay of Fundy and Gulf of Maine," *J. Phys. Oceanogr.*, 13, 5, 886-904, 1983.
- <sup>17</sup>Heaps, N. S., "Development of a Three-Dimensional Numerical Model of the Irish Sea," *Rapp. P.-v. Reun., Cons. in. Explor. Mer.*, 167, 146-162, 1974.
- <sup>18</sup>Hebenstreit, G. T., E. N. Bernard, and A. C. Vastano, "Application of Improved Numerical Techniques to the Tsunami Response of Island Systems," *J. Phys. Oceanogr.*, 10, 1134-1140, 1980.
- <sup>19</sup>Lamb, H., *Hydrodynamics*, 6th edition, Dover Press, London, 1945.
- <sup>20</sup>Lewis, J. K., R. E. Whitaker, and W. J. Merrell, Jr., "The Effects of Stretched-Grid Coordinate System on Long-Wave Dispersion and Energy Characteristics," *J. Geophys. Res.*, 87, C6, 4265-4267, 1982.
- <sup>21</sup>Lilly, D. K., "On the Computational Stability of Numerical Solutions of Time-Dependent Non-Linear Geophysical Fluid Dynamic Problems," *Monthly Weather Review*, 93, 1, 11-26, 1965.
- <sup>22</sup>Miller, M. J. and A. J. Thorpe, "Radiation Conditions for the Lateral Boundaries of Limited-Area Numerical Models," *Quart. J. R. Met. Soc.*, 107, 615-628, 1981.
- <sup>23</sup>Mungall, J. C. H., and R. O. Reid, "A Radiation Condition for Radially - Spreading Non-Dispersive Gravity Waves," TR 78-2-T, Dept. of Oceanography, Texas A&M, 63 pp., 1978.



- <sup>24</sup>Orlanski, I., "A Simple Boundary Condition for Unbounded Hyperbolic Flows," *J. Comp. Phys.*, 21, 251-269, 1976.
- <sup>25</sup>Ramming, H. G. and Z. Kowalik, Numerical Modelling of Marine Hydrodynamics, Elsevier Scientific, New York, 1980.
- <sup>26</sup>Reid, R. O., "Comment on 'Three-Dimensional Structure of Storm-Generated Currents' by G. Z. Forristall," *J. Geophys. Res.*, 80, 9, 1184-1185, 1975.
- <sup>27</sup>Reid, R. O., and B. R. Bodine, "Numerical Model for Storm Surges in Galveston Bay," *ASCE, WW1*, 33-57, 1968.
- <sup>28</sup>Røed, L. P., and O. M. Smedstad, "Open Boundary Conditions for Forced Waves in a Rotating Fluid," *SIAM J. Sci. Stat. Comput.*, 5, 2, 1984.
- <sup>29</sup>Thompson, J. D., "The Coastal Upwelling Cycle on a Beta-Phase Hydrodynamics and Thermodynamics," TR 22, Dept. of Met., Florida State, Tallahassee, 140 pp., 1974.
- <sup>30</sup>Townsend, A. A., The Structure of Turbulent Flow, Cambridge Univ. Press, 429 pp., 1976.
- <sup>40</sup>Vastano, A. C., and R. O. Reid, "Tsunami Response at Wake Island: Comparison of the Hydraulic and Numerical Approaches," *J. Marine Res.*, 28, 3, 345-356, 1970.
- <sup>41</sup>Vastano, A. C., and R. O. Reid, "Tsunami Response for Islands: Verification of a Numerical Procedure," *J. Marine Res.*, 25, 2, 129-139, 1967.
- <sup>42</sup>Wurtele, M. G., J. Paegle, and A. Sielecki, "The Use of Open Boundary Conditions with the Storm-Surge Equations," *Monthly Weather Review*, 99, 6, 537-544, 1971.

## CHAPTER ONE HUNDRED FIFTY NINE

### REPRODUCTION OF NEARSHORE CURRENTS BY A MATHEMATICAL MODEL

Hiroyoshi Tanaka\* and Akira Wada\*\*

#### ABSTRACT

In order to cope with such environmental problems as shoreline change and diffusion of discharged warm water and contaminations in the surf zone, it is necessary to predict velocity vector field due to nearshore currents accurately.

The present study is aimed at establishing a mathematical model applicable to the prediction of nearshore currents on actual coasts which have complicated bottom configurations. First, to investigate the mechanism of nearshore current generation hydraulic experiments were carried out. By the experiment it was made clear that the generation of a longshore current depends mainly upon a difference in mean water level in the longshore direction. After investigating estimation of radiation stress terms on the basis of the information obtained from the basic experiments a mathematical model of nearshore currents was developed and validity of the model was verified by both hydraulic model tests and field survey.

#### I. INTRODUCTION

On a coast having a gentle slope the surf zone is relatively wide, and consequently physical phenomena such as breaking of waves, nearshore currents, etc. may have some effects on the diffusion and shoreline change in and near the surf zone. In the case where the nearshore currents fluctuate as wave condition changes hourly, the currents may exert a great effect on the advective diffusion of small time-scale. Meanwhile, in case that nearshore current pattern doesn't change very much even if wave condition varies to some extent, the currents may also have some effects on the shoreline change of long-term scale.

To cope with the aforementioned environmental problems in and near the surf zone, therefore, it is necessary to accurately predict the velocity vector field due to nearshore currents. Many mathematical models of nearshore currents<sup>1),2),3),4),5)</sup> have been proposed so far, but they have applied the small amplitude wave theory even to the estimation of physical phenomena in and near the surf zone. Consequently, none of the existing models may reproduce well the nearshore currents on actual coasts which have complicated bottom configurations. Recently, field surveys on nearshore currents have been carried out positively. Although those are very important from the standpoint of understanding the

\* Senior Research Engineer, Environment Department, Central Research Institute of Electric Power Industry, Abiko, Chiba Pref., Japan

\*\* Manager of Environment Department, Central Research Institute of Electric Power Industry, Abiko, Chiba Pref., Japan

actual phenomena it is very difficult to minutely grasp the mechanism and main characteristics of nearshore currents from complicated phenomena on a real coast.

In the present study, first, the mechanism of nearshore currents was clarified by hydraulic experiments. Especially, this experimental study attached great importance to the grasp of transient phenomena, regarding it as a clue for elucidating the physical processes and mechanisms.

Next, a mathematical model was developed for the prediction of nearshore currents in the field. In this model, estimation of radiation stress terms was mainly studied so that it was compatible with the mechanism of nearshore current generation. Then, validity of the present mathematical model was examined by comparing the results of the numerical simulation with those of the hydraulic model tests and the field survey.

## II. MAIN CAUSE OF NEARSHORE CURRENT GENERATION

### 2.1 Contents of the hydraulic experiments

The basin used for the present hydraulic experiments has dimensions of  $50\text{m} \times 22.6\text{m} \times 1.5\text{m}$ . On one end of the basin three units of wave generators are installed and on the other end there is a 1/150 non-distorted model of a certain actual sea region. Regular waves were used in the experiments. The normally incident waves were generated by the wave generator and the obliquely incident waves were made by a simple wave maker installed temporarily. As for the wave condition used in the experiments the ranges of the average breaking wave height and the wave period were 2.5~3.6cm (3.8~5.4m in the prototype) and 1.25~2.5s (15.3~30.6s in the prototype) respectively. Thus, the wave height and the wave period were exaggerated in the experiments compared with those appearing in the field, in order to grasp clearly the physical phenomena and processes in the surf zone.

Measurement of water surface level was made by using capacitance type wave gauge, and velocity and direction of nearshore currents were measured with ultra sonic current meters. Great precision was required in measuring wave set-up. Hence, after confirming that no zero drift took place during the measurement, one or several cycles of analog time series data of the water surface level written on pen recorder charts were traced on section papers and the elevation due to wave set-up was estimated by counting the area put between the time variation curve of the water surface and the still water level by means of 1mm section.

### 2.2 Experimental results and discussion

For the purpose of making clear the cause of nearshore current generation, the experiment was at first carried out by applying waves whose average breaking wave height and period were 3.6cm and 2.5s (5.4m and 30.6s in the prototype). Figure 1 shows the horizontal distribution of wave set-up in a steady state with the velocity vector field due to nearshore currents under the offing condition of normal incidence of waves. From the figure it can be seen that longshore currents are governed mainly by a difference in mean water level in the longshore direction. A result of the field survey<sup>6)</sup> carried out by Tokyo Electric Power Company is shown in Fig. 2. This result also tells the directions of longshore currents correlate with a difference in mean water level

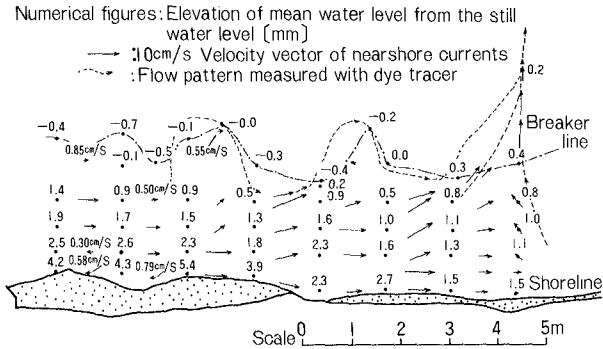


Fig.1 Relation between velocity vector field due to neashore currents and horizontal distribution of mean water level (Experimental result)

Breaking wave height: 0.6m  
 Wave period : 8.6s

⇨: Direction of nearshore currents  
 obtained by the field survey

Numerical figures: Values of mean water level (The base level is the lowest one)  
 [unit; cm]

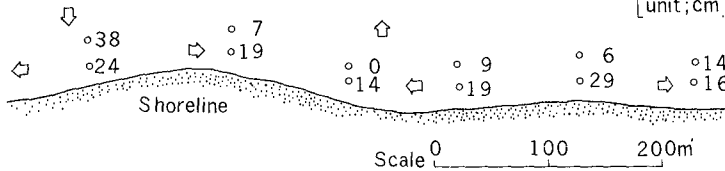


Fig.2 Relation between longshore current directions and horizontal distribution of mean water level (Result of field survey)

in the longshore direction.

The above investigations were performed in steady state conditions.

Another kind of experiment was carried out in a transient state to examine the cause of longshore current generation. In this experiment the relation between the acceleration of a longshore current and the longshore gradient of mean water level was examined at the beginning of wave action, that is, at the time when the effects of friction force, eddy viscosity and inertia can be ignored. The several kinds of regular waves used in the experiment have 2.5~3.6cm in average breaking wave height, 1.25~2.5s in period and 0°~54° in incident angle. An example of the experimental results is shown in Fig. 3. Figure 3(a) shows how to obtain an initial acceleration  $\partial v/\partial t$  from the velocity change of a longshore current in a transient state and Fig. 3(b) shows how to obtain the initial force  $-g \cdot \partial \eta/\partial y$  from the initial difference in mean water level at two points near the velocity sampling point. From these figures it

is found that the acceleration  $\partial v/\partial t$  coincides with the value  $-g \cdot \partial \bar{\eta}/\partial y$  fairly well in the initial state. Figure 4 shows the relation between  $\partial v/\partial t$  and  $-g \cdot \partial \bar{\eta}/\partial y$  at the beginning of the action of various kinds of normally and obliquely incident waves. These data were obtained at various points in the surf zone to the exclusion of the region near breaking points. The experimental result clearly shows that even if waves have any incident angle the initial acceleration  $\partial v/\partial t$  agrees fairly well with the initial force  $-g \cdot \partial \bar{\eta}/\partial y$  based upon a difference in

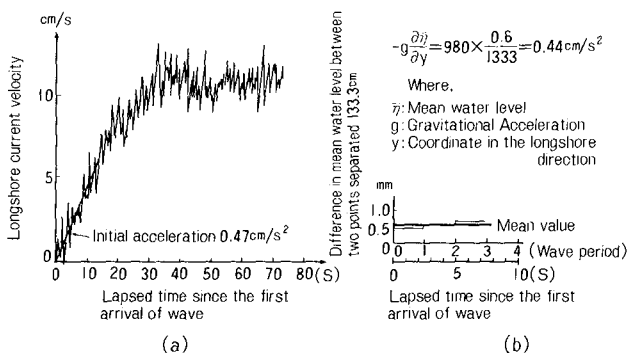


Fig.3 Velocity change of a longshore current and a difference in mean water level in the longshore direction at the beginning of wave action

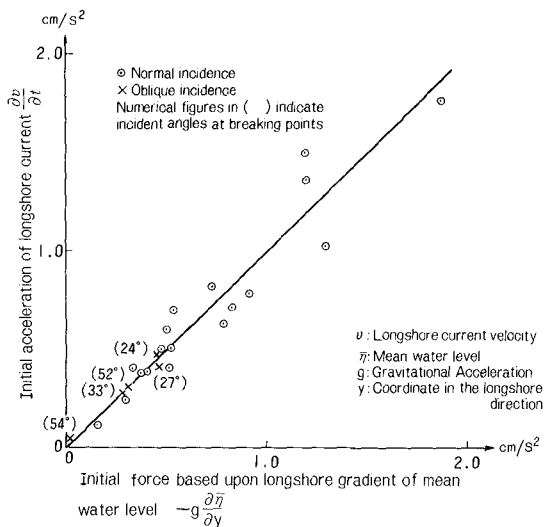


Fig.4 Relation between acceleration of a longshore current and force based upon a difference in mean water level in the longshore direction at the beginning of wave action.

mean water level. Also from this result it can be inferred that the generation of a longshore current depends mainly upon a difference in mean water level in the longshore direction.

### III. FEATURES OF MATHEMATICAL MODELS

#### 3.1 Mathematical model of wave field

The distribution of wave directions is calculated by using the following wave direction equation:

$$C \cdot \vec{i} \cdot \nabla \theta = - \vec{j} \cdot \nabla C \quad (1)$$

where  $C$ ,  $\theta$ ,  $\vec{i}$  and  $\vec{j}$  are wave celerity, wave direction, unit vector in the direction of wave ray, and unit vector in the direction of wave crest line, respectively. This equation shows that the wave direction varies with the spatial change of wave celerity determined by the distribution of water depths. However, as the wave ray method ignores the effects of reflection, diffraction, and energy transfer in the direction of wave crest line, it can be inferred that wave direction as well as wave height cannot be correctly estimated at the places where a space between neighbouring wave rays is very small or where wave rays cross. Hence, wave directions at such places are obtained by interpolating those in the surrounding area where the wave ray method is valid. Such handling as mentioned above removes an unnatural scattering of wave directions.

The plane distribution of wave heights is dealt with independently of wave direction, and the numerical simulation of wave heights is carried out on the basis of the following mathematical model.

Regarding the outside of the surf zone, basic equations are obtained by integrating the continuity equation and the momentum equations in the vertical direction and by applying the small amplitude wave theory. If the two-dimensional momentum equations are applied as it is, numerical instability is liable to occur because variables (water surface elevation and flow rate per unit width) widely fluctuate in a short period. From a physical viewpoint it can be considered that in the actual fluid momentum of waves is diffused due to eddy viscosity. Therefore, the momentum equations should be modified as follows.

$$\partial Q_x / \partial t = - C^2 \cdot \partial \eta / \partial x + K \cdot (\partial^2 Q_x / \partial x^2 + \partial^2 Q_x / \partial y^2) \quad (2)$$

$$\partial Q_y / \partial t = - C^2 \cdot \partial \eta / \partial y + K \cdot (\partial^2 Q_y / \partial x^2 + \partial^2 Q_y / \partial y^2) \quad (3)$$

where  $t$  is the time,  $x$  and  $y$  the horizontal co-ordinates,  $\eta$  the water surface elevation,  $Q_x$  and  $Q_y$  the flow rates per unit width in the  $x$ - and  $y$ - directions respectively, and  $C$  the wave celerity.  $K$  is the apparent horizontal eddy viscosity under the action of waves. By using the continuity equation  $\partial \eta / \partial t + \partial Q_x / \partial x + \partial Q_y / \partial y = 0$  and the momentum equations (2) and (3),  $Q_x$ ,  $Q_y$  and  $\eta$  are calculated from the offshore boundary to the breaking points. Since the result of calculation on the change in wave height is not based on the group velocity but on the wave celerity the actual wave height should be modified as shown below by introducing the coefficient  $f_s$  :

$$H = (\eta_{\max} - \eta_{\min}) (f_s / f_{s0}) \quad (4)$$

where  $\eta_{\max}$  and  $\eta_{\min}$  are the maximum and minimum of  $\eta$  respectively in a wave period. The modifying coefficient  $f_s$  is defined by the following equation :

$$f_s = (1+2kh/\sinh 2kh)^{-1/2} \quad (5)$$

where  $k$  is the wave number and  $h$  the water depth. The subscript  $o$  in Eq.(4) indicates the value of  $f_s$  for the offshore boundary.

The above argument cannot be applied to waves after breaking since it depends on the small amplitude wave theory. In this model, the wave height in the surf zone  $H$  was assumed as follows.

$$H = \gamma h \quad (6)$$

where  $\gamma$  is the ratio of wave height to water depth after breaking. To estimate the ratio  $\gamma$ , an experiment was carried out by using a non-distorted model of scale 1/150. Figure 5 shows the experimental results. The waves used in the experiment had frequencies extending over 0.4-1.2 Hz. The following information is obtained from Fig. 5.

- 1) The ratio of breaking wave height to breaking water depth  $\gamma_b$  (shown by the mark  $\bullet$ ) is about 0.8 even against any wave period.
- 2)  $\gamma$  immediately after breaking (shown by the mark  $\circ$ ) is smaller than  $\gamma_b$  and when the waves advance farther in the surf zone the ratio (shown by the mark  $\circ$ ) becomes much smaller.

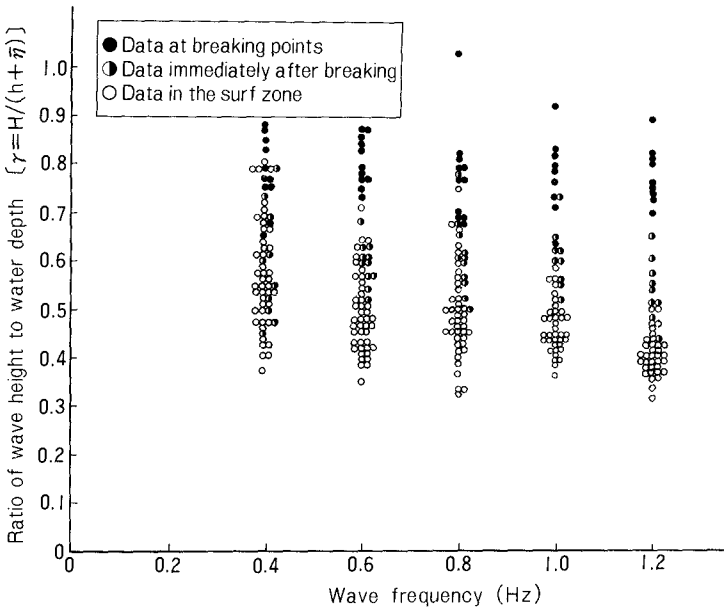


Fig.5 Ratio of wave height to water depth in the surf zone  
(Experimental Result)

3) In the frequency range of 0.4~1.2 Hz, the shorter the wave period, the smaller  $\gamma$  (shown by the mark O) is.

In the present study on nearshore currents, the waves concerned are regular waves (wave period 10.2s) and irregular waves (average wave period 7.3s). With regard to the regular waves, 0.4 is used as the ratio after breaking  $\gamma$  on the basis of Fig. 5 since the wave period 10.2s almost corresponds to the wave frequency 1.2 Hz on the hydraulic model of scale 1/150. In the present study, wave set-up  $\bar{\eta}$  has not been determined yet at the stage of calculating the wave field because the model of wave field is dealt with independently of that of nearshore currents. Ignoring the effect of  $\bar{\eta}$ , therefore, the wave height after breaking  $H$  is approximated by the following equation :

$$H = 0.4h \quad (7)$$

Regarding the irregular waves, 0.55 is used as the ratio of root mean square wave height to water depth in the surf zone and the value is selected based on the results of the field survey<sup>7)</sup>. Breaking wave height is assumed to be 80% of breaking water depth.

### 3.2 Mathematical model of nearshore currents

Basic experiments were conducted on the mechanism of nearshore current generation in parallel to the development of a mathematical model of nearshore currents. Judging from the information obtained by the experiments, it can be inferred that the greatest problem in our previous model<sup>5)</sup> lies in the estimation of radiation stress terms. One problem is the estimation of a wave field related to radiation stresses and another is applicability of the small amplitude wave theory to radiation stresses in and near the surf zone. Since the former problem was discussed in the foregoing paragraph, here follows a discussion on the development of a new mathematical model of nearshore currents in consideration of the latter problem.

The basic equations of the present mathematical model are depth averaged two-dimensional equations which are also averaged over one wave period.

$$\partial \bar{\eta} / \partial t + \partial \bar{M}_x / \partial x + \partial \bar{M}_y / \partial y = 0 \quad (8)$$

$$\begin{aligned} & \partial \bar{M}_x / \partial t + \partial (\bar{U} \bar{M}_x) / \partial x + \partial (\bar{V} \bar{M}_x) / \partial y \\ & = -g \cdot (h + \bar{\eta}) \cdot \partial \bar{\eta} / \partial x - R_x + K_h \cdot (\partial^2 \bar{M}_x / \partial x^2 + \partial^2 \bar{M}_x / \partial y^2) - \gamma_b \cdot \bar{U} \cdot \sqrt{\bar{U}^2 + \bar{V}^2} \end{aligned} \quad (9)$$

$$\begin{aligned} & \partial \bar{M}_y / \partial t + \partial (\bar{U} \bar{M}_y) / \partial x + \partial (\bar{V} \bar{M}_y) / \partial y \\ & = -g \cdot (h + \bar{\eta}) \cdot \partial \bar{\eta} / \partial y - R_y + K_h \cdot (\partial^2 \bar{M}_y / \partial x^2 + \partial^2 \bar{M}_y / \partial y^2) - \gamma_b \cdot \bar{V} \cdot \sqrt{\bar{U}^2 + \bar{V}^2} \end{aligned} \quad (10)$$

where  $x$  and  $y$  are the coordinates in the cross-shore and longshore directions,  $\bar{\eta}$  the mean water level,  $\bar{U}$  and  $\bar{V}$  the mean current velocities in the  $x$ - and  $y$ - directions,  $\bar{M}_x$  and  $\bar{M}_y$  the mean flow rates per unit width in the  $x$ - and  $y$ - directions,  $g$  the gravitational acceleration,  $h$  the water depth,  $R_x$  and  $R_y$  the radiation stress terms in the  $x$ - and  $y$ - directions,  $K_h$  the horizontal eddy viscosity coefficient, and  $\gamma_b$  the bottom friction coefficient.

a) Ry in the surf zone

Based on the basic experiments it is evident that in the surf zone longshore currents are generated mainly due to a difference in wave set-up in the longshore direction. It can therefore be inferred that the



contribution of  $R_y$  to longshore current generation is considerably small. It can be considered that if  $R_y$  is calculated by using the small amplitude wave theory as have been done so far the contribution of  $R_y$  to longshore current generation will be overestimated and consequently the numerical simulation will result in an unrealistic nearshore current field. It can also be supposed that  $R_y$  makes a small contribution to the generation of a longshore current which has a uniform velocity profile below the still water level but that it is connected with the longshore component of mass transport above the still water level. In the present model,  $R_y$  in the surf zone is ignored from an engineering standpoint. But near the breakwater not located in the longshore direction  $R_y$  is estimated with the same weight as that of  $R_x$ . In this case  $R_y$  may make an indirect contribution to the generation of a current because the breakwater interrupts the mass transport flow due to  $R_y$  and changes the mean water level.

b)  $R_x$  in the surf zone

The major cause of nearshore current generation is summarized as follows :

Wave set-up is formed so that it is almost in harmony with the radiation stress term  $R_x$  and usually it is not uniform in the longshore direction. Such a difference in the mean water level in the longshore direction generates a current, and it is important that the above mechanism is appropriately reflected in the mathematical model.

The basic experiments revealed the followings. In the surf zone, there is a narrow range where the mean water level is lower than the still water level but the range is very short in the cross-shore direction. In a very short distance from the breaking point, the mean water level turns out to be higher than the still water level, and the nearer the shoreline the higher the mean water level is. Because, at the place where the breaker line is prominent offshore (called the prominent place), wave set-up begins on the side more offshore than at the place where the breaker line is concave onshore (called the concave place), the mean water level of the prominent place is higher than that of the concave place at the same distance from a shoreline in the surf zone. Consequently, a longshore current flows from the prominent place to the concave one.

On the other hand, since in the previous mathematical model<sup>5)</sup> the wave height and radiation stress tensors  $S_{xx}$  and  $S_{xy}$  are overestimated after breaking,  $R_x$  is underestimated especially immediately after breaking. So, in the computational result, the gradient of the mean water level rise just after breaking is considerably small as compared with the actual phenomenon and the wave set-down range in the surf zone is long in the cross-shore direction. Hence, the model may produce a wrong phenomenon that a longshore current flows from the concave place to the wave set-down range in the prominent place and may distort the whole nearshore current system. Thus, one of the weak points of the previous model seems to be attributable to considerably overestimating radiation stress tensors  $S_{xx}$  and  $S_{xy}$ , especially near the breaking points.

From the above argument, it can be understood that the estimation of  $R_x$  in the surf zone is very important and that it governs the nearshore current pattern. In the present study, the radiation stress term  $R_x$  is estimated as follows by re-examining the existing formulas of radiation stress tensors :

The coefficient  $\alpha$  is determined as Eq.(11) on the basis of the result

of a basic experiment on the distributions of the mean water levels and wave heights in and near the surf zone under the wave condition of normal incidence. Then,  $R_x$  is approximated by multiplying  $R_{XS}$  by  $\alpha$ . Here,  $R_{XS}$  is the value obtained according to the small amplitude wave theory.

$$-g \cdot (h + \bar{\eta}) \cdot \partial \bar{\eta} / \partial x \approx \alpha \cdot (1/\rho) \cdot (\partial S_{XX} / \partial x) s \quad (11)$$

where  $\rho$  is the density of water.  $(\partial S_{XX} / \partial x) s$  is calculated according to the small amplitude wave theory by using the distribution of wave heights. The coefficient  $\alpha$  is inferred from a lot of experimental data related to high waves.  $\alpha$  is assumed to be 1 very near the breaking point and it abruptly decreases to 0.1 at a little more shoreward place where waves begin to be violently deformed to the bore-shape. In the range of  $1/3 \leq S/B \leq 1$  where the bore-shape is completely established  $\alpha$  is assumed to be 0.8 constant. Here,  $S$  is a distance from the breaker line and  $B$  the surf zone width.  $\alpha$  is also assumed to change in linear proportion to  $S$  between the two boundaries where  $\alpha = 0.1$  and  $\alpha = 0.8$ .

c)  $R_y$  on the outside of the surf zone

In the sea region where the small amplitude wave theory is valid the whole  $R_{YS}$  may contribute to current generation, but in the area where the finite amplitude wave theory has to be applied only a certain percentage of  $R_{YS}$  is assumed to contribute to nearshore current generation.  $R_y$  is assumed to be approximated by multiplying  $R_{YS}$  by  $\sqrt{(h-h_b)/(h_s-h_b)}$  because the percentage of  $R_{YS}$ 's contribution to current generation is difficult to estimate quantitatively even by an experiment. Here,  $h_s$  is the minimum water depth in the area where the existing model is applicable,  $h_b$  the breaking water depth and  $R_{YS}$  the value of  $R_y$  based on the small amplitude wave theory.

d)  $R_x$  on the outside of the surf zone

$R_x$  needs a thinking different from the discussion on  $R_y$  because the cross-shore component always has a boundary intersecting the direction. In the present study,  $R_x$  is estimated on the basis of the small amplitude wave theory on the outside of the surf zone from an engineering standpoint.

The above discussion on the estimation of radiation stress terms is summarized as shown in Table-1.

#### IV. CONDITIONS AND METHOD OF NUMERICAL SIMULATION

##### 4.1 Validity verification of the mathematical model by the hydraulic model

(1) Sea region concerned and mesh size for calculation

The numerical simulation was carried out with respect to the sea region shown in Fig. 6. This sea region is characterized by a gently sloping coast facing the Pacific Ocean and by existence of breakwaters. The results of calculations are compared with those of the hydraulic experiment. The comparison is made on the breaker line and the velocity vector field due to nearshore currents. The mesh size for calculation is 20m and the computational time step is 1/100 of wave period.

(2) Incident waves

The incident wave heights and periods are given by converting the values measured by the hydraulic model into those in the prototype. The average wave height and the wave period of usual waves are 0.77m and

Table-1 Estimation of radiation stress terms for calculating nearshore currents

	In the area where a shoreline is monotonous		Near a breakwater or a cape		
	On the outside of the surf zone		In the surf zone	On the outside of the surf zone	In the surf zone
	In the area where the small amplitude wave theory is usually applied	In the area where the finite amplitude wave theory is usually applied			
$R_x$	$R_{xs}$		$\alpha \cdot R_{xs}$ ( $\alpha \leq 1$ )	$R_{xs}$	$\alpha \cdot R_{xs}$
$R_y$	$R_{ys}$	$\sqrt{\frac{h-h_b}{h_s-h_b}} \times R_{ys}$	0	$R_{ys}$	$\alpha \cdot R_{ys}$

$R_x$  ; Radiation stress term in the cross-shore direction

$R_y$  ; Radiation stress term in the longshore direction

$h$  ; Water depth

$h_b$  ; Breaking water depth

$h_s$  ; Minimum water depth in the area where the small amplitude wave theory is valid

$\alpha$  ; Coefficient determined by a basic experiment

Subscript s ; Value calculated on the basis of the small amplitude wave theory

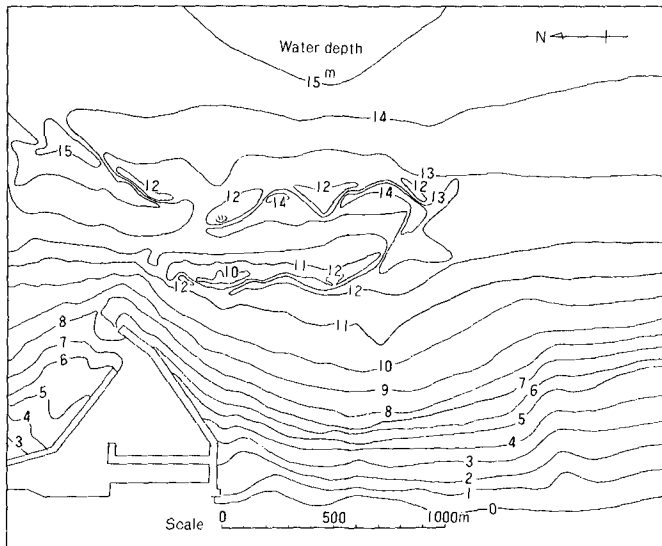


Fig.6 Bottom topography of the sea region concerned

10.2s at a distance 1 km from the shoreline. Those of high waves are 3.1m and 12.9s.

- (3) Horizontal eddy viscosity coefficients  $K_s'$  used for calculating wave fields

1  $m^2/s$  and 2.5  $m^2/s$  are used for calculating usual wave and high wave fields respectively on the basis of the preceding basic experiments.

- (4) Horizontal eddy viscosity coefficients  $K_h'$ s used for calculating nearshore currents

5  $m^2/s$  and 10  $m^2/s$  are used for calculating nearshore currents under the action of usual waves and those under high waves respectively on the basis of the preceding basic experiments.

- (5) Bottom friction coefficient  $\gamma_b$  used for calculating nearshore currents

On the assumption that the friction force is proportional to the square of current speed, 0.02 is taken as the non-dimensional bottom friction coefficient on the basis of the hydraulic model.

- (6) Method of numerical calculation

The wave field is first solved independently of nearshore currents by assuming that the interaction between waves and nearshore currents is small. Then, the computed wave field is used for calculating the values of radiation stress tensors. As the initial conditions, the mean water level and the flow rates are set equal to zero. On the offshore boundary, the mean water level is always equal to zero. At the breakwaters, on the shoreline and on the side boundaries,  $\tilde{M}_n = \partial\tilde{M}_t/\partial n = 0$ , where  $\tilde{M}_n$  and  $\tilde{M}_t$  are the flow rates per unit width, normal and tangent to the boundaries.

In the numerical calculation, the Leap-Frog and Lax-Wendroff schemes are applied in explicit form. The flow rates per unit width  $\tilde{M}_x$ ,  $\tilde{M}_y$  and the mean water elevation  $\tilde{\eta}$  are calculated every time step until they become steady.

#### 4.2 Validity verification of the mathematical model by the field survey

- (1) Sea region concerned and mesh size for calculation

Although the sea region concerned is the same as that described in 4.1 the bottom configuration surveyed in December, 1978 is applied. The sea region for calculation is 12.5km in the longshore direction and 0.8km in the cross-shore direction. The mesh size is 30m in the longshore direction and 20m in the cross-shore direction.

- (2) Incident waves

The applied waves were observed at almost the same time as that of nearshore current survey. The incident direction of waves is normal to the offshore boundary. Two kinds of regular waves are used for calculation. One is the significant wave whose wave height and period are 0.66m and 7.3s. The other is the root mean square wave whose wave height and period are 0.44m and 7.3s respectively.

- (3)  $K$  and  $K_h$

$K=1m^2/s$  and  $K_h=5m^2/s$  are used for the numerical simulation.

- (4)  $\gamma_b$

Since  $\gamma_b$  on the actual sandy coast may be different from that on a hydraulic model covered with mortar, we use 0.00637 which has been proposed so far.

- (5) Effect of the breakwater on wave energy dissipation

The energy dissipation coefficient  $v_d$  is defined by Eq.(12), and the

present mathematical model considers a decrease in wave height due to mounds of concrete armour units in front of the breakwater.

$$\partial(EC_{gx})/\partial x = -v_d k^2 E \quad (12)$$

where  $x$  is the coordinate in the cross-shore direction,  $E$  the wave energy density,  $k$  the wave number, and  $C_{gx}$  the  $x$ -component of group velocity. It is assumed that  $v_d=10^2 \text{ cm}^2/\text{s}$  along the breakwater normal to the shoreline,  $v_d=0 \text{ cm}^2/\text{s}$  at a distance of 400m from the breakwater, and that  $v_d$  linearly changes in the longshore direction between the two boundaries where  $v_d=10^2 \text{ cm}^2/\text{s}$  and  $v_d=0 \text{ cm}^2/\text{s}$ .

(6) Method of numerical calculation

The method is basically the same as that described in 4.1 (6).

## V. RESULTS OF NUMERICAL SIMULATION AND DISCUSSION

### 5.1 Breaker line and distribution of breaking wave heights

Validity of the mathematical model of wave height distribution on the outside of the surf zone has been examined by comparing the position of the breaker lines between the mathematical and experimental results.

As an example of the comparison Fig. 7 shows the breaker lines under the action of usual waves. From this figure it can be concluded that the two breaker lines agree fairly well except for the places where the breaker line is prominent offshore. In the prominent places where shoals grow, there may be some problems with regard to the breaking condition.

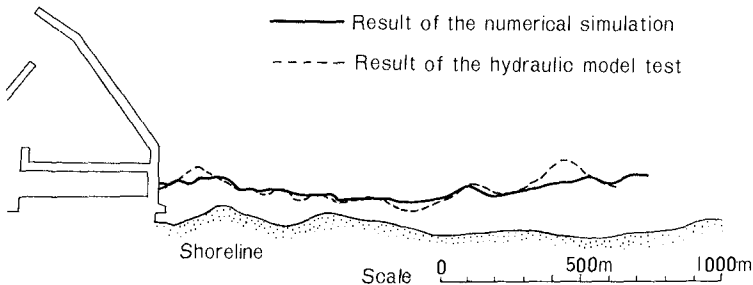


Fig.7 Comparison of the breaker line between the numerical and experimental results

Figure 8 shows comparisons between the results of the field survey and those of the numerical simulation regarding the distribution of breaking wave heights and breaker line. The significant wave trains are concerned in calculating wave field. The distribution of breaking wave heights calculated by the numerical simulation agrees fairly well with the result of the field survey at a long distance from the breakwater, but near the breakwater the calculated wave height is fairly larger than

that of the field observation. It can be considered that the result of the field survey was influenced by cooling water discharge from a foot of the breakwater. The surf zone width obtained by computation is a little smaller than the result of the field survey at the places where both results are almost equal regarding the breaking wave height. This may be due to the fact that the breaker line observed with the eye in the field corresponds to that of wave trains larger than the significant wave.

In conclusion, it can be said that the present mathematical model of wave field reproduces well the distribution characteristics of breaking wave heights and breaking positions on the actual coast.

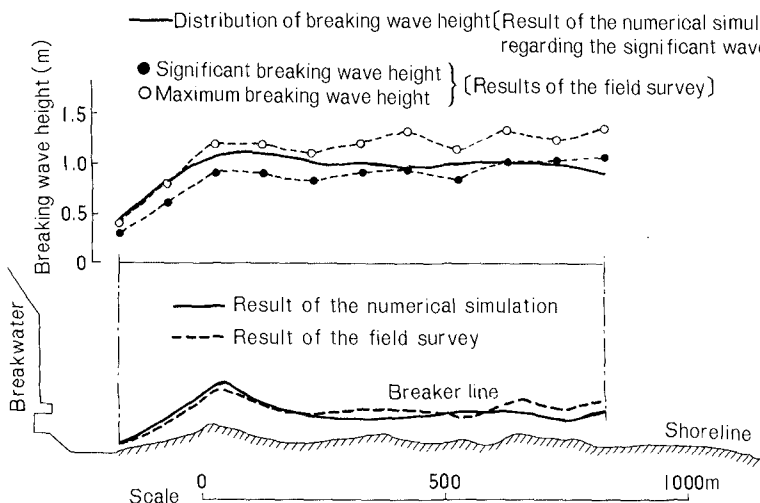


Fig.8 Comparisons of the results of breaking wave height distribution and breaker line between the numerical simulation and the field survey

## 5.2 Velocity vector field due to nearshore currents

Figure 9 shows a comparison of the flow pattern due to nearshore currents under the action of usual waves between the numerical simulation and the hydraulic model test. Figure 10 shows a comparison of nearshore currents under the high waves between the calculation and the experiments.

The followings are revealed from Figs. 9 and 10.

(1) The computed result reproduces the following situation often found in the field. At the place where the breaker line is prominent offshore, the shoreward current is remarkable, while at the place where the breaker line is concave onshore the rip current is predominant.

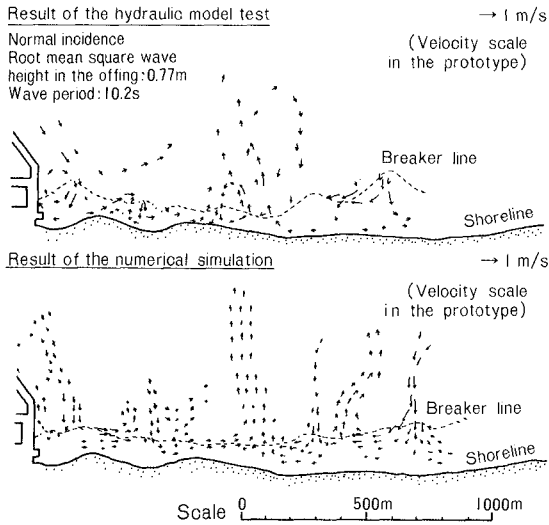


Fig.9 Comparison of the result of nearshore current pattern under the action of usual waves between the numerical simulation and the hydraulic model test

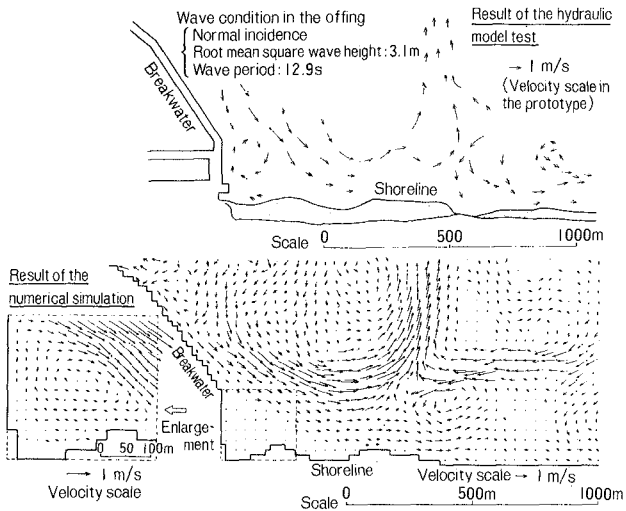


Fig.10 Comparison of the result of nearshore current pattern under the action of high waves between the numerical simulation and the hydraulic model test

(2) The mathematical result agrees fairly well with the experimental result regarding the following phenomena.

- a) A notable rip current reaching the offing at a distance of 800-900m from the foot of the breakwater
- b) Longshore currents in the surf zone
- c) A circulating flow near the breakwater

Next, Fig. 11 shows a comparison of nearshore currents between the present mathematical model and the field survey. The numerical simulation was carried out by using the regular wave condition of root mean square wave obtained from irregular waves in the field. The flow pattern in the field was obtained by using ball floats. Figure 12 shows the velocity vector field due to the previous mathematical model<sup>5)</sup> under the same computational conditions as those of the present model.

The followings are obtained from Figs. 11 and 12.

(1') Considering that a field survey cannot simultaneously grasp the whole flow pattern due to nearshore currents under irregular wave field varying from time to time and that the result may include uncertain factors, it can be said that the present mathematical model makes it possible to reproduce the characteristics of nearshore currents on the actual coast.

(2') The nearshore currents based on the previous mathematical model<sup>5)</sup> don't agree well with those obtained by the field survey especially in the surf zone. It can be understood that the present mathematical model has attained considerable improvement in the accuracy of prediction as compared with the previous model<sup>5)</sup>.

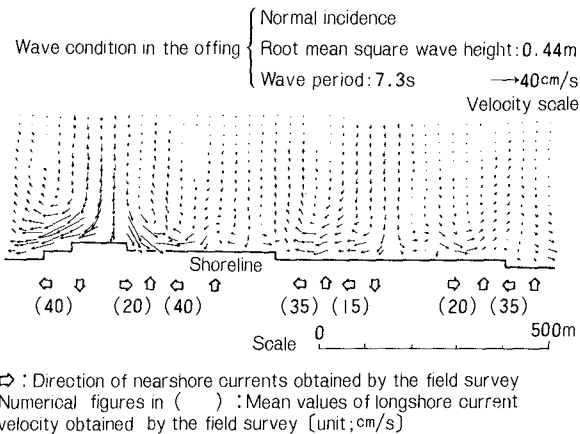


Fig.11 Comparison of the result of nearshore current pattern between the numerical simulation and the field survey



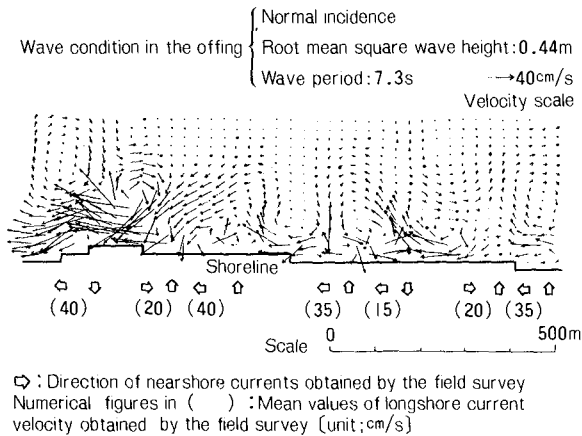


Fig.12 Calculated result of nearshore current pattern  
 on the basis of the previous mathematical model

## VI. CONCLUSION

Main conclusions are summarized as follows.

- (1) Basic experiments showed that longshore currents are generated mainly due to a difference in wave set-up in the longshore direction.
- (2) The results of the numerical simulations well reproduced velocity vector fields due to nearshore currents both under the action of usual waves and under that of high waves.
- (3) Validity of the present mathematical model is verified by both experiments and field survey and it is considered that the model is satisfactorily applicable to predicting nearshore currents in the field, though further study must be made to examine the validity of the model under obliquely incident waves.

## REFERENCES

- 1) Hashimoto, H and Uda, T. : Numerical simulation method on nearshore currents and its application, Proc. 21st Conf. on Coastal Engg. in Japan, JSCE, 1974, pp.355-360 (in Japanese).
- 2) Liu, P.L.F. and Mei, C.C. : Effects of a breakwater on nearshore currents due to breaking waves, Tech. Rep. 192, R.M. Parson Lab., M.I.T., 1974, 265p.
- 3) Noda, E.K. : Wave-induced nearshore circulation, Jour. Geophy. Res., Vol.79, 1974, pp.4097-4106.
- 4) Sato, S., Nagai, T. and Ozasa, H. : Numerical simulation on nearshore currents, Tech. Note, Port and Harbour Res. Inst., No.290, 1978, 16p. (in Japanese).

- 5) Tanaka, H. and Wada, A. : Prediction of the diffusion of discharged warm water influenced by nearshore currents, Coastal Engg. in Japan, Vol.25, 1982, pp.227-238.
- 6) Tokyo Electric Power Company : Field survey report on nearshore currents in and near the surf zone in front of the Fukushima No.1 nuclear Power Station site, Vol.3, 1979, 128p. (in Japanese).
- 7) Tokyo Electric Power Company : Field survey report on nearshore currents in and near the surf zone in front of the Fukushima No.1 Nuclear Power Station site, Vol.7, 1982, 205p. (in Japanese).

## CHAPTER ONE HUNDRED SIXTY

### A TURBULENT TRANSPORT MODEL OF COASTAL PROCESSES

Y. Peter Sheng\*, Member ASCE

#### ABSTRACT

A second-order closure model of turbulent transport and recent model applications to some problems of practical importance in coastal engineering are presented. Particular examples considered are the turbulent wave boundary layer under a linear and a cnoidal wave; current-wave interaction within the bottom boundary layer; mixed layer dynamics; wind-driven currents in a channel. Comparisons are made between the computed results and field/laboratory data.

#### 1. INTRODUCTION

Turbulent transport plays a dominant role in many coastal processes, e.g., sediment dispersion, wave-induced currents in the surf zone, and forces on structures. The accurate prediction of these processes requires a sound understanding of the turbulent transport within various parts of the water column. Existing mathematical models of coastal processes generally utilize relatively simple eddy-viscosity concept to parameterize the complex turbulent transport phenomena. When sufficient data exist to establish the validity of the assumed eddy coefficients in the subject models, the model predictions for a particular application can give reasonable results. However, the required site-specific parameter tuning severely limits the predictability of eddy-viscosity models when little data exist and parameters must be extrapolated from much different flow situations. Moreover, turbulent quantities (e.g., shear stresses) computed by the eddy-viscosity models are often inaccurate due to the inherent model assumption that turbulence is always at local equilibrium condition. The lack of proper physics is why eddy-viscosity model often fails to faithfully simulate highly oscillatory and density-stratified flow situations which are often encountered in coastal waters.

This paper introduces a turbulent transport model (often called "second-order closure model") which allows accurate predictions of coastal processes when data is unavailable or hard to obtain. The basic turbulent transport model (4, 17, 18) retains the dynamic equations of the second-order turbulent correlations which affect the mean flow variables. The added physics contained in the second-order closure model allows direct computation of many of the turbulent transport phenomena without resorting to ad-hoc fixes. Following a brief description of the turbulent transport model, this paper presents some recent model simulations of various coastal processes including: turbulent wave boundary layer, current-wave interaction within the bottom layer, mixed layer dynamics and wind-driven currents.

\*Senior Consultant, Aeronautical Research Associates of Princeton, Inc.  
P. O. Box 2229, Princeton, NJ 08540 U. S. A.

2. A SECOND-ORDER CLOSURE MODEL OF TURBULENT TRANSPORT

The second-order closure model of turbulent transport as described herein has been originally developed by Donaldson and his colleagues at A.R.A.P. The model consists of dynamic equations for the mean flow variables as well as the second-order turbulent correlations (e.g.,  $\overline{u_i u_j}$ ,  $\overline{u_i \rho}$ , and  $\overline{\rho \rho}$ ). Models are developed for the unresolved third-order correlations appearing in the second-order correlation equations. Model constants are derived from analyzing a wide class of flow situations and remain invariant for new applications. As such, the model is often termed as an invariant model.

2.1 MODEL EQUATIONS

The model equations of motion for an incompressible fluid in the presence of both a gravitational and a Coriolis body force, with the mean variables denoted by capitals and the turbulent fluctuations by lower-case, may be written in general tensor notation as follows:

$$\frac{\partial U_i}{\partial t} + U_j \frac{\partial U_i}{\partial x_j} = - \frac{\partial \overline{u_i u_j}}{\partial x_j} - \frac{1}{\rho} \frac{\partial P}{\partial x_i} + g_i \frac{(\Theta - \Theta_0)}{\Theta_0} - 2 \epsilon_{ijk} \Omega_j U_k \tag{1}$$

$$\frac{\partial U_j}{\partial x_j} = 0 \tag{2}$$

$$\frac{\partial \Theta}{\partial t} + U_j \frac{\partial \Theta}{\partial x_j} = - \frac{\partial \overline{u_j \theta}}{\partial x_j} \tag{3}$$

$$\begin{aligned} \frac{\partial \overline{u_i u_j}}{\partial t} + U_k \frac{\partial \overline{u_i u_j}}{\partial x_k} = & - \overline{u_i u_k} \frac{\partial U_j}{\partial x_k} - \overline{u_j u_k} \frac{\partial U_i}{\partial x_k} + g_i \frac{\overline{u_j \theta}}{\Theta_0} + g_j \frac{\overline{u_i \theta}}{\Theta_0} \\ & - 2 \epsilon_{ikl} \Omega_k \overline{u_l u_j} - 2 \epsilon_{jlk} \Omega_l \overline{u_k u_i} \\ & + 0.3 \frac{\partial}{\partial x_k} \left( q \Lambda \frac{\partial \overline{u_i u_j}}{\partial x_k} \right) - \frac{q}{\Lambda} \left( \overline{u_i u_j} - \delta_{ij} \frac{q^2}{3} \right) - \delta_{ij} \frac{q^3}{12 \Lambda} \end{aligned} \tag{4}$$

$$\begin{aligned} \frac{\partial \overline{u_i \theta}}{\partial t} + U_j \frac{\partial \overline{u_i \theta}}{\partial x_j} = & - \overline{u_i u_j} \frac{\partial \Theta}{\partial x_j} - \overline{u_j \theta} \frac{\partial U_i}{\partial x_j} + g_i \frac{\overline{\theta^2}}{\Theta_0} - 2 \epsilon_{ijk} \Omega_j \overline{u_k \theta} \\ & + 0.3 \frac{\partial}{\partial x_j} \left( q \Lambda \frac{\partial \overline{u_i \theta}}{\partial x_j} \right) - \frac{0.75 q}{\Lambda} \overline{u_i \theta} \end{aligned} \tag{5}$$

$$\frac{\partial \overline{\theta^2}}{\partial t} + U_j \frac{\partial \overline{\theta^2}}{\partial x_j} = - 2 \overline{u_j \theta} \frac{\partial \Theta}{\partial x_j} + 0.3 \frac{\partial}{\partial x_j} \left( q \Lambda \frac{\partial \overline{\theta^2}}{\partial x_j} \right) - \frac{0.45 q \overline{\theta^2}}{\Lambda} \tag{6}$$

$$\begin{aligned} \frac{\partial \Lambda}{\partial t} + U_j \frac{\partial \Lambda}{\partial x_j} = & 0.35 \frac{\Lambda}{q^2} \overline{u_i u_j} \frac{\partial U_i}{\partial x_j} + 0.75 q + 0.3 \frac{\partial}{\partial x_i} \left( q \Lambda \frac{\partial \Lambda}{\partial x_i} \right) \\ & - \frac{0.375}{q} \left( \frac{\partial q \Lambda}{\partial x_i} \right)^2 + \frac{0.8}{q^2} q_i \frac{u_i \theta}{\Theta_0} \end{aligned} \tag{7}$$

where  $x_i$  are coordinate axes,  $t$  is time,  $U_i, U_j, U_k$  are the mean velocity components,  $u_i, u_j, u_k$  are the fluctuating velocity components,  $\rho$  is density,  $\Theta$  and  $\theta$  are mean and fluctuating temperatures,  $q$  is total fluctuating velocity,  $\Lambda$  is turbulent macroscale,  $\delta_{ij}$  is Kronecker

delta,  $\epsilon_{ijk}$  is alternating tensor,  $\Omega$  is earth's rotation.

In a first-order closure (or eddy viscosity) model, only the first three equations for the mean variables are resolved. The second-order correlations  $\overline{u_i u_j}$  and  $\overline{u_j \theta}$  appearing in the mean equations are parameterized as the products of eddy coefficients and the mean gradients,  $\partial u_i / \partial x_j$  and  $\partial \theta / \partial x_j$  respectively. The most complete second-order closure model, on the other hand, retains all the dynamic equations for the Reynolds stresses  $\overline{u_i u_j}$ , the heat fluxes  $\overline{u_j \theta}$ , and the temperature variance  $\overline{\theta^2}$ . To close the system, a dynamic equation for the turbulent macroscale  $\Lambda$  is introduced. It should be pointed out that many of the terms in the second-order correlation equations do not require any modeling. These include the turbulent production terms, the buoyancy terms, and the Coriolis terms. The third-order correlation and pressure correlation terms appearing in the original Reynolds stress equations have been modeled as a diffusion term and a tendency toward isotropy term. Model constants for the diffusion term, the tendency toward isotropy term, the dissipation term, and other modeled terms have been determined from analyzing a wide class of flow situations (13) and remain fixed for any new applications.

The complete second-order closure model as described by Equations (1) through (7) has been applied to simulate various atmospheric, oceanic, and laboratory problems of practical importance. The ability of the model to simulate a variety of flow situations with the same set of model constants has been successfully demonstrated. Simplified versions of the second-order closure model have also been formulated by retaining the dynamic equations for only part of the second-order correlation variables. For example, the quasi-equilibrium version retains the dynamic equations for  $q^2$  and  $\Lambda$ , while neglecting the diffusion and time evolution terms in other correlation equations. Such an approximation is valid so long as the turbulent time scale  $\Lambda/q$  is small compared to the mean flow time scale, and is being incorporated into a three-dimensional coastal current model (18).

Most of the following model applications utilize the one-dimensional version of the complete second-order closure model. Multi-dimensional versions of the second-order closure model have been utilized in numerous past and present applications, e.g., the detailed dynamics of wakes behind blunt bodies (5) and flow within the core of a tornado (14).

### 3. TURBULENT WAVE BOUNDARY LAYER

Detailed measurements in turbulent wave boundary layers are scarce. Johnson and Carlsen (9) measured the detailed flow within an oscillating water tunnel with a fixed rough bottom. In their Test I, an 8.39 sec wave with a maximum mean free stream velocity of 2 to 2.22 m/sec and a nearly sinusoidal time variation was imposed on a water depth of 23 cm. Vertical profiles of ensemble-averaged horizontal velocity within the water tunnel were measured at 15° intervals throughout several wave cycles. Multi-layered eddy-viscosity models (10,6,3) and time-varying eddy-viscosity models (8,21) were developed to achieve reasonable simulation of the mean flow variables measured

by Jonsson and Carlsen. Considerable efforts were spent in arriving at the "proper" eddy-viscosity formulation needed to yield good fit of the mean flow data. Using the complete second-order closure model, Sheng (17) successfully simulated Jonsson and Carlsen's turbulent wave boundary layer. Very good agreement was found between the simulated and measured mean velocity, phase lag and shear stress. In addition, model results revealed the transient behavior of a thin classic logarithmic layer modulated by the time-periodic pressure gradient. For simplicity, however, Sheng (17) assumed a sinusoidal free-stream velocity of 2 m/sec amplitude. In the present paper, based on harmonic analysis of the measured data, the following free-stream velocity is used:

$$U_f = A_1 + \sum_{i=2}^{13} \left\{ A_i \cos \left[ (i-1) \theta \right] + B_i \sin \left[ (i-1) \theta \right] \right\} \quad (8)$$

where  $A_i$  and  $B_i$  are coefficients determined from the harmonic analysis of Jonsson and Carlsen's free stream velocity. The boundary conditions for the mean and turbulent variables are basically the same as in Sheng (17).

The mean flow profiles at  $\phi=0^\circ$ ,  $45^\circ$ ,  $90^\circ$ ,  $135^\circ$  are shown in Figure 1(a), while those at  $\phi=180^\circ$ ,  $225^\circ$ ,  $270^\circ$ ,  $315^\circ$  are shown in Figure 1(b). Excellent agreement between the computed and measured data is apparent at all levels and all times. A slight mid-level velocity overshoot at peak free-stream velocity, which was found in the earlier results of Sheng (17), is now eliminated.

Vertical profiles of the Reynolds stress  $-\overline{\rho u w}$  are shown in Figures 2(a) and 2(b). Excellent agreement between the computed and measured results is found at  $\phi=0^\circ$  and  $180^\circ$ , while the worst agreement is found at  $\phi=90^\circ$  and  $\phi=270^\circ$ . This is because Jonsson and Carlsen's Reynolds stresses were not measure directly, but were computed indirectly from the mean flow data via the following equation:

$$\frac{\tau}{\rho} = - \int_0^z \frac{\partial}{\partial t} (U_f - U) dz \quad (9)$$

where  $d$  corresponds to  $\tau=0$  and was taken to be 17 cm. The Reynolds stresses calculated from Equation (9) are very sensitive to the numerical evaluation of the r.h.s., i.e., accuracy of time derivative and vertical profile of the mean velocity. The mean velocities were only measured at 15° intervals. Hence, one expects error in  $\tau$  to be the smallest when time variation of mean velocity is the smallest ( $\phi=0^\circ$  and  $180^\circ$ ) while error is the largest when time variation of mean velocity is the largest ( $\phi=90^\circ$  and  $270^\circ$ ). This explains the discrepancy found in Figure 2. In this regard, the second-order closure model can be used to guide the design of laboratory experiments by pointing out the needed temporal and spatial resolutions of data. Jonsson and Carlsen also calculated the eddy-viscosity values from

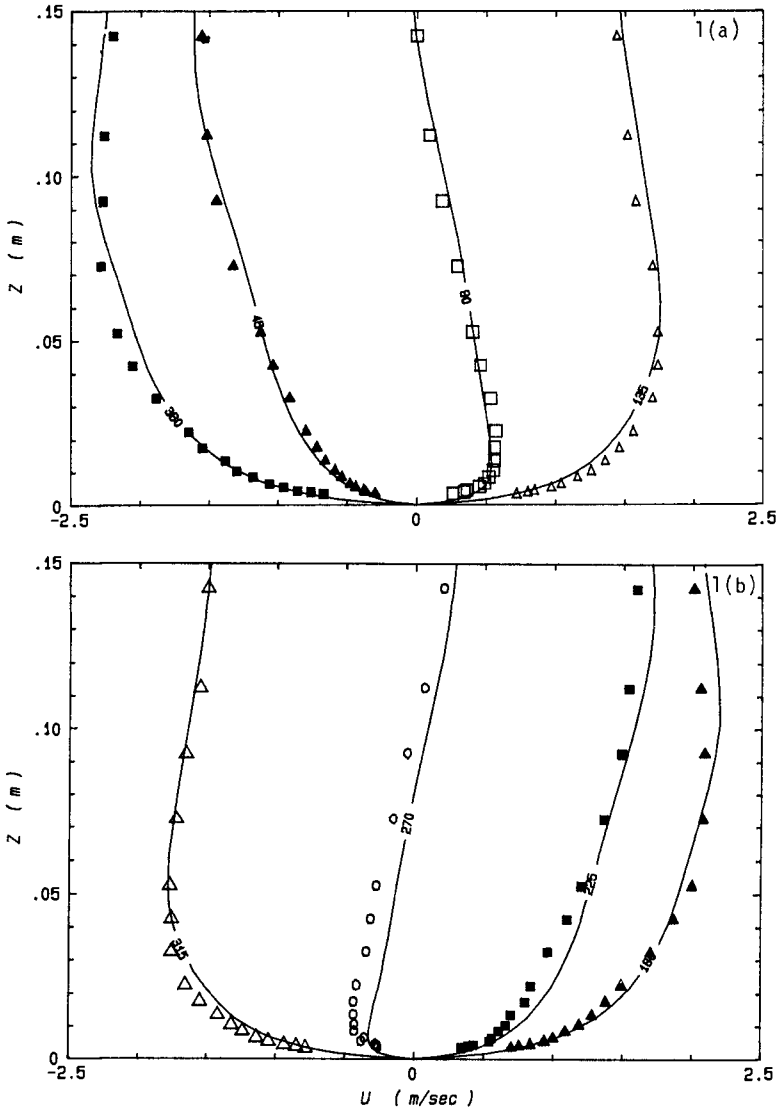


FIGURE 1. Mean velocity vs height in Jonsson and Carlsen's turbulent wave boundary layer (—: model results, symbols: data): (a) at  $\phi=0^\circ, 45^\circ, 90^\circ, 135^\circ$ ; (b) at  $\phi=180^\circ, 225^\circ, 270^\circ, 315^\circ$ .

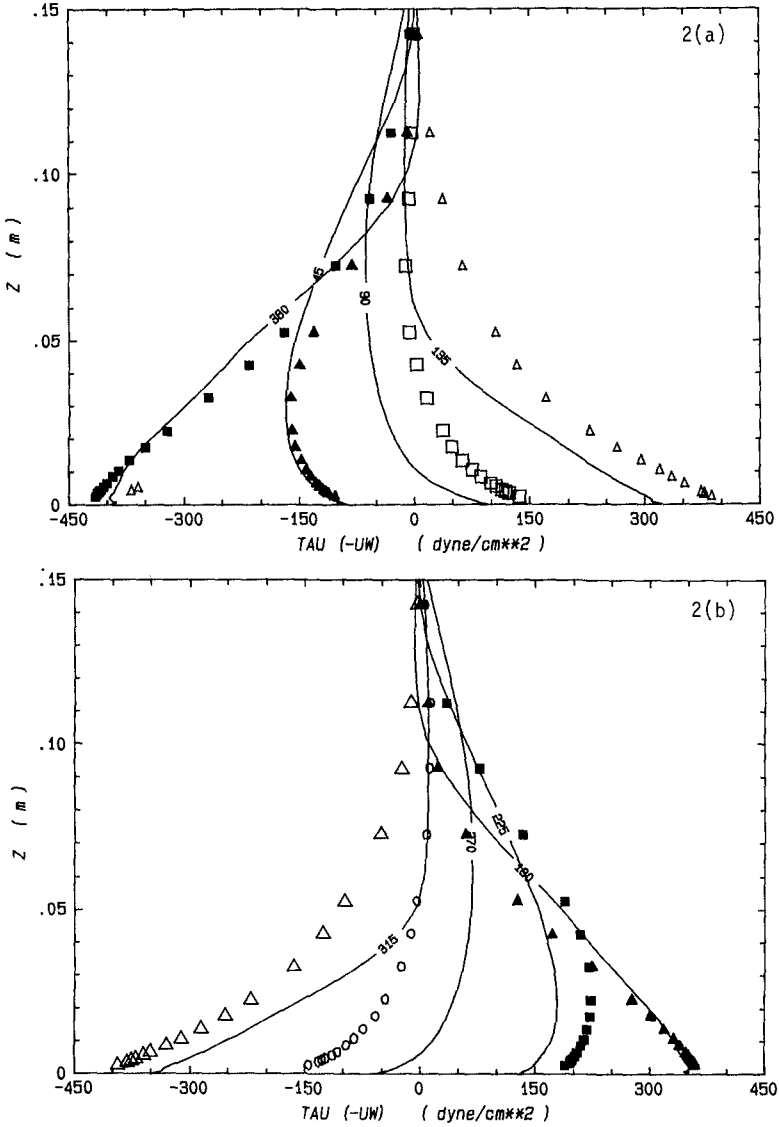


FIGURE 2. Reynolds stress vs height in Jonsson and Carlsen's turbulent wave boundary layer (—: model results, symbols: data): (a) at  $\phi=0^\circ, 45^\circ, 90^\circ, 135^\circ$ ; (b) at  $\phi=180^\circ, 225^\circ, 270^\circ, 315^\circ$ .



the calculated shear stresses and vertical gradients of the measured mean velocities. The resulting eddy viscosities are ill-behaved and often have negative values. Attempt to formulate an eddy viscosity model based on these ill-behaved eddy-viscosity values may lead to good fit of mean flow data, but will not provide physical insight of the turbulent transport processes.

Figure 3 presents the temporal variation of  $U_f$ ,  $U_{1cm}$ ,  $\tau_{bottom}$ ,  $\partial p/\partial x$  and  $z_{log}$  (thickness of the classic logarithmic layer). A phase lag of approximately 0.4 radians is found between  $U_f$  and  $U_{1cm}$  (the mean velocity at 1 cm above the bottom). Similar phase lag is also found between  $U_f$  and  $\tau_{bottom}$  (the bottom stress). The pressure gradient  $\partial p/\partial x$  balances the time variation of  $U_f$  exactly, and obtains maximum absolute value in the neighborhood of  $\phi=90^\circ$  and  $270^\circ$  but is approximately zero at  $0^\circ$  and  $180^\circ$ . The classical logarithmic layer is the layer within which the Reynolds stress  $-\overline{uw}$  varies less than 1% from its bottom value, and the log layer thickness lags behind the pressure gradient by approximately  $27^\circ$ . The maximum thickness of the log layer is only 2.5 cm, or 32 times the roughness height  $z_0$ . This rigorously computed value is substantially smaller than Jonsson and Carlsen's estimate of 6.3 cm and the fixed wave boundary layer thickness assumed by Grant and Madsen (7) in their current-wave boundary layer model.

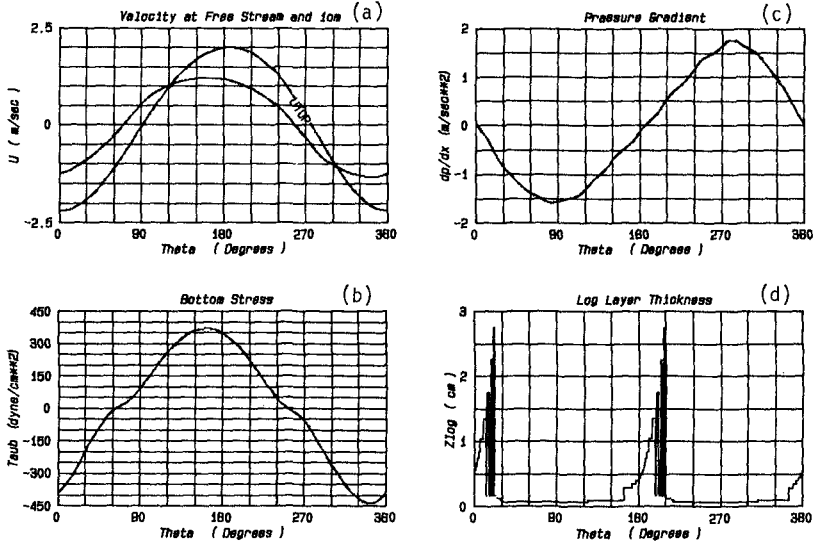


FIGURE 3. Temporal variation of (a) free stream velocity and velocity at 1-cm above the bottom, (b) bottom stress, (c) pressure gradient, and (d) thickness of lag layer over one wave cycle in simulated JC's turbulent wave boundary layer.

#### 4. TURBULENT WAVE BOUNDARY LAYER UNDER A CNOIDAL WAVE

Waves in coastal waters are often nonlinear in nature, particularly when large sea swells are propagated onto very shallow waters. Linear wave theory is often inadequate to describe the wave under these circumstances and cnoidal wave theory has to be used. Cnoidal wave theory is based on the Korteweg-deVries equation (12) and its solution is basically different from those of higher-order Stoke's wave theories. Turbulent wave boundary layer underneath a cnoidal wave has not been previously investigated. The direct extension of the previously mentioned eddy-viscosity models to such cases is questionable. In the following, we present a simulation of the turbulent wave boundary layer underneath a cnoidal wave by means of the second-order closure model.

In a recent physical model study at CERC, the wave parameters within Humboldt Bay, California due to a 11-sec, 10-ft sea swell propagated from the Northwest were measured. Sharp-crested cnoidal waves were clearly observed over much of the Humboldt Bay. At a nearshore station in the vicinity of Buhne Point, the depth ( $d$ ) is only 2.65 m, and the wave height ( $H$ ) is 0.64 m. Values of  $d/gT^2$  and  $H/gT^2$  indicate that cnoidal wave theory should be used. The wave orbital velocities were computed by using the cnoidal wave theory and the linear theory and are shown in Figure 4(a). Based on Kajiura's empirical formula for the bottom friction coefficient underneath a linear wave, the computed bottom stresses over a wave cycle are shown in Figure 4(b). Excessively high bottom stress is found underneath the cnoidal wave.

The turbulent wave boundary layer underneath the cnoidal wave was computed by means of the second-order closure model and considering a water column of 20 cm above the bottom. Figure 5(a) shows the mean velocity profiles over the entire cycle at 45° intervals. The sharp-crested nature of the cnoidal wave is clearly manifested by these velocity profiles. Much of the temporal variation takes place during only half of the wave cycle while little variation is found during the other half cycle. The computed Reynolds stress profiles are shown in Figure 5(b). The Reynolds stresses are generally confined to a layer much thinner than what would be underneath a linear sinusoidal wave. Figure 6 shows the temporal variation of  $U_{\tau}$ ,  $U_{1cm}$ ,  $\tau_{bottom}$ ,  $\partial p/\partial x$  and thickness of the logarithmic layer. Compared to its linear counterpart, the logarithmic layer is thinner during the fast half cycle but somewhat thicker during the slow half cycle. The maximum bottom shear stress as shown in Figure 6 is little over 100 dyne/cm<sup>2</sup>, a value substantially less than the 180 dyne/cm<sup>2</sup> computed by using Kajiura's empirical formula for sinusoidal wave. More detailed computation of the cnoidal wave within the Humboldt Bay can be found in Sheng (20).

#### 5. CURRENT WAVE INTERACTION WITHIN THE BOTTOM BOUNDARY LAYER

Using an eddy-viscosity model, Grant and Madsen (7) produced a theoretical analysis of combined current and wave flow over a rough boundary, predicting an increase in apparent bed roughness and bottom shear stress when waves are superimposed on the current. Similar models and qualitative results have been produced by others (e.g., 2). As pointed out by Kemp and Simon (11), however, no detailed verification of the above eddy-viscosity models has been made. In addition, these models generally require ad-hoc assumptions on the wave boundary layer.

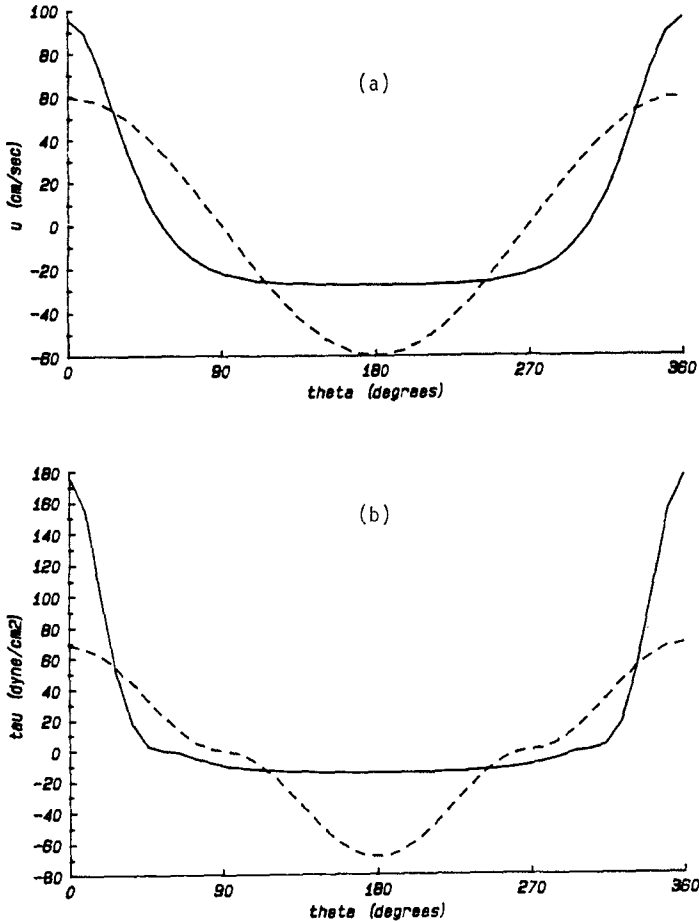


FIGURE 4. Orbital velocity and bottom stress at a station near Buhne Point in Humboldt Bay, CA due to a 11-sec (period) and 10-ft (wave ht.) sea swell propagated from the Northwest (—: cnoidal wave theory, ----: linear wave theory); (a) wave orbital velocity over a wave cycle, (b) bottom stress computed by using Kajiura's empirical formula.

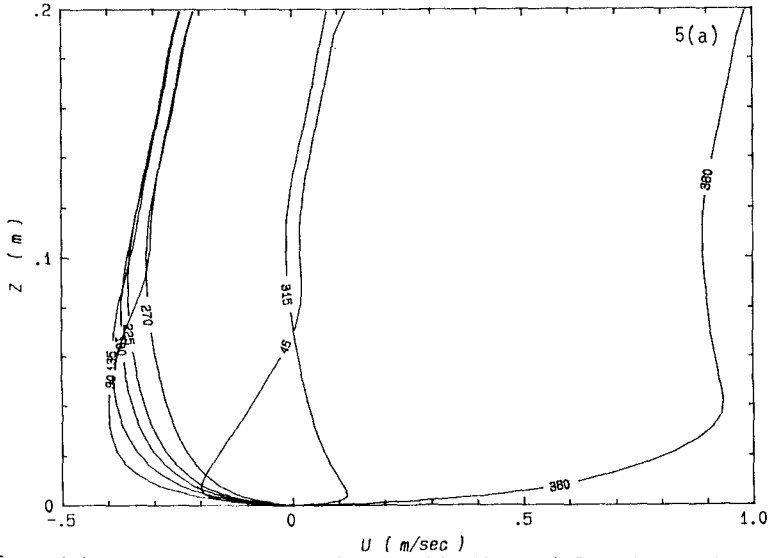


FIGURE 5(a). Mean velocity vs height within the turbulent bottom boundary layer under a cnoidal wave. The profiles are shown at 45° intervals over a wave cycle. Results of second-order closure model.

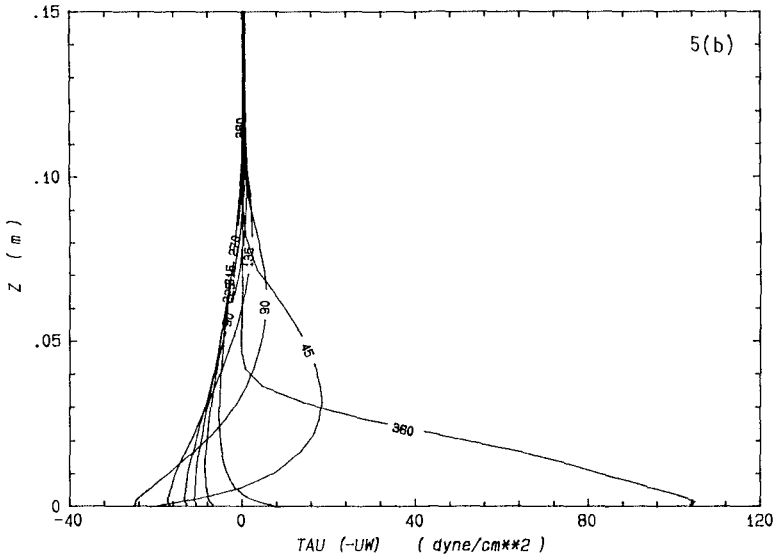


FIGURE 5(b). Reynolds stress vs height within the turbulent bottom boundary layer under a cnoidal wave. The profiles are shown at 45° intervals over a wave cycle.

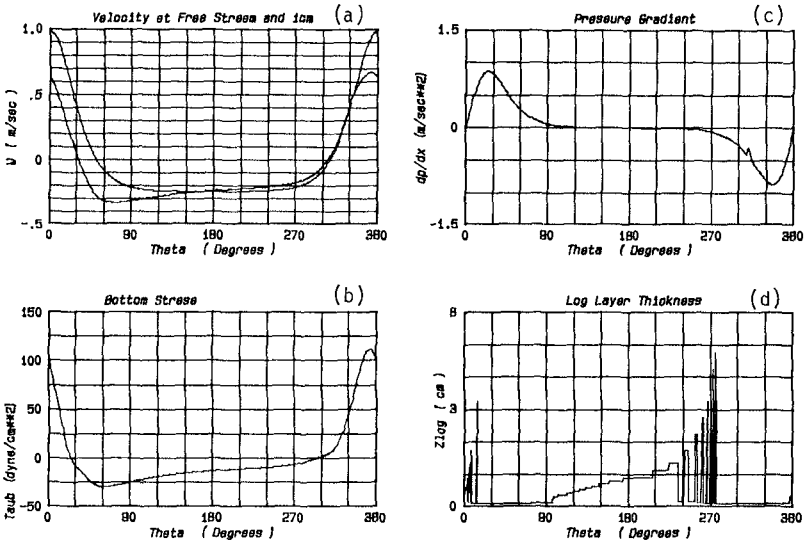


FIGURE 6. Temporal variation of (a) free stream velocity and velocity at 1-cm above the bottom, (b) bottom stress, (c) pressure gradient, and (d) thickness of log layer over one wave cycle in turbulent boundary layer under the cnoidal wave.

In this paper, we present some results on current-wave bottom boundary layer obtained with the second-order closure model. The first simulation is based on some data collected at a CODE site (C3) about 1 km off the California coast. Using  $z_0=0.2$  cm,  $U_{100cm}=10.21$  cm/sec,  $U_w=6.09$  cm/sec, and  $T_w=13.79$  sec, the model computed results (averaged over the wave cycle) within the bottom 1 m are shown in Figure 7. In the absence of any wave, the velocity profile shows a logarithmic variation with depth while the turbulent kinetic energy ( $q^2/2$ ) and Reynolds stress ( $-\overline{uw}$ ) are constant within the bottom boundary layer. When waves are superimposed on the current, the apparent roughness is increased to 0.5 cm while  $q^2$  and  $-\overline{uw}$  are increased by more than 50% near the bottom. The increase in  $-\overline{uw}$  is less than that produced by Grant and Madsen, which was found to be higher than that determined from the logarithmic velocity profile. If Kajiura's empirical formula was used for the bottom friction coefficient, one finds that the wave-induced bottom stress alone is on the order of 1.3 dyne/cm<sup>2</sup> which is much higher than our combined current-wave result.

The second model simulation is based on the current and wave data at a site in the Mississippi Sound (18) where  $z_0=0.1$  cm,  $U_{100cm}=20$  cm/sec,  $U_w=20$  cm/sec and  $T_w=2.5$  sec. The results shown in Figure 8

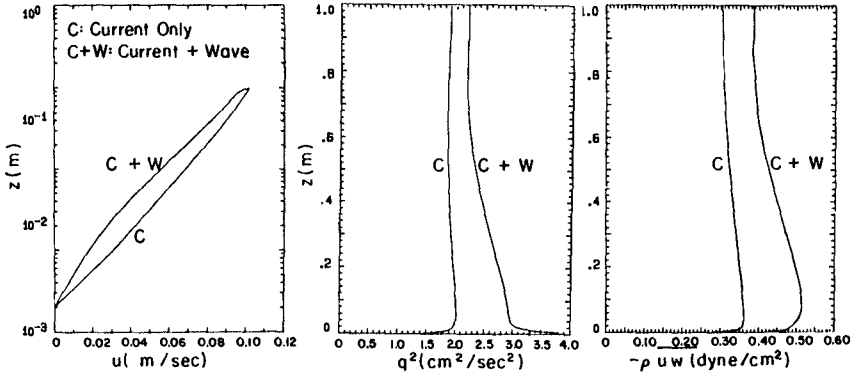


FIGURE 7. Simulated current-wave bottom boundary layer at a CODE site (C3). Vertical profiles of (a) mean velocity, (b) twice the turbulent K.E., and (c) Reynolds stress averaged over the wave cycle.  $z_0 = 0.2$  cm,  $U_{100} = 10.2$  cm/sec,  $U_W = 6.09$  cm/sec,  $T_W = 13.79$  sec.

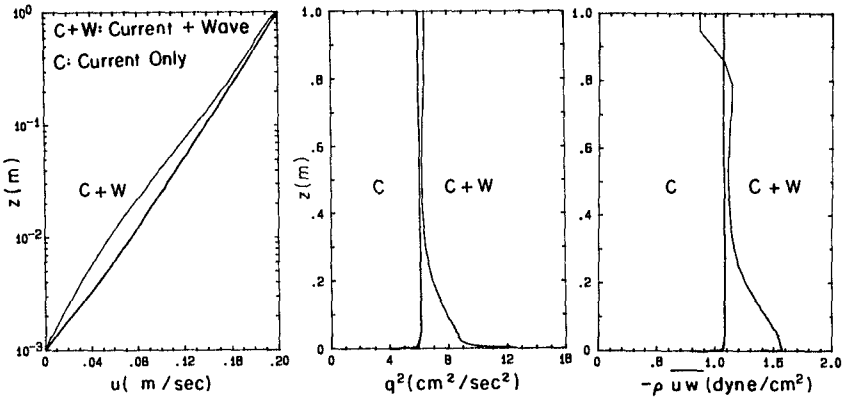


FIGURE 8. Simulated current-wave bottom boundary layer at a site in the Mississippi Sound. Vertical profiles of (a) mean velocity, (b) twice the turbulent K.E., and (c) Reynolds stress averaged over the wave cycle.  $z_0 = 0.1$  cm,  $U_{100} = 20$  cm/sec,  $U_W = 10$  cm/sec,  $T_W = 2.5$  sec.

indicate the wave boundary layer is relatively thinner compared to the CODE simulation, although more than 50% increase is also found in the  $q^2$  and  $-\overline{uw}$  at bottom.

The results presented herein have great engineering implications.

The increased bottom shear stress due to the presence of the wave will lead to enhanced erosion of sediment while the increased turbulent intensity will lead to enhanced mixing of sediment within the water column. In a comprehensive laboratory study of current-wave interaction within the bottom boundary layer, Kemp and Simon (11) found significant phase shift between the turbulent intensity and the bottom stress. Earlier study by van Hoften and Karaki (22) found that presence of the wave may sometimes lead to reduction of the Reynolds stress. To further examine and understand such interesting phenomena, it is essential to use a dynamic turbulent transport model which requires little ad-hoc parameter tuning.

#### 6. MIXED LAYER DYNAMICS

Coastal processes may be affected by density stratification in coastal waters resulting from inhomogeneity in salinity, sediment concentration, and temperature. A predictive model capable of simulating stratified flow situations is highly desirable. Using the second-order closure model, we performed a simulation of the ocean mixed layer measured during MILE (MIXed Layer Experiment) by Miyake (16). Data obtained throughout a 32-day period starting August 2, 1977 exhibited significant temporal variations of the wind stress (between 0 and 5 dynes/cm<sup>2</sup>) and heat flux (diurnal heating and cooling cycle) at the ocean site. The model simulation was performed by using the measured temperature profile on August 2, 1977 as initial condition and the measured wind stress and heat flux during the subsequent 32 days as boundary conditions. As shown in Figure 9(a), the simulated mean temperature profile on the 32nd day agrees well with data. So are the simulated surface temperatures throughout the 32-day period in Figure 9(b). Despite the great variability of the weather, the model was able to correctly track the evolution of the thermocline throughout the simulation period.

More recently, a simplified version of the second-order closure model has been applied to simulate the mixed layer dynamics (19). This simplified model is comparable in complexity to the model of Mellor and Durbin (15) but contains more dynamics by allowing a spatially varying turbulence macroscale.

#### 7. WIND-DRIVEN CURRENTS

A simplified three-dimensional version of the second-order closure model was applied to simulate the wind-driven currents in a laboratory flume measured by Baines and Knapp (1). Figure 10 shows the model results at the middle of the flume obtained with the same  $U_*D/\nu(\sim 51,000)$  of the experiment. Both the mean horizontal velocity  $U$  and the vertical turbulent velocity  $w$  agree very well with measured data. Although the vertical eddy-viscosity  $A_V$  was not measured, the simulated peak  $A_V$  agree well with an estimated peak value based on the measured turbulence profile and a length scale approximately 20% of the water depth.

#### 8. CONCLUDING REMARKS

This paper presents a brief introduction of a second-order closure model of turbulent transport and recent model applications to simulate various coastal processes of practical importance. Due to the added

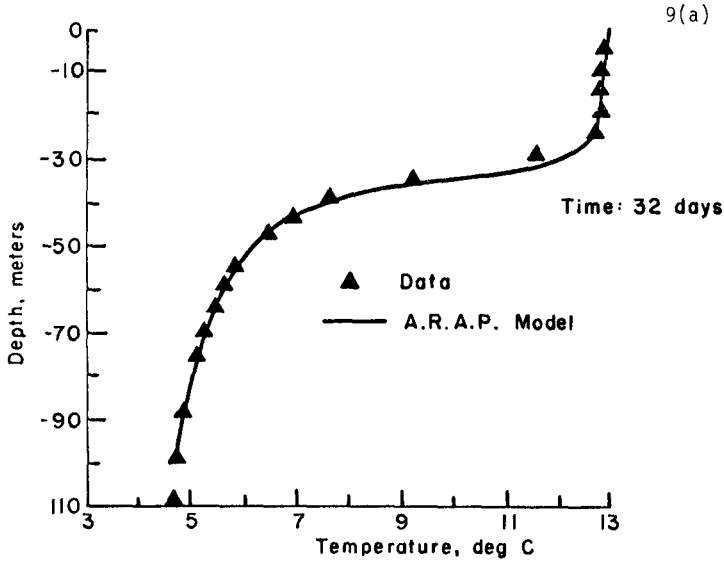


FIGURE 9 (a). Simulated and measured temperature profile at 32 days after the initiation of the MILE ocean mixed layer experiment.

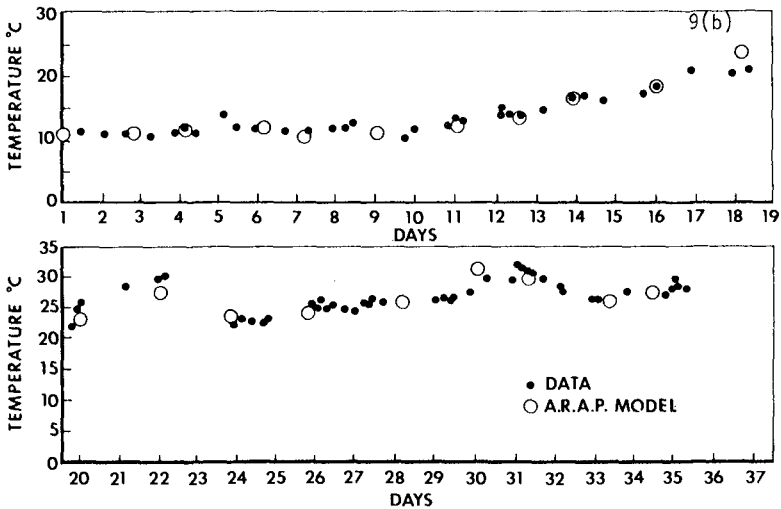


FIGURE 9 (b). Simulated and measured ocean surface temperature during the MILE.



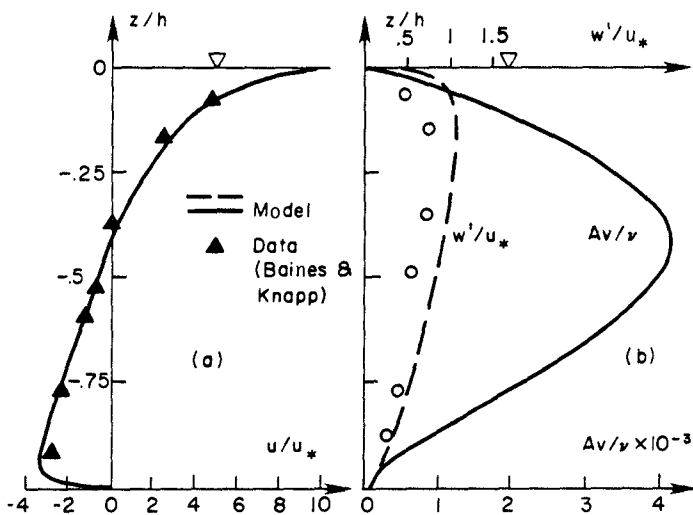


FIGURE 1D. Wind-driven currents in an open channel. Vertical profiles of (a) horizontal velocity, (b) vertical turbulent velocity and eddy viscosity.

physics contained in the model, the model was able to successfully simulate a variety of flow situations without having to perform extensive site-specific tuning of ad-hoc model parameters. Detailed simulations of the turbulent bottom boundary layers and the mixed layer demonstrated that the model may be used to (1) provide detailed understanding of the physical processes, (2) aid the design and interpretation of laboratory/field experiments, and (3) guide the development of first-order closure models (eddy-viscosity models). By combining the turbulent transport model with emerging high-quality laboratory/field data, further understanding on the turbulent current-wave boundary layer can be achieved. Research is also needed to extend the model to study (1) the dispersion of sediments, (2) the hydrodynamic forces on complex structures, and (3) the wave-breaking induced turbulence.

#### 9. ACKNOWLEDGEMENT

This work has been partially supported by the U. S. Army Engineer Waterways Experiment Station under contract DACW 39-8D-C-0D87.

#### 10. REFERENCES

1. Baines, W. D. and D. J. Knapp, 1965: "Wind-Driven Water Currents", *J. Hyd. Div., ASCE*, 91, No. HY2, pp 2D5-221.
2. Bakker, W. T. and Th. Van Doorn, 1978: "Near Bottom Velocities in Waves With a Current", Proc. 16th Conf. on Coastal Engineering.

3. Brevik, I., 1981: "Oscillatory Rough Turbulent Boundary Layers", J. Waterways, Port, Coastal and Ocean Div., ASCE, vol. 107, pp 175-188.
4. Donaldson, C. duP., 1973: "Atmospheric Turbulence and the Dispersion of Atmospheric Pollutants", in AMS Workshop on Micrometeorology, (O.A. Haugen, ed.), Science Press, Boston, pp 313-39D.
5. Donaldson, C. duP., and A. J. Bilanin, 1975: "Vortex Wakes of Conventional Aircraft", AGARDograph, No. 2D4.
6. Grant, W. D. and O. S. Madsen, 1978: "Bottom Friction Under Waves in the Presence of a Weak Current", NOAA Tech Report, ERL-MESA., 150 pp.
7. Grant, W. O. and O. S. Madsen, 1979: "Combined Wave and Current Interaction with a Rough Bottom", J. Geophys. Res., 84, pp 1797-1808.
8. Jonsson, I. G., 1980: "A New Approach to Oscillatory Rough Turbulent Boundary Layers", Ocean Engng., 1, pp 1D9-152.
9. Jonsson, I.G., and N. A. Carlsen, 1976: "Experimental and Theoretical Investigations in an Oscillatory Rough Turbulent Boundary Layer", J. Hydr. Res., 14, pp 45-60.
10. Kajiwara, K., 1968: "A Model of the Bottom Boundary Layer in Water Waves", Bull Earthq. Res. Inst., 46, pp 75-123.
11. Kemp, P. H., and R. R. Simon, 1982: "The Interaction Between Waves and a Turbulent Current: Waves Propagating with the Current", J. Fluid Mech., vol. 116, pp 227-250.
12. Korteweg, D. J., and G. deVries, 1895: "On the Change of Form of Long Waves Advancing in a Rectangular Canal, and on a New Type of Stationary Waves", Phil. Mag., 5th Series, vol. 39, pp 422-443.
13. Lewellen, W. S., 1977: "Use of Invariant Modeling," in Handbook of Turbulence, vol. 1 (W. Frost, ed.), Plenum Publishing Corp., pp 237-280.
14. Lewellen, W. S., and Y. P. Sheng, 1981: "Modeling Tornado Dynamics", U. S. Nuclear Regulatory Commission Report NUREG/CR-1585, 227 pp.
15. Mellor, G. L., and P. A. Ourbain, 1875: "The Structure and Dynamics of the Ocean Surface Mixed Layer", JPO, 5, pp 718-728.
16. Miyake, M., 1978: "Oceanographic Observations at Ocean Station P", Pacific Marine Science Report 78-1, Institute of Ocean Sciences, Sidney, BC.
17. Sheng, Y. P., 1982: "Hydraulic Applications of a Second-Order Closure Model of Turbulent Transport", in Applying Research to Hydraulic Practice, (P. Smith, ed.), ASCE, pp 106-119.
18. Sheng, Y. P., 1983: "Mathematical Modeling of Three-Dimensional Coastal Currents and Sediment Dispersion", Technical Report CERC-83-2, U. S. Army Engineer Waterways Experiment Station, CE, Vicksburg, MS. Also A.R.A.P. Report No. 458, Princeton, NJ, 288 pp.

19. Sheng, Y. P., 1984a: "A One-Dimensional Ocean Current Model", A. R. A. P. Report No. 523.
20. Sheng, Y. P., 1984b: "Numerical Computation of Current- and Wave-induced erosional forcing within the Humboldt Bay", A.R.A.P. Tech. Memo 84-18, Princeton, NJ.
21. Towbridge, J. and O. S. Madsen, 1984: "Turbulent Wave Boundary Layers", JGR, vol. 89, pp 7989-8007.
22. van Hoften, J. O. A., and S. Karaki, 1976: "Interaction of Waves and a Turbulent Current", Proc. 15th International Conf. Coastal Eng.

## CHAPTER ONE HUNDRED SIXTY ONE

### BOTTOM TURBULENT BOUNDARY LAYER IN WAVE-CURRENT CO-EXISTING SYSTEMS

Toshiyuki Asano\* and Yuichi Iwagaki\*\*

#### ABSTRACT

This study presents a new mathematical method calculating the water particle velocity in the wave-current co-existing systems. A boundary layer thickness  $\delta_w$  in the co-existing system is expected to be variable with the water particle velocity ratio of wave component to current component. In this method, the boundary layer equation is solved as a free boundary problem by treating  $\delta_w$  as an unknown boundary value. Several characteristics of the turbulent boundary layer such as the friction factor, friction velocity, boundary layer thickness, etc. are calculated by this method and the effect of the wave-current velocity ratio on them is discussed. Furthermore, the velocity reduction of the current due to wave superimposing is investigated.

In addition, near-bottom velocities are measured by a laser-doppler velocimeter in the pure current, the pure wave and the wave-current co-existing fields. These results are compared with calculated ones by this mathematical method.

#### 1. Introduction

Understanding of near bottom velocity characteristics in wave and current co-existing systems is of considerable importance for sediment transport in the nearshore region, and comprehensive study of the bottom shear stress in the field is essential in developing a more accurate theory to predict nearshore current systems.

Hydrodynamics near the bottom in the co-existing field is complicated because there are mutual interactions between a current and waves. Grant-Madsen<sup>4)</sup> proposed a theoretical model to describe the water particle velocity and the shear stress in the wave-current co-existing field, and pointed out that the current above the wave boundary layer feels a larger resistance due to the presence of the wave than in the pure current field. This is the first theoretical study to investigate

\* Research Associate, Kyoto University

\*\* Professor, Kyoto University, M. of ASCE  
Yoshida-Honmachi, Sakyo-ku Kyoto 606, Japan

not only the wave deformation by a current but also the current deformation by waves. However, their analysis left some problems to be solved.

As an important problem, we point out that convective acceleration terms were neglected in their analysis. When the velocity potential in the wave-current co-existing field is introduced,  $U\partial u/\partial x$  term involved in the boundary conditions at the water surface should be considered because it is regarded to be the same order as the local acceleration term  $\partial u/\partial t$ . The velocity potential and the dispersion equation in the co-existing field can be deduced by considering this term.

Since the water particle velocity obtained by the boundary layer solution and that by the inviscid solution should be matched at a certain level from a bed, this term must be taken into consideration for the consistency in the analysis.

Another problem lies in how to determine the wave boundary layer thickness  $\delta_w$ . This model considers the co-existing field such a way that the current feels different eddy viscosities between inside and outside of the wave boundary layer. However, the current velocity can not be estimated as long as  $\delta_w$  is not determined. Grant-Madsen applied an existing knowledge on  $\delta_w$  in the wave boundary layer straightforwardly to the co-existing field. Therefore, the variation of the boundary layer thickness  $\delta_w$  with the wave-current composing ratio could not be considered in their analysis.

The present study proposes a new mathematical method to predict the water particle velocity in the co-existing field. By using this method, several characteristics of the turbulent boundary layer are calculated and discussed.

Finally, measurements on the near bottom velocity are carried out with a laser doppler velocimeter and the validity of this analytical method is examined by comparing with the experimental results.

## 2. Formulation of boundary layer equation in co-existing field

### (a) Basic assumption

This study is based on Grant-Madsen's model on the wave-current turbulent boundary layer. The basic idea of their model is briefly as follows:

The current is assumed to be a fully developed flow and the associated boundary layer extends over most of the depth. Meanwhile, the wave boundary layer is confined to a relatively thin region close to the bottom. The velocity distributions both for a wave component and a current component are schematically shown in Fig.1. Consequently, the shear stress inside of the wave boundary layer is composed of wave-current interacting effect. They assumed different eddy viscosities both for inside and outside the wave boundary layer regions as follows:

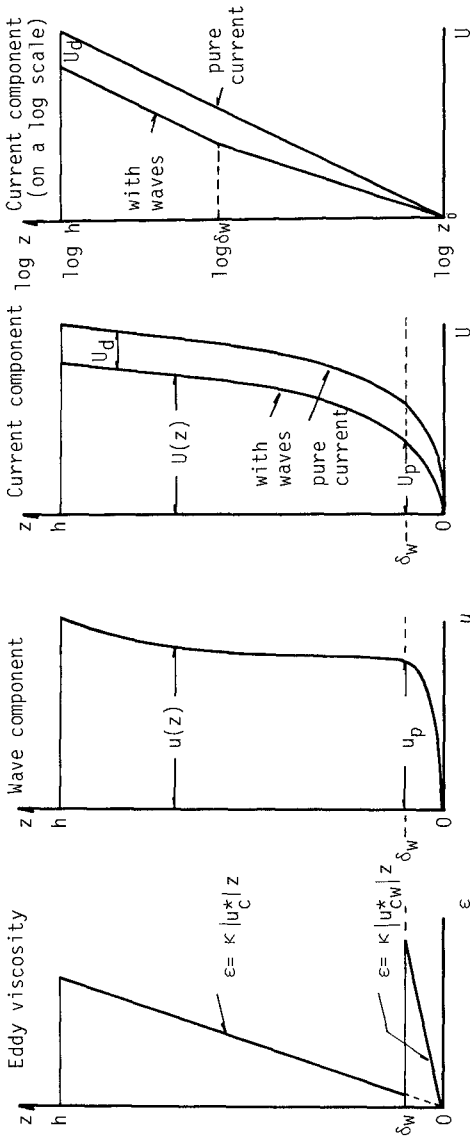


Fig.1 Profiles for eddy viscosity, wave and current components assumed in this model

$$\epsilon = \kappa |u_c^*|^2 z \quad z > \delta_w \quad (1)$$

$$\epsilon = \kappa |u_{cw}^*|^2 z \quad z < \delta_w \quad (2)$$

in which,  $\kappa$  is von Karman's constant,  $z$  the vertical coordinate,  $\delta_w$  the wave boundary layer thickness,  $u_c^*$  and  $u_{cw}^*$  the shear velocities for current and wave-current motions respectively.

This assumption on the eddy viscosity, which increases linearly with the height from the bed, is not sufficient to represent the turbulent boundary layer accurately.

For the wave turbulent boundary layer, Kajiura<sup>5)</sup> and Noda<sup>8)</sup> proposed the elaborate theories by introducing boundary layer stratifications. For the co-existing field, Tanaka-Shuto<sup>9)</sup> and Christoffersen<sup>3)</sup> presented the theoretical analyses on the basis of different assumptions on the eddy viscosity distribution from Grant-Madsen's model.

Their analyses are important for refinement of the Grant-Madsen's model; however, they did not solve the above mentioned problems. Since the primary concern here is to improve the essential weakpoints of Grant-Madsen's model, this study does not consider such modifications on the eddy viscosity, and starts the analysis under the same assumptions as Grant-Madsen's theory.

The shear stress inside the wave boundary layer is calculated by the sum of the wave and current components which are presented respectively as follows:

$$\tau_w = \rho \kappa u_{cw}^* z \frac{\partial u}{\partial z} \quad (3)$$

$$\tau_c = \rho \kappa u_c^* z \frac{\partial U}{\partial z} \quad (4)$$

While, outside the wave boundary layer, the shear stress is also obtained by replacing  $u_{cw}^*$  with  $u_c^*$  in Eqs.(3) and (4). The shear velocity in the co-existing field is assumed to be connected with the maximum bottom shear stress during a wave period  $\tau_{cw, \max}$ ; that is,

$$\tau_{cw, \max} = \tau_c + \tau_w, \max = \rho u_{cw}^{*2} = \rho \kappa u_{cw}^* z \left. \frac{\partial(u+U)}{\partial z} \right|_{\max} \quad (5)$$

in which,  $z_0$  is a constant and denotes a roughness height for fully turbulent flow.

#### (b) Solution for current component

Inside the wave boundary layer, the current velocity  $U$  is obtained from Eq.(4).

$$U = \frac{u_c^{*2}}{\kappa u_{cw}^*} \ln \frac{z}{z_0} \quad z < \delta_w \quad (6)$$

The current velocity at the outer edge of the wave boundary layer  $U_p$  is given by substituting  $z = \delta_w$  into Eq.(6).

$$U_p = -\frac{u_c^{*2}}{\kappa u_c^* z} \ln \frac{\delta_w}{z_0} \tag{7}$$

Outside the wave boundary layer, the relation between the current velocity  $U$  and the current shear stress  $\tau_c$  is represented with the eddy viscosity in Eq. (1) as follows:

$$\tau_c = \rho \kappa u_c^* z \frac{\partial U}{\partial z} \quad z > \delta_w \tag{8}$$

Thus, the current velocity distribution is found from Eqs (7) and (8).

$$U = \frac{u_c^*}{\kappa} \ln \frac{z}{\delta_w} + U_p = \frac{u_c^*}{\kappa} \ln \frac{z}{\delta_w} + \frac{u_c^{*2}}{\kappa u_c^* z} \ln \frac{\delta_w}{z_0} \quad z > \delta_w \tag{9}$$

(c) Solution for wave component

The governing equation in the wave boundary layer is as follows:

$$\frac{\partial u}{\partial t} + U \frac{\partial u}{\partial x} = -\frac{1}{\rho} \frac{\partial p}{\partial x} + \frac{1}{\rho} \frac{\partial \tau_w}{\partial z} \quad z < \delta_w \tag{10}$$

,where the linearized convective acceleration term is involved on the left hand side.

Outside the wave boundary layer, the viscous term on the right hand side of Eq. (10) can be neglected. Thus the following equation is held at just outside the boundary layer:

$$\frac{\partial u_p}{\partial t} + U_p \frac{\partial u_p}{\partial x} = -\frac{1}{\rho} \frac{\partial p_p}{\partial x} \tag{11}$$

in which, the subscript 'p' denotes the value at  $z = \delta_w$ . The vertical pressure gradient is assumed to be negligible on the basis of the boundary layer approximation. The governing equation for the wave component inside the boundary layer is deduced from Eqs. (10) and (11):

$$\frac{\partial(u_p - u)}{\partial t} + U_p \frac{\partial u_p}{\partial x} - U \frac{\partial u}{\partial x} = -\frac{1}{\rho} \frac{\partial \tau_w}{\partial z} = -\frac{\partial}{\partial z} \left( \kappa u_c^* z \frac{\partial u}{\partial z} \right) \tag{12}$$

In the above equation,  $u_p$  is the water particle velocity at the boundary layer edge  $z = \delta_w$  and calculated from the small amplitude wave theory as follows:

$$u_p = \hat{u}_p \cos(kx - \sigma t) = \frac{H}{2} (\sigma - k \mathcal{O}) \frac{\cosh k \delta_w}{\sinh kh} \cos(kx - \sigma t) \tag{13}$$

in which,  $H$  is the wave height,  $\sigma$  the angular frequency,  $k$  the wave number,  $h$  the water depth.

(d) Free boundary problem on boundary layer equation

The wave component in the wave boundary layer is expressed as follows:

$$u = A(z) \cos(kx - \sigma t) + B(z) \sin(kx - \sigma t) \tag{14}$$

Substituting Eq. (14) into Eq. (12), and rewriting the functions  $A$



and  $B$  and their derivatives by  $\vec{\xi}$  and  $\vec{\eta}$  as

$$\vec{\xi} = \begin{pmatrix} A \\ B \end{pmatrix}, \quad \vec{\eta} = \begin{pmatrix} A' \\ B' \end{pmatrix} \tag{15}$$

we get

$$\frac{d\vec{\xi}}{dz} = \vec{\eta}, \quad \frac{d\vec{\eta}}{dz} = D\vec{\eta} + E\vec{\xi} + F \tag{16}$$

in which,

$$D = \begin{pmatrix} -\frac{1}{z}, & 0 \\ 0, & -\frac{1}{z} \end{pmatrix}, \quad E = \begin{pmatrix} 0, & -\frac{\sigma - kU}{\kappa U_{c_w}^* z} \\ \frac{\sigma - kU}{\kappa U_{c_w}^* z}, & 0 \end{pmatrix}, \quad F = \begin{pmatrix} 0 \\ -\frac{\sigma - kU_p \hat{u}_p}{\kappa U_{c_w}^* z} \end{pmatrix} \tag{17}$$

The boundary conditions for Eq. (16) are

$$\vec{\xi} = \begin{pmatrix} 0 \\ 0 \end{pmatrix} \quad z = z_0 \tag{18}$$

$$\vec{\xi} = \begin{pmatrix} \hat{u}_p \\ 0 \end{pmatrix}, \quad \vec{\eta} = \begin{pmatrix} 0 \\ 0 \end{pmatrix} \quad z = \delta_w \tag{19}$$

Eq. (19) shows that the problem we discuss here is a free boundary problem because  $\delta_w$  is an unknown value. The two point boundary value problem as shown in Eqs. (16) ~ (19) is interpreted to be equivalent to the following characteristic equation:

$$\frac{\partial \vec{\xi}}{\partial z} + \frac{\partial \vec{\xi}}{\partial \vec{\eta}} (D\vec{\eta} + E\vec{\xi} + F) = \vec{\eta} \tag{20}$$

This partial differential equation is the so-called invariant imbedding equation, of which value lies in its wide applicability to the numerical solution of various kinds of boundary value problems. The invariant imbedding method is an initial value method for boundary value problems obtained by boundary perturbation techniques<sup>(2),7)</sup>.

An initial value problem is derived from the partial differential equation Eq. (20) by using the following Riccati transformation on  $\vec{\xi}$ :

$$\vec{\xi}(z, \vec{\eta}) = G(z)\vec{\eta} + H(z) \tag{21}$$

Substituting the above in Eq. (20), we obtain

$$\frac{dG}{dz} + GD + GEG = I \tag{22}$$

$$\frac{dH}{dz} + GEH + GF = 0 \tag{23}$$

in which,  $I$  is a  $2 \times 2$  unit matrix and  $0$  is  $2$ -dimensional zero vector. The boundary condition of Eq. (18) is transformed as

$$G(z_0) = 0, \quad H(z_0) = 0 \tag{24}$$

in which,  $0$  is  $2 \times 2$  zero matrix.  $G(z)$  and  $H(z)$  in Eqs. (22) ~ (23) are easily calculated with the initial values shown in Eq. (24). Eq. (21) is

transformed as

$$\bar{\eta}(z) = G^{-1}(z)\{\xi(z) - H(z)\} = G^{-1}(z)\left\{\begin{pmatrix} \hat{u}_c(z) \\ 0 \end{pmatrix} - H(z)\right\} \quad (25)$$

Finally we can obtain the unknown boundary position  $z = \delta_w$  as a  $z$ -value when Eq.(25) is equal to 0. After the upper boundary point  $z = \delta_w$  is determined, the boundary value problem results in an initial value problem; that is, the solution of Eq.(16) can be calculated by the 'terminal condition' at  $z = \delta_w$  as shown in Eq.(19).

The shear velocity of the current  $u^*_C$  is estimated by the velocity distribution of the pure current. However, if only the average current velocity in depth  $\bar{U}$  is obtained for the co-existing system,  $u^*_C$  can be calculated alternatively by integrating Eq.(9) in depth and solving the resultant quadratic equation.

Thus,

$$u^*_c = \frac{-u^*_{c_w}\alpha_2 + \sqrt{u^*_{c_w}\alpha_2^2 + 4\bar{U}\kappa u^*_{c_w}(h-z_0)\alpha_1}}{2\alpha_1} \quad (26)$$

in which,

$$\begin{aligned} \alpha_1 &= h \ln \frac{\delta_w}{z_0} - (\delta_w - z_0) \\ \alpha_2 &= h \ln \frac{h}{\delta_w} - (h - \delta_w) \end{aligned} \quad (27)$$

On the other hand, the shear velocity for the co-existing system is defined by Eq.(5), and rewritten into the following equation with invoking Eq.(6):

$$u^*_{c_w}{}^2 = \kappa u^*_{c_w} z_0 \frac{\partial u}{\partial z} \Big|_{z=z_0} + u^*_{c_w}{}^2 \quad (28)$$

The above equation is a quadratic equation on  $u^*_{CW}$ , therefore if  $(\partial u / \partial z)_{z=z_0}$  is given,  $u^*_{CW}$  can be calculated. However,  $(\partial u / \partial z)_{z=z_0}$  is not known apriori, but obtained from the solution, consequently, several iterations are needed to obtain  $u^*_{CW}$ .

The boundary layer thickness  $\delta_w$  is defined as the height that the maximum shear stress  $\tau_{w,max}$  becomes 0. However it never coincides with exactly 0 unless  $z$  becomes infinitely large, so that, it is considered to be reasonable to define  $\delta_w$  as the  $\tau_{w,max}$  becomes very small relative to the value on the bottom.

In this study,  $\delta_w$  is defined as the height where  $(\partial u / \partial z)_{max}$  becomes 0.01 times of that on the bottom. Therefore,  $\delta_w$  is varied with the multiple rate, however the solution on the water particle velocity is not affected wherever  $\delta_w$  is, because only starting point differs in the calculation.

### 3. Calculating results and discussion

#### (a) Results on characteristics in wave boundary layer

In this section, several characteristics calculated by the above method are discussed and compared with those obtained by Grant-Madsen's theory.

Table 1 shows the results on several characteristics calculated from the both theories in the wave only field. The calculating conditions are as follows. The water depth  $h=30\text{cm}$ , the wave height  $H=10\text{cm}$ , the roughness height on the bottom  $z_0=0.1\text{cm}$  and the wave period  $T=2\text{sec}$  and  $1.25\text{sec}$  for case-I and case-II, respectively. The definition of the friction coefficient  $f_{cw}$  is:

$$\tau_{cw, max} = \rho u_{cw}^{*2} = \frac{\rho}{2} f_{cw} \bar{u}_p^2 \quad (29)$$

It is clear from Table 1 that the results by the authors' method agree with those by Grant-Madsen's theory. However, results on the non-dimensional wave boundary layer thickness  $\delta_w$  show some differences. In the present method,  $\delta_w$  is obtained by a solution of the free boundary problem. On the other hand in Grant-Madsen's theory  $\delta_w$  is assumed to be 2 or 4 times  $\kappa |u_{cw}^*| / \sigma$  (in this calculation  $\delta_w = 4\kappa |u_{cw}^*| / \sigma$ ), so that, the difference of the value is due to the estimation methods.

Table 2 shows the results in the wave current co-existing field. A little difference is seen between the results of Authors' and Grant-Madsen's, because a convective acceleration term is taken into consideration in our method.

Calculations without the convection term are also carried out by our method (indicated as Authors(2) in Table 2), and it is found that these results agree well with those by Grant-Madsen's theory.

Next, variations of the characteristics with the current velocity are discussed. Fig.2 shows the results on the friction coefficient  $f_{cw}$ , where the abscissa is a ratio of the depth averaged current velocity  $\bar{U}$  to the wave celerity  $c$  calculated from the dispersion equation in the co-existing system.

The figure shows that the values of  $f_{cw}$  differ between a following current and an opposite one even if the current has a same absolute velocity. The reason is that the water particle velocity on the bottom becomes larger in the following current co-existing field than that in the pure wave field, whereas in the opposite current co-existing field the water particle velocity on the bottom becomes smaller.

Fig.3 represents the results on the shear velocity  $u_{cw}^*$ , which shows the same tendency as  $f_{cw}$ .

Fig.4 shows the results on the non-dimensional boundary layer thickness  $\delta_w / (\kappa |u_{cw}^*| / \sigma)$ , which indicates that the value decreases with the current velocity and the property is different from Grant-Madsen's assumption that  $\delta_w / (\kappa |u_{cw}^*| / \sigma)$  is a constant independent of the current velocity.

The results on the phase precedence  $\theta$  of the bottom shear stress to the water particle velocity outside the wave boundary layer are shown in Fig.5. It is found that  $\theta$  decreases with the current velocity in the following current case, meanwhile  $\theta$  increases a little with the current velocity in the opposite current case.

Table 1 Calculated results for characteristic values of the boundary layer in the wave-only field.

(CASE-1:  $T=2$  sec,  $h=30$  cm,  $H=10$  cm,  $z_0=0.1$  cm CASE-2:  
 $T=1.25$  sec,  $h=30$  cm,  $H=10$  cm,  $z_0=0.1$  cm)

		$f_{cw}$	$u_{cw}^*$ (cm/sec)	$\delta_w$ (cm)	$\theta$ (rad.)
CASE-1	Authors	0.097	5.68	3.15	0.55
	Grant-Madsen	0.098	5.68	2.89	0.52
CASE-2	Authors	0.139	5.58	2.45	0.58
	Grant-Madsen	0.140	5.59	1.78	0.55

Table 2 Calculated results for characteristic values of the boundary layer in the wave-current co-existing field (CASE-1).

		$f_{cw}$	$ u_{cw}^* $ (cm/sec)	$\delta_w$ (cm)	$\theta$ (rad.)	$\delta_w/(k u_{cw}^* /\sigma)$
$\mathcal{U}=30$ (cm/sec)	Authors (1)	0.144	7.13	3.55	0.51	3.91
	Authors (2)	0.154	7.38	3.55	0.54	3.78
	Grant-Madsen	0.156	7.42	3.78	0.51	4.00
$\mathcal{U}=-30$ (cm/sec)	Authors (1)	0.184	7.35	3.55	0.56	3.79
	Authors (2)	0.168	7.02	3.50	0.54	3.92
	Grant-Madsen	0.169	7.05	3.59	0.51	4.00
$\mathcal{U}=60$ (cm/sec)	Authors (1)	0.225	9.08	4.15	0.47	3.59
	Authors (2)	0.249	9.55	4.00	0.52	3.29
	Grant-Madsen	0.254	9.65	4.92	0.49	4.00
$\mathcal{U}=-60$ (cm/sec)	Authors (1)	0.416	9.33	4.10	0.61	3.45
	Authors (2)	0.351	8.55	3.80	0.53	3.49
	Grant-Madsen	0.354	8.62	4.39	0.50	4.00

Authors (2) denotes case of "without convection term"

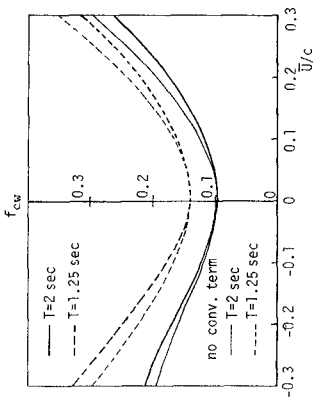


Fig. 2 Friction factor  $f_{cw}$

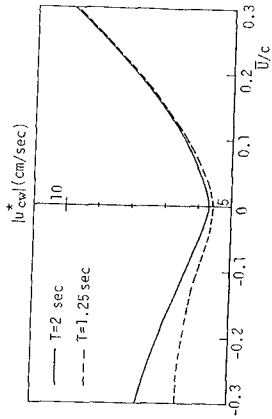


Fig. 3 Friction velocity  $u_{cw}^*$

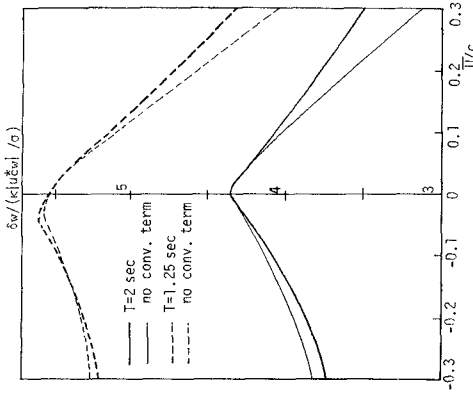


Fig. 4 Non-dimensional boundary layer thickness  $\delta_w / (\kappa |u_{cw}| / \sigma)$

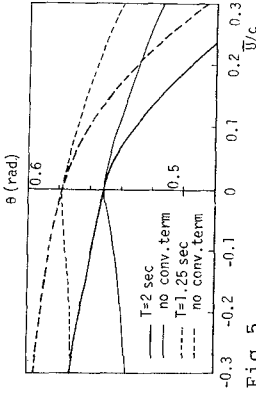


Fig. 5 Phase precedence of bottom shear stress relative to water particle velocity outside boundary layer  $\theta$

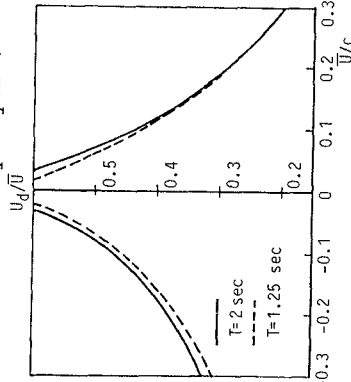


Fig. 6 Non-dimensional current velocity reduction  $U_d / U$

**(b) Current velocity reduction**

As mentioned above, the current in the co-existing field experiences larger hydrodynamic resistance than that in the pure current field. Furthermore, the associated mean bottom shear stress is possible to differ from that in the pure current field. The current velocity without waves  $U_{n.w.}$  is expressed as the well known logarithmic law.

$$U_{n.w.} = \frac{u_c^*}{\kappa} \ln \frac{z}{z_0} \quad (30)$$

Meanwhile, the current velocity in the co-existing field is represented in Eq.(9). Thus, the reduction of velocity  $U_d$  due to wave superimposing above the wave boundary layer is obtained by subtracting Eq.(9) from Eq.(30) as follows:

$$U_d = U_{n.w.} - U = \left( \frac{u_c^*}{\kappa} - \frac{u_c^{*2}}{\kappa u_{cw}^*} \right) \ln \frac{\delta_w}{z_0} \quad (31)$$

The above equation shows that the reduction depends directly on the wave boundary layer thickness  $\delta_w$ .

This method treats  $\delta_w$  as a variable with the wave-current composing ratio and estimates it as a solution of the free boundary problem. Consequently, this method is rational to estimate the current velocity reduction. The calculated results on the non-dimensional reduction velocity  $U_d/U$  are shown in Fig.6.

**(c) Instantaneous water particle velocity**

Fig.7 and Fig.8 are the calculated results on the distribution of water particle velocity for a following and an opposite current cases respectively. The thin curves in the figure show the results calculated from the authors' method without the convective acceleration term. In addition, the results calculated from Grant-Madsen's theory are shown by the dotted curves for comparison. It is found from the figure that the convection term decreases the absolute values of water particle velocity in the following current case, and increases those in the opposite current case.

The effect of the convection term increases as  $U/c$  becomes large, because the ratio of the convective acceleration term  $U \partial u / \partial x$  to the local acceleration term  $\partial u / \partial t$  becomes  $U/c$ . In the actual nearshore regions, however, the value of  $U/c$  is usually small, therefore it occurs rather seldom that the convection term plays an important role.

**4. Measurements on near bottom velocity****(a) Experimental apparatus and procedure**

The experiment was carried out in a 27m long, 0.5m wide and 0.7m high wave tank, in which circulating flow could be generated by a power pump. The water depth was kept constant at 30cm. Test runs were conducted under the conditions that the wave period was 1.67sec, the wave height were 6.3 8.5cm. All the cases of current used in the tests were in the opposite direction to the wave propagation. Two dimensional

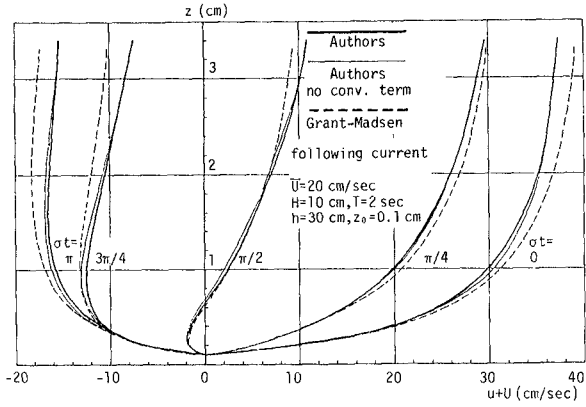


Fig.7 Distributions of horizontal water particle velocity in co-existing field (following current)

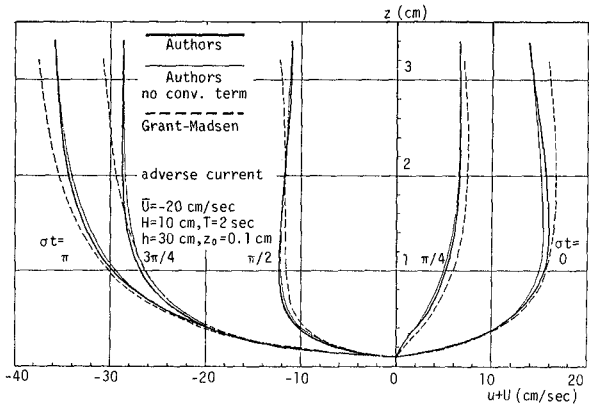


Fig.8 Distributions of horizontal water particle velocity in co-existing field (adverse current)

roughness elements of  $2\text{mm} \times 2\text{mm}$  in cross section and  $15\text{mm}$  interval were added on the bottom.

Water particle velocities were measured with a laser-doppler velocimeter, and at the same location water surface variations were detected simultaneously by a capacitance type wave gauge. The measuring points were located at the lowest  $1.4\text{mm} \sim 1.7\text{mm}$  above the top of the artificial roughness and at the highest  $100\text{mm}$  above that. The total measuring points were 21  $\sim$  23 for each test case. The test conditions are summarized in Table 3, and a schematical view of the experimental apparatus is shown in Fig.9.

**(b) Current component velocity**

The current component velocity in the co-existing system is defined as the time averaged velocity during a wave period. Fig.10 shows the current component velocities both in the pure current field and in the co-existing field.

The velocity reduction of the current component in the co-existing field is clearly seen from the figure.

The dotted line shows the calculated results from the authors' theory, where only the depth averaged velocity of the pure current and the wave conditions are given as inputs of the calculation.

**(c) Instantaneous water particle velocity**

Fig.11 shows the experimental results in the pure wave field, and the calculated results by the authors' and Grant-Madsen's theories are also shown for comparison.

The experimental results take larger values than the calculated ones at the phases 0 and  $\pi/4$  in the region of  $z < 2\text{cm}$ , and the distributions show over-shooting phenomena that the velocity in the boundary layer exceeds the outer velocity. Furthermore, the experimental results become smaller than the calculated ones especially at the phase  $3/4\pi$  and  $\pi$  in the region of  $z < 5\text{mm}$ .

Similar results were found in experimental results performed by Bakker and van Doorn<sup>1)</sup>, who measured water particle velocities under the similar experimental conditions to those of this study.

It also seems to be a reason of the disagreement that the water particle velocities under this test condition were not enough large to generate fully rough turbulent flow near the bottom.

Fig.12 shows the results in the wave-current co-existing field. The agreement between the calculated and experimental results seems to be better in the co-existing field than that in the pure wave field.

The reason can be explained by the fact that in the co-existing field the turbulent flow was produced close to the bottom due to superimposing current, while in the pure wave field under these experimental conditions the laminar sublayer occupied some width on the bottom.

In order to improve the mathematical model for predicting the experimental result more accurately, it is necessary to solve the



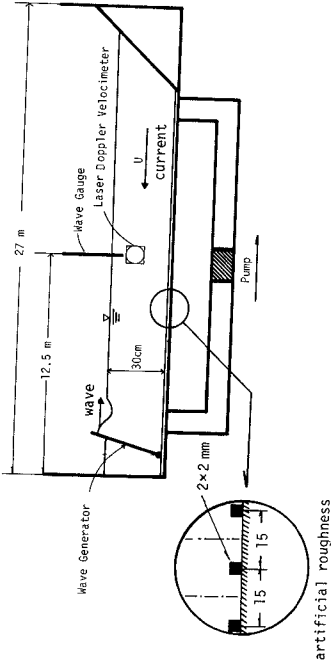


Fig. 9 Experimental apparatus

Table 3 Experimental conditions.

	$\bar{U}$		$H$ (cm)	$T$ (sec)	$h$ (cm)
	(cm/sec)	(cm/sec)			
CASE-I	wave-only	0	8.52	1.67	30
	current-only	-20.0	—		
CASE-II	co-existing	-17.4	7.74	1.67	30
	wave-only	0	7.99		
CASE-III	current-only	-30.3	7.49	1.67	30
	co-existing	-25.9	—		
	wave-only	0	8.22	1.67	30
	current-only	-41.6	—		
	co-existing	-36.7	6.30		

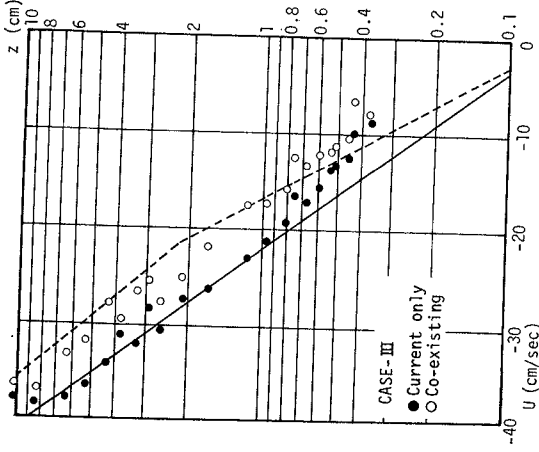


Fig. 10 Distributions of current component in pure current and co-existing fields

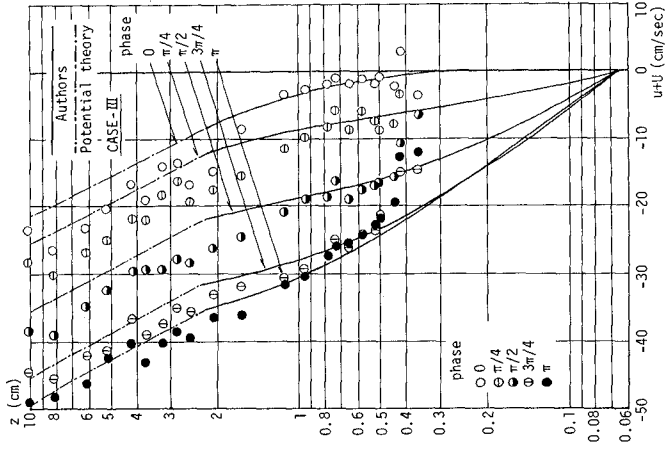


Fig.12 Comparisons between experimental results and theoretical ones in co-existing field

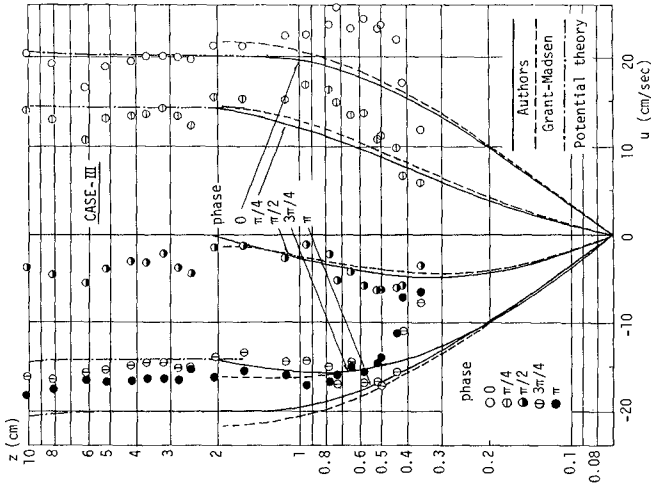


Fig.11 Comparisons between experimental results and theoretical ones in pure wave field

several important problems remained even in the pure wave boundary layer.

One important problem is the finite amplitude effect of waves on the water particle velocity in the wave boundary layer. Another problem lies in the assumption on the eddy viscosity. How to determine the roughness height  $z_0$  in oscillating flow is also one of the problems to be solved.

### 5. Conclusions

This study proposes a new mathematical method to predict near bottom water particle velocities in the wave-current co-existing field. Since this method is capable of expressing the variation of the boundary layer thickness with the wave-current velocity ratio, several characteristics of the boundary layer and the current velocity reduction due to superimposing waves can be estimated reasonably by this method.

Moreover, measurements on the water particle velocity above the artificial rough bottom were carried out in the pure wave, the pure current and the wave-current co-existing fields.

After comparing the calculated results with the experimental data, it was found that this method predicts well the experimental results, however some disagreements between them are obtained. These are partly due to the assumption on the eddy viscosity which is proportional to the height from the bottom, and in addition, due to neglecting the finite amplitude effect of waves.

### Acknowledgement

This study is part of the research sponsored by the Grant-in-Aid for Scientific Research of the Ministry of Science, Culture and Education. The authors wish to express their appreciation to Mr. H. Okamoto, former graduate student at Department of Civil Engineering, Kyoto University, for his assistance in performing the experiments.

### References

- 1) Bakker, W.T. and Th. van Doorn : Experimental investigation of near bottom velocities in water waves without and with a current, Delft Hydraulic Laboratory, M1423, part 1, p. 66, 1981.
- 2) Bellman, R. : Methods on nonlinear analysis, Mathematics in Science and Engineering, Vol. 61-II, Academic Press, p.261, 1973.
- 3) Christoffersen, J. B. : Current depth refraction of dissipative water waves, Inst. of Hydrodynamics and Hydraulic Engineering (ISVA), Technical University of Denmark, Paper No.30, p.177, 1982.
- 4) Grant, W.D. and O.S. Madsen : Combined wave and current interaction with a rough bottom, J. of Geophysical Research, Vol. 84, No. C4, pp.1797-1808, 1979.
- 5) Kajiura, K. : A model of the bottom boundary layer in water waves,

- Bull. of Earthquake Res. Inst., Vol.46, pp.75-123, 1968.
- 6) Kemp, P.H. and R.R. Simons : The interaction between waves and a turbulent current : waves propagating with the current, J. Fluid Mech., Vol.116, pp.227-250, 1982.
  - 7) Mayer, G.H. : Initial value methods for boundary value problems, theory and application of invariant imbedding, Mathematics in Science and Engineering, Vol.100, Academic Press, p.220, 1973.
  - 8) Noda, H. : On the oscillatory flow in turbulent boundary layers induced by water waves, Bull. Disas. Prev. Res. Inst., Kyoto Univ., Vol.20, Part 3, No. 176, March, pp.127-144, 1971.
  - 9) Tanaka, H. and N. Shuto : Friction coefficient for a wave current co-existing system, Coastal Engg. in Japan, Vol.24, pp. 105-128, 1981.

## CHAPTER ONE HUNDRED SIXTY TWO

### NUMERICAL SIMULATION OF SECONDARY CIRCULATION IN THE LEE OF HEADLANDS

by

Roger A. Falconer<sup>1</sup>  
Eric Wolanski<sup>2</sup> and  
Lida Mardapitta-Hadjipandeli<sup>3</sup>

#### ABSTRACT

The paper gives details of a study to refine and further develop a two-dimensional depth average numerical model to predict more accurately the eddy shedding features often observed in the lees of headlands. Details are given of the application of the model to Rattray Island, just east of Bowen, North Queensland, Australia, where the strong tidal currents flowing past the island give rise to separation and hydrodynamic circulation in the lee of the island.

In the governing differential equations used to predict the secondary circulation, particular emphasis has been placed on the representation of the shear stresses associated with the free shear lateral mixing layer in the downstream wake of the headland. Use of an experimentally determined lateral velocity distribution in the shear layer, together with an eddy viscosity approach, have led to the use of a relatively simple turbulence model, including both free shear layer and bed generated turbulence. A comparison of the numerically predicted velocities with corresponding field measured results around Rattray Island has shown an encouraging agreement, although there were some differences. The main difference between both sets of results was that the vorticity strength of the secondary circulation predicted in the numerical model was noticeably less than that measured in the field.

- 
1. Lecturer in Civil Engineering, University of Birmingham, Birmingham.
  2. Principal Research Scientist, Australian Institute of Marine Science, Queensland, Australia.
  3. Research Student in Civil Engineering, University of Birmingham, Birmingham.

## INTRODUCTION

The main objective of the research study outlined herein has been to refine and enhance a two-dimensional depth average numerical model, in an attempt to predict more accurately the tide induced eddy shedding features often observed in the lees of headlands. The model has been applied to Rattray Island, which is located just east of Bowen, North Queensland, Australia, with its geographical location being illustrated in Fig.1. This island is approximately 1.5km long, 300m wide and lies in well mixed water, having a typical depth of about 30m. Its longer axis is inclined at about  $60^\circ$  into the direction of the semi-diurnal tidal current, and strong tidal currents flowing past the island give rise to separation at the most northerly tip of the island and secondary circulation in the downstream lee.

A detailed field study has been undertaken by the Australian Institute of Marine Science to investigate the secondary circulation occurring around Rattray Island and to try and improve the existing knowledge of eddies shed by such headlands. In this study, outlined by Wolanski et al (1984), twenty six current meters were deployed at various sites in the south eastern lee of the island, as shown in Fig.2, with time series sea level recordings being taken around the island. Visual observations of the secondary circulation were also made using landsat imagery and aerial photography, and the surface temperature field was also measured at the time of the aerial observations. The recorded tidal ranges were generally about 3m and a strong south eastwards current was observed and measured during the rising tide. This south easterly current gave rise to a strong clockwise rotating eddy in the south eastern lee of the island. The eddy was observed to be very stable and about twice the size of the island for most of the rising tide. The surface temperature distributions and drogoue trajectories also confirmed the existence of this eddy which, from measurements, was found to be several kilometres long.

The numerical model being used to simulate this eddy shedding phenomenon, for similar hydrodynamic conditions, is of the two-dimensional depth integrated type, with the water surface slope and depth mean velocity fields being evaluated from the conservation equations of mass and momentum. Included in the momentum equations are the effects of the earth's rotation, bed and surface shear forces and a simple turbulence model to represent both bed generated and free shear layer turbulence. In the numerical model, particular emphasis has been placed on: (I) formulating the lateral turbulent shear stresses in the lee of the island, (II) accurately representing the island shape and the associated boundary derivatives, (III) representing the non-linear advective accelerations so that non-linear instabilities were avoided, and (IV) investigating the influence of the Coriolis acceleration on the open boundary conditions.

## GOVERNING EQUATIONS

### *Equations of Motions*

The appropriate equations of mass and momentum conservation were derived by vertical integration of the three-dimensional continuity and Navier-Stokes equations respectively, see Falconer (1976). Thus, for the mass conservation equation in the horizontal plane, integration yields:-

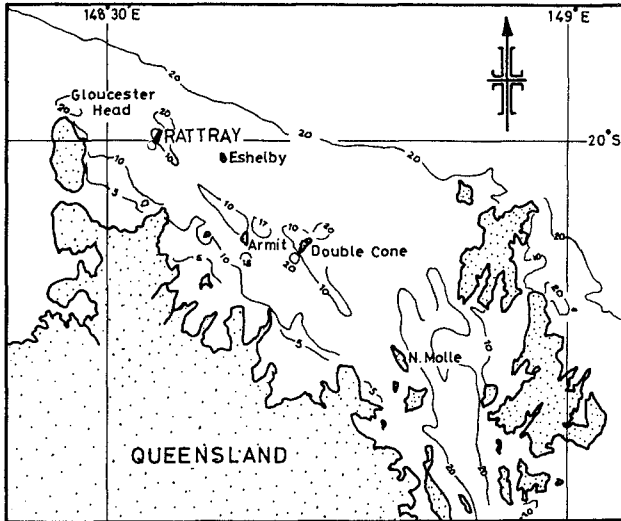


Fig.1 Location of Rattray Island and bathymetry (in fathoms)

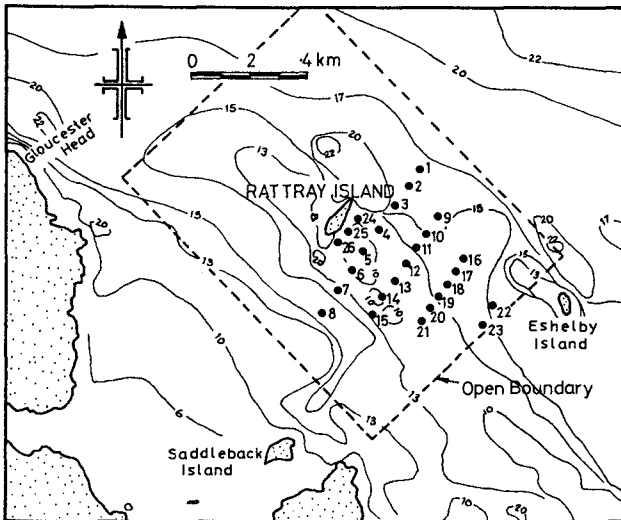


Fig.2 Area around Rattray Island showing location of current meters and model boundary

$$\frac{\partial \eta}{\partial t} + \frac{\partial UH}{\partial x} + \frac{\partial VH}{\partial y} = 0 \quad \dots\dots (1)$$

where  $\eta$  = water surface elevation above mean sea level,  $U, V$  = depth average velocity components in the  $x, y$  co-ordinate directions respectively, and  $H$  = total depth of flow.

Likewise, for an incompressible turbulent fluid flow on a rotating earth, the depth integrated equations for horizontal momentum in the  $x$  and  $y$  directions respectively, can be written as:-

$$\begin{aligned} \frac{\partial UH}{\partial t} + \beta \left[ \frac{\partial U^2 H}{\partial x} + \frac{\partial UVH}{\partial y} \right] - fVH + gH \frac{\partial \eta}{\partial x} - \frac{\tau_{wx}}{\rho} + \frac{\tau_{bx}}{\rho} \\ - \frac{1}{\rho} \left[ \frac{\partial H\sigma_{xx}}{\partial x} + \frac{\partial H\tau_{xy}}{\partial y} \right] = 0 \quad \dots\dots (2) \end{aligned}$$

$$\begin{aligned} \frac{\partial VH}{\partial t} + \beta \left[ \frac{\partial UVH}{\partial x} + \frac{\partial V^2 H}{\partial y} \right] + fUH + gH \frac{\partial \eta}{\partial y} - \frac{\tau_{wy}}{\rho} + \frac{\tau_{by}}{\rho} \\ - \frac{1}{\rho} \left[ \frac{\partial H\tau_{yx}}{\partial x} + \frac{\partial H\sigma_{yy}}{\partial y} \right] = 0 \quad \dots\dots (3) \end{aligned}$$

where  $\beta$  = correction factor for non-uniformity of the vertical velocity profile (assumed to be 1.016 for a seventh power law velocity distribution),  $f$  = Coriolis parameter,  $g$  = gravitational acceleration,  $\rho$  = fluid density,  $\tau_{wx}, \tau_{wy}$  = surface shear stress components due to wind action,  $\tau_{bx}, \tau_{by}$  = bottom shear stress components due to bed friction, and  $\sigma_{xx}, \tau_{xy}, \tau_{yx}, \sigma_{yy}$  = Reynolds stress components in the  $x, y$  directions respectively.

In the present study the effects of wind action have not been considered, and hence  $\tau_{wx}$  and  $\tau_{wy}$  have both been equated to zero. For the bottom stresses, the terms have been represented in a quadratic form (see Dronkers (1964)) giving:-

$$\left. \begin{aligned} \tau_{bx} &= \frac{\rho g U \sqrt{U^2 + V^2}}{C^2} \\ \tau_{by} &= \frac{\rho g V \sqrt{U^2 + V^2}}{C^2} \end{aligned} \right\} \dots\dots (4)$$

where  $C$  = Chezy roughness coefficient (defined by  $H^{1/6}/n$ , where  $n$  is the Manning roughness coefficient).

In the modelling of turbulent flows, particularly where secondary circulation and notable lateral velocity gradients exist, the direct shear stresses  $\sigma_{xx}$  and  $\sigma_{yy}$  are generally small in comparison with the lateral shear stresses  $\tau_{xy}$  and  $\tau_{yx}$ , see Kuipers and Vreugdenhil (1973).



Since this condition appeared to apply in this study, the direct stress components  $\sigma_{xx}$  and  $\sigma_{yy}$  have been neglected from the momentum equations (2) and (3) respectively. However, the significance and importance of the lateral shear stresses is not obvious in any study involving recirculating flows, and hence an analysis of the vorticity transport equation - corresponding to the momentum equations (2) and (3) - has been undertaken in an attempt to indicate the importance of these terms.

*Vorticity Transport Equation*

In order to obtain the appropriate depth mean vorticity transport equation from the momentum equations (2) and (3), the wind stresses and direct stresses were neglected and the momentum correction factor  $\beta$  was assumed to be unity for simplicity. Hence, differentiation of Eqs. (2) and (3) with respect to  $y$  and  $x$  respectively, and subtraction of the corresponding equations gives:-

$$\underbrace{\frac{\partial \omega}{\partial t}}_{(1)} + \underbrace{U \frac{\partial \omega}{\partial x} + V \frac{\partial \omega}{\partial y}}_{(2)} + \underbrace{(\omega - f) \left[ \frac{\partial U}{\partial x} + \frac{\partial V}{\partial y} \right]}_{(3)} + \underbrace{\left[ \frac{\partial}{\partial y} \left( \frac{\tau_{bx}}{\rho H} \right) - \frac{\partial}{\partial x} \left( \frac{\tau_{by}}{\rho H} \right) \right]}_{(4)} - \underbrace{\frac{\partial}{\partial y} \left[ \frac{1}{\rho H} \frac{\partial H \tau_{xy}}{\partial y} \right] + \frac{\partial}{\partial x} \left[ \frac{1}{\rho H} \frac{\partial H \tau_{yx}}{\partial x} \right]}_{(5)} = 0 \dots\dots (5)$$

where  $\omega$  = depth mean vorticity =  $\left( \frac{\partial U}{\partial y} - \frac{\partial V}{\partial x} \right)$

The various terms of Eq. (5) refer to:- (1) the time rate of change of vorticity, (2) advection of vorticity, (3) convergence or divergence of vorticity by the mean flow, (4) effects of bottom friction, and (5) moments of the lateral stresses about a vertical axis.

If a conventional control volume approach is adopted in analysing this equation, it can be shown that the generation of vorticity (or secondary circulation) is only affected by terms (3), (4) and (5) - see Flokstra (1977). Furthermore, the bottom friction term (4) can be shown to have a negative generation effect, i.e. it tends to dissipate any vorticity generated. Such an analysis therefore indicates that secondary circulation (or vorticity) in the lee of a headland, for example, can only be generated by:- (i) the advective terms (3), and (ii) the lateral shear stresses (5). Hence, in this study the representation and inclusion of the lateral shear stresses in the mathematical model is of considerable importance if secondary circulation is to be modelled with any degree of accuracy. In addition to the importance of the lateral shear stresses in recirculating flows, Kuipers and Vreugdenhil (1973) and Flokstra (1977) have shown that the use of a no-slip boundary condition at all solid boundaries is also important in generating vorticity in such flow fields.

*Formulation of Lateral Shear Stresses.*

Having established the importance of the lateral shear stresses in modelling secondary circulation, consideration was then given to formulating these terms as accurately as possible without the use of a multi-equation turbulence model, such as the  $k-\epsilon$  model. The disadvantages of using such refined turbulence models for tide induced secondary circulation are that:- (i) there is a lack of adequate tidal flow data for the empirical constants included in such models, and (ii) there is a significant increase in the computational effort required.

In adopting a simpler approach to the formulation of the lateral shear stresses, the turbulence in the mixing zone in the lee of the headland was first separated into its two components, namely:- (i) bed generated turbulence, and (ii) free shear generated turbulence arising between the main flow and the eddy as a result of relatively large horizontal velocity gradients. However, in the mixing region immediately downstream of the headland, free shear layer generated turbulence tends to dominate over bed generated turbulence and hence more emphasis has to be placed on this component.

In establishing a formulation for the free shear layer turbulence component, use has been made of some of the semi-empirical concepts and approaches developed from extensive experimental studies of the velocity field characteristics in wakes and jet flows. These investigations have been undertaken by a number of authors and are reviewed in Townsend (1956).

The pronounced horizontal velocity gradients occurring in the mixing region downstream of the headland have been approximated in the evaluation of the free shear layer stress components by assuming an observed universal velocity profile of the form given by Townsend (1956). Using the notation illustrated in Fig.3, this velocity profile can be simplified as outlined by Lean and Weare (1979) to give:-

$$U = \frac{U_1}{2} \left\{ 1 + \operatorname{erf} \left[ \frac{y}{x} \left( \frac{Rs}{2} \right)^{\frac{1}{2}} \right] \right\} \quad \dots\dots (6)$$

where  $U_1$  = free stream velocity and  $Rs$  = experimental constant  $\approx 288$ . In adopting an eddy viscosity approach, together with a Boussinesq representation of the shear stresses, observations suggest that a mean eddy viscosity can be applied across the shear layer, see Townsend (1956). In applying this approximation in the mixing layer, the resulting eddy viscosity can be shown to be of the following form:-

$$\epsilon_{\ell} \approx \frac{U_1 x}{2Rs} \quad \dots\dots (7)$$

where  $\epsilon_{\ell}$  = mean eddy viscosity across the mixing layer, and with the rate of spread of the mixing layer being assumed to be constant. In turn, it can be shown that the eddy viscosity, the length scale of turbulence and the width of the shear layer are all linearly dependent upon the longitudinal distance and independent of the lateral distance. Furthermore, although the eddy viscosity increases linearly with  $x$ , the maximum shear stress ( $\tau_{xy}$  at  $y = 0$ ) remains constant since the lateral

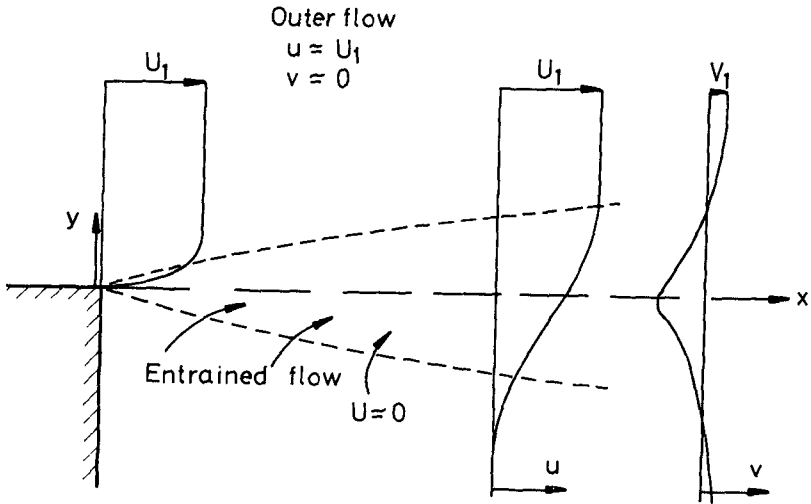


FIG.3 Typical velocity profile occurring in the mixing zone downstream of a headland.

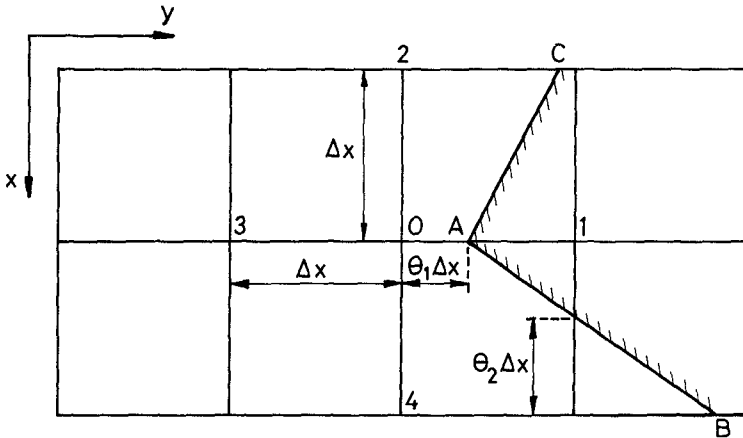


FIG.4 Non-uniform grid spacing around headland for more accurate boundary representation.

velocity gradient  $\frac{\partial U}{\partial y}$  decreases linearly with x (see Lean and Weare (1979)) that is:-

$$\tau_{xy_{max}} = \rho \epsilon_b \frac{\partial U}{\partial y} = \rho \frac{U_1^2}{2} \frac{1}{\sqrt{2\pi R_s}} \approx 0.012 \rho U_1^2 \quad \dots (8)$$

For the bed generated component of turbulence, the vertical velocity profile can be approximated to a logarithmic form - for the purpose of closure of the momentum equations - with the result that the spatially varying eddy viscosity follows the well documented form, as reviewed by Fischer (1973):-

$$\epsilon_b \approx 0.16 U_* H \quad \dots (9)$$

where  $\epsilon_b$  = bed generated eddy viscosity and  $U_*$  = shear velocity =  $\sqrt{gU_s/C}$  - where  $U_s$  is the fluid speed.

In comparing the rate of production of turbulence in the mixing layer with that of the bed, Lean and Weare (1979) have shown that the bed generated turbulence becomes re-established in the mixing layer<sup>2</sup> when:-

$$\frac{x}{H} > \frac{2}{\pi} \frac{C^2}{g} \quad \dots (10)$$

Hence, combining both free shear layer and bed generated turbulence in the momentum equations, the resulting lateral shear stress representation used in the mathematical model can be summarised as follows:-

$$\tau_{xy} = \rho \epsilon \frac{\partial U}{\partial y} = \rho \left\{ \frac{U_1 x}{2R_s} + \frac{0.16 \sqrt{g} U_s}{C} \right\} \frac{\partial U}{\partial y} \quad \dots (11)$$

with the shear stress beyond the mixing layer, i.e.  $x > 2C^2H/(\pi g)$ , being defined simply by bed generated turbulence as:-

$$\tau_{xy} = \rho \left[ \frac{0.16 \sqrt{g} U_s}{C} \right] \frac{\partial U}{\partial y} \quad \dots (12)$$

The boundaries of the mixing layer in the lateral plane were obtained from equation (6), which was assumed to apply within the limits:-

$$0.05 U_1 < U < 0.95 U_1 \quad \dots (13)$$

and with shear generated turbulence again being equated to zero outside these bounds.

NUMERICAL SPECIFICATIONS

*Finite Difference Representations*

The finite difference equations corresponding to the governing differential equations were expressed in an alternating direction implicit form, with all terms being fully centred in time and space - except for the second derivatives of the velocity components immediately adjacent to the island boundary. The non-linear advective acceler-

ations and the second derivatives associated with the lateral shear stresses were time centred by iteration. The second order scheme, with accuracy  $O(\Delta t^2, \Delta x^2)$ , involved discrete values of the variables being represented using a space staggered grid scheme, in which water elevations and velocity components were described at different grid locations.

The only terms requiring special mention are the advective accelerations expressing the lateral transport of momentum in the x and y directions of the momentum equations, i.e. the UV product components of the advective accelerations in equations (2) and (3). These terms were represented in the finite difference scheme using the marker and cell technique, in that the spatial location of the velocity component in the direction of motion under consideration was governed by the direction of the perpendicular velocity component, see Williams and Holmes (1974). This representation was similar to that of upwind differencing and had the advantage that:- (i) the corresponding momentum flux was evaluated nearer to the position where it originated and (ii) no grid scale oscillations were apparent since this scheme included sufficient damping to counteract the occurrence of such oscillations.

In view of the significance of the headland shape on the characteristics of the downstream velocity field, the finite difference representation was refined immediately adjacent to the headland so that the island geometry could be represented as accurately as possible. Hence, instead of using a uniform grid space representation across the whole computational field, the first and second derivatives were adjusted, where necessary, within the grid squares around the headland so that the actual boundary location was defined in the model. An example of the boundary representation for the headland is illustrated in Fig.4, with the corresponding first and second derivatives in the y direction at point O being defined as (see Smith (1978)):-

$$\left. \frac{\partial U}{\partial y} \right|_O = \frac{1}{\Delta x} \left[ \frac{1}{\theta_1(1+\theta_1)} U_A - \frac{(1-\theta_1)}{\theta_1} U_O - \frac{\theta_1}{(1+\theta_1)} U_3 \right] \dots \quad (14)$$

$$\left. \frac{\partial^2 U}{\partial y^2} \right|_O = \frac{1}{\Delta x^2} \left[ \frac{2}{\theta_1(1+\theta_1)} U_A + \frac{2}{(1+\theta_1)} U_3 - \frac{2U_O}{\theta_1} \right] \dots \quad (15)$$

where the subscripts refer to the notation given in Fig.4. The resulting equations have leading errors of  $O(\Delta x^2)$  and  $O(\Delta x)$  respectively, and can be simplified for a no-slip boundary requirement since  $U_A = 0$  for the example given. Tests were undertaken on the application and comparability of this scheme with a regular grid representation for a one-dimensional flat bottomed estuary having similar dimensions and hydrodynamic boundary conditions as for the present study. The numerically predicted water elevations and velocities at the estuary head agreed to within a few percent for the irregular and regular grids, and compared favourably with the analytical results for linear waves (see Ippen (1966)) and the semi-analytical results for non-linear waves (see Proudman (1957)) - which included the effects of the advective accelerations and bottom friction. Hence, no marked numerical diffusion was expected to occur near the headland as a result of using such a

representation, and non-linear instabilities were not encountered in any of the subsequent simulations incorporating Eqs. (14) and (15) and similar representations for the other derivatives.

For the model simulations a mesh of 40 x 29 grid squares was used, with a grid spacing ( $\Delta x$ ) of 300m. At the centre of each grid square a representative depth between mean sea level and the bed was required, with the corresponding data being obtained from bathymetric charts provided by the Australian Institute of Marine Science. The resulting bathymetry used in the mathematical model can be seen in the isoparametric projection illustrated in Fig.5. Since no data was available concerning the characteristics of the bed roughness, all of the mathematical simulations were undertaken for an assumed Manning roughness coefficient of 0.025. This value of  $n$  appeared to be a reasonable choice based on Knight's (1981) measurements in the Conwy Estuary, where similar tidal ranges are experienced.

#### *Open Boundary Conditions*

The boundary conditions for the hydrodynamic model were taken from field measured water elevations and velocities recorded over a period of four tides. At the northernmost boundary water elevations were defined at 10 minute intervals using data recorded around the island perimeter, together with the inclusion of an approximate phase lag of  $L\sqrt{gH}$  - where  $L$  is the distance from the boundary to the island. Two representations of the lateral surface slope were considered in the simulations including:- (i) a horizontal water surface slope with  $\eta = f(t)$  only, or  $\partial\eta/\partial y = 0$ , and (ii) a surface slope governed by the Coriolis acceleration with  $\eta = f(y,t)$ . In both simulations the lateral velocity component along the boundary ( $V$ ) was assumed to be zero, which resulted in the latter and more accurate boundary representation being governed by the resulting form of the momentum equation (3), i.e.:-

$$\frac{\partial\eta}{\partial y} = -\frac{fU}{g} \quad \dots\dots (16)$$

On comparing the two simulations, the use of a horizontal surface slope gave unrealistic velocity field predictions, whereas from a purely observational viewpoint the second representation, i.e. Eq.(16), appeared to give realistic results.

At the western and eastern boundaries a free slip wall was assumed to exist, with only the lateral velocity component ( $V$ ) therefore being zero along the boundary walls. Finally, at the southernmost boundary velocities were defined, again at 10 minute intervals, from field measurements taken at site number 23, which was located as shown in Fig.2. The velocity along this boundary was assumed to be uni-directional, with the result that  $U = f(t)$  only and  $V = 0$ .

The open boundary water elevations and velocities required at every half timestep of 60 seconds were obtained by quadratic interpolation from the field data. The model simulations were always started from rest, i.e.  $U = V = 0$  everywhere, with the initial mean water elevation across the computational domain being coincident with the

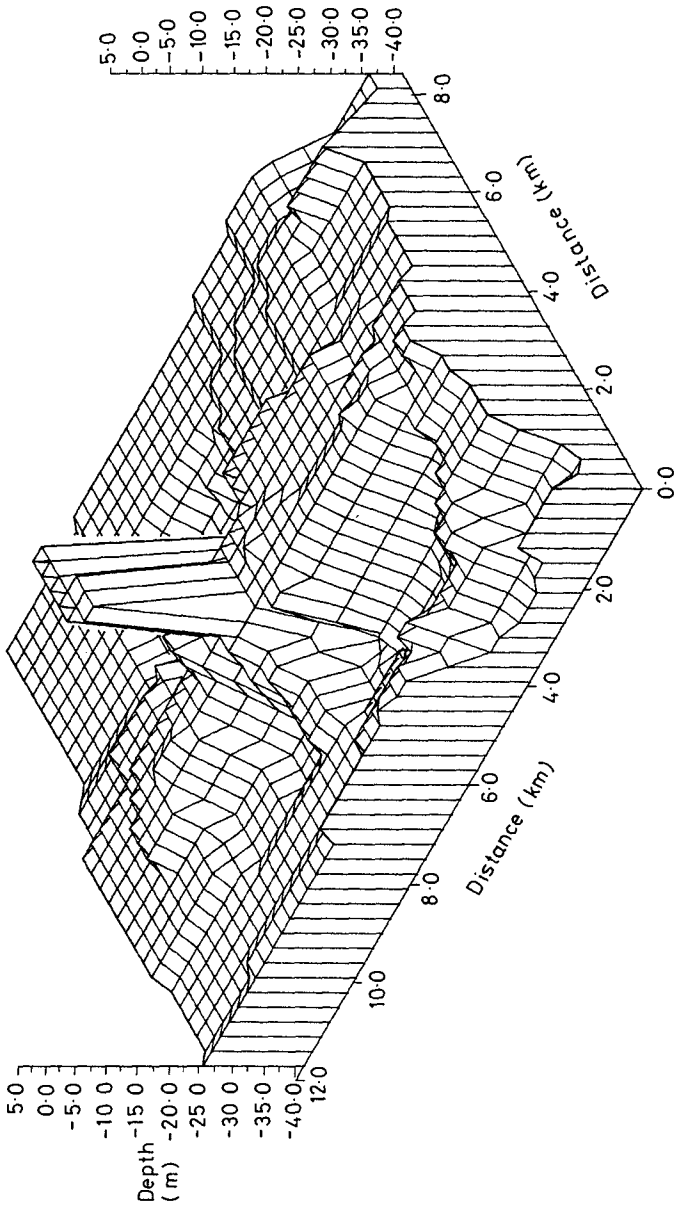


Fig.5 Three-dimensional representation of the bathymetry around Rattray Island

elevation closest to the zero velocity condition obtained from field data.

#### NUMERICAL MODEL RESULTS

Although this study forms part of an on-going research programme on numerical modelling of secondary circulation around headlands, a number of model simulations have been undertaken to date which have allowed comparisons to be made with the field measurements and observations. In all of these simulations the same water elevation and velocity variations were applied at the open boundaries, with the model being run for up to 50 hours, i.e. almost four tides.

In the first of these simulations direct comparisons have been made between the field measured velocities at the current meter positions shown in Fig.2, and the numerically predicted velocities at the grid points closest to these meter positions. Synoptic current meter measurements at three different tidal phases are shown in Fig.6, with the corresponding numerical model predictions for the optimum island geometry being given in Fig.7. When the corresponding results of Figs. 6 and 7 are compared, it can be seen that the overall agreement between the predicted and the measured velocities and field observations is reasonably encouraging, with some distinct similarities. Firstly, the occurrence of the eddy in the lee of the island was first identified some 2 hours into the flood tide. This compared reasonably well with current measurements, in that Wolanski et al (1984) found that the current direction close to and in the lee of the island started to rotate clockwise after one hour into the flood tide. Further similarities between both sets of results were in the dimensions of the eddy, in that predictions and observations indicated that the eddy size was about the same width as the island and that the maximum length of the eddy was about twice the island width.

However, apart from these similarities, there were some important differences between both sets of results, with some of these differences forming the basis of current research in this field by the authors. The main difference between both sets of results was that the vortex strength of the eddy was noticeably less in the numerical model predictions. This was chiefly thought to be due to:- (i) the coarseness of the grid, which is presently being refined for future studies, and (ii) the reduction in size of the lateral shear stress gradient in the model as a consequence of using a finite difference representation for the velocity gradient in the mixing zone, i.e. Eq. (11) within the limits defined by Eq.(13), rather than the semi-empirical velocity gradient defined by Eq.(6). Secondly, the entrainment of the jet flow just downstream of the island tip, along the separation streamline, was found to be less marked in the numerical model - with this discrepancy also thought to be due to the previously mentioned inaccuracies. Finally, the centre of rotation of the eddy in the numerical model predictions was always observed to be too far west of the corresponding field measured and observed eddy centre. This discrepancy was thought to be due to inadequate consideration being given in the model to the flow conditions at the diametrically opposite island tip, where the influence of the separation phenomena on the downstream velocity field was known to be less pronounced.



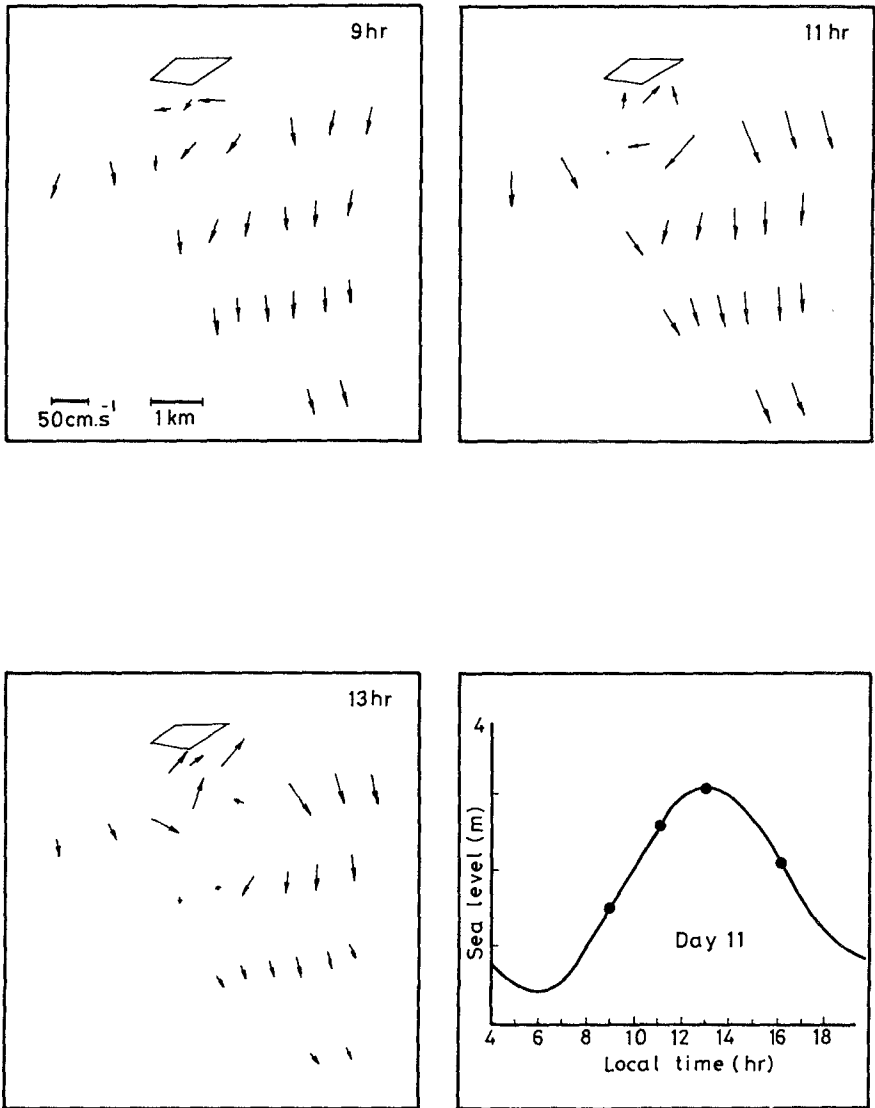


Fig.6 Field measured velocities at the measuring sites

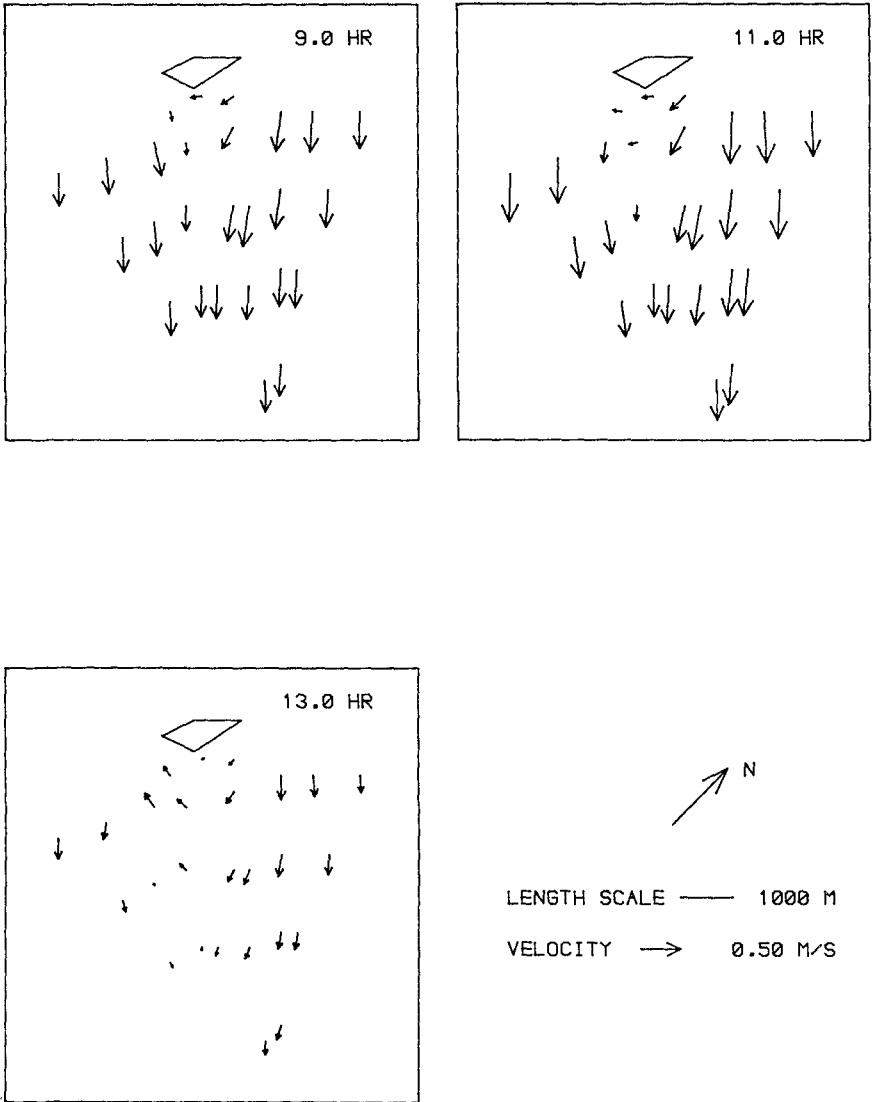


Fig.7 Numerically predicted velocities near the measuring sites using a non-uniform grid around the island

Further similar tests and comparisons were undertaken for different grid representations of the island geometry, see Mardapitta-Hadjipandeli (1984). These tests included the adoption of:- (i) a regular square mesh, and (ii) impermeable thin plate walls for the island, although detailed comparisons with the results for the irregular mesh shown in Fig.7 indicated that the latter gave the closest similarity to the field measured results.

A series of tests were also undertaken to investigate the influence of the various terms of the equations of motion on the secondary circulation characteristics. These results were compared with the velocity field prediction for the whole computational field at 13.3 hours after the start of simulation, i.e. just after high tide, with the corresponding prediction being illustrated in Fig.8.

Although no field measurements have been taken in the northern lee of the island, comparisons were also made with the velocity field predictions at 18.5 hours, where the mathematical model results showed the existence of two well defined counter rotating eddies in the region, see Fig.9. The main results of this series of tests showed that no eddies occurred in either lee of the island when the advective accelerations and the lateral shear stresses were excluded from the model, see Fig.10, and that inclusion of the Coriolis term at the open boundary was essential for realistic velocity field predictions, see Mardapitta-Hadjipandeli (1984).

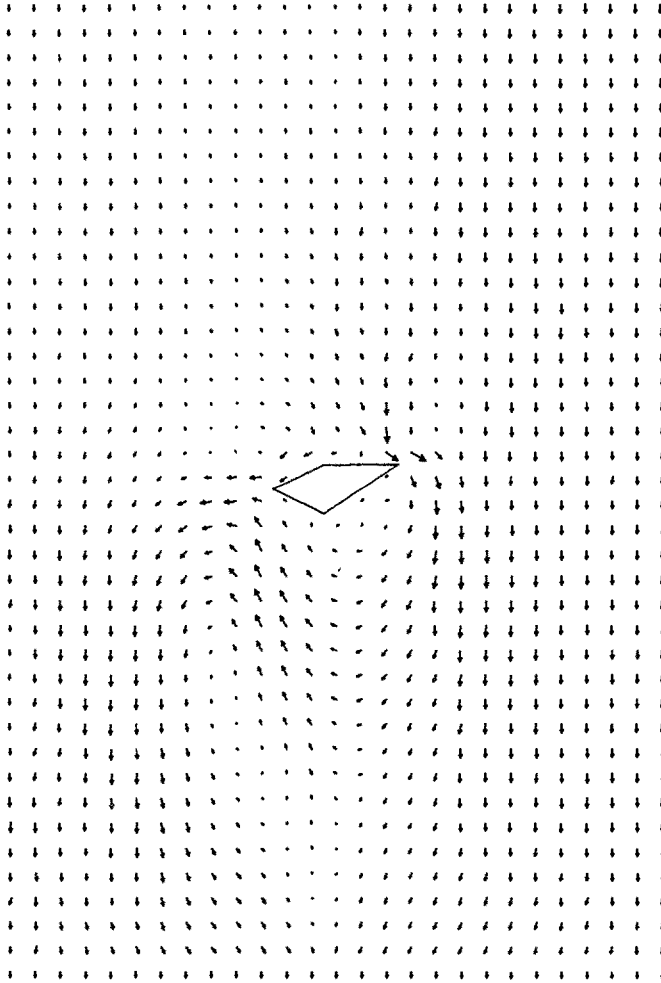
#### CONCLUSIONS

As part of an on-going research programme to develop a reliable mathematical model of secondary circulation in the lee of headlands, such a mathematical model is being developed and refined to predict the tide induced eddies, observed and measured in the field, around Ratray Island. The model includes a relatively simple zero-equation turbulence model, with particular emphasis being placed on the modelling of the free shear layer turbulence occurring in the mixing zone along the separation streamline - formed at the separation point at the island's most easterly tip. This component of the turbulence structure has been included in the model using an eddy viscosity approach, and a universal lateral velocity distribution, which is based on extensive field and experimental measurements for velocity fields in jet flows and wakes.

The numerical model predictions to-date have been compared with extensive field measurements and, although the agreement between both sets of results is reasonably encouraging, there are some important differences. These differences include:- (i) a weaker vortex strength, (ii) less entrainment into the mixing zone, and (iii) a difference in location of the centre of rotation of the eddy between the field measured and the numerically predicted results.

In addition to these comparisons, further tests have been undertaken to investigate the hydrodynamic phenomena being modelled. These tests showed that:- (i) exclusion of the Coriolis acceleration along the water level boundary gave unrealistic results, (ii) use of an irregular grid adjacent to the island gave improved results, with

TIME = 13.3 HR



LENGTH SCALE — 300 M

VELOCITY → 0.50 M/S

AVERAGE DEPTH = 30.3 M

MANNING NUMBER = 0.025

TIDAL HEIGHT = 2.22 M

TIDAL PERIOD = 12.6 HR

Fig.8 Numerically predicted velocities around Rattray Island  
at High Water Level

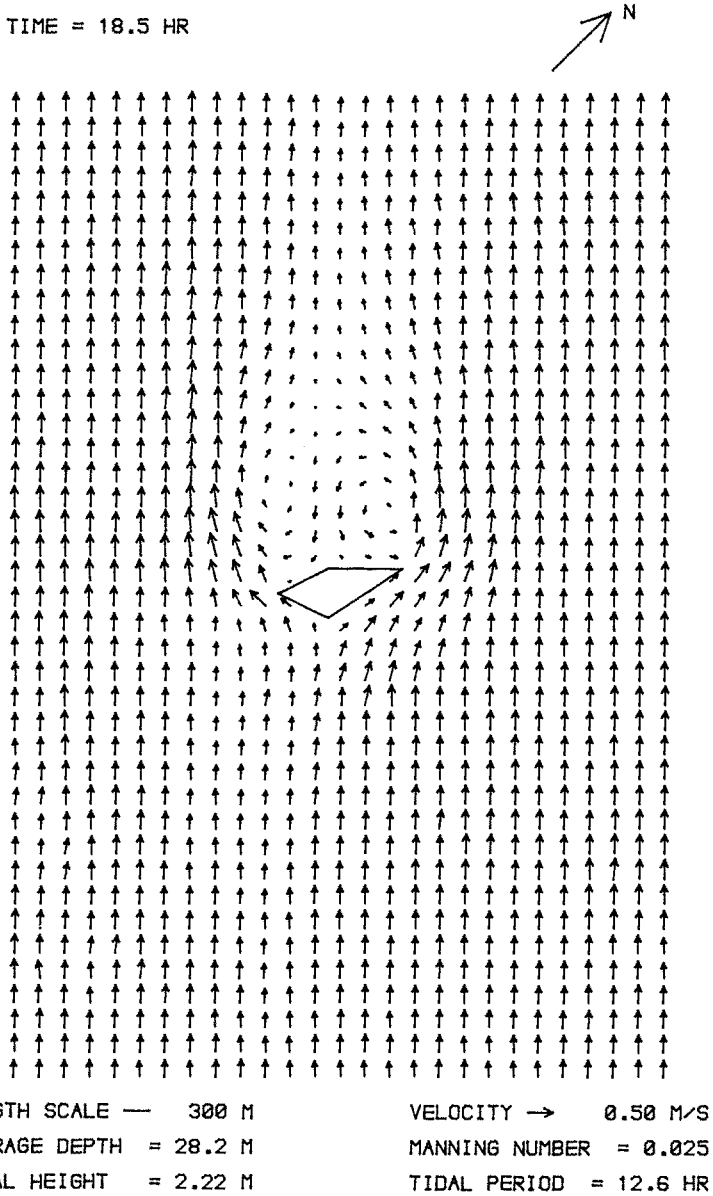
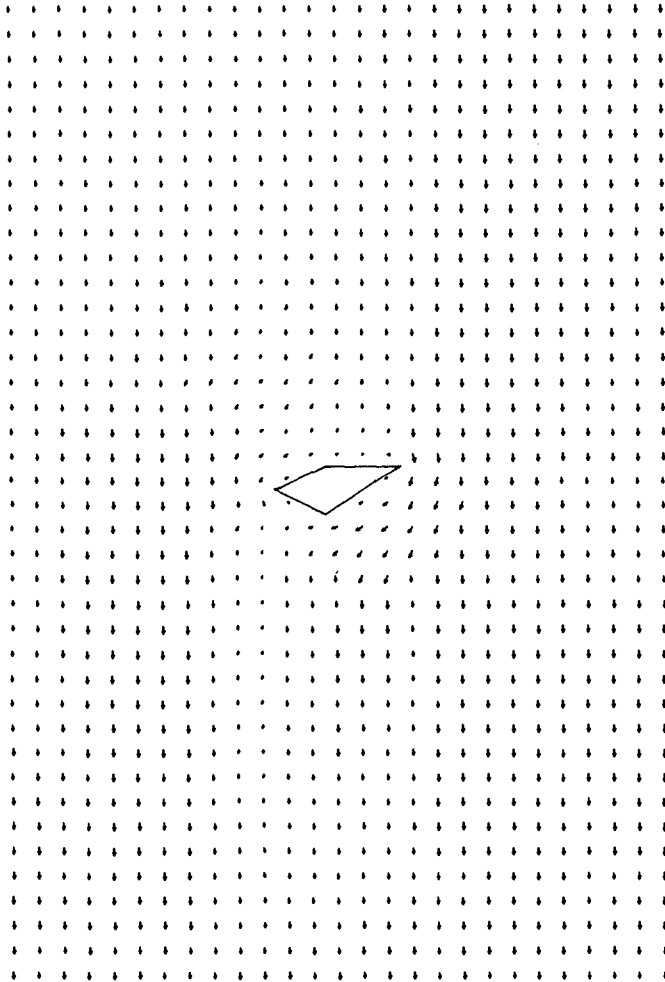


Fig.9 Numerically predicted velocities around Rattray Island near low water level during ebb tide.

TIME = 13.3 HR



LENGTH SCALE — 300 M  
AVERAGE DEPTH = 30.3 M  
TIDAL HEIGHT = 2.22 M

VELOCITY → 0.50 M/S  
MANNING NUMBER = 0.025  
TIDAL PERIOD = 12.6 HR

Fig.10 Numerically predicted velocities around Rattray Island at high water level excluding the advective accelerations

no indications of marked numerical diffusion, and (iii) no secondary circulation was predicted in the model when the advective accelerations and the lateral shear stresses were excluded. The latter conclusion from these tests confirmed the results of an analysis of the vorticity transport equation, where it was shown that the only terms generating vorticity in the model were the advective accelerations and the lateral shear stresses.

#### ACKNOWLEDGEMENTS

The model developments were undertaken at the Department of Civil Engineering, of the University of Birmingham, with the study being partially funded by a Science and Engineering Research Council research studentship.

This study in its present form would not have been possible without the use of extensive field data being made available by the Australian Institute of Marine Science, Queensland, Australia.

#### REFERENCES

1. DRONKERS, J.J. (1964). "Tidal Computations in Rivers and Coastal Seas". North Holland Publishing Company, Amsterdam.
2. FALCONER, R.A. (1976). "Mathematical Modelling of Jet-Forced Circulation in Reservoirs and Harbours". Ph.D. Thesis, University of London, England, 237pp (unpublished)
3. FISCHER, H.B. (1973). "Longitudinal Dispersion and Turbulent Mixing in Open Channel Flow". Annual Review of Fluid Mechanics, Vol.5, pp.59-78.
4. FLOKSTRA, C. (1977). "The Closure Problem for Depth-Averaged Two-Dimensional Flow". Paper A106, 17th International Association for Hydraulic Research Congress, Baden-Baden, Germany, pp.247-256.
5. IPPEN, A.T. (Ed.) (1966). "Estuary and Coastline Hydrodynamics". Engineering Society Monographs, McGraw-Hill Book Company Inc., New York.
6. KNIGHT, D.W. (1981). "Some Field Measurements Concerned with the Behaviour of Resistance Coefficients in a Tidal Channel". Estuarine, Coastal and Shelf Science, Vol.12, pp.303-322.
7. KUIPERS, J. and VREUGDENHIL, C.B. (1973). "Calculations of Two-Dimensional Horizontal Flow". Report No.S163, Part 1, Delft Hydraulics Laboratory, Delft, October.
8. LEAN, G.H. and WEARE, T.J. (1979). "Modelling Two-Dimensional Circulating Flow". Journal of the Hydraulics Division, ASCE, Vol.105, No.HY1, January, pp.17-26.
9. MARDAPITTA-HADJIPANDELI, L. (1984). "The Numerical Modelling of Tide-Induced Circulation." M.Sc. (Qual.) Thesis, University of Birmingham England, 155pp (unpublished).
10. PROUDMAN, J. (1957). "Oscillations of Tide and Surge in an Estuary of Finite Length". Journal of Fluid Mechanics, Vol.2, pp.371-382.
11. SMITH, G.D. (1978). "Numerical Solution of Partial Differential Equations". Oxford University Press, Second Edition.
12. TOWNSEND, A.A. (1956). "The Structure of Turbulent Shear Flow". Cambridge University Press, Cambridge, England.

13. WILLIAMS, J.W. and HOLMES, D.W.(1974). "Marker-and-Cell Technique, a Computed Programme for Transient Stratified Flows with Free Surfaces". Report No.134, Hydraulics Research Station, Wallingford pp.54.
14. WOLANSKI, E., IMBERGER, J. and HERON, M.(1984). "Island Wakes in Shallow Coastal Waters". Journal of Geophysical Research(in Press).

## NOTATION

$C$	= Chezy roughness coefficient
$f$	= Coriolis parameter
$g$	= gravitational acceleration
$H$	= total depth of flow
$L$	= distance from open boundary to island
$n$	= Manning roughness coefficient
$R_s$	= experimental constant
$t$	= time
$U, V$	= depth averaged velocity components in the $x, y$ directions
$U_1$	= free stream velocity
$U_*$	= shear velocity
$U_g$	= fluid speed
$x, y$	= mutually perpendicular co-ordinate axes in the horizontal plane
$\beta$	= correction factor for non-uniformity of the vertical velocity profile
$\Delta t$	= time step
$\Delta x$	= grid spacing
$\epsilon_b$	= eddy viscosity due to bed generated turbulence
$\epsilon_\ell$	= eddy viscosity due to free shear layer generated turbulence
$\eta$	= water surface elevation above mean sea level
$\rho$	= fluid density
$\sigma_{xx}, \sigma_{yy}$	= direct stress components in the $x, y$ directions
$\tau_{xy}, \tau_{yx}$	= lateral shear stress components in the $x, y$ directions
$\tau_{bx}, \tau_{by}$	= bed shear stress components in the $x, y$ directions
$\tau_{wx}, \tau_{wy}$	= wind induced surface shear stress components in the $x, y$ directions
$\omega$	= depth average vorticity about the vertical axis



## CHAPTER ONE HUNDRED SIXTY THREE

### ACCURATE MODELLING OF TWO-DIMENSIONAL MASS TRANSPORT

Lance Bode<sup>1</sup> and Rodney J. Sobey<sup>2</sup>

Any numerical solution of the convective transport equation in an Eulerian framework will exhibit inherent numerical dispersion and solution oscillations. The magnitude of such numerical errors is often so severe as to destroy the value of many computed solutions. A successful and economical algorithm for the convective transport equation in one spatial dimension has been published recently by one of the authors (RJS), in which an exact solution is achieved by means of a moving coordinate system. The present study describes the extension of this work to the more important and challenging two-dimensional case.

#### INTRODUCTION

Numerical methods for the solution of the two-dimensional convection-dispersion or advective-diffusion equation (ADE) abound in the literature of fluid dynamics. In Cartesian coordinates  $(x,y)$  the ADE has the form:

$$\frac{\partial C}{\partial t} + u \frac{\partial C}{\partial x} + v \frac{\partial C}{\partial y} = \nu \left( \frac{\partial^2 C}{\partial x^2} + \frac{\partial^2 C}{\partial y^2} \right), \quad (1)$$

where  $C(x,y,t)$  is the field of the substance that is re-distributed passively by the velocity field  $(u,v)$ ,  $t$  is time and  $\nu$  is the diffusion coefficient. The equation may also contain source and reaction terms.

The attention given to ADE is a measure both of its importance and ubiquity. Physically, an initial distribution  $C(x,y) = C(x,y,0)$  is given and the solution describes the field of  $C$  at any subsequent time over the solution domain, under the dual influences of advection and diffusion. In many instances, and certainly in estuarine and coastal environments, Eq. (1) is advection-dominated, and diffusive effects are minor. To a first approximation,  $\nu$  can be ignored the problem reverts to passive scalar advection.

- 
1. Research Fellow, Department of Civil and Systems Engineering, James Cook University of North Queensland, Townsville, Q. 4811, AUSTRALIA.
  2. Associate Professor, Department of Civil Engineering, 412 O'Brien Hall, University of California, Berkeley, CA 94720, USA.

More importantly however, it is the advective rather than the diffusive terms in Eq. (1) that present numerical problems. Indeed, considerable attention continues to be devoted to the *one-dimensional* ADE (6,7,12,14,15), a sure indicator of dissatisfaction with the current 'state-of-the-art'. The reasons for this are well known, but often ignored. Most solutions of Eq. (1) are Eulerian, in that they use a fixed computational grid. As pointed out by Penton (6), solutions such as conventional finite difference or finite element schemes attempt to solve the equation, with no attempt to take account, let alone advantage, of the nature of the solution. In problems dominated by advection, the performance of Eulerian solutions is often most unsatisfactory. With many such schemes, numerical dispersion and solution oscillations completely degrade the value of the computed solution.

In view of the above, a satisfactory solution of the two-dimensional problem remains to be demonstrated. A successful and economical algorithm for the one-dimensional ADE has been presented recently by Sobey (15,16), in which an exact solution is achieved by means of a moving coordinate system. The present scheme is an extension of this Lagrangian scheme to two spatial dimensions. The primary aim in such an algorithm is to permit the accurate calculation of mass transport (biota, pollutants) in continental shelf waters. In such cases, the velocity field (u,v) that is applied to Eq. (1) would be provided by a conventional two-dimensional hydrodynamic model.

GOVERNING EQUATIONS

Setting  $v = 0$  in Eq. (1) gives the advection equation:

$$\frac{\partial C}{\partial t} + u \frac{\partial C}{\partial x} + v \frac{\partial C}{\partial y} = 0 \quad (2)$$

As the prototype problem, Eq. (2) is to be solved on a square,  $-1 \leq (x,y) \leq 1$ , for  $t > 0$  where the initial field of C is a cone of unit height, radius  $r_0$  and initial location  $(x_0, y_0)$  - by convention (10,18) these parameters are  $r_0 = 1/4$ ,  $x_0 = -1/2$  and  $y_0 = 0$ . The initial conditions are:

$$C(x,y,0) = C_0(x,y) = \begin{cases} 1 - r/r_0, & r < r_0 \\ 0, & r > r_0 \end{cases} \quad (3)$$

where  $r = [(x-x_0)^2 + (y-y_0)^2]^{1/2}$ .

On the boundaries of the square, C is set equal to zero. The velocity field is solid body (anti-clockwise) rotation about the origin:

$$u = -\Omega y, \quad v = +\Omega x \quad (4)$$

where  $\Omega$  is the angular velocity. Perspective and plan views of the initial conditions are shown in Fig. 1.

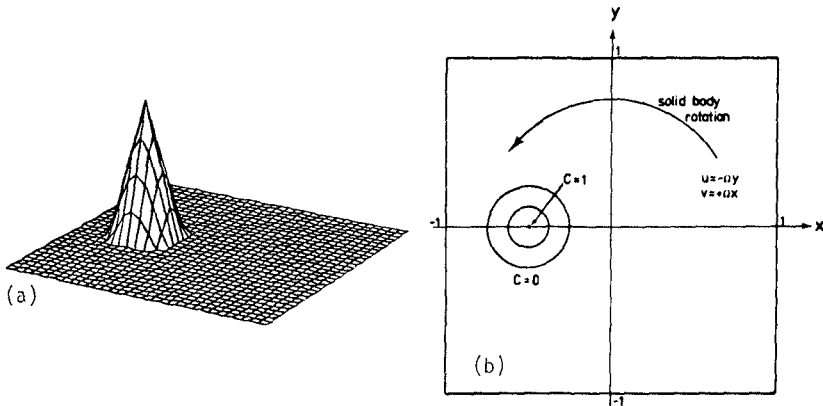


Fig. 1 (a) Perspective and (b) plan views of initial cone configuration.

In the absence of diffusion ( $\nu = 0$ ), the cone should return, undistorted, to its original position after any integral number of periods,  $nT = 2n\pi/\Omega$ ; elements of the cone describe concentric circles with constant angular velocity  $\Omega$ , about the origin. The range of  $C$  should always remain  $[0,1]$ . The rotating cone problem has become the basic prototype problem for two-dimensional advection, and has been used widely as a test bed for numerical algorithms (3,4,10,18). It is undoubtedly demanding, since any dispersion (phase speed errors) immediately truncate the peak of the cone, as will be seen in the following section. However, if such schemes are to be capable of mapping the evolution of point-like sources such as a pollution outfall, then the requirement of high fidelity at short wavelengths is absolutely essential.

#### Jacobian Formulation

For incompressible flow a stream function  $\psi$  can be defined in the conventional manner by

$$u = -\frac{\partial\psi}{\partial y}, \quad v = +\frac{\partial\psi}{\partial x} \quad (5)$$

This allows Eq. (2) to be expressed as

$$\frac{\partial C}{\partial t} + J(C, \psi) = 0 \quad (2')$$

where  $J$  is the usual two-dimensional Jacobian. In this form the equation can be expressed in a variety of ways so that certain quantities are conserved throughout the region of integration. Use of this has been made in particular for finite difference schemes beginning with the work of Arakawa (1), discussed in the following section.

EXISTING TECHNIQUES

Two finite difference (FD) schemes, representative of existing techniques for the solution of Eq. (2) are reviewed below. In order that an objective comparison of the performance and economy of the various schemes can be made with the proposed scheme, these two algorithms have been programmed and selected results are presented.

Arakawa/Jacobian scheme

The Jacobian formulation of Eq. (2') has been used widely to evaluate the advective terms in numerical weather prediction models as well as in a variety of other fluid dynamical applications. For homogeneous boundary conditions in the absence of dissipation, it can be shown that a number of quantities, averaged over the region of integration, must be conserved. For two-dimensional incompressible flow, if  $\zeta$  is vorticity, then  $\bar{\zeta}$ ,  $\overline{\zeta\psi}$  (kinetic energy) and  $\overline{\zeta^2}$  (enthalpy) must be conserved, where the overbar denotes the continuous spatial average. Arakawa (1) was able to show that certain aliasing interactions were minimised by particular second order FD formulations for the Jacobian, resulting in the global conservation of  $\bar{\zeta}$ ,  $\overline{\zeta\psi}$  and  $\overline{\zeta^2}$ .

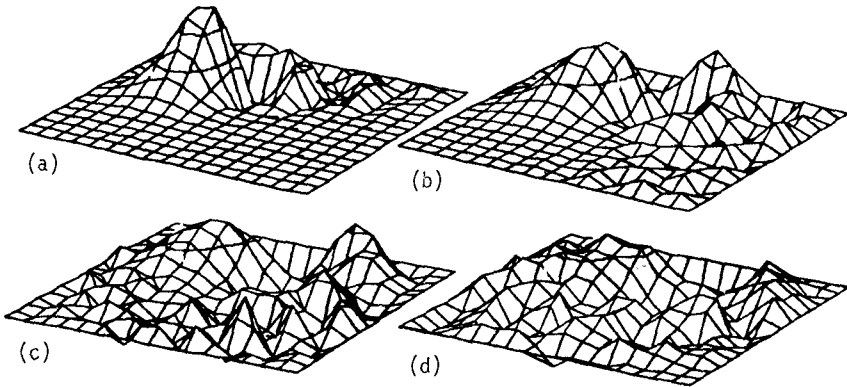
The Jacobian, denoted here by J - see also Ref. (10) - conserves all three quantities. Numerical experiments showed that this formulation prevented instabilities that had caused numerical schemes to 'blow up' and the use of Arakawa Jacobians has become widespread. It is a relatively simple matter to extend this scheme to produce Jacobians that are fourth order accurate spatially. One such formulation (1,10) also conserves all three quantities, and will be referred to as  $J_4$ . Although the conservative properties of  $J_2$  and  $J_4$  apply over the entire region of integration, this does not necessarily hold locally, with the result that the undesirable numerical dispersion can still be severe, particularly at the important shorter wavelengths.

Two basic spatial grid spacings are used,  $\Delta s = 1/8$  and  $1/16$ . These result in uniform  $17 \times 17$  and  $33 \times 33$  square grids applied to the given area of integration. These are denoted as cases A and B respectively. Both second order ( $J_2$ ) and fourth order ( $J_4$ ) Arakawa Jacobians are used, resulting in four cases altogether - A2, A4, B2 and B4. Time stepping is via the conventional 'leapfrog' scheme with periodic averaging to overcome time-splitting and appropriate re-initialisation. Thus, Eq. (2') is integrated by:

$$C_{i,j}^{n+1} = C_{i,j}^{n-1} + 2\Delta t J_{i,j}^n, \tag{6}$$

where  $J_{i,j}^n$  is either  $J_2(C)_{i,j}^n$  or  $J_4(C)_{i,j}^n$ . Temporal accuracy is of order  $(\Delta t)^2$ . The usual stability criterion applies to limit the size of  $\Delta t$  to  $\Delta t < \Delta s/v_{\max} = \Delta s/(\Omega\sqrt{2})$ .

In Fig. 2 the progress of the cone as it rotates through one complete revolution is shown for case A2. In all cases, the perspective views are rotated back to the original position, with the centre at  $(-1/2, 0)$ ,



**Fig. 2** Perspective views of cone at intervals of a quarter rotation for case A2 - see Table I.

for ease of comparison. The defects inherent in such a scheme are immediately apparent. In Fig. 2(a) after a quarter rotation, a wake is observed behind the cone proper for which only the 0.2 and 0.4 contours remain, even at this early stage - the range of  $C$  is  $[-0.25, 0.54]$ . This trailing wake continues to grow at the expense of the cone. By the end of one period - Fig. 2(d) - the structure of the cone is effectively unrecognisable, with the range of  $C$  now being  $[-0.31, 0.30]$ .

For some improvement, equivalent results for case B2 at twice the spatial revolution are presented in Fig. 3. Although a clear improvement, this second-order scheme is still totally inadequate. Numerical dispersion is so severe that short wavelength detail, particularly the cone's peak, trails behind in a wake of ever-increasing extent. After one revolution the original range for  $C$  of  $[0, 1]$  has become  $[-0.23, 0.52]$ . In Fig. 4, the results for case B4 (fourth order Jacobian with  $\Delta s = 1/16$ ) are presented after one and two revolutions. The range of  $C$  at these two times is  $[-0.13, 0.83]$  and  $[-0.16, 0.77]$  respectively. The well-recognised improvement with higher spatial order schemes (4,8,10) is apparent, but these results remain considerably short of theoretical expectations.

The overall results of these computations are listed in Table I. This gives the cone parameters (maximum and minimum values of  $C$  and the coordinates of the maximum  $C$  value) for the various cases at time  $t = 2T$ . These results can, to a limited extent, be compared with the results of a number of studies of the rotating cone problem that have been collated by Christensen and Prahm (3). Unfortunately, there is little uniformity amongst these, especially with regard to the times at which results are obtained. The present discussion will concentrate on the results at  $t = 2T$  - c.f. Ref. (10).

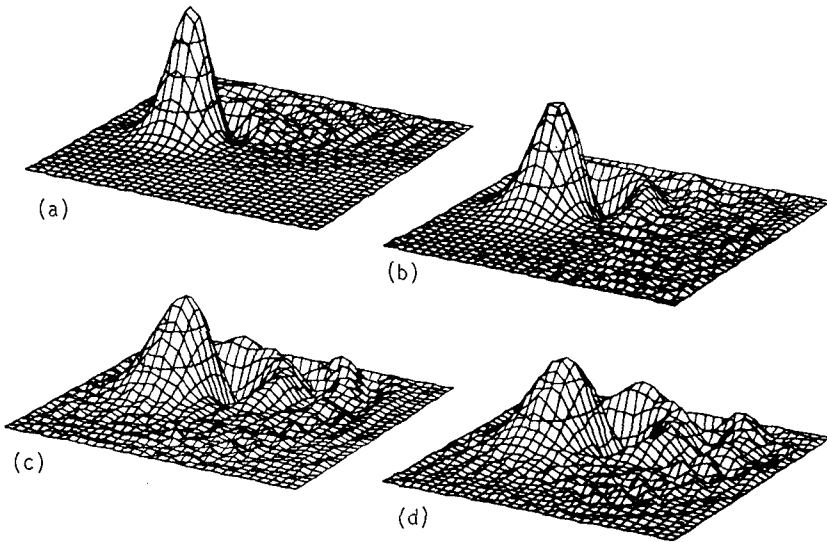


Fig. 3 As for Fig. 2, but case B2.

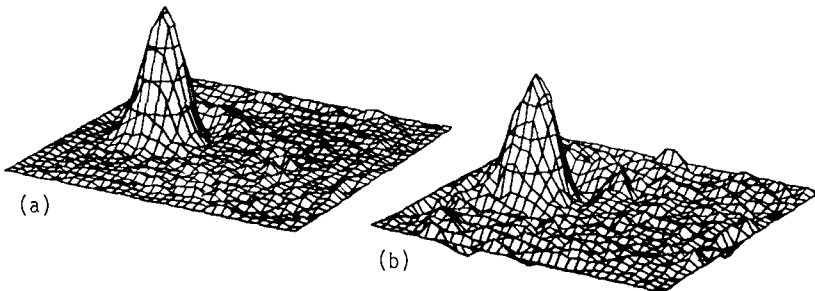


Fig. 4 Perspective views at (a)  $t = T$  and (b)  $t = 2T$  for case B4.

Lax-Wendroff Schemes

Consider the one-dimensional advection problem  $\partial C/\partial t + u (\partial C/\partial x) = 0$ , with  $u$  a constant. The standard Lax-Wendroff (LW) scheme (13) arises if,  $C^0$  is expanded as a Taylor series in time and the advection equation is then used to replace  $C_t$  and higher time derivatives by spatial derivatives. These are then approximated by centred FD approximations. Specifically, the one-dimensional scheme is:

$$C_i^{n+1} = C_i^n - \frac{\mu}{2}(C_{i+1}^n - C_{i-1}^n) + \frac{1}{2}\mu^2(C_{i+1}^n - 2C_i^n + C_{i-1}^n) \quad (7)$$

The LW scheme is both dissipative and quite strongly dispersive at short wavelengths (9). An equivalent two step scheme has also been derived (7). One advantage of the two-step formulation is the ease of extension to two or more spatial dimensions, as well as to higher spatial accuracy, as detailed in Gadd (7,8). In the second paper, Gadd noted that the scheme in two dimensions was not unconditionally stable and introduced a further modification. Like the fourth order Arakawa scheme above, calculations revert to second order at grid points adjacent to the boundaries. The final scheme (8) was shown to have a superior performance for the rotating cone problem over the earlier version.

Selected results for this scheme (8) and the standard second order LW method are presented. The cases that have been calculated are denoted by C and D for grid spacings of  $\Delta s = 1/8$  and  $1/16$  respectively, followed by the numbers 2 or 4 corresponding respectively to standard second order LW or the (fourth order) modified Gadd scheme (8). In Fig. 5 the progress of the cone over one rotation is shown for case D2. The overall impression is that these results are very similar to those exhibited by the corresponding second order Arakawa Jacobian experiments above. Quantitative details are listed in Table I. Again, doubling of spatial resolution does afford some improvement, but overall performance is poor. For example, after one revolution the C range in case D2 is  $[-0.20, 0.49]$  versus  $[-0.23, 0.52]$  for the corresponding case B2. In Fig. 6, case D4 is shown after one and two revolutions, the range for C at  $t = 2T$  being  $[-0.07, 0.76]$ , compared with  $[-0.16, 0.77]$  for the corresponding Arakawa case B4. The Gadd scheme is distinctly faster computationally, with two rotations for D4 taking 168 s on a DEC 10-21 mainframe versus 286 s for B4 - see also Table II. The performance of the Gadd scheme (8) does appear superior, since the negative values of C are not as extreme as those in case B4. However, it can be shown from Fourier analysis (9), that this can be attributed to increased dissipation and not necessarily to reduced dispersion at the shorter wavelengths.

It is apparent from Figs. 2-6 and Table I that the major problem is dispersion, although increased spatial accuracy in the representation of the advective terms can go a long way towards improving this situation. The effects of time differencing errors and spatial resolution are much less important. This defect (dispersion) is common to all Eulerian schemes; it is widely recognised and has been commented upon extensively, often in quite scathing terms (6,11,17). In spite of this, such schemes continue to enjoy widespread usage.

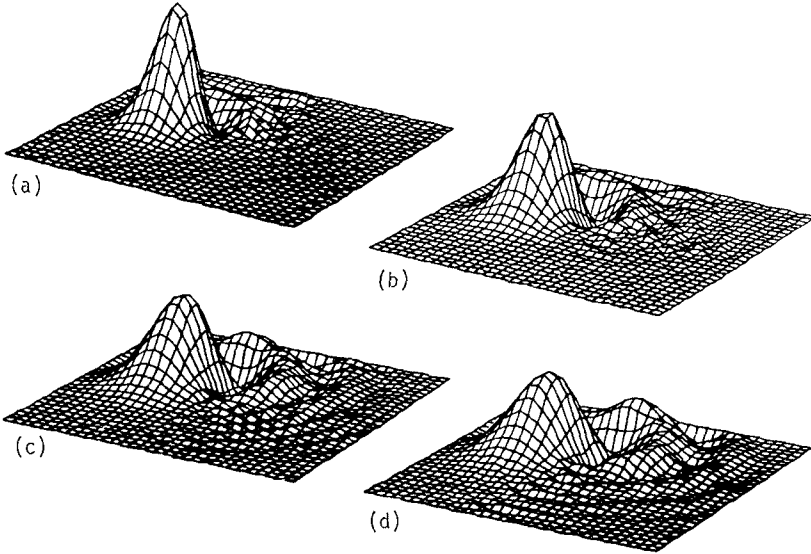


Fig. 5 As for Fig. 2, but case D2.

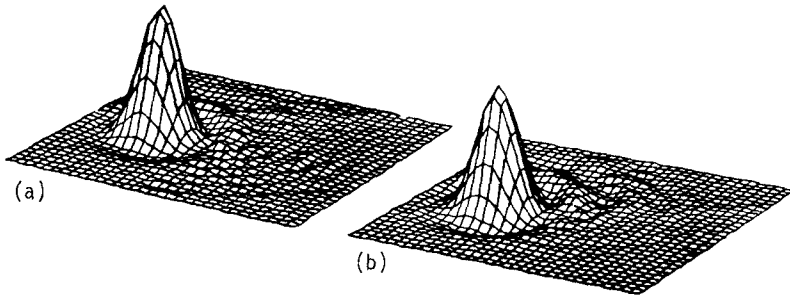


Fig. 6 As for Fig. 4, but case D4.

Spectral Methods

The major problem with the above FD methods, and indeed with all low order polynomial-based Eulerian methods is their failure to resolve spatial structure, particularly in the calculation of first derivatives. The spectral methods introduced by Orszag (10) have, by and large, been able to overcome this problem. They involve the expansion of the C field spatially in a set of suitable basis functions, chosen in general to satisfy the boundary conditions. Initial work used complex



two-dimensional Fourier series for the rotating cone problem which required the boundary conditions to be spatially periodic. Computations are sped up significantly by the use of the Fast Fourier Transform. Simple calculations reveal how with spectral methods, all available points enter the computation of derivatives, resulting in schemes that are markedly more accurate than second or fourth order FD methods. A substantial body of literature has arisen from this pioneering work of Orszag - see the review of Orszag and Israeli (11). The extension to less restrictive boundary conditions than the original periodic case follows with the use of alternative basis functions, such as Chebyshev polynomials.

There is, however, a major problem with spectral methods:- their lack of flexibility. The major motivation behind the present work was stated in the Introduction to be the need for an accurate algorithm for Eq. (1) where the velocity field ( $u,v$ ) is provided by a two-dimensional hydrodynamic model. Often, the boundaries of such models are extremely irregular, since they follow the coastline. Neither Eulerian FD models nor the present Lagrangian scheme have any difficulty in coping with this problem. On the other hand spectral models are totally unable to handle this situation; indeed, they are crucially dependent upon a regular (usually rectangular) geometry. A further related constraint is the lack of flexibility with respect to imposed boundary conditions. Even with regular boundaries, there is no simple way by which spectral methods could cope with, say, time-dependent input of  $C$  at a given point on the boundary, meant to model, for example, a pollutant discharge. Accommodation of this situation by Eulerian FD methods is again straightforward and will be shown below to be the case for the present method. Overall, although it can be demonstrated that spectral methods provide superior performance over more commonly used Eulerian FD schemes, they can offer little in the way of general application to hydrodynamic modelling of two-dimensional mass transport.

TABLE I

ACCURACY OF THE VARIOUS NUMERICAL SCHEMES (at  $t = 2T$ )

Scheme	Description	Spatial Order	Grid Dimensions	$C_{max}$	$C_{min}$
A2	Arakawa	2nd	17 x 17	0.32	-0.29
B2	"	"	33 x 33	0.42	-0.24
A4	"	4th	17 x 17	0.39	-0.24
B4	"	"	33 x 33	0.77	-0.16
C2	Lax-Wendroff	2nd	17 x 17	0.20	-0.18
D2	"	"	33 x 33	0.36	-0.21
C4	Gadd (LW)	4th	17 x 17	0.41	-0.17
D4	"	"	33 x 33	0.76	-0.07
MC	Moving Coords	Exact	17 x 17	1.00	0.00

## MOVING COORDINATE ALGORITHM

It is widely recognised (6,11) that Lagrangian or moving coordinate numerical schemes are the 'natural' method for the solution of the advection equation, Eq. (1). Nevertheless, it would seem that the advantages offered by the simplicity of Eulerian schemes have been allowed to overshadow their considerable disadvantages as highlighted in the previous section. Lagrangian schemes have been proposed only rarely (5), but such work does not appear to have been carried appreciably further.

Lagrangian Solutions of the Advection Equation

Eq. (1) is mathematically equivalent to:

$$\frac{dC}{dt} = 0 \quad (8)$$

along

$$\frac{dx}{dt} = u \quad , \quad \frac{dy}{dt} = v \quad . \quad (9)$$

This is the Lagrangian scheme that forms the basis of the present work. There are complicating factors involved in the use of a Lagrangian scheme and these will be described below, but they are often over-stated. The almost trivial simplicity of Eq. (8) demands further attention. It simply states the well known physical fact that values of C are conserved in time along trajectories or characteristics that are the paths of the fluid particles. The actual integration of Eq. (9) can be performed by any suitable algorithm for ordinary differential equations, once the velocity field is specified. Standard fourth order Runge-Kutta is chosen in the present study.

The basis of Lagrangian schemes is reviewed by Book and Boris (2). A number of disadvantages of such schemes are stated, chief among which is the distortion of an initially uniform grid by a non-uniform velocity field. In specific numerical computations, the flow and hence the grid might become so distorted that the 'bookkeeping' involved in keeping track of the positions of the individual nodes ultimately becomes intractable. However, this argument loses sight of the fact that the very distortion of the grid mirrors the gradients in the flow: it is in regions where either C or the flow varies rapidly that grid points must be concentrated in order to effect an accurate solution. Lagrangian schemes adapt to this situation naturally; Eulerian schemes are simply unable to do so and their consequent and often severe loss of fidelity as the Nyquist limit is approached, can hardly be unexpected.

Previous Lagrangian schemes appear to have concentrated on situations where flow variables altered rapidly. These include flows involving shocks and other large gradients in the flow, for which they are ideal theoretically, but apparently impractical because of mesh distortion. In the present case the proposal is to apply the scheme to mass

transport calculations in slowly varying velocity fields. In this case, the computational grid does not become unmanageably distorted. More importantly, however, the gradients of  $C$  can be preserved accurately and do not suffer from the artificial diffusion and solution oscillations associated with Eulerian schemes. It needs to be recognised that in order to solve Eq. (9) for each element of  $C$ , the velocity field needs to be specified at the actual location of each of these points. For the solid body rotation of the present problem, simple linear interpolation will accomplish this exactly. For slowly varying velocities a low order bivariate interpolation scheme should suffice. This contrasts with the situation for Eulerian schemes where, on a fixed grid, spatial derivatives of  $C$  cannot be calculated accurately by low order Taylor series, especially in regions of high gradients (6).

Another problem that has been associated with Lagrangian schemes, and which has been believed to be to their detriment is associated with inflow and outflow boundaries. At the latter, grid points must leave the computational region; at the former, they must be created. This is by no means an insurmountable obstacle and will be discussed below.

If the solution of the full ADE, Eq. (1) is required, then the question incorporating diffusion on a possibly distorted Lagrangian grid, that may be both gaining and losing mesh points, is obvious. A proposed treatment of this important extension of the present problem is also discussed below. All of the above questions (i.e. method of integration of Eq. (9); boundary conditions and the addition or removal of grid points; incorporation of the diffusion step) have been addressed by Sobey (15,16) in an algorithm for the solution of the one-dimensional ADE. The results of this work were most encouraging, in terms of the high accuracy attained, the relative computational efficiency and the inherent flexibility of the scheme, and suggest that the extension of this Lagrangian approach to the more important and challenging question of two-dimensional advection should be equally worthwhile.

#### Sample Computations

Eqs. (8,9) were solved for the rotating cone problem, with the same spatial resolutions employed for the tests of the two main Eulerian schemes above. The results of these computations for the  $17 \times 17$  grid after two full rotations are presented in Table I and in Fig. 7. The timestep used for these results was  $1/16$  of the period of rotation. This corresponds to a dimensionless timestep of 4.5, compared with 0.5 used for the above Eulerian schemes. The error, which can be measured by the maximum error in the position of the grid elements at  $t = 2T$  was negligible ( $5 \times 10^{-5}$ ). It should be recalled that the range of  $C$  is always  $[0,1]$  with this scheme. It can be reduced by reducing the specified timestep in the solution of Eq. (9), but this increases the CPU time and the present parameters would appear to be satisfactory. The actual CPU times for the various schemes are shown in Table II and the moving coordinate scheme undoubtedly compares favourably with the much less accurate Eulerian methods. Should, on the other hand, the timestep be increased, inaccuracy results inevitably. For example, a dimensionless timestep of 18.0 results in errors of order unity in the position of grid elements at the boundary of the computational region.

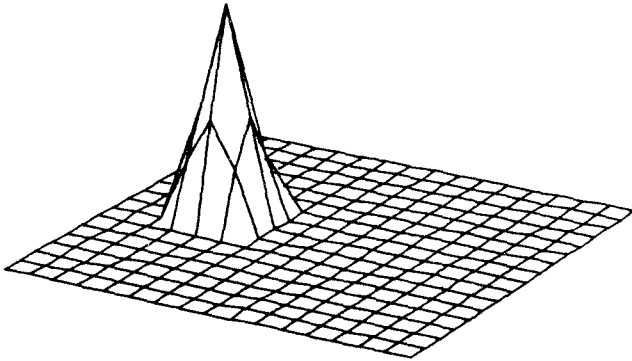


Fig. 7 Perspective view of cone at  $t = 2T$  with the moving coordinate algorithm, with  $\Delta s = 1/8$ .

TABLE II

CPU TIMES FOR VARIOUS INTEGRATION SCHEMES ( $t = 2T$ )

Numerical Scheme	Dimensionless Timestep, $\lambda$	CPU(s)
Arakawa 2nd order	0.5	22.6
Lax-Wendroff 2nd order	0.5	10.9
Arakawa 4th order	0.5	32.3
Gadd (LW) 4th order	0.5	18.3
Moving Coordinates	4.5	6.7

$\lambda = v_{\max} \Delta t / \Delta s$ , with all results for a spatial grid of  $\Delta s = 1/8$ .  
 All computations performed on a DEC 10-21 mainframe computer.

Boundary Conditions

The specification of boundary conditions is exactly analogous to the treatment used in the method of characteristics, and is detailed in Sobey (15). For the rotating cone problem,  $C$  is specified as zero along the boundary of the square computational region, but more general boundary conditions can just as easily be accommodated. Outflow boundaries present no problem. If over a given timestep an element of  $C$  is adjudged to have passed out of the computational region, that element is simply removed from further consideration. At inflow boundaries, additional grid points can be created by integration back along the characteristics, Eq. (9), to the particular inflow boundary (15).

### Extension to the Advection-Diffusion Equation

The essence of this extension is the method of fractional steps employed by Sobey (15) for the one-dimensional ADE. Eq. (1) is equivalent to the following pair of equations:

$$\frac{\partial C}{\partial t} + u' \frac{\partial C}{\partial x} + v' \frac{\partial C}{\partial y} = 0 \quad , \quad (10)$$

$$\frac{\partial C}{\partial t} = \nu' \left( \frac{\partial^2 C}{\partial x^2} + \frac{\partial^2 C}{\partial y^2} \right) \quad (11)$$

Addition of Eqs. (10) and (11) gives Eq. (1), the two-dimensional ADE, provided  $(u', v', \nu') = 2(u, v, \nu)$ . Thus, the full ADE can be thought of as separate, but simultaneous advection and diffusion steps, but with twice the given velocity and diffusion. Numerically, it is simpler to take the two steps as sequential. The solution of C at  $n\Delta t$  is advanced to  $(n+1/2)\Delta t$  by the numerical solution of Eq. (10), the present Lagrangian scheme. The field of C at this intermediate step is then used to solve the diffusion (or heat) equation, Eq. (11).

Because of the Lagrangian solution of the advection equation, this second step necessitates the solution of the diffusion equation on a non-uniform grid. Sobey (16) has presented an optimised solution of this equation in one dimension. The results obtained were most satisfactory, but the extension of this method to two dimensions poses additional problems, and a more pragmatic but less sophisticated approach may be warranted. Although Eulerian schemes have been effectively rejected for the solution of the advective step, there is no reason to do so for the diffusive step. The solution of Eq. (11) by standard low order Taylor series approximations, either FD or FE methods, is satisfactory in this case. Further work is currently being pursued on this important aspect of the problem.

### CONCLUSIONS

The moving coordinate method introduced in the present paper has been shown to have much higher accuracy than is available from conventional and widely-used Eulerian schemes. It is simple in both concept and implementation, and, in addition, it can be interfaced easily with hydrodynamic models used to provide the velocity field.

Extensions to include the diffusive component of Eq. (1) have to take account of the necessarily distorted computational grid. This has already been effected successfully for the one-dimensional equation - Refs. (15,16) - and an analogous procedure for the two-dimensional case has been proposed. With the slowly-varying velocity fields (e.g. continental shelf circulation) for which the method is intended, the mesh will distort, but not unmanageably so. Strategies have also been discussed for the removal or addition of mesh points, should they become too sparse or concentrated. It should be recalled however, that such

distortion mirrors the background gradients and gives a Lagrangian scheme natural advantages over any Eulerian approach. Overall, the present approach is meant to provide the first but also most important step towards the development of accurate and reliable methods for the solution of ADE problems in actual physical environments. Advection-dominated flows are the rule rather than the exception, yet too often the veracity of available solutions would appear to be compromised by an inadequate appreciation of the limitations of available numerical methods. A successful solution of the problem, based on the above principles, provides a resolution of this impasse.

#### ACKNOWLEDGEMENTS

This work has been supported in part by the Marine Sciences and Technologies Grant Scheme of the Australian government. The assistance of Mr. Lou Mason in the preparation of graphical output is also appreciated.

#### APPENDIX - REFERENCES

1. Arakawa, A., "Computational Design for Long-Term Numerical Integration of the Equations of Fluid Motion: Two-Dimensional Incompressible Flow. Part I", *Journal of Computational Physics*, Vol. 1, 1966, pp.119-163.
2. Book, D.L. and Boris, J.P., "Computational Techniques for Solution of Convective Equations", in *Finite-Difference Techniques for Vectorized Fluid Dynamics Calculations*, D.L. Book, editor, Springer-Verlag, 1981, pp.5-28.
3. Christensen, D. and Prahm, L.P., "A Method for Numerical Solution of the Advection Equation", *Journal of Applied Meteorology*, Vol. 15, 1976, pp.1284-1294.
4. Crowley, W.P., "Numerical Advection Experiments", *Monthly Weather Review*, Vol. 96, 1968, pp.1-11.
5. Crowley, W.P., "FLAG, A Free-Lagrange Method for Numerically Simulating Hydrodynamic Flows in Two Dimensions", *Proceedings of the Second International Conference on Numerical Methods in Fluid Dynamics*, Springer-Verlag, 1971, pp.37-43.
6. Fenton, J.D., "On the Numerical Solution of Convective Equations", *Bulletin of the Australian Mathematical Society*, Vol. 26, 1982, pp.81-105.
7. Gadd, A.J., "A Numerical Advection Scheme with Small Phase Speed Errors", *Quarterly Journal of the Royal Meteorological Society*, Vol. 104, 1978, pp.583-594.
8. Gadd, A.J., "Two Refinements of the Split Explicit Integration Scheme", *Quarterly Journal of the Royal Meteorological Society*, Vol. 106, 1980, pp.215-220.
9. Morton, K.W., "Stability and Convergence in Fluid Flow Problems", *Proceedings of the Royal Society of London, Series A*, Vol. 323, 1971, pp.237-253.
10. Orszag, S.A., "Numerical Simulation of Incompressible Flows within Simple Boundaries: Accuracy", *Journal of Fluid Mechanics*, Vol. 49, 1971, pp.75-112.

11. Orszag, S.A. and Israeli, M., "Numerical Simulation of Viscous Incompressible Flows", *Annual Reviews of Fluid Mechanics*, Vol. 6, 1974, pp.281-318.
12. Pironneau, O., "On the Transport-Diffusion Algorithm and its Application to the Navier-Stokes Equations", *Numerische Mathematik*, Vol. 38, 1982, pp.309-332.
13. Richtmyer, R.D. and Morton, K.W., *Difference Methods for Initial-Value Problems*, Wiley Interscience, 1967.
14. Sobey, R.J., "Hermitian Space-Time Finite Elements for Estuarine Mass Transport", *International Journal for Numerical Methods in Fluids*, Vol. 2, 1982, pp.277-297.
15. Sobey, R.J., "Fractional Step Algorithms for Estuarine Mass Transport", *International Journal for Numerical Methods in Fluids*, Vol. 3, 1983, pp.567-581.
16. Sobey, R.J., "An Optimized Solution for the Diffusion Equation on a Non-Uniform Grid", *International Journal for Numerical Methods in Engineering*, Vol. 20, 1984, pp.465-477.
17. Sobey, R.J., "Numerical Alternatives for Transient Stream Response", *Journal of Hydraulic Research*, ASCE, Vol. 110, 1984, pp.749-773.
18. Zlatev, Z., Berkowicz, R. and Prahm, L.P., "Testing Subroutines Solving Advection-Diffusion Equations in Atmospheric Environments", *Computers and Fluids*, Vol. 11, 1983, pp.13-38.



*Five Sisters Breakwater showing accretion behind, Wentthrop Beach, MA*

### **PART III**

## **COASTAL STRUCTURES AND RELATED PROBLEMS**

*Entrance to Wildwood Harbor, Cleveland, OH*







## CHAPTER ONE HUNDRED SIXTY FOUR

### Safety and Reliability of Breakwaters

A. Mol \*)  
R.L. Groeneveld \*)  
A.J. Waanders \*)

#### Abstract

This paper discusses the need to incorporate a reliability analysis in the design procedures for rubble mound breakwaters. Such an analysis is defined and a suggested approach is outlined. Failure mechanisms are analysed and categorized in Damage Event Trees. The probability of failure is computed using a level III simulation method to include time and cumulative effects and to account for skewed probability distributions. Typical outputs of the computer program are shown and compared with results according to traditional design approaches. The paper concludes that there is a definite need to include reliability analysis in the design procedures for larger breakwaters and such an analysis must consider the accuracy of design parameters and methods.

#### 1. Introduction

The design of rubble mound breakwaters is traditionally based upon a combination of experience, engineering skill and hydraulic model studies. The criteria for design are based on a design load having a return period in the order of 50 to 100 years. Under such a design load, typically damage may occur to between 2% and 5% of the armour units. When site information is unreliable the design condition may be defined more conservatively by applying an appropriate safety factor (Figure 1). Even so, a certain risk of failure in the lifetime of the breakwater still exists.

\*) PRC Engineering, Inc, Badhuisweg 11, 2587 CA The Hague,  
the Netherlands

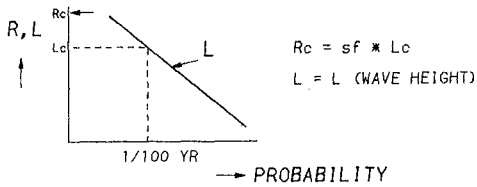


Fig. 1 Traditional Approach

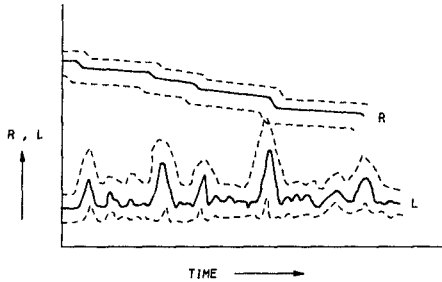


Fig. 2 Load and Strengths versus Time

OBJECTIVE TO ASSESS THE REAL PROBABILITY ON FAILURE

- PROCEDURE
- DESCRIBE FAILURE FUNCTION  
 $F = F(X_1, X_2, X_3, \dots, X_n)$
  - DESCRIBE VARIABLES  $X_n$  by  
 STATISTICAL DISTRIBUTION  $P(X_n)$
  - DETERMINE STATISTICAL DISTRIBUTION  
 $P(F)$  AND PROBABILITY  $F=0$  (DAMAGE EVENT)  
 BY APPROXIMATE METHODS (LEVEL II) OR  
 BY EXACT METHODS (LEVEL III)

Fig. 3 Reliability Analysis Higher Levels

However, the probability and extent of damage is not established solely by the actual wave height exceeding the design wave height. Both the strength of the structure and the imposed loads are influenced by a number of other variables, some of which are a function of time. This results in a typical representation of the breakwater strength 'R' and the applied load 'L' as given in Figure 2. Failure principally occurs when the load exceeds the strength:  $'R-L < 0'$ .

For a breakwater, 'R' and 'L' are functions of a large number of parameters. 'R' is described by parameters which include geotechnical properties, armour weight, density and shape, crest height and slope angle. The load 'L' is a function of parameters which include the offshore wave height, period, direction and refraction. All of these parameters are not precisely defined, but have certain variations due to inaccuracies in studies and measurements, construction constraints, quality of workmanship etc. Furthermore, environmental conditions, including the wave parameters, have significant stochastic characteristics.

A better assessment of the probability of a given degree of damage, then according to the traditional approach outlined above, can be achieved by using more sophisticated probabilistic methods presently available, see Figure 3. The Joint Committee on Structural Safety (Reference 6) has structured the various methods for reliability analysis. In this respect the traditional design approach can be defined as level I. References 1 and 7 describe the application of a level II approach for rubble mound breakwaters. However in the level II method the computations are carried out utilizing a linearisation of the failure function  $'F = R - L'$  and utilizing assumptions for the shape of the probability functions. Also the method does not take into account accumulation of damage in subsequent storms.

This paper discusses the application of a computer program which computes the probability of failure on level III using a time domain simulation approach. Therefore, in contrary to the level II approach, it includes arbitrary statistical distributions of all variables and the response of breakwater structures depending on previous history of damages.

## 2. Failure Mechanisms

With traditional methods as well as with probabilistic approaches, gross errors must be avoided. Such errors may occur due to the neglect of one or more of the possible failure modes. For design conditions well within the existing field of experience this might not be important, but it can be critical when the design concepts are stretched beyond existing experience. Recent failures of deepwater breakwaters have exhibited evidence of neglect of certain failure modes through breakage of armour units and geotechnical instability of slopes.

<u>EXTERNAL EVENTS</u>	<u>MINOR EVENTS</u>	<u>MAJOR EVENTS</u>	<u>FAILURE EVENTS</u>
WATER LEVEL	SCOUR OF FORESHORE	DAMAGE FRONT ARMOUR	SETTLEMENT SLIDING AND OVERTURNING OF CROWN WALL
WAVES	EROSION OF TOE FILTER	DAMAGE REAR ARMOUR	EROSION OF UNDERLAYERS AND CORE
CURRENTS	VENTING THRU BREAKWATER	SETTLEMENT OF CORE AND SUBSOIL	GRADUAL DETERIORATION OF MOUND
TSUNAMIS	INSTABLE FRONT BERM	SLIDING FAILURE OF SLOPES AND SUBSOIL	
EARTHQUAKE	WASHING OUT OF FINES	EROSION AND UPLIFT OF BACKFILL	
		BREAKAGE OF PARAPET WALL	

Table 1 Damage Events

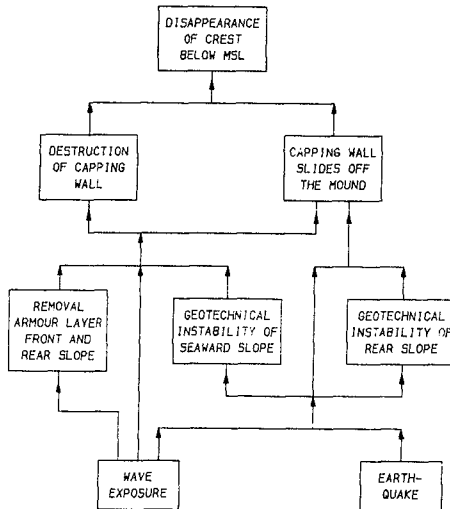


Fig. 4 Main Damage Event Tree

An important step in the probabilistic design method is to list all possible failure modes and to present the interrelation by use of a fault tree consisting of a number of successive or parallel events. Table 1 lists various damage events as they have occurred in failures of breakwaters. The relation between the various damage events is given in 'Damage Event Trees' as shown in Figures 4, 5 and 6. Figure 4 shows the main Damage Event Tree of a breakwater. Based on this, the Damage Event Tree is given for the geotechnical instability of the front slope (Figure 5). Figure 6 concentrates on the hydraulic damage of front and rear slopes.

Significant external loads on a breakwater structure are currents, waves, water level and seismic activities. These loads may cause events such as the hydraulic instability of front and rear armour, geotechnical instability of front and rear slopes, or the destruction or sliding of the capping wall either directly or as a consequence of damage to the slope. For each event the (partial) probability should be defined. Some events are independent whilst others are dependent. However, the total probability of failure of a breakwater is greater than the probability of a single event, for example, the hydraulic instability of the front armour layer only.

Considerations of the probability of failure lead to an important conclusion for the design of the components of a breakwater. If limited finance is available for reducing the overall failure probability, it should be invested in those components which show the largest reduction in overall failure probability for the given amount of money. Generally these comprise the relatively low-cost components to the breakwater which, however, may be vital to the stability of the structure. Examples of such components include filters and berms. The costs of safeguarding these components from failure are minor compared with the costs of achieving a similar increase in overall stability by improving major cost components such as armour or slopes. Hence, from the point of view of both risk analysis and cost, low-cost components may be designed such that the probability of their failure is negligible compared with the probability of failure of high cost items. This also simplifies the Damage Event Trees by virtually eliminating unknown factors and limiting consideration to failure mechanisms which can be quantified.

Figure 6 shows a simplified Damage Event Tree which indicates that, basically, only the problem of hydraulic instability of armour, due to waves, remains. Although not fully understood, hydraulic instability can be analyzed with reasonable accuracy using the results of hydraulic model tests in combination with a stability formula, as is shown in Section 4. The geotechnical response of the structure to external loads can be described by using methods as presented in Reference 2 and this paper does not consider this aspect further.

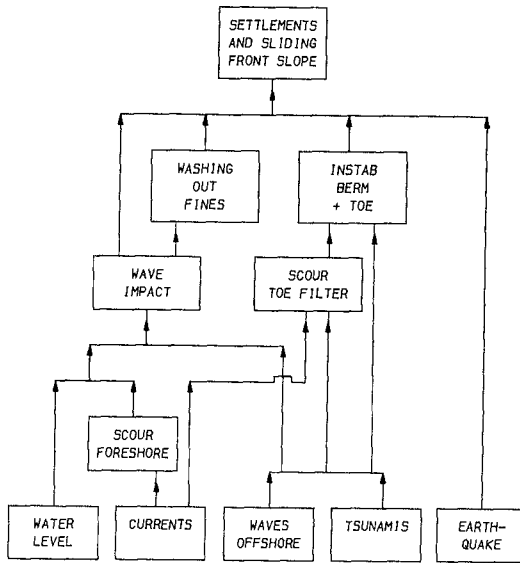


Fig. 5 Damage Event Tree - Geotechnical Instability Front Slope

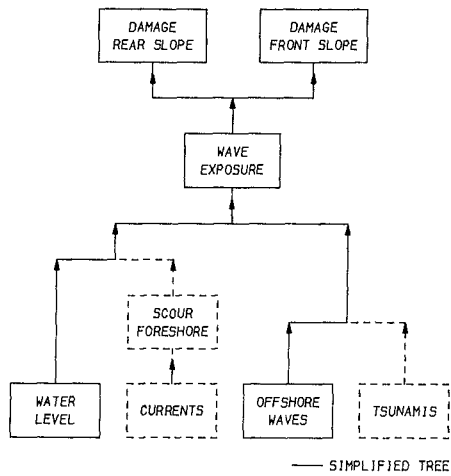


Fig. 6 Hydraulic Damage without Capping Wall

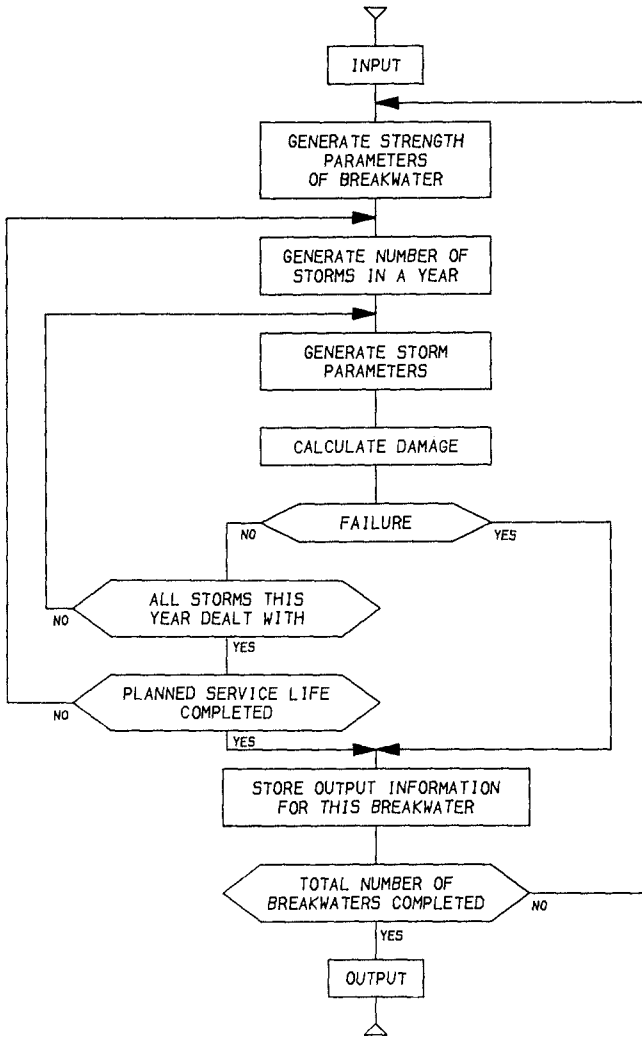


Fig. 7 Flow Diagram - Simulation Model



### 3. A Computermodel for Level III Reliability Analysis

As stated in References 1 and 7 considerable assumptions were necessary to compute the probability on failure. As a result the outcome is not very accurate, and is very limited.

A much more promising method is an approximatel level III approach based on a time domaine simulation of the service life of a large number of breakwaters from which the strength parameters are randomly generated from given statistical distributions. Figure 7 shows a flowchart of the computer program developed to handle this approach. Firstly the properties determining the strength of the breakwater are randomly selected from the given distributions, which can be of an arbitrary shape. Subsequently the impact of various generated storms is recorded over the service life of the breakwater with a range of options on accumulation of damage, historical effects and repair works. The program restarts by generating the properties of a new breakwater and subsequently recording the impact of newly generated storms, up to the required number of simulations.

The computational effort to obtain a reliable result strongly depends on the width of the statistical distributions. Checks on the accuracy are based on comparing the output of runs with various numbers of simulated breakwaters. It was found that for the presented case the computational effort was within acceptable limits.

The Software program can be expanded to include modules for geotechnical instability, (due, for example to wave action) and for seismic activity (generated independently according to given distributions); both simultaneous with the modules for hydraulic instability. In the following section a mathematical description is given of the relation between damage and input parameters for the hydraulic instability of the armour layer.

### 4. Mathematical Description and Quantification of Hydraulic Stability

In order to assess damage as a function of various input parameters, a mathematical description of hydraulic stability is required. This description is complex because it must take account of the load history, as exhibited by settlements of the armour and armour breakage. Although research on this subject continues, it is entering the stage of being used for engineering purposes (References 3, 4 and 9).

The damage function can be assessed using a combination of stability formulae (to include the effects of known parameters), and hydraulic model testing. Model tests help to assess the level of stability of the structure and verify the relationship between parameters, such as wave period, wave groupiness, the time history and the resulting

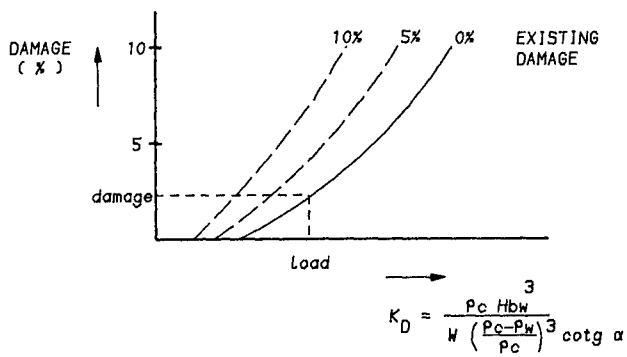


Fig. 8 Shape Factor

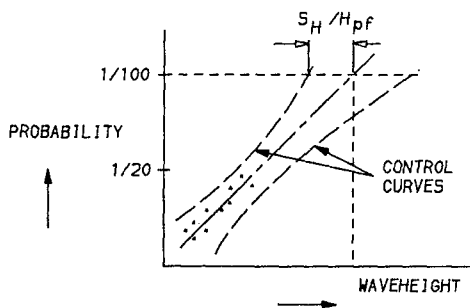


Fig. 9 Scatter Extreme Wave Heights

armour breakage. The graph shown in Figure 8 with damage along the 'y' axis and the Hudson Number 'Kd' along the 'x' axis illustrates. The Hudson Number is computed from the following equation:

$$Kd = \frac{\rho_c H^3}{W \left( \frac{\rho_c - \rho_w}{\rho_w} \right)^3 \cot \alpha}$$

with H = wave-height at the location  
of the breakwater without  
wave breaking  
 $\rho_c$  = density of concrete  
 $\rho_w$  = density of water  
W = armour weight  
 $\alpha$  = slope angle

The relationship in Figure 8 is shown as a function of the starting damage. Damage is expressed as the proportion of broken or displaced armour units related to the total number of units in the structure. Depending upon the sensitivity for wave parameters, tests should include the effect of spectral shape (peak period) and groupiness. Hence, extensive testing is required to provide the necessary input for the reliability analysis. The effects of small variations in input parameters, such as the weight and density of the armour unit and the slope angle, will produce damage of the order predicted by the stability formula. The wave-height excludes the effects of wave breakage (model testing will account for this phenomenon) but includes refraction, modelled numerically or physically.

For input into the model, the statistical distributions of the various parameters must be quantified. Table 2 gives a listing of the various parameters, the interrelation between the parameters, and the assumed modelling for the present study.

The estimated statistical distribution for parameters such as the armour weight is based on the allowable tolerances in the specifications and on the quality of supervision, specified measurement methods and expected quality of workmanship. Other parameters will depend on the quality and quantity of the studies carried out. For parameters describing environmental conditions, this factor for inaccuracy should be superimposed on the natural variation.

In the present study the joint probability distribution of wave-height, period, direction, groupiness and storm surge is equated to relations between the wave-height and other parameters. These other parameters are defined by a scatter parameter and the probability distribution of the wave height.

Particular emphasis should be laid on the scatter of the wave height distribution. Errors may occur due to:

- scatter and inaccuracies of the original data
- selection of probability function
- a considerable extrapolation outside the available period of observations

Table 2  
Listing of Parameters

<u>Parameter</u>	<u>Symbol</u>	<u>Relation</u>	<u>Modelling</u>
concrete density	$\rho_c$	independent	independent
density of water	$\rho_w$	"	"
slope angle	$\alpha$	"	"
armour weight	$W$	"	"
wave height offshore	$H_{so}$	} joint probability distribution of $H_{so}$ , $T$ , $s$ and $GF$	independent
storm surge	$s$		$s = F(H_{so})$
wave period	$T$		$T = F(H_{so})$
wave direction	$\phi$		independent
wave groupiness	$GF$		in model test
tide	$t$	independent	independent
refraction factor	$K_r$	depending on $\phi$ , $T$	$K_r = K_r(\phi, T)$
wave breaking	$K_b$	depending on $H, L,$ $T, s, t$	in model test
stability coefficient - damage relation	$K_d$	depending on $T, GF, s, K_r$	$K_d =$ $F(T, GF, s, t)$

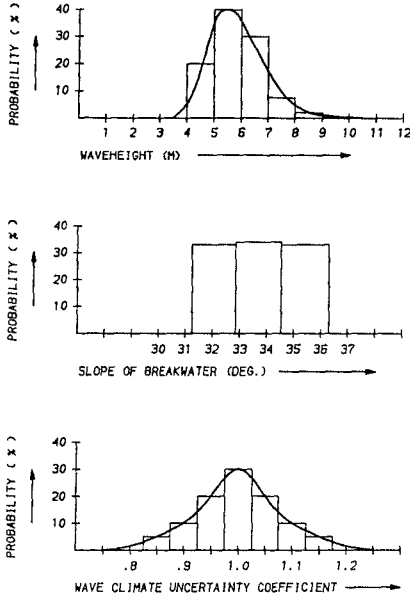


Fig. 10 Probability Density Functions

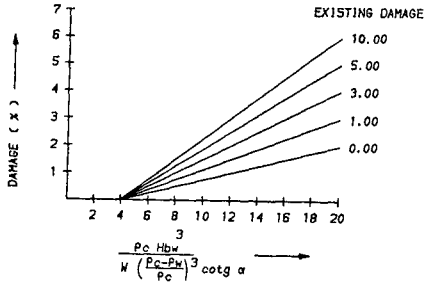


Fig. 11 Response of Structure to Wave Load

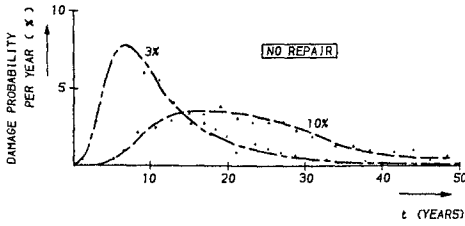


Fig. 12 Probability of Damage versus Time

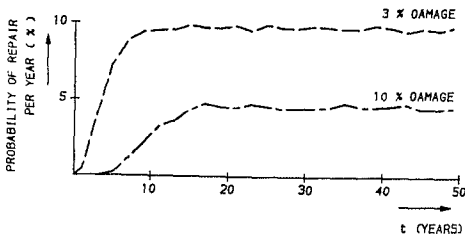


Fig. 13 Probability of Repair versus Time

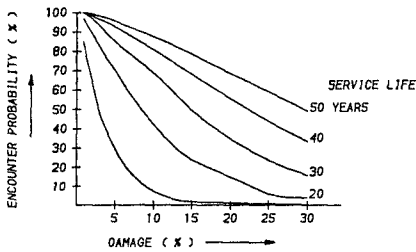


Fig. 14 Encounter Probability of Damage as Function of Service Life

This results in a large confidence band around the extrapolated function and gives standard deviations in the order of 10% to 15% of the average value, as shown in Figure 9 (References 5 and 8).

## 5. Application

An example of the application of the method as described above is shown in this section. It comprises a breakwater with a tetrapod armour layer of 25 tons. The wave climate is characterised by a 100 year return period wave-height of  $H_s = 8.5$  m.

Some examples of applied statistical distribution (wave-height, wave-height inaccuracy and slope distribution) are shown in Figure 10. The relationship between stability parameters and damage is assumed to be as in Figure 11. The concrete density is fixed on 2.43 T/m<sup>3</sup>.

Using the traditional level I approach, the design criterium was set at 3% damage in a 100 year event. Applying a 20% safety factor on the wave-height to include uncertainties, such as breakage of armour, the design wave-height is 10.2 m and, according to Figure 8, the criteria are satisfied.

The output of the level III simulation model is shown in Figures 12, 13 and 14. Figure 12 shows the number of breakwaters per year exceeding the 3% or 10% damage in a certain year of the lifetime. From this it can be seen that, although the traditional design approach suggests that the design criteria are satisfied, in closer reality many breakwaters (85%) will suffer more than 10% damage during a period of 50 years.

Figure 13 shows the number of breakwaters that would need to be repaired based on a 3% damage criteria after a given storm period. This shows that the probability of repair per year is 10%.

Figure 14 shows the encounter probability of damage in a certain service lifetime for a given level of damage. The design criterium based on a certain damage in an event with a 100 year return period results in an encounter probability of 39%. As shown in Figure 14 the encounter probability is much larger (99%). The damage belonging to the required encounter probability of 30% can be defined as severe.

In summary, it is essential that not only the wave-height but all parameters should be treated as statistical variables and that these variables must include the cumulative effects of damage.

## 6. Conclusions

The inaccuracy of the traditional design method is shown in establishing the real probability of damage. It is shown that a more reliable result can be achieved with the proposed level III approach, based on time domain simulation by utilizing a specially developed computer program.

The level selected for design and assessment of the failure probability is only reliable when all possible failure modes are included in the analysis. The neglect of an important mode will lead to an inadequate design. To avoid such errors the designer should be aware of causes and mechanisms of failures such as have occurred recently.

The proposed approach requires the designer to consider the accuracy of the various components of the study. This offers significant advantages over the traditional approach where the question of accuracy is not raised automatically. The proposed approach will further highlight those components where a large study effort is essential to minimize the risk of failure. Examples of these components are wave climate, wave refraction and structure response studies.

The reliability analysis also may lead to conclusions on the relative strengths of components of the breakwater. Components involving a relatively small financial investment can be designed with relatively high factors of safety and should not therefore have a significant contribution to the overall probability of failure.

In addition to variables in the design and in environmental conditions, further variables occur in the construction. Site conditions may impose variations between the design and the actual as-constructed structure. Also inconsistency in quality of the available material and inaccuracy of placement through available construction plant will inevitably play a certain role in the built-in safety of the final product. To what degree the variations will affect the overall quality is often difficult to conclude, in particular when such variation is sensitively related to the design assumptions. The proposed approach described herein will therefore prove to provide a very useful tool also for construction purposes.

## References

1. AGEMA, J.F. and VRIJLING, J.K.;  
Concrete Armour Units and Probabilistic Design of  
Breakwaters;  
Post Doctorate Course on Harbours;  
Delft University of Technology 1981 (in Dutch)



2. BARENDS, B.J.; KOGEL, H.v.d.; UIJTTEWAAL, F.;  
West Breakwater Sines, Dynamic Geotechnical Stability of  
Breakwaters;  
Coastal Structures 1983 Washington
3. BURCHARTH, H.F.;  
Material, Structural Design of Armour Units;  
Seminar on Rubble Mound Breakwaters, Stockholm 1983
4. GROENEVELD, R.L.; MOL, A.; ZWETSLOOT, P.A.J.;  
West Breakwater Sines - New Aspects of Armour Units;  
Coastal Structures 1983, Washington
5. ISAACSON, M. De St.Q.; MACKENZIE, N.G.; Long Term  
Distribution of Ocean Waves: a Review.  
Journal of Waterways, Port, Coastal and Ocean Division, ASCE,  
Vol. 107, No.WW2, 1981 pp. 99-109.
6. JOINT COMMITTEE ON STRUCTURAL SAFETY;  
General Principals on Quality Assurance for Structures;  
Lisbon, January 1981
7. MOL, A.; PAAPE, A.; LIGTERINGEN, H.;  
Risk Analysis in Breakwater Design;  
Conference on Breakwaters, Design and Construction;  
ICE, London May 1983
8. SHEN WANG; LEMEHAUTE, B.  
Duration of Measurements and Long Term Wave Statistics.  
Journal of Waterways, Port, Coastal and Ocean Divison, ASCE,  
1983, pp 236-249.
9. TIMCO, G.W.; MANSARD, E.P.D.;  
On the Interpretation of Rubble Mound Breakwater Tests;  
Coastal Structures 1983, Washington

## CHAPTER ONE HUNDRED SIXTY FIVE

### Rehabilitation Methods for Damaged Breakwaters

R.L. Croeneveld \*  
A. Mol \*  
E.H. Nieuwenhuys \*

#### Abstract

A number of studies have been undertaken recently to select optimum methods for rehabilitating damaged breakwaters in the Mediterranean and in the Atlantic Ocean. This paper outlines the approach to these studies and discusses the relative merits of the various concepts considered for repairing the damaged structures. Based on case studies of two projects, the paper also shows how the principle concepts have been successfully applied.

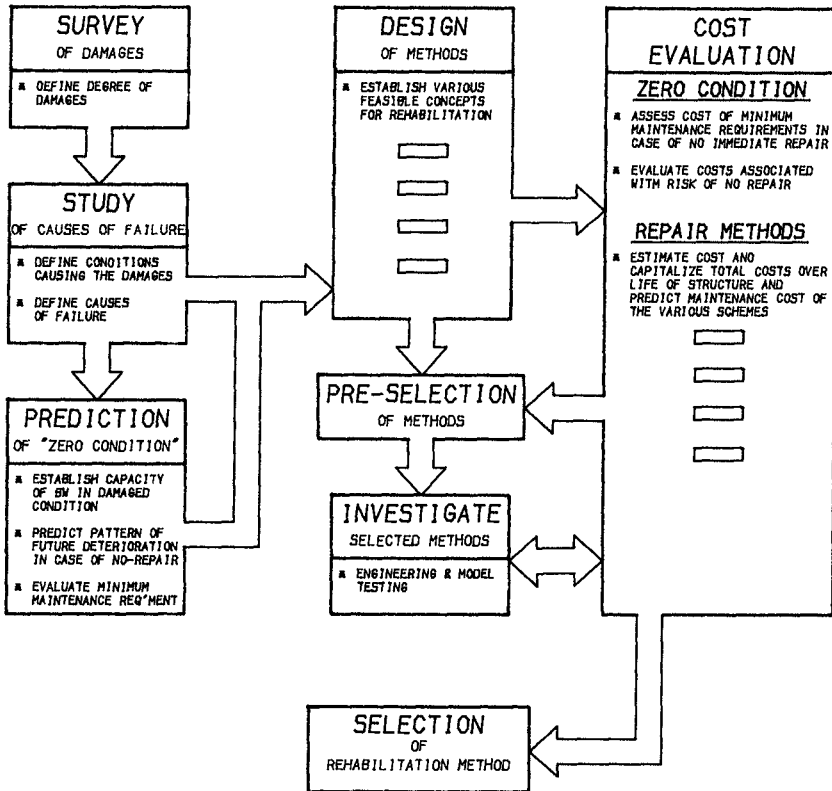
#### 1. Introduction

In recent years many deep-water breakwaters, protecting ports at exposed locations around the world, have exhibited damage to their armour systems or have in some cases suffered complete failure of whole sections. Studies have been carried out to define the causes of these failures and to select the most satisfactory method for rehabilitation in each case.

The optimum method for the rehabilitation of a breakwater depends on many factors which necessarily include:

- the cause of failure (inadequate design, unsatisfactory construction, or extreme environmental conditions)
- the degree and nature of the damage
- the geometry of the structure
- the local topography
- the availability of construction materials and equipment
- the acceptable level of risk to port operations or other facilities

\*) PRC Engineering, Inc., Badhuisweg 11, 2587 CA The Hague, the Netherlands



FLOW DIAGRAM  
EVALUATION OF  
REHABILITATION METHODS  
FIGURE 1

- future requirements for port expansion or other construction works
- financial resources, cash-flow details and requirements on local and foreign elements of the rehabilitation costs

The basis for the evaluation of rehabilitation measures may be termed the "zero-condition" in which no immediate repair work is carried out. Under such a condition, the further deterioration of the breakwater is predicted and the likely additional financial burden, due to any associated restrictions in port operations or damage to other facilities, is assessed.

The general approach to a project study, in order to develop a satisfactory rehabilitation scheme, is shown in Figure 1. This indicates that the first step is to carry out a detailed survey of the historical damages to the breakwater. Wherever possible, this should be directly equated with the history of local environmental conditions. In addition, the causes of damage or failure should be determined as accurately as possible.

Together with the assessment of the "zero-condition", various feasible concepts for rehabilitation are developed, which provide possible permanent solutions. After a pre-selection the most attractive solutions are refined and optimized utilising laboratory model test studies.

The final selection of possible solutions and the "zero-condition" are then re-evaluated taking into account costs and all further relevant aspects including local availability of materials and plant and owner's cash flow policy.

This paper discusses this approach, for the study of any breakwater rehabilitation, in more detail and presents various concepts for repair. Examples of the application of the principle concepts outlined are shown, using case studies of projects along the Atlantic Coast.

## 2. Damage Survey and Causes of Failures

A detailed survey of a damaged breakwater is an essential element in establishing the cause or causes of the damage. The damage events are listed in Table 1. The external events which may be the direct causes of damage or failure of a breakwater are also listed.

Parallel with the breakwater survey the environmental conditions causing the damage have to be established using measurements, observations and, if necessary, hindcasting methods. In this respect, the severity of the event causing damage should be established as a matter of prime importance.

TABLE 1

DAMAGE EVENTS

<u>External Events</u>	<u>Minor Damages</u>	<u>Major Damages</u>	<u>Failure Damages</u>
Water level	Scour of Foreshore	Damage Front Armour	Settlement Sliding and Overturning of Crown Wall
Waves	Erosion of Toe Filter	Damage Rear Armour	
Currents	Venting thru Breakwater	Settlement of Core and Subsoil	Erosion of Underlayers and Core
Tsunamis	Instable Front Berm	Sliding Failure of Slopes and Subsoil	Gradual Deterioration of Mound
Earthquake	Washing Out of fines	Erosion and up-lift of backfill	
		Breakage of Parapet wall	

This study of the extent and causes of failure should also include the comprehensive collection of data on the design and construction stages. In this respect, major aspects to be investigated include:

- quality, extent and accuracy of the design studies
- possible neglect of any failure modes
- design parameters and safety factors
- differences between the design and the as-built condition of the breakwater

The damage or failure of a breakwater is frequently due to a combination of circumstances rather than to any single factor and it is important to identify as accurately as possible the precise causes of such damage of failure. If this is not done, there is a high inherent risk that further damage or failure will occur for the same unidentified reasons.

### 3. Study of the "Zero-Condition"

The severeness of a damage to a breakwater may be classified between two extreme conditions which are:

- a) damage of a nature which does not increase the risks of further damage/failure, and
- b) critical damage which places the breakwater at serious risk to further damage/failure.

Clearly, if the nature of any damage invokes a risk of complete failure, immediate measures will be required. In certain cases, however, the risk of further deterioration of a damaged breakwater may be small and the rate of further deterioration may be low. As an example of this, it is possible that a low percentage of armour units are found to be broken due to rocking and displacement. It is even possible that conditions exist which encourage further compaction of all units (so that they are less subject to rocking and displacement) whereby the broken units continue to be part of an integrated armour system. Under such conditions, the risks of further deterioration are diminishing.

A higher percentage of broken units may create serious weak spots in the armour. The broken units will not all be interlocked with the adjacent units and may be lifted. The secondary layer of armour will then be subjected to direct exposure. Such a condition will require repair, possibly by periodic replacement of broken armour units with new units.

The predictions of future damage can be verified through simulations by model tests, but it should be noted that many factors influencing the causes of failure are difficult or impossible to model. Most scale models are only concerned with the hydraulic behaviour of the armour and with immediate erosion problems. They do not address long term problems such as the loss of fine materials of the core material.

In order to establish the zero condition as a standard of comparison for other alternatives, an evaluation should be carried out in accordance with the following scope:

- define the damages
- investigate the causes of the damages
- evaluate the effect of the damage on the causes
- make a prediction of further damages in time
- estimate the risk of complete failure of the damaged area
- investigate the effect of the complete failure on the overall function of the breakwater with respect to port operations and safety
- evaluate the costs resulting from failure of part of the breakwater with respect to restrictions in port operations and damage to other port structures.

Relevant aspects to be taken into account in the comparison with other alternatives are:

- Owner's investment plan
- Project planning concerning port expansion or reconstruction work
- Availability of construction material and plant in the area

#### 4. Rehabilitation Methods

##### 4.1 General

The technical feasibility of methods of rehabilitation is related to the causes of the failures encountered and the extent of the damage. With respect to the extent of the damages, a classification is given in Table 2. This table shows a classification of damages resulting from hydraulic instability of the armour system.

The correlation between the percentage of displaced units and the description of damage given is based on average conditions.

TABLE 2

Classification of Damage	Percentage of Displaced Units	Description of Damage
(i) Minor	0 - 3%	A few individual units of top layer displaced, but no gaps in top layer larger than 4 units, bottom layer intact.
(ii) Moderate	3 - 5%	No gaps in top layer larger than 6 units, slight displacements of bottom units only
(iii) Major	5 - 30%	Top layer removed over large area, bottom layer over not more than 2 units.
(iv) Total	Over 30%	Armour and underlayers removed over large area, exposure of core material.

Typical concepts for repair (Methods 1 to 4) are set out below. Their application must be considered in the light of the causes of the damage or failure encountered. Figure 2 presents a diagram illustrating applications of each of these rehabilitation concepts. Each concept is related to the degree of damage and the magnitude of the external event (expressed in period of recurrence) which caused the damage.

Minor damage to a breakwater, is generally only noticed if the condition of the breakwater is regularly inspected. If damage is found, repair and strengthening measures may be necessary to avoid the risk of initiating a chain of events which leads to a major failure. If such a risk is not expected, it may be more economic to use the zero option and leave the damage unrepaired.

DAMAGE	RETURN PERIOD EXTERNAL EVENT		
	0-1 YR	10-25 YR	50-100 YR
MINOR	ZERO-CONDITION (0)		
	PROVIDE SHELTERING (4)	RESTORE ORIGINAL DESIGN (1)	
MAYOR	STRENGTHEN DAMAGED COMPONENTS (2)		
TOTAL	RECONSTRUCT RUBBLE MOUND (3)		

FIGURE 2

It is often difficult to strengthen individual components of a breakwater to avoid future minor damage. For example, repair is complicated if venting through the breakwater results in washing out of fine particles of the core material due to large permeability and insufficient filtering of the underlayers. In such cases the consequential risk of a major damage to the structure may be minimized by strengthening other components.

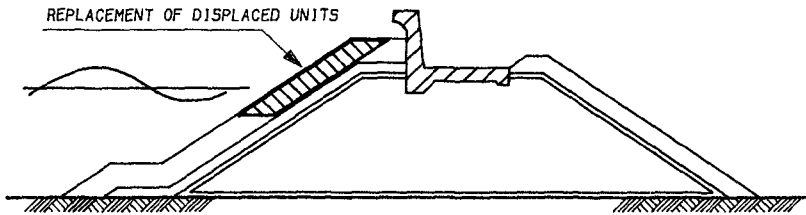
4.2 Repair by replacement of units (Method 1)

Damages classified under (i) and (ii) of Table 2 may be repaired by replacement of units of the same type and size, provided that such damage has been caused by events resembling the design conditions.

The feasibility of replacing the individual units should be considered case by case. Usually, if the units are of the interlocking type, the undamaged original units on the slope above the gap caused by the displaced damaged units, will need to be removed and replaced to provide adequate interlocking between individual elements.



Because the displaced units have most likely been removed from above or just below the water-line, the method of repair can in most cases be carried out with lifting equipment placed on the breakwater, provided that space is available. (Ref. Figure 3)



METHOD 1  
FIGURE 3

If the original units were too light, it may be possible to use reinforced units of the same type. This has the advantage that the units will be heavier and give better resistance against impacts due to initial movements and rocking. The amount of reinforcing steel may however be considerable and the solution may prove expensive. Moreover, the life of the reinforced units may be shortened by corrosion of the reinforcement when seawater seeps through cracks in the concrete. Compared with other possible repair methods, the use of steel reinforcement is seldom an attractive solution.

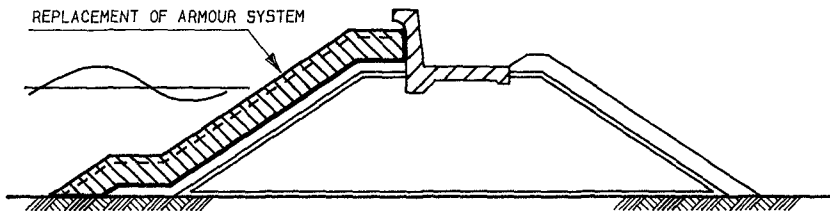
If heavier replacement units are preferred, a slight increase in dimensions can give a considerable increase in weight. It is likely however that this method will require continuous maintenance over a long period and will only be attractive if lifting cranes and labour are readily available when maintenance works are needed. The method can be economically attractive because:

- a) only those areas of the slopes and head of a breakwater, which are critically exposed, will be repaired and the areas where no damage occurs are left untouched
- b) the high direct investment costs are low and those costs required for the repair are spread over a long period

#### 4.3 Repair by replacement of Armour System (Method 2)

This method requires the replacement of the armour units by others of a different type and requires the removal of all original units. The method may be feasible if excessive maintenance to the original system is anticipated over the life of the structure, and capitalized costs of this maintenance exceed the cost of replacement. The underlying material should suit the new armour units and must be checked for layer thickness and compaction. It may be necessary also to place a new layer of secondary armour, in which case an adjustment of the slope may be considered. (Ref. Figure 4)

This method has been applied in cases in which the original choice of armour units proved to be inadequate. In particular this may occur, regarding the structural strength of units with a sophisticated interlocking form. The original units were possibly selected because similar but smaller units proved to be successful for breakwaters in shallower water with less wave action. However, the extrapolation to deepwater breakwaters often yields unsatisfactory results because the larger units have insufficient strength.

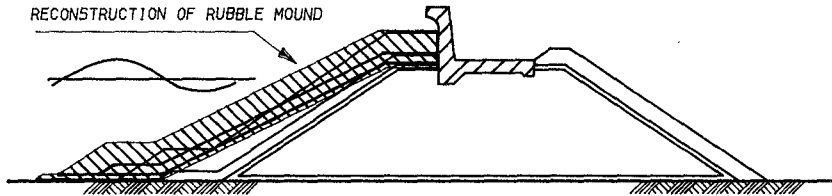


METHOD 2

FIGURE 4

#### 4.4 Repair by reconstruction of rubble mound (Method 3)

This method involves removal of the original armour and underlayers and placement of new layers after preparation of well-compacted core material and the placement of a suitable filter between core and armour material. (Ref. Figure 5)



METHOD 3

FIGURE 5

This ultimate solution may prove necessary to overcome serious problems such as:

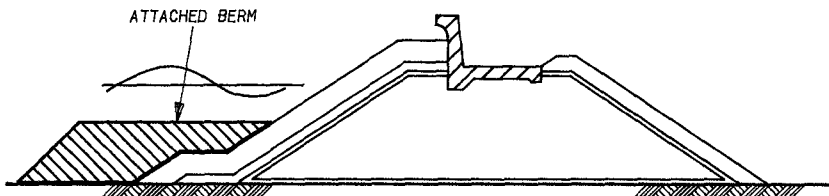
- geotechnical instability e.g. slopes which are too steep in relation to the internal friction of the core, the underlayer material or the sub-soil.
- undue settlements of prime armour and crown due to the loss of core material through the armour system, caused by a lack of adequate filters, or erosion of sub-soil material near the toe of the breakwater because of a lack of sub-soil protection.

#### 4.5 Provision of sheltering against Critical Wave Condition (Method 4)

This method includes the following alternative solutions:

- a) Provision of an Underwater Berm attached to the Breakwater:

This underwater berm should be designed to reduce the energy of the waves, which may be critical to the stability of the slope. (Ref. Figure 6)



METHOD 4 , PROVIDE FOR SHELTERING

FIGURE 6

b) Provision of a Detached Underwater Breakwater:

In this case the additional structure reduces the wave conditions in front of the damaged breakwater to an acceptable level.

It is of interest to compare the merits of the above different methods in specific cases of breakwater projects. For this purpose, two case studies are discussed in this paper.

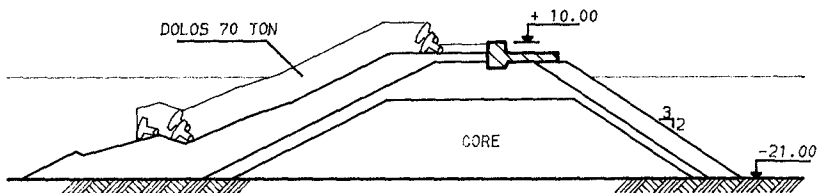
## 5. Case Studies

### 5.1 Case 1

This case study concerns a port along the Northern coast of Spain protected by two breakwaters.

The breakwaters are situated in waterdepths up to 20 m. The location is very exposed, in particular from north-westerly directions, but also from the North and occasionally from the East. Damage to the breakwaters occurred, however, under relatively quiet sea conditions. The first observations of damage were made soon after the completion of the construction of the breakwater. Damage was visually evident because armour units, which consist of 50 ton dolosse on slopes of 1:1.5 and 1:2, were broken.

Breakage of dolosse continued with time. Three years after the construction, over 3000 units were found broken, 17% of the total number of one breakwater and 25% of the total number on the other. In the areas with the greatest concentration of breakage the percentage was almost 50%. In addition, major cracks in the concrete crownwall of the South breakwater were found at several locations as a result of differential settlements.



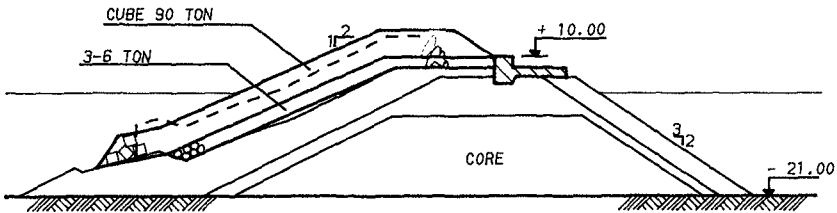
EXISTING SECTION-N.B.

FIGURE 7

A study was undertaken covering an extensive scope including a re-evaluation of the wave climate at the particular location, site investigations, investigations of the causes of failure and evaluation of possible rehabilitation of the breakwaters.

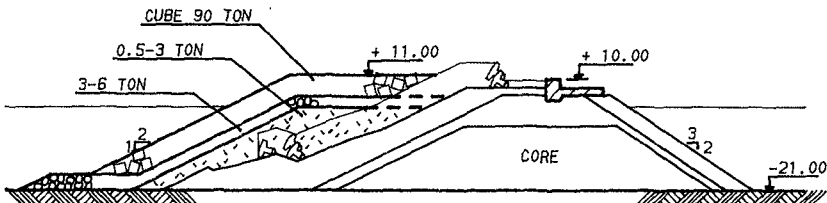
Six alternative methods for rehabilitation of the North breakwater, of which the existing section is shown in Figure 7, were studied:

- (1) Removal of the existing 50 tons dolosse and replacement with a double layer of 90 ton concrete cubes placed at random. New rock armour underlayers would be placed. (Ref. Figure 8).



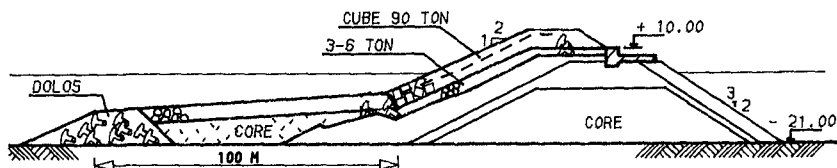
NEW SECTION N.B. - ALT.1  
FIGURE 8

- (2) Placement of a rock dike against the existing section and the voids between the dolosse would be filled with fine quarry run material or gravel whereby the existing dolosse would be left in place. Subsequently, new concrete armour similar to that considered for the first alternative would be placed over the rock dike at a slope of 1 to 2. (Ref. Figure 9).



NEW SECTION N.B. - ALT.2  
FIGURE 9

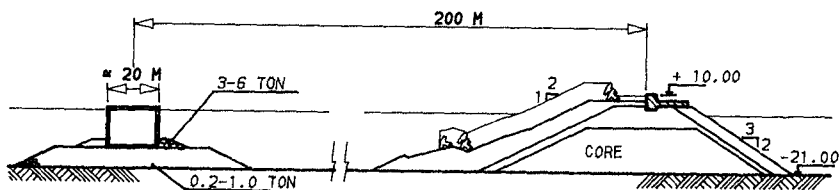
- (3) Installation of a berm at the toe of the breakwater to a level of about one third of the water depth whereby the dolosse would be left in place. New armour would be placed above the berm.
- (4) Installation of a wide berm attached to the breakwater as in alternative 3, but of sufficient size to absorb wave energy and thus reduce the energy acting on the slope of the breakwater. The dolosse would be left in place, except on the breakwater slope above the berm where the dolosse would be replaced by 60 ton solid cubes where necessary. (Ref. Figure 10).



NEW SECTION N.B. - ALT.4

FIGURE 10

- (5) Installation of an underwater breakwater in front of the existing breakwater at a distance sufficient to break up the waves before they reach the existing breakwater, which in principle remains unrepaired. The underwater breakwater would be designed such that the energy of the broken waves or, if unbroken, smaller waves would not cause further damage to the existing breakwater.
- (6) This alternative is the same as the alternative 5 with the exception that the underwater breakwater would consist of a series of concrete caissons in lieu of a rubble mound structure. (Ref. Figure 11)



NEW SECTION N.B.-ALT.6

FIGURE 11

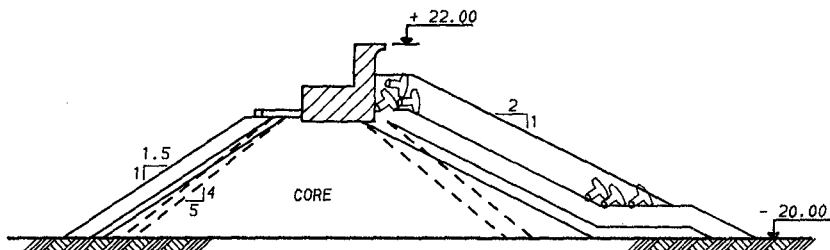
The relative costs of the various alternatives compared to the most conventional type of repair defined in Alternative 1, are 140, 165, 65, 105 and 200 percent for the alternatives 2 thru' 6 respectively. These cost indications are given for a random section of the breakwater in deeper water. The final solution for the whole of the breakwater can of course be a combination of various methods, whereby the overall costs can be optimized. Alternative 1 could be applied for the deep water section, while the dolosse removed from that deep water section could be used as berm material as per the Alternative 4 solution for those sections which are less exposed.

The cost of alternative 2, whereby the dolosse would be left in place, is relatively high despite the fact that removal is not required. An important contribution in the costs is the special provision for pumping gravel between the dolosse to ensure that the underlayer of the new armour and sublayers would be properly compacted with a porosity as required within the overall system.

The cost of the Alternative 6 is high but includes the cost for repair of the head of the breakwater in accordance with Alternative 1. This has been done because the underwater breakwater would not provide effective protection for the head.

For both economical and technical reasons, the scheme finally selected for the rehabilitation of the North breakwater was in accordance with Alternative 1. The risk of exposure of the underlayers during construction, when the existing armour is removed, has been accepted.

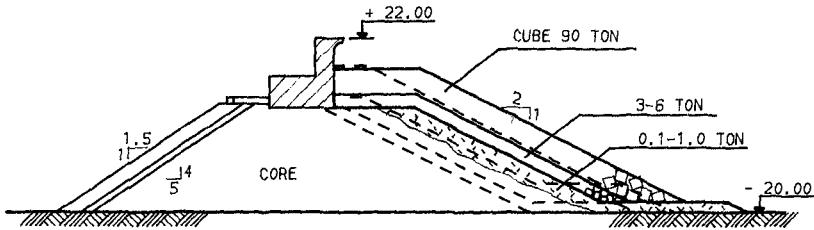
For the rehabilitation of the South Breakwater, of which the existing cross section is shown in Figure 12, the possibilities were limited because this breakwater needed rehabilitation of the armour as well as strengthening to achieve better geotechnical stability. The alternatives considered were:



EXISTING SECTION - S.B.

FIGURE 12

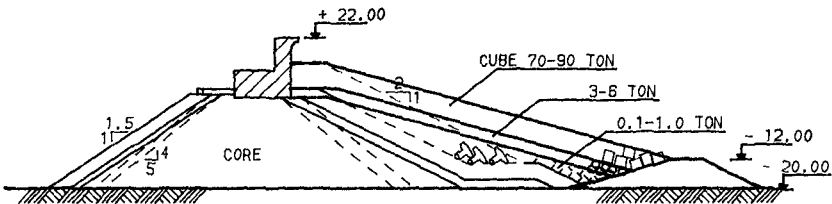
- 1) Removal of the dolosse and placement of filter material over the existing core material at a slope 1 to 2, placing of a new underlayer and the installation of solid block armour units in sizes varying from 50-90 ton. (See Figure 13)



NEW SECTION S.B. - ALT.1  
FIGURE 13

- 2) A second alternative similar to the first, but with all new material placed at a slope of 1 to 3. The prime armour of block units would then be smaller than in Alternative 1. Furthermore, a berm at the toe of the seaward slope of the breakwater would be placed to a level of -12.0 m at waterdepth up to -20.0 m. (Ref. Figure 14)

The cost of the second alternative was estimated to be about 50% higher than the cost of Alternative 1. The second alternative was therefore selected for implementation.



NEW SECTION S.B. - ALT.2  
FIGURE 14

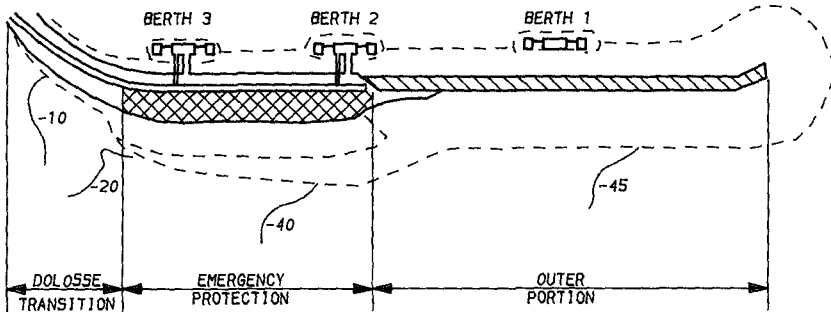


## 5.2 Case 2

This concerns the West Breakwater of the port of Sines, Portugal, located at the Atlantic coast, which was severely damaged during two storms in the winter period of 1978-1979. Figure 15 shows the layout of the breakwater divided in three sections:

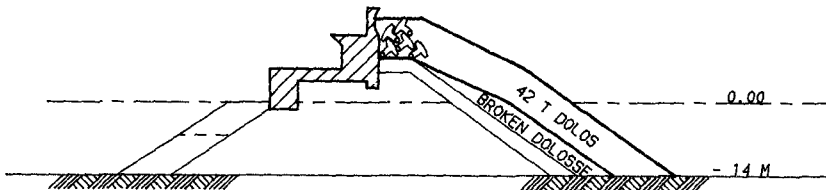
- the Section between berth 3 and the shore protected with dolosse (Figure 16)
- the Section between berths 2 and 3 previously repaired with new 90 ton Antifer type blocks (Figure 17)
- the outer portion, severely affected and at present unrepaired (Figure 18).

The history of the damage of the breakwater was extensively described in Reference 1. The study was commissioned to evaluate the



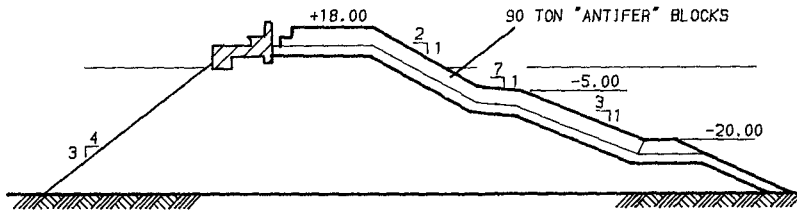
WEST BREAKWATER, SINES PORTUGAL

FIGURE 15

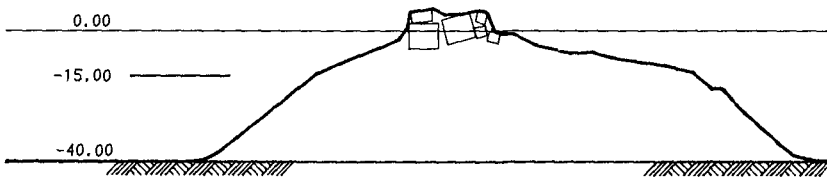


DOLOSSE SECTION

FIGURE 16



EMERGENCY REPAIR  
FIGURE 17

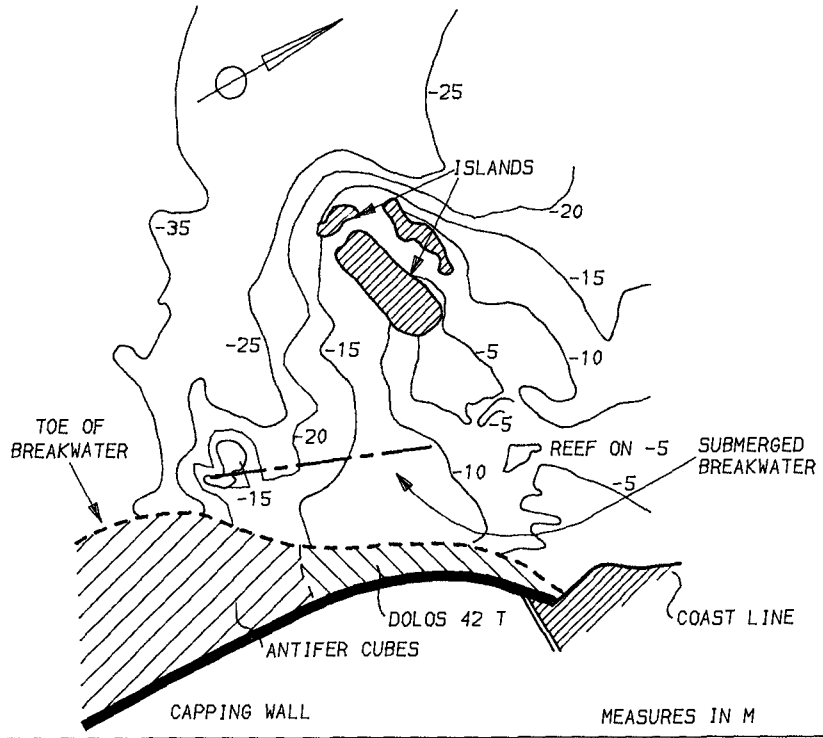


OUTER PORTION, PRESENT SITUATION  
FIGURE 18

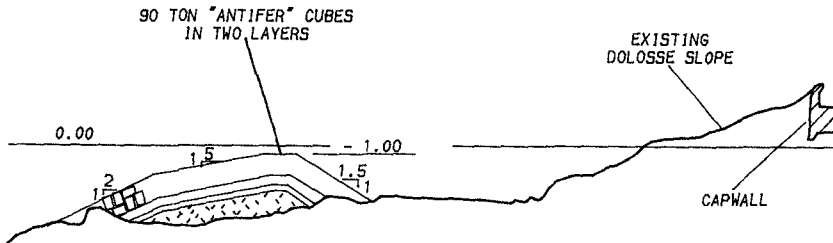
earlier repaired sections, to propose mitigating measures if necessary, and to develop a rehabilitation method for the outer portion. Preliminary results were presented in Reference 2.

The conclusions of the study were as follows:

1. Close to the shore side of the breakwater the original section suffered hardly any damage. The repair should therefore be in accordance with Method 1 described above, and should be limited to replacement of new armour units where necessary. The units would then be of the same type as used in the original design.
2. The section armoured by dolosse, situated close to the previously repaired section, needed improvement. The most economic solution should involve closing the subsea trench south of the Perceveira Islands thereby eliminating the large waves which were penetrating through this trench from westerly directions. A plan and cross section are given in Figures 19 and 20.
3. The repair of the section between berths 2 and 3, where previous repairs had been made, should be in accordance with Method 2. The seaward slope should be modified by placing compact heavy cubes to a more gentle gradient.



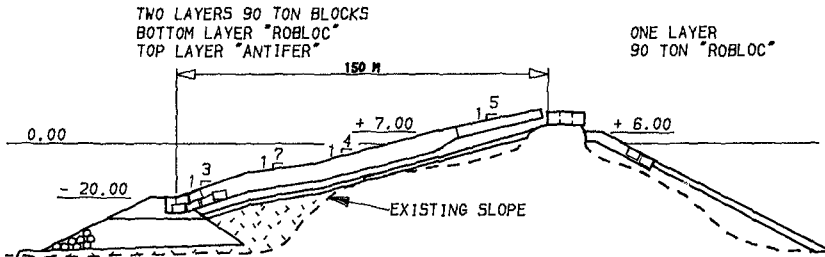
ALIGNMENT SUBMERGED BREAKWATER IN FRONT OF DOLOSSE SECTION  
FIGURE 19



CROSS-SECTION IMPROVED DOLOSSE SECTION  
FIGURE 20

4. The outer portion of the breakwater should be rehabilitated by constructing a new rubble mound over the damaged structure (Figure 21).

In addition, with regard to the last part of the outer portion of the breakwater, a cost-benefit analysis is currently being carried out. Indications are that full reconstruction of this part is not justifiable at present. However, to provide the necessary protection of the port, the crest level of this part of the breakwater may have to be maintained on mean sea level.



REHABILITATION OUTER PORTION  
FIGURE 21

#### 6. Conclusive Remarks

- (1) Damage to a breakwater is often caused by a combination of events. Sufficient effort must be put into the rehabilitation study to recognise all causes so that the deficiencies of the breakwater can be correctly identified and satisfactory methods of rehabilitation can be selected.
- (2) To provide a basis for cost comparison of any rehabilitation method, the "zero-condition" excluding repairs should be studied. This study should include the predictions of further deterioration, the analysis of the costs associated with the risk of a partial failure of the breakwater and the long-term

maintenance requirements to minimize such risks. In some cases it can be justified, technically and economically, to postpone the repair work to suit the owner's requirements or to integrate it in the construction planning of new port facilities.

- (3) Simulation studies by physical or numerical models are an essential part of the overall study of a breakwater. Designers should be aware however of the limitations of such models. Overall conclusions must not be drawn from single model test results but from the interpretation of the study as a whole.

Reference:

1. A.S.C.E. "Failure of the Breakwater at Port Sines, Portugal", 1982.
2. Toppler, J.F. et al. "West Breakwater-Sines Overview of Rehabilitation and Synthesis of Project". Coastal Structure Conference 1983. Washington, U.S.A.

## CHAPTER ONE HUNDRED SIXTY SIX

### STABILITY OF BREAKWATERS WITH VARIATIONS IN CORE PERMEABILITY

G.W. Timco\*, E.P.D. Mansard\* and J. Ploeg\*

#### ABSTRACT

In setting-up a breakwater test in a laboratory flume, the conventional practice is to scale geometrically the armour units, under-layer rocks and core material based on the Froude scaling criteria. However, because some of the properties of the water are not scaled for a model test, the Reynolds scaling law is violated. This can result in improper water flow distribution through the model breakwater. To investigate this problem, a series of tests were performed with a model breakwater in which the permeability (and porosity) of the core was varied over a wide range, and the hydraulic response and breakage of the armour units were measured. It was found that the overall stability of the breakwater could be drastically affected if the flow in the core is scaled incorrectly.

#### 1.0 INTRODUCTION

Physical modelling of rubble-mound breakwaters is a common practice in many hydraulic laboratories. In order to model realistically these structures in a laboratory flume, there are several parameters which must be properly simulated since they can influence the test results. It has been shown, for example, that correct reproduction of the sea state must be made in both the time and frequency domain [6] and that the strength of the armour units must be properly simulated in the model regime [11] for the most reliable results. There are other factors, however, which to date have not been investigated, but which could influence the test results. In this paper, the effects on both the hydraulic and structural stability of a breakwater are investigated in terms of the permeability of the core material. This was done by comparing the response to the same storm conditions of a number of different breakwaters which were identical in all respects except for the permeability of the core.

#### 2.0 STATEMENT OF THE PROBLEM

In physical modelling, the forces involved in a specific interaction process are reduced but, by careful selection of the experimental arrangement, maintained in the same ratio as in the prototype. In this way, the interaction process can be investigated at reduced scale. This is highly desirable since model tests are much more economical to do than a corresponding full scale test, and it allows an examination of the process under controlled experimental conditions. For

\*Hydraulics Laboratory, National Research Council, Ottawa, Ont. K1A 0R6  
Canada

accurate results, however, it is important that all of the forces involved are scaled in the correct proportion. For model tests of rubble-mound breakwaters the forces of interest are gravity  $F_g = Mg = \rho g L^3$  where  $M$  is the mass,  $g$  is gravitational acceleration,  $\rho$  is the density and  $L$  is a linear dimension; the inertial forces  $F_i = Ma = \rho L^3 L t^{-2}$  where  $a$  is acceleration and  $t$  is time; and the viscous forces  $F_v = \mu p t^{-2} L^2$  where  $\mu$  is kinematic viscosity. The relationship between the gravitational and inertial forces is given by the Froude number ( $F_n$ )

$$F_n = \frac{v_p}{\sqrt{L_p g_p}} = \frac{v_m}{\sqrt{L_m g_m}} \quad (1)$$

where  $v$  is velocity and the subscripts  $m$  and  $p$  denote model and prototype respectively. Similarly, the relationship between the viscous forces and inertial forces is given by the Reynolds number ( $Re$ )

$$Re = \frac{L_p v_p}{\nu_p} = \frac{L_m v_m}{\nu_m} \quad (2)$$

To ensure total similitude in the model tests, both these numbers should be satisfied. This is virtually impossible to do unless a tank fluid can be found where (equating equations (1) and (2))  $\nu_p = \lambda^{3/2} \nu_m$  where  $\lambda$  is the linear scale factor of the model test. Since water is the normal working fluid in these tests, this is not accomplished and the viscous forces are not modelled correctly. For flow in the armour layer, it has recently been shown [4,9] that this is not a problem, even in tests with high scale factors. However, for flow in the filter layers and especially the core, this may not be the case due to the much smaller size of units and the correspondingly lower permeability of these regions. To test this is the purpose of the paper.

If the flow distribution in the core is not scaled correctly, this will influence the flow in the armour layer and consequently alter and distort the relative amount of wave energy dissipated in each of these regions. Because a breakwater dissipates the incident wave energy through rocking of the armour units and water turbulence within, the water flow and distribution should be the same in the model as in the prototype. If it is not, then the response of the armour units and energy dissipating processes are not properly reproduced in the model. This can affect the stability of the breakwater. This problem has been discussed by Yalin [12] who predicted that the restoring forces on the armour layer units will be scaled incorrectly and this could affect both the hydraulic and structural stability of the units. Burcharth [3] has suggested that this viscous effect will result in too high an internal water table within the breakwater. For the armour, this means that there will be a larger destabilizing pressure gradient and a reduction in the reservoir effect, thereby leading to larger overflow velocities.

### 3.0 EXPERIMENTAL APPROACH

The severity of this problem can be investigated using the physical modelling techniques which have been developed in this labora-

tory [8,10]. These techniques include: (1) the generation of realistic sea states in which both the variance spectral density and time domain characteristics of the wave field are correctly reproduced in the flume; (2) the use of a material to make the armour units in which the mechanical properties of concrete are scaled correctly for the model test (i.e. the strength of the armour units is scaled correctly based on the modelling laws). This material is a mixture of plaster-of-Paris, sand, iron ore and water. By varying the ratio of plaster to sand, the flexural (tensile) strength of the material can be altered over a wide range of interest ( $40 \geq \lambda \geq 15$ ); whereas by properly choosing the iron ore to sand ratio, the density of the material can be adjusted to that of concrete. Measurements of the mechanical properties of this material have shown that the flexural strength, density and fracture toughness are correctly scaled over a wide range of scale factors. The use of this material allows breakage of the armour units at realistic stress levels, thereby allowing an examination of the structural as well as hydraulic stability of the armour layer in the test; and (3) the use of a photographic technique which automatically takes pictures of the face of the breakwater with both a 16 mm movie camera at every wave trough and a 35 mm SLR camera at every 50 wave troughs. This gives a continuous record of the damage to the breakwater during a storm.

To investigate the influence of the permeability of the core, a very simple approach was taken as follows: A series of different model breakwaters of 0.9 m sections were built in a 1.8 m wide flume. In each case the slope and height of the breakwater, the size and type of the armour units, and primary and secondary underlayer stones were identical. The only difference was the permeability of the core. Each breakwater was subjected to identical storm conditions. After the storm, the damage to each breakwater was assessed in terms of both the number of armour units which either broke or had large displacements, and the amount of underlayer exposed. Since the breakwaters were identical in all respects except for the permeability of the core, any differences in their stability during storm conditions was attributed to differences in the viscous flow in the breakwater.

#### 4.0 TEST SET-UP

The tests were performed in a 1.8 m wide flume (see Figure 1) which was equipped with an hydraulically driven wave generator. The model breakwater was built with four individual layers comprising the core, primary and secondary underlayer and the armour layer. It was built with a 1:1.5 slope. In constructing the breakwater, the armour units were placed by hand in a random fashion with care being taken to ensure that it was of the same density and packing arrangement each time. For all of these tests, the armour layer consisted of dolos units of length 9 cm packed in two layers to a density of 330 units -  $m^{-2}$ . A cross-section profile of the model breakwater indicating the relative dimensions of each layer is shown in Figure 2. It should be noted that since the strength-simulated dolos units must be made individually, it was decided to limit the number of breakable units to 60 for each test. These were placed in a "nest" pattern centered about the mean water level in the centre of the model breakwater. The photographic equipment was set up to provide continuous documentation of the response of each breakwater to the storm conditions. After the storm, the flume was



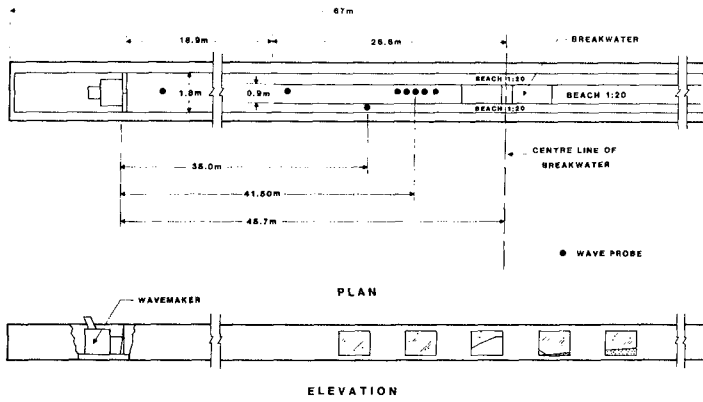


FIGURE 1: WAVE FLUME WITH PROBE LOCATIONS

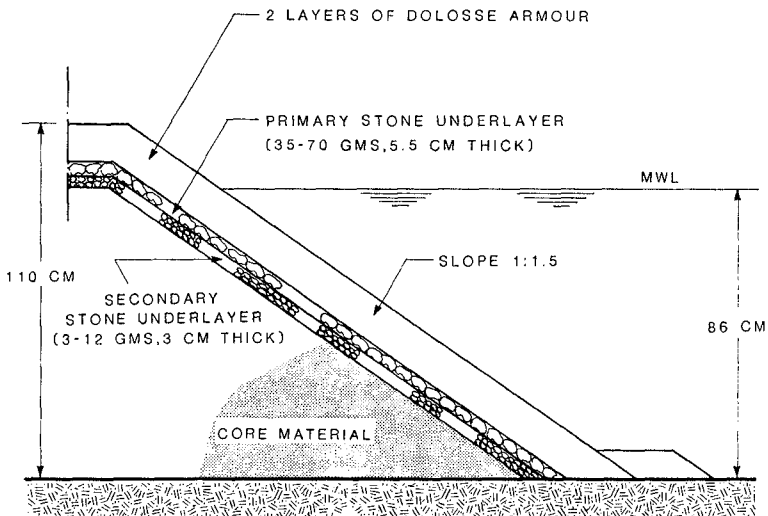


FIGURE 2: CROSS-SECTION PROFILE OF MODEL BREAKWATER

drained and the damage was assessed in terms of the number of broken and displaced armour units.

To alter the permeability of the core, three different core arrangements were used. To represent a very open core, the core was constructed from relatively large angular stones (diameter range from 3 to 6 cm). This was very porous with high permeability and an average Reynolds number of  $6 \times 10^3$ . To represent a more restrictive core, the core was constructed from much smaller angular stones (diameter range from 0.2 to 2 cm) with a correspondingly lower permeability and an average Reynolds number of  $1 \times 10^3$ . A core of this type is used in this laboratory in many tests of rubble-mound breakwaters since it is based on Froude geometric scaling of typical prototype cores. To represent a closed, restrictive core, a thin sheet of polyethylene plastic was inserted at the top of the core at the interface between the core and the secondary underlayer. This prevented flow within the core. In this case, all wave energy dissipated within the breakwater occurred in the armour layer and primary and secondary underlayer. This is the extreme case which represents zero permeability with a corresponding Reynolds number of zero for the core. These three cases were chosen simply to cover as wide a range of core permeabilities as possible. They are not meant to represent any particular prototype situation. This approach of looking at the response to a wide range of core permeabilities was taken since information on the permeability of prototype cores is scarce. Because of this, it is not possible at this time to know what the permeability, pressure and flow distribution should be within the core for a model test. In the present case, the permeability of the core is simply altered over as wide a range as possible in an attempt to determine the sensitivity to the core permeability of the overall stability of the breakwater.

In setting up the experiment, it was necessary to choose a suitable scale factor ( $\lambda$ ) for the test. When using the strength-reduced armour units, it is possible to scale the strength of the units over a wide range of scale factors (15 to 40). Based on the size of the armour units (285 gm dolos units), this would correspond to prototype dolos weights of 1 to 18 tonnes. Since it is known that there is a "size-effect" with concrete armour units such that the larger units will fracture much more readily than the smaller units for the same relative amount of movement [2], and since the problem of incorrect viscous flow becomes more severe with increasing scale factor, a test at any single scale factor produces limited information. Because of this, it was decided to perform the test series for scale factors at both  $\lambda = 15$  and  $\lambda = 40$ . These values bracket the range of scale factors which are typically used for model investigations of rubble-mound breakwaters. The first series was performed with the low scale factor ( $\lambda = 15$ ) since it is known that if there is a difference seen in these tests, it will be much worse at higher scale factors.

In order to test their relative stability, it is important that the storm conditions be identical for each test. This is accomplished since the flume is equipped with a hydraulically driven irregular wave generator which is controlled by an on-line computer. This wave generator can produce a variety of natural sea states and wave transients in the flume. Figure 3 shows the time and frequency characteris-

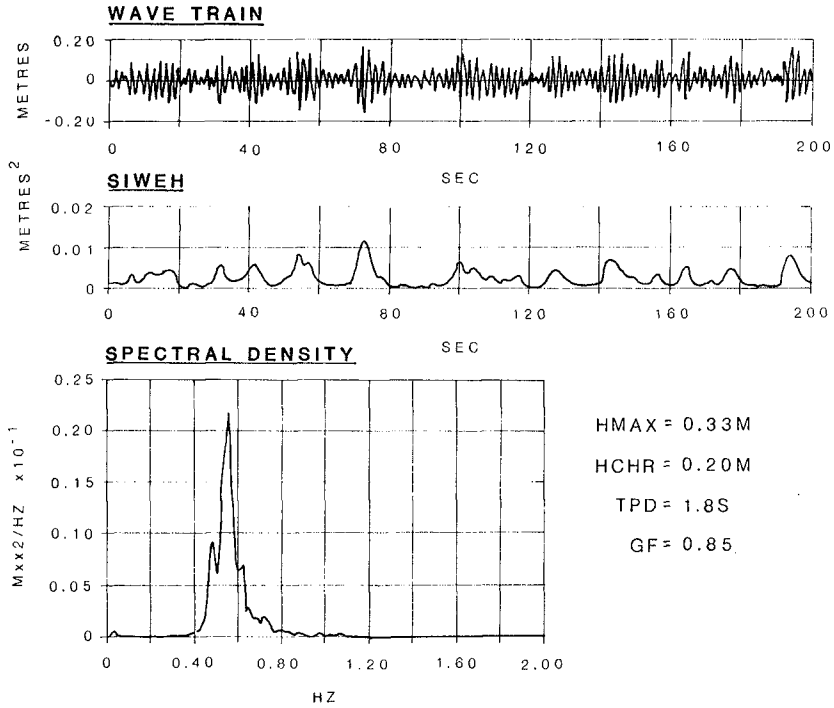


FIGURE 3: WAVE CHARACTERISTICS FOR THE TESTS

tics of the wave conditions generated for each of the test series. The reflection of the waves off of the breakwater was measured using an array of five gauges (see Figure 1) by the least squares method developed by Mansard and Funke [7]. The Smoothed Instantaneous Wave Energy History (SIWEH) which is shown in Figure 2 is used to determine the amount of wave grouping in the wave train [5]. Since the wave board in the flume is controlled by an on-line computer, these wave conditions could be stored and generated in each of the test series. In all tests, the storm conditions were run for 45 minutes.

## 5.0 RESULTS

The results of the tests for series I and II are tabulated in Tables I and II respectively. These tables list the information on the set-up for each test, as well as the damage sustained by the breakwater due to the storm. Note that the reflection coefficient (R) of the primary spectrum ( $R = \sqrt{E_R/E_I}$  where  $E_R$  and  $E_I$  are the total energies of the reflected and incident spectra respectively) was similar for all three types of core. This indicates that, regardless of the type of core, the overall energy transmitted into or dissipated at the front face of the breakwater was always the same (91-93% of the total incident energy) within experimental accuracy.

For test series I at  $\lambda = 15$  representing one ton dolosse, both the regular core and open core had very little damage done to the armour layer due to the storm. There were relatively few broken units or large scale displacements of the dolosse. There was virtually no difference in response between these two cases at this scale factor. For the case of the impermeable core, on the other hand, the response of the breakwater and amount of damage was quite different. In this case there was considerable rocking, displacement and breakage of the units. The destruction was so severe that in several places the underlayer was exposed since a considerable number of dolos units rolled off the face of the breakwater to the toe. This can be seen in Figure 4. During the storm, the whole face of the breakwater was almost continually under water since it took considerably longer for the water to drain off the breakwater than in the other two cases. In many instances for the impermeable core, the water from one wave would still be on the face of the breakwater when the next wave would hit. This caused a constant state of agitation of the dolos armour units. In observing the tests, it was evident that the response of the armour units to improper viscous flow was in agreement with the predictions by Yalin [12] and Burcharth [3] as discussed earlier. The complete hydraulic and structural stability of the armour layer was drastically influenced due to the improper viscous flow in the core.

For test series II at  $\lambda = 40$  representing 18 ton dolosse, the test with the impermeable core was not repeated. Since there was extensive damage for this case at the lower scale factor, there would be considerable damage for any similar test at a higher scale factor representing larger dolosse. For the open and regular core at the low scale factor, there was no difference in response between these two cases. Since the problem of improper viscous flow should become more severe with increasing scale factor, these two cases were repeated at the higher scale factor of  $\lambda = 40$ . At this scale factor, there was a signi-

TABLE I  
TEST SERIES I ( $\lambda = 15$ )

	TEST #1 (Open Core)	TEST #2 (Regular Core)	TEST #3 (Impermeable Core)
<u>TEST SET-UP</u>			
Height of breakwater (cm)	116	116	116
Slope of breakwater	1:1.5	1:1.5	1:1.5
Water depth (cm)	86	86	86
Type of armour unit	dolos	dolos	dolos
Height of armour unit (cm)	9	9	9
Mass of armour unit (gm)	285	285	285
Number of breakable units	60	60	60
Placement density of armour units (units - m <sup>-2</sup> )	330	330	330
Thickness of primary underlayer (cm)	5.5	5.5	5.5
Mass of primary underlayer stones (gm)	35-70	35-70	35-70
Shape of primary underlayer stones	angular	angular	angular
Thickness of secondary underlayer (cm)	3	3	3
Mass of secondary underlayer stones (gm)	3-6	3-6	3-6
Shape of secondary underlayer stones	angular	angular	angular
Diameter of core stones (cm)	3-6	0.2-2	closed
Shape of core stone	angular	angular	-
Porosity of core	0.53	0.29	0
Permeability of core (cm - s <sup>-1</sup> )	10 <sup>0</sup> -10 <sup>-2</sup>	0.6	0
Reynolds number of core	(4-8) x 10 <sup>3</sup>	(.2-2) x 10 <sup>3</sup>	0
Characteristic wave height during storm (cm)	20	20	20
Peak wave period (s)	1.8	1.8	1.8
Groupiness factor - GF	0.85	0.85	0.85
<u>TEST RESULTS</u>			
Mean reflection coefficient (R)	0.27	0.29	0.28
% of energy dissipated by the breakwater (1-R <sup>2</sup> ) x 100	93	91	92
Damage - units broken in trunk section	2	0	8
Damage - units broken in leg	3	6	3
Damage - severe rocking	8	5	21
Damage - large scale displacement	-	7	18

TABLE II

TEST SERIES II ( $\lambda = 40$ )

	TEST #4 (Open Core)	TEST #5 (Regular Core)
<u>TEST SET-UP</u>		
Height of breakwater (cm)	116	116
Slope of breakwater	1:1.5	1:1.5
Water depth (cm)	86	86
Type of armour unit	dolos	dolos
Height of armour unit (cm)	9	9
Mass of armour unit (gm)	285	285
Number of breakable units	65	62
Placement density of armour units (units - m <sup>-2</sup> )	330	330
Thickness of primary underlayer (cm)	5.5	5.5
Mass of primary underlayer stones (gm)	35-70	35-70
Shape of primary underlayer stones	angular	angular
Thickness of secondary underlayer (cm)	3	3
Mass of secondary underlayer stones (gm)	3-12	3-12
Shape of secondary underlayer stones	angular	angular
Diameter of core stones (cm)	3-6	0.2-2
Shape of core stone	angular	angular
Porosity of core	0.53	0.29
Permeability of core (cm - s <sup>-1</sup> )	10 <sup>0</sup> -10 <sup>2</sup>	0.6
Reynolds number of core	(4-8) x 10 <sup>3</sup>	(.2-2) x 10 <sup>3</sup>
Characteristic wave height during storm (cm)	20	20
Peak wave period (s)	1.8	1.8
Groupiness factor - GF	0.85	0.85
<u>TEST RESULTS</u>		
Mean reflection coefficient (R)	0.26	0.29
% of energy dissipated by the breakwater (1-R <sup>2</sup> ) x 100	93	92
Damage - units broken in trunk section	7	15
Damage - units broken in leg	5	25
Damage - severe rocking	3	6
Damage - large scale displacement	1	14



FIGURE 4: PHOTOGRAPH OF THE FACE OF THE BREAKWATER WITH THE IMPERMEABLE CORE AFTER THE STORM. THE ARROWS INDICATE UNITS WHICH HAVE ROLLED DOWN THE FACE OR BROKEN, AND ALSO AREAS WHERE THE UNDERLAYER IS EXPOSED.

ificant difference in the response of the breakwaters. As summarized in Table II, there was considerably more damage to the breakwater built with the regular, less-porous core.

## 6.0 DISCUSSION

These tests clearly show two things. First, the permeability of the core has a very definite effect on the overall stability of a rubble-mound breakwater. The core clearly plays an important role in the overall energy dissipating process of the breakwater. Secondly, for model testing of rubble-mound breakwaters, the influence of incorrect scaling of permeability is a function of the scale factor of the test such that it increases with increasing scale factor because of the size effect. Care must be taken to scale as nearly as possible this aspect of the breakwater for a model test. The generally accepted method of preventing viscous effects is to construct the breakwater such that the Reynolds number for the flow exceeds a certain value (typically  $10^3$  [12]). Recently Burcharth [3] has pointed out that this criterion is not satisfactory for two reasons. First of all, a single value of a Reynolds number cannot represent the complicated and unsteady flow which occurs in the prototype. Secondly, the permeability of prototype cores is very difficult to predict since the permeability is sensitive to small variations in grading and separation of the material when dumped. In general, the prototype flow field is poorly known.

In order to try to minimize this problem, more emphasis must be placed in examining the geotechnical stability of prototype breakwaters [1]. Correct scaling of this property can only be accomplished once tests of the permeability, flow and internal pressure in the prototype core are measured and understood. If this were done, correct viscous flow should be obtainable directly for model tests which use very large armour units. For those tests in which smaller armour units (i.e. high scale factor) are used, a solution may be to run an appropriate math model to determine the internal pressure field and, by adjusting the core permeability, calibrate the small-scale physical model to reproduce correctly the calculated internal pressure field [3]. This type of approach, although it is not ideal, should result in better model-prototype conformity.

The present tests have implications to the understanding of the behaviour and design of prototype breakwaters. First of all, the difference in the results clearly shows that the core plays an important role in the overall energy dissipating properties of a rubble-mound breakwater. Secondly, the tests show that the relative stability of the armour layer can be enhanced if the core is made more porous. If it were, it would assume a relatively higher percentage of the wave energy dissipated within the breakwater than a less porous core. This would decrease the amount of wave energy which would be dissipated in the armour layer and consequently make the armour layer more stable. Of course, this aspect would have to be incorporated into the design of the breakwater with due consideration to the geotechnical stability of the structure.



## 7.0 SUMMARY

Based on the results of the present tests, it is clear that incorrect viscous flow in the core can influence the hydraulic and structural stability of the breakwater. Care must be taken, therefore, to scale this viscous flow as correctly as possible. If this is done, model tests of the stability of rubble-mound breakwaters would be more reliable since they would then be relatively unbiased by viscous effects.

## 8.0 ACKNOWLEDGEMENTS

The authors would like to thank George Ashe for overseeing the construction of the breakwaters and for technical assistance during the tests, and to Rob Bowen for making the strength-reduced armour units.

## 9.0 REFERENCES

1. Barends, B.J., van der Kogel, H., Uijttewaal, F.J. and Hagenaar, J., 1983, "West Breakwater-Sines, Dynamic-Geotechnical Stability of Breakwaters", in Proc. Coastal Structures 83, p. 31-44, A.S.C.E., Arlington, Virginia, U.S.A.
2. Burcharth, H.F., 1981, "Full Scale Dynamic Testing of Dolosse to Destruction", Coast. Eng. 4, p. 229-251.
3. Burcharth, H.F., 1983, "The Way Ahead", in Proc. Conf. on Breakwaters - Design and Construction, Institute of Civil Engineers, London, England.
4. Burcharth, H.F. and Thompson, A.C., 1983, "Stability of Armour Units in Oscillatory Flow", in Proc. Coastal Structures 83, p. 71-82, A.S.C.E., Arlington, Virginia, U.S.A.
5. Funke, E.R. and Mansard, E.P.D., 1980, "On the Synthesis of Realistic Sea States", in Proc. 17th Int. Conf. on Coastal Engineering, p. 2228-2243, Sydney, Australia.
6. Johnson, R.R., Mansard, E.P.D. and Ploeg, J., 1978, "Effects of Wave Grouping on Breakwater Stability", in Proc. 16th Int. Conf. on Coastal Eng., Hamburg, Germany.
7. Mansard, E.P.D. and Funke, E.R., 1980, "Measurement of Incident and Reflected Spectra by the Least Squares Method", in Proc. 17th Int. Conf. on Coastal Eng., Sydney, Australia.
8. Mansard, E.P.D. and Timco, G.W., 1983, "A Review of Breakwater Testing at NRCC", in Proc. 6th CSCE Hydrotech. Conf., Vol. 2, p. 787-803, Ottawa, Canada.
9. Mol, A., Ligteringen, H., Groeneveld, R.L. and Pita, C., 1983, "West Breakwater - Sines, Study of Armour Stability", in Proc. Coastal Structures 83, p. 57-70, A.S.C.E. Arlington, Virginia, U.S.A.

10. Timco, G.W. and Mansard, E.P.D., 1982, "Improvements in Modelling Rubble-Mound Breakwaters", in Proc. 18th Int. Conf. on Coastal Eng., p. 2047-2061, Cape Town, South Africa.
11. Timco, G.W. and Mansard, E.P.D., 1983, "On the Interpretation of Rubble-Mound Breakwater Tests", in Proc. Coastal Structures 83, p. 83-93, A.S.C.E., Arlington, Virginia, U.S.A.
12. Yalin, M.S., 1983, "Physical Modelling of Wave Breakers", in Proc. Workshop on Shallow Water Ocean Eng. Research, Technical Rept. No. 56, U. Hawaii-Look Lab-83-3, Honolulu, Hawaii.

## CHAPTER ONE HUNDRED SIXTY SEVEN

### PHOTOGRAMMETRIC MONITORING OF DOLOS STABILITY, MANASQUAN INLET, NEW JERSEY

Jeffrey A. Gebert<sup>1</sup> and James Clausner<sup>2</sup>

#### ABSTRACT

Photogrammetry has been applied as a technique to monitor the stability of dolosse on the Manasquan Inlet, New Jersey jetties. These jetties were rehabilitated between 1979 and 1982 with 16-ton steel-reinforced dolosse. The jetties have been exposed to a number of storms since 1982, including a design-level storm in March 1984. The photogrammetric measurements have provided a detailed record of the magnitude and direction of dolos movements in response to these storm events. Standard leveling techniques have been used to check the accuracy of the elevation data derived from photogrammetry. This paper describes the methods used in this monitoring effort and the results obtained from the photogrammetric measurements. Also presented are data on the structural integrity of the steel-reinforced dolosse.

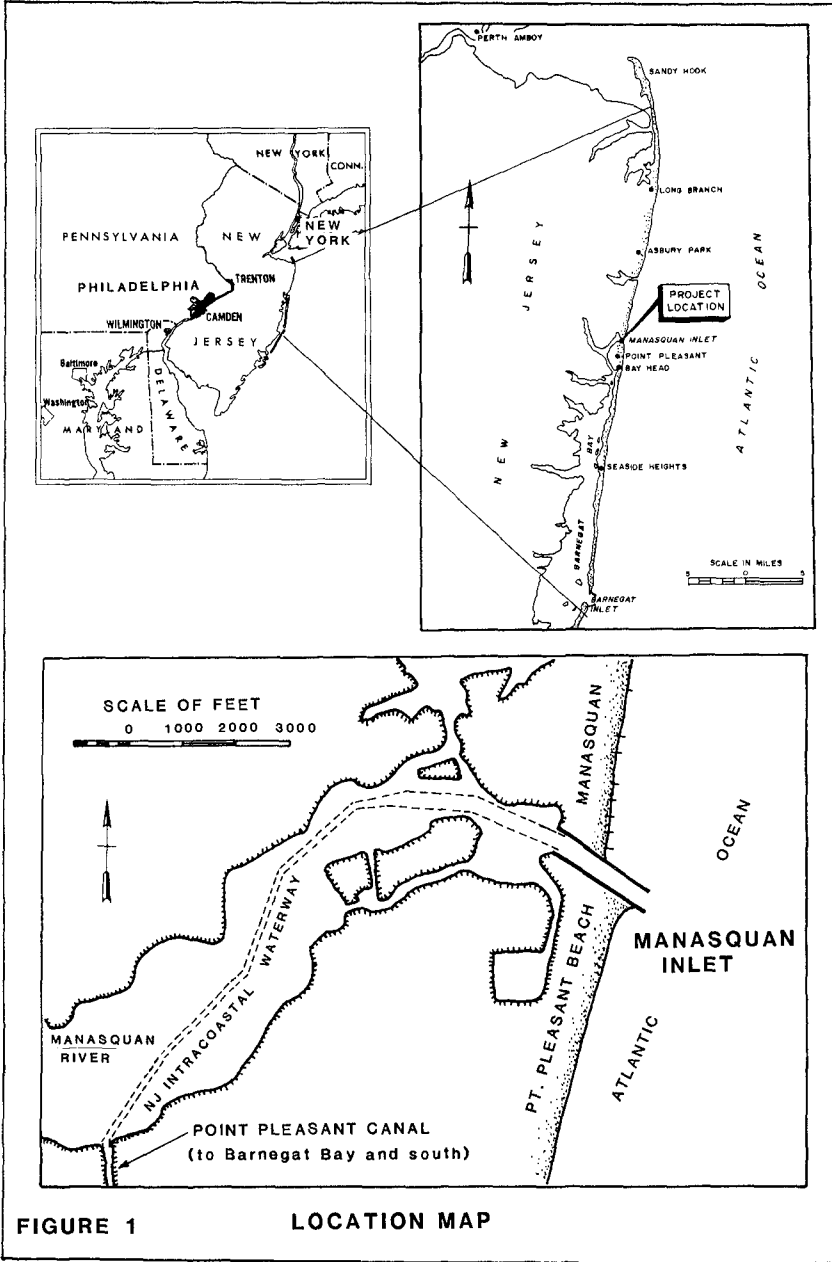
#### INTRODUCTION.

The Federal navigation project at Manasquan Inlet, New Jersey consists of a channel stabilized by parallel jetties, and provides the northernmost connection between the Atlantic Ocean and the New Jersey Intracoastal Waterway. Manasquan Inlet is located about 40 miles (64 km) south of New York City and about 60 miles (96 km) northeast of Philadelphia (Figure 1). The inlet is used year-round by a large commercial and party boat fishing fleet, and is most heavily used in summer when there is a large influx of recreational boaters.

Construction of the original rubblemound jetties and dredged channel was completed in 1931. The jetties are about 1200 feet (366 m) long, spaced 400 feet (122 m) apart, and protect the 250 feet (76 m) wide by 14 feet (4.3 m) deep (MLW) channel. Over the 1935 to 1975 period, the jetties suffered recurrent storm-related damages, primarily to the head sections of the jetties. In this period there were no less than nine contracts awarded for rehabilitation of one or both jetties. These rehabilitation efforts typically consisted of placement of additional and larger stone armor units, such that by 1975 the original 2-ton (1816 kg) stone size had been upgraded to 12-ton (10,896 kg) units in the most exposed portions of the jetties.

<sup>1</sup>Oceanographer, U.S. Army Engineer District, Philadelphia, PA, 19106

<sup>2</sup>Hydraulic Engineer, U.S. Army Engineer Waterways Experiment Station, Vicksburg, MS 39180



**FIGURE 1**                      **LOCATION MAP**

Despite the increase in stone size, the jetties continued to experience damage. This led to the 1978 investigation of alternative rehabilitation methods which concluded that dolosse would be used along the seaward portions of the jetties. Hydraulic design criteria of the U.S. Army Corps of Engineers in effect in 1978 resulted in required armor unit weights of 16 tons (14,528 kg) for dolosse and about 60 tons (54,480 kg) for quarystone given the design breaking wave height of 25 feet (7.6 m). Dolosse were selected as armor units because 60-ton quarystone was beyond the practical range of stone sizes available at this site. The jetties were rehabilitated under two separate contracts, with the south jetty completed in December 1980 and the north jetty in December 1982. A total of about 1300 steel-reinforced, 16-ton dolosse were used in the rehabilitation of the two jetties.

#### MONITORING PROGRAM

The effectiveness of the jetty rehabilitation has been observed and evaluated since 1982 through a monitoring program which is part of the U.S. Army Corps of Engineers Monitoring Completed Coastal Projects (MCCP) program. The monitoring program is a cooperative effort of the Coastal Engineering Research Center of the U.S. Army Engineer Waterways Experiment Station and the Philadelphia District of the U.S. Army Corps of Engineers. The Manasquan Inlet monitoring program has included the following types of measurements:

- o recording wave gage ("Waverider")
- o recording tide gage
- o littoral environment observer (LEO)
- o inlet tidal prism
- o hydrographic surveys of inlet and adjacent beaches
- o side scan sonar
- o aerial photography
- o photogrammetric mapping of dolosse
- o dolos elevations by leveling

This paper describes the procedures used and results obtained in the application of photogrammetry to monitor the stability of the dolosse since initial placement, and also presents findings regarding the structural integrity of the steel-reinforced dolosse.

## PHYSICAL/ENVIRONMENTAL CONDITIONS

Manasquan Inlet is located at the mouth of the Manasquan River, a small stream which originates 17 miles (27 km) above the inlet and is tidal for 5 miles (8 km) upstream of the inlet. At a point 2 miles (3 km) upstream of the inlet, the Manasquan River intersects the Point Pleasant Canal, a man-made channel which extends south 2 miles (3 km) and provides a hydraulic connection to the head of Barnegat Bay. Shark River Inlet is located 6 miles (10 km) north of Manasquan Inlet and is the only breach in the coastline from Manasquan north to Sandy Hook. The first inlet south of Manasquan is Barnegat Inlet, at a distance of 23 miles (37 km).

The hydraulics of Manasquan Inlet are tidally dominated, with a 4.0 feet (1.2 m) mean tidal range and semi-diurnal tides. The spring tidal prism has been measured to be on the order of  $3.5 \times 10^9$  cubic feet ( $9.9 \times 10^6$  cubic meters). The offshore contours are approximately shore parallel out to a depth of 40 feet (12.2 m), and there is no ebb shoal present. Since 1982 the actual depths in the navigation channel between the jetties range from 15 to 20 feet (4.6 to 6.1 m). From the outer ends of the jetties, the bottom drops off to a depth of 30 feet (9.1 m) below mean low water within about 500 feet (152 m) of the north jetty.

The beaches adjacent to Manasquan Inlet (Manasquan to the north, Point Pleasant Beach to the south) are formed against a headland of sandy Atlantic Coastal Plain sediments. The net longshore transport direction is to the north, as evidenced by the shoreline offset shown in Figure 2.

Prior to 1880, when the first timber jetties were built at Manasquan Inlet, the inlet location had been unstable within a zone extending several thousand feet (about 1 km) north of the present location. The first jetties failed by 1886, and no further attempts were made to stabilize the inlet until 1922, when the state of New Jersey built new timber jetty structures. These also failed and the inlet closed naturally on several occasions between 1922 and 1930. The inlet was closed in 1930 at the time that construction began on the present Federal navigation project.

## DOLOS STABILITY MONITORING

Background. In view of the historic problems with maintaining the integrity of the quarystone armor layers of the jetties, and also in view of the relative lack of prototype experience with dolosse on the U.S. east coast, a technique was needed to accurately monitor the performance of the dolosse at Manasquan Inlet and to verify the validity of the design procedures and assumptions used in the rehabilitation effort. Therefore, as an experiment in the Manasquan Inlet monitoring program, the use of precision photogrammetry was proposed as a means to answer the following questions:



**FIGURE 2**  
**MANASQUAN INLET**  
**24 JUNE 1983**

1. Do the dolosse move, particularly under storm conditions?
2. If they do move, then how far, and at which locations on the jetties?
3. Do dolos movements compromise the predicted project performance?
4. How accurate are the photogrammetric measurements and what is the resolution (vertical and horizontal) of photogrammetry in this application?
5. Was jetty rehabilitation with dolosse successful? and
6. Is photogrammetry a cost-effective method of monitoring the stability and performance of armor units on coastal structures?

The following sections provide the answers to these questions developed as of September 1984.

Procedures. The initial step in constructing photogrammetric maps of the south and north jetties at Manasquan Inlet was to establish primary targets on stable portions of the jetties and adjacent land area. The targets were surveyed in from nearby geodetic and vertical control benchmarks, and were visible in the aerial photography. These primary targets were used to define the horizontal (x and y) and vertical (z) datums to which all measurements on the dolosse are referred. The primary targets on the jetties were located along the centerline of the concrete cap. Each concrete cap section is a monolith 20 feet (6.1 m) square by 6 feet (1.8 m) thick, weighing 180 tons (163,000 kg), and supported by the core material of the jetty. The primary targets were surveyed periodically to determine their stability as reference points.

Low altitude black and white aerial photography was obtained with a shore-parallel flight line at an altitude of 600 feet (183 m), resulting in a contact scale of 1:1200 (or 1 inch = 100 feet). The photographic flights were scheduled to coincide with times of low tide and high sun angle conditions. All photography in this monitoring program was obtained with the same precision cartographic camera, a Zeiss RMK A 15/23. A total of three exposures were required to prepare the photogrammetric maps of the jetties; the southern and middle exposures were used for the stereo model of the south jetty, and the middle and northern exposures were used for the stereo model of the north jetty.

The final step in constructing the photogrammetric maps was compilation. A Kern PG 2-AT stereo restitution instrument was used to compile the selected features, in this case the plan view outlines of the dolosse, concrete cap sections, and armor stone. These features were superimposed on a grid based on the New Jersey State Plane Coordinate System, which graphically defined location and orientation of features in the horizontal plane. Vertical data were recorded numerically as spot elevations at selected points on the



same features. Using an enlargement factor of 20 times the contact scale, the finished scale of the maps was 1:60 (or 1 inch = 5 feet). A portion of a south jetty map is shown in Figure 3.

The photogrammetric maps were plotted on stable-base transparent drafting material. In this manner, the stability of a dolos from one flight date to the next was determined by overlaying and registering the two maps, then visually comparing the location of the feature of interest on the earlier and later dates. If a dolos moved in the time interval, the horizontal component of movement was evident as a displacement of the outline of the dolos, which was then scaled from the 1:60 maps. Experience with a number of Manasquan Inlet jetty maps has shown that horizontal movements of as little as 0.3 feet (9 cm) can reliably be detected. The vertical component of movement was determined by comparison of the spot elevation data for a particular point. A later section of this report addresses the accuracy and resolution of the vertical measurements.

Data Obtained. Aerial photography suitable for photogrammetric mapping was obtained on the dates indicated with a "P" in Table 1. Also shown are the dates of the three most significant storm events which have occurred during the course of the Manasquan Inlet monitoring program. The symbols "S" and "N" refer to the south and north jetties respectively, and the numbers (1,2, etc) refer to successive photogrammetric maps prepared for each jetty. Note that a north jetty map was not prepared from the 9 January 1982 photography because the north jetty rehabilitation was in progress at the time.

DATE		SOUTH JETTY	NORTH JETTY
P	9 Jan 1982	S 1	-
	24-26 Oct 1982	Storm	
P	29 Jan 1983	S 2	N 1
	12-13 Feb 1983	Storm	
P	15 Sep 1983	S 3	N 2
P	27 Mar 1984	S 4	N 3
	28-30 Mar 1984	Storm	
P	9 May 1984	S 5	N 4

The initial maps for the south jetty (S1) and north jetty (N1) are the most detailed of the maps prepared in this monitoring program. Spot elevations were determined at two or three locations



on all fully visible dolosse and cap sections, with one or two elevations determined for partially visible dolosse and armor stones. Maps S1 and N1 together document the location, orientation and elevation of 754 dolosse, about 57% of the 1326 units placed on the two jetties during the 1979 to 1982 rehabilitation. The remaining 43% of the dolosse were not mapped because they were either underwater or beneath the top layer of dolosse, and thus not visible in the photography. Subsequent photogrammetric maps have typically included from 20 to 30% of the 754 dolosse shown on maps S1 and N1. This smaller sample size reduces the cost of map compilation, while still obtaining representative coverage of armor units on the two jetties.

Leveling Measurements. As a check on the accuracy of photogrammetric methods which were previously untested in mapping armor units, standard leveling techniques have been used to record two or three spot elevations on a representative sample of both dolosse and armor stones. These level data were obtained for 65 south jetty dolosse on 27 April 1982, 14 March 1983, and 8 September 1983, and for 95 north jetty dolosse on 15 March, 9 June and 7 September 1983.

Prior to the 7-8 September 1983 leveling and 15 September 1983 photography, the comparisons of photogrammetric and standard leveling data suggested that accuracy of the photogrammetrically derived elevations was on the order of  $\pm 0.3$  feet (9.1 cm). However, there were two factors identified which could have been contributing to the differences between leveling and photogrammetric elevation data. The first factor was that the dates of leveling differed by as much as 2 or 3 months from the closest dates of photography. It was possible that dolos movement occurred during such periods, which would then contribute to apparent differences between photogrammetric and leveling measurements on the same point. For example, note that the February 1983 storm occurred in the six-week interval between the January 1983 photography and the March 1983 leveling. The second factor was that prior to September 1983, there were no visual targets on the dolosse to insure that the field leveling crew and the photogrammetrist were observing exactly the same point when measuring an elevation. Features such as "center of face of vertical fluke", for example, were the nominal targets used by the surveyors and photogrammetrist for spot elevations. If such surfaces are inclined relative to the horizontal, as are almost all dolos surfaces on a jetty, then small differences in horizontal location can contribute to comparable differences in measured elevation.

The best data set for determining the accuracy of the photogrammetric elevations was obtained in the period 7-15 September 1983, when both leveling measurements and aerial photography were performed. For these observations, one-foot (30 cm) black targets (crosses) were painted onto 111 dolosse distributed over the two jetties, assuring that both the field crew and the photogrammetrist would determine elevations at exactly the same points within a storm-free period of 8 days. Elevations were determined to the nearest 0.01 foot (3 mm) for both methods. Comparison of the elevation data from the two methods demonstrated that 84% of the photogrammetric

values were within  $\pm 0.1$  feet (3 cm) of the elevations determined by leveling, and 98% were within  $\pm 0.2$  feet (6 cm). The largest discrepancy between the two methods at any point was 0.27 feet (8.2 cm). These findings strongly suggested that earlier uncertainties regarding accuracy and resolution of the photogrammetric elevations were due to the time interval between measurements and the lack of point targets on the dolosse. These findings also showed that photogrammetry was capable of accurately resolving a scale of movement of individual armor units which would permit a detailed evaluation of dolos stability.

The leveling data were essential in verifying the accuracy of the photogrammetric elevations. However, the leveling data do not provide any information on horizontal displacement, whereas both elevation and planimetric data are provided by photogrammetry. Nevertheless, the leveling data summarized below in Table 2 suggest a relationship between dolos movement and storm exposure. Note that level measurements on the south jetty were obtained from April 1982 to September 1983, during which time two northeasters occurred (October 1982 and February 1983). The north jetty level measurements were obtained between March and September 1983, a relatively storm-free period. The data in Table 2 show that the south jetty dolosse experienced more frequent and greater downward vertical displacements than did the north jetty dolosse.

$\Delta z$ (feet)	SOUTH JETTY April 1982 to September 1983	NORTH JETTY March 1983 to September 1983
$\Delta z = 0$	3	18
$0 < \Delta z \leq 0.1$	22	32
$0.1 < \Delta z \leq 0.2$	1	3
$0.2 < \Delta z \leq 0.3$	1	3
$\Delta z > 0.3$ (Total upward)	2 (26)	1 (39)
$-0.1 \leq \Delta z < 0$	36	35
$-0.2 \leq \Delta z < -0.1$	13	6
$-0.3 \leq \Delta z < -0.2$	11	0
$\Delta z < -0.3$ (Total downward)	11 (71)	2 (43)

Note: positive  $\Delta z$  is upward movement, negative is downward.

Photogrammetric Measurements - Results through September 1983.

South jetty maps S1, S2, and S3 and north jetty maps N1 and N2 were prepared from aerial photography obtained through 15 September 1983. As previously discussed, these photogrammetric maps did not achieve as high a degree of accuracy in measuring dolos movement as did later maps due to the lack of point targets on the dolosse. However, analysis of the photogrammetric displacement data through September 1983 did show that 65% of the 250 observed points were within  $\pm 0.3$  feet (9.1 cm), and 91% were within  $\pm 1.0$  feet (30.5 cm) of their initial elevations. The maximum vertical change detected was a drop of 4.2 feet (1.3 m) on a dolos at the head of the south jetty. Ninety percent of the vertical displacements which exceeded 1.0 feet (30.5 cm) occurred on dolosse at the heads of the two jetties. The largest horizontal displacement detected was about 6.0 feet (1.8 m) on a dolos on the channel side of the south jetty. The next largest horizontal displacement was only 3.5 feet (1.1 m), and also occurred at the head of the south jetty. The mean horizontal movement of all monitored dolosse through September 1983 was about 1.0 feet (30.5 cm). The movements were predominantly rotation around the vertical axis (yaw) and displacement in a downslope direction relative to the jetty structures.

Photogrammetric Measurements - September 1983 through May

1984. All photogrammetric measurements on maps for this period utilized the dolos targets established in September 1983 and are therefore assumed to be of comparable accuracy. Note from Table 1 that the time interval from 15 September 1983 to 27 March 1984 was relatively storm-free, whereas the interval from 27 March to 9 May 1984 was not. Measurements of vertical and horizontal displacements over these two intervals reinforced the earlier findings that dolos movements were predominantly related to storm effects.

In the six-month period from 15 September 1983 to 27 March 1984, the mean vertical displacement for all points monitored on the two jetties was -0.15 feet (-4.6 cm) and only 10% of the monitored dolosse experienced detectable horizontal displacements, the largest of which was about 1 foot (30.5 cm).

Between 28 and 30 March 1984, an intense coastal storm affected the mid-Atlantic states. During the 29th, there was a maximum of about 4.5 feet (1.4 m) of storm surge above the predicted tide levels. The maximum still water elevation recorded at the long-term tide gage at Atlantic City, about 50 miles (80 km) to the south was only 0.1 feet (3 cm) below that attained during the March 1962 "storm of record". The maximum stage recorded at Manasquan was 0.2 feet (6.1 cm) below that at Atlantic City on 29 March 1984. However, coastal damage was less in March 1984 because the highest waves coincided with only one high tide, in contrast to the "five high tide" duration of the March 1962 storm. The wave gage at Manasquan, located about 1 mile (1.6 km) northeast of the inlet where the depth is about 50 feet (15.2 m), recorded a maximum 20-minute significant wave height of 22 feet (6.7 m) with a corresponding peak period of about 11.5 seconds. The peak of the wave record coincided with the maximum of the ocean stage, and thus exposed the jetties to what is believed to be the equivalent of the design storm. The significant

wave height at the gage exceeded 20 feet (6.1 m) for 5 hours and exceeded 10 feet (3.0 m) for 30 hours. Note that the 27 March 1984 photography was obtained only 24 hours before the arrival of the first storm effects at Manasquan.

The mean vertical displacement of all monitored dolosse due to the March 1984 storm was -0.46 feet (-14 cm). Table 3 summarizes the elevation change data from this storm, and utilizes the same notation as in Table 2. Approximately 3% of the dolosse moved in excess of 1.0 feet (30.5 cm) vertically, with a maximum value of a 2.03 feet (62 cm) drop.

$\Delta z$ (feet)	SOUTH JETTY	NORTH JETTY
$\Delta z = 0$	3	4
$0 < \Delta z \leq 0.1$	3	23
$0.1 < \Delta z \leq 0.2$	0	7
$0.2 < \Delta z \leq 0.3$	1	0
$\Delta z > 0.3$	2	0
(Total upward)	(6)	(30)
$-0.1 \leq \Delta z < 0$	24	26
$-0.2 \leq \Delta z < -0.1$	22	10
$-0.3 \leq \Delta z < -0.2$	14	10
$\Delta z < -0.3$	31	20
(Total downward)	(91)	(66)

The largest horizontal displacement caused by the March 1984 storm was 7.0 feet (2.1 m) at the head of the south jetty. There were 3 other dolosse which moved about 5 feet (1.5 m) horizontally. Altogether only 9% of the monitored dolosse moved in excess of 2 feet (61 cm) horizontally, with 31% moving from zero to 2 feet. About 60% of the dolosse experienced no detectable horizontal displacement.

Dolos Breakage. As a result of the March 1984 storm, 3 dolosse broke on the north jetty, all within a zone about 35 feet (10.7 m)

wide at the head of the structure. Two of the breaks resulted in the loss of some concrete from the shank portions of the dolosse, but the presence of the epoxy-coated reinforcing steel kept the dolosse substantially intact. The third north jetty dolos suffered a hairline crack through one fluke. One south jetty dolos, located near the head on the channel side of the structure, broke at the junction of the shank and a fluke. This dolos is also essentially intact because of the reinforcing steel.

Prior to the March 1984 storm, one other dolos at the head of the north jetty had broken. Therefore, a total of 5 out of the 1326 dolosse (only 0.4%) used in the 1979 to 1982 rehabilitation have broken despite exposure to the design storm event. It is interesting to note that of the five dolosse which have broken, only one has experienced a net horizontal displacement in excess of 2 feet (0.6 m) from its initial location. Other dolosse have moved greater distances, up to 7 feet (2.1 m) between dates of photography, yet have not broken.

Based on several years monitoring at Manasquan Inlet, it is evident that steel-reinforced dolosse in a weight range up to 16 tons can exhibit a degree of mobility on the jetty surface in response to storm conditions, yet not incur significant damage due to breakage of individual units.

## CONCLUSIONS

Photogrammetry has been found to be a highly useful technique for monitoring the stability of armor units on coastal structures. The application described in this paper has involved dolosse, but the technique would be equally applicable for monitoring structures with quarystone or other concrete armor units. Comparison of photogrammetric measurements with standard land survey techniques has shown that photogrammetry provides a degree of accuracy and resolution more than adequate to evaluate armor unit stability. At the scale of mapping used in this project, vertical accuracy of  $\pm 0.1$  feet (3.1 cm) and horizontal accuracy of about  $\pm 0.3$  feet (9.1 cm) have been attained. Periodic photogrammetric mapping of a coastal structure would permit detection of incipient or progressive failure along any visible portion of the structure before such a problem was readily detected by other means. This would allow for early assessment and possible correction of the problem.

Photogrammetry offers several advantages over conventional land survey techniques. First, it is possible to map armor units at or near the waterline of the structure which would be inaccessible or too hazardous to access on foot. Secondly, photogrammetry is flexible in that all the information needed to perform the photogrammetric mapping can be obtained almost instantaneously, permanently and at a fixed cost with one aerial photographic flight. The mapping itself can then be performed at any time thereafter, or not at all, depending on available resources, need for

information, etc. In contrast, land survey methods capable of obtaining the location, orientation, and elevation data for mapping every visible armor unit are labor-intensive and would require considerably more time and expense than the photogrammetry. If the land survey measurements are not made on a given date, they are then permanently lost. Thirdly, the standard data product of photogrammetric mapping is graphical, and thus readily interpreted with respect to location and magnitude of any armor unit displacements.

Despite the relatively short period of monitoring at Manasquan Inlet since completion of the jetty rehabilitation, monitoring measurements have shown that the jetties have already been exposed to their design level storm event (in March 1984). The photogrammetric measurements have documented that the dolosse do move, particularly in response to storm exposure. These measurements have quantitatively shown which dolosse have moved, how far, and in which direction. However, there is presently no indication that the range of dolos displacements experienced to date has in any way compromised the effectiveness of the most recent rehabilitation project. The photogrammetric measurements have also shown that none of the monitored dolosse has experienced a displacement, either horizontal or vertical, in excess of about 70% of the unit dimension (11 feet, or 3.4 m) of a 16-ton dolos.

The rehabilitation of the Manasquan Inlet jetties with these units has been fully successful to date. The overall performance of the jetties and in particular the low percentage of broken dolosse in response to the March 1984 storm serve to verify the design and construction procedures utilized in the rehabilitation of the jetties.

The initial photogrammetric maps prepared for the Manasquan Inlet jetties provide a complete and somewhat unique set of baseline data against which future performance of the dolosse can be readily compared. The information obtained by monitoring of the dolosse and jetties at Manasquan Inlet should provide an important quantitative contribution on prototype structure performance to complement the more extensive body of knowledge on armor unit stability derived from physical model studies.

#### ACKNOWLEDGEMENTS.

The research reported in this paper has been funded by the U.S. Army Corps of Engineers Monitoring Completed Coastal Projects (MCCP) program. Support by the office of the Chief of Engineers and the Coastal Engineering Research Center, Waterways Experiment Station is appreciated. The authors also wish to express appreciation to Mr. David K. Nale of A.D.R. Associates, Pennsauken, N.J. for continued valuable technical advice on the photogrammetric aspects of this work, and to Mrs. Clare McAneny for assistance in manuscript preparation.



## CHAPTER ONE HUNDRED SIXTY EIGHT

### SHIP-WAVE ATTENUATION TESTS OF A PROTOTYPE FLOATING BREAKWATER

Ronald E. Nece<sup>1</sup>, F. ASCE and Norman K. Skjelbreia<sup>2</sup>

#### ABSTRACT

Limited data are presented for the ship-wave attenuation of a prototype concrete pontoon floating breakwater. Results are compared with wave attenuation performance of a breakwater of identical cross-section and similar anchoring configuration as predicted by model tests using monochromatic waves. Field test procedures and limitations are described.

#### Introduction

Often the most severe wave climate impressed on floating breakwaters used in sheltered waters may originate not from wind-generated waves but from ship or boat waves. This paper presents limited boat wave attenuation test results for a prototype concrete pontoon breakwater. These specific tests were conducted as part of a U.S. Army Corps of Engineers prototype test program initiated to establish design criteria for floating breakwater applications in semi-protected coastal waters, lakes, and reservoirs.

The prototype testing program was established to obtain field information on, among other things, wave transmission characteristics, anchor loads, and structural forces. In particular, this paper describes the boat wave attenuation performance of a particular type of floating breakwater quite commonly used in semi-protected waters of the North Pacific coast in the United States and Canada.

Data from model tests using monochromatic waves typical to laboratory tests of such floating structures were available for a breakwater of identical cross-section and comparable anchoring scheme. Some data on wind wave performance of the prototype structure discussed in this paper also were available. This paper then takes the opportunity to compare, even if on a limited basis, laboratory, wind wave, and boat wave data for the same breakwater. Reasons why the test results are limited are indicated, and why boat wave performance tests of prototype floating structures may be limited in general is discussed.

- 
1. Professor, Dept. of Civil Engineering, University of Washington, Seattle, Washington, U.S.A.
  2. Hydraulic Engineer, U.S. Army Corps of Engineers, Seattle, Washington, U.S.A.

### Description of Test Site and Breakwater

The prototype structure was installed at a test site at West Point, near Seattle, in Puget Sound, Washington. The site was in an exposed location, selected so that within the time frame of the tests the structure would be exposed to wave conditions more severe than those existing at sites currently considered as suitable for floating breakwaters. The water depths at the site varied between 40 and 50 feet (12.2 and 15.2 m) at mean lower low water (MLLW), the diurnal tide at the site is 11.3 feet (3.5 m) and the currents are variable.

The prototype breakwater consisted of two rectangular modules, each 75 feet (22.87 m) long and 16 feet (4.96 m) wide, with a draft of 3.5 feet (1.07 m) and a freeboard of 1.5 feet (0.46 m). During the boat-wave tests, the two modules were rigidly fastened together to form a single, 150-foot (45.73 m) long structure. The breakwater was anchored in place by 10 anchor lines attached to H-piles embedded in the sand and gravel bottom. Anchor lines consisted of 1-3/8-inch (35-mm) stud link chain at each end, with a one ton clump weight attached to minimize lateral displacement of the breakwater. The anchor lines had a minimum scope of 1 vertical to 4.5 horizontal, and were pre-tensioned to  $5,000 \pm 1,000$  pounds ( $22,200 \pm 4,450$  N). The breakwater is shown schematically in Figure 1.

Waves were measured by resistance-wire wave staffs mounted on spar buoys equipped with damping plates and having natural periods in heave and roll of 18 and 12 seconds, respectively, both much greater than periods of either windwaves or boatwaves at the test site. For the tests discussed in detail here the wave gages were located as shown in Figure 2; they were attached to the breakwater anchor lines. The gages were connected to a microprocessor-based data acquisition system designed to handle 80 analog input channels from wave gages, and force, pressure, and motion measuring transducers used in the monitoring project. Strip-chart records were also obtained during the boatwave tests. Details of the breakwater design and the instrumentation have been provided respectively by Nelson et al. (5) and Christensen (2).

### Boat-Wave Tests

Two tests are discussed here; each involved a different vessel.

The test discussed in more detail used a U.S. Coast Guard utility boat with a modified deep 'V' planing-type aluminum hull and having the following dimensions: length, 40.7 feet (12.4 m); beam, 13.4 feet (4.1 m); maximum draft, 4.9 feet (1.5 m); full load displacement, 15 tons. Nominal speeds for the constant speed, straight line courses run during the test were 12, 16, and 20 knots; at the 16-knot speed the boat is just beginning to plane and generates its largest waves.

Vertical photographs were taken during the boat runs, using a conventional aerial camera. The plane elevation was about 1,000 feet (305 m), so that the nominal scale was 1:2000. Those timed, sequential photographs which included the moving boat and the breakwater provided the necessary measure of boat speed, with the breakwater providing the

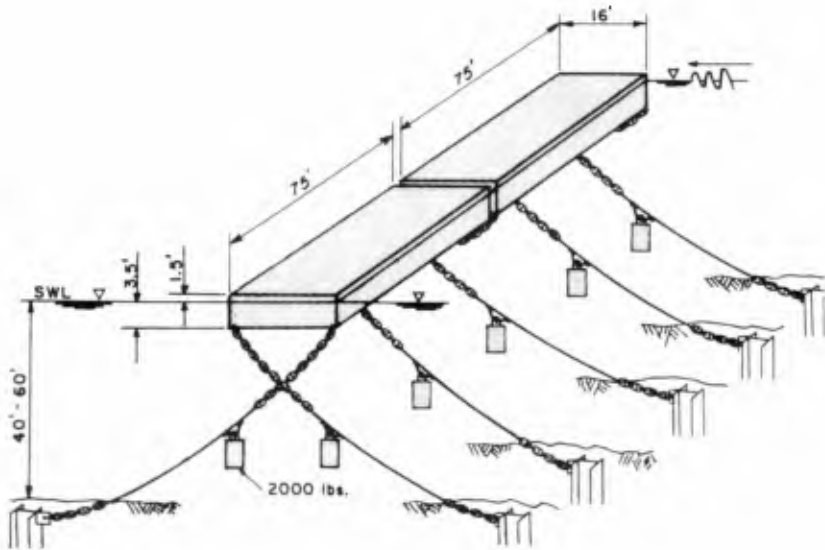


Figure 1. Schematic drawing of breakwater.

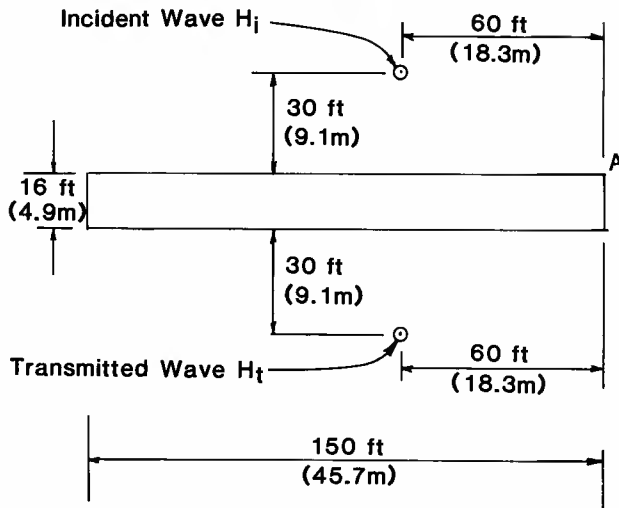


Figure 2. Wave gage locations.

horizontal scale, as well as boat direction and sailing line distance with respect to the breakwater. An example photograph is shown in Figure 3. A pipe-tire breakwater, not discussed in this paper, also appears in Figure 3. Successful photographs were not obtained for all runs. Boat speed was determined from the photographs for only one (the 16-knot) speed, so the same ratio between measured speed and that indicated by on-board instrumentation was assumed in the reduction of data. The actual speeds were thus determined to be 11.1, 14.9, and 18.6 knots. Boat wave patterns were obtained for the two higher speeds; the wave pattern angles for the "12-knot" speed had to be estimated by extrapolation. Where aerial photos were not available (when, for example, the airplane and the boat did not pass the breakwater at the same time) boat directions and distances from the breakwater were estimated on the basis of the test design and visual observations from the boat and breakwater. The breakwater corner 'A' identified in Figure 2 and in definition sketch Figure 4, was used as the reference point in distance measurements and calculations. Incident wave properties were defined at the position of the incident wave gage, as shown in Figure 4.

Wave angles  $\beta$ , and therefore  $\theta$  (measured with respect to the sailing line direction) of the diverging waves which were the dominant waves in the boat-wave pattern were measured at various distances from the sailing line on the aerial photographs. The solid lines on Figure 5 for the 14.9 and 18.6-knot speeds are each based on over twenty individual measurements of wave crest directions on a photograph; as indicated previously, the curve for the 11.1-knot speed was obtained by extrapolation.

The nearness of the wave staff to the breakwater posed a problem with respect to measurement of  $H_i$ , the height of the incident wave. To avoid possible effects of wave reflection from the breakwater, the following procedure was adopted. On the strip-chart records used in the present data analysis, the boat wave envelope was identified, and the vertical distance from the crest of the second wave in the boat-wave envelope to the following trough (using the gage scale factor) was defined as  $H_i$ . This is illustrated in Figure 6, traced from an expanded plot produced from the data acquisition system. The sampling rate was 4 Hz; frequencies below 0.1 Hz and above 0.8 Hz were filtered out to eliminate electronic drift and high frequency noise, respectively. Wind waves at the site were generally in the 2 to 4-second period range. The representative trace in Figure 6 was obtained from a separate piling-mounted wave gage located 150 feet (45.7 m) from the end of the breakwater opposite to the end containing point 'A', and on the longitudinal axis of the breakwater, so that there were no reflected waves. The record was obtained during tests using a 110-foot (33.5 m) tug, as described below. Figure 6 indicates that the error in the definition of  $H_i$  was small. The height  $H_t$  of the transmitted wave was the maximum wave height measured at the gage 'behind' the breakwater. Figure 6 shows the boat-wave envelope, and also indicates that at the time of the test the wind-waves were small enough so that for purposes of the present test the boat-wave heights could be measured directly from the strip-chart records.

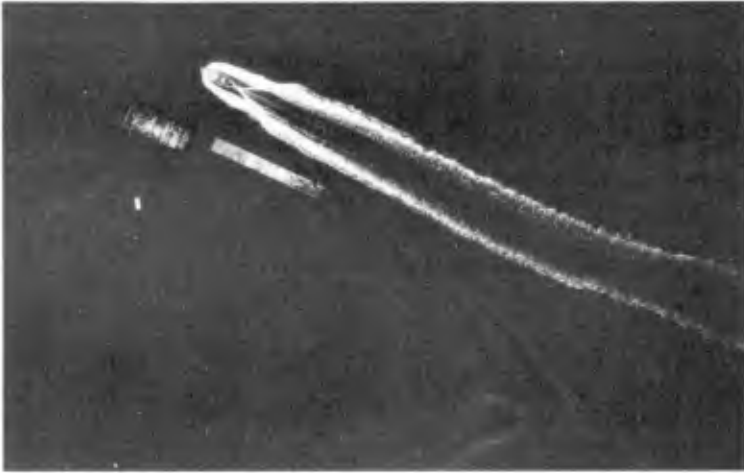


Figure 3. Vertical aerial photograph, Coast Guard utility boat.

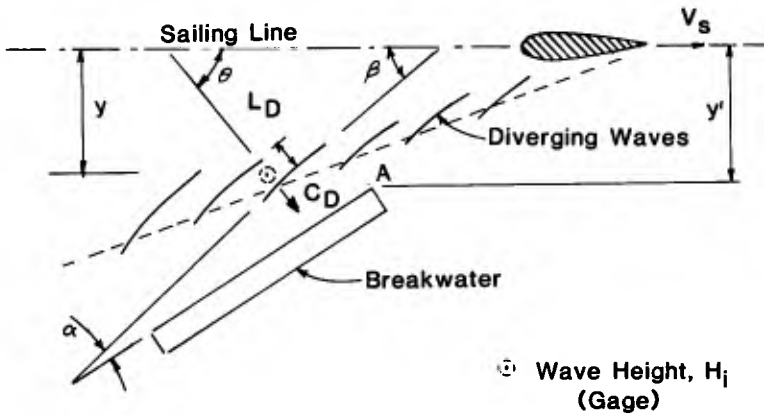


Figure 4. Definition sketch.

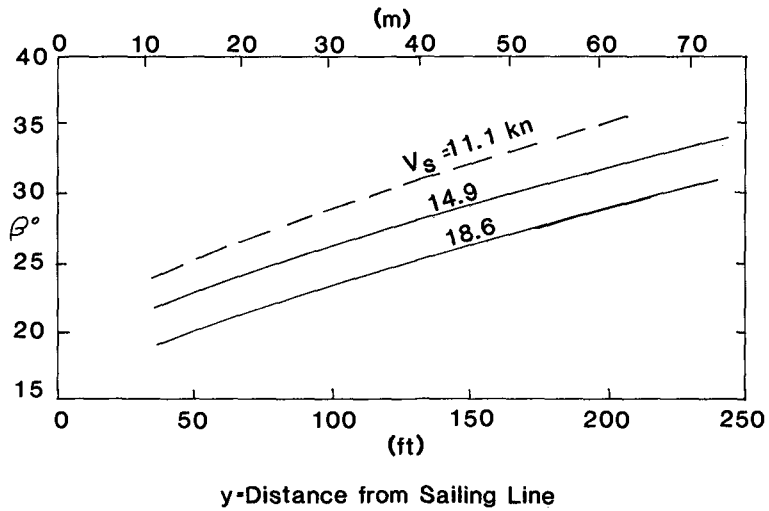


Figure 5. Wave crest direction vs. distance from sailing line, Coast Guard utility boat.

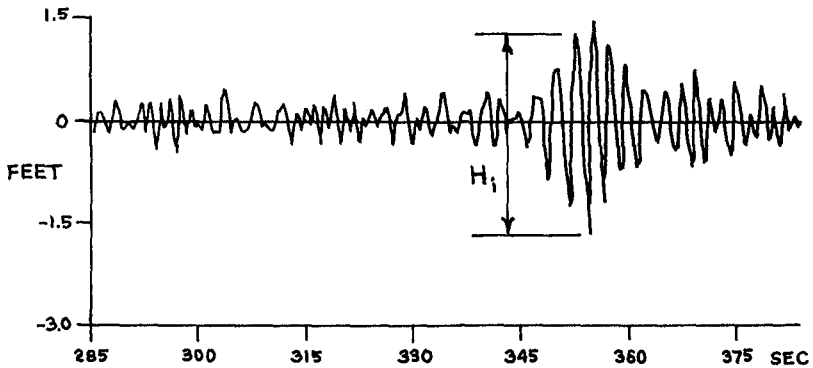


Figure 6. Representative wave trace (marine tug) and selected value of incident wave height  $H_1$ .

Figure 7 indicates the measured decay of wave height with normal distance  $y$  from the sailing line, for each of the three boat speeds. This decay is comparable to that reported by Sorensen for a Coast Guard cutter of length and speed range close to that of the boat used in the present test (8). Wave half-periods (time from crest to trough of the boat waves, as measured at the staff gage) ranged between 1.2 and 1.4 seconds, also comparable to the values reported by Sorensen.

The second test mentioned here utilized a marine tug having the following dimensions: length, 110 feet (33.5 m); beam 34 feet (10.4 m); draft, 10 feet (3.1 m); displacement, 193 tons (gross). The nominal speed was 11 knots for all runs. Aerial photographs were taken for some runs; however, the photographs were taken at oblique angles from a small airplane by a hand-held camera. Figure 8 is an example of these oblique photos. General features of the boat-waves as they acted upon the breakwater were visible, but vessel speeds and wave angles could not be determined. Consequently, no detailed treatment of the wave height data could be made. More details of this test, and of two other short boat-wave tests of the prototype breakwater in which aerial photography was not employed have been given by Skjelbreia (7).

#### Model Data

Model tests had been conducted on a floating breakwater proposed for (but not eventually, so constructed) a site near East Bay, Olympia, on Puget Sound Washington. Results, here all expressed in equivalent full-scale values, were reported by Carver (1). Monochromatic waves only were used in the 1:10 scale model tests.

Two configurations were tested, as shown in Figure 9. The cross-section of Plan 2 is identical to that of the prototype breakwater used in the boat wave tests. Anchoring systems are similar but not identical and the East Bay water depths are less than at West Point, so the East bay tests did not fully model the prototype of the present tests. Trends in wave transmission characteristics, however, would be expected to be similar. Conventional two-dimensional test results are shown in Figure 9 in the form of transmission coefficient  $C_t$  vs.  $L/W$ , where

$$C_t = H_t / H_i$$

$$W = b_{\text{breakwater width}}$$

$$L = \text{length of incident wave.}$$

To remain within the range of wave heights measured in the Coast Guard boat tests,  $H_i$  values of only 1.5 and 2 feet (0.46 and 0.61 m) from the model test data, were used in plotting Figure 9.

Plan 1 was also tested with waves having crests at an angle of obliquity  $\theta$  with respect to the face of the breakwater. Information concerning these tests is shown in Figure 10. Transmitted wave heights plotted in Figure 10 were maxima measured at the wave gage location shown; measurements from this gage were used because it most closely

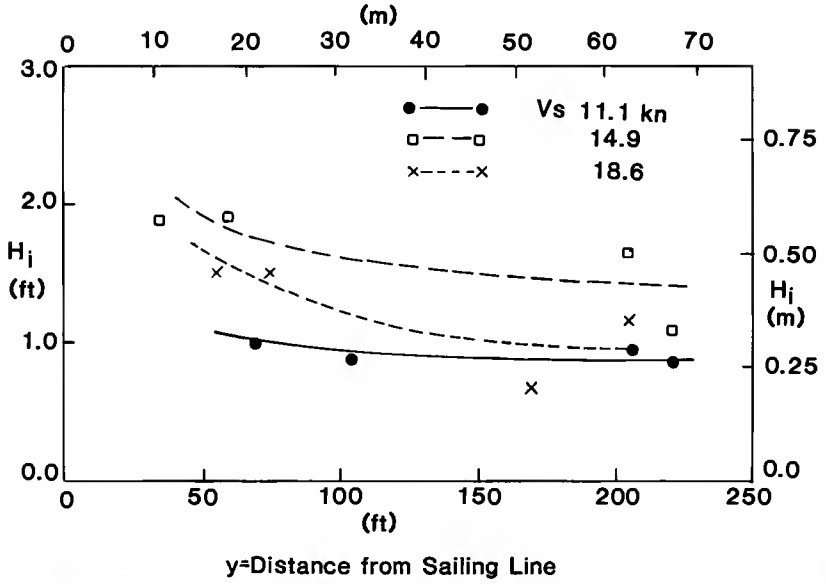


Figure 7. Decay of boat wave height with distance.



Figure 8. Oblique aerial photograph, marine tug.



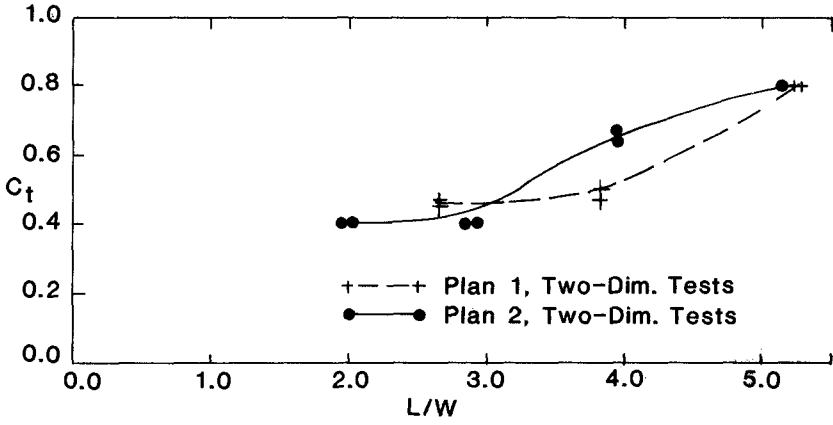
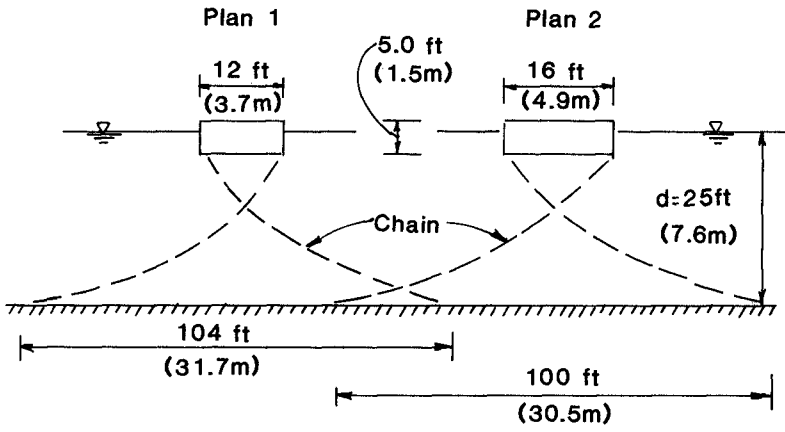


Figure 9. East Bay models, test data.

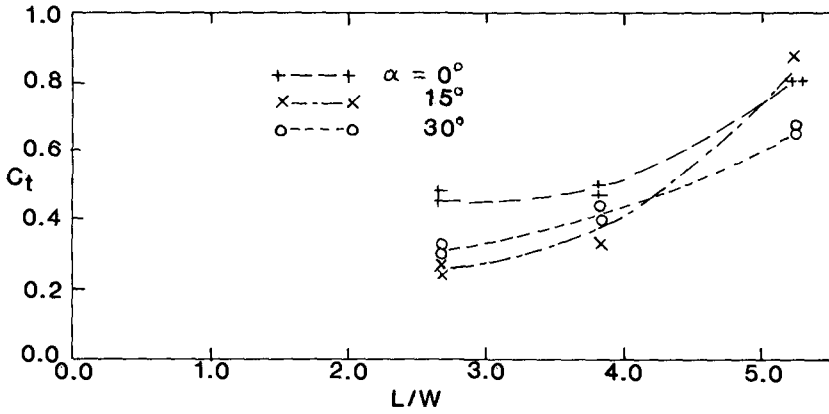
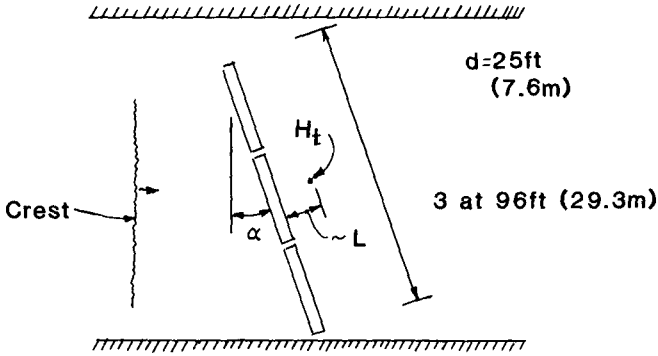


Figure 10. East Bay model data, Plan 1.

simulated the location of the transmitted wave staff in the boat wave tests.

### Results of Prototype Tests

In order that the boat wave data be compared with laboratory data such as shown in Figure 10, it is necessary that  $\alpha$  and  $L$  be determined for the divergent waves of the boat wake which were the incident waves at the breakwater. Since it has long been established, e.g. (4) that boat wave patterns depend upon vessel speed and hull form (3), the aerial phototographs were necessary. Wave periods and water depths at the test site allowed deep-water equations for linear wave theory to be employed in the analysis.

Since the Kelvin-type wave pattern as a whole moves with the vessel, the wave crest (phase velocity) of the divergent wave is

$$C_D = V_s \cos \theta$$

in the direction normal to the wave crest as shown in Figure 4. Using the deep-water relations, the other wave properties are obtained:

$$T_D = \frac{2\pi C_D}{g} = \frac{2\pi V_s \cos \theta}{g}$$

$$L_D = \frac{g T_D^2}{2\pi} = \frac{2\pi V_s^2 \cos^2 \theta}{g}$$

The period  $T_D$  is not that recorded by a stationary wave gage as the diverging waves pass it. Wave lengths so calculated for the boat wave tests did agree well with wave lengths measured directly from the aerial photographs. The quality of the photographs was such, however, that wave crest angles could be measured more accurately than lengths; hence, the procedure followed.

Results of twelve passes of the boat past the breakwater are recorded in Table I. As noted, boat directions and distances from the breakwater could be obtained from only four photographs; other values are best estimates. To conserve space, only the foot units originally used are tabulated. Calculated incidence angles  $\alpha$  are listed, and compared with values estimated by an observer on the breakwater and with those few which could be measured from the photographs. Disparities in results indicate the need for a complete set of good quality photographs if a good, full set of data is to be obtained.

Wave transmission results are plotted as a function of wave length in Figure 11, and in conventional dimensionless form in Figure 12. The  $L$  and  $T$  in both figures apply to the diverging waves as they reached the incident wave gage. For the shorter boat waves, the transmission coefficient agrees with the results from the monochromatic wave model tests. For longer wave lengths  $L_D$ , however,  $C_t$  values for the boat

Table I

Run No.	Vessel Speed knots	Angle <sup>a</sup> degrees	Dist. $v^1$ feet	Dist. $y$ feet	$\beta$ degrees	Calc. $\alpha$ degrees	Estimated $\alpha$ (Field Notes) <sup>b</sup> degrees
12-1	11.1	0	250	220	36	36	-
12-2	11.1	30	200	205	35	-5	-
12-3	11.1	0	100	70	27	27	20
12-4	11.1	50	75	105	29	20	15
16-1	14.9	0	250	220	33	33	15
16-2	14.9	45	200	205	32	13	5-10
16-3	14.9	1 <sup>c</sup>	65 <sup>c</sup>	35	22	22	20+(30) <sup>c</sup>
16-4	14.9	51 <sup>c</sup>	54 <sup>c</sup>	85	25	26	15-20(18) <sup>c</sup>
20-1	18.6	0	200	170	27	27	5
20-2	18.6	45	200	205	29	16	20
20-3	18.6	0 <sup>c</sup>	85 <sup>c</sup>	55	20	20	20(24) <sup>c</sup>
20-4	18.6	55 <sup>c</sup>	44 <sup>c</sup>	75	21	24	25-30(35) <sup>c</sup>

Run No.	Calculated Values,			Measured		$C_t$	$\frac{L_D}{W}$
	Diverging Waves $\theta$ degrees	$T_D$ sec	$L_D$ feet	Wave Heights $H_i$ feet $H_t$ feet			
12-1	54	2.19	24.5	0.87	0.33	0.38	1.53
12-2	55	2.11	22.8	0.95	0.42	0.44	1.43
12-3	63	1.73	15.4	1.00	0.33	0.33	0.96
12-4	61	1.79	16.5	0.87	0.2	0.23	1.03
16-1	57	2.68	36.7	1.09	0.6	0.55	2.29
16-2	58	2.60	34.5	1.67	0.7	0.42	2.16
16-3	68	1.83	17.2	1.92	0.9	0.47	1.08
16-4	65	2.07	22.0	1.92	0.8	0.42	1.37
20-1	63	2.78	39.4	0.67	0.4	0.60	2.46
20-2	61	2.98	45.3	1.17	0.8	0.68	2.83
20-3	70	2.19	24.6	1.50	0.7	0.47	1.53
20-4	69	2.19	24.6	1.50	0.7	0.47	1.53

<sup>a</sup>: Angle between sailing line and breakwater longitudinal axis

<sup>b</sup>: Visual estimates by observer on the breakwater

<sup>c</sup>: Measured from aerial photographs

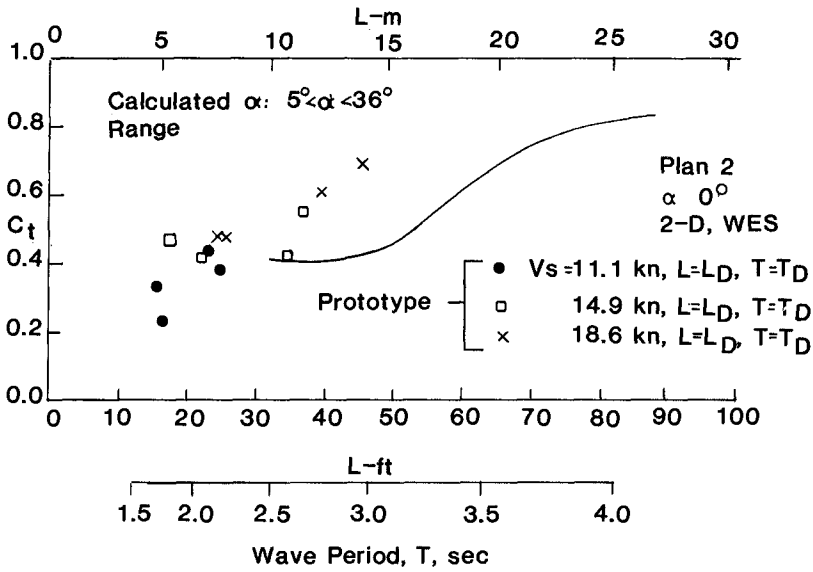


Figure 11. Boat wave data, Coast Guard utility boat.

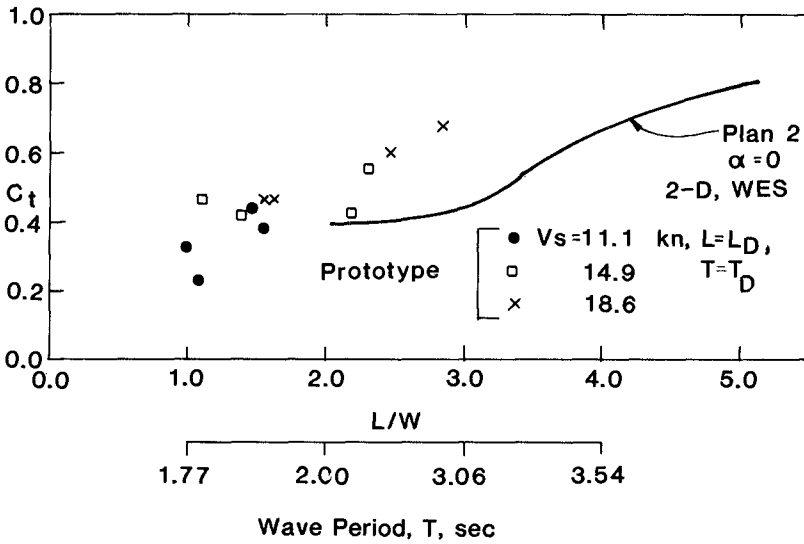


Figure 12. Boat wave data, Coast Guard utility boat.

waves appear to be larger than those for the model tests. There is no discernible relationship of  $C_r$  to the obliquity angle  $\alpha$ , within the  $\alpha$  range indicated. The data are too limited for conclusive statements. One possible reason for the differences in  $C_r$  at the longer wave lengths could be the differences in the anchor line tensions.

Figure 13 shows some results reported by Nelson and Broderick (6) for wind waves at the prototype structure. The wave crests were essentially parallel to the breakwater axis for waves generated by southerly winds. The incident wave gage used was the pile-mounted gage referred to earlier, so that wave reflections from the breakwater posed no problem. The period shown is that at the spectral energy peak, obtained from spectral analysis of 2,048-point, approximately 8-1/2 minute records. The significant wave height was taken as four times the variance (standard deviation squared) of the wave record, an approximate result for calculations based on the Rayleigh distribution function (9).

No correlation of boat wave data from the test using the marine tug are given in this paper. Incident waves were of the order of magnitude 2-3 feet (0.6-0.9 m) as typified by the trace in Figure 6, and transmitted wave heights were approximately 0.5 foot (0.15 m). It was difficult to separate the transmitted boat-waves from the surface chop on the "transmitted" side of the breakwater on the day of the tests, just as it was difficult to identify the transmitted boat waves by visual observation. There was water on the deck of the breakwater when it was impacted by the waves generated by the tug. This breaking of waves on the breakwater provided an additional wave attenuation mechanism which may not have been relatively so significant in the laboratory studies; hence, wave attenuation by the prototype was greater than would be predicted by the laboratory model tests. Again, differences in anchor line restraint could be a major cause for the differences in performance of the laboratory model under monochromatic waves and the prototype breakwater subjected to boat waves.

### Conclusions

The limited data did not allow identification or separation of effects of the many variables involved in correlating wave transmission performances of a floating breakwater for continuous, monochromatic waves typical of model studies and for the finite envelope of waves experienced in boat wakes.

It appears that for shorter wave lengths (say  $L/W = 2$  or less) boat wave transmission of a breakwater can be predicted reasonably well from monochromatic wave model tests. At many sites where floating breakwaters may be feasible, this range of  $L/W$  might cover the anticipated range of boat waves that might be generated by smaller vessels such as pleasure craft.

For  $L/W > 2$ , results reported here are not conclusive. For the Coast Guard boat waves, transmitted waves were greater than predicted using the model test results, while the opposite was true for the tug-generated waves. This difference is perhaps due mostly to non-similitude in the anchoring systems. The pre-tensioned anchor lines

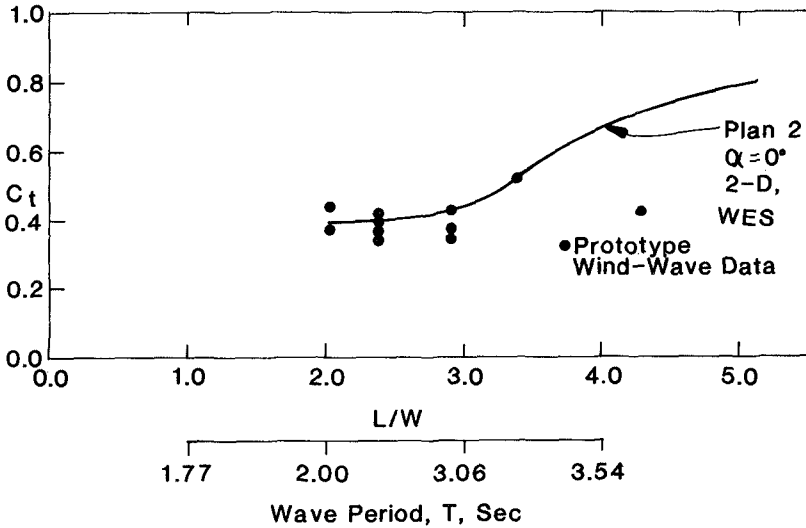


Figure 13. Wind wave data.

in the prototype may have kept the breakwater, while responding to the boat wave envelope, from achieving the motions obtained under continuous waves in the laboratory. For waves of moderate height the model data were not conservative, while they were for higher steeper waves which broke over the prototype.

In almost all cases for both model and prototype wave crests were inclined at angles of 30 degrees or less from the breakwater longitudinal axis. No significant effect of wave incidence angle on wave transmission was detected in the field test data.

Aerial photography is an important, and almost necessary, component of a comprehensive field test of the behavior of a floating structure to ship-generated waves. Tests involving aerial photography require careful planning and coordination, and must be responsive to such constraints as visibility conditions, sea state, and perhaps, elevations at which the aircraft used are allowed to fly if other air traffic is a concern. These requirements indicate why availability of such data may, in general, be limited.

#### Acknowledgements

The testing program was conducted under the direct supervision of the Seattle District, Corps of Engineers. Monitoring of the prototype performance was performed by the Department of Civil Engineering, University of Washington.

References

1. Carver, R.D., "Floating Breakwater Wave-Attenuation Tests for East Bay Marina Olympia Harbor, Washington", Technical Report HL-79-13, U.S. Army Waterways Experiment Station, Vicksburg, Mississippi, U.S.A., Aug., 1979.
2. Christensen, D.R., "Installation, Operation, and Maintenance Manual for Breakwater Data Acquisition and Analysis System", Draft report submitted by University of Washington to U.S. Army Engineer District, Seattle, Washington, U.S.A., 1984.
3. Comstock, J.P. (ed.), "Principles of Naval Architecture", The Society of Naval Architects and Marine Engineers, New York, New York, U.S.A., 1967, pp. 301-303.
4. Hovgaard, W., "Diverging Waves", Transactions, Institution of Naval Architecture, London, England, Vol. 51, 1909, pp. 251-263.
5. Nelson, E.E., Christensen, D.R., and Schuldt, A.D., "Floating Breakwater Prototype Test Program", Proceedings Coastal Structures '83, American Society of Civil Engineers, Mar., 1983, pp. 433-446.
6. Nelson, E.E., and Broderick, L.L., "Floating Breakwater Prototype Test Program", Proceedings 41st Meeting of the Coastal Engineering Research Board, U.S. Army Coastal Engineering Research Center, May 5-7, 1984.
7. Skjelbreia, Norman, K., "Boat Wake Transmission Tests of a Prototype Floating Breakwater", thesis presented to the University of Washington, Seattle, Washington, U.S.A., in 1984, in partial fulfillment of the requirements for the degree of Master of Science in Civil Engineering.
8. Sorensen, R.M., "Investigation of Ship-Generated Waves", Proceedings, American Society of Civil Engineers, Vol. No. 93, No. WW1, Feb., 1967, pp. 85-99.
9. U.S. Army Coastal Engineering Research Center, "Shore Protection Manual", Vol. I, Fort Belvoir, Virginia, U.S.A., 1977, pp. 3-11 to 3-13.



## CHAPTER ONE HUNDRED SIXTY NINE

Case History of a Spaced Pile Breakwater at Half Moon Bay Marina  
Auckland, New Zealand

P.S. HUTCHINSON\*  
A.J. RAUDKIVI\*\*

### Introduction

Half Moon Bay Marina is a privately owned small boat harbour located on the Tamaki Estuary of the Auckland Harbour. The marina was built in 1970 for 485 boats moored to floating marina berths, Fig. 1, and is sheltered by a spaced pile breakwater.



Figure 1 : View of Half Moon Bay Marina

- \* Partner, Bruce Wallace and Partners Consulting Engineers,  
P.O. Box 9123 Auckland, New Zealand
- \*\* Professor of Civil Engineering, University of Auckland,  
New Zealand

The marina is well protected by land from the prevailing south-westerly winds and from the north-easterly gales which are experienced in the region, Fig. 2. However, the marina entrance is exposed to the less frequent north-westerly and westerly winds blowing across the Tamaki River. For winds from a northerly direction at high tides the calculated significant wave height is 1 metre with a 3 second period and 0.7 metres with a 2.7 second period with westerly winds. During low water the fetch is further reduced to the relatively narrow width of the estuary by the drying shallows at the opposite side of the river.

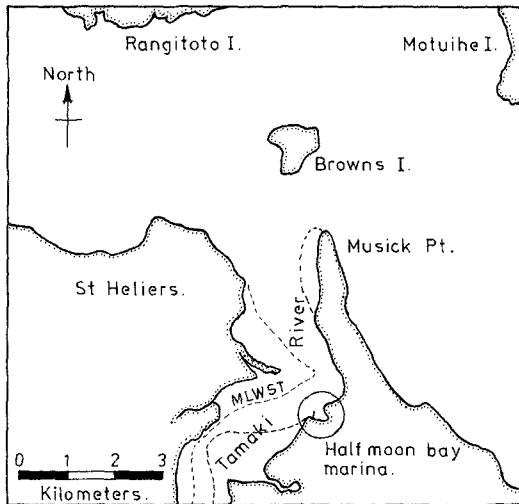


Figure 2 : Location map of the marina showing the narrow sector of exposure to wind waves

Because of space restriction and cost it was not desirable to use a cover breakwater to protect the entrance and no such shelter was provided. The entrance to the marina was kept narrow, at 33 m width, in order to minimise the amount of wave energy entering. However, even with this narrow entrance full height waves can enter the marina and affect the boats and outer marina berths.

#### Aims

The object of the breakwater design was to provide shelter for the marina at least cost. A stone breakwater in the 4 m deep water would have been very expensive and would have occupied an unacceptable width of the river channel. A steel sheet pile breakwater would have been even more expensive and would have both reflected waves across the navigation channel and deflected some of the tidal flow. Floating breakwaters were considered but were not considered to provide a sufficiently positive breakwater. The final design used a spaced pile breakwater which has proved satisfactory when used in conjunction with robust steel tube marina berths in the area facing the entrance.

## Breakwater Design

Model tests to a 1:12 scale, were carried out in a wave flume at the Auckland University School of Engineering, and showed that a 50% reduction of wave height could be obtained by using vertical 300 mm timber piles spaced 37 m apart. This spacing gave a horizontal force of 22 kN per linear metre of breakwater. The force on a solid breakwater would have amounted to 53 kN per metre. These results compare well with those reported by Grüne and Kohlhasse (1) and Hayashi et al. (2).

This reduced load from spaced piles allowed a breakwater to be built using treated pine piles supported on an orthodox plumb and raker pile structure, Fig. 3.

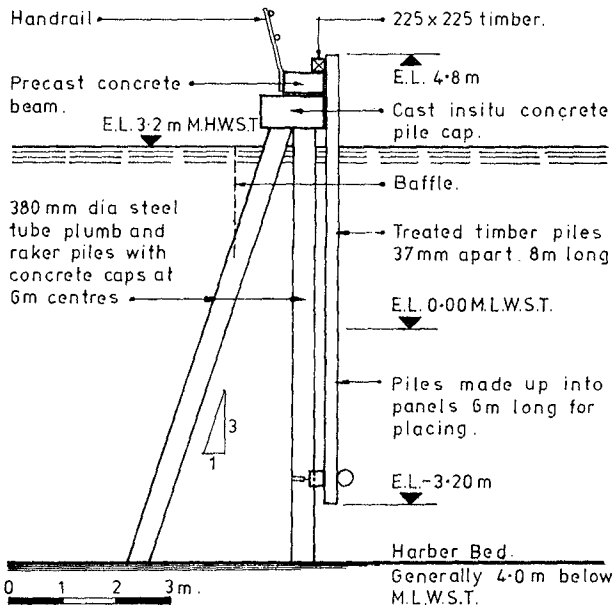


Figure 3 : Typical cross section of the breakwater

It was also found that a barrier 2 m deep, 1.5 m behind the spaced pile breakwater provided very effective additional wave energy dissipation without significantly increasing the loading. The water level in this gap oscillated gently up and down. With this additional skirt the wave height transmitted was reduced to 30%. However, this secondary barrier was not used in final design.

### Breakwater Construction

Site investigations showed that there was no firm ground at a reasonable depth on which to found point bearing piles. It was therefore decided to use friction piles. To assess their friction capacity a factor of safety was applied to the shear strengths of the clays encountered. The 6 mm thick 380 mm diameter plumb and raker piles at 6 m spacing were driven using a 1 ton hammer striking on a pad about 2 m of sand and gravel in the bottom of the pile. The piles were filled with sand to 3 metres below the top and the top portion was filled with concrete reinforced to connect the piles to the cast in situ cap which supported the longitudinal precast concrete beam.

The upper 10 m of piles were sandblasted and treated with epoxy tar. The lower sections of the piles, which were in the harbour bed, were left untreated.

The spaced timber piles were prefabricated ashore into 6 m long panels and placed by a crane into position. The panels were supported by the precast concrete at the top and were fixed to the vertical steel piles at the lower end.

### Breakwater Maintenance

Virtually no maintenance has been required during the first twelve years of the breakwater's life, except that in 1983 it was found that some of the timber piles were loose and inspection by divers found that the bolts fixing the piles to the lower walings were pulling out. It was also found that the U bolts used to fasten the lower end of the panels to the vertical steel piles had failed.

In 1984 a contract for NZ\$56,000 was let for the repair of the breakwater. A detail, using 19 mm mild steel plate and 36 mm mild steel bolts was used to replace the original U bolts and timber yokes. The exposed steel bolts and nuts were wrapped in 'Denso tape'. It was found that the original 19 mm bolts and their threads were sound and that in all cases the nuts had corroded, sometimes completely, leaving the thread intact. The vertical piles bolted to the horizontal walers had also come loose due to the corrosion of the nuts with the bolts again left relatively intact.

Analysis of the steel has shown that different steels had been used to make the nuts and bolts and this led to an electrolytic action and corrosion of the nuts.

The pinus radiata piles had been treated with a copper chrome treatment to a concentration of 22 lbs per cubic foot (350 kg per m<sup>3</sup>). To date there has been no indication of marine borer attack of the piles.

### Marine Design

The floating marina was constructed using timber walkways supported on fibreglass pontoons. In New Zealand, because of the frequent strong winds experienced, boats are usually moored in marinas to float

clear of piles and the marina structure, using four mooring lines, Fig. 4. With this method of mooring boats need little supervision and fenders are not required. At Half Moon Bay it is only the marina berths near the entrance where the sea condition has caused deterioration of the timber marina structure. During northerly winds the waves which enter the marina through the entrance, combined with the half wave height entering through the spaced pile breakwater, cause a considerable amount of wave disturbance over the area just inside the entrance.

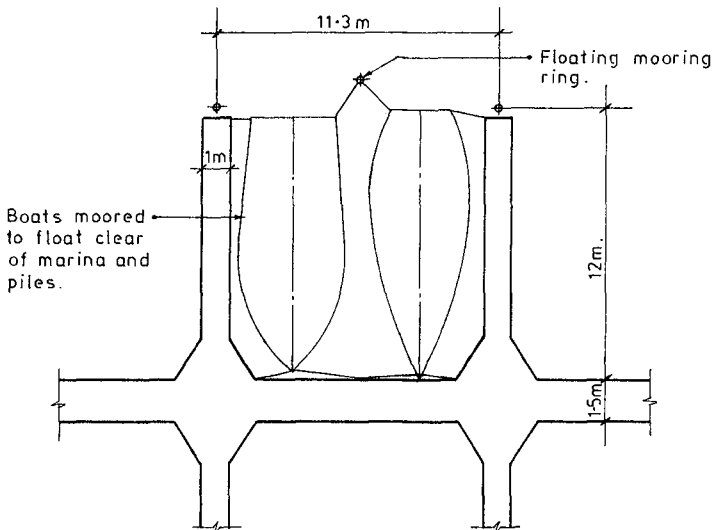


Figure 4 : Typical dimensions of the marina, showing the four line mooring system

The end fingers near the entrance have now been replaced using continuous 600 mm diameter steel pipe, Fig. 5, to support the walkway and fingers. This construction was first used over 20 years ago when the first marina berths were built by the Auckland Harbour Board at the Westhaven boat harbour.

#### Conclusion

A spaced pile breakwater has provided satisfactory economical shelter to a 485 boat marina. Only near the entrance did the original timber structure of the marina berths deteriorate due to wave action and it has been necessary to replace the light timber and fibreglass marina and fingers with more robust continuous 600 mm diameter steel pipes. Boats are moored to float clear of the fingers and do not require fenders.

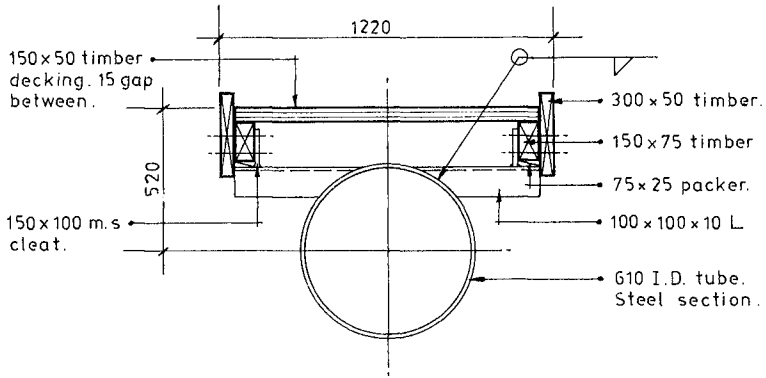


Figure 5 : Typical section through walkway

#### Acknowledgements

The authors wish to thank the Auckland Maritime Trust for permission to publish this paper.

#### References

1. GRÜNE, J. and KOHLHASE, S., Wellentransmission an Schlitzwänden, Die Küste, Vol. 27, 1975, 74-82
2. HAYASHI, T., KANO, T. and SHIRAI, M., Hydraulic Research on closely spaced pile breakwater. Proc. 10th Conference on Coastal Engineering, Tokyo, 1966, Vol. 2, 873-884

## CHAPTER ONE HUNDRED SEVENTY

### NEW TYPE BLOCKS FOR SEAWALL SLOPE PROTECTION

Osamu Toyoshima\*

#### 1. INTRODUCTION

Japan is a mountaineous country, and coastal areas have been looked upon quite valuable.

In most cases, shorelines were slightly advancing until 1950, although there are some exceptional coasts which have been under continuous erosion for more than a thousand years.

However, in the last thirty years, beaches began to be eroded one after another, and the countermeasure against beach erosion has become one of the most important problems in the national land preservation.

Since the early 1960's, many seawalls against the beach erosion have been constructed. The table shows the amounts of the shore protection works constructed in the last twenty years.

Total length of the coastline of Japan	34 064 km		
Year	1962	1972	1982
length of seadikes	1818 km	2566 km	2889 km
length of seawalls	2686 km	4752 km	5665 km
number of groins	5448	8747	9790
number of detached breakwaters	205	544	2831

Seadikes have been extended gradually year by year, seawalls and groins show great elongation. And, detached breakwaters also show a remarkable development in the last ten years. The elongation percentages of these shore protection works in these twenty years is seadikes 1.59, seawalls 2.11, groins 1.80 and detached breakwaters 13.81.

Most of the seawalls constructed before 1975 were vertical ones, and mechanism of beach erosion had not exactly been known those days. As a result, some of the seawalls even encouraged the beach erosion contrary to expectation.

The author then, proposed new types of seawalls. The first type was the "Block faced seawall" whose front slope was covered with some artificial concrete blocks such as armour units, and the second type was the "Lattice type seawall".

---

\* Prof. Dr. Faculty of Marine Sci. & Tech. Tokai University  
Orido 3-20-1, Shimizu-shi, 424, JAPAN

The details of these works were presented by the author, on the 16th I.C.C.E., titled "Effectiveness of seawalls with rough slope".

Block faced seawalls have been used on several coasts in Japan for the past ten years or so. Most of these seawalls have turned out to be successful, in spite of the fact that they have to be connected with extra hooks to attain sufficient solidarity.

Recently, the author invented a new type of concrete blocks for slope protection works of seawalls, which need no hooks for connection, named "Lotus-Uni".

This paper describes the characteristics of "Lotus-Uni" and experimental works of seawalls using them.

## 2. DEFECTS OF VERTICAL TYPE SEAWALLS

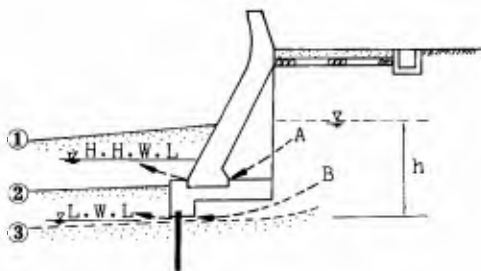


Fig.1 Typical vertical type seawall

In Fig.1,

- ① is the shore just after the construction of the seawall.
- ② incident waves were violently reflected on the steep front slope of seawalls, and foreshore and the toe of seawalls were washed out with the reflected waves like this.
- ③ then, sand is completely washed out.

And furthermore, by the water pressure difference ( $h$ ) between outside and inside of the seawall facing, not a little amount of sand are drawn out with jet streams like A and B in Fig.1 through the small hall in the seawall facing.



Photo.1 Backfill sand is drawn out



Photo.1 shows a typical case where the backfill sand is drawn out. Soon after these phenomena, vertical type seawalls collapsed like Photo.2



Photo.2 Vertical type seawalls collapsed

### 3. AN EXAMPLE OF BLOCK FACED SEAWALLS IN SHIZUOKA COAST

After many field experiences, the author pointed out that, the problems to be considered for the new seawalls were as follows;

- 1) to decrease the reflected waves from the front of seawalls as much as possible.
- 2) to make the front face more rough.
- 3) to make the front face permeable.
- 4) some partial collapses should be allowed, but never be destroyed the whole body of the seawalls.
- 5) repair and reinforcement should be easy.
- 6) structure should be simple and low cost.

The author proposed block faced seawalls as a new type seawalls, and the first large-scale works have been carried out on the restoration works of collapsed seawalls in Shizuoka Coast under the author's guidance.

Fig.2 shows the previous structure and cross section of Shizuoka Coast before the destruction which occurred in March 1977. Since the 1970's, the Shizuoka Coast has turned into a erosive coast. The seawalls of this coast were constructed before 1970.

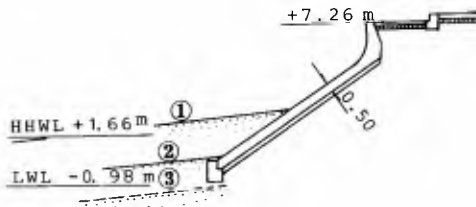


Fig.2 Structure and cross section before the destruction

In Fig.2,

- ① is the shore when the seawalls were constructed in 1961.
- ② just before the destruction in March 1977.
- ③ just after the destruction.

After the first destruction in March 1977, the seawalls in Shizuoka Coast have been broken down by the violent waves one after another. The position of collapsed seawalls are shown in Fig.3.

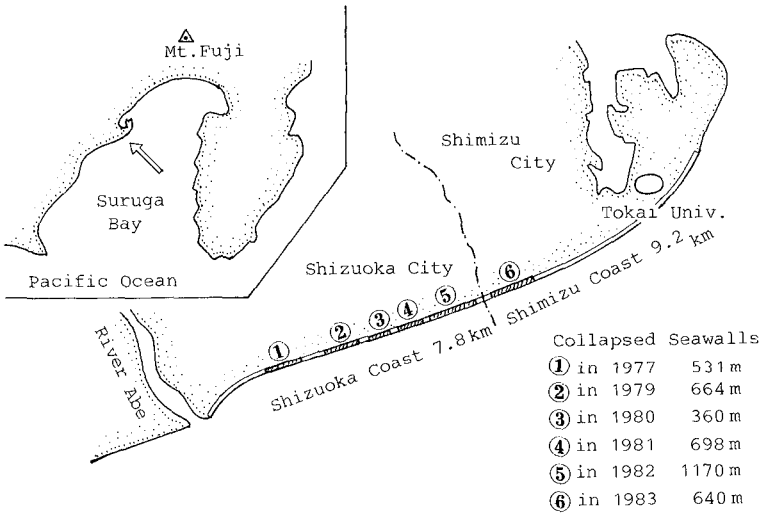


Fig.3 Position of collapsed seawalls

Instead of usual concrete facing, concrete block facing works was used as the restoration works, according to my proposal. Fig.4 shows the structure of the restoration works using the block facing.

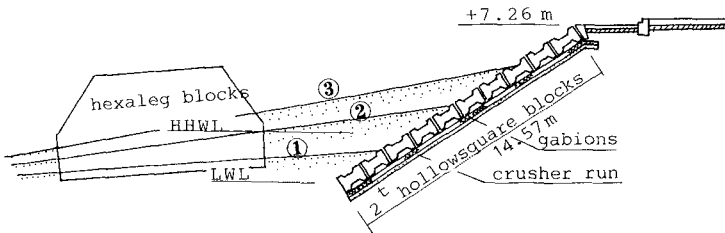


Fig.4 Structure of restored seawalls with block facing

In Fig.4,

- ① is the shore at the starting works, in August 1977.
- ② is the shore at the completion of the works, in May 1978.
- ③ is the shore in May 1984.

Before the destruction, the beach had been eroded year by year. But, after the restoration works, the beach finely recovered and sand accumulated as about ten years ago.

Photo.3 shows the seawalls in 1978 one year after the restoration works. Four blocks are under the beach, and six are seen.

Photo.4 is the later view of the coast. The blocks are covered with sand up to the second step, then eight blocks are under the sand beach. Now the beach looks very stable.



Photo.3 Restoration works completed (1978)



Photo.4 The beach recovered finely (May 1984)

We have been talking about the first destruction in Shizuoka Coast, the position (1) in Fig.3.

After this restoration works, another destructions from the position (2) to (5) occurred consecutively, and all of them are restored in the same way as the above.

All of these restored seawalls were never destroyed again, and these block faced seawalls have proved to be successful.

However, they had to be connected with extra hooks to attain sufficient solidarity.

Recently, the author invented a new blocks, which need no hooks for connection, named "Lotus-Uni".

#### 4. CHARACTERISTICS OF THE "LOTUS-UNI" BLOCK

Fig.5 shows the plane and profile of the Lotus-Uni block. The block has three models according to its weight. Each model has same face, only the thickness is different.

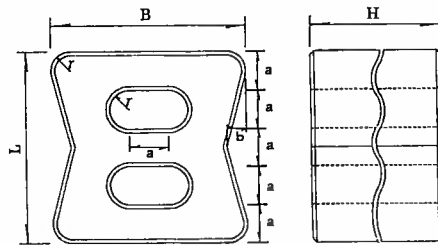


Fig.5 Lotus-Uni block

Model	B	L	H	Weight
50H			50 cm	2 ton
75H	1.5 m	1.5 m	75 cm	3 ton
100H			100 cm	4 ton



Photo.5 Lotus-Uni block ( Model 50H, 2 ton)

The blocks have good close connection with one another, and there is no necessity for hooks (Fig.6).

Even if a block (black one in Fig.7) is removed, there is little room to move for the six blocks around(hatched), because blocks are holding mutually.

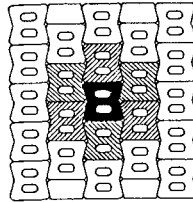
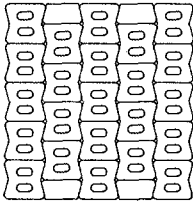


Fig.6 Facing style      Fig.7 Remove a block(black one)

## 5. NEW TYPE SEAWALLS FACED WITH "LOTUS-UNI"

### 5.1 Characteristics

Standard cross section of the seawalls faced with Lotus- Uni is shown in Fig.8.

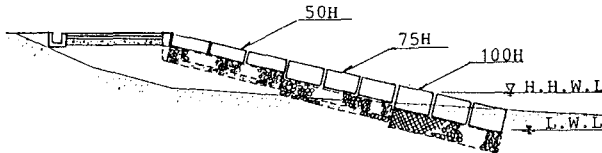


Fig.8 Seawalls faced with Lotus-Uni block

Characteristics of this type seawalls are as follows.

- 1) There is no use for foundation, cut-off walls or steel sheet piles.
- 2) Blocks differ only in thickness, and different type of blocks can be used together on one slope as Fig.8.
- 3) The structure of this type of seawalls have flexibility, roughness, looseness, and chain connection like gabions. Once faced, these blocks shall hardly be decomposed by wave powers.

### 5.2 Example works

An experimental work of the new type seawall using Lotus- Uni block has been carried out on Muroran Coast, Hokkaido prefecture, Japan, facing the Pacific Ocean.

In this work, model 50H (2 ton) block is used on all the slope. The cross section of the work is like Fig.8.

There are no foundation and other shore protection works. The grade of the front slope is 1:3, and the number of blocks per slope is nine.



Photo.6 Soon after the completion (1982)

Photo.6 shows the seawall soon after the completion in 1982. The foundation blocks were set on the shoreline of the low water level, and there was no foreshore in front of the seawall. The uprush runs up with sand and gravel on the slope.



Photo.7 Uprush are sucked into the holes

Some of the uprushes are sucked into the holes of the block, and the back rush decreases.

The velocity and the volume of the backrush become slow and small. Then, the reflected waves become weaker, and the erosive beach turn into an accumulative one.



Photo.8 Gravel are left on the toe of the seawall

Sand and gravel, came from the offshore and included in the uprush, are left on the slope, in the holes and the toe of the slope of the seawall.

Eight or nine blocks are seen on the slope.



Photo.9 One year after the photo.8

More than ten meters long foreshore has grown in front of the seawall. Four or five block are to be seen, and five or four blocks are under the sand beach.

Sand has accumulated gradually and surely.



Photo.10 The latest view of the beach (1984)

The shoreline has advanced substantially, and the sand beach has grown extensively.

#### 6. CONCLUSION

The author invented a new type blocks for seawall slope protection. Now, twenty or more experimental works using the Lotus-Uni block are being carried out in Japan for the countermeasures against the beach erosion.

The collapsed seawalls in Shimizu Coast, the position(6) in Fig.3, were restored with Lotus-Uni block lately.

Most of these works are apparently successful.

#### 7. REFERENCES

Toyoshima, O. 1978: Effectiveness of seadikes with rough slope. Proceedings of the sixteenth Conference on Coastal Engineering, ASCE, Vol.3, pp.2528-2539.



## CHAPTER ONE HUNDRED SEVENTY ONE

### DETAILED DESIGN OF A WAVE ENERGY CONVERSION PLANT

G de F Retief<sup>1</sup>, FPJ Müller<sup>2</sup>, GK Prestedge<sup>3</sup>,  
LC Geustyn<sup>4</sup>, DH Swart<sup>5</sup>

#### ABSTRACT

A preliminary assessment of wave energy conversion by means of the Stellenbosch Wave Energy Converter (SWEC) has indicated the viability of this system as a supplementary source of electric power.

In order to refine the preliminary estimates of the cost of power delivered, detailed design of a 770 MW (rated output) installation at a site 60 km north of Cape Town has been undertaken.

This paper describes the power conversion characteristics of the SWEC at the proposed site, structural design of the collector arms and generating tower for both mass gravity or piled solutions, a construction scenario involving a casting harbour in nearby Saldanha Bay and the towing and placement of 53 m long precast modules, and finally an assessment of the environmental impact of the proposed 40 km array on the adjacent coastline.

The proposed system is found to be both technically and economically feasible and offers a useful contribution towards future electric power supply.

#### 1. INTRODUCTION

The Stellenbosch Wave Energy Converter (SWEC) is a shallow water device developed over a number of years to meet the specific requirements for wave power utilisation along the south western coast of South Africa. An analysis of the wave power resource along this coast as well as a full description of the development of the SWEC are presented in Retief et al. (1982).

- 
1. Professor, Ocean Engineering, University of Stellenbosch, Stellenbosch, South Africa, 7600.
  - 2,4. Research Engineer, Ocean Engineering Research Group, University of Stellenbosch, South Africa, 7600.
  3. Associate, Watermeyer, Legge, Piesold & Uhlmann, P O Box 6433, Roggebaai, South Africa, 8012.
  5. Sediment Dynamics Division, National Research Institute for Oceanology, C.S.I.R., P O Box 320, Stellenbosch, South Africa, 7600.

The objective of the present project was to produce an in-depth analysis of a potential application of the SWEC with reliable projections of future costs and operation management. The site chosen had been identified in the previous study as one of the more favourable locations for wave power conversion and the overall design philosophy described in Retief et al. (1982) was adhered to throughout this investigation.

Although the general characteristics of the device had been determined in the previous study a further series of field and hydraulic model studies were required for the determination of design parameters and power conversion characteristics specific to the site. Model studies of the rectified airflow, generated by the SWEC, led to a detailed design of the air turbine/power generation system. A theoretical analysis of prevailing littoral processes provided input for an environmental impact assessment of the proposed array on the adjacent coastline. Sedimentation in the immediate vicinity of the converter was studied both theoretically and empirically. Final costing was based on a construction and management scenario developed in conjunction with a team of coastal engineering consultants and contractors.

## 2. CONVERTER CONCEPT

A typical converter unit, which would form part of the total power conversion array, is shown in Figure 1. For the site under consideration in this project the unit is to be installed in an average water depth of 14 m (i.e. 2 m submergence), approximately 1,5 km off-shore. The two collector arms forming the "V" are 160 m long orientated at 45° to the predominant direction of energy flux at the site. Each arm comprises three precast concrete modules, each containing four chambers in which the water level oscillates. Each oscillation chamber is connected via rectification flap valves to the high and low pressure, closed-system air ducts which merge at the apex of the "V" to form the two legs of the generator tower. An axial flow air turbine mounted horizontally in the tower cabin converts the differential pressure between the two air ducts to mechanical power which in turn drives an alternating current electric generator. The module section shown in Figure 1 relates to the gravity design option - the alternative piled option is shown in Figure 14.

## 3. PROPOSED SITE

The proposed site for the converter array is shown in Figure 2. This 40 km long stretch of coastline, consisting of North and South Bays, is directly exposed to the almost unrefracted south westerly swells which are the cause of the peak levels of wave energy occurring along this section of the Southern African coast (Geustyn, 1983).

The study area has been well instrumented in the past and reliable wave height and direction data for the site are available. Mean annual wave power levels of about 30 kW/m are found in-shore at the generator site, which is conveniently situated, between the urban growth points of Saldanha and Cape Town, near to the national electric power network. The converter array will consist of 154 "V" units with a 770 MWe rating and mean winter capacity of 450 MWe.

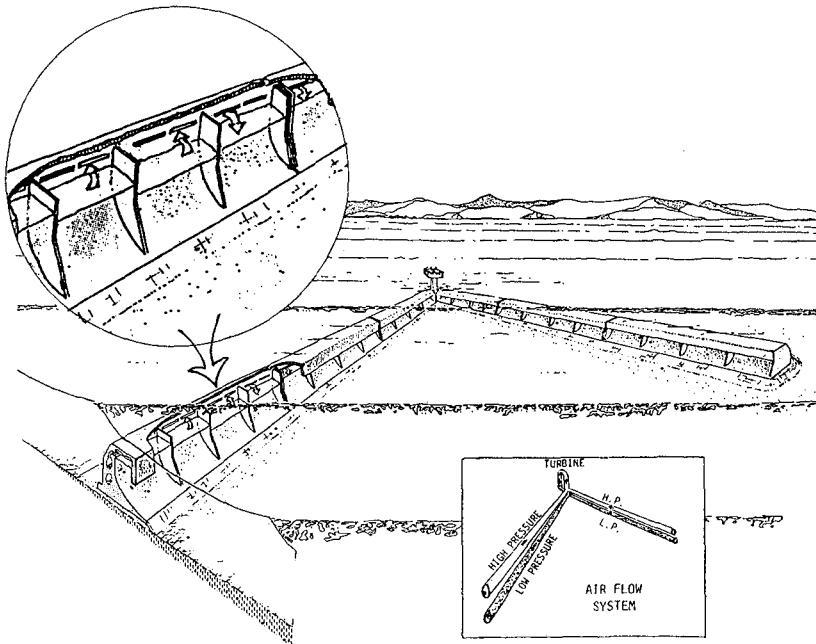


FIGURE 1: Typical Layout of Wave Energy Converter

The two bays comprise sandy beaches with an average off-shore slope of 1:100, bounded at each end by a rocky headland. Nett littoral drift is northwards. Off-shore currents are weak and variable and the mean tidal range is 1,0 m diurnal.

A variety of analyses were performed on the available wave data - typical seasonal distributions of wave power were presented in Retief et al. (1982), wave direction characteristics are shown in Figure 3 and long term fluctuations (measured over a five year period at a station at the southern end of the array in 23 m water depth) are shown in Figure 4. The long term analysis produced a maximum deviation from the five year mean of  $\pm 5\%$  for the mean annual power level and  $\pm 20\%$  to  $30\%$  for the mean seasonal power level. As with all forms of fluctuating alternative energy sources a feasibility study of wave power utilisation should include an analysis of the probable occurrence and duration of periods during which the power available falls below some prescribed demand level. Figure 5 shows a Weibull distribution, based on five year's data, of the return period and duration of "calm" events where "calm" is defined by the level of wave power not exceeded during that period.

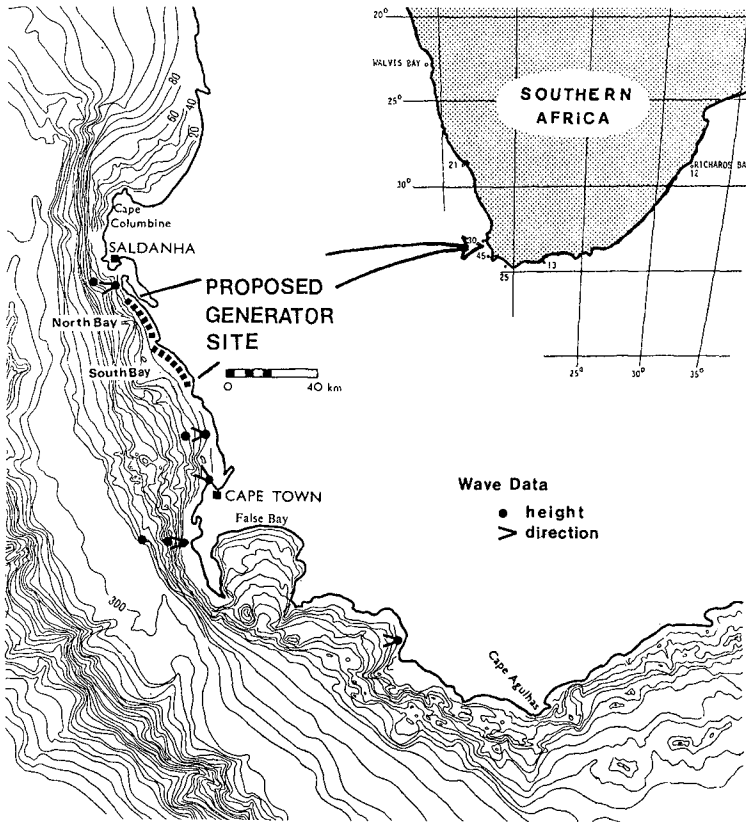


FIGURE 2: Proposed Generator Site

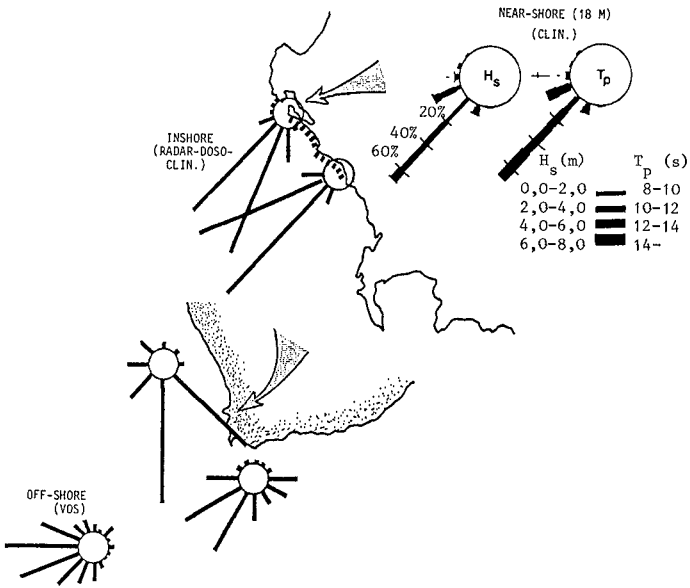


FIGURE 3: Wave Direction Analysis

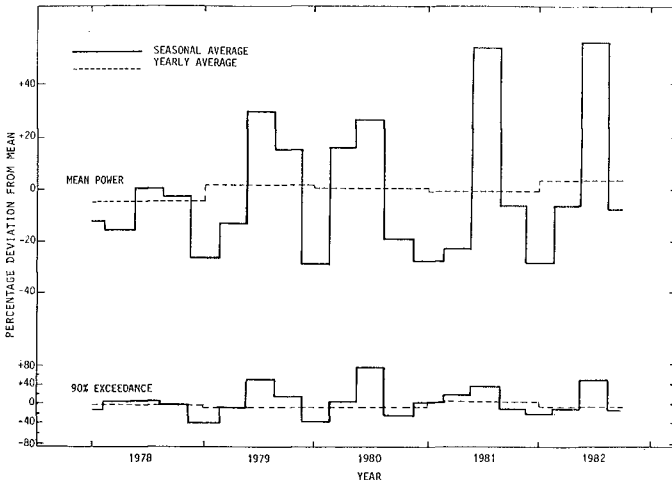


FIGURE 4: Seasonal and Yearly Variation in Wave Power

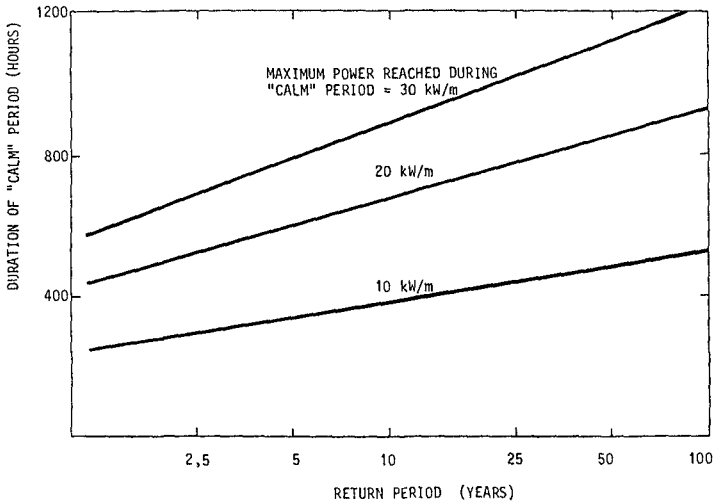


FIGURE 5: Duration of "Calm" Periods vs. Return Period

4. MODEL STUDIES

The physical and theoretical models which were used in the optimisation of the converter array design are summarised in Table 1.

Hydraulic Models	1:60	3-D	Irregular Wave	Conversion Design
				Sediment Studies
	1:50	2-0	Regular Wave	Internal Geometry
	1:100	2-0	Regular / Irregular	Structural Design
Theoretical Studies	LINREF Model (Crowley 1984)			Wave Refraction
	Regression Model (Swart 1976)			Extent of On-/Off-shore Transport
	Analysis based on Evans (1982)			Collector Arm Optimisation

TABLE 1: Model Studies for Converter Design

4.1 Power Conversion

Figure 6 shows the 1:60 scale three-dimensional model of a "V" unit being tested in the irregular wave tank of the National Research Institute for Oceanology of the South African Council for Scientific and Industrial Research. A schematic section of the model in Figure 8 shows the submerged oscillation chamber scaled according to Froude and the airflow system constructed to Reynolds scaling above water level.

Parameters monitored continuously by computer included air pressure at various locations, airflow in both collector arms, and water level both inside and outside the collector arms. The airflow throttle was set at an optimum pressure/flow ratio of 30 pascals per  $m^3/sec$ . Although the air system was not a correct reproduction of the prototype unit, non-linear duct losses are greater at model scale than at full scale (especially for irregular wave spectra at higher energy periods) and the results were considered to be conservative.

An example of a typical Pierson Moskowitz test spectrum is shown in Figure 7. Variables considered in the test series included water depth/structure height, submergence depth, angle of wave attack, swept angle of "V", collector arm geometry, incident and transmitted wave characteristics.



FIGURE 6: Three-dimensional Irregular Wave Tests

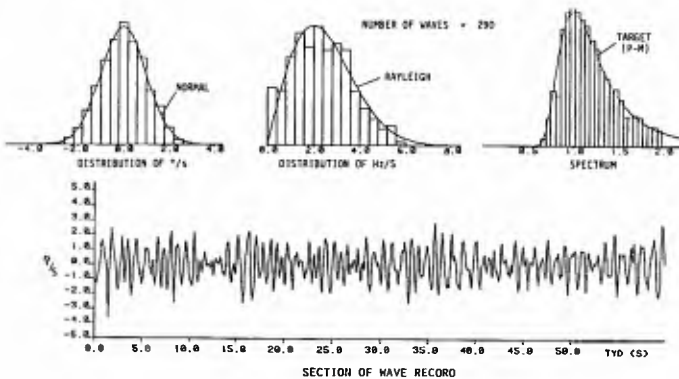


FIGURE 7: Analysis of Generated Irregular Waves

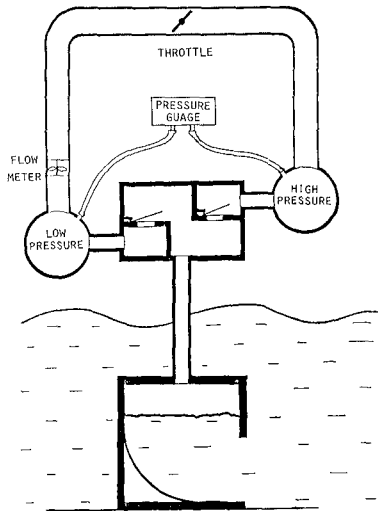


FIGURE 8: Schematic Diagram of Three-dimensional (1:60 scale) Model

The "V" shape of the collector arms not only enhances wave power conversion capability by reflecting "trapped" energy from one arm to the other, it also transmits the greater proportion of the unconverted energy shorewards. This relatively high transmission coefficient reduces the potential impact of the device on the shoreline, and is probably caused by non-linear effects along the collector arm which reduce the effective reflection angle of a wave slug.

In studying the frequency response of the "V" for different collector arm lengths it was found that the converter responds optimally to the zero crossing period,  $T_z$ , of the spectrum and not the peak or energy periods as had been expected. As the SWEC is not a tuned resonator it can be theorised that optimum "coupling" with the incident wave profile would occur at a period which reflects average fluctuation of the water surface ( $T_z$ ).

Directional sensitivity produced very favourable results when compared with the narrow direction spectrum measured at the proposed site. Figure 9 shows that 90% of the wave directions measured at the site fall within the 95% direction dependent conversion efficiency.

The percentage occurrence of power generated at discrete power intervals for one "V" converter is shown in Figure 10. This analysis was based on a 22 month wave record from the proposed site. The average rate of power conversion for the 22 month period is 2,2 MWe per "V", while the winter average was found to be 2,9 MWe per "V" (450 MWe winter average for the full array). The available and generated power in percentage exceedence form is given in Figure 11.



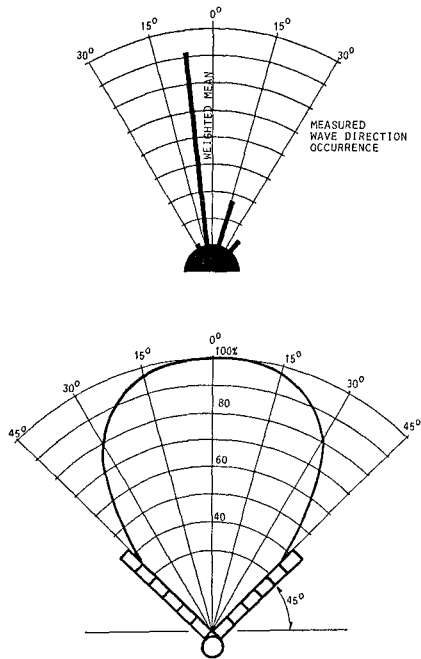


FIGURE 9: Relative Conversion Efficiency with Direction

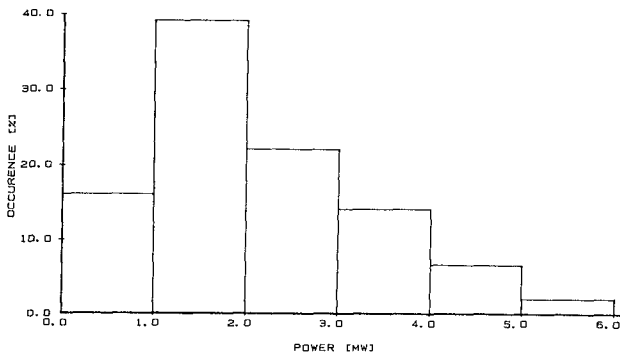


FIGURE 10: Occurrence of Power Generated for Period June '80-April '82

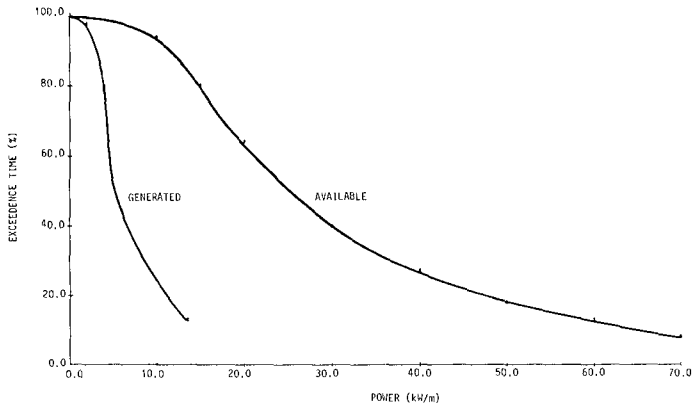


FIGURE 11: Cumulative Power Exceedence (Available and Generated)

## 4.2 Stability Design

The SWEC has a relatively complicated form compared with the cylinders or spheres for which wave force data have previously been published. As no data were available for structures with water depth to structure height ratios as low as 1,4 (an area where modelling of the free surface becomes significant) it was decided to revert to a two-dimensional model study as a first attempt at determining design forces. The tests were conducted at scales of 1:100 and 1:60 and are described in Morrison and Geustyn (1984). Figure 12 shows peak values of the normalised horizontal force ( $f_x$ ) acting on the converter plotted against a dimensionless wave amplitude for various water depth/structure height ratios, where:

$$f_x = F_{x\max} / \rho g a a_0$$

and

$$a = \text{structure height}$$

$$a_0 = \text{amplitude of incident linear wave } (= H/2)$$

$$k = \text{wave number}$$

The measured curves are compared with those of previous similar studies and are found to display similar trends but with a more rapid reduction in force for higher  $ka$  values due probably to the compliant nature of the front face caused by the opening.

By ignoring wave period and assuming a linear relationship between wave height and applied force Morrison et al. were able to compile a set of simple design curves for various water depths, which were used in the later structural design.

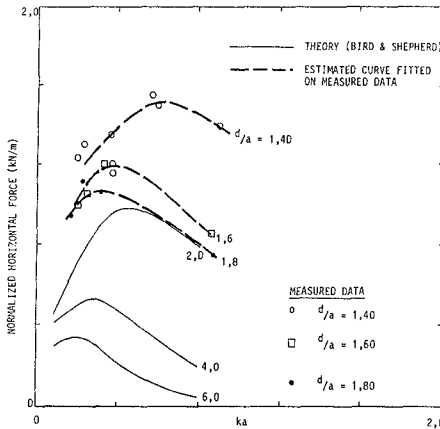


FIGURE 12: Horizontal Wave Force on Structure. Theoretical and Measured (Morrison & Geustyn 1984)

To resist forces acting on the structure two design options were pursued. The one made use of a mass gravity solution which was model studied at a scale of 1:60 (Figure 13). The other solution entailed a theoretical analysis of a piled structure. Both were based on a maximum wave height/depth limited design condition. The design of the generator tower was handled in a similar manner. The force on the deck slab due to water column deceleration against the entrapped air cushion was determined by analytical modelling.

The finally selected sections are shown in Figure 14. Both would be placed by barge onto a prepared rubble bed. The gravity section is designed to be fully stable, immediately after placement, in the flooded mode. The mass surcharge introduced by the backfill, which is later placed by barge, is designed to accommodate the instability introduced by pumping air into the system when power generation commences. As the construction window on the piled option is more limited, driving of the 1,5 m diameter steel piles from a jack-up rig would commence immediately after placement. Both sections caused severe erosion of the seaward toe and a bitumen grouted apron of 2 t selected rubble was found to solve this problem. After the units have been secured on the bed the air ducts will be joined underwater by means of a flexible coupling specially designed for this purpose.

#### 4.3 Sediment Studies

Sediment deposition and erosion in the immediate vicinity of the converter was studied in the three-dimensional 1:60 scale model, qualified by a theoretical prediction of seabed stability. It was found that under the predominant wave conditions the position off-shore is such



FIGURE 13: Two-dimensional (1:60 scale) Stability Tests

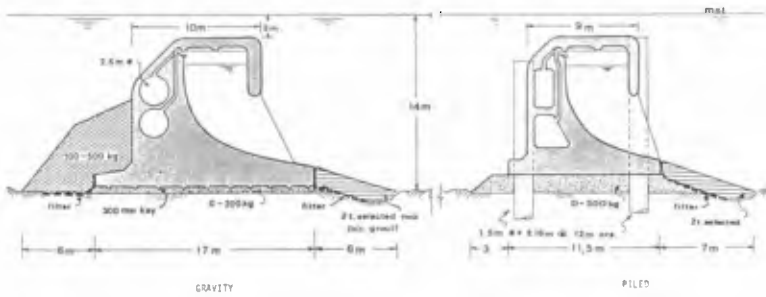


FIGURE 14: Alternative Installation Methods

as to be beyond the dynamic sediment swept prism. Under storm conditions a bar was found to occur in the apex of the "V". Further long term build-up or dissipation of this mound has yet to be determined in a more rigorous analysis of the processes involved. The possible need for a sand by-pass or maintenance pumping station has thus not yet been determined. From the data of wave transmission across the converter, determined in the 1:60 scale three-dimensional model, an estimate was made of the overall impact that the array would have on the prevailing on-shore/off-shore sediment processes in the bays. The anticipated seawards shift of the beach line is likely to be between 10 m and 20 m. An anomalous situation could occur at each end of the array due to a discontinuity in long-shore drift rates. To reduce this effect the array is planned to extend as far as the bordering headlands in each bay.

#### 4.4 Airflow System Design

The rectification valves mounted in the plenum chamber above each oscillating water column will consist of 300 mm high plied rubber or neoprene flaps, with directional reinforcing, housed in a removable module. A buoyant splash flap will be installed at each valve opening immediately below the air cushion chamber. It is anticipated that an annual clean-up of the valves will be required to remove marine growth. This will probably entail removal of the complete valve module and its replacement with a serviced module while the converter is in a flooded mode.

Each collector arm will have an airflow throttle control, housed in the generator tower, to damp vertical displacement of the water surface in the oscillation chamber and limit power conversion during storm events. A typical example of airflow surging through the turbine caused by wave-beat is shown in Figure 15.

#### 4.5 Electro-Mechanical Power Conversion

Design parameters for the 3.5 m diameter, 8 m long axial flow variable pitch turbine are summarised in Figure 16. Airflow speeds of up to 100 m/sec will be experienced at the turbine. To counteract water drop erosion of the blades a nickel-aluminium-bronze or stainless-steel tipped G.R.P. construction is being considered. Anticipated maintenance includes an annual cleaning and inspection and 25 year replacement of the turbine. Conversion efficiency of the electro-mechanical system is estimated at 75%.

The variable pitch constant speed turbine will be directly coupled to a 5 MVA, 22 kV synchronous electric generator. The "V" units will be interconnected in groups of six, with each group connected directly to the national electricity supply grid by means of a 1.5 km long 22 kV, 35 MVA seabed cable.

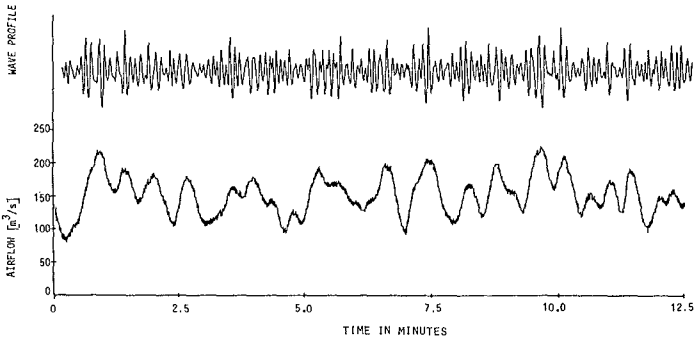


FIGURE 15: Typical Wave Train with Resulting Airflow through Turbine

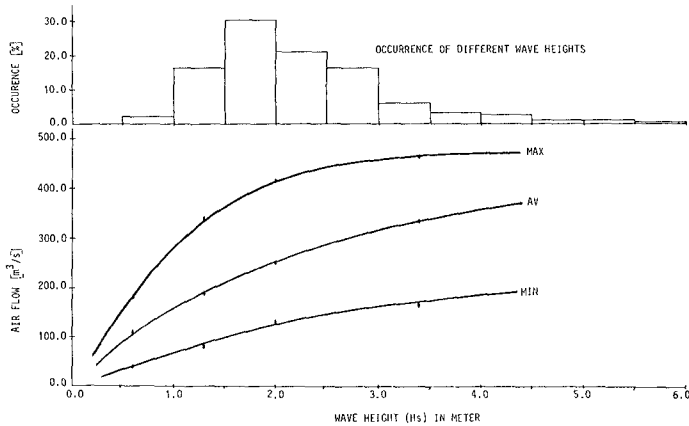


FIGURE 16: Airflow vs. Wave Height

5. LAYOUT AND CONSTRUCTION

A full set of wave refraction diagrams covering five deepsea directions ( $180^{\circ}$ ,  $210^{\circ}$ ,  $240^{\circ}$ ,  $270^{\circ}$ ,  $300^{\circ}$ ) and six periods (10,5; 12,3; 13,9; 15,2; 16,4; 17,5 secs) were compiled for the proposed site. This analysis identified the distribution of wave power along the shore, the long-shore energy flux along the 15 m contour and the optimum orientation for installation of the converter units. Figure 17 is an example

of the most dominant south westerly swell ( $240^{\circ}$ , 12,3 sec) approaching North Bay with a series of typical direction roses used for optimum converter orientation.

Figure 18 shows an artists rendering of the construction phases envisaged. Construction of the complete array has been planned to extend over a five year period after an initial preparation lead time of two years. The precast modules will be assembled in a specially constructed casting harbour within Saldanha Bay and towed to site suspended from a placement barge. The lowering of units onto the horizontal berm will commence at the apex of the "V". Each subsequent unit will be winched up to the previously placed unit to a tolerance of 500 mm and the flexible duct connectors will be installed, followed by the ballast rubble or piling by jack-up rig. The turbine/generator unit will be winched up directly into the tower cabin from a transport barge which will be temporarily moored between the tower legs.

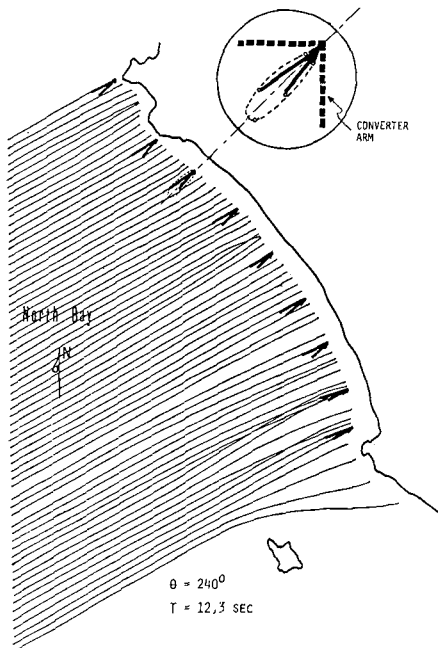


FIGURE 17: Converter Orientation Studies

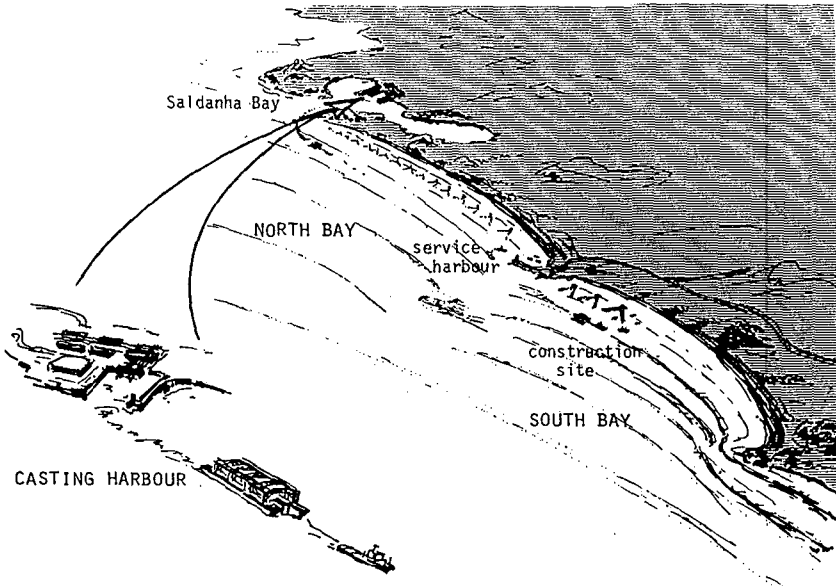


FIGURE 18: Construction Scenario

## 6. MAINTENANCE AND COSTING

Apart from the annual servicing of the flap valves and generator unit, maintenance of the converter is expected to be relatively low and not to exceed an average present day cost of (RSA) 0,6 cents per kWh over the design lifetime of 50 years. Marine growth in the submerged section of the oscillating chamber is expected to stabilize at a thickness of 120 mm and has not been found to affect conversion efficiency. Water is expected to accumulate in the air ducts and turbine chamber and will be drained to collector points and automatically pumped out. An optimum air volume in the converter will be maintained by an electricaly driven air pump housed in the generator tower. Navigation lights will be mounted at each end of the "V" and on the generator tower.

As the "elasticity" of the national electricity supply network can easily accommodate the expected variability in supply from this relatively minor source of power, costing has been based on total utilisation of the output from the converter array, which for an average year is 2,2 GWh of power delivered to the network (i.e. 14300 MWh per "V" per year).

The capital cost of a single "V" unit (based on the gravity option which was found to be less than the piled structure) is estimated at (RSA) R8,3 m. The projected cost of power delivered covers a range of values depending on the combination of financial parameters assumed. For an economic horizon of 30 years, an interest rate of 15% and an inflation rate of 12%, the present day cost of power delivered (discounted at 10%)



ranges from 2,6c/kWh (for a power tariff coupled to inflation) to 4,3c/kWh (for a tariff increase rate equal to 80% of inflation rate).

These figures compare very favourably with the present cost of nuclear power (RSA 5,6c/kWh) and coal fired power (RSA 4,7c/kWh) for the same area (SAICE, 1984).

## 7. CONCLUSION

The proposed 770 MW (rated output) wave power converter has been studied in sufficient detail to establish both a predictable means of implementation at what is considered to be a reliable estimate of the costs involved. An attempt has been made throughout the study to adopt a conservative approach to those areas which are as yet unproven. The system proposed is however well within the capability of present day technology and as there is scope for further reduction in the projected costs (by more rigorous optimisation of the civil engineering design vis-a-vis power conversion) the SWEC is considered to be a viable and attractive supplementary source of power.

## ACKNOWLEDGEMENTS

The authors gratefully acknowledge the financial and technical support of their sponsors and the various organisations who made their time and facilities available for this study.

## REFERENCES

- CROWLEY, JB, (1984): The use of the LINREF-Refraction Program on the CDC. NRIO Technical Report - In Preparation. CSIR, Stellenbosch.
- EVANS, DV, (1982): A comparison of the relative hydrodynamic efficiencies of alternator and terminator wave energy devices. Proc. 2nd Intl. Symp. on Wave Energy Utilization, Trondheim, 1982.
- GEUSTYN, LC (1983): Wave energy along the South African coastline - an evaluation of the time and spatial distribution. Presented in partial fulfillment of the M.Eng. degree at the University of Stellenbosch (in Afrikaans), Stellenbosch, 1983.
- MORRISON, DG and GEUSTYN, LC, (1984): Determining submerged wave energy structure design forces in shallow water. To be presented at the 4th Intl. Symp. on Offshore Mechanics, Dallas, Feb. 1985.
- RETIEF, G DE F, PRESTEDGE, GK and MÜLLER, FPJ, (1982): A proposal for wave energy conversion near Cape Town. Proc. 18th Intl. Conf. Coastal Eng., Cape Town, Nov. 1982.
- SAICE (1984): The Civil Engineer in South Africa. Vol. 26, No. 6, June 1984, p. 301.
- SWART, DH (1976): Predictive Equations Regarding Coastal Transports. Proc. 15th Intl. Conf. Coastal Eng., Hawaii, July 1976.

## CHAPTER ONE HUNDRED SEVENTY TWO

### STRUCTURAL DESIGN PROCEDURES FOR CONCRETE ARMOUR UNITS

Kevin R. Hall, P.Eng.\*, W.F. Baird, P.Eng.\* and D.J. Turcke, P.Eng.\*\*

#### ABSTRACT

A rational design procedure for rubblemound breakwater protection which will ensure both the structural integrity and hydraulic stability of individual concrete armour units and the overall armour system is presented. The procedure involves new experimental techniques for measuring strains in model concrete armour units in a hydraulic model of a breakwater subjected to simulated prototype wave attack and analytical techniques for determining equivalent prototype loads on units. Selected design loads are used to define the resultant stress distribution to allow the designer to take the necessary measures to ensure the structural performance of the unit in a breakwater environment.

#### INTRODUCTION

In recent years, extensive damage has occurred to the armour layers of many breakwaters. In many cases this damage has led to a partial or complete failure of the entire breakwater structure including the core, filter layers and superstructure. In some instances, breakage of individual concrete armour units has been identified as the cause of the damage to the armour layer. This individual unit breakage has clearly demonstrated the inadequacy of existing procedures for successfully designing the armour layer of the breakwater.

Although specific concrete units such as the dolos and tetrapod can be identified as being more prone to structural failure, many other types of units including cubes have been observed to break in the breakwater environment. For this reason it is not sufficient to eliminate the use of units such as the dolos or to design the armour layer with large cubes placed on very flat slopes (to restrict motion). This does not achieve the desired objective of breakwater design which is to provide a safe, reliable, structure as economically as possible.

Existing design procedures must be updated to reflect the current state of the art in other scientific disciplines such as structural design, instrumentation techniques and materials modelling.

A review of existing breakwater design procedures reveals that designers have, consciously or not, accepted that undefined tensile

\* W.F. Baird & Associates, Coastal Engineers Ltd., 1390 Prince of Wales Drive, Suite 309, Ottawa, Ontario, K2C 3N6, Canada

\*\*T& C Engineering, Cartwright Point, Kingston, Ontario

stresses can occur in the armour units since movement of the units has been accepted. The procedure outlined in this paper has been developed so that these previously undefined stresses can now be determined and the appropriate action taken to ensure both the structural integrity and hydraulic stability of the armour units.

Several of the technical studies required to develop this rational design procedure are described in this paper. It is important to note that the design procedure was developed using existing technology from other areas of engineering, such as materials modelling, instrumentation, finite element methods and structural design techniques. These technologies were adapted for use in a hydraulic model and to take into account the uniqueness of a breakwater environment. These studies considered the following:

- A review of instrumentation or measuring techniques that could be adapted for use in a hydraulic model study to define the loads (or resulting stresses or strains) that occur on an armour unit. The instrumentation techniques reviewed included accelerometers and high speed photography to define unit movements and load cells, strain gauges, photoelastic techniques and full field strain measuring techniques to determine stress or strain levels in the units. The practicality of working at specified scales and in a hydraulic environment precluded the effective use of some of the identified techniques. As a result of this review, a system utilizing strain gauges placed at strategic locations on the model armour units used in the hydraulic model and directly measuring the strain level during simulated prototype wave attack was selected.
- A review of model materials was undertaken. Selection of a material was made in relation to the scaling down of prototype properties so that the requirements of similitude between the model and prototype are met. However, since the displacement related to the deformation of the prototype units is small, a certain level of strain distortion is permissible in the model and it was therefore advantageous to select a material with a low modulus of elasticity (resulting in a magnification of the low level strains in the model). A reinforced epoxy resin was selected which permitted the use of acceptable geometric scales with an appropriate scaling of material properties.
- A series of specifications for the design of the instrumentation system were developed based on the model material, hydraulic testing techniques, anticipated strain levels and minimum performance criteria.
- A thorough assessment of the reliability and repeatability of the instrumentation system was made for a range of static, dynamic and combined static-dynamic loading. A number of prototype tests described in the literature were duplicated to assist in assessing the accuracy of the system.
- Analysis of measured model data was completed using finite element procedures. Post processing colour graphics capabilities were developed to assist in presenting the data.

Each of these technical studies is described in more detail in the following sections. The component studies have been integrated into a rational design procedure. This is used to produce a design for a breakwater armour layer which is made both economical and reliable by combining structural integrity with hydraulic performance.

OVERVIEW OF THE DESIGN PROCEDURE

The rational design procedure involves techniques to define the loadings imposed on a model armour unit on a breakwater subjected to simulated prototype wave attack and subsequently, using conventional structural engineering techniques to determine the resulting stress distribution in the armour unit. A detailed design of the individual units can then be undertaken using standard structural engineering procedures that utilize reinforcing (bar, fibre and prestressing) or make use of changes in the geometry of the unit. A general outline of the overall design procedure is given below. The procedure is illustrated in Figure 1.

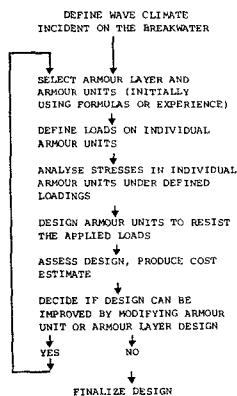


Fig. 1 Design Chart

Initially, it is necessary to fully understand the environmental conditions to which the breakwater is exposed, of which the most important parameter is the wave climate.

The choice of armour unit is up to the designer and should depend upon a number of variables including economics, material availability, form availability and construction equipment availability. Initially, the design should be developed using a hydraulic model study so that the armour units are not displaced from the armour layer under the design wave conditions. The assumption will be made at this point that each unit has sufficient strength to resist the applied forces.

Model armour units instrumented with a number of strain gauges placed at strategic locations on the unit are placed at random through the design test section. Values of strain are recorded continuously throughout the testing. Tests are undertaken for a variety of instrumented unit placement locations. From the results of the measured data, a history of the internal forces and moments occurring at the instrumented cross-section can be derived. The measured internal forces will include dynamic loads resulting from wave action on the breakwater, from collision between adjacent units and from static loads that are imposed by adjacent units or as a result of differential settlement of the structure.

Simplified equivalent external load conditions and constraints are derived, using numerical analysis, from the internal forces and moments

determined at the instrumented cross-section. The equivalent loads produce the selected measured stress (strain) distribution at the instrumentation location. Because of the random nature of the applied loads in a breakwater environment, it is necessary to undertake a statistical interpretation of the measured data. For each set of strains measured (flexure, torque, shear and axial) a frequency of occurrence distribution is determined. Extreme events from a selected set of strain data are combined with the other corresponding strains to determine equivalent design loads.

The design loads are applied to a finite element model of the armour unit to calculate the resulting stress distribution within the armour unit. The armour unit can now be structurally designed to resist the applied loadings using conventional structural engineering procedures. This may include the use of reinforced concrete, fibre reinforced concrete, prestressed concrete, the use of alternative materials or modification to the geometry of the unit (development of a new unit or armour layer system).

If additional changes to the design are implemented as a result of construction constraints and limitations, then the process of defining the loads in the hydraulic model would be repeated for the new design. The result of this procedure is the development of a breakwater armour design which provides the most economical solution combined with optimum hydraulic and structural performance.

#### DESCRIPTION OF THE COMPONENTS OF THE PROCEDURE

##### 1. Model Material Selection

Selection of the appropriate model material was based on the fundamental requirements of similitude between the model and prototype. This requires that the relationship between certain strength characteristics of the model material and the geometric scaling factor (in relationship to prototype) be properly assessed. A static dimensional analysis was carried out (Hall 1984, Baird et al, 1983) which showed that for complete similarity the geometric scaling must be identical to the material scaling. However, since the displacements related to the deformations of the prototype are sufficiently small, and not critical to the overall behaviour of the breakwater, some strain distortion and differences in Poisson's ratio is permissible. The results of the dimensional analysis yield,

$$\Theta_m = \frac{E_p}{E_m} \frac{h_m}{h_p} \Theta_p \quad (1)$$

where,  $\Theta$  = strain level;  $E$  = modulus of elasticity;  $h$  = geometric linear dimension; the subscript m denotes model and the subscript p denotes prototype.

Clearly, the choice of model size or geometric scale has a direct influence on the expected model strain levels. Since the strain gauging system has a limited resolution, the model material was selected so that the strains induced in the relatively small scale hydraulic model

studies would be of sufficient magnitude to be measured by the gauges.

Consequently, the following general requirements were identified. The material should:

- 1) have approximately the same density as concrete
- 2) be linear, elastic, homogeneous and isotropic
- 3) have a strength that would produce minimum model strain levels in the order of 50 microstrains to ensure that the behaviour of the units could easily be monitored within the resolution of the instrumentation
- 4) have reproducible mechanical properties
- 5) be easily strain gauged
- 6) be easy to use in a casting process
- 7) be relatively inexpensive.

Three major types of material are available for the construction of elastic models - plastics, cementitious materials and metals. It was determined that plastics meet most of the general requirements. Metals could not be found with the critical combination of the correct density and the desired elastic modulus required to ensure measurable strains and cementitious materials could not provide the long term stability required in a hydraulic environment and they are not easy to strain gauge.

There are a wide variety of thermoplastics and thermosetting plastics available with a diverse range of chemical composition and mechanical properties. Thermosetting plastics were identified as the best available material for the following reasons:

- 1) thermosetting plastics have a limited development of heat of polymerization which assures a homogeneous hardening process and results in a relatively consistent modulus throughout the material.
- 2) the relatively lower shrinkage that occurs in epoxy compounds after casting results in a significant decrease in the internal stresses.
- 3) the density, elastic modulus and curing rate can be easily modified by adjusting the amount of hardener or adding an inert material (filler) dispersed homogeneously throughout the model unit.

The material used to construct the model armour units was a steel fibre reinforced epoxy resin which had a bulk density of approximately 2000 kg/cubic metres and a Young's Modulus of Elasticity of 5 GPa.

## 2. Design of the Instrumentation System

The selection of the type of strain gauges and their placement location on the model armour units requires careful consideration since the forces acting on the unit and hence the stress/strain distributions are unknown. The design of the instrumentation has the fundamental objective of providing an economical, efficient strain gauging system capable of withstanding the environment in which it is operating. This design can only be achieved by taking into account the following

fundamental issues:

- 1) Environmental Operating Conditions - Factors such as temperature fluctuations, abrasion and hydraulic considerations.
- 2) Loading-Environment - Qualitative loads must be identified, such as static loads due to mound settlement, self-weight and weight of adjacent units and dynamic loads due to interunit and projectile collisions and hydrodynamic impact pressures.
- 3) Geometry - The geometric size of the model unit and the material used to construct the unit must be optimized.
- 4) Gauge Location - The density and placement of the strain gauging array must be selected to ensure adequate definition of stresses induced by torsional, flexural, shear, and axial loading conditions.
- 5) Strain Level - The possible magnitude of strains that will occur in the model must be defined so that the appropriate instrumentation can be selected.
- 6) Installation - The method of installing the gauges and subsequent water-proofing of the system must be defined.

Based on the requirements listed above and on a review of available strain gauging techniques and systems the following type of instrumentation package was developed.

For bending, torque and shear measurements, the gauge type used is a Vishay Micro-Measurement No. EA-06-125TW-120. The characteristics of this gauge type are as follows:

- constantan (A-alloy) in self-temperature-compensated form
- flexible polyimide backing
- self-temperature-compensation number = 06 in/in/degrees F
- 3 mm (.125 in) gauge length
- grid and tab geometry "TW"
- 120 ohms resistance

The gauge type used to measure axial strains is an EA-06-125TE-120 and differs from the EA-06-125TW-120 gauge only in its grid and tab geometry.

The gauge arrays should all be self-temperature-compensating (full bridge) to eliminate the effects of apparent strain in the system.

The EA series of gauges are a constantan (A-alloy) foil in combination with a tough, flexible polyimide backing, which is capable of operating in a temperature of -75 to +175 degrees Celcius. The constantan alloy has a high strain sensitivity (gauge factor) which is relatively insensitive to strain level and temperature and its resistivity is high enough to achieve suitable resistance values in very small grids. The polyimide backing is a tough, flexible carrier and can be contoured readily to fit very small radii. This backing is also

capable of very large elongation and can be used to measure plastic strains in excess of 20%.

Strain gauge performance is easily degraded by the effects of moisture damage and as a result, gauges require varying degrees of protection according to the severity of the environment in which they operate. For use in a hydraulic model study, the gauges will be subjected to a changing wet-dry environment and may be susceptible to abrasion; therefore, a good protection system is required. The work completed to date has used a system protected with Micro-Measurement M-Coat-G, a polysulfide modified epoxy compound and M-Coat B, a solvent thinned nitrite rubber compound. This system was found to provide excellent protection to the strain gauges.

### 3. Data Measurement

The instrumented model armour units are placed in the model breakwater which is subjected to simulated prototype design waves. Several considerations must be made at this point.

The random placement of armour units in the armour layer, results in a random pattern of constraint points and loading locations, and as a consequence, the forces acting on a unit will show a large variability based on the units location within the armour layer.

Therefore, it is important to determine the number of units and their placement within the armour layer required to accurately provide a definition of the stress envelope describing all possible unit locations on the breakwater. That is, it is necessary to understand how many instrumented units are required in a given test and how many tests are required (each test will require the test section to be rebuilt) to define this envelope.

Observations of prototype structures indicate that the most extensive breakage of prototype units occurs in the vicinity of the mean water level where the wave induced velocities in the armour layer are the greatest. This would indicate that forces on individual units are probably the largest in this area.

As the breakwater is tested, output from the gauges is a continuous voltage readout. Typically, voltage signals are relayed through a signal conditioner-amplifier and filtered through a high speed data acquisition. Experience has shown that a sampling rate of 100 to 200 samples per second (per channel) provides a suitable definition of the dynamic loads, although more study is required in this area. The signal can then be converted to a digital signal and stored on a computer for subsequent analysis.

In any particular test of a breakwater, in which the instrumented units are placed, the time history of the strains from all gauges is recorded simultaneously, resulting in a large quantity of data. The data must be pre-processed so that the design loads (at a desired level of exceedance) can be determined with a minimal amount of numerical analysis.



Several alternatives have been used; however, this is an area in which more research will be conducted in a future study to optimize this part of the design process. In one technique, equivalent load conditions on each instrumented unit are determined for each wave event based on the measured strains. Resultant stress values are then calculated for selected locations in the armour unit. However, because of the large number of events it is necessary that some preselection of the data be undertaken. Alternatively, statistical interpretation of the measured strain data can be made. For each set of strains measured (i.e. either flexure, torque, shear or axial strain) a frequency of occurrence distribution would be determined. Extreme events from a selected set would then be combined with the other corresponding strains to determine equivalent design loads and resulting stress distributions.

#### 4. Data Analysis and Presentation

The objective of the design procedure is to take the strain components measured during the hydraulic model tests and derive, using numerical analysis, loads that can be used for the structural design of the concrete armour units.

Finite element methods and colour graphics postprocessing are used extensively to determine the loads and view the stress distributions throughout the unit. The finite element technique is well established as a powerful tool capable of carrying out complex dynamic non-linear material and geometric analysis. The graphics package permits the analyst to quickly see the flow of stress throughout the model and verify that the model is behaving correctly.

Using the numerical techniques, simplified equivalent load conditions that produce the selected measured stress distributions at the instrumented section location are determined. These equivalent loads or, in fact, imposed boundary conditions are selected in such a way as to maximize the internal generalized forces and moments which are viewed as contributing most to the failure of prototype units at preselected locations.

Figure 2 shows a finite element grid model developed for a dolos.

Several techniques are available for viewing the resultant stress distribution in the armour units including stress flow diagrams which show the magnitude and location of tensile and compressive stress flow patterns and stress block techniques which indicate the intensity of surface stresses in the various elements. Figures 3, 4 and 5 show stress flow patterns for the dolos, tetrapod and tribar units for predetermined load conditions.

#### 6. Model-Prototype Relationship

The relationship between model and prototype is of fundamental importance to the design procedure. Two techniques are available; the first approach is to relate model strains directly to prototype strains and then determine the appropriate loads, while the second approach consists of first determining the model loads and then calculating the

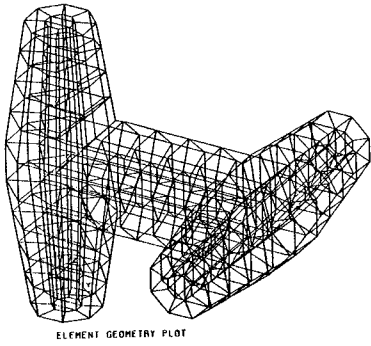


Fig. 2 Discretized Dolos

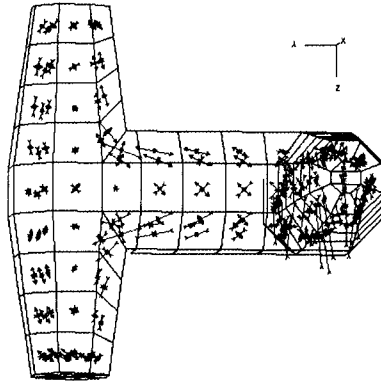


Fig. 3 Stress Flow Diagram - Dolos

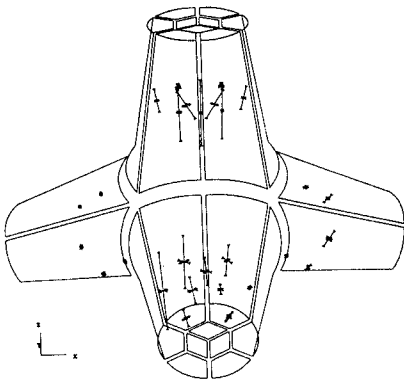


Fig. 4 Stress Flow Diagram - Tetrapod

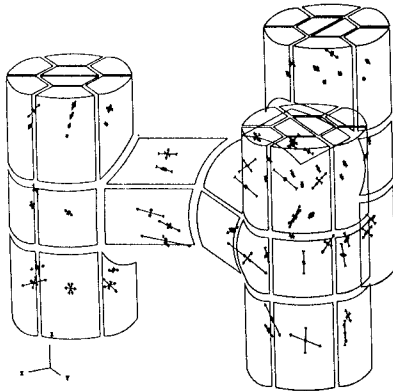


Fig. 5 Stress Flow Diagram - Tribar

prototype values of load and strain. A discussion of both approaches is made below.

In the first approach the ability to relate strains between the model and prototype requires that the model material replicates all the fundamental material properties of the prototype. As a result, with the model material selected, which is essentially homogeneous linear elastic, model and prototype strains can only be related up to cracking for both unreinforced and reinforced concrete prototype units. This type of simplified relationship has been developed and is presented in Hall (1984).

For those units that are reinforced this structural model will not provide direct prototype strain information. In addition, any complete relationship must also take into account the static and dynamic attributes of both the model and prototype materials. Consequently, a direct relationship between model and prototype strains is both complex to develop and limited in its range of application.

An alternative to the above is the second approach which only involves establishing a model to prototype load relationship. Essentially, this method requires that the model material be well defined, that is both the static and dynamic properties be established, and the model loads be determined from the measured model strains. Once these loads are defined, the appropriate model to prototype load factor, based on the geometric scale, can be used to determine the equivalent prototype loadings.

It is important to note that there has been no restriction placed on the prototype material, since the determination of these loads did not require a prototype material definition.

Consequently, this approach can be applied to reinforced concrete units or units made of any other material. Thus the analysis and design of prototype units can be based on the appropriate codes of practice once these design loads are determined.

#### EXAMPLE APPLICATION

In this section of the paper an example of the design and performance of an instrumented model armour unit is given. The units used as an example are 110 mm dolos units which were subjected to extensive testing consisting of singular static and dynamic loadings in a dry environment and hydraulic model testing using both regular and irregular waves. Complete details of the tests are given in Hall et al (1984).

The design of the instrumentation package for the dolos unit required careful consideration since the forces acting on the unit and hence the strain distribution were unknown.

An approximation of the strain levels anticipated in the model dolos units was made using finite element analysis in which simplistic loading cases were imposed on a discretized dolos unit. Based on the results of

this analysis, it was anticipated that strain levels would be in the order of 40 to 200 microstrains for 110 mm units constructed of steel fibre reinforced epoxy resin.

The instrumented unit is shown in Figure 6.

Single point static loads were applied at a number of locations on the unit to place the instrumented section in pure flexure, torsion and axial strain and combined flexure, shear, torque and axial strain conditions. The units were restrained in a fixture designed to provide a solid restraint without inducing apparent stress within the units. Figure 7 shows a sample of the load versus strain curve for a typical test and indicates a linear relationship for both the loading and unloading curves.

A number of tests were performed in which an instrumented unit was placed in an armour layer and consequently, subjected to multiple static loads. Variation was made in the number of layers of dolos, placement density and slope of the armour layer. Figure 8 shows the response for one particular set up and illustrates the variation of static strain with a change in slope of the armour layer.

A number of dynamic tests were also undertaken in a dry environment. These tests consisted of short duration single event dynamic impacts created by dropping the unit onto one of its flukes or fluke ends. Figure 9 shows the type of tests conducted and Figure 10 shows a typical response. The sharp response at the moment of impact is clearly visible in Figure 10. However, the magnitude of the induced strains measured at the centre of the shank of the dolos are relatively small. Subsequent numerical analysis has shown that strain levels near the fluke-shank interface may be 3 to 5 times larger than those in the middle of the shank during this type of loading event.

The most interesting example of the use of instrumented units is given by observing the performance of the instrumentation during a breakwater model test in which the test section is subjected to simulated prototype waves. The units were subjected to both static loads, resulting from self-weight, the weight of adjacent units and mound settlement and readjustment, and dynamic loads resulting from hydrodynamic forces and impact with adjacent units. The instrumented units were placed at random within the breakwater armour layer. The test section was initially subjected to low wave conditions which were increased in small increments until significant armour unit movement was observed. Figure 11 shows the instrumented units in a typical test set up. Figure 12 shows the breakwater being subjected to wave attack.

Figure 13 shows an example of the output measured during a test conducted with regular waves. The repeatability of the strain signal at the same period as the period of the waves is excellent and illustrates the capability of the instrumentation. The strain level recorded exhibited a marked increase with an associated increase in wave height.

Figure 14 illustrates the response of the instrumented unit during tests ran with irregular wave conditions having a peak model wave period



Fig. 6 Instrumented Dolos Unit

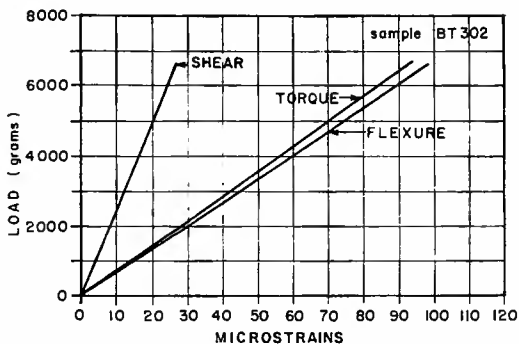


Fig. 7 Load Versus Strain Plot for Static Load

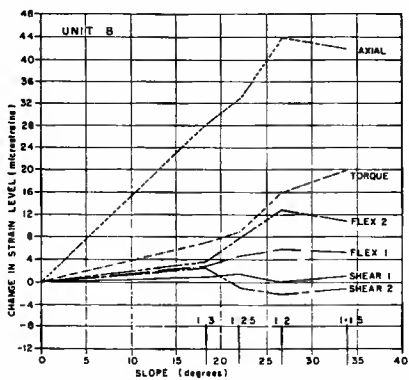


Fig. 8 Variation in Strain with Armour Slope

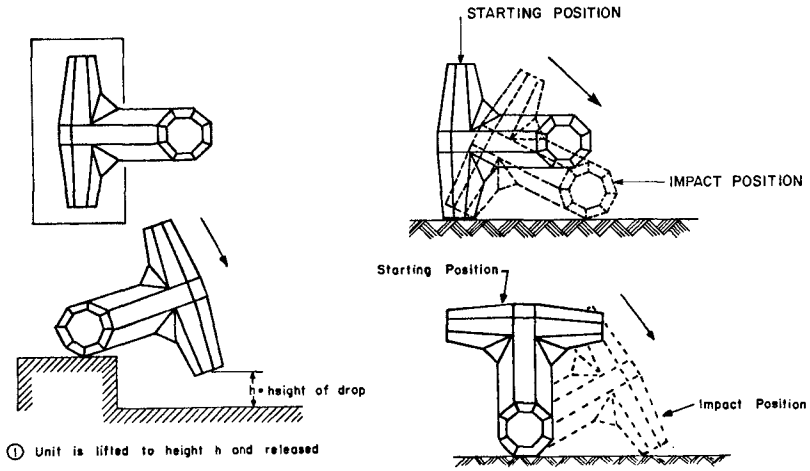


Fig. 9 Types of Dynamic Load Tests

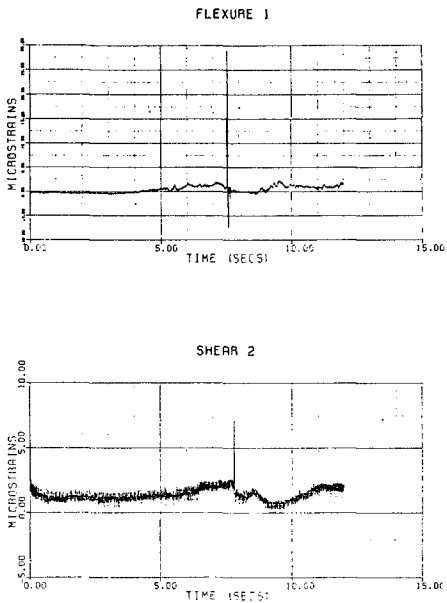


Fig. 10 Dynamic Impact Response - Strain vs Time



Fig. 11 Example of Instrumented Unit  
Placement in the Armour Layer



Fig. 12 Wave Impact on the Instrumented  
Unit

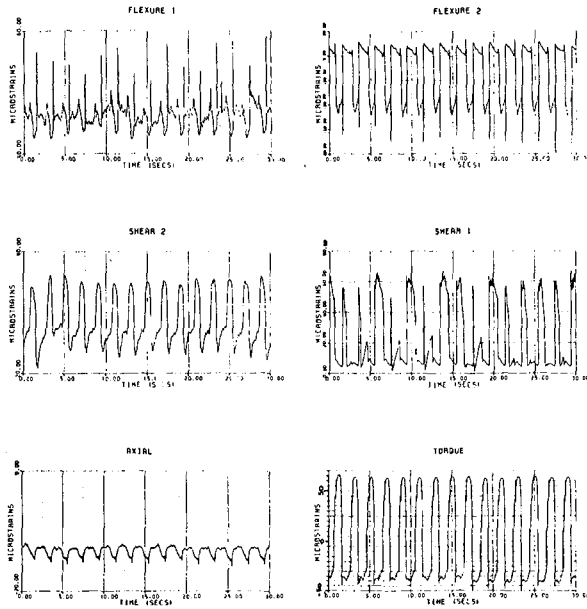


Fig. 13 Strain Response - Regular Wave Test

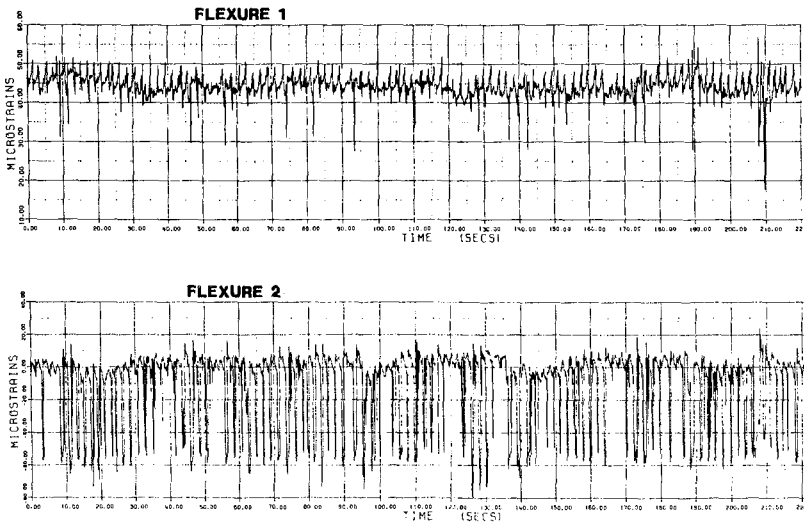


Fig. 14 Strain Response - Irregular Wave Test



of approximately 2 seconds. Both the magnitude of the peak strain levels and the period between peaks is irregular and in fact, in some instances, the strain levels exhibit a groupiness similar to that observed in the irregular wave trace.

The following comments can be made with respect to the performance of the instrumentation used during these tests:

- 1) individual strain levels exceeding the tensile cracking strain level for concrete were recorded in wave conditions in which armour unit motion was observed.
- 2) the response of the instrumentation in irregular waves exhibited excellent repeatability in phase with the period of the waves.
- 3) the instrumentation is not affected by the hydraulic environment of the breakwater.
- 4) the instrumentation is not affected by abrasion occurring as a result of adjacent units moving over the surface and colliding directly onto the gauges.
- 5) the lead wires from the gauges do not affect the movement of the instrumented units or the units adjacent to them.

In general it is concluded that the strain gauging system provides a viable system of measuring strain levels in model armour units subjected to simulated prototype wave attack in a hydraulic wave flume.

#### CONCLUSIONS

A rational procedure for designing concrete armour units so that the structural and hydraulic performance can be simultaneously guaranteed has been presented. The various aspects that require consideration when designing the instrumentation and developing the prototype design criteria were discussed. The general objectives of utilizing this design procedure is to permit the widespread use of precast concrete units throughout the design life of the structure and represent a least cost investment.

A procedure for defining the loads that occur on a breakwater which enables the engineer to structurally design the unit has been developed and its performance evaluated.

Based on the design loads, the designer can determine the size of unit required, and the necessity for reinforcement (and type of reinforcement required). If necessary the geometry of the unit can be altered to reduce the occurrence of stress concentrations. This may ultimately result in the development of new units which optimize the combined structural and hydraulic performance.

In addition, if fatigue analysis is required, the defined loads can be employed to determine the expected life of a unit so that estimates of maintenance costs over a given period of time, related to replacement of armour units, can be determined.

Alternatively, these procedures could be used to develop codes of practice for concrete armour unit design which would provide a

description of the design loads for the many types of armour units used in breakwater design and for many of the variations in the physical environment of a breakwater.

#### ACKNOWLEDGEMENTS

The authors would like to thank the National Research Council of Canada, Hydraulics Laboratory and Public Works Canada for funding of various parts of the development of the overall design procedure.

#### REFERENCES

1. Baird, W.F., Hall, K.R., Turcke, D.J. and Chadwick, D.C., "Development of a Procedure for the Design of Concrete Armour Units for Rubblemound Breakwaters", Unpublished report for Public Works Canada, March 1983.
2. Hall, K.R., Baird, W.F., Turcke, D.J. and Scott, D.C., "Design and Evaluation of an Instrumentation Package for Measuring Strain Levels in Model Dolos Units", Unpublished report prepared for Public Works Canada and the National Research Council of Canada, March 1984.
3. Hall, K.R., "Design of Concrete Armour Units for Rubblemound Breakwater Protection", Coastal Engineering in Canada, Queen's University, April 1984.
4. Hall, K.R. and Turcke, D.J., "Modelling Strain Levels in Concrete Breakwater Armour Units", Fifth ASCE Engineering Mechanics Specialty Conference, University of Wyoming, August 1984.

## CHAPTER ONE HUNDRED SEVENTY THREE

### THE DESIGN OF BREAKWATERS USING QUARRIED STONES

W.F. Baird, MASCE, P.Eng.\* and K.R. Hall, AMASCE, P.Eng.\*

#### 1.0 Introduction

The majority of rubble mound breakwaters built in North America that use quarried stones in their armour layer contain either one or two layers of armour stone, one or two filter layers and a core of quarry run.

Preparation of a design normally involves use of the Hudson equation and may be supported by physical model tests. Once the design wave conditions are defined the size of armour stones are only a function of the outer slope of the breakwater.

In this paper an alternative approach to the design of quarried stone breakwaters is discussed. The basic principal involved in this concept is the use of locally available materials. It is established that the greater the thickness of the armour layer, the smaller the stones that are required to provide stable protection against wave action. Therefore, the thickness of the armour layer for a specific breakwater is determined by the gradation of the available armour stones and the incident wave climate. The final cross-section makes allowance for the practical considerations of breakwater construction. New concepts for breakwaters that have resulted from the use of this alternative design procedure are described. Construction of these breakwaters in 1983-84 has demonstrated that significant cost savings are obtained.

#### 2.0 Traditional Design

The traditional design approach is described in many texts, and in greatest detail in the U.S. Corps of Engineers Shore and Protection Manuals (4). A breakwater design that may result from the use of this procedure is shown in Figure 1.

A number of possible difficulties with the construction of this design can be identified and include the following:

- Large Armour Stones Required. At many locations the wave climate dictates (through the design formula) large stones that may be very expensive to obtain or are not available.

In the latter case the designer must specify concrete armour units which will significantly increase the cost of the project.

\* W.F. Baird & Associates, Coastal Engineers Ltd., 1390 Prince of Wales Drive, Suite 309, Ottawa, Ontario, K2C 3N6, Canada

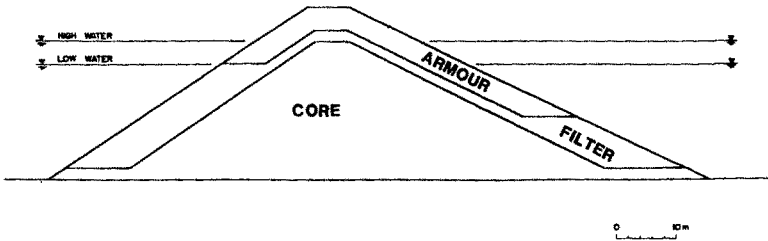


Figure 1. Example of Conventional Armour Stone Breakwater

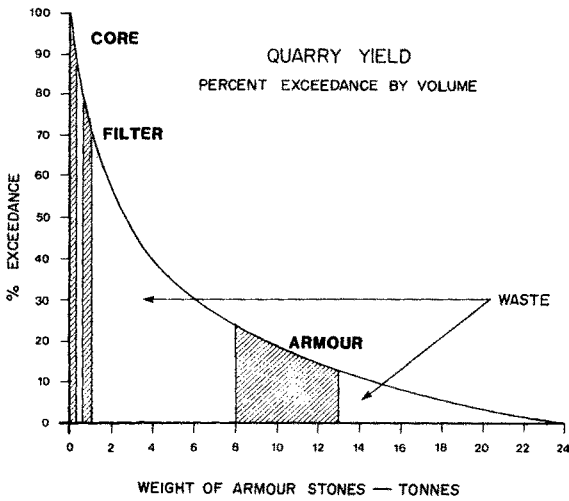


Figure 2. Quarry Yield and Stone Weights Required By Conventional Breakwater

- Wastage at the Quarry. The volume of armour and filter stones of the specified weights used may represent only a small percentage of the volume that must be quarried to obtain these stones. This problem is illustrated in Figure 2, which shows the yield of a typical quarry and the range of stone weights that can and cannot be used for a breakwater. This breakwater is designed for a significant wave height of 5 m and has a front slope of 2 horizontal to 1 vertical.

The relative proportions of material required to build this breakwater in 12 m of water are compared to the relative proportions of the usable volumes of the quarry yield in Table 1. In this example, over-production of armour stones will be required to produce the required volume of core material, although quite often the converse is true.

- Costly Quarry Operations. The quarry operation must be geared to produce armour stones, filter stones and core material. This may require differing blasting procedures. All other material that results from the quarried operations must be sorted and placed in a waste pile.
- Difficult to Construct. Placing continuous layers of armour and filter stones to specified tolerances for location and slope below water requires very careful supervision and inspection, which may be restricted by poor visibility. This may be very problematic in deeper water and/or at locations where there is little calm weather. Construction problems may also be associated with requirements to place core, filter and armour material in close succession to avoid damage to a partly built breakwater by wave action. The supply of materials along the breakwater can cause major logistical problems.
- Speed of Construction. The rate of placement of armour stones on a traditional breakwater is limited by crane operations, which are relatively slow.

The conventional design procedure based on the Hudson formula provides very little flexibility to the designer to overcome these problems and provide what could be a more cost effective design.

### 3.0 Alternative Design Approach

The basis of the design procedure described in this section is the optimization of the use of locally available material and the preparation of a design that requires relatively simple but effective construction methods.

The objective of the design process is to prepare a least cost and stable breakwater.

In order to develop the design, the following procedure is used:

- i) Study the properties of locally available stones.
- ii) Define the range of sizes of the locally available material, typically the gradation of curve of a quarry.

TABLE 1

COMPARISON OF RELATIVE PROPORTIONS OF MATERIAL VOLUMES  
REQUIRED FOR BREAKWATER TO THE USABLE QUARRY YIELD

	Percent of Breakwater Volume	Percent of Usable Quarry Yield
Armour	25	36
Filter	25	26
Core	50	38

TABLE 2

COMPARISON OF STONE SIZES POSSIBLE WITH BERM DESIGN  
AND CONVENTIONAL DESIGN

Design Significant Wave Height (Metres)	Range of Armour Stone In New Design (Tonnes)	Stone Weight For Conventional Design (Tonnes)	
		Slope	
4	0.2 - 1.1	1:1.5	1:2
		7.1	5.3
6	0.7 - 3.5	24	18
8	1.8 - 8.4	57	43

Note: The size of armour stones used in the proposed concept should be dictated by the yield of the local quarry and may be larger than shown. The above indicates possible lower limits that may be considered.

- iii) Use the smaller fraction of the available material for the core of the structure, as illustrated in Figure 3.
- iv) Use the large fraction of the available material for the armour, as illustrated in Figure 3.
- v) Determine the shape and dimensions of the armour protection, which typically involves increasing the thickness of the armour layer, so that during design wave conditions, a stable structure is obtained. This activity is completed using physical hydraulic model studies. As the dimensions of the armour protection are determined, the relative sizes of core material and armour material (items iii and iv) will vary to accommodate changes in the relative percentages of armour stone and core material required.
- vi) Finalize the geometry of the cross-section of the armour to allow for simple construction operations.

The design concept that has resulted from this approach contains armour stones placed in the form of a horizontal berm as illustrated in Figure 4. It is the horizontal dimension "L" that is to be determined in the model studies. This dimension is a function of the armour stone gradation and incident wave height. In Figure 4 comparison is made between a conventional breakwater and this alternative design when designed for the same wave conditions. This breakwater concept has the following features.

- The armour stones can be less than one-fifth the weight of the stones required in a conventional design, as illustrated in Table 2. However, the important point is that the concept is intended to make use of the available stones and not necessarily the use of smaller stones.
- Maximum use of quarry yield, as illustrated in Figure 3.
- Simple Design. Filter layers and toe scour protection berms are usually not required.
- The quarry operation consists only of blasting and sorting the stones into two categories (the larger fraction and the smaller fraction).
- The breakwater can be built using land based equipment only. In most cases a dump and push operation can be utilized and no crane placement is required. Plenty of room is available on the breakwater for construction roads. Wave action during construction is relatively of little concern.
- Construction tolerances can be relaxed and the requirement for extensive underwater inspection can be replaced by relatively simple surveys.
- The performance of the breakwater when subjected to waves exceeding the design condition is significantly better than the performance of a conventional structure exposed to similar conditions. The structure

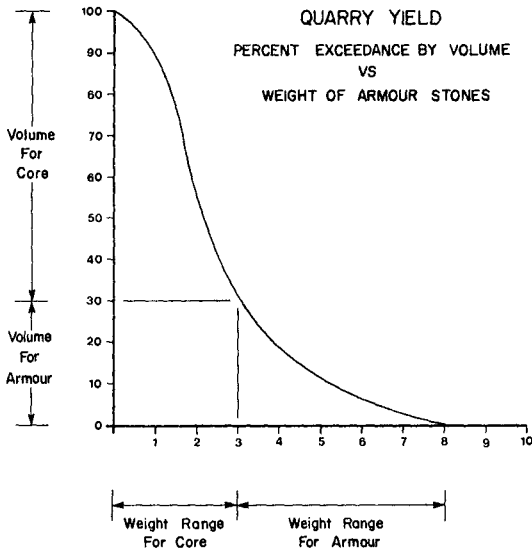


Figure 3. Quarry Yield and Stone Weights Required By Berm Breakwater

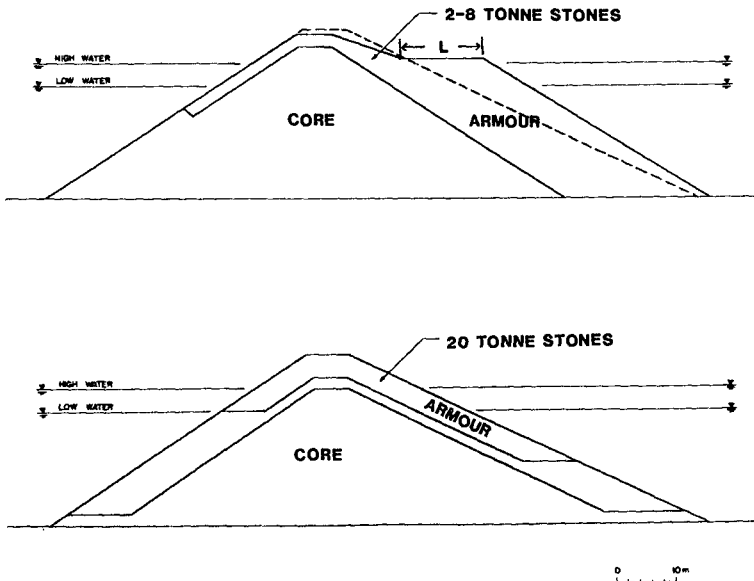


Figure 4. Example of Berm Breakwater Compared to Conventional Breakwater



will not fail in a rapid catastrophic manner.

- The total volume of the structure, compared to a conventional structure, depends on the depth of water and the size of stones available. Typically, it may be 10 to 20 per cent greater in depths of 10 to 20 metres.
- The cost of construction of this breakwater in Canada has been found to be between 50 and 70 per cent of the cost of an equivalent traditional structure.

The improved performance of the structure compared to conventional structures is achieved because of the permeable berm of armour stones that consolidates into a well 'nested' and armoured surface. In the following discussion the main armour protection, which is in the form of an armour stone berm, is referred to as the berm.

The relatively high porosity of the berm allows the waves to propagate into the armour stones and dissipate their energy over a large area within the berm. In a conventional two stone armour layer, the flow produced by the incident wave is restricted by the relatively impermeable filter and core and, consequently, there are large velocities produced by the wave uprushing or downrushing within the narrow armour layer. In the berm the flow has a larger area into which it can move and as a result localized velocities are greatly reduced thereby decreasing the external hydrodynamic forces applied to the stones. A considerable increase in stability is achieved as a consequence of this dissipation of wave energy within the permeable berm of armour stones.

The berm also increases its stability as a result of progressive wave action exceeding a threshold that will cause motion of the stones in the berm. The berm is consolidated as a result of nesting of stones and this increases the shear strength of the berm. This nesting process also results in an increase in the frictional restraint on individual stones. Depending on the size of stones available and the design wave conditions, movement of stones on the outer surface may occur to varying degrees. Movement takes place during the early stages of exposure to wave action. The stones eventually find a geometrically similar space in the berm surface into which they nest. The result of this process is a natural armouring of the outer layer of the berm. A typical armoured profile is illustrated in Figure 5, where it can be seen that the final profile has been consolidated to approximately 85 to 90 per cent of the as-placed volume.

Although the final shape of the cross-section may be similar to the 'S' shape profile reported by other investigators (3), there are several subtle differences. The berm does not change profile below a certain depth. Stones are not rolled out of the top of the berm and carried down to the seabed. The berm is consolidated because the stones that move eventually find a geometrically similar void into which they nest. Also, the profile of the berm is quite regular through the water line, typically in the order of 1:5, whereas an 'S' shaped profile tends to have a curvature to it in the region of the waterline.

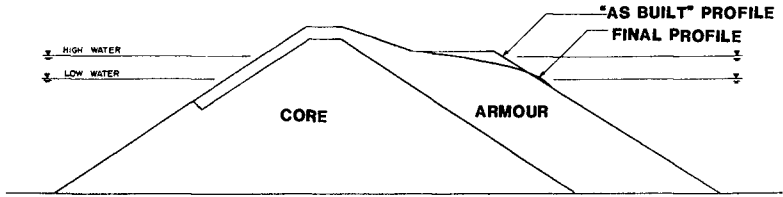


Figure 5. Profile Development on Berm Breakwater

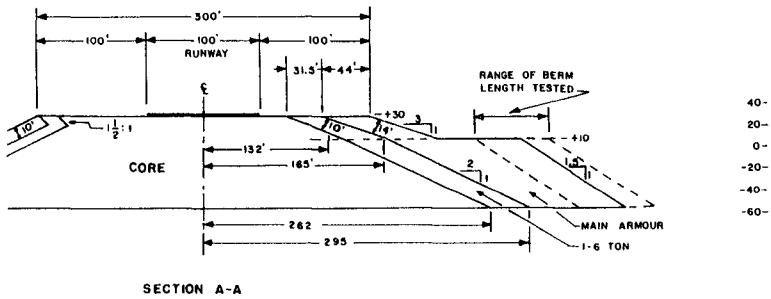


Figure 6. Cross-section of Unalaska Design

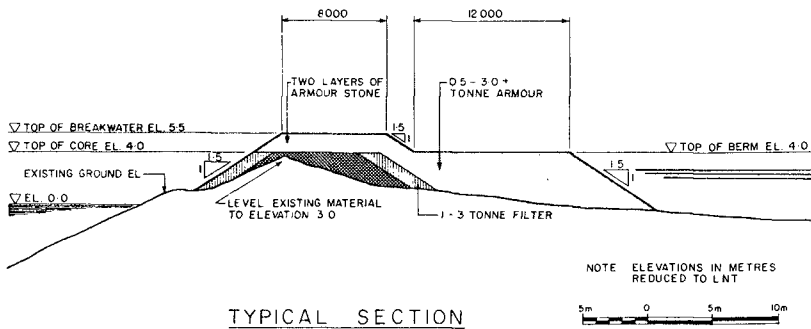


Figure 7. Cross-section of Codroy Breakwater

A formula to assist with the design of this concept of breakwater cannot be introduced because of the site specific nature of each design.

#### 4.0 Summary of Recent Experience

In the following section some designs that have been developed are summarized.

##### i) Runway Extension, Unalaska, Alaska

Protection against a design significant wave height of 10.5 m was required for a runway extending into a maximum water depth of 17 m. The armour consisted of a 23 m wide berm of 3.5 to 17 tonne stones. This design is reported in references (1) and (2). The cross-section is illustrated in Figure 6.

This design was prepared for Dames & Moore, Anchorage, who were responsible to the State of Alaska for this project.

##### ii) Helguvik Bay, Iceland

The breakwater was designed for a significant wave height of 6 m in a water depth of 20 m. The armour consisted of a 14 m wide berm of 1.7 to 7 tonne stones.

The design was prepared for Bernard Johnson Inc. of Bethesda who were responsible to the U.S. Navy for this project.

##### iii) Codroy, Newfoundland

The breakwater was designed for a maximum wave height of 6.8 m. The armour consists of a 12 m wide berm of 0.5 to 4.0 tonne stones. This breakwater is illustrated in Figures 7, 8, and 9.

Construction was completed in the summer of 1984. The work was completed for the Department of Public Works of Canada.

##### iv) North Bay, Ontario

The breakwater is designed to protect a marina. The design significant wave height is 1.5 m and the maximum water depth is 5 m. The breakwater was built out of 2 to 750 kg stones. The breakwater is illustrated in Figure 10.

Construction was completed in the summer of 1984. The work was completed for the Department of Public Works of Canada.

##### v) Breakwaters in Iceland

Four breakwaters based on this concept were built in Iceland by the Harbour and Lighthouse Authority in 1983-84. Contractors were invited to bid on conventional designs as well as the berm design. The berm design was found to be significantly less expensive.



Figure 8. Codroy Breakwater After Construction. Breakwater Extends From Beach (in foreground) to an island



Figure 9. Berm of Codroy Breakwater During Construction Showing 0.5 to 4.0 Tonne Stones

### 5.0 Model Investigations

The designs described above, with the exception of the Icelandic Harbour and Lighthouse Authority breakwaters, were based on extensive model investigations. These studies involved in excess of sixty complete tests (simulating a full storm profile) in three dimensions using irregular waves at scales between 1:30 and 1:50, and have considered the following variables:

- stone sizes and gradations
- width of the berm
- wave attack at an angle to the breakwater
- changes in water levels
- duration of storm and storm profile
- more than one consecutive design storm
- angular and rounded stones
- crest elevation and overtopping

Verification of the prototype performance of these structures has been the subject of discussion during the review of all of these designs. Review of the literature shows that extensive prototype data describing the performance of quarried stone structures of a similar nature exist. Since the 1800's many breakwaters have been built by dumping all quarried material at the breakwater site. The breakwater at Cherbourg, France; Plymouth, England; Fishguard and Holyhead, Wales; Aldernay, Channel Islands; Port Elliot and Encounter Bay, Australia are some examples where a major part of the structure was built in this way. Extensive surveys of many of these structures exist, although difficult to obtain, and provide support to the performance of the structures observed in the model tests. The question is whether the hydraulic model studies undertaken of these site specific designs fully represent the prototype processes. Consequently, in the development of these designs the size of the model, the simulation of storm waves, and the properties of the stones were very carefully reviewed.

### 6.0 Conclusions

The following conclusions can be drawn:

- i) The potential of quarried stones for protecting breakwaters from wave action is not realized with traditional designs.
- ii) Quarried stones could be used at many locations where expensive and problematic concrete units have been used in the past.
- iii) Significant cost savings compared to conventional structures can be achieved because of minimum wastage of available material, use of smaller stone sizes and simple construction methods. Cost savings of between 50 to 70 per cent of the cost of conventional structures have been achieved in Canada.
- iv) Improved stability, compared to traditional designs, is achieved for wave conditions equal to, or exceeding, the design event.

- v) The design for a specific project depends on the characteristics of the local quarry and the wave climate of the site.
- vi) The traditional design with two layers of armour stones can be considered a special case of this more general concept.

#### 7.0 References

1. Hall, K.R. and Baird, W.F., May 1982, "Offshore Runway Extension of Unalaska Airport, Alaska - The Development of Structures to Protect the Runway Extension From Wave Action Using a Hydraulic Model Study". Unpublished report prepared for Dames and Moore, Los Angeles.
2. Hall, K.R., Baird, W.F. and Rauw, C.I., 1983, "Development of a Wave Protection Scheme for a Proposed Offshore Runway Extension at Unalaska Airport, Alaska", Coastal Structures 83, Washington.
3. Naheer, E. and Buslov, V., 1983, "On rubble-mound breakwaters of composite slope", Coastal Eng.,7:253-270.
4. U.S. Army Coastal Engineering Research Center, 1973. Shore Protection Manual, Volume II.



Figure 10. North Bay Breakwater During Construction. Construction Required Only Trucks and a Bulldozer

## CHAPTER ONE HUNDRED SEVENTY FOUR

### FATIGUE IN BREAKWATER CONCRETE ARMOUR UNITS

Hans F. Burcharth <sup>★</sup>

#### ABSTRACT

The reliability of rubble mound breakwaters depends on the hydraulic stability and the mechanical strength of the armour units. The paper deals with the important aspect of fatigue related to the strength of concrete armour units.

Results showing significant fatigue from impact tests with Dolosse made of unreinforced and steel fibre reinforced flyash concrete are presented. Moreover universal graphs for fatigue in armour units made of conventional unreinforced concrete exposed to impact load and pulsating load are presented. The effect of fibre reinforcement and the implementation of fatigue in a stochastic design process are discussed.

#### INTRODUCTION

Many of the recent failures of large rubble mound breakwaters are due to unexpected fracture of the concrete armour units. Traditionally the design process is based on hydraulic model tests and the design criterion chosen with consideration only to the hydraulic stability. Although progress has been made during the last years there exists no consistent armour layer design method in which both the hydraulic and the mechanical stability are considered. A discussion on the state of the art of this problem is given in Burcharth, 1983 (ref. 1 and 2).

The different types of loads on armour units and their origin are listed in Fig. 1.

TYPES OF LOADS		ORIGIN OF LOADS
STATIC	}	Weight of units
		Prestressing due to: Settlement of underlayers Wedge effect and arching due to movements under dynamic loads
ABRASION	}	Suspended material
DYNAMIC	Impact	Rocking/rolling of units Missiles of broken units Placing during construction
	Pulsating	Earthquake Gradually varying wave force
THERMAL	}	Stresses due to temperature differences during hardening process Freeze-thaw
CHEMICAL	}	Corrosion of reinforcement Sulfate reactions etc.

*Fig. 1. Types of loads on armour units.*

<sup>★</sup> Professor of Marine Civil Engineering, University of Aalborg, Denmark.

This paper deals with fatigue due to repeated dynamic loads from the waves. Fatigue is the reduction in material strength by increasing number of load cycles.

FATIGUE

The waves will cause *pulsating* (gradually varying) flow forces and also *impact* forces when the units are rocking. The number of cycles of wave loadings will be in the order of 200 million during a 50 years' period in the North Atlantic period. Since 1903 it has been known that concrete shows significant fatigue. Considering the high stress level in the large slender types of units such as Dolosse and Tetrapods it is important to evaluate the fatigue effect on the stability.

Fig. 2 shows the results from uniaxial fatigue tests with small specimens by Tepfers et al., 1979 (ref. 3 and 4), Fagerlund et al., 1979 (ref. 5), Zielinski et al., 1981 (ref. 6). The size of the specimens were 150 mm cubes, 100 mm and 74 mm diameter cylinders.

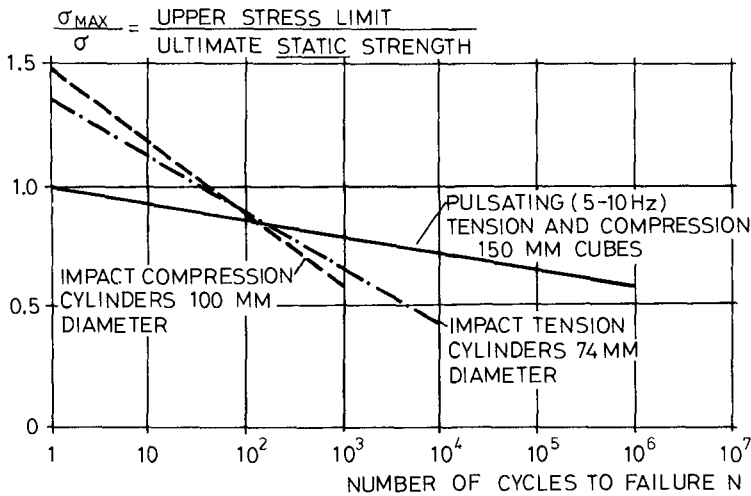


Fig. 2. Fatigue. Uniaxial impact and pulsating loading of small specimens (Tepfers et al. 1979, Fagerlund et al. 1979, Zielinski et al. 1981).

The results of the static test shown in Fig. 2 compare very well to the results by Tait et al., 1980 (ref. 7) for 25 kg model Dolosse of 300 mm height exposed to a pulsating load which created mainly uniaxial tensile stresses in the critical section, see Fig. 3.

Impact tests by M.G.A. Silva, 1983 (ref. 8) with full scale cubes in the range 1 ton to 27 tonnes also revealed significant fatigue as shown in Fig. 4. In the tests one cube impacted side to side a resting cube of the same size.



From the above mentioned tests it is seen that impact loads create the most drastic reduction in strength. Regarding the application in practical breakwater design of the tests presented in Fig. 2 and 3 it might be argued that the size of the specimens could be too small to re-

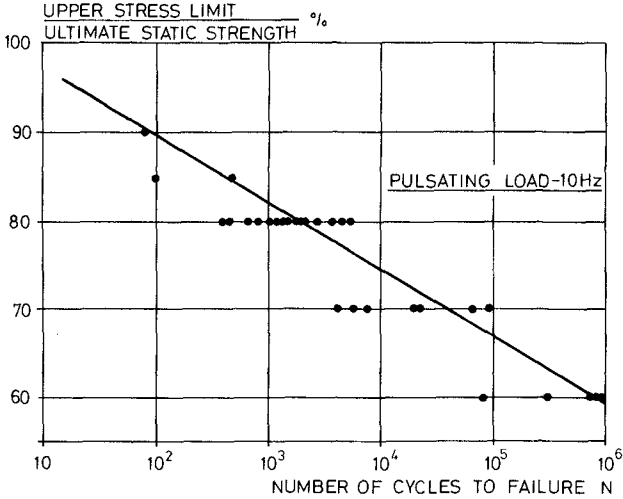


Fig. 3. Fatigue. Uniaxial pulsating tension loading of model Dolosse of 300 mm height (Tait et al. 1980).

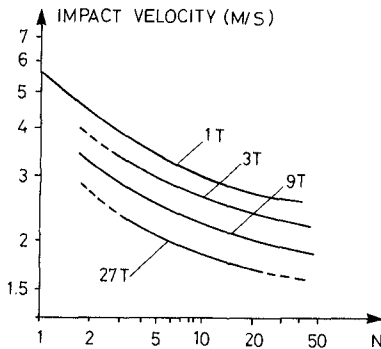


Fig. 4. Fatigue. Impact tests with full scale cubes (M. G. A. Silva 1983).

present the properties of prototype concrete. Also the stresses are uniaxial whereas in prototype the stresses in critical sections are often flexural stresses. To evaluate these questions series of impact fatigue flexural stress tests with 200 kg Dolosse were performed at the University of Aalborg from 1981 to 1983. Both unreinforced and steel fibre reinforced concrete were tested.

FATIGUE TEST SET UP AND TEST PROGRAMME

The test set up is shown in Fig. 5.

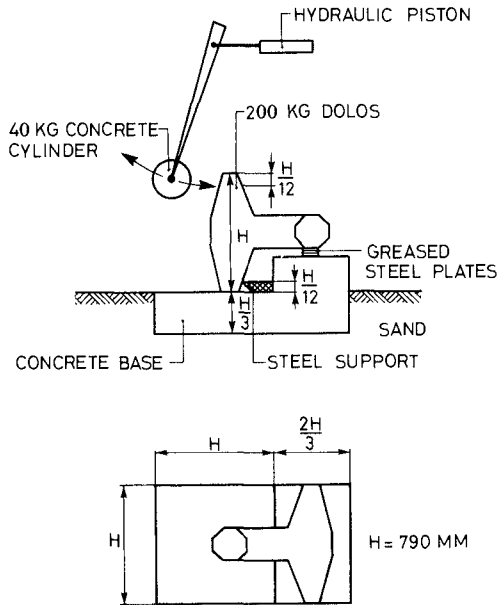


Fig. 5. Set up of Dolosse impact fatigue tests.

The support of the Dolos compares to the set up used in prototype dynamic testing of Dolosse proposed by Burcharth 1980 and 1981 (ref. 9 and 10) and since widely used by other researchers. The set up is designed to generate mainly flexural stresses in the critical sections of the stem and the leg near the stem/leg corner. The pendulum was automatically operated by a hydraulic piston which could be set to any draw back distance from which the pendulum was released, thus reaching a specific impact speed. The number of impacts were recorded automatically. The operating speed was approximately one impact per 2 sec, somewhat dependent on the draw back distance.

Apart from disintegration also the first sign of crack and a specific width of the crack were taken as failure modes to be registered. This necessitated careful visual observation of the Dolosse throughout the tests.

To prevent material scale effects the size of the Dolosse was chosen such that concrete with normal size of aggregates could be used. This resulted in a Dolos height of 790 mm, a stem diameter of 261 mm giving a waist ratio of 0.33 and a mass of approximately 200 kg. The diagonal of the stem leg corner fillets was 48 mm.

A total of 45 Dolosse were tested included some pilot tests. Two types of concrete, unreinforced flyash concrete and steel fibre reinforced flyash concrete, were tested. The specifications and the material properties are listed in Table 1.

Table 1. Specifications of concretes.

	Unreinforced units	Steelfibre reinforced units
Cement content kg/m <sup>3</sup>	380 portland	435 portland flyash cement
Flyash kg/m <sup>3</sup>	125	
Sand kg/m <sup>3</sup>	525	788
4-8 mm pebbles kg/m <sup>3</sup>	80	none
8-16 mm pebbles kg/m <sup>3</sup>	1095	416
16-32 mm stones kg/m <sup>3</sup>	none	416
Water cement ratio	0.45	0.40
Additives	app. 4% air in Dolosse	3.3 kg plastisizer BV 40 app. 6% air in Dolosse
Reinforcement kg/m <sup>3</sup>	none	160, Wirex steel fibre 45 × 1 mm plain round (2% by volume)
Mean static compressive strength 100 × 200 mm cyl. $\bar{\sigma}_c$ N/mm <sup>2</sup>	44.4	27.0 *)
Mean static tensile strength 100 × 200 mm cyl. splitting test $\bar{\sigma}_{T \text{ split}}$ N/mm <sup>2</sup>	3.65	3.47 *)
Mean modulus of elasticity determined by ultrasound measurement $\bar{E}$ N/mm <sup>2</sup>	4.4 × 10 <sup>4</sup>	
Mean mass density of concrete in Dolosse $\bar{\rho}$ kg/m <sup>3</sup>	2330	2300

\*) Absolute values not fully representative for the Dolosse concrete strength due to boundary effect of the small cylinders on the concrete containing large fibres and coarse aggregates. This resulted in app. 4% higher air content and accordingly lower strength properties for the cylinder specimens. On this base the strength of the concrete in the Dolosse is estimated to  $\bar{\sigma}_c = 30$  N/m<sup>2</sup> and  $\bar{\sigma}_T = 3.85$  N/mm<sup>2</sup>.

A fairly high fibre content of 160 kg per m<sup>3</sup> of concrete or 2% by volume was used to make sure that it was well above the limit where fibre has no effect. According to full scale tests with 30 t Dolosse (static test and drop test) conducted by the author a steel fibre content below 70 kg/m<sup>3</sup> has only negligible effect on the strength.

Pilot's tests with beams reinforced with various types of steel fibres showed that a fibre length of app. 45 mm ensured a good toughness. A somewhat smaller diameter of the fibre than the applied 1 mm would probably have been more effective in terms of toughness per kilo of steel.

Although the amount of fibres was high no problems with mixing of the fibres were observed and the distribution of the fibres in the concrete Dolosse was good. However, the air content came out higher than expected and the strengths lower.

The age of all units when tested were approximately one year.

**THEORETICAL CONSIDERATIONS ON THE PROCESSING AND REPRESENTATION OF THE TEST RESULTS**

In fatigue tests each specimen is exposed to repeated load representing a specific stress range,  $\Delta\sigma$ .

Neglecting the influence of the rate of strain on stress and the variation of Poisson's ration Burcharth 1981 (ref. 10) derived formulae for the maximum tensile stress in a Dolosse exposed to impact load in a drop test and a pendulum test. Taking the waist ratio as a constant (0.33 in the present tests) the two formulae is given by

$$\frac{\sigma_T}{mghH^{-3}} \sim \left(\frac{E}{\rho gh}\right)^{0.5} \tag{1}$$

where  $\sim$  means proportional to

- $\sigma_T$  the max tensile stress
- m the pendulum mass (or the Dolos mass in the drop test)
- h the pendulum fall height (or the Dolos centre of gravity fall height in the drop test)
- H the Dolos height
- g the gravitational constant
- E the dynamic or static modulus of elasticity
- $\rho$  the mass density of pendulum and Dolos

In this it is assumed that for each type of concrete there is a constant ratio between the dynamic and the static modulus of elasticity. Thus the variation of this ratio with the stress level and the amount of internal fracture is neglected.

Eq. (1) is based on the assumption that the duration of the impact  $\Delta t$  can be taken as the time which elapses for a longitudinal shock wave to travel from the point of impact to a free edge of the concrete and back again, i.e.  $\Delta t$  is proportional to a characteristic length, H. However, actual recordings of the impact time in the present tests showed bigger values of  $\Delta t$ . A reanalysis based on the assumption of  $\Delta t$  being half of the natural period for the first mode of vibration of the Dolos when hit revealed good agreement between measured and calculated values of  $\Delta t$ . Fortunately this finding do not change eq. (1) as also the vibration model involves proportionality between  $\Delta t$  and a characteristic length.

Since the stresses range from approximately zero for each impact in the tests, the maximum stresses also represent the stress range. Thus in eq. (1)  $\sigma_T = \Delta\sigma_T$ .

The present fatigue test results are presented in diagrams where the ratio of the ultimate dynamic tensile stress range for N Impacts,  $\Delta\sigma_N$  to the same quantity for one impact,  $\Delta\sigma_{N=1}$

is plotted against the number of impacts at failure,  $N$ . Since the stresses were not directly recorded in the tests the ratio  $\Delta\sigma_N/\Delta\sigma_{N=1}$  was determined from the impact speed (or fall height) of the pendulum as follows:

For a system with constant values of  $g$ ,  $m$  and  $H$  eq (1) reduces to

$$\Delta\sigma_T \sim \left(\frac{Eh}{\rho}\right)^{0.5} \quad (2)$$

Moreover since  $\rho$  and  $E$  were approximately constants for each type of concrete we get

$$\Delta\sigma_T \sim h^{0.5} = \frac{v}{(2g)^{0.5}}, \quad (3)$$

where  $v$  is the pendulum impact velocity.

Since the material properties of concrete produced to identical specifications vary, corrections for this variation should be implemented in the results. For this reason 6 cylinders (100 x 200 mm) were cast from the batch of each Dolos. 4 or 3 cylinders were used to determine the splitting tensile strength,  $\sigma_{T\text{split}}$  and 3 or 4 cylinders were used to determine the compressive strength,  $\sigma_C$ . As testing of the cylinders and the corresponding Dolos took place at the same time it is assumed that the mean values  $\bar{\sigma}_{T\text{split}}$  and  $\bar{\sigma}_C$  characterize the actual strength properties of the Dolos.

In the impact fatigue tests the relevant strength property is the dynamic tensile strength  $\sigma_{T\text{dyn}}$  and not  $\sigma_{T\text{split}}$  which, due to the splitting test procedure, is a static tensile strength property. However, in what follows the reasonable assumption of proportionality between the two tensile strengths is used for each specific type of concrete.

To make it possible to compare fatigue in Dolosse of different concrete strength, corrections for the variations as found from the cylinder splitting test can be made by means of eq. (3). Thus a measure of a characteristic stress range for a tested Dolos is

$$\Delta\sigma_a = k \frac{h_a^{0.5}}{\sigma_{T\text{split},a}} \quad (4)$$

where  $k$  is an unknown constant and indices  $a$  corresponds to a specific Dolos.

From this we obtain

$$\frac{\Delta\sigma_{N,a}}{\Delta\sigma_{N=1,b}} = \frac{h_{N,a}^{0.5} / \sigma_{T\text{split},a}}{h_{N=1,b}^{0.5} / \sigma_{T\text{split},b}} \quad (5)$$

where indices  $b$  refers to a specific Dolos.

It should be noted that the use of eq. (4) in the present tests is somewhat invalidated by the uncertainty on estimating  $\sigma_{T\text{split}}$  from relatively small cylinders, cf. the footnote in Table 1. However, the test result presented by the graphs in Figs. 8 - 10 are based on eq. (5) which is not significantly biased because  $\sigma_{T\text{split}}$  appears both in the nominator and the denominator.

$h_{N=1}$  in eq. (5) could not be found directly from a test because it is impossible to determine the pendulum speed which in just one impact on an untested unit causes exactly the ulti-

mate stress where the first crack appears. Therefore  $\Delta\sigma_{N=1}$  was determined by extrapolation to  $N = 1$  of the fatigue test results in a log-linear representation, see Figs. 6 and 7.

LEGEND:

● — TEST RESULTS, FIRST SIGN OF CRACK.

$$\frac{\Delta\sigma_N}{k} = \frac{\sqrt{h_N}}{\sigma_{Tsplit}}$$

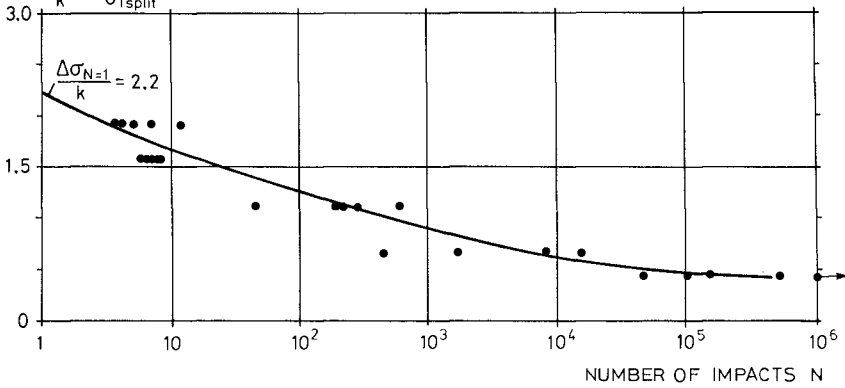


Fig. 6. Determination of  $\Delta\sigma_{N=1}$  for unreinforced flyash concrete Dolosse. Flexural stress.

LEGEND:

● — TEST RESULTS, FIRST SIGN OF CRACK.

$$\frac{\Delta\sigma}{k} = \frac{\sqrt{h_N}}{\sigma_{Tsplit}}$$

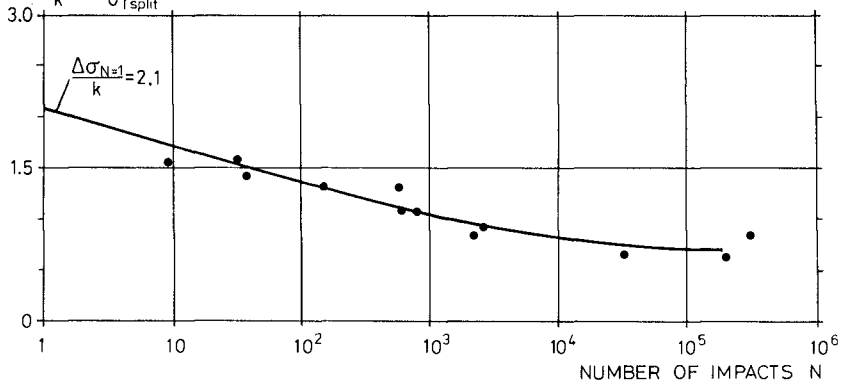


Fig. 7. Determination of  $\Delta\sigma_{N=1}$  for steel fibre reinforced concrete Dolosse. Flexural stress.

TEST RESULTS

Fig. 8 shows the result of the fatigue tests with unreinforced Dolosse.

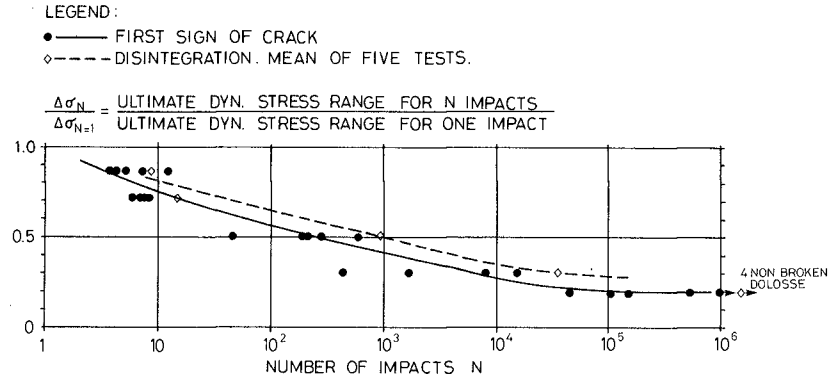


Fig. 8. Fatigue. Impact loaded Dolosse of unreinforced flyash concrete. Flexural stress.

The ordinate represents the ratio between two dynamic stresses, namely the ultimate dynamic stress range for N impacts to the same quantity for one impact, N = 1. Very often in such Wöhler diagrams the denominator is the static strength (cf. Fig. 2), but the presentation in Fig. 8 demonstrates the fatigue effect more clearly.

The full line corresponds to the first sign of crack, thus representing the design graph. The dotted line shows the state of disintegration. No sign of damage or indentation of the impacted Dolos-surfaces was seen in the test series with unreinforced concrete.

The results for the fibre reinforced units are shown in Fig. 9.

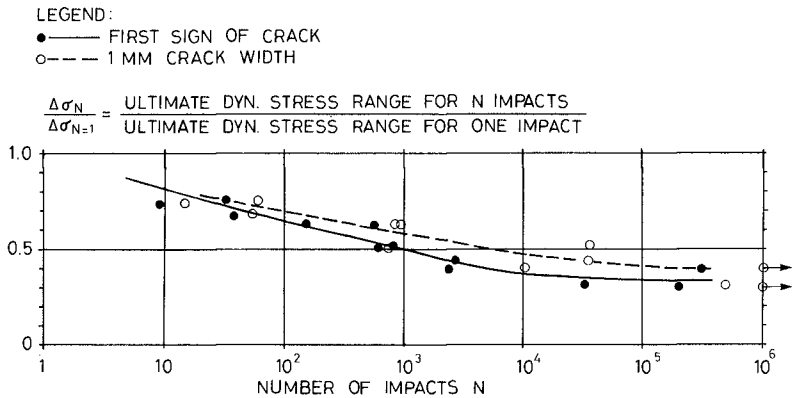


Fig. 9. Fatigue. Impact loaded Dolosse of steel fibre reinforced fly ash concrete. Flexural stress.

The full line corresponds to the first sign of crack and the dotted line to a crack width of 1 mm. For design purpose, the full line should be used since a crack width of 1 mm implies fast corrosion of the tiny steel fibres. If non-corrosive fibres are used cracks of some size might be acceptable. By large numbers of impacts an indentation was clearly seen on the impacted surface — quite contrary to the case of unreinforced concrete.

A comparison of the fatigue properties of the two types of concrete is presented in Fig. 10.

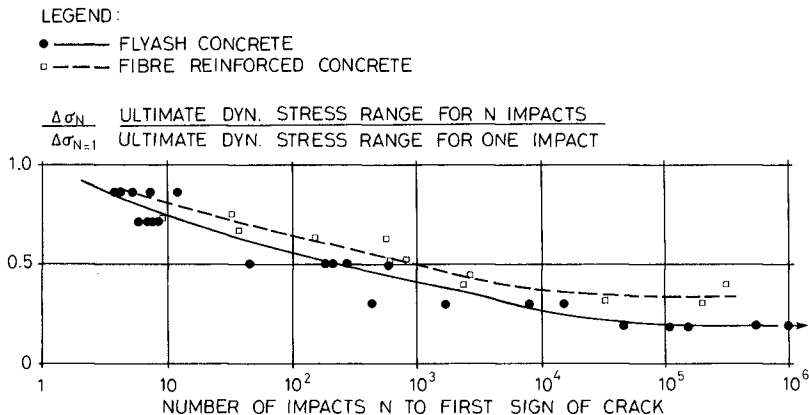


Fig. 10. Comparison of fatigue in impact loaded Dolosse of unreinforced and steel fibre reinforced flyash concrete. Flexural stress.

It is seen that the fatigue effect is smaller in the fibre reinforced units as it stabilizes at a stress range twice as big as for the unreinforced units for  $N \geq 10^5$ . This better performance is properly partly due to the development of a more soft impact surface, cf. the observed indentation.

Fig. 11 shows a comparison of the ultimate impact energy at the first sign of a crack. The impact energy, taken as the maximum kinetic energy of the pendulum, is dimensionless by dividing by  $gMH$ , where  $g$  is the gravitational constant,  $M$  the mass of the Dolos and  $H$  the height of the Dolos.

It is seen that, the fatigue life of the steel fibre reinforced concrete is the best of the two except for small number of impacts. However, the difference is fairly small and probably much smaller than most people expect since it is often said in the literature that fibres increase the energy absorbtions at failure many times, compared to plain concrete.

For example in ref. (11) a factor of "at least ten times" is related to a steel fibre content of  $100 \text{ kg/m}^3$ .

The reason for this discrepancy is the fact that most testing of fibre reinforced concrete reported in the literature is done with rather slender specimens, such as beams, where large deflection creates only very small cracks, contrary to what is the case with stiff bodies like Dolosse and Tetrapods. Another important reason is that in the case of armour units failure must be defined as the appearance of a crack, while in the concrete literature failure of tested specimens is usually taken as the state of complete disintegration or some high level of deformation.



LEGEND:  
 ○ — FLYASH CONCRETE  $\bar{\sigma}_f = 3.65 \text{ N/MM}^2$   
 ● — FIBRE REINFORCED CONCRETE,  $\bar{\sigma}_f = 3.85 \text{ N/MM}^2$ , STEEL FIBRE  $45 \times 1 \text{ MM} - 160 \text{ KG/M}^3$   
 m AND v MASS AND VELOCITY OF PENDULUM.  
 M AND H MASS AND HEIGHT OF DOLOS.  
 g GRAVITATIONAL CONSTANT.

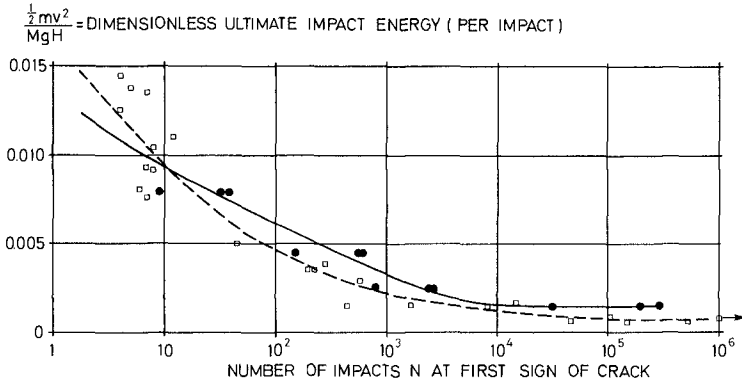


Fig. 11. Fatigue. Comparison of ultimate impact energy for impact loaded Dolosse of unreinforced and steel fibre reinforced flyash concrete. Flexural stress.

The effect of steel fibres on the fatigue life and on the impact strength of slender armour units seems to be small and is certainly much smaller than the effect of similar quantities of steel in a conventional bar reinforcement, cf. also discussion of reinforcement in ref. (1).

In Fig. 12 the results of the present flexural impact tests with unreinforced concrete (Fig. 8) are shown together with the results of the uniaxial impact tests with small specimens (Fig. 2).

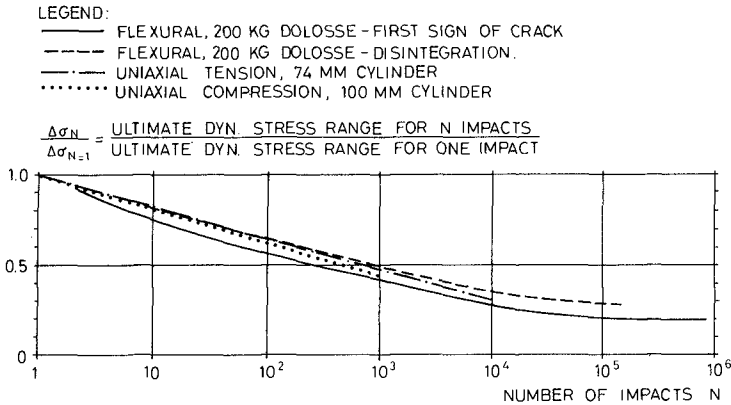


Fig. 12. Fatigue. Unreinforced concrete. Impact load.

It is seen that the graphs almost collapse into one single graph which then represents a universal curve for fatigue of *impact* loaded unreinforced concrete. Moreover, the graphs in Figs. 2 and 3 representing fatigue due to *pulsating* uniaxial loads fall into one graph. Because it seems most likely that also in this case fatigue due to pulsating flexural load follows this graph one can then produce two universal graphs as shown in Fig. 13, one representing fatigue by impact load and one representing pulsating load.

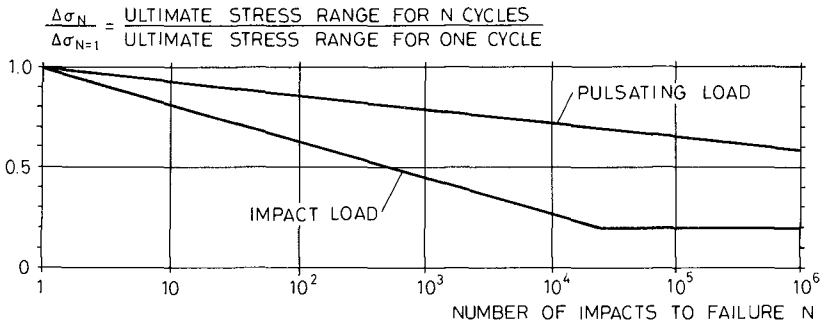


Fig. 13. Fatigue in conventional unreinforced concrete. Uniaxial and flexural stress.

Having in mind the uncertainties on the important parameters involved in rubble mound breakwater design, the graphs in Fig. 13 are regarded accurate enough for practical design of armour layers made of conventional unreinforced concrete blocks. It should be noted that the ultimate *impact load* strength for one cycle is in the order of 1.4 and 1.5 times the ultimate *pulsating load* strength in the case of uniaxial tension and compression respectively, cf. Fig. 2. For flexural stresses a factor of app. 1.4 should be used.

The ultimate pulsating load strength properties for one cycle can be taken equal to the static ones.

**IMPLEMENTATION OF FATIGUE IN THE DESIGN PROCESS**

The fatigue life is usually evaluated according to the *Palmgren-Minor accumulated damage theory* on the basis of a propiate Wöhler diagram, e.g. Fig. 13.

The Palmgren-Minor rule expressing the cumulative damage ration, D reads

$$D = \sum_{i=1}^K \frac{\eta_i}{N_i} \leq 1 \quad , \quad (6)$$

where  $\eta_i$  is the number of cycles within the stress range interval  $i$ ,  $N_i$  is the number of cycles to failure at the same stress range derived from the Wöhler diagram and  $K$  is the total num-

ber of stress range intervals. This implies that the number of stress cycles and the corresponding stress ranges throughout the lifetime of the structure, i.e.  $\eta$ ,  $N$  and  $K$  in eq. (6), must be estimated. This again means that the *load history* and the *relationship between the load and the stresses* must be established.

Pure deterministic calculations are impossible. More realistic is a *stochastic* approach.

In breakwater engineering the load history is closely tied up with the wave history. In most places a reasonable estimate on the wave history can be obtained from hindcast studies or observations. The wave history may be presented as the variation in significant wave height,  $H_s$  with the time,  $t$ , see Fig. 14.

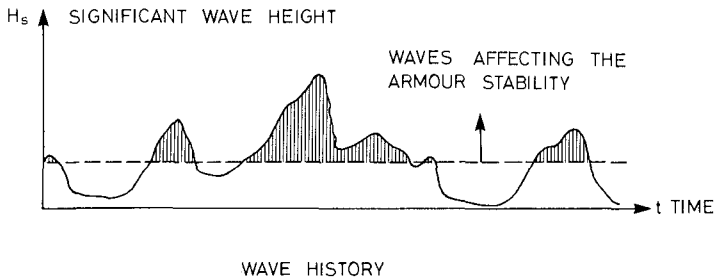


Fig. 14. Wave history.

The wave period which is also of great importance is included in this representation if a relationship between wave height and period is established; for example is a power relationship often found. Only waves or storms over a certain size will contribute to the stability conditions of the armour block. The cut-off level, shown as a dotted line in the figure, depends on many things of which the type, the size, the material strength properties and the location on the structure of the armour blocks are the most important. The cut-off level will be relatively low for complex types of units, especially for the big ones where the stresses are high due to their own weight alone. The cut-off level might vary with time due to change in the strength properties of the concrete or change in hydraulic stability, for example caused by abrasion of the blocks.

The storm history can be modelled as a weakly stationary, stochastic process with a specific intensity, and following a specific extreme distribution, for example a Weibull distribution. Further, if independence between storm event is assumed the starting times of the storms can be characterized by a Poisson counting process. The wave heights are Rayleigh distributed in intervals of stationarity.

The stresses in an armour unit can be split into three terms, cf. Fig. 1: The *static* stresses mainly due to gravity, the *pulsating* stresses due to flow forces generated by the waves and the *impact* stresses generated when units are rocking, displaced and hit by other units. The problem is to find the stress transfer functions i.e. the relationship between the stresses and the wave action on the specific location of the breakwater structure, as illustrated in Fig. 15.

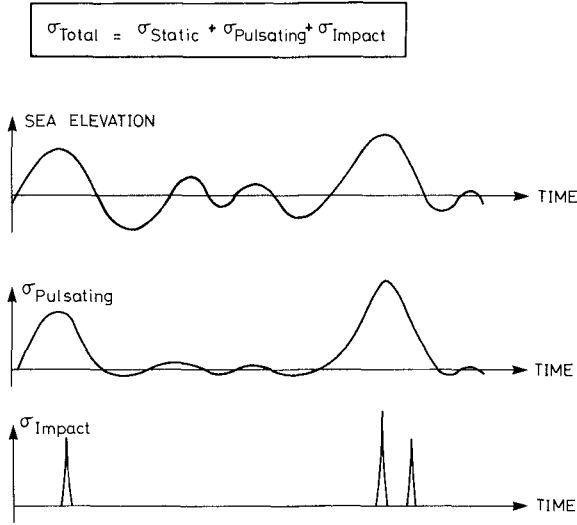


Fig. 15. Realization of wave induced stresses in an armour unit.

Due to the random placement of the armour units the stress transfer functions must be characterized by reference values (as for example the mean) and the distribution functions as illustrated on Fig. 16.

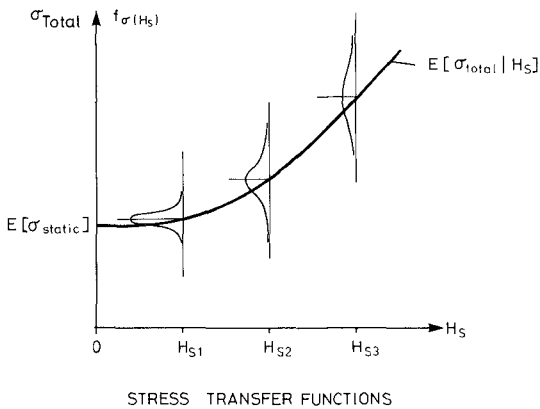


Fig. 16. Qualitatively illustration of dependence of stress transfer frequency functions on wave parameter.

The static stress field might be established from strain gauge measurements on large scale model armour layers in the dry combined with similarity considerations.

The dynamic stress field is much more difficult to assess. Because prototype measurements are very difficult and expensive the problem must be studied in large scale hydraulic models mainly by strain gauge measurements. The huge amount of work necessary to meet the needs of the practical designer calls for international sponsorship and cooperation.

In a consistent design process the above discussed strength aspects must be linked to the hydraulic stability aspects. Ref. (12) titled "Stochastic design of rubble mound breakwaters" deals with this problem taking into account also impact fatigue based on an estimated simple stress transfer function.

#### ACKNOWLEDGEMENTS

The study was sponsored by The Danish Council for Scientific and Industrial Research. The cooperation of Mr. Sven Hvid Nielsen and Mr. J.Kr. Jehrbo Jensen, the help of Aalborg Portland Cement and Concrete Laboratory in preparing pilot tests with fibre reinforced beams and the discussions with Prof. D. Krajinovic and Dr. A.J. Zielinski are gratefully acknowledged. N.B. Beton Aps and S.N. Simonsen & Co. are thanked for the supply of concrete and fibres.

#### REFERENCES

1. Burcharth, H.F.: Material, Structural Design of Armour Units. Proc. Seminar on Rubble Mound Breakwaters. Royal Inst. of Technology, Stockholm, Sweden. Bulletin No. TRITA-VBI-120, 1983.
2. Burcharth, H.F.: The Way Ahead. Proc. Conf. on Breakwaters — Design and Construction. Inst. of Civil Engineers, London, 1983.
3. Tepfers, R., Kutti, T.: Fatigue strength of plain ordinary and lightweight concrete. ACI-Journal, May 1979.
4. Tepfers, R.: Tensile fatigue strength of plain concrete. ACI-Journal, August 1979.
5. Fagerlund, G., Larsson, B.: Betongs slaghallfasthed (in Swedish). Swedish Cement and Concrete Research Institute at the Institute of Technology, Stockholm, 1979.
6. Zielinski, A.J., Reinhardt, H.W., Körmeling, H.A.: Experiments on concrete under repeated uniaxial impact tensile loading. RILEM Matériaux et Constructions, Vol. 14, No. 81, 1981.
7. Tait, R.B., Mills, R.D.W.B.: An investigation into the material limitations of breakwater Dolosse. ECOR newsletter No. 12, 1980.
8. Silva, M.G.A.: On the mechanical strength of cubic armour blocks. Proc. Coastal Structures '83, Washington, USA, 1983.
9. Burcharth, H.F.: Full scale trials of Dolosse to destruction. Proc. 17th Int. Conf. on Coastal Engineering, Sydney, 1980.
10. Burcharth, H.F.: Full scale dynamic testing of Dolosse to destruction. Coastal Engineering, 4, 1981.

11. Hippert, A.P., Hannant, D.J.: Impact resistance of fibre concrete. TRRL Supplementary Report 654. Transport and Road Research Laboratory, Dept. of the Environment. Berkshire, U.K.
12. Nielsen, S.R.K., Burcharth, H.F.: Stochastic design of rubble mound breakwaters. Laboratoriet for Hydraulik og Havnebygning, Aalborg University, June 1983. Short version: Proc. 11th IFIP Conf. on System Modelling and Optimization, Copenhagen 1983.

## CHAPTER ONE HUNDRED SEVENTY FIVE

### Stability of Armour Units in Flow Through a Layer

Alex C. Thompson \*  
Hans F. Burcharth \*\*

#### Abstract

As part of a program to study the hydraulics of wave attack on rubble mound breakwaters tests were made on model armour units in a steady flow through a layer laid on a slope. The flow angle has little effect on stability for dolosse or rock layers. The head drop at failure across each type of layer is similar but the dolosse layer is more permeable and fails as a whole. There was no viscous scale effect. These results and earlier tests in oscillating flow suggest a 'reservoir' effect is important in the stability in steep waves.

#### Introduction

Many types of concrete unit for armouring rubble mound breakwaters have been designed to try and achieve a good stability to weight ratio and low costs of production. The designer of a breakwater often finds it difficult to choose between these different units as no systematic information on their stability exists. The physics behind the differences in stability of slender and bulky units is still poorly understood despite the large number of model tests and investigations of flow in rubble mound structures that have been performed.

Generally for units of the same weight and density, slender ones like dolosse exhibit a better hydraulic stability than bulky ones like cubes. However the different types of armour do not respond in the same way to changes in wave characteristics. Whillock and Price (7) for example, showed that oblique wave attack can dislodge dolosse much more easily than waves approaching at right angles and Burcharth (3) has demonstrated that the stability of a dolosse slope decreases as the wave period increases. Both effects are in contrast to the behaviour of slopes made of rocks.

It is thought that the explanation for this is the 'reservoir effect' by which the greater volume of voids in a dolosse pack can absorb a larger fraction of the uprushing wave than a rock slope. This idea emerged from work by the present authors (4) on oscillating flow over the surface of dolosse and rock layers. They found that the dolosse were only slightly more stable than stones of the same weight in this fully submerged flow, a similar result to that of Brebner (2) who tested dolosse and rocks in steady flow. The present work investigated the stability of dolosse and rocks on a slope in flow from underneath at various angles to the layer. The flow is uni-directional and through the

\* Lecturer, University of Sheffield, England

\*\* Professor of Marine Civil Engineering, Aalborg University, Denmark

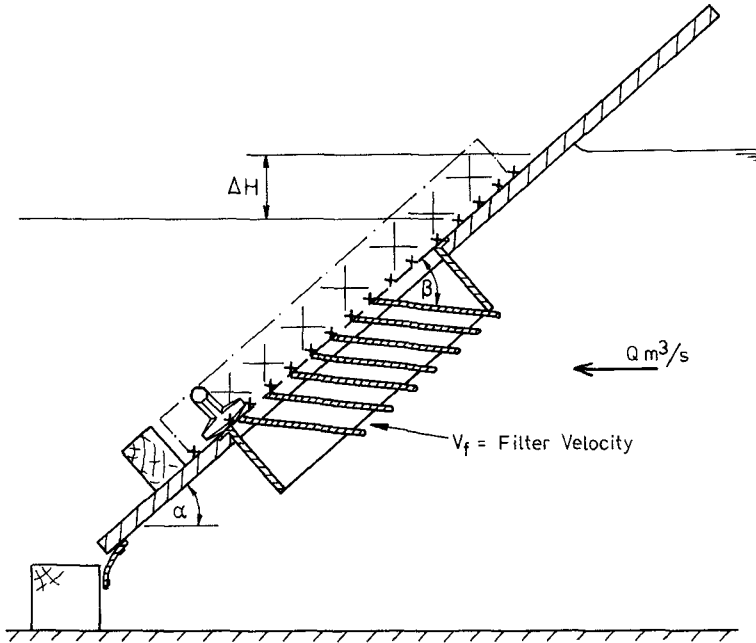


Figure 1 Throughflow Test Rig

layer. The object was to see if the differences in stability of slender and bulky units could be due to a difference in their response to flow through the cover layer, rather than to flow parallel to the surface. It was thought that at some instants of the wave motion on a breakwater the flow emerging through the slope may have a similar effect to the test flow.

A secondary object was to examine a further scale effect which might arise in models of rubble mound breakwaters, if flow through the layers was important as well as flow over the surface. To this end a scale model of the relevant parts of the main rig was made and tested.

#### Experimental Method

Layers of dolosse and rocks laid on a slope were subjected to flow through the slope, and through the layer. The head drop and flow rate at which the layer failed, as defined below, were found for different slope angles,  $\alpha$  and flow angles,  $\beta$ . A sketch of the apparatus is shown in fig. 1.



The test rig consisted of a plywood board thickness 20mm, width 0.9m and height 1.2m which formed the test slope. This was mounted so that its slope could be varied between  $15^\circ$  and  $45^\circ$  in the high head flume at the Hydraulics Research Station, Wallingford. This is a glass sided flume with a wooden floor and cross-section of 0.9 x 0.9m. Rubber seals were arranged round the edge of the board so that flow took place only through a hole of dimensions 0.6m wide by 0.34m deep in the lower half of the board, under the area covered by the armour units. The bottom units rested on a wooden ledge running the width of the board, and all units lay on an expanded metal mesh covering the board and the flow opening. In the flow opening one of three sets of vanes fixed at angles of  $20^\circ$ ,  $45^\circ$  and  $90^\circ$  to the slope could be mounted. These were made from aluminium plates of thickness 3mm and length 150mm mounted with a gap of 20mm between each in a rigid frame made from 12mm plastic plates. The flume was supplied with water from a large sump via a pump feeding a constant head tank. The water then flowed through a control valve into the inlet tank of the flume, over a 'V' notch where the discharge was measured, into a settling section through various screens and into the working section of the flume. The slope was mounted halfway along the 10m working length and at the end of the flume an adjustable over-shot tailgate allowed the water level downstream of the test slope to be varied.

The armour units used for the test were plastic dolosse with metal bars embedded in the limbs to give a weight of 130 gms, a height of 70cm and an average density of  $2.40 \text{ gm/cm}^3$ . The rock was selected from a supply of crushed rock by eye to match a number of individually weighed rocks and to have a reasonably cube-like shape. The average weight of the rocks was then found to be 124 gm and the density  $3.0 \text{ gm/cm}^3$ .

The number of dolosse used was 297 and the same number of rocks were employed in building a test layer. A single layer of units was used, placed by hand starting from the bottom of the slope but with no overall system of laying other than to get all the units in an area of 0.9m x 0.5m and to fill any obvious holes. This area was chosen so that the flow opening was covered, the full width of the channel occupied by units and because initial trials with the units showed that the number used filled this area naturally. The photographs 1 and 2 show views of the layers as completed.

The procedure for each test was to set the slope at the desired angle using a protractor in the form of an adjustable set square with a spirit level attached to it. The layer of units was then laid as described above and the flume filled using a slow rate of flow to avoid a large head drop across the slope before the flume downstream of the slope filled up. The rate of flow was then increased slightly and the water levels immediately upstream and downstream of the slope measured, while the slope was observed closely for signs of failure. The water levels were measured with point gauges attached to metre rules. The rules were held against the metal rails at the top of the flume, which had been accurately levelled, and read from the top edge of the rails. This system was adopted to follow the fast change in water levels which occurred after increasing the flow, so that the levels at the point of failure could be measured. As soon as holes appeared in

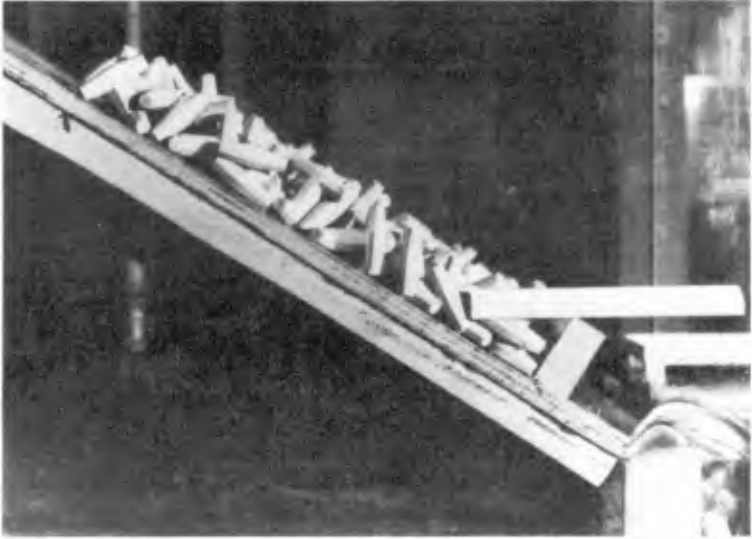


Photo 1 Dolosse layer.



Photo 2 Rock layer.

the layer the water levels would change again. The experiment was performed with two observers so that the water levels could be followed and so that one was always watching the slope. After these levels had been measured the water level upstream of the V notch was read using a pointer gauge mounted on a calibrated screw in a stilling tube. If the slope had not failed the flow rate was increased slightly and further readings taken.

The occurrence of failure was usually quite obvious but with careful control of the flow rate different stages could be observed, and the conditions just prior to failure established. Without close observation and control the failure flow could be exceeded giving complete collapse of the dolosse layer or large holes in the rock layer, as the first change noted. With a layer of dolosse a slight settling down the slope could be observed before failure, followed by the opening of gaps in the layer at a slightly larger flow, this is the failure condition and any further increase in flow would usually result in all the dolosse sliding down and off the slope. Occasionally larger gaps would open before total failure happened. With a layer of rocks the indication of failure was the displacement of individual rocks from their original position to positions lower down the slope, leaving holes in the layer. When 2 or 3 rocks had been moved in this way the flow could be increased without increasing the head drop and further rocks would move leaving more holes, as the flow was raised. The displacement of 2-3 rocks was taken as the failure condition for rock slopes. The rock layers never slid right off the slope as the dolosse layer often did.

Once the failure condition had been determined the flume was emptied, the slope angle changed and the layer rebuilt for another test. Slope angles  $\alpha$  of  $43.5^\circ$ ,  $36.7^\circ$ ,  $23.6^\circ$  and  $18.6^\circ$  were tested, first with dolosse and then with rock. The next set of vanes was then fitted to the test rig and the tests repeated so that results were obtained for vane angles  $\beta$  of  $90^\circ$ ,  $45^\circ$  and  $20^\circ$ . The head loss through the apparatus without a layer of armour units in place was found so that the head drop across the layer of units could be estimated.

After the main test had been completed a scale model of the apparatus was built based on the size of small dolosse available. These weighed 14.5 gm and had a height of 3.7cm. A plate to fit over the original flow opening was built, containing an opening scaled down in the ratio  $3.7/7.0 = 0.486$ . A set of vanes set at  $\beta = 90^\circ$  was also built to this scale and a step to hold the bottom of the layer. Expanded metal mesh of very nearly the correct scale (0.5) was used for the base of the layer. The flow and head drop at failure was found for the dolosse layer and for a layer of 14.5 gm stones, using this scaled down version of the original test.

A short series of tests which we refer to as 'overflow' tests was performed by blocking the hole in the sloping board and letting water flow over the top. The layers were built on the top half of the board supported by a new step fixed above the original opening. Layers of the large units were tested at several slope angles. In each run the slope of the board was set and the layer was built in the same way as for the throughflow test. The flow rate was gradually increased until the layer failed or the maximum flow rate was reached. The depth of flow above

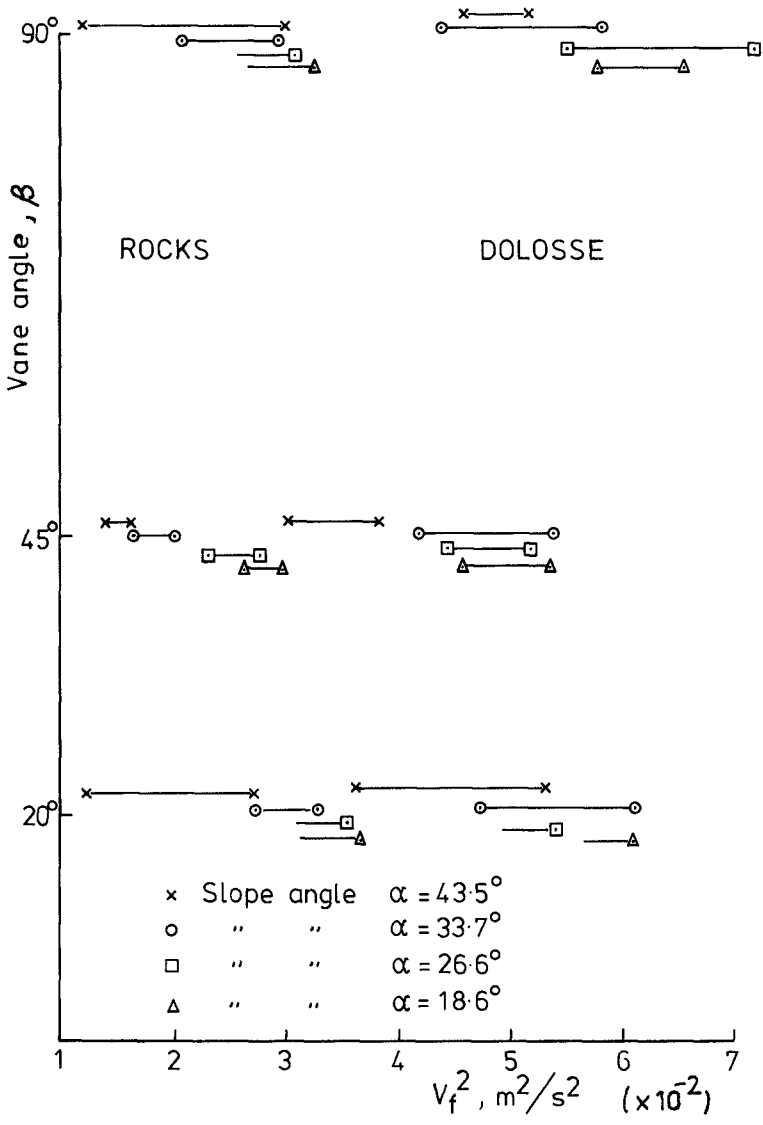


Figure 2 Filter Velocity Squared at Failure

the board and the flow rate were measured at several settings below failure. Depth was measured using a rule looking through the glass side of the flume half way down the slope where water surface is roughly parallel to the bed. This measurement was inevitably approximate until the water surface was well above the surface of the layer and became smooth.

#### Test Results

The test results were plotted in three graphs shown in figs. 2, 3 and 4. In the first of these the square of the filter velocity,  $V_f^2$ , at failure was plotted against vane angle,  $\beta$ . These results for the large units only. The slope angle  $\alpha$  was indicated by the different symbols shown in the figure and the failure condition is indicated by a range of values in some cases.  $V_f$  was defined as the discharge at failure divided by the area of the opening in the slope. This plot shows that the vane angle had little effect on the stability of either type of layer. The dolosse could withstand a higher filter velocity but this was because the permeability was higher as discussed below. It is interesting that the effect of slope angle,  $\alpha$ , is not great, with only  $\alpha = 43.5^\circ$  giving obviously lower  $V_f^2$  at failure, in this figure.

The second plot, fig. 3, shows the hydraulic gradient,  $i$ , across the layer at failure, versus the slope angle. This is expressed in a non dimensional form as follows. The hydraulic gradient  $i$  was calculated from:

$$i = \frac{(\Delta H - VL)}{t} \quad (1)$$

where  $\Delta H$  = total measured head loss  
 $VL$  = Vane loss of same flow rate  
 $t$  = thickness of layer

The layer thickness,  $t$ , is difficult to measure directly but an average value was found from the equation

$$t = \frac{W'N}{A(\rho_s - \rho)g(1 - n)} \quad (2)$$

where  $W'$  = submerged weight of a unit  
 $N$  = number of units in layer  
 $A$  = area covered by layer  
 $n$  = porosity of layer  
 $\rho_s$  = density of armour unit material  
 $\rho$  = density of water

A critical hydraulic gradient  $i_c$  was calculated for the condition that the pressure force across the layer is equal to the component of the weight of units and water in the layer at right angles to the layer. This gives the expression

$$i_c = - \left( \frac{\rho_s}{\rho} - 1 \right) (1 - n) \cos \alpha \quad (3)$$

Equations (1), (2) and (3) were then combined to give the quantity

$$\frac{i}{i_c} = \frac{(\Delta H - VL) \rho g A \left(\frac{\rho_s}{\rho} - 1\right) (1 - n)}{W'N \left(\frac{\rho_s}{\rho} - 1\right) (1 - n) \cos \alpha}$$

i.e.

$$\frac{i}{i_c} = \frac{\rho g (\Delta H - VL) A}{W'N \cos \alpha} \quad (4)$$

Figure 3 shows  $i/i_c$  versus slope angle  $\alpha$ . These results are for a vane angle  $\beta$  of  $90^\circ$  and include the tests on the small units. For the two lowest slope angles  $\alpha$  of  $18.6^\circ$  and  $26.6^\circ$  the layer fails for  $i/i_c$  between 0.85 and 1.0 for rocks and dolosse of both sizes tested. At  $\alpha = 33.7^\circ$  there was slightly more variation in the results with most layers failing at  $i/i_c$  between 0.8 and 1.0, and the small dolosse failing at  $i/i_c$  between 0.75 and 0.8. At the highest slope  $\alpha = 43.5^\circ$ , all layers except the small stones failed at lower values of  $i/i_c$  between 0.65 and 0.8. Although rock and dolosse layers failed at similar values of  $i/i_c$  the mode of failure was different. In rock layers individual units were removed from the layer leaving holes and were deposited lower down the slope. Dolosse layers failed by the whole layer sliding down the slope. Sometimes a slight settlement or bowing out of the layer can be seen shortly before the complete collapse.

The third graph, fig. 4, gives the head drop across a layer  $(\Delta H - VL)$  against the filter velocity squared,  $V_f^2$ . Results for the small units are plotted scaled up according to a Froudian law using the length scale  $\lambda = 0.486$ . The results for large rocks and large dolosse fall on straight lines indicating that the flow is turbulent and viscous scaling effects are absent in this size of model. The results from the small units fall mainly on or below the same lines.

The results of the overflow tests are given in table 1. Both types of layer dolosse and rock failed in a similar way. A few units were removed from the layer soon after the water covered most units. The flow could then be increased without further losses until a level where units began to be removed again, and once 2 or 3 had been removed the layer failed completely, being progressively washed away by the flow. A dolosse layer that was slightly looser in build than normal failed by sliding at a low flow rate, when the water just covered most units. The water which flowed through the layer and out at the toe never removed any units from the outflow region, with either dolosse or rock.

#### Interpretation of Results

The first fact apparent from the results is that the angle of flow at the bottom of the layer,  $\beta$ , does not affect the failure conditions of dolosse or rock. The higher stability dolosse under attack by steep waves is not due to an effect of the angle of flow through the layer.

The results did show a difference in permeability between dolosse and rock but an equal drop in total head across the layers required to produce failure. The critical head gradient  $i_c$  is much lower for

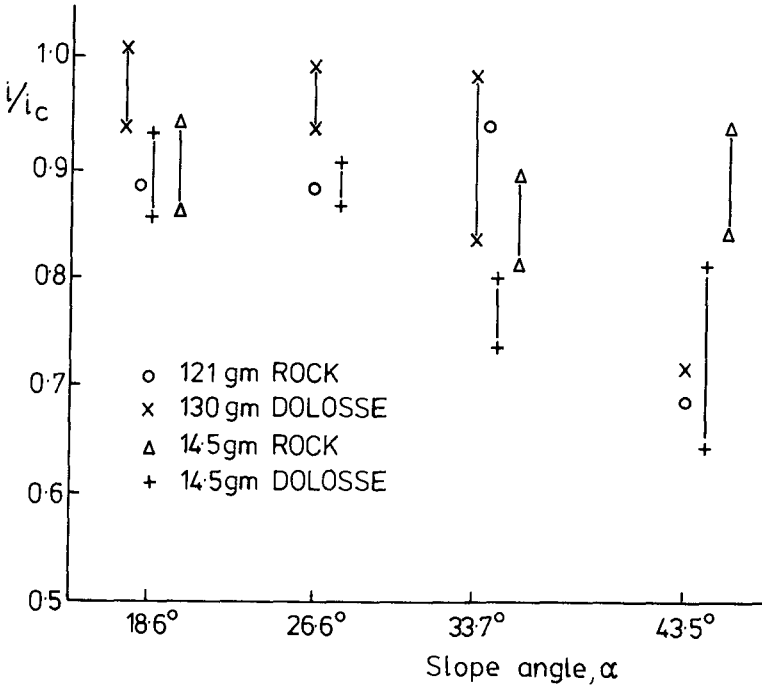


Figure 3 Hydraulic Gradient at Failure.

dolosse than rock but must act over the greater thickness of the dolosse layer. For example calculating  $i_c$  from equation (2) we find

For rock  $(\frac{\rho_s}{\rho} - 1) = 1.65, n = 0.4, i_c = 0.99 \cos \alpha$

For dolosse  $(\frac{\rho_s}{\rho}) = 1.4, n = 0.6, i_c = 0.56 \cos \alpha$

It is perhaps surprising that the angle of slope does not influence the head gradient at failure more than the  $\cos \alpha$  factor, at lower slopes than  $\alpha = 43.5^\circ$ . This is particularly so for rock where at  $\cot \alpha$  term appears in Hudson's Equation. This may be due to the placing of the rock layer by hand, rather than pell-mell dumping. Dolosse layers are often laid at steeper slopes and their structure does seem to make them less sensitive to slope than rock layers. The type of failure in throughflow, blanket as opposed to individual movement, may mean that dolosse layers will be more resistant to a localised critical head gradient. Certainly the gradient required to remove individual dolosse must be greater than that measured in the present experiments.

If it can be shown that the head gradient across the cover layer is near the critical value in a breakwater attacked by waves then these differences may explain the differences in stability between bulky and slender units in waves. Some evidence on this is provided by the results of Bavends et al (1). Calculations and measurements on a large physical model of Sines breakwater repaired section, both give the pressures in the region of maximum outflow. The wave height of 20m is sufficient to cause some damage according to the results of Mol et al (6). The parameter  $\xi = \tan \alpha / \sqrt{H/L_0}$  can be estimated as between 2.05 and 1.083 if the wave period is in the same range, 22 to 16 secs. as that used by Mol et al. (6). The pressures under the first filter layer and above the cover layer are given. Calculating the thickness of the two armour layers and the filter layers from the details given by Barends the head gradient can be estimated as  $i \approx 0.44$ . This is well below the critical value. Evidence from the overflow experiment described above is that water rushing down through the cover layer and then out at the toe of the slope is unable to dislodge either dolosse or rocks. Finally in model tests on breakwater sections with a cover layer of dolosse damage occurs with single units being removed. That is, a different type of failure than in the throughflow test takes place. All this suggests that on a conventional design of rubble breakwater the cover layer is not damaged by throughflow before other types of damage start. In an earlier series of tests, Burcharth and Thompson (4) the authors showed that fully submerged layers of dolosse and rock have about the same stability in oscillatory flow parallel to the surface of the layer. It is suggested that the good stability of dolosse in steep waves is due partly to interlocking and partly to a reservoir effect. That is, the large voids in the dolosse layer absorb a significant proportion of the uprushing wave, and this water then runs down within the layer so that it cannot remove units from the layer.

Calculations by Koutitas (5) on a breakwater section of uniform permeability, indicate that hydraulic gradient  $i$ , can exceed the critical values found in the present tests. Throughflow might therefore cause damage in a breakwater with unusually permeable underlayers. This point can probably be explored by further calculations.

The measurements of head drop across the layers show no evidence of a scaling effect due to viscosity. The points predicted by scaling up results from the small units using Froude scaling fall close to the results from the large units. The units span the usual range of sizes used in models except in giant flumes. The Reynolds number of the flow through the small rock is  $V_p D / \nu = 1.9 - 5.2 \times 10^3$ . This is just above the limit of  $2 \times 10^3$  for viscous effects in porous media suggested by Yalin (8). In the region of high outflows through the cover layer there should therefore be little viscous scale effect in models. A possible scale effect of a different sort is the force exerted in building the models. This will be relatively greater in small models where the units are placed by hand and could be responsible for the high strength of the small rock layer at  $\alpha = 43.5^\circ$  in the present results. A similar effect was noted in the oscillatory flow tests.

#### Acknowledgement

The model tests described in this paper were carried out at



Table 1 Overflow Results

Q m <sup>3</sup> /s	y m	Remarks
.0127 .0180 .0215 .0257 .0296 .0325 .0390 .0458	.05 approx. .06 " .07 " .075 " .08 " .0825 " .085 " .09 - .10	<u>Dolosse <math>\alpha = 33.7^\circ</math></u> No movement " " - Layer just covered " " 3 lost No more losses 2 Lost at slightly higher flow Failure
.0571 .0839	.095 approx .12 " .13 "	<u>Dolosse <math>\alpha = 26.6^\circ</math></u> About 10 lost Failure
.0172 .0172 .0335 .0946	.07 approx .09 " .15 "	<u>Dolosse <math>\alpha = 18.4^\circ</math></u> Layer nearly submerged 1 lost No movement, max. flow
.00963 .0182 .0223 .0283	.03 approx .05 " .055 .06	<u>Rock <math>\alpha = 33.7^\circ</math></u> Layer submerged, 2 rocked 1 lost then failure (RH half)
.0074 .0144 .0177 .0257 .0314	.03 approx. .04 " .05 " .06 .065	<u>Rock <math>\alpha = 26.6^\circ</math></u> Most rocks covered 2 lost 2 lost then failure (RH half)

Hydraulics Research Wallingford. The authors express their thanks to the Director and his staff for their kind assistance and permission to use the photographs presented here.

REFERENCES

1. Barends, B.J., Van der Kogel, H., Uijtewaal, F.H. and Hagenaar, J. "West Breakwater Sines - Dynamic - Geotechnical Stability of Breakwaters". Coastal Structures '83, ASDC Conf. Washington 1983.
2. Brebner, A., "Performance of Dolosse Blocks in an Open Channel Situation". Proc. 16th ICCE Hamburg 1978.
3. Burcharth, H.F. 'The Effect of Wave Grouping on On-Shore Structures', Coastal Engineering, Vol.2, 1979.
4. Burcharth, H.F. and Thompson, A.C. "Stability of Armour Units in Oscillatory Flow". Coastal Structures '83, ASCE Conf., Washington 1983.
5. Koutitas, C. 'A Numerical Model for Rubble Mound Breakwater Stability'. Coastal Eng. (in press), 1982.
6. Mol, A., Ligtevingen, H., Groenweld, R.L. and Pita, C.R.A.M. 'West Breakwater Sines - Study of Armour Stability', Coastal Structures '83. ASCE Conf., Washington, 1983.
7. Willcock, A.F. and Price, W.A. 'Armour Blocks as Slope Protection'. Proc. 15th ICCE, Honolulu, 1976.
8. Yalin, M.S. 'Theory of Hydraulic Models'. Macmillan.

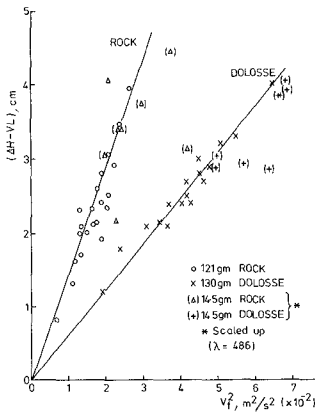


Figure 4 Head Drop Across Layers versus  $V_f^2$ .

## CHAPTER ONE HUNDRED SEVENTY SIX

### Stability of Rubble Mound Slopes under Random Wave Attack

J.W. van der Meer\* and K.W. Pilarczyk\*\*

#### Abstract

The objective of the present research project is to give new practical design formulae for rubble mound slopes under random wave attack. The study is based upon a series of model tests. More than two hundred tests have been performed in order to vary systematically all the relevant variables. The main shortcomings in Hudson-type formulae have been solved as a result of the present series of investigations. Stability formulae are given which include the influence of wave period, number of waves, armour grading, spectrum shape, groupiness of waves and the permeability of the core.

#### Introduction

The use of coarse materials, such as gravel and natural stone for slope revetments, is very common in civil engineering. In recent years, there has been an increasing demand for reliable design formulae, to cope with the ever growing dimensions of the structures and the necessity to move into more hostile environments.

In 1981, the Netherlands Public Works Department commissioned the Delft Hydraulics Laboratory to perform a systematic study with the objective of developing design rules for both statically and dynamically stable slope revetments. The first results of this study, the design data for statically stable revetments, are given in this paper. Design criteria for dynamically stable gravel revetments have been reported earlier [5]. Research on profile development for rock material is still in progress. Reference should be made to [7] for a preliminary review of the complete study.

The Hudson formula is well known because of its simplicity. In the last decade, however, it has been found by many users to have a lot of shortcomings. It does not include the influence of the wave period and no data are available for random waves. The study of Ahrens [1] in a large wave tank showed the importance of the wave period on the stability of riprap. The tests, however, were performed with regular waves. Evaluation of Ahrens' data by Pilarczyk and den Boer [7] produced stability formulae which included the wave period. Losada

---

\* Delft Hydraulics Laboratory, P.O. Box 117, 2600 MH Delft,  
The Netherlands

\*\* Delta Department, Rijkswaterstaat, P.O. Box 20904, 2500 EX  
The Hague, The Netherlands

and Giménez-Curto [6] gave formulae for stability of rubble mound slopes under regular wave attack which also included the wave period.

An extensive investigation has been performed by Thompson and Shuttler [9] on the stability of rubble mound slopes under random waves. One of their main conclusions was, that within the scatter of the results, the erosion damage showed no clear dependence on the wave period. Reanalyzing their data, the authors, however, have found a very clear dependence on the wave period! The analysis also showed that only steep waves were used with a small range of wave periods. The work of Thompson and Shuttler has, therefore, been used as a starting point for the present research. By performing tests with longer wave periods, the dependence of erosion damage on wave period has been confirmed for a wider range of conditions. In addition the dependency on other variables has been investigated.

#### Governing Variables

A design formula for armour units should give a method of determining the minimum mass of individual armour units for given mass densities, required for stability as a function of all the variables involved. In the following the average mass of graded rubble is referred to as  $W_{50}$  or to the nominal diameter,  $D_{n50}$ , where:

$$D_{n50} = (W_{50}/\rho_a)^{1/3} \quad (1)$$

where:  $D_{n50}$  = nominal diameter (m)  
 $W_{50}$  = 50% value of the mass distribution curve (kg)  
 $\rho_a$  = mass density of stone (kg/m<sup>3</sup>)

The relative mass density of the stone in water can be expressed by:

$$\Delta = \rho_a/\rho - 1 \quad (2)$$

where:  $\Delta$  = relative mass density (-)  
 $\rho$  = mass density of water (kg/m<sup>3</sup>)

As shown by many authors there are a large number of variables affecting armour stability. The primary variables are shown in Table 1.

The wave height can be normalized by dividing the significant wave height,  $H_s$ , by the relative mass density and the nominal diameter. This dimensionless wave height is the same as the often used stability number  $N_s$  and reduces the Hudson formula to a very simple form:

$$H_s/\Delta D_{n50} = (K_D \cot \alpha)^{1/3} \quad (3)$$

The wave period can be related to external processes, waves breaking on a slope, by the dimensionless surf similarity parameter,  $\xi_z$ , where:

$$\xi_z = \tan \alpha / \sqrt{2\pi H_s/g T_z^2} \quad (4)$$

Table 1 Primary variables affecting armour stability

variable	symbol	dimension
nominal diameter	$D_{n50}$	m
relative mass density	$\Delta$	-
significant wave height	$H_s$	m
average wave period	$T_z$	s
slope angle	$\alpha$	degr
damage level	$S_2$	-
number of waves	$N$	-
armour grading	$D_{85}/D_{15}$	-
spectrum shape	$\epsilon_{5\%}, Q_p$	-
groupiness of waves	$G.F., J_1, J_2$	-
permeability of core	-	-

Plots of  $H_s/\Delta D_{n50}$  or  $N_s$  versus  $\xi_z$  are used by many authors to show the influence of wave period on armour stability. The wave period  $T_z$  can be related to internal processes as initiation of damage and transport of material, by coupling it to the nominal diameter:

$$\text{dimensionless wave period} = \sqrt{g T_z^2 / D_{n50}} \quad (5)$$

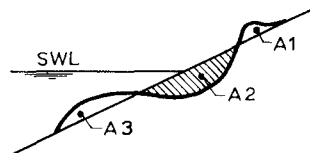
This wave period is also used in the investigations of van Hijum and Pilarczyk [5], on the stability of gravel beaches. Using (5) instead of (4) means that the influence of the wave height and the wave period on stability can be treated independently.

The dimensionless damage level,  $S_2$ , is described by:

$$S_2 = A_2 / D_{n50}^2 \quad (6)$$

where:

- $A_1$  = accretion above water level [m<sup>2</sup>]
- $A_2$  = eroded area of the profile [m<sup>2</sup>]
- $A_3$  = accretion below erosion area [m<sup>2</sup>]



A physical description for  $S_2$  is the number of cubical stones with a side of  $1 D_{n50}$ , eroded over a width of  $1 D_{n50}$ . The "no damage" criterion of Hudson and Ahrens is taken generally to be when  $S_2$  is between 1 and 3 stones eroded and "failure" of the slope is assumed when  $S_2$  is between 8 and 17. The exact value of  $S_2$  is dependent to some extent on the slope of the revetment.

#### Test Equipment, Materials and Procedure

All tests were conducted in a 1.0 m wide, 1.2 m deep and 50.0 m long wave flume with test sections installed about 44 m from the

random wave generator. This wave generator is capable of performing both translatory and rotational motions by means of a hydraulic actuator, programmed by a closed loop servo-system. The command signal of this loop is obtained from a punched tape, representing a random signal with a predetermined wave energy spectrum. A new system developed by the Delft Hydraulics Laboratory was used to measure and compensate for reflected waves at the wave board. With this system standing waves and basin resonance are avoided.

For the investigation a surface profiler was developed with nine gauges placed 0.10 m apart on a computer controlled-carriage. The surface along the slope was measured every 0.040 m. Depending on the slope angle every survey consisted between 500 and 1600 data points. Successive soundings were taken at exactly the same points using the relocatability of the profiler. An average profile was calculated and plotted by computer and used for determining the erosion damage,  $S_2$ .

Broken stone was used for the armour layer, the main characteristics of which were:  $W_{50} = 0.123$  kg;  $\rho_a = 2630$  kg/m<sup>3</sup>;  $D_{n50} = 0.036$  m; layer thickness 0.080 m. The sieve analysis curves were straight lines on a log-linear plot, see Fig. 1. Two gradings were used with  $D_{85}/D_{15} = 2.25$  (riprap) and 1.25 (uniform stones) respectively. The filter layer was defined by  $D_{n50}$  (armour)/ $D_{n50}$  (filter) = 4.5 and  $D_{85}/D_{15} = 2.25$ . The thickness of the filter layer was 0.02 m. This layer was placed directly on a slope constructed of mortar when an impermeable core was being tested. When a permeable core was tested the armour layer was placed directly on this core.

Each complete test consisted of a pre-test sounding, a test of 1000 waves, an intermediate sounding, a test of 2000 more waves and a final sounding. After each complete test the armour layer was removed and rebuilt. A test series consisted generally of 5 tests with the same wave period, but different significant wave heights. Wave heights ranged from 0.05 m to 0.26 m and wave periods from 1.3 to 3.2 seconds. A water depth of 0.80 m was applied for all tests. A damage curve was drawn for  $N = 1000$ , and  $N = 3000$ , for each test series, as shown in Fig. 2. From this the  $H_s/\Delta D_{n50}$  value was taken for three damage levels and the surf similarity parameter,  $\xi_z$ , given in (4) was calculated. The following three damage levels were chosen:

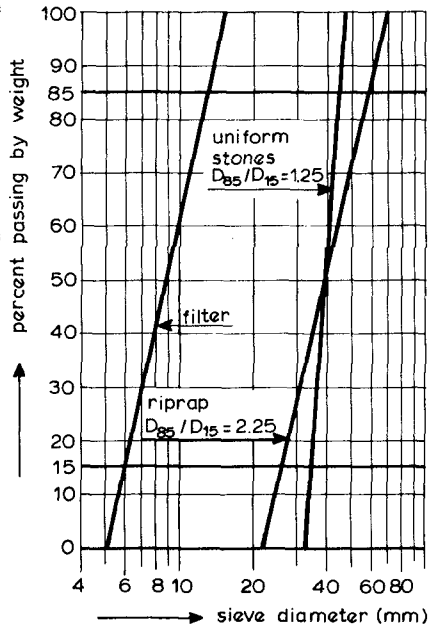


Fig. 1 Sieve curves

- start of damage (the  $H_D=0$  for Hudson)
- intermediate damage
- failure: filter layer is visible.

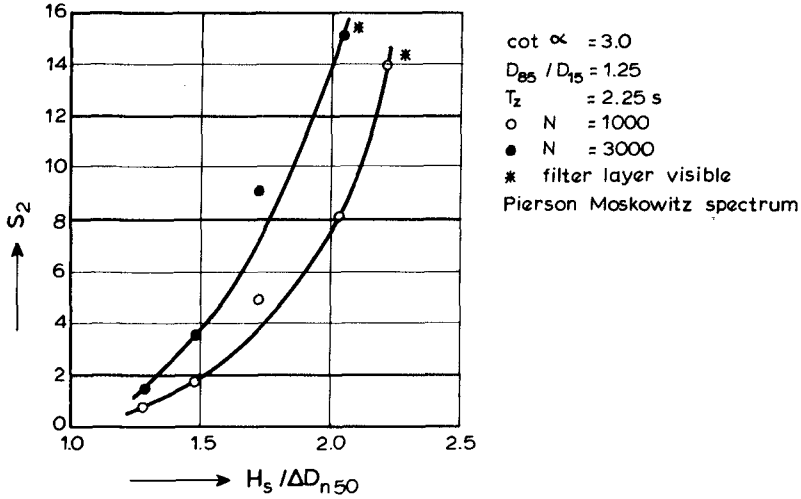


Fig. 2 Example of damage curves

Test Programme

The test programme is shown below.

Table 2 Test programme

slope angle $\cot \alpha$	grading $D_{85} / D_{15}$	spectrum shape	permeable core	number of tests
2	2.25	PM	no	19
3	2.25	PM	no	20
4	2.25	PM	no	21
6	2.25	PM	no	26
3	1.25	PM	no	21
4	1.25	PM	no	20
3	2.25	narrow	no	19
3	2.25	wide	no	20
3	1.25	PM	yes	19

PM = Pierson Moskowitz spectrum

Results

The influence of the primary variables on armour stability, shown in Table 1 is discussed below and new practical stability formulae, obtained from the results, presented.

Influence of Number of Waves

In the investigation of Thompson and Shuttler [9] profiles were sounded after each 1000 waves, up to  $N = 5000$ . Analyzing their results gives the relationship between damage and number of waves shown in Fig. 3. Data points are based on 50 tests and are independent of slope angle, wave period and damage level. Since a clear relationship was found between  $S_2$  and  $N$ , it was decided to decrease the total number of waves in the present study to  $N = 3000$  and to conduct one intermediate sounding after  $N = 1000$ . Analyzing the ratio of damage after 3000 and 1000 waves and using the damage after 3000 waves as a reference, gave a new point (\*) in Fig. 3. The difference between the two investigations is small.

The relationship between  $S_2$  and  $N$  can be described by the following formula:

$$S_2(N) = 0.014 \sqrt{N} * S_2(5000) \tag{7}$$

Since (7) is a square root function it is easy to find a parameter which describes the influence of the number of waves on the damage. This parameter is  $S_2/\sqrt{N}$ . The constant 0.014 becomes a part of a stability coefficient. The parameter  $S_2/\sqrt{N}$  can be used for  $N$  in the range of, approximately, 1000 to 7000. For  $N < 1000$  a linear relationship fits the data better, see Fig. 3. It is, however, very clear that with random waves a stable profile is not found with less than

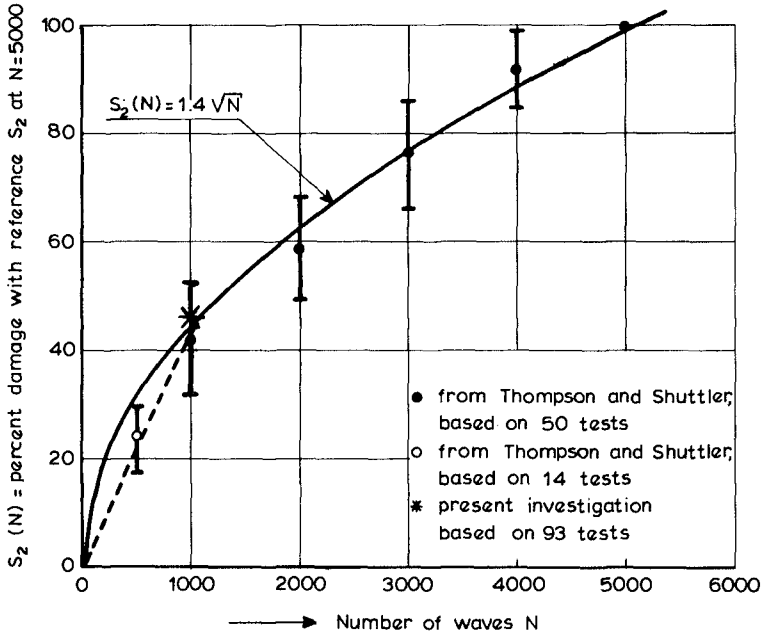


Fig. 3 Influence of number of waves on damage:  $S_2/\sqrt{N}$



10,000 waves. This is very different to regular waves where equilibrium is generally found within 1000 - 2000 waves.

#### Influence of Wave Period and Slope Angle

The extent of damage depends on the slope angle. More stones have to be displaced for gentler slopes before the failure criterion is reached. From the investigations the lower and upper damage levels were determined as shown in Table 3.

Table 3 Lower and upper damage levels

$\cot\alpha$	start of damage	failure
2	$S_2 = 2$	$S_2 = 8$
3	$S_2 = 2$	$S_2 = 12$
4	$S_2 = 3$	$S_2 = 17$
6	$S_2 = 3$	$S_2 = 17$

The  $H_s/\Delta D_{n50}$  and  $\xi_z$  values for the three damage levels have been plotted for each slope angle and for  $N = 3000$  in Figs. 4 and 5. Although there is a little scatter the influence of the wave period is very clear, especially for the gentler slopes. The influence of the wave period is evidently larger for breaking waves ( $\xi_z < 2.5 - 3.5$ ) than for non-breaking waves ( $\xi_z > 2.5 - 3.5$ ).

#### Influence of Armour Layer Grading

For slopes with  $\cot\alpha = 3.0$  and  $\cot\alpha = 4.0$  the tests were repeated with different grading of the armour. The wide grading with,  $D_{85}/D_{15} = 2.25$  (riprap), was replaced by a narrow grading with  $D_{85}/D_{15} = 1.25$  (uniform stones). Test results are plotted on Figs. 4b and 5a (open symbols). No difference in damage was found for the two gradings. It can be concluded that the grading of the armour within the range tested has no influence on the stability and that the armour layer can be described by the nominal diameter,  $D_{n50}$ , only. This conclusion is in contrast to the use of different  $K_D$  values for riprap ( $K_D = 2.2$ ) and for uniform stones ( $K_D = 3.2$ ). It should be stated that the difference between the Hudson formula and the work of Ahrens [1] can not be explained by the different grading of the armour. Probably, this difference is due to the difference in core permeability of the two investigations.

#### Influence of Spectrum Shape and Groupiness of Waves

The main part of the present series of tests was conducted with a Pierson Moskowitz (PM) spectrum. The test series with a slope angle with  $\cot\alpha = 3.0$  were performed with both a very narrow spectrum and a wide spectrum. Although the last word has not yet been written about the description of spectrum shape and groupiness of waves the following parameters give a reasonable idea.

$$\epsilon_{5\%} = (1 - m_2^2/m_0 m_4)^{0.5} \quad (8)$$

Fig. 4a Cot  $\alpha = 2.0$

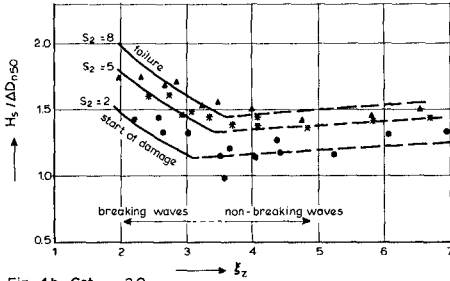


Fig. 4b Cot  $\alpha = 3.0$

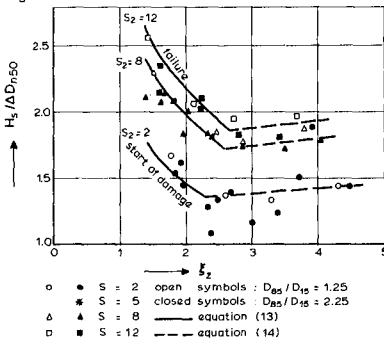


Fig. 4 Stability formulae and test results for  $N = 3000$  and an impermeable core

Fig. 5a Cot  $\alpha = 4.0$

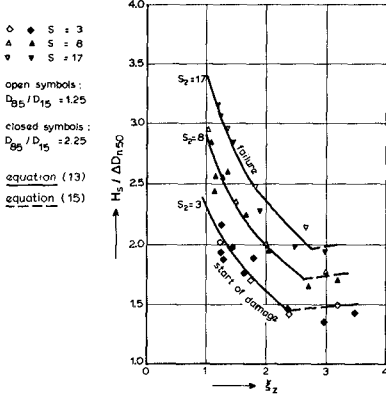


Fig. 5b Cot  $\alpha = 6.0$

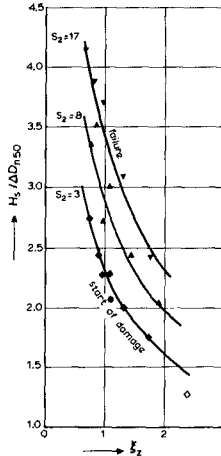


Fig. 5 Stability formulae and test results for  $N = 3000$  and an impermeable core

$$Q_p = \frac{2}{m_0} \int_0^\infty f[S(f)]^2 df \tag{9}$$

$$GF = \text{groupiness factor} = (m_{0,\text{group}})^{0.5} / m_0 \tag{10}$$

$$\bar{j}_1(A) = \text{mean length of wave group above level A} \tag{11}$$

$$\bar{j}_2(A) = \text{mean total length of wave group (Goda [3])} \tag{12}$$

where:  $\epsilon_{5\%}, Q_p$  = spectral width parameters  
 $m_n$  = nth spectral moment of the energy density spectrum  
 $f$  = frequency  
 $S(f)$  = energy density as function of  $f$   
 $m_{0,\text{group}}$  = spectral moment of the SIWEH spectrum (Funke and Mansard [2])

Parameter values for the narrow, PM and wide spectra mentioned above are given in Table 4.

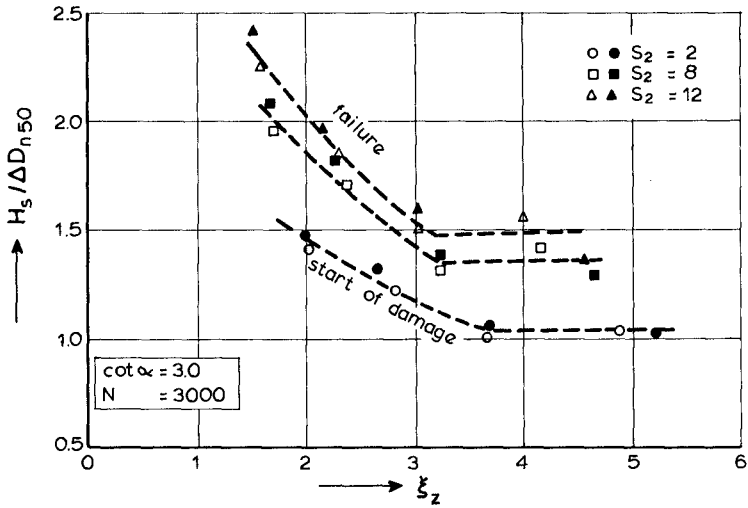
Table 4 Spectral parameters and groupiness of waves

parameter	narrow spectrum	PM spectrum	wide spectrum
$\epsilon_{5\%}$	0.10 ± 8%	0.39 ± 3%	0.59 ± 5%
$Q_p$	13.4 ± 14%	2.60 ± 3%	1.47 ± 11%
GF	0.99 ± 8%	0.77 ± 6%	0.72 ± 8%
$\bar{j}_1(H)$	5.43 ± 12%	2.60 ± 3%	2.16 ± 6%
$\bar{j}_2(H)$	12.6 ± 13%	5.60 ± 3%	4.76 ± 3%
$\bar{j}_1(H_s)$	2.95 ± 6%	1.54 ± 5%	1.35 ± 5%
$\bar{j}_2(H_s)$	22.0 ± 6%	11.3 ± 6%	10.3 ± 6%

The difference in width of the three spectra is clear. A strong wave groupiness was present for the narrow spectrum. Some groupiness existed for both the PM and wide spectrum but the difference between the GF factors is small. Although the width of the wide spectrum is much larger than for the PM spectrum ( $\epsilon_{5\%} = 0.6$  and  $0.4$  respectively), the groupiness of waves was almost the same ( $0.72$  and  $0.77$  respectively).

Test results for the narrow and wide spectrum are shown, for  $N = 3000$ , in Fig. 6.

Using the average wave period,  $T_z$ , for calculating  $\xi_z$  (4) gives good agreement between the test results for a narrow and a wide spectrum. It can be stated, therefore, that stability is not influenced by the spectrum shape or by the groupiness of waves. This conclusion was also reached for the profile development of gravel beaches, by van Hijum and Pilarczyk [5]. Wave runup and rundown, however, depend strongly on the groupiness of waves.



open symbols : wide spectrum,  $\epsilon_{5\%} = 0.59, GF = 0.72$   
 closed symbols : narrow spectrum,  $\epsilon_{5\%} = 0.10, GF = 0.99$

Fig. 6 Influence of spectrum shape and wave groupiness on stability

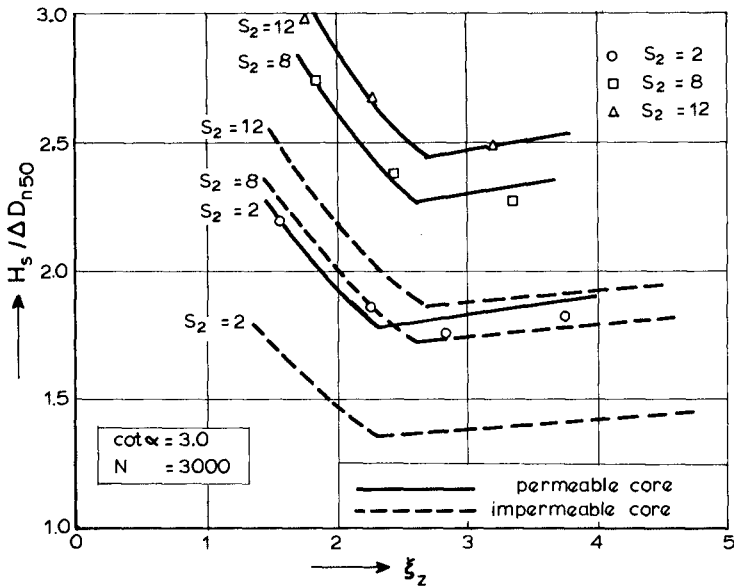


Fig. 7 Influence of core permeability

## Influence of Core Permeability

Tests were performed on a slope with  $\cot \alpha = 3.0$  with a permeable core. The armour layer was constructed directly on the core. The relative dimensions of the core were  $D_{n50}(\text{armour})/D_{n50}(\text{core}) = 3.2$  and  $D_{85}/D_{15} = 1.5$ . Test results are shown in Fig. 7.

The difference in results with an impermeable core (dotted lines) is appreciable which means that its influence on the stability is large. This was also found by Hedar [4] in 1960 for regular waves. Although stability is higher with a permeable core the same trend for the influence of wave period is shown.

## New Practical Stability Formulae

The list of variables given in Table 1 can be shortened using the results described above. The influence of the number of waves is given by  $S_2/\sqrt{N}$ . Armour grading, spectrum shape and wave groupiness have no influence on the stability and can, therefore, be deleted. The stability of rubble mound slopes can then be described by the following dimensionless variables:

$$H_s/\Delta D_{n50}; \xi_z \text{ or } \sqrt{g T_z^2/D_{n50}}; \cot \alpha; S_2/\sqrt{N}; \text{ permeability}$$

Stability formulae are given below for an impermeable core (lower boundary). The permeability of the core can be included in the formulae by adjusting coefficients. There is distinct difference between breaking and non-breaking waves, see Figs. 4 and 5, and different formulae have, therefore, to be applied for  $\xi_z < 2.5 - 3.5$  and for  $\xi_z > 2.5 - 3.5$ . Non-linear regression analysis gives the following stability formulae for an impermeable core.

for breaking waves:  $\xi_z < 2.5 - 3.5$

$$H_s/\Delta D_{n50} = 4.4 (S_2/\sqrt{N})^{0.22} \xi_z^{-0.54} \quad (13)$$

for non-breaking waves:  $\xi_z > 2.5 - 3.5$  and  $\cot \alpha < 3$

$$H_s/\Delta D_{n50} = 1.25 \sqrt{\cot \alpha} (S_2/\sqrt{N})^{1/6} \xi_z^{0.1} \quad (14)$$

for non-breaking waves:  $\xi_z > 2.5 - 3.5$  and  $\cot \alpha > 3$

$$H_s/\Delta D_{n50} = 1.25 \sqrt{3} (S_2/\sqrt{N})^{1/6} \xi_z^{0.1} \quad (15)$$

Eqs. (13), 14 and (15) become straight lines on log-log paper as shown in Fig. 8.  $H_s/\Delta D_{n50}$  is plotted in this figure against  $\xi_z$  and lines for several damage levels,  $S_2$ , are given for  $N = 3000$ .  $\xi_z^{-0.54}$  and  $\xi_z^{0.1}$  give the slope for the lines and also the influence of the wave period.

The damage level to be taken for design depends on the wave conditions, but must always be within the limits mentioned in Table 3. For storms with a recurrence interval of a few years  $S_2$  can be taken close to the lower limit ( $S_2 = 2 - 3$ ), for very severe storms an intermediate or even the upper limit should be chosen. Figures can be drawn with (13) (14) and (15) for any number of waves required. The stability formulae are also plotted in Figs. 4 and 5, and show good agreement with the test results.

Another way of describing the influence of the wave period is to use the variable  $\sqrt{g T_z^2/D_{n50}}$  instead of  $\xi_z$ . The following simple power function has been found for breaking waves:

$$\boxed{H_s / \Delta D_{n50} * \sqrt{g T_z^2 / D_{n50}} * \tan \alpha = 31 (S_2 / \sqrt{N})^{1/3}} \quad (16)$$

The correlation coefficient, in this case, is 0.90. The formula is based on the actual test results but with the restriction  $S_2 > 2$ . 225 data points were used for the regression analysis. Fig. 9 gives (16) for all test results. 156 data points could be used from Thompson and Shuttler [9] and 171 data points from the present investigation. The results of four different slope angles and two gradings are summarized in the figure.

The following relationships between wave height and damage for constant wave period, slope angle and number of waves can be determined from (14), (15) and (16).

$$S_2 = A H_s^3 \quad \text{for breaking waves} \quad (17)$$

$$S_2 = A H_s^6 \quad \text{for non-breaking waves} \quad (18)$$

where: A = a constant

A third and sixth power function are found. From (17) and (18) it can be concluded that for non-breaking waves the curve is steeper and the damage more progressive. This is also clear in Fig. 4a.

Although it seems that (13) is very different from (16), equation (13) can be rewritten in almost the same form as (16):

$$(H_s / \Delta D_{n50})^{1.35} * \sqrt{g T_z^2 / D_{n50}} * \tan \alpha = 39 (S_2 / \sqrt{N})^{0.41} \quad (19)$$

Using this formula the relationship between wave height and damage becomes:

$$S_2 = A H_s^{3.3}, \quad (20)$$

which is almost the same as found in (17). The agreement between (13) and (16) is good.

Higher stability was found for the permeable core, but with the same trend for the influence of the wave period, see Fig. 7. This

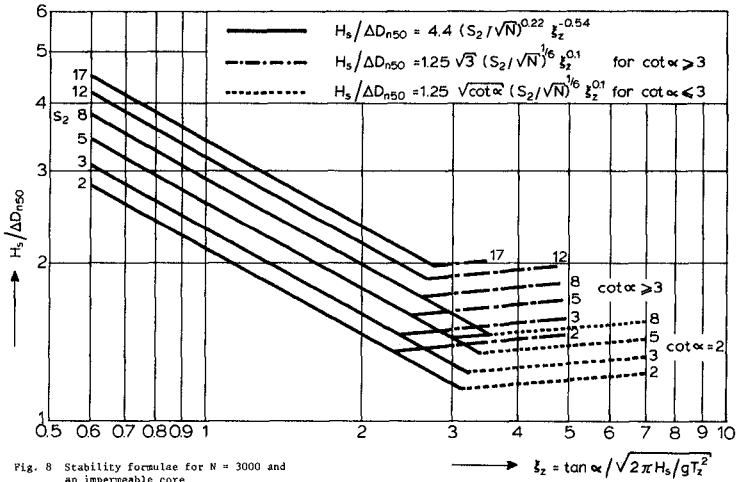


Fig. 8 Stability formulae for  $N = 3000$  and an impermeable core

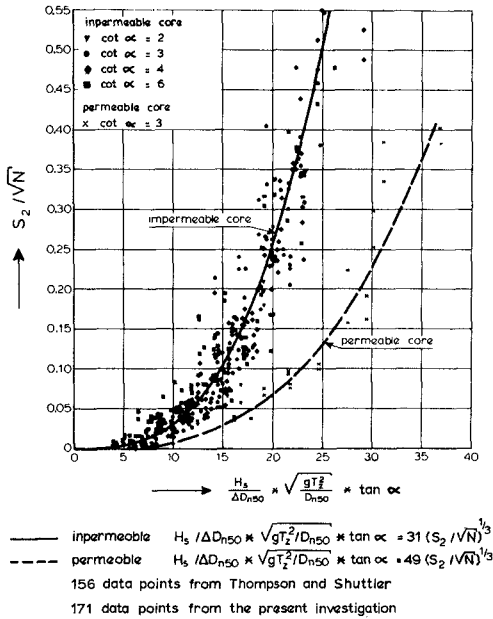


Fig. 9 Stability formulae and test results for breaking waves ( $z_2 < 2.5$ )

makes it possible to use the same stability formulae (13) to (16) but with adjusted coefficients. For a permeable core the formulae become:

$$H_s/\Delta D_{n50} = 5.8 (S_2/\sqrt{N})^{0.22} \xi_z^{-0.54} \quad (13a)$$

$$H_s/\Delta D_{n50} = 1.65 \sqrt{\cot \alpha} (S_2/\sqrt{N})^{1/6} \xi_z^{0.1} \quad (14a)$$

$$H_s/\Delta D_{n50} = 1.65 \sqrt{3} (S_2/\sqrt{N})^{1/6} \xi_z^{0.1} \quad (15a)$$

$$H_s/\Delta D_{n50} * \sqrt{g T_z^2/D_{n50}} * \tan \alpha = 49 (S_2/\sqrt{N})^{1/3} \quad (16a)$$

The increase of stability for (13a), (14a) and (15a), is 32% and for (16a) 58%. Since there is no known simple parameter which describes the permeability of a structure it is left to the engineers judgement to use (13) to (16) or (13a) to (16a) or even intermediate values. The stability formulae (13a) to (16a) are shown on Figs. 7 and 9 and correspond well with the test results. Further investigation is still necessary with other values of core permeability and with other slope angles in order to solve this problem.

#### Conclusions

1. Based on more than two hundred tests and on the work of Thompson and Shuttler [9] practical design formulae have been developed for rubble mound slopes under random wave attack.
2. The stability, in a dimensionless form, has been determined using
  - the significant wave height:  $H_s/\Delta D_{n50}$
  - the average wave period:  $\xi_z$  or  $\sqrt{g T_z^2/D_{n50}}$
  - the slope angle:  $\cot \alpha$
  - the damage as function of number of waves:  $S_2/\sqrt{N}$
  - the permeability of the core.
3. Within the conditions tested the following had no influence on the stability:
  - the grading of the armour
  - the spectrum shape
  - the groupiness of waves.

#### References

- 1 AHRENS, J.P., Large Wave Tank Tests of Riprap Stability. C.E.R.C. Technical Memorandum No. 51, May 1975.
- 2 FUNKE, E.R.; MANSARD, E.P.D., On the synthesis of realistic sea states in a laboratory flume. Hydraulics Laboratory, Ottawa, Canada, August 1979.
- 3 GODA, Y., Numerical experiments on wave statistics with spectral simulation. Rep. Port Harbour Res. Inst., Min. Transport, Vol. 9, No. 3, (1970).
- 4 HEDAR, P.A., Stability of rock-fill breakwaters. Göteborg, 1960.



- 5 HIJUM E. van and PILARCZYK, K.W., Gravel beaches: equilibrium profile and longshore transport of coarse material under regular and irregular wave attack. Delft Hydraulics Laboratory, Publication No. 274, July 1982.
- 6 LOSADA, M.A., GIMENEZ-CURTO, L.A., The joint effect of wave height and period on the stability of rubble-mound breakwaters using Irribarren's number. Coastal Engineering 3 (1979) 77-96.
- 7 PILARCZYK, K.W. and BOER, K. den, Stability and profile development of coarse material and their application in coastal engineering. Delft Hydraulics Laboratory, Publication No. 293, January 1983.
- 8 SIGURDSSON, G., Wave forces on breakwater capstones. Proceedings ASCE, WW3, 1962.
- 9 THOMPSON D.M., and SHUTTLE, R.M., Riprap design for wind wave attack. A laboratory study in random waves. Wallingford, EX 707, September 1975.

## Notation

$H_s/\Delta D_{n50}$	= dimensionless wave height	
$\xi_z$	= surf similarity parameter: $\xi_z = \tan \alpha / \sqrt{2\pi H_s/gT_z^2}$	
$\sqrt{gT_z^2/D_{n50}}$	= dimensionless wave period	
$S_2/\sqrt{N}$	= dimensionless damage as function of number of waves	
$A_2$	= area of erosion profile	(m <sup>2</sup> )
$D_{n50}$	= nominal diameter; $D_{n50} = (W_{50}/\rho_a)^{1/3}$	(m)
$D_{15}$	= 15% value of sieve curve	(m)
$D_{85}$	= 85% value of sieve curve	(m)
GF	= groupiness factor	(-)
$H_s$	= significant wave height	(m)
$K_D$	= stability coefficient	(-)
N	= number of waves	(-)
$N_s$	= stability number; $N_s = H_s/\Delta D_{n50}$	(-)
$Q_p$	= parameter for spectral width	(-)
$S_2$	= damage level; $S_2 = A_2/D_{n50}^2$	(-)
$T_z$	= average wave period	(s)
$W_{50}$	= 50% value of mass distribution curve	(kg)
g	= acceleration due to gravity	(m/s <sup>2</sup> )
$\bar{j}_1$	= mean length of wave group	(-)
$\bar{j}_2$	= mean total length of wave group	(-)
$\alpha$	= slope angle	(degr)
$\Delta$	= relative mass density; $\Delta = \rho_a/\rho - 1$	(-)
$\epsilon_{5\%}$	= variable for spectral width	(-)
$\rho$	= mass density of water	(kg/m <sup>3</sup> )
$\rho_a$	= mass density of stone	(kg/m <sup>3</sup> )

## CHAPTER ONE HUNDRED SEVENTY SEVEN

### Surveys of Coastal Structures Using Geophysical Techniques

John R. Dingler and Roberto J. Anima\*

Coastal engineers have long relied upon bathymetric surveys to determine the extent of underwater damage to jetties and breakwaters. Though such surveys supply important information about variations in water depth around structures, they alone do not show in sufficient detail the nature of the material on the structure, the extent of subbottom features, or the nature of the subbottom upon which the structure sits. However, by conducting bathymetric surveys in conjunction with other remote-sensing techniques and diving observations, it is possible to obtain more complete knowledge of the subsurface condition of coastal structures.

During the summer of 1983 and the spring and summer of 1984, we conducted side scan sonar and shallow subbottom surveys in conjunction with bathymetric and diving surveys along three northern California coastal structures to determine the condition of the structures before extensive damage occurred. Then, we evaluated the applicability of the data collection techniques for condition surveys in general.

Two of the structures surveyed are the parallel jetties that protect the entrance to Humboldt Bay, California, and the third structure is the outer breakwater at Crescent City, California. Bathymetric records and sonographs from Humboldt Bay show deep holes along much of the inside of the south jetty and off the heads of both jetties. The subbottom record from inside Humboldt Bay shows a subsurface fault, the extension of which would run under the south jetty.

Sonographs from Crescent City show significant bedrock outcrops throughout the area outside the breakwater, making it difficult in places to identify the toe of the structure. The subbottom record shows that pockets of sand exist amidst the bedrock, but they are generally less than 2 m (6 ft) in thickness.

We found that the side scan sonar is an excellent tool for defining the toe of the structure; also, when waves are low, it can be useful in determining armor types and the slope of structures. Our subbottom system provided information on fault and bedrock locations; however, other systems need to be tested to see if any of them can locate buried armor near the structures.

\* Oceanographer and Geologist, respectively, United States Geological Survey, 345 Middlefield Road, Menlo Park, CA 94025.

## INTRODUCTION

Currently, it is difficult to evaluate the condition of a coastal structure before it fails. Damage from individual waves or storms may slowly undermine structural integrity, eventually causing a seemingly sudden failure and necessitating stop-gap repair measures until more permanent, and usually costly repairs, can be undertaken. Although coastal structures are built to withstand a prespecified wave (usually the significant wave according to the U.S. Army, 1973, p. 7-168), the combination of wave activity, tidal currents, and longshore transport slowly causes structural weakening. When damage becomes severe enough--usually after a visible failure of the structure--engineers inspect the structure above water and conduct a localized bathymetry survey to assess the damage. Prefailure surveys to determine the condition of a structure are rarely, if ever, conducted.

The cost of repairing coastal structures is high; consequently, techniques are needed to determine their integrity. Recently, the Los Angeles District of the Corps of Engineers initiated a program to determine the present condition of man-made structures along the California coast. During the summer of 1983, we conducted geophysical surveys in the vicinity of the jetties at Humboldt Bay, California, and the outer breakwater at Crescent City, California. In the spring of 1984, we repeated some of the Humboldt Bay surveys to document changes produced by winter waves. In the summer of 1984, we dove around the structures to see if we could improve our interpretation of the sonographs. The goals of these surveys were (1) to develop a general survey methodology that could be used to inspect other such structures along the California coast and (2) to test the methodology by ascertaining in situ the condition of the structures at the two sites.

## LOCATION AND DESCRIPTION

Humboldt Bay, the harbor for the city of Eureka and the largest bay on the northern California coast, is about 400 km (215 nmi) north of San Francisco. Crescent City, located on the south side of Point St. George, is about 120 km (65 nmi) north of Eureka. Figure 1 shows the location of the study area; figure 2 shows the jetties at the entrance to Humboldt Bay, and figure 3 shows the outer breakwater configuration at Crescent City. Both the jetties and the breakwater are rubble-mound structures with large, cast-armor units in selected places.

Stabilizing the entrance to Humboldt Bay commenced in 1881 and has continued sporadically to the present. Repairs have been so extensive that Hagwood (1981, p. 176) stated that the quantity of stone used to repair the Humboldt Bay jetties has been, in total, greater than that used for the original structures. At present, Humboldt Bay has parallel jetties that are 610 m (2,000 ft) apart; each jetty is over 2,000 m (6,560 ft) long. Repeated dredging maintains a navigation channel, 152 m (500 ft) wide by 13 m (43 ft) deep, near the south jetty.

Because of strong storm waves in the area, both jetties have experienced repeated damage and repair. Because traditional designs were unable to protect the jetty heads, in 1971 both were widened and

armored with 38- and 39-t (42- and 43-ton) dolosse. This was the first use of these units in the United States (Hagwood, 1981, p. 348). At present, the heads of both jetties have settled, and in one place the inside flank of the south jetty has separated from the cap.

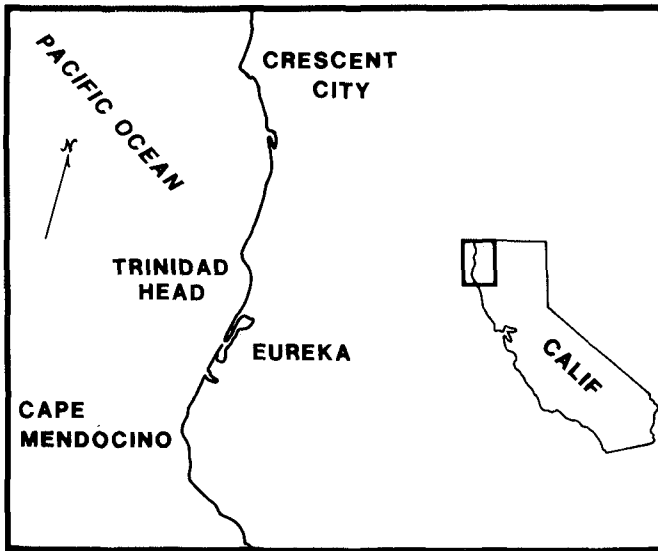


Figure 1: Location of the study sites at Crescent City and Eureka, northwestern California.

The outer breakwater at Crescent City is knee-shaped, extending southeast from the shore for about 1,128 m (3,700 ft) and then turning east for about 305 m (1,000 ft). Construction of the initial breakwater was finished in 1930. That first section extended 914 m (1,000 ft) southeast from the shore toward Round Rock. Later, engineers decided to extend the breakwater to Round Rock, forming a breakwater about 1,740 m (5,700 ft) long. That plan proved to be unfeasible, and the easterly arm was added instead, leaving a submerged rocky reef extending to the southeast.

Model studies at the Waterways Experiment Station, Vicksburg, Mississippi led, in 1956, to the placement of 23-t (25-ton) tetrapods on the easterly arm, the first use of these units in the western hemisphere (Hagwood, 1981, p. 341). Because of further storm damage, 38-t (42-ton) dolosse were added to protect the corner in 1974.

#### Equipment and Procedures

Although this survey was the first of its kind on the west coast, the various instruments have been used separately in similar

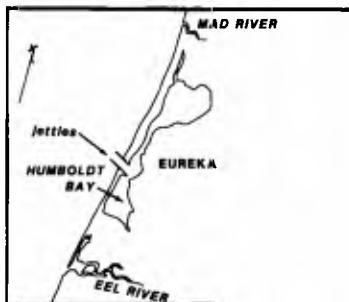


Figure 2: Entrance to Humboldt Bay at Eureka, California.

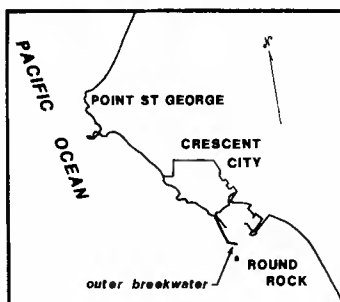


Figure 3: Harbor at Crescent City, California.

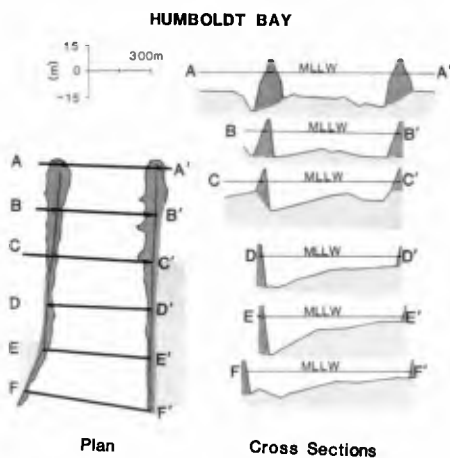


Figure 4: Plan view (left) of the jetties at Humboldt Bay, California showing the location of cross sections plotted on the right.

situations. Bathymetric surveys are commonly conducted around coastal structures. Patterson and Pope (1983) used side scan sonar to inspect structures in quiet waters; Mazel (1984) described how to use side scan sonar to inspect vertical surfaces; and surface-towed seismic transducers are often used to study surficial sand bodies.

Equipment used during this study included precision depth recorders, 100- and 500-kHz side-scan sonars, and a surface-towed 3.5-kHz subbottom profiler. The instruments were deployed from the (43 ft) R/V David Johnston or from a small (21 ft) boat. Instruments were chosen to fulfill specific objectives: the precision depth recorders were used to survey the bottom in the vicinity of the structures and to determine structure slopes; the side-scan sonar provided images of the toes of the structures and of surficial features on the adjacent sandy bottom; and the subbottom profiler determined the depth to bedrock and type of near-surface internal structure.

During the summer of 1984, scuba divers swam along the toes of, and occasionally onto, the three structures, and their direct observations were used to clarify the sonographs.

## RESULTS

The 1983 and 1984 geophysical surveys and the 1984 scuba dives produced accurate data on the toes of the three structures, detailed bathymetric maps and slope profiles, and a rough picture of the subsurface. These surveys failed to produce detailed information on the distribution of armor on the structures or the location of buried armor. Sub-bottom techniques capable of accurately locating objects as large as the armor units failed to do so because of adverse conditions.

### Humboldt Bay

Water depth varies considerably and systematically throughout the inlet and adjacent nearshore zone, as shown in figure 4. Whereas water is deep on the southwest side of both jetties, only along the south jetty is the water deep adjacent to the inlet-side (inside) flank. Figure 5, a plot of additional profiles run perpendicular to the south jetty, shows the disparity in depth between its outside and inside flanks. Near the head of the south jetty, the water is deeper on the south (outside) flank; however, landward from the back of the head, the water is deeper on the inside.

The seismic profiles showed that the shallow subsurface is sandy. Transects in the bay that crossed the center lines of both jetties show subsurface faulting that would lie under the south jetty when extended (fig. 6). However, over 20 m (66 ft) of unfaulted sediment overlies the faults. Waves distorted the offshore records to the extent that subbottom features could not be discerned. Attempts to locate buried armor were not successful.

The sonographs delineate the toes of the jetties and large subaqueous dunes in shallow parts of the inlet; slope changes and individual armor upon the jetties were identified. The location of the

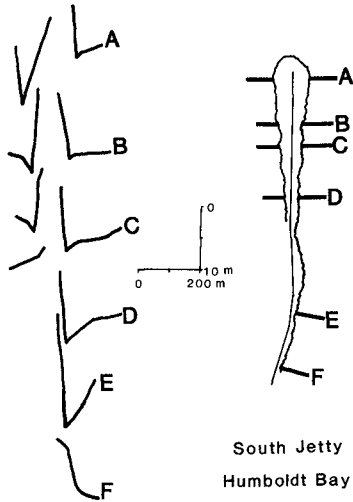


Figure 5: Profiles along the south jetty at Humboldt Bay, California. Zero on the abscissa is at the centerline of the jetty. Station numbers represent distances in hundreds of feet, with the largest value being at the jetty head.

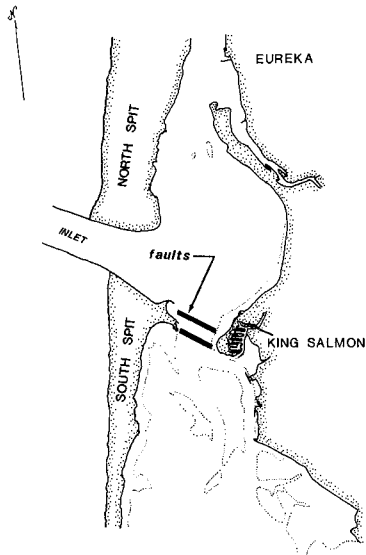


Figure 6: Location and trend of subsurface faults inshore of the south jetty at Humboldt Bay, California.

jetty toes, as calculated from the sonographs, are shown in figure 4.

The scuba dives, although conducted when water visibility was poor, led to the discovery that the jetty toes have different makeups. As shown on figure 7, the toe of the south jetty varies from large rock, to dolosse, to large rock with extensive sand that forms ramps up the flank, whereas the toe of the north jetty varies from large rock, to dolosse, to large areas covered with gravel and small rock.

#### Crescent City

Surveys at Crescent City covered the area between the outer breakwater and Round Rock to the south and Steamboat Rock to the west and the area adjacent to the inside of the arm (see fig. 3). Outside the Crescent City breakwater, the bottom is irregular because of extensive bedrock outcrops, is gently sloping, and is punctuated by rocky pinnacles that occasionally reach the sea surface. Depths along the outside of the shore-attached breakwater are as much as 9 m (30 ft) at the corner of the breakwater, maintaining that depth along the east-trending arm. The bottom shallows over the rocky reef, which nearly reaches the surface in places. One notable difference from the Humboldt Bay bathymetry data is the absence of depressions along the breakwater toe.

The sonographs showed extensive bedrock outcrops. On many records, such as the one shown in figure 8, it was hard to separate the breakwater toe from the naturally outcropping material. Figure 9 shows the location of the toe of the breakwater and of features thought to be outcrops rather than the breakwater itself. At one site just west of the corner of the breakwater, divers noted that the bulge is actually bedrock and that the toe is straight.

Seismic profiling confirmed that bedrock lies at or near the surface throughout the region. Typically, sand is restricted to depressions, forming patches less than 2 m (6 ft) thick. The only areas where sand completely covers the bedrock are east of the breakwater head and along the inside of the arm.

#### DISCUSSION

At Humboldt Bay, the bottom is sandy, and depth varies with location such that the greatest depths occur between the entrance channel and the south jetty and adjacent to the south sides of both jetty heads. The flanks of the south jetty slope as much as 42°, and the adjacent bottom drops off from the channel to the jetty without forming a channel wall (fig. 5). Continuing that profile to the ocean side of the jetty revealed highly unequal water depths on the two sides of the jetty--the outside being much shallower. That discrepancy is typical except at the head where, it reverses so that the deep scour appears on the outside. For interpretative purposes we divided the sea floor around and between the jetties into five parts: (1) the areas southwest of both heads, (2) elsewhere along the outside of the jetties, (3) the inside of the south jetty, (4) the entrance channel, and (5) elsewhere in the inlet.



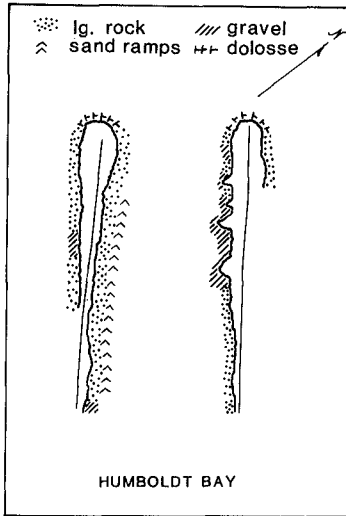


Figure 7: Location of armor types and sand ramps along the jetties at Humboldt Bay, California.

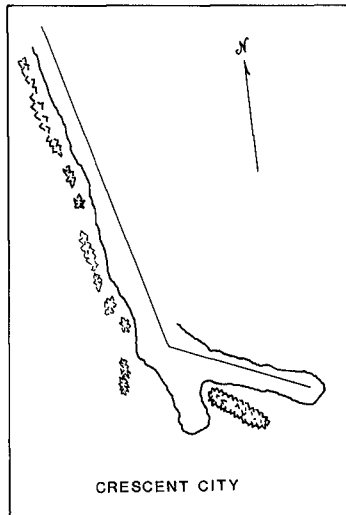


Figure 9: Location of the toe of the outer breakwater at Crescent City, California, as interpreted from sonographs. Also shown are bedrock outcrops near the breakwater.

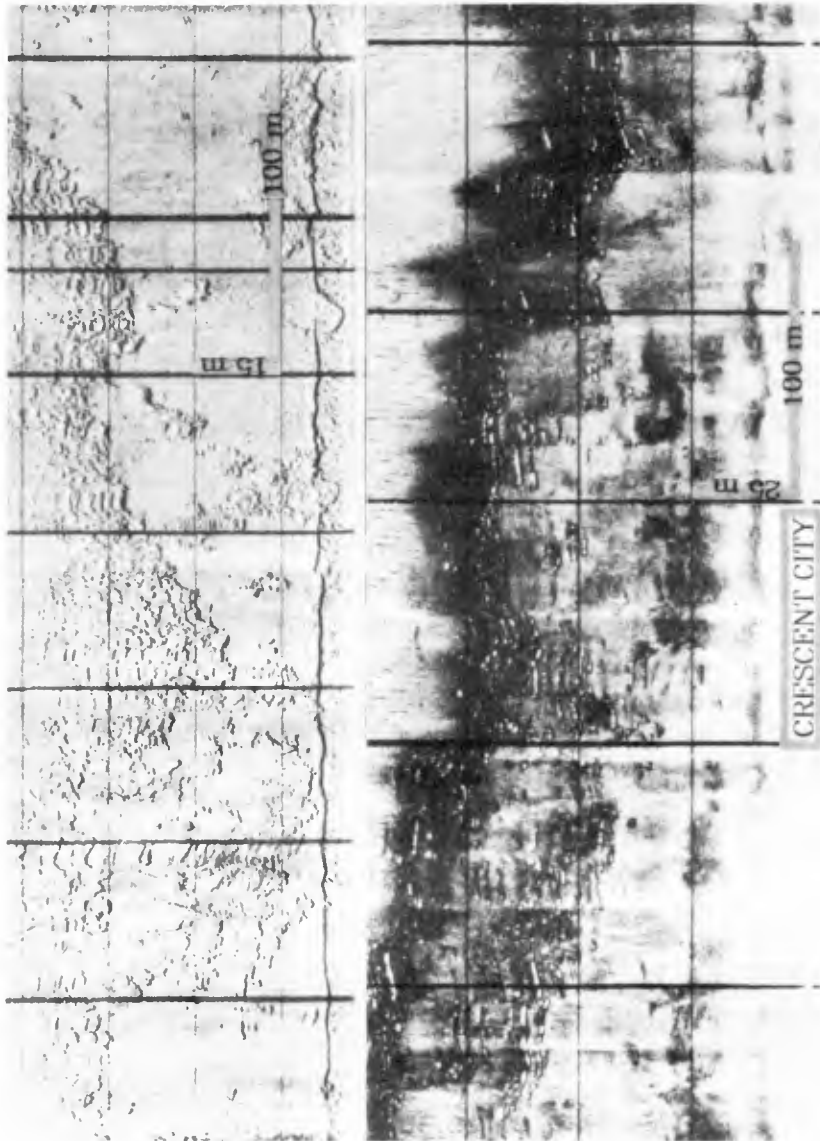


Figure 8: Sonographs of the bottom adjacent to the corner of the outer breakwater at Crescent City, California. Strong reflectors are bedrock outcrops. A 500-kHz sonograph is to the left, and a 100-kHz sonograph to the right.

Southwest of both heads, storm waves produce large, year-round, scour holes along the heads that are slightly deeper in the winter. Perhaps tidal flows or shelf currents contribute to the extensive erosion in this area. Overlaying the bathymetry on the construction drawings shows that the jetty toes have been extensively undermined in this area (Doug Pirie, oral commun., 1984).

Farther onshore, the waves have not created large depressions along the outsides of the jetties. Instead, the bathymetric data show a shallowing shoreward trend. Going from north to south there is about a 610-m (2,000-ft) shoreward offset of the shoreline.

Along the inside of the south jetty, strong tidal currents appear to have eroded the bottom, creating a continuous depression. Here, the divers found sand that formed ramps from the floor up the flank. The location and orientation of these sand ramps--abutting the east side of large armor and whose axes are tilted slightly shoreward-- suggest either flood-tide control or control by the distribution of armor. The entrance channel is periodically dredged to 13 m (43 ft). Its proximity to the inside of the south jetty may contribute to the extreme scour along that stretch of the toe.

Waves and tides interact to control the rest of the inlet. The traces of old groins, which were built to inhibit erosion along the north jetty (Chuck Orvis, oral commun., 1984), on both summer and winter sonographs suggest that tidal flows limit the depositional depth of the wave-driven sand in that area. Large bedforms in the central part of the inlet also suggest strong wave and tidal currents.

At the Crescent City study area bedrock dominates. Because the breakwater sits on bedrock, scour at the toe is minimal. Divers found, in places where sand or gravel abutted the breakwater, that the slope is gentle up to approximately 1 m (3 ft) of the armor and then steep down to the base of the armor; wave activity probably causes this pattern. Tidal currents appear to be relatively unimportant around the breakwater. Outside, waves attack the breakwater; inside, the water is often quiescent.

Wave action reduced the quality of the various records. Records collected on the (rare) calm days showed much more detail; furthermore, records could be collected over the structures only on such days. Most of the records, however, were affected by wave activity to the extent that details were missing. Each of the aspects of the study-- bathymetry, seismic profiling, side scanning, and diving--could have contributed more information under better conditions.

Wave activity affected the bathymetric surveys by introducing large offsets to the bottom traces and by preventing us from surveying over the steep slopes of the structures. To a great extent, wave noise can be visually removed from the bathymetric records, but fine detail is lost. However, not being able to survey over the structures made it difficult to accurately locate the toes of the structures.

Side scan sonar helped in determining toe location when working

over the structure was not possible. However, if, as in the case of the south jetty at Humboldt Bay, the bottom depth was much different at the toe than at the point where the side scan fish was being towed, the distance measured from the sonograph would not be the horizontal distance from the ship's track to the toe. To obtain that distance a correction had to be made that depended on the depth at the toe, which necessitated knowing the location of the toe. Nevertheless, the error in toe location could be satisfactorily minimized by towing the fish near the bottom and knowing the approximate depth of the toe.

Patterson and Pope (1983) showed that side scan sonar can be used to recognize individual armor units and perhaps to recognize slope changes and missing armor. However, such detailed work requires ideal conditions, which, in many areas, occur only a few days per year. Those who plan surveys must, therefore, decide on whether or not it is economically feasible to wait for the right conditions. Although during this study wave conditions precluded our identifying individual armor or slope changes, variations in armor size between areas showed on the sonographs. Divers found that the groins along the north jetty at Humboldt Bay contain small rock, whereas the rest of that jetty has large rock or dolosse at the toe. Figure 10 shows how these differences appear on a sonograph.

Although the 500-kHz side scan sonar produced records with much more detail on them than did the 100-kHz sonar, both provided enough detail to determine toe location in most cases. However, the 500-kHz unit should be used when searching for small features.

Boat speed must be considered when looking for small features. If, for example, one wants to identify the sand ramps, which sit in 2- to 3-m (6- to 10-ft) gaps between large armor, boat speeds must be less than 1 m/s (2 kt). Otherwise, that section of the sonograph will be too narrow, making it impossible to resolve the feature.

Seismic profiling requires calm conditions to obtain interpretable records. This is especially true of a surface-towed unit. Again, detail is lost during wavy conditions. We attempted to find buried armor, which would show up on the record as point-source parabolas, but saw none. Although there may not have been any to find, excessive motion of the sled would have masked their presence.

Diving also requires calm conditions, both to improve visibility and to permit swimming around the structure. We were able to follow the toe, but unable to see far enough to assess large-scale irregularities.

#### CONCLUSIONS AND RECOMMENDATIONS

1. At Humboldt Bay extensive scour has taken place on the south sides of the heads of both jetties and along the south jetty between the inside flank and the entrance channel.
2. On all three structures, large rock is the predominant material found along the toes. At Crescent City, there are a few dolosse at the corner and tetrapods along much of the easterly extension. At

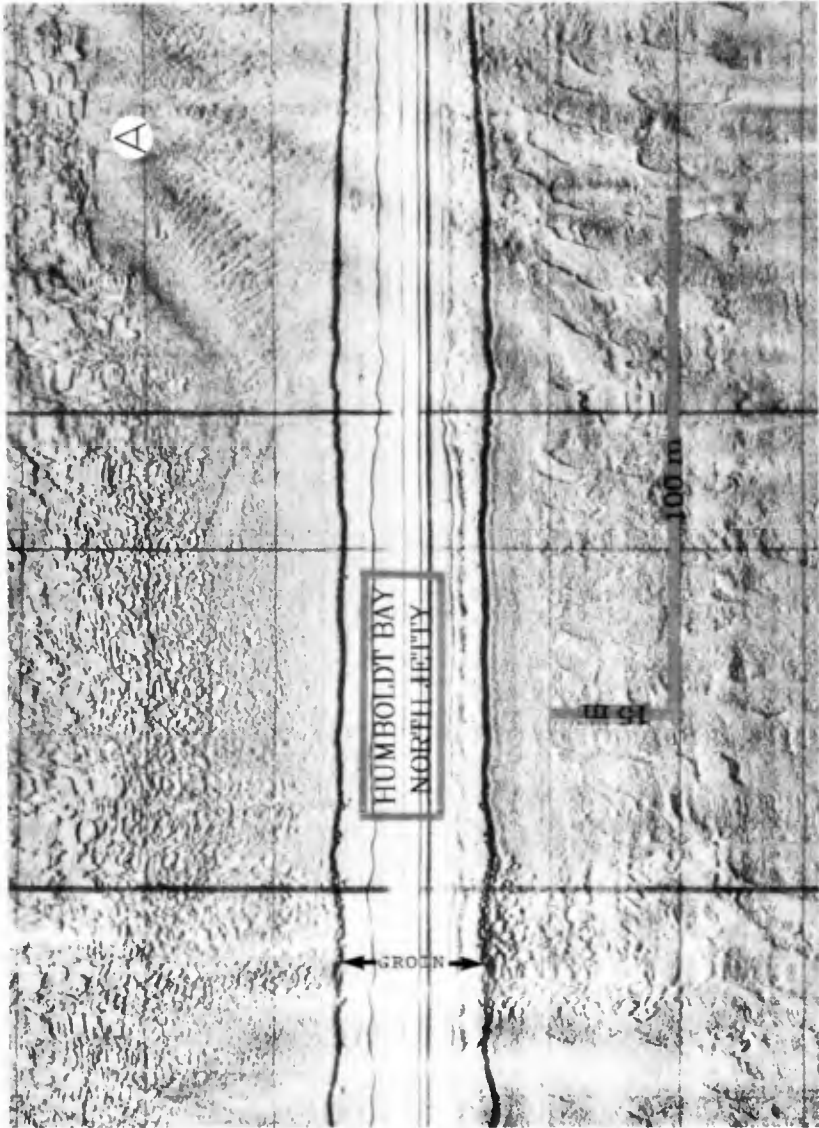


Figure 10: Sonograph of a groin along the inside of the north jetty at Humboldt Bay, California. The patterns on the sonograph indicate that the size of the material composing the groin and adjacent toe is smaller than the size of the material farther shoreward (A).

Humboldt Bay, there are dolosse on the bottom around both heads and smaller rock in a few places, primarily around the groins.

3. At Humboldt Bay, the subsurface is sandy; faulting extends under the south jetty but does not break the surface. At Crescent City, bedrock is present at or near the bottom throughout the study area.

The surveys showed that some techniques have general applicability and that others are more specialized. Also, they showed the extent to which such surveys depend on calm seas. On the basis of our work around these structures, we make the following recommendations:

1. Bathymetric surveys are fundamental to conducting condition surveys on coastal structures. They can be used under more severe conditions than the other techniques, and most wave noise can be filtered from the records.
2. Side scan sonar is an important adjunct to bathymetry in determining the location of the toe of the structure and the position of bottom features. It also can be used to look for features on the structures, but only when seas are calm.
3. Seismic profiling is useful when large-scale features are to be resolved. More work with different devices, however, must be done before it will be known if seismic techniques can locate buried armor.
4. Diving is a useful tool when visibility and wave climate permit. It can provide information on small features that often cannot be resolved with the geophysical tools.

#### ACKNOWLEDGMENTS

This study was sponsored by the Los Angeles District, U.S. Army, Corps of Engineers. We thank the many people from the U.S. Geological Survey, the Corps of Engineers, and the Humboldt Bay Coast Guard Station who helped us during the study. Chuck Orvis of the Los Angeles District and the staff of the Eureka office of the Corps of Engineers were especially helpful. Beth Laband and George Tait improved this manuscript with their reviews.

#### REFERENCES

- Hagwood, J. J., 1981: Engineers at the Golden Gate. U.S. Army, Corps of Engineers, 453 p.
- Mazel, C.H., 1984: Inspection of surfaces by side scan sonar. in Remotely Operated Vehicles, The Marine Technology Society, San Diego Section, 375 p.
- Patterson, D.R. and J. Pope, 1983: Coastal applications of side scan sonar. Proceedings, Coastal Structures '83, 9D2-91D.
- U.S. Army, 1973: Shore Protection Manual. Coastal Engineering Research Center, 3 v.

## CHAPTER ONE HUNDRED SEVENTY EIGHT

### Reef Type Breakwaters

John P. Ahrens, Aff. M. ASCE\*

#### Introduction

Reef type breakwaters refers to a low-crested rubble mound breakwater without the traditional multilayer cross section. This type of breakwater is little more than a homogenous pile of stones with individual stone weights sufficient to resist wave attack.

In recent years a number of low-crested breakwaters has been built or considered for use at a variety of locations. Most of these structures are intended to protect a beach or reduce the cost of beach maintenance. Other applications include protecting the water intakes for power plants, the entrance channel for small boat harbors, and providing an alternative to revetment for stabilizing an eroding shore line. In situations where only partial attenuation of the waves on the leeside of the structure is required, or possibly even advantageous, a low-crested rubble mound breakwater is a logical selection. Since the cost of a rubble mound increases rapidly with the height of the crest, the economic advantage of a low-crested structure over a traditional breakwater that is infrequently overtopped is obvious. Because the reef type breakwater represents the ultimate in design simplicity it could be the optimum structure for many situations. Unfortunately, the performance of low-crested rubble mound structures, and particularly a reef type breakwater, is not well documented or understood.

#### Background and Objectives

A number of papers have noted that the armor on the landside slope of a low-crested breakwater is more likely to be displaced by heavy overtopping than the armor on the seaward face, Lording and Scott (1971), Raichlen (1972), and Lillevang (1977). Raichlen discusses the characteristics of the overtopping over the crest and the inherent complexity of the problem. Walker, et al. (1975) give a carefully reasoned discussion of the many factors influencing the stability of heavily overtopped rubble mound breakwaters. Walker, et al. also show a figure which suggests what armor weight might be required for stability on the beachside of a low-crested breakwater. Unfortunately, the data scatter shown in the figure undermines confidence in the suggested armor weights.

In Australia the breakwater at Rosslyn Bay was damaged severely during cyclone "David" in 1976, Bremner, et al. (1980). The crest height of the structure was reduced as much as four meters but still functioned effectively as a submerged breakwater for over two years until it was

\*Oceanographer, Coastal Engineering Research Center, U. S. Army Engineer Waterways Experiment Station, P. O. Box 631, Vicksburg, MS 39180

repaired. Based on the surprisingly good performance of the damaged Rosslyn Bay breakwater and the findings from model tests, a low-crested design was chosen for the breakwater at Townsville Harbor, Australia. This breakwater is unusual because it was built entirely of stone in the 3- to 5-ton range, Bremner et al. Reef breakwaters, as described in this paper, are very similar to the Townsville breakwater except a wider gradation of stone was used in the model breakwater tests discussed herein.

Seelig (1979) conducted an extensive series of model tests to determine the wave transmission and reflection characteristics of low-crested breakwaters, including submerged structures. From these tests Seelig concluded that the component of transmission due to wave overtopping was very strongly dependent on the relative freeboard, i.e. the freeboard divided by the incident significant wave height. Recent work by Allsop (1983) with multilayered, low-crested breakwaters showed that the wave transmission was strongly dependent on a dimensionless freeboard parameter which included the zero-crossing period of the irregular wave conditions. Allsop did not find much wave period dependency in his evaluation of breakwater stability but indicates that since the wave transmission (which is largely due to overtopping) is dependent on the period, then possibly the stability of the backface would also be a function of wave period.

A study currently being conducted at the Coastal Engineering Research Center (CERC) is intended to document the performance of low-crested breakwaters. This paper discusses laboratory model tests of reef type breakwaters and provides information on their stability to wave attack and the wave transmission and reflection characteristics of the structures.

#### Techniques Used

To date 205 two-dimensional laboratory tests of reef breakwaters have been completed. These tests were conducted in a 61-centimeter-wide channel within CERC's 1.2- by 4.6- by 42.7-meter wave tank (see Figure 1 for a plan view of the tank and test setup).

All tests were conducted with irregular waves. The spectra used have wave periods of peak energy density,  $T_p$ , ranging from about 1.45 to 3.60 seconds. The signals to control the wave blade were stored on magnetic tape and were transferred to the wave generator through a data acquisition computer system (DAS). For this study there were four files on the tape which would produce a distinct spectrum for each file. Table 1 gives the nominal period of peak energy density for each file.

<u>Tape File</u>	<u>Approximate <math>T_p</math> (sec)</u>
1	1.45
2	2.25
3	2.86
4	3.60

Table 1. Period of peak energy density for each file.



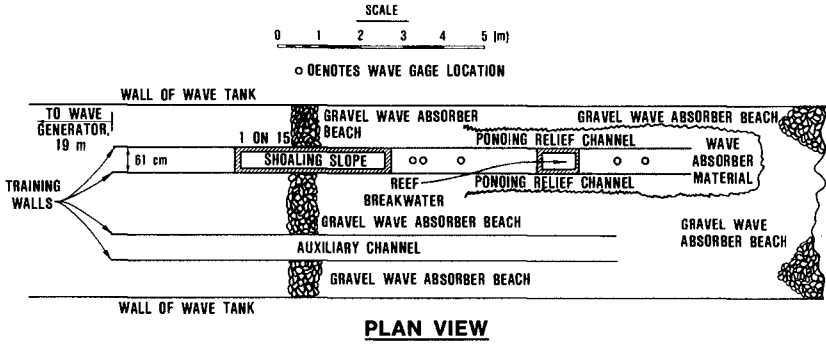


Figure 1. Plan view of wave tank and test setup.

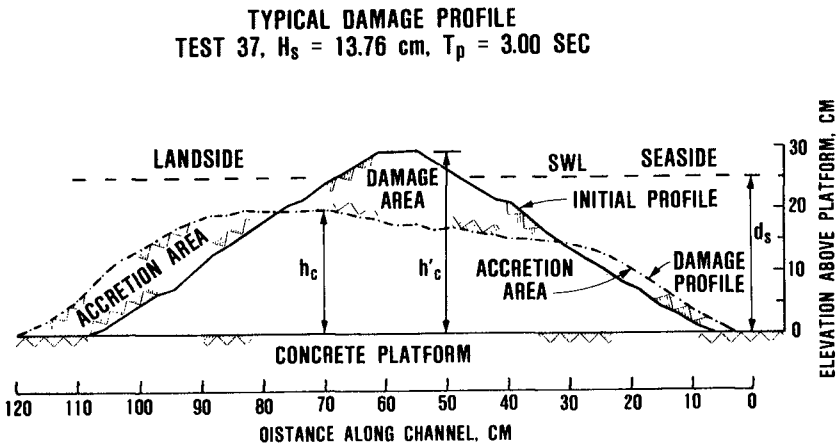


Figure 2. Cross sectional view of the initial and damaged breakwater profile.

If there were no attenuation of the signal to the wave generator the files used were intended to produce a saturated spectrum at all frequencies above the frequency of peak energy density for the water depth at the wave blade. For frequencies lower than that of the peak, the energy density falls off rapidly. This procedure produced a spectrum of the Kitaigorodshii type as described by Vincent (1981). The amplitude of the signal to the wave generator could be attenuated by a 10-turn potentiometer in a voltage divider network which allowed control of the wave heights generated. In addition, the waves were generated in a water depth 25 centimeters greater than at the breakwater and shoaled to the water depth of the structure over a 1 on 15 slope (see Figure 1). This setup ensures that very severe conditions can be developed at the structure site. Incident zero-moment wave heights ranged from about 1 to 18 centimeters.

Three parallel wire resistance-type wave gages were used in front of the breakwater to resolve the incident and reflected wave spectrum using the method of Goda and Suzuki (1976). Two wave gages were behind the structure to measure the transmitted wave height. The location of the gages is shown in Figure 1. During data collection the gages were sampled at a rate of 16 times per second for 256 seconds by the same DAS which controlled the wave generator motion.

Two distinct types of model tests were conducted during this study. They will be referred to as "stability" tests and "previous damage" tests. For a stability test the following test sequence was used:

1. Rebuild the breakwater from the previously damaged condition.
2. Survey the breakwater to document its initial condition.
3. Calibrate the wave gages.
4. Select the wave file and signal attenuation setting.
5. Start the wave generator and run waves.
6. Collect wave data (several or more times).
7. Stop the wave generator.
8. Survey the breakwater to document its final condition.

The duration of wave action lasted from 1-1/2 hours for a test using the File 1 spectrum to 3-1/2 hours for a File 4 spectrum. Generally, the technicians observing the tests thought that most of the stone movement occurred during the first 10 or 15 minutes of wave generation, so the final survey is regarded as an equilibrium profile for the structure. In rebuilding the breakwater the technicians rarely touched the stone but merely pushed it around by foot until the shape conformed to the desired initial profile. This procedure was a conscious effort to avoid overly careful placement of the stone. Outlines of the desired initial profile were fixed to the walls of the testing channel and a moveable template was used to ensure that the initial profile was reasonably close to the desired profile. Initial configuration of the breakwater for a stability test is a narrow, trapezoidal shape with the seaward and landward slopes of 1 on 1-1/2 (see Figure 2). Figure 2 also shows a typical profile after moderately severe wave attack during a stability test. Wave transmission and reflection also were measured during a stability test.

Tests referred to as previous damage were conducted to answer the question of how the breakwater would perform for typical wave conditions after it had been damaged by very severe wave conditions. For previous damage tests there was very little readjustment of the damage profile from test to test since the breakwater is not rebuilt at the end of a test. There really was no stability information obtained from these tests and the duration of wave action is only half an hour, but wave transmission and reflection were measured. Previous damage tests had the following sequence of events:

1. Final survey of the breakwater for the last test which becomes the initial survey for this test.
2. Calibrate wave gages.
3. Select the wave file and signal attenuation setting.
4. Start generator and run waves for half an hour.
5. Collect wave data (two or three times).
6. Stop the wave generator.
7. Survey breakwater as noted above in Step 1.

All 205 of the completed tests of this study logically can be divided into 10 subsets or test series. Because of the test plan stability test series have odd numbers and previous damage test series have even numbers. Table 2 gives the basic information about each subset.

<u>Subset No.</u>	<u>No. of Tests</u>	<u>Water Depth (cm)</u>	<u>Crest Height as Built (cm)</u>	<u>Median Stone Weight (gr).</u>	<u>Area of Breakwater Cross Section (cm<sup>2</sup>)</u>
1	27	25	25	17	1170
2	3	25	NA	17	1170
3	29	25	30	17	1560
4	12	25	NA	17	1560
5	41	25	35	17	2190
6	11	25	NA	17	2190
7	38	25	32	71	1900
8	26	25	NA	71	1900
9	13	30	32	71	1900
10	5	30	NA	71	1900

Table 2. Basic data for each subset.

Two different sizes of stone were used during this study. For subsets 1 through 6 an angular quartzite with a median weight of 17 grams was used and for subsets 7 through 10 a blocky to angular diorite was used. Table 3 summarizes the information about the stone used in this study.

<u>Characteristic</u>	<u>Quartzite</u>	<u>Stone Type Diorite</u>
Median weight (gr)	17.0	71.0
Density	2.63	2.83
$W_{98}/W_2$	3.9	10

Table 3. Stone and gradation characteristics.

Table 4 provides a summary of the definitions for variables used in this study.

Symbol, Definition (units)

$H_S$	, incident zero-moment wave height (cm)
$H_T$	, zero-moment transmitted wave height (cm)
$H_c$	, zero-moment wave height at transmitted gage locations with no breakwater in channel (cm)
$T_p$	, wave period of peak energy density of spectrum (sec)
$d_s$	, water depth at breakwater (cm)
$L_p$	, Airy wave length calculated using $T_p$ and $d_s$ (cm)
$W_{50}$	, median stone weight, subscript indicates percent of total weight of gradation contributed by stones of lesser weight (gr)
$w_r$	, density of stone
$w_w$	, density of water, tests conducted in fresh water $w_w = 1.0$
$h_c$	, crest height of breakwater as built (cm)
$h_c$	, crest height of breakwater after wave attack (cm)
$A_t$	, cross sectional area of breakwater (cm <sup>2</sup> )
$A_D$	, area of damage to breakwater (cm <sup>2</sup> )
$K_R$	, reflection coefficient of breakwater as defined and calculated by method of Goda and Suzuki (1976)

Results

Stability. To prevent confusion it should be mentioned that the stability will be quantified by the damage or lack of damage during a test. For reef breakwaters, stability logically can be viewed from two perspectives. One perspective is volumetric damage. This type of damage is related to the number of stones displaced from their original location and possibly includes where the stones were deposited. Information regarding volumetric damage is important when considering maintenance requirements for the structure. The second aspect of stability is the reduction in the crest height of the breakwater due to wave action. Since the performance of a reef breakwater will be judged largely by its wave transmission characteristics, this aspect of stability is quite important because wave transmission is very sensitive to the crest height

of the structure relative to the water depth. Two dimensionless variables are used to define these two aspects of the stability of the breakwater; they are the relative crest height,  $h_c/d_s$ , and the dimensionless damage,  $D'$ , which is defined as

$$D' = \frac{A_d}{(w_{50}/w_r)^{2/3}}$$

The relative crest height is the ratio of the equilibrium or stable crest height to the water depth at the site for the given wave conditions and  $D'$  is a measure of the number of stones removed from the damaged area. Experience indicates that damage to a rubble mound breakwater will be strongly dependent on Hudson's stability number  $N_s$ , Hudson (1959). The stability number is defined for irregular waves as

$$N_s = \frac{H_s}{(w_{50}/w_r)^{1/3} \left( \frac{w_r}{w_w} - 1 \right)}$$

In Figures 3a and 3b  $h_c/d_s$  and  $D'$  are plotted versus  $N_s$  for data of subset 1. These data trends generally are what would be expected: as the severity of wave attack increases, i.e. increasing  $N_s$ , the volume of stone displaced increases at an ever-increasing rate and the height of the breakwater decreases gradually. On the whole, the stability number does a fairly good job of explaining the damage to the structure but careful inspection of the data points in Figures 3a and 3b suggests that there is a wave period effect. The effect indicated is that wave spectra with large  $T_p$ 's do more damage than spectra with small  $T_p$ 's, other factors being equal. This finding is consistent with the findings of Gravesen, et al. (1980) who have conducted an extensive study of the stability of rubble mound breakwaters to irregular wave attack. The breakwaters studies by Gravesen, et al. are considerably different from reef breakwaters in that they are high multilayered structures with large concrete caps designed so the structure is rarely overtopped. Gravesen's, et al. work suggested that a modified stability number which took into account the period of peak energy density of the spectrum might describe damage to the breakwaters better than the traditional stability number. Following Gravesen, et al. the spectral stability number,  $N_s^*$  is defined

$$N_s^* = \frac{(H_s^2 L_p)^{1/3}}{(w_{50}/w_r)^{1/3} \left( \frac{w_r}{w_w} - 1 \right)} \quad \text{Eq. 1}$$

When the data shown in Figures 3a and 3b are replotted versus  $N_s^*$  in Figures 4a and 4b there is a considerable reduction in the data scatter. When the other stability data subsets are compared as in Figures 3 and 4 it is found that using  $N_s^*$  reduces the scatter in all subsets, eg. see Figure 5 which shows the data for Subset 5.

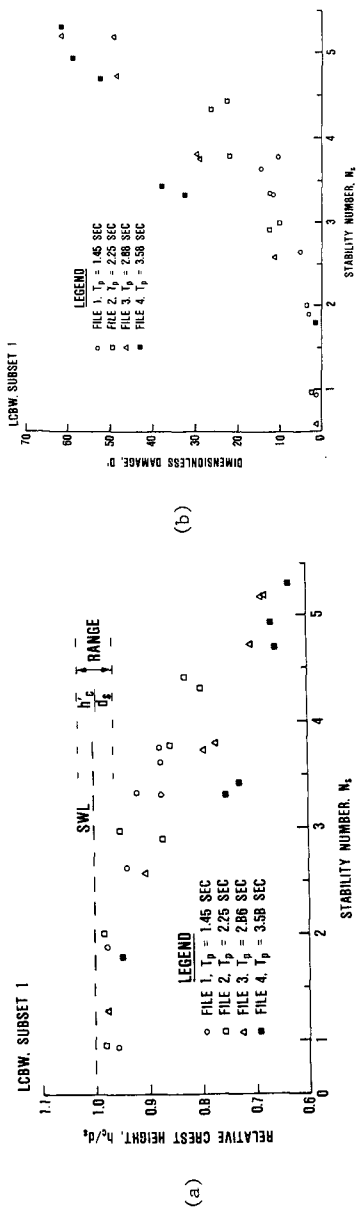


Figure 3. Damage response of breakwater as a function of stability number for data subset 1.

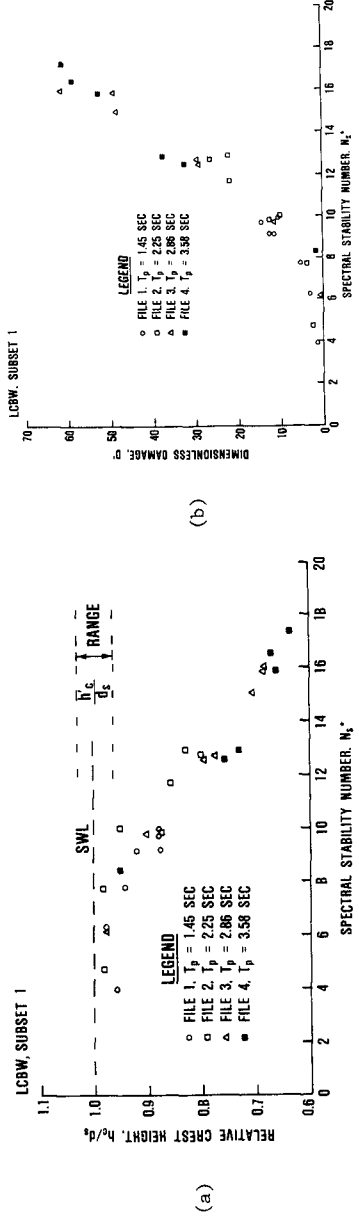
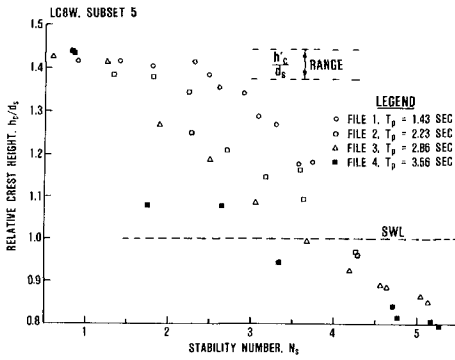
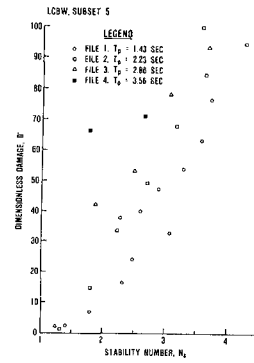


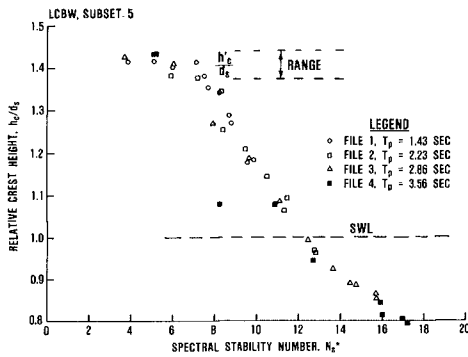
Figure 4. Damage response of breakwater as a function of the spectral stability number for data subset 1.



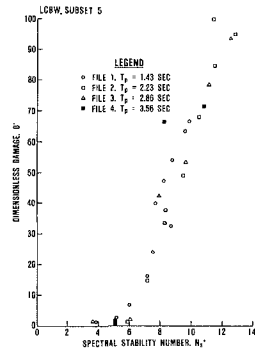
(a)



(b)



(c)



(d)

Figure 5. Damage response of breakwater for data subset 5.

Although the reason is not entirely clear, it appears that  $H_s^2 L_p$  is a better measure of wave severity than  $H_s^3$ , at least as far as reef breakwaters are concerned. Part of the reason may be due to relating damage to the zero-moment wave height rather than a larger wave in the height distribution. It is convenient to relate damage to the zero-moment wave height because of the statistical stability of the parameter and because of its relation to the area under the spectrum; however, it is commonly observed that the larger waves in the distribution move most of the stone. In addition, for a given water depth, the maximum stable wave height increases with period; therefore, for a fixed water depth and zero-moment wave height it would be the file with the longer period of peak energy density which would have the larger waves striking the breakwater. Another factor which might cause longer waves to be more damaging could be called the runup factor. Generally, on rough porous slopes, longer period waves have higher runup than shorter waves if other conditions are equal (see Figure 12 in Seelig 1980). A longer period and higher runup mean a greater return flow which can cause damage on a high structure and a greater volume and celerity of overtopping flow to cause damage on a low-crested breakwater.

Somewhat surprisingly, the classic picture of a large wave curling over and breaking on the structure was rarely observed during this study. Possibly because of the porous nature of the breakwater, waves appeared to be partly absorbed into the structure before they could break on it. Usually it was the drag forces caused by heavy overtopping flow which moved most of the stones rather than wave impact.

Since the relative height of the breakwater was so strongly dependent on  $N_s^*$  for all the stability subsets it is instructive to look at all five trends together in one Figure. Figure 6 shows these trends which indicate that there is little or no degradation of the breakwater for  $N_s^* \leq 6$ , but for the higher structures there is quite noticeable degradation for  $N_s^* \geq 8$ . Figure 6 also shows that the damage rate is reduced after the crest has been battered down to about the still water level by wave attack. Once the structure is submerged the overlying water provides considerable protection from further damage. This tendency has been observed in the field for a number of damaged breakwaters, Wiegell (1982).

#### Wave Transmission

For these tests the wave transmission coefficient  $K_T$  is defined as:

$$K_T = \frac{H_t}{H_c}$$

Although this is not the most commonly used definition of  $K_T$  it has some advantages over the traditional definition which is given by the ratio of  $H_T$  to  $H_s$ . The definition given above can be stated as



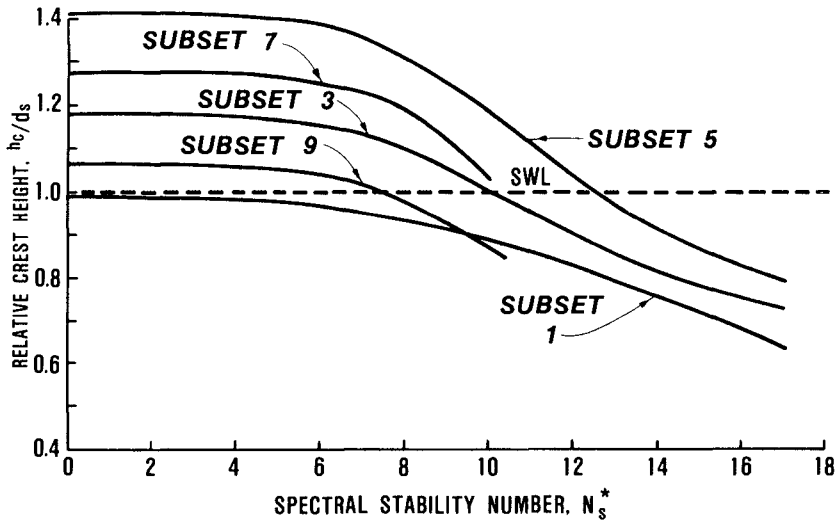


Figure 6. Damage trends as a function of the spectral stability number for data subsets 1, 3, 5, 7, and 9.

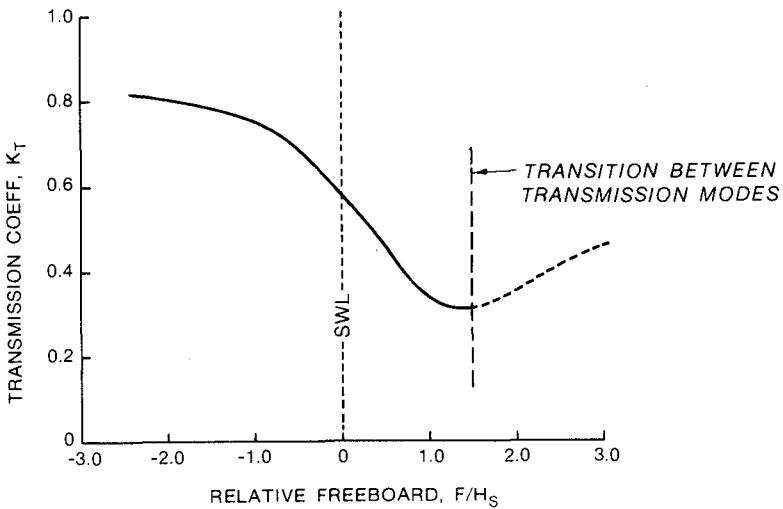


Figure 7. Wave transmission as a function of the relative freeboard.

the ratio of the transmitted wave height to the wave height which would be observed at the same location without the breakwater in the channel. This definition eliminates wave energy losses occurring between the incident and transmitted gages in the absence of a breakwater in the testing channel. These losses were observed to be considerable for the most severe wave conditions during calibration of the channel. In effect  $K_T$  measures the attenuation of wave energy due strictly to the presence of the breakwater and eliminates additional energy losses due to natural wave breaking processes occurring between the incident and transmitted wave gages. Because of this definition  $K_T$  should be somewhat conservative.

In an extensive study of wave transmission, Seelig (1979) concluded that the relative freeboard  $F/H_s$  was the most important variable in explaining the transmission characteristics of submerged and overtopped breakwaters, where  $F = h_c - d_s$ . Figure 7 shows a trend curve for  $K_T$  as a function of  $F/H_s$  based on results from this study. The curve shown in Figure 7 is schematic in nature because it tries to follow the trend of the data from all 10 subsets. There are some small inconsistencies introduced by using this approach because the larger structures will attenuate the waves better than the smaller structures for the same relative freeboard, i.e. the broader the crest of the breakwater, the greater the reduction in the transmitted wave height. Another problem is that for relatively high breakwaters transmission is no longer dominated by wave overtopping but by energy transmission through the structure which is a function of, among other things, wave steepness,  $H_s/L_p$ . It is this changing role in the dependence of  $K_T$  on  $H_s$  which causes the paradoxical trend in the data which is suggested by the dashed curve in Figure 7. The transition in modes of transmission occurs at approximately  $F/H = 1.5$  for reef breakwaters. In Figure 7 the dashed curve is not intended to suggest that for a fixed incident height the transmitted height will increase if the freeboard is increased but rather that with a fixed freeboard the transmission coefficient will increase if the incident wave height is reduced. Despite its limitations Figure 7 provides a reasonably good idea about the performance of reef breakwaters over a wide range of conditions. The problem is a typical one: the phenomena of interest is not a function of one variable over the entire range of interest.

Analysis of the wave transmission data is continuing. It appears that  $F/H_s$  and  $H_s/L_p$  provide a reasonably good way to parameterize wave transmission due to overtopping and through the breakwater, respectively. However, the work of Allsop (1983) suggests that there should be some influence of wave period in the portion of wave transmission due to overtopping.

#### Wave Reflection and Energy Dissipation

Wave reflection from the breakwater is more strongly dependent on wave period or wave length than is the wave transmission. Reflection, however, also is strongly dependent on  $F/H_s$  which provides an opportunity to plot wave reflection data along with wave transmission data.

A figure showing both wave reflection and transmission can be used to estimate the amount of wave energy dissipated by the structure. Generally, the more wave energy dissipated the more effectively the breakwater is functioning since both reflection and high levels of transmission are undesirable. The following equation represents the energy balance in the vicinity of the reef breakwater.

$$K_R^2 + K_R^2 + \text{dissipation} = 1.0 \quad \text{Eq. 2}$$

where  $K_R$  is the energy-weighted reflection coefficient given by Goda and Suzuki (1976) as

$$K_R = \sqrt{E_R/E_I}$$

where  $E_R$  and  $E_I$  are the reflected and incident wave energy, respectively, and "dissipation" is the fractional part of the wave energy remaining after the transmitted and reflected energy are subtracted from the total incident wave energy. Since the water depth is the same on both sides of the breakwater and the period of peak energy density is usually about the same on both sides of the breakwater, Equation 2 should be approximately correct. Figure 8 shows the results of using Equation 2 for the data collected during this study. In Figure 8 energy is plotted versus the relative freeboard with the transmitted energy to be read against the scale on the left side of the figure and the reflected energy to be read against the scale on the right side of the figure. Wave energy dissipated by the structure is the energy remaining in the central part of the figure after the reflected and transmitted energy are subtracted from the total incident wave energy. Figure 8 is schematic in nature because there are variables affecting reflection and transmission which cannot be taken into account by the figure, but it illustrates in a reasonably accurate way the most important function of the breakwater, i.e. to dissipate wave energy.

#### Conclusions

The severity of irregular wave attack is measured better by the parameter  $H_s^2 L_p$  than it is using  $H_s^3$ , at least for reef breakwaters.

If a stability number similar to Hudson's (1959) is defined using  $H_s^2 L_p$ , a variable is formed which is a very useful measure of the cause of damage to the breakwater for irregular wave conditions. This variable is referred to as the spectral stability number,  $N_s^*$ , and is defined by Equation 1. All of the test series used to evaluate stability indicate there is a threshold for stone movement around  $N_s^* = 7$ . When  $N_s^* \leq 6$  there is little or no stone movement and when  $N_s^* \geq 8$  there is noticeable stone movement and damage to the breakwater.

Wave transmission is caused by wave overtopping and transmission through the breakwater which for a given structure are primarily functions of  $(h_c - d_s)/H_s$  and  $H_s/L_p$ , respectively.

Wave reflection from the breakwater was measured during these tests. By subtracting the reflected and transmitted energy from the total incident energy an estimate of the wave energy dissipation by the breakwater as a function of  $(h_c - d_s)/H_s$  was obtained (see Figure 8).

Acknowledgements

The tests described and the resulting data presented herein, unless otherwise noted, were obtained from research conducted under the program, Coastal Structure Evaluation and Design of the United States Army Corps of Engineers by the Coastal Engineering Research Center. Permission was granted by the Chief of Engineers to publish this information.

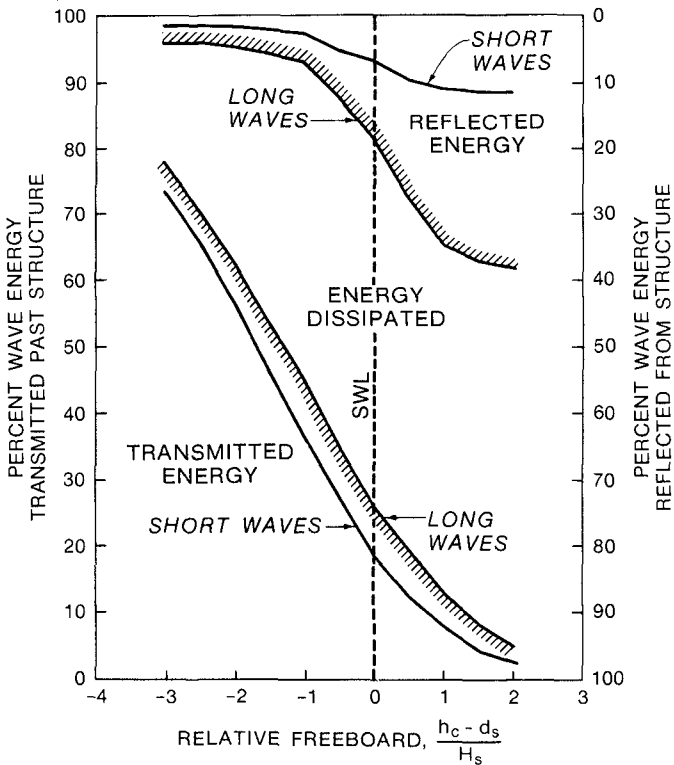


Figure 8. Wave energy allocation in the vicinity of a reef breakwater.

References

- Allsop, N. W. H., "Low-Crest Breakwater, Studies in Random Waves," Proceedings of Coastal Structures 83, Arlington, Virginia, March 1983, pp 94-107.
- Bremner, W. D., N. Foster, C. W. Miller, and B. C. Wallace, "The Design Concept of Dual Breakwaters and its Application to Townsville, Australia," Proceedings of the 17th Coastal Engineering Conference, Vol 2, Sydney, Australia, 1980, pp 1898-1908.
- Goda, T. and Y. Suzuki, "Estimation of Incident and Reflected Waves in Random Wave Experiments," Proceedings of the 15th Coastal Engineering Conference, Honolulu, Hawaii, 1976, pp 828-845.
- Gravesen, H., Jensen, O. J., and Sorensen, T., "Stability of Rubble Mound Breakwaters II," Danish Hydraulic Institute, 1980.
- Hudson, R. Y., "Laboratory Investigations of Rubble-Mound Breakwaters," Proceedings of the Waterways and Harbors Division, American Society of Civil Engineers, Vol 83, No WW3, 1959.
- Lillevang, O. J., "A Breakwater Subject to Heavy Overtopping: Concept, Design, Construction, and Experience," Proceedings of ASCE Specialty Conference Ports 77, Long Beach, California, March 1977.
- Lording, P. T. and J. R. Scott, "Armor Stability of Overtopped Breakwater," Journal of Waterways, Harbors and Coastal Engineering Division, ASCE WW2, May 1971, Paper 8138, pp 341-354.
- Raichlen, F., "Armor Stability of Overtopped Breakwater," Journal of Waterways, Harbors, and Coastal Engineering, ASCE, WW2, May 1972, Discussion of paper 8138, pp 273-279.
- Seelig, W. N., "Effect of Breakwaters on Waves: Laboratory Tests of Wave Transmission by Overtopping," Vol 2, Proceedings of Coastal Structures 79, Vol 2, Alexandria, Virginia, March 1979, pp 941-961.
- Seelig, W. N., "Two-Dimensional Tests of Wave Transmission and Reflection Characteristics of Laboratory Breakwaters," Coastal Engineering Research Center Technical Report No. 80-1, Ft. Belvoir, Virginia, June 1980.
- Vincent, C. L., "A Method for Estimating Depth-Limited Wave Energy," CETA 81-6, U. S. Army Corps of Engineers, Coastal Engineering Research Center, Ft. Belvoir, Virginia, November 1981.
- Walker, J. R., R. Q. Palmer, and J. W. Dunham, "Breakwater Back Slope Stability," Proceedings of Civil Engineering in the Oceans/III, Vol 2, Newark, Delaware, June 1975, pp 879-898.
- Wiegel, R. "Breakwater Damage by Severe Storm Waves and Tsunami Waves," Prepared for Pacific Gas and Electric Co., Berkeley, California, March 1982.

## CHAPTER ONE HUNDRED SEVENTY NINE

### RIGID BODY MOTION OF A FLOATING BREAKWATER

Robert W. Miller<sup>1</sup> and Derald R. Christensen<sup>2</sup>

#### ABSTRACT

Predictions of the dynamic response of a floating breakwater obtained from a frequency domain analysis are compared with full-scale field measurements. Those parameters prominently affecting accurate response predictions are identified and discussed.

#### I Introduction

##### A) Overview

While concrete pontoon floating breakwaters have been successfully used under certain conditions to provide wave attenuation, their design has been primarily based upon empirical considerations. It has only been in the last decade that both the analytical tools and the field data have reached a state of refinement and sophistication which enables the reliable construction and calibration of breakwater response models.

This paper presents a simplified mathematical model of breakwater motion response. The model uses a frequency-domain approach to predict the harmonic responses of a breakwater to short-crested seas for five degrees-of-freedom of rigid-body motion. Rigid-body accelerations for three degrees of freedom as predicted by the model were compared with the corresponding full-scale field measurements. An attempt has been made to identify those parameters which most heavily affect the ability of the model to produce accurate results.

The funding for both the field-measurements and model development was provided by the United States Army Corps of Engineers as part of the West Point Prototype Breakwater Test Project. This project and its scope are more fully described in "Ship-Wake Attenuation Tests Of A Prototype Floating Breakwater" (1984) by Nece and Skjelbreia.

#### II Field Data

The project site and layout of the instruments of interest to this report are depicted in Figure 1. The two pontoons pictured were rigidly bolted together during the period under discussion. The project site was chosen to maximize exposure to wave attack. Measured

- 
1. Associate Member, ASCE, Tongass Engineers, Inc., Juneau, Alaska, U.S.A.
  2. Senior Research Associate, Dept. of Civil Engineering, University of Washington, Seattle, Washington, U.S.A.

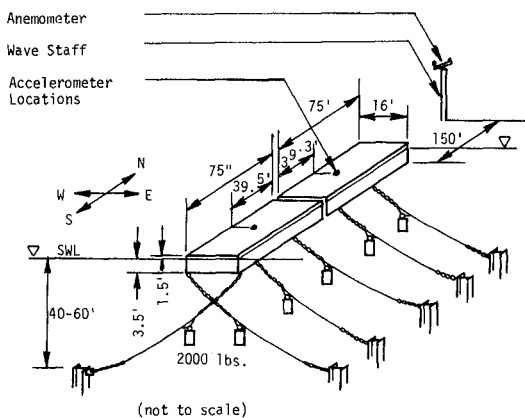


Figure 1. West Point Prototype Floating Breakwater: Project Site Instrument Layout

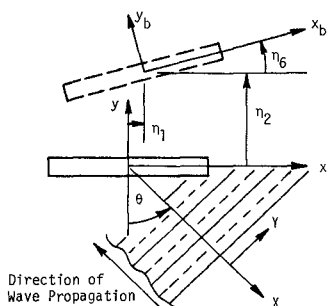


Figure 2. Top View.

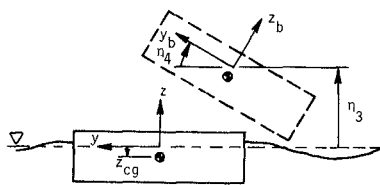


Figure 3. End View.

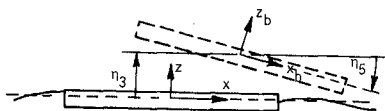


Figure 4. Side View.

Coordinate Definitions

Global:  $x, y, z$   
 Equilibrium:  $x, y, z$   
 Body:  $x_b, y_b, z_b$

Relative Motion

$\eta_1$  = surge       $\eta_4$  = roll  
 $\eta_2$  = sway       $\eta_5$  = pitch  
 $\eta_3$  = heave       $\eta_6$  = yaw

quantities which were used in this study were incident wave height, breakwater accelerations, and wind direction. Timeseries of all measured quantities contained 2048 samples (4 samples per second for 8 1/2 minutes).

Incident wave measurements were made at a location 150 feet from the breakwater and located such that wave diffraction or reflection due to the breakwater itself was minimal. Timeseries of incident wave heights were converted into autospectral estimates by means of Fast Fourier Transform techniques. These estimates were used as inputs into the analytical model. Servo-accelerometers measuring sway, heave, and roll were located approximately at the center of mass of each pontoon. Timeseries of these quantities were also transformed and the resulting spectral estimates used for comparison with the model output.

Measurements of wind direction were used to estimate the principal angle of wave attack. This angle was assumed to be coincident with the mean wind direction. The extent to which this assumption is valid is very likely dependent upon the length of time the wind has been blowing in approximately the same direction.

### III Description of Model

The analytical techniques employed in breakwater motion prediction are essentially those of ship motion or seakeeping theory as described in St. Denis, 1953; Ochi, 1974; Salveson, 1970. Strip theory is used to estimate the hydrodynamic properties of the body and linear second order differential equations of motion are solved at each discrete frequency of interest. Motion response is therefore confined to the frequency of the excitation with harmonics and second-order effects neglected by the model.

This methodology has been applied to barges (Hutchison, 1977) and breakwaters (Hutchison, 1982; Adee, 1976), but, to the knowledge of the authors, never in a directional sea with the benefit of extensive full-scale data. As pointed out by Hutchison, (1976), barges (and therefore concrete pontoon breakwaters) should be excellent shapes for such an analysis. Many of the problems which have troubled ship motion predictions such as forward speed corrections, bilge keels etc. are absent in breakwaters. Discontinuities in the submerged perimeter are localized in the ends which should provide a suitable situation for strip theory. However, successful treatment of nonlinear phenomenon such as square-law damping or the load-displacement relationships of mooring lines may present additional problems.

#### B) Coordinates

The coordinate systems used in this analysis are depicted in Figures 2-4. Global coordinates X,Y,Z remain stationary with respect to a fixed point on the earth. The origin of the equilibrium coordinate system is located at the mean still water level in the vertical direction and at the mean position of the center of mass in the horizontal plane. In traditional seakeeping analysis, the



equilibrium frame frequently translates or rotates at a constant rate with respect to the global frame. For a moored breakwater, the distinction between the two frames would only become apparent as a result of long-term changes in mean position of the body due to tide, current, or wind. This distinction, therefore, serves no further purpose in the present analysis.

The body coordinate system ( $x_b, y_b, z_b$ ) remains fixed in the breakwater itself and is the frame of reference implicitly held by the accelerometers attached to the breakwater.

### C) Equations of Motion

The basic equation of motion for the six-degree-of-freedom rigid body response is:

$$\sum_{j=1}^6 (I_{ij} + A_{ij}(\omega)) \ddot{\eta}_j + B_{ij}(\omega) \dot{\eta}_j + (C_{ij} + K_{ij}) \eta_j = F_i e^{i\omega t};$$

for  $i = 1$  to  $6$  3.1

where

I	is the inertia coefficients matrix,
A	is the added mass coefficients matrix,
B	is the hydrodynamic damping coefficients matrix
C	is the hydrostatic restoration coefficients matrix,
K	is the linearized mooring force restoration matrix,
F	is a complex amplitude vector consisting of 6 wave excitation forces,
$\omega$	is the angular frequency of the incident wave,
$\eta_j$	is a complex vector describing the amplitude and phase of the motion in the $j$ th direction in the equilibrium frame,
$e^{i\omega t}$	is a unit vector rotating with angular frequency $\omega$ ,
	and the dots indicate differentiation with respect to time.

The use of the term "coefficients" is in contrast to "variable" and is not intended to imply non-dimensionality.

The values of the hydrodynamic mass and damping terms as well as the wave excitation forces were determined by the NSRDC Ship Motion and Sea Loads Computer Program (Meyers, 1975), which has exhibited success in the accurate prediction of the motion of destroyer hulls (Salveson, 1970).

Linearized mooring force restoration stiffnesses were obtained from Program BRKMOOR (Adee, 1976) which uses a finite-element approach to establish the equilibrium position of the breakwater. Restoring constants are then determined by perturbing the breakwater from its equilibrium position and calculating the change in mooring tension that

results.

D) Modeling of Square-Law Roll-Damping

The hydrodynamic damping terms presented in the previous section produce damping forces which are linearly proportional to the velocity of the motion. It has been found (Salveson, 1970; Ochi, 1976) in the case of ships that such neglect of higher order (e.g. damping proportional to the square or cube of the velocity) produces satisfactory response prediction except in the case of roll motion. If significant wave energy is present near the roll natural frequency, then the predicted roll response will be much too great. In the case of the West Point floating breakwater, it was also found necessary to include an accounting of square-law roll damping in the analytical model in order to avoid overprediction.

While space limitations preclude a detailed treatment in this report, a thorough development of the following equations may be found in (Schmitke, 1978) for the interested reader. Since a floating breakwater has no mean forward velocity, the only sources of square-law roll damping considered were those due to eddy-making and those due to hull-friction. The approach employed was to calculate the amount of work done by the aforementioned nonlinear damping forces during a complete roll cycle. An equivalent linear roll damping coefficient,  $B^*44$  was then defined which dissipates the same amount of energy during the cycle. Since the amplitude of the roll motion must be known to calculate the energy dissipation, the procedure involved is iterative, requiring repetitive solution of the equations of motion until the calculated and assumed roll amplitudes are in sufficiently close agreement.

Equation 3.1 described above is solved repeatedly at each discrete angle of wave attack and frequency of interest. If the excitation force used is that which would be caused by a wave of unit amplitude incident upon the structure, the solution results in a complex vector termed the frequency response operator or FRO. This quantity is also referred to in the literature as the transfer function. The FRO provides a linear transformation between the amplitude and phase of the wave and that of the motion response of the breakwater. For a particular frequency and angle of wave attack this relationship is:

$$S_{\eta}(\omega, \theta) = H_{\eta}(\omega, \theta) S_{\xi}(\omega, \theta) H_{\eta}^*(\omega, \theta) \quad 3.2$$

where  $S_{\eta}(\omega, \theta)$  is the response autospectrum for a given frequency and angle

$S_{\xi}(\omega, \theta)$  is the incident wave height autospectrum for that frequency and angle

and  $H_{\eta}(\omega, \theta)$  is the FRO for the frequency  $\omega$  and angle  $\theta$  and the superscript \* denotes the complex conjugate

Since a random short-crested sea-state may be represented at the summation of monochromatic waves of different frequencies and direction (St. Denis, 1953), it is possible, by means of linear superposition, to

predict the response to a variety of sea states given a complete set of appropriate FROs. This is done using the following form of equation 3.2 given in discrete form:

$$S_{\eta}(\omega) = \xi [H_{\eta}(\omega, \theta) S_{\xi}(\omega, \theta) H_{\eta}^*(\omega, \theta)] \quad 3.2a$$

Since directional spectra for the project site were not known, it was assumed that

$$\begin{aligned} S_{\xi}(\omega, \theta) &= S_{\xi}(\omega) \Psi(\theta) & 3.3 \\ \int_{-\pi}^{\pi} \Psi(\theta) d\theta &= 1.0 & 3.4 \end{aligned}$$

The form of  $\Psi(\theta)$  employed was

$$\begin{aligned} \Psi(\theta) &= K \cos^n(\theta - \theta_0), \quad -\pi/2 \leq \theta \leq \pi/2 & 3.5 \\ \Psi(\theta) &= 0 \quad \text{otherwise} \end{aligned}$$

where  $\Psi(\theta)$  is referred to as the spreading function  
 $\theta_0$  is the principal or mean angle of wave attack  
 and  $K$  is a constant chosen to satisfy equation 3.4

#### F) Operator Transformations

As mentioned previously, solution of the equations of motion in the form in which they have been presented results in displacement frequency response operators about the origin of the x y z coordinate frame. To enable direct comparison of predicted with measured results these operators must i) relate to accelerations, not displacements ii) be valid at the physical location of the instruments and iii) be written in the body rather than equilibrium coordinate system. These transformations will be briefly outlined.

##### i) Acceleration FRO

since  $H_{\eta}(\omega, \theta)$  is assumed to be of the form

$$H_{\eta}(\omega, \theta) = /H_{\eta}(\theta) / e^{i\omega t} \quad 3.6$$

it follows that

$$H_{\eta}''(\omega, \theta) = -\omega^2 /H_{\eta}(\theta) / e^{i\omega t} \quad 3.7$$

$H_{\eta}''(\omega, \theta)$  is referred to as the Acceleration FRO.

##### ii) Spatial Transformation

In general if  $\{A\}$  and  $\{R\}$  are translational and rotational vectors respectively then

$$\{A(x, y, z)\} = \{A_0(x_0, y_0, z_0)\} + \{R_0\} X \{r\} \quad 3.8$$

where the subscript '0' denotes the original (untransformed) location,  $r$  is the position vector from  $(x_0, y_0, z_0)$  to  $(x, y, z)$  and 'X'

denotes the vector cross-product.

iii) Transformation to Body Coordinates

Acceleration in the body coordinate system is defined by the following relation:

$$\{\ddot{A}_b\} = [T] \{A\} \quad 3.9$$

where the subscript 'b' denotes the body coordinate system and [T] is the transformation vector for a sequence of rotation of the Euler angles  $\eta_6, \eta_5, \eta_4$ . For small angles,

$$[T] = \begin{bmatrix} 1 & \eta_6 & \eta_5 \\ \eta_6 & 1 & \eta_4 \\ \eta_5 & \eta_4 & 1 \end{bmatrix}$$

It is to be noted that vectors of rotational quantities are invariant to the foregoing two transformations.

IV Analysis and Discussion

General Method

Many of the parameters required as input into the analytical model just described are not known with certainty. Since one of the purposes of this work was to establish estimates of these values which yielded acceptable response predictions, a consistent method was desired for varying the input parameters. Because much of the processing was done on relatively slow microcomputers, it was necessary to allow flexibility in the application of this method to insure that a reasonable amount of data was examined.

Unknown quantities which appeared to have the largest influence upon the shape and magnitude of the predicted results include the value of the exponent in the cosine-power spreading function, the mooring stiffnesses, the value of the effective bilge radius of the breakwater cross-section, and the reciprocal wave steepness,  $1/WS$  which is defined as the wave length divided by the wave height. The latter two quantities primarily influence roll while it is shown later that the mooring stiffness only significantly affect the sway response. The value of 'n' is therefore the only value of large uncertainty which has a substantial influence over the heave response.

Calibration of  $R_e$ , the bilge radius, was performed by selecting an input wave spectrum based upon measurement taken during a strong steady wind which blew for several hours directly to beam. A value of n was found which appeared to give good results for heave acceleration response. The values of  $R_e$  and the wave steepness were then varied until good results in roll were obtained. While the wave steepness could be expected to change with variations in the wave climate, the bilge radius is a property of the breakwater cross-section and should not change, although its proper value for a cross-section with flat

sides and sharp corners is not obvious. Therefore, after initial calibration, its value was not altered in subsequent runs.

#### Statistical Measures of Predictive Accuracy

It is appropriate to mention that the spectral density functions derived from measurements are estimates. The 95% confidence band ranges between 0.65 and 1.75 of the plotted ordinate. In most cases, differences between analytical model outputs and spectral estimates fall well within the 95% confidence band. For this reason, conclusions should be drawn based upon trends in the analysis which appear over several runs rather than upon one record only.

In order to present and discuss the results meaningfully for a large number of runs, it was desirable to develop some quantitative measures of closeness of the predicted and measured autospectral estimates. Two quantities were used for this purpose: the predicted variance normalized by the measured variance, henceforth referred to as the variance ratio, VR;

$$VR = \frac{\sigma^2 \text{ predicted}}{\sigma^2 \text{ measured}} \quad \text{where } \sigma^2 \text{ is the response variance} \quad 4.2$$

and the normalized squared error,  $E_n^2$  as defined by the following:

$$E_{n,4.2}^2 = \frac{\epsilon}{\omega} [ \{ (S_{\eta}^{\ddot{}}(\omega) \text{ measured} / \sigma^2 \text{ measured}) - (S_{\eta}^{\ddot{}} \text{ pred.}(\omega) / \sigma^2 \text{ pred.}) \}^2 ]$$

where the summation is over each of the discrete frequencies analyzed.

The variance ratio is intended as an indication of the closeness of the predicted to the measured response magnitudes with 1.0 expressing perfect agreement, numbers greater than 1.0 indicating over-prediction, and numbers less than 1.0 indicating underprediction of the acceleration response magnitude. This statistic, however, does not consider the closeness of the shapes of the curves under comparison, which may differ appreciably while enclosing the same area. When both spectra to be compared to one another are normalized so that each encloses a unit area, the extent to which  $E_n^2$  differs from zero is strictly a result of differences in general shape between the two curves. Identical curves, translated with respect to one another along the frequency axis, however, would have different values of  $E_n^2$ . The unidirectional wind duration, uwd, was defined as the number of hours that the mean wind direction remained within 20 degrees of the mean for the record under consideration.

#### Evaluation of Results

Table 1 summarizes the results obtained for all model runs made. Overall agreement is generally good except where the wind direction was not steady for several hours or when the significant wave height was low. No obvious overall trends were evident, except perhaps for the

Date 1983	Run#	H <sub>s</sub> feet	Wind Angle degrees	Unidir Wind Dur hours	1/WS nd	n nd	HEAVE		ROLL		SWAY	
							VR nd	E <sub>n</sub> <sup>2</sup> sec <sup>2</sup>	VR nd	E <sub>n</sub> <sup>2</sup> sec <sup>2</sup>	VR nd	E <sub>n</sub> <sup>2</sup> sec <sup>2</sup>
4/24	1	2.1	3.5	6	125	9	1.02	4.6	.95	5.7	.90	13.7
4/24	2	1.4	4.2	10	125	*	0.99	7.2	1.03	7.5	1.10	11.4
4/8	3	1.8	16.5	0	125	7	0.56	7.6	0.46	16.84	0.54	5.5
4/8	4	1.6	10.0	8	125	7	1.06	2.6	0.93	15.5	0.87	15.3
4/9	5	1.5	19.0	8	175	18	0.98	5.7	0.98	19.8	0.96	5.9
4/12	6	0.8	24.5	2	400	7	1.21	18.0	0.54	93.9	0.53	58.4
4/13	7	0.6	25.0	0	400	1	1.27	24.8	0.43	101.0	0.47	58.0
4/24	8	1.8	4.3	8	125	18	1.02	21.4	0.89	14.8	0.93	11.1
4/24	9	1.9	8.5	2	125	7	1.04	25.3	1.20	20.2	0.65	74.4
5/28	10	0.9	27.0	6	300	5	0.73	22.1	0.55	63.4	0.47	21.5
4/23	11	1.0	24.2	8	125	9	1.13	97.0	0.85	100.0	0.50	51.2
4/12	12	1.0	3.3	8	175	12	1.00	85.6	0.97	28.8	0.83	11.2
5/6	13	1.0	2.6	8	135	12	1.21	24.1	0.88	41.6	1.02	19.6

\* unidirectional wave: n = infinity  
 nd = non-dimensional

Table 1 Summary Statistics for all Model Runs (1983)

sway and roll variance ratios to be low rather than high while in heave they tended to be high rather than low. It is encouraging that no degree of freedom experienced inordinately poorer results than the others suggesting a proper balance of terms in the equations of motion. Figure 5 through 7 show typical graphical results obtain for the three degrees of freedom examined.

#### Heave

In general, more consistent results over a wider range of conditions were obtained for heave than for the other two degrees of freedom, particularly on the records examined which had short wind duration and those with recent wind directional shifts. Even when magnitude discrepancies occurred in heave, the predicted maximum response was at the correct frequency. This is not surprising in view of the fewer uncertain input parameters in heave, the relatively small stiffness provided by mooring restraints in this mode, and the absence of significant higher order damping effects.

Heave acceleration variance ratios ranged approximately from 0.55 to 1.25. The mean variance ratio, averaged over all runs was 1.02 while the normalized squared error,  $E_n^2$  in heave averaged 22.8 over all runs. This value is lower than for the other two degrees of freedom, and if one outlier is discarded, it drops to 16.6.

#### Roll

The general level of agreement obtained in predicting roll motions is quite good. If only records with fairly constant wind directions for at least four hours are considered, then the ratio of predicted to measured variances ranges from 0.85 to 1.03 with a mean of 0.93. A glance at Table 1 shows that a slight tendency toward underprediction exists overall. If only records are considered during which the breakwater underwent wave attacks within ten degrees of beam, then the mean variance ratio improves to 0.98.

The estimated roll natural frequency is approximately 0.3 hertz which agrees well with both model output and measurements. In runs 6, 7, and 9 the measured peak roll response appears to be shifted slightly toward lower frequencies. Runs 6, 7, and 9 were all of short unidirectional wind duration and records 6 and 7 both exhibit low significant wave heights and relatively large angles of wave attack with respect to beam. Oblique wave attack angles tend to shift the forcing functions to lower frequencies but this should be correctly predicted by the analytical model. Since square law roll damping was only modeled in a narrow frequency range (0.289 to 0.32 hertz) it is difficult to explain a shift of the entire response by means of inaccurate estimation of square law damping parameters.

#### Sway

Sway is only marginally a harmonic response mode due to the absence of a hydrostatic restoring constant. The mooring restraints do provide

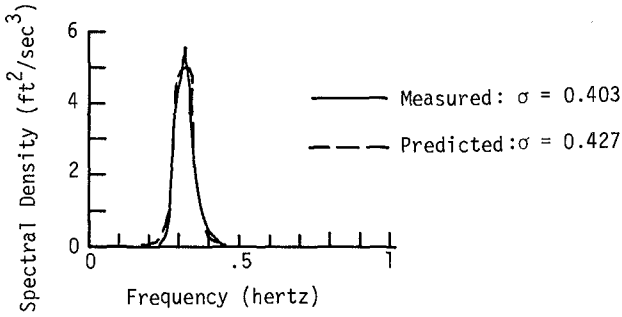


Figure 5. Measured and Predicted Heave Acceleration Autospectral Estimates for West Pontoon: Run 4.

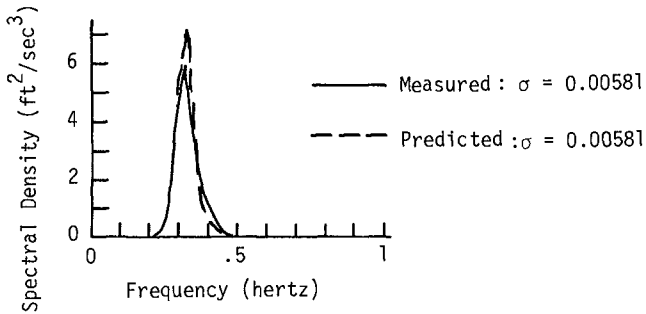


Figure 6. Measured and Predicted Roll Acceleration Autospectral Estimates for West Pontoon: Run 4.

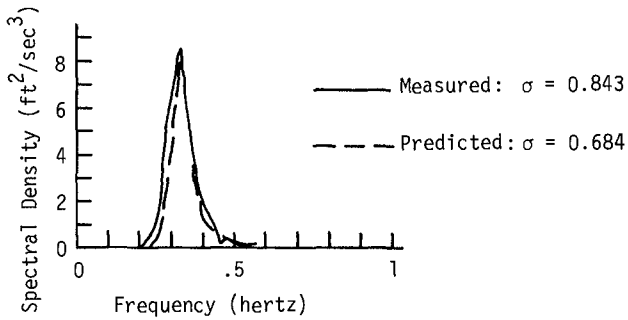


Figure 7. Measured and Predicted Sway Acceleration Autospectral Estimates for West Pontoon: Run 4.



a small restoring force but this does not produce much effect on the acceleration of the body except in the low frequency range. The sway response, however, is harmonic in character due to the periodic nature of the wave excitation force and coupling with other truly harmonic degrees of freedom such as roll. Prediction of sway motions can be difficult because other causes such as wind, tides, and currents can produce significant sways excitations. Long period or steady drift-type forces may have a large effect on mooring stiffnesses which could certainly influence the displacement response and can affect the acceleration response in the low frequency range (Oppenheim, 1980).

It is therefore quite encouraging that the sway variance ratios do not appear to be seriously worse than those of heave or roll. Predicted variance ratios ranged from about 0.5 to 1.1 with a mean of 0.75 over all runs indicating a tendency toward underestimation, particularly as the wind direction veered away from beam. If only records are considered with a mean wind direction within 25 degrees of beam and at least four hours unidirectional wind duration, then the mean variance ratio improves to 0.89. The sway mode was generally more sensitive to input parameters relating to the state of the wave field than either heave or, to a lesser extent, roll.

Although the variance ratios obtained for sway showed poorer agreement than in roll or heave, the mean sway normalized squared error,  $E_n^2$  averaged over all runs was 25.8. This is only slightly higher than for heave (24.5) and significantly lower than roll (40.5). Underestimation of response magnitudes accompanied by good agreement of shape could indicate an underestimation of the forcing functions in the frequency range of maximum wave energy. Such an underestimation would not severely affect the shape of the response curves if it were consistent over attack angles and frequencies of interest, but would cause a depression of the response magnitude.

While these results suggest that a reasonable estimate may be made of the time-varying transverse horizontal inertial force on the body, it should be remembered that some of the considerations mentioned previously would have to be adequately addressed to correctly estimate the lower-frequency forces on the body due to mooring, current etc.

#### Discussion of Important Parameters

##### Significant Wave Height

The quantitative measures of closeness, VR and  $E_n^2$  are displayed by significant wave height in figures 8 through 13. A distinction was made between the data records in which the unidirectional wind duration was four hours or greater than those in which it was not.

The accuracy of the heave response predictions shows no particular dependency on  $H_s$  while both roll and sway acceleration had noticeably poorer agreement at smaller significant wave heights. There may be a tendency for milder sea states to have a more complex directional character due to higher frequency components in the spectrum. Such

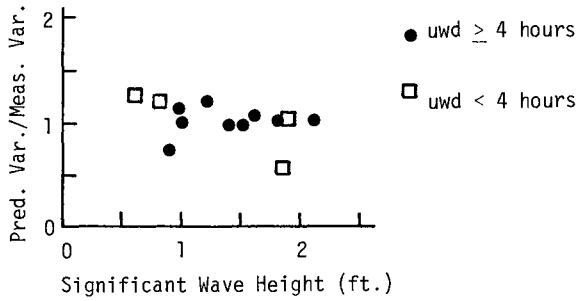


Figure 8. Variance Ratios in Heave Mode versus Significant Wave Height for All Runs.

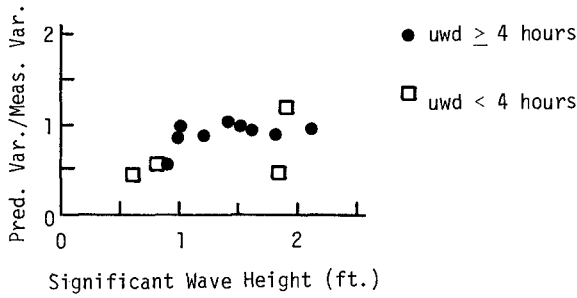


Figure 9. Variance Ratios in Roll Mode versus Significant Wave Height for All Runs.

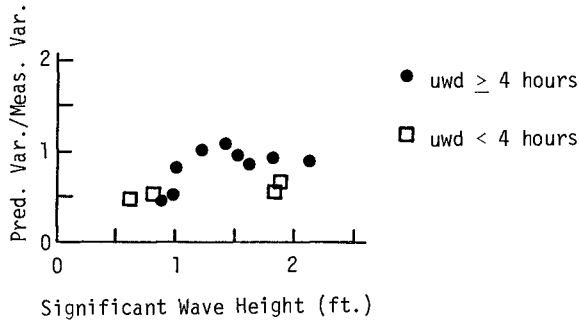


Figure 10. Variance Ratios in Sway Mode versus Significant Wave Height for All Runs.

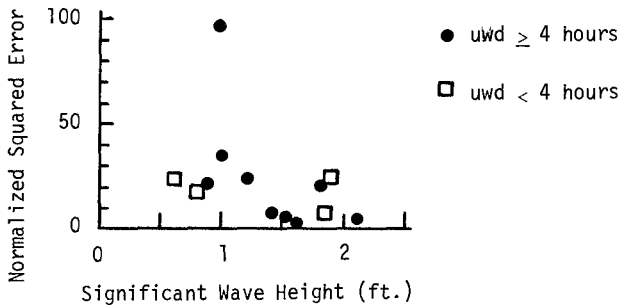


Figure 11. Normalized Squared Error in Heave Mode versus Significant Wave Height for All Runs.

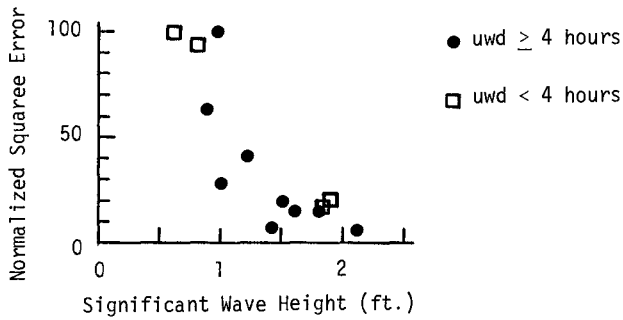


Figure 12. Normal Squared Error in Roll Mode versus Significant Wave Height for All Runs.

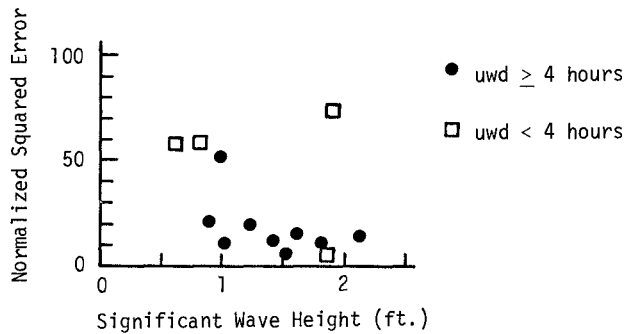


Figure 13. Normalized Squared Error in Sway Mode versus Significant Wave Height for All Runs.

seas would arise and decay faster and respond more quickly to wind shifts. This condition would affect roll and sway more than heave due to the greater sensitivity of these modes to the principal angle of attack. Some of the apparent decline in accuracy, however, is undoubtedly due to the fact that the records with the four smallest significant wave heights all have wind headings of about 25 degrees off beam, so it is unclear which parameter had the greatest effect in reducing agreement.

#### Wind Direction

Predictive accuracy, as quantified by VR and  $E_n^2$ , was less in the sway and roll modes as the wind direction moved off beam. The data examined only contained wind angles from 0 to 30 degrees off beam, but even this amount of obliqueness appeared to adversely influence the accuracy of the predictions. Since the purpose of a floating breakwater is to provide shelter from incident waves, the ability to accurately predict response to beam seas is of paramount importance, but a lessening of predictive accuracy with such small shifts of the wave attack off beam could indicate a problem with the model. Increments of 10 degrees were used to compute excitation forces, and smaller increments might have been more appropriate.

#### Directional Spreading Function

The directional characteristics of the limited-fetch short-crested seaway is a subject for which only a very limited amount of data is available. While various methods for modeling this phenomenon exist, the presence of only one node in this analysis made a long-crested superposition approach by far the most straightforward.

Opinions differ as to appropriate values of the exponent,  $n$ , in equation 3.5. Generally accepted values range between 2 and 10 for the Puget Sound Region (Langen, 1981).

Some of the values of  $n$  found to result in the best agreement between measured and predicted autospectra are higher than can be justified in the literature. Powers of 18 were used twice and on one occasion a unidirectional sea was found to provide the best agreement with the data. The best agreement with the response data was usually obtained when powers of 7 to 12 were employed. It is worthy of mention that values of  $n$  which gave the best agreement tended to increase with increasing unidirectional wind duration.

#### Mooring Forces

The procedure whereby mooring forces are modeled in a frequency domain analysis is a weakness of the method. It is well known that the forces exerted by a non-taut hanging cable are not a linear function of displacement. The question is not so much whether such forces respond linearly to displacements, but over what range of conditions is the error incurred by making such an assumption acceptable.

If second order forces are small and the mooring cables do not lose their hanging catenary shape, the magnitude of the mooring forces are small compared with other forces present such as inertial, wave excitation, and damping. Reasonable estimates of maximum dynamic transverse shear stresses in the major portions of the pontoons themselves could therefore be made despite the rough nature of the mooring force estimates provided by the method of analysis described in this report. Economical design of the mooring system itself, as well as local reinforcement detail in the pontoon near the points of attachment, however, might be better pursued with the aid of a supplementary low-frequency analysis such as described by Oppenheim (1981) or Standing (1981.)

### Conclusions

Reasonable agreement was found between acceleration response statistics obtained from a frequency domain model and those based upon measurements from a full-scale floating breakwater. Predicted response variances typically ranged from 0.5 to 1.3 of those obtained from field measurements. Within the limits of the data, predictive accuracy appeared to increase with increasing significant wave height.

The best results were obtained for the heave or vertical degree of freedom. Response magnitudes tended to be underpredicted in many cases in the sway or transverse mode and (to a lesser extent) in the roll of longitudinal rotation modes.

Predictive accuracy appears to be high enough to produce reasonable estimates of the internal forces in the breakwater itself. Caution should be exercised, however, in the sway mode in the low frequency range where slowly varying forces unaccountable by this model may be significant. While the method might therefore be appropriate as a tool in floating breakwater design, other more accurate (and costly) methods may be more appropriate in the prediction of mooring forces.

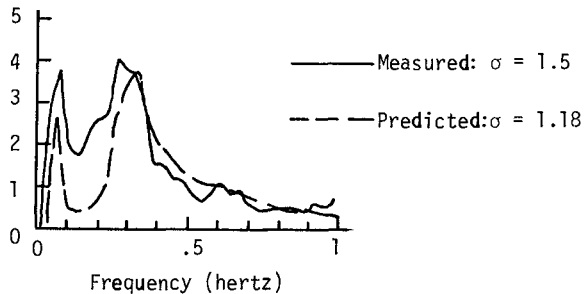


Figure 14. Measured and Predicted Sway Acceleration FRD Moduli for East Pontoon, Run 1: Mooring Stiffnesses from Program BRKMOOR.

References

1. Hutchinson, Bruce L. The Prediction and Analysis of the Motions of Offshore Deck Cargo Barges, MS Thesis, University of Washington, 1977.
2. Hutchinson, Bruce L. "Impulse Response Techniques for Floating Bridges and Breakwaters Subject to Short-Crested Seas," presented at Pacific Northwest Section, Society of Naval Architects and Marine Engineers, 1982.
3. Meyers, W.G. et al, "Manual: NSRDC Ship-Motion and Sea-Load Computer Program," Naval Ship Research and Development Center Report 3376, Washington D.C. February, 1975.
4. Nece, R.E., Skjelbreia, N.K., "Ship-Wake Attenuation Tests Of A Prototype Floating Breakwater", presented at ASCE Conference, Houston, Texas, August, 1984.
5. Ochi, Michel K., "Review of Recent Progress in Theoretical Prediction of Ship Responses to Random Seas," Seakeeping 1953-1973 SNAME T & R Symposium S-3, June 1974, pp. 129-192.
6. Oppenheim, B.W. and Wilson, P.A., Low-Frequency Dynamics of Moored Vessels, Giannotti and Associates, Inc. February, 1980.
7. St. Denis, Manley and Pierson, William J. Jr., "On the Motion of Ships in Confused Seas," Trans. SNAME, Vol. 61, 1953, pp. 280-357
8. Salvesson, N., Tuck, E.O., and Faltinsen, O.M., "Ship Motions and Sea Loads," Trans. SNAME, Vol. 78, 1970, pp. 250-287.
9. Schmitke, Rodney T., "Ship Sway, Roll, and Yaw Motions in Oblique Seas," presented at Annual Meeting, SNAME, New York, N.Y., November 16-18, 1978.
10. Standing, R.G., et al., "Slowly-Varying Second-Order Wave Forces: Theory and Experiment", National Maritime Inst. Feltham England, 1981.

## CHAPTER ONE HUNDRED EIGHTY

### ASPHALT STABILIZATION OF RUBBLE SLOPES

E.J.Schmeltz, M.ASCE<sup>1</sup>, M.J.McCarthy, A.M.ASCE<sup>2</sup>, N.Lopez<sup>3</sup>

#### ABSTRACT

During the spring of 1982 a new container terminal was under construction at the Port of Haina, Dominican Republic. Changes in design conditions due to damages to the protective breakwaters at the port entrance required modifications to the design of slope protection under the pier. The stabilization of the rubble slope was, in fact, a stop gap measure in that repairs would be instituted on the breakwaters in the near future.

Due to a lack of suitable stone, the location of structural elements already in place and severe time constraints, an asphalt coating over relatively light weight rubble was selected to armor the slopes under the pier. The asphalt coating was prepared in a locally available batching plant and placed on-site using a crane equipped with a 4 cubic yard bucket. As a result of the use of the asphalt coating, construction delays were minimized and adequate slope protection was provided for the container pier without extensive design modifications.

The purpose of this paper is to discuss the advantages and disadvantages of the use of asphalt in the construction of shore protection facilities in the context of the site specific application at the Port of Haina.

#### INTRODUCTION

The Dominican Republic occupies the eastern portion of the island of Hispaniola in the Caribbean Sea. The Port of Haina is located on the southern coast of the Dominican Republic at the mouth of the Haina River, as shown in Figure 1. The Port is approximately 12 kilometers west of Santo Domingo, the capital city of the Dominican Republic.

The Port of Haina is a fully developed port complex with a wide spectrum of cargo handling capabilities. The complex includes a major sugar processing and loading facility, fertilizer and ferronickel loading wharf, Sealand container offloading facility, diesel fuel unloading area, container wharf under construction as described herein and a proposed coal offloading facility for a planned generating station.

---

1. PRC Engineering, 300 East 42nd Street, New York, NY, USA

2. PRC Engineering, 300 East 42nd Street, New York, NY, USA

3. Department of Public Works, Santo Domingo, Dominican Republic

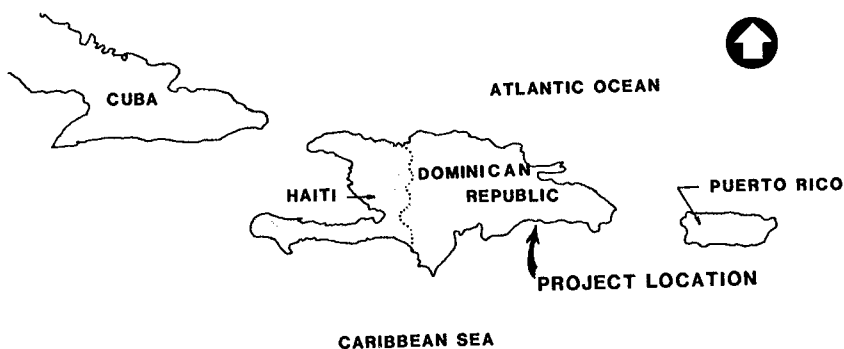


Figure 1  
Location Plan

The harbor is protected against incoming waves by two breakwaters as shown in Figure 2. During the fall of 1979, the site was affected by two hurricanes, Frederick and David, which resulted in considerable damage to the breakwaters. 110 meters of the east breakwater and 65 meters of the west breakwater were essentially destroyed. Since that time, progressive deterioration of the structures has resulted in increased exposure of the south end of the container terminal which was under construction.

The design of the container terminal pier included a pile supported relieving platform constructed over a rock armored dike which surrounded fill material used for the container storage area, as shown in Figure 3. The armor layer consisted of stone with a median weight of 300 kilograms and an average specific gravity of 2.6. Based on Hudson's equation (Reference 1), using a design slope of 1:1.75, this stone was found to be stable for wave heights of up to 1.25 meters. At the time of this study, in April 1983, exposure of the site had increased to a point where the original one meter design wave height could be as high as 2.6 meters. Since this wave height was in excess of the stable wave height for the proposed stone armor layer, a study was initiated to determine alternative methods of temporary reinforcement.



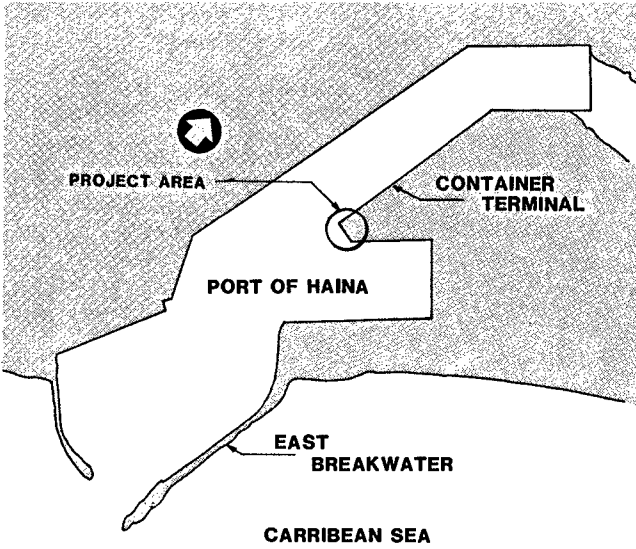


Figure 2  
Site Plan

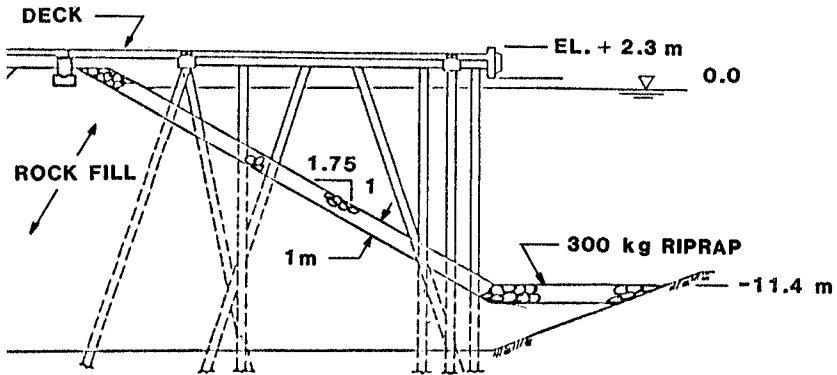


Figure 3  
Typical Section of Container Berth As Designed

It should be noted that at the time of this effort, a substantial amount of construction was completed on the container berth. Piles and pile caps were in place and the majority of the deck was completed. Figure 4 provides an aerial view of the facility around this time. Only the southern end of the structure was of concern since the deterioration of the breakwaters resulted in a high exposure level to southerly waves at this "head" section. A total of approximately 150 linear meters of the structure were involved.



Figure 4  
Container Facility Under Construction  
(View from the north)

Modifications to the original design of the section were not instituted earlier in the project because reconstruction of the breakwaters was anticipated. This reconstruction, which would have reduced the wave action to an acceptable level, was delayed for a variety of reasons beyond the scope of this discussion. Suffice it to say that the net result was a severe time constraint on design and construction of any possible alternative. Due to the inherent difficulties associated with the repair of the rubble dike under the relieving platform, completion of the head section was not judged to be prudent as discussed in the following paragraphs.

## ALTERNATIVES CONSIDERED

Various slope protection alternatives were considered in light of the expected 2.6 meter design waves, including:

- increase the primary armor stone size
- addition of artificial armor units to the slope
- placement of concrete filled mats
- construction of a wave skirt on the fender panels
- placement of asphalt grout or stone asphalt on the slope protection stone

The following paragraphs discuss these alternatives and present the rationale for the final selection of asphalt grout. The basic criteria utilized to assess the effectiveness of the alternatives were:

- constructibility
- cost
- engineering adequacy.

**Do Nothing:** The do nothing alternative implied construction of the dike slope protection as originally designed and acceptance of damages during periods with wave heights exceeding 1.25 meters at the structure. This alternative was deemed unacceptable due to the unknown period of time until the breakwaters were repaired and the consequences of a slope failure. In addition, after construction of the deck was completed, a major reconstruction effort would be required to make repairs to the rubble slope.

**Increased Stone Sizes:** Utilizing Hudson's equation for quarystone randomly placed in two layers, the required median stone size was found to be on the order of 2.3 metric tons for the design wave of 2.6 meters. Increasing the size of the rock used as the primary armor layer in this area to 2.3 metric tons was not an acceptable option since rock of the size and quality necessary is not locally available. As a consequence, material would have to be brought in from distant sources at high cost and would result in unacceptable delays in the completion of the facility. Discussions with the contractor on site confirmed this finding.

Additionally, the increased thickness of the required two layers and underlayers would necessitate removal of materials already placed in order to avoid intrusion on the berth area, and placement between piles would be, at best, difficult. As a result of the high anticipated costs, delayed construction and the encroachment problem, this alternative was ruled out.

**Concrete Filled Mats:** Concrete filled mats have been used in some shore protection applications and in numerous hydraulic structures. They are not, however, generally used in structures subject to large wave heights. Several questions were raised about the application of concrete filled mats to the project at the Port of Haina, including:

- the effects of the expected increase in wave runup due to the relatively smooth slopes
- the possibility of cracking the relatively thin mats during design wave events and disintegration of the slope
- lack of availability on short notice of the mats and equipment necessary for placement

Further, placement between existing piles and caps would be difficult. Consequently, this alternative was dropped from further consideration.

**Wave Skirt:** An indirect method of increasing the stability of the rock dike involved reducing the wave heights affecting the slope. Due to the relatively low deck elevation, a wave skirt placed below the fender face would function on the principle of stopping the wave energy in the upper part of the water column from reaching the rock dike under the structure. Energy during storm conditions would be decreased on the dike via reflection from the skirt and overtopping of the deck. Although technically feasible, this type of structure has not apparently been employed for this purpose. Additionally, structural connections would be difficult and might cause excessive loadings on the deck structure. It was felt that this option would require a significant amount of engineering, and further that construction might also be somewhat complicated causing further delays in the project. This option was not considered appropriate for further consideration.

**Asphalt Grout Or Stone Asphalt:** The final alternative consisted of the placement of an asphaltic compound in the interstices of the armor stone; or mixing armor stone with an asphaltic compound and placement on the structure. The asphalt then acts as a binder increasing the effective "weight" of the armor layer and therefore its stability. This type of approach has been employed successfully in both Holland (References 2 through 7) and the United States (References 2 , 5) on similar projects in the past. The material can be placed either as a grout or as a stone asphalt layer.

The use of asphalt had several distinct advantages for stabilization of rubble slopes, particularly from the standpoint of this project. First, the basic materials were available locally. Secondly, construction could be accomplished with standard construction equipment, e.g. cranes and buckets already at the site. Third, the basic cross section of the dike would be essentially unchanged so encroachment in the berth area would not pose a problem. Construction could presumably be accomplished before placement of the deck sections without significant delays in the contractor's work. The end result then would be stabilization of the structure at a relatively low cost to the owner.

Discussions with a specialty contractor involved in this type of construction revealed that the mixes utilized, although slightly different from routine pavement asphalt, could be manufactured in any asphalt plant in good working order. A limiting wave height on these structures of around 4.0 meters is normally assumed. This level was certainly within those anticipated at this location, and this alternative was selected for further analysis.

## HISTORICAL USES OF ASPHALT

A review of available literature (References 2 through 7) was conducted to develop a basis for the design of the asphalt grout for use at the Port of Haina. Based on this review, it was found that asphalt had been used in marine structures since the late 1920's, but it was not until the early 1930's that systematic applications began (Reference 3).

Some of the earliest uses of asphalt involved the construction or rehabilitation of groins, primarily along the coast of Holland. These structures utilized asphalt both as a grout over stones and in sand mixtures which could stand alone. Typical

mixes used in the asphalt grout included 70-72 percent sand, 10 percent filler and 18-20 percent asphalt (Reference 3).

Later uses of asphalt in marine structures along the coast of Holland included an asphalt and sand mixture for the Harlingen Harbor Breakwater. This structure, constructed in 1948, was subject to severe overtopping due to its low crest elevation. A second structure, the breakwater at Scheveningen, was grouted using an asphalt mix during this same year. Eight ton blocks on the Scheveningen Breakwater were successfully grouted during a repair project (Reference 3).

A number of additional examples of the use of asphalt and asphalt grout were found throughout the European Coastline (Reference 6). These included the asphalt grouting of 4 ton blocks forming the foundation of a vertical wall breakwater located in Marseilles, France. The blocks were located at a depth of approximately 12 meters (40 feet). A mix consisting of 60 percent fine sand, 20 percent limestone filler and 20 percent bitumen, 40-50 penetration was used. The asphalt was lowered in a bucket which was opened just above the rock surface. The initial temperature of the asphalt was 180 degrees C. Grouting of large concrete blocks was also accomplished at the River Adour northern breakwater also located in France. At this structure, 15 ton concrete blocks were grouted. Another example was the Pointe de Grave breakwater in France, where three to five ton stones were grouted using a mix consisting of 12 percent filler, 34 percent beach sand up to 6.0 mm, 34 percent dune sand up to 0.05 mm and 13 percent bitumen, 60-70 penetration.

At Porto Levante on the Po Delta in Italy, an asphalt grout consisting of 70 percent fine sea sand, 10 percent filler and 20 percent bitumen, 40-50 penetration, was placed on a breakwater at temperatures of 180 to 200 degrees C. Finally, a breakwater at Hirtshals Harbor in Denmark was grouted from 4.0 meters below the zero datum to 1.5 meters above. The mix used on this structure consisted of 72 percent sand, 10 percent limestone filler and 18 percent bitumen, 80-100 penetration.

In the United States, one of the earliest and most successful uses of asphalt grouting was during the rehabilitation of the Galveston, Texas jetty in 1935-1936 (References 2, 5). The armor on the south jetty at Galveston consisted of 6 to 10 ton stone, and the jetty cross section had deteriorated and become porous. After several mixes were tried, the jetty was grouted with a mix consisting of 70 percent Galveston beach sand, 12 percent Mississippi River loess (filler) and 18 percent asphalt cement, 30-40 penetration. The asphalt was placed at 204 degrees C (400 degrees F.).

## SELECTED DESIGN

The evaluation of the available literature on the use of asphalt in shore protection structures made one major factor eminently clear: very little published information exists on the design of such structures. The choice, however, was still desirable given the historical successes of the basic method, the rapid construction necessitated by project requirements, locally available materials and relatively low cost.

The basic design for this project consisted of placement of asphalt as a grout to fill the interstices of the existing primary armor. From the top of structure to a level 4.0 meters below the datum, the asphalt would be placed as a continuous cover. The lower level was selected since it is approximately 1.5 times the design wave height below the surface. Below - 4.0 meters, the material would be "pattern"

grouted to result in approximately 50% coverage. The purpose of the pattern grouting was to permit relief of pore pressures in the rock-fill. Penetration of the asphalt to a depth of 0.3 meters was judged to be adequate to bind the primary armor. The design section is shown in Figure 5.

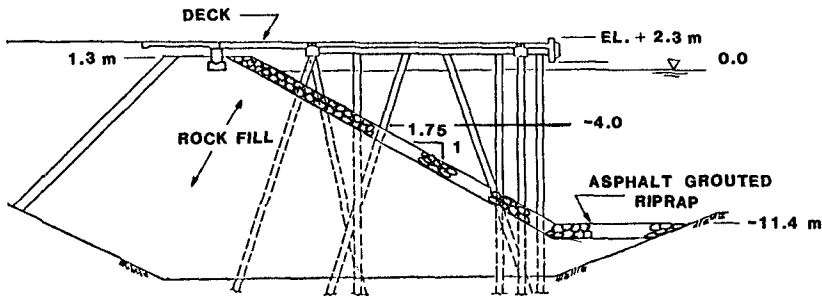


Figure 5  
Revised Cross Section With Asphalt Grout

Critical to the successful placement of the asphalt was the determination of a reasonable mix for the material. Some valuable information was obtained from work by Mulders (Reference 8), however due to the lack of available detailed design information, selection of the mix was an iterative process.

The initial mix selected for use is shown in Table 1 along with several iterations leading to the final mix. The initial proportions were selected based on information in the literature from past uses. Prior to placement, however, the mix was modified because of the highly fluid nature of the original mix. It appeared that penetration into the rock might be too great therefore increasing the volume of asphalt necessary to complete the work.

The second mix, with 25% one half inch aggregate, retarded flow of the material in the interstitial spaces to a greater extent than desirable. The final mix shown in Table 1 resulted in a reasonable level of flow and good filling of the voids in the armor layer.

TABLE 1  
ASPHALT MIXES

	INITIAL MIX	2nd TRIAL	FINAL MIX
ASPHALT	15	12	12
SAND	70	52	58
FILLER	15	11	15
GRAVEL	—	25	15

- NOTES: 1. Asphalt penetration 60-70  
2. Asphalt mixes and temperatures were controlled to some extent by the capabilities of the existing plants

Placement temperatures ranged from a low of 99° C (210 °F) to a high of 215° C (410°F). Both the low and high ends of the temperature range were troublesome since low temperatures resulted in poor flow; high temperatures in a spongy mass in the water and excess steam formation. The majority of the material was placed at approximately 165° C (330° F) which resulted in good flow and reasonable under water placement. The asphalt was supplied from a plant approximately 10 kilometers from the site. Delivered to the site in 15 cubic meter batches by truck, the material was dumped into a rock bin (steel holding box) as shown in Figure 6.

The material was placed on the structure with a 4 cubic yard clamshell as shown in Figure 7. When placed above water workmen utilized shovels and rakes to move the asphalt as required, although on the slopes it flowed well. Below water, the clamshell was opened near the water surface and material was dropped in mass to the rock surface. The pattern was obtained by locating the bucket relative to the pile caps and horizontal members already in place.

Two hundred and sixty cubic meters of asphalt were delivered and placed on the structure. With an adequate supply, approximately 60 cubic meters were placed in a working day. A total of 1150 square meters of rock protection surface between elevation +1.3 and -4.0 meters were completely grouted; 1450 square meters from -4.0 to -10.8 meters were pattern grouted with approximately 50% coverage achieved. Figures 8 and 9 provide views of the above water section and near the water line, respectively.

Unfortunately, photographs below water are not available, however sections under-water were inspected by divers who reported both adequate penetration, coverage and a durable mass.



Figure 6  
Asphalt Being Dumped into Rock Bin at the Site



Figure 7  
Asphalt Placement With Four Cubic Yard Bucket





Figure 8  
**Asphalt Grout Partially in Place Near the Crest**



Figure 9  
**Asphalt Grouted Rock Slope Near Water Line**

## SUMMARY AND CONCLUSIONS

Initial placement of the asphalt began on 26 April 1983 and was completed on 11 May 1983. As a result of the timely manner in which the redesign and construction of the armor layer was conducted, the contractor was able to maintain his work schedule and ultimately completed overall construction ahead of schedule.

Based on the experience gained on this project in the use of asphalt grout at the Port of Haina, the major advantages of the material included:

- the use of locally available materials
- a flexible finished structure
- minimized armor stone size
- relative ease of construction

The disadvantages of the asphalt grout included a lack of available design criteria, potentially increased runup and pore pressure buildup. One further aspect of the use of asphalt which may be of great concern in some areas is the environmental impact of placement in the water. Although no information could be found in the literature, several on site observations are worthy of note.

Placement of the material resulted in a substantial cloud of steam which was anticipated because of the high temperatures. Shortly after placement, a film of oil was visible on the water surface which dissipated relatively quickly. Fish normally seen around the structure returned within an hour or two of placement and seemed to be feeding on the asphalt surface. It is difficult to draw any firm conclusions from these observations, and environmental impacts of this method of slope stabilization should be considered where appropriate.

In conclusion, the placement of asphalt at the Port of Haina project has manifested itself as a technically and economically feasible method of increasing the stability of the stone armor layer to withstand wave attack. Inspection of the armor layer after slightly more than one year indicated that the asphalt grouted slope was stable and performing satisfactorily. Several periods of severe wave conditions occurred during this time, although it is unlikely that the design conditions were experienced.

## ACKNOWLEDGMENTS

The authors would like to express their appreciation to the Department of Public Works Executive Unit of the Port of Haina, Dominican Republic for their support in this project. We would also like to thank the on-site personnel of the contractor, Conde-Meisner, for their assistance and valuable suggestions during the construction of this work.

## REFERENCES

1. Shore Protection Manual, Vol. II, U.S. Army Coastal Engineering Research Center, Fort Belvoir, Virginia, 1977.
2. Asphalt Institute, The, Asphalt in Hydraulics, Manual Series No. 12, November 1976.

3. Asbeck, Baron W.F. van, "A Review of Asphalt Construction in Hydraulics in Europe," Proceedings of the First Western Conference on Asphalt in Hydraulics, University of Utah, 1955.
4. Asbeck, Baron W.F. van, "Bitumen in Coastal Engineering," Proceedings of the Fifth Conference on Coastal Engineering, Grenoble, 1954.
5. Carey, Walter C., "Asphalt in River and Harbor Work," Proceedings of the First Western Conference on Asphalt in Hydraulics, University of Utah, 1955.
6. Asbeck, Baron W.F. van, Bitumen in Hydraulic Engineering, Volume II, Elsevier Publishing Co., 1964.
7. Garderen, A.P. van and Mulders, G.L.M., "The Use of Bitumen in Coastal Structures," Proceedings of Coastal Structures '83, Arlington, Virginia, 1983.
8. Mulders, G.L.M., "Designing Hydraulic Structures with Asphaltic Materials," Dredging and Port Construction, October, 1982.

## CHAPTER ONE HUNDRED EIGHTY ONE

### REEF RUNWAY WAVE PROTECTIVE STRUCTURE, HONOLULU INTERNATIONAL AIRPORT, OAHU, HAWAII, STABILITY PERFORMANCE EVALUATION

Robert S. Chun\*, Edward K. Noda\*\*, Elaine E. Tamaye\*\*\*

#### Abstract

An inspection survey of the Reef Runway Wave Protective Structure at the Honolulu International Airport was accomplished in 1982 to assess the performance of the dolos and rock armored structure to date. The inspection showed the structure to be performing adequately considering that the design wave conditions were experienced.

#### Introduction

In 1972, the State of Hawaii began construction of an offshore runway at the Honolulu International Airport. This project, called the Reef Runway, was undertaken to alleviate aircraft noise and safety concerns over metropolitan Honolulu, provide more flexibility for aircraft takeoff and landings, and increase airfield capacity. The project encompasses dredged fill on 1,240 acres of offshore coral reef with a 16,100 foot-long wave protective structure, a 12,000 foot-long by 200 foot-wide runway, 1,350 feet of apron and clear zone bordering the runway, and taxiways and service roads which connect the runway to shore. The protective structure is of rubblemound construction and armored with 4 and 6 ton dolos concrete units along the deepwater sections. Figure 1 shows a General Plan view of the Reef Runway at the Honolulu International Airport. The project was the subject of environmental controversy, and was held up for approximately one year due to various court actions. Finally, the U.S. Supreme Court allowed the project to proceed after declining to hear appeals from environmental groups on the adequacy of the Environmental Impact Statement. In 1975, the Reef Runway protective structure was completed, and in 1977, the Reef Runway was dedicated and operational. The Reef Runway was named one of the Ten Outstanding Engineering achievements of 1977 by the National Society of Professional Engineers, and one of Outstanding Projects of 1977 by the American Society of Civil Engineers. The Federal Aviation Administration also elected the Reef Runway an Environmental Excellence Award.

\*Engineering Program Manager, Airports Division, Department of Transportation, State of Hawaii

\*\*Principal, Edward K. Noda & Associates, Honolulu, Hawaii

\*\*\*Ocean Engineer, Edward K. Noda & Associates, Honolulu, HI

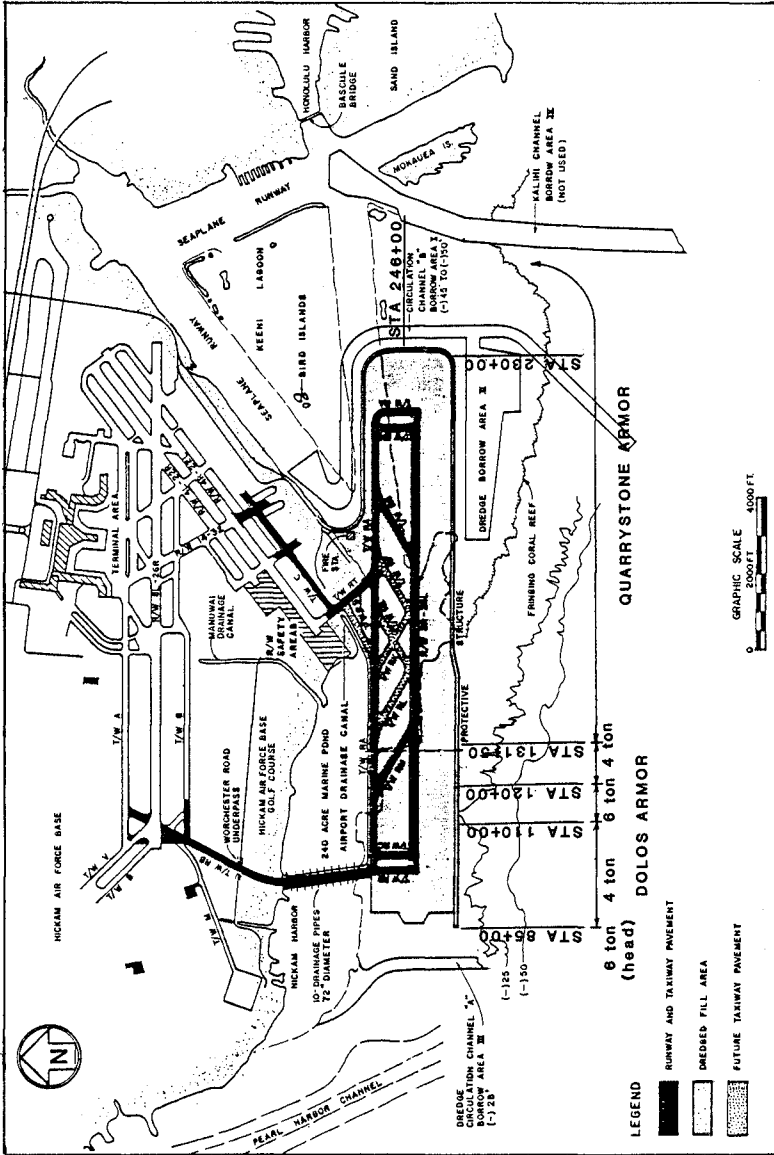


FIG. 1 GENERAL PLAN OF THE REEF RUNWAY AT HONOLULU INTERNATIONAL AIRPORT

In mid 1982, a detailed inspection of the Reef Runway protective structure was initiated by Edward K. Noda & Associates for the Reef Runway Managing Consultant at the request of the State of Hawaii. The survey was undertaken as a precautionary measure to assess the performance of the structure to date. In view of the controversy which has developed as to the viability of existing stability criteria for concrete armor units in rubblemound structures, stemming from the breakwater failure at Port Sines on the Atlantic coast of Portugal in 1978, the results of the survey were expected to serve as verification of the design criteria as well as to provide a baseline data set for future inspection and maintenance surveys. The inspection revealed no significant damages, and the protective structure was found to be performing as designed. The evaluation of the stability performance of the wave protective structure was two-fold. First, the physical condition of the structure was assessed to determine the percent damage to the armor units. Second, the wave conditions to which the structure has been subjected to date were evaluated to determine whether the design wave criteria were experienced. This paper summarizes the results of the inspection and stability performance evaluation of the Reef Runway protective structure.

### **Reef Runway Protective Structure Design**

The basic design criteria for the Reef Runway wave protective structure was developed by Tetra Tech of Pasadena, California, in 1972 for the Reef Runway Managing Consultant, the Ralph M. Parsons Company.

#### Oceanographic Design Criteria

Tetra Tech recommended a design stillwater elevation of +3.0 feet above Mean Sea Level (MSL) based on evaluation of the following factors:

- \*Set-up due to wind stress components
- \*Water level increase due to atmospheric pressure reduction associated with storm centers
- \*Wave set-up due to breaking waves
- \*Astronomical tide

It is interesting to note that the highest tide recorded to 1981 was 2.39 feet above MSL. The Mean Higher High Water (MHHW) level is 1.08 feet above MSL.

The design wave criteria was based on the maximum possible wave height,  $H_{max}$ , that could theoretically exist at the toe of the structure. For the deepwater dolos-armored section, the maximum wave height was given by:

$$H_{max} = (0.73 + 5.6 S)D \quad (1)$$

where:

S = the ocean bottom slope seaward of the toe  
 D = the total water depth at the toe

Thus, the design wave height varied as a function of the local bottom slope and water depth along the toe of the structure, and the highest computed  $H_{max}$  was 25.2 feet at Station 116+00. To determine the maximum wave height for the shallow water section fronted by fringing reef, S, in the above equation, was set to zero.

Tetra Tech also reviewed and evaluated previously measured and hindcasted storm events to verify that waves as large as  $H_{max}$  could physically be generated in the region, and concluded that 25 foot waves could be expected to occur once in ten years.

#### Armor Stability Criteria

Primary armor design for stability was evaluated using the Hudson equation:

$$W = \frac{w_r H^3}{K_D (S_r - 1)^3 \cot \phi} \quad (2)$$

where:

W = weight of individual armor units (lbs)  
 $w_r$  = unit weight of the armor unit (lbs/ft<sup>3</sup>)  
 H = design wave height at the structure (ft)  
 $S_r$  = specific gravity of the armor unit relative to seawater = ( $w_r/w_w$ )  
 $w_w$  = unit weight of seawater = 64 lbs/ft<sup>3</sup>  
 $\phi$  = angle of the structure face measured from horizontal  
 $K_D$  = stability coefficient (varies primarily as a function of the shape of the armor units, roughness of the armor units, and degree of interlocking obtained in placement)

The layer thickness of the primary armor units is given by:

$$t = n k_t (W/w_r)^{1/3} \quad (3)$$

where:

t = thickness of primary armor layer (ft)  
 n = the number of units comprising the armor layer thickness  
 $k_t$  = layer coefficient (varies as a function of the type of armor unit)

Finally, the density of units in the primary armor layer is given by:

$$N = n k_e (1 - P/100) (w_r/W)^{2/3} \quad (4)$$

where:

$N$  = the number of armor units per square feet of surface area

$P$  = the average porosity of the primary armor layer (%)

For the exposed deepwater section of the wave protective structure, various primary cover layer designs were assessed and designs completed for five alternative protection schemes. In the competitive bidding process, Hawaiian Dredging and Construction Company was the low bidder, and chose a design consisting of 4 and 6 ton dolos concrete armor units. It has been recognized that rubblemound structures can accept some level of damage and still remain stable. In view of this, and the acceptability of a degree of risk associated with the recurrences of significant storm events, the stability coefficient  $K_D$  was selected to yield an acceptable damage level of 4% and 2% for the 6 and 4 ton dolos trunk sections, respectively. Tests conducted by the USAE Waterways Experiment Station (Davidson & Markle, 1976) indicate that stability is affected only when random breakage exceeds 15% and cluster breakage exceeds 3 units. Table 1 summarizes the stability criteria adopted for the final design of the dolos covered sections.

Table 1. Stability Criteria for Dolos Armor  
(Sta 85+00 to 131+50)

	Breakwater Head	Trunk Sections	
	Sta 85-86	Sta 110-120	All other
Nominal weight of units	6 ton	6 ton	4 ton
Unit weight, $w_r$	147 lb/ft <sup>3</sup>	147 lb/ft <sup>3</sup>	147 lb/ft <sup>3</sup>
Design wave height, $H_{max}$	13.8 ft	25.2 ft	<18 ft*
Cot structure slope	2.25	1.5	1.5
Stability coefficient, $K_D$	6.8	64	32
Allowable damage	0%	4%	2%
Layer thickness, $t$	11.3 ft	11.3 ft	9.9 ft
Number of units thick, $n$	2	2	2
Layer coefficient, $k_e$	1.3	1.3	1.3
Density of armor units, $N$	.055/ft <sup>2</sup>	.055/ft <sup>2</sup>	.075/ft <sup>2</sup>
Porosity of armor layer, $P$	60%	60%	60%
Crest elevation above MSL	16 ft	20 ft	16-20 ft

\*While maximum wave heights were typically less than 18 feet, within a short reach maximum wave heights to 19.3 feet can be expected.

The armor layer extends down to the toe of the structure, where the maximum water depth is 27 feet below MSL at



Station 116+00. Figure 2 depicts typical cross sections for the protective structure. Figure 3 depicts the relative dolos dimensions and Table 2 lists the design dimensions for the 4 and 6 ton units, based on a unit weight of 147 lb/ft<sup>3</sup> for concrete.

Table 2. Design Dimensions for Individual Dolos Units

	Nominal Weight of Units	
	4 ton	6 ton
Volume = 0.16 C <sup>3</sup>	54.9 ft <sup>3</sup>	81.9 ft <sup>3</sup>
Overall dimension, C	7 ft	8 ft
Waist dimension, B = 0.32 C	2' 1''	2' 5''
Fluke dimension, A = 0.20 C	1' 5''	1' 7''
Fillet dimension, D = 0.057 C	5''	6''

#### Inspection and Damage Assessment

The inspection survey was performed during the period July 1982 through January 1983, and involved a visual, photographic and underwater reconnaissance of the entire Reef Runway protective structure. Although a major portion of the structure is fronted by shallow reef which facilitated the inspection, approximately 7,000 lineal feet is in deeper water sometimes exceeding 25 feet. Inspection of the underwater regions of the deepwater sections were hampered by poor visibility water conditions, resulting in three months of delay from September to December 1982 before conditions improved sufficiently to enable completion of the survey.

A total of 301 dolos armor units were damaged out of a total of 18,009 units originally placed, yielding an overall damage of 1.67% to the primary armor cover. An estimated 71 out of the 4,317 6-ton units placed and 230 out of 13,692 4-ton units placed were broken or displaced, yielding damages of 1.64% for the 6-ton and 1.68% for the 4-ton units. Table 3 provides a detailed damage assessment. The number of dolos placed per various reaches are estimated based on the total number of dolos known to have been placed and the percent of square footage covered within the given reach, assuming reasonably uniform density of placement for given dolos size.

Since the water depth at the toe varies considerably over short distances, the maximum design wave height and actual  $K_D$  vary within given reaches of a specified nominal dolos size. For the head section to Sta 86+00, the design  $K_D$  of 6.8 is slightly conservative over the actual  $K_D$  of 6.6; however, the actual damage is greater than the no-damage design criteria. For Sta 110+00 to 120+00 which also utilized 6 ton dolos, the design  $K_D$  of 6.4 is

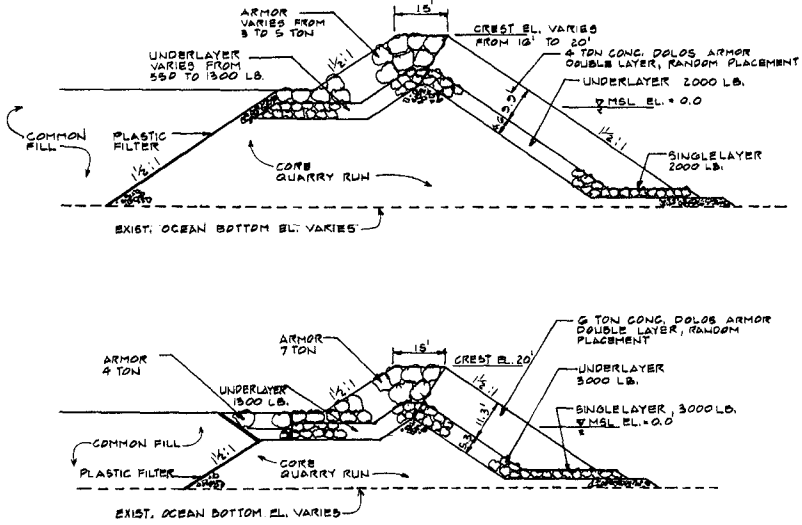


FIG.2 TYPICAL DOLOS ARMOR PROTECTIVE STRUCTURE SECTIONS

(Not To Scale)

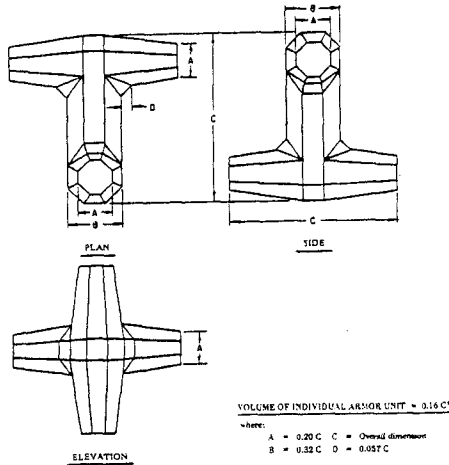


FIG.3 RELATIVE DOLOS DIMENSIONS

Table 3. Damage Assessment of Dolos Armor Units, Reef Runway Wave Protective Structure  
(Based on 1982 Inspection)

Station Location		No. of Damaged Dolos			Dolos	Design	Stability Coef. K <sub>s</sub>		No. Dolos	Percent Damage	
From	To	U/Water	A/Water	Total	Size	H <sub>max</sub> (ft)	Design	Actual	Placed	Design	Actual
Breakwater Head		2	0	2	6T	13.8		6.6			
85+00	86+00	6	2	8	6T	13.8		6.6			
Head	86+00	8	2	10	6T		6.8	6.6	1,234	0%	0.81%
86+00	88+64	16	5	21	4T	13.8-12.7		14.8-11.5			
88+64	91+64	22	8	30	4T	12.7-16.8		11.5-26.6			
91+64	95+25	31	6	37	4T	16.8-19.3		26.6-40.4			
95+25	96+25	14	4	18	4T	19.3-18.5		40.4-35.6			
98+25	101+25	12	6	18	4T	18.5-15.4		35.6-20.5			
101+25	104+25	14	4	18	4T	15.4-15.2		20.5-19.7			
104+25	107+25	13	9	21	4T	15.2-13.1		19.7-12.6			
107+25	110+00	13	6	19	4T	13.1-15.1		12.6-19.3			
86+00	110+00	135	47	182	4T		32	11.5-40.4	9,510	2%	1.91%
110+00	113+25	12	4	16	6T	15.1-20.2		12.9-30.9			
113+25	116+25	9	1	10	6T	20.2-25.2		30.9-59.9			
116+25	120+00	28	7	35	6T	25.2-16.1		59.9-15.6			
110+00	120+00	49	12	61	6T		64	12.9-59.9	3,083	4%	1.98%
120+00	125+25	19	5	24	4T	16.1-11.8		23.4- 9.2			
125+25	128+25	7	4	11	4T	11.8-16.8		9.2-26.6			
128+25	131+50	10	3	13	4T	16.8- 9.3		26.6- 4.5			
120+00	131+50	36	12	48	4T		32	4.5-26.6	4,182	2%	1.15%
TOTAL		228	73	301					18,009		1.67%
6 ton Total		57	14	71					4,317		1.64%
4 ton Total		171	59	230					13,692		1.68%

similarly conservative over the actual range of  $K_D$ ; and in this reach the actual damage overall is well within the 4% design damage criteria. For the reaches with 4 ton dolos, the actual  $K_D$  sometimes exceeded the design  $K_D$  of 32; however, the actual damage overall was within the 2% design damage criteria.

For those reaches with 4 ton dolos, the actual  $K_D$  is as high as 40 in one area. However, test results (Zwamborn, 1980) indicate that for the design packing density, the  $K_D$  of 40 is still within the envelope of data for 2% damage. For a relative packing density of 0.075 units/ft<sup>2</sup>  $\times V^{-2/3} = 1.08$  for the 4 ton dolos, the test data indicate a minimum  $K_D$  of 16, mean  $K_D$  of 25.5, and maximum  $K_D$  of 41. The data indicates an optimum double-layer packing density of 0.9 to 1.0  $V^{-2/3}$ , with corresponding mean  $K_D$  of 32 to 28. The design packing densities of 0.055 units/ft<sup>2</sup>  $= 1.04 V^{-2/3}$  for the 6 ton dolos and 0.075 units/ft<sup>2</sup>  $= 1.08 V^{-2/3}$  for the 4 ton dolos would indicate less stability than optimum. In fact, Darling (1976) indicates that the required packing densities resulted in a three-layer cover, with a large percentage of the total 1.4% breakage during placing operations resulting from trying to fit the top layer of dolos.

In general, the damaged units were found scattered randomly throughout the structure, and the primary armor cover appeared to retain its original integrity. The broken dolos were intermixed with the unbroken units, and a few units were displaced from the structure. However, it was difficult to determine where the displaced units came from. Figures 4 and 5 show typical damages to the dolos.

During the period when the survey was delayed due to poor visibility water conditions, Hurricane Iwa struck the Hawaiian Islands. Both above water and underwater inspections indicated no evident additional damage as a result of the storm. Apparently, most of the damage to the dolos occurred prior to the wave attack from Hurricane Iwa.

### Wave Evaluation

In order to provide a credible assessment of the performance of the Reef Runway wave protective structure, an evaluation of the types and magnitudes of the largest waves to have attacked the structure following completion of construction in the fall of 1975 to the completion of the inspection survey in January 1983 was accomplished. Figure 6 depicts the general location of the project site within the Hawaiian Islands, and Figure 7 shows the site in relation to adjacent facilities along the south coast of Oahu. Three distinct wave types have attacked the structure during this period:



**FIG.4 TYPICAL DOLOS BREAKAGE (6-TON UNITS AT STA 119+25)**



**FIG.5 TYPICAL DOLOS BREAKAGE (4-TON UNITS AT STA 128+50)**

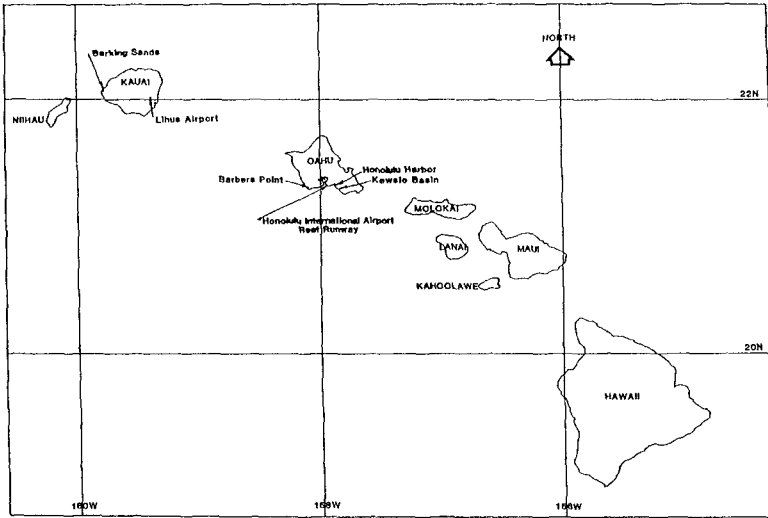


FIG.6 MAP OF THE HAWAIIAN ISLANDS SHOWING THE PROJECT SITE LOCATION

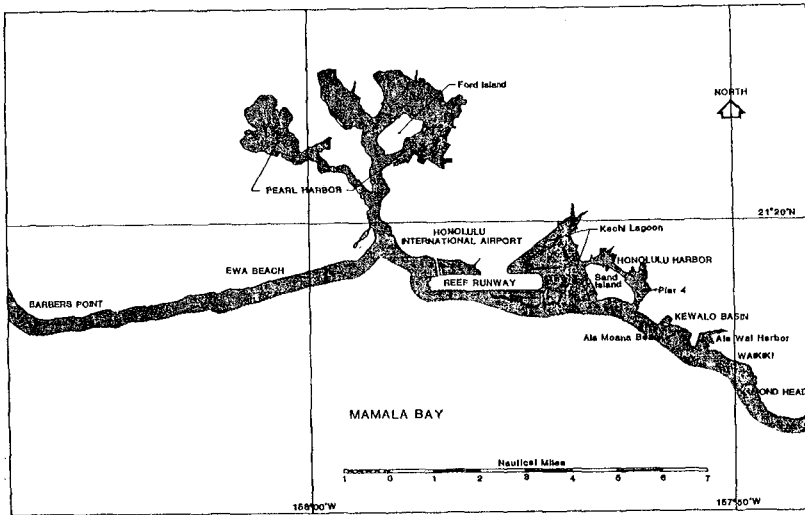


FIG.7 VICINITY MAP OF PROJECT SITE ON SOUTH SHORE OF OAHU

- \*Locally generated "Kona" storm waves
- \*Southerly swell generated by Southern Hemisphere storms
- \*Hurricane Iwa waves

#### Kona Storm waves and Southerly swell

Nov 24, 1975 storm: South and southeast winds generated estimated maximum surf of about 6 feet at Ala Moana. Although winds were not particularly strong at the Honolulu International Airport, estimated 25 to 30 mph winds generated waves large enough to wash a 118-foot fishing vessel aground at the entrance to Honolulu Harbor. A 41-foot Coast Guard rescue boat trying to help the fishing vessel ran aground nearby.

Feb 5-6, 1976 storm: This was a major storm which generated large southwest waves offshore the Reef Runway for about two days. Peak gust at Lihue Airport, Kauai, was 46 mph from the southwest. The average wind speed at Honolulu International Airport was 17.5 mph, with the fastest mile of 26 mph. Although the wind data at Honolulu Airport did not indicate exceptionally strong southwest winds, the waters southwest of the Reef Runway did experience strong Kona winds. Estimated surf was about 6 feet at Ala Moana.

Jan 8-10, 1980 storm: Up to that time, this storm caused the greatest monetary loss ever recorded in the State. Heavy rains, Kona winds, high waves, and two tornadoes accompanied the passage of two successive cold fronts. Wind gusts of 100 mph were recorded on Mt. Haleakala, Maui. Honolulu International Airport recorded gusts of 52 mph. The long duration of strong winds generated high waves which battered the south and west shores of all the islands. Estimated maximum surf was about 6 feet at Ala Moana, with surf to 15 feet reported in other areas. Bretschneider (1984) reports hindcast deepwater significant wave heights of 29 feet with significant period of 13.5 seconds.

Southerly swell: During the summer months, large swell from Southern Hemisphere storms frequently cause high surf conditions along the southern shores of the Hawaiian Islands. The following are occurrences of estimated high surf conditions:

- \*July 27-28, 1976: 8 feet
- \*July 29, 1976 : 7 to 9 feet, max 10-12 feet
- \*May 25, 1977 : 8 feet

#### Hurricane Iwa waves

On November 23, 1982, the most destructive storm in Hawaiian history, Hurricane Iwa, struck the Hawaiian

Islands. Hardest hit were the islands of Niihau, Kauai, and Oahu, where storm surge and waves inundated the southern coast of Kauai and the leeward and portions of the southeast coast of Oahu. Statewide storm-related damages exceeded \$310 million.

A hindcast analysis of the expected hurricane waves at the Reef Runway was accomplished utilizing the significant wave approach by Bretschneider (1970, 1972a, 1972b, 1976). The hurricane parameters used in the hindcast are as follows:

Central Pressure,  $P_c$  = 28.6 inches Hg (measured)  
Pressure depression,  $\Delta P$  = 1.32 inches Hg  
Radius of maximum wind,  $R$  = 20 nautical miles  
(estimated)  
Latitude,  $\phi$  = 22 degrees  
Average forward speed,  $V_F$  = 20 knots

Figure 8 shows the track of Hurricane Iwa, where the storm center passed within 110 to 120 nautical miles of the Reef Runway at its closest point of approach. The hindcast indicated maximum significant wave heights of 39.8 feet with wave period of 13.3 seconds, and expected significant wave heights offshore the Reef Runway of about 31 feet associated with sustained winds of 35 knots. Bretschneider (1984) suggests that the radius of maximum wind was probably as large as 50 nautical miles, with hindcast maximum significant wave heights of 41 to 43 feet and periods of 14.2 to 14.7 seconds. Based on his hindcast analysis, expected significant wave heights offshore the site were on the order of 35 feet.

No instrument measurements are available to confirm the hindcast wave heights. However, the US Navy reported that its guided missile destroyer USS Goldsborough was hit by a "30 foot" wave about 2 miles offshore the entrance to Pearl Harbor at 4:30 pm, on 23 November 1982, which killed a crew member on the forward deck and washed a second crew member overboard. While direct wave measurements are not available, wind speed measurements at the Honolulu International Airport confirm the hindcast 35 knot sustained wind speeds.

Measurements of the rise in water level elevation due to the passage of Hurricane Iwa are also available. Data from gage measurements in Kewalo Basin, approximately 3 miles from the Reef Runway, indicates that the difference between measured water levels and predicted tide levels was a maximum of 41 inches (3.4 feet) due to the storm. The design water level for the Reef Runway wave protective structure was 3.0 feet above MSL.



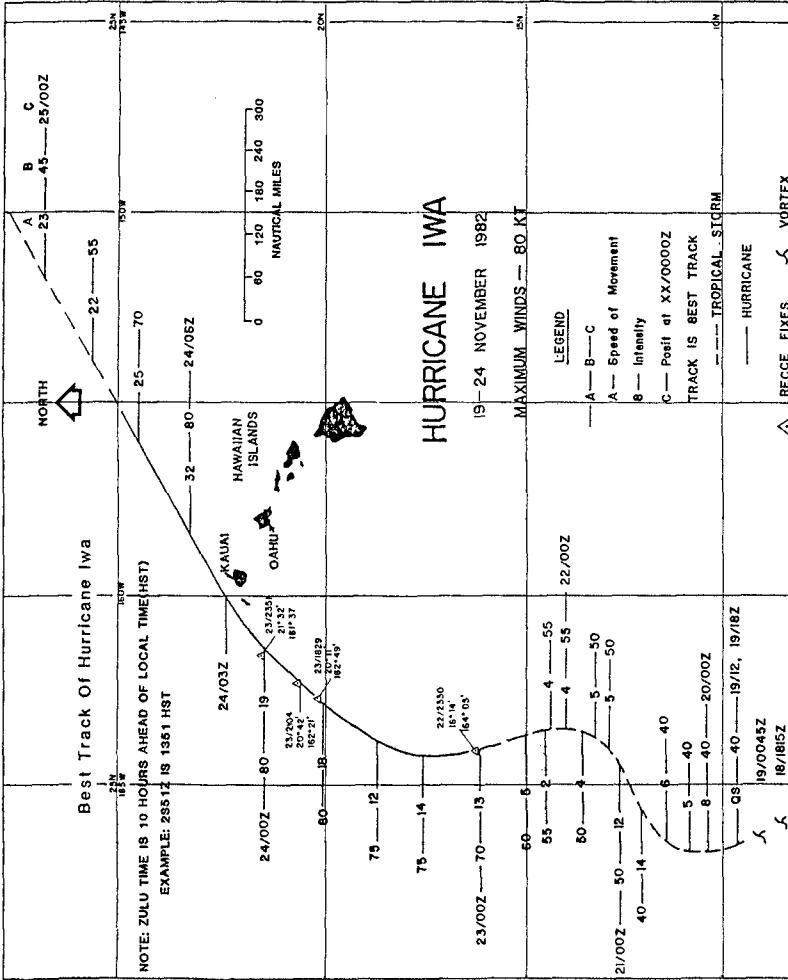


FIG. 8 TRACK OF HURRICANE IWA, NOVEMBER 1982

### Summary and Conclusions

A visual and photographic inspection of the wave protective structure for the Reef Runway, Honolulu International Airport, has been performed to assess the present physical state of the structure. The performance of the protective structure was assessed by reviewing the basic design criteria and design practices utilized for construction, and evaluation of the maximum waves which have attacked the structure.

A review of the design procedure for the wave protective structure performed in 1972 indicates that the design practice implemented for the Reef Runway protective structure is still consistent with present day techniques. Hindcasts of the wind-generated waves from Hurricane Iwa indicates that significant wave heights of up to 35 feet would be expected offshore the Reef Runway located approximately 110-120 nautical miles from the hurricane center. Comparison of these hurricane hindcast waves with the design maximum breaking waves along the exposed deepwater sections of the protective structure shows that Hurricane Iwa most probably generated maximum design wave conditions for the structure.

The design water level for the wave protective structure was 3.0 feet above MSL, and water level measurements at Kewalo Basin during Hurricane Iwa indicate a maximum measured rise of about 36 inches above MSL. When analysis is performed subtracting expected tidal fluctuations from measured water level, a maximum water level rise due only to Hurricane Iwa is calculated at 41 inches.

In general, the Reef Runway wave protective structure is in very good condition. The exposed deepwater section protected by 4 and 6 ton dolos concrete armor units has undergone the most severe wave attack and is the only major region where wave damage is evident. Underwater and above water visual inspection surveys were performed both prior to and after wave attack from Hurricane Iwa. These inspections indicate that no visually discernable damage to the dolos armored sections occurred due to Hurricane Iwa wave attack.

A numerical count of broken dolos by station locations was performed and the results show that 301 units were found broken, comprising about 71 each 6-ton units and 230 each 4-ton units. At the completion of construction in late 1975, 4,317 each 6-ton and 13,692 each 4-ton dolos units were installed yielding a percent damage of 1.64% for the 6-ton and 1.68% for the 4-ton units, with an overall damage percentage of 1.67% for all dolos installed.

The design criteria utilized a 2% damage level for the 4-ton dolos, a no-damage criteria for the 6-ton dolos at the

breakwater head, and a 4% damage level for the 6-ton dolos along the trunk section. Comparison of this design damage level versus the existing damage indicates that the structure is performing adequately following the design wave attack.

Underwater visual inspections show that the dolos protected deepwater sections remain integrally intact, and that broken dolos parts generally still remain imbedded in the structure cover layer. At Station 88+00 is the only area which was noted to have a small void region on the slope face with some broken dolos sighted 10-15 away from the structure toe.

Historically, scale-model experiments of dolos protected rubblemound structures indicate that the stability characteristics increase with small levels of damage. The reason is attributed to the condition that under wave attack, usually by relatively smaller waves than the design waves, units which were placed in an unstable position would either move and break or would be displaced off the structure, thereby resulting in a small percent damage. Those units not broken or displaced would nest and stabilize, thereby developing greater interlocking stability with a consequent capability to remain stable under the design wave attack. This condition is believed to have occurred for those sections of the Reef Runway protective structure utilizing dolos armor units. Following construction, wave attack from Kona storm waves and Southern Hemisphere generated swell, generally smaller than the design wave heights, served to increase stability by increasing the as-constructed interlocking capability of the random placed dolos units, with the inherent consequences of suffering a small level of damage. It is believed that the overall 1.67% dolos damage level noted during this survey occurred prior to wave attack from Hurricane Iwa. With an increased stability capability, the dolos armored structure was able to withstand wave attack from Hurricane Iwa with no increase in damage as compared to prior visual surveys.

**References**

- American Society of Civil Engineers (1982), *Failure of the Breakwater at Port Sines, Portugal*, prepared by the Port Sines Investigating Panel, Coastal Engineering Research Council, ASCE.
- Bretschneider, C.L. (1970), *Forecasting Relations for Wave Generation*, Look/Lab Hawaii, Vol. 1, No.3.
- Bretschneider, C.L. (1972a), *A Non-Dimensional Stationary Hurricane Wave Model*, Proceedings 1972 Offshore Technology Conference, Paper No. OTC 1517.
- Bretschneider, C.L. (1972b), *Revisions to Hurricane Design Wave Practices*, Proceedings 13th Coastal Engineering Conference, ASCE.
- Bretschneider, C.L. and E. Tamaye (1976), *Hurricane Wind and Wave Forecasting Techniques*, Look Lab/Hawaii, Vol.6, No.1.
- Bretschneider, C.L. (1984), *HOTEC Design Hurricane Waves off Kahe Point, Oahu*, prepared for Hawaiian Dredging and Construction Co., Honolulu.
- Darling, W.D. (1976), *Design and Construction of Protective Structure for New Reef Runway, Honolulu International Airport*, Proceedings 15th Coastal Engineering Conference, ASCE.
- Davidson, D.D. and D.G. Markle (1976), *Effect of Broken Dolosse on Breakwater Stability*, Proceedings 15th Coastal Engineering Conference, ASCE.
- Tetra Tech, Inc. (1972), *Design Analysis for the Protective Structure for the Proposed Reef Runway at Honolulu International Airport*, Tetra Tech Report No. TC-274.
- Tetra Tech, Inc. (1972), *Model Tests of the Reef Runway Protective Structure for Honolulu International Airport*.
- Zwamborn, J.A. (1979), *Analysis of Causes of Damage to Sines Breakwater*, Proceedings Coastal Structures '79, ASCE.
- Zwamborn, J.A., D.E. Bosman, J. Moes (1980), *Dolosse, Past, Present, Future?*, Proceedings 17th Coastal Engineering Conference, ASCE.

## CHAPTER ONE HUNDRED EIGHTY TWO

### MARINE ROUGHENED CYLINDER WAVE FORCE COEFFICIENTS

John H. Nath, Fellow, ASCE\*

#### ABSTRACT

Steel cylinders were submerged on a platform in the South Pass region of the Gulf of Mexico for one year to accumulate biofouling for later laboratory testing to determine wave force transfer coefficients. They were positioned at -55, -140, and -190 feet below the still water surface. Laboratory tests comprised steady tow up to Reynolds number of  $7 \times 10^5$ , and periodic waves up to Reynolds number of  $1.6 \times 10^5$  and Keulegan-Carpenter number up to 25. The force transfer coefficients for the -55 cylinder were about equal to those for a sand roughened cylinder with relative cylinder roughness,  $\epsilon/D$ , of .03, where  $\epsilon$  is the height of the equivalent sand roughness size and  $D$  is the smooth cylinder diameter. The drag coefficient for very high Keulegan-Carpenter number, or steady tow, is about 1.0 if the effective cylinder diameter is taken into account, for the rougher cylinders.

#### INTRODUCTION

Most information about force transfer coefficients for cylinders in waves or in steady flow is based on smooth cylinders or cylinders uniformly roughened with glued-on sand. Biofouling, however, can be very irregular, have a much thicker accumulation, and protrude much further into the flow field from the cylinder surface than any sand coated cylinder ever tested.

In order to gather wave force information on cylinders roughened with real marine growths, three 8-5/8 inch diameter steel cylinders were positioned at -55, -140, and -190 feet below the still water surface at a platform positioned in the Gulf of Mexico near the mouth of the Mississippi River at the coordinates 89° 23' East and 28° 50' North. Three cylinders were positioned at each level so that they could be tested after 1, 2, and 3 years' of growth. This paper reports on the results obtained from the 1-year old cylinders.

---

\*Professor, Ocean Engineering Program, Dept. of Civil Engineering, Oregon State University, Corvallis, OR 97331.

## EQUIPMENT

The cylinders were constructed from 8-5/8 inch diameter steel pipes, 2 feet long. They were split longitudinally so they could be attached to a test beam for the laboratory tests in steady flow and waves (4,5,6), using countersunk, flush-headed machine screws. The test beam was about 10 feet long, mounted horizontally between 2 vertically suspended low-drag support members that were positioned close to the wave flume walls. The support members hung from a tow carriage. The Oregon State University (OSU) Wave Research Laboratory (WRL), the tow carriage, and the test beam are further described in (4,5,6).

The half cylinders were mounted to strain gage force dynamometers so that the total horizontal and vertical forces could be measured on the 2-foot long test section. They were carefully calibrated in all directions before and after each test with the test beam submerged. The calibration constants were linear and varied by less than 2% between the calibrations prior to the tests and those after the tests. The water surface fluctuation was measured directly above the beam. A current meter was positioned 2 cylinder diameters above the cylinder surface, but the measurements therefrom have not been used in the analysis because of the modification to the rotating flow from the presence of the cylinder.

Two dummy cylinders (each were split) were attached to the test beam to provide a continuous cylindrical surface. They were roughened artificially with glued-on sand, barnacles, corks and fuzzy material to provide a roughness about equal to that of the center test surface. The position of the test section relative to the water surface and wave flume floor is shown in Fig. 1. There was a space of less than 1/8 inch between the test section and the dummy section that did not influence the results, as proved in other testing (6).

Data were recorded digitally on a PDP-11 minicomputer. For reliability there were 2 channels for horizontal force, 2 for vertical force, 1 each for the horizontal and vertical current measurement and 1 for the water surface profile.

Photographs of the cylinders were made by personnel at the ocean platform prior to mounting them in shipping containers of sea water. They were shipped quickly by air freight to OSU, where they arrived with almost all of the organisms still alive. At OSU they were photographed, aerated, and removed from their mounting core prior to placement under water (fresh water) on the test beam. A photograph of the cylinder from -55 feet is shown in Fig. 2.

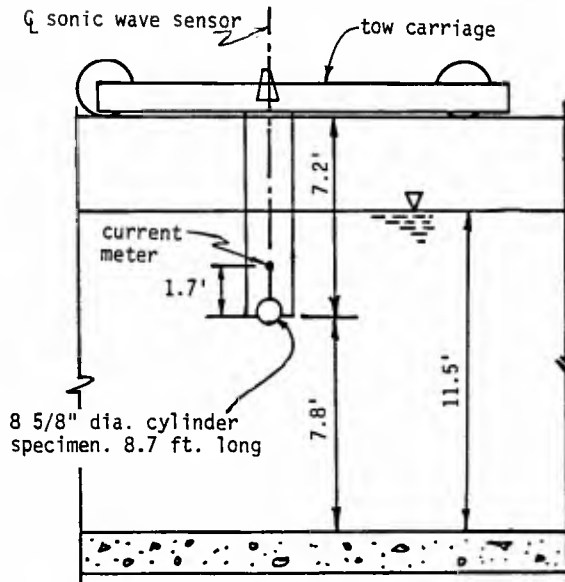


Fig. 1 Horizontal cylinder location in the wave flume.



Fig. 2 Cylinder from -55 feet, South Pass platform.

Most of the organisms stayed alive until placed in fresh water, whereupon the cylinders were immediately tested in steady state towing. They soon died in the fresh water, but they generally remained attached to the cylinder for the remainder of the testing. The test results showed that the death of the organisms caused no appreciable change in the force transfer coefficients.

#### TESTS

There have been earlier tests on smooth and sand roughened cylinders at OSU (5), some results of which will be repeated here for comparison with the marine roughened cylinders. The South Pass cylinders were first towed at speeds from 1 to 10 fps. Then the ends of the carriage test beam were guyed to the WRL walls for tests in periodic and random waves. (The tests in random waves are not reported on herein.) After the wave tests, the cylinders were again towed to see if there was a detectable change in the steady state drag coefficients due to a loss of biofouling from the fresh water and the vigorous action from waves. The cylinders were then dried and the soft (now crisp) organisms were brushed off. The cylinders were tested again in steady tow to see if there was a detectable change in the steady state drag coefficients due to the loss of the soft, flexible organisms. These 3 conditions of the organisms during the tests are termed "live", "after" and "dried" for this report.

The various cylinder roughnesses are given abbreviated designations in this report for ease in referring to them. These designations are summarized in Table 1.

Table 1. Cylinder designators.

Designation	Explanation
SMC	Smooth cylinder
SRC.02	Sand roughened cylinder with $\epsilon/D = .023$
SRC.03	Sand roughened cylinder with $\epsilon/D = .032$
SP1-55	South Pass cylinder, 1 year old, -55 ft,
SP1-140	South Pass cylinder, 1 year old, -140 ft,
SP1-190	South Pass cylinder, 1 year old, -190 ft,



## ANALYSIS

The steady state tow drag coefficient,  $C_{ds}$ , was calculated from

$$C_{ds} = \frac{F}{\frac{1}{2} DL\rho U^2 \delta} \quad (1)$$

where  $F$  is the average force on the test section,  $D$  is the smooth cylinder diameter,  $L$  is the test section length (2 feet),  $\rho$  is the water mass density,  $U$  is the steady tow speed (the carriage was timed over a measured distance), and  $\delta$  is the effective diameter coefficient ( $\delta \geq 1$ ). For very rough and irregular growths, and for significant, flexible biofouling, like heavy accumulations of kelp, it is sometimes difficult to define an effective diameter that can be universally accepted. Therefore, for much of the analysis for this work the coefficient,  $\delta$  was set equal to 1. Much of the data presented here were so calculated, but for some data  $\delta$  was computed from the circumferential measurements of the cylinders.

The force transfer coefficients were computed with least squares methods using a vector form of the Morison equation that is reviewed in more detail in (5,11). During a test, measurements were made for 4 wave periods, from which 3 complete crest-to-crest waves could be defined. Coefficients were calculated for each of the 3 waves and averaged. These average values are reported herein.

The Morison equation for the force per unit of length,  $\vec{F}$ , on a horizontal cylinder is then written as

$$\vec{F} = \frac{1}{2} C_d \delta D \rho \vec{q} |\vec{q}| + C_m \pi \frac{(\delta D)^2}{4} \rho \vec{\dot{q}} \quad (2)$$

where  $\vec{q}$  is the velocity vector and  $\vec{\dot{q}}$  is the acceleration vector. In the least squares analysis,  $C_d$  and  $C_m$  are assumed to be constant with time. If  $\delta$  is assumed to be 1, the increase in diameter due to biofouling is included in  $C_d$  and  $C_m$ . Where  $C_d$  and  $C_m$  are so computed, they can be corrected with appropriate manipulations with the  $\delta$  desired.

It is well known with respect to wave forces on cylinders that are small in diameter compared to the wave lengths that the averaged force transfer coefficients computed from least squares techniques are functions of the Keulegan-Carpenter number and the Reynolds number. They are defined, respectively, as

$$K = \frac{u_{\mu} T}{D\delta} \quad (3)$$

$$\text{and } R = \frac{u_{\mu} D\delta}{\nu} \quad (4)$$

where  $u_{\mu}$  is the maximum horizontal water speed at the cylinder $_{\mu}$  position,  $T$  is the wave period, and  $\nu$  is the kinematic viscosity.

More recently the particle orbit shape has been found to influence force transfer coefficients for vertical smooth cylinders. The orbit shape is usually quantified with the ratio

$$\Omega = \frac{u_{\mu}}{w_{\mu}} \quad (5)$$

where  $w_{\mu}$  is the maximum vertical velocity.

For a horizontal cylinder with the axis parallel to the wave crests the vortex shedding characteristics are influenced considerably by  $\Omega$ . Without the cylinder present the velocity vector rotates, at the position of the center of the cylinder, in a clockwise direction if the progressing wave is travelling from left to right. The vector changes in magnitude with time if the wave is not a linear, deep water wave. Otherwise, the magnitude remains constant and  $\Omega = 1$ .

For this work  $.4 < \Omega < 1.0$ , as detailed in ref. (5). However, the wave conditions were such that  $K$  and  $R$  could not be varied through the full range for each value of  $\Omega$ . Therefore, the lower values of  $\Omega$  are usually associated with the higher values of  $K$  and  $R$ .

Another way to consider the wave forces is through the maximum force coefficient,  $C_{\mu}$ , and the phase shift,  $\hat{\phi}$ . The first is defined as

$$C_{\mu} = \frac{F_{\mu}}{\frac{1}{2} DL\rho u_{\mu}^2 \delta} \quad (6)$$

and the phase shift is (please refer to Fig. 3)

$$\hat{\phi} = \frac{\phi_f}{\phi_a} \quad (7)$$

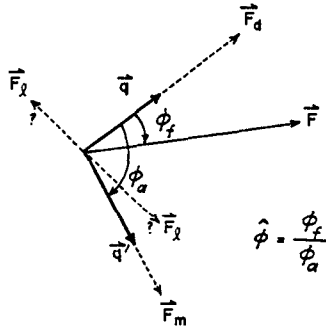


Fig. 3 The velocity vector,  $\vec{q}$ , drag force,  $\vec{F}_d$ , acceleration vector,  $\dot{\vec{q}}$ , inertia force,  $\vec{F}_m$ , "lift" force,  $\vec{F}_l$ , and the phase angles for a wave with the crest parallel to the axis of a submerged horizontal cylinder.

It can be shown (7) that as  $K$  gets very large,  $C_u \rightarrow C_{ds}$  in Eq. (6). Where  $\phi_f$  is the instantaneous phase shift (in space) between the velocity vector and the total force vector, and  $\phi_a$  is the phase shift between the velocity vector and the acceleration vector (which =  $90^\circ$  only for deep water small amplitude waves). Note that the "lift" force,  $\vec{F}_l$ , which is orthogonal to the velocity vector, is not included in Eq. (2), so the somewhat random influence from vortex shedding will appear as scatter in both  $C_d$  and  $C_m$ . However, Eq. (6) should not be influenced quite so much from such effects, so one would expect less scatter in the results for  $C_u$ . On the other hand,  $\hat{\phi}$  should be very sensitive to vortex shedding and one would expect considerable scatter in experimental values for  $\hat{\phi}$ .

There is as much information about the wave force in Eqs. (6) and (7) as in Eq. (2) if one considers  $\hat{\phi}$  to be a function of time. Actually,  $\hat{\phi}$  is evaluated when  $F$  is  $F_u$ . An advantage for Eqs. (6) and (7) is that they conceivably can be based on measurements only. There is no theory involved if  $\dot{\vec{q}}$  is measured in some way. In this paper  $\dot{\vec{q}}$  is based on the water surface profile and Dean's stream function wave theory. For vertical cylinders it is easier to base Eq. (6) on pure measurements. It also turned out that there was much less scatter in the  $C_u$  plots than for  $C_d$  and  $C_m$ . In this case there is more scatter in  $\hat{\phi}$  because of its sensitivity to vortex shedding. Another advantage to Eq. (6) is that  $u$  need not be measured right at the cylinder, but can be any distance away, at the same depth. But measurement of the water surface profile,  $\eta(t)$ , or theory, must be used to be able to evaluate  $\hat{\phi}$ . Herein the stream function theory is used.

Another advantage in considering Eq. (7) is in the

clear realization of whether the wave force is dominated by water acceleration or velocity effects. If  $\phi$  is 1.0, clearly the force is acceleration dependent. If it is 0.0 it is velocity (drag) dependent. Further discussion on this point can be seen in (7).

#### RESULTS

The SRC.03 could not be towed, so no  $C_{ds}$  values are presented for it. The results of circumferential measurement of the various cylinders are given in Table 2.

Table 2. Effective diameter coefficients for the various cylinders from circumferential measurements and sand sizes.

Designation	$\epsilon/D$	$\delta$
SMC	0	1.00
SRC.02	.023	1.046
SRC.03	.032	1.064
SP1-55	.037	1.074
SP1-140	small	1.00
SP1-190	0	1.00

The SP1-190 cylinder was so smooth that it was not tested. The SP1-140 only had a few very small anemones and a few other crusty organisms. The SP1-55 cylinder had a large number of acorn barnacles attached and one tintinnabulum balanus with average heights of 0.34 inches and a standard deviation of .23 inches. However, the average of several circumferential measurements yielded the results given in Table 2.

Steady tow test results for the SMC, SRC.02, SP1-140 and SP1-55 cylinders are shown in Figs. 4 through 7. There is some obvious scatter in Fig. 5, the true source of which is unknown. Some of it is probably due to small amplitude vibrations of the tow carriage, modifying the wake separation points to some degree. Figure 5 also indicates that the  $C_{ds}$  values may be influenced about 2.9% or less because of limited water space above the cylinder (surface effects). This magnitude of difference was later verified with additional testing. Figure 6 shows that the SP1-140 cylinder had a roughness between that of the SMC and the SRC.02. Figure 7 shows that the roughness of the SP1-55 cylinder did not change appreciably between the live, after, and dried conditions. In addition, its roughness appeared to be about equal to that for the SRC.02.

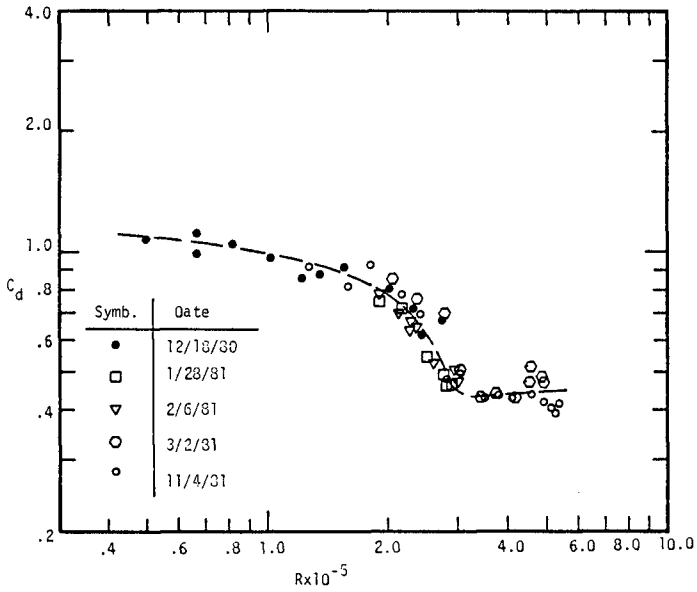


Fig. 4 Steady state tow  $C_{dS}$  for SMC.

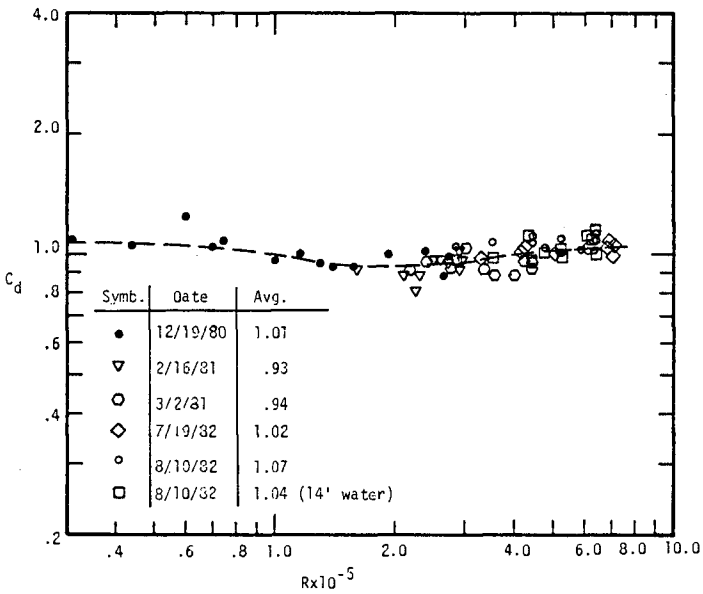


Fig. 5 Steady state tow  $C_{dS}$  for SRC.02.

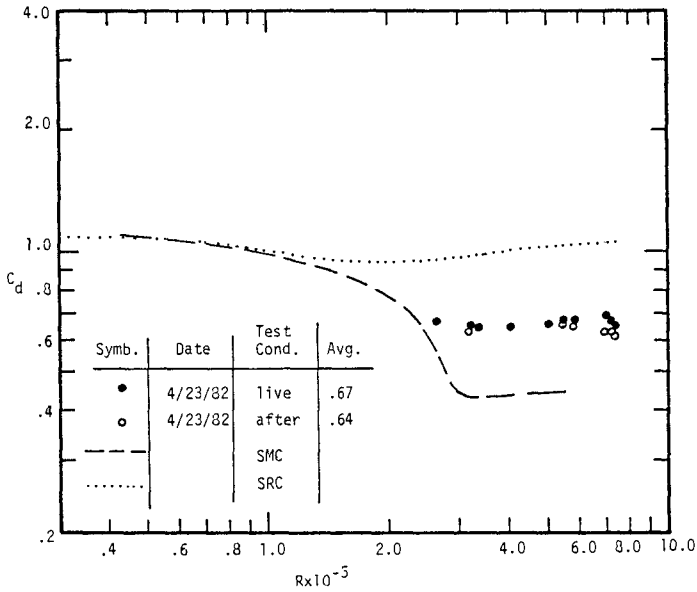


Fig. 6 Steady state tow  $C_{ds}$  for SPL-140.

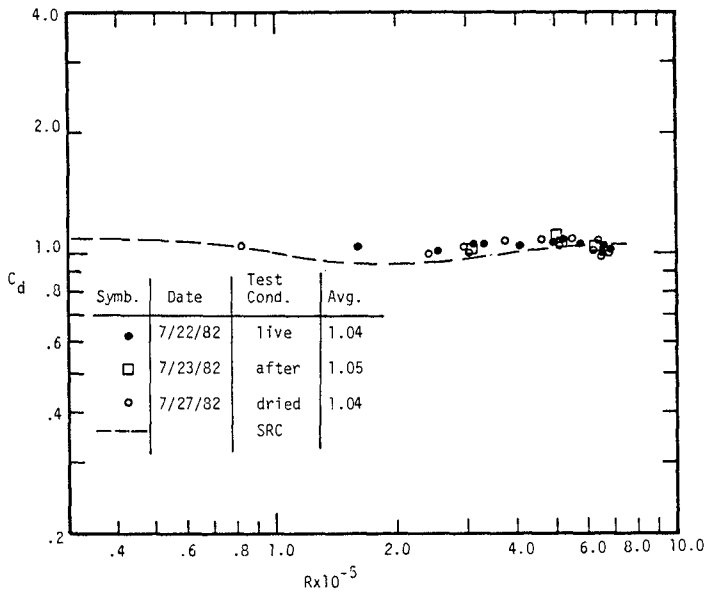


Fig. 7 Steady state tow  $C_{ds}$  for SPL-55.

Figure 8 shows the results for  $C_d$  from periodic waves for the SMC, SRC.02 and SRC.03 cylinders for  $15 < K < 25$ . All results fall below those for the results from (8) for oscillatory flow ( $\Omega = 0$ ), for  $K = 20$ . The results for the SMC have a lot of scatter around  $R = 1.8 \times 10^5$ , the true source of which is not yet known.

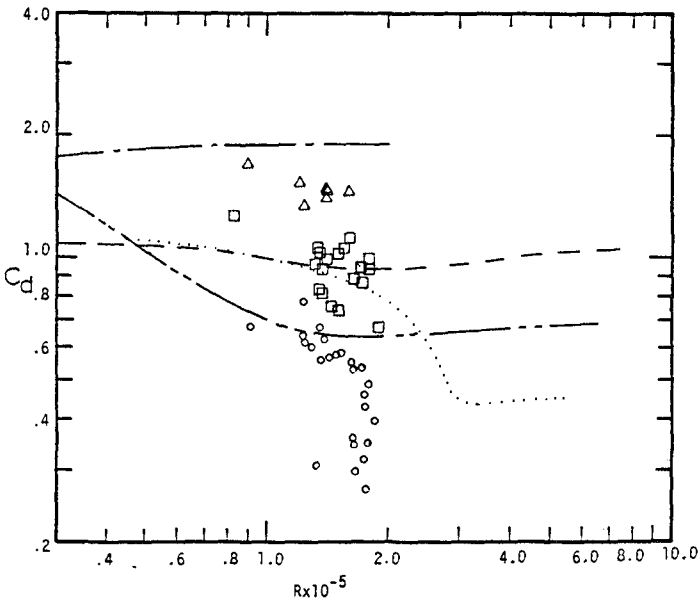


Fig. 8 Drag coefficients in steady tow and wavs for:  
 - - - - - Sarpkaya (8),  $\epsilon/D = .02$ ,  $K = 20$ ; - - - - - Sarpkaya  
 (8), smooth,  $K = 20$ ; — — — — —  $C_{ds}$ , SRC.02; ······  $C_{ds}$ ,  
 smooth;  $\Delta$  SRC.03,  $15 < K < 25$ ;  $\square$  SRC.02,  $15 < K < 25$ ;  $\circ$   
 smooth,  $15 < K < 25$ .

Figure 9 shows the same results for the SP1-140 and SP1-55 cylinders. Figures 10 and 11 are the counterparts of 9 and 10, only for  $C_m$ . These results show very approximately that the SP1-55 cylinder has an equivalent  $\epsilon/D \approx .03$  and the SP1-140 is somewhere between the smooth condition and  $\epsilon/D \approx .02$ .

The data for the SRC.02, SRC.03, and the SP1-55 were also processed according to Eqs. 6 and 7 using the  $\delta$  values indicated in Table 2. The results are plotted in Figs. 12 and 13. Figure 12 fairly clearly shows how  $C_\mu$  increases with roughness in the range of  $4 < K < 15$ . In addition, the  $C_{ds}$  values for SP1-55 and the SRC.02 are plotted at high  $K$  in Fig. 12. In the range  $15 < K < 25$  the differences in  $C_\mu$  are less clear. The figure indicates that the experimental  $C_\mu$  values may well merge with the  $C_{ds}$  values at high  $K$  and that  $C_{ds} \approx 1.0$  for both  $\epsilon/D \approx .03$  and  $\epsilon/D \approx .02$  providing the proper  $\delta$  is used. This figure may have considerable importance because it implies the  $C_\mu$  values for the region of  $25 < K < 200$ , which includes the full scale values of  $K$  for ocean platforms.

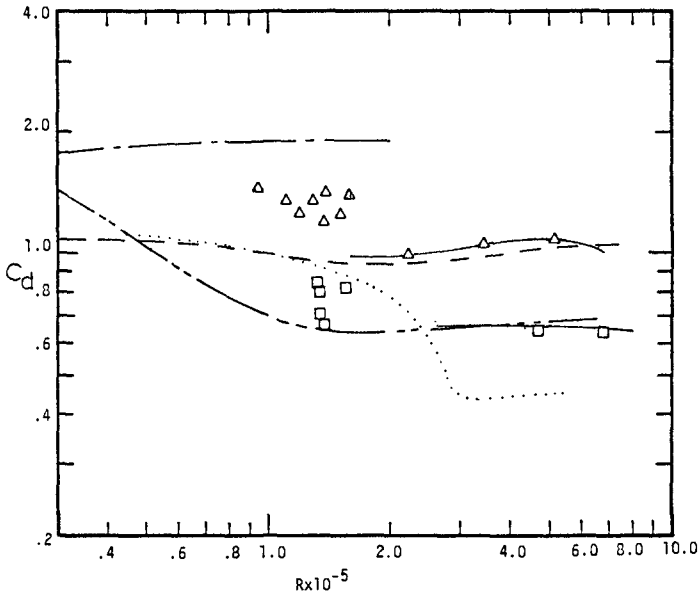


Fig. 9 Drag coefficients in steady tow and waves for: ——— Sarpkaya (8),  $\epsilon/D = .02$ ,  $K = 20$ ; - - - Sarpkaya (8), smooth,  $K = 20$ ; - · -  $C_{ds}$ , SRC.02; —△—  $C_{ds}$ , SP1-55; —□—  $C_{ds}$ , SP1-140; △ SP1-55,  $15 < K < 25$ ; □ SP1-140,  $15 < K < 25$ .



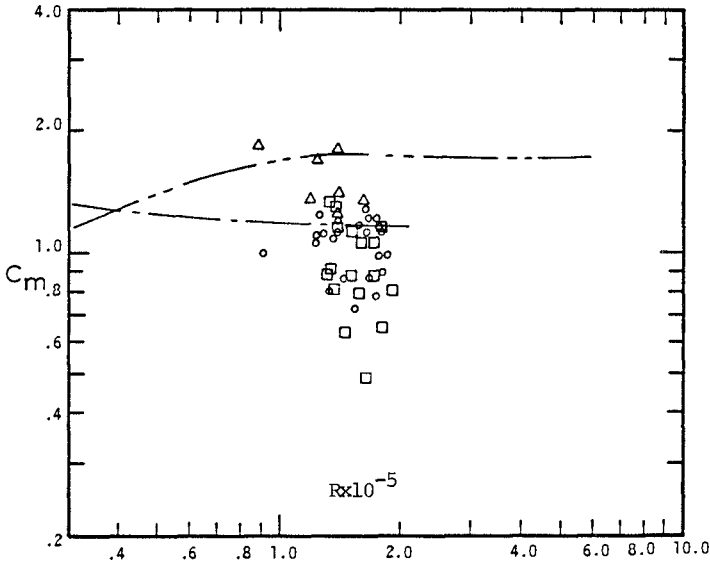


Fig. 10 Inertia coefficients for: ——— Sarpkaya (8),  $\epsilon/D = .02$ ,  $K = 20$ ; - - - Sarpkaya (8), smooth,  $K = 20$ ;  $\Delta$  SRC.03,  $15 < K < 25$ ;  $\square$  SRC.02;  $15 < K < 25$ ;  $\circ$  smooth,  $15 < K < 25$ .

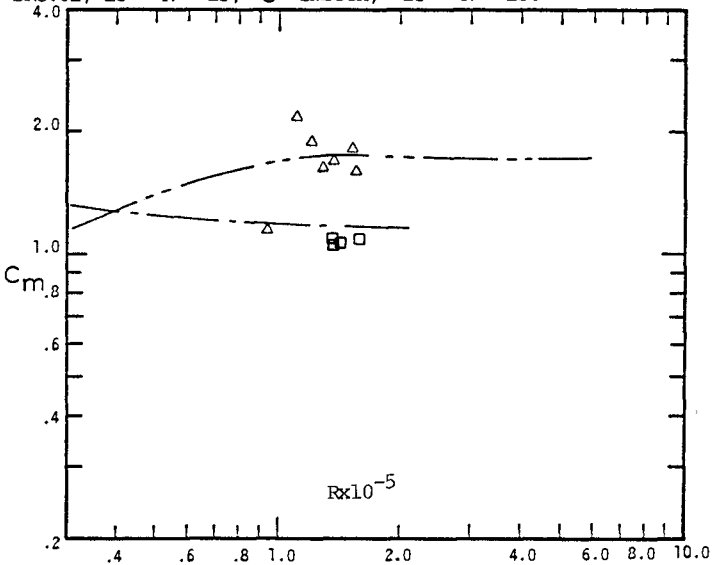


Fig. 11 Inertia coefficients in waves for: ——— Sarpkaya (8),  $\epsilon/D = .02$ ,  $K = 20$ ; - - - Sarpkaya (8), smooth,  $K = 20$ ;  $\Delta$  SP1-55,  $15 < K < 25$ ;  $\square$  SP1-140,  $15 < K < 25$ .

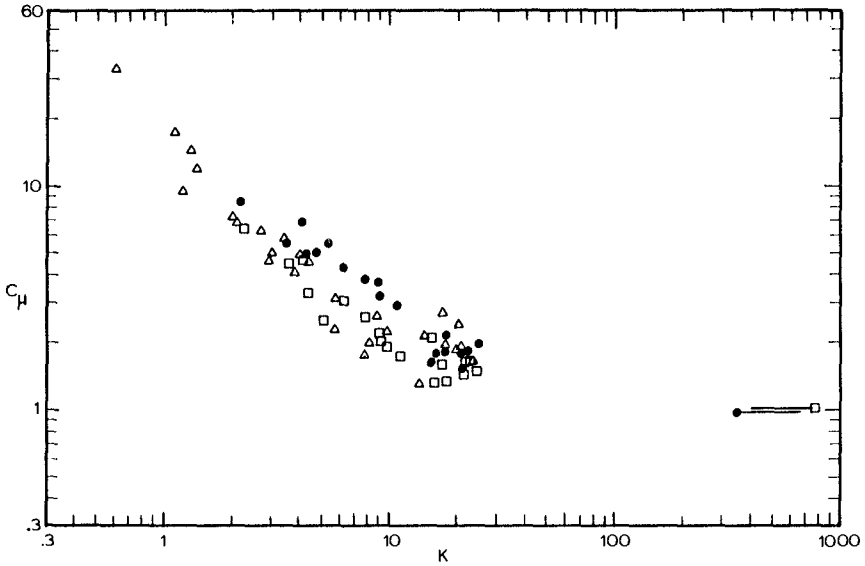


Fig. 12 Maximum force coefficient, horizontal cylinder in waves for: ● SPI-55; △ SRC.03; □ SRC.02; —□  $C_{ds}'$ , SRC.02; ●—  $C_{ds}'$ , SPI-55.

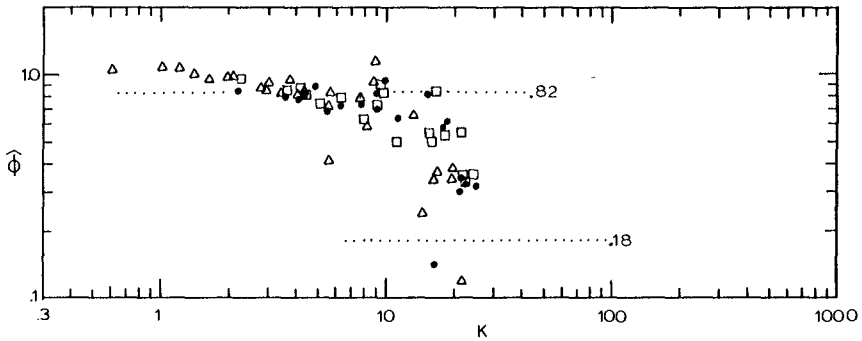


Fig. 13 Phase shift, horizontal cylinder in waves for: ● SPI-55; △ SRC.02; □ SRC.02.

The phase shift results are plotted in Fig. 13. Not surprisingly, scatter is more prevalent in the range  $6 < K < 20$ . It is clear that as  $K$  increases, the maximum force on the cylinder becomes more velocity (drag) dependent. What is not clear, surprisingly, is that the rougher cylinders are not more drag dependent in the range  $10 < K < 20$ . More data are required to determine relationships on a statistical basis for so much scatter. However, at  $K = 25$  the few data available indicate that the SP1-55 is more drag dominated than the SRC.02; furthermore,  $\phi$  is about the same for SP1-55 and the SRC.03. Perhaps the differences in roughness in this study do not have an important influence on the value of  $\phi$  because as  $K$  increases due to an increase in  $\epsilon/D$ ,  $\phi$  tends to increase because  $K$  becomes smaller ( $K = u_T/D\delta$ ); but, as the surface roughness increases, the flow should become more drag dependent, tending to make  $\phi$  decrease. These opposing trends tend to compensate.

#### CONCLUSIONS

Within the range of tests herein the soft fuzzy growths that covered the barnacle-type growths neither appreciably increased nor decreased the drag or inertia coefficients.

The effective roughness of the SP1-55 cylinder was about  $\epsilon/D \approx .03$  and the effective diameter coefficient was about  $\delta \approx 1.07$ .

For drag dominated flow and high  $K$  values, the maximum force coefficient should approach the value of  $C_{ds}$ . Furthermore, within these tests,  $C_{ds} \approx 1.0$  for all rough cylinders providing appropriate values of  $\delta$  are used, which can be determined from circumferential measurements.

#### ACKNOWLEDGEMENTS

The placement and retrieval of the cylinder was done by Chevron USA. Support for the tests and the transfer coefficient analysis was from the American Petroleum Institute. The  $C_u$  and  $\phi$  analysis support was provided partially by the OSU Sea Grant Program, Grant No. NA 81AA-D-00086, and partially by the National Science Foundation, Grant No. CEE-8310732. The author gratefully acknowledges the support from each of these organizations.

## REFERENCES

1. Hudspeth, R.T., Jones, D., and J.H. Nath, "Design of Hinged Wave makers for Random Waves," International Conference on Coastal Engineering, Hamburg, Germany, August 1978.
2. Nath, J.H. and K. Kobune, "Periodic Theory Velocity Prediction in Random Waves," International Conference on Coastal Engineering, Hamburg, Germany, August 1978.
3. Nath, J.H., "Drift Speed of Buoys in Waves," (with appendix by M.S. Longuet-Higgins), International Conference on Coastal Engineering, Hamburg, Germany, August 1978.
4. Nath, J.H., "Hydrodynamic Coefficients for Macro-Roughness," Proceedings of Offshore Technology Conference, OTS 3989, May 1981.
5. Nath, J.H., "Heavily Roughened Horizontal Cylinders in Waves," Proceedings of BOSS82, Massachusetts Institute of Technology, August 1982.
6. Nath, J.H., "Hydrodynamic Coefficients for Cylinders Roughened by Marine Growths from the Gulf of Mexico," Final Report to the American Petroleum Institute, Ocean Engineering Program, Department of Civil Engineering, Oregon State University, January 1983.
7. Nath, J.H., et.al., "Laboratory Wave Forces on Vertical Cylinders," Proceedings of the Ocean Structural Dynamics Symposium, Oregon State University, September 1984.
8. Sarpkaya, T., and M. Isaacson, "Mechanics of Wave Forces on Offshore Structures," Van Nostrand-Reinhold, 1981.
9. Sarpkaya, T., Discussion of Ref. 10, Journal of Waterway, Port, Coastal and Ocean Division of ASCE, February 1984.
10. Stansby, P.K., Bullock, G.N., and I. Short, "Quasi-2-D Forces on a Vertical Cylinder in Waves," Journal of Waterway, Port, Coastal and Ocean Division, ASCE, February, 1983.
11. Teng, C.C., and J.H. Nath, "Wave and Current Forces on Cylinders," Proceedings of the Ocean Structural Dynamics Symposium, Oregon State University, September 1984.

## CHAPTER ONE HUNDRED EIGHTY THREE

### TIME AND FREQUENCY LOADING ANALYSIS OF SUBMARINE PIPELINES

H. C. Alexander, P. L. Allen and J. L. Warner\*

#### ABSTRACT

Fatigue damage to marine pipelines subjected to wave forces is evaluated using time-domain and frequency-domain methods. Spectral techniques are applied to North Sea, Gulf of Mexico and offshore Atlantic Canada wave conditions. Time-domain analysis is applied to wave conditions in the Canadian North Atlantic Ocean.

The frequency-domain analysis is performed using spectral and probabilistic techniques suggested by L. Borgman (2). The pipeline dynamic characteristics are described by classical analytical descriptions. The time-domain analysis computes time histories of wave force loading on the submerged pipeline from actual wave records. The traditional Morison wave force equation is used to obtain the time history of the loading on the pipeline. Empirically determined wave spectra are shown not to produce as good a correlation with the deterministic results as the actual wave spectra.

Free spanning submarine pipelines subjected to cyclic surface wave loading accumulate strength reductions leading to failure from material fatigue. The Palmgren-Miner rule for the linear accumulation of fatigue damage is applied to evaluate the time to failure. The American Welding Society X-X stress accumulation curve is applied.

The results of the deterministic analysis were compared with those of the more efficient spectral analysis. It is shown that comparable results can be obtained from the spectral analysis provided the actual spectra of the water surface elevation is employed in the spectral analysis.

\*H. C. Alexander, Associate Professor, California State University, Long Beach, Long Beach, California.  
P. L. Allen, Assistant Professor and J. L. Warner, Associate Professor, Technical University of Nova Scotia, Halifax, Nova Scotia, Canada.

## NOMENCLATURE

$A_n$	amplitude of nth wave component
$a_i$	water particle acceleration in the ith time interval
$C_D$	drag force coefficient
$C_M$	inertia Force Coefficient
$C_1, C_2$	Morison wave force equation coefficients
$D_o$	outer diameter of steel linepipe
$D_{Con}$	outer diameter of concrete coating
$d$	water depth
$F$	wave force per unit length of pipe
$F_i$	wave force in the ith time interval
$F_M$	magnitude of the Mth Fourier force coefficient
$f$	wave frequency
$g$	gravitational acceleration
$H_s$	significant wave height
$L$	length of unsupported span of pipeline
$S_{nn}(f)$	spectral density of water surface elevation
$t_{Con}$	thickness of concrete jacket
$t_w$	wall thickness of steel pipeline
$U_{19.5}$	wind velocity at a height of 19.5 meters
$u_i$	water particle velocity at the ith time interval
$Z$	distance above the sea bed
$\alpha, \beta$	empirically derived constants that appear in the P-M formulation of the wave spectrum
$\eta$	water surface elevation
$\sigma_i$	bending stress in the ith time interval
$\rho_{con}$	density of concrete
$\rho_{fl}$	density of fluid
$\phi_n$	nth Fourier cosine series phase angle

## 1.0 INTRODUCTION

Extensive production of petroleum and natural gas now takes place in coastal waters with the move being to exploration, and in the near future, production in deep ocean waters. Studies show that the most efficient way of transporting the hydrocarbon products onshore is by submarine pipelines, where possible. Some structures offshore have been at a particular site for over 20 years. Engineers have recognized that these structures have undergone long-term cyclic loading and have developed methods of evaluating the accumulated damage caused by the cyclic wave loading. The analyses have been predominantly probabilistic in nature, and have been extended by Alexander (1) to evaluate the fatigue life of a free span of submarine pipeline.

An increasing amount of actual water surface elevation records for particular sites are becoming available. More accurate probabilistic analyses are now possible and as well deterministic (time-domain) analyses which involve no assumptions regarding wave spectra or the linearization of the drag term in the Morison (6) wave force equation, are also available.

The line pipe, Figure 1, used in the offshore industry is of circular cross-section, seamless, fabricated from steel and is generally jacketed in concrete to provide protection and insure negative buoyancy. Moybo (5) has shown that the concrete jacket does not appreciably alter the flexible stiffness of the submerged steel pipe. The scour of sediment and sand from around a pipeline laid on the ocean bottom, due to the action of both surface waves and bottom currents, can cause submarine pipelines to be exposed and suspended as shown in Figure 2. Herbich (3) and Strating (9) have documented many cases of submarine pipelines becoming free spanning. These free-spans of submarine pipelines have the potential to fail from fatigue due to surface-wave induced, generally low level, cyclic loads. Vortex induced loading also caused by surface-waves and bottom currents, which may also contribute to the fatigue damage, are not included in this analysis.

In order for a structure to suffer from fatigue damage it must undergo a displacement process. Anytime a structure is displaced in a cyclic manner the possibility of the displacement of the structure being dynamically amplified exists. This analysis involved an evaluation of the range of frequencies over which the hydrodynamic loading might dynamically amplify the response of the free-spanning submarine pipeline structure. The range of natural frequency for a typical pipe span length is shown in Figure 3. Where dynamic amplification was significantly small a more efficient quasi-static method was used to evaluate pipeline response.

Airy wave theory was employed to describe surface-wave induced water particle kinematics. This theory allowed water particle velocity and acceleration to be determined at the elevation of the free-spanning pipeline. An Airy wave description is shown in Figure 4.

## 2.0 WAVE RECORD AND FORCE ANALYSIS

An ocean engineer faced with the task of analysing the wave climate at a particular location can proceed in two different directions. The traditional method developed by Pierson and Moskowitz (8) was to relate wave amplitude as a function of wave frequency and with further analysis the spectral energy density  $S_{\eta}(f)$  as a function of the wave frequency as given by Equation 1<sup>n</sup>

$$S_{\eta}(f) = \alpha \frac{g^2}{[(2\pi)^4 f^5]} \exp [-\beta (g/2\pi U_{19.5} f)^4] \quad (1)$$

where  $\alpha$  and  $\beta$  are empirically derived coefficients, respectively equal to 0.0081 and 0.74 and valid for fully arisen sea conditions. Significant wave height,  $H_s$ , and significant wave period may be determined from the spectral density relationship. Fully arisen seas are rarely encountered in coastal waters off the coast of Atlantic Canada. The spectral density of the water surface elevation is not accurately represented by the P-M spectrum at these locations.

When time histories of water surface elevation are available for a particular location the ocean engineer can proceed with an alternate analysis. Of late, extensive libraries of time histories of water surface elevation, in the coastal waters of Atlantic Canada, are available from the Marine Environment Data Service (MEDS) of Fisheries and Oceans Canada. Such a record is shown in Figure 6, for station 144 near the Sable Island region of offshore Atlantic Canada. This record will be presented as an example analysis. The twenty minute records available are assumed to represent the sea conditions which exist over a three hour period. Assuming that the water surface elevation function  $\eta(t)$  repeats itself every twenty minutes a Fourier cosine series of the record may be written such that  $N$  equations describing the water surface elevation would be of the form

$$\eta_i = \sum_{n=1}^N A_n \cos(\pi i n/N + \phi_n) \quad (2)$$

where  $A_n$  is the amplitude of the  $n^{\text{th}}$  wave component and  $\phi_n$  is its corresponding phase angle. Similarly water particle velocity and acceleration,  $u_i$  and  $a_i$  can be written in discrete form. The Morrison equation can now be used in discrete form

$$F_i = C_1 u_i |u_i| + C_2 a_i \quad (3)$$

to obtain the response of the submarine pipeline to wave loading. Even efficient fast fourier transforms require significant computer time to analyze several twenty minute records each consisting of two thousand points.

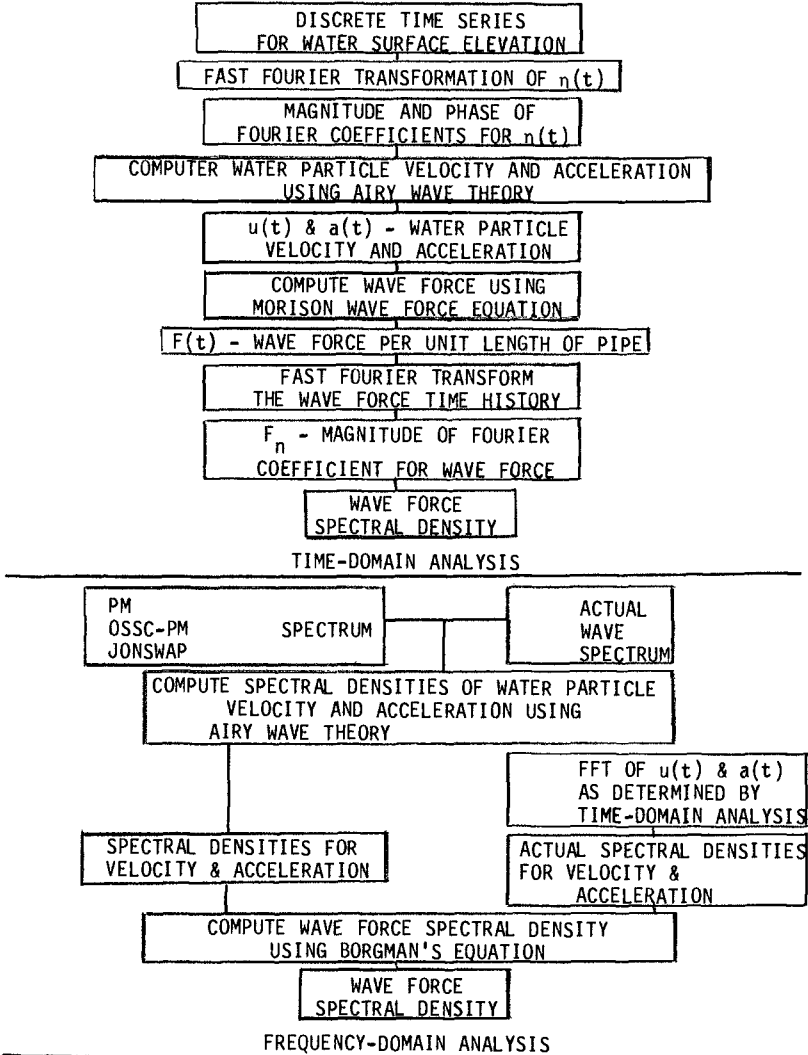
A more efficient method when the actual wave records are available is to obtain the actual spectral density of the surface elevation. The actual spectral density for wave record station 144 is shown compared with other empirically derived spectra in Figure 5. Little correlation exists between the actual and the P-M and the modified P-M spectra. The Jonswap spectrum shows acceptable correlation but only when the necessary coefficients are determined from the actual spectrum. This cannot be done a priori. Clearly, actual wave spectra should be employed when determining the hydrodynamic loading.

The spectral density for the wave force can be evaluated by several methods. Firstly, the wave force can be assessed in the time-domain using equation 3. A high degree of confidence can be placed in this method. Secondly, Borgman's transformation can be used to obtain the spectral density of the wave force from the Fourier transformation of the discrete time series. This hybrid time-frequency-domain analysis and results appear to be acceptable. The third method employs the Borgman transformation from an empirically formulated energy spectrum. Since poor correlation exists between



the actual spectrum and the empirically formulated spectra only marginal confidence can be placed in this method.

Flow charts of the evaluation of the force spectral density for the time-domain analysis (method 1) and the frequency-domain analysis (method 2 and 3) follow:



### 3.0 FATIGUE ANALYSIS

Offshore structures which are subjected to cyclic hydrodynamic loading suffer a reduction in strength, which may eventually cause failure, through a process called fatigue. The fatigue life of structure may be determined by applying the Palmgren (7) and Miner (4) law of linear-accumulated damage. It states that fatigue failure will occur when

$$\sum_i \frac{m_i}{N_i} = 1 \quad (4)$$

where  $m_i$  is the actual number of occurrences of stress magnitude  $\sigma_i$  determined from the wave loading spectrum.  $N_i$  is the permissible number of occurrences of stress determined from S-N curves which relate the number of cycles to failure to a certain stress range. The American Welding Society S-N curve, ASW-X was used as the failure criteria. The fatigue damage sustained by a submarine pipeline was assessed for a year. The reciprocal of this value was taken as the fatigue life.

The relationship between the force spectral density and the stress spectral density is determined by considering the force spectral density as an input to the linear free-spanning submarine pipeline system. The displacement response and the stress response are directly related and expressed in the frequency-domain.

In the time-domain analysis the uniformly distributed wave load is replaced by a concentrated wave load applied at the center of the pipe span, which produces the same maximum bending stress. This concentrated load is used as the forcing term in the dynamic equation of the pipeline motion. An iterative procedure is included to solve for the relative velocity between the structure and the water particles. Once the structure displacement is determined, bending stresses are calculated from simple beam theory assuming that the suspended line-pipe has pinned-supports. The exact procedure required to determine the stress-history in the time-domain is complex and time consuming even on high-speed digital computer.

### 4.0 RESULTS

The following pipeline and environmental parameters were used in the fatigue analysis as applied to six 20 minute wave records from Station 144.

Pipe diameter ( $D_0$ )	600 mm (24 inches)
Pipe wall thickness ( $t_w$ )	13 mm (0.5 inches)
Concrete jacket thickness ( $t_{con}$ )	38 mm (1.5 inches)
Concrete density ( $\rho_{con}$ )	2400 kg/m <sup>3</sup> (150)

	$1b_m/ft^3$ )
Hydrocarbon density ( $\rho_{f1}$ )	800 $kg/m^3$ (50 $1b_m/ft^3$ )
Length of span (L)	40 m (131 ft)
Water depth (d)	20 m (66 ft)
Height of span above sea bed (Z)	2 m (6.5 ft)
Inertia coefficient ( $C_m$ )	2.5
Drag coefficient ( $C_D$ )	1.5

When the fatigue damage incurred during the twenty minute period was extrapolated to one year by assuming that the particular record persisted for the entire year the following fatigue life was determined for each record from the time-history analysis.

Wave record	1	2	3	4	5	6
$H_s$ (m)	2.0	2.15	2.59	2.44	2.16	3.19
Fatigue Life (years)	8187	5048	515	214	1284	14

The value for the fatigue life yielded in this manner is only representative of the actual fatigue life in so far as the particular sea state chosen is representative of the wave climate averaged over one year. However, if the twenty minute wave record were analyzed statistically then there appears the probability of encountering larger waves and thus higher stress ranges than actually detected during the twenty minute time-domain analysis. Fatigue life results for each record assuming a statistical analysis of the twenty minute wave record are now:

Wave record	1	2	3	4	5	6
$H_s$ (m)	2.0	2.15	2.59	2.44	2.16	3.19
Fatigue life (years)	2320	1690	1750	453	1150	18

The fatigue life predictions by the spectral method are presented for the actual wave spectrum, the P-M spectrum, the modified P-M spectrum and the JONSWAP spectrum.

Wave record	1	2	3	4	5	6
$H_s$ (m)	2.0	2.15	2.59	2.44	2.16	3.19
Fatigue life (years)						
Actual Spectrum	2085	1561	2300	670	1573	47
P-M	7868	3350	420	795	3175	45
Modified P-M	2130	1295	4598	578	1687	46
JONSWAP	1628	860	160	269	799	40

It is shown that a particular empirical formulation for wave spectrum performs acceptably in a spectral fatigue analysis when it acceptably matches the actual spectrum. Fatigue life predictions by the spectral method are comparable when actual wave spectrum is employed.

#### 5.0 CONCLUSIONS

Extensive wave record analysis would predict fatigue life by deterministic methods. This is expensive, often not possible and not necessary.

Segmented wave records provide sufficient data for an acceptably accurate fatigue life analysis by deterministic methods. This is still costly.

Spectral techniques, when applied using the actual wave spectrum are efficient and correlate reasonably well with the deterministic evaluation.

Submarine pipelines subjected to seas with significant wave heights less than 2.0 m (6.5 feet) need not be analyzed for fatigue failure.

Analysis of only six-twenty minute wave records predicts fatigue failure from 14 to 47 years. This is a matter of concern.

#### REFERENCES

1. Alexander, H. C., Warner, J. L. and Allen, P. L., "Fatigue Considerations for Offshore Pipelines," Second Offshore Mechanics and Arctic Engineering Symposium, Houston, Texas, 1983.
2. Borgman, L. E., "The Spectral Density for Ocean Wave Forces," Technical Report H-9-8, Hydraulic Engineering Laboratory, Univ. of California, Berkeley, 1965.
3. Herbich, J. B., "Wave-Induced Scour Around Offshore Pipelines," Offshore Technology Conference, OTC Paper 2968, Houston Texas, 1977.
4. Miner, M. A., "Cumulative Damage in Fatigue," Journal of Applied Mechanics, American Society of Mechanical Engineers, Vol. 12, 1945.
5. Mogbo, N. C., Jirsa, T. D. and Wilhort, J. C., "Effective Stiffness of Concrete Coated Line Pipe," Petroleum and Mechanical Engineering with Under Water Technology Conference, Houston, Texas, 1971.
6. Morison, J. R., O'Brien, M. P., Johnson, J. W., and Schaaf, S. A.,

"The Force Exerted by Surface Waves on Pipes," Transactions of the American Institute of Mining and Metallurgical Engineers, Vol. 189, 1950.

7. Palmgren, A. "Die Lebensdauer Von Kugellagern," VDI ZEIT, VOL. 68, 1924.
8. Pierson, W. J. and Moskowitz, L., "A Proposed Spectral Form for Fully Developed Wind Seas Based on the Similarity theory of Kitaigorodski," Journal of Geophysical Research, Vol. 69, 1964.
9. Strating, John, "A Survey of Pipelines in the North Sea: Incidents during Installation, Testing, and Operation," Offshore Technology Conference, OTC Paper 4069, 1981.

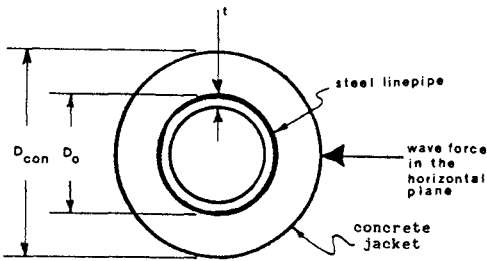


Figure 1. Concrete Jacketed Pipeline

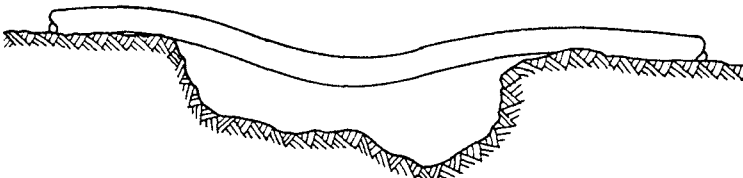


Figure 2. Free-Spanning Pipeline

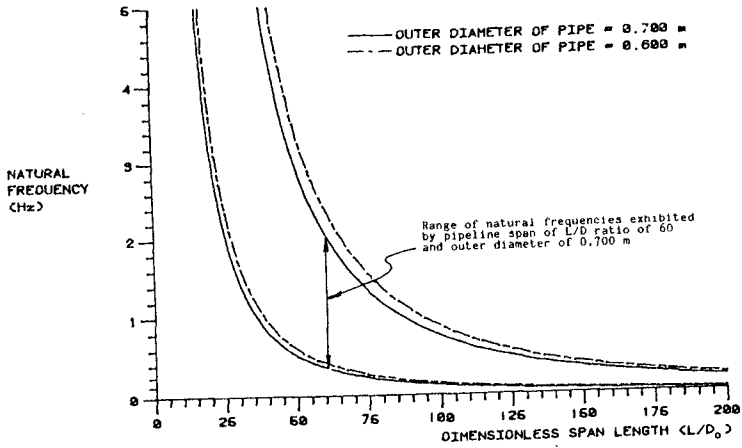


Figure 3. Natural Frequency of Vibration

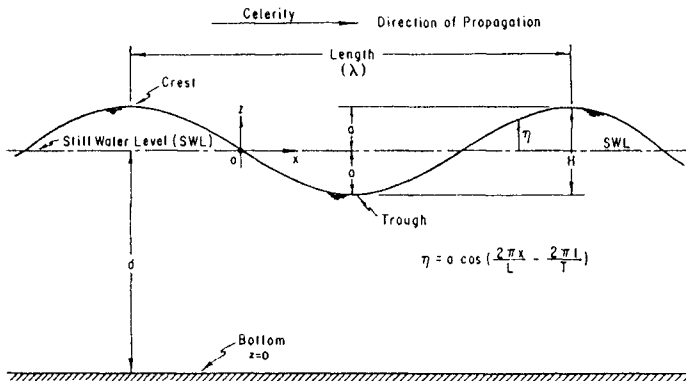


Figure 4. Airy Theory Wave Description

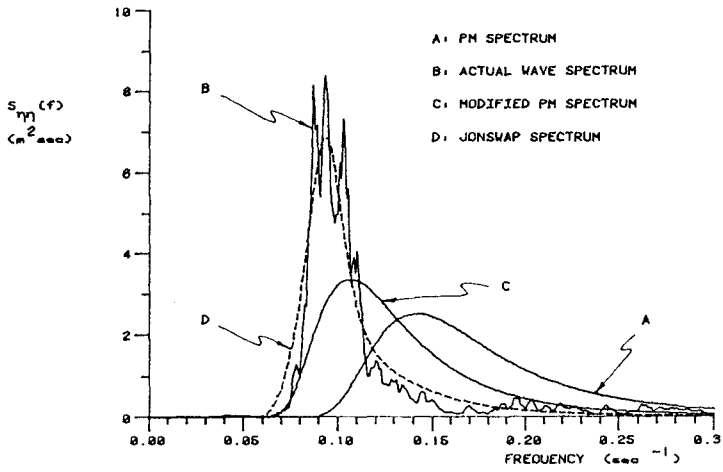


Figure 5. Water Surface Elevation Spectral Density

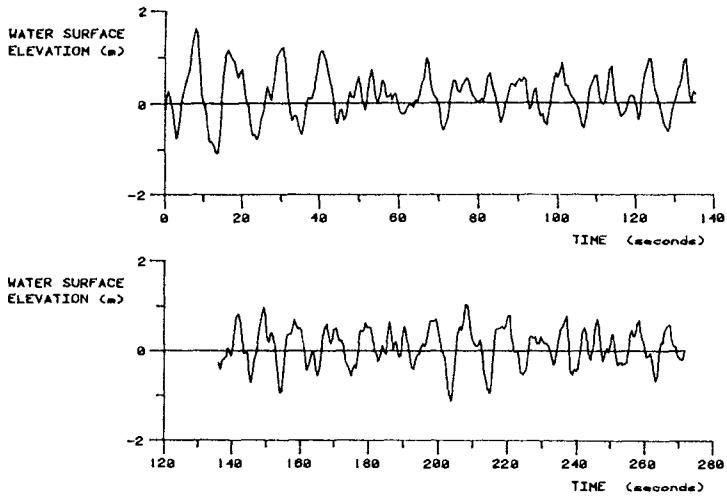


Figure 6. Water Surface Elevation Station 144

## CHAPTER ONE HUNDRED EIGHTY FOUR

### The use of sand in breakwater design

ir. L.V. Van Damme \*  
ir. P.A. Kerckaert \*  
ir. R.L. Carpentier \*\*  
ir. J.N. De Rouck \*\*\*  
ir. A. Bernard \*\*\*\*

#### Abstract

The design scheme of the Zeebrugge Outer Harbour, Belgium, consists of two breakwaters protruding into the sea as far as 1,750 m beyond the existing môle or 3,000 m out from the coastline. The west outer breakwater is 4,280 m long, the east breakwater runs 4,030 m out from the sea-wall. The east outer harbour will accommodate terminals for liquid bulk products such as LNG. The west outer harbour will provide space to install two harbour basins to suit general cargo, hazardous cargo, container and ferry traffic.

In the paper emphasis is put on the use of sand in the design of the breakwaters, firstly as part of the foundation by replacing the little resistant top layers by dumped sand, and secondly as part of the core, by dumping sand above the original sea-bottom. In as far as proposed criteria were not fulfilled, the dumped sand had to be compacted. Two methods are discussed : compaction by vibrating needles and compaction using explosives.

#### 1. INTRODUCTION

The construction of the existing port of Zeebrugge has been a royal decision pronounced by H.M. King Leopold II in 1881. Almost a century later, in 1970, the Belgian Government decided to build a new inner harbour and finally in 1976 the decision was taken to the extension of the outer harbour. The outer harbour should provide a protection for the access channel to the new inner harbour. Moreover the outer harbour was necessary to accommodate the national LNG-terminal.

\* Ministry of Public Works, Coastal Department, Ostend, Belgium.

\*\* Belgian Geotechnical Institute, Zwijnaarde, Belgium.

\*\*\* Harbour and Engineering Consultants, HAECON NV, Ghent, Belgium

\*\*\*\*Joint Venture Zeebouw-Zeezand, Knokke-Heist, Belgium.



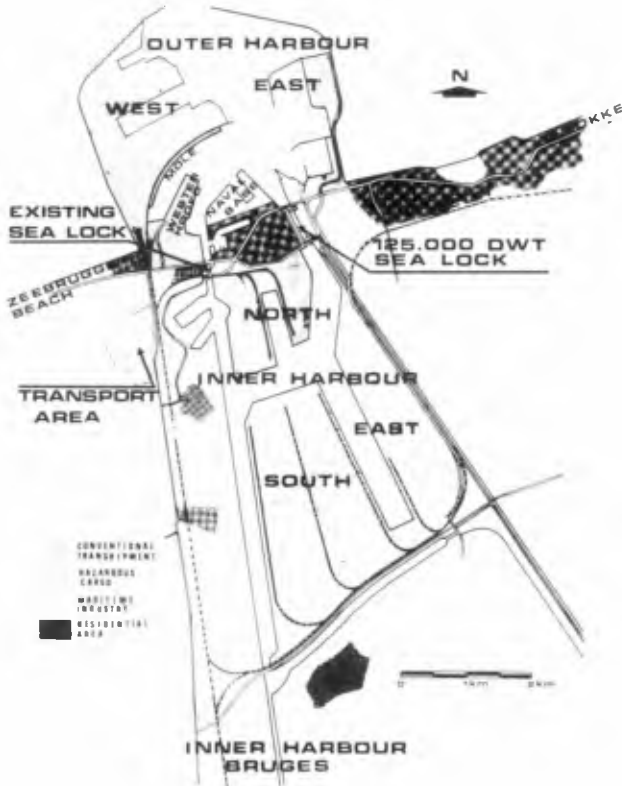


Fig. 1 : general layout of the Zeebrugge Port Extension Scheme

The masterplan finally adopted provides 3,370 ha sub-divided as follows (fig. 1) :

- outer harbour, including the existing port	1,165 ha
- inner harbour	1,705 ha
- port area of Bruges	450 ha
- transport area	50 ha.

The design scheme of the outer harbour consists mainly of two breakwaters protruding into the sea as far as 1,750 m beyond the existing môle.

The breakwaters are from the rubble-mound type. The west outer harbour breakwater is 4,280 m long. The east breakwater runs 4,030 m out from the sea-wall (fig. 2). The east outer harbour will accommodate terminals for liquid bulk products, such as LNG. A LNG-terminal is at present under construction and will be operational mid 1987. The west outer harbour will provide space to install two harbour basins to suit hazardous cargo, general cargo, container and ferry traffic.

## 2. DESIGN OF THE BREAKWATERS

The design of the breakwaters has been discussed in a paper on the Coastal Engineering Conference in Cape Town.

By developing the design the rubble-mound breakwater has been judged to be the best viable alternative taking into account costs, technical risks, construction problems and flexibility by changing environmental conditions.

An important economization in the design was the use of sand in the breakwater as soil replacement and as raised foundation.

Indeed, because the existing and future navigation channels to the harbour have to be deepened, some 30 million m<sup>3</sup> of relatively coarse sea-sand was available.

The quarry stone is won at distances of 100 km to 200 km off Zeebrugge and is rather expensive. So every possible substitution of quarry stone by sea-sand was an economical operation.

Technically the design with soil replacement has been assessed by evaluating the alternative of a breakwater built directly on the existing sea-bed, where the overall stability is given by equilibrium embankments at both sides.

## 3. ENVIRONMENTAL DESIGN CONDITIONS

### 3.1. Bottom depth

The bottom depth in the alignment of the outer harbour breakwaters ranges fairly between Z - 5.00 and Z - 7.00 (chart datum Z = mean low low water spring + 0.08).

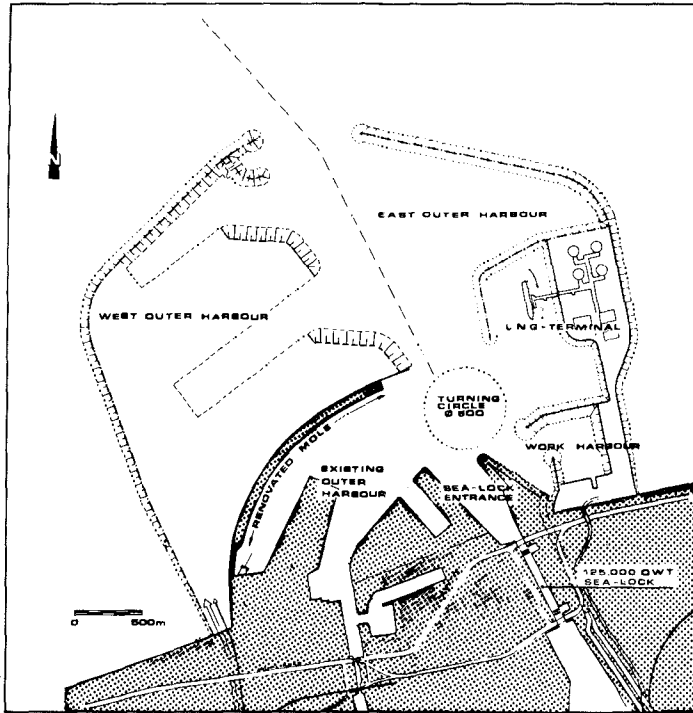


Fig. 2 : layout Masterplan Zeebrugge Outer Harbour

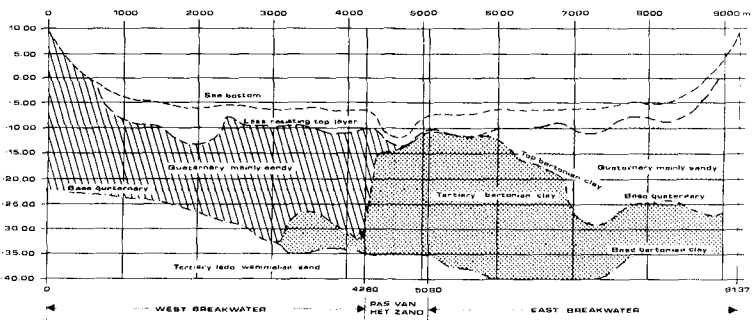


Fig. 3 : geological profile outer harbour breakwater alignment

### 3.2. Tidal conditions

The tide is semi-diurnal with levels ranging from amplitudes of 4.30 m at mean spring tide to 2.80 m at mean neap tide. The meteorological set-up is up to 2.45 m in the defined design period and probability of exceedance. The tidal currents at the final breakwater alignment will be (at surface) 1.2 m/s to 2.00 m/s at spring flood tide and 1.0 m/s to 1.6 m/s at spring ebb tide.

### 3.3. Soil conditions

The new outer harbour at Zeebrugge is located in the Scheldt Estuary which is characterized by a very heterogeneous soil composition of the top layers. In behalf of the construction of the new outer harbour a very extensive site investigation program consisting of continuous seismic profiling, CPT tests type M4 and borings with undisturbed sampling and laboratory tests is performed.

A geological profile along the axis of the breakwaters, resulting from the performed site investigation, is shown in fig. 3.

At the location of the new harbour the quaternary cover consists of loose sands and soft clays to a depth of about 4 to 6 m, underlain by a medium dense to dense sand layer. In the north eastern part of the new outer harbour the dense sand layer is not present and the top loose sands and soft clays are immediately resting on a stiff tertiary clay layer (Bartonian Clay).

The layer of soft clay and loose sand has cone resistances ranging between 0 and 1.5 MN/m<sup>2</sup>.

## 4. SAND USED AS PART OF THE BREAKWATER

### 4.1. As part of the foundation : soil replacement

Over large lengths of the breakwaters the bearing capacity of the surface layers was insufficient.

Only locally it was possible to construct the breakwaters directly on the natural soil layers on condition to provide a heavy toe construction.

Based on technical and economical considerations a soil replacement was decided over about 8 km of the breakwaters. The top loose sands and soft clays are dredged by large sea-going cutter suction dredgers and hopper suction dredgers and are replaced by relatively coarse sea-sand won in the existing and future navigation channels to the harbour. The mean diameter of the dumped sand is about 170 to 300  $\mu$ m. The cross-section of the dredged trench with a width of about 100 m is shown in fig. 4.

It is generally known that by the execution of a soil replacement by dredging and filling a trench, a transitional layer occurs at the bottom of the dredged trench. Special precautions had to be taken to

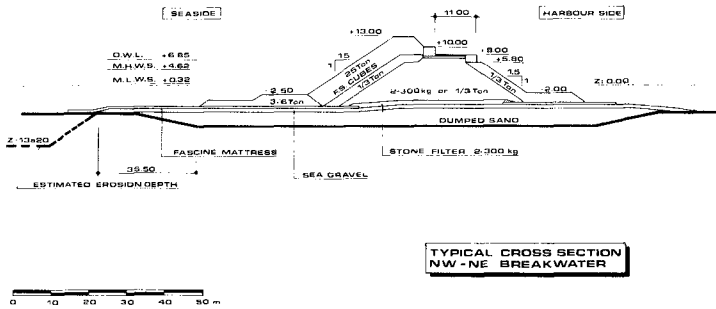


Fig. 4 : typical cross-section NW-NE breakwater

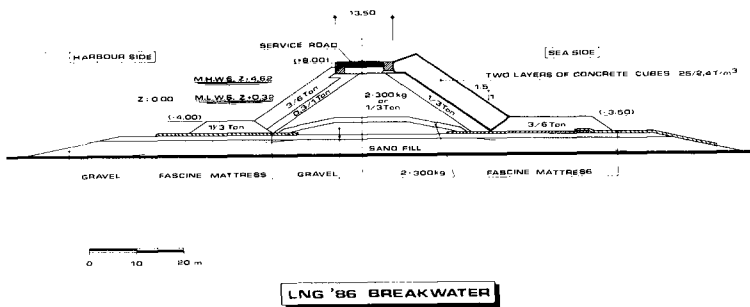


Fig. 5 : typical cross-section LNG '86-breakwater

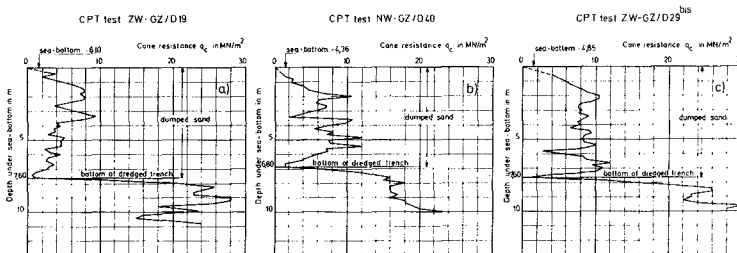


Fig. 6 : results of 3 CPT tests performed in the dumped sand

minimize the extent and thickness of that layer. In addition to that phenomenon, at Zeebrugge a supplementary supply of mud in the dredged trench is caused by waves and strong tidal currents. In order to minimize the sedimentation of mud in the dredged trench, immediately after preparing a compartment with a length of about 150 to 250 m, the sand was dumped at a quick rate with hopper suction dredgers.

The sand dumping was done with advancing slope in order to push forward the eventual mud sediments in the direction of the open part of the trench, where the mud was sucked by the hopper dredger after completing its dumping activity (the so-called cleaning phase).

The theoretical bottom line of the trench could be reached very smoothly. The deviation in depth varied between 0 and 1.00 m. The trench slopes varied between 1:10 to 1:15 for hopper suction dredgers and between 1:4 to 1:6 for cutter suction dredgers. In the case of hopper suction dredgers, the transition layer consisting of silty mud at the bottom of the excavated trench was less pronounced.

In order to reduce the cost of the superstructure of the breakwaters, the sand was dumped as high as possible, on an average about 1 m above the original sea-bottom. This was only possible by using hopper suction dredgers with slidebottomdoors and split-hopper trailer dredgers. In order to limit the loss of dumped sand by the tide-run the sand was covered as soon as possible with about 1 m of unscreened sea-gravel.

The controlled dumping of the sand was executed without any mooring. High accuracy in positioning could be reached especially by using hoppers equipped with bow thrusts or propellers.

#### 4.2. As part of the core : raised foundation

In the zone of the LNG-breakwater, where the soft and loose top soil layers were dredged for the exploitation of the existing harbour, sand was dumped immediately on the sea-bed over a height of about 5 m in order to reduce the quantity of quarry stone of the breakwater. The sand was on both sides protected with gravel banks (fig. 5).

### 5. SOIL IMPROVEMENT

#### 5.1. Mechanical characteristics of the dumped sand

To control the quality of the soil replacement, CPT tests type M4 are performed at regular distances in the soil replacement areas. In fig. 6 the results of 3 CPT tests are given as an example. On each CPT diagram of fig. 6 the bottom of the dredged trench is indicated. Although precautions were taken to minimize the quantity of mud at the bottom of the trench before dumping the sand, it can be deduced from the results of the CPT tests that this could not be prevented completely. In each diagram of fig. 6, a thin layer with relatively small cone resistances can be distinguished at the bottom of the previously dredged trench, indicating the presence of a relatively thin layer of silty or clayey sand. In general however, from a depth of about 1 or

2m underneath the top of the dumped sand layer, the cone resistance in the dumped sand layer reaches values of about 6 to 10 MN/m<sup>2</sup>, or even more. The gradual increase of the cone resistance in the upper 1 to 4m of the dumped sand is to be attributed to the effect of depth.

The design criteria of the quality of the dumped sand were made bearing in mind that liquefaction of the dumped sand foundation of the breakwaters was not admitted.

Based on practical experience with natural soil layers and with hydraulic sand-fills on land, and considering CPT tests type M4 with measurements of the cone resistance every 20 cm, the following criteria were put forward for the evaluation of the quality of the dumped sand :

- underneath the critical depth in the CPT test, the mean cone resistance over any meter of depth must be higher than 5 MN/m<sup>2</sup> :  $q_{c,mean} > 5 \text{ MN/m}^2$  ;
- over any meter of depth, at most 2 values of the cone resistance may be smaller than 4 MN/m<sup>2</sup>.

Answering to the criteria was checked by one CPT test M4 per area of about 4000 m<sup>2</sup>.

Considering for instance the CPT test diagrams of fig. 6 :

- at the vertical of the CPT test ZW-GZ/D29 of fig 6.c the dumped sand layer has a thickness of 7.60 m. At the bottom of the backfilled trench only one relatively small value of the cone resistance is found indicating the presence of a thin clayey sand layer. Up to a depth of 2.00 m underneath the sea-bottom the cone resistance increases nearly linearly with depth and reaches values ranging between about 7 MN/m<sup>2</sup> and about 10 MN/m<sup>2</sup>. Only at a depth of 5.80 m one value of the cone resistance smaller than 4 MN/m<sup>2</sup> is measured. The above-mentioned evaluation criteria are thus fulfilled over the whole depth of the dumped sand layer.
- At the vertical of the CPT test NW-GZ/D40 of fig. 6.b the dumped sand layer has a thickness of 6.80 m. At the bottom of the backfilled trench a layer with relatively small cone resistance is found over a thickness of about 0.40 m. Apart from that layer only at a depth of 3.40 m one value of the cone resistance is smaller than 4 MN/m<sup>2</sup> and the evaluation criteria can be considered as fulfilled.
- At the vertical of the CPT test ZW-GZ/D19 of fig. 6.a the dumped sand layer has a thickness of 7.60 m. At the bottom of the backfilled trench a layer with relatively small cone resistances is found over a thickness of about 0.40 m. The evaluation criteria are fulfilled up to a depth of 3.80 m. From that depth and up to the bottom of the trench the criteria are not fulfilled. In as far as the criteria were not fulfilled, the dumped sand had to be compacted.

Handling the criterion for density control, compaction was only necessary over a length of about 25 % of the breakwaters where dumped sand has been used.

### 5.2. Deep compaction using vibrating needles

At Zeebrugge a compaction in depth based on vertical vibration is applied using a patented vibration probe constituted of three steel plates welded together with a cross-section of a three pronged star, hence the name "starprofile". The probe is hung in an electric or hydraulic vibrator block and is lowered into the dumped sand from a jack-up platform by means of a heavy crane. The energy of the vertically vibrating probe is transferred to the soil mainly through a series of ribs working as individual pounders (fig. 7). The vibrating probe is introduced in the ground to a depth of about 2m into the natural soil layers underneath the bottom of the filled trench.

Based on experience a vibration time of 15 minutes per "compaction prick" has been used. The distance between the compaction centres on a triangular pattern was determined depending on the results of the CPT tests performed before compaction, and on the cone resistance to be obtained in the dumped sand after compaction.

For the compaction of the dumped sand foundation layer of the northern breakwater of the Workharbour, compaction grids of one prick per 4 m<sup>2</sup>, one prick per 6 m<sup>2</sup> and one prick per 8 m<sup>2</sup> have been used. Fig. 8 shows the results of CPT tests performed before and after compaction, according to the different spacings of the compaction centres on a triangular pattern. The post-compaction tests were positioned in the centre of the treatment pattern remote from the compaction centres. Fig. 8.a gives the influence on the cone resistance in the dumped sand layer of one compaction prick per area of 8 m<sup>2</sup>. Fig. 8.b gives the influence of one prick per area of 6 m<sup>2</sup> and fig. 8.c of one prick per area of 4 m<sup>2</sup>. From fig. 8 it can be deduced that the influence of the compaction on the cone resistance in the dumped sand layer is higher the smaller the spacing of the compaction centres. It may be remarked that the transitional layer at the bottom of the previously dredged trench could not be eliminated completely by compaction, which is to be attributed to the clay content of that layer.

A diagrammatic picture of CPT tests performed before and after compaction is given in fig. 9. Before compaction, due to the influence of depth, the cone resistance in the dumped sand layer increases nearly linearly with depth from the sea-bottom up to a depth  $z_0$  where the cone resistance reaches a value  $q_{c,z_0}$ .

After compaction the cone resistance increases more rapidly with depth from the sea-bottom up to approximately the same depth  $z_0$ , but reaches a higher value  $q_{c,z_0}^n$  at that depth.



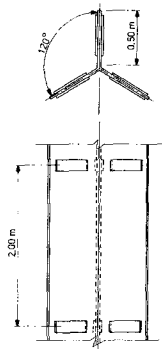


Fig. 7 : vertically vibrating probe

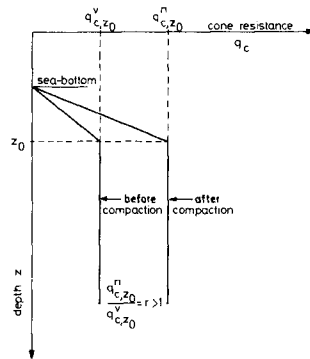


Fig. 9 : diagrammatic picture of CPT tests before and after compaction

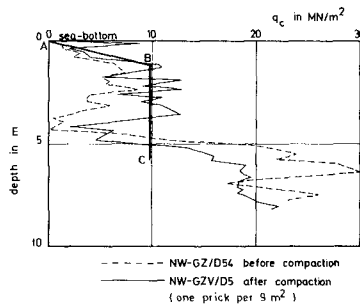


Fig. 10 : comparison of predicted and measured cone resistance profile after compaction

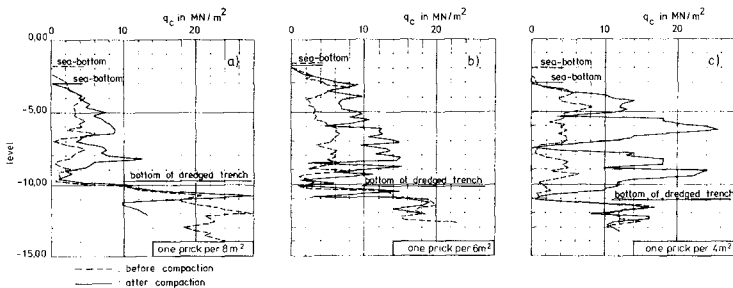


Fig. 8 : results of CPT tests before and after compaction

The ratio of the cone resistance at the depth  $z_0$  after and before compaction is given by

$$r = \frac{q_{c,z_0}^n}{q_{c,z_0}^v} > 1$$

From a systematic analysis of 14 pairs of CPT tests performed in a zone with a compaction grid of one prick per 6 m<sup>2</sup> a ratio  $r$  could be derived, ranging between 3.3 and 1.5, with a central value  $r_6 = 2.4$ . From 11 pairs of CPT tests performed in a zone with a compaction grid of one prick per 9 m<sup>2</sup> a ratio  $r$ , ranging between 2.7 and 1.2, with a central value  $r_9 = 1.7$  was deduced. From 16 pairs of CPT tests performed in a zone with a compaction grid of one prick per 12 m<sup>2</sup> a ratio  $r$ , ranging between 2.9 and 1.1, with a central value  $r_{12} = 1.5$  was obtained. The values of  $r_6$ ,  $r_9$  and  $r_{12}$  reflect the effectiveness of the different compaction grids. Having at disposal the results of CPT tests which doesn't fulfil the quality criteria, a rough estimation of the cone resistance profile after compaction can thus be made and thus a choice of the compaction grid.

In fig. 10 the schematic cone resistance profile ABC, predicted from the results of CPT test NW-GZ/D54 for a compaction grid of 1 prick per 9 m<sup>2</sup>, is compared with the results of CPT test NW-GZ/D5, performed after compaction. The prediction can be considered as fairly good.

### 5.3. Deep compaction using explosives

Although the deep compaction with the vibrating probe has given satisfactory results, a program was set up to examine the feasibility of in situ densification using explosives.

#### 5.3.1. Design of the blast program

-----

The impact of the explosive charge causes momentary liquefaction of loose saturated sands which subsequently adopt a more dense, stable structure under the weight of the overburden and increased drainage. Literature presents empirical relationships for single concentrated charges relating size of charge, depth of charge and spacing of blast holes based on extensive field and laboratory test data. However, no clear information is presented in the literature about size and depth of two concentrated charges placed at different depths in the same blast hole.

The depth of the lower charge was selected considering that the upper layer was liquefied by the upper charge and thus could be neglected when the lower charge was detonated; in this reasoning the lower charge was detonated within one to two seconds after the detonation of the upper charge.

The sequence of blasting was planned bearing in mind that successive blasts are more effective than a single heavy blast or different small blasts at the same moment. For the time interval between successive blasts at least 4 hours was chosen as suggested in literature.

### 5.3.2. Set-up of charges

-----

#### 5.3.2.1. Explosive

A high explosive "Blastogel" with a density of 1.4 kg/dm<sup>3</sup>, primarily composed of nitroglycerine (50-60 %) and containing no ammoniumnitrate (NH<sub>4</sub>NO<sub>3</sub>) was used. This explosive is initially waterresistant but decomposes under water in about one month. An eventually not detonated charge couldn't present a latent danger for the achieved breakwater. Blastogel has an equivalence factor of 1.0915 with regard to TNT. Blastogel was delivered in cylindrical blocks  $\varnothing$  85 mm of 5 kg mass.

#### 5.3.2.2. Firing system

As the electrical firing system and the use of detonating cord were excluded for underwater blasting, a non-electrical firing system NONEL was chosen, being waterresistant and presenting sufficient strength against water currents and accidental pull.

#### 5.3.2.3. Charges

The upper and lower charges of one vertical were prefabricated on the deck of the drilling platform. A scheme of the building up is given in fig. 11. The upper charge weights 4.5 kg, the lower charge 5.5 kg.

#### 5.3.2.4. Round

For sake of security each charge was fitted with two detonators NONEL with suitable delay. The four NONEL tubes of the upper and lower charge of one vertical were connected together above the waterlevel and bundled with the NONEL tubes of the charges placed in the other boreholes of the same blasting series. An electric detonator was then coupled to the bundle of NONEL tubes and was detonated from a blasting initiator placed on the deck of the drilling platform.

### 5.3.3. Blasting program

-----

The blasting program was carried out in the foundation layers at the extremity of the north western breakwater. The jack-up platform was equipped with three jetting rigs and the platform was moved in parallel lanes in order to minimize movements of the platform anchors.

The charge holes are jetted in parallel lines at distances of 7.5 m and the explosive charges are placed at depths of 4.5 m and 9.0 m below the sea-bottom. Blasting is executed in a triangular pattern, the charges at the corners of one triangle are detonated at least four hours after detonation of the charges of the adjacent triangle. The

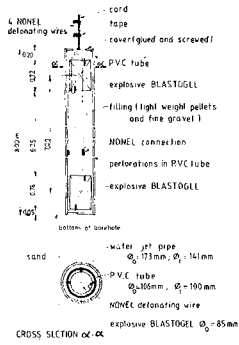


Fig. 11 : prefabricated couple of charges

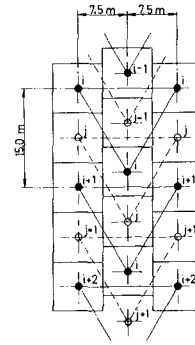


Fig. 12 : principle of arrangement

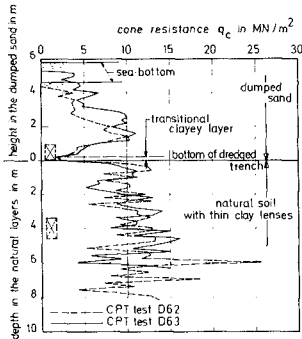


Fig. 13 : CPT tests D62 and D63

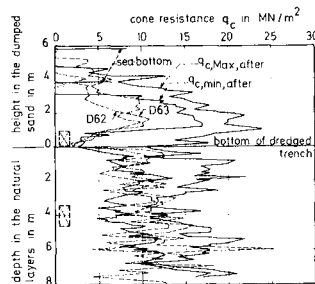


Fig. 14 : min. and max.  $q_c$  values of tests S10 to S13 after blasting with tests D62 and D63 before blasting

principle of the arrangement for the blasting is shown in fig. 12. In a first pass of the platform in a lane the charges of triangles  $i-1$ ,  $i$ ,  $i+1$ , ... are detonated consecutively ; the charges of triangles  $j-1$ ,  $j$ ,  $j+1$ , ... are detonated consecutively in a second pass of the platform in the same lane. After all charges of one lane were detonated, the platform was moved to the adjacent lane. In this way the same volume of soil was influenced by different blasts at different times.

A total surface area of about 14,000 m<sup>2</sup> was compacted over a period of fifteen days. Compaction was carried out over a thickness of layer of about 11 m using about 15.3 g of Blastogel per m<sup>3</sup> of soil. In the compacted area 242 borings with a total length of 2,180 m were carried out in waterdepths varying between 8 and 13 m, 2,300 kg of explosives were detonated.

The increase in density of the sand after blasting was evaluated by performing a number of CPT tests.

#### 5.3.4. Blast results

-----

Before starting the blast program, two CPT tests numbered D62 and D63, are performed (fig. 13).

After completion of the whole blasting program over an area of 13,612 m<sup>2</sup>, another 4 CPT tests numbered S10 to S13, were performed. In fig. 14 the maximum and minimum cone resistances of these tests are compared with the results of the two virgin tests D62 and D63. The results of the tests S10 to S13 confirmed the rather important increase of the cone resistances in the dumped sand layer. In the natural layer above the level of the lower charge, the minimum cone resistances in the tests S10 to S13 are of the same magnitude as the minimum cone resistances in the virgin tests D62 and D63 ; however, the maximum cone resistances after blasting are higher than in the tests before blasting. The thin clay lenses after blasting thus influence the minimum cone resistances as before blasting ; in the sand between the clay seams higher cone resistances are obtained after blasting.

## 6. CONCLUSIONS

- 6.1. The soil improvement technique by replacing in open sea the soft top layers by dumped sand was successfully developed.
- 6.2. Even by equal costs, the soil improvement profile still offers a more controlled construction and a foundation pad with a higher quality level. By using this profile less settlements may be expected.
- 6.3. Compaction of the dumped sand can be done as well by using a vertical vibrating probe as by using explosives.

## CHAPTER ONE HUNDRED EIGHTY FIVE

### A Review of Breakwater Development in Australia

D.N. Foster\* M.I.E. (AUST), M.A.S.C.E.

#### 1. Introduction

Prior to 1970 rubble mound breakwaters in Australia were armoured with rock or concrete rectangular prisms. Model testing was rarely undertaken. During storms some damage to the breakwaters was tolerated with repairs being undertaken as and when necessary. This procedure is still successfully used today. However since 1970 there has been a move towards designing breakwaters to minimise or eliminate maintenance and to optimise costs. This paper reviews some of the less conventional developments that have taken place over this period, with references to reports and papers for those who wish to obtain more detailed information on any of the projects.

#### 2. Sea-Wall Mascot Airport N.S.W.

The extension of Mascot airport into Botany Bay required that the perimeter be protected from wave attack. The design wave conditions were 4.6 m significant height with a depth limited upper wave height of 5.8 m in a water depth of 7.6 m. The designers were the Department of Housing and Construction. Model tests were undertaken at the Water Research Laboratory (Ref 9).

Interesting features related to the project are:

- i. Dry construction was specified. An initial bund of sand was pumped along the alignment of the seawall to above the reach of normal tides and waves. A trench was then cut through the sand bund and the seawall placed in the dry. The offshore sand was then pumped onto the reclamation area and the seawall completed to its design height. This technique worked extremely well with substantial cost savings.
- ii. Uniform placed Tribars were used as armour. The mass of the unit was 5 tonnes designed according to conventional practice. As it was known that the seawall would be constructed in the dry the benefits that might be achieved by pattern placement of the units was studied. The first pattern tested was the most dense possible (lowest porosity) with the legs of a Tribar abutting the webs of the adjacent units. Rather surprisingly (at that time), this section failed at wave heights very much less than the design wave as the legs of the Tribar could easily rotate about the webs and interlocking was lost. Model testing (Ref 9) showed that the most

\* Director, Water Research Laboratory, University of New South Wales, King Street, Manly Vale, N.S.W., 2093, Australia.

structurally stable pattern was one such that all the legs were in contact. This had the added advantage that it was the least dense (highest porosity) with a consequent cost saving in concrete and number of units to be placed. With this configuration Hudson damage coefficients in excess of 100 could be achieved. However, as failure tended to be catastrophic the pattern placement was used only as an added factor of safety and to reduce concrete and placement costs.

The seawall was constructed in 1970 and no maintenance has been required. However as a result of configuration dredging for port development (Ref 24), wave conditions at the site have been significantly reduced and the structure has not and will never be subjected to the design wave conditions. Some minor breakage of the legs of the Tribars have occurred as a result of settlement.

### 3. Seawall Banksmeadow N.S.W.

The development by the Maritime Services Board of Botany Bay as a major port for N.S.W. is described in Ref 23. An interesting feature was the use of configuration dredging to reduce wave action in the shipping lanes (Ref 24).

The development required the construction of a revetment/breakwater to provide protection to the harbour area. The design offshore wave conditions were a significant wave height of 7.8 m. Water depths at the toe of the structure varied between zero and 13.5 m and limited the height of the maximum wave. Model testing of the structure was undertaken by the Water Research Laboratory of the University of N.S.W. (Refs 6, 8, 16 and 17) and the Hydraulic Research Station Wallingford (Ref 19).

Features of interest are:

- i. The initial design was a copy of the Mascot seawall using pattern placed uniform Tribars of 2, 8 and 20 tonnes depending upon the water depth.
- ii. Construction methods were not specified and the contractor elected to undertake the work in the wet.
- iii. The pattern placement was extremely difficult to achieve as divers were required for the placement of each unit. As a consequence primary armour placement lagged behind the placement of the core and secondary armour.
- iv. Storms in May/June 1974 (Ref 10) caused major damage to the unprotected core and secondary armour. As a result the contractor was in considerable difficulty to meet his obligations and requested consideration be given to a re-design of the remainder of the breakwater using Dolosse.
- v. Model testing indicated Dolosse would be a suitable alternative armour. However, as a stockpile of Tribar units had already been

produced, a composite armour of Dolosse below water and pattern placed Tribars above water was tested and finally adopted.

- vi. Model testing indicated that in the composite design the junction between the Tribar and Dolosse units was a weak point and vulnerable to damage. It was initially thought that the best junction would be to anchor a leg of the Dolosse below the Tribar. However, this proved to be negative as movement of the Dolosse acted as a catapult to dislodge the Tribar. The best joint developed was simply a butt joint.

The prototype performance has been satisfactory. The structure has been subjected to near design wave conditions on two occasions. Some breakages of Dolosse units have occurred. A lot of this damage is towards the bed and is the result of settlement. There has been negligible damage of the Tribar armouring.

The composite armour used arose from the construction difficulties of pattern placing Tribars below water. Despite its adequate performance use of a composite section is not recommended as the junction between the units is a definite weak spot.

#### 4. Rock Breakwater Little Crassy Bay Tasmania

This rather unconventional breakwater arose from the availability of large quantities of waste rock overburden from a nearby sheelite mine. Five per cent of the rock was in the range 2 to 10 tonnes, with 95% being run of quarry less than 2 tonne.

Design wave conditions were estimated to be 10.5 m significant with a depth limited upper wave associated with a 18 m water depth.

The proposal was to push a core of run of the quarry material out to an adjacent offshore island which would act as a roundhead. The core would be allowed to pull down under wave action to form a beach on which would be placed selected 6 to 10 tonne armour rock as required. The purpose of this armour was to increase the stability of the breakwater and to reduce losses from littoral drift along the breakwater.

The initial crest width of the core was 60 m to allow for an adjustment of the face slope to 1 in 10.

The breakwater was designed by Maunsell and Partners, Consulting Engineers. Testing by the Water Research Laboratory (Ref 7) indicated that the proposal was feasible. Construction commenced in 1972 and was completed in 1974.

Construction and behaviour of the prototype is discussed in Ref 5. During construction the seaward face rapidly pulled down to a slope of 1 in 3.5. During storm action it can be expected that this will pull down to a flatter slope. Model tests indicated that the equilibrium slope of the core material (without armouring) would be between 1 in 7 and 1 in 10. However prototype experience indicates that the actual slopes may be somewhat steeper than that predicted by the model. Over



the 10 year period since its completion the breakwater has satisfactorily performed its design function.

#### 5. Rosslyn Bay Breakwater Queensland

Rosslyn Bay is a small fishing and recreational port in mid Queensland. Normal wave conditions are moderate; however, during cyclones (hurricanes, typhoons) the site is subject to design waves of significant height of 4.6 m superimposed on storm tide levels of 3 to 8.5 m on low water datum as compared to H.A.T. of 4.8 m. The high storm surge presents problems in the design of breakwaters in the lower latitudes which covers much of Australia's coastline as economics normally require a crest level subject to overtopping under extreme conditions.

The original breakwater was constructed in 1966 and suffered severe damage during Cyclone David in 1976 as a result of overtopping of the crest. A detailed account of this failure is given in Ref 14. Some notable features of the failure were:

- i. The failure was catastrophic taking place over a few hours.
- ii. After failure the structure continued to give substantial protection, significantly reducing damage to the harbour infrastructure and enabling the harbour to be used for its design function under the more common weather conditions that followed.
- iii. Model testing (Ref 11) was able to closely simulate the failure and the breakwater profile after failure.

Repairs to the breakwater were designed by Blain Bremner and Williams, Consulting Engineers. The repair made as much use of the failed breakwater as possible. The seaward face was flattened to 1 on 4 and the landward face to 1 on 2. Armour mass was increased to 5 tonne nominal and was carried over the crest and down the leeward face to allow for overtopping. The tests indicated that damage to the crest is a function of wave period and water levels as well as wave height and there was a critical combination of these variables which resulted in the highest damage. Further studies related to this aspect are given in Ref 13.

After the quarry was opened up the yield of 5 tonne rock was less than anticipated. For this reason the crest was actually armoured with 3.2 tonne modified cubes and the seaward and leeward face with a composite armour of 6 tonne rock and 3.2 tonne modified cubes which provided a dense interlocking combination which has proved very satisfactory.

Construction of the breakwater was completed in 1978 and has been subjected to several severe cyclonic storms with no significant damage.

#### 6. Breakwater and Seawall Townsville Queensland

To provide additional infrastructure to the port facilities at Townsville an area of land was to be reclaimed. The seaward face of the reclamation was to be protected against a significant wave height of

4.15 m superimposed on a storm tide level of 4.45 m corresponding to the 1 in 100 year event. The high value bulk and containerised cargoes required that the system be designed for zero overtopping.

Three alternatives were considered:

- i. A seawall along the face of the reclamation using conventional design practice.
- ii. A shore parallel offshore breakwater to provide protection to the reclamation area using conventional breakwater techniques.
- iii. A shore parallel submerged breakwater to provide protection to the reclamation area.

Economic analysis indicated that the third proposal offered cost savings of about 40 per cent over the other two. However, as all breakwater construction in Australia is undertaken using land based plant, there was difficulty in constructing such a breakwater in its final form. The failure of the Rossllyn Bay breakwater had indicated that damage to a breakwater of this type occurs in a controlled manner and that model testing could be used to simulate this damage. The concept was therefore to construct a mound of nominal 4T rock which would be allowed to reform as a submerged breakwater under the action of storm waves. The design was undertaken by Blaim Bremner and Williams, Consulting Engineers, and was model tested by the Water Research Laboratory. Details of the investigations are given in Refs 1 and 15 which demonstrated the feasibility of the proposal. Construction was undertaken in 1980. To date no significant cyclones have occurred at the site and the prototype performance can not as yet be evaluated.

#### 7. The Hanbar Unit

Many of the older breakwaters in N.S.W. have been armoured with rock or concrete rectangular prism dumped at their natural angle of repose. A commonly adopted size of the concrete units is 40 tonnes on the trunk and 60 tonnes on the head.

Along this section of coast extreme deep water significant wave heights are 8 to 10 m (May 1974, 9.5 m Ref 10; March 1978, 7.7 m with a maximum recorded wave of 16.4 m Ref 20). Under these conditions some damage to the breakwaters resulted requiring maintenance to be undertaken. Following damage to a number of breakwaters in the storms of May 1974, the N.S.W. Department of Public Works undertook an investigation into other forms of armour which might have a better performance. The restricted access, uneven slope and size of existing armour and the immediate need for patch repairs using readily available equipment, often in remote locations, suggested the need for a tippable unit. The unit finally adopted was a modification of British Transport Dock Board Tripod to simplify form work and to reduce construction costs. In Australia the unit is known as the "Hanbar". Prototype tests on both reinforced and un-reinforced units showed that when tipped on the Port Kembla breakwater they fell a distance of 7 m down the slope without breaking, and with only minor damage to the extremities. Consequently

all future units have been un-reinforced. Between 1975 and 1980, some 1,500 units have been used for repair of existing breakwaters.

Model tests by the Department of Public Works (Ref 21) indicate values of Hudson damage coefficient under depth limited breaking waves of approximately 7 for 0 to 5 per cent damage.

Since development of the Hanbar it has proved to be competitive with other units such as the Dolosse because of its relatively low construction cost, and has been used recently in seawalls at Port Kembla and Hay Point.

#### 8. Abbott Point Mole Queensland

Armouring of the mole at Abbott Point, Queensland, against a depth limited 4.3 m wave height was undertaken using the recently developed Seabee unit (Refs 2-4) at a cost significantly lower than other armour units. This unit is hexagonal in cross-section and is placed in an array. The length, mass and porosity of the unit can be varied to suit design and construction requirements. The unit was developed by Chris Brown, Consulting Engineer, and has been extensively tested by the Water Research Laboratory.

The mole was designed by MacDonald Wagner and Priddle, Consulting Engineers. The characteristics of the units adopted were Trunk (diameter 1800, length 900, porosity 36.5%, mass 2.9 tonne) and Head (diameter 1800, length 1200, porosity 36.5%, mass 3.9 tonne).

Model testing of the structure was undertaken by the Water Research Laboratory and considerable effort was made to determine the minimum acceptable standard of construction (i.e. surface condition of underlay, gaps between units, etc.). As a result of this work it was established that acceptable minimum standards of placement were 90% on the trunk and 80% on the roundhead of the theoretical maximum cover provided gaps greater than half a meter were filled with in situ concrete.

Construction was completed in 1982. The breakwater has been subjected to near design wave conditions and has performed to design expectations.

#### 9. Hay Point Tug Harbour Queensland

This breakwater is proposed to provide protection to a harbour for tugs used to berth bulk coal carriers at the Hay Point offshore coal loading terminal. At present these tugs have to operate out of MacKay some 20 km away. The design wave and storm tide conditions for the 1 in 100 year return period are 5 m significant height with a 7 second peak period superimposed on a storm tide level of 4.50 m. Offshore depth limits the maximum wave height at the structure to approximately 7 to 8 m.

The breakwater has been under consideration since 1977. The initial proposal was for a conventional breakwater armoured with a 6 to 8 tonne Dolosse (Ref 18). This proved to be too expensive and a modified design was undertaken of an overtopped structure using 12 tonne Dolosse

on a slope of 1.5:1 with a cap designed to be overtopped with cast in situ concrete blocks each of 400 tonnes in weight (Ref 22). However, the cost of the breakwater was still substantial and raised doubts of its economic viability. Further investigation of quarries in the region indicated the possibility of obtaining large quantities of rock ranging in size between 3 to 7 tonnes and a modified design was considered using a similar principal to that adopted at Little Grassy, Tasmania. The concept was to place a mound of sufficient size to allow storm waves to pull it down to a stable profile.

The breakwater was designed by Blain Bremner and Williams, Consulting Engineers, and was model tested at the Water Research Laboratory (Ref 12). Some of the interesting aspects of the tests were:

- i. Damage was much less than anticipated.
- ii. Whilst severe overtopping was expected this did not occur.
- iii. Provided the initial estimates of rock quantities from the quarry are proven, the cost will be approximately 30 per cent less than that of a conventional breakwater.

#### 10. Conclusions

Breakwater construction in Australia over the past 25 years has seen some developments which might be described as non-conventional. These have achieved improved performance and most importantly, cost savings. The paper summarises some of these developments. For further details the reader is referred to the references, most of which can be obtained on request from the Water Research Laboratory of The University of New South Wales.

## REFERENCES

- [1] Bremner, W., Foster, D.N., Miller, C.A. and Wallace, B.C. "The design concept of dual breakwaters and its application to Townsville, Australia". Proc. 17th Internat. Conf. on Coastal Engineering, Sydney, 1980.
- [2] Brown, C.T. "Armour units - random mass or disciplined array". A.S.C.E. Coastal Structures, Alexandria, March, 1979.
- [3] Brown, C.T. "Blanket theory and low cost revetments". A.S.C.E. 16th Internat. Conf. on Coastal Engineering, Hamburg, August 1978.
- [4] Brown, C.T. "Seabees, a third generation armour unit". 7th Internat. Harbour Congress, Antwerp, Royal Society for Flemish Engineers, May 1978.
- [5] Burren, K.R. "Investigation, design and construction of a harbour on King Island Tasmania". Institution of Engineers, Aust., Civil Eng. Trans. Vol. CE17 No. 1, 1975.
- [6] Foster, D.N. "Banksmeadow breakwater - stability of a combined face of uniform random and pattern placed tribar armouring". Uni. of N.S.W., Water Research Lab., Tech. Report 73/1, 1973.
- [7] Foster, D.N. "Investigation of quarry run breakwater - Little Grassy, King Island". Uni. of N.S.W., Water Research Lab. Tech. Report 69/20, 1969.
- [8] Foster, D.N. and Adams, J. "Banksmeadow revetment Botany Bay - tests on the stability of toe cubes". Uni. of N.S.W., Water Research Lab., Tech. Report 75/12, 1975.
- [9] Foster, D.N. and Dudgeon, C.R. "Model studies of seawall for Mascot runway extensions". Uni. of N.S.W., Water Research Lab., Tech. Report 70/6, 1970.
- [10] Foster, D.N., Gordon, A.D. and Lawson, N.V. "The storms of May-June 1974 Sydney N.S.W." Proc. Second Conf. Coastal & Ocean Eng., Inst. of Eng. August 1975.
- [11] Foster, D.N. and Haradasa, D.K. "Rosslyn Bay boat harbour breakwater model studies". Uni. of N.S.W., Water Research Lab., Tech. Report 77/6, 1977.
- [12] Foster, D.N., Haradasa, D.K.C. and Foster, S.J. "Half tide tug harbour, hydraulic model studies". Uni. of N.S.W., Water Research Lab., Tech. Report 83/15, 1983.
- [13] Foster, D.N. and Khan, S. "Stability of overtopped rock breakwaters". Uni. of N.S.W., Water Research Lab., Research Report 161, 1984.

- [14] Foster, D.N., McCrath, B.L., and Bremner, W. "Rosslyn Bay breakwater, Queensland, Australia." Proc. 16th Internat. Conf. on Coastal Engineering, Hamburg, 1978.
- [15] Foster, D.N., Miller, C.A. and Wallace, B.C. "Townsville harbour eastern breakwater extension hydraulic model studies". Uni. of N.S.W., Water Research Lab., Tech. Report 80/1, 1980.
- [16] Foster, D.N. and Nagle, B. "Banksmeadow revetment Botany Bay - stability of Dolosse and composite Tribar and Dolosse armour". Uni. of N.S.W., Water Research Lab., Tech. Report 74/10, 1974.
- [17] Gordon, A.D. "Breakwater stability stage 1 revetment, Botany Bay" Uni. of N.S.W., Water Research Lab. Tech. Report 72/11, 1972.
- [18] Higgs, K. and Foster, D.N. "Model testing of the eastern breakwater Hay Point tug harbour". Uni. of N.S.W., Water Research Lab. Tech. Report 77/12, 1977.
- [19] Hydraulic Research Station, Wallingford. "Banksmeadow breakwater - model tests on stability of Tribar armouring". Report No. EX538, March 1971.
- [20] Lawson, N.V. "Wave climate around Australia". Water Research Foundation Symposium, Energy and Economics of Water Utilization, Wollongong, Feb. 1983.
- [21] N.S.W. Public Works Department Hydraulic Laboratory. "Port Kembla sea wall model". Manly Vale Laboratory Report No. 272, Sept. 1979.
- [22] Queensland Government Hydraulic Laboratory. "Hay Point tug harbour structural model of an overtopped breakwater". Deakon Lab., Dept. of Harbours & Marine Report M11/1, June 1981.
- [23] Silva, E.J. "Hydraulic investigations associated with the development of port facilities in Botany Bay, Sydney". Australia and New Zealand Association for the Advancement of Science 44th Congress Sydney, Aug. 1972.
- [24] Wallace, J.M. "Control of wave action by configuration dredging at the entrance to Botany Bay, Sydney, Australia". 1977 P.T.A.N.C. Congress Leningrad.

## CHAPTER ONE HUNDRED EIGHTY SIX

### BREAKWATER ARMOR DISPLACEMENT THRESHOLDS: A POSSIBLE CORRELATION WITH CUMULATIVE WAVE ENERGY

Daniel L. Behnke, A.M. ASCE<sup>1</sup>  
Fredric Raichlen, F. ASCE<sup>2</sup>

#### Abstract

An extensive program of stability experiments in a highly detailed three-dimensional model has recently been completed to define a reconstruction technique for a damaged breakwater (Lillevang, Raichlen, Cox, and Behnke, 1984). Tests were conducted with both regular waves and irregular waves from various directions incident upon the breakwater. In comparison of the results of the regular wave tests to those of the irregular wave tests, a relation appeared to exist between breakwater damage and the accumulated energy to which the structure had been exposed. The energy delivered per wave is defined, as an approximation, as relating to the product of  $H^2$  and  $L$ , where  $H$  is the significant height of a train of irregular waves and  $L$  is the wave length at a selected depth, calculated according to small amplitude wave theory using a wave period corresponding to the peak energy of the spectrum. As applied in regular wave testing,  $H$  is the uniform wave height and  $L$  is that associated with the period of the simple wave train. The damage in the model due to regular waves and that caused by irregular waves has been related through the use of the cumulative wave energy contained in those waves which have an energy greater than a threshold value for the breakwater.

#### Introduction

To properly design a breakwater and its armor and to evaluate any damage that a structure has received, it is necessary to characterize the wave conditions in a meaningful way. Most often breakwater armor stability has been evaluated using hydraulic models exposed to regular waves. More recently irregular waves have been used in the laboratory to simulate the actual wave climate to which the breakwater would be exposed. Usually the irregular waves which are used for design purposes are characterized by an energy density spectrum. The spectrum may be described in general terms by using: a statistical measure of the wave height, the period of the maximum energy density of the spectrum, and a description of the shape of the spectrum. There are other

<sup>1</sup> Consulting Engineer, ARCTEC, Incorporated, Columbia, MD, U.S.A.

<sup>2</sup> Professor of Civil Engineering, W. M. Keck Laboratory of Hydraulics and Water Resources, California Institute of Technology, Pasadena, CA, U.S.A.

variables which may be important for a design, such as the wave direction, the storm duration, the stillwater level, and the wave groupiness. Each of these descriptors of the irregular wave train can change with time during a particular storm, and they can also occur in different combination over the lifetime of a structure. Therefore, the design wave conditions for a structure must be defined by a combination of wave characteristics which will be the most serious to the particular breakwater under consideration.

For breakwater armor experiments which are conducted with regular waves, the degree of damage of the breakwater is usually a function of the number of waves of a given wave height to which the breakwater is exposed. In other words, a group of waves of a given height and duration may slightly damage a structure whereas an increase in duration may destroy it. In most tests which are conducted, the experimental conditions include a range of wave periods and stillwater levels to more realistically account for changes in the prototype wave climate in addition to wave duration. The design wave height which is used in regular wave tests often is defined in terms of a statistical height related to the ocean waves such as the significant wave, i.e., the average of the highest one-third waves in a wave train, or some other higher wave average; the latter might be used to incorporate a higher degree of conservatism into the design. The shape of the armor pieces, their weight, and the seaward and landward slopes of the breakwater are chosen based on the model results so that under exposure to regular waves of a given height an acceptable amount of damage occurs. This may range from no movement of units to a significant displacement of armor units depending upon economics and the function of the structure.

In any event, the height of the regular waves which would be used in laboratory model tests generally is "numerically equal" to a statistically defined design wave height. (The term "numerically equal" is used to emphasize the difference between a wave height which characterizes a train of irregular waves and the height of waves in a periodic train). One has to be careful in this definition because, for example, a group of regular waves with height  $H$  has twice the energy of a group of irregular waves where heights follow a Rayleigh distribution with a significant wave height equal to  $H$ . In addition, it is recalled that the irregular wave train could include waves more than twice the height of the significant wave as well as waves which are much smaller. Therefore, a priori, it is not clear how the results of breakwater model tests with regular waves can be used to define the design where the actual breakwater will be exposed to a train of complex waves.

Many of the questions which have been raised could be avoided by the use of irregular waves in two-dimensional and three-dimensional models of coastal structures. This method of testing is becoming increasingly common and important since a variety of wave spectra can be used to simulate the design wave conditions at a site. The spectra can be varied throughout a test program to reproduce the growth and decay of waves from a storm, and the shape of a spectrum and the frequency of the maximum energy can be varied also to examine these effects on the



stability of the breakwater. A major difficulty with this technique is the number of experiments required to cover the possible combinations of wave heights, periods, and growth and decay characteristics which would be combined to give the worst conditions. In three-dimensional models additional experiments would be required to evaluate the effect of wave direction.

The resistance of breakwater armor to wave damage has been related to the wave height without regard for the wave period in the commonly used equations of Irribarren and Nogales (1953) and Hudson (1959). The basis for these equations has been described by Raichlen (1975) where the simplifications made in their developments are summarized. More recently experimental data have demonstrated the effect of wave period or wave length on armor stability. A summary paper published by the Permanent International Association of Navigation Congresses (1976) lists sixteen different formulae of which twelve use a term proportional to  $H^3$ , two use a term proportional to  $H^2L$ , and two use a term proportional to  $H^2T$ ; where  $H$  is the design wave height,  $L$  is the wave length, and  $T$  is the wave period. Thus, the importance of wave length has been incorporated in several design approaches.

In this paper the results of a limited series of experiments with a three-dimensional hydraulic model of a breakwater armored with Tribars will be used to suggest a possible correlation of the stability of the breakwater to a measure of the energy in groups of regular and irregular waves. If this is valid for a wider range of conditions than those tested, such a method may be able to resolve some of the problems of correlating the results of regular wave testing with those from irregular wave programs.

#### The Hydraulic Model

The hydraulic model from which these results were obtained was a three-dimensional model of the west and east breakwaters at the Diablo Canyon Nuclear Power Plant where an extremely complex offshore bathymetry was carefully reproduced in an undistorted model built to a scale of 1 foot in the model corresponding to 45 feet in the prototype. The breakwater is armored with a single layer of pattern place Tribars with weights of 21.6 tons (19.6 metric tons) and 36.8 tons (33.4 metric tons) and slopes of 1.5 horizontal to 1 vertical on the landward side of the trunk of the breakwater and 2.25 horizontal to 1 vertical on the seaward face of the trunk; the terminus cone has a slope of 3 horizontal to 1 vertical. The interested reader is referred to Lillevang, Raichlen, Cox and Behnke (1984) for the details of the breakwater cross-section, its construction, a complete description of the model, and the testing program. The model was needed for engineering design purposes because the west breakwater had been damaged by waves from a storm on January 28, 1981 and a reconstruction scheme was required so the structure could withstand future expected storm waves. The model was exposed to both regular waves and irregular waves representing the most severe storms in the past 85 years as determined by storm wave hindcasts and also from available buoy measurements. In addition, the directions of these waves were varied.

Since the model was not constructed for basic research on breakwater stability, the results presented herein are limited to a single unique breakwater design. However, as mentioned earlier, it is hoped that the concepts developed in this study may be useful evaluating other breakwater designs and testing programs.

#### Presentation and Discussion of Results

A series of regular wave experiments were conducted using the hydraulic model discussed by Lillevang et al. (1984) to examine the effect of the wave length on the stability of 36.8 ton (33.4 metric ton) Tribars which armored the terminus cone of the breakwater. The duration of the tests extended until damage began, with the initiation of damage for the structure defined as the removal of four contiguous Tribars from the armor blanket. This number was based on the observation that the removal of four adjacent Tribars generally led to rapid failure of the armored slope whereas the removal of less Tribars from an area did not appear to affect the armor stability.

The variation of the wave height necessary to initiate damage as a function of the number of waves to which the structure was exposed until that damage was observed is presented in Figure 1. It is apparent in Figure 1 that for a given wave height regular waves with larger wave periods are more damaging than those waves with the same wave height but smaller wave periods. In addition, for each wave period there is a threshold wave height below which no damage to the breakwater occurs regardless of the number of waves.

Considering the observed effect of wave period, or wave length, on the armor stability, the variation of the stability with the parameter  $H^2L$  was investigated. This parameter is of interest since it is proportional to the energy contained in a periodic wave with height  $H$  and wave length  $L$ . The data which were shown in Figure 1 are presented in Figure 2 in terms of the parameter  $H^2L$  as the ordinate with the number of waves to initiate damage as the abscissa. (The wave length has been calculated from small amplitude wave theory for a depth of about 75 feet (23 m) which represents the region just offshore of the west breakwater terminus.) The data appear to be less scattered when presented in this manner which indicates that the effect of wave length on Tribar stability may be related to the energy to which the structure is exposed. The solid curve shown in the figure was fitted to the data and the dashed curves represent a variation of plus or minus 10 percent from the solid curve. The data still exhibit scatter which may be due to the fact that each data point represents damage at a somewhat different location on the structure which is probably a function of the variation in the fitting of the Tribars in the armor layer. A similar correlation between stability and the energy,  $H^2L$ , has been shown for other breakwater armor types, including rubble mounds by Ahrens (1984) and Gravesen et al. (unpublished); these tests primarily used irregular waves.

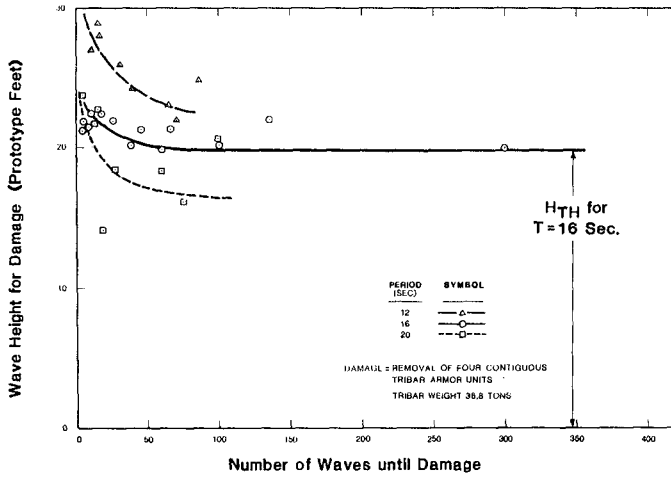


Figure 1. Wave Height to Initiate Damage as a Function of Period and Number of Waves

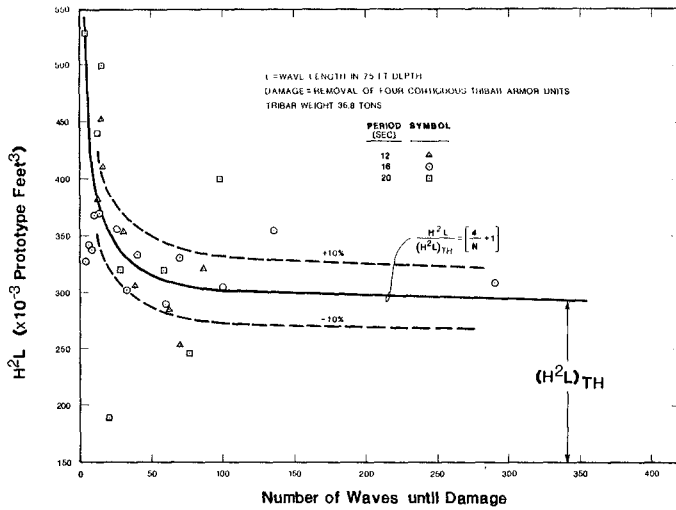


Figure 2. Total Energy,  $H^2L$ , Versus Number of Waves to Initiate Damage

The energy parameter,  $H^2L$ , appears to account for the effect of wave length (wave period) and wave height on the stability of the breakwater armor. However, as such, it does not provide a direct means of comparison of the results of regular wave tests to those from irregular wave experiments where the structure is exposed to a simulated storm wave spectrum. In addition, this does not appear to provide a means for comparing the damage caused by waves from a storm composed of a small number of large waves to the damage due to the waves from a less intense storm with a larger number of small waves. A method is proposed herein to extend the concepts just presented to that situation.

In developing these relationships use will be made of the concept of a "zero damage wave height". This wave height, also denoted as the threshold wave height, was mentioned earlier and refers to the wave height below which no damage occurs for a given breakwater armor and geometry. As could be seen in Figure 2, the threshold also applies to the wave energy parameter,  $H^2L$ , i.e., there is a value of the wave energy parameter below which no damage occurs regardless of the number of waves to which the structure is exposed. This threshold value is denoted as  $(H^2L)_{TH}$ . The assumption is made in this development that the damage due to a single wave greater than this threshold value is proportional to the magnitude of  $H^2L$  for that wave. Furthermore, it is assumed that the total damage to a structure is a result of the cumulative effect of all waves which have a total energy which exceeds the threshold value. Therefore, for a train of  $N$  regular waves with height  $H$  this cumulative energy would be equal to  $NH^2L$ . Note that this implies that waves of different wave height and different wave periods can have the same potential for damage to the same structure.

Applying this concept to irregular waves, the cumulative magnitude of  $H^2L$  for all waves with "energy" greater than the threshold value,  $(H^2L)_{TH}$ , is dependent on the joint probability distribution of wave height and wave period. To simplify the analysis it is assumed that the frequency distribution of wave heights follows a Rayleigh distribution and that the wave length is independent of wave height. Hence, the cumulative "energy" can be written as:

$$\Sigma(H^2L)_{TH} = NL \int_{H_{TH}}^{\infty} H^2P(H)dH \quad (1)$$

where the representative wave length for the storm waves is taken as that defined by the period of the peak of the energy spectrum at the depth of interest, and the probability distribution of wave height is denoted as  $P(H)$ . As mentioned, the Rayleigh distribution is used as a representative probability distribution:

$$P(H) = 4.01 \frac{H}{H^2_{33\%}} \exp \left[ -2.01 \left( \frac{H}{H_{33\%}} \right)^2 \right] \quad (2)$$

Substituting Equation 2 into Equation 1 and performing the integration one obtains the following:

$$\Sigma(H^2L)_{TH} = \frac{1}{2} NLH^2_{33\%} [2.01 \left(\frac{H_{TH}}{H_{33\%}}\right)^2 + 1] \exp [-2.01 \left(\frac{H_{TH}}{H_{33\%}}\right)^2] \quad (3)$$

Equation 3 provides a measure of the cumulative total energy incident on a breakwater which is contained in those waves whose height is greater than the threshold height  $H_{TH}$ . It should be noted that the number of waves  $N$  used is based on the interval of time for which the particular significant wave height applies and the period of the peak of the energy spectrum. Thus, the assumption is made that the spectrum is a narrow band spectrum as is indicated by the use of the Rayleigh distribution.

A series of breakwater stability tests that were conducted in connection with the reconstruction efforts of the Diablo Canyon breakwater have been analyzed using the concept of the cumulative energy,  $\Sigma(H^2L)_{TH}$ . These tests were conducted with both regular and irregular waves so that there was an opportunity to compare stability for a particular structure with these different waves. For these experiments in the Diablo Canyon breakwater model, the breakwater was armored with 21.6 ton (19.6 metric ton) Tribars. The regular waves had a wave period of 16 seconds and the peak of the energy spectrum for the irregular waves was 16 seconds also. The geometry of the breakwater was identical in all experiments. To have a basis for comparison, the damage to the breakwater armor was defined in terms of the total number of Tribars displaced, since for a pattern placed armor consisting of a single layer the number of units which were displaced could be evaluated easily. Another criterion for comparison of the effect of regular and irregular waves is the displacement of the cap-blocks which form the crest of the breakwater (see Lillevang et al., 1984). The concrete cap-blocks consisted of individual cast in place concrete blocks, each approximately 30 feet (9.1 m) long, 21 feet (6.4 m) wide, and 7 feet (2.1 m) thick with a weight of about 300 tons (270 metric tons) In the prototype, a number of these cap-blocks were displaced in a storm which occurred in January 1981. In the model the displacement of the blocks was useful in comparing the results of regular and irregular wave tests.

The damage to the breakwater is shown in Figure 3 in terms of the number of dislodged Tribars as a function of the cumulative energy. For 16 second waves a threshold wave height of 17.5 feet (5.3 m) was determined from the experiments and this was used in Equation 3. It should be noted that the threshold wave height is less than that shown in Figure 2 because 36.8 ton (33.4 metric ton) Tribars had been used in the former case and the smaller 21.6 ton (19.6 metric ton) Tribars were used for these data. Two forms of testing were used for the periodic waves: either exposing the structure to bursts of 9 waves with a 16 second period or to a continuous train of these waves. There does not appear to be a significant difference in the results from these two different types of regular wave tests. The irregular and regular wave

tests are specifically denoted in Figure 3. It can be seen that the results of these two types of experiments are similar. An important fact related to the experiments is that a greater number of waves (and greater total cumulative wave energy) impacted the breakwater during the irregular wave tests. However, because only the energy in those waves greater than a threshold limit was summed, the damage potential for the irregular waves was accounted for in a way similar to that for the regular wave experiments.

In a similar manner the number of dislodged cap-blocks versus the cumulative energy is shown in Figure 4. The cap-blocks were cast for each separate experiment and were not reused in a subsequent experiment once they had been displaced. Generally there is considerably more scatter of the data in Figure 4 compared to Figure 3, although the irregular wave damage results agree well with the regular wave damage for Tests 1 and 4. There appears to be a much greater resistance of the cap-blocks to motion for Test 3 which was conducted using regular waves. It is believed that this was a result of the underside of the cap-blocks for these experiments being much rougher than in other tests, which resulted in a greater interlocking with the underlying intermediate stone layers and thus an increased resistance to sliding. This increased roughness was due to a different method of casting the cap-blocks for this particular test. Also shown in the figure is the best estimate of displacement of the prototype cap-blocks which occurred on January 28, 1981 (see Lillevang et al., 1984). The data shown are based on observations of the time of cap-block motion and estimates of storm wave conditions based on wave measurements from a National Oceanographic and Atmospheric Administration (NOAA) buoy located 18 miles from the site. It is postulated that the slower rate of damage of the prototype cap-blocks as compared to those in the model tests may be due to differences between the roughness of the underside of the blocks in the prototype and the model. Since there were no direct measurements possible of the actual prototype cap-block roughness, it cannot be determined whether this was accurately reproduced in the model. Of course, there are certainly other difference which could contribute to the differences. Not the least of these is the water surface time history used in the model, which had to be synthesized from a measured spectrum without wave phase information. The results shown in Figure 4 indicate that design conclusions for the rate of damage of the cap-blocks based on this model are probably conservative, leading to a factor of safety in the interpretation of the model results. Even though the rate of damage in the model was in some cases different, the mode of failure of the breakwater was accurately described by the model.

The relation of the breakwater armor displacement to cumulative wave energy has been developed based on limited data from experiments on this particular breakwater design. However, it appears that this approach has potential for providing a means of characterizing storm waves for breakwater design and model testing which could be much more generally applicable.

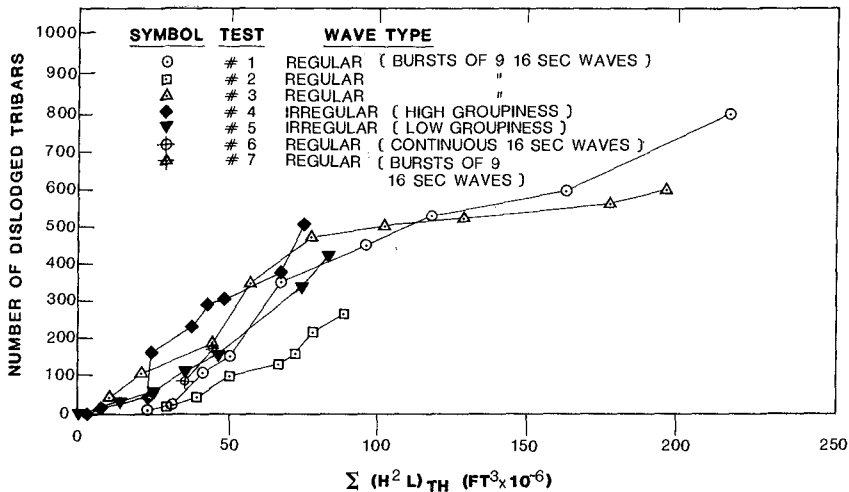


Figure 3. Tribar Displacement Versus Cumulative Wave Energy. Based on  $(H^2L)_{TH}$  of 230,000 ft<sup>3</sup>. Each Tribar Weighs 21.6 tons.

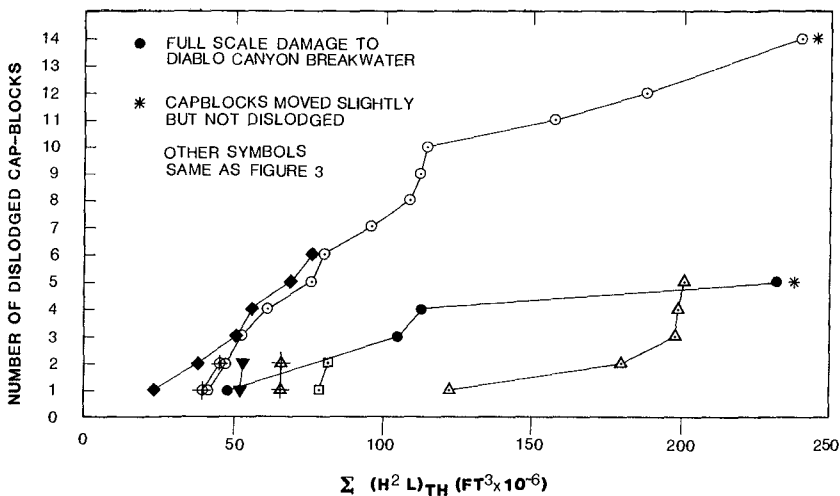


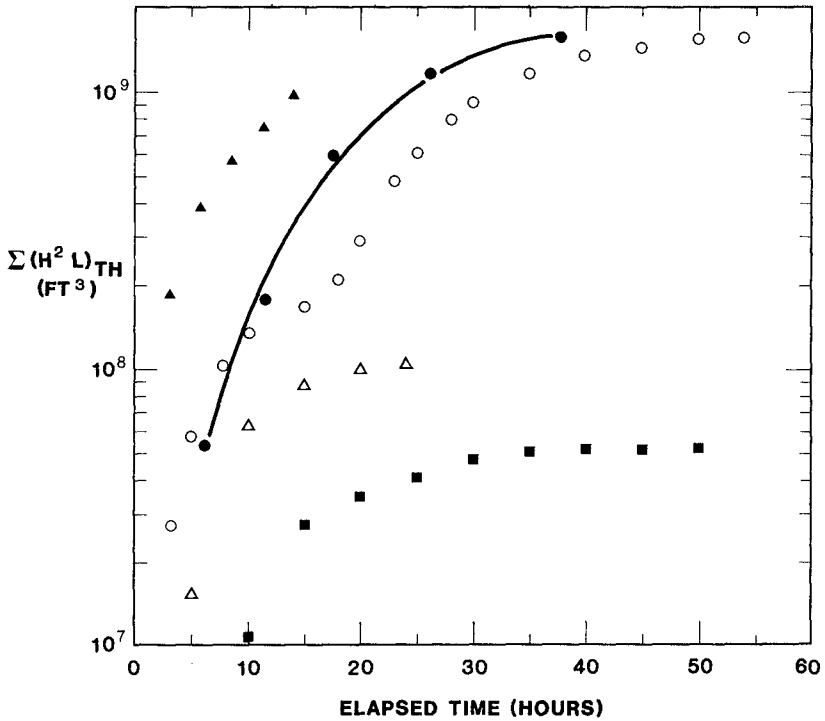
Figure 4. Cap-block Displacement Versus Cumulative Wave Energy. Based on  $(H^2L)_{TH}$  of 230,000 ft<sup>3</sup>. Each Tribar weighs 21.6 tons.

One question which occurred in this investigation related to storm events which took place after the model tests were completed. A series of storms occurred in the winter and spring of 1983 offshore of the west coast of the United States which caused significant damage along the California coast. Since the model tests were completed and there was not opportunity to expose the hydraulic model to a spectrum representing the waves from those storms, the question was raised as to what the effect of recent storms on the reconstructed breakwater could have been, compared to the results of the storm waves to which the breakwater model had been exposed during the extensive model testing program. The characteristics of the most serious irregular wave system the breakwater had been exposed to in the testing program was obtained from hindcasts of a storm which occurred in March 12 and 13, 1905. This storm was hindcast to have had a maximum significant wave height of about 31 feet (9.4 m) with the period of the peak of the spectrum of about 15 seconds. The storm of March 1983 had considerably larger wave periods which varied from about 13 seconds to 25 seconds and about the same maximum significant wave height. The wave data from this recent event were obtained from the NOAA buoy mentioned earlier, so that the variation of the period of the peak energy of the spectrum as the storm grew and subsided could be incorporated in computations. The proposed method was applied to this storm (and several others measured with the NOAA buoy) and compared to the hindcast 1905 storm waves. These results are shown in Figure 5 where the cumulative total energy has been plotted as a function of the elapsed time of the storm as the abscissa. The cumulated energy from the model experiments using the 1905 storm waves are shown along with that for the 1983 storm. It is seen that the storms to which the model was exposed had about the same total maximum cumulative energy as the recent (1983) storm waves, but the former occurred in a shorter elapsed time. The major reason for this is that the storm to which the model was exposed grew and decayed more rapidly than the 1983 storm did. Thus, if the concept of cumulative energy is correct, it would be expected that the effect of the 1983 storm on the breakwaters would not be more serious than the storms to which the model had been exposed in the testing program. Several other storms which are of lesser consequence are also shown in the figure.

As shown, the method of cumulative energy can be applied in assisting in the interpretation of hydraulic model results in light of prototype wave measurements. There are additional applications of this approach which can be mentioned.

The first might be the use of the term  $H^2_{33\%}L$  to characterize the peak intensity of a storm, instead of  $H_{33\%}$  as is commonly done. This would allow the effect of period on breakwater armor stability to be accounted for when selecting a design storm or storms for use in breakwater model testing. The second would be to characterize storms whose spectral characteristics vary throughout their duration into a single parameter,  $\Sigma H^2_{33\%}L$ , which accounts for variations in wave height, periods, and duration. Thus, a large number of storms could be evaluated as to their total potential for damage, instead of simply using the significant wave height associated with the peak of the





SYMBOL	DATE	COMMENT
—●—	3/12/05 - 3/13/05	USED IN MODEL (978A-984F)
○	3/1/83 - 3/3/83	FROM NOAA BUOY
△	2/21/83	FROM NOAA BUOY
▲	3/12/05 - 3/13/05	USED IN MODEL (989A-993A)
■	1/26/83 - 1/28/83	FROM NOAA BUOY

Figure 5. Comparison of Cumulative Wave Energy Used In Model Tests for March 1905 Storm to That Inferred From NOAA Buoy 46011 Data at A Nearshore Location. Based on a Threshold Wave Height of 17.5 feet.

storm, for instance, in the development of storm return periods. A third application of the proposed method would be in breakwater model testing for design purposes. Instead of testing the breakwater design over a wide range of spectral characteristics and durations, regular wave tests could be used to determine  $(H^2L)_{TH}$ . The potential of damage due to any storm of given wave characteristics and duration could then be compared to results of damage due to a limited number of regular and irregular wave tests which would characterize the response of the breakwater design to  $\Sigma(H^2L)_{TH}$ . This could reduce the number of tests required, and allow a wider range of potential storms to be evaluated.

### Conclusions

A relationship between breakwater armor displacement and wave energy has been demonstrated for a single breakwater design. The armor consisted of both Tribar and crest cap-blocks. In addition, the damage in the model due to regular waves and that caused by irregular waves for the same structure has been related through the use of the cumulative total wave energy contained in those waves which have an energy greater than a threshold value for the breakwater. The threshold damage value is that magnitude of wave energy which will do no damage to the breakwater independent of the number of waves which impinge on the structure. For a given wave period, the threshold wave energy  $(H^2L)_{TH}$  can be related to a threshold wave height  $H_{TH}$  for which there is no damage to the breakwater. The application of experiments with irregular waves to situations which have not been tested is described in these results. It should be emphasized that these results were for a specific breakwater model, so that additional studies would be necessary to demonstrate the applicability of this approach to a wider range of breakwater armor types and breakwater geometries.

### Acknowledgments

The authors would like to express their appreciation to Mr. Omar J. Lillevang, the project engineer for the breakwater study. It was his initial comment regarding the possible importance of wave energy which led to the development described herein. The Pacific Gas and Electric Company is also acknowledged for their support of the project, as well as their permission to publish this paper.

### Bibliography

- Aherns, John P., "Reef Type Breakwaters," Proceedings of the 19th International Conference on Coastal Engineering, Houston, Texas, 1984.
- Gravesen, H., O. J. Jensen, and T. Sorensen, "Stability of Rubble Mound Breakwaters II," Danish Hydraulic Institute, unpublished.
- Hudson, R. Y., "Laboratory Investigations of Rubble-Mound Breakwaters", ASCE, Journal of Waterways and Harbors Division, Vol. 85, No. WW3, 1959.

- Irribarren, C. R., and O. C. Nogales, "Report on Breakwaters," XVIII, Permanent International Association of Navigation Congresses, Section II, Subj. 3:119-39, 1953.
- Lillevang, Omar J., Fredric Raichlen, Jack C. Cox, and Daniel L. Behnke, "A Detailed Model Study of Damage to a Large Breakwater and Model Verification of Concepts for Repair and Upgraded Strength," Proceedings of the 19th International Conference on Coastal Engineering, Houston, Texas, 1984.
- Permanent International Association of Navigation Congresses, 1976. Report of the International Commission for the "Study of Waves". Annex to Bulletin No. 25, Vol. III, 1976.
- Raichlen, F., "The Effect of Waves on Rubble-Mound Structures," Annual Review of Fluid Mechanics, Vol. 7, 1975.

## CHAPTER ONE HUNDRED EIGHTY SEVEN

### A DETAILED MODEL STUDY OF DAMAGE TO A LARGE BREAKWATER AND MODEL VERIFICATION OF CONCEPTS FOR REPAIR AND UPGRADED STRENGTH

Omar J. Lillevang, P.E., F.ASCE<sup>1</sup>  
Fredric Raichlen, P.E., F.ASCE<sup>2</sup>  
Jack C. Cox, P.E., A.M.ASCE<sup>3</sup>  
Daniel L. Behnke, P.E., A.M.ASCE<sup>4</sup>

#### ABSTRACT

Ten years after it was completed, and intact as originally built, West Breakwater at Diablo Canyon on the central coast of California was severely damaged during a wave storm in January 1981. The paper describes uncommonly detailed site investigations that followed and the development of a large three-dimensional hydraulic model for discovering the specific mechanism that precipitated the damage, and then for verification of the effectiveness of concepts for rebuilding the breakwater to resist greater storm events than had been used for the original design. Unique procedures for modelling contorted terrain, for producing reflection-corrected irregular wave systems, for eliminating abnormal waves at the start and at the end of test runs are discussed. The tested final concept for reconstruction is described and surveyed results of closely packed Tribar armoring, as reconstructed in 1983-84, are illustrated.

The authors conclude that investigations of problems involving wave attack on the termini of rubble mound breakwaters should always be undertaken with the aid of three-dimensional physical modelling unless owner and engineer are in a position knowingly to take large risks. Further, that physical modelling at suitably large scale is virtually mandated if the submerged terrain at a site is not regular.

#### INTRODUCTION

At dawn on January 28, 1981, the first five massive concrete blocks capping the seaward 150 feet of Diablo Canyon West Breakwater was observed to slide into the sea, in reaction to attack by a strong wave storm. Three of the other four sections, averaging 300 tons each, followed in quick succession and the fifth, now unsupported under much of its 600 square feet base at 13 feet above tidal datum, went in finally, about two months later.

The two breakwaters at Diablo Canyon Nuclear Power Plant were built in 1970-71 initially to provide sufficient wave shelter to enable

- (1) Consulting Engineer, Whittier, California USA
- (2) Professor of Civil Engineering, Pasadena, California USA
- (3) Vice President, ARCTEC, Inc., Columbia, Maryland USA
- (4) Consulting Engineer, ARCTEC, Inc., Columbia, Maryland USA

construction of intake pumping facilities for the first two generating units at the site. Each of four sea water circulation pumps in the intake structure would deliver approximately 900 cubic feet of cold sea water per second (25.5 cubic meters per second). The rotating parts of the pumping equipment, single impeller vertical turbines, and the rotors of their electric motors would provide sufficient flywheel effect that quick suction-side variations of water level of 5 feet would be acceptable. Consequently it was determined by the project owner that the breakwaters need not provide their full sheltering effect except at such future times that construction might again be undertaken; that it would be economically appropriate to restore deteriorated breakwaters periodically rather than incur the added costs of construction to resist extreme storms of infrequent occurrence. With parts of West Breakwater extending to depths as great as 70 feet on an unprotected coast, the breakwaters that were built were massive. As shown by Figure 1, West Breakwater's trunk slopes at 2.25:1 on the seaward side and is armored by Tribars weighing 21.5 tons each that abut on concrete crest blocks 7 feet thick by 21 feet wide. Their upper surfaces are 20 feet above datum. The sheltered side of the trunk slopes at 1.5:1 and is armored by 36.8 ton Tribars. The conical terminus slopes at 3:1 and was armored by the smaller Tribars. The profile, at 20 feet above Mean Lower Low water, was not high enough to prevent heavy overtopping and the designs were developed so as to survive such overtopping during the ordinary heavy storms of each winter. The original project was described in detail by the senior author in a paper published in 1977 (4).

The design engineer, on site during the latter hours of the damaging storm, identified for the owners three fundamental questions that needed to be answered:

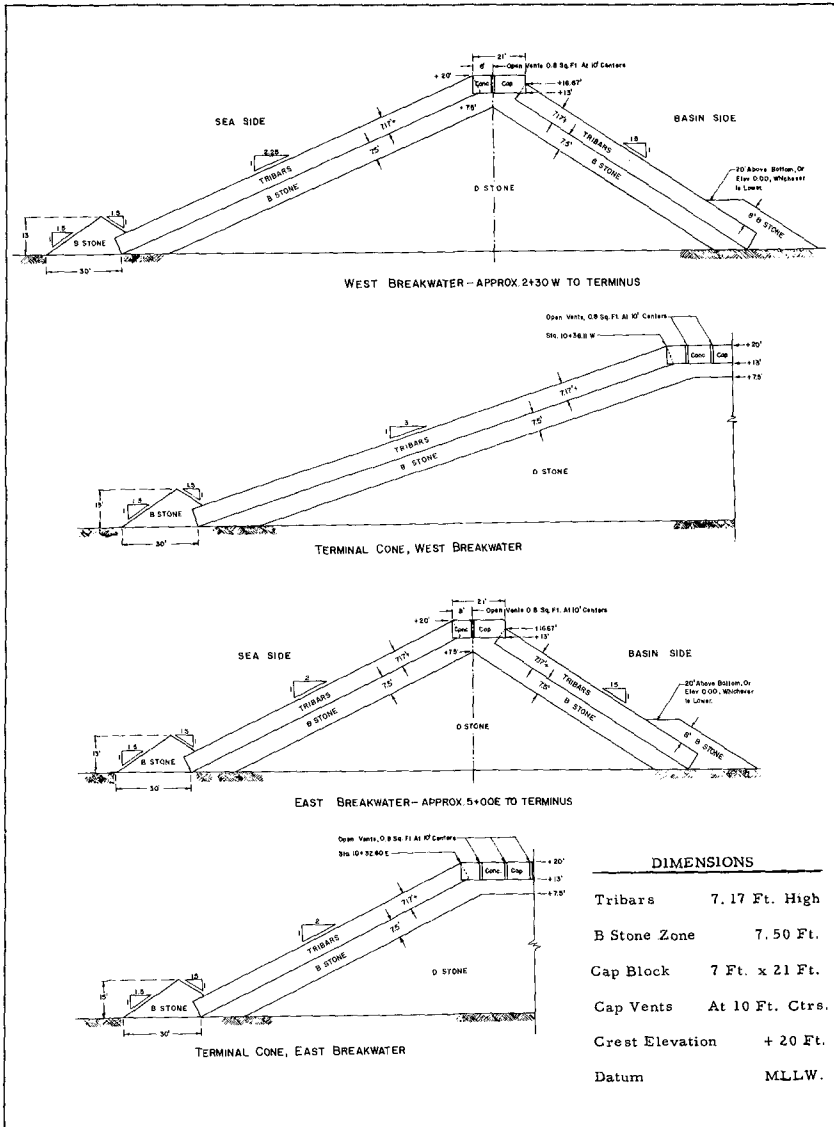
1. What is the extent and significance of the damage done by the storm?
2. How was the damage done; what was the mechanism of the damage?
3. What could or should be done in a reconstruction effort?

It was pointed out and accepted, that until there were solidly based answers to the first two questions, the third one at that time could only be answered by speculation. That would be unworthy, and attention therefore was initially concentrated on the prerequisites. Instructions were issued, that the answers to all three questions be pursued.

#### SITE AND CONDITION SURVEYS

Towill, Incorporated, with long experience at surveys in the marine environment, was engaged to provide detailed maps of the damaged areas of West Breakwater and of the location and configuration of debris shoals from the damaged areas. They also were to identify, by serial numbers that had been cast into the concrete, and to locate precisely in three dimensions all Tribars that remained intact in their original positions. Towill in turn acquired the services of engineer

Figure 1  
ORIGINAL CROSS-SECTIONS, 1970-71  
(Ref. 4)



divers from Ames and Associates, Consulting Engineers, to assist in the Tribar inventory surveys. The center at the top of each leg of each Tribar was located horizontally by the intersection of lines of sight from two transits. The elevation of the top center of each leg was derived from vertical angles read from the transits, which had made their observations on a painted band on a pole held vertically by a swimmer at the water surface, while his partner, in diving gear and with cable communication with one of the transmitters, held the pole at the required point on each leg of each Tribar. On the seaward side, landward of the damage, only the toe Tribars and the Tribars above water were surveyed. Figure 2 is reduced from a part of the resultant "map inventory" of the intact Tribars. It was of great interest, that the map showed virtually no damage had occurred below the breakwater armor zone region at 15 to 20 feet below Mean Lower Low Water. The map also showed that the debris from the damaged areas above about -15 feet had not been carried into the entrance channel between East and West Breakwaters. It had all been dropped by the waves on the channelward slope of the West Breakwater's terminal cone.

When original construction of the breakwaters was under way in 1970 and 1971, and during the nearly ten years that passed before West Breakwater was damaged in January of 1981, there had been wave behavior that suggested the presence of bottom terrain features that the available hydrographic maps did not show or, if suggested by the maps, were not delineated with enough detail for adequately explaining how they affected the waves. Towill, Inc. was therefore also asked to map the ocean floor out to the 110 foot depth contour, designing their survey coverage appropriately to define contours at two-foot depth intervals, at a horizontal scale of 1"=20' (1:240) within 1,000 feet West of West Breakwater and similar radial distances from its terminus, and at 1"=100' (1:1200) the rest of the way to the limiting 110 foot depth contour. Obviously they could not resurvey the ocean floor where the breakwaters had already been built, and it was not deemed necessary to do new mapping of the intake basin, so the maps that finally were compiled were composites made up from the new and densely covered areas West and South of West Breakwater, and the earlier surveys which had been done in 1967 by the same firm. Figure 3 is a reduction of the composite map. It represents sea floor terrain over a width from East to West of one mile, or 1600 meters, and a width at its greatest of 0.7 miles, or 1100 meters. The sea floor is essentially free of sediments above elevation -70 feet and the details of its features are extremely contorted and abrupt in relief. A massive rock mound referred to as "The Wash Rock", just 350 feet West of West Breakwater, proved to be so steep that two-foot contours could not be drawn at its flanks as separately distinguishable lines, so there the contours are drawn only for each 10 feet.

#### THE STORM, IN DEEP WATERS

With the peak of the storm of January 28, 1981 occurring in the early morning hours, there were no qualified engineers on site at that time to note technical details of the wave attacks. Hindcasts from meteorological data were acquired therefore from marine meteorologist R. Rea Strange III. He described the deep water wave system offshore

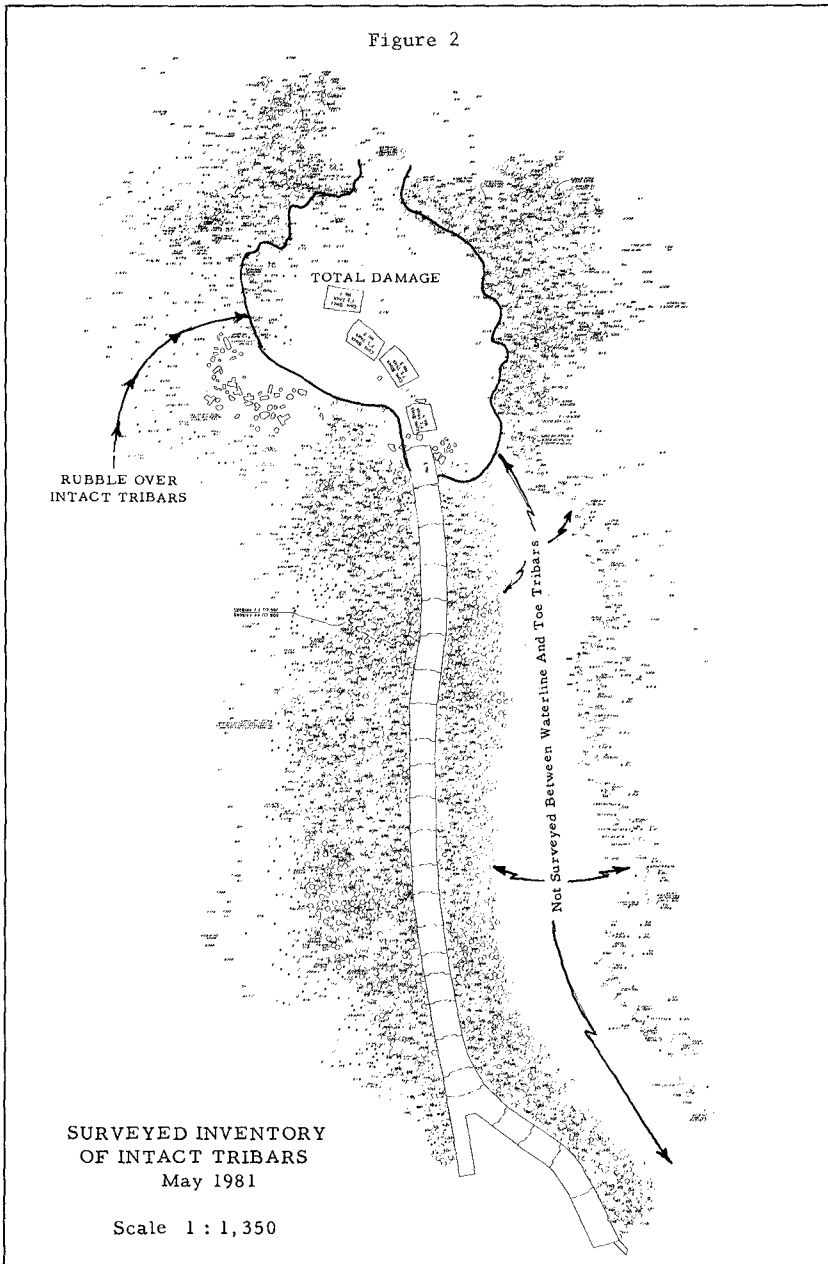
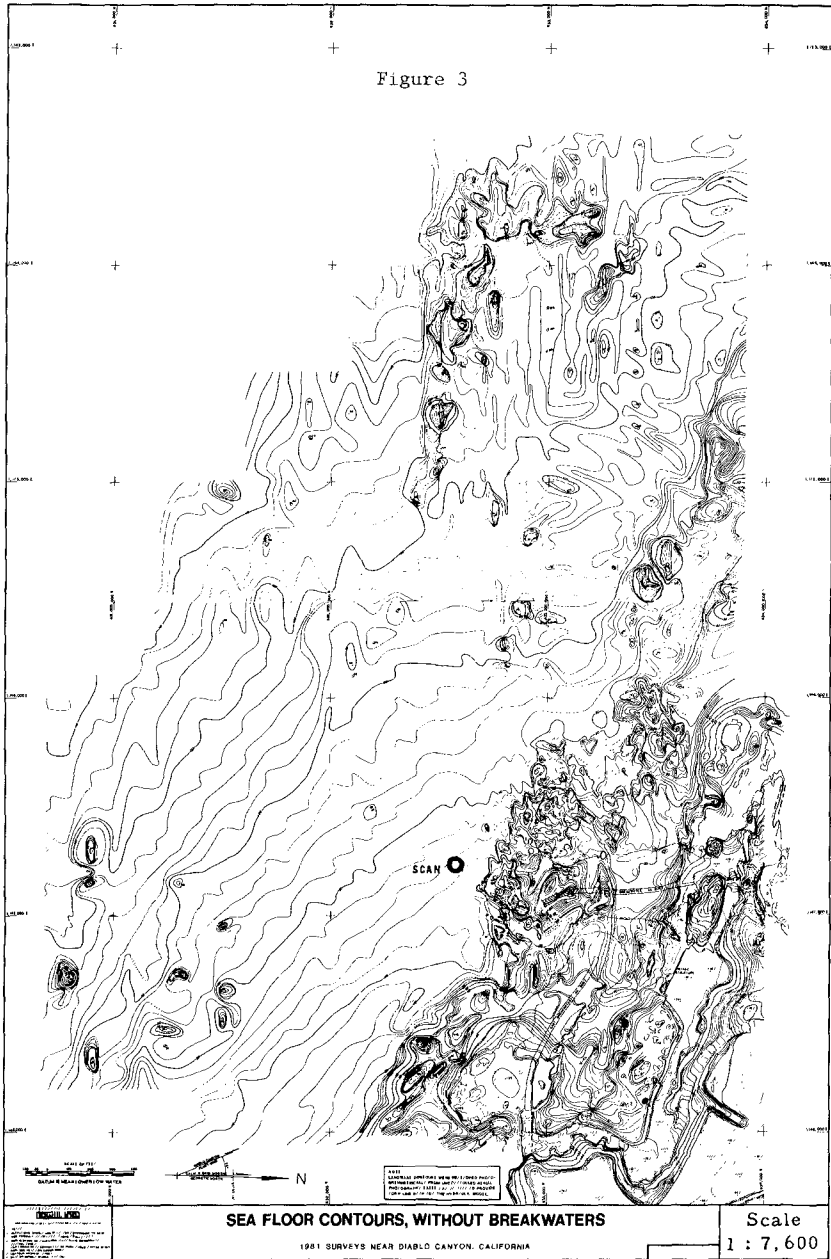




Figure 3



as being composed of seas that were being generated by a local storm, with winds from azimuth 225°, which for 12 hours had "significant" heights of 13.5 feet, and of swells from a storm 900 miles distant at azimuth 260°. The swells rose very abruptly after the seas had begun to drop. The maximum significant height of the combined swells and seas was 20.8 feet; the peak of the combined spectra was 17.5 seconds. The significant height of the swell component was 19.9 feet, of the seas, 6.1. The periods, respectively, were 17.5 and 8.5 seconds. About two weeks after submitting his hindcasts, Mr. Strange discovered the existence of a wave data buoy, anchored in deep water by the National Oceanic and Atmospheric Administration at a location only 18.6 nautical miles from Diablo Canyon Site. Apparently the buoy had recorded the waves on January 28, 1981, without any lapses. The investigators acquired duplicate magnetic tapes of the data transmitted by the NOAA buoy, number 46011, that had been recorded at its shore station in Mississippi. They were not raw data, so a factual water surface time profile could not be taken from the tape. Instead, the tape had spectral data which had been refined at the shore station from partially processed accelerometer records compiled by a microprocessor aboard the buoy. The raw data were processed aboard the buoy for each 20 minutes of record. They were sampled each two-thirds of a second. When the twenty minutes of partially processed data were transmitted to shore by radio satellite, records for the next 20 minutes were processed on the buoy, eradicating what had been there before.

Figure 4 shows the hourly variations of the NOAA buoy's spectral energy data, by separate frequency bands, through the two days of the storm. The presence and persistence of energy in the lower frequencies is worthy of note. Figure 5 breaks the energy data down to show the variations during the storm's strongest hours of the significant wave height ( $H_{33}$ ) as calculated from total energy, of the period at the peak of the spectral energy, of the deep water wave length for the peak energy component, and of the variation of  $H_{33}^2-L$ , a characterization of the energy per wave in the deep water condition.

The investigators had no basis for confirming in detail how well the accelerations of the NOAA buoy were interpreted to yield the energy data it preserved, so no conclusions could be reached as to the comparative qualities of the buoy's data and the hindcast data. If all else should be equal, there were advantages in the buoy recordings in their being available at 20-minute intervals instead of the 3 hours for hindcasts, and they did of course give clear indications of the time of rise and fall of the storm. They could not, however, provide any information as to the directions of the waves. The hindcasts did provide that information.

#### THE STORM, IN SHALLOW WATERS

The NOAA buoy was located in 133 fathoms depth. Thus, with normal criteria considered, its recordings were deep water data for all wave frequencies above 0.055 Hertz ( $T=18$  seconds). Hindcasts also yield deep water data, so it was necessary to determine the adjustments that should be made to the deep water storm descriptions in order to describe the waves at Diablo Canyon site that had damaged West

Figure 4

GROWTH AND DECLINE OF ENERGY  
WITHIN SPECIFIC FREQUENCY BANDS  
AT BUOY 46011  
JANUARY 28-29 1981

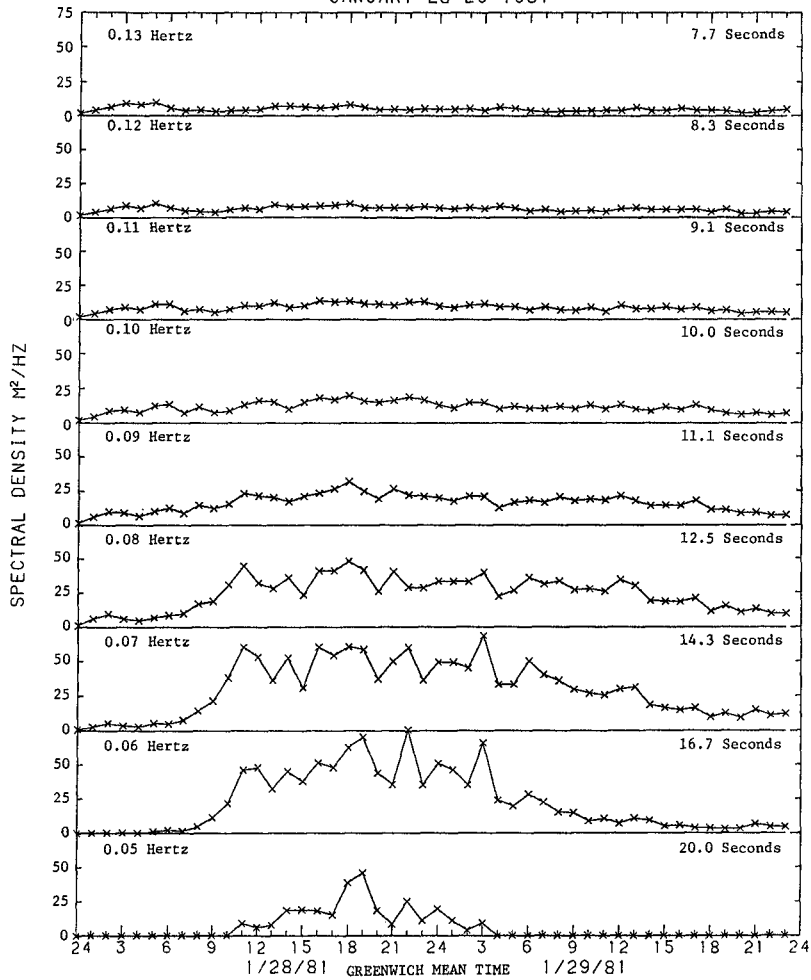
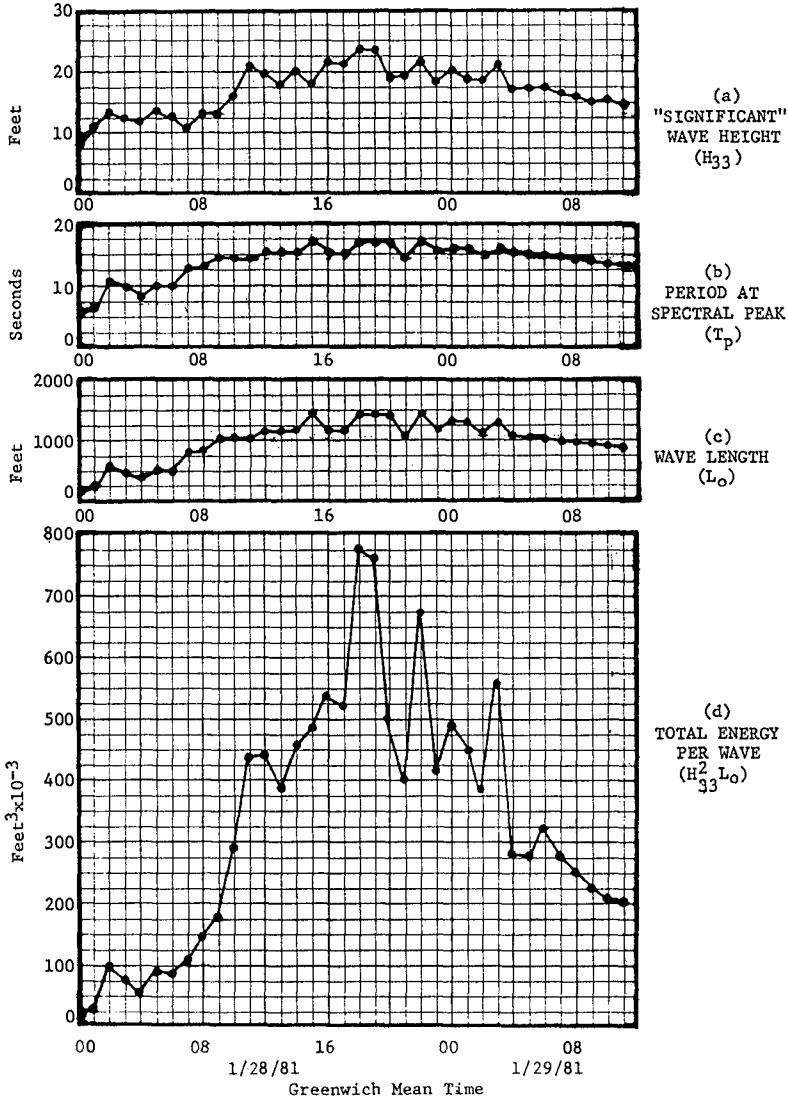


Figure 5  
 WAVE TRAIN CHARACTERISTICS AT NOAA BUOY 46011  
 DURING PEAK OF STORM ON JANUARY 28-29, 1981



Breakwater. To enable making the appropriate adjustments, to deep water waves of any period from any azimuthal direction, a numerical model of the ocean floor was created and used with a refraction program elaborated by Dr. R.C.Y. Koh at California Institute of Technology from concepts developed by Professor Fredric Raichlen and published in 1970 (1). The model extends 15 miles from the coast out to the 206 fathoms depth contour and reaches from 35 miles downcoast from Diablo Canyon to 6 miles upcoast. Elevation data were entered at grid intervals of 250 feet between the coast and about the 40 fathoms curve. Between the 40 fathoms contour and 75 fathoms, data were entered for each 500 feet, and seaward from the 75 fathoms depth the elevations were stored for each 1,000 feet. Twenty thousand such points were input from manual takeoffs, using the new maps by Towill Inc. close in and several of the "smooth sheets" from the mid-1930s archives of the United States Coast and Geodetic Survey for the rest of the modelled area that would be used for wave refraction calculations. Seventeen thousand more elevations were computer interpolated between the input points and stored to define a "fine grid" of 250 feet mesh out to the 40 fathoms area and to define a coarse grid of 500 feet spacing for the rest of the model. Unused areas of a rectangular outline enclosing the above also had to be stored in the model, so pseudo elevations were used for such points. Thus the model consequently contained 109,000 data points. Figure 6 provides a locality map showing the Diablo Canyon Site between Point Buchon at the North and Point Arguello at the South, the NOAA buoy and the physical extent of the numerical model.

Fan diagrams were used, with a ray emanating from each 2.5 degrees of azimuth at an arbitrary point named SCAN at 75 feet depth, close to West Breakwater, to discover the deep water locations from which to propagate waves of selected deep water directions at various periods or frequencies that would bracket the coastal site. The location of SCAN is shown on Figure 3. With tabular as well as graphic output from the program to work from, representing calculations for over 500 wave refraction rays, a matrix was compiled that can be interpolated to give the refracted energy or height and the refracted azimuth at SCAN of waves of any deep water period up to 22 seconds with any deep water azimuth between 180 and 300 degrees.

With use of the numerical refraction model and accepting the hind-cast estimates of direction in deep water of the storm waves, the January 28, 1981 recordings by the NOAA buoy were transformed to represent shallow water waves at Diablo Canyon Site. Figure 7 shows both the deep water spectra and the spectra of the refracted waves at the 100 foot depth locality. The data for the 100 foot depth condition were used later for programming random wave generation in the physical hydraulic scale model that is described following.

#### THE HYDRAULIC MODEL

The extremely contorted submarine terrain that has previously been shown on Figure 3 was a major contributor to the assumptions that complex three-dimensional wave phenomena are present at Diablo Canyon Site that would be best reproduced by competent three-dimensional physical modelling. A new basin to hold such a model was built in Escondido,

Figure 6

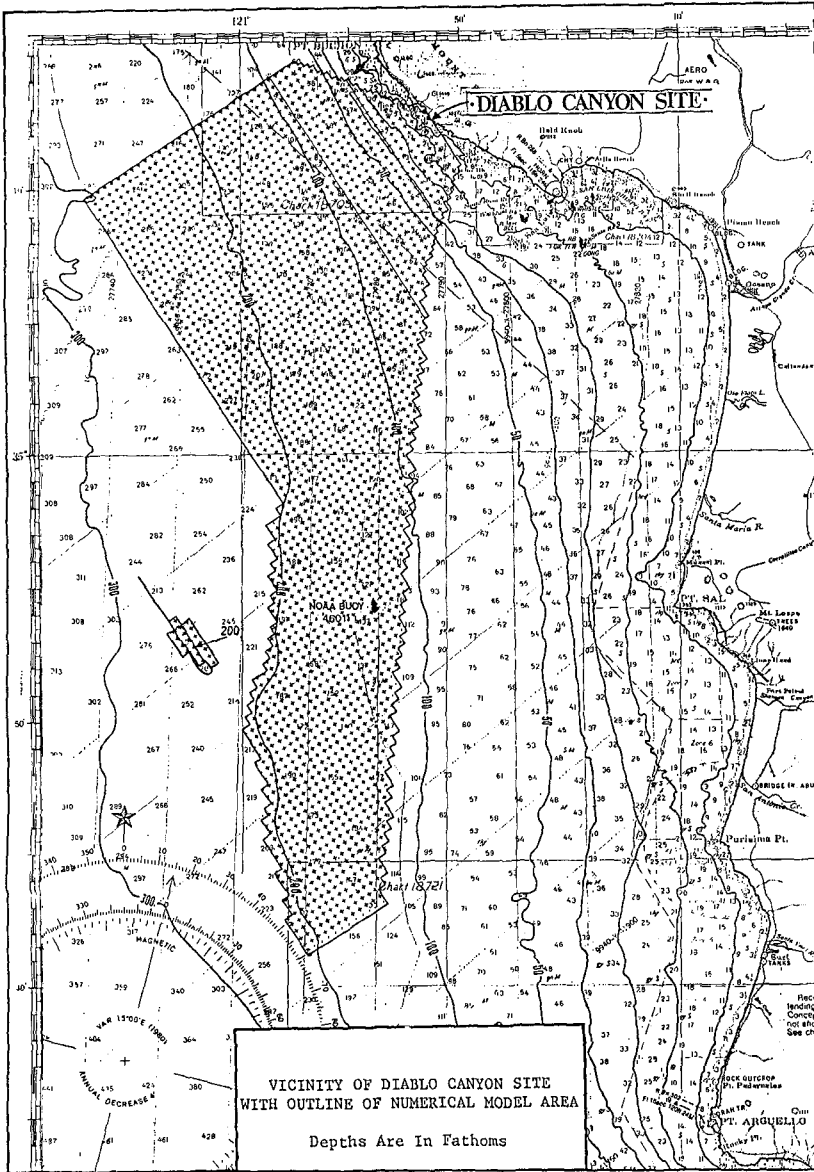
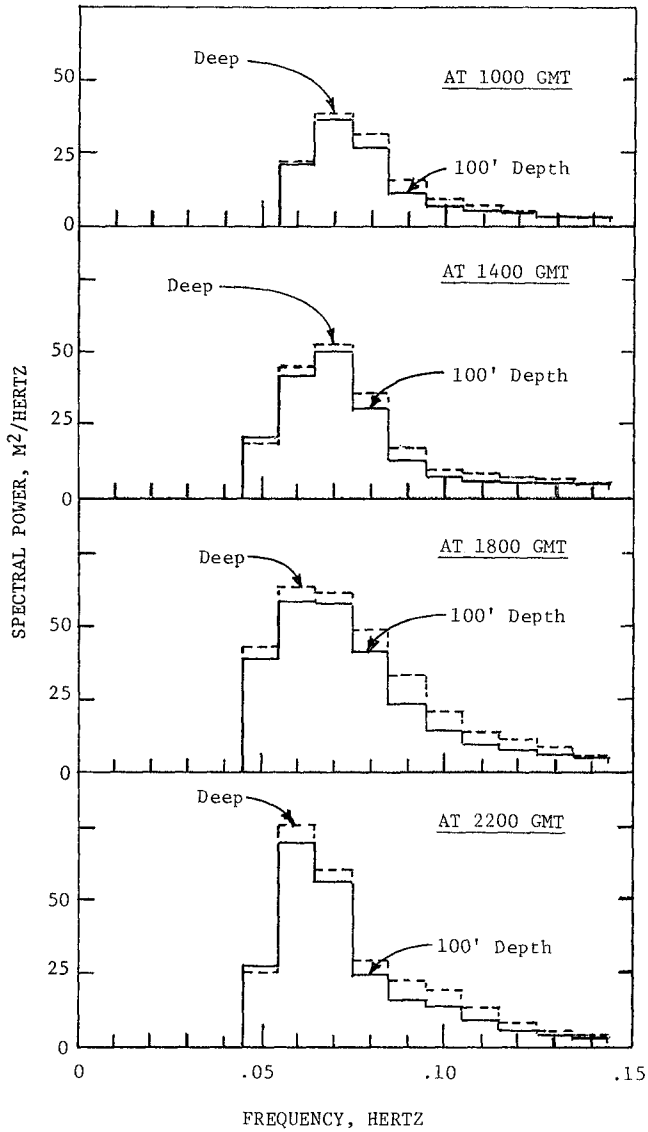


Figure 7

WAVE SPECTRA IN DEEP AND IN SHALLOW WATER  
FROM NOAA BUOY RECORDS ON JANUARY 28, 1981



California, alongside Offshore Technology Corporation's existing facilities. With a model scale of 1 to 45, the terrain above the 100 feet contour that is mapped on Figure 3 was fitted into the 80 feet by 120 feet basin. The basin's walls were at the edge of the Figure 3 map.

Several known techniques for molding the terrain accurately in the model were considered, but the great irregularity of the contours and the firm commitment to make the model as accurate a representation of the mapped features as possible, ruled those traditional methods out and a unique approach was developed. First, photographic enlargements of each 150' x 200' rectangular extent of the maps on sheets 40 by 54 inches in size were printed at 1:45 scale. Those sheets then were glued as a controlled mosaic on the floor of the model basin. Along every contour, typically at about eight-inch intervals, angle-iron clips were fastened to the floor with power-actuated stud drivers, the clips being so placed that their standing legs were tangent to the contour line. Galvanized steel strips, or "ribbons", were then bowed to follow each contour on the map and were spot welded to the angles after a surveyor had verified, by differential levelling, that the upper edges of each of the ribbons were positioned accurately to scale at the elevation defined by the contour. At single points representing peaks or hollows in the terrain, or at features where contours were too closely spaced or too tightly curved to leave room for the angles and ribbons, 10-inch galvanized spikes that are sold for eaves gutter fastening were driven to prescribed model elevations so they could be used like grade hubs. With the ribbons and spikes properly in place, sand was laid on the basin floor up to within 2 or 3 inches of the surfaces represented by the upper edges of the ribbons and the spikes, and then the remaining 2 or 3 inches were filled with sand-cement concrete and shaped to the contour controls by trowelling. Figure 8 shows the angles fastened along contours of the mosaic, steel ribbons temporarily



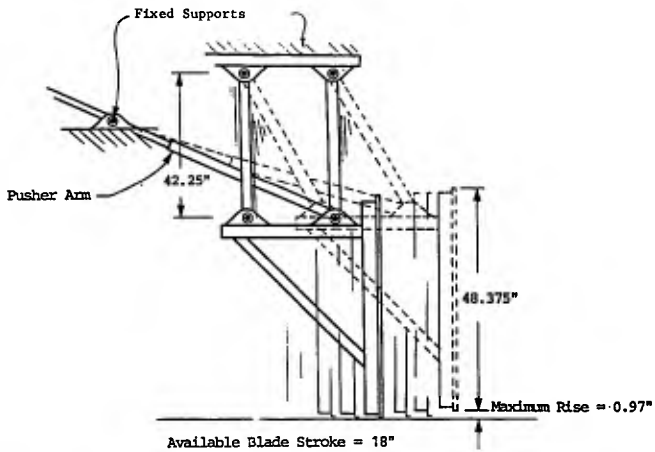


clamped to the angles, surveyors confirming the accuracy of the clamping and technicians with a portable spot welder fastening the ribbons permanently in place.

Four existing wave makers, each 11 feet long, were re-built to a modified configuration and a fifth was built to the new design, in which the moving blade's suspension was an articulated parallelogram support that caused the blade to remain aligned vertically throughout its stroke rather than swinging through a long radius arc from a single axis, like a door on edge. The re-built linkage is shown schematically by Figure 9. Screw jack castered wheels were included that could be

Figure 9

ARTICULATION OF WAVE BLADES



cranked down to make moving the modules relatively easy. Thus various alignments of the wave machines could be achieved for propagating waves across the model terrain toward the breakwaters. The five modules were aligned with a straight front and their blades were moved identically and simultaneously to produce continuous wave crests 55 feet long. Perpendicular to the 55 feet long blade at each end a wave guide fence that self-adjusted to profile features was extended toward the area under test, to control losses of wave energy laterally from the waves. Wherever reflections were seen that were caused by model boundaries but would not occur at the coastal site, open barred cages filled with lathe shavings of stainless steel were deployed to absorb the energy that otherwise would be reflected.

The wave blades were moved through the water by two-way hydraulic cylinders that tapped an open loop of a circulating oil supply at near constant pressure. Servo valves controlled the displacement time-history of the blade and these valves functioned in response to a voltage time-history that was constructed from spectra, either hindcast or measured, using the method proposed in 1970 by Goda (2). The variable voltage signals were recorded and played back during wave generation on conventional C-60 audio tape cassettes.

The testing program was devised to determine the effects on the model breakwaters of either uniform waves or of trains of random waves of equivalent energy. Except for the largest wave periods, where six or seven waves was the limit, the uniform waves were sent against the model breakwaters in bursts of nine and the machines then were stopped until the basin was suitably calm again. Then another burst of nine would continue the test. Two interesting techniques that had evolved in previous studies at California Institute of Technology were used with these uniform waves that were important improvements over traditional ones. First, instead of sinusoidal waves, which would not be a stable profile for gravity waves in depths as shallow as 100 feet, the variable voltage signals to the wave makers were programmed so that cnoidal wave profiles were produced within very short intervals of travel away from the blades of the wave machines, usually before those waves began to cross the modelled sea floor terrain. The other innovation eliminated a nuisance that historically has confused interpretations of model experiments. The first wave or two and the last one in a test run are almost always abnormal. Often the last wave has been compounded by reflections off of the blade and can be a high energy "rogue" that can do damage that the preceding train's series of prescribed waves had not been capable of doing. A simple concept was employed that essentially eliminated these first and last wave anomalies. No matter what phase of generating motion the blade might be in when a test run was completed, and a halt command was sent, sensing circuitry automatically delayed the effect of the halt instruction until the blade had completed its programmed traversal to its fully retracted position, and only then did it stop moving. At that phase of wave generation the blade's translatory velocity is zero; extraordinary waves do not result and start-up for following sets of waves is smooth and free of the lurching that is frequent when reactions to instantaneous demands of the system occur for motion.

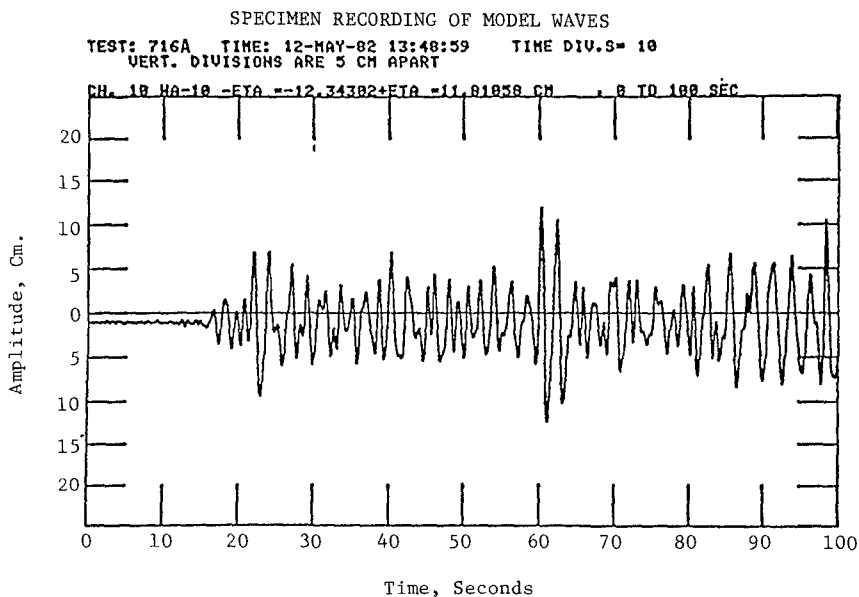
Capacitance type probes were utilized to sense wave heights at various separate locations within the basin. The capacitance probes were essentially copper rods which had been insulated by continuous heat shrink tubing. As a probe becomes immersed in water, a change in capacitance is sensed between the copper rod core and the surrounding body of water. This change in capacitance is sensed by an electronic circuit which transforms it to a change in voltage which then is correlated with different degrees of immersion so that the change in water level due to the passing of the wave is sensed and related to wave height. As many as sixteen wave probes were deployed in the model basin at selected locations in different runs. They were mounted on tripod stands with adjustable legs that facilitated placement in various water depths and over the complex bottom topography. To relate the signal from a wave probe to the change in water level each probe was frequently calibrated by use of centrally controlled motors that drove them up and down in the water for known amounts of displacement. Information on the voltage reading of the probe and the displacement was supplied to a Tektronix 4052 computer which calculated the calibration value for each wave probe as a function of voltage and displacement. The results were highly linear and stable with time.

Measured wave heights were compiled by digital sampling, utilizing the Tektronix 4052 computer. Up to 16 channels of analog wave information were converted to digital form and were input to the computer. Once detected and processed by computer software, the information could then be permanently stored on floppy disk and also be presented in a hardcopy form for evaluation, through a graphics printer. The data were taken in unfiltered form and sampled at a rate of 10 Hertz. Lengths of test records were limited to the maximum number of samples that could be stored in the memory of the computer. A total of 128,000 samples could normally be stored using 12-bit format, limiting the maximum duration for compiling a record of a wave train to approximately 13 minutes of a test. With a slightly less accurate 8-bit format 256,000 samples could be stored, which made it possible to record as much as 26 minutes of testing.

Standard data that was output for both tests with regular waves and tests using irregular waves included wave time histories at each of the wave probes and basic statistical information on the waves that were measured including significant wave height and peak wave height. An example of a series of waves recorded during a test is shown by Figure 10, along with statistical information derived by the computer during the test. More sophisticated analyses that were also made from the probe records included presentation of actually measured wave spectra and the decomposition of the wave signals from two or more of the probes into incident and reflected wave components.

All relevant wave data were stored in computer compatible form for easy retrieval and analysis. Data were read to the Tektronix 4907 floppy disk memory unit, which transcribed the information onto 8 inch soft disks. The data were stored in an uncalibrated form with calibration factors stored in a separate header. The calibration factors were stored with each test run, rather than in one file only, to minimize or avoid any wrong calibration factors inadvertently being applied to

Figure 10



the raw data.

When test runs were made that used random waves the succession of wave bursts and intervening rests that were used for the uniform wave tests was not acceptable. The random wave sequences ran for tens of model minutes. With periods at peak energy of the random waves being 12 to 14 prototype seconds, which would be 1.8 to 2.1 seconds in the model, roughly 300 waves would be generated each ten minutes in the model. Such prolonged episodes provided considerable opportunity for wave reflections to build up between the model breakwaters and the wave machines. Routines were devised to adapt concepts to a three-dimensional wave basin that were described by Goda (3) for two-dimensional wave tests in flumes, for separating reflected wave components from the incident. The procedures involved comparing the histories of the water surfaces at two probes closely located one to the other along the direction of wave motion and near the wave machine, determining the separate incident and reflected spectra by harmonic analysis and computing adjusted signals to send to the servomechanisms to produce the effect of the desired net incident wave spectrum.

An office trailer placed alongside the test basin housed all central electronic gear and control stations, as well as computers,

plotters, printers and physical storage of records. Video recording terminals and monitors, with titling equipment and cameras, both video and film, standby equipment, etc., were housed in a smaller portable building alongside. Two-way speaker-microphone stations were installed to cover the whole model basin and in both portable buildings, so that all personnel could hear or contribute to voice communication.

Catwalks and booms, adjustable for height and rotatable from a mainmast to any location were cantilevered from the mast at the basin's edge. Fixed video and film cameras were mounted which could be activated remotely. All test runs included a recorded running commentary by the test engineers that later was transcribed. Parts of the commentary also were on the video cassettes that were recorded continuously during every test run. Parts of selected tests also were recorded on moving picture film exposed at 128 frames per second. When exposed at normal projection speeds, the moving images slowed to approach full-scale time of wave motion. That made more acute observation possible of fast acting events that had occurred in the model.

The model breakwaters were built over the molded sea floor terrain in close compliance with the original design. The core in the model breakwaters was made of coarse sand that was generally larger than the 1:45 linear model scaling of the prototype material would call for. That was deliberate, so viscous effects with smaller grain sizes would not distort the experimental results. The intermediate zone between the core and the Tribar armor layer, either B Stone or E Stone, was modelled to scale of volumes, i.e.  $1/45^3$ . The gradation called for the median stone's volume to be twice the volume of the minimum piece and the maximum stone to be twice the volume of the median. In either B or E Stone, the median size was 10 per cent of the volume of the Tribar armor piece. That gradation produces a voids volume approximating 45 per cent of gross volume occupied by the mixture. With nominal diameters of the scaled-down stones ranging between 2.1 and 3.3 centimeters for the smaller B Stone and between 2.5 and 3.9 centimeters for the E Stone it was determined that viscosity effects would be unimportant so it was scaled linearly. The model B and E Stone mixtures were made from crushed rock of appropriate specific weight. Proper shape and size distributions were obtained by hand selection and weighing each individual stone and classifying into two bins, using median size as the separation. Then equal weights of the two classifications were combined and mixed to produce a practical model gradation of the specified stone.

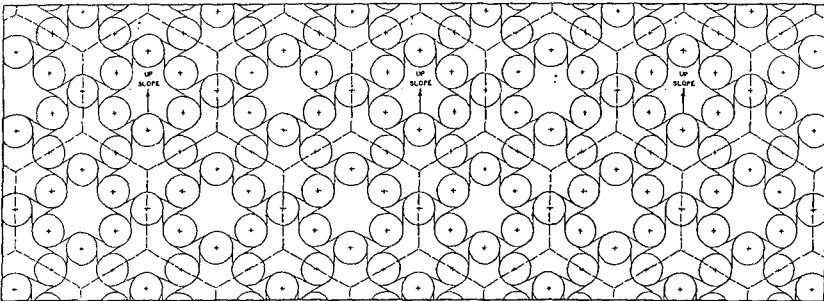
The model Tribars were cast under tightly controlled procedures in RTV molds, each of which was discarded after about 80 castings had been made from it. Thermal-setting resins were used to which industrial grade barium sulfate (barite) was added to obtain the correct specific gravity. Liquid catalyst was added to harden the pour before the finely divided weighting mineral could settle out of the honey consistency resin. Air that was entrained during the mixing of the parts was extracted from the catalyzed mixture under a vacuum bell jar before the mixture was poured into the molds. The heat of the catalyst is ineffective, however, where the mold and the resin interface, so external heat is necessary to harden the resin there. To provide the surface

heat the molds were first placed in controlled temperature ovens and then were removed just as the resin-barite-catalyst mixture was ready for pouring. Minimal flashing that resulted was removed from the castings after they were taken from the mold. After the hardened pouring chimney material had also been ground away each of the Tribars was weighed and one in ten was tested for specific gravity. No pieces were overweight and the specific gravity was almost without exception on target. None of the Tribars of 296 cubic feet size was as much as 3 per cent off on weight and the pieces of most accurate weight, ranging between 0 and 0.14% underweight, were code painted blue and were used in the model where surveys had shown removals by the January 28, 1981 wave storm. Those that were underweight by between 0.14 and 1.00% were painted green and were placed adjoining the historically damaged zones. The rest, sometimes painted black but mostly left in their unpainted milk chocolate brown color, were used elsewhere on West Breakwater beyond expected aggravated damage and on East Breakwater.

Figure 11 illustrates one of two possible geometric patterns for placing Tribars that represents the so-called 100 per cent pack. All pieces are in juxtaposition. In that configuration, one Tribar occupies  $5.008d^2$  units of area,  $d$  being the common diameter of each cylindrical leg or spoke in the Tribar. The theoretical perfect pack, at

Figure 11

## GEOMETRICAL ARRANGEMENT OF TRIBARS IN 100% PACK



100 per cent, cannot be achieved in actual construction but tight packing is an important objective for a Tribar armor zone. With close fitting, each Tribar is restrained by its abutting neighbors from tilting out of the "fabric" if it becomes unstable due to uneven support by the stones underneath and suffers displacing forces from the moving water. With the possibility under consideration that reconstruction specifications might require the builder to document achievement of a 90 per cent pack, the model breakwater armoring was placed to approximate 85 per cent, a consciously conservative modelling provision. Limits were also imposed on how much the legs of one Tribar could extend above or below those of an adjoining one, and as to how far the plane defined by the

ends of the three legs of any Tribar could tilt from the surface slopes defined by the design cross-sections.

A fast hardening and water resistant material named "Duracal" by one of several firms marketing it, and normally used for thin patches on deteriorated surfaces of concrete slabs, curbs or steps, was used for casting the model crest blocks. Barite was blended in to bring the material to appropriate density. The cap blocks were cast in place on the model breakwater, with a double layer of woven plastic screen cloth overlaid with a paper towel sheet being used to keep the simulated concrete from intruding the voids in the quarrrstones that support the crest block. In the prototype, chain link fencing mesh had been used, with asphaltic felt paper as an overlay, for this same purpose. After the blocks had hardened and their side forms had been taken away, each block was carefully lifted out, the mesh and paper towel membrane were removed, the tops were sanded smooth and the vent holes specified in the design were drilled. Each block was then put very carefully back in its original place. Each time that the breakwater was restored, in preparation for another test, new cap blocks were poured in place to replace the ones that the waves had removed during the preceding test. The displaced ones were not used again.

Figure 12 shows several of the features that have been discussed. The model's West Breakwater can be seen, ready for the first tests. The extreme relief characteristics of the terrain features are evident. Five of the wave recording probes on their tripods, with full-thread rods for adjustable legs, are aligned just West of West Breakwater, one of the profile-accommodating wave guide fences for containing the ends of waves is seen in the background, as is one of the crates containing stainless steel shavings for absorbing unwanted reflections at borders of the model. Figure 13 is a view from East of the Intake Structure of a test in progress. Water in the model basin is at extreme high tide stage +7.5 feet, while uniform waves 19 feet high and with 16 seconds period are attacking from a shallow water azimuth of 249 degrees. The catwalk for observations and camera station is also to be seen. Due to either a kind providence or Southern California weather this outdoor operation was at no time shut down because of wind conditions compromising testing conditions. On only one occasion was it necessary briefly to suspend progress due to rain. Much of the restructuring of the model breakwater extended into night shifts and on occasion test runs were made on the night shift.

#### THE MODEL CONFIRMED - THE DAMAGE MECHANISM IDENTIFIED

Five separate test runs were made that each confirmed the model's ability to reproduce the damage that was done to West Breakwater on January 28, 1981. The model was also consistent in that each of the tests produced the same damage. It was of considerable interest that essentially identical results were displayed by the three tests that were made with successive bursts of nine uniform height waves and that were made by the two continuous tests where the breakwaters were subjected to attack by random height waves. The wave series in the random heights tests carefully reproduced the energy characteristics at the 100 feet depth region of the model that had been derived from the

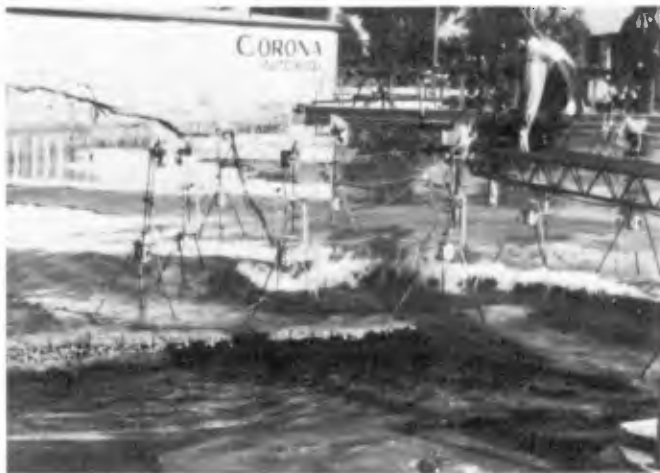
Figure 12

DETAIL OF THE MODEL



Figure 13

TESTING UNDER WAY





records made during the January 28, 1981 storm by the NOAA wave buoy. In all five of the test runs the wave machines were oriented to agree with azimuths that were derived by use of the numerical model for refraction, with input of Strange's hindcasts of deep water azimuths for that storm. Tide variations for January 28, 1981 at the site were not great through the hours of the storm's stronger phases, so no variation of water level was used during these five test runs, all being made with a tide stage in the model basin representing elevation +3.7 feet.

The damage sequence began with displacement by the waves of a Tribar on the edge of the armor pattern, at a specific point at the toe of the slope of the terminal cone. That specific location is where a blunt rocky ridge with its crest at elevation -15 feet was partly covered by the breakwater. Water rushing back down the conical surface of the breakwater's terminal cone, after passage of the preceding wave crest, proved to be capable of shifting the bottom row Tribar away from those upslope Tribars against which it had been tightly fitted during construction. After being moved downslope, away from the abutting support of the upslope Tribars the force of a following wave's uprush was sufficient to lift the shifted Tribar off of its base and then to tumble it across the breakwater's conical terminal surface toward deeper water on the sheltered quarter of the cone. Tribars that had been installed at the same -15 feet elevation either side of this localized high toe were not moved because they were in the middle of a pattern of Tribars and packed closely, so that freedom to move sufficiently to be tipped out was not available. The Tribars that shifted and then came out did so because of what was clearly an edge phenomenon. After the first Tribar was carried away its former immediate upslope neighbors became edge pieces and in succession they were loosened downslope by downrushing phases of the waves and then, newly without buttressing restraint from their former upslope neighbors, they were tilted out and carried over to a developing shoal of Tribar debris on the back slope. Every removal of a Tribar expanded the "unhemmed" edge of the pattern of remaining intact elements and the progress of damage increased rapidly as the perimeter of unsupported Tribars grew longer.

For some time the stripped off area's "downstream" boundary did not grow beyond the conical element of the terminus that paralleled the crests of the waves. That was the high point of the armoring crossed by the transiting waves. Beyond that "ridge line" there was no backrush of water after a wave's passage. The only forces by moving water that was felt by those Tribars tended to drive the edge pieces more firmly against their buttressing neighbors. In later tests that were carried on with long durations those edge Tribars did finally come loose, but due to a different cause. They tipped backward into the stripped off area after persisting high velocity forward wash of the waves eroded the stripped off area to a lowered profile. That eventually under-cut the quarrystone that had been supporting those Tribars, and they fell back and then were carried away forward to the debris shoal.

Once the rapid removal of the Tribar armor had grown to an area roughly elliptical in outline, with the major axis of the ellipse extending from the -15 feet initial point up to the near corner of the

end cap block (Cap Block No. 1), the rapid growth continued at its edge toward the breakwater's root. The other edge, along the "ridge line" of the cone as described above, did not grow very much at that phase. At the lower parts of the growing edge of the ellipse uprushing waves passed over Tribars whose upslope neighbors had already been carried away. Those lower Tribars were dislodged by the uprushing waves, transported upslope to come to rest momentarily against the crest block for a wave or two, rolling short distances up and down slope. They were then carried parallel with the breakwater's axis toward the breakwater's end and thence across the terminal cone for eventual deposition in the debris shoal. As the Tribars at the bottom parts of the ellipse came away, Tribars on the upper reaches of that edge lost support from below and were dislodged, and the cycle continued. The edge toward the breakwater's root of the stripped off area maintained its curved configuration as the damaged area grew.

Generally, there was no detectable rocking or movement of the crest block above the area currently being stripped of Tribars until right after all of the Tribars immediately below that block had been carried away. At about that time the full undiffused force of the uprushing waves was impacting against the 7 feet vertical extent of the block. The block could be seen to rock upward very slightly as each wave struck and was pivoted more or less on the opposite edge of its base. Simultaneously there was a violent diversion of energy downward and upward at the block face. The upward diversion was visibly evident by the splash from the wave. The downward diversion caused vertical downward jet just as the confining weight of the crest block on its foundation quarrrystones was momentarily relaxed through the upward rocking of the block. The large quarrrystones on which the cap normally was supported were quickly picked away in the split second that the block tended to rock upward. The progressive undercutting soon removed a third or more of the support and then the block slid toward the sea, badly tilted and no longer an effective element of the breakwater.

Figure 14, in three parts, shows in (a) and (c) the damage in the model after eight crest blocks had been dislodged after an extended run during the first model confirmation test. Part (b) is a reduced size excerpt from the map of the surveys of condition that were made at Diablo Canyon Site just after the storm of January 28, 1981. The curved and rising edge of the stripped away areas are seen in all three illustrations. Figure 15 is reproduced from the test records and shows outlines of the growing area of Triabar removals in the model that were sketched from vertical photographs at nine stages of the testing. The position of the dislodged crest blocks is not sketched, but as noted in Figure 15 Blocks 1 through 12 were dislodged in this test. It was continued well beyond the conditions that reproduced the historical damage, primarily to see if the storm in nature might have destroyed West Breakwater completely, had it persisted long enough.

Test 1, which Figure 15 summarizes, was made with regular waves that were delivered in bursts of nine. As shown by the Figure the test began with 54 waves that increased from 13 to 17 feet in prototype height and with a period in prototype time of 16 seconds. No damage resulted. Then, without changing the period, the wave height was

Figure 14

DAMAGE IN NATURE AND IN THE MODEL.



Model, Test 1



Model, Test 1



Survey At Site  
1981

Figure 15

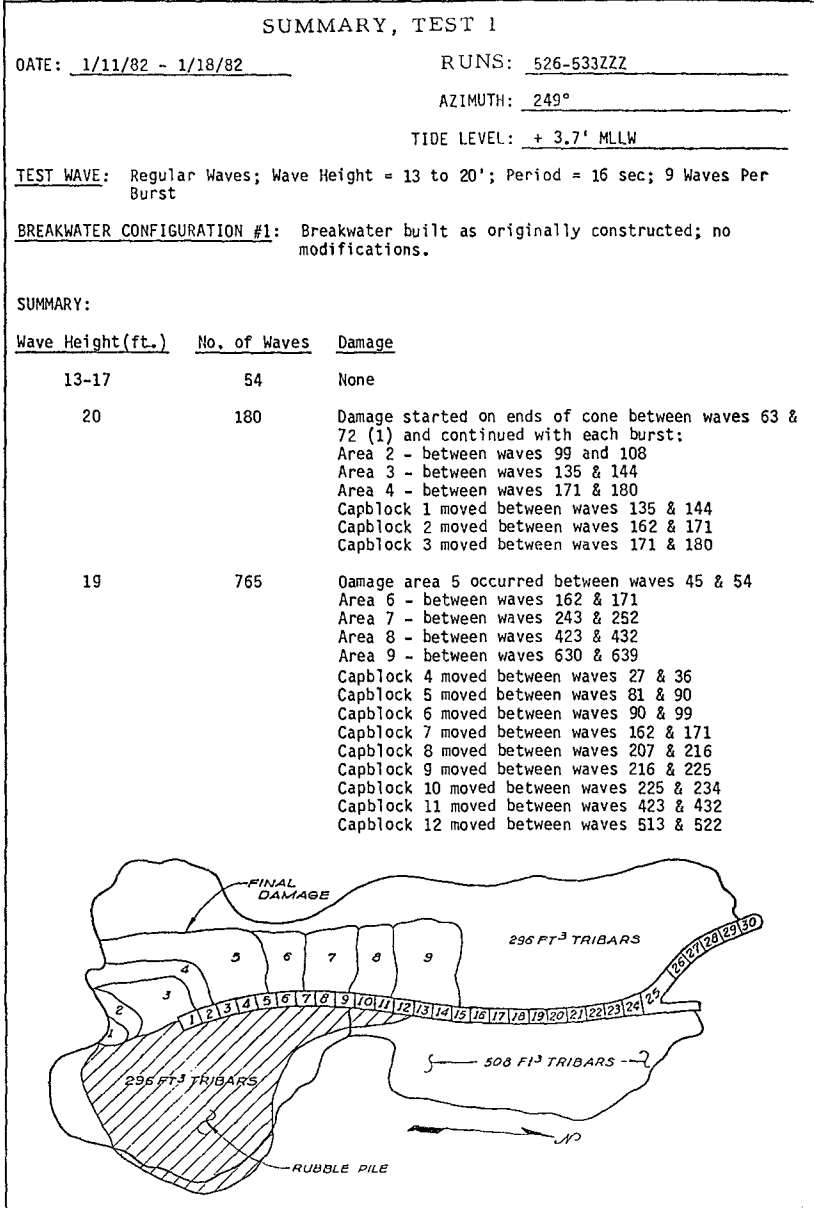


Table A  
 RATES AND EXTENT OF DAMAGE DURING TEST NO. 1  
 RELATIVE TO NUMBERS OF UNIFORM WAVES

<u>Area No. (Fig. 15)</u>	<u>Areas Stripped of Tribars</u>		<u>Cumulative Number of Waves</u>	<u>Crest Blocks Displaced</u>	
	<u>No. of Waves Per Area</u>			<u>No. of Waves Per Block</u>	<u>Block Number</u>
1	72		72		
2	36		108		
3	36		144	144	1
			171	27	2
4	36		180	9	3
			216	36	4
5	54		234		
			270	54	5
			279	9	6
6	117		351	72	7
			396	45	8
			405	9	9
			414	9	10
7	261		432		
8	180		612	198	11
			702	90	12
9	207		819		

increased to 30 feet and shortly damage began to develop. Table A is a timing breakdown of the data in Figure 15. The center column shows the total number of large waves (greater than 17 feet) that had attacked the breakwater during Test 1 when each numbered area on Figure 15 was observed to have developed, and when each crest block was displaced.

The damage to the Tribar armor grew more and more slowly as the Tribar removals passed the general locality of Crest Block Number 5. By the time the seaward face of the breakwater was denuded as far back as the limit of Area 9, at Block Number 15, the rate of growth of the damage was hardly perceptible. Reasons for this were not rigorously investigated but are believed to be uniquely related to the site, with particular relationship to the path the waves moved over submerged terrain features toward the landward part of West Breakwater's alignment.

Test runs 2 and 3 duplicated Run Number 1. Runs 4 and 5 also tested the original configuration of the breakwaters but random waves were generated instead, in which the spectral energy equaled the energy at SCAN that was derived from the records made by the NOAA buoy during the actual storm of January 28, 1981. The synthesized trains of random height waves that were generated in the model differed however between Run Number 4 and Run Number 5 in one respect. The wave train of Test Number 5 was one of "high groupiness" and the one generated for Test Number 4 was of "low groupiness". The groupiness factor relates to the concept that the higher waves in a random set often are found together in the train. If the large amplitude waves occur together, that can be referred to as high groupiness, but if the high waves are dispersed more evenly it can be referred to as low groupiness.

There was no difference to be seen in any of the five tests as to how and exactly where the Tribar removals began, or in how the striping away of Tribars progressed. Neither were any differences apparent in the tests as to the sequence of events that led to displacement of each crest block. There were noticeable differences shown in the resistance to displacement by individual crest blocks and in exactly where they had come to rest when a test was completed. Those differences were known to relate to the impossibility of duplicating exactly the quarystone beddings on which the blocks were poured.

Those first five tests, with the breakwaters modelled as the prototype originally had been designed, and attacked in the model by waves that are believed to be closely comparable in energy with the historical wave event of January 27, 1981, produced essentially identical results in steps that were closely alike. The results they produced closely matched the conditions that site surveys showed immediately after the 1981 storm and in each test the damage began at exactly the same point.

#### HEMMING THE EDGE

The edge Tribars at the -15 feet locality of West Breakwater's terminal cone were given restraint against downslope displacement by the downrushing of waves by embedding their legs in simulated pumped-in-place concrete. Two rows of Tribars at that locality of the toe

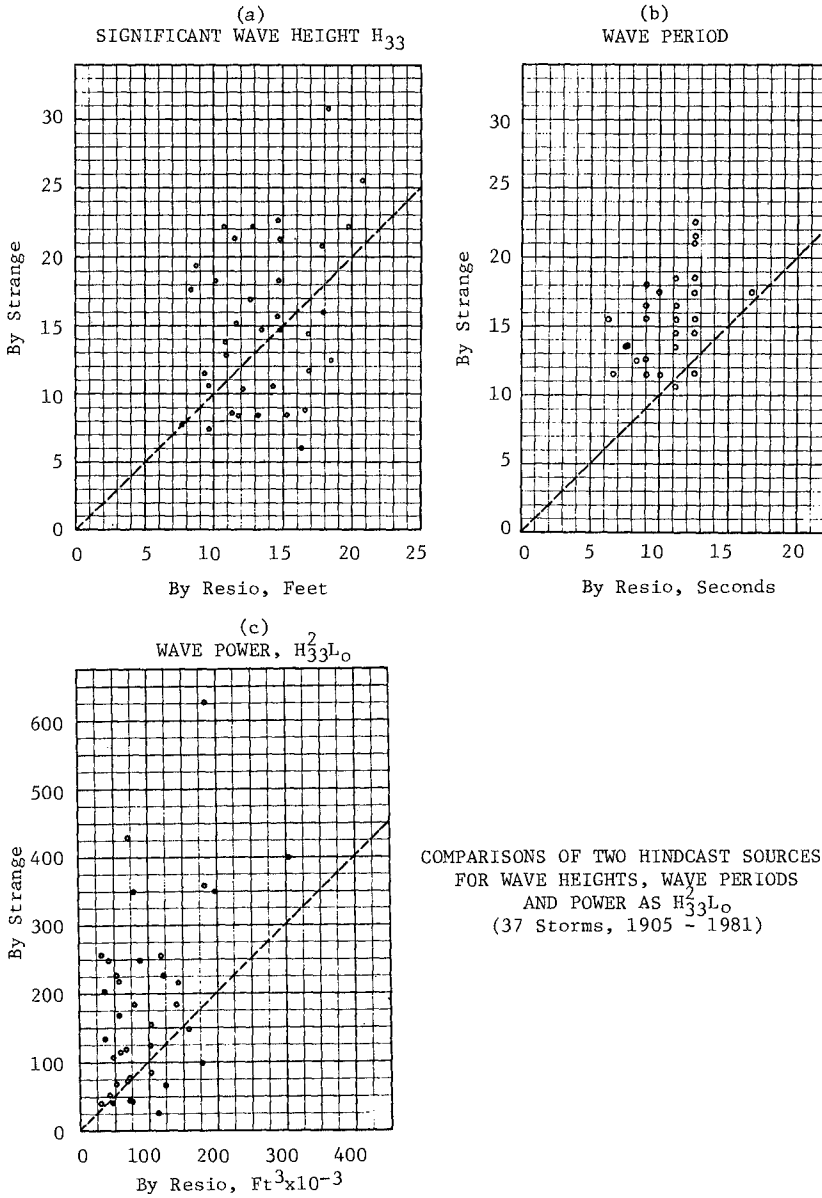
of the slope were embedded to a thickness equal to one-half the Tribars' height. This procedure was first used in 1975 to solve an edge restraint problem on the toe of East Breakwater's sheltered side and proved to be effective and was found in 1981 to be entirely intact (4, pgs 87-91). To be conservative, the embedment was continued along the toe of slope until it reached to the -30 feet contour on both sides of the -15 feet rock. The whole breakwater was again rebuilt, otherwise exactly according to the original design, and again tested with both uniform wave trains of up to 21 feet heights and random wave trains like those of January 28, 1981, in which the significant height of the wave train was 19 feet. The results at the embedded toe were good, the edge Tribars were successfully restrained from shifting.

#### UPGRADED RECONSTRUCTION GOALS

The weak link in West Breakwater's resistance to the original design goals had been found and was remedied by the pumped concrete "hem" at the high level toe of the terminal slope. However, with prolonged attack in the model by the January 28, 1981 peak wave train it was eventually able to remove a cluster of three or four Tribars on the far side of the terminus. Once such a cluster of Tribars had tediously been removed by prolonged attack, another analogy to the behavior of the ravellable fabrics was evident. Like a hole in the middle of some fabric meshes, the cluster of stripped away Tribars grew rapidly. It was obviously the edge effect again. With clusters of only 2 or possibly 3 Tribars removed by waves the perimeter Tribars around the cluster area appeared to be giving mutual restraint, each to the adjoining two, against being shifted by moving water. It was much as arch stones carry higher structural loads laterally and then down to a masonry building's foundation. But when the three or four Tribars were gone such arching action between peripheral remaining pieces diminished and the wave overwash shifted, then tipped, then rolled out and carried away the edge pieces in rapid succession. It was evident that the January 28, 1981 storm, which had at its peak an  $H_{3/3}^L$  value per wave of 350,000 at SCAN as contrasted with the original design's value of 205,400, would eventually have damaged West Breakwater if the "weak link" at the high edge of the terminus' toe had not existed at all.

The project owners needed to know the probable recurrence interval for the 1981 storm in order to have a decision basis for questions of upgrading vs. reproducing the original structure. Identical wave hindcast assignments were separately given to two qualified marine meteorologists, to identify all storms in the weather maps that had been compiled since the earliest days that had inferrable potential for severe attack in the inshore waters at Diablo Canyon Site. They collaborated only in searches of the records, beginning with those of 1899 and continuing through January of 1981, and reached a consensus on forty events. It was understood that either hindcaster was free to make further additions or deletions as he got deeper into his assignment. R. Rea Strange III compiled 47 hindcasts of his expanded list of storms and D. T. Resio submitted 41. The results from the two efforts were carefully compared and, as shown by Figure 16(a), their wave height hindcast data were fairly well centered on a 1:1 comparison line, though quite scattered. Figure 16(b) however shows consistent

Figure 16



COMPARISONS OF TWO HINDCAST SOURCES  
 FOR WAVE HEIGHTS, WAVE PERIODS  
 AND POWER AS  $H_{33}^2 L_0$   
 (37 Storms, 1905 - 1981)



disagreement between the peak frequencies of the spectra from the two hindcasters. In most storms the frequency according to Strange was lower than the values from Resio. Each hindcaster's data are also compared by using the wave periods to calculate wave lengths and thus to derive the  $H_{3/3}^2L$  characteristics at the peak of each storm. That comparison appears in Figure 16(c). With the typically larger wave periods thus affecting the comparison it was clear that use of Strange's hindcasts would be the more conservative choice. That the periods hindcast by Strange also compared satisfactorily with the periods found in the few buoy records of storms that had also been independently hindcast, confirmed the conclusion that Strange's results should be used in the present studies when wave storms that had not been recorded would be generated in the model basin.

The most severe storm in the hindcast report, between 1899 and 1981, occurred on March 13, 1905. According to Professor Leon E. Borgman, who analyzed the storms statistically for the principal investigator, that storm has a probable return frequency of 100 years at SCAN if the wave height is used for ranking, and of 80 years when the  $H_{3/3}^2L$  characteristic is used to rank the storms' strength. The respective values for the January 28, 1981 storm he found to be 13 and 18 years. The original design criteria would fall on Borgman's return frequency curves at 8 years for wave height and 8 years also for  $H_{3/3}^2L$ .

The project owner instructed that an upgraded design be developed for West Breakwater, to provide a level of resistance to storm attack that would provide undiminished shelter for the intake basin on a continuous basis. An important constraint on an upgraded West Breakwater design was however defined by the owner, namely that for environmental concerns a rebuilt breakwater had to fit within the cross-section, profile and planform limits of the original structure. With that limitation sharply in focus, the investigators tested to see how strong a storm an upgrade concept might be able to resist. After proving the effectiveness of embedding the toe Tribars at the high parts of the terminal cone, the West Breakwater model was rebuilt with 36.8 tons Tribars in the damaged area instead of the 21.5 tons pieces of the original design and of all of the preceding tests. The model was then subjected to several tests with the January 28, 1981 spectrum of irregular waves, and with regular waves whose height was built up from burst to burst until they were on the order of the highest 1 per cent of the waves in the corresponding irregular wave train, or even higher. Eventually in each test several Tribars did come out of the pattern on the back side of the terminal cone and then, as described before, the damage spread quickly. The embedment concept was then adapted to this type of damage evolution, by creating parallel "ribs" of embedded Tribars across the terminal cone. Gaps were left between parallel adjoining ribs so that air that might otherwise be trapped by uprushing waves in the voids of the quarrystone supporting the Tribars could vent harmlessly away. Like rows of stitching across a banner to limit tearing or unravelling of the fabric, the ribs minimized or eliminated the development of clustered Tribar removals. Consequently edge removals of intact Tribars did not grow after single Tribars might be carried away from the gaps between ribs.

Compressive strength of concrete in the prototype specifications was set at 4,500 pounds per square inch at 28 days. Scale strength for the 1:45 model would then be 100 pounds per square inch. A mixture was prepared for the model concrete that was composed of Plaster of Paris, sand, barite and water. It could easily be made to the correct density, had good pouring qualities and the correct scaled compressive strength. However, it was found after several test runs that extended immersion caused the material to become so weak that it could easily be crumbled by pinching it between finger and thumb. Its use was discontinued. Interestingly, however, the embedment functioned effectively in its saturated weak condition, restraining the model Tribars from movement by big waves. Although the embedment concrete undoubtedly should be strong, to achieve longevity of the embedment, the compressive loading on the mass of embedment concrete by Tribars that are being attacked by the waves is low. The function of the embedment is simply to provide a passive restraint against initial movement.

Instead of the Plaster of Paris mixture another material named "Modcrete" was used for both the toe embedment and the rib embedment of Tribars in all the remaining tests. It was developed for the work by personnel of ARCTEC, Incorporated, by adapting and altering that firm's model scaled ice compound, changing its strength and elastic properties by adjustment of proportions of its ingredients and weighting it with barite to achieve the correct specific weight.

A pattern of ribs evolved as the tests proceeded with the 1981 storm conditions. Those ribs stabilized the breakwater for that storm condition, but survival of higher attack levels was desired.

Table B shows the characteristics at the 100 feet depth locality of ten greatest storms at Diablo Canyon Site among the 47 that were selected and hindcast by Strange.

Table B

CHARACTERISTICS AT 100 FEET LOCALITY OF TEN GREATEST STORMS

<u>Date</u>	<u>H<sub>33</sub>Ft.</u>	<u>T<sub>p</sub>Sec.</u>	<u>Azimuth</u>	<u>H<sub>33</sub>L</u>
3/13/05	30.8	14.5	233°	626,500
12/06/69	20.0	22.5	249°	428,900
4/05/58	22.1	17.5	260°	398,900
2/03/15	25.4	12.5	247°	357,300
1/28/81	20.7	17.5	249°	350,000
2/17/80	22.1	15.5	242°	348,800
12/28/31	17.7	17.5	247°	255,900
2/09/60	22.6	11.5	264°	255,100
2/10/63	19.4	14.5	246°	248,500
1/06/39	16.9	18.5	260°	248,000

The hindcasts were reviewed to identify the historical storms that had been most severe from each of four subdivisions of the whole sector from which any damaging waves had reached the site. Three of the four sub-sectors had storms among the ten most severe in the 81 years

covered by the hindcasts. In the remaining sub-sector, the most southerly one, the worst storm was that of January 25, 1914, It was ranked as the 17th strongest of the 47 in the 80 years of hindcasts. The events in March 1905, January 1914, February 1960 and January 1981 were selected for the four events that should be reproduced in continuing test series to discover whether or not additional measures for upgrading West Breakwater should be taken and, if so, to test such measures for effectiveness.

Table C presents the maximum wave conditions from each of the four sub-sectors of approach to which the model breakwaters were exposed. The sets of tests were not done in the order they appear in the table. Each set began with runs using small regular waves and then they were built up toward the maxima until substantial damage developed. At that point the run was halted. The damage was mapped by a surveyor, photos were taken and modifications of the rib patterns were decided upon. The breakwater was then rebuilt accordingly. The maximum heights of regular waves that were reached generally approximated or exceeded the 1 per cent wave height for the hindcast waves of the maximum historical storm for that sector of approach.

After the attacks by the maximum hindcast storm spectra from the four sub-sectors of approach had been made, and in each test the embedded ribs had been improved so that West Breakwater survived without progressive damage, the 1905 storm spectrum was generated from each of the four sectors at several tide stages for each direction. As indicated by the  $H^2L$  factors shown in the last column at the right of Table C, those tests using the 1905 spectrum substantially exceeded the attack levels of the historical storms in each of the other three sectors. Furthermore, the durations of the test runs from the 1905 storm in its own sector,  $233^\circ$ , at fixed tide levels rather than naturally transient levels, constituted attacks that were more drastic than the historical. Single Tribars at randomly scattered locations were removed by waves during some of the 1905 storm tests, two adjoining Tribars in one case, but none of those areas then grew larger during persistent continuing attack by these final extreme condition tests. In fact, these small opened areas shrank slightly, enough that a Tribar could not be reinserted in the remaining space.

Figure 17 shows the plan that was recommended for the restoration and upgrading of West Breakwater; Figure 18 presents the related cross-sections. During the final verification testing, when extreme storm conditions were imposed, some vulnerability of the Tribars was seen at two shallow toe features and at the emergent edge of the armoring where East Breakwater springs from a reef at its root. As shown on Figures 17 and 18 embedment of the toe at those locations was included in the recommended plan. The recommendations were adopted and the breakwater was reconstructed accordingly. Packing the Tribars to 90 per cent of the theoretically perfect pack was specified. As each Tribar was set in place the three coordinate values for the center at the top of each of the 3 legs of the piece were determined by instrument surveys and field computer, to determine if an acceptable placement had been achieved before the Tribar was released from the setting crane's tackle. No new work shift was started by the contractor until it had

BREAKWATER DAMAGE MODEL

2805

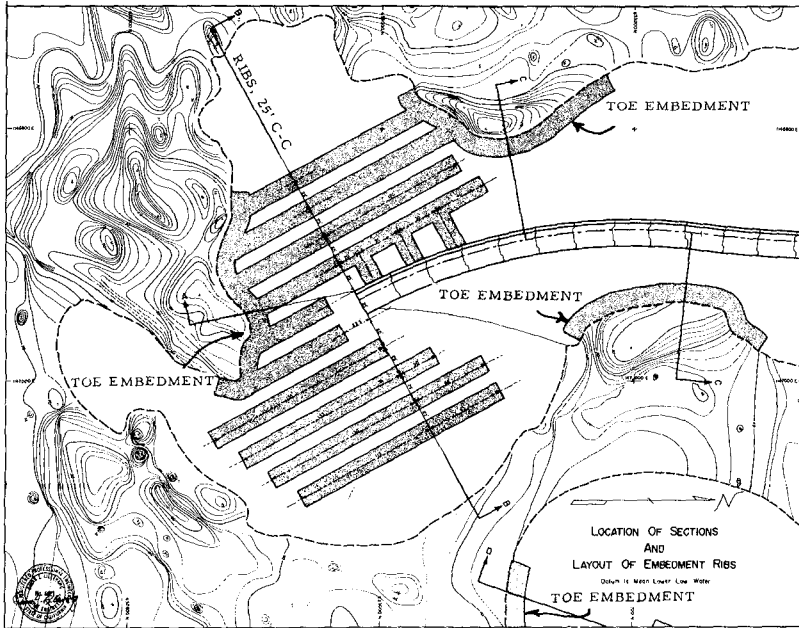
Table C

MAXIMUM CONDITIONS GENERATED AT 100 FEET DEPTH LOCALITY  
DURING 47 TESTS ON DIABLO MODEL BREAKWATERS

Azimuth At 100' Depth	REGULAR WAVES				IRREGULAR WAVES				
	Tide (Ft)	H (Ft)	T (Sec)	Length (Ft)	Spectrum Of:	Tide (Ft)	H <sub>33</sub> (Ft)	T <sub>p</sub> (Sec)	H <sub>33</sub> <sup>2</sup> L 1000
270°	+7.5	37	18	987	2/09/60	+7.5	24	18	568
	-2.0	41	18	948		-2.0	25	18	593
	+7.5	37.5	11.5	564					
	-2.0	39	11.5	548					
					3/13/05	+7.5	30	14.5	687
						+5.3	32	14.5	775
						+2.8	30	14.5	675
						0.0	31	14.5	713
						-2.0	34	14.5	851
	249°	+3.7	33	16	848	1/28/81	+7.5	25.5	17.5
+3.7							26	17.5	636
-2.0							24	17.5	529
					3/13/05	+7.5	32	14.5	782
						-2.0	31	14.5	708
233°	+7.5	35	14.5	763	3/13/05	+7.5	31	14.5	733
	-2.0	45	14.5	736		-2.0	29	14.5	619
217°	+7.5	35	12.5	631	1/25/14	+3.7	19.5	12.5	237
	+3.7	35.5	12.5	624					
	-2.0	35	12.5	611					
					3/13/05	+7.5	30	14.5	681
						+5.3	27	14.5	552
						+2.8	25.5	14.5	488
						0.0	25	14.5	464
						-2.0	25	14.5	460

Figure 17

## RECOMMENDED PLAN FOR RIBS AND TOE EMBEDMENT



SCALE 1 : 1325

been demonstrated to the Resident Engineer by computer analysis that the preceding shift's placing results had met or exceeded the packing requirement that was specified. Figure 19 is printed at greatly reduced scale from the map at 1"-20' (1:240). It shows a computer plot of the surveyed Tribars as built in the prototype in 1983-84.

#### CONCLUSION

The solution for upgrading the breakwater's resistance to storms that has been described is by no means conventional; that is mostly due to the constraint that had been laid down, that the original alignment, profile and cross-section limits had to enclose the upgraded structure. However, the unique character of the terrain effects at the site and the conventional influences of cost for larger structures in the sea might well have made this an appropriate solution even if the environmentally related limits had not been imposed.

The authors conclude that investigations of problems involving wave attack on the termini of rubble mound breakwaters should always be undertaken with the aid of three-dimensional physical modelling unless

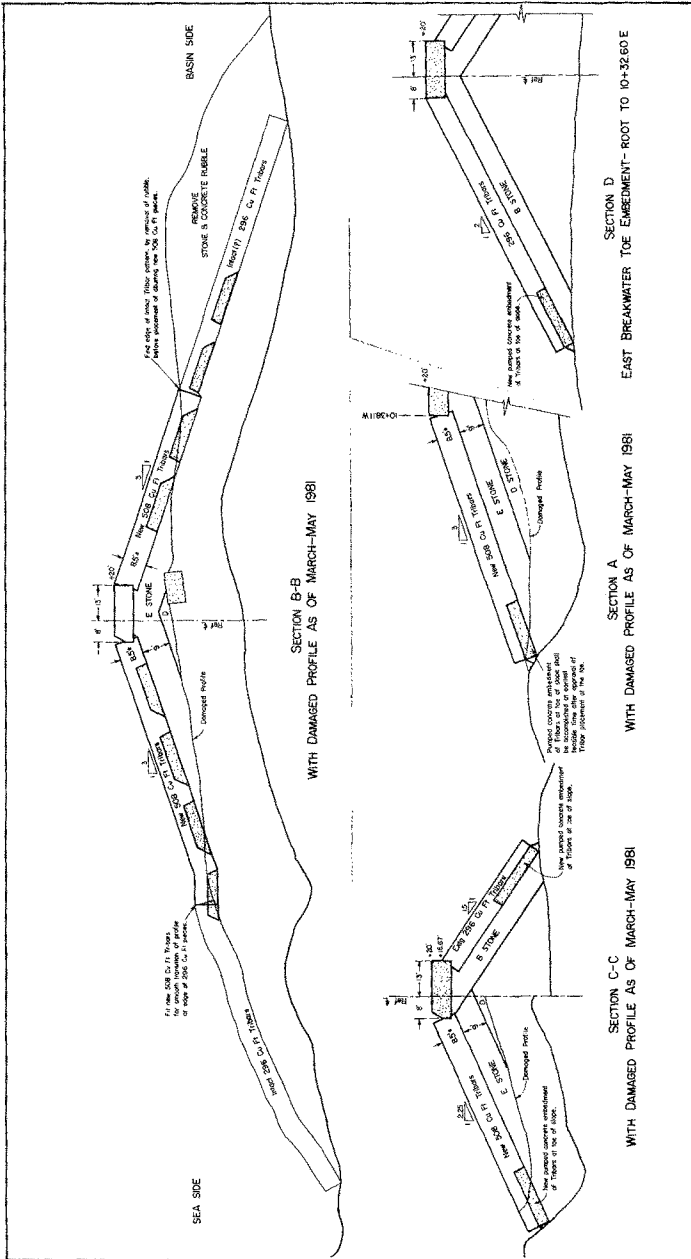
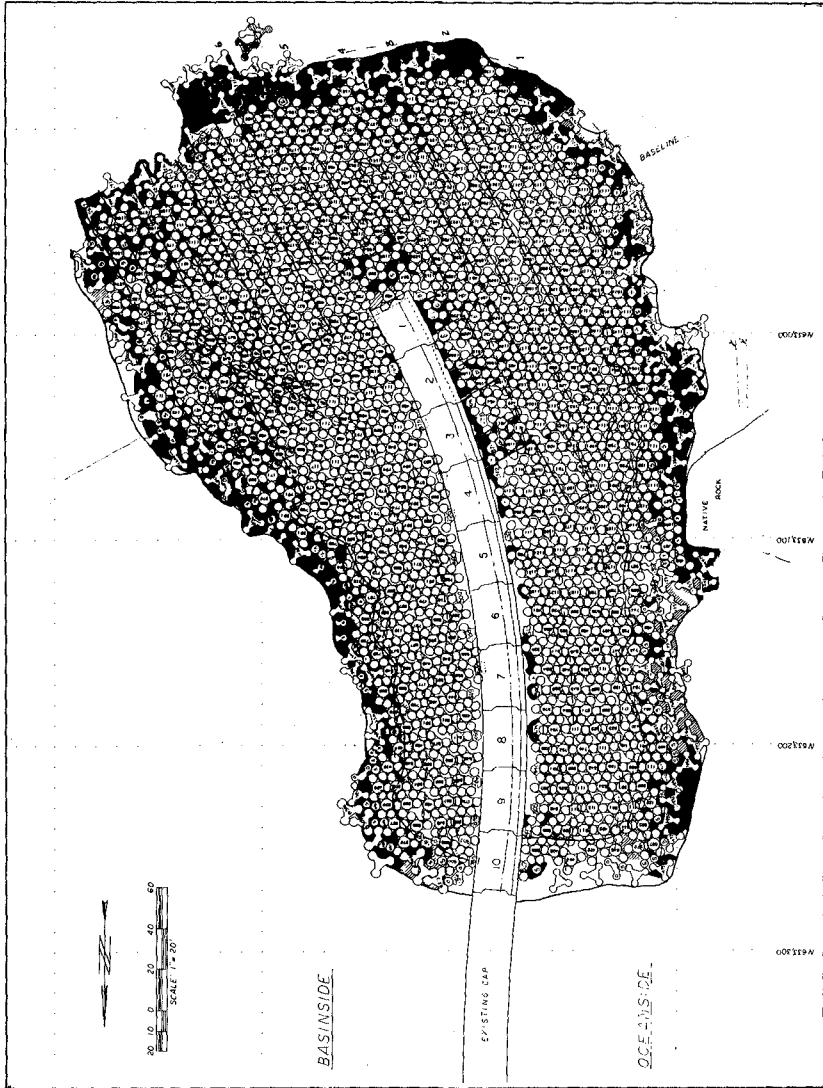


Figure 18  
CROSS-SECTIONS SHOWING RECOMMENDED RIBS AND TOE EMBEDMENTS

Figure 19

SURVEYED POSITIONS OF TRIBARS  
AS BUILT AT DIABLO CANYON WEST BREAKWATER  
1984



owner and engineer are in a position knowingly to take large risks. Further, that physical modelling at suitably large scale is virtually mandated if the submerged terrain at a site is not regular.

#### ACKNOWLEDGMENTS

Michele M. Monde, A.M.ASCE, with the authors, completed the team of professionals that carried out the model studies to which this paper relates.

The authors' appreciation is expressed to the owner of the project, Pacific Gas and Electric Company of San Francisco, California, for permission to publish this paper. The support provided to the investigators by the Company has been exceptional and is gratefully acknowledged.

#### REFERENCES

- (1) Coudert, J. F. and Raichlen, F., Discussion of "Wave Refraction Near San Pedro Bay, California", Journal, Waterways, Harbors and Coastal Engineering, American Society of Civil Engineers, August 1970.
- (2) Goda, Y, "Numerical Experiments on Wave Statistics With Spectral Simulation", Report of the Port and Harbor Institute of Japan, Vol. 9, No. 3, Sept. 1970.
- (3) Goda, Y, and Suzuki, Y, "Estimation of Incident and Reflected Waves in Random Wave Experiments", Proceedings of the XVth Coastal Engineering Conference, Chapter 48, 1976.
- (4) Lillevang, Omar J., "Breakwater Subject to Heavy Overtopping; Concept, Design, Construction and Experience", ASCE Ports '77, Vol. II pgs. 61-93, 1977.



## CHAPTER ONE HUNDRED EIGHTY EIGHT

### ANALYSIS OF UPRIGHT STRUCTURE FOR WAVE DISSIPATION USING INTEGRAL EQUATION

Kazuhiro Hagiwara

#### ABSTRACT

A theoretical analysis using an integral equation derived for the unknown horizontal velocity component in a pervious wall is proposed for estimating the reflection and transmission coefficients of upright structures for wave dissipation, and various factors related to wave and structural conditions having influences on the wave dissipating characteristics are investigated for a breakwater with pervious vertical walls at both seaward and landward sides.

In two-dimensional experiments, the theoretical results are in good agreement with experimental data with respect to reflection and transmission coefficients, and therefore, the wave dissipating characteristics of upright structures for wave dissipation can be explained by the integral equation method theory.

#### INTRODUCTION

Recently, the decline of water quality in harbors has become a serious problem in Japan. Therefore, upright breakwaters for wave dissipation such as those with pervious vertical walls at both seaward and landward sides have been constructed for the purposes of reducing reflected wave heights in the harbor, and facilitating exchange of water inside and outside of the harbor. With this type of breakwater, sea water in the protected area can be kept relatively clean to allow the water to pass through the breakwater, but calmness inside the harbor is liable to be disturbed. Consequently, the structural dimensions of this type of breakwater which is required to satisfy the contrasting demands for wave dissipation and water passage must be carefully examined.

A number of theoretical studies such as by Sawaragi and Iwata have been conducted regarding the problem of wave transmission through and reflection from upright structures for wave dissipation. However, equations for calculating the reflection and transmission coefficients are not easily derived.

In this paper, a theoretical method for estimating reflection and

---

Research Engineer, The Research Institute of Shimizu Construction Co., Ltd., 4-17, Etchujima 3-Chome, Kotoku, Tokyo 135, Japan

transmission coefficients of an upright structure for wave dissipation based on an integral equation is proposed while examining various factors related to wave and structural conditions having influences on the dissipating characteristics. In addition, experimental data are utilized to substantiate this theory.

THEORY

Suppose a breakwater, as shown in Figure 1, with pervious vertical walls at both seaward and landward sides, the origin of the coordinate system being taken at the still water surface at the center of the reservoir space with the  $x$  axis horizontal and  $z$  axis vertical and pointing upward. The pervious parts of the front wall with thickness  $b_1$  at  $x = -l$  and of the rear wall with thickness  $b_2$  at  $x = l$  are  $-d_2 \leq z \leq -d_1$  and  $-d_4 \leq z \leq -d_3$ , respectively. Also, suppose that the influence of the discontinuity of water stream is within the limits of  $x_{-2} \leq x \leq x_{-1}$  at the front wall and  $x_1 \leq x \leq x_2$  at the rear wall, respectively, and is very small compared with the wave length. The water area is divided into three regions, (I), (II), and (III).

Assuming a small-amplitude wave in an incompressible perfect liquid in two dimensions with the velocity potential in each region  $\phi_s(x, z; t) = \phi_s(x, z)e^{i\sigma t}$  ( $s=1,2,3$ ), where  $\sigma$  is the incident wave of frequency, then, solutions for Laplace's equation which satisfy surface and boundary conditions are expressed as follows:

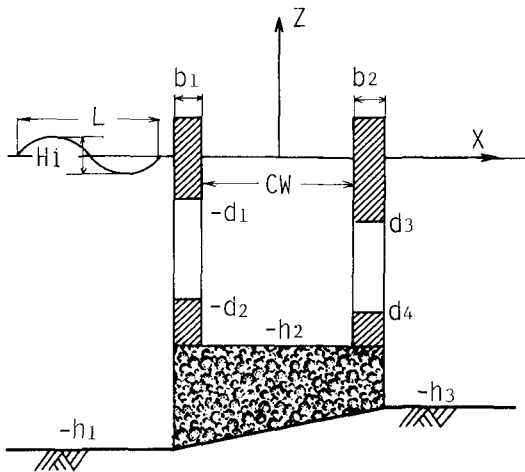


Figure 1 Definition sketch of breakwater with pervious vertical walls at both seaward and landward sides.

$$\begin{aligned} \phi_1(x, z) = & \{A \exp(-ik(x+l+b_1)) + B \exp(ik(x+l+b_1))\} \frac{\cosh k(z+h_1)}{\cosh kh_1} \\ & + \sum_{m=1}^{\infty} C_m \exp(k_m(x+l+b_1)) \frac{\cos k_m(z+h_1)}{\cos k_m h_1} \quad \dots (1) \end{aligned}$$

$$\begin{aligned} \phi_2(x, z) = & (D \frac{\cos k'x}{\cos k'l} + E \frac{\sin k'x}{\sin k'l}) \frac{\cosh k'(z+h_2)}{\cosh k'h_2} \\ & + \sum_{n=1}^{\infty} (F_n \frac{\cosh k_n'x}{\cosh k_n'l} + G_n \frac{\sinh k_n'x}{\sinh k_n'l}) \frac{\cos k_n'(z+h_2)}{\cos k_n'h_2} \quad \dots (2) \end{aligned}$$

$$\begin{aligned} \phi_3(x, z) = & I \exp(-ik''(x-l-b_2)) \frac{\cosh k''(z+h_3)}{\cosh k''h_3} \\ & + \sum_{s=1}^{\infty} J_s \exp(-k_s''(x-l-b_2)) \frac{\cos k_s''(z+h_3)}{\cos k_s''h_3} \quad \dots (3) \end{aligned}$$

where,  $A$  is the known complex constant which represents the incident wave.  $B$  and  $I$  are unknown complex constants representing reflected and transmitted waves, respectively. Also,  $D$ ,  $E$  and  $C_m$ ,  $F_n$ ,  $G_n$ ,  $J_s$  are unknown complex constants for standing and scattered waves, respectively. Further,  $k$ ,  $k_m$ ,  $k'$ ,  $k_n'$  and  $k''$ ,  $k_s''$  are eigenvalues determined by the following relations:

$$\sigma^2 = gk \tanh kh_1 = -gk_m \tan k_m h_1 \quad (m=1, 2, 3, \dots) \quad \dots (4)$$

$$\sigma^2 = gk' \tanh k'h_2 = -gk_n' \tan k_n' h_2 \quad (n=1, 2, 3, \dots) \quad \dots (5)$$

$$\sigma^2 = gk'' \tanh k''h_3 = -gk_s'' \tan k_s'' h_3 \quad (s=1, 2, 3, \dots) \quad \dots (6)$$

where,  $g$  is gravitational acceleration,

Let the horizontal velocity of the pervious part of the vertical wall be  $U_1(z)$  and  $U_2(z)$  at the front and rear walls, respectively. Then the principle of conservation of mass requires the following conditions;

$$U_1(z) = \frac{1}{\epsilon_1} \frac{\partial \phi_1}{\partial x} \Big|_{x_2 \approx -(l+b_1)} = \frac{1}{\epsilon_1} \frac{\partial \phi_2}{\partial x} \Big|_{x_1 \approx -l} \quad \dots (7)$$

$$U_2(z) = \frac{1}{\epsilon_2} \frac{\partial \phi_2}{\partial x} \Big|_{x_1 \approx l} = \frac{1}{\epsilon_2} \frac{\partial \phi_3}{\partial x} \Big|_{x_2 \approx l+b_2} \quad \dots (8)$$

where,  $\epsilon_1$  and  $\epsilon_2$  are opening ratios of the pervious parts of the front and rear walls, respectively. Substituting Eqs. (1), (2) and (3) into Eqs. (7) and (8), we have the following equations:

$$\begin{aligned} \epsilon_1 U_1(z) = & -i(A-B) \frac{k \cosh k(z+h_1)}{\cosh kh_1} + \sum_{m=1}^{\infty} C_m \frac{k_m \cos k_m(z+h_1)}{\cos k_m h_1} \quad \dots (9) \\ = & (D \tan k'l + E \cot k'l) \frac{k' \cosh k'(z+h_2)}{\cosh k'h_2} \end{aligned}$$

$$-\sum_{n=1}^{\infty} (F_n \tanh k_n' l - G_n \coth k_n' l) \frac{k_n' \cos k_n'(z+h_2)}{\cosh k_n' h_2} \dots, (10)$$

$$\begin{aligned} \epsilon_2 U_2(z) = & -(D \tan k' l - E \cot k' l) \frac{k' \cosh k'(z+h_2)}{\cosh k' h_2} \\ & + \sum_{n=1}^{\infty} (F_n \tanh k_n' l + G_n \coth k_n' l) \frac{k_n' \cos k_n'(z+h_2)}{\cosh k_n' h_2} \dots, (11) \end{aligned}$$

$$= -i I \frac{k'' \cosh k''(z+h_3)}{\cosh k'' h_3} - \sum_{s=1}^{\infty} J_s \frac{k_s'' \cos k_s''(z+h_3)}{\cosh k_s'' h_3} \dots, (12)$$

Considering the orthogonality of the function hyperbolic sine and sine, we multiply each term of Eq. (9) by  $\cosh k(z+h_1)$  and  $\cos k_m(z+h_1)$ , of Eqs. (10) and (11) by  $\cosh k'(z+h_2)$  and  $\cos k_n'(z+h_2)$ , and of Eq. (12) by  $\cosh k''(z+h_3)$  and  $\cos k_s''(z+h_3)$ . In consideration of  $U_1(z) = U_2(z) = 0$  except for  $-\bar{d}_2 \leq z \leq -\bar{d}_1$  and  $-\bar{d}_4 \leq z \leq -\bar{d}_3$ , integrating from  $z = -h_1$  to  $z = 0$ ,  $z = -h_2$  to  $z = 0$ , and  $z = -h_3$  to  $z = 0$  at each region with respect to  $z$ , we can write the unknown complex constants included in Eqs. (1), (2) and (3).

$$B = A - i \frac{1}{N_0} \int_{-\bar{d}_2}^{-\bar{d}_1} \epsilon_1 U_1(\xi) \cosh k(\xi+h_1) d\xi \dots (13)$$

$$C_m = \frac{1}{N_m} \int_{-\bar{d}_2}^{-\bar{d}_1} \epsilon_1 U_1(\xi) \cos k_m(\xi+h_1) d\xi \dots (14)$$

$$\begin{aligned} D = & \frac{1}{2 N_0' \tan k' l} \left[ \int_{-\bar{d}_2}^{-\bar{d}_1} \epsilon_1 U_1(\xi) \cosh k'(\xi+h_2) d\xi \right. \\ & \left. - \int_{-\bar{d}_4}^{-\bar{d}_3} \epsilon_2 U_2(\xi) \cosh k'(\xi+h_2) d\xi \right] \dots (15) \end{aligned}$$

$$\begin{aligned} E = & \frac{1}{2 N_0' \cot k' l} \left[ \int_{-\bar{d}_2}^{-\bar{d}_1} \epsilon_1 U_1(\xi) \cosh k'(\xi+h_2) d\xi \right. \\ & \left. + \int_{-\bar{d}_4}^{-\bar{d}_3} \epsilon_2 U_2(\xi) \cosh k'(\xi+h_2) d\xi \right] \dots (16) \end{aligned}$$

$$\begin{aligned} F_n = & \frac{1}{2 N_n' \tanh k_n' l} \left[ \int_{-\bar{d}_2}^{-\bar{d}_1} \epsilon_1 U_1(\xi) \cos k_n'(\xi+h_2) d\xi \right. \\ & \left. + \int_{-\bar{d}_4}^{-\bar{d}_3} \epsilon_2 U_2(\xi) \cos k_n'(\xi+h_2) d\xi \right] \dots (17) \end{aligned}$$

$$\begin{aligned} G_n = & \frac{1}{2 N_n' \coth k_n' l} \left[ \int_{-\bar{d}_2}^{-\bar{d}_1} \epsilon_1 U_1(\xi) \cos k_n'(\xi+h_2) d\xi \right. \\ & \left. + \int_{-\bar{d}_4}^{-\bar{d}_3} \epsilon_2 U_2(\xi) \cos k_n'(\xi+h_2) d\xi \right] \dots (18) \end{aligned}$$

$$I = i \frac{1}{N_0''} \int_{-\bar{d}_4}^{-\bar{d}_3} \epsilon_2 U_2(\xi) \cosh k''(\xi+h_3) d\xi \dots (19)$$

$$J_3 = -\frac{1}{N_3''} \int_{-d_4}^{-d_3} \epsilon_2 U_2(\xi) \cos k_S''(\xi+h_3) d\xi \quad \dots\dots(20)$$

where,

$$\left. \begin{aligned} N_0 &= \frac{\sinh 2 kh_1 + 2 kh_1}{4 \cosh kh_1}, & N_m &= \frac{\sin 2 kmh_1 + 2 kmh_1}{4 \cos kmh_1} \\ N_0' &= \frac{\sinh 2 k'h_2 + 2 k'h_2}{4 \cosh k'h_2}, & N_m' &= \frac{\sin 2 k_n'h_2 + 2 k_n'h_2}{4 \cos k_n'h_2} \\ N_0'' &= \frac{\sinh 2 k''h_3 + 2 k''h_3}{4 \cosh k''h_3}, & N_3'' &= \frac{\sin 2 k_S''h_3 + 2 k_S''h_3}{4 \cos k_S''h_3} \end{aligned} \right\} \dots\dots(21)$$

The principle of conservation of momentum at the pervious part of the front wall requires the following condition as shown by Mei et al.:

$$P_{x-2} = P_{x-1} + \rho \left( \frac{1}{2} C_1^* |U_1 e^{i\sigma t}| U_1 e^{i\sigma t} + L_1^* \frac{\partial}{\partial t} (U_1 e^{i\sigma t}) \right) \quad \dots\dots(22)$$

where,  $P$  is fluid pressure,  $\rho$  is fluid density,  $C^*$  is head loss coefficient, and  $L^*$  is apparent orifice length. From the condition in which the energy loss for one period in a linear system is equivalent to that in a non-linear system, the linear resistance coefficient  $f$  is given as follows:

$$f_1^* = \frac{4}{3\pi} C_1^* \bar{U}_1 \quad \dots\dots(23)$$

where,  $u_1 = \bar{U}_1 \sin \sigma t$ . Consequently, Eq. (22) is expressed by the velocity potential as follows:

$$\phi_2|_{x-1} - \phi_1|_{x-2} + \beta_1 \left. \frac{\partial \phi_2}{\partial x} \right|_{x-1} = 0 \quad \dots\dots(24)$$

$$\beta_1 = \frac{1}{\epsilon_1} \left( i \frac{f_1^*}{\sigma} - L_1^* \right) \quad \dots\dots(25)$$

In the same way, we obtain the relationships below with respect to the rear wall,

$$\phi_3|x_2 - \phi_2|x_1 + \beta_2 \left. \frac{\partial \phi_2}{\partial x} \right|_{x_1} = 0 \quad \dots\dots(26)$$

$$\left. \begin{aligned} \beta_2 &= \frac{1}{\epsilon_2} \left( i \frac{f_2^*}{\sigma} - L_2^* \right) \\ f_2^* &= \frac{4}{3\pi} C_2^* \bar{U}_2 \end{aligned} \right\} \dots\dots(27)$$

Substituting Eqs. (1) to (3) into Eqs. (24) and (26), we have the following relationships:

$$\{D(1 + \beta_1 k^t \tan k'l) - E(1 - \beta_1 k^t \cot k'l)\} \cdot \frac{\cosh k'(z+h_2)}{\cosh k'h_2}$$

$$\begin{aligned}
 & + \sum_{n=1}^{\infty} \{F_n(1 - \beta_1 k_n' \tanh k_n' l) - G_n(1 - \beta_1 k_n' \coth k_n' l)\} \\
 & \frac{\cos k_n'(z+h_2)}{\cos k_n'h_2} - (A+B) \frac{\cosh k(z+h_1)}{\cosh kh_1} - \sum_{m=1}^{\infty} C_m \frac{\cos k_m(z+h_1)}{\cos k_m h_1} = 0
 \end{aligned}
 \tag{28}$$

$$\begin{aligned}
 & \{D(1 + \beta_2 k' \tan k'l) + E(1 - \beta_2 k' \cot k'l)\} \cdot \frac{\cosh k'(z+h_2)}{\cosh k'h_2} \\
 & + \sum_{n=1}^{\infty} \{F_n(1 - \beta_2 k_n' \tanh k_n' l) + G_n(1 - \beta_2 k_n' \coth k_n' l)\} \\
 & \frac{\cos k_n'(z+h_2)}{\cos k_n'h_2} - \frac{\cosh k''(z+h_3)}{\cosh k''h_3} - \sum_{s=1}^{\infty} J_s \frac{\cos k_s''(z+h_3)}{\cos k_s''h_3} = 0
 \end{aligned}
 \tag{29}$$

Then, substituting Eqs. (13) to (20) into Eqs. (28) and (29) and making a rearrangement, we get, finally, the following results:

$$\epsilon_1 \int_{-d_2}^{-d_1} S_1(z, \xi) U_1(\xi) d\xi + \epsilon_2 \int_{-d_4}^{-d_3} S_2(z, \xi) U_2(\xi) d\xi = A\zeta(z) \dots \tag{30}$$

$$\epsilon_1 \int_{-d_2}^{-d_1} T_1(z, \xi) U_1(\xi) d\xi + \epsilon_2 \int_{-d_4}^{-d_3} T_2(z, \xi) U_2(\xi) d\xi = 0 \dots \tag{31}$$

where,

$$\zeta(z) = \frac{2 \cosh k(z+h_1)}{\cosh kh_1} \dots \tag{32}$$

$$\begin{aligned}
 S_1(z, \xi) = & \frac{\beta_1 k' + \cot 2k'l}{N_0' \cosh k'h_2} \cosh k'(z+h_2) \cosh k'(\xi+h_2) \\
 & + i \frac{1}{N_0' \cosh kh_1} \cosh k(z+h_1) \cosh k(\xi+h_1) \\
 & + \sum_{n=1}^{\infty} \frac{\beta_1 k_n' - \coth 2k_n'l}{N_n' \cos k_n'h_2} \cos k_n'(z+h_2) \cos k_n'(\xi+h_2) \\
 & - \sum_{m=1}^{\infty} \frac{1}{N_m \cos k_m h_1} \cos k_m(z+h_1) \cos k_m(\xi+h_1) \dots \tag{33}
 \end{aligned}$$

$$\begin{aligned}
 S_2(z, \xi) = & - \frac{1}{N_0' \sin 2k'l} \frac{1}{\cosh k'h_2} \cosh k'(z+h_2) \cosh k'(\xi+h_2) \\
 & + \sum_{n=1}^{\infty} \frac{1}{N_n' \sin 2k_n'l} \frac{1}{\cosh k_n'h_2} \cos k_n'(z+h_2) \cos k_n'(\xi+h_2) \dots \tag{34}
 \end{aligned}$$

$$T_1(z, \xi) = S_2(z, \xi) \dots \tag{35}$$

$$\begin{aligned}
 T_2(z, \xi) = & \frac{\beta_2 k'' + \cot 2k''l}{N_0'' \cosh k''h_3} \cosh k''(z+h_3) \cosh k''(\xi+h_3) \\
 & + i \frac{1}{N_0'' \cosh k''h_3} \cosh k''(z+h_3) \cosh k''(\xi+h_3)
 \end{aligned}$$

$$\begin{aligned}
 & + \sum_{n=1}^{\infty} \frac{\beta_2 k_n' - \coth 2k_n' l}{N_n' \cos k_n' h_2} \cos k_n'(z+h_2) \cos k_n'(\xi+h_2) \\
 & - \sum_{s=1}^{\infty} \frac{1}{N_s'' \cos k_s'' h_3} \cos k_s''(z+h_3) \cos k_s''(\xi+h_3) \dots\dots(36)
 \end{aligned}$$

Eqs. (30) and (31) are Fredholm's simultaneous integral equations of the first kind. The integral kernels  $S_1(z, \xi)$ ,  $S_2(z, \xi)$ ,  $T_1(z, \xi)$  and  $T_2(z, \xi)$  are known, while  $U_1(\xi)$  and  $U_2(\xi)$  are unknown functions. These functions cannot be determined analytically except for special problems, and so, they must be solved numerically in terms of approximate values. Then, using weight coefficient  $R_i^n$ , we discretize the integrals of Eqs. (30) and (31) as follows:

$$\left. \begin{aligned}
 \int_{-d_2}^{-d_1} S_1(z, \xi) U_1(\xi) d\xi &= \sum_{i=1}^n R_i^n S_1(z, \xi_i) U_1(\xi_i) (d_2 - d_1) \\
 \int_{-d_4}^{-d_3} S_2(z_1, \xi) U_2(\xi) d\xi &= \sum_{i=1}^n R_i^n S_2(z, \xi_i) U_2(\xi_i) (d_4 - d_3) \\
 \int_{-d_2}^{-d_1} T_1(z, \xi) U_1(\xi) d\xi &= \sum_{i=1}^n R_i^n T_1(z, \xi_i) U_1(\xi_i) (d_2 - d_1) \\
 \int_{-d_4}^{-d_3} T_2(z, \xi) U_2(\xi) d\xi &= \sum_{i=1}^n R_i^n T_2(z, \xi_i) U_2(\xi_i) (d_4 - d_3)
 \end{aligned} \right\} \dots\dots(37)$$

Now, with

$$\begin{aligned}
 f_j &= Af(z_j), \quad U_i^{(1)} = \epsilon_1 (d_2 - d_1) U_1(\xi_i) \\
 U_i^{(2)} &= \epsilon_2 (d_4 - d_3) U_2(\xi_i) \dots\dots(38) \\
 S_{ji}^{(1)} &= S_1(z_j, \xi_i), \quad S_{ji}^{(2)} = S_2(z_j, \xi_i) \\
 T_{ji}^{(1)} &= T_1(z_j, \xi_i), \quad T_{ji}^{(2)} = T_2(z_j, \xi_i)
 \end{aligned}$$

Eqs. (30) and (31) to be finally solved will be the following in terms of matrix expression:

$$\begin{bmatrix} R_1^n S_{11}^{(1)} & \dots & R_n^n S_{1n}^{(1)} & R_1^n S_{11}^{(2)} & \dots & R_n^n S_{1n}^{(2)} \\ \vdots & & \vdots & \vdots & & \vdots \\ R_1^n S_{n1}^{(1)} & \dots & R_n^n S_{nn}^{(1)} & R_1^n S_{n1}^{(2)} & \dots & R_n^n S_{nn}^{(2)} \\ R_1^n T_{11}^{(1)} & \dots & R_n^n T_{1n}^{(1)} & R_1^n T_{11}^{(2)} & \dots & R_n^n T_{1n}^{(2)} \\ \vdots & & \vdots & \vdots & & \vdots \\ R_1^n T_{n1}^{(1)} & \dots & R_n^n T_{nn}^{(1)} & R_1^n T_{n1}^{(2)} & \dots & R_n^n T_{nn}^{(2)} \end{bmatrix} \begin{bmatrix} U_1^{(1)} \\ \vdots \\ U_n^{(1)} \\ U_1^{(2)} \\ \vdots \\ U_n^{(2)} \end{bmatrix} = \begin{bmatrix} f_1 \\ \vdots \\ f_n \\ 0 \\ \vdots \\ 0 \end{bmatrix} \dots\dots(39)$$

For incident wave of  $\eta = (H_I/2) \cdot \cos(kx - \sigma t)$ , we have constant A in region (I) as follows:

$$A = i \frac{H_I}{2} \frac{g}{\sigma} \exp(ik(l+bt_1)) \quad \dots, (40)$$

The values of  $U_i(1)$  and  $U_i(2)$  were determined in this study using the Gauss-Moor method as shown by Hidaka. On obtaining the values, reflection coefficient  $K_R$  and transmission coefficient  $K_T$  can be calculated by Eqs. (13) and (19), respectively.

#### LABORATORY EXPERIMENTS

##### 1. Experimentation Equipment and Procedures

Tests were performed in a two-dimensional wave channel made of steel, 20.0 m long, 0.6 m wide, and 1.0 m deep. The breakwater model having two slotted walls of 2.6-cm thickness was made of vinyl chloride and the front wall was fixed at 14.0 m from the wave generator plate.

The depth of water was maintained constant at 50 cm in the experiments. For wave period of 1.2 sec and incident wave height of 2 cm, the opening ratios  $\epsilon_1$  and  $\epsilon_2$  of the front and rear walls, and the chamber width  $C_w (= 2L)$  were suitably varied.

Capacitance-type wave gages were used to measure wave height. Partial clapotis was measured on the front of the model using a mobile carriage equipped with the wave gages, the reflection coefficient being calculated by Healy's method. The transmitted wave height at a location one-fourth of a wave length back of the model was determined by average of five consecutive wave heights.

##### 2. $C^*$ and $L^*$ of Slotted Wall

The head loss coefficient  $C^*$  and the apparent orifice length  $L^*$  must be determined to calculate the reflection and transmission coefficients. For one slotted wall, Mei et al. gave  $C^*$  as a function of the discharge coefficient and the opening ratio of the wall, and indicated  $L^*$  by the geometric dimensions of the wall on the basis of acoustics. Kondo and Sato connected  $C^*$  and  $L^*$  of one perforated wall with drag coefficient  $C_D$  and inertia coefficient  $C_M$  of the wall, respectively, and gave  $C^*$  as a function of both opening ratio and Reynolds number. Also, they gave the non-dimensional parameter  $L^*/L$  ( $L$ : incident wave length) as a function of the Keulegan-Carpenter number. For a caisson with a slotted front wall, Tanimoto and Yoshimoto gave  $C^*$  as a function of the opening ratio of the wall, and also, the non-dimensional parameter of  $L^*$  and the wall thickness as a function of the ratio of chamber width to wave length of the chamber. They obtained an experimental formula of  $C^*$  and  $L^*$  by minimizing the square sum of the difference between the calculated and experimental values related to the reflection coefficient. In this paper,  $C^*$  and  $L^*$  are related to  $C_D$ ,  $C_M$  and the geometric dimensions of the slotted wall, respectively, on the basis of an approach similar to that of Kondo and Sato.

To consider the equilibrium of force on the pervious wall in unsteady flow, it can be expressed as "forces generating flow" = "inertia force of fluid" + "force acting on body." The force acting on the body



can then be expressed separating into drag force and inertia force as follows:

$$Fd = \rho V_f \frac{dq}{dt} + (\rho C_D A_S \frac{|q| \cdot q}{2} + \rho C_M V_S \frac{dq}{dt}) \quad \dots (41)$$

where,  $q$ : fluid velocity in the opening part of the pervious wall,  $V_f$ : volume of fluid,  $V_S$ : volume of the non-opening part of the pervious wall,  $A_S$ : projected area of the non-opening part of the pervious wall.

As the forces which generate flow are due to the pressure gradient between the front and back of the pervious wall, Eq. (41) may be re-written as follows:

$$-\frac{1}{\rho} \frac{\partial P}{\partial x} = C_D \left( \frac{A_S}{V_T} \right) \frac{|q|q}{2} + \left( \frac{V_f}{V_T} + C_M \frac{V_S}{V_T} \right) \frac{dq}{dt} \quad \dots (42)$$

Using the opening ratio  $\epsilon$  and the wall thickness  $\Delta x$ , Eq. (42) may be expressed as:

$$-\frac{1}{\rho} \frac{\partial P}{\partial x} = C_D \frac{1-\epsilon}{\Delta x} \frac{|q|q}{2} + \{ \epsilon + C_M(1-\epsilon) \} \frac{dq}{dt} \quad \dots (43)$$

Meanwhile, the equation of motion of flow in the vicinity of the pervious wall is expressed by Eq. (22) which can be rewritten as follows:

$$-\frac{1}{\rho} \frac{P}{x} = C^* \frac{1}{\Delta x} \frac{|q|q}{2} + L^* \frac{1}{\Delta x} \frac{\partial q}{\partial t} \quad \dots (44)$$

As Eqs. (43) and (44) are equivalent,  $C^*$  and  $L^*$  will be the following:

$$\left. \begin{aligned} C^* &= C_D(1-\epsilon) \\ L^* &= \epsilon \{ 1 + C_M(1-\epsilon) \} \Delta x \end{aligned} \right\} \quad \dots (45)$$

For the inertia coefficient, we use  $C_M = 2.19$  obtained from the potential theory for a square pillar. For the drag coefficient, the following is considered. From Hino and Yamasaki, the quantity of energy dissipation per period is expressed as shown below.

$$\delta = \int_0^T F(t)q(t)dt \quad \dots (46)$$

where, the force  $F(t)$  on the pervious wall and the velocity  $q(t)$  at the opening part of the pervious wall are hypothesized as follows:

$$\left. \begin{aligned} F(t) &= \frac{1}{2} C_D \rho (1-\epsilon) h |q(t)|q(t) \\ q(t) &= q_0 \sin \sigma t \end{aligned} \right\} \quad \dots (47)$$

Substituting Eq. (47) into Eq. (46), we have the following relationship:

$$\delta = \frac{2TC_D \cdot \rho(1-\epsilon)h q_0^3}{3\pi} \dots\dots(48)$$

With  $q_0$  as the average value of the  $Z$  direction at the time phase when  $q(t)$  in Eq. (47) is at the maximum,  $q_0$  is expressed as follows:

$$q_0 = \frac{1}{h} \int_{-h}^0 \frac{1}{\epsilon} \frac{\pi H I}{T} \frac{\cosh k(z+h)}{\sinh kh} dz \dots\dots(49)$$

Consequently, substituting Eq. (49) into Eq. (48),  $\delta$  will be as follows:

$$\delta = \frac{2\pi^2 H I^3 (1-\epsilon) \rho C_D h}{3T^2 \epsilon^3 (kh)^3} \dots\dots(50)$$

or

$$\frac{\delta}{W} = C_D \frac{1-\epsilon}{\epsilon^3} \frac{1}{(kh)^3} \dots\dots(51)$$

where,

$$W = \frac{2\pi^2 H I^3 h}{3g T^2} \dots\dots(52)$$

In this case,  $\delta/W$  indicates the non-dimensional quantity concerning energy dissipation at the pervious wall. We examine  $C_D$  by means of comparing the calculated results with the experimental ones.

The ratio of energy dissipation  $E_I$  for the incident wave is expressed by the reflection coefficient  $K_R$  and the transmission coefficient  $K_T$  as follows:

$$E_I = 1 - K_R^2 - K_T^2 \dots\dots(53)$$

Hence, the quantity of energy dissipation is obtained by multiplying  $E_I$  by the energy and period of the incident wave:

$$\delta = E_t(E \cdot C_g) i \cdot T = (1 - K_R^2 - K_T^2) \cdot \frac{1}{8} \rho g H i^2 \cdot C_g i \cdot T \dots\dots(54)$$

where,  $C_g i$  indicates the group velocity of the incident wave, and is expressed as follows:

$$\left. \begin{aligned} C_g i &= n \cdot C_i \\ n &= \frac{1}{2} \left[ 1 + \frac{2 kh}{\sinh 2 kh} \right] \end{aligned} \right\} \dots\dots(55)$$

where,  $C_i$  is wave velocity. Dividing Eq. (54) by  $W$ , the non-dimensional expression with  $C_D$  corresponding to Eq. (51) as the parameter is obtained.

Figure 2 presents comparisons of  $\delta/W$  between the calculated results by Eq. (51) and the measured ones for the single-slotted wall. These results indicate that the measured values can be approximated by the calculated curve for  $C_D = 2.05$ . Also, Urashima et al. found  $C_D =$

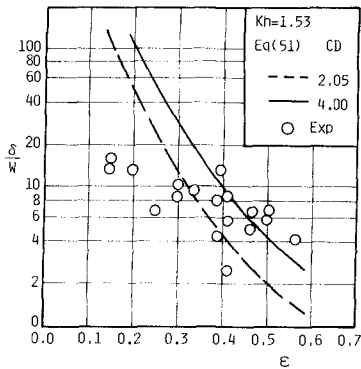


Figure 2 Experimental and theoretical  $\delta/W$ .

2.05 and  $C_M = 2.19$  could be approached when flow velocity was defined by the actual velocity in the slot, and consequently, in this paper,  $C_D = 2.05$  was adopted for both the front and rear walls.

3. Comparisons Between Experiment and Theory

Figure 3 shows comparisons of the reflection and transmission coefficients between experiments and theory for a breakwater having a single vertical slotted wall. The measured values are in good agreement with the theory.

Figures 4 and 5 show comparisons of the experimental and theoretical reflection and transmission coefficients for a breakwater having vertical slotted walls at both the seaward and landward sides. These figures indicate a tendency for theoretical values to be in agreement with measured values, though the latter are generally smaller than the calculated results in Figure 4.

This theory is then compared with the experimental results of other researchers, Figure 6 shows comparisons of the reflection and transmission coefficients from experiments by Kono and Tsukayama and from this theory for a submerged breakwater. As for Figure 7, it shows a comparison of the transmission coefficient from experiments by Kato and Jouman and this theory for double rigid thin barriers. The theoretical results for each type of breakwater are in good agreement with

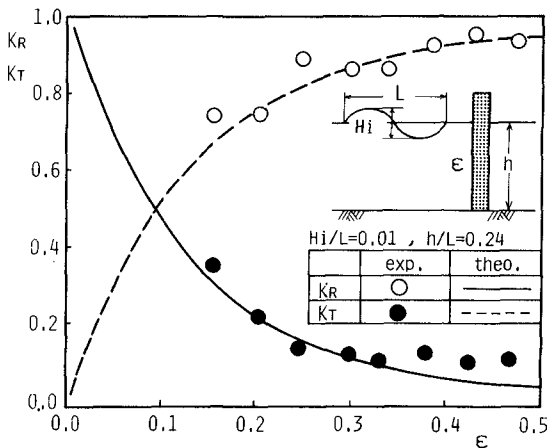


Figure 3 Breakwater with single vertical slotted wall.

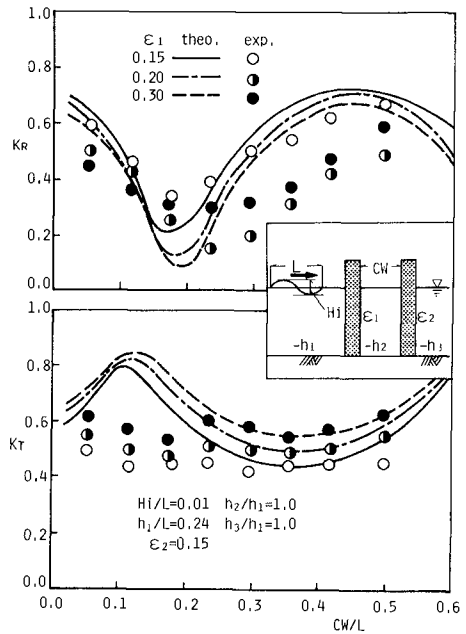


Figure 4 Breakwater with double vertical slotted walls. Plots of  $K_R$ ,  $K_T$  versus  $CW/L$ .

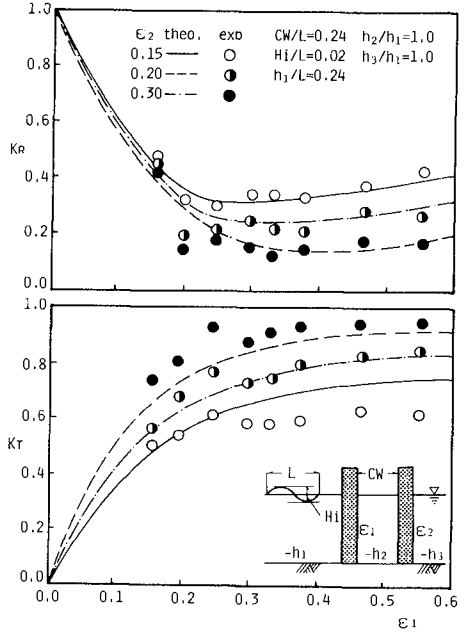


Figure 5 Breakwater with double vertical slotted walls. Plots of  $K_R$ ,  $K_T$  versus  $\epsilon_1$ .

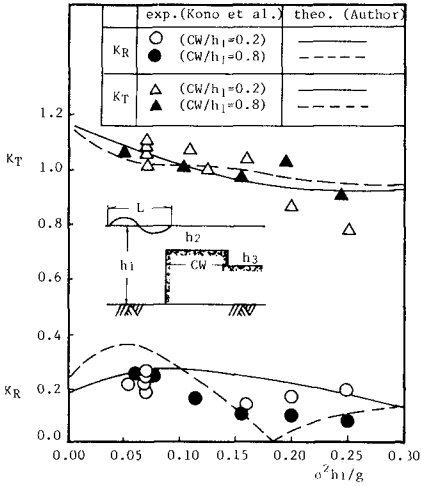


Figure 6 Submerged breakwater.

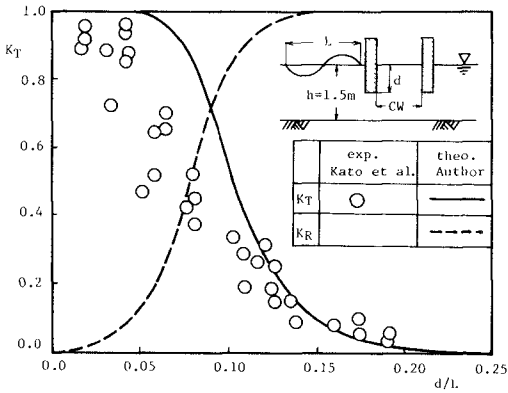


Figure 7 Double rigid thin barriers.

measured results of other researchers. Consequently, it has been found that the wave dissipating characteristics of the upright structures can be explained well by the integral equation method theory.

VARIOUS FACTORS HAVING INFLUENCES ON REFLECTION AND TRANSMISSION COEFFICIENTS

Suppose a prototype breakwater with pervious vertical walls at both seaward and landward sides and examine various factors having influences on the reflection and transmission coefficients, numerically.

Figure 8 shows the relationships between the reflection and

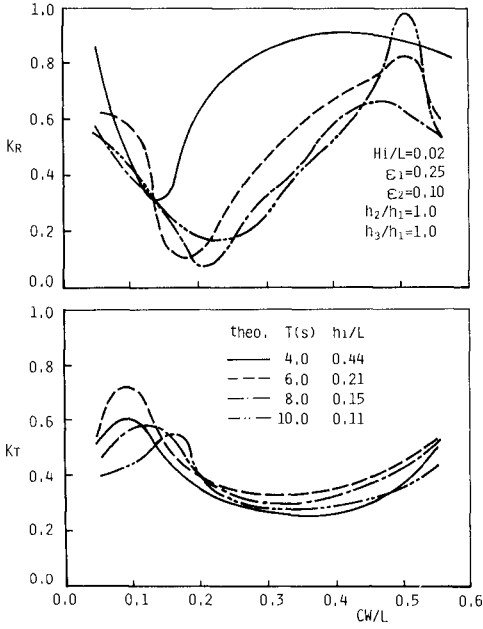


Figure 8  $K_R$ ,  $K_T$  and  $C_W/L$ .

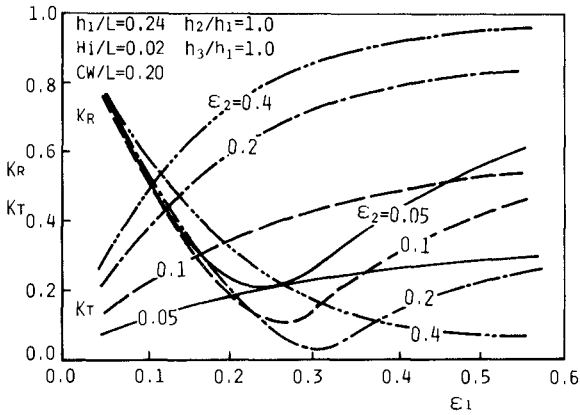


Figure 9  $K_R$ ,  $K_T$  and  $\epsilon$ .

transmission coefficients  $K_R$ ,  $K_T$  and the relative chamber width  $C_W/L$  under the conditions of  $\epsilon_1 = 0.25$ ,  $\epsilon_2 = 0.1$  and  $H_I/L = 0.02$ . The reflection coefficient is a minimum at  $C_{W0}/L$  making the wave energy dissipation maximum. The value of  $C_{W0}/L$  changes by the period  $T$ , that is, the relative water depth  $h_1/L$ , and becomes large for the smaller values of  $h_1/L$ . The transmission coefficient does not change as much as the reflection coefficient for the relative chamber width and the period.

Figure 9 shows the relationships between the reflection and transmission coefficients and the opening ratios for the front and rear pervious walls under the conditions of  $H_I = 1.0$  m,  $T = 6.0$  sec, and  $C_W/L = 0.2$ .

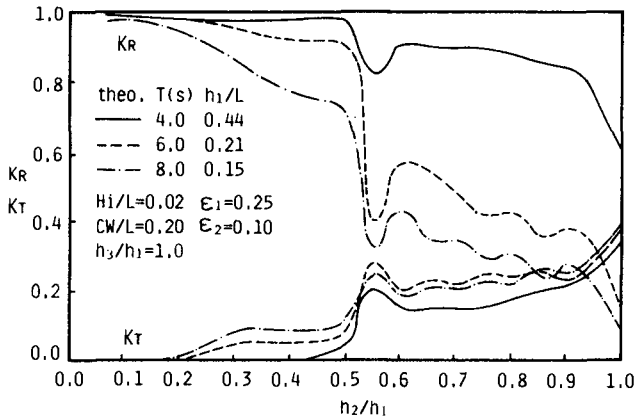


Figure 10  $K_R$ ,  $K_T$  and  $h_2/h_1$ .

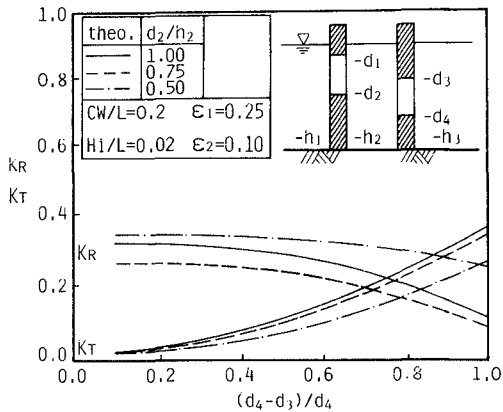


Figure 11  $K_R$ ,  $K_T$  and depth of pervious wall.

The value of  $\epsilon_1$  taking the minimum value of  $K_R$  is small as  $\epsilon_2$  decreases, but the minimum value of  $K_R$  is small as  $\epsilon_2$  increases.  $K_T$  increases as the values of both  $\epsilon_1$  and  $\epsilon_2$  become larger and larger. Consequently, the opening ratios of the front and rear pervious walls having influences on  $K_R$  and  $K_T$  are important, so it is possible to make the values of both  $K_R$  and  $K_T$  small by choosing the opening ratios appropriately.

The relationships between the reflection and transmission coefficients and the water depth in the chamber under the conditions of  $\epsilon_1 = 0.25$ ,  $\epsilon_2 = 0.1$ , and  $C_W/L = 0.25$  are shown in Figure 10. As the values of relative water depth  $h_2/h_1$  become larger and larger,  $K_R$  decreases and  $K_T$  increases, that is, as the water depth in the chamber becomes deeper than one-half of the water depth in front of the breakwater,  $K_R$  decreases suddenly depending on the period, although some amount of waves is let through to the back.

Figure 11 shows the relationships between the reflection and transmission coefficients and depth of the pervious wall under the conditions of  $H_I = 1.0$  m,  $T = 6.0$  sec,  $\epsilon_1 = 0.25$ ,  $\epsilon_2 = 0.1$ , and  $C_W/L = 0.2$ . As the depth of the rear pervious wall becomes greater,  $K_R$  decreases slightly although  $K_T$  increases gradually. Also, the depth of the front pervious wall has a great influence on  $K_R$  more than on  $K_T$ .

#### CONCLUSIONS

- (1) An analytical solution of reflection and transmission coefficients has been derived for an upright breakwater with pervious walls at both seaward and landward sides based upon an integral equation.
- (2) The head loss coefficient and apparent orifice length in the present theory have been related to the drag and inertia coefficients in the wave force equation and the geometric dimensions of the slotted wall, respectively.
- (3) The theoretical results of each type of upright breakwater have been compared with the experimental results of the author and other researchers, and as a result, it has been found that the wave dissipating characteristics of the upright structure with the pervious wall can be explained well by the present theory.
- (4) For the purpose of making both the values of the reflection and transmission coefficients small, it is important to determine the relative chamber width and the opening ratio of the pervious wall appropriately.

#### REFERENCES

- For example, Hidaka, K., "Theory of Applied Integral Equation," Gendai-sha, 1974 (in Japanese).
- Hino, M., and Yamasaki, T., "Reflection and Transmission Coefficient, and Energy Loss of Surface Wave by a Vertical Barrier," Proc. of Japan



Society of Civil Engineers, No. 190, 1971 (in Japanese).

Kato, J., and Jouman, T., "Wave Dissipating Effect of Double Curtain-Wall Breakwater," Proc. of 15th Coastal Engineering Conf. in Japan, 1968 (in Japanese)

Kondo H., and Sato, R., "Presumption of Head Loss and Apparent Orifice Length of Porous Walls," Proc. of 26th Coastal Engineering Conf. in Japan, 1976 (in Japanese).

Kono, T., and Tsukayama, S., "Wave Deformation on a Barrier Reef," Proc. of Japan Society of Civil Engineers, No. 307, 1981 (in Japanese).

Mei, C. C., Liu, P. L. F., and Ippen, A. T., "Quadratic Loss and Scattering of Long Waves," Proc. ASCE, Vol. 100, No. WW3, 1974.

For Example, Sawaragi., T., and Iwata, K., "On Wave Absorber of Two Permeable Walls Type Breakwater Quay," Proc. of Japan Society of Civil Engineers, No. 262, 1977 (in Japanese).

Tanimoto, K., and Yoshimoto, Y., "Various Factors Having Influences on the Reflection Coefficient for Wave Dissipating Caisson with a Slotted Front Wall," Proc. of 29th Coastal Engineering Conf. in Japan, 1982 (in Japanese).

Urashima, S., Ishizuka, K., and Kondo, H., "Characteristics of Wave Force on a Slotted Wall," Tomakomai Technical College, No. 17, 1982 (in Japanese).

## CHAPTER ONE HUNDRED EIGHTY NINE

### COASTAL DESIGN CRITERIA IN SOUTHERN CALIFORNIA

James R. Walker<sup>1</sup> Ph.D., P.E., M. ASCE

Robert A. Nathan<sup>2</sup> P.E., A.M. ASCE

Richard J. Seymour<sup>3</sup> Ph.D., M. ASCE

R. Rea Strange III<sup>4</sup>

#### ABSTRACT

Southern California was subjected to a series of severe winter storms in 1983 that caused record damages to the coast. In the aftermath of the storms, emergency repairs were made and new designs were developed that responded to the severe conditions. These designs were often considerably more conservative than those previously undertaken. Agencies, owners, and engineers were compelled to use both higher design criteria and longer recurrence intervals to account for the wave characteristics and water levels that caused damages along the coast. This paper briefly discusses the unusual circumstances of the storm conditions and the associated damages. The primary purpose of the paper is to present new data that incorporates the effects of the 1983 winter storms to estimate the change in perception of what the wave climate and design criteria may be in this highly developed coastline. The results indicate that the design wave height for a given recurrence interval has increased approximately 26 percent, the wave periods are longer than previously used, and the severe storms tend to coincide with the extreme water levels. The engineer should consider the impacts of the 1983 winter storms in future designs. Despite the record damages, many structures survived. Merely using the highest water elevations and most severe waves of record may not be the most prudent design criteria. The concept of project life and economics must be employed to develop a design.

---

<sup>1</sup>Chief Coastal Engineer, Moffatt & Nichol, Engineers, Long Beach, Ca.

<sup>2</sup>Coastal Engineer, Moffatt & Nichol, Engineers, Long Beach, Ca.

<sup>3</sup>Head, Ocean Engineering Research Group, Scripps Institution of Oceanography, La Jolla, Ca.

<sup>4</sup>President, Pacific Weather Analysis, Santa Barbara, Ca.

## INTRODUCTION

A series of intense storms during the winter of 1983 caused extensive damages to the Southern California coast. Several piers, breakwaters, revetments, homes and beaches were damaged due to a combination of unusually high waves with long periods from an unusual direction of approach coincident with high water elevations. In the aftermath of the storms, public outcry was for more stringent design criteria. Newspapers across the state quoted expert opinion that the wave conditions and water elevations experienced in 1983 were only the beginning of a long-term trend of severe weather for the state and the 1983 storms should be used as the new design storms. The addition of new storm waves and water levels plus the increase of design recurrence intervals may result in an unwarranted compounded increase in design criteria.

## RECENT COASTAL DAMAGES

The winter of 1983 was characterized by several extreme extratropical storm events that occurred during high water levels. The storm events were among the strongest of recorded history; the water levels were the highest of recorded history. The severity of the storm events and the high water levels have been associated with the El Nino-Southern Oscillation (ENSO) as described by Seymour, Strange, Cayan and Nathan (11). These storms were estimated by the U.S. Army Corps of Engineers and the State of California (14) to have caused in excess of \$116 million to coastal structures. Figure 1 shows a summary of the piers that were damaged and Figure 2 is a summary of the breakwaters and jetties that were damaged. Over 70 percent of the damages occurred in Southern California. Several beaches lost considerable quantities of sand and there was conjecture that these beaches would never return because the sand was carried too far offshore to return under normal wave conditions. Many coastal streets, utilities, homes and restaurants were flooded by overtopping waves and high water levels. An oil island located off Seal Beach was completely destroyed. Many of the destroyed structures had survived for 80 years with only minor repairs. Other structures were in need of repair prior to the storms. The primary factors in the damaged structures appear to be the extreme high water level and the high waves with unusually long wave periods approaching from a westerly direction.

Two examples of damages were the San Pedro Breakwater and the San Clemente Pier. The San Pedro Breakwater that protects Los Angeles Harbor was built in the early 1900's. Overtopping waves caused a 400-foot (122 meters) long gap after 80 years of service. A post-storm survey by the U.S. Army Corps of Engineers (13) indicated that there were 166 repair areas to the breakwater and that 87 percent of the failures were on the backslope. Walker, et al. (15) explains the failure mechanism due to excessive water levels and wave heights in relation to the crest elevation. Another mode of failure was the possibility that the stone size was not sufficient for the storm event. The breakwater was repaired by the U.S. Army Corps of Engineers in a manner similar to the original construction.

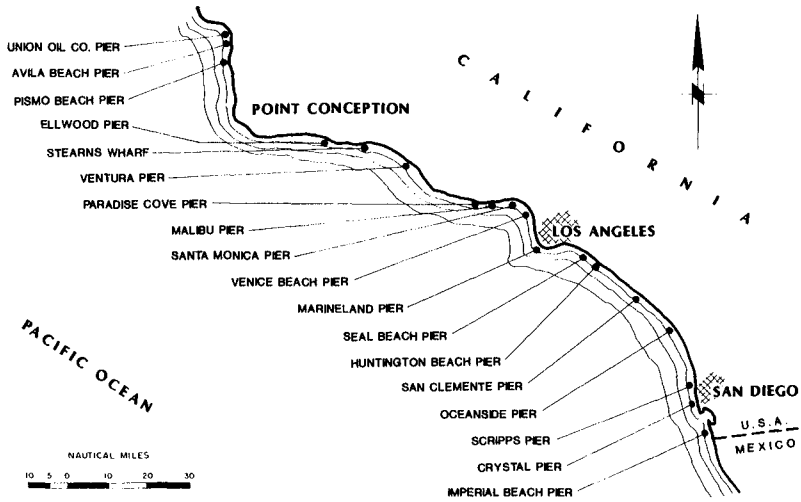


Figure 1. Pier Damage

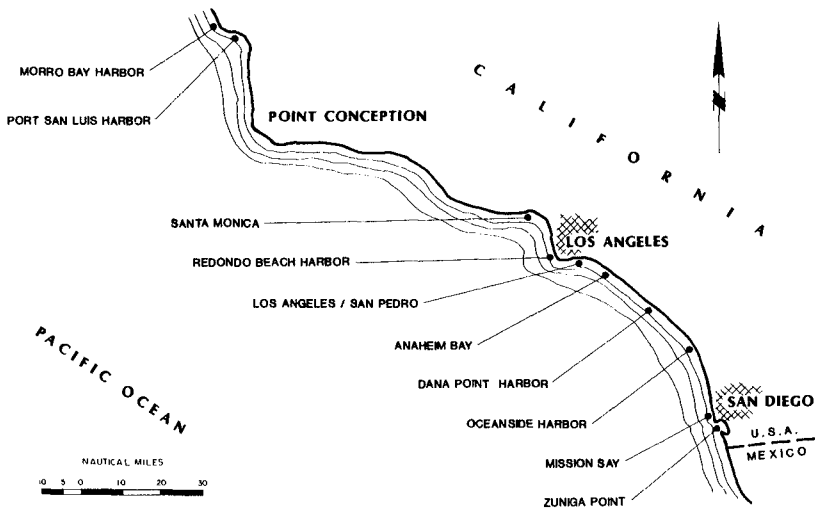


Figure 2. Breakwater and Jetty Damage

The San Clemente Pier was a wooden pile structure that lost approximately 500 feet of the seaward end. Figure 3 shows the existing pier elevation and depth-controlled breakers. Two wave crest elevations are given. The one labeled "prior to 1983" represents the depth-controlled breaker on a 6.0-foot (1.8 meters) mean lower low water elevation that was used as the original design criterion. The wave crest elevation labeled "1983" represents the depth-controlled breaker on a recorded 7.5-foot (2.3 meters) mean lower low water elevation that was measured in San Diego Harbor during one of the events in 1983 that damaged the pier. In this case, damage was attributed to the combination of the wave crest exceeding the pier deck, scour at the sea bed, excessive wave-induced forces on deteriorated piles, and broken pile debris impacting on other piles. Arbitrarily raising design criteria in one aspect may not solve all of the problems. The damage can be readily described using normal water elevations without the need to resort to wave setup and other factors that could raise the water level by 2.0 to 3.0 feet (0.6 to 0.9 meters).

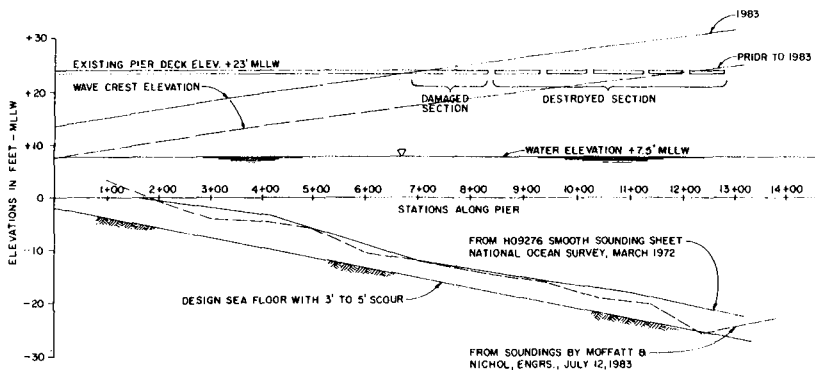


Figure 3. San Clemente Pier

#### EFFECTS OF 1982-1983 WINTER

The ENSO of 1982-1983 was exceptionally strong and had several effects that lead scientists and engineers to suspect that there may be a correlation between high water levels and storm events. When strong ENSOs occur, the water levels are increased, the extratropical cyclones approach from more westerly directions and are closer to the coast, wave heights are higher and periods are greater [see Seymour, et al. (11)]. Shoreline segments that are typically sheltered by the offshore islands and refraction effects from northwesterly waves were more directly exposed to the westerly waves.

### Water Elevations

Prior to 1983, water levels were based primarily on the recordings of nearby harbors such as the gages at Los Angeles and San Diego. These gages incorporated the effects of astronomical tides, ENSO anomalies and some components of storm surge such as the barometric effect. Designers would often add a foot to some water level to account for storm surge and wave setup.

Table 1 is a summary of design water elevations taken from design documents<sup>1</sup> over the last 40 years for typical shore protection structures. Design water elevations were typically lower than the highest of record. The rationale for this was that the probability of the design wave occurring at the same time as the highest water elevation is small. Design water elevations for shore protection structures have increased from mean higher high water [5.4 feet (1.6 meters) above mean lower low water] in the 1940's and 1950's to 10.0 feet (3.0 meters) above mean lower low water in 1984. Design reports showed an increase of 2.0 to 4.0 feet (0.6 to 1.2 meters) following the 1983 winter storms.

TABLE 1

#### Design Water Elevations

1940's - 50's: 5.4 to 6.0 feet (1.6 to 1.8 meters) above MLLW  
1960's - 70's: 6.0 to 7.0 feet (1.8 to 2.1 meters) above MLLW  
1980's: 7.0 to 7.5 feet (2.1 to 2.3 meters) above MLLW  
After 1983 storms: 8.0 to 10.0 feet (2.4 to 3.0 meters) above MLLW

In Southern California, the highest tides of the year usually occur in January; the same month which extratropical storms frequently occur. Record-high water elevations of 7.96 feet (2.43 meters) above mean lower low water and 8.35 feet (2.55 meters) above mean lower low water were recorded on January 27, 1983 at Los Angeles and San Diego, respectively. At the same time, deepwater significant wave heights up to 27.0 feet (8.2 meters) were recorded offshore. The previous record-high water elevations occurred on November 30, 1982. The recorded elevations were 8.09 feet (2.47 meters) above mean lower low water at San Diego and 7.76 feet (2.37 meters) above mean lower low water at Los Angeles.

Recorded annual extreme high water elevations obtained from the National Ocean Service for the San Diego Bay and Los Angeles Outer Harbor reference tide stations were statistically analyzed using the Gumbel (also termed Fisher-Tippett I) distribution. The "tide year" was defined as September to the following August such that the winter season is included within the year. Water elevation records from the San Diego station are available from 1926; Los Angeles water elevation records are available from 1923.

---

<sup>1</sup>The principal source is U.S. Army Corps of Engineers, Los Angeles District, General Design Memorandums.

Figure 4 is a plot of the annual extreme high water elevations versus recurrence intervals for the San Diego and Los Angeles stations, respectively. For each station, the dashed line is a plot of the annual extremes prior to the 1982-1983 record-high water elevation; the solid line is a plot of the annual extremes which have incorporated the record-high water elevation into the data set.

Comparing annual extreme high water elevations at the Los Angeles tide station before and after the 1982-1983 record-high water elevations show that an 8.0-foot (2.4 meters) mean lower low water elevation prior to 1982-1983 has a recurrence interval of approximately 130 years. When the record-high water elevation is added to the data set, the recurrence interval for an 8.0-foot (2.4 meters) water elevation is now approximately 80 years. A 10.0-foot (3.0 meters) mean lower low water elevation with the 1982-1983 water elevation included in the data set has a recurrence interval greater than 500 years. A similar trend is shown for the San Diego Harbor station.

#### Wave Characteristics

Selection of design wave characteristics for coastal structures in Southern California is either based on published hindcasted wave data for a station in deep water or on a hindcast for a specific site. The published data sources typically used in Southern California are hindcasted wave data from the most severe storms occurring between 1900 and 1957 by Marine Advisers (5), from 3-year hindcasts by Marine Advisers (6) and by National Marine Consultants (9), or from once-daily wave computations from 1951 to 1974 by Meteorology International Incorporated (7). Measured wave data which was available during these periods formed short records or records with notable gaps during high wave episodes. Design waves were therefore obtained strictly through hindcast techniques, which differed considerably as a result of a number of factors. First, and most important, is the lack of good meteorological data from ships at sea prior to the mid-1940's. Compounding the problem is the fact that wave forecast techniques differ appreciably among themselves and all utilize empirical wave data collected in the Atlantic, not the Pacific. The same forecast techniques can produce different results when used independently by meteorologists whose experience in the field may differ.

The Marine Advisers (6) and National Marine Consultants (9) wave hindcasts were presented as monthly and annual averages and do not include specific storm wave characteristics. The Marine Advisers (5) and Meteorology International Incorporated (7) do include extreme storm wave characteristics over periods of 58 and 24 years, respectively. The Marine Advisers hindcasts have been used extensively but the Meteorology International Incorporated hindcasts have been judged to be deficient [see Cross (12) and Strange (12)]. For example, only four storms producing combined wave heights of 16 feet (5 meters) or more in twenty-four years were noted. Two of these were not during the storm season, and none of the well-documented high wave episodes are reflected in the statistics. Results of this hindcast have been studied in detail with the conclusion that there are major problems with the methods employed. Therefore, no further

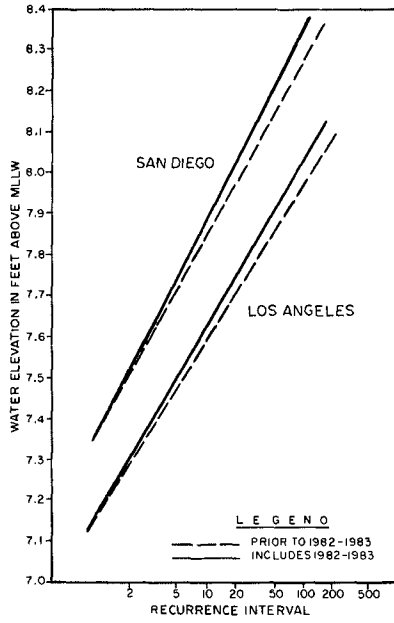


Figure 4. Water Elevation vs. Recurrence Interval

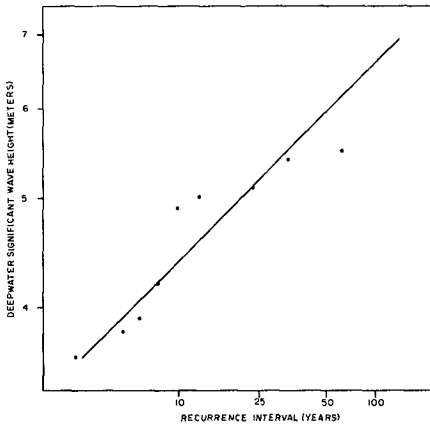


Figure 5. Wave Height Distribution, 1900-1957

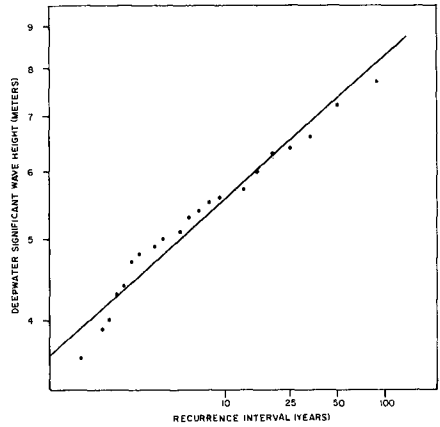


Figure 6. Wave Height Distribution, 1900-1983



consideration is given to the Meteorology International Incorporated wave hindcasted data for purposes of this paper.

The Marine Advisers (5) hindcast study was prepared for the U.S. Army Corps of Engineers to evaluate characteristics of severest probable waves as a basis for design of small-craft harbor protective structures at Oceanside and Dana Point. This study has subsequently been used to determine design waves for other marinas, seawalls, and offshore oil platforms from San Diego County to Los Angeles County. Weather maps, newspapers, and ship observations from 1900 to 1957 were examined. Fifteen storms were selected based on reports for their general severity or coastal damage. Two of the fifteen selected storms gave lower wave heights than anticipated and were thus excluded. Table 2 is a list of the hindcasted results in an exposed deepwater location for the remaining 13 storms.

TABLE 2

Hindcasted Maximum Significant Wave Characteristics  
in Deep Water for 1900 to 1957

<u>Date</u>	<u>H<sub>s</sub></u> <u>(Feet)</u>	<u>T</u> <u>(Seconds)</u>	<u>Azimuth</u> <u>(Degrees)</u>
9-10 Mar 1904	17.9	12.0	225
8-10 Mar 1912	17.5	11.5	270
16-17 Dec 1914	13.0	9.9	180
28-30 Jan 1915	16.3	11.8	205
1-3 Feb 1915	16.5	12.4	280
26-28 Jan 1916	14.0	9.6	250
1-2 Feb 1926	12.6	16.0	260
6-8 Apr 1926	11.8	13.8	270
6-12 Dec 1937	11.6	16.4	270
15-25 Sep 1939 <sup>a</sup>	26.9	14.0	205
20-23 Jan 1943	16.2	10.8	180
13-14 Mar 1952	11.7	11.7 <sub>p</sub>	250
6-8 Jan 1953	16.0	19.2 <sup>b</sup>	260

<sup>a</sup>tropical storm

<sup>b</sup>15.0 to 15.8 seconds was recorded at Camp Pendleton

Source: Marine Advisers (5).

Following the 1983 storms, the Marine Advisers severe storm hindcasted wave data set was updated with wave hindcasts prepared by Pacific Weather Analysis (10) for severe storms occurring between 1958 and 1983 in Southern California in deep water outside the offshore islands. Table 3 is a summary of the maximum wave characteristics hindcasted for each of the storms by Pacific Weather Analysis.

Direct comparison of Tables 2 and 3 is not statistically valid. The wave hindcasts were prepared using different procedures, different quantities of synoptic data, different time periods, and varying degrees of experience which have calibrated wave hindcasts with

TABLE 3

Hindcasted Maximum Significant Wave Characteristics  
in Deep Water for 1958 to 1983

<u>Date</u>	<u>Classification</u>	<u>H<sub>s</sub></u> <u>(Feet)</u>	<u>T</u> <u>(Seconds)</u>	<u>Azimuth</u> <u>(Degrees)</u>
Jan 1958	sea	9.0	9-10	280
	swell	15.2	13-14	270
	summation	18.1	13-14	-
Apr 1958	sea	7.4	8-9	280
	swell	20.0	17-18	293
	summation	25.1	17-18	-
Feb 1960	sea	14.2	11-12	290
	swell	15.3	18-19	294
	summation	18.3	18-19	-
Feb 1963	sea	11.8	10-11	150
	swell	15.9	14-15	269
	summation	19.5	13-14	-
Sept 1963 <sup>a</sup>	swell	10.3	14-15	167
Feb 1969	sea	7.5	8-9	280
	swell	14.3	14-15	284
	summation	15.6	14-15	-
Dec 1969	swell	14.4	20-21	276
Aug 1972 <sup>a</sup>	swell	11.6	17-18	156
Jan 1978	sea	5.1	7-8	290
	swell	16.6	16-17	284
	summation	18.6	16-17	-
Feb 1980	sea	10.3	9-10	220
	swell	15.3	13-14	255
	summation	15.6	14-15	-
Jan 1981	swell	15.4	17-18	265
Jan 1981	sea	4.8	6-7	210
	swell	21.1	15-16	269
	summation	21.5	15-16	-
Sept 1982 <sup>a</sup>	swell	10.1	17-18	158
Nov 1982	sea	17.1	12-13	290
	swell	17.6	14-15	293
	summation	20.4	10-11	-
Jan 1983	sea	7.3	8-9	160
	swell	19.7	20-21	283
	summation	21.0	20-21	-
Feb 1983	sea	3.5	5-6	320-340
	swell	16.7	16-17	275
	summation	17.1	16-17	-
Mar 1983	sea	12.6	11-12	160
	swell	22.3	18-19	263
	summation	23.6	18-19	-

<sup>a</sup>tropical storm

Source: Pacific Weather Analysis (10)

recent wave measurements. The proper procedure would be to update all storms of record using similar hindcast procedures. Such an effort was not possible for the purposes of this paper. It was assumed that the methodologies of the two hindcasts are similar enough to permit a reasonable estimate of wave height distribution over the entire period of record.

The extreme wave statistics presented in Tables 2 and 3 have waves from two meteorological sources: extratropical storms and tropical storms. The most frequent and severe waves are due to the extratropical storms. However, the largest hindcasted wave event of record was the 1939 tropical storm that made landfall in Southern California. The three maximum tropical storm swells in Table 3 are included for comparison with the 1939 event. The 1939 tropical storm is usually treated as a rare event and is not included as a design condition for most structures. However, the consequences of damages in the event that another tropical storm similar to the 1939 storm occurs should be considered in design of structures.

The distribution of wave heights without the tropical storms which were used prior to 1983 and after 1983 are compared. Rather than select one probability distribution a priori, five different distributions as described by Isaacson and MacKenzie (4) are fitted to the wave data using a least squares fit; the best-fit curve is then selected among the log-normal, Gumbel, Fretchet, Weibull lower-bound, and Weibull upper-bound distributions. The selected distribution for both data sets is the Weibull lower-bound.

The deepwater wave height distribution for Southern California using the Marine Advisers data set without the 1939 tropical storm is shown in Figure 5. The 100-year recurrence interval wave height is 6.6 meters (21.7 feet). Figure 6 shows the effect of including the severe waves of 1983 and the addition of hindcasts from 1958 to 1983 without the tropical storms. The 100-year recurrence interval wave height is now 8.3 meters (27.2 feet). The additional data increased the 100-year recurrence interval wave height in deep water outside the offshore islands by 25.8 percent.

Measured and hindcasted wave data indicated that peak energy periods were much longer than previously considered. The measured data were from NOAA buoys recently installed in deep water off the coast of California. Prior to the recent storms, typical design waves had periods of 10 to 14 seconds. Some previously used hindcasted data sets indicated that waves of 14 seconds or more existed only as low forerunners. The buoy data on the other hand as shown in Table 4, indicate that rarely is there a high wave episode with peak energy periods below 14 seconds. The peak wave energy periods for the 1983 winter storms ranged from 14 to 25 seconds and these were associated with the peak wave heights.

TABLE 4

Storm Summary of Wave Period

Wave Period (seconds)	Number of Events			
	Marine Advisers 1900-1957	Meteorology International Inc. 1951-1974	Pacific Weather Analysis 1958-1983	NOAA Data Buoy 1980-1984
9				
10	1	3		
11	2	1	1	
12	2			
13				
14	1		2	
15			2	
16			1	
17			2	4
18			2	1
19	1		2	
20				2
21			2	
22				1
23				
24				
25				1

Another characteristic of the 1983 storms was the direction of wave approach. The storm waves approached from a more westerly direction than normal; 280 degrees in the 1982-1983 winter as opposed to a long term average of 290 degrees. Areas typically sheltered by offshore islands or by refraction effects, such as the Los Angeles Harbor were directly exposed to storm waves as shown in Figure 7. The pre-frontal winds also generated local seas from the south that were higher than normal, and in some cases arrived simultaneously with the westerly swell.

## DISCUSSION

The recent storm events of 1983 have dramatically changed the concept of design criteria. Not only have the individual parameters of wave height, wave period, and water level changed, but also the simultaneous occurrence has been revealed as more likely. The extreme storm events of 1983 would have been classified as having wave heights with over 100-year recurrence intervals prior to their occurrence. The storm waves are now considered to have recurrence intervals on the order of 40 years. These individual storm waves must be brought to shore past the offshore islands and refracted across locally complex bathymetry to nearshore sites. Recurrence intervals are therefore likely to show wide variation from site to site. For instance, design calculations for the San Clemente Pier indicate that the recurrence interval for wave heights hindcasted during the March 1983 storm which would be directly exposed to the site is 100 to 150 years.. [see Moffatt & Nichol, Engineers (8)]. A blanket acceptance

of this storm and the exceptional water levels for all coastal sites and problems may lead to unrealistic design requirements. The engineer needs to analyze the data at the particular site including the particular design circumstances such as safety aspects, economic consequences of the design parameters being exceeded, and the particular experience with similar structures. These data should be discussed with the client to evaluate the risk levels involved; it should be recognized that rare and unusual events can and do occur.

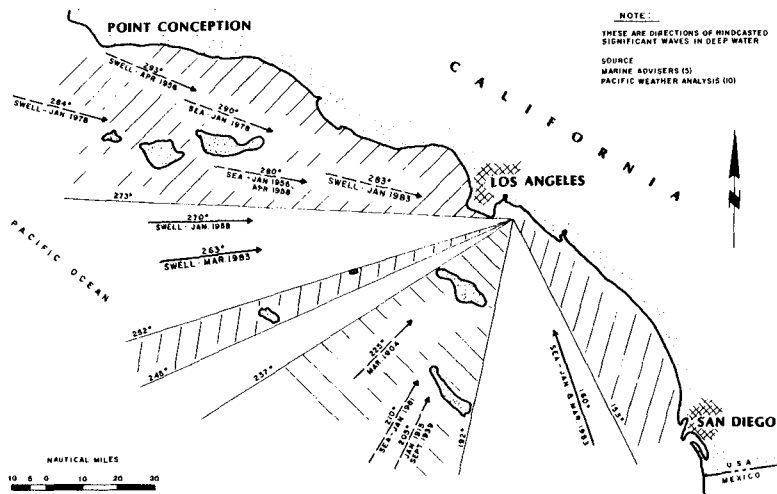


Figure 7. Wave Exposure

The extreme high water levels measured in 1983 coincident with the severe storm waves have caused coastal flooding that has not occurred in the past. This has prompted designers to look for justification for higher design water levels. Review of some of the recent design reports by the authors indicate a compounding of water levels has occurred. For instance, the record-high water level measurements include astronomical tide, barometric tide, sea level rises, and ENSO effects. Addition of 1.0 or 2.0 feet (0.3 to 0.6 meters) to account for these effects appears to be a duplication of the effects. Review of Figure 4 indicates that the 100-year recurrence interval water elevation should be on the order of 8.0 feet (2.4 meters) above mean lower low water at Los Angeles Harbor and about 8.3 feet (2.5 meters) above mean lower low water at San Diego Harbor.

Care should also be exercised in application of the wave setup term. Wave setup varies as a function of the breaking wave characteristics and relative position in the surf zone. For instance, the breaker point has a set down and setup is a maximum at the beach. Large waves persistently breaking offshore may induce a setup on the beach which raises the water level near the shoreline, but not at the seaward end of a pier.

## CONCLUSIONS

The following specific conclusions regarding the relation of the 1983 winter storms to previously used criteria which has been used in design of many coastal projects in Southern California are presented. These conclusions are presented to document the relative importance of the recent storms and to discuss their potential impact on future design policies. No attempt is made herein to establish a specific design criteria.

1. The deepwater wave height for a 20-year recurrence interval and a 50-year recurrence interval has increased from 16.5 and 19.5 feet (5.0 and 6.0 meters) to 21.5 and 25.0 feet (6.5 and 7.6 meters), respectively.
2. The wave period associated with an extratropical storm has increased from a range of 10 to 14 seconds to 14 to 25 seconds.
3. Severe storms usually approach from a more westerly direction during ENSO events.
4. The simultaneous occurrence of an extreme water level and extreme wave event must be considered as dependent events to a greater degree than has been customary.
5. The 1982-1983 winter had three of the top five extreme wave events in deep water over the past 80 years.
6. The coastal damages which occurred were due to a combination of factors including extreme water level, extreme wave height, extreme wave period, direction of approach which exposed segments of shoreline that are traditionally protected by the offshore islands, and to the aged condition of some of the pile structures.
7. Employing all of the considerations cited above may lead to a significant increase in design criteria which could lead to some very conservative and expensive designs.

## RECOMMENDATIONS

It is recommended that designers of coastal structures consider the effects of the 1983 winter storms in their new designs, but that the increase in water level and wave characteristics be evaluated in terms of how neighboring structures performed during the storms and the economical and safety consequences of the design being exceeded by larger waves. It may be very difficult for the engineer to use a 100-year design storm and water level criteria based on the new data set and current design procedures with non-linear waves compared to a 20-year design storm and water level using statistics developed in 1960 and linear wave theories. For instance, most of the breakwaters on the Southern California coast were built using previous criteria. The local rock quarries can supply up to about 12 to 16 ton armor stone and these structures have functioned reasonably well over their project life. If strict application of the data set with the 1983

storms included, quarry stone would be considered impractical and more expensive precast concrete armor units would be required. Then the engineering design must more seriously consider the economics of repairs to the stone structures and the risk of damages. While these optimization design procedures are documented by Bruun (1) and the Delft University of Technology (3), they are rarely explicitly applied in Southern California because local traditional methods have been satisfactory until 1983.

## REFERENCES

1. Bruun, Per, Port Engineering, Gulf Publishing Company, Houston, Texas, 1973.
2. Cross, Ralph H., "Ocean Wave Statistics for San Francisco," Journal of the American Shore and Beach Preservation Association, Vol. 48, No. 3, July 1980, pp. 26-29.
3. Delft University of Technology, "Coastal Engineering, Breakwater Design", edited by W.W. Massie, Coastal Engineering Group, Department of Civil Engineering, Vol. III, December 1979.
4. Isaacson, Michael de St. Q., and MacKenzie, Neil G., "Long-Term Distributions of Ocean Waves: A Review," Journal of the Waterways, Port, Coastal and Ocean Division, ASCE, Vol. 107, No. WW2, May 1981, pp. 93-109.
5. Marine Advisers, "Design Waves for Proposed Small Craft Harbor at Oceanside, California," prepared for U.S. Army Engineer District, Los Angeles, March 1960.
6. Marine Advisers, "A Statistical Survey of Ocean Wave Characteristics in Southern California Waters," prepared for U.S. Army Engineer District, Los Angeles, January 1961.
7. Meteorology International Incorporated, "Deep-Water Wave Statistics for the California Coast," Volumes 1-6, prepared for State of California, Department of Navigation and Ocean Development (now Department of Boating and Waterways), February 1977.
8. Moffatt & Nichol, Engineers, "Oceanographic Design Conditions for the Repair of the San Clemente Pier", prepared for the City of San Clemente, August 1983.
9. National Marine Consultants, "Wave Statistics for Seven Deep Water Stations Along the California Coast," prepared for U.S. Army Engineer Districts, Los Angeles and San Francisco, December 1960.
10. Pacific Weather Analysis, preparation of wave hindcasts for Moffatt & Nichol, Engineers, 1983.

11. Seymour, Richard J., Strange III, R. Rea, Cayan, Daniel R., Nathan, Robert A., "Influence of El Ninos on California's Wave Climate," Proceedings 19th International Conference on Coastal Engineering, 1984.
12. Strange, R. Rea III, "On the Accuracy of Wave Hindcasts Relevant to the Proposed LNG Terminal near Point Conception, California", prepared for Hollister Ranch Owners Association, unpublished, April 1978.
13. U.S. Army Corps of Engineers, "Specifications for Restoration of San Pedro Breakwater at Los Angeles County, California," DACW09-83-B-0040, July 1983.
14. U.S. Army Corps of Engineers, Los Angeles District and State of California, "Coastal Storm Damage, Winter 1983", April 1984.
15. Walker, James R., Palmer, Robert Q. and Dunham, James W., "Breakwater Back Slope Stability," Proceedings Civil Engineering in the Oceans/III, Vol. 2, June 1975, pp. 879-898.



## CHAPTER ONE HUNDRED NINETY

### A SIMULATION METHOD FOR SMALL CRAFT HARBOUR MODELS

by

Dov Sergiu Rosen<sup>1</sup>, M.ASCE and Eliezer Kit<sup>2</sup>

#### ABSTRACT

A simulation method is presented to improve small craft harbour design by studying the behaviour of moored vessels in small craft harbours, using physical modelling in medium size wave basins, available at most laboratories. Instead of carrying the study in an agitation model with moored vessel models and built in a large wave basin at a large geometric scale, it is performed in two consecutive models of different scales, in a medium size basin. Transfer functions of vessel movements and mooring and fender forces are determined in the first model, for representative types of vessels moored alternately at a solitary berth, under simulated inside harbour conditions and for various sea states and directions. Near berth wave spectra are obtained in the second (agitation) model for sea states covering the local climate. Integration of the wave spectra with the transfer functions leads to response spectra of vessel movements and forces. Finally, maximum movements and forces are determined from the response spectra and are used together with limiting criteria and the long term wave statistics to choose the optimum configuration of: harbour layout, types of berth structures and mooring and fendering systems.

#### INTRODUCTION

The design of small craft harbours has usually been based on agitation models in which only waves were measured inside and in the surroundings of the simulated breakwaters' layout of a small craft harbour model, for various incident wave heights, periods and directions. The types of wave disturbance studied were short wave disturbance induced by gravity waves (periods 3-30 sec) and seiche disturbance induced by infragravity waves (periods 30-180 sec). The wave disturbance data required in the agitation model have been used to determine the optimum layout and the optimum types of structures of the designed small craft harbour, on the basis of empirical rules regarding allowable wave heights and current strength. Such rules, specifying only the maximum allowable wave height near a harbour berth were presented by Dunham and Finn (4), Le Mehaute (7), Mercer et al. (8). It was clear that such criteria could be used only as general guidance for small craft harbour design but that they were not sufficient for an optimum design

---

<sup>1</sup> Chief Engineer, M.Sc., CAMERI-Coastal and Marine Engineering Research Institute, Technion City, Haifa 32000, Israel.

<sup>2</sup> Senior Researcher, Ph.D., CAMERI-Coastal and Marine Engineering Research Institute, Technion City, Haifa 32000, Israel.

including harbour layout, inner harbour configuration, type of berth structure for each berth and mooring and fendering systems. Therefore, it is not surprising that the importance of simulating moored vessel behaviour in the model for reliable design of large commercial harbours has been recognized many years ago Vasco Costa(13), and nowadays has become the usual modelling procedure. Although the same importance was attributed to simulating moored vessels for the design of small craft harbours, its application was performed only in few small craft harbour studies, e.g. Isaacson and Mercer (5). Most of the model studies of small craft harbours however, continued to be carried out in agitation models lacking the presence of moored vessel models, Stickland (12). The lack of moored vessels in the simulated models seems to be due to the difficulty to fulfill simultaneously the two following requirements:

- a) The harbour model should cover the area of the harbour and its surroundings. Hence, it has to be built at a relatively small geometric scale (1:80 - 1:125) in order to fit into a medium size wave basin (available at most laboratories).
- b) The models of small vessels (sailboats, lighters, trawlers, patrol boats, etc.) have to be made at relatively large geometric scales (1:20 - 1:50). Since such vessels are light and have small displacements (compared to commercial ships) this requirement is necessary in order to allow the correct simulation of loading conditions (displacement, mass distributions) and natural periods of oscillation(roll,pitch) as well as accurate measurements of vessel movements and of forces in the mooring lines and into the berth fenders.

Obviously, these requirements could be fulfilled only when a large size wave basin was available. Even then, vessel models were usually not used, due to the much increased costs for building the model and carrying out the study of the small craft harbour at a large scale relatively to the expenses of a model built at a small geometric scale (about 4:1).

This paper presents a simulation method which includes the study of moored small craft vessels, but which allows to carry out the model study in a medium size basin and at competitive costs performance, relatively to those of an agitation model without vessel models. (Costs about 1.5 - 2 times more than those of an agitation model). Furthermore, using this simulation method, the simultaneous fulfillment of the above requirements a) and b) is no longer necessary. This method was applied at CAMERI for the design study of a relatively large fishing harbour.

#### DESCRIPTION OF THE MODEL SIMULATION METHOD

##### General Concept

Two basic concepts stay behind the present simulation method. The first one, known as the Froude-Kriloff hypothesis (see Korvin-Kroukovsky (6)) states that the effect of a vessel located in a wave field on that wave field can be considered negligible. Consequently, the measurements of the wave field in an agitation model are expected to provide all the necessary information required to forecast the behaviour of a vessel

in that wave field, if the transfer functions relating the input waves with the response behaviour of the vessel are known.

The second concept, known as the Froude hypothesis on linear superposition, states that the resulting amplitudes of movements of a vessel located in an irregular wave field can be determined by linear superposition of the separate contributions of regular waves of corresponding wave energy at each frequency band to that existing in the irregular field at that frequency band.

On the basis of these two concepts, the simulation procedure assumes that the results which would be obtained from a physical model with moored vessel models built at a large geometric scale (say 1:30-1:50), may also be sufficiently accurately determined in the case of a small craft harbour built in shallow water, by dividing the study into two separate physical models and by combining analytically the results of these two studies.

The first model would be a "moored seakeeping model study" in which the transfer functions of vessel movements and mooring and fender forces are determined for various wave conditions, while the second model would be an "agitation model" in which near-berth wave spectra are measured and logged for various harbour configurations and for various representative sea states covering the wave climate at the site of the proposed small craft harbour. The application of the measured wave spectra on the transfer functions determined, would provide response spectra of moored vessel movements and mooring and fender forces, from which maximum movements and forces can be determined. The combination of the results obtained for various types of vessels, and for various types of harbour configurations due to various sea states, with the limiting criteria of vessel movements, mooring and fender forces and harbour entrance wave heights and with the statistics of the long term wave climate, would allow the choice of the optimum configuration of breakwaters layout, berth structures and mooring and fendering systems and would ensure the optimum operability and safety of the small craft harbour design.

Since each of the above mentioned models can be carried out separately, each of them can be performed at its optimum geometric scale. Each one would usually fit in a medium size wave basin and they may be carried out in two consecutive testing stages.

The general simulation procedure is schematically presented in Figure 1.

#### Moored Seakeeping Model Study

In order to obtain the transfer functions of the vessel movements and of the mooring and fender forces for relevant vessels representing the fleet determined to be serviced by the proposed fishing harbour, a moored seakeeping model study was carried out. The model was built in a wave tank of limited overall dimensions (24x 26m), at a geometric scale of 1:50, large enough for the simulation of the vessels considered. Two types of vessels were chosen for the study, namely a trawler of 800 DWT and a tuna boat of 400 DWT. Each of the vessel models was calibrated for two loading conditions, one of ballast at departure, the other of laden at arrival.

The vessel models were alternately moored at a solitary berth in a number of alternative mooring and fendering systems of varying stiffness,

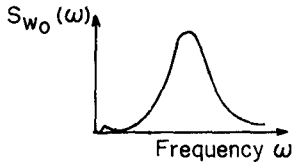



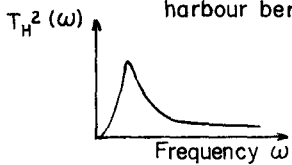
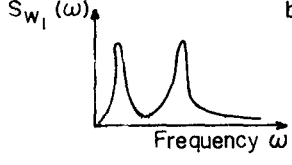

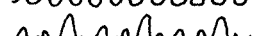
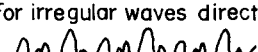
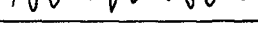
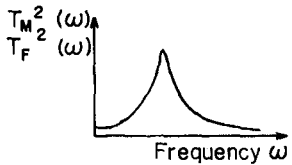
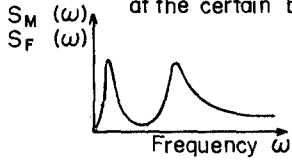



	FREQUENCY DOMAIN	TIME DOMAIN
Stage 2 - Agitation model study	Incident wave energy spectrum (outside harbour) 	+  +  • • • = 
	Transfer function of the waves energy at a certain harbour berth 	Response (height of regular waves near berth) = Incident wave height (outside harbour)
	Response wave energy spectrum at a certain harbour berth 	For regular waves by calculation +  +  • • • =  For irregular waves directly 
Stage 1 - Moored seakeeping model study	Transfer function (of movement or of a force) 	Response amplitude (of movement or force) = Wave height near berth
Stage 3 - Integration of the results of stage 1 and stage 2	Response spectrum (of movement or force when a vessel is moored at the certain berth) 	+  +  • • • = 

Fig. 1. Schematic description of the procedure to obtain response spectra of vessel movements and forces in mooring lines and in fenders by linear superposition.

while the berth structure was alternately changed to represent three types of berth structure; an open structure on piles, an impervious wave reflecting sheet pile structure and an impervious but wave absorbing rubble slope beneath a piles supported structure. The models of mooring lines and fenders were made in such a way as to correctly represent the nonlinear load deflection curves of the mooring lines and the nonlinear load compression curves of the fender units. For the model of a mooring line the correct load deflection was achieved by attaching one of the ends of a stiff thread representing the mooring line to two linear springs located on the vessel model and the other end to a force transducer located on the berth. Of the two springs only one worked at the beginning while after a certain loading was achieved both springs worked together (see Fig. 2).

For the model of a fender unit the non linear load compression curve was obtained also with the aid of two linear springs located one inside the other and working in a similar way as the springs of a mooring line model (see Fig. 3).

Vessel movements were measured with the aid of rotational potentiometers, forces were measured by means of linear displacement voltage transducers and waves were measured by resistance type wave gauges, (see Fig. 7). Unidirectional incident waves of regular and irregular type were separately generated in transient water depth. The incident waves were adequately shoaled by sloping bottom and then were propagated over a constant water depth section on which the solitary berth was located. The water depth at that section corresponded to the designed water depth inside the proposed harbour. In this way the direct excitation of near-berth shoaled waves on the moored vessel model was obtained for various conditions tested.

The measured movements, forces and wave data were statistically analyzed in real time and logged on magnetic media by a minicomputer system which controlled also the wave generation.

The tests with regular waves covered the wave periods range corresponding to gravity and infragravity waves (3-30 sec and 30-60 sec). The tests with irregular waves were performed to study the additional effects of drift forces (induced by wave groups) on the moored vessels, because these forces are not obtained with regular waves. For both wave types a few wave heights (calibrated in the absence of vessels) were tested with various configurations. The wave heights range was from 0.2 m to 0.8 m (prototype). Care was taken to remove parasitic components of the waves generated. Under these circumstances, the response amplitude operators (RAO), i.e. the transfer functions of the vessel movements and forces were determined for three angles of wave incidence considered relevant in this study ( $0^\circ$ ,  $30^\circ$ ,  $60^\circ$ ) relative to the vessel longitudinal axis.

#### Agitation Model Study

After the moored seakeeping model study was finished, an agitation model in fix bed was built in the same wave tank at a geometric scale of 1:100. The model covered the harbour and its surroundings in order to allow the correct simulation of boundary conditions. Various sea states, covering the local climate at the site of the proposed harbour were generated using unidirectional irregular waves (in situ recorded) for various configurations (i.e. for various layouts

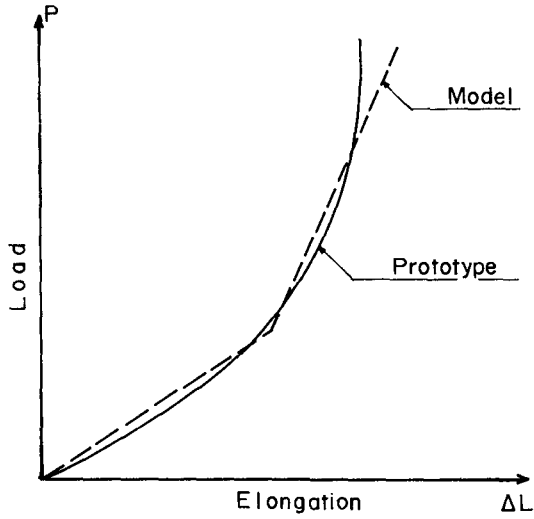


Fig. 2. Schematic modelling of load-elongation characteristics of a mooring line.

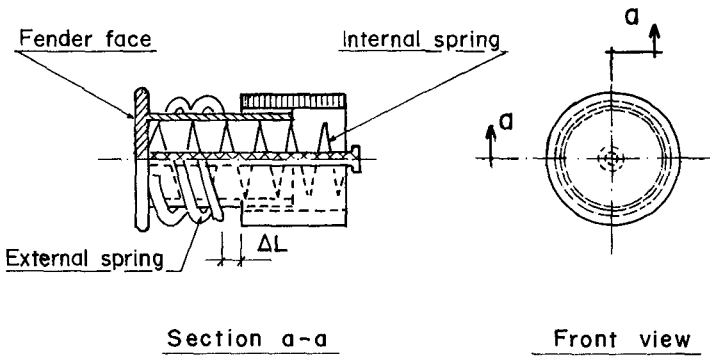


Fig. 3. Schematic description of a fender model.

of the protecting breakwaters, for various inner harbour layouts of the berths and for various types of berth structure). The wave data measured at the various harbour berths as well as these measured at the harbour entrance and at various locations in the surroundings of the harbour were statistically processed in real time and were logged on magnetic media by a minicomputer system. Off line spectral processing of the logged wave data yielded the response wave spectra of the harbour at every berth as induced by the various incident deep water sea states. These response wave spectra of the harbour to the external wave excitation became the input wave spectra which would be applied on vessels moored at the harbour berths. The wave spectra measured for various wave conditions at a majority of harbour berths showed wave energy concentration in two frequency ranges: one with less energy in the high frequency range, the other with equal or more energy in the low frequency range.

It is estimated that the concentration of wave energy in the low frequency range is related to the interaction between the wave groups with the harbour geometry.

Examples of incident wave spectra in deep water and in shallow water and for the corresponding inside harbour wave spectra, are shown for four sea states in Fig. 4, 5 and 6.

Since the wave field inside the harbour is composed of incident waves entering the harbour and of reflected waves from the harbour structures, the directional spectrum of the waves at any harbour berth would be important for the correct determination of the response spectra of the vessel movements and forces.

However, for the present model directional spectra could not be measured and consequently some simplifications have been adopted. Firstly, it was realized that the direction of wave incidence inside the harbour at a berth is almost independent of the direction of incidence of the waves outside harbour. Secondly, the general wave pattern in the harbour could be determined visually by photography. From the analysis of pictures, it was observed that the waves approaching any berth of the harbour have mainly a two dimensional nature (as can be seen in Fig. 8). Furthermore, the variance spectrum of the waves measured at each berth included already possible reflected waves. On the basis of these remarks it was possible to proceed further with the determination of the response spectra of the vessel movements and forces, considering the waves approaching any berth to behave like unidirectional waves.

#### Determination of Response Spectra of Vessel Movements and Forces

Assuming the Froude hypothesis mentioned before to be true under the excitation of relatively small waves (below 1 m significant height), the behaviour of the oscillating system composed by a vessel and its moorings and fenders may be considered linear. Consequently, one may obtain in such a case the response spectra of the various movements and forces according to the following formula:

$$(1) \quad S_R(f) = T^2(f) \cdot S_W(f).$$

where:  $f$  - frequency;  $S_R(f)$  - response variance spectrum of a movement or force;  $S_W(f)$  - wave energy (variance) spectrum measured at a certain berth for a certain sea state and harbour layout;  $T(f)$  - transfer

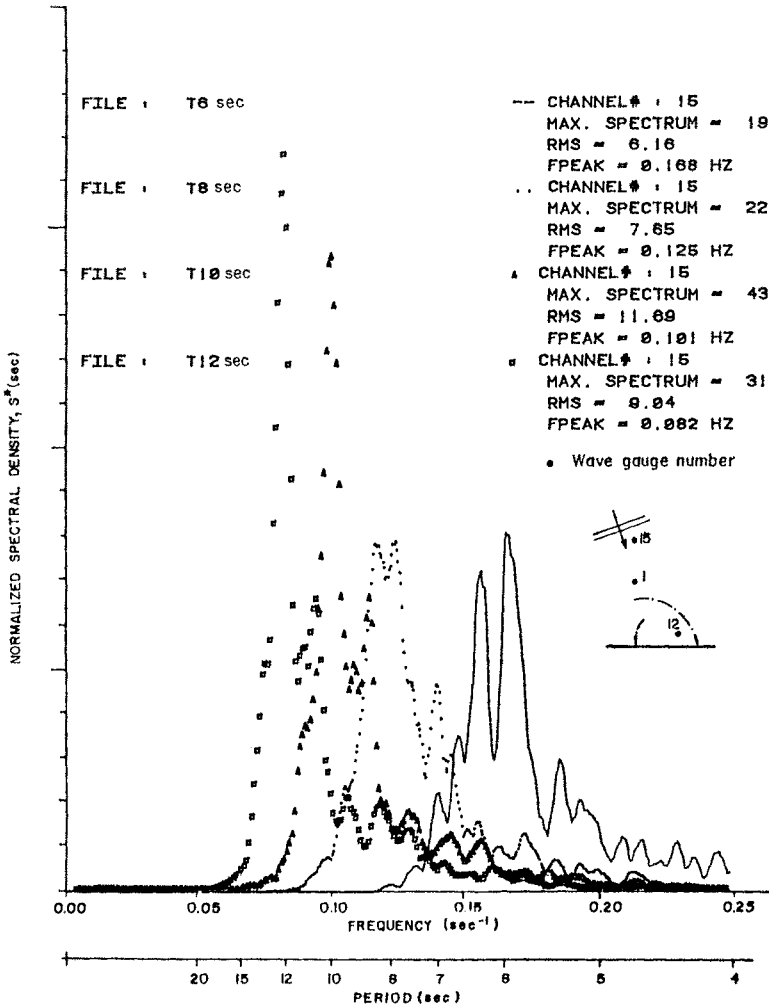


Fig. 4. Incident deep water wave spectra for four peak periods generated and measured in agitation model.



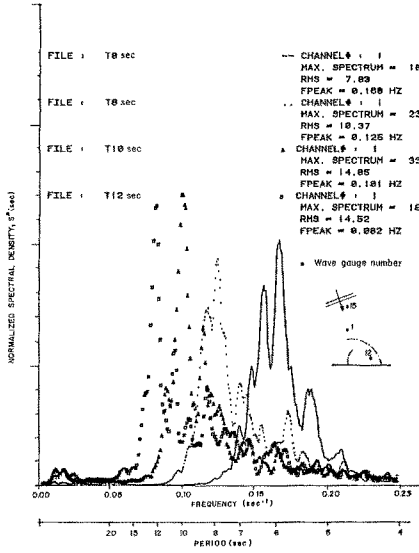


Fig. 5. Shallow water wave spectra in front of harbour entrance measured in agitation model.

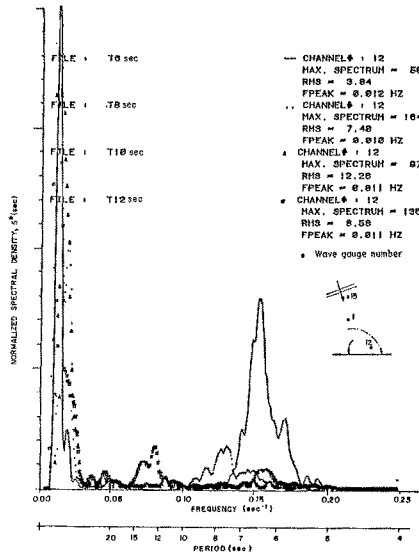


Fig. 6. Example of inside harbour near berth wave spectra obtained in agitation model.

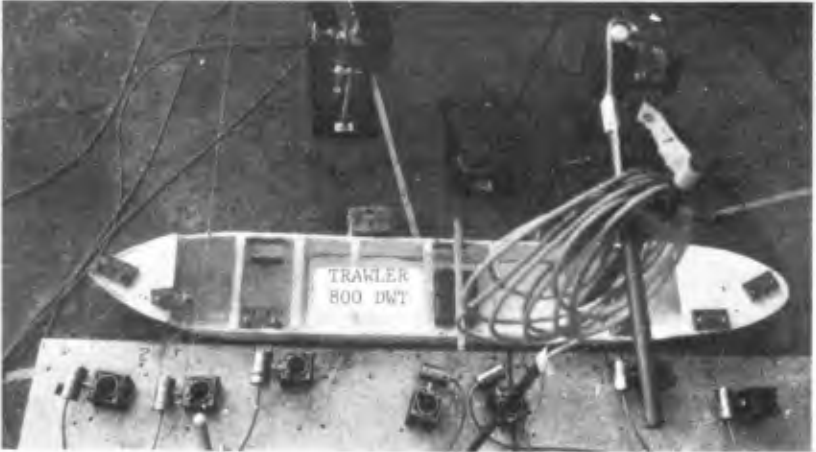


Fig. 7. Instrumentation set-up used in moored seakeeping model study.



Fig. 8. Wave incidence pattern observed in agitation model.

function of a movement or of a mooring or fender force.

A problem arose in the evaluation of the response spectrum regarding the choice of the correct transfer function, among the three transfer functions obtained for the three directions of wave incidence.

The logical procedure would be to determine the optimum orientation of the harbour berths on the basis of the values of the response amplitude operators (RAO) of the transfer functions of the predominant vessel movements. However, in the present study the berth orientations were predetermined by the designers on the basis of backland constraints. In view of these conditions it was decided to use for every movement or force of a vessel, only one transfer function, possessing the largest RAO values among those obtained for the three wave directions in the moored seakeeping model. Care was taken not to use the function obtained for a wave direction which was unreasonable in view of the wave pattern observed by photography. Still, the transfer functions obtained in this way lacked the contribution of the additional effects induced inside the harbour by the wave groups. Nevertheless, these effects could be discarded in the case of a small craft harbour because of the following two reasons:

- a) The effect of drift forces induced by wave groups inside the harbour was in general small because the wave energy of the short waves was small too.
- b) The spectral energies of the long waves induced in the harbour at the various berths were in general of the same order of magnitude or greater than the spectral energies of the short waves (see Fig.6 ). Therefore, the direct effect of the long waves was in general much larger than the one induced by the drift forces.

However, if the spectral energy would be larger than that in the low frequency range, the contribution of the drift forces becomes important and can not be neglected. In such a case, it would be necessary to determine transfer functions on the basis of irregular waves to add the contribution of the second order drift forces, but this was not the case in

Consequently, in the case of a small craft harbour located in shallow water the proposed simulation method was applicable and the response spectra were estimated to lead to slightly conservative results. An example of a response spectrum is shown in Fig. 9 for surge movement.

#### Evaluation of Maximum Movements and Forces

From the response spectra, maximum vessel movements and mooring and fender forces occurring in various sea states and layouts were determined by the following procedure: Firstly, for each response spectrum obtained, the spectral variance  $\sigma_R^2$  and the zero crossing wave period  $T_z$  of the response were evaluated using the formulas:

$$(2) \quad \sigma_R^2 = \int_0^{\infty} S_R(f) df$$

and

$$(3) \quad T_z \approx T_{m_0,2} = \sqrt{m_0/m_2}$$

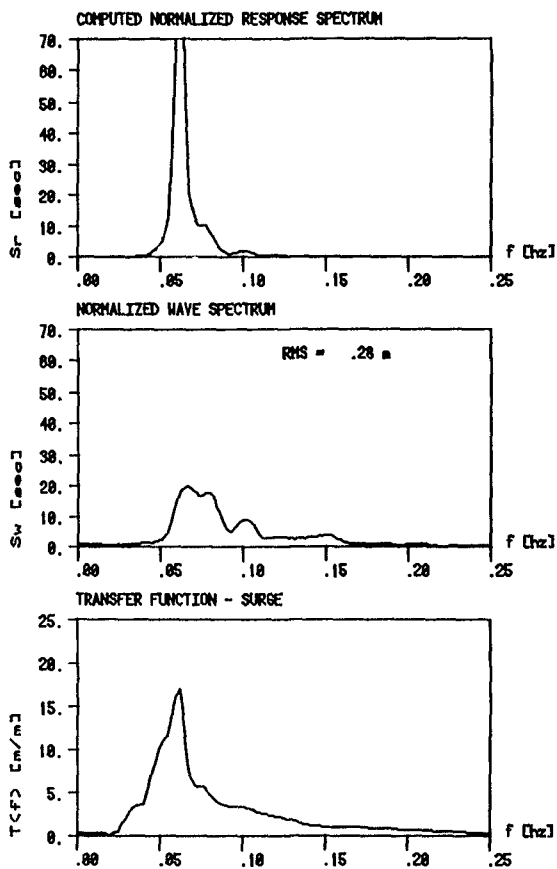


Fig. 9. Example of computer plot of computed response spectrum for surge movement (trawler vessel, full)

where  $T_{m_{0,2}}$  is the spectral estimate of the zero crossing period and  $m_0$  and  $m_2$  are the zeroth and second spectral moments of the response. Secondly, assuming a quasi-stationary sea state to prevail for a time period  $t$ , the average number of reversals ( $N$ ) of a movement or force, was obtained from

$$(4) \quad N = t/T_z$$

Finally, assuming the movements and the forces during a quasi-stationary sea state to be Rayleigh distributed the maximum value of the response  $R_{max}$  was determined from the formula (Ochi (9)):

$$(5) \quad R_{max} = \sigma_R \left( \frac{1}{2} \ln N \right)^{1/2}$$

Though the assumption of Rayleigh distribution for mooring and fender forces is not quite true due to their non linear characteristics, it was estimated that this assumption led to conservative values.

A problem arose regarding the determination of maximum values for the many cases of two peaked response spectra. To solve this, it was decided to divide the response spectrum into two separate response spectra, one covering the high frequency range and the other covering the low frequency range and treat them as individual spectra, following the procedure outlined above. The maximum value of the response spectrum was obtained in this case by the summation of the individual maximum values obtained from the two divisions of the response spectrum.

## HARBOUR OPTIMIZATION

### Limiting Criteria

In order to determine limiting criteria regarding maximum allowable values of vessel movements and mooring and fender forces for safe operation at the harbour berths, a literature survey and discussions with a number of skippers and marina operators were carried out. Limiting values regarding mooring and fender forces were presented by mooring lines manufacturers (Samson Ocean Systems(10), British Ropes (2)) and by PIANC (9), while limiting values of vessel movements are presented by Bruun (3). The discussions conducted led to the conclusion that beside the forces in moorings and fenders, the safety of mooring and loading or unloading operations is affected more by crew behaviour on vessel than by the amplitudes of vessel movements, though the latter are usually assumed to determine the crew behaviour. However, as shown by various studies of human behaviour during aircraft flight or seakeeping (e.g. Arwas and Rolnick (1)), the main factor in influencing human behaviour is the acceleration of the body and not the body velocity of movement.

After studying the information collected, the following criteria have been established as safety limit criteria.

- maximum linear acceleration : 0.4 m/sec<sup>2</sup>
- maximum angular acceleration : 2.0 deg/sec<sup>2</sup>
- maximum peak to peak roll : 6.0 degrees
- maximum force in a mooring : 20% of breaking load
- maximum force in a fender : 60% of ultimate load

Here the movement limitation for roll was needed to prevent

entanglement of vessel masts while mooring side by side.

In order to determine maximum accelerations, response spectra of the accelerations corresponding to the six vessel movements were evaluated. The method described previously on response spectra was used, by applying the following formula:

$$(6) \quad S_a(f) = (2\pi f)^4 \cdot T^2(f) \cdot S_w(f)$$

where:  $S_a(f)$  - acceleration response variance spectrum. Maximum accelerations were obtained assuming again the values to follow the Rayleigh distribution.

#### Determination of Yearly Average Operability

The maximum values obtained were combined with the wave statistics and the above criteria, yielding average yearly operabilities at every berth for the various layouts. From these results, the optimum harbour configuration was chosen.

#### CONCLUSIONS

A relatively inexpensive simulation method has been derived for the study of small craft harbours. This is estimated to allow sufficiently reliable determination of optimum harbour layout (breakwaters, quays) and optimum type of structure for each berth, in respect to safe operational conditions for the vessels serviced by the small craft harbour, using small to medium size wave basins which are available at most laboratories. In order to further increase its reliability a model study has been initiated at CAMERI, to compare this method with the results of direct measurements of vessel behaviour in a harbour model.

#### REFERENCES

1. Arwas S., and Rolnick A., (1984), "Ship Motion Effects on Naval Crew", Abstracts of 18th Israel Conference on Mechanical Engineering, June 27-28, Technion City, Haifa.
2. British Ropes, (1977), "Mooring Lines" Publ. No. 1050/1, Publ. ny Publicity Dept. of British Ropes Ltd, London, England.
3. Bruun P., (1979) "An Alternative to Conventional Fendering", Rep. No. 3, Div. of Port and Ocean Engrg., Norwegian Inst of Technology. (Revised version of Sept. 1979).
4. Dunham J.W., and Finn A.A., (1974), "Small-Craft Harbors: Design, Construction, and Operation", U.S. Army Corps. of Engineers, Coastal Engineering Research Center, Special Report No. 2.
5. Isaacson M., and Mercer A.G., (1982), "The Response of Small Craft to Wave Action", Proc. 18th Intl. Conf. on Coastal Engrg., Cape Town, cap. 165, pp. 2723-2742, ASCE.

6. Korvin-Kroukovsky B.V., (1961), "Theory of Seakeeping", Publ. of Soc. of Naval Architects and Marine Engineers, New York.
7. Le Mehaute B., (1977), "Wave Agitation Criteria for Harbours", Proc. Ports '77 - 4th Annual Symp. of Waterways, Port Coastal and Ocean Division, ASCE, vol. I, pp. 366-372.
8. Mercer A.C., Isaacson M., and Mulcahy M.W., "Design Wave Climate in Small Craft Harbours", Abstracts 18th I.C.C.E, Cape Town, pp. 334-335, ASCE.
9. Ochi M.K., (1973), "On Prediction of Extreme Values", Journal of Ship Research, No. 17, pp. 29-37.
10. PIANC(Permanent Intl. Assoc. of Navigation Congresses), (1981), "Improving Fender Design Systems" Interim Rep. to be discussed at 25th PIANC Congress, Edinburg, March 1981.
11. Samson Ocean Systems Inc, (1977), "Samson Rope Manual", 2nd Edition, Boston, U.S.A.
12. Stickland I.W., (1972), "Site Investigation and Hydraulic Model Studies" in Webber N.W. editor-Marinas and Small Craft Harbours, Symp. at Univ. of Southampton, April 1972, Southampton Univ. Press, 1973, pp. 105-128.
13. Vasco-Costa F., (1965), "Physical Model of the Moored Ship as an Oscillating System", Proc. NATO Advanced Study Institute on Analytical Treatment of Problems of BERTHING & MOORING SHIPS, Lisbon, Portugal, July 1965, Publ. ASCE, Aug. 1970.

#### ACKNOWLEDGEMENTS

The present study was conducted in connection with a model study for a fishing harbour designed by Richard Scheiner and Assoc., Consulting Engineers, who also participated in the definition of the limiting criteria. The financial support provided for the publication of this study by the CAMERI-Coastal and Marine Engineering Research Institute, Haifa, is acknowledged.

## CHAPTER ONE HUNDRED NINETY ONE

### Hydrodynamic Forces on a Circular Cylinder due to Combined Wave and Current Loading

Yuichi Iwagaki\* and Toshiyuki Asano\*\*

#### ABSTRACT

The hydrodynamic force acting on a circular cylinder in a wave-current co-existing field and its generating mechanism are discussed. This study focuses on the asymmetries of both the water particle movement and the resultant vortex property with respect to the cylinder, which produce inherent characteristics in the hydrodynamic forces in the wave-current co-existing field.

First of all, the vortex property around a circular cylinder in the wave-adverse current co-existing field has been examined by flow visualization tests. It has been found that the vortex property depends on the flow characteristics around the trough phase when the wave-current composite velocity becomes maximum and can be represented with a newly proposed  $K.C.$  number for the co-existing field.

Secondly, the characteristics of the in-line force has been made clear by evaluating the drag coefficient and the mass coefficient in the expanded Morison's equation for the co-existing field. These coefficients can be well arranged by  $(K.C.)^{\frac{1}{2}}$ , which is one of the newly proposed  $K.C.$  numbers, and their characteristics coincide with the existing results in the wave only field. The in-line hydrodynamic force in the co-existing field can be explained sufficiently by considering the vortex property in the same manner as clarified in the wave only field.

Thirdly, the characteristics of the transverse force (lift force) are discussed in connection with the vortex properties. It has also been found that the fluctuating frequency of the lift force is synchronized with the loading wave frequency.

#### 1. Introduction

Evaluation of wave forces acting on a circular cylinder is one of the most important subjects in coastal and ocean engineering. Recently, Sarpkaya and Isaacson<sup>1)</sup> systematically assembled and organized comprehensive research efforts in this field, and they pointed out several problems which remain unsolved. The study on hydrodynamic forces

\* Professor, Dept. of Civil Eng., Kyoto University, M. of ASCE

\*\* Research Associate, Dept. of Civil Eng., Kyoto University  
Yoshida-honmachi, Sakyo-ku, Kyoto 606 Japan



in wave-current co-existing fields is one of such problems. However, researches on this subject are scarce and as yet there is not a sufficient understanding.

A quasi wave-current co-existing field can be easily obtained either by oscillating a cylinder in the in-line direction in a uniform flow, or by moving it at a constant speed in a harmonically oscillating flow. Verley and Moe<sup>1,2)</sup> examined the drag and the mass coefficients by using the former field, while Horikawa et al.<sup>2)</sup> treated them in the latter field. However, the existing studies have not sufficiently discussed the hydrodynamic forces based on the vortex properties around a cylinder.

As an essential difference of the generation mechanism of the hydrodynamic forces in the wave-current co-existing field from that in the wave-only field, this study focuses on the asymmetry of a water particle movement with respect to a cylinder.

In the wave-only field, the water particle moves almost symmetrically in both phases of wave crest and wave trough, while in the co-existing field it does asymmetrically due to a superimposed current. Consequently, the properties of the vortex formation, development and shedding become different from the wave-only field, and they produce inherent characteristics in the hydrodynamic forces.

From the above mentioned viewpoint, in this study first of all, flow visualization tests are performed in wave and adverse current co-existing fields to examine the vortex properties.

Secondly, the characteristics of the in-line force are made clear through the experimental data of the drag and the mass coefficients in the expanded Morison's equation to the co-existing field. Moreover, the generation mechanism of the in-line force associated with the vortex properties is discussed in detail.

Thirdly, the characteristics of the lift force are examined in regard to both the lift coefficients and the fluctuating frequencies. Further, "synchronization" between the lift force fluctuation and the loading wave frequency in the co-existing field is examined.

## 2. Vortex properties around a circular cylinder in co-existing fields

### (1) Flow visualization test

Experiments were carried out in a wave tank, 27m long, 0.5m wide and 0.7m high, in which a circulating flow can be generated by a power pump. The water depth was kept constant 30cm. The vertical circular cylinders used in this test were 30 mm and 60mm in diameter.

Test runs were conducted under conditions that the wave frequency  $f$  was 0.5Hz, the wave heights  $H$  were 1.1~3.9cm, the currents were in the opposite direction to the wave propagation and their velocities varied 0~13.9 cm/sec. The flow visualization around the cylinder was performed with aluminum powder, and photographs of fluid motion at the water surface were taken with a motor-drive camera at the speed of 3 frames per second.

## (2) Experimental results and discussion

To clarify the effect of the current on the vortex properties, the experiments were carried out under the condition that the wave height and period are almost constant, and only the current velocity is varied.

Fig.1 shows the results of experiments when the surface  $K.C.$  numbers  $K.C._s$  calculated from the water particle velocity of only the wave component, are approximately equal to 3 and only the current velocity is varied.

$K.C._s$  is defined as follows:

$$K.C._s = u_{ms} T / D \quad (1)$$

in which,  $u_{ms}$  is the velocity amplitude of wave component at the still water level,  $T$  the wave period and  $D$  the diameter of a cylinder.  $u_{ms}$  was calculated from the small amplitude wave theory. The subscript 's' denotes the value at the water surface.

$(K.C._s)_\dagger$  and  $(K.C._s)_\ddagger$  in Fig.1 are introduced as new  $K.C.$  numbers in the co-existing field. Their definition will be described later. In these numbers, the water particle velocity is represented by a composite velocity of the wave and current components at the trough phase. The direction of the wave propagation in Fig.1 is from left to right, and that of current is from right to left.

Fig.1(a), which is the case of the wave-only field, shows that a pair of symmetric vortices are generated and they are not shed from the cylinder. Fig.1(b) shows the case when a current of 6.3 cm/sec in velocity is superimposed on the waves. In this figure, it is observed that a pair of symmetric vortices are generated at the phase III, when the composite velocity becomes large, and they develop, decay and vanish as the phase proceeds. Fig.1(c) is the case when a faster current than in the case of (b) is superimposed, so that the movement of the water particles is uni-directional throughout all phases. It is observed that one vortex is generated in one wave period at one side, and in the following wave period one vortex is generated at the other side. As the current velocity still increases, a pair of asymmetric vortices are generated as shown in Fig.1(d).

From Fig.1 and other visualization tests, the following vortex properties were made clear.

The vortices which are generated at the trough phase when the composite velocity becomes maximum dominate the vortex pattern all over the wave phases. The relation between the vortex pattern and  $(K.C._s)_\dagger$  or  $(K.C._s)_\ddagger$  coincides with that of existing results in the wave-only field.<sup>9), 10)</sup> It cannot be decided here which  $K.C.$  number best represents the vortex properties in the co-existing field, since the number of the experimental data is not sufficiently large. However, concerning the coefficients of the hydrodynamic force,  $(K.C._s)_\ddagger$  was found to be the better parameter to describe them than  $(K.C._s)_\dagger$ .

Meanwhile, the flow properties during the crest phase are so affected by the still existing vortices generated during the trough phase that the vortex properties cannot be explained by the

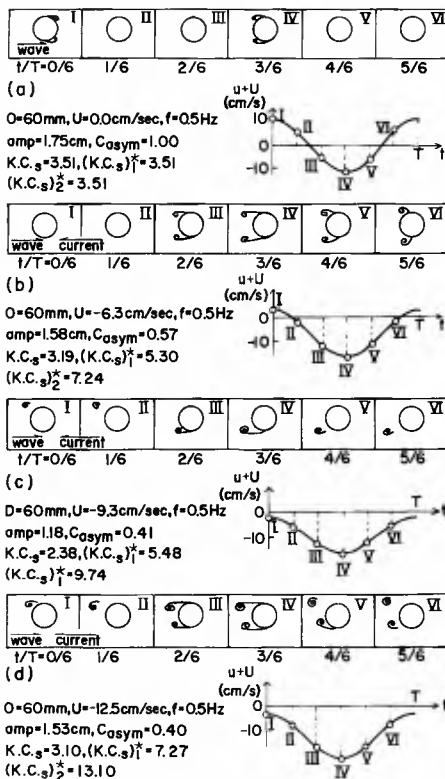


Fig.1 Changes of vortex pattern due to currents



Photo.1 An example of visual observations  
 (this photograph corresponds to Fig.1(c),  $t/T=4/6$ )

characteristics of the water particle movement.

The vortex properties clarified here are considered to control not only the characteristics of the in-line force but also those of the lift force.

### 3. Characteristics of in-line force acting on a circular cylinder

#### (1) Experimental procedure

The experimental apparatus was almost same as that used in the flow visualization test. Two vertically supported circular cylinders having  $D=30\text{mm}$  and  $60\text{mm}$  diameters are mainly used in this experiment. Test runs using a cylinder of  $20\text{mm}$  in diameter were added in order to obtain large  $K.C.$  numbers.

The experiments were conducted under the conditions of the wave frequencies  $f=0.5\sim 1.6\text{Hz}$  and the wave heights  $H=0\sim 21.0\text{cm/sec}$ . The currents were opposite direction to the wave propagation and their velocities varied  $U=0\sim 27.1\text{cm/sec}$ . The total number of the test runs was 80 for the wave only field, and 104 for the co-existing field. The water depth was kept constant  $40\text{cm}$ . The hydrodynamic forces were detected as moments by two strain gauges.

#### (2) Procedure of analysis

The hydrodynamic forces acting on a cylinder are represented by the following Morison's equation taking into account the effect of currents:

$$dF(z) = \frac{\rho}{2} C_D (u(z) + U(z)) |u(z) + U(z)| Dz + \frac{\rho\pi}{4} C_M D^2 \frac{\partial u(z)}{\partial t} dz \quad (2)$$

in which,  $dF$  is the horizontal hydrodynamic force acting on a segment  $dz$ ,  $\rho$  the density of fluid and  $C_D$  and  $C_M$  the drag and the mass coefficients respectively.

The wave component in the water particle velocity  $u(z)$  was assumed to be expressed by the small amplitude wave theory. The current velocity  $U(z)$  was assumed to be uniform in depth.

In this study two estimation methods of  $C_D$  and  $C_M$  were used. The first one is that either  $C_D$  or  $C_M$  is calculated at the specific phase when the inertia force or the drag force becomes zero respectively. Although this method is simple for calculation, it has some defects. That is to say, the reliability for the calculated value decreases significantly under such a wave and current composing condition that the water particle velocity or acceleration becomes small. Furthermore, for the case when the current velocity is larger than the amplitude velocity of the wave component,  $C_M$  cannot be calculated since the composite velocity never becomes zero throughout the wave phases.

Therefore, this method is applicable only for estimating  $C_D$  at the trough phase when the composite velocity becomes maximum.  $C_D$  estimated by the above mentioned method is expressed as  $(C_D)_{tr}$ , in which the subscript 'tr' means the value at the trough phase.

The second method estimating  $C_D$  and  $C_M$  is that proposed by Reid.<sup>5)</sup> By this method, water particle velocity  $u$  and acceleration  $\dot{u}$  are calculated from the water surface deviation  $\eta$  by using a numerical filter, and  $C_D$  and  $C_M$  are estimated from the measured hydrodynamic force by using the least squares method. The frequency response functions on  $\eta \sim u$  and  $\eta \sim \dot{u}$  with consideration of a current should be used.

The hydrodynamic force coefficients estimated by the above method are denoted as  $(C_D)_{b.f.}$  and  $(C_M)_{b.f.}$ , in which the subscript 'b.f.' means the best fit value.

### (3) Predominant parameters for expressing hydrodynamic force coefficients

Existing studies have treated the  $K.C.$  number and the Reynolds number as the predominant parameters expressing the hydrodynamic force coefficients in the wave only field. However, in the range of the Reynolds number in this experiment was between  $2 \cdot 10^3 \sim 2 \cdot 10^4$  where Sarpkaya<sup>6)</sup> reported that the changes of  $C_D$  and  $C_M$  with the Reynolds number are not so much. Accordingly, this study focuses on only the  $K.C.$  number as the predominant parameter for the force coefficients.

In the present study, two definitions are proposed as new  $K.C.$  numbers in the co-existing field. As shown in Chapter 2, the vortex properties around a cylinder throughout the phases are dominated by the water particle motion around the trough phase when the composite velocity becomes maximum.

As the first  $K.C.$  number, considering the composite velocity at the trough phase, the following parameter is introduced:

$$(K.C.)_1^* = (u_m + |U|)T/D \quad (3)$$

The physical meaning of the  $K.C.$  number can be considered as the ratio of the moving distance of a water particle in the one side direction of the cylinder  $s$  to the cylinder diameter  $D$ .

$$K.C. = \pi s/D \quad (4)$$

The second  $K.C.$  number is defined by the following equation expanding the above mentioned idea to the co-existing field.

For  $U \leq u_m$

$$(K.C.)_2^* = 2\pi \int_{t^*}^{T/2} |U + u_m \cos \sigma t| dt/D \quad (5)$$

in which,  $t^*$  denotes the time when the composite velocity becomes zero;

$$t^* = \cos^{-1}(-U/u_m)/\sigma \quad (6)$$

For  $U > u_m$

$$(K.C.)_2^* = \pi UT/D \quad (7)$$

As an expression for the component ratio of the wave and the current, the following parameter is introduced:

$$C_{asym} = u_m / (u_m + |U|) \tag{8}$$

This ratio becomes 1 at the limit of wave-only and tends to 0 as the current component becomes large compared with the wave component. Since this parameter represents the degree of asymmetry of the flow with respect to the center of a cylinder, the subscript of 'asym' denotes the abbreviation of asymmetry. In Eqs.(3), (5), (6) and (8), the velocity amplitude of the wave component  $u_m$  is defined as the root mean square value in the range from the water surface to the bottom.

Next, the ratio of the drag force to the inertia force is discussed. The maximum values of the drag and inertia forces throughout the wave phases,  $dF_{D,max}^r$  and  $dF_{M,max}^r$  are expressed by,

$$dF_{D,max}^r = (1/2) \rho C_D D (u_m + |U|)^2 dz \tag{9}$$

$$dF_{M,max}^r = (1/2) \rho \pi^2 C_M D^2 (u_m/T) dz \tag{10}$$

Accordingly, the ratio of both forces is calculated as follows:

$$\frac{dF_{D,max}^r}{dF_{M,max}^r} = \frac{C_D}{C_M} \left( \frac{u_m T}{D} \right) / \pi^2 \left( \frac{u_m}{u_m + |U|} \right)^2 = \frac{C_D}{C_M} (K.C.) / (\pi^2 C_{asym}^2) \tag{11}$$

The condition that the drag force is just equal to the inertia force is examined by using Eq.(11) under the assumption that  $C_D=1$  and  $C_M=2$ , independently of  $K.C.$  and  $C_{asym}$ . The result is shown in Fig.2, in which the predominant region of the drag or the inertia force is illustrated.

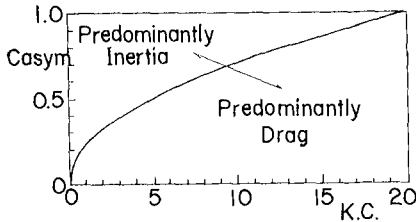


Fig.2 Predominant region of either drag or inertia force

(4) Experimental results and discussions

At first, preliminary experiments in the wave-only field were carried out. It is confirmed that the results coincide well with the existing ones in the wave-only field.

Next, the results obtained in the co-existing field are discussed. Fig.3 shows the relation between  $(C_D)_{tr}$  calculated at the wave trough phase and the  $K.C.$  number. It is observed that the characteristics of  $(C_D)_{tr}$  are not made clear by the  $K.C.$  number only, but they become evident after classifying the data into several ranges of  $C_{asym}$ . Also

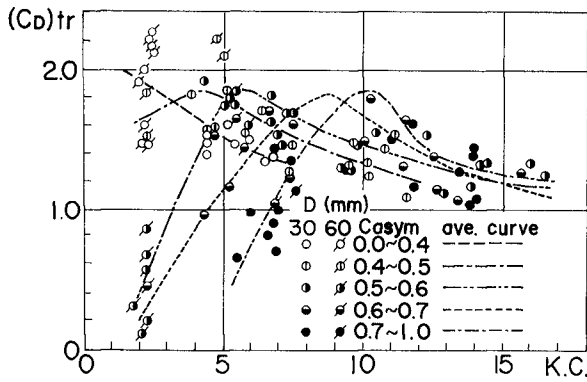


Fig.3 Drag coefficient  $(C_D)_{tr}$  at trough phase versus K.C. number (co-existing field)

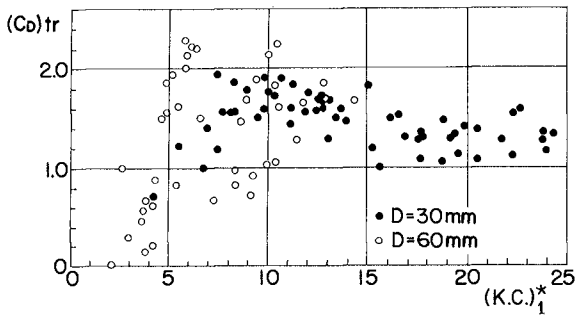


Fig.4 Drag coefficient  $(C_D)_{tr}$  at trough phase versus  $(K.C.)_1^*$  (co-existing field)

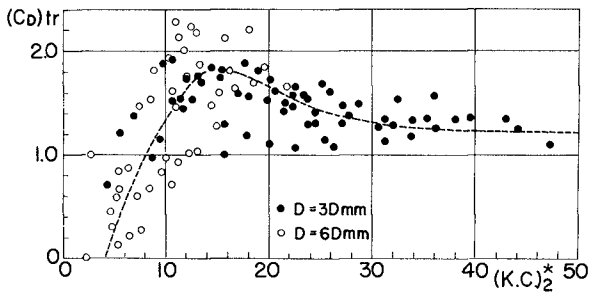


Fig.5 Drag coefficient  $(C_D)_{tr}$  at trough phase versus  $(K.C.)_2^*$  (co-existing field)

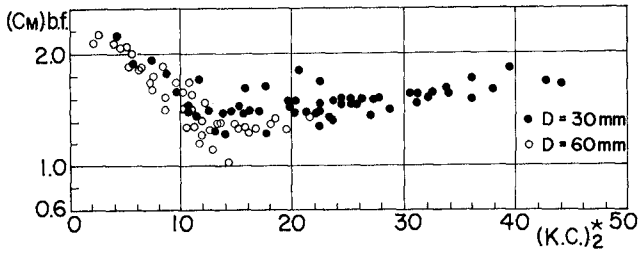


Fig.6 Mass coefficient  $(C_M)_{b.f.}$  fitting best with measured forces throughout wave phases versus  $(K.C.)^*_2$  (co-existing field)

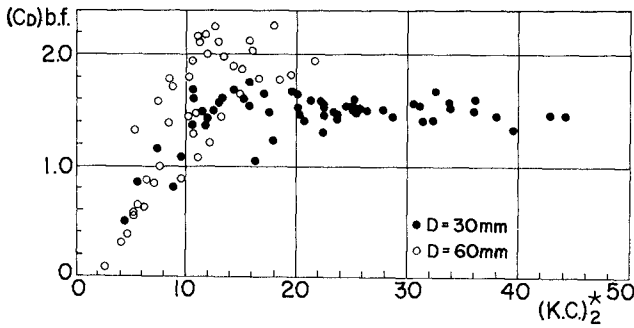


Fig.7 Drag coefficient  $(C_D)_{b.f.}$  fitting best with measured forces throughout wave phases versus  $(K.C.)^*_2$  (co-existing field)

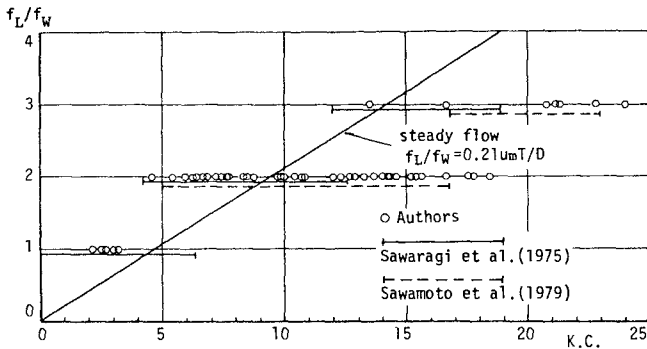


Fig.8 Ratio of lift force frequency  $f_L$  to loading wave frequency  $f_W$  versus  $K.C.$  (wave only field)



the peaks of the averaged curves shift in the direction of an increase in the  $K.C.$  number as  $Casym$  increases.

The results arranged by  $(K.C.)_1^*$  and  $(K.C.)_2^*$ , proposed as the new parameters in the co-existing field, are shown in Figs.4 and 5, respectively. In comparing both plots, the degree of scattering in Fig.5 using  $(K.C.)_2^*$  is less than that in Fig.4 using  $(K.C.)_1^*$ . In addition to this, from the view point of the physical meaning of the  $K.C.$  number, it is concluded that  $(K.C.)_2^*$  is a more appropriate parameter than  $(K.C.)_1^*$ .

The results of  $(C_D)_{b.f.}$  and  $(C_M)_{b.f.}$ , which are obtained by the least squares method in order to best fit the calculated values with the measured one, are discussed. Since  $(K.C.)_2^*$  is found to be the most suitable parameter as mentioned above, the data of  $(C_D)_{b.f.}$  and  $(C_M)_{b.f.}$  are also arranged by it. The results are shown in Figs.6 and 7 respectively.

Comparing Fig.5 with Fig.6, not much difference of the  $C_D$  values by the estimating methods is found. Furthermore, it is also made clear that the characteristics of the hydrodynamic force coefficients in the co-existing field show a good agreement with those in the wave-only field.

The reason why  $C_D$  and  $C_M$  are expressed well by  $(K.C.)_2^*$ , which represents the flow property around the trough phase, is considered that this flow property dominates the whole one throughout the wave phases. These characteristics of  $C_D$  and  $C_M$  can be explained by the established physical views in the wave only field<sup>4)</sup>.

Furthermore, several examinations on  $C_D$  and  $C_M$ , such as an effect of convective acceleration on them, were carried out and they were reported at the previous paper<sup>4)</sup>.

#### 4. Characteristics of lift force acting on a circular cylinder

##### (1) Experimental procedure

The experimental apparatus was almost same as that used in the flow visualization test and the in-line force measurements. Lift forces were measured by using two vertically supported cylinder of which diameters were 30mm and 60mm.

The experiments were conducted under the conditions of the wave frequency  $f=0.5\sim 0.8\text{Hz}$  and the velocities of adverse currents  $U=0\sim 25\text{cm/sec}$ . The water depth  $h$  was kept constant 40cm; however, several test runs were added under the condition of the water depth  $h$  reduced to 30cm to make current velocity large.

##### (2) Synchronization between lift force fluctuating frequency and loading wave frequency

Generation mechanism of lift force can be explained by vortex shedding around a cylinder. Accordingly, the vortex shedding frequency  $f_V$  generally coincides with the lift force fluctuating frequency  $f_L$ .

For a steady current, the relation between the current velocity  $U$  and the lift force fluctuating frequency  $f_C$  due to the current, which is

called here as Strouhal frequency, are described by Strouhal number  $S_t$ .

$$S_t = f_c D / U \quad (12)$$

The value of  $S_t$  is nearly constant at 0.2 in wide ranges of Reynolds number; therefore, the value of  $f_c$  increases continuously as the current velocity increases.

For the wave only field, however, it has been pointed out that  $f_L$  varies stepwisely with increasing in  $K.C.$ . Fig.8 shows the experimental results on the relation of  $f_L/f_W$  and  $K.C.$ . This result shows that even if the water particle velocity increases so far as the  $K.C.$  number does not exceed a certain value,  $f_L$  still remains constant. Namely, it is considered that the lift force fluctuation is strongly controlled by the loading wave frequency. This phenomenon is named here "synchronization".

The wave current co-existing field is considered as a transitional field connecting between the current only field and the wave only field; therefore, it is interesting to examine which property of currents or waves dominates in the co-existing field.

### (3) Experimental results on lift force fluctuation

Fig.9 shows some examples on the relation between lift force fluctuations and water surface deviations. Fig.9(a) is a result in the wave-only field, and shows that the frequency of the lift force is twice that of the wave. Fig.9(b) shows a result in the wave-current co-existing field. It is found in other many cases that  $f_L/f_W$  takes half odd numbers such as 0.5, 1.5, 2.5, ..., and this is considered to be an inherent property in the co-existing field.

Thus, in this study, the term of "synchronization" is used extensively for the case that  $2 \cdot f_L/f_W$  becomes an integer in addition to the case that  $f_L/f_W$  is an integer.

Fig.9(c) is a result of a relatively strong current and small waves combined loading. The figure shows that there is no obvious relation between the lift force fluctuations and the water surface deviations, and the value of  $f_L$  coincides with the Strouhal frequency  $f_c$  estimated from Eq.(12); therefore, it can be decided that the synchronization exists no longer in this case.

However, it is rather difficult to distinguish the case that  $f_L$  coincides with the Strouhal frequency  $f_c$  from the case that synchronization occurs, because when the value of  $f_L/f_W$  becomes larger than around 3, the lift force becomes irregular.

The experimental results on  $f_L/f_W$  are plotted in Fig.10. As the current velocity becomes large relative to the wave component, the value of  $f_L/f_W$  becomes large and finally  $f_L$  reaches to  $f_c$ . The data that  $f_L=f_c$  are plotted as a sign of "x" in the figure. In such cases that decision whether  $f_L$  is a multiple of  $f_W$  or equal to  $f_c$  is difficult, both signs are plotted in the figure.

It is noticeable in Fig.10 that  $2 \cdot f_L/f_W$  remains an integer even when the current velocity becomes large compared with the wave component

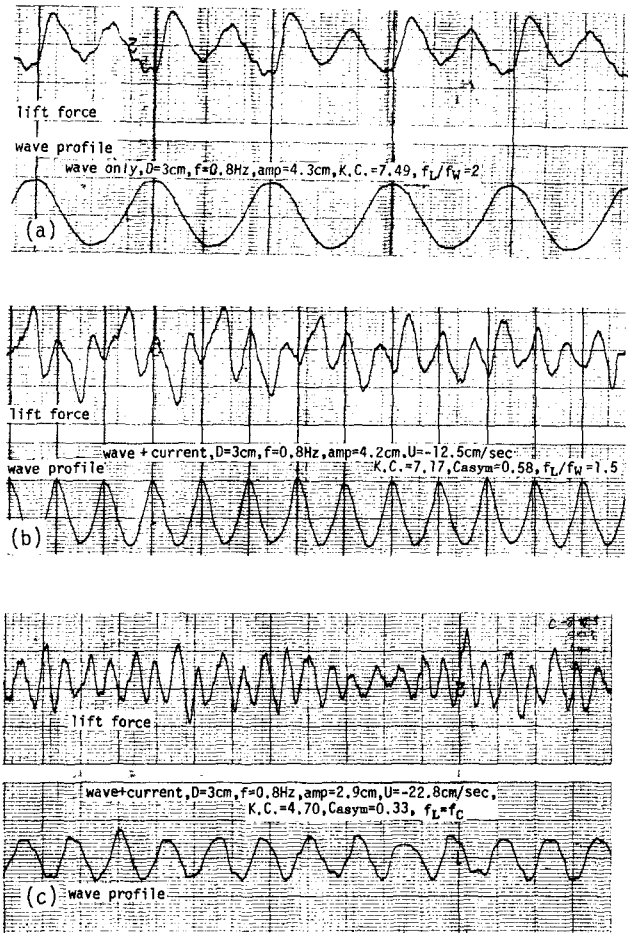


Fig.9 Records of lift force fluctuations and water surface deviations

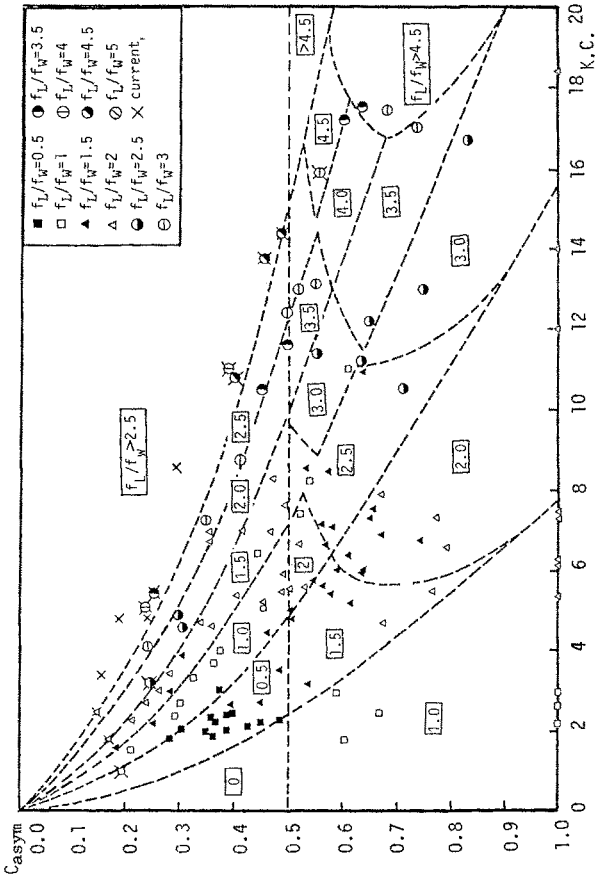


Fig.10 Comparisons of experimental results with calculated ones on a ratio of lift force frequency  $f_L$  to loading wave frequency  $f_w$

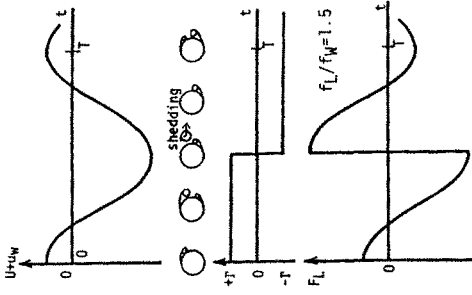


Fig.11 Schematic illustration of a model on  $f_L/f_w$

of water particle velocity.

It can be concluded that the lift force frequency or the vortex shedding frequency is strongly dominated by the loading wave frequency in the wave-current co-existing field.

This phenomenon is similar to the well known "synchronization" for a steady current field<sup>8)</sup>: When a cylinder is oscillated in a steady current, the forced oscillation locks the vortex-shedding frequency and controls the shedding process. Recently, a similar phenomenon is reported on aerodynamic responses on a bridge that a turbulent fluctuation of wind is possible to control the vortex-shedding<sup>9)</sup>.

#### (4) A model for predicting $f_L/f_W$

In this section, a simple model for predicting the experimental results on  $f_L/f_W$  is proposed.

Concerning an approximate estimation on the fluctuating frequency of lift force  $f_L$ , it is sufficient to consider only both properties of vortex shedding and mean flow velocity variation. It is not necessary to consider vortex generation, decay and movement.

Here, therefore, the lift force variations are approximated with the following Kutta-Joukowski type equation:

$$F_L = -\rho V \Gamma \quad (13)$$

in which  $\Gamma$  is a circulation around a cylinder.

Sawamoto and Kikuchi<sup>10)</sup> proposed a model to estimate lift forces in wave only field under the following assumptions: In a steady flow, a pair of vortices are shed from a cylinder when the moving distance of a water particle  $s$  exceeds 5 times the cylinder diameter  $D$ , which is easily obtained from the relationship of Eq.(12). They applied this idea extensively to the wave only fields, and estimated the number of shedding vortices during a wave period. Furthermore, they considered the variation of the circulation around a circular cylinder in the following way: Whenever a vortex sheds from a cylinder, the same magnitude and opposite sign circulation is added according to Kelvin's circulation theory.

Here, this study applied Sawamotos' idea to the wave-current coexisting field. Fig.11 shows schematically the variation of the circulation around a cylinder, the water particle velocity and the estimated lift force fluctuation.

In the wave only field, a water particle moves symmetrically with respect to the cylinder so far as non-linearity is ignored; therefore, equal number of vortices are shed from up-stream and down-stream sides of the cylinder. The number of shedding vortices while a water particle moves in one direction is presented by "n", then the total number of shedding vortices during a wave period is equal to  $2n$ . Consequently, the circulation  $\Gamma$  changes its sign  $2n$  times during a wave period. Meanwhile, the main stream velocity  $U+u_m \cos \omega t$  changes its sign 2 times during a wave period. Accordingly,  $f_L/f_W$  is given as

$$f_L/f_W = n + 1 \quad (14)$$

In the wave-current co-existing field, water particles move asymmetrically due to a superimposed current, so that the number of vortices from each side of the cylinder becomes different.

At first, we consider a case that current velocity  $U$  is smaller than the amplitude velocity of the wave component  $u_m$ . The numbers of shedding vortices from both sides of the cylinder are denoted as  $n_1$  and  $n_2$ . Since the circulation  $\Gamma$  changes its sign  $n_1 + n_2$  times and the main stream velocity does 2 times, the value of  $f_L/f_W$  for this case is calculated as follows:

For  $|U| \leq u_m$

$$f_L/f_W = (n_1 + n_2 + 2)/2 \quad (15)$$

Next, for another case of  $|U| \leq u_m$ , a water particle moves in the uni-direction throughout a wave period.  $\Gamma$  changes its sign  $n$  times, in which  $n$  denotes the number of shedding vortices during a wave period, while  $U + u_m \cos \omega t$  never changes its sign. Consequently, the following equation is obtained:

For  $|U| > u_m$

$$f_L/f_W = n/2 \quad (16)$$

It is easily confirmed from Eqs.(15) and (16) that  $f_L/f_W$  is possible to take a value of half odd number. The numbers of  $n_1$ ,  $n_2$ ,  $n$  are calculated based on the assumption that one vortex is shed when the moving distance  $s$  exceeds 2.5 times the cylinder diameter  $D$ . For example,  $n_1$  in Eq.(15) is calculated by following equation:

$$\begin{aligned} n_1 &= \left\{ 2 * \int_0^{t^*} (U + u_m \cos \omega t) dt / (2.5D) \right\} \\ &= \left\{ \frac{2}{5} \cdot \frac{K.C.}{\pi} \left( \sin \omega t^* + 2\pi \frac{U}{u_m} \frac{t^*}{T} \right) \right\} \end{aligned} \quad (17)$$

in which,  $\{ \}$  shows the maximum integer not to exceed the inside value of the bracket.  $t^*$  denotes the time when the wave-current component velocity becomes zero as shown in Eq.(6). If two parameters of  $K.C.$  (Eq.(1)) and  $C_{asym}$  (Eq.(8)) are given, all the values of  $n_1$ ,  $n_2$  and  $n$  can be calculated and then  $f_L/f_W$  also can be estimated from these values.

The results on  $f_L/f_W$  estimated by this model are shown in Fig.10 with the experimental results, where the boundaries on the values of  $f_L/f_W$  are drawn by dotted curves. The reason why the calculated  $f_L/f_W$  values vary at  $C_{asym}=0.5$  is that the model estimates them using the different equations between for  $|U| > u_m$  and for  $|U| \leq u_m$ .

From the comparison of calculated results with experimental ones, it is found that this simple model predicts satisfactorily well the experimental results including the property that  $f_L/f_W$  has a value of half odd number.

#### (5) Lift force coefficient in wave-current co-existing fields

In this section, the lift force coefficient and the predominant

parameters are discussed. The lift coefficient  $C_L$  in the co-existing field are defined as the following equation:

$$C_L = F_L / \{0.5\rho D(u_m + |U|)^2\} \quad (18)$$

in which,  $F_L$  is the individual peak value of the lift force fluctuation. Since lift forces generally do not show regular fluctuations even if regular forces load on a cylinder, it is necessary to use statistic representatives on  $C_L$ .

Here three representatives are used, such as, the mean, the one-third and the one-tenth largest lift coefficients which are denoted as  $\overline{C_L}$ ,  $C_{L1/3}$ , and  $C_{L1/10}$ , respectively.

In the wave only field, it has already been pointed out that  $C_L$  becomes the maximum when  $K.C.$  is around 10~12. Fig.12 shows the experimental results on the one-tenth largest lift force coefficient performed by the authors and Sawaragi-Nakamura<sup>9)</sup>.

Fig.13 shows the results on the mean lift coefficient  $\overline{C_L}$  in the wave-current co-existing field against  $K.C.$ . Since the parameter  $K.C.$  does not consider the current component, there appears much scatter.

Next, the same results are arranged by the newly proposed  $K.C.$  number in the co-existing field  $(K.C.)_{\frac{1}{2}}$  which is defined by Eqs. (5) and (7). The results are shown in Fig.14 and similar results on the one-third and the one-tenth largest lift coefficients  $C_{L1/3}$  and  $C_{L1/10}$  are shown in Figs.15 and 16 respectively.

It is found from these figures that the lift force co-efficients are well arranged by  $(K.C.)_{\frac{1}{2}}$  and take their maximum around  $(K.C.)_{\frac{1}{2}} = 10 \sim 12$ . This fact coincides with the property obtained in the wave only field as shown in Fig.12. The property that  $C_L$  takes the maximum around  $(K.C.)_{\frac{1}{2}} = 10 \sim 12$  is explained by the vortex property obtained in Chapter 2; that is, asymmetric vortices are generated in the flow condition when  $(K.C.)_{\frac{1}{2}} = 10 \sim 12$ .

It is concluded that  $(K.C.)_{\frac{1}{2}}$  which expresses the vortex property in the wave current co-existing field can represent the property of the lift force coefficient as well as the in-line force coefficients.

## 5. Conclusions

The vortex properties around a circular cylinder depend on the flow properties around the phase when the wave-current composite velocity is maximum.

The force coefficients for both in-line and transverse forces are arranged well by  $(K.C.)_{\frac{1}{2}}$  which is proposed as a new  $K.C.$  number in the wave-current co-existing field. The relations between these coefficients and  $(K.C.)_{\frac{1}{2}}$  are in good agreement with the results on the relations between the coefficients and  $K.C.$  established in the wave only field.

Furthermore, on the lift force frequency the following inherent properties in the co-existing field are obtained: the ratio of its

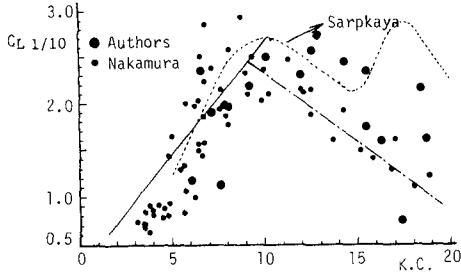


Fig.12 One-tenth largest lift coefficient  $C_{L1/10}$  versus K.C. (wave only field)

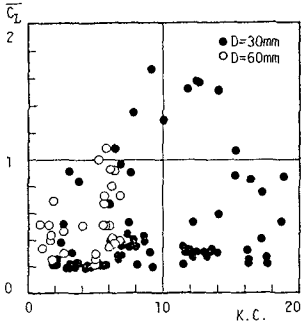


Fig.13 Mean lift force coefficient  $\overline{C_L}$  versus K.C.

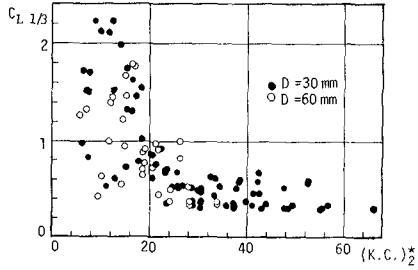


Fig.15 One-third largest lift coefficient  $C_{L1/3}$  versus  $(K.C.)^{1/2}$

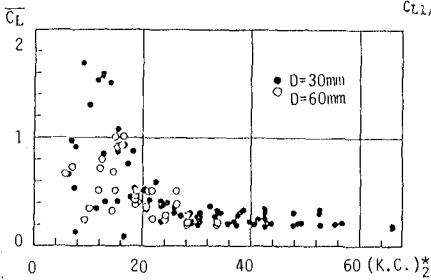


Fig.14 Mean lift coefficient  $\overline{C_L}$  versus  $(K.C.)^{1/2}$

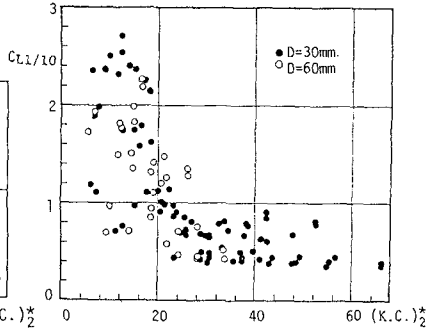


Fig.16 One-tenth largest lift coefficient  $C_{L1/10}$  versus  $(K.C.)^{1/2}$



frequency to the loading wave frequency is possible to take a half odd numbers, and the both fluctuations synchronize each other.

#### Acknowledgement

This study is part of the research sponsored by the Grant-in-Aid for Scientific Research of the Ministry of Science, Culture and Education. The authors wish to express their appreciation to Messrs. F. Nagai and T. Yamada, former students at Department of Civil Engineering, Kyoto University, for their help in performing the experiments.

#### Reference

- 1) Bishop, R.E.D. and A.Y. Hassan : The lift and drag forces on a circular cylinder oscillating in a flowing fluid, Proc. Royal Soc. London, A277, pp.51-75, 1964.
- 2) Horikawa, K., M. Mizuguchi, O. Kitazawa and Y. Yanagimoto : On hydrodynamic force in wave-current field (part.1), Proc. 23th Conf. Coastal Eng. in Japan, pp.39-44, 1976 (in Japanese).
- 3) Iwagaki, Y. and H. Ishida : Flow separation, wake vortices and pressure distribution around a circular cylinder under oscillatory waves, Proc. 15th Coastal Eng. Conf., ASCE, pp.2341-2356, 1976.
- 4) Iwagaki Y., T. Asano and F. Nagai : Hydrodynamic forces on a circular cylinder placed in wave-current co-existing fields, Memoirs of Faculty of Eng., Kyoto Univ., Vol.45 No.1, pp.11-23, 1983.
- 5) Reid, R.O. : Correlation of water level variations with wave forces on a vertical pile for non-periodic waves, Proc. 6th Conf. Coastal Eng., pp.749-783, 1957.
- 6) Sarpkaya, T. : In-line and transverse forces on cylinders in oscillatory flow at high Reynolds number, Proc. of Offshore Technology Conference, Vol.2, pp.95-108, 1976.
- 7) Sarpkaya, T. and M. Isaacson : Mechanics of wave forces on offshore structures, Van Nostrand Reinhold Co., p.651, 1981.
- 8) Sawamoto, M. and K. Kikuchi : Lift forces on circular cylinder in an oscillating fluid, Proc. 26th Conf. Coastal Eng. in Japan, pp.429-433, 1979 (in Japanese).
- 9) Sawaragi T., T. Nakamura and H. Kita : Characteristics of lift forces on a circular pile in waves, Coastal Engineering in Japan, Vol.19, pp.59-71, 1976.
- 10) Sawaragi, T. and T. Nakamura : Analytical study of wave force on a cylinder in oscillatory flow, Coastal Structures 79, Vol.1, pp.154-173, 1979.
- 11) Shiraishi, N., M. Matsumoto and H. Okanan : Aeroelastic galloping of prismatic tower in the turbulent flow, Symposium on Wind Engineering, pp.273-279, 1982 (in Japanese).
- 12) Verley, R.L.P. and G. Moe : The forces on a cylinder oscillating in a current, The Norwegian Institute of Technology, Rep. No. STF60, A79061, p.58, 1979.

## CHAPTER ONE HUNDRED NINETY TWO

### WAVE POWER EXTRACTION AT COASTAL STRUCTURE BY MEANS OF MOVING BODY IN THE CHAMBER

Hideo KONDO<sup>1</sup>, M.ASCE, Tomiji WATABE<sup>2</sup> and Kenji YANO<sup>3</sup>

#### Abstract

A series of study on wave power extractors which may utilize a part of the coastal structures has been performed by the group of faculties of Muroran Institute of Technology since 1978. Three kinds of extractor belonging to the so-called fixed type had been developed and studied in the laboratory. They are the air chamber with flap, the wave turbine system and the pendolor system. The last two systems have been subsequently studied at the field test plant constructed at Port Muroran. The study shows that the pendolor system brings an excellent power conversion efficiency.

#### 1 INTRODUCTION

Numerous apparatus have been proposed for the purpose of extracting usable energy from sea waves. However, none of them except the Masuda air buoy as navigational markers are in practice because of the economical difficulty to cope with oil. These extractors are classified roughly into two types, namely, the floating and the fixed ones. Table 1 presents a further classification of the two types of extractors from the viewpoint of dynamic property and direction of body or water, etc.

Much effort had been devoted to develop the floating type extractors just after the 1973 oil crisis. Generally speaking, they require large floating bodies with durable mooring equipments, which raises the cost of energy to be produced. The idea of so-called fixed coastal type has a longer history than the floating one but less attention had been paid for it in the 70's. The drawback of the floating type made a few groups reexamine the merit of fixed type.

Coastal defensive structures, namely, breakwaters, dykes, and revetments have been so designed as to reflect and/or to dissipate the incoming waves. If we could extract a considerable amount of the incident wave energy at these structures without spoiling their essential functions, the cost of energy must be remarkably decreased from that by the conventional apparatus. With this line of thought, the group of civil, mechanical and electric engi-

---

1 Professor of Civil Engineering, Muroran Institute of Technology, 27-1 Mizumoto-Cho, Muroran, 050 JAPAN

2 Professor of Mechanical Engineering, ditto

3 Research Assistant of Civil Engineering, ditto

Table 1 Classification of Wave Power Extractors  
 [ Notations in the parenthesis after the name of extractors are as follows.  
 Fin;Finland, US;United States of America, UK;United Kingdom, J;Japan, NY;  
 Norway, RSA;Republic of South Africa ]

	DYNAMIC PROPERTY	DIRECTION OF BODY MOTION OR WATER, ETC.	NAME OF EXTRACTOR(COUNTRY)	
FLOATING TYPE	PASSIVE SYSTEM (ISLAND SYSTEM)	Wave Pressur	Tömkvist(Fin)	
		Wave Run-up	Dam Atoll(US)	
		Wave Pressure	Flexible Bag(UK), CLAM(UK) Masuda Air Buoy(J), Belfast(UK) Point Absorber(NY), Tail Tube(UK)	
		Heaving	Buoy	Kaimisi(J)
			Attenuator	OWC(UK), Plunger Shaped(UK)
	RESONANT SYSTEM	Terminator	Salter Duck(UK)	
		Rolling	Cockrell Raft(UK)	
		Pitching	Oscillating Cylinder(UK)	
		Underwater		
FIXED TYPE	PASSIVE SYSTEM (PROGRESSIVE WAVE)	Wave Pressure	Bottom Pressure(US)	
		Inflow	Pressure Diaphragm(J) HRS Rectifier(UK)	
		Overtopping	Wave-Current(J)	
		Vertical	NEL-OWC(UK), SWEC(RSA)	
		Horizontal	Air Chamber with Flap(J)	
	RESONANT SYSTEM (SAWING WAVE)	Vertical	Wave Turbine(J)	
		Horizontal	Pendulor(J)	

neering faculties of the institute headed by the senior author had tried to find the fixed type extractors which can be set within coastal structures and be easily operated , since 1978. The three extractors developed are the resonant fixed type ones and are those underlined in Table 1.

2 AIR CHAMBER WITH FLAP

The first extractor studied consists of an air chamber with the oscillating flap hinged at the top, which pushes and draws the air confined in the chamber to rotate the turbine on it while the incoming waves swing the flap, as shown in Fig. 1. The chamber may be surrounded with the curving backwall, the partision walls and the coping in which the air duct locates. The cofiguration of backwall looks like those of common seawalls and of dykes.

The experiment in a 24 meter long, 0.6 meter wide and 1 meter deep wave channel with regular waves, showed 20 to 50 % of the incident wave power was converted to the air pressure power, as shown in Fig. 2. The conversion efficiency  $\eta_a$  of the vertical axis in the figure is that defined as

$$\eta_a = \frac{\bar{w}_a}{B \cdot \bar{w}_i} \times 100 \quad (1)$$

where  $\bar{w}_i$  is the incident wave power per unit crest width and is given by the following equation for the regular waves.

$$\bar{w}_i = \bar{E} \cdot C_g = \frac{1}{8} \rho g H^2 C_g \quad (2)$$

where  $C_g$  is the group velocity of the incident wave.  $\bar{w}_a$  is the average air pressure power absorbed by the system of length  $B$  and is estimated as

$$\bar{w}_a = \frac{1}{T} \int p \cdot dV \quad (3)$$

where  $T$  is the wave period,  $p$  is the air pressure and  $V$  denotes the volume of air in chamber.

The effect of the opening ratio of air duct  $e$  is not clear. There are two apparent peaks of the efficiency, for  $T/T_N = 1.5$  and 2.1.  $T_N$  is the natural period of the pendular.

Because of the efficiency of model air turbine being low, torque of air turbine remains about 2 % of the regular incident wave power. This figure, of course, will be much improved by employing a more efficient air turbine.

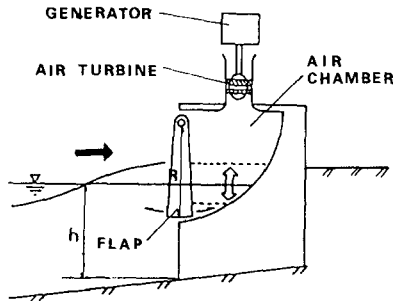


FIG.1 SKETCH OF AIR CHAMBER WITH FLAP

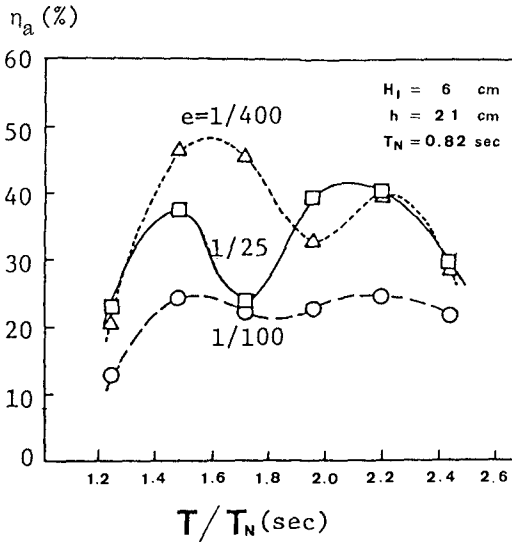


FIG.2 CONVERSION EFFICIENCY FROM  
WAVE TO AIR

### 3 WAVE TURBINE SYSTEM

The next system has a three-vane Savonius turbine rotating around the vertical axis fixed in the rectangular water chamber formed in the reinforced concrete caisson without the seaward wall as seen in Fig. 3. The plane form of the turbine is asymmetric in order to rotate it in the same direction in spite of the reciprocating wave force acting on it. The guide plates are attached to the partition walls and aim to concentrate the flow near the turbine and eventually to increase the torque of it. A standing wave occurs in the chamber. Thus the highest conversion efficiency is expected where the distance between the axis and the backwall is about the one quarter of the wave length in the chamber. That means the axis lies near the node of the standing wave. For the cases of relatively larger wave length, the caisson may be installed on a solid or a rubble base mound to decrease the depth of chamber, in which case the wave length becomes short so

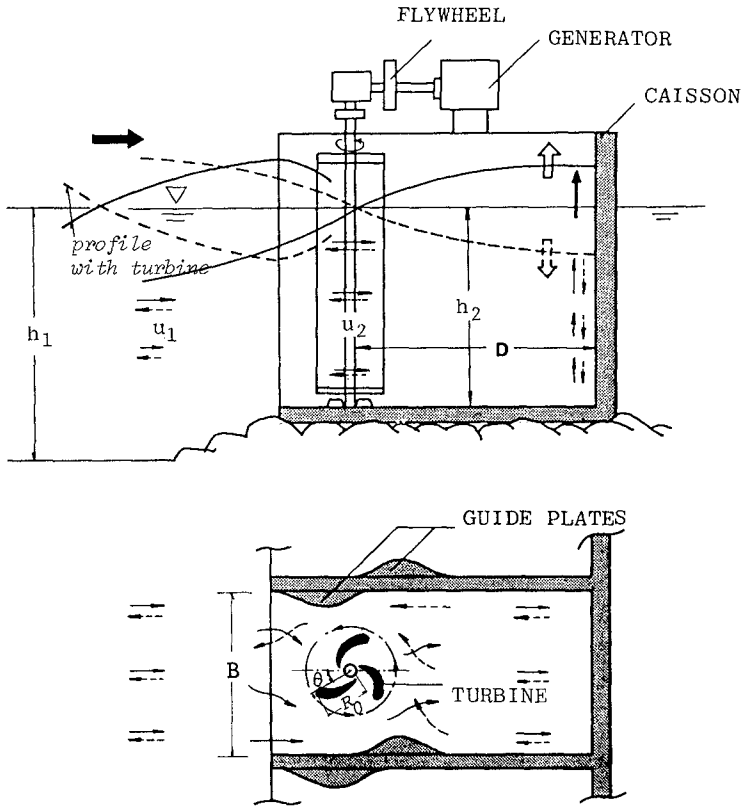


FIG. 3 SKETCH OF WAVE TURBINE SYSTEM AND WATER PARTICLE MOTION AROUND IT

that the caisson width can be decreased for the given wave period and for the original depth  $h_1$ .

The experiment was performed for the power extraction, wave reflection and wave force characteristics of the system in the same channel described in the section 2. The details of the result had been reported by KONDO et al. (1980, 1981). The average power extracted by the turbine  $\bar{w}_t$  was evaluated by

$$\bar{w}_t = \tau \bar{\dot{\theta}} \quad (4)$$

where  $\tau$  is the load torque and  $\dot{\theta}$  is the angular velocity of turbine. The conversion efficiency  $\eta_t$  from incident wave power to torque of turbine of length is defined as

$$\eta_t = \frac{\bar{w}_t}{B \cdot \bar{w}_i} \times 100 (\%) \quad (5)$$

The actual efficiency of mechanical conversion for the system with  $h_1 \neq h_2$  in which a part of incident wave power is reflected, should be defined as

$$\eta_e = \frac{\bar{w}_t}{B \cdot \bar{w}_i'} \times 100 (\%) \quad (6)$$

where  $\bar{w}_i'$  is the transmitted wave power into the chamber per unit crest width without the system.  $\eta_e$  should be  $\eta_t$  for the case  $h_1 = h_2$ . The efficiency  $\eta_e$  takes the maximum for the relative distance of axis from backwall  $D/L$  around 0.25 as expected, which can be seen in Fig. 4. The guide plates are much effective to increase the extracted power as shown in the figure. However,  $\eta_e$  remains 20 % at most. The theoretical values of  $\eta_e$  shown with solid and broken lines in the figure were those of calculated with the approach presented in the Appendix.

The reflection coefficient of the structure as a whole is almost less than 0.4 and is comparable to that of common rubble mound breakwaters. Fig. 5 presents the critical wave height to slide the caisson with the system, from which the horizontal wave force against the structure as a whole is estimated to be 50 % or less of that on the imperious upright breakwaters.

#### 4 PENDULOR SYSTEM

The last system has an oscillating pendulor around the horizontal axis perpendicular to it, and transmits the power of pendulor to that of oil pressure through the reciprocating cylinder connected to the pendulor at the top, as illustrated in Fig. 6.

The experiment had been performed on the horizontal bottom in a 18.5 meter long, 0.4 meter wide and 1 meter deep wave channel at the initial stage and later in the 24 meter channel stated in the section 2. The average power extracted to the oil pressure was determined in the experiment by

$$\bar{w}_p = \frac{1}{T} \int F_C r_C \dot{\theta} dt \quad (7)$$

where  $r_C$  is the distance between the neutral position of pendular and the center of cylinder, and  $\dot{\theta}$  is the angular velocity of pendulor.  $F_C$  is the reaction force of cylinder.

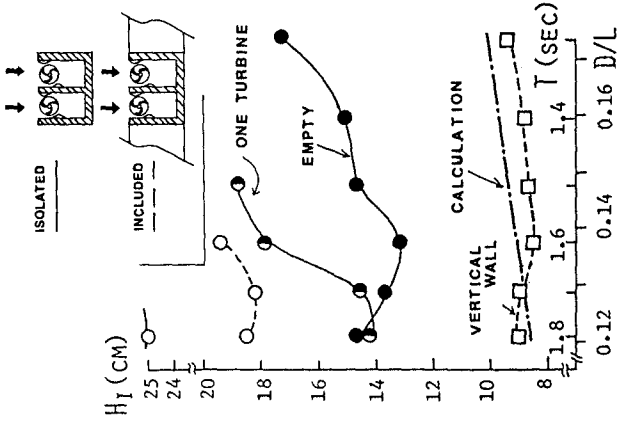


FIG. 5 CRITICAL INCIDENT WAVE HEIGHT FOR SLIDING OF CAISSON

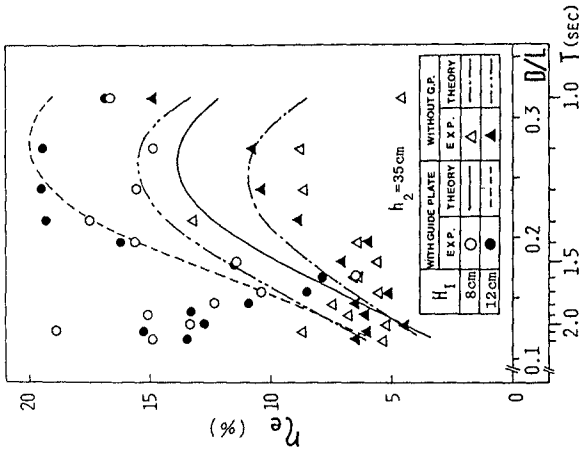


FIG. 4 CONVERSION EFFICIENCY FROM THE TRANSMITTED WAVE POWER INTO THE CHAMBER TO THE TORQUE



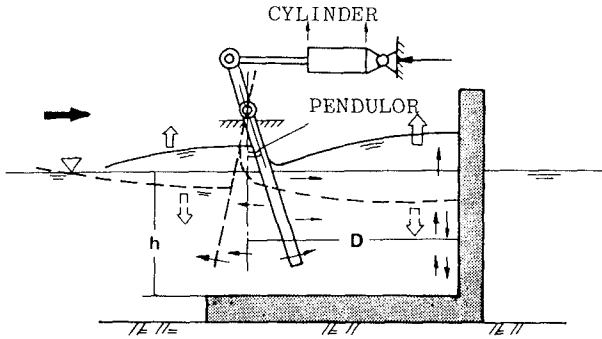


FIG. 6 SKETCH OF THE PENDULOR SYSTEM

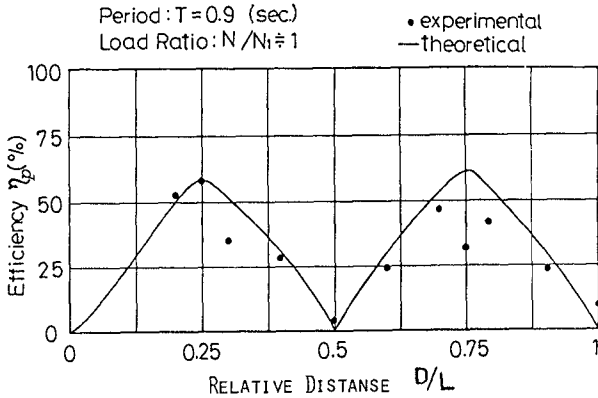


FIG. 7 CONVERSION EFFICIENCY FROM WAVE TO OIL PRESSURE VERSUS RELATIVE DISTANCE OF THE PENDULOR AXIS FROM BACKWALL

der and is evaluated as

$$F_C = F_O + \beta (r_C \dot{\theta})^2 \quad (8)$$

where  $F_O$  is the frictional force of cylinder and  $\beta$  is the load coefficient due to the orifice restrictor. Then the conversion efficiency of the system with length  $B$  is

$$\eta_p = \frac{\bar{W}_p}{B \cdot \bar{W}_i} \times 100 \quad (\%) \quad (9)$$

The system also brings the maximal of  $\eta_p$  where the neutral position of pendular coincides the location of node of the standing waves formed in the chamber, as clearly seen in Fig. 7. The maximum value of  $\eta_p$  was 80 % in the experiment . The two dimensional analysis for the small amplitude wave had been derived by Asano (1980), outline of which will be introduced in the paper by Ando et al. (1984). Fig. 8 presents the result of comparison of theoretical efficiency with experimental one. The theory successfully predicts the experimental data or the cases of relatively lighter load condition and of shorter wave period, as shown in Fig. 8.

5 FIELD EXPERIMENT

In order to investigating feasibility of the last two systems at the sea, a series of the field test has been carried out employing a test caisson. It is 6.1 meter long,

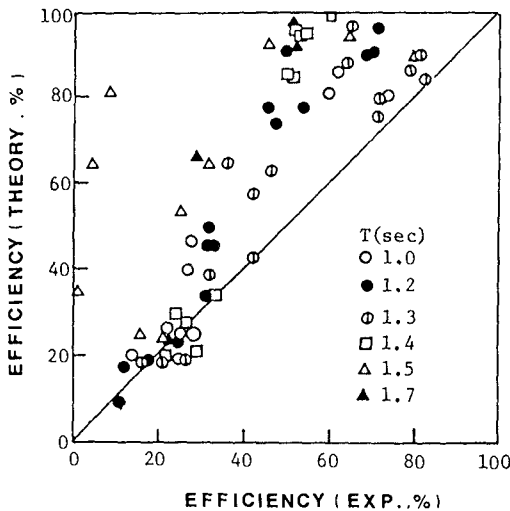


FIG.8 COMPARISON OF THE EFFICIENCIES OF THEORY AND OF EXPERIMENT

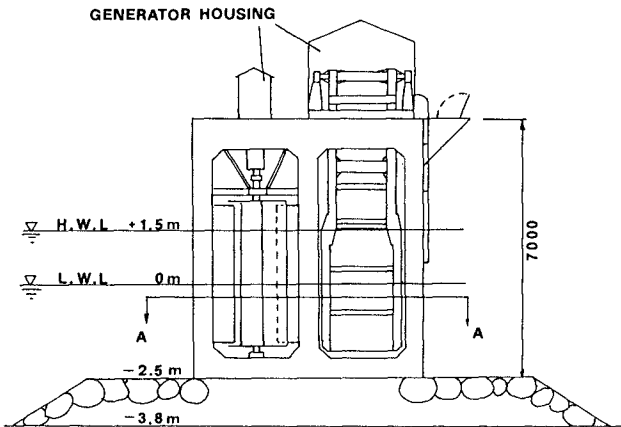
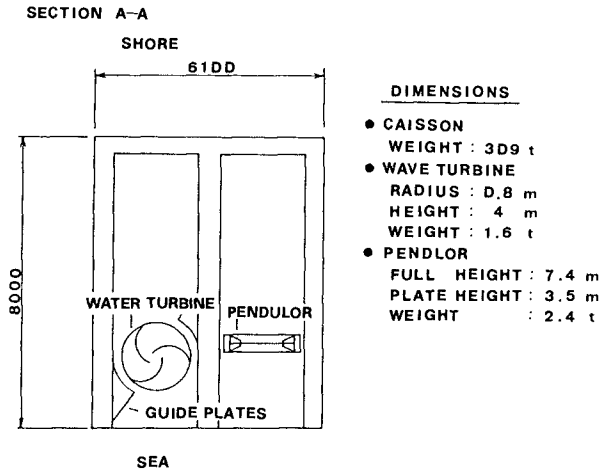


FIG.9 THE FIELD TEST PLANT AT PORT MURORAN

Photo. 1

Test Plant Caisson before installation - Wave Turbine and Guide Plates had been set in the left hand side Chamber



Photo. 2

Test Plant just after installation at seaward of South Breakwater of Port Murooran in April 1980

Photo. 3

The Pendolor is being set in the another Chamber of Test Plant in March 1983



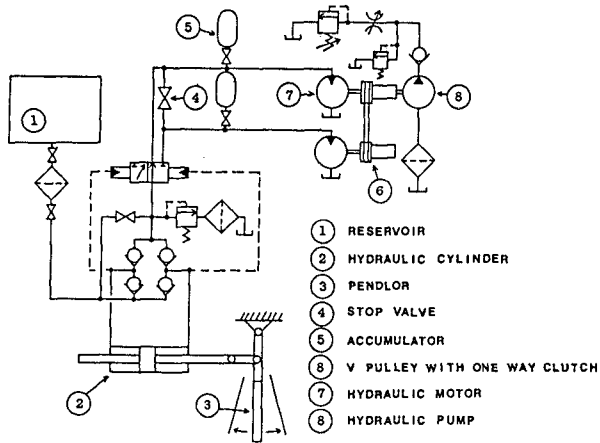


FIG.10 THE OIL PRESSURE CIRCUIT OF TEST PLANT

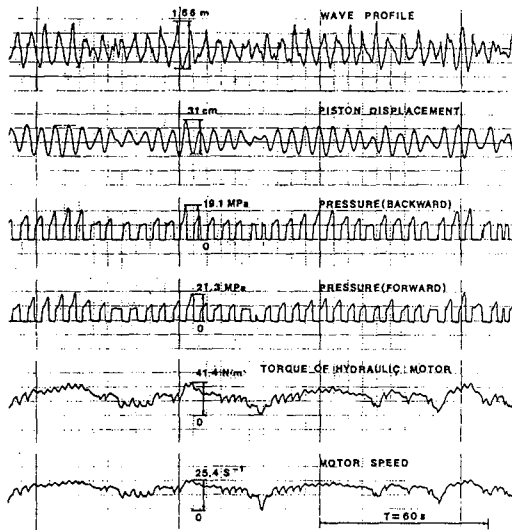


FIG.11 EXAMPLE OF THE DATA MEASURED AT TEST PLANT

7 meter high and 8 meter wide, and had been constructed seaward of the south breakwater of Port Muroran in the spring of 1980 ( see Fig.9 and Photo.1 and 2 ). As seen from Photo. 1, the caisson has two chambers to be able to install two kinds of systems. Since the port faces to a bay on the Pacific south west coast of Hokkaido Island, the waves of  $H_{1/3} \geq 1.0$  meter is approximately 12 % and appear mostly in winter.

The power extracted by the wave turbine system at the caisson transmits via a flywheel to the 2 kW D.C. generator. The extracted power measured in front of the generator was in the range of 3 to 8 % of the incident wave power, and much fluctuated. The incident wave power of the sea waves was estimated with the following equation to the Bretschneider-Mitsuyasu spectrum, provided that the waves belong to those of deep water.

$$\bar{w}_i = \int_0^{\infty} S(f) \cdot C_G \cdot df = 0.44 \cdot H_{1/3}^2 \cdot T_{1/3} \quad (kW/m) \quad (10)$$

where  $S(f)$  is the frequency spectrum, and  $H_{1/3}$  and  $T_{1/3}$  are the significant wave height and period, respectively. About 60 % of the torque power was converted to the electric power. The wave data used were of 2 km offshore.

The pendulum system which had been installed in the another chamber of caisson in 1983 is of 2.5 ton of weight and the length from the rotational axis to the lower end is 7.1 meter, as shown in Fig. 9. The plate to receive wave force at the lower part of it is 2 meter wide and 3.5 meter high ( see Fig.9 and Photo.3 ). The secondary conversion block consists of the oil circuit which outputs the oil pressure with employing an oil pump instead of a generator which is illustrated in Fig. 10. The circuit can be used in the three ways, namely, the smoothing, the nonlinear and the linear ones, respectively. Fig. 11 presents an example of the measured data of the pendulum system. The

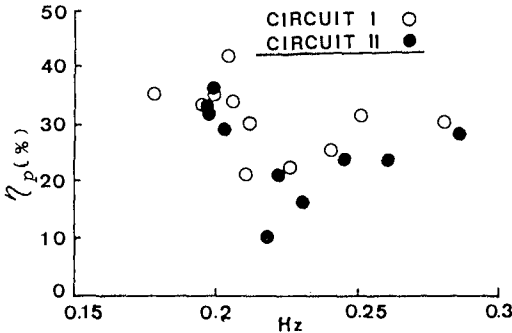


FIG.12 CONVERSION EFFICIENCY VERSUS WAVE FREQUENCY OF THE FIELD TEST

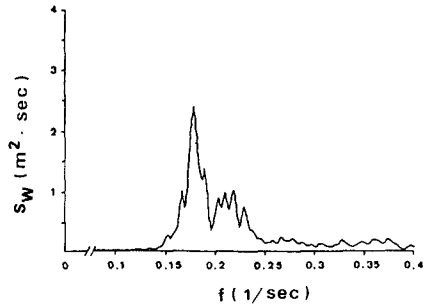


FIG.13 WAVE SPECTRUM SEAWARD OF THE CAISSON

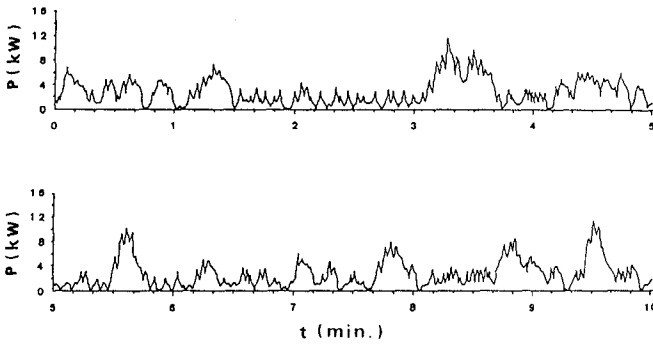


FIG.14 TIME HISTORY OF EXTRACTED OIL PRESSURE POWER

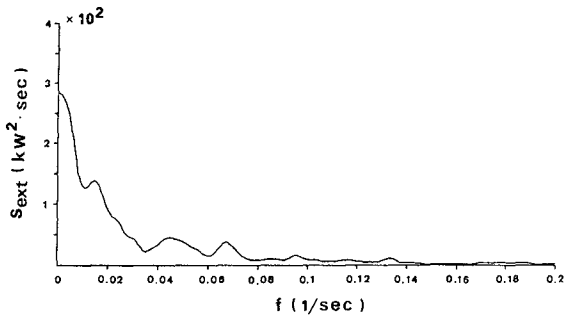


FIG.15 THE SPECTRUM OF THE EXTRACTED POWER

circuit I (smoothing) gave higher efficiency than the circuit II (nonlinear) did as shown in Fig. 12. The pendulum system with the smoothing circuit could convert about 35 % of the incident wave power to the oil pressure power. This figure seems to be a remarkably higher value as the data in real sea.

Figs. 13, 14 and 15 give examples of the wave spectrum from the datum measured 5 meter apart from the caisson with the ultrasonic wave gage set over the water surface, the time history of extracted power, and the spectrum of extracted power, respectively. The extracted power is much smoothed with the aid of the smoothing circuit.

## 6 CONCLUDING REMARKS

The cost of electricity to be produced by the pendulum system in prototype commercial plant is estimated to be approximately 26 Yen/kWh or 11 US cents/kWh at the price of the year of 1982 in Japan, provided the average incident wave power  $\bar{w}_i = 25$  kW/m and the overall efficiency 20% (Ref. 5)). This figure can be reduced to about 60 % of that for the cases of construction cost of caisson being exempted, which may occur when it serves also as any breakwater, dyke or revetment. The pendulum system seems to be one of the most prospective wave power extractors, though there remains several engineering problems to be solved before the commercial use.

A small pilot plant of the pendulum system has been operated at Mashike Town, in the Japan Sea coast of Hokkaido, the details of which will be reported by Ando, et al. (1984).

## ACKNOWLEDGEMENTS

The authors are much appreciative for the co-operation of those who had been or are presently the members of the group for wave power utilization study at the institute, Professors K. Orikasa, S. Ozaki, K. Okuda, T. Matsuda and Y. Dote. Thanks must go to the some forty former graduate and undergraduate students of the institute, who had participated with the study during the period 1976 - 83.

We also wishes to express our appreciation to Drs. A. Ando and M. Takagi, Mr. M. Kuroi, and the late Mr. S. Asano of Hitachi Zosen Corporation who have studied the pendulum system jointly with us and had made the plant of Mashike.

Major part of the present study has been supported by Science Research Fund of the Ministry of Education.

## APPENDIX - The Simplified Analysis of the Power Extraction for the Wave Turbine System

The dynamic equation for the wave turbine of vertical axis set in the chamber as illustrated in Fig. 3 can be expressed as

$$(I + I_a) \ddot{\theta} + N_w \dot{\theta} + k\theta = \tau_w - \tau \quad (11)$$

where  $I$  is moment of inertia of the turbine,  $I_a$  added moment of inertia,  $N_w$  damping coefficient due to radiation



waves generated by the turbine,  $k$  restoring coefficient of the turbine,  $\tau_w$  wave exciting torque on the turbine,  $\tau$  torque of load,  $\theta$  rotational angle of the turbine. The dot denotes the time derivative.

The torque  $\tau_w$  on the turbine such as shown in Fig. 3 is approximated as

$$\tau_w = \rho C_t U_2^2 R_0^2 h_2 / 2 \quad (12)$$

where  $\rho$  is the density of fluid and  $C_t$  coefficient of torque on the turbine.

The horizontal water particle velocity  $u_2$  is expressed as

$$u_2 = U_2 \cos(\sigma t - \delta) \quad (13)$$

Then, the time average of  $\tau_w$  in Eq.11 is given by

$$\bar{\tau}_w = \rho R_0^2 h_2 U_2^2 C_t / 4 \quad (14)$$

The load torque  $\tau$  may be expressed as

$$\tau = N_t \dot{\theta} + \tau_{t0}$$

where  $N_t$  and  $\tau_{t0}$  are the coefficients related to load resistance. Since the coefficient  $k$  may be relatively small for the system, Eq.11 becomes

$$\ddot{\theta} + p\dot{\theta} = r \cos 2(\sigma t - \delta) + s \quad (15)$$

wh

$$p = \frac{N_t + N_t}{I + I_a}, \quad r = \frac{\bar{\tau}_w}{I + I_a}, \quad s = \frac{\bar{\tau}_w - \tau_{t0}}{I + I_a}$$

The solution of Eq.15 is given as follows.

$$\theta = \frac{r}{2\sigma\sqrt{4\sigma^2 + p^2}} \cdot \sin[2(\sigma t - \delta) + \gamma] + \frac{q}{p}t + Ce^{-pt} \quad (16)$$

where  $\gamma = \tan^{-1}(\frac{2\sigma}{p})$

After calculating  $\theta$ , the power extracted by the turbine is obtained with Eq.4 in section 3.  $U_2$  of Eq.4 may be approximated with wave deformation theory for the stepwise previous structure by Kondo (1983).

#### REFERENCES

- 1) Ando, A., S. Ohtani, M. Takagi, M. Kuroi, H. Kondo, K. Yano and T. Watabe: On a flap type wave energy converter, Paper to be presented at ECOR International Conf., 1984.
- 2) Asano, S.: Energy absorption efficiency of flap type wave energy converter, JTTC, SK60-14, 1980 (in Japanese).
- 3) Kondo, H. (Ed.): Study on the fixed type wave power generating systems to be installed in coastal structures, Rept. of Science Research Fund of Ministry of Education, 1978 - 79, 1980 (in Japanese).
- 4) Kondo, H., K. Yano, M. Takahashi, T. Watabe and K. Okuda: A Device for wave power extraction in Coastal Structure - Wave turbine system-, Proc. of 28th Japanese Conf. on Coastal Eng., JSCE, 1981 (in Japanese).
- 5) Kondo, H. (Ed.): Ocean Energy Utilization Technology, Research Rept., No.1, Hokkaido Port & Coastal Research Assoc., 1983 (in Japanese).

- 6) Kondo, H.: Reflection and transmission of shallow water waves at the pervious coastal structures on solid step, Proc. of XX Congress of IAHR, Vol.VII, 1983.
- 7) Watabe, T., H. Kondo, K. Yano, H. Takeda and M. Kuroi: A device for wave power extraction in coastal structure (2) -Pendulor system-, Proc. of 29th Japanese Conf. on Coastal Eng., JSCE, 1982(in Japanese).
- 8) Watabe. T., H. Kondo and K. Yano: Wave energy conversion by wave pendulor - Design of experimental plant outside the Port of Muroran, Proc. of JSME, in press (in Japanese).

## CHAPTER ONE HUNDRED NINETY THREE

### FULL-SCALE WAVE FORCES ON PILES IN SHALLOW WATER

by

Uwe Sparboom <sup>+</sup>

Nico Efthimiou <sup>++</sup>

Andreas Voigt <sup>++</sup>

#### ABSTRACT

This paper presents some results of simultaneous full-scale wave kinematic and local force measurements (field and laboratory) on a slender, vertical cylindrical pile (test-section) under shallow water conditions. The usual application of Morison's equation is taken under critical consideration due to the real flow regime near the surf zone. The data were analyzed in the time domain as well as in the amplitude and frequency domain. Two estimation methods for force coefficients were tested and compared.

#### INTRODUCTION

Pile-supported substructures are often needed for various coastal engineering structures. There are still many difficulties in the design of cylindrical slender structures in shallow water regions which are characterized by surf zones with an important dissipation of energy, especially under storm surge conditions. A decisive advance in determining reliable force coefficients is to measure the water particle kinematics synchronously with the surface elevations (waves) and wave pressures or wave forces in the field (Dean (/2/)). Results of field-measurements and added two-dimensional full-scale laboratory investigations with the same test-pile used in the field enable to describe the mechanism of wave-structure interactions more sufficiently. The real wave attack in the experiments reported in this paper occurred at supercritical Reynolds number conditions.

+ Research Engineer, Dipl.-Ing., LARGE WAVE CHANNEL-Joint Institution of University of Hannover and Technical University of Braunschweig, Merkurstrasse 11, D-3000 Hannover 21, West Germany

++ Senior Student of Electrical Eng., cand.-ing., University of Hannover, West Germany

The authors are members of "SONDERFORSCHUNGSBEREICH 205-COASTAL ENGINEERING" at University of Hannover, West Germany, sponsored by the German Research Foundation

### FIELD MEASUREMENTS

In order to obtain field-data at high Reynolds numbers the measuring facilities were installed in the nearshore area of the Eastfrisian Island Norderney on the German North Sea Coast. Detailed informations can be found in Sparboom (/8/). In Fig.1 the configuration of the measuring devices which were used for this paper is drawn up schematically. Wave pressures were measured at a test-section in 16 points at even spaces on the circumference of the pile (diameter 0.7 m). In a distance of about 5.0 m from the pile the surface elevations and the velocities of the water particle motions (two components in a vertical plane and two components in a horizontal plane) were measured synchronously. It should be noted here, that the test-section of the pile is structurally combined with a calibrated two-component strain gauge unit measuring the total wave forces acting on the test-section. These force signals were used to control the forces obtained by integrating the pressures which were measured synchronously by 16 single transducers. Representative samples of field data were recorded in some winter-seasons under different storm surge conditions at high tide water levels. Simultaneous records of wave kinematics and wave forces can be seen exemplarily in Fig.2. It could be assumed that the wave kinematics (horizontal velocities and accelerations, surface elevations) were always unaffected by the pile. The direction nearly normal to the shore was defined as mean inline direction (X-axis), because it coincided with the mean direction of the incoming waves. The direction nearly parallel to the shore was similarly defined as mean transverse direction (Y-axis).

### LABORATORY FULL-SCALE TESTS

With the end of the winter-season 1982/83 the research program was changed to systematic full-scale tests in the new Large Wave Channel (Grüne and Führböter, (/4/); Führböter, (/3/)). The part of the test-pile in the field which contains the test-section was recovered and used for first laboratory investigations with respect to regularly generated waves (periods from 5.0 to 8.0 seconds, wave heights from 1.0 to 2.0 meters). The configuration of the installed sensors and transducers is given in Fig.3. Regarding the configuration in Fig.1 care was taken to realize the laboratory full-scale tests under equal conditions as used in the field. An example for simultaneous records of the first tests in the Large Wave Channel is plotted in Fig.4. The measured values of the horizontal transverse velocity components were very small. Therefore they were neglected for further calculations.

### WAVE FORCE ANALYSIS IN THE TIME DOMAIN

The mostly used approach in the course of estimating the loading of vertical cylindrical structures is as follows: For a given set of wave height  $H$  and wave period  $T$  the wave kinematics  $u$  and  $\dot{u}$  are calculated theoretically; with a suitably chosen pair of coefficients  $C_d$  and  $C_m$  and application of Morison's equation maximum wave forces are estimated. This method contains uncertainties arising from the validity or not of wave theories proposed for the actual sea state, particularly in the nearshore zone. With measured kinematics only the uncertainty in determining  $C_d$  and  $C_m$  remains. This problem will be subject of this paper.

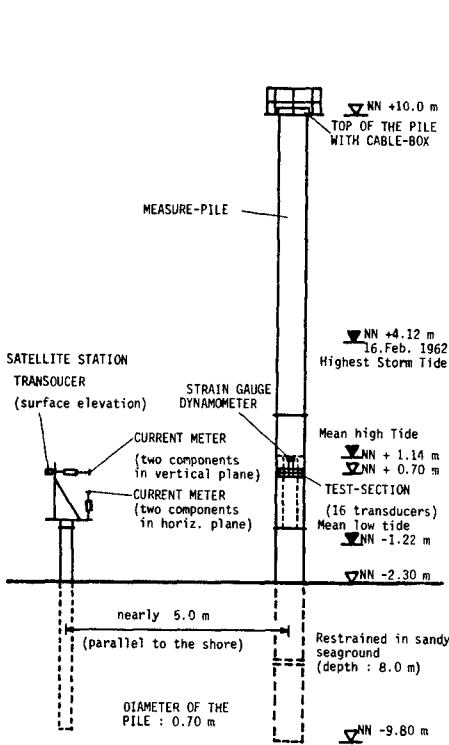


Fig. 1:

Full-Scale Configuration in the Field

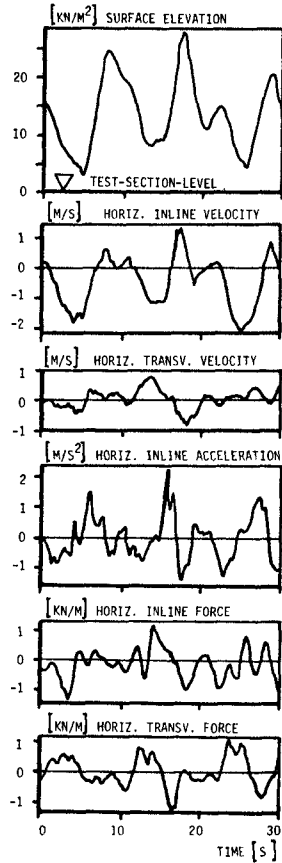
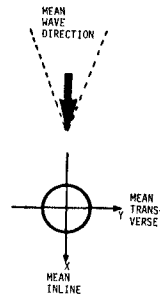


Fig. 2:  
Simultaneous Field Records  
of Wave Kinematics and  
Wave Forces in the  
Test-Section Level



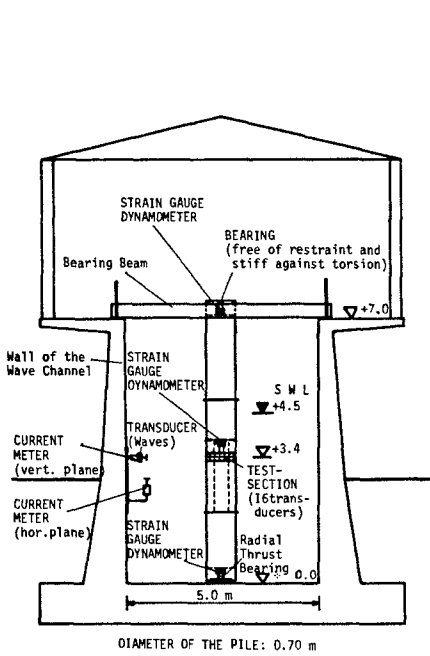


Fig. 3:  
Full-Scale Configuration  
in the Laboratory

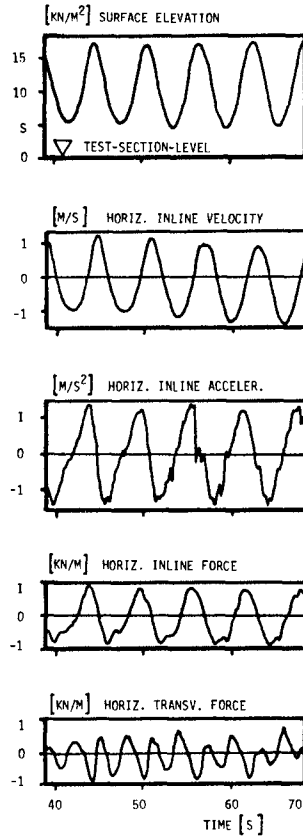
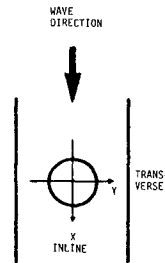


Fig. 4:  
Simultaneous Laboratory  
Records of Wave Kinematics  
and Wave Forces in the  
Test-Section Level



Utilizing the first simultaneous field data it was found that the values of the force coefficients plotted against Reynolds and Keulegan-Carpenter numbers displayed high scatter (Sparboom (/8/)). The main reasons for the large amount of scatter are as follows:

- three-dimensional effects; large variability of wave kinematics direction
- interactions of wave kinematics and test-structure (test-section) due to vortex shedding
- superposed long-periodic oscillations; presence of trend values
- wave deformation near the breaker zone.

Fig.5 gives an example for the time-dependent development of simultaneously measured horizontal velocity and wave force vectors (single step equal to 0.192 seconds). The plotted traces represent a record of about 40 seconds.

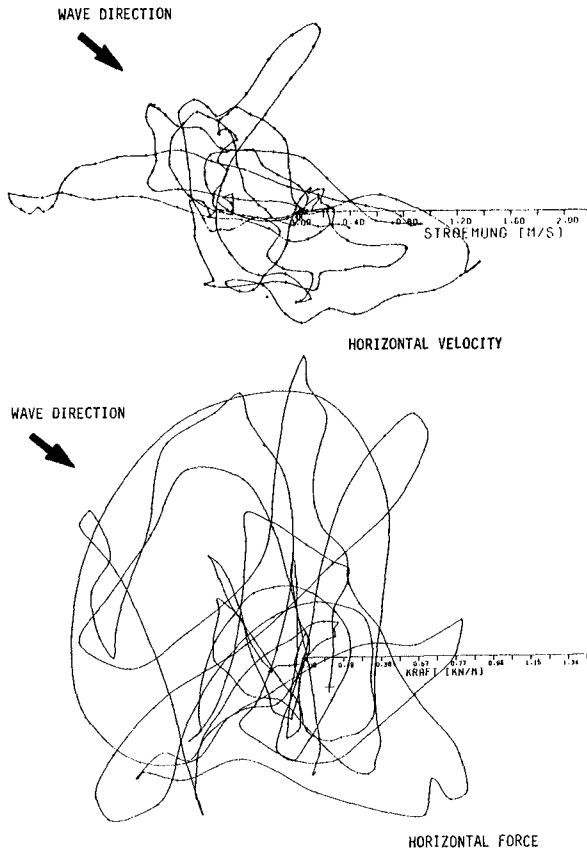


Fig. 5: Measured Vector Traces of Horizontal Velocity and Test-Section Wave Forces

In order to check the reliability of Morison's equation under shallow water conditions a statistically based method was applied to determine force coefficients. With reference to Pearcey and Bishop (/6/) the mean square method was utilized and computed.

A definition sketch for the apparatus used in full-scale investigations of wave-loading can be seen in Fig.6.

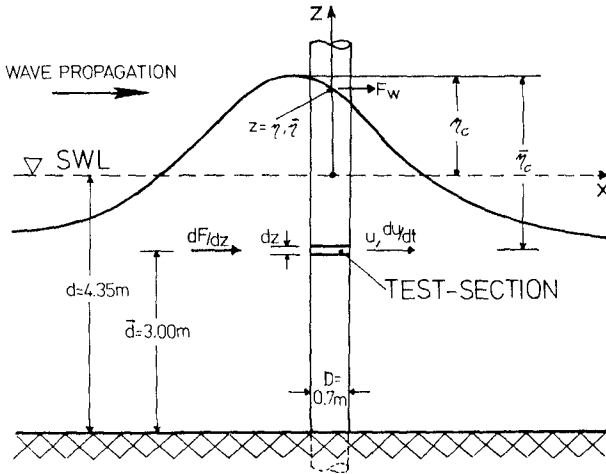


Fig. 6: Definition Sketch of Test-Section Wave-Loading

A complete analysis for the loading of cylindrical piles from the hydrodynamic considerations is beyond the scope of this paper. It is, however, instructive to recall some of the basic assumptions associated with the derivation of Morison's equation. This formula depends on the linear superposition of wave force terms as a result of water particle motions (velocity and acceleration or drag and inertia portions). One classical approach to the derivation of Morison's equation starts with the fluid power equilibrium (Lighthill (/5/)). The inertial term in Morison's equation is derived by equating the time rate of work done by the inertial force on a Newtonian fluid to the time rate of change of the fluid kinetic energy due to irrotational flow, under the assumptions of flow field uniformity (no convective accelerations) and existence of a potential function. Similarly, the drag term is derived by equating the power by drag forces to the sum of the time rate of change of kinetic energy in the wake (rotational flow) plus the power dissipation in the wake due to viscous effects. Again, uniformity of flow is assumed; additionally, this term is derived by assuming that the velocity is constant or very slowly varying. Taking into consideration the contribution to the pressure gradient due to the interaction between velocity and vorticity an additional lift force term may be derived. In this case the following assumptions are made: The vorticity is uniformly distributed; the vorticity is proportional to the velocity.



The wave force acting on a vertical, smooth slender cylinder in the horizontal plane then becomes

$$\vec{F} = \vec{F}_{\text{drag}} + \vec{F}_{\text{inertia}} + \vec{F}_{\text{lift}} + \vec{F}_w \quad (1)$$

with  $\vec{F}_w$  = Waterline Force.

The first three terms are usually determined by integrating with respect to  $z$  the force per unit length of the submerged portion of the cylinder given in cartesian coordinates by

$$\begin{pmatrix} f_x \\ f_y \end{pmatrix} = \frac{1}{2} C_d \rho D \sqrt{(u_x - \dot{x})^2 + (u_y - \dot{y})^2} \begin{pmatrix} u_x - \dot{x} \\ u_y - \dot{y} \end{pmatrix} \quad (2a)$$

$$+ \rho \frac{\pi D^2}{4} \begin{bmatrix} 1 + C_{xx} & 1 + C_{xy} \\ 1 + C_{yx} & 1 + C_{yy} \end{bmatrix} \begin{pmatrix} \dot{u}_x \\ \dot{u}_y \end{pmatrix} - \begin{bmatrix} C_{xx} & C_{xy} \\ C_{yx} & C_{yy} \end{bmatrix} \begin{pmatrix} \ddot{x} \\ \ddot{y} \end{pmatrix} \quad (2b)$$

$$\pm \frac{1}{2} C_l \rho D \sqrt{(u_x - \dot{x})^2 + (u_y - \dot{y})^2} \begin{pmatrix} u_y - \dot{y} \\ u_x - \dot{x} \end{pmatrix} \quad (2c)$$

- $f_x, f_y$  = wave force per unit length  
 $\rho$  = water density  
 $D$  = diameter of the vertical cylindrical pile  
 $C_d$  = drag coefficient  
 $C_{xx}, C_{yy}$  = added mass coefficients  
 $C_l$  = lift coefficient  
 $u_x, u_y$  = horizontal orbital velocity  
 $\dot{u}_x, \dot{u}_y$  = temporal derivatives of  $u_x$  and  $u_y$   
 $\dot{x}, \dot{y}$  = horizontal displacement velocity  
 $\ddot{x}, \ddot{y}$  = horizontal displacement acceleration

The reducing assumptions that pile movements are of very small value and therefore ineffective regarding force generation, and that the potential field is axial-symmetric, i.e.  $1 + C_{xx} = 1 + C_{yy} = C_m$  (inertia coefficient), yield

$$\begin{pmatrix} f_x \\ f_y \end{pmatrix} = \frac{1}{2} D \rho C_d |\vec{u}| \begin{pmatrix} u_x \\ u_y \end{pmatrix} + \frac{\pi}{4} \rho D^2 C_m \begin{pmatrix} \dot{u}_x \\ \dot{u}_y \end{pmatrix} \pm \frac{1}{2} \rho D C_l |\vec{u}| \begin{pmatrix} u_y \\ u_x \end{pmatrix} \quad (3)$$

with  $|\vec{u}| = \sqrt{u_x^2 + u_y^2}$ .

Due to the complex vorticity mechanism the sign of the lift term cannot be defined theoretically. The inline force in X-direction becomes

$$f_x = \frac{1}{2} \rho D C_d u_x |\vec{u}| + \frac{\pi}{4} \rho D^2 C_m \dot{u}_x \pm \frac{1}{2} \rho D C_l u_y |\vec{u}|. \quad (4)$$

Neglecting the lift term we get

$$f_x = \frac{1}{2} \rho D C_d u_x |\vec{u}| + \frac{\pi}{4} \rho D^2 C_m \dot{u}_x. \quad (5)$$

For the two-dimensional case in the wave channel  $u_y$  in equation (3) disappears so that equation (5) gives the well-known Morison's equation

$$f_x = \frac{1}{2} \rho D C_d u_x |u_x| + \frac{\pi}{4} \rho D^2 C_m \dot{u}_x \quad (6)$$

For determining Morison coefficients from time-averaged field measurements the mean square method was applied (/6/). Equation (5) goes over in

$$\overline{f_x^2} = A^2 \overline{u_x^2 |u_x|^2} + B^2 \overline{\dot{u}_x^2} + 2 A B \overline{u_x \dot{u}_x |u_x|} \quad (7)$$

The bars indicate mean values of the squares of the measured quantities ( $f_x$ ,  $u_x$ ,  $|u_x|$ ,  $\dot{u}_x$ ) integrated over a chosen interval. Assuming linear independence between  $u_x |u_x|$  and  $\dot{u}_x$  the cross product can be neglected. The solution of a pair of linear equations for consecutive intervals gives the unknown coefficients A and B and also the Morison coefficients

$$C_d = \frac{A}{\frac{1}{2} \rho D} \quad , \quad C_m = \frac{B}{\frac{\pi}{4} \rho D^2} \quad .$$

It should be noted here, that the solution of the linear system of equations (7) will be valid if the flow is stationary and if the parameters are time-invariant.

Mean squared equation (6) becomes

$$\overline{f_x^2} = A^2 \overline{u_x^4} + B^2 \overline{\dot{u}_x^2} + 2 A B \overline{u_x \dot{u}_x |u_x|} \quad (8)$$

The mean squares corresponding to equation (4) lead to a more complicated formula

$$\overline{f_x^2} = A^2 \overline{u_x^2 |u_x|^2} + B^2 \overline{\dot{u}_x^2} + C^2 \overline{u_y^2 |u_x|^2} + 2 A C \overline{u_x u_y |u_x|^2} + 2 B C \overline{\dot{u}_x u_y |u_x|} + 2 A B \overline{u_x \dot{u}_x |u_x|} \quad (9)$$

Due to linear independence the last term can be neglected again. Because there are nonvanishing cross terms in (9), there exists no linear solution. Instead of solving equation (9) the square of the error E which is defined as the difference between the right and left hand side of equation (9) is minimized:

$$\frac{1}{2} \sum_{i=1}^N E_i^2 \quad (A, B, C) \xrightarrow{!} \text{Min} \quad (10)$$

N = number of averaged intervals

The unknown coefficients for the feedback to equation (4) are

$$C_d = \frac{A}{\frac{1}{2} \rho D} \quad , \quad C_m = \frac{B}{\frac{\pi}{4} \rho D^2} \quad , \quad C_l = \frac{C}{\frac{1}{2} \rho D} \quad .$$

The minimization is performed by an iterative gradient technique. The essentially same method can be used to minimize the two-parametric equations (7) and (8). Two independent solutions for the parameters from the same time-averaged record can therefore be obtained and compared.

## ANALYSIS IN THE AMPLITUDE AND FREQUENCY DOMAIN

Measured field data and wave channel data were analyzed using similar procedures (except for minor differences in their smoothing requirements detailed later on). The analysis was performed in the frequency domain and in the amplitude domain.

At the first stage, data were checked for stationarity. To this purpose, the original record was partitioned in equal time intervals (about 30 sec) for each of which a sample mean was calculated. Next, the number of runs about the mean value calculated for the entire record was counted and compared to the values for the run distribution. The hypothesis of stationarity was rejected at the  $\alpha = 0.05$  level of significance because the number of runs counted was considerably lower than the lower bound of the acceptance region (this was especially true for the surface elevation record, less so far the horizontal orbital velocity). This implies that there is a non-negligible contribution to the surface elevation with a period at least one order of magnitude longer than the wave periods. This phenomenon may be attributed to surf beat due to wave groupiness.

Now, letting  $z(t)$  be the nonstationary surface elevation,  $\eta(t)$  a random process with a stationary mean value of zero, and  $G(t)$  a very slow process (henceforth called the trend of  $z(t)$ ) compared to  $\eta(t)$ , we may write

$$z(t) = G(t) + \eta(t) \quad (11)$$

It can then be shown (Bendat and Piersol (/1/)) that the expected value of  $z(t)$  is  $G(t)$ . The mean square value of  $z(t)$  is

$$E [(G + \eta)^2] = E [G^2] + E [\eta^2] + 2 E [G \cdot \eta] \quad (12)$$

where the last term turns out to be of negligible magnitude compared to the other two, implying that  $G(t)$  and  $\eta(t)$  are linearly independent; for, in this case,  $E [G \cdot \eta] = E [G] \cdot E [\eta]$  and  $E [\eta]$  is zero by definition. Equation (12) shows that the mean square value of the surface elevation would be overestimated by the amount  $E [G^2]$  if the trend portion is not removed. It is by precisely this amount that the spectral density function would also be overestimated (specifically, in the lower frequency range). In fact, the trend would nullify the estimation of low frequency spectral content. It is for these reasons that it was decided to remove the trend. An appropriate estimate for  $G(t)$  is given by short time averaging as follows:

$$\hat{G}(t) = \frac{1}{2T} \int_{t-T}^{t+T} z(\tau) d\tau \quad (13)$$

It was found that a satisfactory trade-off between bias error and random error for  $G(t)$  could be achieved for  $2T = 47$  sec. For a digitized  $z(t)$  with sampling rate  $t$ , this operation is equivalent to the application of a finite-impulse-response digital filter with transfer function

$$H(\omega \Delta t) = \frac{\sin(\omega T)}{\sin \frac{\omega \Delta t}{2}} \cdot \frac{\Delta t}{2T} \quad (14)$$

The transfer function being real-valued, there is no phase distortion associated with the filtering operation. Additionally, if the same

linear operation is performed on two different records (e.g. surface elevation and horizontal orbital velocity), then the transfer function and associated coherence remain unchanged. This prompted us to use the trend filter on all processed signals. Data analysis in the frequency domain concentrated on the estimation of power spectral density functions  $\hat{S}_{ii}(f)$ , gain functions  $|\hat{H}_{ij}(f)|$  and coherence functions  $\hat{\gamma}_{ij}(f)$ . Preliminary tests showed that there are no significant contributions above 0.6 Hz. The estimates obtained were therefore plotted up to that frequency (some up to 0.5 Hz), not up to the Nyquist frequency, this being 2.6 Hz for field measurements and 20 Hz for wave channel measurements. Since records of various length were used (15 to 20 min for the field), it was decided to keep the number of degrees of freedom for the spectral estimates practically constant at  $n = 40$ . This means the normalised standard error

$$\epsilon_r = \left(\frac{1}{2} \cdot n\right)^{-\frac{1}{2}} = 0.22$$

The reasons leading to the choice for  $n$  are:

- a smaller number of degrees of freedom would appreciably increase the random error in the spectral estimates. For instance,  $n = 22$  would give  $\epsilon_r = 0.3$ .
- a larger number of degrees of freedom would not lead to a corresponding reduction of random error. For example, to achieve  $\epsilon_r = 0.1$ , we would require  $n = 200$  (five times more degrees of freedom). Such a disproportionate increase in the number of degrees of freedom would require increasing the resolution bandwidth (and thus increasing the bias error) or increasing the record length (and thereby violating the stationary assumption).

Frequency smoothing need not be performed on regular wave data obtained under laboratory conditions.

Standard FFT procedures are used to obtain all estimates from the time records. For the power spectral density estimate  $\hat{S}_{\dot{u}\dot{u}}$  of the horizontal acceleration  $\partial u / \partial t$  for field data, however, use of the well-known identity

$$\mathcal{F}\left[\frac{\partial u}{\partial t}\right] = j\omega \mathcal{F}[u]$$

where  $\mathcal{F}[\ ]$  is the Fourier Transform and  $j = \sqrt{-1}$  was made,

RESULTS AND CONCLUSIONS

The application of the mean square method in two-dimensional case (equ. (8) for regular waves in the laboratory) seems to be quite satisfactory. The mean parameters  $C_d$  and  $C_m$  corresponding to various time-averaged intervals were plotted in Fig. 7 for the linear solution and for the minimization of the squared error.  $C_m$  is almost independent from the length of intervals. The values for  $C_d$  differ significantly between the estimation methods used and display considerable scatter.

Feeding back a suitable pair of force coefficients ( $C_d = 1.0$ ;  $C_m = 1.5$ ; Dean's reliability ratio  $r = 0.8$  to  $1.8$ ) to equation (6) and operating with measured kinematics, the force was obtained in comparison to the real measured force (Fig.8). A quite good agreement of measured and calculated force plots can be observed. The goodness of mean square based estimations was also verified by the gain and coherence functions

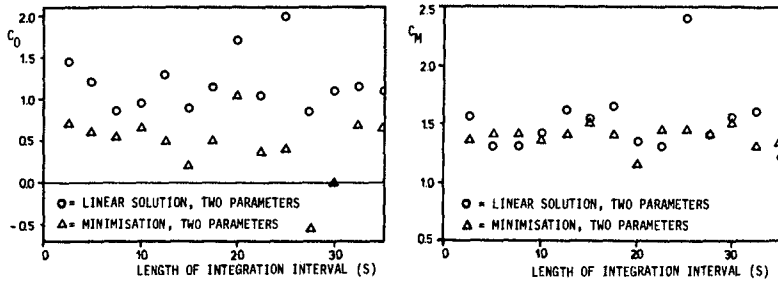


Fig. 7: Calculated Force Coefficients from Laboratory

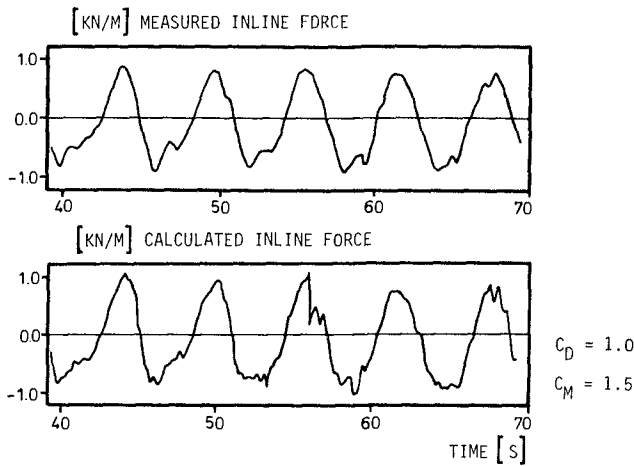


Fig. 8: Time History of Measured and Calculated Test-Section Wave Forces

between measured and calculated forces (Fig.9). The gain function shows that a proportional relation exists in the range of high coherence; the value of  $|H_{xy}|$  is nearly unity. Utilizing mean square method in field data processing equations (7) and (9) were computed. Fig.10 displays results for two- and three-parametrical cases. It should be noted, that the lift term in equation (9) is superposed in inline direction because the present velocity in transverse direction generates this lift force, theoretically. Again, the coefficient  $C_m$  is nearly independent from the length of intervals and from the estimation methods. Values of  $C_d$  are somewhat smaller in the three-parametrical case. Feeding back suitable pairs of estimated force coefficients to equation (5) with the simultaneously measured kinema-

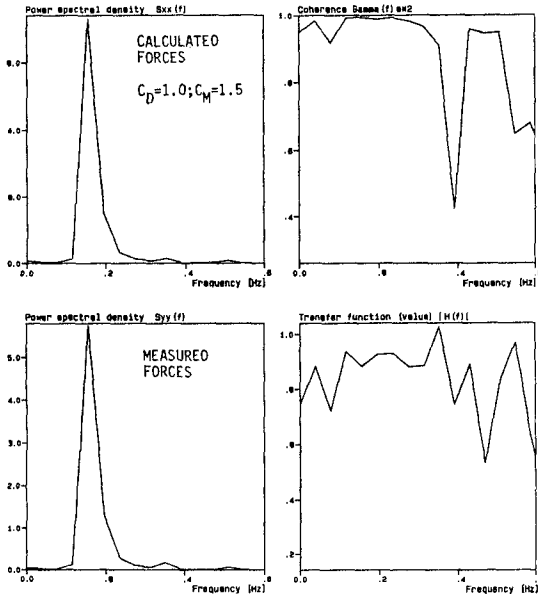


Fig. 9: Frequency Characteristics of Measured and Calculated Forces-Laboratory (Regular Waves)

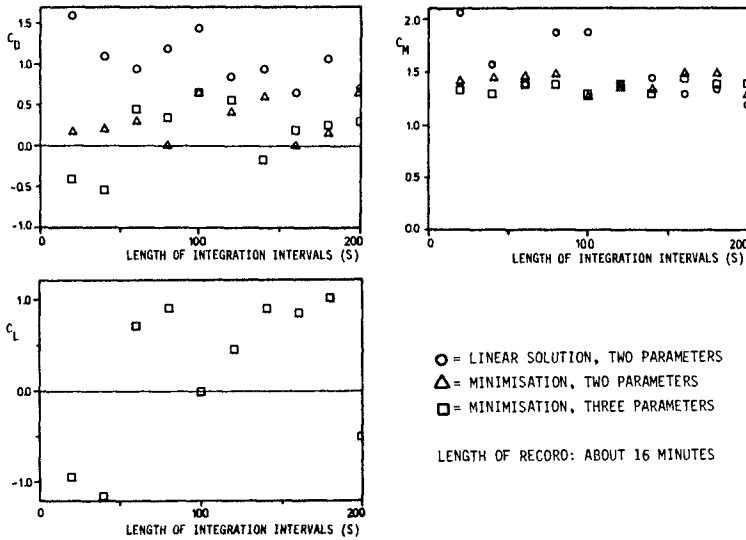


Fig.10: Calculated Force Coefficients from Field Data

tics, time records of calculated forces were obtained. These time records matched poorly with the measured force. Inclusion of the lift term in equation (4) didn't give any better fit. These comparisons indicate that Morison's equation may be deemed adequate in predicting the inline force for simple flow structures (harmonic unidirectional waves and no current) as encountered under laboratory conditions; this is not the case for complex flow regimes as found in the nearshore area, in particular predicting maximum forces. This should not be surprising, since the assumptions associated with the derivation of Morison's equation are valid to a much higher degree for laboratory conditions than in the real irregular sea.

On the other hand it can be noted that the power (zero order moment) of the calculated force spectrum ( $C_d = 0.8$ ;  $C_m = 1.4$ ;  $r = 1.2$  to  $2.0$ ) has nearly the same value as that of the measured force (Fig.11). For lower frequencies the calculated forces are somewhat overestimated and in the range of higher frequencies they are underestimated. The amount of total energy within a 16 minute record is fairly good represented by recalculations with Morison's equation using measured kinematics and mean square estimated coefficients. This was expected, because Morison's equation is derived from power equilibrium considerations. Due to rapid changes in the flow (Sarpkaya (/7/)) inline force components at higher frequencies than those considered by Morison's equation occurred in the field. The interaction between transverse and inline forces, further influenced by nearshore currents, might be responsible for the higher frequency contributions to the inline force spectrum.

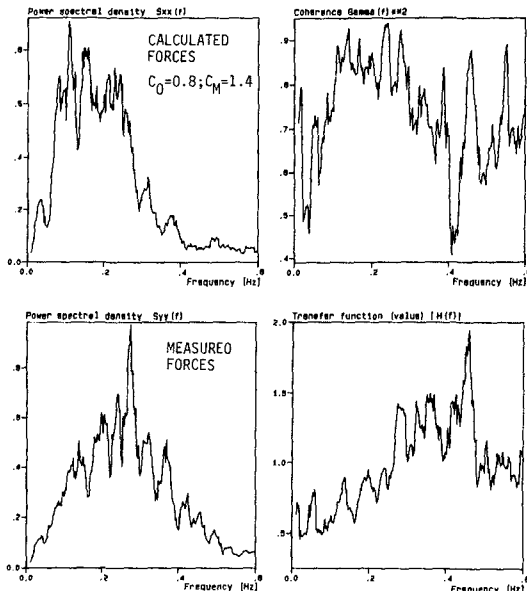
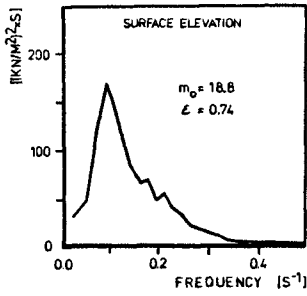


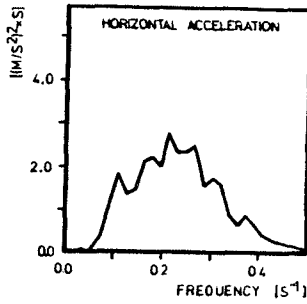
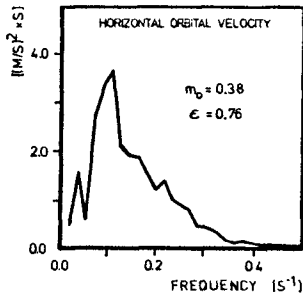
Fig.11: Frequency Characteristics of Measured and Calculated Forces-Field (Irregular Sea State)

Frequency analysis of field data, performed as described in the previous section, resulted in power spectra for the surface elevation, measured wave kinematics and measured forces, resolved in quasi-inline and quasi-transverse directions. Representative plots for several processed tests are given in Fig.12. Contrary to reported data obtained from deepwater offshore structures (Pearcey and Bishop (/6/)), it can be readily ascertained that the quasi-transverse force spectrum has a comparable amount of spectral content to the quasi-inline force spectrum. This prompted some additional investigations regarding the directionality of force calculating the force spectra for several pertinent directions. Fig.13 illustrates the directionality of force power spectra associated with a cylindrical nearshore pile (test-section) under the influence of storm surge conditions. At first, it may seem surprising that the spectral content (which is best summarised by the  $m_0$  parameter) is maximum about  $45^\circ$  from the mean incident wave direction, falling off gradually from this maximum to both sides and reaching a minimum at  $-45^\circ$  from the mean wave direction; the ratio of the maximum to the minimum value being 1.6 to 1.0. If, however, we consider the slowly varying velocity component established by the trend removal procedure, then the disparity between mean wave direction and "mean force direction" may be accounted for. This gradually varying current  $V$  (magnitude 0.4 m/s to 0.7 m/s), moving obliquely against wave propagation direction, conspires with the wave-induced velocities to produce an asymmetric flow pattern. An idealized model derived for this flow situation suggests that the clockwise-directed vortex is consistently reenforced to the detriment of the anti-clockwise vortex. This should result in a force component in "mean force direction". The observed effect due to complex interactions in the surf zone might explain reported failures of nearshore structures which often demonstrated material fatigue nearly transverse to the mean incident wave direction. In conclusion, only two-dimensional full-scale laboratory investigations with respect to lift force interactions will not suffice to determine the magnitude of these forces as measured nearshore at storm surge conditions.





WAVE KINEMATICS



WAVE FORCES

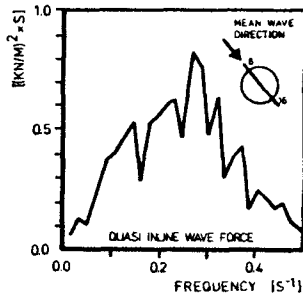
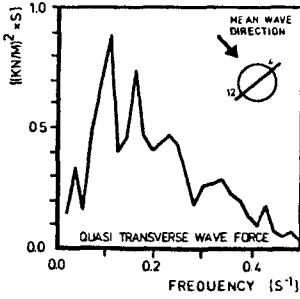


Fig.12: Power Spectral Density of Surface Elevation, Wave Kinematics and Wave Forces

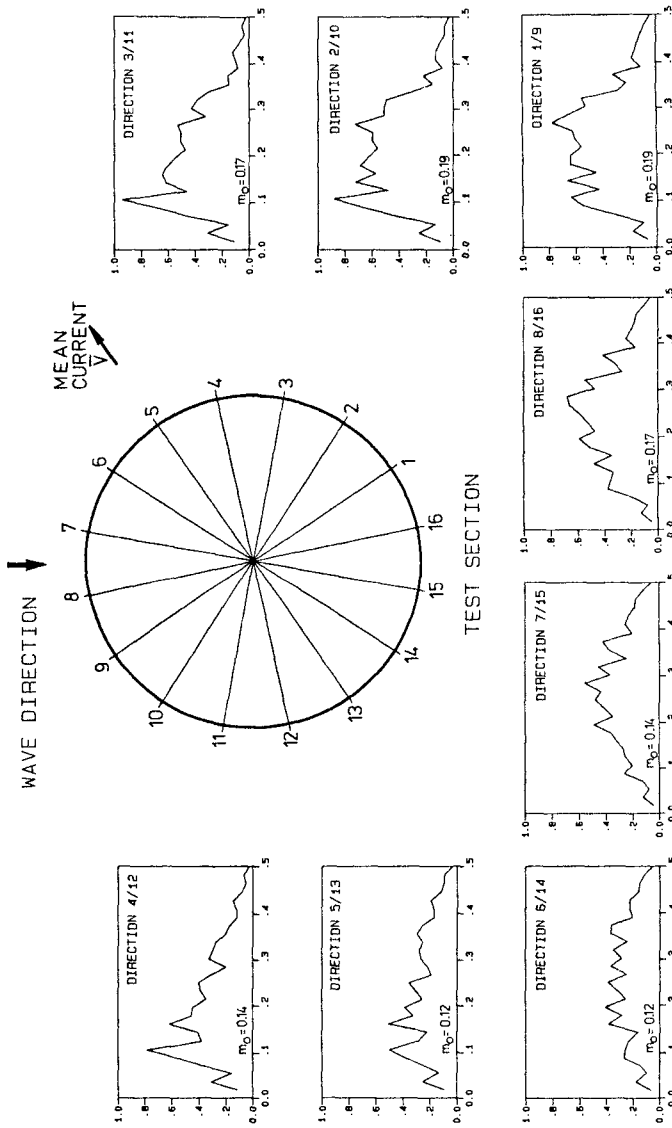


Fig.13: Multi-Directional Wave Force Spectra Versus Frequency

## ACKNOWLEDGEMENTS

The fundamental research program is sponsored by the German Research Foundation through the "SFB 205-Coastal Engineering" at the University of Hannover. The authors wish to thank Prof. Dr.-Ing. A. Führböter, Head of Division of Hydrodynamics and Coastal Engineering at the Technical University of Braunschweig and Head of the Large Wave Channel, for his support in the investigations.

## REFERENCES

- (/1/) Bendat, J.S. and Piersol, A.G., 1971: Random Data: Analysis and Measurement Procedures. J. Wiley, New York
- (/2/) Dean, R.G., 1976: Methodology for Evaluating Suitability of Wave and Wave Force Data for Determining Drag and Inertia Coefficients. Proc. of BOSS'76, Trondheim
- (/3/) Führböter, A., 1982: Prototype Facility "Grosser Wellenkanal" (Hannover) and its Research Tasks. Proc. of INTERMARITEC'82, Hamburg
- (/4/) Grüne, J. and Führböter, A., 1975: A Large Wave Channel for Full-Scale Modeling of Wave Dynamics in Surf Zones. Proc. of Int. Symposium on Modeling Techniques, San Francisco
- (/5/) Lighthill, J.: Waves and Hydrodynamic Loading. Proc. of BOSS'79, London
- (/6/) Pearcy, H.H. and Bishop, J.R., 1979: Wave Loading in the Drag and Drag Inertia Regimes; Routes to Design Data. Proc. of BOSS'79, London
- (/7/) Sarpkaya, T., 1981: A Critical Assessment of Morison's Equation. Proc. of Int. Symposium on Hydrodynamics in Ocean Eng., Trondheim
- (/8/) Sparboom, U., 1981: Wave Pressure on a Vertical Cylindrical Pile in Shallow Water. Proc. of 5th Australian Conf. on Coastal and Ocean Eng.-Offshore Structures, Perth

## CHAPTER ONE HUNDRED NINETY FOUR

### THE WAVE PRESSING PLATE FOR PROTECTING COOLING WATERWAYS OF COASTAL POWER PLANTS

by

S. C. Chow<sup>1</sup>      Frederick L.W. Tang<sup>2</sup>  
H. H. Hwung<sup>3</sup>

#### ABSTRACT

A horizontal plate laid on water surface to reduce the wave motion is proved to be effective theoretically and verified by model tests done at Tainan Hydraulics Laboratory. This principle has been put into practice on the northern coast of Taiwan for protecting a nuclear power plant cooling water intake against intruding waves.

The design and construction of wave prevention works of such type are described succinctly in the paper. Also the effect of wave diminishing has been affirmed by measuring the respective waves heights outside and inside of the wave pressing plate.

#### INTRODUCTION

Almost all of the nuclear and fossil power plants in Taiwan are constructed on coast of the island with cooling water intakes and outlets facing open sea. For many years the traditional layout of breakwaters has normally been used to protect these cooling waterway structures against typhoon and monsoon waves and the sheltering effect of breakwaters is efficient. However, as these waterways are not intended for navigation, the traditional layout of breakwaters may be unnecessary and too expensive. An attractive alternative is presented herein.

1. Vice President, Taiwan Power Company, Retired since August 1, 1984 and presently Senior Adviser of Sinotech Engineering Consultants, Inc. R.O.C.
2. Dr. Eng. Professor, National Cheng Kung University, Taiwan, R.O.C.
3. Dr. Eng. Associate Professor and Director of Tainan Hydraulics Laboratory, National Cheng Kung University, Taiwan, R.O.C.

Basis of this paper originates from the idea described by J. J. Stoker in his book "Water Waves" that a horizontal plate placed on water surface is able to reduce the waves transmitting under it. Following that idea, the authors thought that some practical arrangements could be developed to keep off the waves intruding into the cooling water intake basin of coastal power plants without resorting to the building of conventional breakwaters. When the second nuclear power plant located on the northern coast of Taiwan was planned in 1974, the authors started to investigate the feasibility of applying such type of wave prevention system. Then elaborate model tests were carried out and verified that such an idea is feasible. Furthermore, the construction cost will be much less in comparison with building breakwaters, approximately in the ratio of one to three. An estimated saving of US\$ 10 million can be achieved for Taipower Fourth Nuclear Project by adopting the wave pressing plate intake system constructed on rock against an intake system of traditional breakwaters constructed on beach.

#### THEORETICAL CONSIDERATION

Now, if we consider a horizontal plate located on water surface as shown in Fig-1

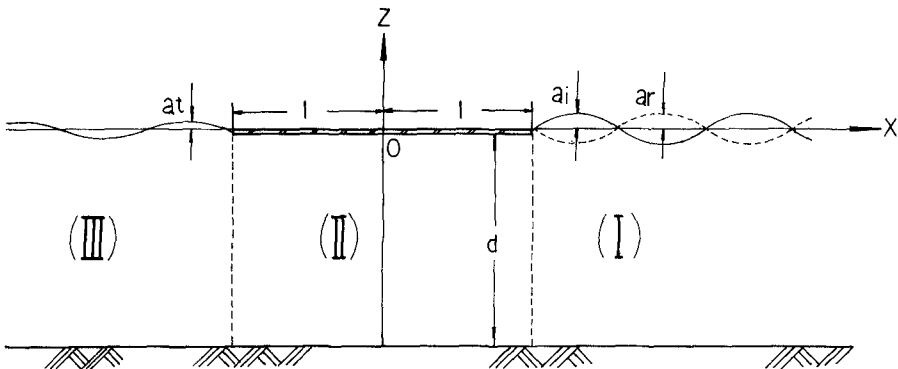


Fig - 1

From this figure, the wave motion can be divided into three regions, (I) an incidental wave region, (II) the wave motion being pressed by a horizontal plate and (III) a transmitting wave region. Since the wave motion is an inviscid, incompressible, irrotational flow and the water depth of such water way is small enough to assume the incidental wave as a long wave, the potential function of

wave motion can be written as

$$\Phi = \left. \begin{aligned} & \frac{A \cosh [k_0 (z+d)]}{\cosh (k_0 d)} \exp [i (k_0 x + \omega t)] \\ & + \frac{B \cosh [k_0 (z+d)]}{\cosh (k_0 d)} \exp [i (k_0 x - \omega t)] \\ & + \sum_{n=1}^{\infty} \frac{C_n \cos (k_n' (z+d))}{\cos (k_n' d)} \exp (k_n' x + i \omega t) \\ & + \sum_{n=1}^{\infty} \frac{D_n \cos [k_n' (z+d)]}{\cos (k_n' d)} \exp (k_n' x - i \omega t) \end{aligned} \right\} \quad (1)$$

Here, A, B, C<sub>n</sub>, D<sub>n</sub> are the arbitrary constants of integration. And the potential function will be satisfied with Laplace's equation.

$$\frac{\partial^2 \Phi}{\partial x^2} + \frac{\partial^2 \Phi}{\partial z^2} = 0 \quad (2)$$

Then applying the method of separation of variables and the boundary conditions of the above wave motion, we can obtain the potential functions in regions (I)(II)(III) respectively as follows:

$$\Phi_1 = A \exp [i (k_0 x + \omega t)] + B \exp [-i (k_0 x - \omega t)] \quad (3)$$

$$\Phi_2 = (C + D x) \exp (i \omega t) \quad (4)$$

$$\Phi_3 = E \exp [i (k_0 x + \omega t)] \quad (5)$$

And A, B, C, D, E will be solved from the continuous conditions of wave motion at the boundary of the horizontal plate, we got

$$\left. \begin{aligned} B &= \frac{i \lambda \pi \exp (2 i \lambda \pi)}{1 + i \lambda \pi} A \\ C &= A \exp (i \lambda \pi) \\ D &= \frac{i \lambda \pi \exp (i \lambda \pi)}{\ell (1 + i \lambda \pi)} A \\ E &= \frac{\exp (2 i \lambda \pi)}{1 + i \lambda \pi} A \end{aligned} \right\} \quad (6)$$

and the coefficient of wave reflection  $K_r$  and transmission  $K_t$  will be worked out respectively

$$\left. \begin{aligned} K_r &= \left| \frac{B}{A} \right| = \frac{\lambda \pi}{\sqrt{1 + (\lambda \pi)^2}} \\ K_t &= \left| \frac{E}{A} \right| = \frac{1}{\sqrt{1 + (\lambda \pi)^2}} \end{aligned} \right\} \quad (7)$$

where  $\lambda$  is the ratio of the horizontal plate length  $2\ell$  to wave length  $L$ , and  $A$ ,  $B$ ,  $E$  represent the amplitudes of incidental wave, reflecting wave and transmitting wave respectively. Equation (7) shows that the wave height behind the horizontal plate will be reduced effectively as the plate is made long enough.

#### HYDRAULIC MODEL TESTS

Before we commenced the hydraulic model tests for the cooling water intake of the nuclear power plant, various calculations had to be performed to estimate the water elevations of tide, storm surge, tsunami and intensity of waves due to lack of available field records except meteorological and tidal data in the vicinity of the plant site.

From the numerical calculations, the highest surge deviation caused by typhoons was determined to be 1.20m. Then based on the past records of submarine earthquakes from 1904 to 1963 in the north-east of Taiwan Island, the largest wave height and period of tsunami were calculated to be 10 meters and 49 minutes by Wilson's formula, and the height of run-up to be about 8 meters by Iida's empirical data which is close to the recorded value of 7.5 meter experienced at Keelung Harbor in 1918.

Furthermore, waves of typhoons were also calculated by numerical method. Four real typhoons passing through the northern coast of Taiwan were picked out, and in addition, three model typhoons advancing from east to west were also assumed into the computer program. The routes of these typhoons are shown in Fig-2, and the calculated result of the maximum wave height is 7.86 meters and the period is 8.78 seconds in NNE direction.

Finally, the numerical calculations of wave reflection in shallow water region in front of the second nuclear power plant were also performed.

Based on the above mentioned calculations, we proceeded with three dimensional physical model tests to measure wave features and to verify whether the general intake

layout of the second nuclear power plant was proper or not. Fifty-one test runs of experiments had been carried out and the best layout was determined.

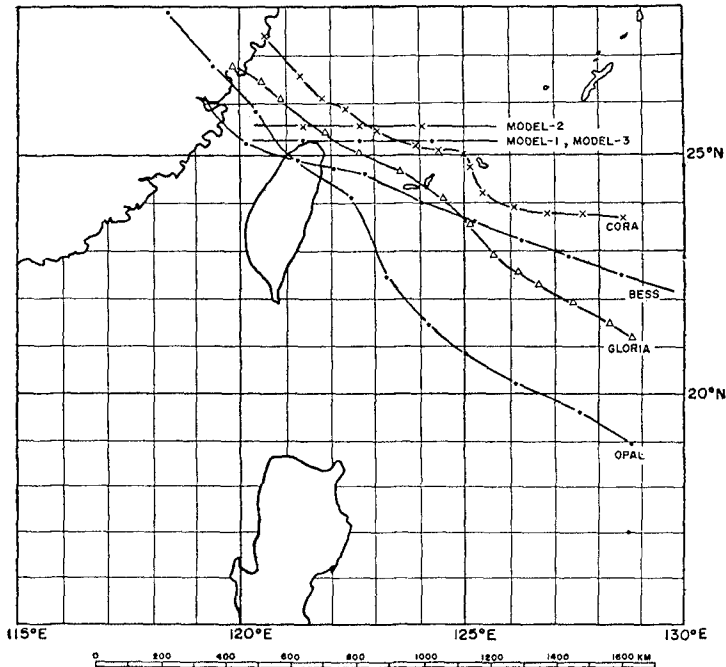


Fig - 2

Time interval between points: 6 hrs.

Afterwards, according to the best intake layout, the detailed experiments on the arrangement of wave dissipation structures were performed in a wave channel with circulation water system to simulate the coexistent situation of waves being acting on various structures and water being sucked through the intake basin. The scale of the model was decided to be 1:36, and wave features, water elevations and intake cooling water discharge were incorporated in this model. After a number of testing runs, we found that it was very important to determine the elevation of the horizontal plate located across the cooling water entrance and the tetrapod blocks installed in front of intake basin.

Experimental results indicated that with the horizontal plate, 18 meters in length, placed on the elevation of



+1.70 m and the tetrapod blocks raised to elevation +3.50m, the cooling water pumping system was able to suck cooling water through intake basin satisfactorily, because in most test runs, water surface fluctuations in front of the pump house were less than 40 cm. Such intake arrangement, though relatively complicate, will be more economical. And the flow patterns in the basin were observed incidentally. Eddies were recognized on both left and right portions of the basin, and flow velocity across the entrance was found to be smaller than 90 cm/sec. As a refinement splitter walls were added just downstream of the entrance, so that the flow would be more regulated to reduce the eddies. The plan view and side view of intake system of the second nuclear power plant were shown in Fig-3.

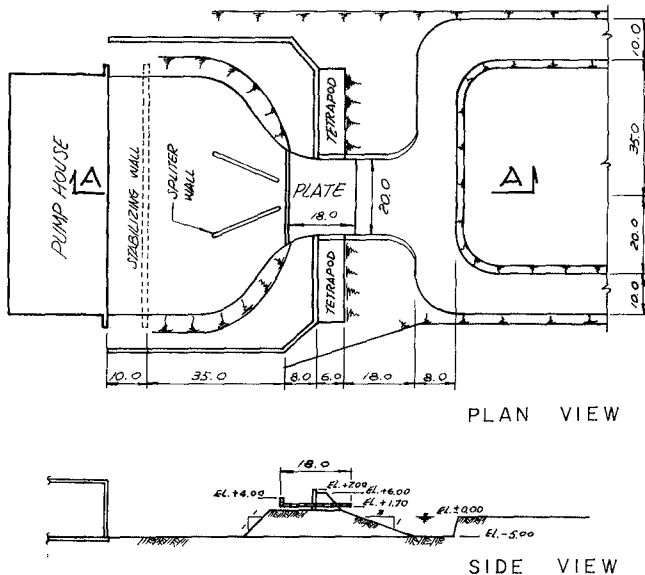


Fig - 3

After obtaining the test results of physical model, the authors set the vital design guides of the wave protection works for intake system of the second nuclear power plant: (1) a horizontal plate of 18 meters in length be placed on the waterway connecting lead channel with intake basin, (2) elevation of the horizontal plate be set at +1.70m and (3) tetrapod blocks be raised to elevation +3.5 m in front of the intake entrance. Moreover, two straight

piles of tetrapod blocks, one on each side, have been built to elevation +7.0 m for reducing wave overtopping in case of extraordinary high tide caused by typhoon.

Incidentally the lead channel arrangement also contribute to wave dissipation. Two parallel channels about 150 meters long and 50 meters apart are tied together by a cross channel to form a U-loop in front of the intake. Flow to the horizontal wave pressing plate is taken from the central portion of the cross channel so that waves rushing in along the parallel channels will have to make a right angle turn to enter into the tie channel in opposite directions. The opposing flows cause waves to die down considerably as can be seen from Photo-1.

#### CONSTRUCTION RESULTS

The construction works were completed in 1980 as shown in the following photos. Photo-1 is a birds-eye view of the intake system of the second nuclear power plant. Photo-2 is a rear view of intake structures taken from the pump house. Photo-3 is a front view of the horizontal pressing plate and entrance taken from lead channel and Photo-4 is a side view of the horizontal pressing plate with two splitter walls extending into the intake basin.



PHOTO - 1



PHOTO — 2



PHOTO — 3



PHOTO - 4

After operation of the second nuclear power plant, waves at an offshore point of 15 m deep below the low water level and water surface fluctuation in the intake basin have been measured constantly. Several typhoons attacked the coast and from records of the intake basin we found only five times when the maximum wave height exceeded 0.5m, but all the significant wave heights measured in those two years were below 0.3m. Fig-4 shows the wave records measured from 7th to 17th, August, 1982; the solid line record wave height at an offshore point of 15m deep below the low water level and dashed line recorded wave height in intake basin respectively. It is seen that the wave heights are greatly reduced while waves pass through under the wave pressing plate of the intake structure. The intake structure design has therefore been proven to be completely successful.

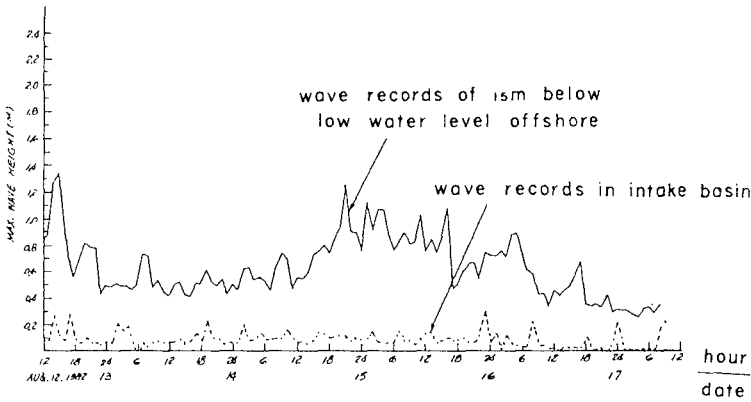
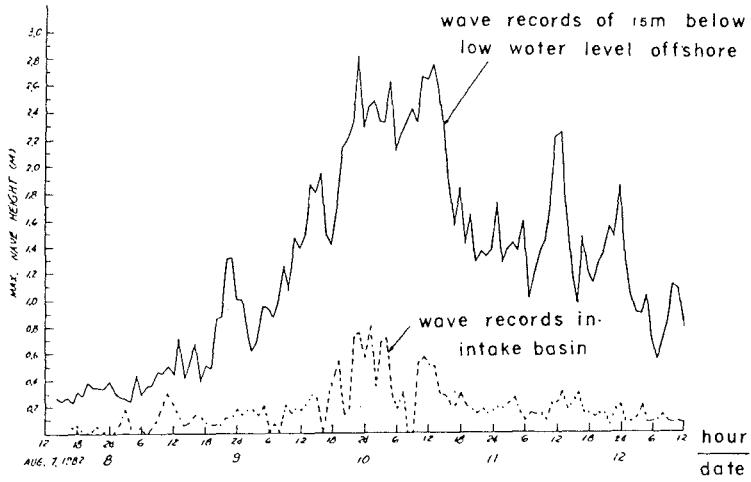


Fig-4 wave comparison of outside and inside of the horizontal pressing plate

CONCLUSION

According to the experience obtained from the model tests and the construction works in prototype, it would be worthwhile to introduce to the technical community the effectiveness of the wave pressing plate in protecting the cooling waterways and the potential saving in construction costs due to adoption of the wave pressing design. However, the application is limited to rocky coast for cooling water intake. Where sandy beach is near the rocky intake, the designer should be alert to sedimentation problem since during sustained rough weather more and more fine sand particles would be in suspension and move with the cooling water flow.

The wave pressing plate idea is also applicable to cooling water discharge on beach in a reversed direction of water flow. One typical example is the cooling water discharge at Hsinta Fossil Power Plant where two 500 MW units are in operation and two 550 MW units are under construction.

REFERENCES

1. J. J. Stoker "Water Waves" Institute of Mathematics of Science, New York University, 1968.
2. "Report on the model study of cooling water intake for the second nuclear power plant" Bulletin No.23, Tainan Hydraulics Laboratory, National Cheng-Kung University, Taiwan, R.O.C. 1974.
3. Frederick, L. W. Tang "Researches on the calculation of waves on long shoaling beaches" Vol.1, Journal of Civil and Hydraulics Engineering, National Cheng-Kung University, 1970.
4. Frederick L. W. Tang, Theodore, T. M. Lee and K. S. Liu "Researches on the waves in harbor basin" Proceeding of 20th Conference on Coastal Engineering, Japan Society of Civil Engineering, Oct. 1973.

## CHAPTER ONE HUNDRED NINETY FIVE

### Wave Forces and Impacts on a Circular and Square Caisson

J.W. van der Meer\* and E. Benassai\*\*

#### Abstract

The existing breakwater at Civitavecchia Harbour, Italy, will be extended with a part of caissons. In order to investigate wave forces for this caisson, the Ministero dei Lavori Pubblici commissioned the Delft Hydraulics Laboratory to perform a model investigation on the proposed extension. In the first part of the study quasi-static wave forces on the entire caisson were measured by means of a force measuring frame. In the second part wave impacts were recorded by pressure cells at 22 positions of the caisson.

The investigation contained two main items which are discussed in this paper:

- Comparison of quasi-static wave forces with maximum forces by wave impacts.
- Comparison of forces and impacts for a circular caisson with those measured for a square caisson.

#### Introduction

The stability of a caisson against wave attack can be described by external parameters (loads) and internal parameters (strength). External parameters are for example, wave height, wave period, foreshore and structure geometry. Internal parameters are dimensions, mass and mass distribution of the caisson and the friction coefficient between the bottom of the caisson and the foundation. If the loads are known for a given external geometry of the caisson, the mass and dimensions required for stability can be calculated. These calculations are simple when quasi-static wave forces are assumed, i.e. forces which vary with the wave period. They can be found in most handbooks. The measuring of the loads and the calculations on stability become more complicated, when also wave impacts have to be considered. For stability calculations which include the time-dependent dynamic forces one is referred to [1].

In this paper an investigation is described on wave forces on a caisson subject to both quasi-static wave forces and wave impacts. Both a caisson with a circular and a rectangular cross-section was examined.

---

\* Delft Hydraulics Laboratory, P.O. Box 177, 2600 MH Delft, The Netherlands

\*\* Professor of Maritime Constructions at Hydraulics and Hydraulic Engineering, Naples, Italy

The main dimensions of the caisson are shown in Fig. 1. Both caissons consisted of a base plate with dimensions of  $20 \times 22 \text{ m}^2$  and a curved crest wall with the top elevation 8.5 m above Mean Sea Level (M.S.L.). The cylindrical caisson had a diameter of 19 m, for a square caisson the dimensions were  $19 \times 20 \text{ m}$ . The caissons were founded on a berm 18.5 m below M.S.L. The water depth in front of the caisson was approximately 30 m.

The design conditions were established at a significant wave height of 8.0 m and an average wave period of 10.5 s. The linear scale factor used for the investigation was 38. All tests were conducted in a 1.0 m wide, 1.2 m deep and 50.0 m long wave flume with the test section installed about 45 m from the random wave generator. This wave generator is capable of performing both translatory and rotational motions by means of a hydraulic actuator, programmed by a closed loop servo-system. The command signal of this loop is obtained from a punched tape, representing a random signal with a predetermined wave energy density spectrum.

#### Quasi-Static Wave Forces

Sliding and overturning are the failure mechanisms for an entire caisson. This means that only the total horizontal and vertical wave force and the total overturning moment on the caisson are of interest for stability calculations. One is not interested in the distribution of the wave pressures on the caisson. In this case the wave forces can simply be measured by a caisson attached to a force metering frame.

Tests on quasi-static wave forces were performed on one caisson in the middle of the flume with on each side another half caisson. The middle caisson was suspended above the floor of the flume by rigid metal plates attached to the inner section of the Laboratories force metering frame, see Fig. 2. The inner section of the metering frame was supported by a rigidly mounted external frame section through five suspensions with strain gauges, two in the horizontal and three in the vertical planes. A clearance of approximately 3 mm was left around the front and sides of the middle caisson to ensure complete freedom of movement during the force measuring tests. A pressure cell in front of the caisson measured the variation in water level.

Typical signal recordings of the five gauges and the pressure cell are shown in Fig. 3. Impact forces will cause resonance of the suspended caisson at its natural frequency. Second-order low-pass electrical filters of 5 Hz were installed in the force metering recording circuits to eliminate this effect. This means, however, that only the quasi-static forces and no wave impacts were present in the measured signals.

The signals of the strain gauges were recorded by a HP 1000 computer with a sampling frequency of 25 Hz. The time histories of the total horizontal force ( $F_h$ ), the total vertical force ( $F_v$ ) and the total overturning moment ( $M_A$ ) were calculated from the signals of the strain gauges, using the equations given in Fig. 2. The maximum force and moment for each wave crest were calculated from these time histories and with these data exceedance curves were calculated. Fig. 4



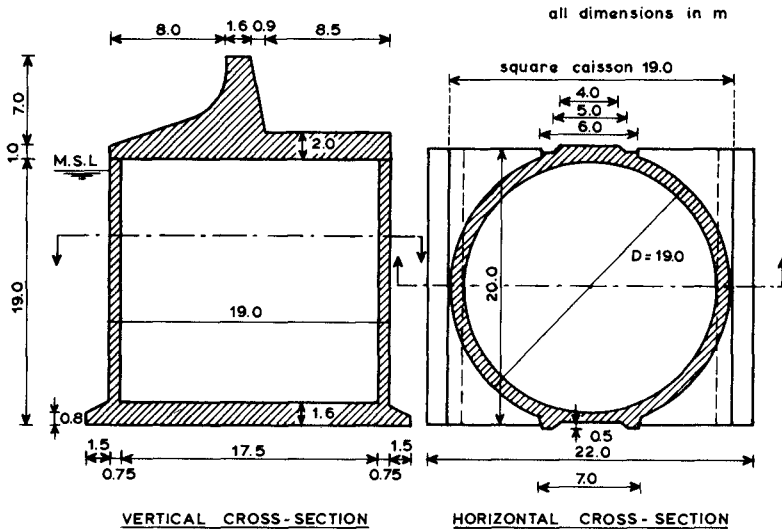
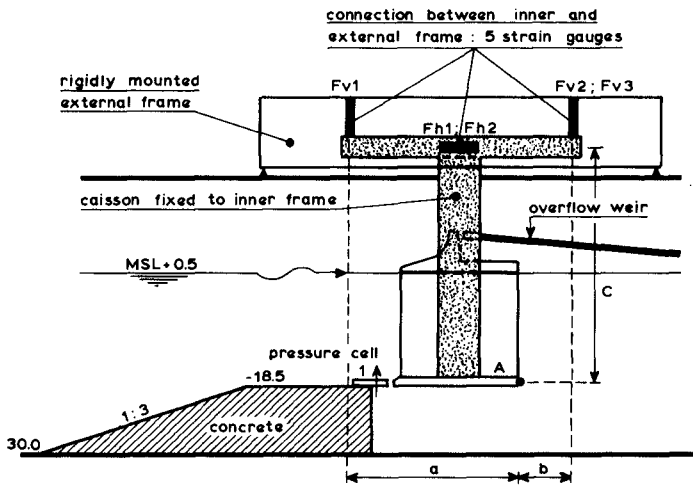
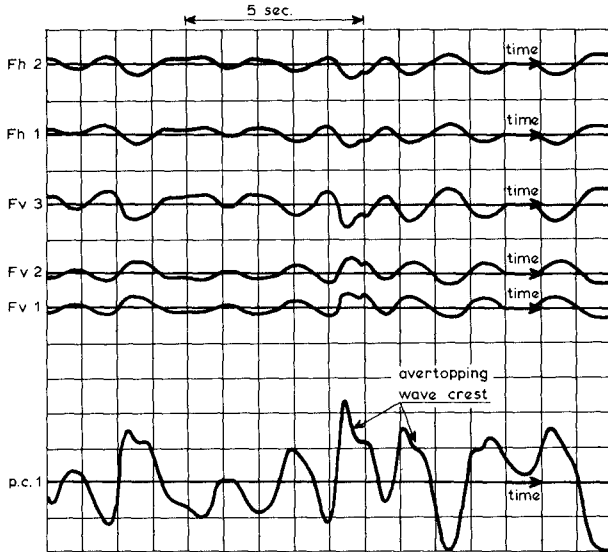


FIGURE 1. DIMENSIONS OF THE CAISSON



vertical force :  $F_v = F_{v1} + F_{v2} + F_{v3}$   
 horizontal force :  $F_h = F_{h1} + F_{h2}$   
 moment :  $M_A = F_{v1} \cdot a - (F_{v2} + F_{v3}) \cdot b + (F_{h1} \cdot F_{h2}) \cdot c$

FIGURE 2. FRAME FOR MEASURING QUASI-STATIC WAVE FORCES



p.c. 1 - pressure cell 1, see figure 2  
 Fv 1, Fv 2, Fv 3 - vertical forces of the measuring frame, see figure 2  
 Fh 1, Fh 2 - horizontal forces of the measuring frame, see figure 2  
 total vertical force  $F_v = F_{v1} + F_{v2} + F_{v3}$   
 total horizontal force  $F_h = F_{h1} + F_{h2}$

FIGURE 3. TYPICAL RECORDINGS OF THE FORCE MEASURING FRAME

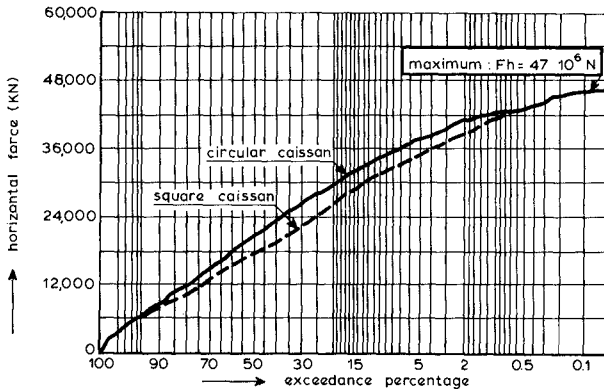


FIGURE 4. EXCEEDANCE CURVE FOR THE TOTAL HORIZONTAL FORCE

gives the exceedance curve for the horizontal force, both for a circular and a square caisson.

Although a small difference exists for the two exceedance curves, the maximum horizontal force is the same for a circular and a square caisson. This maximum horizontal force amounted to 47 MN, full scale value. It can be concluded that the shape of the caisson has hardly any influence on the quasi-static horizontal wave forces.

#### Wave Impacts

Wave impacts can cause very high local pressures, exceeding the hydrostatic pressures by a factor 10-50. The parts of a structure where impacts occur should be designed for these high pressures. For this reason wave impacts were measured on the caisson.

The front side of one caisson with on each side another half caisson was constructed of 10 mm thick steel, see Fig. 5. The rear side was strengthened by steel diaphragms to ensure a rigid model construction. The caissons were founded on a rigid steel base, the berm in front of the caisson was constructed of concrete. Six or seven pressure cells were applied for each test to measure wave impacts simultaneously along a vertical or horizontal axis. A front view of the positions of the pressure cells is given in Fig. 6. In this way impacts were measured at 22 positions of the caisson. Tests 1..4 refer to the circular caisson. In test 5 the square caisson was investigated. To maintain a constant water level the overtopped water at the rear side of the caisson was pumped back to the sea side.

For the tests 0.8 cm diameter DRUCK PDCR 10 miniature pressure transducers were used, each having operating pressure of 100 kPa with 400% overpressure capability. The pressure cells were mounted on a brass plate. The transducer calibrations supplied by the manufacturer were confirmed by static pressure tests. The natural frequency in air was 28,000 Hz and mounted on the caisson and in water approximately 10,000-15,000 Hz. Outputs from the pressure transducers were fed into a RACAL magnetic tape recorder for off-line processing. Seven data channels were available for the RACAL tape recorder. For a recording speed of 15 inch/s (0.38 m/s) the recorder had a 100% frequency response up to 4000 Hz and up to 5000 Hz for an accuracy of 70%. The ten highest impacts, determined from a Honeywell oscillographic visicorder (model 1858) were recorded on a second RACAL tape recorder with a time expansion of 16 times. These analog signals were used, again with a time expansion of 16 times, for sampling by means of a HP1000 computer with a sampling frequency of 100 Hz. Therefore the sampling frequency of the original pressure outputs was  $16 \times 16 \times 100 = 25,600$  Hz. The overall frequency of the measuring system was about 4,000 Hz.

Digital processing of data give a fast method to combine all pressure signals into a total force by multiplying with different factors, representing the respective working area. Two impacts, plotted at different time scales, are shown in Fig. 7.

For each test and for each pressure cell the ten highest impacts were plotted. The schematization and the location of these impacts on

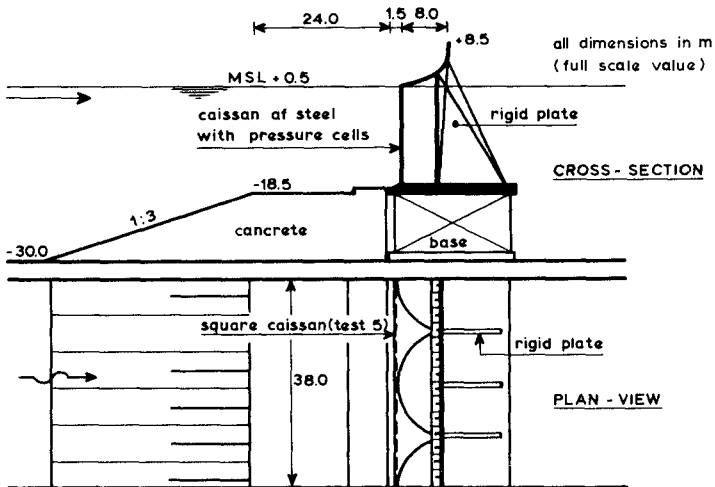


FIGURE 5. TEST SET - UP FOR WAVE IMPACT STUDY

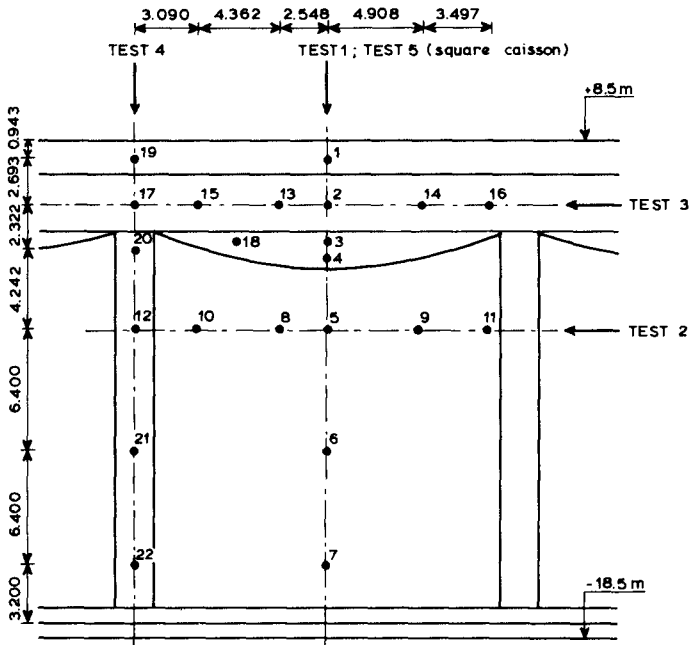


FIGURE 6. FRONT VIEW OF CAISSON WITH POSITIONS OF PRESSURE CELLS

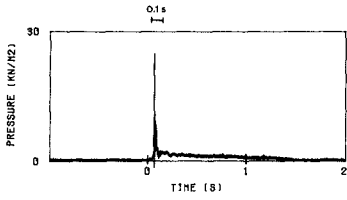


Fig a. impact due to wave tongue

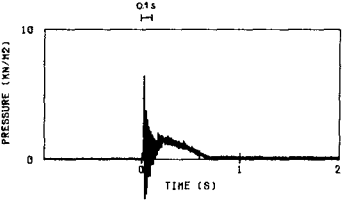
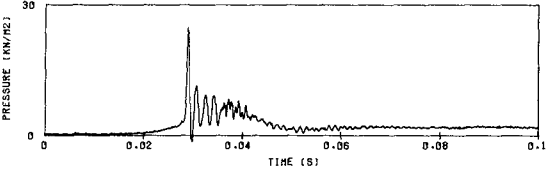
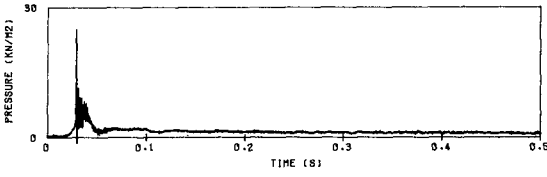


Fig b. impact due to enclosed air pocket

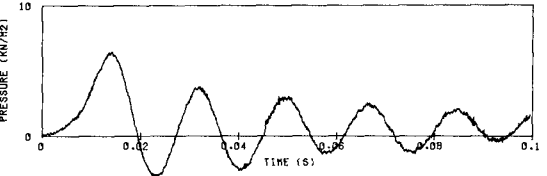
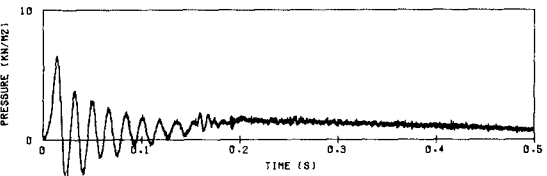


FIGURE 7. IMPACTS AT DIFFERENT TIME SCALE

the caisson are shown in Fig. 8. All local impacts could be described by four diagrams, two with the shape of one or two triangles and two with the shape of a damped oscillation. Fig. 8 shows also the moment just before the impacts occurs. The wave front rises along the vertical wall and a wave tongue falls on the upper part of the crest wall, whilst an air pocket is formed for the lower section of the crest wall. At the upper part high impacts occur under the wave tongue with impact type 1 or 2. At the lower part of the crest wall, oscillation of the air pocket was observed. Pressures are less high and the rising time longer (type 3). This oscillation generates pressure waves which travel through the water and give impact pressures at the pressure cells below M.S.L. (type 4) with a fast damping. Impact types 1 and 2 have been found for breaking waves on a slope and type 3 was found by Ramkema [2].

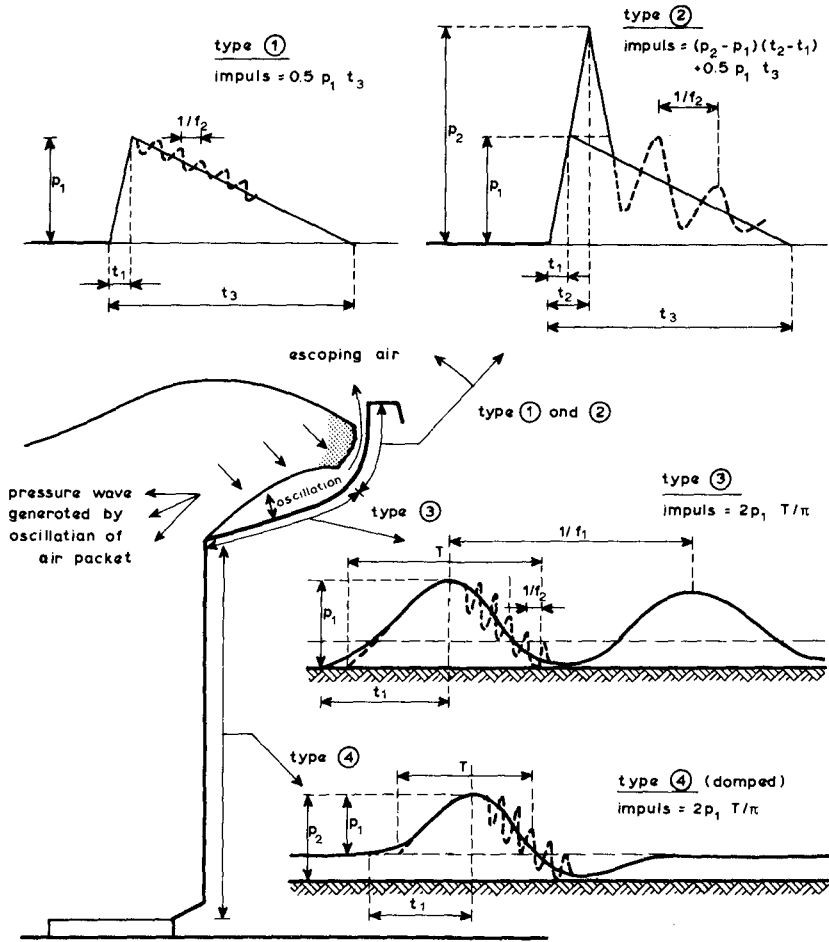
Every impact is completely described by the pressure  $p_1$  and  $p_2$ , the rising times  $t_1$  and  $t_2$ , the impact duration  $t_3$ , the duration  $T$  of the first half oscillation (type 3), the frequency of this oscillation  $f_1$  and the frequency  $f_2$  of oscillations during the decrease of the pressure. The impulse of the impact can be calculated with the above mentioned characteristics and formulae are given in Fig. 8. The impact by the wave tongue (type 2) gives the highest pressures, up to  $44.5 \text{ kN/m}^2$ , model value. The frequency of the oscillation of the air pocket is within the range of  $33 < f_1 < 80 \text{ Hz}$ . Oscillation of little air bubbles was observed with frequencies in the range of  $200 < f_2 < 2000 \text{ Hz}$ .

#### Comparison Wave Impacts for Circular and Square Caisson

For each test six or seven impacts were recorded simultaneously, see Fig. 6. The sum of the signals was calculated, taking into account the area corresponding to each cell, the direction of the resultant force and the scale of the model. No correct scaling laws are available for all types of impacts observed for the tests. Maybe the model law given by Ramkema [2] may be applied for impact types 3 and 4, the higher impacts types 1 and 2 are not scaled correctly with this law. The common relationship (Froude) is  $n_p = n_l$  and  $n_t = \sqrt{n_l}$ . As this relationship gives the most conservative results it was used for all impacts. The scale factor for the pressure was  $n_p = 38$  and for the time  $n_t = 6.16$ . The time history of the total force per meter width for test 1 (circular caisson) and test 5 (square caisson) is shown in Fig. 9 for the highest impact. From this figure the following conclusions can be derived for the maximum horizontal force per meter width:

The maximum horizontal force for the circular and square caisson are almost the same and amounted to  $4.4 \text{ MN/m}$  and  $5.0 \text{ MN/m}$  respectively. The impulse, however, was 1.8 times larger for the square caisson ( $i = 0.188 \text{ MNs/m}$  and  $i = 0.347 \text{ MNs/m}$  for the circular and square caisson, respectively).

For the circular caisson the impacts on 22 pressure cells were measured. Combination of these signals obtained from tests 1..4 gives the total horizontal signal for the circular caisson. The total horizontal force per meter width for test 5 (see Fig. 9) multiplied by 20 m gives the total horizontal force for the square caisson. The time history of the horizontal force for the circular caisson and for the



$t_1, t_2$  = rising time  
 $t_3$  = impact duration  
 $p_1, p_2$  = maximum pressures  
 $\Delta t_f$  = phase lag between maximum of two pressure cells

$f_2$  = frequency of air bubble oscillation in the wave front  
 $f_1$  = frequency of air packet enclosed by overlapping wave  
 $T$  = duration of half a sine

FIGURE 8. SCHEMATIZATION OF WAVE IMPACTS AND CORRESPONDING LOCATION

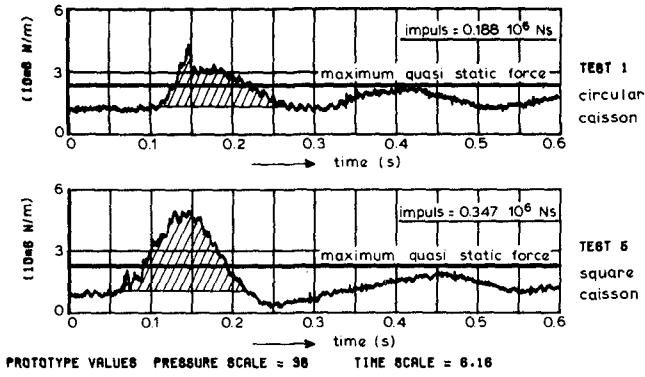


FIGURE 9. TIME HISTORY OF THE MAXIMUM HORIZONTAL IMPACT FORCE FOR TESTS 1 AND 5

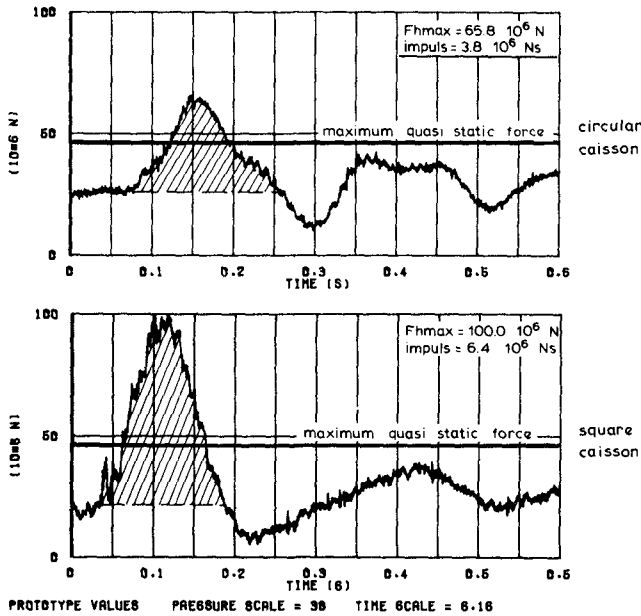


FIGURE 10. TIME HISTORY OF THE MAXIMUM TOTAL HORIZONTAL IMPACT FORCE FOR THE ENTIRE CAISSON



square caisson are shown in Fig. 10 for the highest impact. From this figure the following conclusions can be derived for the total maximum horizontal impact force for the entire caisson:

- The maximum horizontal forces for the square caisson are 1.5 times higher than for the circular caisson. The average maximum horizontal force was  $F_h = 65.8$  MN for the circular caisson and  $F_h = 100.0$  MN for the square caisson.
- The impulse is also about 1.5 times higher for the square caisson. The impulse for the circular caisson was  $i = 3.8$  MNs and for the square caisson  $i = 6.4$  MNs.
- Rising time and duration of the impacts are almost the same for the circular and square caisson. The rising time is about  $t_1 = 0.07$  sec and the total duration of the impact  $t_3 = 0.17$  sec.

#### Comparison Quasi-Static Wave Forces and Wave Impacts

The maximum quasi-static force was established at 47 MN for both the circular and square caisson. This value is also given in Fig. 10. Scaling impact forces according to the Froude number, as was done in Figs. 9 and 10, gives maximum impact forces which are 2 times higher for the square caisson and 1.3 times higher for the circular caisson than the maximum quasi-static force.

The model law for iso-thermal compression, described by Ramkema [2] can be used for impact types 3 and 4. Although this law is not correct for impact types 1 and 2 it will be used in order to calculate a lower boundary for the impact force. In this case the maximum impact for the square caisson was used, where even the highest located impacts could be described by impact type 3, see Fig. 11. Results are given in Fig. 12 for the impact pressures and in Fig. 13 for the total maximum impact force for the caisson. The force signal of Fig. 10 (Froude scaling) has been added to Fig. 13.

Scaling according to the model law for iso-thermal compression shows much lower impacts than for scaling to the Froude number. The maximum horizontal force is about 40 MN for the compression model, whilst a force of 100 MN was calculated according to the Froude number. The actual maximum force in nature will be within this range and probably close to 50 MN, as impact types 1 and 2 are only present on a small part of the caisson.

#### Main Conclusions

- 1 Horizontal quasi-static wave forces on a circular and square caisson are almost the same.
- 2 All local impacts could be described by four diagrams, two with the shape of one or two triangles and two with the shape of a damped oscillation, see Fig. 8. The triangular types are caused by the impact of the wave tongue and can be compared with a wave breaking on a slope. The damped oscillation is caused by the compression of an enclosed air pocket as found by Ramkema [2]. The impact by the wave tongue gives the highest pressures, (up to  $44.5$  kN/m<sup>2</sup>). The frequency of the oscillation of the air pocket is within the range

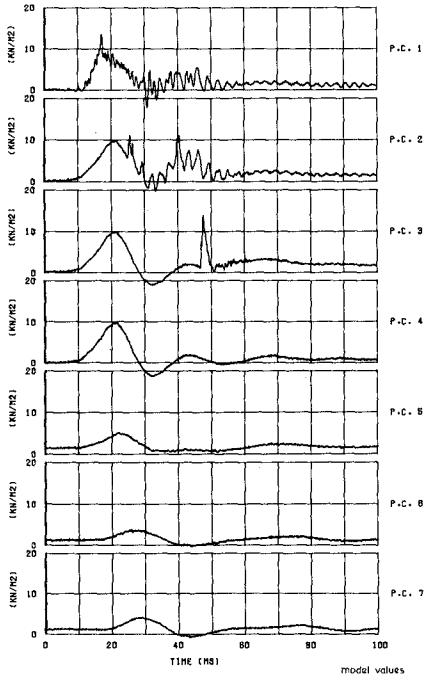


FIGURE 11. MAXIMUM IMPACT PRESSURES FOR THE SQUARE CAISSON

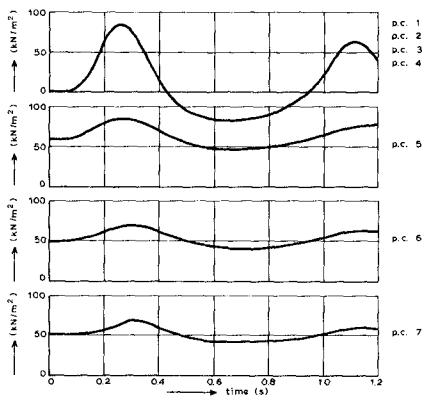


FIGURE 12. PRESSURES OF TEST 5 SCALED ACCORDING TO THE COMPRESSION MODEL

of  $33 < f_1 < 80$  Hz. Oscillation of little air bubbles was observed with frequencies in the range of  $200 < f_2 < 2000$  Hz.

- 3 Total impact forces for a square caisson are 1.5 times higher than for a circular caisson, whilst also the impulse is about 1.5 times higher. Rising time and duration are almost the same for the circular and square caisson, see Fig. 10.
- 4 Scaling impact pressures according to the Froude number gives maximum impact forces which are 2 times higher for the square caisson and 1.3 times higher for the circular caisson than the maximum quasi-static force. Scaling according the model law for iso-thermal compression (Ramkema [2]) shows impact forces with the same values as the maximum quasi-static wave force.

#### References

- 1 BENASSAI, E., The stability against sliding of breakwaters under the action of breaking waves. PIANC Bulletin No. 21, 1975.
- 2 RAMKEMA, C., A model law for wave impacts on coastal structures. Proc. Coastal Engineering Conf., Hamburg, 1978.

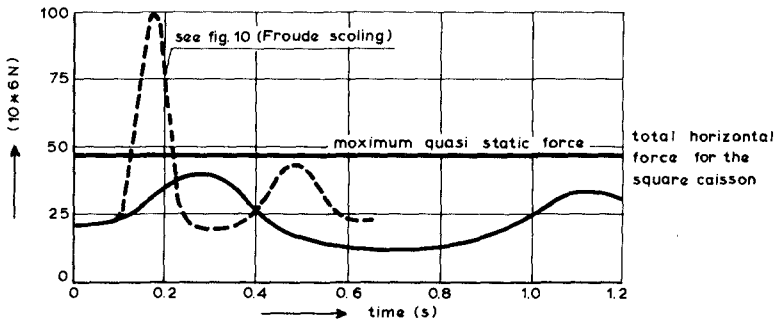


FIGURE 13. TIME HISTORY OF THE MAXIMUM HORIZONTAL FORCE, SCALED ACCORDING TO THE COMPRESSION MODEL

## CHAPTER ONE HUNDRED NINETY SIX

### ATTENUATION OF WAVE INDUCED OSCILLATION IN PORTS BY IMPROVING THE CONDITIONS AT THE HARBOR ENTRANCE

M. Kubo<sup>1</sup>, S. Aoki<sup>2</sup> and J.J. Avitia Segura<sup>3</sup>

#### ABSTRACT

The authors developed the numerical method to calculate the wave height distribution around a pair of breakwaters with arbitrary shape of the edge. The effect of the resonators equipped in the breakwaters on the diffracted wave height is simulated by using this method. Simulated results show that the resonators have remarkable effect to reduce wave heights in a harbor. However, in the experiments, resonators are not so effective as predicted by the theory.

#### I. INTRODUCTION

A harbor should be a protected zone of water, able to bring safety for ships to permit the activities of traffic of merchandises and persons at all time. However, in harbors suffering from storm waves, cargo handlings are often interrupted and sometimes mooring lines are broken by large ship motions.

In order to protect a harbor from waves, a lot of money have been spent in constructing breakwaters. No matter how effective breakwater may be, waves pass through the breakwater gap inevitably. Once waves enter the harbor, it is difficult to absorb these energy in the harbor surrounded with vertical walls, and sometimes harbor resonance is induced when the wave period is close to the natural period of the harbor.

So the development of a new method to trap the wave energy before the waves enter the harbor is desired. As a new method to trap the wave energy, a resonator was introduced by Valembos in 1953 and defined as a wave absorber which can trap the wave energy by taking advantage of the resonance phenomenon. After that, some researchers investigated the wave resonators built in a channel and showed that they were sufficiently effective. (for example, W. James (1968,1970))

In this paper, we deal with diffraction problem by the breakwaters equipped with a resonator. The mathematical model is proposed to predict the diffracted wave height distribution for arbitrary shape of entrance and for any angle of the wave incidence. By using this

- 
1. Associate Professor, Kobe Univ. of Mercantile Marine, Kobe, Japan
  2. Research Associate, Osaka Univ., Osaka, Japan
  3. Planeacion y Proyectos S.C., Mexico

model, wave transformation around the wave resonators is simulated. The calculated wave height are discussed by comparing with the experimental results.

## II. THEORY AND NUMERICAL PROCEDURE

In this section, first, the theoretical analysis to predict the diffracted wave height distribution for arbitrary shape of entrance is developed by modifying Lee's method (1970) which is widely used to calculate the wave height distribution in a harbor. Then, the numerical procedure to simulate diffracted waves are shown. Finally, the procedure is verified by comparing with the analytical solutions.

### (A) Theory

Let us take  $z$  axis upward from the still water level and assume that the fluid is invicid and the motion is irrotational. The equation of continuity for an incompressible fluid is expressed by the Laplace equation by using the velocity potential  $\Phi(x, y, z, t)$ :

$$\frac{\partial^2 \Phi}{\partial x^2} + \frac{\partial^2 \Phi}{\partial y^2} + \frac{\partial^2 \Phi}{\partial z^2} = 0 \quad (1)$$

For a sinusoidal wave with frequency  $\omega$ ,  $\Phi$  which satisfies the boundary condition at  $z=-h$ ,  $\partial\Phi/\partial z = 0$  is expressed as

$$\Phi(x, y, z, t) = A \frac{\cosh k(h+z)}{\cosh kh} f(x, y) e^{-i\omega t} \quad (2)$$

where  $A$  : constant,  
 $h$  : constant water depth,  
 $k$  : wave number,  
 $i = \sqrt{-1}$ ,

and  $f(x, y)$  is the wave function which satisfies the Helmholtz equation:

$$\frac{\partial^2 f(x, y)}{\partial x^2} + \frac{\partial^2 f(x, y)}{\partial y^2} + k^2 f(x, y) = 0 \quad (3)$$

The velocity potential of the fluid motion is determined by solving Eq. (3) under boundary conditions.

Fig. 1 shows a pair of straight breakwaters with arbitrary shape of edges and a coordinate system. To solve Eq.(3) in the domain of interest shown in Fig.1, we divide it into three regions. I is the open sea region, II is the entrance region and III is the harbor region.

The velocity potential in each region is described as  $\Phi_I$ ,  $\Phi_{II}$  and  $\Phi_{III}$ .  $\Phi_I$  can be divided into two terms  $\Phi_{I0}$  and  $\Phi_{I1}$  and described as follows:

$$\Phi_I = \Phi_{I0} + \Phi_{I1} = A \frac{\cosh k(h+z)}{\cosh kh} (f_0 + f_1) e^{-i\omega t} \quad (4)$$

where suffix 0 represents the composite waves of the incident and reflected waves when the boundary  $C_1$  is closed, and suffix 1 indicates the quantities concerning with the correction term due to the scattering waves from the region II.

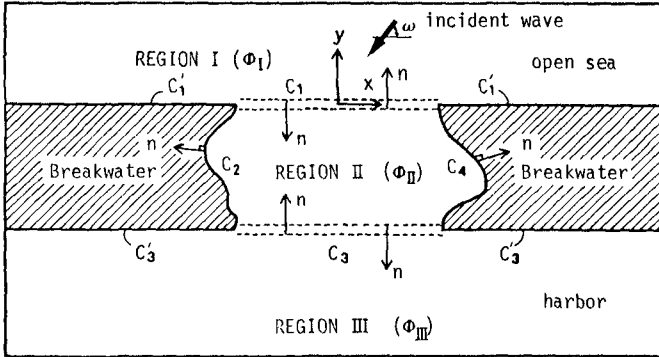


Fig.1 The domain of interest and the coordinate

If the incident wave profile  $\zeta_I$  is given by the following equation:

$$\zeta_I = \zeta_0 \exp \{ -i (k_x x \cos \omega + k_y y \sin \omega + \omega t) \}, \tag{5}$$

the surface profile of the composite waves  $\zeta_I + \zeta_R$  becomes

$$\zeta_I + \zeta_R = 2 \zeta_0 \cos(k_y y \sin \omega) e^{-i k_x x \cos \omega} \cdot e^{-i \omega t} \tag{6}$$

where  $\zeta_0$  is the amplitude of the incident waves and  $\omega$  is the angle of the wave incidence defined in Fig.1. Another description of the surface profile is given by the dynamic condition on the free surface.

$$\zeta_I + \zeta_R = -\frac{1}{g} \left( \frac{\partial \Phi_{I0}}{\partial t} \right)_{z=0} = \frac{i \omega}{g} A f_0 e^{-i \omega t} \tag{7}$$

Comparing Eq.(6) and Eq.(7) and taking  $A = \frac{g \zeta_0}{i \omega}$ ,  $\Phi_I$  is expressed by

$$\Phi_I = \frac{g \zeta_0}{i \omega} \frac{\cosh k(h+z)}{\cosh k h} (f_0 + f_1) e^{-i \omega t} \tag{8}$$

where

$$f_0 = z \cos(k_y y \sin \omega) e^{-i k_x x \cos \omega} \tag{9}$$

Similarly the velocity potentials in region II and III can be expressed as

$$\Phi_{II} = \frac{g\zeta_0}{\lambda\sigma} \cdot \frac{\cosh kR(R+z)}{\cosh kR} f_2 e^{-i\omega t} \quad (10)$$

$$\Phi_{III} = \frac{g\zeta_0}{\lambda\sigma} \cdot \frac{\cosh kR(R+z)}{\cosh kR} f_3 e^{-i\omega t} \quad (11)$$

Taking the normal vector  $n$  of each region outward, the conditions of continuity of pressure and velocity between each region are described as follows:

on  $C_1$

$$f_0 + f_1 = f_2 \quad (12)$$

$$\frac{\partial f_1}{\partial n} = -\frac{\partial f_2}{\partial n} \quad (\because \frac{\partial f_0}{\partial n} = 0) \quad (13)$$

on  $C'_1$

$$\frac{\partial f_1}{\partial n} = 0 \quad (\because \frac{\partial f_0}{\partial n} = 0) \quad (14)$$

on  $C_2, C_4$

$$\frac{\partial f_2}{\partial n} = 0 \quad (15)$$

on  $C_3$

$$f_2 = f_3 \quad (16)$$

$$\frac{\partial f_2}{\partial n} = -\frac{\partial f_3}{\partial n} \quad (17)$$

on  $C'_3$

$$\frac{\partial f_3}{\partial n} = 0 \quad (18)$$

Furthermore the radiation condition must be considered:

$$f_i \rightarrow 0, \quad f_3 \rightarrow 0 \quad ; \quad \text{when } \sqrt{x^2+y^2} \rightarrow \infty \quad (19)$$

While, the wave function  $f_i$  ( $i=1,2,3$ ) at any position inside each region can be expressed in terms of  $f_i$  and  $\frac{\partial f_i}{\partial n}$  at the boundary of each region by applying Weber's solution of Helmholtz equation and Eq.(19).

$$f_1 = -\frac{\lambda}{4} \int_{C_1+C'_1} \left\{ f_1 \frac{\partial}{\partial n} H_0^{(1)}(kR) - H_0^{(1)}(kR) \frac{\partial f_1}{\partial n} \right\} ds \quad (20)$$

$$f_2 = -\frac{\lambda}{4} \int_{C_1+C_2+C_3+C_4} \left\{ f_2 \frac{\partial}{\partial n} H_0^{(1)}(kR) - H_0^{(1)}(kR) \frac{\partial f_2}{\partial n} \right\} ds \quad (21)$$

$$f_3 = -\frac{\lambda}{4} \int_{C_3+C'_3} \left\{ f_3 \frac{\partial}{\partial n} H_0^{(1)}(kR) - H_0^{(1)}(kR) \frac{\partial f_3}{\partial n} \right\} ds \quad (22)$$

,where  $H_0^{(1)}(kr)$  is the zeroth order Hankel function of the first kind and  $r$  is the distance between the point inside the region and that on the boundary. Similarly,  $f_i$  on the boundary is expressed in terms of  $f_i$  and  $\partial f_i / \partial n$  on the boundary as follows:

$$f_1(\text{on } C_1, C_1') = -\frac{i}{2} \int_{C_1+C_1'} \left\{ f_1 \frac{\partial}{\partial n} H_0^{(1)}(kr) - H_0^{(1)}(kr) \frac{\partial f_1}{\partial n} \right\} ds$$

$$= -\frac{i}{2} \int_{C_1} H_0^{(1)}(kr) \frac{\partial f_1}{\partial n} ds \tag{23}$$

$$(\because \partial f_1 / \partial n = 0 \text{ on } C_1 \text{ and } \frac{\partial}{\partial n} H_0^{(1)}(kr) = 0 \text{ on } C_1 \text{ and } C_1')$$

$$f_2(\text{on } C_1, C_2, C_3, C_4) = -\frac{i}{2} \int_{C_1+C_2+C_3+C_4} \left\{ f_2 \frac{\partial}{\partial n} H_0^{(1)}(kr) - H_0^{(1)}(kr) \frac{\partial f_2}{\partial n} \right\} ds \tag{24}$$

$$f_3(\text{on } C_3, C_3') = -\frac{i}{2} \int_{C_3+C_3'} \left\{ f_3 \frac{\partial}{\partial n} H_0^{(1)}(kr) - H_0^{(1)}(kr) \frac{\partial f_3}{\partial n} \right\} ds$$

$$= -\frac{i}{2} \int_{C_3} H_0^{(1)}(kr) \frac{\partial f_3}{\partial n} ds \tag{25}$$

Using Eqs. (12), (13) and (23),

$$f_2 = f_0 - \frac{i}{2} \int_{C_1} H_0^{(1)}(kr) \frac{\partial f_2}{\partial n} ds \quad (\text{on } C_1) \tag{26}$$

Eqs. (15) and (24) give the relation

$$f_2 = -\frac{i}{2} \int_{C_1+C_2+C_3+C_4} f_2 \frac{\partial}{\partial n} H_0^{(1)}(kr) ds + \frac{i}{2} \int_{C_1+C_3} H_0^{(1)}(kr) \frac{\partial f_2}{\partial n} ds \tag{27}$$

(on  $C_1+C_2+C_3+C_4$ )

and Eqs. (16), (17) and (25) lead to the equation

$$f_2 = -\frac{i}{2} \int_{C_3} H_0^{(1)}(kr) \frac{\partial f_2}{\partial n} ds \quad (\text{on } C_3) \tag{28}$$

The wave function  $f_2$  and  $\partial f_2 / \partial n$  are determined by solving Eqs. (26), (27) and (28). While, Eqs. (20) and (22) can be rewritten as follows, by using Eqs. (12), (13), (16) and (17):

$$f_1 = -\frac{i}{4} \int_{C_1} \left\{ f_2 \frac{\partial}{\partial n} H_0^{(1)}(kr) + H_0^{(1)}(kr) \frac{\partial f_1}{\partial n} \right\} ds$$

$$- \frac{i}{4} \int_{C_1'} f_1 \frac{\partial}{\partial n} H_0^{(1)}(kr) ds \tag{29}$$

$$f_3 = -\frac{i}{4} \int_{C_3} \left\{ f_2 \frac{\partial}{\partial n} H_0^{(1)}(kr) + H_0^{(1)}(kr) \frac{\partial f_3}{\partial n} \right\} ds$$

$$- \frac{i}{4} \int_{C_3'} f_3 \frac{\partial}{\partial n} H_0^{(1)}(kr) ds \tag{30}$$



In these equations,  $f_1$  on  $C'_1$  and  $f_3$  on  $C'_3$  are given by substituting Eqs. (13) and (17) into Eqs. (23) and (25):

$$f_1 = -\frac{\lambda}{2} \int_{C_1} H_0^{(1)}(kr) \frac{\partial f_2}{\partial n} ds \quad (\text{on } C'_1) \tag{31}$$

$$f_3 = -\frac{\lambda}{2} \int_{C_3} H_0^{(1)}(kr) \frac{\partial f_2}{\partial n} ds \quad (\text{on } C'_3) \tag{32}$$

Consequently,  $f_1$  and  $f_3$  inside each region are expressed in terms of  $f_2$  and  $\frac{\partial f_2}{\partial n}$  on the boundary as follows:

$$f_1 = -\frac{\lambda}{4} \int_{C_1} \left\{ f_2 \frac{\partial}{\partial n} H_0^{(1)}(kr) + H_0^{(1)}(kr) \frac{\partial f_2}{\partial n} \right\} ds - \frac{\lambda}{4} \int_{C'_1} \left\{ -\frac{\lambda}{2} \int_{C_1} H_0^{(1)}(kr) \frac{\partial f_2}{\partial n} ds \right\} \frac{\partial}{\partial n} H_0^{(1)}(kr) ds \tag{33}$$

$$f_3 = -\frac{\lambda}{4} \int_{C_3} \left\{ f_2 \frac{\partial}{\partial n} H_0^{(1)}(kr) + H_0^{(1)}(kr) \frac{\partial f_2}{\partial n} \right\} ds - \frac{\lambda}{4} \int_{C'_3} \left\{ -\frac{\lambda}{2} \int_{C_3} H_0^{(1)}(kr) \frac{\partial f_2}{\partial n} ds \right\} \frac{\partial}{\partial n} H_0^{(1)}(kr) ds \tag{34}$$

Finally, the variations of the free surface in each region are given as follows:

$$\zeta_1 = -\frac{1}{g} \left( \frac{\partial \Phi_I}{\partial t} \right)_{z=0} = \zeta_0 (\zeta_0 + f_1) e^{-\lambda \alpha t} \tag{35}$$

$$\zeta_2 = -\frac{1}{g} \left( \frac{\partial \Phi_{II}}{\partial t} \right)_{z=0} = \zeta_0 f_2 e^{-\lambda \alpha t} \tag{36}$$

$$\zeta_3 = -\frac{1}{g} \left( \frac{\partial \Phi_{III}}{\partial t} \right)_{z=0} = \zeta_0 f_3 e^{-\lambda \alpha t} \tag{37}$$

Therefore, the diffraction coefficient  $K_d$  is determined by

$$K_d = \left| \frac{\zeta_3}{\zeta_2} \right| = \left| \frac{\zeta_0 f_3 e^{-\lambda \alpha t}}{\zeta_0 e^{-\lambda(kx \cos \omega + ky \sin \omega)} e^{-\lambda \alpha t}} \right| = |f_3| \tag{38}$$

(C) Numerical Procedure

In order to solve Eqs. (26), (27) and (28) numerically, we divided the boundaries into some segments as shown in Fig.2, and then these equations are described in discrete form at each segment as follows:

$$f_2(\lambda) = f_0(\lambda) - \frac{\lambda}{2} R \sum_{j=1}^{N_1} H_0^{(1)}(kR_j) \bar{f}_2(j) \Delta S_j \quad (\lambda=1, N_1) \tag{39}$$

$$f_2(\lambda) = \frac{i}{2} R \sum_{j=1}^{N_1+N_2+N_3+N_4} f_2(j) H_1^{(1)}(Rr_{\lambda j}) \Delta s_j - \frac{i}{2} R \sum_{j=1}^{N_1+N_3} H_0^{(1)}(Rr_{\lambda j}) \bar{f}_2(j) \Delta s_j \quad (\lambda=1, N_1+N_2+N_3+N_4) \quad (40)$$

$$f_2(\lambda) = -\frac{i}{2} R \sum_{j=1}^{N_3} H_0^{(1)}(Rr_{\lambda j}) \bar{f}_2(j) \Delta s_j \quad (\lambda=1, N_3) \quad (41)$$

where  $\bar{f}_2(j) = \frac{1}{R} \frac{\partial f_2(j)}{\partial n}$ ,  $H_0^{(1)}(Rr_{\lambda j})$  is the first order Hankel function of the first kind,  $i$  and  $j$  are the calculation points on the boundary.

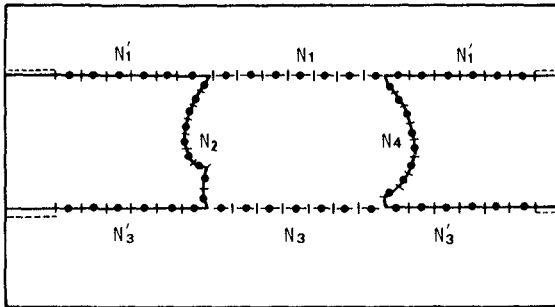


Fig.2 Segmentation of boundaries

The number of unknowns  $f_2$  and  $\bar{f}_2$  is  $2N_1+N_2+2N_3+N_4$  and the number of equations is the same. So,  $f_2$  and  $\bar{f}_2$  on the boundaries  $C_1, C_2, C_3$  and  $C_4$  are given by solving Eqs. (39), (40) and (41).

Eqs. (33) and (34) are also rewritten as follows:

$$f_1(x, y) = -\frac{i}{4} R \sum_{j=1}^{N_1} \{ f_2(j) H_1^{(1)}(Rr_{xj}) + H_0^{(1)}(Rr_{xj}) \bar{f}_2 \} \Delta s_j - \frac{i}{4} R \sum_{j=1}^{2N_1} \left\{ -\frac{i}{2} R \sum_{\ell=1}^{N_1} H_0^{(1)}(Rr_{j\ell}) \bar{f}_2(\ell) \Delta s_\ell \right\} H_1^{(1)}(Rr_{xj}) \Delta s_j \quad (42)$$

$$f_3(x, y) = -\frac{i}{4} R \sum_{j=1}^{N_3} \{ f_2(j) H_1^{(1)}(Rr_{xj}) + H_0^{(1)}(Rr_{xj}) \bar{f}_2 \} \Delta s_j - \frac{i}{4} R \sum_{j=1}^{2N_3} \left\{ -\frac{i}{2} R \sum_{\ell=1}^{N_3} H_0^{(1)}(Rr_{j\ell}) \bar{f}_2(\ell) \Delta s_\ell \right\} H_1^{(1)}(Rr_{xj}) \Delta s_j \quad (43)$$

Although the number of segments  $N_1$  and  $N_3$  must be infinite, we put them finite because the influence of the point far away from the region II is very small. Here, the length of  $C_1$  and  $C_3$  is taken 10 times of wave length.

## (c) Verification of numerical solution

Here, the validity of the numerical method and the stability of the solution are discussed. Fig.3 shows a pair of breakwaters with square edge. For this type of breakwaters, some analytical solutions of diffraction were obtained. However, there is the limitation in these solutions that the width of a breakwater is infinitely small. So, the numerical solutions used in this study are compared with the analytical solutions proposed by Takayama (1981) for the case of small width of a breakwater.

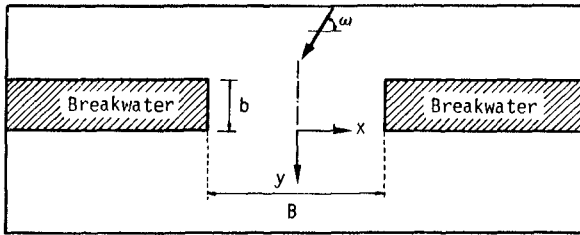


Fig.3 A pair of straight breakwaters with square edges

Figs. 4 (a) to (d) show the diffraction coefficient  $K_d$  at the point of  $Y/L=0.1, 0.5$  and  $1.0$  for the case of  $b/L=0.01, B/L=0.5$  and  $\omega = 90^\circ, 150^\circ$  and  $165^\circ$ . In these cases, the maximum length of a segment  $D_{max} \leq L/10$  ( $L$ : wave length), namely, each boundary is divided into small segments whose length is smaller than  $L/10$ .

As can be seen from these figures, the solutions of the proposed numerical method (shown by the broken lines) are a little smaller than the exact solutions shown by the solid lines. These small differences are not improved by shortening the length of a segment. It is not clear whether these differences come from the influence of the width of a breakwater or from the numerical error. However, the results of our numerical method sufficiently agree with the analytical solutions.

Next we calculated the wave height distribution for rectangular resonators shown in Fig.5. Fig.6 shows the diffraction coefficient  $K_d$  with wave resonators at the point of  $X/B=0.0$  and  $Y/B=1.33$  and the amplification factor  $\zeta_A/\zeta_I$  for the case of  $L/B=0.5, B_R/B=0.08$  and  $b_R/B=0.03$ . The solid lines represent the case where the maximum length of a segment  $D_{max}$  is smaller than  $L/20$  and the broken lines represent the case of  $D_{max} \leq L/50$ .

It is noted that the difference between two curves is remarkable especially near the resonant point in the resonator. It is also found that it is impossible to stabilize the numerical solution even in the case of  $D_{max} \leq L/100$  when the resonance takes place. The reason for this instability is supposed that the value of a calculation point does not correspond to the value on a segment owing to the marked variation of  $f_z$  and  $\partial^2 \zeta / \partial n^2$  in the resonators. So it is difficult to obtain stable solutions (especially in the state of resonance) even if

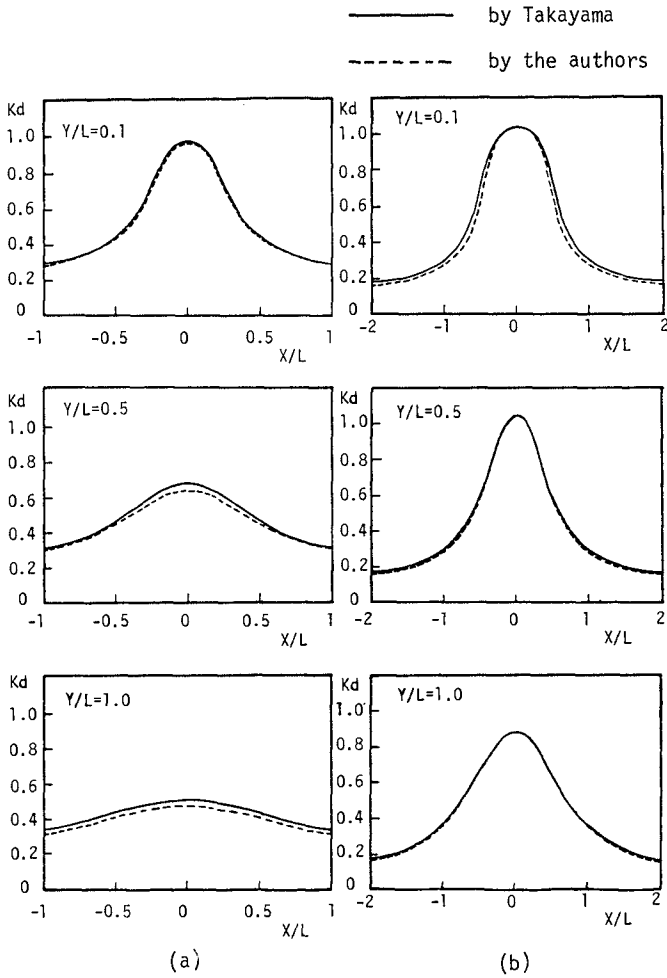


Fig.4 Diffraction coefficients  $K_d$

(a)  $\omega = 90^\circ$ ,  $B/L = 0.5$ ,  $b/L = 0.01$ ,  $D_{max}/L = 0.08$

(b)  $\omega = 90^\circ$ ,  $B/L = 1.0$ ,  $b/L = 0.01$ ,  $D_{max}/L = 0.09$

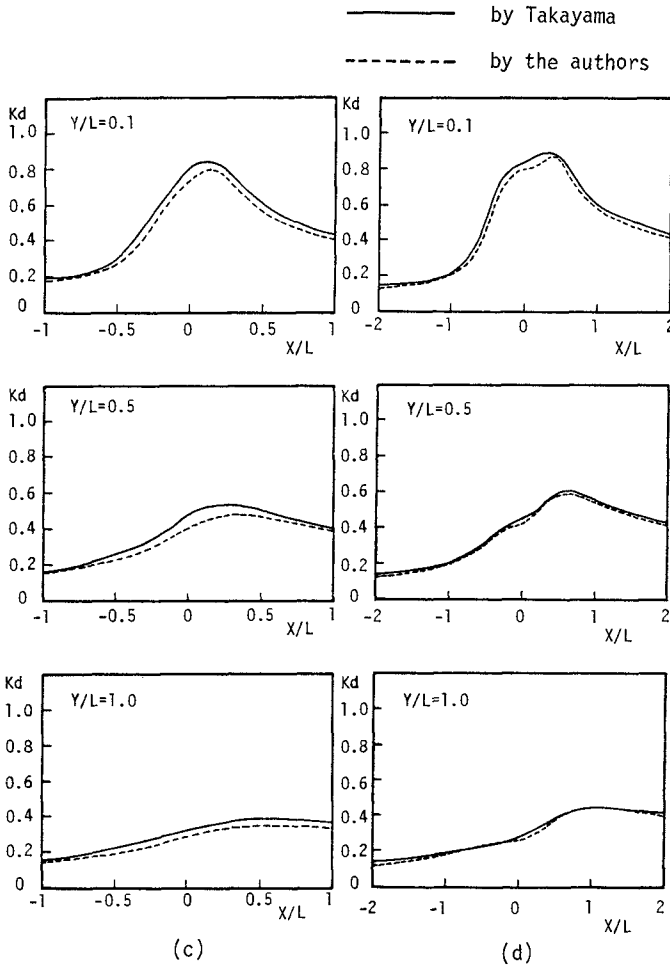


Fig.4 Diffraction coefficients  $K_d$

(c)  $\omega = 150^\circ$ ,  $B/L = 0.5$ ,  $b/L = 0.01$ ,  $D_{max}/L = 0.08$

(d)  $\omega = 165^\circ$ ,  $B/L = 1.0$ ,  $b/L = 0.01$ ,  $D_{max}/L = 0.09$

the length of the segment is considerably small. However, judging from the results shown in Fig.6, it is reasonable to consider that our numerical method is applicable to discuss the variation of diffraction coefficients qualitatively because the variation of  $K_d$  with varying  $L/B$  calculated from different  $D_{max}$  are similar.

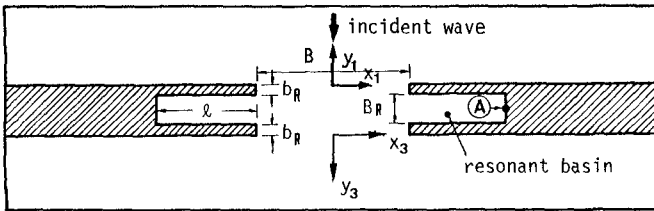


Fig.5 Wave resonators in breakwaters and the coordinates

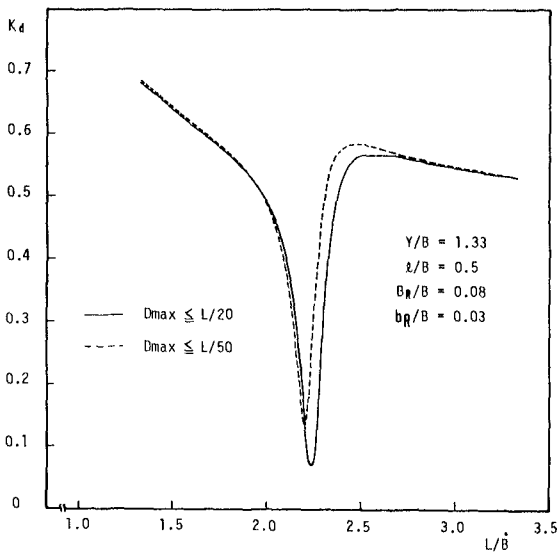


Fig.6-(a) Variations of diffraction coefficient  $K_d$  with wave resonators

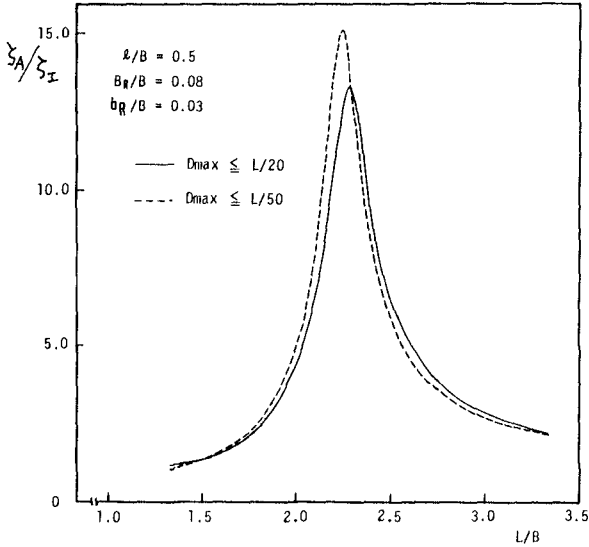


Fig.6-(b) Amplification factor  $\zeta_A/\zeta_I$  at the point of (A)

III. THEORETICAL DEFINITION AND EFFECTS OF A WAVE RESONATOR

As shown in Fig.6, the diffraction coefficients in the case with resonators are strongly dependent on the wave length (i.e. wave period) and indicate a remarkable decrease at the point where the resonance occurs in the resonators ( $L/B = 2.2$ ). In this section, the function of a wave resonator that diminishes the diffracted wave height is investigated theoretically.

Firstly, let us divide  $f_1$  and  $f_3$  in Eqs.(8) and (11) into two components respectively:

$$f_1 = f_{10} + f_{1R} \tag{44}$$

$$f_3 = f_{30} + f_{3R} \tag{45}$$

where  $f_{10}$  and  $f_{30}$  are the wave function in the case without resonator and  $f_{1R}$  and  $f_{3R}$  represent the influence of resonators on  $f_1$  and  $f_3$  and are called here after the wave functions of radiated waves from resonators.  $f_{1R}$  and  $f_{3R}$  are obtained by calculating  $f_1$ ,  $f_3$ ,  $f_{10}$  and  $f_{30}$ .

Fig.7 and Fig.8 illustrate the wave height distribution in region I and III when  $\omega=90^\circ$ . Fig.(a) in each figures shows the wave height distribution around breakwaters without resonators, Fig.(b) represents the radiated waves from resonators obtained by using Eqs.(44) and (45) and Fig.(c) shows the wave height distribution in the case with resonators. The wave height distribution in Fig.(c) can be regarded as the composite waves of the diffracted waves in Fig.(a) and the radiated waves in Fig.(b). The numerals in these figures indicate the ratio of the wave height to the incident wave height  $H/H_1$ .

The geometric profile and dimensions of the resonator in Figs. 7 and 8 corresponds to that in Fig.6. Fig.7 shows the wave height distributions in the case of  $L/B=2.5$ . In this case, the amplification factor at the point A in the resonator  $\zeta_A/\zeta_1$  is small as shown in Fig.6 (b). Fig.8 shows the wave height distribution in the case of  $L/B=2.2$  and it is found from Fig.6 (b) that the resonance occurs in the resonators.

In the case of Fig.7, the radiated wave height is relatively small. Therefore the difference of the wave height distribution in Fig.(c) is similar to that in Fig.(a). On the other hand, in the case of Fig.8, the composite wave height in the harbor region becomes very small, and at the same time, the radiated wave height shown in Fig.8(b) is much larger than Fig.7-(b). The distribution of the radiated waves in the harbor (Fig.8-(b)) is similar to that of diffracted waves without resonators shown in Fig.8-(a).

So it is clear that the effectiveness of resonators comes from the phase interaction between diffracted waves in the case without resonator and the radiated waves from resonators. However, it must be paid attention to the fact that the wave heights in the open sea region becomes larger than those in the case without resonator. (See Fig.8-(c))

Fig.9 and Fig.10 show the wave height distribution in the case where resonance takes place when the entrance width  $B$  is larger than the wave length  $L$ . These figures demonstrate that each resonator located at the edge of breakwater has a tendency to function independently as the ratio  $L/B$  becomes small. The wave height distribution is much different from that shown in Fig.8 and the resonators is not so effective to reduce the diffracted wave height.



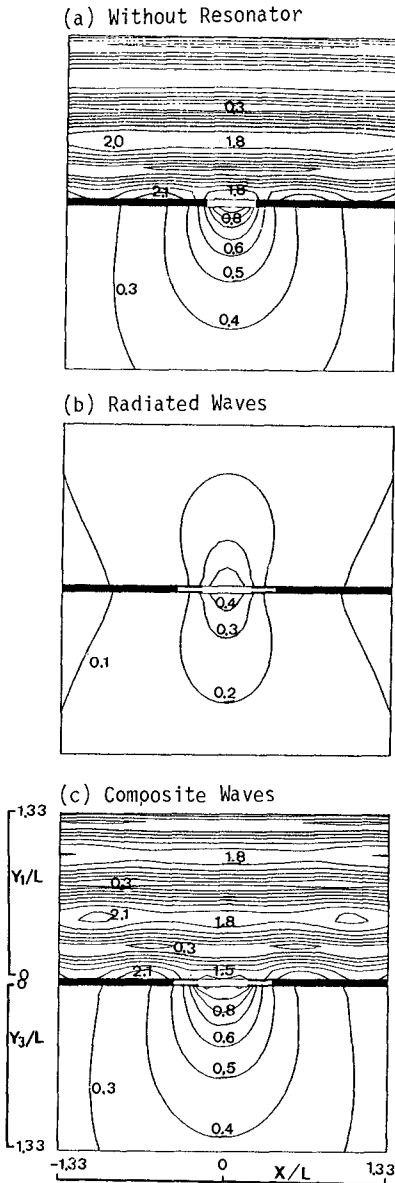


Fig.7 Wave height distribution  
( $L/B=2.5, B/B=0.5, B/B=0.08, b/B=0.03$ )

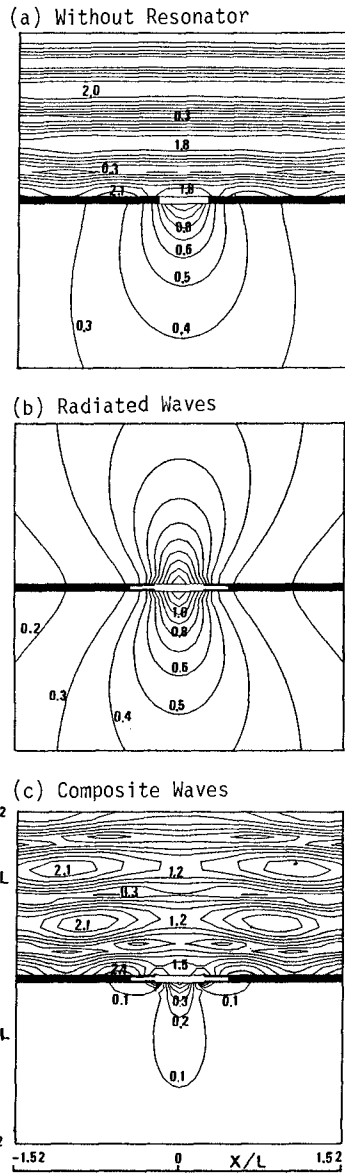
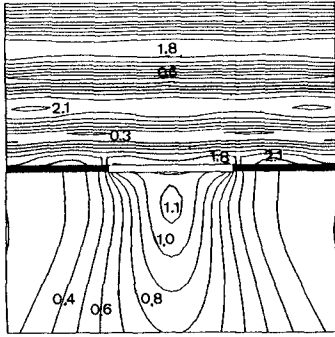
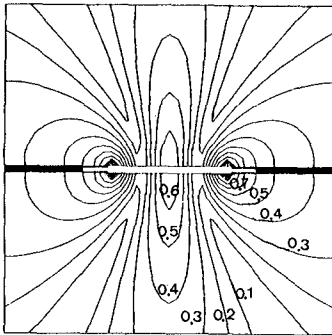


Fig.8 Wave height distribution  
( $L/B=2.2, B/B=0.5, B/B=0.08, b/B=0.03$ )

(a) Without Resonator



(b) Radiated Waves



(c) Composite Waves

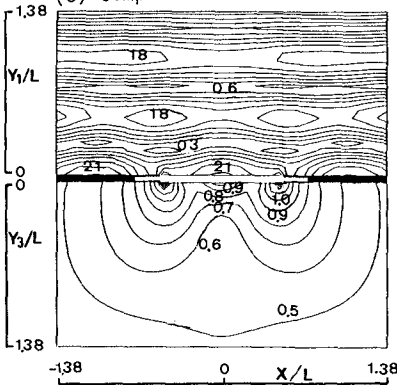
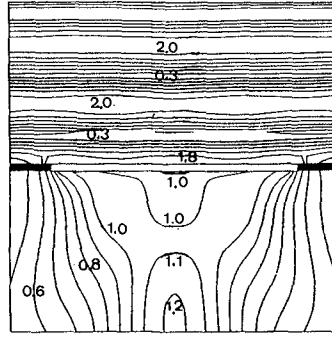
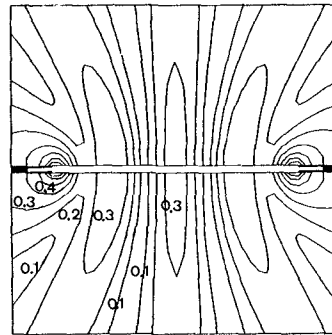


Fig.9 Wave height distribution  
( $L/B=0.97$ ,  $\gamma/B=0.2$ ,  $\beta/B=0.03$ ,  $b/B=0.013$ )

(a) Without Resonator



(b) Radiated Waves



(c) Composite Waves

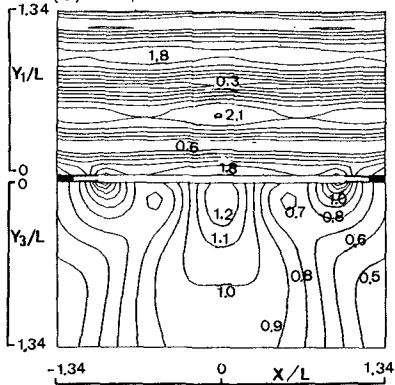


Fig.10 Wave height distribution  
( $L/B=0.5$ ,  $\gamma/B=0.1$ ,  $\beta/B=0.015$ ,  $b/B=0.007$ )

## IV. EXPERIMENTAL VERIFICATION

Judging from the numerical calculation, resonators are very effective to diminish the diffracted wave height and are expected to reduce harbor oscillation. In order to verify these results, model tests were carried out in a wave basin of 15m x 5m and 0.6m deep shown in Fig.11.

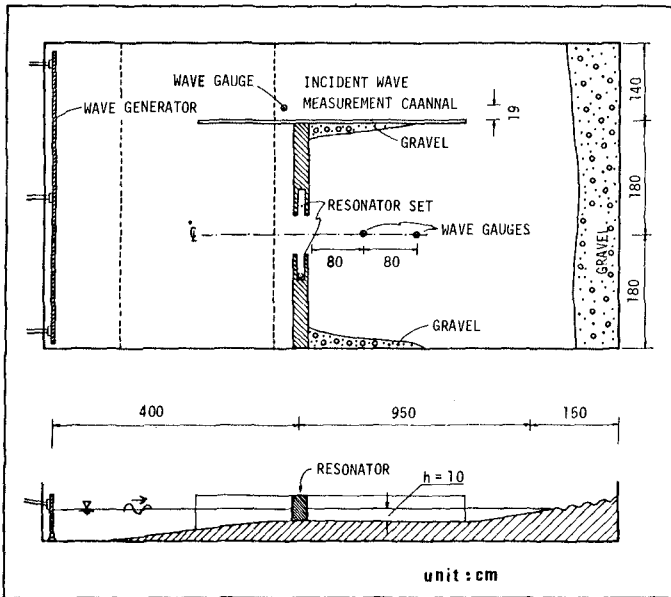


Fig.11 Wave basin

In the wave basin, an over floor made of wood was constructed in order to generate waves of about 2cm height at the depth of 10cm. A flap type wave generator located at one end of the basin was used. At the other end, a gravel sloped beach was equipped as a wave absorber. A lateral wave channel to measure the incident waves during the experiments was also prepared.

Three types of resonators (Case-A, Case-B and Case-C) shown in Fig. 12 (a), (b) and (c) were tested. The results obtained in these cases are shown in Fig.13, 14 and 15 by comparing with theoretical results. The theoretical results in the case C was calculated by using Lee's method.

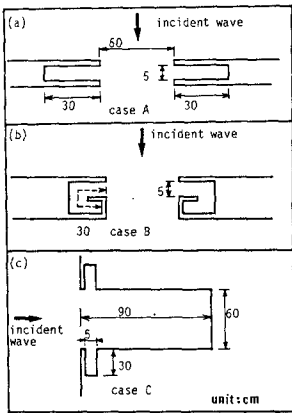


Fig. 12 Experimental cases

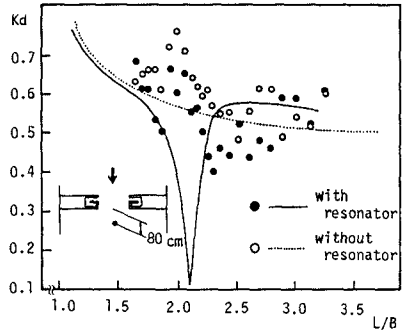


Fig. 14 Diffraction coefficient (Case-B)

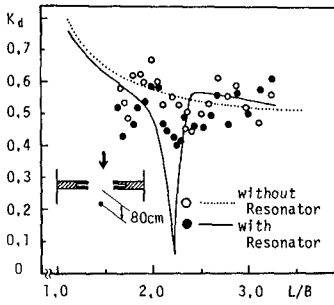


Fig. 13 Diffraction coefficient (Case-A)

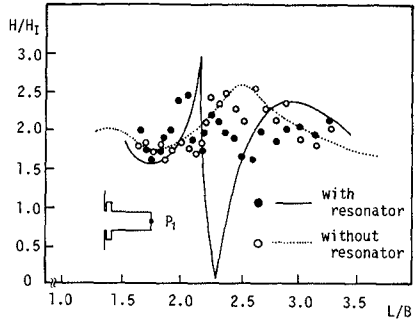


Fig. 15 Amplification factor at  $P_1$  (Case-C)

In all these cases, the abscissas represent the ratio of the wave length to the width of the harbor entrance  $L/B$ . The ordinates in Figs. 13 and 14 are the diffraction coefficient  $K_d$  at the point of 80cm away from the breakwaters in the harbor region. The ordinate in Fig.15 shows the amplification factor at the point  $P_1$  in Fig.15. The dotted lines represent the calculated response in the case without resonator and the open circles are the experimental results. The solid lines are the calculated response in the case with resonators and closed circles show the experimental results.

The calculated results indicate an apparent decrease of wave height when a resonance takes place in the resonator, but such a decrease can not be seen in all experiments as shown in Figs. 13 to 15. It is also found that the agreement between experimental results and theoretical ones is not good even in the case without resonator. The cause of this is assumed that the transversal oscillation in the wave basin exists. Of course, in the case where the resonator was equipped, this transversal oscillation also affected the experimental results. However, this is not the main reason why the experimental results do not show a significant decrease.

As mentioned above, only when the resonance occurs in the resonators the resonators become effective to reduce the diffracted wave height. So the response in the resonator was investigated based on the experimental results obtained in Case-A. Fig. 16 shows the amplification factor  $H/H_x$  at the point (A) in the resonator shown in Fig.5. Clearly, the resonance in the experiments is not as remarkable as that in the calculated results and the measured peak of the response appears at the different position from the calculated response. This is probably due to the energy dissipation at the resonator mouth.

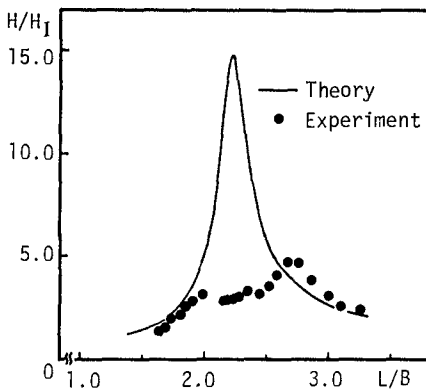


Fig.16 Amplification factor at (A) in the resonator (Case-A)

Consequently, it must be concluded that the wave resonators treated here are not so effective as predicted by the theory, and the reason is considered that sufficient resonance to reduce the diffracted wave height does not occur in the resonator.

#### V. CONCLUSIONS

In this paper, the effect of wave resonators on wave diffraction by breakwaters was investigated theoretically and experimentally. The numerical method developed here shows that resonators equipped at the edge of a breakwater are very effective to reduce diffracted wave heights when resonance occurs in resonators. This effect comes from the phase interaction between the diffracted waves in the case without resonator and the radiated waves from resonators.

The effectiveness of resonators predicted by the numerical simulation was not verified by experiments. The main reason of this is supposed to be the energy dissipation at the resonator mouth which prevents from occurring the sufficient resonance in the resonator.

#### REFERENCES

- James W. (1968) : Rectangular Resonators for Harbour Entrances, Proc. of 11th ICCE, Chapter 98
- James W. (1970) : Spectral Response of Harbor Resonator Configurations, Proc. of 12th ICCE, Chapter 132
- Lee J.J. and Raichlen F. (1970) : Resonance in Harbors of Arbitrary Shape, Proc. of 12th ICCE, Chapter 131
- Takayama T. (1981) : Wave Diffraction and Wave Height Distribution inside a Harbor, Doctral Thesis, Kyoto University
- Valembois J. (1953) : Etude de l'Action d'Ouvrages Resonants et leur Applicayion a la Protection de la Houle, Minnesota International Hydraulic Convention

## CHAPTER ONE HUNDRED NINETY SEVEN

### DYNAMIC ANALYSIS OF PILE STRUCTURES TO PERIODIC WAVES

Hajime Ishida  
Associate Professor, Department of Civil Engineering,  
Kanazawa University, Kanazawa, Japan

and

Yoshinori Konda  
Staff, Aichi Prefectural Government, Nagoya, Japan

#### ABSTRACT

This paper has dealt with the dynamic response of offshore structures to the ocean waves. In order to establish the calculation scheme for offshore structures, the methods of transfer matrices and of structural-property matrices have been introduced and applied to the analysis of dynamic response of pile structures. The validity of these calculation methods have been verified by the experiments in the laboratory.

#### INTRODUCTION

The need for drilling oil from the sea bed has induced the progress of ocean structures until now, and much more structures should be constructed to extract the new sources and energies from the oceans in the future. Then, more precise design of structures should be demanded with considering the dynamic behaviours from the viewpoint of reliability and economical efficiency.

The purpose of this paper is to advance the calculation scheme of dynamic analysis of offshore structures and to clarify the characteristics of the dynamic response to waves. The structural forms treated in this paper are as follows: (1) a vertical small diameter pile, (2) a platform supported by four small diameter piles and (3) a vertical large diameter pile. These three structures are analysed with modeling as a multi-degrees-of freedom system by using the methods of transfer matrices and of structural-property matrices.

The method of transfer matrices is suitable for the analysis of harmonic vibrations, and this method has already been applied to the vibrational analysis of offshore structures by Gaither and Billington.<sup>1)</sup> However, only the monochromatic concentrating forces were used as the

external forces and no calculations have been performed by using the wave forces in their study. Then, in this paper, the authors advance their study and indicate the calculation method for the ocean waves. In the case of a small diameter pile, not only the small amplitude wave theory but also the Stokes wave theory are applied to the Morison's formula to explain the resonant characteristics. In the case of a large diameter pile, MacCamy-Fuchs' diffraction theory<sup>2)</sup> is used as the equation of wave force in stead of Morison's formula.

The method of structural-property matrices<sup>3)</sup> is convenient for calculating the transient response with including the initial conditions or the random vibrations induced by irregular waves. In this paper, this calculation method and the results of some model calculations are shown mainly in the case of periodic waves.

In order to discuss the validity of these calculation methods and to find the characteristics of real vibrations, the laboratory experiments are conducted in the wave tanks by using the model structures mentioned above.

METHOD OF TRANSFER MATRICES

EVALUATION OF TRANSFER MATRICES<sup>1)</sup>

The coordinate system is shown in Fig.1. The share force in the direction of the z-axis and the corresponding displacement are denoted by  $V_z$  and  $w$  respectively. The bending moment around the y-axis and the corresponding slope are denoted by  $M_y$  and  $\psi$  respectively. Henceforth,  $V_z$ ,  $M_y$ ,  $w$  and  $\psi$  are used as the complex amplitudes. The amplitudes are generated by eliminating from their real quantities the time part oscillating with an angular frequency  $\Omega$ ,  $exp(j\Omega t)$ , in which  $t$  is the time and  $j=\sqrt{-1}$ .

The vertical column vector constructed by their real and imaginary parts is called the state vector and is denoted by  $\{z\}$  as follows:

$$\{z\} = \underbrace{\{-w, \psi, M_y, V_z\}}_{\text{Real}} \underbrace{| -w, \psi, M_y, V_z | 1 \}_{1}}_{\text{Imaginary Unit}}^T \cdot (1)$$

To apply the method of transfer matrices, the continuous member is idealized as a discrete series of masses and beams as shown in Fig.2. The external forces are considered to act upon the masses.

Using the compatibility and equilibrium conditions at the beam  $i$ , the relationship between the state vector of the upper side of the mass  $i-1$  denoted by  $\{z\}_{i-1}^U$ , and that of lower side of the mass  $i$  denoted by  $\{z\}_i^L$ , can be described by the matrix equation

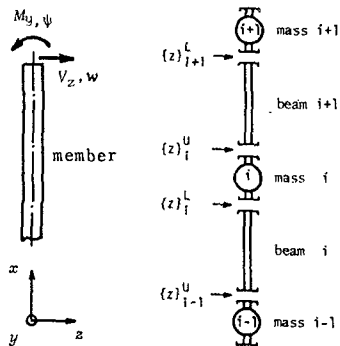


Fig.1 Coordinate system<sup>4)</sup>.

Fig.2 Mass-beam system<sup>4)</sup>.



$$\{z\}_i^L = [F]_i \{z\}_{i-1}^U, \dots \dots \dots (2)$$

in which  $[F]_i$  is called the field transfer matrix and given by

$$[F]_i = \left[ \begin{array}{ccc|ccc} 1 & L & \frac{L^3}{2EI(1+\epsilon^2)} & \frac{L^3}{6EI(1+\epsilon^2)} & 0 & 0 & \frac{\epsilon L^2}{2EI(1+\epsilon^2)} & \frac{\epsilon L^2}{6EI(1+\epsilon^2)} & 0 \\ 0 & 1 & \frac{L}{EI(1+\epsilon^2)} & \frac{L^2}{2EI(1+\epsilon^2)} & 0 & 0 & \frac{\epsilon L}{EI(1+\epsilon^2)} & \frac{\epsilon L^2}{2EI(1+\epsilon^2)} & 0 \\ 0 & 0 & 1 & L & 0 & 0 & 0 & 0 & 0 \\ 0 & 0 & 0 & 1 & 0 & 0 & 0 & 0 & 0 \\ \hline 0 & 0 & \frac{-\epsilon L^2}{2EI(1+\epsilon^2)} & \frac{-\epsilon L^2}{6EI(1+\epsilon^2)} & 1 & L & \frac{L^2}{2EI(1+\epsilon^2)} & \frac{L^3}{6EI(1+\epsilon^2)} & 0 \\ 0 & 0 & \frac{-\epsilon L}{EI(1+\epsilon^2)} & \frac{-\epsilon L^2}{2EI(1+\epsilon^2)} & 0 & 1 & \frac{L}{EI(1+\epsilon^2)} & \frac{L^2}{2EI(1+\epsilon^2)} & 0 \\ 0 & 0 & 0 & 0 & 0 & 0 & 1 & L & 0 \\ 0 & 0 & 0 & 0 & 0 & 0 & 0 & 1 & 0 \\ \hline 0 & 0 & 0 & 0 & 0 & 0 & 0 & 0 & 1 \end{array} \right]_i \dots \dots \dots (3)$$

In Eq.(3),  $E$  is the elastic modulus,  $A$  is the cross-sectional area,  $I$  is the second moment of inertia about the  $y$ -axis,  $L$  is the beam length between the two masses, and  $\epsilon$  is a constant number driven by considering the structural damping to the beam. The range of values is commonly indicated as  $\epsilon=0 \sim 0.015$ .

By applying the same conditions to the mass  $i$ , the relationship between the state vectors  $\{z\}_i^U$  and  $\{z\}_i^L$  is obtained as follows:

$$\{z\}_i^U = [P]_i \{z\}_i^L, \dots \dots \dots (4)$$

in which  $[P]_i$  is the point transfer matrix and given by

$$[P]_i = \left[ \begin{array}{ccc|ccc} 1 & 0 & 0 & 0 & 0 & 0 \\ 0 & 1 & 0 & 0 & 0 & 0 \\ 0 & I_y \Omega^2 & 1 & 0 & c_z \Omega & -f_z \\ m \Omega^2 & 0 & 0 & c_z \Omega & 0 & -f_z \\ \hline 0 & 0 & 0 & 1 & 0 & 0 \\ 0 & 0 & 0 & 0 & 1 & 0 \\ 0 & -c_\psi \Omega & 0 & 0 & I_y \Omega^2 & 1 \\ -c_\psi \Omega & 0 & 0 & m \Omega^2 & 0 & 0 \\ \hline 0 & 0 & 0 & 0 & 0 & 1 \end{array} \right]_i \dots \dots \dots (5)$$

In Eq.(5),  $m$  is the mass,  $I_y$  is the mass moment of inertia about the  $y$ -axis, and  $c_z$  and  $c_\psi$  are the coefficients of viscous damping in the direction of the  $z$ -axis and around the  $y$ -axis respectively.  $f_z$  and  $f_\psi$  are amplitudes of the external forces in the direction of the  $z$ -axis and the external moment around the  $y$ -axis respectively.

Fig.3 shows the pile idealized as the mass-beam system. Transferring the state

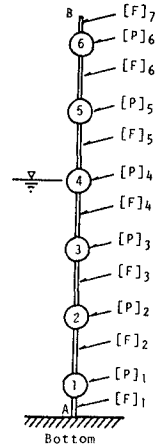


Fig.3 Idealized pile as mass-beam system<sup>4)</sup>.

vector  $\{z\}$  from the fixed base at A to the free end at B by using Eqs. (2) and (4), the following equation which gives the relationship between the state vector at the location A denoted by  $\{z\}_A$  and that of the location B denoted by  $\{z\}_B$  is obtained:

$$\{z\}_B = [F]_7 [P]_6 [F]_6 \dots [P]_1 [F]_1 \{z\}_A = [U]_{BA} \{z\}_A \dots \dots \dots (6)$$

The boundary conditions for this case are given as follows:

for the location A :  $w = 0, \psi = 0, \dots \dots \dots (7)$   
 for the location B :  $V_z = 0, M_y = 0.$

Substituting Eq.(7) to Eq.(6),  $M_y$  and  $V_z$  at the location A, and  $w$  and  $\psi$  at the location B can be obtained, that is  $\{z\}_A$  and  $\{z\}_B$  can be determined so as to satisfy the boundary conditions. The state vector of each location, therefore, can be calculated by using Eqs.(2),(4) and the state vector  $\{z\}_A$ .

EXTERNAL FORCE TERMS DUE TO WAVES

In the following, the coordinate system is taken as shown in Fig.4.  $\xi$  denotes the displacement of pile in the direction of the x-axis.  $u$  and  $\dot{u}$  denote respectively the water particle velocity and its acceleration in the direction of the x-axis.

Applying Morison's formula and using the relative velocities to express the wave forces on the pile in the direction of the x-axis, the equation about the transverse vibration of pile is expressed as follows:

$$\rho A \xi_{tt} + c_1 \xi_t + EI \xi_{zzzz} = \frac{1}{2} C_D \rho_w D (u - \xi_t) |u - \xi_t| + (C_M - 1) \rho_w A (\dot{u} - \xi_{tt}) + \rho_w A \dot{u} \dots \dots (8)$$

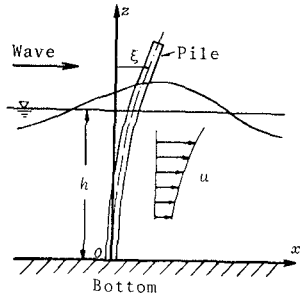


Fig.4 Coordinate system of wave field.

in which,  $\rho$  and  $\rho_w$  are the densities of pile and water respectively,  $c_1$  is the damping coefficient,  $D$  is the diameter of pile, and  $C_D$  and  $C_M$  are the drag and inertia coefficients respectively. The lower indices of  $\xi$ ,  $t$  and  $z$ , indicate the differentiation  $\xi$  with respect to  $t$  and  $z$  respectively.

Eq.(8) is nonlinear with respect to  $\xi$ , however, if the assumption that  $u \gg \xi$  is made, the Eq.(8) becomes linear as follows:

$$(\rho A + K \rho_w A) \xi_{tt} + (c_1 + 2C_D' |u|) \xi_t + EI \xi_{zzzz} = C_D' u |u| + C_M' \dot{u} \dots \dots \dots (9)$$

in which,  $C_D' = C_D \rho_w D / 2$ ,  $C_M' = C_M \rho_w A$ ,  $K = C_M - 1$ , and  $K$  is called the added mass coefficient.

By using the small amplitude wave theory, the water level variation  $\eta$ , the water particle velocity  $u$  and its acceleration  $\dot{u}$  at the location  $x=0$  are described as follows:

$$\eta = a \cos \sigma t, \dots\dots\dots(10)$$

$$u = a\sigma (\cosh kz / \sinh kh) \cos \sigma t, \dots\dots\dots(11)$$

$$\dot{u} = -a\sigma^2 (\cosh kz / \sinh kh) \sin \sigma t, \dots\dots\dots(12)$$

Substituting Eqs.(11) and (12) into Eq.(9), and integrating Eq.(9) along the divided length  $\Delta z_i = z_i - z_{i-1}$  shown in Fig.5,  $m_i$  and  $C_{z_i}$  included in  $[P]_i$  of Eq.(5) can be obtained as follows:

$$m_i = (\rho A + K\rho_w A) \Delta z_i, \dots\dots\dots(13)$$

$$c_{z_i} = c_1 \Delta z_i + 2C'_D a\sigma \{ (\sinh kz_i - \sinh kz_{i-1}) / (k \sinh kh) \} | \cos \sigma t |, \dots\dots\dots(14)$$

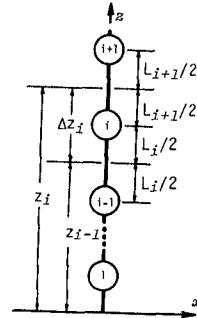


Fig.5 Range of the integration.

The wave forces acting on the mass  $i$  can be expressed as follows:

$$f_i(t) = X_i \cos \sigma t | \cos \sigma t | + Y_i \sin \sigma t, \dots\dots\dots(15)$$

in which,

$$X_i = C'_D (a^2 g k / \sinh 2kh) \{ (\sinh 2kz_i - \sinh 2kz_{i-1}) / 2k + \Delta z_i \}, \dots\dots\dots(16)$$

$$Y_i = -C'_M (ag / \cosh kh) (\sinh kz_i - \sinh kz_{i-1}), \dots\dots\dots(17)$$

If we expand the part  $\cos \sigma t | \cos \sigma t |$  in Eq.(15) into the Fourier series and take up to the third term, the Eq.(15) yields

$$f_i(t) = \frac{8}{3\pi} X_i \cos \sigma t + \frac{8}{15\pi} X_i \cos 3\sigma t - \frac{8}{105\pi} X_i \cos 5\sigma t + Y_i \sin \sigma t, \dots\dots\dots(18)$$

It can be recognized that the four terms  $(8/3\pi)X_i$ ,  $(8/15\pi)X_i$ ,  $(8/105\pi)X_i$  and  $Y_i$  are generated as the amplitudes of external forces  $f_{z_i}$  included in  $[P]_i$  of Eq.(5), and that  $\Omega_i$  in this case becomes  $\Omega$ ,  $3\Omega$ ,  $5\Omega$  and  $\Omega$  corresponding to each amplitude. Therefore, in order to obtain the actual state vector including the time part, each  $\{z\}$  must be calculated by using each  $f_{z_i}$  and  $\Omega_i$ . Then each  $\{z\} \exp(j\Omega t)$  must be calculated, and the real part or imaginary part of  $\{z\} \exp(j\Omega t)$  must be chosen whether the phase of the terms of external force is  $\cos$  or  $\sin$  respectively. Finally, these must be composed.

In the actual calculations,  $f_\psi$ ,  $I_y \Omega^2$  and  $C_\psi \Omega$  included in Eq.(5) are all neglected because they are ascertained as not greatly effecting the values of state vectors by performing some model calculations. Moreover,  $c_1$  in  $C_{z_i}$  of Eq.(14) is also neglected because of being small compared with  $2C'_D |u|$ .

RESONANCE OF PILE DUE TO SMALL AMPLITUDE WAVE

In order to explain some characteristics of the vibrations of a vertical circular cylinder, some calculations have been performed by using the method indicated above. The calculating conditions are determined by considering the scale of the experiments.

The water depth  $h$  is 40cm. The diameter of the cylinder  $D$  is 3cm, the length 60cm, the specific density 1.12, and the elastic modulus  $E$  500Kg/cm<sup>2</sup>. It is inappropriate to always give the drag and inertia coefficients  $C_D$  and  $C_M$  definite values, therefore they should be changed according to the various cases. Practically, however, it is difficult to choose appropriate values in each case because these values cannot be determined only by the Reynolds number and Keulegan-Carpenters' number<sup>9)</sup> In this paper, therefore,  $C_M=2.0$  and  $C_D=1.0$  were ventured to be used as the design criteria<sup>6)</sup> in all cases. Moreover, the added mass coefficient  $K$  is fixed to 1.0 and structural damping is neglected as  $c=0$ . The cylinder is idealized by 6 masses and 7 beams as shown in Fig.3. The lengths of the beams are 5cm at the locations of the fixed bottom and top, and 10cm at the other locations.

Fig.6 shows the characteristics of resonance, taking the horizontal axis as wave period  $T$  and the vertical axis as maximum values of the displacement at the top point in the direction of wave propagation. The dotted lines in this figure indicate that the waves exceed their breaking limit  $H/L=0.14$ .

It can be seen from this figure that the resonance occurs at  $T=0.44$ sec and 1.32sec ( $=3 \times 0.44$ sec) because of the first and fourth terms having the angular frequency  $\sigma$ , and the second term having  $3\sigma$  in the right hand side of Eq.(18), respectively. However, as the wave height increases, the resonant effects at  $T=2.20$ sec ( $=5 \times 0.44$ sec) become more indistinguishable at the displacement of the positive side (not of the negative side) because of the negative sign of the third term having the angular frequency  $5\sigma$  of Eq.(18).

Generally speaking, the resonance of pile structures appears at the wave periods of odd number intervals' natural period in the case where the small amplitude wave theory is used.

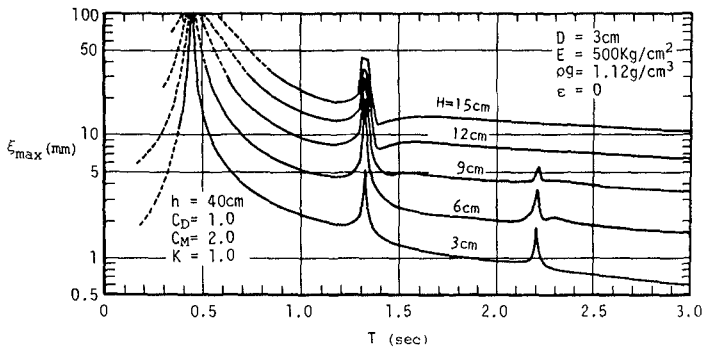


Fig.6 Characteristics of resonance due to small amplitude waves<sup>4)</sup>.

Fig.7 shows the time variations of the displacement at the top point during a cycle of waves by successively changing the wave periods.  $t/T=0$  and  $\pm 0.5$  express the phases of the wave crests and troughs coming to the position of the cylinder respectively. The displacements are divided by their maximum value in each case to standardize them. In all cases, the ratio of the maximum inertia forces to the maximum drag forces are 2:1, and therefore, the high frequency components of the drag forces are not so large. However, it can be seen from this figure that high frequency vibrations appear in the time variations of displacement in the cases  $T=1.30\text{sec}$  or  $1.35\text{sec}$  and  $2.20\text{sec}$  because of resonant effects.

#### RESONANCE OF PILE DUE TO STOKES WAVE

An experiment concerning vibrations of a circular cylinder has been performed at the Department of Civil Engineering of Kanazawa University. The experimental apparatus is shown in Fig.8. The dimension of the wave tank used in this experiment was 50cm wide, 60cm high and 14m long. A wave generator of the plunging type was installed at the end of this wave tank. A circular cylinder of which end the plate spring was attached was vertically installed 4.5m apart from this wave generator. The diameter of this cylinder  $D$  was 3cm, the length 60cm, the specific gravity 1.60, and the elastic modulus of the plate spring  $E$  400Kg/cm<sup>2</sup>. The dynamic displacements of this cylinder were measured at its top part, at which a copper plate was attached, by using the electromagnetic displacement meter of the non-contact type. The water depth  $h$  was 40cm.

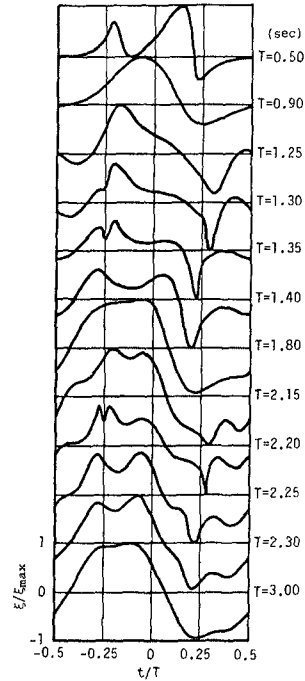


Fig.7 Time variations of the displacement at the top point of cylinder<sup>4)</sup>.

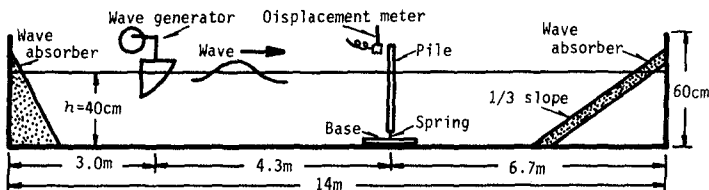
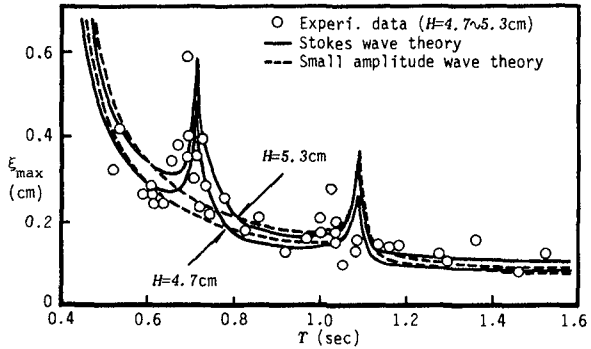


Fig.8 Experimental apparatus in the case of a pile.

In this experiment, the resonance appears by the waves of which period is integer times natural period of the cylinder. This phenomenon cannot be explained by using the small amplitude wave theory but the Stokes wave theory. This reason is that the inertia force contains the frequency terms of  $\sin\omega t, \sin 2\omega t, \sin 3\omega t, \sin 4\omega t, \dots$  and the drag force produces the frequency terms  $\cos\omega t, \cos 2\omega t, \cos 3\omega t, \cos 4\omega t, \dots$  when the Stokes wave theory is applied to the Morison's formula.

Fig.9 shows the comparison between the experimental data and the calculated values by using the small amplitude wave theory and the Stokes wave theory. In this figure, it is recognized that the calculated values by using the Stokes wave theory agree roughly well with the experimental ones near the resonant point  $T=0.71$ sec which is two times the natural period of cylinder  $T=0.354$ sec.

Fig.9 Characteristics of resonance in the case of small diameter cylinder due to Stokes wave.



DYNAMIC RESPONSE OF PLATFORM

In the case of a platform, the axial force  $N$  and its displacement  $u$  shown in Fig.10 should be introduced. Therefore, the state vector is denoted as follows:

$$\{z\} = \underbrace{\{u, -w, \psi, M_y, V_z, N\}}_{\text{Real}} \underbrace{|u, -w, \psi, M_y, V_z, N|}_{\text{Imaginary}} \underbrace{1}_{\text{Unit}} \}^T \dots \dots (19)$$

The portion of the corner idealized as mass-beam system is shown in Fig.11, in which the corner transfer matrix  $[C]$  is newly introduced to change the direction of the neutral axis at the corner. The corner transfer matrix is indicated by Eq.(20) in the case that the neutral axis turns 270 degrees clockwise. The point transfer matrix and the field transfer matrix are indicated by Eqs.(21) and (22) respectively. The state vectors can be determined by multiplying these matrices in the same manner as the vertical pile<sup>1)</sup>.

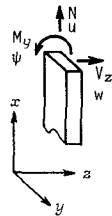


Fig.10 Coordinate system.



The experiment has been carried out to the platform shown in Photo. 1. Four vertical piles supporting the aluminum plate are made of rubber, and their diameter is 3cm, the elastic modulus  $600\text{Kg/cm}^2$ . Idealizing this platform as mass-beam system as shown in Fig.12, the analyses have been performed by using the small amplitude wave theory to simplify the calculations.

One of the model calculations about resonance is shown in Fig.13, in which the horizontal axis is the wave period  $T$ , and the vertical one is the maximum value of the displacement at the corner point B. The wave steepness is kept  $H/L=0.1$ , and the added mass coefficient  $K$  is changed 0, 1 and 2. From this figure, it can be seen that the resonant wave period decreases as  $K$  decreases from 2 to 0, and the value of the displacement becomes minimum at the wave period  $T=0.54\text{sec}$ . The minimum point of the displacement appears when the wave length becomes about two times distance between piles because the directions of wave forces acting on the piles become opposite with each other.

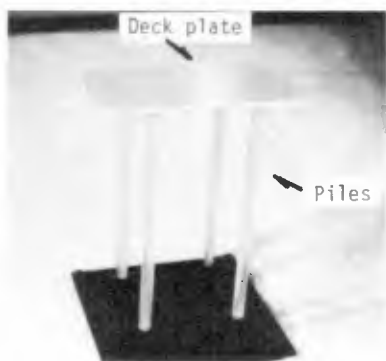


Photo.1 Model of platform.

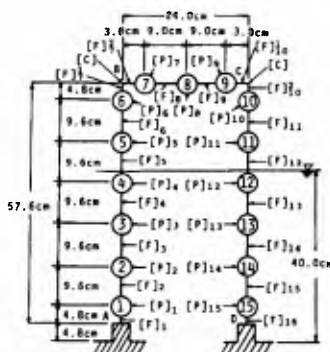


Fig.12 Idealized platform as mass-beam system.

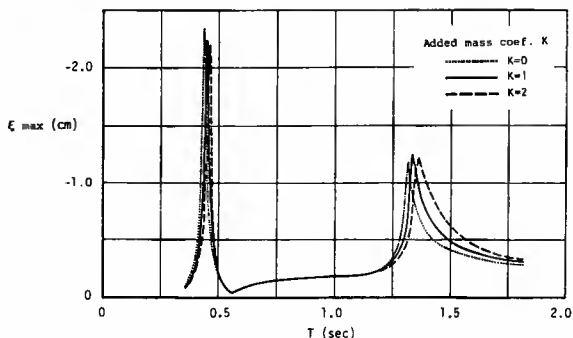


Fig.13 Characteristics of resonance of the platform.



Fig.14 shows the comparison of the time variations of the displacement at the point B between the experimental values and the calculated ones. From this figure, it is recognized that the calculated values shown by chain lines agree well with the experimental ones shown by solid lines.

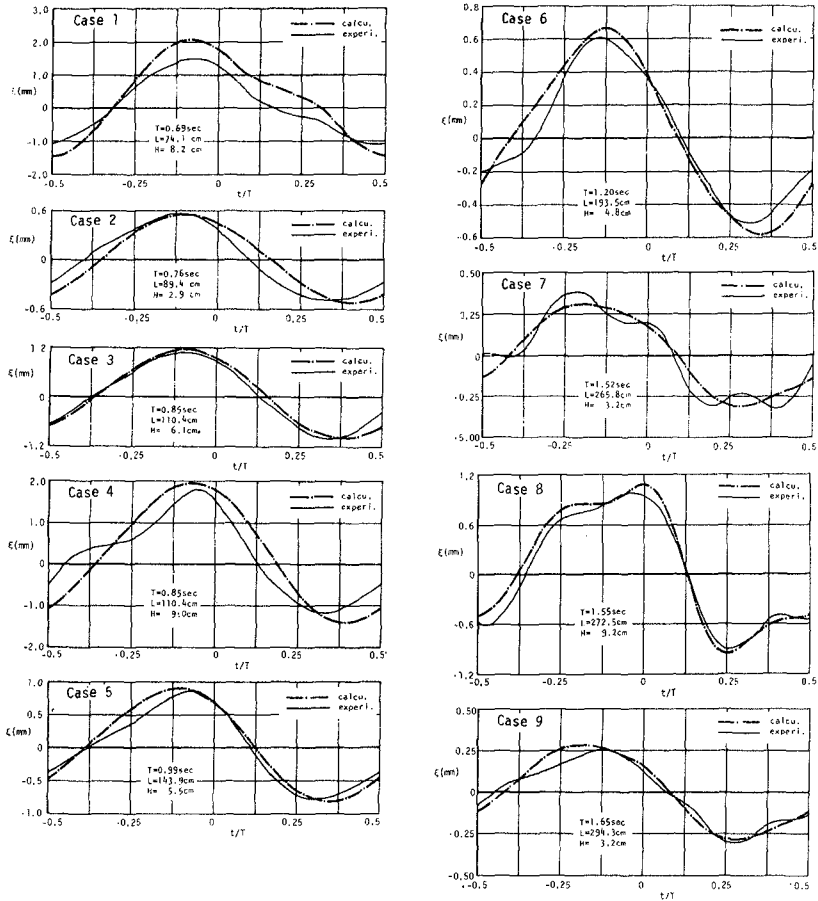


Fig.14 Comparison of the time variations of displacement between the experimental values and the calculated.

DYNAMIC RESPONSE OF LARGE DIAMETER PILE

In the case of a large diameter pile, MacCamy-Fuchs' diffraction theory can be applied to the equation of wave forces instead of Morison's formula in its calculations. On the occasion of this experiment, the circular cylinder shown in Fig.15 has been used. The diameter of this cylinder is 40cm and the experimental apparatus is shown in Photo.2. The dimension of the wave tank is 6.7m long, 4.3m wide and 55cm deep. The water depth was kept 35cm, and the displacement was measured by using the contact type displacement meter. The natural period of this cylinder is 0.56sec in the still water.

Fig.16 shows the characteristic of resonance of this cylinder with comparing the experimental values with the calculated ones. From this figure it is recognized that the solid line calculated by using  $K=0$  is closer to the experimental values than the broken line calculated by using  $K=1$ . This fact may indicate that the added mass coefficient  $K$  decreases from 1.0 with according to the increase in magnitude of the displacement.

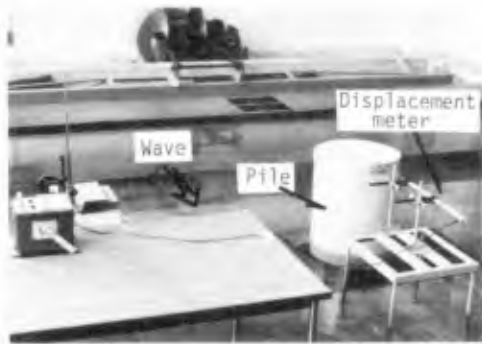


Photo.2 Experimental apparatus.

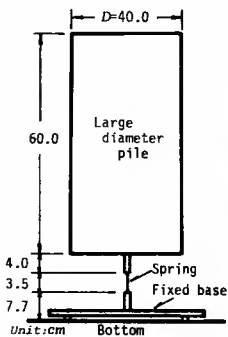


Fig.15 Large diameter pile.

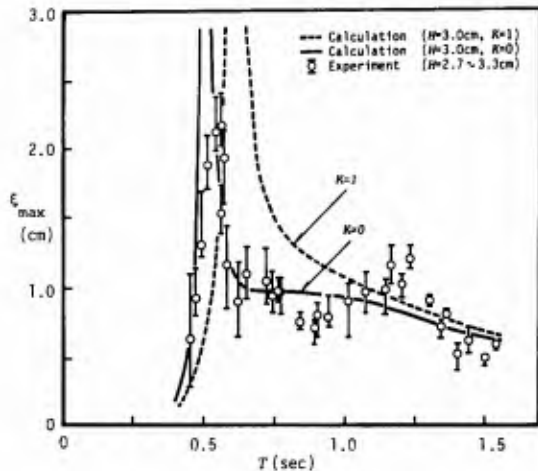


Fig.16 Characteristics of resonance.

METHOD OF STRUCTURAL-PROPERTY MATRICES

EVALUATION OF STRUCTURAL-PROPERTY MATRICES

The method of transfer matrices has been proved most effective for the analysis of harmonic vibrations. On the other hand, the method of structural property matrices is available for the non-harmonic vibrations. In this approach, the structure is assumed to be divided into a system of discrete elements which are interconnected only at a finite number of nodal point. The properties of the complete structure are then found by evaluating the properties of the individual finite elements and superposing them appropriately<sup>3</sup>.

Fig.17 shows the beam element of number i, in which the displacements and rotations at node i and i-1 are denoted by  $\xi_i, \xi_{i-1}$  and  $\theta_i, \theta_{i-1}$  respectively. The deflected shape of the element  $\xi(x)$  can be expressed in terms of its nodal rotations and displacements as follows:

$$\xi(x) = \psi_1(x)\xi_{i-1} + \psi_2(x)\xi_i + \psi_3(x)\theta_{i-1} + \psi_4(x)\theta_i, \dots (23)$$

in which,  $\psi_n(x)$  (n=1,2,3,4) are the deflections developed in the element subjected to the unit nodal displacements which can be expressed as follows:

for $\xi_{i-1}=1$ ;	$\psi_1(x) = 1 - 3(x/l)^2 + 2(x/l)^3$	} .....	(24)
for $\xi_i = 1$ ;	$\psi_2(x) = 3(x/l)^2 - 2(x/l)^3$		
for $\theta_{i-1}=1$ ;	$\psi_3(x) = x(1 - x/l)^2$		
for $\theta_i = 1$ ;	$\psi_4(x) = (x^2/l)(x/l - 1)$		

Here, the displacement vector of i-th beam is defined in terms of its nodal rotations and displacements as follows:

$$u_i = (\xi_{i-1}, \theta_{i-1}, \xi_i, \theta_i)^T \dots (25)$$

The external forces and moments applied to a beam element are assumed to act only upon its nodes as shown in Fig.17. The force vector of j-th beam is defined in terms of these forces and moments as follows:

$$F_j = (P_{i-1}^j, M_{i-1}^j, P_i^j, M_i^j)^T \dots (26)$$

When the force vector  $F_j$  acts upon the i-th element, the equation of motion about the i-th element is given as follows:

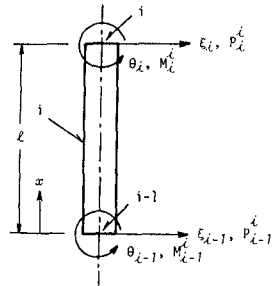


Fig.17 Notation of forces and displacements at beam element.

$$[M]_i \ddot{u}_i + [C]_i \dot{u}_i + [K]_i u_i = F_i, \dots\dots\dots(27)$$

in which,  $[K]_i$ ,  $[M]_i$  and  $[C]_i$  are called the stiffness matrix, the mass matrix and the damping matrix respectively. By applying the principle of virtual work to the element, these matrices can be evaluated as shown in Eqs.(28), (29) and (30) respectively, in which,  $\psi_n'' = d^2\psi_n/dx^2$ ,  $\bar{m}$  and  $\bar{c}$  is the mass and the damping coefficient per unit length which can be calculated from Eqs.(13) and (14) respectively. Moreover, the force vectors can be evaluated by using the Morison's formula, and however, the moments may be neglected when their magnitudes are small.

Evaluating the equations of motion for the individual finite elements and superposing them, the equation of motion for the complete structure can be obtained. The time variations of the displacement vectors can be calculated from this equation.

$$[K]_i = \left[ EI \int_0^l \psi_j'' \psi_k'' dx \right]_i = \left( \frac{2EI}{l^3} \right) \begin{bmatrix} 6 & 3l & -6 & 3l \\ & 2l^2 & -3l & l^2 \\ \text{Sym.} & & 6 & -3l \\ & & & 2l^2 \end{bmatrix}_i, \dots\dots\dots(28)$$

$$[M]_i = \left[ \bar{m} \int_0^l \psi_j \psi_k dx \right]_i = (\bar{m}l)_i \begin{bmatrix} \frac{13}{35} & \frac{11}{210}l & \frac{9}{70} & -\frac{13}{420}l \\ & \frac{1}{105}l^2 & \frac{13}{420}l & -\frac{1}{140}l^2 \\ \text{Sym.} & & \frac{13}{35} & -\frac{11}{210}l \\ & & & \frac{1}{105}l^2 \end{bmatrix}_i, \dots\dots\dots(29)$$

$$[C]_i = \left[ \bar{c} \int_0^l \psi_j \psi_k dx \right]_i = \left( \frac{\bar{c}}{\bar{m}} \right)_i [M]_i, \dots\dots\dots(30)$$

TIME VARIATION OF PILE DISPLACEMENT

Some experiments and calculations have been performed for the small diameter cylinder, of which end the plate spring is attached. The length of this cylinder is 60cm and the diameter is 4cm. The flexural rigidity of the plate spring  $EI$  is  $1.93 \times 10^5$  Kg.cm<sup>2</sup>. The natural period of the cylinder was changed appropriately by arranging the length of plate spring. In the experiment, the water depth was always kept 40cm. In the calculations, this cylinder is divided into seven elements as shown in Fig.18. The Newmark's  $\beta$  method has been applied to calculate the time variations of the displacement vector with selecting  $\beta=0.25$ .

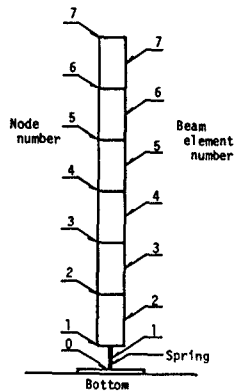
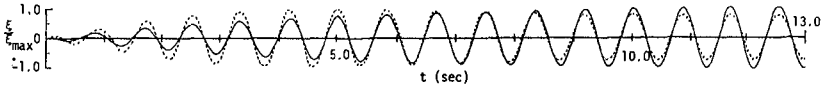


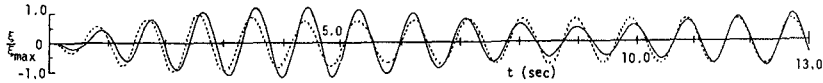
Fig.18 Division of pile into elements.

Fig.19 shows the time variations of the displacement at the cylinder top, in which the dotted lines and solid lines indicate the experimental values and the calculated ones respectively. In Fig.19(a), the displacements become larger to a certain magnitude as the time proceeds, because the wave period  $T=0.84\text{sec}$  is close to the natural period  $0.80\text{sec}$ . In Fig.19(b), the displacements are beating, because the wave period  $T=0.92\text{sec}$  is slightly different from the natural period. In Fig.19(c), the calculated values agree well with the experimental.

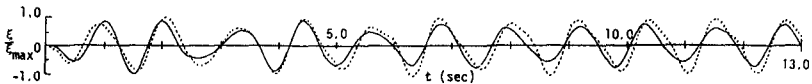
Fig.20 is one of the examples applied to the case of hyperbolic waves, in which the upper figure shows the water level variation  $\eta$  and the lower one is the displacement  $\xi$  calculated from  $\eta$ . In the displacement, the natural vibrations are generated by the high frequency component waves included in the wave crests.



(a)  $T=0.84\text{sec}$ ,  $H=1.9\text{cm}$ ,  $\xi_{\text{max}}=4.85\text{cm}$ .



(b)  $T=0.92\text{sec}$ ,  $H=4.1\text{cm}$ ,  $\xi_{\text{max}}=4.91\text{cm}$ .



(c)  $T=1.18\text{sec}$ ,  $H=4.6\text{cm}$ ,  $\xi_{\text{max}}=1.98\text{cm}$ .

Fig.19 Time variations of displacement of small diameter pile.  
(Solid line: Calculated. Dotted line: Experiment)

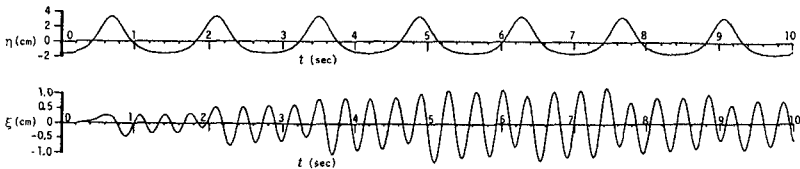


Fig.20 Time variations of hyperbolic waves and the displacement of small diameter pile.

In the case of irregular waves,  $\xi$  can be calculated only from  $\eta$  by using the linear filters<sup>2)</sup>. Fig.21 is one of the examples of irregular waves, in which, the calculated values of the displacement shown by solid line agree well with the experimental ones shown by dotted line.

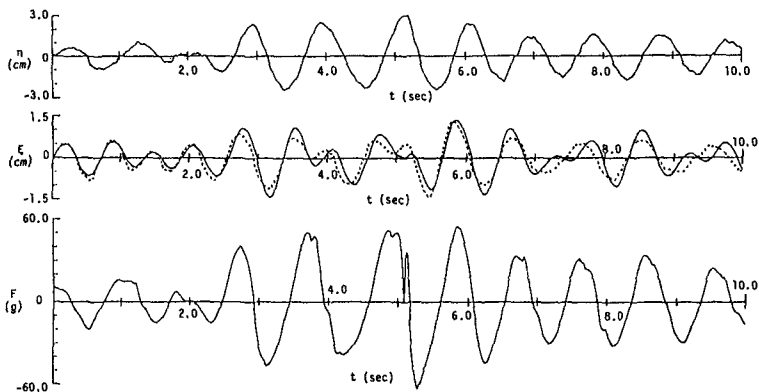


Fig.21 Time variations of displacements in case of irregular wave. ( $\eta$ : water level variation,  $\xi$ : displacement, F: wave force)

## CONCLUSIONS

The harmonic vibrations of structures can be calculated by the method of transfer matrices. On the other hand, in order to calculate the transient response with considering initial conditions or the random vibrations induced by irregular waves, the method of structural-property matrices should be used. In these calculations, the added mass coefficient should be given an appropriate value in the range from 0 to 1 in accordance with the magnitude of a displacement, and also the damping coefficient should be determined with considering the interaction effect between structures and waves.

The resonance of a small diameter pile occurs at the wave periods of integer times natural period, which has been confirmed by the experiments and the calculations. The time variations of the displacement of structures can be calculated correctly by using the matrix methods shown in this paper.

## ACKNOWLEDGEMENT

The authors wish to express their gratitudes to Mr. H.Sawaki, Mr. H.Masuya and Mr. T.Hosogai (who were postgraduate students at that time) for their assistances through this investigation.

## REFERENCES

- 1) Gaither, W.S. and D.P. Billington "The dynamic response of offshore structures to time dependent forces", Proc. 9th Conf. on Coastal Engg., pp.453-471, 1964.
- 2) Sarpkaya, T. and M. Isaacson "Mechanics of wave forces on offshore structures", Van Nostrand Reinhold Company, pp.381-472, 1981.
- 3) Clough, R.W. and J. Penzien "Dynamics of structures", MacGraw-Hill, 1975.
- 4) Hajime Ishida "Dynamic response of vertical pile to periodic waves by transfer matrix method", Symposium Engg. in Marine Environment, in Brugge, pp.2.102-2.114, 1982.
- 5) Iwagaki, Y., Ishida, H. and T. Senda "Irregular wave forces on a circular cylinder", Proc. 20th Conf. on Coastal Engg. in Japan, pp.1-5, 1973. (in Japanese)
- 6) JSCE "Index to design offshore steel structures", JSCE, 1973. (in Japanese)
- 7) Ishida, H. and Y. Iwagaki "Wave forces induced by irregular waves on a vertical circular cylinder", Proc. 16th Conf. on Coastal Engg., pp.2397-2414, 1979.



*Fishing Harbor, Homer, AK*

#### **PART IV**

### **COASTAL ESTUARINE AND ENVIRONMENTAL PROBLEMS**

*Boardwalk, Cape May, N.J.*







## CHAPTER ONE HUNDRED NINETY EIGHT

### EVOLUTION OF INTERFACIAL WAVES ALONG AN UNSTEADY SALT WEDGE

by

Wataru Nakano\* and Isao Yakuwa\*\*

#### ABSTRACT

Field measurements of the receding salt wedge were made at the mouth of the Ishikari River in October 1981. The gradually growing interfacial waves and the diffusion pattern of salinity are visualized by the Ultrasonic Method. The evolution mechanisms of waves are analysed in detail by calculating the power spectra of wave records. It is pointed out that the wave breaking, the wave-eddy interaction and the nonlinearity of waves are factors dominating the evolution. The nonlinear property of interfacial waves is studied further by watertank experiments.

#### INTRODUCTION

Because a salt wedge influences the flow structure and water quality in the estuary, many studies about it have been carried out by various research methods. The theoretical study and laboratory experiment have found out the importance of internal waves in the dynamics of the stratified shear flow[8]. The results of field observations, however, shows that in the steady state of the salt wedge the interfacial waves are not the factor controlling the diffusion process because the amplitudes of interfacial waves are small under this condition. Do the interfacial waves, on the other hand, play an important role in the unsteady salt wedge? Regrettably, there is not enough observational research of the unsteady salt wedge. So we planned to observe the interfacial waves along the unsteady salt wedge in the Ishikari River.

The Ishikari River, which has a length of 262 km, flows through the Ishikari Plain and pours into the Japan Sea (Fig. 1). The normal discharge of this river is about  $300 \text{ m}^3/\text{sec}$ . Because the critical discharge  $Q_c$  for the intrusion of the salt wedge into the river mouth is about  $600 \text{ m}^3/\text{sec}$  [3], the salt wedge steadily lies in the water course to a point about 8 km upstream from the river mouth under the usual river flow.

---

\* Postgraduate Student, Division of Applied Physics,  
Hokkaido University, Sapporo 060, Japan.

\*\* Professor, Department of Engineering Science,  
Hokkaido University, Sapporo 060, Japan.

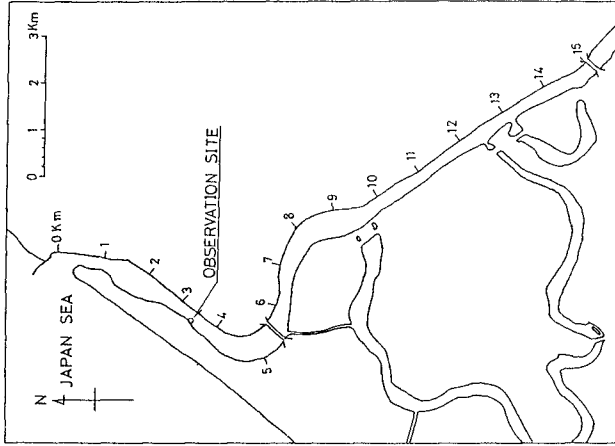


Fig.2 Location map

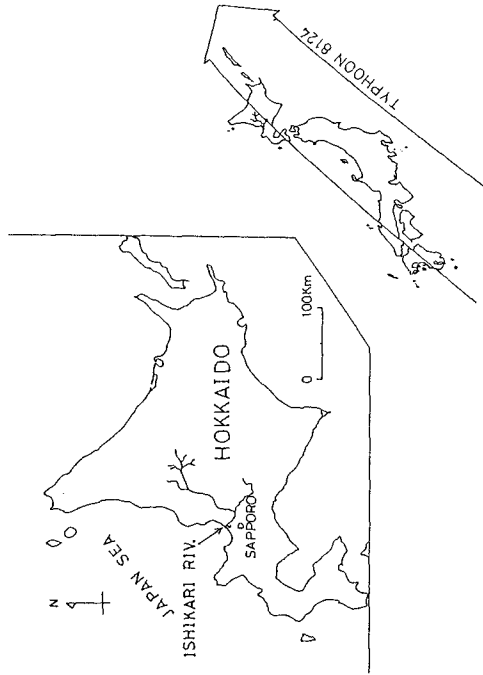


Fig.1 The Ishikari River and the route of the Typhoon 8124

From October 22 to October 23, 1981, a severe 960-millibar typhoon (the Typhoon 8124) hit and passed through the Japanese Islands as shown in Fig.1. Because of the heavy rain brought about by this typhoon in the drainage basin of the Ishikari River, the river discharge increased from 300 to 2,250 m<sup>3</sup>/sec beyond the critical value  $Q_c$ . On these two days, we had a chance to observe the interfacial gravity waves propagating along the interface of the unsteady salt wedge. The purpose of this paper is to report the observational results and to make clear the evolution mechanisms of the interfacial waves along an unsteady salt wedge.

### FIELD OBSERVATION

The estuary of the Ishikari River is drawn in Fig.2. The observation was conducted on a pier which locates 3.5 km upstream from the river mouth. As shown in Fig.3, the displacement of interface was measured with two echo-sounder transducers, No.1 and No.2. No.1 was settled facing downwards slightly under the water surface, whereas, No.2 was settled facing upwards on the riverbed to record the both of the water level and the displacement of interface.

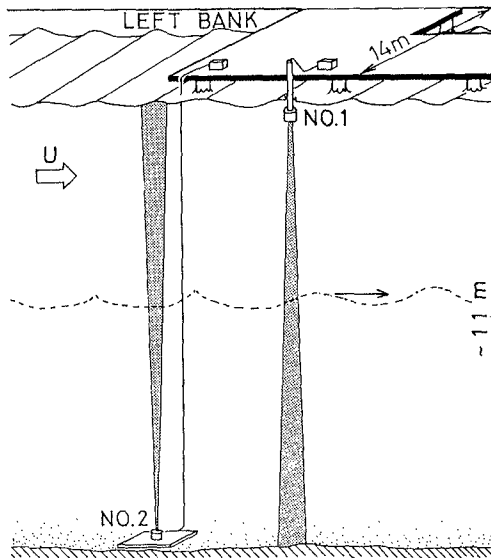


Fig.3 Pier station and two echo-sounder transducers

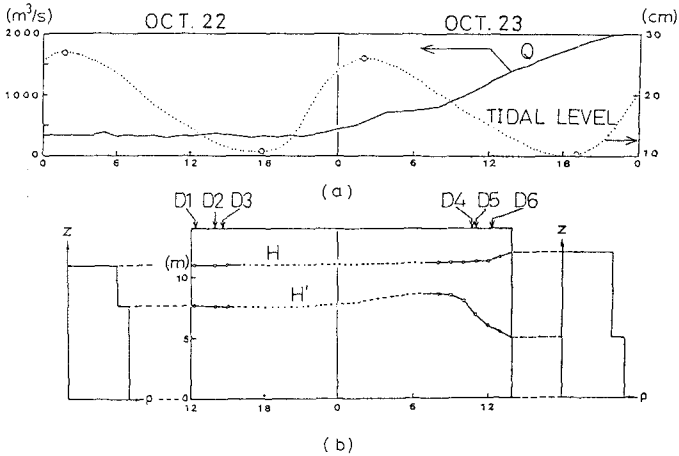


Fig.4 Hydraulic conditions. (a)History of river discharge  $Q$  and tidal level. (b)History of the level of surface  $H$  and interface  $H'$ .

The hydraulic conditions during the observation are summarized in Fig.4. Fig.4(a) shows the history of the river discharge and the tidal level. The latter has been observed at Otaru Port which locates about 30 km west from the river mouth. Fig.4(b) shows the history of the surface level  $H$  and the interface level  $H'$  measured at the station. After a weak tidal motion, the interface level  $H'$  begins to lower rapidly at 9:00 on October 23 according to the increase of river discharge. The echo-sounder measurement was performed from 11:00 to 15:00 on October 22 and from 8:00 to 13:00 on October 23. The six series of wave records were sampled at short time intervals numbered from D1 to D6 in Fig.4(b). Because we had to use the clearer image to analyse the data accurately, the data D1, D2 and D3 are sampled from the chart of echo-sounder No.1, and the data D4, D5 and D6 are sampled from that of No.2.

The charts D1, D2 and D3 in Fig.5(a) were recorded on October 22. At these stages the river charged almost steady discharge of  $350 m^3/sec$  that was fairly smaller than the critical value  $Q_c$  of  $600 m^3/sec$ . The depth at the observation point was about 11 m. The river bed cannot be seen in these figures. The chart D1 shows that several waves of small amplitude are intermittently propagating along the interface lying at 3.5 m depth. The wave height and the wave period are about 30 cm and 18 sec respectively. In the stage of D2, the waves are going through more frequently, and in the stage of D3, the wave height attains to 50 cm and the waves become short-crested. It

will also be noted that the wave breaking and the destruction of interface are taking place.

On October 23, the river discharge abruptly increased beyond the critical discharge  $Q_c$ . The recorded charts are shown in Fig.5(b). D4 shows the large scale random and modulated waves, which are propagating along the interface lying at 6 m depth and are causing violent wave breaking. It may be seen that the interfacial waves are playing an important role in salinity diffusion. The wave height is about 80 cm and the wave period is obtained as about 21 sec. The waves shown in D5 have longer period of 30 sec and waves are propagating more periodically. After 85 minutes, in the stage shown in D6, the waves recur to the modulated state and the wave period lengthens up to 40 sec and the wave height attains to 2 m.

### SPECTRAL ANALYSIS

To make clear the evolution mechanism of interfacial waves, we calculated the power spectra of recorded waves, which are shown in Fig.6. Each spectrum was calculated by FFT method with 512 data sampled from the recorder charts shown in Fig.5(a) and (b). In each figure the spectrum is drawn with a solid line. Further, the spectrum of preceding step is drawn with a broken line for a convenience of comparison.

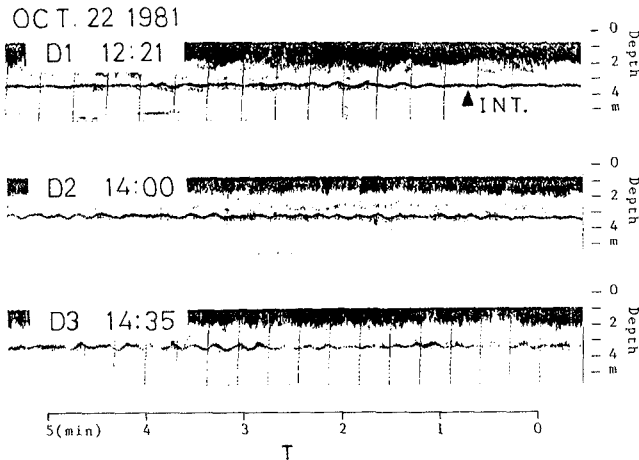


Fig.5(a) Echo-sounding images recorded on Oct. 22.

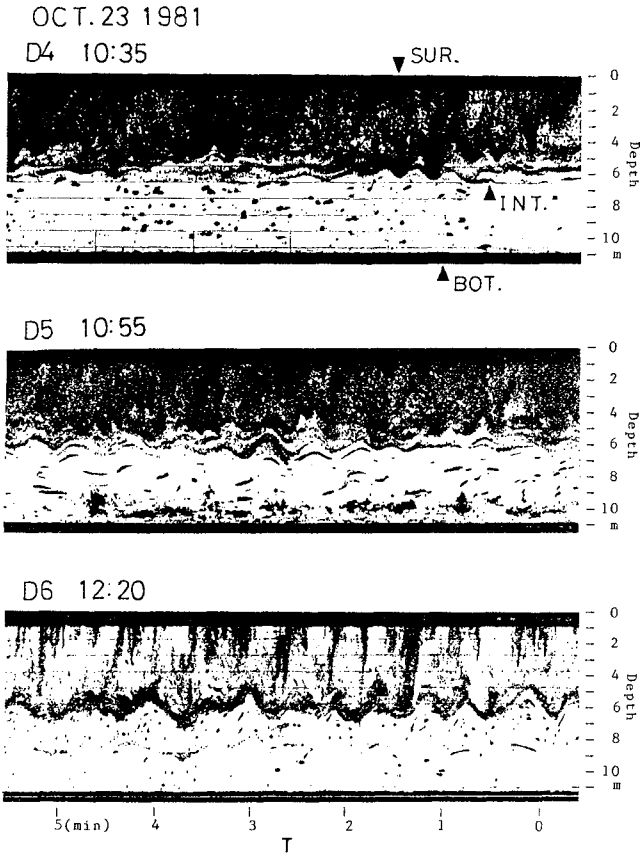


Fig.5(b) Echo-sounding images recorded on Oct. 23.

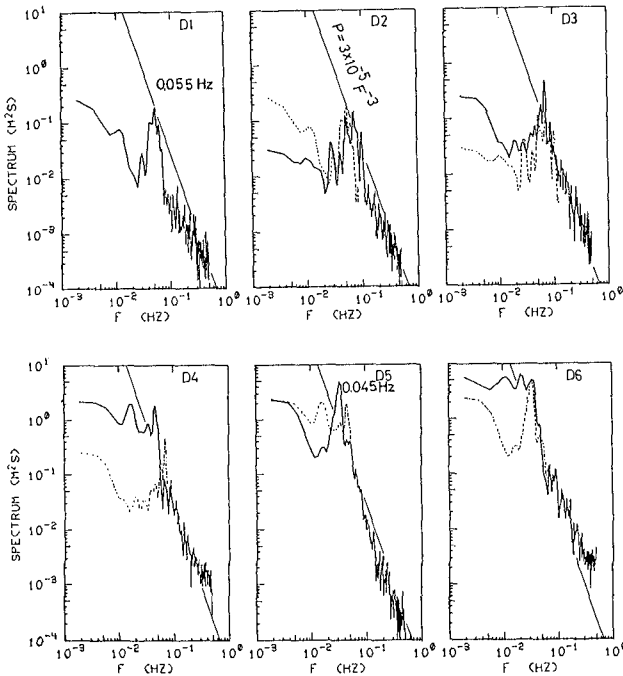


Fig.6 Power spectra of interfacial waves (solid lines). The broken line in each figure represents the spectrum of the preceding step.

Corresponding to the mean wave period of 18 sec shown in the chart of Fig.5(a), the spectrum of D1 has a distinct spectral peak at 0.055 Hz. In this stage, the power spectra in higher frequency range decreases with frequency  $f$  more dully than  $f^{-3}$ . After this stage the spectrum approaches a saturated spectral form in high frequency range which decreases with  $f$  as  $f^{-3}$  as shown in D2 and D3. Spectral form of this type has been observed in the spectra of ocean internal waves [2] and theoretical explanation of this spectral form has been proposed by Phillips[6]. Phillips[6] derived the  $f^{-3}$ -spectrum by assuming the local breakdown of internal waves caused by shear stress in wave motion. Therefore, the growth of spectrum from D1 to D3 indicates that the local breakdown process of the interfacial waves is beginning at this stage. The local breakdown process must be the mechanism controlling the earlier stage of evolution.

Though the  $f^{-3}$ -spectrum in high frequency range is maintained also in the later stage, another feature is noted in D4, D5 and D6 of



Fig.6. The spectrum of D4 has one small peak and two larger peaks. The small one grows the narrow dominant peak in D5. After this stage, the lower side components of this peak grow the new maximum peak in D6. This result indicates that in these stages the waves go through a modulation-demodulation cycle and the frequency of dominant components shifts to the lower frequency side. These phenomena are explained in the following section.

### TWO MECHANISMS OF EVOLUTION

The process of modulation-demodulation and frequency downshift of interfacial waves can be interpreted by assuming two different mechanisms:

The first mechanism is an interaction between the interfacial waves and turbulent eddies in the upper layer. The upper figure of Fig.7 is same as the chart D5 of Fig.5(a). The diffusion patterns of salinity in the upper layer indicates the existence of large scale turbulent eddies in this layer. It seems that these eddies have a mean vertical scale comparable to the thickness of the upper layer and have a mean period comparable to that of the interfacial waves. These eddies will cause the pressure disturbance along the interface. This pressure disturbance will supply its energy to the interfacial waves of the same horizontal scale as that of eddies as shown in Fig.8(a). By the way, the scales of the eddies are restricted under the thickness of the upper layer, which increases with discharge. It follows that the length and period of interfacial waves increase as the discharge increases. Further, if the horizontal scales of waves and eddies are mismatched, the wavetrain will modulated as shown in Fig.8(b). The cycle of matching and mismatching of two scales will lead the waves to the process of modulation-demodulation.

The second mechanism is based on the nonlinearity of interfacial waves. Both of the modulation-demodulation cycle and the downshift of frequency were observed by Lake et al.[5] in the laboratory experiment of finite amplitude surface waves. The former phenomenon was explained by the nonlinear Schrödinger equation for complex amplitude  $A(x,t)$ :

$$i\left(\frac{\partial A}{\partial t} + \frac{d\omega}{dk} \frac{\partial A}{\partial x}\right) + \mu \frac{\partial^2 A}{\partial x^2} + \nu |A|^2 A = 0, \quad (1)$$

where  $k$  and  $\omega$  are carrier wave number and carrier frequency respectively, and  $\mu$  and  $\nu$  are coefficients characteristic of the system. The displacement  $\eta(x,t)$  is related to  $A(x,t)$  by

$$\eta(x,t) = A(x,t)\exp[i(kx-\omega t)] + c.c. \quad (2)$$

The nonlinear modulational instability described by the equation(1) is summarised as follows: The nonlinear plane wave shown in Fig.9(a) is unstable to small disturbances in the form of a pair of side-band modes; at initial stage the modulational disturbances grow

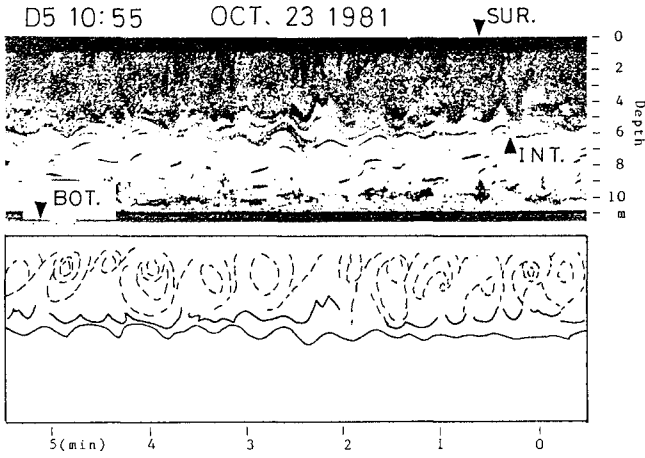


Fig.7 Large scale turbulent eddies in the upper layer.

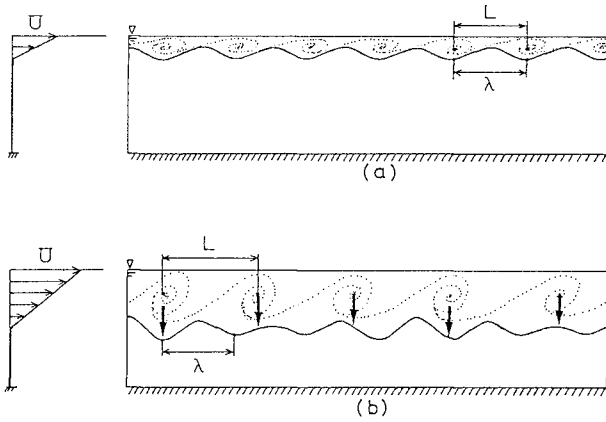


Fig.8 Eddy-wave interaction

exponentially with time; the long-time evolution is completely recursive and the side-band modes are symmetric throughout the evolution as shown in Fig.9(c)-(e). In the experiments performed by Lake et al.[5], however, the side-band components grew asymmetrically as shown in Fig.9(f)-(h) and the downshift of wave frequency was observed.

At present stage, the data is not sufficient to conclude this problem. In the following chapter, the nonlinear instability of interfacial waves is investigated by laboratory experiment.

EXPERIMENT

The apparatus used is depicted in Fig.10. The experiments were performed in the 25cmx50cmx600 cm watertank in which a two-layer density stratification had been formed by fresh water (specific gravity of 1.004) and salt water (specific gravity of 1.061). The thickness of fresh water layer was 20.5 cm and that of salt water layer was 19.5 cm. Modulated waves were generated by a wave maker at one end of the tank and absorbed by a wave absorbing beach at the opposite end. The evolution of waves was measured with seven infrared type wave amplitude gauges located at the stations 0.5m, 1m, 2m, 3m, 4m, 5m, and 5.4 m downstream of the wave maker. The wave gauges are similar to that imploved by Koop et al.[4]. The data measured at all stations were recorded on the chart of multi-pen recorder and the data

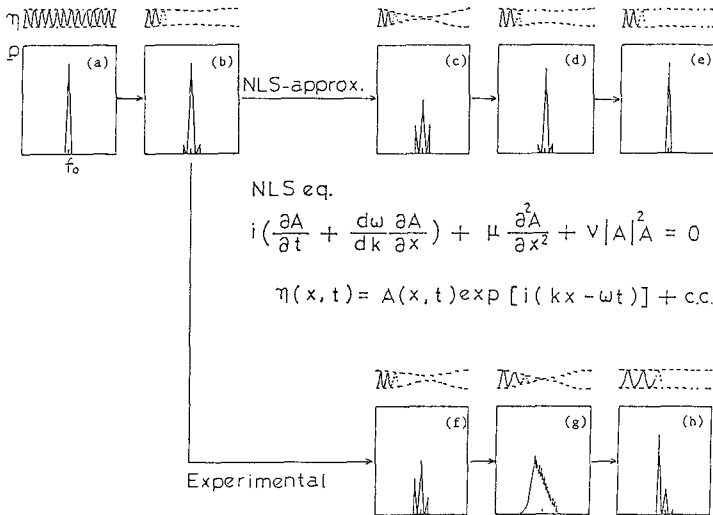


Fig.9 Nonlinear modulational instability of surface waves. Theoretical prediction based on the nonlinear Schrödinger equation and the experimental result of Lake et al.[5].

measured at stations 0.5m, 1m, 2m and 3m were recorded also in a 4-ch FM data-recorder to calculate power spectra of interfacial waves.

It is well known that wave train is unstable to modulational disturbance if the coefficients of the nonlinear Schrödinger equation(1)  $\mu$  and  $\nu$  satisfy the inequality:

$$\mu\nu > 0 \quad (3)$$

Tanaka[7] derived formulae which express the coefficients characteristic of interfacial waves as functions of the wave number, the density of two fluids and the thickness of each layer. Since the wave length is 31 cm in our experiments, the coefficients are calculated as  $\mu=8.5 \text{ cm}^2\text{sec}^{-1}$  and  $\nu=0.049 \text{ sec}^{-1}\text{cm}^{-2}$  by Tanaka's formulae[7]. Because  $\mu\nu=0.42 \text{ sec}^{-2}>0$ , the modulational instability can be expected under this condition. The growth of modulational disturbance, however, depended on the strength of initial modulation given by the wave generator because the viscosity dumped the power of small amplitude disturbance. For example, the waves which had not been modulated at the wave generator were never modulated throughout the propagation even when it satisfied the instability condition (3).

When the waves had been initially modulated, modulation-demodulation cycles were found, as shown in Fig.11. Initially modulated waves have large modulation amplitude at the station of 0.5 m, and become almost unmodulated state at 1.0 m. At the station of 2.0 m, strong modulation appears for the second time, and at 3.0 m the modulation becomes relatively weak. After these stages, waves are separated into many wave pulses. This figure resembles that measured by Lake et al.[5].

To examine whether the recurrence observed in the experiment is a nonlinear phenomenon or not, we calculated power spectra of the data measured at the stations 0.5 m, 1.0 m, 2.0 m and 3.0 m. The calculated spectra are shown in Fig.12. In Fig.12(a) the spectrum has one large peak at frequency 0.36 Hz and two smaller side-band peaks at frequencies  $0.36 \pm 0.039$  Hz. These side-band components are severely modulating the carrier waves in this stage, but they decrease in the stage of Fig.12(b) showing that the modulation are weakened. In the following stages shown in Figs.11(c) and (d), the lower side-band components increase a little as shown in Fig.12(d), whereas the fundamental components and higher side-band components decrease, in consequence, it may be regarded that the lower side-band components are growing in relative sense. This mutual exchange of spectral power between different modes indicates that the modulation-demodulation process observed in the experiment is the nonlinear process in essence.

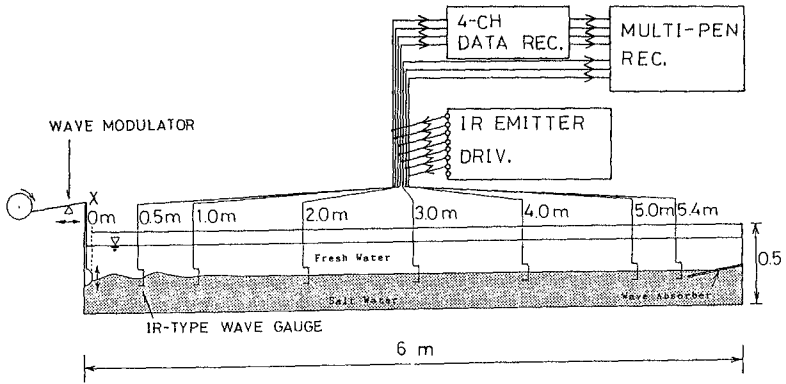


Fig.10 Experimental apparatus.

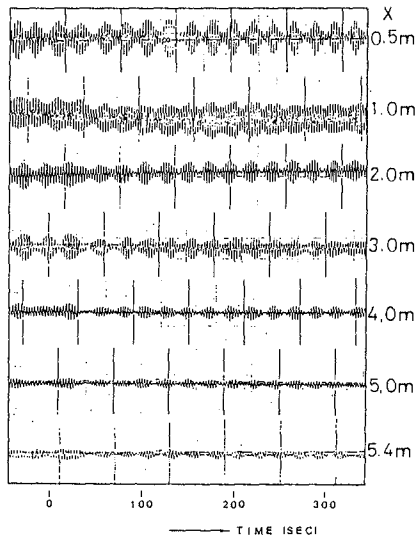


Fig.11 Wave shape observed at seven points.

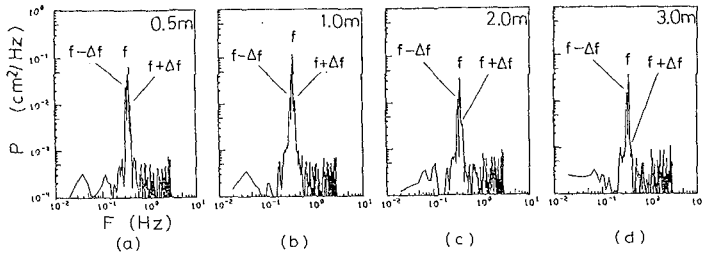


Fig.12 Power spectra.

### CONCLUSIONS

Based on the results of the field measurement of an unsteady salt wedge, it is concluded that:

1. When the river discharge increases beyond a critical value, the salt wedge recedes and interfacial waves of considerable amplitude appear along the interface of fresh and salt water.
2. These interfacial waves grow through following two stages:

In the earlier stage, the interfacial waves of small amplitude grow and become short-crested. The growth of waves in this stage is controlled by the mechanism of local breakdown discovered by Phillips[6].

In the later stage the violent wave breaking begins and the interfacial waves become an important factor of salinity diffusion.

3. The process of modulation-demodulation and frequency downshift observed in the later stage may be interpreted by either or both of the following mechanisms: (a) Interaction between interfacial waves and turbulent eddies in the fresh water layer, (b) Nonlinear modulation mechanism in large amplitude interfacial waves. But at present stage, the data are not sufficient to conclude.
4. In laboratory scale, the nonlinear modulational instability takes place also in interfacial waves if the initial modulation is sufficiently strong.

## REFERENCES

1. Benjamin, T. B. and J. E. Fair, 1967, "The disintegration of wave trains on deep water, Part 1. Theory," *J. Fluid Mech.*, Vol.27, 417-430.
2. Brekhovskikh, K., K. V. Konjaev, K. D. Sabinin and A. N. Serikov, 1975, "Short-period internal waves in the sea," *J. Geophys. Res.*, Vol.80, No.6, 856-864.
3. Fukushima, H., M. Kashiwamura and I. Yakuwa, 1966, "Studies on salt wedge by ultrasonic method," *Proc. Coastal Engg.*, 1435-1447.
4. Koop, C. G., H. Rungaldier and J. D. Sherman, 1979, "Infrared optical sensor for measuring internal interfacial wave motions," *Rev. Sci. Instrum.*, Vol.50, No.1, 20-23.
5. Lake, B. M., H. C. Yuen, H. R. Rungaldier and W. E. Ferguson, 1977, "Nonlinear deep-water waves: theory and experiment, Part 2. Evolution of continuous wave train," *J. Fluid Mech.*, Vol.83, 49-74.
6. Phillips, O. M., 1977, "The dynamics of the upper ocean," 2nd ed., Cambridge, Cambridge University Press.
7. Tanaka, M., 1982, "Nonlinear self-modulation of interfacial waves," *J. Phys. Soc. Jpn.*, Vol.51, No.6, 2016-2023.
8. Thorpe, S. A., 1971, "Experiments on the instability of stratified shear flows: miscible fluids," *J. Fluid Mech.*, Vol.46, 299-319.

## CHAPTER ONE HUNDRED NINETY NINE

### MODELING ESTUARIAL COHESIVE SEDIMENT TRANSPORT

By E. J. Hayter,<sup>1</sup> A.M. ASCE and A. J. Mehta,<sup>2</sup> M. ASCE

#### ABSTRACT

Cohesive sediment related problems in estuaries include shoaling in navigable waterways and water pollution. A two-dimensional, depth-averaged, finite element cohesive sediment transport model, CSTM-H, has been developed and may be used to assist in predicting the fate of sorbed pollutants and the frequency and quantity of dredging required to maintain navigable depths. Algorithms which describe the transport processes of redispersion, resuspension, dispersive transport, settling, deposition, bed formation and bed consolidation are incorporated in CSTM-H.

The Galerkin weighted residual method is used to solve the advection-dispersion equation with appropriate source/sink terms at each time step for the nodal suspended sediment concentrations. The model yields stable and converging solutions. Verification was carried out against a series of erosion-deposition experiments in the laboratory using kaolinite and a natural mud as sediment. A model application under prototype conditions is described.

#### INTRODUCTION

Fine, cohesive sediments in estuaries are comprised largely of terrigenous clay-sized particles. The remainder may include fine silts, biogenic detritus, organic matter, waste materials and sometimes small quantities of very fine sand. The electrical surface repulsive forces which act on each elementary clay particle are several orders of magnitude larger than the gravitational force. As a result, the physico-chemical properties of fine sediments are controlled mostly by the surface forces.

In water with a very low salinity (less than about one part per thousand, ppt) the elementary particles are usually found in a dispersed state. A slight increase in the salinity (up to 2-3 ppt) is sufficient to repress the repulsive surface forces between the particles, with the result that the particles coagulate to form units known as flocs. Each floc may consist of thousands of elementary particles. Coagulation depends upon inter-particle collision and cohesion resulting from collision. The three principle mechanisms of inter-particle collision in suspension are Brownian motion, internal fluid shearing and differential sedimentation. Cohesion of particles

<sup>1</sup>Asst. Prof., Dept. of Civil Engrg., Clemson Univ., Clemson, SC 29631.

<sup>2</sup>Assoc. Prof., Coastal and Oceanographic Engrg. Dept., Univ. of Florida, Gainesville, Fla. 32611.



is caused by the presence of net attractive surface forces. The latter condition is caused by the increased concentration of dissolved ions, which serves to depress the double layer around each particle and allow the attractive forces to predominate.

Flocs have a tendency to build up or combine under favorable fluid shearing rates to form larger units known as aggregates. The transport of aggregates in estuaries is affected by the hydrodynamic conditions and by the chemical composition of the suspending fluid. Most estuaries contain abundant quantities of cohesive sediments which usually occur in the coagulated form in various orders or degrees of aggregation. The orders of aggregation classify aggregates according to their density and shear strength. Therefore, an understanding of the transport properties of these sediments requires a knowledge of the manner in which the aggregates are transported in estuarial waters.

Fine sediment related problems in estuaries include sedimentation and water pollution. Under low flow velocities, sometimes coupled with turbulent conditions which favor the formation of large aggregates, fine sediments have a tendency to deposit in dredged cuts and navigation channels, in harbors and marinas, and behind pilings placed in water (9). In addition, the mixing zone between upland fresh water and sea water in estuaries is a favorable site for bottom sediment accumulation. Inasmuch as estuaries are often used as transportation routes, it is desirable to be able to accurately estimate the amount of dredging required to maintain navigable depths in these water bodies, and also to predict the effect of new estuarial development projects such as the construction of a port facility or dredging of additional navigation channels.

A significant portion of the pollution load in water is quite often transported sorbed to cohesive sediments rather than in the non-sorbed state (16). Thus, the importance of considering the movement of cohesive sediments in predicting the fate of pollutants (e.g. pesticides, radioisotopes, and toxic elements such as lead, mercury, cadmium and nickel) cannot be over emphasized. The properties of cohesive sediments, and in particular clays, which cause the sorption of pollutants are the large surface area to volume ratio, the net negative electrical charges on their surfaces and their cation exchange capacity.

#### TRANSPORT MODEL

Prediction of the fate of sorbed pollutants or the annual dredging requirements of a harbor can be accomplished by modeling the movement of cohesive sediments. This requires mathematical descriptions of the various physical processes which govern cohesive sediment transport under turbulent flow. Algorithms which represent the processes of redispersion, resuspension, dispersive transport, settling, deposition, bed formation and consolidation have been developed and incorporated in a two-dimensional transport model which solves the depth-averaged advection-dispersion equation (Eq. 1) using the finite element method.

$$\frac{\partial C}{\partial t} + u \frac{\partial C}{\partial x} + v \frac{\partial C}{\partial y} = \frac{\partial}{\partial x} (D_{xx} \frac{\partial C}{\partial x} + D_{xy} \frac{\partial C}{\partial y}) + \frac{\partial}{\partial y} (D_{yx} \frac{\partial C}{\partial x} + D_{yy} \frac{\partial C}{\partial y}) + S \quad (1)$$

where  $C$  = depth-averaged suspension concentration,  $u, v$  = local depth-averaged water velocity components in the  $x$  and  $y$  directions,  $D_{ij}$  = effective sediment dispersivity tensor, and  $S$  = source/sink term which accounts for the rate of sediment addition (source) due to erosion and the rate of sediment removal (sink) due to deposition. The resulting transport model, CSTM-H, is capable of predicting the horizontal and temporal variations of the depth-averaged suspended sediment concentrations and bed surface elevations in an estuary, coastal waterway or river. Previous models are not as comprehensive as they use mathematical descriptions (or algorithms) of the considered transport processes that are based on limited studies conducted prior to the early 1970's. In this study field evidence and the considerable amount of experimental research that has been conducted on cohesive sediment transport mechanics since that time have been used to develop new algorithms. A description of the algorithms is given below.

Surficial layers of estuarial beds, typically composed of flow-deposited cohesive sediment aggregates, are stratified with respect to bed shear strength and density, and occur in three different states: stationary suspensions, partially consolidated (or consolidating) beds and settled (fully consolidated) beds. Stationary suspensions, which may be regarded as extremely under-consolidated soil, develop whenever the settling rate of concentrated mobile suspensions exceeds the rate of self-weight consolidation. They tend to have a very high water content and low shear strength and are redispersed, or mass eroded, when subjected to an excess bed shear stress, i.e. when the bed shear stress is greater than the mechanical shear strength of the bed surface. That portion of the suspension that is not redispersed undergoes: 1) consolidation, due to overburden resulting from the weight of the overlying sediment which crushes the aggregate network below, and 2) thixotropic effects, i.e. slow rearrangement of deposited aggregates attributed to internal energy and unbalanced internal stresses, both of which alter the order of aggregation of the sub-surface bed layers. This results in a vertical stratification of the bed with respect to density and shear strength, with both properties typically increasing with depth (11). Differential settling caused by sorting processes is another cause of stratified bed formation.

Partially consolidated deposits have a somewhat lower water content and higher shear strength, and are eroded aggregate by aggregate when subjected to an excess shear stress. Settled beds possess a much lower water content, a much higher shear strength and as well are resuspended aggregate by aggregate when subjected to an excess shear, unless the excess shear stress is very large in which case large chunks of material may detach from the bed and be entrained. Both stationary suspensions and partially consolidated beds undergo consolidation, with the bed density and shear strength increasing with time of consolidation. In settled beds, the shear strength and density profiles exhibit relatively uniform properties over depth.

To facilitate the modeling of changes in the bed surface elevation due to erosion, deposition and consolidation, the bed is treated in the following manner: 1) it is discretized into layers and 2) bed properties, i.e. density and shear strength, are assumed to be spatially (in the x-y plane) invariant within each element, but not so from element to element, in order to account for inter-element spatial variances in shoaling and/or scouring patterns. These two factors are explained below.

The bed in each element is considered to be composed of two sections: 1) the original, settled bed that is present at the start of modeling and 2) new deposits located on top of the original bed, that result from deposition during model simulation. Each of these two sections is divided into a number of layers in order to specify the actual shear strength and bulk density profiles in the model. The new deposit section is subdivided into two sub-sections, the top referred to as unconsolidated new deposit (UND) layers and the bottom as partially consolidated new deposit (PCND) layers (Fig. 1). The number of layers indicated in Fig. 1 for each of the three bed sections are not fixed, as each section can be assigned any number of layers. Within each layer the bed shear strength and density are assumed to vary in a linear manner with depth. Previous models have used a constant bed shear strength and density for each layer, and only a single layer for the partially consolidated bed section. Therefore, the stratified nature of partially consolidated beds is not represented in these models.

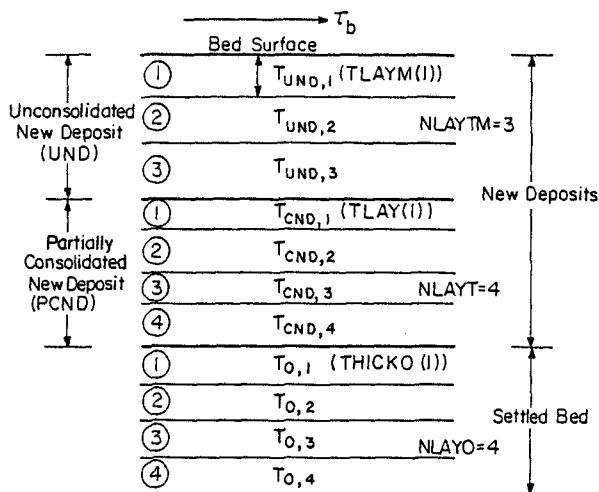


Fig. 1 Bed Schematization Used in Bed Formation Algorithm (4).

Stationary suspensions are represented as being the top section of the layered bed model, even though they do not constitute a true bed, in order to account for the subsequent redispersion and/or consolidation of these suspensions. However, the time-varying thickness of the bed in each element is equal to the sum of only the NLAYT (number of PCND layers) PCND layers and the MLAYO settled bed layers.

The bed formation algorithm uses the following procedure to form the new deposit bed layer(s). The dry sediment mass per unit bed area per element,  $M_D$ , read in as an initial condition if a new deposit is initially present on top of the settled bed in any element, or deposited during the modeling (as determined by the deposition algorithm) is used in conjunction with the assumed linear bed density profiles in the UND and PCND layers to iteratively solve for the thickness of bed formed by  $M_D$  for each element where  $M_D > 0$ . The bed structure (i.e. bed shear strength and density profiles) of the existing bed is adjusted to account for the added sediment mass. During periods of deposition, first the UND layers are filled and then the PCND layers. The bottom PCND layer can never fill up; therefore, continuing deposition is accounted for by increasing the thickness of this layer, while the thicknesses of the overlying UND and PCND layers remain the same. This particular filling sequence was used in order to account for the consolidation of the sediment bed due to overburden during the bed formation phase by virtue of the increasing bed shear strength and density values with depth. Previous models use the assumed constant bed density value in each layer to solve explicitly for the bed thickness formed by  $M_D$ .

The erosion algorithm simulates the erosion of saturated, flow-deposited cohesive sediment beds on an element by element basis in the following manner. Redispersion of stationary suspensions (i.e. the UND layers) is represented by instantly reentraining the thickness of the bed above the level at which the bed shear stress,  $\tau_b$ , is equal to the bed shear strength,  $\tau_c$ . The mass of sediment that is redispersed per time-step is determined from the linearly varying  $\tau_c$  and dry sediment bed density,  $\rho$ , profiles in each stationary suspension layer. The average resuspension rate,  $\epsilon$ , of partially consolidated bed layers over one time-step,  $\Delta t$ , is given by the following empirical law that is analogous to the rate expression which results from a heuristic interpretation of the rate process theory of chemical reactions (11):

$$\epsilon = \epsilon_{0i} \exp\left\{\alpha_i \left(\frac{\tau_b - \tau_c}{\tau_c}\right)\right\} \quad (2)$$

where  $\epsilon_{0i}$  and  $\alpha_i$  are empirical coefficients for the  $i$ -th PCND layer. In Eq. 2,  $\tau_c$  is taken to vary linearly with  $z_b$ , the depth below the sediment-fluid interface, in the discretized manner explained previously. The rate expression given by Eq. 2 for PCND layers indicates that the resuspension rate varies exponentially with the excess bed shear stress,  $\tau_b - \tau_c$ . The average resuspension rate of settled bed layers is given by an empirical expression that is proportional to the first term of a Taylor series expansion of Eq. 2, and thus is linearly proportional to the excess shear stress (8). The proportionality coefficient is termed the erodibility constant,  $M_i$ , where the subscript  $i$  represents the value of  $M$  for the  $i$ -th settled bed layer

below the new deposit bed sections. The dry sediment mass and bed thickness of PCND or settled bed layers eroded per time-step are determined with the appropriate rate expression as functions of the time-varying  $\tau_c$  and  $\rho$  profiles using an iteration routine. New layer thicknesses and  $\tau_c$  and  $\rho$  profiles are then determined.

The effect of salinity,  $S$ , on the bed shear strength and hence on the erosion rate of that bed, as determined from laboratory resuspension tests is incorporated into the erosion algorithm. The bed shear strength of a natural mud was found to nearly double in value, in a linear manner, between  $S \approx 0$  and 2 ppt, and thereafter (for  $S > 2$  ppt) was found to remain practically constant (5). Consequently, the rate of erosion is predicted to decrease with increasing salinity up to 2 ppt, where it becomes essentially invariant with respect to salinity. The mud used in these tests was from Lake Francis, Nebraska, and consisted of particles 50% of which were finer than  $2\mu\text{m}$ , with montmorillonite, illite, kaolinite and quartz being the predominant minerals. It had a cation exchange capacity (CEC) of 100 milliequivalents/100 grams. This high CEC value indicates a higher percentage of montmorillonite than the other two clay minerals.

In the erosion algorithm, redispersion and resuspension are simulated to occur in unsteady flows only during temporally accelerating flows, i.e.  $\tau_b(t+\Delta t) > \tau_b(t)$ . Thus, even though  $\tau_b(t+\Delta t)$  and/or  $\tau_b(t)$  may be greater than  $\tau_c(z_b=0)$ , no erosion will be predicted if  $\tau_b(t+\Delta t) < \tau_b(t)$ . This stipulation for the occurrence of erosion, and an analogous one for deposition, is based on an interpretation of typically observed Eulerian concentration-time records in estuaries. Laboratory evidence further suggests that under accelerating flows, erosion occurs without redeposition of the eroded sediment, and that during decelerating flows, sediment deposits without reentrainment of the deposits (10,11,16). During periods of steady flows, erosion or deposition may occur, but never simultaneously.

The dispersive transport terms in Eq. 1 account for the transport of sediment by processes other than advective transport. Some of these processes include the effects of transverse and vertical velocity variations in bounded shear flows and turbulent diffusion. Thus, the effective sediment dispersion coefficients in Eq. 1 must include the effect of all processes whose scale is less than the grid size of the model or what has been averaged over time and space.

In modeling dispersion of a nonconservative constituent, e.g. sediment, it is essential to determine which of the four primary dispersion mechanisms - baroclinic circulation, shear-flow dispersion, bathymetry induced dispersion and wind-induced circulations - are important in the water body being modeled. Because of well-known problems in identifying, describing and modeling the combined effects of the various dispersion mechanisms, the dispersion algorithm in CSTM-H includes only shear flow dispersion. Following the analysis of Holley (6), it is assumed that the dispersion in wide, vertically well mixed estuaries is associated primarily with the vertical shear. The limitations of this assumption, which determine the applicability of such a dispersion algorithm, are consistent with those associated with a two-dimensional, depth-averaged model.

The shear flow dispersion algorithm uses the Reynolds analogy between mass and momentum transfer, which was verified by Jobson and Sayre (7) for sediment particles less than about 100  $\mu\text{m}$  in diameter, and calculates the four components of the two-dimensional sediment dispersivity tensor (Eq. 3) using the following formulation derived by Fischer (3) for bounded shear flows:

$$D_{ij} = 0.04 u_i u_j d^2 I_{ij} / \bar{E} \quad i, j = 1, 2 \quad (3)$$

in which  $u_i$  = local depth-averaged velocity in the  $x_i$ -direction,  $\bar{E}$  = depth-averaged diffusion coefficient in the  $z$  (vertical) direction, and  $I_{ij}$  is a dimensionless triple integral which expresses correlation between the rate of cross-stream mixing and the slope of the vertical velocity profile. Fischer (3) recommended that a value of 0.10 be used for  $I_{ij}$  since 1) in most investigations the vertical velocity profiles,  $u(z)$  and  $v(z)$ , and the vertical turbulent diffusion coefficient,  $E_z$ , are not known with a high degree of accuracy, and 2) the value of  $I_{ij}$  is fairly insensitive to the shape of the vertical velocity profile. The value of  $\bar{E}$  is given by  $0.067 u_* d$ , in which  $u_*$  = friction velocity. This expression for  $\bar{E}$  results from integrating the expression for  $E_z$  obtained by Elder (2) for shear flow down an infinitely wide inclined plane over  $d$ . Values of  $D_{ij}$  are calculated at each time step using the specified nodal values of  $u$ ,  $v$ ,  $u_*$  and  $d$ .

The deposition algorithm integrates the concepts proposed by various investigators (9,10) and represents a unified model of this process. The rate of deposition is given by

$$\frac{dC}{dt} = \frac{W'_s C}{d} \quad (4)$$

where  $W'_s$  = apparent sediment settling velocity. Laboratory experiments have shown that  $W'_s$  is a function of the bed shear stress, suspension concentration,  $C$ , and salinity,  $S$ . Figure 2 shows various ranges in which  $W'_s$  is defined. Deposition is predicted to occur only in decelerating flows, i.e.  $\tau_b(t + \Delta t) < \tau_b(t)$ , when  $\tau_b$  is less than the maximum shear stress at which deposition can occur,  $\tau_{b\text{max}}$ . In Ranges IA and IIA the sediment aggregates settle independently without much mutual interference, and therefore  $W'_s$  is independent of  $C$ . In Range IB, which corresponds to concentrations between approximately  $C_1 = 0.1 - 0.7$  gram/liter (g/l) and  $C_2 = 10-15$  g/l,  $W'_s$  increases with increasing concentration due to accompanying increase in inter-aggregate collisions, and therefore increased mutual interference. In Range IC (for  $C > C_2$ ),  $W'_s$  decreases with increasing concentration. At such high concentrations the sediment suspension, often referred to as fluid mud or mud cake, hinders the upward flux of water expelled by consolidation of the lower suspension (9). This type of settling is referred to as hindered settling. In Range IIB,  $W'_s$  increases with increasing suspension concentration and is obtained from a log-normal relationship (10). Expressions for  $W'_s$  as a function of  $C$ ,  $\tau_b$  and  $S$  for the five settling domains are given by Hayter (4).

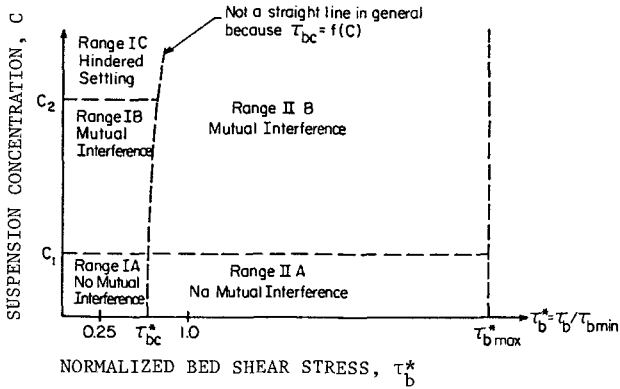


Fig. 2 Apparent Settling Velocity Description in Domains Defined by Suspended Sediment Concentration and Bed Shear Stress.  $\tau_{bmin}^*$ ,  $\tau_{bmax}^*$ ,  $\tau_{bc}^*$  and  $\tau_b^*$  are characteristic values of  $\tau_{bm}^*$  (4).

The deposition rates of the Lake Francis mud were found to have a slight dependence on salinity. A power relationship between  $W_s$  and  $S$  of the form  $W_s \propto S^n$ , with  $n = 0.13$ , was determined from analysis of deposition tests conducted at salinities ranging from 0 to 35 ppt and under bed shear stresses varying from 0.0 to 0.30  $N/m^2$  (5).

The amount of sediment deposited onto the bed per time-step is determined on an element-by-element basis by integrating Eq. 4 over  $\Delta t$ , and the thickness and structure (i.e. density and shear strength profiles) of the bed are adjusted accordingly by the previously described bed formation algorithm. When deposition is not occurring (i.e. after bed formation) the bed is simulated to undergo consolidation, which is the result of soil mass volume reduction accompanied by outflow of water from the soil pores (primary consolidation), and plastic deformation of the bed (i.e. soil aggregates) under overburden forces (secondary consolidation).

The consolidation algorithm accounts for the consolidation of a stationary suspension and partially consolidated bed by increasing the bed density and bed shear strength and decreasing the bed thickness with time. Consolidation is considered to begin after the bed formation process is complete, at which time the bed thickness will be maximum. Laboratory experiments have revealed that after a consolidation time,  $T_{dc}$ , of a certain magnitude,  $T_{dc1}$ , stationary suspensions undergo resuspension (as opposed to redispersion with  $T_{dc} < T_{dc1}$ ) when subjected to an excess shear stress (4). Accordingly, the dry sediment mass in a stationary suspension for which  $T_{dc} = T_{dc1}$  ( $T_{dc1}$  was determined to be equal to three hours in a laboratory test using kaolinite) is incorporated into the partially consolidated bed, and therefore will undergo resuspension when subjected to an excess bed shear.

The following normalized relationship was found between the depth-averaged dry sediment density  $\bar{\rho}$  and  $T_{dc}$  and is used in the consolidation algorithm to determine  $\bar{\rho}$  (4).

$$\frac{\bar{\rho}}{\bar{\rho}_{\infty}} = 1 - \alpha \exp(-\lambda T_{dc}) \quad (5)$$

where  $T_{dc}^1 = T_{dc}/T_{dc\infty}$ ,  $\bar{\rho}_{\infty}$  = final (i.e. fully consolidated) mean bed density at consolidation time  $T_{dc\infty}$ . Least squares analysis gave  $\alpha = 0.845$ ,  $\lambda = 6.58$ . Owen (14) found  $\bar{\rho}_{\infty}$  to vary linearly with the initial suspension concentration.

The dry sediment density profile,  $\rho(z_b)$ , found by Owen (15) and Thorn and Parsons (17) for four natural muds with  $T_{dc} \geq 48$  hours can be expressed as

$$\frac{\rho(z_b)}{\bar{\rho}} = \beta \left(\frac{H-z_b}{z_b}\right)^{\delta} \quad (6)$$

where  $z_b$  = depth below the bed surface and  $H$  = bed thickness. Both  $\beta$  and  $\delta$  were found to be constants for  $T_{dc} > 48$  hours (4). Using  $\bar{\rho}$  determined by Eq. 5, the density profile  $\rho(z_b)$  is determined from Eq. 6.

Due to the limited available information on bed shear strength profiles in cohesive sediment beds, the increase of the shear strength,  $\tau_c$ , of a bed with  $T_{dc}$  is accounted for in the algorithm through use of a power law relationship between  $\rho$  and  $\tau_c$  (14,17)

$$\tau_c = \zeta \rho^{\xi} \quad (7)$$

with  $\zeta = 6.85 \times 10^{-6}$  and  $\xi = 2.44$  for Avonmouth mud (14).

The variation of  $\rho(z_b)$  and  $\tau_c(z_b)$  with  $T_{dc}$  is determined using the empirically determined relationships given by Eqs. 5-7. The thickness of the bed is reduced to account for the expulsion of pore water during consolidation, and to insure that sediment mass in the bed is conserved. The new deposit bed section (composed of stationary suspension and partially consolidated bed) of the layered bed is further divided into a finite number of strata in order to account for repeated periods of deposition, as typically occur in estuaries due to the oscillatory tidal flow. The top stratum may be composed of a stationary suspension and partially consolidated bed, whereas the buried strata are composed of just partially consolidated sections. The degree of consolidation of a particular stratum is accounted for by using a separate consolidation time for each stratum.

The finite element solution routine developed by Ariathurai (1) was modified to include the two cross product dispersion coefficients,  $D_{xy}$  and  $D_{yx}$ . The Galerkin weighted residual method is used to solve the advection-dispersion equation (Eq. 1) for the nodal depth-averaged suspended sediment concentrations, and a Crank-Nicholson type finite difference formulation is used to solve the temporal problem, i.e. advance the spatial solution in time. The model yields stable and converging solutions. The accuracy of the solution is affected when



the Peclet number becomes too large (greater than  $10^2$ ) or too small (less than  $10^{-3}$ ).

#### MODEL SYNOPSISIS

A synopsis of the operations performed by CSTM-H during each time-step and the data required is given below.

The average bed shear stress induced by the turbulent flow velocity of the suspending fluid is calculated for each element. Then the amount of sediment, if any, that is deposited onto or resuspended from the bed in each element during the current time-step is determined using the deposition and erosion algorithms, respectively. The dispersion algorithm then calculates the values of the four components of the two-dimensional sediment dispersivity tensor. Using these values and the prescribed velocity field and concentration boundary conditions, Eq. 1 is solved for the depth-averaged suspended sediment concentration at each node for the next time-step. The new bed elevation in each element is determined by adding or subtracting the thickness of sediment deposited onto or resuspended from, respectively, the bed profile that existed during the previous time-step. Lastly, the consolidation algorithm calculates for each element the increase in bed density and shear strength and the decrease in bed thickness due to consolidation during the previous time-step.

The following four types of data are required: 1) finite element grid of the system to be modeled, 2) two-dimensional depth-averaged velocity and salinity fields, 3) concentration initial and boundary conditions and 4) properties of the cohesive sediments which characterize their erosion, deposition, bed formation and consolidation.

#### VERIFICATION

Model verification was carried out against four erosion-deposition experiments, three of which were performed in an 18m long, 0.61 m wide recirculating flume and the fourth in an 0.76 m mean radius rotating annular flume. The bed shear stress history for one of the three experiments performed in the recirculating flume using kaolinite in tap water was the following: bed shear stress  $\tau_b = 0.06$  N/m<sup>2</sup> for two hours, then increased to 0.12 N/m<sup>2</sup> for the third and fourth hours, and finally decreased to 0.03 N/m<sup>2</sup> for the final five hours. In this nine hour experiment the bed was prepared by mixing the sediment-water suspension at a shear stress of approximately 0.5 N/m<sup>2</sup> for four hours, after which the flow was reduced to a shear stress of approximately 0.025 N/m<sup>2</sup> for eight hours. The flow in the flume was then completely stopped and the flow deposited bed was allowed to undergo consolidation for 3 hours. Figure 3 shows both the measured and predicted depth-averaged suspension concentration-time record. Satisfactory agreement between measurement and prediction is seen for this experiment, and a similar degree of agreement was obtained for the other two experiments.

The experiment in the rotating flume was conducted using the Lake Francis mud in water with 10 ppt sodium chloride concentration. The

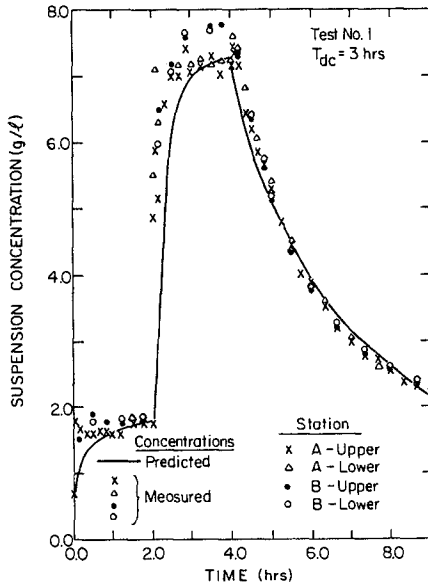


Fig. 3 Measured and Predicted Suspension Concentration for Experiment in Recirculating Flume (4).

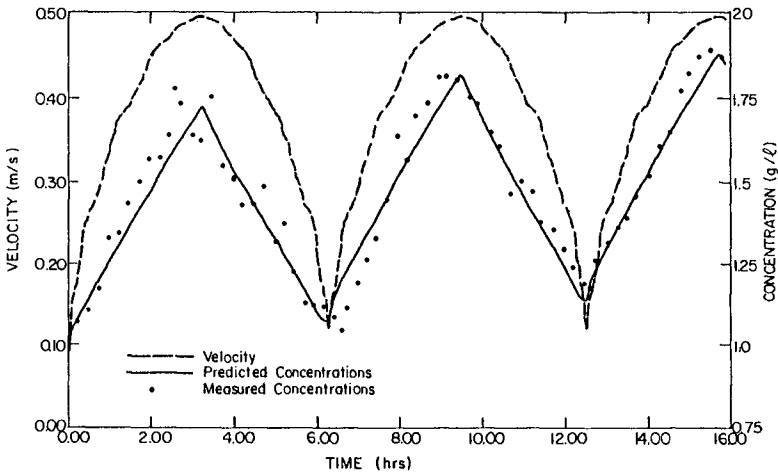


Fig. 4 Velocity - Time Record and the Measured and Predicted Suspension Concentrations for Experiment in Rotating Flume (4).

sediment-water mixture was mixed at a shear stress of  $1.7 \text{ N/m}^2$  for 24 hours, after which the flume was stopped and the sediment allowed to deposit and undergo consolidation for 40 hours. A micro-computer driven flow control system was used to generate semi-diurnal, constant water depth (30 cm) tidal flow shown in Fig. 4. Also shown in this figure are the measured and predicted suspension concentration-time records. Except for the short time-lags between predicted and measured concentrations at the times of maximum and minimum velocities, satisfactory agreement was again achieved. The empirical parameters which characterize erosion, deposition and consolidation of the sediment used in each experiment were determined in laboratory tests. An important conclusion from the verification process is that laboratory measured, transport-related parameters can be successfully used for model simulation.

#### APPLICATION

The utility of the model was shown by simulation of sedimentation in Camachee Cove Yacht Harbor, located adjacent to the Intercoastal Waterway in St. Augustine, Florida. An aerial view of the basin is shown in Fig. 5. The semi-rectangular shaped basin has approximate dimensions of 300 m in length and 100 m in width, and the entrance channel is 60 m wide. The mean depth of the basin is approximately 3 m. The hydrographic and sediment data required to model both the predominantly tide-induced circulation and fine sediment transport in the basin were collected by the Coastal Engineering Laboratory of the University of Florida. The hydrodynamic modeling was performed using the two-dimensional (depth-averaged) finite element flow model RMA2 (13). Results from flow modeling as well as the required sediment data measured during the field study were used in modeling sediment transport in the basin. The results are shown in Fig. 6, which shows contours of the predicted amount (thickness) of sediment deposition in centimeters per year. The observed shoaling pattern is not unexpected, as the greatest amount of sediment deposition would occur near the entrance because of the extremely small flow velocities (maximum  $\sim 10^{-2} \text{ m/sec}$ ) in that vicinity and throughout the basin as well. A mean shoaling rate of 15.1 cm/year was predicted, which is reasonably close to the measured 14.6 cm/year (12). The latter value was obtained by comparing bathymetric surveys conducted in March, 1980 and September, 1982.

#### SUMMARY AND CONCLUSIONS

Previous fine, cohesive sediment transport models have used transport algorithms based on limited studies conducted prior to the early 1970's. Utilization of contemporary laboratory experimental and field evidence to develop algorithms which describe erosion, dispersion, settling, deposition and bed consolidation has resulted in a model with predictive capability. The following is a summary of improvements over previous models: 1) The model includes the cross product dispersion coefficients in the two-dimensional advection-dispersion equation; 2) includes a dispersion and bed consolidation algorithm; 3) calculates the erosion rate of partially consolidated beds as an exponential function of the excess bed shear stress; 4)



Fig. 5 Aerial View of Camachee Cove Yacht Basin (4).

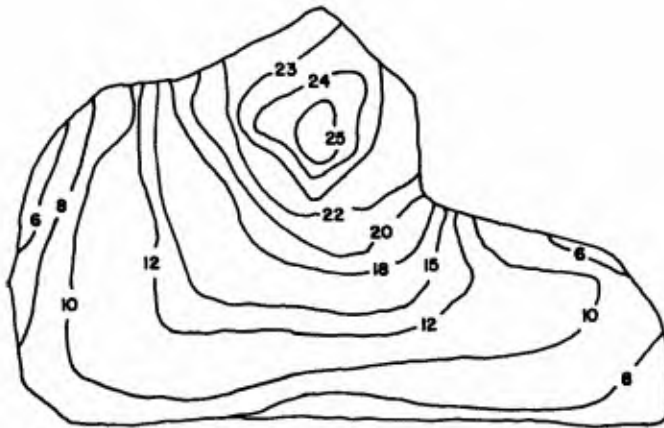


Fig. 6 Predicted Sedimentation Contours for Camachee Cove Yacht Basin, in cm/year (12).

represents the stratified nature of consolidating sediment beds by assuming a linear intra-layer bed density and shear strength variation (instead of constant values) in the layered bed model in determining the mass of sediment eroded or thickness of bed formed by deposition of a given sediment mass; 5) accounts for flow acceleration in determining occurrence of erosion or deposition under a given bed shear stress; 6) predicts that deposition occurs in decelerating flows when  $\tau_b < \tau_{bmax}$ , whereas previous models predict deposition only when  $\tau_b < \tau_{bmin}$  in either accelerating or decelerating flows. Thus, deposition is predicted to occur in the previous models during only a small percentage (e.g. 20% for kaolinite in tap water) of the shear stress range in which deposition has been observed to occur in laboratory steady flow experiments. 7) The model accounts for the effect of salinity on the rates of erosion and deposition of fine sediments. This feature of the model is particularly important in upstream estuarial reaches as well as in downstream regions when high runoff due to storms reduces the salinity.

A two-dimensional, depth-averaged model such as CSTM-H can strictly be applied only to well-mixed estuaries, harbors and basins where the horizontal dimensions of the water body are at least one order of magnitude greater than the vertical dimension. Applications to partially mixed water bodies or especially to highly stratified water bodies should be made when only extremely rough estimates of some sedimentary process, e.g. shoaling rate, are required.

A significant conclusion from this study was that laboratory measured transport-related parameters can satisfactorily reproduce the concentration-time history in laboratory erosion-deposition experiments and a mean sedimentation rate in the prototype, given settling velocity values derived from field measurements in the latter case.

#### ACKNOWLEDGMENT

The work was performed while the first author was a graduate student at the University of Florida. Support by the Water Resources Division of the U.S. Geological Survey under their thesis support program is gratefully acknowledged. Simulation of sedimentation in Camachee Cove Yacht Harbor was carried out with the help of support from Florida Sea Grant College, NOAA, through project R/C-6.

#### REFERENCES

1. Ariathurai, R., "A Finite Element Model for Sediment Transport in Estuaries," Ph.D. Dissertation, University of California, Davis, California, 1974.
2. Elder, J.W., "The Dispersion of Marked Fluid in Turbulent Shear Flow," Journal of Fluid Mechanics, Vol. 5, 1959, pp. 544-560.
3. Fischer, H.B., "On the Tensor Form of the Bulk Dispersion Coefficient in a Bounded Skewed Shear Flow," Journal of Geophysical Research, Vol. 83, No. C5, May, 1978, pp. 2373-2375.

4. Hayter, E.J., "Prediction of Cohesive Sediment Transport in Estuarial Waters," Ph.D. Dissertation, University of Florida, Gainesville, Florida, 1983.
5. Hayter, E.J., and Mehta, A.J., "Modeling of Estuarial Fine Sediment Transport for Tracking Pollutant Movement," UFL/COEL-82/009, Coastal and Oceanographic Engineering Department, University of Florida, Gainesville, Florida, December, 1982.
6. Holley, E.R., "Unified View of Diffusion and Dispersion," Journal of the Hydraulics Division, ASCE, Vol. 95, No. HY2, March, 1969, pp. 621-631.
7. Jobson, H.E., and Sayre, W.W., "Vertical Transfer in Open Channel Flow," Journal of the Hydraulics Division, ASCE, Vol. 96, No. HY3, March, 1970, pp. 703-724.
8. Kandiah, A., "Fundamental Aspects of Surface Erosion of Cohesive Soils," Ph.D. Dissertation, University of California, Davis, 1974.
9. Krone, R.B., "Flume Studies of the Transport of Sediment in Estuarial Shoaling Processes," Final Report, Hydraulic Engineering Laboratory and Sanitary Engineering Research Laboratory, University of California, Berkeley, California, June 1962.
10. Mehta, A.J., "Depositional Behavior of Cohesive Sediments," Ph.D. Dissertation, University of Florida, Gainesville, Florida, 1973.
11. Mehta, A.J., Parchure, T.M., Dixit, J.G., and Ariathurai, R., "Resuspension Potential of Deposited Cohesive Sediment Beds," in Estuarine Comparisons, V.S. Kennedy Editor, Academic Press, New York, 1982, pp. 591-609.
12. Mehta, A.J., Ariathurai, R., Maa, P., and Hayter, E.J., "Fine Sedimentation in Small Harbors," UFL COEL-TR/051, Coastal and Oceanographic Engineering Department, University of Florida, Gainesville, Florida, September, 1984.
13. Norton, W.R., King, I.P., and Orlob, G.T., "A Finite Element Model for Lower Granite Reservoir," Walla Walla District U.S. Army Report, prepared by Water Resources Engineer, Inc., Walnut Creek, California, March 1973.
14. Owen, M.W., "A Detailed Study of the Settling Velocities of an Estuary Mud," Report No. INT 78, Hydraulics Research Station, Wallingford, England, September, 1970.
15. Owen, M.W., "Erosion of Avonmouth Mud," Report No. INT 150, Hydraulics Research Station, Wallingford, England, September, 1975.

16. Parchure, T.M., "Erosional Behavior of Deposited Cohesive Sediments," Ph.D. Dissertation, University of Florida, Gainesville, Florida, 1984.
17. Thorn, M.F.C., and Parsons, J.G., "Erosion of Cohesive Sediments in Estuaries: An Engineering Guide," Proc. Third International Symposium on Dredging Technology, Paper F1, Bordeaux, France, March, 1980.

## CHAPTER TWO HUNDRED

WATERQUANTITY AND -QUALITY RESEARCH FOR THE RHINE MEUSE ESTUARY

BY  
A. Roelfzema<sup>1)</sup>, M. Karelse<sup>2)</sup>, A.J. Struijk<sup>3)</sup> and M. Adriaanse<sup>4)</sup>

### ABSTRACT

In commission of the Dutch Government (Ministry of Public Works), the Delft Hydraulics Laboratory carries out a long term research programme on the water quantity and water quality of the Rhine-Meuse estuary. The researchprogramme has to provide the necessary hydraulic data as input for a management decision-making process. The programme is based on an "integrated approach philosophy" with respect to the various subjects to be studied and the research tools to be used (data from nature, hydraulic model, mathematical models and fundamental research). The paper presents the essentials and backgrounds of the research programme and discusses some first results.

### 1. INTRODUCTION

Estuaries play an important role in life and economy. Many important cities have developed on their shores where navigation meets the inland transport systems and man has tried to interfere with estuarine systems in various ways. Hydraulically speaking estuaries are far from simple (e.g. Fischer et al, 1979). The tide penetrates, causing the water to rise and fall and to flow in and out with the regularity of its astronomical cause. Seasonal flows of fresh water from the river(s) traverse the estuaries and mix with the waters of the sea. The heavier sea water tries to intrude along the bottom, which is counteracted by internal friction and mixing with the fresh water.

Estuarine waters are far from pure. Salt penetrates from the sea, but also the "fresh" river flows carry a "natural" load of millions of tons of dissolved matter. Moreover, estuaries are often polluted by a diversity of wastes and heat from cities, industries and agriculture. Especially the suspended fine sediments absorb large quantities of chemical substances, thus contributing to the transportation and deposition of pollutants in the system.

Estuarine management tries to obtain an optimum balance between the different, often conflicting, interests. Essential for the management decision making process on estuarine system is the input of water quantity and water quality parameters, see figure 1.1. These parameters must be estimated by hydraulic research.

1) Project-leader, Delft Hydraulics Laboratory, The Netherlands

2) Research engineer, Delft Hydraulics Laboratory, The Netherlands

3) Senior-engineer, Ministry of Public Works (Rijkswaterstaat)

4) Research engineer, Ministry of Public Works (Rijkswaterstaat)



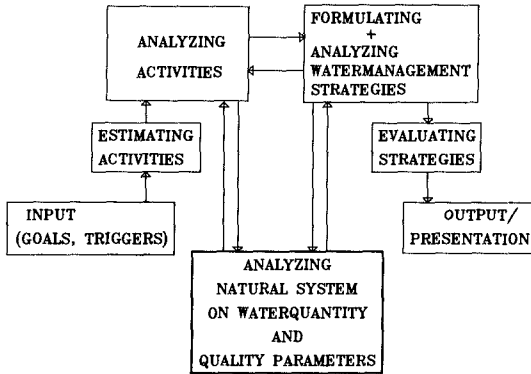


Fig.1.1 PROCESS WATERMANAGEMENT ANALYSIS

The Rhine-Meuse estuary is situated in the south-western part of the Netherlands and covers a densely populated area. The estuary system consists of various branches, forming a network with the Rotterdam harbours in the northern part and large tidal areas in the southern part, see figure 1.2. At the upstream side the system is bounded by three fresh-water river branches, the downstream salt tidal boundary consists of a free and a regulated outflow into the North sea.

Salinity intrusion is of the partly mixed and layered type (Van der Heijden, de Jong, Kuijper, Roelfzema, 1984) and regularly reaches upstream of Rotterdam. The Rijkswaterstaat (Dutch Government, Ministry of Public Works) is responsible for the management of the Rhine Meuse estuary. The water quantity and -quality problems that play a role are safety against inundation, maintenance of infrastructural works, water supply for industrial, agriculture and public use, discharging and flushing the system and the accessibility for navigation. These management aspects show interferences and conflicting interests. The management aspects have been translated into a number of subjects on which hydraulic research is carried out. These interrelated subjects, are :

- flood and flood control
- morphological stability of the system (sedimentation and erosion)
- distribution and discharge of (fresh) water
- salinity intrusion (intake locations of fresh water)
- siltation (dredging of harbours and ecological impacts)
- dispersion of heat and waste
- discharge of ice

Guidelines for the management and therefore also for the research on these subjects are, amongst others, the economy (e.g. with respect to the dredging) and laws and legal statements with respect to the distribution of fresh water, pollution of surface water and to salinity intrusion.

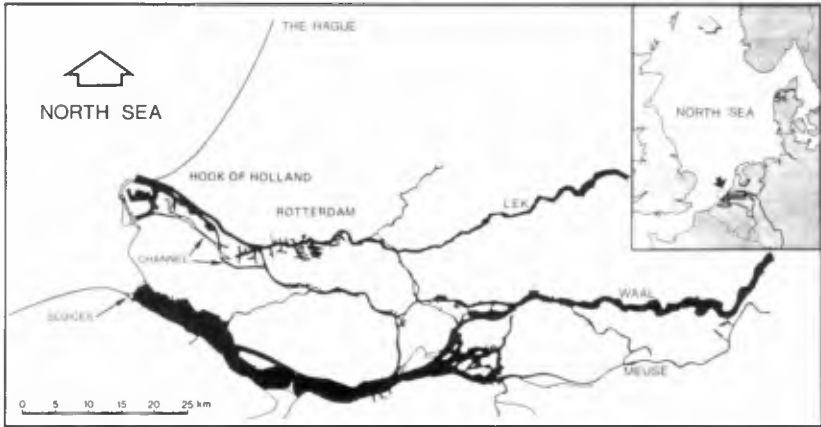


Fig. 1.2 PLAN VIEW RHINE-MEUSE ESTUARY



## 2. THE RESEARCH PROGRAMME

Relevant for the set up of the research programme are the complexity of the physical processes in the estuary system, the variety of water quantity and -quality problems to be studied and the required accuracies of the answers to be given. The physical processes and the variety of problems have a common basis: the inhomogeneous tidal flows in the system (= affected by the density differences between sea and rivers). These inhomogeneous tidal flows are primary determining the physics in the system.

Understanding these flow phenomena under various hydraulic and geometrical circumstances is therefore essential for analyzing and interpreting research results on the different problems, separately and with their interference, see figure 2.1. A systematic investigation on these various conditions, in this way, forms the core of the long term research programme. Within this systematic investigation the main objectives are to solve practical problems on water quantity and/or quality and to provide data based on which optimum water management strategies can be developed. Additional objectives are the development of mathematical models and the development of techniques for research and interpretation.

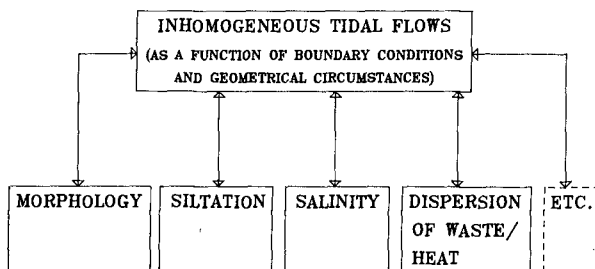


Fig.2.1 PHYSICAL RELATIONS

The systematic investigation on various hydraulic and geometrical circumstances includes seven groups of similar subjects. The groups are a result of an analysis of the physics of nature and of the water quantity and -quality problems. The question has been to estimate the ranges of the hydraulic and geometrical conditions, regarding the present situation of the estuary system and the possible changes due to nature or due to man-made measures. The resulting groups are:

- boundary conditions (tides, including meteorological effects on mean sea levels, and riverdischarges)
- closing or opening harbours or branches
- withdrawals and changing the discharges between riverbranches
- deepening or raising bottom levels of branches
- resistance and mixing of branches
- dispersion of heat and waste, and
- small scale measures like groynes, bars (to be removed), bottomgroynes (to be build), cut-off bends, etc.

For these groups the relevant parameters have to be investigated in a systematic way for a wide, but realistic, range including the direct practical problems. Because of the necessity of an unambiguous comparison of research results the total programme is carried out under standardized boundary conditions. Depending on the accents to be laid, different combinations of boundary conditions, resulting from the first group, can be used (neap tide/spring tide time series, change of the mean sea level due to meteorological effects and the discharge of the fresh water river inflows).

In the research programme, as described above, emphasis is laid on (the changes in) the inhomogeneous tidal flows as a common basis for analyses and interpretations. This "integrated approach philosophy" is employed also with respect to the research tools. For each specific problem an adequate set of research tools is used; the hydraulic scale model of the Rhine-Meuse estuary, various mathematical models, measurements in nature and, for general support, fundamental studies. The set-up serves two objects: the solving of the water quantity and water quality problems and the development of mathematical models, gradually making the hydraulic scale model redundant.

With respect to the solving of the practical problems, up to now the hydraulic model is the core of the programme. Field data, and mathematical models are mainly used as a guide for the measurements in the hydraulic model, by providing in a systematic way tendencies and (rough) indications. Subsequently a restricted selection of tests in the hydraulic model gives the detailed information with the required accuracies for the practical use. For example: changes in salinity distributions near intake points have to be obtained with an inaccuracy in the order of 100 mg Cl/1. On the other hand the hydraulic model provides input for mathematical models. For example detailed measurements of the inhomogeneous tidal flows serve as input for calculations on siltation or water quality processes, see figure 2.2.

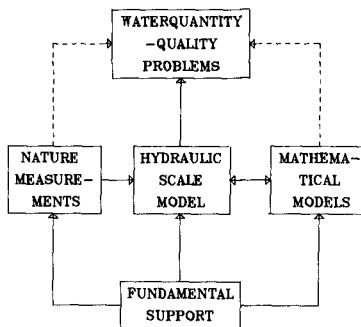


Fig. 2.2 OPERATIONAL USE RESEARCH TOOLS

With respect to the development of mathematical models one has to distinguish several phases. The actual development takes place in the fundamental framework, including estimation of numerical scheme, treatment of boundaries, research on and the description of turbulent

processes on momentum and mass etc. The hydraulic scale model is used to verify the models under systematically varied circumstances with respect to geometry and boundary conditions.

Finally a relatively restricted verification (or validation) on field data proceeds the operational use of the mathematical models. This set-up implies an interactive development process between the various research tools, see figure 2.3.

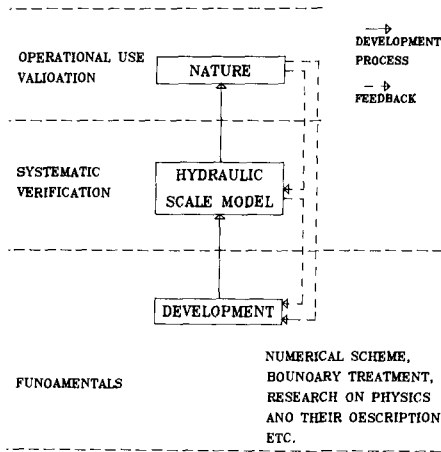


Fig. 2.3 DEVELOPMENT MATHEMATICAL MODELS

### 3. FACILITIES

In this chapter, a brief description will be given of the facilities "field measurements", hydraulic scale model, mathematical models and fundamental support.

#### 3.1- Field measurements

The measurements can be divided into two types: continuous measurements of waterlevels and salinities and "special purpose" measurements. The former includes estimation on fixed locations all over the estuary system of some 40 waterlevels and of some 10 salinities. The measurements are mainly meant for long term system control.

The latter may include calibration measurements with, in addition to the permanent measurements, extensive measurements with boats of flows and salinity distributions (Van der Heijden, Kuijper, de Jong, Roelfzema, 1984), verification measurements and measurements on specific locations and on phenomena such as exchange processes between harbour and river, dispersion processes, streampattern on junctions, etc.

All the field measurements are performed by the Ministry of Public Works.

### 3.2- Hydraulic scale model

The hydraulic scale model of the Rhine-Meuse estuary, simulating tidal flows and salinities, is operational since summer 1982, see figure 3.1. The model covers the area of figure 1.2 and is the rebuilt and extended version of the earlier Rotterdam Waterweg hydraulic model (Van Rees, Van der Kuur, Stroband; 1972), (Breusers, Van Os; 1980). Its scale factors are therefore the same: 1 : 64 for the vertical and 1 : 640 for the horizontal scale. The model has been calibrated and verified with extensive field data showing a good simulation of the dominant physical processes, viz, tidal flows, changes of the mean sea level due to meteorological effects, river discharges, vertical gravitational circulations and vertical turbulent diffusion (Van der Heijden, Kuijper, de Jong, Roelfzema, 1984). The area where salinity intrusion occurs has been modelled, in plan view, similar to nature. The sea area and the

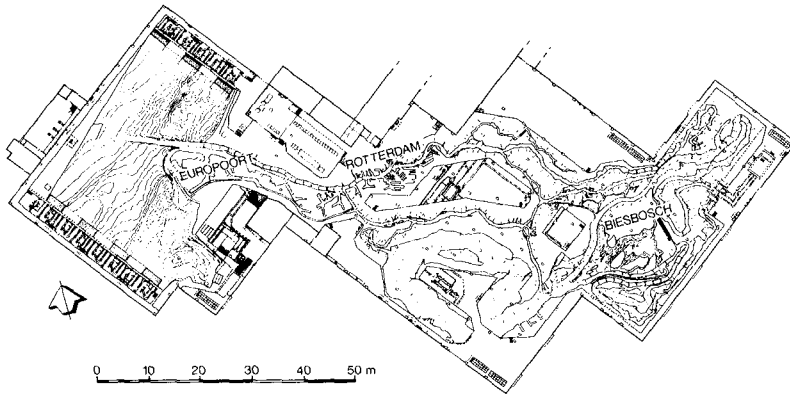
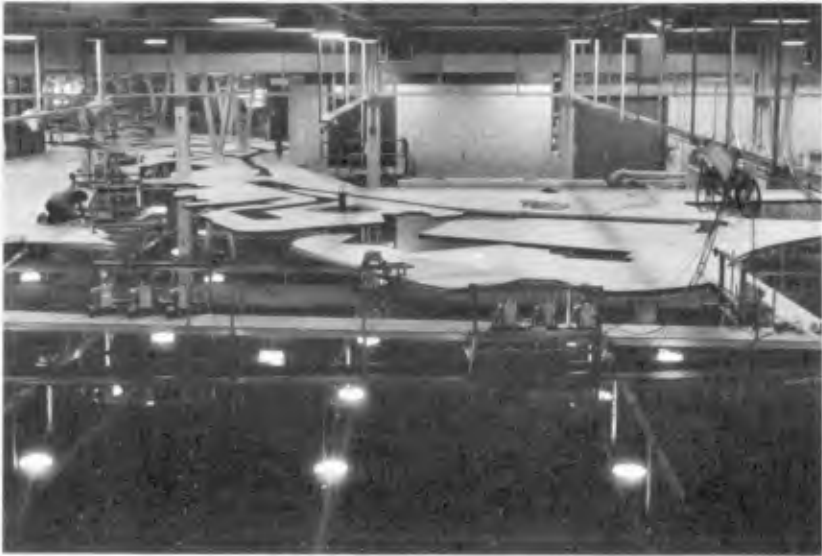


Fig. 3.1 HYDRAULIC SCALE MODEL

upstream parts of the model are mainly meant to provide the correct boundary conditions. Measurements include waterlevels, velocities, discharges and temperatures and conductivities which are combined to densities. The discharges are measured on 14 locations near the junctions of branches in the network by means of acoustic instruments. Using the doppler-principle and by integrating the signals over their cross-sections, these instruments present continuously cross-sectional discharges. For the measurements of conductivities, besides of the conventional "one-point" probes, the Delft Hydraulics Laboratory developed bar-type conductivity probes. Every bar includes conductivity probes, which makes it possible to present the conductivities in 12 positions in the vertical. In the model more than 20 of these conductivity bars are operated. Combined with temperatures, these bars allow continuous measurements of the vertical salinity distribution under tidal time series.



HYDRAULIC SCALE MODEL



ACOUSTIC DISCHARGE  
MEASUREMENT INSTRUMENT



CONDUCTIVITY PROBE



### 3.3- Mathematical models

It is the intention to replace the hydraulic model by a set of mathematical models as soon as possible. The main reasons for this are the relatively high cost of exploitation of the hydraulic model and the necessity to have facilities to study, beside the water motion and salt distribution, the transport of sediment (especially mudtransport), the transport of cooling water and the waterquality. The set of mathematical models will be a system consisting of a base model that simulates the water motion and salt distribution and several transport models coupled to the base model for the computation of sediment transport, cooling water transport or water quality.

#### - Choice of the base model

For the selection of the most adequate model with predictive properties for the Rhine-Meuse estuary it is necessary to have insight into the physical mechanisms that are dominating in the problems under study. Important for the choice is the geometry of the area and the stratification of the estuary. In this respect the Rhine-Meuse estuary can be divided into 4 areas:

- the homogeneous network of tidal rivers which are relatively narrow (width/depth ratio  $B/H < 100$ ). Generally a one dimensional (1D) basemodel is sufficient in this area
- the wide homogeneous southern part of the estuary. A twodimensional depth averaged (2Dh) model gives generally sufficient information
- the inhomogeneous, narrow ( $B/H < 100$ ) tidal area Rotterdamse Waterweg, New- and Old Meuse in which a stratified salinity distribution is present (see figure 3.2) while gravitational circulation and exchange phenomena are important. So the phenomena in the vertical plane through the axes of the river are important and at least a twodimensionally laterally averaged (2Dv) branched model is necessary.

#### STRATIFICATION RWW + N.MAAS

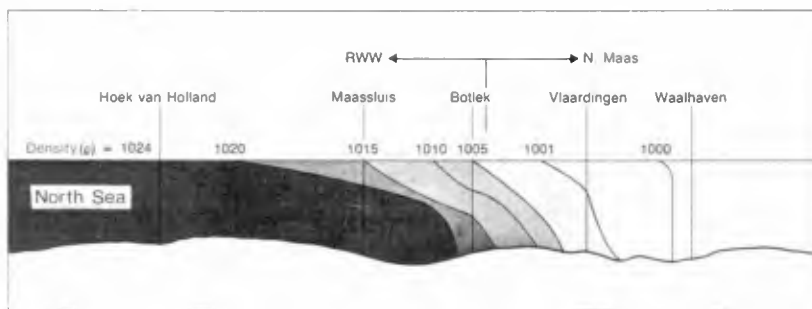
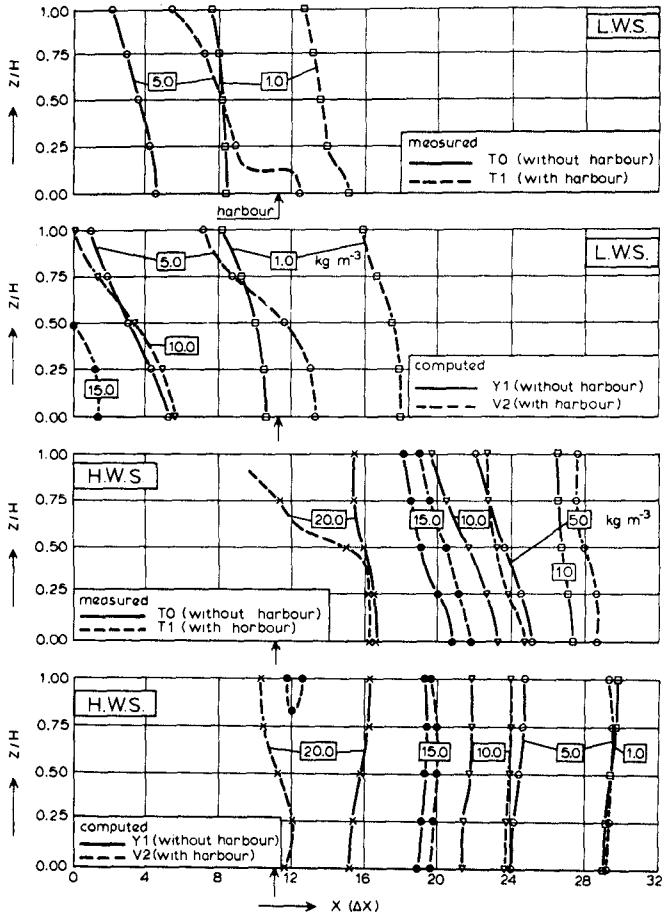


Fig. 3.2

- the stratified, wide sea-area at the mouth of the Rhine-Meuse estuary. Beside the two horizontal dimensions along the coast a stratified situation is often present because of river discharge from the estuary and so the vertical dimension is important too: a 3D model will be needed.



For the choice of the base model other important factors are the availability (now and in the future) and the cost of development and operational use. A 1D model for the whole estuary, called ZWENDL, is available, which has been calibrated for the water motion. A 2Dv model for the salt intrusion part of the estuary, called DISTRO, has been build, which was developed from a tidal flume version [Perrels and Karelse, 1981], see figure 3.3



COMPARISON OF MEASURED AND COMPUTED INFLUENCE OF THE HARBOUR ON THE LONGITUDINAL DENSITY DISTRIBUTION AT L.W.S. AND AT H.W.S.

Fig. 3.3 2-Dv MODEL

These considerations have resulted in the choice for a base model consisting of a combination of a 3D, a 2Dv (DISTRO) and a 1D (ZWENDL) model which are coupled with each other, see figure 3.4. A two-layer model will serve as an alternative for the 2Dv model and as a special purpose model for the simulation of silt transport processes in the inhomogeneous part of the estuary.

With respect to the modelling of sediment transport, cooling water transport and water quality for each area the type of modelling still has to be chosen (the choice is limited by the choice of the base model).

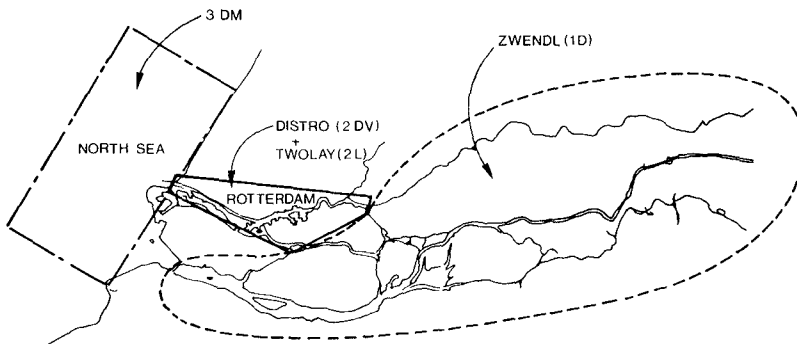


Fig. 3.4 BASE MODEL

The coupling of these models to the base model will present numerical problems. At this moment the 2Dh (preceeding the 3D development)/1D coupling is under research. Another important problem using 3 types of models and comparing computational results with each other and with measured results from prototype or hydraulic model is to get a unification of

- . geometry schematization
- . initial- and boundary conditions
- . in- and output and the databases
- . presentation of results
- . way of calibration and interpretation

Activities on these aspects are carried out.

As mentioned before the 1D model ZWENDL is an operational model with respect to the water motion for the whole Rhine-Meuse estuary.

#### Description ZWENDL

The one-dimensional model "ZWENDL" covers the tidal part of the rivers. The sea boundary is situated near Hook of Holland. Longitudinal dispersion is modelled as a gradient type transport. At first a "Thatcher Harleman"-like approach was followed for the dispersion coefficient and the sea boundary conditions for salt.

The results of the calibration and verification of ZWENDL with this formulation for the tidal motion and salinity distribution in the Rhine-Meuse estuary were unsatisfactory. So the study is going continued to obtain best formulation for the dispersion relation as function of location, time and circumstances and the best formulation of the sea boundary for salt as function of time and conditions.

LD models for sediment transport and waterquality in estuaries are available, they have to be coupled to ZWENDL.

#### Description "DISTRO"

The two-dimensional vertical model DISTRO covers the salt influenced part of the rivers (see fig. 3.4).

The vertical diffusion is modelled with a mixing length approach. The reduction of vertical diffusion due to density differences is modelled as a first approach with damping functions to represent the effect of stratification. A  $K-\epsilon$  modelling is in study. The horizontal dispersion is modelled as a gradient type transport. The sea boundary condition is similar with the one-dimensional (Thatcher-Harleman-like) approach but now for each layer in the vertical [Perrels, Karelse, 1981].

Besides DISTRO a 2 Dv cooling watermodel and water quantity model is available and a silt transport model will be developed in the near future.

The development of a 3D model for the sea part of the estuary is still in a begin stage of development

### 3.4- Fundamental support

A basic part of the set of research facilities is formed by the fundamental support. Also in commission of the Dutch Ministry of Public Works the Delft Hydraulics Laboratory carries out a long term research programme on inhomogeneous flows and silt transport processes. The programme includes research on turbulent mixing in stratified flows and on the transport mechanisms of silt and silt layers under inhomogeneous circumstances. Based on these studies, theoretical as well as experimental, also the mathematical models for the Rhine-Meuse estuary are developed and improved. For this fundamental research, the Delft Hydraulics Laboratory will again have the possession of a tidal silt/salinity flume (of 130 m length), to replace the flume that was destroyed by a fire in 1979.

## 4. RESULTS/DISCUSSION

In the research programme, systematic studies have been carried out on the effect of boundary conditions (tides, including wind effects and river discharges) and on the effect of changes in the tidal area (building or closing harbours). Tests, carried out under cyclic and under time series conditions of several weeks show the importance of the interaction of harbours with the tidal boundary conditions. Wind effects generating elevations of the mean sea level introduce complex effects on the salinities, see figures 4.1 up to 4.2). The mixing influence of harbours on the salinity distribution appeared to be significant. Closing all the harbours, implying decreased tidal filling- and emptying

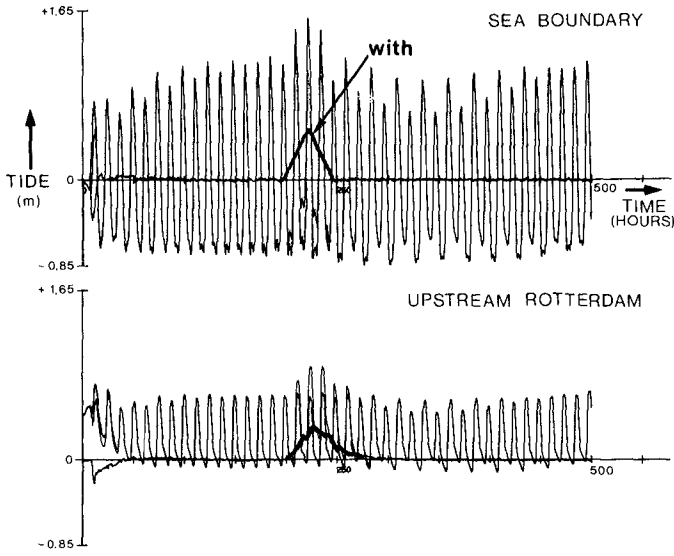


Fig. 4.1 VERTICAL TIDES AT TWO LOCATIONS, WITH- AND WITHOUT ELEVATION OF MEAN SEALEVEL

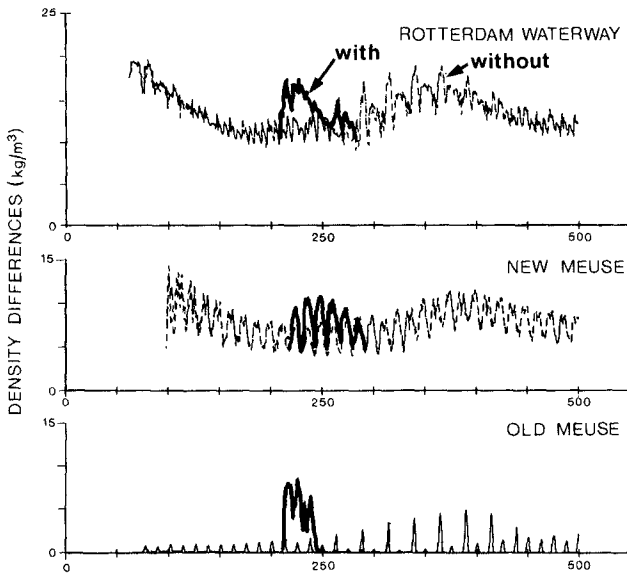


Fig. 4.2 TIME SERIES SALINITIES

volumes results in a smaller salinity intrusion on the one hand. On the other hand closing the harbours results in smaller tidal amplitudes causing less vertical mixing and therefore resulting in a larger salinity intrusion. For the Rhine-Meuse estuary, closing all the harbours results in an increase of vertical stratification and thereby an increase of salinity intrusion, figure 4.3). The same tendencies result from closing single harbours on the Nieuwe Maas, (see also: Abraham, De Jong, Van Kruiningen, 1984).

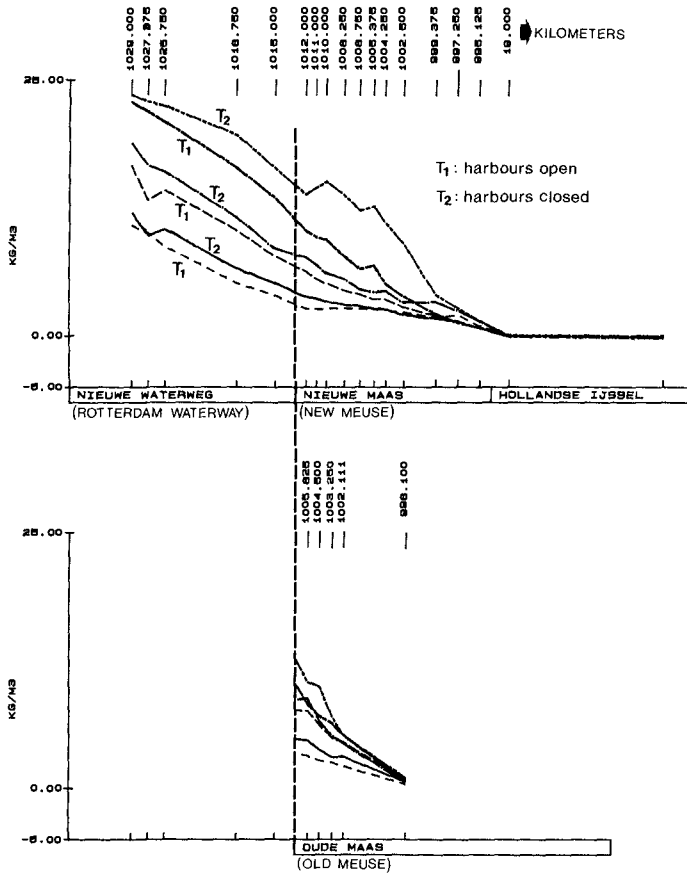


Fig. 4.3 ISOHALINES AT HWS

These experiences are relevant for the mathematical modelling, especially with respect to the length of the time series to be simulated and the density of data to be acquired. On the short run the experiences are used for the improvement of the inhomogeneous 1-D dispersion description and for the further verification of the 2-Dv model. Tests in the hydraulic scale model provide velocity- and salinity distributions on the base of which, in an inverse way, one-dimensional dispersion coefficients are estimated. Analyses of these coefficients may lead to an improved dispersion formulation.

A first test of the 2-Dv model with damping functions to represent the effect of stratification, resulted in a systematic difference between the model and nature; the model generates too much mixing. Besides of the implementation of the more sophisticated  $K-\epsilon$  modelling, the schematization has to be refined resulting in the lay-out of fig. 4.4. Subsequently a systematic research on the sensitivity for numerical, geometrical and hydraulic parameters has to be carried out (gridsize, boundaries, harbours, junctions, roughness, longitudinal viscosity and dispersion and stratification).

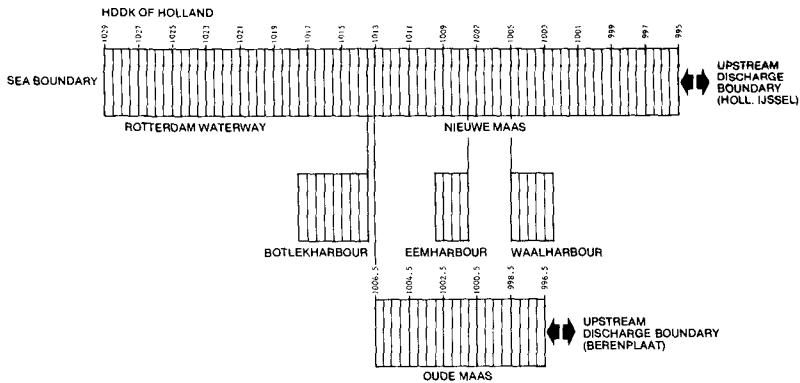


Fig. 4.4 SCHEMATIZATION OF SALT INTRUSION PART OF RHINE MEUSE ESTUARY  
IN DISTRO MODELLING  $\Delta X = 500$  m

In this integrated approach as described above, the results of the research programme provide information for the practical management of the estuary system. For example on the effect on the inhomogeneous tidal flows due to the eventual closing of smaller Rotterdam harbours, or on the impact of exchange phenomena between harbours and rivers on local siltation processes.

5. REFERENCES

- Abraham, G., Jong, P. de, Kruiningen, F.E. van, 1984:  
"Large scale influences on salinity intrusion in partly mixed estuaries". Symposium physics of shallow estuaries and of bays, Miami, USA.
- Breusers, H.N.C., Os, A.G. van, 1981:  
"Physical modelling of Rotterdam Waterway estuary", Proc. ASCE, Vol. 107, no HY 11, pp. 1351-1370
- Fischer, H.B., et al, 1979,  
"Mixing in Inland and Coastal Waters", Academic Press, New York
- Heijden, H.N.C.M., van der, Jong, P. de, Kuijper, C., Roelfzema, A., 1984:  
"Calibration and Adjustment procedures for the Rhine-Meuse estuary scale model", 19th Int. Conf. on Coastal Eng., Houston, USA
- Perrels, P.A.J., Karelse, M., 1981:  
"A two-dimensional laterally averaged model for salt intrusion in estuary", in "Transport Models for Inland and coastal waters", Acad. Press, p.p. 483-535
- Rees, A.J. van, Kuur, P. van der, Stroband, H.J., 1972:  
"Expierence with tidal Salinity model Europoort", 13th Int. Conf. Coastal Eng. Vancouver, July 1972, Vol III, Chapter 135, New York, 1973, ASCE, pp. 2355-2378, 8 figs., 7 refs.

## CHAPTER TWO HUNDRED ONE

### SEDIMENTATION PATTERNS IN A TIDAL INLET SYSTEM MORICHES INLET, NEW YORK

Michael J. Vogel and Timothy W. Kana  
RPI Coastal Science and Engineering, Inc.  
Columbia, South Carolina

#### ABSTRACT

A detailed study of the historical development of Moriches Inlet, Long Island (New York), was completed to determine the morphodynamic interaction of tidally influenced processes and the effects of man-made alterations on the inlet channel and affiliated flood and ebb-tidal deltas. The south shore of Long Island in the vicinity of Moriches Inlet is a microtidal, wave-dominated (mixed-energy) environment. Characteristic of this setting, the inlet bisects a low-lying barrier island backed by an open bay and has a prominent flood-tidal delta.

In this study, bathymetric charts of the inlet, bay, and barrier nearshore zones were contoured for analysis. Using a polar planimeter, the areas between isobaths from mean high water to the bottom surface were measured. This information was used to determine the volumetric distribution of sediment and water in the system. In addition, harmonic analysis was applied on digitized bay-tide records to ascertain the relationships of the semidiurnal overtide constituents. From the results, mean rise/fall duration differences, related to the conservation of mass, were calculated.

The results of the quantitative spatial analysis indicate that Moriches Inlet was flood-dominant from breach in 1931 until closure in 1951. After reopening in 1953, the inlet became ebb-dominant as a result of inlet stabilization and extensive dredge-and-spoil operations in the inlet and bay. Good correlations exist between net sedimentation in the inlet with (1) bay-surface area change, (2) water storage capabilities of the flood-tidal delta, and (3) the cross-sectional area of the inlet. The relationship among these variables suggests that there is a system-wide response to the change in the hydrodynamics caused by man-made alterations, resulting in ebb dominance.

#### INTRODUCTION

Research in coastal processes and geomorphology has recognized the relationship between the scope and distribution of morphologic features and the hydrodynamic regime of the environment. The interaction of the morphology with tidal and wave energy, or the morphodynamics of a system, involves continual change toward an equilibrium condition. Through detailed examination of an environment, process/



response models have been developed to help understand this interaction.

This study focuses on the morphodynamics controlling the tidally influenced sedimentation patterns in a tidal inlet/bay system at Moriches Inlet, Long Island (New York). Through modifications of the inlet and bay configurations, the hydrodynamic adjustment resulted in a reversal in tidal dominance. In order to quantify this reversal and to identify the controlling factors of tidal dominance in the system, an historical analysis of the evolution of the inlet and associated depositional bodies was completed. Detailed bathymetric charts of the entire inlet system that document the morphological changes, supplemented with bay-tidal records, comprise the data base for this study.

### INLET DYNAMICS

The dynamics of flow in an inlet/bay system can be described by two governing principles: (1) the equation of motion (or conservation of momentum) and (2) the continuity equation (or conservation of mass). Assuming that the velocity in the inlet is constant (i.e., local acceleration is neglected) and that the tidal wave is much longer than the inlet length, the one-dimensional equation of motion can be integrated to yield:

$$g(h_o - h_b) = L \frac{du}{dt} + \frac{1}{2}(1 + \frac{2r}{h})ul \quad (1)$$

where  $g$  is the acceleration of gravity,  $h_o$  is the ocean water-surface elevation,  $h_b$  is the bay water-surface elevation,  $L$  is the entrance length,  $u$  is the average inlet velocity,  $h$  is the water depth in the inlet, and  $r$  is the square law friction coefficient defined as:

$$r = \sigma/\gamma u^2$$

where  $\sigma$  is the bottom shear stress and  $\gamma$  is the density of water. This equation represents the difference in bay and ocean water levels as proportional to the flow velocity squared, through a channel of a given geometry based on its length, depth, and the effects of inertia.

The equation of continuity can be stated as:

$$UA_c + Q = A_b [dh_b/dt] \quad (2)$$

where  $A$  is the cross-sectional area of the inlet,  $A_b$  is the bay surface area, and  $Q$  is discharge from river flow or sources other than the inlet. This equation relates the velocity to (1) the rate of change of the bay water level and (2) the ratio of the bay surface area over the inlet cross-sectional area. As  $A_c$  and  $A_b$  vary over a tidal cycle, the peak ebb and flood velocities, as well as their duration will differ.

### STUDY AREA

Moriches Inlet is located on Fire Island, off the south shore of Long Island, New York (Fig. 1). One of five inlets on the south shore, Moriches Inlet connects Moriches Bay and the Atlantic Ocean. The inlet is 80 miles (mi), by water, east of The Battery (New York

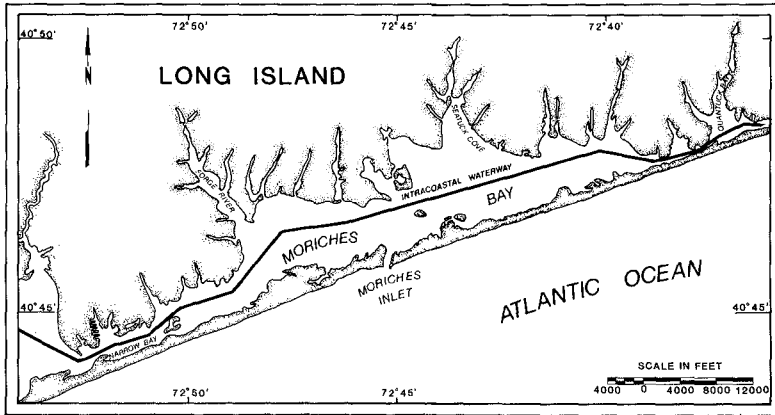
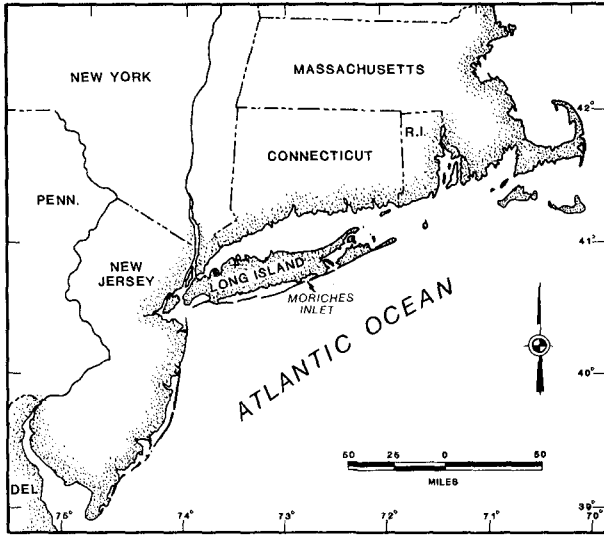


FIGURE 1. Location map of Long Island, New York, and Moriches Inlet on the south shore.

City) and is 52 mi west of Montauk Point. The inlet separates Great South Beach (Fire Island) on the west and Cupsogue Spit, or Pike's Beach (eastern end of Westhampton Beach), on the east.

Moriches Bay is 12.8 mi long, including the adjacent Narrow Bay. The width of the bay varies from 0.75 mi to 2.5 mi, whereas Narrow Bay, which connects Moriches Bay to Great South Bay to the west, has widths of 1,000 to 4,000 feet (ft). The total water surface area of the combined bay is approximately 20 square miles (mi<sup>2</sup>). Moriches Bay also connects with Shinnecock Bay to the east through Quantuck and Quogue Canals. The largest streams which drain into Moriches Bay are the Forge River and Seatuck Creek; a total of 60 mi<sup>2</sup> of land area drain into the bay.

The astronomic tides at Moriches Inlet are semidiurnal with a mean range of 2.9 ft. The mean spring and neap tidal ranges are 3.5 ft and 2.1 ft, respectively. Visual observations of the nearshore wave climate were compiled by the Coastal Engineering Research Center from June 1970 to May 1973. The average breaker height, based on these observations, was 2.25 ft, and the average breaker period was 7.9 seconds.

#### GEOMORPHIC/HYDRAULIC HISTORY

The geomorphic and hydraulic history of Moriches Inlet and Bay from 1931 to 1967 can be described by two phases: (1) an initial post-breach period during which the inlet system was relatively natural and eventually shoaled closed, and (2) a period beginning after the inlet was stabilized and artificially reopened--characterized by human manipulation of the inlet and bay. The apparent contrast in sedimentation patterns between these two periods provided the basis for this study on tidal inlet dominance.

##### 1931-1951

The modern Moriches Inlet was breached on 4 March 1931 by a severe extratropical storm. A July 1931 survey shows an initial configuration of the inlet 800 ft wide and 1,500 ft long with channel depths up to 18 ft. A prominent flood-tidal delta with an intertidal perimeter existed landward of the inlet. A line of breakers indicated on the sheet suggest that an ebb-tidal delta had formed also. The bay tidal range was measured at 0.4 ft.

From the breach in 1931 to 1940, the inlet migrated westward a distance of 3,500 ft from its original breach position. During this time, the inlet/bay system was a sediment trap, as net sedimentation continued on both the ebb- and flood-tidal deltas. The morphology and the hydraulics of the inlet adjusted to the tidal flow demonstrated by a small increase in the bay tidal range as well as an increase in the inlet length and width. These processes were probably enhanced by the impact of storms in 1934, 1938, and 1940.

In 1947, a jetty was constructed on the west side of the inlet in an attempt to stop its westward migration. The construction was

performed in conjunction with channel dredging to the west of the inlet. The combined effects of this artificial manipulation of the inlet caused increased shoaling. The updrift barrier, Cupsogue Spit, laterally accreted westward and narrowed the inlet throat and length. A highly detailed survey taken in 1949 reveals a developed ebb-tidal delta and a large flood-tidal delta, mostly supratidal. By July 1951, the inlet closed naturally.

Hydrographic measurements taken by current-float observations during the 1949 survey show that peak ebb and flood velocities were nearly equal at 5.2 and 5.3 ft/sec, respectively. The bay high tide followed peak flood flow by 24 minutes, while peak ebb flow trailed low water by 1.5 minutes. The close phase relationship of the vertical tidal curve and current velocities denotes a progressive tidal wave condition at the inlet.

#### 1952-1967

In 1952, jetty construction was initiated to reopen and stabilize Moriches Inlet in response to local interests. An eastern jetty was built approximately 800 ft from the western jetty. In 1953, when construction was completed across the barrier island, dredging began to reestablish the inlet. On 6 November 1953, before channel completion, an extratropical storm impacted the area and breached the new opening.

For the remainder of the study period, the geomorphic and hydraulic history of the inlet was dominated by dredge/spoil operations (Table 1). During this time, 2 million yd<sup>3</sup> of sediment were dredged from the inlet and bay, with much of the spoils placed on the flood-tidal delta. As a result of the excavation projects and natural scouring, the hydraulic radius of the inlet increased, accompanied by an increase in the bay tidal range from 0.6 ft in 1955 to 1.5 ft in 1967.

The changes in the inlet delta morphology and tidal current regime indicate that the sedimentation patterns changed. A marked decrease in size of the flood-tidal delta simultaneous with an increase in size of the ebb-tidal delta suggest bay flushing had begun. Current velocity measurements taken in 1955-56 and in 1967 confirm that the inlet was hydraulically ebb-dominant. In November 1955 through May 1956, inlet velocities were measured at 5.2 ft/sec during flood and 6.5 ft/sec during ebb. In 1967, current velocity measurements taken mid-channel at an intermediate depth gave peak flood velocities at 2.4 ft/sec while peak ebb velocities were recorded at 4.3 ft/sec.

#### METHODOLOGY

The primary data base for analysis is a time-series of bathymetric surveys of Moriches Inlet and Bay, including coverage of the inlet, adjacent barrier islands, ebb-tidal delta, flood-tidal delta, and the surrounding bay. A spatial analysis was undertaken on each chart in an attempt to distinguish the morphological components of the system and their changes through time. The objective is that this type of

analysis should yield time-averaged results of net sediment transport within the surveyed areas.

TABLE 1. Moriches Inlet improvement projects based on published and unpublished records of the New York District (U.S. Army Corps of Engineers) and Suffolk County Department of Public Works.

Date	Project	Agency
1933	Dredge: 600 ft x 35 ft x 6 ft channel = 4,600 yd <sup>3</sup>	Local Interests
1935	Dredge: 3,360 yd <sup>3</sup>	Suffolk County
1947	Construction: West jetty	Suffolk County
	Dredge: Northwest Channel	
1952	Construction: Jetties spaced 800 ft	New York State
	East jetty (846 ft long)	
	West jetty (1,461 ft long)	
1953	Dredge: 747,310 inlet cut	Suffolk County
1954	Construction: Jetties extended	Suffolk County
	Spoil: Close Northwest Channel	New York State
1958	Dredge: 365,715 yd <sup>3</sup> - Northwest Channel (200 ft x 10 ft channel)	Suffolk County
1962	Dredge: 1,014,834 yd <sup>3</sup> - dredge inlet	Suffolk County
	Spoil: Close Northwest Channel	
1966	Dredge: 677,850 yd <sup>3</sup> - Northwest Channel (1,300 ft wide x 12 ft deep)	Suffolk County

In addition to documenting the changes of the inlet/bay system, critical parameters were examined in order to develop a process/response relationship for ebb-tidal dominance. One of the more significant factors influencing tidal dominance is the change in bay surface area over a tidal period (Oliviera, 1970; King, 1974; Seelig and Sorensen, 1978; FitzGerald and Nummedal, 1983). None of the surveys available to this study, however, covered the entire bay. As a result, the soundings were confined to the flood-tidal delta in the immediate inlet vicinity.

The selection of surveys with adequate coverage of the features aforementioned produced five working maps—a composite of 1932 and 1933 surveys, 1940, 1949, 1955, and 1967. A control grid of the study area was also constructed. The size of the grid was dictated by the survey of minimum areal coverage (Fig. 2). The establishment and utilization of this grid allow quantitative comparisons of the inlet/bay system to be made.

A survey of Moriches Bay and Fire Island from 1891, when no inlet existed, provided a baseline for comparison of the development of the flood-tidal delta. At that time, maximum depths in the bay were 8 ft. However, no available bathymetry of the nearshore zone exists which could serve as a baseline for ebb-delta growth. Soundings were

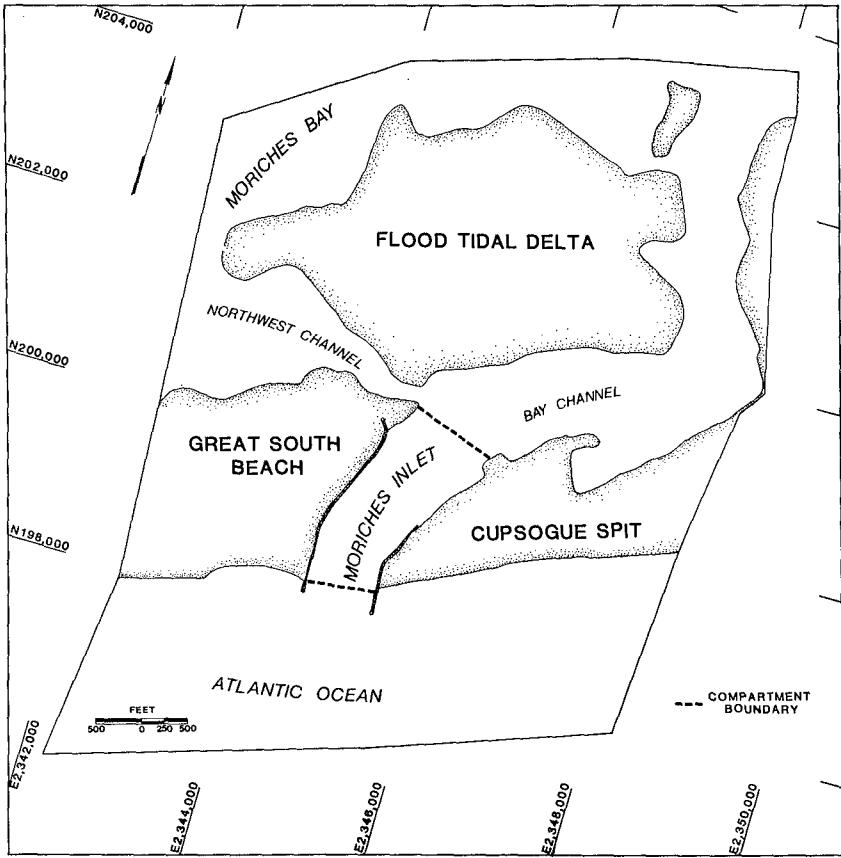


FIGURE 2. Control grid dimensions and compartment locations. MSL shoreline shown based on USACE 1955 survey.

taken, though, in 1951 when the inlet had naturally closed. Using the technique developed by Dean and Walton (1975), a hypothetical shoreline was created based on these soundings in which contour lines parallel the coast. The idealized bathymetry was then used in conjunction with the 1891 bay for analysis. For reference, the control grid was superimposed on the site of the stabilized inlet.

For the purposes of this study, the Moriches Inlet and Bay system was divided into three compartments within the control grid:

- 1) The bay, which represents the area landward of the bay shoreline.
- 2) The inlet proper.
- 3) The ocean or nearshore zone—that area oceanward of the inlet including subtidal segments of the barrier islands.

These subdivisions allow independent analysis of the inlet and the ebb- and flood-tidal deltas (Fig. 2).

The areal distribution of the geomorphic features on the individual charts was measured using a digital compensating polar planimeter. Areas enclosed between isobaths within the control grid were obtained to the nearest 1,000 ft<sup>2</sup>. The area measured for each interval supplied the data for volumetric analysis.

The areas measured at each isobath by planimetry were multiplied by the contour interval to produce a volumetric "slice" of water. The sum of all slices is a close measure of the total amount of water in that compartment. In this way, the amount of sediment deposited in the ebb and flood deltas of each survey can be directly compared.

## HARMONIC ANALYSIS

In the absence of complete velocity measurements, vertical tide records taken at the U.S. Coast Guard Station in Moriches Bay were obtained. Four 29-day continuous records were selected which roughly corresponded with the bathymetric surveys or significant events from 1944, 1955, 1966, and 1967. Based on the equation of continuity (2) and following the work of Boon and Byrne (1981), the tidal signatures of the bay can be related to the dynamics of the tidal flow through the system.

Harmonic analysis used on filtered, digitized bay-tidal curves supplied the amplitude and phase relationships of the principal tidal constituents. In a semidiurnal system, the constituents which can sufficiently represent the bay tidal curves are the  $M_2$  [the principal lunar semidiurnal constituent with a period of 12.42 hours (hr)],  $M_4$  (6.21-hr period), and  $M_6$  (4.14-hr period) harmonics (Shureman, 1958). These overtides have speeds (frequencies) which are exact multiples of the elementary constituent. Therefore, the combination of the overtides can represent the distortion of the mean bay tidal curve, and rise/fall durations can be observed.

## RESULTS

## VOLUMETRIC RESULTS

The results of the volume calculations are presented in Table 2. These are calculations of the water volume for each compartment referenced to MSL. This datum plane is considered constant through the study period.

TABLE 2. Compartment and total water volumes. Reference datum is mean sea level. Unit of measure is  $\times 10^3$  ft<sup>3</sup>.

Survey Date	Inlet Compartment Volume	Bay Compartment Volume	Ocean Compartment Volume	Total Volume
Hypothetical	0	146,168	198,106	344,274
1932-1933	4,782	127,900	186,334	319,016
1940	22,784	27,546	131,116	181,446
1949	1,710	56,136	202,462	260,308
1955	14,590	61,964	195,466	272,020
1967	17,134	128,568	124,640	270,342

The raw volumes are not adjusted for any dredge and spoil quantities listed in Table 1. While these quantities alter the results to some degree, the exact location of the dredging projects and the distribution of spoils are not known. Therefore, it is difficult to calculate the amount of sediment which has truly been removed from the control area.

The water volumes for the bay and ocean compartment both show an increase in sedimentation from the time of the breach until 1949, or approximately the time of the inlet closure. The 1940 survey results show that period as the 'richest' in sediment. From 1955 to 1967 (or extrapolating back to the reopening in 1953), the bay and ocean compartments show a complementary trend. As the bay compartment exported sediment as indicated by the increase in water volume, the sedimentation in the ocean compartment increased. These results are clear evidence that Moriches Inlet became ebb-dominated after reopening.

The totals shown in Table 2 also signify that the inlet system was stable after jetty construction, measured by the total sediment flux. The total water volume varied by only  $10 \times 10^6$  ft<sup>3</sup> from 1949 to 1967. As expected, sediment volume was lowest in the pre-breach and 1932-1933 composites due to the relative immaturity of the inlet/bay system.



## INLET MEASUREMENTS

Inlet dimensions, parameters in the governing equations of the dynamics of tidal flow (Equations 1 and 2), were measured from the base maps. With a known inlet volume previously identified, the mean cross-sectional area can be calculated using the inlet length. Table 3 lists inlet lengths, widths, and cross-sectional areas at MSL.

TABLE 3. Moriches Inlet dimensions.

Date	Inlet Length (ft)	Width (ft)	Mean Cross-sectional Area (ft <sup>2</sup> ) (MSL datum)
1932-1933	520	1,420	9,196
1940	3,108	2,442	7,331
1949	652	337	2,623
1955	2,100	800	6,948
1967	1,384	800	12,380

Moriches Inlet reached its greatest cross-sectional area of 12,380 ft<sup>2</sup> in 1967 from scouring and dredging. In the 1932-1933 composite, the inlet had a large hydraulic radius, producing a relatively high mean cross-sectional area of 9,196 ft<sup>2</sup>. The inlet was most constricted in 1949 with a mean area of 2,623 ft<sup>2</sup>. After construction of the jet-ties (1952), inlet size increased again to 6,948 ft<sup>2</sup> by 1955.

## INTERTIDAL AREA

The change in bay area over a tidal cycle is an important quantity affecting net sediment transport (Equation 2). According to King (1974), a large area change produces net offshore transport. In Moriches Inlet, the amount of intertidal area change within the control grid is a function of a combination of factors. These factors include the size of the flood-tidal delta, the slopes of the flood-tidal delta margins, and perhaps most significant, the varying tidal range in the bay.

Table 4 lists the intertidal area changes in both the bay and inlet compartments as determined by measurement and hypsometric analysis. The inlet compartment, which was included to account for the water storage of the 1940 survey, had a significant amount of intertidal area within the long waterway. The tabulated totals for each survey show a correlation with the magnitude of the tide range at that time. In 1967, when the bay tidal range was 1.5 ft, the corresponding intertidal area was  $9,638 \times 10^3$  ft<sup>2</sup>, while in 1932-1933 when the tidal range was only 0.4 ft, the intertidal area was also the lowest at  $1,132 \times 10^3$  ft<sup>2</sup>. The data from 1940, 1949, and 1955 (when the tidal range was

nearly constant) show that the smaller-scale variations in intertidal area were the result of the flood-tidal delta morphology.

TABLE 4. Intertidal areas of the bay and inlet compartments. Unit of measure =  $\times 10^3$  ft<sup>2</sup>. (1) MHW to MSL area from measured results. (2) MSL to MLW area from hypsometric function.

Date	Inlet <sup>1</sup>	Inlet <sup>2</sup>	Bay <sup>1</sup>	Bay <sup>2</sup>	Total
1932-1933	34	46	648	404	1,132
1940	440	701	2,055	1,347	4,543
1949	12	14	2,865	1,992	4,883
1955	14	16	3,812	1,986	5,828
1967	0	4	6,260	3,374	9,638

#### HARMONIC ANALYSIS

In contrast to the work of Boon and Byrne (1981), the results from the harmonic analysis of the bay tidal records show no mean rise/fall duration differences. Mean sinusoidal curves produced from the amplitudes and phase angles of the  $M_2$ ,  $M_4$ , and  $M_6$  constituents for each digitized record were constructed. In the resultant curve of each tide record, the rise duration equals the fall duration within the resolution of the five-minute increment used in calculation.

The type and degree of distortion in the combined tidal signature are primarily a function of the phase angle relationship among the overtides. The distortion, however, only appears significant when the ratio of the  $M_4$  and  $M_2$  amplitudes are greater than 0.1. Table 5 illustrates that while the phase angles of the overtides do change, the  $M_4/M_2$  amplitude ratios never exceed 0.04. The effect, then, of the  $M_4$  and  $M_6$  overtides on the principal semidiurnal component are so small that any distortion created is minimal.

The hydrographic data from Moriches Inlet show a small phase lag between bay tidal elevations and channel velocities, indicating a progressive tidal wave condition in the inlet/bay system. Under these circumstances, it appears that, without distortion of the bay tidal elevations, there are still ebb- and flood-velocity differences evidenced by the hydrographic measurements as well as changes in the sizes of the ebb- and flood-tidal deltas. Therefore, other morphodynamic factors such as the frictional effects of a change in bay surface area or channel dimensions must be influencing the direction of net sediment transport.

TABLE 5. Moriches Bay overtide constituents phase angle (degrees) and amplitude (ft).

	$M_2$	$M_4$	$M_6$	$M_4/M_2$ Ratio
1944				0.03786
Amplitude	0.1215	0.0046	0.0040	
Phase	215.07	269.54	203.06	
1955				0.01563
Amplitude	0.0896	0.0014	0.0015	
Phase	124.64	214.49	146.91	
1966				0.0238
Amplitude	0.3992	0.0095	0.0155	
Phase	147.99	147.92	75.14	
1967				0.01521
Amplitude	0.4603	0.0070	0.0044	
Phase	61.66	12.39	254.71	

## DISCUSSION

The morphodynamics of an estuarine environment are fundamentally dependent upon wave and tidal energy, and sediment input. In Moriches Inlet and Bay, modulations in tidal range and available sediment appear to be closely related to the variation in morphology and tidal dominance. These changes are primarily the result of man-made modifications through stabilization and dredging of the inlet/bay system.

Relating these factors to the study, it has been demonstrated that the tidal energy in Moriches Inlet has changed over the course of this study. No available data covering the entire study period exist, but it is assumed that wave energy has been relatively constant. Long-shore transport rates, storm deposition, jetty trapping, and inlet bypassing--all affect the sediment flux to the inlet/bay system which has been further altered by dredge and spoil operations.

To account for changes in sediment input, the measured volumes were normalized by creating percentiles of the sum of total water volume in the control grid and (1) the inlet and bay total and (2) the ocean compartment. In this way, any decrease or increase of sediment that would affect the system as a whole is taken into consideration.

Figure 3 is a graph showing the distribution of water volume in the control grid for each survey. Incorporated in this figure are pertinent dredge volumes which alter the relative percentage. This correction is based on an assumption that dredged sediment within the control grid is removed from the subtidal system. A decrease in the percent of water in a compartment indicates an increase in sedimentation. Comparing the proportions of volume with a semihypothetical pre-inlet condition, the volume of sediment in the bay and inlet compartments increased to 1949. This trend reversed between 1949 and

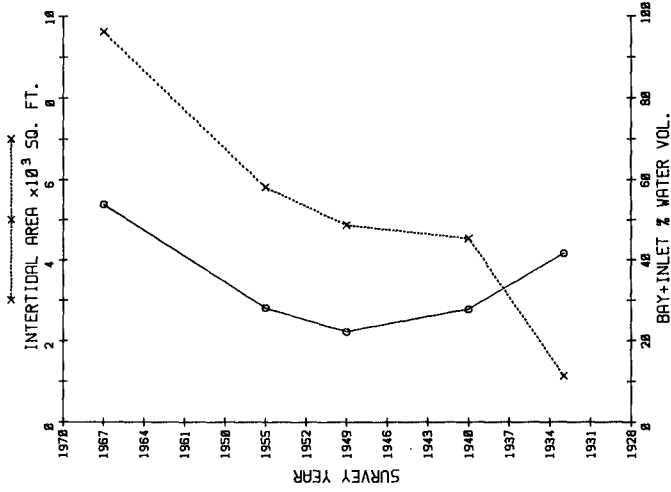


FIGURE 4. Correlation between percent water volume (indicating net sedimentation) and intertidal area of bay and inlet compartments. Note favorable correlation from 1949 to 1967.

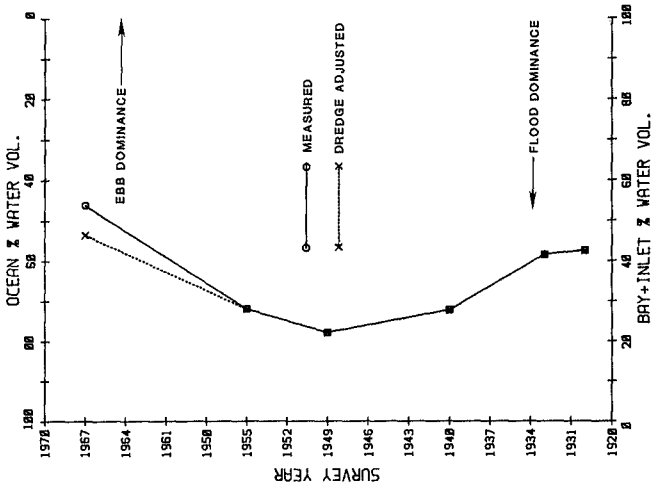


FIGURE 3. Relative percentage of water volume within the control grid. Movement to the left represents flood dominance; movement to the right represents ebb dominance.

1967 when the majority of sedimentation took place in the ocean compartment or ebb-tidal delta. Figure 3 can be interpreted by describing the inlet/bay system as flood-dominant from breach to closure in 1951 and as ebb-dominant from the reopening of the inlet in 1953 to 1967.

The net sedimentation in the bay during flood dominance is due to a combination of factors. Modelers (Oliviera, 1970; King, 1974; Seelig and Sorensen, 1978) have shown that net bayward transport is possible when there is negligible change in the bay-surface area over a tidal period. Flood currents carrying a bedload of sand can lose competence upon entering the static, deeper bay from the confined flow of the inlet, analogous to the formation of a river delta. Other possibilities for bay sedimentation processes include storm and wash-over deposits, or increase in the flood-tidal delta volumes attributable to spoil operations.

In order to determine the extent of tidal influence on net sedimentation patterns, the principal factors relating to tidal dominance were examined in relation to the volumetric distributions of Figure 3. As mentioned, the variation in intertidal area is considered a dominant factor for bay flushing. Figure 4 shows the relationship of the change in area between MHW and MLW within the control grid plotted against the volumetric percentage of the ocean compartment.

Of the five survey dates, there is a favorable correlation in 1949, 1955, and 1967. The lack of association between the variables of the earlier surveys is due possibly to (1) the lower precision of the 1940 survey and, therefore, more significant error and (2) a lack of equilibration of the immature system in 1932-1933. However, both these surveys were taken within two years after the impact of major storms on the area. This suggests that the morphology in 1932-1933 and 1940 was shaped more by the occurrence of storms than by tidal flow.

In Figure 5, the intertidal water volumes in the bay and inlet are presented with the same volumetric distributions. The volume of water was obtained by multiplying the intertidal areas by the tidal range. This calculation emphasizes the change in area due to increased tidal range rather than the size and shape of the ebb-tidal delta. The correlation in this graph implies that the water-storage capacity of the flood-tidal delta or the degree of flow through the intertidal areas is also closely related to tidal dominance and not just to the change in area over a tidal period. The greater flow would have higher frictional distortions which indirectly determine the magnitude and direction of tidal dominance.

The tidal range for a given bay-surface area, or more directly the tidal prism, is related to the cross-sectional area of the inlet, according to the work of O'Brien (1931, 1969) and Jarrett (1976). The cross-sectional area and its variation is also an indication of inlet stability (O'Brien and Dean, 1972) and the degree of inlet channelization. Since net transport is sensitive to inlet depth and channel dimensions (King, 1974), the mean cross-sectional areas from Table 3 were plotted against the volumetric distribution as in Figures 4 and 5. From the graph in Figure 6, the cross-sectional area correlated well with the

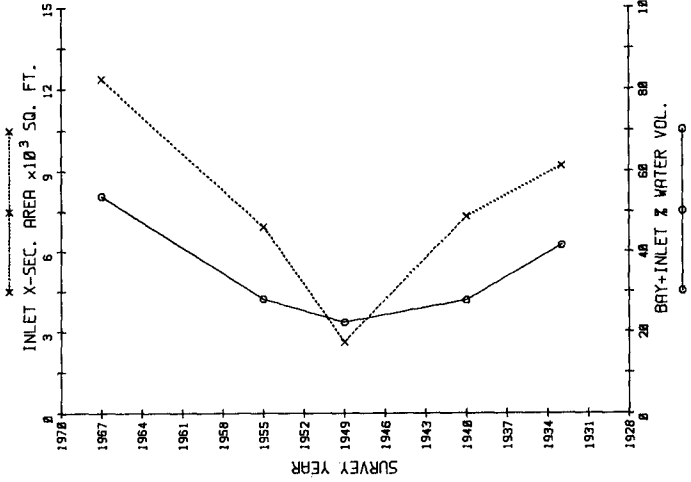


FIGURE 6. Good correlation between percent water volume and inlet cross-sectional area. The control of channel dimensions reflects ebb dominance.

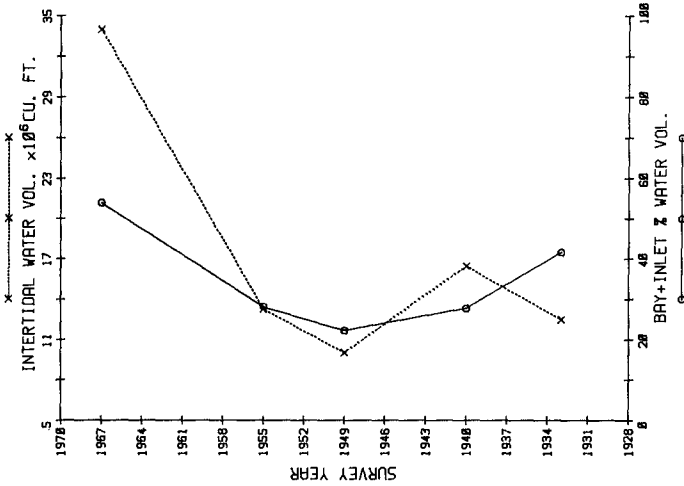


FIGURE 5. Correlation between water volume and interstitial water volume in the bay and inlet compartments. Note the improved correlation from previous figure, suggesting the importance of the bay-tidal range.

percentage of water volume in the bay and inlet compartments. Both variables decreased to a minimum in 1949 and subsequently increased to 1967.

It is worth noting that the changes in mean cross-sectional area qualitatively correspond with the amount of channelization in the flood-tidal delta, as indicated by the hypsometric analysis and bathymetric charts. One can conclude from Figure 6 that as the degree of flow through the inlet increased with the tidal prism, this flow became more confined by the flood-tidal delta complex. The system response was an increase in effective channelization (i.e., more efficient flow) and ebb-dominant, net-sediment transport.

By examining the process/response relationships of the inlet/bay system, one can construct an interpretational history of the evolution of Moriches Inlet and Bay. The natural setting of Fire Island is a typically long, low-lying, microtidal barrier island backed by a broad open bay. Through the impact of storms, the barrier has been breached frequently, creating temporary inlets with deltas forming from the excess available sediment. With minimum tidal flow and perpetual longshore transport of sediment, Moriches Inlet migrated west-erly with gradual inlet shoaling. As the inlet laterally migrated, it successfully receded from the flood-tidal delta complex, leaving the easternmost portions inactive. With the migration, the inlet faced a portion of the open bay, which enabled further sedimentation through bay trapping.

This natural process was interrupted initially by the construction of the western downdrift jetty. By preventing continued migration, sediment from longshore transport accelerated the rate of shoaling in the inlet throat, resulting finally in inlet closure.

When Moriches Inlet was reopened, the twin jetties were emplaced at an 800-ft spacing, much narrower than any inlet width that had been maintained naturally. The jetties also prevented the inlet from migrating away from the flood-tidal delta in addition to trapping sand from longshore transport. The effect was to initiate scouring through the inlet and contiguous flood-tidal delta. The system responded with an increase in channelized flow, increase in the tidal range, and the initiation of bay flushing and net oceanward sediment transport.

The subsequent dredging and spoil operations in the inlet and bay enhanced this response by increasing the scale of channelized flow through the inlet and bay, the inlet cross-sectional area, the bay-tidal range, and the change in bay surface area. By 1967, Moriches Inlet had become ebb-dominant as a result of these man-made alterations to the system.

## CONCLUSIONS

An historical spatial analysis of the Moriches Inlet and Bay system revealed that:

- 1) Moriches Inlet experienced a reversal in net sedimentation from flood-dominant during 1931-1951 to ebb-dominant during 1953-1967.
- 2) This reversal was initiated by modifications of the system by dredging and inlet stabilization. The modifications enhanced system-wide variations indicated by changes in:
  - a) Intertidal bay surface area.
  - b) Inlet cross-sectional area.
  - c) Tidal range.
  - d) Channelized tidal flow.These factors control the direction and magnitude of tidal dominance.
- 3) Harmonic analysis of Moriches Bay tidal records for 29-day periods in 1944, 1955, 1966, and 1967 indicate that no rise/fall duration differences exist in the mean tidal curve to account for dominant tidal flow.

## REFERENCES

- Boon, J. D. and R. J. Byrne, 1981, On basin hypsometry and morphodynamic response of coastal inlet systems: *Marine Geology*, Vol. 40, pp. 27-48.
- Dean, R. C. and T. L. Walton, 1975, Sediment transport processes in the vicinity of inlets with special reference to sand trapping: in Cronin, L. E. (ed.), *Estuarine Research*, Vol. 2, Academic Press, New York, N.Y., pp. 129-150.
- FitzGerald, D. M. and D. Nummedal, 1983, Response characteristics of an ebb-dominated tidal inlet channel, *Jour. Sed. Petrol.*, Vol. 53, pp. 833-847.
- Jarrett, J. T., 1976, Tidal prism - inlet area relationships, U.S. Army Coastal Eng. Res. Cont., Fort Belvoir, Vir., GITI Rept. 3, 31 pp.
- King, Jr., D. B., 1974, The dynamics of inlets and bays, College of Engineering, Univ. Florida, Tech. Rept. No. 22, 82 pp.
- O'Brien, M. P., 1931, Estuary tidal prisms related to entrance areas, *Civil Engineering*, Vol. 1, No. 8, pp. 738-739.
- O'Brien, M. P., 1969, Equilibrium flow areas of inlets on sandy coasts: *Amer. Soc. Civ. Eng., Proc. Jour. Waterways Harbors Div.*, WW1, pp. 43-52.
- O'Brien, M. P. and R. C. Dean, 1972, Hydraulics and sedimentary stability of coastal inlets: in *Proc. 13th Coastal Eng. Conf.*, ASCE, New York, N.Y., pp. 761-780.
- Oliveira, Mota, I. B., 1970, Natural flushing ability in tidal inlets, *Amer. Soc. Civ. Eng. Proc. 12th Coastal Eng. Conf.*, Washington, D.C., pp. 1827-1845.
- Schureman, P., 1958, *Manual of harmonic analysis and prediction of tides*, U.S. Dept. Commerce, Coastal Geodetic Surv., Wash., D.C., Spec. Publ. 98, 317 pp.
- Seelig, W. N. and R. M. Sorensen, 1978, Numerical model investigation of selected tidal inlet-bay system characteristics: in *Proc. 16th Coastal Eng. Conf. (Hamburg, West Germany)*, ASCE, New York, N.Y., pp. 1302-1319.



## CHAPTER TWO HUNDRED TWO

### NUMERICAL MODELING OF SHORELINE EVOLUTION AROUND THE RIVER MOUTH

MING-CHUNG LIN\* and JYH-CHERNG WANG\*\*

#### 1.0 INTRODUCTION

The river sediments transport into coastal water together with wave-induced longshore sediment transport make shoreline evolution much complicated. Fig.1 shows typical feature of shoreline shape around a river mouth. Recently there are some investigators treated this problem (Grijm, 1964, Bakker & Edelman, 1964; Komar, 1973; Tsuchiya & Yasuda, 1978), and had developed some mathematical or numerical models. This paper proposes a numerical model for predicting long-term shoreline evolution around a river mouth by incorporation certain river parameters into the Willis beach evolution model (1978). The proposed model is at first applied to four ideal cases to investigate its general characteristics and adaptability, and reasonable results are found. In our results the accretion on updrift side is faster than downdrift side under the oblique incident wave condition and the width of the river mouth increase steadily. These results are different from other approaches that the shoreline shape is always nearly symmetrical with respect to the centerline of the river mouth. Finally, as an field case application of the model, a numerical simulation of shoreline changes around the Cho-shui River mouth is performed and compared with field data.

#### 2.0 FORMULATION OF THE MODEL

##### 2.1 Assumptions

In order to make the problem tractable, we make some basic assumptions:

- (1) A year is divided into some periods, and in each period the wave characteristics such as height  $H_0$ , period  $T_0$  and length  $L_0$  are const..
- (2) Wave will break at the place where water depth is equal to  $1.25 H_0$ .
- (3) The energy of breaking wave will not exceed five times of offshore wave. The exuding energy, if any, will be distributed to the elements of each side.
- (4) The upper swash limit of waves equal to mean high water level plus one breaking wave height; the critical water depth of sediment movement is twice breaking waves height below the mean low water level.
- (5) The sand transport by wind, tidal current and the artificial effect will leave out of consideration.
- (6) The wave-induced alongshore discharge and the river-induced alongshore discharge can be a linear accumulation.

\*Professor, Dept. of Naval Architecture, National Taiwan University, Taipei, Taiwan, 107, R.O.C.

\*\*Senior Coastal Engineer, China Engineering Consultants, Inc., Taipei, Taiwan, R.O.C.

- (7) A year is divided into some periods, and the discharge, and the sediment concentration of the river in a period are constant.

## 2.2 Shoreline Evolution Equations

In the proposed model we consider two regions. One is coastal region away from river mouth, in which no river discharge and sediment directly flow into the elements. The other is river mouth region.

### (1) Coastal region

As Willis (1978), the sand transport zone is schematized as a triangle prism bounded by the instantaneous mean water level, the flat sloping bed and a depth equal to twice the average breaking wave height (Fig. 2). The alongshore discharge and sediment flow into the element equal to  $Q_x \Delta t$  and  $C_n Q_x \Delta t$  respectively. The amount of flowing out are

$$\left[ Q_x + \frac{\partial Q_x}{\partial x} \Delta x \right] \Delta t + Q_{nw} \Delta t$$

$$\left[ C_n + \frac{\partial C_n}{\partial x} \Delta x \right] \left[ Q_x + \frac{\partial Q_x}{\partial x} \Delta x \right] \Delta t + C_{nw} Q_n \Delta t$$

According to the continuity of discharge we will get

$$Q_{nw} = - \frac{\partial Q_x}{\partial x} \Delta x \quad (1)$$

by applying the continuity to sediment transport within the element, it yields

$$\begin{aligned} & \left[ C_n + \frac{\partial C_n}{\partial x} \Delta x \right] \left[ Q_x + \frac{\partial Q_x}{\partial x} \Delta x \right] \Delta t + C_{nw} Q_{nw} \Delta t \\ & = C_n Q_x \Delta t - (D2-F) \Delta Y \Delta x \end{aligned} \quad (2)$$

here the sediment transport is expressed as the product of flow discharge and sediment concentration.

Substituting Eq.(1) into Eq.(2) then yields

$$(D2-F) \frac{\Delta Y}{\Delta t} + (C_n - C_{nw}) \frac{\partial Q_x}{\partial x} + Q_x \frac{\partial C_n}{\partial x} + \frac{\partial C_n}{\partial x} \frac{\partial Q_x}{\partial x} \Delta x = 0 \quad (3)$$

where

(D2-F) = vertical distance from the upper swash limit of waves to the critical water depth of sediment movement

$Q_x$  = alongshore discharge which is equal to  $Q_L + Q_{W_x}$ ;  $Q_L$

denotes the river-induced alongshore discharge,  $QW_x$   
denotes the wave-induced alongshore discharge.

$Q_n$  = onshore-offshore discharge.

$C_n$  = alongshore sediment concentration.

$C_{n\omega}$  = onshore-offshore sediment concentration

The shoreline change  $\Delta y$  of coastal region can be calculated by Eq. (3). The form of this equation (3) is the same as that of Willis. But we must point out that herein  $Q_x$  is different from that of the Willis equation.

## (2) River mouth region

In this region river discharge  $QR_n$  and river sediment  $C_{nR}$   $QR_n$  are taken into account in the elements. By the continuity equation of discharge we can get

$$Q_{n\omega} = - \frac{\partial Q_x}{\partial x} \Delta x + QR_n \quad (4)$$

By the sediment continuity equation we get

$$Q_x C_n \Delta t + QR_n C_{nR} \Delta t - \left[ Q_x + \frac{\partial Q_x}{\partial x} \Delta x \right] \left[ C_n + \frac{\partial C_n}{\partial x} \Delta x \right] \Delta t - C_{n\omega} Q_{n\omega} \Delta t = (D2-F) \Delta Y \Delta x \quad (5)$$

From Eq.(4) and Eq.(5) it yields readily

$$(D2-F) \frac{\Delta Y}{\Delta x} + (C_n - C_{n\omega}) \frac{\partial Q_x}{\partial x} + Q_x \frac{\partial C_n}{\partial x} + \frac{\partial C_n}{\partial x} \frac{\partial Q_x}{\partial x} \Delta x + (C_{n\omega} - C_{nR}) \frac{QR_n}{\Delta x} = 0 \quad (6)$$

The shoreline change  $\Delta y$  of river mouth region then can be computed by Eq.(7). For solving Eq.(3) and Eq.(6) the evaluations of  $QL_n$ ,  $QW_x$ ,  $C_n$  and  $C_{n\omega}$  are needed in advance.

## 2.3 The River-induced Alongshore Discharge

We here model the flow at river mouth by a turbulent plane jet flow. Fig. 3 shows the elements schemed and the flow distribution. For the center element 1, the river discharge flowing in is  $QR_1$  and the jet discharge flowing out is  $QO_1$ . By applying continuity equation, we get alongshore current discharge induced by river at element 1

$$QL_1 = KR \frac{QR_1 - QO_1}{2} \quad (7)$$

where KR is a modification factor. When performing numerical calculation afterward, we take it to be 1.0. Similarly, the river-induced alongshore current discharge in the element n can be expressed as

$$QL_n = KR (QR_n - QO_n) + QL_{n-1} \tag{8}$$

If  $|x|$  is larger than  $b_0$ , the  $QR_n$  is equal to zero. If the  $|x|$  is larger than the boundary of the jet velocity distribution, we assume the alongshore discharge will be decreased in the manner of the form:

$$QL_{n+m} = QL_n / (1+m)^2 \tag{9}$$

Where  $QO_n$  can be obtained by integrating the velocity distribution of a turbulent plane jet flow. In the present study, the velocity distribution in turbulent plane jet interacting with obliquely incident wave developed by Hwang & Chen (1981) is used. Fig. 4 shows the coordinate system they used. Hwang and Chen assumed that the velocity distribution be a Gaussian distribution for a wave period average.

$$\frac{\bar{u}(x,y)}{[\bar{u}(0,y)]_{\max}} = \exp\left(-\frac{x^2}{2C_1 y^2}\right) \tag{10}$$

in which  $C_1$  is a velocity distribution coefficient. By momentum conservation concept, it reads

$$[u(0,y)]_{\max} = \left\{ \frac{2 b_0}{1+0.5\alpha^2(y,\theta)\sqrt{\pi} C_1 y} \right\}^{0.5} u_0 \tag{11}$$

where

$$\alpha(y,\theta) = \frac{\frac{\bar{u}_w^2}{u_0^2} - \sqrt{\pi} C_1 \frac{y}{b_0} \cos^2\theta}{2 - \frac{\bar{u}_w^2}{u_0^2} - \sqrt{\pi} C_1 \frac{y}{b_0} \cos^2\theta} \tag{12}$$

$$\bar{u}_w^2 = \frac{\pi H^2}{2T^2} \coth^2\left(\frac{2\pi h}{L}\right) \tag{13}$$

Where h denotes water depth.

The width of velocity distribution is expressed as

$$\frac{b(y,\theta)}{b_0} = \sqrt{\frac{\pi}{2}} C_1 \frac{y}{b_0} + \frac{\varepsilon(y,\theta)}{b_0 \alpha(y,\theta)} \tag{14}$$

Where

$$\varepsilon(y,\theta) = \frac{\pi H}{L} \coth\left(\frac{2\pi d}{L}\right) \sqrt{\pi} C_1 y \cos^2\theta \tag{15}$$

Here  $H$ ,  $L$ ,  $d$  denote the wave height, wave length, and water depth respectively. From Eq.(11) - Eq.(16)  $\bar{u}(x,y)$  can be calculated and then  $QO_n$  can be obtained.

In the present study, when numerical calculation is performed, wave refraction is calculated by the Brampton model (1977), wave-induced long-shore current and discharge by the Willis (1978a) work and sediment concentration by the Willis (1978b) formula.

### 3.0 NUMERICAL FORMULATION

#### 3.1 Difference Form of Shoreline Evolution Equation

Fig. 5 shows the differential element layout, in which  $y_n$  is the distance from baseline to the middle of the upper swash limit and the critical water depth of sediment movement. We set

$$y_{n-\frac{1}{2}} = \frac{1}{2} (y_{n-1} + y_n) \quad (16)$$

And the angle between shoreline and baseline  $A_S$  at gride  $n$  is

$$A_S(n,t) = \tan^{-1} \left[ \frac{y(n+\frac{1}{2},t) - y(n-\frac{1}{2},t)}{\Delta x} \right] \quad (17)$$

The angle between shoreline and wave crest line  $A_{br}$  then can be got by  $A_S$ . Now let

$$DQ = Q_x(n+1,t) - Q_x(n,t)$$

$$DC = C_n(n+1,t) - C_n(n,t)$$

$$Q_{ave} = \frac{1}{2} [Q_x(n+1,t) + Q_x(n,t)]$$

$$QR_{ave} = \frac{1}{2} [QR(n+1,t) + QR(n,t)]$$

$$DNC = \frac{1}{2} [C_n(n+1,t) + C_n(n,t) - C_{n\omega}(n+1,t) - C_{n\omega}(n,t)]$$

$$DNR = \frac{1}{2} [C_{n\omega}(n+1,t) + C_{n\omega}(n,t) - C_{nr}(n+1,t) - C_{nr}(n,t)]$$

then, from Eq.(3), difference equation for coastal region is

$$DY = \frac{\Delta t}{(D2-F)\Delta x} [DQ \times DNC + Q_{ave} \times DC + DC \times DQ] \quad (18)$$

and the difference form of Eq.(6) in river mouth region is

$$DY = \frac{\Delta t}{(D2-F)\Delta x} [DQ \times DNC + Q_{ave} \times DC + DC \times DQ + DNR \times QR_{ave}] \quad (19)$$

### 3.2 Input Data

The proposed model needs the following input data

- (1) The height, direction, period and length of incident wave in each calculated period, and the duration of each period in a year.
- (2) The location, discharge, sediment concentration and width of river in each period, and the duration of each period in a year.
- (3) The kinematic viscosity and density of sea water.
- (4) Density, porosity,  $D_{50}$  of sand, and the relative roughness.
- (5) Mean high water level and mean low water level.
- (6) The initial water depth chart.
- (7) The other special data, such as no-erosible region or coastal structure.

## 4.0 NUMERICAL RESULTS OF FOUR IDEAL CASES

### 4.1 Input Data of Four Ideal Cases

For investigating the general characteristics and adaptability of the proposed model, we run four ideal cases. The same part of input data are as follows:

- (1) beach slope 0.01
- (2) Kinematic viscosity of fluid  $1.3 \times 10^{-6} \text{ m}^2/\text{S}$
- (3) Density of sea water  $1020 \text{ kg/m}^3$
- (4) Density of sand  $2650 \text{ kg/m}^3$
- (5) Porosity of sand 0.35
- (6) Central grain diameter 0.0002 m.
- (7) Width of river mouth 1.2 Km
- (8) Relative roughness of sand 0.0007m
- (9) River flow velocity at mouth 0.6 m/S
- (10) Incident wave height 2 m

Table 1 shows the other input data for each case.

Table 1 Input data for four ideal cases

	The depth of river (m)	River Discharge (cms)	River sediment concentration	Wave incident angle (°)
Case A	1.5	1080	0.0004	45
B	1.0	720	0.0006	45
C	1.0	720	0.0004	45
0	1.0	720	0.0004	30

#### 4.2 The Features of the Present Model

The numerical results are shown in Fig.6. From these results, some important features can be described as follows.

- (1) In all cases the accretion on updrift side is faster than downdrift side under the assumed oblique incident wave condition.
- (2) In all cases the width of the river mouth increase steadily and the center lines are always refracted to the direction of nearshore current.
- (3) Fig. 6a shows the results of case A and B, which indicate that when the total sediment transport of river is constant, an increase in river discharge will decrease the accretion of downdrift side.
- (4) Fig. 6b shows the results of case B and C, which indicate that when river discharge is equal, the accretion of each drift side is in proportion to sediment concentration.
- (5) Fig. 6c shows the results of case A and C, which indicate that if sediment concentration is equal, the accretion of updrift side increases with river discharge increase, but in downdrift side is just opposite.
- (6) Fig. 6d shows the results of case C and D, which indicate that if all input data of the river is the same, the accretion of updrift side increases with wave-induced nearshore current velocity increase, but in downdrift side is just opposite.

### 5.0 FIELD CASE APPLICATION OF THE MODEL

#### 5.1 Introduction

Cho-Shui River, located in the mid-west Taiwan, is the biggest one in Taiwan. The annual total discharge is about  $4.65 \times 10^9$  m<sup>3</sup>/year. The total sediment load is about  $4 \times 10^7$  m<sup>3</sup>/year, among which  $1 \times 10^7$  m<sup>3</sup>/year of sediment load being deposited on the river bed and the left  $3 \times 10^7$  m<sup>3</sup>/year sediment load flowing into the coastal water and settled down the river mouth. Due to the river flow and incident wave, the shoreline evolution is severe and complicated. Fig. 7 shows the change of the shoreline around the Cho-Shui river between 1903 and 1972. Before 1911 the Cho-Shui river use the channel of the old Cho-Shui river, but after a work of channel regulation done in 1911, the mouth of the Cho-Shui river was changed to the present location. The change get a severe erosion of the shoreline around the Old Cho-Shui river mouth and a great accretion around the Present Cho-Shui river mouth.

#### 5.2 Description of Input Data

- (1) The variation of the discharge and the sediment concentration of the Cho-Shui river is very large. Table 2 shows the various data of discharge in a year at the Silo station. It is quite difficult to choose the amount of discharge in each period

Table 2. Discharge of Cho-Shui River (Unit: Cms)

Month Item	1	2	3	4	5	6	7	8	9	10	11	12
Monthly average	6.91	6.61	17.39	30.05	122.30	412.43	170.77	317.36	194.70	91.26	30.86	18.77
Max. monthly average	31.28	51.40	108.07	195.98	364.22	1,058.03	569.90	878.68	480.32	269.26	226.10	70.38
Min. monthly average	0.33	0.31	0.46	0.49	4.19	24.96	8.70	22.01	14.16	5.43	3.24	5.31
Average discharge	Max. annual average		Min. annual average		Max. day average			Min. day average				
122.95	208.34		36.23		6,610.00			0.09				

Table 3. Input data combination

Item Time step	Duration (month)	Wave direction	Wave height (m)	Waver period (s)	Discharge (cms)	Sediment concentration	Sediment load (m <sup>3</sup> /month)
1	8.3	NE	1.63	5.50	2,100	0.0006	3.26x10 <sup>6</sup>
2	3.7	SW	0.70	5.00	500	0.0006	7.78x10 <sup>5</sup>



for use. It is also not easy for selecting correctly the sediment concentration by its large variation from 40 ppm to 3500 ppm. For deciding feasonably the discharge and the sediment concentration of the river, we had made a several tests for several combinations. Considering the fact that the proposed model is more suitable for large discharge, we finally suggest taking a discharge larger than the real discharge in each period. This discharge combining with the sediment concentration, which is little than the real average concentration, make sure the total sediment load equal to the real total load. The combination we take is shown in table 3.

- (2) According to the report of Taichung Harbour Bureau (1973), we decide the incident wave height and period in monsoon and summer season as shown in table 3.
- (3) For the initial water depth chart we used the sea chart No.234 of Japanese Navy Waterway survey department in 1903. Fig.8 shows the water depth in the scope we decided. This scope includes the old Cho-Shui River in order to understand the effect of the Cho-Shui river channel regulation in 1911.
- (4) The other input data we used just as follow:

kinematic viscosity of sea water	$1.3 \times 10^{-6} \text{ m}^2/\text{s}$
density of sea water	$1020 \text{ kg}/\text{m}^3$
density of sand	$2650 \text{ kg}/\text{m}^3$
width of river mouth	2.1 km
central grain diameter	0.0002 m
sand relative roughness	0.0007 m
porosity of sand	0.35

### 5.3 The Result of The Numerical Simulation

Fig. 9 shows the simulated result. The centerline of the Cho-Shui river is at the grid 27.5 in x-axis. The result is not good enough because we had not considered the artificial effect just like oyster and other water fowls growth. In the following some discussions about the result is described for three regions.

- (1) The region 1 is from grid 40 to grid 55, being just at the south side of the old Cho-Shui river mouth. Either the sea chart or our simulation result show this region had a quickly accretion from 1903 to 1972. But the accretion velocity of the sea chart is large than the simulation one. For understanding the reason we investigated the shoreline of this region and found that there were many oyster growth fields there. These oyster growth fields had made a large deposition of the longshore sediment load beyond the nature quantity. It seems that the existence of this artificial oyster fields make the deviation of numerical result.
- (2) The region 2 from grid 20 to grid 40 is just at the Cho-Shui river

mouth. Either the field or numerical result showed this region also had a quickly accretion from 1903 to 1972, and a delta had been grown. The location of the delta in our simulation result is at the north side of the field one, but the accretion velocity was almost equal, and the area of accretion in region 1 and region 2 in simulation is almost equal to that of the field result. Consequently this unagreement between numerical and field result might be due to the over deposition in region 1.

- (3) In the region 3 from grid 10 to gride 20, which is at the south side of the Cho-Shui river mouth, there are no artificial oyster growth and other coastal structures. The simulation result agree the field data very well.

From the fact metioned above, if there are no artificial effects, the present model would be able to give a reasonable agreement.

## 6.0 CONCLUSIONS

According to the results described above, we get some conclusions:

- (1) The proposed model assumes that the river flow in the coast around the river mouth is a turbulent plane jet. So the model is more suitable for the rivers with large discharge and velocity.
- (2) The other approachs either mathematical solutions or numerical simulations always lead to unreasonable results that the shoreline shape is nearly symmetrical with respect to the centerline of river mouth even if oblique wave approachs, and that under constant river sediment supply the shape of shoreline at the river mouth maintains no change even though the river discharge or sediment concentration is changed. The proposed model, in contrast, can give more reasonable results with more general conditions.
- (3) The proposed model can be used readily for field cases to predict the shoreline evolution around the river mouth.

## REFERENCES

- Acker, P. and W. R. White, 1973: Sediment Transport, New Approach and Analysis, Proc. ASCE, Vol.99, No. HY-11, 2041-2060.
- Brampton, A. H., 1977: A Computer Method for Wave Refraction, Hydraulic Research Station, Rept. No. IT-172.
- Bakker, W. T. and T. Edelman, 1964: The Coastline of River-Delats, Proc. of the 9th Conf. on Coastal Eng., ASCE, 199-218.
- Grijm, W., 1964: Theoretical Formes of Shorelines, Proc. of the 9th Conf. on Coastal Eng., ASCE, 219-235.

- Hwung, H.H. and Y.Y. Chen, 1981: The Development of the Velocity Distribution in Turbulent Plane Jet Interacting with Obliquely Wave, Proc. of the 5th Conf. on Ocean Eng. in Taiwan, 219-234 (in Chinese).
- Jonsson, I.G., 1966: Wave Boundary Layers and Friction Factor, Proc. of the 10th Conf. on Coastal Eng., ASCE, 127-148.
- Komar, P.D., 1973: Computer Models of Delta Growth Due to Sediment Input from Rivers and Longshore Transport, Soc. American Bull., Vol. 84, 2217-2226.
- Longuet-Higgins, M. S., 1970: Longshore Currents Generated by Obliquely Incident Sea Waves, 1, 2, J. Geophys. Res., Vol. 75, No. 33, 6778-6789.
- Tsuchiya, Y. and S. Yasuda, 1978: A Simple Model for Beach Evolution, Proc. the 25th Japanese Conf. on Coastal Eng., JSCE, 189-193 (in Japanese).
- Willis, D. H., 1978a: An Alongshore Current Beach Evolution Model, Hydraulic Laboratory, Division of Mechanical Eng., National Res. Council of Canada, Rept. No. HY-92.
- Willis, D. H., 1978b: Sediment Load Under Waves and Current, Proc. of the 16th Conf. on Coastal Eng., ASCE, 1627-1635.

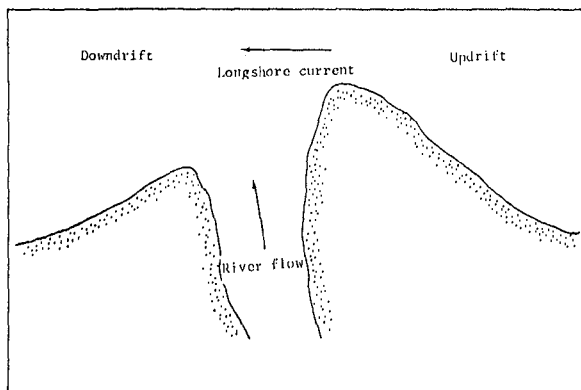
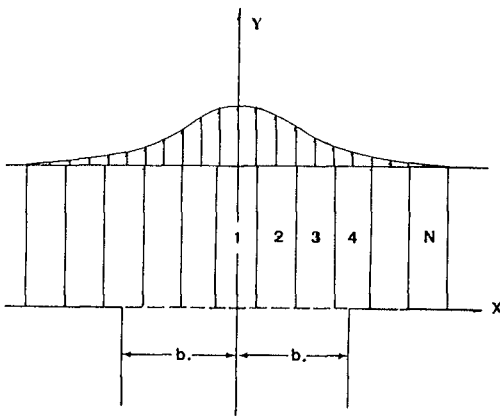
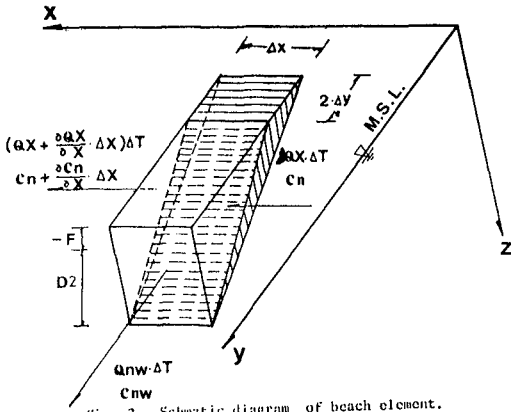


Fig. 1. Typical shoreline shape around a river mouth.



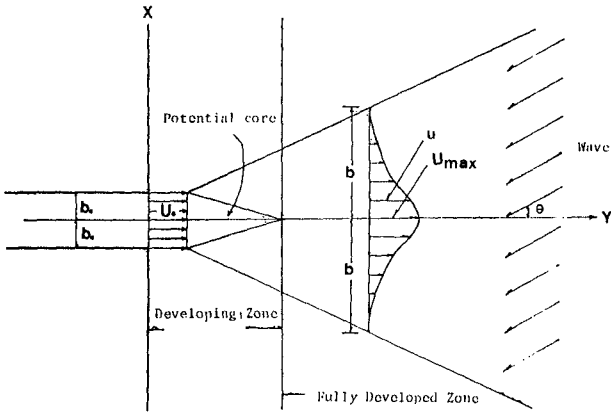
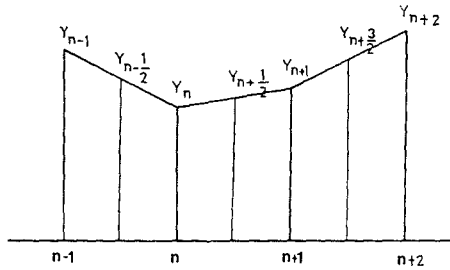
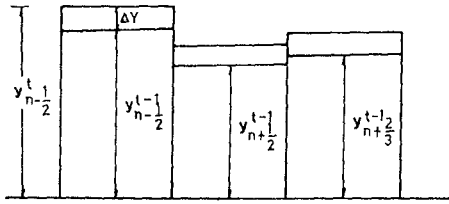


Fig. 4. Turbulent jet flow profile.



(a)



(b)

Fig. 5. Schematic diagram of grid element.

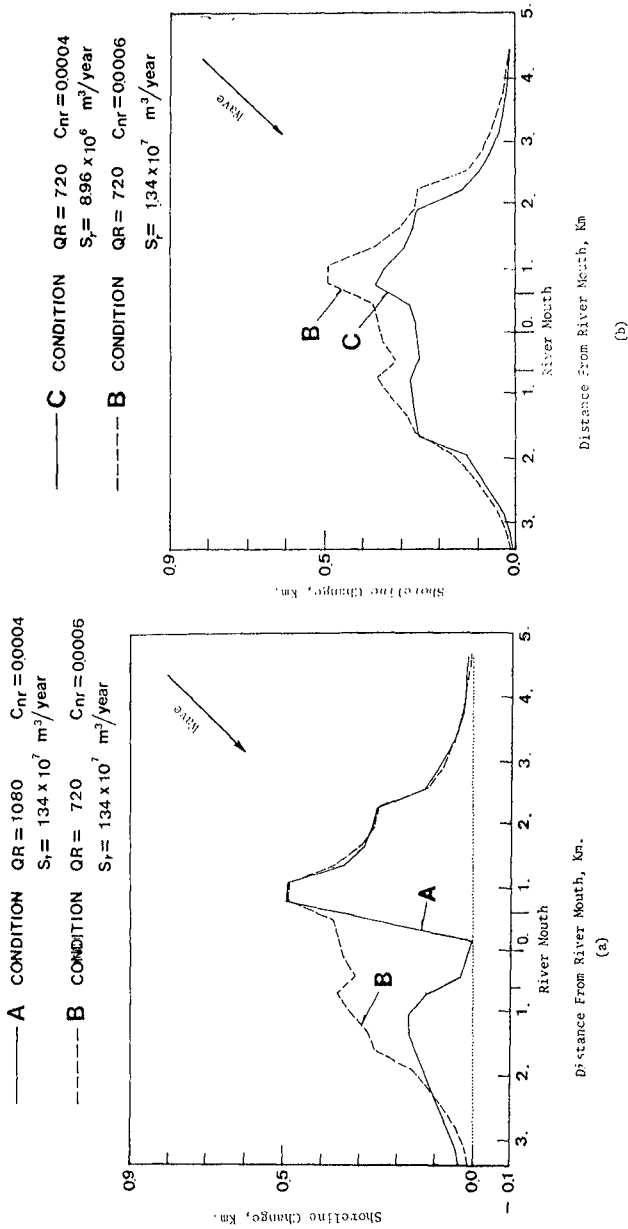


Fig. 6. Computed shoreline evolution around a river mouth. (Note that the scales used for horizontal and vertical coordinates are taken to be different).

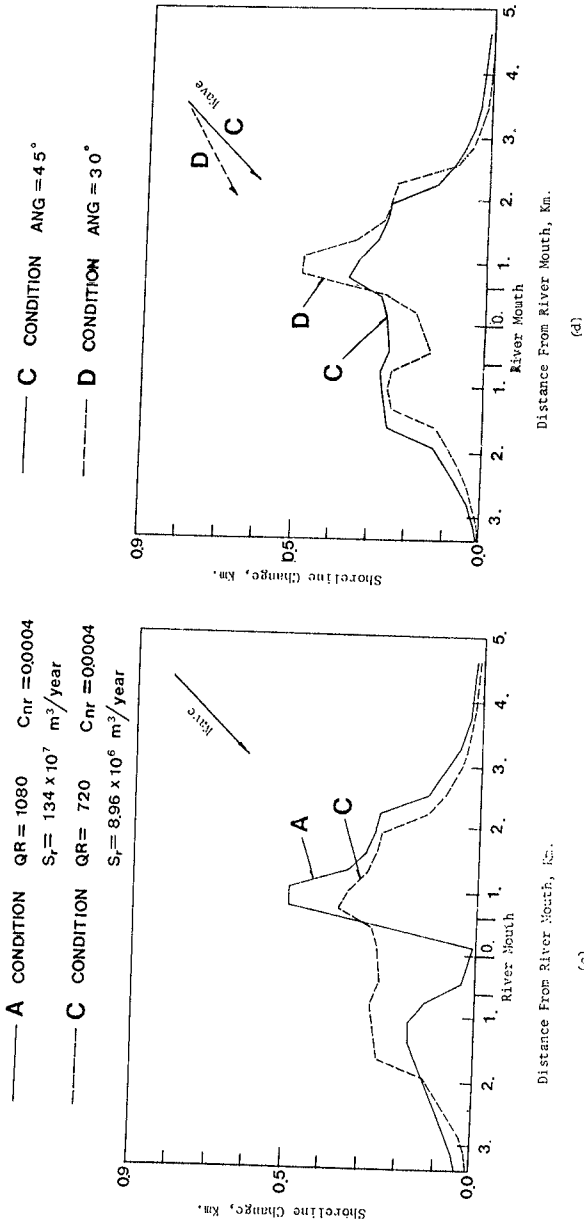


Fig. 6. Computed shoreline evolution around a river mouth. (Note that the scales used for horizontal and vertical coordinates are taken to be different).

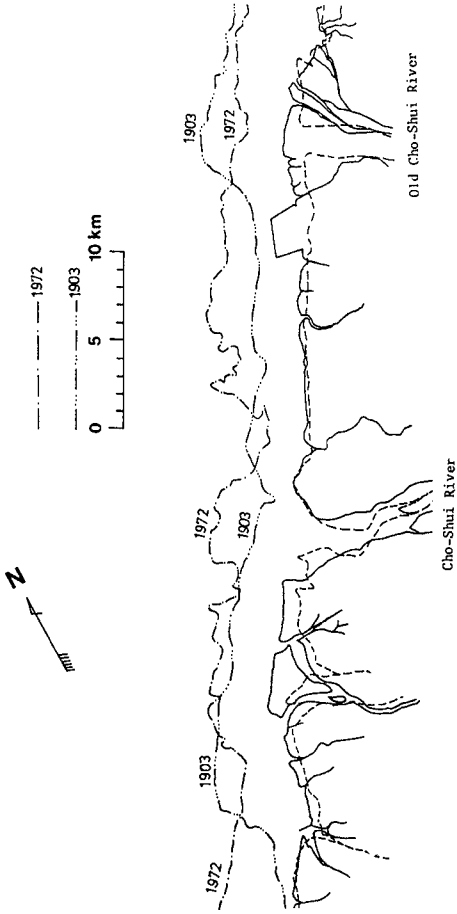


Fig. 7. Actual shoreline changes around the Cho-Shui River mouth. (The shoreline is based on the minimum low tide).



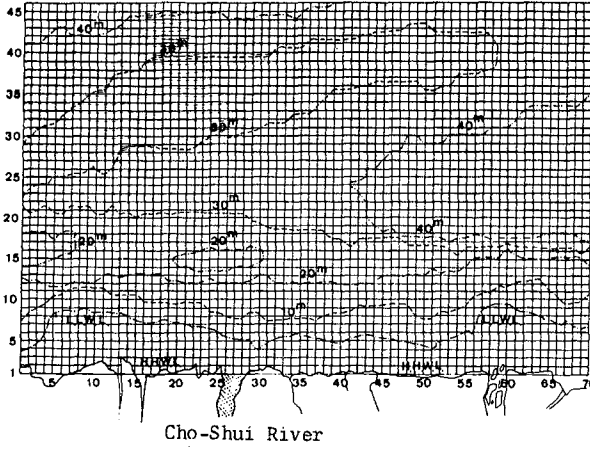


Fig. 8. Schematic diagram at net-grid layout.

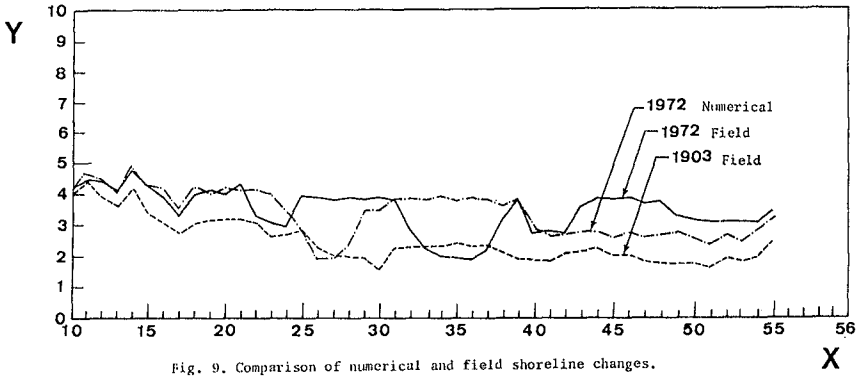


Fig. 9. Comparison of numerical and field shoreline changes.

## CHAPTER TWO HUNDRED THREE

### SEDIMENTATION PROCESSES ALONG THE EAST FRIESIAN ISLANDS, WEST GERMANY

Duncan M. FitzGerald<sup>1</sup>

Shea Penland<sup>2</sup>

Dag Nummedal<sup>3</sup>

#### ABSTRACT

The East Friesian Islands are located on a high energy shoreline. The average deepwater significant wave height exceeds 1.0 m and the spring tidal range varies from 2.7 to 2.9 m. A large easterly net longshore transport rate has caused eastward growth of the barrier islands. Reclamation of tidal flats has significantly reduced the backbarrier area and has resulted in a decrease in the ratio of inlet width to barrier island length from 42% to 16% during the past 300 years.

The headwaters of the major channel dissecting the tidal flats erode in an eastward direction in response to tidal and wave driven currents, wave suspension, and eastward barrier island elongation. Consequently, the drainage systems of most of the inlets are highly asymmetric with 70-80% of the tidal prism coming from the east. This pattern results in a hooked main channel. The location of the channel at the inlet throat is controlled by the westward ebb flow in the main channel, the inertia of ebb flow in the tributary creeks, eastward longshore sediment transport, and the regional stratigraphy.

The position and orientation of the main ebb channel controls the symmetry of the ebb-tidal delta about the inlet shoreline. This, in turn, affects the location of swash bar attachment to the beach and overall trends of erosion and deposition along the downdrift barrier.

#### INTRODUCTION

The East Friesian Islands are a barrier chain that has

- 
1. Department of Geology, Boston University, Boston, MA 02215
  2. Coastal Geology Program, Louisiana Geological Survey, Baton Rouge, LA 70893
  3. Department of Geology, Louisiana State University, Baton Rouge, LA 70803

undergone a great amount of change during the past 300 years. These changes are the result of natural processes and man's influences. It is the objective of this paper to report the historical changes that have occurred to these barriers and to show that these changes can be explained in terms of the regional stratigraphy and the sedimentation processes active in this area.

This paper represents a summary of several papers published by the authors dealing with the morphodynamics of the East Friesian Islands. These works include a discussion of sediment transport patterns at Norderneyer Seegat (Nummedal and Penland, 1981), control of barrier island morphology by inlet sediment bypassing processes (FitzGerald et al, 1984A), and the correlation that exists between inlet narrowing and backbarrier filling (FitzGerald et al, 1984B).

#### PHYSICAL ENVIRONMENT

The East Friesian Islands consist of six barriers and five tidal inlets, spanning a 90 km stretch of shoreline along the West German North Sea coast (Fig. 1). The barriers are separated from the mainland by a 4-12 km wide tidal flat and creek system. The tidal flats are comprised of medium-fine sand near the inlets fining to muds toward the drainage divides (Fig. 2).

The winds in this area blow out of the westerly quadrant during the entire year with an average velocity of 8-15 kt (Luck, 1976A). This produces a net eastward long-

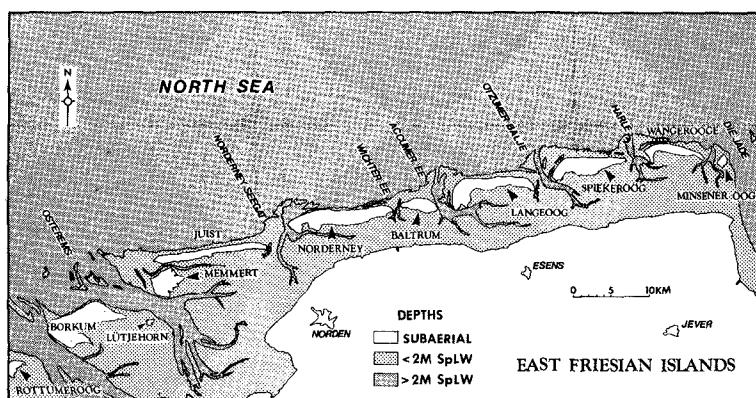


Figure 1. Location map of the East Friesian Islands.



Figure 2. Aerial photograph of Baltrum and Langeoog looking east. Note the coastal structures on the western ends of the islands.

shore power component of  $4.44 \times 10^3 \text{ W-m}^{-1}$  (azimuth= $101^\circ$ ) (Fig. 3) (Nummedal and Penland, 1981). It has been estimated, using morphological data, that a minimum of  $2.7 \times 10^5 \text{ m}^3$  of sand is transported to east yearly (FitzGerald et al, 1984A).

The tides in the North Sea are semi-diurnal and propagate in an easterly direction along the coast. The tidal lag between the islands of Juist and Wangerooge is approximately one hour. Spring tidal range varies from 2.5 m at the mouth of Osterems to 2.9 m at Die Jade.

#### HISTORICAL ANALYSIS

Historical changes of the East Friesian Islands were determined from sequential maps compiled by Homeier and Luck (1969). One of the overlays that were constructed from these maps is shown in Figure 4. During the 310 year period of record the Island of Norderney prograded 12 km to the east. Note, however, that the eastward growth of Norderney was accommodated not only through inlet migration but also by the narrowing of Wichter Ee. This same trait is apparent at Accumer Ee and repeated along the rest of the barrier island chain.

During the past 310 years an abundant sediment supply has led to an 80% increase in aerial extent of the barrier islands (Fig. 4). Of this increase, 45% was due to land reclamation along the backsides of the barrier (Fig. 2), while the rest of the growth (35%) was caused by natural

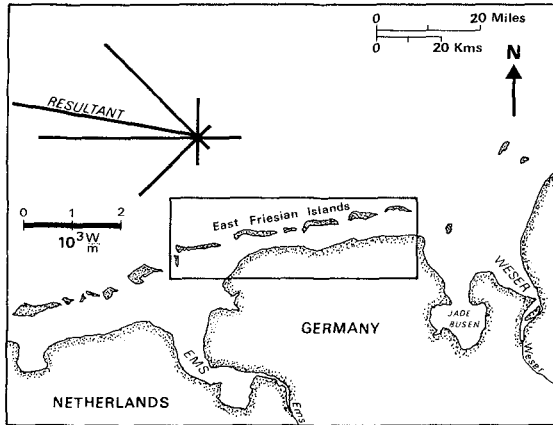


Figure 3. Deep-water wave power distributions for the Bremerhaven data square as determined from the Summary of Synoptic Meteorologic Observations. The northwesterly resultant component of wave energy produces a large easterly longshore transport rate (from Nummedal and Penland, 1981).

processes including spit accretion and beach progradation. During this same time span empoldering was also occurring along the mainland shoreline (Fig. 4). Since 1650 the backbarrier drainage area has been reduced by 30%. As discussed by FitzGerald et al (1984B), the decrease in bay area has caused a reduction in the inlet tidal prisms. This, in turn, has resulted in smaller equilibrium inlet cross sectional areas (O'Brien, 1931, 1969). One reflection of this has been a continued decrease in total inlet width from 20.4 km in 1650 to 9.4 in 1960. One other consequence of the smaller tidal prisms has been a decrease in the size of the ebb-tidal deltas (Walton and Adams, 1976; FitzGerald et al, 1984B).

#### BACKBARRIER PROCESSES

From the historical analysis it is known that most of the East Friesian barrier islands and some of the tidal inlets have migrated in an easterly direction. Therefore, it would be expected that if the backbarrier channels had remained relatively static then through time they would have become hook-shaped and oriented toward the west. However, just the opposite pattern has developed. As seen in Figure 5, the channels are indeed hook-shaped, but they are oriented west, not east. The reason for this is that

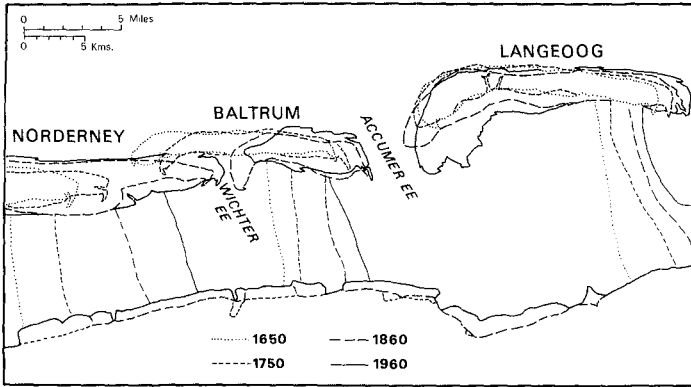


Figure 4. Historical changes for a portion of the East Friesian barrier island chain. Constructed from maps produced by Homeier and Luck (1969).

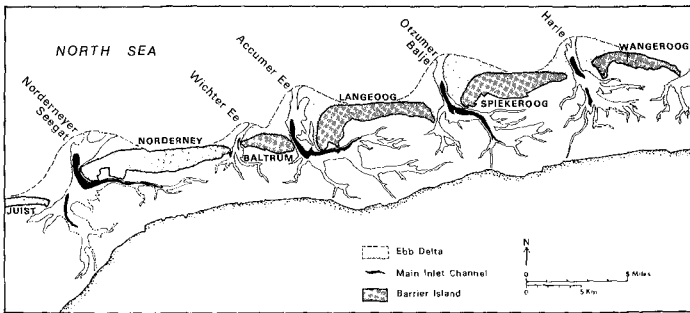


Figure 5. Positions of the main ebb channels and configurations of the ebb-tidal deltas.

through time the drainage divides have also migrated in an easterly direction, keeping pace with the growth of the barrier islands (Fig. 4). The easterly extension of the backbarrier channel systems is a product of headward erosion with a net transport fine-grained material to the east across the drainage divides.

The processes affecting sedimentation in the back-barrier include tidal current 1) time asymmetry and 2) velocity asymmetry. Time asymmetry, as first put forth

by Van Straaten and Kuenen (1957), Postma (1961, 1967), Groen (1967), Reineck (1967) and others, refers to the condition when maximum current velocities do not take place at mid-tide but rather occur early or late in the tidal cycle. This condition was used by the above workers to develop the concepts of scour and settling lags to explain the net landward movement of fine-grained sediment on Dutch and German tidal flats. Velocity asymmetry occurs when the maximum current velocities are unequal during the flood and ebb cycles. In the East Friesian Island backbarrier flood tidal currents predominate. This velocity asymmetry is attributed primarily to: 1) a steepening of the tidal wave and 2) wind effects.

Redfield (1978) has shown that as the tidal wave propagates across a wide shallow shelf it steepens in a manner similar to a wind generated wave along a beach. This steepening produces a shorter period in the rise of the tide than its fall. In the main inlet channels of the East Friesian Islands this difference in tidal duration amounts to approximately one half hour. Because the water has a shorter time to enter the inlet than to exit the currents must move more swiftly, hence, the stronger flood tidal currents.

As mentioned earlier, the winds along this portion of the North Sea blow out of the westerly quadrant during the entire year. This direction coincides with the longest fetch length of the backbarrier region (E-W). Consequently, superimposed on the tidal regime is an easterly movement of water driven by wind stresses. Winds of 15-30 kph are capable of producing current velocities of 10-20 cm/sec. The effect of the winds on the backbarrier water circulation, if tidal currents were symmetrical, would be to cause stronger flood currents in the eastern portion of the inlet drainage and to increase ebb flow in the western part of the drainage system.

Current velocities recorded by Koch and Luck (1974) behind the island of Juist show the effects of the factors that have been discussed above (Fig. 6). Stations #7 and 8 on the western side of the drainage divide have stronger flood than ebb tidal currents. On the opposite side of the divide stations #9 and 10 are clearly dominated by ebb currents.

Thus it is proposed that the easterly migration of the drainage divides is the result of net sediment transport to the east. This is caused primarily by wind-generated currents augmenting and retarding the tidal currents.

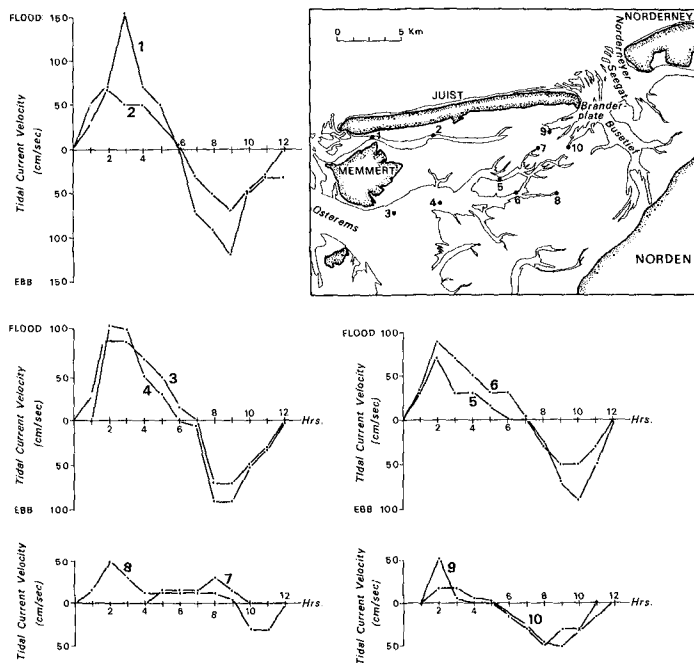


Figure 6. Velocity curves in the tidal channels behind the island of Juist. Note the flood dominance of stations #7 and 8 and the ebb dominance of stations #9 and 10. Velocity data from Koch and Luck (1974).

TIDAL INLETS

Morphology

Tidal inlets along the East Frisian Islands are classified in Hayes' (1979) and Nummedal and Fischer's (1978) mixed energy (tide-dominated) coastal setting. They are fronted by well developed ebb-tidal deltas and have main ebb channels that are dominated by ebb-tidal currents. Inlet throat geometry exhibits a large degree of variability along the island chain. Most often, the channels are highly asymmetric with their thalwegs abutting the updrift or downdrift shoreline (Fig. 5). The factors that control channel morphology include: 1) easterly longshore sediment transport, 2) stratigraphy of the area, 3) backbarrier tidal channel distribution and 4) stabilization projects. Changes in tidal inlet morphology



have been discussed by Luck (1976B).

The strong easterly longshore transport system would seem to dictate that all the Friesian inlets should have channel thalwegs along their eastern downdrift sides. However, this is not the case (Fig. 5). As Sindowski's (1973) stratigraphic study of the barriers has revealed, several of the inlets have scoured into semi-indurated marine clays or glacial tills. The resistance of these sediments to erosion has served to naturally stabilize these inlets and control their geometry. For example, the thalweg at Accumer Ee is anchored along the western side of the inlet, having eroded into glacial tills. While the position of inlet thalweg was stabilizing at Accumer Ee, the back-barrier tidal channels continued to erode in an easterly direction. In this hook-shaped configuration the ebb-tidal flow in the main backbarrier channel is directed toward the western side of the inlet. This further stabilizes the thalweg along the updrift inlet shoreline.

At Nordeneyer Seegat the deepest portion of the inlet channel abuts the island of Norderney (Fig. 5) and has eroded laterally into compacted glacial sediments (Sindowski, 1973). The downdrift location of the channel thalweg is a product of the position and orientation of Buse Tief (a tributary creek with a northwesterly orientation) and the downdrift offset inlet shoreline configuration which affords greater exposure of the inlet channel to the dominant westerly wave energy.

It should be mentioned that during the past 100-150 years many of the inlets have been stabilized with groins and seawalls of various constructions (Fig. 2). A jetty has also been built at Harle Inlet.

#### Inlet Processes

Tidal inlet hydraulics and sediment transport patterns have been studied in detail at Nordeneyer Seegat by Nummedal and Penland (1981) and at Harle Inlet by Hanisch (1981). The data base for these investigations consisted of historical information, grain size data, box cores, bedform measurements, velocity profiles and tracer experiments. Although in each of the studies different sediment transport processes were deemed most important similar sediment transport trends were envisioned. Nummedal and Penland's (1981) sediment transport model for Nordeneyer Seegat is shown in Figure 7. The bedform data at Wichter Ee (Fig. 8) corroborate these general sand transport patterns.

Sand bypasses tidal inlets along the East Friesian Islands by a combination of wave and tidal processes in a manner first described by Brunn and Gerritsen (1959).

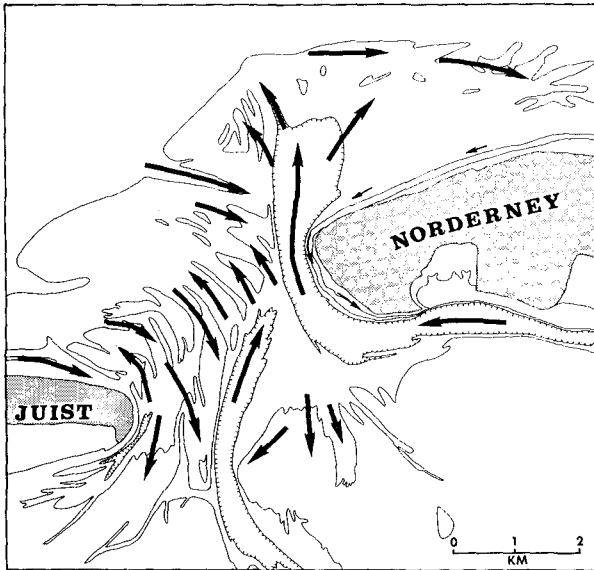


Figure 7. Sediment transport patterns at Norderney Seegat (from Nummedal and Penland, 1981).

One of the end products of inlet sediment bypassing process is the attachment of large bar complexes to the downdrift beach. Sand is transported to the inlets by wave action from the west. Once in the vicinity of the ebb-tidal delta sand is moved toward the inlet through marginal flood channels by flood tidal currents and wave-generated currents. Most of the sand that is delivered to the main ebb channel is transported in a net seaward direction by dominant ebb tidal flow. This sand is deposited along an arcuate series of bars (reef bow) that comprise the outer portion of the ebb-tidal delta. These bars migrate in an easterly fashion along the periphery of the delta (Fig. 9) (Homeier and Kramer, 1957). Aerial views of the ebb-tidal delta bars at Norderney Seegat and Wichter Ee are shown in Figure 10.

Sand from the ebb-tidal delta is ultimately added to the downdrift beach through the landward migration of large swash bars, which may be more than 1 km in length. Bar complexes in the process of welding to the shoreline of Baltrum are illustrated in Figure 11. It should be emphasized that as much as half of the volume of sand that bypasses the inlet is moved onshore by wave action

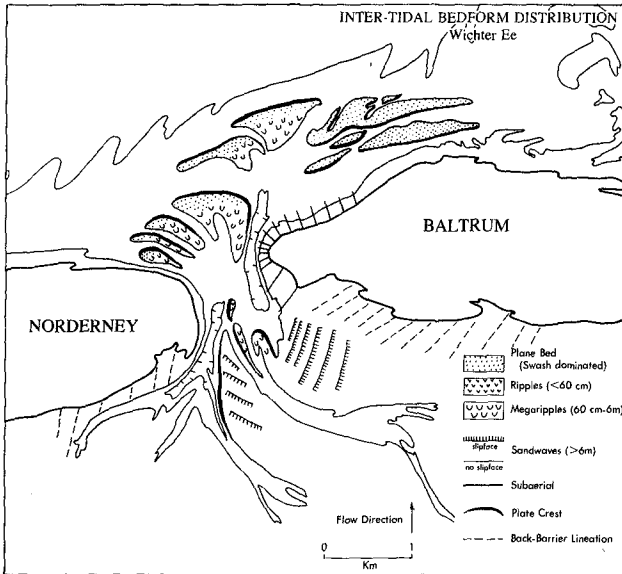


Figure 8. Bedford distribution map for Wichter Ee.

independent of the bar complexes.

#### BARRIER ISLAND PROCESSES

Erosional-depositional trends along the East Friesian Islands are discussed in detail by Luck (1975 and 1976B). These trends correlate well with the location where bars weld to the beach and the local longshore transport patterns. If the bars move onshore some distance down-drift of the inlet shoreline then the updrift end of the barrier is likely to be erosional. Conversely, the site where the bars weld to the beach and the shoreline down-drift of this location are normally accretionary (Luck, 1975).

FitzGerald et al (1984) have also shown that the shape of the East Friesian barriers is tied closely to the bar welding process (Fig. 12). If the bars move onshore close to the inlet mouth then a drumstick barrier develops, as would be predicted by Hayes and Kana (1976). However, when the bar complexes attach to the beach some distance away from the inlet a humpbacked or down-drift bulbous barrier is formed (FitzGerald et al, 1984A).

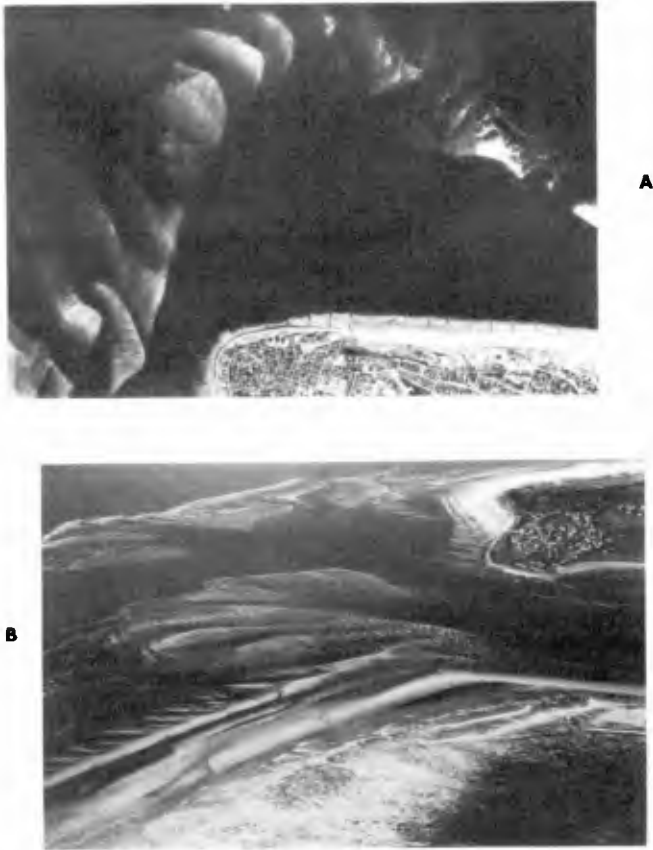


Figure 9. Aerial photographs of A. Norderneyer Seegat and B. Wichter Ee.

The position along the downdrift barrier island shoreline where the bar complexes weld to the beach is a product of the size and symmetry of the ebb-tidal delta. These factors control the amount of overlap of the ebb-tidal delta and therefore the distance from the inlet that the sediment bypassing process is completed. The size of inlet is a function of the backbarrier drainage area. The symmetry of the ebb delta is controlled by the position of the main ebb channel at the inlet throat. The influence of these various factors is demonstrated in Figure 5. Note that the large size of Norderneyer Seegat coupled with the downdrift location of the main channel at the inlet throat have produced a highly asymmetric ebb-tidal delta that



Figure 10. Pathways of bar movement at Wichter Ee and Accumer Ee (from Homeier and Kramer, 1957).

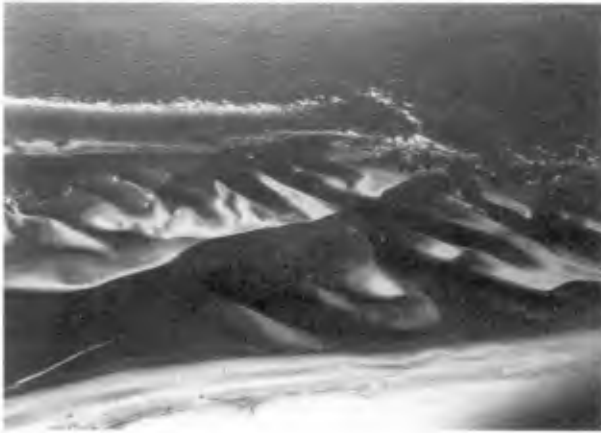


Figure 11. View of swash bars welding to the beach along Baltrum.

greatly overlaps the downdrift beach (5.0 km). This explains the humpbacked development of the island of Norderney. Contrastingly, the western position of the main ebb channel at Accumer Ee has resulted in a symmetrically-shaped delta. Bar welding along Langeoog occurs close to the inlet and thus Langeoog has a drumstick shape.

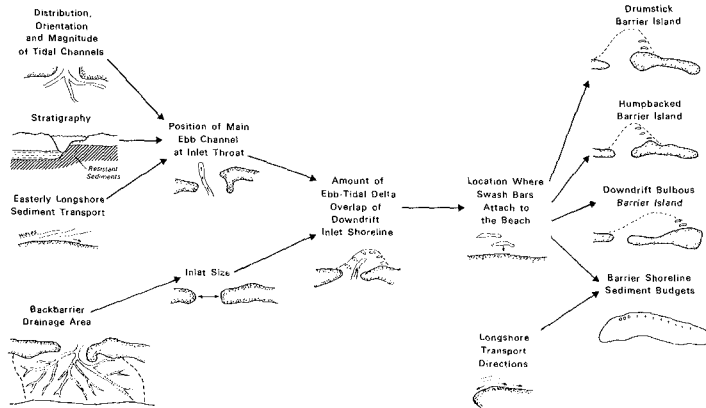


Figure 12. Model of the morphological development of East Friesian barrier islands.

SUMMARY

- 1) The East Friesian Islands have undergone dramatic changes since 1650. An abundant sediment supply has resulted in a 35% increase in aerial extent of the barrier islands. Coincident with this growth was a 30% decrease in backbarrier drainage area due to land reclamation efforts. This decrease in bay size has caused a reduction in the tidal prisms and smaller equilibrium tidal inlet cross sectional areas.
- 2) The strong westerly wind regime of this region produces a dominant easterly longshore transport direction. This easterly transport of sediment has caused an eastward extension of the barrier islands. Some of this eastward growth has occurred through an easterly migration of the tidal inlets. However, most of the growth has been accommodated by a narrowing of the inlets.
- 3) There has been a long-term eastward migration of the backbarrier drainage systems caused by the dominant westerly winds. Wind driven currents augment and retard the tidal currents resulting in a net easterly transport of sediment and headward erosion of the tidal

creeks. This has produced hook-shaped backbarrier channels. The position of the main channel at the inlet throat and the degree of hook-shape of the backbarrier channels are controlled by the stratigraphy of the region. Norderneyer Seegat and Accumer Ee have scoured into resistance sediments and thus have stabilized. At these locations there has been little inlet migration and their main channels are highly hooked. Conversely, Harle Inlet has had a history of easterly migration prior to jetty construction and its main channel is fairly straight.

- 4) Sediment bypasses the inlets in the form of landward migrating swash bars. Sand is also bypassed independent of the bars along the periphery of the delta. The location where the bars weld to the beach is controlled by the overlap of the ebb-tidal delta which, in turn, is a function of inlet size and position of the main ebb channel at the inlet throat. The site where swash bars move onshore coincides with the bulbous portion of the barriers. This accretionary process is responsible for barriers of various shape.

#### REFERENCES

- Brunn, P. and Gerritsen, F., 1959. Natural by-passing of sand at coastal inlets. *Jour. of Waterways, Harbors Div., Am. Assoc. Civ. Eng.*, v. 85, p. 75-107.
- FitzGerald, D.M., Penland, S., and Nummedal, D., 1984A. Control of Barrier Island shape by inlet sediment by-passing: East Friesian Islands, West Germany. *Marine Geology*, v. 60, p. 355-376.
- \_\_\_\_\_, \_\_\_\_\_, \_\_\_\_\_, 1984B. Changes in tidal inlet geometry due to backbarrier filling: East Friesian Islands, West Germany. *Shore and Beach*, v. 52, p. 2-8.
- Groen, P., 1967. On the residual transport of suspended matter by an alternating current: Netherlands. *Jour. Sea Res.*, v. 3, p. 564-574.
- Hanisch, J., 1981. Sand transport in the tidal inlet between Wangerooge and Spickeroog: West Germany. *Spec. Publ. Int. Assoc. Sedimentology*, v. 5, p. 175-185.
- Hayes, M.O., 1979. Barrier Island morphology as a function of tidal and wave regime: *in* Leatherman, S.P., ed., *Barrier Islands: From the Gulf of St. Lawrence to the Gulf of Mexico*. New York, Academic Press, p. 1-28.
- \_\_\_\_\_, and Kana, T., 1976. Terrigenous clastic depositional Environments. *Tech. Rpt. 11, CRD, Dept. of Geol.*,

- University of South Carolina, Columbia, SC, 364 p.
- Homeier, H. and Kramer, J., 1957. Verlagerung der Platen im Riffbogen von Norgerney und ihre Anlandung an den Strand. Jber. Forschungstelle Norderney, v. 8, p. 37-60.
- \_\_\_\_\_, and Luck, G., 1970. Untersuchung morphologischer Gestaltungsvorgänge im Bereich der Accumer Ee als Grundlage für die Beuxteilung der Strand und Dunenentwicklung im Western und Nordwesten Langeoogs. Jber. Forschungstelle Norderney, v. 22, p. 7-42.
- Koch, M. and Luck, G., 1974. Untersuchung zu den Stromungsverhältnissen auf dem westlichen Juister Watt. Jber. Forschungstelle Norderney, v. 13, p. 29-33.
- Luck, G., 1975. Der Einfluss der Schutzwerke der ostfriesischen Inseln auf die morphologischen Vorgänge im Bereich der Seegaten und ihre Einzugsgebiete. Mitt. Leichtweiss Inst., Braunschweig, v. 47, p. 1-22.
- \_\_\_\_\_, 1976A. Protection of the littoral and seabed against erosion. Jber. Forschungstelle Norderney, v. 27, p. 9-78.
- \_\_\_\_\_, 1976B, Inlet changes of the East Friesian Islands. Am. Soc. Civ. Eng., Proc. 15th Conf. Coastal Eng., New York, v. 2, p. 1938-1957.
- Nummedal, D. and Fischer, I., 1978. Process-response models for depositional shorelines: The German and Georgia Bights. Am. Soc. Civ. Eng., Proc. 16th Conf. Coastal Eng., New York, v. 2, p. 1212-1231.
- \_\_\_\_\_, and Penland, S., 1981. Sediment dispersal in Norderneyer Seegat, West Germany. Spc. Publ. Int. Assoc. Sedimentology, v. 5, p. 187-210.
- O'Brien, M.P., 1931, Estuary tidal prisms related to entrance areas. Civ. Eng., v. 1, p. 738-739.
- \_\_\_\_\_, 1969, Equilibrium flow areas of inlets on sandy coasts. Jour. of Waterways, Harbors and Coastal Eng., Proc. 13th Coastal Eng. Cong., p. 761-780.
- Postma, H., 1961. Suspended matter and secchi disc visibility in coastal waters. Neth. Jour. Sea. Res., v. 1, p. 359-390.
- \_\_\_\_\_, 1967. Sediment transport and sedimentation in the estuarine environment: in Lauff, C.H., ed., Estuaries. A.A.A.S., Washington, p. 158-179.



- Redfield, A.C., 1980. Introduction to Tides. Marine Science International, Woods Hole, MA, 198 p.
- Reineck, A.E., 1967, Layered sediments of tidal flats, beaches, and shelf bottoms of the North Sea: in Lauff, G.H., ed., Estuaries. A.A.A.A., Washington, p. 191-206.
- Sindowski, K., 1973. Das ostfriesische kustengebiet. Sammlung Geologischer Fuhrer, v. 57, 103 p.
- VanStraaten, L.M.S.U., and Kuenen, P.H., 1957. Accumulation of fine-grained sediments in the Dutch Wadden Sea. Geol. Mijnbouw, v. 19, p. 329-354.
- Walton, T.L. and Adams, W.D., 1976. Capacity of inlet outer bars to store sand. Am. Soc. of Civ. Eng., Proc. 15th Coastal Eng. Conf., v. 2, p. 1919-1937.

## CHAPTER TWO HUNDRED FOUR

### Lateral Distributions of Water, Salt and Sediment Transport in a Partly Mixed Estuary

R.J. Uncles, R.C.A. Elliott and S.A. Weston\*

The transverse structure of the residual transport of water, salt and suspended sediment in the upper reaches of the Tamar Estuary is investigated. Data were obtained at three cross-sections for spring and neap tides. The transport for each variable is analyzed in terms of the governing physical processes.

#### Introduction

The objectives of this paper are to investigate transverse variations in the transport of water, salt and suspended sediment in the upper reaches of the Tamar Estuary, which is a partly mixed estuary in the southwest of England (Figure 1). Tides are semi-diurnal, with mean neap and spring ranges of 2.2 and 4.7 m, respectively.

Observations of the transverse structure of currents and salinity have been made for some other estuaries, generally with a view to investigating dispersion processes (4,6,7,8,10,11). In this work we present data on the transverse variations in the advective, tidal pumping and vertical shear components of the salt and sediment transport.

#### Observations

Three sections (1, 2 and 3 in Figure 1) were worked for spring and neap tidal cycles. Velocity, temperature, salinity and suspended sediment were profiled at either four or five positions over each section. Some of these stations dried out near low water. Measurements were made at half-hourly intervals from a seatruck anchored in the centre of a section, and at approximately three-quarter-hourly to hourly intervals at the remaining stations. Transverse topography at the experimental sections is shown in Figure 2. Positions of the high and low water lines for the spring and neap tide surveys are drawn, together with the station positions. The mean, axial, depth averaged current speeds in the deepest parts of the sections were roughly  $0.4 - 0.5 \text{ m s}^{-1}$  during spring tides, and less than half this at neap tides.

Table 1 shows background data for sections 1 to 3. Up-estuary flows are negative. The estimated residual flow due to diurnal inequality over each observed tidal cycle is given, together with the sum of flows due to run-off and inequality,  $Q$ .

None of the sections were vertically well mixed for salinity, and

\* Principal, Higher and Assistant Scientific Officers, Natural Environment Research Council, Institute for Marine Environmental Research, Prospect Place, The Hoe, Plymouth PL1 3DH, UK.

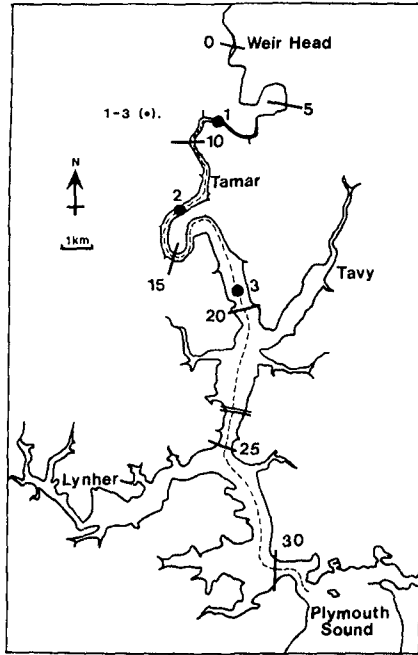


Figure 1. Sketch chart of the Tamar Estuary, showing its sub-division into 5 km sections and the locations of sections 1 to 3.

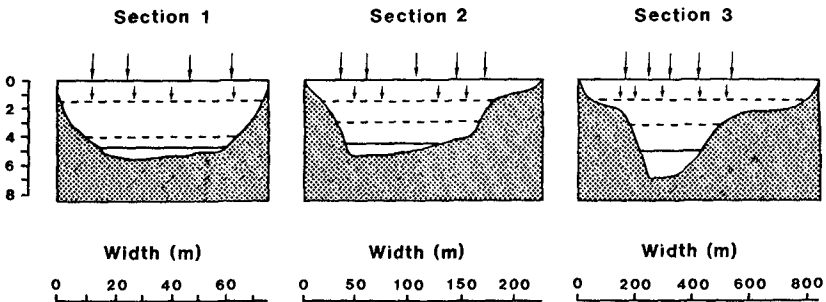


Figure 2. Transverse topography at sections 1 to 3, showing station positions and depths (m) below the high water springs line.

TABLE 1: Background data for sections 1-3, springs (S) and neaps (N). Residual flows due to daily-averaged run-off, diurnal inequality and their sum, Q, are shown (negative up-estuary).

Section	Date	Tidal Range (m)	Run-off ( $\text{m}^3 \text{ s}^{-1}$ )	Inequality ( $\text{m}^3 \text{ s}^{-1}$ )	Q ( $\text{m}^3 \text{ s}^{-1}$ )
1(N)	18/5/82	2.3	3.7	-0.5	3.2
2(N)	19/3/82	1.6	41.8	-1.8	40.0
3(N)	18/2/82	1.8	21.3	3.8	25.1
1(S)	25/5/82	4.9	3.6	0.0	3.6
2(S)	27/4/82	4.6	5.9	0.0	5.9
3(S)	26/2/82	4.9	25.9	14.3	40.2

section 2 (Neaps) was strongly stratified, owing to high run-off (see Table 1). Consequently, at section 2 (Neaps) the residual (tidally averaged) current was directed down-estuary throughout the column. The residual currents at sections 1 and 3 (Neaps) showed classical gravitational circulation. At spring tides, the stronger residual tidal wave (Stokes) transport generated compensating down-estuary residual currents which greatly reduced the gravitational circulation at all sections.

Concentrations of suspended sediment were much higher during spring tides, and increased towards the bed. Therefore, local resuspension of sediment was important. During neap tides, concentrations were typical of those associated with freshwater and marine inputs, although the slight increase in suspended sediment with depth at section 1 (Neaps) showed that a small amount of local resuspension occurred.

#### Calculation of Transport

If  $\bar{Q}$  is the volume transport of water per unit width,  $\bar{Q} = H\bar{U}$ , where H is total depth, U velocity and the overbar denotes a depth average, then the residual transport is given by:

$$\langle \bar{Q} \rangle = \langle H\bar{U} \rangle = Q_E + Q_S = Q_L$$

in which the diamond bracket denotes a tidal average, and where:

$$Q_E = \langle H \langle \bar{U} \rangle \rangle \quad (1)$$

$$Q_S = \langle \hat{H}\hat{U} \rangle \quad (2)$$

with  $\hat{U} = \bar{U} - \langle \bar{U} \rangle$  and  $\hat{H} = H - \langle H \rangle$

$$\text{and } Q_L = Q_E + Q_S \quad (3)$$

Therefore,  $Q_E$  is the Eulerian residual transport per unit width,  $Q_L$  is the residual transport of water per unit width, and  $Q_S$  is the residual transport associated with the tidal wave (equivalent to the Stokes transport for one-dimensional flows (12)). On intertidal areas,  $Q_E$  is also defined from equation (1), except that the substitution  $\bar{U} = 0$  is made during times when a station is not submerged;  $Q_S$  is then defined from equation (3) rather than from equation (2).

The residual, depth averaged rate of transport of salt per unit width is (in ppt  $m^2 s^{-1}$ ):

$$F = F_L + F_{TP} + F_V \quad (4)$$

where  $F_L$  is due to the residual flow of water,  $Q_L$ , and  $F_{TP}$  and  $F_V$  are due to tidal pumping and vertical shear, respectively (5, 9, 13). If  $S$  denotes the instantaneous salinity and  $\hat{S} = S - \langle S \rangle$ , then:

$$F = \langle \overline{HUS} \rangle \quad (5)$$

$$F_L = Q_L \langle \bar{S} \rangle \quad (6)$$

$$F_{TP} = \langle \overline{QS} \rangle \quad (7)$$

$$\text{and } F_V = \langle \overline{HU'S'} \rangle \quad (8)$$

where  $S' = S - \bar{S}$  and  $U' = U - \bar{U}$ . Fluxes are taken to be zero in these tidal averages when a station is not submerged on the intertidal areas.

The residual, depth averaged rate of transport of sediment per unit width is (in ppm  $m^2 s^{-1}$ , where ppm = parts per million by weight of water):

$$G = G_L + G_{TP} + G_V \quad (9)$$

Subscripts have the same meaning as those for the salt transport (equation (4)). If  $P$  denotes the instantaneous suspended sediment concentration, and  $\hat{P} = P - \langle P \rangle$ , then:

$$G = \langle \overline{HUP} \rangle \quad (10)$$

$$G_L = Q_L \langle \bar{P} \rangle \quad (11)$$

$$G_{TP} = \langle \overline{QP} \rangle \quad (12)$$

$$\text{and } G_V = \langle \overline{HU'P'} \rangle \quad (13)$$

where  $P' = P - \bar{P}$ .

Results

The cross-sectionally averaged currents, salinity and suspended sediment load over a tidal cycle are shown in Figure 3. An overbar is used to denote a cross-sectional average, rather than a depth average, in this figure. The cross-sectional area is denoted by A. Cross-sectional values were deduced by interpolating observed data onto a rectangular grid of points covering each section. The interpolation program has been widely used for such problems ( 2, 3 ). The program was also used to extrapolate data from the outer stations on each section (Figure 2) to the banks. Extrapolation is least accurate for the velocity, owing to its large spatial variations. Because of this, a condition of zero velocity was applied at the bed over the region of extrapolation, and on the banks, so that the problem reverted to one of interpolation.

Typical maximum current speeds were of order  $1 \text{ m s}^{-1}$  during spring tides. Speeds were less than half of this during neap tides. Currents

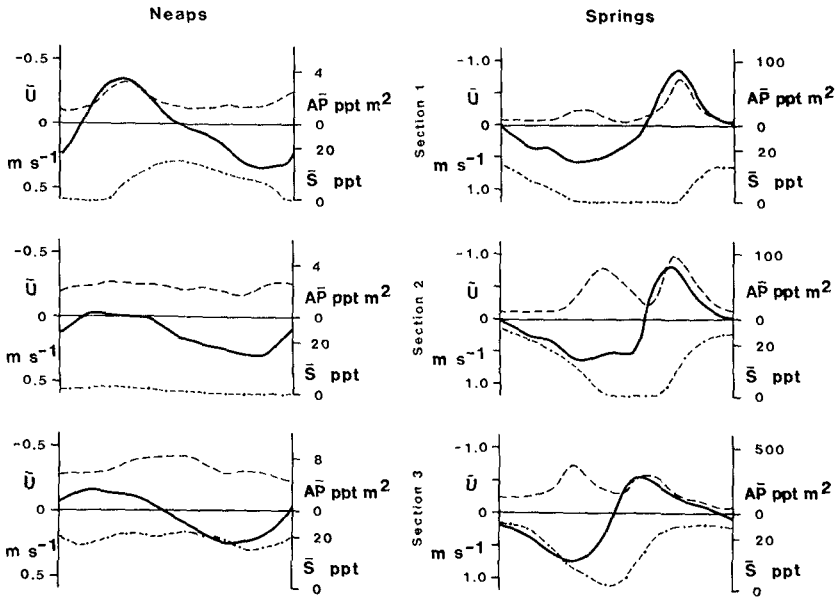


Figure 3. Tidal cycles of sectionally-averaged velocity (—), sediment load (---) and salinity (●-●-●).

were much more distorted during spring tides. At sections 1 and 2 the flood currents exceeded the ebb currents and were of shorter duration.

This tidal asymmetry is typical of estuarine flows in shallow water (14,1). At the seaward section (section 3) the tidal asymmetry was very small and the down-estuary-directed Eulerian residual current was sufficiently strong to generate an ebb-dominated flow.

Asymmetry in the tidal currents affected the suspended sediment load during spring tides. At sections 1 and 2 the enhanced flood currents produced more resuspension and a higher suspended sediment load than during the ebb tides (Figure 3). At section 3 the suspended load maximized during the ebb tide. Sediment loads during spring tides were very much higher than during neap tides. There is some indication that slight resuspension of sediment occurred during maximum flood currents at section 1 (Neaps).

Cross-sectionally averaged salinity is shown in Figure 3. Near the head, at sections 1 and 2, the salinity was zero near low water as the fresh water-brackish water interface swept through the section. Salinity was very low throughout the tidal cycle at section 2 (Neaps) owing to the high freshwater run-off (Table 1).

#### Water Transport

Transverse distributions of the residual rates of transport of water per unit width of estuary are shown in Figure 4. Data are given for neap

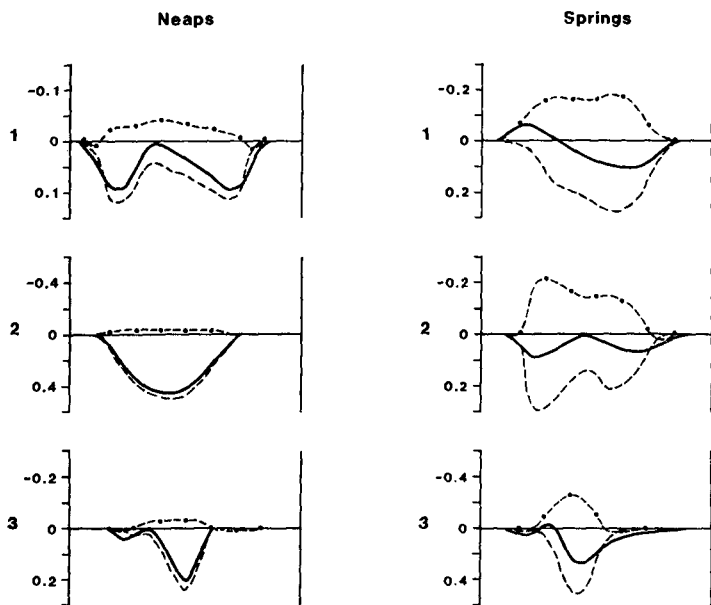


Figure 4. Lateral profiles of residual water transport per unit width ( $m^2s^{-1}$ ). Stokes (-.-), Eulerian (- - -), Total (—).

and spring tides at sections 1 to 3. The tidal wave (Stokes) transport  $Q_S$  was directed up-estuary over the deeper parts of each cross-section, and was small and directed down-estuary over the intertidal areas. This transport was much higher during spring than neap tides. The Eulerian transport  $Q_E$  was always directed down-estuary, and was driven by surface slopes generated by the overall up-estuary tidal wave transport, as well as those due to freshwater inputs to the estuary, density effects and non-linear tidal effects. At section 2 (Neaps) the Eulerian transport had a simple river-like form, with fastest speeds in the deeper, central part of the section. Physical conditions were governed by the high run-off at that time.

Transverse distributions of the total residual rates of water transport per unit width  $Q_T$  were similar to those for the Eulerian transport at neap tides, owing to the smaller tidal wave (Stokes) transport. The distributions at sections 1 and 3 (Neaps) and 2 and 3 (Springs) showed a systematic pattern of circulation. Transport in the central, deeper part of the section was small, whereas over the shallower subtidal and intertidal areas the transport was stronger and directed down-estuary. This pattern consisted of three components: a run-off induced residual flow which was directed down-estuary everywhere; a density-driven component which was down-estuary in the shallow subtidal and intertidal areas, and up-estuary in the deeper, central parts of a section; and a tidally-induced component, which acted to enforce the density-driven flow. The density-driven and tidally-induced flows opposed the river-like circulation in the centre of the sections, leading to small transport there. The opposite occurred in the shallow areas.

#### Salt Transport

Transverse distributions of the residual rate of salt transport per unit width ( $\text{ppt m}^2 \text{ s}^{-1}$ ) are given for sections 1 to 3 in Figure 5. Rates of transport due to vertical shear ( $F_V$  in equation (8)), tidal pumping ( $F_{TP}$  in equation (7)) and advection ( $F_L$  in equation (6)) are shown.

Transport due to vertical shear was always directed up-estuary, and was largest in the deeper, central parts of a section. Here, the vertical variations in both currents and salinity were largest, and pronounced gravitational circulations occurred. Transport due to tidal pumping was directed up-estuary in the deeper parts of a section, but sometimes reversed direction in the shallow areas. With the exception of section 1 (Neaps), this down-estuary transport due to tidal pumping was extremely small, and is thought to be due to the reduced phases of the tidal currents (a response to the increased frictional drag in these areas) relative to those in the deeper regions.

The advective transport of salt due to the residual flow of water had a very similar pattern to the residual flow of water (compare Figures 4 and 5). This is because of the relative insignificance of transverse variations in salinity when compared with sectionally-averaged values. Thus, the advective transport of salt tended to be small in the deeper parts of a section, and large and directed down-estuary in the shallower areas. Rates of transport due to vertical shear and tidal pumping were large and directed up-estuary in the deeper part of a section. Therefore,



the residual transport was directed up-estuary in the central, deeper part of a section, and directed down-estuary in the shallow regions.

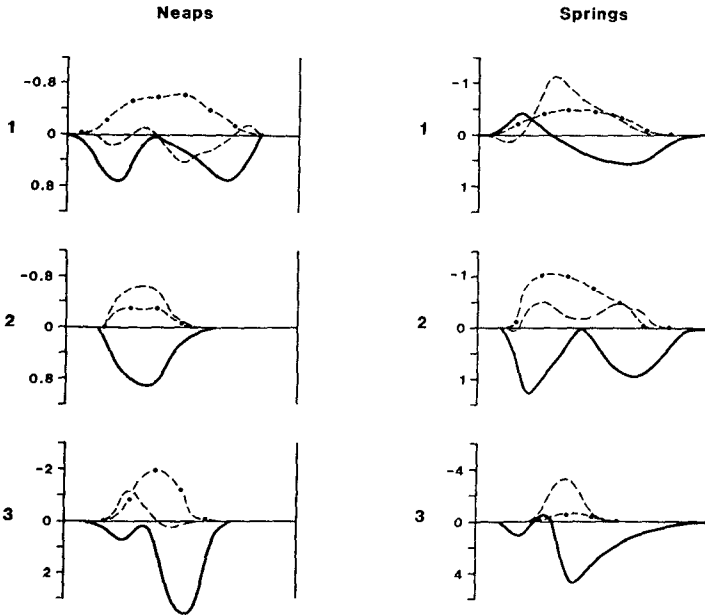


Figure 5. Lateral profiles of residual salt transport per unit width ( $\text{ppt m}^2 \text{s}^{-1}$ ). Advection (—), Pumping (- - -), Shear (-.-).

#### Sediment Transport

Transverse distributions of the residual sediment transport per unit width ( $\text{ppm m}^2 \text{s}^{-1}$ ) are given for sections 1 to 3 in Figure 6. Rates of transport due to vertical shear ( $G_v$  in equation (13)) were negligible and are not plotted. This is because of the low and fairly uniform concentrations of suspended sediment during neap tides; marine and freshwater concentrations were comparable (5-10 ppm). During spring tides the much higher concentrations were generated by local resuspension at maximum flood and ebb currents, and temporal correlations of the vertical shear transport were small.

The advective transport of suspended sediment due to the residual flow of water had a very similar pattern to the residual flow of water (compare Figures 4 and 6). Transport during spring tides was between one and two orders of magnitude larger than during neap tides.

Tidal pumping of sediment was directed up-estuary at section 1, and was considerably larger during the spring tide. The residual, up-estuary transport due to tidal pumping was a consequence of enhanced re-suspension of sediment, and associated up-estuary transport during peak flood currents (see also Figure 3). Flood currents also exceeded ebb currents at section 2 (Springs), and up-estuary tidal pumping occurred in the shallow areas. However, weak down-estuary pumping occurred in the deeper part of the section. This was possibly due to the absence of easily erodible bed sediment in the deepest part of the section. Tidal pumping of non-locally suspended sediment acted in the opposite way to that for salt (salinity increased down-estuary, whereas suspended sediment concentrations decreased), and so pumped sediment out of the estuary. Asymmetry between flood and ebb currents was small at section 3 (Springs). Here, the associated up-estuary pumping in the shallow areas was weak, and the down-estuary pumping in the deeper part of the section was large.

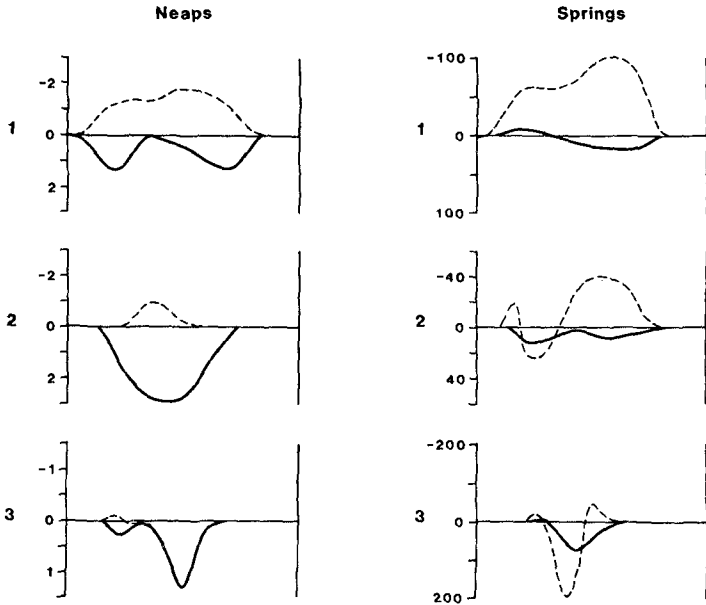


Figure 6. Lateral profiles of residual sediment transport per unit width ( $\text{ppm m s}^{-2}$ ). Advection (—), Pumping (---).

#### Conclusions

Spring tidal currents showed a strong asymmetry in the upper reaches of the estuary with flood currents exceeding ebb currents. Maximum current speeds were more than twice those at neap tides. Suspended sediment concentrations at spring tides were between one and two orders of magnitude higher than those at neap tides, owing to strong local resuspension of

sediment in the faster tidal currents.

The residual, tidal wave (Stokes) transport of water was much higher during spring tides. The transport was directed up-estuary in the deeper parts of a section, but could reverse direction in the shallow intertidal areas. The Eulerian residual transport was always directed down-estuary. The total residual rate of transport tended to be directed down-estuary over the shallow and intertidal areas, whereas in the deeper parts of a section it tended to be smaller, and could be directed up or down-estuary.

Tidal pumping of salt was directed up-estuary in the deepest part of a section, whereas it was small and could be directed down-estuary in shallow and intertidal areas. This was possibly due to reduced phases of the tidal currents (slack water occurring earlier) in the shallow areas. Vertical shear transport of salt was always directed up-estuary, and was largest in the deeper regions where vertical stratification was more pronounced and gravitational circulation was present. Residual salt transport due to local advection by the residual flow of water closely followed the pattern of residual water flow, owing to the relative insignificance of cross-estuary variations in salinity. The total residual transport of salt was directed up-estuary in the deeper parts of a section, and down-estuary in the shallower regions.

Tidal pumping dominated the suspended sediment transport during spring tides. Pumping was directed up-estuary over the whole section near the head. This was because of the much stronger flood currents (and associated erosion stresses) and the existence of a plentiful supply of bed sediment for erosion and resuspension. The asymmetry in the tidal currents was weaker further down-estuary. Tidal pumping was directed down-estuary in the deeper part of a section. This is thought to be due to the absence of easily erodible bed sediment in the deep channel. In absence of local resuspension, the tidal pumping of sediment acted in the opposite way to the tidal pumping of salt (salinity decreased up-estuary whereas suspended sediment concentrations increased). Fine sediment was present in the shallow and intertidal areas further down-estuary, and the tidal pumping there was weak but directed up-estuary.

Vertical shear transport of sediment was very much smaller than that due to pumping and advection. Pumping dominated advection at spring tides, whereas the reverse was true at neap tides. Transport was much smaller at neap tides, but weak resuspension and tidal pumping occurred near the head.

#### Acknowledgements

This work forms part of the Physical Processes programme of the Institute for Marine Environmental Research, a component of the Natural Environment Research Council (NERC). It was partly supported by the Department of the Environment on contract No. DGR 480/48.

## Appendix - References

1. Allen, G.P., Salomon, J.C., Bassoullet, P., Du Perihout, Y., and De Grandpre, C., "Effects of tides on mixing and suspended sediment transport in macrotidal estuaries," Sedimentary Geology, 26, 1980, pp. 69-90.
2. Applications Consultants Inc., "Surface approximations and contour mapping (SACM)," Houston, Texas, USA.
3. Batcha, J.P., and Reese, J.R., "Surface determination and automatic contouring for mineral exploration, extraction, and processing," Quarterly J. Colorado Sch. of mines, 59, 1964, pp. 1-14.
4. Dyer, K.R., "The salt balance in stratified estuaries," Estuar. Coastal Mar. Sci., 2, 1974, pp. 273-281.
5. Fischer, H.B., List, E.J., Koh, R.C.Y., Imberger, J., and Brooks, N.H., "Mixing in inland and coastal waters," Academic Press, N.Y., 1979, 484 pp.
6. Hansen, D.V., "Currents and mixing in the Columbia River Estuary," Trans. Joint Conf. on Ocean Sci. and Ocean Engineering, 1965, pp. 943-955.
7. Hughs, F.W., and Rattray, M., "Salt fluxes and mixing in the Columbia River Estuary," Estuar. Coastal Mar. Sci., 10, 1980, pp. 479-493.
8. Hunkins, K., "Salt dispersion in the Hudson Estuary," J. Phys. Oceanogr., 11, 1981, pp. 729-738.
9. Lewis, R.E., and Lewis, J.O., "The principal factors contributing to the flux of salt in a narrow, partially stratified estuary," Estuar. Coastal Shelf Sci., 16, 1983, pp. 599-626.
10. Murray, S.P., and Siripong, A., "Role of lateral gradients and longitudinal dispersion in the salt balance of a shallow well mixed estuary," Estuarine Transport Processes (Kjerfve, B., ed.) Univ. S. Carolina Press, 1978, pp. 113-124.
11. Rattray, M., and Dworski, J.G., "Comparison of methods for analysis of the transverse and vertical circulation contributions to the longitudinal advective salt flux in estuaries," Estuar. Coastal Mar. Sci., 11, 1980, pp. 515-536.
12. Uncles, R.J., and Jordan, M.B., "A one-dimensional representation of residual currents in the Severn Estuary and associated observations," Estuar. Coastal Mar. Sci., 10, 1980, pp. 39-60.
13. Uncles, R.J., Bale, A.J., Howland, R.J.M., Morris, A.W., and Elliott, R.C.A., "Salinity of surface water in a partially-mixed estuary, and its dispersion at low run-off," Oceanologica Acta, 6, 1983, pp. 289-296.
14. Uncles, R.J., Elliott, R.C.A., and Weston, S.A., "Observed fluxes of water, salt and suspended sediment in a partly mixed estuary," Estuar. Coastal Shelf Sci., (in press).

## CHAPTER TWO HUNDRED FIVE

### STABILITY PARAMETERS OF WESTERN SCHELDT ESTUARY

by

H. de Jong<sup>1</sup> and F. Gerritsen<sup>2</sup>

#### 1. INTRODUCTION

The Western Scheldt is a major estuary in the Southern part of The Netherlands and the Northern part of Belgium. It is an important navigational route connecting the city of Antwerp with the North Sea. At the entrance Vlissingen is a major Dutch port. (Figure 1)

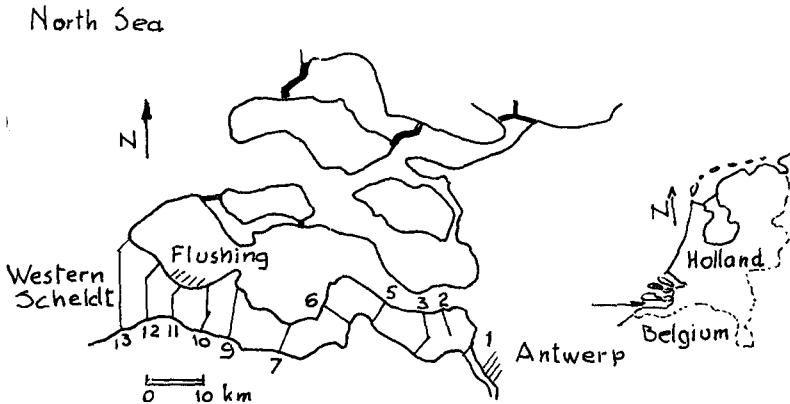


Figure 1: Western Scheldt Estuary

During recent years much dredging work has been carried out by the Belgian Government (16 million m<sup>3</sup> in 1977) to remove shoals and improve channel alignments in the estuary, in view of increasing vessel drafts and traffic density to the port of Antwerp (Belgium).

It is of great importance to predict the effects of future dredging operations, carried out in the outer shoals and in major navigation channels on tidal regime (tides and currents) and on morphological changes in other parts of the estuary.

<sup>1</sup> Researcher, Rijkswaterstaat, Vlissingen, The Netherlands

<sup>2</sup> Professor and Chairman, Dept. of Ocean Engineering, Univ. of Hawaii Honolulu, HI

Calculations based on detailed hydrographic surveys have indicated that where the estuary used to be subject to sedimentation, the situation may now have changed to one of dominant erosion.

## 2. MORPHOLOGICAL STABILITY OF TIDAL CHANNELS

### The stability equation

The morphological stability of tidal channels has two major components:

- (a) location stability
- (b) cross-sectional stability

The location stability has to do with the meandering of channels, where the channel migrates gradually within the physical boundaries of the estuary. The nature of this process is strongly affected by the type of estuary, by the nature of bottom conditions (presence of silt layers) and by the type of coastal protection works (if present) along the estuary's boundaries.

Migration of tidal channels in the outer part of the estuary is often a cyclic process with a period of a number of years which is governed by the external boundary conditions related to tide, waves and littoral drift. The process of cyclic changes can be arrested or slowed down by high capacity dredging operations.

The development and migration of tidal channels in an estuary is connected with the system of flood and ebb channels in an estuary. Flood channels are characterized by dominating flood flow; they have a shoal at their inner end. In ebb channels the ebb flow dominates and a shoal is usually present at their seaward ends. Tidal channels are neutral when flood and ebb flow are of equal magnitude.

Cross-sectional stability relates to the variability of the cross-sectional area of tidal channel and to its dependency on tidal flow characteristics.

Tidal inlets are often characterized by a gorge, in which the tidal flow is well organized and where channel migration does not play a major role.

In this paper we will particularly be concerned about the cross-sectional stability of tidal channels whereby we will examine the total channel, as well as the individual flood or ebb channels, if they can be clearly identified.

The cross-sectional stability of a tidal channel is in general governed by the equation:

$$\frac{\partial Q_s}{\partial x} = 0 \quad (1)$$

if  $Q_s$  represents the sediment transport rate ( $m^3/sec$ ) and  $x$  the mean direction of the flow through a channel.

For (1) to be valid it is necessary that the mean sediment concentration over the channel cross-section does not vary with time.

For channels subject to tidal flow the stability equation must be intergrated over time and gives the condition ( $T$  = tidal period):

$$\frac{\partial}{\partial x} \int_0^T Q_s dt = 0 \quad (2)$$

under the assumption that the transport process repeats itself in equal manner during subsequent tidal cycles.

In case a strong difference exists between neap tide and spring tide cycles the integration is to be performed over a series of cycles to cover a sequency which repeats itself:

$$\frac{\partial}{\partial x} \int_0^t Q_s dt = 0 \quad (3)$$

where  $t \gg T$ .

Unfortunately the detailed knowledge about the sediment transport process is not adequate enough at the present time to use equation (3) with confidence to predict changes in bottom configuration.

#### Solutions to the stability problem

For many years the relation between the cross-section of a tidal channel and the tidal flow characteristics has been recognized.

A classical paper is that of M.P. O'Brien (9) who arrived at an empirical relationship between cross-sectional area and tidal prism for inlets on the U.S. West Coast. The tidal prism was calculated as the product of tidal storage area and tidal range. For the latter the difference between MHHW and MLLW was assumed.

The relation obtained was purely empirical because no consideration was given to relevant physical parameters such as:

- grain size
- littoral drift transport in relation to tidal transport,
- river discharge
- relative depth of channel (Chézy)
- presence of jetties
- presence of shoals, etc.

Because of the complexity of the problem it may be expected that certain empirical relationships would not be universally valid for other situations.

In more recent papers O'Brien and several other authors recognized this problem and certain modifications of the relationship were proposed.

In 1960 and in subsequent years Bruun and Gerritsen (3) attempted to evaluate the effect of various physical parameters on the empirical stability equations. They introduced the concept of stability shear stress  $\tau_s$  and found that this parameter was a useful parameter to define inlet stability. The variability of  $\tau_s$  with a number of physical parameters affecting inlet stability was thereby investigated. A comprehensive analysis is presented by Bruun (4).

A satisfactory solution to the stability equation (3) can only be obtained if the process of sediment transport through the channels can be accurately described by a sediment transport formula.

At present existing knowledge does allow the description and calculation of tides and currents in an estuary in a satisfactory manner. Work of fundamental importance was done by Dronkers (6) for one-dimensional flow and by Leendertse (8) for two-dimensional tidal problems. However the state of the art regarding the description of the sediment transport phenomenon in an estuary is not accurate enough to predict erosion and sedimentation rates according to equation (3).

The Kalinske and Morra formulation has been used in combination with a one-dimensional tidal model to predict morphological changes in the form of erosion and sedimentation rates for the Western Scheldt. The one-dimensional tidal model does not adequately distinguish between transport through channels and over shoals. Results of this approach can at best be qualitative.

The problem is magnified in the outer estuary where a formulation is required describing the sediment transport as a function of waves and currents combined. Such a formulation was proposed by Bijker (2).

Until a sufficiently accurate formulation for the sediment transport processes has been found an interim solution may be utilized, in which a mathematical model for flow is utilized to calculate the changes in water levels and currents, and where the changes in bottom configuration are predicted from empirical relationships between flow parameters and channel dimensions. For this, however, it is necessary that these empirical relationships, which have a statistical nature, are sufficiently accurate to use them as a predictive tool. The method to be applied is an iterative scheme: the changes in tide conditions are predicted using the numerical tidal hydraulics model; then channel profiles are adjusted based on the empirical relationship between tide parameters and channel dimensions. The process is repeated until stability conditions are fulfilled. It is the purpose of this paper to investigate a number of empirical relationships for the whole of the Western Scheldt, whereby the channel cross-section is related to a variety of tidal parameters such as velocity, tidal discharge, tidal prism, bottom shear stress, Chézy coefficient, etc.

The assumption is made that certain empirical relationships are not only valid for the entrance area but are applicable to the inner tidal channels as well.

It is furthermore assumed and verified that river discharge is negligible compared to tidal discharge and that density differences have no appreciable effect on the sediment transport equation.

The usefulness of various relationships will be evaluated from the calculated values of correlation coefficients obtained from the regression analysis.

In the study the cross-sectional area is treated as the independent variable, plotted on the horizontal axis of the regression diagrams.



Flow parameters are then considered as a function of the cross-sectional area.

Furthermore it must be noted that all tidal characteristics refer to mean tidal conditions, unless otherwise stated.

### 3. METHOD OF INVESTIGATION

#### Data used for analysis

The data have been obtained from extensive field measurements carried out by the Hydraulic Advisory section of the Rijkswaterstaat at Vlissingen over a number of years.

The basis is the set of velocity measurements, simultaneously carried out in different stations, at depths ranging from a little below the surface to a short distance above the bottom. Most of the measurements were carried out with the Ott current meter, and included current directions. The measurements were always done twice on successive days. Velocity measurements were integrated to flow values and flow values to tidal volumes. All flow data were reduced to mean tide conditions valid for the year in which the measurements were carried out. For this reduction the tidal range of the nearest tidal station was used as a reference. The reduction was done in a linear fashion, which has been shown to be an adequate procedure. Simultaneous measurements were usually carried out in 5-7 stations in one profile in cross-sections numbered 1-11 in Figure 1. Simultaneous measurements were carried out in a reference station. The vertical tide was measured (continuously) at 5 fixed tidal stations along the estuary. A discussion on the tidal regime for the Western Scheldt is presented by Daamen (5). The bottom of the Western Scheldt consists of fine alluvial sands, diameter  $d_{50} = 40-450\mu$ . For the profiles 12 and 13, situated in the outer part of the estuary (see Figure 1) insufficient velocity measurements were available to form a reliable base for the calculation of tidal flow and tidal prism. Therefore these values were calculated from the flow values for Profile 11, using the continuity equation. The possible error in the flow data is estimated at  $\pm 10\%$ .

The cross-sectional area was used in two different ways in the analysis of regression relationships:

- (1) the area  $A_c$  measured between bottom and the standard reference level N.A.P. (approximately equal to Mean Sea level)
- (2) the area  $A_c^1$  measured between the bottom and the water level at the time the flow (Q) has its maximum value ( $Q_{max}$ )

Reference is made to Figure 2. For the ebb situation  $A_c$  and  $A_c^1$  are not much different. For the flood, however, there is a considerable difference between  $A_c$  and  $A_c^1$ .

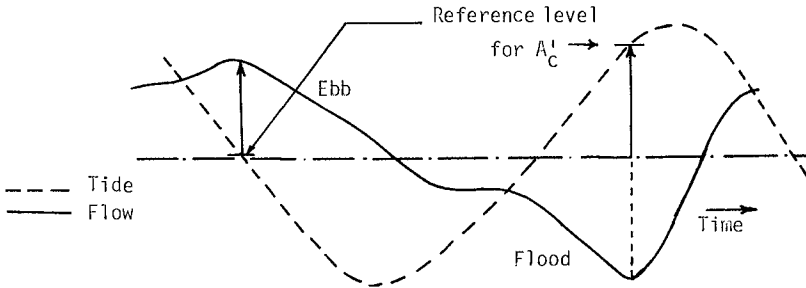


Figure 2: Tide and Flow Characteristics

### Method of Analysis

The following hydraulic and morphological parameters were included in the analysis:

$\bar{v}$ : mean velocity over tidal period ( $\text{m sec}^{-1}$ )

$v_{\text{max}}$ : maximum velocity  $\frac{Q_{\text{max}}}{A}$  ( $\text{m sec}^{-1}$ )

$Q_{\text{max}}$ : maximum tidal flow through cross-section ( $\text{m}^3/\text{sec}$ )

$\Omega_{\text{flood}}$ : tidal volume ( $\int Q dt$ ) during flood ( $\text{m}^3$ )

$\Omega_{\text{ebb}}$ : tidal volume during ebb ( $\text{m}^3$ )

$A_C$ : cross-sectional area below NAP ( $\sim$ MSL) ( $\text{m}^2$ )

$A'_C$ : cross sectional area below level at which  $Q_{\text{max}}$  occurs ( $\text{m}^2$ )

$\tau_s$ : stability shear stress ( $\text{N}/\text{m}^2$ )

$C$ : Chézy coefficient ( $\text{m}^{1/2} \text{sec}^{-1}$ )

A regression analysis between morphological and hydraulic parameters has been carried out for various cross-sections (Fig. 1). The statistical significance of the relationship tested is expressed by the value of the calculated correlation coefficient.

In the regression analysis the cross-section is used as the independent parameter, and is plotted horizontally in various graphs.

In Bruun and Gerritsen (3) the stability shear stress was used as a parameter of tidal inlet cross-sectional stability. It was defined as the mean bottom shear stress along a cross-sectional profile at maximum flow conditions during spring tide.

The use of springtide was selected because bedforming flow conditions occur during that phase of the tide. To some degree this corresponds with the calculation of the tidal prism in O'Brien (9) where for the U.S. West Coast the difference between MHHW and MLLW is used as basis for the calculations.

In this study all data have been referenced to mean tide conditions; regarding the stability shear stress values with reference to both mean tide and springtide were calculated.

The general formulation of the mean shear stress in a channel cross-section may be given by:

$$\tau = \rho g R S \quad (4)$$

where R is the hydraulic radius of the channel and S the slope of the energy gradient line.

Using the Chézy expression for the average channel velocity v:

$$v = C \sqrt{RS} \quad (5)$$

The mean shear stress can be expressed in terms of v:

$$\tau = \rho g \frac{v^2}{C^2} \quad (6)$$

and since  $v = \frac{Q}{A}$ , also in terms of Q:

$$\tau = \rho g \frac{Q^2}{C^2 A^2} \quad (7)$$

From equation (7) the stability shear stress is defined by:

$$\tau_s = \rho g \frac{Q_{\max}^2}{C^2 A^2} \quad (8)$$

where  $Q_{\max}$  is the maximum tidal flow during springtide for either ebb or flood conditions.

From equation (8) the cross-sectional area A can be expressed in terms of stability shear stress by the equation:

$$A = \frac{Q_{\max}}{C \sqrt{\tau_s / \rho g}} \quad (9)$$

In a correlation diagram between  $\frac{Q_{\max}}{C \sqrt{\tau_s / \rho g}}$  and A a line under  $45^\circ$  will be obtained if proper values for C and  $\tau_s$  are introduced.

For the cross-section value in equation (9) both the quantities  $A_c$  and  $A_c^2$  have been utilized in the regression analysis.

Stability shear stress for a combined effect of current and wave conditions.

In the outer part of the estuary the sediment transport by tidal currents is affected by waves.

As a first attempt to evaluate the effect of wave action on the stability shear stress parameter the formula developed by Bijker (2) was used to describe the bedload transport as a function of waves and currents. It is realized that the bottom sediment in this area is comparatively fine and therefore transport in suspension dominates. The use of the Bijker formula may still be valid because of the relationship between bedload transport and transport in suspension.

The Bijker formula can be written in the form:

$$Q_b = BD \frac{v}{C} \sqrt{\frac{\tau_c}{\rho}} e^{-\frac{0.27 \Delta D \rho g}{\mu \tau_c \left\{ 1 + \frac{1}{2} \left( \xi \frac{u_0}{v} \right)^2 \right\}}} \quad (10)$$

where  $Q_b$  = bedload transport

$B$  = dimensionless coefficient

$C$  = Chézy coefficient

$\tau_c$  = bottom shear stress from currents only

$v$  = mean velocity over profile

$u_0$  = maximum orbital velocity near the bottom induced by waves

$\Delta$  = relative sediment density =  $\frac{\rho_s - \rho}{\rho}$

$\rho$  = density of sea water

$\rho_s$  = density of sediment

$g$  = acceleration of gravity

$\mu$  = ripple coefficient

$\xi$  = factor to increase shear stress in a combination of current and waves

An equivalent shear stress  $\tau'$  is now defined in such a manner that transport by currents and waves and shear stress  $\tau'_s$  is equal to the transport without waves and shear stress  $\tau_s$ .

This gives the relationship:

$$\tau_s e^{-\frac{0.27 \Delta D \rho g}{\mu \tau_s}} = \tau'_s e^{-\frac{0.27 \Delta D \rho g}{\mu \tau'_s \left\{ 1 + \frac{1}{2} \left( \xi \frac{u_0}{v} \right)^2 \right\}}} \quad (11)$$

The values of  $\tau_s^i$  can be calculated using the above relationship and can be used in stability relationships for the outer estuary (profiles 12, 13, Figure 1). The value of  $u_0$  is related to wave height, wave period and depth.

4. RESULTS OF INVESTIGATIONS

Mean tidal velocity ( $\bar{v}$ )

In past studies (v.d. Kreeke and Haring, (7)), the mean tidal velocity has been used as a reference velocity for stability. Its value is defined by:

$$\bar{v} = \frac{\Omega_{flood} + \Omega_{ebb}}{AT}$$

where  $\Omega_{flood}$ ,  $\Omega_{ebb}$  are respectively the flood and ebb volumes of a tidal cycle, also called tidal prism.

Figure 3 shows the value of this velocity along the axis of the estuary, as well as the cross-sectional areas at the same locations.

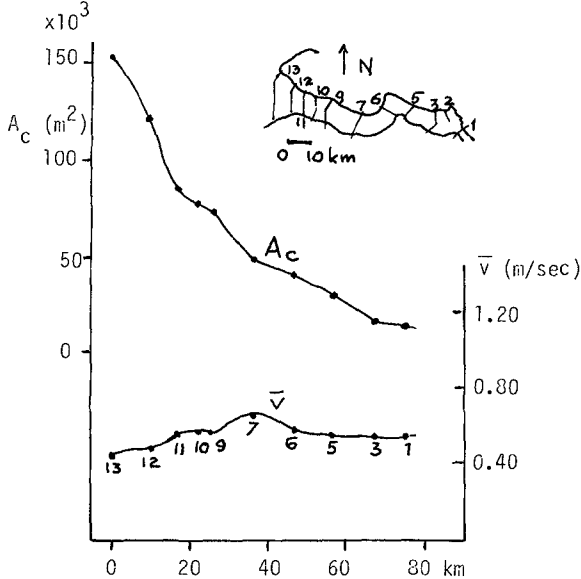


Figure 3: Variation in cross-sectional area and tidal velocity,  $\bar{v}$ , along longitudinal axis of the estuary.

The geometry of the estuary shows profiles at stations 7 and 11 to be smaller than would be expected from the general trend due to restrictions in the natural width at these locations. The graph for the mean tidal velocities show bumps in these locations (7,11) accordingly.

The general trend is a fairly constant value of 0.55 m/sec for  $\bar{v}$  for the upper 30 km and a decrease in value for the outer portion of the estuary (profiles 12, 13) to 0.45 m/sec.

#### Maximum tidal velocities ( $V_{max}$ )

The trend in maximum velocities is shown in Figure 4. Maximum flood velocities are considerably higher than maximum ebb velocities and show greater modulations. Part of this is due to the width restrictions in profiles 7 and 11. In profile 7 the maximum flood velocity (averaged over profile) is 1.25 m/sec.

Seaward of profile 11 maximum velocities also decrease significantly in seaward direction.

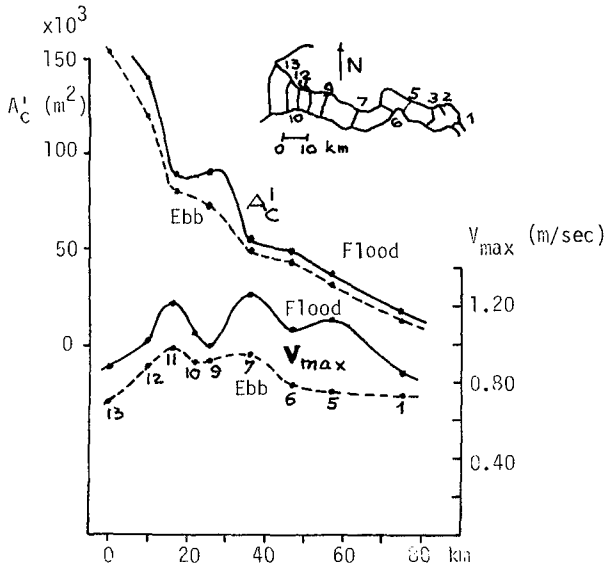


Figure 4: Variation in cross-sectional area and maximum tidal velocity,  $V_{max}$ , along longitudinal axis of the estuary.

#### Maximum flow ( $Q_{max}$ )

In earlier studies (Bruun and Gerritsen, (3)), it was found that  $Q_{max}$  was a useful parameter to characterize a stable channel. This was confirmed in this study.

It appears from the analysis that the use of  $A_C$  gives a slightly better result than that of  $A_C^i$  (contrary to expectations).

Figure 5 gives the regression using the  $A_C^i$  for flood and ebb.

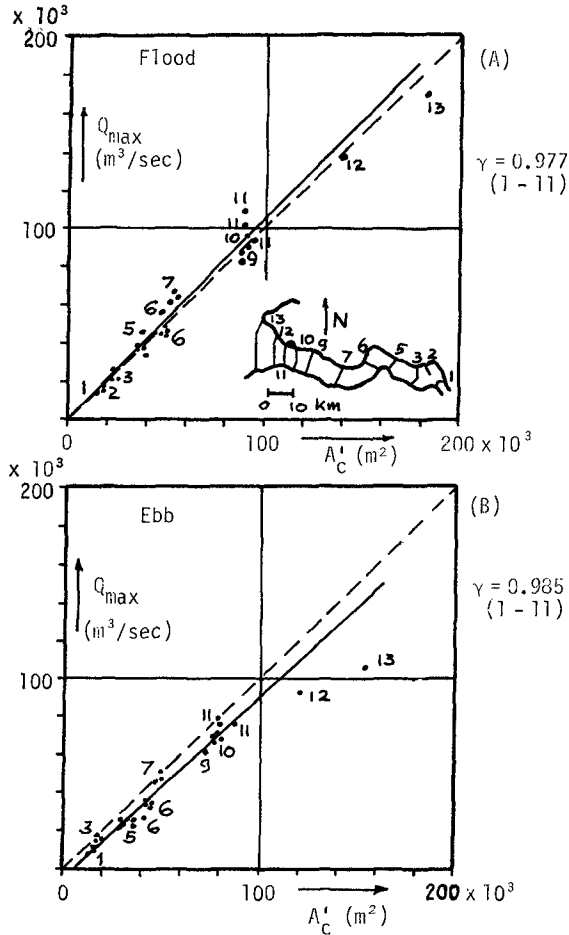


Figure 5: Regression  $Q_{max}$  versus  $A_c^1$   
(A) Flood; (B) Ebb.

The dotted line is for  $Q_{max} = A_c^1$  (in metric units). Flood flows are somewhat higher and ebb flows somewhat lower than this dotted line relationship.

This corresponds to higher maximum flood currents compared to the maximum ebb current as shown in Figure 4. The profiles 12 and 13 do fit the general relationship for flood but they do not fit the relationship for ebb.

The sinusoidal maximum flow ( $\hat{Q}$ )

Another useful parameter for regression analysis is the sinusoidal maximum flow,  $\hat{Q}$ , defined by

$$\hat{Q} = \frac{\pi(\Omega_{\text{flood}} + \Omega_{\text{ebb}})}{2T}$$

The correlation  $\hat{Q}$  versus  $A_C$ , has a correlation coefficient of 0.990, for profiles 1-11.

Van de Kreeke and Haring (7) found for the relation between  $\hat{Q}$  and  $A_C$  (for inlet portion only):

$$A_C = 1.117 \hat{Q}$$

This study gives (for profiles 1-11 only)

$$A_C = 1.08 \hat{Q}$$

with profiles 12 and 13 deviating from this relationship.

Tidal prism ( $\Omega$ )

The correlation between tidal prism and cross-sectional area  $A_C$  is shown in Figure 6 for flood and ebb.

The solid lines represent the average regression for profiles 1-11. The difference between the lines for  $\Omega_{\text{flood}}$  and for  $\Omega_{\text{ebb}}$  is very small.

Again the profiles 12 and 13 do not fit the average relationship for the profiles 1-11. The deviations are almost equal for flood and for ebb.

Stability shear stress ( $\tau_s$ )

In order to satisfy the identity expressed in equation (9) a certain value for the stability shear stress must be selected. Again it was found that the behavior of profiles 12 and 13 differed from the other profiles (1-11). The values of the stability shear stress which had to be introduced to obtain a satisfactory identity are presented in table 1. Values are given for mean tide as well as for spring tide.



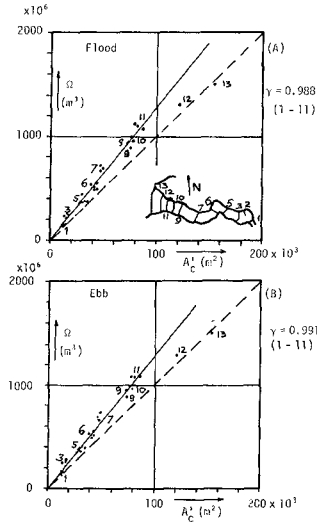


Figure 6: Regression  $\Omega$  versus  $A_c^1$   
(A) Flood; (B) Ebb.

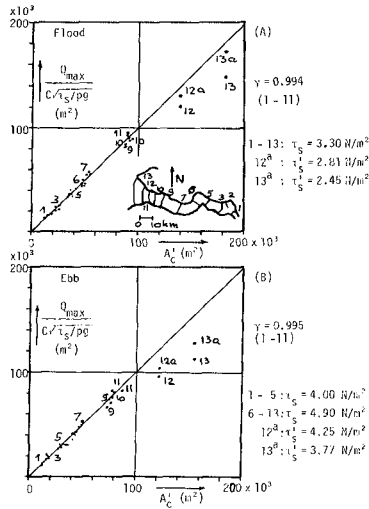


Figure 7: Regression  $\frac{Q_{max}}{C \sqrt{\tau_s} \rho g}$  versus  $A_c^1$   
(A) Flood; (B) Ebb.

Table 1. Values of stability shear stress, profiles 1-11 (N/m<sup>2</sup>)

Tide	Average $\tau_s$ (1-11)	$\tau_s$ (ebb)		$\tau_s$ (flood) (1-11)
		(1-5)	(6-11)	
Mean tide	3.90	4.00	4.90	3.30
Spring tide	5.00	5.00	6.50	4.30

For the calculation of the required values of  $\tau_s$ , values for the Chézy coefficient must be introduced. Based on earlier studies in the Western Scheldt (Beyl (1)), the following relationships were used to calculate C:

$$\text{flood: } C = 56.9 v^{0.48} \text{ m}^{1/2}/\text{sec.}$$

$$\text{ebb: } C = 42.9 v^{0.28} \text{ m}^{1/2}/\text{sec.}$$

The results of the regression analysis (based on  $A_C^1$ ) are shown in Figure 7, indicating good agreement for profiles 1-11. In section 3 it was proposed to adjust the stability shear stress in areas where currents and waves affect the sediment transport. A method to calculate a representative shear stress, based on the Bijker formula, was suggested.

Introducing the modified stability shear stress  $\tau_s^1$  as proposed in section 3, corrections for the profiles 12 and 13 can be made. These are shown as 12<sup>a</sup> and 13<sup>a</sup> in Figures 7A and B. Regarding Figure 7A which describes flood conditions, the corrections for profiles 12 and 13 to points 12<sup>a</sup> and 13<sup>a</sup> bring the latter very well in agreement with the other profiles. For the ebb, (Figure 7B) there is considerable improvement but the fitting of 12<sup>a</sup> and 13<sup>a</sup> into the general curve is not quite satisfactory. A possible reason for the difference between flood and ebb may lie in the way the Chézy coefficients were calculated. The C-values used in the calculations may deviate from the actual C-values for those profiles.

Overall, however, the method suggested seems to be promising to bring all data of the entire estuary into one regression relationship.

#### Flood and ebb channels

For various flow parameters correlations have been determined for a number of well defined flood and ebb channels.

In general correlation coefficients of the same order of magnitude were found.

## 5. CONCLUSIONS

The study of the stability relationships for the Western Scheldt Estuary has led to the following conclusions:

- (1) The correlation coefficient ( $\gamma$ ) for the regression between various flow parameters and the cross-sectional area, for profiles 1-11, decreases in the following order:

1. $\frac{Q_{\max}}{C \sqrt{\tau_s / \rho g}}$	versus $A_C^1$ :	$\gamma_{\text{flood}} = 0.994$
		$\gamma_{\text{ebb}} = 0.995$
2. $\Omega$	versus $A_C$ :	$\gamma_{\text{flood}} = 0.988$
		$\gamma_{\text{ebb}} = 0.991$
3. $Q_{\max}$	versus $A_C$ :	$\gamma_{\text{flood}} = 0.978$
		$\gamma_{\text{ebb}} = 0.985$

- (2) For the separate tidal channels the same sequence is found for the flood channels. For the ebb channels the sequence is 1-3-2.
- (3) Profiles 12 and 13 generally deviate from the regression relationships established for profiles 1-11. Exceptions are the relationships  $Q_{\max}$  versus  $A_C$  and  $Q_{\max}$  versus  $A_C^1$  for flood.
- (4) Profiles 12 and 13 also fit in the relationship  $\frac{Q_{\max}}{C \sqrt{\tau_s / \rho g}}$  versus  $A_C^1$ , for flood if  $\tau_s$  is adjusted to  $\tau_s^1$  accounting for wave action.
- (5) The values for  $\tau_s$  found for the Western Scheldt corresponds very well with the values established by Bruun and Gerritsen (3).
- (6) The established relationships have correlation coefficients between 0.95 and 0.99. It appears that these relationships may be utilized in one-dimensional tidal models for the calculation of changes in profiles as a result of changes in external boundary conditions such as in dredging operations.

## 6. REFERENCES

1. Beyl, P.R. (1977): Determination of the accuracy of sandtransport calculations using the Bijker -Einstein method, in the Western Scheldt. Report as part of graduation requirements for the Degree of Civil Engineering, Delft University of Technology.
2. Bijker, E.W. (1967): Some considerations about scales for coastal models with movable bed. Doctoral Dissertation, Delft University of Technology.
3. Bruun, P. and F. Gerritsen, (1960): Stability of coastal inlets. North Holland Publishing Company, Amsterdam.
4. Bruun, P. (1978): Stability of Tidal inlets, theory and engineering. Elsevier Scientific Publishing Company, Amsterdam-Oxford-New York.
5. Daamen, J.W. (1983): Tidal regime of Western Scheldt. Report Adviesdienst Vlissingen, Rijkswaterstaat, WWKZ-83 V297.
6. Dronkers, J.J. (1964): Tidal computations North Holland Publishing Co. - Amsterdam.
7. Kreeke, J.v.d. and Jac. Haring (1979): Equilibrium flow areas in the Rhine-Meuse Delta. J. Coastal Engineering, 3, 97-111.
8. Leendertse, J.J. (1967): Aspects of a computational model for long-period water-wave propagation. Doctoral Dissertation, Delft University of Technology.
9. O'Brien, M.P. (1931): Estuary tidal prisms related to entrance areas, Civil Engineering, May, 1931.

## CHAPTER TWO HUNDRED SIX

### EFFLUENT DISPERSAL IN EUROPEAN COASTAL WATERS

D. PRANDLE

Institute of Oceanographic Sciences, Bidston Observatory,  
Merseyside, L43 7RA, U.K.

#### ABSTRACT

The mixing of dissolved material discharged from the Windscale nuclear re-processing plant is examined. The first phase involves a numerical modelling study of large-scale long-term mixing over the entire Continental Shelf. The second phase involves a similar modelling study of near-source mixing processes over a region some 100 km square immediately adjacent to the discharge position. In this latter phase, reproduction of instantaneous peak concentrations is required.

The first phase of this simulation has been successfully completed while the second phase is presently being considered. Ironically, it is shown that this second phase poses far more difficult modelling problems and hence the accuracy of simulation attained in the first phase may not be reproduced. The contrasts in these two modelling approaches are examined and their varying complexities explained.

#### 1. INTRODUCTION

The long-term residual circulation of the waters over the European Continental Shelf is of interest for studies such as : the dispersal of pollutants, the dynamics of marine biology and marine chemistry, sediment transport etc. Several numerical models have been formulated to simulate both the tidal and wind-driven dynamics, these models have provided estimates of residual circulation. Some of these estimates are in reasonable agreement as might be expected from the basic similarity in the models. Confidence in such models must be established by verification against actual observed data. However, a preponderance of small-scale variability allied to inadequate instrumental accuracy obstructs direct measurement of the residual circulation.

Since 1963 various substances have been discharged at monitored rates by pipeline into these coastal waters from the nuclear re-processing plant at Windscale (see figure 1). A number of these substances are non-existent in natural form and their introduction is almost exclusively from Windscale. Thus by modelling the mixing processes of such substances and comparing, through time, observed and calculated distributions the validity of the calculated residual circulation can be established. In the present study, Caesium 137 ( $^{137}\text{Cs}$ ) was adopted as a suitable trace material since it remains almost entirely in dilution and with a half-life of 30.1y retains sufficient mass over the time scale of interest.

Regular monitoring of the spread of  $^{137}\text{Cs}$  has revealed a net transport northwards out of the Irish Sea, then proceeding in a confined coastal zone around the Scottish Coast into the North Sea. Much of the material then flows in an anti-clockwise gyre southwards along the English coast, eastwards along the Continental coast and finally, some 5 years after the discharge, the material flows northwards along the Norwegian Coast.

The spread of  $^{137}\text{Cs}$  may be conveniently partitioned into two phases. The first phase concerns movement over a region approximately 1500 km square embracing the entire Continental Shelf region while the second phase covers movement over a region some 100 km square immediately adjacent to the discharge point. In the first case, the aim was to reproduce mean concentrations averaged over large spatial areas and long time periods while in the second case maximum instantaneous peak concentrations are of concern. (Chatwin and Allen (1985) emphasise the important difference in such requirements). The large scale simulation has been successfully completed (Prandle 1984). Here we summarise the approach used in this simulation and thence outline the related difficulties associated with the near-source simulation.

Perhaps unexpectedly, the near-source problem is shown to be more complex, as a simple illustration of this finding we now examine the relative values of advection and dispersion in mixing processes. The time scale,  $t_A$ , for a pollutant to travel a distance  $L$  when transported by an advective velocity  $U$  is simply  $L/U$ . The time scale,  $t_D$ , for a pollutant to spread over a region  $L$  squared by dispersive processes is  $L^2/K$  where  $K$  is the horizontal dispersion coefficient. Thus a rough comparison of the relative effectiveness of these two processes is given by the Peclet Number,  $Pe$  where

$$Pe = \frac{t_A}{t_D} = \frac{L/U}{L^2/K} = \frac{K}{LU} \quad (1)$$

For values of  $Pe \ll 1$  advection predominates whereas for  $Pe \gg 1$  dispersion predominates. In the present region residual velocities

are of the order of  $1 \text{ cm s}^{-1}$  and  $K \approx 10 \text{ cm}^2 \text{ s}^{-1}$ , hence for distance greater than 100 km from the source advection predominates whereas for distances less than 1 km dispersion predominates. Thus we immediately see that the near-source problem is likely to be more complex since both mixing processes are equally important.

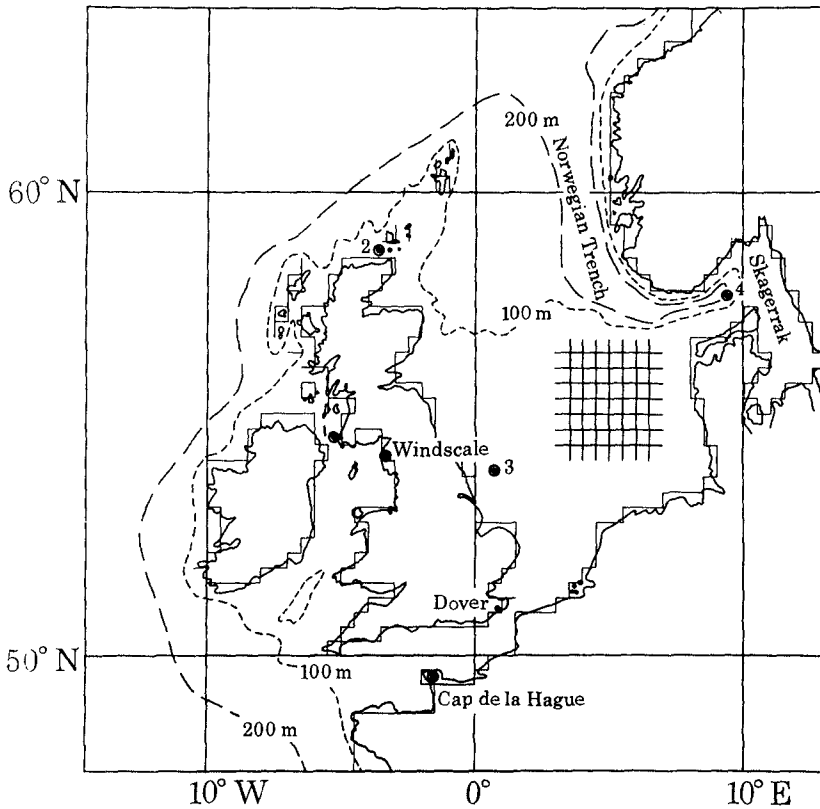


Figure 1.  
Extent of the numerical model of the European Continental Shelf.

## 2. HYDRODYNAMIC MODEL OF THE CONTINENTAL SHELF

The boundaries of the numerical model extend over the complete region shown in figure 1. The location of these open-boundaries in deep oceanic waters beyond the Shelf Edge allowed two important assumptions to be introduced into the prescription of external boundary conditions.

- (i) Variations in mean sea level or any attendant residual flow in the ocean can be neglected since numerical simulations show that the Shelf is effectively isolated from such residual forcing terms.
- (ii) The concentration of  $^{137}\text{Cs}$  was set to zero, reflecting the near-infinite sink capacity of the deep ocean.

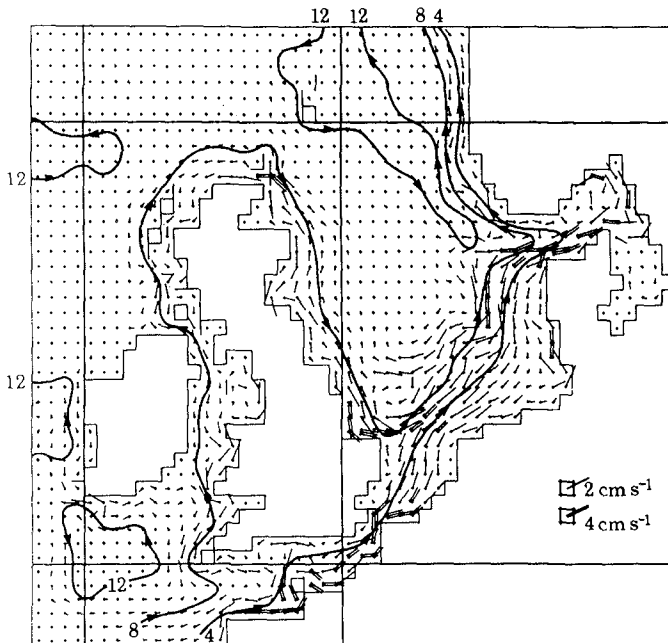


Figure 2.

Residual tidal flow, streamlines in  $10^4 \text{ m}^3 \text{ s}^{-1}$ .



Tidal forcing, emanating from the North Atlantic, is the major energy source driving the Shelf Seas. Moreover, within this tidal forcing, the single lunar semi-diurnal constituent  $M_2$  predominates to an extent that in most locations the amplitude of  $M_2$  is greater than the sum of all other constituent amplitudes. These two characteristics permit the following assumptions to be made in the large-scale long-term simulation.

- (i) the net tidal residual may be approximated by the  $M_2$  residual
- (ii) the equations of motion for wind-driven and density-driven flows may be linearised using coefficients derived simply from the  $M_2$  tide.

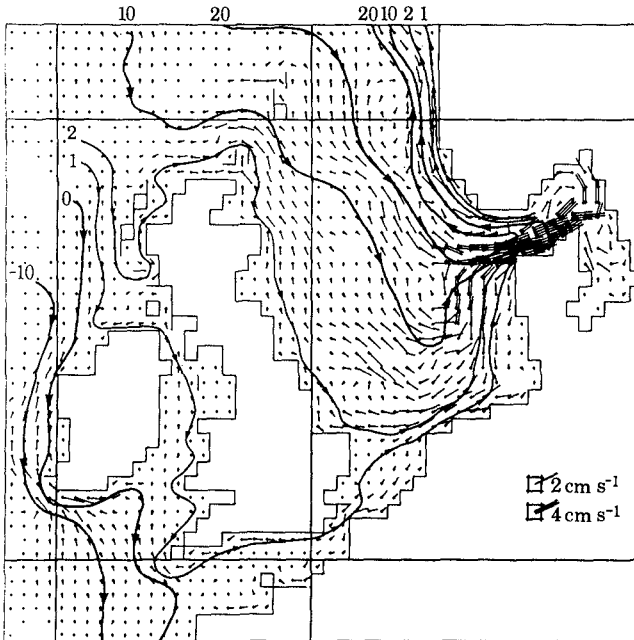


Figure 3.  
Response to a westerly wind (mean stress of  $0.529 \text{ dyn cm}^{-2}$ ),  
streamlines in  $10^4 \text{ m}^3 \text{ s}^{-1}$ .

In consequence of (i) and (ii), the net residual motion at any time can be reasonably approximated by linear superposition. Thus, first we computed the (linear) response to (a) a westerly wind stress of unit magnitude and (b) a southerly wind stress of unit magnitude. Then for any specific period we simply add to the tidal residual the results from (a) multiplied by the relevant westerly wind stress and likewise for (b).

Limitation of computer capacity (even using a Cray machine) dictated the use of a vertically-averaged numerical model. Some allowance for density-driven residuals was made by including longitudinal density gradients. However, in general these were shown to be small except for certain localised regions and hence this forcing term was neglected in subsequent simulations.

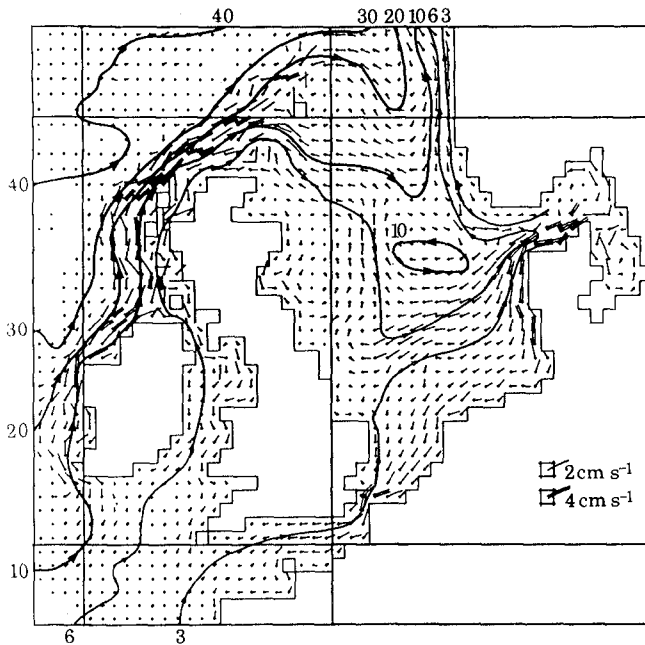


Figure 4.

Response to a southerly wind (mean stress of  $0.435 \text{ dyn cm}^{-2}$ ),  
streamlines in  $10^4 \text{ m}^3 \text{ s}^{-1}$ .

Figure 2 shows the  $M_2$  tidal residual flow, figures 3 and 4 the residual flows corresponding to the long-term mean wind stress from the west and south respectively. In obtaining these results it is important to recognise the reliance on earlier work namely :

- (i) oceanic tidal measurements made by Cartwright et al. (1980)
- (ii) modelling of North Atlantic tides by Flather, IOS Bidston - to be published
- (iii) evaluation of appropriate long-term wind stress data (Thompson et al. 1983)

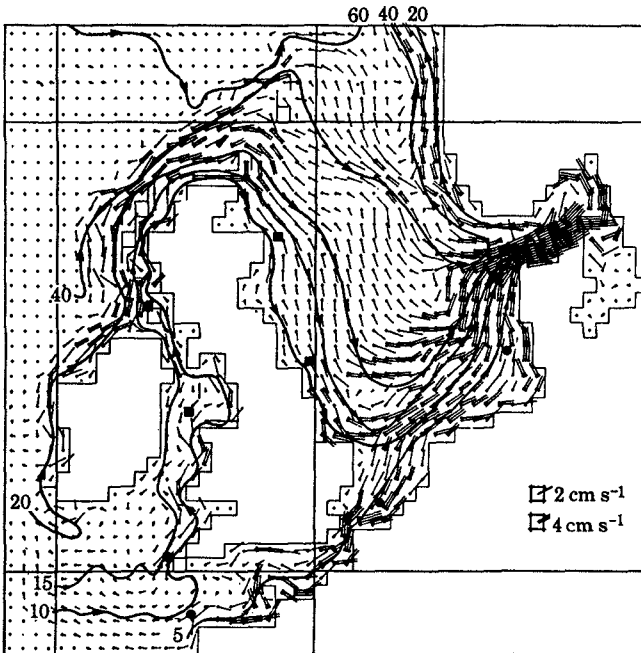


Figure 5.

Net residual flow (tide + winds), streamlines in  $10^4 \text{ m}^3 \text{ s}^{-1}$ .

Early confidence in the results shown in figures 2 to 4 was established by comparison with (a) related modelling studies and (b) indirect observational data. With residual currents of typically 1 or 2  $\text{cm s}^{-1}$  superimposed on to tidal currents often exceeding  $100 \text{ cm s}^{-1}$  it is difficult to obtain reliable observational data using existing current meters. However, the validity of the net residual flow pattern (figure 5) was finally established by comparing the computed mean sea level variations (which coincide with the residual flow distributions) with the observed variations in m.s.l. deduced by Rossiter (1967). The close agreement illustrated in figure 6 provided the necessary confidence in the hydrodynamic model to proceed to the development of a mixing model.

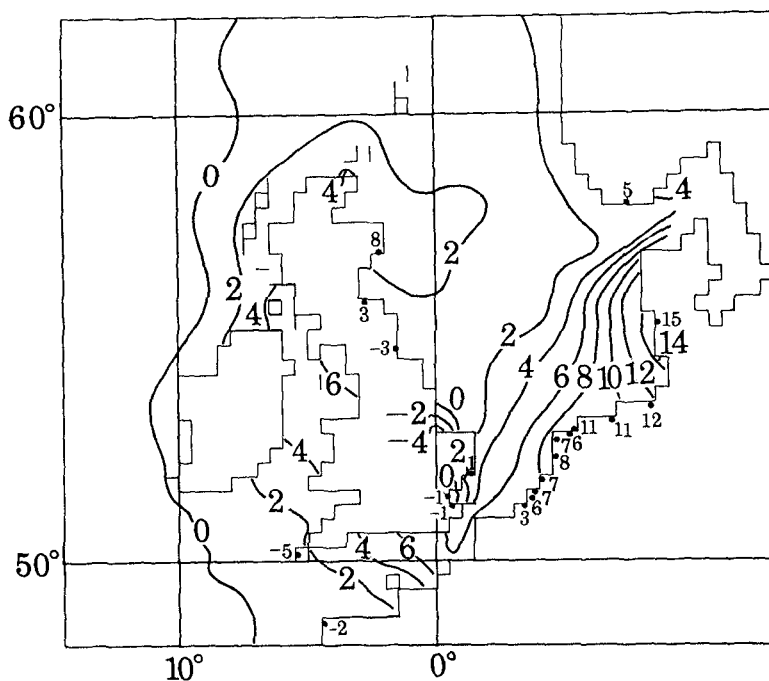


Figure 6.

Mean sea level variation (tide + winds) in cm,  $\bullet$  observed value from Rossiter (1967).

### 3. MIXING MODEL OF THE CONTINENTAL SHELF

Tides represent a well-ordered spectrally narrow phenomenon and thus their propagation is more amenable to numerical simulation than mixing processes which occur over a much wider spectral range and involve random processes.

#### 3.1 Numerical dispersion

A low-order difference scheme was used, this scheme introduces additional numerical dispersion such that the dispersion coefficient  $K$  is increased by  $\delta K$  given by (Roache 1976)

$$\delta K = \frac{1}{2} (u \Delta x - u^2 \Delta t) \quad (2)$$

Since stability requires  $\Delta x / \Delta t > u$ , in most cases  $\delta K \rightarrow \frac{1}{2} u \Delta x$ . The model grid size  $\Delta x = 35$  km and hence to keep  $\delta K < K$  ( $\approx 5 \times 10^6 \text{ cm}^2 \text{ s}^{-1}$ ) required  $U < 3 \text{ cm s}^{-1}$ . Thus to avoid excessive numerical dispersion it was necessary to drive the mixing model using only the residual flow field. Dispersion due to oscillatory tidal motions was introduced by defining the dispersion coefficients  $K_x$  and  $K_y$  in terms of the  $M_2$  tidal current amplitudes  $\hat{U}$  and  $\hat{V}$  (along orthogonal  $x$  and  $y$  axes respectively) as follows :

$$K_x = 1000 \hat{U} (\hat{U}^2 + \hat{V}^2)^{1/2} \quad \text{and} \quad K_y = 1000 \hat{V} (\hat{U}^2 + \hat{V}^2)^{1/2} \quad (\text{cm}^2 \text{ s}^{-1}) \quad (3)$$

The inclusion of only residual motions yielded the advantage of enabling a time step of  $\Delta t = 12\text{h}$  (from  $\Delta t < \Delta x / u$ ) to be used in the mixing model, whereas simulation of oscillatory tidal motion would require  $\Delta t \approx 0.5\text{h}$ .

#### 3.2 Model evaluation

Discharges of  $^{137}\text{Cs}$  from Windscale started in 1963 with the major discharges occurring in the decade 1970 to 1980. Discharges from other sources may be neglected in comparison with Windscale. Using wind stress data from this period from Thompson (1983). Figure 7 indicates observed and computed concentrations over the Shelf for May 1983 and August 1979. In view of the many simplifications and approximations inherent in the modelling approach, the level of agreement shown was judged to be highly satisfactory.

Sensitivity tests were carried out setting (i)  $K_x = K_y = 0$  and (ii) increasing both  $K_x$  and  $K_y$  by a factor of 5. The computed concentrations showed significant changes in both cases thus indicating that the level of agreement illustrated in figure 7 was a consequence of accurate specification of  $K_x$  and  $K_y$ . Similar sensitivity tests were carried out setting wind stress values to zero, these tests indicated that good reproduction of  $^{137}\text{Cs}$  distributions also depended on accurate specification of the wind-induced advective transport. Thus it was shown that correct simulation of the spread of  $^{137}\text{Cs}$  depends on accurate reproduction of both advection and dispersion.

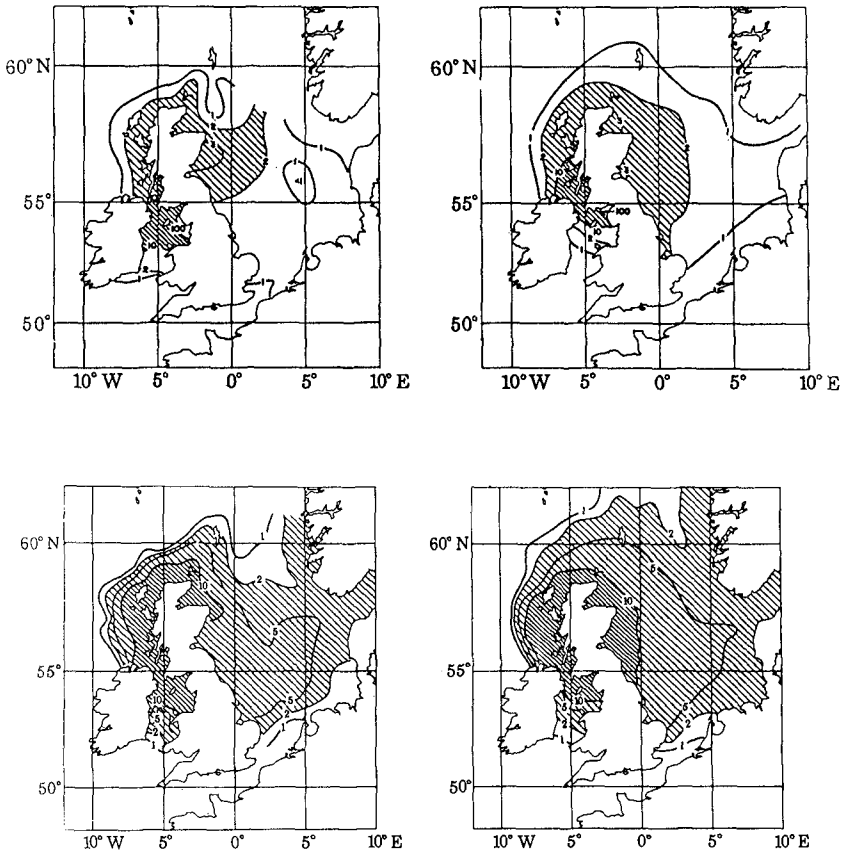


Figure 7.

Observed (left) against computed (right) levels of  $^{137}\text{Cs}$  ( $\mu\text{Ci l}^{-1}$ ) in May 1973 (top) and August 1979 (bottom)

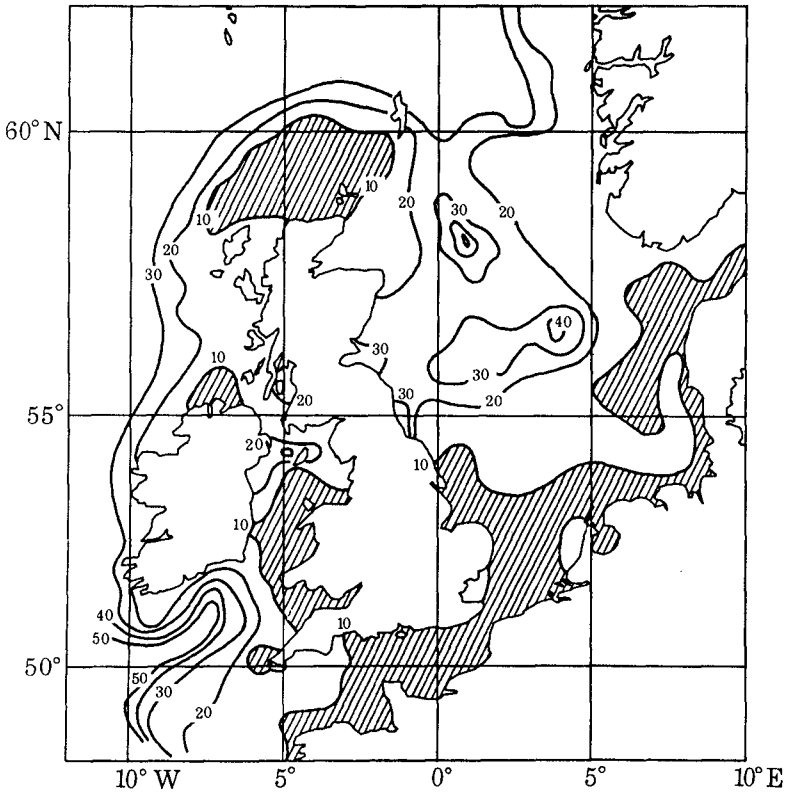


Figure 8.

'Turn-over-times' for model grid-boxes in days, (grid size 20' lat. x 30' long.)

## 4. MIXING TIME SCALES OF THE CONTINENTAL SHELF

Having validated both the hydrodynamic and mixing models it is useful to calculate pertinent time-scales associated with water quality studies.

Figure 8 shows,  $T_f$ , the 'turn-over-time', or 'flushing time' associated with each grid box of the model. The value  $T_f$  corresponds to the time taken for the concentration within a grid box to be reduced by a factor  $1/e \approx 0.37$  when all surrounding boxes have an initial zero concentration. The actual values of  $T_f$  are a function of grid size, however the variation in values is of interest. In particular, when areas of large  $T_f$  (sluggish circulation) lie close to areas of small  $T_f$  (vigorous circulation) we might expect to see the formation of thermal fronts at certain seasons.

Figure 9 shows the 'age',  $T_a$  of material released from Windscale where  $T_a$  represents the average travel time between discharge and arrival at any location. In simple terms, the distribution of  $T_a$  is shown to be a combination of radial dispersion from the source modified by the advective transport paths shown earlier.

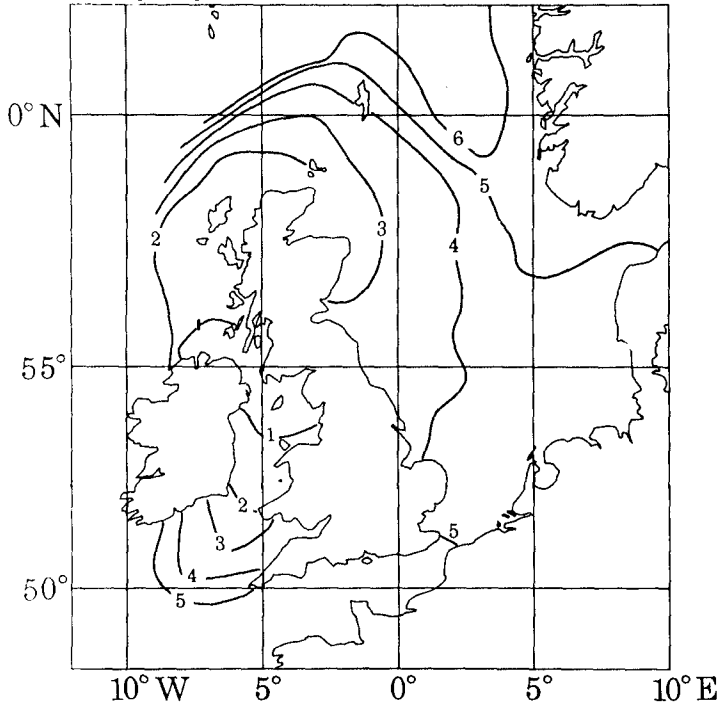


Figure 9. Age (in years) of material discharged from Windscale.



## 5. SIMULATION OF NEAR-SOURCE MIXING

The interest in localised instantaneous peak concentrations in this region precludes the approach used in the earlier study whereby wind-driven residual flows and tidal residuals were superposed. The requirement to simulate hour by hour motions dictates that real-time surge-tide and tide-tide non-linear interactions must be incorporated (Prandle and Wolf 1978).

In the hydrodynamic section of the model the above requirements mean that boundary conditions must be supplied from an external model dynamically meshed with the 100 km square region of immediate interest. Similarly the specification of concentrations along the boundary of this inner region must involve some real-time simulation of the external region. In both cases, the extent of the meshed external region will be governed by the duration of events to be simulated. For the hydrodynamic model, the speed of propagation of surface gravity waves means that far-distant boundaries are necessary to avoid spurious reflections. However, for the mixing model, lower mass-propagation speeds allow for closer location of external boundaries.

The success of the earlier study suggested that, in most regions, vertical mixing was sufficiently intense to render the problem effectively two-dimensional. Moreover, careful examination of the wind and tidally-driven residual streamlines reveals a close similarity which may be explained by the existence over large areas of a near-geostrophic balance which produces topographic steering of flow along depth contours. Thus, what appears initially to be a three-dimensional mixing problem is effectively reduced to a one-dimensional problem. To a large extent, one-dimensional mixing problems enjoy a self-correcting mechanism whereby an excess of wind-driven advection for one month may be effectively counter-balanced by a corresponding reduction in the next. Unfortunately, the near-source mixing problem is fully three-dimensional with complications including density fronts.

One advantage in the smaller model concerns numerical dispersion. Thus from (2) with a grid size of 1 km and tidal currents less than 50 cm/s, the level of numerical dispersion may be sufficiently contained to allow simulation of tidal oscillatory motions, such simulation is clearly required. If numerical dispersion is found to be troublesome some corrective scheme would have to be employed (see for example Zalesak 1979, Smolarkiewicz 1984).

## 6. SUMMARY AND CONCLUSIONS

The success of the large-scale long-term simulation of mixing over the Continental Shelf can be attributed to the following :

- (i) Siting of open-sea boundaries beyond the Shelf edge thereby providing suitable boundary conditions for both the hydrodynamic and mixing models.
- (ii) Predominance of the  $M_2$  tidal constituent, obviating the necessity to consider other tidal constituents and permitting wind-driven residual flow to be linearly superposed.
- (iii) Availability of excellent field data including oceanic and coastal tide gauges and comprehensive surveys of  $^{137}\text{Cs}$  distributions.
- (iv) Strong vertical mixing combined with a near-geostrophic balance for residual flows effectively reduce a 3 dimensional problem to a one-dimensional problem with flow confined to fixed streamlines. Under these conditions a degree of self-correction exists in relation to temporal variations in the advective motions.

The second phase of this study involves a near-source simulation with particular interest in maximum instantaneous concentrations. This study is directly analogous to typical coastal engineering problems involving dispersion from power stations or sewage treatment plants. Unfortunately, none of the above factors apply to this second phase and hence, ironically, a more complex modelling approach is required and the accuracy of simulation is likely to be reduced.

The work described in this paper was funded by the Natural Environment Research Council and by the Ministry of Agriculture, Fisheries and Food.

## REFERENCES

- CARTWRIGHT D.E., EDDEN A.C., SPENCER R & VASSIE J.M. 1980, The tides of the northeast Atlantic Ocean. Phil.Trans.R.Soc.A , 298, 87-139.
- CHATWIN P.C. & ALLEN C.M. 1985, Mathematical models of dispersion in rivers and estuaries. To appear in Vol. 17. Ann. Review of Fluid Mechanics.
- PRANDLE D. 1984, A modelling study of the mixing of Cs in the seas of the European Continental Shelf. Phil.Trans.R.Soc.A , 310, 407-436.
- PRANDLE D. & WOLF J. 1978, The interaction of Surge and Tide in the North Sea and River Thames. Geophys.J.R.astr.Soc. 55(1), 203-216.
- ROACHE P.J. 1976, Computational Fluid Dynamics. Albuquerque, N.M. Hermosa.
- ROSSITER J.R. 1967, An analysis of annual sea level variations in European waters. Geophys.J.R.astr.Soc. 12, 259-299.
- SMOLARKIEWICZ P.K. 1984, A fully multidimensional positive definite advection transport algorithm with small implicit diffusion. J.Comp.Phys. 54, (2), 325-362.
- THOMPSON K.R., MARSDEN R.F. & WRIGHT D.G. 1983, Estimation of low frequency wind stress fluctuations over the open ocean. J.Phys.Ocean , 13, 1003-1011.
- ZALESAK S.T. 1979, Fully multidimensional flux-corrected transport algorithms for fluids. J.Comp.Phys. 31, 335-362.

## CHAPTER TWO HUNDRED SEVEN

### Mathematical Modelling of Water-quality for long time periods

P Huizinga\*

#### ABSTRACT

This paper presents a one-dimensional dynamic water-quality model suitable for long-term application to estuaries. The computation techniques used in the model are very simple, but very good results have been obtained both for theoretical test cases and from applications to estuaries when compared with prototype measurements.

#### 1. INTRODUCTION

To investigate water-quality problems in several narrow tidal estuaries in South Africa a mathematical model was required which could be applied easily and economically for long-period investigations. The model presented in this paper has certain features similar to that described by Orlob (1972) and in applying the model in combination with a one-dimensional explicit hydrodynamic model, very good results were obtained.

A brief description is given of the method employed. Some test results are shown of simulations in theoretical channels. The paper includes calibration and verification results of an application to the Knysna estuary, which is located 500 km east of Cape Town on the south coast of South Africa, as well as results of investigations of the effect of changes in fresh-water inflow on the salinity distributions in this estuary.

#### 2. THE COMPUTATIONAL METHOD

##### 2.1 General

One-dimensional advection and dispersion is described by the formula (see list of symbols):

$$\frac{\partial(\text{Vol}.C)}{\partial t} = \frac{\partial(Ax.K.\frac{\partial C}{\partial x})}{\partial x}.dx - \frac{\partial(Ax.u.C)}{\partial x}.dx \quad (2-1)$$

Extra terms can be included for other phenomena such as breakdown and growth or lateral inflows of contaminants.

Computational schemes are often designed for a simplified version of this equation in which constant velocity, depth and cross-sectional area are assumed:

\* National Research Institute for Oceanology, Stellenbosch, Republic of South Africa.

$$\frac{\partial C}{\partial t} + u \frac{\partial C}{\partial x} = K \frac{\partial^2 C}{\partial x^2} \quad (2-2)$$

Mathematical models based on this formula can give very good results if applied to channels and rivers with almost constant flow and cross-sectional area. They should not be applied to estuaries with complex topography and under tidal influence.

The computational method on which this model is based is similar in certain respects to that described by Orlob (1972). In principle it is based on a finite difference approximation of the equation 2-1. It consists of two stages per timestep, first, the total advective and diffusive transport between nodes are computed, in other words the right-hand side of formula 2-1 is computed. Then, knowing the change in volume in a node and also the in- and outflow volumes and concentrations, the new concentration for each node can be computed. Special routines are used to handle side branches with splitting points and positions where pollutants are released.

## 2.2 Advective Transport Computation

The advective transport through a cross-section during a time-step can be computed directly from the flow through that cross-section for that timestep multiplied by the average concentration. For section M-1 or between nodes N-1 and N on Figure 1 this transport is:

$$ATR_{M-1} = Q_{M-1} \cdot C_{M-1} \cdot \Delta t \quad (2-3)$$

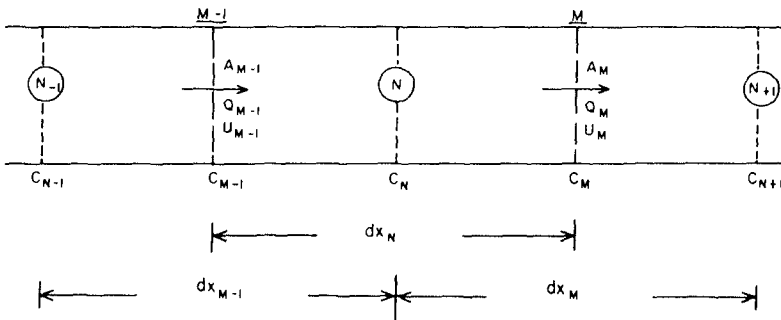


Figure 1.

Similarly for section M:

$$ATR_M = Q_M \cdot C_M \cdot \Delta t \quad (2-4)$$

If there are no side branches at nodes N-1, N or N+1 a linear interpolation together with a slight correction due to the velocity U can be made to determine C<sub>M</sub>.

$$C_M = C_N + (C_{N+1} - C_N) \cdot (0,5 \cdot dx_M - 0,5 \cdot U_N \cdot \Delta t) / dx_M \quad (2-5)$$

and

$$C_{M-1} = C_{N-1} + (C_N - C_{N-1}) \cdot (0,5 \cdot dx_{M-1} - 0,5 \cdot U_{M-1} \cdot \Delta t) / dx_{M-1} \quad (2-6)$$

At release positions and at splitting points sudden changes of concentrations can occur. For those situations other interpolation routines are used to estimate concentrations through cross-sections ( $C_M$ ). If  $C_{N+1}$  is a splitting point and  $C_N$  not, then  $C_M$  is determined by linear extrapolation from  $C_{N-1}$  and  $C_N$ . If this would cause negative values for  $C_M$ , then  $C_M$  is set equal to zero. If  $C_N$  and  $C_{N+1}$  are splitting points and the flow is to the right then  $C_M$  is taken to be equal to  $C_N$ .

### 2.3 Dispersive Transport Computation (Figure 1)

Dispersion in estuaries has been extensively described by many authors (see for example, Fisher, 1979), but no predictive formula exists that can be generally applied to determine the dispersion coefficient ( $K$ ) For a number of tests described in this report the coefficient was determined as suggested by Leendertse (1970). This consists of a constant part and a part dependent on velocity, depth and Chezy-coefficient.

$$K = \frac{Df/U \cdot R}{C_F} + D_w \quad (2-7)$$

In the salinity tests for the Knysna estuary the dispersion coefficient was determined from the salinity distribution in the estuary and the inflow of fresh water.

$$K = \frac{(\partial S / \partial x)}{(U_n) \cdot S} \quad (2-8)$$

$U_n$  is the net downstream velocity caused by the freshwater discharge.

The dispersive transport through a cross-section (Figure 1) during a timestep ( $\Delta t$ ) is computed by:

$$DTR_{M-1} = -K_{M-1} \cdot (C_N - C_{N-1}) \cdot \Delta t \cdot A_{M-1} / dx_{M-1} \quad (2-9)$$

and

$$DTR_M = K_M (C_{N+1} - C_N) \cdot \Delta t \cdot A_M / dx_M \quad (2-10)$$

### 2.4 Computation of Concentrations

After having computed the transports through all the cross-sections and also knowing the changes in volumes for all the nodes, the next step is to compute the new concentrations at all the nodal points.  $CTR_N$ , the total transport through all the sections leading to nodal point N, is then used to compute the new concentration at node N.

$$C_N^1 = (C_N \cdot \text{Vol}_N + \text{CTR}_N) / \text{Vol}_N^1 \quad (2-11)$$

If N is also an outfall release position, the extra transport towards N due to this outflow is also included in  $\text{CTR}_N$ .

## 2.5 Stability and Accuracy

The water quality model is connected to an explicit one-dimensional hydrodynamic model (CSIR, 1976) and is operated at the same schematization and timestep. This set-up implies certain disadvantages but model simulations have shown that it is a practical combination.

For stability reasons the timestep of the hydrodynamic computation is limited due to the Courant criterion.

$$\Delta t < \frac{\Delta x}{\sqrt{gR}} \quad (2-12)$$

For advective transport only a similar criterion is valid for the water quality computation.

$$\Delta t < \frac{\Delta x}{u} \quad (2-13)$$

The celerity of the long wave ( $\sqrt{gR}$ ) is normally an order of magnitude faster than the water velocity. Therefore, if both models are operated on the same timestep, the Courant criterion for the hydrodynamic model determines the timestep of the computation.

Normally the water level variation with time and distance is gradual, but, variations of concentrations can be sudden which means that the section lengths in the water quality model must be small.

Therefore, in this model combination, the section length is selected first, based on the topography and on the accuracy wanted from the water quality computation, and then the timestep is set, based on the Courant criterion for the hydrodynamic computation.

## 2.6 Adaptation to Topography

The model has facilities to adapt cross-sectional areas, hydraulic radii, surface areas and volumes for increasing and decreasing of water levels, which makes it particularly suitable for applications to tidal estuaries.

# 3. RESULTS IN THEORETICAL CHANNELS

## 3.1 General

A few model tests were done for theoretical channels with rectangular cross-sections to test the quality of the computation techniques.

3.2 Channel with Rectangular Cross-section

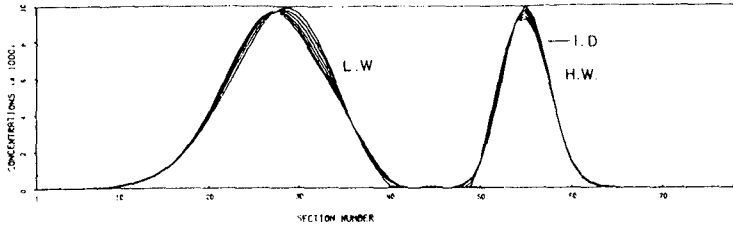


Figure 2.

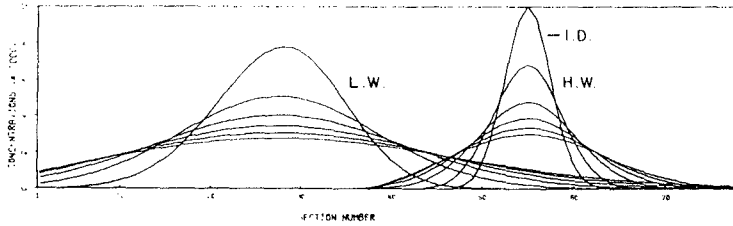


Figure 3.

The results of tests on numerical dispersion in a straight channel are shown in Figures 2 and 3. The channel has a depth of 2 m and a length of 15 400 m. It is open on the left-hand side where a water level variation with an amplitude of 1 m and a period of 12,5 hours was applied, and it is closed off on the right-hand side. The initial distribution of a conservative pollutant is indicated by I.D. and the computed concentrations at high and low water are marked by H.W. and L.W. The graphs at high and low water are plotted at intervals of 25 hours. In the first test (Figure 2) only advective transport was taken into account and in the second test (Figure 3) dispersive transport was computed as well, with a dispersion coefficient of  $6,0 \text{ m}^2/\text{s}$ . The very small deformation of the graphs on Figure 2 shows that the numerical dispersion is very small compared to the dispersion in the second test (Figure 3).

3.3 Channel with Branching

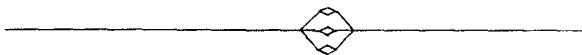


Figure 4.



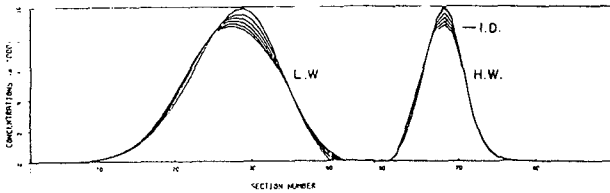


Figure 5.

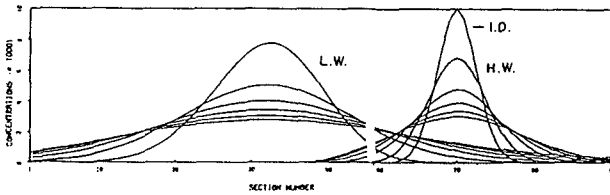


Figure 6.

The test described under 3.2 was repeated for a channel in which a portion of the channel was split up into several branches as shown in Figure 4. Figure 5 shows the results from a computation with only advective transport; for those in Figure 6 dispersive transport was also taken into account. The numerical dispersion (Figure 5) is slightly more than in the previous test (Figure 2) but still very small when compared with the simulation in which dispersive transport was included (Figure 6).

3.4 Channel with Constriction

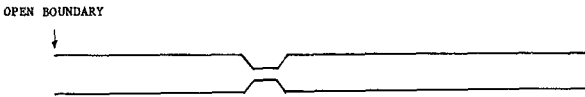


Figure 7.

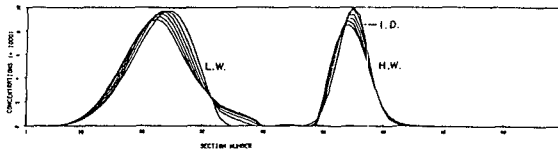


Figure 8.

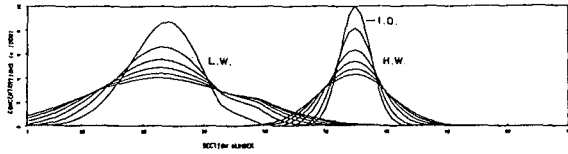


Figure 9.

The same test (3.2) as repeated for a channel with a constriction in it (Figure 7). Again the numerical dispersion with only advective transport (Figure 8) is very small compared to the model test in which dispersive transport was also taken into account (Figure 9).

4. APPLICATION TO KNYSNA ESTUARY

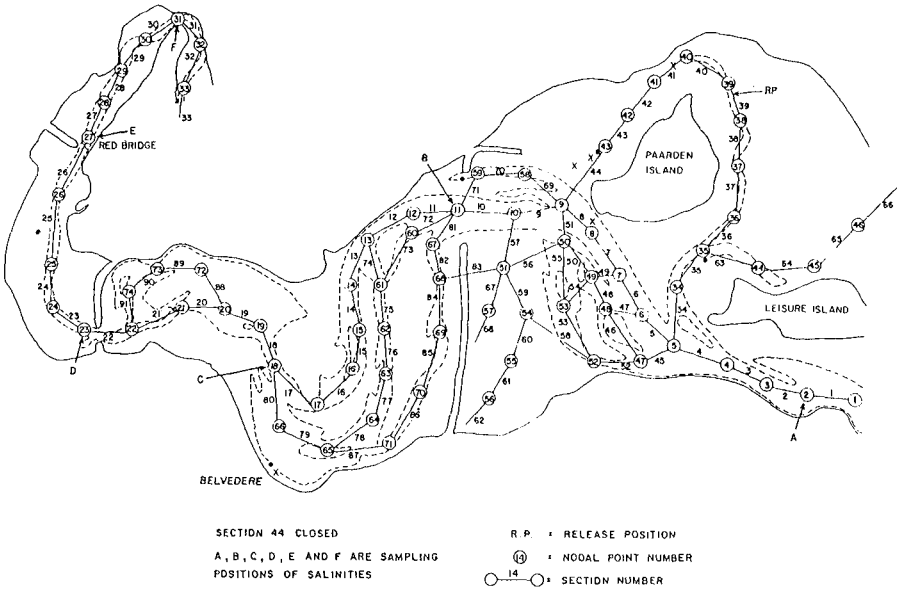


Figure 10.

4.1 General

The Knysna estuary on the south coast of South Africa has a complicated channel system, with extensive flood plains in the downstream area (Figure 10). At the upstream end fresh water from the Knysna river enters the estuary causing gradients in salinity concentrations along

the estuary. Increasing demands for fresh water have led to investigations of the feasibility of extracting water from the Knysna river upstream of the estuary. The problem is to determine the effect this could have on the salinity distributions and variations and on the ecology of the estuary. Salinity concentrations were measured on a certain day, then the river flow was monitored and after a period of about seven days the salinities were measured again. An estimation was made for the dispersion coefficients in the estuary. With these data available, model simulations were done. The starting conditions were the salinity distributions of the beginning of a period. At the open sea boundary a recorded tidal variation was used and at the upstream end the recorded river flow was used for boundary conditions. The salinities computed with the model after the period were then compared with the measured salinities of the corresponding time. A reassessment was then made of the dispersion coefficients and the model simulation was repeated. After a few tests good agreement was achieved between model results and prototype data and the model was considered to be calibrated. Verification runs were done for other periods with equally good results. A number of model tests were then done under different flow conditions for investigating salinity distributions under these circumstances.

#### 4.2 Calibration Tests

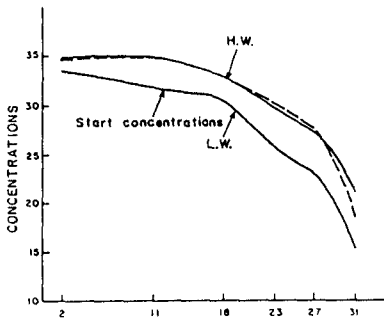
In Figure 11A the start condition is shown, which was measured at low water on 18 January 1984 and which was used for the calibration runs. The period covered by the tests was from 18 till 25 January 1984. The river flow was constant at  $0,8 \text{ m}^3/\text{s}$  and at the open sea boundary the water level variation was recorded. A first estimation of the dispersion coefficient ( $K$ ) was made using formula 2.8. In the first calibration test  $K = 45 \text{ m}^2/\text{s}$  was used for all the sections. The model results are compared on Figure 11B for 25 January 1984. The model results are slightly higher compared to the field data in the upstream region (Sections 23 to 33) of the estuary.

A second calibration test was done in which  $K = 45$  for all sections except  $K = 35$  for Sections 23 to 26 and  $K = 25$  for Sections 27 to 32. The model results are now slightly too low at the upstream region of the estuary indicating that the adaptation was a little too drastic (Figure 11C).

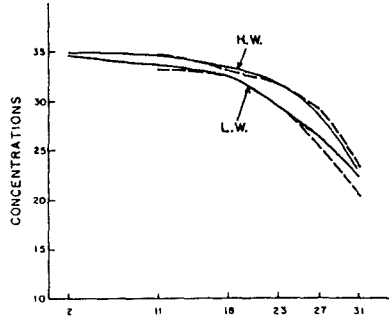
A third calibration test was therefore done in which  $K = 45$  for all sections except  $K = 40$  for Sections 23 to 26 and  $K = 35$  for Sections 27 to 32. Figure 11D shows that excellent agreement between model results and field data was achieved. In all further tests these dispersion coefficients were used.

#### 4.3 Verification Tests

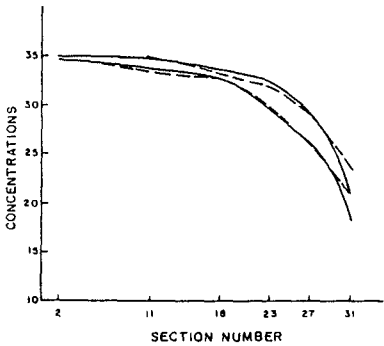
The first verification test was done for the period 10 to 17 March 1984. The flow was variable from  $1,82 \text{ m}^3/\text{s}$  on 10/03/1984 to  $2,90 \text{ m}^3/\text{s}$  on 13/03/1984 to  $1,15 \text{ m}^3/\text{s}$  on 17/03/1984. The agreement between model results and prototype data was still good for 17/03/1984, although the river flow data was probably not very accurate (Figure 12B).



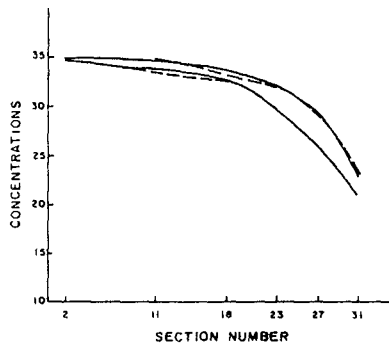
A. Simulation 1  
 Date: 18.1.1984  
 Start conditions at L.W.  
 $K = 45.00$  for all sections  
 Flow =  $0.8 \text{ m}^3/\text{s}$ .



B. Simulation 1  
 Date: 25.1.1984  
 $K = 45.00$  for all sections  
 Flow =  $0.8 \text{ m}^3/\text{s}$ .



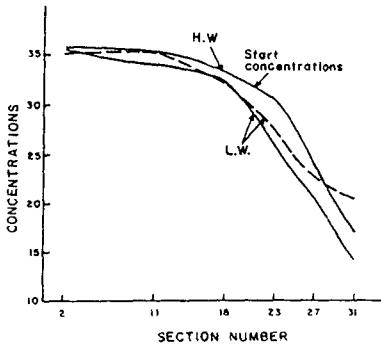
C. Simulation 2  
 Date: 25.1.1984  
 $K = 45.00$  Sections 1-22, 33-74  
 $K = 35.00$  Sections 23-26  
 $K = 25.00$  Sections 27-32  
 Flow =  $0.8 \text{ m}^3/\text{s}$ .



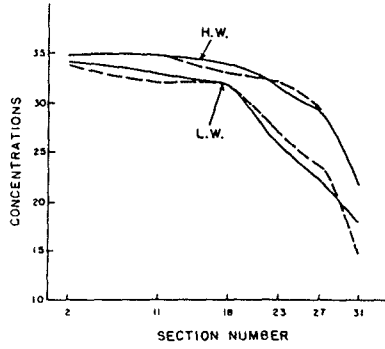
D. Simulation 3  
 Date: 25.1.1984  
 $K = 45.00$  Sections 1-22, 33-74  
 $K = 40.00$  Sections 23-26  
 $K = 35.00$  Sections 27-32  
 Flow =  $0.8 \text{ m}^3/\text{s}$ .

— = computed concentrations  
 - - - = field measurements

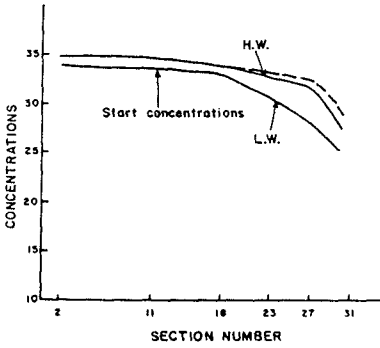
Figure 11



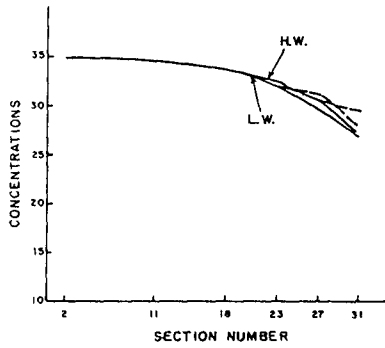
A. Simulation 4  
 Date: 10.3.1984  
 Start conditions at H.W.  
 $K = 45.00$  Sections 1-22, 33-74  
 $K = 40.00$  Sections 23-26  
 $K = 35.00$  Sections 27-32



B. Simulation 4  
 Date: 17.3.1984  
 Flow: Variable



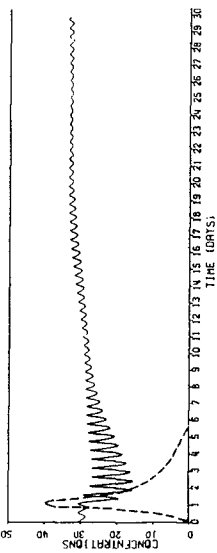
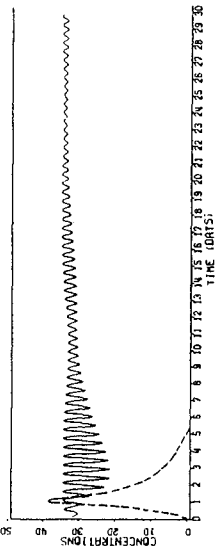
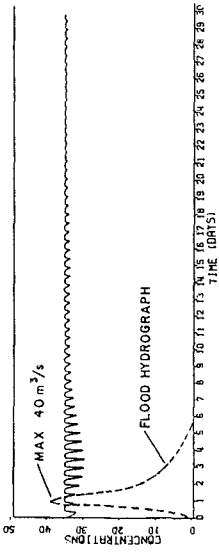
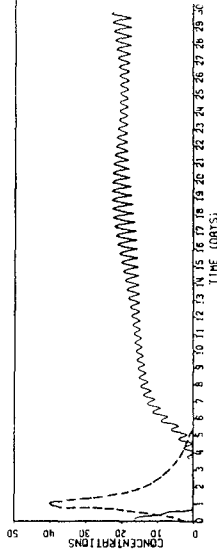
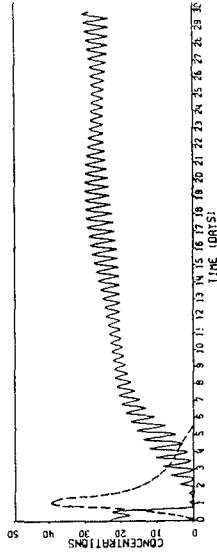
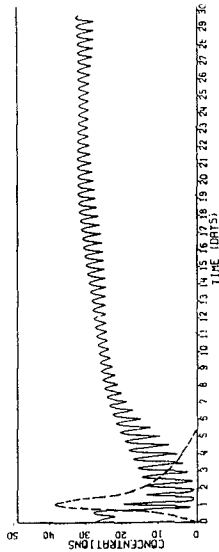
C. Simulation 5  
 Date: 16.4.1984  
 $K = \text{same as simulation 4}$   
 Flow: variable.

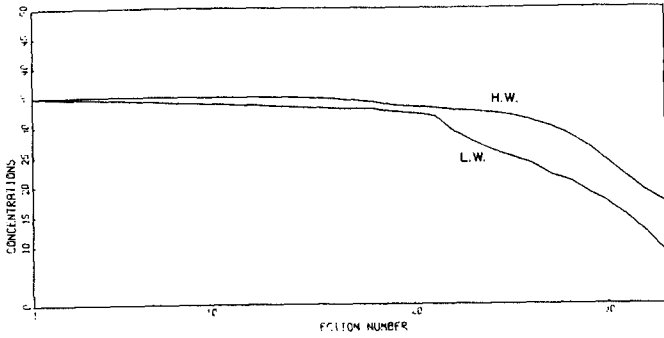


D. Simulation 5  
 Date: 23.4.1984  
 $K = \text{same as simulation 4}$   
 Flow: variable.

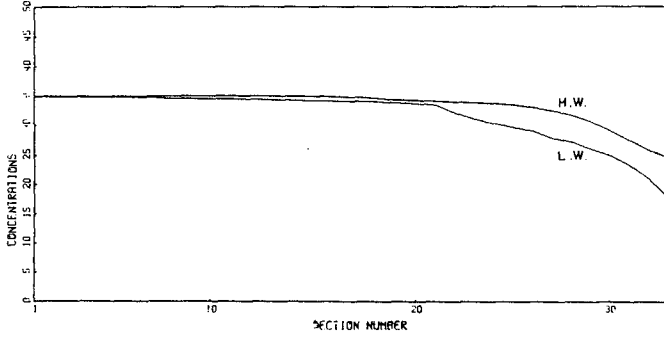
— = computed concentrations  
 - - - = field measurements

Figure 12

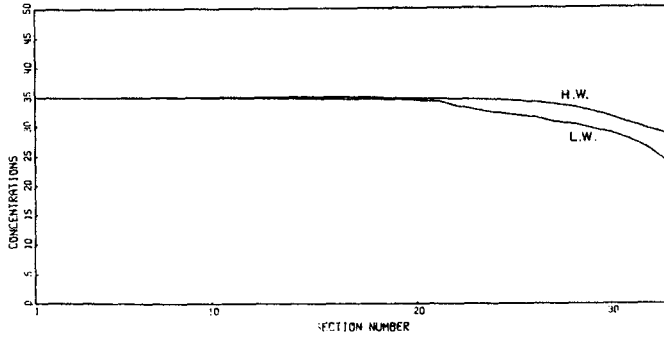




A. SALINITIES AT SPRINGTIDE AND RIVER FLOW OF 1.0 m<sup>3</sup>/s



B. SALINITIES AT SPRINGTIDE AND RIVER FLOW OF 0.5 m<sup>3</sup>/s



C. SALINITIES AT SPRINGTIDE AND RIVER FLOW OF 0.3 m<sup>3</sup>/s

Figure 14

A second verification test was done for the period 16 to 23 April 1984. The flow data used was  $0,85 \text{ m}^3/\text{s}$  for 16 to 19/04/1984,  $0,70 \text{ m}^3/\text{s}$  for 20 and 21 April 1984 and  $0,60 \text{ m}^3/\text{s}$  for 22 and 23 April 1984. The results again show good agreement between model and prototype results (Figure 12D).

#### 4.4 River Flood Test

On Figure 13 the effects of a minor river flood on the salinities in the estuary is shown. The shape of the hydrograph with a maximum flow of  $40 \text{ m}^3/\text{s}$  is shown on each graph.

At the upstream end of the estuary, positions E and F (see also Figure 10), the salinities drop down to zero but later return to their normal values. The graphs for positions A, B, C and D all show the effects of this flood, with the strongest influence upstream in the estuary and the weakest effect near the estuary mouth. On all the graphs the effect of the spring-neap-spring tidal variation is also visible.

#### 4.5 Tests under different constant-flow conditions (1,0, 0,5 and $0,3 \text{ m}^3/\text{s}$ )

The start condition in all these tests was the salinity distributions as measured at low water on 18 January 1984. The results are shown as graphs of distributions in the main channel of the estuary in Figure 14.

For Sections 1 to 22 all the graphs show little difference between high and low water, but considerably bigger differences for Sections 23 to 33, in the narrow upper channel of the estuary. It can also be seen that the influence of the fresh water inflow is considerable at the upper end of the estuary, but small in the downstream part (Sections 1 to 22).

#### 4.6 Details of Computation

The Knysna model tests were done at a timestep of 30 seconds to fulfil the Courant criterion for the hydrodynamic computation (formula 2-12). As stated before (Section 2.5) the hydrodynamic and water quality computations were done at the same timestep. The operation of the Knysna model on the CDC-cyber 750 computer could be done at a cost of about \$10 a day (prototype time).

### 5. CONCLUSIONS

The model presented is one-dimensional and is also 100 per cent conservative. Simulations with test models of simple geometrical structure show that the numerical dispersion is very small. This numerical dispersion increases slightly at models with irregular topography and networks, but for the test cases described here this dispersion was always very small.

As shown by its application to the Knysna estuary, the model is easily applicable to suitable estuaries, which means estuaries that are



vertically well-mixed and in which two-dimensional horizontal current patterns are negligible.

The calibration and verification runs for the Knysna estuary in particular show the reliability of the model and the subsequent tests for different flow conditions show the potential of the model as a tool for investigations of the influences of these conditions on salinities and these results can be used for further ecological studies.

The model could be developed further to simulate chemical and biological processes, but it would probably be better to use the other existing models, like the Dynamic Estuary Model (DEM) from the Environmental Protection Agency (EPA) in the USA. As mentioned before, the model presented here has similar features to this DEM.

Finally, the present combination of the hydro-dynamical with the water-quality model computations has the disadvantage that the model has to be operated on a small section length (100 to 500 m) and time-step (30 to 60 seconds). It was possible though to carry out the tests at relatively low cost. The Knysna model for example, was operated at about \$10 per day or \$300 per month. This shows that the model can be a practical tool for many investigations at reasonable cost.

#### LIST OF SYMBOLS

ATR	=	advective transport
$A_x, A_N$	=	cross-sectional area at x or N ( $m^2$ )
C	=	concentration ( $kg/m^3$ )
$C_N$	=	concentration of position N ( $kg/m^3$ )
$C_f$	=	Chezy coefficient ( $m^{1/2}/s$ )
CTR	=	sum of all advective and diffusive transport to and from a nodal position
Df	=	constant used which is actually $Df = Df^1 \cdot \sqrt{2g}$ in formula for diffusion coefficient (2-7)
DTR	=	diffusive transport
DW	=	diffusion coefficient ( $m^2/s$ )
$dx_N, dx_M$	=	nodal length at N, section length at M (m)
K	=	dispersion coefficient ( $m^2/s$ )
<u>M</u>	=	identification of section number (also as subscript)
N	=	identification of nodal number (also as subscript)
Q, $Q_M$	=	flow through cross-section (M) ( $m^3/s$ )
R	=	hydraulic radius (m)
S	=	salinity concentration (mg/l)
t	=	time (s)
$\Delta t$	=	timestep of computation (s)
$u_M$	=	mean velocity (m/s)

$u_N$  = net downstream velocity due to fresh water discharge  
Vol = volume ( $m^3$ )  
 $x$  = distance (m)  
<sup>1</sup> = all variables marked like this are on a new time level

## LIST OF REFERENCES

CSIR (1976). Saldanha Bay, the assessment of field data, the mathematical model and the physical model, Volume II. CSIR Report C/SEA 7620/2.

FISHER, H B, LIST, E J, KOH, R C Y, IMBERGER, J and BROOKS, N H (1979). Mixing in inland and coastal waters. New York.

LEENDERTSE, J J (1970). A water-quality simulation model for well-mixed estuaries and coastal seas. Volume I, principles of computation. RM-6230-RC.

ORLOB, G T (1972). Mathematical modelling of estuarial systems. International symposium on modelling techniques in water resources systems. Ottawa.

## CHAPTER TWO HUNDRED FOUR

### THE EXCHANGE OF WATER IN FJORDS: A SIMPLE MODEL OF TWO-LAYER ADVECTIVE REACHES SEPARATED BY MIXING ZONES

E.D. Cokelet<sup>1</sup>  
R.J. Stewart<sup>2</sup>  
C.C. Ebbesmeyer<sup>3</sup>

We propose a model for the two-layer, mean transport within a branched, recirculating fjord system. The recirculation is parameterized in terms of efflux/reflux coefficients at distinct mixing zones. The mass fluxes and efflux/reflux coefficients are determined from long-term salinity and current meter observations. The model provides a way to predict the mean concentrations of pollutants introduced within the system. An application to Puget Sound shows that different discharge sites markedly affect the concentrations landward of the sites themselves.

#### 1. Introduction

The task of predicting the long-term build-up of pollutants within estuaries is becoming more important with increasing urban and industrial pressure and environmental awareness. Historical data sets are often available on only the density of the seawater via temperature and salinity observations. Modern time-dependent computational models have the potential for being up to the task, but they are expensive to run over simulation periods of several years. We have developed a model for the steady-state circulation within a fjord system based upon the principal of conservation of mass.

In a classical fjord the long-term mean circulation pattern is two-layered with runoff-laden brackish water flowing seaward at the surface and entraining salt water from the slow, landward-flowing lower layer. In such a system a soluble, conservative pollutant added to the upper layer would simply be carried out to sea as if on a conveyor belt. Unfortunately many actual fjords are more complex than this. They consist of a sequence of deep, stratified reaches separated by shallower sills formed by past glaciers. Sometimes one fjord arm may branch into two or more arms at a junction. Mixing

---

<sup>1</sup> NOAA/Pacific Marine Environmental Laboratory, 7600 Sand Point Way N.E., Seattle, WA 98115-0070 U.S.A.

<sup>2</sup> Formerly at NOAA/PMEL. Presently at 4116 55th Ave SW, Seattle, WA 98116 U.S.A.

<sup>3</sup> Evans-Hamilton, Inc., 6306 21st Ave. N.E., Seattle, WA 98115 U.S.A.

Contribution No. 750 from PMEL

between the layers often occurs at these sills and junctions due to enhanced tidal currents. This intermixing complicates the "conveyor-belt" view of pollutant flushing.

2. Simple Junctions

Our premise is that many fjord systems can be thought of as made of two different components, reaches and mixing zones. In a two-layered reach the mean motion is purely horizontal advection. The two layers communicate only at mixing zones at the ends of each reach. These zones are complex regions where turbulent transport by tidal currents or shorter-period features often dominate the slow mean circulation, but it is not necessary to consider in detail the flows there. The net effect of the mixing zones is expressible solely in terms of the properties of the layers entering and leaving them.

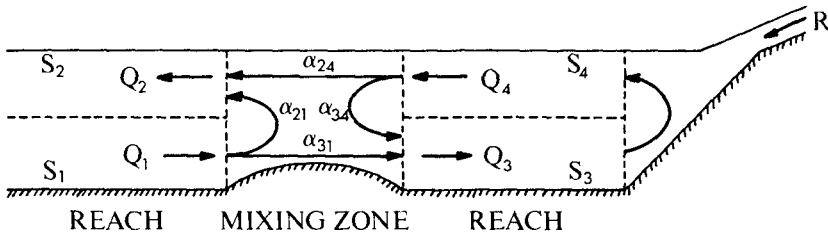


Figure 1. Two reaches meeting at a simple junction mixing zone.

A model for two reaches meeting at a simple junction is shown in Figure 1. The steady mass flux,  $Q_i$ , in any reach layer can be expressed in terms of the salinity,  $S_i$ , and runoff,  $R$ , by Knudsen's Hydrographic Theorem (ref. 3), i.e.,

$$Q_1 = \frac{S_2}{S_1 - S_2} R, \quad Q_2 = \frac{S_1}{S_1 - S_2} R. \quad (1)$$

$S_i$  is the flux-weighted salinity which must be determined from hydrographic and current observations. It is defined by

$$S_i = \frac{1}{Q_i} \int_{A_i} \bar{\rho} \bar{S} \bar{u} \cdot \mathbf{n} \, dA \quad (2)$$

with

$$Q_i = \int_{A_i} \bar{\rho} \bar{u} \cdot \mathbf{n} \, dA. \quad (3)$$

Each integral is evaluated over the cross-sectional area,  $A_i$ , of layer  $i$  with a downstream unit normal  $\mathbf{n}$ . The long-time-mean density, salinity and velocity are  $\bar{\rho}$ ,  $\bar{S}$  and  $\bar{\mathbf{u}}$ , respectively. These equations come from volume integrals of the steady continuity and salinity equations. Molecular diffusivity of salt is neglected as well as mean, turbulent salt transport within the reaches. Furthermore it is assumed that only salinity contributes to the density, hence temperature effects are neglected. Further details can be found in reference 1.

The flow in any layer is apportioned into two parts when it enters a mixing zone. A fraction,  $\alpha_{34}$ , of the landward reach's outflow (layer 4) mixes downward and refluxes into that reach's lower layer 3. The remaining fraction,  $\alpha_{24}$ , effluxes into layer 2. Likewise a fraction,  $\alpha_{21}$ , of layer 1's inflow refluxes seaward in layer 2, and the remainder,  $\alpha_{31}$ , effluxes landward. Conservation of water and salt lead to the following matrix equation for the efflux/reflux coefficients,  $\alpha_{ij}$ :

$$\begin{bmatrix} Q_1 & Q_4 & 0 & 0 \\ S_1 Q_1 & S_4 Q_4 & 0 & 0 \\ 0 & 0 & Q_1 & Q_4 \\ 0 & 0 & S_1 Q_1 & S_4 Q_4 \end{bmatrix} \begin{bmatrix} \alpha_{21} \\ \alpha_{24} \\ \alpha_{31} \\ \alpha_{34} \end{bmatrix} = \begin{bmatrix} Q_2 \\ S_2 Q_2 \\ Q_3 \\ S_3 Q_3 \end{bmatrix} . \quad (4)$$

With the aid of Knudsen's relations the solution becomes

$$\begin{aligned} \alpha_{21} &= \frac{S_1 S_2 - S_4}{S_2 S_1 - S_4} & \alpha_{24} &= \frac{S_1 S_3 - S_4}{S_3 S_1 - S_4} \\ \alpha_{31} &= \frac{S_4 S_1 - S_2}{S_2 S_1 - S_4} & \alpha_{34} &= \frac{S_4 S_1 - S_3}{S_3 S_1 - S_4} . \end{aligned} \quad (5)$$

Hence the flux-weighted salinities lead directly to the efflux/reflux coefficients.

The sum of all coefficients emanating from a layer, i.e. with constant second subscript, must be unity. The  $\alpha_{ij}$  lie between zero and one. For instance, the reflux coefficient in the inner reach,  $\alpha_{34}$ , is zero when the two lower-layer salinities are equal,  $S_1 = S_3$ . It approaches unity and complete recirculation as  $S_3$  approaches  $S_4$  — a limit which can never be reached unless the runoff is negligible.

### 3. N-Tuple Junctions

An N-tuple junction is a mixing zone in which N reaches meet. Figure 2 shows a schematic of one reach branching into two more at a triple junction. The layers are drawn side-by-side for convenience, but usually they are superposed.

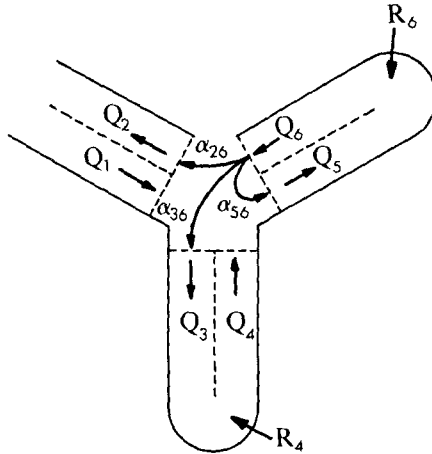


Figure 2. Schematic diagram of three reaches meeting at a triple junction. Only three of the nine efflux/reflux coefficients are shown for clarity.

In general  $N$  tracers (fresh water and salt being two) are needed to determine completely the  $N$  efflux/reflux coefficients at an  $N$ -tuple junction. The problem may be formulated in terms of a matrix equation similar to (4). The tracer concentrations must be independent of one another for a solution to exist. If through local knowledge or an independent set of measurements,  $N(N-2)$  efflux/reflux coefficients can be specified, then water and salt conservation are sufficient to determine the system.

An  $N$ -tuple junction with  $M$  rivers directly entering the mixing zone is treated the same as an  $(N+M)$ -tuple junction. The efflux/reflux matrix formulation also applies to a sequence of reaches and mixing zones.

#### 4. Pollutant Fluxes

Suppose a conservative pollutant is continuously injected at a mass rate  $p_i$  by a perfect diffuser at the upstream end of each layer of a simple junction fjord system as in Figure 1. Mass conservation

of the pollutant with concentration  $C_i$  in each layer leads to the following equation:

$$\begin{bmatrix} 1 & 0 & 0 & 0 \\ -\alpha_{21} & 1 & 0 & -\alpha_{24} \\ -\alpha_{31} & 0 & 1 & -\alpha_{34} \\ 0 & 0 & -1 & 1 \end{bmatrix} \begin{bmatrix} C_1 Q_1 \\ C_2 Q_2 \\ C_3 Q_3 \\ C_4 Q_4 \end{bmatrix} = \begin{bmatrix} P_1 \\ P_2 \\ P_3 \\ P_4 \end{bmatrix} \quad (6)$$

Here we have assumed that the pollutant mass input rate is negligible compared to the layer fluxes,  $Q_i$ . Inverting yields the steady state concentrations as a function of the efflux/reflux coefficients, mass fluxes, and inputs, i.e.

$$\begin{bmatrix} C_1 \\ C_2 \\ C_3 \\ C_4 \end{bmatrix} = \begin{bmatrix} \frac{1}{Q_1} & 0 & 0 & 0 \\ \frac{1}{Q_2} & \frac{1}{Q_2} & \frac{1}{Q_2} & \frac{1}{Q_2} \\ \frac{\alpha_{31}}{\alpha_{24} Q_3} & 0 & \frac{1}{\alpha_{24} Q_3} & \frac{\alpha_{34}}{\alpha_{24} Q_3} \\ \frac{\alpha_{31}}{\alpha_{24} Q_4} & 0 & \frac{1}{\alpha_{24} Q_4} & \frac{1}{\alpha_{24} Q_4} \end{bmatrix} \begin{bmatrix} P_1 \\ P_2 \\ P_3 \\ P_4 \end{bmatrix} \quad (7)$$

The coefficient  $\alpha_{24}$  plays a crucial role since the concentrations within the landward reach vary as its reciprocal. Hence a small value corresponding to large refluxing will lead to high pollutant concentrations. Equations (6) and (7) can be generalized to more complex fjord geometries, an example of which is given below.

##### 5. The Puget Sound Refluxing Model

The theory outlined above and given more completely in reference 4 has been applied to Puget Sound to provide the first quantitative examination of the long-term behavior of conservative pollutants in the entire system. Figure 3 shows a map of the region which consists of a series of deep, glacially carved channels with typical depths of 60 m to 200 m. Sills due to glacial hanging valleys or terminal moraines separate the various reaches. The main basin off Seattle is about 200 m deep along its axis with a sill at Admiralty Inlet to the north which shoals to 60 m. Near Tacoma the main basin shoals at the Narrows whose sill depth is approximately 40 m. There two sill zones have strong tidal currents (1.5-2.5 m/sec) with vigorous mixing.





Figure 4 shows a schematic of the model with the Puget Sound system divided into 9 two-layer reaches. Usually each seaward flowing layer lies above a landward flowing one, but layers 7 and 8 are an exception. Current meter observations indicate that the mean flow is juxtaposed with a surface-to-bottom mean circulation flowing clockwise around Vashon Island due to tidal rectification. No modifications to the theory are necessary for this case.

Mixing zones occur either at sills, river mouths or multiple junctions. Five mixing zones are simple junctions with rivers entering directly. The indeterminacy associated with each is dispensed with by assuming that all of the buoyant, freshwater river flow leaves the zone via the outflowing surface layer; hence none enters the outflowing bottom layer. The remaining efflux/reflux coefficients for each of the five mixing zones are then uniquely determined from water and salt conservation.

At the head of layer 18 a "leak" through Deception Pass allows salt water and some river water from the second largest river in the system, the Skagit River, to flow directly into layer 4. This is accounted for by making three assumptions based upon limited local observations (ref. 2):

1. 60% of the Skagit River flow exits directly into layer 4, i.e.  $\beta_{4,18} = 0.6$ ,
2. the mean volume flux through Deception Pass is  $1125 \text{ m}^3/\text{sec}$ , and
3. no layer-3 water flows over the shallow, ten-meter-deep sill in the Pass, i.e.  $\alpha_{18,3} = 0$ .

Here  $\beta_{ij}$  represents the efflux coefficient to layer  $i$  from river  $j$  which enters at the head of surface layer  $j$ .

One Puget Sound mixing zone, Admiralty Inlet, is a quadruple junction with a river ( $R_4$ ) entering directly. Water and salt conservation give 8 equations for 20 efflux/reflux coefficients. A variety of possible assumptions have been tried to close the system. The one considered here is that the three surface layers and the river flowing into the mixing zone combine to form an intermediate salinity water. Then this mixes in varying proportions with the inflowing bottom water of layer 3 to supply bottom layers 5, 13 and 17. This leads to the following 12 independent equations which close the system:

$$\begin{aligned}
 \alpha_{4,6} &= \alpha_{4,14} = \alpha_{4,18} = \beta_{4,4} \\
 \alpha_{5,6} &= \alpha_{5,14} = \alpha_{5,18} = \beta_{5,4} \\
 \alpha_{13,6} &= \alpha_{13,14} = \alpha_{13,18} = \beta_{13,4} \\
 \alpha_{17,6} &= \alpha_{17,14} = \alpha_{17,18} = \beta_{17,4}.
 \end{aligned}
 \tag{8}$$

We are interested in the mean circulation over time scales of about one year. The mass fluxes and efflux/reflux coefficients depend critically upon the observed salinity and current distributions through the flux-weighted salinities. Even though Puget Sound has been studied extensively for over 50 years only during one year, December 1953 to November 1954, do sufficient salinity profiles exist at monthly intervals for each reach in the model. Current meter data does not exist for this time but is available sporadically, being principally concentrated in the 1970's with a varying degree of spatial coverage. Thus we use a synthesized data set consisting of 1953-54 runoff and salinity data and available current observations. The technique of combining this data to provide rational estimates of the flux-weighted salinities is beyond the scope of this paper but is presented in reference 4.

Typically the flux-weighted annual mean salinities in the system are about 30‰. Landward of layers 5 and 6 the total runoff is about 400 m<sup>3</sup>/sec which, combined with a bottom-to-surface salinity difference of about 1‰, gives a net volume flux from Knudsen's relations (1) of approximately 12,000 m<sup>3</sup>/sec. Column 2 of Table 1 shows the calculated volume fluxes for each layer. Fluxes in layers 1 and 2, the Strait of Juan de Fuca, are large due to the large runoff from river 2 (the Fraser River) of over 5000 m<sup>3</sup>/sec. The flux values are somewhat dependent upon how the salinity and current meter data are analyzed as explained in reference 4.

Table 1. Predicted Volume Fluxes and Pollutant Concentrations, C<sub>i</sub>, in Puget Sound.

Layer i	Volume Flux (10 <sup>3</sup> m <sup>3</sup> /sec)	C <sub>i</sub> due to Layer-6 Input (µg/kg)	C <sub>i</sub> due to Layer-7 Input (µg/kg)
1	116	0	0
2	123	8	8
3	40	21	21
4	42	44	44
5	13	66	66
6	14	137	137
7	19	65	141
8	19	64	139
9	14	64	139
10	14	63	137
11	4.3	64	138
12	4.4	63	136
13	6.3	60	60
14	6.5	58	58
15	2.2	60	60
16	2.4	56	56
17	2.1	79	79
18	1.6	67	67

The model in Figure 4 has 54 efflux/reflux coefficients of which 12 are specified by the assumptions of the previous paragraphs. The remaining 42 are determined uniquely from the flux-weighted salinities via mass conservation and equations (8).

#### 6. Puget Sound Pollutant Concentrations Due To Alternative Sources

One way to utilize the model is to contrast the difference between discharging a conservative pollutant at two different input sites. The simple example of equation (7) shows that given the pollutant input rates,  $p_i$ , we can calculate their steady-state concentrations,  $C_i$ , and this holds true for the complex model of Figure 4.

Let us suppose that we wish to discharge 1 kg/sec of an arbitrary, conservative pollutant through a perfect diffuser (such that it mixes into its discharge layer completely) at the head of either layer 6 or layer 7. Columns 3 and 4 of Table 1 show the predicted concentrations due to the discharge sites. Pollutants introduced at either site are broadcast throughout the system owing to recirculation. They appear at the landwardmost reaches of all of the fjord arms.

In layers 1-6 and 13-18, mean concentrations do not depend upon the location of the discharge. This is because these layers are seaward of the seawardmost discharge site. As with conservative pollutants discharged into a river, the downstream concentration cannot be altered by simply relocating discharge sites already upstream of the observation point.

Reach layers 7-12, landward of the discharge sites, have equilibrium concentrations which depend significantly upon the sites. This is in stark contrast to the "conveyor-belt" view of fjord flushing in which no landward layer could receive pollutants. Layer-7 discharge leads to about twice the layer-6 discharge concentrations due to the fact that layer 7 flows landward coupled with the effluxing/refluxing at various mixing zones.

#### 7. Summary

We have developed a theory for recirculation within a fjord system composed of a sequence of advective reaches separated by mixing zones. Long-term salinity and current observations lead to the efflux/reflux coefficients which relate directly to conservative pollutant concentrations. An application to Puget Sound has shown one potential use for the model, that of predicting steady-state pollutant concentrations as a function of various discharge sites. Investigations are underway to compare the Puget Sound Refluxing Model predictions with observations of various trace metals, especially dissolved copper. Also work is in progress to determine the residence time of such a system.

## B. References

1. Cokelet, E.D. and R.J. Stewart (1985) The exchange of water in fjords: The efflux/reflux theory of advective reaches separated by mixing zones, to appear in J. Geophysical Research.
2. Collias, E.E., C.A. Barnes and J.H. Lincoln (1973) Skagit Bay study dynamical oceanography final report, Department of Oceanography, University of Washington, 197 pp.
3. Knudsen, M. (1900) Ein hydrographischer Lehrsatz, Ann. d. Hydr. u. Marit. Meteorol., 28, 316-320.
4. Stewart, R.J., E.D. Cokelet and C.C. Ebbesmeyer (1985) Mass transport in Puget Sound: An application of the refluxing theory, in preparation.

## CHAPTER TWO HUNDRED FIVE

### SEWAGE DISPOSAL IN SHALLOW COASTAL WATERS

by

Hans H. Dette

#### Abstract

The disposal of sewage effluent into coastal waters for dilution and final disposal requires an effective mixing of sewage with the seawater in order to achieve the necessary or demanded reduction of bacterial population. Most of the design parameters originate from work done on ocean outfalls. RAWN et al. (1960) developed curves from field data for the determination of initial dilution in a waste issuing from a horizontal port. ABRAHAM (1963) extended these curves to show that the dilution is a function of the depth of discharge port, the diameter of the discharge orifice  $D$  and the FROUDE number  $F$ .

The question, to which extent this calculation method is also valid for outfalls in shallow water regions, is still open. In connection with the actual design of a diffuser in shallow coastal water the method of ABRAHAM was applied together with a new method derived by BERGEN (1980) which is based upon experiments which were carried out in the Leichtweiss-Institute at semi-technical scale. After the diffuser had been taken into operation by means of in-situ measurements the demanded dilution could be checked and herewith also the reliability of the applied design method for practical use.

#### Experimental investigations on concentration ratio

For a comprehensive application, especially in case of discharges at low jet velocities (FROUDE number  $F < 1$ ), the calculation method of ABRAHAM (1963) is insufficient. Therefore investigations were carried out in order to extend ABRAHAM'S work into a wider range of validity (Table 1).

The experiments were carried out in a water tank with a depth of 3.5 m. For the measurement of instantaneous concentrations along the axis of freshwater upwelling in seawater the conductivity method was selected. For this purpose a grid of horizontal and vertical tungsten wires was installed in the tank so that disturbances on the dispersion in the tank were reduced to a minimum (Fig. 1).

It was the aim of the investigation to describe approximately by means of a 1st order theory diffusion processes. All derivations are related to an axially symmetrical and vertical buoyant jet originating from the discharge of a lighter fluid into a heavier one at still water.

Chief Engineer, Leichtweiss-Institute, Technical University of  
Braunschweig, Fed. Rep. of Germany M. A.S.C.E.

Table 1: Parameter variations in the experiments of the Leichtweiss-Institute and of ABRAHAM

Parameter	Range of variations			
	LEICHTWEISS-INSTITUTE		ABRAHAM	
	from	to	from	to
FROUDE number	0.0001	11.7	1	95
REYNOLDS' number	$0.15 \cdot 10^3$	$45 \cdot 10^3$	$1.8 \cdot 10^3$	$8.7 \cdot 10^3$
outlet velocity	0.0014 m/s	0.45 m/s	0.1 m/s	0.68 m/s
concentration ratio $c_m/c_o$	0.76	0.001	0.67	0.085
dilution	1 : 1.3	1 : 1000	1 : 1.5	1 : 12

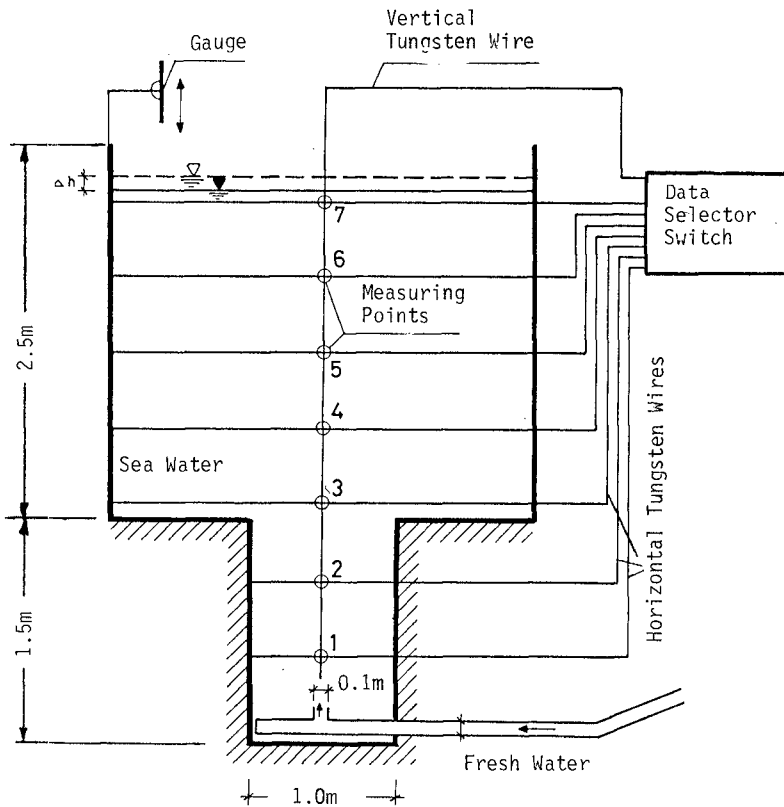


Fig. 1: View of the test facility for measuring concentrations along the axis of jet

In case of low outlet velocities the distribution profile of concentration is not so distinct as in case of high velocities; besides the mean upwelling velocity in the axis of jet is much higher than in cross direction. As for design purpose mostly maximal data are needed an uniform distribution of concentration  $c$  and velocity  $v$  is assumed in the cross-section of the jet. It follows that the concentration at any point of the cross-section is equal that along the axis.

Table 2 shows as example the results of one test series. For different outlet velocities ranging from very low ( $v = 0.0014$  m/s) up to velocities of 0.45 m/s the connected FROUDE and REYNOLDS' numbers are listed together with the measured concentration ratios at different levels  $\frac{x}{D}$ .

Table 2: Test results of concentration ratio measurements (BERGEN, 1980)

TEST SERIES II $\Delta\rho_o / \rho_o = 0.02192$						
No.	TEST	$\frac{x}{D}$	$v_o$ [m/s]	Fr	Re	$\frac{c_m}{c_o}$
31	1	3,5	0.0015	0.0001	148	0.0080
32		8,5				0.0040
33		18,5				0.0040
34		23,5				0.0001
35		28,5				0.0015
36		33,5				0.0015
37	2	3,5	0.0020	0.0002	197	0.0121
38		8,5				0.0078
39		18,5				0.0043
40		23,5				0.0042
41		28,5				0.0019
42		33,5				0.0024
43	3	3,5	0.0048	0.0011	483	0.0406
44		8,5				0.0188
45		18,5				0.0185
46		23,5				0.0068
47		28,5				0.0046
48		4				3,5
49	8,5		0.0366			
50	18,5		0.0081			
51	23,5		0.0359			
52	28,5		0.0109			
53	33,5		0.0083			
54	5	3,5	0.2315	2.4920	23150	0.7715
55		8,5				0.1736
56		18,5				0.0616
57		23,5				0.0321
58		28,5				0.0046
59		33,5				0.0173

In Fig. 2 these data are plotted through which for each test linear curves were drawn for further use.

A qualitative analysis of the test results revealed that at low jet velocities (e.g.  $v_o = 0.0015$  m/s. Curve A in Fig. 3 a relatively high initial dilution  $v_o$  is obtained in the direct vicinity of the outlet,

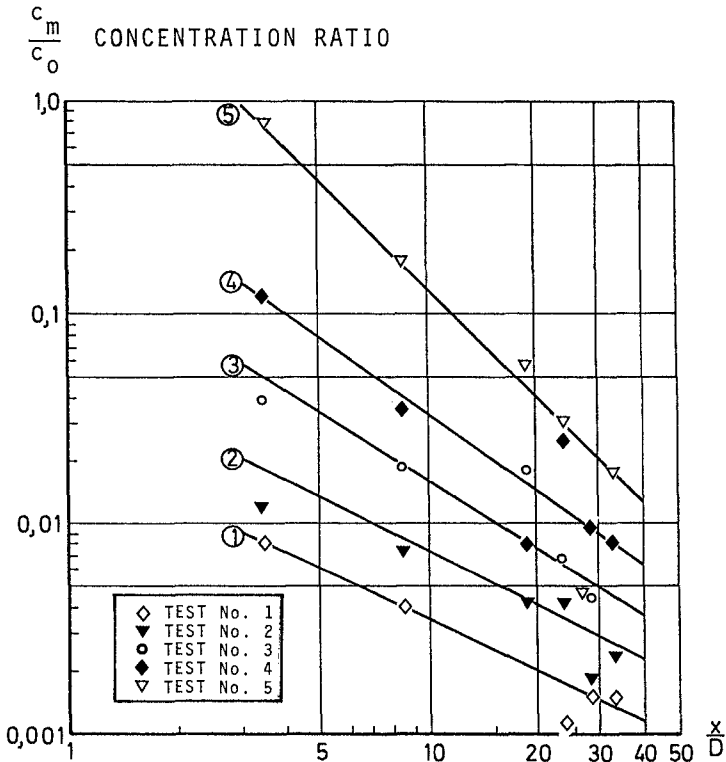


Fig. 2: Correction curves for measured concentration ratios (BERGEN, 1980)

here demonstrated by the lowest point of curve A (at  $x/D = 3.5$ , with  $x$  = vertical distance from outlet and  $D$  = diameter of outlet pipe = 0.10 m in the tests). In the course of further upwelling the dilution further increases by a factor between 4 to 6 (at  $x/D = 35$ ).

At higher jet velocities (e.g.  $v_0 = 0.2315$  m/s, which is more than two orders of magnitude higher than the previous example, curve B (in Fig. 3) the initial dilution is considerably lower but increases by a factor between 20 and 50 (at  $x/D = 35$ ). These results are in agreement with the statement of ABRAHAM (1959) that for Froude numbers  $\rightarrow 0$  (low velocity) the mean concentration  $c_m$  decreases faster than for Froude numbers  $\rightarrow \infty$ .



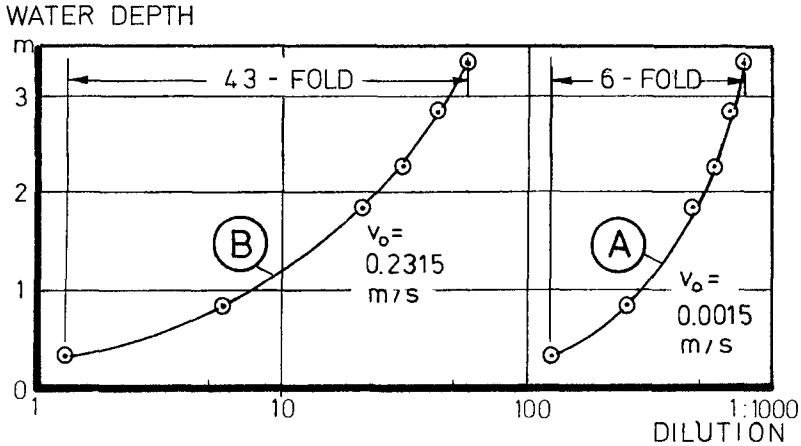


Fig. 3: Test results of dilution distribution at low (curve A) and at higher (curve B) jet velocities

Computation method for the determination of the concentration ratio

Based upon the already mentioned assumptions and approximations BERGEN (1980) derived an equation for the computation of concentration ratio by means of experimental data.

The following linear approach

$$\frac{c_m}{c_o} = \left[ \frac{x}{D} \right]^{-1} \left[ B_1 \cdot \left[ \frac{x}{D} \right]^2 + B_2 \right]^{-1/2}$$

was abandoned in favour of a nonlinear approach in which a hyperbolic cross-sectional shape of the jet is assumed (Fig. 4)

After certain transformations BERGEN (1980) obtained the following equation:

$$\frac{c_m}{c_o} = 2 \left[ \frac{b-3}{2} \right] \sqrt{\frac{Fr}{b}} \cdot D \left[ \frac{5-b}{2} - \frac{2}{5} \right] \cdot \left[ \frac{x}{D} \right]^{-\frac{2}{5}}$$

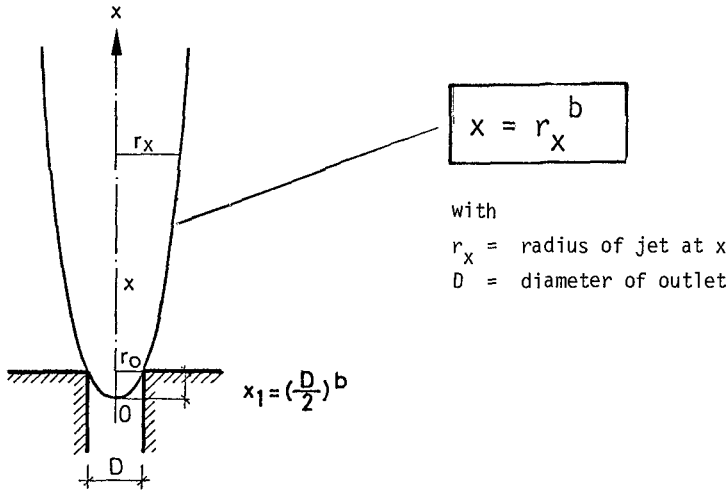


Fig. 4: Hyperbolic cross-sectional shape of jet (schematic)

By introducing three coefficients which are functions of two known parameters (Froude number  $F$  and outlet diameter  $D$ ) and only one unknown (parameter  $b$ )

$$B_3 = 2 \left[ \frac{b-3}{2} \right] \cdot \sqrt{\frac{Fr}{b}} \quad (B_3 = f(b, Fr))$$

$$B_4 = D \left[ \frac{5-b}{2} - \frac{2}{b} \right] \quad (B_4 = f(b, D))$$

$$B_5 = \frac{2}{b} \quad (B_5 = f(b))$$

the above equation can be written

$$\frac{c_m}{c_0} = B_3 \cdot B_4 \cdot \left[ \frac{x}{D} \right]^{-B_5}$$

For the determinations of the three coefficients the iteration method was applied so far until the computed concentration ratio was equal the measured one

$$\frac{c_m}{c_0} (\text{theory}) \cong \frac{c_m}{c_0} (\text{experiment})$$

Table 3 shows as example the computed coefficients obtained by iteration for the measured concentration ratio  $c_m/c_o$  (experiment). The scattering of the value b can be explained by the fact that in the equation no distinction is made between the direct vicinity of jet release and the further distant where upwelling is more defined.

Table 3: Computation of coefficients  $B_3$ ,  $B_4$  and  $B_5$  and parameter b by iteration for measured concentration ratio (BERGEN, 1980)

TEST SERIES II $\Delta\rho_o / \rho_o = 0,02192$								
No.	TEST	$\frac{x}{D}$	$v_o$ [m/s]	$\frac{c_m}{c_o}$ experim.	$B_3$	$B_4$	$B_5$	b
31	1	3,5	0,0015	0,0080	0,0081	1,701	0,436	4,59
32		8,5		0,0039	0,0077	1,364	0,460	4,35
33		18,5		0,0021	0,0073	1,160	0,480	4,17
34		23,5		0,0018	0,0073	1,110	0,485	4,12
35		28,5		0,0015	0,0072	1,072	0,490	4,08
36		33,5		0,0013	0,0071	1,035	0,495	4,04
37	2	3,5	0,0020	0,0175	0,0119	2,417	0,403	4,96
38		8,5		0,0083	0,0111	1,851	0,427	4,68
39		18,5		0,0043	0,0110	1,508	0,448	4,46
40		23,5		0,0036	0,0104	1,441	0,454	4,41
41		28,5		0,0030	0,0103	1,364	0,460	4,35
42		33,5		0,0026	0,0102	1,304	0,465	4,30
43	3	3,5	0,0048	0,0500	0,023	2,715	0,394	5,08
44		8,5		0,0195	0,027	1,800	0,430	4,65
45		18,5		0,0085	0,025	1,315	0,464	4,31
46		23,5		0,0065	0,024	1,202	0,475	4,21
47		28,5		0,0055	0,024	1,140	0,482	4,15
48	4	3,5	0,0190	0,1170	0,107	1,851	0,427	4,68
49		8,5		0,0410	0,096	1,192	0,476	4,20
50		18,5		0,0160	0,088	0,844	0,526	3,80
51		23,5		0,0120	0,086	0,771	0,542	3,69
52		28,5		0,0095	0,084	0,723	0,554	3,61
53		33,5		0,0080	0,083	0,689	0,563	3,55
54	5	3,5	0,2315	0,7600	1,165	1,181	0,477	4,19
55		8,5		0,1720	0,983	0,614	0,588	3,40
56		18,5		0,0460	0,882	0,414	0,712	2,81
57		23,5		0,0320	0,864	0,388	0,743	2,69
58		28,5		0,0230	0,848	0,366	0,778	2,57
59		33,5		0,0175	0,837	0,352	0,806	2,48

With respect to a parameter b which is independent of the distance x from outlet a parameter  $B_e$  is introduced as follows:

$$B_e = \frac{\sum_{i=1}^n b_i}{n}$$

with n = number of data from one test

By assuming  $b \equiv B_e$  then only the parameter b has to be replaced in the derived equation.

If a satisfactory relation between parameter  $B_e$  and a given experimental or design parameter can be found the derived equation can be applied for actual design.

Fig. 5 shows for the parameter  $Be$  related to the REYNOLDS' number  $Re$  a relative good agreement so that this graph can be used as key curve for design purpose.

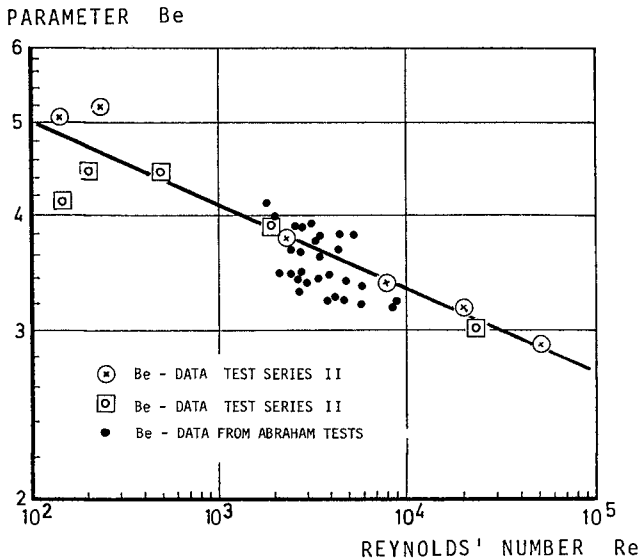


Fig. 5: Key curve for the calculation of concentration ratio (BERGEN, 1980)  
Application of the computation method for design

As could be shown in the preceding chapter the single design parameters on concentration ratio depend from each other so that the optimal values have to be found by iteration. In order to facilitate the computation of the concentration ratio number according to BERGEN'S equation for engineering purpose three diagrams (II, III, IV) in relation to diagram I as the key curve (Fig. 5) were developed (Fig. 6).

Actual design of a multiport diffuser in shallow coastal water

The sewage of the city of Kiel for many years was released through a single point outlet into the Baltic Sea. The distance from the shoreline was 250 m (Fig. 7).

Due to bacterial population above the allowed boundary values and odour nuisance the recreational beaches adjacent to the point of release had to be restricted for public use. In order to re-establish bathing water quality it was demanded to extend the outlet up to 1.500 m distant from the shoreline in order to prevent further shore pollution. By extensive field measurements (DETTE, 1984) it was concluded that a multiport

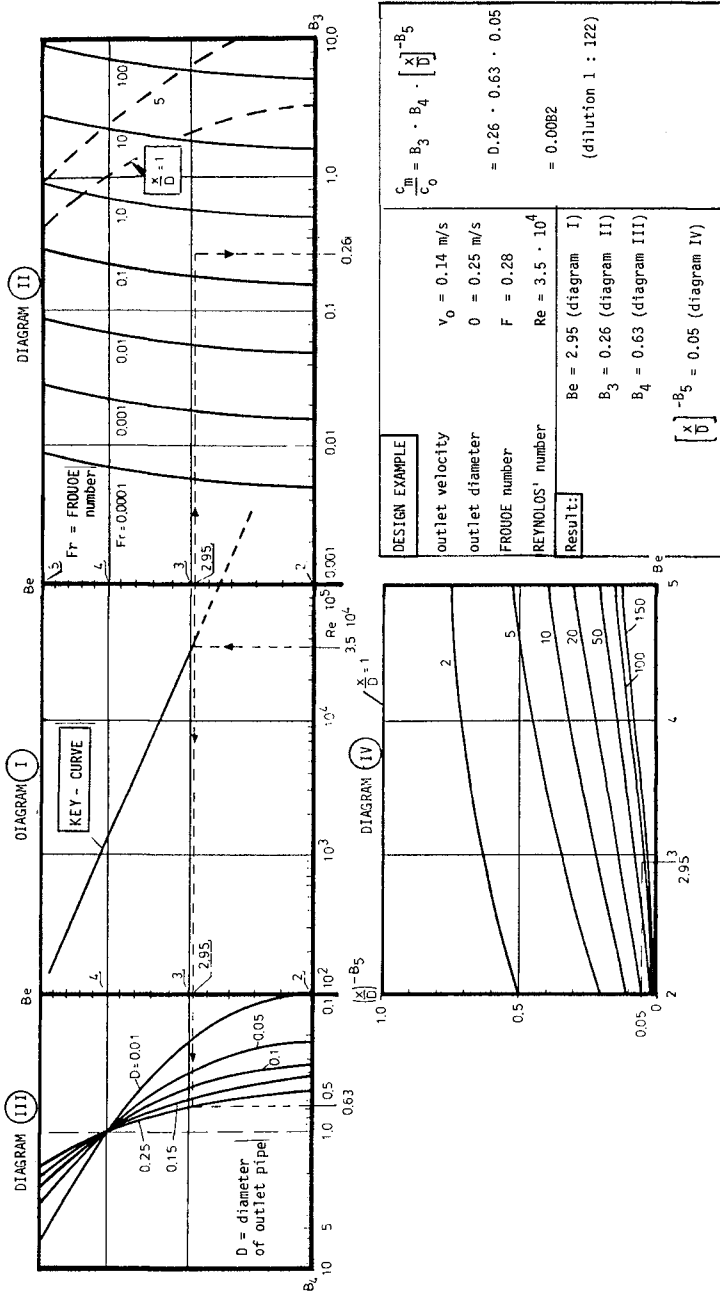


Fig. 6: Application diagrams for the computation of the concentration ratio  $c_m/c_0$  (BERGEN, 1980)

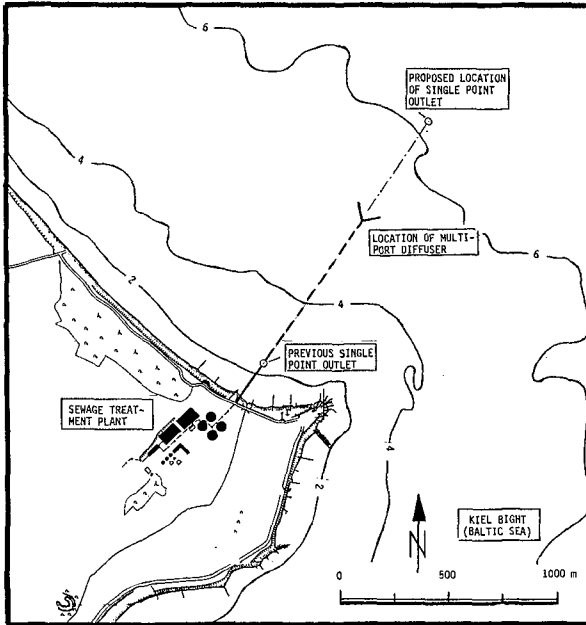


Fig. 7: Sewage release in shallow coastal water

y-shaped diffuser should be built at a distance of 1.000 m from the shoreline (Fig. 7).

As design criteria for the diffuser it was demanded that a dilution of 1 to 10 should be obtained at the water surface above the diffusers. With respect to the optimization of porthole diameter and number of portholes for a given sewage discharge of  $Q = 0.7 \text{ m}^3/\text{s}$  in one arm of the y-shaped diffuser the calculation methods of ABRAHAM (1959) and that of BERGEN (1980) were applied.

The results are plotted in Fig. 8.

In order to obtain an uniform outflow from all portholes variable distances between the single portholes were calculated and suggested for execution (Fig. 9). Details of the diffuser system are shown in Fig. 10. For the 1000 m long submarine pipeline of DN 1500 mm (diameter) tubes of 6 m length were welded together on land to lengths of 50 m which were afterwards brought into the water and transported as floating elements to their final position. For the underwater connection of the sections special couplings (type: Straub Flex) were used.

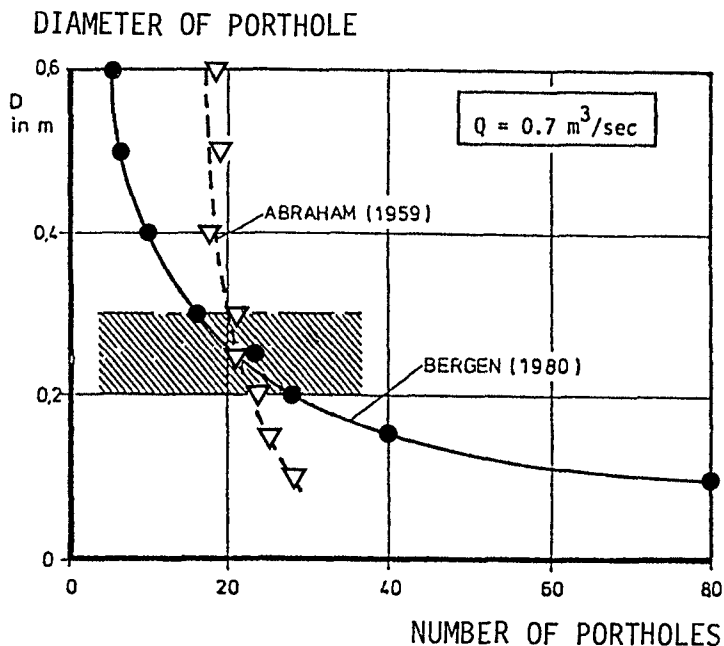


Fig. 8: Computation of porthole numbers in relation to outlet diameter according to ABRAHAM (1959) and BERGEN (1980)

#### Control measurements on initial dilution

After the new diffuser had been taken into operation control measurements were carried out in the direct vicinity of the diffuser in order to know to which extent the number of coliforms has been reduced in comparison to those values sampled at the plant itself. The reduction in the number of coliforms can be regarded in shallow water as direct indicator of the obtained dilution. Fig. 11 shows the locations where samples have been taken from the water surface. In Table 4 the results are listed. With respect to the number of total coliforms a mean reduction to approx. 3 percent is obtained directly above the diffuser in comparison to a demanded reduction to 10 percent. At a distance of 10 m from the diffuser already a further reduction of one order of magnitude is reached (0.3 percent).

It is therefore concluded that the applied calculation method on concentration ratio and the layout of the diffuser fulfilled the targets so that a general application for sewage release in shallow water can be recommended.

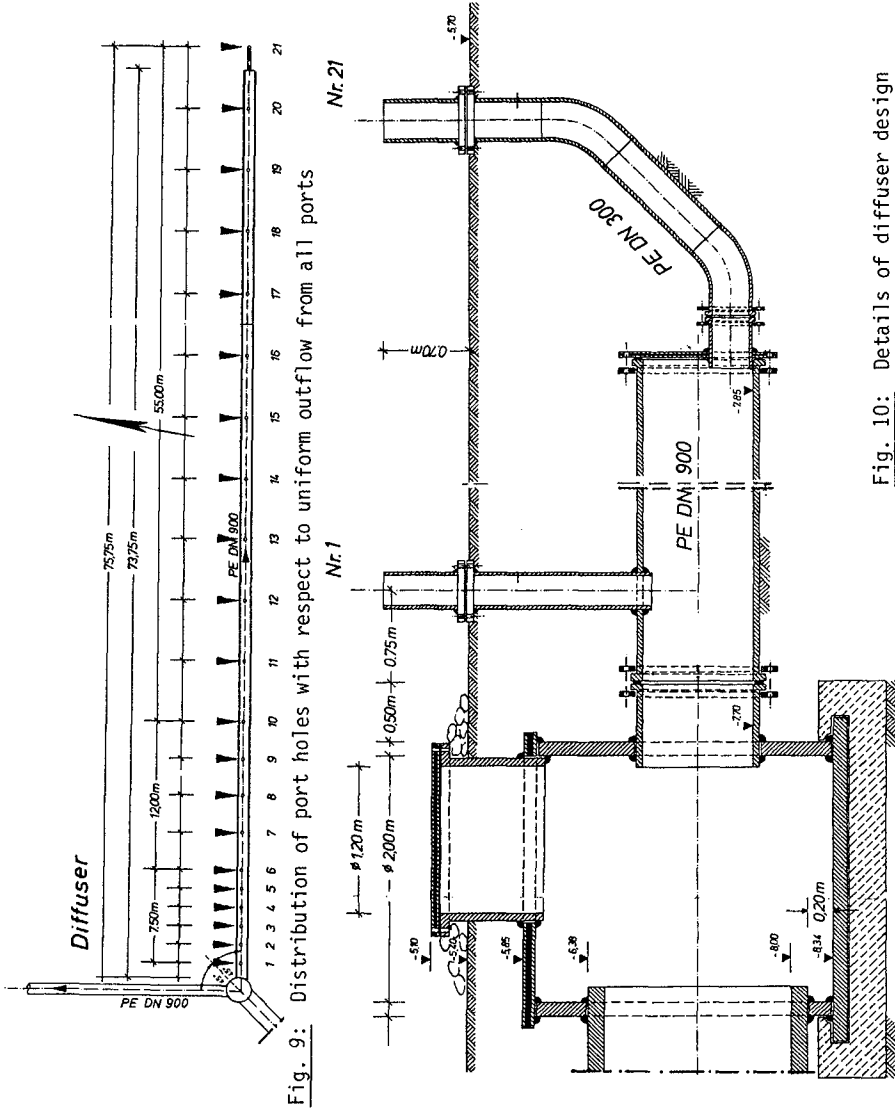




Table 4: In-Situ measurements of coliforms in the vicinity of the diffuser carried out by Institute of Marine Microbiology at University of Kiel

Sample	Temperature	Salinity	Coliforms		Remark
			Total (37°C)	Fecal (44°C)	
-	°C	%	10 <sup>3</sup> mg/l	10 <sup>3</sup> mg/l	-
Sewage plant	-	-	254	13	-
1	10.8	12.5	5	0.8	<u>A B O V E</u> the diffusers
2	10.8	12.5	6	0.7	
3	10.8	12.5	8	1.1	
4	10.5	12.5	8	1.5	
5	10.8	12.5	8	1.0	
6	10.8	12.5	5	1.6	
7	10.5	12.5	4	1.0	
8	10.8	12.5	10	1.4	
Mean value	10.8	12.5	7	1.1	
Percent of plant value	-	-	2.8 %	8.5 %	
9	10.8	12.8	0.2	0.08	<u>10 m</u> <u>distance</u> from diffusers
10	10.8	12.8	0.6	0.15	
11	10.5	12.8	0.6	0.13	
12	10.8	12.8	0.8	0.26	
13	10.8	12.8	1.1	0.26	
14	10.8	12.8	1.0	0.17	
Mean value	10.8	12.8	0.7	0.18	
Percent of plant value	-	-	0.3 %	1.4 %	

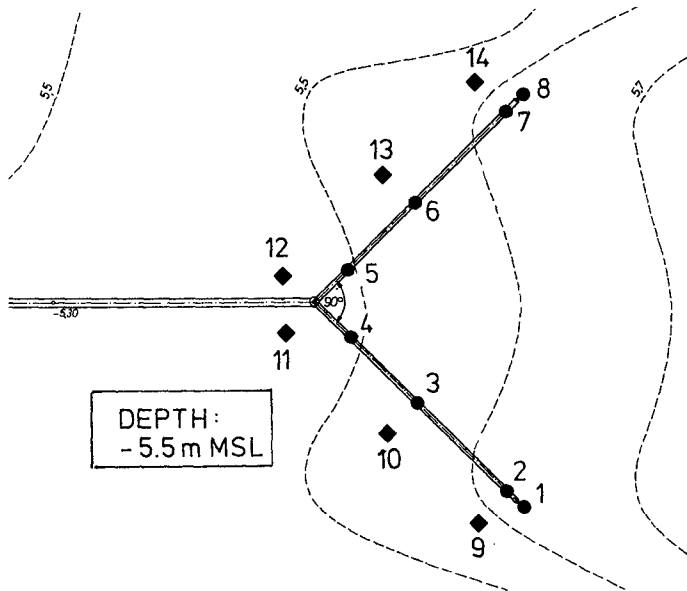


Fig. 11: Location of control measurements on coliforms

#### References

- Abraham, G. 1959 in Streeter, 1961: Handbook of Fluid Dynamics. Mc. Graw-Hill Book Comp., N. York
- Bergen, G. 1980: Über die Diffusion beim Einleiten von Abwasser in Meerwasser. Mitteilungen Leichtweiss-Institut, Techn. Universität Braunschweig, Heft 69.
- Rawn, M.; Bowerman F.R. and Brooks, N. H. 1960: Diffusers for Disposal of Sewage in Sea Water Journal of the Sanitary Division, A.S.C.E., March, 1960

## CHAPTER TWO HUNDRED TEN

### LARGE DIAMETER POLYETHYLENE SUBMARINE OUTFALLS

L. A. Jackson \*

#### 1.0 INTRODUCTION

This paper presents the state of the art that has now evolved in Australia and shows the trend towards using high density polyethylene pipes for submarine conditions and the varying techniques and materials utilised.

Prior to 1981 High Density Polyethylene (H.D.P.E.) was not produced in Australia in diameters larger than 630mm and even in the available sizes submarine outfalls were in the main constructed of mild steel or concrete pipes.

In 1980 the Gold Coast City Council called tenders for the supply and installation of a 1500 metre, 1 metre diameter, outfall across the Southport Broadwater which is an active tidal estuary area. The proposed route crossed a main navigation channel and required trenching up to 8 metres into sand and sandstone. After consideration of the special requirements and high tender prices for conventional materials, Council constructed a temporary 400mm diameter H.D.P.E. outfall while the design of the permanent outfall was re-evaluated. The outfall was eventually constructed by day labour utilising a 1 metre diameter H.D.P.E. at a cost saving of approximately \$1.5 million over the lowest tender price utilising steel pipes.

Manufacturing facilities were imported into Australia for this job and now other large diameter submarine H.D.P.E. outfalls have been constructed in Australia and this material is now gaining acceptance.

\* Special Projects Engineer, Gold Coast City Council, Bundall Road, Surfers Paradise, Gold Coast, Queensland, Australia, 4217.

## 2.0 MATERIAL AND DESIGN CONSIDERATIONS

H.D.P.E. is a flexible material and as such the design and installation techniques vary considerably from conventional pipe materials.

The properties are summarised as below:-

Density	- 0.96
Min. Bending Radius	- 33 x Pipe O.D.
Flow Characteristics	- $C(20^{\circ}) \approx 155$ (max.)
Tensile Strength	- 24 MPa
Impact Strength	- 18 mj/mm <sup>2</sup>
Flexural Strength	- 32 MPa
Hardness	- 63
Co-efficient of	
Linear Expansion	- $2 \times 10^{-4}/^{\circ}\text{C}$
Thermal Conductivity	- 0.37 K. Cal/M.L. <sup>^{\circ}\text{C}</sup>
Crystalline Melting	
Point	- 130 <sup>^{\circ}\text{C}</sup>
Chemical Resistance	- Not affected except by strong oxidising agents.

Thus in general H.D.P.E. is a material which has good flow characteristics, chemical resistance and is flexible but due to its low S.G. requires weighting to provide negative buoyancy. The minimum S.G. of the pipeline weighted system will depend on the wave, current and backfill material characteristics. Experience has shown that as the pipe is flexible, then unless the final weight is adequate and the weight spacing is not excessive, floatation can occur during backfilling.

Due to the flexibility and buoyancy of H.D.P.E. pipe, various construction techniques can be utilised as listed:-

- (a) Fabricate the entire length, float into position and sink.
- (b) Progressively fabricate on, and lay off, a barge.
- (c) Progressively fabricate and bottom pull into place.
- (d) Progressively fabricate and flange join each length above or below water.

The pipe may either be laid in place on the seabed or in a prepared trench, or, due to its flexibility, jetted into the seabed material or undercut and lowered by dredging alongside the sunken pipeline.

Because of its light weight, flexibility, and ease of welding, H.D.P.E. can be assembled and laid without expensive specialised equipment and with a minimum of construction personnel. Overheads are therefore low and the cost of stand downs during adverse weather conditions is minimal.

### 3.0 CASE HISTORIES

Three case histories of major H.D.P.E. pipelines which have been constructed recently in Australia follow. Each job involved construction problems associated with the site conditions but the total job budget could not accommodate the use of large expensive specialised equipment. Different techniques were evolved for each job to suit the conditions and each was able to be carried out using readily available equipment and labour at a cost less than on comparable pipelines of alternate materials. The location of each job is shown in Fig. 1.

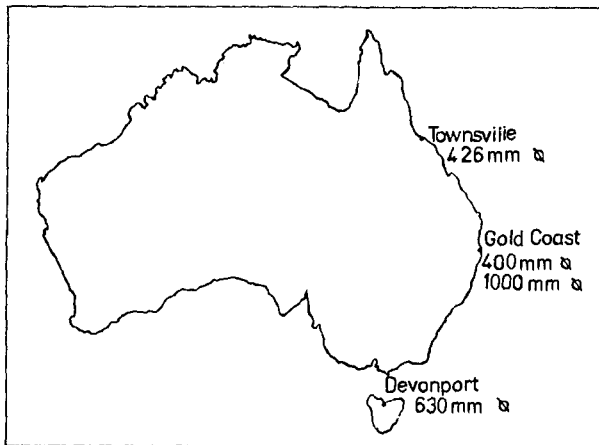


FIG. 1

(a) Gold Coast, Queensland (1982) (ref. Jackson, 1983 (2))

Location: Southport Broadwater (Nerang River Estuary)

Use: The pipeline serves as a submarine outfall to dispose of effluent from the recently constructed Coombabah carousel type sewerage treatment plant (50,000 e.p. capacity). Tenders for the pipeline construction were originally called but due to excessive costs the lowest tender utilising concrete lined mild steel was not accepted. Due to these delays it was necessary to provide a temporary outfall which

was constructed by Council's day labour force utilising 400 mm H.O.P.E. at a cost of \$200,000.

Site Description: The route traversed the wide estuary located at the mouth of the Nerang River and crossed two major navigation channels, which could not be closed, and the active sand bars of the internal delta. In the sand bar area up to 7m of sand and 1.5m of sandstone needed to be removed by dredging. The high tidal velocities made work difficult and caused rapid siltation/scour of the trench.

Length: 1450 m

Oiameter: 1000 mm (nom.) O.D.

Wall Thickness: 43.5 mm to 50.9 mm

Pressure Rating: 45 m

Average Flow: 1800 l/s

S.G.: 1.26 (too low!)

Costs: Total = \$2.5 million

Pipe Materials = \$730,000 of MSCL	\$745,645
Concrete	\$538,013
F.R.P.	\$731,612

Contractor: Day Labour (Gold Coast City Council)

Consultant: Camp Scott & Furphy

#### Fabrication:

- (1) 12 m plain ended pipes were butt fusion welded on land into lengths approximately 200 m long and progressively winched over steel rollers into a shallow holding area as each length added.
- (2) Each fabricated length hydrostatically tested and refloated.
- (3) Concrete weights were then attached to the floating length using a catamaran barge with lifting gantry.

#### Installation:

- (1) Oredge trench progressively.
- (2) Tow fabricated length and sink into position as trench prepared (end left afloat for dry attachment of next length).
- (3) Level and backfill each length as laid.
- (4) Attach next length above water using catamaran barge as trench prepared and then sink.
- (5) Place prefabricated flexible concrete scour mattresses under channels.



(b) Townsville, Qld (ref Bryne & Reidel, 1983 (1))

Location: Cleveland Bay between Townsville and Magnetic Island (Fig 2).

Use: In order to provide water to the growing population on Magnetic Island, a new water supply pipe was required.

The material was not specified, but H.D.P.E. was nominated by the successful tenderer.

Site Description: The route traversed Cleveland Bay which is up to 5m deep with waves of 2.0m maximum and currents up to 1.5 km/hr. The bottom material varied from coral to soft mud in the intertidal zone.

Diameter:	426mm O.D.
Length:	5610m
Working Pressure (max):	0.7 MPa
Minimum Flow	155 l/sec
Burial 1.5m in the surf zone	
Water Temperature:	26 <sup>0</sup> ± 8 <sup>0</sup> C
Design Waves: Height	4 metres
Period	8.5 seconds
S.G.:	1.5
Wall Thickness:	40mm
Cost:	\$1.8 million (\$321/m)
Contractor:	Construct Pty Ltd
Consultant:	Reidel & Byrne Consulting Engineers Pty Ltd

## Fabrication:

- (1) 17m plain ended pipes butt fusion welded into 400m lengths on beach.
- (2) Concrete weights attached prior to launching by lifting and dragging.

## Installation:

- (1) Excavate trench progressively in reef, surf and intertidal zones using amphibious excavator.
- (2) Lift pipe into water and tow with additional floats into place and sink completely into 1.5m (max) deep trench.
- (3) Flange joint next pipe under water when next 400m of trench prepared.
- (4) Bury seabed sections of pipeline using the diving operated jetting machine.

Jointing: Epoxy coated steel flanges and galvanised bolts (all cathodically protected).



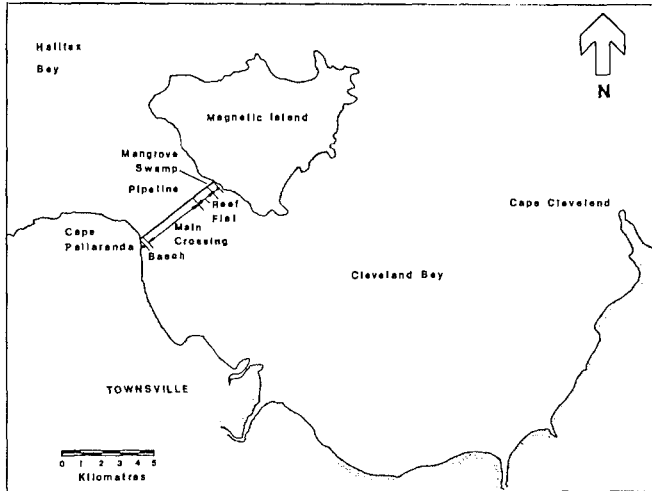


FIG. 4

(c) Devonport, Tasmania (1982)

Location: Mersey River

Use: The main carries raw sewage to the new East Devonport Plant.

Site Description: The main crosses the deep Mersey River which carries a high volume of commercial marine traffic which includes the Melbourne to Tasmania Ferry. In order to prevent excessive disruption the river could not be closed for more than 12 hours at any one time. Due to the site conditions, the need to be corrosive resistant both internally and externally and the need to be laid quickly at a reasonable cost, the Council selected H.D.P.E. over steel and concrete.

Length:	288m
Diameter:	630 mm
Wall Thickness:	30 mm
S.G.:	1.3
Costs:	\$250,000 (\$868/m)
Construction:	Day Labour (Devonport City Council)
Consultant:	(Reidel & Bryne Consulting Engineers Pty Ltd)

## Installation:

- (1) Dredge 2m deep trench
- (2) Fabricate one 288m length from 12m plain ended pipes using butt fusion welds on a nearby beach (4 days)
- (3) The lower half of the 54 concrete weights were laid out on the beach along side the pipe and the pipe lifted onto the weights using a fleet of front end loaders. The top sections of the weights were then bolted on top. The operation was completed in 8 hours.
- (4) The weighted pipe was then towed into the water over greased timber skids at high tide.
- (5) Using a tug and several small work boats the pipe was towed into position and sunk into the trench by flooding with town water in 3 hours.

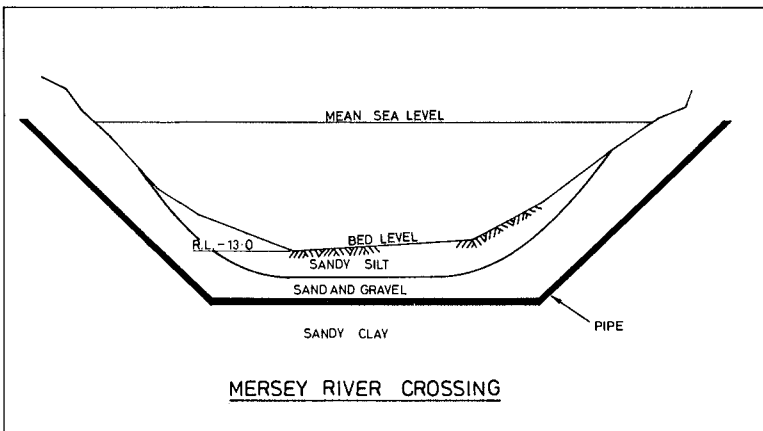


FIG. 5

#### 4.0 OVERVIEW

The three cases cited all involved difficult conditions but as illustrated by utilising the inherent flexibility of H.D.P.E., construction techniques such as prefabrication and above water flange joining were utilised to enable these projects to be carried out economically without the need for specialised equipment or labour. Due to the nature of the pipe, detailed design of the weighting system, scour protection and corrosion protection/minimisation of joint materials are necessary.

#### References

1. Byrne Gt Reidel, H.P.: Townsville to Magnetic Island Submarine Pipeline - 6th Aust Conference on Coastal and Ocean Engineering, 1983.
2. Jackson, L. A.: Construction of a 1000 mm dia Polyethylene Effluent Outfall across the Southport Broadwater - 6th Aust Conference on Coastal and Ocean Engineering, 1983

## CHAPTER TWO HUNDRED ELEVEN

### OPTIMIZING DUMPING SITES NEAR DREDGED CHANNELS

Dipl.-Ing. Ulrich Kögel           \*  
Dipl.-Ing. Friedrich Ohlmeyer   \*\*

#### ABSTRACT

To maintain the depth of the deepwater channel of the Elbe-Waterway extensive dredging has to be done permanently. Dumping should be optimized, choosing sites near the dredging area but with a small risk of recirculation of the dumped material. In order to estimate this risk field measurements with current meters and radioactive tracer tests in field and model were carried out.

#### 1.0 INTRODUCTION

The deepwater channel of the river Elbe from Hamburg to the North Sea has been deepened to an average depth of 13,5 m below chart datum. The mean tidal range is about 3 m.

The channel has to be kept free by constant dredging. A volume of 8 to  $10 \cdot 10^6 \text{ m}^3$  fine and medium sand has to be dredged annually from the North Sea up to Hamburg. The dredged volume has increased the last three years nearly up to twice the amount before. This caused the Board of Waterway in Cuxhaven to look for the most economical way of dredging. The dredged material could be dumped near the dredging

---

Bauberrat,	Federal Waterways and Shipping Administration / Agency Cuxhaven 2190 Cuxhaven, Deichstraße 12
Research engineer,	Hydraulics Research Station of the Federal Institute of Waterways 2000 Hamburg, Wedeler Landstr. 157

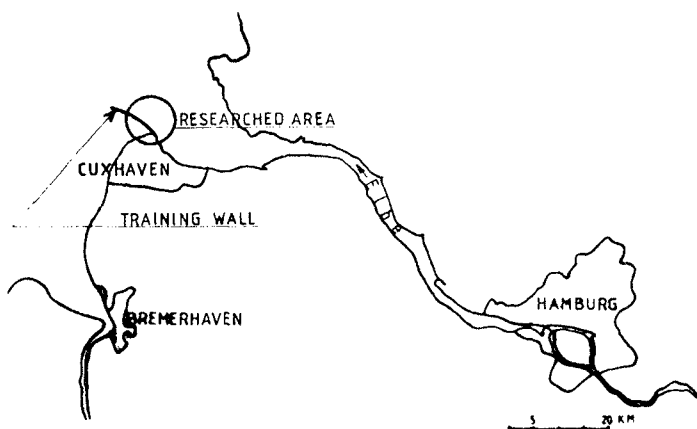


fig. 1 geographical location

sites as very deep areas are situated on both sides of the deepwater channel. But this method is only acceptable if there is no recirculation of dumped material into the deepwater channel within a short time. One of the main dredging sites with a dredging volume up to  $2.8 \cdot 10^6 \text{ m}^3$  p.a. is the training wall area near Cuxhaven (Fig. 1). This area has been researched to find out the reasons of accretion, especially as two dumping sites had been opened up on both sides of the dredging area. Recognizing a constant depth at the two dumping sites a flux of the dumped material is evident.

The dumping sites were checked for their suitability. For this, measurements in field using current meters and several investigations with radioactive tracers in a hydraulic model and in field were carried out with the aim to get informations of direction of the sediment transport. The influence of wave pressure and direction was neglected, because the wave height is very small in comparison with the water depth.

## 2.0 PRELIMINARY SURVEY

The sounding maps (fig. 2) of this area gives a picture of the sites of accretion and of the depth situation below mean spring low water. By investigations it was found that the highest inflow was from the south. Most dredging had to be done there. A comparison between the dredged and the dumped volume in this area of the year 1983 shows, that the dredged volume was up to 2,4 times the amount of the volume dumped in the vicinity. Therefore the dumping of the material on both sides of the deepwater channel cannot be the only reason of the increased sedimentation.

## 3.0 INVESTIGATION OF THE DUMPING SITE I

### 3.1 MEASUREMENTS WITH CURRENT METERS

At first field measurements with recording current meters were carried out. The aim of this investigations was determine the direction of sediment transport and also to estimate the amount of accretion

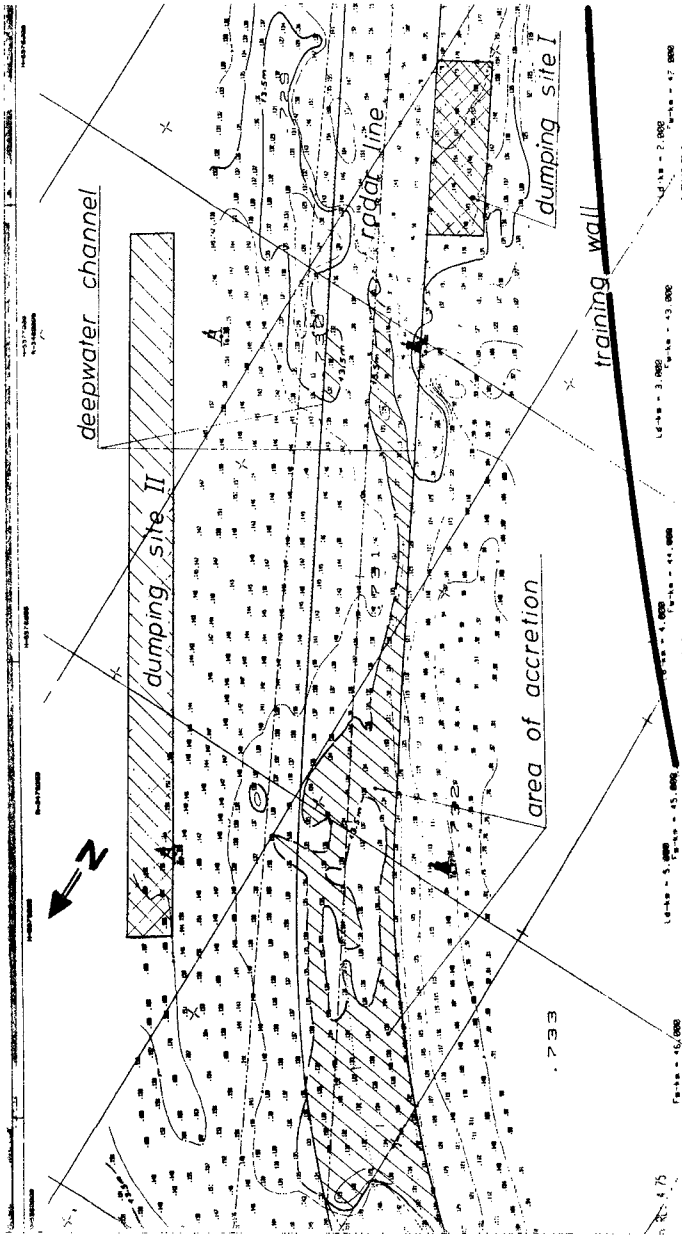


fig. 2 Sounding map with dumping and dredging areas

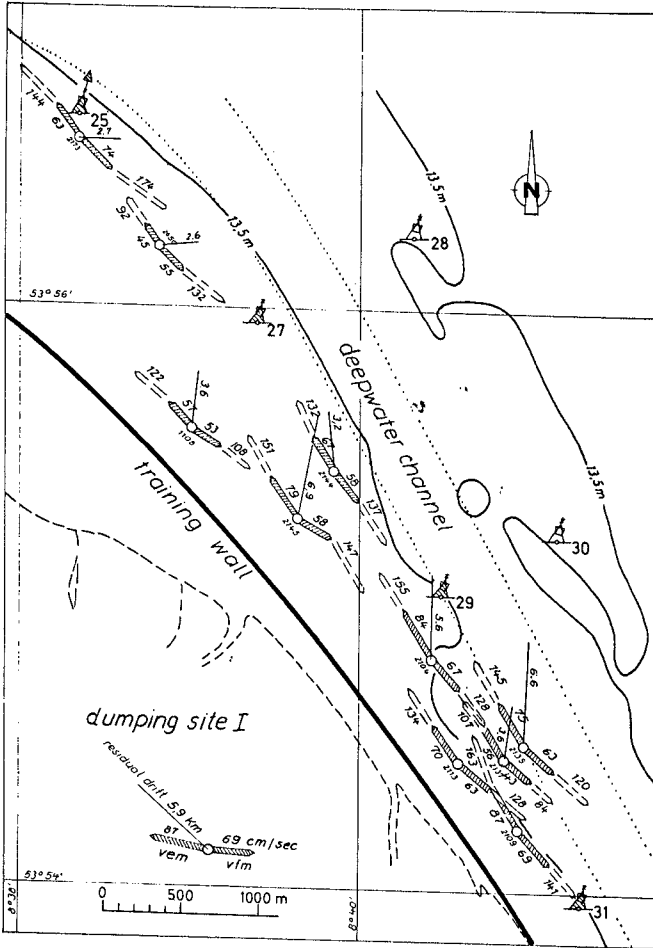


fig. 3 Bed current measurements in field, I



dependant on conditions of ebb- and flood current. The velocity and direction of current are recorded with current meters, moored 0,5 m above the bed. The currents measured at that level are regarded as relevant for sediment transport in this case. The results are stored on magnetic tapes. Mostly the measurements were carried out continuously. The 14 days measurements took into account the effect of the mean, the spring and the neap tides. The data showed, that up to 1000 m downstream from buoy 29 the ebb current dominates, but from buoy 27 onwards the mean ebb and flood velocities are equal. Downstream from buoy 27 the mean flood velocity prevails (fig. 3).

The ebb- and flood-current in this area reaches 45 - 87 cm/s. The highest rate 84 - 174 cm/s. There is a residual drift of 2.6 - 6.9 km/tide towards downstream or upstream and towards the deepwater channel depending on the dominating ebb or flood current. The residual drift is calculated from the vectoral additions of the ebb and flood current data measured in 5 minutes intervals.

All measurements were evaluated by means of tapereader, desk-top computer and plotter. A good overall picture of the expected sediment transport can be obtained by consulting the current velocity rose, which shows the current velocity and directions (fig. 4). The direction of ebb- and flood currents oscillates in an angle-scope of 25 degrees. The ebb current dominates in this case, ebb and flood direction diametrically opposed to each other. The residual drift vector calculated of it, shows the direc-

## DISTRIBUTION OF CURRENT VELOCITY/DIRECT.

POSITION 53°55'44"N 08°40'48"E  
 DATE 14.03.-28.03.84  
 LOCATION DUMPING SITE II / BUOY 28-30  
 HEIGHT OVER BOTTOM 0,50 m  
 FLOOD  $V_{\text{mean}} = 41 \text{ cm/s}$   $V_{\text{max}} = 103 \text{ cm/s}$   
 EBB  $V_{\text{mean}} = 51 \text{ cm/s}$   $V_{\text{max}} = 151 \text{ cm/s}$

Strömungsgeschwindigkeits- und -richtungsverteilung

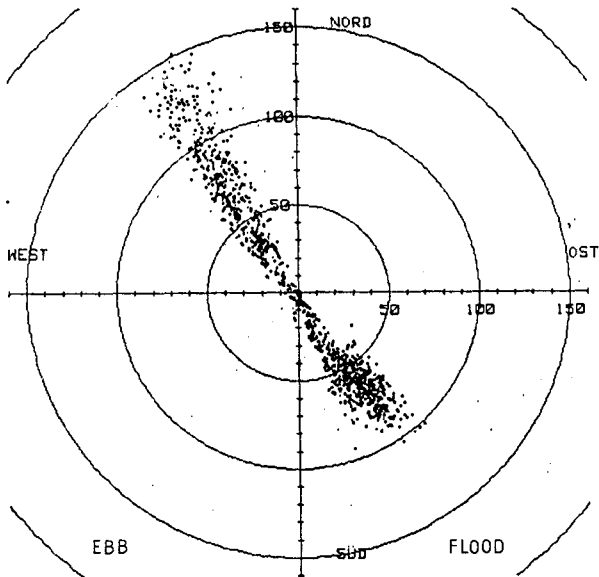


fig. 4 current velocity rose

tion of the mean ebb current from which one can deduce that the sediment is transported in this case in the direction of ebb current. The measurements of the individual measuring points were compared with the results of neighbouring points. By this the following overall result was reached:

Because of the prevailing ebb current upstream from buoy 27 and the prevailing flood current downstream from this buoy and the respective residual drifts towards the deepwater channel, sediment transport must be expected from the south into the deepwater channel up- and downstream from buoy 27.

The direction of the residual drift indicates, that the greater part of the dumped material from dumping site I moves back into the deepwater channel between buoy 27 and 29. This assumption is confirmed by comparing the grain sizes of the material ( $d_{50} = 0.16$  mm) dumped in dumping site I and being dredged on the southern sides of the dredging area between buoy 27 and 29.

### 3.2 MEASUREMENTS WITH RADIOACTIVE TRACERS IN MODEL

The results of the field measurements were confirmed by investigations in a hydraulic model with movable bed using a radioactive tracer. This model of the Elbe estuary is managed by the Bundesanstalt für Wasserbau in Hamburg. The model scales are 1 : 800 horizontal and 1 : 100 vertical. The hydrodynamic time-scale is non Froudeian; one tidal period of semi-diurnal type lasts 13.03 min. The bed material consists of polystyrene grains with  $d_m = 2.0$  mm and a density of  $1.035$  g/cm<sup>3</sup>. The theory is referred to Vollmers/Giese, (2) and aims in a natural simulation of dune structures.

The  $\gamma$ -radiating isotope Br 82 with a half-life of 36 hours was used to label 25 g of the polystyrene-grains, which were put into the model at high water

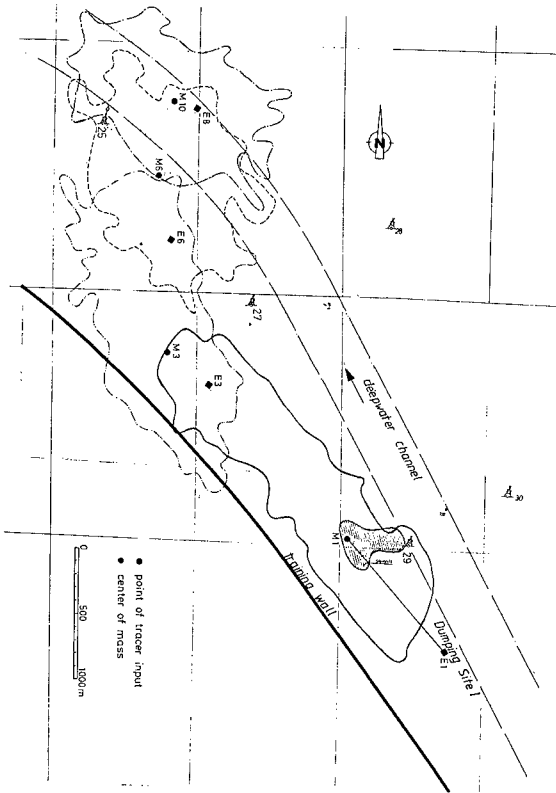


fig. 5 Radioactive tracer spreading in model, 1

slack. After a run of 150 tides in model the tracer has spread over an area of several square meters due to current and turbulence activities. The spreading area was scanned in a grid of 10 to 15 cm using a radiation detector and a scintillation counter. Detailed informations about this subject were given by Rohde, (1).

Between training wall and navigation channel 4 investigations were carried out in the model. (fig. 5). The spreading figures of the tracer-only the lines of the weakest radiation with 20 impulses per minute are depicted - can be interpreted in two ways. The one is to consider the direction of the longer main axis of the figures and the other is to draw the vectors from the input points to the centers of mass.

The results are in good conformance with the current measurements in field. The dominating ebb-current moves the material from dumping site I first parallel to the training wall. 2000 m downstream from the point of tracer input it sweeps round towards the deepwater channel and causes here a considerable accretion.

### 3.3 CONCLUSION

The results of the investigations led to the conclusion the recirculation -rate between dumping site and dredging area to be very high. Therefore the dumping activities at point I were stopped.

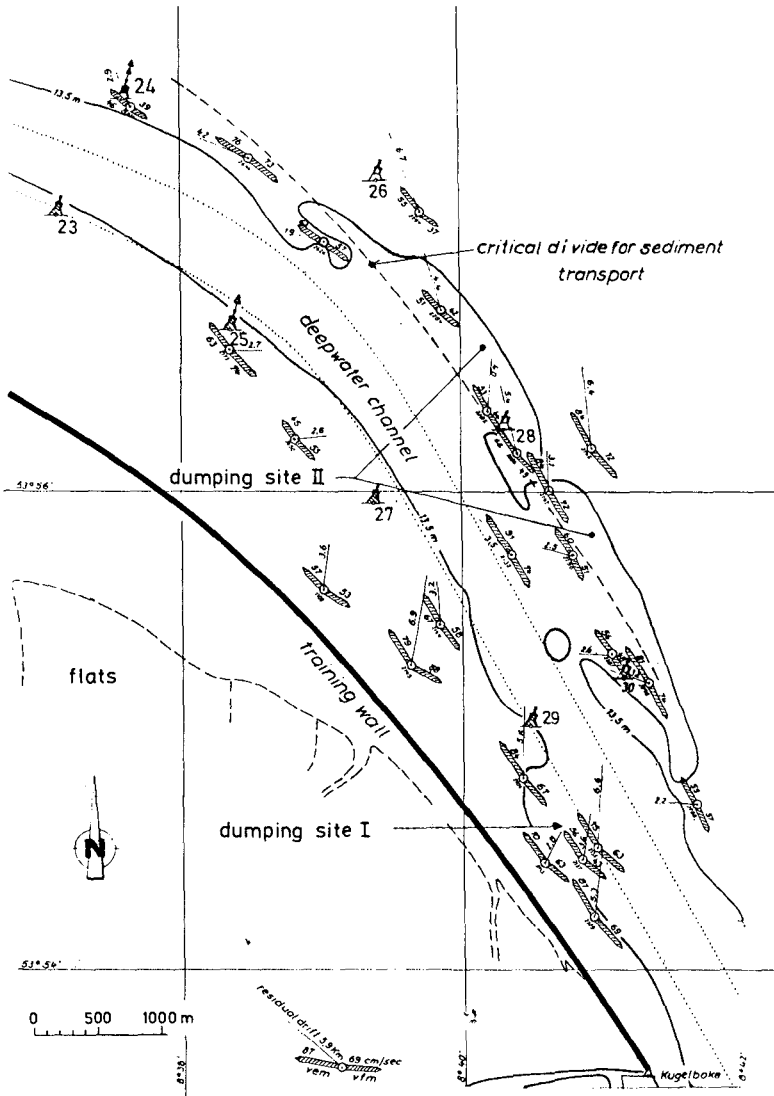


fig. 6 Bed current measurements in field, II

#### 4.0 INVESTIGATION OF THE DUMPING SITE II

The dumping site II was investigated by current measurements in the field and radioactive tracers experiments in model and the field.

#### 4.1 MEASUREMENTS WITH CURRENTS METERS

The results of the current measurements can be assumed as following (Fig. 6):

1. The mean and maximum ebb current velocities are higher than the corresponding flood velocities.
2. The residual drifts are clearly directed downstream, but one is directed to the north and the other towards the deepwater channel. The residual drift vectors are directed on the one hand to the north and on the other hand towards the deepwater channel separated by a dividing line.
3. In all cases the ebb current dominates and a dominating ebb-transport can be suggested.

#### 4.2 TRACER TESTS IN MODEL

This general tendency obtained with current meters is confirmed by research with radioactive tracers in the model. The tracer dumped in the middle of dumping site II spreads out to buoy 28 in a very soft angle towards the deepwater channel, from there it moves more steeply towards the deepwater channel and reaches it at buoy 25. The paths of the mass-centers are shown in fig. 7. A general tendency of decreasing vector lengths can be recognized.

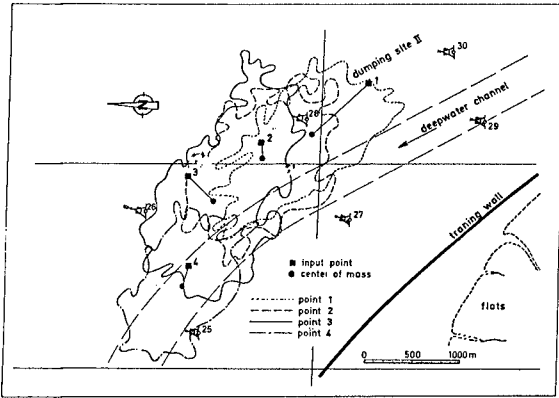


fig. 7 Radioactive tracer spreading in model, II

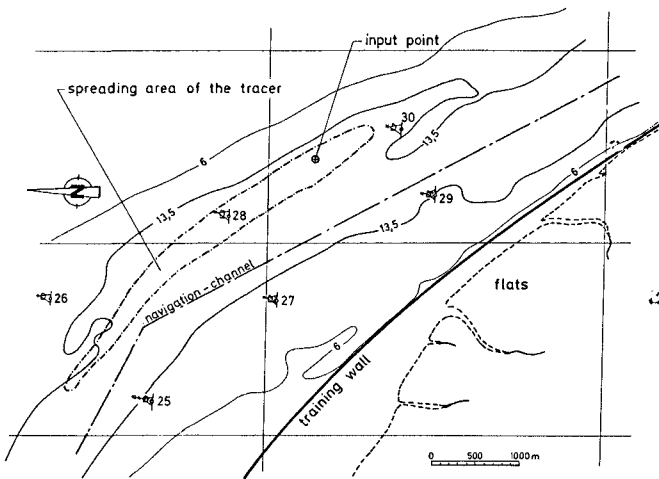


fig. 8 Radioactive tracer spreading in field



#### 4.3 MEASUREMENTS WITH RADIOACTIVE TRACERS IN NATURE

For better estimation of the suitability of the dumping site an additional investigation with radioactive sand was carried out in the field.

To prepare the tracer 10 kg fine to medium sand with a  $d_{50} = 0.26$  mm was taken from the river bottom and with the help of waterglass labelled with scandium (half-life 84 days). A heavy sledge with a scintillation detector was used to measure the radiation. The sledge was pulled over the river bed by a towing boat. The radioactivity was recorded by a scintillation counter. Hifix digital navigation system was employed for the location. More details about the tracer experiment are published by Rohde, (1).

The radioactive sand was introduced into the center of dumping site II. The area in which radioactive material could be found is shown on Fig. 8. In the first stages the tracer spread from the point of input downstream in a small plume, almost parallel to the axis of the deepwater channel. From buoy 28 on, the material moved towards the northern side of the waterway. The spreading of the tracer in lateral direction did not extend more than 300 m. It was possible to keep track of the tracer for about 3500 m downstream from the input point only. The tracer was suggested to be transported into the deepwater channel and passing on its northern side.

#### 4.4 CONCLUSION

These results of the different measurements led to the following procedure of dumping: The dumping site is restricted to an area downstream from buoy 28 and very close to the 13.5 m -line. It is supposed the transported sediment will not affect the deep-water channel essentially.

#### 5.0 RÉSUMÉ

Current measurements in field, radioactive tracer test in the field and in a model with movable bed are good tools in optimizing dredging and dumping procedure. These three methods have to complete each other as long as there is no better understanding of the complex physical process of sediment transport in tidal areas.

---

#### REFERENCES:

- (1) ROHDE, H. Sand Movement Investigations by Means of Radioactive Tracers in a Hydraulic Model and in the Field. Proc. Coastal Eng., Honolulu 1976
- (2) VOLLMERS, H. and GIESE, E. Elbe Tidal Model with Movable Bed. Proc. Coastal Eng., Vol. III Vancouver 1972.

## CHAPTER TWO HUNDRED TWELVE

### A New Nuclear Density Gauge to Measure Directly High Turbidities in Muddy Areas

A. Caillot, G. Meyer, D. Chambellan, J.C. Tanguy\*

#### Foreword

A better knowledge of the characteristics of muddy areas, in access fairways and port basins, and of the behaviour of ships during their crossing, presents the double interest of enhancing the navigation possibilities, through a more precise adjustment of the ship draught to the status of the bottoms, and permitting a more rational organization of the maintenance dredging campaigns. Considerable savings will be obtained through the development of such knowledges for harbours management.

These improvements imply the use of measuring equipments which must be handy, sturdy, reliable and which give accurate measurements.

The JTD3 gauge presented by the Radioisotopes Applications Service of the French Atomic Energy Commission is an important step in the development of such measuring equipments. It is now in running order, and commercially available, after thorough test campaigns, undertaken during many months in different french harbours.

New developments are already engaged, namely through the design of a turbidity gauge able to make dynamic measurements.

P. Monadier  
Head Central Technical Service  
Harbours and Maritime Navigation Directorate  
French Sea Ministry

#### I - Introduction

The depth necessary for sailing includes the free space between the keel and the bed of the channel, called keelclearance (Fig. 1a). However in muddy areas, it is quite possible for ships to sail through non consolidated silt (Fig. 1b) without reducing the safety.

The usual method to determine the water depth is based on the traditional hydrographic survey. But the upper trace recorded by echosounder appears as the bottom of the channel. In these conditions it is very difficult to say exactly where the nautical depth is, and the maintenance dredging takes two aspects:

- when, where to dredge and to which depth ?
- how to control dredging works cost ?

In assessing the nautical as well as the dredging aspects, an important factor is the density of the silt/water mixture. For this purpose, a nuclear scattering gauge, called SAPRA JTD3, has been developed to measure directly in the mud layer, vertical density (or concentration) profiles versus depth.

\* Commissariat à l'Energie Atomique, Service d'Applications des Radioéléments, Saclay (France).

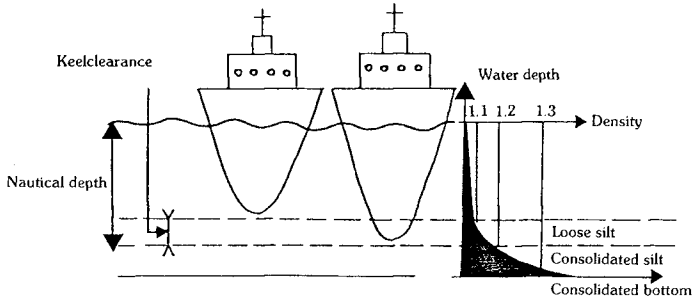


Fig. 1 - Scheme of keelclearance showing the consolidated bottom, the consolidated silt layer, and the loose silt layer.

II - Principle and Description of the Scattering Gauge

II.1 - Principle

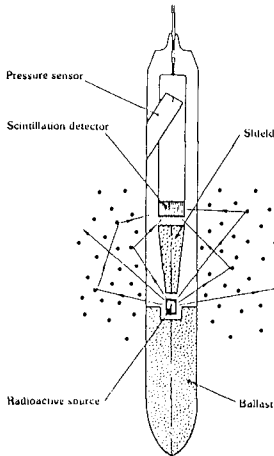


Fig. 2 - Scheme of the SAPRA JTD3 probe.

Gamma rays emitted in all directions by a very small cesium 137 sealed source (500  $\mu$ Ci or 18.5 MBq - Energy 661 keV - half life 30.18 years), are scattered through the sediment (Fig. 2).

The detector is shielded from direct gamma rays emitted by the source by the mean of a conical shaped tungsten plug set between the detector and the source housing (Fig. 3). The source to detector spacing is nominally 5 cm.

Gamma rays emitted by the source interact with the electrons of matter through two main ways: Compton effect and photoelectric absorption. Figure 4 shows the relative importance of those interactions versus gamma energy and atomic number Z.

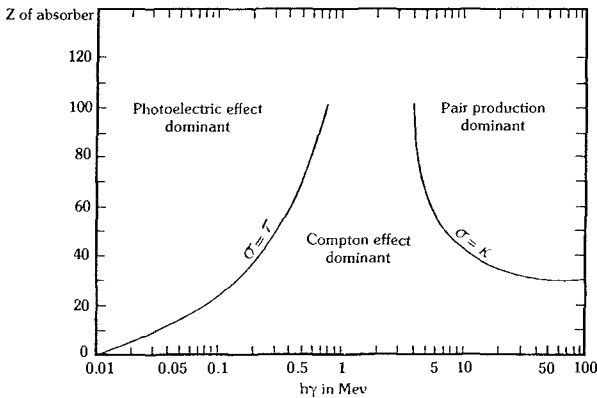


Fig. 4 - Relative importance of the different interaction effects between X or  $\gamma$  rays with matter.

The probability of occurrence of Compton effect is proportional to the ratio  $Z/A$  of an atom ( $A$  atomic mass of the element). This ratio is nearly the same for all the element, except hydrogen. That means that the diffusion effect is nearly independent of the chemical constitution of the sediment one wants to measure the concentration. But the probability of occurrence of photoelectric effect is proportional to the ratio  $Z^5/A$  of an atom. So this absorption effect will increase with the presence of mineral element of higher mean atomic number than classical  $SiO_2$ ,  $CaO$ ,  $Al_2O_3$ ,  $K_2O$ ... and so on.

As the two effects occur in competition in the same media, one must be careful to calibrate the probe in a media of chemical composition, more precisely mean atomic number not too different from the material which will be measured in situ.

#### 11.2 - Description

The probe device consists in a stainless steel pencil-shaped tube (Fig. 3). Length: 1000 mm, diameter: 55 mm, weight about 20 kg. Due to its shape, this gauge penetrates easily into the mud layer up to a density of 1.3 (about  $500 \text{ gl}^{-1}$ ). It is connected with an electronic data acquisition system through a four conductors steel cable (diameter 4.6 mm - tensile strength 1200 daN) stored on an electric winch.

This gauge can be connected (Fig. 5) to a small computer (APPLE 11) which controls the winch and calculates the sediment concentration profile.

The submersion depth is determined by a pressure sensor up to a maximum depth of 100 m. Winch and data processing equipment are powered by a gasoline or oil fired generator providing an AC 220 V supply.

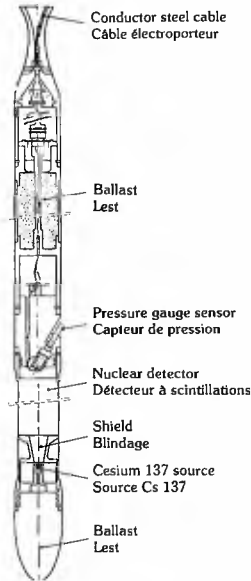


Fig. 5 - Photograph of the SA70-JD3 gauge showing the probe, the winch, the computer and the printer.

### II.3 - Safety

The radioactive source is certified as "material under special form" ISO CE 65 535 in agreement with international standards.

Maximum dose equivalent rate in contact with the gauge close to the source is less than 10 mrem/h when the probe is out of its transport shielding. In these conditions the handling of the probe requires minimum radiation safety.

### III - Measurements in Practice

#### III.1 - Calibration

The calibration will be done in large barrels (called infinite medium size ones). The probe hanging in medias ranging from water (fresh or salt water) up to mud suspension in the range density from 1 to 1.5.

Reference measurements  $N_W$  is taken in water. Table I and Fig. 6 give typical results.

Table I - Calibration of the gauge

Concentrations G in g/l	0	195	262	306	359	413	484	542	629
Densities $\rho$	1	1,12	1,16	1,18	1,21	1,25	1,29	1,32	1,37
$R = \frac{N_e}{N_W}$	1	1,037	1,040	1,054	1,063	1,074	1,083	1,094	1,113

A least square fit (first order) gives the following calibration relation:

$$\frac{N}{N_W} = 0.700 + (0.301 \pm 0.01) \rho$$

Such coefficients must be entered in the computer by the operator.

#### III.2 - Field Measurements

Operational density measurements using SAPRA JTD3 gauges have been performed in harbours and channels like ZEEBRUGE (Belgium), SINGAPORE, LOIRE esturay, ROGHEFORT (France),...etc.

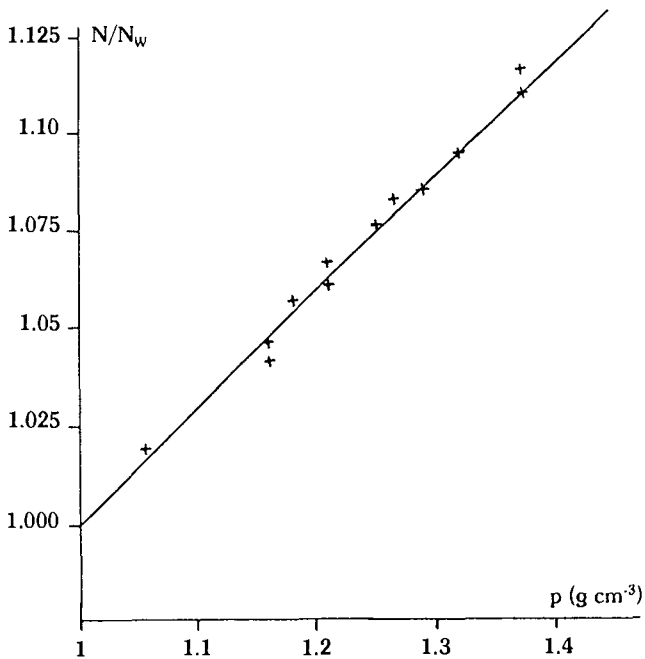


Fig. 6 - Calibration of the gauge.

The motor boat is neither morred nor anchored. The lowering speed of the probe is fixed between 0 to 30 cm/s (the usual lowering speed is 5 to 10 cm/s). Every second a measurement is realised, however the accuracy increases as the counting time increases too (typically this counting time is 5 seconds).

Typical concentration profiles are given on Fig. 7.

### III.3 - Performances

The instrument has a measurement range densities of 1.020 to 1.350 (about 30 to 580 g/l).



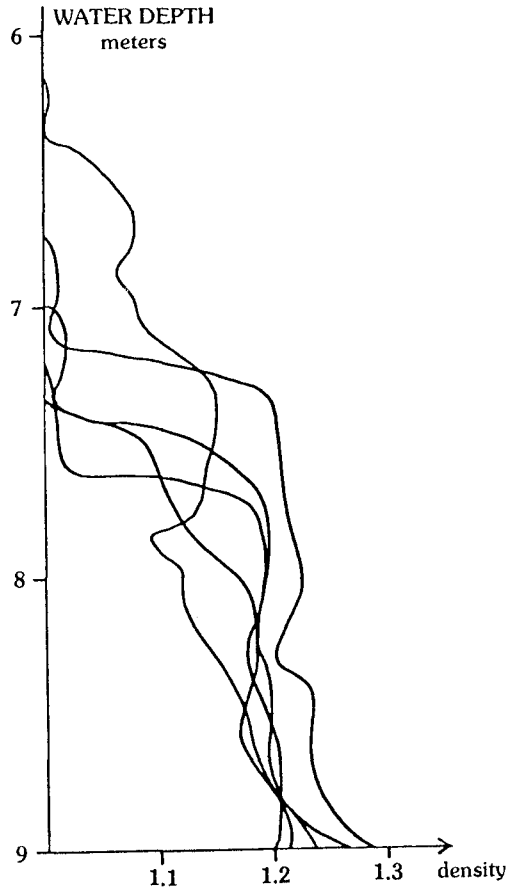


Fig. 7 - Typical density profiles in Rochefort harbour.

The accuracy is about  $\pm 0.010$  with a confidence level 95%.

The volume "seen" by the gauge is a horizontal cylinder (diameter: 60 cm - height: 15 cm).

Ten to fifteen vertical profiles per hour are recorded if the water current is lower than 2 m/s.

## IV - Conclusion

In muddy areas, such as access channels and harbours, where repeatable in situ measurements of the density in sediment layers are necessary, the SAPRA JTD3 gauge and the echosounder are complementary tools. This nuclear gauge's use permits to get an optimization of the dredging schedules.

## CHAPTER TWO HUNDRED THIRTEEN

### CALIBRATION AND ADJUSTMENT PROCEDURES FOR THE RHINE-MEUSE ESTUARY SCALE MODEL

H.N.C.M. van der Heijden<sup>1)2)</sup><sup>BY</sup>, P. de Jong<sup>1)</sup>, C. Kuijper<sup>1)</sup>,  
and A. Roelfzema<sup>3)</sup>

#### ABSTRACT

At the Delft Hydraulics Laboratory the hydraulic model of the Rhine-Meuse estuary has been rebuilt and extended after being destroyed by fire in 1979. The new model has been operational since the summer of 1982 for water quantity and water quality research. The present paper deals with the calibration and adjustment procedures for this hydraulic model. Successively the (physical) backgrounds for the calibration process, the techniques used for provision of boundary conditions and the procedures for adjusting flows and salinity distribution are discussed. Finally, the results of calibration and verification and the experiences gained on the employed techniques will be analysed.

#### 1. INTRODUCTION

The new hydraulic scale model is, in commission of Rijkswaterstaat (Ministry of Public Works), employed as one of the research tools in the framework of a long term research programme on water quantity- and water quality problems of the Rhine-Meuse estuary (Roelfzema, Karelse, Struijk, Adriaanse, 1984). See fig. 1.1 and 1.2. The model has, for practical reasons the same scales as those of the earlier model, i.e. the vertical scale factor is 64 and the horizontal scale factor is 640. Reviews of the earlier model are given by Van Rees, van der Kuur, Stroband (1972) and by Breusers and Van Os (1981).

Hydraulic modelling of the complicated inhomogeneous flows of the Rhine-Meuse estuary implies that the various physical mechanisms are simulated in an integrated way. A basic requirement for such a simulation is knowledge of these physical mechanisms. Based on this knowledge the appropriate scale laws and scale factors have to be estimated (or, in this case reanalysed) and the most adequate type of additional roughness - and mixing elements has to be chosen, section 2.

Section 3 and 4 deal with the time variant boundaries of the rivers and sea, section 5 describes the adjustment of the "roughness" of the river system. To adjust the flows of the complex network a procedure based on a least squares method, with a general applicability for the convergence of the calibration processes has been developed.

Adjusting the salinity distribution was achieved with more conventional methods. The actual calibration process is discussed in section 6, while in section 7 the results of calibration and verification are analysed and some concluding remarks are made.

- 1) Research engineer, Delft Hydraulics Laboratory, the Netherlands
- 2) Present affiliation: Shell Research, Rijswijk, the Netherlands
- 3) Project leader, Delft Hydraulics Laboratory, the Netherlands

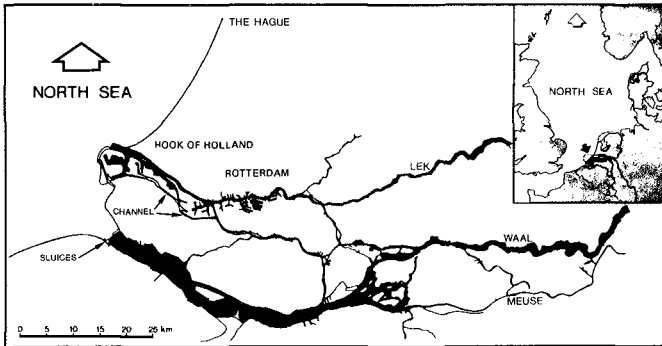


Fig. 1.1 PLAN VIEW RHINE-MEUSE ESTUARY

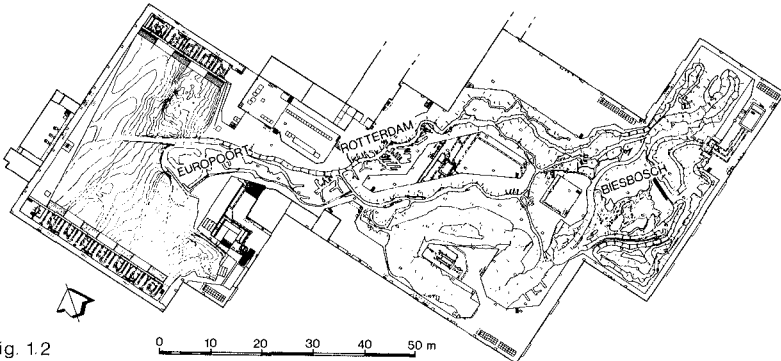


Fig. 1.2  
HYDRAULIC SCALE MODEL

## 2. BACKGROUNDS HYDRAULIC MODELLING

Characteristic for the geometry of the Rhine-Meuse estuary is its network system, consisting of a number of rivers with almost rectangular cross-sections. Only in the upstream parts of the system there are branches with flow and storage areas. In the northern part the Rotterdam harbours are found while in the southern part large, flat storage areas are present, forming about the half of the total tidal area of the estuary system.

The system is bounded at the upstream part by three river inflows, with a total discharge ranging from about  $600 \text{ m}^3/\text{s}$  up to about  $8500 \text{ m}^3/\text{s}$ . The downstream part is bounded by a free and a regulated outflow into the North Sea. The water levels show a dominant semi-diurnal tidal variation of about 2,20 m and 1.50 m at springtide and neaptide respectively.

The density difference between the sea and the fresh river inflow is about  $25 \text{ kg/m}^3$ .

The resulting inhomogeneous tidal flows show tidal influences to more than 100 km upstream from the mouth of the Rotterdam Waterway and salinity intrusion ranging from 30 up to 50 km.

Analyses of the physics of the system has been made possible by various

measurements carried out in the last few decades. Applying the internal estuarine number  $E_d$  according to Thatcher and Harleman (1972), the estuary system appears to be a partly mixed or layered type with normal values between 2,5 and 0,5. Amongst other approaches as dimensional analyses and decomposition methods, these measurements show that the dominant mechanisms are the vertical tidal effects, including the meteorological influences on the mean sea level, the river discharges, the vertical gravitational circulations due to density differences between sea and rivers and between rivers and harbours and the vertical turbulent diffusion. Of minor importance or negligible are horizontal circulations, lateral effects, longitudinal and lateral turbulent diffusion and wind effects on mixing. Applying the Froude-law, a basic condition for the modelling of gravitational and inertial forces has been satisfied, and thus for the modelling the dominating mechanisms of tides, river discharges and gravitational circulations.

The vertical scale factor of 64, taken over from the former model, allows in general a sufficiently high Reynolds number to simulate the overall structure of turbulence. A resulting representative Reynolds number is of the order of  $10^4$ . In this way the large scale turbulent eddies are reproduced correctly, satisfying a necessary modelling condition.

While the vertical scale factor had to be determined by principal considerations, the horizontal scale factor in general is determined on practical considerations of costs/economics. The horizontal scale factor of 640, also taken over from the former model, meets a reasonable optimum between the practical considerations and the experiences gained on distorted, inhomogeneous tidal models, (van Rees, et al 1972).

With these scale factors, the model (fig. 1.2) includes the research part of the estuary system along with a part of the North Sea and the fresh water rivers. These rivers have the correct scale for all hydraulic relevant parameters (length, depth, cross-sectional area etc.), but they have been bent to limit the total area of the building. In the Rhine-Meuse estuary the bottom influence on turbulent shear stress and on mixing are strongly dominating the side wall influences. The additional bottom roughness- and mixing elements, necessary because of the distorted scales, effectuates that in the model bottom influences are also dominating. To find the most adequate type of elements, analyses and flume tests have been carried out.

Premises for these activities were that the bottom elements have to be as small as possible to minimize local disturbances. Also they have to provide the model with non-directional resistance. Furthermore the elements have to facilitate flows near the model bottom in order to allow (analyses of) sediment transport processes, they have to allow occasional cleaning of the model and they have to be removed and to be replaced easily in order to facilitate the calibration process. Several types of elements have been investigated (viz. blocks, plates, bars, etc.), finally resulting in the choice for cross-shaped elements, fixed with a short bar on the modelbottom, fig. 2.1.

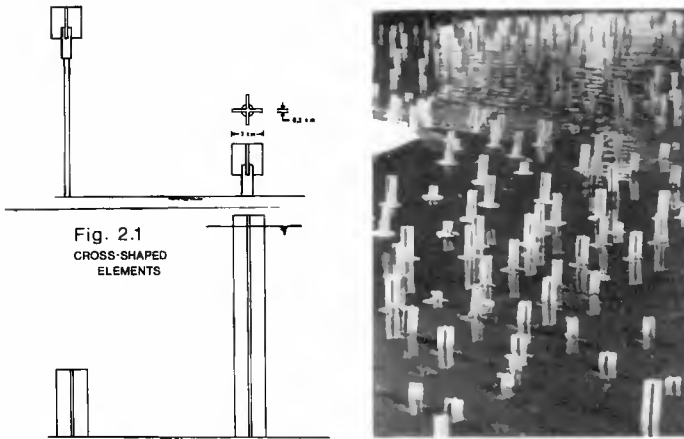


Fig. 2.1  
CROSS-SHAPED  
ELEMENTS

With respect to the geometry to be modelled it is very hard to estimate the actual differences between a model of concrete and a prototype under water. However, experience from past models has shown that no systematic differences could be found if every possible precaution was taken to make the model as accurate as possible. The results of new economic techniques involving concrete blocks of model, cast on polystyrene moulds were carefully compared to the more labour intensive ways of manually modelling a river. Although the result does not look as natural, no systematic differences could be found.

### 3. THE RIVER BOUNDARIES

From a research point of view only the central part of the model is of interest. The upstream river branches and the downstream model sea serve as generators of non-reflective boundary conditions for the area of interest.

The three upstream river branches begin in the model at places where the tide is negligible or that coincide with weirs. It is necessary to prescribe discharges at the river boundaries which may vary smoothly in time. In general these discharges are derived from water levels by means of a rating curve.

Tests in mathematical models showed that accuracy of the flow control should be so good that the mean over one minute should deviate less than 0.2% of the prescribed value within the whole range from 1.8 l/s (600 m<sup>3</sup>/s) to 26 l/s (8500 m<sup>3</sup>/s). This could be accomplished by using a constant head water tank and a system with several flow meters and valves, that switches slowly and automatically from one valve and flowmeter to the next.

### 4. THE SEAWARD BOUNDARY.

The conditions in the river mouth are described by the time variant water level and by the density, which is a function of time and depth. This water level and density are not directly controlled but are generated by the real flow field in the model sea. As there is hardly any stratification in the prototype at the position of the boundaries in

the sea, these boundaries have been constructed in the model as actively mixed sections (each of four meters length) where the total flow is accurately controlled (fig. 4.1). The layout is the same as in the old model (see Van Rees et al.), but all boundaries are now flow controlled. The electronics and the real time software are comparable to that of the old model (see Adriaanse et al.), but have been updated (completely digital) and highly integrated.

The problem with the control of these boundaries is that usually when prototype measurements on the river take place, the measurements in the sea are very limited in number. The procedures described in this section make the generation of reliable boundary conditions for such periods possible by using the measurements of other periods. The time series used to control these boundaries are derived from measurements as follows:

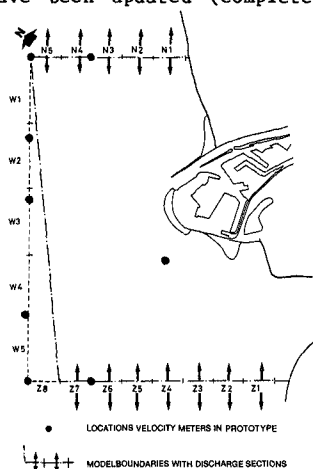
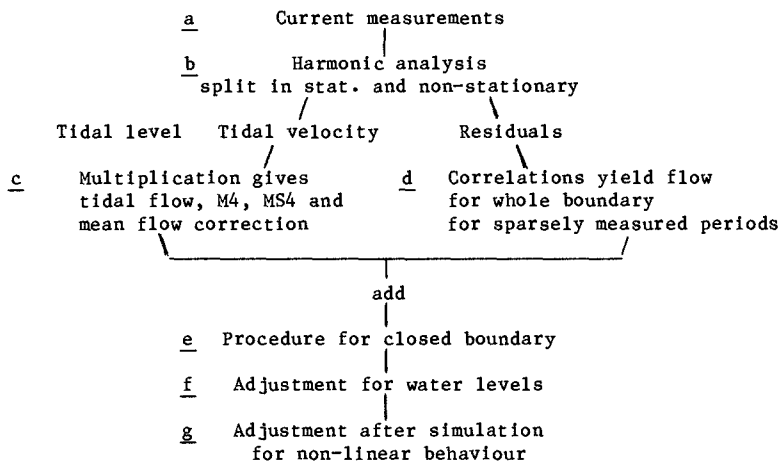


Fig. 4.1



- a. The currents at sea were measured at about 8 points during various periods of about one month. (fig. 4.1). Several measurements were simultaneous, others were not.
- b. According to good practise in time series analysis, the non-stationary part of the signal was separated from the stationary (this is the part for which the expectation does not change with

- time). Harmonic analysis was used to compute the tidal part and the stationary residual was assumed to consist of meteorological effect and noise.
- c. The tidal flow through each of the sections was then computed as the product of the velocity component perpendicular to the boundary and the time variant cross sectional area. This product yielded relevant higher harmonics (M4 and MS4) and gave a large correction to the mean flow. Gaps were filled in using correlations from short (13 hours) manual measurements made at many points on the boundaries.
  - d. For the meteo part of the flow no relevant correlations were found between the residuals of water levels and currents. Correlations between the residuals of simultaneous current meters at different positions were found to be significant for longer period variations (over 12 hours). In this way the residuals of current measurements at one position gave information about the flow through each of the model sections during the periods to be simulated.
  - e. As the flow pattern at sea is mainly parallel to the coast the north-western boundary of the model is a closed boundary (for economic reasons). Therefore procedures were developed in the old model to add the flow through this boundary to specific sections of the other boundaries (mainly the northern section of the north-east boundary). Afterwards these procedures were checked by studying the behaviour of the fresh water wedge in the prototype and the model sea.
  - f. The basic time series of the flow will not necessarily result in the correct water level in the model. Therefore cross-spectral analysis (of initial simulations) between the total volume of water in the model and the water level at the mouth of the river was used to compute a transfer function. It shows very clearly a resonance period of about 70 s. This function was measured for periods of 1125 s (= 25 hours prototype) to 56 s and extended to 28 s to give a smooth damped time representation used for convolution. Applying this function to the desired water level at the mouth of the river gives the desired total volume of water in the model. Comparing this with the basic flow of the model sections gives a correction to the flow into the model. This correction was then distributed over all model sections in proportion to their cross sectional area. The correction is small and will not affect the flow pattern in the model sea.
  - g. Then the period is simulated in the model. As the cross-spectral analysis uses linear relations there will be some differences between the desired and realized water levels. The same response function as used in paragraph f is then used to make another extremely small update for the flow sections to compensate for the non-linearities. A slow back-coupling from water levels to the flow sections is used to facilitate starting up and to compensate for drift in flow meters or intentional changes in river discharges.

##### 5. ADJUSTING ROUGHNESS

The damping of the tide wave, penetrating into the system from sea is caused by loss of momentum due to turbulent momentum exchange between the flow and the geometry. Though the loss of momentum on a river is often described with a "roughness-constant" (e.g. Chezy, Manning) it is clear that the hydraulic conditions are of primary importance in determining the turbulent structure of the flow. Since, in practice, it



is not possible to measure the momentum-exchange directly in prototype or model, calibrating the flow in a distorted model implies the adjustment of the correct amount of roughness-elements in order to achieve a proper reproduction of the flow. In that case loss of momentum on a river is correctly scaled, as can be derived from the momentum equation.

Apart from the problem how to direct the adjustment of the roughness in a new and complicated model one of the first problems seems to be the enormous amount of information it generates and how to control this. Changing the roughness in one branch might cause the water to take another route and although there would certainly be a human damping factor in the procedures a tedious trial and error procedure would not be welcomed. This section describes how the dataset was reduced to give overall picture of the model as compared to the prototype. It shows how this set was then used to interactively give information about the changes in roughness to be made. For this purpose it was necessary to estimate the effect of changes in roughness from the behaviour of a mathematical model. This behaviour also gives a broad idea of the situation that will emerge after these changes have been implemented. It was shown for a non-dendritic system (a system with islands) that the adjustment should be done on water levels and discharges simultaneously if the circumference of the islands is small with respect to the tidal wavelength. This problem was solved by using acoustic open channel flow meters at several points in the model that gave the total instantaneous flow in one reading instead of one position in a cross section (see Botma, 1978 and Roelfzema et al., 1984).

In the following sections the procedures used will be described in detail. Section 5.1 shows the principle of least squares as used for the optimisation and in section 5.2 the solution procedure is described. Section 5.3 gives an idea of how the procedures were implemented.

### 5.1 Least squares for optimisation

The purpose of the adjustment may be formulated as getting the best possible reproduction of the water levels and discharges in the model. "Best" was then defined to be the situation with the smallest sum  $F$  of the standard deviations of the difference between the time function  $f$  of model ( $m$ ) and prototype ( $n$  for nature).

$$F = \sum_p \frac{1}{s_p^2 T} \int_T (f_n - f_m)^2 dt \quad (1)$$

where  $p$  is the number of measured locations,  $T$  is the measured period and  $s_p$  is a weight function, that is taken to be the inaccuracy of the measurement at the point  $p$  in prototype and model combined.  $s_p$  makes  $F$  dimensionless and creates the possibility of incorporating water levels and discharges in one object function. Furthermore it was decided to compute  $F$  only for the mean and for the most relevant tidal components ( $M_2$ ,  $S_2$ ,  $M_4$ ,  $MS_4$ ,  $O_1$ ) or their fourier equivalents as far as they may be computed from the measured period. Each such component is called a characteristic. This leads to an enormous data reduction. Actually the calibration aimed at a correct reproduction of these characteristics, giving an overall good reproduction and discarding minor deviations.

Using Parseval's theorem  $F$  may now be written as

$$F = \sum_p \frac{1}{s_p^2} \left\{ (\Delta A_o)^2 + \frac{1}{2} \sum_j ((\Delta a_j)^2 + (\Delta b_j)^2) \right\} \quad (2)$$

where  $\Delta A_0$  is the difference in the mean value and  $j$  is the counter for the relevant fourier component,  $\Delta a_j$  and  $\Delta b_j$  are computed from the amplitude  $A_j$  and the phase  $\phi_j$  as follows:

$$A_j \cos(\omega_j t - \phi_j) = a_j \cos \omega_j t + b_j \sin \omega_j t \quad (3)$$

$$\Delta a_j = a_{j,n} - a_{j,m} \quad (4)$$

$$\Delta b_j = b_{j,n} - b_{j,m}$$

It is clear that  $F$  is a function of the roughness  $R_k$  in all the river branches  $k$  as the amplitudes  $a_{j,m}$  and  $b_{j,m}$  depend on  $R_k$ .  $F$  is also a function of the boundary conditions of the model; if, for example, a discharge was measured on a river branch which was different from the discharge at the boundary (both measures with the same accuracy) then one might take the discharge for the model to be somewhere in between, resulting in a lower  $F$  over the two points. By distinguishing between the boundary conditions and the measured values at the boundaries of the model one eliminates the overweight usually present there. So in the following one should not only think of roughness when  $R$  is used but also of several characteristic features of the boundary conditions that may be adjusted during the process of calibration. Six boundary conditions were used (three discharges, mean sea level and the amplitude and phase of the semidiurnal tide) and 19 sections of river branches where the roughness may be changed.

Could one be more explicit about the relation between  $F$  and  $R_k$ ? In the study phase for the adjustment an analytical harmonic model was build which behaved astonishing well. From such a model (as fully described by Dronkers (1964)) the following assumptions were derived:

1. For the roughness parameter  $R_k$  the formula  $R = g/C^2$  may be used where  $g$  is the acceleration of gravity and  $C$  is Chezy's  $C$ .
2. A change in  $R_k$  will give a change in the mean components  $A_0$ , proportional to the change in  $R_k$ . Actually this only applies to the tidal region but for small changes in  $R_k$  it may also be used for the upstream branches of the model where the quadratic nature of the resistance becomes significant.
3. A change in  $R$  will give a change in the amplitude  $A_j$  in proportion to the change in  $R$  and the value of  $A_j$ .
4. A change in  $R_k$  will give a change in phase that is proportional to this change.

In formula:

$$\begin{aligned} A_0^{\text{new}} &= A_0^{\text{old}} + \alpha_1 \Delta R_1 + \alpha_2 \Delta R_2 \dots \\ \ln(A_j^{\text{new}}) &= \ln(A_j^{\text{old}}) + \Delta R_1 \ln(1+\beta_1) + \Delta R_2 \ln(1+\beta_2) \dots \quad (5) \\ \phi_j^{\text{new}} &= \phi_j^{\text{old}} + \Delta R_1 \omega \gamma_2 + \Delta R_2 \omega \gamma_2 \dots \end{aligned}$$

As stated the  $\alpha$ ,  $\beta$  and  $\gamma$ 's are constants and valid in a very wide range of circumstances. This is a linear mathematical model of the estuary. To make  $F$  an explicit function of the change in roughness one would like to have equations in the form of

$$\begin{aligned} A_0^{\text{new}} &= A_0^{\text{old}} + \alpha_1 \Delta R_1 + \alpha_2 \Delta R_2 \dots \\ a_j^{\text{new}} &= a_j^{\text{old}} + \delta_1 \Delta R_1 + \delta_2 \Delta R_2 \dots \quad (6) \end{aligned}$$

$$b_j^{new} = b_j^{old} + \epsilon_1 \Delta R_1 + \epsilon_2 \Delta R_2 \dots$$

It can be shown that

$$\delta_i \approx a_m \beta_i - b_m \sin \omega \gamma_i \tag{7}$$

$$\epsilon_i \approx b_m \beta_i + a_m \sin \omega \gamma_i$$

The substitution of the actual  $a_m$  and  $b_m$  is the reason why (6) is valid in a much smaller range of circumstances. But (6) may now be substituted into (2) making F an explicit quadratic function of all  $R_k$ . To find the minimum of F the normal least squares is followed:

$$\frac{\delta F}{\delta R_k} = 0 \text{ for each } K \tag{8}$$

which results in (9) if we do not include the weighting factor  $1/s_p$  and use the notation of the first equation of (6) uniformly for the other two equations of (6) (numbering the  $\alpha$ 's with one more index i which runs continuously through all equations).

$$\begin{bmatrix} B & B & B & B \\ \sum_{i=1} \alpha_{i1}^2 & \sum_{i=1} \alpha_{i1}\alpha_{i2} & \sum_{i=1} \alpha_{i1}\alpha_{i3} \dots & \sum_{i=1} \alpha_{i1}\alpha_{iK} \\ B & B & B & B \\ \sum_{i=1} \alpha_{i2}\alpha_{i1} & \sum_{i=1} \alpha_{i2}^2 & \sum_{i=1} \alpha_{i2}\alpha_{i3} \dots & \sum_{i=1} \alpha_{i2}\alpha_{iK} \\ \dots & \dots & \dots & \dots \\ B & B & B & B \\ \sum_{i=1} \alpha_{iK}\alpha_{i1} & \sum_{i=1} \alpha_{iK}\alpha_{i2} & \sum_{i=1} \alpha_{iK}\alpha_{i3} \dots & \sum_{i=1} \alpha_{iK}^2 \end{bmatrix} \begin{bmatrix} \Delta R_1 \\ \Delta R_2 \\ \dots \\ \Delta R_K \end{bmatrix} = \begin{bmatrix} B \\ \sum_{i=1} \alpha_{i1} \Delta A_i \\ B \\ \sum_{i=1} \alpha_{i2} \Delta A_i \\ \dots \\ B \\ \sum_{i=1} \alpha_{iK} \Delta A_i \end{bmatrix} \tag{9}$$

where K is the total number of  $R_k$  and B is the total number of characteristics of all points.

The linear mathematical model (the  $\alpha$ 's) is obtained from successive simulations in a mathematical model, changing one roughness parameter ( $g/C^2$ ) or boundary condition at a time. As the coefficients  $\alpha$ ,  $\beta$ ,  $\gamma$  are valid for every period and are not very sensitive for the period used in simulation they are determined by simulating periods of 25 hours. The mathematical model does not need to be very sophisticated or to have a fine grid, small inaccuracies in the linear mathematical model (the  $\alpha$ 's) will only result in a somewhat slower optimisation. In the study phase  $\alpha$ 's from an analytical harmonic model were used quite successfully to adjust a finite difference model. Although differences in the roughness effects between the hydraulic model and the mathematical model may exist, obtaining the  $\alpha$ 's from the hydraulic model would be a tedious job. Solving (9) now gives a set of changes of the roughness  $\Delta R$ 's that will result in a lower F.

5.2 Options

It would not be very satisfactory if one were only to get a set of changes to be made to all the roughness parameters and all the boundary conditions together; one would like to see if the mean water levels and discharges relate to the same changes as the semidiurnal water levels and discharges do and so on. One might like to exclude certain  $R_k$ 's; for example the boundary conditions should not yet be changed after the first simulation. One might like to get a more regional impression of the changes to be made in several branches combined, or the change to be

made in all deep and narrow branches to see whether there are systematic deviations from the expected roughness. And most of all one would like to have an impression of the accuracy and the effect of the changes to be made.

This section gives some indications how this may be accomplished within the scope of least squares procedures.

It will be clear that equation (9) may be computed for each characteristic as defined in section (5.1). The building of the matrices should then be done by summation not from 1 to B but over specified subsets. The sum may be a weighted sum, stressing one characteristic over the others. The same applies to the function F that may be related to each of the characteristics. The equation (9) to be used then consists of the sum of several or all of the subsets. After the simulation, when all the characteristics from the model have been calculated the matrix (9) and the value of F is computed for each of the characteristics and put in a file. Thus in this way, it is possible to solve (9) once for a set that includes the mean water levels and the mean discharges and then for a set that includes the semidiurnals or both.

Before starting to solve the set of equations one might like to exclude certain  $R_k$ 's by omitting the corresponding rows and columns from the matrices and lower the dimension. The solution will then never indicate a change in this  $R_k$ .

Another important operation to be done on equation (9) is the combination of several  $R_k$ 's. This may be done by adding the corresponding elements of the rows and columns to one new row and column and lower the dimension accordingly. The resulting change in  $R_k$  should then be used for all the members of the combination; in this way one may get an indication of a trend, for example that the initial roughness of all the deep and narrow river branches has been overestimated.

It is outside the scope of this paper to describe how the matrix (9) may be inverted but it is good to notice the following: F is a quadratic function of all the  $R_k$ 's and (9) may be written as:

$$\begin{bmatrix} \frac{\partial^2 F}{\partial R_1^2} & \frac{\partial^2 F}{\partial R_1 \partial R_2} & \dots & \frac{\partial^2 F}{\partial R_1 \partial R_K} \\ \ddots & \ddots & \dots & \ddots \\ \frac{\partial^2 F}{\partial R_1 \partial R_K} & \frac{\partial^2 F}{\partial R_K \partial R_2} & \dots & \frac{\partial^2 F}{\partial R_K^2} \end{bmatrix} \begin{bmatrix} \Delta R_1 \\ \dots \\ \Delta R_K \end{bmatrix} = \begin{bmatrix} \frac{\partial F}{\partial R_1} \\ \dots \\ \frac{\partial F}{\partial R_K} \end{bmatrix} \quad (10)$$

so with a Taylor series expansion (9) gives a complete description of F as a function of all  $R_k$ 's (as far as (6) is valid). The procedures used for inverting the set of equations compute the change of F simultaneously with the step by step inversion. If it is now assumed that F has a normal distribution then one can give a simple statistical indication of the importance of a certain change in  $R_k$ , based on the decrease of F, the resulting F and the number of measured locations and  $R_k$ 's involved. A good description of these statistics may be found in Himmelblau (1970). The actual inversion procedure may be found in Efronson (1959). It does not give the solution of the whole set (9) at once, but it selects first the  $R_k$  that is most effective (that gives the greatest decrease of F). It then computes how big the change in  $R_k$  should be if this were the only change to be made; it computes the

resulting  $F$  and gives an indication of the accuracy of the change in  $R_k$ . In the next step it takes one more  $R_k$ , computes the desired change in each of them, the change in  $F$ , the accuracy of each of the individual changes and so on. The procedure may go as far as producing a completely inverted matrix (9) but obviously was stopped at the point where  $F$  does not decrease significantly any more.

Substitution of the indicated changes into the equations (5) or (6) then gives the values to be expected at the individual measured locations. Comparing these values with the values from prototype and from the previous simulation in the model gives then a very detailed view of the progress of the calibration.

### 5.3 Implementation

A series of programs was written for the DEC BASIC compiler. After a simulation these calculated the characteristics of the model, the matrices (9) and the  $F$ 's for each of the characteristics summed over all water levels or over the discharges. Then an interactive program was run that combines a selected set of characteristics, deletes and combines  $R$ 's and solves the equations step by step, printing information about the accuracies, the resulting  $F$  and so on. In each step the  $F$  that is related to each of the individual characteristics may be computed from a Taylor series using (10) giving information about the improvement of other characteristics. After this terminal session an even better idea of what may be expected may be obtained by substitution of the intended changes into (5) and plotting the expected characteristics together with the last simulation and the prototype (compare fig. 7.2-7.4). After this the change in roughness (which is still in  $g/C^2$ ) is converted to a change in the number of roughness elements.

## 6. CALIBRATION AND VERIFICATION

For the calibration and verification of the model an extensive measurement campaign has been carried out by Rijkswaterstaat (Ministry of Public Works) in 1979. Four periods of three days in May and September were used for the measurement of flows and salinity distribution, with 35 boats simultaneously. These periods included the weekends when nautical activities on the river are less. In this way detailed information about the vertical velocity- and salinity profiles was obtained. From the velocity profiles discharges were derived in the main branches of the estuary. During the whole period of May and September 1979 waterlevels all over the system and salinities at some locations were measured continuously, thereby providing data about springtide-neap tide-springtide time series. Finally some automatically monitoring instruments were used for measurements at sea. Considerations with respect to salinity intrusion, meteorological influences (wind), possible withdrawals and the integral quality of the measurements resulted in the choice of September for calibration of the model (relatively low river discharges) and of May for the verification. Within September the first period of three days with the 13 hours discharge- and salinity vertical measurements was selected for the adjustment process (wind influences being almost negligible in this period). In order to verify the model on hydraulic conditions with extreme low river discharges, which are especially of interest from a research point of view, use was made of available prototype data of August 1976. For that period only time series of waterlevels and a restricted number of salinity recordings are available. Essential for the above described

prototype data is the possibility to adjust the model on large scale phenomena under time series conditions, thereby allowing an assessment of the time-fluctuating dominant phenomena of the tide, mean sea level, river discharge and gravitational circulation. Within these time series the consistency of the detailed reproduction of the vertical velocity and salinity profiles can be considered, giving also insight into the simulation of the vertical turbulent diffusion process.

The actual calibration and verification was then carried out as follows. Based on experiences with one-dimensional models and on a reanalysis of the characteristics of the network system, the hydraulic model was provided with an initial amount of additional roughness.

Subsequently the flows of the September time series were adjusted in a first approximation by means of the procedures as described in chapter 5. By doing so, also the density distribution will be simulated in a global sense as it is primarily determined by the advective transport processes. Then the next phase is the final adjustment by optimizing in an alternating way flows (of the September timeseries) and density distribution, based on the first period with detailed information about the vertical salinity profiles. This optimisation completes the calibration resulting in a mix of various additional roughness- and mixing elements. Based on this model lay-out the verification was performed on the timeseries and vertical salinity profiles of May 1979 and on the timeseries of August 1976.

## 7. RESULTS/DISCUSSION

The provision of boundary conditions was straight forward. Updates could easily and quickly be made. The water levels in the mouth of the river are accurately reproduced from prototype data (see fig. 7.1).

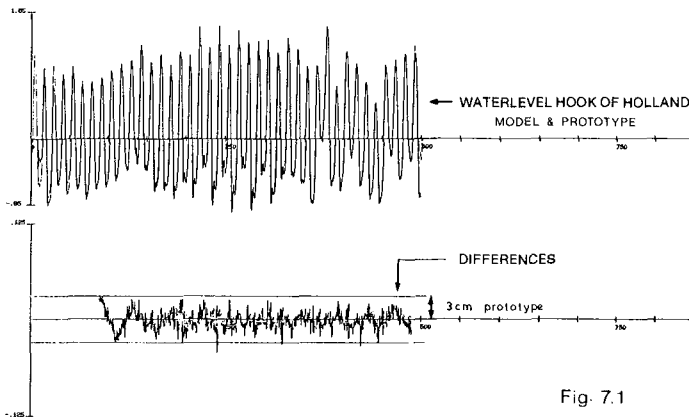


Fig. 7.1

The flow field at sea in front of the river mouth is rather satisfactory, according to comparisons of floats from model and prototype and according to the behaviour of the fresh water wedge at sea.

For optimisation of the salt boundary conditions at the mouth of the Rotterdam Waterway a calibration on tidal flows and on salinity distribution (thin fresh layer due to the river outflow) appeared to be necessary. For this reason additional field measurements in the sea near

the mouth of the Rotterdam Waterway have been carried out in order to verify the model on these data, which may lead to a combined (flows and salinities) improvement of the downstream boundary provision. In this respect it is relevant that the accuracy of the prediction of tidal currents may be considerable less than the accuracy of the prediction of water levels (Godin, 1983).

The adjustment procedures for the waterflows gave very good results. For the complicated network system the final accuracy of the reproduction of the vertical and horizontal tides was met in a few steps. It is very well possible to adjust the roughness in several branches at a time without losing control. The linear mathematical model may be derived from a simpler model than the model that has to be adjusted. The procedures aided in stopping the process of calibration at the point when the result of going on would have been negligible. In this way, this part of the calibration process was accelerated manifold with respect to conventional methods. Based on these experiences, the principles of this optimisation technique will be used also for the development (calibration/optimisation) of mathematical models for the Rhine-Meuse estuary network system (Roelfzema, et al., 1984).

The final result of the calibration and verification shows a fairly good agreement with the prototypedata. Flow characteristics of the vertical tides generally are reproduced within inaccuracies of about 1%, horizontal tides within about 5 to 10%. With this respect figures 7.2 up to 7.4 show some illustrations of the reproduction quality of the mean waterlevels, the semidiurnal amplitude of the vertical tide and its phase as mean values over a neap tide/spring tide/neap tide time series, while figures 7.5 and 7.6 show the reproduction of waterlevels and discharges as functions of time.

Instantaneous inaccuracies of the densities generally vary between 1 to 10%. Tidal mean values show considerable lower inaccuracies. It is important to remark that, in spite of instantaneous differences between model and prototype, the long term tendencies, in general are reproduced fairly, thereby showing the capability of the model to reproduce the overall, dominant characteristics of nature, see figures 7.7 and 7.8.

A remark has to be made with respect to the verification quality of the second period in September 1979. In this period with a combination of neap tide and strong gradients in the mean waterlevels the model probably generates insufficient turbulent diffusion, resulting in larger differences between the vertical salinity distribution of model and prototype, see figure 7.9. For smooth parts of some river branches an opposite effect appeared in the contribution of the additional roughness— an mixing elements in their contribution to the resistance on the one hand and to the mixing on the other. These parts required less resistance and more mixing so an optimum had to be found.

This evidence and the result according to figure 7.9 emphasize the importance of studies on the quantitative knowledge about the vertical diffusion process and requires fundamental research work in a tidal salinity flume on the turbulent exchange processes on mass and momentum and their modelling (physical and mathematical).

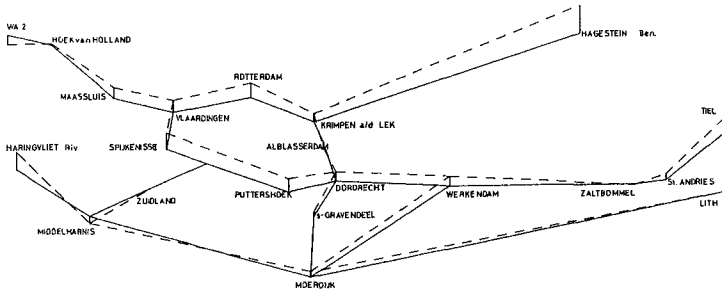


Fig. 7.2  
DIFFERENCES  
MEANWATERLEVEL: (model - proto)  
3 SEPT. 1979 - 17 SEPT. 1979

0.04 ■ prototype  
--- MODEL - PROTO

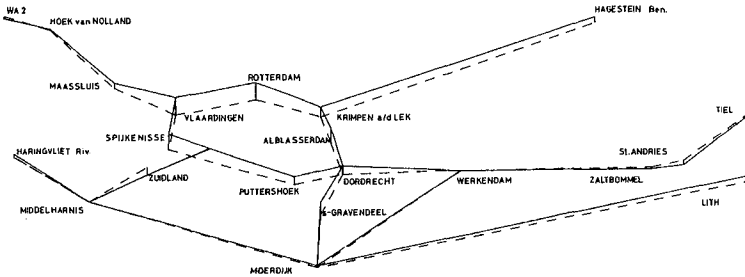


Fig. 7.3  
DIFFERENCE M2-AMPLITUDE (model - proto)  
3 SEPT 1979 - 17 SEPT. 1979

0.04 ■ prototype  
--- MODEL - PROTO

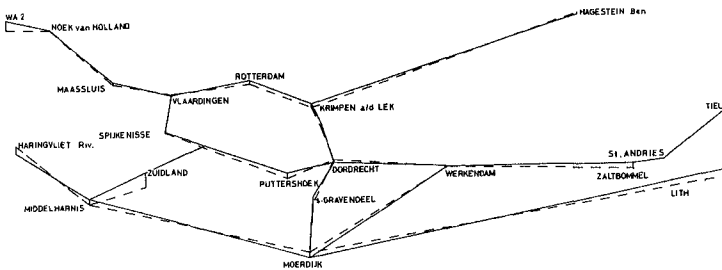


Fig. 7.4  
DIFFERENCE M2-PHASE (model - proto)  
3 SEPT. 1979 - 17 SEPT. 1979

7.2° ■ prototype  
--- MODEL - PROTO



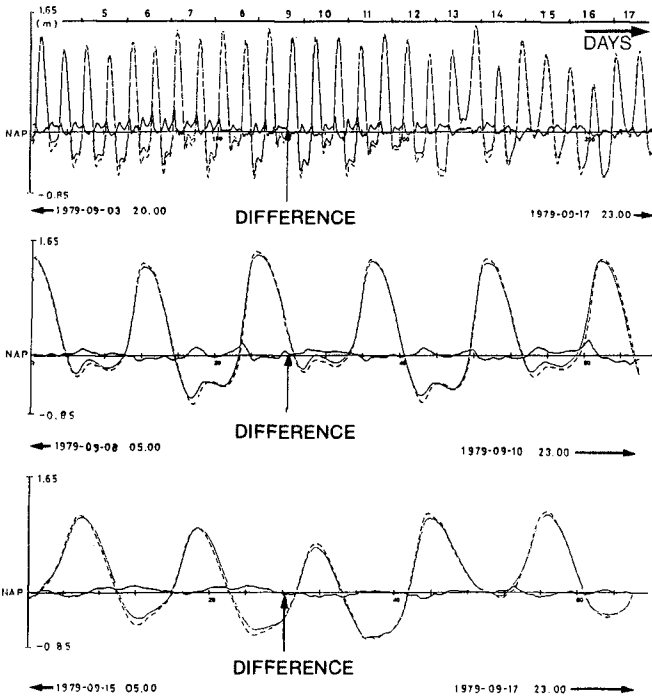


Fig. 7.5 WATERLEVELS ROTTERDAM — — — PROTOTYPE  
 ——— MODEL

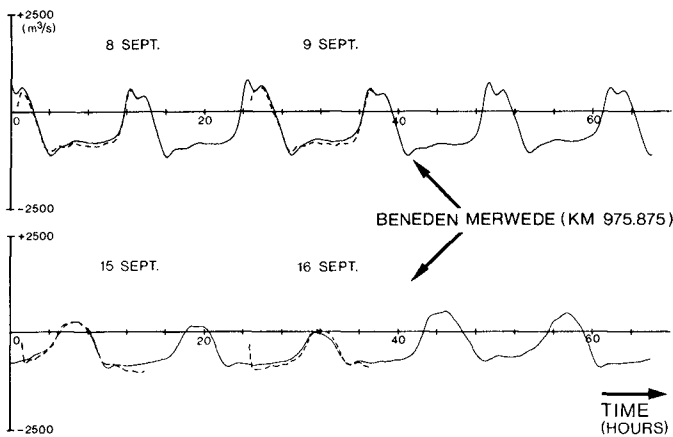


Fig. 7.6 DISCHARGES

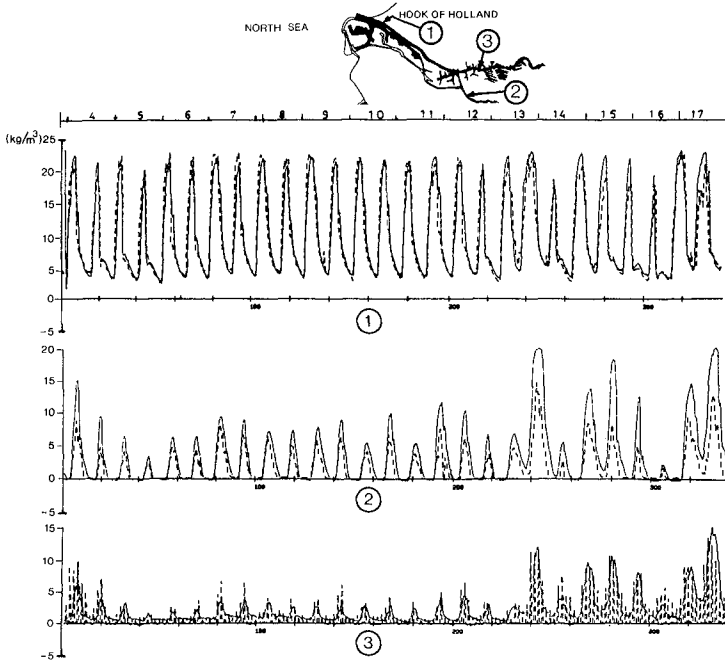


Fig. 7.7 DENSITY AS FUNCTION OF TIME (CALIBRATION) - - - - PROTO  
 \_\_\_\_\_ MODEL

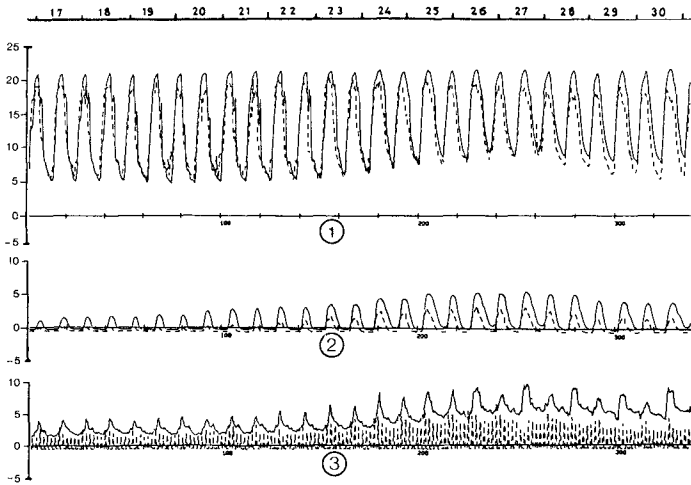


Fig. 7.8 DENSITY AS FUNCTION OF TIME (VERIFICATION) - - - - PROTO  
 \_\_\_\_\_ MODEL

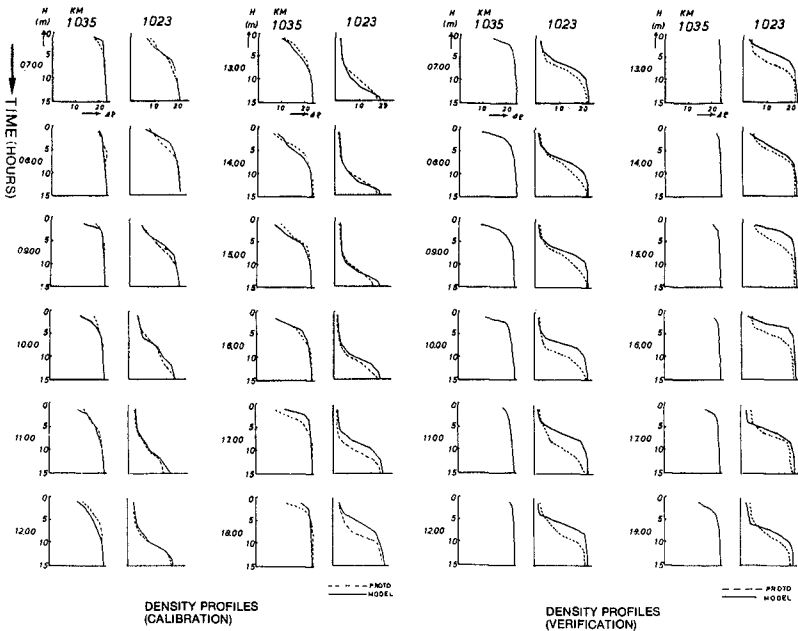


Fig. 7.9

## 8. REFERENCES

- Adriaanse, P., Cslldwell, C.R. and Droppert, L.J., 1979  
Rijnmond tidal model control system, Journal A, Volume 19, no 1,  
Botma, H.C., 1978  
Acoustic flowmeter for use with hydrsulic models, in Flow  
Measurements of fluids, Dijsstelbergen and Spencer (eds.), Centrsl  
Org. TNO, The Hague, North Holl. Publ. Comp., Amsterdsm,  
Breusers, H.N.C., and Os, A. vsn, 1981  
Physical Modelling of the Rotterdamse Waterweg Estuary, Proc. ASCE,  
Hydrsulic Division, Vol. 107, no HY 11, pp 1351-1370  
Dronkers, J.J., 1964  
Tidal computations in rivers and coasts1 water, North Hollsnd  
Publishing Comp. Amsterdam, 1964  
Efroymsn, M.A., 1959  
Multiple Regressionssion Analysis, in Mathematical Methods for Digital  
Computers, Rslston and Wilf (eds.), John Wiley and S, New York,  
Godin, G., 1983:  
On the predictability of currents, Internstional Hydrogrsphic  
Review, p.p. 119-126  
Himmelblau, D.M., 1970  
Process Ansls1s by Ststistical Methods, John Wiley and S, New York,  
Rees, A.J. vsn, Kuur, P. vsn der and Strobsnd, H.J., 1972  
Experiences with Tidsl Salinity Model Europoort, Proc. 13th Int.  
Conf. on Coastal Eng. Vancouver, ASCE, VOL. III, pp 2355-2378  
Roelfzems, A., Karelse, M., Struijk, A.J., Adriaanse, M., 1984:  
Waterquantity and -qualsty research for the Rhine-Meuse estuary,  
19th Int. Conf. on Coastal Engineering, Houston, USA  
Thatcher, M.L., Harleman, D.R.F., 1972  
A mathematical model for the prediction of unsteady salinity  
intrusion in estuaries, MIT-report 144,

## CHAPTER TWO HUNDRED FOURTEEN

### COMPARISON OF TURBULENT LATERAL MIXING MODELS

William G. McDougal and Robert T. Hudspeth<sup>1</sup>

#### ABSTRACT

A variety of different lateral mixing models have been employed in the equation of motion for determining wave-induced longshore currents. The equation of motion is cast into a general form which enables a comparison of the various models. Analytic solutions for longshore currents are developed for seven different mixing models. A nonplanar beach profile is employed because it has been found to be representative of many beaches and it allows for a distinction between offshore and depth scaling of eddies. The seven different mixing models include models which vary monotonically with horizontal distance offshore and models which change form at the breaker line. Numerical results indicate that the longshore current profile is rather insensitive to the form of the mixing model for nonplanar beach profiles.

#### INTRODUCTION

Horizontal mixing due to turbulence has a significant influence on the longshore current profile. The equation of motion describing the longshore velocity is not forced seaward of the breaker line if energy flux is conserved. In the absence of lateral turbulent mixing, a discontinuity is developed in the longshore current at the breaker line for simple periodic waves. This physically unrealistic solution is improved by the inclusion of lateral turbulent mixing. The lateral diffusion of momentum flux couples the solutions across the breaker line and eliminates the velocity discontinuity.

There is a general consensus that lateral mixing should be included in the equation of motion. However, there is little agreement on the exact mathematical form of the mixing term and several different models may be found in the literature.

One of the earliest models is that of Inman, et al. (1971) in which an empirical relationship was determined from field studies of dye dispersion. Two physical discussions were presented to justify the model, a mixing length approach and a friction velocity based on the radiation stresses. For a given wave and beach, the model predicted a constant eddy viscosity. Bowen (1969) had assumed a constant eddy viscosity for estimating longshore currents and provided an estimate of the eddy viscosity based on laboratory measurements. Thornton (1970)

---

<sup>1</sup>Ocean Engineering Program, Department of Civil Engineering, Oregon State University, Corvallis, Oregon 97331.

proposed a model based on the product of the water particle velocity and excursion length to develop a mean Reynolds stress due to wave motion. The magnitude of the eddy viscosity increased out to the breaker line, but decreased seaward of the breaker line. Longuet-Higgins (1970b) suggested that the scaling for the eddies is proportional to the horizontal distance offshore and the shallow water wave celerity. This eddy viscosity increases monotonically with distance offshore. Jones (1975) developed an eddy viscosity by analogy with mass transport and Fickian flux. The model provided reasonable estimates for laboratory data, but was in very poor agreement with the field measurements of Inman, et al. (1971). Kraus and Sasaki (1979) following Madsen, et al. (1978) used a model which was proportional to the maximum wave orbital velocity at the bottom. Battjes (1975) provided an energy dissipation derivation that led to an eddy viscosity similar to the Longuet-Higgins model for planar beaches. However, this similarity was only for planar beaches because the Battjes model was slope-dependent. This model has been extended by Battjes (1983) to include the diffusive transport of turbulence and a solution for the model was presented by Visser (1984).

In order to evaluate the effects of these various mathematical models for mixing, a general expression for the equation of motion is developed which allows examination of the different mixing models. Analytical solutions for longshore current on a nonplanar beach profile are developed for a variety of mixing models. Numerical results indicate that the longshore current profile is rather insensitive to the choice of any of these individual lateral mixing models. This insensitivity has also been noted by several other investigators. Wu (personal communication) employing a two-dimensional nonlinear numerical model observed little change in the longshore current profile for very different eddy viscosity models. Kraus, et al. (1980) examined a variety of mixing models and again noted a lack of sensitivity. The method employed to compare different mixing models in this paper is similar to the technique used by Kraus, et al. (1980).

#### EQUATION OF MOTION

The time- and depth-averaged longshore equation of motion for the nonplanar beach profile shown in Fig. 1 is given by [Longuet-Higgins (1970b)]

$$-\frac{d}{dx} S_{xy} + \tau_{by} + \frac{d}{dx} (\mu_e d \frac{d}{dx} v) = 0 \quad (1)$$

in which  $S_{xy}$  is the onshore-longshore component of radiation stress;  $\tau_{by}$  is the bottom stress;  $\mu_e$  is an eddy viscosity;  $d$  is the total depth (still-water-depth plus the wave-induced setup); and  $v$  is the longshore current. Implicit in this equation are the assumptions of steady state; of no longshore gradients, of slowly varying depth, of no surface stresses, of small viscous transport of momentum with respect to the turbulent transport, and of an eddy viscosity model. The eddy viscosity model may be represented by a general expression that will permit comparisons between various mathematical models that have been used to represent the turbulent stress.

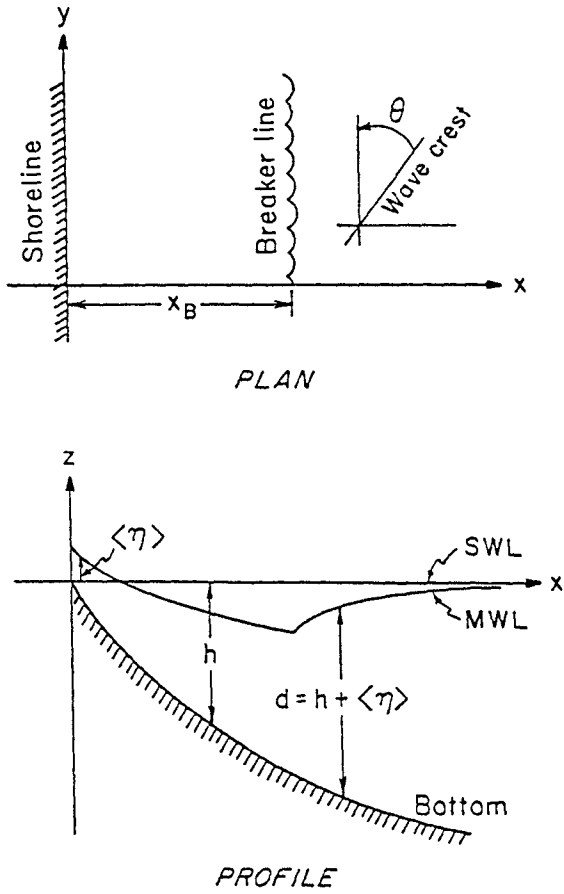


Figure 1. Definition Sketch

The divergence of the radiation stress is given by

$$\frac{d}{dx} S_{xy} = \begin{cases} -\frac{5}{16} \rho g \kappa^2 d \sqrt{d/d_B} \sin \theta_B \frac{d}{dx} d & ; x < x_B \\ 0 & ; x > x_B \end{cases} \quad (2a)$$

$$(2b)$$

in which  $\rho$  is the density of water;  $g$  is the acceleration due to gravity;  $\kappa$  is a breaker index;  $\theta$  is the wave angle; and the subscript B denotes the value at the breaker line. It is assumed that wave energy flux is conserved seaward of the breaker line, that wave angles are small, that shallow-water wave conditions exist shoreward of the breaker line, and that the breaking wave height is proportional to the local water depth ( $H = \kappa d$ ).

The bottom shear stress may be approximated using linear, shallow water wave theory and small-angle relationships [cf. Liu and Dalrymple (1978)]

$$\tau_{by} = -\frac{C_f}{\pi} \kappa \rho \sqrt{gd} v \quad (3)$$

in which  $C_f$  is an empirically determined friction coefficient of order 0.01 and  $\pi$  is a numerical constant.

Longuet-Higgins (1970b) assumed that the eddy viscosity coefficient is proportional to a velocity scale and a length scale was taken to be a linear function of the horizontal distance offshore. This particular choice for horizontal scale of the turbulent eddies is limited by the shoreline boundary inside the surf zone. However, for a planar beach this scaling gives the same offshore dependency as eddies which are limited by the depth. Therefore, it is of interest to examine a non-planar, concave-up beach profile where these two types of eddy scaling may be treated differently. An eddy viscosity model similar to that used by Longuet-Higgins (1970b) will be adopted, but the length scale of the eddies will be considered to be an arbitrary exponential function of the horizontal distance offshore. The following general expression allows comparison with other turbulence models by varying the exponent to represent the scale of the eddy size; i.e.,

$$\mu_e = N\rho (gd)^{1/2} \frac{x^p}{x_B^{p-1}} \quad (4)$$

where  $N$  is a numerical constant and  $p$  is a shape factor for scaling the eddy size.

Introducing (2), (3), and (4) into (1) gives

$$\frac{N\pi}{C_f \kappa} x_B^{1-p} \frac{d}{dx} (x^p d^{3/2} \frac{d}{dx} v) - d^{1/2} v = \begin{cases} -\frac{5}{16} \frac{\pi}{C_f} g^{1/2} \kappa \frac{\sin \theta_B}{d_B^{1/2}} d^{3/2} \frac{d}{dx} d & ; x < x_B \\ 0 & ; x > x_B \end{cases} \quad (5a)$$

$$(5b)$$

Nondimensionalizing all length scales by the horizontal surf zone width,  $x_B$ , and the velocity scales by the no-mixing planar beach velocity at the breaker line,  $v_{BL}$ , given by Longuet-Higgins (1970a), the dimensionless longshore equation of motion (denoted by upper case letters) becomes

$$\frac{N\pi}{C_f \kappa} \frac{d}{dX} (X^p D^{3/2} \frac{dV}{dX}) - D^{1/2} V = \begin{cases} -\Delta D^{3/2} \frac{dD}{dX} & ; X < 1 \\ 0 & ; X > 1 \end{cases} \quad (6a)$$

$$(6b)$$

in which

$$X = x/x_b \quad (6c)$$

$$V = v/v_{BL} \quad (6d)$$

$$\Delta = \left(\frac{x_B}{d_B}\right)^2 \quad (6e)$$

$$v_{BL} = \frac{5}{16} \frac{\pi \kappa}{C_f} s v \sin \theta_B \sqrt{gd} \quad (6f)$$

and  $s$  is the planar beach slope including setup.

The boundary conditions which are to be imposed to determine the integration constants require that the velocities be bounded at both the shoreline ( $X = 0$ ) and offshore ( $X \sim \infty$ ) and that both the magnitude of and the gradient of velocity be continuous at the breaker line ( $X = 1$ ).



## BEACH PROFILE

Equations (6) are expressed in terms of an arbitrary total water depth,  $D(X)$ . However, this depth profile must increase monotonically with horizontal distance offshore. This restriction is due to the breaker index which relies on the so-called spilling breaker assumption in which the breaking wave height is considered to be proportional to the local water depth. This assumption is frequently employed in analytical longshore current models and is obviously a weak assumption. However, it is not the intent of this paper to improve on breaking wave models, but rather to cast the equation of motion into a somewhat standard form and to then examine the influence of various mathematical expressions for the lateral mixing models on the longshore current profile.

The monotonically increasing depth profile is required to avoid wave heights which increase over inshore troughs. An arbitrary, but monotonic, depth profile is given by

$$D = B X^q \quad (7)$$

in which  $q$  is an arbitrary shape factor that need not be an integer and  $B$  is analogous to slope. Equation (7) allows the equation of motion to be expressed in terms of a general depth profile according to

$$P \frac{d}{dX} \left[ X^{(3/2 + q + p)} \frac{d}{dX} v \right] - X^{1/2 + q} v = \begin{cases} -q X^{5/2 + q - 1} & ; X < 1 \quad (8a) \\ 0 & ; X > 1 \quad (8b) \end{cases}$$

in which  $P$  is a mixing strength parameter defined by

$$P = \frac{N\pi}{C_f \kappa} B \quad (8c)$$

Equations (8) are general and may be applied to a variety of beach profiles which increase monotonically in depth offshore. For  $p=q=1$ , (8) reduce to the planar beach equation of Longuet-Higgins (1970b). For  $p=1$ ,  $q=1/2$  (8) reduce to the Bruun profile evaluated by McDougal and Hudspeth (1983a). Rather complex beach profiles may be modeled piecewise using (8) along with appropriate matching of boundary conditions at the ends of each piecewise segment. This approach was employed by McDougal and Hudspeth (1984a) to model a composite beach having a non-planar, concave-up beach profile in the offshore segment with a planar beach face on the nearshore segment.

Natural beaches tend to be concave-up rather than planar. A beach profile in which the still-water-depth is proportional to the horizontal

distance offshore raised to the 2/3 power has been deduced from physical arguments by Bruun (1954), Dean (1977), and Bowen (1978). In an examination of a total of 502 beach profiles along the Atlantic and Gulf coasts of the United States, Dean (1977) estimated a relationship between the coefficient of proportionality and the grain size. The 2/3 power profile has also been observed along the Danish coast by Bruun (1954).

McDougal and Hudspeth (1983) determined the setup/setdown on this 2/3 type beach profile and found the total depth (still-water-depth plus wave-induced setup) to be well approximated by a total water depth profile that is proportional to the horizontal distance offshore raised to the 1/2 power. This 1/2 power total depth profile will be employed in this study. This profile enables a distinction between the length scale associated with the offshore distance and local depth length scale in the eddy viscosity.

#### EDDY VISCOSITY MODELS

Analytical solutions are developed for seven different eddy viscosity models for the 1/2 power beach profile. Accordingly,  $q = 1/2$  in (8) for all values of  $p$  used below. The relevant parameters for comparing the models are summarized in Table 1. Solutions to (8) have been given by Hildebrand (1976). Longshore current profiles are plotted for each model in Figures 2 and 3 for mixing strengths of 0.1 and 1.0, respectively.

Linear Scale:  $p = 1$

The eddy viscosity model employed by Longuet-Higgins (1970b) assumed that the velocity and length scales were proportional to the shallow-water wave celerity and the horizontal distance offshore. This corresponds to a value of  $p=1$  in (8). Solutions to the equation of motion satisfying the boundary conditions are given in McDougal and Hudspeth (1984b).

Depth Scale:  $p = 1/2$

Battjes (1975) has suggested that a more appropriate length scale for eddies is the depth rather than the horizontal distance offshore. For an eddy length scale proportional to the depth this yields  $p = 1/2$  for a nonplanar,  $X^{1/2}$  concave-up profile.

Maximum Scale:  $p = 3/2$

It may be shown by the method of Frobenius (Hildebrand, 1976) that the maximum value  $p$  may obtain is 3/2.

Constant Scale:  $p = -1/4$

Bowen (1969) assumed and Inman, et al. (1970) observed that the eddy viscosity was a constant independent of the horizontal distance offshore. For an  $X^{1/2}$  beach profile, a constant eddy viscosity given by (4) requires that  $p = -1/4$ .

Table 1. Summary of Mixing Models for Nonplanar Beaches (q=1/2)

Model	p	Mixing Strength (P)
Linear Scale	1	$\frac{N\pi}{C_f \kappa} B$
Depth Scale	1/2	$\frac{N\pi}{C_f \kappa} B$
Maximum Scale	3/2	$\frac{N\pi}{C_f \kappa} B$
Constant Scale	-1/4	$\frac{N\pi}{C_f \kappa} B$
Wave Kinematic Scale	1/4 ; X < 1 -7/4 ; X > 1	$\frac{\pi \kappa}{8 C_f} \frac{B^2}{\omega} \left(\frac{g}{d}\right)^{1/2}$
Modified Linear Scale	1 ; X < 1 1/2 ; X > 1	$\frac{N\pi}{C_f \kappa} \beta$
Energy Dissipation Scale	1/3 ; X < 1 (4r <sub>2</sub> +3)/12 ; X > 1	$\frac{N\pi}{C_f} \left(\frac{5}{32} \kappa^2 B^7\right)^{1/3}$

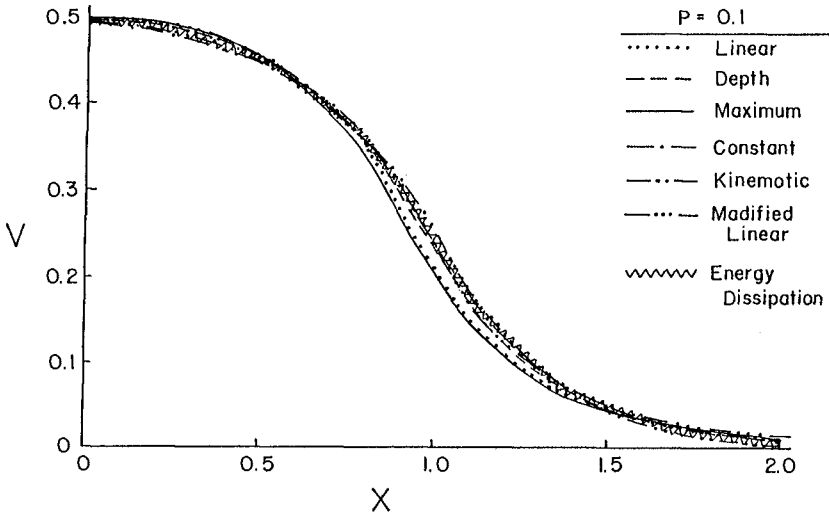


Figure 2. Comparison of Longshore Current Profiles (P = 0.1, q = 0.5)

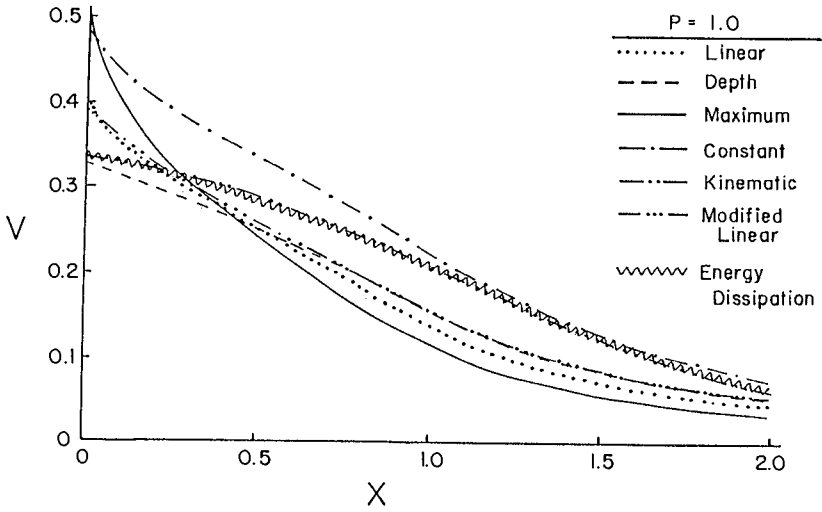


Figure 3. Comparison of Longshore Current Profiles ( $P = 1.0, q = 0.5$ )

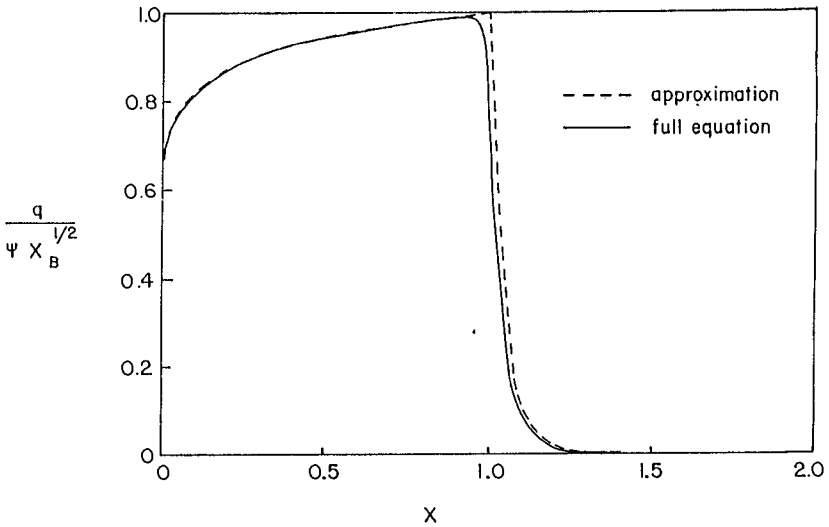


Figure 4. Comparison of Actual and Approximate Velocity Scales for the Energy Dissipation Model

Thornton Model Scale:  $p = 1/4, -7/4$

Thornton (1970) proposed a model which relates the eddy viscosity to the absolute value of the time-averaged product between the water particle excursion due to the wave motion,  $l'$ , and the water particle velocity fluctuation due to the waves,  $u'$ . This model is given by

$$\mu_e = \rho \langle |u' l'| \rangle \quad (9)$$

where  $\langle \cdot \rangle$  is the temporal averaging operator over the wave period.

Evoking the both small wave angle assumption and linear wave theory at the bottom, (9) may be written as

$$\mu_e = \frac{\rho \omega H^2}{8 \sinh^2 kd} \quad (10)$$

in which  $k$  is the wave number and  $\omega$  is the radian wave frequency. Inside the breaker line shallow water assumptions are made and the eddy viscosity is given by

$$\mu_e = \rho g \frac{\kappa^2}{8\omega} d \quad (11)$$

Substitution of this eddy viscosity into (1) instead of using (4) results in a different mixing strength parameter,  $P_T$ , given by

$$P_T = \frac{\pi \kappa B^2}{8 C_f \omega} \left( \frac{g}{d_B} \right)^{1/2} \quad (12)$$

and the resulting equation of motion is equivalent to  $p = 1/4$ .

Seaward of the breaker line the wave-induced turbulence is much less. The eddy viscosity model proposed by Thornton (1970) changes form at the breaker line. The waves are no longer breaking and the shallow water assumption is inappropriate. In this relatively deeper region, the eddy viscosity decays approximately hyperbolically with increasing distance from shore. Assuming deep water conditions, using the concave beach profile and requiring  $\mu_e$  to be continuous at the breaker line, the offshore eddy viscosity is approximately given by

$$\mu_e = \rho g \frac{\kappa^2}{4\omega} d_B \left( \frac{d}{d_B} \right)^{3/2} \quad (13)$$

The mixing strength parameter is the same as for  $X < 1$  given by (16) and the resulting equation of motion is equivalent to  $p = -7/4$ .

Modified Linear Scale:  $p = 1, 1/2$

Kraus and Sasaki (1979) developed a model which is applicable in the offshore employing results from Madsen, et al. (1978). Requiring continuity of the eddy viscosity at the breaker line, this model may be approximated as

$$\mu_e = \begin{cases} N\rho \times \sqrt{gd} & ; X < X_B & (14a) \\ N\rho \times \sqrt{gd} \frac{d_B}{d} & ; X > X_B & (14b) \end{cases}$$

which is the same as the Longuet-Higgins model shoreward of the breaker line. The modification in the offshore region reduces the rate at which the eddy viscosity increases, but it still increases monotonically. The resulting mixing strength parameter is given by (8c) and the equation of motion corresponds to  $p = 1$  for  $X < 1$  and  $p = 1/2$  for  $X > 1$ .

Energy Dissipation Scale:  $p = 1/3, (4r_2 + 3)/12$

Battjes (1975) estimated the horizontal turbulent momentum exchange from an examination of the turbulent energy dissipation. The model turns out to be similar in form to an eddy viscosity model, but this assumption was not made a priori. However, this similarity was only for planar beaches because the model was slope-dependent. This model was not applicable seaward of the breaker line. Citing results from dye studies in the surf zone, Battjes (1975) observed that the turbulence is primarily contained within the surf zone, but that there must be some production of turbulence seaward of the breakers to avoid a velocity discontinuity at the breaker line. By including the diffusive transport of the turbulent momentum, Battjes (1983) extended the range of application of the turbulence model to include the entire nearshore region. A solution to the equation proposed by Battjes (1983) for the balance of turbulent energy was presented by Visser (1984).

$$\mu_e = M \rho \kappa d q \tag{15a}$$

in which

$$q = \begin{cases} [A_1 x^{r_1} + \frac{5}{16} \kappa^2 g^{3/2} d^{3/2} \frac{d}{dx} d]^{1/3} & ; x < x_p & (15b) \\ [A_2(x-a)^{r_2}]^{1/3} & ; x > x_p & (15c) \end{cases}$$

and  $M$  is an empirical coefficient of order 1;  $r_1$ ,  $r_2$ , and  $a$  are wave field parameters; and  $A_1$  and  $A_2$  are integration constants which can be

determined by requiring continuity of  $q$  and the gradient of  $q$  at the plunge point,  $x_p$ . The production of turbulence begins at the location of actual breaking,  $x_p$ , not the location of the initiation of breaking,  $x_{B1}$  and this effect was included in the Visser solution. However, this effect was not included in any of the other models. To allow direct comparison of the models it will be assumed that  $x_p = x_B$ .

When the nonplanar beach profile is employed in Eqs. (15) and the wave field parameters are evaluated, the resulting forms for the eddy viscosity are not compatible with Eq. (4). Therefore, the following approximations are used

$$q = \begin{cases} \psi x^{1/12} = \psi x_B^{1/12} X^{1/12} & ; X < 1 & (16a) \\ \psi x_B^{1/12} \left(\frac{x}{x_B}\right)^{1/3} r_2 = \psi x_B^{1/12} X^{1/3} r_2 & ; X > 1 & (16b) \end{cases}$$

where

$$\psi = \left(\frac{5}{32} \kappa^2 g^{3/2} \beta^{5/2}\right)^{1/3} \quad (16c)$$

These approximations are compared with the full equation for a nonplanar profile and with  $x_p = x_B$  in Figure 4. Upon substitution into the equation of motion, a different mixing strength parameter,  $P_B$ , results.

$$P_B = \frac{M\pi}{c_f} \left(\frac{5\kappa^2}{16} B^7\right)^{1/3} \quad (17)$$

The resulting eddy scale of (4) requires that  $p = 1/3$  and  $p = (4r_2+3)/12$  for  $x < 1$  and  $x > 1$ , respectively. The solution is sensitive to the breaking wave height. Larger wave heights yield velocity profiles which appear to have lower lateral turbulent mixing strengths. The numerical results shown in Figures 2 and 3 are for small wave height conditions.

#### DISCUSSION

Solutions to the longshore equation of motion have been developed for seven different lateral mixing models on a nonplanar beach profile which are summarized in Table 1. Longshore velocity profiles obtained for these solutions are shown in Figures 2 and 3 for each mixing model for mixing strengths of  $P = 0.1$  and  $P = 1.0$ , respectively. There are relatively small differences between these velocity profiles, and these differences decrease as the mixing strength decreases due to the obvious requirement that all of the models must converge for  $P = 0$ .

The differences between the equations listed in Table 1 for the mixing strength parameters defined by Battjes and by Thornton compared to the other four models appear to be significant. However, the dif-

ferences in the numerical values for the longshore current computed by each of these models are rather small and most of the models have similar dependencies on the various parameters. Each of the models exhibit similar dependencies on mixing for nonplanar beaches in that steeper slopes yield greater mixing strengths. Increasing the bottom roughness results in decreasing the strength of lateral mixing in each model. All of the models listed in Table 1, except the wave kinematic and the energy dissipation, are inversely related to the breaker index. This implies that if the spilling wave longshore current models are applied to plunging or surging breakers the mixing should be reduced. The wave kinematic model is linearly dependent on the wave period such that longer waves will be more mixed than shorter waves. The energy dissipation model is also a function of the wave conditions with larger wave heights being less mixed.

These numerical results demonstrate that the longshore current profile is only weakly dependent on the analytical form of the lateral mixing model employed. This observation suggests that any reasonable analytical model for the lateral turbulent mixing may be selected for a particular application based solely on its computational efficiencies. However, the kinematic and energy dissipation models provide more physically realistic estimates of mixing. The velocity profiles are obviously sensitive to the strength of mixing. Komar (1975) suggests that values for the mixing strength should generally be less than 0.4.

#### REFERENCES

- Battjes, J.A. (1975). Modeling of turbulence in the surf zone. Proc. Symp. on Modeling Techniques, 1050-1061.
- Battjes, J.A. (1983). Surf zone turbulence. Proc. XXth Congress of IAHR.
- Bowen, A.J. (1969). The generation of longshore currents on a plane beach. J. of Mar. Res., 27:206-215.
- Bowen, A.J. (1978). Simple models of nearshore sedimentation; beach profiles and longshore bars. Proc. Conf. Coastlines of Canada.
- Bruun, P. (1954). Coastal Erosion and Development of Beach Profiles, Beach Erosion Board Tech. Memo. No. 44, 82 pp.
- Dean, R.G. (1977). Equilibrium Beach Profiles; U.S. Atlantic and Gulf Coasts, University of Delaware Ocean Engr. Rept. No. 12, 45 pp.
- Hildebrand, F.B. (1962). Advanced Calculus for Applications, 2nd Edition, Prentice-Hall, Inc., New Jersey, 733 pp.
- Inman, D.L., R.J. Tait and C.E. Nordstrom (1971). Mixing in the surf zone. J. of Geophys. Res., 76:3493-3514.
- Jones, D.L. (1975). The Effect of Vertical Seawalls on Longshore Currents, Ph.D. Thesis, University of Florida, 189 pp.



- Komar, P.D. (1975). Longshore currents and sand transport on beaches. Proc. Civil Engr. in the Oceans/III, 1:333-354.
- Kraus, N.C. and T.O. Sasaki (1979). Influence of wave angle and lateral mixing on longshore current. Marine Sci. Comm., 5:91-126.
- Kraus, N.C., N. Mimura, and K. Horikawa (1980). Investigations of dispersion in and around the surf zone. Proc. 27th Conf. on Coast. Engr. in Jap., ISCE, pp. 173-177 (in Japanese).
- Liu, P.L-F and R.A. Dalrymple (1978). Bottom frictional stresses and longshore current due to wave with large angles of incident. J. of Mar. Res., 36:357-375.
- Longuet-Higgins, M.S. (1970a). Longshore currents generated by obliquely incident sea waves, 1. J. of Geophys. Res., 75:6778-6789.
- Longuet-Higgins, M.S. (1970b). Longshore currents generated by obliquely incident sea waves, 2. J. of Geophys. Res., 75:6790-6801.
- Madsen, O.S., D.W. Oslendorf, and A.S. Reyman (1978). A longshore current model. Proc. Coastal Zone 78, ASCE, 3:2332-2341.
- McDougal, W.G. and R.T. Hudspeth (1983). Wave setup/setdown and longshore currents on nonplanar beaches. Coast. Engr., 7:103-117.
- McDougal, W.G. and R.T. Hudspeth (1984a). Longshore sediment transport on Dean beach profiles. Proc. 19th Coast. Engr. Conf.
- McDougal, W.G. and R.T. Hudspeth (1984b). Influence of turbulent mixing on longshore currents. Ocean Engr., in review.
- Thornton, E.B. (1970). Variation of longshore current across the surf zone. Proc. 12th Coast. Engr. Conf., 291-308.
- Visser, P.J. (1984). Uniform longshore current measurements and calculations. Coast. Engr. Conf. Abstracts, pp. 212-213.

#### ACKNOWLEDGEMENTS

The authors wish to thank J.A. Battjes, P.J. Visser, N.C. Kraus, and C.S. Wu for their comments and the information which they generously provided.

This research was supported by the Oregon State University Sea Grant College Program, National Oceanic and Atmospheric Administration Office of Sea Grant, Department of Commerce, under Grant No. NA81AA-D-00086 (Project No. R/CE-13). The U.S. government is authorized to produce and distribute reprints for governmental purposes, notwithstanding any copyright notation that may appear hereon.



*Fishing Harbor, Nakuek, AK*

**PART V**

**SHIP MOTIONS**

*Hopper dredge at Port Canaveral, FL*





## CHAPTER TWO HUNDRED FIFTEEN

### Surges and Waves Generated by Ships in a Constricted Channel

John B. Herbich\* and Robert E. Schiller, Jr.\*\*

#### Introduction

A study of surges and waves was initiated because of serious bank erosion along the Sabine-Neches Waterway, located in East Texas. The Waterway provides ship access from the Gulf of Mexico to Port Arthur and Beaumont. The design water depth in the ship channel is 12.12 m (40 ft). The 1978 tonnage of ships using the waterway was 69,740,900 tons (1). The highway on the east bank of the Waterway between Port Arthur and Mesquite Pt. leading to Louisiana had to be relocated several times because of bank erosion. The erosion was thought to be principally caused by ship traffic generating surges and waves.

The main purpose of the study was to:

1. evaluate the magnitude of surges and waves generated by ships using the Waterway,
2. evaluate bank erosion potential, and
3. evaluate and recommend the most economical structural measures to prevent further bank erosion.

The results of this first part of the study are reported in this paper.

#### Literature Review

The literature on waves and surges created by ships in dredged navigational channels is rather limited, but occurrences of such phenomena have been observed in many countries. The most severe problem occurs in an artificial channel dredged in a shallow inlet or a tidal estuary. Large ships passing through such a confined deep channel cause a significant initial drop in water level and a resulting surge as the ships proceed along the channel. The waves generated by such ships are relatively small as compared with the magnitude of the generated surge. Small, high-speed vessels generate only insignificant surges, but may create relatively high waves.

Lee and Bowers (5) conducted tests for the Panama Canal and made extensive drawdown measurements for a wide range of channel depths,

---

\*Professor of Ocean and Civil Engineering and Director, Center for Dredging Studies, Texas A&M University, College Station, TX, USA.

\*\*Professor, Civil and Ocean Engineering, Texas A&M University, College Station, TX, USA.

widths, and ship speeds. Helm and Woltinger (4) stated that the speed of the return flow (surge) provides an indication of the magnitude of the soil erosion problem.

Gelencser (3) confirmed the occurrence of drawdown created by ships in the St. Lawrence Seaway.

Dand and White (2) reported on the studies conducted in the Suez Canal and indicated that one of the disadvantages of a horizontal berm at the western side of the Canal is the generation of surge waves. A dimensionless plot of the vessels Froude Number, as a function of the blockage ratio, was developed to indicate the possibility of creating a drawdown at the berm.

Balanin, et al. (1) and Van de Kaa (8) also addressed the problem of the drawdown that occurs with ship's passage. Maynard (7) conducted field studies on the Sacramento River Deep Water Ship Channel concerning riprap protection in navigation channels.

#### Generation of Surges and Waves

In an artificially-dredged channel, in otherwise shallow water, a large ship displaces a large volume of water which must then follow in the opposite direction to the ship's movement along both sides of the ship (Figure 1). This causes a surge which moves perpendicularly to the bank at a high velocity, thus causing bank erosion (Figure 2). Surges as high as 3.3 m (10 ft) have been observed during the passage of large vessels moving at a relatively high speed. In addition, bow and stern waves are generated by the vessels, but these are of small magnitude as compared with generated surges. Small work boats and tugs generate only insignificant surges but generate waves which may be of the order of 1 to 1.2 m (3 to 4 ft) when travelling at high speed.

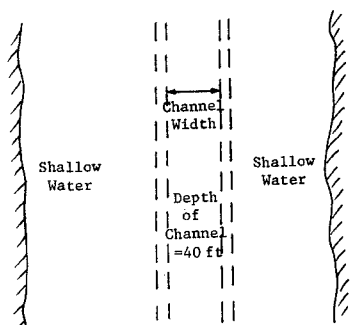


Figure 1. Dredged Ship Channel

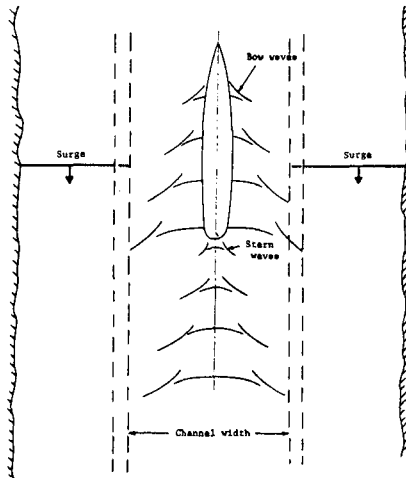


Figure 2. Waves and Surges Generated by a Ship in a Constricted Channel

### Field Measurements

Field measurements of ship's speed, draft, generated waves and surges were taken with a video tape recorder, movie camera and pressure transducers installed at several locations along the banks of the Waterway. Pressure transducers were installed in about 2.1 to 2.4 m (7 to 8 ft) of water and connected to a recorder on land.

Transducers, approximately 6.4 cm (2.5 inches) diameter at the base and 18.5 cm (7.25 inches) long, were constructed of stainless steel. The transducers were connected to an electronic recorder which traced the water level as a function of time. Since the recorders were powered by batteries, they were only turned on when a vessel passed through the Waterway.

A typical recorded surge trace by a deep-draft vessel is shown in Figure 4 and a typical recorded wave trace is shown in Figure 5. A sample surge trace as a function of time is shown in Figure 5 for a 4.7 m (15.5 ft) draft vessel moving at 9.77 knots. It will be noted that surging continued for several minutes (the recorder was turned off after 5 minutes.). In some cases, surging was observed for 20 minutes or more.

### Data Analysis

#### Surge height for a range of ship drafts

The surge height as a function of Froude Number for a range of ship drafts is shown in Figures 6 and 7. The surge height is shown in

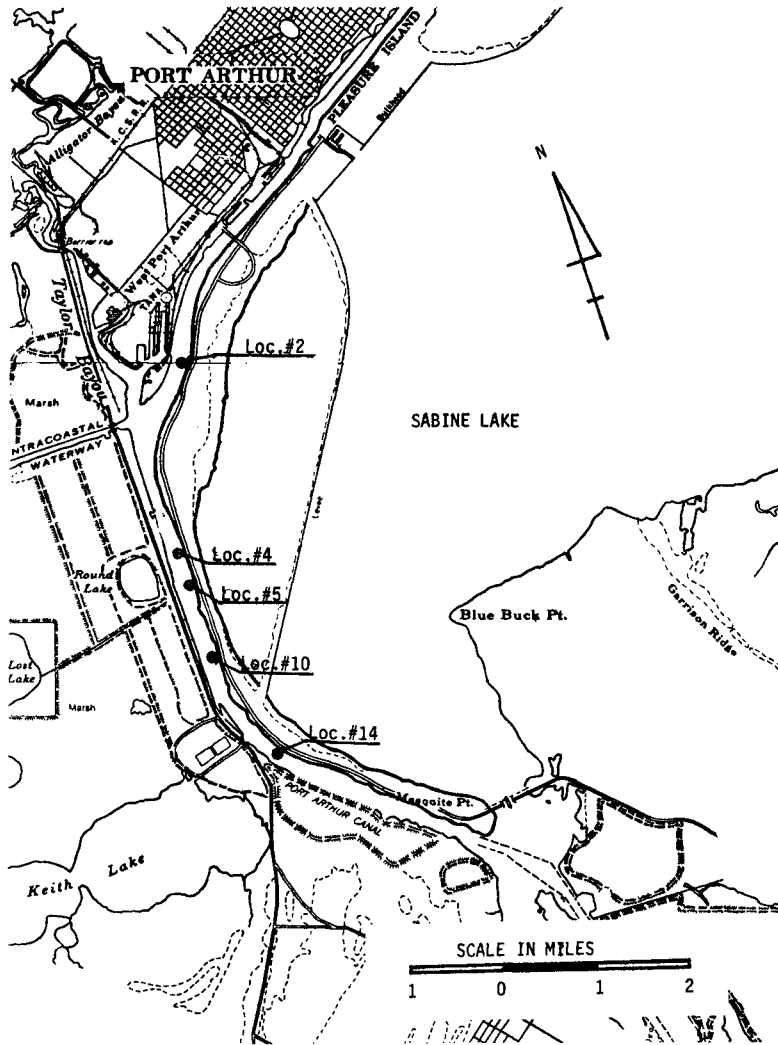


Figure 3. Sabine-Neches Waterway between Port Arthur and Mesquite Pt. (Texas)

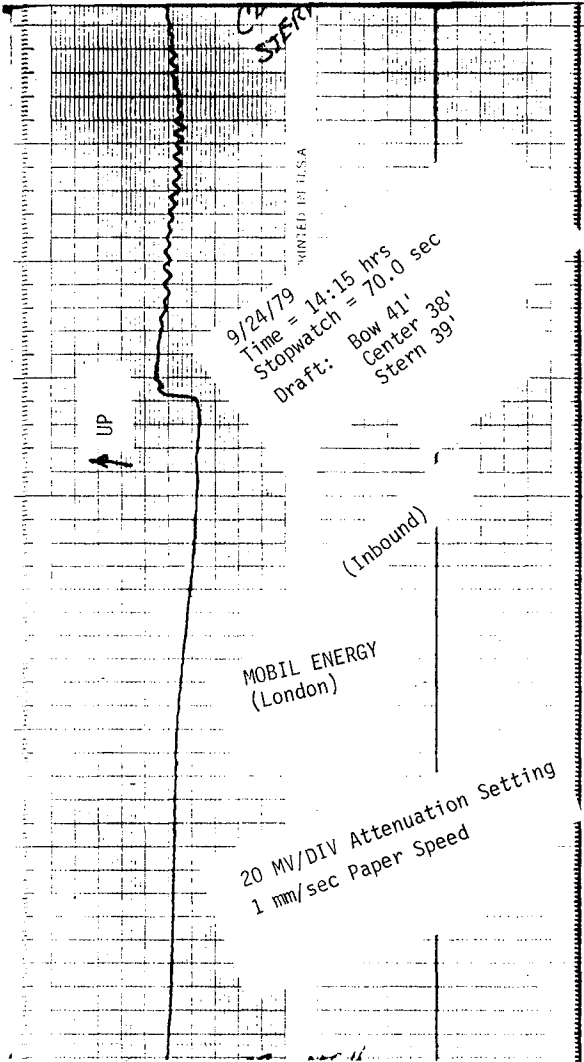


Figure 4. Typical Recorder Trace of Surge Due to Passage of a Ship



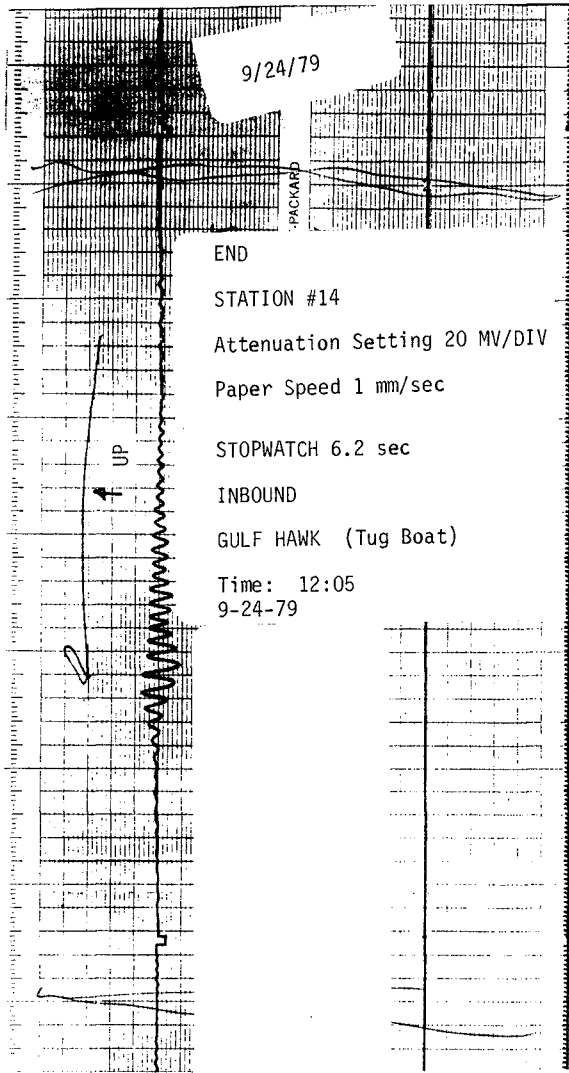


Figure 5. Typical Recorder Trace of Waves from Wake Due to Passage of a Tug Boat

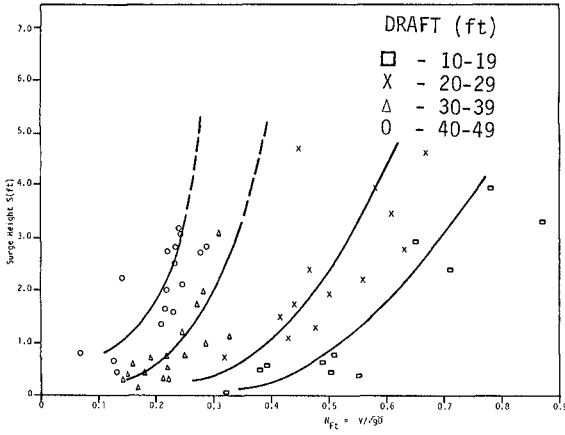


Figure 6. Surge Height Vs. Froude Number at Location #2 for Inbound Ships (Equal Draft)

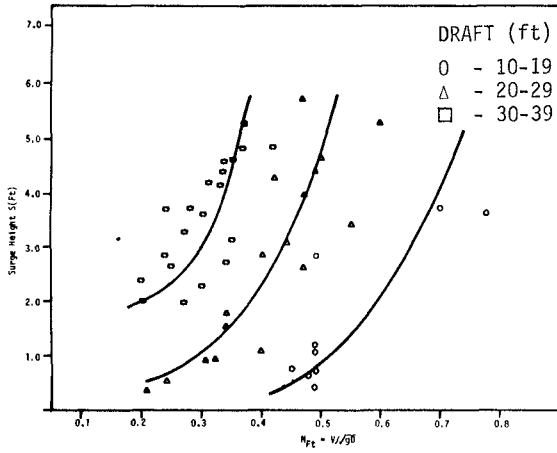


Figure 7. Surge Height Vs. Froude Number at Location #2 for Outbound Ships (Equal Draft)

feet (1 ft = 0.3048 m) and the Froude number is defined as

$$\frac{V}{\sqrt{gD}}$$

where

V = vessel's speed,  
g = acceleration due to gravity, and  
D = vessel's draft.

The vessel's draft is also shown in feet.

Figure 6 represents the data for inbound ships at location No. 2 (see Figure 3 for actual location) and Figure 7 shows similar information for outbound ships. The lines are drawn for ships of equal draft ranges. It is quite clear from the figures that the surge height is a function of the Froude Number and the ship's draft. The surge height increases rapidly with the Froude Number.

#### **Surge height for a range of ship speeds**

The surge height as a function of Froude Number for a range of ship speeds is shown in Figures 8 and 9 for outbound ships.

#### **Surge height for a range of ship drafts and observed ship speeds**

Figure 10 presents the surge height measurements for outbound ships at location No. 2 as a function of ship's speed, and Figure 11 presents the surge height measurements for inbound ships at location No. 14.

#### **Surge height/length of ship (B.P.) for a range of ship drafts**

Figures 12 through 14 present the surge height data in a dimensionless form (surge height/length of ship between perpendiculars) as a function of Froude Number for two locations, No. 2 and No. 14. Figures 12 and 13 are for location No. 2 for inbound and outbound ships respectively and Figure 14 is for location No. 14.

#### **Occurrences of surge heights**

Figure 15 presents the number of surge height occurrences measured at location No. 2, and Figure 16 shows the number of occurrences of ship-generated wave heights measured at location No. 14. Figure 15 presents the data for deep-draft vessels and Figure 16 is for small vessels moving at low speeds.

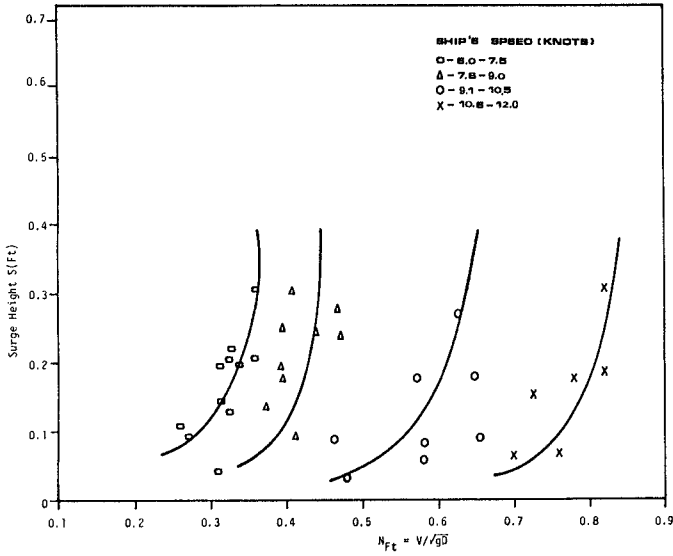


Figure 8. Surge Height Vs. Froude Number at Location #14 for Inbound Ships (Equal Speed)

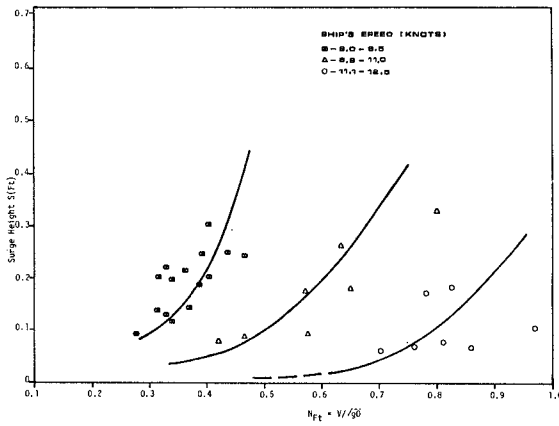


Figure 9. Surge Height Vs. Froude Number at Location #14 for Outbound Ships (Equal Speed)

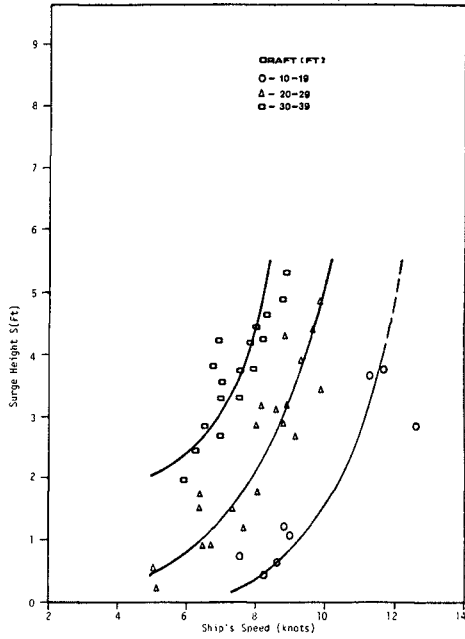


Figure 10. Surge Height Vs. Ship's Speed at Location #2 for Outbound Ships (Equal Draft)

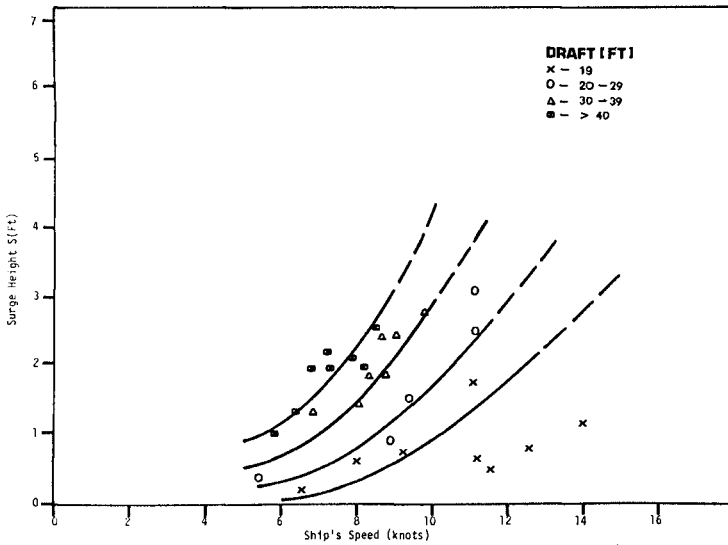


Figure 11. Surge Height Vs. Ship's Speed at Location #2 for Outbound Ships (Equal Draft)

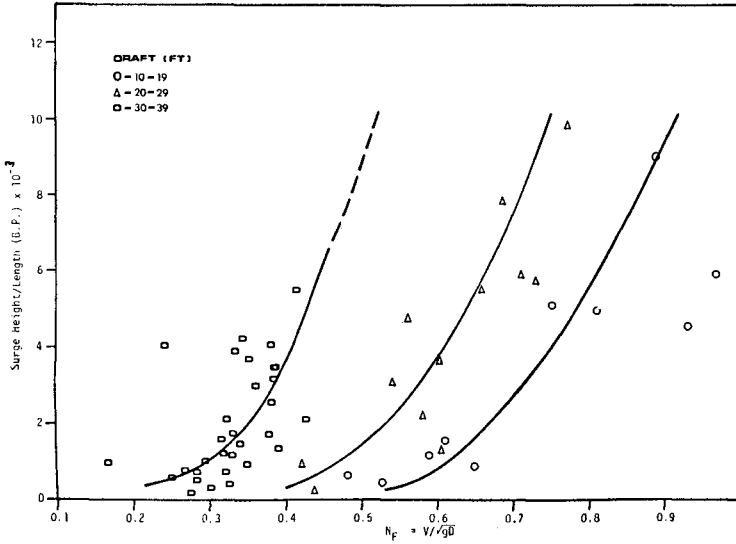


Figure 12. Surge Height/Length of Ship (B.P.) Vs. Froude Number at Location #2 for Inbound Ships

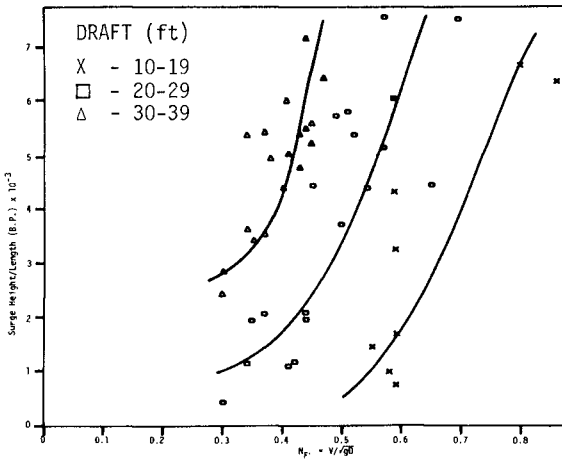


Figure 13. Surge Height/Length of Ship (B.P.) Vs. Froude Number at Location #2 for Outbound Ships

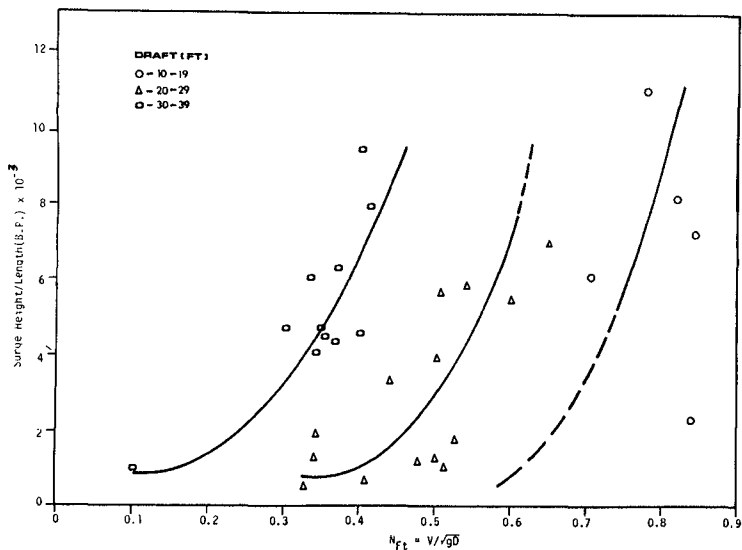


Figure 14. Surge Height/Length of Ship (B.P.) Vs. Froude Number at Location #14 for Outbound Ships (Equal Draft)

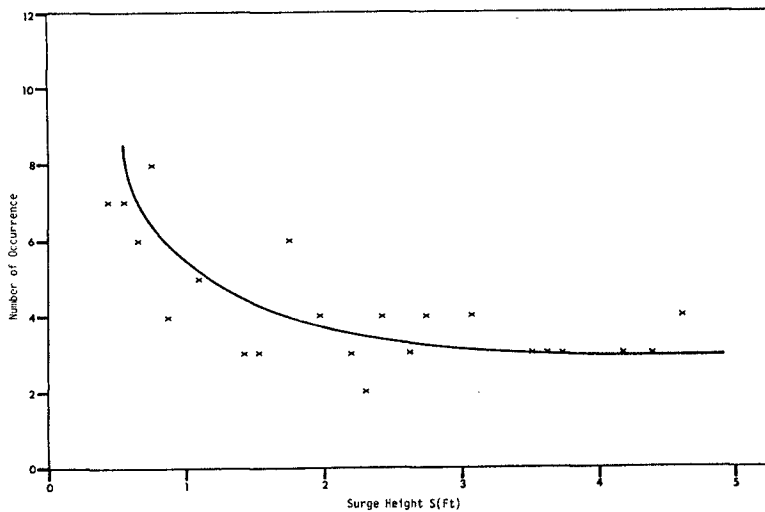


Figure 15. Number of Occurrence Vs. Surge Height at Location #2

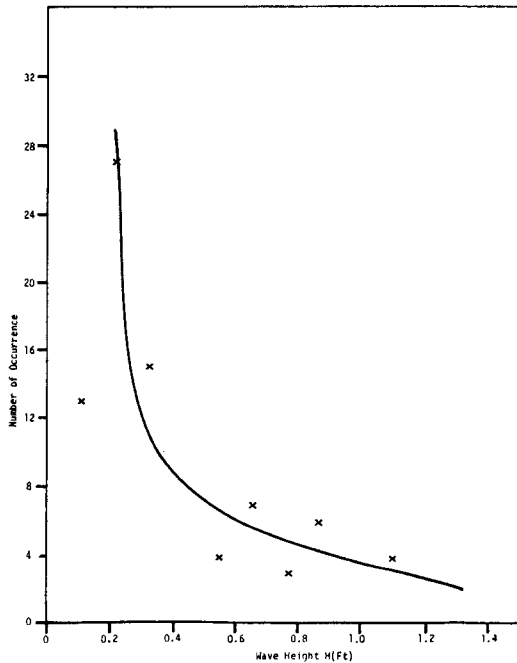


Figure 16. Number of Occurrence Vs. Wave Height at Location #14

### Conclusions

1. Considerable surges and waves generated by ships were observed in the Sabine-Neches Waterway. Such surges and waves are the principal cause of bank erosion along the Waterway.
2. The surge height generated by large vessels in a dredged channel, in an otherwise shallow estuary or inlet, is a function of ship's draft and ship's speed. In general, the greater the ship's draft and ship's speed, the greater the generated surge and drawdown.
3. The waves generated by small vessels are principally a function of ship's speed.
4. The surge height generated by large vessels is considerably higher than the waves generated by such vessels.
5. The wave heights generated by small vessels are very large in comparison with surges generated by such vessels. In fact, the surges generated by small vessels can be considered insignificant.



**Acknowledgment**

The study was sponsored by the Texas State Department of Highways and Public Transportation in cooperation with the Texas Transportation Institute. The cooperation of Mr. Franklin C. Young and Mr. William A. Potter, III is gratefully acknowledged. Mr. K. Kim and T.Y. Lee, graduate students in ocean engineering, assisted in data collection and analysis. Mr. A. R. Toussaint, an undergraduate student in Ocean Engineering, did most of the pressure transducer installations.

**Appendix - References**

1. Balanin, V., Zernov, D., Kirjakov, S., Metelitsina, G., Polunin, A., Schegolev, V. (1977). "Peculiarities of Navigation on Canals and Restricted Channels, Originating Hydraulic Phenomena Associated with Them and Their Effect on the Canal Bed; Measures Preventing Slope Deterioration," 24th International Navigation Congress, PIANC, Leningrad, Section I, Subject 3.
2. Dand, I.W. and White, W.R. (1977). "Design of Navigation Canals," Symposium on Aspects of Navigability of Constraint Waterways, Including Harbour Entrances, Delft, The Netherlands, Vol. 2.
3. Gelencser, G.J. (1977). "Drawdown Surge and Slope Protection, Experimental Results," 24th International Navigation Congress, PIANC, Leningrad, Section I, Subject 3.
4. Helm, K. and Woetinger, O. (1953). "Conditions Requisites pour la Section Transversale de Navigation," 18th International Navigation Congress, PIANC, Rome, Section I, Communication I.
5. Lee, C. and Bowers, C. (1947). "Restricted Channel Tests for the Panama Canal," Navy Department, David Taylor Model Basin, Bethesda, MD.
6. Marine Board, National Research Council (1983). "Criteria for the Depths of Dredged Navigational Channels," National Academy Press, Washington, DC.
7. Van de Kaa, E.J. (1978). "Power and Speed of Push Tows in Canals," Symposium on Aspects of Navigability of Constraint Waterways, Including Harbour Entrances, Delft, The Netherlands, Vol. 3.
8. Maynard, S.T. (1984). "Riprap Protection on Navigable Waterways," T.R. HL-84-3, U.S. Army Engineer Waterways Experiment Station, Vicksburg, MS.

## CHAPTER TWO HUNDRED SIXTEEN

### DEVELOPMENT OF SHIP WAVE DESIGN INFORMATION

Robert M. Sorensen, F. ASCE\*  
J. Richard Weggel, F. ASCE\*\*

#### ABSTRACT

During the last three decades several field and laboratory investigations have been conducted in which the waves generated by a wide variety of vessels have been measured. There is a need to synthesize the data published from these studies and to develop general ship wave prediction methods for designers. To complete this task some additional ship wave data must be collected. This paper initiates the effort to develop these prediction methods. A summary and critique of available data are given. Then, the appropriate portion of these data is employed to develop a ship wave height predictor model that gives the maximum ship wave height as a function of ship speed and displacement, water depth, and distance from the sailing line. This is an interim model that is quite applicable but can be improved pending additional data. Finally, planned future efforts to further develop design wave prediction methods are discussed.

#### INTRODUCTION

The design of various waterway features such as bank erosion control structures and marina protective works, as well as the establishment of allowable ship speeds in navigable waterways, require a knowledge of the characteristics of the waves generated by the ship traffic using the waterway. The characteristics of the ship waves (wave heights, periods, crest orientations) depend on the ship speed and direction, the water depth, the ship hull form and draft, and the distance from the sailing line.

During the later 19th Century, Kelvin developed the first ship wave theory and Froude conducted towing tank experiments to measure ship wave resistance. However, only during the last twenty-five years has there been a serious effort to conduct field and laboratory measurements of the characteristics of ship-generated waves. Data has been collected in towing tanks and in restricted and open waterways, for deep and shallow water wave conditions generated by a variety of vessels. Typically, for a given test run, reported data consists of the height of the highest wave in a wave record generated by the passing ship and its associated half period, for the particular speed and distance from the sailing line.

Available experimental data covers a wide range of ship types and speeds and waterway conditions; however, certain data deficiencies do

---

\* Professor of Civil Engineering, Lehigh University, Bethlehem, PA 18015  
\*\*Associate Professor of Civil Engineering, Drexel University,  
Philadelphia, PA 19104

exit. Specifically, there is insufficient data for large ship draft to water depth ratios. Also, hull forms for the vessels studied are inadequately defined.

The data that are available (plus additional data to be collected) need to be synthesized and analysed to develop a coherent procedure for predicting ship wave heights and periods for given ships, ship speeds, water depths and distances from the sailing line.

Also, design analyses often require more information on ship wave characteristics than the maximum wave height and associated half-period. Of more value, for example, would be a representative wave height similar to the significant wave height from a wind wave record and the typical distribution of wave heights in a ship wave record for given conditions.

With these deficiencies in view, the authors have initiated a study to improve ship wave design information and procedures. This paper presents initial results of the study.

#### SHIP-GENERATED WAVE CHARACTERISTICS

A brief summary of ship wave characteristics is presented here; see Sorensen (1973) for more details.

As water flows past the bow of a ship, a pressure gradient develops and waves are generated. The pressure gradient and resulting height of generated waves depend on the relative water velocity (i.e. ship speed), the bow shape, the ship draft, and the clearance below the keel (i.e. ship draft to water depth ratio). The resulting pattern of wave crests generated by the bow of a ship moving in deep water (Figure 1) consists of a symmetrical set of diverging waves that move obliquely out from the sailing line and a single group of transverse waves that move in the direction of the sailing line. The transverse and diverging waves meet to form cusps located along lines  $19^{\circ}28'$  out from the sailing line. If the ship speed is increased, this pattern retains the same geometric shape but grows in size as the wave lengths increase. A similar pattern of waves typically with lower wave heights is generated at the ship's stern.

At increasing distances from the bow, diffraction increases the wave crest length and decreases the wave amplitude. Havelock (1908, 1914) demonstrated analytically that the wave heights at the cusp points decrease at a rate inversely proportional to the cube root of the distance from the bow while the transverse wave heights along the sailing line decrease at a rate inversely proportional to the square root of the distance from the bow. Thus, at greater distances from the ship, the diverging waves become more prominent than the transverse waves.

Figure 2 show a typical water surface-time history measured at a point during the passage of a ship. Most published data on ship waves present the maximum wave height,  $H_m$ , and the associated half-period,  $T/2$ , from such a record.

The transverse waves have a celerity equal to the speed of the ship. Thus, using linear wave theory, their length and period can be calculated for a given ship speed and water depth. The diverging waves have a celerity that is less than the ship speed and equal to  $V \cos \theta$ , where  $V$  is the ship speed and  $\theta$ , defined in Figure 1, is approximately  $55^{\circ}$ . Thus, the diverging wave length and period can also be calculated (see Sorensen, 1967).

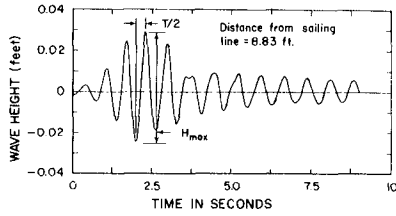


Figure 2 Water Surface Time History at Point For Waves From Mariner Model Ship (Das 1969).

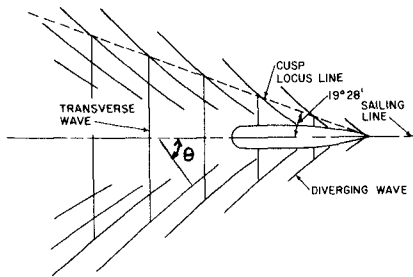


Figure 1 Deep Water Wave Crest Pattern Generated by Ship's Bow

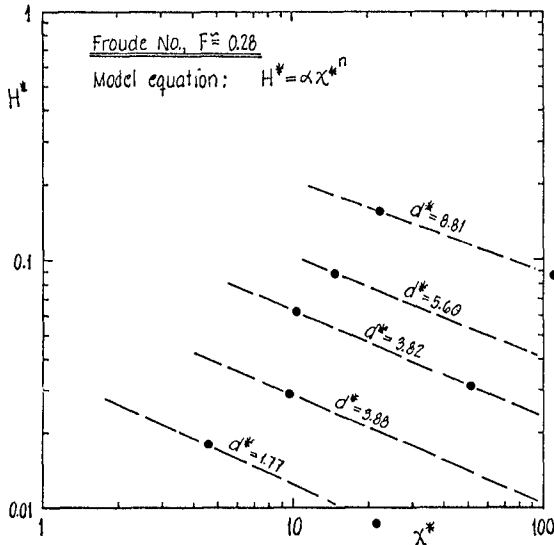


Figure 3 Variation of  $H^*$  with  $x^*$  for Various Values of  $d^*$ . Froude Number = 0.28.

When the water depth is less than about one half the length of the ship waves, the waves "feel" bottom and their characteristics and crest pattern are significantly modified. This "shallow water" condition occurs for depth Froude numbers,  $F$ , in excess of approximately 0.6 (Sorensen, 1966), where  $F = V/\sqrt{gd}$ , and  $d$  equals the water depth.

In shallow water, as  $F$  increases from 0.6 to 1.0 the cusp locus angle increases from  $19^{\circ}28'$  to  $90^{\circ}$ . The leading transverse and diverging wave heights are accentuated at the expense of the following waves. At  $F = 1.0$ ,  $V = \sqrt{gd}$  and the transverse and diverging waves combine to form a single wave having a crest line perpendicular to the sailing line. Thus, as would be expected,  $H_m$  and  $T/2$  increase at an increasing rate through this range of Froude numbers. Ships rarely operate at speeds exceeding a Froude number of unity (see Schofield, 1974) so the wave pattern and characteristics in this region will not be considered here.

For a given vessel shape and speed, water depth, and distance from the sailing line, there is a significant increase in  $H_m$  as the ship draft increases (see Johnson, 1958). On the other hand, light vessels that increase their speed may plane before reaching a Froude number of unity and once planing commences there is essentially no increase in wave height with increasing ship speed.

#### EXPERIMENTAL DATA

Several laboratory and field investigations of ship-generated waves have been conducted during the last twenty-five years. Table 1 summarizes the test conditions and data collected from published investigations.

Typically, in each investigation the water surface time history was measured at one or a few points (distances from the sailing line) as the ship passes. Few of the actual time history records have been published; most authors just present data on  $H_m$  and  $T/2$  as a function of ship speed and distance from the sailing line. Some authors have published an average period,  $\bar{T}$ , equal to the number of waves divided into the duration of the "wave packet". Wave records with a strong contribution from both diverging and transverse waves would have a bimodal distribution of wave periods so an "average" period could be misleading.

Zabawa and Ostrom (1980) also present ship wave energy density data (for each test run) based on the root mean square wave height for the waves in a given record. Similarly, Ofuya (1970) presents data on the total energy in a ship wave record based on the root mean square wave height and the period of  $H_m$ . Das (1969) presents energy spectra for eight of his test runs.

Usually, experiments were conducted with whatever model or prototype vessels were available and most experiments, particularly in the field, were conducted with a small ship-draft to water-depth ratio ( $D/d$ ). Consequently, the data do not cover waves generated by a uniform range of hull forms and in almost all cases  $D/d$  is less than 0.5. Also, for most data sets, the ship hull geometry was very inadequately defined or reported, making it difficult or impossible to quantify the hull form geometry with respect to its wave generating capability. For some data sources, block coefficients (displaced volume/length x beam x draft) could be defined. For others, the

Table 1 - Ship Wave Data Summary

Reference	Model or Prototype	F range	Vessels	D/d	V/LBD	Data Presented
Johnson, 1958	M	0.6-2.0	Power boat	0.25	0.37	Only selected Hm, T/2 versus Vs, x data presented.
			Barge	0.44,0.23,0.13	0.58	
			Canoe	0.37	0.82	
			Rectangle with V-bow(3)	0.52 0.19	0.56 0.93	
Brebner, et al., 1966	M	0.29-0.89	Ocean liner	0.16,0.60	0.51	Hm versus Vs, x for all conditions;curves only,no data points shown.
			Bulk carrier	0.16,0.60	0.40	
Sorensen, 1966	M	0.4-0.9	Rectangle with V-bow(3)	0.33	0.87	Hm versus Vs, x for 81 test runs.
		0.69-1.58	Idealized hull form	0.50	0.53	Contour plot of wave surface for 7 test runs.
Sorensen, 1967	P	0.25-0.92	Tug	0.16	0.25	Hm,T/2 versus Vs, x. Planing for some cabin cruiser test runs.
			Tug(fire boat)	0.28	0.36	
			USCG Cutter	0.09	0.22	
			Fishing boat	0.08	0.44	
			Cabin cruiser	0.04	0.31	
			Misc. other vessels	-	-	
Hay, 1968	M	0.36-0.76	Cargo ship	0.73, 0.5, 0.4, 0.29	0.52	Hm versus Vs, x for 270 test runs.
			David Taylor Series 60 Tanker		0.56	
			Aux. supply vessel	0.69		
			Barge	0.63		
Tug	0.73,0.33	0.86	0.48			

Table I (continued) - Ship Wave Data Summary

Reference	Model or Prototype	F range	Vessels	D/d	W/LBD	Data Presented
Bidde, 1968	M	0.43-0.85	Cargo ship Barge	0.5, 0.43, 0.40, 0.38 0.40, 0.33 0.25, 0.22	0.52 0.87	Hm versus Vs, x for constant and decreasing water depths out from sailing line, 245 test runs.
Das, 1969	M	0.27-0.96	Cargo ship Cruiser	0.73, 0.12 0.48, 0.08	0.52 -	Hm, T/2 versus Vs, x for 71 test runs; water surface time histories for 8 runs.
Ofuya, 1970	P	0.1-1.0	Cruiser 92 other vessels of opportunity	0.05 -	0.23 -	Hm, Hrms, $\bar{T}$ versus Vs, x; planing for some cruiser runs.
Zabawa and Ostrom, 1980	P	0.46-4.86	Cruiser Boston Whaler	<0.3 <0.3	- -	Hm, Hrms, $\bar{T}$ versus Vs, x for 60 test runs; planing for many runs.
Bhowmik et al. 1982	P	0.10-0.65	59 barge tows of opportunity	0.06-0.3 (approx.)	varied	Hm versus Vs, x; river currents with/against tow; blockage ratio: 14.7-226.9.
Maynord and Oswalt, 1984	M	0.3-0.62	Barge tows	0.90-0.64	varied	Hm versus Vs, x at channel bank; blockage ratio: 4.6-16.4.

block coefficient could at best be estimated, or only a verbal description of the hull form could be obtained.

#### INTERIM MODEL TO PREDICT SHIP-GENERATED WAVE HEIGHTS

An interim model has been developed to predict ship-generated wave heights at a given location when a ship's speed and displacement, water depth, and distance from the sailing line are known. Obviously, the heights of ship-generated waves depend on hull characteristics other than just the ship's displacement; for example, factors such as the beam to length ratio, beam to draft ratio, and the ratio of the displaced volume to the product of the beam, draft and length (block coefficient) affect wave heights. The model presently considers only the ship's displacement but work is underway to improve the model by considering other relevant hull-shape parameters. Some progress in this direction is presented here.

The data used for developing the interim model was the field data presented by Sorensen (1967) and includes wave height data from seven different ships having displacements ranging from 3 to 18,800 tons, lengths ranging from 23 to 504 feet and drafts ranging from 1.7 feet to 28 feet.

The important variables considered in the interim model to describe the ship-wave generation problem and their dimensions are:

- H = ship-generated wave height, (L)
- d = water depth, (L)
- x = distance from the sailing line to the point where the wave height is measured, (L)
- V = ship speed, (L/T), and
- $\Psi$  = volume of water displaced by the ship, (L<sup>3</sup>)

In addition, the length, beam, and draft of the ship are important although they are not initially considered in the interim model. Their influence will be discussed later.

Dimensional analysis of the above variables yields four dimensionless variables. The form for each of the dimensionless variables selected for the present analysis was largely dictated by the available data; that is, the dimensionless parameters were selected so that the functional relationship between two variables could be investigated while the remaining variables were held constant or nearly constant. One set of dimensionless variables meeting this criterion is:

$$\frac{V}{\sqrt{gd}} = \text{Froude number}$$

$$\frac{H}{(\Psi)^{1/3}} = \text{dimensionless wave height (dependent variable),}$$

$$\frac{x}{(\Psi)^{1/3}} = \text{dimensionless distance from sailing line,}$$

$$\frac{d}{(\Psi)^{1/3}} = \text{dimensionless depth.}$$

where the term,  $\Psi^{1/3}$ , is a characteristic length dimension of the ship.



In the interim model, all of the ship's characteristics are embodied in this parameter which may be physically interpreted as the length of the side of a cube having the same displacement as the ship. If the length, beam, and draft of a ship are also considered, at least three additional dimensionless variables must be added to the above. For example, they could be defined,

$$\frac{L}{(\Psi)^{1/3}} = \text{dimensionless length}$$

$$\frac{B}{(\Psi)^{1/3}} = \text{dimensionless beam}$$

$$\frac{D}{(\Psi)^{1/3}} = \text{dimensionless draft}$$

Other parameters have been used to describe hull forms including the block coefficient, or a parameter suggested by Brebner et al. (1966) defined as the square root of the maximum cross-sectional area of the hull divided by the distance from the bow to the cross-section of maximum area.

#### EMPIRICAL RELATIONSHIPS

Letting  $F$ ,  $H^*$ ,  $x^*$ , and  $d^*$  be the Froude number, dimensionless wave height, dimensionless distance from the sailing line, and dimensionless water depth, respectively, empirical relationships were established among these variables. Havelock (1908) found that the wave height decreases as the one-third power of the distance from the sailing line; hence, the dimensionless wave height,  $H^*$ , was assumed to decrease exponentially with distance from the sailing line. Figures 3, 4 and 5 show the decrease of  $H^*$  with  $x^*$  for three different values of the Froude number. Each figure also shows how  $H^*$  varies with the dimensionless depth,  $d^*$ . In general form, the assumed variation is given by,

$$H^* = \alpha x^{*n} \quad (1)$$

where the exponent  $n$  and coefficient  $\alpha$  are functions of the remaining dimensionless variables. Actually, both  $n$  and  $\alpha$  were found to be functions of the Froude number and the dimensionless water depth  $d^*$ . As shown in Figure 6  $n$  could be expressed as,

$$n = \beta d^{*\delta} \quad (2)$$

$$\text{where} \quad \beta = -0.225 F^{-0.699} \quad 0.2 \leq F \leq 0.55 \quad (3)$$

$$\beta = -0.342 \quad 0.55 \leq F \leq 0.8$$

$$\text{and,} \quad \delta = -0.118 F^{-0.356} \quad 0.2 \leq F \leq 0.55 \quad (4)$$

$$\delta = -0.146 \quad 0.55 \leq F \leq 0.8$$

as shown in Figure 7. Note that the lower and upper bounds for the definitions of  $\beta$  and  $\delta$  are assumed to be 0.2 and 0.8 respectively since the interim model should not be used much beyond the range of the data from which it was derived.

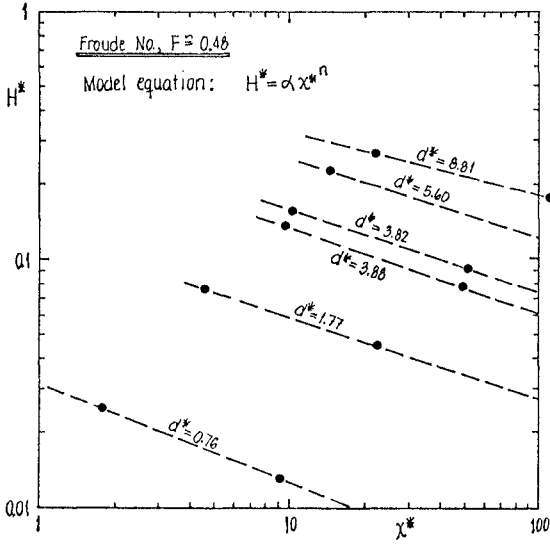


Figure 4 Variation of  $H^*$  with  $x^*$  for Various Values of  $d^*$ . Froude Number = 0.48.

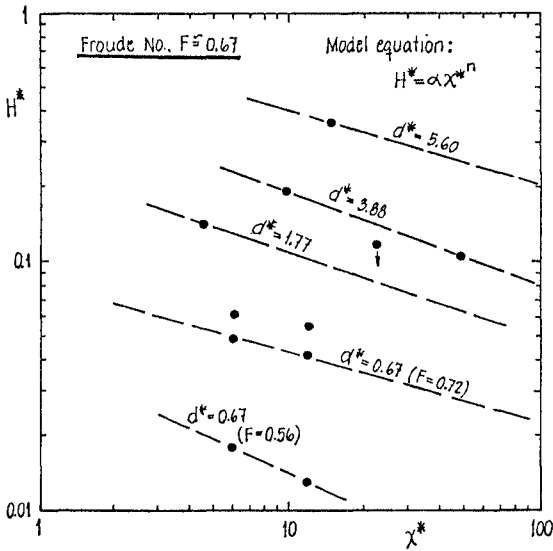


Figure 5 Variation of  $H^*$  with  $x^*$  for Various Values of  $d^*$ . Froude Number = 0.67.

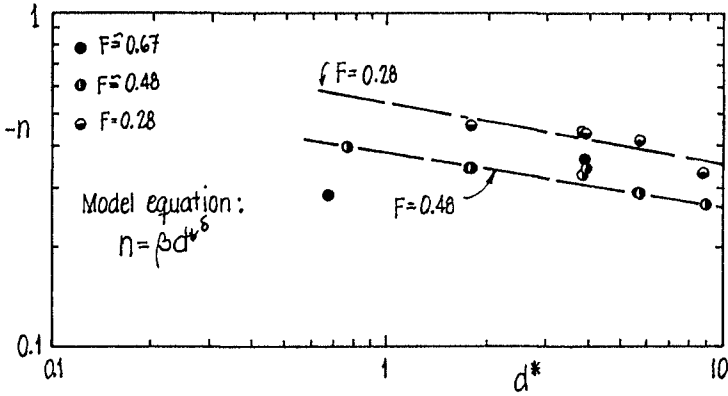


Figure 6 Exponent  $n$  as a Function of  $d^*$  and  $F$ .

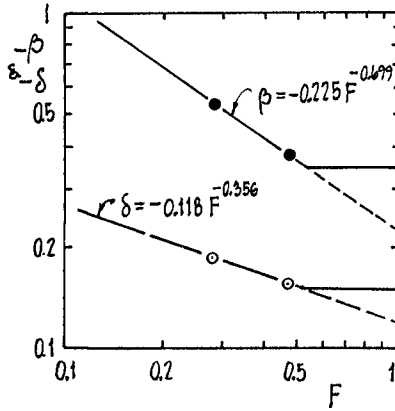


Figure 7 Coefficients  $\beta$  and  $\delta$  as Functions of Froude Number.

Figure 8 shows the variation of  $\alpha$  with  $d^*$  for three values of  $F$ . An empirical expression for  $\alpha$  is given by,

$$\log \alpha = a + b \log (d^*) + c (\log^2 (d^*)) \quad (5)$$

As shown in Figures 9 and 10, empirical expressions for the coefficients are given by,

$$a = -0.6/F \quad (6)$$

$$b = 0.75 F^{-1.125} \quad (7)$$

and 
$$c = 2.6531 F^{-1.95} \quad (8)$$

Equations 1 through 8 permit calculation of ship-generated wave heights at a location given the ship's displacement and speed, the distance between the location and the ship's sailing line, and the water depth. A comparison between the wave heights predicted by equations 1 through 8 and the original data used to develop the empirical relationships is given in Figure 11. The predicted wave heights are plotted against the measured wave heights used to develop the model. While there is some scatter, the equations do a fair job of predicting the data considering that the ship's characteristics have been embodied into a single parameter, the cube root of the displaced volume,  $\Psi$ .

The interim model was subsequently checked against three other data sets for several ships with known hull forms. Figure 12 compares values of  $H^*$  calculated using the interim model with the data obtained by Sorensen (1967) for five geometrically similar box-like models. (For clarity, only data from three of Sorensen's models are shown in the figure. All of Sorensen's data follow the same trend.) The models were basically rectangular boxes with pointed bows, each having the same shape but at a different scale. Their lengths varied from 1.5 feet to 4.0 feet. Figure 12 shows that the waves generated by the box hulls exceed those predicted by the interim model; however, measured and calculated values of  $H^*$  vary linearly suggesting a correction equation given by,

$$H^*_{\text{meas}} = 2.427 H^*_{\text{calc}} - 0.0728 \quad (9)$$

The interim model was also evaluated against the laboratory data obtained by Das (1969) for two ships with distinctly different hull forms, a "Cruiser" hull with a relatively broad beam and a "Mariner" tanker hull with a more streamlined form. A comparison of measured values of  $H^*$  with values of  $H^*$  predicted by the interim model for the "Cruiser" model is shown in Figure 13. Generally, the "Cruiser" data also suggest a linear correction to bring measured and calculated values together. For the "Cruiser" data the correction equation is given by,

$$H^*_{\text{meas}} = 3.158 H^*_{\text{calc}} - 0.1105 \quad (10)$$

The "Cruiser" data also suggest that the hull is more efficient for generating waves than the interim model predicts.

Several data points in Figure 13 are given by Das as being "Cruiser" data in the tables appended to his report. The points, however, are not consistent with the majority of the "Cruiser" data and are suspected of having been obtained from the "Mariner" tanker model.

The "Mariner" data is shown in Figure 14. Again the deviation of

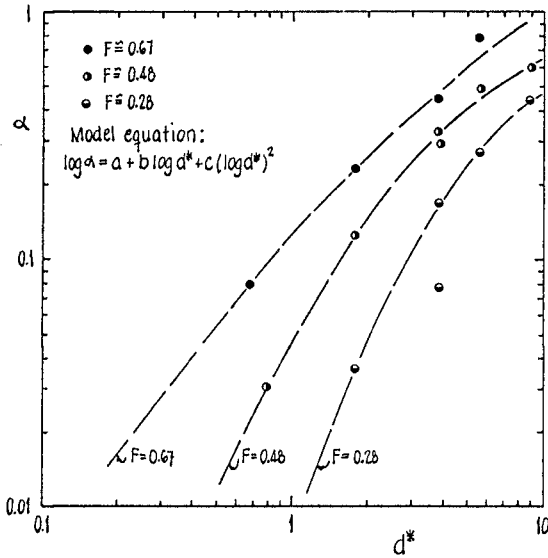


Figure 8 Coefficient  $\alpha$  as a Function of  $d^*$  and Froude Number.

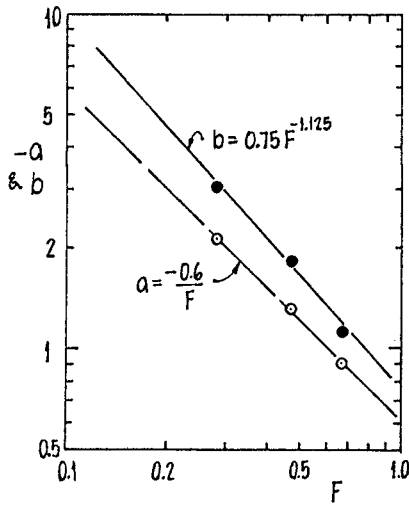


Figure 9 Coefficients  $a$  and  $b$  as Functions of Froude Number.

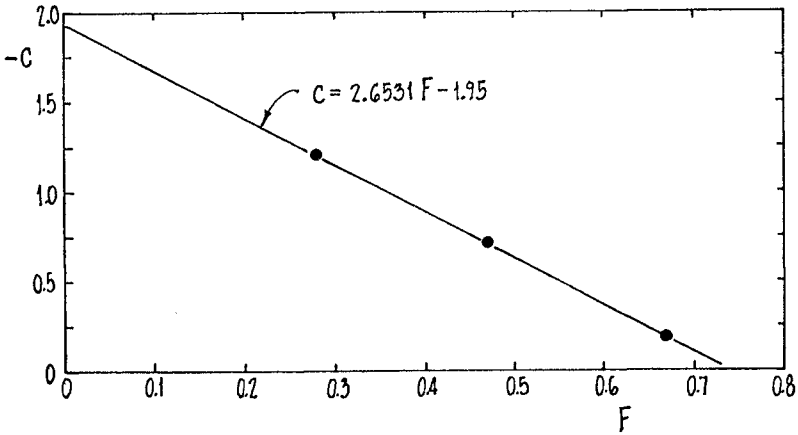


Figure 10 Coefficient  $c$  as a Function of Froude Number.

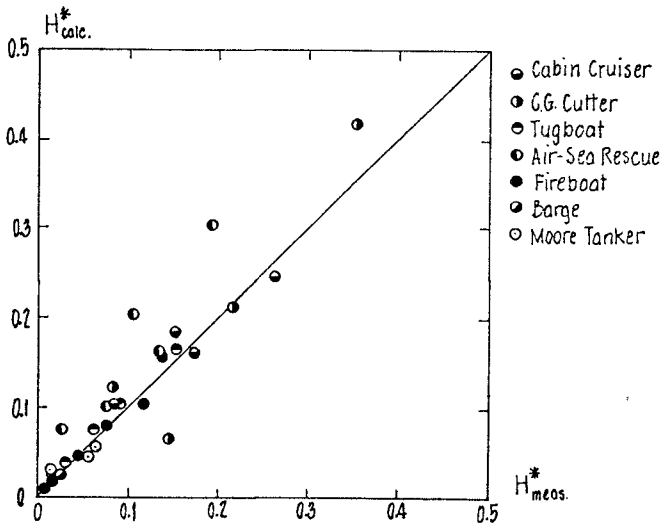


Figure 11 Comparison Between Measured and Calculated Values of  $H^*$  for Data Used to Develop Model.

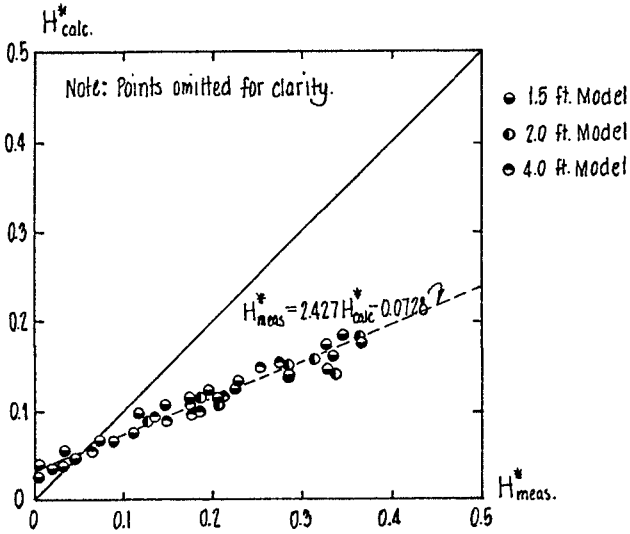


Figure 12 Comparison Between Measured and Calculated Values of  $H^*$  for Sorensen's (1967) Model Data.

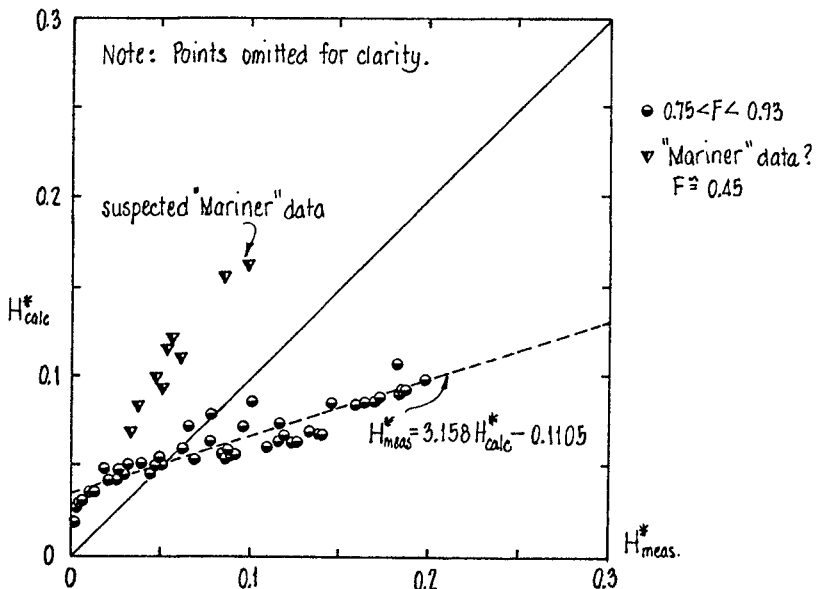


Figure 13 Comparison Between Measured and Calculated Values of  $H^*$  for Das' (1969) "Cruiser" Data.

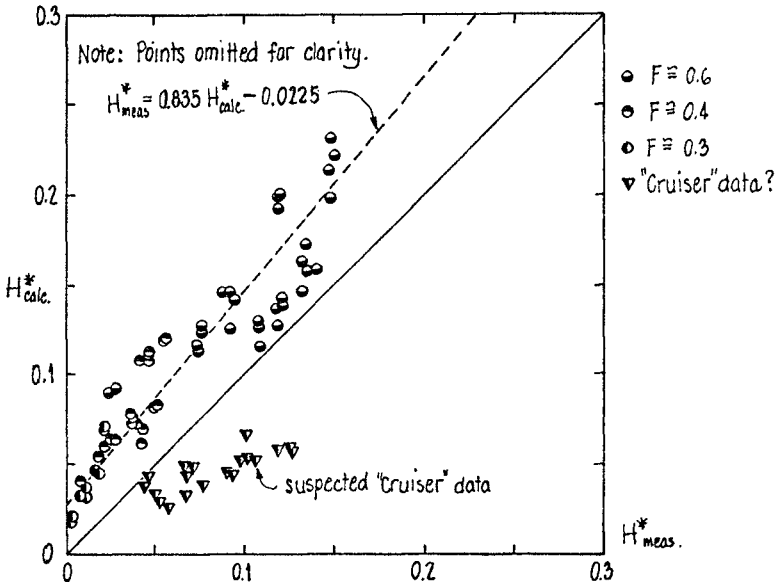


Figure 14 Comparison Between Measured and Calculated Values of  $H^*$  for Das's (1969) "Mariner" Data.

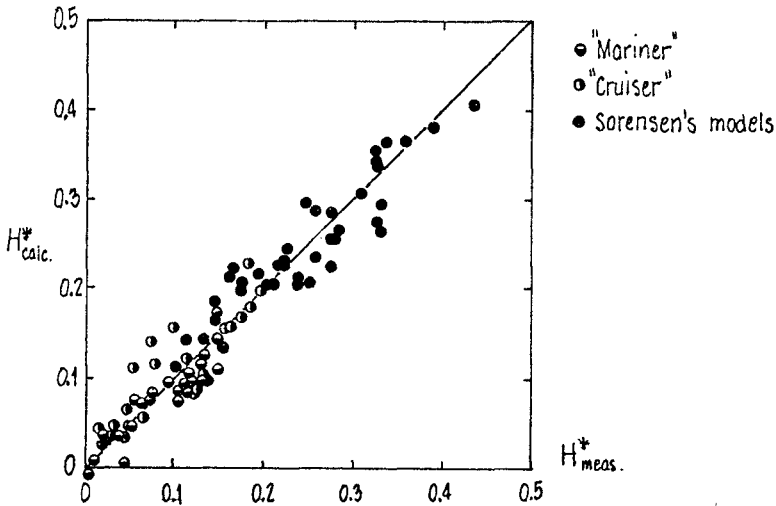


Figure 15 Comparison Between Measured and Calculated Values of  $H^*$ . Linear Corrections to Sorensen's and Das's Data.



the data from the interim model can be adjusted through a linear correction, in this case given by,

$$H^*_{\text{meas}} = 0.835 H^*_{\text{calc}} - 0.0225 \quad (11)$$

A number of data points in Figure 14 are not consistent with the remainder of the "Mariner" data. These points are suspected of being "Cruiser" data instead of "Mariner" data. The "Mariner" data shows that this more streamlined tanker hull is not as efficient in generating waves than is the "Cruiser" hull or Sorensen's box hulls. Generally, the coefficient of  $H^*$  in equations 9 through 11 is a measure of how efficiently the hull generates waves. The larger the coefficient, the greater the hull's efficiency in generating waves. In fact, the two coefficients in the correction equations should be related to hull characteristics such as the block coefficient or Brebner's parameter. For example, Brebner's parameter (the ratio of the square root of the ship's maximum cross-sectional area to the distance from the bow to the cross-section of maximum area) is believed to be larger for the "Cruiser" hull and for Sorensen's box model hulls than for the more streamlined "Mariner" hull. Unfortunately, the information to calculate Brebner's parameter for the "Cruiser" and "Mariner" hulls is not available. Investigators usually report basic hull dimensions such as length, beam, and draft but rarely report relevant cross-section dimensions that would allow this parameter to be determined.

The interim model was also evaluated against the barge-tow data obtained on the Illinois River by Bhowmik et al. (1982), but without success.

#### FUTURE WORK

Future work will initially be directed toward obtaining available wave data from various ships for which hull shape is reported in sufficient detail to calculate the relevant hull parameters. These data will be used to refine the interim model to account for hull shape in determining ship-generated wave heights. Specifically, the coefficients of the linear correction equations (equations 9 through 11) will be empirically related to the various dimensionless parameters describing the hull. Since data appears to be available for only a limited number of hulls, additional wave data from hulls with known configuration will need to be collected. Also, data are needed for a wider range of ship-draft to water-depth ratios.

The preceding analysis provides only a method for estimating  $H_{\text{max}}$  which may or may not be the relevant parameter to predict the effects of ship-generated waves on structures or shorelines. Information on the energy contained within the wave packet and its distribution with frequency might, in fact, be more relevant; hence, spectral descriptions of ship generated waves need to be investigated.

#### REFERENCES

- BALANIN, V.V. & L.S. BYKOV (1965), "Selection of Leading Dimensions of Navigation Canal Sections and Modern Methods of Bank Protection," PIANC, Section 1, Subject 4, Stockholm, Sweden, 1965.
- BIDDE, D.D. (1968), "Ship Waves in Shoaling Water," Technical Report HEL 12-6, Hydraulic Engineering Laboratory, University of California, Berkeley, January 1968, 32 p.

- BHOWMIK, N.G., M. DEMISSIE, & C-Y GUO (1982), "Waves Generated by River Traffic and Wind on the Illinois and Mississippi Rivers," Water Resources Center Report WRC 167, University of Illinois at Urbana-Champaign, March, 1982, 90 p.
- BREBNER, A., P.C. HELWIG, & J. CARRUTHERS (1966), "Waves Produced by Ocean-Going Vessels: A Laboratory and Field Study," Proceedings, Tenth International Conference on Coastal Engineering, Tokyo, Japan, pp. 455-465.
- DAS, M.M. (1969), "Relative Effects of Waves Generated by Large Ships and Small Boats in Restricted Waterways," Technical Report HEL 12-9, Hydraulic Engineering Laboratory, University of California, Berkeley, 112 p.
- HAY, D. (1968), "Ship Waves in Navigable Waterways," Proceedings, Eleventh International Conference on Coastal Engineering, London, England, pp 1472-1487.
- HAVELOCK, T.H. (1908), "The Propagation of Groups of Waves in Dispersive Media, with Application to Waves on Water Produced by a Traveling Disturbance," Proceedings of the Royal Society of London, Series A, pp 398-430.
- HAVELOCK, T.H. (1914), "The Propagation of Disturbances in Dispersive Media," Cambridge University Press, Cambridge, England.
- JOHNSON, J.W. (1958), "Ship Waves in Navigation Channels," Proceedings, Sixth International Conference on Coastal Engineering, Gainesville, Florida, pp 666-690.
- MAYNARD, S.T. & N.R. OSWALT (1984), "Navigation Tests for the Divide-Cut Section, Tennessee - Tombigbee Waterway, U.S. Army Waterways Experiment Station, Vicksburg, Mississippi (in press).
- OFUYA, A.O. (1970), "Shore Erosion - Ship and Wind Waves," Report 21, Marine Engineering Division, Department of Public Works, Ottawa, Canada.
- SCHOFIELD, R.B. (1974), "Speed of Ships in Restricted Navigation Channels," Journal of the Waterways, Harbors and Coastal Engineering Division, ASCE, May, 1974, pp 133-150.
- SORENSEN, R.M. (1966), "Ship Waves," Technical Report HEL 12-2, Hydraulic Engineering Laboratory, University of California, Berkeley, 163 p.
- SORENSEN, R.M. (1967), "Investigation of Ship-Generated Waves," Journal of the Waterways and Harbors Division, ASCE, February, 1967, pp 85-99.
- SORENSEN, R.M. (1973), "Ship-Generated Waves," Advances in Hydroscience, Academic Press, New York, Vol. 9, pp 49-83.
- U.S. ARMY CORPS OF ENGINEERS (1980), "Gallipolis Lock and Dam Replacement, Ohio River, Phase I Advance Engineering and Design Study," General Design Memorandum, Vol. I, Appendix J.
- ZABAWA, C. & C. OSTROM (1980), "The Role of Boat Wakes in Shore Erosion in Anne Arundel County, MD," Coastal Resources Division, Maryland Department of Natural Resources, December 1980.

## CHAPTER TWO HUNDRED SEVENTEEN

### The Effect of Wave Direction on Ship Motions in a Harbour Entrance Channel - Model Study Approach

A C van Wyk\* and J A Zwamborn\*

#### ABSTRACT

Basic knowledge of a ship's vertical motions in waves of different angles of approach is an essential requirement in the formulation of allowance criteria on which to base harbour accessibility under extreme wave conditions.

A comprehensive series of scale model tests are being undertaken to establish minimum underkeel clearance for given channel depths and sea states using two models representing typical 150 000 and 270 000 dwt bulk carriers.

#### 1. INTRODUCTION

The increasing demand for harbour utilization by deeper-draught ships has necessitated a more critical look at harbour accessibility in terms of accepted safety criteria. Based on experience gained at Richards Bay, South Africa's major coal export port (Campbell and Zwamborn, 1977 and 1984; see also figure 1), it was realized that sufficient knowledge of the effect of wave direction on the motions of bulk carriers in limited depths of water is a primary requirement.



Figure 1. Aerial view of Richards Bay harbour entrance

\* Maritime Structures Division, National Research Institute for Oceanology, CSIR, Stellenbosch, RSA.

Details of field measurements of ship motions in the approaches to South Africa's major export ports were given by Zwamborn and Van Wyk (1981) and Van Wyk (1982). The measurements have confirmed the excessive vertical motions of large coal carriers induced by quartering to near-beam swells in the approach channel to Richards Bay harbour. These swells, up to 3 m in height and with periods ranging between 12 and 17 s, have resulted in maximum draught increases of up to twice the significant wave height (Figure 2).

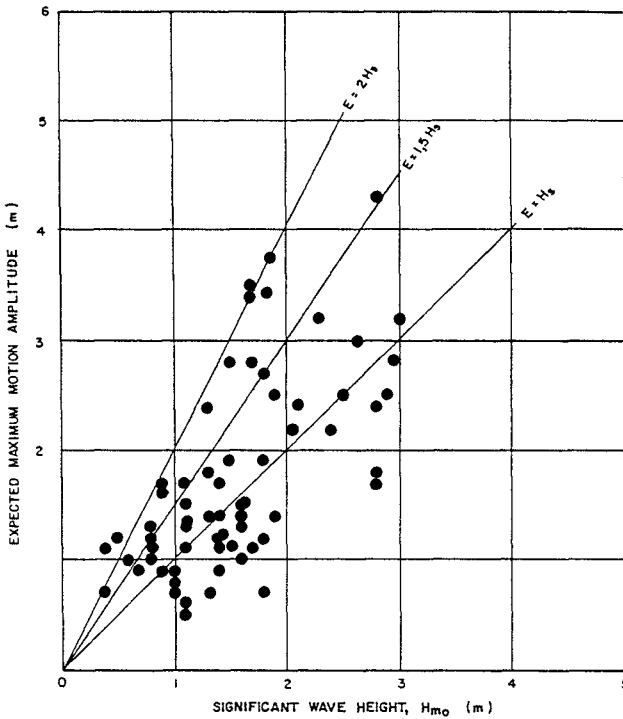


Figure 2. Maximum vertical ship motions at Richards Bay harbour

To assist in the optimum operation of Richards Bay harbour and to determine minimum dredging requirements in the entrance channel for ships up to 250 000 dwt, an extensive programme of research was undertaken, including both physical and mathematical modelling techniques and further prototype measurements.

A start was made with this programme of research during the second half of 1982 with the acquisition of a computer program, based on the 3-D source technique, to calculate ship motions, preparations for the development of suitable scale model ships and laboratory equipment, and the construction of a test basin equipped with irregular wave generators.

The establishment of these facilities, including the wave generators, took almost two years, so that the basic testing only started just before the conference. The present paper, therefore, includes a brief description of the main objectives of the model studies, the required facilities and equipment and their calibration, the approach adopted for the model studies and some initial results.

## 2. STUDY OBJECTIVES

The main objective of this study is to determine **vertical ship motions** as function of wave direction. This implies determination of a ship's behaviour, firstly, as a result of her own inherent properties, and, secondly, as a result of the prevailing environmental conditions.

The ship's inherent properties are the principal dimensions, hull shape (as well as appendages), the loading condition, the speed of advance and the manoeuvrability characteristics. The environment comprises the channel dimensions (including the depth of water), the wave conditions, and possibly currents and wind.

The main objective is being met by conducting a series of basic tests, using scale model ships, assisted by the use of the mathematical model.

## 3. TEST FACILITIES AND EQUIPMENT

Two 1-in-100 scale model ships, representing 150 000 and 270 000 dwt bulk carriers, were built for the basic model tests. The hulls were accurately scaled-down from line drawings of existing prototype vessels and were made of glass fibre (Figure 3).



Figure 3. Mould for construction of glass fibre model hull



Figure 4. Distribution of lead weights for proper loading

The required model loading was obtained by proper distribution of lead weights during inclining experiments in air and in water (Figure 4). Provision was made for both a 'short' and long' period natural roll at full load.

The models are self-propelled and self-steered with true-to-scale speed and rudder response (Figure 5).



Figure 5. Model propulsion unit

The basic tests are conducted in a  $23 \times 28 \text{ m}^2$  flat-bottomed basin, with a maximum depth of 0,35 m, equipped with a bank of SEASIM programmable irregular wavemakers (Figure 6).

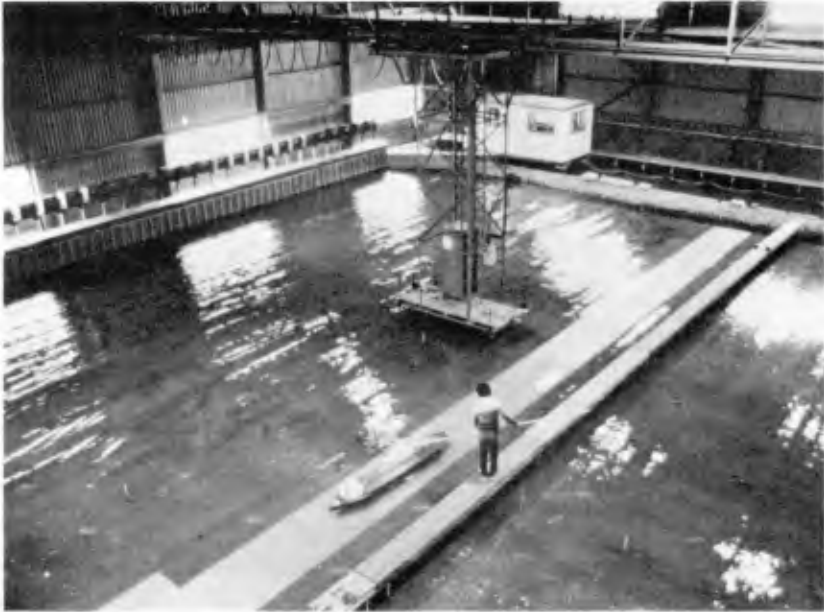


Figure 6. Model test basin with Seasim irregular wavemakers

During testing, the model is run along a straight course, at different angles to the waves, covering a distance of about 20 m (2 km prototype). Measurement of the resistance between four electrodes attached to the model's hull/keel (Figure 7) and galvanised steel plates fixed to the basin floor allows continuous recording of the underkeel clearance (UKC) at the ships quarters and shoulders.



Figure 7. Electrodes attached to model's keel for UKC measurement

Simultaneously with the UKC measurements, the following are recorded: the waves encountered (using a wave probe on the ship's bow) and the rudder deflections and propeller rpm's.

At present, both model control and data transmission are done via a light-weight ship/shore cable but this will soon be replaced by a remote-controlled radio telemetry system, which will also include an autopilot system with feedback to shore.

The ship's horizontal excursions are monitored by two remote-controlled overhead cameras which can be triggered as fast as every 0,2 s (Figure 8). This, together with the feedback from the ship, gives information on the course-keeping ability of the model during tests.



Figure 8. Overhead camera to record model's horizontal excursions

Data handling and analysis are catered for by a shore-based data acquisition system, featuring 16 channel A-to-D conversion and an H.P. mini-computer with on-site graphics terminal (Figure 9).

The ship's vertical response will also be calculated using the mathematical model with the ship's hull simulated by a representative number of panels and with the loading conditions in accordance with those of the scale models. This model makes possible a frequency domain solution of the coupled equations of motion. The resulting response amplitude operators (RAO) can also be combined with a wave spectrum to obtain short-term statistical averages of the vessel's motions.





Figure 9. Data acquisition system in the control room

4. APPROACH OF MODEL STUDIES

The studies are conducted in two successive stages, namely Stage I, calibration (Figure 10) and Stage II, the actual model tests (Figure 11).

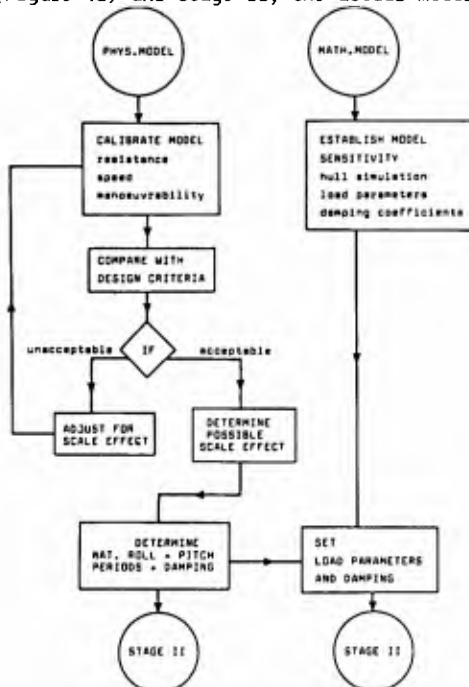


Figure 10. Approach of model studies - stage I

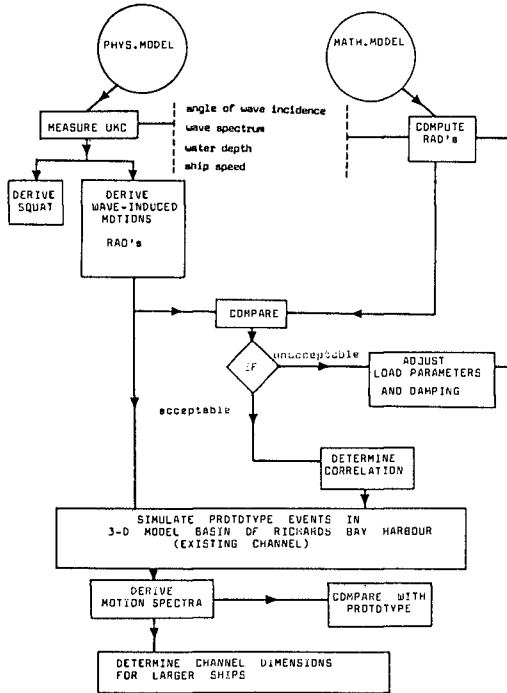


Figure 11. Approach of model studies - stage II

**Stage I** comprises the basic setting-up procedures and the calibration of the two model ships with respect to resistance in water, speed of advance and manoeuvrability. The natural periods of oscillation in roll and pitch as well as the damping coefficients as functions of water depth were also established for various load conditions.

Stage I also includes a series of sensitivity runs with the mathematical model. The experimentally derived natural periods and viscous damping coefficients will be used as input for the mathematical model runs of Stage II.

**Stage II** involves a series of model tests concentrated on the two ship sizes selected. The RAO's for the wave-induced vertical motions will be determined for the two ship sizes as function of angle of wave incidence, wave height and period, water depth and ship speed. The physical model test results will then be compared to predicted RAO's obtained from the mathematical model.

5. RESULTS OF MODEL CALIBRATION TESTS

At the time of the conference, most of the Stage I tests were completed with respect to the smaller model ship and the Stage II tests had just started.

The results of the towing resistance and model speed tests for the 150 000 dwt model ship are shown in Figure 12.

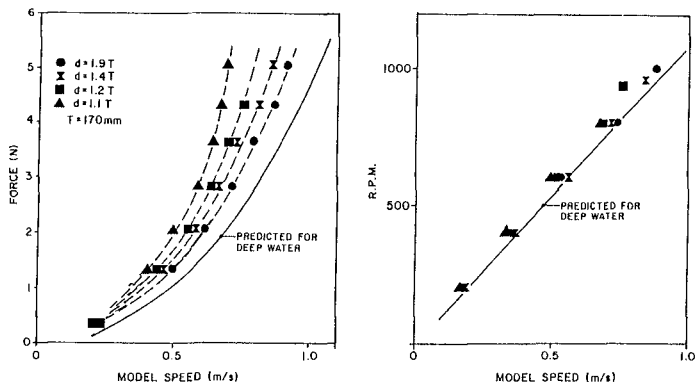


Figure 12. Model towing resistance and speed

The model's towing resistance for a depth-over-draught ratio of  $d/T = 1,9$  was found to agree reasonably closely to the predicted value for deep water. The model speeds for  $d/T = 1,9$  are about 10 per cent less than the calculated deep water values. Since  $d/T > 2$  is usually accepted to represent deep water conditions it means that the model's resistance is, perhaps, only slightly too high.

A significant reduction in speed, for the same propulsion force, is evident in shallower water. This reduction is also shown clearly by the relationship between propeller rpm and model speed (Figure 12).

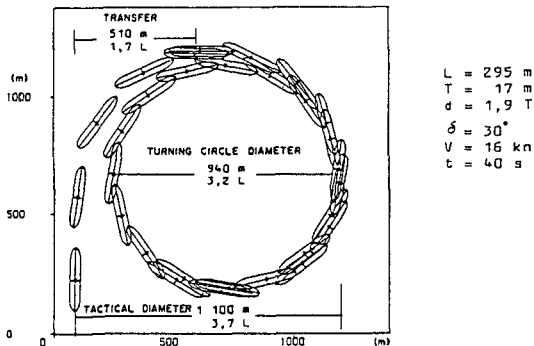


Figure 13. Results of turning circle test

A typical result of a turning circle test is shown in Figure 13. The diameter of the turning circle, the position of the point of maximum advance (transfer) and the tactical diameter are all in agreement with prototype data, obtained under similar conditions.

The effect of  $d/T$  on the model roll period and the damping coefficient is shown in Figure 14. The tests were done under full load conditions but with two different load distributions, resulting in 'deep' water roll periods of 1,26 and 1,66 s respectively.

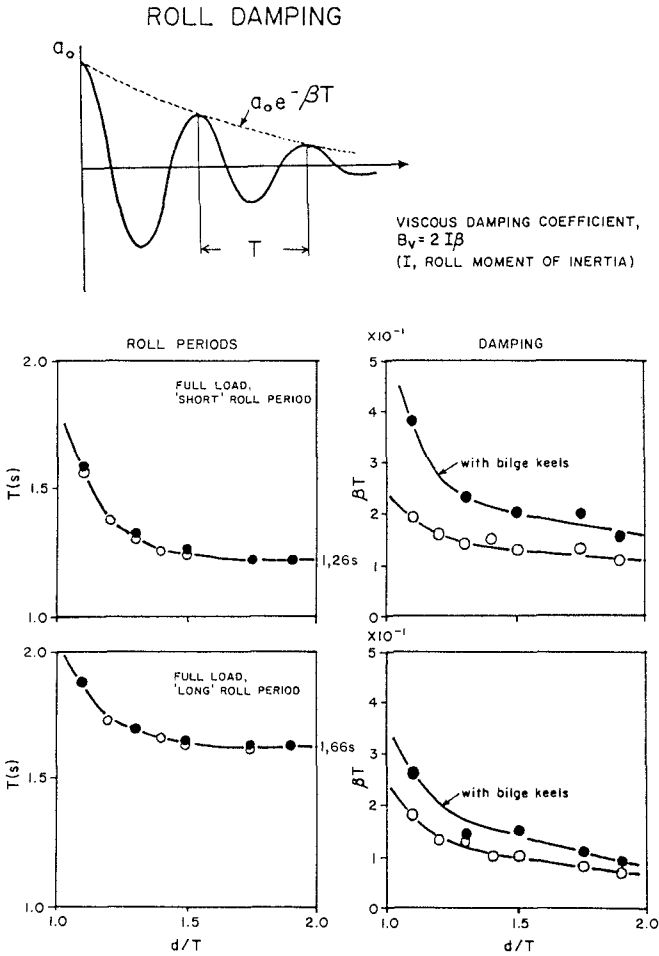


Figure 14. Roll periods and damping for various depth-over-draught ratios

The results show significantly longer roll periods for smaller under-keel clearance, particularly for the 'short' roll period case. A similar trend is visible for the damping coefficients which are much greater in shallower water.

As could be expected, the roll periods are not affected by the presence of bilge keels but the damping coefficients increase considerably (by 30 to 100 per cent) with the presence of bilge keels on the model ship.

#### 6. PRELIMINARY RESULTS OF ACTUAL MODEL TESTS

All the scale-model tests are conducted in unidirectional waves of various spectral shape. Angles of wave incidence will be varied in steps of  $15^\circ$  in the regions where the ship's response is very sensitive to wave direction and in steps of  $30^\circ$  for the remainder of the directions (Figure 15).



Figure 15. Model test run with  $90^\circ$  wave approach

Most of the tests are done with waves which have a spectral shape based on actual recorded wave spectra. Figure 16 shows 128 normalised spectra, recorded at Richards Bay. These cover conditions with  $H_{m0} = 1$  to  $= 5$  m and  $T_p = 11$  to  $17$  s, which are the most relevant conditions with regard to ship motions. The spectra are seen to be remarkably similar with quite a narrow variation, and the mean spectral shape was considered representative for conditions at Richards Bay. This spectrum was therefore used for most of the tests although tests with different spectral shapes are also done to check on sensitivity.

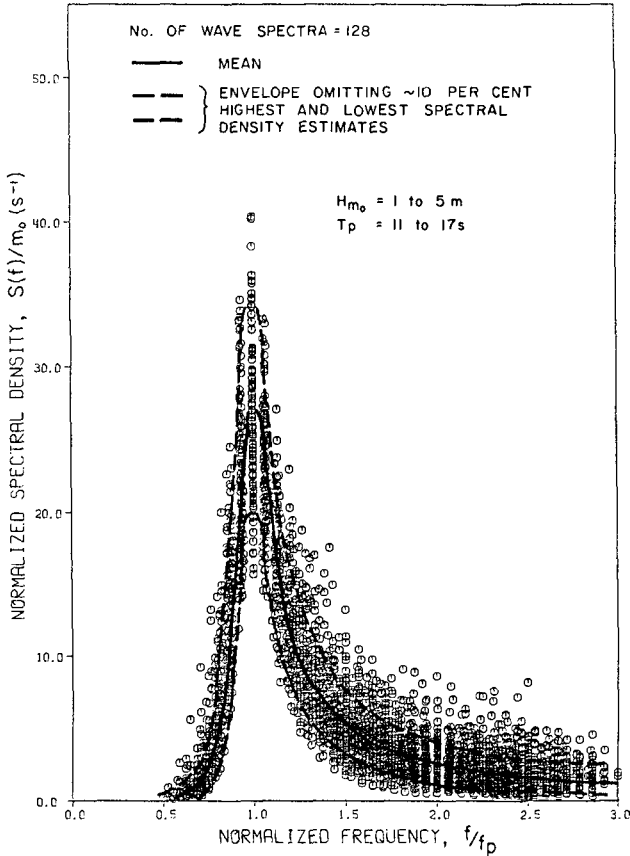


Figure 16. Normalized Richards Bay wave spectra

Sample amplitude response functions for the starboard and port shoulders of the 150 000 dwt model ship for beam waves are shown in Figure 17. These results are based on a model run of 20 m length. The amplitude response (RAO) was determined by dividing the response spectra by the wave input spectrum. Maximum response is seen to occur at about 13 s which is the ship's natural roll period for a depth-overdraught ratio of 1,3. A peak response (mainly roll because of beam waves) of 5 m/m was found for both shoulders.

Some preliminary results of the mathematical model are shown in Figure 18. This figure clearly shows the influence of wave direction on the ship's roll response.

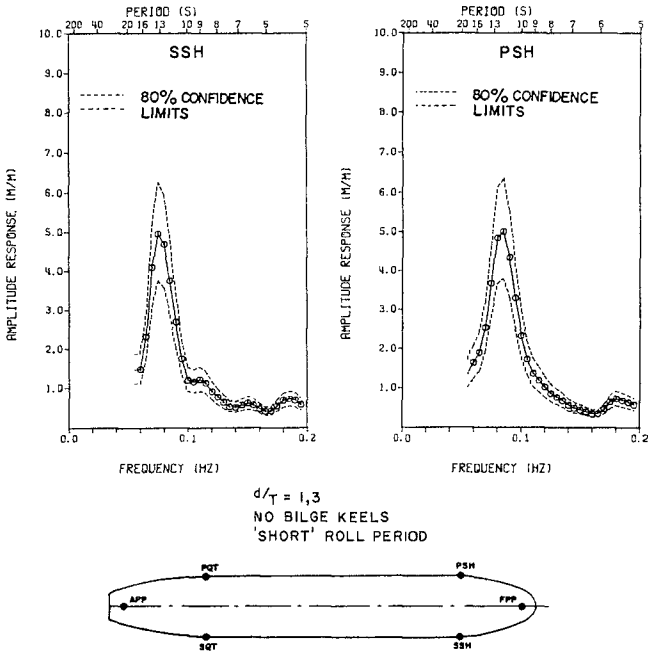


Figure 17. Sample amplitude response functions, 90° wave approach

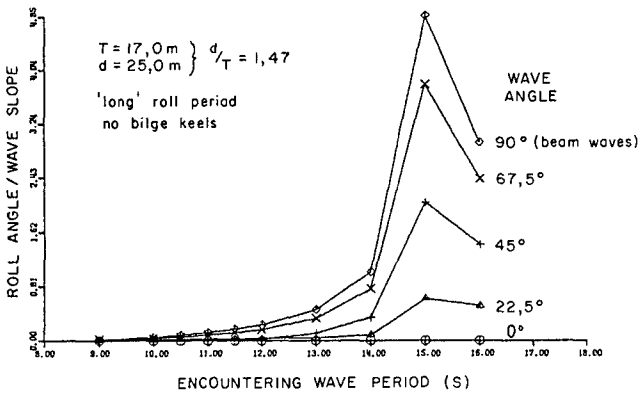


Figure 18. Mathematical model roll response for different wave directions

## 7. CONCLUDING REMARKS

The results of these studies will be applied to formulate allowance criteria on which to base optimum harbour usage under all wave conditions. This will serve to update and improve the present operational manual being used at Richards Bay harbour (Campbell and Zwamborn, 1984 and Zwamborn and Cox, 1982).

On completion of the basic tests, a series of tests are planned in a 1-in-100 scale model of the Richards Bay harbour entrance channel. These tests will involve simulation of prototype events/conditions to compare the 150 000 dwt model behaviour to field measurements as well as tests using the 270 000 dwt model to determine channel dimensions (dredging requirements) for possible future extensions.

## ACKNOWLEDGEMENT

The work described in this paper is carried out by the CSIR under contract for the South African Transport Services. Their permission to publish this paper is acknowledged with thanks.

## REFERENCES

- CAMPBELL, N P and ZWAMBORN, J A (1977). Special features in the design and construction of the new harbour for bulk cargoes at Richards Bay, Republic of South Africa. Proc. 24th PIANC Congress, Leningrad.
- CAMPBELL, N P and ZWAMBORN, J A (1984). Richards Bay harbour. Port Operation Manual, Mark I. PIANC Bulletin No. 45, Brussels.
- VAN WYK, A C (1982). Wave-induced motions in harbour entrances: a field study. Proc. 18th ICCE, Cape Town.
- ZWAMBORN, J A and VAN WYK, A C (1981). Monitoring of ship motions in the Richards Bay harbour entrance channel. Proc. 25th PIANC Congress, Edinburgh.
- ZWAMBORN, J A and COX, P J (1982). Operational procedures, Richards Bay harbour. Proc. 18th ICCE, Cape Town.



## CHAPTER TWO HUNDRED EIGHTEEN

SHIP WAVES IN SHALLOW WATER AND THEIR EFFECTS ON MOORED SMALL VESSEL

by

Katsuhiko Kurata\* and Kazuki Oda\*\*, M.ASCE

### ABSTRACT

The characteristics of ship-generated waves in shallow water and the motions of moored small vessel induced by the ship waves were investigated in a wide range of water-depth and ship-length Froude Numbers.

The maximum heights and periods of ship waves were obtained as functions of Froude Number. The relationships between maximum angular and translatory displacements of moored vessel and the maximum ship waves were determined.

### INTRODUCTION

The waves resulting from passages of ships have relatively large heights compared with their lengths, and hence the surface slopes of ship-generated waves are steep so as to cause large motions of small vessels moored at the structures adjacent to waterways such as wharves, quays and piers.

Since the pioneer's work by W.Froude, many experimental and theoretical studies about ship waves have been performed primarily in the fields of naval architecture and partly in coastal and harbor engineering. (1)-(3), (11), (13)-(15) The first theoretical treatment about ship waves was the application of the solution for the problem of "Waves generated by a point impulse moving with a constant speed on water surface", which gives the similar wave pattern to the actual one. (3), (13) Applying the thin ship theory and/or the slender body theory to the problems about flows around ships, the more strict solutions for the water surface undulations around ships can be obtained using the point source distributions or the Green's functions to satisfy the adequate boundary and radiation conditions under such assumptions that the beam and/or draft of ship are negligibly small compared with its length. (7), (18) More improved theories have been developed taking the effects of the curvature and thickness of ship-hull shape on the flow around the ship into account. (9), (19) Most of those studies in naval architecture, however, were conducted from the standpoint as to how the waves affected the resistances of ships. While, from the standpoint of coastal and harbor engineering, the significance of ship wave influences on the bank erosions of canals, the safety navigations and moorings of small vessels have been emphasized. (6), (10), (15), (17) In a harbor, a canal and a navigation channel the ship wave generated by a small tug boat has

---

\*Assist. Prof., Dept. of Civil Eng., Osaka City University

\*\*Dr., Prof., Dept. of Civil Eng., Osaka City University

Sugimoto-3, Sumiyoshi-Ku, Osaka 558, JAPAN

a significant influence on moored vessel rather than a large ship, because the small boat passes nearer the moored vessel with faster speed than the large ship. However, there are little quantitative data available on ship wave influences on moored vessel.

According to the results of model and field tests, the hydraulic model tests are efficient for investigating the ship waves because they yield the results similar to the prototypes.(16)

In the present paper, (1)the characteristics of ship waves generated by a large ferry boat and a small tug boat in relatively shallow water and (2)the motions of moored small cargo ship induced by the ship waves will be discussed.

#### MODEL TESTS

The model tests were carried out based on the Froude law of similarity at the Hydraulic Engineering Laboratory of Osaka City University, Osaka, Japan. The model scale was 1/60.

#### SHIP WAVES

Models of a car ferry boat and a tug boat were towed at various speeds in water of various uniform depths. A basin was approximately 40 m long and about 6 m wide.

The straight guide-rail was placed above the basin. The model ship was attached fore by short string to a carriage on the rail connected with a taut line which passed over pulleys at both ends of rail and was driven by an electric motor.(See Figs.1 and 2) The speed of ship was accurately computed from the time interval between marks made on charts during each advancing every 2 meters of ship.

The ship waves were measured by capacitance-type wave gages at five positions along a perpendicular to the sailing line as shown in Fig.3, and they were recorded on charts by using a multi-pens recorder.

The dimensions of towed ships, the ship speeds,  $V$ , and the water depths of basin,  $h$ , for the tests were listed on Table 1.

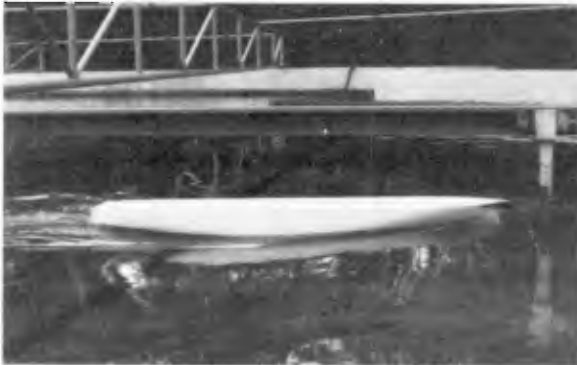


Fig.1 Model Ship Towed by Carriage

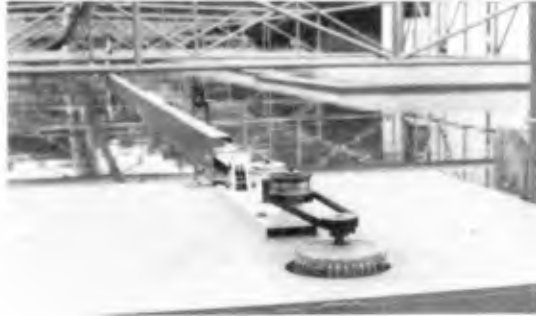
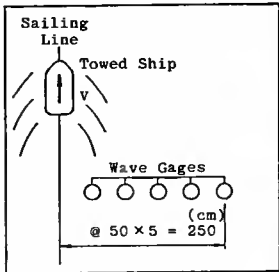
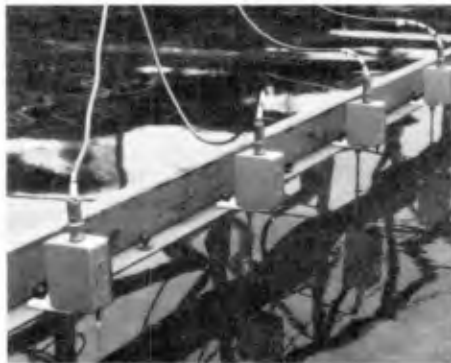


Fig.2 Electric-Motor and Pulleys



(a) Positions of Wave Gages



(b) Capacitance-Type Wave Gages

Fig.3 Wave Measurement

Table 1 Test Conditions for Ship Waves

	Ferry Boat (3624G.T.)	Tug Boat (199G.T.)
Length (cm)	136.7 (82m)	46.7 (28m)
Beam (cm)	24.3 (14.6m)	14.3 (8.6m)
Draft (cm)	9.8 (5.9m)	4.3 (2.6m)
Speed (cm/s)	55.6 - 188 (8.6knots - 29knots)	48.5 - 129 (7.5knots - 20knots)
Water Depth (cm)	14.6 - 24.6 (8.8m - 14.8m)	10.8 , 18.3 (6.5m , 11.0m)

( ) : in Prototype

MOTIONS OF MOORED VESSEL

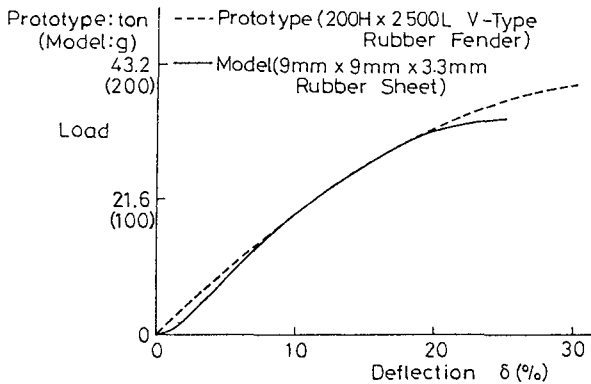
Model of small cargo ship was moored at a wharf in a usual manner with fenders and mooring lines. The model fender was made by rubber-sheet with 3.3 mm thickness, 9 mm length and 9 mm height. Its characteristic curve was similar to that of prototype as shown in Fig.4(a). Although the characteristic curve of mooring line in model, which was rubber-string with 0.9 mm square section, was different from that in prototype as seen in Fig.4(b), the slopes of tangents of those curves were almost the same each other in the test range so that the mooring line in model and prototype were considered to have the similar load-elongation relationships. Then, the rubber-string used in the tests was supposed to be suitable for the model of mooring line.

As the incident ship waves to the moored vessel were assumed the waves measured by a servo-type wave gage at a symmetrical position of the center of gravity of moored vessel, *C.G.*, in a state of rest with respect to the sailing line. (See Figs. 5 and 6)

The motions of moored vessel induced by the ship waves were measured by a ship-motion meter using potentiometers shown in Fig.7. Angular displacements around *C.G.* (rolling, pitching and yawing) and translatory displacements of *C.G.* (surging, swaying and heaving) were obtained from the measurements of current-variations through potentiometers installed at *C.G.* and at the upper carriage of the meter, which were linearly proportional to the vessel motions. (See Fig.8)

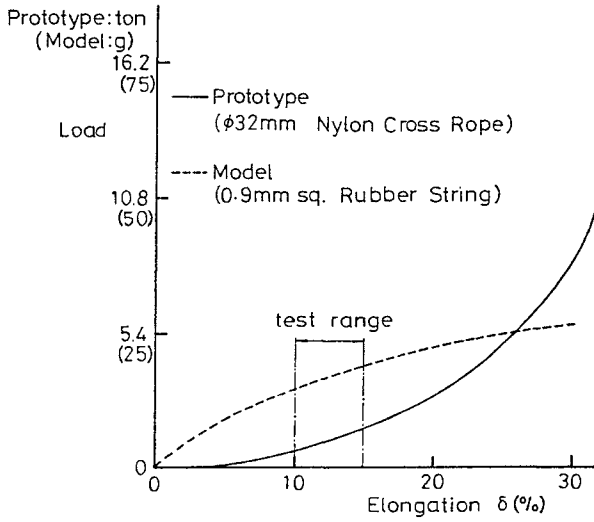
The ship waves and motions of vessel as shown in Fig.9 were recorded on magnetic-tapes by using a multi-channels data-recorder.

The dimensions of moored vessel and towed ship, the speeds of towed ship, *V*, the water depths at navigation channel, *h*, and at the wharf and natural periods of moored vessel motions were listed on Table 2.



(a) Fender

Fig.4 Characteristic Curves of Mooring Facilities



(b) Mooring Line

Fig.4 Characteristic Curves of Mooring Facilities

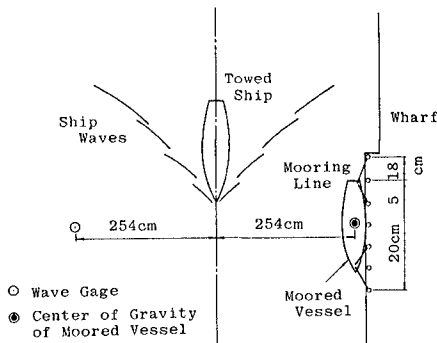


Fig.5 Model Set-Up



Fig.6 Servo-Type Wave Gage



Fig.7 Ship-Motion Meter



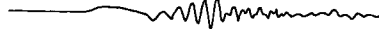
(a) Potentio-Meters Installed at *C.G.*



(b) Potentio-Meters Equipped on Upper Carriage

Fig.8 Measurement of Vessel Motion

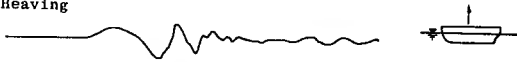
Incident Ship Wave ( $Fr = 0.86$ )



Pitching



Heaving



Rolling



Swaying



Fig.9 Time-Histories of Ship Waves and Vessel Motions

## RESULTS AND DISCUSSIONS

## DEFINITIONS

The maximum wave height,  $H_{max}$ , and the maximum wave period,  $T_{max}$ , in ship wave train were defined as Fig.10.(3) The maximum wave height is the vertical distance of the maximum crest above the following trough, and the maximum wave period is twice as long as the related time interval.

Maximum angular and translatory displacements of moored vessel were defined like the maximum wave height.

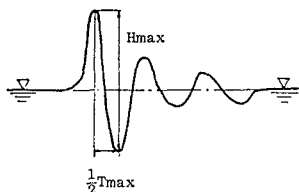


Fig.10 Definition of Maximum Ship Wave

Table 2 Test Conditions for Moored Vessel Motions

	Moored Vessel (Cargo Ship, 199G.T.)		Towed Ship (Ferry Boat, 3624G.T.)
Length (cm)	83.3 (50m)		136.7 (82m)
Beam (cm)	15.0 (9m)		24.3 (14.6m)
Draft (cm)	Full Condition	Light Condition	9.8 (5.9m)
	5.5 (3.3m)	2.3 (1.4m)	
Water Depth (cm)	8.2 (4.9m) at Wharf		18.3 (11m) at Navigation Channel
Speed (cm/s)	—		53 - 185 (8.2knots-29knots)
Natural Period (Moored at Wharf) (sec)			
	Full Condition	Light Condition	
Pitching	0.6 - 0.7 (4.6 - 5.4)	0.6 - 0.7 (4.6 - 5.4)	
Rolling	1.2 - 1.25 (9.3 - 9.7)	0.6 - 0.7 (4.6 - 5.4)	
Yawing	3.7 - 4.5 (28.7-34.9)	2.7 - 3.2 (20.9-24.8)	
Surging	1.75- 2.4 (13.6-18.6)	—	
Swaying	1.0 (7.7)	—	
Heaving	0.55- 0.65 (4.3 - 5.0)	0.45- 0.6 (3.5 - 4.6)	

( ) : in Prototype



MAXIMUM WAVE PERIOD

The diverging waves are predominant in the ship waves, which originate from the hump of water surface at the bow and the hollow at the stern advancing with together the ship. Then, the characteristic period  $T_0 = 2\pi V/g$  ( $g$ :acceleration of gravity) was introduced to represent the inherent period of waves generated by the ship going with the speed of  $V$ . The values of  $T_{max}/T_0$  indicate which the ship waves with period  $T_{max}$  are "deep water waves" or "shallow water waves", because  $T_0$  corresponds to the period of deep water wave with the phase velocity of  $V$ . The ratios of  $T_{max}$  to  $T_0$  were obtained as shown in Fig.11. Circles and triangles in Fig.11 denote the mean values of  $T_{max}/T_0$  for the cases of tug boat and ferry boat at each water-depth Froude Number,  $Fr = V/\sqrt{gh}$ , respectively. A hatched region means the results from field tests by Sorensen. (12)

In a region of  $Fr < 0.8$ , the mean values are approximately 0.8 to 0.9 for the tug boat and 0.6 to 0.8 for the ferry boat, and hence the ship waves are considered as the deep water waves. While, due to the definition of  $T_0$ , when  $Fr > 0.56$  the ship waves are expected as the shallow water waves. The discrepancy between the test and the theory may be due to the fact that the apparent propagation direction of ship waves is oblique to the sailing line so that the apparent propagation velocity is less than  $V$ . From Fig.11 it is clear that the model test results agree reasonably well with the field test results, and hence there are little scale effects on the test results found.

When  $0.8 < Fr < 1.0$ , the mean values are almost constant to be 0.9 to 1.0 for the tug boat and around 1.2 for the ferry boat. In this range the ship waves may have the characteristics of the shallow water waves.

The region of  $Fr > 1.0$  is called as the super-critical region where no waves have the greater phase velocity than the ship speed, because  $\sqrt{gh}$  corresponds to the maximum wave velocity which can exist in water of depth  $h$ . In this region only the diverging waves were observed and no transverse waves were seen. The mean values of  $T_{max}/T_0$  take the peak values at  $Fr \sim 1.0$  and decrease to become almost constant with  $Fr$ .

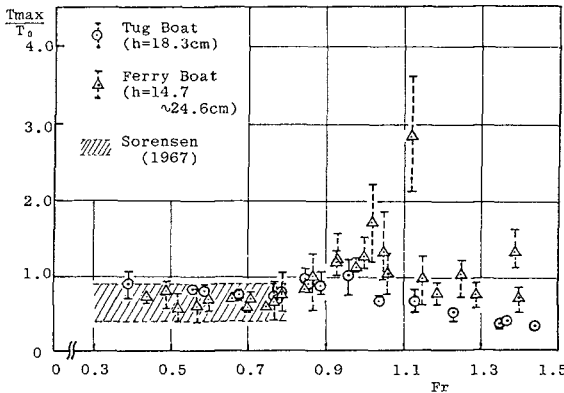


Fig.11 Ratios of  $T_{max}$  to  $T_0$

From the results in Fig.11, the ratio of  $T_{max}$  to  $T_0$  is supposed to relate only to Froude Number. Here, we let

$$T_{max}/T_0 = C \quad (1)$$

where  $C$  is a coefficient dependent upon  $Fr$ . Then

$$T_{max} = C \cdot 2\pi V/g \quad (2)$$

At a field far from a vertical cylinder in a steady free surface flow with a uniform current velocity,  $V$ , and a uniform depth,  $h$ , a wave number,  $k$ , of water surface undulation is approximately given as follows.(5)

$$\tanh kh/kh = A \cdot Fr^2 \quad (3)$$

$$Fr = V/\sqrt{gh} < 1.0$$

where  $A$  is a constant equal to 3/4 or 1/2.

The period of progressive wave,  $T$ , which has the same wave number as  $k$  obtained by Eq.(3), is yielded by using the small amplitude wave theory as Eq.(4).

$$T = (\sqrt{A}/\tanh kh) \cdot 2\pi V/g \quad (4)$$

If we put

$$T_{max} = T \quad (5)$$

then

$$C = \sqrt{A}/\tanh kh \quad (6)$$

The comparisons of the maximum wave periods  $T_{max}$  with the calculated periods  $T$  by Eqs.(3) and (4) are shown in Fig.12 for the cases of  $Fr < 1.0$ . The calculated values of  $T$  agree well with the values of  $T_{max}$ . The calculated values of  $\sqrt{A}/\tanh kh$  were approximately 0.9 to 1.0 for the tug boat and 0.7 for the ferry boat under the test conditions. Those values are in a good agreement with the values of  $C = T_{max}/T_0$  shown in Fig.11. From the comparisons of  $T_{max}$  with  $T$ , namely  $C$  with  $\sqrt{A}/\tanh kh$ , it may be concluded that (1) the wave period at the field far from the origin of waves have no reference to the draft and shape of the object producing the waves, (2) the maximum wave period can be theoretically estimated by using Eqs.(3) and (4) when the water-depth Froude Number is once determined. However, the difficulties still remain to decide precisely the value of the constant  $A$  for the specified ship-hull shape.

### MAXIMUM WAVE HEIGHT

The ship wave height is closely related to wave-making resistance of ship which varies with ship-length Froude Number,  $F_L = V/\sqrt{gLs}$  ( $Ls$  : ship length). (8) The maximum wave height is inversely proportional to a cubic root of a distance from the sailing line,  $x$ . (2), (4) Considering the facts above mentioned, the non-dimensional maximum wave height  $(H_{max}/B)(x/L)^{1/3}$  was introduced to be investigated their changes with  $F_L$ .  $B$  is a ship beam and  $L$  a wave length for the period  $T_{max}$  and the water depth  $h$ .

As shown in Fig.13, the non-dimensional maximum wave height for both the ferry and tug boats increase with  $F_L$  until critical value. At  $F_L \sim 0.5$  they attain the peak values. When  $F_L > 0.5$ , those values decrease with  $F_L$ . The changes of non-dimensional maximum wave heights with  $F_L$  seem similar to those of wave-making resistance coefficients as expected. Although the data show some scattering, it is clear that the non-dimensional maximum wave heights depend mainly upon the ship-length Froude Number but slightly upon the ratio of water depth to ship draft and the water-depth Froude Number.

### MOTIONS OF MOORED VESSEL

As shown in Fig.14, the ship waves are so small that the motions of moored vessel induced by them are also small in a region of  $Fr < 0.7$  to 0.8.

In a range of  $0.7 < Fr < 1.0$ , the wave height increases rapidly with  $Fr$ . The exciting force on the moored vessel might be considered proportional to  $H_{max}^2$ . As a sequence, the rolling and swaying motions of vessel rapidly increase with  $Fr$ . The cusp line, namely the apparent crest line, of ship waves approaches perpendicular to the bow-stern line of moored vessel, hence the pitching and surging motions become large. The ship waves with large height and long length go into the gap between the moored vessel and the wharf, and the phase lag between the exciting forces on the bow and the stern of the vessel cause the large yawing motion of vessel.

In the super-critical region of  $Fr > 1.0$ , the motions of moored vessel increase with  $Fr$  as well as the maximum wave period, although the maximum wave height decrease to become almost constant.

Thus, the motions of moored vessel seem to depend upon the wave heights, wave length and wave direction. The heaving motion, however, may be considered dependent upon the vertical motion of the water surface (wave height). The maximum heaving motion seems to have almost the same amplitude as the maximum wave in a range of  $0.6 < Fr < 1.4$  without regard to the wave conditions and the mooring conditions as presented in Fig.15.

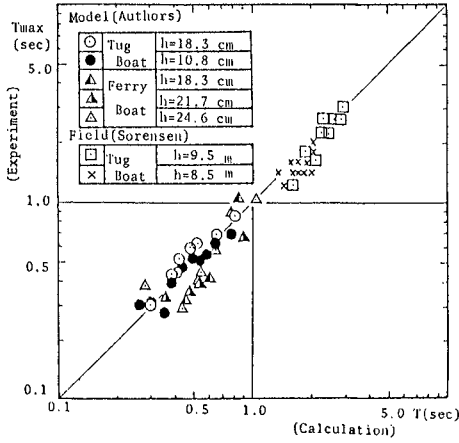


Fig.12 Comparisons of  $T_{max}$  with  $T$

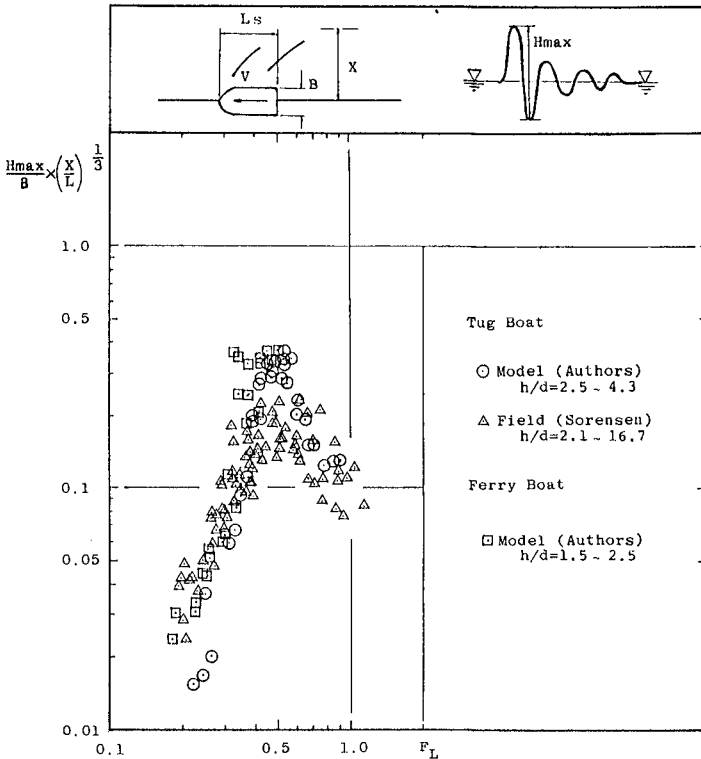


Fig.13 Non-Dimensional Maximum Wave Heights

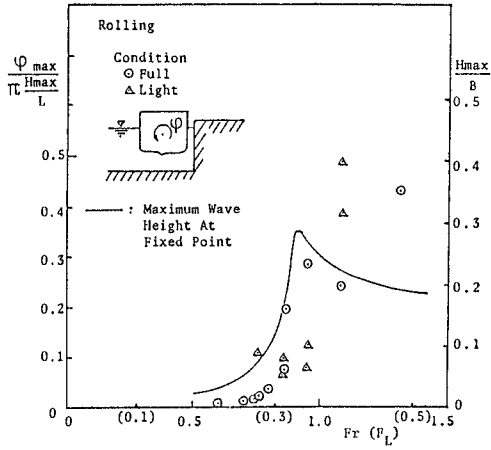


Fig.14 Maximum Rolling Motions of Moored Vessel

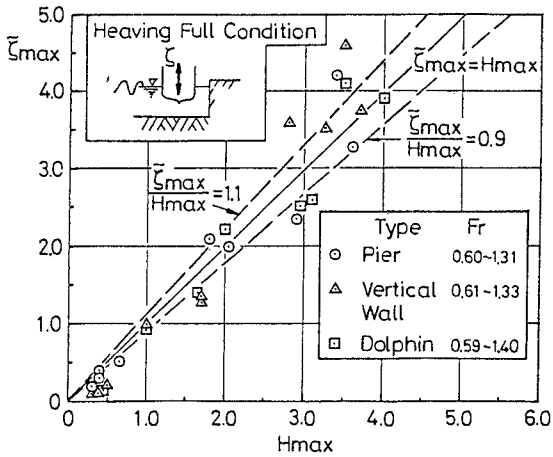


Fig.15 Maximum Heaving Motion of Moored Vessel

FOURIER TRANSFORMS

For analyzing the transient phenomena such as the ship waves and the moored vessel motions induced by them shown in Fig.9, the Fourier transform is generally used.

According to the results by the Fourier transforms of the incident ship waves and the motions of moored vessel, the motion of vessel resonate to have a large amplitude at the natural period in each mode as shown in Fig.16. At the period when the maximum amplitude of ship wave component occurs, the amplitude of motion of vessel is also large. From the results by the Fourier transforms, the response factors of moored vessel to the waves might be obtained. The moored vessel motion to the arbitrary incident waves may be predicted by using those factors.

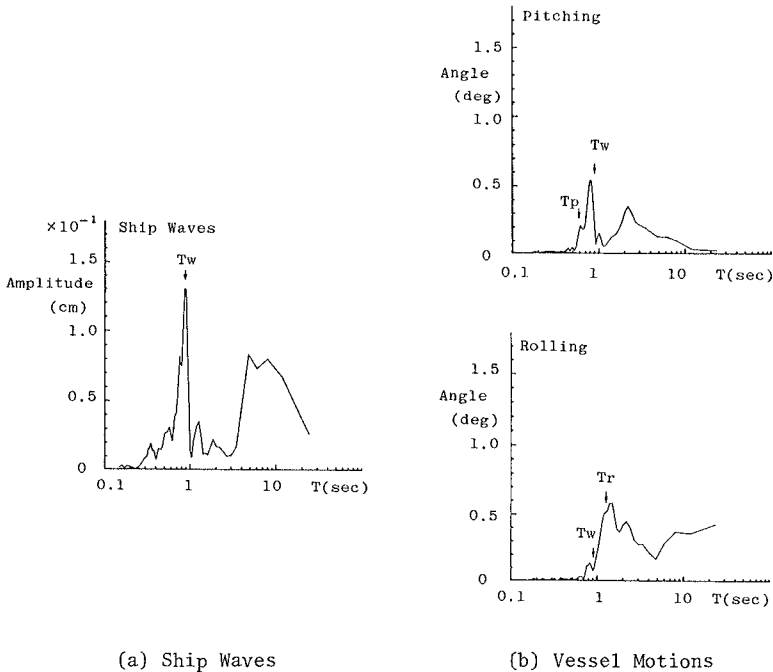


Fig.16 Fourier Amplitudes of Ship Waves and Vessel Motions

### CONCLUSIONS

The maximum height and the maximum period of ship wave and the motions of moored vessel induced by the ship waves were investigated in a wide range of the water-depth and ship-length Froude Numbers.

The maximum wave period is related to the water-depth Froude Number and can be estimated theoretically when its value is once specified.

The non-dimensional maximum wave height depends upon the ship-length Froude Number. The wave length refers to the wave period, which is decided by the water-depth Froude Number. Then, the maximum wave height is considered as a function of the ship-length and water-depth Froude Numbers.

The relationships between the maximum angular and translatory displacements of moored vessel and the maximum ship waves were obtained. The maximum displacements of vessel are related to wave height, wave period and wave direction.

The responses of moored vessel to the ship waves were investigated by using the Fourier transforms. The vessel motion responses are large at the natural period and at the period when the maximum amplitude of component wave occurs.

The influences of the passing ships, with the speeds of 10 knots or less (usually  $Fr < 0.5 \sim 0.6$ ) through fareways or navigation channels, are considered not to be significant on the small cargo ships moored at the wharves.

### ACKNOWLEDGEMENTS

The authors thank to Mr.T.Kimura, a technical staff, Mr.S.Hirai and Mr.A.Kitaura, post-graduate students, Mr.Y.Kouzaki and Mr.K.Matsui, under-graduate students of Dept. of Civil Eng., Osaka City University, for their help with conducting the tests.

REFERENCES

- (1) Brebner, A., P.C. Helwig and J. Carruthers : Waves Produced by Ocean-Going Vessels, A Laboratory and Field Study, Proc. of 10th Conf. on Coastal Eng., pp.455-465, 1966
- (2) Havelock, T.H. : The Propagation of Groups of Waves in Dispersive Media, with Application to Waves on Water Produced by a Traveling Disturbance, Proc. Roy. Soc., Ser. A 81, pp.398-430, 1908
- (3) Johnson, J.W. : Ship Waves in Navigation Channels, Proc. of 6th Conf. on Coastal Eng., pp.666-690, 1958
- (4) Kurata, K., K. Oda and S. Hirai : Ship Waves in Shallow Water and Their Effects on Moored Vessel, Proc. of 30th Japanese Conf. on Coastal Eng., pp.598-602, Nov. 1983 (in Japanese)
- (5) Kurata, K. : Free Surface Flow around Vertical Cylindrical Object, 1984 (unpublished)
- (6) Lee, T.T. : Ship Generated Waves in Navy Marina at Pearl Harbor, Tech. Rep. No.38, James K.K. Look Laboratory of Oceanographic Eng., Univ. of Hawaii, Apr. 1976
- (7) Mei, C.C. : Flow around a Thin Body Moving in Shallow Water, Jour. of Fluid Mech., Vol.77, Part 4, pp.737-751, 1976
- (8) Newmann, J.N. : Marine Hydrodynamics, 1980
- (9) Okamura, H., T. Inui and H. Kajitani : Analysis of Ship Waves Propagating on a Non-Uniform Flow, Jour. of the Soc. of Naval Architects of Japan, Vol.138, pp.37-45, Dec. 1975 (in Japanese)
- (10) Powell, A. and W.R. McCreight : Effect of Ship Waves on Vessels and Ocean Structures, US-JAPAN Conf. on Development and Utilization of Natural Resources, Tokyo, 1982
- (11) Saunders, H.E. : Hydrodynamics in Ship Design, Vol.1, Chap.10, p.168-p.184, The Soc. of Naval Architects and Marine Engineers, New York, 1957
- (12) Sorensen, R.M. : Investigation of Ship-Generated Waves, Jour. of the Waterways and Harbors Div., Vol.93, WW1, pp.85-99, ASCE, 1967
- (13) Sorensen, R.M. : Ship-Generated Waves, Advances in Hydroscience, Vol.9, p.49-p.83, Academic Press, New York, 1973
- (14) Stoker, J.J. : Water Waves, p.219-p.243, Interscience Publishers, New York, 1957
- (15) Takenouchi, Y. and K. Nanasawa : About "Gunkan-Nami" (Warship Wave) which Reaches on the Imabari Beach as Significant Breakers, The Jour. of the Oceanographical Soc. of Japan, Vol.17, No.2, pp.20-30, June 1961 (in Japanese)
- (16) Tanaka, H. et al. : Some Application of the Wave Analysis on the Geomi-Models and Their Actual Ship, Jour. of the Soc. of Naval Architects of Japan, Vol.126, pp.11-24, Dec. 1969 (in Japanese)
- (17) Tanaka, H. and H. Adachi : Influence of Waves due to Large Ship upon Small Ships and Ocean Structures, US-JAPAN Conf. on Development and Utilization of Natural Resources, Tokyo, 1982
- (18) Tuck, E.O. : Shallow-Water Flows Past Slender Bodies, Jour. of Fluid Mech., Vol.26, Part 1, pp.81-95, 1966
- (19) Ursell, F. : On Kelvin's Ship-Wave Pattern, Jour. of Fluid Mech., Vol.8, Part 3, pp.418-431, 1960





## SUBJECT INDEX

Page number refers to first page of paper.

- Adjustment, 3180  
Airport runways, 2693  
Analytical techniques, 968, 1161  
Armor units, 2487, 2500, 2563, 2580,  
2592, 2608, 2760  
Asphalts, 2680  
Asymmetry, 1016  
Australia, 1522, 1952, 2751, 3148
- Bank erosion, 3213  
Barrier islands, 2339, 3051  
Bathymetry, 2635  
Beach cusps, 1311  
Beach erosion, 257, 1553, 1584, 1650,  
2140, 2536  
Beach nourishment, 1471, 1522, 2140  
Beaches, 1, 328, 678, 708, 1016, 1342,  
1386, 1420, 1539, 1732, 1879, 1896,  
1968, 1983, 1997, 2124, 2150, 2165  
Beaches erosion, 1244  
Bed load, 1325  
Bed load movement, 1252, 1306  
Bed ripples, 2293  
Bed roughness, 1149  
Bedforms, 1952  
Boating, 1635  
Boundary conditions, 858, 1057  
Boundary layer, 1161  
Boundary layer flow, 2232, 2293  
Breaking waves, 15, 31, 82, 649, 912,  
1016, 1132, 1420  
Breakwaters, 741, 1715, 1929, 2008,  
2107, 2451, 2467, 2487, 2530, 2648,  
2680, 2737, 2751, 2760, 2773
- Caissons, 2920  
Calibration, 3180  
California, 577, 886, 2827  
Case reports, 2530, 3148  
Channel improvements, 1863  
Channels, waterways, 2063, 3078,  
3157, 3172, 3213  
Cnoidal waves, 1118  
Coastal engineering, 1, 217, 831  
Coastal morphology, 625, 1437  
Coastal processes, 516, 1600, 1650,  
1830, 1913, 2380, 3094  
Coastal structures, 15, 316, 2635,  
2827, 2875  
Cohesive sediment, 2985  
Compaction, 2737  
Computation, 955
- Concrete, 2592  
Conformal mapping, 1192  
Continental shelves, 1799, 1952, 2346  
Cooling water, 2909  
Core walls, 2487  
Currents, 983, 1073, 1103, 1132, 1161,  
2232, 2263, 2346, 2363, 2397, 2857  
Cylinders, 2710, 2857
- Damage assessment, 1539, 2773  
Data collection, 243, 304  
Deep water, 661  
Deltas, 1600  
Design, 2737  
Design criteria, 31, 2563, 2827  
Design waves, 362, 3227  
Differential equations, 1057  
Diffusers, 3134  
Dikes, 199, 316  
Dissipation, 2810  
Drainage, 532  
Dredge spoil, 2042  
Dredging, 1668, 1816, 1863, 3078,  
3157, 3172  
Dunes, 1553, 1584  
Dynamic analysis, 2952  
Dynamic response, 2952
- Eddy viscosity, 2263  
Effluents, 3094, 3134  
Energy conversion, 2546, 2875  
Energy dissipation, 54, 82, 649, 968  
Erosion, 1600  
Erosion control, 2536  
Estuaries, 199, 782, 1863, 2181, 2985,  
3001, 3067, 3078, 3109, 3180  
Exploration, 831
- Failures, investigations, 2773  
Fatigue, 2592, 2726  
Fiber reinforced materials, 2592  
Field investigations, 1765, 1786, 1830  
Field tests, 678  
Finite differences, 846, 858  
Finite element method, 1090, 1209  
Fisheries, 2091  
Fjords, 3124  
Floating breakwaters, 2514, 2663  
Floating structures, 15  
Flow resistance, 1306  
Forecasting, 452

- Geophysical surveys, 2635
- Grain size, 2322
- Gravity waves, 1028, 1073, 1103
- Great Barrier Reef, 226
- Great Lakes, 1571, 1635, 1929
- Groins, 1522
- Groins, structures, 2026, 2107
- Gulf of Mexico, 2339
  
- Harbor engineering, 2842
- Harbor structures, 1635
- Harbors, 846, 929, 1040, 1929, 2091, 2933, 3244
- Houses, 1539
- Hurricanes, 147, 162, 243, 257
- Hydraulic models, 3180
- Hydrodynamics, 226, 831, 2857
- Hydroelectric power generation, 1252
  
- Inlets, waterways, 1360, 1668, 3017
- Intakes, 2909
- Integral equations, 2810
  
- Japan, 1403, 2536
- Jetties, 2500
  
- Laboratory tests, 724, 1311, 1715, 2124, 2192
- Lakes, 1571
- Littoral currents, 2192, 2208, 2363, 3197
- Littoral drift, 1291, 1454, 1488, 1765, 1786, 1846, 2140
- Load combinations, 2857
  
- Marinas, 2530
- Mass transport, 1149, 2124, 2434
- Mathematical models, 1437, 1685, 1732, 2192, 2363, 3109
- Measurement, 2077
- Mediterranean Sea, 1600
- Mixing, 3094, 3124, 3134, 3197
- Model studies, 2773
- Model verification, 1178, 1342, 2773
- Models, 147, 501, 831, 858
- Monitoring, 1816, 2077, 2500
- Morphology, 2165
- Movable bed models, 1227, 1342, 2322
  
- National Flood Insurance Program, 217
- Navigation, 1635
- Nearshore circulation, 383, 1252, 1371, 1507, 1703, 1732, 1786, 2208, 2280, 2363
- Netherlands, 625, 1830, 2026
- Nile River, 1600
- North Sea, 1749, 1816
- Norway, 2346
- Nuclear density meters, 3172
- Numerical analysis, 1584
- Numerical calculations, 1040, 1161
- Numerical models, 15, 174, 190, 226, 501, 815, 846, 1057, 1118, 1244, 1553, 2414, 2434, 3034
  
- Ocean disposal, 3134
- Ocean Waves, 1, 383
- Offshore drilling, 831
- Offshore structures, 2693
- Oscillations, 132, 625, 846, 929, 1559, 2933
- Outwash, 2339
- Overtopping, 316, 532
  
- Permeability, 2487, 2608, 2620
- Photogrammetry, 2500
- Pile structures, 2952
- Piles, 2530, 2892
- Plates, 2909
- Pollutants, 3094, 3124
- Polyethylene, 3148
- Porosity, 2487
- Pressure gages, 271, 755
- Probability, 162
- Probability distribution, 415, 516, 532, 610, 741
- Profiles, 1342, 1386, 1507, 1522, 1879, 1913, 1940, 1983, 2124, 2232
- Prototypes, 243
  
- Quays, 929
  
- Radioactive tracers, 2042, 2063
- Radioisotopes, 1252, 2063
- Random waves, 593, 649, 1420
- Reconstruction, 2760
- Reefs, 2648, 2693
- Rehabilitation, 2467
- Reliability analysis, 2451
- Repairing, 2773
- Reservoir storage, 532
- Resonance, 846
- Response time, 2150
- Reynolds stress, 42
- Rigid-body dynamics, 2663
- Rip currents, 2091
- Rivers, 3034
- Roughness, 2710
- Rubble-mound breakwaters, 2451, 2563, 2580, 2592, 2620

- Safety, 2451  
Saline water-freshwater interfaces, 2971  
Sand, 1265, 1282, 1765, 2063, 2293, 2322, 2737  
Sandbars, 2140  
Scale effect, 1227, 2322, 2487  
Scale models, 1386, 3180  
Scour, 1715  
Sea floor, 1132, 1192, 1403, 1685, 1715, 1952  
Sea level, 886, 899  
Sea state, 501, 610, 798  
Sea walls, 316, 532, 1522, 2536  
Secondary flow, 2414  
Sediment, 1371, 1403, 1799, 1968, 2008  
Sediment concentration, 1325, 1618, 2077, 2310  
Sediment deposits, 2181  
Sediment transport, 1244, 1252, 1282, 1325, 1420, 1454, 1488, 1559, 1600, 1703, 1732, 1765, 1830, 1952, 1997, 2063, 2077, 2280, 2985  
Sedimentation, 1227, 1816, 3017, 3051  
Sewage disposal, 3134  
Shallow water, 287, 370, 435, 547, 649, 724, 999, 1057, 1209, 2892, 3258  
Shear stress, 1685, 1799  
Ship motion, 2514, 3213, 3227, 3244, 3258  
Shipping, 2077, 3172  
Shoaling, 798, 1016, 1118, 1863, 2091  
Shore protection, 1650  
Shoreline changes, 257, 1227, 1244, 1403, 1522, 1571, 1913, 2107, 2165, 3034  
Simulation, 770  
Simulation models, 1584, 2842  
Slope stability, 2620  
Slope stabilization, 2680  
Slopes, 328, 593, 708, 1132, 2124  
Small crafts, 1635, 2842, 3258  
Solitons, 435  
Spatial distribution, 383  
Spectral analysis, 484  
Stability, 2500, 2608, 2620, 2693  
Stability analysis, 1360  
State-of-the-art reviews, 2751  
Statistical analysis, 516  
Statistics, 345, 642, 770  
Steady flow, 2280, 2608  
Stochastic processes, 199  
Stones, 2580, 2648  
Storm surges, 115, 162, 174, 190, 199, 243, 257, 886, 899, 1209, 1584, 1749, 2346  
Storms, 1539  
Structural design, 2563  
Submarine pipelines, 3148  
Surf beat, 724, 871  
Surf zone, 42, 54, 70, 99, 625, 1765, 1786, 1846, 1940, 1997, 2150, 2363  
Surface waves, 271, 1073, 1103  
Surveying, 1879  
Suspended load, 1325  
Suspended sediments, 1765, 1786, 1846, 1983, 2181, 2310, 3067  
Taiwan, 452  
Tidal effects, 115, 1846  
Tides, 115, 1749  
Time series analysis, 1968, 2150  
Tombolo, 1403, 2008  
Topography, 1732, 2165  
Transport phenomena, 1265, 1282  
Transport rate, 1291, 1325  
Tropical cyclones, 2339  
Tsunamis, 132, 815  
Turbidity, 3172  
Turbulence, 42, 70, 99, 3197  
Turbulent boundary layers, 2380, 2397  
Turbulent flow, 2310  
Two-dimensional, 2434  
Typhoons, 115, 561  
Undertow, 2246  
Underwater pipelines, 2726  
Water depth, 516, 1028, 1103, 2008  
Water flow, 2487  
Water level fluctuation, 1571  
Water quality, 3001, 3109  
Water speed, 912  
Water surface, 955  
Water tunnels, 1559  
Wave attenuation, 54, 2514, 2933  
Wave climatology, 287, 304, 577, 782  
Wave diffraction, 999, 1040, 1090, 1178  
Wave energy, 70, 328, 399, 941, 968, 2546, 2760, 2810, 2875  
Wave equations, 941  
Wave forces, 2710, 2726, 2892, 2920  
Wave generation, 642  
Wave groups, 642, 661, 695, 724, 770, 798  
Wave height, 31, 54, 328, 345, 362, 415, 452, 561, 610, 741, 968, 1028, 1118, 2933, 3227

- Wave measurement, 271, 399, 755
- Wave pressure, 741
- Wave propagation, 435, 1178
- Wave reflection, 467, 1040
- Wave refraction, 968, 999, 1040, 1090, 1103, 1118, 1178
- Wave runup, 328, 399, 415, 593, 678, 708, 1553, 1896, 1968, 1997
- Wave spectra, 362, 370, 467, 484, 501, 547, 661, 678, 755, 1040, 2208
- Waves, 316, 345, 516, 955, 983, 1057, 1161, 2008, 2232, 2397, 2857, 2909, 2952
- West Germany, 3051
- Wind, 516, 1265, 2263
- Wind direction, 782
- Wind speed, 2220.

## AUTHOR INDEX

Page number refers to first page of paper.

- Abe, Tetsuo, 132  
Adriaanse, M., 3001  
Ahrens, John P., 2648  
Alexander, H. C., 2726  
Allen, P. L., 2726  
Anima, Roberto J., 2635  
Aoki, S., 2933  
Asano, Toshiyuki, 2397, 2857
- Bailard, J. A., 1454  
Baird, W. F., 1929, 2563, 2580  
Bakker, W. T., 1161, 2026  
Barthel, V., 782, 798  
Basco, David R., 99  
Battjes, J. A., 642, 649, 1420  
Beaulieu, G. T., 1929  
Behnke, Daniel L., 2760, 2773  
Behrendt, Lars, 941, 1090  
Benassai, E., 2920  
Bernard, A., 2737  
Binglai, Zhao, 741  
Birkemeier, William A., 1507, 1913  
Blake, W., 1471  
Bode, L., 226  
Bode, Lance, 2434  
Bodge, Kevin R., 755  
Boer, S., 1437  
Booij, N., 1178  
Borgman, Leon E., 162  
Botes, W. A. M., 846  
Bowen, A. J., 1703  
Bretschneider, Charles L., 147  
Briggs, Michael J., 484  
Buchan, S. J., 287  
Burcharth, Hans F., 2592, 2608  
Butler, H. Lee, 162, 815, 858
- Caillot, A., 2042, 3172  
Carlson, Christopher T., 399  
Carmel, Zev, 1282  
Carpentier, R. L., 2737  
Cayan, Daniel R., 577, 886  
Chambellan, D., 3172  
Chen, Yang Yih, 1028  
Chien, C. C., 561  
Chow, S. C., 2909  
Christensen, Derald R., 2663  
Christoffersen, J. B., 1103  
Chu, Hsao-Ling, 1118  
Chun, Robert S., 2693  
Clausner, James, 2500  
Coeffe, Y., 1209
- Coffey, Felicity C., 2232  
Cokelet, E. D., 3124  
Cooper, Cortis K., 2346  
Courtois, G., 2042  
Cox, Jack C., 2773
- Dal Secco, S., 1209  
Dally, William R., 82  
Dalrymple, Robert A., 82, 999, 1650  
Davidsen, Elias, 501  
Davison, A., 2063  
de Jong, H., 3078  
de Jong, P., 3180  
De Rouck, J. N., 2737  
de Smit, C., 2026  
de Vriend, H. J., 1437  
Dean, Robert G., 82, 755, 1584  
Deguchi, Ichiro, 1325  
Derks, H., 1830  
Dette, Hans H., 3134  
Dick, Jennifer E., 1650  
Dingemans, M. W., 1178  
Dingler, John R., 2635  
Doering, J. C., 1703  
Dold, J. W., 955  
Douglass, Scott L., 316  
Downing, John P., 1765, 1786  
Doyle, Lynn C., 1539  
Drapeau, Georges, 1252  
Dube, S. K., 190
- Ebbesmeyer, C. C., 3124  
Edge, Billy L., 1635  
Efthimiou, Nico, 2892  
Elgar, Steve, 770  
Elliott, R. C. A., 3067  
Erchinger, Heie Focken, 2140  
Esposito, P., 1209
- Falconer, Roger A., 2414  
Fisher, J. S., 1553  
Fisher, John S., 1635  
FitzGerald, Duncan M., 3051  
Flick, Reinhard E., 886  
Flor, Thomas H., 243  
Forman, James W., Jr., 1668  
Foster, D. N., 2751  
Fox, William L., 1539  
Fry, William G., 217  
Funke, E. R., 782
- Gable, Christopher G., 1879

- Gaillard, P., 1040  
 Garrow, Holly C., 2165  
 Gebert, Jeffrey A., 2500  
 Gerritsen, F., 625, 3078  
 Geustyn, L. C., 2546  
 Golik, Abraham, 1282  
 Gordon, A. D., 1952  
 Gordon, Angus D., 1799  
 Gourlez, P., 2042  
 Green, M. O., 2150  
 Groeneveld, R. L., 2451, 2467  
 Guimarães, J. C., 1342  
 Guza, R. T., 31, 708, 770
- Hagiwara, Kazuhiro, 2810  
 Haines, John W., 2280  
 Hall, K. R., 2580  
 Hall, Kevin R., 2563  
 Hallermeier, R., 1227  
 Hanes, Daniel M., 1306  
 Hansen, J. Buhr, 2246  
 Hansen, M., 1471  
 Hanson, Hans, 2107  
 Hardy, Thomas A., 162  
 Harikai, Soichi, 2107  
 Hayter, E. J., 2985  
 Headland, John R., 1118  
 Hemsley, J. Michael, 304  
 Herbich, John B., 3213  
 Hino, Mikio, 1192  
 Hoffman, J. G., 1952  
 Holman, R. A., 708, 1896, 1968  
 Holman, Robert A., 1913, 1940  
 Horikawa, Kiyoshi, 1265  
 Hoslin, R., 2042  
 Hotta, Shintaro, 1265  
 Houston, J. R., 1244  
 Houston, James R., 815  
 Howd, P. A., 1968  
 Hsu, S. A., 2220  
 Hubertz, Jon M., 2208  
 Hudspeth, Robert T., 1488, 3197  
 Hughes, Steven A., 383  
 Huizinga, P., 846, 3109  
 Hulsbergen, C. H., 2026  
 Huntley, David A., 871  
 Hutchinson, P. S., 2530  
 Hwang, Paul A., 1016  
 Hwung, H. H., 2909
- Ijima, Takeshi, 929  
 Inman, Douglas L., 1282, 1600  
 Irie, Isao, 1715, 1846  
 Ishida, Hajime, 2952  
 Ismail, Nabil M., 1073  
 Isobe, Masahiko, 467
- Ito, Masahiro, 1386  
 Iwagaki, Yuichi, 593, 2124, 2397,  
 2857  
 Iwata, Koichiro, 415
- Jackson, L. A., 3148  
 Jaffe, Bruce E., 1983  
 Jenkins, Scott A., 1600  
 Jensen, Robert E., 547  
 Jonsson, I. G., 1103  
 Jonsson, Ivar G., 941, 1090, 2310  
 Juang, Jea-Tzyy, 452
- Kamphuis, J. W., 2322  
 Kana, Timothy W., 3017  
 Kaneko, Arata, 1311  
 Karelse, M., 3001  
 Katoh, Kazumasa, 1846  
 Katori, Sadakazu, 1265  
 Kawata, Yoshiaki, 115  
 Kerckaert, P. A., 2737  
 Kim, Chang S., 871  
 Kimura, Akira, 532  
 King, David B., Jr., 1559  
 Kirby, James T., 999  
 Kit, Elizzer, 2842  
 Kjeldsen, Soren Peter, 15  
 Kögel, U., 3157  
 Komiya, Yoshihiro, 1403  
 Konda, Yoshinori, 2952  
 Kondo, Hideo, 2875  
 Kondo, Kosuke, 467  
 Kostense, J. K., 724  
 Kraus, Nicholas C., 2107  
 Kriebel, David L., 1584  
 Kubo, M., 2933  
 Kubota, Susumu, 1265  
 Kuijper, C., 3180  
 Kuik, A. J., 1178  
 Kurata, Katsuhiko, 3258
- Latteux, B., 1209  
 Le Mehaute, Bernard, 345  
 Lee, Dong-Young, 271  
 Lee, J. J., 983  
 Leendertse, Jan J., 831  
 Leeuwenstein, W., 1685  
 Liang, N. K., 561  
 Lillevang, Omar J., 2773  
 Lin, Ming-Chung, 3034  
 Liu, Paul C., 362  
 Liu, Philip L. -F., 999  
 Liu, Shiao-Kung, 831  
 Lo, Jen-Men, 147  
 Long, Bernard, 1252  
 Lopez, N., 2680

- Lundgren, H., 501
- McCarthy, M. J., 2680  
Macdonald, H. V., 1522  
McDougal, William G., 1488, 3197  
Machen, P. C., 912  
Mangor, Karsten, 1816  
Mansard, E. P. D., 798, 2487  
Mardapitta-Hadjipandeli, Lida, 2414  
Mase, Hajme, 593  
Mason, Curtis, 1913  
Mason, L. B., 226  
Massias, J., 2042  
May, S. K., 2150  
Mehta, A. J., 2985  
Meyer, G., 3172  
Miller, Robert W., 2663  
Mimura, Nobuo, 2293  
Mizuguchi, Masaru, 678  
Mol, A., 2451, 2467  
Müller, F. P. J., 2546  
Murray, Stephen P., 2263
- Nadaoka, Kazuo, 1192, 1715  
Nairn, R. B., 2322  
Nakano, Wataru, 2971  
Nath, John H., 2710  
Nathan, Robert A., 577, 2827  
Navntoft, Erling, 1816  
Nece, Ronald E., 2514  
Nelson, Arthur R., 661  
Nielsen, Alexander F., 1799  
Nielsen, Peter, 968, 2232  
Nieuwenhuys, E. H., 2467  
Nishioka, Yōichi, 1732  
Noda, Edward K., 2693  
Noda, Hideaki, 2008  
Nummedal, Dag, 3051
- O'Brien, Morrrough P., 1  
Ochi, Michel K., 516  
Oda, Kazuki, 3258  
Ogawa, Yoshinobu, 328  
Ohlmeyer, F., 3157  
Okuzono, Hideaki, 929  
Overton, M. F., 1553
- Pae, Wi-Gwang, 2124  
Patterson, D. C., 1522  
Peiji, Huang, 741  
Penland, Shea, 2339, 3051  
Peregrine, D. H., 955  
Pilarczyk, K. W., 2620  
Ploeg, J., 2487  
Powell, John D., 1559  
Prandle, D., 3094
- Prater, Mark D., 162  
Prestedge, G. K., 2546  
Provis, D. G., 287
- Quesney, M., 2042
- Radder, A. C., 1178  
Raichlen, F., 983  
Raichlen, Fredric, 2760, 2773  
Raudkivi, A. J., 2530  
Read, W. W., 695  
Renger, Eberhard, 2077  
Retief, G. de F., 2546  
Rhodes, Perry A., 217  
Richmond, Bruce M., 1997  
Roelfzema, A., 3001, 3180  
Roelse, P., 2026  
Roelvink, J. A., 1618  
Rohde, Hans, 899  
Rosen, Dov Sergiu, 2842  
Roy, G. D., 190  
Russell, K. S., 846
- Saeki, Hiroshi, 1132  
Sakai, Shigeki, 1132  
Sakai, T., 42  
Sakuramoto, Hiroshi, 2091  
Sallenger, A. H., Jr., 1896  
Sallenger, Asbury H., 1913, 1983  
Sallenger, Asbury H., Jr., 1940, 1997  
Sánchez-Arcilla, A., 610  
Sandanbata, I., 42  
Sas, Marc, 199  
Sasaki, Tamio O., 2091  
Sato, Shinji, 2293  
Sauzay, G., 2042  
Savage, R. P., 257  
Sawaragi, Toru, 415, 1325  
Sayão, S. F. J., 1342  
Schaper, H., 1057  
Schiller, Robert E., Jr., 3213  
Schmeltz, E. J., 2680  
Scott, Susan C., 243  
Sedivy, Dean G., 661  
Segura, J. J. Avitia, 2933  
Seyama, Akira, 532  
Seymour, R. J., 770  
Seymour, Richard J., 577, 1559, 2827  
Sheng, Y. P., 858  
Sheng, Y. Peter, 2380  
Shi, N. C., 1786  
Shigemura, Toshiyuki, 1403  
Short, A. D., 2150  
Shuto, Nobuo, 328  
Siefert, Winfried, 1749  
Sill, Ben L., 1635



- Silvester, Richard, 1291  
 Sinha, P. C., 190  
 Skafel, M. G., 1929  
 Skjelbreia, Norman K., 2514  
 Skovgaard, Ove, 1090  
 Sleath, J. F. A., 1149  
 Sobey, R. J., 695  
 Sobey, Rodney J., 2434  
 Sorensen, Robert M., 3227  
 Sørensen, Torben, 1816  
 Sparboom, Uwe, 2892  
 Stark, K. P., 226  
 Staub, Carsten, 2310  
 Stauble, D. K., 1471  
 Steedman, R. K., 287  
 Sternberg, R. W., 1786  
 Sternberg, Richard W., 1983  
 Stewart, R. J., 3124  
 Stive, M. J. F., 70, 649, 1178, 1420, 1830  
 Strange, R. Rea, III, 577, 2827  
 Stroud, S. A., 287  
 Struijk, A. J., 3001  
 Su, Jilan, 2181  
 Suter, John R., 2339  
 Svasek, J. N., 2026  
 Svendsen, I. A., 54, 2246  
 Svendsen, Ib A., 99, 2310  
 Swain, A., 1244  
 Swart, D. H., 1371, 2546  
 Swartzmiller, James A., 1635  
  
 Takasugi, Jouji, 1403  
 Tamaye, Elaine E., 2693  
 Tanaka, Hiroyoshi, 2363  
 Tanaka, Norio, 1846  
 Tang, F. L. W., 2909  
 Tang, Frederick L. W., 452, 1028  
 Tanguy, J. C., 3172  
 Thompson, Alex C., 2608  
 Thompson, Warren C., 661  
 Thornton, E. B., 31, 708  
 Timco, G. W., 2487  
 Tola, F., 2042  
 Toyoshima, Osamu, 2536  
 Tsuchiya, Y., 435  
 Tsuchiya, Yoshito, 115, 174, 1386  
 Turcke, D. J., 2563  
  
 Uchida, M., 42  
  
 Uncles, R. J., 3067  
 Uva, L. P., 1863  
  
 Vallianos, Limberios, 1668  
 Van Damme, L. V., 2737  
 van de Graaff, J., 1618  
 van de Kreeke, Jacobus, 1360  
 van der Heijden, H. N. C. M., 3180  
 van der Meer, J. W., 2620, 2920  
 van Heteren, J., 70, 625  
 van Kesteren, W. G. M., 1161  
 van Vledder, G. Ph., 642  
 van Wyk, A. C., 3244  
 Vicente, C. M., 1863  
 Vincent, Charles L., 370  
 Visser, P. J., 2192  
 Vogel, Michael J., 3017  
 Voigt, Andreas, 2892  
  
 Waanders, A. J., 2451  
 Wada, Akira, 2363  
 Walker, James R., 2827  
 Wanetick, Jerome R., 1879  
 Wang, Hsiang, 271  
 Wang, Jyh-Cherng, 3034  
 Wang, Shen, 345  
 Wang, Wei-Chi, 516  
 Warner, J. L., 2726  
 Watabe, Tomiji, 2875  
 Watanabe, Akira, 2293  
 Weggel, J. Richard, 3227  
 Weishar, Lee L., 1571  
 Weston, S. A., 3067  
 Wind, H. G., 1437, 1685  
 Wolanski, Eric, 2414  
 Wood, William L., 1571  
 Wright, L. D., 2150  
 Wu, C. S., 31  
  
 Xu, Weiyi, 2181  
  
 Yakuwa, Isao, 2971  
 Yamaguchi, Masataka, 1732  
 Yamashita, Takao, 174  
 Yano, Kenji, 2875  
 Yasuda, T., 435  
 Yoon, Sung B., 999  
 Yoshida, Akinori, 929  
 Young, Myron H., 2263  
  
 Zielke, W., 1057  
 Zwamborn, J. A., 3244